Investigation of thermochromism in a series of side-chain, liquid-crystalline, azobenzene-containing polymers

Stephan Freiberg, François Lagugné-Labarthet, Paul Rochon, and Almeria Natansohn

Abstract: The thermochromic properties of a series of liquid crystalline polymethacrylates, containing azobenzene side-chains with variable spacer lengths, were investigated. Annealing the amorphous polymer thin films above the glass transition temperature results in a rearrangement of the azobenzene moieties, causing a hypsochromic shift in the electronic absorption spectra. A detailed investigation of the spectral shift was performed by in situ UV–vis spectroscopy and indicated the formation of H-type aggregates by the side-chain chromophores above the glass transition temperature. The rate at which the hypsochromic shift occurs is faster for polymers with shorter spacers since their high glass transition temperature results in a higher thermal energy during the thermochromic effect. Experimentally determined activation energies show that the aggregation occurs primarily due to side-chain relaxation (β-relaxation) and main-chain relaxation (α-relaxation). Further annealing above the isotropization temperature resulted in the onset of deaggregation and in most cases showed that the chromophores were freed from the ordered state.

Key words: liquid-crystalline polymer, thermochromic properties, chain relaxation, aggregation, thin films, azobenzene mesogens.

Résumé : Les propriétés thermochromes d'une série de films minces de polymères liquide-cristallins contenant des mésogènes azobenzène sont présentées. Des mesures in situ en spectroscopie UV–vis mettent en évidence la formation d'agrégats de type H lorsque de tels films minces sont chauffés proche de leur température de transition vitreuse. L'analyse des spectres UV–vis permet d'identifier les différentes étapes mises en jeu pendant la formation des agrégats. L'étude dynamique de la formation d'agrégats montre que la relaxation des groupes mésogènes (relaxation de type β) prédomine indépendamment de la longueur des espaceurs tandis que la relaxation de la chaine principale (relaxation de type α) joue un rôle moindre tout en étant dépendant de la taille des espaceurs.

Mots clés : polymères liquide-cristallins, propriétés thermochromes, relaxation de chaîne, agrégation, films minces, mésogènes azobenzènes.

Introduction

In the past decade, the optical properties of azobenzene-containing, side-chain liquid crystal polymers (SCLCPs) have drawn considerable attention from both fundamental and applied aspects. Similar to amorphous azopolymers, the optical properties of azo-containing SCLCPs, such as birefringence and dichroism, can be modulated through *trans-cis-trans* photoisomerization. Molecular photoinduced orientation — created by an angular redistribution of the azobenzene moieties in a direction perpendicular to the polarization direction of the actinic light — is stable, can be triggered rapidly, and can be completely erased. This property is of great interest for photonic applications, making these materials appropriate for all-optical data storage purposes, optical switching, and other photonic devices (1–6).

In a previous work (7), we have shown that a high degree of remnant molecular orientation could be achieved in SCLCPs but that the stability of the photoinduced orientation was strongly influenced by the formation of aggregation. The formation of aggregates in the azobenzene SCLCP thin films is dictated by various parameters such as the molecular weight of the polymer, the length of the spacer that decouples the chromophore from the main chain, and, subsequently, its glass transition temperature (T_g). The formation of aggregates under annealing conditions induces large wavelength shifts that vary from $\Delta\lambda$ = 10 to 60 nm, depending on the spacer length, and that can be accompanied by the

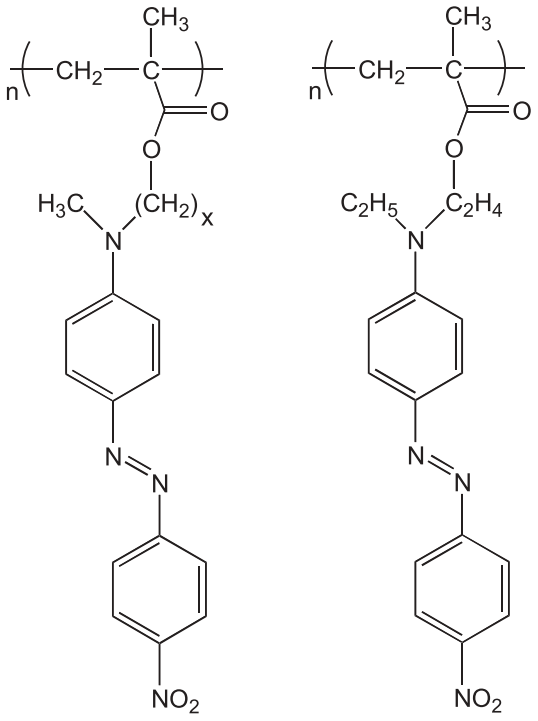
Received 7 July 2003. Published on the NRC Research Press Web site at http://canjchem.nrc.ca on 5 November 2003.

S. Freiberg and A. Natansohn. Department of Chemistry, Queen's University, Kingston, ON K7L 3N6, Canada.
F. Lagugné-Labarthet.[1] LPCM, UMR 5803-CNRS, Université Bordeaux I, 351 Cours de la Libération, 33405 Talence, France.
P. Rochon. Department of Physics, Royal Military College, Kingston, ON K7K 5L0, Canada.

[1]Corresponding author (e-mail: f.lagugne@lpcm.u-bordeaux1.fr).

 doi: 10.1139/V03-170 © 2003 NRC Canada

Chart 1.



formation of a smectic mesophase (7, 8). The shift in absorption wavelength is caused by the interaction of chromophores as they self-organize in an anti-parallel fashion during the formation of smectic domains.

The backbone flexibility and the side-chain relaxation are the two dominant factors responsible for the formation and stability of organized domains. Their effect has been extensively investigated on Langmuir–Blodgett films of polyglutamates containing azobenzene moieties, using UV–vis polarized spectroscopy and X-ray reflectivity (9). The results obtained by Menzel et al. (9) have led to a deeper insight into the various possible types of aggregation at different photoisomerization and annealing steps.

There are, however, no in-depth reports of temperature-dependent aggregation studies for a series of SCLCP films with variable spacer lengths. In the present study we have systematically investigated the thermochromic properties of a series of azobenzene SCLCPs; we emphasize the role of main-chain and side-chain relaxation on the nature of the aggregate formation. This concludes our work on a series of manuscripts on SCLCPs as examined by the Natansohn group (7, 8, 10).

Experimental

The synthesis and the spectroscopic and optical characterization of this series of polymers (pXMAN) are described elsewhere (8). Their general structure is shown in Chart 1, where X is the number of methylene units and varies from 2 to 12. The physical data of pDR1M and the pXMAN series are summarized in Table 1.

Table 1. Physical data of the pXMAN series and pDR1M.

Material	T_g (°C)	Mn	Amorphous state λ_{max} (nm)
PDR1M	129	2000 – 10 000	466
P2MAN	110	5000	455
P3MAN	80	4400	436
P4MAN	85	4400	431
P5MAN	68	3500	428
P6MAN	70	4000	455
P7MAN	57	8600	431
P8MAN	45	4600	428
P9MAN	31	3500	412
P10MAN	25	3200	410
P11MAN	30	4000	411
P12MAN	25	4800	410

All of the films were spin-cast, from solutions containing 15–20 mg of polymer per 1 mL of dichloromethane, onto clean glass substrates at about 1500 rpm, to obtain an absorbance in the visible range of about 1 and a thickness between 200 and 400 nm. Heat treatment was performed using an Instec HS 400 thermal hot stage, and the data were collected on a Beckman DU 7400 series photo-diode array spectrophotometer.

Fitting the UV spectra

The UV spectra can be described using two Gaussian functions, as shown in Fig. 1. The Gaussian function G1 is assigned to H-aggregated azobenzene while the Gaussian function G2 is assigned to free, unaggregated azobenzene, as reported previously (7). Whatever the considered state — unaggregated mesogens of the amorphous state (Fig. 1A) or H-aggregated mesogens (Fig. 1B) — the fitted curves are very close to the experimental spectra. The parameters of G1 (height, width, and λ_{max}) were allowed to vary freely throughout the entire fitting process. The wavelength of maximum absorption (λ_{max}) and the full width at half maximum (width) of G2 were determined from the UV spectra of isotropic samples and were held constant throughout the fitting for all spectra, but the height was allowed to vary.

The areas of G1 and G2 were plotted against time for isothermal experiments (variation of absorbance at a fixed temperature) and could be fitted using a bi-exponential function. For the hypsochromic shift induced by annealing the thin film, the time-dependent variation of G1 is fit to a bi-exponential rise

$$[1] \qquad Y = Y_0 + A(1 - e^{-k_a t}) + B(1 - e^{-k_b t})$$

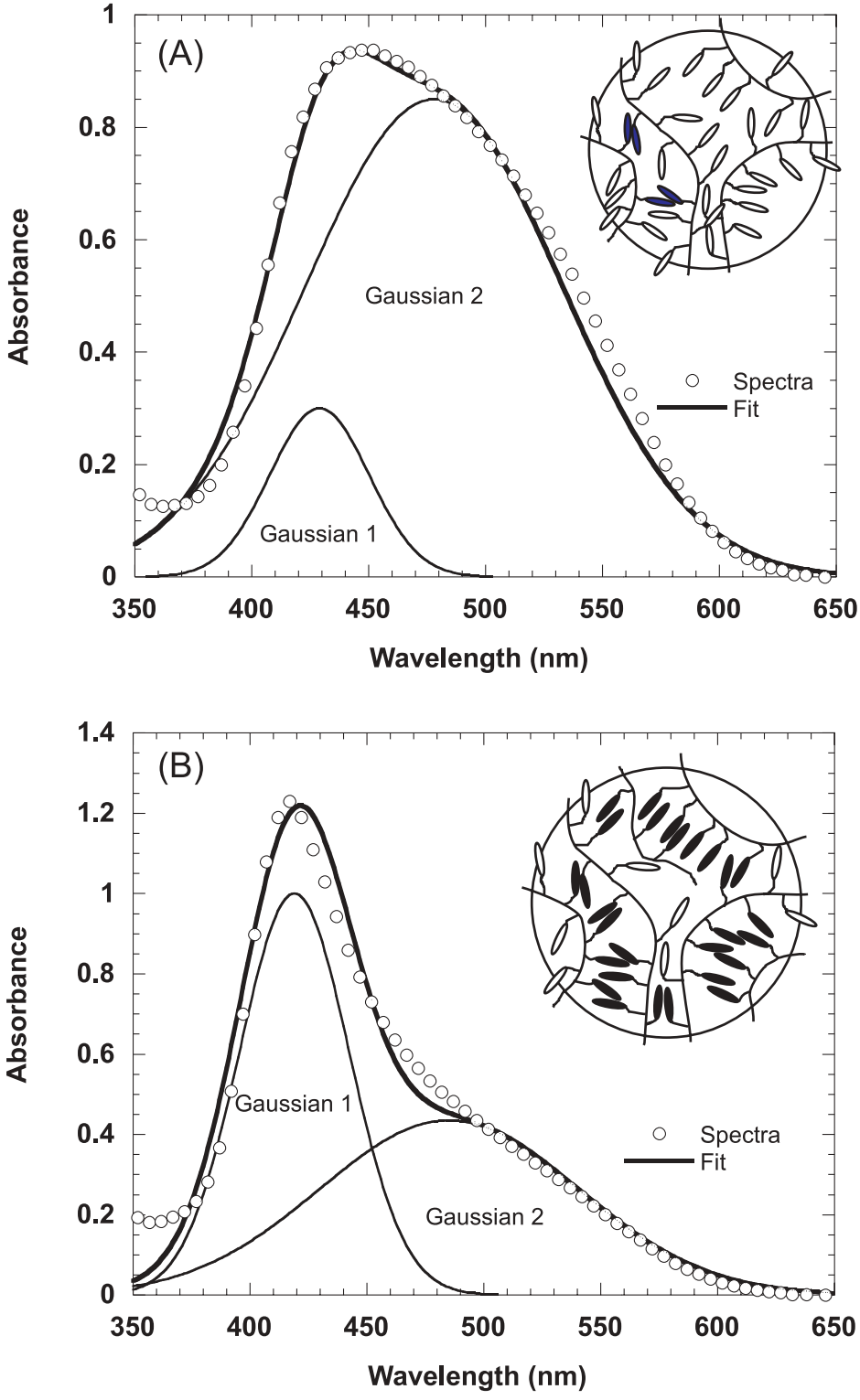
The variation of G2 is fit to a bi-exponential decay process as described by

$$[2] \qquad Y = Y_0 + Ae^{-k_a t} + Be^{-k_b t}$$

The amplitude A and the rate constant k_a are defined as the fast contribution to the process while the amplitude B and the rate constant k_b are defined as the slow contribution of the process.

© 2003 NRC Canada

Fig. 1. Illustrative example for the fitting procedure. Gaussian 1 (G1) is the fitting function related to the H-aggregated azobenzene moieties. Gaussian 2 (G2) is the fitting function related to the free unaggregated azobenzene contribution. After spin-coating (A), the spectrum shows a dominant contribution of the free azobenzene moieties. After annealing at 120 °C for 20 min (B), a clear hypsochromic shift is observed, and the contribution of the aggregated chromophores is dominant. The agreement between the experimental spectrum (○) and the resulting fitting curve G1 + G2 (full line) is quite good.



© 2003 NRC Canada

Results and discussion

The thermochromic effects are mainly observed through the intense absorption band in the visible range, which is assigned to a vibronic coupling between n–π^* and π–π^* electronic transitions; this spectral absorption is due to the strong charge transfer between the electron-donor group (amino) and the electron-withdrawing (nitro) acceptor group. As previously reported, the thermochromism exhibited by the polymers of the pXMAN series varies with the spacer length (8).

(*i*) For the polymer with the shortest spacer, p2MAN, no thermochromic effect is observed. The polymer is amorphous and has properties similar to homopolymers or copolymers with similar structures, such as pDR1M, which differs only by an N-ethyl group in the place of the N-methyl group (Chart 1). The presence of a short spacer does not provide the mesogen with enough mobility to allow rearrangement of the chromophores.

(*ii*) The thin films of the polymers with the shorter spacers, p3MAN to p8MAN, undergo a hypsochromic shift after heating to the glass transition temperature. Annealing these films at temperatures within the isotropization range results in the destruction of the ordered phase and a bathochromic shift.

(*iii*) For the polymers with longer spacers, p9MAN to p12MAN, the hypsochromic shift occurs readily at room temperature, owing to their low T_g (25–31 °C). A recovery of the isotropic state can be observed when annealing in the isotropization range.

To investigate the thermochromic properties, two sets of experiments were conducted. First, variable temperature (ramping) experiments were performed by recording UV–vis spectra between room temperature and the isotropization or decomposition temperature at a ramp rate of 2 degrees per minute (dpm) and by collecting spectra every minute. Each spectrum was deconvolved into two Gaussian curves, allowing the aggregation process to be followed as a function of the annealing temperature. In a second set of experiments, the spectra were collected during isothermal runs where UV spectra were recorded at a given annealing temperature as a function of time. Isothermal experiments were performed primarily on p3MAN–p8MAN, to examine the first color change (hypsochromic shift). The second color change (bathochromic shift) was examined by experimenting with the thin films of selected polymers; namely, p4MAN, p5MAN, p8MAN, p9MAN, p11MAN, and p12MAN.

Ramping experiments

As an illustrative example, Fig. 2 shows the results of a ramping experiment performed on p4MAN (T_g = 74 °C), and it is representative of all pXMAN ramping experiments with X = 3–8. It can be seen that a first color change (blue shift) starts to occur at about the glass transition temperature (about 80 °C), where the area of G1 increases and, conversely, the area of G2 decreases. At a temperature of 116 °C, G1 reaches a maximum and G2 reaches a minimum. At about 130 °C, G1 starts to decrease and G2 starts to increase, suggesting the onset of the second color change (red shift). At this point, the amount of free azobenzenes starts to increase while the amount of aggregates starts to decrease, owing to the onset of isotropization.

The increase in G1 at a temperature close to T_g is assigned to the formation of H-aggregates, in agreement with the classification made by Kunitake and co-workers (11). The fact that the electronic transition undergoes a blue shift and becomes narrower suggests that the chromophore moities are interdigitated with their dipolar moments opposite to the adjacent chromophores. Such organization produces a weaker charge transfer between the donor amino group and the withdrawing nitro group. Subsequently, if the charge transfer decreases, the electronic transition has a π–π character rather than an n–π^* character, and a blue shift is observed. The second color change (red shift) occurs during the isotropization range where aggregation is destroyed during melting.

The results of ramping experiments for polymers p9MAN to p12MAN exhibit a different trend, since their glass transition temperature is lower. Shown in Fig. 3, the ramping experiment for p11MAN (T_g = 40 °C) exhibits additional features. Immediately, after spin coating, the absorption spectrum shows two contributions related to free and H-aggregated azobenzene moieties. The contribution of aggregated azobenzene increases when annealing, until 80 °C. Above this temperature, the aggregates are disappearing and the absorption band can be fitted with a single Gaussian function, as seen in the inset of Fig. 3. Its normalized absorbance reaches 1.2, indicating that the absorption coefficient depends strongly on the environment around the chromophores, in particular the inhomogeneous intermolecular chromophore interactions.

Isothermal experiments

The dynamic measurements performed at fixed temperatures allow us to obtain greater insight into the dynamic rates involved in the formation of aggregates. For a given annealing temperature, the changes in absorption of the electronic transition can be correlated to the activation energy of both the backbone chain and the side-chain chromophores. Both hypsochromic and bathochromic shifts are discussed for the pXMAN series.

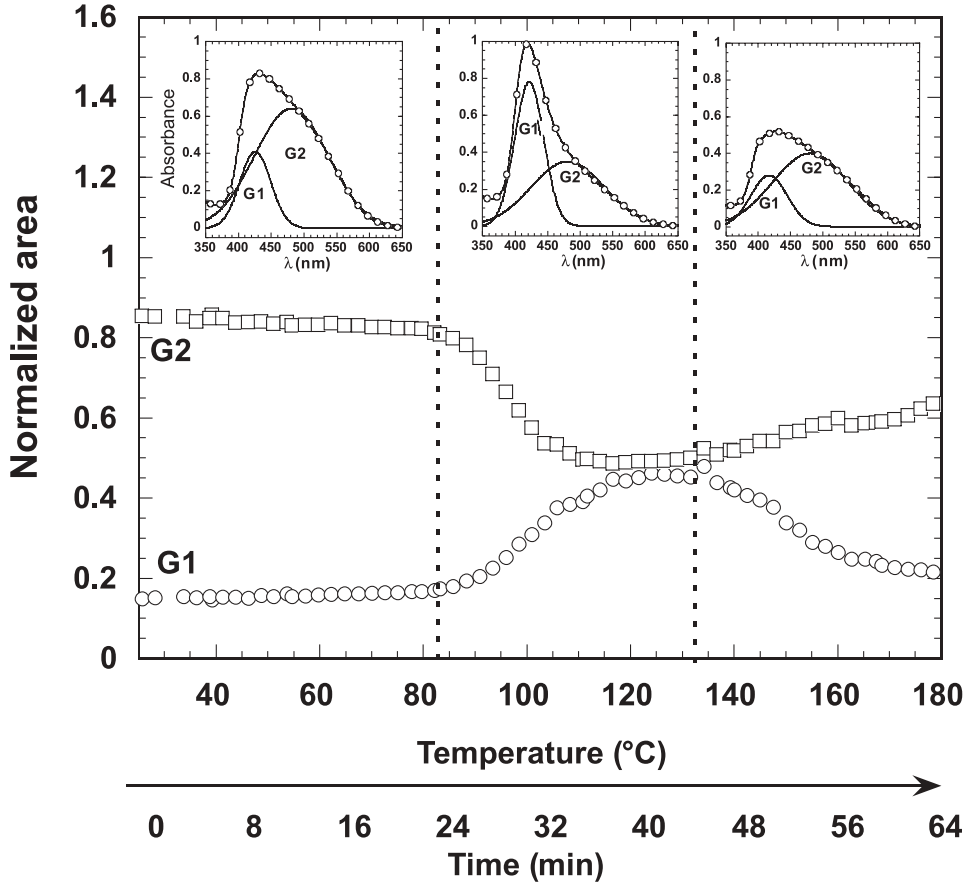
Hypsochromic shift

The plots shown in Figs. 4A and 4B for p7MAN are representative of the evolution of G1 and G2, respectively, during a typical isothermal experiment. Both curve sequences show that the rate at which the thermochromism occurs increases significantly with temperature.

Fitting the curves to a bi-exponential process results in two amplitude constants, A and B, and two rate constants, k_a and k_b. The fast amplitude constant, A, tends to increase with temperature while the slow contribution, B, decreases. The rate constants k_a and k_b represent the fast and slow processes, respectively, and also increase with temperature. In general, it is also observed that the rates at which thermochromism occurs (at $T - T_g$) are larger for polymers with shorter spacers. This is illustrated in Fig. 5, which shows that p3MAN and p4MAN have higher k_a and k_b values (at $T - T_g$) than p7MAN; this trend is observed for p3MAN to p8MAN. It is also noteworthy that thermochromism occurs

© 2003 NRC Canada

Fig. 2. Temperature-dependent variation of the area of fitting functions G1 and G2 for p4MAN. Two transitions can be clearly observed with an initial hypsochromic shift followed by a bathochromic shift at higher temperature, as shown in the inset. At a temperature of 135 °C, the bathochromic shift is accompanied by the formation of a smectic mesophase. This variation is typical for the series from p3MAN to p8MAN.



at T_g for p3MAN and p4MAN but occurs at T_g + 20 °C for the polymers p5MAN to p8MAN. Intuitively, these results are unexpected, since polymers containing longer spacers (lower T_gs) should have more freedom of motion to undergo aggregation. The results show that the aggregation process occurs more readily at T_g for p3MAN and p4MAN than for the polymers with longer spacers. A rigorous explanation of these results will be discussed in the "activation energies" section.

For the longer side-chains polymers, p9MAN–p12MAN, the dynamics of the first color change is less readily observable since it appears to be, in part, complete after spin-casting. Likely, the low T_g associated with these materials support immediate aggregation during the spin-casting procedure.

Activation energies

Activation energies (E_as) were estimated for the fast and slow processes, using the k_a and k_b constants obtained from the isothermal experiments. The validity of the Arrhenius law has been widely demonstrated for the study of liquid-crystalline polymers. The activation energy related to the fast and slow contributions obtained at different temperatures was determined using the Arrhenius equation

$$[3] \qquad \ln(k_i) = A - \frac{E_a}{R}\frac{1}{T}$$

where k_i is the considered rate constant (s^{-1}), A is a constant, R is the molar gas constant (R = 8.31 $J \cdot mol^{-1} \cdot K^{-1}$), and T is the temperature in Kelvin. From eq. [3], the activation energy is proportional to the slope of the natural logarithm of k_i (s^{-1}) vs. reciprocal temperature (Kelvin). The activation energies for the fast and slow processes are deduced from the slopes of the $k_i = f(T - T_g)$ plots (Fig. 5) and are reported in Table 2.

In general, the activation energy required to induce polymer backbone motion (α-relaxation) is typically in the range of 70–150 $kJ \cdot mol^{-1}$, depending on the spacer length, and occurs at the glass transition temperature (12–15). Activation energies for the mesogen relaxation (β-relaxation) are, rather, in the range of 50–100 $kJ \cdot mol^{-1}$ and are observable at temperatures lower than T_g (T_g – 20 °C). (12, 13, 15–19). In addition the β-relaxation is generally independent of the spacer length (20, 21). As reported in Table 2, the activation energy values associated with the slow rate, k_b, tend to decrease with spacer length. Polymers with short spacers have a larger E_a value (80–100 $kJ \cdot mol^{-1}$) while the LCPs with longer spacers have smaller activation energies (30–

© 2003 NRC Canada

Fig. 3. Temperature-dependent variation of the area of fitting functions G1 and G2 for p11MAN. Two transitions can be clearly observed with an initial hypsochromic shift following by a bathochromic shift at higher temperature, as shown in the inset.

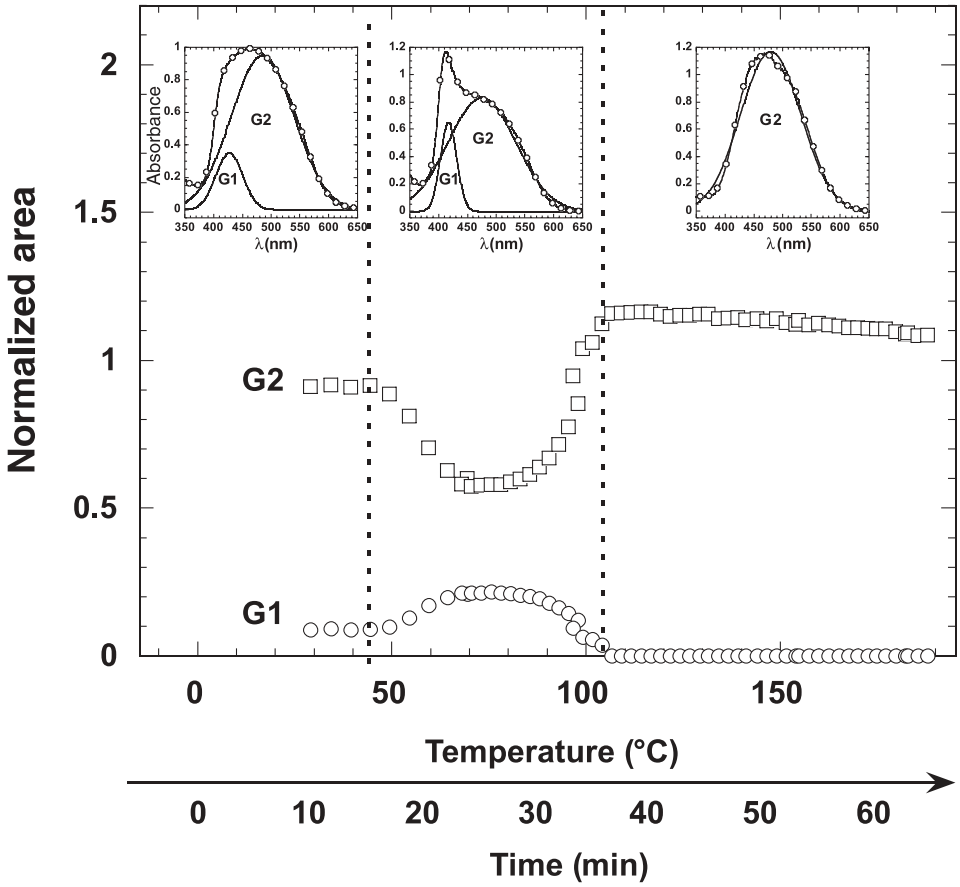


Table 2. Activation energies (E_a) extracted from ramping experiments during the hypsochromic shift for the polymers from p3MAN to p8MAN.

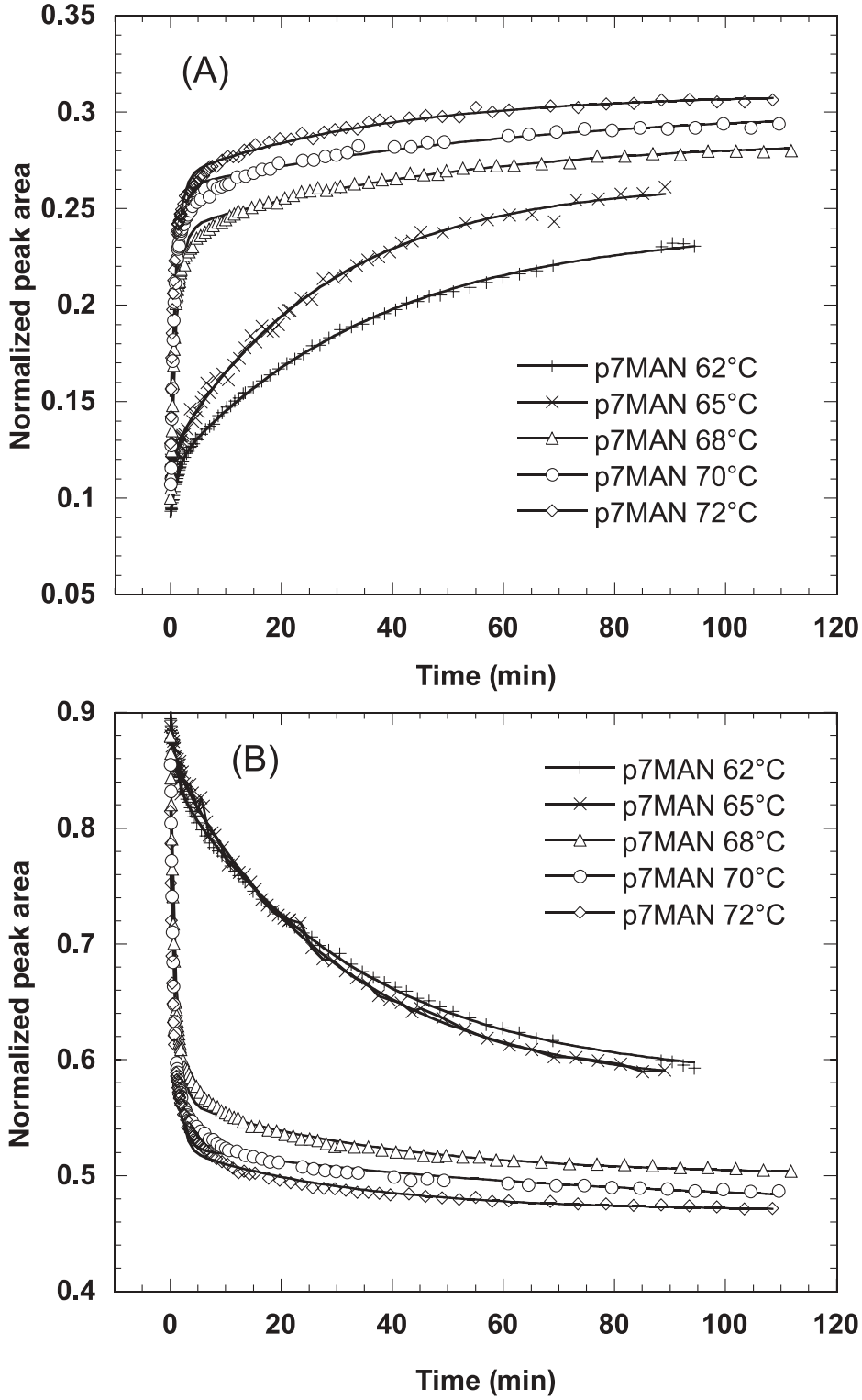
		Aggregated chromophores G1		Non-aggregated chromophores G2	
	T_g (°C)	E_a (kJ·mol^{-1}) (from k_a)	E_a (kJ·mol^{-1}) (from k_b)	E_a (kJ·mol^{-1}) (from k_a)	E_a (kJ·mol^{-1}) (from k_b)
P3MAN	80	62	116	51	108
P4MAN	85	66	82	73	87
P5MAN	68	50	69	41	92
P6MAN	70	66	26	62	50
P7MAN	57	66	66	75	75
P8MAN	45	50	55	33	60

50 kJ·mol^{-1}). The activation energies associated with the fast rate constants appear to remain stable within experimental uncertainty (30–70 kJ·mol^{-1}) and are independent of the spacer length. By analogy with previous studies (12, 13, 15–19), the values of the activation energies determined experimentally suggest that the fast process is, presumably, associated with mesogen relaxation, and the slow process is due to main-chain relaxation.

Earlier, when discussing Fig. 5, we mentioned that polymers with longer spacers tend to undergo the first color change at temperatures of about T_g + 20 °C, while p3MAN and p4MAN undergo the first color change at about T_g. In addition, the rate constants k_a and k_b, associated with the thermochromic process, are greater at $T - T_g$ for the polymers with shorter spacers, as shown in Fig. 5. These results are unexpected since polymers with longer spacers are expected to be more mobile than the polymers with shorter spacers. However, when annealed at about their respective glass transition temperature, the polymers with shorter chains (p3MAN, p4MAN) are supplied with more energy than their counterparts with longer chains. Since the mesogen relaxation activation energy is independent of the spacer length, it is the same for all polymers. However, the glass transition temperature increases with decreasing spacer

© 2003 NRC Canada

Fig. 4. Isothermal experiments performed during the hypsochromic shift for p7MAN. The measurements were done at different annealing temperatures and were fitted with a bi-exponential function for both G1 (A) and G2 (B).



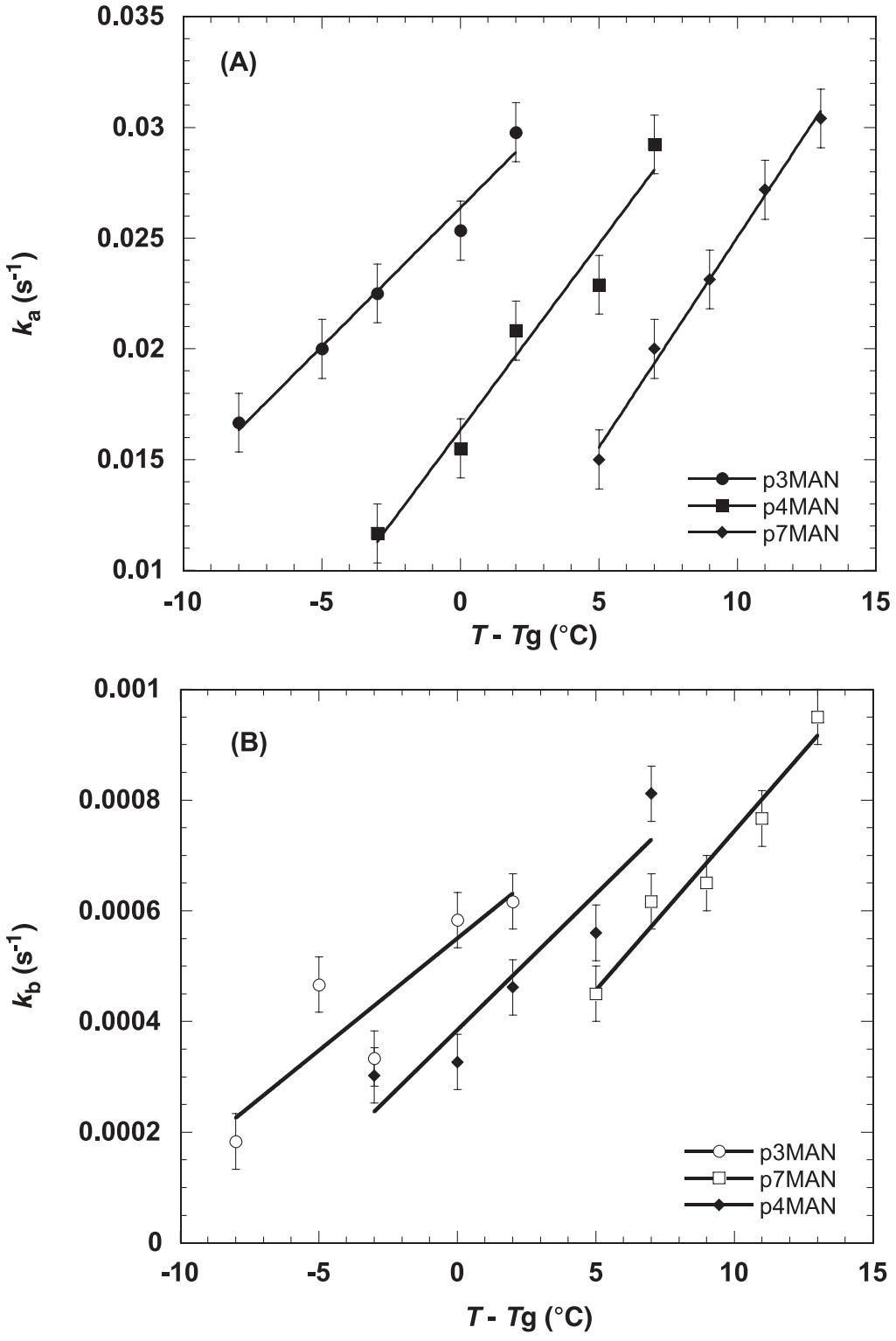
length, and excess of thermal energy is supplied at T_g for polymers with the shortest spacers. The excess thermal energy supplied for the same process in different polymers implies that the color change will occur more readily for polymers with shorter spacers, as observed in Fig. 5.

Bathochromic shift

The evolution of G1 for p4MAN, p5MAN, and p8MAN experiments shows a decrease in curve area at temperatures inside the isotropization range with a concurrent increase in the area of G2 (shown for p4MAN in Figs. 6A and 6B). Al-

© 2003 NRC Canada

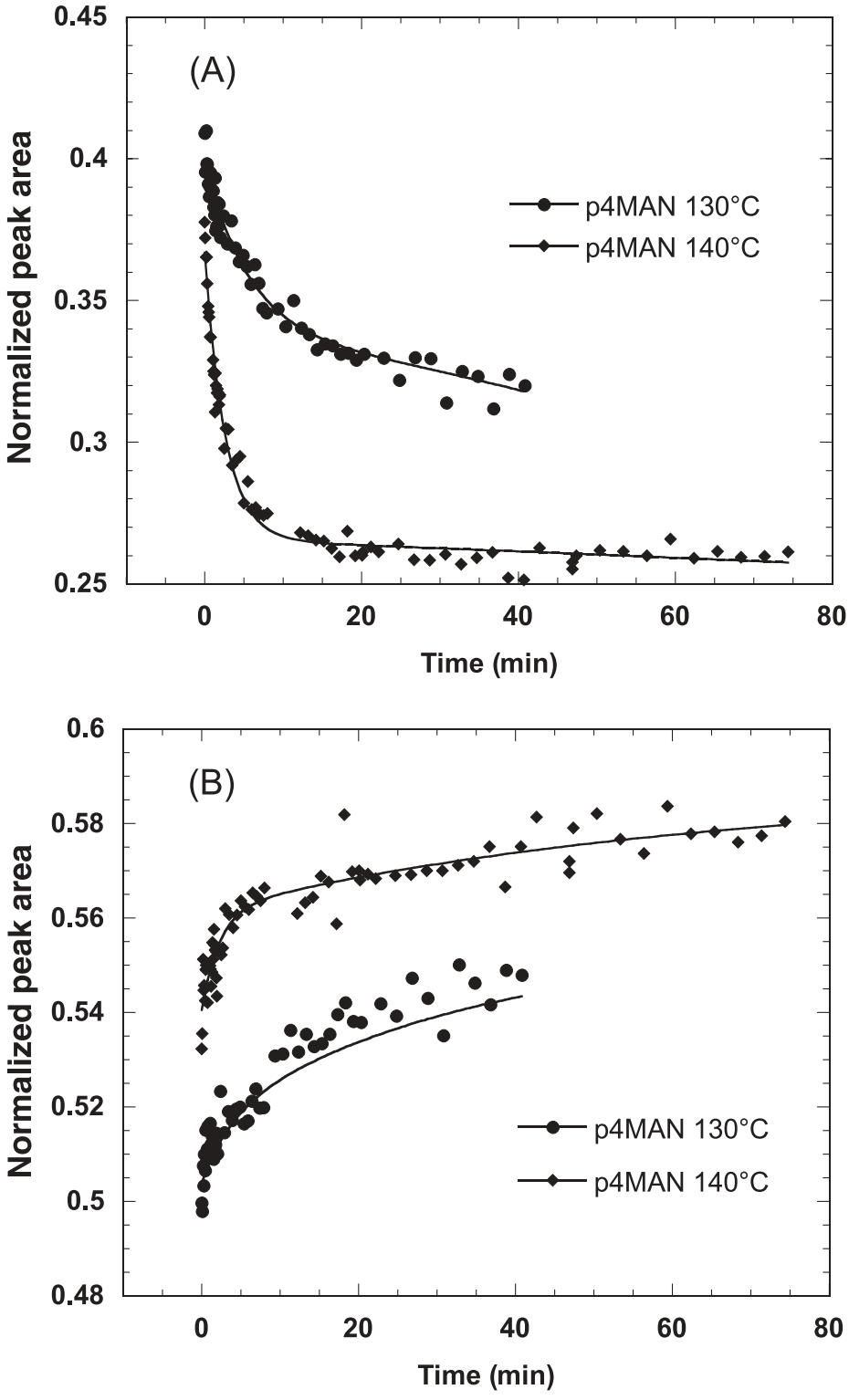
Fig. 5. (A) Fast constant rates, k_a, for p3MAN, p4MAN, and p7MAN vs. $T - T_g$ for G1; the rates are larger near T_g for the polymers with shorter spacers; (B) Slow constant rates, k_b, for p3MAN, p4MAN, and p7MAN vs. $T - T_g$ for G1; the rates are larger near T_g for the polymers with shorter spacers.



though quantitative information is not gathered from these experiments, qualitative observation shows that the aggregates generally undergo destruction at temperatures inside the isotropization range. Similarly, the second color change for p9MAN–p12MAN inside the isotropization range results in a disappearance of the aggregation peak (G1), while the

© 2003 NRC Canada

Fig. 6. Isothermal experiments performed during the bathochromic shift for p4MAN. The decrease of G1 (A) and concomitant increase of G2 (B) were measured at 130 and 140 °C, but the erratic behavior does not allow a quantitative analysis of the activation energies.



peak relative to free chromophores becomes almost symmetric, as shown in Fig. 3 for temperature above 100 °C. Therefore, the bathochromic shift observed above the isotropization temperature confirms destruction of the smectic phase. However, isotropization is not complete in the cases of the polymers with the shortest spacers (p3MAN and p4MAN) since they are prone to decomposition before they reach an isotropization temperature.

© 2003 NRC Canada

Conclusion

The thermochromic properties of a series of azobenzene-containing, liquid-crystalline polymers were investigated. A hypsochromic shift in the absorption spectra at the glass transition temperature is attributed to H-aggregation of the chromophores during smectic phase formation. A bathochromic shift during isotropization is attributed to deaggregation of the chromophores during melting.

Isothermal experiments were of particular interest in estimating the contribution of backbone relaxation and side-chain relaxation. The activation energies for the fast process were found to be similar for all of the polymers in the series and were assigned to the mesogen relaxation. On the other hand, E_as associated with the slow process decreased with increasing spacer length, which is characteristic of the main-chain relaxation.

The results of experiments within the isotropization range confirmed that the bathochromic shift is due to deaggregation of the side-chain chromophores.

Acknowledgment

The authors are dedicating this work to Almeria Natansohn, our guide, who greatly spawned the multiple interests of azopolymers in the chemistry and physics communities in Canada and in many other countries.

References

1. M. Eich, J. Wendorff, B. Reck, and H. Ringsdorf. Makromol. Chem. Rapid Commun. **8**, 59 (1987).
2. R. Hagen and T. Bieringer. Adv. Mater. **13**, 1805 (2001).
3. L.-X. Liao, D. Junge, and D. McGrath. Macromolecules, **35**, 319 (2002).
4. C. Ruslim and K. Ichimura. Adv. Mater. **18**, 624 (2001).
5. K. Ichimura, S.-K. Oh, and M. Nakagawa. Science (Washington, D.C.), **288**, 161 (2000).
6. F. Lagugné-Labarthet, P. Rochon, and A. Natansohn. Appl. Phys. Lett. **75**, 1377 (1999).
7. F. Lagugné-Labarthet, S. Freiberg, C. Pellerin, M. Pézolet, A. Natansohn, and P. Rochon. Macromolecules, **33**, 6815 (2000).
8. S. Freiberg, F. Lagugné-Labarthet, P. Rochon, and A. Natansohn. Macromolecules, **36**, 2680 (2003).
9. H. Menzel, B. Weichart, A. Schmidt, S. Paul, W. Knoll, J. Stumpe, and T. Fisher. Langmuir, **10**, 1926 (1994).
10. G. Iftime, F. Lagugné-Labarthet, A. Natansohn, and P. Rochon. J. Am. Chem. Soc. **122**, 12 646 (2000).
11. M. Shimomura, R. Ando, and T. Kunitake. Ber. Bunsen-Ges. Phys. Chem. **87**, 1134 (1983).
12. R. Zental, G. Strobl, and H. Ringsdorf. Macromolecules, **18**, 960 (1985).
13. G. Simon. Polymer, **30**, 2227 (1989).
14. G. Day and W. Jackson. Eur. Polym. J. **32**, 1361 (1996).
15. A. Schonhals, D. Wolff, and J. Springer. Macromolecules, **31**, 9019 (1998).
16. F. Bormuth, W. Haase, and R. Zental. Mol. Cryst. Liq. Cryst. **148**, 1 (1987).
17. M. Laus and D. Ferri. J. Polym. Sci. B, **34**, 1085 (1996).
18. A. Krupicka, J. Aberg, M. Trollsas, F. Sahlen, A. Hult, U. Gedde, and R. Boyd. Polymer, **38**, 3463 (1997).
19. U. Gedde, F. Liu, A. Hult, F. Sahlen, and R. Boyd. Polymer, **35**, 2056 (1994).
20. A. Schonhals, D. Wolff, and J. Springer. Macromolecules, **28**, 6254 (1995).
21. K. Ngai and A. Schonhals. J. Polym. Sci. B, **36**, 1927 (1998).

© 2003 NRC Canada

Theoretical studies of model compounds of lathyrane-type diterpenes

Yukimasa Terada, Tomoo Matsuura, Yukari Mori, and Shosuke Yamamura

Abstract: The conformation of the 11-membered ring of the lathyrane skeleton has been investigated using NMR spectra and theoretical calculations. Some other skeletons, such as jatrophane, jatrapholane, and tigliane, seem to be derived from this framework, and the conformation is important in connection with the configuration of the resultant diterpenes. The conformation of lathyrane is principally defined by the orientation of the two methyl groups; namely, the methyl groups on C_1 and C_6 directed above or below the ring plane. Theoretical calculations revealed that the predominant conformation is altered depending on the oxygen functional groups on the ring. As far as the bond lengths, bond angles, and dihedral angles are concerned, all calculation methods afforded reasonable results. In contrast, as regards conformational stability, only the ab initio molecular orbital method (RHF/6-31G*) predicted the most stable conformation, consistent with NOE experiments. On the other hand, the stable conformations predicted by the ab initio method (RHF/STO-3G), the semi-empirical molecular orbital method (MOPAC(PM3)), and the molecular mechanics calculations (MM3) did not necessarily agree with the conformers suggested by the NOE experiments.

Key words: ab initio MO, semi-empirical MO, molecular mechanics, 11-membered ring conformation, NOE.

Résumé : On a étudié la conformation du cycle à onze chaînons du squelette lathyrane en faisant appel à la spectroscopie RMN et à des calculs théoriques. Il semble que d'autres squelettes, tels ceux du jatrophane, du jatrapholane et du tigliane, sont dérivés de celui-ci et sa conformation est importante en relation avec la configuration des diterpènes qui en résultent. La conformation du lathyrane est définie principalement par l'orientation des deux groupes méthyles, à savoir les groupes méthyles en C_1 et en C_6 orientés vers le dessus ou le dessous du plan du cycle. Les calculs théoriques révèlent que la conformation privilégiée varie avec la nature des groupes fonctionnels oxygénés présents sur le cycle. En ce qui concerne les longueurs des liaisons, des angles des liaisons et des angles dièdres, toutes les méthodes de calcul conduisent à des résultats raisonnables. Ce n'est toutefois pas le cas pour la stabilité conformationnelle; en effet, seule la méthode ab initio d'orbitales moléculaires (RHF/6-31G*) permet de prédire la conformation la plus stable, telle qu'observée par des expériences d'effet Overhauser nucléaire (eOn). Toutefois les conformations les plus stables prédites par la méthode ab initio (RHF/STO-3G), la méthode d'orbitales moléculaires semi-expérimentale (MOPAC(PM3)) et les calculs de mécanique moléculaire (MM3) ne correspondent pas nécessairement avec les conformères suggérés par les expériences d'eOn.

Mots clés : OM ab initio, OM semi-empirique, mécanique moléculaire, conformation d'un cycle à onze chaînons, eOn.

[Traduit par la Rédaction]

Introduction

A variety of diterpenes with a unique structure have been isolated from the plant species *Euphorbiacea* and *Thymeleacea*. A number of these compounds have remarkable bioactivities, such as skin-irritant, tumor-promotion, and proinflammatory properties. It is noteworthy that some macro- and polycyclic diterpenes have exhibited anti-tumor activities (1). Therefore, discovery of a synthetic route to these diterpenes will contribute to the development of a new class of medicines.

Diterpenes are divided into several groups by their molecular framework. One key intermediate of these skeletons is the lathyrane type (2). Some other skeletons, such as jatrophane, jatrapholane, and tigliane, seem to be derived from this framework, as shown in Scheme 1. For example, we reported transformation of the lathyrane skeleton to jatrapholane and daphnane types (3). Recently, we also reported the transannular cyclization of the lathyrane type to the jatrapholane type (4). Moreover, in the course of these cyclization reactions, we synthesized several lathyrane derivatives that have some oxygen functional groups, as shown in Fig. 1. We studied the conformation of these lathyrane derivatives based on the NMR spectra. NOE experiments suggested that the predominant conformation is affected by the type and location of the oxygen functional groups. The conformation of the 11-membered ring of lathyrane can be roughly classified into four groups by the orientation of the two methyl groups on the double bonds. However, the re-

Received 15 July 2002. Published on the NRC Research Press Web site at http://canjchem.nrc.ca on 27 November 2003.

Y. Terada[1] and Y. Mori. Faculty of Pharmacy, Meijo University, Tenpaku, Nagoya 468-8503, Japan.
T. Matsuura and S. Yamamura. Department of Chemistry, Faculty of Science and Technology, Keio University, Hiyoshi, Yokohama 223-8522, Japan.

[1]Corresponding author (e-mail: yterada@ccmfs.meijo-u.ac.jp).

 doi: 10.1139/V03-171 © 2003 NRC Canada

Scheme 1.

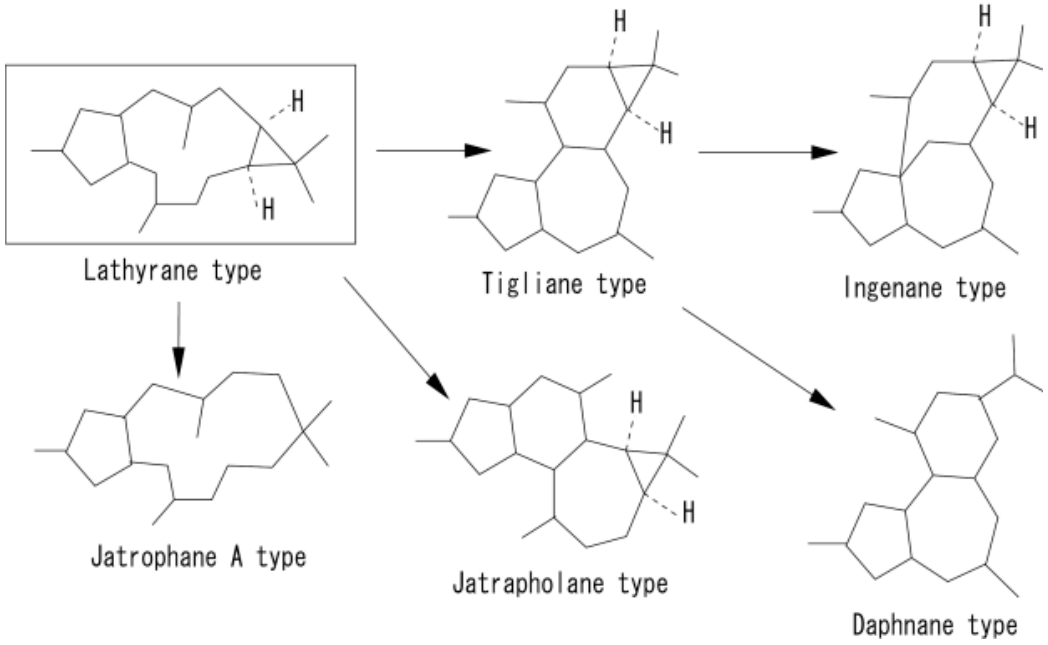
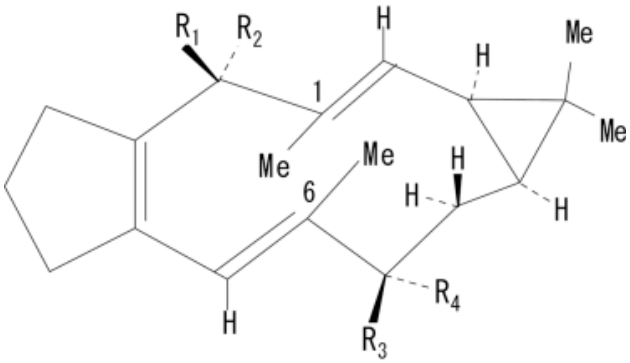


Fig. 1. The structure and the oxygen functional groups of lathyrane derivatives (**1**~**5**).



	R_1	R_2	R_3	R_4
1	H	OH	OH	H
2	H	OH	H	OH
3	H	OH	= O	
4		= O	= O	
5		= O	OH	H

sults of NOE experiments could not specify one of the four conformational groups. Therefore, we started conformational analysis of the 11-membered ring by several theoretical methods, because the conformation is important in determining the configuration of the transannular reaction product (4, 5).

To simplify the calculation and to save time, a truncated lathyrane model was postulated, as shown in Fig. 2. Namely, the cyclopentene ring was simplified to a double bond and the dimethyl group on the cyclopropane ring was replaced by hydrogen atoms. The letter m represents these postulated model structures.

We sought the minimum energy conformer within each conformational group of 5 lathyrane model structures. The "stochastic search for conformers" option in the MM3(96) program was used to generate a number of conformers in a group. Subsequently, the obtained, unique conformers were optimized by MM3(96), MOPAC(PM3), or ab initio (RHF/STO-3G and RHF/6-31G*) MO programs. The conformational stability predicted by these theoretical methods were compared with the NOE results.

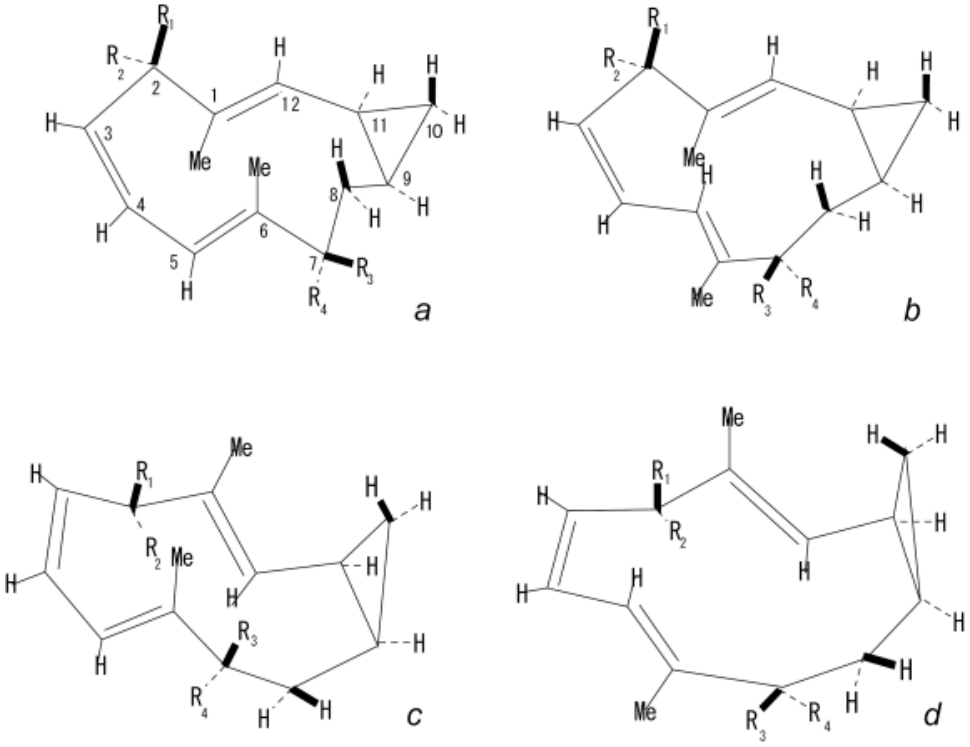
In addition, the transition state for conformational interchange was identified by the RHF/6-31G* optimization and subsequent one-point calculation at the B3LYP/6-31G* level of theory. The activation energy estimated for the model compound **m2** suggested free interchange between the **m2a** and **m2b** conformations.

Results

Structure optimization of the truncated lathyrane model was performed by the ab initio and semi-empirical molecular orbital (MO) methods, as well as the molecular mechanics (MM) method. The conformation of the 11-membered ring of the lathyrane skeleton can be classified into four groups by the orientation of the C_1 and C_6 methyl groups; that is: $\alpha - \beta$ (**a**), $\alpha - \alpha$ (**b**), $\beta - \beta$ (**c**), and $\beta - \alpha$ (**d**), respectively, as shown in Fig. 2. The relative conformational energies of **a**, **b**, **c**, and **d** of the model compounds (**m1**~**m5**) and the relative population calculated at 25 °C under the assumption of the Boltzmann distribution are shown in Table 1. The stable conformers of the model compounds optimized by RHF/6-31G* calculations are shown in Fig. 3. Except for the model compound **m4**, the conformers with the β-oriented C_1 methyl group were distinctly less stable than the conformers with the α-oriented C_1 methyl group. The observed NOE enhancements (%), together with the calculated nonbonding hydrogen—hydrogen interatomic distances, are shown in Table 2.

© 2003 NRC Canada

Fig. 2. The four conformations of the truncated model of lathyrane derivatives (**m1**~**m5**). The orientation of the methyl groups on C_1 and C_6 are (*a*) α – β, (*b*) α – α, (*c*) β – β, and (*d*) β – α, respectively.



	R_1	R_2	R_3	R_4
m1	H	OH	OH	H
m2	H	OH	H	OH
m3	H	OH	= O	
m4	= O		= O	
m5	= O		OH	H

In Table 3, the resultant bond lengths, bond angles, and dihedral angles of the 11-membered ring of the model compound **m2a** are shown and compared with the result of the X-ray crystallographic analysis of 3,8,14,20-tetraacetyl-7-(2-methyl-butanoyl)-synadenol (6). The model compound **m2** was selected, since the configuration of the oxygen functional groups on C_2 and C_7 were comparable to that of the compound analyzed by X-ray analysis. For comparison of the predictability of the theoretical methods, standard errors were calculated by the following equation:

$$\mathrm{SE} = \sqrt{\frac{\sum_{i=1}^{n}(P_{x_i} - P_{c_i})^2}{n}}$$

where P_{x_i} and P_{c_i} indicate geometric parameters obtained by the X-ray analysis and the theoretical calculation; these are shown in Table 3.

We also investigated the transition state for conformational interconversion between **m2a** and **m2b**. The transition structure with a single imaginary frequency (65.6 *i* cm^{-1}) was identified at the RHF/6-31G* level. The stable conformers and the transition structure are shown in Fig. 4. The C_5=C_6 double bond seems to turn around with almost no effect on other parts of the 11-membered ring. The C_3-C_4-C_5-C_6 dihedral angle of **m2a**, **m2b**, and the transition state were 69.9°, –101.7°, and 147.7°, respectively. Furthermore, the activation free energies of the conformational interconversion, starting from **m2a** and **m2b**, were estimated at 31.02 kJ mol^{-1} and 37.18 kJ mol^{-1}, respectively.

Discussion

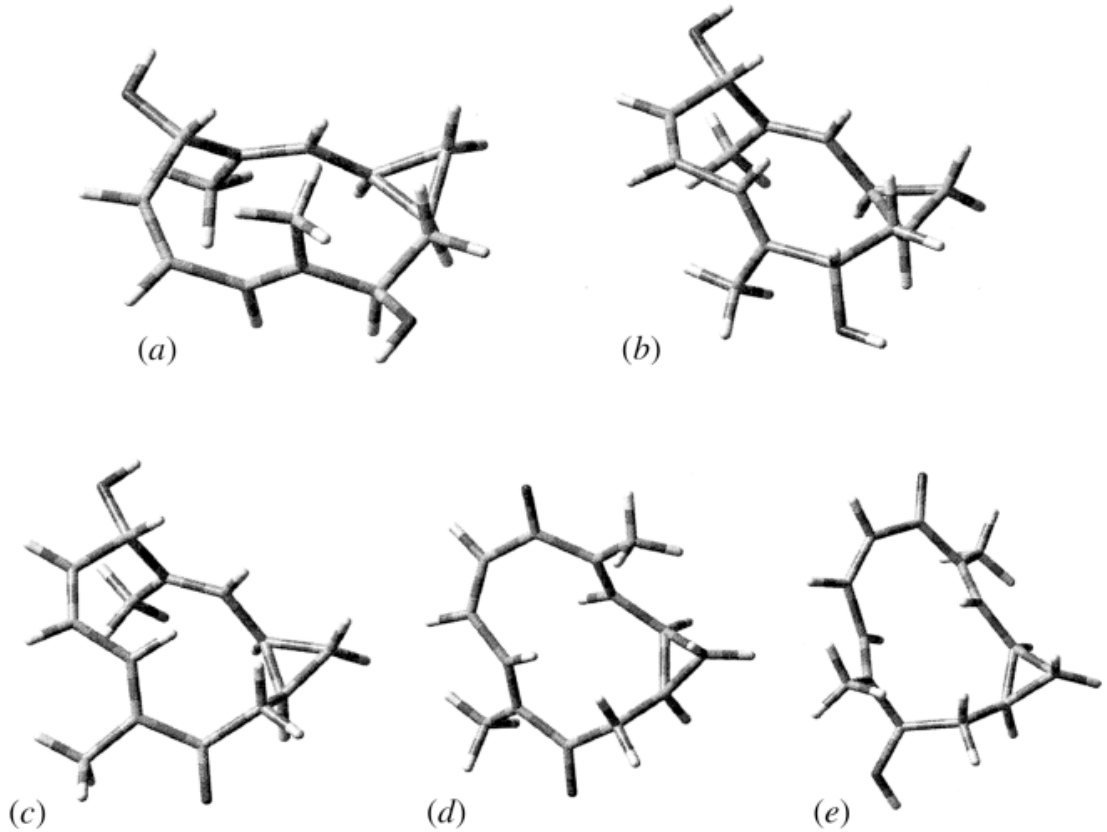
In solution, a molecule exists in an equilibrium mixture of various conformational isomers. The best way to find the global minimum conformation must be to optimize all such possible conformers. Actually, Saunders et al. (7) calculated the conformational energy of cycloheptadecane and discussed the method to find the global minimum conformation of a flexible molecule. Since the 11-membered ring of the lathyrane model compounds includes 3 double bonds and condenses with a cyclopropane ring, the conformational flexibility is considerably restricted. Therefore, paying attention to the C_7-C_8 torsion angle, the conformation of the 11-membered ring can be classified into four groups by the relative orientation of the two methyl groups on C_1 and C_6, as

© 2003 NRC Canada

Table 1. Theoretically calculated relative conformational energies (kJ mol^{-1}) and the relative population (%) calculated at 25 °C under the assumption of the Boltzmann distribution.

Compound	Conformation	B3LYP	(%)	6-31G*	(%)	STO-3G	(%)	PM3	(%)	MM3	(%)
m1	**a**	0.00	96	0.00	92	0.23	48	6.65	6	0.00	63
	b	8.04	4	5.94	8	0.00	52	0.00	93	1.33	37
	c	36.71	0	41.08	0	28.60	0	20.17	0	29.52	0
	d	53.86	0	38.81	0	28.04	0	13.71	0	24.33	0
m2	**a**	1.25	38	5.19	11	5.78	9	6.77	5	0.00	97
	b	0.00	62	0.00	89	0.00	91	0.00	84	8.85	3
	c	31.22	0	42.55	0	21.89	0	5.05	11	19.48	0
	d	27.70	0	30.47	0	27.38	0	16.64	0	17.49	0
m3	**a**	22.66	0	19.51	0	13.57	0	0.00	86	15.36	0
	b	0.00	100	0.00	100	0.00	100	4.52	14	0.00	100
	c	59.95	0	60.62	0	46.58	0	35.35	0	42.98	0
	d	33.45	0	38.35	0	35.36	0	25.58	0	21.72	0
m4	**a**	21.04	0	12.29	0	6.61	6	2.01	30	6.72	6
	b	10.75	1	2.20	29	0.00	92	0.00	69	0.00	93
	c	28.77	0	24.04	0	21.34	0	11.09	1	15.68	0
	d	0.00	99	0.00	70	9.38	2	16.57	0	13.19	0
m5	**a**	0.00	100	0.00	98	0.00	92	13.31	0	0.00	93
	b	14.80	0	9.53	2	6.19	8	0.00	99	6.48	7
	c	31.49	0	30.31	0	30.28	0	15.98	0	26.10	0
	d	31.77	0	25.91	0	23.91	0	22.38	0	15.41	0

Fig. 3. The most stable conformation obtained by the RHF/6-31G* optimization; (*a*) **m1a**, (*b*) **m2b**, (*c*) **m3b**, (*d*) **m4d**, and (*e*) **m5a**.



shown in Fig. 2. By inspection of the Dreiding model, we generated initial coordinates of each group and evolved 200 conformers using the "stochastic search for conformers" option of the MM3(96) program. Subsequently, unique conformers (having a dihedral angle differing by more than 15° from other conformers) were selected and optimized using the above-mentioned theoretical methods.

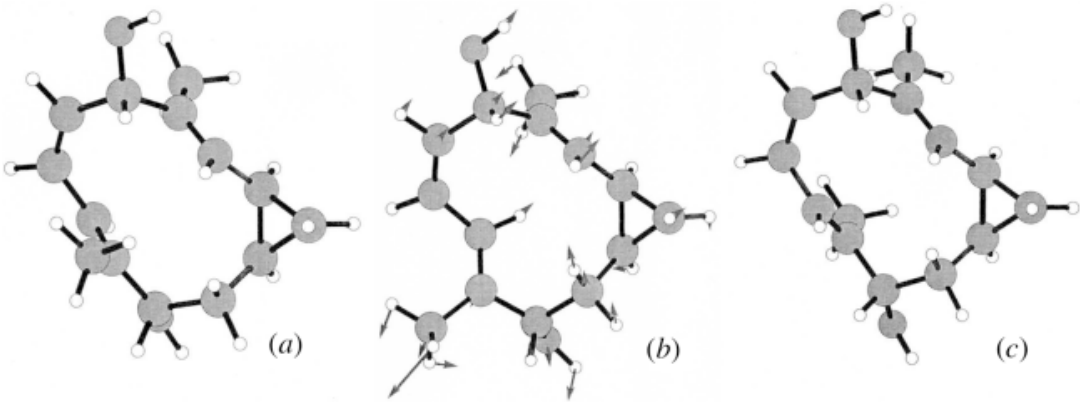
The accuracy of the calculation methods was confirmed by comparison with the experimental result. In Table 3, the calculation results of the model compound **m2a** and, as

© 2003 NRC Canada

Table 2. Observed NOE enhancement and nonbonding H—H distances (Å) calculated by the Gaussian 98, MOPAC(PM3), and MM3 programs.

			6-31G*				STO-3G				PM3				MM3			
Compound	Hydrogen	NOE (%)	**a**	**b**	**c**	**d**	**a**	**b**	**c**	**d**	**a**	**b**	**c**	**d**	**a**	**b**	**c**	**d**
m1	H_5–$H_{7\alpha}$	9	2.2	3.6	2.9	3.4	2.3	3.7	2.9	3.5	2.3	3.7	2.8	3.7	2.3	3.7	3.1	3.5
	$H_{8\alpha}$–$H_{7\alpha}$	4	2.6	2.4	2.6	2.4	2.7	2.5	2.5	2.5	2.8	2.6	2.6	2.6	2.6	2.5	2.6	2.5
	H_9–$H_{7\alpha}$	5	2.6	2.7	2.6	4.1	2.6	2.7	4.2	4.2	2.5	2.4	4.1	4.1	2.7	2.8	4.2	4.3
m2	H_5–$H_{7\beta}$	5	3.5	2.4	3.5	2.2	3.5	2.6	3.7	2.3	3.6	2.5	3.8	2.3	3.5	2.4	3.7	2.3
m3	H_5–$H_{8\beta}$	15	4.3	2.0	3.7	1.9	4.3	2.1	4.5	2.1	3.8	1.8	3.7	1.8	4.4	2.0	3.1	1.9
	H_5–H_{12}	5	4.3	2.4	2.3	2.7	4.1	2.5	2.5	3.1	3.8	2.7	1.8	3.2	4.3	2.4	2.1	2.9
	H_5–$H_{2\beta}$	3	4.3	2.7	3.9	2.7	4.3	2.7	4.1	3.0	4.0	2.9	4.1	3.0	4.4	2.7	3.8	3.2
m4	H_5–$H_{8\beta}$	16	4.3	1.9	3.5	1.9	4.4	2.0	2.0	2.0	3.9	1.8	1.8	1.8	4.4	1.9	1.9	1.9
	H_5–H_{12}	6	4.6	2.6	2.4	2.7	4.5	2.6	2.5	3.0	3.6	2.7	2.7	3.6	4.5	2.5	2.5	2.9
m5	H_5–$H_{7\alpha}$	13	2.3	3.6	2.6	3.4	2.3	3.7	2.9	3.5	2.3	3.7	2.8	3.6	2.3	3.7	3.1	3.5
	H_9–$H_{7\alpha}$	5	2.7	2.5	4.2	3.8	2.6	2.6	4.2	4.2	2.5	2.3	4.1	4.2	2.6	2.6	4.2	4.3

Fig. 4. Two stable conformations and the transition structure for the conformational interconversion. (*a*) **m2a**, (*b*) the transition structure with vibration vectors, and (*c*) **m2b**.



a standard of comparison, the reported results of an X-ray crystallographic analysis of 3,8,14,20-tetraacetyl-7-(2-methylbutanoyl)-synadenol (6) are shown. Regardless of the difference in the molecular structure, all calculation methods afforded bond lengths, bond angles, and dihedral angles in good agreement with the X-ray results. In addition, all standard errors by different calculation methods were comparable. Therefore, as far as the geometrical accuracy is concerned, there is little difference in these theoretical methods.

Moreover, no distinct difference was detected between the geometrical parameters of the diterpene structure (**2**) in Fig. 1 and the truncated model structure (**m2**) in Fig. 2 (the data are not shown). Thus, the removal of the 5-membered ring or the cyclopropane dimethyl group did not seriously influence the conformation of the 11-membered ring. Since all atoms bonding to the C_3=C_4 double bond were fixed in a plane and the cyclopropane dimethyl group did not contact the 11-membered ring, they must have little steric influence on the 11-membered ring. Accordingly, the calculations on the truncated models caused no inconsistency in the 11-membered ring conformation.

The resultant relative values of the minimum energy of each group are listed in Table 1. Excluding the exceptional result of the model compound **m4**, conformers with the β-oriented C_1 methyl group were considerably less stable than the conformers with the α-oriented C_1 methyl group. Actually, the reported conformation of the lathyrane derivatives with a C_1=C_{12} double bond had the α-oriented C_1 Me group (3, 6, 8). To direct the C_1 methyl group upward, two single bonds (namely, C_1—C_2 and C_{11}—C_{12}) must be rotated. As a result of this rotation, the cyclopropane ring becomes almost perpendicular to the 11-membered ring; moreover, this rotation also affects the relative position of C_7 and C_8. Because of these conformational requirements, the conformations with the β-oriented C_1 methyl group must be more destabilized than the α-oriented C_1 methyl conformers. In fact, the effect of flipping the C_1 methyl group is much larger than that of the C_6 methyl group (see Table 1). Moreover, since the cyclopropane ring of the β-oriented C_1 methyl conformation is approximately perpendicular to the 11-membered ring, one of the cyclopropane methyl groups causes steric hindrance with the 11-membered ring. Therefore, conformations with the β-oriented C_1 methyl group must be further destabilized in the lathyrane skeleton when compared with the truncated model compounds. On the assumption of a Boltzmann distribution, the 11 kJ mol^{-1} difference in stability corresponds to the overwhelming existence (99%) of the stable conformer; therefore, the less stable conformer must have no effect on the NMR spectra.

In the case of the dicarbonyl compound (**m4**), the **d** con-

© 2003 NRC Canada

Table 3. Comparison of bond lengths, bond angles, and dihedral angles between the X-ray results and the theoretical calculations for model compound **m2a**.

	X-ray[a]	6-31G*	STO-3G	PM3	MM3
Bond lengths (Å)					
1—2	1.5163	1.5149	1.5437	1.5130	1.5110
2—3	1.5347	1.5197	1.5414	1.5085	1.5141
4—5	1.4662	1.4861	1.5065	1.4592	1.4968
5—6	1.3363	1.3225	1.3144	1.3388	1.3475
6—7	1.5042	1.5181	1.5419	1.5123	1.5172
7—8	1.5161	1.5473	1.5729	1.5453	1.5468
8—9	1.5252	1.5215	1.5364	1.5045	1.5285
9—10	1.4896	1.4982	1.5055	1.5041	1.5120
9—11	1.5228	1.5147	1.5189	1.5171	1.5300
10—11	1.5080	1.5019	1.5085	1.5013	1.5188
11—12	1.5015	1.4813	1.5024	1.4691	1.4739
1—13	1.5308	1.5125	1.5245	1.4847	1.5099
6—14	1.5133	1.5109	1.5304	1.4896	1.5119
Standard error		0.0150	0.0252	0.0217	0.0186
Bond angles (°)					
1-2-3	112.2	112.5	112.3	112.4	115.9
2-1-12	122.1	118.8	119.3	118.9	120.3
4-5-6	128.8	127.1	125.6	125.2	124.6
5-6-7	120.5	121.8	121.4	122.9	123.1
6-7-8	111.8	113.4	111.9	111.4	114.0
7-8-9	116.8	117.1	115.6	116.4	120.0
9-10-11	61.1	60.6	60.5	60.6	60.6
8-9-11	125.2	125.9	124.7	123.6	122.3
9-11-12	119.7	120.4	120.7	119.6	118.9
1-12-11	123.6	126.2	127.2	123.4	128.0
12-1-13	124.8	124.7	126.1	123.9	124.0
5-6-14	122.8	123.7	122.9	121.8	122.0
Standard error		1.5	1.8	1.7	2.7
Dihedral angles (°)					
1-2-3-4	34.7	43.1	35.6	45.7	35.5
2-1-12-11	168.9	164.0	170.2	168.4	172.4
3-4-5-6	104.2	69.5	83.1	84.3	71.5
4-5-6-7	179.2	–176.1	–179.0	179.3	178.6
5-6-7-8	88.0	110.0	107.8	101.3	113.0
6-7-8-9	–89.8	–81.8	–88.0	–86.0	–82.5
7-8-9-10	159.7	153.5	152.2	153.9	148.7
7-8-9-11	85.8	81.0	79.9	83.2	78.6
8-9-11-12	–2.4	–5.4	–3.3	–5.2	–6.6
1-12-11-9	–136.7	–125.1	–127.0	–133.7	–123.2
3-2-1-13	81.9	62.0	68.8	64.9	61.6
4-5-6-14	–0.7	4.5	0.6	–0.9	3.8
Standard error		14.4	10.0	9.4	14.6

[a]Reference 6.

former was stabilized — especially the RHF/6-31G* optimized conformation — and the one-point calculation by B3LYP/6-31G* demonstrated that **m4d** was the most stable.[2] This is exceptional, because other compounds in this work and in previous results (3, 6, 8) exhibited a predominance of the α-oriented C_1 methyl conformation. All unsaturated bonds of **m4** (namely, C_{12}—C_1, C_2—O_{19}, C_3—C_4, C_5—C_6, and C_7—O_{20}) are conjugated; moreover, C_{12}—C_1 and C_2—O_{19}, as well as C_5—C_6 and C_7—O_{20} of the calculated **m4d**, were nearly co-planar. The *s-trans* arrangement of this conformation seems to be strainless; therefore, the disadvantage of the β-oriented C_1-methyl conformation may be overcome by the conjugation effect of these nearly planar unsaturated systems. While **m5** also has the C_2—O_{19} carbonyl group, the conformational change caused by the saturation of the C_7 carbon must force the C_{12}=C_1—C_2=O_{19} system to deviate from planarity. Because of this conformational change, **m5a** was the most stable conformation of this compound.

The relative energies of the minimum conformations of the individual conformational groups and their proportion at 25 °C under the assumption of Boltzmann distribution are shown in Table 1. From this relative population, the predominant conformation of the model compounds (**m1**~**m5**) and the possibility of conformational equilibrium are indicated. The NOE enhancement (%) and the calculated nonbonding hydrogen—hydrogen distance are also shown in Table 2. Since NOE is observed at the inverse sixth power of the interatomic distance (9), it is favorably observed between hydrogens located as close as possible. Except for the 6-31G* calculation, the calculated relative stability was not necessarily consistent with the NOE observation as shown in Table 2. The stable conformations predicted by both the RHF/6-31G* minimization and single-point DFT calculation based on the RHF/6-31G* optimized structure were always consistent with the NOE observation. For example, RHF/6-31G* calculations predicted that **m1a** is the most stable, and all hydrogen—hydrogen distances in **m1a** were short enough, whereas other conformers of **m1** had at least one distant H–H pair for NOE observation. Since both α-oriented C—H bonds on C_5 and C_7 of **m1a** were almost perpendicular to the average ring plane, these protons were close to each other. In contrast, the corresponding protons of **m1c** were not so close, because the quasi-equatorial C_7 proton was extended to the outside of the 11-membered ring. Similarly, the 6-31G* prediction of other compounds agreed well with the NOE observation. In contrast, the STO-3G, PM3, and MM3 calculations did not necessarily agree with the NOE observation. Namely, the STO-3G and PM3 calculations incorrectly predicted that **m1b** was the most stable. For the model compound **m2**, the MM3 method incorrectly predicted that the predominant conformation is **m2a**, and this disagrees with the NOE observation between H_5 and $H_{7\beta}$. As regards the model compound **m3**, all calculations except for PM3 suggested that **m3b** is the overwhelmingly predominant conformation.

Based on the energy difference between the conformers of the DFT single-point calculation in Table 1, the populations were estimated, for **m2a** and **m2b**, as 38% and 62%, respectively. Therefore, if the interchange is possible at room temperature, this compound may be a conformational mixture. However, all NMR spectra consist of only one set of signals, indicating that each compound adopts one conformation or exists in a conformational mixture by rapid interchange. The estimated, relatively low activation energy of the inversion of the C_5=C_6 double bond suggests free inversion of the dou-

[2]The 6-31G* optimized conformation of **m4d** was consistent with the NOE observation (see Table 2).

© 2003 NRC Canada

ble bond. When the flipping of the double bond is faster than the NMR time scale, the observed NOE is the average of all the conformations present in the solution. In such a case, we cannot rule out the co-existence of **m2a**, though there was no NOE observation suggesting **m2a**. Differing from **m2**, the calculated large energy difference revealed that compounds **m1**, **m3**, **m4**, and **m5** adopt, exclusively, a single conformation regardless of the activation energy.

Conclusion

All calculation methods used in this work afforded comparable bond lengths, bond angles, and dihedral angles, as shown in Table 2. In contrast, the predominant conformations predicted by the different methods differed. Only the 6-31G* calculations always predicted the predominant conformations that agreed with the NOE results. Thus, the conformational stability predicted by the MM3, PM3, and STO-3G methods is not necessarily correct. Therefore, ab initio calculations using a larger basis set are desirable for such peculiar ring systems as the lathyrane type.

Methods

The structure of lathyrane derivatives, together with the type and location of the oxygen functional groups, are shown in Fig. 1.[3] ^{1}H NMR spectra were obtained at 400 MHz on a JEOL JNM-GX400 spectrometer using $CDCl_3$ solutions, as follows: **1**: δ: 5.66 (1H, br s), 4.93 (1H, d, *J* = 11.6 Hz), 4.63 (1H, br s), 4.02 (1H, d, *J* = 8.5 Hz), 2.54 (1H, m), 2.37 (2H, m), 2.29 (1H, m), 1.94 (1H, dd, *J* = 4.3, 12.1 Hz), 1.75 (3H, complex), 1.45 (3H, d, *J* = 1.5 Hz), 1.42 (3H, d, *J* = 1.5 Hz), 1.19 (1H, dd, *J* = 8.5, 11.6 Hz), 1.03 (3H, s), 1.00 (3H, s), 0.74 (1H, ddd, *J* = 3.9, 8.5, 11.2 Hz); **2**: δ: 5.54 (1H, br s), 4.83 (1H, d, *J* = 11.4 Hz), 4.65 (1H, br s), 4.30 (1H, br s), 2.58 (2H, m), 2.40 (1H, m), 2.19 (1H, m), 2.16 (1H, ddd, *J* = 3.6, 5.3, 14.8 Hz), 1.80 (2H, m), 1.58 (1H, m), 1.54 (3H, s), 1.42 (3H, s), 1.25 (1H, dd, *J* = 9.3, 11.8 Hz), 1.11 (3H, s), 1.04 (3H, s), 0.99 (1H, ddd, *J* = 3.6, 9.3, 11.8 Hz); **4**: δ: 7.02 (1H, br s), 5.71 (1H, dd, *J* = 1.5, 9.8 Hz), 3.03 (1H, dd, *J* = 11.7, 12.1 Hz), 2.80–2.65 (3H, complex), 2.59 (1H, m), 2.46 (1H, dd, *J* = 4.4, 12.1 Hz), 1.93 (2H, m), 1.67 (3H, d, *J* = 1.5 Hz), 1.66 (3H, d, *J* = 2.0 Hz), 1.31 (1H, dd, *J* = 9.3, 9.8 Hz), 1.11 (6H, s), 1.06 (1H, ddd, *J* = 4.4, 9.3, 11.7 Hz); **5**: δ: 5.98 (1H, br s), 5.60 (1H, dd, *J* = 1.0, 11.6 Hz), 4.20 (1H, d, *J* = 9.2 Hz), 2.76 (1H, m), 2.64–2.51 (3H, complex), 2.01 (1H, dd, *J* = 6.4, 13.6 Hz), 1.90–1.81 (2H, complex), 1.77 (3H, d, *J* = 1.0 Hz), 1.74 (1H, m), 1.51 (3H, s), 1.38 (1H, dd, *J* = 8.8, 11.6 Hz), 1.12 (3H, s), 1.08 (1H, overlapped), 1.07 (3H, s).

The calculations were performed on the truncated model structures, as shown in Fig. 2. The starting coordinates of each conformation of the truncated model structures (**m1**~**m5**) were generated by inspection of the Dreiding molecular model using standard bond lengths and bond angles. Then, 200 conformers were evolved using the stochastic search option of the MM3(96) program (10). Similar conformers whose dihedral angles were within ±15° from the corresponding angles of an already selected conformation and unsuitable conformers having a sterically isomerized double bond or a cyclopropane ring were removed. Intramolecular flexibility of the surviving conformers was optimized by the following theoretical methods: namely, the ab initio MO, semi-empirical MO, and MM methods.

Ab initio calculations of MO were carried out using the Gaussian 98 program package (11). The structure was optimized at the RHF/STO-3G or RHF/6-31G* level. To introduce more correlation effects, a single-point calculation was performed on the 6-31G* optimized structure, employing the B3LYP/6-31G* level of theory (12). All ab initio MO calculations were performed on a FACOM VPP5000/56 super computer at Nagoya University Computation Center.

Semi-empirical MO calculations were done by employing the PM3 method in MOPAC Ver. 6.01 (13). All the geometric variables were completely optimized for each conformer in order to locate the minimum energy conformation. The calculations were carried out on a FACOM GP7000F at Nagoya University Computation Center.

Molecular mechanics calculations were performed using the MM3(96) program package downloaded from QCPE (10). Force constants not parameterized in the program were estimated using the parameter estimation routine. All the geometric variables were completely optimized by block-diagonal, then full-matrix, minimization methods. Calculations were performed on an IBM RS/6000 UNIX work station.

Barrier height for the flipping of the 11-membered ring of the model compound (**m2**) was estimated by RHF/6-31G* level calculations of Gaussian 98 (11). The transition structure of the pseudo-rotation of the C_5=C_6 double bond was searched using the QST3 key word; then, the resultant conformation was optimized under the TS key word. Furthermore, the frequency analysis was performed on the transition state and the two stable conformers (**m2a** and **m2b**); then they were confirmed by existence or absence of a single imaginary mode. The activation energy was the difference in the Gibbs free energy between the transition state and either stable conformation.

Acknowledgements

The authors are grateful to Professor Hiroaki Wasada of Gifu University for his kind advice on the Gaussian 98 program.

References

1. F.J. Evans and S.E. Taylor. *In* Progress in the chemistry of organic natural products. *Edited by* L. Zechmeister, W. Herz, G. Grisebach, and W. Kirby. Springer-Verlag, Wien. 1983. Chap 44. p. 1.
2. (*a*) T. Matsuura, S. Yamamura, and Y. Terada. Tetrahedron Lett. **41**, 2189 (2000); (*b*) A.B. Smith III, B.D. Dorsey, M. Visnick, T. Maeda, and M.S. Malamas. J. Am. Chem. Soc. **108**, 3110 (1986); (*c*) G. Appendino, G.C. Tron, T. Jarevang, and O. Sterner. Org. Lett. **3**, 1609 (2001).
3. Y. Shizuri, J. Ohtsuka, S. Kosemura, Y. Terada, and S. Yamamura. Tetrahedron Lett. **25**, 5547 (1984).

[3] T. Matsuura and S. Yamamura. Unpublished results.

© 2003 NRC Canada

4. T. Matsuura and S. Yamamura. Tetrahedron Lett. **41**, 4805 (2000).
5. T. Matsuura, Y. Terada, and S. Yamamura. Tetrahedron Lett. **42**, 4163 (2001).
6. G.W.J. Oliver, M.G. Rowan, S.K. Branch, M.F. Mahon, and K.C. Molloy. J. Chem. Soc. Perkin Trans. **1**, 1831 (1992).
7. M. Saunders, K.N. Houk, Y.-D. Wu, W.C. Still, M. Lipton, G. Chang, and W.C. Guida. J. Am. Chem. Soc. **112**, 1419 (1990).
8. (*a*) Y. Shizuri, S. Kosemura, J. Ohtsuka, Y. Terada, and S. Yamamura. Tetrahedron Lett. **24**, 2577 (1983); (*b*) J. Hohmann, F. Evanics, A. Vasas, G. Dombi, G. Jerkovich, and I. Mathe. J. Nat. Prod. **62**, 176 (1999); (*c*) G. Appendino, E. Belloro, G.C. Tron, J. Jakupovic, and M. Ballero. J. Nat. Prod. **62**, 1399 (1999).
9. F.A.L. Anet and A.J.R. Brown. J. Am. Chem. Soc. **87**, 5250 (1965), and refs. cited therein.
10. N.L. Allinger. MM3(96) [computer program]. QCPE No. 698. Quantum chemistry program exchange, Department of Chemistry, Indiana University, Bloomington. 1996.
11. M.J. Fisch, G.W. Trucks, H.B. Schlegel, G.E. Scuseria, M.A. Robb, J.R. Cheeseman, V.G. Zakrzewski, J.A. Montgomery, R.E. Stratmann, J.C. Burant, S. Dapprich, J.M. Millam, A.D. Daniels, K.N. Kudin, M.C. Strain, O. Farkas, J. Tomasi, V. Borone, M. Cossi, R. Cammi, B. Mennucci, C. Pomelli, C. Adamo, S. Clifford, J. Ochterski, A. Petersson, P.J. Ayala, Q. Cui, K. Morokuma, D.K. Malick, A.D. Rabuck, K. Raghavachari, J.B. Foresman, J. Cioslowski, J.V. Ortiz, B.B. Stefanov, B. B.; A. Liu, Liashenko, P. Piskorz, I. Komaromi, R. Gomperts, R.L. Martin, D.J. Fox, T. Keith, M.A. Al-Laham, C.Y. Peng, A. Nanayakkara, C. Gonzalez, M. Challacombe, P.M.W. Gill, B.G. Johnson, W. Chen, M.W. Wong, J.L. Andres, M. Head-Gordon, E.S. Replogle, and J.A. Pople. Gaussian 98 [computer program]. Revision A.1. Gaussian, Inc., Pittsburgh. 1998.
12. RG. Parr and W. Yang. Density-functional theory of atoms and molecules. Oxford University Press, New York. 1994.
13. J.J.P. Stewart. MOPAC Ver6.0 [computer program]. Version 6.01. QCPE No.455. *Revised by* Y. Inoue. Green Cross Corporation, Osaka. 1990.

© 2003 NRC Canada

Theoretical studies on the one- and two-photon absorption of tetrabenzoporphyrins and phthalocyanines

Xin Zhou, Ai-Min Ren, Ji-Kang Feng, and Xiao-Juan Liu

Abstract: The one-photon absorption (OPA) properties of tetrabenzoporphyrins (TBPs) and phthalocyanines (Pcs) were studied using the semiempirical ZINDO method and time-dependent density functional theory (TDDFT), respectively. The compared results confirmed that the semiempirical ZINDO method was reasonably reliable when calculating the OPA of tetrabenzoporphyrins and phthalocyanines. On the basis of the OPA properties obtained from the ZINDO method, two-photon absorption (TPA) properties of two series of molecules were investigated, using ZINDO and sum-over-states (SOS) methods. The results showed that the TPA cross-sections of all molecules were in the range of $220.6 \times 10^{-50} - 345.9 \times 10^{-50}$ $cm^4 \cdot s \cdot photon^{-1}$, which were in the same order of magnitude as the values reported in the literature. The relatively larger $\delta(\omega)$ value for Pcs with respect to that for corresponding TBPs originates from larger intramolecular charge transfer, which can be characterized by the difference of dipole moment between S_0 and S_1 and the transition dipole moment between S_1 and S_5.

Key words: two-photon absorption, ZINDO, sum-over-states, tetrabenzoporphyrin, phthalocyanines.

Résumé : On a étudié les propriétés d'absorption monophotoniques (« OPA ») de tétrabenzoporphyrines (TBPs) et de phtalocyanines (Pcs) à l'aide de la méthode semi-empirique ZINDO et de la théorie fonctionnelle de la densité dépendante du temps (« TDDFT »). Une comparaison des résultats confirme que pour le calcul des « OPA » des tétrabenzoporphyrines et des phtalocyanines, la méthode semi-empirique ZINDO donne des valeurs raisonnablement fiables. Sur la base des « OPA » obtenus par la méthode ZINDO, on a étudié les propriétés d'absorption biphotoniques (« TPA ») de deux séries de molécules ont été étudiées à l'aide des méthodes ZINDO et de la somme de tous les états (« SOS »). Les résultats montrent que les sections droites des « TPA » de toutes les molécules se situent dans la fourchette $220{,}6 \times 10^{-50}$ à $345{,}9 \times 10^{-50}$ $cm^4 \cdot s \cdot photon^{-1}$, valeurs qui sont du même ordre de grandeur que celles rapportées dans la littérature. La valeur de $\delta(\omega)$ relativement plus élevée pour les Pcs par rapport aux THBs résulte d'un plus grand transfert de charge qui peut être caractérisé par la différence entre les moments dipolaires S_0 et S_1 et le moment dipolaire de transition entre S_1 et S_5.

Mots clés : absorption biphotonique, ZINDO, somme de tous les états, tétrabenzoporphyrine, phtalocyanine.

[Traduit par la Rédaction]

Introduction

The phthalocyanines (Pcs) and tetrabenzoporphyrins (TBPs) have attracted considerable attention because of their applications in a wide variety of important chemical, physical, and biological processes, including electrophotographic systems (1), photonvoltaic cells for energy conversion (2), optical power limiting (3, 4), photosensitizers (5), and photodynamic therapy (6–9). Much theoretical and experimental effort has been exerted in attempts to elucidate the electronic, spectroscopic, and optical properties of these molecules (10–17). Experimentally, the spectroscopic properties of Pcs in the vapor phase and in solvents were measures by Edwards and Goutermans (14). The spectroscopic studies of TBPs were carried out by Ehrenberg and Johnson (15). They examined the basic absorption and fluorescence properties of TBPs in a variety of solvents and mixtures and pointed out the potential applications of these dyes as either ultrasensitive probes or photosensitizers. Ortí et al. (16) used the valence effective Hamiltonian quantum-chemical method to theoretically determine the molecular and solid-state electronic structures of metal-free phthalocyanine. Nguyen and Pachter (17) investigated and compared the ground-state electronic structures and spectra of ZnTBP and ZnPc using density functional theory.

Previous experimental observations and theoretical investigations of TBPs and Pcs have focused on the study of one-photon absorption (OPA) properties, although the potential significance of two-photon absorption (TPA) properties has also been paid attention (10, 18, 19). In recent years, the TPA of molecules has become a more and more exciting nonlinear optical phenomenon that possesses great potential for application in photonic and biological areas, such as

Received 4 May 2003. Published on the NRC Research Press Web site at http://canjchem.nrc.ca on 27 November 2003.

X. Zhou, A.-M. Ren, J.-K. Feng,[1] and X.-J. Liu. State Key Laboratory of Theoretical and Computational Chemistry, Institute of Theoretical Chemistry, Jilin University, 125 Jie Fang Road, Changchun 130023, China.

[1]Corresponding author (e-mail: jikangf@yahoo.com).

 doi: 10.1139/V03-175 © 2003 NRC Canada

three-dimensional optical storage (20, 21), two-photon fluorescence excitation microscopy (22, 23), and two-photon upconverted lasing (24, 25). To find organic molecules with large TPA cross-sections, many efforts were devoted to experimentally developing chromophores with novel structures and conjugation patterns (26, 27). Meanwhile, theoretical calculations were also employed, to establish the structure–property relationships for a large number of TPA dyes and to understand the underlying mechanisms for increasing the TPA cross-section (28–30).

Recently, Karotki et al. (10) investigated the increase of TPA in a series of porphyrins and tetraazaporphyrins by measuring the absolute TPA cross-section with 100-fs-duration pulses in two ranges of laser wavelengths, from 1100 to 1500 nm and from 700 to 800 nm. The cross-section in the Q transition region was $1 \times 10^{-50} - 10 \times 10^{-50}$ cm^4·s·photon^{-1}, and in the Soret transition region they found an enhancement of the TPA cross-section by one order of magnitude. In symmetrically substituted tetraazaporphyrins with strong electron acceptors, further enhancement of the TPA cross-section — up to 1600×10^{-50} cm^4·s·photon^{-1} — was found.

In this paper, we have first investigated the OPA properties of tetrabenzoporphyrin (H_2TBP), metallo-TBPs (MgTBP, ZnTBP), phthalocyanine (H_2Pc), and metallo-Pcs (MgPc, ZnPc) by means of time-dependent density functional theory (TDDFT) and ZINDO and then compared the results obtained from the two methods. Then, ZINDO and sum-over-states (SOS) were employed to calculate the second hyperpolarizability and TPA properties of six molecules on the basis of geometries optimized by B3LYP/6-31G and the OPA properties obtained from the ZINDO method.

Theoretical methodology

The TPA process corresponds to simultaneous absorption of two photons. The TPA efficiency of an organic molecule at optical frequency $\omega/2\pi$ can be characterized by the TPA cross-section $\delta(\omega)$. It can be directly related to the imaginary part of the second hyperpolarizability $\gamma(-\omega;\omega,\omega,-\omega)$ by the following equation (31):

$$[1] \qquad \delta(\omega) = \frac{8\pi^2\hbar\omega^2}{n^2c^2} L^4 \operatorname{Im}\gamma(-\omega;\omega,\omega,-\omega)$$

where $\hbar$ is Planck's constant divided by 2π; n is the refractive index of medium; c is the speed of light; and L is a local field factor (equal to 1 for vacuum).

The SOS expression to evaluate the components of the second hyperpolarizability γ_{ijkl} can be induced using perturbation theory and the density matrix method. By considering a power expansion of the energy with respect to the applied field, the γ_{ijkl} Cartesian components are given by the following equation (32, 33):

$$[2] \qquad \gamma_{ijkl}(-\omega_\sigma;\omega_1,\omega_2,\omega_3) = \frac{4\pi^3}{3h^3} \mathrm{P}(i,j,k,l;-\omega_\sigma;\omega_1,\omega_2,\omega_3) \times \left[\sum_{m\neq o}\sum_{n\neq o}\sum_{p\neq o} \frac{\langle o|\mu_i|m\rangle\langle m|\bar{\mu}_j|n\rangle\langle n|\bar{\mu}_k|p\rangle\langle p|\mu_l|o\rangle}{(\omega_{mo}-\omega_\sigma-i\Gamma_{mo})(\omega_{no}-\omega_2-\omega_3-i\Gamma_{no})(\omega_{po}-\omega_3-i\Gamma_{po})} - \sum_{m\neq o}\sum_{n\neq o} \frac{\langle o|\mu_i|m\rangle\langle m|\mu_j|o\rangle\langle o|\mu_k|n\rangle\langle n|\mu_l|o\rangle}{(\omega_{mo}-\omega_\sigma-i\Gamma_{mo})(\omega_{no}-\omega_3-i\Gamma_{no})(\omega_{no}+\omega_2-i\Gamma_{no})} \right]$$

where P(i, j, k, l;$-\omega_\sigma$; ω_1, ω_2, ω_3) is a permutation operator defined in such a way that for any permutation of (i, j, k, l), an equivalent permutation of ($-\omega_\sigma$; ω_1, ω_2, ω_3) is made simultaneously; $\omega_\sigma = \omega_1 + \omega_2 + \omega_3$ is the polarization response frequency; ω_1, ω_2, ω_3 indicate the frequencies of the perturbing radiation fields (considering the degenerate TPA, $\omega_1 = \omega_2 = \omega$ and $\omega_3 = -\omega$); i, j, k, and l correspond to the molecular axes x, y, and z; m, n, and p denote excited states and o, the ground state; μ_j is the j (= x, y, z)th component of the dipole operator; ($\langle m|\bar{\mu}_j|n\rangle = \langle m|\mu_j|n\rangle - \langle o|\mu_j|o\rangle$); $(h/2\pi)\omega_{mo}$ is the transition energy between the m and o states; and Γ_{mo} is the damping factor of the excited state m. Considering that the higher the excited state, the shorter is its lifetime, the Γ_{mo} is expressed as follows (34):

$$[3] \qquad \Gamma_{mo} = 0.08 \times \frac{\omega_{mo}}{\omega_{1o}}$$

To compare the calculated δ value with the experimental value measured in solution, the orientationally averaged (isotropic) value of γ is evaluated, which is defined as

$$[4] \qquad \langle\gamma\rangle = \frac{1}{15}\sum_{i,j}(\gamma_{iijj} + \gamma_{ijij} + \gamma_{ijji}); \qquad i,j = x,y,z$$

Generally, the position and relative strength of the two-photon resonance for centrosymmetric molecules are to be predicted using the following simplified form of the SOS expression (28, 32):

$$[5] \qquad \delta \propto \frac{M_{0k}{}^2 M_{kn}{}^2}{(E_{0k} - E_{0n}/2)^2\Gamma}$$

where M_{ij} is the transition dipole moment from the state i to the state j; E_{ij} is the corresponding excitation energy; the subscripts 0, k, and n refer to the ground state S_0, the intermediate state S_k, and the TPA final state S_n, respectively;

© 2003 NRC Canada

and the damping factor Γ has been calculated according to eq. [3].

In principle, any kind of self-consistent field molecular orbital (SCFMO) procedure combined with configuration interaction (CI) can be used to calculate the physical values in the above expression. In the present paper, the B3LYP/6-31G method was first used to calculate molecular equilibrium geometry. Then, the property of the electronic excited state was obtained by single and double electron excitation configuration interaction (SDCI), using the ZINDO program and TDDFT, respectively. Furthermore, on the basis of the OPA parameters obtained from the ZINDO method, TPA properties of the molecules are provided. Then, according to eqs. [1]–[4], the second hyperpolarizability γ and the TPA cross-section δ(ω) were calculated.

Results and discussion

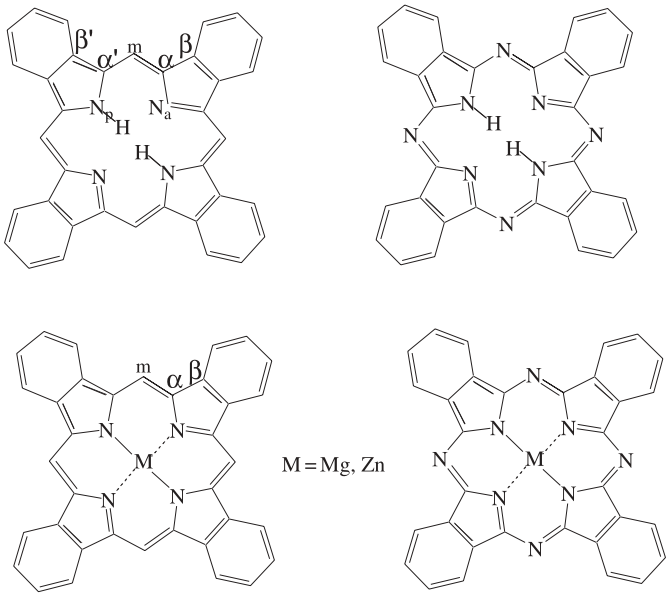
Molecular structures

The compounds studied in this paper are shown in Fig. 1. Since the molecular structures used in the calculations have an important effect on the accuracy of the computed spectra, it is necessary to compare the calculated structural parameters with theoretical and experimental results. In this paper, the molecular geometries were optimized by the B3LYP method in the Gaussian 98 program package, using the 6-31G basis set under the following symmetry constraints: D_{4h} for bivalent metallic derivatives and D_{2h} for metal-free phthalocyanine or tetrabenzoporphyrin (35). Figure 1 and Table 1 display the molecular labels and structural parameters. For H_2Pc, the parameters obtained by the B3LYP/6-31G method are consistent with the PM3-optimized parameters (15). Although, for the C_α—N_m and C_α—N_m bonds, the lengths of 1.324 and 1.340 Å are smaller than the PM3-optimized values of 1.344 and 1.349 Å, they are in line with the X-ray value of 1.330 Å reported for α-H_2Pc (38). Compared with the literature value (15), the N_p—C_α distance of H_2Pc (1.388 Å) is overestimated by 0.023 Å, which is comparable with the value reported in ref. 38 (1.36–1.38 Å). As far as ZnPc is concerned, the geometric parameters are in good agreement with the previous DFT calculation (17). The predicted Zn—N bond distance is slightly longer than those obtained from experimental observation. The C—C and C—N distances are well within 0.02 Å of the experimental values. The calculated bond angles are almost within 2° of the experimental values.

One-photon absorption

On the basis of the geometries optimized by B3LYP/6-31G, we have studied the OPA properties for all molecules. For comparison, the semi-empirical ZINDO and TDDFT are, respectively, used to obtain the OPA wavelength $\lambda^{(1)}$ and the corresponding oscillator strength, which are included in Tables 2 and 3, along with the experimental results. As shown in Table 2, in comparison with the results of the TDDFT calculations, the Q-band absorption peaks of all six compounds predicted by the ZINDO method are in better agreement with the experimental observations. For example, for ZnTBP, the result is 602.8 nm, which is longer than the TDDFT result (561.3 nm) and almost equal to the datum (601.8 nm) taken from the gas-phase supersonic jet (32). As

Fig. 1. Molecular structures and labels for the compounds studied.



can be seen in Table 3, the Q-band absorption peak of ZnPc calculated by ZINDO is at 609.9 nm, which is close to the value obtained from the gas-phase supersonic jet (635.8 nm) (37), while the TDDFT result is 584.2 nm. The results calculated by ZINDO suggest, for either TBPs or Pcs, that the presence of the metal ion makes the Q-band absorption peak exhibit blue-shifts to a certain extent (from 638.0 nm of H_2TBP to 603.4 nm of MgTBP and to 602.8 nm of ZnTBP; from 642.0 nm of H_2Pc to 611.3 nm of MgPc and to 609.9 nm of ZnPc). It is known that the Q-bands of TBPs and Pcs arise from π-electron transitions from occupied to unoccupied orbitals. From the HOMO–LUMO gaps of all compounds in Table 4 we see that, since there are coordination bonds between metals (Mg, Zn) and pyrrole nitrogens, the HOMO–LUMO gaps of metal phthalocyanines and tetrabenzoporphyrins (MPcs and MTBPs) are larger than those of metal-free phthalocyanine and tetrabenzoporphyrin (H_2Pc and H_2TBP), and so maximum absorption wavelengths of MPcs and MTBPs are shorter than those of H_2TBP and H_2Pc. The difference in the central metal has little effect on the Q-band absorption of TBPs and Pcs, which is in good agreement with the conclusion found in the literature (35).

The B-band absorption is dominated by transitions from the HOMO-1 to the two degenerate LUMOs. For the B-bands of the Pcs, the semi-empirical ZINDO results are in line with the TDDFT calculations, and they are consistent with the experimental data. For H_2Pc, the ZINDO result is 351.5 nm with an oscillator strength of 0.28, and TDDFT predicts an absorption peak at 343.5 nm with an oscillator strength of 0.26. These values are in agreement with the experimental values (340 nm) obtained in vapor-phase absorption spectra (14). As far as MgPc is concerned, the B-band gained by ZINDO is predicted to appear at 328.1 nm (oscillator strength f = 0.04), and TDDFT indicates that it is located at 335.2 nm with a stronger oscillator strength of 0.68. The result in the literature (14) is 332 nm, which accords

© 2003 NRC Canada

Table 1. Geometry parameters (in Å and °) for the compounds.

	MgTBP	ZnTBP	MgPc	ZnPc			
	B3LYP	B3LYP	B3LYP	B3LYP	Theor (18)	Expt (36)	Expt (37)
Bond lengths (Å)							
M—N	2.087	2.070	2.015	2.003	2.001	1.980	1.954
C_β—C_β	1.417	1.410	1.410	1.410	1.411	1.400	1.550
C_α—$C(N)_m$	1.393	1.380	1.330	1.330	1.331	1.369	1.372
Bond angles (°)							
α(Zn-N-C_α)	125.7	125.8	125.2	125.4	125.1	125.4	126.5
α(C_β-C_α-$C(N)_m$)	125.5	125.5	124.8	124.4	123.9	123.3	121.3
α(N-C_α-$C(N)_m$)	125.4	125.5	125.1	125.1	127.6	127.8	125.7
	H_2TBP	H_2Pc					
	B3LYP	B3LYP	Theor (18)				
Bond lengths (Å)							
N_p—C_α	1.284	1.388	1.411				
C_β—C_β	1.423	1.420	1.420				
C_α—$C(N)_m$	1.388	1.324	1.344				
N_a—$C_{\alpha'}$	1.379	1.381	1.386				
C_β—$C_{\beta'}$	1.415	1.412	1.423				
$C_{\alpha'}$—$C(N)_m$	1.397	1.340	1.349				
Bond angles (°)							
α(N_p-C_α-$C(N)_m$)	126.1	127.7	128.6				
α(C_β-C_α-$C(N)_m$)	127.7	126.0	124.8				
α(N_a-$C_{\alpha'}$-$C(N)_m$)	125.7	126.9	125.5				
α($C_{\beta'}$-$C_{\alpha'}$-$C(N)_m$)	124.1	122.6	125.6				
α(C_a-$C(N)_m$-$C_{a'}$)	128.2	124.9	125.9				

Table 2. The one-photon absorption parameters of tetrabenzoporphyrins.

H_2TBP			MgTBP			ZnTBP		
ZINDO $\lambda^{(1)}$ (nm) (*f*)	TDDFT $\lambda^{(1)}$ (nm) (*f*)	Expt (16)	ZINDO $\lambda^{(1)}$ (nm) (*f*)	TDDFT $\lambda^{(1)}$ (nm) (*f*)	Expt (3)	ZINDO $\lambda^{(1)}$ (nm) (*f*)	TDDFT $\lambda^{(1)}$ (nm) (*f*)	Expt
638.0(0.12)	582.4(0.06)	662	603.4(0.25)	568.7(0.15)	626	602.8(0.25)	561.3(0.16)	601.8(39)
565.7(0.31)	567.9(0.21)	595.7	347.5(1.55)	379.5(1.24)	432	344.6(1.60)	375.6(1.18)	389(39)
363.2(1.56)	396.9(1.10)	429.3		325.5(0.07)		313.7(0.48)	323.4(0.09)	320(40)
	375.4(1.11)		315.0(0.39)	304.2(0.08)	305		317.8(0.04)	
340.0(0.80)	343.8(0.52)			297.6(0.14)			296.2(0.14)	295.9(41)
317.6(0.58)			257.1(0.18)	259.7(0.08)	258	270.3(0.01)	274.6(<0.01)	269.5(41)
300.4(0.24)	307.6(0.07)		238.2(0.36)	239.8(0.03)	239	255.1(0.13)	258.8(0.07)	253.5(40)
293.2(0.73)	291.6(0.21)		231.5(0.06)	231.3(0.03)		237.4(0.31)	239.8(0.04)	247.9(41)
273.3(0.61)	265.1(0.11)		227.6(0.01)	226.6(0.01)		230.8(0.07)	231.1(0.03)	
257.6(0.08)	255.4(0.04)					226.8(0.01)	229.5(<0.01)	
236.1(0.12)	236.2(0.02)					224.3(<0.01)	225.4(0.19)	
232.5(0.22)								
226.2(0.24)	224.6(0.06)							
232.5(0.22)								
226.2(0.24)	224.6(0.06)							

with our calculations. For ZnPc, the ZINDO result of 327.9 nm (*f* = 0.04) and the TDDFT value of 325.3 nm (*f* = 0.34) are almost equal to the value found in the experiment (14) (326.5 nm) and the result (326 nm) found in the literature (42). In the terms of TBPs, the B-bands obtained from TDDFT exhibit more reasonable values to the experimental results than those of ZINDO. The B-band of H_2TBP, predicted by TDDFT, is 396.9 nm (*f* = 1.10); the ZNIDO result is 363.2 nm with a stronger oscillator strength of 1.55, and the corresponding experimental value is 429.3 nm (16). As to MgTBP and ZnTBP, the differences between TDDFT and ZINDO in the B-band are about 30 nm. The results suggest that for predicting the B-band absorptions of TBPs, the TDDFT method can give better results than the ZINDO

© 2003 NRC Canada

Table 3. The one-photon absorption parameters of phthalocyanines.

H_2Pc			MgPc			ZnPc	ZnPc	
ZINDO $\lambda^{(1)}$ (nm) (*f*)	TDDFT $\lambda^{(1)}$ (nm) (*f*)	Expt (14)	ZINDO $\lambda^{(1)}$ (nm) (*f*)	TDDFT $\lambda^{(1)}$ (nm) (*f*)	Expt (14)	ZINDO $\lambda^{(1)}$ (nm) (*f*)	TDDFT $\lambda^{(1)}$ (nm) (*f*)	Expt
642.0(0.53)	591.2(0.33)	686	611.3(0.61)	589.7(0.39)	666	609.9(0.62)	584.2(0.40)	661(9), 635.8(37)
596.7(0.59)	588.3(0.43)	622.5	328.1(0.04)	335.2(0.68)	332		341.4(0.18)	
351.5(0.28)	343.5(0.26)	340		331.3(0.31)			334.1(0.45)	334(37)
340.1(0.09)	342.8(0.43)		282.1(0.62)	285.6(0.21)	280.3	327.9(0.04)	325.3(0.34)	326.5(14)
	334.7(0.15)		278.3(0.66)			280.7(0.38)	284.5(0.21)	
321.4(0.23)	330.8(0.78)		266.2(0.47)			277.7(0.99)		276.1(14)
282.3(1.31)	286.9(0.35)	280	257.7(0.6)			266.3(0.45)		263.8(42)
273.1(1.22)	281.6(0.16)	270	222.3(0.19)	236.6(0.10)		239.6(0.01)	236.8(0.14)	239.8(14)
253.5(0.23)	251.2(0.06)		211.3(0.08)	210.5(0.43)		222.9(0.18)	217.7(0.05)	
236.6(0.17)	236.4(0.04)	240	203.6(0.46)	205.8(0.03)		211.3(0.08)	212.6(0.16)	
214.6(0.08)	210.4(0.16)	220				203.7(0.40)	210.1(0.26)	
205.4(0.29)	208.8(0.03)	210						
204.2(0.32)								

Table 4. The energies (eV) of the HOMO and LUMO and the gaps (ΔE_g (e vV)) for compounds.

	H_2TBP	MgTBP	ZnTBP	H_2Pc	MgPc	ZnPc
LUMO	–2.322	–2.141	–2.140	–2.993	–2.876	–2.878
HOMO	–4.765	–4.676	–4.694	–5.162	–5.094	–5.120
ΔE_g	2.443	2.535	2.554	2.169	2.218	2.242

method. In general, compared with the calculated TDDFT and the experimental results, the OPA spectra predicted by the semi-empirical ZINDO method are reasonably reliable.

Two-photon absorption property

According to eqs. [1]–[4], we compiled a program that calculated the average second hyperpolarizability <γ> and TPA cross-section δ(ω) by ourselves. By using the program combined with the ZINDO method, we calculated the real and imaginary parts of <γ>, as well as the δ(ω) value (ω = $2\pi/\lambda^{(2)}$ is the speed of light) and the corresponding two-photon absorption wavelength $\lambda^{(2)}_{max}$ and transition nature (configurations and weight) for the maximum TPA (shown in Table 5). To verify the accuracy of the method used, we chose stilbene (molecule A in Table 5) and 4,4′-bis(dimethylamino)stilbene (molecule B in Table 5) as comparison samples, and the corresponding experimental values are given in parentheses. We can see from Table 5 that the results we calculated are in good agreement with experimental values. It was observed that, from H_2TBP to MTBP (M = Mg, Zn), $\lambda^{(2)}_{max}$ is slightly blue-shifted. From H_2Pc to MPc, $\lambda^{(2)}_{max}$ is blue-shifted by 24~25 nm. Compared with $\lambda^{(2)}_{max}$ of H_2TBP (729 nm), the TPA wavelength of H_2Pc (817.2 nm) is red-shifted by 88 nm. The $\lambda^{(2)}_{max}$ of MPc are about 55 nm longer than that of the corresponding MTBP (M = Mg, Zn). However, the difference of the metal ion has little effect on the TPA wavelength.

From Table 5, one can obtain the information that the TPA final state of the six compounds is S_5, which is described mainly by mixing the two-electron promotion from the (HOMO, HOMO) to the (LUMO, LUMO) and from the (HOMO, HOMO) to the (LUMO+1, LUMO+1). It can be seen that for TBPs and Pcs, the two-electron promotion plays an important role in the TPA of the investigated molecules. So, to analyze the TPA properties of TBPs and Pcs, it is very necessary to add the double configuration interaction to the calculations. The results show that because of the similar structure between TBPs and Pcs from the metal-free system to the metallo-system, the changes of the TPA wavelengths exhibit a similar trend.

To verify whether we have gained $\lambda^{(2)}_{max}$ when δ(ω) is maximized by our method, we selected molecule ZnTBP as an example and considered the 5 lowest two-photon allowed excited states as the TPA final state. It is known that the selection rule for TPA is different from that of OPA (44). One change of parity is required for a one-photon transition, while two-photon transitions must have initial and final states with the same parity. For molecules that, like all molecules studied in this paper, have central symmetry, a change in parity between the initial and final states (wave functions) is required for every photon involved in the transition for electric dipole transitions. So, for ZnTBP, the 5 lowest two-photon allowed excited states are S_3, S_4, S_5, S_8, and S_9, respectively. In term of eqs. [1] and [2], we have calculated δ(ω) (shown in Fig. 2). The results listed in Fig. 2 indicates that at S_5, $\lambda^{(2)}$ surely corresponds to the maximum δ(ω), 274.9×10^{-50} $cm^4 \cdot s \cdot photon^{-1}$, at 728.6 nm. Both theoretical and experimental results indicate that there is no evident one-photon absorption in the range of 700–950 nm, and TPA can be expected in this range. Our calculated TPA wavelength of ZnTBP is just in this range.

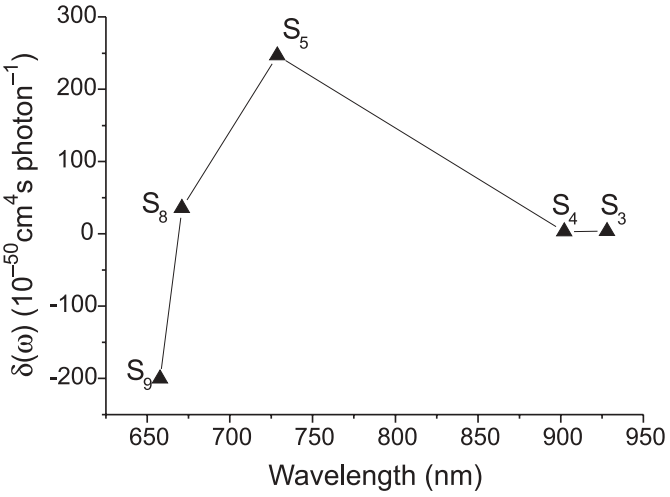
Now, we pay attention to the TPA cross-sections of these compounds. As can be seen in Table 5, we first compared the TPA cross-section of H_2TBP and MTBP. The magnitude of δ(ω) for H_2TBP is 220.6×10^{-50} $cm^4 \cdot s \cdot photon^{-1}$, while for MgTBP, it is 278.3×10^{-50} $cm^4 \cdot s \cdot photon^{-1}$, and for ZnTBP, it is 274.9×10^{-50} $cm^4 \cdot s \cdot photon^{-1}$. It was found that since the addition of metal ions in the molecule forms coordination

© 2003 NRC Canada

Table 5. The two-photon absorption properties of six molecules.

Molecule	$\lambda^{(2)}_{max}$ (nm)	Transition	Configurations and weights	$\langle\gamma\rangle\times10^{-34}$ (esu)	$\delta_{(max)}\times10^{-50}$ ($cm^4\cdot s\cdot photon^{-1}$)
H_2TBP	729.0 (724)(19)	$S_0\rightarrow S_5$	(HOMO,HOMO)→(LUMO+1,LUMO+1) 24% (HOMO,HOMO)→(LUMO,LUMO) 21% (HOMO–1,HOMO)→(LUMO,LUMO+1) 13%	–7.55+35.6*i*	220.4(57) (19)
MgTBP	727.0	$S_0\rightarrow S_5$	(HOMO,HOMO)→(LUMO,LUMO) 34% (HOMO,HOMO)→(LUMO+1,LUMO+1) 34%	–20.5+44.7*i*	278.3
ZnTBP	728.6	$S_0\rightarrow S_5$	(HOMO,HOMO)→(LUMO,LUMO) 34% (HOMO,HOMO)→(LUMO+1,LUMO+1) 34%	–19.7+44.4*i*	274.9
H_2Pc	817.2	$S_0\rightarrow S_5$	(HOMO,HOMO)→(LUMO,LUMO) 39% (HOMO,HOMO)→(LUMO+1,LUMO+1) 33%	–103+59.4*i*	292.6
MgPc	782.2	$S_0\rightarrow S_5$	(HOMO,HOMO)→(LUMO,LUMO) 39% (HOMO,HOMO)→(LUMO+1,LUMO+1) 39%	–119+64.6*i*	345.9
ZnPc	783.2	$S_0\rightarrow S_5$	(HOMO,HOMO)→(LUMO,LUMO) 39% (HOMO,HOMO)→(LUMO+1,LUMO+1) 39%	–120+63.4*i*	340.9
A	432 (425)(43)	$S_0\rightarrow S_3$	(HOMO,0)→(LUMO+3,0) 65% (HOMO, HOMO)→(LUMO,LUMO) 13%	0.44+5.33*i*	93.81(54) (43)
B	517.4 (529)(43)	$S_0\rightarrow S_3$	(HOMO–1,0)→(LUMO,0) 84%	–0.51+34.9*i*	429.71(411) (43)

Fig. 2. The TPA spectrum of ZnTBP.



bonds, the conjugation range of molecule enlargers and the TPA cross-section of the molecule drastically increases. But the effect of the difference of the metal atom on the TPA cross-section is very small, which is similar to the trend of the OPA parameters in the same molecules, as well as the results obtained from ref. 35. The same trend can be obtained when one studies the TPA cross-sections of the Pcs.

From Table 4, one can find that the TPA cross-sections of Pcs are bigger than those of corresponding TBPs. For example, the TPA cross-section maximum of MgPc is 345.9 × 10^{-50} $cm^4\cdot s\cdot photon^{-1}$, while that of MgTBP is equal to 278.3 × 10^{-50} $cm^4\cdot s\cdot photon^{-1}$. The maximum TPA cross-section of H_2Pc is 292.6 × 10^{-50} $cm^4\cdot s\cdot photon^{-1}$, while that of H_2TBP is equal to 220.4 × 10^{-50} $cm^4\cdot s\cdot photon^{-1}$. In the literature (10, 19), the TPA properties of porphyrins have been experimentally measured. For H_2TBP, the $\delta(\omega)$ is equal to 57 × 10^{-50} $cm^4\cdot s\cdot photon^{-1}$ when the incident laser frequency reaches 13 800 cm^{-1} (λ = 724 nm). The experimental value of H_2TBP is about one fourth of our calculation (220.4 × 10^{-50} $cm^4\cdot s\cdot photon^{-1}$). However, experimentally there is no TPA peak in the TPA spectrum of H_2TBP. In other words, it is possible to reach a larger TPA cross-section value if one changes the incident laser frequency. Moreover, the authors in ref. 19 also pointed out that the gained results only provide a qualitative explanation of the TPA spectra, and a quantitative description of the absolute TPA cross-section values is not readily available. In addition, a theoretical investigation of the one- and two-photon properties of porphyrins is presented by Masthay et al. (18). The results in this reference suggest that if both photons are linearly polarized, the TPA cross-section of free-base porphyrin (FBP) — the analogue of TBPs — is 585.715 × 10^{-50} $cm^4\cdot s\cdot photon^{-1}$. In contrast, the TPA cross-section value of FBP reaches a maximum of 143.886 × 10^{-50} $cm^4\cdot s$ $photon^{-1}$ if both photons are circularly polarized.

The above reports suggest that because of the differences in calculation methods and experimental conditions, the TPA cross-section for the same compound differs a lot. As a whole, the maximum TPA cross-sections of all compounds calculated in this paper are the same order of magnitude as the values reported in the literature, which suggests that the above discussions about the TPA properties can give some useful information in the understanding of the structure–property relationships of porphyrins, phthalocyanines, and their analogs.

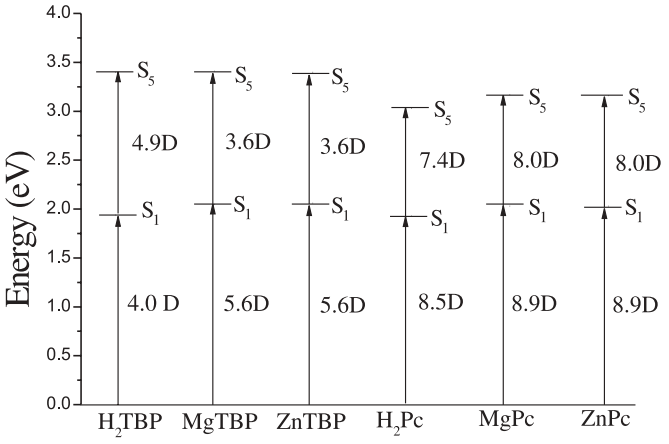
On the basis of the results of the calculations, as shown in Fig. 3, we can rationalize the increase in the TPA cross-section on going from TBPs to Pcs on the basis of (*i*) an increase in the S_0 to S_1 transition dipole moment (M_{01}) from 4.0 to 8.5 D (from H_2TBP to H_2Pc) and from 5.6 to 8.9 D (from MTBP to MPc, M = Mg, Zn); (*ii*) an increase in the S_1 to S_5 transition dipole moment (M_{15}) from 4.9 to 7.4 D (from H_2TBP to H_2Pc) and from 3.6 to 8.0 D (from MTBP to MPc, M = Mg, Zn). According to eq. [5], we find that the major contributors to the enhanced $\delta(\omega)$ value of Pcs with respect to that of TBPs are the increase in the S_0 to S_1 transi-

© 2003 NRC Canada

Table 6. The charge distribution of central moieties of molecules H2TBP and H2Pc.

	H_2TBP			H_2Pc		
Atom labels	Q_0	Q_1	DQ	Q_0	Q_1	DQ
N_p	–0.221844	–0.221588	0.000256	–0.225622	–0.215784	0.009838
N_a	–0.775620	–0.783878	–0.008258	–0.798404	–0.844138	–0.045734
C_α	0.429472	0.500896	0.071424	0.894016	1.046960	0.152944
$C_{\alpha'}$	0.339828	0.340940	0.001112	0.865872	0.930660	0.064788
C_m	–0.172760	–0.189300	–0.016540	–1.324540	–1.426828	–0.102288
Sum	–0.400924	–0.352930	0.047994	–0.588678	–0.509130	0.079548

Fig. 3. Scheme of the calculated energy levels and transition dipole moments (in debyes) for the three lowest singlet states for the investigated compounds.



tion dipole moment and the increase in the S_1 to S_5 transition dipole moment.

To further understand the micromechanism of the difference in the TPA cross-sections of TBPs and Pcs, we also analyzed the changed value of the charge ΔQ, from the ground state Q_0 to the excited state Q_1 of the molecules. Here, we take H_2TBP and H_2Pc as comparison examples and analyze the charge distribution of the moiety, including pyrrole N atoms (N_p, N_a), C_α, and meso N or C (N_m, C_m) in the two compounds. The detailed data are collected in Table 6, and the relative labels of atoms are shown in Fig. 1. As can be seen from Table 6 and Fig. 1, the ΔQ of H_2Pc (0.079548) is larger than that of H_2TBP (0.047994). The results illustrate that the relatively larger $\delta(\omega)$ value for Pcs, in comparison with that for TBPs, originates from a larger intramolecular charge transfer, which can be characterized by the transition dipole moment between the S_0 and S_1 and the transition dipole moment between S_1 and S_5.

Analyzing the above results, one can find that, whether looking at the OPA properties or the TPA properties, TBPs and Pcs have many similar points. Figure 4 depicts the relationship between the one-photon Q-band absorptions obtained by the ZINDO method and TPA cross-sections of the two series. The two similarly shaped lines appear in Fig. 4. It is obvious that from the changing tendency in the two quantities of TBPs we can obtain similar information about Pcs. In other words, when one examines the one- and two-photon absorption properties of Pcs, they can gain some enlightenment about the absorption property rules of TBPs.

Fig. 4. The relationship between the Q-band wavelength and TPA cross-section of TBPs and Pcs.

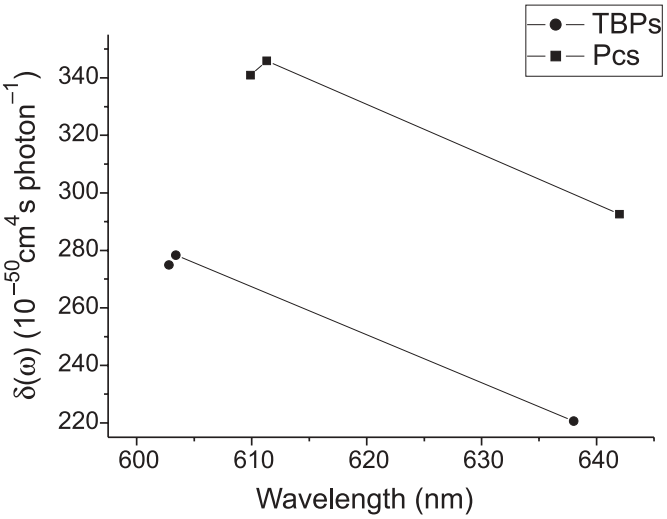
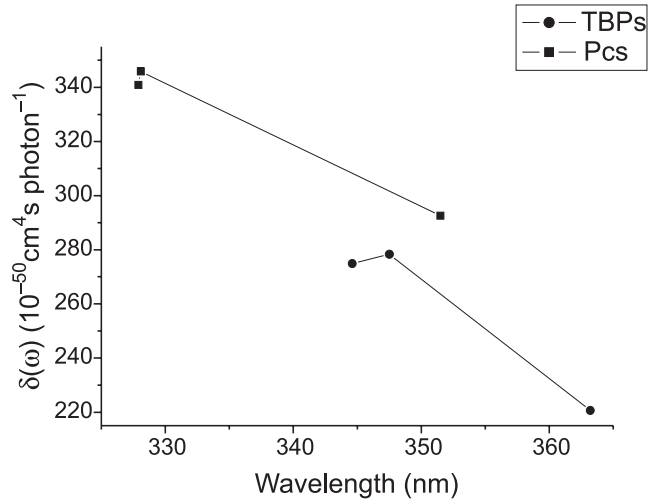


Fig. 5. The relationship between the B-band wavelength and TPA cross-section of TBPs and Pcs.



The relationships between the B-band absorption and the TPA cross-section of all molecules are shown in Fig. 5. The results, as exhibited, are similar.

Summary

We have studied the theoretical one- and two-photon absorption properties of tetrabenzoporphyrins and phthalo-

© 2003 NRC Canada

cyanines. The calculated results are in good agreement with the experimental values. The results suggest for the two series of molecules that there are some similarities in both one-photon absorption and two-photon absorption properties. From the changing trend in one- and two-photon absorption properties of TBPs (or Pcs), one can gain some enlightenment on the nonlinear optical properties of Pcs (or TBPs). The increase in the S_0 to S_1 transition dipole moment and the increase in the S_1 to S_5 transition dipole moment are the major contributors to the enhanced $\delta(\omega)$ value of Pcs with respect to those of the corresponding TBPs.

Acknowledgements

This work is supported by the National Nature Science Foundation of China (20273023, 90101026) and the Key Laboratory for Supramolecular Structure and Material of Jilin University.

Reference

1. R.O. Loutfy and J.H. Sharp. J. Chem. Phys. **71**, 1211 (1979).
2. O. Stenzel, A. Stendal, K. Voigtsberger, and C. von Borczyskowski. Sol. Energy Mater. Sol. Cell. **37**, 337 (1995).
3. H. Stiel, A. Volkmer, I. Rüchmann, A. Zeug, B. Ehrenberg, and B. Röder. Opt. Commun. **155**, 135 (1998).
4. K.J. McEwan, G. Bourhill, J.M. Robertson, and H.L. Anderson. J. Nonlinear Opt. Phys. Mater. **9**, 451 (2000).
5. M. Ambroz, A. Beeby, A.J. MacRobert, M.S.C. Simpson, R.K. Svensen, and D. Phillips. J. Photochem. Photobiol. B Biol. **9**(1), 87 (1991).
6. B.W. Henderson and T.J. Dougherty. Photochem. Photobiol. **55**, 147 (1992).
7. R. Bonnett. Chem. Soc. Rev. **24**, 19 (1995).
8. R.L. Goyan and D.T. Cramb. Photochem. Photobiol. **72**(6), 821 (2000).
9. K.S. Samkoe and D.T. Cramb. J. Bio. Opt. **8**, 410 (2003).
10. A. Karotki, M. Drobizhev, M. Kruk, C. Spangler, E. Nickel, N. Mamardashvili, and A. Rebane. J. Opt. Soc. Am. B, **20**(2), 321 (2003).
11. S. Maree, D. Phillips, and T. Nyokong. J. Porphyrins Phthalocyanines, **6**(1), 17 (2002).
12. W.D. Edwards and M.C. Zerner. Int. J. Quantum. Chem. **23**, 1407 (1983).
13. G.L. Wood, M.J. Miller, and A.G. Mott. Opt. Lett. **20**, 973 (1995).
14. L. Edwards and M. Goutermans. J. Mol. Spectrosc. **33**, 292 (1970).
15. B. Ehrenberg and F.M. Johnson. Spectrochim. Acta, **46A**, 1521 (1990).
16. E. Ortí, R. Crespo, M.C. Piqueras, and F. Tomás. J. Mater. Chem. **6**(11), 1751 (1996).
17. K.A. Nguyen and R. Pachter. J. Chem. Phys. **114**, 10 757 (2001).
18. M.B. Masthay, L.A. Findsen, B.M. Pierce, D.F. Bocian, J.S. Lindsey, and R.R. Birge. J. Chem. Phys. **84**, 3901 (1986).
19. M. Drobizhev, A. Karotki, M. Kruk, and A. Rebane. Chem. Phys. Lett. **355**, 175 (2002).
20. A.S. Dvornikov and P.M. Rentzepis. Opt. Commun. **119**, 341 (1995)
21. B.H. Cumpston, S.P. Ananthavel, S. Barlow, D.L. Dyer, J.E. Ehrlich, L.L. Erskine, A.A. Heikal, S.M. Kuebler, I.-Y.S. Lee, D. McCord-Maughon, J. Qin, H. Röckel, M. Rumi, X.-L. Wu, S.R. Marder, and J.W. Perry. Nature (London), **398**, 51 (1999).
22. W. Denk, J.H. Strickler, and W.W. Webb. Science (Washington, D.C.), **248**, 73 (1990).
23. R.H. Köhler, J. Cao, W.R. Zipfel, W.W. Webb, and M.R. Hansen. Science (Washington, D.C.), **276**, 2039 (1997).
24. J.D. Bhawalkar, G.S. He, and P.N. Prasad. Rep. Prog. Phys. **59**, 1041 (1996).
25. G.S. He, C.F. Zhao, J.D. Bhawalkar, and P.N. Prasad. Appl. Phys. Lett. **67**, 3703 (1995).
26. J.E. Ehrlich, X.L. Wu, I.-Y.S. Lee, Z.-Y. Hu, H. Röckel, S.R. Marder, and J.W. Perry. Opt. Lett. **22**, 1843 (1997).
27. B.A. Reinhardt, L.L. Brott, S.J. Clarson, A.G. Dillard, J.C. Bhatt, R. Kannan, L. Yuan, G.S. He, and P.N. Prasad. Chem. Mater. **10**, 1863 (1998).
28. M. Albota, D. Beljonne, J.L. Brédas, J.E. Ehrlich, J. Fu, A.A. Heikal, E. Hess, T. Kogej, M.D. Levin, S.R. Marder, D. McCord-Maughon, J.W. Perry, H. RÖeckel, M. Rumi, G. Subramaniam, W.W. Webb, X. Wu, and C. Xu. Science (Washington, D.C.), **281**, 1653 (1998).
29. B.R. Cho, K.H. Son, S.H. Lee, Y.-S. Song, Y.-K. Lee, S.-J. Jeon, J.H. Choi, and M. Cho. J. Am. Chem. Soc. **123**, 10 039 (2001).
30. X. Zhou, A.-M. Ren, J.-K. Feng, X.-J. Liu. Chem. Phy. Lett. **362**, 541 (2002).
31. C.L. Caylor, I. Dobrianow, C. Kimmr, R.E. Thome, W. Zipfel, and W.W. Webb. Phys. Rev. E, **59**(4), R3831 (1999).
32. B. Dick, R.M. Hochstrasser, and H.P. Trommsdorff. *In* Nonlinear Optical properties of organic molecules and crystals. Vol. 2. *Edited by* D.S. Chemla and J. Zyss. Academic Press, Orlando, Fl. 1987. pp. 167–170.
33. B.J. Orr and J.F.Ward. Mol. Phys. **20**, 513 (1971).
34. D. Beljonne, J. Cornil, Z. Shuai, J.L. Bredas, F. Rohlfing, D.D.C. Bradlley, W.E. Torruellas, V. Ricci, and G.I. Stegeman. Phys. Rev.B, **55**, 1505 (1997).
35. J.O. Morley and M.H. Charlton. J. Phys. Chem. **99**, 1928 (1995).
36. W.R. Scheidtnd W. Dow. J. Am. Chem. Soc. **99**, 1101 (1977).
37. F.L. Plows and A.C. Jones. J. Mol. Spectrosc. **194**, 163 (1999).
38. K. Yase, N. Yasuoka, T. Kobayashi, and N. Uyeda. Acta Crystallogr. Sect. C, **44**, 514 (1988).
39. U. Even, J. Jortner, and J. Friedman. J. Phys. Chem. **86**, 2273 (1982).
40. A.J. McHugh, M. Gouterman, and C.W. Weiss, Jr. Theor. Chim. Acta, **24**, 346 (1972).
41. T.C. Vancott, M. Koralewski, D.H. Metcalf, P.N. Schatz, and B.E. Williamson. J. Phys. Chem. **97**, 7417 (1993).
42. T.C. Van Cott, J.L. Rose, G.C. Misener, B.E. Wiiliamson, A.E. Schrimpf, M.E. Boyle, and P.N. Schatz. J. Phys. Chem. **93**, 2999 (1989).
43. Y. Morel, A. Irimia, P. Najechalski, Y. Kervella, O. Stephan, P.L. Baldeck, and C. Andraud. J. Chem. Phys. **114**, 5391 (2001).
44. W.M. McClain. Acc. Chem. Res. **7**, 129 (1974).

© 2003 NRC Canada

Phosphorus magnetic shielding tensors for transition-metal compounds containing phosphine, phosphido, and phosphinidene ligands: Insights from computational chemistry

Kirk W. Feindel and Roderick E. Wasylishen

Abstract: The present study examines the quality of the restricted Hartree–Fock (RHF) ab initio, B3LYP hybrid density functional theory (DFT), and relativistic zeroth-order regular approximation (ZORA) DFT methods for the calculation of phosphorus chemical shift (CS) tensors in phosphine, phosphido, and phosphinidene transition-metal complexes. A detailed comparison of calculated and experimental ^{31}P CS tensors allows us to identify the characteristic advantages of each computational method. The results from B3LYP and ZORA-DFT calculations indicate that a double-ζ quality basis set reproduces experimental values of the principal components of the ^{31}P CS tensor in many of the phosphorus-containing transition-metal complexes investigated, whereas the RHF method requires a triple-ζ doubly polarized basis set, yet fails in the case of the terminal phosphido group. Inclusion of the spin-orbit relativistic correction with the ZORA-DFT formalism requires a triple-ζ quality basis set to reproduce the experimental data. We demonstrate the merit of modern computational methods for investigating theoretically the effect of geometric variations upon the phosphorus CS tensor by systematically altering the W—P bond length and the W-P-C_{Me} bond angle in $W(CO)_5(PMe_3)$. Additionally, a previously reported correlation, determined experimentally, relating the ^{31}P CS tensor to the Fe-P-Fe bond angle in a series of iron phosphido-bridging compounds, has been reproduced with calculations using the model compound $Fe_2(CO)_6(\mu_2\text{-}PPh_2)(\mu_2\text{-}Cl)$. The results presented demonstrate the value of modern computational techniques for obtaining a greater understanding of the relationship between phosphorus chemical shifts and molecular structure.

Key words: ^{31}P chemical shift, phosphine, phosphido, phosphinidene, RHF, B3LYP, relativistic, ZORA-DFT.

Résumé : Dans le présent travail, on examine la qualité de la théorie de densité fonctionnelle hybride B3LYP (« DFT »), une méthode ab initio de Hartree–Fock restreinte (« RHF »), ainsi que les méthodes « DFT » relativistes d'approximation régulière d'ordre zéro (« ZORA ») pour le calcul des tenseurs des déplacements chimiques (DC) du phosphore dans les complexes de métaux de transition contenant des groupes phosphine, phosphido et phosphinidène. Une comparaison détaillée des tenseurs calculés et expérimentaux des DC du ^{31}P a permis d'identifier les avantages caractéristiques de chacune de ces méthodes de calcul. Les résultats obtenus par les calculs B3YLP et « ZORA-DFT » indiquent qu'un ensemble de base de qualité double-ζ permet de reproduire les valeurs expérimentales des principaux composants du tenseur du DC du ^{31}P de plusieurs des complexes étudiés de métaux de transition contenant du phosphore; par ailleurs, la méthode RHF qui nécessite un ensemble de base doublement polarisé triple-ζ ne donne même pas de bons résultats avec le groupe phosphido terminal. Pour pouvoir reproduire les résultats expérimentaux en incluant la correction relativiste spin-orbite dans le formalisme « ZORA-DFT », il est nécessaire d'utiliser un ensemble de base de qualité triple-ζ. On démontre les mérites des méthodes modernes de calcul pour étudier d'une façon théorique l'effet des variations géométriques sur le tenseur du DC du ^{31}P en faisant varier d'une façon systématique la longueur de la liaison W—P et l'angle de liaison W-P-C_{Me} dans $W(CO)_5(PMe_3)$. De plus, des calculs sur le composé modèle $Fe_2(CO)_6(\mu_2\text{-}PPh_2)(\mu_2\text{-}Cl)$ ont permis de reproduire une corrélation rapportée antérieurement, déterminée de façon expérimentale et qui permet de relier le tenseur du DC du ^{31}P à l'angle de la liaison Fe-P-Fe dans une série de composés du fer contenant un pont phosphido. Les résultats présentés démontrent la valeur des techniques modernes de calculs théoriques pour arriver à une meilleure compréhension de la relation entre les déplacements chimiques du phosphore et la structure moléculaire.

Mots clés : déplacement chimique du ^{31}P, phosphine, phosphido, phosphinidène, « RHF », B3LYP, relativiste, « ZORA-DFT ».

[Traduit par la Rédaction]

Received 7 September 2003. Published on the NRC Research Press Web site at http://canjchem.nrc.ca on 27 November 2003.

Dedicated to Professor Donald R. Arnold for his contributions to chemistry in Canada.

K.W. Feindel and R.E. Wasylishen.[1] Department of Chemistry, University of Alberta, Edmonton, AB T6G 2G2, Canada.

[1]Corresponding author (e-mail: roderick.wasylishen@ualberta.ca).

 doi: 10.1139/V03-176 © 2003 NRC Canada

Introduction

Phosphorus compounds containing one or more formal localized electron lone pairs are important ligands in transition-metal chemistry. Phosphorus ligands possess the ability to act as σ-donors and π-acceptors simultaneously, allowing the ligand to adapt to the electronic characteristics of a metallic centre (1). Transition-metal-containing phosphorus compounds have found use in numerous applications, ranging from catalysis (2–7) to medicine (8–10). Phosphorus-31 nuclear magnetic resonance (NMR) spectroscopy is one of the most important techniques for characterizing such compounds (11), and therefore, understanding the origin of phosphorus chemical shifts and their relationship with molecular structure is essential.

Phosphorus-31 NMR spectroscopic studies are very common in both the liquid (solution) and solid states, and there are several reviews that deal specifically with solution ^{31}P NMR of phosphorus ligands in transition-metal complexes (12, 13). Despite this, phosphorus chemical shifts are generally not well understood (13–15). Considerable effort has been devoted to identifying empirical correlations between isotropic ^{31}P chemical shifts and molecular structure, such as in the presence or absence of metal–metal bonds in phosphido-bridging complexes (16), or correlations between chemical shifts and electronic transitions (17) or electron density (18), with little attempt to understand the theoretical origin of these observed empirical trends. More than ten years ago, Randall and Carty (19) recognized the importance of attempting to characterize phosphorus chemical shift (CS) tensors to rationalize chemical shift – structure relationships in transition-metal complexes. The magnetic shielding experienced by a particular nucleus in a molecule is generally characterized by a symmetric, second-rank tensor that can be described by three principal components and three Euler angles, which relate the principal axis system (PAS) of the tensor to the molecular framework of the molecule (20).

The last decade has yielded prodigious advances in the efficiency and affordability of desktop computers, thereby allowing many aspects of computational chemistry to become more accessible. The development of user-friendly software such as Gaussian 98W (21) enables experimentalists to readily calculate molecular properties such as nuclear magnetic shielding tensors (σ) based on first principles (ab initio) or density functional theory (DFT). For relatively small molecules containing first-row elements, the agreement between ab initio calculated magnetic shielding tensors and experiment is almost quantitative (22, 23). The success of theoretical methods for calculating magnetic shielding tensors at heavier nuclei continues to improve (24). Quantum chemical calculations of magnetic shielding tensors can provide the missing link that relates experimentally measured chemical shifts and structural parameters (25). Computational results may serve to complement experimental data and can provide information that may be difficult to obtain experimentally, such as the orientation of the PAS of the CS tensor (26). Single-crystal NMR or dipolar chemical shift NMR experiments often yield, at best, a twofold ambiguity in the orientation of CS tensors (27–29), whereas calculations yield a single orientation. Using an ab initio calculated orientation to interpret experimental results is often invaluable; it allows a confident assignment of the CS tensor orientation in the molecular frame of reference, as we recently demonstrated for the ^{31}P CS tensor in several phosphido-bridging complexes (27). However, one must take a cautious approach to the assignment of the tensor orientation if two of the components are quantitatively similar either experimentally or theoretically (i.e., tensors approaching axial symmetry); in these cases the calculated data may be as ambiguous as the experimental data one is trying to interpret. Of course, for a CS tensor that is truly axially symmetric, the question of the orientation of the two degenerate components becomes irrelevant.

Establishing the reliability of quantum chemical methods for the calculation of CS tensors in a variety of systems is important. In the past many computational papers have focussed on isotropic phosphorus chemical shifts (30–33). From an experimentalist's perspective, computational methods should ideally reproduce not only the isotropic value but also the three principal components of the tensor and their orientation. One needs to recognize that although the calculated isotropic value and span of the CS tensor (see Definitions and background theory) may be well reproduced, the agreement could be the result of a fortuitous cancellation of errors in the values of the tensor principal components (vide infra) (34).

Theoretical studies of phosphorus CS tensors have shown that ab initio and DFT methods are capable of reproducing experimental data for small phosphorus-containing compounds (30–33, 35–47) and for transition-metal-containing phosphorus compounds (27, 48–50). These calculations *qualitatively* reproduce experimental isotropic CS data and have enabled easy investigation of the effects of geometric structural variations on phosphorus magnetic shielding (27, 30, 32, 40, 42, 44, 46, 51–54). Several studies have indicated that in many cases inclusion of electron correlation generally improves agreement with experiment (30, 33, 35, 44). However, *quantitative* reproduction of experimental CS tensors for light nuclei such as ^{13}C, ^{15}N, ^{17}O, and ^{19}F in small molecules remains a challenge (25, 55). For example, Auer, Gauss, and Stanton (55) have shown that quantitative reproduction of gas-phase ^{13}C CS tensors requires large (quadrupule-ζ) uncontracted basis set CCSD(T) (coupled-cluster singles and doubles augmented by perturbation corrections for triple excitations) calculations with consideration of vibrational effects. In small molecules (e.g., C_3H_4, CF_4) a standard deviation of 1–2 ppm can be achieved. For a recent review on electron-correlated methods and quantitative reproduction of experimental chemical shifts, see ref. 25.

A number of studies have been published that explicitly compare experimental and theoretical phosphorus CS tensors (27, 35, 38, 40–43, 46, 47, 49, 53–56). Only a few investigations involve complexes containing nuclei heavier than sulfur (27, 33, 45, 48–50, 57), and although limited, the quantum chemical studies involving transition-metal-containing phosphorus compounds (predominantly phosphines) have provided a basis for the interpretation of phosphorus chemical shifts. Kaupp (48) was the first to investigate theoretically ^{31}P chemical shifts in a series of transition-metal phosphines, using sum-over-states density-functional perturbation theory (SOS-DFPT) with individual gauges for localized orbitals (IGLO). Later, Ruiz-Morales and Ziegler (49) employed a gauge-including atomic orbitals (GIAO) DFT

© 2003 NRC Canada

method for a similar series of complexes, analyzing specific paramagnetic couplings between occupied and virtual orbitals. Bühl et al. (50), also using the SOS-DFPT-IGLO method, have demonstrated that calculations on larger systems containing multiple metal centres are feasible, and in the case of $Ru_4(CO)_{13}(\mu_3\text{-PPh})$ they accurately reproduce the experimental ^{31}P CS tensor. More recently, van Wüllen (33) explored various DFT approaches and the ab initio Hartree–Fock (HF) and second-order Møller–Plesset perturbation theory (MP2) methods, using both IGLO and GIAO variants, as well as the method proposed by Wilson, Amos, and Handy (58). Eichele et al. (27) employed the restricted Hartree–Fock (RHF) method to calculate the phosphorus CS tensor of phosphido ligands in several ruthenium carbonyl compounds, reproducing the orientations found experimentally. However, a more comprehensive investigation, involving a greater number of phosphorus-containing transition-metal compounds, is still lacking.

The purpose of the present investigation is twofold. First, to provide the experimentalist with an indication of the reliability of ab initio (RHF), hybrid DFT (B3LYP), and pure DFT (ZORA-DFT) methods for the reproduction of experimental ^{31}P CS tensors in transition-metal-containing complexes. Second, to demonstrate the value of quantum chemical calculations as a method to examine the effect of molecular geometry on phosphorus magnetic shielding tensors in model compounds. Relativistic effects on phosphorus magnetic shielding tensors are also investigated for select compounds, using the ZORA-DFT method.

Definitions and background theory

Experimental NMR spectroscopists measure chemical shifts and CS tensors, while first-principles calculations provide magnetic shielding constants and magnetic shielding tensors. The relationship between chemical shift (δ) and magnetic shielding (σ) is described by

$$[1] \qquad \delta_{ii} = \frac{\sigma_{ref} - \sigma_{ii}}{1 - \sigma_{ref}}$$

where i = 1, 2, 3 represents the principal components of the CS and magnetic shielding tensors and σ_{ref} is the isotropic magnetic shielding of some reference compound. For comparison of experimental with calculated data, experimental ^{31}P chemical shifts have been converted to magnetic shielding (or vice versa) using the ^{31}P absolute magnetic shielding scale established by Jameson et al. (59), σ_{ref} = 328.35 ppm (85% aq H_3PO_4). Since σ_{ref} is small relative to one, eq. [1] can be simplified to

$$[2] \qquad \sigma_{ii} \approx 328.35 - \delta_{ii}$$

The principal components of the magnetic shielding tensor are defined such that $\sigma_{11} \leq \sigma_{22} \leq \sigma_{33}$; thus, σ_{33} represents the most shielded principal component. The isotropic shielding, σ_{iso}, is equal to one third the trace of the tensor

$$[3] \qquad \sigma_{iso} = \frac{\sigma_{11} + \sigma_{22} + \sigma_{33}}{3}$$

The span, Ω (60), describes the maximum orientation dependence of the magnetic shielding interaction and is defined as

$$[4] \qquad \Omega = \sigma_{33} - \sigma_{11} = \frac{(\delta_{11} - \delta_{33})}{1 - \sigma_{ref}} \approx \delta_{11} - \delta_{33}$$

Computational methods

The RHF ab initio non-relativistic method imposes doubly occupied (degenerate) spatial orbitals (61), and in practice the computational requirement for HF methods scale between N^2 and N^3, where N is the number of basis functions (62). The HF method does not include electron correlation effects; it treats electron–electron interactions as an average effect, and thus is not expected to give quantitatively accurate results, particularly if the nucleus in question bears a lone pair (23) (vide infra).

In the DFT formalism (63), electron correlation effects are accounted for implicitly through the use of an exchange-correlation (XC) functional. Current DFT methods do not yield exact results, since the functional form of the exact XC energy is unknown. Calculations converge toward a certain value as the basis set size is increased, but theory does not allow an evaluation of the errors inherent in this limit. The quality of the result can only be determined through comparison with experiment (64). For the purposes of our hybrid-DFT studies, Becke's B3LYP functional (65, 66), which mixes the Kohn–Sham orbital exchange energy functional, E_x, with gradient-corrected E_x and E_c (correlation contribution to the functional), has been employed. B3LYP is acknowledged as one of the most successful and widely used hybrid XC functionals (67, 68).

For heavy nuclei, relativistic effects become important as the core electrons move with speeds approaching that of light. Scalar relativistic effects include the mass–velocity correction, which results from the dependence of the electron mass on the velocity, and the Darwin correction, which accounts for the high-frequency oscillation of the electron around its mean position. These two contributors to scalar relativistic effects have opposite sign and, in practice, often essentially cancel each other. The spin-orbit relativistic term arises from the interaction of the nuclear magnetic moment with the magnetic field that is generated by the movement of an electron (69).

Relativistic effects should be considered if elements with $Z > 36$ are present in the molecule of interest (70). For very heavy elements (i.e., Au, Hg, Pt, etc.), relativistic effects also perturb valence orbitals, resulting in significant changes in fundamental properties such as magnetic shielding (71). The inclusion of relativistic effects is most important when calculating absolute values of magnetic shielding. In the case of chemical shift calculations, relativistic effects tend to cancel (72, 73); thus, to a first approximation, they are often ignored. Both the RHF and B3LYP-DFT methods, although non-relativistic, can employ quasi-relativistic effective core potentials (RECPs) on heavy atoms to correct for scalar, and in some cases spin-orbit, relativistic effects. While RECPs are not recommended for the calculation of magnetic shielding involving the heavy nuclei, they have been successful for neighbouring nuclei (72, 74). The ZORA-DFT method (75, 76) provides the benefits of the efficient DFT procedure with the ability to account for scalar and spin-orbit relativistic effects without the use of RECPs.

© 2003 NRC Canada

Table 1. Descriptive information of Slater-type ZORA relativistic basis sets.

	ZORA (I)	ZORA (II)	ZORA (III)	ZORA (IV)	ZORA (V)
	Single-ζ	Double-ζ	Double-ζ polarized	Valence triple-ζ polarized	Valence triple-ζ doubly polarized
H	1*s*	2*s*	2*s*, 2*p*	3*s*, 1*p*	3*s*, 1*p*, 1*d*
C, O	2*s*, 1*p*	4*s*, 2*p*	4*s*, 2*p*, 1*d*	5*s*, 3*p*, 1*d*	5*s*, 3*p*, 1*d*, 1*f*
P, S, Cl	3*s*, 2*p*	6*s*, 4*p*	6*s*, 4*p*, 1*d*	7*s*, 5*p*, 1*d*	7*s*, 5*p*, 1*d*, 1*f*
Cr, Fe	4*s*, 3*p*, 1*d*	8*s*, 5*p*, 3*d*	—	9*s*, 5*p*, 3*d*	9*s*, 6*p*, 3*d*, 1*f*
Mo, Ru	—	11*s*, 7*p*, 5*d*	—	12*s*, 8*p*, 6*d*	12*s*, 8*p*, 6*d*, 1*f*
W	—	14*s*, 10*p*, 6*d*, 3*f*	—	14*s*, 10*p*, 7*d*, 3*f*	14*s*, 10*p*, 7*d*, 4*f*

Computational details: Methods and molecular structures

Calculations of magnetic shielding tensors were performed using the gauge-including atomic orbital (GIAO) (77) method with Gaussian 98W (revision A.7) (21), Gaussian 98 (revision A.4) (78) (RHF and B3LYP), and the NMR module (79) of the Amsterdam density functional (ADF 2000.02, 2002.01, 2002.02) package (80) (ZORA-DFT). Gaussian 98 calculations were performed on an IBM RS/6000 workstation or a Windows-based PC. ADF calculations were performed on an IBM RS/6000 workstation or an AMD-based Linux PC or 8 processor cluster. RHF and B3LYP calculations employed locally dense Gaussian-type basis sets, which are part of the standard Gaussian 98 package. The full potential Slater-type ZORA basis sets used are available in the standard ADF package (see Table 1 for a description of ZORA basis sets). For all ADF calculations, the XC functional employed the local density approximation (LDA) given by Vosko, Wilk, and Nusair (VWN) (81) and the generalized gradient approximation (GGA) of Becke 88 (82) and Perdew 86 (83). All ZORA-DFT calculations include scalar relativistic corrections.

Atomic coordinates were calculated from X-ray structures (Table 2). Phenyl and cyclopentadienyl rings were assumed planar with hydrogens added at a fixed C—H bond length of 1.08 Å (104). Hydrogens were added to methyl and ethyl groups with an assumed tetrahedral geometry and a fixed bond length of 1.09 Å. To reduce computational time, one of the two similar phosphorus sites in compounds **3**, **13**, and **15** was modified by replacing the existing phenyl groups with methyl groups. The P—CH_3 bond length was fixed to the P—C_{ipso} bond length. The geometry of the hydrogen nuclei added to **15** was optimized at the HF/3-21G level of theory.

Unless noted otherwise, RHF and B3LYP calculations were performed for compounds **1**–**17** by employing the 6-31G(d) or 6-311+G(2d) diffuse basis set for phosphorus and directly bonded atoms, the LANL2DZ RECP for metallic centres, and 3-21G on the remainder of the molecule. ZORA-DFT calculations, including only scalar relativistic corrections, were performed using the ZORA (II) basis set on all nuclei.

Results and discussion

Phosphorus nuclear magnetic shielding tensors were calculated for the transition-metal-containing phosphine, phosphido, and phosphinidine compounds (**1**–**17**), shown in Fig. 1, using the RHF, B3LYP, and relativistic ZORA-DFT methods in an effort to determine the minimum basis set required to qualitatively reproduce experimental ^{31}P CS tensors. Many of the compounds investigated contain relatively heavy metal nuclei, for which the viability of these methods has not been tested previously. Phosphorus CS tensors for all compounds chosen have been formerly characterized by solid-state ^{31}P NMR techniques. For example, the calculated orientation of the phosphorus CS tensor principal components for compounds **6**, **7**, **9**, and **17** are compared with previously obtained data from single-crystal ^{31}P NMR experiments (28, 29, 92, 103).

Practical considerations

Chemical shift range

The CS range of ^{31}P is approximately 2000 ppm, extending from δ_{iso} = 1362 ppm for *t*-BuP[$(Cr(CO)_5]_2$ to δ_{iso} = –552 ppm for gaseous P_4 (105) with respect to 85% aq H_3PO_4. Differences between observed and calculated shifts should be considered relative to the CS range of phosphorus. For comparison of calculated with experimental values, agreement within 10% of the average of the experimentally measured spans for the compounds studied herein is considered excellent.

Errors owing to molecular geometry

The most reliable experimental structures have been employed for the shielding calculations herein; however, phosphorus CS tensors are known to be dependent on bond lengths and bond angles (27, 30, 32, 40, 44, 54). For example, in the case of phosphine, PH_3, Jameson et al. (51) have estimated $\partial\sigma(^{31}P)/\partial r \cong -150$ ppm/Å. Thus, any errors in the assumed structure make a *quantitative* comparison of calculated phosphorus magnetic shielding tensors with experiment difficult.

Intermolecular effects

The experimental data discussed herein, as well as the structural data used, are for compounds in the solid state. The experimental solid-state data intrinsically include intermolecular effects, which will affect the observed chemical shift to some extent. The calculations are performed on a single isolated molecule without consideration of intermolecular effects. Intermolecular effects are known to be predominantly *deshielding* for the isotropic value (106, 107); thus, one might expect systematic deviations in our gas-phase model from experimental values. Using phosphine as an example, the ^{31}P gas-to-liquid chemical shift is approximately 20 ppm (note, the phosphorus nucleus is more shielded in the gas phase) (59). In general, intermolecular ef-

© 2003 NRC Canada

Table 2. Compounds for which calculations have been performed.

	Compound	Structure ref.	NMR ref.
Phosphine			
$Cr(CO)_5(PMe_3)$	**1**	84	85
$Cr(CO)_5(DBP)$	**2**	86	87
cis-$Cr(CO)_4(DBP)_2$	**3**	86	87
trans-$Cr(CO)_4CS(PPh_3)$	**4**	88	88
$Mo(CO)_5(PMe_3)$	**5**	89	85
$Mo(CO)_5(MeDBP)$	**6**	28	28
$Mo(CO)_5(\eta^1$-dppm)	**7**	29	29
$W(CO)_5(PMe_3)$	**8**	90	85
$RhCl(PPh_3)_3$	**9**	91	92
Phosphido-bridging			
$Fe_2(CO)_6(\mu_2$-Cl)$(\mu_2$-$PPh_2)$	**10**	93	94
$Ru_2(CO)_6(\mu_2$-η^2-C≡C-*t*-Bu)$(\mu_2$-$PPh_2)$	**11**	95	27
$Ru_2(CO)_6(\mu_2$-η^2-C≡C-Ph)$(\mu_2$-$PPh_2)$	**12**	96	27
$Ru_2(CO)_6(\mu_2$-$PPh_2)_2$	**13**	97	27
$Ru_3(CO)_9(\mu_2$-H)$(\mu_2$-$PPh_2)$	**14**	98	27
$Ru_4(CO)_{13}(\mu_2$-$PPh_2)_2$	**15**	99	27
Terminal phosphido			
$Mo(P)[N(t$-Bu)(3,5-$C_6H_3Me_2)]_3$	**16**	100	101
Phosphinidine			
$Ru_4(CO)_{13}(\mu_3$-PPh)	**17**	102	103

Note: For computational efficiency, one of the two similar phosphorus sites in compounds **3**, **13**, and **15** was modified by replacing the phenyl groups with methyl groups. Reported magnetic shielding tensors are for the phosphorus bearing the phenyl group.

fects, rovibrational averaging, and differences between assumed and actual molecular structure are expected to have a minor effect on chemical shifts compared with the experimental trends we are attempting to reproduce with the calculations (vide infra). In the discussion that follows, experimental and calculated chemical shifts will be compared without further explicit discussion of the gas-to-solid shifts.

Spin-orbit relativistic correction

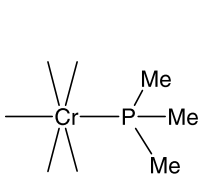
The effect of the spin-orbit relativistic correction with the ZORA-DFT method on the phosphorus magnetic shielding has been investigated for phosphines **1**, **5**, and **8** using the ZORA (V) basis set and for **13** using the ZORA (II) and locally dense ZORA (I/V) (i.e., ZORA (V) for metallic centres, phosphorus, and directly bonded nuclei and ZORA (I) for the remainder of the molecule) basis sets. Compounds **1**, **5**, and **8** are isostructural, each with a different group VI transition metal. Previous calculations for this series did not include spin-orbit corrections, and Kaupp (48) postulated this as the reason for the observed deviation of the SOS-DFPT-IGLO calculation of the $W(CO)_5(PMe_3)$ phosphorus CS tensor from experimental values. Herein, both scalar-only and scalar + spin-orbit relativistic calculations have been performed. Table 3 provides a comparison of experimental and calculated values. Although the results for the tungsten compound (**8**) are poorest in both calculations, the spin-orbit calculation yields significant improvement over the scalar-only calculation (Fig. 2). Relative to experimental values, the scalar-only ZORA-DFT calculation underestimates all three phosphorus magnetic shielding tensor principal components and yields a larger span. The effect of including the spin-orbit correction increases when progressing down group VI from Cr to W. In all three cases, including the spin-orbit correction improves agreement with experiment, and as expected, the most noticeable effect is for **8**. For this complex, the agreement with experiment improves by over 10% for the tensor principal components and reduces the span from 72 to 32 ppm (relative to 12 ppm experimentally). The deviation of the calculated values from experiment (Δ = calcd – expt), averaged for the three complexes, are as follows: $\Delta\sigma_{iso} = -1$, $\Delta\sigma_{11} = -7$, $\Delta\sigma_{22} = -1$, $\Delta\sigma_{33} = 3$, and $\Delta\Omega = 10$ ppm. Inclusion of spin-orbit relativistic effects increased the computational time by approximately four, relative to the scalar-only calculation for **1**, **5**, and **8**.

For **13**, the ZORA (IV) and (V) scalar-only calculations yield isotropic values (inclusive of locally dense combinations) deshielded relative to experimental data by approximately 65 ppm (σ_{11} is affected predominantly).[2] The scalar-only ZORA (II) calculation provides values in excellent agreement with experiment. Inclusion of spin-orbit relativis-

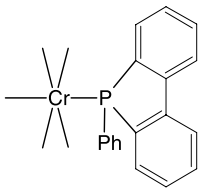
[2] Numeric data for **13** are available in Supplementary Table D1. Supplementary data may be purchased from the Depository of Unpublished Data, Document Delivery, CISTI, National Research Council Canada, Ottawa, ON K1A 0S2, Canada (http://www.nrc.ca/cisti/irm/unpub_e.shtml for information on ordering electronically).

© 2003 NRC Canada

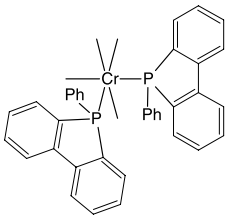
Fig. 1. Transition-metal-containing phosphine (**1**–**9**), phosphido-bridging (**10**–**15**), terminal phosphido (**16**), and phosphinidene (**17**) complexes for which ^{31}P magnetic shielding tensors have been investigated via GIAO RHF, B3LYP, and relativistic ZORA-DFT calculations. DBP = 5-phenyldibenzophosphole; MeDBP = 5-methyldibenzophosphole; dppm = bis(diphenylphosphino)methane.



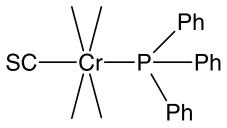
$Cr(CO)_5(PMe_3)$
1



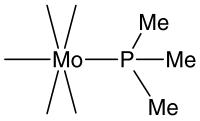
$Cr(CO)_5(DBP)$
2



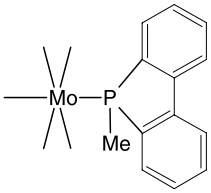
cis-$Cr(CO)_4(DBP)_2$
3



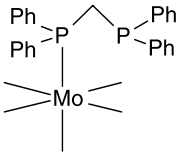
trans-$Cr(CO)_4CS(PPh_3)$
4



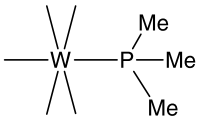
$Mo(CO)_5(PMe_3)$
5



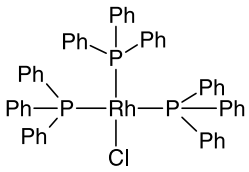
$Mo(CO)_5(MeDBP)$
6



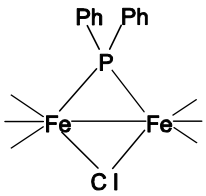
$Mo(CO)_5(\eta^1\text{-dppm})$
7



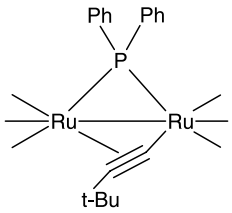
$W(CO)_5(PMe_3)$
8



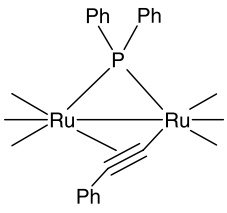
$RhCl(PPh_3)_3$
9



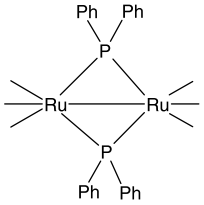
$Fe_2(CO)_6(\mu_2\text{-Cl})(\mu_2\text{-PPh}_2)$
10



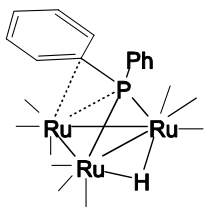
$Ru_2(CO)_6(\mu_2\text{-}\eta^2\text{-C}\equiv\text{C-}t\text{-Bu})(\mu_2\text{-PPh}_2)$
11



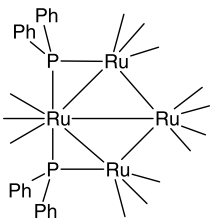
$Ru_2(CO)_6(\mu_2\text{-}\eta^2\text{-C}\equiv\text{C-Ph})(\mu_2\text{-PPh}_2)$
12



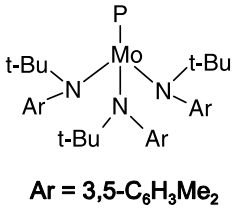
$Ru_2(CO)_6(\mu_2\text{-PPh}_2)_2$
13



$Ru_3(CO)_9(\mu_2\text{-H})(\mu_2\text{-PPh}_2)$
14

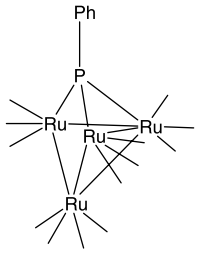


$Ru_4(CO)_{13}(\mu_2\text{-PPh}_2)_2$
15



$Ar = 3,5\text{-}C_6H_3Me_2$

$Mo(P)[N(t\text{-Bu})Ar]_3$
16



$Ru_4(CO)_{13}(\mu_3\text{-PPh})$
17

tic effects for **13** with the ZORA (II) and locally dense ZORA (I/V) basis sets leads to an increase in shielding for all three principal components, with the greatest effect observed for σ_{33}, and an increased isotropic shielding of 33 ppm for both calculations. Thus, the effective deshielding observed when employing larger triple-ζ basis sets with the scalar-ZORA-DFT method may be due to the exclusion of the spin-orbit relativistic correction. The scalar-only ZORA (II) calculation is in best agreement with experiment and requires much less computational time.

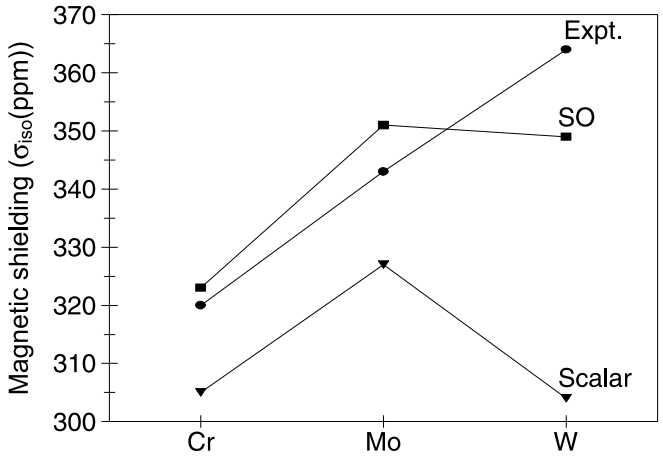
© 2003 NRC Canada

Table 3. Experimental[a] and calculated ^{31}P magnetic shielding tensors for $M(CO)_5(PMe_3)$ (M = Cr, Mo, W) (ppm).

Compound		σ_{iso}	σ_{11}	σ_{22}	σ_{33}	Ω
$Cr(CO)_5(PMe_3)$	Exptl.	320	290	299	370	80
	ZORA SO[b,c]	323	283	309	378	95
	ZORA scalar[b,d]	305	264	289	363	99
	SOS-DFPT[e]	326	296	296	391	95
	DFT[f]	313	283	283	373	90
$Mo(CO)_5(PMe_3)$	Exptl.	343	315	334	380	65
	ZORA SO[b,c]	351	328	335	388	60
	ZORA scalar[b,d]	327	300	307	375	75
	SOS-DFPT[e]	350	327	327	396	69
	DFT[f]	339	322	322	378	56
$W(CO)_5(PMe_3)$	Exptl.	364	359	364	370	11
	ZORA SO[b,c]	349	332	351	364	32
	ZORA scalar[b,d]	304	277	287	349	72
	SOS-DFPT[e]	350	328	328	395	67

[a]Reference 85.
[b]This work. Calculation employed the ZORA (V) basis set uniformly.
[c]Scalar + spin-orbit correction.
[d]Scalar correction only.
[e]Reference 48.
[f]Reference 49.

Fig. 2. Experimental (●), ZORA scalar-only (▼), and ZORA scalar + spin-orbit (■) calculations of isotropic ^{31}P magnetic shielding values for $M(CO)_5(PMe_3)$ (M = Cr, Mo, W). Calculations employed the ZORA (V) basis set uniformly.



Choice of basis sets

A series of calculations was performed on $Ru_2(CO)_6(\mu_2\text{-}PPh_2)_2$ (**13**), for which high-quality experimental X-ray (97) and solid-state NMR (27) data are available, to investigate the basis set dependence for the RHF, B3LYP, and ZORA-DFT methods (see Appendix A for discussion). Results are summarized in Fig. 3.[3] After examining these results, with consideration of computational time, as well as results obtained from investigation of the spin-orbit relativistic correction (vide supra), basis sets for calculations on the remaining compounds were chosen. RHF and B3LYP calculations were performed for compounds **1**–**17**, employing the 6-31G(d) or 6-311+G(2d) diffuse basis set for phosphorus and directly bonded atoms, the LANL2DZ RECP for metallic centres, and 3-21G on the remainder of the molecule. ZORA-DFT calculations, including only scalar relativistic corrections, were performed using the ZORA (II) basis set on all nuclei.

Comparison of calculated and experimental chemical shift tensors

The following discussion will deal with results obtained for both the 6-31G(d) and the 6-311+G(2d) locally dense basis sets (RHF and B3LYP) and the ZORA (II) basis set.[4] Discussion of observed trends for each of the computational methods will be divided into the following three general sections: (*i*) transition-metal phosphines (**1**–**8**), (*ii*) phosphido-bridging clusters (**10**–**15**), and (*iii*) terminal phosphido and phosphinidene (**16** and **17**). Compound **9** is treated separately from the other phosphines, as the metal centre is in a distorted square-planar bonding arrangement, not pseudo-octahedral as are **1**–**8**. The phosphorus nuclei in these compounds exhibit the following characteristic isotropic chemical shifts and spans: for the phosphines (**1**–**8**), δ_{iso} = –36 to 52 ppm and Ω = 11 to 158 ppm; for the three phosphorus sites in Wilkinson's catalyst (**9**), δ_{iso} = –50 to 76 ppm and Ω = 150 to 271 ppm; for the phosphido-bridging clusters (**10**–**15**), δ_{iso} = 114 to 185 ppm and Ω = 179 to 308 ppm; for the terminal phosphido (**16**), δ_{iso} = 1208 ppm and Ω = 2308 ppm; and for the phosphinidene (**17**), δ_{iso} = 414 ppm and Ω = 829 ppm. Figure 4 compares the RHF/6-311+G(2d), B3LYP/6-31(d), and ZORA (II) results with experimental values. Average deviations of calculated from experimental (Δ = calcd – exptl) ^{31}P magnetic shielding values for the phosphines (**1**–**8**) and phosphido-bridging compounds (**10**–**15**) are provided in Table 4.

[3]Numeric data are available in Supplementary Tables D1 and D2.
[4]Numeric data for compounds **1**–**17** are available in Supplementary Table D3.

© 2003 NRC Canada

Fig. 3. Investigation of locally dense basis set performance for reproduction of experimental ^{31}P magnetic shielding tensors for $Ru_2(CO)_6(\mu_2\text{-}PPh_2)_2$ (**13**). σ_{iso} = ●, σ_{11} = ▼, σ_{22} = ■, σ_{33} = ▲. Solid lines indicate experimental values. Experimental and RHF/6-311+G(2d) data are from ref. 27.

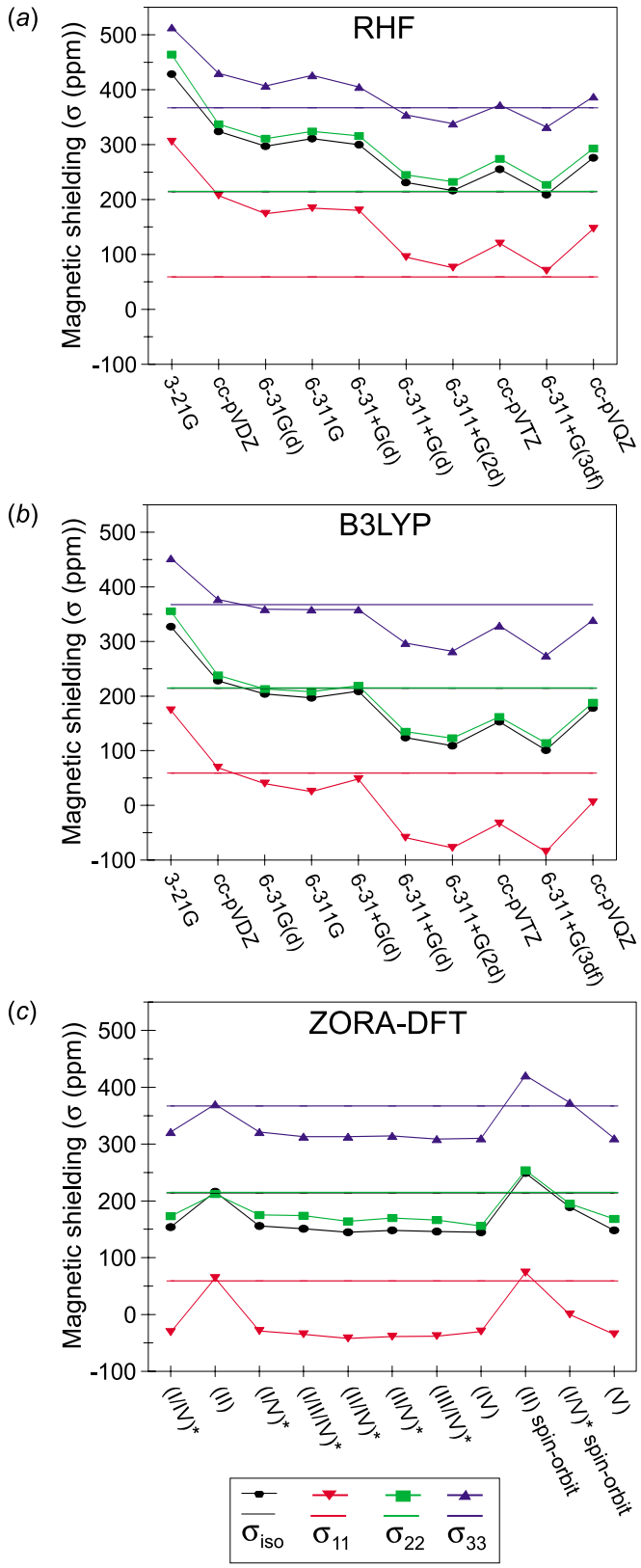
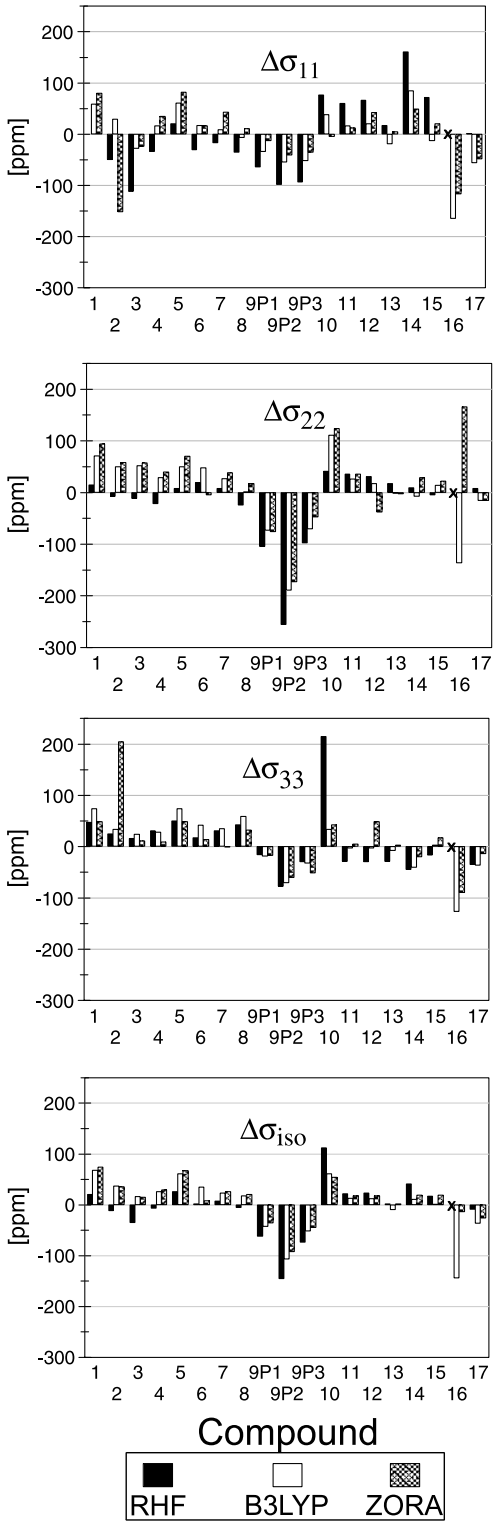


Fig. 4. Deviation in ppm of calculated ^{31}P magnetic shielding tensor principal component and isotropic values from experimental results (calcd – exptl) for **1**–**17**. Negative values indicate that the calculated results are deshielded relative to the experiment. Calculated values are for the RHF/6-311+G(2d) and the B3LYP/6-31G(d) locally dense basis sets, and the ZORA (II) scalar-only calculation. Note: RHF data for compound **16** are not included (see text).



© 2003 NRC Canada

Table 4. Average deviation of calculated[a] from experimental (Δ = calcd – exptl) ^{31}P magnetic shielding values for the phosphines (**1**–**8**) and phosphido-bridging (**10**–**15**) complexes (ppm).

	Method	$\Delta\sigma_{iso}$	$\Delta\sigma_{11}$	$\Delta\sigma_{22}$	$\Delta\sigma_{33}$	$\Delta\Omega$
Phosphines						
	RHF/6-31G(d)	80	59	84	96	36
	RHF/ 6-311+G(2d)	–1	–33	–2	32	66
	B3LYP/6-31G(d)	35	19	41	46	27
	B3LYP/ 6-311+G(2d)	–54	–79	–52	–33	46
	ZORA (II)	37	13	48	49	36
Phosphido-bridging						
	RHF/6-31G(d)	121	170	106	89	–81
	RHF/ 6-311+G(2d)	36	76	22	11	–65
	B3LYP/6-31G(d)	15	21	26	–3	–24
	B3LYP/ 6-311+G(2d)	–66	–78	–52	–67	12
	ZORA (II)	22	21	28	16	–4

[a]RHF and B3LYP calculations employed locally dense basis sets; the indicated basis set was used for P and directly bonded nuclei, the LANL2DZ ECP was used for metallic centres, and 3-21G on all remaining nuclei. The ZORA-DFT calculation includes only scalar relativistic corrections.

Transition-metal phosphines

Transition-metal phosphine complexes exhibit ^{31}P isotropic magnetic *shieldings*, ranging from approximately 200 to 350 ppm (i.e., $\delta_{iso} \cong 130$ to –20 ppm) with spans less than 200 ppm. As already mentioned, previous theoretical investigations of the ^{31}P CS tensor in phosphines containing transition metals have been made by Kaupp (48), Ruiz-Morales and Ziegler (49), and van Wüllen (33). Kaupp concluded that proper interpretation of ^{31}P chemical shifts of substituted phosphine ligands in transition-metal complexes requires a detailed analysis of the electronic structure of the ligand; the increase in ^{31}P magnetic shielding observed when moving down the periodic table in the $M(CO)_5(PX_3)$ (M = Cr, Mo, W; X = H, Me, F, Cl) systems is the result of contributions from the perpendicular components of the shielding tensor ($\sigma_\perp$) (48). A subsequent study by Ruiz-Morales and Ziegler (49) (excluding M = W, including X = Ph) identified both positive and, in the case of X = F, Cl, negative contributions to the ^{31}P chemical shift from paramagnetic couplings between specific ligand and complex orbitals. In the present study we report calculated phosphorus magnetic shielding tensors for large phosphine ligands (e.g., PPh_3, DBP (5-phenyldibenzophosphole)) and the group VI $M(CO)_5(PMe_3)$ systems, including spin-orbit relativistic effects. In addition, we investigate the influence of varying the W—P bond length, as well as the W-P-C_{Me} bond angle in **8**, and examine the phosphorus CS tensors for the three unique phosphorus nuclei in Wilkinson's catalyst (**9**).

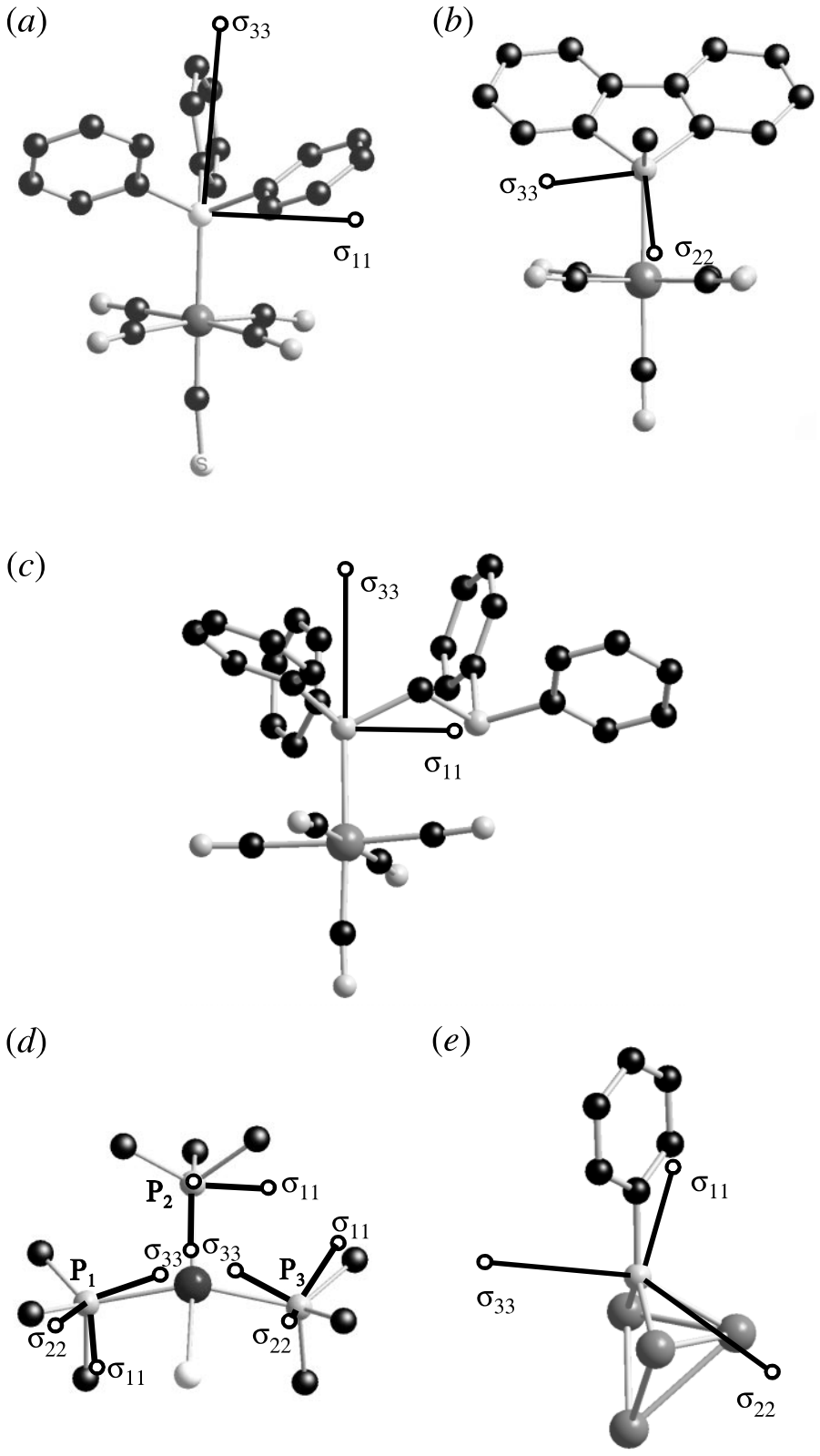
Comparison of the calculated and experimental values of the phosphorus magnetic shielding tensor principal components yields several insights. For **1**–**8**, the RHF/6-311+G(2d) calculations provide the most accurate results for the isotropic shielding and the three principal components of the magnetic shielding tensor; however, the span is consistently overestimated, as follows: $\Delta\sigma_{iso} = -1$, $\Delta\sigma_{11} = -33$, $\Delta\sigma_{22} = -2$, $\Delta\sigma_{33} = 32$, and $\Delta\Omega = 66$ ppm. In most cases σ_{11} (except **5**) is deshielded and σ_{33} is shielded relative to experimental values. Both the B3LYP and ZORA-DFT calculations with only a double-ζ quality basis set provide results that are surprisingly accurate. For the B3LYP/6-31G(d) calculations, the average deviations from experiment are $\Delta\sigma_{iso} = 35$, $\Delta\sigma_{11} = 19$, $\Delta\sigma_{22} = 41$, $\Delta\sigma_{33} = 46$, and $\Delta\Omega = 27$ ppm. The ZORA (II) calculation overestimates the isotropic shielding, σ_{22}, and σ_{33} in most cases (except σ_{33} for **7**), as follows: $\Delta\sigma_{iso} = 37$, $\Delta\sigma_{11} = 13$, $\Delta\sigma_{22} = 48$, $\Delta\sigma_{33} = 49$, and $\Delta\Omega = 36$ ppm. The RHF/6-31G(d) calculations do not give qualitatively accurate results relative to experiment (except for the span that is fortuitously reproduced with $\Delta\Omega = 36$ ppm). The RHF and B3LYP results with the 6-31G(d) basis set display similar trends, and apart from σ_{11} for **3**, the calculated tensor principal components, and thus the isotropic values, are shielded relative to experiment. Consistently, the calculated span is greater than the experimental span. In principle, one should expect an improvement in calculated values upon increasing the basis set to 6-311+G(2d) (vide supra); in practice, however, with the B3LYP method, calculated results worsened relative to experiment. For all compounds, the tensor principal components and the isotropic values are deshielded relative to the experimental values, and the calculated spans exceed those measured.

In an experimental ^{31}P NMR study of compound **4** the direction of greatest shielding at the phosphorus site was assumed to be along the P—Cr bond axis (88). Since the approximate local mirror plane of the PPh_3 ligand is preserved, the principal component of least shielding is either in the local mirror plane or perpendicular to it (88). Experimentally the two perpendicular components are reported to exhibit the same chemical shift, even though the local mirror plane is only approximate. The RHF and B3LYP methods indicate that σ_{33} is 8.5 ± 1.5° off the Cr—P bond axis (supporting the assumption made in the experimental study) and that σ_{11} is perpendicular to the local mirror plane (Fig. 5*a*). The ZORA (II) calculation predicts σ_{33} at an angle of 15° with the Cr—P bond axis.

The phosphorus CS tensor orientation for **6** has been determined experimentally via a single-crystal ^{31}P NMR study (28). This compound provides an important example as to why one should not always assume that the most shielded component of the phosphorus CS tensor in these systems would be approximately along the metal–phosphorus bond.

© 2003 NRC Canada

Fig. 5. Orientation of the ^{31}P CS tensor in its PAS for (*a*) *trans*-$Cr(CO)_4CS(PPh_3)$ (**4**), (*b*) $Mo(CO)_5$(MeDBP) (**6**), (*c*) $Mo(CO)_5(\eta^1$-dppm) (**7**), (*d*) $RhCl(PPh_3)_3$ (**9**), and (*e*) $Ru_4(CO)_{13}(\mu_3$-PPh) (**17**). For clarity, hydrogen nuclei have been omitted; (*d*) only *ipso*-carbons of the phenyl rings are shown; and (*e*) carbonyl groups are omitted.



© 2003 NRC Canada

In this case, the electronic environment about phosphorus was found to deviate considerably from axial symmetry; σ_{33} is not along the Mo—P bond axis. In fact, both σ_{11} and σ_{33} are perpendicular to the Mo—P axis, with σ_{33} approximately perpendicular to the local mirror plane. Experimentally the Mo-P-σ_{ii} angles are 87°, 8°, and 83° for i = 1, 2, and 3, respectively. The RHF and B3LYP calculations with the 6-31G(d) basis set and the ZORA (II) calculation provide qualitatively accurate orientations (Fig. 5*b*), whereas the RHF and B3LYP calculations with the triple-ζ basis set switch the placement of σ_{22} and σ_{33}. Experimentally these two components differ by only 18 ppm. The difference between σ_{22} and σ_{33} in the calculations ranges from 6 ppm for the ZORA (II) calculation to 15 ppm for the RHF/6-311+G(2d) calculation. When the CS tensor for a particular nucleus nears axial symmetry, one must take care to accurately determine the proper orientation of the two components that are close in chemical shift. The RHF and B3LYP methods indicate an Mo-P-σ_{11} angle of 92.5 ± 2.5° (ZORA (II) 101°). Excluding orientations obtained from the 6-311+G(2d) calculations, the Mo-P-σ_{22} angle ranges from 10° (B3LYP) to 17° (RHF) and the Mo-P-σ_{33} angle ranges from 73° (RHF) to 89° (ZORA (II)).

For **7**, all three computational methods are in agreement with the experimental phosphorus CS tensor orientation determined via a single-crystal ^{31}P NMR study (29); σ_{33} is 11.2° off the Mo—P bond axis and σ_{11} is approximately perpendicular to one of the Mo-P-C_{ipso} planes (Fig. 5*c*). The RHF and B3LYP results indicate that the Mo-P-σ_{33} angle is 14 ± 2° and σ_{11} is 19 ± 1° off the normal to the plane. The ZORA (II) calculation indicates an Mo-P-σ_{33} angle of 36° and that σ_{11} is 13° off the normal to the plane.

Wilkinson's catalyst, $RhCl(PPh_3)_3$ (**9**), contains three crystallographically and magnetically non-equivalent phosphorus nuclei. The orientations of the phosphorus CS tensors in their PAS have been proposed from a single-crystal ^{31}P NMR study (92), and thus **9** is a suitable system for investigating the reliability of quantum chemical calculations for the reproduction of the tensor orientations. This compound proved challenging for all computational methods employed. The calculations employing double-ζ quality basis sets provided results closest to the experimental values. The RHF/6-31G(d) calculation performed best; average deviations for the three phosphorus nuclei are $\Delta\sigma_{iso}$ = –28, $\Delta\sigma_{11}$ = –10, $\Delta\sigma_{22}$ = –80, $\Delta\sigma_{33}$ = 9, and $\Delta\Omega$ = 19 ppm. Both the RHF and B3LYP methods with the 6-311+G(2d) basis set yield values deshielded on the order of 100 ppm. The values of the phosphorus magnetic shielding tensor principal components were calculated to be deshielded relative to experiment, except in the case of the RHF/6-31G(d) calculations. These trends are different from those observed for the other phosphines investigated. As noted, the other eight phosphines studied are in a pseudo-octahedral bonding arrangement, whereas $RhCl(PPh_3)_3$ is in a slightly distorted square planar arrangement. Intermolecular effects are expected to be more significant for this structure, and ligands are expected to display magnetic shielding trends characteristic of the structural environment of the metal. However, because of the large triphenylphosphine ligands, distances from the metal to nuclei of neighbouring molecules are greater than 4.4 Å. Although we cannot conclude that the difference in magnetic shielding trends observed here is solely a result of the structural environment of the metal, a study investigating observed trends in calculated shieldings for various structural systems could be conducted. Experimentally, the orientation of the three phosphorus CS tensors was assigned by assuming that σ_{33} lies approximately along the P—Rh bond in each case. All methods employed herein qualitatively reproduce the experimental CS tensor orientation for each of the three phosphorus sites, indicating the same general orientation (Fig. 5*d*). Numerical values are presented in Table 5.

Table 5. Calculated[a] orientation of the three ^{31}P magnetic shielding tensors in Wilkinson's catalyst, $RhCl(PPh_3)_3$ (**9**).

Site	Rh-P-σ_{ii}	Angle (°)	
P_1	i = 1	85	(ZORA (II) = 92)
	i = 2	90±1	
	i = 3	176.5±1.5	
P_2	i = 1	89.5±2.5	
	i = 2	90.5±2.5	
	i = 3	177±1	
P_3	i = 1	96±1	
	i = 2	78.5±1.5	(ZORA (II) = 63)
	i = 3	166.5±1.5	(ZORA (II) = 153)

[a]Unless otherwise stated, the angle given is the average of the angles obtained from the RHF, B3LYP, and ZORA (II) calculations. RHF and B3LYP calculations employed locally dense basis sets; 6-31G(d) or 6-311+G(2d) was used for P and directly bonded nuclei, the LANL2DZ ECP for metallic centres, and 3-21G on all remaining nuclei.

Phosphido-bridging clusters

Phosphido-bridging groups in transition-metal complexes normally exhibit ^{31}P isotropic shieldings between 100 and 600 ppm (i.e., $\delta_{iso} \cong$ 230 to –270 ppm) with spans of less than 500 ppm. Recently, Eichele et al. (27) reported an in-depth experimental and theoretical study of phosphorus CS tensors in ruthenium phosphido-bridging complexes. In the present study we investigate the ability of various theoretical methods to reproduce the available experimental data for phosphido-bridging compounds containing first- and second-row transition metals. The data discussed below includes only the phosphido-bridging compounds (**10**–**15**).

As with the phosphines, the B3LYP/6-31G(d), ZORA (II), and RHF/6-311+G(2d) calculations yield the most accurate results relative to experiment. For the phosphido-bridging compounds, the B3LYP/6-31G(d) method provides excellent results, as follows: $\Delta\sigma_{iso}$ = 15, $\Delta\sigma_{11}$ = 21, $\Delta\sigma_{22}$ = 26, $\Delta\sigma_{33}$ = –3, and $\Delta\Omega$ = –24 ppm. With the double-ζ ZORA (II) basis set, the ZORA-DFT method yields results comparable to the B3LYP/6-31G(d) calculations but reproduces the span more accurately; $\Delta\Omega$ = –4 ppm. The RHF/6-311+G(2d) calculations provide results in good agreement with experiment, although the calculated isotropic shielding and σ_{11} are consistently overestimated. The average deviations are $\Delta\sigma_{iso}$ = 36, $\Delta\sigma_{11}$ = 76, $\Delta\sigma_{22}$ = 22, $\Delta\sigma_{33}$ = 11, and $\Delta\Omega$ = –65 ppm. Since σ_{11} is not well reproduced, the accuracy of σ_{iso} is clearly the result of the superb values calculated for σ_{22} and σ_{33}. This illustrates the importance of studying the tensor principal components obtained from a calculation rather than relying solely on the isotropic value. Similar to results ob-

© 2003 NRC Canada

tained for the phosphine complexes, employing the 6-311+G(2d) basis set with the B3LYP functional for the phosphido-bridging complexes provides values in poor agreement with experiment relative to the double-ζ calculation. The average deviations from experiment with the larger basis set are $\Delta\sigma_{iso} = -66$, $\Delta\sigma_{11} = -78$, $\Delta\sigma_{22} = -52$, and $\Delta\sigma_{33} = -67$ ppm; σ_{11} and σ_{33} are always underestimated relative to experimental values. Despite the deviations exhibited for the tensor principal components, the span is fortuitously reproduced with $\Delta\Omega = 12$ ppm. Disappointing results are realized with the RHF/6-31G(d) calculations. In all cases, the calculated principal components and isotropic values are greatly overestimated with $\Delta\sigma_{iso} = 121$, $\Delta\sigma_{11} = 170$, $\Delta\sigma_{22} = 106$, $\Delta\sigma_{33} = 89$, and $\Delta\Omega = -81$ ppm.

The importance of considering the three principal components of the magnetic shielding tensor is illustrated in Fig. 6. The ^{31}P NMR powder pattern simulated from experimental data is compared with results from the three computational methods employed for **12**, a phosphido-bridging ruthenium cluster. There is obviously great variation in the calculation of the ^{31}P CS tensor, depending on the computational method and basis set employed. The RHF/6-311+G(2d), B3LYP/6-31G(d), and ZORA (II) calculations all yield excellent values of the isotropic shielding. The RHF/6-311+G(2d) method underestimates the span by 96 ppm, as σ_{11} is shielded by 66 ppm and σ_{33} is deshielded by 30 ppm relative to experiment. The ZORA (II) method reproduces the span very well, but σ_{11} and σ_{33} are shielded by 42 and 49 ppm, respectively, and σ_{22} is deshielded by 38 ppm relative to experiment. These observations bring a key point to the forefront: calculations may reproduce the isotropic shift (and (or) span) regardless of the agreement between experimental and calculated values of the CS tensor principal components.

Although the orientation of the phosphorus CS tensor in the molecular framework of the iron phosphido-bridging complex (**10**) has not been investigated experimentally, Eichele et al. (27) have recently proposed the orientation of the phosphorus CS tensor in ruthenium phosphido-bridging compounds. Their single-crystal ^{31}P NMR study of **13** (denoted compound **4** in ref. 27) yielded two possible orientations of the phosphorus CS tensor, placing σ_{11} either 25° above or below the phosphorus–phosphorus internuclear vector as depicted in Fig. 7. Using RHF GIAO calculations, σ_{11} was predicted to be oriented above the internuclear vector. In the present study, the B3LYP and ZORA (II) methods indicate the same orientation for **10** and **13** as was proposed in ref. 27, placing the least-shielded component (σ_{11}) approximately 25° above the bridging ligand internuclear vector. Curiously, the RHF calculations provide a different orientation for **10**, placing σ_{11} approximately 25° below and σ_{33} 65° above the bridging ligand internuclear vector. In this study we have not otherwise encountered orientations from the RHF, B3LYP, and ZORA methods that are in disagreement, except for **6**, where two of the tensor principal components exhibit similar chemical shifts (vide supra). Perhaps proper treatment of electron correlation is necessary to obtain the correct orientation of the phosphorus CS tensor in compound **10**, which contains a μ_2-Cl ligand, and thus, in this case the RHF method is inadequate.

Fig. 6. Simulated ^{31}P powder patterns for compound **12**. Experimental values (ref. 27). The RHF and B3LYP calculations employed locally dense basis sets. Solid vertical line indicates δ_{iso}. Note: the scale is chemical shift, δ, not magnetic shielding, σ.

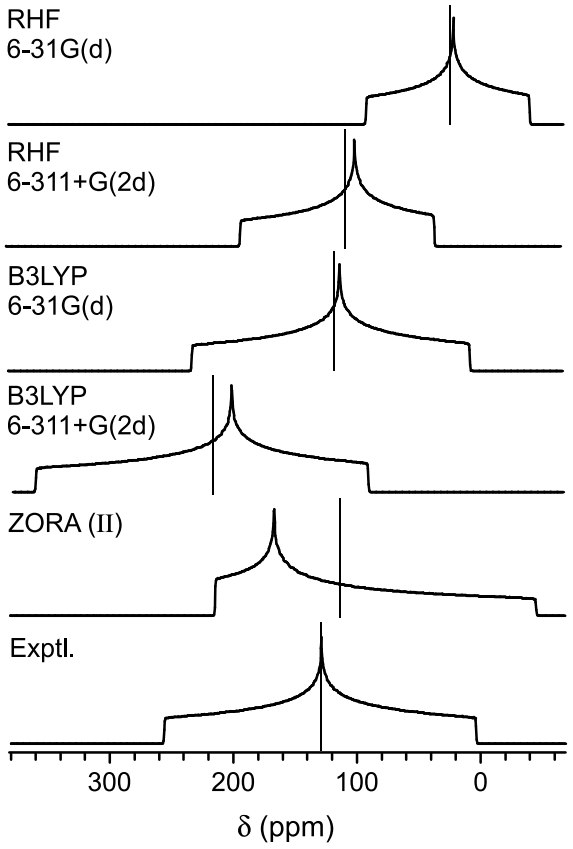
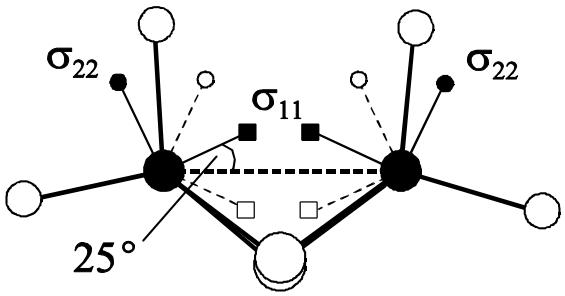


Fig. 7. Two possible orientations of the ^{31}P CS tensor for $Ru_2(CO)_6(\mu_2\text{-}PPh_2)_2$ (**13**) obtained from a single-crystal NMR study (adapted from ref. 27). For clarity, only the metallic centres, phosphorus nuclei (shaded), and *ipso*-carbons of the phenyl groups are shown. B3LYP and ZORA-DFT calculations for $Fe_2(CO)_6(\mu_2\text{-}Cl)(\mu_2\text{-}PPh_2)$ (**10**) and **13** reproduce the orientation, placing σ_{11} 25° above the bridging ligand internuclear vector.



Terminal phosphido and phosphinidene

Terminal phosphido complexes represent a class of compounds that exhibit the largest observed ^{31}P chemical shifts (101). For example, compound **16** has an isotropic chemical shift of 1208 ppm and a span of over 2300 ppm. Both the B3LYP and ZORA-DFT methods produce results in agreement with experiment. Experimentally, the values of σ_{11} and

© 2003 NRC Canada

σ_{22} are identical, –1650 ppm. The B3LYP/6-311+G(2d) method performs well, reproducing values of σ_{11} and σ_{22} that are closest to each other and experimental values, and the span is within 35 ppm. The ZORA (II) method most accurately calculates the isotropic shielding and the span, differing from experiment by –14 and 27 ppm, respectively. Although the σ_{11} and σ_{22} values obtained with the ZORA-DFT method are not similar, their average, –1626 ppm, is only 24 ppm greater than the experimental value. The RHF calculations fail completely, likely due to the combination of the demands of representing the bonding arrangement and the formally localized lone pair of electrons on the phosphorus (vide supra). The advantage of DFT methods is clearly demonstrated by this example; despite the difficulty of this calculation, the performance of both the B3LYP and ZORA (II) methods is outstanding.

Phosphorus CS tensors have been investigated experimentally for several phosphinidenes. Transition-metal phosphinidenes generally exhibit phosphorus CS tensor spans greater than 500 ppm and isotropic shieldings for μ_3 and μ_4 complexes, including those containing second- and third-row transition metals, ranging from –200 to 300 ppm (108). However, many contain four or more transition metals and large ligands with complex bonding arrangements, thus hindering computational studies. At this time we limit our study to $Ru_4(CO)_{13}(\mu_3\text{-PPh})$ (**17**), for which the phosphorus CS tensor orientation was determined in a single-crystal ^{31}P NMR study (compound **2**, ref. 103). Experimentally, σ_{11} is highly deshielded, resulting in a large span of 829 ppm. Bühl et al. (50) have previously calculated the phosphorus CS tensor for **17** employing the SOS-DFPT-IGLO formalism, reporting values for the tensor principal components and their orientation in the PAS. Relative to experiment, the values reported are $\Delta\sigma_{iso}$ = 16, $\Delta\sigma_{11}$ = 41, $\Delta\sigma_{22}$ = 12, $\Delta\sigma_{33}$ = –5, and $\Delta\Omega$ = –46 ppm.

Herein, the RHF/6-311+G(2d), B3LYP/6-31G(d), and ZORA (II) methods outperform the RHF/6-31G(d) and B3LYP/6-311+G(2d) calculations. RHF/6-311+G(2d) provides the most impressive agreement with experiment. The isotropic shielding and σ_{33} are deshielded by 9 and 35 ppm; σ_{11} and σ_{22} are shielded by only 1 and 8 ppm, respectively; and the span is underestimated by 37 ppm relative to experiment. The B3LYP/6-31G(d) and ZORA (II) results are also excellent, considering the span of the CS tensor. The experimental ^{31}P CS tensor orientation for **17** was rationalized via frontier molecular orbital calculations, which determined that σ_{33} is perpendicular to the open face formed by the cluster of Ru nuclei and that σ_{11} forms an angle of 8° with the C—P bond axis. Calculations of Bühl et al. (50) reproduce the experimental orientation, predicting σ_{11} to be 9° off the C—P bond. The angle reported herein for σ_{33} relative to the open face of the cluster is the average of the three angles obtained by considering the three different planes that may be formed by the phosphorus nucleus and any two of the three ruthenium nuclei. The RHF and B3LYP methods indicate that σ_{33} forms an angle of 107.5 ± 2° with the open face and σ_{11} an angle of approximately 14° with the C—P bond axis (Fig. 5*e*). From the ZORA (II) calculation, σ_{33} forms an angle of 103° with the open face and σ_{11} is at an angle of 9° with respect to the C—P bond axis.

Effect of systematic geometric variation on nuclear magnetic shielding

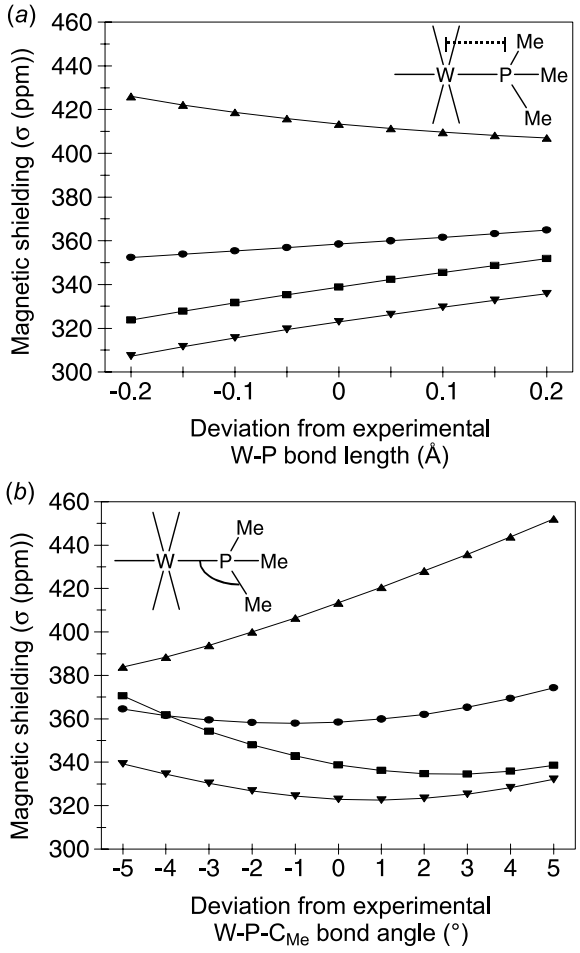
Quantum chemical calculations are able to provide direct information regarding the effects of systematic geometric variations on magnetic shielding tensors (109). However, experimentally, different ligands must be used to alter the system geometry, resulting in uncertainty as to what portion of the observed change in the CS tensor is actually due to the geometric variation and not the ligand change. Numerous quantum chemical studies have investigated the effects of geometric variations on the ^{31}P magnetic shielding tensor in smaller phosphorus-containing compounds (30, 32, 40, 42, 44, 46, 51–54). Recently, Avalle et al. (110) performed B3LYP-DFT calculations of ^{119}Sn chemical shifts for a series of organometallic compounds and found that the Sn-N-C bond angle strongly influences the calculated chemical shift. As well, we have previously studied the effect of varying the Ru-P-Ru bond angle in **13** via alteration of the Ru—P bond length (27), supporting an experimental correlation established by Carty et al. (94). As expected, a general ^{31}P deshielding trend was observed upon decrease of the Ru-P-Ru angle (increase of the Ru—P bond lengths).

The impact of systematic geometric variation on the phosphorus magnetic shielding tensor of the transition-metal phosphine $W(CO)_5(PMe_3)$ (**8**) was investigated using the RHF/6-311+G(2d) method. The W—P bond length was varied by ±0.2 Å in 0.05 Å increments. The W-P-C_{Me} angles were varied by ±4° in increments of 1°. The phosphorus magnetic shielding tensor for phosphine ligands bound to transition metals is often oriented such that σ_{33} lies approximately along the M—P bond, as is the case with **8**. As such, one would expect that a change in the bond length will have the least impact on the shielding component along this direction, while the perpendicular components will be more influenced. As evident in Fig. 8*a*, σ_{33}, which lies along the W—P bond axis, is more shielded for shorter W—P bond lengths (47 ppm/Å), while the perpendicular tensor components display more prominent deshielding trends (–70 ppm/Å). As expected, the isotropic shielding exhibits a less dramatic dependence; for shorter W—P bond lengths a moderate decrease in shielding is observed (–31 ppm/Å). Varying the W-P-C_{Me} bond angles produces some interesting trends in the values of the tensor principal components (Fig. 8*b*). For W-P-C_{Me} bond angles smaller than experimental values, σ_{33} exhibits an almost linear decrease in shielding while σ_{22} becomes more shielded. Bond angles up to 3° from experimental geometry result in deshielding of σ_{22}, while larger angles cause σ_{22} to increase. Any change in the W-P-C_{Me} bond angles leads to an increase in shielding for σ_{11}.

We have employed the iron phosphido-bridging complex (**10**) as a model system to investigate theoretically an experimentally determined correlation between the ligand bond angle (Fe-P-Fe) and the observed ^{31}P isotropic chemical shift in iron phosphido-bridging compounds. Compound **10** was included in the experimental study by Carty et al. (94). Herein, the Fe-P-Fe bond angle in **10** was varied from 69° to 76° in 1° increments by proportionally changing the Fe—P bond lengths. The B3LYP/6-311+G(2d) locally dense method was employed for this study. Similar trends in the phosphorus magnetic shielding tensor isotropic and principal

© 2003 NRC Canada

Fig. 8. Effect of systematic geometric variation of the W—P bond length (*a*) or the W-P-C_{Me} bond angle (*b*), relative to experimental values, on the calculated ^{31}P magnetic shielding for $W(CO)_5(PMe_3)$ (**8**). σ_{iso} = ●, σ_{11} = ▼, σ_{22} = ■, σ_{33} = ▲. Calculated values obtained with the RHF/6-311+G(2d) locally dense basis set method.

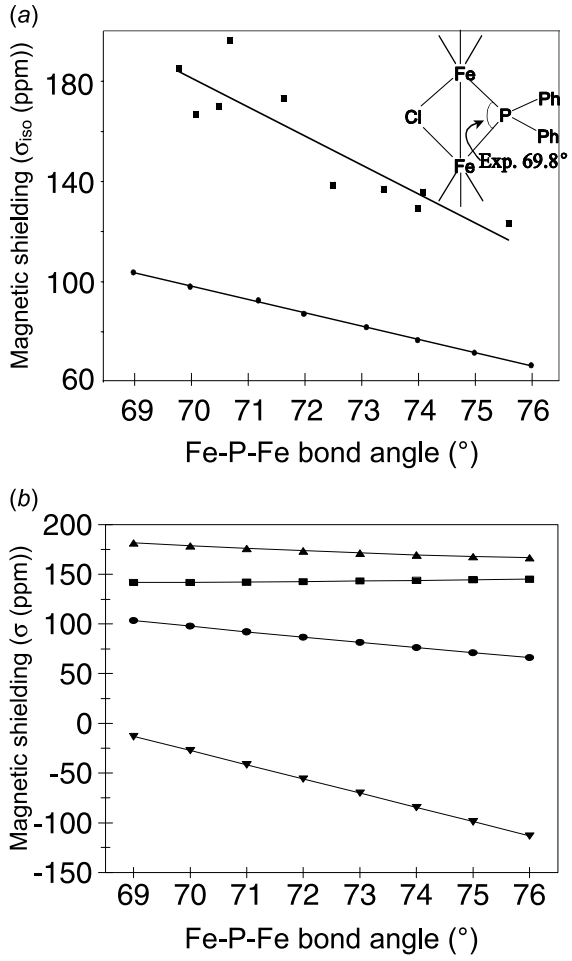


component values were observed for both **10** and the ruthenium analogue, **13** (27). As the M-P-M bond angle increases, a general deshielding of σ_{iso} is observed, with the trend being dictated by σ_{11}, in agreement with experimental results (94) (Fig. 9). Interestingly, when employing the RHF method in this study of **10**, the deshielding trend is dominated by σ_{33}. In all cases the trend is controlled by the phosphorus CS tensor principal component that is above the internuclear vector between the bridging ligands (vide supra). By fixing the ligand—metal bond length and varying the metal—metal bond length in a model phosphido compound, correlations between the degree of metal—metal interaction and ^{31}P chemical shift could also be investigated.

Conclusions

Experimental ^{31}P CS tensor data for a range of transition-metal-containing phosphine, phosphido, and phosphinidene complexes have been compared with results obtained from quantum chemical calculations employing GIAO RHF, B3LYP, and relativistic ZORA-DFT methods. The results

Fig. 9. Relationship between the Fe-P-Fe angle in $Fe_2(CO)_6(\mu_2\text{-}Cl)(\mu_2\text{-}PPh_2)$ (**10**) and the calculated ^{31}P magnetic shielding tensor. (*a*) The calculations confirm the experimentally observed (ref. 94) general deshielding trend as the Fe-P-Fe bond angle increases in a series of $Fe_2(CO)_6(\mu_2\text{-}PPh_2)(\mu_2\text{-}X)$ (X = ligand) complexes. Illustrated in (*b*) is the dependence of the calculated principal components on the Fe-P-Fe angle. σ_{iso} = ●, σ_{11} = ▼, σ_{22} = ■, σ_{33} = ▲. Calculated values obtained with the B3LYP/6-311+G(2d) locally dense basis set method.



presented are indicative of the viability and dependability of these methods for the computation of phosphorus magnetic shielding tensors in transition-metal-containing compounds. Numerous trends are observed in the deviation of calculated from experimental values of the magnetic shielding tensors. As well, the usefulness of employing computational methods for the investigation of geometric dependencies of the nuclear magnetic shielding tensor has been demonstrated. The present work indicates that a double-ζ quality basis set with either the B3LYP functional or the scalar-ZORA-DFT method *qualitatively* reproduce experimental ^{31}P CS tensors in phosphorus compounds containing first-, second-, or third-row transition metals. Use of larger, triple-ζ basis sets with these methods yields values that deviated farther from experiment. The RHF method requires a triple-ζ doubly polarized diffuse basis set to approach experimental values of the ^{31}P CS tensor principal components, yet completely fails

© 2003 NRC Canada

for the terminal phosphido group in compound **16**. Inclusion of the spin-orbit relativistic correction with the ZORA-DFT method requires use of the triple-ζ basis set to reproduce experimental data. These methods will, in most cases, qualitatively reproduce the experimental orientation of the ^{31}P CS tensor in its PAS, although the RHF method should be avoided in systems where electron-correlation may be very important.

Systematic trends in the deviation of calculated from experimental phosphorus magnetic shielding tensors for the phosphines investigated herein have been observed, as follows: RHF and B3LYP calculations at the 6-31G(d) level always overestimate the tensor principal components (i.e., more shielded than experiment) and the span; the RHF/6-311+G(2d) method usually underestimates σ_{11} and always overestimates σ_{33} and Ω; the B3LYP/6-311+G(2d) calculations provide values that are always deshielded and a span greater than experiment; and in most cases, the ZORA (II) method overestimates σ_{iso}, σ_{22}, and σ_{33}. For the phosphido-bridging compounds investigated herein, all values from the RHF/6-31G(d) calculations are more shielded and provide larger spans than experiment; the RHF/6-311+G(2d) values for σ_{iso} and σ_{11} are overestimated; the B3LYP/6-311+G(2d) results for σ_{11} and σ_{33} are deshielded relative to experiment; and σ_{iso} from the ZORA (II) method is too large. In general, with the same basis sets, the RHF calculations converged more rapidly than those with the B3LYP functional. Although, in most cases, the B3LYP/6-31G(d) and ZORA (II) calculations yield values in excellent agreement with experiment, one should note that the ZORA (II) method requires more computational time. Clearly, for more quantitative agreement with experiment, much larger basis sets, medium effects, and rovibrational averaging would need to be considered. At this time such computations on molecules as large as those considered here are not feasible.

With continual improvements in technology and the development of new computational techniques, the outlook for the calculation of magnetic shielding tensors in systems containing heavy nuclei is very bright. Recent developments correcting for self-interaction in approximate DFT methods (111) and the introduction and success of magnetically corrected basis sets for magnetic shielding tensor calculations (112) is extremely promising. The results presented here clearly demonstrate that modern computational techniques are a valuable resource to experimentalists interested in a greater understanding of the relationship between phosphorus chemical shifts and molecular structure.

Acknowledgments

The authors thank all members of the solid-state NMR group at the University of Alberta and Prof. Cynthia Jameson for helpful comments and discussions. Dr. David Bryce is thanked for assistance with the ZORA-DFT calculations and several useful suggestions. Prof. P.-N. Roy is thanked for allowing use of his AMD-based cluster, *Plethora*, sponsored by the Canadian Foundation for Innovation (CFI). R.E.W. is a Canada Research Chair in Physical Chemistry at the University of Alberta and thanks the Natural Sciences and Engineering Research Council of Canada (NSERC) and the University of Alberta for research grants. K.W.F. thanks NSERC, the Alberta Ingenuity Fund, and the University of Alberta for post-graduate scholarships.

References

1. (*a*) F.A. Cotton and G. Wilkinson. Advanced Inorganic chemistry: A comprehensive text. John Wiley and Sons, Toronto. 1980; (*b*) G.L. Miessler and D.A. Tarr. Inorganic chemistry. Prentice-Hall, Inc., Upper Saddle River, New Jersey. 1999.
2. R.R. Schrock and J.A. Osborn. J. Am. Chem. Soc. **98**, 2134 (1976).
3. F. Jachimowicz and J.W. Raksis. J. Org. Chem. **47**, 445 (1982).
4. A.K. Fazlur-Rahman, J.C. Tsai, and K.M. Nicholas. J. Chem. Soc. Chem. Commun. 1334 (1992).
5. (*a*) P.G. Pringle and M.B. Smith. J. Chem. Soc. Chem. Commun. 1701 (1990); (*b*) E. Costa, P.G. Pringle, M.B. Smith, and K. Worboys. J. Chem. Soc. Dalton Trans. 4277 (1997).
6. D. Ferraris, B. Young, T. Dudding, and T. Lectka. J. Am. Chem. Soc. **120**, 4548 (1998).
7. W.Y. Wong, F.L. Ting, and W.L. Lam. J. Chem. Soc. Dalton Trans. 2981 (2001).
8. D.V. Griffiths, J.C. Caesar, J.M. Hughes, P.M. Mahoney, S.P. Swetnam, G. Walton, and D.C. York. Phosphorus Sulfur Silicon Relat. Elem. **146**, 485 (1999).
9. S.L. Queiroz and A.A. Batista. Quim. Nova, **19**, 651 (1996).
10. (*a*) P.J. Sadler. *In* Advances in inorganic chemistry. Vol. 36. *Edited by* A.G. Sykes. Academic Press, Inc., San Diego. 1991. p. 1; (*b*) Z. Guo and P.J. Sadler. *In* Advances in inorganic chemistry. Vol. 49. *Edited by* A.G. Sykes. Academic Press, Inc., San Diego. 2000. p. 183.
11. (*a*) J.H. Nelson. Concepts Magn. Reson. **14**, 19 (2002); (*b*) J.H. Nelson. Nuclear magnetic resonance spectroscopy. Pearson Education, Inc., Upper Saddle River, New Jersey. 2003.
12. (*a*) J.F. Nixon and A. Pidcock. Annu. Rep. NMR Spectrosc. **2**, 345 (1969); (*b*) P.E. Garrou. Chem. Rev. **81**, 229 (1981).
13. P.S. Pregosin and R.W. Kunz. *In* NMR basic principles and progress. Vol. 16. *Edited by* P. Diehl, E. Fluck, and R. Kosfeld. Springer-Verlag, Berlin. 1979. p. 1.
14. W. Kutzelnigg, U. Fleischer, and M. Schindler. *In* NMR basic principles and progress. Vol. 23. *Edited by* P. Diehl, E. Fluck, and R. Kosfeld. Springer-Verlag, Berlin. 1979. p. 1.
15. K.R. Dixon. *In* Multinuclear NMR. *Edited by* J. Mason. Plenum Press, New York. 1987. p. 369.
16. E. Fluck and G. Heckman. *In* Methods in stereochemical analysis 8. *Edited by* J.G. Verkade and L.D. Quin. VCH Publishers Inc., Deerfield Beach. 1987. p. 61.
17. (*a*) G. Huttner and K. Knoll. Angew. Chem. Int. Ed. Engl. **26**, 743 (1987); (*b*) G. Huttner. J. Organomet. Chem. **308**, C11 (1986); (*c*) G. Huttner and H. Lang. *In* Multiple bonds and low coordination in phosphorus chemistry. *Edited by* M. Regitz and O. Scherer. Georg Thieme Verlag, Stuttgart. 1990. p. 48.
18. T. Kuivalainen, J. El-Bahraoui, R. Uggla, R. Kostiainen, and M.R. Sundberg. J. Am. Chem. Soc. **122**, 8073 (2000).
19. L.H. Randall and A.J. Carty. Inorg. Chem. **28**, 1194 (1989).
20. (*a*) F.A.L. Anet and D.J. O'Leary. Concepts Magn. Reson. **3**, 193 (1991); (*b*) **4**, 35 (1992).
21. M.J. Frisch, G.W. Trucks, H.B. Schlegel, G.E. Scuseria, M.A. Robb, J.R. Cheeseman, V.G. Zakrzewski, J.A. Montgomery, Jr., R.E. Stratmann, J.C. Burant, S. Dapprich, J.M. Millam, A.D. Daniels, K.N. Kudin, M.C. Strain, O. Farkas, J. Tomasi,

© 2003 NRC Canada

V. Barone, M. Cossi, R. Cammi, B. Mennucci, C. Pomelli, C. Adamo, S. Clifford, J. Ochterski, G.A. Petersson, P.Y. Ayala, Q. Cui, K. Morokuma, D.K. Malick, A.D. Rabuck, K. Raghavachari, J.B. Foresman, J. Cioslowski, J.V. Ortiz, A.G. Baboul, B.B. Stefanov, G. Liu, A. Liashenko, P. Piskorz, I. Komaromi, R. Gomperts, R.L. Martin, D.J. Fox, T. Keith, M.A. Al-Laham, C.Y. Peng, A. Nanayakkara, C. Gonzalez, M. Challacombe, P.M.W. Gill, B. Johnson, W. Chen, M.W. Wong, J.L. Andres, C. Gonzalez, M. Head-Gordon, E.S. Replogle, and J.A. Pople. Gaussian 98. Revision A.7. Gaussian, Inc., Pittsburgh, Pa. 1998.

22. R.E. Wasylishen and D.L. Bryce. J. Chem. Phys. **117**, 10 061 (2002).
23. T. Helgaker, M. Jaszuński, and K. Ruud. Chem. Rev. **99**, 293 (1999).
24. For example, see C.J. Jameson and A.C. de Dios. Theoretical and physcial aspects of nuclear shielding. *In* Specialist periodical reports, nuclear magnetic resonance. Vol. 32. The Royal Society of Chemistry, Cambridge. 2003. p. 43.
25. J. Gauss and J.F. Stanton. Electron-correlated approaches for the calculation of NMR chemical shifts. *In* Advances in chemical physics. Vol. 123. *Edited by* I. Prigogine and A. Rice. John Wiley and Sons, Inc., New York. 2002. p. 355.
26. J.C. Facelli. Shielding tensor calculations. *In* Encyclopedia of nuclear magnetic resonance. *Edited by* D.M. Grant and R.K. Harris. John Wiley and Sons Ltd., New York. 1996. p. 4327.
27. K. Eichele, R.E. Wasylishen, J.F. Corrigan, N.J. Taylor, A.J. Carty, K.W. Feindel, and G.M. Bernard. J. Am. Chem. Soc. **124**, 1541 (2002).
28. K. Eichele, R.E. Wasylishen, K. Maitra, J.H. Nelson, and J.F. Britten. Inorg. Chem. **36**, 3539 (1997).
29. K. Eichele, G.C. Ossenkamp, R.E. Wasylishen, and T.S. Cameron. Inorg. Chem. **38**, 639 (1999).
30. A. Dransfeld and D.B. Chesnut. Chem. Phys. **234**, 69 (1998).
31. G.D. Cody, B. Mysen, G. Sághi-Szabó, and J.A. Tossell. Geochim. Cosmochim. Acta, **65**, 2395 (2001).
32. D.B. Chesnut and L.D. Quin. Heteroatom Chem. **10**, 566 (1999).
33. C. van Wüllen. Phys. Chem. Chem. Phys. **2**, 2137 (2000)
34. A.M. Orendt, J.C. Facelli, A.J. Beeler, K. Reuter, W.J. Horton, P. Cutts, D.M. Grant, and J. Michl. J. Am. Chem. Soc. **110**, 3386 (1988).
35. K. Wolinski, C.L. Hsu, J.F. Hinton, and P. Pulay. J. Chem. Phys. **99**, 7819 (1993).
36. D.B. Chesnut, L.D. Quin, and S.B. Wild. Heteroatom Chem. **8**, 451 (1997).
37. T.M. Alam. Ab initio calculation of nuclear magnetic resonance chemical shift anisotropy tensors. I. Influence of basis set on the calculation of ^{31}P chemical shifts. Sandia National Laboratories, Albuquerque, N.M. 1998.
38. D. Gudat, E. Niecke, G. Grossmann, and K. Krüger. Magn. Res. Chem. **37**, 43 (1999).
39. A.B. Rozhenko, W.W. Schoeller, and M.I. Povolotskii. Magn. Res. Chem. **37**, 551 (1999).
40. M.J.T. Ditty and W.P. Power. Can. J. Chem. **77**, 1951 (1999).
41. G.M. Bernard, G. Wu, M.D. Lumsden, R.E. Wasylishen, N. Maigrot, C. Charrier, and F. Mathey. J. Phys. Chem. A, **103**, 1029 (1999).
42. K. Krüger, G. Grossmann, U. Fleischer, R. Franke, and W. Kutzelnigg. Magn. Res. Chem. **32**, 596 (1994).
43. M. Gee, R.E. Wasylishen, K. Eichele, G. Wu, T.S. Cameron, F. Mathey, and F. Laporte. Can. J. Chem. **78**, 118 (2000).
44. D.B. Chesnut and E.F.C. Byrd. Heteroatom Chem. **7**, 307 (1996).
45. M. Kaupp, C. Aubauer, G. Engelhardt, T.M. Klapötke, and O.L. Malkina. J. Chem. Phys. **110**, 3897 (1999).
46. M.J. Potrzebowski, X. Assfeld, K. Ganicz, S. Olejniczak, A. Cartier, C. Gardiennet, and P. Tekely. J. Am. Chem. Soc. **125**, 4223 (2003).
47. M. Gee, R.E. Wasylishen, K. Eichele, and J.F. Britten. J. Phys. Chem. A, **104**, 4598 (2000).
48. M. Kaupp. Chem. Ber. **129**, 535 (1996).
49. Y. Ruiz-Morales and T. Ziegler. J. Phys. Chem. A, **102**, 3970 (1998).
50. M. Bühl, M. Kaupp, O.L. Malkina, and V.G. Malkin. J. Comp. Chem. **20**, 91 (1999).
51. C.J. Jameson, A.C. de Dios, and A.K. Jameson. J. Chem. Phys. **95**, 9042 (1991).
52. A. Dransfeld and D.B. Chesnut. Phosphorus Sulfur Silicon Relat. Elem. **146**, 653 (1999).
53. M.J. Potrzebowski, G. Grossmann, K. Ganicz, S. Olejniczak, W. Ciesielski, A.E. Kozioł, I. Wawrzycka, G. Bujacz, U. Haeberlen, and H. Schmitt. Chem. Eur. J. **8**, 2691 (2002).
54. N. Asakawa, D. Sato, M. Sakurai, and Y. Inoue. J. Phys. Chem. A, **104**, 2716 (2000).
55. A.A. Auer, J. Gauss, and J.F. Stanton. J. Chem. Phys. **118**, 10 407 (2003).
56. D. Gudat, W. Hoffbauer, E. Niecke, W.W. Schoeller, U. Fleischer, and W. Kutzelnigg. J. Am. Chem. Soc. **116**, 7325 (1994).
57. G. Grossmann, D. Scheller, O.L. Malkina, V.G. Malkin, G. Zahn, H. Schmitt, and U. Haeberlen. Solid State Nucl. Magn. Reson. **17**, 22 (2000).
58. P.J. Wilson, R.D. Amos, and N.C. Handy. Chem. Phys. Lett. **312**, 475 (1999).
59. C.J. Jameson, A.C. de Dios, and A.K. Jameson. Chem. Phys. Lett. **167**, 575 (1990).
60. J. Mason. Solid State Nucl. Magn. Reson. **2**, 285 (1993).
61. W. Koch and M.C. Holthausen. A chemists guide to density functional theory. Wiley-VCH. Weinheim. 2000. Section 1.4.
62. W. Koch and M.C. Holthausen. A chemists guide to density functional theory. Wiley-VCH. Weinheim. 2000. Section 1.5.
63. (*a*) P. Hohenberg and W. Kohn. Phys. Rev. B, **136**, 864 (1964); (*b*) W. Kohn and L.J. Sham. Phys. Rev. A, **140**, 1133 (1965).
64. F. Jensen. Introduction to computational chemistry. John Wiley and Sons, Chichester. 2001. Chap 6.
65. A.D. Becke. J. Chem. Phys. **98**, 5648 (1993).
66. C. Lee, W. Yang, and R.G. Parr. Phys. Rev. B, **37**, 785 (1988).
67. W. Koch and M.C. Holthausen. A chemists guide to density functional theory. Wiley-VCH. Weinheim. 2000. Section 6.6.
68. (*a*) M. Bühl. Chem. Phys. Lett. **267**, 251 (1997); (*b*) N. Godbout, R. Havlin, R. Salzmann, P.G. Debrunner, and E. Oldfield. J. Phys. Chem. A, **102**, 2342 (1998); (*c*) N. Godbout and E. Oldfield. J. Am. Chem. Soc. **119**, 8065 (1997).
69. F. Jensen. Introduction to computational chemistry. John Wiley and Sons, Chichester. 2001. Chap 8.
70. U. Fleischer, C. van Wüllen, and W. Kutzelnigg. NMR chemical shift computation: Ab initio. *In* Encyclopedia of computational chemisty. *Edited by* P. Schleyer. John Wiley and Sons, Chichester. 1998. p. 1827.
71. K. Balasubramanian. Relativistic effective core potential techniques for molecules containing very heavy atoms. *In* Encyclopedia of computational chemistry. *Edited by* P. Schleyer. John Wiley and Sons, Chichester. 1998. p. 1835.
72. W. Koch and M.C. Holthausen. A chemists guide to density functional theory. Wiley-VCH. Weinheim. 2000. Section 11.2.
73. R. Bouten, E.J. Baerends, E. van Lenthe, L. Visscher, G.

© 2003 NRC Canada

Schreckenbach, and T. Ziegler. J. Phys. Chem. A, **104**, 5600 (2000).
74. J. Autschbach and T. Ziegler. Relativistic computation of NMR shieldings and spin-spin coupling constants. *In* Encyclopedia of nuclear magnetic resonance. Vol. 9. *Edited by* D.M. Grant and R.K. Harris. John Wiley and Sons Ltd., New York. 2002. p. 306.
75. E. van Lenthe, E.J. Baerends, and J.G. Snijders. J. Chem. Phys. **99**, 4597 (1993).
76. (*a*) E. van Lenthe, E.J. Baerends, and J.G. Snijders. J. Chem. Phys. **101**, 9783 (1994); (*b*) E. van Lenthe, A. Ehlers, and E.J. Baerends. J. Chem. Phys. **110**, 8943 (1999); (*c*) E. van Lenthe, J.G. Snijders, and E.J. Baerends. J. Chem. Phys. **105**, 6505 (1996); (*d*) E. van Lenthe, R. van Leeuwen, E.J. Baerends, and J.G. Snijders. Int. J. Quantum Chem. **57**, 281 (1996).
77. (*a*) R. Ditchfield. Mol. Phys. **27**, 789 (1974); (*b*) K. Wolinski, J.F. Hinton, and P. Pulay. J. Am. Chem. Soc. **112**, 8251 (1990); (*c*) G. Rauhut, S. Puyear, K. Wolinski, and P. Pulay. J. Phys. Chem. **100**, 6310 (1996); (*d*) P. Pulay and J.F. Hinton. Shielding theory: GIAO method. *In* Encyclopedia of nuclear magnetic resonance. *Edited by* D.M. Grant and R.K. Harris. John Wiley and Sons Ltd., New York. 1996. p. 4334.
78. M.J. Frisch, G.W. Trucks, H.B. Schlegel, G.E. Scuseria, M.A. Robb, J.R. Cheeseman, V.G. Zakrzewski, J.A. Montgomery, Jr., R.E. Stratmann, J.C. Burant, S. Dapprich, J.M. Millam, A.D. Daniels, K.N. Kudin, M.C. Strain, O. Farkas, J. Tomasi, V. Barone, M. Cossi, R. Cammi, B. Mennucci, C. Pomelli, C. Adamo, S. Clifford, J. Ochterski, G.A. Petersson, P.Y. Ayala, Q. Cui, K. Morokuma, D.K. Malick, A.D. Rabuck, K. Raghavachari, J.B. Foresman, J. Cioslowski, J.V. Ortiz, B.B. Stefanov, G. Liu, A. Liashenko, P. Piskorz, I. Komaromi, R. Gomperts, R.L. Martin, D.J. Fox, T. Keith, M.A. Al-Laham, C.Y. Peng, A. Nanayakkara, C. Gonzalez, M. Challacombe, P.M.W. Gill, B. Johnson, W. Chen, M.W. Wong, J.L. Andres, C. Gonzalez, M. Head-Gordon, E.S. Replogle, and J.A. Pople. Gaussian 98. Revision A.4. Gaussian, Inc., Pittsburgh PA, 1998.
79. (*a*) G. Schreckenbach and T. Ziegler. J. Phys. Chem. **99**, 606 (1995); (*b*) G. Schreckenbach and T. Ziegler. Int. J. Quantum Chem. **60**, 753 (1996); (*c*) G. Schreckenbach and T. Ziegler. Int. J. Quantum Chem. **61**, 899 (1997); (*d*) S.K. Wolff and T. Ziegler. J. Chem. Phys. **109**, 895 (1998); (*e*) S.K. Wolff, T. Ziegler, E. van Lenthe, and E.J. Baerends. J. Chem. Phys. **110**, 7689 (1999).
80. (*a*) C.F. Guerra, J.G. Snijders, G. te Velde, and E.J. Baerends. Theor. Chem. Acc. **99**, 391 (1998); (*b*) ADF 2000.02, 2002.01, 2002.02, SCM [online]. Theoretical Chemistry, Vrije Universiteit, Amsterdam, The Netherlands. Available from http://www.scm.com [cited 10 July 2002].
81. S.H. Vosko, L. Wilk, and M. Nusair. Can. J. Phys. **58**, 1200 (1980).
82. A.D. Becke. Phys. Rev. A, **38**, 3098 (1988).
83. (*a*) J.P. Perdew. Phys. Rev. B, **33**, 8822 (1986); (*b*) J.P. Perdew. Phys. Rev. B, **34**, 7406 (1986).
84. K.J. Lee and T.L. Brown. Inorg. Chem. **31**, 289 (1992).
85. J.H. Wosnick, F.G. Morin, and D.F.R. Gilson. Can. J. Chem. **76**, 1280 (1998).
86. S. Affandi, J.H. Nelson, N.W. Alcock, O.W. Howarth, E.C. Alyea, and G.M. Sheldrick. Organometallics, **7**, 1724 (1988).
87. K. Eichele, R.E. Wasylishen, J.M. Kessler, L. Solujić, and J.H. Nelson. Inorg. Chem. **35**, 3904 (1996).
88. Y. Huang, H.L. Uhm, D.F.R. Gilson, and I.S. Butler. Inorg. Chem. **36**, 435 (1997).
89. M.S. Davies, M.J. Aroney, I.E. Buys, T.W. Hambley, and J.L. Calvert. Inorg. Chem. **34**, 330 (1995).
90. F.A. Cotton, D.J. Darensbourg, and B.W.S. Kolthammer. Inorg. Chem. **20**, 4440 (1981).
91. M.J. Bennett and P.B. Donaldson. Inorg. Chem. **16**, 655 (1977).
92. A. Naito, D.L. Sastry, and C.A. McDowell. Chem. Phys. Lett. **115**, 19 (1985).
93. N.J. Taylor, G.N. Mott, and A.J. Carty. Inorg. Chem. **19**, 560 (1980).
94. A.J. Carty, C.A. Fyfe, M. Lettinga, S. Johnson, and L.H. Randall. Inorg. Chem. **28**, 4120 (1989).
95. A.A. Cherkas, L.H. Randall, S.A. MacLaughlin, G.N. Mott, N.J. Taylor, and A.J. Carty. Organometallics, **7**, 969 (1988).
96. A.A. Cherkas. Ph.D. dissertation. Department of Chemistry. University of Waterloo. 1989.
97. L.M. Bullock, J.S. Field, R.J. Haines, E. Minshall, M.H. Moore, F. Mulla, D.N. Smit, and L.M. Steer. J. Organomet. Chem. **381**, 429 (1990).
98. S.A. MacLaughlin, A.J. Carty, and N.J. Taylor. Can. J. Chem. **60**, 87 (1982).
99. G. Hogarth, J.A. Phillips, F. Van Gastel, N.J. Taylor, T.B. Marder, and A.J. Carty. J. Chem. Soc. Chem. Commun. 1570 (1988).
100. C.E. Laplaza, W.M. Davis, and C.C. Cummins. Angew. Chem. Int. Ed. Engl. **34**, 2042 (1995).
101. G. Wu, D. Rovnyak, M.J.A. Johnson, N.C. Zanetti, D.G. Musaev, K. Morokuma, R.R. Schrock, R.G. Griffin, and C.C. Cummins. J. Am. Chem. Soc. **118**, 10 654 (1996).
102. A.A. Cherkas, J.F. Corrigan, S. Doherty, S.A. MacLaughlin, F. van Gastel, N.J. Taylor, and A.J. Carty. Inorg. Chem. **32**, 1662 (1993).
103. K. Eichele, R.E. Wasylishen, J.F. Corrigan, N.J. Taylor, and A.J. Carty. J. Am. Chem. Soc. **117**, 6961 (1995).
104. G.A. Jeffrey, J.R. Ruble, R.K. McMullan, and J.A. Pople. Proc. R. Soc. Lond. A, **414**, 47 (1987). p. 3612.
105. K. Karaghiosoff. Phosphorus-31 NMR. *In* Encyclopedia of nuclear magnetic resonance. *Edited by* D.M. Grant and R.K. Harris. John Wiley and Sons Ltd., New York. 1996. p. 3612.
106. (*a*) C.J. Jameson. Bull. Magn. Reson. **3**, 3 (1980); (*b*) F.H.A. Rummens. *In* NMR basic principles and progress. Vol. 10. *Edited by* P. Diehl, E. Fluck, and R. Kosfeld. Springer-Verlag, Berlin. 1975. p. 1.
107. C.J. Jameson, A.K. Jameson, D. Oppusunggu, and S. Wille. J. Chem. Phys. **76**, 152 (1982).
108. A.J. Carty, S.A. MacLaughlin, and D. Nucciarone. *In* Methods in stereochemical analysis 8. *Edited by* J.G. Verkade and L.D. Quin. VCH Publishers Inc., Deerfield Beach. 1987. p. 559.
109. M. Bühl. NMR chemical shift computation: Structural applications. *In* Encyclopedia of computational chemisty. *Edited by* P. Schleyer. John Wiley and Sons, Chichester. 1998. p. 1835.
110. P. Avalle, R.K Harris, and R.D. Fischer. Phys. Chem. Chem. Phys. **4**, 3558 (2002).
111. S. Patchkovskii and T. Ziegler. J. Phys. Chem. A, **106**, 1088 (2002).
112. V.V. Rossikhin, S.I. Okovytyy, L.I. Kasyan, E.O. Voronkov, L.K. Umrikhina, and J. Leszczynski. J. Phys. Chem. A, **106**, 4176 (2002).

© 2003 NRC Canada

Appendix A: Investigation of basis set performance.

To investigate the effectiveness and efficiency of various locally dense (A1) basis set combinations with the RHF and B3LYP methods, a series of calculations was performed on $Ru_2(CO)_6(u_2\text{-}PPh_2)_2$ (**13**). Results are summarized in Fig. 3.[5] This compound is a typical phosphido-bridging, transition-metal carbonyl complex with $\delta_{iso}(^{31}P)$ = 114 ppm (σ_{iso} = 214 ppm) and Ω = 308 ppm (A2). The basis sets for the phosphorus and directly bonded nuclei were varied in each calculation, while the LANL2DZ RECP (A3) was used for transition metals, and 3-21G was employed for the remainder of the molecule. The RHF method, with the small 3-21G basis set, does not reproduce experimental isotropic values (Fig. 3*a*). A significant improvement is noted upon use of a double-ζ quality basis set (cc-pVDZ or 6-31G(d)), but inclusion of diffuse functions yields no greater accuracy for the increased computational requirement. The RHF results appear to converge to the experimental values of the ^{31}P CS tensor principal components upon addition of a third outer valence function and the inclusion of diffuse functions and a single polarization function (6-311+G(d)). The addition of a second polarization function yields calculated values that effectively reproduce experimental data. As depicted in Fig. 3*b*, the B3LYP functional reproduces experimental values of the principal components of the ^{31}P magnetic shielding tensor in **13** with only a singly polarized double-ζ quality basis set. The basis set dependence is similar to that of the RHF method, except that the values obtained with the B3LYP method are deshielded; use of a triple-ζ basis set with the B3LYP functional provides results that are deshielded on the order of 100 ppm relative to experiment and RHF results. However, calculations employing the quadruple-ζ basis set cc-pVQZ begin to approach the experimental values. In general, the addition of polarization functions had a deshielding effect with both the RHF and B3LYP methods. Based on these results, RHF and B3LYP calculations were performed for **1**–**17**, employing the 6-31G(d) or 6-311+G(2d) diffuse basis set for phosphorus and directly bonded atoms.

ZORA-DFT calculations were performed for compound **13**, employing the full potential Slater-type ZORA (II), (IV), and (V) relativistic basis sets, as well as numerous locally dense combinations. The notation used for indication of locally dense basis sets is as follows: ZORA (I/V) signifies the ZORA (V) basis set for metallic centres, phosphorus, and directly bonded atoms and the ZORA (I) basis set for the remainder of the molecule. Calculations for **13** indicate that the use of locally dense basis sets for relativistic ZORA-DFT calculations yield similar data to those obtained through the use of uniform basis sets (Fig. 3*c*).[6] The largest discrepancy for the isotropic magnetic shielding was observed for the ZORA (I/IV) combination relative to the ZORA (IV) results (+9 ppm). In most cases, σ_{11} (except for ZORA (I/V)) is deshielded, while σ_{22} and σ_{33} (except for ZORA (III/IV)) are shielded relative to the results obtained from use of the larger basis set only. Upon use of a locally dense basis set the span increased 9 ppm on average. The use of locally dense basis sets substantially reduces the required computational time; the ZORA (I/V) calculation required approximately one fifth the time of the ZORA (V) calculation. For efficiency, when a triple-ζ level of theory with the ZORA-DFT method is desired, with little compromise to the results of the calculation, the use of locally dense basis sets is highly recommended for magnetic shielding calculations.

References

A1. (*a*) D.B. Chesnut and K.D. Moore. J. Comp. Chem. **10**, 648 (1989); (*b*) D.B. Chesnut, B.E. Rusiloski, K.D. Moore, and D.A. Egolf. J. Comp. Chem. **14**, 1364 (1993); (*c*) D.B. Chesnut and E.F.C. Byrd. Chem. Phys. **213**, 153 (1996).

A2. K. Eichele, R.E. Wasylishen, J.F. Corrigan, N.J. Taylor, A.J. Carty, K.W. Feindel, and G.M. Bernard. J. Am. Chem. Soc. **124**, 1541 (2002).

A3. (*a*) W.R. Wadt and P.J. Hay. J. Chem. Phys. **82**, 284 (1985); (*b*) J.V. Ortiz, P.J. Hay, and R.L. Martin. J. Am. Chem. Soc. **114**, 2736 (1992).

[5] Numeric data are available in Supplementary Table D2.
[6] Numeric data are available in Supplementary Table D1.

© 2003 NRC Canada

Inclusion complexation involving sugar-containing species: β-cyclodextrin and sugar surfactants

Vincent C. Reinsborough and Vanessa C. Stephenson

Abstract: Surface tension, proton NMR, and computer modeling studies were undertaken in nonionic alkylpolyglycoside (APG) solutions containing β-cyclodextrin (β-CD) with a view to characterize the inclusion complexes formed and to determine if the sugar entities of the host and guest molecules played a significant role in the process. The APGs investigated were four glucopyranosides (octyl G8, decyl G10, dodecyl G12, tetradecyl G14) and two maltosides (decyl M10, dodecyl M12). Critical micelle concentrations (CMC) were obtained in the surfactant–β-CD systems, which in all cases increased with increasing β-CD concentration. The 1:1 APG–β-CD inclusion complex was principally formed with binding constants of 425 (mol $L^{-1})^{-1}$ for the G12 complex, 340 (mol $L^{-1})^{-1}$ for the G10 complex, and 125 (mol $L^{-1})^{-1}$ for the M12 complex. The preferred configuration of the G-12–β-CD complex has the surfactant tail coiled in the CD cavity with the surfactant sugar moiety sealing off the narrower opening of the CD torus.

Key words: alkylpolyglycoside, β-cyclodextrin, NMR, critical micelle concentration, surface tension.

Résumé : Afin de caractériser les complexes d'inclusion qui se forment et pour déterminer si les sucres des molécules hôtes et invitées jouent un rôle significatif dans le processus, on a entrepris des études de tension superficielle, de RMN du proton et de modélisation moléculaire de solutions de polyglucosides d'alkyle non ioniques (PGA) contenant de la β-cyclodextrine (β-CD). Les PGA étudiés sont quatre glucopyranosides (d'octyle G8, de décyle G10, de dodécyle G12 et de tétradécyle G14) et deux maltosides (de décyle M10 et de dodécyle M12). On a déterminé les concentrations micellaires critiques (CMC) dans les systèmes agent de surface–β-CD qui augmentent dans tous les cas avec une augmentation de la concentration de β-CD. Le complexe d'inclusion principal est le PGA–β-CD 1:1 avec le G12 (constante de fixation = 425 (mol $L^{-1})^{-1}$), le G10 (constante de fixation = 340 (mol $L^{-1})^{-1}$) et le M12 (constante de fixation = 125 (mol $L^{-1})^{-1}$). Dans la configuration privilégiée par le complexe G1–β-CD, la queue de la chaîne de l'agent de surface est repliée dans la cavité de la CD alors que la portion sucrée de l'agent de surface ferme l'ouverture moins large du tore de la CD.

Mots clés : polyglycoside d'alkyle, β-cyclodextrine, RMN, concentration micellaire critique, tension superficielle. .

[Traduit par la Rédaction]

Introduction

Cyclodextrins are cyclical sugars composed of α-D-glucopyranose units bound end-on-end, which can incorporate within their cavities molecules of the correct fit and hydrophobicity in solution or in solid form (1, 2). The complexes thus formed find a wide range of uses in pharmaceutical (3), industrial (4), and reaction chemistry (5, 6). Because of its relatively low cost, high purity, and snug accommodation of a large number of common guest molecular moieties — notably the phenyl group — in primarily 1:1 complexes, the most common cyclodextrin investigated has been β-cyclodextrin (β-CD), which consists of seven end-on-end, interconnected glucose residues.

Surfactants are particularly strongly complexed by β-cyclodextrin, with the hydrophobic hydrocarbon chain tail usually enfolded within the cavity. A particular group of surfactants that is of current interest is the nonionic alkylpolyglycosides (APGs), which consist of hydrocarbon chains attached to sugar groups (Fig. 1). APGs are often termed "green" detergents because they environmentally degrade relatively innocuously (7). When β-CD and an APG form complexes, it is of some interest what influence the sugar–sugar interaction has upon the inclusion process and structure. The usual surfactant–CD situation finds the surfactant head situated in the mouth of the cyclodextrin torus, with the principal interaction in the complex being that between the included surfactant tail and the inside of the β-CD torus (Fig. 2). Binding constants determined through proton NMR and critical micelle concentrations (CMC) determined through surface tension can provide valuable insights into this situation. In this report, computer modelling has been coupled with the results of the foregoing investigations to obtain a more detailed picture of the positioning of the surfactant within the CD torus.

Received 2 July 2003. Published on the NRC Research Press Web site at http://canjchem.nrc.ca on 28 November 2003.

V.C. Reinsborough[1] and V.C. Stephenson. Department of Chemistry, Mount Allison University, Sackville, NB E4L 1G8, Canada.

[1]Corresponding author (e-mail: vcreinsb@mta.ca).

Experimental

Surface tensions of the surfactant solutions were obtained by the duNouy platinum ring suspension method. Calibration of the instrument was performed with distilled,

 doi: 10.1139/V03-180 © 2003 NRC Canada

Fig. 1. Alkylpolyglycoside (APG), where m = 1 (glucopyranoside) or 2 (maltoside) and n = 6–12.

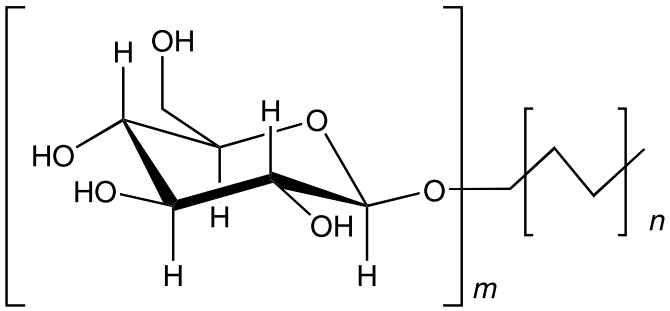
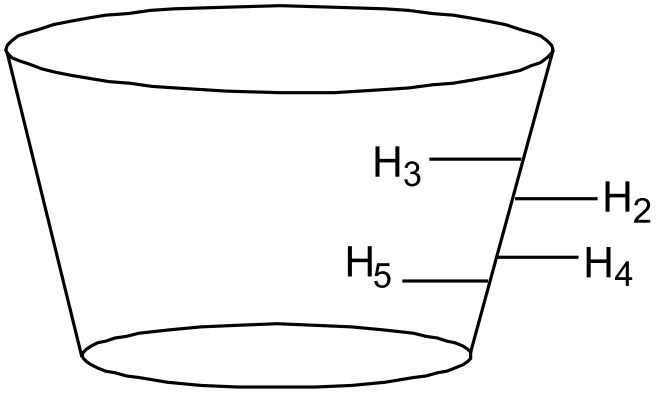


Fig. 2. Cyclodextrin (CD) torus with locations of particular H atoms important to NMR.



deionized water, using the value of 72.6 dyne cm^{-1} (1 dyne = 10 μN) as the surface tension of pure water. In each surfactant system, β-CD concentrations of 0.25, 0.50, 0.75, 1.0, 1.5, and 2.0 mmol L^{-1} were used to obtain the surface tension data. The critical micelle concentration (CMC) for each system was determined in the normal manner, as the intersection of the surface tension vs. log[surfactant] plot (Fig. 3).

Proton NMR data for the surfactant–β-CD systems were collected on a JEOL 270 MHz spectrometer. Of particular interest were the peak shifts of the H_3 and H_5 protons located on the interior wall of the β-CD torus (Fig. 2). Surfactant addition resulted in these peaks being shifted upfield while the exterior H_2 and H_4 peaks were unaffected. With surfactants G8 and M10 (see below), interference from surfactant peaks rendered the assignment of the β-CD H_3 and H_5 peaks problematic, a situation commonly encountered with β-CD inclusion complexes (8). Association constants for complex formation between β-CD and surfactant (K_a) were obtained by the NMR titration technique (9, 10), whereby surfactant was added incrementally to β-CD solutions and the peak shifts of either the β-CD H_3 or H_5 protons were noted until no further change occurred (Fig. 4).

Molecular mechanics studies were undertaken to decide the most favourable orientation of the sugar surfactant G12 within the CD torus upon complexation. Systems were modeled using the PC Spartan Pro Computational Program via the MMFF94 force field while employing solvation parameters available in the program. Initial attempts to model the β-CD molecule foundered because the torus folded in on itself on energy minimization, owing, in part, to the solvation model. Crystallographic data were obtained from K.B. Lipkowitz (Indiana University, Purdue University, U.S.A.), and dihedral angles of the core structure were fixed so as to allow the bond lengths and angles of the core to vary while keeping its cyclic shape during geometry optimizations. This approach proved very successful.

Table 1. CMC values for pure alkylpolyglycosides in water at 25 °C.

Sugar surfactant	CMC (mM) – this work	CMC (mM) – literature values
G12	0.16	0.12 (11), 0.13 (12), 0.14 (13)
G10	2.0	1.99 (11), 2.0 (14), 2–3 (15), 4.2 (13)
G8	17	17.4 (16), 20–25 (15), 25 (17), 25.4 (13)
M14	0.012	—
M12	0.15	0.14 (13), 0.15 (18), 0.16 (11, 16, 17, 19), 0.1–0.6 (15), 0.2 (14)
M10	1.8	1.4 (13), 1.6 (14), 3.23 (11).

The sugar surfactants used were octyl-β-D-glucopyranoside (G8), decyl-β-D-glucopyranoside (G10), dodecyl-β-D-glucopyranoside (G12), tetradecyl-β-D-glucopyranoside (G14), decyl-β-D-maltoside (M10), and dodecyl-β-D-maltoside (M12). All were purchased from Fluka, except for G8 (Sigma) and G14 (Sigma). β-CD was obtained from Aldrich and dried in vacuo at room temperature before use. All chemicals were supplied as 98%–99% purity and were not further treated.

Results and discussion

The CMC values for the pure alkylpolyglycosides, as determined by surface tension at 25 °C, are shown in Table 1, together with the corresponding literature values. The usual observation with surfactants that possess hydrocarbon tails — that a decrease of two carbons in the tail results in an increase of an order of magnitude in the CMC value — appears to hold with the alkylpolyglycosides. Adding β-CD to sugar surfactant solutions always brought about an increase in the CMC, which is not unexpected because of the competing β-CD–surfactant complexation equilibrium (Figs. 5 and 6) thus introduced. Determination of the CMC of short-chained surfactants such as G8 is fraught with more error because of the greater instability of the micelle, viz. Fig. 5. It is of interest that, in all the systems investigated, subtracting the surfactant concentration from the CMC value reproduced approximately the CMC value of the pure surfactant. This argues for a 1:1 complexation as the principal interaction that occurs between the surfactant and the non-surface-active cyclodextrin.

Association constants, determined by NMR analysis, for the binding of β-CD and G12 (undertaken in 2.0 and 1.0 mmol L^{-1} β-CD) were in reasonable agreement at 440 ± 40 (mol $L^{-1})^{-1}$ and 410 ± 40 (mol $L^{-1})^{-1}$, respectively, when the ring interior H_5 proton peak shift was followed. For G10 and M12, when the chemical shifts for the same peak were used, association constants of 340 ± 30 (mol $L^{-1})^{-1}$ and

© 2003 NRC Canada

Fig. 3. Surface tension of G12 solutions.

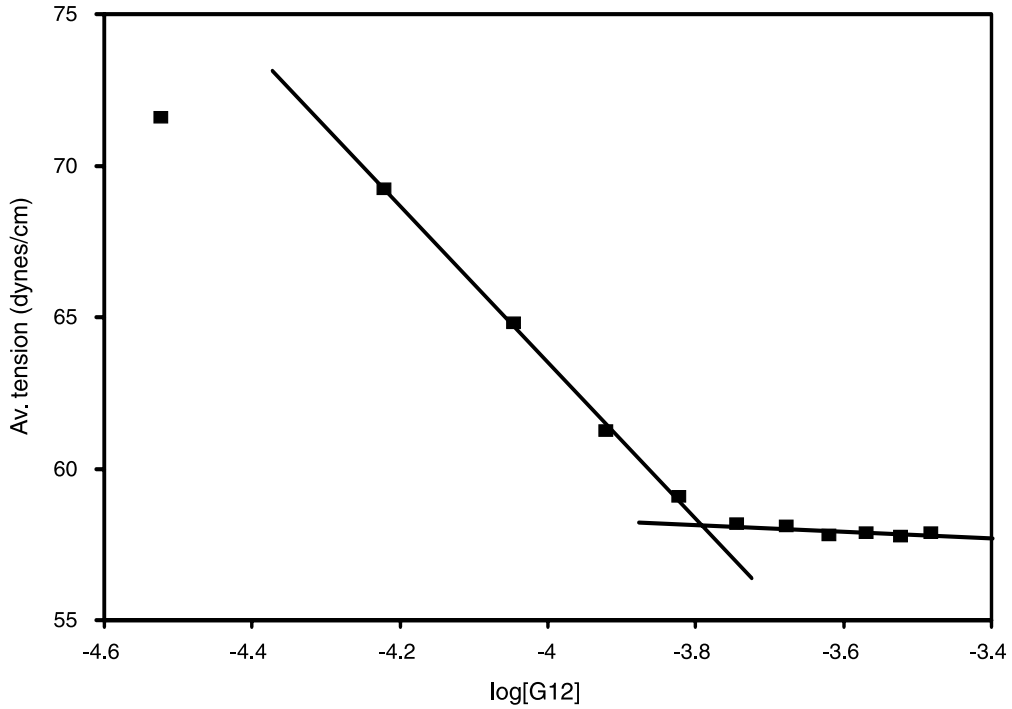
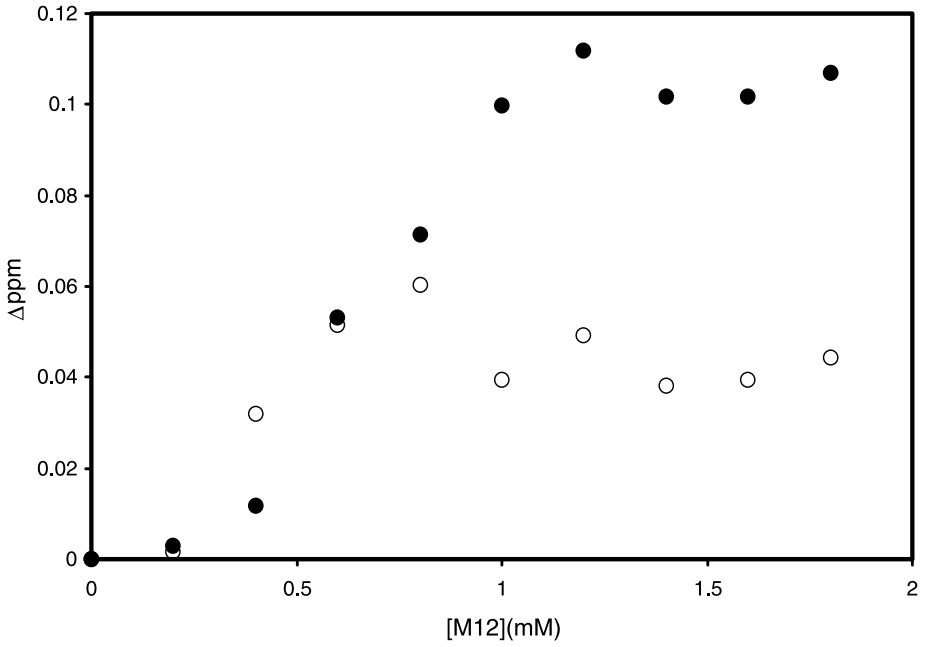


Fig. 4. NMR peak shifts of the H_3 and H_5 atoms of the inner torus of β-CD in 1.0 mmol L^{-1} β-CD solution with M12 addition.



125 ± 10 (mol L^{-1})$^{-1}$, respectively, were obtained in 1.0 mmol L^{-1} β-CD. The ring interior H_3 proton peak shifts gave inconsistent results, possibly due to signal interference from surfactant protons. Lengthening the surfactant hydrocarbon chain increases the binding strength, as is generally found with cyclodextrin–surfactant complexations. This is consistent with the surfactant tail residing in the hydrophobic CD cavity in the complex formed. A comparison of the binding constants for G12 and M12 indicates that the extra sugar moiety in the M12 surfactant head decreases the strength of the β-CD complex. The negative effect on the binding generated by the second sugar molecule points to no significant sugar–sugar interaction being involved in the binding; therefore, the surfactant head is not in the CD cavity in the complex but is likely in the mouth of the cavity where water–sugar interactions predominate. Also, the observation that the NMR peak shifts reached a plateau at 1 and 2 mmol L^{-1} surfactant in the 1.0 and 2.0 mmol L^{-1} β-CD systems, respectively, supported the CMC results that allowed us to assign a 1:1 stoichiometry to the principal com-

© 2003 NRC Canada

Fig. 5. Dependence of CMC of alkylglucopyranosides on β-CD concentration: G8, ▲; G10, ●; G12, ○.

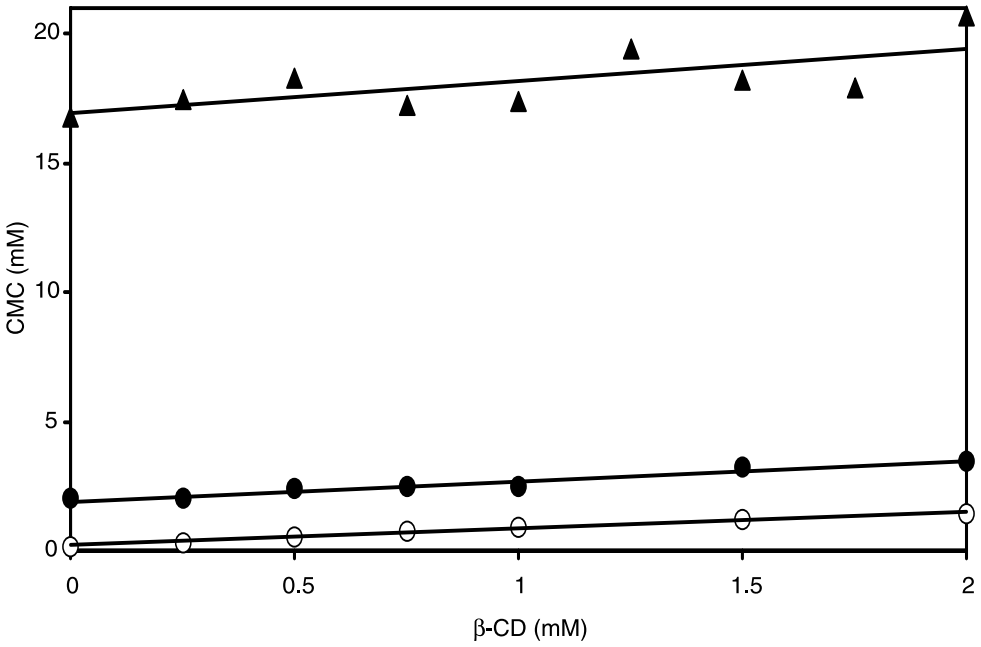
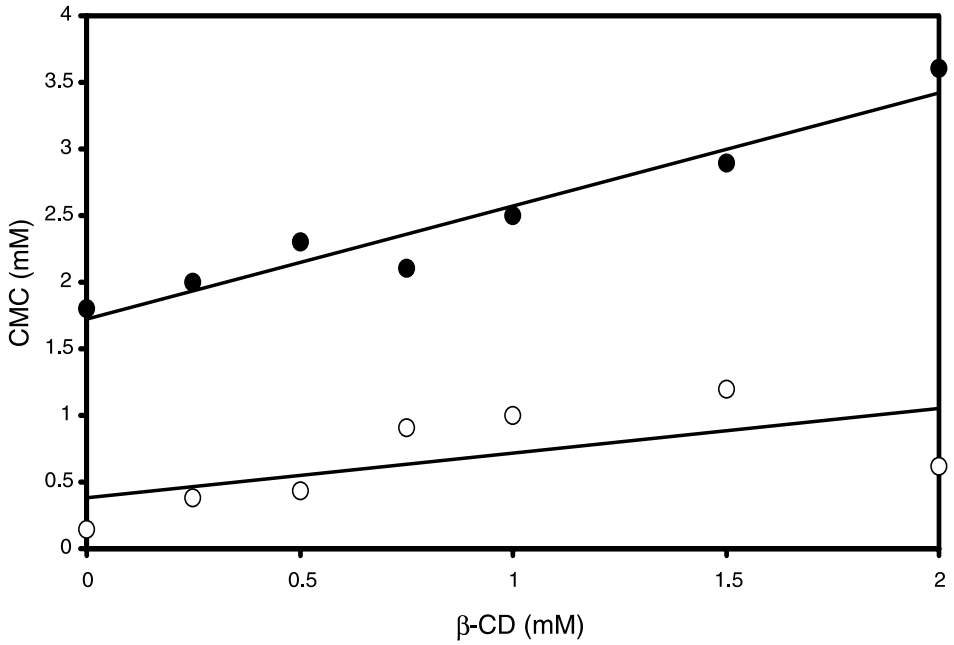


Fig. 6. Dependence of CMC of alkylmaltosides on β-CD concentration: M10, ●; M12, ○.

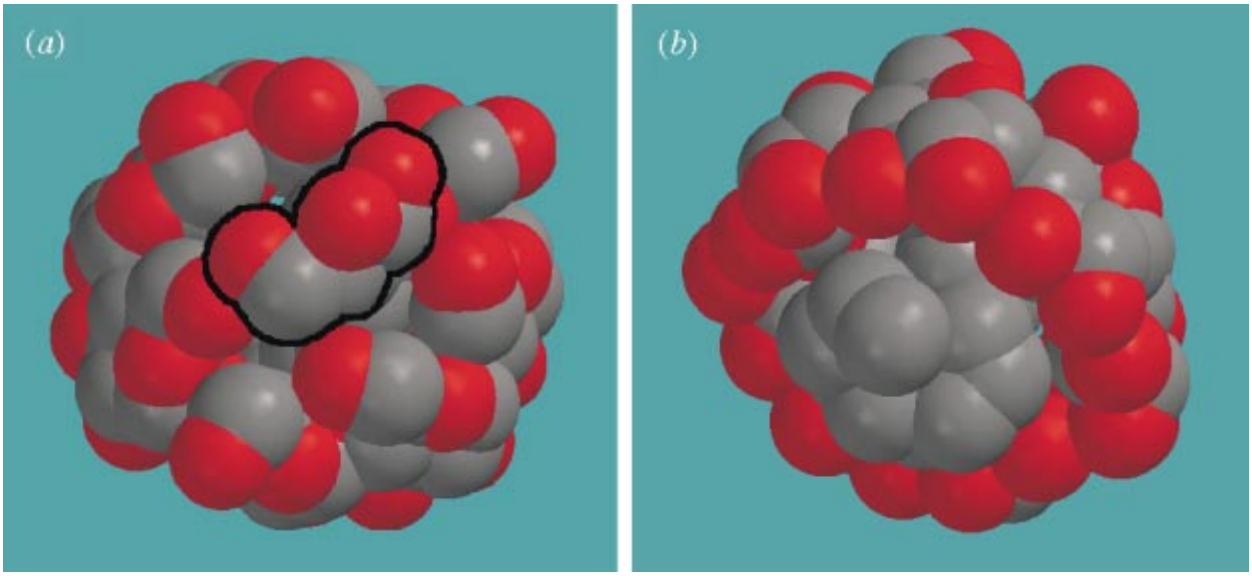


plex being formed. The magnitudes of the binding constants are consistent with binding constants of other β-CD complexes with surfactants with 10–12 carbon atoms in the hydrocarbon tail (8).

Having the surfactant head located in the narrower rather than the wider opening of the β-CD torus led to a more stable structure by roughly 196 kJ mol^{-1} when computational calculations were performed on 10 various conformers of the 1:1 β-CD–G12 complex. In each of the optimized conformers, the sugar head-group remained in its boat conformation and oriented itself in such a fashion as to maximize the number of hydrogen bonds to the hydroxyl groups lining the rim of the CD cavity. The advantage of the narrower CD opening is that it possesses freely rotating primary hydroxyl groups, which leads to extra hydrogen bonding possibilities. Hydrophobic forces also play a significant role, as the surfactant tail bends and folds into the wider opening of the CD cavity. In the lowest energy conformer found, the coiled tail resides in the cavity with the sugar moiety of the surfactant, blocking completely the narrower CD entrance (Fig. 7). Even though the calculations were conducted only for the β-CD–G12 complex, the situation with G10 and G8 is expected to be similar. Modeling the maltosyl surfactants, M14, M12, and M10, even at an elementary level, is more

© 2003 NRC Canada

Fig. 7. Space-filled model showing (*a*) the G12 sugar head-group in its snug conformation within the narrow β-CD opening and, in a view from the opposite side of the complex, (*b*) the coiled hydrocarbon tail of G12 tucked into the wider β-CD opening. The hydrogen atoms have been omitted to assist in viewing. The carbon atoms are shown in grey while the oxygen atoms are in red.



difficult and was not attempted. However, simple steric considerations suggest that the structure of the 1:1 complexes of these sugar surfactants with β-CD would be similarly disposed. With the narrower cavity of the α-CD molecule and the wider cavity of the γ-CD molecule, as compared with the β-CD molecule, the stereochemical fit of the sugar moiety in both these complexes would likely be less snug, giving rise to lower binding constants, unless a compensatory shift in the insertion position were to occur within the cavity. It would be of interest to pursue these studies, to delineate further the CD inclusion process.

Conclusion

Sugar surfactants form stable 1:1 complexes with β-CD in which the coiled surfactant occupies the CD cavity with the sugar head-group occupying, snugly, the narrower CD opening.

Acknowledgment

Funding for this research was provided by the Natural Sciences and Engineering Research Council of Canada (NSERC). Thanks are owing also to S.D. Wetmore (Mount Allison University) and K.P. Lipkowitz (Indiana University – Purdue University) for assistance with the molecular mechanics calculations.

References

1. R.J. Clarke, J.H. Coates, and S.F. Lincoln. Adv. Carbohydr. Chem. **46**, 205 (1988).
2. J. Szejtli. Chem. Rev. **98**, 1743 (1998).
3. K.-H. Frömming and J. Szejtli. *In* Cyclodextrins in pharmacy. Kluwer, Dordrecht, Netherlands. 1994.
4. A.R. Hedges. Chem. Rev. **98**, 2035 (1998).
5. K. Takahashi. Chem. Rev. **98**, 2045 (1998).
6. W.S. Li, W.S. Chung, and I Chao. Chem. Eur. J. **9**, 951 (2003).
7. K. Hill, W. Rybinski, and G. Stoll. *In* Alkyl polyglycosides. VCH, Weinheim, Germany. 1996.
8. L.D. Wilson and R.E. Verrall. Can. J. Chem. **76**, 25 (1998).
9. Z.J. Tan, X.X. Zhu, and G.R. Brown. Langmuir, **10**, 1034 (1994).
10. R.E. Heath, G.M. Dykes, H. Fish, and D.K. Smith. Chem. Eur. J. **9**, 850 (2003).
11. M.L. Sierra and M. Svensson. Langmuir, **15,** 2301 (1999).
12. C.M. Deber and L.C. Hsu. Biochem. Biophys. Res. Commun. **134**, 731 (1986).
13. J.R. Casey and R.A.F. Reithmeier. Biochem. **32**, 1172 (1993).
14. R. Aveyard, B.P. Binks, J. Chen, J. Esquena, and P.D.I. Fletcher. Langmuir, **14**, 4699 (1998).
15. J. Neugebauer. *In* A guide to the properties and uses of detergents in biology and biochemistry. Calbiochem-Novabiochem Corp., La Jolla, Cal., U.S.A. 1988.
16. W. Kuehlbrandt. Quart. Rev. Biophys. **21**, 429 (1988).
17. L. Lebeau, F. Lach, C. Vénien-Bryan, A. Renault, J. Dietrich, T. Jahn, M.G. Palmgren, W. Kühlbrandt, and C.J. Mioskowski. J. Mol. Biol. **308**, 639 (2001).
18. C.J. Drummond, G.G. Warr, F. Grieser, B.W. Ninham, and D.F. Evans. J. Phys. Chem. **89**, 2103 (1985).
19. J.D. Hines, R.K. Thomas, P.R. Garrett, G.K. Rennie, and J. Penfold. J. Phys. Chem. B, **101**, 9216 (1997).

© 2003 NRC Canada

Azabenzenes (azines) — The nitrogen derivatives of benzene with one to six N atoms: Stability, homodesmotic stabilization energy, electron distribution, and magnetic ring current; a computational study

Jürgen Fabian and E. Lewars

Abstract: The twelve azabenzenes — the species formed by replacing CH groups of benzene by N — were examined computationally (with emphasis on the six contiguous-nitrogen species). MP2(fc)/6-31G*, B3LYP/6-31G*, CCSD(T)/6-31G*//MP2(fc)/6-31G*, and G3(MP2) calculations were used to probe kinetic and thermodynamic stabilities, homodesmotic ring-opening energies, electron distribution (bond orders and lengths, Bird index), and NICS values, primarily to discern where the transition occurs from reasonably stable to highly fragile species. Some azabenzenes with three and those with four or more nitrogens are thermodynamically unstable, but kinetic stabilities indicated that, with the possible exception of hexaazabenzene, all the azabenzenes should be isolable, although some with four nitrogens might decompose at room temperature, and pentaazabenzene would require matrix isolation techniques. Although homodesmotic ring-opening reactions showed an almost monotonic decrease in the stability of the cyclic relative to the open-chain species (in appropriate ring-opening reactions) on going from benzene to hexaazabenzene, bond-order variation and NICS suggested this may be because of increasing destabilization by nitrogen lone pairs rather than because of a decrease in electron delocalization (in aromaticity).

Key words: azines, azabenzenes, pentazine, hexazine, ab initio, DFT, aromaticity.

Résumé : On a fait des calculs théoriques sur douze azabenzènes, les espèces qui se forment en remplaçant des groupes CH du benzène par un N, en portant une attention spéciale aux espèces comportant des azotes contigus. On utilisé les calculs MP2(fc)6-31G*, B3LYP/6-31G*, CCSD(T)/6-31G*//MP2(fc)/6-31G* et G3(MP2) pour étudier les stabilités cinétiques et thermodynamiques, les énergies d'ouvertures de cycles homodesmotiques, les distributions d'électrons (ordres et longueurs des liaisons et indice de Bird) ainsi que les valeurs NICS, principalement pour déceler l'endroit où se produit la transition d'une espèce raisonnablement stable vers une qui est extrêmement fragile. Quelques azabenzènes comportant trois azotes et tous ceux qui en contiennent quatre ou plus sont thermodynamiquement instables; toutefois, les stabilités cinétiques indiquent que, à l'exception de l'hexaazabenzène, on devrait pouvoir isoler tous les azabenzènes même si quelques-uns de ceux qui contiennent quatre azotes pourraient se décomposer à la température ambiante et que pour le pentaazabenzène il faudrait probablement faire appel à des techniques d'isolation dans une matrice. Même si les réactions d'ouverture de cycle homodesmotiques présentent toutes une diminution monotone de la stabilité du cycle par rapport aux espèces en chaînes ouvertes (dans des réactions appropriées d'ouverture de cycle) lorsqu'on passe du benzène à l'hexaazabenzène, la variation dans l'ordre de liaison et dans les valeurs de NICS suggèrent que cette tendance pourrait être due à une augmentation de la déstabilisation par des doublets non appariés de l'azote plutôt qu'à une diminution dans la délocalisation électronique (dans l'aromaticité).

Mots clés : azines, azabenzènes, pentazine, hexazine, ab initio, DFT, aromaticité.

[Traduit par la Rédaction]

Introduction

General

This paper describes our computational study of the nitrogen analogues of benzene: the molecules formally derived from benzene (with which we compare them) by replacing CH groups by nitrogen atoms. Figures 1 and 2 show these molecules and the designations (**N0**, **N1**, etc.) that will be

Received 23 May 2003. Published on the NRC Research Press Web site at http://canjchem.nrc.ca on 9 December 2003.

J. Fabian. Institut für Organische Chemie, Technische Universität Dresden, Mommsenstrasse 13, D-01062 Dresden, Germany.
E. Lewars.[1,2] Department of Chemistry, Trent University, Peterborough, ON K9J 7B8, Canada.

[1]Adjunct Professor, Queen's University, Kingston, ON K7L 3N6, Canada.
[2]Corresponding author (e-mail: elewars@trentu.ca).

 doi: 10.1139/V03-178 © 2003 NRC Canada

used here for brevity, along with parameters that are discussed below. The species are conveniently divided into those with contiguous (1,2-, 1,2,3-, etc.) and noncontiguous (1,3-, 1,4-, etc.) nitrogens. It is convenient to take benzene as the first (**N0**) member of the contiguous-N class. The heterocycles can be named by replacement nomenclature as azabenzene, 1,2-diazabenzene, …, hexaazabenzene or by the less elegant Hantsch–Widman system as azines (i.e., azine, 1,2-diazene, …, hexazine) (1). The properties examined are (*i*) activation energies and reaction energies (i.e., kinetic and thermodynamic stabilities) for decomposition to stable two-heavy-atom triply bonded fragments, e.g., $N_6 \rightarrow 3N_2$; (*ii*) homodesmotic ring-opening, e.g., N_6 + 2 HN=NH $\rightarrow$ hexaazahexatriene + tetraazabutadiene; (*iii*) electron distribution, as indicated by bond order – bond length variation; (*iv*) ring-current effects, as indicated by calculated nucleus-independent chemical shifts (NICS).

There are at least four reasons why these compounds are interesting, namely: (*a*) any chemist with imagination must be intrigued by the possibility of obtaining an oligomeric version of a widespread element known so far only as a diatomic molecule. This would be realized in the molecule at the end of the replacement series, N_6; (*b*) benzene and pyridine (the **N0** and **N1** replacement members) are well-known, very stable substances, but hexaazabenzene is (as indicated so far only by computations) exceedingly unstable. One wonders where and why the transition to extreme instability occurs; (*c*) benzene and pyridine are unequivocally "aromatic" (2). It would be interesting to see if continued replacement of CH by N suppresses this (admittedly elusive) characteristic; (*d*) nitrogen oligomers have been considered as possible high-energy-density materials; their kinetic and thermodynamic stabilities are relevant to this (and to *a*, *b*, and, to some extent, *c*).

Our main objective was to examine the trends in properties as CH is replaced by N and to locate the point or region between highly stable molecules like benzene and pyridine and the unstable hexaazabenzene. For this reason, we concentrate on the N-contiguous species and discuss the noncontiguous ones somewhat peripherally.

Literature

All these heterocycles have been reviewed up to 1995 in the latest edition of the encyclopedia edited by Katritzky et al. (3). First, we briefly describe what is known *experimentally* about azabenzenes, then consider the computational literature.

Experimental literature

N0, N1

Benzene and pyridine are commercially important compounds known for almost two centuries (4).

N2

1,2-Diazabenzene (pyridazine) (5), 1,3-diazabenzene (pyrimidine) (6), and 1,4-diazabenzene (pyrazine) (7) are well-known, stable compounds, regarded as normal aromatic heterocycles. The 1,3-system is the motif of nucleic acid pyrimidine bases and, fused to a five-membered ring, of purine bases. The 1,4-system has long been well known (8) and is even found in natural products of potential utility (9).

N3

1,2,3-Triazabenzene was first made in 1981 and is, as expected from the known fragility of chains and rings with contiguous nitrogen atoms (10), the least stable triazabenzene, but it is still readily handled at room temperature (11). A colorless crystalline solid, it melts at 71 °C and decomposes at 130 °C to form mainly tar. The molecule is readily attacked by nucleophiles and undergoes Diels–Alder reactions with alkynes. 1,2,4-Triazabenzene has been known since 1966 (12). 1,3,5-Triazabenzene (cyanuric acid) was isolated in 1895, although the correct structure was not assigned till 1954 (13).

N4–N6

The systems with four to six nitrogens atoms are of more interest to theorists. 1,2,4,5-Tetraazabenzene is well known, having been made in 1900 (14). 1,2,3,4-Tetraazabenzene and 1,2,3,5-tetraazabenzene are unknown (15).

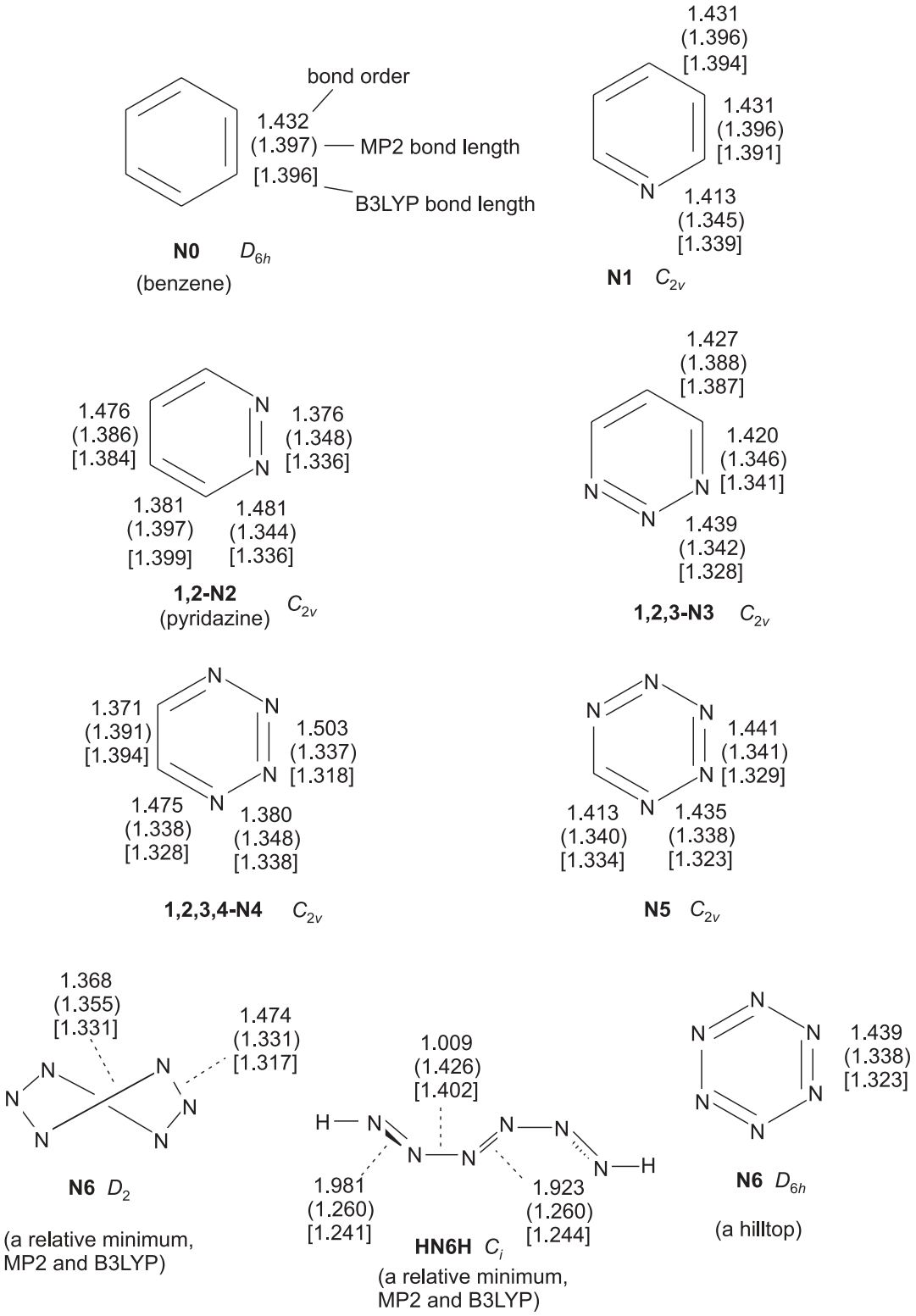
Pentaazabenzene (15) and hexaazabenzene (15) are unknown; there have been tentative speculations on the possible experimental generation of N_6 species by azide dimerization under electron pulse radiolysis (16), polarographic conditions (17), and the low-temperature photolysis of an azide-platinum complex (18).

Computational literature

Most of the computational literature on the azabenzenes is somewhat eclectic, in that few papers are devoted to just one compound or to a narrow group of compounds like, say, the N_2 or N_3 species. Therefore, we cannot review this literature in a strict nitrogen-sequential (i.e., N_1, N_2, …) order. There have been a few theoretical papers in which benzene and some or all of the azabenzenes were examined for one particular property (some of these papers are discussed below in connection with our investigation of the property; for example, aromaticity). Maksić et al. (19) investigated π-electron correlation energy and NICS in pyridine, **1,2-N2**, **1,2,3-N3**, and **1,2,4,5-N4**. Rauhut (20) reviewed computations on various heterocycles, mentioning, among the azabenzenes, the diaza- and triazabenzenes and the tetraazabenzenes **1,2,4,5-N4** and **1,2,3,4-N4**. Gambiagi et al. (21) investigated the aromaticity of the azabenzenes, subjecting AM1 geometries to PM3 calculations of a bond index that reflects electronic charge in bonds. Williams and Whitehead (22) used MNDO, AM1, PM3, and noncorrelated ab initio methods to calculate their heats of formation, while Doerksen and Thakkar (23) studied the polarizabilities of the N_3–N_6 members. Politzer and co-workers (24, 25) studied the electrostatic potentials and local ionization energies of some azabenzenes. Katritzky and Barczynski (26), in a study of the aromaticity of five- and six-membered heterocycles with the AM1 method and geometric, energetic, and magnetic criteria, examined **1,2,3-N3**, **1,2,4,5-N4**, and **1,2,3,4-N4** and concluded that the evidence was "that pyridine-like nitrogen atoms have relatively little effect on "classical" aromaticity". Sanz et al. (27) calculated the basicities of pyridine, the diazabenzenes, the triazabenzenes, and the tetraazabenzenes at the MNDO, AM1, and Hartree–Fock levels. A study by Wiberg et al.

© 2003 NRC Canada

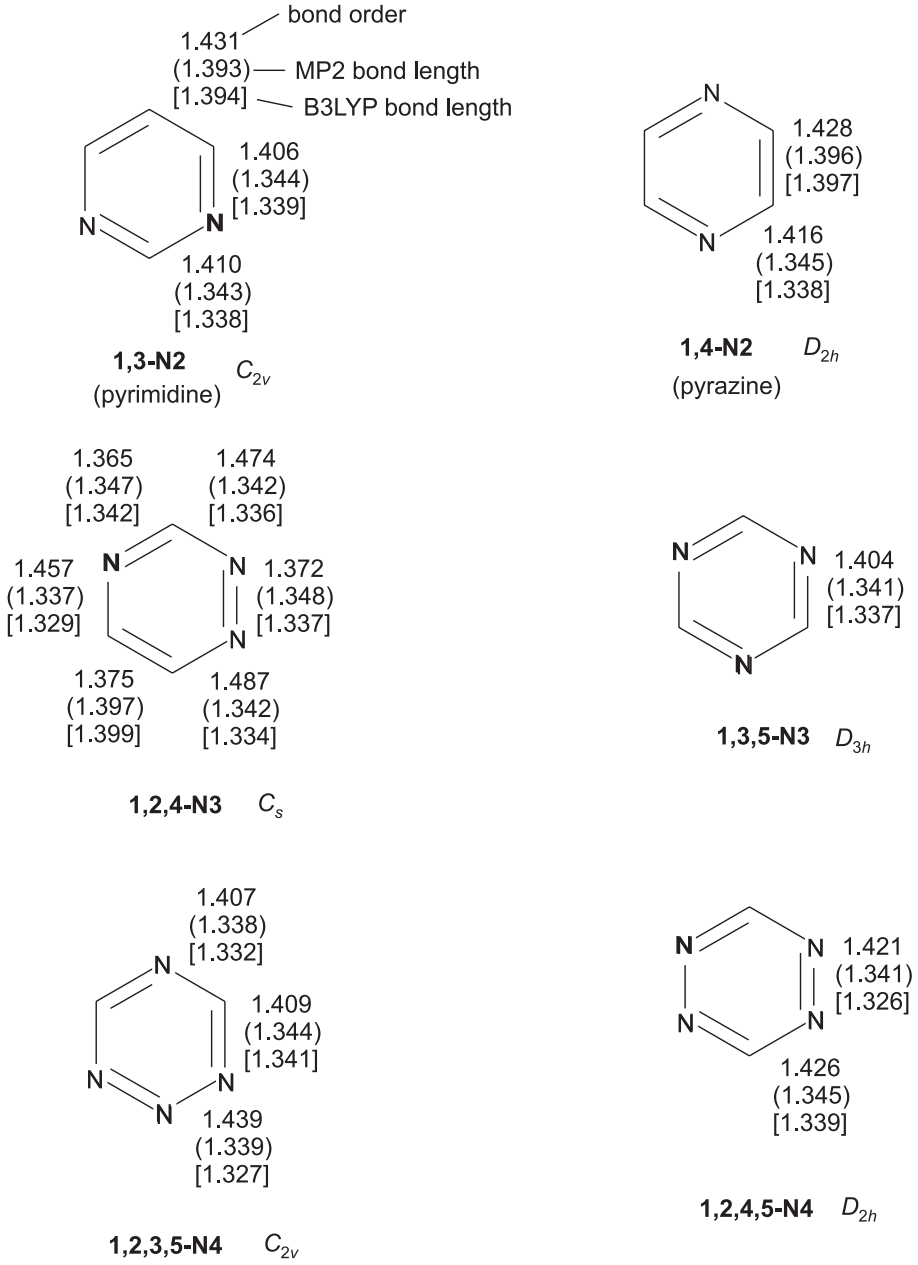
Fig. 1. The six azabenzenes with contiguous nitrogens; also, benzene and HN_6H. Bond orders are Wiberg bond orders from single-point HF/3-21G calculations on MP2(fc)/6-31G* geometries. Bond lengths (Å) are MP2(fc)/6-31G* and B3LYP/6-31G*.



(28) of benzene, pyridine, the diazabenzenes, **1,3,5-N3**, **1,2,4,5-N4**, and **N6** at the MP2 and MP3 levels examined experimental UV spectra and addressed the question of aromaticity with isodesmic-type and hydrogenation reactions and electron density calculations. The basicities and ionization energies of pyridine, the diazabenzenes, the

© 2003 NRC Canada

Fig. 2. The six azabenzenes with noncontiguous nitrogens. Bond orders are Wiberg bond orders from single-point HF/3-21G calculations on MP2(fc)/6-31G* geometries. Bond lengths (Å) are MP2(fc)/6-31G* and B3LYP/6-31G*.



triazabenzenes, and the tetraazabenzenes were investigated with the help of Hartree–Fock 6-31G* single-point calculations on lower-level geometries by Mó et al. (29). Fos et al. (30) compared the accuracy of MNDO and HF/4-31G calculations for the heats of formation of the N_2–N_4 azabenzenes.

In a pioneering study of hexaazabenzene, Saxe and Schaefer (31) briefly reviewed the experimental status of the entire azabenzene series and the computational work thus far on hexaazabenzene and reported their Hartree–Fock and preliminary correlated (configuration interaction) work, which predicted that planar (D_{6h}) hexaazabenzene is "a dimple on top of a mountain". They wisely qualified this whimsical but apt characterization with the caveat that the prediction "carries with it not a trace of infallibility". Early work by Engelke (32, 33) on hexaazabenzene and other nitrogen-rich species established that the planar (D_{6h}) species, although a relative minimum on the potential energy surface (PES) at the Hartree–Fock level, is a hilltop with correlated (MP2) calculations. Using correlated ab initio calculations, Glukhovtsev and Schleyer (34) compared hexaazabenzene to open-chain isomers and showed that the cyclic structure adopts a twisted (D_2) shape, and they used isodesmic-type reactions (below) to show that this is destabilized, rather than stabilized like benzene, with regard to ring-opening; these workers also commented on reports of the preparation of N_6 species and clarified some results for N_6 species reported by Engelke (33), Nguyen and co-workers (35–37), and Ramek (38). Simkin et al. (39), in a review of aroma-

© 2003 NRC Canada

ticity in connection with heterocycles, summarized work comparing the resonance energies of benzene, pyridine, the diazabenzenes, **1,3,5-N3**, **1,2,4,5-N4**, and **N6** and reviewed the role of σ-to-σ* electron transfer in **N6**.

Computational methods

Calculations were done with Gaussian 98 for Windows (G98W) (40) and visualized with GaussView 2.1 for Windows (41) on a 933 Pentium 3 or a 1.5 GHz Pentium 4 computer equipped with Microsoft Windows NT 4.00, 1 GB of memory, and 15 360 MB of scratch space. Ab initio (42) MP2 (frozen-core, MP2(fc)) and DFT (43) B3LYP calculations were full geometry optimizations followed by frequency calculations (44). Zero-point energies (ZPEs) from the frequency jobs were multiplied by the appropriate correction factors (0.9670 for MP2(fc)/6-31G* and 0.9806 for B3LYP/6-31G*) recommended by Scott and Radom (45) and added to the raw energies to give the ZPE-corrected energies. Coupled-cluster calculations were CCSD(T) (46) single-point calculations on MP2 geometries, and the basis set was 6-31G*. The coupled-cluster energies were corrected with the MP2/6-31G* ZPEs. G3(MP2) energies (47), which are almost as accurate as G3 values (48) but considerably faster, refer to G3MP2 (0 K) values. Absolute total energies, ZPEs, and ZPE-corrected energies are given in the supplementary material.[3] All transition states were checked by intrinsic reaction coordinate (IRC) calculations (49), which showed that they connect the cyclic molecule with its fragmentation products in a concerted reaction, except for anomalies connected with reactions 3a and (or) 3a′ and possibly 4a (Fig. 3) for the MP2 PES.

For reaction 3a, we were unable to find an MP2 transition state linking **1,2-N2** and 2 HCCH + N_2, but we located instead **ts-rxn3a** (rxn = reaction) (Fig. 3), which connects **1,2-N2** with a van der Waals complex of a species CHCHCHCH and N_2. There appears to be a series of these loosely bound complexes, and **c3a** (Fig. 3) may not be exactly the one to which **ts-rxn3a** leads (the IRC was unable to travel downhill all the way to the complex). The complex **c3a** decomposes via a transition state **ts-rxn3a′** to 2HCCH + N_2. The relative energies of **1,2-N2**, **ts-rxn3a**, **c3a**, and **ts-rxn3a′** indicate that **c3a** decomposes readily to 2 HCCH + N_2. Indeed, the CC energies of **c3a** and **ts-rxn3a′**, 361.1 and 359.5 kJ mol^{-1}, place the latter marginally below its precursor, but this is not unusual when single-point calculations are performed on a minimum and a transition state representing a very low barrier — this is seen also for reaction 9a, discussed below. Because of the fragility of complexes of the type **c3a**, in the following discussion we regard the first step, reaction 3a, as the critical one in the two-step (rxn 3a, rxn 3a′) fragmentation of **1,2-N2** to 2HCCH + N_2. For reaction 4a we found an MP2 transition state, **ts-rxn4a**, which led from **1,2-N2** to what appeared to be a complex, CHCHCHN + HCN; however, when the IRC run was allowed to proceed well toward this supposed complex and the resulting non-stationary point was optimized, it dissociated to HCCH + 2HCN. Attempts to find an MP2 transition state unambiguously linking **1,2-N2** with HCCH + 2HCN failed, and we consider **ts-rxn4a** to lead directly to the products or to pass through a complex resembling only a dimple on the MP2 PES.

Discussion

Activation energies and reaction energies

We calculated the activation and reaction energies for fragmentation of the azabenzenes into two-heavy-atom fragments, e.g., $N_6 \rightarrow 3N_2$. That the energies of this particular reaction mode should be a good indication of the kinetic (from activation energy) and thermodynamic (from reaction energy) stabilities of the cyclic systems is intuitively apparent for hexaazabenzene (it is hard to imagine any other reasonable decomposition mode for N_6) at one end of the substitution continuum and is demonstrated for benzene, at the other end, by its formation from ethyne thermally or under catalysis (50). Kinetic and thermodynamic stabilities are very important probes of the properties of exotic molecules because they address directly the question of their possible existence, their stability, and their ease of experimental manipulation. Because of the importance of activation and reaction energies, we examined the results of calculations at the four levels shown in Figs. 3 and 4 (see computational methods section for details). For simplicity we use relative energies (activation and reaction energies) from the differences in the ZPE-corrected "absolute" energies; these represent 0 K enthalpy differences (51). These relative energies should show the same trends as, and not differ greatly from, relative energies that take into account the increase in translational, rotational, and vibrational energy of a molecule on going to room temperature (51).

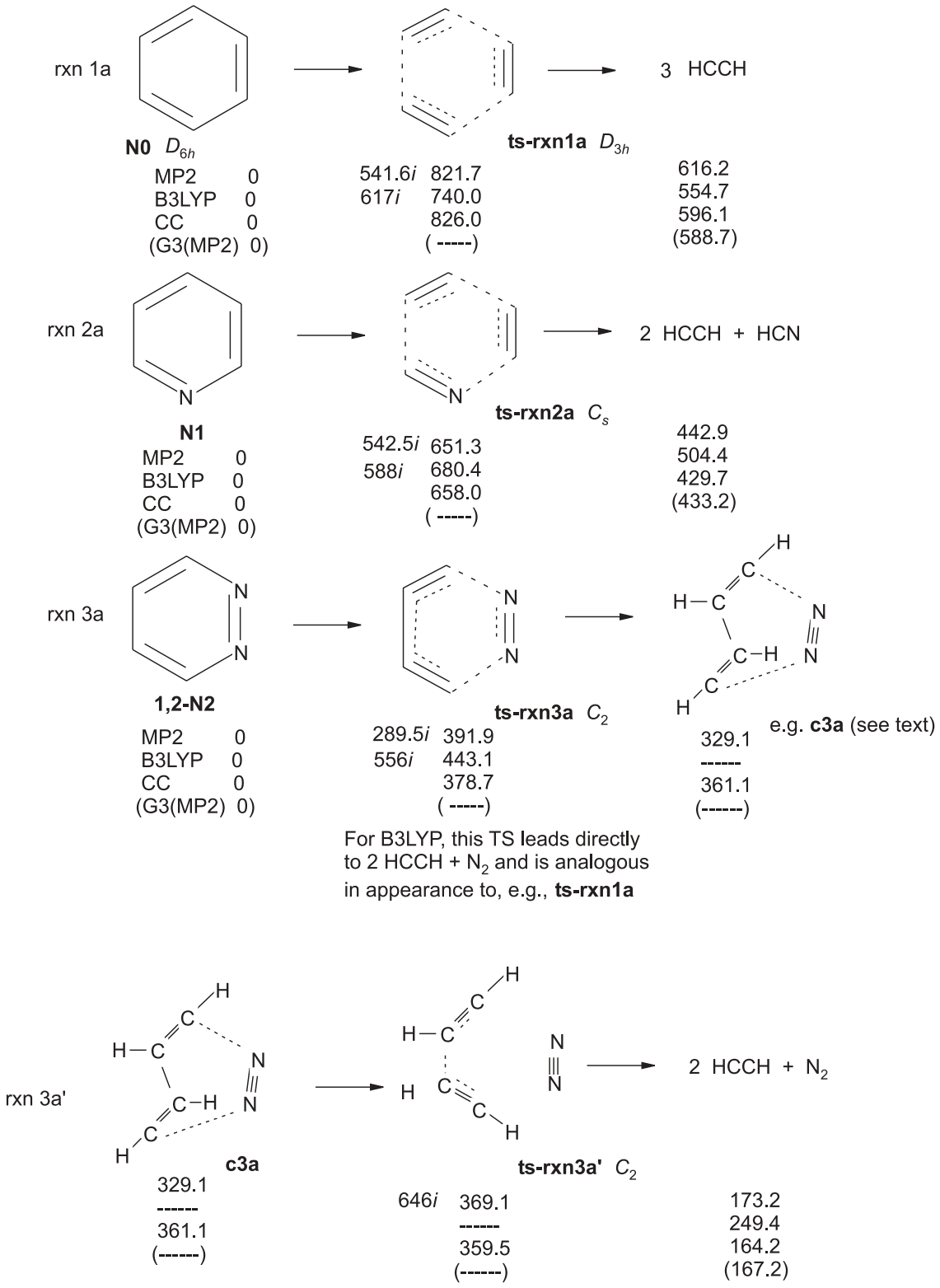
Inspection of Figs. 3 and 4 shows that the MP2, B3LYP, and CCSD(T) calculations all agree on the trends in activation and reaction energies as the number of nitrogens increases: the activation and reaction energies are predicted to fall, as one would expect to actually be the case. The reaction energies become negative when we reach molecules with three contiguous or four noncontiguous nitrogens (actually, **1,2,4-N3** is predicted by MP2 and CC to have slightly negative reaction energies). Comparing MP2, B3LYP, and CC, we see that MP2 and CC agree to within 20 kJ mol^{-1} for activation and reaction energies (for reaction 1a, the CC reaction energy is 20 kJ mol^{-1} lower and for reaction 3b, the CC activation energy is 19 kJ mol^{-1} higher than for the MP2 values, and the other deviations are less), except for reaction 6a, for which the activation energy from the CC method is 35 kJ mol^{-1} higher than that from the MP2 method, and reaction 9a, for which the CC reaction energy is 24 kJ mol^{-1} higher than the MP2.

In contrast to the fair consonance of MP2 and CC energies, the B3LYP activation and reaction energies usually differ considerably from the MP2 and CC values and are almost always higher. For the nine contiguous-N species activation energies (reactions 1a–9a), only for reactions 2a, 7a, and 8a is the B3LYP energy within 30 kJ mol^{-1} of the MP2 and the CC values; for 6a it is 6 kJ mol^{-1} higher than the CC but 40 kJ mol^{-1} higher than the MP2. For reactions 1a, 3a,

[3] Supplementary data may be purchased from the Depository of Unpublished Data, Document Delivery, CISTI, National Research Council Canada, Ottawa, ON K1A 0S2, Canada (http://www.nrc.ca/cisti/irm/unpub_e.shtml for information on ordering electronically).

© 2003 NRC Canada

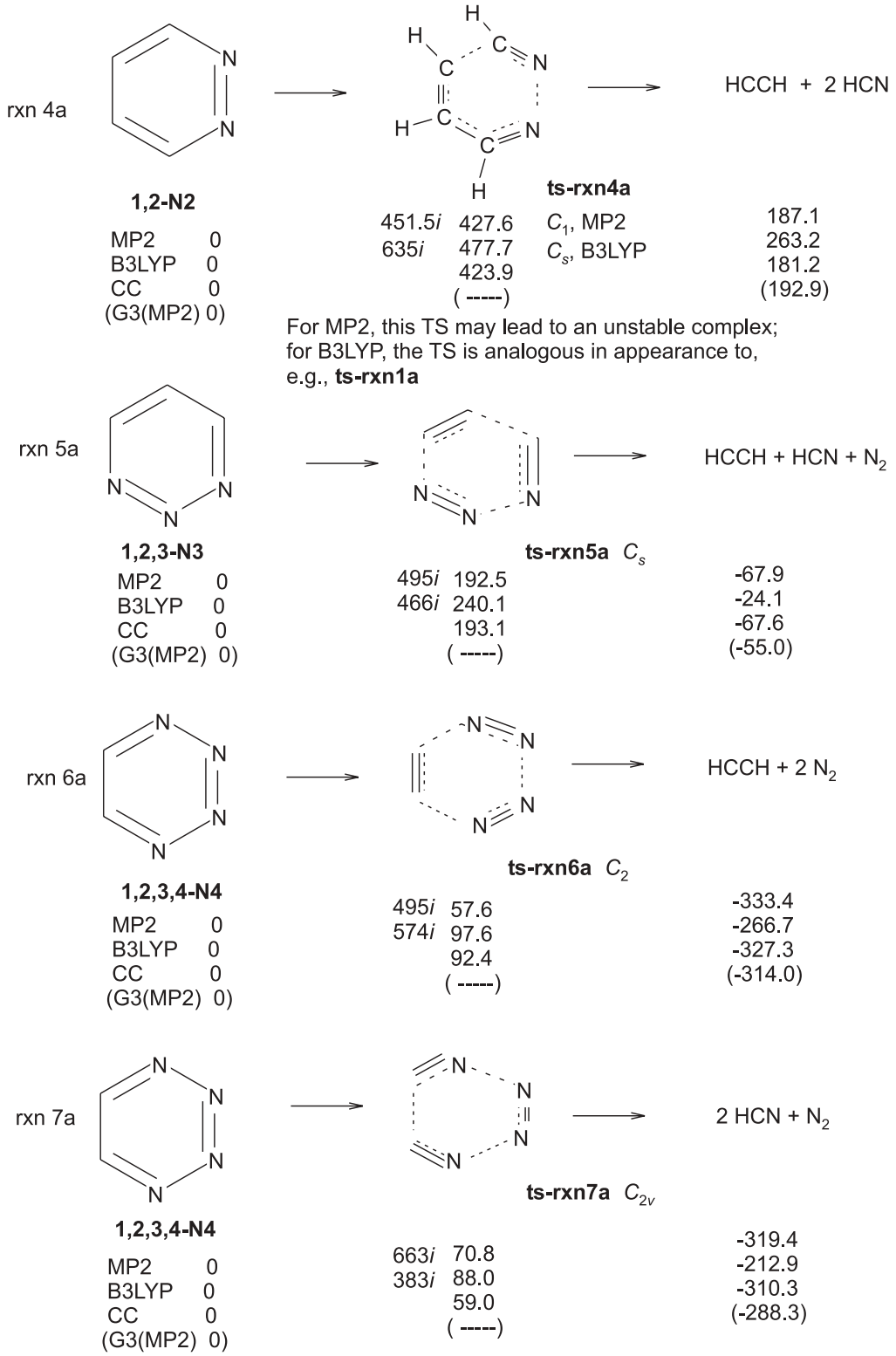
Fig. 3. Activation and reaction energies for fragmentation of contiguous-N azabenzenes into stable two-heavy-atom triply bonded fragments. See text for computational details.



4a, and 5a, the B3LYP deviations are from 47 to 86 kJ mol^{-1}. For the nine contiguous-N species reaction energies, the B3LYP values exceed the MP2 and CC ones from 60 (6a) to 137 kJ mol^{-1} (9a), except for reaction 1a (61 and 41 kJ mol^{-1} smaller than the MP2 and CC values). For the seven non-contiguous-N species (reactions 1b–7b) activation energies, the B3LYP deviations (all positive) are less than for the contiguous-N set. For reactions 1b, 5b, 6b, and 7b, the B3LYP

© 2003 NRC Canada

Fig. 3 (*continued*).

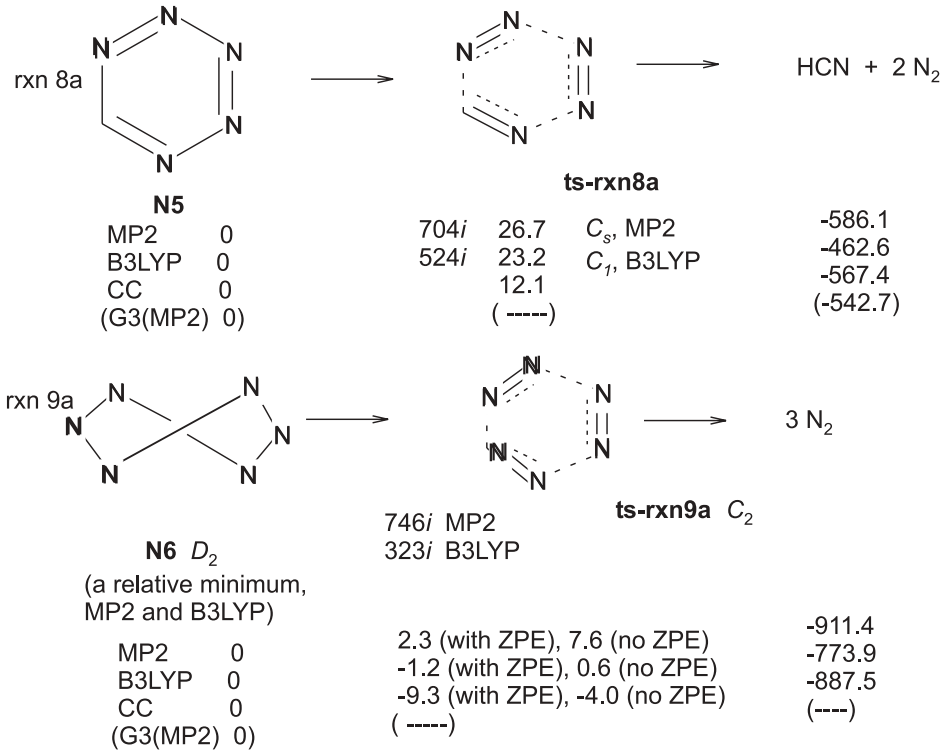


values are within about 30 kJ mol^{-1} of the MP2 and CC ones; for 2b, 3b, and 4b, we find deviations of 38–46 kJ mol^{-1}, except for 3b, where the B3LYP value lies only 18 kJ mol^{-1} above the CC one. For the seven noncontiguous-N species reaction energies, the B3LYP values exceed the MP2 and CC ones from 77 (2b) to 111 kJ mol^{-1} (6b).

To obtain an independent indication of which set of energies, the B3LYP or the MP2 and CC ones (these two latter being quite similar to each other), were the more reliable, we obtained the G3(MP2) reaction energies for reactions 1a–8a (Fig. 3). G3(MP2) activation energies and the reaction energy for reaction 9a are not reported because the Hartree–

© 2003 NRC Canada

Fig. 3 (*concluded*).



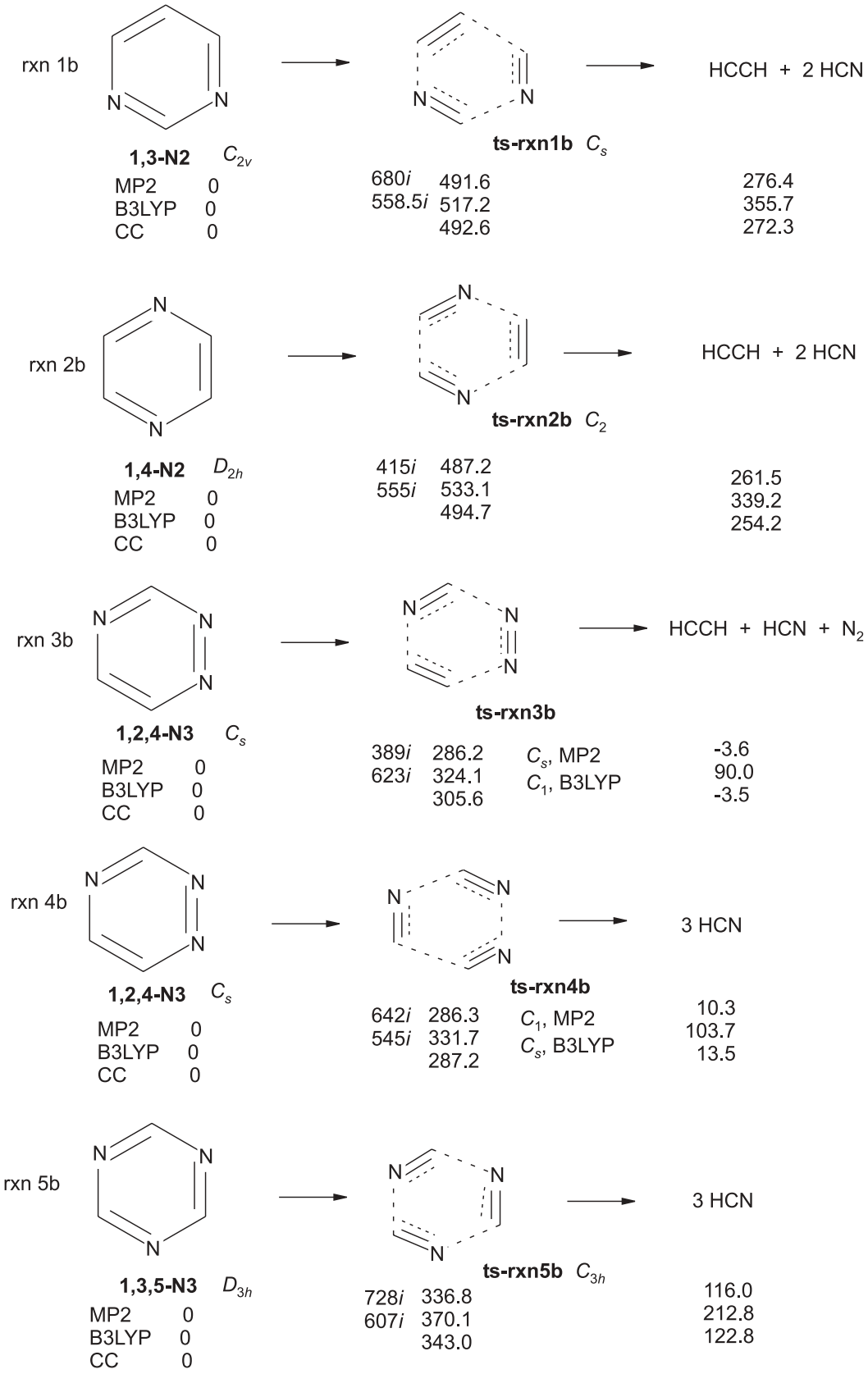
Fock (HF) level geometry optimization step in the G3(MP2) procedure does not always lead to a reasonable approximation of the transition-state geometry found on the correlated (B3LYP or MP2) potential energy surface and because, for reaction 9a, calculations at the HF and correlated (46, 52) levels give qualitatively different results. For a process like the fragmentation of a closed-shell molecule into closed-shell products, G3(MP2) calculations should reliably give relative energies to within 10 kJ mol^{-1} (47, 48) (reactions involving uncoupling of paired electrons are problematic (53)). Table 1 shows that the G3(MP2) reaction energies agree quite well with the CC values (average of absolute deviations 12 kJ mol^{-1}; maximum deviation 25 kJ mol^{-1}) and fairly well with the MP2 values (average of absolute deviations 19 kJ mol^{-1}) but deviate significantly more from the B3LYP relative energies (average of absolute deviations 62 kJ mol^{-1}). The MP2 and CC activation energies agree to within 20 kJ mol^{-1} (reaction 3b) but deviate by up to 86 kJ mol^{-1} from the B3LYP values (reaction 1a) (except for the case of reaction 6a, which is anomalous in that here it is the CC and B3LYP activation energies that are similar and lie 35–40 kJ mol^{-1} above the MP2 energy; careful checking of the calculations left this anomaly unexplained). As a further check on the accuracy of the CC relative energies for our reactions, we compared the calculated and experimental activation energies for two well-studied six-electron pericyclic reactions, namely the Diels–Alder reaction of 1,3-butadiene with ethene and the Cope rearrangement of 1,5-hexadiene. Our CCSD(T)/6-31G*//MP2(fc)/6-31G* values for the Diels–Alder reaction were 114 kJ mol^{-1}, cf. 105 kJ mol^{-1} from experiment (54), and for the Cope rearrangement, they were 161 kJ mol^{-1}, cf. 140 kJ mol^{-1} from experiment (55), approximating the Cope transition state as a bis(allyl radical) species à la Houk et al. (56). For these reasons, we regard the CC relative energies, activation and reaction, as reliable and will refer to these in evaluating the kinetic and thermodynamic stabilities of these species. These results suggest that these CC energies (0 K enthalpy differences) are accurate to within ca. 30 kJ mol^{-1} and that they thus reflect fairly well the relative and even the absolute stabilities (kinetic and thermodynamic) of these molecules. Some discrepancies between our MP2 reaction energies and those of Wiberg et al. may be because of their use, in some cases, of estimated ZPEs (28).

We briefly address the considerable differences in MP2 and B3LYP activation and reaction energies. It has very recently been claimed that diffuse (plus) functions are "vital" for calculating relative energies (57). We examined the effect of diffuse functions (6-31+G* basis) on some of these reactions; the activation and reaction energies do indeed move closer to the MP2 values, but only modestly (ca. 10–20 kJ mol^{-1} in most cases; for reaction 1a, however, the reaction energy increases from 554.7 to 629.4 kJ mol^{-1}, cf. the MP2 value of 616.2 kJ mol^{-1}). Much improvement for B3LYP beyond the 6-31G* basis set would be somewhat unexpected, as it is now well established that DFT is much less responsive to large basis sets than is ab initio (43*a*, 58). We are inclined to attribute the moderately inferior showing of DFT here to the fact that current functionals are semiempirical — there is no purely theoretical DFT way to improve DFT functionals (59) — and so may prove inadequate outside their sphere of parameterization. There are even cases in which ab initio works but DFT simply fails (60).

The MP2 and B3LYP geometries of benzene and the azabenzenes (Figs. 1 and 2) agree well, the biggest difference being ca. 0.02 Å (found in **1,2,3,4-N4**, **N5**, and **N6**),

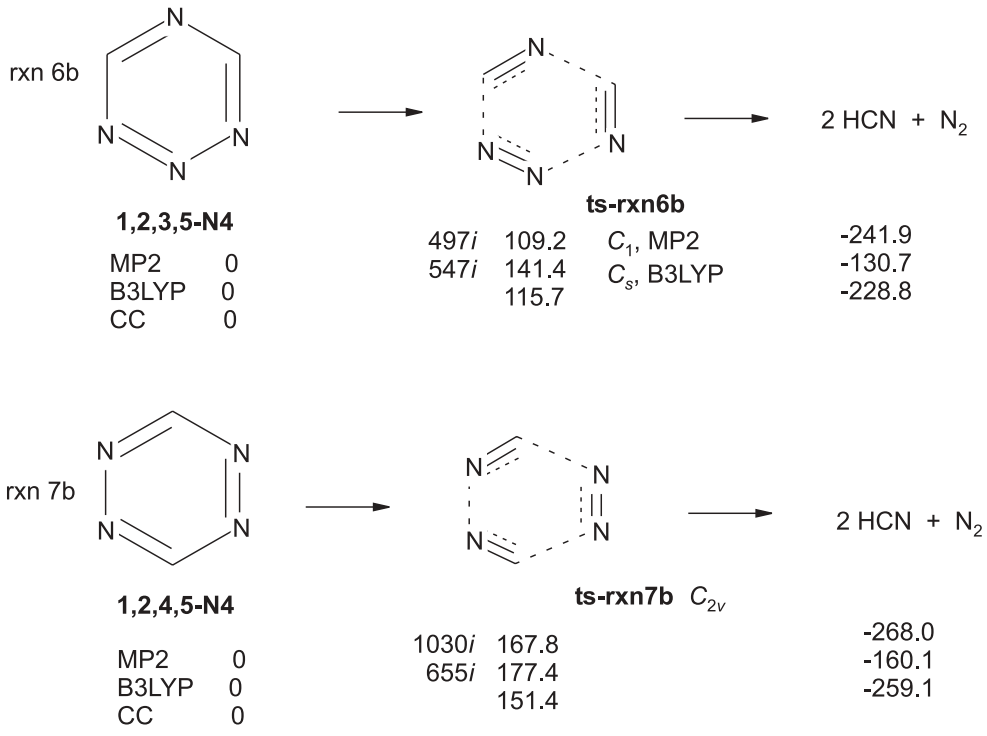
© 2003 NRC Canada

Fig. 4. Activation and reaction energies for fragmentation of noncontiguous-N azabenzenes into stable two-heavy-atom triply bonded fragments. See text for computational details.



© 2003 NRC Canada

Fig. 4 (*concluded*).



with the MP2 lengths almost always being the longer (exceptions are found in **1,2-N2**, **1,2,3,4-N4**, **1,4-N2**, and **1,2,4-N3**).

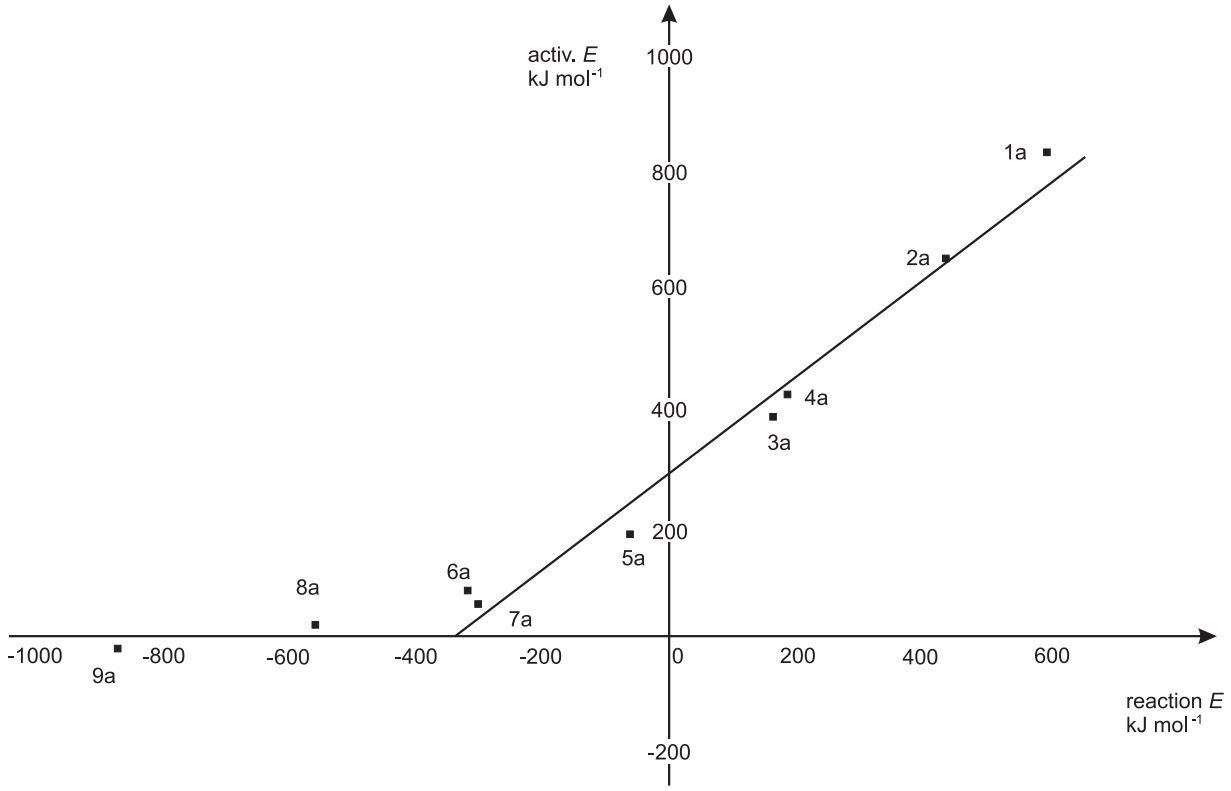
Figure 5 shows a plot of the CCSD(T)/6-31G*//MP2(fc)/6-31G* (Fig. 3) activation energies against reaction energies for reactions 1a–9a (the significance of this graph is discussed below). Focusing first on the (CC) reaction energies, we see that among the seven contiguous-N (including benzene here, **N0**–**N6**) species (Fig. 3) only three, those with 0, 1, and 2 nitrogens (reactions 1a–4a), are predicted to be thermodynamically stable with respect to fragmentation to their two-heavy-atom "components". Among the six noncontiguous-N species (Fig. 4; not included in Fig. 5), three, **1,3-N2**, **1,4-N2**, and **1,3,5-N3** (reactions 1b, 2b, and 5b), are predicted to be thermodynamically stable, and **1,2,4-N3** (reactions 3b and 4b) is a borderline "neutral" case, in that one fragmentation mode (3b) is very slightly exothermic and the other (4b) is only slightly endothermic (–3.5 and 13.5 kJ mol^{-1}, respectively). Where more than one fragmentation mode is possible (reactions 3a–4a, 6a–7a, and 3b–4b), there is little difference (less than 20 kJ mol^{-1}) between their reaction energies (this is true too for the activation energies — discussed below — except for 6a–7a, which differ by 33 kJ mol^{-1}). Note that the azabenzenes are predicted to be *thermodynamically* either robustly stable (reaction energies over 167 kJ mol^{-1}, 3a), or distinctly unstable (reaction energies less than –229 kJ mol^{-1}, 6b), except possibly for **1,2,3-N3** (reaction 5a is calculated to be mildly exothermic, –67.6 kJ mol^{-1}) and **1,2,4-N3** (the borderline reactions 3b and 4b, above).

Let us now examine the CCSD(T)/6-31G*//MP2(fc)/6-31G* activation energies and their relationship to the reaction energies. We point out that from experience a barrier to decomposition of ca. 100 kJ mol^{-1} represents the threshold for isolating a compound at room temperature. For example, pentazole, HN_5, and its conjugate base, N_5^-, have been estimated by extrapolation from data for derivatives to have room temperature activation energies and half-lives of 75 kJ mol^{-1} and 10 min and 106 kJ mol^{-1} and 2 days, respectively (61), while (*E*)-cycloheptene, with an (*E*)-to-(*Z*) activation energy of 71 kJ mol^{-1}, has an extrapolated room temperature half-life of tens of seconds (62). It is clear that in accord with the facts, benzene, pyridine, **1,2-N2**, **1,3-N2**, **1,4-N2**, and **1,3,5-N3** (reactions 1a, 2a, 3a/4a, 1b, 2b, and 5b, respectively) are predicted to be unambiguously stable: the thermodynamic and kinetic obstacles (over 100 and over 300 kJ mol^{-1}, respectively) to their fragmentation are substantial. For **1,2,4-N3** (reactions 3b and 4b), the activation energy (ca. 300 kJ mol^{-1}) is expected to ensure that this compound is isolable at room temperature, whatever may be the uncertainty (above) about its thermodynamic stability; the compound is known and "stable" (12). Similarly, for **1,2,3-N3**, for which the reaction energy (reaction 5a, –67.6 kJ mol^{-1}) appears to be but is not quite unequivocally negative, the fairly high calculated activation energy (193.1 kJ mol^{-1}) indicates that this compound should be fairly stable at room temperature, and indeed, 1,2,3-triazabenzene can be handled at room temperature but decomposes at 130 °C (11).

The tetraazabenzenes form an interesting mix of stable and unstable species. **1,2,3,5-N4** is likely to be kinetically stable at or somewhat below room temperature (reaction 6b, activation energy 115.7 kJ mol^{-1}) but should decompose on heating to give HCN and N_2. Interestingly, this molecule was calculated (55) by CISD to be 33 kJ mol^{-1} lower in energy than the well-known (14) **1,2,4,5-N4**. Our CCSD(T)/6-31G*//MP2(fc)/6-31G* (with MP2(fc)/6-31G* ZPE correc-

© 2003 NRC Canada

Fig. 5. Activation energy vs. reaction energy for the fragmentation reactions 1a, etc., of the contiguous-N azabenzenes at the CCSD(T)/6-31G*//MP2(fc)/6-31G* level (Fig. 3 shows the reactions and energies). The least-squares linear fit to points 1a–7a corresponds to activation E = 0.816 reaction E + 297, with r^2 = 0.979.



tions) energies were as follows: **1,2,3,5-N4**, –295.50198 au; **1,2,4,5-N4**, –295.49044 au. This indeed places the unknown **1,2,3,5-N4** below **1,2,4,5-N4**, by 0.01154 au or 30.3 kJ mol^{-1}.

1,2,4,5-N4 is predicted, correctly, to have substantial kinetic stability (reaction 7b, activation energy 151.4 kJ mol^{-1}) against decomposition to HCN and N_2. This tetraazabenzene has been known for over a century (14). It indeed undergoes thermal decomposition to HCN and N_2 but is stable enough to participate in Diels–Alder reactions (14), and derivatives of it are well known and have been used as reagents, e.g., as oxidants (63). **1,2,3,4-N4** is expected to decompose at about room temperature to HCN and N_2 (reaction 7a), possibly in competition with decomposition to HCCH and N_2 (reaction 6a), the calculated activation energies being 59.0 and 92.4 kJ mol^{-1}, respectively. Early calculations (semiempirical AM1) by Kaihoh et al. (64) suggested that this molecule would decompose to 2HCN and N_2 in a concerted reaction with an activation energy of 298 kJ mol^{-1} and to HCCH and $2N_2$ by a stepwise path with an activation energy of 145 kJ mol^{-1} for the rate-determining step.

We now come to systems of particular interest: those with five and six nitrogens. The fair linear correlation between calculated reaction energy and calculated activation energy (Fig. 5 plots the data for the contiguous-N molecules) that holds for benzene and all the **N1** to **N4** molecules (i.e., for reactions 1a–7a and 1b–7b) breaks down for pentaazabenzene and hexaazabenzene; their activation energies, being perforce positive, "should" correspond to reaction energies of ca. –400 kJ mol^{-1}, but in fact the calculated reaction energies are –567.4 and –887.5 kJ mol^{-1}, respectively. These molecules are thus more energy-rich than would be suggested by comparison of their activation energies with those of other azabenzenes; alternatively, one might say that they are in a sense stabler than they have a right to be, since their reaction energies are those "expected" for quite negative (!) activation energies. Pentaazabenzene, with a calculated fragmentation activation energy of 12.1 kJ mol^{-1} (the MP2 and B3LYP calculations essentially concur with the single-point CC in this, their values being only ca. 13 kJ mol^{-1} higher) is expected to require matrix isolation techniques (65) for its spectroscopic study but should be observable.

Hexaazabenzene surely is a holy grail of the synthetic chemist seeking nitrogen allotropes N_x. Both MP2(fc)/6-31G* and B3LYP/6-31G* optimizations yield a twisted, D_2 geometry as the potential energy surface *relative* minimum for cyclic N_6 (in agreement with the MP2(full) optimizations with a bigger basis set by Glukhovtsev and Schleyer (34)). Unfortunately, our calculations strongly indicate that it has, at best, an exceedingly low barrier for decomposition to dinitrogen. The three methods (MP2, B3LYP, CC) give activation energies without ZPE of 7.6, 0.6, and –4.0 kJ mol^{-1}; adding ZPE alters the values to 2.3, –1.2, and –9.3 kJ mol^{-1}. The negative energy without ZPE is probably simply because of the error inherent in calculating a small energy difference with single-point calculations (CC on MP2 geometries), and the negative values with ZPE are presumably just the result of errors in the ZPE, possibly combined with (for the CC value) the aforementioned single-point-method error (that **ts-rxn9a** is indeed the desired transition

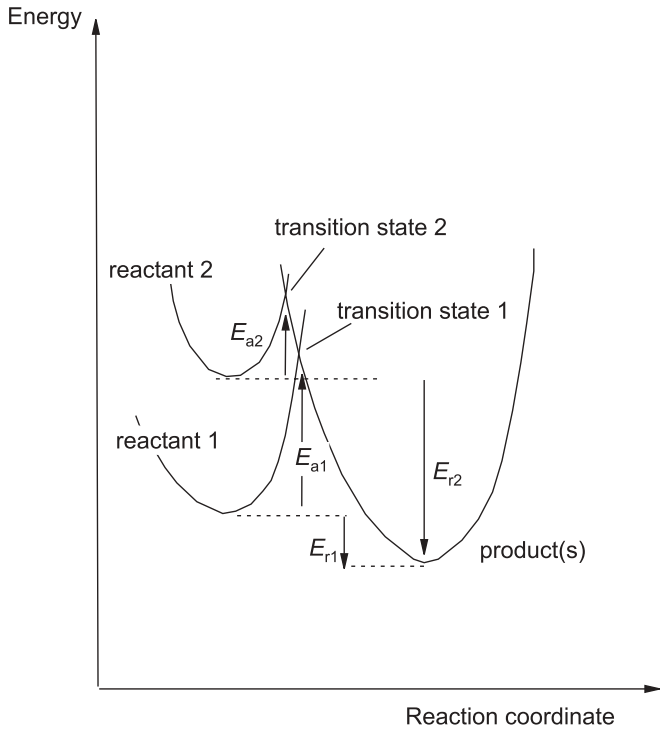
© 2003 NRC Canada

state was shown the B3LYP and MP2 IRC calculations). In any case, the barrier is so small that it is swamped by the errors in all three calculational levels; a barrier of less than 20, and perhaps less than 10 kJ mol^{-1}, is indicated. In fact, the calculated barrier is so close to zero that it is even possible that cyclic N_6 is not really a potential energy surface relative minimum (the acyclic C_2 symmetry N_6 species calculated (34) to be 109 kJ mol^{-1} stabler than hexaazabenzene, is perhaps a more viable synthetic objective, although we have not calculated its kinetic stability).

We now briefly comment further on the relationship between activation and reaction energies for the azabenzenes, as depicted in Fig. 5 for the contiguous-N molecules. For the nine reactions 1a–9a, the plot of activation energy vs. reaction energy is reasonably linear, with the exception of the points corresponding to reactions 8a (pentaazabenzene fragmentation) and 9a (hexaazabenzene fragmentation). This correlation of activation energy with reaction energy (the noncontiguous-N molecules also show a rough linear relationship) is in accord with the Bell–Evans–Polanyi principle (66, 67), which asserts that in a series of related reactions, as the reactions grow more exothermic, the barriers should decrease proportionately. Although apparently not resting on a rigorous theoretical basis, the principle has been manifested as a linear activation vs. reaction energy plot in another series of unimolecular organic reactions involving bond breaking, namely the cleavage of three-, four-, and five-membered rings fused to a cyclohexane ring (68). The concept behind the principle is that in an energy–reaction coordinate plot, the transition state can be regarded as the point where the curves for the reactant and the product cross. Factors that raise the energy of the reactant relative to that of the product then decrease the activation energy and also make the reaction more exergonic, or less endergonic (Fig. 6). The anomalous energetic situation of pentaaza- and hexaazabenzene has been noted above. Reactions with such a low barrier should have transition states resembling the reactants rather than the products, in accord with the Hammond (Hammond–Leffler) principle (66, 69, 70), and this is clearly seen in Fig. 7, which compares reactants with fragmentation transition states for benzene and hexaazabenzene. For benzene, the bonds that break are ca. 80% (according to the bond order change) or ca. 60% (according to the bond length change) broken in the transition state. Thus this transition state is quite product-like. For hexaazabenzene, bond breaking (the lower symmetry cf. benzene presents us with two kinds of breaking bonds) has progressed by only ca. 20% using bond-order changes and only ca. 6%–8% using bond-length changes, making for a reactant-like transition state; the geometry needs to distort but little for the molecule to start falling apart.

The benzene fragmentation transition state has been studied by Wagenseller et al. (71) at several levels; their best (MP4SDTQ/6-31+G*//MP2/6-31G* + ZPE) activation energy was 215 kJ mol^{-1} for the trimerization reaction, the reverse reaction from our viewpoint, cf. our CC single-point value of 826.0 – 596.1 (Fig. 3) = 230 kJ mol^{-1}. Jiao and Schleyer (72) investigated the transition state with emphasis on the question of its aromaticity and obtained, with DFT (B3LYP) and ab initio (MP4SDTQ//MP2), using the 6-311+G** basis set, activation and reaction energies of ca. 790 and 584 kJ mol^{-1}, respectively. In connection with a sophisticated NICS analysis, Morao and Cossío (73) obtained (B3LYP/6-31+G*) activation and reaction energies of 830 and 628 kJ mol^{-1}, respectively. These compare quite well with our CC values of 826 and 591 kJ mol^{-1}, particularly in view of our reservations about the accuracy of DFT here.

Fig. 6. The Bell–Evans–Polanyi principle. Here, reactant 2 is of higher energy than reactant 1 relative to the product(s) in a series of related reactions. See text.

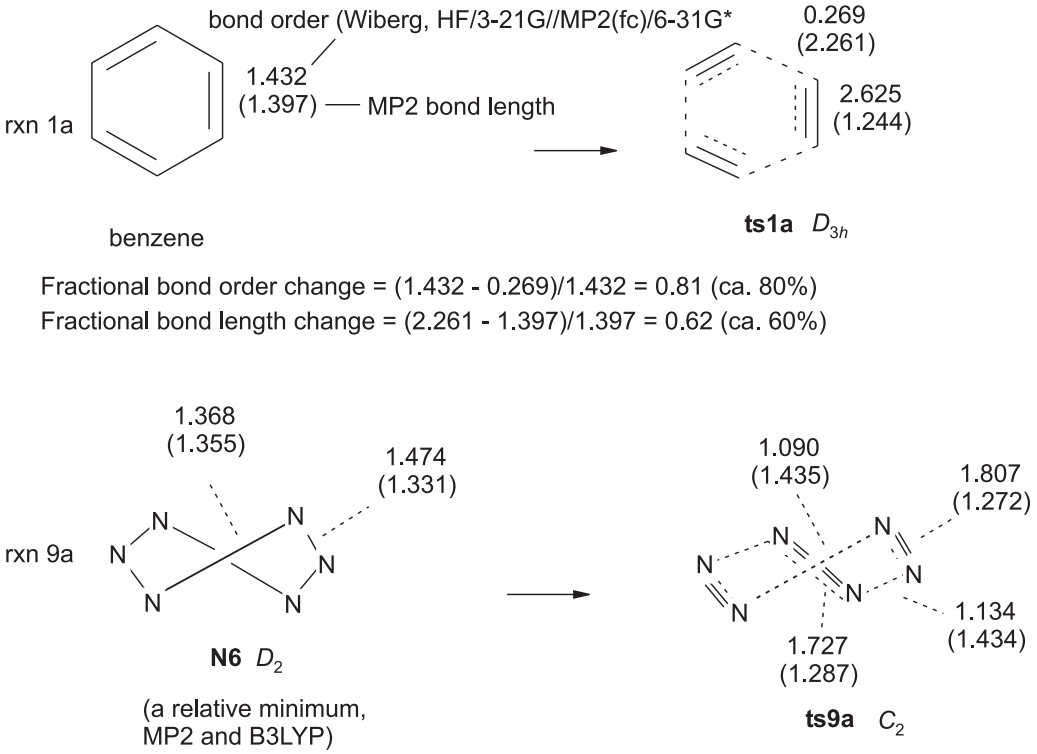


Homodesmotic ring-opening

These calculations were performed on the reactions shown in Fig. 8 and were limited to the contiguous-N azabenzenes. They were designed to assess the stabilization of these molecules relative to their open-chain analogues (e.g., benzene, cf. 1,3,5-hexatriene). With a caveat (below), this is a measure of cyclic conjugation energies or resonance energies, i.e., of aromaticity. Isodesmic reactions are reactions, usually hypothetical, which conserve the numbers of each kind of bond (74). They have the desirable feature that errors, owing to inaccuracies in the non-evenhanded way (mainly because of the imperfect treatment of electron correlation) that energy is calculated for different kinds of molecules, tend to cancel. Several kinds of isodesmic reactions have been developed in an attempt to improve the similarity of the bonds on the two sides of the equation. Williams and Whitehead (22) used an "isolabal" scheme, involving only aromatic rings, to calculate the heats of formation of all twelve (**N1**–**N6**) azabenzenes, employing semiempirical and noncorrelated ab initio (HF/4-31G and 6-31G**) methods. Chesnut (75) found that bond separation isodesmic reactions with ab initio and DFT methods (MP2 and BLYP) gave reasonably good resonance energies, and Chesnut and Davis (76) later reviewed the proliferating varieties of isodesmic reactions and introduced their "homomolecular differential bond separa-

© 2003 NRC Canada

Fig. 7. Comparison of changes in bond order and length on going to the transition state for benzene and hexaazabenzene.

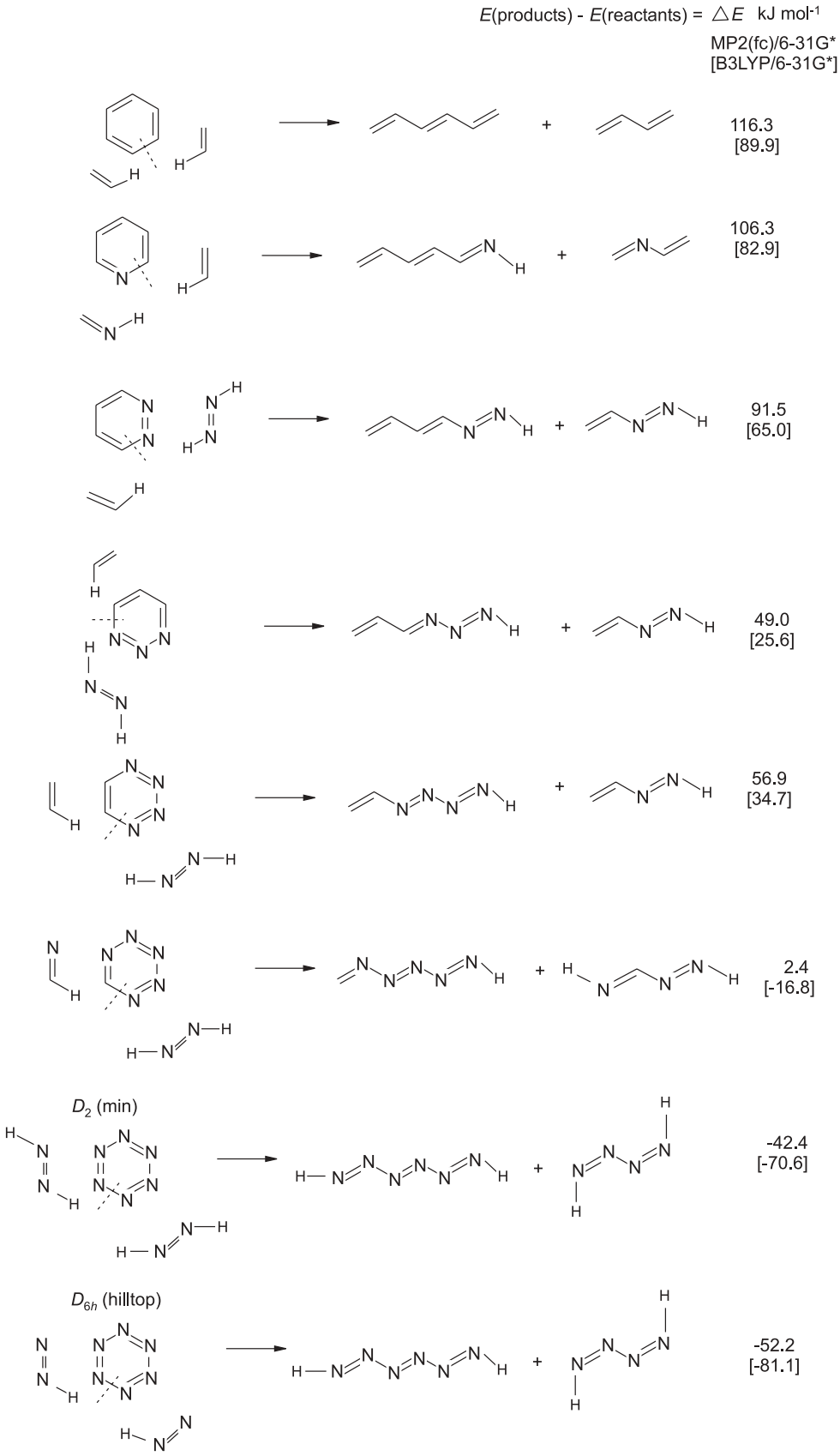


tion" reactions. Glukhovtsev et al. (77) showed that homodesmotic isodesmic reactions (e.g., breaking benzene into three 1,3-butadiene molecules using three ethene molecules, thus conserving the number of sp^2–sp^2 bonds (Fig. 9*a*)) give good values of resonance energies. Delamere et al. (78) used a simple version of homodesmotic reactions to probe the aromaticity of the pentalenoquinones; the molecules were unzipped to acyclic trienediones, preserving the number of sp^2–sp^2 bonds. This unzipping method gives virtually the same results as the more conventional "fragmentation" homodesmic reactions; reactions (*a*) and (*b*) in Fig. 9 are endothermic by 97.0 and 94.0 kJ mol^{-1}, respectively, using the pBP* DFT method (78). We use this homodesmic approach (Fig. 8) here for its simplicity and concur that "the (homodesmotic energy) scheme…has become the most dependable tool for obtaining numerical values of RE" (79). This "resonance energy" (RE) is, essentially, the widely used aromatic stabilization energy, ASE (80).

Figure 8 shows that homodesmic ring-opening is endothermic (the products contain more energy than the reactants) for benzene and the **N1**–**N4** molecules, essentially thermoneutral or slightly exothermic for pentaazabenzene (MP2: 2.4, B3LYP: –16.8 kJ mol^{-1}), and exothermic for hexaazabenzene, with the D_{6h} hilltop being more energy-rich than the D_2 relative minimum by 10 kJ mol^{-1}, according to both MP2 and B3LYP. The decrease in ΔE (Fig. 8) from **N1**–**N5** is qualitatively almost monotonic (ΔE is ca. 10 kJ mol^{-1} bigger for **N4** than for **N3**). Good isodesmic-type reactions essentially eliminate energy differences between reactants and products due to bond energy differences, so ΔE for such reactions is usually due to differences in electron delocalization energy (differences in resonance energy) and (or) differences in strain energy. The resonance energy of the cyclic species is obtained by adding its strain energy to ΔE. This is illustrated by calculations of the resonance energies of benzene, cyclobutadiene, and planar cyclooctatetraene (77). The strain energy (a concept associated with distortion of σ bonds from their normal angles) of benzene is taken as being small or zero and that of smaller rings as being positive (77, 78). The ΔE values in Fig. 8 show that benzene and the **N1**–**N4** molecules are distinctly stabilized with respect to bond-energy-compensated ring opening to acyclic analogues; **N5** is about neutral in this regard; and **N6** is distinctly unstable in this sense. Our values of ΔE for benzene (MP2: 116.3, B3LYP: 89.9 kJ mol^{-1}) and D_2 hexaazabenzene (MP2: –42.4, B3LYP: –70.6 kJ mol^{-1}) using reactions of Fig. 9, type *b*, lead to the same conclusions as those obtained by Glukhovtsev and Schleyer (34) from MP4SDTQ/6-31G(d,p)//MP2(full)/6-31G(d,p) calculations on reactions of Fig. 9, type *a* (benzene 100.0; D_2 hexaazabenzene –73.6 kJ mol^{-1}). The ca. 100 kJ mol^{-1} stabilization of benzene can be ascribed to cyclic electron dissociation — its resonance energy (77). Does the nearly monotonic decrease in ΔE with increasing numbers of nitrogens result

© 2003 NRC Canada

Fig. 8. Homodesmotic ring opening of the contiguous-N azabenzenes. The energies were calculated at the MP2/6-31G* and (in brackets) B3LYP/6-31G* levels.



© 2003 NRC Canada

Fig. 9. Homodesmotic fragmentation (*a*) and unzipping (*b*) reactions (both of which conserve sp^2–sp^2 bonds) give essentially the same results (DFT pBP/DN* calculations (71)).

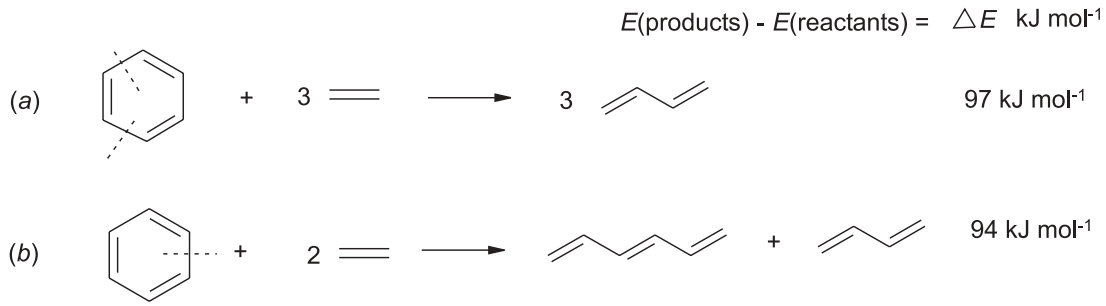


Table 1. Deviation of G3(MP2) reaction energies (kJ mol^{-1}) from those calculated at the CCSD(T)/6-31G*//MP2(fc)/6-31G*, MP2(fc)/6-31G*, and B3LYP/6-31G* levels, for reactions 1a–8a (Fig. 3).

Reaction	Deviation from CC	Deviation from MP2[a]	Deviation from B3LYP[a]
1a	–3	–27	34
2a	4	–10	29
3a	3	–6	–82
4a	12	6	–70
5a	13	13	–79
6a	13	19	–47
7a	22	31	–75
8a	25	43	–80
Average	12	19	62

[a]Deviation = G3(MP2) reaction energy — coupled cluster, etc., reaction energy. The averages are the arithmetic means of the absolute values of the deviations.

from a progressive decrease in resonance energy? This would be the case if there were no factors other than resonance at work in the series. In fact, however, replacing CH groups with nitrogens introduces electron lone pairs, and an obvious way that these may destabilize these molecules is by simple electrostatic repulsion, a possibility considered by Glukhovtsev and Schleyer (77). A subtler way in which lone pairs might effect destabilization is by weakening C—N or N—N bonds, by donating nonbonding electrons into σ* orbitals (81). In any case it seems likely that some destabilizing effect associated with nitrogen lone pairs is operating and, thus, that the homodesmotic Δ*E* values beyond the **N2** or **N3** molecules would have to be somehow corrected for this destabilizing effect, to extract the resonance energy of the heterocycle; cf. the correction of Δ*E* for strain for some molecules (77, 78). The effect of lone-pair interactions on the proton affinities of the azabenzenes has been noted by Sanz et al. (27) and by Mó et al. (29), the latter finding no correlation with lone-pair energies. Katritzky and Barczynski (26) concluded from an AM1 probe of aromaticity using geometric, energetic, and magnetic criteria that the azabenzene nitrogens have little effect on "classical" aromaticity, but they studied only **1,2,3-N3**, **1,2,4,5-N4**, and **1,2,3,4-N4** among the azabenzenes. Wiberg et al. (28) performed at the HF, MP2, and MP3 levels isodesmic-type hydrogen transfer reaction calculations (e.g., cyclohexadiene plus pyridine giving dihydropyridine plus benzene), as well as hydrogenation energy calculations (a kind of isodesmic calculation), and concluded that the resonance energies of benzene, pyridine, **1,3-N2**, and **1,4-N2** are essentially the same.

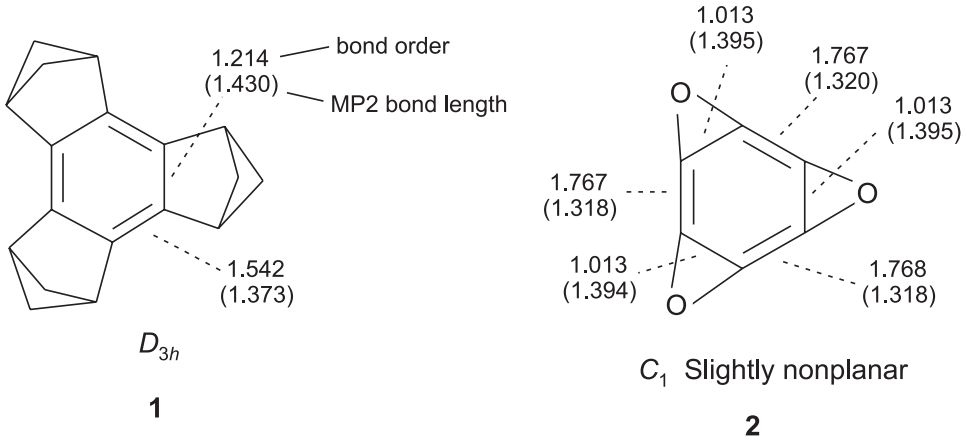
Electron distribution as indicated by bond order – bond length variation

These were calculated for benzene and the six contiguous-N azabenzenes (Fig. 1) and for the six noncontiguous-N azabenzenes (Fig. 2). The idea here is that an aromatic, cyclically delocalized ring should show less variation in bond order than one with localized single and double bonds. For example, for the cyclopentadienyl cation, the relative minimum on the potential energy surface is a C_{2v} species with three kinds of bonds (82), but for the anion the minimum is a D_{5h} species with only one kind of bond and, thus, with an even electron distribution (83). Several, somewhat complex, indexes based essentially on deviations from uniformity of bond length or bond order have been suggested as probes of aromaticity (84); simple indexes that are essentially deviations from an average bond length have also been used (85). We are skeptical of the usefulness of such indexes in probing aromaticity in the series pyridine–pentaazabenzene, because unlike the case of carbocycles like benzene, cyclopropenyl species, cyclopentadienyl species, etc. — and even azulene and benzocyclobutene (85) — one expects (and finds) an uneven electron distribution due to the presence of C—C, C—N, and N—N bonds, which makes it uncertain what the electron distribution "should" be in the absence of aromatic delocalization. This makes it hard to draw reliable conclusions beyond that given simply by the symmetry (e.g., that **1,3,5-N3**, being D_{3h}, has only one kind of C—N bond and so is cyclically delocalized like benzene, rather than possessing single and double bonds like the hypothetical cyclohexatriene). Nevertheless, we document calculated bond orders and lengths for benzene and all the azabenzenes (Figs. 1 and 2) and use these bond orders to calculate the Bird aromaticity index (86). This is essentially the standard deviation (more precisely, a somewhat biased version of the variance) of the bond orders, adjusted (for six-membered potentially aromatic rings) so that benzene gets an index of 100 (*V*, below, = 0) and Kekulé benzene (cyclohexatriene, with bond orders 1,2,1,2,1,2; V_K, below, = 33.3) an index of zero.

$$[1] \qquad V = \frac{100}{\bar{N}}\sqrt{\frac{\sum (N_i - \bar{N})^2}{n}}$$

© 2003 NRC Canada

Fig. 10. Tris(bicyclo[2.2.1]hexeno)benzene (**1**) and tris(oxireno)benzene (**2**); HF/3-21G Wiberg bond indexes on MP2(fc)/6-31G* geometries.



$$[2] \qquad I = 100\left(1 - \frac{V}{V_K}\right)$$

where V_K = 33.3, using Kekulé bond orders 1,2,1,2,1,2.

For six-membered rings, the summation in eq. [1] is over the six bond orders N_i; $\bar{N}$ is the arithmetic mean of the bond orders; and n = 6. V is commonly denoted σ_n. V_K in eq. [2] is V for Kekulé benzene (cyclohexatriene). The Bird index (I, eq. [2]) was chosen because, unlike some other indexes, it can be calculated for any cyclic species for which bond orders are available; because it is straightforward; and because it is probably as good as any other index based on deviations from bond order or bond length. Obviously the value of I depends on the bond orders used, and since there is no single, correct bond order (87), there is no uniquely correct Bird index for any molecule. Bird used bond orders estimated from experimental or from estimated bond lengths, presumably because, at the time, good fully optimized molecular geometries were not available for sizable molecules. We use here Wiberg bond orders (88) calculated at the HF/3-21G level on MP2(fc)/6-31G* geometries (the algorithm that implements bond order and related calculations in Gaussian 98 is by Glendening et al. (89)); all these geometries were checked by frequency calculations at the same (MP2) level to ensure they were potential energy surface relative minima.

Table 2 shows the results of our Bird index calculations for the azabenzenes; to put these values in perspective we also show our values for some five-membered-ring aromatics and for two potentially cyclohexatriene-like benzene rings: **1**, tris(bicyclo[2.1.1]hexeno)benzene, and **2**, tris(oxireno)benzene (Fig. 10), which we briefly discuss below. Values obtained by Bird (Table 2) often differ considerably from ours, showing the effect of using different bond order values. If bond-order variation were the only criterion for aromaticity, the Bird index could be regarded as a measure of how aromatic a molecule is, percentage-wise, compared with benzene. For example, pyridine could be said to be 98.2% (Wiberg bond orders) as aromatic as benzene. The index probably does reflect to some extent the amount of cyclic delocalization in a potentially aromatic ring; the five-membered heterocycles in the table have considerably smaller I values than benzene, with furan having the smallest value, in accord with the conventionally accepted order of their aromaticity. Particularly interesting are the I values for **1** and **2**, molecules designed to impose bond alternation on benzene by diverting electron density from formal double bonds: the former to avoid strain in the bicyclic moieties, the latter to avoid, in the oxirene moieties, strain and antiaromaticity. The aromaticity of **1** has been evaluated from magnetic properties and isodesmic reactions, with the conclusion that, in accord with previous work on the molecule, it "retains a substantial degree of aromaticity" (90), which accords with I = 64.3. Molecule **2** has the astonishingly small Bird index of 18.5, suggesting it is essentially a cyclohexatriene; bond fixation in benzooxirenes has been exam-

Table 2. Bird indexes (79) for benzene, the azabenzenes, thiophene, pyrrole, furan, and the bond-localized benzenes **1** and **2**.

	Bird index, I	
Molecule	From Wiberg BOs	From estimated BOs (Bird (86*a* and 86*b*))
Benzene	100	100 (86*b*)
N1 (pyridine)	98.2	85.7 (86*b*)
1,2-N2	89.5	78.9 (86*b*)
1,2,3-N3	98.4	76.9 (86*b*)
1,2,3,4-N4	88.5	
N5	97.5	
N6 (D_2)	89.6	
N6 (D_{6h}) (a hilltop)	100	
1,3-N2	97.7	
1,4-N2	98.8	
1,2,4-N3	89.1	86.1 (86*b*)
1,3,5-N3	100	100 (86*b*)
1,2,3,4-N4	96.9	
1,2,4,5-N4	99.5	97.8 (86*b*)
Thiophene	52.1	66 (86*a*)
Pyrrole	58.4	59 (86*a*)
Furan	23.2	43 (86*a*)
1 (Fig. 10)	64.3	
2 (Fig. 10)	18.5	

Note: Bond orders: HF/3-21G Wiberg bond orders on MP2(fc)/6-31G* geometries. Where available, values calculated by Bird (79*a*, 79*b*) from estimated bond orders are given.

© 2003 NRC Canada

ined computationally, and the pronounced bond length fixation in **2** was noted (91). Like oxirenes in general, **2** is unknown (92). Bond-order variation indicates that all twelve azabenzenes are about as delocalized (as "aromatic") as benzene, with Bird indexes of 89–100.

Ring-current effects as indicated by calculated nucleus-independent chemical shifts (NICS)

The calculated magnetic shielding of a ring on a probe nucleus without charge — the nucleus-independent chemical shift or NICS — has become a popular method of testing cyclic molecules for the ring-current effects believed to be associated with aromaticity or antiaromaticity. Since its introduction by Schleyer et al. in 1996 (93), the NICS method has been applied widely, e.g., to the putative homoaromatic compound triquinacene (94); to the correlation of magnetic with other criteria for aromaticity (95); to novel sulfur-containing compounds (96); to inorganic rings (97); to pentafulvene and silicon, germanium, and tin derivatives thereof (98); and to transition states (99). There are variations of the method in which the probe nucleus is placed above the ring to avoid local σ-bond effects (100), and the variation of shielding with distance above the ring has been analyzed theoretically (73).

Our NICS results for the contiguous-N azabenzenes are shown in Fig. 11. These are from GIAO HF/6-31G* calculations on MP2(fc)/6-31G* geometries; in our experience, this level generally gives essentially the same results as HF/6-31+G*//B3LYP/6-31G* calculations, one level that was used in the original NICS work (93). The shielding was calculated at 0, 0.5, 1, 1.5, 2, and 2.5 Å above the ring center, and Fig. 11 actually shows, for convenience, –NICS (= BQ isotropic (93); BQ, for Banquo, is Gaussian's designation of a ghost atom) rather than NICS values, since the NICS values are all negative except for NICS 0 of D_{6h} **N6**. In work on the quinones of pentalene, Delamere et al. (78) showed that plots of –NICS against distance above the ring center ("NICS curves") could be useful in examining related molecules for aromatic, nonaromatic, or antiaromatic character. Although we have not plotted actual curves here, the data in Fig. 11 show that by this magnetic test all eight species are aromatic: the –NICS 1 values are all ca. 12–13, and the –NICS 2 values are all ca. 5–6, cf. the benzene values of 12.81 and 5.46, respectively (for convenience we omit the NICS units of NMR ppm). This inclusiveness comfortably accommodates the suggestion that a molecule be considered nonaromatic if it has "less than half the magnitude of property in comparison to benzene" (101). The only considerable divergence from the values for benzene is in the –NICS 0 values, which, for all six planar molecules, benzene to **N5** (D_2 **N6** is twisted and D_{6h} **N6** is not a "real" molecule but rather a hilltop), fall monotonically and dramatically from 11.54 to 1.67. We attribute this to an effect involving the in-plane σ electrons and (or) lone pairs (97) and draw attention to the importance of calculating shielding above the ring plane, as has been recognized by others (100).

Integrating the results

Despite the nearly monotonic decrease in kinetic and thermodynamic stabilities for all the azabenzenes (e.g., Fig. 5) and in "resistance" to homodesmotic ring opening for the contiguous-N species (Fig. 8), the indication from bond-order variation (Table 2) and, more strongly, from NICS (Fig. 11) is that all the azabenzenes are delocalized much like benzene, i.e., are "aromatic" (2). The question of correlation between "classical" energetic criteria on the one hand and magnetic and other criteria on the other has been discussed at length in the literature, with conclusions ranging from significant correlation (95, 102) to little correlation (103) and even to the view that different magnetic criteria can diverge strongly as probes of aromaticity (101).

Fig. 11. NICS values (ppm) for the contiguous-N azabenzenes, at 0, 0.5, 1, 1.5, 2, and 2.5 Å above the ring center. From HF/6-31G* GIAO calculations on MP2(fc)/6-31G* geometries.

N0 (benzene)

r (Å)	–NICS
0	11.54
0.5	13.27
1	12.81
1.5	8.99
2	5.46
2.5	3.30

N1 (pyridine)

r (Å)	–NICS
0	9.62
0.5	12.08
1	12.38
1.5	8.85
2	5.42
2.5	3.29

N2 (1,2-diazabenzene)

r (Å)	–NICS
0	7.66
0.5	11.23
1	12.50
1.5	9.06
2	5.59
2.5	3.42

N3 (1,2,3-triazabenzene)

r (Å)	–NICS
0	6.08
0.5	10.51
1	12.48
1.5	9.14
2	5.66
2.5	3.49

N4 (1,2,3,4-tetraazabenzene)

r (Å)	–NICS
0	4.05
0.5	9.61
1	12.47
1.5	9.21
2	5.73
2.5	3.55

N5 (pentaazabenzene)

r (Å)	–NICS
0	1.67
0.5	8.35
1	12.14
1.5	9.11
2	5.71
2.5	3.51

N6, D_2, a minimum

r (Å)	–NICS
0	6.81
0.5	12.64
1	14.79
1.5	10.51
2	6.48
2.5	4.02

N6, D_{6h}, a hilltop

r (Å)	–NICS
0	−0.29 (sic, -0.29)
0.5	7.61
1	12.24
1.5	9.20
2	5.77
2.5	3.61

Conclusions

These calculations indicate that all the azabenzenes are probably "aromatic" in the sense of resembling benzene in sustaining a diatropic ring current (as measured by NICS values) and in evenness of electron distribution around the ring (as measured by the Bird bond order uniformity index). However, increasing nitrogen substitution causes a steady (in the contiguous-N series, a nearly monotonic) decrease in kinetic and thermodynamic stability (as measured by comparison of the energies of reactants with the energies of

© 2003 NRC Canada

transition states for fragmentation and with the energies of fragmentation products). A study of the stability of the contiguous-N series toward ring opening (as measured by homodesmotic ring-opening energies) also showed a steady decrease in stability with increasing nitrogen substitution. We ascribe these decreases in stability to the lone pairs on nitrogen, which may act by simple electrostatic repulsion and (or) by weakening C—N and N—N bonds by donation of *n* electrons into σ* orbitals. The still-unknown azabenzenes (1,2,3,4-, 1,2,3,5-, pentaaza-, and hexaazabenzene) are relative minima on the MP2/6-31G* and B3LYP/6-31G* potential energy surfaces, but for hexaazabenzene, the barrier to fragmentation is so low (e.g., 2.3 kJ mol^{-1} with MP2/6-31G*) that this species may in reality not be able to exist.

References

1. D. Hellwinkel. Systematic nomenclature of organic chemistry. Chapter 1. Springer-Verlag, Berlin. 2001.
2. (*a*) V.I. Minkin, M.N. Glukhovtsev, and B. Ya. Simkin. Aromaticity and antiaromaticity. Wiley, New York. 1994; (*b*) Chem. Rev. **101**(5) (2001).
3. A.J. Boulton (*Editor*). *In* Comprehensive heterocyclic chemistry. A review of the literature 1982–1995. Vol. 6. Elsevier Science, Oxford. 1996.
4. (*a*) K. Schofield. Benzene. University of Exeter, Exeter. 1974; O.T. Benfet (*Editor*). Kekulé symposium. American Chemical Society, Washington, D.C. 1966; (*b*) D.T. Davies. Aromatic heterocyclic chemistry. Oxford University Press, New York. 1992.
5. W.J. Coates. *In* Comprehensive heterocyclic chemistry. A review of the literature 1982–1995. Vol. 6. *Edited by* A.J. Boulton. Elsevier Science, Oxford. 1996.
6. K. Undheim and T. Benneche. *In* Comprehensive heterocyclic chemistry. A review of the literature 1982–1995. Vol. 6. *Edited by* A.J. Boulton. Elsevier Science, Oxford. 1996.
7. N. Sato. *In* Comprehensive heterocyclic chemistry. A review of the literature 1982–1995. Vol. 6. *Edited by* A.J. Boulton. Elsevier Science, Oxford. 1996.
8. D.J. Brown. The pyrazines: Supplement I. The Chemistry of heterocyclic compounds. Vol. 58. Wiley-Interscience, New York. 2002.
9. C. Guo, S. Bhandaru, P.L. Fuchs, and M.R. Boyd. J. Am. Chem. Soc. **118**, 10 672 (1996).
10. F.R. Benson. The high nitrogen compounds. Wiley, New York. 1984.
11. A. Ohsawa and T. Itoh. *In* Comprehensive heterocyclic chemistry. A review of the literature 1982–1995. Vol. 6. *Edited by* A.J. Boulton. Elsevier Science, Oxford. 1996.
12. H. Neunhofer. *In* Comprehensive heterocyclic chemistry. A review of the literature 1982–1995. Vol. 6. *Edited by* A.J. Boulton. Elsevier Science, Oxford. 1996.
13. D. Bartholomew. *In* Comprehensive heterocyclic chemistry. A review of the literature 1982–1995. Vol. 6. *Edited by* A.J. Boulton. Elsevier Science, Oxford. 1996.
14. J. Sauer. *In* Comprehensive heterocyclic chemistry. A review of the literature 1982–1995. Vol. 6. *Edited by* A.J. Boulton. Elsevier Science, Oxford. 1996.
15. D.T. Hurst. *In* Comprehensive heterocyclic chemistry. A review of the literature 1982–1995. Vol. 6. *Edited by* A.J. Boulton. Elsevier Science, Oxford. 1996.
16. E. Hayon and M. Simic. J. Am. Chem. Soc. **92**, 7486 (1970).
17. V. Pizak and H. Wendt. Ber. Bunsenges. Physik. Chem. **83**, 481 (1979).
18. A. Vogler, R.E. Wright, and H. Kunkley. Angew. Chem. Int. Ed. Engl. **19**, 717 (1980).
19. Z.B. Maksić, D.M. Smith, and D. Barić. Chem. Phys. **269**, 11 (2001)
20. G. Rauhut. *In* Advances in heterocyclic chemistry. *Edited by* A.R. Katritzky. Academic Press, New York. 2001.
21. M. Gambiagi, M.S. de Gambiagi, C.D. Silva, and A.P. De Figueiredo. Phys. Chem. Chem. Phys. **2**, 3381 (2000).
22. C.I. Williams and M.A. Whitehead. J. Mol. Struct. (Theochem), **393**, 9 (1997).
23. R.J. Doerksen and A.J. Thakkar. Int. J. Quant. Chem. **30**, 1633 (1996).
24. P. Politzer, J.S. Murray, J.M. Seminario, and R.S. Miller. J. Mol. Struct. (Theochem), **262**, 155 (1992).
25. J.S. Murray, J.M. Seminario, and P. Politzer. J. Mol. Struct. (Theochem), **187**, 95 (1989).
26. A.R. Katritzky and P. Barczynski. J. Prakt. Chem. **332**, 885 (1990).
27. J.F. Sanz, J. Anguiano, and J. Vilarrasa. J. Comp. Chem. **9**, 784 (1988).
28. K.B. Wiberg, D. Nakaji, and C.M. Brennan. J. Am. Chem. Soc. **111**, 4178 (1989).
29. O. Mó, J.L.G. De Paz, and M. Yañez. J. Mol. Struct. (Theochem), **150**, 135 (1987).
30. E. Fos, J. Vilarrasa, and J. Fernández. J. Org. Chem. **50**, 4894 (1985).
31. P. Saxe and H.F. Schaefer. J. Am. Chem. Soc. **105**, 1760 (1983).
32. R. Engelke. J. Phys. Chem. **96**, 10 789 (1992).
33. R. Engelke. J. Phys. Chem. **94**, 6924 (1990).
34. M.N. Glukhovtsev and P.v.R. Schleyer. Chem. Phys. Lett. **198**, 547 (1992); *Erratum* **204**, 394 (1993).
35. T.-K. Ha and M.T. Nguyen. Chem. Phys. Lett. **195**, 179 (1992).
36. M.T. Nguyen. J. Phys. Chem. **94**, 6923 (1990).
37. H. Huber, T.K. Ha, and M.T. Nguyen. J. Mol. Struct. (Theochem), **105**, 351 (1983).
38. M. Ramek. J. Mol. Struct. (Theochem), **109**, 391 (1984).
39. B. Ya. Simkin, V.I. Minkin, and M.N. Glukhovtsev. *In* Advances in heterocyclic chemistry. *Edited by* A.R. Katritzky. Academic Press, New York. 1993.
40. R.E. Stratman, J.C. Burant, S. Dapprich, J.M. Millam, A.D. Daniels, K.N. Kudin, M.C. Strain, O. Farkas, J. Tomasi, V. Barone, M. Cossi, R. Cammi, B. Mennucci, C. Pomelli, C. Adamo, S. Clifford, J. Ochterski, G.A. Petersson, P.Y. Ayala, Q. Cui, K. Morokuma, D.K. Malick, A.D. Rabuck, K. Raghavachari, J.B. Foresman, J. Cioslowski, J.V. Ortiz, A.G. Baboul, B.B. Stefanov, G.Liu, A. Liashenko, P. Piskorz, I. Komaromi, R. Gomperts, R.L. Martin, D.J. Fox, T. Keith, M.a. Al-Laham, B. Johnson, W. Chen, M.W. Wong, J.L. Andres, C. Gonzalez, M. Head-Gordon, E.S. Replogle, and J.A. Pople. Gaussian 98 [computer program]. Revision a.9. Gaussian, Inc., Pittsburgh, Pa. 1998.
41. Gaussian, Inc. GaussView 2.1 [computer program]. Gaussian, Inc., Pittsburgh, Pa. 2000.
42. (*a*) W.J. Hehre, L. Radom, P.v.R. Schleyer, and J.A. Pople. Ab initio molecular orbital theory. Wiley-Interscience, New York. 1986; (*b*) J.B. Foresman and A. Frisch. Exploring chemistry with electronic structure methods. 2nd ed. Gaussian, Inc., Pittsburgh, Pa. 1996.
43. (*a*) G.N. Merrill, S. Gronert, and S.R. Kass. J. Phys. Chem. A, **101**, 208 (1997); (*b*) W. Kohn, A.D. Becke, and R.G. Parr. J. Phys. Chem. **100**, 12 974 (1996); (*c*) L.J. Bartolotti and K.

© 2003 NRC Canada

Flurchick. Rev. Comput. Chem. **7**, 187 (1996); (*d*) A. St.-Amant. Rev. Comput. Chem. **7**, 217 (1996).
44. J.B. Foresman and A. Frisch. Exploring chemistry with electronic structure methods. 2nd ed. Gaussian, Inc., Pittsburgh, Pa. 1996. Chap 4.
45. A.P. Scott and L. Radom. J. Phys. Chem. **100**, 16 502 (1996).
46. T.H. Dunning. J. Phys. Chem. **104**, 9062 (2000), and refs. therein.
47. (*a*) L.A. Curtiss, P.C. Redfern, K. Raghavachari, V. Rassolov, and J.A. Pople. J. Chem. Phys. **110**, 4703 (1999); (*b*) L.A. Curtiss, K. Raghavachari, P.C. Redfern, and J.A. Pople. J. Chem. Phys. **112**, 7374 (2000).
48. L.A. Curtiss, K. Raghavachari, P.C. Redfern, V. Rassolov, and J.A. Pople. J. Chem. Phys. **109**, 7764 (1998).
49. J.B. Foresman and A. Frisch. Exploring chemistry with electronic structure methods. 2nd ed. Gaussian, Inc., Pittsburgh, Pa. 1996. Chap 8.
50. K.P.C. Vollhardt. Angew. Chem. Int. Ed. Engl. **23**, 539 (1984), and refs. therein.
51. E. Lewars. Computational chemistry. Introduction to the theory and applications of molecular and quantum mechanics. Kluwer Academic Publishers, New York. 2003. Section 5.5.2.
52. (*a*) K. Raghavachari and J.B. Anderson. J. Phys. Chem. **100**, 12 960 (1996); (*b*) M. Head-Gordon. J. Phys. Chem. **100**, 13 213 (1996).
53. C. Cramer. Essentials of computational chemistry. Wiley, New York. 2002. p. 226.
54. M. Uchiyama, T. Tomioka, and A. Amano. J. Phys. Chem. **68**, 1878 (1964).
55. H.M. Frey and R. Walsh. Chem. Rev. **69**, 103 (1969).
56. K.N. Houk, S.M. Gustafson, and K.A. Black. J. Am. Chem. Soc. **114**, 8565 (1992).
57. B.J. Lynch, Y. Zhao, and D.G. Truhlar. J. Phys. Chem. A, **107**, 1384 (2003).
58. P.J. Stephens, F.J. Devlin, C.F. Chablowski, and M.J. Frisch. J. Phys. Chem. **98**, 11 623 (1994).
59. A.M. Mattsson. Science (Washington, D.C.), **298**, 759 (2002).
60. (*a*) S. Gronert, G.L. Merrill, and S.R. Klass. J. Org. Chem. **60**, 488 (1995); (*b*) D.A. Plattner and K.N. Houk. J. Am. Chem. Soc. **117**, 4405 (1995); (*c*) M.T. Nguyen, S. Creve, and L.G. Vanquickenborne. J. Phys. Chem. **100**, 18 422 (1996).
61. V. Benin, P. Kaszynski, and J.G. Radziszki. J. Org. Chem. **67**, 1354 (2002).
62. Y. Inoue, T. Ueoka, and T. Hakushi. J. Chem. Soc. Perkin 2, 983 (1983).
62. J.R. Thomas, G.E. Quelch, and H.F. Schaefer. J. Org. Chem. **56**, 539 (1991).
63. R.E. Sammelson, M.M. Olmstead, M.J. Haddadin, and M.J. Kurth. J. Org. Chem. **65**, 9265 (2000).
64. T. Kaihoh, T. Itoh, K. Yamaguchi, and A. Ohsawa. Chem. Pharm. Bull. **38**, 3191 (1990).
65. I.R. Dunkin. Matrix isolation techniques: A practical approach. The practical approach in chemistry series. Oxford University Press, New York. 1998.
66. S.S. Shaik, H.B. Schlegel, and S. Wolfe. Theoretical aspects of physical organic chemistry. Wiley, New York. 1992. Chap 1 and refs. therein.
67. W.P. Jencks. Chem Rev. **85**, 511 (1985).
68. D. Sawicka, S. Wilsey, and K.N. Houk. J. Am. Chem. Soc. **121**, 864 (1999).
69. N.M. Donahue. J. Phys. Chem. A, **105**, 1489 (2001).
70. D.G. Wales. Science (Washington, D.C.), **293**, 2067 (2001).
71. P. Wagenseller, D.M. Birney, and D. Roy. J. Org. Chem. **60**, 2853 (1995).
72. H. Jiao and P.v.R. Schleyer. J. Phys. Org. Chem. **11**, 655 (1998).
73. I. Morao and F.P. Cossío. J. Org. Chem. **64**, 1868 (1999).
74. D.A. Ponomarev and V.V. Takhistov. J. Chem. Educ. **74**, 201 (1997).
75. D.B. Chesnut. J. Comp. Chem. **16**, 1227 (1995).
76. D.B. Chesnut and D.M. Davis. J. Comp. Chem. **18**, 584 (1997).
77. M.N. Glukhovtsev, R.D. Bach, and S. Laiter. J. Mol. Struct. (Theochem), **417**, 123 (1997).
78. C. Delamere, C. Jakins, and E. Lewars. Can. J. Chem. **79**, 1492 (2001), and refs. therein.
79. V.I. Minkin, M.N. Glukhovtsev, and B. Ya. Simkin. Aromaticity and antiaromaticity. Wiley, New York. 1994. p. 37.
80. (*a*) P.v.R. Schleyer, H Jiao, and B. Goldfuss. Angew. Chem. Int. Ed. Engl. **34**, 337 (1995); (*b*) P. George, M. Trachtman, A.M. Brett, and C.W. Bock. J. Chem. Soc. Perkin Trans. 2, 1036 (1977); (*c*) W.J. Hehre, R.T. McIver, J.A. Pople, and P.v.R. Schleyer. J. Am. Chem. Soc. **96**, 7162 (1974); (*d*) L. Radom. J. Chem. Soc. Chem. Commun. 403 (1974).
81. S. Inagaki and N. Goto. J. Am. Chem. Soc. **109**, 3234 (1987).
82. (*a*) H. Jiao, P.v.R. Schleyer, Y. Mo, M.A. McAllister, and T.T. Tidwell. J. Am. Chem. Soc. **119**, 7075 (1997), and refs. therein; (*b*) P. Gölitz. Angew. Chem. Int. Ed. **41**, 2211 (2002), and refs. therein.
83. V.I. Minkin, M.N. Glukhovtsev, and B. Ya. Simkin. Aromaticity and antiaromaticity. Wiley, New York. 1994. p. 183.
84. (*a*) D. Glossman-Mitnik. J. Mol. Struct. (Theochem), **549**, 285 (2001); (*b*) B.S. Jursic. J. Mol. Struct. (Theochem), **468**, 171 (1999); (*c*) B.S. Jursic. J. Heterocyc. Chem. **34**, 1387 (1997).
85. (*a*) Y.L. Lu, D.M. Lemal, and J.P. Jasinski. J. Am. Chem. Soc. **122**, 2440 (2000); (*b*) M.-C. Ou and S.-Y. Chu. J. Phys. Chem. **98**, 1087 (1994).
86. (*a*) C.W. Bird. Tetrahedron, **41**, 1409 (1985); (*b*) **42**, 89 (1986); (*c*) **43**, 4725 (1987); (*d*) **46**, 5697 (1990).
87. E. Lewars. Computational chemistry. Introduction to the theory and applications of molecular and quantum mechanics. Kluwer Academic publishers, New York. 2003. Section 5.5.4.
88. K.B. Wiberg. Tetrahedron, **24**, 1083 (1996).
89. E.D. Glendening, A.E. Reed, J.E. Carpenter, and F. Weinhold. Gaussian NBO [computer program]. Version 3.1. As implemented in Gaussian 98, Revision A9. 1998.
90. A. Matsuura and K. Komatsu. J. Am. Chem. Soc. **123**, 1768 (2001), and refs. therein.
91. E. Lewars. Can. J. Chem. **78**, 297 (2000).
92. C. Delamere, C. Jakins, and E. Lewars. Can. J. Chem. **80**, 94 (2002), and refs. therein.
93. P.v.R. Schleyer, C. Maerker, A. Dransfeld, H. Jiao, and N.J.R. van Eikema Hommes. J. Am. Chem. Soc. **118**, 6317 (1996).
94. S.P. Verevkin, H.-D. Beckhaus, C. Rüchardt, R. Haag, S.I. Kozhushkov, T. Zywietz, A. de Meijere, H. Jiao, and P.v.R. Schleyer. J. Am. Chem. Soc. **120**, 11 130 (1998).
95. M.K. Cyrañski, T.M. Krygowski, A.R. Katritzky, and P.v.R. Schleyer. J. Org. Chem. **67**, 1333 (2002).
96. J. Fabian and A. Hess. Int. J. Quantum Chem. **90**, 1055 (2002).
97. P.v.R. Schleyer, H. Jiao, N.J.R. van Eikema Hommes, V.G. Malkin, and O.L. Malkina. J. Am. Chem. Soc. **119**, 12 669 (1997).
98. W. Collier, S. Saebø, and C.U. Pittman. J. Mol. Struct. (Theochem), **549**, 1 (2001).
99. (*a*) H. Jiao and P.v.R. Schleyer. J. Phys. Org. Chem. **11**, 655 (1998); (*b*) F.P. Cossío, I. Morao, H. Jiao, and P.v.R. Schleyer. J. Am. Chem. Soc. **121**, 6737 (1999).

© 2003 NRC Canada

100. (*a*) R. West, J.J. Buffy, M. Haaf, T. Müller, B. Gehrhus, M.F. Lappert, and Y. Apeloig. J. Am. Chem. Soc. **120**, 1639 (1998); (*b*) T. Veszprémi, M. Takahashi, B. Hajgató, J. Ogasawara, K. Sakamoto, and M. Kira. J. Phys. Chem. A, **102**, 10 530 (1998); (*c*) T.K. Zywietz, H. Jiao, P.v.R. Schleyer, and A. De Meijere. J. Org. Chem. **63**, 3417 (1998).
101. E.D. Jemmis and B. Kiran. Inorg. Chem. **37**, 2110 (1998).
102. K. Jug and A.M. Köster. J. Phys. Org. Chem. **4**, 163 (1991).
103. A.R. Katritzky, P. Barczynski, G. Musumarra, D. Pisano, and M. Szafran. J. Am. Chem. Soc. **111**, 7 (1989).

© 2003 NRC Canada

Bismuth-mediated reductive dehalogenation of α-halocarbonyl compounds[1]

Yoon Joo Lee and Tak Hang Chan

Abstract: Bismuth metal, activated by ammonium hydrogen fluoride, was found to reduce various α-halocarbonyl compounds efficiently and chemoselectively in aqueous media to give the dehalogenated reduction products in excellent yields.

Key words: bismuth, reduction, α-halocarbonyl compounds, fluoride salts, aqueous media, bismuth enolates, aldol reaction.

Résumé : On a observé que le bismuth métallique activé par du fluorure d'ammonium permet de réduire en milieu aqueux divers composés α-halocarbonylés de façon efficace et chimiosélective pour conduire avec de bons rendements à la formation des produits de réduction déshalogénés.

Mots clés : bismuth, réduction, composés α-halocarbonylés, fluorures, milieu aqueux, énolates de bismuth, réaction aldolique.

[Traduit par la Rédaction]

Introduction

The reductive dehalogenation of α-halocarbonyl compounds (without affecting the carbonyl group) has received considerable attention in organic chemistry. A number of reagents have been developed for this selective reduction, including: (*i*) reducing agents, such as zinc in acetic acid (1), sodium dithionate (2), organotin hydrides (3), borohydride (4), and low-valent transition metal salts (e.g., titanium(III) (5), vanadium(II) (6), and chromium(II) (7)); (*ii*) strong nucleophiles that may act as reducing agents, such as iodide ions (8), phosphines (9), iodophosphines (10), iodotrimethylsilane (11), thiols (12), selenols (13), tellurolates (14), and amines (15); (*iii*) stoichiometric amounts of zero-valent transition metal carbonyls of iron (16), cobalt (17), and molybdenum (18); (*iv*) heterogeneous hydrogenation catalysts involving transition metal surfaces (19); and (*v*) composite reducing systems of tin or silicon hydrides with transition metal catalysts, such as palladium (20) and molybdenum (21). The choice of a reducing agent usually depends on what other functional groups are present. Typically, these methods have to be carried out with organic solvents as the reaction media. Recently, Ranu et al. (22) reported an efficient and general methodology for the chemoselective reduction of α-halocarbonyl compounds in aqueous media. They discovered that indium metal could reduce α-halocarbonyl compounds to the corresponding dehalogenated carbonyl compounds in water under sonication. A wide range of structurally diverse α-bromo and α-iodoketones and esters was found to undergo the reductive dehalogenation by this procedure, to provide the corresponding reduction products in excellent yields. More recently, a useful employment of indium metal for the reductive dehalogenation reaction in aqueous media was reported by Chae et al. (23). One very important aspect of these reduction systems involving indium metal is the use of water as a reaction medium, which has attracted considerable interest in recent years in the context of green chemistry (24). We are interested in seeking an alternative to indium for aqueous reactions because of the high cost of indium and its potential toxicity. In this connection, among the heavy metals such as indium, antimony, mercury, and lead, bismuth metal is relatively inexpensive and nontoxic (25). In 1995, Ren et al. (26) reported the selective reduction of carbon–carbon double bonds in α,β-unsaturated esters by sodium borohydride in combination with bismuth chloride in ethanol. Subsequently, they also found the $NaBH_4$–$BiCl_3$ system to be very effective for the reduction of nitroarenes to primary amines (27). More recently, $BiCl_3$–Al and $BiCl_3$–Sm have been used to mediate the coupling of α-bromocarbonyl compounds with aldehydes (28). In all these cases, it was presumed that activated bismuth was generated by the reduction of the bismuth chloride, even though bismuth metal by itself was not active. Recently, we found that many metals can be rendered reactive in aqueous media by the activation of fluoride salts (29). We have therefore examined the possibility of activating bismuth metal by fluoride salts in aqueous media for various reactions.

Received 24 May 2003. Published on the NRC Research Press Web site at http://canjchem.nrc.ca on 28 November 2003.

Y.J. Lee and T.H. Chan.[2] Department of Chemistry, McGill University, Montreal, QC H3A 2K6, Canada.

[1]This article is part of a Special Issue dedicated to professor Ed Piers.

[2]Corresponding author (e-mail: tak-hang.chan@mcgill.ca).

Results and discussion

During our investigation into the allylation of carbonyl compounds mediated by bismuth metal, ammonium hydrogen fluoride was found to be an effective promoter in aque-

 doi: 10.1139/V03-172 © 2003 NRC Canada

Table 1. Reduction of α-halocarbonyl compounds mediated by bismuth metal in the presence of NH_4HF_2 in aqueous media.

Entry	α-Halocarbonyl compound	Time (h)	Product		Isolated yield (%)
1	$MeCOCHMeBr$	2	$MeCOCH_2Me$	**2a**	100[a]
2	$EtCOCH_2Br$	5	$EtCOCH_3$	**2a**	100[a]
3	$MeCOCH_2Cl$	14 days	$MeCOCH_3$	**2b**	63[a]
4	$PhCOCH_2Br$	2	$PhCOCH_3$	**2c**	88
5	$PhCOCHMeBr$	4	$PhCOCH_2Me$	**2d**	92
6	$PhCOCMe_2Br$	5	$PhCOCHMe_2$	**2e**	95
7	$HO_2CCHMeBr$	24	HO_2CCH_2Me	**2f**	100[a]
8	$HO_2CCHPhBr$	1	HO_2CCH_2Ph	**2g**	65
9	HO_2CCOCH_2Br	4	HO_2CCOCH_3	**2h**	100[a]
10	MeO_2CCH_2Br	16	MeO_2CCH_3	**2i**	100[a]
11	*p*-$NO_2PhCOCH_2Br$	3	*p*-$NO_2PhCOCH_3$	**2j**	94
12	*p*-$BrPhCOCH_2Br$	20	*p*-$BrPhCOCH_3$	**2k**	92

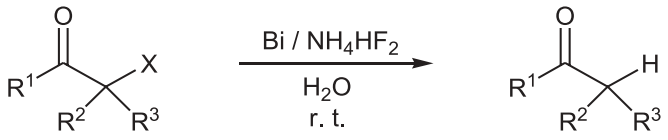
[a]Determined by ^1H NMR. The product was not isolated, owing to its low boiling point or solubility.

ous media (30). This prompted us to initiate a systematic investigation into the reduction of α-halocarbonyl compounds (**1**) by bismuth metal with ammonium hydrogen fluoride in aqueous media (Scheme 1). The results are summarized in Table 1.

As can be seen in Table 1, bismuth metal activated by ammonium hydrogen fluoride could effectively reduce various α-halocarbonyl compounds in aqueous media at room temperature, to provide the corresponding dehalogenated reduction products in fairly high yields. It should be emphasized that in the absence of the fluoride salt, the reduction with bismuth did not proceed to any significant extent. The reduction of the chloro compound (entry 3) was found to be much slower in comparison with those of the bromo compounds. It is important to note that this reduction system is highly chemoselective. Usually, the nitro group is very sensitive to reduction by metals. However, under these reduction conditions, *p*-nitroacetophenone could be obtained successfully without reducing the nitro group (entry 11). This should be compared with the $BiCl_3$–$NaBH_4$ system, which reduces nitro function as well (27). Furthermore, in the case of 2,4′-dibromoacetophenone, the bromo group on the aromatic ring also remained unaffected (entry 12). These results indicate that the present reaction conditions for the reduction of α-halocarbonyl compounds to dehalogenated carbonyl compounds are compatible with the nitro groups and the haloaryl, as well as the carbonyl, groups (ketone, acid, and ester). Finally, no reductive pinacol coupling products, derived from the carbonyl function, were observed (29*a*).

The exact role of the fluoride salt in the activation of metal in aqueous media is not known. Many metals may be unreactive in water because of the formation of water-insoluble metal oxide on the metal surface. Previously, it was suggested that the fluoride anion may render the metal oxide water soluble through formation of complex fluoride salts and allow further reaction at the metal surface to take place (29*a*). Metal-mediated reactions in aqueous media may proceed by different mechanisms, depending on the metal used. In many cases, it is considered that metal-mediated aqueous reactions go through a single electron transfer (SET) process on the metal surface, generating a radical anion intermediate **3** (31). While the precise mechanism for the bismuth-mediated reductive dehalogenation of α-halocarbonyl compounds is not known at this point, the fact that the radical self-coupling product **4** was not observed as a side product under the reaction condition suggests that the reduction did not undergo the SET process (Scheme 2, path a). It is more likely that the reduction by bismuth metal in the presence of ammonium hydrogen fluoride in aqueous media proceeds through the formation of a bismuth enolate intermediate **5** (Scheme 2, path b), which, on protonation, gives the reduction product **2**. Similar bismuth enolates have been invoked for the $BiCl_3$–Al mediated aldol condensation (28).

Scheme 1.

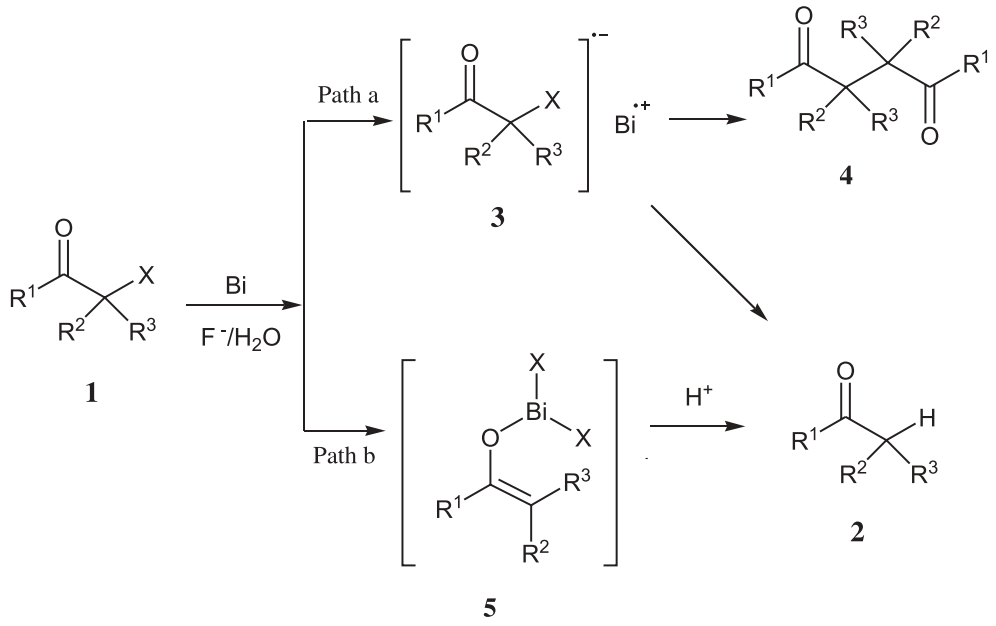


1 **2**

Supporting evidence for the intermediacy of bismuth enolate was obtained by carrying out an aldol condensation under the same reaction conditions. 3-Bromoisobutyrophenone (**1e**) and benzaldehyde in the presence of bismuth and NH_4HF_2 were stirred in water at room temperature overnight. The reaction proceeded cleanly, and the starting **1e** was completely consumed. In addition to the reduction product **2e** in 63% yield, the aldol product **6** was obtained in 37% yield (Scheme 3). It appeared that, in the competition between protonation and aldol reaction, the protonation process was favoured. One should be able to increase the yield of the aldol product **6** by increasing the rate of aldol condensation or suppressing the protonation reaction. This can be achieved by decreasing the amount of water (Table 2, entry 2), since the rate of the aldol reaction is dependant on the concentration of aldehyde. Alternatively, one can also reduce the rate of protonation by replacing water with D_2O, taking advantage of the kinetic isotope effect (32). This was indeed found to be the case (Table 2, entries 3 and 4). These results suggest that bismuth metal, under fluoride activation, may

© 2003 NRC Canada

Scheme 2.



Scheme 3.

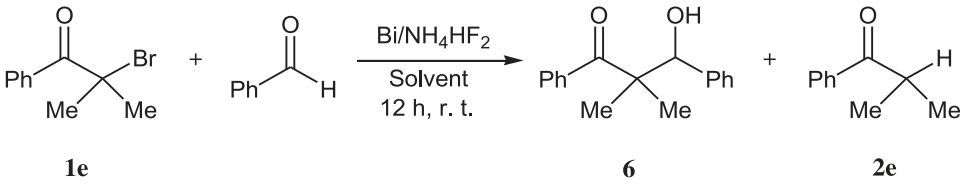


Table 2. Bismuth-mediated crossed aldol type reaction of 2-bromoisobutyrophenone (**1e**) with benzaldehyde in the presence of NH_4HF_2 in aqueous media.

Entry	Solvent (mL)	Yield (%) of **6**[a]	Yield (%) of **2e**[a]
1	H_2O (5)	37	63
2	H_2O (1)	56	44
3	D_2O (5)	76	24
4	D_2O (1)	82	18

Note: Ratio **1e**:benzaldehyde:Bi:NH_4HF_2 = 1:1.1:1.5:1.5 mmol.
[a]Determined by ^{1}H NMR of the crude product.

be a viable method to mediate crossed aldol type reactions, and its scope should be further explored (33).

Conclusion

The bismuth-mediated reductive dehalogenation of α-halocarbonyl compounds in aqueous media was investigated. Bismuth metal, activated by ammonium hydrogen fluoride, was found to reduce various α-halocarbonyl compounds efficiently under mild conditions, to afford the corresponding dehalogenated reduction products in excellent yields. The results showed that the reduction was highly chemoselective and suggested that the reduction products were presumably formed from the bismuth enolate intermediate.

Experimental

General information

Chemicals were purchased from Aldrich or Alfa Aesar Chemical Company. Thin layer chromatography was performed on plastic plates precoated with silica gel (60 F_{254}), which were developed using a mixture of hexane and ethyl acetate as the eluent. Analytes were visualized by UV light or by dipping the plate into a developing agent (a solution of ammonium molybdate and ceric sulfate in dilute sulfuric acid) and heating with a heat gun. Column chromatography was performed on 230–400 mesh silica gel. Melting points were determined using a Gallenkamp apparatus and were uncorrected. ^{1}H NMR spectra and ^{13}C NMR spectra were recorded on a Varian Mercury 300 MHz spectrometer at ambient temperature. Chemical shifts (δ) were reported in parts per million (ppm) and referenced to $CDCl_3$ at δ 7.25 ppm for ^{1}H and δ 77.00 ppm for ^{13}C. The multiplicity of each signal was indicated by s (singlet), d (doublet), t (triplet), q (quartet), quint (quintet), sept (septet), and m (multiplet). Coupling constants (*J*) were reported in Hertz (Hz).

General procedure for bismuth-mediated reductive dehalogenation

To a mixture of an α-halocarbonyl compound (1 mmol), bismuth powder (1.5 mmol), and NH_4HF_2 (1.5 mmol) was added distilled water (1 mL). The reaction mixture was vigorously stirred at room temperature until the reaction was

© 2003 NRC Canada

completed (1–24 h). Additional distilled water (10 mL) was added to the reaction mixture, and the product was extracted with diethyl ether (3 × 30 mL). The combined organic layer was dried over anhydrous Na_2SO_4 and filtered. After the evaporation of solvent under reduced pressure, the crude product was purified by flash column chromatography on silica gel, using 2% ethyl acetate in hexane as the eluent, to give the corresponding pure reduction product. Their identities were confirmed by comparison with authentic samples.

Bismuth-mediated aldol type reaction

To a mixture of 2-bromoisobutyrophenone (1 mmol), benzaldehyde (1.1 mmol), bismuth powder (1.5 mmol), and NH_4HF_2 (1.5 mmol) was added water or D_2O (1 or 5 mL). The reaction mixture was vigorously stirred at room temperature for 12 h. Additional distilled water (10 mL) was added to the reaction mixture, and the product was extracted with diethyl ether (3 × 30 mL). The combined organic layer was dried over anhydrous Na_2SO_4 and filtered. After the evaporation of solvent under reduced pressure, the crude product was analyzed by ^{1}H NMR for product distribution. The mixture was purified by flash column chromatography on silica gel, using 5% ethyl acetate in hexane as the eluent, to give the reduction product **2e** and the aldol product **6** (34) as a white solid. mp 105–107 °C. IR ($CHCl_3$) (cm^{-1}): 3475 (O—H), 1672 (C=O). ^{1}H NMR (300 MHz, $CDCl_3$) δ: 7.58–7.54 (m, 2H), 7.48–7.25 (m, 8H), 5.15 (d, J = 3.8 Hz, 1H), 2.92 (d, J = 3.8 Hz, 1H), 1.27 (s, 3H), 1.22 (s, 3H). ^{13}C NMR (75 MHz, $CDCl_3$) δ: 211.59, 140.04, 139.51, 130.37, 127.86, 127.81, 127.64, 127.58, 126.98, 78.82, 52.52, 24.34, 19.70.

Acknowledgment

We thank the Natural Sciences and Engineering Research Council of Canada (NSERC) for financial support of this research.

References

1. (*a*) H.E. Zimmerman and A. Mais. J. Am. Chem. Soc. **81**, 3644 (1959); (*b*) R.R. Sauers and C.K. Hu. J. Org. Chem. **36**, 1153 (1971); (*c*) P.A. Grieco. J. Org. Chem. **37**, 2363 (1972).
2. (*a*) T.L. Ho and C.M. Wong. J. Org. Chem. **39**, 562 (1974); (*b*) S.K. Chung and Q.Y. Hu. Synth. Commun. **12**, 261 (1982).
3. H.G. Kuivila and L.W. Menapace. J. Org. Chem. **28**, 2165 (1963).
4. T. Goto and Y. Kishi. Tetrahedron Lett. **2**, 513 (1961).
5. (*a*) T.L. Ho and C.M. Wong. Synth. Commun. **3**, 237 (1973); (*b*) J.E. McMurry. Acc. Chem. Res. **7**, 281 (1974).
6. T.L. Ho and G.A. Olah. Synthesis, 807 (1976).
7. C.E. Castro and W.C. Kray, Jr. J. Am. Chem. Soc. **85**, 2768 (1963).
8. (*a*) G.A. Fleisker and E.C. Kendall. J. Org. Chem. **16**, 573 (1951); (*b*) J.M. Townsend and T.A. Spencer. Tetrahedron Lett. **12**, 137 (1971); (*c*) A.L. Gemel and J.L. Luche. Tetrahedron Lett. **21**, 3195 (1980).
9. (*a*) H. Hoffmann and H.J. Dier. Tetrahedron Lett. **3**, 583 (1962); (*b*) P.A. Chopard, R.F. Hudson, and G. Klopman. J. Chem. Soc. 1379 (1965); (*c*) I.J. Borowitz and H. Parnes. J. Org. Chem. **32**, 3560 (1967); (*d*) I.J. Borowitz, K.C. Kirby, Jr., P.E. Rusek, and E. Lord. J. Org. Chem. **34**, 2687 (1969).
10. J.N. Denis and A. Krief. Tetrahedron Lett. **22**, 1431 (1981).
11. (*a*) T.L. Ho. Synth. Commun. **11**, 101 (1981); (*b*) G.A. Olah, A. Husain, B.P. Singh, and A.K. Mehrotra. J. Org. Chem. **48**, 3667 (1983).
12. (*a*) M. Oki, W. Funakoshi, and A. Nakamura. Bull. Soc. Chem. Jpn. **44**, 828 (1971); (*b*) H. Inoue, H. Hata, and E. Imoto. Chem. Lett. 1241 (1975); (*c*) K. Fuji, M. Node, T. Kawabata, and M. Fujimoto. Chem. Lett. 1153 (1984).
13. R. Seshadri, W.J. Pegg, and M. Israel. J. Org. Chem. **46**, 2596 (1981).
14. (*a*) D.L. Clive and P.L. Beaulieu. J. Org. Chem. **47**, 1124 (1982); (*b*) L. Engman and M.P. Cava. J. Org. Chem. **47**, 3946 (1982); (*c*) A. Osuka and H. Suzuki. Chem. Lett. 119 (1983).
15. R.E. Lyle and R.A. Covey. J. Am. Chem. Soc. **75**, 4973 (1953).
16. (*a*) S.J. Nelson, G. Detre, and M. Tanabe. Tetrahedron Lett. **14**, 447 (1973); (*b*) H. Alper. Tetrahedron Lett. **16**, 2257 (1975); (*c*) R. Noyori, Y. Hayakawa, H. Takaya, S. Murai, R, Kobayashi, and N. Sonoda. J. Am. Chem. Soc. **100**, 1759 (1978); (*d*) T.Y. Luh, C.H. Lai, K.L. Lei, and S.W. Tam. J. Org. Chem. **44**, 641 (1979).
17. H. Alper, K.D. Logbo, and H. des Abbayes. Tetrahedron Lett. **18**, 2861 (1977).
18. (*a*) H. Alper and D. Des Roches. J. Org. Chem. **41**, 806 (1976); (*b*) H. Alper and L. Pattee. J. Org. Chem. **44**, 2568 (1979).
19. (*a*) L.J. Sargent and J.H. Agar. J. Org. Chem. **23**, 1938 (1958); (*b*) D.A. Denton, F.J. McQuillin, and P.L. Simpson. J. Chem. Soc. 5535 (1964).
20. (*a*) E. Keinan and P.A. Gleize. Tetrahedron Lett. **23**, 477 (1982); (*b*) E. Keinan and N. Greenspoon. J. Am. Chem. Soc. **108**, 7314 (1986).
21. (*a*) E. Keinan and D. Perez. J. Org. Chem. **52**, 2576 (1987); (*b*) D. Perez, N. Greenspoon, and E. Keinan. J. Org. Chem. **52**, 5570 (1987).
22. B.C. Ranu, P. Dutta, and A. Sarkar. J. Chem. Soc. Perkin Trans. 1, 1139 (1999).
23. H.S. Chae, S.W. Cho, G.C. Keum, S.B. Kang, A.N. Pae, and Y.S. Kim. Tetrahedron Lett. **41**, 3899 (2000).
24. (*a*) C.J. Li and T.H. Chan. Organic reactions in aqueous media. John Wiley & Sons, New York. 1997; (*b*) P.A. Grieco (*Editor*). Organic synthesis in water. Blackie Academic and Professional, London. 1998.
25. N.C. Norman (*Editor*). Chemistry of arsenic, antimony, and bismuth. Blackie Academic & Professional, London. 1998.
26. P.D. Ren, S.F. Pan, T.W. Dong, and S.H. Wu. Synth. Commun. **25**, 3395 (1995).
27. P.D. Ren, S.F. Pan, T.W. Dong, and S.W. Wu. Synth. Commun. **25**, 3799 (1995).
28. (*a*) Z. Shen, J. Zhang, H. Zou, and M. Yang. Tetrahedron Lett. **38**, 2733 (1997); (*b*) J.M. Zhang and Y.M. Zhang. Chin. J. Chem. **20**, 111 (2002).
29. For the fluoride activation of (*a*) aluminum: L.H. Li and T.H. Chan. Org. Lett. **2**, 1129 (2000); (*b*) antimony: L.H. Li and T.H. Chan. Tetrahedron Lett. **41**, 5009 (2000).
30. T.H. Chan, L.-H. Li, Y. Yang, and W. Lu. *In* Clean solvents. ACS symposium series 819. *Edited by* M.A. Abraham and L. Moens. American Chemical Society, Washington, D.C. 2002.
31. (*a*) T.H. Chan, C.J. Li, M.C. Lee, and Z.Y. Wei. Can. J. Chem. **72**, 1181 (1994); (*b*) C.J. Li. Tetrahedron, **52**, 5643 (1996).
32. L. Melander and W.H. Saunders, Jr. Reaction rates of isotopic molecules. Wiley-Interscience, New York. 1980.
33. J.Y.J. Lee and T.H. Chan. Can. J. Chem. **81**, 1402 (2003).
34. C.H. Harrison. Tetrahedron Lett. **28**, 4135 (1987).

© 2003 NRC Canada

The β-(acyloxy)alkyl radical rearrangement revisited[1]

David Crich and Dae-Hwan Suk

Abstract: A β-(acyloxy)alkyl radical precursor, containing a carboxylate residue suitably placed for the trapping of any intermediate alkene radical cations, has been constructed. In nonpolar solutions the probe, in the form of either the free acid or its tetrabutylammonium salt, undergoes the typical rearrangement reaction with no evidence of trapping, leading to the conclusion that the reaction is either concerted or that collapse of any intermediate contact ion pair is so rapid as to preclude the possibility of trapping.

Key words: radical, rearrangement, contact ion pair.

Résumé : Un précurseur de transposition d'un radical β-(acyloxy)alkyle, equippé d'un résidu carboxylate convenablement placé pour piéger des intermediares alcene cation radicalaire, a été construit. En milieu apolaire la sonde, sous forme d'acide carboxylique ou sel de tetrabutylammonium quaternaire, subit la transposition typique et ne manifest aucune évidence de piègage, ce qui mène à la conclusion que la réaction est soit concertée, soit a lieu par l'intermédiaire d'une paire d'ions intime qui se réunit trop rapidement pour admettere la possibilité de piègage.

Mots clés : transposition radicalaire, paire d'ions intime.

Introduction

Initially thought to be concerted (1), the β-(phosphatoxy)alkyl radical rearrangement has recently been shown to involve a rate-determining radical ionic fragmentation to a contact radical ion pair with subsequent collapse to the product radical (Scheme 1, X = $P(OR)_2$) (2, 3). The jury is still out, however, in the case of the closely related β-(acyloxy)alkyl radical rearrangement (1), otherwise known as the Surzur–Tanner rearrangement (4). In this paper we describe attempts at trapping any intermediate contact ion pair, which attest, at the least, to the rapidity of its collapse to the product radical.

The evidence for the fragmentation mechanism in the rearrangement of β-(phosphatoxy)alkyl radicals is spectroscopic and kinetic (2, 3, 5) and is well supported by a range of trapping experiments (6–10). Thus, in more polar solvents, β-phenyl-β-(phosphatoxy)ethyl radicals fragment to give the styryl radical cation, which is readily detected in time-resolved laser flash photolytic experiments, and the phosphate anion. Kinetic experiments reveal the Arrhenius parameters for the fragmentation, with log(A) values typically in the vicinity of 10–12 (2, 3, 11). When the same experiments are conducted in nonpolar solvents only the rearranged radical is observed, but the Arrhenius parameters for these rearrangements closely resemble those for the fragmentations in more polar solvents (2, 3, 12, 13). The congruence between the two sets of Arrhenius parameters leads to the conclusion that both involve rate-determining fragmentation to a contact radical ionic pair, but that in nonpolar solvents rapid collapse to the product radical precludes the possibility of cage escape and spectroscopic detection of the radical cation. Note that, owing to the nanosecond timescale of the instrument used in the LFP experiments and the expected sub-nanosecond times anticipated for the escape of ions from contact ion pairs (14), only those radical cations that live long enough to escape the initial contact pair can be observed spectroscopically. Numerous trapping studies (6–10) have pointed to the ability of nucleophiles to intervene in this mechanism by trapping the alkene radical cation, and the stereochemical information retained in some of them (9) indicates that, with appropriate nucleophiles, trapping can take place at the level of the contact radical ion pair.

Significant effort has also been focused on the mechanism of the β-(acyloxy)alkyl radical rearrangement (15). A variety of stereochemical and isotopic labeling studies point to a reaction that is the formal equivalent of a 2,3-sigmatropic shift (Scheme 2) (1, 15). However, kinetic studies conducted by classical competition and (or) ESR spectroscopic methods (1, 15) and by time-resolved laser flash photolysis methods (13) have revealed Arrhenius parameters, especially typical log(A) values of 11.0–14.0, which closely parallel those of the β-(phosphatoxy)alkyl radical rearrangements, thereby strongly suggesting an analogous rate-determining fragmentation followed by an extremely rapid collapse to the product

Received 1 July 2003. Published on the NRC Research Press Web site at http://canjchem.nrc.ca on 1 December 2003.

This paper is dedicated to Professor Ed Piers (UBC) in recognition of his many valuable contributions to organic chemistry.

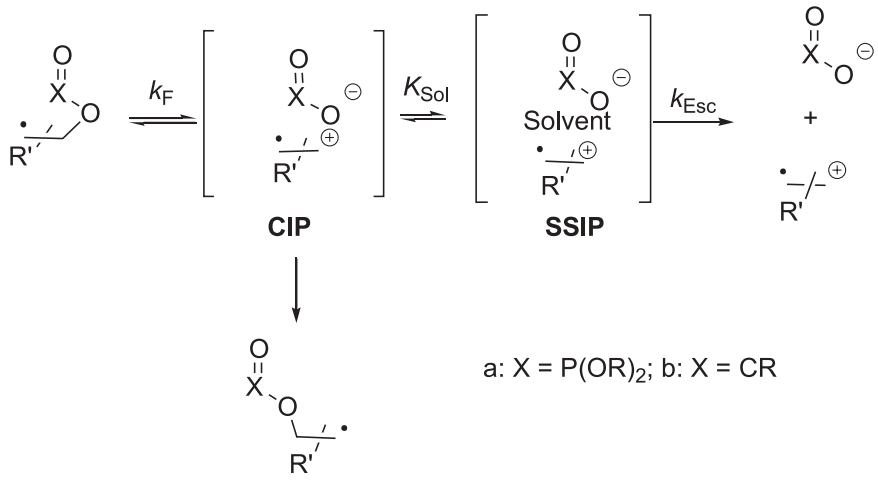
D. Crich[2] and D.-H. Suk. Department of Chemistry, University of Illinois at Chicago, 845 West Taylor Street, Chicago, IL 60607, U.S.A.

[1]This article is part of a Special Issue dedicated to Professor Ed Piers.

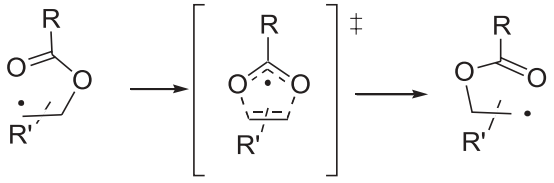
[2]Corresponding author (email: dcrich@uic.edu).

 doi: 10.1139/V03-148 © 2003 NRC Canada

Scheme 1. The fragmentation–recombination mechanism for the rearrangement of ester-substituted radicals.



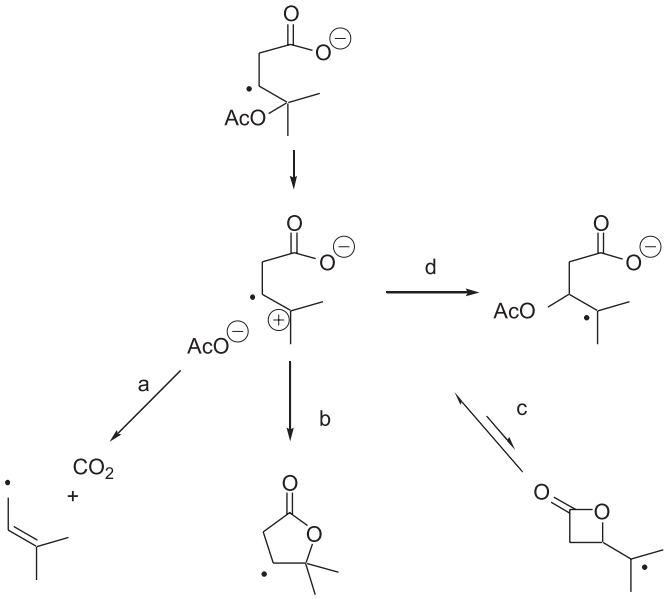
Scheme 2. A concerted mechanism for the [2,3]-rearrangement of β-(acyloxy)alkyl radicals.



radical (Scheme 1, X = CR). In contrast to the phosphates, though, is the failure of several trapping studies to subvert the rearrangement reaction and the lack of any direct observation of the intermediate alkene radical cation in such a mechanism. These apparent inconsistencies may be reconciled with the fragmentation mechanism if it is supposed that the carboxylate anion is much more basic than the diphenylphosphate anion, which leads to an even more rapid collapse of the contact ion pair, with which neither trapping nor cage escape can compete (16–18).[3]

The investigations reported in this paper were spurred by the possibility that carboxylates homoallylic to alkene radical cations might undergo facile decarboxylation (Scheme 3, path a) (19), analogous to the way in which glycine-based aminium radical cations suffer rapid decarboxylation (20, 21). Alternatively, it was considered possible that the radical cation might be trapped in a 5-endo-trig manner to yield γ-lactone-based products (Scheme 3, path b). There also exists the possibility that the alkene radical cation takes part in a 4-exo-cyclization to afford an azetidinone-substituted methyl radical (Scheme 3, path c), but, as these are known to fragment with rate constants of 10^5–10^6 s^{-1} at 80 °C (19), any equilibrium of this kind was expected to favor the open-chain product. Any or all of these processes could possibly divert the initial contact ion pair from collapse to the rearranged radical (Scheme 3, path d) and so potentially provide evidence for the intervention of alkene radical cations in the β-(acyloxy)alkyl radical rearrangement.

Scheme 3. Possible reaction pathways for carboxy-substituted β-(acyloxy)alkyl radicals.

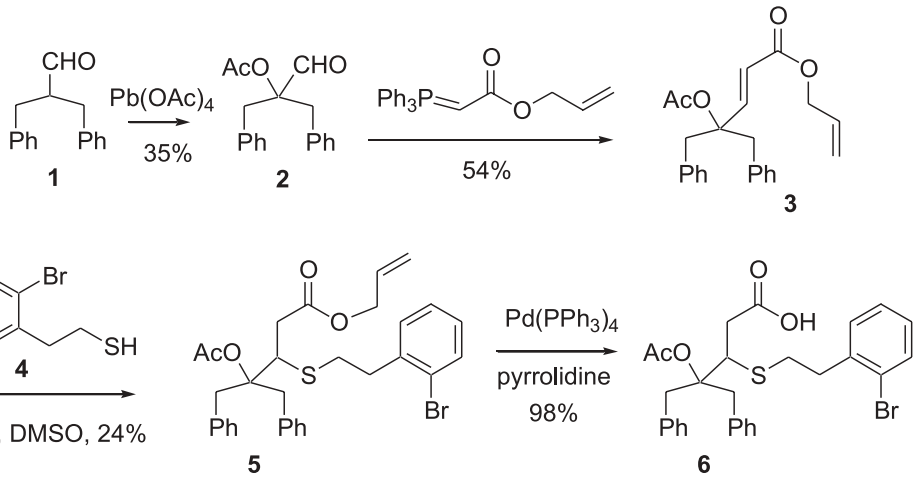


A suitable radical precursor was synthesized, as outlined in Scheme 4, with the main design feature being the use of the 2-(2-bromophenyl)ethanesulfenyl group (22) as a stable radical precursor β to the potentially enolizable carboxylate function. Thus, oxidation of 2-benzyl dihydrocinnamaldehyde **1** with lead tetraacetate afforded the acetoxyaldehyde **2**, which was immediately converted to the allyl ester **3** by Wittig olefination. Conjugate addition of 2-(2-bromophenyl)ethanethiol **4** (23) gave adduct **5** in poor but sufficient yield. Finally, removal of the allyl ester to give the product **6** was achieved with palladium(0) catalysis in the presence of pyrrolidine as nucleophile, the choice of ester and cleavage conditions being dictated by the desire to minimize elimination of the sulfide group.

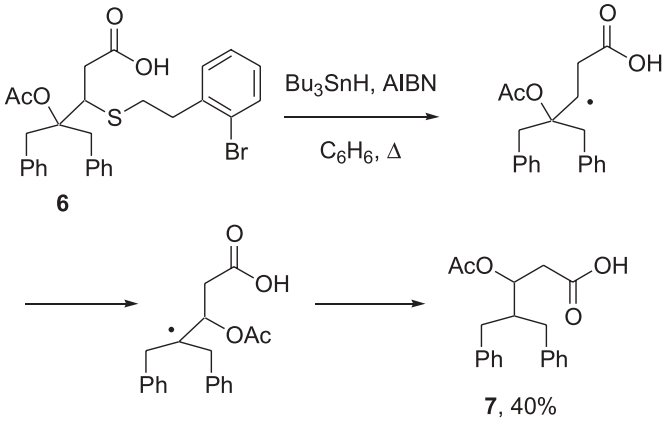
[3] Against this background of experimental evidence it must be recognized that a series of computational investigations have supported the concerted mechanisms for rearrangement, although the more recent versions admit the possibility of a dissociative mechanism (16–18).

© 2003 NRC Canada

Scheme 4. Synthesis of the radical precursor **6**.



Scheme 5. Rearrangement of **6** to **7**.



Exposure of **6** to tributyltin hydride and benzene at reflux, with initiation by AIBN, afforded the rearrangement product **7** in 40% isolated yield, thereby establishing the viability of the rearrangement in question (Scheme 5, Table 1).

Similar results were obtained (Table 1) when **6** was first converted to its tetrabutylammonium salt before exposure to tributyltin hydride and AIBN in both benzene and THF at reflux. Careful inspection of the ^{1}H NMR spectra of the reaction mixtures in each case did not provide any evidence for the formation of products that may have been anticipated as arising from pathways a, b, and c of Scheme 3. In each case the only discernible products were **7**, arising from the rearrangement and the unreacted substrate **6**. Finally, neutralization of a methanolic solution of **6** with potassium hydroxide followed by azeotroping to dryness, then treatment with tributyltin hydride and AIBN in benzene at reflux also resulted only in the formation of the rearranged product **7** (Table 1). The relatively poor mass balances in some of these reactions are attributed to decomposition on silica gel chromatography, particularly the elimination of acetate from **7**. Under most conditions significant amounts of unreacted substrate **6** remained after prolonged treatment with tributyltin hydride and AIBN. While other explanations are possible, this is most likely symptomatic of the difficulty of sustaining good chain propagation under the dilute conditions employed to minimize the possibility of premature radical trapping by the hydride.

Table 1. Rearrangement of acid **6** and its salts.

Substrate	Solvent	Recovered **6** (%)[a]	Yield **7** (%)[a]
6	Benzene	9	40
6 Bu_4N^+ salt	Benzene	45	35
6 Bu_4N^+ salt	Tetrahydrofuran	49	20
6 K^+ salt	Benzene	0	63

[a]Yields refer to isolated material.

Overall we are driven to the conclusion that in nonpolar solvents the β-acyloxyalkyl rearrangement is either concerted or proceeds via a contact ion pair in which the rate of recombination to give the rearranged radical significantly exceeds that of trapping by intramolecular carboxylates. Given that the rate constant for intermolecular attack of acetate anion on the resonance-stabilized, photochemically generated 4-methoxystyrene radical cation in acetonitrile solution is 4×10^{10} (mol $L^{-1})^{-1}$ s^{-1} (24), it is perhaps not surprising that collapse of the acetate onto the alkene radical cation, within the confines of the putative contact ion pair, out-competes other modes of trapping, even intramolecular.

Experimental part

2-Acetoxy-2-benzyldihydrocinnamaldehyde (2)

To a solution of 2-benzyldihydrocinnamaldehyde **1** (27.1 g, 0.12 mol) and $Pb(OAc)_4$ (58.9 g, 0.13 mol) in benzene (250 mL) was added BF_3OEt_2 (15.3 mL, 0.12 mol) (25). After stirring overnight at room temperature, the reaction mixture was washed with Na_2CO_3 solution and the washings back extracted with Et_2O (100 mL). The combined organic layer was washed with brine and then dried over $MgSO_4$. Evaporation of the solvent under reduced pressure followed by column chromatography on silica gel (eluent: hexane → hexane–EtOAc, 20:1) gave the title product (11.9 g, 35%), which was used immediately in the next step. ^{1}H NMR ($CDCl_3$) δ: 2.11 (s, 3H), 3.16 (d, 2H, J = 8.6 Hz), 3.23 (d, 2H, J = 8.6 Hz), 7.13–7.31 (m, 10H), 9.26 (s, 1H).

© 2003 NRC Canada

^{13}C NMR ($CDCl_3$) δ: 21.5, 40.3, 86.4, 127.5, 128.8, 131.0, 134.8, 171.3, 201.6.

Allyl 4-acetoxy-4-benzyl-5-phenyl-2*E*-pentenoate (3)

To a solution of **2** (12.9 g, 45.7 mmol) in benzene (200 mL) was added (allyloxycarbonylmethylidene)triphenylphosphorane (16.5 g, 45.7 mmol) (26). The mixture was heated to reflux overnight, then cooled to room temperature, diluted with EtOAc, and washed with water and brine, then dried over $MgSO_4$. Evaporation of the solvent under reduced pressure followed by column chromatography on silica gel (eluent: hexane) gave the target product **3** (9.1 g, 54%). ^{1}H NMR ($CDCl_3$) δ: 1.95 (s, 3H), 3.20 (d, 2H, J = 8.3 Hz), 3.63 (d, 2H, J = 8.3 Hz), 4.62–4.64 (m, 2H), 5.23–5.31 (m, 2H), 5.64 (d, 1H, J = 9.5 Hz), 5.86–5.94 (m, 1H), 6.90 (d, 1H, J = 9.5 Hz), 7.10–7.27 (m, 10H). ^{13}C NMR ($CDCl_3$) δ: 22.5, 43.4, 65.4, 84.8, 118.4, 120.9, 127.3, 128.5, 131.0, 132.5, 135.7, 150.1, 165.9, 170.7. Anal. calcd. for $C_{23}H_{24}O_4$: C 75.80, H 6.64; found: C 75.96, H 6.69.

Allyl 4-acetoxy-4-benzyl-3-[2-(2-bromophenyl)ethylsulfanyl]-5-phenylpentanoate (5)

To an ice-cooled solution of **3** (4.5 g, 12.3 mmol) and 2-(2-bromophenyl)ethylthiol **4** (23) (2.7 g, 12.3 mmol) in DMSO (20 mL) was added NaH (50 mg, 1.2 mmol). The reaction mixture was stirred overnight at room temperature before it was diluted with CH_2Cl_2, then washed with water and brine, and dried over $MgSO_4$. Evaporation of the solvent under reduced pressure followed by column chromatography on silica gel (eluent: hexane → hexane–EtOAc, 10:1) gave the thioether **5** (1.7 g, 24% based on 0.52 g recovered starting material). ^{1}H NMR ($CDCl_3$) δ: 1.81–1.87 (m, 1H), 2.05 (s, 3H), 2.21–2.25 (m, 1H), 2.92–3.07 (m, 4H), 3.22 (s, 2H), 3.57(d, 1H, J = 8.5 Hz), 3.71 (d, 1H J = 8.5 Hz), 4.08–4.10 (m, 1H), 4.44–4.49 (m, 2H), 5.14–5.23 (m, 2H), 5.77–5.83 (m, 1H), 7.05–7.54 (m, 14H). ^{13}C NMR ($CDCl_3$) δ: 22.9, 35.3, 37.0, 38.4, 41.1, 41.7, 49.8, 65.6, 89.0, 118.5, 124.8, 127.2, 127.3, 127.9, 128.55, 128.61, 128.67, 131.2 131.4, 132.5, 133.3, 136.9, 137.2, 140.0 171.1, 171.8. Anal. calcd. for $C_{31}H_{33}BrO_4S$: C 64.02, H 5.72; found: C 64.44, H 5.69.

4-Acetoxy-4-benzyl-3-[2-(2-bromophenyl)ethylsulfanyl]-5-phenylpentanoic acid (6)

To an ice-cooled solution of **5** (1.1 g, 1.9 mmol), $Pd(PPh_3)_4$ (55 mg, 0.05 mmol), and PPh_3 (25 mg, 0.1 mmol) in CH_2Cl_2 (50 mL) was added pyrrolidine (1.6 mL). After stirring for 1.5 h at room temperature, the reaction mixture was washed with 1 N HCl, water, and brine, then dried over $MgSO_4$. Evaporation of the solvent under reduced pressure followed by column chromatography on silica gel (eluent: hexane–EtOAc, 5:1 → 1:3) gave the title acid **6** (1.0 g, 98%). ^{1}H NMR ($CDCl_3$) δ: 1.72–1.78 (m, 1H), 2.04 (s, 3H), 2.15–2.20 (m, 1H), 2.96–3.01 (m, 4H), 3.18 (s, 2H), 3.54 (d, 1H, J = 8.5Hz), 3.69 (d, 1H, J = 8.5Hz), 4.01–4.04 (m, 1H), 7.05–7.51 (m, 14H). ^{13}C NMR ($CDCl_3$) δ: 22.9, 35.5, 36.9, 37.9, 41.1, 41.7, 49.5, 89.1, 124.8, 127.3, 127.4, 127.9, 128.6, 128.7, 131.1, 131.4, 133.3, 136.8, 137.1, 139.9, 171.2, 176.7. Anal. calcd. for $C_{28}H_{29}BrO_4S$: C 62.11, H 5.40; found: C 62.33, H 5.40.

3-Acetoxy-4-benzyl-5-phenylpentanoic acid (7)

A solution of Bu_3SnH (59.6 μL, 0.22 mmol) and AIBN (1.5 mg, 9.2 μmol) in benzene (3.1 mL) was added dropwise over 3 h with the aid of a syringe pump to a solution of **6** (100 mg, 0.18 mmol) in benzene (3.1 mL) at reflux under Ar. After heating to reflux for a further 1 h, the reaction mixture was cooled to room temperature and concentrated under reduced pressure. The residue was dissolved in MeCN (1 mL) and extracted with hexanes (3 × 3 mL). The acetonitrile layer was concentrated under reduced pressure and purified by column chromatography on silica gel (eluent: hexane–EtOAc, 2:1) to afford **7** (24.1 mg, 40%) ^{1}H NMR ($CDCl_3$) δ: 1.96 (s, 3H), 2.42–2.46 (m, 1H), 2.55–2.71 (m, 6H), 5.23–5.26 (m, 1H), 7.07–7.30 (m, 10H). ^{13}C NMR ($CDCl_3$) δ: 21.3, 36.3, 36.6, 45.4, 71.8, 126.6, 126.7, 128.8, 128.9, 129.33, 129.39, 140.1, 140.3, 170.8, 175.6: ESI-HR-MS calcd. for $C_{20}H_{22}NaO_4$: 349.1416; found: 349.1428 ($[M + Na]^+$).

Acknowledgement

We thank the National Science Foundation (NSF) (CHE 9986200) for support of this work.

References

1. A.L.J. Beckwith, D. Crich, P.J. Duggan, and Q. Yao. Chem. Rev. **97**, 3273 (1997).
2. P.O. Whitted, J.H. Horner, M. Newcomb, X. Huang, and D. Crich. Org. Lett. **1**, 153 (1999).
3. M. Newcomb, J.H. Horner, P.O. Whitted, D. Crich, X. Huang, Q. Yao, and H. Zipse. J. Am. Chem. Soc. **121**, 10 685 (1999).
4. (*a*) J.-M. Surzur and P. Teissier. C. R. Acad. Sci. Fr. Ser. C, **264**, 1981 (1967); (*b*) D.D. Tanner and F.C. Law. J. Am. Chem. Soc. **91**, 7535 (1969).
5. M. Newcomb, N. Miranda, X. Huang, and D. Crich. J. Am. Chem. Soc. **122**, 6128 (2000).
6. D. Crich, X. Huang, and M. Newcomb. J. Org. Chem. **65**, 523 (2000).
7. D. Crich and W. Huang. J. Am. Chem. Soc. **123**, 9239 (2001).
8. D. Crich, K. Ranganathan, and X. Huang. Org. Lett. **3**, 1917 (2001).
9. D. Crich and K. Ranganathan. J. Am. Chem. Soc. **124**, 12 422 (2002).
10. B.C. Bales, J.H. Horner, X. Huang, M. Newcomb, D. Crich, and M.M. Greenberg. J. Am. Chem. Soc. **123**, 3623 (2001).
11. J.H. Horner, E. Taxil, and M. Newcomb. J. Am. Chem. Soc. **124**, 5402 (2002).
12. D. Crich and X.-Y. Jiao. J. Am. Chem. Soc. **118**, 6666 (1996).
13. S.-Y. Choi, D. Crich, J.H. Horner, X. Huang, M. Newcomb, and P.O. Whitted. Tetrahedron, **59**, 3317 (1999).
14. B.R. Arnold, D. Noukakis, S. Farid, J.L. Goodman, and I.R. Gould. J. Am. Chem. Soc. **117**, 4399 (1995).
15. Pertinent earlier mechanistic studies: (*a*) L.R.C. Barclay, D. Griller, and K.U. Ingold. J. Am. Chem. Soc. **104**, 4399 (1982); (*b*) A.L.J. Beckwith and C.B. Thomas. J. Chem. Soc. Perkin Trans. 2, 861 (1973); (*c*) L.R.C. Barclay, J. Lusztyk, and K.U. Ingold. J. Am. Chem. Soc. **106**, 1793 (1984); (*d*) P. Kocovsky, I. Stary, and F. Turecek. Tetrahedron Lett. **27**, 1513 (1986); (*e*) A. L.J. Beckwith and P.J. Duggan. J. Am. Chem. Soc. **118**, 12 838 (1996).
16. S. Saebo, A.L.J. Beckwith, and L. Radom. J. Am. Chem. Soc. **106**, 5119 (1984).

© 2003 NRC Canada

17. H. Zipse. J. Am. Chem. Soc. **119**, 1087 (1997).
18. H. Zipse and M. Bootz. J. Chem. Soc. Perkin Trans. 2, 1566 (2001).
19. D. Crich and X.-S. Mo. J. Am. Chem. Soc. **120**, 8298 (1998).
20. M. Bonifacic, I. Stefanic, G.L. Hug, D.A. Armstrong, and K.-D. Asmus. J. Am. Chem. Soc. **120**, 9930 (1998).
21. Z. Su, P.S. Mariano, D.E. Falvey, U.C. Yoon, and S.W. Oh. J. Am. Chem. Soc. **120**, 10 676 (1998).
22. For radical generation by intramolecular homolytic substitution at sulfur see (*a*) K.U. Ingold and B.P. Roberts. Free radical substitution reactions: Bimolecular homolytic substitutions at saturated multivalent atoms. Wiley, New York. 1971; (*b*) J.A. Kampmeier, R.B. Jordan, M.S. Liu, H. Yamanaka, and D.J. Bishop. *In* Organic free radicals. ACS Symposium Series. No 69. *Edited by* W.A. Pryor. ACS, Washington. 1978. pp. 275; (*c*) C.H. Schiesser and L.M. Wild. Tetrahedron, **52**, 13 265 (1996); (*d*) T. Ooi, M. Furuya, D. Sakai, and K. Maruoka. Adv. Synth. Catal. **343**, 166 (2001); (*e*) D. Crich and Q. Yao. J. Org. Chem. **61**, 3566 (1996).
23. D. Crich, D.-H. Suk, and X. Hao. Tetrahedron, **58**, 5789 (2002).
24. L.J. Johnston and N.P. Schepp. J. Am. Chem. Soc. **115**, 6564 (1993).
25. P. Calinaud and J. Gelas. Bull. Soc. Chim. Fr. 1155 (1974).
26. Y. Elemes and C.S. Foote. J. Am. Chem. Soc. **114**, 6044 (1992).

© 2003 NRC Canada

Vacuum pyrolysis of *N*,*N*-dimethylbicyclo-[3.2.0]hepta-3,6-dien-1-amine — He I ultraviolet photoelectron spectroscopic and computational studies[1]

Tom Bajorek and Nick H. Werstiuk

Abstract: The photoelectron spectra of *N*,*N*-dimethylbicyclo[3.2.0]hepta-3,6-dien-1-amine (**1**) and its pyrolysate were obtained using an unique ultraviolet (UV) photoelectron (PE) spectrometer interfaced with a CW CO_2 laser. Pyrolysis of **1** in the source chamber of the PE spectrometer initially generates the transient *N*,*N*-dimethylcyclohepta-1*E*,3*Z*,5*Z*-trien-1-amine (**2**) — the computed barrier is 21.5 kcal mol^{-1} — that isomerizes to the all-cis isomer with a barrier of only 5.0 kcal mol^{-1}. There is no evidence for the formation of *N*,*N*-dimethycyclohepta-1*Z*,3*E*,5*Z*-trien-1-amine (**4**), formation of which has an zero-point-energy corrected barrier of 28.4 kcal mol^{-1}. A PE spectrum of an authentic sample of *N*,*N*-dimethylcyclohepta-1*Z*,3*Z*,5*Z*-trien-1-amine (**3**) correlated well with the pyrolysis spectrum. Molecular orbitals and their energies were obtained with Becke3LYP calculations.

Key words: vacuum pyrolysis, *N*,*N*-dimethylbicyclo[3.2.0]hepta-3,6-dien-1-amine, photoelectron spectroscopy, DFT calculations.

Résumé : Faisant appel à un spectrophotomètre photoélectronique (PE) ultraviolet (UV) unique lié à un laser à CO_2 « CW », on a déterminé les spectres photoélectroniques de la *N*,*N*-diméthylbicyclo[3.20]hepta-3,6-dién-1-amine (**1**) et de son produit de pyrolyse. La pyrolyse du composé **1** dans la source du spectrophotomètre PE conduit initialement à la formation d'une espèce transitoire, la *N*,*N*-diméthylcyclohepta-1*E*,3*Z*,5*Z*-trién-1-amine (**2**) avec une barrière calculée de 21,5 kcal mol^{-1}; celle-ci s'isomérise en isomère complètement cis avec une barrière de 5,0 kcal mol^{-1}. On n'a observé aucune indication pour suggérer la formation de la *N*,*N*-diméthylcyclohepta-1*Z*,3*E*,5*Z*-trién-1-amine (**4**) pour laquelle la barrière corrigée à l'énergie au point zéro est de 28,4 kcal mol^{-1}. Un spectre PE d'un échantillon authentique de *N*,*N*-diméthylcyclohepta-1*Z*,3*Z*,5*Z*-trién-1-amine (**3**) présente une bonne corrélation avec celui du spectre du produit de la pyrolyse. On a aussi obtenu les orbitales moléculaires et leurs énergies à l'aide de calculs Becke3LYP.

Mots clés : pyrolyse sous vide, *N*,*N*-diméthylbicyclo[3.20]hepta-3,6-dién-1-amine, spectroscopie photoélectronique, calculs « DTF ».

Introduction

Combining ab initio calculations with UV-PE spectroscopy yields information about the bonding and electronic structure of stable molecules and transient species that is provided by no other technique. We have recently shown through the pyrolysis of bicyclo[3.2.0]hept-6-en-2-one that *E*,*Z* isomers of cyclohepta-2,4-dien-1-one may be differentiated and identified with the combination of PE spectroscopy and MO calculations (1). The cyclobutene moiety of bicyclo[3.2.0]hept-6-en-2-one undergoes a thermal conrotatory electrocyclic reaction in accord with the Woodward–Hoffmann rules with two products being possible, one with the trans double bond at the C1-C2 position and one with the trans double bond at the C3-C4 position. It was observed experimentally that only the product with the trans double bond between C4 and C5 was generated. This was also confirmed by DFT calculations. Houk and co-workers (2) have computationally investigated the preferential direction of twisting of the breaking σ bond in thermal electrocyclic reactions of substituted cyclobutenes and found a computational way of predicting the stereoselectivity of the thermal cyclobutene ring opening. The term "torquoselectivity" was introduced to describe this type of stereoselective process (2*c*). Based on their finding the authors have concluded that electron-donating substituents preferentially rotate outward while electron-withdrawing substituents preferentially rotate inward. It has been shown that electronic control dominates over the steric influence in the conrotatory ring opening both computationally and experimentally (2, 3). The results we obtained on bicyclo[3.2.0]hept-6-en-2-one are in accord with the proposal by Houk.

Previous studies on bicyclo[3.2.0]hepta-3,6-diene established the product to be *Z*,*Z*,*Z*-1,3,5-cycloheptatriene, sug-

Received 4 June 2003. Published on the NRC Research Press Web site at http://canjchem.nrc.ca on 9 December 2003.

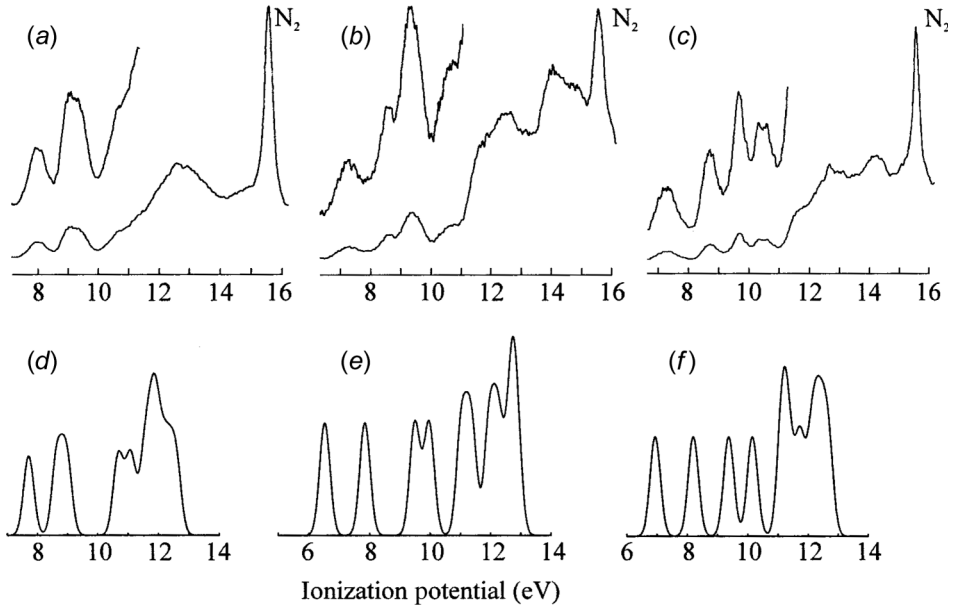
T. Bajorek and N.H. Werstiuk.[2] Department of Chemistry, McMaster University, Hamilton, ON L8S 4M1, Canada.

[1]This article is part of a Special Issue dedicated to Professor Ed Piers.

[2]Corresponding author (e-mail: werstiuk@mcmaster.ca).

 doi: 10.1139/V03-158 © 2003 NRC Canada

Fig. 1. Experimental and simulated partial PE spectra of: (*a*) **1**; (*b*) pyrolysate of **1**; (*c*) **3**; (*d*) simulated partial PE spectrum of **1**; (*e*) simulated partial PE spectrum of **2**; and (*f*) simulated partial PE spectrum of **3**.



gesting that the thermal ring opening occurs via the thermally forbidden disrotatory path (4, 5). We undertook the photoelectron spectroscopic and computational investigation of the pyrolysis of *N*,*N*-dimethylbicyclo[3.2.0]hepta-3,6-dien-1-amine (**1**) to study the electrocyclic ring opening of the cyclobutene moiety of a fused ring system substituted with an electron-donating group. This work was aimed at the determinating whether this bicyclic system substituted with a strong electron-donating group undergoes the thermally allowed conrotatory ring expansion or follows the thermally forbidden disrotatory path. This study also allowed us to establish whether the theory of torquoselectivity applies to a bicyclic system. The results of our computational and experimental studies are reported in this paper.

Experimental

The PE spectra in this investigation were recorded using a locally build PE spectrometer interfaced with a CW CO_2 laser and calibrated using the IP band of N_2, which is seen at 15.6 eV in the experimental spectra (6). The linearity of the spectral scale was established by using the two lowest IP bands of methyl iodide at 9.54 and 10.16 eV, as well, prior to the experiments. Pyrolysis of the starting material was accomplished using the CW CO_2 laser focused on a tip of a quartz nozzle of the probe directly in the source chamber of the PE spectrometer. In this way, the laser is used as a directed heat source that produces a 2 to 3 mm hot zone 10 mm away from the ionization zone. Laser settings and temperatures at the nozzle were calibrated by measuring the temperature with a thermocouple inserted into a closed tip quartz probe positioned in the source of the PE spectrometer. The temperature of approximately 600 °C used in these experiments was obtained with a laser power setting of approximately 55 W.

Becke3LYP/6-31+G(*d*) DFT (7) calculations predict ionization potentials (IPs) with good accuracy (8) and simulated PE spectra calculated from MO energies with a FORTRAN program PESPEC (9) can be used for assigning the bands of experimental PE spectra and for identifying products of pyrolysis reactions. DFT calculations were performed with Gaussian 98 (10). Initial molecular geometries were generated using HyperChem (11). Displays of molecular orbitals and molecular geometries were obtained with Molekel (12).

Results and discussion

The photoelectron spectrum of **1** shows two distinct, broad IPs with vertical ionization potentials (IP_vs) at 8.0 and 9.1 eV as shown in Fig. 1*a*. The first IP corresponds to the highest occupied molecular orbital (HOMO) which is mainly the lone pair of nitrogen with a contribution from the bridging σ bond that is illustrated as $n_N(\sigma)$ in Fig. 2. The experimental and calculated IP_vs are listed in Table 1. The predicted first IP is lower than the experimentally observed IP_v by 0.29 eV. A similar difference between the predicted and experimental IP_vs is observed for the second band that results from the overlap of two IPs. The predicted IP_vs at 8.65 and 8.97 eV correspond to HOMO-1 and HOMO-2, both of which have π character (Fig. 2). Taking the average between these two calculated IP_vs and comparing the value to the observed IP yields a difference of 0.29 eV. Overall, the simulated PE spectrum of **1** (Fig. 1*d*) correlates well with the experimental spectrum. The simulation shows two broad bands that are similar in shape and intensity to the IPs observed experimentally.

Upon pyrolysis, **1** yields a new PE spectrum (Fig. 1*b*). A new band appears at 7.3 eV and broad second and third bands are found at 8.7 and 9.7 eV, respectively. A fourth IP at approximately 10.4 eV appears as a shoulder on the very broad feature beginning at 11 eV. While the calculated first IP_v of the *E*,*Z*,*Z* isomer **2** is at 6.52 eV, a band is not seen below 7 eV in the pyrolysis spectrum when the spectrum was scanned between 6–16 eV. The simulated spectrum of **2**

© 2003 NRC Canada

Fig. 2. Becke3LYP molecular orbitals of 1. MO contour value is 0.08.

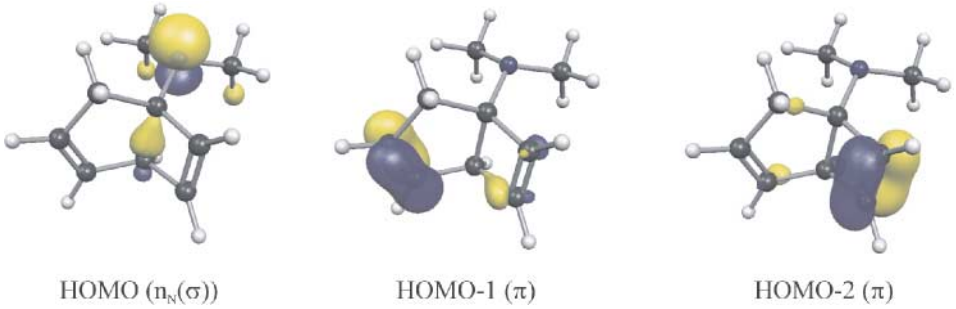


Table 1. Experimental and calculated Becke3LYP ionization potentials.

Compound	Ionization potential (eV)				
1	Exp.	8.0	-------9.1-------		—
	B3LYP	7.71	8.65	8.97	10.68
PY[a]	Exp.	7.30	8.7	9.4	10.4
2	Exp.	—	—	—	—
	B3LYP	6.52	7.84	9.49	9.96
4	Exp.	—	—	—	—
	B3LYP	7.19	7.82	8.64	9.74
3	Exp.	7.3	8.7	9.7	10.4
	B3LYP	6.94	8.21	9.38	10.16

[a]The pyrolysate of **1**.

is displayed as Fig. 1*e*. The difference between the first calculated IP_v of **2** and the first experimentally observed IP_v of the pyrolysate is 0.78 eV. Similarly, the difference between the second computed IP_v and the second experimental IP_v is 0.86 eV. These differences between the theoretical and experimental ionization potential are too large to allow for the assignment of the pyrolysis spectrum to **2**.

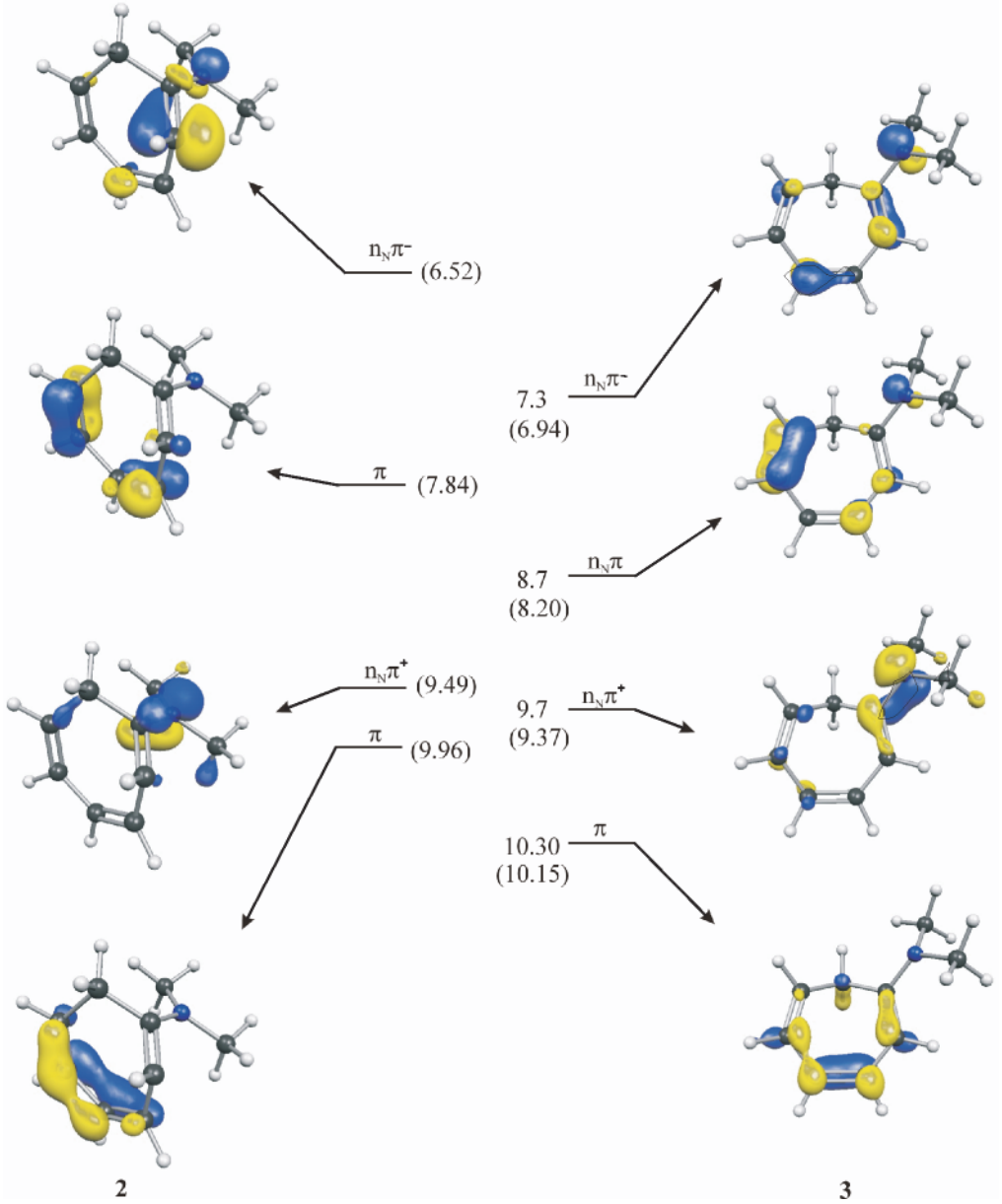
We also synthesized an authentic sample of *N*,*N*-dimethylcyclohepta-1*Z*,3*Z*,5*Z*-trien-1-amine (**3**) (13) and recorded its spectrum (Fig. 1*c*) as it is a potential product of the forbidden disrotatory ring opening of **1**. The PE spectrum of **3** shows four distinct bands at 7.3, 8.7, 9.7, and 10.4 eV. The differences between the experimental and calculated IP_vs are 0.36, 0.50, 0.33, and 0.25 eV. The simulated spectrum of **3** (Fig. 1*f*) correlates very well with the experimentally observed one showing four distinct IPs. These IPs of **3** correlate with the four Becke MOs HOMO to HOMO-3 shown in Fig. 3. The HOMO has antibonding character between the nitrogen lone pair and the π system of the adjacent C1-C2 double bond and is denoted as $n_N\pi^-$. HOMO-1, which is denoted as $n_N\pi$, also exhibits mixing between the nitrogen lone pair and the π system of the cycloheptatrienyl group. In HOMO-2 the nitrogen lone pair and the π system of the adjacent double bond mix with bonding character and are shown as $n_N\pi^+$ in Fig. 3. The fourth MO (HOMO-3) has π-bonding character that includes the three double bonds of the cycloheptatriene ring and no contribution from the nitrogen lone pair. Figure 3 displays the first four MOs of **2** and **3** and their ionization potentials. The HOMO of **2** is also a $n_N\pi^-$ MO but it exhibits a larger p coefficient on the strained trans double bond than is observed in the HOMO of **3**. HOMO-1 of **2** is π rather than $n_N\pi$ type as observed in **3** and exhibits mixing with the nitrogen lone pair. HOMO-2 of **2** also has a $n_N\pi^+$ character as seen in **3**. In this case, the bonding interaction is predominantly localized at the C1—N bond because the double bond is twisted, unlike the case for **3** where the bonding interaction in HOMO-2 includes N, C1, and C2. HOMO-3 of **2** has π-bonding character between C3-C4-C5-C6 and there is no contribution from the trans double bond, unlike HOMO-3 of **3** that includes all three double bonds.

It is known that *N*,*N*-dimethylcyclohepta-1,3,5-trien-7-amine (**9**) yields **3** via a 1,5-hydrogen shift (13) upon pyrolysis. Consequently we prepared **9** — its PE spectrum is displayed as Fig. 4*a* — and studied its pyrolysis. In fact, the spectrum obtained from the pyrolysis of **9** (Fig. 4*b*) also exhibits broadened second and third bands and the PE spectra obtained upon pyrolysis of **1** (Fig. 1*b*) and **9** show common features. The broadening of the bands observed in the pyrolysis spectra of **1** and **9** at 8.7 and 9.4 eV undoubtedly results from the free rotation of the dimethylamino group and there is a change in the conformation populations at the elevated temperatures of the pyrolysis experiments. Calculations show that *N*,*N*-dimethylcyclohepta-1,3,5-trien-1-amine (**3**) can exist in two conformations. One where the lone pair of the nitrogen of the dimethylamino group points in a direction opposite to the C7 methylene group (Fig. 5, **3a**), and one where the dimethylamino lone pair points in the same direction as the C7 methylene group (Fig. 5, **3b**). The energy barrier for the rotation of the dimethylamino group was found to be 8.3 kcal mol^{-1}. The calculated first four IP_vs of **3a** are: 6.94, 8.21, 9.38, and 10.16 eV. The predicted first four IP_vs of **3b** are: 6.87, 8.31, 9.47, and 10.21 eV; the rotation of the dimethylamino group has the largest impact on the second and third IPs. We also found that heating **3** under the pyrolysis conditions yields a spectrum (Fig. 4*c*) with broadened second and third bands. The calculations predict that the second and third IP bands should be affected most by the free rotation of the dimethylamino group and this appears to be in accord with experiment. It is apparent that **3** is the product of the pyrolysis of **1**.

That **1** yields **3** suggests that the thermal electrocyclic reaction follows the forbidden disrotatory path. Yet a transition state calculation — the zero-point-energy corrected barrier being 21.5 kcal mol^{-1} — for the ring opening of **1** located transition state **TS1** that leads to **2**. The computed, zero-point-energy corrected barrier — the transition state is **TS3** — for the ring opening of **1** to **4**, which is the *E*,*Z*,*E* isomer is 28.4 kcal mol^{-1}. The transition state for the forbidden disrotatory process that would link **1** and **3** could not be located. Exhaustive attempts to locate this transition state

© 2003 NRC Canada

Fig. 3. Becke3LYP molecular orbitals (HOMO–HOMO-3) of **2** and **3** with assignment of ionization potentials. Values in brackets are the calculated IPs. MO contour value is 0.08.



resulted in the generation of **TS1**. Since **2** is not observed upon the pyrolysis of **1**, we located the transition state for the isomerization of the *E*,*Z*,*Z* isomer **2** to the *Z*,*Z*,*Z* isomer **3**. The transition state **TS2** for this process lies only 5.0 kcal mol^{-1} above **2**. The rearrangement of **1** is illustrated in Scheme 1. In the case of **1**, the dimethylamino group is pyramidalized with the dihedral angle between C1-C8-C9-N being 28.2°. In the case of **2**, this dihedral angle is only 9.3°. This planarization facilitates the n-π interaction of the lone pair with the adjacent trans double bond and may lower the barrier for isomerization with the driving force being the release of strain and the formation of a conjugated cyclic π system. Comparing HOMO-3 of **3** and **2** (Fig. 3), triene **3** is 29.7 kcal mol^{-1} lower in energy than **1** and 22.3 kcal mol^{-1} lower in energy than **2**. According to our calculations, **1** initially undergoes a thermal conrotatory ring opening to yield **2** that isomerizes to **3**. The total and relative energies of the four compounds and the transition states are listed in Table 2.

That barrier for ring opening of **1** is relatively low was confirmed by ^{1}H NMR spectroscopy. A spectrum of **1** was recorded and the sample was allowed to stand at room temperature in the dark. A spectrum obtained after 24 h showed signals due to **3** as determined from the ^{1}H NMR spectrum of an authentic sample of **3**. After 5 days, **1** and **3** were present in a 1:1 ratio.

According to the theory of torquoselectivity, electron donors preferentially favor the formation of a trans double bond to which the electron-donating group is attached, while electron acceptors yield a cis double bond when both substituents are in the cis position on the starting cyclobutene. Thus, an electron-donating group rotates outward upon

© 2003 NRC Canada

Fig. 4. PE spectra of: (*a*) **9**; (*b*) pyrolysate of **9**; (*c*) pyrolysate of **3**.

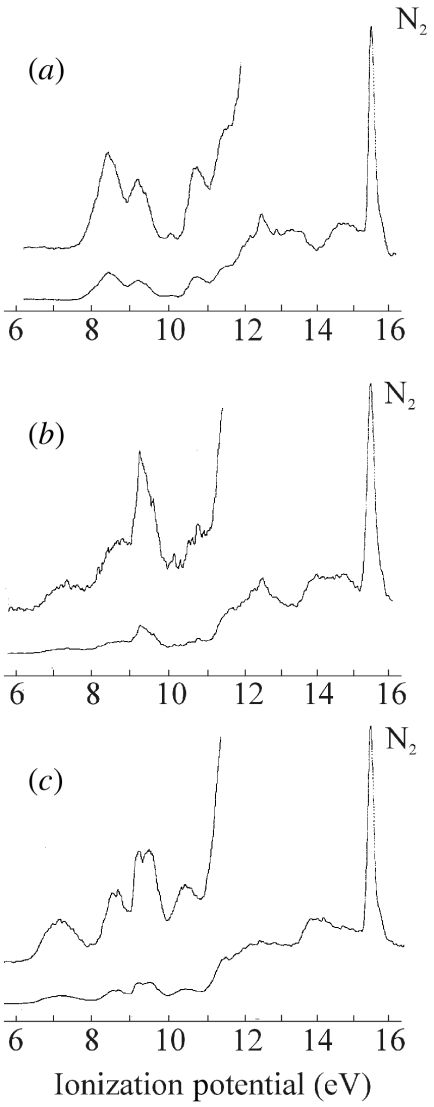
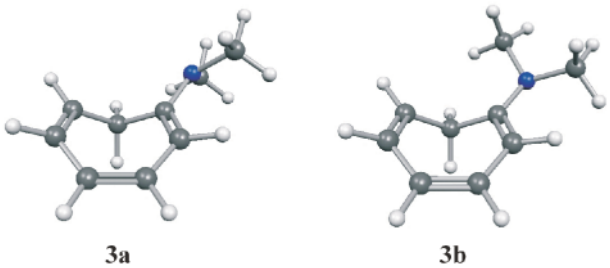


Fig. 5. Becke3LYP equilibrium geometries of **3a** and **3b**.



breaking of the σ bond in the cyclobutene moiety, while an electron acceptor substituent rotates inward (2). In the case of the cyclobutene conrotatory ring opening of **1**, we have found that the inward–outward rotation terminology does not apply in the way described by Houk. The constrained geometry of the bicyclic system does not allow for the rotation of the substituents at the bridgehead carbons of the

Scheme 1. The rearrangement of **1** to **3**.

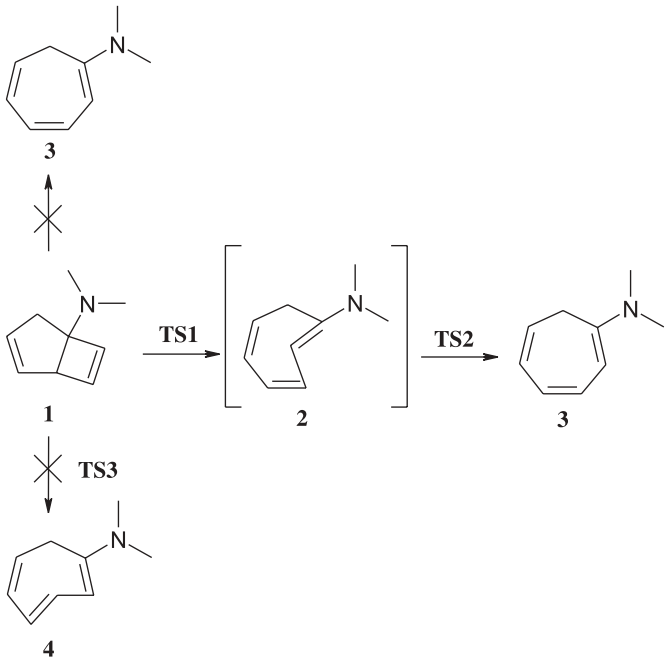


Table 2. ZPVE corrected relative energies of **1**–**4**, **TS1**, **TS2**, **TS3**, and **5**–**8**.

	B3LYP/6-31+G(d) ZPVE corrected relative energy (kcal mol^{-1})
1	0.0
2	7.4
4	20.3
3	–29.7
TS1	21.5
TS2	5.0[a]
TS3	28.4
5	—
6	0.0
7	7.5
8	—
8a	2.9
8b	0.0

[a]The relative energy between **2** and **TS2**.

breaking σ bond. The bridgehead carbons C1 and C4 move away from each other in the transition state as shown by the displacement vectors displayed in Fig. 6*c*, while the substituent undergoes planarization through the movement of the C1—N bond. Fig. 6*a* shows the front view of the transition-state geometry and Fig. 6*b* shows the view along the C1—C2 bond. The dimethylamino group shows marginal movement inward rather that outward, which is contrary to the theoretical predictions that donors preferentially rotate outward. The hydrogen at the C4 position in **1** rotates outward while C5 shows no apparent movement. Nevertheless, the stereochemical outcome is in accord with the theory of torquoselectivity; the electron-donating dimethylamino group leads to the formation of a trans double bond in the final

© 2003 NRC Canada

Fig. 6. Becke3LYP molecular geometries of **TS1**: (*a*) front view with atom numbers; (*b*) view along C2—C1 bond; and (*c*) displacement vectors corresponding to the negative frequency.

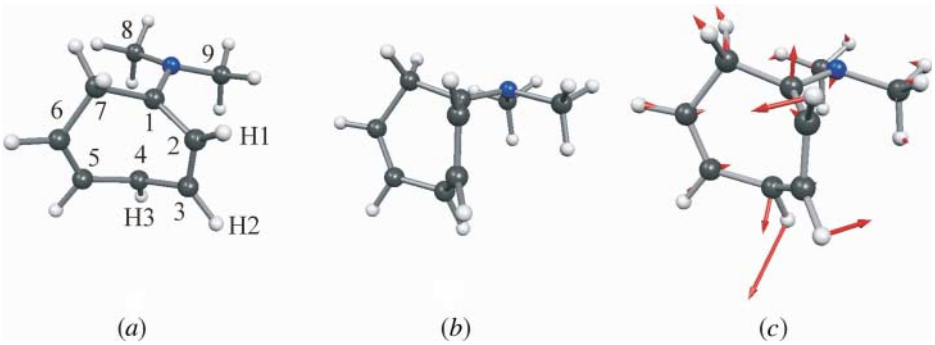


Table 3. Selected Becke3LYP/6-31+G(*d*) bond lengths (Å) and dihedral angles (°).

	1	TS1	2	3	4	5
Bond lengths (Å)						
N—C1	1.460	1.374	1.370	1.393	1.412	1.388
C1—C2	1.525	1.484	1.389	1.374	1.342	1.348
C2—C3	1.340	1.353	1.461	1.437	1.472	
C3—C4	1.529	1.462	1.367	1.373	1.330	
C4—C5	1.504	1.472	1.478	1.441	1.476	
C5—C6	1.341	1.351	1.362	1.355	1.329	
C6—C7	1.510	1.513	1.530	1.506	1.538	
C7—C1	1.559	1.505	1.498	1.523	1.555	
C1—C4	1.613	2.254	2.781	3.143	2.814	
Dihedral angles (°)						
C1-C8-C9-N	28.2	20.3	9.3	18.4	22.6	19.7[a]
N-C1-C2-H1	60.8	94.6	156.9	13.3	8.7	
H2-C3-C4-H3	67.8	33.8	7.0	0.2	175.9	

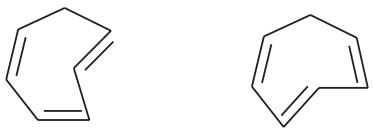
[a]The dihedral angle between C1, the carbons of the methyls of the dimethyamino group, and the nitrogen atom.

product. In going from **1** to **2**, the N—C1 bond becomes shorter by 0.09 Å and the C1—C2 distance decreases by 0.136 Å as the single bond is converted into the strained trans double bond of **2** that is 0.015 Å longer than the corresponding C1-C2 cis double bond of **3** (Table 3). Since there is a break in the conjugation of the π system introduced by the trans double bond between C3-C4 of **4**, all three double bonds are shorter that those in **2** and **3** (Table 3). A calculation on *N*,*N*-dimethyl-*N*-vinylamine (**5**) showed that the amine is pyramidalized with a dihedral angle of 19.7° among C1, the two methyl groups of the amine, and the nitrogen. The C1—N bond of **5** is slightly shorter than in **3** and the C1-C2 double bond is also shorter than in **3** and **2** by 0.026 and 0.041 Å, respectively, but it is only slightly longer than in **4**. Not unexpectedly, conjugation plays a significant role in determining the bond lengths in these molecules.

The thermal conrotatory ring opening of **1** yields **2** and not **4** most likely because **2** has two coplanar double bonds that extend the conjugation. In **4** this conjugation is broken by the trans double bond between C3-C4. Our calculations on unsubstituted cycloheptatriene indicate a difference in energy of 7.5 kcal mol^{-1} between cyclohepta-1(E),3(Z),5(Z)-triene (**6**) and cyclohepta-1*Z*,3*E*,5*Z*-triene (**7**), **6** being lower in energy than **7** (Fig. 7).

A calculation on hexa-1,3,5-triene (**8**) also shows a considerable difference in energy between two hexatrienes that

Fig. 7. Schematic representation of **6** and **7**

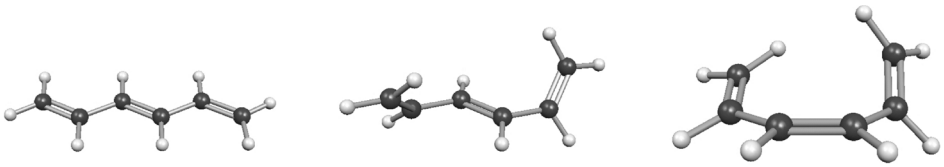


6 **7**

have constrained dihedral angles to resemble those of **6** and **7** (Fig. 8). In hexatriene **8a** the dihedral angles between C1-C2-C3-C4 and C3-C4-C5-C6 have been constrained to 57° to resemble **7**. Similarly in hexatriene **8b**, the dihedral angle between C1-C2-C3-C4 has also been constrained to 57° to resemble **6**. The difference in energy between the two hexatrienes was found to be 2.9 kcal mol^{-1}. The total and relative energies are listed in Table 2. The conjugation of the double bonds in **8b** is reduced, thus increasing the energy. The energy of the system is higher in a case where none of the double bonds are coplanar as in **7** and **4** and it is lower in a case where at least two of the double bonds are conjugated and coplanar as in **6** and **2**. Therefore, the formation of **2** is favored over **4** since in **2** the conjugation is preserved between two double bonds where as in **4** there is a complete break in the conjugation of the π system.

© 2003 NRC Canada

Fig. 8. Becke3LYP optimized geometries of hexatrienes **8**, **8a**, and **8b**.



8 **8a** **8b**

Conclusions

Our computational and PES study of the pyrolysis of *N*,*N*-dimethylbicyclo[3.2.0]hepta-3,6-dien-1-amine (**1**) has shown that the initial product of this reaction is *N*,*N*-dimethylcyclohepta-1*E*,3*Z*,5*Z*-trien-1-amine (**2**) which then isomerizes to *N*,*N*-dimethylcyclohepta-1*Z*,3*Z*,5*Z*-trien-1-amine (**3**) with an energy barrier of 5.9 kcal mol^{-1}. Transition-state calculations at B3LYP/6-31+G(*d*) have shown that the ring opening of the cyclobutene moiety of **1** follows the conrotatory path to give **2** with an energy barrier of 22.8 kcal mol^{-1}. The energy barrier for the ring opening to yield **4** was found to be 30.5 kcal mol^{-1}. Therefore, the PE spectrum of **4** was not observed. The PE spectrum of **2** was also not observed because of the low-energy barrier for the isomerization of the trans double bond in **2** to a cis double bond, which yielded **3** as the product of the pyrolysis. Thus, the thermal reaction of **1** still follows the Woodward–Hoffmann rules. The driving force of this reaction is the release of ring strain and the formation of a thermodynamically more stable **3**, which preserves the coplanarity and resonance of the three conjugated double bonds of the cycloheptatriene ring with the contribution of the resonance from the dimethylamino group.[3]

Acknowledgements

Financial support by the Natural Sciences and Engineering Research Council of Canada (NSERC) is gratefully acknowledged.

References

1. T. Bajorek and N.H. Werstiuk. Chem. Commun. (Cambridge), 648, (2002).
2. (*a*) W. Kirmse, N.G. Rondan, and K.N. Houk. J. Am. Chem. Soc. **106**, 7989 (1984); (*b*) N.G. Rondan and K.N. Houk. J. Am. Chem. Soc. **107**, 2099 (1985); (*c*) W.R. Dolbier, Jr., H. Koroniak, K.N. Houk, and C. Sheu. Acc. Chem. Res. **29**, 471, (1996).
3. K.N. Houk, D.C. Spellmeyer, C.W. Jefford, C.G. Rimbault, Y. Wang, and R.D. Miller. J. Org. Chem. **53**, 2125 (1988).
4. M.R. Willcott and E. Goerland. Tetrahedron Lett. **51**, 6341 (1966).
5. E.W. Otterbacher and J.J. Gajewski. J. Am. Chem. Soc. **103**, 5862 (1981).
6. N.H. Werstiuk, D.N. Butler, and E. Shahid. Can. J. Chem. **65**, 760 (1986).
7. (*a*) A.D. Becke. J. Chem. Phys. **98**, 5648 (1993); (*b*) C. Lee, W. Yang, and R.G. Parr. Phys. Rev. B, **37**, 785 (1988).
8. (*a*) H.M. Muchall, N.H. Werstiuk, and B. Choudhury. Can. J. Chem. **78**, 221 (1998); (*b*) H.M. Muchall, N.H. Werstuik, J.L. Pitters, and M.S. Workentin. Tetrahedron, **55**, 3767 (1999); (*c*) N.H. Werstiuk, H.M. Muchall, J. Ma, and M.T.H. Liu. Can. J. Chem. **76**, 1162 (1998).
9. N.H. Werstiuk, G. Timmins, J. Ma, and T.A. Wildman. Can. J. Chem. **70**, 1971 (1992).
10. M.J. Frisch, G.W. Trucks, H.B. Schlegel, G.E. Scuseria, M.A. Robb, J.R. Cheeseman, V.G. Zakrzewski, J.A. Montgomery, Jr., R.E. Stratmann, J.C. Burant, S. Dapprich, J.M. Millam, A.D. Daniels, K.N. Kudin, M.C. Strain, O. Farkas, J. Tomasi, V. Barone, M. Cossi, R. Cammi, B. Mennucci, C. Pomelli, C. Adamo, S. Clifford, J. Ochterski, G.A. Petersson, P.Y. Ayala, Q. Cui, K. Morokuma, D.K. Malick, A.D. Rabuck, K. Raghavachari, J.B. Foresman, J. Cioslowski, J.V. Ortiz, A.G. Baboul, B.B. Stefanov, G. Liu, A. Liashenko, P. Piskorz, I. Komaromi, R. Gomperts, R.L. Martin, D.J. Fox, T. Keith, M.A. Al-Laham, C.Y. Peng, A. Nanayakkara, M. Challacombe, P.M.W. Gill, B. Johnson, W. Chen, M.W. Wong, J.L. Andres, C. Gonzalez, M. Head-Gordon, E.S. Replogle, and J.A. Pople. Gaussian 98. Revision A.9 [computer program]. Gaussian, Inc., Pittsburgh Penn. 1998.
11. HyperChem™. Hypercube, Inc., 1115 NW 4th Street, Gainesville, Fla.
12. (*a*) P. Flükiger, H.P. Lüthi, S. Portmann, and J. Weber. MOLEKEL 4.3 [computer program]. Swiss Center for Scientific Computing, Manno, Switzerland. 2000–2002; (*b*) S. Portmann and H.P. Luthi. Chimia, **54**, 766 (2000).
13. A.P. Ter Borg, E. Razenberg, and H. Kloosterziel. Rec. Trav. Chim. Pays–Bas, **85**, 774 (1966).

[3] Supplementary data may be purchased from the Directory of Unpublished Data, Document Delivery, CISTI, National Research Council Canada, Ottawa, ON K1A 0S2, Canada (http://www.nrc.ca/cisti/irm/unpub_e.shtml for information on ordering electronically). These data can be obtained, free of charge, via www.ccdc.cam.ac.uk/conts/retrieving.html (or from the Cambridge Crystallographic Data Centre, 12 Union Road, Cambridge CB2 1EZ, U.K.; fax +44 1223 336033; or deposit@ccdc.cam.ac.uk).

© 2003 NRC Canada

Diastereoselective reduction of α-aminoketones: Synthesis of *anti*- and *syn*-β-aminoalcohols[1]

David S. Fraser, Sheldon B. Park, and J. Michael Chong

Abstract: Reduction of *N*-*t*-BOC-protected-*N*-alkyl α-aminoketones with $LiEt_3BH$ or Li(*s*-Bu)$_3$BH furnishes protected *syn*-β-aminoalcohols with high selectivities. In contrast, removal of the BOC group followed by reduction of the aminoketone gives *anti*-β-aminoalcohols with variable selectivities. With aromatic ketones, selectivities are typically high while aliphatic ketones show mediocre to high selectivities depending on steric considerations.

Key words: β-aminoalcohol, diastereoselective reduction.

Résumé : La réduction, à l'aide de $LiEt_3BH$ ou de Li(*s*-Bu)$_3$BH, de *N*-alkyl-α-aminocétones portant un groupe protecteur *N*-*t*-BOC conduit à la formation de *syn*-β-aminoalcools protégés avec des sélectivités élevées. Par ailleurs, si on enlève le groupe BOC, la réduction de l'aminocétone conduit à la formation de β-aminoalcools anti avec des sélectivités variables. Avec les cétones aromatiques, les sélectivités sont généralement élevées alors que les sélectivités obtenues avec les cétones aliphatiques varient de médiocres à élevées suivant l'encombrement stérique.

Mots clés : β-aminoalcool, réduction diastéréosélective.

[Traduit par la Rédaction]

Introduction

The β-aminoalcohol moiety is found in many natural products, pharmaceuticals, and ligands used for asymmetric synthesis (1). Stereoselective approaches to this important class of compounds include nucleophilic additions to α-aminoaldehydes (2) or chiral imine derivatives (3), manipulations of chiral cyanohydrins (4), and reductions of α-aminoketones (5–7).

The stereoselective reduction of α-aminoketones has been a common route to specific diastereomers of β-aminoalcohols and much of the early work in this area has been reviewed by Tramontini (5). This early work consisted only of reductions of arylketones and only a very few good selectivities were achieved. Since then, considerably more research has been carried out and a reasonable understanding of factors affecting syn- and anti-diastereoselectivity is beginning to emerge (6).

As part of our work with α-aminoorganostannanes, we showed that *N*-BOC-*N*-alkyl-aminostannanes can be transmetalated with alkyllithiums and the resulting α-aminoorganolithiums can be trapped with aldehydes to provide β-amino alcohols with complete retention of stereochemistry at the amino centre (8). However, a 1:1 mixture of diastereomers is usually produced (Scheme 1).

Thus, we decided to examine the diastereoselective reduction of α-aminoketones (Scheme 2). We anticipated that the *N*-BOC-amino group would act as the large group in Cram–Felkin-Ahn type reductions such that the syn products **4** would be favoured. Removal of the BOC group would then provide *syn*-aminoalcohols **5**. Conversely, initial removal of the BOC group would give ketones **6** wherein the amino group would be expected to act as a coordinating group in chelation–Cram type reductions so that *anti*-aminoalcohols **7** would predominate. Since either enantiomer of stannane **1** could be prepared from the corresponding acylstannane, this approach would allow for the preparation of any of the four possible diastereomers of β-aminoalcohols from the same acylstannane (9).

Results and discussions

Synthesis of aminoketones

In some cases, aminoketones could be prepared in good yields directly from the corresponding organolithium by reaction with dimethylamides. However, this route gave low yields with hindered organolithiums. Thus, trapping with aldehydes followed by oxidation was usually used. For aromatic aldehydes, yields of trapped products were typically 80%–95% while aliphatic aldehydes usually gave lower (65%–78%) yields, consistent with the expectation that enolization may be a competing side-reaction. Oxidation of alcohols under Swern conditions yielded no identifiable products while the chromium reagents PDC and PCC gave only modest yields. Eventually it was found that TPAP oxidation (10) gave excellent (80%–95%) yields of ketones **3** (Table 1).

Received 14 July 2003. Published on the NRC Research Press Web site at http://canjchem.nrc.ca on 10 December 2003.

This paper is dedicated to Professor Ed Piers, a true master of organic chemistry.

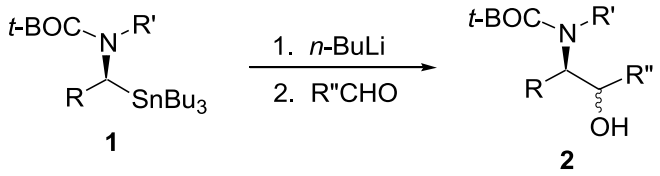
D.S. Fraser, S.B. Park, and J.M. Chong.[2] Guelph–Waterloo Centre for Graduate Work in Chemistry and Biochemistry (GWC[2]), Department of Chemistry, University of Waterloo, Waterloo, ON N2L 3G1, Canada.

[1]This article is part of a Special Issue dedicated to Professor Ed Piers.

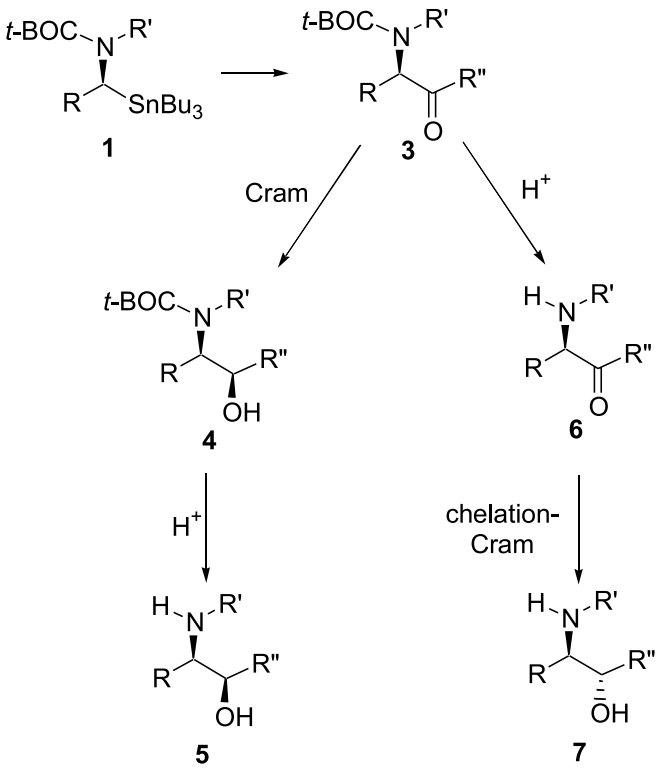
[2]Corresponding author (e-mail: jmchong@uwaterloo.ca).

 doi: 10.1139/V03-165 © 2003 NRC Canada

Scheme 1.



Scheme 2.

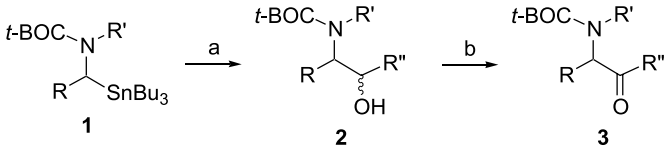


Cram-selective reduction of *t*-BOC-protected aminoketones

Reductions of ketone **3a** with DIBAL-H (toluene, –78 °C) or $Zn(BH_4)_2$ proceeded with poor selectivities to give mixtures of diastereomeric alcohols in ratios of 60:40 and 65:35, respectively. In contrast, reduction of **3a** with L-selectride® ($Li(s\text{-}Bu)_3BH$) gave a near quantitative yield of a single alcohol (Table 2, entry 1). L-Selectride® also reduced the more hindered ketone **3b** with essentially complete diastereoselectivity; however, complete reduction of ketone **3b** could not be achieved, even with a large excess (10 equiv.) of reagent. Fortunately, the related but less-bulky reagent Super-hydride® (lithium triethylborohydride) reduced ketone **3b** to afford alcohol **4b** in near quantitative yield, albeit with slightly diminished stereoselectivity (Table 2, entry 3).

Other ketones were also reduced with Super-hydride®. In general, arylketones (Table 2, entries 4–8) provided the syn-isomer as the only one detectable by ^{1}H NMR spectroscopy. For the arylketones examined, only the isopropyl=substituted ketone **3b** gave some of the anti-isomer. This is consistent with expectations based on a Felkin-Anh model where the BOC-amino group acts as the large group; with R = *n*-alkyl, essentially complete diastereoselectivity is observed

Table 1. Preparation of aminoketones from α-aminoorganostannanes.[a]



1a: R = Et, R' = Me
1b: R = *i*-Pr, R' = Me
1c: R = Me, R' = Me
1d: R = *n*-C_5H_{11}, R' = Me
1e: R = *c*-C_6H_{11}, R' = Me
1f: R = Me, R' = Bn
1g: R = *n*-C_5H_{11}, R' = Bn

Entry	Stannane	R″	Ketone	Yield of **2**/**3**[b] (%/%)
1	**1a**	Ph	**3a**	81[c]
2	**1b**	Ph	**3b**	94/83
3	**1c**	Ph	**3c**	91/92
4	**1d**	Ph	**3d**	84/91
5	**1e**	Ph	**3e**	81/86
6	**1f**	Ph	**3f**	92/96
7	**1g**	Ph	**3g**	88/95
8	**1f**	*n*-C_5H_{11}	**3h**	67/90
9	**1d**	Et	**3i**	70/89
10	**1d**	*n*-C_5H_{11}	**3j**	66/82
11	**1d**	*i*-Pr	**3k**	77/94
12	**1d**	*t*-Bu	**3l**	78/84
12	**1b**	*n*-C_5H_{11}	**3m**	65/80
14	**1c**	*n*-C_5H_{11}	**3n**	77/87

[a]Conditions: a (*n*-BuLi, THF, –78 °C then R"CHO); b (NMO, cat. TPAP, $CH2Cl_2$, rt).
[b]Isolated yields of purified (flash chromatography) **2** and **3**.
[c]Prepared directly from stannane **1a** using *n*-BuLi then $PhC(O)NMe_2$.

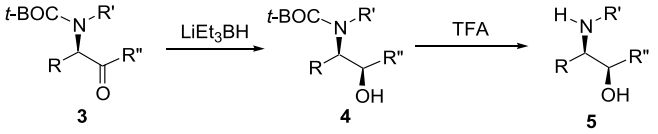
but with R = *i*-Pr, the larger isopropyl group offers a small amount of competition. With alkyl ketones, selectivities were not perfect but still very good (Table 2, entires 9–16). There is a general trend in which the selectivity increases as the steric bulk of R″ increases (Table 2, compare entries 11–13). The lowest selectivity was observed with the isopropyl-substituted ketone **3m**, which gave a 91:9 mixture of diastereomers. Reduction of **3m** with L-Selectride® gave only the syn-isomer but the reaction was sluggish and only low conversion was observed (Table 2, entry 15), a result comparable to that previously noted for isopropyl-substituted ketone **3b** (Table 2, entries 2, 3). In contrast, the relatively unhindered ketone **3i** was efficiently reduced with L-Selectride® to provide **4i** in high yield (Table 2, entry 10). Thus, it is apparent that the very bulky L-Selectride® can give very high selectivities but is subject to steric constraints while Super-hydride® consistently gives good to excellent selectivities, even for hindered systems. High syn selectivity could be achieved for all of the compounds studied.

Preparation of aminoalcohols 5 and analysis of their ^{1}H NMR spectra

Analysis of the ^{1}H NMR spectra of the alcohols **4** was complicated by the presence of carbamate rotamers which often led to broad lines. Deprotection with TFA gave the products **5**. The yields for these deprotections were lower than would normally be expected for this sort of procedure,

© 2003 NRC Canada

Table 2. syn-Selective reductions of *t*-BOC-protected α-aminoketones.



Entry	**3**	R	R′	R″	Yield of **4x**[a]	syn:anti[b]	Yield of **5x**[a]
1[c]	**3a**	Et	Me	Ph	—	>99:<1	100[d]
2[c]	**3b**	*i*-Pr	Me	Ph	70	>99:<1	nd
3	**3b**	*i*-Pr	Me	Ph	100	98:2	75
4	**3c**	Me	Me	Ph	98	>99:<1	63
5	**3d**	*n*-C_5H_{11}	Me	Ph	100	>99:<1	74
6	**3e**	*c*-C_6H_{11}	Me	Ph	93	>99:<1	71
7	**3f**	Me	Bn	Ph	100	>99:<1	90
8	**3g**	*n*-C_5H_{11}	Bn	Ph	94	>99:<1	89
9	**3i**	*n*-C_5H_{11}	Me	Et	81	96:4	86
10[c]	**3i**	*n*-C_5H_{11}	Me	Et	99	>99:<1	nd
11	**3j**	*n*-C_5H_{11}	Me	*n*-C_5H_{11}	86	96:4	79
12	**3k**	*n*-C_5H_{11}	Me	*i*-Pr	81	97:3	38
13	**3l**	*n*-C_5H_{11}	Me	*t*-Bu	99	>99:<1	85
14	**3m**	*i*-Pr	Me	*n*-C_5H_{11}	82	91:9	77
15[c]	**3m**	*i*-Pr	Me	*n*-C_5H_{11}	25	>99:<1	nd
16	**3n**	Me	Me	*n*-C_5H_{11}	87	96:4	75

Note: nd is not detected.
[a]Isolated yields. **x** = same letter as ketone precursor.
[b]Determined by ^{1}H NMR spectroscopy. ">99:<1" denotes no signal for the other isomer was detected.
[c]Reduction was carried out with Li(*s*-Bu)$_3$BH.
[d]Yield of **5a** from **3a**.

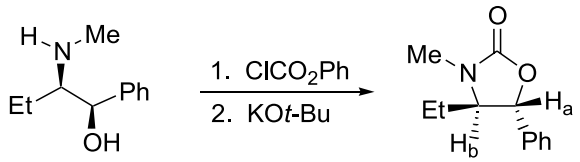
possibly because the β-aminoalcohols are somewhat soluble in water, and complete extraction from the basic aqueous phase is not easily achieved.

With the aminoalcohols in hand, they could be converted to their corresponding oxazolidinones, a method previously used to determine the relative configuration of β-aminoalcohols (11). Thus, it is known that cyclization of a *syn*-β-aminoalcohol leads to a *trans*-oxazolidinone, which has a smaller J_{ab} than the corresponding *cis*-oxazolidinone derived from an *anti*-β-aminoalcohol, consistent with expectations based on Karplus relationships. For example, cyclization of **5a** using Wuts and Pruitt's method (12) gave oxazolidinone **8a** which exhibited J_{ab} = 6.0 Hz, confirming trans stereochemistry for **8a** and hence syn stereochemistry for **5a** (Scheme 3).

Rather than convert all of the aminoalcohols to oxazolidinones, we determined the stereoselectivity of the reductions based on the observation that the carbinol protons (H_a) of all of the *N*-methyl-β-aminoalcohols prepared have significantly different chemical shifts for the syn- and anti-diastereomers (Table 3).

There is a signal separation of at least 0.15 ppm and usually 0.3–0.5 ppm in each case that allows a positive identification of each diastereomer. In addition, the important trend is that H_a of the anti-diastereomer always appears downfield of the syn-isomer. This allows the assignment of stereochemistry without the need to prepare oxazolidinone derivatives if spectral data for both isomers is available.

Scheme 3.



5a J_{ab} = 6.0 Hz **8a**

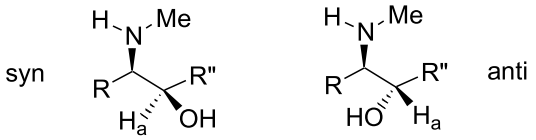
Chelation-controlled reduction with $Zn(BH_4)_2$

Removal of the BOC protecting group from ketones **3** with TFA gave quantitative yields of the aminoketones **6**. These ketones were not very stable and were used immediately. Subsequent reduction with $Zn(BH_4)_2$ gave predominantly the anti-aminoalcohols in the yields and selectivities shown in Table 4. Reductions with $NaBH_4$ generally gave lower selectivities (e.g., **6a** afforded a syn:anti ratio of 10:90) and were not explored further.

For the phenylketones examined (Table 4, entries 1–7), selectivities were generally excellent. In many cases, only the anti-diastereomer was detected. The lowest selectivity was observed with ketone **6c** (R = Me), where 7% of the syn-diastereomer was formed. The lower selectivity can be attributed to the relatively small size of the CH_3 group, which would be less effective at blocking the disfavoured side of the carbonyl in the Cram chelation model.

© 2003 NRC Canada

Table 3. Partial ^{1}H NMR data for *N*-methyl β-aminoalcohols.[a]



5 **7**

β-Aminoalcohol	R	R′	δ H_a syn	δ H_a anti
5a/7a	Et	Ph	4.30	4.83
5b/7b	*i*-Pr	Ph	4.43	4.77
5c/7c	CH_3	Ph	4.06	4.70
5d/7d	*n*-C_5H_{11}	Ph	4.32	4.89
5e/7e	*c*-C_6H_{11}	Ph	4.51	4.81
5i/7i	*n*-C_5H_{11}	Ph	3.24	3.55
5j/7j	*n*-C_5H_{11}	*n*-C_5H_{11}	3.31	3.70
5k/7k	*n*-C_5H_{11}	*i*-Pr	3.10	3.25
5l/7l	*n*-C_5H_{11}	*t*-Bu	2.94	3.38
5m/7m	*i*-Pr	*n*-C_5H_{11}	3.40	3.65
5n/7n	CH_3	*n*-C_5H_{11}	3.09	3.59

[a]Spectra were recorded in dilute $CDCl_3$ solution.

The yields for these reductions were moderate. As no starting material was recovered from these reductions, it seems likely that the relatively high degree of water solubility of the β-aminoalcohols is at least partially responsible.

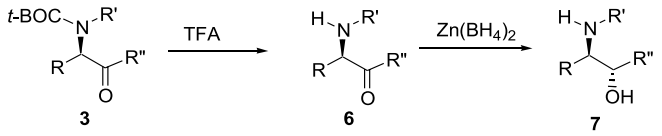
With aliphatic ketones (Table 4, entries 8–14), reductions were generally not very selective. In some cases (Table 4, entries 9–11), essentially no selectivity was observed. These results can be explained by invoking the Felkin–Anh model. For example, ketone **6i** has no obviously larger group so little selectivity is expected. If we consider ketone **6m**, the isopropyl side chain becomes the large group, so the predominant diastereomer is actually the Cram control product. The reduction of **6l** can be explained via this same model, but in this case the bulky *tert*-butyl group in the R′′ position provides the Cram control, as observed by Cherest et al. (13) Thus, the aliphatic α-aminoketones do not seem to be reduced by $Zn(BH_4)_2$ in a true chelation-controlled fashion. The desired anti stereochemistry is obtained only when the side chains are sterically bulky enough to direct the reduction via a Felkin-Anh type transition state.

Enantiomerically enriched β-aminoalcohols

It was of interest to apply the oxidation–reduction protocol established to compounds of high enantiomeric purity. If the amino centre is epimerized in any of the steps, then the value of this route would be greatly lessened.

To investigate whether the stereochemistry at the amino centre was preserved, the sequence shown in Scheme 4 was followed. Trans-metalation and trapping of stannane (*S*)-**1b** yielded (*R*)-**2b** as a mixture of diastereomers. HPLC analysis (ChiralCel OD) indicated that (*R*)-**2b** had an ee of 96%. TPAP oxidation of the mixture and subsequent reduction with Super-hydride® yielded (*R*)-**4b** (Scheme 4). HPLC analysis of the product showed that (*R*)-**4b** had 94% ee. This established that the TPAP oxidation and Super-hydride® reduction occur with only a small amount (2%) of racemization. Similarly, a sample of (*R*)-**2b** was prepared in 94% ee, and oxidized to (*R*)-**3b** with TPAP. (*R*)-**3b** was subjected to the procedure for chelation-controlled reduction with zinc borohydride, and the BOC group was then reinstated to allow HPLC analysis. HPLC subsequently showed that (*R*)-**7b** had an ee of 92%. Thus, the extent of epimerization is relatively minor for the overall conversion to either syn or anti aminoalcohols.

Table 4. Chelation-controlled reduction of α-aminoketones **6**.



3 **6** **7**

Entry	**6**	R	R′	R′′	syn:anti[a]	Yield of **7x**[b]
1	**6a**	Et	Me	Ph	2:98	65
2	**6b**	*i*-Pr	Me	Ph	<1:>99	56
3	**6c**	Me	Me	Ph	7:93	63
4	**6d**	*n*-C_5H_{11}	Me	Ph	<1:>99	61
5	**6e**	*c*-C_6H_{11}	Me	Ph	<1:>99	63
6	**6f**	Me	Bn	Ph	1:99	77
7	**6g**	*n*-C_5H_{11}	Bn	Ph	<1:>99	61
8	**6h**	Me	Bn	*n*-C_5H_{11}	20:80	75
9	**6i**	*n*-C_5H_{11}	Me	Et	55:45	76
10	**6j**	*n*-C_5H_{11}	Me	*n*-C_5H_{11}	50:50	65
11	**6k**	*n*-C_5H_{11}	Me	*i*-Pr	59:41	69
12	**6l**	*n*-C_5H_{11}	Me	*t*-Bu	4:96	63
13	**6m**	*i*-Pr	Me	*n*-C_5H_{11}	4:96	81
14	**6n**	Me	Me	*n*-C_5H_{11}	37:63	66

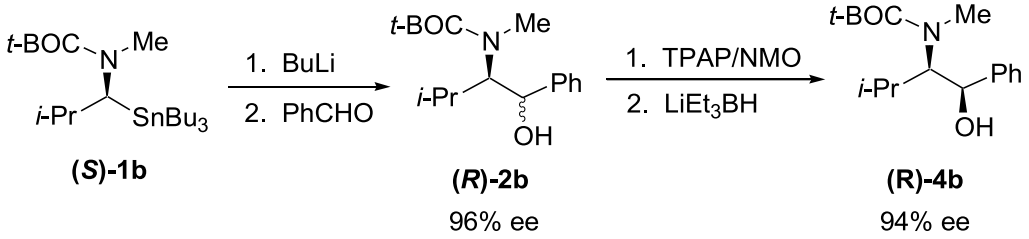
[a]Determined by ^{1}H NMR spectroscopy. "< 1:>99" denotes no signal for the other isomer was detected.
[b]Isolated yields. **x** = same letter as ketone precursor.

Conclusions

Tributylstannylalkylcarbamates **1** may be converted to either *syn*- or *anti*-β-aminoalcohols as shown in Scheme 1. The tributylstannylalkylcarbamates are easily transmetalated and trapped to yield a diastereomeric mixture of β-aminoalcohols. Trapping with non-enolizable aldehydes results in 80%–95% yields of alcohol; enolizable aldehydes result in 50%–75% yields of alcohol. Oxidation of the diastereomeric mixture of β-aminoalcohols to α-aminoketones with TPAP– NMO proceeds in 80%–95% yield. These α-aminoketones may be directly reduced with $LiEt_3BH$ to give the *syn*-β-aminoalcohol in 82% – >99% de. Removal of the BOC group followed by chelation-controlled reduction with $Zn(BH_4)_2$ gives the *anti*-β-aminoalcohol in 86% – >98% de for arylketones and certain alkylketones. Chelation-controlled reduction proceeds with low selectivity for unbranched alkylketones. The reaction sequence proceeds with only 2% racemization of the amino centre for enantiomerically enriched examples.

© 2003 NRC Canada

Scheme 4.



(*S*)-1b **(*R*)-2b** 96% ee **(R)-4b** 94% ee

Experimental section

All reactions were carried out in dry glassware under an atmosphere of argon unless otherwise noted. Low-temperature baths were prepared as follows: –60 °C, dry ice – $CHCl_3$; –78 °C, dry ice – acetone; –95 °C, liquid N_2 – MeOH. Diethyl ether and THF were distilled from Na – benzophenone ketyl. CH_2Cl_2 was distilled from CaH_2. DMF was distilled from CaH_2 and stored over 3 Å molecular sieves. Aldehydes were distilled or purified by chromatography on basic alumina. Carbamates **1a**–**1e** were prepared as previously described (8). Zinc borohydride solution was prepared according to the method of Gensler et al. (14) Other reagents were used as purchased (Aldrich). Thin layer chromatography was performed with silica gel 60 F_{254} aluminum sheets (Merck 5554). Developed plates were visualized with 4% phosphomolybdic acid in EtOH. Flash chromatography was performed using Merck 9385 silica gel (230–400 mesh). Melting points were determined on a Mel-Temp melting point apparatus and are uncorrected. Optical rotations were measured on a PerkinElmer 241 digital polarimeter. Infrared spectra were obtained as thin films between NaCl plates or as KBr pellets on an MB-100 FT IR spectrometer. NMR spectra were obtained on Bruker AM-250 or AC-200 spectrometers using $CDCl_3$ or C_6D_6 as solvent. Internal references were TMS (δ 0.0) in ^{1}H spectra and $CDCl_3$ (δ 77.0) or C_6D_6 (δ 128.0) in ^{13}C spectra. NMR data is presented in the following order: (multiplicity, integration, coupling constants in Hz, assignment). An asterisk (*) denotes the major rotamer or diastereomer where a positive distinction could be made. Mass spectrometry was done by electrospray ionization on a VG Quattro II mass spectrometer using CH_3CN or CH_2C_2 as solvent. Elemental analyses were done by M-H-W Laboratories, Phoenix, Ariz.

tert-Butyl *N*-benzyl-*N*-(1-tributylstannylethyl)carbamate (1f)

This compound was prepared from *tert*-butyl *N*-(1-tributylstannylethyl)carbamate (8) and benzyl bromide. It was obtained in 92% yield as a clear colourless oil. IR (neat) (cm^{-1}): 2922, 1675, 1457, 1166. ^{1}H NMR (250 MHz, $CDCl_3$) δ: 7.4–7.2 (m, 5H, ArH), 4.41 (ABq, 2H, J = 15.3 Hz, Δδ = 0.43, $ArCH_2N$), 2.80 (q, 1H, J = 7.3 Hz, CHN), 1.7–1.1 (m, 15H, $SnCH_2CH_2CH_2CH_3$ and CH_3CHN), 1.43 (s, 9H, $C(CH_3)_3$), 1.0–0.6 (m, 15H, $SnCH_2CH_2CH_2CH_3$). ^{13}C NMR (63 MHz, $CDCl_3$) δ: 155.51, 139.05, 128.79, 128.19, 127.58, 126.96, 79.03, 51.96, 42.80 (^1J = 383, 365 Hz), 29.09 (^2J = 17 Hz), 28.36, 27.51 (^3J = 56 Hz), 17.44, 13.65, 10.44 (^1J = 326, 313 Hz). ES-MS *m/e*: 524 [M + 1 (^{118}Sn), 65], 526 [M + 1 (^{120}Sn), 100]. Anal. calcd. for $C_{25}H_{47}NO_2Sn$: C 58.61, H 9.25, N 2.73; found: C 58.76, H 9.02, N 2.68.

tert-Butyl *N*-benzyl-*N*-(1-tributylstannylhexyl)carbamate (1g)

This compound was prepared from *tert*-butyl *N*-(1-tributylstannylhexyl)carbamate (8) and benzyl bromide. It was obtained in 94% yield as a clear colourless oil. IR (neat) (cm^{-1}): 2917, 1676, 1457, 1167. ^{1}H NMR (250 MHz, $CDCl_3$) δ: 7.4–7.1 (m, 5H, ArH), 4.39 (ABq, 2H, J = 15.1 Hz, Δδ = 0.57, $ArCH_2N$), 2.77 (m, 1H, CHN), 1.8–1.0 (m, 20H, $SnCH_2CH_2CH_2CH_3$ and $CH_3(CH_2)_4CHN$), 1.44 (s, 9H, $C(CH_3)_3$), 1.0–0.75 (m, 12H, $SnCH_2CH_2CH_2CH_3$ and $CH_3(CH_2)_4CHN$), 0.75–0.50 (m, 6H, $SnCH_2CH_2CH_2CH_3$). ^{13}C NMR (63 MHz, $CDCl_3$) δ: 156.15, *155.45, 138.90, 128.20, 127.08, *78.99, 72.10, 53.28, 49.22 (^1J = 380, 360 Hz), 32.36, 31.77, 29.11 (^2J = 18 Hz), 28.44, 27.76, 27.51 (^3J = 56 Hz), 22.56, 13.95, 13.64, 10.62 (^1J = 321, 310 Hz). ES-MS *m/e*: 580 [M + 1 (^{118}Sn), 85], 582 [M + 1 (^{120}Sn), 100]. Anal. calcd. for $C_{29}H_{55}NO_2Sn$: C 61.28, H 9.75, N 2.46; found: C 61.30, H 9.78, N 2.43.

2-(*N*-*tert*-Butoxycarbonyl-*N*-methylamino)-1-phenyl-1-butanone (3a)

To a cooled (–78 °C) stirred solution of stannane **1a** (2.00 g, 4.33 mmol) in THF (20 mL) was added BuLi (1.6 mol/L in hexanes, 3.25 mL, 5.20 mmol) dropwise and the resulting solution was stirred for 10 min. A solution of *N*,*N*-dimethylbenzamide (0.839 g, 5.97 mmol) in THF (2 mL) was added and stirring was continued for 5 min. The reaction was quenched with sa. NH_4Cl and diluted with ether. Standard aqueous workup followed by flash chromatography on silica gel (80 g, hexanes:ether (12:1)) afforded ketone **3a** as a colourless oil. IR (neat) (cm^{-1}): 1689, 1388, 1150. ^{1}H NMR (200 MHz, $CDCl_3$) δ: 8.1–7.9 (m, 2H, ArH), 7.6–7.4 (m, 3H, ArH), 5.54 (dd, 0.6H, J = 5.8, 9.2 Hz, CHN), 5.20 (dd, 0.4H, J = 5.7, 9.1 Hz, CHN), 2.69 (s, 1.2H, NCH_3), 2.61 (s, 1.8H, NCH_3), 1.9 (m, 2H, CH_3CH_2), 1.52 (s, 3.6H, $C(CH_3)_3$), 1.46 (s, 5.4H, $C(CH_3)_3$), 0.95 (m, 3H, CH_3CH_2). ^{13}C NMR (50 MHz, $CDCl_3$) δ: *199.23, 198.55, *155.87, 154.96, *135.76, 133.01, 128.42, 128.08, 80.41, *79.94, 61.60, *59.56, 29.61, *29.27, 28.23, 20.94, *20.60, 10.35, *10.11. EI-MS *m/e*: 278 [M + 1, 3], 222 (21), 204 (19), 172 (76), 116 (100), 105 (71), 72 (96). Anal. calcd. for $C_{16}H_{23}NO_3$: C 69.29, H 8.36, N 5.05; found: C 69.40, H 8.12, N 4.91.

General procedure A: Preparation of racemic 2-(*N*-*tert*-butoxycarbonyl-*N*-alkylamino)-1-aryl-1-alkanols and 1-alkyl-1-alkanols 2 and TPAP–NMO oxidations to ketones 3

To a cooled (–78 °C) solution of the appropriate *tert*-butyl-*N*-methyl-*N*-(1-tributylstannylalkyl)carbamate in THF (0.25 mol/L) was added dropwise BuLi (1.6 mol/L in hex-

© 2003 NRC Canada

anes, 1.1 equiv.) and the resulting solution was stirred for 15 min. The appropriate aldehyde (1.1 equiv.) was then syringed into the flask and the solution was stirred for a further 15 min. The reaction was quenched with sat. NH_4Cl solution and Et_2O was added. The solution was washed 3 times with H_2O, dried on $MgSO_4$, filtered, and concentrated in vacuo. Flash chromatography (30 g silica/g substrate, hexanes–Et_2O (4:1)) furnished the desired alcohol **2**.

To a 0.5 mol/L solution of the appropriate alcohol in CH_2Cl_2 was added *N*-methylmorpholine-*N*-oxide (1.5 equiv.) and powdered 4 Å mol sieves (500 mg/mmol). Tetrapropylammonium perruthenate (0.05 equiv.) was then added in one portion. The solution was stirred for 1 h, then filtered through a short pad of silica. Concentration of the filtrate in vacuo yielded the crude ketone. Flash chromatography (20 g silica/g substrate, hexane–Et_2O (3:1)) afforded the pure ketone **3** as a colourless oil (10).

*2-(*N-tert-*Butoxycarbonyl*-N-*methylamino)-3-methyl-1-phenyl-1-butanone (3b)*

Stannane **1b** and benzaldehyde were allowed to react according to *General procedure A* to give alcohol **2b** in 94% yield as a mixture of diastereomers. Oxidation of **2b** then gave **3b** in 83% yield as a clear colourless oil. IR (neat) (cm^{-1}): 2955, 1690, 1598, 1459, 1380. ^{1}H NMR (250 MHz, $CDCl_3$) δ: 8.12 (m, 1.3H, ArH), 8.02 (m, 0.7H, ArH), 7.6–7.4 (m, 3H, ArH), 5.31 (d, 0.7H, *J* = 10.6 Hz, CHN), 5.05 (d, 0.3H, *J* = 10.6 Hz, CHN), 2.66 (s, 1H, NCH_3), 2.62 (s, 2H, NCH_3), 2.41 (m, 1H, C*H*$(CH_3)_2$), 1.54 (s, 3H, $C(CH_3)_3$), 1.44 (s, 6H, $C(CH_3)_3$), 0.93 (m, 6H, $CH(CH_3)_2$). ^{13}C NMR (63 MHz, $CDCl_3$) δ: *197.67, 196.64, *155.71, 154.75, 136.39, *136.08, 133.07, 128.50, 128.35, 128.25, 80.29, *79.79, 63.86, *62.41, *29.00, 28.87, 28.25, *28.08, 25.86, *25.59, 19.84, *19.65, 18.34, *17.99. ES-MS *m/e*: 292 [M + 1, 100]. Anal. calcd. for $C_{17}H_{25}NO_3$: C 70.07, H 8.65, N 4.81; found: C 70.09, H 8.54, N 4.82.

*2-(*N-tert-*Butoxycarbonyl*-N-*methylamino)-1-phenyl-1-propanone (3c)*

Stannane **1c** and benzaldehyde were allowed to react according to *General procedure A* to give alcohol **2c** in 91% yield as a mixture of diastereomers. Oxidation of **2c** then gave **3c** in 92% yield as a clear colourless oil. IR (neat) (cm^{-1}): 2963, 1691, 1597, 1449, 1389. ^{1}H NMR (250 MHz, $CDCl_3$) δ: 8.1–7.9 (m, 2H, ArH), 7.6–7.4 (m, 3H, ArH), 5.69 (q, 0.6H, *J* = 6.8 Hz, CHN), 5.17 (q, 0.4H, *J* = 6.6 Hz, CHN), 2.80 (s, 1.1H, NCH_3), 2.63 (s, 1.9H, NCH_3), 1.45 (s, 6.9H, $C(CH_3)_3$), 1.42 (s, 2.1H, $C(CH_3)_3$), 1.37 (d, 3H, *J* = 7.0 Hz, CHC*H*$_3$). ^{13}C NMR (63 MHz, $CDCl_3$) δ: *198.98, 198.15, *154.92, 154.09, 135.20, *132.58, 128.06, 127.89, 127.71, 79.99, *79.57, 56.64, *54.30, 30.37, *29.17, 27.83, 13.33, *12.80. ES-MS *m/e*: 264 [M + 1, 100]. Anal. calcd. for $C_{15}H_{21}NO_3$: C 68.42, H 8.04, N 5.13; found: C 68.24, H 7.87, N 5.13.

*2-(*N-tert-*Butoxycarbonyl*-N-*methylamino)-1-phenyl-1-heptanone (3d)*

Stannane **1d** and benzaldehyde were allowed to react according to *General procedure A* to give alcohol **2d** in 84% yield as a mixture of diastereomers. Oxidation of **2d** then gave **3d** in 91% yield as a clear colourless oil. IR (neat) (cm^{-1}): 2930, 1692, 1598, 1457, 1388. ^{1}H NMR (250 MHz, $CDCl_3$) δ: 8.03 (m, 1.2H, ArH), 7.94 (m, 0.8H, ArH), 7.6–7.4 (m, 3H, ArH), 5.61 (dd, 0.6H, *J* = 5.8 Hz, 9.2, CHN), 5.3 (dd, 0.4H, *J* = 5.8, 9.2 Hz, CHN), 2.69 (s, 1.2H, NCH_3), 2.61 (s, 1.8H, NCH_3), 1.8 (br m, 2H, C*H*$_2$CHN), 1.50 (s, 3.6H, $C(CH_3)_3$), 1.45 (s, 5.4H, $C(CH_3)_3$), 1.34 (br, 6H, $CH_3(CH_2)_3$), 0.9 (br, 3H, $CH_3(CH_2)_3$). ^{13}C NMR (63 MHz, $CDCl_3$) δ: *198.94, 198.29, *155.54, 154.63, 135.83, *135.61, 132.78, 128.22, 127.90, 80.11, *79.65, 59.46, *57.84, 31.28, 29.39, *29.12, 28.01, 27.46, *27.16, 25.25, *25.09, 22.27, 13.66. ES-MS *m/e*: 320 [M + 1, 100]. Anal. calcd. for $C_{19}H_{29}NO_3$: C 71.44, H 9.15, N 4.38; found: C 71.29, H 8.96, N 4.38.

*2-Cyclohexyl-2-(*N-tert-*butoxycarbonyl*-N-*methylamino)-1-phenylethanone (3e)*

Stannane **1e** and benzaldehyde were allowed to react according to *General procedure A* to give alcohol **2e** in 81% yield as a mixture of diastereomers. Oxidation of **2e** then gave **3e** in 86% yield as a clear colourless oil. IR (neat) (cm^{-1}): 2928, 2853, 1688, 1597, 1447, 1390. ^{1}H NMR (250 MHz, $CDCl_3$) δ: 8.11 (m, 1.3H, ArH), 8.01 (m, 0.7H, ArH), 7.6–7.4 (m, 3H, ArH), 5.41 (d, 0.7H, *J* = 10.6 Hz, CHN), 5.16 (d, 0.3H, *J* = 10.6 Hz, CHN), 2.67 (s, 1H, NCH_3), 2.62 (s, 2H, NCH_3), 2.15 (m, 1H, CHNC*H*$(CH_2)_2$), 1.9–0.8 (br, 10H, *c*-$CH(CH_2)_5$), 1.53 (s, 3H, $C(CH_3)_3$), 1.44 (s, 6H, $C(CH_3)_3$). ^{13}C NMR (63 MHz, $CDCl_3$) δ: *197.51, 196.81, *155.58, 154.70, 136.47, *136.16, 132.95, 128.40, 128.27, 128.18, 80.08, *79.63, 62.13, *60.85, 35.03, *34.67, 30.36, *30.13, *29.00, 28.83, 28.42, 28.16, 28.00, 27.90, 26.16, 25.57, 25.41. ES-MS *m/e*: 332 [M + 1, 100]. Anal. calcd. for $C_{20}H_{29}NO_3$: C 72.47, H 8.82, N 4.23; found: C 72.35, H 8.77, N 4.17.

*2-(*N-*Benzyl*-N-tert-*butoxycarbonylamino)-1-phenyl-1-propanone (3f)*

Aminoalcohol **2f** was prepared from stannane **1f** and benzaldehyde according to *General procedure A* in 92% yield as a clear colourless oil. TPAP oxidation of **2f** gave ketone **3f** in 96% yield as a viscous clear oil. IR (neat) (cm^{-1}): 2962, 1692, 1598, 1452, 1167. ^{1}H NMR (250 MHz, $CDCl_3$) δ: 8.05–7.0 (m, 10H, ArH), 5.9–5.6 (m, 0.7H, CHN), 4.95 (m, 0.3H, CHN), 4.8–4.1 (m, 2H, ArCH_2N), 1.33 (br s, 12H, $C(CH_3)_3$ and C*H*$_3$CHN). ^{13}C NMR (63 MHz, $CDCl_3$) δ: *199.41, 198.54, 155.20, *138.95, 138.34, 135.65, 132.59, 128.16, 127.92, 126.62, 80.75, *80.30, 57.33, *55.08, 49.52, *47.83, 27.90, 14.41. ES-MS *m/e*: 340 [M + 1, 100]. Anal. calcd. for $C_{21}H_{25}NO_3$: C 74.31, H 7.42, N 4.13; found: C 74.36, H 7.50, N 4.16.

*2-(*N-*Benzyl*-N-tert-*butoxycarbonylamino)-1-phenyl-1-heptanone (3g)*

Aminoalcohol **2g** was prepared from stannane **1g** and benzaldehyde according to *General procedure A* in 88% yield as a clear colourless oil. TPAP oxidation of **2g** gave ketone **3g** in 95% yield as a viscous clear oil. IR (neat) (cm^{-1}): 3063, 2943, 1690, 1598, 1453, 1403, 1366, 1255, 1167. ^{1}H NMR (250 MHz, $CDCl_3$) δ: 7.98 (m, 1.5H, ArH), 7.76 (m, 0.7H, ArH), 7.6–7.3 (m, 3.3H, ArH), 7.2–6.9 (m, 4.5H, ArH), 5.73 (br t, 0.6H, *J* = 7.1 Hz, CHN), 5.24 (m, 0.4H, CHN), 4.5–4.1 (m, 2H, ArCH_2N), 2.0–1.1 (m, 8H,

© 2003 NRC Canada

$CH_3(CH_2)_4$), 1.51 (s, 3H, $C(CH_3)_3$), 1.34 (s, 6H, $C(CH_3)_3$), 0.84 (m, 3H, $CH_3(CH_2)_4$). ^{13}C NMR (63 MHz, $CDCl_3$) δ: *198.42, 197.69, *155.42, 155.03, *138.59, 138.12, 135.81, *132.60, 132.32, 128.06, 127.58, 127.52, 126.70, 126.18, 80.03, 59.92, 58.07, *47.76, 47.09, 37.76, 31.23, 28.23, *27.73, 26.02, *25.32, 22.26, *22.11, 13.72, *13.57. ES-MS *m/e*: 396 [M + 1, 100]. Anal. calcd. for $C_{25}H_{33}NO_3$: C 75.92, H 8.41, N 3.54; found: C 76.03, H 8.48, N 3.61. The ^{1}H NMR (200 MHz, DMSO-d_6) signal for CHN coalesced at or below 352 K. The barrier to rotation ($\Delta G_c^{\ddagger}$) was estimated to be 17.2 kcal/mol.

2-*(N-*Benzyl*-N-tert-*butoxycarbonylamino)-3-octanone (3h)

Aminoalcohol **2h** was prepared from stannane **1f** and hexanal according to *General procedure A* in 67% yield as a clear colourless oil. TPAP oxidation of **2h** gave ketone **3h** in 90% yield as a viscous clear oil. IR (neat) (cm^{-1}): 2934, 1702, 1416, 1367, 1249, 1163. ^{1}H NMR (250 MHz, $CDCl_3$) δ: 7.4–7.1 (m, 5H, ArH), 4.9–4.5 (m, 1.1H, $ArCH_2N$), 4.3–4.1 (m, 1.3H, $ArCH_2N$ and CHN), 3.7–3.5 (m, 0.6H, CHN), 2.4–1.9 (m, 2H, $CH_2C(O)$), 1.5–1.0 (m, 9H, CH_3CHN and $CH_3(CH_2)_3CH_2$), 1.43 (s, 9H, $C(CH_3)_3$), 0.85 (m, 3H, $CH_3(CH_2)_4$) ^{13}C NMR (63 MHz, $CDCl_3$) δ: 208.84, *208.12, 154.93, 138.70, *137.90, 128.44, 127.50, 127.27, *80.98, 80.49, *61.19, 60.37, *51.09, 49.75, 38.54, *37.97, 31.27, 28.15, 23.28, 22.24, *13.77, 13.57. ES-MS *m/e*: 334 [M + 1, 100]. Anal. calcd. for $C_{20}H_{31}NO_3$: C 72.04, H 9.37, N 4.20; found: C 72.08, H 9.50, N 4.15.

4-*(N-tert-*Butoxycarbonyl-N-methylamino)-3-nonanone (3i)

Aminoalcohol **2i** was prepared according to *General procedure A* from stannane **1d** and propionaldehyde in 70% yield as a mixture of diastereomers. The title compound was prepared from aminoalcohol **2i** in 87% yield as a clear colourless oil. IR (neat) (cm^{-1}): 2926, 1701, 1460, 1355, 1150. ^{1}H NMR (250 MHz, $CDCl_3$) δ: 4.66 (dd, 0.55H, *J* = 5.1, 9.9 Hz, CHN), 4.27 (dd, 0.45H, *J* = 4.9, 10.0 Hz, CHN), 2.77 (s, 1.4H, CH_3N), 2.69 (s, 1.6H, CH_3N), 2.6–2.3 (m, 2H, CH_3CH_2CO), 1.95–1.45 (m, 2H, CH_2CHN), 1.49 (s, 5H, $C(CH_3)_3$), 1.47 (s, 4H, $C(CH_3)_3$), 1.4–1.15 (m, 6H, $CH_3(CH_2)_3CH_2CHN$), 1.15–0.95 (overlapping t, 3H, *J* = 7.2 Hz, $COCH_2CH_3$), 0.95–0.8 [m, 3H, $CH_3(CH_2)_4CHN$). ^{13}C NMR (63 MHz, $CDCl_3$) δ: *209.16, 208.63, *155.79, 154.91, 79.71, *79.38, 64.41, 62.54, *32.38, 31.98, 30.99, 30.79, *29.87, 27.82, 26.81, *26.32, 25.12, 22.04, 13.44, 7.14. ES-MS *m/e*: 272 [M + 1, 100]. Anal. calcd. for $C_{15}H_{29}NO_3$: C 66.38, H 10.77, N 5.16; found: C 66.22, H 10.55, N 4.96.

7-*(N-tert-*Butoxycarbonyl*-N-*methylamino)-6-dodecanone (3j)

Aminoalcohol **2j** was prepared according to *General procedure A* from stannane **1d** and hexanal in 66% yield as a mixture of diastereomers. The title compound was prepared from aminoalcohol **2j** in 82% yield as a clear colourless oil. IR (neat) (cm^{-1}): 2943, 2866, 1702, 1459, 1389, 1155. ^{1}H NMR (250 MHz, $CDCl_3$) δ: 4.66 (dd, 0.5H, *J* = 5.3, 9.8 Hz, CHN), 4.27 (dd, 0.5H, *J* = 4.7, 9.8 Hz, CHN), 2.76 (s, 1.5H, CH_3N), 2.68 (s, 1.5H, CH_3N), 2.41 (t, 2H, *J* = 7.3 Hz, CH_2CO), 1.9–1.7 (m, 2H, CH_2CHN), 1.7–1.5 (m, 2H, CH_2CH_2CO), 1.48 (s, 4.5H,$C(CH_3)_3$), 1.47 (s, 4.5H, $C(CH_3)_3$), 1.4–1.1 (m, 10H, $CH_3CH_2CH_2CH_2CH_2CO$ and $CH_3CH_2CH_2CH_2CH_2CHN$), 1.0–0.8 (m, 6H, $CH_3(CH_2)_4CO$ and $CH_3(CH_2)_4CHN$). ^{13}C NMR (63 MHz, $CDCl_3$) δ: *208.62, 208.15, *155.77, 154.91, 79.64, *79.31, 64.43, 62.51, *39.18, 38.77, 30.98, 30.60, *29.76, 27.79, 26.67, *26.21, 25.10, 22.90, *22.79, *22.03, 21.94, 13.41, *13.35. ES-MS *m/e*: 314 [M + 1, 100]. Anal. calcd. for $C_{18}H_{35}NO_3$: C 68.97, H 11.25, N 4.47; found: C 68.79, H 11.12, N 4.32.

4-*(N-tert-*Butoxycarbonyl*-N-*methylamino)-2-methyl-3-nonanone (3k)

Aminoalcohol **2k** was prepared according to *General procedure A* from stannane **1d** and isobutyraldehyde in 77% yield as a mixture of diastereomers. The title compound was prepared from alcohol **2k** in 94% yield as a clear colourless oil. IR (neat) (cm^{-1}): 2928, 1701, 1461, 1380, 1154. ^{1}H NMR (250 MHz, $CDCl_3$) δ: 4.86 (dd, 0.5H, *J* = 5.7, 9.1 Hz, CHN), 4.52 (dd, 0.5H, *J* = 4.9, 9.6 Hz, CHN), 2.95–2.75 (m, 1H, CH_3CHCH_3), 2.74 (s, 1.5H, CH_3N), 2.67 (s, 1.5H, CH_3N), 1.9–1.5 (m, 2H, CH_2CHN), 1.48 (s, 9H, $C(CH_3)_3$), 1.40–1.15 (br m, 6H, $CH_3CH_2CH_2CH_2$), 1.15–1.00 (m, 6H, CH_3CHCH_3), 1.0–0.8 (br m, 3H, $CH_3(CH_2)_4$). ^{13}C NMR (63 MHz, $CDCl_3$) δ: *212.16, 211.68, *155.71, 154.93, 79.73, *79.39, 61.88, 60.29, *36.93, 36.23, 31.04, 30.30, *29.68, 27.84, 26.75, *26.39, 25.10, 22.08, 18.63, *18.42, *17.34, 17.23, 13.47. ES-MS *m/e*: 286 [M + 1, 100].

4-*(N-tert-*Butoxycarbonyl*-N-*methylamino)-2,2-dimethyl-3-nonanone (3l)

Aminoalcohol **2l** was prepared according to *General procedure A* from stannane **1d** and pivaldehyde in 78% yield as a mixture of diastereomers. The title compound was prepared from alcohol **2l** in 84% yield as a clear colourless oil. IR (neat) (cm^{-1}): 2927, 1696, 1462, 1380, 1320, 1154. ^{1}H NMR (250 MHz, $CDCl_3$) δ: 5.24 (apparent t, 0.6H, *J* = 7.5 Hz, CHN), 5.04 (dd, 0.4H, *J* = 5.6, 9.4 Hz, CHN), 2.70 (s, 1H, CH_3N), 2.66 (s, 2H, CH_3N), 1.70–1.40 (m, 2H, CH_2CHN), 1.50 (s, 3H, $OC(CH_3)_3$), 1.46 (s, 6H, $OC(CH_3)_3$), 1.40–1.20 (m, 6H, $CH_3(CH_2)_3CH_2$), 1.16 (s, 3H, $COC(CH_3)_3$), 1.15 (s, 6H, $COC(CH_3)_3$), 0.95–0.80 (br m, 3H, $CH_3(CH_2)_4$). ^{13}C NMR (63 MHz, $CDCl_3$) δ: *212.49, 211.85, *155.13, 154.51, 79.58, *79.21, 55.80, 54.49, 43.61, *31.12, 31.00, 28.53, 28.24, 27.88, 25.84, *25.54, 24.83, 22.09, 13.50. ES-MS *m/e*: 300 [M + 1, 100]. Anal. calcd. for $C_{17}H_{33}NO_3$: C 68.19, H 11.11, N 4.68; found: C 68.40, H 10.90, N 4.73.

3-*(N-tert-*Butoxycarbonyl*-N-*methylamino)-2-methyl-4-nonanone (3m)

Aminoalcohol **2m** was prepared according to *General procedure A* from stannane **1b** and hexanal in 65% yield as a mixture of diastereomers. The title compound was prepared from alcohol **2m** in 80% yield as a clear colourless oil. IR (neat) (cm^{-1}): 2945, 1695, 1457, 1379, 1304, 1154. ^{1}H NMR (250 MHz, $CDCl_3$) δ: 4.44 (d, 0.6H, *J* = 10.8 Hz, CHN), 4.07 (d, 0.4H, *J* = 10.4 Hz, CHN), 2.69 (s, 1.2H, CH_3N), 2.62 (s, 1.8H, CH_3N), 2.6–2.25 (m, 2H, CH_2CO), 2.25–2.1 (m, 1H, CHCHN), 1.55–1.45 (m, 2H, CH_2CH_2CO), 1.49 (s, 3.6H, $C(CH_3)_3$), 1.48 (s, 5.4H, $C(CH_3)_3$), 1.4–1.15 (m, 4H, $CH_2(CH_2)_2CH_3$), 1.0–0.75 (m, 9H, $(CH_3)_2CH$ and

© 2003 NRC Canada

$CH_3(CH_2)_3$). ^{13}C NMR (63 MHz, $CDCl_3$) δ: *207.33, 206.56, *155.92, 154.96, 79.78, *79.46, 68.72, 66.51, *41.37, 40.80, 30.99, 30.88, *29.76, 29.13, 27.87, 25.20, *24.71, 22.91, *22.74, 21.94, 19.78, *19.32, 18.18, *17.86, 13.41. ES-MS *m/e*: 286 [M + 1, 100]. Anal. calcd. for $C_{16}H_{31}NO_3$: C 67.33, H 10.95, N 4.91; found: C 67.43, H 11.03, N 4.82.

*2-(*N-tert-*Butoxycarbonyl*-N-*methylamino)-3-octanone (3n)*

Aminoalcohol **2n** was prepared according to *General procedure A* from stannane **1c** and hexanal in 77% yield as a mixture of diastereomers. The title compound was prepared from alcohol **2n** in 87% yield as a clear colourless oil. IR (neat) (cm^{-1}): 2930, 1702, 1460, 1382, 1315, 1252, 1154. ^1H NMR (250 MHz, $CDCl_3$) δ: 4.75–4.55 (br, 0.5H, CHN), 4.30–4.05 (br, 0.5H, CHN), 2.84 (br s, 1.5H, CH_3N), 2.73 (br s, 1.5H, CH_3N), 2.43 (t, 2H, *J* = 7.2 Hz, CH_2CO), 1.65–1.45 (m, 2H, CH_2CH_2CO), 1.47 (br s, 9H, $C(CH_3)_3$), 1.40–1.15 (m, 7H, CH_3CHN and $CH_3CH_2CH_2$), 0.89 (t, 3H, *J* = 6.8 Hz, $CH_3(CH_2)_4$). ^{13}C NMR (63 MHz, $CDCl_3$) δ: 208.87, 208.50, 155.35, 154.20, 79.90, 79.52, 61.04, 58.98, *38.38, 38.09, 31.49, 31.00, 30.28, 27.84, 22.89, 21.98, 13.41, 12.79, 12.27. ES-MS *m/e*: 258 [M + 1, 100].

General procedure B: Reduction of ketones with Super-hydride®

To a –78 °C solution of the appropriate ketone in THF (0.25 mol/L) was slowly added Super-hydride® (1.0 mol/L in THF, 3.0 equiv.). The reaction mixture was stirred for 15 min and then quenched with 4 N NaOH solution. While the reaction mixture was still cold, 30% H_2O_2 solution was added dropwise (*vigorous reaction*). The reaction mixture was taken up in Et_2O, washed twice with water, and then brine. The organic layer was dried on $MgSO_4$, filtered through Celite, and concentrated in vacuo to yield the alcohol, which did not require purification.

syn-*2-(*N-tert-*Butoxycarbonyl*-N-*methylamino)-3-methyl-1-phenyl-1-butanol (4b)*

This compound was prepared from aminoketone **3b** according to *General procedure B* as a 98:2 mixture of diastereomers. **4b** was obtained in 97% yield as a white, oily solid, mp 106–110.5 °C. IR (melt) (cm^{-1}): 3409, 2955, 1672, 1463, 1356, 1162. ^1H NMR (250 MHz, $CDCl_3$) δ: 7.4–7.1 (m, 4.5H, ArH), 6.8–6.4 (br, 0.5H, ArH), 5.02 (d, 0.5H, *J* = 8.5 Hz, C*H*OH), 5.01 (d, 0.5H, *J* = 8.5 Hz, C*H*OH), 3.8–3.6 (br d, 0.3H, CHN), 3.0–2.0 (m, 4.7H, NCH_3, CHN, and $(CH_3)_2CH$), 1.7–1.2 (br s, 7.5H, $C(CH_3)_3$), 1.2–1.0 (m, 5H, $C(CH_3)_3$ and $(CH_3)_2CH$), 1.0–0.7 (m, 3.5H, $(CH_3)CH$). ^{13}C NMR (63 MHz, $CDCl_3$) δ: 157.50 (br), *155.89, 143.46, *143.26, 127.68, 126.73, 126.46, *125.96, 125.31, 79.94, *78.39, *73.79, 73.53, 66.07, 40.48, 30.44, *28.13, 27.79, *26.69, 26.56, *20.13, 19.97. ES-MS *m/e*: 294 [M + 1, 100]. Anal. calcd. for $C_{17}H_{27}NO_3$: C 69.59, H 9.28, N 4.77; found: C 69.76, H 9.03, N 4.59.

syn-*2-(*N-tert-*Butoxycarbonyl*-N-*methylamino)-1-phenyl-1-propanol (4c)*

This compound was prepared from aminoketone **3c** according to *General procedure B* as a >99:<1 mixture of diastereomers in 98% yield as a clear oil. IR (neat) (cm^{-1}): 3416, 2949, 1675, 1448, 1349, 1155. ^1H NMR (250 MHz, $CDCl_3$) δ: 7.4–7.25 (m, 5H, ArH), 4.56 (d, 1H, *J* = 8.3 Hz, C*H*OH), 4.16 (br, 1H, CHN), 2.75 (br, 3H, NCH_3), 1.47 (s, 9H, $C(CH_3)_3$), 1.03 (br d, 3H, CH_3CHN). ^{13}C NMR (63 MHz, $CDCl_3$) δ: *156.47 (br), 155.63 (br), 142.08, 127.58, 126.85, 126.16, 78.94 (br), 75.48, 67.14, *57.03 (br), 56.20 (br), 30.22 (br), 27.77, 24.93, 13.95. ES-MS *m/e*: 266 [M + 1, 100]. Anal. calcd. for $C_{15}H_{23}NO_3$: C 67.90, H 8.74, N 5.28; found: C 67.84, H 8.59, N 5.10. This is a previously reported compound (15).

syn-*2-(*N-tert-*Butoxycarbonyl*-N-*methylamino)-1-phenyl-1-heptanol (4d)*

This compound was prepared from aminoketone **3d** according to *General procedure B* as a >99:<1 mixture of diastereomers in 100% yield as a clear, colourless oil. IR (neat) (cm^{-1}): 3418, 2924, 1676, 1455, 1357, 1160. ^1H NMR (250 MHz, $CDCl_3$) δ: 7.5–7.1 (m, 5H, ArH), 4.8–4.4 (br m, 1H, C*H*OH), 4.4–3.6 (br m, 1H, CHN), 2.84 (br s, 1.5H, NCH_3), 2.61 (br s, 1.5H, NCH_3), 1.45 (s, 7H, $C(CH_3)_3$), 1.41 (s, 2H, $C(CH_3)_3$), 1.23 (m, 8H, $(CH_2)_4CH_3$), 0.84 (br, 3H, $(CH_2)_4CH_3$). ^{13}C NMR (63 MHz, $CDCl_3$) δ: *157.52, 156.59, *142.58, 142.18, 128.16, *128.05, 127.55, *127.20, 126.68, *126.31, *79.68, 79.34, 75.58, 60.52 (br), *31.30, 31.13, 28.19, *25.81, 25.47, 22.32, 13.77. ES-MS *m/e*: 322 [M + 1, 100]. Anal. calcd. for $C_{19}H_{31}NO_3$: C 70.99, H 9.72, N 4.36; found: C 71.20, H 9.73, N 4.20.

syn-*2-Cyclohexyl-2-(*N-tert-*butoxycarbonyl*-N-*methylamino)-1-phenylethanol (4e)*

This compound was prepared from aminoketone **3e** according to *General procedure B* as a >99:<1 mixture of diastereomers except that 2.0 equiv. of Super-hydride® were used and flash chromatography (30g silica/g substrate, hex–Et_2O (2:1)) was required to remove a small amount (~6%) of starting material. Alcohol **4e** was obtained in 93% yield as a clear viscous oil (99% based on recovered starting material). IR (neat) (cm^{-1}): 3403, 2918, 1670, 1461, 1397, 1163. ^1H NMR (200 MHz, $CDCl_3$) δ: 7.5–7.1 (m, 5H, ArH), 5.01 (d, 1H, *J* = 3.5 Hz, C*H*OH), 3.79 (br d, 1H, CHN), 3.0–2.4 (br m, 3H, NCH_3), 2.4–0.8 (br m, 11H, *c*-C_6H_{11}), 1.5–1.3 (br s, 9H, $C(CH_3)_3$). ^{13}C NMR (50 MHz, $CDCl_3$) δ: 157.60, *155.87, 143.34, 127.58, 126.52, 126.34, *125.93, 125.22, 80.01, 78.22, 75.48, 73.03, *72.87, 64.39, 40.52, 35.48, *35.25, 30.59, 30.45, 30.27, 30.04, 28.07, 27.69, 26.27, 25.80, 25.68. ES-MS *m/e*: 334 [M + 1, 100]. Anal. calcd. for $C_{20}H_{31}NO_3$: C 72.04, H 9.37, N 4.20; found: C 71.95, H 9.20, N 4.12.

syn-*2-(*N-*Benzyl*-N-tert-*butoxycarbonylamino)-1-phenyl-1-propanol (4f)*

This compound was prepared from ketone **3f** according to *General procedure B* as a >99:<1 mixture of diastereomers. The diastereomeric ratio was determined by integration of the carbinol H signals in the ^1H NMR spectrum of the deprotected aminoalcohol **5f**. **4f** was obtained in 100% yield as a clear viscous oil. IR (neat) (cm^{-1}): 3401, 3063, 2959, 1675, 1604, 1450, 1262. ^1H NMR (250 MHz, $CDCl_3$) δ: 7.7–6.9 (m, 10H, ArH), 4.67 (d, 1H, *J* = 7.0 Hz, $ArCH_2N$), 4.5–4.2 (m, 1H, $ArCH_2N$), 4.0–3.6 (m, 2H, C*H*OH and CHN),

© 2003 NRC Canada

1.45 (br s, 9H, $C(CH_3)_3$), 1.14 (m, 3H, CH_3CHN). ^{13}C NMR (63 MHz, $CDCl_3$) δ: 156.82, 142.52, 138.69, 128.03, 127.91, 127.07, 126.90, 126.61, 126.07, 80.06, 76.52, 59.66, 51.02, 28.05, 15.25. ES-MS *m/e*: 342 [M + 1, 100]. Anal. calcd. for $C_{21}H_{27}NO_3$: C 73.87, H 7.97, N 4.10; found: C 73.69, H 8.18, N 3.98.

syn-*2-(*N-*Benzyl*-N-tert-*butoxycarbonylamino)-1-phenyl-1-heptanol (4g)

This compound was prepared from ketone **3g** according to *General procedure B* as a >99:<1 mixture of diastereomers. The diastereomeric ratio was determined by integration of the carbinol H signals in the ^1H NMR spectrum of the deprotected aminoalcohol **5g**. **4g** was obtained in 94% yield as a clear viscous oil. IR (neat) (cm^{-1}): 3399, 3029, 2942, 1675, 1459, 1365, 1248, 1167. ^1H NMR (250 MHz, $CDCl_3$) δ: 7.5–6.9 (m, 10H, ArH), 4.75 (m, 1H, $ArCH_2N$), 4.30 (m, 1H, $ArCH_2N$), 3.45 (m, 2H, C*H*OH and CHN), 1.7–1.4 (m, 2H, CH_2CHN), 1.44 (br s, 9H, $C(CH_3)_3$), 1.2–0.9 (m, 6H, $CH_3(CH_2)_3CH_2$), 0.78 (m, 3H, $CH_3(CH_2)_4$). ^{13}C NMR (63 MHz, $CDCl_3$) δ: 157.67, 143.00, 138.30, 128.23, 127.80, 127.12, 126.09, 125.85, 80.65, 75.53, 74.55, 38.82, 31.40, *29.09, 28.34, 27.93, 26.23, 22.35, 13.85. ES-MS *m/e*: 398 [M + 1, 100]. Anal. calcd. for $C_{25}H_{35}NO_3$: C 75.53, H 8.87, N 3.52; found: C 75.64, H 8.66, N 3.52. The ^1H NMR (200 MHz, DMSO-d_6) signal for $C(CH_3)_3$ coalesced at or below 352 K. The barrier to rotation ($\Delta G_c^{\ddagger}$) was estimated to be 17.8 kcal/mol.

syn-*4-(*N-tert-*Butoxycarbonyl*-N-*methylamino)-3-nonanol (4i)

This compound was prepared according to *General procedure B* from ketone **3i** in 81% yield as a syn–anti (96:4) mixture of diastereomers. The diastereomeric ratio was determined by integration of the carbinol H signals in the ^1H NMR spectrum of the deprotected aminoalcohol **5i**. **4i** was obtained as a clear colourless oil. IR (neat) (cm^{-1}): 3438, 2925, 1675, 1458, 1355, 1157. ^1H NMR (250 MHz, $CDCl_3$) δ: 3.47 (m, 2H, C*H*OH and CHN), 2.78 (s, 3H, CH_3N), 1.70–1.15 (m, 10H, $CH_3(CH_2)_4CHN$ and CH_2CHOH), 1.46 (s, 9H, $C(CH_3)_3$), 1.00 (app. t, 3H, J = 7.4 Hz, CH_3CH_2CHOH), 0.89 (m, 3H, $CH_3(CH_2)_4CHN$). ^{13}C NMR (63 MHz, $CDCl_3$) δ: *157.20, 156.64, 79.24, 73.92, 31.39, 28.13, 27.23, 26.73, *25.65, 25.48, 22.32, 13.71, *9.83, 9.61. ES-MS *m/e*: 274 [M + 1, 100]. Anal. calcd. for $C_{15}H_{31}NO_3$: C 65.89, H 11.43, N 5.12; found: C 66.01, H 11.18, N 5.05.

syn-*7-(*N-tert-*Butoxycarbonyl*-N-*methylamino)-6-dodecanol (4j)

This compound was prepared according to *General procedure B* from ketone **3j** in 86% yield as a syn–anti (96:4) mixture of diastereomers. The diastereomeric ratio was determined by integration of the carbinol H signals in the ^1H NMR spectrum of the deprotected aminoalcohol **5j**. **4j** was obtained as a clear colourless oil. IR (neat) (cm^{-1}): 3433, 2921, 1674, 1457, 1366, 1157. ^1H NMR (250 MHz, $CDCl_3$) δ: 3.52 (m, 2H, C*H*OH and CHN), 2.78 (s, 3H, CH_3N), 1.7–1.1 (m, 16H, $CH_3(CH_2)_4CHN$ and $CH_3(CH_2)_4CHOH$), 1.45 (s, 9H, $C(CH_3)_3$), 1.0–0.8 (m, 6H, $CH_3(CH_2)_4CHN$ and $CH_3(CH_2)_4CHOH$). ^{13}C NMR (63 MHz, $CDCl_3$) δ: *157.31, 156.70, 79.41, 72.66, *34.58, 34.13, *31.83, 31.50, 28.24, *25.79, 25.61, 25.20, 22.47, 13.86. ES-MS *m/e*: 316 [M + 1, 100]. Anal. calcd. for $C_{18}H_{37}NO_3$: C 68.53, H 11.82, N 4.44; found: C 68.76, H 11.68, N 4.35.

syn-*4-(*N-tert-*Butoxycarbonyl*-N-*methylamino)-2-methyl-3-nonanol (4k)

This compound was prepared according to *General procedure B* from ketone **3k** in 81% yield as a syn–anti (97:3) mixture of diastereomers. The diastereomeric ratio was determined by integration of the carbinol H signals in the ^1H NMR spectrum of the deprotected aminoalcohol **5k**. **4k** was obtained as a clear colourless oil. IR (neat) (cm^{-1}): 3449, 2925, 1743, 1676, 1458, 1360, 1157. ^1H NMR (250 MHz, $CDCl_3$) δ: 4.1–3.8 (m, 1H, C*H*OH), 3.29 (m, 1H, CHN), 2.83 (s, 0.5 H, CH_3N), 2.77 (s, 2.5H, CH_3N), 1.9–1.6 (m, 1H, CH_3CHCH_3), 1.46 (s, 9H, $C(CH_3)_3$), 1.4–1.1 (m, 8H, $CH_3(CH_2)_4CHN$), 1.1–0.8 (m, 9H, CH_3CHCH_3 and $CH_3(CH_2)_4$). ^{13}C NMR (63 MHz, $CDCl_3$) δ: *157.64, 156.87, 82.70, 79.53, *76.87, 76.34, 59.62, 57.05, *32.28, 32.01, 31.49, 30.35, *29.68, 28.67, 28.25, 28.13, *25.67, 25.49, 22.45, 20.07, 17.45, *16.45, 15.23, 13.84. ES-MS *m/e*: 288 [M + 1, 100]. Anal. calcd. for $C_{16}H_{33}NO_3$: C 66.86, H 11.57, N 4.87; found: C 66.86, H 11.72, N 4.95.

syn-*4-(*N-tert-*Butoxycarbonyl*-N-*methylamino)-2,2-dimethyl-3-nonanol (4l)

This compound was prepared according to *General procedure B* from ketone **3l** in 99% yield as a clear colourless oil. IR (neat) (cm^{-1}): 3461, 2926, 1675, 1463, 1396, 1364, 1159. ^1H NMR (250 MHz, $CDCl_3$) δ: 4.18 (m, 0.6H, C*H*OH), 3.75 (m, 0.25H, C*H*OH), 3.45 (m, 0.15H, C*H*OH), 3.18 (m, 1H, CHN), 3.0–2.7 (m, 3H, CH_3N), 2.3–1.6 (m, 2H,CH_2CHN), 1.45 (s, 9H, $OC(CH_3)_3$), 1.40–1.15 (m, 6H, $CH_3(CH_2)_3CH_2CHN$), 0.95 (s, 9H,$CHOHC(CH_3)_3$), 0.95–0.80 (m, 3H, $CH_3(CH_2)_4$). ^{13}C NMR (63 MHz, $CDCl_3$) δ: 157 (br), *156.06, 85.01, *81.46, 81 (br), *79.10, 78.5 (br), 65 (br), 57.40, *54.29, 53.5 (br), 40 (br), 35.37, *35.09, 31.46, 31.27, 31.02, 30.35 (br), 29.75 (br), 28.14, 26.17, 26.06, 25.39, 24.05, 22.40, 22.30, 13.71. ES-MS *m/e*: 302 [M + 1, 100]. Anal. calcd. for $C_{17}H_{35}NO_3$: C 67.73, H 11.70, N 4.65; found: C 67.93, H 11.59, N 4.66.

syn-*3-(*N-tert-*Butoxycarbonyl*-N-*methylamino)-2-methyl-4-nonanol (4m)

This compound was prepared according to the *General procedure B* from ketone **3m** in 82% yield as a syn–anti (91:9) mixture of diastereomers. The diastereomeric ratio was determined by integration of the carbinol H signals in the ^1H NMR spectrum of the deprotected aminoalcohol **5m**. **4m** was obtained as a clear colourless oil. IR (neat) (cm^{-1}): 3445, 2928, 1675, 1462, 1362, 1158. ^1H NMR (250 MHz, $CDCl_3$) δ: 3.95–3.70 (m, 1H, CHN), 3.50 (m, 1H, C*H*OH), 2.88 (s, 3H, CH_3N), 1.7–1.2 (m, 9H, CH_3CHCH_3 and $CH_3(CH_2)_4CHOH$), 1.46 (s, 9H, $C(CH_3)_3$), 1.01 (d, 3H, J = 6.4 Hz, CH_3CHCH_3), 0.95–0.8 (m, 6H, CH_3CHCH_3 and $CH_3(CH_2)_4$). ^{13}C NMR (63 MHz, $CDCl_3$) δ: *157.11, 156.63, *79.54, 79.08, 71.36, *71.20, 64.17, *35.09, 34.67, 31.90, 28.27, *26.41, 26.22, *25.81, 25.62, 22.51, 19.96, 13.90. ES-MS *m/e*: 288 [M + 1, 100]. Anal. calcd. for

© 2003 NRC Canada

$C_{16}H_{33}NO_3$: C 66.86, H 11.57, N 4.87; found: C 66.93, H 11.42, N 4.73.

syn-*2-(*N-tert-*Butoxycarbonyl-*N-*methylamino)-3-octanol (4n)

This compound was prepared according to *General procedure B* from ketone **3n** in 87% yield as a syn–anti (96:4) mixture of diastereomers. The diastereomeric ratio was determined by integration of the carbinol H signals in the ^{1}H NMR spectrum of the deprotected aminoalcohol **5n**. It was obtained as a clear colourless oil. IR (neat) (cm^{-1}): 3433, 2925, 1676, 1460, 1348, 1156. ^{1}H NMR (250 MHz, $CDCl_3$) δ: 3.89 (app. quintet, 1H, *J* = 7.1 Hz, CHN), 3.51 (m, 1H, C*H*OH), 2.79 (s, 3H, CH_3N), 1.60–1.25 (m, 8H, $CH_3(CH_2)_4CHOH$), 1.46 (s, 9H, $C(CH_3)_3$), 1.15 (d, 3H, *J* = 6.9, CH_3CHN), 0.89 (m, 3H, $CH_3(CH_2)_4$). ^{13}C NMR (63 MHz, $CDCl_3$) δ: 157.18 (br), 79.73, 73.24, 56.29, 34.36, 31.94, 28.41, 25.14, 22.61, 14.69, 14.01. ES-MS *m/e*: 260 [M + 1, 100].

General procedure C: Conversion of BOC-protected amines to aminoalcohols 5

To a 6.4 mol/L (50% v/v, 15 mmol) solution of trifluoroacetic acid in CH_2Cl_2 was added anisole (1.5 mmol). A solution of **4** (1 mmol) in CH_2Cl_2 (1.2 mL) was slowly added to the acid solution. The mixture was stirred for 45 min, taken up in Et_2O (40 mL), extracted with 1 N HCl (3 × 25 mL), and basified with 30% w/v NaOH in brine. NaCl was added to make a sat. solution, which was extracted with CH_2Cl_2 (5 × 15 mL). The organic layer was then dried on $MgSO_4$, filtered through a cotton plug, and concentrated in vacuo to yield amino alcohol **5**.

syn-*2-(*N-*Methylamino)-1-phenyl-1-butanol (5a)

To a cooled (–78 °C) solution of ketone **3a** (100 mg, 0.36 mmol) in THF (2 mL) was added L-Selectride® (1.0 mol/L in THF, 0.72 mL. 0.72 mmol) and the resulting mixture was stirred for 10 min. Water (2 mL) was added dropwise followed by 4 mol/L HCl (2 mL). The mixture was heated at reflux overnight. The mixture was diluted with ether (10 mL) and extracted with 1 mol/L HCl (3 × 10 mL). The acid extracts were basified with 4 mol/L NaOH and extracted with ether (30, 20, 20 mL). The ethereal extracts were dried ($MgSO_4$) and concentrated in vacuo to provide 65 mg (100%) of the known (16) **5a** as a white solid, mp 112–114 °C. ^{1}H NMR (250 MHz, $CDCl_3$) δ: 7.35–7.20 (m, 5H, ArH), 4.30 (d, 1H, *J* = 7.8 Hz, CHOH), 2.90 (br s, 2H, NH and OH), 2.48 (m, 1H, CHN), 2.39 (s, 3H, NCH_3), 1.40 (m, 2H, CH_2CH_3), 0.83 (t, 3H, *J* = 7.4 Hz, CH_2CH_3).

syn-*2-(*N-*Methylamino)-3-methyl-1-phenyl-1-butanol (5b)

Following *General procedure C*, 0.296 g (1.0 mmol) of **4b** was converted to **5b** (0.147 g, 75%) as a pale yellow oil. IR (neat) (cm^{-1}): 3344, 2929, 1603, 1460, 1390. ^{1}H NMR (200 MHz, C_6D_6) δ: 7.4 (m, 2H, ArH), 7.2 (m, 3H, ArH), 4.43 (d, 1H, *J* = 5.1 Hz, C*H*OH), 2.24 (dd, 1H, *J* = 4.4, 5.0 Hz, CHN), 2.03 (s, 3H, NCH_3), 1.57 (d of sept., 1H, *J* = 4.3, 6.9 Hz, CH_3CHCH_3), 0.76 (d, 3H, *J* = 6.9 Hz, CH_3CH), 0.69 (d, 3H, *J* = 6.9 Hz, CH_3CH). ^{13}C NMR (50 MHz, C_6D_6) δ: 145.65, 128.35, 127.10, 126.72, 72.54, 72.14, 37.38, 30.21, 20.42, 17.88. ES-MS *m/e*: 194 [M + 1, 100]. Anal. calcd. for $C_{12}H_{19}NO$: C 74.57, H 9.91, N 7.25; found: C 74.68, H 9.84, N 6.96. The ^{1}H NMR spectrum showed a signal for the carbinol proton of the anti-diastereomer (δ 4.77), which integrated to 2%.

syn-*2-(*N-*Methylamino)-1-phenyl-1-propanol (5c)

This compound was prepared according to *General procedure C* from **4c** in 63% yield as a white solid, mp 116 to 117 °C (lit. (17) value, 118 °C). IR (KBr pellet) (cm^{-1}): 3071, 2981, 2789, 1476, 1384, 1060. ^{1}H NMR (250 MHz, C_6D_6) δ: 7.4 (m, 2H, ArH), 7.2 (m, 3H, ArH), 4.06 (d, 1H, *J* = 8.0 Hz, C*H*OH), 2.35 (dq, 1H, *J* = 8.0, 6.4 Hz, CHN), 2.00 (s, 3H, NCH_3), 0.64 (d, 3H, *J* = 6.4 Hz, CH_3CHN). ^{13}C NMR (63 MHz, C_6D_6) δ: 143.68, 127.67, 126.85, 77.61, 61.79, 33.23, 15.39. ES-MS *m/e*: 166 [M + 1, 100]. Anal. calcd. for $C_{10}H_{15}NO$: C 72.69, H 9.15, N 8.48; found: C 72.47, H 8.99, N, 8.49. There was only a small signal for the carbinol H (δ 4.70) of the anti-diastereomer in the ^{1}H NMR spectrum, which integrated to <1%. This compound has been previously reported.

syn-*2-(*N-*Methylamino)-1-phenyl-1-heptanol (5d)

This compound was prepared according to *General procedure C* from **4d** in 74% yield as a clear yellow oil. IR (neat) (cm^{-1}): 3320, 3030, 2937, 1603, 1457, 1340. ^{1}H NMR (250 MHz, C_6D_6) δ: 7.4 (m, 2H, ArH), 7.2 (m, 3H, ArH), 4.32 (d, 1H, *J* = 7.3 Hz, C*H*OH), 2.42 (dt, 1H, *J* = 4.9, 7.1 Hz, CHN), 2.03 (s, 3H, NCH_3), 1.4–0.9 (m, 8H, $CH_3CH_2CH_2CH_2CH_2CH$), 0.82 (t, 3H, *J* = 7.0 Hz, CH_3CH_2). ^{13}C NMR (63 MHz, C_6D_6) δ: 144.26, 128.35, 127.44, 127.32, 74.74, 65.80, 33.08, 32.27, 29.83, 25.72, 22.85, 14.19. ES-MS *m/e*: 222 [M + 1, 100]. Anal. calcd. for $C_{14}H_{23}NO$: C 75.97, H 10.47, N 6.33; found: C 75.76, H 10.56, N 6.13. There was only a small signal for the carbinol H (δ 4.89) of the anti-diastereomer in the ^{1}H NMR spectrum, which integrated to <1%.

syn-*2-Cyclohexyl-2-(*N-*methylamino)-1-phenylethanol (5e)

This compound was prepared according *General procedure C* from **4e** in 71% yield as a clear yellow oil that crystallized on standing, mp 37 to 38 °C. IR (neat) (cm^{-1}): 3136, 2920, 1446, 1351. ^{1}H NMR (250 MHz, C_6D_6) δ: 7.4 (m, 2H, ArH), 7.2 (m, 3H, ArH), 4.51 (d, 1H, *J* = 4.6 Hz, C*H*OH), 2.24 (t, 1H, *J* = 4.5 Hz, CHN), 2.03 (s, 3H, NCH_3), 1.8–1.4 (br, 5H, *c*-C_6H_{11}), 1.4–1.2 (br, 1H, *c*-C_6H_{11}), 1.2–0.9 (br, 4H, *c*-C_6H_{11}), 0.9–0.7 (br, 1H, *c*-C_6H_{11}). ^{13}C NMR (63 MHz, C_6D_6) δ: 146.17, 128.39, 126.97, 126.57, 72.03, 71.45, 41.15, 37.44, 30.85, 29.00, 26.86, 26.80. ES-MS *m/e*: 234 [M + 1, 100]. Anal. calcd. for $C_{15}H_{23}NO$: C 77.21, H 9.93, N 6.00; found: C 77.39, H 9.71, N 5.91. There was only a small signal for the carbinol H (δ 4.81) of the anti-diastereomer in the ^{1}H NMR spectrum, which integrated to <1%.

syn-*2-(*N-*Benzylamino)-1-phenyl-1-propanol (5f)

This compound was prepared from alcohol **4f** according to *General procedure C* except that the final extraction was performed with Et_2O. It was obtained in 90% yield as a white solid, mp 93.0–94.5 °C. IR (KBr pellet) (cm^{-1}): 3091, 2829, 1434, 1384, 1052. ^{1}H NMR (250 MHz, C_6D_6) δ: 7.5–7.0 (m, 10H, ArH), 4.14 (d, 1H, *J* = 8.0 Hz, C*H*OH), 3.37

© 2003 NRC Canada

(ABq, 2H, J = 13.0 Hz, $\Delta\delta$ = 0.19, $ArCH_2N$), 2.62 (m, 1H, CHN), 0.72 (d, 3H, J = 6.3 Hz, CH_3CHN). ^{13}C NMR (63 MHz, C_6D_6) δ: 143.47, 140.64, 128.63, 128.41, 128.34, 127.61, 127.47, 127.21, 77.79, 59.68, 51.34, 16.22. ES-MS *m/e*: 242 [M + 1, 100]. Anal. calcd. for $C_{16}H_{19}NO$: C 79.63, H 7.94. N 5.80; found: C 79.50, H 7.79, N 5.71. The ^1H NMR spectrum showed a signal for the carbinol proton of the anti-diastereomer (δ 4.72), which integrated to <1%.

syn-*2-(*N-*Benzylamino)-1-phenyl-1-heptanol (5g)*

This compound was prepared from alcohol **4g** according to *General procedure C*, except that the final extraction was performed with Et_2O. It was obtained in 89% yield as a white solid, mp 48.5–51.5 °C. IR (KBr pellet) (cm^{-1}): 3122, 2938, 2862, 1449, 1384, 1046. ^1H NMR (250 MHz, C_6D_6) δ: 7.5–7.0 (m, 10H, ArH), 4.38 (d, 1H, J = 6.7 Hz, C*H*OH), 3.47 (ABq, 2H, J = 12.9 Hz, $\Delta\delta$ = 0.08, $ArCH_2N$), 2.64 (m, 1H, CHN), 1.45–0.90 (m, 8H, $CH_3(CH_2)_4$), 0.82 (m, 3H, $CH_3(CH_2)_4$). ^{13}C NMR (63 MHz, C_6D_6) δ: 144.59, 141.10, 129.00, 128.87, 128.74, 127.82, 127.57, 75.32, 64.17, 51.91, 32.59, 31.32, 26.08, 23.22, 14.58. ES-MS *m/e*: 298 [M + 1, 100]. Anal. calcd. for $C_{20}H_{27}NO$: C 80.76, H 9.15, N 4.71; found: C 80.86, H 8.98, N 4.69. The ^1H NMR spectrum showed a signal for the carbinol proton of the anti-diastereomer (δ 4.89), which integrated to <1%.

syn-*4-(*N-*Methylamino)-3-nonanol (5i)*

Following *General procedure C*, (0.179 g, 0.65 mmol) of *syn*-4-(*N*-tert-butoxycarbonyl-*N*-methylamino)-3-nonanol (**4i**) was converted to 0.097 g (86%) of **5i** as a clear oil. IR (neat) (cm^{-1}): 3337, 2921, 1421, 1106. ^1H NMR (250 MHz, C_6D_6) δ: 3.24 (dt, 1H, J = 3.4, 7.8 Hz, C*H*OH), 2.14 (s, 3H, CH_3N), 2.11 (m, 1H, CHN), 1.65–1.10 (m, 10H, CH_2CHOH and $CH_3(CH_2)_4CHN$), 1.12 (app. t, 3H, J = 7.3 Hz, CH_3CH_2CHOH), 0.90 (app. t, 3H, J = 6.9 Hz, $CH_3(CH_2)_4CHN$). ^{13}C NMR (63 MHz, C_6D_6) δ: 73.11, 63.62, 33.55, 32.53, 30.23, 27.66, 25.71, 22.95, 14.23, 10.61. ES-MS *m/e*: 174 [M + 1, 100]. Anal. calcd. for $C_{10}H_{23}NO$: C 70.12, H 13.53, N 8.18; found: C 70.00, H 13.66, N 8.12. The ^1H NMR spectrum showed a signal for the carbinol proton of the anti-diastereomer (δ 3.55), which integrated to 4%.

syn-*7-(*N-*Methylamino)-6-dodecanol (5j)*

This compound was prepared according to *General procedure C* from **4j** in 79% yield as a clear colourless oil. IR (neat) (cm^{-1}): 3345, 2910, 2798, 1460, 1378, 1089. ^1H NMR (250 MHz, C_6D_6) δ: 3.31 (app. td, 1H, J = 7.4, 3.4 Hz, C*H*OH), 2.14 (m, 1H, CHN), 2.12 (s, 3H, CH_3N), 1.8–1.0 (m, 16H, $CH_3(CH_2)_4CHN$ and $CH_3(CH_2)_4CHOH$), 1.0–0.8 (m, 6H, $CH_3(CH_2)_4CHN$ and $CH_3(CH_2)_4CHOH$). ^{13}C NMR (63 MHz, C_6D_6) δ: 71.78, 64.04, 35.08, 33.56, 32.53, 30.28, 26.212, 25.74, 23.15, 22.96, 14.31, 14.25. ES-MS *m/e*: 216 [M + 1, 100]. Anal. calcd. for $C_{13}H_{29}NO$: C 72.50, H 13.57, N 6.50; found: C 72.38, H 13.50, N 6.34. The ^1H NMR spectrum showed a signal for the carbinol proton of the anti-diastereomer (δ 3.70), which integrated to 4%.

syn-*4-(*N-*Methylamino)-2-methyl-3-nonanol (5k)*

This compound was prepared according to *General procedure C* from **4k** in 38% yield as a clear colourless oil. IR (neat) (cm^{-1}): 3380, 2920, 1459. ^1H NMR (250 MHz, C_6D_6) δ: 3.10 (dd, 1H, J = 4.2, 7.1 Hz, C*H*OH), 2.26 (m, 1H, CHN), 2.10 (s, 3H, CH_3N), 1.68 (d of sept., 1H, J = 4.1, 6.8 Hz, CH_3CHCH_3) 1.45–1.10 (m, 8H, $CH_3(CH_2)_4$), 1.12 (d, 3H, J = 6.8 Hz, CH_3CHCH_3), 1.04 (d, 3H, J = 6.8 Hz, CH_3CHCH_3), 0.89 (app. t, 3H, $CH_3(CH_2)_4$). ^{13}C NMR (63 MHz, C_6D_6) δ: 75.93, 60.83, 33.23, 32.46, 30.59, 30.29, 25.47, 22.94, 20.78, 16.25, 14.24. ES-MS *m/e*: 188 [M + 1, 100]. Anal. calcd. for $C_{11}H_{25}NO$: C 70.53, H 13.45, N 7.48; found: C 70.60, H 13.33, N 7.50. The ^1H NMR spectrum showed a signal for the carbinol proton of the anti-diastereomer (δ 3.25), which integrated to 3%.

syn-*4-(*N-*Methylamino)-2,2-dimethyl-3-nonanol (5l)*

This compound was prepared according *General procedure C* from **4l** in 85% yield as a clear colourless oil. IR (neat) (cm^{-1}): 3326, 2921, 1460, 1089. ^1H NMR (250 MHz, C_6D_6) δ: 2.94 (d, 1H, J = 3.9 Hz, C*H*OH), 2.17 (m, 1H, CHN), 2.12 (s, 3H, CH_3N), 1.45–1.05 (m, 8H, $CH_3(CH_2)_4$), 1.00 (s, 9H, $C(CH_3)_3$), 0.89 (t, 3H, J = 6.9 Hz, $CH_3(CH_2)_4$). ^{13}C NMR (63 MHz, C_6D_6) δ: 78.90, 59.11, 36.37, 35.64, 35.14, 32.33, 26.26, 26.00, 22.98, 14.23. ES-MS *m/e*: 202 [M + 1, 100]. The ^1H NMR spectrum showed no detectable signal for the carbinol proton of the anti-diastereomer (δ 3.38).

syn-*3-(*N-*Methylamino)-2-methyl-4-nonanol (5m)*

This compound was prepared according to *General procedure C* from **4m** in 77% yield as a clear colourless oil. IR (neat) (cm^{-1}): 3340, 2927, 1462, 1120. ^1H NMR (250 MHz, C_6D_6) δ: 3.40 (m, 1H, C*H*OH), 2.22 (s, 3H, CH_3N), 1.85 (app. t, 1H, J = 4.7 Hz, CHN), 1.8–1.2 (m, 9H, CH_3CHCH_3 and $CH_3(CH_2)_4$), 0.92 (m, 3H, $CH_3(CH_2)_4$), 0.82 (d, 3H, J = 6.9 Hz, CH_3CHCH_3), 0.71 (d, 3H, J = 6.9 Hz, CH_3CHCH_3). ^{13}C NMR (63 MHz, C_6D_6) δ: 70.34, 69.71, 37.61, 37.02, 32.45, 30.56, 26.29, 23.12, 20.16, 17.98, 14.31. ES-MS *m/e*: 188 [M + 1, 100]. The ^1H NMR spectrum showed a signal for the carbinol proton of the anti-diastereomer (δ 3.65), which integrated to 9%.

syn-*2-(*N-*Methylamino)-3-octanol (5n)*

This compound was prepared according to *General procedure C* from **4n** in 75% yield as a clear colourless oil. IR (neat) (cm^{-1}): 3328, 2920, 1454, 1112. ^1H NMR (250 MHz, C_6D_6) δ: 3.09 (app. td, 1H, J = 8.2, 3.0 Hz, C*H*OH), 2.09 (m, 1H, CHN), 2.06 (s, 3H, CH_3N), 1.60–1.15 (m, 8H, $CH_3(CH_2)_4$), 0.92 (m, 3H, $CH_3(CH_2)_4$), 0.74 (d, 3H, J = 6.3 Hz, CH_3CHN). ^{13}C NMR (63 MHz, C_6D_6) δ: 74.25, 60.19, 34.39, 33.29, 32.48, 25.90, 23.11, 15.39, 14.31. ES-MS *m/e*: 160 [M + 1, 100]. The ^1H NMR spectrum showed a signal for the carbinol proton of the anti-diastereomer (δ 3.59), which integrated to 4%.

General procedure D: Preparation of ketones 6 and reduction with $Zn(BH_4)_2$ to alcohols 7

To a solution of trifluoroacetic acid (6.4 mol/L in CH_2Cl_2, 4.5 mL, 28 mmol) was added anisole (0.310 g, 2.8 mmol). A solution of ketone **3** (0.498 g, 1.9 mmol) in CH_2Cl_2 (4.5 mL) was added dropwise. Gas evolution was evident and the reaction mixture turned pale yellow. The mixture was stirred for 45 min, taken up in Et_2O (50 mL), and extracted with

© 2003 NRC Canada

1 N HCl (3 × 40 mL). The acid extract was basified with 30% w/v NaOH in brine and extracted with CH_2Cl_2 (3 × 40 mL). The CH_2Cl_2 extracts were dried on $MgSO_4$, filtered through Celite, and concentrated in vacuo to yield the crude deprotected ketone **6**.

Ketone **6** was dissolved in Et_2O (3 mL) and syringed into a –78 °C solution of $Zn(BH_4)_2$ (0.15 mol/L in Et_2O, 2 equiv.). The mixture was stirred for 1 h and then quenched with 2 N HCl (15 mL). The mixture was diluted with 1 N HCl (40 mL) and extracted with Et_2O (40 mL). The acid layer was basified with 30% w/v NaOH in brine and then extracted with CH_2Cl_2 (3 × 40 mL). The CH_2Cl_2 extracts were dried on $MgSO_4$, filtered through Celite, and concentrated in vacuo to yield alcohol **7**.

*Preparation of 2-(*N*-methylamino)-1-phenyl-1-butanone (6a) and reduction with $Zn(BH_4)_2$*

Ketone **6a** was obtained from ketone **3a** according to *General procedure D* as a colourless oil in 97% yield. ^{1}H NMR (250 MHz, $CDCl_3$) δ: 7.96 (m, 2H, ArH), 7.6–7.4(m, 3H, ArH), 4.12 (dd, 1H, *J* = 5.0, 6.0 Hz, CHN), 2.80 (s, 1H, NH), 2.37 (s, 3H, NCH_3), 1.82–1.60 (m, 2H, CH_2CH_3), 0.93 (t, 3H, *J* = 7.3 Hz, CH_2CH_3).

anti-2-(*N*-Methylamino)-1-phenyl-1-butanol (**7a**) was prepared in 65% yield as a white solid, mp 87.5–88.0 °C. ^{1}H NMR (250 MHz, $CDCl_3$) δ: 7.3 (m, 5H, ArH), 4.83 (d, 1H, *J* = 4.0 Hz, C*H*OH), 2.52 (m, 1H, CHN), 2.50 (s, 3H, NCH_3), 1.20 (m, 2H, CH_2CH_3), 0.82 (t, 3H, *J* = 7.4 Hz, CH_2CH_3). This compound has been previously reported (18).

*Preparation of 2-(*N*-methylamino)-3-methyl-1-phenyl-1-butanone (6b) and reduction with $Zn(BH_4)_2$*

Ketone **6b** was obtained from ketone **3b** according to *General procedure D* as yellow oil. IR (neat) (cm^{-1}): 3337, 2927, 2796, 1679, 1598, 1460. ^{1}H NMR (250 MHz, C_6D_6) δ: 7.87 (m, 2H, ArH), 7.1–7.0 (m, 3H, ArH), 3.71 (d, 1H, *J* = 4.5 Hz, CHN), 2.24 (s, 3H, NCH_3), 1.91 (d sept, 1H, *J* = 4.5, 6.8 Hz, C*H*CHN), 1.15 (d, 3H, *J* = 6.8 Hz, CH_3CHCH_3), 0.81 (d, 3H, *J* = 6.8 Hz, CH_3CHCH_3). ^{13}C NMR (63 MHz, C_6D_6) δ: 203.25, 137.58, 132.96, 128.85, 128.37, 69.84, 35.87, 31.60, 20.56, 17.03.

anti-2-(*N*-Methylamino)-3-methyl-1-phenyl-1-butanol (**7b**) was prepared in 56% yield (for two steps) as a clear yellow oil. IR (neat) (cm^{-1}): 3355, 2923, 1603, 1465, 1390. ^{1}H NMR (250 MHz, C_6D_6) δ: 7.4 (m, 2H, ArH), 7.15 (m, 3H, ArH), 4.77 (d, 1H, *J* = 5.0 Hz, C*H*OH), 2.30 (dd, 1H, *J* = 3.6, 5.0 Hz, C*H*NHCH$_3$), 2.12 (s, 3H, NCH_3), 1.6 (d sept., 1H, *J* = 3.6, 6.9 Hz, CH_3CHCH_3), 0.82 (d, 3H, *J* = 6.9 Hz, CH_3CH), 0.66 (d, 3H, *J* = 6.9 Hz, CH_3CH). ^{13}C NMR (63 MHz, C_6D_6) δ: 143.48, 128.27, 127.03, 126.69, 73.00, 70.50, 35.97, 28.22, 21.47, 17.53. ES-MS *m*/*e*: 194 [M + 1, 100]. Anal. calcd. for $C_{12}H_{19}NO$: C 74.57, H 9.91, N 7.25; found: C 74.52, H 10.00, N 7.42. There was only a small signal for the carbinol H (δ 4.43) of the syn-diastereomer in the ^{1}H NMR spectrum, which integrated to <1%.

*2-(*N*-Methylamino)-1-phenyl-1-propanone (6c) and reduction with $Zn(BH_4)_2$*

Ketone **6c** was prepared according to *General procedure D*. From 0.498 g (1.9 mmol) of **3c** there was obtained 0.327 g of **6c** as a yellow oil. IR (neat) (cm^{-1}): 3331, 2939, 2797, 1684, 1597, 1449. ^{1}H NMR (250 MHz, C_6D_6) δ: 7.85 (m, 2H, ArH), 7.15–6.95 (m, 3H, ArH), 3.85 (q, 1H, *J* = 7.0 Hz, CHN), 2.21 (s, 3H, NCH_3), 1.11 (d, 3H, *J* = 7.0 Hz, CH_3CHN). ^{13}C NMR (63 MHz, C_6D_6) δ: 202.81, 136.40, 133.04, 128.82, 128.51, 59.76, 34.51, 19.34. This crude material was reduced to give a pale yellow solid (0.198 g). The carbinol H signals (δ 4.06 (syn), 4.70 (anti)) in the ^{1}H NMR spectrum of this material indicated that there was a 93:7 anti:syn mixture of diastereomers present. Flash chromatography (3 g SiO_2, ethyl acetate/0.5% Et_3N) afforded 0.098 g (31%) of *anti*-2-(*N*-methylamino)-1-phenyl-1-propanol (**7c**) as a white solid, mp 73.5–74.5 °C (lit (17) mp value 79 °C). IR (KBr pellet) (cm^{-1}): 3080, 2967, 2816, 1452, 1384, 1042. ^{1}H NMR (250 MHz, C_6D_6) δ: 7.4 (m, 2H, ArH), 7.2 (m, 3H, ArH), 4.70 (d, 1H, *J* = 5.7 Hz, C*H*OH), 2.48 (m, 1H, CHN), 2.05 (s, 3H, NCH_3), 0.63 (d, 3H, *J* = 6.5 Hz, CH_3CHN). ^{13}C NMR (63 MHz, C_6D_6) δ: 143.03, 128.24, 127.00, 126.52, 73.14, 60.95, 33.73, 13.65. ES-MS *m*/*e*: 166 [M + 1, 100]. Anal. calcd. for $C_{10}H_{15}NO$: C 72.69, H 9.15, N 8.48; found: C 72.72, H 8.97, N 8.50.

*Preparation of 2-(*N*-methylamino)-1-phenyl-1-heptanone (6d) and reduction with $Zn(BH_4)_2$*

This compound was prepared from ketone **3d** according to *General procedure D* except that the final extraction was performed with Et_2O instead of CH_2Cl_2 and the flash chromatography was omitted. The crude deprotected ketone **6d** was obtained as a yellow oil. IR (neat) (cm^{-1}): 3350, 2913, 1682, 1597, 1457, 1232. ^{1}H NMR (250 MHz, C_6D_6) δ: 7.93 (m, 2H, ArH), 7.15–7.0 (m, 3H, ArH), 4.40 (dd, 1H, *J* = 7.3, 4.3 Hz, CHN), 2.26 (s, 3H, NCH_3), 1.65–1.55 (m, 2H, $(CH_2)_4CH_3$), 1.55–1.30 (m, 3H, $(CH_2)_4CH_3$), 1.30–1.00 (m, 3H, $(CH_2)_4CH_3$), 0.81 (t, 3H, *J* = 6.8 Hz, $(CH_2)_4CH_3$). ^{13}C NMR (63 MHz, C_6D_6) δ: 202.90, 137.00, 133.00, 128.84, 128.42, 64.68, 35.11, 33.97, 32.11, 25.98, 22.82, 14.15.

anti-2-(*N*-Methylamino)-1-phenyl-1-heptanol (**7d**) was prepared in 61% yield as a white solid, mp 56–57.5 °C. IR (KBr pellet) (cm^{-1}): 3309, 3120, 2931, 2854, 1561, 1466, 1384, 1049. ^{1}H NMR (250 MHz, C_6D_6) δ: 7.4 (m, 2H, ArH), 7.2 (m, 3H, ArH), 4.89 (d, 1H, *J* = 3.3 Hz, C*H*OH), 2.46, (m, 1H, CHN), 2.19 (s, 3H, NCH_3), 1.25–0.85 (m, 8H, $CH_3CH_2CH_2CH_2CH_2$), 0.77 (t, 3H, *J* = 7.0 Hz, $CH_3CH_2CH_2CH_2CH_2$). ^{13}C NMR (63 MHz, C_6D_6) δ: 146.76, 128.24, 126.97, 126.55, 71.90, 66.04, 34.40, 32.18, 28.41, 26.52, 22.85, 14.16. ES-MS *m*/*e*: 222 [M + 1, 100]. Anal. calcd. for $C_{14}H_{23}NO$: C 75.97, H 10.47, N 6.33; found: C 76.10, H 10.38, N 6.32. There was only a small signal for the carbinol H (δ 4.32) of the syn-diastereomer in the ^{1}H NMR spectrum, which integrated to <1%.

*Preparation of 2-cyclohexyl-2-(*N*-methylamino)-1-phenylethanone (6e) and reduction with $Zn(BH_4)_2$*

This compound was prepared from ketone **3e** according to the procedure described in *General procedure D* except that the final extraction was performed with Et_2O instead of CH_2Cl_2 and flash chromatography was omitted. The crude deprotected ketone **6e** was obtained as a yellow oil. IR (neat) (cm^{-1}): 3350, 2904, 1679, 1597, 1449, 1217. ^{1}H NMR (250 MHz, C_6D_6) δ: 7.93 (m, 2H, ArH), 7.1–7.0 (m, 3H, ArH), 3.78 (d, 1H, *J* = 4.5 Hz, CHN), 2.25 (s, 3H, NCH_3), 2.0–1.4 (m, 7H, *c*-C_6H_{11}), 1.3–0.8 (m, 4H, *c*-C_6H_{11}). ^{13}C NMR (63 MHz, C_6D_6) δ: 203.42, 137.84, 133.01, 128.90,

© 2003 NRC Canada

128.40, 69.62, 41.88, 35.90, 31.11, 28.11, 26.80, 26.62, 26.56.

anti-2-Cyclohexyl-2-(*N*-methylamino)-1-phenylethanol (**7e**) was prepared in 63% yield (for both steps) as a white solid, mp 94.5–96 °C. IR (KBr pellet) (cm^{-1}): 3316, 3076, 2918, 2851, 1561, 1452, 1385, 1056. ^{1}H NMR (250 MHz, C_6D_6) δ: 7.4 (m, 2H, ArH), 7.2 (m, 3H, ArH), 4.81 (d, 1H, *J* = 5.0 Hz, C*H*OH), 2.30 (dd, 1H, *J* = 4.9, 4.6 Hz, CHN), 2.16 (s, 3H, NCH_3), 1.85 (m, 1H, C*H*CHN), 1.7–1.2 (m, 5H, *c*-C_6H_{11}), 1.1–0.8 (m, 5H, *c*-C_6H_{11}). ^{13}C NMR (63 MHz, C_6D_6) δ: 143.37, 128.25, 127.06, 126.72, 72.75, 70.62, 38.98, 36.14, 31.84, 28.35, 26.86, 26.74. ES-MS *m*/*e*: 234 [M + 1, 100]. Anal. calcd. for $C_{15}H_{23}NO$: C 77.21, H 9.93, N 6.00; found: C 76.96, H 9.79, N 5.90. There was only a small signal for the carbinol H (δ 4.51) of the syn-diastereomer in the ^{1}H NMR spectrum, which integrated to <1%.

*Preparation of 2-(*N*-Benzylamino)-1-phenyl-1-propanone (6f) and Reduction with $Zn(BH_4)_2$*

This compound was prepared from ketone **3f** according to *General procedure D*. It was obtained in 92% yield as a pale yellow oil. IR (neat) (cm^{-1}): 3330, 3029, 2975, 1683, 1597, 1449, 1217, 1152. ^{1}H NMR (250 MHz, C_6D_6) δ: 7.78 (m, 2H, ArH), 7.4–6.95 (m, 8H, ArH), 4.06 (q, 1H, *J* = 7.0 Hz, CHN), 3.62 (ABq, 2H, *J* = 13.1 Hz, Δδ = 0.21, $ArCH_2N$), 1.11 (d, 3H, *J* = 7.0 Hz, CH_3CHN). ^{13}C NMR (63 MHz, C_6D_6) δ: 202.48, 140.62, 135.89, 132.60, 128.15, 128.10, 127.22, 126.73, 56.84, 51.66, 19.44.

anti-2-(*N*-Benzylamino)-1-phenyl-1-propanol (**7f**) was obtained in 77% yield (for both steps) as a clear oil. IR (neat) (cm^{-1}): 3355, 2880, 1603, 1494, 1454, 1199, 1065. ^{1}H NMR (250 MHz, C_6D_6) δ: 7.5–7.0 (m, 10H, ArH), 4.72 (d, 1H, *J* = 3.5 Hz, C*H*OH), 3.52 (ABq, 2H, *J* = 13.3 Hz, Δδ = 0.04, $ArCH_2N$), 2.74 (dq, 1H, *J* = 3.5, 6.5 Hz, CHN), 0.70 (d, 3H, *J* = 6.5 Hz, CH_3CHN). ^{13}C NMR (63 MHz, C_6D_6) δ: 142.83, 140.54, 128.61, 128.36, 128.22, 127.18, 127.01, 126.51, 73.59, 58.17, 51.15, 14.09. ES-MS *m*/*e*: 242 [M + 1, 100]. Anal. calcd. for $C_{16}H_{19}NO$: C 79.63, H 7.94, N 5.80; found: C 79.83, H 7.85, N 5.80. The ^{1}H NMR spectrum showed a signal for the carbinol proton of the syn-diastereomer (δ 4.14), which integrated to 1%. This is a previously reported compound (4).

*Preparation of 2-(*N*-benzylamino)-1-phenyl-1-heptanone (6g) and reduction with $Zn(BH_4)_2$*

This compound was prepared from ketone **3g** according to *General procedure D*. It was obtained in 65% yield as a pale yellow oil. IR (neat) (cm^{-1}): 3331, 2909, 1685, 1592, 1455. ^{1}H NMR (250 MHz, C_6D_6) δ: 7.88 (m, 2H, ArH), 7.36 (m, 2H, ArH), 7.3–6.9 (m, 6H, ArH), 4.12 (m, 1H, CHN), 3.66 (ABq, 2H, *J* = 13.1 Hz, Δδ = 0.24, $ArCH_2N$), 1.85–0.85 (m, 8H, $CH_3(CH_2)_4$), 0.81 (m, 3H, $CH_3(CH_2)_4$). ^{13}C NMR (63 MHz, C_6D_6) δ: 203.00, 141.01, 136.90, 132.99, 128.83, 128.70, 128.54, 127.19, 61.80, 52.46, 34.22, 31.99, 25.87, 22.80, 14.16.

anti-2-(*N*-Benzylamino)-1-phenyl-1-heptanol (**7g**) was obtained in 61% yield (for both steps) as a clear viscous oil. IR (neat) (cm^{-1}): 3402, 2915, 1455, 1051. ^{1}H NMR (250 MHz, C_6D_6) δ: 7.5–6.9 (m, 10H, ArH), 4.89 (d, 1H, *J* = 3.5 Hz, C*H*OH), 3.64 (ABq, 2H, *J* = 13.2 Hz, Δδ = 0.12, $ArCH_2N$), 2.66 (m, 1H, CHN), 1.4–0.8 (m, 8H, $CH_3(CH_2)_4$), 0.75 (m, 3H, $CH_3(CH_2)_4$). ^{13}C NMR (63 MHz, C_6D_6) δ: 142.50, 140.64, 128.69, 128.52, 128.27, 127.34, 127.03, 126.48, 72.33, 62.86, 51.77, 31.99, 28.49, 26.32, 22.80, 14.13. ES-MS *m*/*e*: 298 [M + 1, 100]. Anal. calcd. for $C_{20}H_{27}NO$: C 80.76, H 9.15, N 4.71; found: C 81.00, H 9.20, N 4.71. The ^{1}H NMR spectrum showed a signal for the carbinol proton of the syn-diastereomer (δ 4.38), which integrated to <1%.

*Preparation of 2-(*N*-benzylamino)-3-octanone (6h) and reduction with $Zn(BH_4)_2$*

This compound was prepared from ketone **3h** according to *General procedure D*. It was obtained in 88% yield as a pale yellow oil. IR (neat) (cm^{-1}): 3333, 3028, 2923, 1712, 1457, 1128. ^{1}H NMR (250 MHz, C_6D_6) δ: 7.4–7.0 (m, 5H, ArH), 3.56 (ABq, 2H, *J* = 13.2 Hz, Δδ = 0.10, $ArCH_2N$), 3.08 (q, 1H, *J* = 7.0 Hz, CHN), 2.08 (AB of app. ABX_2, 2H, *J* = 17.1, 7.4 Hz, Δδ = 0.11, $CH_2C(O)$), 1.53 (app. p, 2H, *J* = 7.4 Hz, $CH_2CH_2C(O)$), 1.4–1.05 (m, 4H, $CH_3CH_2CH_2CH_2CH_2C(O)$), 0.96 (d, 3H, *J* = 7.0 Hz, CH_3CHN], 0.85 (m, 3H, $CH_3(CH_2)_4C(O)$). ^{13}C NMR (63 MHz, C_6D_6) δ: 212.40, 140.93, 128.54, 128.40, 127.15, 61.89, 52.06, 39.18, 31.75, 23.59, 22.81, 18.07, 14.10.

anti-2-(*N*-Benzylamino)-3-octanol (7h) was obtained in 75% yield (for both steps) as an ~80:20 mixture of anti- and syn-diastereomers, respectively. Spectral data for **7h** are as follows: IR (neat) (cm^{-1}): 3378, 2934, 1456, 1108. ^{1}H NMR (250 MHz, C_6D_6) δ: 7.4–7.0 (m, 5H, ArH), 3.58 (app. dt, 0.8H, *J* = 3.0, 6.3 Hz, C*H*OH (anti)), 3.56 (s, 1.6H, $ArCH_2N$ (anti)), 3.53 (ABq, 0.4H, *J* = 13.0 Hz, Δδ = 0.21, $ArCH_2N$ (syn)), 3.16 (dt, 0.2H, *J* = 2.8, 8.3 Hz, C*H*OH (syn)), 2.48, (dq, 1H, *J* = 3.0, 6.5 Hz, CHN), 1.8–1.1 (m, 8H, $CH_3(CH_2)_4$), 1.0–0.8 (m, 6H, $CH_3(CH_2)_4$ and CH_3CHN). ^{13}C NMR (63 MHz, C_6D_6) δ: 141.38, 129.00, 128.75, 75.11 (syn), 71.86 (anti), 58.25 (syn), 57.12 (anti), 51.85, 34.66 (syn), 33.59, 32.81, 27.02, 26.32 (syn), 23.47, 16.76 (syn), 14.70, 14.43. ES-MS *m*/*e*: 236 [M + 1, 100]. Anal. calcd. for $C_{15}H_{25}NO$: C 76.55, H 10.71, N 5.95; found: C 76.48, H 10.52, N 6.07.

*Preparation of 4-(*N*-methylamino)-3-nonanone (6i) and reduction with $Zn(BH_4)_2$*

Ketone **3i** was deprotected according to *General procedure D* in quantitative yield as a pale yellow oil. IR (neat) (cm^{-1}): 3362, 2919, 2797, 1712, 1460, 1378, 1124. ^{1}H NMR (250 MHz, C_6D_6) δ: 2.88 (m, 1H, CHN), 2.10 (AB of ABX_3, 2H, Δδ = 0.18, *J* = 17.7, 7.4 Hz, CH_2CO), 2.14 (s, 3H, CH_3N), 1.50–1.05 (m, 8H, $CH_3(CH_2)_4CHN$), 0.99 (t, 3H, *J* = 7.3 Hz, CH_3CH_2CO), 0.86 (t, 3H, *J* = 7.6 Hz, $CH_3(CH_2)_4CHN$). ^{13}C NMR (63 MHz, C_6D_6) δ: 213.00, 69.44, 34.96, 32.66, 32.54, 32.17, 25.81, 22.83, 14.16, 7.77.

The deprotected ketone **6i** was reduced according to *General procedure D* except that the final extraction was done with Et_2O and the chromatography was omitted. A 69% yield (for both steps) of alcohols **5i** and **7i** in a 55:45 syn:anti ratio was obtained. ^{1}H NMR (250 MHz, C_6D_6) δ: 3.55 (dt, 0.45H, *J* = 9.1, 3.6 Hz, C*H*OH (anti)), 3.23 (dt, 0.55H, *J* = 3.4, 7.2, C*H*OH (syn)), 2.18 (s, 1.35H, CH_3N (anti)), 2.15 (m, 1H, CHN), 2.12 (s, 1.65H, CH_3N (syn)), 1.6–1.0 (m, 10H, $CH_3(CH_2)_4CHN$ and CH_2CHOH), 1.0–0.85 (m, 6H, $CH_3(CH_2)_4CHN$ and CH_3CH_2CHOH). ^{13}C

© 2003 NRC Canada

NMR (63 MHz, C_6D_6) δ: 73.14 (syn), 71.84 (anti), 64.26 (anti), 63.59 (syn), 34.56 (anti), 33.63 (syn), 32.53, 30.29 (syn), 28.89 (anti), 27.70, 26.65 (anti), 25.71, 22.97 (syn), 14.25, 11.31 (anti), 10.63 (syn).

*Preparation of 7-(*N*-methylamino)-6-dodecanone (6j) and reduction with $Zn(BH_4)_2$*

Ketone **3j** was deprotected according to *General procedure D* in ~77% yield as a pale yellow oil. IR (neat) (cm^{-1}): 3341, 2913, 2797, 1711, 1460, 1371, 1133. ^1H NMR (250 MHz, C_6D_6) δ: 2.92 (m, 1H, CHN), 2.20 (AB of app. ABX_2, 2H, Δδ = 0.14, *J* = 17.0, 7.3 Hz, CH_2CO), 2.18 (s, 3H, CH_3N), 1.60 (p, 2H, *J* = 7.3 Hz, CH_2CH_2CO), 1.50–1.05 (m, 12H, $CH_3(CH_2)_4CHN$ and $CH_3CH_2CH_2CH_2CH_2CO$), 1.0–0.75 (overlapping t, 6H, $CH_3(CH_2)_4CHN$ and $CH_3(CH_2)_4CO$). ^{13}C NMR (63 MHz, C_6D_6) δ: 212.41, 69.66, 39.57, 35.05, 32.50, 31.85, 25.86, 23.62, 22.86, 14.18, 14.10.

The ketone **6j** was reduced according to *General procedure D* except that the final extraction was done with Et_2O and the chromatography was omitted. The alcohols **5j/7j** was obtained in 65% yield (for both steps) as a white solid, which was a 50:50 mixture of diastereomers. ^1H NMR (250 MHz, C_6D_6) δ: 3.72 (br m, 0.5H, C*H*OH (anti)), 3.39 (br m, 0.5H, C*H*OH (syn)), 2.4–2.0 (br m, 4H, CH_3N and CHN), 1.65–1.1 (m, 16H, $CH_3(CH_2)_4CHN$ and $CH_3(CH_2)_4CHOH$), 1.1–0.7 (m, 6H, $CH_3(CH_2)_4CHN$ and $CH_3(CH_2)_4CHOH$).

*Preparation of 4-(*N*-methylamino)-2-methyl-3-nonanone (6k) and reduction with $Zn(BH_4)_2$*

Ketone **3k** was deprotected according to *General procedure D* in quantitative yield as a pale yellow oil. IR (neat) (cm^{-1}): 3338, 2919, 2797, 1711, 1462, 1381, 1135, 1039. ^1H NMR (250 MHz, C_6D_6) δ: 3.03 (dd, 1H, *J* = 4.5, 7.4 Hz, CHN), 2.45 (sept., 1H, *J* = 6.8 Hz, CH_3CHCH_3), 2.16 (s, 3H, CH_3N), 1.55–1.05 (m, 8H, $CH_3(CH_2)_4CHN$), 1.01 (d, 3H, *J* = 6.7 Hz, CH_3CHCH_3), 0.91 (d, 3H, *J* = 6.7 Hz, CH_3CHCH_3), 0.87 (t, 3H, *J* = 7.0 Hz, $CH_3(CH_2)_4CHN$]. ^{13}C NMR (63 MHz, C_6D_6) δ: 215.91, 67.90, 37.84, 35.08, 32.53, 32.22, 26.07, 22.89, 18.84, 17.93, 14.19.

The ketone **6k** was reduced according to *General procedure D* except that the final extraction was performed with Et_2O and the chromatography was omitted. A 69% yield of alcohols **5k/7k** (for both steps) was obtained as a clear oil, which was a 59:41 syn:anti mixture of diastereomers. ^1H NMR (250 MHz, C_6D_6) δ: 3.25 (dd, 0.4H, *J* = 3.1, 8.9 Hz, C*H*OH (anti)], 3.09 (dd, 0.6H, *J* = 4.4, 7.1 Hz, C*H*OH (syn)), 2.4–2.2 (m, 1H, CHN), 2.14 (s, 1.2H, CH_3N (anti)), 2.10 (s, 1.8H, CH_3N (syn)), 1.9–1.6 (m, 1H, CH_3CHCH_3), 1.5–1.0 (m, 8H, $CH_3(CH_2)_4CHN$), 1.24 (d, 1.2H, *J* = 6.5 Hz, CH_3CHCH_3 (anti)), 1.12 (d, 1.8H, *J* = 6.8 Hz, CH_3CHCH_3 (syn)), 1.05 (d, 1.8H, *J* = 6.7 Hz, CH_3CHCH_3 (syn)), 1.0–0.8 (m, 3H, $CH_3(CH_2)_4CHN$), 0.78 (d, 1.2H, *J* = 6.7 Hz, CH_3CHCH_3 (anti)). ^{13}C NMR (63 MHz, C_6D_6) δ: 75.93 (syn), 75.11 (anti), 62.00 (anti), 60.95 (syn), 34.12 (anti), 33.26 (syn), 32.50, 30.54 (syn), 30.39 (anti), 30.22 (syn), 27.77 (anti), 26.60 (anti), 25.50 (syn), 23.01 (anti), 22.96 (syn), 20.78 (syn), 20.67 (anti), 18.67 (anti), 16.28 (syn), 14.26.

*Preparation of 4-(*N*-methylamino)-2,2-dimethyl-3-nonanone (6l) and reduction with $Zn(BH_4)_2$*

Ketone **3l** was deprotected according to *General procedure D* in 91% yield as a clear oil. IR (neat) (cm^{-1}): 3331, 2920, 2795, 1703, 1468, 1365, 1133, 1057. ^1H NMR (250 MHz, C_6D_6) δ: 3.34 (dd, 1H, *J* = 3.2, 8.4 Hz, CHN), 2.12 (s, 3H, CH_3N), 1.65–1.10 (m, 8H, $CH_3(CH_2)_4CHN$), 1.02 (s, 9H, $C(CH_3)_3$), 0.88 (t, 3H, *J* = 6.8 Hz, $CH_3(CH_2)_4CHN$). ^{13}C NMR (63 MHz, C_6D_6) δ: 217.38, 63.16, 43.15, 35.04, 35.57, 32.16, 26.39, 22.94, 14.22.

The ketone **6l** was reduced according to *General procedure D* except that the last extraction was performed with Et_2O and the chromatography was omitted. The alcohol was obtained in 63% yield (for both steps) as a clear oil, which was a 96:4 anti:syn mixture of diastereomers. *anti*-4-(*N*-methylamino)-2,2-dimethyl-3-nonanol (**7l**) exhibited the following spectral characteristics: IR (neat) (cm^{-1}): 3319, 2916, 1467, 1361, 1089, 1014. ^1H NMR (250 MHz, C_6D_6) δ: 3.38 (d, 1H, *J* = 1.9, C*H*OH), 2.37 (dt, 1H, *J* = 2.2, 8.8 Hz, CHN), 2.19 (s, 3H, CH_3N), 1.45–1.10 (m, 8H, $CH_3(CH_2)_4$), 1.07 (s, 9H, $C(CH_3)_3$), 0.89 [t, 3H, *J* = 6.7 Hz, $CH_3(CH2)_4$). ^{13}C NMR (63 MHz, C_6D_6) δ: 77.82, 62.40, 34.63, 32.64, 30.07, 27.41, 27.13, 26.26, 23.08, 14.29. ES-MS *m/e*: 202 [M + 1, 100].

*Preparation of 3-(*N*-methylamino)-2-methyl-4-nonanone (6m) and reduction with $Zn(BH_4)_2$*

Ketone **3m** was deprotected according to *General procedure D* in quantitative yield as a pale yellow oil. IR (neat) (cm^{-1}): 3362, 2929, 2797, 1708, 1463, 1373, 1135. ^1H NMR (250 MHz, C_6D_6) δ: 2.69 (d, 1H, *J* = 5.2 Hz, CHN), 2.13 (AB of app. ABX2, 2H, Δδ = 0.18, *J* = 17.0, 7.5 Hz, CH_2CO), 2.17 (s, 3H, CH_3N), 1.74 (d of sept., 1H, *J* = 5.2, 6.8 Hz, CH_3CHCH_3), 1.57 (p, 2H, *J* = 7.4 Hz, CH_2CH_2CO), 1.35–1.05 (m, 4H, $CH_3CH_2CH_2CH_2CH_2CO$), 0.95 (d, 3H, *J* = 6.8 Hz, CH_3CHCH_3), 0.86 (t, 3H, *J* = 8.8 Hz, $CH_3(CH_2)_4CO$), 0.77 (d, 3H, *J* = 6.8 Hz, CH_3CHCH_3). ^{13}C NMR (63 MHz, C_6D_6) δ: 212.55, 75.20, 40.82, 35.91, 31.83, 30.54, 23.57, 22.86, 20.39, 17.49. 14.07.

The ketone **6m** was reduced according to *General procedure D* except that the final extraction was performed with Et_2O and the chromatography was omitted. The alcohol was obtained in 81% yield (for both steps) as a clear oil, which was a 96:4 anti:syn mixture of diastereomers. *anti*-3-(*N*-Methylamino)-2-methyl-4-nonanol (**7m**) exhibited the following spectral characteristics: IR (neat) (cm^{-1}): 3380, 2916, 1462, 1103. ^1H NMR (250 MHz, C_6D_6) δ: 3.65 (m, 1H, C*H*OH), 2.24 (s, 3H, CH_3N), 1.98 (dd, 1H, *J* = 5.2, 4.8 Hz, CHN), 1.72 (d of sept., 1H, *J* = 5.2, 6.9 Hz, CH_3CHCH_3), 1.50–1.25 (m, 8H, $CH_3(CH_2)_4CHOH$), 0.93 (t, 3H, *J* = 6.7 Hz, $CH_3(CH_2)_4$), 0.91 (d, 3H, *J* = 6.9 Hz, CH_3CHCH_3), 0.79 (d, 3H, *J* = 6.9 Hz, CH_3CHCH_3). ^{13}C NMR (63 MHz, C_6D_6) δ: 70.65, 69.42, 36.48, 32.84, 32.52, 29.08, 26.74, 23.14, 21.11, 18.65, 14.31. ES-MS *m/e*: 188 [M + 1, 100].

*Preparation of 2-(*N*-methylamino)-3-octanone (6n) and reduction with $Zn(BH_4)_2$*

Ketone **3n** was deprotected according to *General procedure D* in ~87% yield as a pale yellow oil. IR (neat) (cm^{-1}): 3341, 2916, 2797, 1712, 1457, 1371, 1135. ^1H NMR (250 MHz, C_6D_6) δ: 2.91 (q, 1H, *J* = 7.0 Hz, CHN), 2.15

© 2003 NRC Canada

(AB of ABX_3, 2H, $\Delta\delta$ = 0.09, J = 17.0, 7.4 Hz, CH_2CO), 2.14 (s, 3H, CH_3N), 1.55 (p, 2H, J = 7.4 Hz, CH_2CH_2CO), 1.45–1.05 (m, 4H, $CH_3CH_2CH_2CH_2CH2CO$), 0.96 (d, 3H, J = 7.0 Hz, CH_3CHN), 0.85 (t, 3H, J = 6.9 Hz, $CH_3(CH_2)_4CO$). ^{13}C NMR (63 MHz, C_6D_6) δ: 212.34, 64.55, 38.99, 34.51, 31.78, 23.56, 22.82, 17.65, 14.07.

The ketone **6n** was reduced according to *General procedure D* except that the final extraction was performed with Et_2O and the chromatography was omitted. The alcohols **5n/7n** were obtained in 66% yield (for both steps) as a yellow oil, which was a 37:63 syn:anti mixture of diastereomers. ^{1}H NMR (250 MHz, C_6D_6) δ: 3.58 (dt, 0.4H, J = 8.8, 3.4 Hz, C*H*OH (anti)), 3.15 (dt, 0.6H, J = 2.9, 8.3 Hz, C*H*OH (syn)), 2.3–2.1 (m, 1H, CHN), 2.12 (s, 1.2H, CH_3N (anti)), 2.11 (s, 1.8H, CH_3N (syn)), 1.8–1.1 (m, 8H, $CH_3(CH_2)_4CHOH$), 0.93 (m, 3H, $CH_3(CH_2)_4CHOH$), 0.85 (d, 1.2H, J = 6.5 Hz, CH_3CHN (anti)), 0.79 (d, 1.8H, CH_3CHN (syn)). ^{13}C NMR (63 MHz, C_6D_6) δ: 74.32 (syn), 71.32 (anti), 60.23 (syn), 59.40 (anti), 34.39 (syn), 33.64 (anti), 33.40, 32.50, 26.64 (anti), 25.91 (syn), 23.12, 15.45 (syn), 14.31, 13.14 (anti).

Experimental for the preparation of enantiomerically enriched β-aminoalcohols

(2*R*)-2-(*N-tert*-Butoxycarbonyl-*N*-methylamino)-3-methyl-1-phenyl-1-butanol ((***R***)-**2b**). This compound was prepared from (***S***)-**1b** and benzaldehyde according to *General procedure A* except that the reaction was run at –95 °C and was stirred for 10 min. Aminoalcohol (***R***)-**2b** was obtained in 71% yield as a mixture of diastereomers. HPLC (Chiralcel OD, 4.6 mm × 150 mm, 98:2 hex./*i*-PrOH, 0.25 mL/min) indicated that the product was 94% ee. Another sample of this compound was prepared that had an ee of 96%.

*(*R*)-2-(*N-tert-*Butoxycarbonyl-*N-*methylamino)-3-methyl-1-phenyl-1-butanone ((R)-3b)*

This compound was prepared according to *General procedure A* from (***R***)-**2b** (94% ee) in 95% yield. It exhibited spectral data as for racemic **3b** and optical rotation $[\alpha]_D$ = +254.9 (*c* 1.10, THF).

*(1*R*,2*R*)-2-(*N-tert-*Butoxycarbonyl-*N-*methylamino)-3-methyl-1-phenyl-1-butanol ((R)-4b)*

This compound was prepared from ketone (***R***)-**3b** (made from (***R***)-**2b** of 96% ee) according to *General procedure B* in 88% yield. It exhibited spectral data as described for compound **4b**. HPLC (Chiralcel OD, 4.6 mm × 150 mm, 98:2 hex./*i*-PrOH, 0.25 mL/min) indicated that it had an ee of 94%.

Acknowledgments

We thank the Natural Sciences and Engineering Research Council of Canada (NSERC) for financial support.

References

1. Review: D.J. Ager, I. Prakash, and D.R. Schaad. Chem. Rev. **96**, 835 (1996).
2. M.T. Reetz. Angew. Chem. Int. Ed. **30**, 1531 (1991), and refs. cited therein.
3. (*a*) T.P. Tang, S.K. Volkman, and J.A. Ellman. J. Org. Chem. **66**, 8772 (2001); (*b*) J.C. Barrow, P.L. Ngo, J.M. Pellicore, H.G. Selnick, and P.G. Nantermet. Tetrahedron Lett. **42**, 2051 (2001).
4. W.R. Jackson, H.A. Jacobs, G.S. Jayatilake, B.R. Matthews, and K.G. Watson. Aust. J. Chem. **43**, 2045 (1990).
5. M. Tramontini. Synthesis, 605 (1982).
6. R.V. Hoffman, N. Maslouh, and F. Cervantes-Lee. J. Org. Chem. **67**, 1045 (2002).
7. (*a*) D. Nadkarni, J. Hallissey, and C. Mojica. J. Org. Chem. **68**, 594 (2003); (*b*) S. Sengupta and D.S. Sarma. Tetrahedron Lett. **42**, 485 (2001); (*c*) S. Sengupta and D.S. Sarma. Tetrahedron: Asymmetry, **10**, 4633 (1999); (*d*) M.J. Palmer, J.R. Studley, T.C. Walsgrove, and M. Wills. Tetrahedron, **54**, 8827 (1998).
8. (*a*) J.M. Chong and S.B. Park. J. Org. Chem. **57**, 2220 (1992); (*b*) A. Ncube, S.B. Park, and J.M. Chong. J. Org. Chem. **67**, 3625 (2002).
9. P.C.-M. Chan and J.M. Chong. J. Org. Chem. **53**, 5584 (1998).
11. M.-N. Dufour, P. Jouin, J. Poncet, A. Pantaloni, and B.J. Castro. J. Chem. Soc. Perkin Trans. 1, 1895–1899 (1986).
12. P.G.M. Wuts and L.E. Pruitt. Synthesis, 622 (1989).
13. M. Cherest, H. Felkin, and N. Prudent. Tetrahedron Lett. 2199 (1968).
14. W.J. Gensler, F.A. Johnson, and A.D.B. Sloan. J. Am. Chem. Soc. **82**, 6074 (1960).
15. C. Agami, F. Couty, L. Hamon, and O. Venier. Tetrahedron Lett. **34**, 4509 (1993).
16. K. Everaere, A. Mortreux, M. Bulliard, J. Brussee, A. van der Gen, G. Nowogrocki, and J.-F. Carpentier. Eur. J. Org. Chem. 275 (2001).
17. S. Budavari (*Editor*). Merck index. 11th ed. Merck and Co. Rahway, N.J. 1989. p. 565.
18. K. Lovgren and J.L. Nilsson. G. Acta Pharmaceutica Suecica, **14**, 30 (1977).

© 2003 NRC Canada

Pachymoside A — A novel glycolipid isolated from the marine sponge *Pachymatisma johnstonia*[1]

Kaoru Warabi, William T. Zimmerman, Jingkai Shen, Annick Gauthier, Marilyn Robertson, B. Brett Finlay, Rob van Soest, and Raymond J. Andersen

Abstract: Crude extracts of the North Sea marine sponge *Pachymatisma johnstonia* showed promising activity in a new assay for inhibitors of bacterial type III secretion. Bioassay-guided fractionation resulted in the isolation of the pachymosides, a new family of sponge glycolipids. A major part of the structural diversity in this family of glycolipids involves increasing degrees of acetylation and differing positions of acetylation on a common pachymoside glycolipid template. All of the metabolites with these variations in acetylation pattern were converted into the same peracetylpachymoside methyl ester (**2**) for purification and spectroscopic analysis. Pachymoside A (**1**) is the component of the mixture that has natural acetylation at the eight galactose hydroxyls and at the C-6 hydroxyls of glucose-B and glucose-D. Chemical degradation and transformation in conjunction with extensive analysis of 800 MHz NMR data was used to elucidate the structure of pachymoside A (**1**).

Key words: Pachymatisma johnstonia, marine sponge, pachymoside, glycolipid.

Résumé : Les produits bruts extraits de l'éponge marine de la mer du Nord *Pachymatisma Johnstonia* présentent une activité intéressante dans un nouvel essai pour les inhibiteurs de la sécrétion bactérienne de type III. Des fractionnements orientés par des bioessais ont permis d'isoler les pachymosides, une nouvelle famille de glycolipides des éponges. Une partie importante de la diversité structurelle de cette famille de glycolipides implique des degrés croissants d'acétylation et des différences dans les positions de l'acétylation sur un gabarit commun du glycolipide pachymoside. Tous les métabolites comportant ces variations dans le patron d'acétylation ont été transformés dans le même ester méthylique du peracétylpachymoside (**2**) aux fins de purification et d'analyse spectroscopique. Le pachymoside A (**1**) est le composant du mélange qui correspond à l'acétylation naturelle au niveau des huit hydroxyles du galactose et aux hydroxyles en C-6 du glucose-B et du glucose-D. Afin d'élucider la structure du pachymoside A (**1**), on a utilisé une dégradation et une transformation chimique de concert avec une analyse extensive des données RMN à 800 MHz.

Mots clés : Pachymatisma johnstonia, éponge marine, pachymoside, glycolipide.

[Traduit par la Rédaction]

Introduction

Several important gram-negative pathogenic bacteria deliver virulence factors directly into host cells via a "type III secretion system" (TTSS) (1–4). These include *Bordetella pertussis*, the cause of whooping cough, *Chlamydia trachomatis*, the cause of a sexually transmitted disease that leads to blindness, enterohemorrhagic *Escherichia coli* (EHEC), the cause of "hamburger" disease, and *Salmonella typhi*, the cause of typhoid fever. EHEC (5) and the closely related enteropathogenic *E. coli* (EPEC) (6), the major cause of infantile diaherria that kills several thousand children worldwide each year, have served as important models for studying TTSSs and their role in pathogenicity. While many bacterial pathogens attach themselves to host cell proteins, these pathogenic *E. coli* are remarkable because they use a TTSS to deliver their own receptors into the host cells to which they attach. The bacterial protein receptor delivered into the host cell by the *E. coli* TTSS is called Tir for "translocated intimin receptor". Once inside the host cell, Tir binds to an *E. coli* protein "intimin" on the surface of the bacterium to give intimate attachment, a required prelude to

Received 23 June 2003. Published on the NRC Research Press Web site at http://canjchem.nrc.ca on 15 December 2003.

Dedicated to Professor Edward Piers, a wonderful colleague and friend.

K. Warabi, W.T. Zimmerman,[2] J. Shen, and R.J. Andersen.[3] Departments of Chemistry, Earth and Ocean Sciences, University of British Columbia, 2036 Main Mall, Vancouver, BC V6T 1Z1, Canada.
A. Gauthier, M. Robertson, and B.B. Finlay. Departments of Biochemistry and Microbiology, University of British Columbia, Vancouver, BC V6T 1Z3, Canada.
R. van Soest. Department of Coelenterates and Porifera, Zoologisch Museum, University of Amsterdam, Amsterdam, The Netherlands.

[1]This article is part of a Special Issue dedicated to Professor Ed Piers.
[2]On leave from DuPont Crop Protection, Stine-Haskell Research Center, Newark, DE, U.S.A.
[3]Corresponding author (email: randersn@interchange.ubc.ca).

 doi: 10.1139/V03-183 © 2003 NRC Canada

virulence. The TTSS, which forms a syringe-like pore that spans both bacterial and host cell membranes, consists of more than 20 proteins. Deleting or mutating any part of the TTSS significantly reduces the virulence of the affected *E. coli*. Non-pathogenic intestinal *E. coli* do not have TTSSs.

The TTSS is considered an attractive target for the development of new antibiotics that would selectively target pathogenic gram negative bacteria but would not harm the ordinary microflora that do not possess this virulence mechanism (1, 7–9). An added benefit of this type of hypothetical antibacterial agent is that by targeting a virulence mechanism, there would be little or no selective pressure for viability, potentially reducing the development of resistance. No TTSS inhibitors were known at the outset of our research. Consequently, there was a significant need to discover TTSS inhibitors that could be used to provide proof principle demonstrations and drug leads for this novel approach to treating important infectious diseases.

Marine sponges, which are the richest source of bioactive marine natural products (10, 11), are constantly exposed to bacteria in seawater and it has frequently been proposed that they contain chemical agents that have evolved to prevent pathogenic bacteria from infecting them (12, 13). We have screened a library of crude extracts from marine sponges for their ability to inhibit type III secretion of *E. coli* secreted proteins (Esps) by EPEC without affecting the growth or general secretion of the bacterium (1). Two extracts showed promising activity in the screen. Recently, we reported the structure of caminoside A, an antimicrobial glycolipid isolated from the Caribbean sponge *Caminus sphaeroconia* that was the first compound active in the TTSS inhibition screen (14, 15).[4] The second active extract came from the sponge *Pachymatisma johnstonia* (Bowerbank, 1842) collected along the coast of the Isle of Mann. Bioassay-guided fractionation of the *P. johnstonia* extract yielded a complex family of glycolipids that were active in the TTSS assay. The structure elucidation of pachymoside A (**1**), a novel glycolipid that is a representative member of this family, is described below.

Results and discussion

The TTSS inhibitory fraction obtained from an initial Sephadex LH20 chromatographic separation (eluent: MeOH) of the crude *P. johnstonia* extract gave spectroscopic data that was indicative of a complex mixture of closely related glycolipids. LR-FAB-MS analysis of the mixture revealed a series of clusters of molecular ions with centres at *m/z* 1918, 1932, 1944, 1961, 1973, 1988, 2003, 2015, and 2046. The ^{1}H and ^{13}C NMR spectra of the mixture showed evidence for the presence of a number of monosaccharide anomeric carbons, a large number of carbinol methines and methylenes, extensive acetylation, and a long aliphatic chain. All chromatographic attempts to resolve the complex mixture of natural products into individual components failed. To facilitate purification of the mixture, it was first methylated with (trimethylsilyl)diazomethane and then acetylated with Ac_2O–pyridine in the presence of DMAP. Reversed-phase HPLC separation of the mixture of derivatized natural products gave a pure peracetylpachymoside A methyl ester (**2**) as a colourless glass.

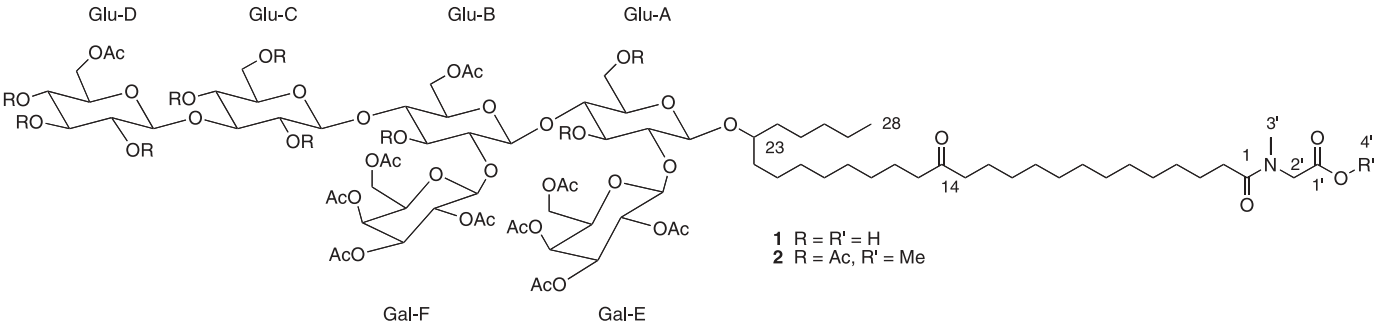
Peracetylpachymoside A methyl ester (**2**) gave a $[M + Na]^+$ ion at *m/z* 2333.9639 in the ESI-HR-MS consistent with a molecular formula of $C_{106}H_{159}NO_{54}$ (calcd. for $^{12}C_{105}{}^{13}CH_{159}NO_{54}Na$, 2333.9658), requiring 28 sites of unsaturation. The ^{13}C NMR spectrum of **2** (100 MHz) recorded in C_6D_6 showed the same general features of a glycolipid observed in the spectrum of the natural product mixture. Thus, it was possible to attribute clusters of peaks to ester or amide carbonyls (δ 168–170), monosaccharide anomeric carbons (δ 100–102), carbinol methines and methylenes (δ 67–81), methyl groups attached to O or N (δ 49–52), acetate methyl carbons (δ 29–31), and a significant saturated aliphatic fragment (δ 14–43). The ^{1}H NMR spectrum of **2** was very congested at 500 MHz so all of the ^{1}H 1D and 2D data used in the structure elucidation was recorded at 800 MHz in C_6D_6, which gave excellent dispersion.

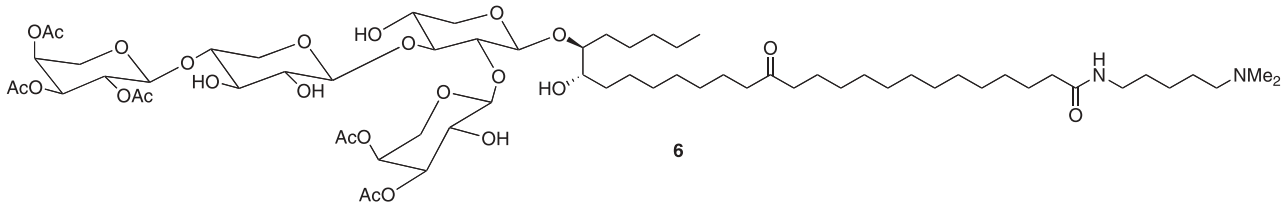
The first step in the structure elucidation of **2** involved chemical degradation of the mixture of natural pachymosides to liberate the individual monosaccharides. Treatment of the pachymoside mixture with acetyl chloride in dry MeOH cleaved the glycosidic linkages and converted the individual monosaccharides into mixtures of α- and β-methylglycopyranosides. After removal of the reagents in vacuo, the resulting residue was acetylated with Ac_2O in pyridine and a catalytic amount of DMAP to give the peracetylated methylglycosides of the individual monosaccharides. Fractionation of the peracetylated methylglycosides via reversed-phase HPLC gave an inseparable mixture of methyl 2,3,4,6-tetra-*O*-acetyl-α-glucopyranoside (**3**) and methyl 2,3,4,6-tetra-*O*-acetyl-α-galactopyranoside (**4**) in a ratio of ≈2:1, respectively. The difference in intensities of the resonances for each of **3** and **4** made it possible to identify each of the component compounds by analysis of the 1D and 2D NMR data obtained for the mixture. To confirm the assigned structures of **3** and **4**, authentic samples of D-glucose and D-galactose were converted into their peractylated methyl α-glycopyranosides and the NMR chemical shifts of the authentic compounds were compared with the degradation products. Chiral GC analysis of the alditol acetates prepared from authentic L- and D-glucose and D-galactose and the alditol acetates prepared from the monosaccharides obtained by aqueous hydrolysis of the pachymoside mixture showed that the glucose and galactose residues in the pachymosides had the D configuration.

A very non-polar fraction, which contained a mixture of the aglycon portions of the pachymosides, was also obtained

[4] While the current study was underway, another group reported screening a chemical library for inhibition of YopE transcription with a luciferase reporter assay, yielding three compounds that inhibited the reporter signal expressed from the *yopE* promoter and effector protein secretion with little effect on bacterial growth (15). One compound appears to be affecting type III regulation, and this and one other compound are specific to the virulence-associated TTSS, and do not affect flagellum assembly and motility. Overall, these results are evidence in support of TTSS-specific inhibitors, although the bacterial target(s) and ability to inhibit TTSS in infected host cells awaits further study.

© 2003 NRC Canada





from the methanolysis reaction on the pachymoside mixture described above. HPLC fractionation of the mixture of aglycons yielded a number of closely related compounds. Methanolysis of pure peracetylpachymoside A methyl ester (**2**), followed by analysis of the non-polar product by HPLC, ^{1}H NMR, and EI-MS, revealed that the methyl ester **5** obtained from the large-scale methanolysis of the mixture of pachymosides corresponded to the aglycon fragment of **2**. The ester **5** gave a M^+ ion at *m/z* 539.4567 in the EI-HR-MS appropriate for a molecular formula of $C_{32}H_{61}NO_5$ (calcd. 539.4550), requiring three sites of unsaturation.

Three associated pairs of singlets were apparent in the ^{1}H NMR spectrum of **5**, each of which exhibited an intensity ratio of ca. 4:1. A singlet at δ 3.71 in the ^{1}H NMR spectrum (associated peak at δ 3.77), which showed a HMQC correlation to a carbon at δ 52.5 and a HMBC correlation to a carbon at δ 170.0, was assigned to a methyl ester. A second singlet at δ 3.05 (associated peak at δ 2.95), which showed an HMQC correlation to a carbon at δ 36.5 and HMBC correlations to carbons at δ 172.0 and 49.0, was assigned to a *N*-methyl amide. The third singlet at δ 4.11 (associated peak at δ 4.03), integrated for only two protons relative to the other singlets. It showed a HMQC correlation to a carbon at δ 49.0 and HMBC correlations to the ester carbonyl at δ 170.0, the amide carbonyl at δ 172.0, and the *N*-methyl carbon at δ 36.5, and was assigned to the α carbon of an *N*-acyl-*N*-methylglycine methyl ester fragment. As is typical for tertiary amides, slow rotation about the *N*-acyl-*N*-methylglycine amide bond is presumed to be responsible for the presence of associated pairs of peaks observed in the ^{1}H NMR spectrum for the *N*-methyl, methyl ester, and glycine α-methylene resonances.

Additional features in the ^{1}H NMR spectrum of **5** included a six proton multiplet at δ 2.36, a deshielded one proton multiplet at δ 3.55, and a three proton triplet at δ 0.87. The six proton multiplet (δ 2.36) showed HMQC correlations into carbon resonances at δ 38.1 and 42.8, and HMBC correlations into the amide carbonyl resonance at δ 172.0 and into a deshielded carbon resonance at δ 211.0, assigned to a saturated ketone. These correlations indicated that the six proton multiplet was comprised of three separate but coincidentally chemical shift-equivalent methylene resonances that were assigned to a methylene α to the amide carbonyl and two methylenes α to a saturated ketone. Consistent with these assignments, there was a small triplet at δ 2.20 in the ^{1}H NMR spectrum that was assigned to the methylene α to the amide carbonyl in the minor rotamer of **5**. The methine resonance at δ 3.55 showed a HMQC correlation to the carbon resonance at δ 72.5 consistent with the presence of a secondary alcohol in **5**, and the triplet at δ 0.87 was assigned to a methyl at the end of a linear aliphatic chain. Since the methyl ester, *N*-methylamide, and ketone carbonyls accounted for the three sites of unsaturation in **5**, and the only terminal residues identified in the NMR data were the methyl ester and aliphatic methyl groups, the aglycon had to have a 27-carbon linear chain extending from the *N*-acyl amide carbonyl to the terminal methyl group, and there had to be saturated ketone and secondary alcohol functionalities situated along the chain.

The positions of the ketone and secondary alcohol functionalities in **5** were determined by analysis of the EI-HR-MS data obtained for the compound as shown in Fig. 1. A major peak at *m/z* 145.0739 ($C_6H_{11}NO_3$) was attributed to a McLafferty rearrangement involving the C-4 amide carbonyl that results in cleavage of the C-5—C-6 bond, confirming the presence of the *N*-acyl-*N*-methylglycine methyl ester fragment at one terminus of the aglycon. A pair of peaks at *m/z* 284.2232 ($C_{16}H_{30}NO_3$) and 341.2557 ($C_{19}H_{35}NO_4$) were attributed to McLafferty rearrangements occurring on both sides of the ketone functionality, which located the ketone at C-14. Finally, a peak at *m/z* 468.3697 ($C_{27}H_{50}NO_5$) was assigned to an α cleavage adjacent to the secondary alcohol, which had to be at C-23. The base peak in the mass spectrum of **5** resulted from a cleavage of the amide bond to

© 2003 NRC Canada

Fig. 1. HR-EI-MS analysis of the aglycon methyl ester **5**.

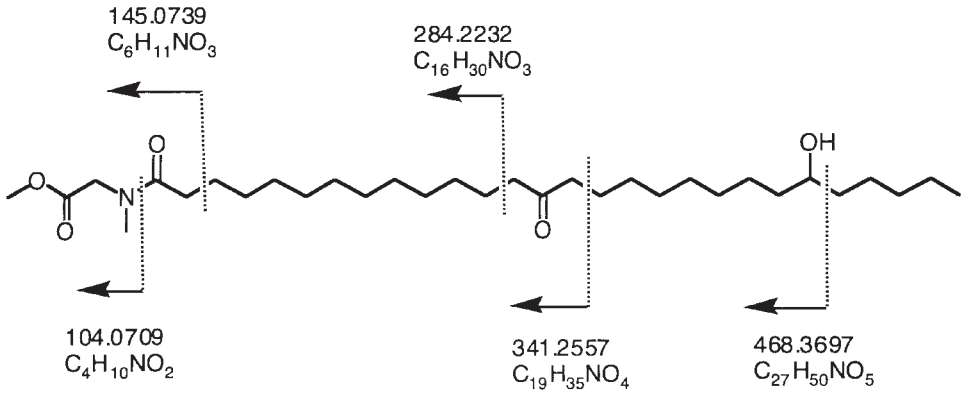
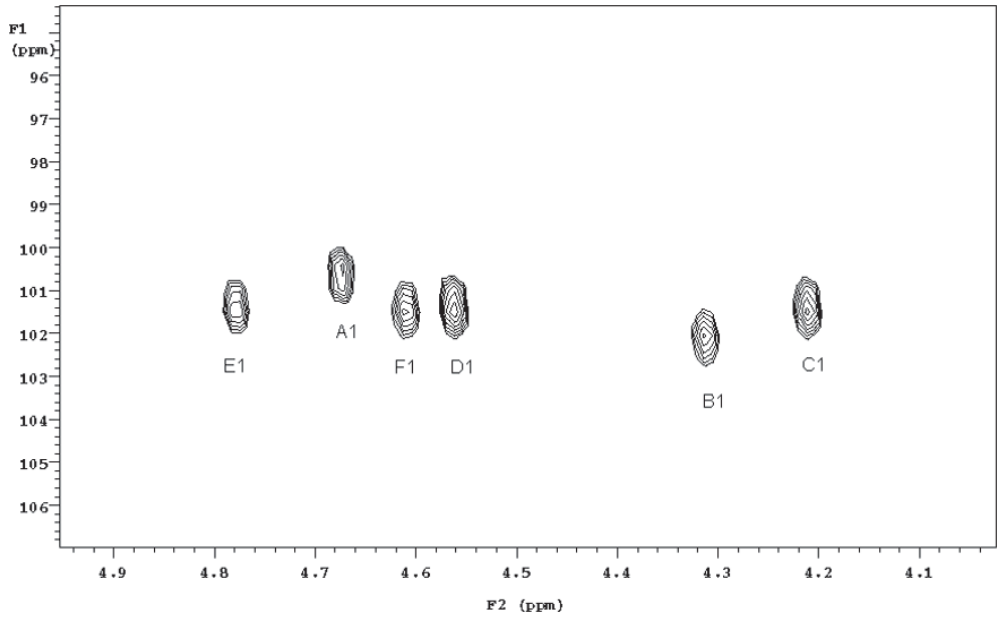


Fig. 2. Expansion of gHSQC spectrum of peracetylpachymoside A methylester (**2**) acquired in C_6D_6 at 800 MHz. Anomeric carbon correlations are shown.



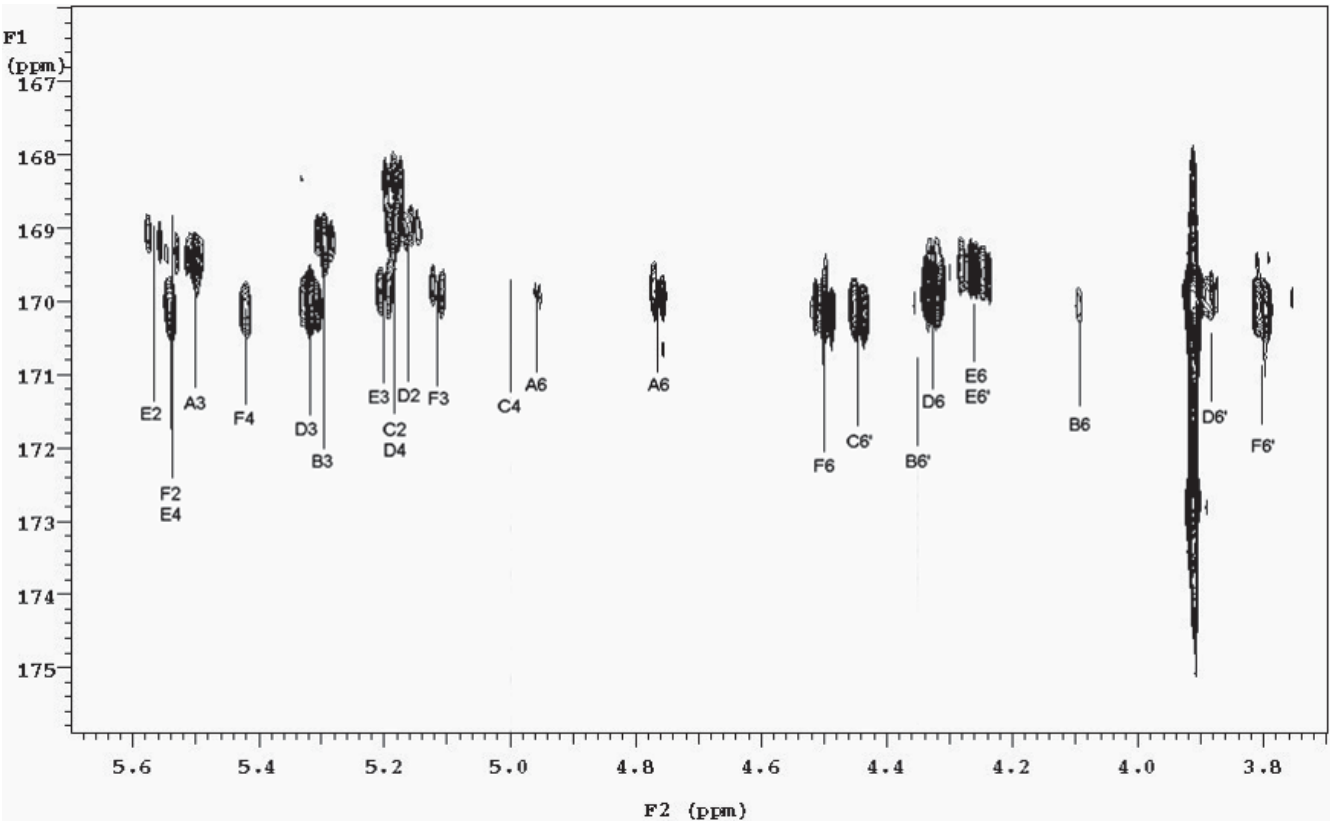
give a fragment ion at *m/z* 104.0709 ($C_4H_{10}NO_2$), which had the molecular formula of protonated *N*-methylglycine methyl ester.

Subtracting the atoms present in the aglycon ($C_{32}H_{60}NO_5$) from the molecular formula of peracetylpachymoside A methyl ester (**2**) ($C_{106}H_{159}NO_{54}$) left $C_{74}H_{99}O_{49}$ and 25 sites of unsaturation unaccounted for. Preliminary analysis of the NMR data obtained for **2**, in conjunction with the degradation studies, indicated the remaining atoms had to be part of glucose, galactose, or acetate residues. Six anomeric carbons and their attached protons (δ ^{13}C: ^{1}H; 100.7:4.67; 101.4:4.21; 101.4:4.56; 101.4:4.78; 101.5:4.61; 102.1:4.31) could be readily identified in the HSQC spectrum of **2** (Fig. 2). Subtracting the 36 carbons of six hexose monosaccharides (glucose and galactose) from the 74 carbons remaining to be accounted for, left 38 carbons, which corresponded to 19 acetate residues. The six sites of unsaturation accounted for by the putative monosaccharide rings, along with the 19 sites of unsaturation associated with the acetate residues and the three sites of unsaturation in the aglycon, accounted for all of the unsaturation required by the molecular formula of **2**. Therefore, what remained was to determine the connectivity among the aglycon, the six monosaccharide residues, and the 19 acetates, as well as determining the relative stereochemistry of the polysaccharide portion of the molecule. These features of **2** were elucidated by detailed analysis of its 800 MHz NMR data (Figs. 3 and 4).

Starting with the six well-resolved anomeric proton resonances, it was possible by careful analysis of the COSY, 1D-TOCSY, 2D-TOCSY, HSQC, and HMBC data to assign resonances to all of the hydrogen and carbon atoms in each of the six monosaccharide residues as listed in Table 1. Degradation had shown that the pachymosides contained only D-glucose and D-galactose monomers. Analysis of the ^{1}H vicinal NMR coupling constants for each of the monosaccharide residues A to F confirmed that there were four glucose units (A–D) and two galactose units (F and E) in **2**. In addition, all six of the anomeric proton resonances appeared as doublets with coupling constants between 7.0 and 8.2 Hz, indi-

© 2003 NRC Canada

Fig. 3. Expansion of gHMBC of peracetylpachymoside A methyl ester (**2**), (natural abundance) acquired at 800 MHz in C_6D_6. Assignments for carbinol methine and methylene HMBC correlations to acetate carbonyls are indicated. No coupling for C-4 to its attached acetate carbonyl is observed for the unlabeled sample.



cating that all of the glycosidic linkages were β. Examination of the proton chemical shifts (Table 1) in each of the monosaccharide residues for acyl shifts predicted that glucose-A was acetylated at C-3 and C-6, glucose-B was acetylated at C-3 and C-6, glucose-C was acetylated at C-2, C-4, and C-6, glucose-D was acetylated at C-2, C-3, C-4, and C-6, galactose-E was acetylated at C-2, C-3, C-4, and C-6, and galactose-F was also acetylated at C-2, C-3, C-4, and C-6. This acetylation pattern, which was confirmed by HMBC correlations from the corresponding monosaccharide protons to the acetate carbonyls (Fig. 3), was consistent with the presence of 19 acetate residues in **2**. Finally, HMBC and ROESY correlations (Table 1 and Fig. 4) provided the information required to identify the linkages between the six monosaccharide residues A–F and the aglycon as shown in Fig. 4.

NMR analysis of the crude mixture of pachymosides showed that the natural products are partially acetylated. Information about the natural acetylation pattern was lost during the peracetylation step required for isolation of pure peracetylpachymoside A methyl ester (**2**). To locate the sites of introduced acetylation in **2**, a second portion of the crude pachymoside mixture was methylated with (trimethylsilyl)diazomethane and then acetylated with $(CH_3{}^{13}CO)_2O$, pyridine, and DMAP as before. The crude reaction mixture was fractionated to give peracetylpachymoside A methyl ester (**2**) labelled at the sites of synthetic acetylation with $CH_3{}^{13}CO$. The ESI-LR-MS of the unlabeled peracetylpachymoside A methyl ester (**2**) gave a $[M + Na]^+$ at *m*/*z* 2335, while the corresponding ESI-LR-MS of the ^{13}C-acetate labelled compound gave two $[M + Na]^+$ major peaks at *m*/*z* 2343/2344, indicating the addition of eight and nine ^{13}C-acetyl groups. An HMBC spectrum collected on the ^{13}C-labelled sample of **2** showed intense peaks for the monosaccharide proton to acetyl carbonyl correlations involving ^{13}C-labelled acetate residues and essentially no correlations for the natural abundance acetates (Fig. 5). Using this intensity difference as a marker of introduced acetate, it was possible to show that ^{13}C-acetate had been introduced at 10 sites in the molecule (A-3, A-6, B-3, B-6, C-2, C-6, D-2, D-3, D-4, D-6; see Fig. 5). Evidence for labelled acetate introduction at C-4 came from the observation of additional scalar coupling in the glucose-C H-4 resonance observed at 400 MHz, which was attributed to three bond ^{1}H/^{13}C coupling. The absence of a corresponding HMBC cross peak in the 800 MHz spectrum is an anomaly produced by the line broadening of the C residue H-4 resonance at high field (vide infra). There was no evidence for introduction of ^{13}C-labelled acetate at any of the hydroxyl positions of the galactose-E and galactose-F residues, indicating that they are fully acetylated in all of the natural pachymosides. Since there is evidence for introduction of labelled acetate at 11 hydroxyls in **2** and the MS data indicates that only eight or nine labelled acetates have been introduced in individual molecules, the natural pachymoside mixture must consist in part of a major group of compounds that have the same aglycon **5**, are peracetylated on the galactose residues E and F, and have either two or three acetates distributed among

© 2003 NRC Canada

Table 1. 1D- and 2D-NMR data for pachymoside A peracetate methyl ester (**2**).[a]

Position	δ ^{13}C NMR	δ ^{1}H NMR	Multiplicity	*J* (Hz)	COSY (H → H)	HMBC (H → C)	TOCSY (H → H)	ROESY (H → H)
Aglycon[b]								
1	172.8	—						
2	33.0/32.8	2.04/1.98	t	7.5		1	3,4	
3	25.3	1.72/1.74			2, 4	2, 4	2,4	
4	29.7	1.30			3	3	2,3	
5–10		1.26–1.32						
11	29.7	1.23			12	12, 13	12,13	
12	24.2	1.58	qn	7.5	11,13	13, 14	11,13	
13	42.7	2.09	t	7.5	12	12, 14	11,12	
14	208.9	—						
15	42.7	2.12	t	7.5	16	14, 16	16,17,18,19,20,21	
16	24.2	1.64	qn	7.5	15, 17	14, 15	15,17,18,19,20,20′, 21	
17	30	1.33			16	15, 16	15,16,18	
18	30	1.44				17/19(vw)	15,16,17	
19	30	1.32				16,17,20,21	18,20	
20	30	1.44			20′,21	18/19(vw)	20′,21,21′	
20′	—	1.38			20	18/19	19,20,21,22,23,24	
21	25.3	1.55			20	20(w)	20,22	
22	34.5	1.70			22′	21,23	20,20′,21,22′,23	
22′	—	1.57			22	21,23	20,22	
23	80.2	3.71			22,22′, 24,24′	22, 24, A1	20-22/20′-22′,24-26/24′26′	A1,22,22′,24,24′
24	35.3	1.70			24′	23,25	23,25,25′,26	
24′	—	1.63			24	25(w)	24,25,26	
25	25.3	1.52					24,24′(w),26,26′	
25′	—	1.54				27(vw)	24,24′,26	
26	32.4	1.39			28	25, 27	23,24,24′,25,25′	
26′	—	1.34				27	25,25′,26,27	
27	23.1	1.40			28	26, 28	28,26,25,24,23	
28	14.4	0.97	t	7.4	27	26, 27	27,26,25,24,23	
1′	169.9	—						
2′	49.2/51.0	3.91/3.42	s			1, 1′		
3′	35.7/34.5	2.44/2.79	s			1, 2′		
4′	51.3/*	3.27/3.24	s			1′		
Glu-A[c]								
A-1	100.7	4.67	d	7.2	A2	23, A5		23
A-2	78.7	3.79	dd	7.2, 9.0	A1, A3	A1, A3, E1		E1
A-3	75.1	5.50	t	9.0	A2, A4	A2, A4		
A-4	78.8	3.73	dd	9.0, 9.6	A3, A5	A3, A6, B1		B1
A-5	72.4	3.82	ddd	2.6,4.5,9.6	A4, A6, A6′	A4		
A-6	62.2	4.76	dd	4.3, 12.0	A5, A6′	A4		
A-6′	—	4.95	dd	2.8, 12.0	A5, A6′	A4, A5		
Glu-B								
B-1	102.1	4.31	d	7.0	B2	A4		A4
B-2	78.1	3.62	dd	7.0, 8.6	B1, B3	B1, B3, F1		F1
B-3	74.0	5.29	dd	8.6, 9.6	B2, B4	B2, B4		
B-4	76.6	3.50	dd	9.6, 11.2	B3, B5	B3, B5, C1		
B-5	72.2	3.08	ddd	1.6,5.3,11.3	B4, B6, B6′	B1		B1
B-6	62.8	4.10	dd	5.2, 11.9	B5,B6′	B5		
B-6′	—	4.35	dd	1.9, 11.9	B5, B6	B4, B5		
Glu-C								
C-1	101.4	4.21	d	8.2	C2	B4	C(2,3,4,5)[d]	B4, C3, C6(w)[e]
C-2	73.2	5.18	dd	8.2, 9.4	C1, C3	C1, C3	C(1,3,4,5)	C4(vw)
C-3	79.1	3.89	nco[f]		C2, C4	(nco)	C1, C2	D1, C1(w)
C-4	68.4	5.00	t[f]	9.6	C3, C5	(nco)	C1	C6′(w)

© 2003 NRC Canada

Table 1 (*concluded*).

Position	δ ^{13}C NMR	δ ^{1}H NMR	Multiplicity	*J* (Hz)	COSY (H → H)	HMBC (H → C)	TOCSY (H → H)	ROESY (H → H)
C-5	72.7	3.51	nco[f]		C4, C6, C6′	C1[g]	C6, C6′	C2, C6
C-6	61.9	4.11	dd	2.5, 12.7	C5, C6′	C4, C5	C5, C6′	C5, C6′
C-6′	—	4.44	dd	4.2, 12.3	C5, C6	C5(w)	C5, C6	C6
Glu-D								
D-1	101.4	4.56	d	8.2	D2	C3		C3
D-2	71.6	5.15	dd	8.2, 9.8	D1, D3	D1, D3		
D-3	73.3	5.32	dd	9.4, 9.8	D2, D4	D2, D4		
D-4	68.1	5.18	dd	9.4, 10.4	D3, D5	D3, D5		
D-5	72.2	3.05	ddd	2.1,3.9,10.2	D4, D6, D6′	D1(w)		
D-6	61.5	4.32	dd	3.9, 12.5	D5, D6′	(nco)		
D-6′	—	3.88	dd	2.1, 12.5	D5, D6	D4, D5		
Gal-E								
E-1	101.4	4.78	d	8.0	E2	A2		A2
E-2	69.7	5.56	dd	8.0, 10.5	E1, E3	E1, E3		
E-3	71.6	5.20	dd	3.4, 10.5	E2, E4	E2, E4		
E-4	67.3	5.54	dd	0.8, 3.4	E3, E5(w)	E2, E3		
E-5	70.9	3.49	ddd	0.8,6.2,7.8	E4(w),E(6/6′)	E4, E6		
E-6	60.9	4.25	dd[h]	6.2, 11.0	E5	E4, E5		
E-6′	—	4.27	dd[h]	7.7, 11.0	E5	E4, E5		
Gal-F								
F-1	101.5	4.61	d	8.0	F2	B2		B2
F-2	68.9	5.54	dd	8.0, 10.6	F1, F3	F1, F3		
F-3	71.4	5.11	dd	3.4, 10.6	F2, F4	F2, F4(w)		
F-4	67.5	5.42	dd	0.8, 3.4	F3, F5(w)	F2, F3		
F-5	71.2	3.33	ddd	0.8,5.3,8.1	F4(w), F6, F6′	F4, F6		
F-6	61.3	4.50	dd	7.7, 11.3	F5, F6′	F4, F5		
F-6′	—	3.80	dd	5.3, 11.3	F5, F6	F4, F5		

Note: (w) denotes a weak but detectable correlation, (vw) very weak; singlet (s), doublet (d), triplet (t), quartet (q), quintet (qn), unresolved multiplet (m); no coupling observed (nco).

[a]Spectra recorded in C_6D_6 at 800 MHz.

[b]Major and (or) minor rotomeric forms indicated where observed.

[c]Acetate resonances not indicated.

[d]1D-TOCSY shows correlations: C1-C2, C3, C4, C5 and C6-C2, C4, C5, C6′.

[e]Possible overlap with B-4 → C1 in HMBC.

[f]Peaks broadened at 800 MHz, C4 appears as a triplet at 400 MHz; (nco)

[g]1D-NOE (400 MHz) shows C1-C3-C5 (negative enhancement).

[h]Non-first-order coupling (see *J* resolved in *Supplementary information*[5]), COSY cross peaks coincident.

the 11 hydroxyl functionalities of the four glucose residues A–D.

The mass of a pachymoside having the aglycon **5** and acetylation at 10 sites is 1918, a mass found in the FAB-MS of the crude mixture of natural pachymosides prior to derivatization. Adding an additional acetate to the sugar alcohols generates a natural pachymoside with a mass of 1960, which was also represented in the FAB-MS of the crude mixture. Therefore, it appears that a major part of the structural diversity in this family of glycolipids involves increasing degrees of acetylation and differing positions of acetylation on the pachymoside template. All of these variations in acetylation pattern would have been converted into the same peracetylpachymoside A methyl ester (**2**) upon derivatization for purification. We have arbitrarily chosen to define pachymoside A (**1**) as the component that has natural acetylation at the eight galactose hydroxyls and at B-6 and D-6, since the HMBC correlation intensities in the ^{13}C-labelled compound indicate that these latter two positions have the greatest degree of natural acetylation.

It was clear from the NMR data obtained for the mixture of natural pachymosides and the aglycons liberated by methanolysis that there are also natural variations in the aglycon. There was evidence for aliphatic methyl doublets in the ^{1}H NMR spectrum of both the mixture of aglycon methyl esters and the natural pachymoside mixture indicating the presence of internal methyl branches on the aglycon fatty acyl chain. The detailed structures of the various aglycons other than **5** have not been determined due to the difficulties of locating branching methyls in a long aliphatic chain.

During the course of analyzing the NMR data for peracetylpachymoside A methyl ester (**2**), an unexpected difference in the data obtained at 400, 500, and 800 MHz in

[5] Supplementary data may be purchased from the Directory of Unpublished Data, Document Delivery, CISTI, National Research Council Canada, Ottawa, ON K1A 0S2, Canada (http://www.nrc.ca/cisti/irm/unpub_e.shtml for information on ordering electronically).

© 2003 NRC Canada

Fig. 4. A minimal set of unambiguous ROESY and HMBC correlations linking the substructures of **2**.

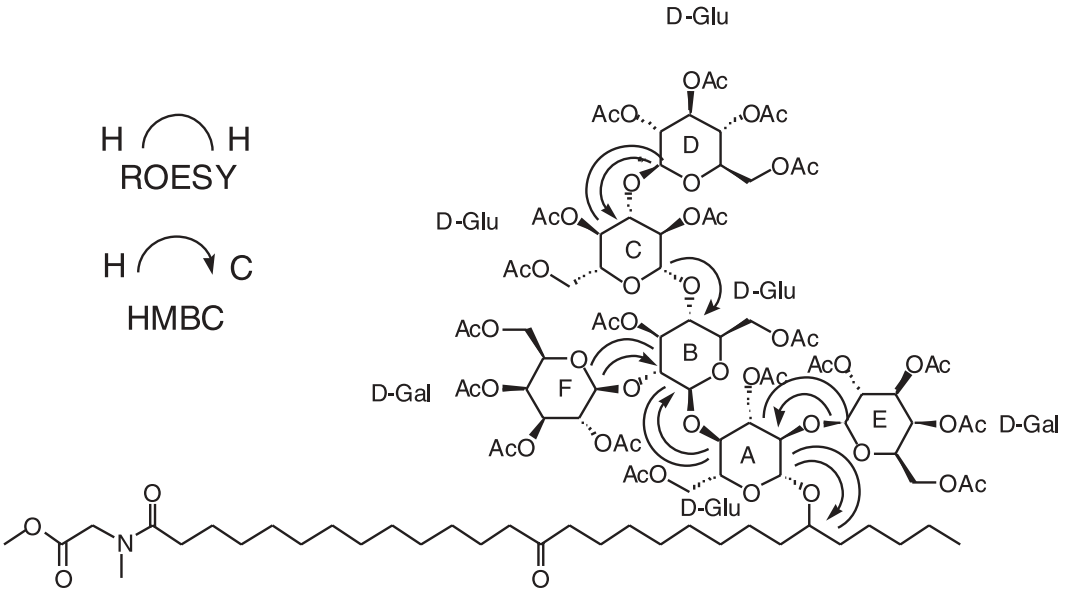
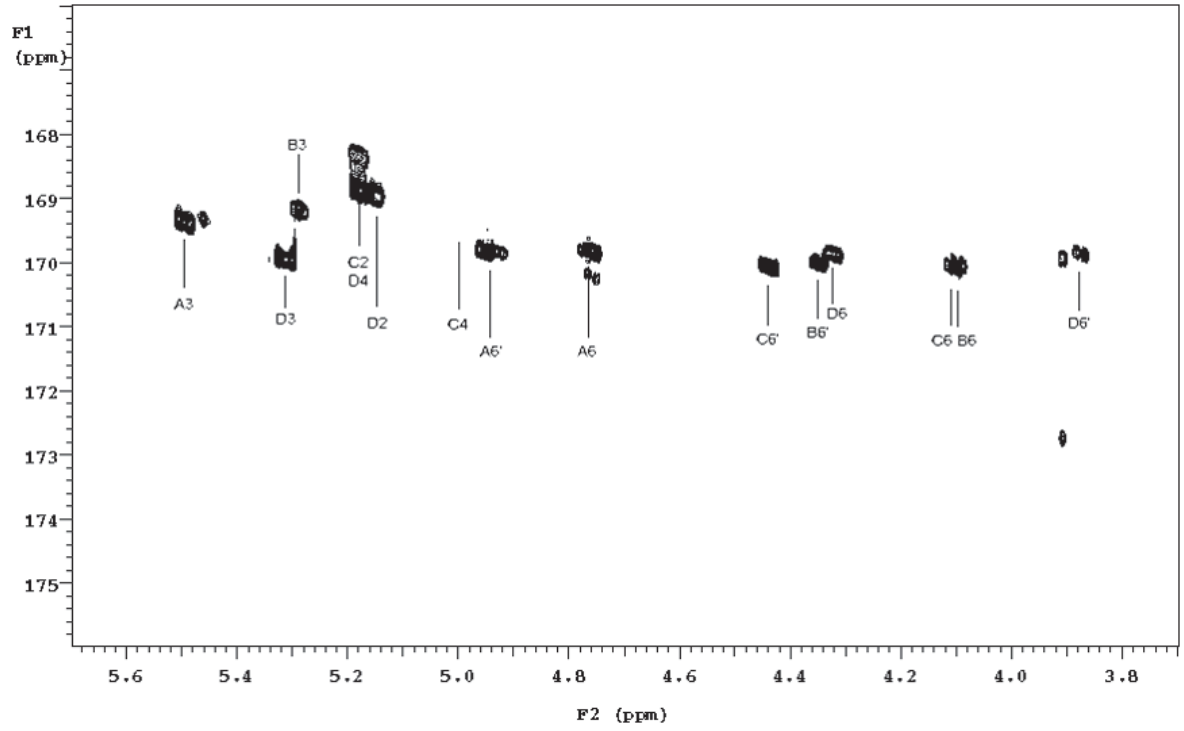


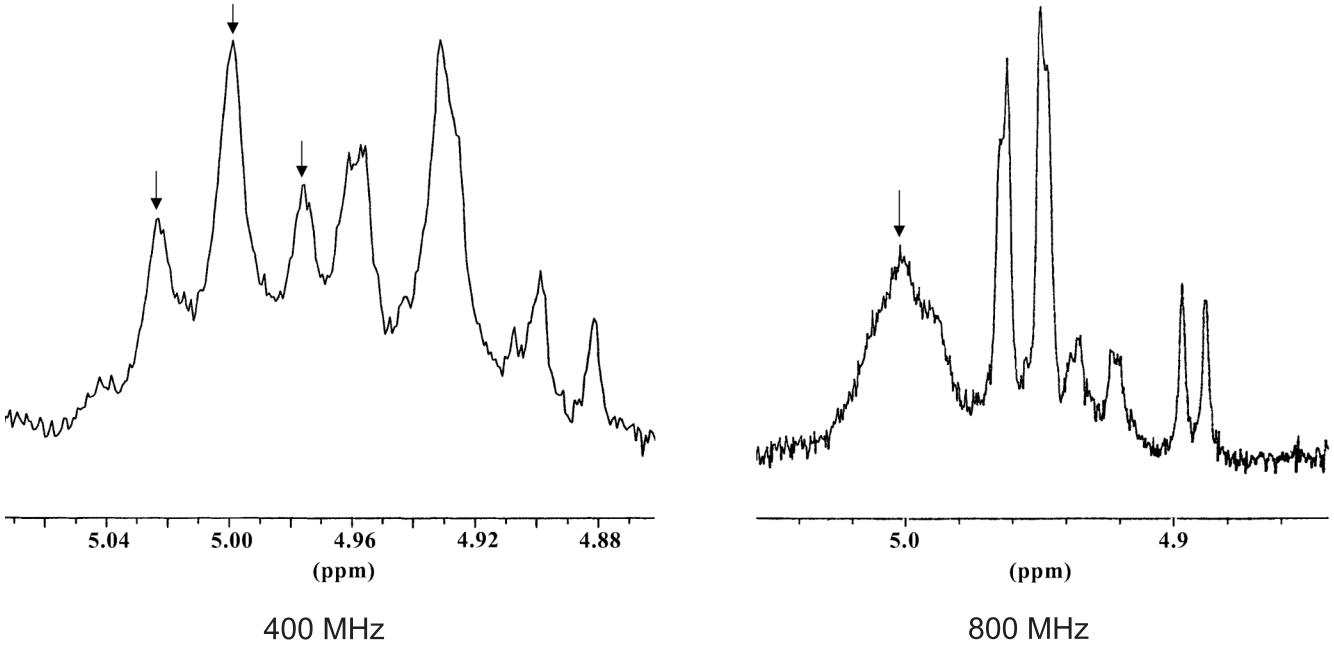
Fig. 5. Expansion of gHMBC spectrum of peracetylpachymoside A methyl ester (**2**) ($CH_3{}^{13}CO$-labeled) acquired at 800 MHz in C_6D_6. Assignments of methines and methylenes coupled to ^{13}C-labeled acetates are indicated. The methine at C-4 exhibits weak coupling at 500 MHz (2D data), while none is observed at 800 MHz. 1D proton data (400 MHz) for this methine exhibits additional splitting (unlabeled appears as triplet, ^{13}C-labeled appears as triplet of doublets). Cross peaks for the methylene to carbonyl coupling are of generally weaker intensity than the methines and vary in order of decreasing intensity as follows: C6 > A6 > B6 > D6.



C_6D_6 was encountered. As shown in Fig. 6, the resonance assigned to the glucose-C H-4 resonance appeared as a clear dd (J = 9.9, 9.6 Hz) at 400 and 500 MHz as expected, but appeared as a broad unresolved multiplet at 800 MHz. Normally the increased dispersion at 800 MHz simplifies multiplets by removing many second-order effects and signal overlap. Therefore, the deterioration of the multiplet structure on going from 400 to 800 MHz was contrary to our usual experience with 800 MHz data. One possible explanation for the observation is restricted conformational mobility at C-4 of glucose-C that is fast on the NMR timescale at 400 MHz leading to a single sharp resonance, but slow on

© 2003 NRC Canada

Fig. 6. NMR spectra (400 and 800 MHz) (C_6D_6) of the glucose-C residue H-4 resonance.



the NMR timescale at 800 MHz leading to a broadening of the resonance. Since the H-1, H-2, and H-6/H-6′ resonances in residue C are sharp at 800 MHz, the conformational equilibrium probably does not involve a change in the pyranose conformation. The existence of at least two conformers for rotation about the C-4 oxygen to acetate carbonyl bond that interconvert slowly on the 800 MHz NMR timescale, is a probable explanation for the observed field-dependent NMR behaviour of H-4 on glucose-C. We are not aware of any literature reports of similar observations of peak shape change as a function of increasing field strength.

Glycolipids are emerging as an important class of structurally diverse sponge metabolites that frequently have interesting biological activities (14, 16–21). The pachymosides represent a novel family of sponge glycolipids that have unprecedented glycon and aglycon fragments. The fatty acyl component of their aglycon has the same number of carbons and identical positioning of ketone and glycon attachments as the fatty acyl component of erylusamine E (**6**), one of a family of IL-6 receptor antagonists isolated from sponges in the genus *Erylus* (19, 20). However, the sugar residues in **1** (D-glucose and D-galactose) and **6** (D-arabinose and L-xylose) are different, the number and connectivity of the sugars are different, and the amino components of the aglycon amides are different. The pachymosides have an acidic aglycon while the erylusamines all have basic aglycons. One interesting structural feature of the pachymosides is the complete acetylation of the galactose residues and only partial acetylation of the glucose residues. Further investigation of the biological activity of the pachymosides revealed that although they showed promising activity in the TTSS inhibition assay, they are not true TTSS inhibitors. Rather, their observed activity appears to stem from their ability to effectively activate extracellular bacterial proteases that rapidly degrade the excreted Esps, resulting in a false indication of TTSS inhibition in the assay (1).

Experimental

General experimental procedures

^{1}H, COSY-gr, HMBC-gr (optimized for $^{2,3}J$ = 8 Hz), and HMQC-gr for (peracetyl pachymoside A methyl ester) were initially recorded on a Bruker AMX500 NMR spectrometer. These experiments plus 1D- and 2D-TOCSY, ROESY, HSQC, eCOSY, and *J*-resolved experiments were repeated on a Varian INOVA 800 MHz spectrometer at the NANUC facility at the University of Alberta. ^{13}C NMR data were recorded on a Bruker AM400 NMR spectrometer. Chemical shifts were referenced to solvent peaks (δ_H 7.15 ppm, δ_C 128.0 ppm for C_6D_6). Low-resolution electrospray (ES) mass spectra were recorded on a Bruker Esquire LC mass spectrometer, operated by direct infusion. High-resolution ES mass spectra were recorded on a Micromass LCT mass spectrometer. Both low- and high-resolution EI mass spectra were recorded on an AEI MS-50 mass spectrometer. Flash silica gel column chromatography was performed using 230–400 mesh silica gel 60 (Silicycle). Preparative HPLC separations were performed using a Waters 515 pump and a Waters 2487 dual tunable absorbance detector. Solvents were all HPLC grade (Fisher) and filtered prior to use. Thin layer chromatography (TLC) was performed with Merck silica gel 60 F_{254} aluminum sheets, and visualized with vanillin – sulfuric acid spray reagent. Pyridine, methanol, benzene, acetic anhydride, 4-(dimethylamino)pyridine (DMAP), and (trimethylsilyl)diazomethane (solution in hexanes) used in derivatization reactions were anhydrous and (or) reagent grade (Aldrich) and used without further purification. Acetic anhydride (1,1′-$^{13}C_2$, 99%) was purchased from Cambridge Isotope Laboratories, Inc.

Biological material and isolation of pachymosides

Specimens of *P. johnstonia* (650 g wet weight) were collected by hand using SCUBA from rocky subtidal marine

© 2003 NRC Canada

habitats along the coast of the Isle of Mann. A voucher sample (ZMA 17065) has been deposited at the Zoologisch Museum, University of Amsterdam. Freshly collected sponge material was frozen immediately and stored at –15 °C until workup. A portion of the frozen sponge (wet wt 111 g) was cut into pieces and extracted twice with MeOH over a six day period. The combined MeOH extracts were filtered and concentrated by rotary evaporation to an amber semisolid. This residue was partitioned between water (50 mL) and ethyl acetate (ea) (100 mL), and the aqueous layer extracted twice more with ethyl acetate (100 mL ea). The yellow-colored ethyl acetate solution was evaporated to dryness in vacuo to afford 1.60 g of a greenish amber amorphous solid. A portion of this material (0.16 g) was purified by Sephadex™ LH-20 size exclusion chromatography (28 mm ID × 100 cm bed length) eluting with 100% MeOH. Early eluting like fractions (as detected by TLC developed with 15% MeOH–CH_2Cl_2) were combined and concentrated in vacuo to give a mixture of pachymosides as a white amorphous solid (0.106 g). This material exhibited a distribution of molecular ion clusters centred at *m/z* 1973/1974 in the LR-FAB-MS.

Methanolysis of the pachymoside mixture

Pachymosides (60 mg) were dissolved in 10 mL of anhydrous methanol and 0.2 mL of CH_3COCl was slowly added. The reaction mixture was stirred at 70 °C with refluxing for 2 h. MeOH was removed from the reaction mixture in vacuo and the resulting residue was partitioned between H_2O and Et_2O. The aglycon methyl esters (25 mg) went into the organic phase and the methyl glycosides (30mg) went into the aqueous phase.

Acetylation of monosaccharide methylglycosides

The mixture of monosaccharide methyl glycosides (20 mg) obtained from methanolysis of the pachymosides was added to 9 mL of anhydrous pyridine, 3 mL of acetic anhydride, and ~1 mg of DMAP as catalyst. The reaction mixture was stirred overnight at room temperature. After removal of the pyridine and acetic anhydride under high vacuum, the crude product was partitioned between H_2O and Et_2O. The organic extract soluble materials were purified by isocratic normal phase HPLC (eluent: 31% EtOAc:69% hexanes) monitored with a RI detector to give one fraction containing peracetylated glucose/galactose α-methyl glycopyranosides and a second fraction containing peracetylated glucose/galactose β-methyl glycopyranosides.

Preparation of monosaccharide standards

Commercial D-glucose or D-galactose (20 mg, 0.11 mmol) were dissolved in 10 mL MeOH with 0.2 mL of CH_3COCl (2 mmol) and stirred with refluxing at 70 °C for 2 h. The solvent was then removed in vacuo to give a residue that was partitioned between H_2O and Et_2O. The aqueous fraction was dried and added to 9 mL (100 mmol) of anhydrous pyridine and 3 mL of acetic anhydride (30 mmol) with ~1 mg of DMAP as a catalyst. The acetylation mixture was stirred at room temperature overnight. After removal of the pyridine and acetic anhydride under high vacuum, the crude product was partitioned between H_2O and Et_2O and the organic extract was purified by normal-phase HPLC as described above to give pure samples of methyl 2,3,4,6-tetra-*O*-acetyl-α-D-glucopyranoside (**3**) and methyl 2,3,4,6-tetra-*O*-acetyl-α-D-galactopyranoside (**4**).

Chiral GC analysis of alditol acetates

The pachymoside mixture was hydrolyzed for 1 h at reflux in H_2O (20 mL) and 0.25 mL of 6 N HCl. The reaction was worked up by evaporating the H_2O to dryness under high vacuum and the residue was partitioned between H_2O and Et_2O. The water soluble materials were concentrated to dryness via lyophilization and reduced with $NaBH_4$ in MeOH at rt. After removing the MeOH in vacuo, the residue was treated with acetic anhydride and pyridine and a catalytic amount of DMAP to give a mixture of alditol acetates. Normal-phase flash chromatography separated the mixture into glucitol peracetate and galactitol peracetate. Commercial samples of D-glucose, L-glucose, and D-galactose were also converted to their alditol peracetates using the same reaction conditions. The alditol peracetates were analyzed by GC on a Chrial Select 1000 β-Dex-390 column using flame ionization detection. The GC analysis showed that the glucose and galactose obtained from hydrolysis of the pachymoside mixture both had the D configuration.

Aglycon (5)

The Et_2O soluble fraction (25mg) from methanolysis of the pachymoside mixture was loaded on a normal phase silica gel flash column and eluted with a gradient of hexanes–EtOAc (5% EtOAc:95% hexanes – 100%EtOAc). The fractions eluting with 20% EtOAc:80% hexanes contained one major component and one minor component by TLC analysis. The more polar major component was fractionated further by isocratic reversed-phase HPLC (eluent: 88% MeOH:12% H_2O (monitored at 206.0 nm)) to give pure methyl ester **5** (see *Results and discussion* for spectroscopic data).

Esterification of the pachymoside mixture

A 45 mg (ca. 0.024 mmol) sample of the pachymoside mixture was dissolved in a mixture of 0.5 mL each of MeOH and benzene and treated with 0.080 mL of (trimethylsilyl)diazomethane (2.0 mol L^{-1} solution in hexanes) and stirred at ambient temperature for 24 min. The reaction mixture was diluted with 5 mL EtOAc, evaporated to dryness (aspirator), then redissolved in EtOAc (6 mL), washed with sat. NaCl solution, dried (Na_2 SO_4) and again evaporated in vacuo to a film (38 mg). A short reaction time was found to be critical in this step. If left to react overnight, most of the acetate groups appeared to be lost, as determined by NMR. Mass spectroscopy (ES) on this sample again exhibited a distribution of molecular ion clusters centered at 2012 (Na^+ adducts) with a nearly identical pattern to that found for the underivatized material. This represents a shift in molecular weight of plus 14 amu, which is correct for the methyl ester derivative, and confirms that the acetate groups of the pachymosides remained fully intact in this step.

LR-ESI-MS data[a]: (Na^+ adducts) *1956* (55), 1969 (75), *1998* (70), 2012 (100), *2040* (65), 2053 (80); exchanged with CD_3OD: *1965* (50), 1979 (75), *2006* (55), 2018 (100), *2046* (50), 2060 (70). (Italic indicates homolog ions that

© 2003 NRC Canada

would afford pachymoside A peracetate upon full acetylation).

Acetylation of the pachymoside methyl ester mixture

The sample of mixed pachymoside methyl esters (38 mg) was dissolved in anhydrous pyridine (3.0 mL) under argon and treated with 1.3 mg DMAP, then with 1 g of acetic anhydride (or 1,1′-$^{13}C_2$ acetic anhydride) and stirred for 15 h at ambient temperature. After evaporation under high vacuum, the residue was taken up in EtOAc–hexanes (1:1) and subjected to flash column chromatography (12 × 210 mm) eluting with EtOAc–hexanes (4:1) to afford 35 mg of a white solid. TLC in this solvent system showed a spot at 0.18 R_f for the desired derivative. This was taken up in MeOH (2.0 mL) and fractionated by reverse-phase HPLC (Inertsil C_{18} 9.4 × 250 mm, eluting with H_2O–1-PrOH (7:4). UV detection at 202 and 280 nm, up to 3 mg per injection) to give pachymoside A methyl ester (**2**), peracetate (4.0 mg) (or its corresponding 1-^{13}C-acetylated analog).

Data for unlabeled analog

HR-ESI-MS: *m*/*z* 2333.9639 (calcd. for $^{12}C_{105}{}^{13}CH_{159}NO_{54}Na$ 2333.9658); ^{1}H and ^{13}C NMR (800 and 100 MHz, respectively) see Table 1.

LR-ESI-MS: Unlabeled acetate derivative: 2335 (100, Na^+), 1178 ($2Na^+$). ^{13}C-acetate derivative: 2343/2344 (100, Na^+), 1183 (10, $2Na^+$), indicating the presence of eight to nine ^{13}C-acetyl groups.

(Note: LR-ESI-MS data *m*/*z* absolute values estimated at ±1 amu at these values; relative values of the weighted cluster center are reported. Each molecular ion cluster generally shows three or more sequential peaks owing to naturally abundant ^{13}C).

Acknowledgements

Financial support was provided by the Natural Sciences and Engineering Research Council of Canada (NSERC) (RJA), Canadian Institutes for Health Research (CIHR) (AG, BBF), and the Canadian Bacterial Disease Network Center of Excellence (BBF). The authors thank M. LeBlanc and D. Williams for collecting *P. johnstonia* and the Canadian National High Field NMR Centre (NANUC) for their assistance and use of the facilities. NANUC is funded by CIHR, NSERC, and the University of Alberta.

References

1. A. Gauthier and B.B. Finlay. ASM News, **68**, 383 (2002).
2. B.A. Vallance and B.B. Finlay. Proc. Natl. Acad. Sci. U.S.A. **97**, 8799 (2000).
3. B. Kenny, R. DeVinney, M. Stein, D. Reinscheid, E.A. Frey, and B.B. Finlay. Cell (Cambridge, Mass.), **91**, 511 (1997).
4. C. Deibel, S. Kramer, T. Chakraborty, and F. Ebel. Mol. Microbiol. **28**, 463 (1998).
5. S.S. Park, R.W. Worobo, and R.A. Durst. Crit. Rev. Biotechnol. **21**, 27 (2001).
6. J. Nataro and J. Kaper. Clin. Microbiol. Rev. **11**, 142 (1998).
7. J. Mecsas and E.J. Strauss. Emerging Infect. Dis. **2**, 271 (1996).
8. C.J. Hueck. Microbiol. Mol. Biol Rev **62**, 379 (1998).
9. G.R. Cornelis and F. Van Gijsegem. Ann. Rev. Microbiol. **54**, 735 (2000).
10. D.J. Faulkner. Nat. Prod. Rep. **19**, 1 (2002), and previous reviews in this series.
11. J.W. Blunt, B.R. Copp, M.H.G. Munro, P.T. Northcote, and M.R. Prinsep. Nat. Prod. Rep. **20**, 1 (2003).
12. R.W. Newbold, P.R. Jensen, W. Fenical, and J.R. Pawlik. Aquat. Microb. Ecol. **19**, 279 (1999).
13. J.E. Thompson, R.P. Walker, and D.J. Faulkner. Mar. Biol. (Berlin), **88**, 11 (1985).
14. R.G. Linington, M. Robertson, A. Gauthier, B.B. Finlay, R. Van Soest, and R.J. Andersen. Org. Lett. **4**, 4089 (2002).
15. A. Kauppi, R. Nordfelth, H. Uvell, H. Wolf-Watz, and M. Elofsson. Chem. Biol. **10**, 241 (2003)
16. E. Fattorusso and A. Mangoni. Marine glycolipids. *In* Progress in the chemistry of organic natural products. *Edited by* W. Hertz, G.W. Kirby, R.E. Moore, W. Steiglich, and Ch. Tamm. Springer, Wein. 1997. pp. 215–301.
17. V. Costantino, E. Fattorusso, and A. Mangoni. Tetrahedron, **56**, 5953 (2000).
18. V. Costantino, E. Fattorusso, C. Imperatore, and A. Mangoni. Eur. J. Org. Chem. 4457 (2001).
19. V. Costantino, E. Fattorusso, A. Mangoni, M. Di Rosa, and A. Ianaro. J. Am. Chem. Soc. **119**, 12 465 (1997).
20. N. Sata, N. Asai, S. Matsunaga, and N. Fusetani. Tetrahedron, **50**, 1105 (1994).
21. R. Goobes, A. Rudi, Y. Kashman, M. Ilan, and Y. Loya. Tetrahedron, **52**, 7921 (1996).

© 2003 NRC Canada

Generic synthesis of β-sultams via domino alkylation of bromomethanesulfonamides[1]

William R.S. Barton and Leo A. Paquette

Abstract: Reaction of *N*-substituted bromomethanesulfonamides with 2 equiv of potassium carbonate and an α-halo ketone, ester, or nitrile leads directly to 3-substituted β-sultams. The first step is intermolecular and is followed by an intramolecular alkylation. The process is particularly efficient when diethyl bromomalonate and 3-chloro-2-butanone are involved. In the latter example, no competitive cyclization to form a six-membered ring is seen. The functional groups in certain of the β-sultam products can be subsequently manipulated to give bicyclic products.

Key words: β-sultams, intramolecular S_N2 displacement, sulfonamides, ring closing metathesis, four-membered heterocycles.

Résumé : La réaction de bromométhanesulfonamides *N*-substitués avec deux équivalents de carbonate de potassium et des cétones, des esters ou des nitriles α-halogénés conduit directement à des β-sultames substitués en position 3. La première étape est intermoléculaire et elle est suivie par une alkylation intramoléculaire. La méthode est particulièrement efficace avec le bromomalonate de diéthyle et la 3-chlorobutan-2-one. Dans ce dernier cas, on n'a pas observé de cyclisation compétitive conduisant à la formation d'un cycle à six chaînons. Les groupes fonctionnels dans certains β-sultames formés comme produits peuvent être manipulés subséquemment pour conduire à des produits bicycliques.

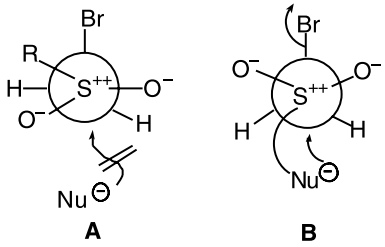
Mots clés : β-sultames, déplacement S_N2 intramoléculaire, sulfonamides, métathèse avec fermeture de cycle, hétérocycles à quatre chaînons.

[Traduit par la Rédaction]

Introduction

As a result of their close structural similarity to β-lactams, β-sultams have been rather extensively investigated for their antibacterial properties. Despite the significantly heightened reactivity (ca. 10^3-fold) toward hydrolysis resident in these strained sulfur analogues (1), none have exhibited truly remarkable antibiotic features. However, other biological activities have surfaced. For example, the irreversible inhibition of human neutrophile elastase has recently been documented for a member of this class (2). In part, the quest for more structurally varied β-sultams has been limited by existing synthetic methodology (3). Since the hydrogen atoms at C-3 are not activated by any neighboring group, the direct introduction of substituents at this site has often proven troublesome.

Reported herein is a direct, flexible approach to C-3 functionalized β-sultams. This new methodology is based on the inertness of α-bromomethanesulfonamides to intermolecular S_N2 displacement and the contrasting ease of intramolecular ejection of bromide ion (4). The dramatically different transition-state characteristics for these allied reactions are depicted in **A** and **B**.



In the intermolecular process **A**, the field effect exerted by the two sulfonyl oxygens requires close approach of the nucleophile to at least one atom of high electron density, thus strongly decelerating backside attack (5). When intramolecularity is involved, as in **B**, geometric factors conspire to require orientation of the sulfonyl oxygens as remote as possible from the attacking nucleophile. As a consequence, cyclization reactions are facilitated, in line with a cooperative inductive effect (6).

Received 3 September 2003. Published on the NRC Research Press Web site at http://canjchem.nrc.ca on 12 December 2003.

This paper is dedicated with respect and admiration to Ed Piers who has provided us with a rich legacy of important milestones in synthetic methodology and total synthesis.

W.R.S. Barton and L.A. Paquette.[2] Evans Chemical Laboratories, The Ohio State University, Columbus, OH 43210, U.S.A.

[1]This article is part of a Special Issue dedicated to Professor Ed Piers.
[2]Corresponding author (e-mail: paquette.1@osu.edu).

 doi: 10.1139/V03-174 © 2003 NRC Canada

Results and discussion

The sulfonamides **1a**–**1c** were conveniently prepared by the reaction of readily available bromomethanesulfonyl chloride (7) with the relevant primary amine in CH_2Cl_2, containing both DMAP and Hünig's base, at –10 °C (8). Treatment of these sulfonamides with 2 equiv of potassium carbonate and an α-halo ketone, ester, or nitrile in DMF at various nonoptimized temperatures generated the β-sultams **4** (Scheme 1). The simple alkylation products **2** can be isolated in high yield if the reaction is performed instead at room temperature (rt) in the same solvent and quenched after approximately 3 h. Presumably, further deprotonation ensues upon continued reaction to give **3**, the nucleophilic site in which gives indication of being well disposed to cyclization.

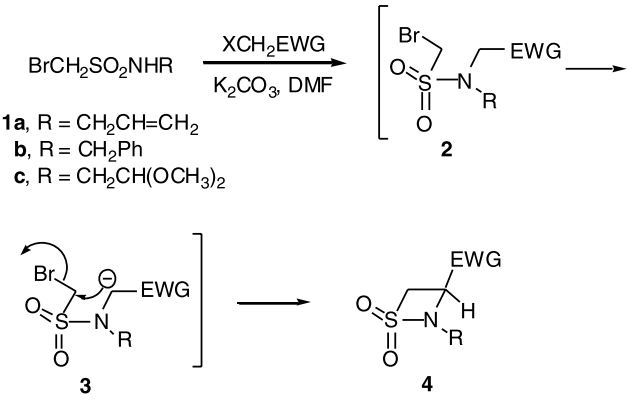
The overall process is not limited to activated primary halides and proceeds with notably high efficiency when diethyl bromomalonate and 3-chloro-2-butanone are involved (Scheme 2). The latter example holds considerable mechanistic significance. In this case, the closure of **7** with elaboration of β-sultam **9** can a priori be viewed as competitive, with the formation and cyclization of enolate **8**. Were **8** to experience intramolecular displacement, the six-membered isomer **10** would result. While no information is available regarding the possible intervention of **8**, it is patently clear that no **10** is formed. This outcome is regarded to be a reflection of the fact that the relatively elongated C—S and N—S bonds of acyclic α-bromosulfonamides (9) are more ideally suited to the reaction trajectory defined by **7** than that prevailing in **8** (10). An impressively regioselective one-pot, two-step domino (11) alkylative sequence is the result.

The direct availability of the functionalized β-sultams **4** provides an unrivaled opportunity to synthesize bicyclic derivatives in a straightforward manner. Several preparative options that can deliver these targets are illustrated below. As shown in Scheme 3, the controlled addition of methylmagnesium bromide to ester **4f** gave rise to a chromatographically separable mixture of **4d** and **11**, thereby setting the stage for their independent conversion to diene **12** (Scheme 3). For this purpose, **4d** was subjected to a Wittig olefination with methylenetriphenylphosphorane, and **11** was dehydrated with phosphorus oxychloride in pyridine. Ring-closing metathesis (RCM) of **12** in the presence of tricyclohexylphosphine[1,3-bis(2,4,6-trimethylphenyl)-4,5-dihydroimidazole-2-ylidene][benzylidene]ruthenium(IV) dichloride (**14**) (12) was then exploited to generate **13** in near quantitative yield.

Compound **15** was produced by a related route that involved the condensation of **4f** with an equivalent of allylmagnesium bromide. The coupling step was followed by migration of the double bond into conjugation with the ketone carbonyl. In this way, the stage was set for application of RCM technology for the conversion of **15** to **16** (Scheme 4).

When esters **4f** and **4h** were subjected to the action of sodium borohydride in wet THF, alcohols **17a** and **17b** were obtained. As shown in Scheme 5, the first of these was conveniently transformed via mesylate **18** into primary iodide **19**. In the *N*-benzyl series, bromide **20** was prepared more directly by reaction of **17b** with triphenylphosphine

Scheme 1.



	R	X	EWG	Yield of 4, %
4d	$-CH_2CH=CH_2$	Cl	$-COCH_3$	59
4e	$-CH_2CH=CH_2$	Br	–COPh	81
4f	$-CH_2CH=CH_2$	Br	$-COOC_2H_5$	56
4g	$-CH_2CH=CH_2$	Br	–CN	61
4h	$-CH_2Ph$	Br	$-COOC_2H_5$	70

dibromide. When **19** was heated with tributyltin hydride in benzene, 5-exo cyclization (13) operated predominantly, to deliver bicyclic sultam **28** as a 3:1 mixture of diastereomers in nonoptimized 47% yield. In contrast, the primary radical did not enter into homolytic aromatic substitution (14). Instead, the kinetically preferred reaction involved fragmentation of the strained heterocyclic ring with formation of **22**.

Conclusion

N-Substituted bromomethanesulfonamides are amenable to base-promoted condensation with α-halo ketones, esters, and nitriles under conditions where a second S_N2 displacement, now intramolecular, can operate in tandem fashion. This domino alkylation sequence exhibits a reactivity order where ketone > nitrile > ester. Evidence has been obtained that the formation of four-membered β-sultam products is kinetically favored over cyclization to give the six-membered analogs. Although β-lactams have previously been generated by the stepwise closure of α-haloacetamides (15), in only one report has azetidinone construction been described from cyclic precursors in a single operation (16). The protocol described herein is tailored to the ready introduction of useful functional groups at C-3, such that arrival at bicyclic β-sultams of varied type is conveniently feasible. In this connection, the preferred cyclization of **19** to **21** under free-radical conditions without competitive homolytic fragmentation is noteworthy.

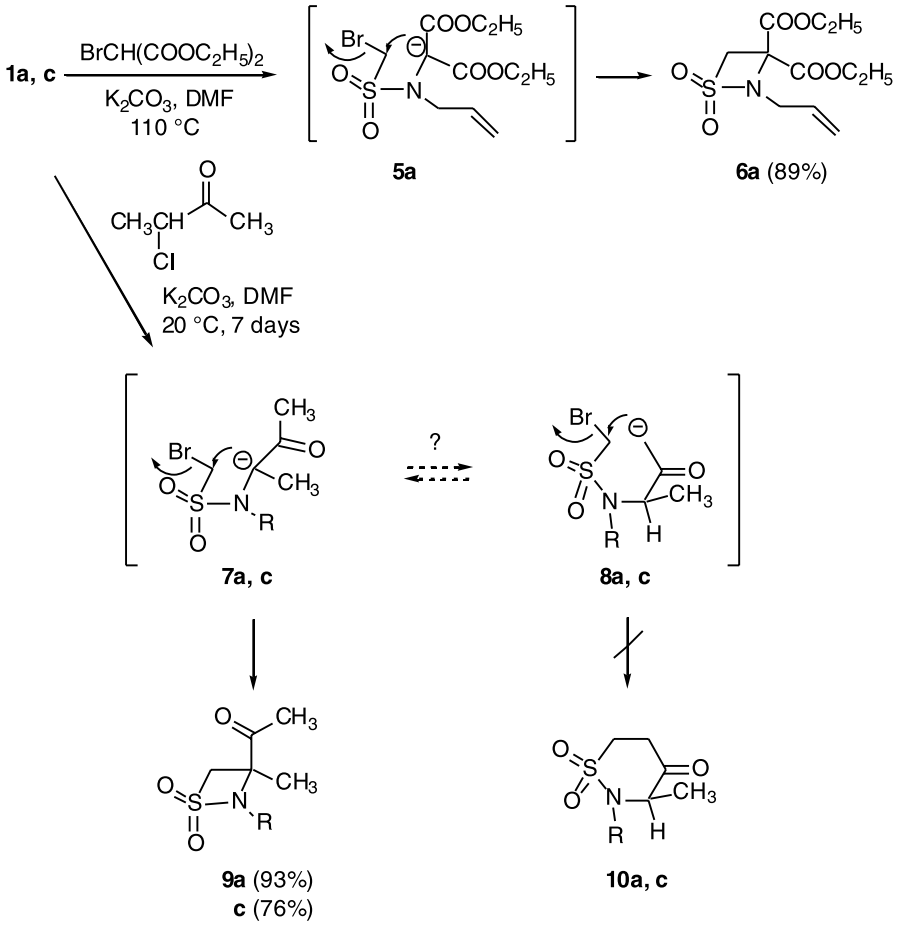
Experimental

β-Sultam 4d

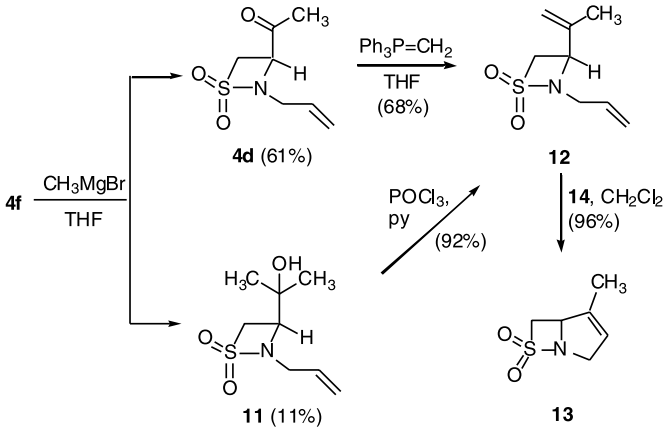
A solution of **1a** (100 mg, 0.467 mmol) in DMF (1.5 mL) was stirred with potassium carbonate (129 mg, 0.934 mmol) for 20 min, treated with a solution of chloroacetone (48 mg, 0.51 mmol) in DMF (1.5 mL), and allowed to react for 48 h.

© 2003 NRC Canada

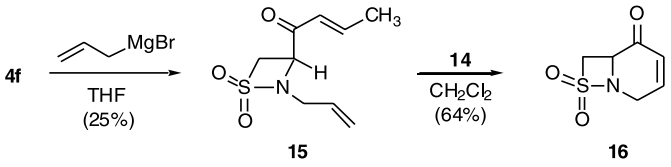
Scheme 2.



Scheme 3.



Scheme 4.



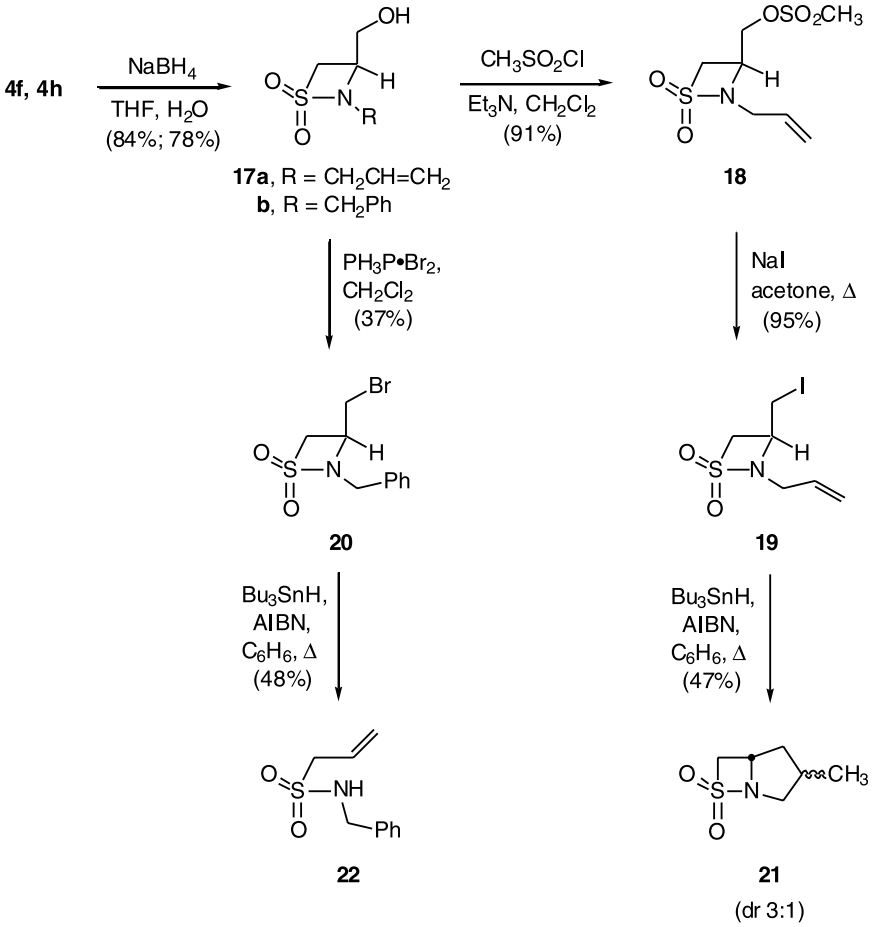
The reaction mixture was quenched with water and extracted with ethyl acetate (3×). The combined organic layers were washed with water and brine (2×), dried, and evaporated. The residue was chromatographed on silica gel (elution with hexanes – ethyl acetate 3:2) to give **4d** as a colorless oil (53 mg, 59%). ^{1}H NMR (300 MHz, $CDCl_3$) δ: 5.89–5.78 (m, 1 H), 5.40–5.25 (m, 2 H), 4.26 (dd, *J* = 8.8, 12.7 Hz, 1 H), 4.09 (dd, *J* = 6.4, 12.7 Hz, 1 H), 3.92–3.84 (m, 1 H), 3.69–3.57 (m, 2 H), 2.29 (s, 3 H). ^{13}C NMR (75 MHz, $CDCl_3$) δ: 203.3, 130.4, 121.0, 60.1, 52.1, 49.5, 25.5. ES-HR-MS (*m*/*z*) ([M+Na]$^+$) calcd: 212.0352; obsd: 212.0357.

β-Sultam 4e

Analogous reaction of **1a** (100 mg, 0.467 mmol) with potassium carbonate (130 mg, 0.934 mmol) and phenacyl bromide (93 mg, 0.467 mmol) in DMF (3 mL total) at rt for 6 days furnished 95 mg (81%) of **4e** as a colorless oil. ^{1}H NMR (300 MHz, $CDCl_3$) δ: 7.93–7.88 (m, 2 H), 7.66–7.60 (m, 1 H), 7.53–7.47 (m, 2 H), 5.80 (m, 1 H), 5.34–5.26 (m, 1 H), 5.20–5.16 (m, 1 H), 4.68 (dd, *J* = 6.5, 8.3 Hz, 1 H), 4.40 (dd, *J* = 8.3, 12.2 Hz, 1 H), 4.19 (dd, *J* = 6.5, 12.2 Hz, 1 H), 3.88–3.81 (m, 1 H), 3.75–3.70 (m, 1 H). ^{13}C NMR (75 MHz, $CDCl_3$) δ: 192.5, 134.5, 134.2, 131.1, 129.2, 128.5, 120.6, 60.9, 48.9, 48.7. ES-HR-MS *m*/*z* ([M+Na]$^+$) calcd: 274.0508; obsd: 274.0523.

© 2003 NRC Canada

Scheme 5.



β-Sultam 4f

Compound **1a** (2.00 g, 9.34 mmol), ethyl bromoacetate (1.04 mL, 9.34 mmol), and potassium carbonate (2.84 g, 20.6 mmol) in DMF (80 mL) was stirred overnight at rt and heated to 105 °C for 3.5 h. Following the predescribed workup, there was isolated 1.14 g (56%) of **4f** as a colorless oil. ^{1}H NMR (300 MHz, $CDCl_3$) δ: 5.95–5.82 (m, 1 H), 5.40–5.24 (m, 2 H), 4.33–4.18 (m, 4 H), 3.88–3.71 (m, 3 H), 1.30 (t, J = 7.1 Hz, 3 H). ^{13}C NMR (75 MHz, $CDCl_3$) δ: 168.0, 130.7, 120.5, 62.4, 60.5, 49.0, 46.5, 14.0. ES-HR-MS m/z ([M+Na]$^+$) calcd: 242.0457; obsd: 242.0458.

β-Sultam 4g

A mixture of **1a** (200 mg, 0.934 mmol), bromoacetonitrile (123 mg, 0.934 mmol), and potassium carbonate (260 mg, 1.87 mmol) was stirred at rt for 72 h and processed as detailed above. There was isolated 98 mg (61%) of **4g** as a colorless oil. ^{1}H NMR (300 MHz, $CDCl_3$) δ: 5.88–5.80 (m, 1 H), 5.52–5.37 (m, 2 H), 4.46 (dd, J = 7.9, 12.7 Hz, 1 H), 4.37 (dd, J = 4.5, 12.7 Hz, 1 H), 4.18 (dd, J = 4.5, 7.9 Hz, 1 H), 3.94–3.79 (m, 2 H). ^{13}C NMR (75 MHz, $CDCl_3$) δ: 129.2, 122.0, 114.8, 62.1, 48.3, 35.7. ES-HR-MS m/z ([M+Na]$^+$) calcd: 195.0199; obsd: 195.0237.

β-Sultam 4h

Comparable reaction of **1b** (2.08 g, 7.87 mmol) with ethyl bromoacetate (0.87 mL, 7.87 mmol) and potassium carbonate (2.18 g, 15.7 mmol) in DMF (40 mL) for 18 h at rt and 4 h at 110 °C afforded 1.48 g (70%) of **4h** as a colorless oil. ^{1}H NMR (300 MHz, $CDCl_3$) δ: 7.40–7.30 (m, 5 H), 4.46 (d, J = 14.2 Hz, 1 H), 4.35–4.18 (m, 3 H), 4.17–4.05 (m, 2 H), 3.78 (dd, J = 6.1, 8.1 Hz, 1 H), 1.19 (t, J = 7.1 Hz, 3 H). ^{13}C NMR (75 MHz, $CDCl_3$) δ: 167.9, 133.8, 129.0, 128.7, 128.2, 60.5, 49.9, 46.7, 13.9. ES-HR-MS m/z ([M+Na]$^+$) calcd: 292.0614; obsd: 292.0604.

β-Sultam 6a

A mixture of **1a** (500 mg, 234 mmol) and potassium carbonate (650 mg, 4.68 mmol) in DMF (2.5 mL) was treated with diethyl bromomalonate (0.38 mL, 2.34 mmol) and stirred overnight at rt and at 110 °C for 3 h. The reaction mixture was quenched with water and extracted with ethyl acetate (3×). The usual workup yielded 0.61 g (89%) of **6a** as a colorless oil. ^{1}H NMR (300 MHz, $CDCl_3$) δ: 6.00–5.87 (m, 1 H), 5.43–5.21 (m, 2 H), 4.50 (s, 2 H), 4.32 (q, J = 7.1 Hz, 4 H), 3.99–3.96 (m, 2 H), 1.32 (t, J = 7.1 Hz, 6 H). ^{13}C NMR (75 MHz, $CDCl_3$) δ: 165.9, 131.7, 119.4, 64.7, 63.3, 57.7, 46.8, 14.0. ES-HR-MS m/z ([M+Na]$^+$) calcd: 314.0667; obsd: 314.0678.

β-Sultam 9a

Analogous reaction of **1a** (100 mg, 0.467 mmol) with 3-chloro-2-butanone (55 mg, 0.467 mmol) and potassium carbonate (129 mg, 0.93 mmol) in DMF (2.5 mL) at rt for 7 days provided 94 mg (93%) of **9a** as a colorless oil. ^{1}H

© 2003 NRC Canada

NMR (300 MHz, $CDCl_3$) δ: 5.90–5.79 (m, 1 H), 5.44–5.37 (m, 1 H), 5.29–5.24 (m, 1 H), 4.26 (d, *J* = 12.8 Hz, 1 H), 3.94–3.86 (m, 1 H), 3.81 (d, *J* = 12.8 Hz, 1 H), 3.51–3.43 (m, 1 H), 2.37 (s, 3 H), 1.50 (s, 3 H). ^{13}C NMR (75 MHz, $CDCl_3$) δ: 205.5, 131.0, 120.3, 66.6, 57.1, 45.2, 24.2, 17.1. ES-HR-MS *m/z* ($[M+Na]^+$) calcd: 226.0508; obsd: 226.0512.

β-Sultam 9c

Bromomethanesulfonyl chloride (from 20.00 g (0.107 mmol) of sodium bromomethanesulfonate and 22.20 g (0.102 mmol) of phosphorus pentachloride) dissolved in CH_2Cl_2 (100 mL) was added to aminoacetaldehyde dimethyl acetal (12.29 mL, 0.112 mmol), DMAP (20 mg), and triethylamine (15.60 mL, 0.112 mmol) in CH_2Cl_2 (100 mL) at 0 °C over 30 min. Stirring was maintained at this cold temperature for 4 h, at which point the reaction mixture was allowed to warm to rt, stirred overnight, quenched with saturated $NaHSO_4$ solution, and extracted with CH_2Cl_2 (3×). The combined organic phases were washed with brine, dried, and evaporated to yield 12.97 g (50% over two steps) of **1c** as a colorless oil. ^{1}H NMR (300 MHz, $CDCl_3$) δ: 5.05 (t, *J* = 6.0 Hz, 1 H), 4.47 (s, 2 H), 4.42 (t, *J* = 5.0 Hz, 1 H), 3.42 (s, 6 H), 3.31 (dd, *J* = 6.0, 5.0 Hz, 2 H). ^{13}C NMR (75 MHz, $CDCl_3$) δ: 102.9, 54.7, 45.3, 41.9. ES-HR-MS *m/z* ($[M+Na]^+$) calcd: 283.9563; obsd: 283.9548.

To a solution of **1c** (123 mg, 0.467 mmol) and 3-chloro-2-butanone (55 mg, 0.467 mmol) in DMF (25 mL) was added potassium carbonate (129 mg, 0.734 mmol). The mixture was stirred at rt for 6 days and processed as described above to give 89 mg (76%) of **9c** as a colorless oil. ^{1}H NMR (300 MHz, $CDCl_3$) δ: 4.43 (dd, *J* = 4.1, 6.1 Hz, 1 H), 4.23 (d, *J* = 12.8 Hz, 1 H), 3.82 (d, *J* = 12.8 Hz, 1 H), 3.45–3.39 (m, 4 H), 3.35 (s, 3 H), 2.93 (dd, *J* = 6.1, 14.3 Hz, 1 H), 2.39 (s, 3 H), 1.57 (s, 3 H). ^{13}C NMR (75 MHz, $CDCl_3$) δ: 205.2, 107.8, 66.7, 57.2, 54.7, 54.6, 43.4, 23.5, 16.8.

Addition of methylmagnesium bromide to 4f

A solution of methylmagnesium bromide in THF (7.28 mL of 3.0 mol L^{-1}, 21.9 mmol) was added over a 20 min period to a solution of **4f** (1.20 g, 5.46 mmol) in the same solvent (100 mL) previously cooled to –78 °C. The mixture was stirred in the cold for 5 h, quenched with saturated NH_4Cl solution, warmed to rt, and extracted with CH_2Cl_2 (2×). The combined organic layers were washed with brine, dried, and evaporated. The residue was chromatographed on silica gel (elution with hexanes – ethyl acetate 3:2) and afforded 630 mg (61%) of **4d** (identical to the sample prepared above) and 126 mg (11%) of **11** as a colorless oil. ^{1}H NMR (300 MHz, $CDCl_3$) δ: 5.98–5.87 (m, 1 H), 5.42–5.26 (m, 2 H), 4.15 (dd, *J* = 6.1, 12.4 Hz, 1 H), 4.02 (dd, *J* = 8.3, 12.4 Hz, 1 H), 3.92 (dd, *J* = 6.1, 15.5 Hz, 1 H), 3.66–3.58 (m, 1 H), 3.16 (dd, *J* = 6.1, 8.3 Hz, 1 H), 2.32–2.30 (m, 1 H), 1.26 (s, 3 H) 1.16 (s, 3 H). ^{13}C NMR (75 MHz, $CDCl_3$) δ: 132.0, 119.7, 70.3, 58.6, 54.6, 50.7, 27.4, 24.8. ES-HR-MS *m/z* ($[M+Na]^+$) calcd: 228.0665; obsd: 228.0667.

Dienyl sultam 12

Olefination of 4d

A solution of *n*-butyllithium in hexanes (0.94 mL of 1.6 mol L^{-1}, 1.50 mmol) was added dropwise to a stirred solution of methyltriphenylphosphonium bromide (536 mg, 1.5 mmol) in THF (10 mL) at 0 °C. After being stirred for 20 min in the cold, the reaction mixture was brought to –42 °C and a solution of **4d** (189 mg, 1.0 mmol) in THF (10 mL) was introduced over 20 min, prior to warming to rt 30 min later. After overnight stirring, saturated NH_4Cl solution was added, and the product was extracted into ether (3×). The combined organic phases were dried and evaporated to leave a residue that was purified by chromatography on silica gel. Elution with 5:1 hexanes – ethyl acetate gave 127 mg (68%) of **12** as a colorless oil. ^{1}H NMR (300 MHz, $CDCl_3$) δ: 5.95–5.81 (m, 1 H), 5.43 (dd, *J* = 1.1, 17.1 Hz, 1 H), 5.23 (dd, *J* = 1.1, 10.2 Hz, 1 H), 5.16 (s, 1 H), 5.04 (d, *J* = 1.1 Hz, 1 H), 4.11 (dd, *J* = 7.9, 12.2 Hz, 1 H), 3.90 (dd, *J* = 6.5, 12.2 Hz, 1 H), 3.77–3.70 (m, 2 H), 3.52 (dd, *J* = 5.6, 14.8 Hz, 1 H), 1.81 (s, 3 H). ^{13}C NMR (75 MHz, $CDCl_3$) δ: 139.9, 131.3, 119.7, 116.1, 61.7, 52.0, 48.3, 30.3. ES-HR-MS *m/z* ($[M+Na]^+$) calcd: 210.0559; obsd: 210.0562.

Dehydration of 11

A solution of **11** (131 mg, 0.64 mmol) in pyridine (10 mL) was treated dropwise with phosphorus oxychloride (0.59 mL, 6.40 mmol) over 5 min. The reaction mixture was stirred overnight at rt, cooled in an ice bath, and cautiously quenched with warm water. After 30 min, the aqueous layer was extracted with ether (2×), and the combined organic layers were washed with 0.5 mol L^{-1} hydrochloric acid, followed by water; dried; and freed of solvent. There was isolated 110 mg (92%) of **12**, identical in all respects to the material generated in the above section (Olefination of 4d).

Ring closing metathesis of 12

β-Sultam **12** (118 mg, 0.63 mmol) dissolved in CH_2Cl_2 (10 mL) was added to a deoxygenated solution of **14** (27 mg, 0.032 mmol) in the same solvent (40 mL). The reaction mixture was heated to a gentle reflux, periodically evacuated to remove ethylene, cooled to rt, and evaporated to dryness. Chromatography of the residue on silica gel provided 96 mg (96%) of **13** as a white solid, mp 85–86 °C. ^{1}H NMR (300 MHz, $CDCl_3$) δ: 5.61 (m, 1 H), 4.49–4.41 (m, 2 H), 4.38–4.36 (m, 1 H), 4.09 (ddd, *J* = 0.7, 3.7, 12.4 Hz, 1 H), 3.76–3.71 (m, 1 H), 1.79–1.77 (m, 3 H). ^{13}C NMR (75 MHz, $CDCl_3$) δ: 135.8, 125.7, 65.0, 55.7, 54.3, 12.0. ES-HR-MS *m/z* ($[M+Na]^+$) calcd: 182.0246; obsd: 182.0253.

Addition of allylmagnesium bromide to 4f

Allylmagnesium bromide (273 mL of 1.0 mol L^{-1} in THF) was added over 10 min to **4f** (0.20 g, 0.91 mmol) in THF (20 mL) at –78 °C. The reaction mixture was stirred in the cold for 3.5 h, quenched carefully with concentrated NH_4Cl solution at –78 °C, warmed to rt, stirred for 3.5 h, and extracted with ethyl acetate (3×). The customary workup (elution with 3:1 hexane – ethyl acetate) gave 48 mg (25%) of **15**. ^{1}H NMR (300 MHz, $CDCl_3$) δ: 7.17–7.07 (m, 1 H), 6.63–6.56 (m, 1 H), 5.88–5.77 (m, 1 H), 5.39–5.24 (m, 2 H), 4.25 (dd, *J* = 8.6, 12.5 Hz, 1 H), 4.08 (dd, *J* = 6.5, 12.5 Hz, 1 H), 3.90–3.80 (m, 2 H), 3.67–3.60 (m, 1 H), 1.98 (dd, *J* = 1.7, 7.0 Hz, 3 H). ^{13}C NMR (75 MHz, $CDCl_3$) δ: 193.1, 148.0, 130.4, 125.3, 121.1, 60.6, 51.1, 49.4, 18.8. ES-HR-MS *m/z* ($[M+Na]^+$) calcd: 238.0508; obsd: 238.0507.

© 2003 NRC Canada

Ring closing metathesis of 15

To a solution of **15** (43 mg, 0.20 mmol) dissolved in CH_2Cl_2 (60 mL) was added a deoxygenated solution of **14** (8.5 mg, 0.001 mmol) in the same solvent (2 mL); this was gently refluxed during 2.5 h, with periodic evacuation of the vessel to remove ethylene, and evaporated to dryness. Chromatographic purification of the residue on silica gel furnished 22 mg (64%) of **16** as a colorless oil. ^{1}H NMR (300 MHz, $CDCl_3$) δ: 6.99 (ddd, *J* = 2.3, 4.0, 10.8 Hz, 1 H), 6.25 (ddd, *J* = 2.3, 2.4, 10.8 Hz, 1 H), 4.61 (dd, *J* = 8.3, 12.8 Hz, 1 H), 4.33 (dd, *J* = 2.8, 12.8 Hz, 1 H), 4.26–4.16 (m, 2 H), 3.93–3.84 (m, 1 H). ^{13}C NMR (75 MHz, $CDCl_3$) δ: 190.8, 146.4, 127.0, 64.6, 45.9, 38.8. ES-HR-MS *m/z* ($[M+Na]^+$) calcd: 196.0039; obsd: 196.0039.

Hydride reduction of 4f

β-Sultam **4f** (0.60 g, 2.73 mmol) dissolved in THF (5 mL) was introduced into a cold (0 °C), vigorously stirred suspension of sodium borohydride (0.52 g, 13.7 mmol) in THF (25 mL), followed by the slow addition of water (10 mL), also at 0 °C. The reaction mixture was stirred at rt for 10 min, treated successively with ethyl acetate and 1.0 mol L^{-1} hydrochloric acid (20 mL), and agitated for a further 20 min. The separated aqueous layer was extracted with ethyl acetate, and the combined organic layers were washed with saturated $NaHCO_3$ solution and brine, dried, and evaporated to give 405 mg (84%) of **17a** as a colorless oil. ^{1}H NMR (300 MHz, $CDCl_3$) δ: 5.96–5.83 (m, 1 H), 5.42–5.35 (m, 1 H), 5.27 (dd, *J* = 1.1, 10.0 Hz, 1H), 4.16 (dd, *J* = 6.3, 12.4 Hz, 1 H), 4.06 (dd, *J* = 7.8, 12.4 Hz, 1 H), 3.90–3.77 (m, 2 H), 3.65 (dd, *J* = 3.1, 12.1 Hz, 1 H), 3.56 (dd, *J* = 6.4, 14.6 Hz, 1 H), 3.42–3.37 (m, 1 H), 2.42 (s, 1 H). ^{13}C NMR (75 MHz, $CDCl_3$) δ: 131.7, 120.0, 61.4, 58.9, 48.9, 48.4. ES-HR-MS *m/z* ($[M+Na]^+$) calcd: 200.0358; obsd: 200.0353.

Hydride reduction of 4h

A 0.50 g (1.86 mmol) sample of **4h** was reduced with sodium borohydride (0.70 g, 18.6 mmol) in the predescribed manner. After chromatography, there was isolated 335 mg (78%) of **17b** as a colorless oil. ^{1}H NMR (300 MHz, $CDCl_3$) δ: 7.40–7.30 (m, 5 H), 4.49 (d, *J* = 13.2 Hz, 1 H), 4.18–4.01 (m, 3 H), 3.49–3.36 (m, 3 H), 2.05 (dd, *J* = 4.2, 8.0 Hz, 1 H). ^{13}C NMR (75 MHz, $CDCl_3$) δ: 134.8, 129.0, 128.7, 128.4, 61.3, 59.0, 50.1, 49.0. ES-HR-MS *m/z* ($[M+Na]^+$) calcd: 250.0508; obsd: 250.0500.

Mesylation of 17a

Samples of **17a** (0.38 g, 2.14 mmol) and Et_3N (0.75 mL, 5.35 mmol) were dissolved in CH_2Cl_2 (40 mL) and treated dropwise with a solution of methanesulfonyl chloride (0.20 mL, 2.57 mmol) in CH_2Cl_2 (5 mL). The reaction mixture was stirred for 3 h, quenched with water, and extracted with CH_2Cl_2 (2×). The combined organic layers were washed with brine, dried, and freed of solvent to provide 0.50 g (91%) of **18** as a colorless oil. ^{1}H NMR (300 MHz, $CDCl_3$) δ: 5.93–5.82 (m, 1 H), 5.43–5.37 (m, 1 H), 5.32–5.27 (m, 1 H), 4.40 (dd, *J* = 4.7, 11.3 Hz, 1 H), 4.30 (dd, *J* = 4.5, 11.3 Hz, 1 H), 4.20 (dd, *J* = 8.1, 12.7 Hz, 1 H), 4.04 (m, *J* = 5.9, 12.7 Hz, 1 H), 3.90–3.83 (m, 1 H), 3.66–3.54 (m, 2 H), 3.11 (s, 3 H). ^{13}C NMR (75 MHz, $CDCl_3$) δ: 131.2, 120.6, 67.9, 60.1, 49.0, 45.6, 35.0. ES-HR-MS *m/z* ($[M+Na]^+$) calcd: 278.0127; obsd: 278.0125.

Formation of iodide 19

A solution of **18** (200 mg, 0.78 mmol) in acetone (15 mL) was treated with sodium iodide (1.17 g, 780 mmol), heated to reflux for 24 h in the absence of light, cooled to rt, and evaporated to dryness. The residue was slurried with ether (3×) and filtered. The dark oily residue resulting from evaporation of the ether was chromatographed on silica gel. Elution with 10:1 to 6:1 hexane – ethyl acetate afforded **19** (212 mg, 95%) as a colorless oil. ^{1}H NMR (300 MHz, $CDCl_3$) δ: 5.93–5.82 (m, 1 H), 5.44–5.37 (m, 1 H), 5.30–5.27 (m, 1 H, 4.21 (dd, *J* = 12.7, 7.5 Hz, 1 H), 3.91–3.83 (m, 2 H), 3.61 (dd, *J* = 14.6, 6.4 Hz, 1 H), 3.45–3.39 (m, 2 H), 3.23–3.17 (m, 1 H). ^{13}C NMR (75 MHz, $CDCl_3$) δ: 131.4, 120.4, 64.5, 48.6, 48.5, 5.5. ES-HR-MS *m/z* ($[M+Na]^+$) calcd: 309.9369; obsd: 309.9374.

Generation of bromide 20

Alcohol **17b** (1.29 g, 5.58 mmol) in CH_2Cl_2 (10 mL) was added dropwise to a stirred suspension of triphenylphosphine dibromide (2.59 g, 6.14 mmol) in CH_2Cl_2 (15 mL) at 0 °C. The mixture was stirred for 30 min, warmed to rt, stirred for 3 h, quenched with saturated $NaHCO_3$ solution, and extracted with CH_2Cl_2 (2×). The combined organic phases were dried and evaporated. The resulting residue was purified by chromatography on silica gel to give 605 mg (37%) of **20** as a colorless oil. ^{1}H NMR (300 MHz, $CDCl_3$) δ: 7.40–7.32 (m, 5 H), 4.45 (d, *J* = 14.1 Hz, 1 H), 4.21 (dd, *J* = 17.7, 7.8 Hz, 1 H), 4.11 (d, *J* = 14.1 Hz, 1 H), 3.96 (dd, *J* = 12.7, 5.7 Hz, 1 H), 3.56–3.49 (m, 1 H), 3.23–3.15 (m, 2 H). ^{13}C NMR (75 MHz, $CDCl_3$) δ: 134.3, 129.0 (2 C), 128.8 (2 C), 128.5, 63.0, 49.9, 48.1, 32.7. ES-HR-MS *m/z* ($[M+Na]^+$) calcd: 311.9664; obsd: 311.9677.

Radical cyclization of 19

A solution of tributylstannane (0.16 mL, 0.60 mmol) and AIBN (17 mg, 0.10 mmol) in benzene (10 mL) was added to a solution of **19** (144 mg, 0.503 mmol) in benzene (50 mL) at the reflux temperature over a period of 12 h. The cooled reaction mixture was evaporated to dryess and the residue was chromatographed on silica gel to give **21** as a colorless oily 3:1 mixture of diastereomers. ^{1}H NMR (300 MHz, C_6D_6) δ: 3.65 (dd, *J* = 12.7, 7.0 Hz, 1 H), 3.56 (dd, *J* = 12.8, 7.0 Hz, 1 H), 3.23–3.15 (m, 1 H), 3.10 (dd, *J* = 12.7, 4.9 Hz, 1 H), 3.00–2.96 (m, 1 H), 2.77 (dd, *J* = 10.2, 7.5 Hz, 1 H), 2.25–2.08 (m, 2 H), 1.77–1.71 (m, 1 H), 1.42–1.23 (m, 2 H), 1.17–1.07 (m, 1 H), 1.00–0.82 (m, 4 H), 0.71 (d, *J* = 6.5 Hz, 3 H), 0.55 (d, *J* = 6.4 Hz, 3 H). ^{13}C NMR (75 MHz, C_6D_6) δ: (major isomer) 66.0, 55.0, 46.5, 38.6, 34.0, 16.4. ES-HR-MS *m/z* ($[M+Na]^+$) calcd: 184.0403; obsd: 184.0411.

Radical fragmentation of 20

A solution of tributylstannane (123 mg, 0.424 mmol) and AIBN (67 mg, 0.41 mmol) in benzene (2.5 mL) was added to a solution of **20** (107 mg, 0.369 mmol) in benzene (20 mL) at the reflux temperature over a period of 9 h. Workup in the predescribed manner afforded 37 mg (48%) of **22** as a colorless oil contaminated with a very minor

© 2003 NRC Canada

amount of the uncleaved reduction product. ^{1}H NMR (300 MHz, C_6D_6) δ: 7.40–7.23 (m, 5 H), 5.90–5.76 (m, 1 H), 5.38–5.35 (m, 1 H), 5.28–5.21 (m, 1 H), 5.00–4.96 (m, 1 H), 4.27 (d, J = 6.2 Hz, 2 H), 3.64 (dd, J = 8.1, 0.8 Hz, 2 H). ^{13}C NMR (75 MHz, C_6D_6) δ: 137.7, 128.6, 128.1 (2 C), 128.0 (2 C), 126.4, 122.8, 57.2, 47.1. ES-HR-MS m/z ($[M+Na]^+$) calcd: 234.0539; obsd: 234.0553.

Acknowledgment

We thank the S.T. Li Foundation for an unrestricted grant. Technical assistance has been provided by Claire E. Barton and Kavita Bhatt.

References

1. (*a*) N.J. Baxter, L.J.M. Rigoreau, A.P. Laws, and M.I. Page. J. Am. Chem. Soc. **122**, 3375 (2000); (*b*) J.M. Wood, P.S. Hinchcliffe, A.P. Laws, and M.I. Page. J. Chem. Soc. Perkin Trans. **2**, 938 (2002); (*c*) P.S. Hinchcliffe, J.M. Wood, A.M. Davis, R.P. Austin, R.P. Beckett, and M.I. Page. Org. Biomol. Chem. 67 (2003).
2. M. Beardsell, P.S. Hinchcliffe, J.M. Wood, R.C. Wilmouth, C.J. Schofield, and M.I. Page. J. Chem. Soc. Chem. Commun. 497 (2001).
3. (*a*) T. Iwama and T. Kataoka. Rev. Heteroatom. Chem. **15**, 25 (1996); (*b*) J. Chanet-Ray and R. Vessiere. Org. Prep. Proced. Int. **18**, 157 (1986).
4. L.A. Paquette. Synlett, 1 (2001).
5. F.G. Bordwell and W.T. Brannen, Jr. J. Am. Chem. Soc. **86**, 4645 (1964).
6. J.D. Schloss, S.M. Leit, and L.A. Paquette. J. Org. Chem. **65**, 7119 (2000).
7. M.-J. Brienne, D. Varech, M. Leclercq, J. Jacques, N. Radembrino, M.-C. Dessalles, G. Mahuzier, C. Gueyouche, C. Borias, P. Loiseau, and P. Gayral. J. Med. Chem. **30**, 2232 (1987).
8. S.M. Leit and L.A. Paquette. J. Org. Chem. **64**, 9225 (1999).
9. For an early compilation of crystallographic data, see R.L. Beddoes, L. Dalton, J.A. Joule, O.S. Mills, J.D. Street, and C.I.F. Watt. J. Chem. Soc. Perkin Trans. 2, 787 (1986).
10. The situation is reminiscent of that noted in the kinetically controlled base-promoted cyclization of epoxy nitriles: G. Stork and J. F. Cohen. J. Am. Chem. Soc. **96**, 5270 (1974).
11. For the initial introduction of this term, see L.A. Paquette and M.J. Wyvratt. J. Am. Chem. Soc. **96**, 4671 (1974).
12. For recent reviews, consult: (*a*) R.H. Grubbs and S. Chang. Tetrahedron, **54**, 4413 (1998); (*b*) A. Fürstner. Angew. Chem. Int. Ed. **39**, 3012 (2000); (*c*) T.M. Trnka and R.H. Grubbs. Acc. Chem. Res. **34**, 18 (2001); (*d*) S.J. Connon and S. Blechert. Angew. Chem. Int. Ed. **42**, 1900 (2003).
13. G.F. Meijs, J.F. Bunnett, and A.L.J. Beckwith. J. Am. Chem. Soc. **108**, 4899 (1986).
14. (*a*) W.R. Bowman, C.F. Bridge, P. Brookes, M.O. Cloonan, and D.C. Leach. J. Chem. Soc. Perkin Trans 1, 58 (2002); (*b*) D.P. Curran, H. Yu, and H. Liu. Tetrahedron, **50**, 7343 (1994).
15. (*a*) J.C. Sheehan and A.K. Bose. J. Am. Chem. Soc. **72**, 5158 (1950); (*b*) J.C. Sheehan and A.K. Bose. J. Am. Chem. Soc. **73**, 1761 (1951); (*c*) T. Okawara and K. Harada. J. Org. Chem. **37**, 3286 (1972); (*d*) A.K. Bose, M.S. Manhas, and B.N. Ghosh-Mazumder. J. Org. Chem. **27**, 1458 (1962); (*e*) B.G. Chatterjee and P.N. Moza. J. Med. Chem. **9**, 259 (1966); (*f*) B.G. Chatterjee and V.V. Rao. Tetrahedron, **23**, 487 (1967).
16. B.G. Chatterjee, P.N. Moza, and S.K. Roy. J. Org. Chem. **28**, 1418 (1963).

© 2003 NRC Canada

Diastereoselectivity in asymmetric allylations: The role of vicinal chirality in the allyl nucleophile for S_E2' reactions with aldehydes[1]

David R. Williams, Kevin G. Meyer, Khalida Shamim, and Samarjit Patnaik

Abstract: A series of nonracemic homoallylic alcohols have been prepared by asymmetric allylation using the (*R*,*R*)- and (*S*,*S*)-1,2-diamino-1,2-diphenylethane bis-sulfonamide controller ligands for in situ formation of chiral B-allyl-1,3,2-diazaborolidines. Diastereofacial selectivity is influenced by adjacent stereochemistry incorporated into the allyl moiety at C-2, in addition to the expected role of the chiral auxiliary. Additional asymmetry in the aldehyde reactant introduces threefold stereodifferentiation. A model is developed to identify reinforcing stereochemical relationships, and examples have ascertained the relative significance of these factors. The methodology supports the construction of complex homoallylic alcohols in a highly convergent fashion.

Key words: asymmetric allylation, diastereofacial selectivity, 1,4-stereocontrol, homoallylic alcohols.

Résumé : On a préparé une série d'alcools homoallyliques non racémiques en procédant à l'allylation asymétrique à l'aide des ligands de contrôle (*R*,*R*)- et (*S*,*S*)-1,2-diamino-1,2-diphényléthane bis-sulfonamide pour la formation in situ de B-allyl-1,3,2-diazaborolidines chirales. La sélectivité diastéréofaciale est influencée par la stéréochimie adjacente qui est incorporée dans la portion allyle au niveau C-2, en plus du rôle attendu de l'auxiliaire chiral. Une asymétrie additionnelle dans l'aldéhyde utilisé comme réactif introduit une triple stéréodifférenciation. On a développé un modèle pour identifier les relations stéréochimiques qui se renforcent et divers exemples ont permis de confirmer la signification relative de ces facteurs. La méthodologie se prête à la construction d'alcools homoallyliques complexes d'une façon extrêmement convergente.

Mots clés : allylation asymétrique, sélectivité diastéréofaciale, stéréocontrôle 1,4, alcools homoallyliques.

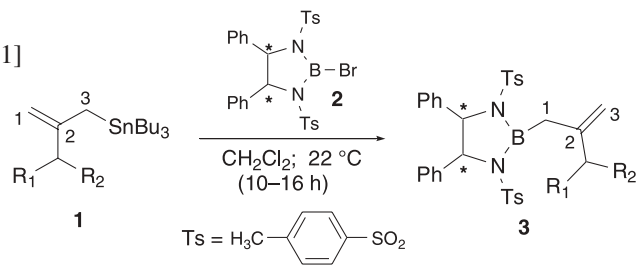
[Traduit par la Rédaction]

Introduction

Asymmetric allylation processes are generally recognized as important tools for stereocontrolled synthesis (1). Impressive levels of stereoselectivity have been achieved for the reactions of allyl and crotyl nucleophiles with aldehydes, leading to the formation of nonracemic homoallylic alcohols (2). Iterations of this scheme are propagated by oxidative cleavage of the terminal olefin and the generation of an aldehyde for sequentially increasing complexity. As often utilized in combination with aldol reactions, asymmetric allylation has provided, in large measure, a significant advance for syntheses of natural products of polyacetate and polypropionate origin (3).

In 1989, Corey and co-workers (4, 5) reported (*R*,*R*)- and (*S*,*S*)-1,2-diamino-1,2-diphenylethane *N*,*N*-sulfonamides as effective chiral auxiliaries to enable enantioselective Diels–Alder, aldol, and allylation reactions. We recognized that the mild conditions needed for transmetalation (eq. [1]) of allylstannanes **1** to nonracemic B-allyl-1,3,2-diazaborolidines **3** with bromoborane **2** would support molecular complexity and functionalization in the allyl segment with substitution at C-2. Thus, asymmetric allylation could prove widely useful for strategic bond formation in a convergent synthesis approach. Recent successes along these lines in our programs, towards hennoxazole A (6), amphidinolide K (7), and phorboxazole A (8), have been encouraging. This study will examine, in detail, the role of vicinal chirality in the allyl component as a result of substitution at the adjacent methylene ($R_1 \neq R_2$ in **1**) of the nascent nucleophile. We will explore the impact of this additional element of asymmetry for stereochemically reinforcing and nonreinforcing relationships with the auxiliary of **3** in the production of diastereomeric alcohols.

[1]



Received 1 August 2003. Published on the NRC Research Press Web site at http://canjchem.nrc.ca on 9 January 2004.

Dedicated to Professor Ed Piers for his many contributions to organic chemistry.

D. Williams,[2] K.G. Meyer, K. Shamim, and S. Patnaik. Department of Chemistry, Indiana University, 800 East Kirkwood Avenue, Bloomington, IN 47405-7102, U.S.A.

[1]This article is part of a Special Issue dedicated to Professor Ed Piers.

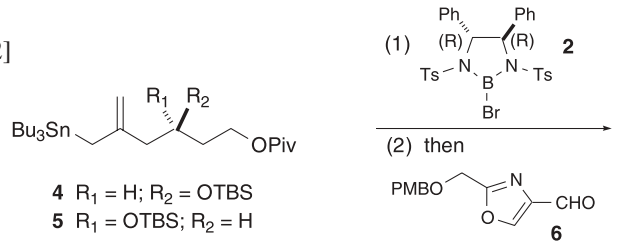
[2]Corresponding author (e-mail: williamd@indiana.edu).

 doi: 10.1139/V03-168 © 2004 NRC Canada

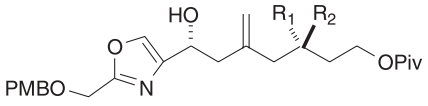
Results and discussion

Our preliminary studies (9) have shown that a range of functionality is tolerated under the ambient conditions of transmetalation of **1** to borane **2**. Examples of compatible functional groups include isolated alkenes, dithioacetals, *para*-methoxybenzyl, and benzyl ethers, esters, vinylstannanes, and most silyl ethers. The presence of Lewis-acid-sensitive protecting groups, such as methoxymethyl (MOM), β-methoxyethoxymethyl (MEM), and tetrahydropyranyl (THP) ethers, as well as other ketals and acetals, are incompatible with bromoborane **2**. Additionally, most allylsilanes do not undergo a productive transmetalation with bromoborane **2**. Upon the in situ formation of allylborane **3** at room temperature, reactions are cooled to –78 °C for the introduction of stoichiometric aldehyde, leading to complete condensations within 2 to 3 h. A variety of functionality may also be incorporated in the aldehyde component. As demonstrated by the reactions of enantiomeric stannanes **4** and **5**, the introduction of a stereogenic center that is separated by at least one methylene unit from the reactive allyl moiety plays little or no role in determining the diastereoselectivity of the condensation. The chiral auxiliary is the major factor to consider in the production of the new chiral alcohols **7** and **8**.

[2]



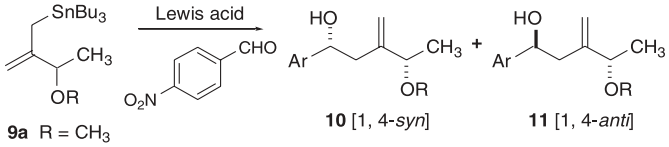
4 R_1 = H; R_2 = OTBS
5 R_1 = OTBS; R_2 = H



7 R_1 = H; R_2 = OTBS
98% yield; >20 : 1 dr
8 R_1 = OTBS; R_2 = H
98% yield; >20 : 1 dr

In previous studies by Nishigaichi et al. (10), moderate stereocontrol in the addition of racemic allylstannanes **9ab** to simple aldehydes was observed. Thus, the placement of methoxy or acetoxy substituents directly adjacent to the reactive allyl component resulted in a diastereofacial preference, which was strongly influenced by the choice of Lewis acid. Related chromium- and indium-mediated allylations (11) have produced 1,4-syn-diol derivatives with diastereomeric excesses of 60–90%.

[3]



9a R = CH_3
9b R = Ac

10 [1, 4-*syn*] **11** [1, 4-*anti*]

With these observations in mind, we have examined the role of adjacent stereogenicity as a control factor for our asymmetric allylations (eq. [1]; $R_1 \neq R_2$). Two general pathways were deployed for the preparation of starting stannanes bearing a chiral carbon at the C-2 allylic position by the introduction of a methyl or hydroxyl substituent.

In the former case, we have utilized our asymmetric conjugate addition methodology (12) for reactions of the alkenylcopper species derived from the Grignard reagent of 2-bromo-3-trimethylsilyl-1-propene (13) with *N*-enoyl-4-phenyl-1,3-oxazolidinone **12**. The imide **13** (diastereomeric ratio (dr) 25:1) was purified by flash chromatography and reduced to yield alcohol **14**, which was subsequently O-protected as the corresponding *tert*-butyldiphenylsilyl ether **15**. Additional complexity was introduced by direct conversion of **14** to the primary iodide **16** for alkylation with 2-lithio-1,3-dithiane, providing the allylsilane **17**. The allylic silanes **15** and **17** were transformed into the desired stannanes **18** and **19** via quantitative, low-temperature reactions to yield the intermediate bromides (R = Br) with subsequent displacement with tri-*n*-butylstannylcopper dimethylsulfide complex (14). In analogous fashion, we also prepared *ent*-**18**.[3] While other routes have been devised and reduced to practice, Scheme 1 offers simplicity and generality.[4]

For the preparation of stannanes bearing an allylic hydroxyl substituent, the aliphatic aldehydes **20** (R = H and R = $CH_2CH{=}CHCH_3$) were converted into the chiral epoxy-alcohols **21** via Wittig olefination, reduction, and Sharpless asymmetric epoxidation (15), as illustrated in Scheme 2.

Mesylation and immediate reduction of crude epoxy sulfonate with zinc dust in the presence of sodium iodide (16) gave optically active **22** in excellent yield. The secondary alcohol in **22** was then used to direct allylic lithiation (17) for C-alkylation with tri-*n*-butylstannyl iodide. Acylation with benzoic anhydride led to pure **23a** (R = H) or **23b** (R = $CH_2CH{=}CH{-}CH_3$) for our allylation experiments.[5]

Results of our allylation studies are assembled in Table 1.[6] Data regarding the stereoselectivity of each condensation reaction was obtained by an initial flash silica-gel column to separate product diastereomers from other organic components, including the chiral auxiliary, which can be recovered and recycled. Thus, overall yields of these attempts were readily assessed, and the ratios of diastereomeric products

[3] Experimental details for the preparation of allylstannanes **18**, **19**, and *ent*-**18** will be published in the full account of the synthesis of leucascandrolide A.

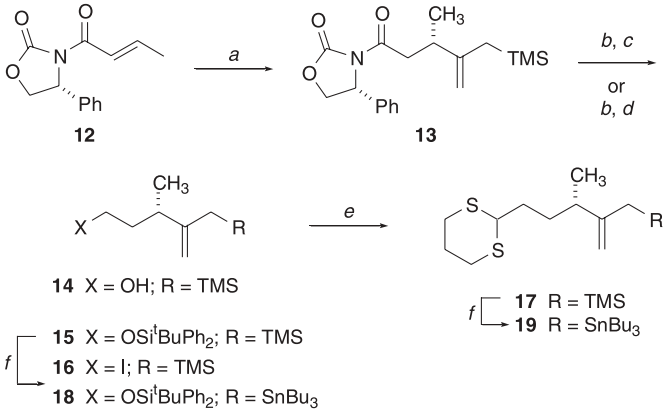
[4] An alternative method for general introduction of the allylic silane uses methyl ketones for kinetic deprotonation, and transformation to their corresponding vinyl triflates. Cross-coupling with (trimethylsilyl)methyl magnesium chloride in the presence of $Ni(acac)_2$ (THF at 22 °C) yields the C-2-substituted allylic silanes.

[5] Experimental details for the preparation of stannanes **23a**, **23b**, and (*R*)-**23b** will be published in the full account of our total synthesis of amphidinolide K (see also ref. 7).

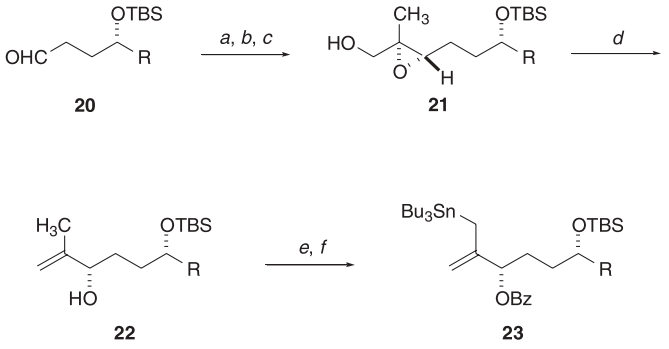
[6] We have used a standard set of conditions for these examples of asymmetric allylation, and further attempts to optimize yields or product ratios have not been made in most cases.

© 2004 NRC Canada

Scheme 1. (*a*) CH_2=C(MgBr)CH_2SiMe_3, CuBr·DMS, THF, –78 °C to –30 °C, 90% (>90% diastereomeric excess (de)); (*b*) $LiBH_4$, MeOH, Et_2O, 0 °C, 80%; (*c*) *t*-$BuPh_2SiCl$, imid, DMF, room temperature (rt), 95%; (*d*) DCC·MeI, THF, 88%; (*e*) 2-lithiodithiane, THF, –78 °C to –5 °C, 90%; (*f*) NBS, propylene oxide, –78 °C, CH_2Cl_2:DMF (3:4); then add Bu_3SnLi, CuBr·DMS to crude allyl bromide, 70%–80%.

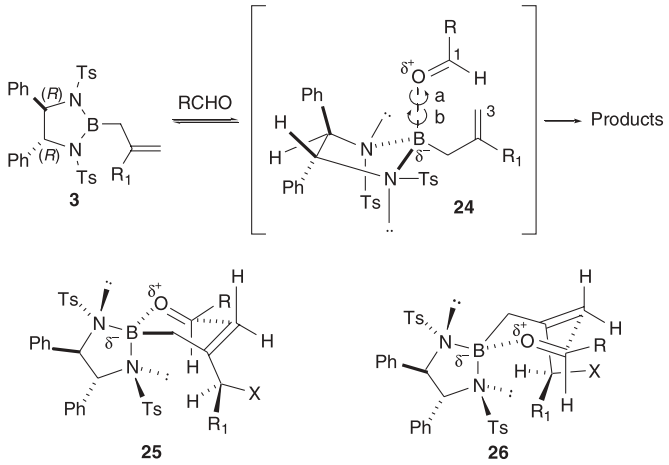


Scheme 2. For R = H or R = CH_2CH=$CHCH_3$; (*a*) $Ph_3PC(CH_3)COOEt$, CH_2Cl_2, rt, 82%; (*b*) DIBAL, CH_2Cl_2, –78 °C, 93%; (*c*) L-(+)-DET, Ti(O-*i*-Pr)$_4$, *t*-BuOOH, CaH_2, 4 Å molecular sieves, CH_2Cl_2, –25 °C, 89% (>97% de); (*d*) MsCl, Et_3N, CH_2Cl_2; then NaI, Zn dust, 2-butanone, 80 °C, 90%; (*e*) *n*-BuLi, TMEDA, Et_2O, rt; then Bu_3SnI, 50%; (*f*) benzoic anhydride, Et_3N, CH_2Cl_2, catalytic amount DMAP, 93%.



were obtained by the integration of selected proton signals in the NMR (400 MHz) spectra. Further confirmations of product ratios in most examples were available via analytical HPLC. In cases that provided a reasonable level of stereoselectivity, the major products were isolated and purified by silica-gel flash chromatography or preparative thin-layer chromatography for complete spectroscopic characterizations. Trace amounts of minor diastereomers or challenging separations from reactions that afforded little selectivity hampered our efforts for full characterization of these materials. However, the stereochemical redundance of our study provided fully characterized major products, which were then compared and identified as minor components in related examples. The assignment of absolute stereochemistry of each purified homoallylic alcohol of Table 1 was determined by Kakisawa analysis of the corresponding Mosher esters (18). Initially, these studies examined reactions with simple aldehydes, as summarized in entries 1 and 2 of Table 1. Reactions were evaluated using bromoborane **2**, bearing the (*R*,*R*)- and the (*S*,*S*)-sulfonamides. The presence of α-stereogenicity in the stannanes **19** and **23a** produced reactions consistent with stereochemically-reinforcing and nonreinforcing relationships with the auxiliaries (19).[7] Best results were obtained using the (*R*,*R*)-**2**, which yielded the 1,4-*syn*-diastereoisomers as major products. The benzoate substituent of **23a** in entry 2 was more effective in reinforcing, as well as countering, the bias of the auxiliary compared with the methyl substitution of **19** in entry 1.

Fig. 1. Diastereofacial selection in allylation reactions.

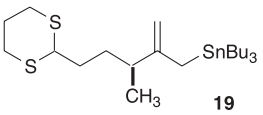
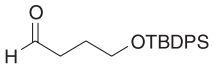
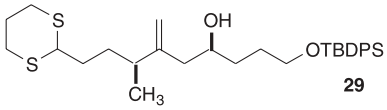
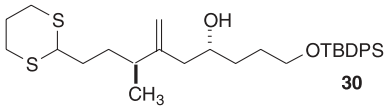
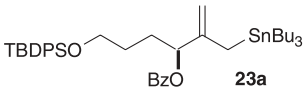
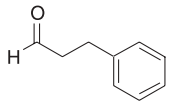
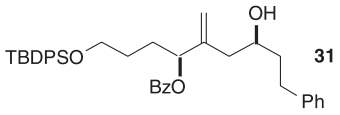
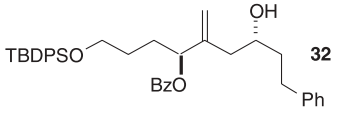
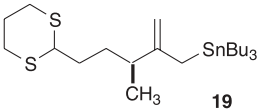
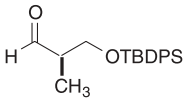
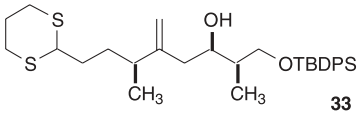
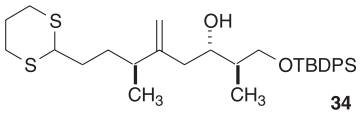
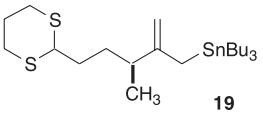
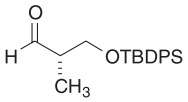
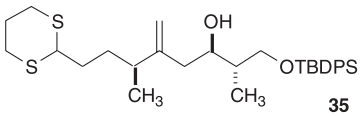
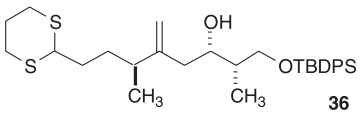
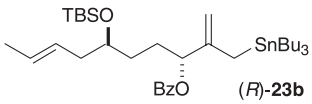
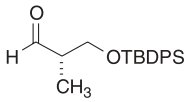
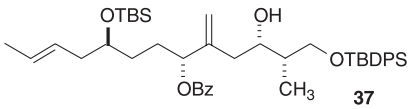
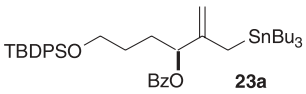
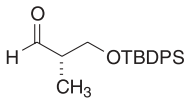
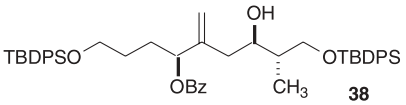
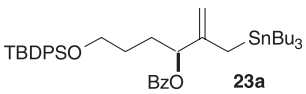
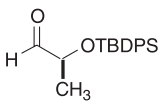
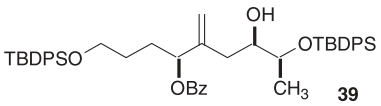


Our rationale for the stereoselectivity of these reactions is illustrated in the diagrams of Fig. 1. Transmetalation gives the sp^2 hybridized borane **3**, which reversibly binds the aldehyde in the axial orientation **24** and provides a synclinal disposition of the Lewis acid with respect to the aldehydic hydrogen. This complexation serves to activate the electrophilic carbonyl, as well as to trigger nucleophilicity of the allyl moiety. Structure **24** also presents a rehybridization of boron to a tetrahedral geometry, and the five-membered heterocyclic ring assumes a conformation that minimizes the nonbonded interactions of sulfonyl and phenyl substituents. Facial selectivity in **24** is determined by the relative energies of diastereomeric transition states as the reactive C_1 and C_3 carbons approach bonding proximity. Thus, our arguments consider bonding via the closed, chair-like arrangements of **25** and **26** as useful models to depict interactions that may contribute to a difference in transition-state energies. Since facial selectivity is not determined by the initial complexation, we offer the following contrivance to aid the visualization of **24** to **25** and **26** (Fig. 1): This process can be visualized from **24** by a rotation (arrow a) of the carbonyl (approximately 90°) and subsequent attack at the *re* face, as depicted in the favored situation in **25** wherein the illustration of **24** is reoriented by a 90° rotation (allyl is projected forward). On the other hand, rotation of the aldehyde in the clockwise direction in **24** (arrow b) results in the unfavorable nonbonded interactions of the aldehydic hydrogen with the

[7] We have utilized the terms "reinforcing" and "nonreinforcing", as introduced by Evans et al. (19), to describe the relationships of stereochemical elements within a reactant.

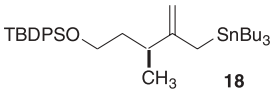
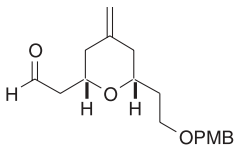
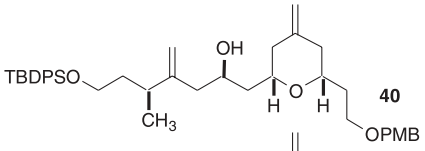
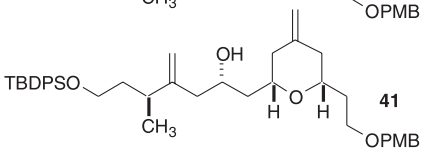
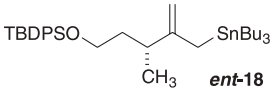
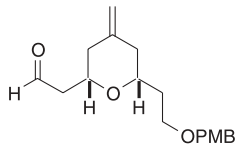
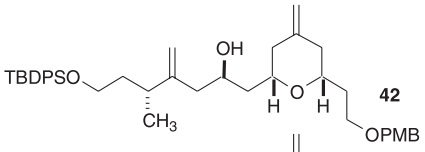
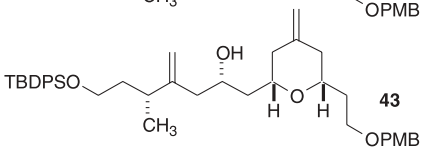
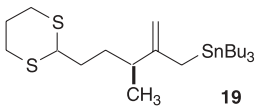
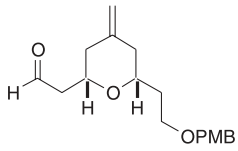
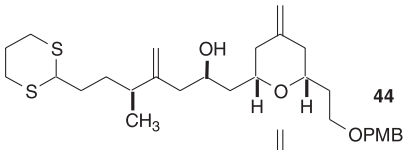
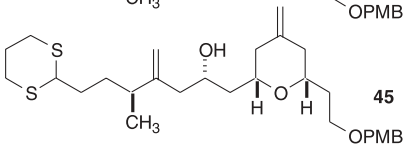
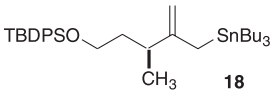
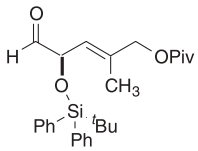
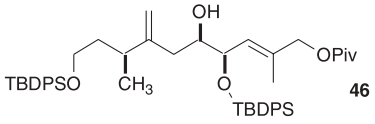
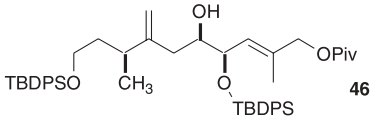
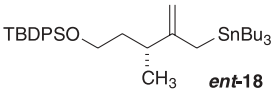
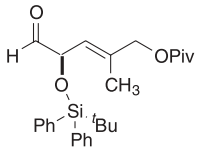
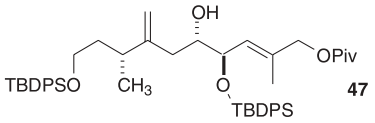
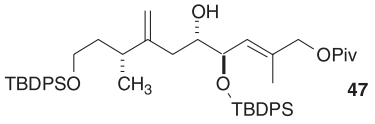
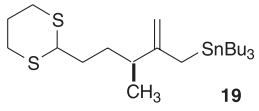
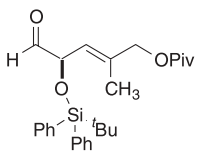
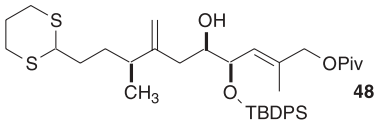
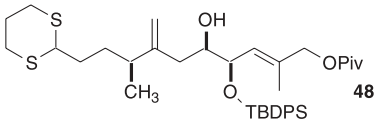
© 2004 NRC Canada

Table 1. Asymmetric allylations.

Entry	Stannane	Aldehyde	Sulfonamide	Major Product	Yield[a] dr
1	 **19**		(*R*,*R*)	 **29**	85% 7.7:1[b]
			(*S*,*S*)	 **30**	80% 4:1[b]
2	 **23a**		(*R*,*R*)	 **31**	96% >20:1[c]
			(*S*,*S*)	 **32**	94% 1:1[c]
3	 **19**		(*R*,*R*)	 **33**	77% 15:1[d]
			(*S*,*S*)	 **34**	70% 1.3:1[d]
4	 **19**		(*R*,*R*)	 **35**	75% 5.4:1[d]
			(*S*,*S*)	 **36**	76% 1.7:1[d]
5	 (*R*)-**23b**		(*S*,*S*)	 **37**	56% >25:1[c]
6	 **23a**		(*R*,*R*)	 **38**	83% >20:1[c]
7	 **23a**		(*R*,*R*)	 **39**	56% >20:1[c]

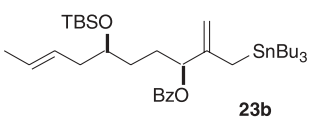
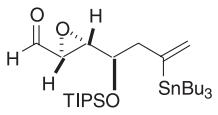
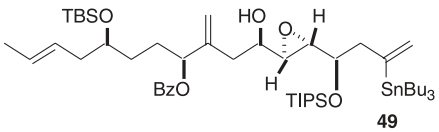
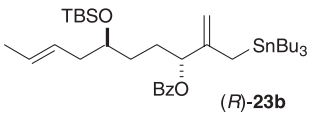
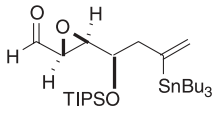
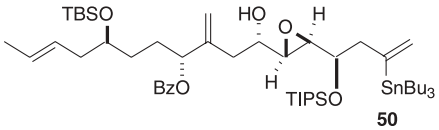
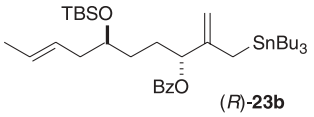
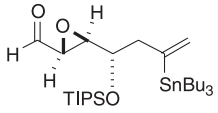
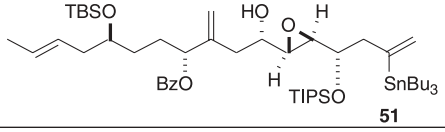
© 2004 NRC Canada

Table 1 (*continued*).

Entry	Stannane	Aldehyde	Sulfonamide	Major Product	Yield[a] dr
8	 **18**		(*R*,*R*)	 **40**	100% 10:1[c]
			(*S*,*S*)	 **41**	98% 2:1[c]
9	 ***ent*-18**		(*R*,*R*)	 **42**	97% 2.2:1[c]
			(*S*,*S*)	 **43**	93% 7:1[c]
10	 **19**		(*R*,*R*)	 **44**	100% 10:1[c]
			(*S*,*S*)	 **45**	78% 2.5:1[c]
11	 **18**		(*R*,*R*)	 **46**	60%[e] 7:1[b]
			(*S*,*S*)	 **46**	77%[e] 1.4:1[b]
12	 ***ent*-18**		(*R*,*R*)	 **47**	80%[e] 1.2:1[b]
			(*S*,*S*)	 **47**	70%[e] 4:1[b]
13	 **19**		(*R*,*R*)	 **48**	82%[e] 4.2:1[b]
			(*S*,*S*)	 **48**	82%[e] 1.5:1[b]

© 2004 NRC Canada

Table 1 (*concluded*).

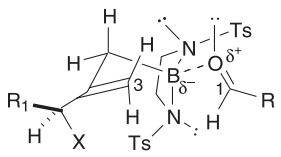
Entry	Stannane	Aldehyde	Sulfonamide	Major Product	Yield[a] dr
14	 **23b**		(*R*,*R*)	 **49**	72% 17:1[b]
15	 (*R*)-**23b**		(*S*,*S*)	 **50**	75% 17:1[b]
16	 (*R*)-**23b**		(*S*,*S*)	 **51**	65% 15:1[b]

Note: TBS = Si-*t*-BuMe$_2$; TBDPS = Si-*t*-BuPh$_2$; Bz = benzoate; Piv = pivaloate.
[a]Yields are based on purified products from flash silica-gel chromatography.
[b]Ratios were determined by HPLC separations of diastereomers on a Zorbax silica column by elution with 1% isopropanol in hexanes.
[c]Ratios were calculated from ^{1}H NMR (400 MHz) data in C_6D_6 via the integration of alkenylic hydrogen signals.
[d]Ratios were determined by HPLC separations on a Chiralpak AD column via elution with 1% isopropanol in hexanes.
[e]Unreacted aldehyde (15%–25%) was recovered in these reactions.

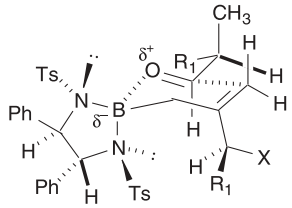
equatorial toluenesulfonyl group of the auxiliary, as shown in **26** (a 90° rotation of **24** with aldehyde projected forward). Thus, our modeling suggests that this nonbonded interaction raises the transition-state energy for *si* face reactions in the case of the (*R*,*R*)-chiral controller (20).

The consequences of steric interactions resulting from allylic branching of the C-2 substituent of **3** introduce an additional level of complexity. As illustrated in Fig. 1, the stereogenic center derived from stannanes such as **19** and **23ab** provides a stereochemically reinforcing scenario in **25** (X = CH_3 or OBz) by a minimization of the A(1,3)-strain, which also directs the methine hydrogen into the region near the sulfonyl group of the auxiliary (21, 22).[8,9] This becomes problematic in the nonreinforcing case, **26**. Aside from steric arguments, the allylic oxygen in the benzoate conformer of **25** (X = OBz) is also anticipated to have electronic effects, which favor the nucleophilic character of the olefin. The composite picture for these allylations suggests that the consequences of isopropyl substitution at C-2 in **25** (X and R_1 = CH_3) is less significant than the interaction of the aldehydic hydrogen and toluenesulfonyl moiety in **26**. This aspect is addressed with greater clarity in Fig. 2, where the proximity of reactive centers at C-1 and C-3 in **27** directs the C-2-branched substituent away from the developing chair. Alternatively, the situation in **26** (Fig. 1) projects the aldehydic hydrogen directly under the six-membered transition state and into the neighboring sulfonyl group. Finally, our models have also incorporated the role of α-chirality in the aldehyde. Diagram **28** in Fig. 2 describes a model for Felkin–Anh addition to the carbonyl while maintaining the favorable relationships of asymmetry, as previously described in **25** (23).[10]

Fig. 2. Preferred transition-state arrangements for asymmetric allylation using (*R*,*R*)-**2**.



27 (Ph's of the (*R*,*R*)-auxiliary have been removed for clarity.)



28

Since the feature of chirality in the aldehyde component multiplies the complexity of the reaction twofold, this aspect was first evaluated with the enantiomerically pure (*R*)- and (*S*)-2-methyl-3-hydroxypropanal derivatives, as shown in entries 3 and 4. The influence of α-stereochemistry in the aldehyde accentuated the reinforcing characteristics of the stannane and the (*R*,*R*)-auxiliary through the expected mode of Felkin–Anh addition (entry 3), yielding predominantly the all-*syn* adduct **33**. On the other hand, it was not sufficient to merely coordinate the chirality of the aldehyde with the (*S*,*S*)-auxiliary **2** in entry 4. This example led to a 1.7:1 mixture of diastereomers; and this points out the importance of allylic stereochemistry in the starting stannane. As observed in reactions with achiral aldehydes, the allylic benzoates **23a** and **23b** led to excellent diastereoselectivity in the matched

[8]The energy requirements for the A(1,3)-strain in **25** (X = CH_3) are estimated to be in the range of 0.4–0.7 kcal/mol, compared with the 1,3-H/H interaction. See ref. 21.
[9]Interestingly, the preferred transition state **25** (X = OBz) may present characteristics that resemble the "inside alkoxy effect" proposed by Stork, Houk, and Jäger for allylic ethers and alcohols. See ref. 22.
[10]Factors for the diastereoselectivity of the aldol reaction using boron enolates derived from chiral ethyl ketones pose some related concerns. Some examples include those found in ref. 23.

© 2004 NRC Canada

cases for Felkin–Anh addition (entries 5 and 7). However, it seems sufficient to coordinate the stereochemically reinforcing asymmetry of the allylic benzoate **23a** with **2** (*R*,*R*) for stereocontrolled condensations via the anti-Felkin mode (entry 6).

Our experiments have also evaluated the effect of β-chirality in the aldehyde, as precipitated by our studies toward leucascandrolide A (24). Tabulated by the results of entries 8, 9, and 10, threefold stereodifferentiation was observed. As documented in previous cases, the cooperation of allylic chirality in the stannane with the auxiliary **2** was a dominant feature. However, the resulting stereochemistry of the major adduct does not conform to the expected result of the Evans polar model for reactions of β-alkoxy aldehydes (19). A challenging situation was also presented by the nonracemic β,γ-unsaturated aldehyde (25)[11] used in entries 11, 12, and 13. Epimerization of this sensitive substrate was avoided, and good yields of condensation products were obtained in spite of considerable steric hindrance. Thus, while the anticipated cooperation of the asymmetry of the stannane and **2** remained intact, the nature of the α-substitution in the aldehyde failed to deliver a clear preference for Felkin or anti-Felkin arrangements. More extensive studies will be needed to probe the issues raised by these entries.

Finally, the versatility of this approach is displayed by the functional complexity of the aldehydes used for entries 14, 15, and 16.[12] Our plans recognized the reinforcing characteristics of stannane **23b** and (*R*,*R*)-**2**, as well as the inherent Felkin–Anh face selectivity for the nonracemic epoxy–aldehyde, as shown in entry 14. This situation is remarkably predictable, as demonstrated by the use of the diastereomeric stannane (*R*)-**23b** in entry 15, which yielded a productive reaction with the (*S*,*S*)-sulfonamide auxiliary and provided for Felkin–Anh addition to give the homoallylic alcohol **50**. The presence of the additional stereocenter at C-4 in the aldehyde (OTIPS of entries 15 and 16) did not impact the stereoselectivity in a major way and demonstrates the flexibility of this methodology for the synthesis of a family of complex diastereoisomers.

Experimental section

General

Infrared spectra were recorded on a Mattson Galaxy 4020 FT-IR instrument with use of an internal standard. Proton and carbon spectra were recorded on a 400 MHz spectrometer in FT mode. Proton chemical shifts are reported in δ, using as a reference the appropriate signal for residual solvent protons, as follows: 7.26 for *d*-chloroform and 7.20 for d_6-benzene. Carbon chemical shifts are reported in δ, using the center peak of the solvent signal as a reference, as follows: 77.0 for $CDCl_3$. Mass spectra were obtained on a Kratos MS80 RFAQQ instrument. Optical rotations were measured using a PerkinElmer 241 polarimeter. Concentration (*c*) is reported as g/100 mL, and temperature is room temperature. Tetrahydrofuran (THF) and diethyl ether (Et_2O) were freshly distilled from sodium benzophenone ketyl. Dimethylformamide (DMF), methylene chloride (CH_2Cl_2), pyridine, oxalyl chloride, triethylamine (Et_3N), benzene, and toluene were distilled from calcium hydride. Ethyl acetate (EtOAc) and hexanes for chromatography were distilled from glass prior to use. Column chromatography was conducted using silica gel 60 (230–400 mesh) from E.M. Science. Precoated glass plates 60F-254 (E. Merck, 0.25 mm and 0.50 mm thickness) were used for analytical and preparative thin layer chromatography (TLC). Reactions were carried out in flame-dried glassware under an inert atmosphere. Elemental analyses were performed by Galbraith Laboratories, Tenn., U.S.A.

General allylation procedure

A 35 mL Schlenk flask was charged with (*S*,*S*) or (*R*,*R*)-*N*,*N*′-bis-*para*-toluenesulfonyl-1,2-diamino-1,2-diphenylethane (0.22 g, 0.42 mmol) and heated to ~90 °C under vacuum (30 Pa). After 12 h, the resulting white solid was cooled to room temperature and CH_2Cl_2 (4 mL) was added under an argon atmosphere. The resultant solution was cooled to 0 °C and treated with fresh boron tribromide (0.42 mL of a 1.0 mol L^{-1} solution in CH_2Cl_2 (Aldrich®), 0.42 mmol). The resulting orange solution was stirred at 0 °C for 10 min, warmed to room temperature, and stirred for 1 h. The solvent and HBr were removed carefully under reduced pressure (0.2 mmHg). The resulting solid was dissolved in CH_2Cl_2 (4 mL), stirred for 10 min, and concentrated under high vacuum. The yellow solid was diluted again with CH_2Cl_2 (4 mL) and cooled to 0 °C, and a solution of the allylstannane (0.47 mmol) in CH_2Cl_2 (~1 mL) was added. The yellow solution was stirred for 16 h at room temperature. After this time the reaction was cooled to –78 °C, and a solution of aldehyde (0.31 mmol) in CH_2Cl_2 (~1 mL) was added. The reaction mixture was stirred at –78 °C for 2 h and then quenched with pH 7 buffer (1 mL). The mixture was allowed to warm to room temperature and diluted with CH_2Cl_2 (15 mL). The organic phase was washed with saturated aqueous $NaHCO_3$ (15 mL). The aqueous phase was extracted with CH_2Cl_2 (15 mL). The combined organic phases were dried ($MgSO_4$), filtered, and concentrated in vacuo. The resulting solid was dissolved in Et_2O and filtered to recover the sparingly soluble bis-sulfonamide chiral auxiliary. The filtrate was concentrated in vacuo, and the residue was purified by flash silica-gel chromatography to yield the mixture of secondary homoallylic alcohols. Diastereomeric ratios were initially determined by the integration of selected proton signals in NMR (400 MHz) spectra. Product ratios were also obtained by analytical HPLC (see notes of Table 1 for conditions). Major diastereomers were purified by flash column chromatography or preparative TLC (silica gel) for full characterization. Solvents for chromatography and data for full characterization of major adducts are included below.

(4*S*,7*S*)-1-(*tert*-Butyldiphenylsilanyloxy)-9-([1,3]dithian-2-yl)-7-methyl-6-methylene-nonan-4-ol (29)

Application of the allylation procedure above led to the

[11]The route for preparation of the nonracemic β,γ-unsaturated aldehyde (entries 11, 12, and 13 of Table 1) has been previously described; see ref. 25 and also ref. 8.

[12]The preparation of optically active aldehydes for entries 14, 15, and 16 has been described in the course of our total synthesis of amphidinolide K. Experimental details are found in the supporting information of ref. 7.

© 2004 NRC Canada

isolation of **29** (entry 1, Table 1) as the major adduct, which was characterized as follows: R_f = 0.52 in 10% EtOAc–hexanes. IR (neat) (cm^{-1}): 3453, 3070, 3043, 2952, 2926, 2850, 1109. ^1H NMR (400 MHz, $CDCl_3$) δ: 7.70–7.67 (m, 4H), 7.45–7.36 (m, 6H), 4.91 (s, 1H), 4.87 (s, 1H), 4.02 (t, *J* = 6.4 Hz, 1H), 3.78–3.69 (m, 3H), 2.95–2.78 (m, 4H), 2.22 (dd, *J* = 3.8, 14.4 Hz, 1H), 2.18 (br s, 1H), 2.14–2.04 (m, 3H), 1.91–1.78 (m, 1H), 1.77–1.46 (m, 8H), 1.06 (s, 9H), 1.04 (d, *J* = 7.2 Hz, 3H). ^{13}C NMR (101 MHz, $CDCl_3$) δ: 150.7, 135.5, 133.7, 129.5, 127.6, 110.9, 69.1, 64.0, 47.7, 42.5, 39.4, 33.7, 33.2, 32.0, 30.4, 28.8, 26.8, 25.9, 20.1, 19.1. HR-MS *m/e* calcd. for $C_{31}H_{44}OS_2Si$ ($[M - H_2O]^+$): 524.2603; found: 524.2607.

(4*R*,7*S*)-1-(*tert*-Butyldiphenylsilanyloxy)-9-([1,3]dithian-2-yl)-7-methyl-6-methylene-nonan-4-ol (30)

Application of the allylation procedure above led to the isolation of **30** (entry 1, Table 1) as the major adduct, which was characterized as follows: R_f = 0.54 in 10% EtOAc–hexanes. IR (neat) (cm^{-1}): 3448, 3071, 3045, 2930, 2856, 2850, 1111. ^1H NMR (400 MHz, $CDCl_3$) δ: 7.70–7.65 (m, 4H), 7.45–7.36 (m, 6H), 4.92 (s, 1H), 4.88 (s, 1H), 4.02 (t, *J* = 6.4 Hz, 1H), 3.80–3.68 (m, 3H), 2.90–2.80 (m, 4H), 2.22 (dd, *J* = 3.8, 14.4 Hz, 1H), 2.17 (br s, 1H), 2.15–2.04 (m, 3H), 1.91–1.80 (m, 1H), 1.76–1.48 (m, 8H), 1.08–1.02 (m, 12H). ^{13}C NMR (101 MHz, $CDCl_3$) δ: 150.8, 135.5, 133.8, 129.6, 127.5, 111.1, 69.0, 64.1, 47.7, 42.8, 38.9, 33.8, 33.3, 32.4, 30.4, 28.8, 26.8, 26.0, 19.7, 19.1. HR-MS *m/e* calcd. for $C_{31}H_{44}OS_2Si$ ($[M - H_2O]^+$): 524.2603; found: 524.2598.

(3*S*,6*S*)-6-Benzoyloxy-9-(*tert*-butyldiphenylsiloxy)-5-methylene-1-phenyl-nonan-3-ol (31)

The allylation procedure above led to alcohol **31** (entry 2, Table 1) as a single diastereoisomer, characterized as follows: R_f = 0.40 in 30% EtOAc–hexanes. $[\alpha]_D$ +17.6 (*c* 3.95, $CHCl_3$). IR (neat) (cm^{-1}): 3493, 3070, 2930, 2856, 1711, 1502, 1273, 1072. ^1H NMR (400 MHz, $CDCl_3$) δ: 8.04 (m, 2H), 7.75–7.15 (m, 18H), 5.32 (dd, *J* = 8.0, 4.5 Hz, 1H), 5.14 (s, 1H), 4.98 (s, 1H), X of ABX (δ: 3.81, m, 1H), 3.71 (m, 2H), 3.24 (br s, 1H), 2.85 (m, 1H), 2.70 (m, 1H), AB of ABX (δ_A: 2.31, δ_B: 2.03, J_{AB} = 13.8 Hz, J_{AX} = 5.7 Hz, J_{BX} = 6.1 Hz, 2H), 2.00–1.60 (m, 6H), 1.06 (s, 9H). ^{13}C NMR (101 MHz, $CDCl_3$) δ: 166.5, 146.1, 142.3, 135.5, 134.7, 133.9, 133.1, 130.1, 129.6, 128.4, 128.3, 127.7, 127.6, 125.7, 113.2, 77.9, 71.6, 63.4, 41.5, 39.0, 32.1, 29.9, 28.7, 26.8, 19.2. HR-MS *m/z* calcd. for $C_{39}H_{46}O_4Si$ ($[M]^+$): 606.3165; found: 606.3119.

(3*R*,6*S*)-6-Benzoyloxy-9-(*tert*-butyldiphenylsiloxy)-5-methylene-1-phenyl-nonan-3-ol (32)

Application of the allylation procedure above led to compound **32** (entry 2, Table 1), which was characterized as follows: R_f = 0.40 in 30% EtOAc–hexanes. $[\alpha]_D$ +17.2 (*c* 3.67, $CHCl_3$). IR (neat) (cm^{-1}): 3491 (br), 3070, 2937, 1961, 1888, 1822, 1712, 1602, 1471. ^1H NMR (400 MHz, $CDCl_3$) δ: 8.05 (m, 2H), 7.75–7.15 (m, 18H), 5.23 (dd, *J* = 8.0, 3.9 Hz, 1H), 5.13 (s, 1H), 4.98 (s, 1H), X of ABX (δ: 4.00, m, 1H), 3.71 (m, 2H), 2.88 (m, 1H), 2.83 (br s, 1H), 2.70 (m, 1H), AB of ABX (δ_A: 2.30, δ_B: 2.22, J_{AB} = 13.8 Hz, J_{AX} = 5.7 Hz, J_{BX} = 6.1 Hz, 2H), 2.00–1.60 (m, 6H), 1.06 (s, 9H). ^{13}C NMR (101 MHz, $CDCl_3$) δ: 166.4, 144.9, 142.3, 135.5, 134.7, 133.8, 133.1, 130.1, 129.6, 128.4, 128.3, 127.7, 127.6, 125.7, 113.4, 75.9, 67.9, 63.3, 42.5, 38.6, 32.4, 30.2, 28.6, 25.8, 19.2. HR-MS *m/z* calcd. for $C_{39}H_{46}O_4Si$ ($[M]^+$): 606.3165; found: 606.3169.

(2*R*,3*R*,6*S*)-1-(*tert*-Butyldiphenylsilanyloxy)-8-([1,3]dithian-2-yl)-2,6-dimethyl-5-methylene-octan-3-ol (33)

Application of the allylation procedure above led to the isolation of **33** (entry 3, Table 1) as the major adduct, which was characterized as follows: R_f = 0.55 in 25% EtOAc–hexanes. IR (neat) (cm^{-1}): 3504, 3071, 3046, 2955, 2932, 2857, 1639, 1428, 1113. ^1H NMR (400 MHz, $CDCl_3$) δ: 7.70–7.65 (m, 4H), 7.46–7.38 (m, 6H), 4.91–4.86 (m, 2H), 4.07–3.99 (m, 2H), 3.74–3.65 (m, 2H), 2.90–2.76 (m, 4H), 2.47 (br s, 1H), 2.20–2.06 (m, 4H), 1.91–1.61 (m, 5H), 1.61–1.51 (m, 1H), 1.07 (s, 9H), 1.04 (d, *J* = 7.2 Hz, 3H), 0.94 (d, *J* = 6.8 Hz, 3H). ^{13}C NMR (101 MHz, $CDCl_3$) δ: 150.8, 135.6, 135.5, 133.3, 133.1, 129.7, 129.7, 127.6, 110.6, 70.9, 67.9, 47.7, 39.5, 39.2, 33.2, 32.2, 30.4, 26.8, 26.0, 20.1, 19.1, 10.3. HR-MS *m/e* calcd. for $C_{31}H_{44}O_1S_2Si$ ($[M - H_2O]^+$): 524.2603; found: 524.2600.

(2*S*,3*R*,6*S*)-1-(*tert*-Butyldiphenylsilanyloxy)-8-([1,3]dithian-2-yl)-2,6-dimethyl-5-methylene-octan-3-ol (35)

Application of the allylation procedure above led to the isolation of **35** (entry 4, Table 1) as the major adduct, which was characterized as follows: R_f = 0.55 in 25% EtOAc–hexanes. IR (neat) (cm^{-1}): 3506, 3071, 3048, 2958, 2931, 2857, 1639, 1427, 1112. ^1H NMR (400 MHz, $CDCl_3$) δ: 7.71–7.66 (m, 4H), 7.46–7.36 (m, 6H), 4.91 (s, 1H), 4.89 (s, 1H), 4.02 (t, *J* = 6.4 Hz, 1H), 3.84–3.76 (m, 1H), 3.79 (dd, *J* = 4.8, 10.0 Hz, 1H), 3.68 (dd, *J* = 6.2, 10.0 Hz, 1H), 2.90–2.76 (m, 4H), 2.31 (dd, *J* = 2.4, 14.8 Hz, 1H), 2.20–2.05 (m, 3H), 1.90–1.62 (m, 5 H), 1.61–1.51 (m, 1H), 1.07 (s, 9H), 1.04 (d, *J* = 6.8 Hz, 3H), 0.96 (d, *J* = 7.2 Hz, 3H). ^{13}C NMR (101 MHz, $CDCl_3$) δ: 151.0, 135.6, 133.2, 130.0, 127.7, 110.6, 72.3, 67.1, 47.7, 40.2, 39.7, 39.3, 33.3, 32.1, 30.4, 26.8, 26.0, 20.2, 19.2, 13.6. HR-MS *m/e* calcd. for $C_{31}H_{44}O_1S_2Si$ ($[M - H_2O]^+$): 524.2603; found: 524.2609.

(2*S*,3*S*,6*R*,9*S*)-6-Benzoyloxy-9-(*tert*-butyldimethylsilyloxy)-1-(*tert*-butyldiphenylsilyloxy)-2-methyl-5-methylene-tridec-11-(*E*)-en-3-ol (37)

The general allylation procedure described above led to the isolation of **37** (entry 5; Table 1) as a single diastereoisomer, as characterized by the following data: R_f = 0.20 in 5% EtOAc–hexanes. $[\alpha]_D$ –24.1 (*c* 1.10, $CHCl_3$). IR (neat) (cm^{-1}): 3503 (br), 3067, 2933, 2860, 1714, 1464, 1273, 1105, 706. ^1H NMR (400 MHz, $CDCl_3$) δ: 8.15 (m, 2H), 7.68 (m, 4H), 7.56 (m, 1H), 7.41 (m, 8H), 5.42 (m, 2H), 5.33 (m, 1H), 5.15 (s, 1H), 5.01 (s, 1H), 4.10 (m, 1H), 3.70 (m, 3H), 3.36 (d, *J* = 2.4 Hz, 1H), 2.29 (dd, A of ABX, J_{AB} = 14.2 Hz, J_{AX} = 4.1 Hz, 1H), 2.22 (dd, B of ABX, J_{BA} = 14.2 Hz, J_{BX} = 9.2 Hz, 1H), 2.14 (app t, *J* = 5.7 Hz, 2H), 1.90 (m, 1H), 1.79 (m, 1H), 1.63 (d, *J* = 5.1 Hz, 3H), 1.62 (m, 1H), 1.48 (m, 1H), 1.06 (s, 9H), 0.96 (d, *J* = 7.0 Hz, 3H), 0.88 (s, 9H), 0.04 (s, 3H), 0.03 (s, 3H). ^{13}C NMR (101 MHz, $CDCl_3$) δ: 166.1, 146.0, 135.7, 135.6, 133.0, 130.3, 129.7, 129.5, 128.3, 127.7, 127.5, 127.4, 112.8, 77.7, 73.0, 71.9, 68.0, 40.4, 39.5, 38.2, 32.5, 29.1, 26.9, 25.9, 19.2, 18.0, 10.5, –4.4, –4.6. HR-MS (FAB, NBA)

© 2004 NRC Canada

m/*z* calcd. for $C_{44}H_{65}O_5Si_2$ ([M + H]$^+$): 729.4371; found: 729.4363.

(2*S*,3*R*,6*S*)-6-Benzoyloxy-1,9-bis-(*tert*-butyldiphenylsilyloxy)-2-methyl-5-methylene-nonan-3-ol (38)

The allylation procedure above led to the isolation of **38** (entry 6, Table 1) as a single diastereoisomer, characterized as follows: R_f = 0.45 in 50% EtOAc–hexanes. $[\alpha]_D$ +22.3 (*c* 2.80, $CHCl_3$). IR (neat) (cm^{-1}): 3504 (br), 3070, 2957, 2930, 2856, 1709, 1427, 1273, 1111, 702. ^{1}H NMR (400 MHz, $CDCl_3$) δ: 8.05 (d, *J* = 7.2 Hz, 2H), 7.74–7.35 (m, 23H), 5.41 (dd, *J* = 7.5, 4.8 Hz, 1H), 5.18 (9s, 1H), 5.06 (s, 1H), 3.86 (m, 1H), 3.72 (m, 4H), 3.63 (br s, 1H), 2.44 (dd, A of ABX, J_{AB} = 14.2 Hz, J_{AX} = 1.9 Hz, 1H), 2.14 (dd, B of ABX, J_{BA} = 14.2 Hz, J_{BX} = 10.0 Hz, 1H), 1.90 (m, 3H), 1.70 (m, 2H), 1.07 (s, 9H), 0.98 (d, *J* = 7.0 Hz, 3H). ^{13}C NMR (101 MHz, $CDCl_3$) δ: 166.2, 146.0, 135.6, 135.5, 133.9, 133.8, 133.4, 133.0, 130.3, 129.6, 129.5, 129.5′, 128.4, 127.7, 127.6, 113.2, 77.7, 74.4, 66.9, 63.5, 40.5, 38.3, 29.8, 28.7, 26.8, 19.1, 13.7. HR-MS (FAB, NBA, Na$^+$) *m*/*z* calcd. for $C_{50}H_{62}O_5Si_2Na$ ([M + Na]$^+$): 821.4034; found: 821.4039.

(2*S*,3*R*,6*S*)-6-Benzoyloxy-2,9-bis-(*tert*-butyldiphenylsilyloxy)-5-methylene-nonan-3-ol (39)

The allylation procedure above led to the isolation of **39** (entry 7, Table 1) as a single diastereoisomer, characterized as follows: R_f = 0.45 in 10% EtOAc–hexanes. $[\alpha]_D$ +9.5 (*c* 1.84, $CHCl_3$). IR (neat) (cm^{-1}): 3489 (br), 3070, 2932, 2858, 1718, 1427, 1271, 1109, 702. ^{1}H NMR (400 MHz, $CDCl_3$) δ: 8.04 (d, *J* = 7.2 Hz, 2H), 7.68 (m, 8H), 7.56 (m, 1H), 7.40 (m, 14H), 5.39 (t, *J* = 6.4 Hz, 1H), 5.13 (s, 1H), 4.94 (s, 1H), 3.86 (m, 1H), 3.78 (m, 1H), 3.69 (app t, *J* = 6.1 Hz, 2H), 2.77 (br s, 1H), 2.34 (dd, A of ABX, J_{AB} = 14.6 Hz, J_{AX} = 3.0 Hz, 1H), 2.08 (dd, B of ABX, J_{BA} = 14.6 Hz, J_{BX} = 9.6 Hz, 1H), 1.86 (m, 2H), 1.64 (m, 2H), 1.08 (s, 9H), 1.06 (s, 9H). ^{13}C NMR (101 MHz, $CDCl_3$) δ: 166.0, 145.1, 135.8, 135.5, 134.3, 133.9, 133.6, 132.9, 130.3, 129.7, 129.6, 128.4, 127.7, 127.5, 113.4, 77.6, 74.7, 72.4, 63.5, 35.5, 29.6, 28.6, 27.0, 26.9, 19.3, 19.2, 17.7. MS (CI, NH_3) *m*/*z* (relative intensity) 606 (25), 349 (42),302 (47), 235 (56). HR-MS *m*/*z* calcd. for $C_{45}H_{51}O_5Si_2$ ([M – *t*-Bu]$^+$): 727.3295; found: 727.3252.

(2*R*,5*S*)-7-(*tert*-Butyldiphenylsilanyloxy)-1-{(2*S*,6*R*)-6-[2-(4-methoxy-benzyloxy)-ethyl]-4-methylene-tetrahydro-pyran-2-yl}-5-methyl-4-methylene-heptan-2-ol (40)

Application of the allylation procedure above led to the isolation of **40** (entry 8, Table 1) as the major adduct, which was characterized as follows: R_f = 0.45 in 25% EtOAc–hexanes. IR (neat) (cm^{-1}): 3496, 3070, 2932, 2857, 1649, 1610, 1513, 1427, 1248, 1111. ^{1}H NMR (400 MHz, $CDCl_3$) δ: 7.70–7.65 (m, 4H), 7.44–7.35 (m, 6H), 7.25 (d, *J* = 8.6 Hz, 2H), 6.87 (d, *J* = 8.6 Hz, 2H), 4.83 (s, 1H), 4.80 (s, 1H), 4.71 (app s, 2H), 4.45–4.39 (m, 2H), 4.00 (m, 1H), 3.80 (s, 3H), 3.71–3.63 (m, 2H), 3.67 (br s, 1H), 3.55–3.48 (m, 4H), 2.35 (ddt, *J* = 6.8, 6.8, 6.8 Hz, 1H), 2.27–2.14 (m, 3H), 2.08 (dd, *J* = 6.4, 14.8 Hz, 1H), 2.00–1.93 (m, 2H), 1.88–1.48 (m, 6H), 1.05 (s, 9H), 0.99 (d, *J* = 6.8 Hz, 3H). ^{13}C NMR (101 MHz, $CDCl_3$) δ: 159.1, 151.3, 143.8, 135.6, 134.7, 130.6, 129.5, 129.3, 127.6, 113.8, 110.1, 108.9, 79.2, 76.1, 72.7, 70.0, 66.5, 62.1, 55.2, 42.5, 42.3, 41.1, 40.6, 38.4, 36.3, 36.1, 26.9, 19.8, 19.2. HR-MS *m*/*e* calcd. for $C_{37}H_{47}O_5Si$ ([M – *t*-Bu]$^+$): 599.3193; found: 599.3193.

(2*S*,5*R*)-7-(*tert*-Butyldiphenylsilanyloxy)-1-{(2*S*,6*R*)-6-[2-(4-methoxy-benzyloxy)-ethyl]-4-methylene-tetrahydro-pyran-2-yl}-5-methyl-4-methylene-heptan-2-ol (43)

Application of the allylation procedure above led to the isolation of **43** (entry 9, Table 1) as the major adduct, which was characterized as follows: R_f = 0.47 in 25% EtOAc–hexanes. IR (neat) (cm^{-1}): 3477, 3071, 2932, 2857, 1646, 1603, 1513, 1425, 1248, 1111. ^{1}H NMR (400 MHz, $CDCl_3$) δ: 7.70–7.68 (m, 4H), 7.45–7.35 (m, 6H), 7.26 (d, *J* = 8.8 Hz, 2H), 6.89 (d, *J* = 8.8 Hz, 2H), 4.85 (s, 1H), 4.81 (s, 1H), 4.72 (app s, 2H), 4.44–4.37 (m, 2H), 4.06 (m 1H), 3.80 (s, 3H), 3.72–3.65 (m, 2H), 3.63–3.45 (m, 4H), 2.80 (br s, 1H), 2.36 (ddt, *J* = 6.8, 6.8, 6.8 Hz, 1H), 2.25–1.52 (m, 12H), 1.07 (s, 9H), 1.00 (d, *J* = 6.8 Hz, 3H). ^{13}C NMR (101 MHz, $CDCl_3$) δ: 159.1, 151.2, 144.3, 135.5, 134.0, 130.6, 129.5, 129.2, 127.6, 113.8, 110.3, 108.7, 76.0, 75.8, 72.6, 66.6, 66.4, 62.1, 55.2, 42.5, 42.1, 40.7, 40.5, 38.2, 36.4, 36.1, 26.9, 20.0, 19.2. HR-MS *m*/*e* calcd. for $C_{37}H_{47}O_5Si$ ([M – *t*-Bu]$^+$): 599.3193; found: 599.3201.

(2*R*,5*S*)-7-([1,3]Dithian-2-yl)-1-{(2*S*,6*R*)-6-[2-(4-methoxy-benzyloxy)-ethyl]-4-methylene-tetrahydro-pyran-2-yl}-5-methyl-4-methylene-heptan-2-ol (44)

The same procedure for allylation was applied here and led to the isolation of **44** (entry 10, Table 1): R_f = 0.32 in 25% EtOAc–hexanes. IR (neat) (cm^{-1}): 3480, 3070, 2935, 1650, 1607, 1512, 1247, 1095. ^{1}H NMR (400 MHz, $CDCl_3$) δ: 7.25 (d, *J* = 8.6 Hz, 2H), 6.88 (d, *J* = 8.6 Hz, 2H), 4.86 (s, 1H), 4.83 (s, 1H), 4.71 (app s, 2H), 4.45–4.39 (m, 2H), 4.04–3.98 (m, 2H), 3.80 (s, 3H), 3.58–3.50 (m, 4H), 2.90–2.78 (m, 4H), 2.27–2.05 (m, 6H), 2.02–1.92 (m, 2H), 1.89–1.50 (m, 10H), 1.03 (d, *J* = 6.8 Hz, 3H). ^{13}C NMR (101 MHz, $CDCl_3$) δ: 159.1, 150.5, 143.7, 130.5, 129.3, 113.7, 110.7, 109.0, 79.4, 76.0, 72.7, 70.1, 66.4, 55.2, 47.8, 42.3, 42.1, 41.0, 40.5, 39.4, 36.2, 33.1, 32.3, 30.4, 26.0, 20.0. HR-MS *m*/*e* calcd. for $C_{29}H_{44}O_4S_2Na$ ([M + Na]$^+$): 543.2591; found: 543.2581.

2,2-Dimethylpropionic acid (4*R*,5*R*,8*S*)-(*E*)-4,10-bis-(*tert*-butyldiphenylsilanyloxy)-5-hydroxy-2,8-dimethyl-7-methylene-dec-2-enyl ester (46)

Application of the allylation procedure above led to the isolation of **46** (entry 11, Table 1) as the major adduct, which was characterized as follows: R_f = 0.68 in 33% EtOAc–hexanes. IR (neat) (cm^{-1}): 3445, 3071, 3049, 2959, 2931, 2857, 1731, 1428, 1282, 1112. ^{1}H NMR (400 MHz, $CDCl_3$) δ: 7.73–7.63 (m, 8H), 7.45–7.30 (m, 12H), 5.38 (d, *J* = 9.6 Hz, 1H), 4.81 (s, 1H), 4.80 (s, 1H), 4.27 (dd, *J* = 6.4, 9.2 Hz, 1H), 4.14 (s, 2H), 3.73–3.60 (m, 3H), 2.54 (d, *J* = 3.6 Hz, 1H), 2.33 (ddt, *J* = 6.8, 6.8, 6.8 Hz, 1H), 2.16 (m, 1H), 1.94 (dd, *J* = 9.6, 14.8 Hz, 1H), 1.79–1.70 (m, 1H), 1.56–1.46 (m, 1H), 1.15 (s, 9H), 1.07–1.02 (m, 21 H), 0.94 (d, *J* = 6.8 Hz, 3H). ^{13}C NMR (101 MHz, $CDCl_3$) δ: 178.0, 150.7, 135.9, 135.8, 135.5, 134.0, 133.6, 129.8, 129.6, 129.5, 127.7, 127.6, 127.4, 126.0, 72.9, 72.6, 68.8, 62.1, 38.8, 38.1, 36.7, 35.8, 27.2, 27.0, 26.9, 19.9, 19.3, 19.2,

© 2004 NRC Canada

14.2. HR-MS *m/e* calcd. for $C_{46}H_{59}O_5Si$ ([M – *t*-Bu]$^+$): 747.3901; found: 747.3909.

2,2-Dimethylpropionic acid (4*R*,5*S*,8*R*)-(*E*)-4,10-bis-(*tert*-butyldiphenylsilanyloxy)-5-hydroxy-2,8-dimethyl-7-methylene-dec-2-enyl ester (47)

Application of the allylation procedure above led to the isolation of **47** (entry 12, Table 1) as the major adduct, which was characterized as follows: R_f = 0.68 in 33% EtOAc–hexanes. IR (neat) (cm^{-1}): 3513, 3071, 3047, 2959, 2930, 2857, 1731, 1427, 1282, 1149, 1112. ^{1}H NMR (400 MHz, $CDCl_3$) δ: 7.70–7.60 (m, 8H), 7.45–7.34 (m, 12H), 5.52 (d, *J* = 9.2 Hz, 1H), 4.74 (s, 1H), 4.66 (s, 1H), 4.32 (dd, *J* = 4.0, 9.6 Hz, 1H), 4.26 (s, 2H), 3.8 (m, 1H), 3.70–3.60 (m, 2H), 2.28 (br s, 1H), 2.28–2.10 (m, 2H), 2.02 (dd, *J* = 8.8, 15.2 Hz, 1H), 1.74–1.66 (m, 1H), 1.52–1.43 (m, 1H), 1.17 (s, 9H), 1.05–1.02 (m, 21 H), 0.90 (d, *J* = 6.8 Hz, 3H). ^{13}C NMR (101 MHz, $CDCl_3$) δ: 178.0, 151.1, 135.9, 135.9, 135.5, 133.4, 134.0, 133.4, 129.7, 129.6, 129.5, 127.6, 127.6, 127.4, 126.8, 73.6, 73.5, 68.5, 62.1, 38.8, 38.1, 37.3, 35.5, 27.2, 27.0, 26.9, 20.0, 19.4, 19.2, 14.1. HR-MS *m/e* calcd. for $C_{46}H_{59}O_5Si$ ([M – *t*-Bu]$^+$): 747.3901; found: 747.3897.

2,2-Dimethylpropionic acid (4*R*,5*R*,8*S*)-(*E*)-4-(*tert*-butyldiphenylsilanyloxy)-5-hydroxy-10-([1,3]dithian-2-yl)-2,8-dimethyl-7-methylene-dec-2-enyl ester (48)

The same procedure for allylation was applied here and led to the isolation of **48** (entry 13, Table 1): R_f = 0.59 in 33% EtOAc–hexanes. IR (neat) (cm^{-1}): 3551, 3071, 2952, 2929, 2852, 1728, 1432, 1275, 1145, 1110. ^{1}H NMR (400 MHz, $CDCl_3$) δ: 7.69–7.62 (m, 4H), 7.43–7.32 (m, 6H), 5.39 (d, *J* = 9.6 Hz, 1H), 4.85 (s, 1H), 4.84 (s, 1H), 4.29 (dd, *J* = 6.2, 9.4 Hz, 1H), 4.16 (s, 2H), 4.00 (t, *J* = 6.8 Hz, 1H), 3.67 (m, 1H), 2.90–2.76 (m. 4H), 2.53 (d, *J* = 4 Hz, 1H), 2.21–2.05 (m, 3H), 1.95 (dd, *J* = 9.6, 15.2 Hz, 1H), 1.90–1.80 (m, 1H), 1.76–1.60 (m, 2H), 1.55–1.46 (m, 1H), 1.16 (s, 9H), 1.07 (s, 3H), 1.05 (s, 9H), 0.98 (d, *J* = 6.8 Hz, 3H). ^{13}C NMR (101 MHz, $CDCl_3$) δ: 178.0, 150.5, 136.0, 136.0, 135.9, 134.1, 133.7, 133.5, 129.8, 129.7, 127.7, 127.4, 126.7, 73.8, 73.4, 68.5, 47.8, 39.2, 38.8, 37.0, 33.2, 32.1, 30.4, 27.1, 27.0, 26.0, 20.0, 19.4, 14.1. HR-MS *m/e* calcd. for $C_{34}H_{47}O_4S_2Si$ ([M – *t*-Bu]$^+$): 611.2685; found: 611.2690.

(4*R*,5*R*,6*S*,7*R*,10*S*,13*S*)-10-Benzoyloxy-13-(*tert*-butyldimethylsiloxy)-5,6-epoxy-9-methylene-2-tributylstannyl-4-triisopropylsiloxy-heptadeca-1,15-(*E*)-dien-7-ol (49)

The allylation procedure above led to the isolation of **49** (entry 14, Table 1) as a single diastereoisomer, characterized as follows: R_f = 0.20 in 5% EtOAc–hexanes. $[\alpha]_D$ +6.69 (*c* 1.44, $CHCl_3$). IR (neat) (cm^{-1}): 3489 (br), 2955, 2928, 2854, 1720, 1462, 1271, 1113, 1068. ^{1}H NMR (400 MHz, $CDCl_3$) δ: 8.04 (d, *J* = 7.2 Hz, 2H), 7.57 (m, 1H), 7.44 (m, 2H), 5.81 (s, 1H), 5.50–5.30 (m, 3H), 5.23 (d, *J* = 2.2 Hz, 1H), 5.18 (s, 1H), 5.06 (s, 1H), 4.12 (m, 1H), 3.90 (m, 1H), 3.69 (dddd, *J* = 5.9, 5.9, 5.7, 5.3 Hz, 1H), 3.15 (dd, *J* = 4.0, 2.0 Hz, 1H), 3.05 (dd, *J* = 2.2, 2.1 Hz, 1H), 2.85 (d, *J* = 2.0 Hz, 1H), 2.71 (dd, *J* = 13.7, 4.2 Hz, 1H), 2.50–2.40 (m, 2H), 2.18 (dd, *J* = 14.2, 9.4 Hz, 1H), 2.14 (m, 2H), 1.84 (m, 2H), 1.62 (d, *J* = 5.9 Hz, 3H), 1.59–1.44 (m, 8H), 1.32 (m, 6H), 1.06 (m, 21H), 0.94–0.86 (m, 24H), 0.04 (s, 6H). ^{13}C NMR (101 MHz, $CDCl_3$) δ: 166.2, 149.9, 144.8, 133.0, 130.2, 129.6, 128.3, 127.5, 127.4, 113.7, 77.7, 71.8, 69.5, 67.9, 57.9, 56.2, 48.5, 40.5, 37.6, 32.4, 29.0, 27.4, 25.9, 18.1, 18.0, 13.6, 12.5, 9.6, –4.4, –4.5. HR-MS (FAB, NBA, Na$^+$) *m/z* calcd. for $C_{52}H_{94}O_6Si_2Sn^{120}Na$ ([M + Na]$^+$): 1013.5509; found: 1013.5549. Anal. calcd. for $C_{52}H_{94}O_6Si_2Sn$ (%): C 63.08, H 9.57; found: C 62.93, H 9.42.

(4*R*,5*S*,6*R*,7*S*,10*R*,13*S*)-10-Benzoyloxy-13-(*tert*-butyldimethylsiloxy)-5,6-epoxy-9-methylene-2-tributylstannyl-4-triisopropylsiloxy-heptadeca-1,15-(*E*)-dien-7-ol (50)

The allylation procedure above led to the isolation of **50** (entry 15, Table 1) as a single diastereoisomer, characterized as follows: R_f = 0.15 in 5% EtOAc–hexanes. $[\alpha]_D$ –25.5 (*c* 2.25, $CHCl_3$). IR (neat) (cm^{-1}): 3483 (br), 2928, 2666, 1720, 1462, 1271, 1113. ^{1}H NMR (400 MHz, $CDCl_3$) δ: 8.03 (m, 2H), 7.56 (m, 1H), 7.44 (m, 2H), 5.81 (m, 1H), 5.41 (m, 1H), 5.34 (dd, *J* = 7.8, 4.9 Hz, 1H), 5.25 (d, *J* = 2.7 Hz, 1H), 5.17 (s, 1H), 5.05 (s, 1H), 3.86 (m, 1H), 3.75–3.66 (m, 2H), 3.01 (dd, *J* = 3.9, 2.1 Hz, 1H), 2.94 (dd, *J* = 3.9, 2.1 Hz, 1H), 2.89 (d, *J* = 1.7 Hz, 1H), 2.59 (m, 2H), 2.39 (dd, *J* = 14.5, 2.2 Hz, 1H), 2.16–2.10 (m, 3H), 1.89 (m, 1H), 1.75 (m, 1H), 1.63 (d, *J* = 5.3 Hz, 3H), 1.61 (m, 1H), 1.52–1.40 (m, 7H), 1.31 (m, 6H), 1.12–1.02 (m, 21H), 0.98–0.84 (m, 2H), 0.04 (s, 3H), 0.03 (s, 3H). ^{13}C NMR (101 MHz, $CDCl_3$) δ: 166.2, 149.8, 144.9, 133.0, 130.2, 129.6, 129.1, 128.3, 127.4, 127.3, 113.6, 77.8, 71.9, 71.7, 70.0, 59.4, 58.8, 47.3, 40.4, 37.1, 32.5, 29.1, 27.4, 25.9, 18.2, 17.9, 13.7, 12.6, 9.6, –4.4, –4.6.

(4*S*,5*S*,6*R*,7*S*,10*R*,13*S*)-10-Benzoyloxy-13-(*tert*-butyldimethylsiloxy)-5,6-epoxy-9-methylene-2-tributylstannyl-4-triisopropylsiloxy-heptadeca-1,15-(*E*)-dien-7-ol (51)

The allylation procedure above led to the isolation of **51** (entry 16, Table 1) as a single diastereoisomer, characterized as follows: R_f = 0.20 in 5% EtOAc–hexanes. $[\alpha]_D$ –11.2 (*c* 1.35, $CHCl_3$). IR (neat) (cm^{-1}): 3475 (br), 2955, 2928, 2866, 1722, 1462, 1271, 1116. ^{1}H NMR (400 MHz, $CDCl_3$) δ: 8.04 (m, 2H), 7.57 (m, 1H), 7.44 (m, 2H), 5.81 (s, 1H), 5.42 (m, 2H), 5.35 (m, 1H), 5.24 (d, *J* = 2.2 Hz, 1H), 5.18 (s, 1H), 5.06 (s, 1H), 4.12 (m, 1H), 3.90 (m, 1H), 3.69 (dddd, *J* = 5.9, 5.9, 5.7, 5.3 Hz, 1H), 3.15 (dd, *J* = 4.0, 2.1 Hz, 1H), 3.05 (dd, *J* = 2.4, 2.2 Hz, 1H), 2.87 (d, *J* = 1.9 Hz, 1H), 2.71 (dd, *J* = 13.8, 4.3 Hz, 1H), 2.46 (dd, *J* = 19.0, 9.8 Hz, 1H), 2.44 (dd, *J* = 14.2, 3.1 Hz, 1H), 2.18 (dd, *J* = 14.2, 9.5 Hz, 1H), 2.14 (dd, *J* = 5.7, 5.7 Hz, 2H), 1.90 (m, 1H), 1.76 (m, 1H), 1.63 (d, *J* = 5.2 Hz, 3H), 1.61 (m, 1H), 1.50 (m, 7H), 1.30 (m, 6H), 1.24 (m, 21H), 0.90 (m, 24H), 0.30 (s, 6H). ^{13}C NMR (101 MHz, $CDCl_3$) δ: 166.2, 149.9, 144.8, 133.0, 130.2, 129.6, 128.3, 127.4, 127.3, 113.7, 77.7, 77.2, 71.9, 69.5, 67.9, 57.9, 56.2, 48.5, 40.4, 37.5, 32.4, 29.0, 27.4, 25.8, 18.0, 17.9, 13.6, 12.5, 9.6, –4.4, –4.5. MS (FAB, NBA, Na$^+$) *m/z* ([M – *t*-Bu]$^+$): 933.

Conclusion

In summary, a powerfully convergent strategy for the diastereoselective synthesis of homoallylic alcohols has been described. Our asymmetric allylation reaction incorporates three elements of stereodifferentiation. Optimal results are provided when adjacent asymmetry in the starting stannane

© 2004 NRC Canada

is stereochemically reinforcing with respect to chirality of the bis-sulfonamide auxiliary. Products featuring 1,4-*syn*-stereochemistry are favored. The incorporation of α- or β-stereogenecity in the starting aldehyde has been documented. The diastereofacial selectivity of reactions with α-substituted aldehydes is predicted by the Felkin–Anh model. Overall, this methodology permits the construction of complex arrangements of stereochemistry and functionality as a useful tool for the synthesis of complex natural products.

Acknowledgements

We gratefully acknowledge the National Institutes of Health (GM-41560 and GM-42897) for generous support of this work.

References

1. For a general review: Y. Yamamoto and N. Asao. Chem. Rev. **93**, 2207 (1993).
2. (*a*) W.R. Roush. Comprehensive organic synthesis. Vol. 2. *Edited by* B.A. Trost and I. Fleming. Pergamon Press, Oxford. 1991; (*b*) P.V. Ramachandran. Aldrichimica Acta, **35**, 23 (2002).
3. S.R. Chemler and W.R. Roush. Recent applications of the allylation reaction to the synthesis of natural products. *In* Modern carbonyl chemistry. *Edited by* J. Otera. Wiley-VCH, Weinheim, Germany. 2000.
4. E.J. Corey, C.-M. Yu, and S.S. Kim. J. Am. Chem. Soc. **111**, 5495 (1989).
5. E.J. Corey, C.-M. Yu, and D.-H. Lee. J. Am. Chem. Soc. **112**, 878 (1990).
6. D.R. Williams, D.A. Brooks, and M.A. Berliner. J. Am. Chem. Soc. **121**, 4924 (1999).
7. D.R. Williams and K.G. Meyer. J. Am. Chem. Soc. **123**, 765 (2001).
8. D.R. Williams, A.A. Kiryanov, U. Emde, M.P. Clark, M.A. Berliner, and J.T. Reeves. Angew. Chem. Int. Ed. **42**, 1258 (2003).
9. D.R. Williams, D.A. Brooks, K.G. Meyer, and M.P. Clark. Tetrahedron Lett. **39**, 7251 (1998).
10. Y. Nishigaichi, H. Kuramoto, and A. Takuwa. Tetrahedron Lett. **36**, 3353 (1995).
11. R.J. Maguire, J. Mulzer, and J.W. Bats. J. Org. Chem. **61**, 6936 (1996); (*b*) R.J. Maguire, J. Mulzer, and J.W. Bats. Tetrahedron Lett. **37**, 5487 (1996).
12. D.R. Williams, W.S. Kissel, and J.J. Li. Tetrahedron Lett. **39**, 8593 (1998).
13. B.M. Trost, T.A. Grese, and D.M.T. Chan. J. Am. Chem. Soc. **113**, 7350 (1991).
14. E. Piers, J.M. Chong, K. Gustafson, and R.J. Andersen. Can. J. Chem. **62**, 1 (1984).
15. Sharpless asymmetric epoxidations proceeded with >97% de; see: Y. Gao, R.M. Hanson, J.M. Klunder, S.Y. Ko, H. Masamune, and K.B. Sharpless. J. Am. Chem. Soc. **109**, 5765 (1987).
16. S.D. Burke, J.L. Buchanan, and J.D. Rovin. Tetrahedron Lett. **32**, 3961 (1991).
17. B.M. Trost and S.A. King. J. Am. Chem. Soc. **112**, 408 (1990).
18. (*a*) I. Ohtani, T. Kusumi, Y. Kashman, and H. Kakisawa. J. Am. Chem. Soc. **113**, 4092 (1991); (*b*) J.A. Dale and H.S. Mosher. J. Am. Chem. Soc. **95**, 512 (1973).
19. D.A. Evans, M.J. Dart, J.L. Duffy, and M.G. Yang. J. Am. Chem. Soc. **118**, 4322 (1996).
20. For a related discussion: W.R. Roush and L. Banfi. J. Am. Chem. Soc. **110**, 3979 (1988).
21. R. W. Hoffmann. Chem. Rev. **89**, 1841 (1989).
22. For a leading reference: J. Haller, T. Strassner, and K.N. Houk. J. Am. Chem. Soc. **119**, 8031 (1997).
23. (*a*) D.A. Evans, H.P. Ng, J.S. Clark, and D.L. Rieger. Tetrahedron, **48**, 2127 (1992); (*b*) I. Paterson. Pure Appl. Chem. **64**, 1821 (1992); (*c*) D.A. Evans and M.A. Calter. Tetrahedron Lett. **34**, 6871 (1993); (*d*) I. Paterson, D.J. Wallace, and S.M. Velázquez. Tetrahedron Lett. **35**, 9083 (1994).
24. D.R. Williams, S.V. Plummer, and S. Patnaik. Angew. Chem. Int. Ed. **42**, 3934 (2003).
25. D. R. Williams, M. P. Clark, U. Emde, and M. A. Berliner. Org. Lett. **2**, 3023 (2000).

© 2004 NRC Canada

The Diels–Alder reactions of quinone imine ketals[1]

Scott C. Banfield and Michael A. Kerr

Abstract: *N*-Benzoyl- and *N*-arylsulfonyl-*p*-benzoquinone-mono-imine ketals (QIKs) undergo smooth Diels–Alder cycloadditions with typical 1,3-butadienes to yield the expected *endo* adducts. Treatment with catalytic acid rapidly converts the adducts to dihydronaphthalenes. The *N*-benzoyl derivatives require high pressures for cycloadditions while the *N*-tosyl and *N*-nosyl derivatives proceed under thermal (ambient pressure) conditions. In all cases the cycloadditions are completely regioselective.

Key words: Diels–Alder, quinone imine ketal, hyperbaric chemistry.

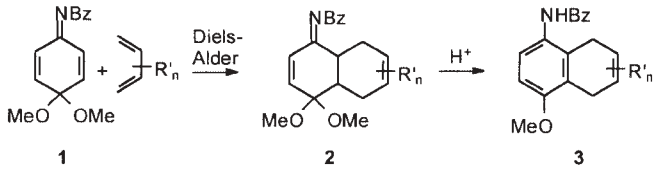
Résumé : Les cétals des *N*-benzoyl- et *N*-arylsulfonyl-*p*-benzoquinonemonoimines donnent facilement des réactions de cycloaddition de Diels–Alder avec les buta-1,3-dienes typiques et ils conduisent à la formation des adduits *endo* attendus. Le traitement avec une quantité catalytique d'acide provoque une transposition des adduits en dihydronaphtalènes. Les dérivés *N*-benzoylés nécessitent de hautes pressions pour donner les réactions de cycloaddition alors que les dérivés *N*-tosyl- et *N*-nosyl- se produisent à des conditions de température et de pression ambiantes. Dans tous les cas, les réactions de cycloadditions sont complètement diastéréosélectives.

Mots clés : Diels–Alder, cétal de la quinoneimine, chimie hyperbarique.

Introduction

The synthetic utility of the Diels–Alder reaction is questioned by no one. Its versatile ability to form a cyclohexene ring (with up to four new stereocenters) with exquisite control is well documented (1). So much work has been done to expand our understanding of this process over the years that one may now plan a complex synthesis involving a Diels–Alder reaction with a high degree of confidence for success. Even though the Diels–Alder reaction is a "mature reaction" in terms of its development, many opportunities exist to expand its utility. These include new dienophiles, dienes, and catalysts. Such developments allow the synthetic chemist the opportunity to tackle new and exciting challenges. Several years ago, we reported the participation of a benzoylated quinone imine ketal **1** in [4+2]-cycloadditions at ultra-high pressures (Scheme 1) (2). Prior to that work, the only report of such reactivity was made by Coutts et al. (3), in which several examples of sulphonylated quinone imine ketals as dienophiles were reported, although Swenton and coworkers (4) have explored the otherwise rich chemistry of benzoylated quinone imine ketals. The stable cycloadducts **2** could be isolated and purified or treated with acid to yield a dihydronaphthalene **3**. Subsequent to our initial report, we disclosed the synthesis of the tricyclic ergot skeleton using this reaction (5). This in turn inspired us to explore a general strategy for the synthesis of 5-methoxy indoles, which we recently reported in preliminary form (6). In the present paper we report the full details and an expanded scope of the hyperbaric Diels–Alder reactions of *N*-benzoyl quinone imine ketals, as well as a more generally usable and scalable thermal variant involving the *N*-arylsulphonyl counterparts.

Scheme 1.



Results and discussion

Synthesis of quinone imine ketals

The *N*-benzoyl quinone imine ketals **5a–d** were prepared by a simplification of the anodic oxidation method reported by Swenton et al. (4*a*) (Table 1). The oxidation is technically simple and is carried out in an open beaker on a stir plate with a platinum mesh electrode at a constant current of 0.3 A. Although other *N*-acyl derivatives (pivaloyl, acetyl, *tert*-butoxycarbonyl) were considered, the low reactivity of these compounds in a Diels–Alder sense, compared with the *N*-arylsulphonyl compounds (vide infra), led us to pursue the *N*-tosyl and *N*-nosyl derivatives instead.

While anodic oxidation yielded the desired products in the preparation of the *N*-arylsulphonyl QIKs, the yields were less than optimal and the reactions somewhat messy. We turned to oxidation with phenyliodo bis acetate (PIBA) (7). The preparation of QIKs by oxidation with this reagent has

Received 8 July 2003. Published on the NRC Research Press Web site at http://canjchem.nrc.ca on 9 January 2004.

This paper is dedicated to Ed Piers who continues to be an inspirational role model to so many.

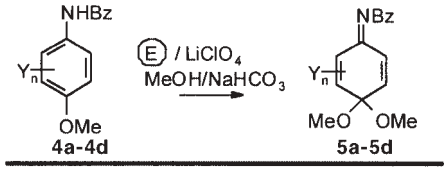
S.C. Banfield and M.A. Kerr.[2] Department of Chemistry, The University of Western Ontario, London, ON N6A 5B7, Canada.

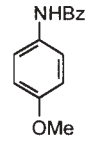
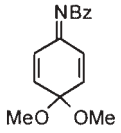
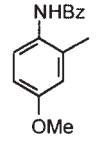
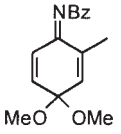
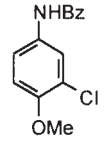
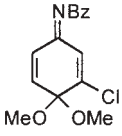
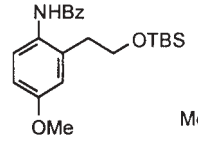
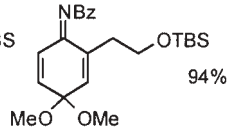
[1]This article is part of a Special Issue dedicated to Professor Ed Piers.

[2]Corresponding author (e-mail: makerr@uwo.ca).

 doi: 10.1139/V03-188 © 2004 NRC Canada

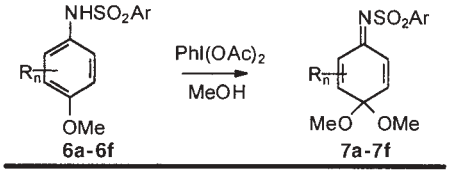
Table 1. Synthesis of *N*-benzoyl quinone imine ketals (QIK).

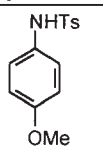
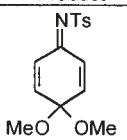
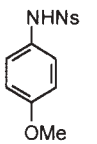
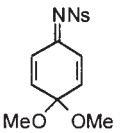
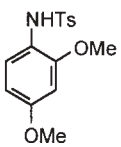
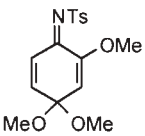
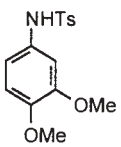
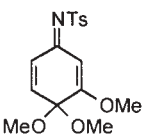
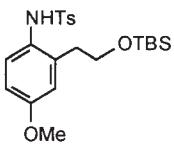
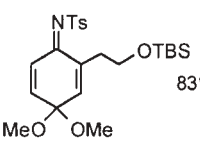
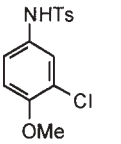
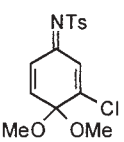


Entry	Anilide	Product	Yield
a			92%
b			96%
c			59%
d			94%

not been reported. Table 2 shows the results for the preparation of a series of *N*-arylsulphonyl QIKs **7a–f** by chemical oxidation of arylsulfonanilides **6a–f**.

Table 2. The synthesis of arylsulfonyl QIKs.



Entry	Anilide	Product	Yield
a			89%
b			74%
c			72%
d			87%
e			83%
f			81%

The Diels–Alder reactivity of QIKs

As expected, the removal of one carbonyl from conjugation with the dienophilic double bond greatly attenuates the dienophilicity of QIKs with respect to the parent *p*-benzoquinones. In fact, when QIKs **5** were subjected to reaction with a variety of 1,3-butadienes at elevated temperatures (150 °C), only decomposition was observed after 3 days. At this stage, high pressures were examined for several reasons, as follows: (*i*) The thermal activation ($\Delta H^{\ddagger}$) can be replaced by entropic activation ($\Delta V^{\ddagger}$) without the problem of thermal decomposition, and (*ii*) it is suspected that much of the low reactivity of these systems stems from the steric encumbrance imposed by the quaternary center adjacent to the reacting π-system, an encumbrance that can be overcome by the use of high pressures (8). In the case of the arylsulfonyl QIKs **7**, the increased electron-withdrawing ability of the tosyl or nosyl groups may overcome the inherent lack of reactivity, and a thermal process may be viable.

A key positive attribute of QIKs as dienophiles resides in the very properties that cause problems with reactivity. The presence of only one LUMO – lowering group on the reacting dienophilic π-bond imparts a degree of regioselectivity often missing in the parent quinones. In addition, the ketal moiety, which is restricted to be essentially orthogonal to the reacting π-systems, all but precludes the transition state A′ leading to the pseudo-*meta* regioisomer B′ (Fig. 1).

High pressure Diels–Alder reactions

The *N*-benzoyl QIK **5a** was subjected to reaction with a series of 5 dienes at 13 kbar (1 bar = 10^5 Pa) at ambient temperature[3] (Table 3). Typically, the reactions took about 7 days to proceed to completion and generally led to clean conversion to the *endo* cycloadducts.[4] These adducts are surprisingly stable to isolation and chromatography, although prolonged exposure to silica gel leads to small conversions to the aromatized species (vide infra). A consideration when using 2,3-dimethylbutadiene (entry d) is competitive polymerization of the diene. Use of a large excess of the diene often resulted in the solidification of the entire reaction mixture. This result is typical of our experiences using dienes that are unsubstituted at both termini of the diene moiety at elevated pressures. The fact that 1-*tert*-butyldimethylsilyloxy-1,3-butadiene (entry e) underwent reaction in higher

[3] This excludes the heating of the sample, which undoubtedly occurs upon compression of the high-pressure apparatus.
[4] The fact that these are *endo* adducts has been confirmed by NOESY experiments and has been published (ref. 2).

© 2004 NRC Canada

Fig. 1. Possible regiochemical outcomes for Diels–Alder reactions.

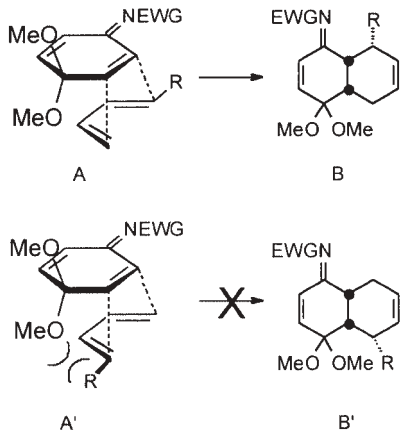
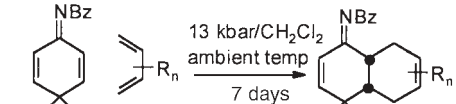
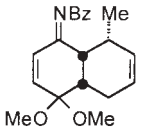
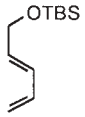
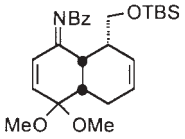
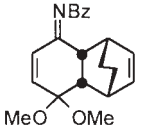
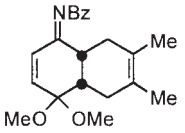
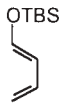
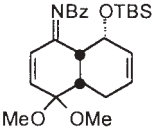


Table 3. Isolation of the initial adducts.



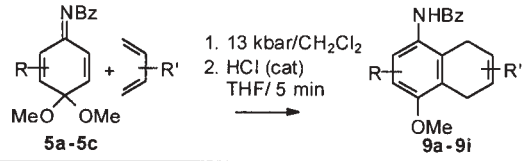
Entry	Diene	Product	Yield
a			89%
b			74%
c			72%
d			87%
e[a]			96%

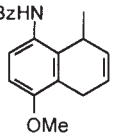
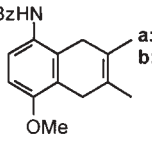
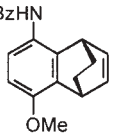
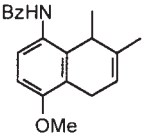
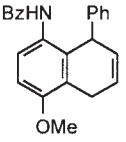
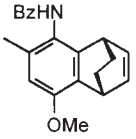
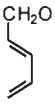
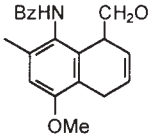
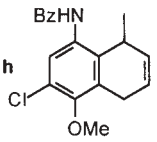
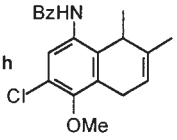
[a] Entry e had a reaction time of 3 days

yield and in less time is not surprising, since it is highly activated by the electron-donating silyloxy substituent.

Of interest to us for the synthesis of alkaloids was the fact that treatment of the adducts with a trace of acid effected the smooth aromatization to a dihydronaphthalene (i.e., **2**→**3** in Scheme 1). Table 4 shows the results of a series of reactions in which the initially formed adduct was isolated and the crude material treated with a drop of concentrated HCl in

Table 4. Hyperbaric Diels–Alder–aromatization results.



Entry	QIK	Diene	Conditions	Product	Yield
a	5a		a: 50 °C/12 h b: r.t/ 5 days		a: 97% b: 93%
b	5a		a: 50 °C/12 h b: r.t/ 7 days		a: 87% b: 91%
c	5a		a: 50 °C/12 h b: r.t/ 5 days		a: 92% b: 89%
d	5a		50 °C/12 h		81%
e	5a		r.t/ 7days		54%
f	5b		50 °C/12 h		92%
g	5b		50 °C/12 h		70%
h	5c		50 °C/12 h		85%
i	5c		50 °C/12 h		90%

THF to effect the formation of the dihydronaphthalene. It is important to note that for some cases in this series of reactions the temperature of the high-pressure reactor was raised

© 2004 NRC Canada

to 50 °C. This relatively minor increase in temperature reduced the reaction times from 7 days to 12 h.

The method of aromatization was also investigated. Mild acid sources such as silica gel were ineffective in promoting the transformation, while a mild Lewis acid such as ytterbium triflate resulted in decomposition. Use of *p*-toluenesulfonic acid resulted in the formation of desired product but also produced the free phenol, possibly because of hydrolysis by the water of hydration in the tosic acid.

Ambient pressure Diels–Alder reactions

In an attempt to make this reaction more widely applicable, we examined the Diels–Alder cycloadditions of *N*-tosyl and *N*-nosyl QIKs in the cycloadditions process. Replacement of the benzoyl moiety with the more electron-withdrawing aryl sulfonyl group should serve to enhance the dienophilicity of the QIK. To this end, **7a–c** and **7f** were heated in toluene with a series of 1,3-butadienes (Table 5). The *N*-tosyl QIKs underwent cycloadditions smoothly at 140 °C (sealed tube), while the more reactive nosyl derivatives required 100 °C as the reaction temperature. In most cases, a substantial amount of conversion to the dihydronaphthalene was observed. The aromatization was driven to completion by treatment with acid, as before, to yield the dihydronaphthalenes **10** in excellent yields. Other than the milder reaction temperatures, an advantage of using a nosyl group is the ease of removal of such a group from the adduct (9). On a larger scale, the reaction was performed in refluxing xylenes, using a standard reflux apparatus, and the aromatization was performed by addition of HCl directly to the xylenes solution. The dihydronaphthalene precipitated from the reaction mixture upon cooling with no significant reduction in chemical yield.

The cycloadducts themselves are suitable substrates for further oxidation and cycloadditions (Scheme 2). Adduct **10c** was hydrogenated to yield **11**, which could be oxidized as before in excellent yield to the QIK **12**. Cycloaddition of **12** with 3-methyl-1,3-pentadiene proceeded to give, after aromatization with catalytic HCl, the linear tricycle **13**.

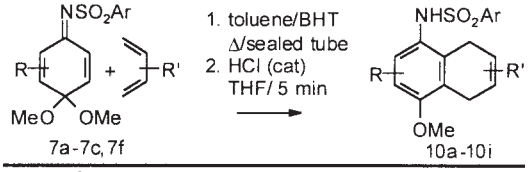
In summary, we have shown that quinone imine ketals bearing an electron-withdrawing group on the nitrogen atom are willing participants in hyperbaric or thermal Diels–Alder reactions. The adducts are readily aromatized with loss of methanol to produce dihydronaphthalenes in excellent yields. The synthetic utility of this process, including the conversion to 5-methoxyindoles, will be the subject of upcoming reports from our lab.

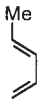
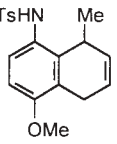
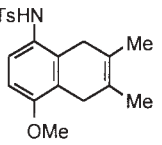
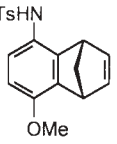
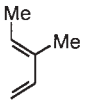
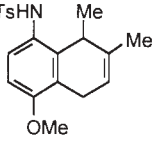
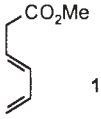
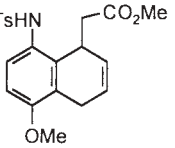
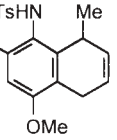
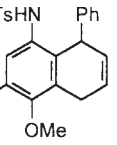
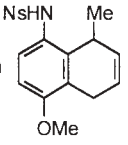
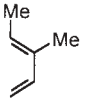
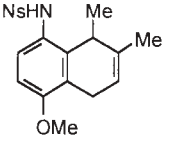
Experimental section

General considerations

Infrared spectra were obtained as thin films on NaCl plates. NMR spectra were obtained at 600 or 400 MHz (^{1}H) and 150 or 100 MHz (^{13}C). Spectra were obtained in $CDCl_3$ (referenced at 7.26 ppm for ^{1}H and 77.0 ppm for ^{13}C) or DMSO-d_6 (referenced at 2.49 ppm for ^{1}H and 39.5 ppm for ^{13}C). Coupling values (J) are in Hz. EI Mass spectra were obtained at an ionizing voltage of 70 eV. Hyperbaric conditions were achieved using a LECO^{TM} Tempres high-pressure chemical reactor. Dichloromethane, toluene, and THF were distilled prior to use, according to the standard procedures

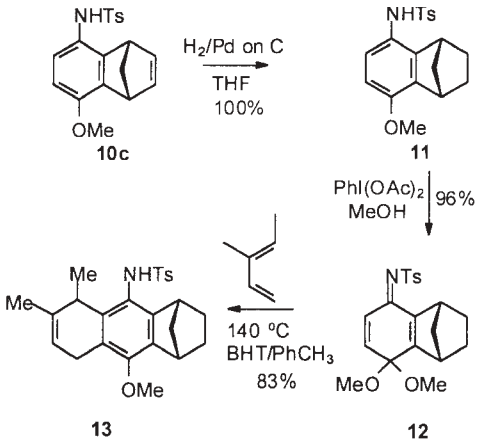
Table 5. Thermal Diels–Alder reactions of QIKs.



Entry	QIK	Diene	Conditions	Product	Yield
a	7a		140 °C/24 h		90%
b	7a		140 °C/24 h		88%
c	7a		140 °C/24 h		98%
d	7a		140 °C/24 h		96%
e	7a		140 °C/24 h		76%
f	7c		140 °C/24 h		85%
g	7f		140 °C/24 h		98%
h	7b		100 °C/7 h		99%
i	7b		100 °C/8 h		85%

© 2004 NRC Canada

Scheme 2.



(10). All other reagents were used as purchased from Aldrich or Lancaster and without purification. Reactions were checked for completion by TLC (EM Science, silica gel 60 F_{254}) and (or) ^{1}H NMR. Flash chromatography was performed using silica gel purchased from Silicycle Chemical Division Inc. (230–400 mesh). The synthesis of the *N*-benzoyl quinone imine ketals was carried out in the manner described by Swenton et al. (4*a*) with the only change being that the reaction was performed in an open beaker using a simple power source capable of producing a constant current of 0.3 A. The anode was a 2.5 cm × 5 cm Pt mesh cylinder, and the cathode was a 1 cm diameter Pt wire hoop. A simple laboratory power source was employed in the anodic oxidations. The Diels–Alder chemistry of the *N*-benzoyl quinone imine ketals has been described by us (2, 5, 6); however, a representative example for the preparation and Diels–Alder reaction of **5a** is given below.

General procedure for the preparation of *N*-benzoyl quinone imine ketals via anodic oxidation

Preparation of 5a

N-(4-Methoxyphenyl)benzamide (3.00 g, 13.2 mmol) was dissolved in 300 mL of a 2% solution of $LiClO_4$–CH_3OH. The mixture was cooled to 0 °C, and $NaHCO_3$ (6.00 g) was added. The mixture was rapidly stirred and anodically oxidized at a constant current (0.3 A) until consumption of the starting material was complete by TLC (approximately 140 min). The oxidation was stopped, and additional benzamide (2.62 g, 11.5 mmol) was added and allowed to dissolve, and the oxidation resumed until complete by TLC, approximately 140 min. The mixture was then poured into water and extracted several times with CH_2Cl_2. The combined organic layers were then washed with brine, dried (Na_2SO_4), filtered, and concentrated. The crude dienophile was then purified via flash chromatography (30%EtOAc–hexane) to yield 5.79 g (22.5 mmol, 91% yield) of the desired quinone imine ketal **5a**. ^{1}H NMR (400 MHz, $CDCl_3$) δ: 7.91 (d, *J* = 8.2 Hz, 2H), 7.60–7.56 (m, 1H), 7.48–7.44 (m, 2H), 6.57 (d, *J* = 9.0 Hz, 2H), 6.46 (d, *J* = 8.6 Hz, 2H), 3.34 (s, 6H). ^{13}C NMR (100 MHz, $CDCl_3$) δ: 180.3, 155.3, 139.6, 133.8, 132.9, 129.7, 128.9, 127.1, 93.2, 50.4. HR-MS (EI 70 eV) calcd. for $C_{15}H_{15}NO_3$: 257.1052; found: 257.1047.

General procedure for the high-pressure Diels–Alder reactions of *N*-benzoyl quinone imine ketals

Preparation of 8a and 9a

The quinone imine ketal **5a** (0.257 g, 1 mmol) was placed in a length (7″ (1″ = 25.4 mm)) of heat-shrinkable Teflon tubing. Dry CH_2Cl_2 (2 mL) was added, followed by an excess (0.5 mL) of technical grade piperylene. The tube was closed with a brass clamp and placed in the LECO^{TM} Tempres high-pressure chemical reactor. The pressure was raised to 13 kbar for a period of 7 days. The reaction mixture was poured directly onto a flash column of silica gel and eluted with 20% EtOAc in hexanes to produce 290 mg (90% yield) of a pure product, **8a**. ^{1}H NMR (250 MHz, $CDCl_3$) δ: 7.89 (d, *J* = 7.5 Hz, 2H), 7.52 (t, *J* = 7.5 Hz, 1H), 7.40 (t, *J* = 7.5, Hz, 2H), 6.09 (dd, *J* = 10.2, 2.1 Hz, 1H), 6.01 (d, *J* = 10.4 Hz, 1H), 5.71–5.68 (m, 2H), 3.28 (s, 3H), 3.25 (s, 3H), 3.27–3.22 (m, 1H), 2.72–2.64 (m, 2H), 2.20–1.88 (m, 2H), 1.48 (d, *J* = 7.6 Hz, 3H). ^{13}C NMR (63 MHz, $CDCl_3$) δ: 179.5, 164.7, 138.8, 133.4, 133.0, 132.9, 129.4, 128.5, 125.0, 123.8, 99.5, 49.7, 47.7, 43.7 (two signals), 35.0, 24.3, 18.7. IR (thin film) (cm^{-1}) ν: 3050, 3010, 2950, 2920, 2815, 1655, 1640, 1440, 1255. MS *m*/*z* (relative intensity): 326 (12, [M + 1]), 325 (48, $[M]^+$), 294 (15), 293 (21), 258 (43), 237 (20), 105 (100). HR-MS (EI 70 eV) calcd. for $C_{20}H_{23}NO_3$: 325.1678; found: 325.1687.

Preparation of 9a

The reaction performed, as for the preparation of **8a**, using **5a** (0.776 g, 3.0 mmol) and piperylene (0.613 g, 9.0 mmol) resulted in the formation of crude **8a**, which was taken up in 20 mL THF. Concentrated HCl (1 drop) was added, and the mixture was stirred for 30 min, after which time solid $NaHCO_3$ was added. The mixture was then stirred for an additional 10 min, and anhyd $MgSO_4$ was then added; stirring continued for 10 min further. The mixture was filtered, washed with THF, and concentrated. The crude residue was purified via trituration with cold hexanes; the solid was filtered and dried. The yield was 0.857 g (97%). ^{1}H NMR (400 MHz, DMSO) δ: 9.79 (s, 1H), 7.97 (app d, *J* = 6.8 Hz, 2H), 7.59–7.49 (m, 3H), 7.12 (d, *J* = 8.6 Hz, 1H), 6.85 (d, *J* = 8.6 Hz, 1Hz), 5.91–5.84 (m, 2H), 3.80 (s, 3H), 3.63–3.56 (m, 1H), 3.28–3.24 (m, 1H), 3.09–3.02 (m, 1H), 1.05 (d, *J* = 7.0 Hz, 3H). ^{13}C NMR (100 MHz, DMSO) δ: 165.9, 154.8, 137.7, 134.6, 131.4, 130.6, 128.4, 127.7, 127.5, 127.0, 122.8, 122.7, 107.5, 55.4, 29.9, 24.0, 22.4. IR (thin films) ν: 3276, 1643. MS *m*/*z* (relative intensity): 294 (14, [M + 1]), 293 (66, $[M]^+$), 188 (21), 105 (100), 77 (43). HR-MS (EI 70 eV) calcd. for $C_{19}H_{19}NO_2$: 293.1416; found: 293.1409.

Typical procedure for the synthesis of *N*-arylsulfonyl quinone imine ketals

Preparation of 7a

In a 250 mL round-bottom flask, containing 125 mL of methanol, was dissolved 10.00 g (36 mmol) of **6a**. The solution was cooled to 0 °C; then 11.70 g (36 mmol) of diacetoxyiodobenzene was added portion-wise over 5 min. The flask was purged with argon and stirred until complete by TLC (approximately 30 min). The reaction mixture was then poured into water and extracted with EtOAc, then washed

© 2004 NRC Canada

successively with water, saturated $NaHCO_3$ (aq), and brine; then it was dried with $MgSO_4$, filtered, and concentrated. The crude product was then purified via recrystalization from CH_2Cl_2 to yield 9.87 g (32 mmol, 89% yield) of the product **7a** as a white solid. mp 109–111 °C. ^{1}H NMR (600 MHz, DMSO-d_6) δ: 7.81 (d, J = 8.2 Hz, 2H), 7.45 (d, J = 8.2 Hz, 2H), 7.36 (dd, J = 10.5, 2.2 Hz, 1H), 7.12 (dd, J = 10.5, 2.9 Hz, 1H), 7.01 (dd, J = 10.2, 2.9 Hz, 1H), 6.36 (dd, J = 10.2, 2.2 Hz, 1H), 3.28 (s, 6H), 2.40 (s, 3H). ^{13}C NMR (100 MHz, $CDCl_3$) δ: 162.8, 143.9, 143.2, 141.9, 137.4, 130.4, 129.4, 127.1, 123.0, 91.9, 50.3, 21.7. IR (thin film) (cm^{-1}) ν: 2835, 1555, 1321, 1156. MS *m/z* (relative intensity): 308 (3, [M + 1]), 307 (19, [M]$^+$), 276 (27), 152 (100), 139 (13), 121 (14), 91 (33). HR-MS (EI 70 eV) calcd. for $C_{15}H_{17}NO_4S$: 307.0878; found: 307.0879.

Quinone imine ketal (7b)

Oxidation of 11.10 g (36 mmol) of the nosylated *p*-anisidine **6b** with 11.62 g (36 mmol) of diacetoxyiodobenzene in 125 mL of methanol was performed in a similar manner to the preparation of compound **7a**, method A. The crude product was purified via a mixed recrystalization from EtOAc–MeOH to yield 9.00 g (26.6 mmol, 74% yield) of the product **7b** as an off-white solid. mp 132–135 °C. ^{1}H NMR (400 MHz, $CDCl_3$) δ: 8.39 and 8.18 (AA′BB′ system, 4H), 7.52 (dd, J = 10.5, 2.0 Hz, 1H), 6.87 (dd, J = 10.5, 2.7 Hz, 1H), 6.80 (dd, J = 10.2, 2.7 Hz, 1H), 6.34 (dd, J = 10.2, 2.0 Hz, 1H), 3.38 (s, 6H). ^{13}C NMR (100 MHz, $CDCl_3$) δ: 164.3, 150.2, 146.1, 144.7, 143.4, 129.9, 128.5, 124.1, 123.1, 91.7, 50.3. IR (thin film) (cm^{-1}) ν: 1532, 1326, 1154. MS *m/z* (relative intensity): 338 (5, [M]$^+$), 307 (46), 170 (14), 152 (100), 121 (28), 106 (17). HR-MS (EI 70 eV) calcd. for $C_{14}H_{14}N_2O_6S$: 338.0573; found: 338.0568.

Quinone imine ketal (7c)

Oxidation of 3.85 g (12.5 mmol) of the tosylated *p*-anisidine **6c** with 4.03 g (12.5 mmol) of diacetoxyiodobenzene in 50 mL of methanol was performed in a similar manner to the preparation of compound **7a**, method A. The crude product was purified via a recrystalization from CH_2Cl_2 to yield 3.05 g (9.0 mmol, 72% yield) of the product **7c** as a yellow solid. mp 137–140 °C. ^{1}H NMR (400 MHz, DMSO-d_6) δ: 7.80 (d, J = 8.4 Hz, 2H), 7.45 (d, J = 8.4 Hz, 2H), 7.30 (d, J = 10.5 Hz, 1H), 7.05 (dd, J = 10.5, 2.5 Hz, 1H), 5.98 (d, J = 2.5 Hz, 1H), 3.60 (s, 3H), 3.27 (s, 6H), 2.41 (s, 3H). ^{13}C NMR (100 MHz, DMSO-d_6) δ: 159.1, 150.2, 144.7, 144.0, 137.3, 129.7, 126.7, 120.9, 111.6, 94.3, 55.3, 49.9, 21.1. IR (thin film) (cm^{-1}) ν: 2938, 1313, 1147. MS *m/z* (relative intensity): 338 (2, [M + 1]), 337 (10, [M]$^+$), 306 (100), 182 (51), 151 (43), 91 (35). HR-MS (EI 70 eV) calcd. for $C_{16}H_{19}NO_5S$: 337.0984; found: 337.0992.

Quinone imine ketal (7d)

Oxidation of 5.00 g (16.3 mmol) of the tosylated *p*-anisidine **6d** with 5.25 g (16.3 mmol) of diacetoxyiodobenzene in 50 mL of methanol was performed in a similar manner to the preparation of compound **7a**, method A. The crude product was purified via recrystalization from CH_2Cl_2 to yield 4.74 g (14.1 mmol, 87% yield) of the product **7d** as a yellow solid and as a (1.8:1) mixture of *trans*- and *cis*-isomers, respectively. mp 110–112 °C. ^{1}H NMR (400 MHz, DMSO-d_6, *trans*-isomer) δ: 7.79 (d, J = 8.3 Hz, 2H), 7.42 (d, J = 8.3 Hz, 2H), 6.79 (d, J = 10.2 Hz, 1H), 6.62 (d, J = 1.6 Hz, 1H), 6.36 (dd, J = 10.2, 1.6 Hz, 1H), 3.85 (s, 3H), 3.20 (s, 6H), 2.39 (s, 3H). ^{1}H NMR (400 MHz, DMSO-d_6, *cis*-isomer) δ: 7.79 (obscured by aryl sulfonyl, 2H), 7.42 (d, J = 8.3 Hz, 2H), 7.42 (obscured by aryl sulfonyl, 1H), 6.89 (d, J = 10.2 Hz, 1H), 5.77 (m, 1H), 3.79 (s, 3H), 3.20 (s, 6H), 2.39 (s, 3H). ^{13}C NMR (100 MHz, DMSO-d_6, both isomers) δ: 170.7, 169.4, 166.3, 165.5, 143.7, 143.6, 142.8, 141.1, 138.4, 138.1, 130.7, 129.7 (two overlapping signals), 126.7, 126.6, 122.8, 102.7, 96.4, 92.7, 92.6, 56.6, 56.5, 50.8 (two overlapping signals), 21.0 (two overlapping signals). IR (thin film) (cm^{-1}) ν: 2835, 1596, 1302, 1146. MS *m/z* (relative intensity): 338 (2, [M + 1]), 337 (9, [M]$^+$), 306 (36), 182 (100), 151 (8), 91 (24). HR-MS (EI 70 eV) calcd. for $C_{16}H_{19}NO_5S$: 337.0984; found: 337.0989.

Quinone imine ketal (7f)

Oxidation of 2.00 g (6.4 mmol) of the tosylated *p*-anisidine **6f** with 2.07 g (6.4 mmol) of diacetoxyiodobenzene in 20 mL of methanol was performed in a similar manner to the preparation of compound **7a**, method B. Filtration and washing with hexanes yielded 1.78 g (5.2 mmol, 81% yield) of the product **7f** as a yellow solid and as a (1.1:1) mixture of *cis*- and *trans*-isomers, respectively. No further purification was required. mp 100–102 °C. ^{1}H NMR (400 MHz, DMSO-d_6, *trans*-isomer) δ: 7.82 (d, J = 8.4 Hz, 2H), 7.57 (dd, J = 10.4, 2.0 Hz, 1H), 7.47–7.45 (m, 2H), 7.18 (d, J = 10.4 Hz, 1H), 6.86 (d, J = 2.0 Hz, 1H), 3.20 (s, 6H), 2.41 (s, 3H). ^{1}H NMR (400 MHz, DMSO-d_6, *cis*-isomer) δ: 7.83 (d, J = 8.4 Hz, 2H), 7.72 (d, J = 2.1 Hz, 1H), 7.47–7.45 (m, 2H), 7.10 (d, J = 10.3 Hz, 1H), 6.60 (dd, J = 10.3, 2.1 Hz, 1H), 3.20 (s, 6H), 2.41 (s, 3H). ^{13}C NMR (100 MHz, DMSO-d_6, both isomers) δ: 161.8, 160.9, 152.8, 149.7, 144.2, 144.1, 143.5, 142.2, 137.1, 137.0, 132.6, 131.6, 129.5 (two overlapping signals), 127.2, 127.1, 125.1, 124.7, 94.34, 94.31, 51.61, 51.58, 21.7 (two overlapping signals). IR (thin film) (cm^{-1}) ν: 2924, 2837, 1320, 1156. MS *m/z* (relative intensity): 343 (9, [M + 2]), 342 (6, [M + 1]), 341 (23, [M]$^+$), 310 (45), 306 (32), 186 (100), 139 (23), 91 (92). HR-MS (EI 70 eV) calcd. for $C_{15}H_{16}ClNO_4S$: 341.0489; found: 341.0494.

Typical procedure for the thermal Diels–Alder–aromatization reactions of quinone imine ketals

Preparation of dihydronaphthalene (10a)

The quinone imine ketal **7a** (0.503 g, 1.6 mmol) and piperylene (0.393 g, 5.8 mmol) were taken up in dry toluene (2.3 mL) in an oven-dried sealed tube. One crystal of the radical inhibitor BHT was added, and the tube was flushed with argon before sealing. The reaction mixture was heated at 140 °C for a period of 24 h, after which time the reaction mixture was concentrated and taken up in dry THF (20 mL). Concentrated HCl (2 drops) was added, and the mixture was stirred under argon for 30 min, after which time solid $NaHCO_3$ was added. The mixture was then stirred for an additional 10 min, and anhyd $MgSO_4$ was then added; stirring continued for 10 min further. The mixture was filtered, washed with THF, and concentrated. The crude residue was purified via trituration with cold hexane; the solid was fil-

© 2004 NRC Canada

tered and dried to yield 0.509 g (1.48 mmol, 90% yield) of the product **10a** as a white solid. mp 152–156 °C. ^{1}H NMR (400 MHz, DMSO-d_6) δ: 9.23 (s, 1H), 7.58 (d, J = 8.3 Hz, 2H), 7.37 (d, J = 8.3 Hz, 2H), 6.60 (d, J = 8.7 Hz, 1H), 6.36 (d, J = 8.7 Hz, 1H), 5.90–5.79 (m, 2H), 3.81–3.71 (m, 1H), 3.69 (s, 3H), 3.27–3.20 (m, 1H), 2.99–2.93 (m, 1H), 2.38 (s, 3H), 1.06 (d, J = 6.8 Hz, 3H). ^{13}C NMR (100 MHz, $CDCl_3$) δ: 155.4, 143.5, 137.7, 136.7, 130.2, 129.5, 127.2, 125.4, 124.9, 124.3, 123.0, 107.2, 55.3, 29.7, 24.2, 22.5, 21.5. IR (thin film) (cm^{-1}) ν: 3244, 1484, 1160. MS *m/z* (relative intensity): 344 (17, [M + 1]), 343 (73, [M]$^+$), 277 (7), 188 (100), 92 (6), 91 (24). HR-MS (EI 70 eV) calcd. for $C_{19}H_{21}NO_3S$: 343.1242; found: 343.1245.

Dihydronaphthalene (10b)

The reaction between quinone imine ketal **7a** (0.504 g, 1.6 mmol) and 2,3-dimethyl-1,3-butadiene (0.509 g, 5.7 mmol) was performed in a similar manner to the preparation of compound **10a**. The crude residue was purified via trituration with cold hexane; the solid was filtered and dried to yield 0.506 g (1.41 mmol, 88% yield) of the product **10b** as a white solid. mp 172–175 °C. ^{1}H NMR (400 MHz, DMSO-d_6) δ: 9.21 (s, 1H), 7.54 (d, J = 8.3 Hz, 2H), 7.34 (d, J = 8.3 Hz, 2H), 6.67–6.61 (m, 2H), 3.71 (s, 3H), 3.02–2.97 (m, 4H), 2.36 (s, 3H), 1.66 (s, 3H), 1.57 (s, 3H). ^{13}C NMR (100 MHz, DMSO-d_6) δ: 154.7, 142.7, 138.1, 133.3, 129.5, 126.7, 126.0, 125.5, 123.4, 122.0, 121.8, 107.2, 55.2, 32.1, 30.8, 20.9, 18.2 (two overlapping signals). IR (thin film) (cm^{-1}) ν: 3274, 1486, 1161. MS *m/z* (relative intensity): 358 (16, [M + 1]), 357 (66, [M]$^+$), 202 (3), 186 (100), 171 (23), 91 (18). HR-MS (EI 70 eV) calcd. for $C_{20}H_{23}NO_3S$: 357.1399; found: 357.1406.

Dihydronaphthalene (10c)

The reaction between quinone imine ketal **7a** (1.00 g, 3.25 mmol) and cyclopentadiene (0.98 mL, 11.8 mmol) was performed in a similar manner to the preparation of compound **10a**. The crude residue was purified via trituration with cold hexane; the solid was filtered and dried to yield 1.082 g (3.17 mmol, 98% yield) of the product **10c** as an off-white solid. mp 137–140 °C. ^{1}H NMR (400 MHz, DMSO-d_6) δ: 9.51 (s, 1H), 7.45 (d, J = 8.1 Hz, 2H), 7.31 (d, J = 8.1 Hz, 2H), 6.65 (dd, J = 5.2, 3.0 Hz, 1H), 6.58 (d, J = 8.8 Hz, 1H), 6.51 (d, J = 8.8 Hz, 1H), 6.26 (dd, J = 5.2, 3.0 Hz, 1H), 3.94 (br s, 1H), 3.76 (br s, 1H), 3.68 (s, 3H), 2.33 (s, 3H), 1.90 (d, J = 7.0 Hz, 1H), 1.67 (d, J = 7.0 Hz, 1H). ^{13}C NMR (150 MHz, DMSO-d_6) δ: 151.6, 149.4, 142.8, 142.7, 142.2, 138.1, 137.1, 129.4, 126.8, 124.1, 123.8, 109.3, 68.8, 55.3, 48.0, 46.2, 20.9. IR (thin film) (cm^{-1}) ν: 3260, 1490, 1161. MS *m/z* (relative intensity): 342 (11, [M + 1]), 341 (43, [M]$^+$), 186 (100), 160 (13), 91 (25). HR-MS (EI 70 eV) calcd. for $C_{19}H_{19}NO_3S$: 341.1086; found: 341.1081.

Dihydronaphthalene (10d)

The reaction between quinone imine ketal **7a** (0.508 g, 1.65 mmol) and 3-methyl-1,3-pentadiene (0.471 g, 5.7 mmol) was performed in a similar manner to the preparation of compound **10a**. The crude residue was purified via trituration with cold hexane; the solid was filtered and dried to yield 0.563 g (1.58 mmol, 96% yield) of the product **10d** as a white solid. mp 160–162 °C. ^{1}H NMR (400 MHz, DMSO) δ: 9.24 (s, 1H), 7.55 (app d, J = 8.3 Hz, 2H), 7.35 (app d, J = 8.3 Hz, 2H), 6.62 (d, J = 8.7 Hz, 1H), 6.50 (d, J = 8.7 Hz, 1H), 5.51–5.50 (m, 1H), 3.70 (s, 3H), 3.45–3.41 (m, 1H), 3.24 (dd, J = 21.6, 5.4 Hz, 1H), 2.89 (dd, J = 21.6, 2.3 Hz, 1H), 2.37 (s, 3H), 1.67 (s, 3H), 1.00 (d, J = 6.8 Hz, 3H). ^{13}C NMR (100 MHz, DMSO) δ: 154.7, 142.5, 140.3, 137.9, 137.1, 129.3, 126.5, 126.0, 125.3, 123.3, 117.8, 107.1, 55.3, 34.1, 24.3, 21.2, 21.0, 20.4. IR (thin film) (cm^{-1}) ν: 3279, 1486, 1161. MS *m/z* (relative intensity): 358 (15, [M + 1]), 357 (62, [M]$^+$), 202 (100), 187 (45), 172 (18), 91 (12). HR-MS (EI 70 eV) calcd. for $C_{20}H_{23}NO_3S$: 357.1399; found: 357.1402.

Dihydronaphthalene (10e)

The reaction between quinone imine ketal **7a** (0.304 g, 0.99 mmol) and methyl (*E*)-3,5-hexadienoate (0.442 g, 3.5 mmol) was performed in a similar manner to the preparation of compound **10a**. The crude residue was purified via flash chromatography (40% EtOAc–hexane) to yield 0.303 g (0.75 mmol, 76% yield) of the product **10e** as a white solid. mp 124–127 °C. ^{1}H NMR (400 MHz, DMSO-d_6) δ: 9.31 (s, 1H), 7.57 (d, J = 8.2 Hz, 2H), 7.37 (d, J = 8.2 Hz, 2H), 6.65 (d, J = 8.7 Hz, 1H), 6.42 (d, J = 8.7 Hz, 1H), 5.95–5.87 (m, 2H), 4.18–4.14 (m, 1H), 3.70 (s, 3H), 3.59 (s, 3H), 3.29–3.22 (m, 1H), 3.00–2.94 (m, 1H), 2.65 (dd, J = 15.4, 3.8 Hz, 1H), 2.38 (s, 3H), 2.14 (dd, J = 15.4, 10.5 Hz, 1H). ^{13}C NMR (100 MHz, DMSO-d_6) δ: 171.5, 155.1, 142.8, 137.9, 137.2, 129.6, 127.8, 126.8, 126.3, 125.8, 125.4, 124.5, 107.8, 55.4, 51.3, 40.5, 31.2, 24.1, 21.0. IR (thin film) (cm^{-1}) ν: 3255, 1735, 1485, 1161. MS *m/z* (relative intensity): 402 (8, [M + 1]), 401 (30, [M]$^+$), 327 (31), 246 (18), 186 (84), 172 (100), 91 (28). HR-MS (EI 70 eV) calcd. for $C_{21}H_{23}NO_5S$: 401.1297; found: 401.1292.

Dihydronaphthalene (10f)

The reaction between quinone imine ketal **7c** (0.501 g, 1.49 mmol) and piperylene (0.357 g, 5.2 mmol) was performed in a similar manner to the preparation of compound **10a**. The crude residue was purified via trituration with cold hexane; the solid was filtered and dried to yield 0.472 g (1.26 mmol, 85% yield) of the product **10f** as an off-white solid. mp 210–213 °C. ^{1}H NMR (400 MHz, DMSO-d_6) δ: 8.90 (s, 1H), 7.50 (d, J = 8.2 Hz, 2H), 7.31 (d, J = 8.2 Hz, 2H), 6.30 (s, 3H), 5.89–5.80 (m, 2H), 3.96–3.95 (m, 1H), 3.75 (s, 3H), 3.23–3.10 (m, 1H), 3.05 (s, 3H), 2.96–2.93 (m, 1H), 2.37 (s, 3H), 1.07 (d, J = 7.0 Hz, 3H). ^{13}C NMR (100 MHz, DMSO-d_6) δ: 156.1, 155.2, 141.9, 141.8, 139.4, 130.8, 128.7, 126.7, 122.6, 114.1, 113.7, 92.9, 55.4, 54.5, 29.8, 23.7, 22.5, 20.9. IR (thin film) (cm^{-1}) ν: 3239, 1591, 1160. MS *m/z* (relative intensity): 374 (6, [M + 1]), 373 (15, [M]$^+$), 218 (100), 186 (18), 91 (16). HR-MS (EI 70 eV) calcd. for $C_{20}H_{23}NO_4S$: 373.1348; found: 373.1352.

Dihydronaphthalene (10g)

The reaction between quinone imine ketal **7f** (0.500 g, 1.46 mmol) and 1-phenyl-1,3-butadiene (0.686 g, 5.27 mmol) was performed in a similar manner to the preparation of compound **10a**. The crude residue was purified via trituration with cold hexane; the solid was filtered and dried to yield 0.631 g (1.43 mmol, 98% yield) of the product **10g**

© 2004 NRC Canada

as a white solid. mp 152–155 °C. ^{1}H NMR (400 MHz, DMSO-d_6) δ: 9.17 (s, 1H), 7.43 (d, J = 8.1 Hz, 2H), 7.31 (d, J = 8.1 Hz, 2H), 7.23 (dd, J = 7.4, 7.2 Hz, 2H), 7.15 (t, J = 7.4 Hz, 1H), 7.06 (d, J = 7.2 Hz, 2H), 6.37 (s, 1H), 5.96–5.88 (m, 2H), 5.19–5.18 (m, 1H), 3.77 (s, 3H), 3.45–3.44 (m, 2H), 2.36 (s, 3H). ^{13}C NMR (100 MHz, DMSO-d_6) δ: 151.4, 144.5, 143.2, 136.5, 135.9, 131.5, 131.1, 129.5, 129.3, 128.4, 127.9, 127.0, 126.0, 124.9, 123.7, 121.8, 60.0, 40.9, 24.9, 21.0. IR (thin film) (cm^{-1}) ν: 3329, 1161. MS *m*/*z* (relative intensity): 440 (12, [M + 1]), 439 (40, [M]$^+$), 311 (16), 284 (100), 249 (45), 234 (30), 130 (42), 91 (78). HR-MS (EI 70 eV) calcd. for $C_{24}H_{22}ClNO_3S$: 439.1009; found: 439.1005.

Dihydronaphthalene (10h)

The quinone imine ketal **7b** (0.511 g, 1.51 mmol) and piperylene were taken up in dry toluene (2.3 mL) in an oven-dried sealed tube. One crystal of the radical inhibitor BHT was added, and the tube was flushed with argon before sealing. The reaction mixture was heated at 100 °C for a period of 7 h, after which time the reaction mixture was concentrated and taken up in dry THF (20 mL). Concentrated HCl (2 drops) was added, and the mixture was stirred under argon for 30 min, after which time solid $NaHCO_3$ was added. The mixture was then stirred for an additional 10 min, and anhyd $MgSO_4$ was then added, stirring for 10 min further. The mixture was then filtered, washed with reagent grade THF, and concentrated. The crude residue was purified via trituration with cold hexane; the solid was filtered and dried to yield 0.564 g (1.50 mmol, 99% yield) of the product **10h** as a white solid. mp 193–195 °C. ^{1}H NMR (400 MHz, DMSO-d_6) δ: 9.74 (s, 1H), 8.41 (d, J = 8.8 Hz, 2H), 7.94 (d, J = 8.8 Hz, 2H), 6.61 (d, J = 8.7 Hz, 1H), 6.35 (d, J = 8.7 Hz, 1H), 5.90–5.75 (m, 2H), 3.78–3.76 (m, 1H), 3.70 (s, 3H), 3.27–3.22 (m, 1H), 3.00–2.94 (m, 1H), 1.07 (d, J = 7.0 Hz, 3H). ^{13}C NMR (100 MHz, DMSO-d_6) δ: 155.5, 149.6, 146.4, 140.1, 130.7, 128.4, 126.3, 125.2, 124.6, 123.8, 122.8, 107.4, 55.3, 29.6, 24.0, 22.4. IR (thin film) (cm^{-1}) ν: 3275, 1588, 1532, 1349, 1167. MS *m*/*z* (relative intensity): 375 (11, [M + 1]), 374 (49, [M]$^+$), 188 (100), 173 (32), 122 (10). HR-MS (EI 70 eV) calcd. for $C_{18}H_{18}N_2O_5S$: 374.0936; found: 374.0940.

Dihydronaphthalene (10i)

The quinone imine ketal **7b** (0.500 g, 1.48 mmol) and 3-methyl-1,3-pentadiene (0.447 g, 5.44 mmol) were taken up in dry toluene (2.3 mL) in an oven-dried sealed tube. One crystal of the radical inhibitor BHT was added, and the tube was flushed with argon before sealing. The reaction mixture was heated at 100 °C for a period of 8 h, at which point NMR analysis revealed 100% conversion to the desired dihydronaphthalene **10i**. The reaction mixture was concentrated, and the crude residue was purified via trituration with cold hexane to yield 0.487 g (1.25 mmol, 85% yield) of the product **10i** as a yellow solid. mp 166–169 °C. ^{1}H NMR (400 MHz, DMSO-d_6) δ: 9.75 (s, 1H), 8.41 (d, J = 8.9 Hz, 2H), 7.92 (d, J = 8.9 Hz, 2H), 6.63 (d, J = 8.8 Hz, 1H), 6.46 (d, J = 8.8 Hz, 1H), 5.53–5.52 (m, 1H), 3.70 (s, 3H), 3.44–3.43 (m, 1H), 3.28–3.21 (m, 1H), 2.94–2.88 (m, 1H), 1.67 (s, 3H), 1.02 (d, J = 6.8 Hz, 3H).^{13}C NMR (100 MHz, DMSO-d_6) δ: 155.3, 149.6, 146.4, 140.7, 137.1, 128.4, 126.4, 124.7, 124.6, 123.8, 118.1, 107.5, 55.3, 34.2, 24.8, 21.1, 20.3. IR (thin film) (cm^{-1}) ν: 3283, 1532, 1349, 1165. MS *m*/*z* (relative intensity): 389 (10), 388 (45), 202 (100), 172 (32), 122 (16), 76 (9). HR-MS (EI 70 eV) calcd. for $C_{19}H_{20}N_2O_5S$: 388.1093; found: 388.1091.

Acknowledgement

We are grateful to the Natural Sciences and Engineering Research Council of Canada (NSERC), The Ontario Ministry of Science and Technology, and MedMira Laboratories for funding. S.C.B. is an NSERC PGSB scholar.

References

1. For an excellent review with many leading references see: K.C. Nicolaou, S.A. Snyder, T. Montagnon, and G. Vassilikogiannakis. Angew. Chem. Int. Ed. **41**, 1668 (2002).
2. M.A. Kerr. Synlett, 1165 (1995).
3. I.G.C.Coutts, N.J. Culbert, M. Edwards, J.A. Hadfield, D.R. Musto, V.H. Pavlidis, and D.J. Richards. J. Chem. Soc. Perkin Trans. 1, **9**, 1829 (1985).
4. (*a*) J.S. Swenton, B.R. Bonke, C.-P. Chen, and C.-T. Chou. J. Org. Chem. **54**, 51 (1989); (*b*) J.S. Swenton, C. Shih, C.-P. Chen, and C.-T. Chou. J. Org. Chem. **55**, 2019 (1990); (*c*) J.S. Swenton, B.R. Bonke, W.M. Clarke, C.-P. Chen, and K.V. Martin. J. Org. Chem. **55**, 2027 (1990).
5. S.C. Banfield and M.A. Kerr. Synlett, 436 (2001).
6. S.C. Banfield, D.B. England, and M.A. Kerr. Org. Lett **3**, 3323 (2001).
7. A. Pelter and S. Elgendy. Tetrahedron Lett. 677 (1988).
8. (*a*) F.-G. Klarner, M.K. Diedrich, and A.E. Wigger. *In* Chemistry under extreme or non-classical conditions. *Edited by* R. van Eldik and C.D. Hubbard. Wiley, New York. 1997. Chap 3; (*b*) J. Jurczak and D.T. Gryko. *In* Chemistry under extreme or non-classical conditions. *Edited by* R. van Eldik and C.D. Hubbard. Wiley, New York. 1997. Chap 4; (*c*) N.S. Isaacs. *In* High-pressure techniques in chemistry and physics. *Edited by* W.B. Holzapfel and N.S. Isaacs. Oxford, New York. 1997. Chap 7.
9. R.E. Heckert and H.R. Snyder. J. Am. Chem. Soc. **74**, 2006 (1952).
10. D.D. Perrin and W.L.F. Armarego. *In* Purification of laboratory chemicals. 3rd ed. Pergamon, New York. 1988.

© 2004 NRC Canada

Nucleophilic additions of lactam-derived enol triflates to aldehydes mediated by nickel(II) and chromium(II) salts[1]

Leah P. Easton and Gregory R. Dake

Abstract: Enol trifluoromethanesulfonates (triflates) derived from *N*-protected lactams undergo nickel(II)-chloride- and chromium(II)-chloride-promoted carbonyl additions to aldehydes. The yields of this process range from 42%–84%.

Key words: nickel(II) chloride, chromium(II) chloride, carbonyl addition, lactam-derived enol triflate.

Résumé : Sous l'influence du chlorure de nickel(II) ou du chlorure de chrome(II), les trifluorométhanesulfonates (triflates) d'énol obtenus à partir de lactames *N*-protégés donnent lieu à des réactions d'addition de carbonyles avec formation d'aldéhydes avec des rendements qui vont de 42% à 84%.

Mots clés : chlorure de nickel(II), chlorure de chrome(II), addition de carbonyle, triflate d'énol dérivé de lactames.

[Traduit par la Rédaction]

Introduction

To investigate the use of semipinacol reactions for the construction of alkaloid natural products (1), our group became interested in the preparation of compounds such as **A** (Scheme 1). Functionalized lactams appeared to be reasonable starting materials for the preparation of compounds like **A**. Currently we use a synthetic protocol that involves the following: (*a*) conversion of the *N*-protected lactam to its enol trifluoromethanesulfonate (triflate); (*b*) formation of a vinylstannane from the enol triflate using a palladium(0)-catalyzed coupling reaction; and (*c*) transmetalation of the stannane to a more nucleophilic lithium or magnesium species, which is reacted with a carbonyl compound. Although this procedure works well and can be scaled up, it does have drawbacks. Specifically, the requirement of hexamethyldistannane in the sequence is a liability because of its expense and toxicity (2).[3] Because of the known facility of mixtures of nickel(II) and chromium(II) salts in promoting additions of vinyl halides or triflates to carbonyl compounds (3), we were intrigued by the possibility of using such a process on a triflate derived from a lactam, thus possibly removing the need for hexamethyldistannane. A precedent for this proposed transformation is the use of a lactone-derived enol triflate in a nickel(II)–chromium(II) salt promoted aldehyde addition reaction, reported by Nicolaou and co-workers (4). Despite the growing use of lactam-derived enol triflates as substrates for metal-promoted (or catalyzed) reactions (5), we were unsure of the plausibility of our hypothesis. We are aware, to the best of our knowledge, of no examples of nickel(II)–chromium(II)-promoted carbonyl addition reactions using lactam-derived enol triflates. Our successful investigations on the feasibility of this process are disclosed in this report.

Results and discussion

The known enol triflate **1**[4] was selected to probe the viability of the nickel(II)–chromium(II)-promoted carbonyl addition. Enol triflate **1** was easily formed by deprotonating *N*-*tert*-butoxycarbonyl-2-piperidone with lithium hexamethyldisilazide followed by enolate quenching with *N*-(5-chloro-2-pyridyl)-triflimide. Unlike enol triflates derived from 5- and 7-membered ring lactams, which can be difficult to store and handle,[5] **1** can be purified by column chromatography on silica gel and can be stored for weeks in the freezer. The reaction between **1** and benzaldehyde, using a variety of different conditions, was initially explored (Scheme 2 and Table 1).

A typical set of reaction conditions suitable for the nickel(II)–chromium(II) carbonyl addition process were

Received 23 June 2003. Published on the NRC Research Press Web site at http://canjchem.nrc.ca on 9 January 2004.

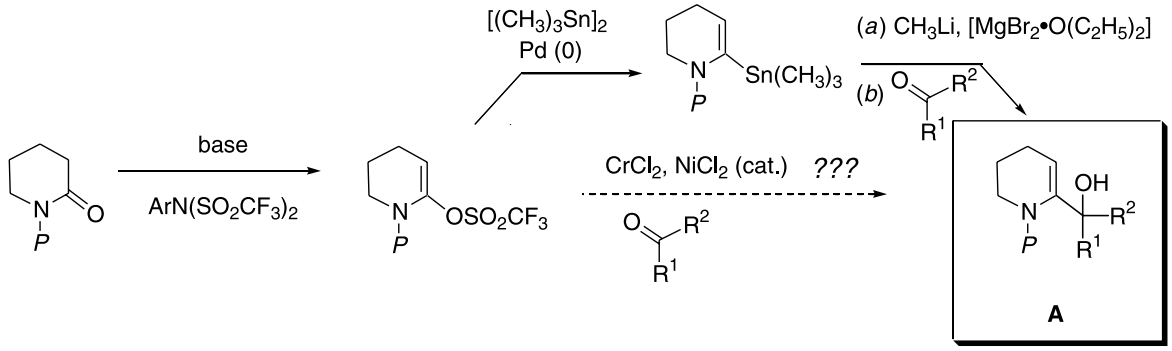
This article is dedicated to my teacher, mentor, and colleague, Professor Edward Piers.

L.P. Easton and G.R. Dake.[2] Department of Chemistry, 2036 Main Mall, University of British Columbia, Vancouver, BC V6T 1Z1, Canada.

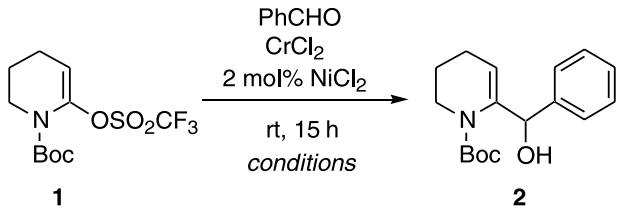
[1]This article is part of a Special Issue dedicated to Professor Ed Piers.
[2]Corresponding author (e-mail: gdake@chem.ubc.ca).
[3]The current cost for 5 g of hexamethyldistannane is Can$141.80 (Aldrich). The cost is even higher when one considers that only one "trimethyltin" group is transferred, and the other is discarded.
[4]References 5(*m*) and 5(*n*).
[5]See, for example, ref. 5(*f*).

 doi: 10.1139/V03-164 © 2004 NRC Canada

Scheme 1.



Scheme 2.



Scheme 3.

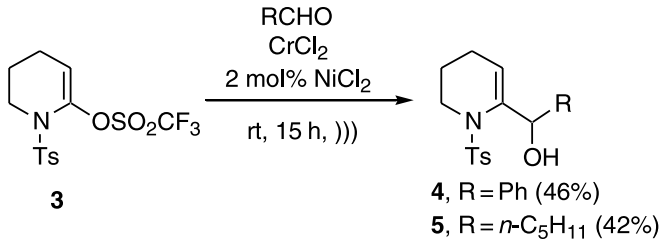


Table 1. Optimization of addition of enol triflate **1** to benzaldehyde.

Entry	equiv. PhCHO	equiv. $CrCl_2$	Solvent	Reaction parameter	Yield **2** (%)[a]
1	6	6	DMF–THF	Sonication	60
2	6	6	DMSO–THF	Sonication	10
3	6	6	DMSO	Sonication	26
4	6	6	DMF	Sonication	66
5	6	6	DMF	Stirring	50
6	6	4	DMF	Sonication	27
7	2	6	DMF	Sonication	63

[a]After isolation and purification.

used. Treatment of **1** with excess benzaldehyde (6 equiv), in the presence of 6 equiv of chromium(II) chloride and nickel(II) chloride (2 mol%), in a 1:1 mixture of degassed DMF–THF mixture at room temperature for 15 h produced the desired adduct **2** in 60% isolated yield (entry 1). The structure of **2** was established by spectroscopic methods. The IR spectrum of **2** contained absorptions typical of both alcohol (3404 cm^{-1}) and carbonyl (1682 cm^{-1}) functional groups. Key signals in the ^1H NMR spectrum of **2** at δ 5.35 ppm (d, J = 9.2 Hz, 1H) and δ 1.29 ppm (s, 9H) could be attributed to the allylic methine proton and the protons on the *tert*-butyl group. It is noteworthy that the alkoxide that is presumably generated after the carbonyl addition does not cyclize into the *tert*-butyl carbamate protecting group to form an oxazolidinone (6).

The choice of solvent had a substantial effect on the course of this reaction. For example, no reaction was observed to take place when using THF as the sole solvent, and using a 1:1 mixture of degassed THF and DMSO produced **2** in only 10% yield (entry 2). Omitting the ether solvent and running the reaction in DMSO alone improved the process somewhat (26% yield of **2**, entry 3). An amide solvent was clearly superior, as running the reaction in DMF alone restored the yield to acceptable levels, 66% (entry 4). Sonication probably better disperses the chromium(II) chloride during the reaction, compared with simple stirring (4). Using stirring to agitate the reaction mixture in DMF resulted in a lowered yield of **2** of 50% (entry 5). Unfortunately, the use of a smaller amount of chromium(II) chloride (4 equiv) drastically reduced the amount of adduct **2** that was isolated after reaction (27%, entry 6). In contrast, the use of a substantial excess of benzaldehyde is not necessary. Adduct **2** was isolated in 63% yield when 2 equiv of benzaldehyde was used with DMF as solvent (entry 7). These conditions (using either 6 or 2 equiv of electrophile) were adapted as our "standard protocol" for this process.

The effect of the different protecting groups on the nitrogen of the enol triflate nucleophile was then examined (Scheme 3). Although the *N*-toluenesulfonyl derivative **3** did react as a nucleophile using these reaction conditions, the efficiency of the reaction was much lower in comparison with the reactions of **1**. For example, the reaction of **3** with benzaldehyde produced allylic alcohol **4** in 46% yield. Hexanal could also be employed as an electrophile. Allylic alcohol **5** was isolated from the reaction of **3** and hexanal in 42% yield. Attempts to use other common protecting groups for

© 2004 NRC Canada

Scheme 4.

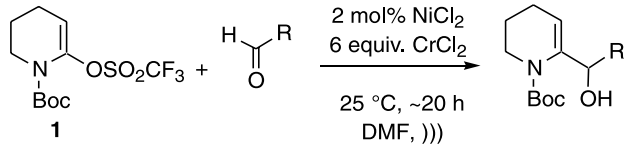
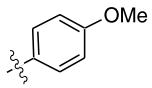
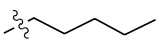
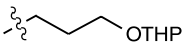
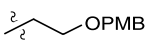
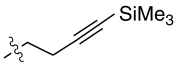


Table 2. Addition of Boc-protected enol triflate **1** to various aldehydes.

Entry	R	equiv. RCHO	Product	Yield (%)[a]
1		6	6	42
2		6	7	49
3		6	8	84
4		6	9	76
5		2	10	62
6		2	11	71
7		6	12	51

[a]After isolation and purification.

nitrogen, such as benzyloxycarbonyl (Cbz), trifluoromethansulfonyl (Tf), or benzoyl, were complicated by either the instability of the enol triflates or the formation of several byproducts during the chromium(II)–nickel(II)-promoted carbonyl addition process.

Using the standard conditions, a variety of aldehydes were then reacted with **1** to probe the scope and limitations of the electrophilic partner (Scheme 4 and Table 2). Electron-rich aromatic aldehydes such as *p*-anisaldehyde (entry 1) or furfural (entry 2) could be used in this reaction, although the yields of the products **6** and **7** were modest: 42% and 49%, respectively. Interestingly, aliphatic aldehydes react more effectively, and the carbonyl addition products could be isolated in much higher yields. As examples, the reactions of **1** with hexanal and isopropanal, using the standard conditions, resulted in the formation of allylic alcohols **8** and **9** in 84% and 76% isolated yields, respectively (entries 3 and 4). Considering the previous use of the chromium(II)–nickel(II)-promoted addition reaction in complex total synthesis (7), it was not surprising that common organic functional groups are compatible with these conditions. Functionalities such as acetals (entry 5, **10**, 62% yield), ethers (entry 6, **11**, 71% yield), and alkynes (entry 7, **12**, 51% yield) were well tolerated in the reaction of **1** under these conditions. Interestingly, attempts to react **1** with cinnamaldehyde were unsuccessful because of problems with decomposition.

Although the desired transformation does occur, this process has its own drawbacks. The first is the large amount of chromium(II) chloride that is required for reaction. Reducing the number of equivalents of chromium(II) salts would substantially improve this process. The lack of reactivity in ethereal solvents is a second handicap that we have uncovered. Although nitrogen-based ligand scaffolds have been used to generate catalytic versions of this carbonyl-addition reaction, those processes typically use THF as a solvent or co-solvent (8). Our preliminary investigations have found that no reaction occurs in THF, despite the presence of external ligands. Finally, the sonication of reaction mixtures is much more easily performed on a small scale. An alternative method for agitation would be required for large-scale reactions. The convenient resolution of all of these issues would generate a generally useful synthetic protocol.

Conclusion

Lactam-derived enol triflates have been demonstrated to undergo nickel(II)–chromium(II) salt mediated carbonyl addition reactions with aldehydes to produce functionalized allylic alcohols. Interestingly, reactions involving aliphatic aldehydes are typically higher yielding compared with aromatic aldehydes. With the feasibility of this protocol established, efforts to render this process *catalytic* in nickel and chromium (9) and to apply this reaction in the construction of nitrogen-containing natural products are underway in our laboratories.

Experimental

General information

All reactions were carried out under a nitrogen atmosphere in flame-dried glassware. Tetrahydrofuran was distilled from sodium, using benzophenone as an indicator. Dimethyl sulfoxide was distilled from calcium hydride under reduced pressure. Dimethyl formamide was dried over molecular sieves (4 Å) and degassed by sparging with nitrogen gas. Commercially available aldehydes (Aldrich) were distilled over sodium sulfate under reduced pressure prior to use. Nickel chloride (98%) was purchased from Aldrich and chromium chloride (99.9%) was purchased from Strem.

Thin-layer chromatography (TLC) was performed on DC-Fertigplatten SIL G-25 UV_{254} pre-coated TLC plates. Sonication was carried out using a Branson 3200 sonicator. Melting points were performed using a Mel-Temp II apparatus (lab devices U.S.A.) and are uncorrected. Infrared (IR) spectra were obtained using a PerkinElmer 1710 FT-IR spectrometer. Proton nuclear magnetic resonance (^{1}H NMR) spectra were recorded in deuterated chloroform, using a Bruker WH-400 spectrometer. Carbon nuclear magnetic resonance (^{13}C NMR) spectra were recorded in deuterated chloroform, using a Bruker AV-300 spectrometer. Chemical shifts (δ) are reported in parts per million (ppm) and are referenced to deuterated chloroform (δ 7.24 ppm ^{1}H NMR; δ 77.0 ppm ^{13}C NMR). Low-resolution mass spectra (LR-MS) were recorded using either a Kratos-AEI model MS 50 or an Aligent 6890 series GC with a 5973 MS. Microanalyses were performed on either a Carlo Erba Elemental Analyzer Model 1106 or a CHN-O Elemental Analyzer Model 1108.

© 2004 NRC Canada

tert-Butyl 6-{[(trifluoromethyl)sulfonyl]oxy}-3,4-dihydropyridine-1(2*H*)-carboxylate (1)

To a solution of 367 mg of 1,1,1,3,3,3-hexamethyldisilazane (2.27 mmol) in 3 mL of THF at –78 °C was added 1.57 mL of *n*-butyllithium in hexane (2.26 mmol, 1.44 mol L^{-1}). After stirring for 20 min, the mixture was transferred via cannula to a solution of 300 mg of 1-(*tert*-butoxycarbonyl)piperidin-2-one (1.50 mmol) in 5 mL of THF at –78 °C. After stirring for 2 h, 1.18 g of *N*-(5-chloro-2-pyridyl)triflimide (3.00 mmol) in 5 mL of THF was added. The cold bath was removed, and the mixture was allowed to warm to 25 °C. After 1 h the reaction was quenched with 8 mL of a 10% aqueous solution of sodium hydroxide. The aqueous phase was extracted with three 5 mL portions of diethyl ether. The combined ethereal extracts were dried over sodium sulfate, filtered, and concentrated using rotary evaporation. Purification via flash chromatography (1:19 ethyl acetate – hexanes, containing 1% triethylamine) on silica gel gave 415 mg (84%) of a clear colourless oil. IR (film) (cm^{-1}): 1726, 1684, 1422, 1211, 1141. ^{1}H NMR (400 MHz, $CDCl_3$) δ: 5.26 (t, *J* = 3.97 Hz, 1H), 3.60–3.56 (m, 2H), 2.24 (td, *J* = 6.71, 3.97 Hz, 2H), 1.77–1.70 (m, 2H), 1.47 (s, H).

Representative procedure for the coupling of lactam-derived enol triflates with aldehydes: _tert_-butyl 6-[hydroxy(phenyl)methyl]-3,4-dihydropyridine-1(2*H*)-carboxylate (2)

A round-bottom flask was charged with 111 mg of chromium(II) chloride (0.91 mmol) and 0.4 mg of nickel(II) chloride (0.003 mmol) and a stirbar. After capping the flask with a septum, DMF (1 mL) was added, and the thick green suspension was stirred for 10 min. Benzaldehyde (96 mg, 0.91 mmol) and a solution of **1** (50 mg, 0.15 mmol) in 1 mL of DMF were added sequentially. The flask containing the reaction mixture was placed in a sonication bath and sonicated for 15 h. Diethyl ether (5 mL) and water (2 mL, containing 1% of triethylamine) was added. The aqueous phase was extracted with three 3 mL portions of diethyl ether. The combined organic extracts were dried over sodium sulfate, filtered, and concentrated in vacuo. Purification via flash chromatography (1:19 ethyl acetate – hexanes, containing 1% triethylamine) on silica gel gave 29 mg (66%) of clear colourless oil. IR (film) (cm^{-1}): 3404, 1682, 1394, 1368, 1256, 1160. ^{1}H NMR (400 MHz, $CDCl_3$) δ: 7.34–7.15 (m, 5H), 5.85 (bs, 1H), 5.45 (t, *J* = 3.66 Hz, 1H), 5.35 (d, *J* = 9.16 Hz, 1H), 3.73 (dt, *J* = 12.51, 4.27 Hz, 1H), 3.03 (t, *J* = 10.99 Hz, 1H), 2.19–2.13 (m, 2H), 1.83–1.68 (m, 2H), 1.29 (s, 9H). ^{13}C NMR (75 MHz, $CDCl_3$) δ: 155.6, 143.7, 142.9, 129.1, 127.9, 127.2, 119.7, 82.6, 67.2, 46.9, 29.4, 24.5, 24.4. LR-MS (EI) *m*/*z* (relative intensity): 289 ([M^+ + 1], 3), 233 (17), 215 (17), 189 (60), 187 (12), 172 (12), 171 (38), 170 (84), 156 (16), 143 (18), 130 (21), 115 (12), 105 (15), 82 (13), 77 (24), 59 (19), 57 (100), 55 (18).

1-[(4-Methylphenyl)sulfonyl]-1,4,5,6-tetrahydropyridin-2-yl trifluoromethanesulfonate (3)

To 1-(*p*-toluenesulfonyl)-piperidin-2-one (200 mg, 0.79 mmol) in THF (6 mL) at –78 °C was added a solution of potassium bis(trimethylsilyl)amide (189 mg, 0.947 mmol) in 2 mL of THF. After stirring for 45 min at –78 °C, a solution of 338 mg of *N*-phenyltriflimide (0.37 mmol) in 3 mL of THF was added. The mixture was allowed to warm to 25 °C. After 1 h the reaction was quenched with 5 mL of a saturated aqueous ammonium chloride solution. The aqueous phase was extracted with three 4 mL portions of dichloromethane. The combined extracts were dried over sodium sulfate, filtered, and concentrated via rotary evaporation. Purification via flash chromatography (1:3 ethyl acetate – hexanes, containing 1% triethylamine) on silica gel gave 195 mg (64%) of white crystals, mp 47 to 48 °C. IR (KBr) (cm^{-1}): 3436, 1674, 1425, 1362, 1213, 1173. ^{1}H NMR (400 MHz, $CDCl_3$) δ: 7.75 (d, *J* = 8.24 Hz, 2H), 7.32 (d, *J* = 8.24 Hz, 2H), 5.43 (t, *J* = 3.97 Hz, 1H), 3.60–3.64 (m, 2H), 2.42 (s, 3H), 2.09–2.14 (m, 2H), 1.53–1.45 (m, 2H).

{1-[(4-Methylphenyl)sulfonyl]-1,4,5,6-tetrahydropyridin-2-yl}(phenyl)methanol (4)

Cloudy colourless oil (yield: 46%). IR (film) (cm^{-1}): 3516, 1715, 1455, 1341, 1163. ^{1}H NMR (400 MHz, $CDCl_3$) δ: 7.61 (d, *J* = 8.55 Hz, 2H), 7.40–7.10 (m, 7H), 5.84 (d, *J* = 1.22 Hz, 1H), 5.46 (t, *J* = 3.66 Hz, 1H), 3.48–3.42 (m, 1H), 3.41–3.35 (m, 1H), 2.40 (s, 3 H), 1.88 (dt, *J* = 10.68, 1.22 Hz, 2H), 1.39–1.29 (m, 2H). ^{13}C NMR (75 MHz, $CDCl_3$) δ: 145.2, 143.4, 142.8, 138.1, 131.1, 129.6, 128.9, 128.8, 128.1, 121.5, 75.9, 48.6, 23.5, 22.9, 21.4. LR-MS (EI) *m*/*z* (relative intensity): 343 ([M^+ + 1], 8), 205 (11), 189 (19), 188 (100), 170 (22), 108 (23), 107 (25), 105 (18), 91 (36), 86 (37), 82 (27), 79 (38), 77 (35), 65 (13), 58 (15), 55 (29), 51 (12).

1-{1-[(4-Methylphenyl)sulfonyl]-1,4,5,6-tetrahydropyridin-2-yl}hexan-1-ol (5)

Clear colourless oil (yield: 42%). IR (film) (cm^{-1}): 3525, 1457, 1343, 1161. ^{1}H NMR (400 MHz, $CDCl_3$) δ: 7.70 (d, *J* = 8.24 Hz, 2H), 7.26 (d, *J* = 7.94 Hz, 2H), 5.60 (t, *J* = 3.66 Hz, 1H), 4.47 (q, *J* = 6.10, 1H), 3.48–3.43 (m, 2 H), 3.19 (d, *J* = 6.10 Hz, 1H), 2.40 (s, 3H), 1.90–1.83 (m, 2H), 1.80–1.60 (m, 2H), 1.42–1.17 (m, 8H), 0.86 (t, *J* = 6.87 Hz, 3H). ^{13}C NMR (75 MHz, $CDCl_3$) δ: 145.2, 142.9, 138.2, 131.1, 128.8, 119.8, 74.9, 48.7, 36.9, 33.1, 27.1, 24.0, 23.3, 23.0, 21.2, 15.4. LR-MS (EI) *m*/*z* (relative intensity): 337 ([M^+ + 1], 6), 182 (37), 126 (12), 112 (100), 111 (12), 91 (20), 82 (11), 55 (25).

tert-Butyl 6-[hydroxy(4-methoxyphenyl)methyl]-3,4-dihydropyridine-1(2*H*)-carboxylate (6)

Clear colourless oil (yield: 42%). IR (film) (cm^{-1}): 3384, 1695, 1683, 1512, 1395, 1368, 1248, 1160. ^{1}H NMR (400 MHz, $CDCl_3$) δ: 7.24–7.20 (m, H), 6.83–6.79 (m, 2H), 5.73 (bs, 1H), 5.43 (t, *J* = 3.66 Hz, 1H), 5.33 (d, *J* = 8.24 Hz, 1H), 3.77 (s, 3H), 3.70 (dt, *J* = 12.21, 3.97 Hz, 1H), 3.05 (t, *J* = 11.60 Hz, 1H), 2.17–2.12 (m, 2H), 1.80–1.69 (m, 2H), 1.32 (s, 9H). ^{13}C NMR (75 MHz, $CDCl_3$) δ: 159.8, 155.6, 143.3, 136.0, 128.4, 119.2, 114.6, 82.6, 76.9, 56.7, 47.0, 29.5, 24.5, 24.4. LR-MS (EI) *m*/*z* (relative intensity): 319 ([M^+ + 1], 4), 246 (11), 245 (53), 219 (19), 202 (19), 201 (86), 200 (69), 187 (15), 186 (100), 171 (11), 170 (55), 160 (22), 158 (13), 146 (13), 137 (18), 135 (30), 128 (10), 121 (10), 115 (12), 91 (13), 77 (32), 65 (11), 63 (11), 59 (90), 57 (85), 56 (12), 55 (21), 51 (16).

© 2004 NRC Canada

***tert*-Butyl 6-[2-furyl(hydroxy)methyl]-3,4-dihydropyridine-1(2*H*)-carboxylate (7)**

Clear colourless oil (yield: 49%). IR (film) (cm^{-1}): 3420, 1681, 1393, 1368, 1161. ^1H NMR (400 MHz, $CDCl_3$) δ: 7.30 (s, 1H), 6.28 (dd, *J* = 3.36, 1.83 Hz, 2H), 5.43 (t, *J* = 3.66 Hz, 1H), 5.35 (s, 1H), 3.72–3.64 (m, 1H), 3.28–3.19 (m, 1H), 2.15 (td, *J* = 7.02, 3.66 Hz, 2H), 1.81–1.71 (m, 2H), 1.40 (s, 9H). ^{13}C NMR (75 MHz, $CDCl_3$) δ: 156.7, 155.8, 142.8, 141.2, 119.3, 111.5, 107.6, 82.8, 72.4, 46.7, 29.6, 24.5, 24.3. LR-MS (EI) *m/z* (relative intensity): 279 ([M^+ + 1], 3), 223 (16), 179 (20), 161 (24), 160 (12), 144 (13), 132 (13), 111 (31), 107 (16), 86 (14), 84 (22), 82 (12), 59 (10), 57 (100), 55 (30).

***tert*-Butyl 6-(1-hydroxyhexyl)-3,4-dihydropyridine-1(2*H*)-carboxylate (8)**

Clear colourless oil (yield: 84%). IR (film) (cm^{-1}): 3424, 1742, 1683, 1393, 1368, 1256, 1163. ^1H NMR (400 MHz, $CDCl_3$) δ: 5.38 (t, *J* = 3.66 Hz, 1H), 5.10 (bs, 1H), 4.05 (dd, *J* = 15.26, 7.32 Hz, 1H), 3.75 (dt, *J* = 11.90, 4.27 Hz, 1H), 3.14 (t, *J* = 8.85 Hz, 1H), 2.13–2.07 (m, 2H), 1.77–1.69 (m, 2H), 1.46 (s, 9H), 1.35–1.20 (m, 6H), 0.90–0.82 (m, 5H). ^{13}C NMR (75 MHz, $CDCl_3$) δ: 156.1, 143.4, 118.0, 82.6, 75.9, 47.0, 36.1, 33.2, 29.7, 27.3, 24.7, 24.3, 24.0, 15.4. LR-MS (GC) *m/z* (relative intensity): 283 ([M^+ + 1], 2), 209 (11), 152 (51), 139 (29), 138 (10), 126 (29), 113 (100), 112 (17), 111 (10), 110 (11), 84 (37), 82 (15), 57 (55), 56 (13), 55 (20), 54 (13).

***tert*-Butyl 6-(1-hydroxy-2-methylpropyl)-3,4-dihydropyridine-1(2*H*)-carboxylate (9)**

White crystals (yield: 76%), mp 58–60 °C. IR (KBr) (cm^{-1}): 3378, 1670, 1656, 1396, 1367, 1166, 1032. ^1H NMR (400 MHz, $CDCl_3$) δ: 5.38 (t, *J* = 3.66 Hz, 1H), 5.14 (bs, 1H), 3.83 (d, *J* = 8.85 Hz, 1H), 3.58 (t, *J* = 9.16 Hz, 1H), 3.04 (t, *J* = 9.77 Hz, 1H), 2.13–2.07 (m, 2H), 1.80–1.66 (m, 2H), 1.45 (s, 9H), 0.98 (d, *J* = 6.71 Hz, 3H), 0.73 (d, *J* = 6.71 Hz, 3H). ^{13}C NMR (75 MHz, $CDCl_3$) δ: 156.2, 142.7, 119.2, 82.7, 82.6, 47.0, 33.0, 29.7, 24.7, 24.3, 21.2, 20.8. LR-MS (GC) *m/z* (relative intensity): 255 ([M^+ + 1], 3), 156 (12), 139 (13), 138 (18), 113 (100), 112 (34), 84 (11), 82 (10), 57 (51), 55 (11). Anal. calcd. for $C_{14}H_{25}NO_3$: C 65.85, H 9.87, N 5.47; found: C 66.25, H 9.98, N 5.28.

***tert*-Butyl 6-[1-hydroxy-4-(tetrahydro-2*H*-pyran-2-yloxy)butyl]-3,4-dihydropyridine-1(2*H*)-carboxylate (10)**

Clear colourless oil (yield: 62%). IR (film) (cm^{-1}): 3441, 2932, 1682, 1393, 1368, 1161. ^1H NMR (400 MHz, $CDCl_3$) δ: 5.39 (t, *J* = 3.66 Hz, 1H), 5.14 (bs, 1H), 4.56–4.51 (m, 1H), 4.10 (q, *J* = 6.71 Hz, 1H), 3.87–3.79 (m, 1H), 3.75–3.65 (m, 2H), 3.50–3.43 (m, 1H), 3.41–3.32 (m, 1H), 3.18 (t, *J* = 10.38 Hz, 1H), 2.10 (td, *J* = 7.02, 3.66 Hz, 2H), 1.84–1.45 (m, 12H), 1.45 (s, 9H). ^{13}C NMR (75 MHz, $CDCl_3$) δ: 156.1, 143.2, 118.0, 100.2, 82.6, 75.7, 75.6, 69.0, 68.9, 63.8, 63.7, 47.0, 33.0, 32.2, 32.1, 29.7, 28.0, 26.9, 24.7, 24.3, 21.1, 21.0. LR-MS (EI) *m/z* (relative intensity): 355 ([M^+ + 1], 2), 198 (14), 197 (18), 196 (38), 171 (40), 170 (45), 167 (11), 155 (11), 154 (37), 152 (20), 149 (22), 126 (24), 113 (67), 112 (11), 110 (24), 97 (23), 85 (62), 82 (10), 67 (14), 57 (100), 55 (21).

***tert*-Butyl 6-{1-hydroxy-3-[(4-methoxybenzyl)oxy]propyl}-3,4-dihydropyridine-1(2*H*)-carboxylate (11)**

Clear colourless oil (yield: 71%). IR (film) (cm^{-1}): 3420, 2932, 2860, 1681, 1515, 1393, 1368, 1249, 1161. ^1H NMR (400 MHz, $CDCl_3$) δ: 7.22 (d, *J* = 8.55 Hz, 2H), 6.84 (d, *J* = 8.55 Hz, 2H), 5.41 (t, *J* = 3.66 Hz, 1H), 5.05 (bs, 1H), 4.41 (dd, *J* = 18.01, 11.29 Hz, 2H), 4.37–3.31 (m, 1H), 3.77 (s, 3H), 3.59 (s, 1H), 3.56–3.44 (m, 2H), 3.19 (s, 1H), 2.10–2.05 (m, 2H), 1.92–1.77 (m, 2H), 1.75–1.65 (m, 2H), 1.45 (s, 9H). ^{13}C NMR (75 MHz, $CDCl_3$) δ: 160.6, 155.9, 143.1, 132.0, 130.7, 117.6, 115.2, 82.6, 74.1, 72.8, 68.9, 56.7, 46.9, 36.2, 29.7, 24.6, 24.2. Anal. calcd. for $C_{21}H_{31}NO_5$: C 66.82, H 8.28, N 3.71; found: C 66.53, H 8.47, N 4.11.

***tert*-Butyl 6-(1-hydroxy-5-trimethylsilanyl-pent-4-ynyl)-3,4-dihydropyridine-1(2*H*)-carboxylate (12)**

Clear colourless oil (yield: 51%). IR (film) (cm^{-1}): 3417, 2961, 2175, 1681, 1392, 1368, 1250, 1162. ^1H NMR (400 MHz, $CDCl_3$) δ: 5.40 (t, *J* = 3.66 Hz, 1H), 5.19 (bs, 1H), 4.19 (dd, *J* = 14.65, 8.24 Hz, 1H), 3.76 (dt, *J* = 11.90, 3.97 Hz, 1H), 3.15 (t, *J* = 10.68 Hz, 1H), 2.24 (t, *J* = 7.63 Hz, 2H), 2.10 (m, 2H) 1.86–1.64 (m, 4H), 1.46 (s, 9H), 0.11 (s, 9H). ^{13}C NMR (75 MHz, $CDCl_3$) δ: 156.1, 142.6, 118.5, 108.5, 86.0, 82.8, 74.7, 47.0, 35.0, 29.7, 24.6, 24.3, 18.3, 1.6. Anal. calcd. for $C_{18}H_{31}NO_3Si$: C 64.05, H 9.26, N 4.15; found: C 64.45, H 9.40, N 4.45.

Acknowledgement

We thank the University of British Columbia and the Natural Sciences and Engineering Research Council of Canada (NSERC) for the financial support of our research program. We also thank the Canadian Foundation for Innovation for enabling specific infrastructure acquisitions.

References

1. M.D.B. Fenster, B.O. Patrick, and G.R. Dake. Org. Lett **3**, 2109 (2001).
2. For the synthetic use of hexamethyldistannane, see: T.N. Mitchell. *In* Encyclopedia of reagents for organic synthesis. Vol. 4. *Edited by* L.A. Paquette. John Wiley, Toronto, Ont. 1995. p. 2664.
3. (*a*) For a recent review, see: A. Fürstner. Chem. Rev. **99**, 991 (1999); also see: (*b*) K. Takai, M. Tagashira, T. Kuroda, K. Oshima, K. Utimoto, and H. Nozaki. J. Am. Chem. Soc. **108**, 6048 (1986); (*c*) H. Jin, J.I. Uenishi, W.J. Christ, and Y. Kishi. J. Am. Chem. Soc. **108**, 5644 (1986)
4. (*a*) K.C. Nicolaou, E.A. Theodorakis, F.P.J.T. Rutjes, J. Tiebes, M. Sato, E. Unterseller, and X.Y. Xiao. J. Am. Chem. Soc. **117**, 1171 (1995); (*b*) K.C. Nicolaou, E.A. Theodorakis, F.P.J.T. Rutjes, M. Sato, J. Tiebes, X.Y. Xiao, C.K. Hwang, M.E. Duggan, Z. Yang, E.A. Couladouros, F. Sato, J. Shin, H.M. He, and T.J. Bleckman. J. Am. Chem. Soc. **117**, 10 239 (1995).
5. Use of lactam-derived enol triflates in metal catalyzed or promoted reactions: (*a*) C.J. Foti and D.L. Comins. J. Org Chem. **60**, 2656 (1995); (*b*) T. Okita and M. Isobe. Synlett, 589 (1994); (*c*) T. Okita and M. Isobe. Tetrahedron, **51**, 3737 (1995); (*d*) T. Luker, H. Hiemstra, and W.N. Speckamp. Tetrahedron Lett. **37**, 8257 (1996); (*e*) T. Luker, H. Hiemstra, and W.N. Speckamp. J. Org. Chem. **62**, 3592 (1997); (*f*) T. Luker, H. Hiemstra, and W.N. Speckamp. J. Org. Chem. **62**, 8131

© 2004 NRC Canada

(1997); (*g*) J.D. Ha and J.K. Cha. J. Org. Chem. **62**, 4550 (1997); (*h*) J.D. Ha, D. Lee, and J.K. Cha. J. Am. Chem. Soc. **121**, 10 012 (1999); (*i*) N. Toyooka, M. Okumura, H. Takahata, and H. Nemoto. Tetrahedron, **55**, 10 673 (1999); (*j*) N. Toyooka, M. Okumura, and H. Takahata. J. Org. Chem. **64**, 2182 (1999); (*k*) J.W. Coe. Org. Lett. **2**, 4205 (2000); (*l*) S. Lindström, L. Ripa, and A. Hallberg. Org. Lett. **2**, 2291 (2000); (*l*) X. Li, Z. Xu, E.F. DiMauro, and M.C. Kozlowski. Tetrahedron Lett. **43**, 3747 (2000); (*m*) E.G. Occhiato, A. Trabocchi, and A. Guarna. Org. Lett. **2**, 1241 (2000); (*n*) E.G. Occhiato, A. Trabocchi, and A. Guarna. J. Org. Chem. **66**, 2459 (2001); (*o*) E.G. Occhiato, C. Prandi, A. Ferrali, A. Guarna, A. Deagostino, and P. Venturello. J. Org. Chem. **67**, 7144 (2002); (*p*) N. Toyooka, A. Fukutome, H. Nemoto, J.W. Daly, T.F. Spande, M. Garraffo, and T. Kaneko. Org. Lett. **4**, 1715 (2002).

6. cf. to: P. Beak and W.K. Lee. J. Org. Chem. **58**, 1109 (1993).
7. For examples, see: (*a*) R.E. Taylor and Y. Chen. Org. Lett. **3**, 2221 (2001); (*b*) O. Corminbeouf, L.E. Overman, and L.D. Pennington. J. Am. Chem. Soc. **125**, 6650 (2003); (*c*) X.T. Chen, S.K. Bhattacharya, B. Zhou, C.E. Gurreridge, T.R.R. Pettus, and S.J. Danishefsky. J. Am. Chem. Soc. **121**, 6563 (1999); (*d*) J.S. Panek and P. Liu. J. Am. Chem. Soc. **122**, 11 090 (2000); (*e*) I. Paterson, D.Y.K. Chen, and A.S. Franklin. Org. Lett. **4**, 391 (2002)
8. For examples, see: (*a*) C. Chen, K. Tagami, and Y. Kishi. J. Org. Chem. **60**, 5386 (1995); (*b*) C. Chen. Synlett, 1311 (1998); (*c*) M. Bandini, P.G. Cozzi, P. Melchiorre, and A. Umani-Ronchi. Angew. Chem. Int. Ed. Eng. **38**, 3357 (1999); (*d*) Z.K. Wan, H-w. Choi, F.A. Kang, K. Nakajima, D. Demeke, and Y. Kishi. Org. Lett. **4**, 4431 (2002); (*e*) H-w. Choi, K. Nakajima, D. Demeke, F.A. Kang, H.S. Jun, Z.K. Wan, and Y. Kishi. Org. Lett. **4**, 4435 (2002); (*f*) M. Inoue, T. Suzuki, and M. Nakada. J. Am. Chem. Soc. **125**, 1140 (2003); (*g*) A. Berkessel, D. Menche, C.A. Sklorz, M. Schroder, and I. Paterson. Angew. Chem. Int. Ed. Eng. **42**, 1032 (2003).
9. (*a*) A. Fürstner and N. Shi. J. Am. Chem. Soc. **118**, 12 349 (1996); (*b*) A. Fürstner. Chem. Eur. J. **4**, 567 (1998).

© 2004 NRC Canada

Synthesis, resolution, and application of 2,2′-bis(diphenylphosphino)-3,3′-binaphtho[*b*]furan (BINAPFu)[1]

Neil G. Andersen, Masood Parvez, Robert McDonald, and Brian A. Keay

Abstract: (±)-2,2′-Bis(diphenylphosphino)-3,3′-binaphtho[2,1-*b*]furan (BINAPFu) was synthesized from 2-naphthoxyacetic acid in a five-step sequence in 62% overall yield. A variety of reported resolution procedures for biaryl bisphosphines did not work with (±)-BINAPFu; thus, a new resolution method was developed, involving the Staudinger reaction of the aforementioned racemate of BINAPFu with an enantiopure camphor sulfonyl azide derivative. The resulting diastereomeric phosphinimines were separated by flash chromatography. Subsequent hydrolysis to the corresponding bis-phosphine oxide and trichlorosilane reduction provided enantiopure BINAPFu. The absolute stereochemical configuration of BINAPFu was established by X-ray crystallography. BINAPFu was compared with commercially available 2,2′-bis(diphenylphosphino)-1,1′-binaphthalene (BINAP) in Pd(0)-catalyzed intermolecular Heck reactions. Investigation of the Heck arylation of 2,3-dihydrofuran showed BINAPFu to be more efficacious than BINAP in dioxane at 30 °C. A variety of phosphorus selenides were prepared, and the $^1J_{P\text{-}Se}$ coupling constants measured, to obtain a comparative scale of parent phosphine basicity. The phosphorus atoms in BINAPFu were found to be electron deficient when compared with BINAP but slightly more electron rich than trifurylphosphine.

Key words: naphthofurans, atropisomers, electron-deficient phosphines, asymmetric Heck reactions, Staudinger reaction.

Résumé : Utilisant l'acide 2-naphtoxyacétique comme produit de départ, on a réalisé la synthèse en cinq étapes du (±)-2,2′-bis(diphénylphosphino)-3,3′-binaphto[2,1-*b*]furane (BINAPFu), avec un rendement global de 62 %. Plusieurs méthodes connues de résolutions ont été tentées sans succès sur le (±)-BINAPFu; on a donc développé une nouvelle méthode de résolution impliquant la réaction du (±)-BINAPFu avec un dérivé énantiopur de l'azoture de camphresulfonyle. On a séparé les phosphinimines diastéréomères résultantes par chromatographie éclair. L'hydrolyse subséquente de l'oxyde de bis-phosphine correspondante et une réduction à l'aide de trichlorosilane ont conduit au BINAPFu énantiopur. La configuration stéréochimique absolue du BINAPFu a été établie par diffraction des rayons X. On a comparé le BINAPFu au 2,2′-bis(diphénylphosphino)-1,1′-binaphtalène (BINAP) dans les réactions intermoléculaires de Heck catalysées par le Pd(0). Une étude de l'arylation de Heck du 2,3-dihydrofurane a montré que le BINAPFu est plus efficace que le BINAP, dans le dioxane, à 30 °C. On a préparé une variété de séléniures de phosphore et on a mesuré les constantes de couplage $^1J_{P\text{-}Se}$ afin d'obtenir une échelle comparative de la basicité de la phosphine de base. On a trouvé que les atomes de phosphore du BINAPFu sont déficients en électron par comparaison avec le BINAP, mais qu'ils sont plus riches en électrons que la trifurylphosphine.

Mots clés : naphtofuranes, atropisomères, phosphine déficiente en électron, réaction de Heck asymétriques, réaction de Staudinger.

[Traduit par la Rédaction]

Introduction

Since Noyori and co-workers' (1) introduction of 2,2′-bis(diphenylphosphino)-1,1′-binaphthyl (BINAP) as a chiral ligand for asymmetric catalysis, numerous workers have shown that remarkably high degrees of enantioselectivity can be obtained using this phosphine in a wide variety of transition-metal-mediated organic reactions (2). Based on the superior results often realized using BINAP in asymmetric transformations, coupled with the recent interest in 2-furyl phosphine ligands (3), a project was undertaken to develop an axially stereogenic diphosphine ligand that incorporates the 2-furyl group. At the onset of this endeavor, a literature search revealed that no such structure had ever been reported. Moreover, it was clear that very little was known about how phosphine σ-donor ability affected the

Received 19 June 2003. Published on the NRC Research Press Web site at http://canjchem.nrc.ca on 9 January 2004.

Dedicated to Dr. E. Piers for his outstanding chemistry contributions and to him as an invaluable mentor over the years.

N.G. Andersen, M. Parvez, and B.A. Keay.[2] Department of Chemistry, University of Calgary, Calgary, AB T2N 1N4, Canada.
R. McDonald. Department of Chemistry, University of Alberta, Edmonton, AB T6G 2G2, Canada.

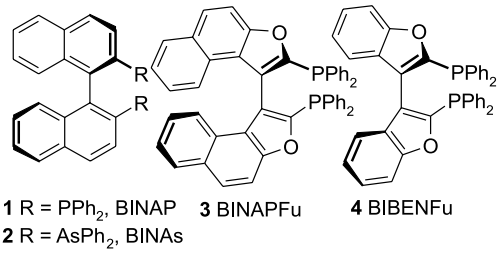
[1]This article is part of a Special Issue dedicated to Professor Ed Piers.
[2]Corresponding author (e-mail: keay@ucalgary.ca).

 doi: 10.1139/V03-173 © 2004 NRC Canada

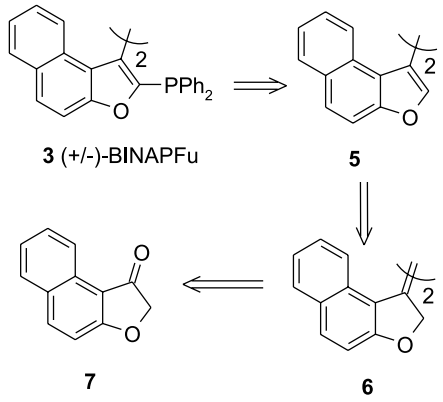
course of enantioselective reactions. However, many workers have now sought to develop chiral 2-furyl phosphine ligands for asymmetric synthesis, and several reports of asymmetric reactions using these ligands have recently been disclosed (4, 5). These investigations have been prompted, in part, by recent evidence that suggests that less electron-rich ligands are or should be advantageous in some metal-mediated organic processes. For example, Shibasaki and co-workers (6) have recently developed 2,2′-bis(diphenylarsino)-1,1′-binaphthyl (**1**, BINAs) and have shown this poorly donating ligand to be more effective than BINAP **2** for an intramolecular asymmetric Heck reaction (Scheme 1) (7). In addition, Amatore and co-workers (8) have studied the oxidative addition of phenyl iodide with in situ generated palladium(0) complexes of triphenylphosphine and TFP, showing that in DMF, $\{Pd(dba)_2 + n(trifurylphosphine)\}$ is always more reactive than $\{Pd(dba)_2 + nPPh_3\}$, for $n \geq 2$ (7). These reports, in conjunction with our interests in the asymmetric polyene cyclization (9), led to the development of a novel 3,3′-bifuryl-derived diphosphine analogue of BINAP (Scheme 1), namely, BINAPFu **3** (10).

To develop a C_2-symmetric furyl phosphine analogue of BINAP, it was conceived that a prudent design would retain the bis(diphenylphosphino) moieties and incorporate the furyl functionality into the biaryl framework. In this way, it was felt that the electronic properties of the phosphine ligand could be altered with minimal perturbation of the chiral pocket structure. Since Benincori and co-workers (5*i*, 11) have concluded that the BIBENFu **4** ligand is not configurationally stable at room temperature, it was decided to prepare the more sterically bulky bisnaphtho[*b*]furan skeleton, as PM3 semi-empirical calculations on **3** indicated that the rotational energy of the bifuryl bond in **3** would be quite high. This paper describes the design aspects, synthesis, resolution, and application of the BINAPFu **3** ligand.

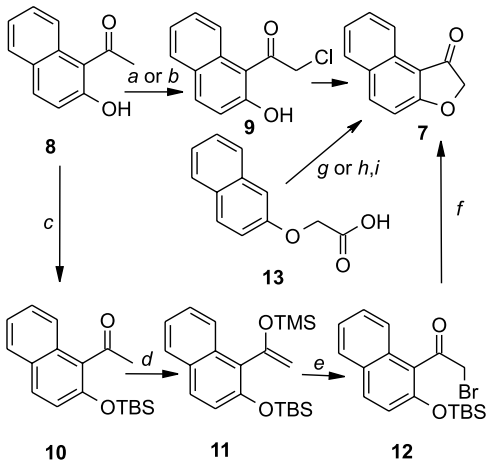
Scheme 1.



Scheme 2.



Scheme 3. (*a*) 1–5 equiv SO_2Cl_2, DCM, reflux, 4.5–12 h, <5%; (*b*) 2 equiv hexachloro-2,4-cyclohexadienone, EtOH, reflux, 18 h, 30%; (*c*) 1.1 equiv TBSCl, Et_3N, DCM, rt, 18 h, 89%; (*d*) 1.0 equiv TMSOTf, Et_3N, DCM, rt, 2 h; (*e*) 1 equiv Br_2, CCl_4; (*f*) 1 equiv TBAF, THF, rt, 0.5 h, 72% (2 steps); (*g*) excess P_2O_5, MsOH, rt, 18 h, 68%; (*h*) 2 equiv $SOCl_2$, benzene, catalytic (cat) Py, reflux, 2 h; (*i*) 1.5 equiv $AlCl_3$, benzene, rt, 12 h, 95% (2 steps).



Synthesis of (±)-BINAPFu 3

Two initial routes to the synthesis of **3** were unsuccessful (12) and led to a design in which the key reaction involved a McMurry coupling. The low-valent titanium homocoupling of aldehydes and ketones, developed independently by Mukaiyama et al. (13), Tyrlik et al. (14), and McMurry et al. (15), has been applied in a wide variety of contexts to prepare symmetrical olefins (16). It was thought that the BINAPFu bifuryl bond could be constructed via a McMurry coupling of ketone **7** followed by DDQ oxidation of the resultant olefin **6** (Scheme 2). Finally, introduction of the diphenylphosphino groups into **5** would give (±)-BINAPFu **3**.

Although ketone **7** has been previously reported (17), the syntheses were characterized by low product yields (<35%) and difficult isolation procedures. It was therefore decided that a new, efficient synthesis of the required ketone **7** should be developed. Since 1-acetyl-2-hydroxynaphthalene (**8**) was readily available, it was reasoned that α-chlorination of the ketone function to give **9**, followed by 5-*exo-trig* ring closure, would provide an expedient route to the desired ketone **7** (Scheme 3). Unfortunately, several chlorination reagents, including sulfuryl chloride (18) and hexachloro-2,4-cyclohexadienone (19), failed to provide α-chloroketone **9** in good yields. Recourse was sought in the three-step α-bromination of ketone **10** via TMS enol ether **11** (Scheme 3). Treatment of hydroxy-ketone **8** with 1.1 equiv of *tert*-butyldimethylsilyl chloride in CH_2Cl_2 and Et_3N furnished TBS ether **10** in 89% yield. Although the TMS enol ether **11** could be formed using LHMDS and TMSCl in an ethereal solvent, much more consistent results were obtained when ketone **10** was treated with TMSOTf in a mixture of CH_2Cl_2 and triethylamine. Bromination of enol silyl ether **11** with

© 2004 NRC Canada

1 equiv of Br_2 in CCl_4 proceeded with loss of TMSBr to furnish α-bromo ketone **12** in modest yield. Cleavage of the TBS ether under standard conditions occurred with concomitant ring closure, to provide the desired naphthoketone **7** in 61% overall yield. Although this four-step synthetic sequence provided the desired ketone **7** in moderate yield, without the need for costly purification routines, the use of expensive protecting groups and reagents rendered this method somewhat infeasible for large-scale preparation.

To address these concerns, an alternative synthesis of compound **7** was conceived whereby readily available 2-naphthoxyacetic acid (**13**) could be subjected to Friedel–Crafts acylation conditions to provide the desired compound directly (Scheme 3). Treatment of acid **13** with Eaton's reagent (20) at ambient temperature for 18 h afforded the desired ketone **7** in 68% yield. Alternatively, preparation of the corresponding acyl chloride, under standard conditions, and subsequent reaction with $AlCl_3$ gave naphthoketone **7** in 95% yield. Interestingly, in both cases, acylation occurred regiospecifically in the 1-position to give the desired product **7** with remarkable purity. This procedure, which does not require any purification steps, can easily be performed on a 50 g scale to provide ketone **7** in excellent yield.

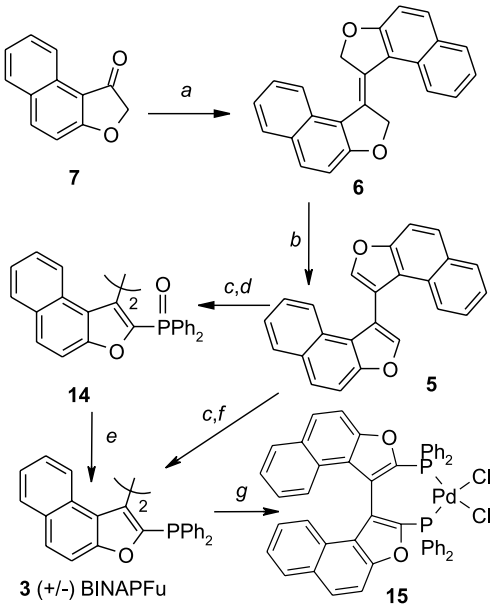
Reductive coupling of compound **7** with $TiCl_4$ and zinc–copper couple (21) in refluxing DME smoothly provided olefin **6** in good yield (Scheme 4). Activated zinc dust (22) worked equally as well for this purpose, giving biaryl **5** in 78% isolated yield after DDQ oxidation (23). ^{1}H NMR analysis of compound **6** showed that the product had been formed essentially as a single isomer (>95%), which was assigned the *E* configuration on the basis of steric arguments. Owing to facile carbon-carbon double bond migration, olefin **6** could not be fully characterized. Upon oxidation with DDQ, the broad singlet (δ: 5.25 ppm) that integrated as four protons in the ^{1}H NMR spectrum of **6** was replaced by a sharp singlet (δ: 7.87 ppm) that represented the two furan α-protons in biaryl **5**.

Installation of the bis(diphenylphosphino) moieties was accomplished by lithiation of the biaryl scaffold **5** with 2.5 equiv of *t*-BuLi and subsequent treatment of the resulting dianion with freshly distilled diphenylphosphinic chloride. This provided phosphine oxide **14** in 88% yield (Scheme 4). Reduction of the oxide **14** with trichlorosilane in a mixture of xylenes and triethylamine furnished (±)-BINAPFu (**3**) in >95% yield. Alternatively, lithiation of biaryl **5** followed by treatment of the resultant dianion with 2.0 equiv of chlorodiphenylphosphine gave (±)-BINAPFu **3** directly in 91% yield.

Structural characterization of (±)-BINAPFu 3

As stated previously, a fundamental aspect of the ligand design required that the 2-furyl groups be incorporated in such a way that the electronic properties of the phosphorus atoms may be altered with as little perturbation of the chiral pocket structure as possible. To investigate the success of the ligand design with respect to this requirement, the palladium(II) chloride complex of BINAPFu **15** was prepared (5*i*) and analyzed by single crystal X-ray diffraction (Fig. 1). Crystals of compound **15** were obtained by slow diffusion of

Scheme 4. 8.2 equiv Zn dust, 2.0 equiv $TiCl_4$, DME, reflux, 18 h; (*b*) 1.0 equiv DDQ, benzene, reflux, 4 h, 78% (2 steps); (*c*) 2.5 equiv *t*-BuLi, Et_2O, rt, 2 h; (*d*) 2.0 equiv $PPh_2(O)Cl$, rt, 12 h, 88%; (*e*) 20 equiv $SiCl_3H$, 24 equiv Et_3N, xylenes, 150 °C, 3 h, >95%; (*f*) 2.0 equiv PPh_2Cl, rt, 12 h, 91%; (*g*) 1.0 equiv $(CH_3CN)_2PdCl_2$, DCM, rt, 28 h, 93%.

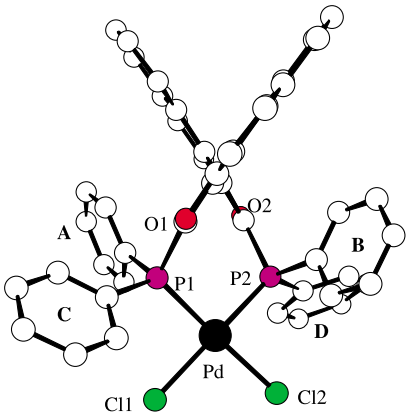


Et_2O into an acetone-saturated solution of the complex under an argon atmosphere.

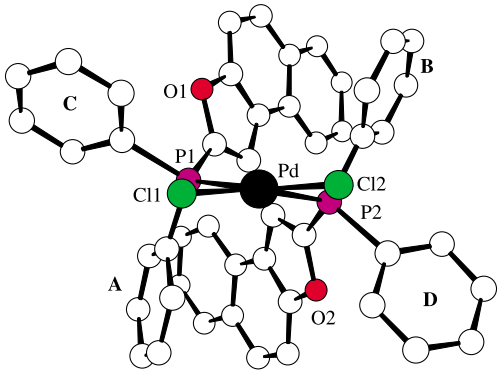
Comparing the projections of [(±)-BINAPFu]$PdCl_2$ (**15**) with Hayashi's [(*R*)-BINAP]$PdCl_2$ structure **16** (24), a few structural differences are immediately apparent. Whereas two of the phenyl rings (A and B) in the [(*R*)-BINAP]$PdCl_2$ complex **16** π-stack with the binaphthalene framework, the corresponding phenyl groups in compound **15** (A and B) do not show perpendicular relationships with the binaphtho[*b*]furan system. Also noteworthy in the [(±)-BINAPFu]$PdCl_2$ structure **15** is that the square planar geometry about the palladium atom seems to be less distorted than in the corresponding (*R*)-BINAP complex **16**. These observations suggest that the chiral pocket formed in the [BINAPFu]$PdCl_2$ complex **15** is somewhat less rigid than that obtained with the BINAP ligand **16**. However, several similarities are also observed upon comparing [BINAP]$PdCl_2$ **16** and [BINAPFu]$PdCl_2$ **15**. In both structures, two of the phenyl rings (C and D) project outward toward the coordination sites occupied by the chloride ligands. The [BINAP]$PdCl_2$ **16** bite angle (25), defined by the P1-Pd-P2 vertex, of 92.7° compares well with that measured for the [BINAPFu]$PdCl_2$ **15** (93.4°). Values for the Pd—P (**16**: 2.245 Å; **15**: 2.264 Å) and Pd—Cl (**16**: 2.350 Å; **15**: 2.333 Å) bond lengths compare quite favorably, although slight differences can be seen because of the reduced electron-donor ability of the BINAPFu ligand. As expected, the mean Pd—P bond length is slightly longer in the [BINAPFu]$PdCl_2$ complex, owing to the reduced σ-donor ability of the phosphorus atoms relative to BINAP. As a result, the Pd—Cl bond lengths are slightly shorter in compound **15**. Given the structural changes that had to be made to incorporate the 2-furyl moieties, it was felt that the struc-

© 2004 NRC Canada

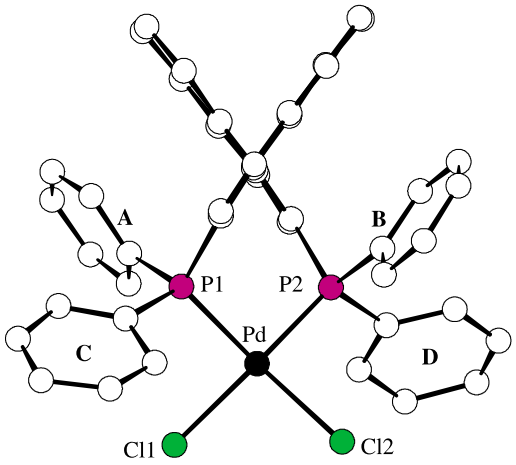
Fig. 1. X-ray crystal structure of [(±)-BINAPFu]$PdCl_2$ (15) vs. Hayashi's (24) [(±)-BINAP]$PdCl_2$ (16) structure (hydrogen atoms omitted for clarity).



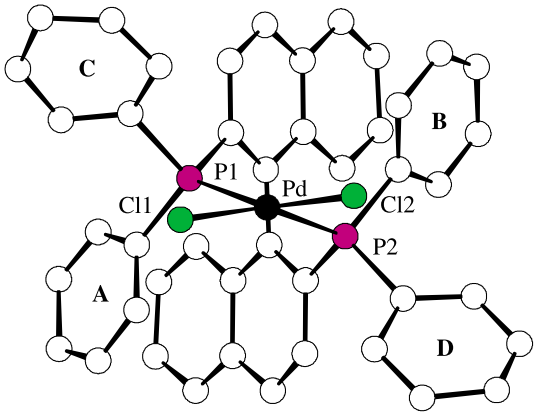
[(±)-BINAPFu]$PdCl_2$ (**15**) top view



[(±)-BINAPFu]$PdCl_2$ (**15**) side view



[(*R*)-BINAP]$PdCl_2$ (**16**) top view



[(*R*)-BINAP]$PdCl_2$ (**16**) side view

tural homology between the two organometallic complexes was great enough to warrant further investigation with the BINAPFu ligand.

Resolution of (±)-BINAPFu 3

Subsequent to developing a simple, highly efficient synthesis of (±)-BINAPFu **3**, attention focused on finding a method for obtaining the two pure optical antipodes. To achieve this goal, it was first necessary to find a convenient method for determining the enantiopurity of diphosphine **3**. Fortunately, (±)-BINAPFu **3** could be readily separated by analytical HPLC using a Chiralcel® OJ column (25 °C; 95:5 MeOH:EtOH; 0.5 mL min^{-1}; 270 nm UV detection), indicating that the rotational barrier of the biaryl axis was of sufficient magnitude to impart optical activity at room temperature. Although preparative HPLC columns employing similar chiral stationary phases are commercially available (26), optical resolution of the BINAPFu ligand in large quantities using this method was deemed to be infeasible.

Although several methods for achieving optical resolution of stereogenic organophosphorus compounds are known (27), efforts were initially focused on procedures that have been applied to BINAP and related C_2-symmetric diphosphines. Unfortunately, the following reported procedures did not afford a suitable resolution method for (±)-BINAPFu **3**: (*a*) co-crystallization of phosphine oxide **14** with (–)-DBTA or (1*S*)-(+)-10-camphorsulfonic acid (28); (*b*) using enantiopure palladium(II) complexes with (*S*)-*N*,*N*-dimethyl-α-phenylethylamine or (*S*)-*N*,*N*-dimethyl-α-(2-naphthyl)ethylamine (29–31); (*c*) via formation of phosphonium salts with enantiopure organohalides like (*S*)-(+)-citronellyl bromide, (*S*)-(+)-citronellyl iodide (32), or (*S*)-(+)-1-iodo-2-methylbutane; and (*d*) attempts to resolve the bis-phosphonium salt

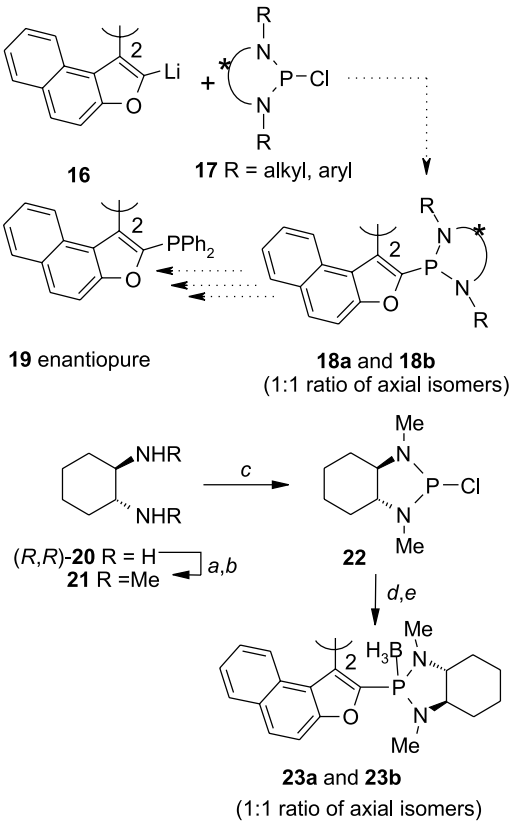
© 2004 NRC Canada

of **3** (generated with 2 equiv of iodomethane) by reaction with silver hydrogen dibenzoyl-L-tartrate (Ag-DBHT) (33) or silver (1*S*)-(+)-10-camphorsulfonate (34).

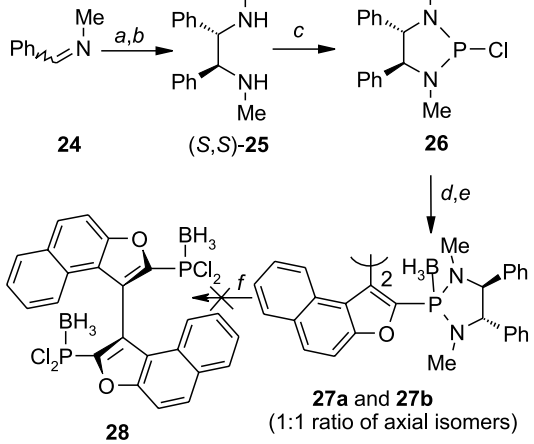
Although the synthesis developed for the BINAPFu ligand (vide supra) is short and efficient, failure to identify a suitable method for obtaining the optically pure material via known resolution methods led to the consideration of alternative synthetic routes. It was postulated that an enantiopure electrophile of type **17** could potentially be reacted with lithiated biaryl **16** to give bis-phosphonamide **18** as a 1:1 mixture of diastereomers (35) (Scheme 5). Such an approach would thus install the required 2,2′-phosphorus atoms while appending a chiral auxiliary for optical resolution. Separation of the resulting diastereomer mixture and subsequent synthetic manipulation of each pure isomer, **18a** and **18b**, would then provide routes to the optically pure BINAPFu antipodes. Following this general scheme, commercially available *trans*-1,2-cyclohexane diamine was resolved (36), and the (*R*,*R*)-isomer (37) **20** was converted to the corresponding *N*,*N*′-dimethyl derivative **21** according to a literature procedure (38) (Scheme 5). Diamine **21**, thus obtained, was treated with 1 molar equivalent of phosphorus trichloride, according to a standard procedure (39), to furnish chlorophosphine **22** in 72% isolated yield. This highly moisture- and oxygen-sensitive (39) compound was prepared using Schlenk techniques under an atmosphere of argon and was used without purification. Trapping dianion **16**, prepared as previously described, with 1,3-diazaphopholidine derivative **22** and subsequent reaction with BH_3·DMS provided a 1:1 mixture of diastereomers **23a** and **23b**, respectively (Scheme 5). Bis-borane complex **23** was prepared in situ to prevent potential complications due to air oxidation of the phosphine precursor (39). Although separation of compounds **23a** and **23b** could not be achieved using standard recrystallization or flash chromatographic techniques, a small sample (~3 mg) of each pure diastereomer was obtained by preparative HPLC, using a reversed-phase C_{18} column. While this labor-intensive and costly separation technique clearly did not provide large quantities of resolved material, the obtainment of diastereomerically pure borane adducts **23a** and **23b** was highly encouraging. Moreover, it was postulated that by simply changing the diamine used to prepare phosphoramidous chloride **17** (Scheme 5), it may be possible to prepare a more readily separable mixture of axial diastereomers.

Diamine **25** was prepared from **24** (40) and resolved (41) according to standard literature procedures (Scheme 6). Diazaphospholidine **26** (42) was subsequently prepared upon treatment of (*S*,*S*)-(–)-diamine **25** with 1 equiv of phosphorus trichloride in Et_3N–Et_2O solution. Further reaction with 2,2′-dilithiated binaphthofuran **16** and BH_3·DMS furnished a 1:1 mixture of axially isomeric borane adducts **27a** and **27b** in 71% yield. Fortunately, separation of stereoisomers **27a** and **27b** was facile by fractional crystallization from a $CHCl_3$–hexanes solvent system. Under these conditions, compound **27a** selectively crystallized, leaving highly enriched (>95%) isomer **27b** in the mother liquor. The latter compound could be further purified by flash chromatography. With pure borane adducts **27a** and **27b** in hand, attention was focused on removing the diamine moiety and installing the required phenyl substituents.

Scheme 5. (*a*) 2.1 equiv ethyl chloroacetate, 4.6 equiv NaOH, H_2O, 0 °C, 2 h, 82%; (*b*) 8.5 equiv $LiAlH_4$, THF, rt, 1 h, 92%; (*c*) 1.0 equiv PCl_3, 2 equiv NEt_3, Et_2O, –40 °C, 72%; (*d*) 0.5 equiv compound **16**, Et_2O, rt, 1.5 h; (*e*) 2 equiv BH_3·DMS, rt, 24 h, 74% (2 steps).



Scheme 6. (*a*) 1.5 equiv Mg, 1.5 equiv $TiCl_4$, 4 mol% $HgCl_2$, THF, 0 °C, 12 h, 61%; (*b*) optical resolution with L-(+)-tartaric acid; (*c*) 1.0 equiv PCl_3, 2 equiv NEt_3, Et_2O, –40 °C, 81%; (*d*) 0.5 equiv compound **16**, Et_2O, rt, 1.5 h; (*e*) 2 equiv BH_3·DMS, rt, 24 h, 71% (2 steps); (*f*) 8 equiv anhyd HCl, Et_2O.



Supported by literature precedent (35, 43), it was envisioned that the diamine chiral auxiliary could be cleaved from borane adduct **27a** upon treatment with anhyd HCl, providing enantiopure chloride **28** (Scheme 6). Subsequent

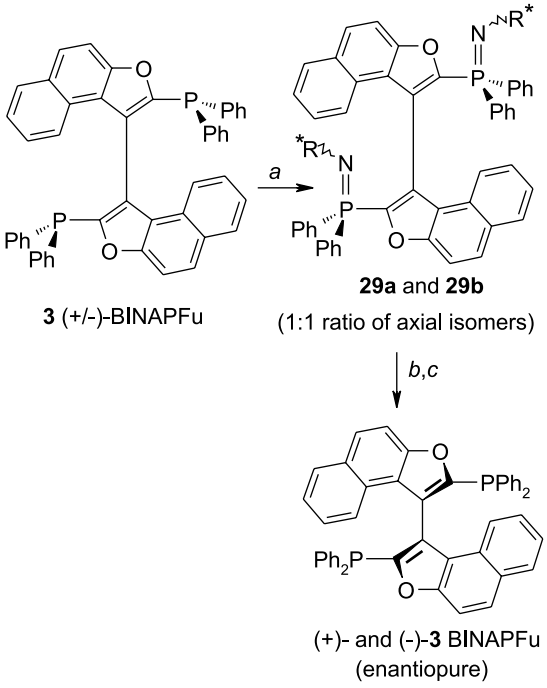
© 2004 NRC Canada

reaction of **28** with 4 equiv of phenyllithium or phenyl Grignard and removal of the BH_3 protecting group would then furnish the desired BINAPFu **3** in optically pure form. Following this approach, isomerically pure compound **27a** was treated with 8 molar equivalents of HCl (1.0 mol L^{-1} solution in Et_2O) at 0 °C for 1 h. The mixture thus obtained was filtered under argon to remove (1*S*,2*S*)-*N*,*N*′-dimethyl-1,2-diphenylethylenediamine dihydrochloride, and the filtrate was treated with 5 equiv of phenyllithium at –40 °C. Under these conditions, a complex mixture of products was obtained, as evidenced by ^{31}P NMR analysis. Lowering the reaction temperature to –40 °C for the acid addition or using phenyl Grignard in place of phenyllithium failed to improve this result. Employing anhyd HCl(g) instead of the 1.0 mol L^{-1} ethereal solution also afforded a complex mixture of products. In all cases, isolation of the unwanted amine hydrochloride salt confirmed that cleavage of the P—N bonds was occurring under the reaction conditions. Low temperature ^{31}P NMR analysis indicated that complex mixture formation was occurring previous to the addition of the organometallic reagent. Other Brönsted acids, including MsOH and TFA in methanolic solution, afforded similar results. The failure to identify suitable conditions for cleaving the diamine chiral auxiliary from borane adduct **27a** led to the development of a new resolution procedure for phosphines.

As several of the known methods for phosphine resolution were unsuccessful, we decided to develop a new resolution to obtain enantiopure BINAPFu **3**. Consideration of the resolution methods already attempted (vide supra) suggested that a newly developed procedure should ideally act directly on BINAPFu **3** or the corresponding bis-phosphine oxide **14** to minimize the number of synthetic steps. Moreover, owing to the difficulties experienced in the CSA and DBTA resolution techniques, it was concluded that a successful route would likely involve appending the resolving agent via a covalent linkage, thus providing two discrete diastereomeric compounds. Based on unsuccessful attempts with the *ortho*-palladated resolving agents (29–31), the diastereomeric compounds obtained by appending a resolving agent to the phosphine ligand should be neutral intermediates, to allow for possible chromatographic separation. Finally, considering the impasse reached with diazaphospholidine compound **27a**, cleavage of the chiral auxiliary to furnish the desired optically pure phosphine **3** or phosphine oxide **14** should not require strongly acidic reaction conditions. With these parameters in mind, it was conceived that a Staudinger reaction (44) between (±)-BINAPFu **3** and 2 equiv of an enantiopure organoazide could potentially give a 1:1 mixture of diastereomeric phosinimines **29a** and **29b** (Scheme 7) if the P=N bond rotational barrier was low enough to prevent geometrical isomerism. A literature survey revealed that the P=N rotational barrier for simple phosphinimines has been calculated to be ca. 2.54 kcal mol^{-1} (45). Hence it was rationalized that P=N geometrical isomerism would likely not complicate the proposed resolution technique. Separation of the phosphinimine mixture and subsequent reductive cleavage of the resolving agent from each pure isomer with $LiAlH_4$ would then furnish the desired, enantiomerically pure antipodes.

To develop a resolution procedure for (±)-BINAPFu based on phosphinimine formation, a readily available and optically pure organoazide needed to be identified (46). (1*S*)-10-camphorsulfonyl azide was chosen as a possible resolving agent; it can be prepared in a single step from commercially available (1*S*)-(+)-10-camphorsulfonyl chloride (47). Treatment of (±)-BINAPFu **3** with 2 molar equivalent of enantiopure sulfonyl azide **30** smoothly provided a 1:1 mixture of diastereomeric phosphinimines **31a** and **32b** in near quantitative yield (Scheme 8). Fortunately, phosphinimines **31a** and **31b** could be readily separated by flash chromatography on silica gel using a 9:1 $CHCl_3$–CH_3CN eluent mixture. With isomerically pure phosphinimines **31a** and **32b** in hand, attention was now focused on identifying a method for removing the chiral auxiliary to give optically pure BINAPFu **3** or the corresponding phosphine oxide **14**.

Scheme 7. (*a*) 2 equiv enantiopure azide ($*RN_3$); (*b*) separate axial stereoisomers; (*c*) H^- reduction, Et_2O.

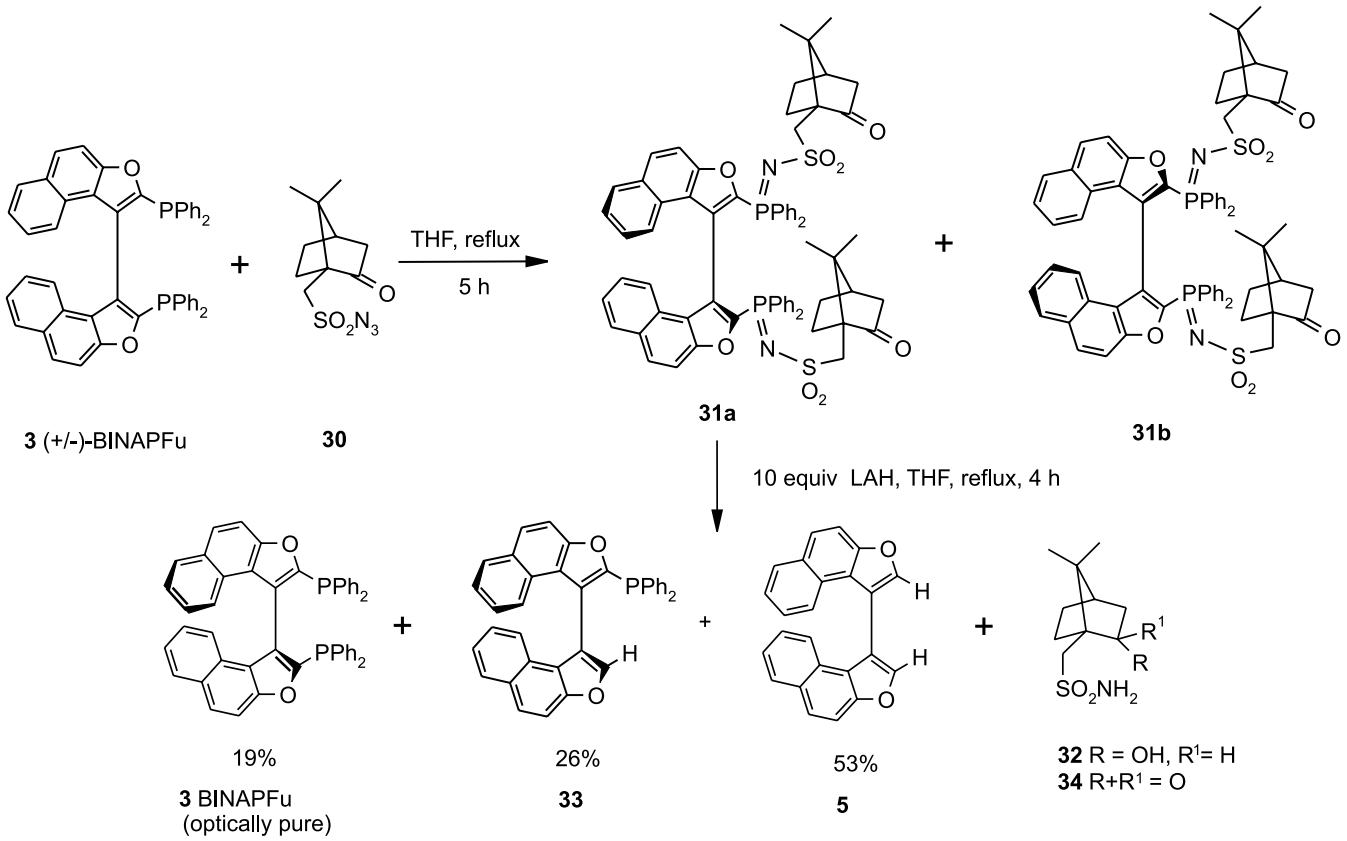


It was postulated that treatment of isomerically pure phosphinimine **31a** with excess $LiAlH_4$ would provide optically pure BINAPFu **3** along with isobornyl-10-sulfonamide **32** (Scheme 8) (48). Interestingly, heating compound **31a** with 10 equiv of LAH in THF resulted in the unexpected formation of 3,3′-binaphtho[*b*]furan (**5**) and monophosphine **33**. Although a small amount of the desired product was obtained and shown to be optically pure by HPLC analysis (Chiralcel® OJ column; 25 °C; 95:5 MeOH:EtOH; 0.5 mL min^{-1}; 270 nm UV detection), conditions to attenuate the formation of byproducts **5** and **33** could not be found. Performing this reaction at ambient temperature resulted in a similar product mixture, while employing weaker reducing agents, such as DIBAL or $NaBH_4$, failed to cleave the P=N bond.

Faced with the failure to prepare optically pure BINAPFu **3** in good yield via direct reduction of phosphinimine **31a**, it was postulated that the P=N bond could be cleaved using an aza-Wittig process (49). Hence, reaction of either compound **31a** or **31b** with CO_2 would afford optically pure phosphine

© 2004 NRC Canada

Scheme 8.



oxide **14** along with (1*S*)-10-camphorsulfonamide **34** (Scheme 8). Subsequent trichlorosilane reduction of phosphine oxide **14** thus obtained would then furnish the desired enantiopure BINAPFu ligand **3**. Surprisingly, bubbling CO_2 gas through a solution of isomerically pure phosphinimine **31a** in THF for a period of 4 h failed to cause any detectable cleavage of the P=N bond. Changing the solvent to acetone and lengthening the exposure time did not improve this result. Moreover, no reaction was observed upon refluxing compound **31a** in carbon disulfide for 24 h, suggesting that an aza-Wittig approach toward cleaving the phosphinimine moiety was not going to be feasible.

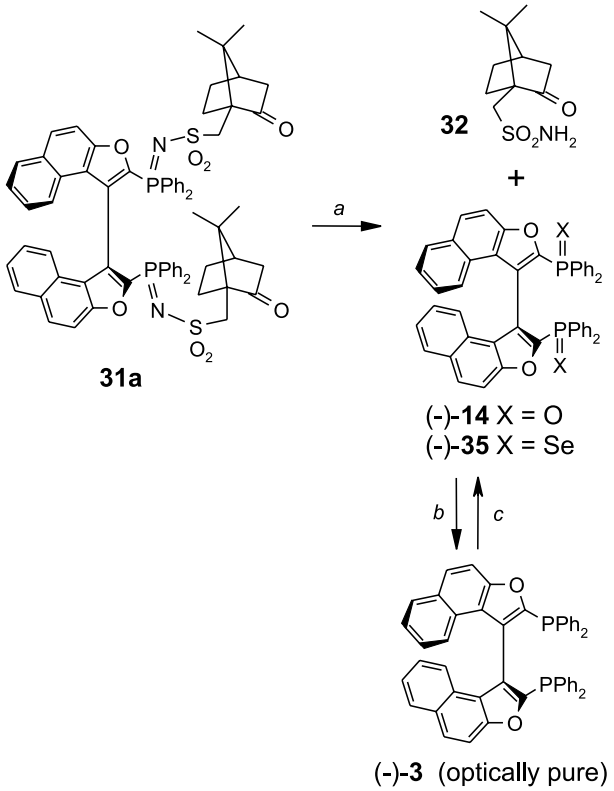
Since phosphinimine **31a** was inert towards aza-Wittig conditions, recourse was sought in the hydrolytic cleavage of the P=N bond using mineral acids (50). Stirring a solution of compound **31a** in THF and 1.5 mol L^{-1} H_2SO_4 at ambient temperature for 24 h failed to give any reaction, as evidenced by ^{31}P NMR analysis. Although this experiment did not result in the cleavage of the P=N bond, it is noteworthy that the binaphtho[*b*]furan system withstood the reaction conditions and was therefore more stable to acid than previously anticipated. Performing the reaction in refluxing THF, under otherwise identical conditions, cleanly provided the desired phosphine oxide, albeit in poor conversion (~15%). Subsequent experimentation revealed phosphine oxide **14** could be obtained in near quantitative yield by refluxing compound **31a** in a 3:2 mixture of 1,4-dioxane and 3 mol L^{-1} H_2SO_4 for 24 h (Scheme 9). Subsequent chromatographic removal of sulfonamide **32** and trichlorosilane reduction of the resulting phosphine oxide **14** provided BINAPFu **3** in excellent yield. HPLC analysis (vide supra) of the bisphosphine thus obtained showed a single peak at R_T = 23.7 min. Finally, optical rotation data revealed that phosphinimine **31a** yielded (–)-BINAPFu ($[\alpha]_D^{19}$ –203.0 (*c* 1.09, $CHCl_3$)). Performing the same hydrolysis–reduction sequence on phosphinimine **31b** provided (+)-BINAPFu **3** in near quantitative yield ($[\alpha]_D^{20}$ +201.8 (*c* 1.28, $CHCl_3$)). Heating the enantiopure (–)-BINAPFu ligand in *p*-xylenes at 150 °C for 7 days did not result in any racemization of the chiral axis, as evidenced by optical rotation and HPLC analysis.

Physical characterization of the BINAPFu ligand: Investigation of the σ-donor ability and absolute configuration assignment

Allen and Taylor (51) have reported that the $^1J(^{31}P\text{-}^{77}Se)$ coupling constant of phosphorus selenides may be used as a measure of parent phosphine basicity. A large coupling constant indicates high *s*-character of the phosphorus lone-pair orbital. In other words, poorly donating phosphine ligands exhibit large $^1J(^{31}P\text{-}^{77}Se)$ coupling constants. To gauge the donor ability of the BINAPFu ligand, a solution of optically pure (–)-**3** in $CHCl_3$ was heated with 10 molar equivalent of selenium powder for 5 h to afford bis-selenide **35** (Scheme 8). ^{31}P NMR analysis of selenide **35** clearly showed a strong singlet at +19.4 ppm with a satellite doublet ($^1J_{P\text{-}Se}$ = 762 Hz) due to $^{31}P\text{-}^{77}Se$ coupling. Performing the same reaction and ^{31}P NMR analysis on a variety of other commonly used phosphine ligands yielded the $^1J_{P\text{-}Se}$ coupling constants shown in Fig. 2. As the data clearly indi-

© 2004 NRC Canada

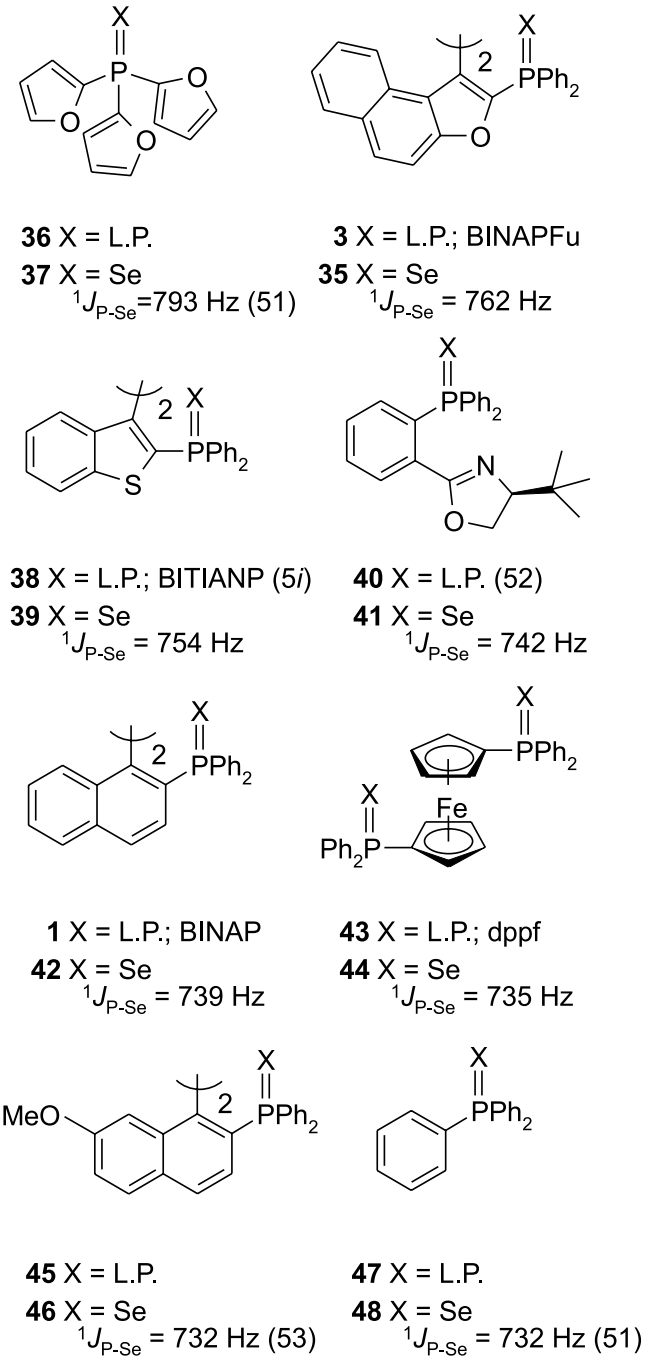
Scheme 9. (*a*) 3 mol L^{-1} H_2SO_4, 1,4-dioxane, 100 °C, 24 h, >95%; (*b*) 20 equiv $SiCl_3H$, 24 equiv Et_3N, xylenes, 150 °C, 3 h, >95%; (*c*) 10 equiv Se powder (100 mesh), $CHCl_3$, 60 °C, 5 h, 97%.



cates, the BINAPFu ligand **3** is far less basic than both triphenylphosphine (**47**) and BINAP (**1**). Moreover, BINAPFu **3** is significantly less basic that Benincori's benzothiophene-derived ligand BITIANP (**38**) (5*i*). Phosphinoaryl oxazoline ligand **40**, which has gained much attention in enantioselective allylic alkylation reactions (52), is also less basic than triphenylphosphine but significantly more basic than either BINAPFu or BITIANP. The small difference observed between the coupling constants for bis-selenides **42** and **46** suggest that this measure of σ-donor ability can be quite a sensitive technique. The latter selenide, derived from 7,7′-dimethoxy-2,2′-bis(diphenylphosphino)-1,1′-binaphthalene (**45**) (53), is slightly more basic than BINAP, owing to the electron-donating capacity of the remote 7,7′-methoxy substituents.

Having demonstrated that the electronic properties of BINAPFu **3** and BINAP **1** are dissimilar, with the former ligand resembling those of tri-2-furylphosphine (**36**), attention was focused on the final task of characterization. The absolute configuration of the biaryl axis needed to be elucidated. With phosphine selenide **35** in hand, prepared from optically pure (–)-BINAPFu (vide supra), it was rationalized that X-ray diffraction using the Bijvoet method (54) could determine the stereochemical assignment. Single crystal analysis of compound **35** furnished the structure depicted in Fig. 3. By refining the inverted structure and evaluating the Flack parameter, it was shown that the *S*-configuration was present in the crystal. Hence, phosphinimine **31a** corresponds to (*S*)-(–)-BINAPFu, while phosphinimine **31b** corresponds to (*R*)-(+)-BINAPFu. This relationship was verified via single crystal X-ray diffraction analysis of phosphinimine **31a** (Fig. 3). In this case, Bijvoet analysis was not required since the absolute stereochemistry of the biaryl axis could be ascertained by simple comparison with the known configurations of the camphor residues. Since (1*S*)-(+)-10-camphorsulfonyl chloride was used to prepare resolving agent **30**, it follows from Fig. 3 that phosphinimine **31a** is the *S*-axial diastereomer.

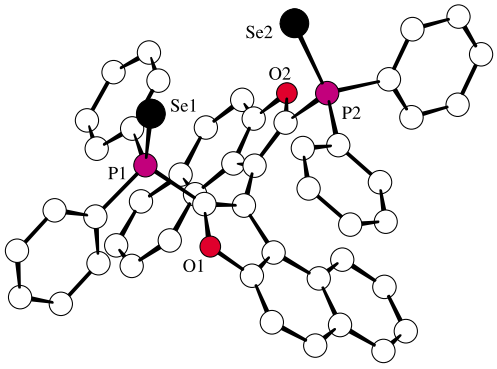
Fig. 2. $^1J_{P\text{-}Se}$ coupling constants for selected phosphine selenides.



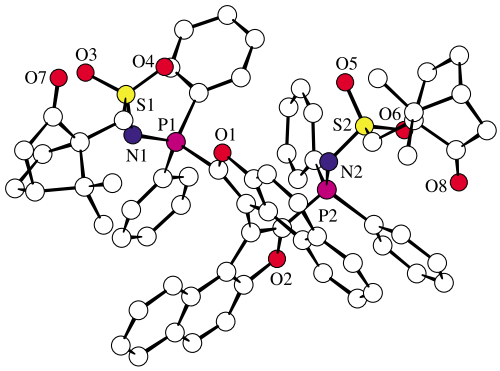
Having attained the goal of preparing and optically resolving a C_2-symmetric bifuran analogue of BINAP, the task of

© 2004 NRC Canada

Fig. 3. X-ray crystal structures of phosphine selenide **35** (one solvent molecule of crystallization (CH_3CN) omitted for clarity) and phosphinimine **31a** (unit cell contains two identical molecules of compound **31a** and five molecules of CH_3CN (not shown)); hydrogen atoms omitted for clarity.



35



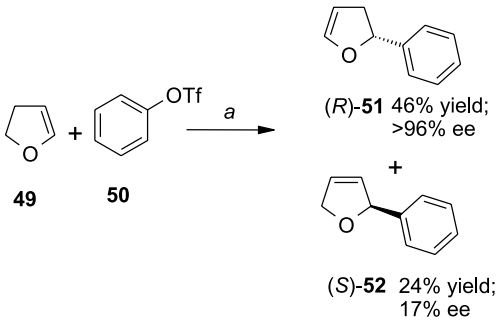
31a

evaluating the performance of this ligand in metal-mediated asymmetric transformations remained.

Application of BINAPFu in the Heck arylation of 2,3-dihydrofuran using (*R*)-BINAP and (*R*)-BINAPFu

The asymmetric Heck arylation of 2,3-dihydrofuran (**49**), first reported by Hayashi and co-workers (24, 55), has been studied extensively and was therefore chosen as a suitable reaction to study using the BINAPFu ligand (Scheme 10). The Heck arylation of 2,3-dihydrofuran (**49**) was performed under a variety of reaction conditions (Table 1) on a 1.0 mmol scale (based on PhOTf) in sealed, screw-cap sample vials. In all cases, the Pd-catalysts (3 mol%) were formed in situ at 60 °C in the presence of an amine base under argon for 30 min. In general, catalysts formed using (*R*)-BINAP were bright orange in color, while catalysts derived from (*R*)-BINAPFu were bright yellow in color. After formation of the catalyst, PhOTf and 2,3-dihydrofuran

Scheme 10. (*a*) 3.0 equiv DIPEA, 3 mol% $Pd(OAc)_2$, 6 mol% (*R*)-BINAP, C_6H_6, 30 °C, 66 h.



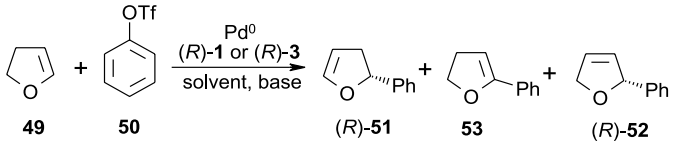
(5.1 mmol) were carefully added by microlitre-syringe. The argon-purged vessels were subsequently sealed and placed in a thermostatically controlled oil bath for a specified period. In light of our inability to repeat Hayashi's experimental results, coupled with the fact that the reported ee values were ascertained using the chiral shift NMR analysis method, it was deemed prudent to perform control experiments using commercially supplied (*R*)-BINAP. To this end, all experiments were performed in parallel, using both the (*R*)-BINAP and (*R*)-BINAPFu catalyst systems, and were analyzed using chiral GC analysis conditions.

Employing Hayashi's original Heck arylation conditions with the (*R*)-BINAP ligand afforded 2,3-dihydrofuran product **51** in 27% yield and 86% ee (entry 1b). However, the reaction was only 30% complete after a 9 day period at 30 °C. In our hands, neither Hayashi's reported yield (78%) (55*a*) nor the enantiomeric excess of the 2,3-dihydrofuran product **51** (93%) (55*a*) were attainable under these reaction conditions. Utilizing (*R*)-BINAPFu under otherwise identical conditions afforded a 21% yield of product **51**, favoring the *R*-configuration in >97% ee. Extraordinarily, the enantiomeric purity of the minor isomer **52** was also greater than when (*R*)-BINAP was employed, and the sense of enantioselection was reversed. In other words, both products **51** and **52** were enriched in the *R*-configuration, suggesting that the reaction with BINAPFu may not follow Hayashi's proposed kinetic resolution mechanism. Repeating this experiment using Proton Sponge® (3.0 equiv) as the base provided much lower product conversion factors (entries 2a and 2b). Since the conditions reported in the literature for this reaction failed to give useful product conversions, alternative palladium sources, solvents, bases, and reaction temperatures were investigated.

A significant increase in product conversion was observed upon using a polar solvent such as 1,4-dioxane with DIPEA as the base (entry 3). The effect was more pronounced for the (*R*)-BINAPFu catalyst, giving a 61% yield of the 2,3-dihydrofuran product **51** (97% ee, entry 3a). Under identical conditions, the (*R*)-BINAP catalyst afforded only 43% yield of **51** (73% ee, entry 3b), albeit with higher regioselectivity. Again, the 2,5-dihydrofuran product **52** was formed with *S*-configuration selectivity using the (*R*)-BINAP catalyst, while the *R*-configuration was preferred with the (*R*)-BINAPFu catalyst. Since NMP has been used successfully in the Stille reaction with trifurylphosphine-derived catalysts (56), it was conceived that this polar solvent may also work well in the present case. Employing NMP as the solvent also afforded

© 2004 NRC Canada

Table 1. Asymmetric Heck results with BINAPFu (3) and BINAP (1).



Entry	Ligand	Solvent	T (°C)	Conversion (%)	Yield (% (% ee))		
					(*R*)-**51**	**53**	(*R*)-**52**
1a	(*R*)-**3**	C_6H_6[a]	30[b]	33	21 (>97)	1	11 (75)
1b	(*R*)-**1**	C_6H_6[a]	30[b]	30	27 (86)	0	3 (51)[c]
2a	(*R*)-**3**	C_6H_6[a]	30[d]	17	1 (—)	3	13 (93)
2b	(*R*)-**1**	C_6H_6[a]	30[d]	1	1 (—)	—	—
3a	(*R*)-**3**	Dioxane[a]	30[b]	71	61 (>97)	1	9 (57)
3b	(*R*)-**1**	Dioxane[a]	30[b]	46	43 (73)	1	2 (46)[c]
4a	(*R*)-**3**	NMP[a]	30[b]	41	32 (>79)	1	8 (22)
4b	(*R*)-**1**	NMP[a]	30[b]	69	67 (72)	1	1 (38)[c]
5a	(*R*)-**3**	Dioxane[e]	50[b]	30	25 (76)	0	5 (37)
5b	(*R*)-**1**	Dioxane[e]	50[b]	56	53 (66)	1	2 (15)
6a	(*R*)-**3**	C_6H_6[e]	70[b]	31	26 (74)	1	4 (61)
6b	(*R*)-**1**	C_6H_6[e]	70[b]	99	77 (54)	3	19 (35)
7a	(*R*)-**3**	THF[e]	70[b]	83	77 (75)	1	5 (61)
7b	(*R*)-**1**	THF[e]	70[b]	100	74 (53)	4	22 (71)
8a	(*R*)-**3**	DME[e]	85[b]	100	95 (73)	1	4 (64)
8b	(*R*)-**1**	DME[e]	85[b]	100	55 (48)	13	32 (72)
9a	(*R*)-**3**	Dioxane[e]	100[b]	100	90 (77)	1	10 (40)
9b	(*R*)-**1**	Dioxane[e]	100[b]	100	73 (41)	9	17 (26)
10a	(*R*)-**3**	DMF[e]	90[b]	100	94 (71)	3	3 (39)
10b	(*R*)-**1**	DMF[e]	90[b]	100	55 (35)	5	41 (47)
11a	(*R*)-**3**	Dioxane[e]	100[f]	100	83 (80)	3	14 (40)
11b	(*R*)-**1**	Dioxane[e]	100[f]	100	62 (50)	5	33 (11)
12a	(*R*)-**3**	Dioxane[e]	100[d]	100	66 (79)	1	33 (44)
12b	(*R*)-**1**	Dioxane[e]	100[d]	100	93 (54)	4	3 (23)
13a	(*R*)-**3**	Dioxane[a]	100[b]	100	94 (74)	1	7 (64)
13b	(*R*)-**1**	Dioxane[a]	100[b]	100	90 (57)	2	12 (79)

[a]3 mol% $Pd(OAc)_2$ for 9 days.
[b](i-Pr)$_2$NEt used as base.
[c]*S*-configuration was favoured.
[d]Proton sponge used as base.
[e]1.5 mol% Pd_2dba_3 for 7 days.
[f]PMP used as base.

higher conversion factors (entries 4a and 4b) than those observed using benzene (entries 1a and 1b), but the ee of the major product **51** was diminished (79%) relative to the result obtained with dioxane (97%). The same general trend in enantioselection was observed, wherein the absolute configuration of the 2,5-dihydrofuran product **52** differed between the two catalyst systems studied. The use of $Pd(OAc)_2$ as the pre-catalyst was not required to achieve good enantioselectivity. Utilizing the $Pd_2(dba)_3$–(*R*)-BINAPFu catalyst system in dioxane at 50 °C with DIPEA as the base afforded a 25% yield of compound **51** in 76% ee (entry 5a). The same conditions in conjunction with a $Pd_2(dba)_3$–(*R*)-BINAP catalyst system furnished compounds **51** and **52** in higher conversion and isomeric selectivity but with reduced enantioselectivity (entry 5b). Using these conditions, both catalysts provided 2,5-dihydrofuran product **52**, favoring the *R*-configuration. Virtually the same product conversion, regioselectivity, and ee were obtained using the (*R*)-BINAPFu ligand in benzene at 70 °C (entry 6a). However, a significant increase in conversion and decrease in isomer selectivity was observed using (*R*)-BINAP in benzene at 70 °C (entry 6b). Although the conversion was certainly poorer with the (*R*)-BINAPFu catalyst, it was encouraging to note that respectable enantioselectivities could also be achieved at higher temperatures. In other words, this result suggested that it may be possible to get this reaction to go to completion while still obtaining reasonable levels of enantioselection.

A study of various ethereal solvents at elevated temperature (entries 7–9) revealed that full conversion was attainable, without a significant loss in enantioselectivity, using 1,4-dioxane as the solvent at 100 °C (entries 9a and 9b). Moreover, at high temperatures, the (*R*)-BINAPFu catalyst

© 2004 NRC Canada

afforded less of the unwanted conjugated isomer **53** and afforded higher selectivity in favor of the 2,3-dihydrofuran product **51**. In all cases, utilization of high-temperature conditions (>50 °C) provided the 2,5-dihydrofuran product **52** enriched in the *R*-isomer, regardless of whether (*R*)-BINAP or (*R*)-BINAPFu was used as the ligand. Conducting the reaction in DMF at 90 °C with DIPEA as the base and an (*R*)-BINAPFu-derived catalyst afforded excellent isomer selectivity with a slight reduction in enantioselectivity (entry 10a). At elevated temperatures, the conditions that employed dioxane as the solvent and PMP as the tertiary amine base yielded the 2,3-dihydrofuran product **51** in 80% ee with only modest regioselectivity (entry 11a). Ozawa, Kubo, and Hayashi have reported (55*b*) higher degrees of enantioselection, at the expense of regioselectivity, using Proton Sponge® as the base. Using this base in dioxane at 100 °C with the (*R*)-BINAPFu catalyst did not result in increased enantioselectivity (entry 12a). However, in accordance with Hayashi's findings, a significant decrease in isomer selectivity was observed. Finally, changing back to the $Pd(OAc)_2$ catalyst and using dioxane as the solvent at 100 °C with DIPEA as the base gave a slight increase in product regioselectivity (entry 13a, cf. entry 9a).

Examining the results listed in Table 1 as a whole, a few general trends immediately emerge. Firstly, the enantiomeric purity of the 2,3-dihydrofuran isomer **51** was always higher when the (*R*)-BINAPFu-derived catalyst system was used. At low temperatures (<50 °C), employing dioxane as the solvent with DIPEA as the base afforded the best balance between conversion (71%) and enantioselectivity of the 2,3-dihydrofuran product **51** (97%). However, in this temperature domain, the (*R*)-BINAP catalyst generally affords a much higher isomer selectivity. The (*R*)-BINAPFu catalyst consistently provides products **51** and **52**, both enriched in the *R*-configuration. In contrast, the (*R*)-BINAP catalyst gives compounds **51** and **52** of opposite configuration only at low temperature (30 °C). At higher temperatures (>70 °C), full conversion of the phenyl triflate can be realized with either catalyst system. Under such conditions, the (*R*)-BINAPFu catalyst typically gives the major product in 71%–80% ee, while the (*R*)-BINAP catalyst produces product **51** in 35%–57% ee. High-temperature conditions, in conjunction with the (*R*)-BINAPFu catalyst system, give rise to higher isomeric ratios in favor of the 2,3-dihydrofuran product **51** and attenuated formation of the conjugated isomer **53**, relative to the corresponding reactions employing the (*R*)-BINAP-derived catalyst. Perhaps of greatest significance is the observation that high enantioselectivity for the 2,3-dihydrofuran isomer **51** does not seem to correlate with poor isomeric selectivity. Recall that Hayashi, Ozawa, and coworkers used this argument as strong evidence supporting a kinetic resolution mechanism (24). Notwithstanding our inability to repeat these workers' findings (vide supra), the experimental results obtained using the BINAPFu ligand suggest that this assertion may indeed be incorrect.

Conclusions

We have designed, synthesized, and resolved a new binaphthofuran ligand (BINAPFu) for use in asymmetric metal-catalyzed reactions. The ligand is easily prepared in 5 steps from readily available starting material. A new resolution procedure was designed for phosphines, involving the Staudinger reaction with a camphor sulfonyl azide derivative. BINAPFu outperformed BINAP in the Heck reaction between phenyl triflate and 2,3-dihydrofuran. Further structural modifications of BINAPFu are currently underway to improve the enantioselectivity of high-temperature Heck arylation reactions.

Experimental section

General comments

Melting points were determined using either an Electrothermal® melting point apparatus in sealed capillary tubes or an A.H. Thomas hot-stage and are uncorrected. Boiling points are uncorrected and refer to measured air-bath temperatures using a Kugelrohr short-path distillation apparatus. Optical rotation data was obtained on a Rudolph Autopol III polarimeter using a quartz cell with a 10 cm path length. Infrared spectra were recorded on a Mattson Galaxy Series 4030 FT-IR spectrometer. ^{1}H and ^{13}C NMR spectra were obtained on a Bruker ACE 200 (^{1}H, 200 MHz; ^{13}C, 50 MHz), a Bruker AM 400 (^{1}H, 400 MHz; ^{13}C, 100 MHz), or a Bruker DRX 400 (^{1}H, 400 MHz; ^{13}C, 100 MHz) spectrometer. Unless otherwise noted, deuteriochloroform was used as the NMR solvent. ^{31}P NMR spectra were obtained on a Varian XL 200 (^{31}P, 81 MHz), a Bruker AMX 300 (^{31}P, 121.5 MHz), or a Bruker DRX 400 (^{31}P, 162 MHz) spectrometer using an external reference of 30% H_3PO_4 in D_2O set to 0 ppm. Unless specified otherwise, ^{31}P NMR samples were prepared using deuteriochloroform as the solvent. GC–MS analysis was performed on a Hewlett-Packard 5890 Series II gas chromatograph equipped with a Hewlett-Packard OV 101, low polarity, 12 m × 0.2 mm column, in conjunction with a Hewlett-Packard 5971A mass selective detector. Low-resolution mass spectra on nonvolatile samples were obtained on a VG 7070 or a Kratos MS80 mass spectrometer using 70 eV ionization with direct probe sample introduction. HR-MS and FAB-MS analyses were obtained using a Kratos MS80 spectrometer. Elemental analyses were obtained from the University of Calgary's Control Equipment Corporation 440 Elemental Analyzer. X-ray structure determination[3] was performed by Dr. M. Parvez (University of Calgary), using a Rigaku AFC6S diffractometer with graphite monochromated Mo Kα radiation, or by Dr. R. McDonald (University of Alberta), using a Bruker P4 diffractometer equipped with a SMART 1000 CCD area detector and 18 kW rotating anode X-ray generator. Column chromatography was performed using silica gel 60 (E. Merck, 0.04–0.063 mm, 230–400 mesh), using the flash method (57). Sol-

[3] Supplementary data may be purchased from the Depository of Unpublished Data, Document Delivery, CISTI, National Research Council Canada, Ottawa, ON K1A 0S2, Canada (http://www.nrc.ca/cisti/irm/unpub_e.shtml for information on ordering electronically). CCDC 221199, 221200, and 147246 contain the supplementary data for this paper. These data can be obtained, free of charge, via www.ccdc.cam.ac.uk/conts/retrieving.html (or from the Cambridge Crystallographic Data Centre, 12 Union Road, Cambridge, U.K.; fax +44 1223 336033; or deposit@ccdc.cam.ac.uk).

© 2004 NRC Canada

vent systems refer to mixtures, by volume, of hexanes and ethyl acetate unless specified otherwise. Analytical HPLC analyses were performed on an ICI LC 1440 instrument equipped with an ICI LC 1150 HPLC Pump (C_{18} column or Chiralcel OJ column with an ICI LC 12010 UV–vis detector) or a Waters 4886 instrument (Nova-Pak C_{18} reverse-phase column or Chiralcel OB column with a Waters 486 UV detector). Preparative HPLC was done on the latter instrument equipped with a 25 mm × 100 mm Water Nova-Pak C_{18} reversed-phase column. Chiral gas chromatography was performed on either a Shimadzu GC-9A gas chromatograph (25 m × 0.33 mm (i.d.) Cydex-B fused silica column with a flame ionization detector) or a Varian Star 3400 CX instrument (30 m × 0.32 mm (i.d.) Cyclodex-B fused silica column with a flame ionization detector).

Chlorination of 1-acetyl-2-hydroxynaphthalene (8)

Method 1

To a solution of 1-acetyl-2-hydroxynaphthalene **8** (100 mg, 0.537 mmol) in CH_2Cl_2 (2 mL), H_2O (11 μL, 0.59 mmol), and MeOH (23 μL, 0.59 mmol), was added SO_2Cl_2 (53 μL, 0.65 mmol). The mixture was refluxed under an N_2 atmosphere for 1 h and subsequently quenched with H_2O (20 mL). The solution was extracted with ether (20 mL), washed with H_2O (2 × 20 mL), and dried ($MgSO_4$). Concentration of the organic phase afforded a greenish yellow oil. Only a trace amount of the desired product **9** was evident in the crude ^{1}H NMR spectrum.

Method 2

Hexachloro-2,4-cyclohexadienone (19) (111 mg, 0.371 mmol) was added to a solution of 1-acetyl-2-hydroxynaphthalene (69 mg, 0.37 mmol) in absolute ethanol (3 mL), and the mixture was refluxed under a nitrogen atmosphere for 15 h. The solvent was removed in vacuo to give a brown residue. ^{1}H NMR analysis showed that the major component of the mixture was unreacted starting material **8**, as well as a minor amount (<30%) of the desired α-chloroketone **9**, as evidenced by a singlet at 4.8 ppm corresponding to H-12. The product was not stable to column chromatography.

1-Acetyl-2-[(*tert*-butyldimethylsilyl)oxy]naphthalene (10)

To a solution of 1-acetyl-2-hydroxynaphthalene (**8**) (21.9 g, 0.117 mol) in Et_3N (75 mL, 0.538 mol) and CH_2Cl_2 (500 mL) was added TBSCl (19.4 g, 0.129 mmol). The mixture was stirred at room temperature (rt) for 18 h before it was quenched with H_2O (500 mL). The mixture was then stirred for 1 h and extracted with ether (3 × 500 mL), and the pooled organic extracts were washed with a 10% HCl solution (2 × 500 mL) and H_2O (2 × 500 mL). The organic layer was dried ($MgSO_4$) and concentrated under reduced pressure to give 31.4 g (89%) of the TBS ether **10** as a light yellow oil. ^{1}H NMR (200 MHz) δ: 0.28 (s, 6H), 1.02 (s, 9H), 2.68 (s, 3H), 7.10 (d, J = 12 Hz, 1H), 7.47 (m, 2H), 7.76 (m, 2H), 7.78 (d, J = 12 Hz, 1H). This material was used in the next step without further purification.

1-[(1-Trimethylsilyl)oxy]ethenyl-2-[(*tert*-butyldimethylsilyl)oxy]naphthalene (11)

To a solution of silyl ether **10** (31.4 g, 0.105 mol) in CH_2Cl_2 (600 mL) and Et_3N (73 mL, 0.52 mol) at 0 °C was added TMSOTf (24 mL, 0.13 mol). The mixture was warmed to rt and stirring was continued for 1 h under an N_2 atmosphere. The mixture was diluted with $CHCl_3$ (100 mL), washed with brine (2 × 300 mL), dried (Na_2SO_4), and evaporated to dryness under reduced pressure to give crude enol ether **11** in quantitative yield. ^{1}H NMR (200 MHz) δ: 0.18 (s, 9H), 0.27 (s, 6H), 1.09 (s, 9H), 4.39 (s, 1H), 4.74 (s, 1H), 7.07 (d, J = 11 Hz, 1H), 7.45 (m, 2H), 7.71 (m, 2H), 8.08 (d, J = 11 Hz, 1H). Trimethylsilyl enol ether **11** was used directly in the subsequent step.

1-(2-Bromoacetyl)-2-[(*tert*-butyldimethylsilyl)oxy]naphthalene (12)

In a flask equipped with a dropping funnel, TMS enol ether **11** (38.9 g, 0.105 mol) was dissolved in CCl_4 (450 mL) and cooled to 0 °C. A solution of bromine (5.66 mL, 0.119 mol) in CCl_4 (100 mL) was placed in the dropping funnel, and 20 mL of this solution was added to the reaction mixture; after warming to rt, the remaining 80 mL of the bromine solution was added over a 30 min period. The mixture was stirred for a further 30 min and diluted with H_2O (200 mL), and the layers were separated. The aqueous layer was extracted with $CHCl_3$ (2 × 100 mL), and the combined organic layers were washed with an $Na_2S_2O_3$ solution (200 mL) and H_2O (2 × 200 mL). The organic fraction was dried (Na_2SO_4) and concentrated in vacuo to furnish 39.5 g of compound **12** as a light orange oil. ^{1}H NMR (200 MHz) δ: 0.29 (s, 6H), 1.05 (s, 9H), 4.58 (s, 2H), 7.08 (d, J = 11 Hz, 1H), 7.50 (m, 2H), 7.78 (m, 2H), 7.85 (d, J = 11 Hz, 1H).

Naphtho[2,1-*b*]furan-3(2H)-one (7) from bromide 12

To a solution of compound **12** (39.7 g, 0.105 mol) in THF (400 mL) at 0 °C was slowly added TBAF (1.0 mol L^{-1} solution in THF, 110 mL, 0.110 mol) under an N_2 atmosphere. The mixture was allowed to stir at 0 °C for 10 min and at rt for 15 min. The dark purple solution was then quenched with NH_4Cl solution (100 mL), and the THF was removed in vacuo. The remaining residue was extracted with ether (3 × 100 mL), and the combined ether layers were washed with brine (100 mL) and H_2O (3 × 150 mL), dried ($MgSO_4$), and evaporated under reduced pressure. The crude product was purified by column chromatography (20:1, hexanes – ethyl acetate) to give 15.1 g (72% from compound **11**) of cyclized ketone **7** as a light yellow solid: mp 133 °C (lit (58) 133 °C). IR (KBr) (cm^{-1}): 1688. ^{1}H NMR (200 MHz, $CDCl_3$) δ: 8.75 (d, J = 8.2 Hz, 1H), 8.05 (d, J = 9.0 Hz, 1H), 7.82 (d, J = 8.0 Hz, 1H), 7.66 (dt, J = 7.6, 0.9 Hz, 1H), 7.47 (dt, J = 7.6, 1.0 Hz, 1H), 7.24 (dd, J = 7.8, 2.4 Hz, 1H), 4.77 (s, 2H). ^{13}C NMR (50 MHz, $CDCl_3$) δ: 199.9 (C), 176.6 (C), 139.7 (CH), 129.8 (CH), 129.2 (C), 129.1 (C), 126.4 (CH), 125.4 (CH), 123.1 (CH), 113.9 (CH), 113.5 (C), 75.5 (CH_2). MS, m/z (relative intensity, %): 184 ($[M]^+$, 74), 155 (87), 126 (100). Exact mass calcd for $C_{12}H_8O$: 184.0524; found: 184.0520.

Naphtho[2,1-*b*]furan-3(2H)-one (7) from 2-naphthoxyacetic acid (13)

2-Naphthoxyacetic acid (20.1 g, 99.3 mmol) in dry benzene (1000 mL) was treated with a catalytic amount of pyridine and 2 equiv $SOCl_2$ (14.4 mL, 198.6 mmol) at reflux under an N_2 atmosphere for 2 h. The cooled solution was

© 2004 NRC Canada

then concentrated in vacuo, and the resulting residue was taken up into C_6H_6 (500 mL) and cooled to 0 °C. To the solution was then added $AlCl_3$ (19.8 g, 148.9 mmol), and the resulting solution was stirred for 12 h at ambient temperature. The mixture was then quenched with brine and extracted with benzene (2 × 100 mL). The combined organic extracts were then washed with water (2 × 100 mL) and filtered through neutral alumina. The filtrate was then concentrated under reduced pressure to afford the desired product **7** (17.2 g, 95%), which was found to be clean by ^{1}H NMR analysis. Spectra were identical to compound **7** made from bromide **12**.

3,3′-Binaphtho[2,1-*b*]furan (5)

Into a 1 L, 3-neck round-bottom flask equipped with an addition funnel was weighed activated zinc dust (29.3 g, 0.448 mol) and DME (300 mL). The mixture was cooled to –78 °C, and to it was carefully added $TiCl_4$ dropwise via syringe over a 30 min period. The resulting blue mixture was warmed to reflux, and the starting naphthoketone **7** (10.0 g, 54.4 mmol in 100 mL DME) was added dropwise over a 20 min period. The resulting mixture was heated to reflux under an N_2 atmosphere for 18 h. The cooled mixture was then filtered through a coarse sintered glass funnel, and the filtrate was concentrated under reduced pressure to give **6** as an orange, gummy residue. This residue was immediately dissolved in C_6H_6 (300 mL) and treated with DDQ (6.17 g, 27.2 mmol) at reflux under an N_2 atmosphere for 4 h. The cooled mixture was then quenched with saturated $Na_2S_2O_3$ and extracted with ether (3 × 100 mL). The combined organic extracts were dried ($MgSO_4$) and concentrated to afford the crude title compound. The product **5** was readily purified by flash chromatography (100:1 hexanes – ethyl acetate) to afford the analytically pure biaryl (7.13 g, 78%). mp 292–294 °C. IR (KBr) (cm^{-1}): 2850, 1436. ^{1}H NMR (200 MHz, $CDCl_3$) δ: 7.94 (d, *J* = 8.2 Hz, 1H), 7.86 (s, 1 H), 7.84 (m, 2H), 7.75 (d, *J* = 8.5 Hz, 1H), 7.35 (dt, *J* = 7.5, 1.0 Hz, 1H), 7.09 (dt, *J* = 7.7, 1.3 Hz, 1H). ^{13}C NMR (50 MHz, $CDCl_3$) δ: 153.5 (C), 142.8 (CH), 130.8 (C), 128.6 (CH), 128.4 (C), 126.4 (CH), 126.3 (CH), 124.5 (CH), 123.3 (CH), 112.1 (C), 113.9 (C), 112.6 (CH). MS, *m*/*z* (relative intensity, %): 334 ([M]$^+$, 100), 305 (31), 276 (32), 138 (18). Exact mass calcd for $C_{24}H_{14}O_2$: 334.0994; found: 334.0970. Anal calcd for $C_{24}H_{14}O_2$: C 86.20, H 4.22; found: C 85.96, H 4.04.

2,2′-Bis(diphenylphosphonyl)-3,3′-binaphtho[2,1-*b*]furan (14)

3,3′-Binaphtho[2,1-*b*]furan **5** (0.593 g, 1.776 mmol) in dry Et_2O (30 mL) was lithiated with *t*-BuLi (2.61 mL, 4.440 mmol, 1.7 mol L^{-1} solution in hexanes) at 0 °C. After 1 h at 0 °C, the vessel was warmed to rt and stirred for a further 2 h under an N_2 atmosphere. To the mixture was then added freshly distilled diphenylphosphinic chloride (0.85 mL, 4.440 mmol), and the resulting white slurry was stirred overnight at room temperature. The reaction mixture was then quenched with water and extracted with $CHCl_3$ (3 × 50 mL). The combined organic extracts were washed with 10% $NaHCO_3$, water, and brine. The organic phase was then dried ($MgSO_4$) and concentrated in vacuo to afford a light yellow solid residue. The crude material **14** was purified by column chromatography (3:1 CH_2Cl_2–EtOAc → 19:1 CH_2Cl_2–MeOH) to afford the title compound (1.150 g, 88%). mp 289–290 °C. IR (KBr) (cm^{-1}): 2924, 1437, 1120. ^{1}H NMR (400 MHz, $CDCl_3$) δ: 7.87 (d, *J* = 8.1 Hz, 1H), 7.83 (d, *J* = 9.1 Hz, 1H), 7.72 (m, 2H), 7.64 (d, *J* = 9.0 Hz, 1H), 7.56 (d, *J* = 7.3 Hz, 1H), 7.53 (d, *J* = 7.3 Hz, 1H), 7.46 (d, *J* = 8.3 Hz, 1H), 7.36 (m, 2H), 7.23 (m, 3H), 7.06 (t, *J* = 7.6 Hz, 1H), 6.96 (dt, *J* = 7.7, 3.1 Hz, 2H). ^{13}C NMR (50 MHz, $CDCl_3$) δ: 155.5 (d, *J* = 8 Hz, C), 145.8 (d, *J* = 128 Hz, C), 132.1 (CH), 132.1 (d, *J* = 35 Hz, C), 132.0 (CH), 131.9 (d, *J* = 3 Hz, CH), 130.8 (C), 129.9 (d, *J* = 31 Hz, C), 128.7 (CH), 128.1 (d, *J* = 13 Hz, CH), 127.6 (d, *J* = 13 Hz, CH), 126.9 (CH), 124.8 (CH), 124.6 (C), 122.7 (CH), 121.5 (d, *J* = 8 Hz, C), 112.6 (CH). ^{31}P NMR (81 MHz, $CDCl_3$) δ: 16.5. MS, *m*/*z* (relative intensity, %): 533 ([M$^+$ – P(O)Ph_2], 100), 201 (54). Exact mass calcd for $C_{48}H_{32}P_2O_4$: 734.1778; found: 734.1731.

(±)-2,2′-Bis(diphenylphosphino)-3,3′-binaphtho[2,1-*b*]furan (3)

3,3′-Binaphtho[2,1-*b*]furan **5** (3.4 g, 10.2 mmol) in dry Et_2O (130 mL) was lithiated with *t*-BuLi (11.2 mL, 22.4 mmol, 2.0 mol L^{-1} solution in hexanes) at 0 °C. After 1 h at 0 °C, the vessel was warmed to rt and stirred for a further 2 h under an N_2 atmosphere. To the mixture was then added freshly distilled chlorodiphenylphosphine (4.0 mL, 22.4 mmol), and the resulting white slurry was stirred overnight at room temperature. The reaction mixture was quenched with water and extracted with $CHCl_3$ (3 × 125 mL). The combined organic extracts were washed with 10% $NaHCO_3$, water, and brine. The organic phase was dried ($MgSO_4$) and concentrated in vacuo to afford a light brown solid residue. The crude material (±)-**3** was purified by crystallization ($CHCl_3$–MeOH) to afford the title compound (6.49 g, 91%). mp 228–229 °C. IR (KBr) (cm^{-1}): 3052, 1433. ^{1}H NMR (400 MHz, $CDCl_3$) δ: 7.90 (d, *J* = 8.1 Hz, 1H), 7.84 (d, *J* = 9.0 Hz, 1H), 7.76 (d, *J* = 9.1 Hz, 1H), 7.62 (d, *J* = 8.3 Hz, 1H), 7.37 (m, 2H), 7.35–7.30 (m, 4H), 7.24–7.14 (m, 5H), 7.04 (td, *J* = 7.4, 1.0 Hz, 1H). ^{13}C NMR (100 MHz, $CDCl_3$) δ: 156.3 (C), 152.9 (d, *J* = 34 Hz, C), 135.4 (d, *J* = 71 Hz, C), 133.7 (CH), 133.6 (CH), 133.5 (CH), 130.7 (C), 128.6 (d, *J* = 4 Hz, CH), 128.5 (CH), 128.3 (C), 128.1 (d, *J* = 2 Hz, CH), 127.4 (CH), 126.5 (d, *J* = 35 Hz, C), 126.7 (CH), 124.5 (CH), 123.0 (CH), 122.5 (C), 112.9 (CH). ^{31}P NMR (81 MHz, $CDCl_3$) δ: –32.3. MS, *m*/*z* (relative intensity, %): 625 ([M$^+$ – Ph], 1), 517 (37), 408 (79), 183 (100). Exact mass calcd for $C_{48}H_{32}P_2O_2$: 702.1878; found: 702.1841.

Preparation of bis-*P*-borane-(R^*_{ax})-2,2′-bis[(8*R*,9*R*)-*N*,*N*′-dimethyl-1,3-diazahexahydro-2-phosphinoindan-2-yl]-3,3′-binaphtho[2,1-*b*]furan complex (23a) and bis-*P*-borane-(S^*_{ax})-2,2′-bis[(8*R*,9*R*)-*N*,*N*′-dimethyl-1,3-diazahexahydro-2-phosphinoindan-2-yl]-3,3′-binaphtho[2,1-*b*]furan complex (23b)

To a solution of naphtho[*b*]furan **5** (0.173 g, 0.518 mmol) in Et_2O (5.0 mL) at –78 °C was added 2.05 equiv of *t*-BuLi (1.7 mol L^{-1} in hexanes, 0.62 mL, 1.1 mmol). The resulting mixture was warmed to 0 °C and stirred under an atmosphere of nitrogen for 1.5 h. To the vessel was then added enantiopure 2-chloro-2,2′-bis[8*R*,9*R*]-*N*,*N*′-dimethyl-1,3-diazahexahydro-2-phosphinoindane (**22**) (38, 39) (0.219 g,

© 2004 NRC Canada

1.06 mmol). The reaction contents were allowed to warm to rt over a 1 h period and subsequently left to stir for 24 h. To the vessel was then added borane – dimethyl sulfide complex (2.0 mol L^{-1} solution in THF, 0.531 mL, 1.06 mmol), and the resulting mixture was left to react for a further 24 h. The reaction contents were then quenched with brine (50 mL) and extracted with $CHCl_3$ (3 × 50 mL). The combined organic extracts were dried ($MgSO_4$) and concentrated under reduced pressure to afford a light yellow oil. The crude material was purified by column chromatography (15:1) to afford a 1:1 mixture of the title compounds (0.270 g, 74%). A small sample (~3 mg) of each pure diastereomer was obtained by exhaustive preparative high performance liquid phase chromatography (Nova-Pak C_{18}, 93:7 $CH_3CN:H_2O$, 1.0 mL min^{-1}, 320 nm detection). The first isomer to elute, compound **23a**, was obtained as a colorless film exhibiting the following analytical data: IR (KBr) (cm^{-1}): 2937, 2387 (BH_3), 1462, 1025. ^{1}H NMR (400 MHz) δ: –0.50 to 0.63 (bq, 3H), 1.10–1.62 (m, 4H), 1.89 (t, *J* = 12.9 Hz, 2H), 2.00–2.13 (m, 2H), 2.19 (d, *J* = 14.5 Hz, 3H), 2.48 (td, *J* = 10.4, 3.0 Hz, 1H), 2.74 (d, *J* = 12.8 Hz, 3H), 3.18 (t, *J* = 9.6 Hz, 1H), 7.02 (t, *J* = 7.0 Hz, 1H), 7.32 (t, *J* = 7.0 Hz, 1H), 7.58 (d, *J* = 7.8 Hz, 1H), 7.82 (d, *J* = 9.1 Hz, 1H), 7.90 (d, *J* = 9.1 Hz, 1H), 7.91 (d, *J* = 7.8 Hz, 1H). ^{13}C NMR (100 MHz) (ppm): 24.7 (CH_2), 24.8 (CH_2), 29.0 (d, *J* = 8 Hz, CH_2), 29.3 (d, *J* = 5 Hz, CH_2), 30.4 (d, *J* = 3 Hz, CH_3), 32.6 (d, *J* = 10 Hz, CH_3), 65.8 (d, *J* = 3 Hz, CH), 68.4 (CH), 113.4 (CH), 122.8 (C), 122.9 (C), 123.5 (CH), 125.1 (CH), 126.4 (d, *J* = 19 Hz, C), 126.8 (CH), 128.9 (CH), 129.3 (CH), 131.3 (C), 150.4 (d, *J* = 30 Hz, C), 155.5 (d, *J* = 4 Hz, C). ^{31}P NMR (162 MHz) (ppm): +94.1 (q, *J* = 71 Hz). FAB-MS, *m/z* (relative intensity, %): 725 (48, $[M + Na]^+$). Compound **23b**, also obtained as a colorless film, had the following properties: IR (KBr) (cm^{-1}): 2935, 2390 (BH_3), 1461, 1003. ^{1}H NMR (400 MHz) δ: –0.48 (qd, *J* = 12.3, 3.6 Hz, 1H), 0.08 (m, 1H), 0.20–1.20 (bq, 3H), 0.78–0.97 (m, 2H), 1.28 (d, *J* = 8.6 Hz, 1H), 1.39 (d, *J* = 9.8 Hz, 2H), 1.65 (d, *J* = 8.9 Hz, 1H), 2.10 (td, *J* = 12.0, 3.2 Hz, 1H), 2.26 (m, 1H), 2.36 (d, *J* = 13.1 Hz, 3H), 2.62 (d, *J* = 14.2 Hz, 3H), 7.13 (t, *J* = 8.0 Hz, 1H), 7.36 (t, *J* = 7.1 Hz, 1H), 7.55 (d, *J* = 8.3 Hz, 1H), 7.88 (ABq, *J* = 9.2 Hz, 2H), 7.94 (d, *J* = 8.1 Hz, 1H). ^{13}C NMR (100 MHz) (ppm): 23.7 (CH_2), 24.1 (CH_2), 27.3 (d, *J* = 5 Hz, CH_2), 28.2 (d, *J* = 8 Hz, CH_2), 30.3 (d, *J* = 2 Hz, CH_3), 32.8 (d, *J* = 10 Hz, CH_3), 64.1 (d, *J* = 3 Hz, CH), 68.2 (CH), 113.5 (CH), 123.1 (d, *J* = 5 Hz, C), 123.2 (d, *J* = 9 Hz, C), 123.7 (CH), 125.3 (CH), 127.1 (CH), 128.7 (CH), 129.0 (C), 129.5 (CH), 131.5 (C), 150.3 (d, *J* = 40 Hz, C), 155.5 (d, *J* = 6 Hz, C). ^{31}P NMR (162 MHz) (ppm): +98.7 (q, *J* = 74 Hz). FAB-MS, *m/z* (relative intensity, %): 725 (7, $[M + Na]^+$).

2-Chloro-1,3-dimethyl-4,5-diphenyl-1,3,2-diazaphospholidine (26)

Under an argon atmosphere, (1*S*,2*S*)-*N*,*N*-dimethyl-1,2-diphenylethylenediamine (**25**) (40, 41) (1.59 g, 6.63 mmol) was dissolved in freshly distilled Et_2O (40 mL) and Et_3N (1.85 mL, 13.3 mmol). The reaction mixture was then cooled to –40 °C; phosphorus trichloride (0.578 mL, 6.63 mmol) was added; and the resultant thick white slurry was stirred for 30 min at –40 °C, for 1 h at 0 °C, and for 24 h at room temperature. The slurry was filtered under an atmosphere of argon, and the filtrate was concentrated under reduced pressure in an inert atmosphere to give a bright yellow solid residue. Crude phosphoramidous chloride **26**: ^{1}H NMR (200 MHz) δ: 2.55 (d, *J* = 19.5 Hz, 3H), 4.28 (d, *J* = 7.4 Hz, 1H), 7.11–7.40 (m, 5H). ^{13}C NMR (50 MHz) (ppm): 31.8 (d, *J* = 21 Hz, CH_3), 78.1 (d, *J* = 11 Hz, CH), 128.2 (CH), 128.7 (CH), 128.8 (CH), 137.1 (d, *J* = 2 Hz, C). ^{31}P NMR (62 MHz) (ppm): +173.6. Compound **26** was used in the subsequent step without further purification.

Bis-*P*-borane-(R^*_{ax})-2,2′-bis[(4*R*,5*R*)-1,3-dimethyl-4,5-diphenyl-1,3,2-diazaphospholidin-2-yl]-3,3′-binaphtho-[2,1-*b*]furan complex (27a) and bis-*P*-borane-(S^*_{ax})-2,2′-bis[(4*R*,5*R*)-1,3-dimethyl-4,5-diphenyl-1,3,2-diazaphospholidin-2-yl]-3,3′-binaphtho[2,1-*b*]furan complex (27b)

To a solution of naphtho[*b*]furan (**5**) (0.245 g, 0.734 mmol) in Et_2O (8.0 mL) at –78 °C was added 2.2 equiv of *t*-BuLi (1.7 mol L^{-1} in hexanes, 0.949 mL, 1.61 mmol). The resulting mixture was warmed to 0 °C and stirred under an atmosphere of nitrogen for 1.5 h. To the vessel was then added enantiopure diazaphospholidine reagent **26** (0.491 g, 1.61 mmol). The reaction contents were allowed to warm to rt over a 1 h period and subsequently left to stir for 3 h. To the vessel was then added borane – dimethyl sulfide complex (2.0 mol L^{-1} solution in THF, 1.10 mL, 2.20 mmol), and the resulting mixture was left to react for a further 4 h. The reaction contents were then quenched with brine (50 mL) and extracted with $CHCl_3$ (3 × 75 mL). The combined organic extracts were dried ($MgSO_4$) and concentrated in vacuo to afford a light yellow solid residue. The crude material was purified by column chromatography (15:1) to afford a 1:1 mixture of the title compounds. Separation of the mixture was achieved by recrystallization from a binary mixture of $CHCl_3$ and hexanes. Under these conditions, compound **27a** crystallized, diastereomerically pure, as long white needles (0.304 g, 46%) characterized by the following analytical data: mp 123–124 °C. IR (KBr) (cm^{-1}): 2869, 2392 (BH_3), 1455, 1147. ^{1}H NMR (300 MHz) δ: –0.32 to 0.84 (bs, 3H), 2.02 (d, *J* = 11.3 Hz, 3H), 2.71 (d, *J* = 13.3 Hz, 3H), 4.00 (d, *J* = 8.7 Hz, 1H), 4.80 (d, *J* = 8.7 Hz, 1H), 7.02–7.45 (m, 12H), 7.74 (d, *J* = 7.9 Hz, 1H), 7.84–8.10 (m, 3H). ^{13}C NMR (75 MHz) (ppm): 31.8 (d, *J* = 3 Hz, CH_3), 32.7 (d, *J* = 11 Hz, CH_3), 75.1 (d, *J* = 3 Hz, CH), 76.3 (CH), 112.7 (CH), 122.4 (C), 122.5 (C), 122.8 (CH), 124.8 (CH), 126.2 (C), 126.9 (CH), 127.7 (CH), 128.0 (CH), 128.5 (CH), 128.6 (CH), 128.8 (CH), 129.1 (CH), 131.1 (C), 137.6 (d, *J* = 9 Hz, C), 138.5 (d, *J* = 4 Hz, C), 151.6 (d, *J* = 26 Hz, C), 155.0 (d, *J* = 3 Hz, C). ^{31}P NMR (81 MHz) (ppm): +98.7 (bs). FAB-MS, *m/z* (relative intensity, %): 899 (1, $[M + H]^+$). Borane adduct **27b** was obtained isomerically pure after flash chromatographic (15:1) purification of the mother liquor. The following analytical data were recorded for this compound: mp 138–140 °C ($CHCl_3$–hexanes). IR (KBr) (cm^{-1}): 2869, 2390 (BH_3), 1455, 1146. ^{1}H NMR (400 MHz) δ: –0.32–1.00 (bs, 3H), 2.11 (d, *J* = 13.7 Hz, 3H), 2.86 (d, *J* = 11.1 Hz, 3H), 4.15 (d, *J* = 8.7 Hz, 1H), 4.61 (d, *J* = 8.7 Hz, 1H), 6.99 (t, *J* = 7.2 Hz, 1H), 7.12–7.23 (m, 2H), 7.25–7.34 (m, 4H), 7.35–7.50 (m, 5H), 7.70 (d, *J* = 8.2 Hz, 1H), 7.91–8.03 (m, 3H). ^{13}C NMR (100 MHz) (ppm): 31.8 (d, *J* = 5 Hz, CH_3), 33.4 (d, *J* = 11 Hz, CH_3), 75.1 (d, *J* = 2 Hz, CH), 76.4 (CH), 113.3

© 2004 NRC Canada

(CH), 122.9 (C), 123.0 (C), 123.5 (CH), 125.2 (CH), 126.7 (C), 126.9 (CH), 128.5 (CH), 128.6 (CH), 128.7 (CH), 128.8 (CH), 128.9 (CH), 129.3 (CH), 129.4 (CH), 131.5 (C), 137.6 (d, J = 9 Hz, C), 138.6 (d, J = 4 Hz, C), 151.3 (d, J = 26 Hz, C), 155.6 (d, J = 3 Hz, C). ^{31}P NMR (81 MHz) (ppm): +91.3 (bs). FAB-MS, *m/z* (relative intensity, %): 899 (4, [M + H]$^+$).

Phosphinimine 31a and 31b

BINAPFu (±)-**3** (2.65 g, 3.78 mmol) in THF (60 mL) was treated with (1*S*)-camphor-10-sulfonyl azide (59) (1.95 g, 7.55 mmol) at reflux under an N_2 atmosphere for 12 h. The cooled mixture was then concentrated under reduced pressure to afford a 1:1 mixture of **31a** and **31b** in quantitative yield. The diastereomeric products were separated by flash chromatography (9:1 $CHCl_3$–CH_3CN). The first spot off the column, **31a**, was determined to be the *S* axial isomer by single crystal X-ray analysis and afforded the following analytical data: mp 175–177 °C. $[\alpha]_D^{21}$ –72.1 (*c* 4.13, $CHCl_3$). IR (KBr) (cm^{-1}): 1745. ^{1}H NMR (200 MHz, $CDCl_3$) δ: 7.97–7.52 (m, 11H), 7.44 (t, J = 8.0 Hz, 1H), 7.38 (d, J = 8.4 Hz, 1H), 7.17 (t, J = 6.6 Hz, 1H), 6.88 (m, 2H), 2.51–2.26 (m, 2H), 2.18 (dt, J = 16.0, 3.0 Hz, 1H), 1.94–1.54 (m, 4H), 1.50–1.07 (m, 2H), 0.90 (s, 3H), 0.53 (s, 3H). ^{13}C NMR (50 MHz, $CDCl_3$) δ: 214.8 (C), 156.3 (d, J = 10 Hz, C), 140.1 (d, J = 154 Hz, C), 134.1 (CH), 134.0 (CH), 133.9 (CH), 133.8 (CH), 133.6 (CH), 133.0 (d, J = 1 Hz, CH), 131.2 (C), 129.9 (CH), 129.5 (CH), 129.4 (CH), 129.3 (CH), 129.0 (C), 128.5 (CH), 128.4 (CH), 128.0 (CH), 127.9 (d, J = 15 Hz, C), 127.4 (d, J = 81 Hz, C), 126.3 (d, J = 84 Hz, C), 125.9 (CH) 123.7 (CH), 122.5 (d, J = 8 Hz, C), 112.5 (CH), 78.0 (CH_2), 58.7 (C), 51.7 (d, J = 4 Hz, CH_2), 47.8 (C), 42.9 (CH), 27.3 (CH_2), 24.6 (CH_2), 20.4 (CH_3), 20.2 (CH_3). ^{31}P NMR (81 MHz, $CDCl_3$) δ: 5.7. MS, *m/z* (relative intensity, %): 531 ([$M^+ - C_{32}H_{40}NO_6PS_2$], 1). FAB-MS, *m/z* (relative intensity, %): 1161 ([M]$^+$, 31), 531 (68). Compound **31b** gave the following analytical data: mp 229 °C (decomposition (dec.)). $[\alpha]_D^{21}$ +66.5 (*c* 1.55, $CHCl_3$). IR (KBr) (cm^{-1}): 1743. ^{1}H NMR (200 MHz, $CDCl_3$) δ: 7.93 (t, J = 9.6, 2H), 7.78 (t, J = 8.5, 4H), 7.70–7.29 (m, 7H), 7.11 (t, J = 8.0, 1H), 6.89–6.71 (m, 2H), 2.59–2.32 (m, 2H), 2.21 (dt, J = 16.0, 3.0, 1H), 1.93–1.60 (m, 4H), 1.49–1.08 (m, 2H), 0.71 (s, 3H), 0.45 (s, 3H). ^{13}C NMR (50 MHz, $CDCl_3$) δ: 215.0 (C), 156.5 (d, J = 9 Hz, C), 140.0 (d, J = 151 Hz, C), 134.1 (CH), 134.0 (CH), 133.7 (CH), 133.6 (CH), 133.5 (CH), 132.9 (d, J = 1 Hz, CH), 130.5 (CH), 129.6 (CH), 129.3 (CH), 129.2 (CH), 128.9 (C), 128.3 (CH), 128.2 (CH), 127.8 (d, J = 15 Hz, C), 127.8 (CH), 127.2 (C), 126.5 (C), 125.7 (CH), 125.5 (C), 123.7 (CH), 122.2 (d, J = 8 Hz, C), 112.6 (CH), 58.3 (C), 51.7 (d, J = 3 Hz, CH_2), 47.6 (C), 42.6 (CH_2), 42.5 (CH), 27.2 (CH_2), 24.8 (CH_2), 20.4 (CH_3), 20.2 (CH_3). ^{31}P NMR (81 MHz, $CDCl_3$) δ: 4.9. MS, *m/z* (relative intensity, %): 531 ([$M^+ - C_{32}H_{40}NO_6PS_2$], 1). FAB MS, *m/z* (relative intensity, %): 1161 ([M]$^+$, 38), 531 (72). Anal calcd for $C_{68}H_{62}P_2S_2O_8N_2$ + $CHCl_3$: C 64.61, H 5.11, N 2.18; found: C 64.75, H 4.98, N 2.37.

X-ray crystallographic analysis on **31a** was performed at the University of Alberta on a Bruker P4 diffractometer equipped with a SMART 1000 CCD area detector, using graphite-monochromated Mo Kα radiation. The following crystal parameters were obtained: monoclinic, $P2_1$ (No. 4); a = 16.248(2) Å; b = 11.0208(16) Å; c = 35.643(5) Å; V = 6372.8(15) Å^3; Z = 4; R = 0.0696; Rw = 0.2355.

(–)-2,2′-Bis(diphenylphosphonyl)-3,3′-binaphtho[2,1-*b*]furan (14)

Phosphinimine **31a** (1.44 g, 1.24 mmol) in dioxane (50 mL) was treated with 3 mol L^{-1} aqueous H_2SO_4 (35 mL), and the resulting mixture was heated to reflux for 12 h. The cooled mixture was then quenched with 10% NaOH and extracted with $CHCl_3$ (3 × 100 mL). The combined organic extracts were dried ($MgSO_4$) and concentrated in vacuo to afford the crude phosphine oxide. The product was purified by flash chromatography on basic alumina (1:1 hexanes – ethyl acetate → 9:1 $CHCl_3$–MeOH) to afford the desired phosphine oxide (–)-**14** in quantitative yield. $[\alpha]_D^{19}$ –166.6 (*c* 1.01, $CHCl_3$). ^{1}H and ^{13}C spectra were indentical to those of (±)-**14**.

(–)-2,2′-Bis(diphenylphosphino)-3,3′-binaphtho[2,1-*b*]furan (3)

Phosphine oxide (–)-**14** (821 mg, 1.12 mmol) was dissolved in a mixture of xylenes (25 mL) and Et_3N (3.75 mL, 26.8 mmol). To the solution was added $SiCl_3H$ (2.26 mL, 22.4 mmol), and the resulting mixture was heated to 100 °C under argon for 1 h. The mixture was then heated to 150 °C for 3 h and subsequently cooled to 65 °C. To the vessel was then added dropwise 30% NaOH (60 mL). The resulting mixture was vigorously stirred for 1 h at 65 °C. The cooled reaction mixture was extracted with $CHCl_3$ (3 × 100 mL), and the combined organic phases were dried ($MgSO_4$) and concentrated in vacuo. The product (–)-**3** was purified by flash chromatography (20:1 hexanes – ethyl acetate) to afford the optically pure (*S*)-BINAPFu (785 mg, 100%). $[\alpha]_D^{19}$ –203.0 (*c* 1.09, $CHCl_3$). Heating the enantiopure ligand in *p*-xylenes at 150 °C for 7 days did not result in any racemization of the chiral axis, as evidenced by optical rotation and HPLC analysis (Chiralcel® OJ, 95:5 MeOH:EtOH, 0.5 mL min^{-1}, 270 nm detection). ^{1}H and ^{13}C spectra were identical to those of (±)-**3**.

(±)-Dichloro[2,2′-bis(diphenylphosphino)-3,3′-binaphtho[2,1-*b*]furan]-palladium (II) (15)

(±)-2,2′-Bis(diphenylphosphino)-3,3′-binaphtho[2,1-*b*]furan (**3**) (300 mg, 0.427 mmol) and bis(acetonitrile)dichloropalladium(II) (111 mg, 0.427 mmol) were stirred in CH_2Cl_2 (20 mL) at rt for 15 h. The solution was concentrated in vacuo, and the residue was purified by recrystallization from acetone–ether to give 349 mg (93%) of palladium adduct **15** as orange crystals: mp 312–314 °C. IR (KBr) (cm^{-1}): 3056, 1095, 999, 690. ^{1}H NMR (400 MHz) δ: 6.59 (m, J = 6.9 Hz, 2H), 6.82 (t, J = 7.3 Hz, 1H), 7.08 (t, J = 7.6 Hz, 1H), 7.27–7.52 (m, 6H), 7.65 (d, J = 7.5 Hz, 1H), 7.67 (d, J = 8.4 Hz, 1H), 7.77 (d, J = 9.1 Hz, 1H), 7.91 (d, J = 8.1 Hz, 1H), 8.11 (d, J = 7.6 Hz, 1H), 8.15 (d, J = 7.6 Hz, 1H). ^{13}C NMR (100 MHz) (ppm): 112.6 (CH), 122.0 (d, J = 2 Hz, C), 123.8 (dd, J = 7, 6 Hz, C), 124.3 (dd, J = 62, 4 Hz, C), 125.8 (CH), 126.8 (dd, J = 68, 5 Hz, C), 127.8 (CH), 128.1 (C), 128.3 (t, J = 6 Hz, CH), 128.5 (t, J = 6 Hz, CH), 128.9 (CH), 129.2 (CH), 131.2 (d, J = 2 Hz, C), 131.6 (CH), 132.0 (CH), 134.3 (t, J = 5 Hz, CH), 136.3 (t, J = 7 Hz, CH), 147.4 (d, J = 73 Hz, C), 158.1 (dd, J = 4, 3 Hz, C). ^{31}P

© 2004 NRC Canada

NMR (162 MHz) (ppm): +11.3. FAB-MS, *m/z* (relative intensity, %): 901 (9, $[M(^{35}Cl_2) + Na]^+$), 878 (9, $[M^+(^{35}Cl_2)]$).

X-ray crystallographic analysis on **15** was performed at the University of Calgary on an Enraf-Nonius CAD-4 diffractometer with graphite monochromated Cu Kα radiation. The following crystal parameters were obtained: monoclinic, $P2_1/n$ (No. 14); a = 16.673(5) Å, b = 18.478(7) Å, c = 13.702(3) Å; V = 4134(2) Å^3; Z = 4; R = 0.053; Rw = 0.041.

(–)-(S_{ax})-2,2′-Bis(selenodiphenylphosphinyl)-3,3′-binaphtho[2,1-*b*]furan (35)

The following procedure is based on a method reported by Allen and Taylor (51). To a 0.02 mol L^{-1} solution of the BINAPFu (–)-**3** (0.119 g, 0.170 mmol) in $CHCl_3$ was added 10 molar equivalents of Se dust (100 mesh). The resulting mixture was heated to reflux under an atmosphere of argon gas for a 5 h period. The cooled mixture was filtered through a pad of Celite®, and the filterings were washed with a small volume of $CHCl_3$. Concentration of the filtrate under reduced pressure furnished the crude phosphine selenide (–)-**35**. The crude product was recrystallized from CH_3CN to furnish the analytically pure product (0.142 g, 97%). X-ray diffraction analysis of a single crystal thus obtained, using the Bijvoet method, showed the *S*-configuration for the biaryl axis. Phosphine selenide (–)-**35** gave the following analytical data: mp 176–178 °C (CH_3CN). IR (KBr) (cm^{-1}): 2923, 1435, 1095, 1003. ^{1}H NMR (400 MHz) δ: 7.04–7.15 (m, 6H), 7.19–7.26 (m, 1H), 7.35 (t, J = 8.0 Hz, 1H), 7.49 (d, J = 8.2 Hz, 1H), 7.61 (d, J = 9.1 Hz, 1H), 7.67–7.79 (m, 4H), 7.82 (d, J = 9.1 Hz, 1H), 7.87 (d, J = 8.1 Hz, 1H). ^{13}C NMR (50 MHz) δ: 112.9 (CH), 122.5 (C), 122.6 (C), 123.2 (CH), 124.9 (d, J = 16 Hz, C), 125.4 (CH), 127.3 (CH), 128.1 (d, J = 3 Hz, CH), 128.2 (CH), 128.3 (CH), 129.2 (d, J = 3 Hz, CH), 129.2 (d, J = 21 Hz, C), 130.3 (d, J = 30 Hz, C), 131.2 (d, J = 3 Hz, C), 131.8 (d, J = 3 Hz, CH), 132.0 (d, J = 3 Hz, CH), 133.1 (d, J = 12 Hz, CH), 133.7 (d, J = 12 Hz, CH), 142.1 (d, J = 99 Hz, C), 155.2 (d, J = 7 Hz, C). ^{31}P NMR (162 MHz) (ppm): +19.4 ($^1J_{P\text{-}Se}$ = 762 Hz). MS, *m/z* (relative intensity, %): 597 (47, $[M^+ - PPh_2Se]$), 517 (100, $[M^+ - PPh_2Se_2]$). Exact mass calcd for $[M^+ - PPh_2{}^{80}Se]$: 597.0523; found: 597.0520. Anal calcd for $C_{48}H_{32}O_2P_2Se_2 + CH_3CN$: C 66.60, H 3.91, N 1.55; found: C 66.41, H 3.91, N 1.70.

X-ray crystallographic analysis on **35** was performed at the University of Calgary on a Rigaku AFC6S diffractometer with graphite-monochromated Mo Kα radiation. The following crystal parameters were obtained: monoclinic, $P2_1$ (No. 4); a = 9.842(4) Å; b = 21.045(5) Å; c = 10.347(3) Å; V = 2031(1) Å^3; Z = 2; R = 0.0406; Rw = 0.0915; Flack parameter (60) = 0.006(19). Bijvoet analysis was performed. A refinement of the inverted structure was carried out and converged with R = 0.0465 (Rw = 0.1043 with Flack parameter = 0.20(2)) and was therefore rejected as the absolute configuration present in the crystal.

General procedure for the Heck arylation of 2,3-dihydrofuran

Into a 2 dram (1 dram = 1.771845 g) screw-cap vial was measured $Pd(OAc)_2$ (2.2 mg, 9.97 μmol), (*S*)-BINAPFu (21.0 mg, 29.9 μmol), Hunig's base (255 μL, 1.46 mmol), and 1,4-dioxane (2.5 mL). The resulting mixture was heated to 60 °C under an argon atmosphere for 30 min. To the vessel was then added 2,3-dihydrofuran (189 μL, 2.50 mmol) and phenyl triflate (79 μL, 0.488 mmol). The mixture was thermostatically heated to 100 °C for a 7 day period. The crude mixture was filtered through a pad of celite and analyzed by chiral GC (Cyclodex B column, 80 °C start temperature, 2 min initial hold time, 1 °C min^{-1} ramp rate, 220 °C final temperature). The reaction products eluted in the following order: (*S*)-2-phenyl-2,3-dihydrofuran T_r = 26.1 min; (*R*)-5-phenyl-2,3-dihydrofuran T_r = 26.7 min; 2-phenyl-4,5-dihydrofuran T_r = 28.9 min; (*R*)-2-phenyl-2,5-dihydrofuran T_r = 31.2 min; (*S*)-2-phenyl-2,5-dihydrofuran T_r = 31.6 min.

Acknowledgments

We thank the Natural Sciences and Engineering Research Council of Canada (NSERC) for financial support. N.G.A. gratefully acknowledges receipt of an NSERC scholarship, a Ralph Steinhauer Award of Distinction from the Alberta Heritage Foundation, and an Honorary Killam Fellowship.

References

1. (*a*) A. Miyashita, H. Takaya, T. Souchi, and R. Noyori. Tetrahedron, **40**, 1245 (1984); (*b*) K. Toriumi, T. Ito, H. Takaya, T. Souchi, and R. Noyori. Acta Crystallogr. Sect. B Struct. Sci. **B38**, 807 (1982); (*c*) A. Miyashita, A. Yasuda, H. Takaya, K. Toriumi, T. Ito, T. Souchi, and R. Noyori. J. Am. Chem. Soc. **102**, 7932 (1980).
2. (*a*) M. McCarthy and P.J. Guiry. Tetrahedron, **57**, 3809 (2001); (*b*) M. Kitamura and R. Noyori. *In* Encyclopedia of reagents for organic synthesis. Vol. 1. *Edited by* L.A. Paquette. John Wiley & Sons, Chichester. 1995. p. 509.
3. N.G. Andersen and B.A. Keay. Chem. Rev. **101**, 997 (2001).
4. N.G. Andersen, R. McDonald, and B.A. Keay. Tetrahedron Asymmetry, **12**, 263 (2001).
5. (*a*) R. Kuwano and Y. Ito. J. Org. Chem. **64**, 1232 (1999); (*b*) R. Kuwano, M. Sawamura, J. Shirai, M. Takahashi, and Y. Ito. Bull. Chem. Soc. Jpn. **73**, 485 (2000); (*c*) B.C. Hamann and J.F. Hartwig. J. Am. Chem. Soc. **120**, 3694 (1998); (*d*) H. Doucet, E. Fernandez, T.P. Layzell, and J.M. Brown. Chem. Eur. J. **5**, 1320 (1999); (*e*) Y. Crameri, J. Foricher, M. Scalone, and R. Schmid. Tetrahedron Asymmetry, **8**, 3617 (1997); (*f*) M. Cereghetti, W. Arnold, E.A. Broger, and A. Rageot. Tetrahedron Lett. **37**, 5347 (1996); (*g*) J.-P. Tranchier, V. Ratovelomanana-Vidal, J.-P. Genêt, S. Tong, and T. Cohen. Tetrahedron Lett. **38**, 2951 (1997); (*h*) R. Schmid, E.A. Broger, M. Cereghetti, Y. Crameri, J. Foricher, M. Lalonde, R.K. Müller, M. Scalone, G. Schoettel, and U. Zutter. Pure Appl. Chem. **68**, 131 (1996); (*i*) T. Benincori, E. Brenna, F. Sannicolò, L. Trimarco, P. Antognazza, E. Cesarotti, F. Demartin, and T. Pilati. J. Org. Chem. **61**, 6244 (1996).
6. A. Kojima, C. Boden, and M. Shibasaki. Tetrahedron Lett. **38**, 3459 (1997).
7. R.F. Heck. Org. React. **27**, 345 (1982).
8. C. Amatore, A. Jutand, G. Meyer, H. Atmani, F. Khalil, and F.O. Chahdi. Organometallics, **17**, 2958 (1998).
9. (*a*) S.Y.W. Lau, N.G. Andersen, and B.A. Keay. Org. Lett. **3**, 181 (2001); (*b*) S.Y.W. Lau and B.A. Keay. Synlett, 605 (1999); (*c*) S.P. Maddaford, N.G. Andersen, W.A. Cristofoli, and B.A. Keay. J. Am. Chem. Soc. **118**, 10 766 (1996); (*d*) W. Cristofoli and B.A. Keay. Synlett, 625 (1994).

© 2004 NRC Canada

10. N.G. Andersen, M. Parvez, and B.A. Keay. Org. Lett. **2**, 2817 (2000).
11. (*a*) T. Benincori, E. Brenna, F. Sannicolò, L. Trimarco, P. Antognazza, and E. Cesarotti, J. Chem. Soc. Chem. Commun. 685 (1995); (*b*) P. Antognazza, T. Benincori, E. Brenna, E. Cesarotti, and R. Sannicolò. International Patent WO 9601831 A1, 1996; (*c*) R. Sannicolò, T. Benincori, and P. Antognazza. International Patent WO 9822484 A1, 1998.
12. N.G. Andersen. Ph.D. thesis. Department of Chemistry, University of Calgary. 2000.
13. T. Mukaiyama, T. Sato, and J. Hanna. Chem. Lett. 1041 (1973).
14. S. Tyrlik and I. Wolochowicz. Bull. Soc. Chim. Fr. 2147 (1973).
15. J.E. McMurry. Acc. Chem. Res. **16**, 405 (1983).
16. A. Fürstner and B. Bogdanovic. Angew. Chem. Int. Ed. Engl. **35**, 2442 (1996).
17. (*a*) B.H. Ingham, H. Stephen, and R. Timpe. J. Chem. Soc. 895 (1931); (*b*) K. Fries and R. Frellstedt. Chem. Ber. **54**, 715 (1921).
18. (*a*) M.F. Wempe and J.R. Grunwell. J. Org. Chem. **60**, 2714 (1995); (*b*) T-L. Ho. Synth. Commun. **11**, 7 (1981); (*c*) D.P. Wyman and P.R. Kaufman. J. Org. Chem. **29**, 1956 (1964).
19. A. Guy, M. Lemaire, and J-P. Guetté. Synthesis, 1018 (1982).
20. T. Inouye, Y. Uchida, and H. Kakisawa. Bull. Chem. Soc. Jpn. **50**, 961 (1977).
21. R.J. Rawson and I.T. Harrison. J. Org. Chem. **35**, 2057 (1970).
22. E. Erdik. Tetrahedron, **43**, 2203 (1987).
23. (*a*) V.K. Ahluwalia and R.S. Jolly. Synthesis, 74 (1982); (*b*) A.N. Starratt and A. Stoessl. Can. J. Chem. **55**, 2360 (1977); (*c*) E.A. Braude, A.G. Brook, and R.P.Linstead. J. Chem. Soc. 3569 (1954).
24. F. Ozawa, A. Kubo, Y. Matsumoto, T. Hayashi, E. Nishioka, K. Yanagi, and K. Moriguchi. Organometallics, **12**, 4188 (1993).
25. (*a*) P. Dierkes and P.W.N.M. van Leeuwen. J. Chem. Soc. Dalton Trans. 1519 (1999); (*b*) P.W.N.M. van Leeuwen, P.C.J. Kamer, J.N.H. Reek, and P. Dierkes. Chem. Rev. **100**, 2741 (2000); (*c*) P.C.J. Kamer, P.W.N.M. van Leeuwen, and J.N.H. Reek. Acc. Chem. Res. **34**, 895 (2001).
26. Chiral Tecnologies Inc. Application guide for chiral column selection. 2nd ed. *Distributed by* J.T. Baker Canada, Toronto. 1995.
27. K.M. Pietrusiewicz and M. Zablocka. Chem. Rev. **94**, 1375 (1994).
28. H. Takaya, K. Mashima, K. Koyano, M. Yagi, H. Kumobayashi, T. Taketomi, S. Akutagawa, and R. Noyori. J. Org. Chem. **51**, 629 (1986).
29. (*a*) K. Tani, L.D. Brown, J. Ahmed, J.A. Ibers, M. Yokota, A. Nakamura, and S.Otsuka. J. Am. Chem. Soc. **99**, 7876 (1977); (*b*) S. Otsuka, A. Nakamura, T. Kano, and K. Tani. J. Am. Chem. Soc. **93**, 4301 (1971).
30. (*a*) P.H. Leung, A.C. Willis, and S.B.Wild. Inorg. Chem. **31**, 1406 (1992); (*b*) J.W.L. Martin, J.A.L. Palmer, and S.B. Wild. Inorg. Chem. **23**, 2664 (1984); (*c*) G. Salem and S.B. Wild. Inorg. Chem. **22**, 4049 (1983); (*d*) D.G. Allen, G.M. McLaughlin, G.B. Robertson, W.L. Steffen, G. Salem, and S.B. Wild. Inorg. Chem. **21**, 1007 (1982); (*e*) N.K. Roberts and S.B. Wild. J. Am. Chem. Soc. **101**, 6254 (1979).
31. N.K. Roberts and S.B. Wild. J. Chem. Soc. Dalton Trans. 2015 (1979).
32. G.L. Lange and C. Gottardo. Synth. Commun. **20**, 1473 (1990).
33. (*a*) N. Gurusamy and K.D. Berlin. J. Am. Chem. Soc. **104**, 3114 (1982); (*b*) K.F. Kumli, C.A. VanderWerf, and W.E. McEwan. J. Am. Chem. Soc. **81**, 248 (1959); (*c*) D.M. Coyne, W.E. McEwen, and C.A. Vanderwerf. J. Am. Chem. Soc. **78**, 3061 (1956).
34. K.L. Marsi and H. Tuinstra. J. Org. Chem. **40**, 1843 (1975).
35. (*a*) H.C.P.F. Roelen, H. Van den Elst, G.A. Van der Marel, and J.H. Van Boom. Tetrahedron Lett. **33**, 2357 (1992); (*b*) P. Jutzi and H. Saleske. Chem. Ber. **117**, 222 (1984); (*c*) H. Nöth and H-J. Vetter. Chem. Ber. 1109 (1963); (*d*) E. Evleth, Jr., L.D. Freeman, and R.I. Wagner. J. Org. Chem. **28**, 2192 (1962).
36. J.F. Larrow and E.N. Jacobsen. J. Org. Chem. **59**, 1939 (1994).
37. F. Galsbøl, P. Steebøl, and B. Søndergaard Sørensen. Acta Chem Scand. **26**, 3605 (1972).
38. Y. Bennani and S. Hanessian. Tetrahedron, **52**, 13 837 (1996).
39. A. Longeau, S. Durand, A. Spiegel, and P. Knochel. Tetrahedron Asymm. **8**, 987 (1997).
40. P. Mangeney, T. Tejero, A. Alexakis, F. Grosjean, and J. Normant. Synthesis, 255 (1988).
41. P. Mangeney, F. Grosjean, A. Alexakis, and J. Normant. Tetrahedron Lett. **29**, 2675 (1988).
42. A. Alexakis, J.C. Frutos, and P. Mangeney. Tetrahedron Lett. **29**, 5125 (1994).
43. A.A. Tolmachev, S.P. Ivonin, A.V. Kharchenko, and A.S. Kozlov. J. Gen. Chem. USSR. 778 (1991).
44. (*a*) H. Staudinger and E. Hauser. Helv. Chim. Acta, **4**, 861 (1921); (*b*) H. Staudinger and J. Meyer. Helv. Chim. Acta, **2**, 635 (1919).
45. J. Koketsu, Y. Ninomiya, Y. Suzuki, and N. Koga. Inorg. Chem. **36**, 694 (1997).
46. (*a*) N.G. Andersen, P.D. Ramsden, D. Che, M. Parvez, and B.A. Keay. J. Org. Chem. **66,** 7478 (2001); (*b*) N.G. Andersen, P.D. Ramsden, D. Che, M. Parvez, and B.A. Keay. Org. Lett. **1**, 2009 (1999).
47. R. Cremlyn, K. Burrell, K. Fish, I. Hough, and D. Mason. Phosphorus Sulfur Relat. Elem. **12**, 197 (1982).
48. G.M. Kosolapoff and L. Maier. *In* Organic phosphorus compounds. Vol. 3. John Wiley & Sons, New York. 1972.
49. A.W. Johnson. *In* Ylid chemistry. Vol. 7. *Edited by* A.T. Blomquist. Academic Press, New York. 1966. Chap 5.
50. J. Emsley and D. Hall. *In* The chemistry of phosphorus. John Wiley & Sons, New York. 1976. Chap 10.
51. D.W. Allen and B.F. Taylor. J. Chem. Soc. Dalton Trans. 51 (1982).
52. G.J. Dawson, C.G. Frost, J.M.J. Williams, and S.J. Coote. Tetrahedron Lett. **34**, 3149 (1993).
53. D. Che, N.G. Andersen, S.Y.W. Lau, M. Parvez, and B.A. Keay. Tetrahedron Asymm. **11**, 1919 (2000).
54. E.L. Eliel, S.H. Wilen, and L.N. Mander. *In* Stereochemistry of organic compounds. John Wiley & Sons, New York. 1994. pp. 113–115.
55. (*a*) F. Ozawa, A. Kubo, and T. Hayashi. J. Am. Chem. Soc. **113**, 1417 (1991); (*b*) F. Ozawa, A. Kubo, and T. Hayashi. Tetrahedron Lett. **33**, 1485 (1992).
56. V. Farina and B. Krishnan. J. Am. Chem. Soc. **113**, 9585 (1991).
57. W.C. Still, M. Kahn, and A. Mitra. J. Org. Chem. **43**, 2923 (1978).
58. K. Fries and R. Frellstedt. Chem. Ber. **54**, 715 (1921).
59. R.J.W. Cremlyn and R. Hornby. J. Chem. Soc. C, 120 (1969).
60. H.D. Flack. Acta Crystallogr. **A39**, 876 (1983).

© 2004 NRC Canada

A new family of monocyclopentadienyl organoscandium *bis*-alkyls supported by a bulky trialkylphosphine oxide ancillary[1]

Lee D. Henderson, Glen D. MacInnis, Warren E. Piers, and Masood Parvez

Abstract: Treatment of the oligomeric compound $[Cp^*ScCl_2]_n$ ($Cp^* = C_5Me_5$) with tri-*tert*-butylphosphine oxide in THF leads to the monocyclopentadienyl scandium dichloride $[Cp^*(t\text{-}Bu_3P{=}O)ScCl_2]$ as a monomeric, THF-free solid in 72% yield. This compound can be alkylated with MeLi to give the corresponding dimethyl derivative, $[Cp^*(t\text{-}Bu_3P{=}O)ScMe_2]$, **1**. The crystal structures of these two compounds have been done and reveal a three-legged piano stool geometry about the scandium center. The coordinated phosphine oxide ligand exchanges with free donor in both compounds via an associative mechanism, as indicated by the activation parameters ($\Delta H^{\ddagger}$ = 6.4–8.4 kcal mol^{-1}; $\Delta S^{\ddagger}$ = –22.5 to –26.6 eu). Thus, the $Cp^*(t\text{-}Bu_3P{=}O)$ ligand set provides a stable platform for organoscandium chemistry. This was demonstrated by the activation of **1** by treatment with $B(C_6F_5)_3$ to form the fully characterized contact ion pair $[Cp^*(t\text{-}Bu_3P{=}O)ScMe]^+[MeB(C_6F_5)_3]^-$, **2**, which is an active ethylene polymerization catalyst.

Key words: organoscandium compounds, olefin polymerization, cationic complexes.

Résumé : Le traitement du produit oligomère $[Cp^*ScCl_2]_n$ ($Cp^* = C_5Me_5$) avec de l'oxyde de tri-*tert*-butylphosphine, dans le THF, conduit à la formation du dichlorure de monocyclopentadiénylscandium, $[Cp^*(t\text{-}Bu_3P{=}O)ScCl_2]$, isolé avec un rendement de 72 %, sous la forme monomère et exempt de THF. Ce composé peut être alkylé avec du MeLi pour donner le dérivé diméthylé correspondant, $[Cp^*(t\text{-}Bu_3P{=}O)ScMe_2]$, **1**. On a déterminé les structures cristallines de ces deux composés qui comportent une géométrie en banc de piano à trois pattes autour du centre scandium. Le ligand oxyde de phosphine qui est coordiné s'échange avec un donneur libre dans les deux composés, par le biais d'un mécanisme associatif suggéré par les paramètres d'activation ($\Delta H^{\ddagger}$ = 6,4 à 8,4 kcal mol^{-1}; $\Delta S^{\ddagger}$ = –22,5 à –26,6 ue). Ainsi, l'ensemble de ligand $Cp^*t\text{-}Bu_3P{=}O$ fournit une plate-forme stable pour la chimie de composés organiques du scandium. Ceci a été démontré par l'activation de **1** par traitement avec du $B(C_6F_5)_3$ qui conduit à la formation de la paire d'ions de contact complètement caractérisé, $[Cp^*(t\text{-}Bu_3P{=}O)ScMe]^+[MeB(C_6F_5)_3]^-$ (**2**), qui est un catalyseur actif pour la polymérisation de l'éthylène.

Mots clés : composés organiques du scandium, polymérisation des oléfines, complexes cationiques.

[Traduit par la Rédaction]

Introduction

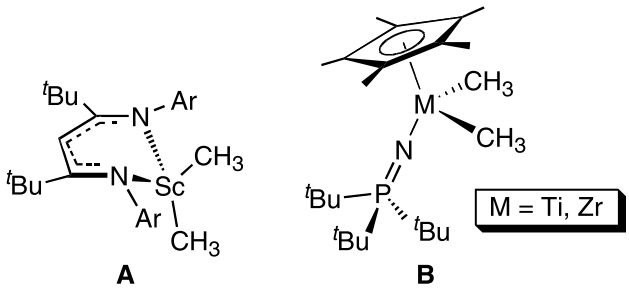
Suitable ligand environments for group 3 metal bis-alkyl functions free from occluded salts or coordinating solvent molecules are rare; this lack of abundance has prevented development of the chemistry of organo group 3 dialkyls to the same degree as the extensively explored group 4 dialkyls (1). A notable exception is the bulky β-diketiminato (nacnac) ligand framework (**A**) and related structures (2), which supports the chemistry of base-free scandium dialkyls (3) and cationic scandium alkyls (4) but cannot eliminate the need for THF ligation in analogous organoyttrium chemistry (5). Despite the success of this ligand ancillary and its derivatives (6), new environments are of interest in the continued expansion of this area of early transition-metal organometallic chemistry.

Received 31 July 2003. Published on the NRC Research Press Web site at http://canjchem.nrc.ca on 12 January 2004.

Dedicated to Professor Edward Piers on the occasion of his 65th birthday and for his many contributions to chemistry in Canada.

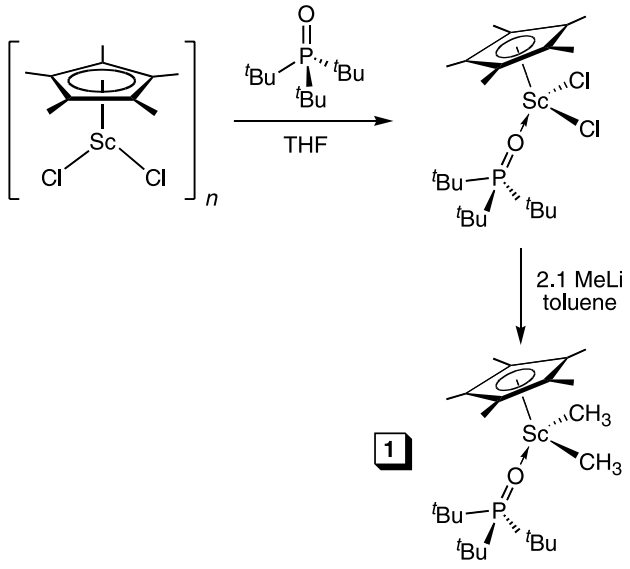
L.D. Henderson, G.D. MacInnis, W.E. Piers,[2,3] and M. Parvez. Department of Chemistry, University of Calgary, 2500 University Drive NW, Calgary, AB T2N 1N4, Canada.

[1]This article is part of a Special Issue dedicated to Professor Ed Piers.
[2]S. Robert Blair Professor of Chemistry (2000–2005).
[3]Corresponding author (e-mail: wpiers@ucalgary.ca).



 doi: 10.1139/V03-157 © 2004 NRC Canada

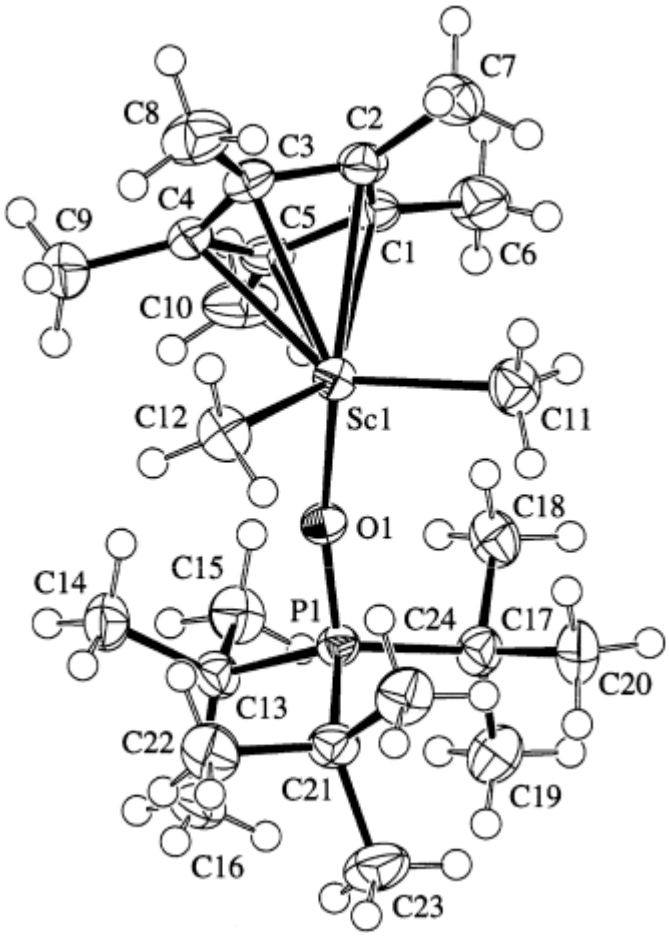
Scheme 1.



Inspiration for possible organo group 3 ligand environments can be found in successful areas of group 4 metal chemistry. Stephan and co-workers (7) and others (8) have demonstrated the efficacy of the bulky phosphinimide ligand t-$Bu_3P{=}N^-$ as a steric replacement for the Cp* ligand ($C_5Me_5^-$), following a strategy originally tendered by Wolczanski and co-workers (9) and embodied in the tri-*tert*-butylmethoxide "tritox" ligand system. Thus, the organotitanium and zirconium compounds **B** are sterically analogous to the more well-known permethylmetallocenes but with a somewhat more open environment in the immediate vicinity of the metal center, which confers high reactivity. Since dialkyl group 3 chemistry requires a monoanionic ancillary ligand set, either the Cp* or the phosphinimide ligand must be neutralized to transfer this general ligand environment to scandium or yttrium. Herein we describe the preparation and some preliminary chemistry of [Cp*(t-$Bu_3P{=}O$)$ScMe_2$], **1**, a new THF-free organoscandium dimethyl complex incorporating a bulky phosphine oxide ligand as a Cp* equivalent.

The synthesis of **1** is straightforward and shown in Scheme 1.[4] Treatment of $[Cp^*ScCl_2]_n$ (10), which possesses an ill-defined oligomeric structure, with t-$Bu_3P{=}O$ (11) leads to deoligomerization and formation of [Cp*(t-$Bu_3P{=}O$)$ScCl_2$] in good yield on a multigram scale. Downfield shifts in the ^1H and ^{31}P NMR spectra (by 0.18 ppm and 24.5 ppm, respectively) are observed for the coordinated t-$Bu_3P{=}O$ relative to the free ligand, mirroring trends observed in other $R_3P{=}O$ coordination compounds of scandium (12). Notably, the material is isolated free of THF even though the reaction is performed in this normally persistent solvent, attesting to the steric satisfaction provided by the Cp* – phosphine oxide combination to the Lewis-acidic scandium center. The dichloride is readily methylated when treated with MeLi in toluene, giving **1** in 45% isolated yield

Fig. 1. Molecular structure of [Cp*(t-$Bu_3P{=}O$)$ScMe_2$], **1**, with hydrogen atoms omitted for clarity. Selected metrical parameters are given below; numbers in parentheses are analogous distances and angles for [Cp*(t-$Bu_3P{=}O$)$ScCl_2$]. Distances (Å): Sc(1)—$Cp^*_{centroid}$, 2.21(1) (2.159(4)); Sc(1)—O(1), 2.072(1) (2.0373(1)); Sc(1)—C(11), 2.251(2) (Sc(1)—Cl(1), 2.3906(6)); Sc(1)—C(12), 2.252(2) (Sc(1)—Cl(2), 2.3995(5)); O(1)—P(1), 1.5225(13) (1.5336(10)). Angles (°): Sc(1)-O(1)-P(1), 162.09(8) (161.12(6)); O(1)-Sc(1)-C(11), 103.22(7) (101.01(3)); O(1)-Sc(1)-C(12), 100.16(7) (100.02(3)); C(11)-Sc(1)-C(12), 104.48(8) (105.54(2)).



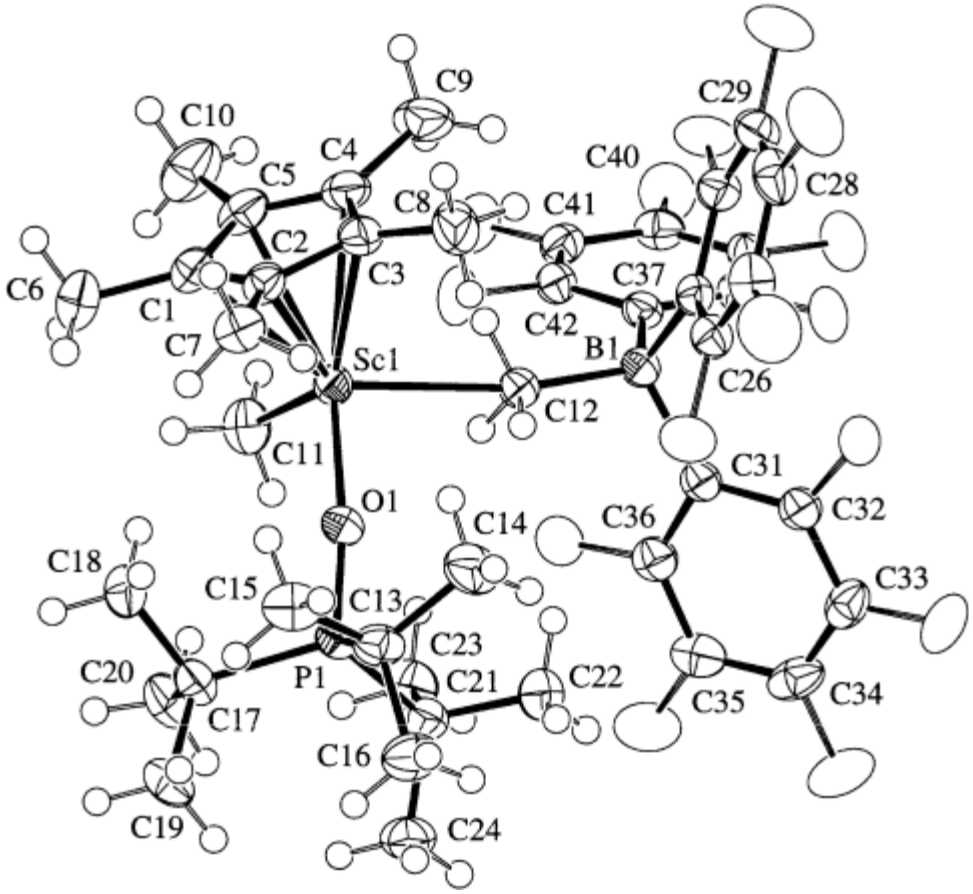
(^1H NMR (Sc—Me) = –0.36 ppm; ^{31}P NMR = 82.2 ppm). Care must be taken not to expose this compound to excess MeLi, to avoid the formation of a side product that we believe to be the scandate complex $[Cp^*ScMe_3]^-[Li]^+$.

Both **1** and its dichloride precursor are monomeric in the solid state as determined by X-ray crystallography; the structure of **1** is shown in Fig. 1, along with selected metrical parameters for both compounds for comparative purposes. The structures are grossly similar to that reported for [Cp*(t-$Bu_3P{=}N$)$TiCl_2$] (7*a*), with the phosphine oxide ligand occupying a roughly equivalent region of coordination space to that of the Cp* ligand in a tetrahedral environment. The

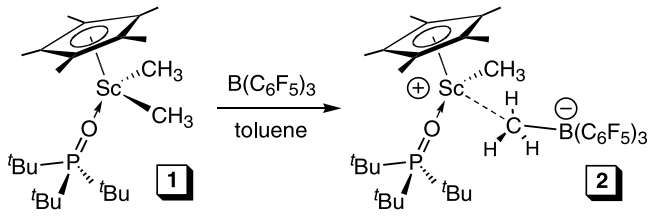
[4] Full experimental details on the synthesis and characterization of new compounds can be found in the Supporting information. Supplementary data may be purchased from the Depository of Unpublished Data, Document Delivery, CISTI, National Research Council Canada, Ottawa, ON K1A 0S2, Canada (http://www.nrc.ca/cisti/irm/unpub_e.shtml for information on ordering electronically). CCDC 215982–215984 contain the supplementary data for this paper. These data can be obtained, free of charge, via www.ccdc.cam.ac.uk/conts/retrieving.html (or from the Cambridge Crystallographic Data Centre, 12 Union Road, Cambridge, U.K.; fax +44 1223 336033; or deposit@ccdc.cam.ac.uk).

© 2004 NRC Canada

Fig. 2. Molecular structure of $[Cp^*(t\text{-}Bu_3P{=}O)ScMe]^+[MeB(C_6F_5)_3]^-$, **2**, with hydrogen atoms omitted for clarity. Selected bond distances (Å): Sc(1)—$Cp^*_{centroid}$, 2.155(1); Sc(1)—O(1), 2.0370(13); Sc(1)—C(11), 2.201(2); Sc(1)—C(12), 2.529(11); O(1)—P(1), 1.536(13); B(1)—C(12), 1.658(7). Selected bond angles (°): Sc(1)-O(1)-P(1), 167.49(8); Sc(1)-C(12)-B(1), 170.00(11); O(1)-Sc(1)-C(11), 102.10(7); O(1)-Sc(1)-C(12), 95.06(5).



Scheme 2.



Sc(1)-O(1)-P(1) angles are about the same for both compounds and are bent slightly away from the Cp* ligand. The Sc(1)—O(1) distances are comparable with those of other phosphine oxide complexes of scandium (12) and intermediate between the typical distances for scandium alkoxides (≈1.90 Å (13)) and scandium ethers (≈2.20 Å (14)). In **1**, the Sc(1)—O(1) distance is elongated relative to the dichloride, reflecting the lower Lewis acidity of the Cp^*ScMe_2 fragment.

Despite the accessibility of these new organoscandium compounds, the dative nature of the phosphine oxide – scandium linkage raises concerns about the kinetic stability of this ligand and its suitability as an ancillary. Indeed, for both the dichloride and **1**, the coordinated $t\text{-}Bu_3P{=}O$ ligand exchanges with free ligand on the NMR timescale. The barriers to exchange, as measured by the coalescence method (15) using variable temperature ^1H NMR spectra, was 11.9(5) kcal mol^{-1} (253 K) for $[Cp^*(t\text{-}Bu_3P{=}O)ScCl_2]$ and 17.7(5) kcal mol^{-1} (363 K) for the less Lewis-acidic dimethyl derivative **1**. The activation parameters were determined by analysis of the rate constants at various temperatures using EXSY methods (16) and the $\Delta S^{\ddagger}$ values are –22.4(8) and –26.6(6) eu for the dichloride and **1**, respectively. These values are consistent with an associative mechanism for ligand exchange and indicate that the compounds are stable towards dissociation of the ligand under ambient conditions. It should be noted, however, that compound **1** decomposes to unknown products when heated to temperatures above 80 °C in toluene, a process that is accelerated in the donor solvent THF.

Treatment of **1** with 1 equiv of $B(C_6F_5)_3$ in toluene leads to a soluble contact ion pair, $[Cp^*(t\text{-}Bu_3P{=}O)ScMe]^+[MeB(C_6F_5)_3]^-$, **2** (Scheme 2), demonstrating that the Cp^*–$t\text{-}Bu_3P{=}O$ ligand set can deliver a stable platform for organometallic chemistry. Although phosphine oxide adducts of $B(C_6F_5)_3$ are known (17), the ^{11}B NMR chemical shift for **2** (–15.2 ppm) and the small difference between the *meta* and *para* fluorine signals in the ^{19}F NMR spectrum ($\Delta_{m,p}$ = 4.1 ppm (18)) clearly establishes **2** as a contact ion pair deriving from methide abstraction (19). Separate, nonexchanging signals for Sc-Me (–0.07 ppm) and B-Me (1.09 ppm, br) in-

© 2004 NRC Canada

dicate that this abstraction is irreversible, at least on the NMR timescale; a similar lack of Sc-Me–B-Me exchange is observed in the organoscandium methyl cation of complex **A** (4*b*). The structure was confirmed by X-ray analysis of colourless crystals of **2** grown from toluene; an ORTEP diagram is shown in Fig. 2, along with selected distances and angles. The carbon-boron distance in the anion is 1.658(7) Å, comparable with that observed in the contact ion pair formed from the β-diketiminato complex **A** (4*b*). In contrast to the nacnac system, however, there are no close Sc···F contacts, and the Sc(1)···C(12) contact of 2.529(11) Å is much closer than the 2.703(6) Å observed in the ion pair formed from **A**. In addition, the B(1)-C(12)-Sc(1) angle of 170.00(11)° is more characteristic of a metallocenium ion pair (19). The decreased steric congestion about scandium relative to **1** allows for a slightly more linearly coordinated phosphine oxide ligand (Sc(1)-O(1)-P(1) = 167.49(8)°).

Compound **2** is relatively thermally stable in solution, and preliminary experiments indicate that **2** is a highly active ethylene polymerization catalyst at room temperature and 1 atm (1 atm = 101.325 kPa) of ethylene (1.3×10^5 g mol^{-1} h^{-1} of polyethylene). However, polymerizations carried out at higher temperatures indicated a decline in activity presumably due to catalyst decomposition, either thermally or via catalyst interaction with the solvent and with monomer feed scrubbers present in the medium.

In summary, we have prepared a new dimethyl scandium derivative with a ligand environment that mimics the metallocene set (20) but provides two reactive hydrocarbyl ligands with which to develop new organoscandium chemistry. The facile preparation of these novel compounds offers an opportunity to open new areas of organoscandium chemistry.

Acknowledgments

Funding for this work came from NOVA Chemicals (Calgary, Alberta) and from the Natural Sciences and Engineering Research Council of Canada (NSERC) in the form of a CRD grant. LDH also thanks NSERC for scholarship support (PGSA and PGSB).

References

1. D.J.H. Emslie and W.E. Piers. Coord. Chem. Rev. **233–234**, 129 (2002).
2. L. Bourget-Merle, M.F. Lappert, and J.R. Severn. Chem. Rev. **102**, 3031 (2002).
3. P.G. Hayes, L.W.M. Lee, L.K. Knight, W.E. Piers, M. Parvez, M.R.J. Elsegood, W. Clegg, and R. McDonald. Organometallics, **20**, 2533 (2001).
4. (*a*) L.W.M. Lee, W.E. Piers, M.R.J. Elsegood, W. Clegg, and M. Parvez. Organometallics, **18**, 2947 (1999); (*b*) P.G. Hayes, W.E. Piers, and R. McDonald. J. Am. Chem. Soc. **124**, 2132 (2002); (*c*) P.G. Hayes, W.E. Piers, and M. Parvez. J. Am. Chem. Soc. **125**, 5622 (2003).
5. (*a*) G.C. Welch, P.G. Hayes, D.J.H. Emslie, C.L. Noack, W.E. Piers, and M. Parvez. Organometallics, **22**, 1577 (2003).
6. (*a*) A.M. Neculai, H.W. Roesky, D. Neculai, and J. Magull. Organometallics, **20**, 5501 (2001); (*b*) A.M. Neculai, D. Neculai, H.W. Roesky, J. Magull, M. Baldus, O. Andreonesi, and M. Jansen. Organometallics, **21**, 2590 (2002).
7. (*a*) D.W. Stephan, J.C. Stewart, F. Guerin, S. Courtenay, J. Kickham, E. Hollink, C. Beddie, A. Hoskin, T. Graham, P. Wei, R.E.v. H. Spence, W. Xu, L. Koch, X. Gao, and D.G. Harrison. Organometallics, **22**, 1937 (2003); (*b*) N. Yue, E. Hollink, F. Guerin, and D.W. Stephan. Organometallics, **20**, 4424 (2001); (*c*) F. Guerin, J.C. Stewart, C. Beddie, and D.W. Stephan. Organometallics, **19**, 2994 (2000); (*d*) D.W. Stephan, J.C. Stewart, F. Guerin, R.E.v.H. Spence, W. Xu, and D.G. Harrison. Organometallics, **18**, 1116 (1999); (*e*) D.W. Stephan, F. Guerin, R.E.v. H. Spence, L. Koch, X. Gao, S.J. Brown, J.W. Swabey, Q. Wang, W. Xu, P. Zoricak, and D.G. Harrison. Organometallics, **18**, 2046 (1999).
8. (*a*) K. Dehnicke, S. Anfang, K. Harms, F. Weller, O. Borgmeier, H. Lueken, and H. Schilder. Z. Anorg. Allg. Chem. **624**, 159 (1998); (*b*) M.J. Sarsfield, M. Said, M. Thornton-Pett, L.A. Gerrad, and M. Bochmann. J. Chem. Soc. Dalton Trans. 822 (2001); (*c*) K. Dehnicke, M. Krieger, and W. Massa. Coord. Chem. Rev. **182**, 19 (1999).
9. T.V. Lubben, P.T. Wolczanski, and G.D. Van Duyne. Organometallics, **3**, 977 (1984).
10. W.E. Piers, E.E. Bunel, and J.E. Bercaw. J. Organomet. Chem. **407**, 51 (1991).
11. H. Schmidbaur and G. Blaschke. Z. Naturforsch. **33B**, 1556 (1978).
12. (*a*) L. Deakin, W. Levanson, M.C. Popham, G. Reid, and M. Webster. J. Chem. Soc. Dalton Trans. 2439 (2000); (*b*) J. Fawcett, A.W.G. Platt, and D.R. Russell. Polyhedron, **21**, 287 (2002); (*c*) N.J. Hill, W. Levason, M.C. Popham, G. Reid, and M. Webster. Polyhedron, **21**, 1579 (2002).
13. (*a*) P.B. Hitchcock, M.F. Lappert, and A. Singh. J. Chem. Soc. Chem. Commun. 1499 (1983); (*b*) G.B. Deacon, P.E. Fanwick, A. Gitlits, I.P. Rothwell, B.W. Skelton, and A.H. White. Eur. J. Inorg. Chem. 1505 (2001).
14. (*a*) J.L. Atwood and K.D. Smith. J. Chem. Soc. Dalton Trans. 921 (1974); (*b*) B. Campion and T.D. Tilley. Organometallics, **12**, 2584 (1993).
15. J. Sandström. Dynamic NMR spectroscopy. Academic Press, Toronto. 1982. pp. 93–97.
16. C.L. Perrin and T.J. Dwyer. Chem. Rev. **90**, 935 (1990).
17. (*a*) M.A. Beckett, D.S. Brassington, S.J. Coles, and M.B. Hursthouse. Inorg. Chem. Commun. **3**, 530 (2000); (*b*) M.A. Beckett, D.S. Brassington, M.E. Light, and M.B. Hursthouse. J. Chem. Soc. Dalton Trans. 1768 (2001).
18. A.D. Horton and J. de With. Organometallics, **16**, 5424 (1997).
19. E.Y.-X. Chen and T.J. Marks. Chem. Rev. **100**, 1391 (2000).
20. M.E. Thompson, S.M. Baxter, A.R. Bulls, B.J. Burger, M.C. Nolan, B.D. Santarsiero, W.P. Schaefer, and J.E. Bercaw. J. Am. Chem. Soc. **109**, 203 (1987).

© 2004 NRC Canada

New 1,3-dihydroazepin-2-one derivatives by [3,3]-sigmatropic rearrangement of suitably substituted 2-alkenylcyclopropyl isocyanates[1]

Hans-Ulrich Reissig, Gesine Böttcher, and Reinhold Zimmer

Abstract: The 2-siloxysubstituted 2-alkenylcyclopropanecarboxylic acids **10**–**14** were converted into the corresponding carbonyl azides by treatment with DPPA (diphenyl phosphorazidate) and triethylamine. On heating to 80 °C these intermediates smoothly furnished azepinone derivatives **19**–**25** in moderate to good overall yields, which are the result of a sequence of Curtius reaction to cyclopropylisocyanates, [3,3]-sigmatropic rearrangement, and a final proton shift. The primary products may undergo desilylation (to afford azepin-2,5-diones such as **23**) or double bond migration (to compound **25**). Cyclopropanecarboxylic acids *cis*-**32**, *cis*-**34**, and *cis*-**35**, which bear no 2-siloxy group, similarly provided azepinone derivatives **36**–**38** in good yields. No influence of the 2-siloxy substituent on the reaction course and rates could be observed in these qualitative studies, which was confirmed by DFT calculations with model compounds **39**–**42** showing similar reaction barriers for rearrangements of cyclopropylisocyanates with or without a 2-hydroxy group.

Key words: vinyl cyclopropanes, carbonylazides, [3.3]-sigmatropic rearrangements, azepinones.

Résumé : Les acides carboxyliques 2-alcénylcyclopropanecarboxyliques portant un substituant 2-siloxy (**10**–**14**) peuvent être transformés en azotures de carbonyle correspondants par traitement avec du phosphorazidate de diphényle (« DPPA ») et de la triéthylamine. Par chauffage à 80 °C, ces intermédiaires peuvent facilement se transformer en dérivés de l'azépinone (**19**–**25**) avec des rendements allant de moyens à bons; cette transformation est le résultat d'une séquence impliquant une réaction de Curtius conduisant aux isocyanates de cyclopropyle, d'un réarrangement sigmatropique [3,3] et d'un déplacement final de proton. Les produits primaires peuvent aussi subir une désilylation (qui conduisent à des azépine-2,5-diones, tel le produit **23**) ou une migration de double liaison (conduisant au composé **25**). Les acides cyclopropanecarboxyliques *cis*-**32**, *cis*-**34** et *cis*-**35** qui ne portent pas de groupe siloxy en position 2 conduisent aussi à des dérivés de l'azépinone (**36**–**38**) avec de bons rendements. Dans ces études qualitatives, on n'a pas observé d'influence du substituant siloxy en position 2 sur l'orientation ou la vitesse des réactions; cette observation a été confirmée par des calculs DFT sur les composés modèles **39**–**42** qui ont montré que les barrières aux réactions de réarrangement sont semblables pour les isocyanates de cyclopropyle avec ou sans groupe hydroxy en position 2.

Mots clés : vinylcyclopropanes, azoture de carbonyle, réarrangements sigmatropiques [3,3], azépinones.

[Traduit par la Rédaction]

Introduction

The Cope rearrangement of divinylcyclopropanes to cycloheptadienes establishes a valuable and stereoselective pathway to seven-membered ring systems often applied in natural product synthesis (1). Seminal contributions are due to the efforts of the Piers group (2). One method to generate functionalized divinylcyclopropane derivatives able to undergo the crucial 3,3-sigmatropic rearrangement employed vinylcyclopropyl ketones **A** that by *O*-silylation provided the corresponding silyl enol ethers **B**. Their thermolysis furnished cycloheptadiene derivatives **C**, and desilylation gave a series of 4-cyclohepten-1-ones **D** (3). Inspired by these results we anticipated that 2-siloxycyclopropanecarboxaldehydes **E** should be convertible into divinylcyclopropane derivatives **F** with an alternative substitution pattern that would finally provide 3-cyclohepten-1-ones via cycloheptadiene derivatives **G**. However, we had to learn that donor–acceptor substituted cyclopropanes (4) such as **E** can not be isolated since they immediately undergo the related [3,3]-

Received 2 July 2003. Published on the NRC Research Press Web site at http://canjchem.nrc.ca on 15 January 2004.

Dedicated with warm affection to Ed Piers, a great synthetic chemist, whom we owe our interest in cyclopropane and organometallic chemistry.

H.-U. Reissig[2,3] and R. Zimmer. Institut für Chemie – Organische Chemie, Freie Universität Berlin, Takustr. 3, D-14195 Berlin, Germany.
G. Böttcher. Institut für Organische Chemie, Technische Universität Dresden, D-01061 Dresden, Germany.

[1]This article is part of a Special Issue dedicated to Professor Ed Piers.
[2]Also at: Institut für Organische Chemie, Technische Universität Dresden, D-01061 Dresden, Germany.
[3]Corresponding author (e-mail: hans-reissig@chemie.fu-berlin.de).

 doi: 10.1139/V03-186 © 2004 NRC Canada

sigmatropic rearrangement involving the CO double bond, smoothly affording functionalized 2,5-dihydrooxepines **H** (5, 6) (Scheme 1).

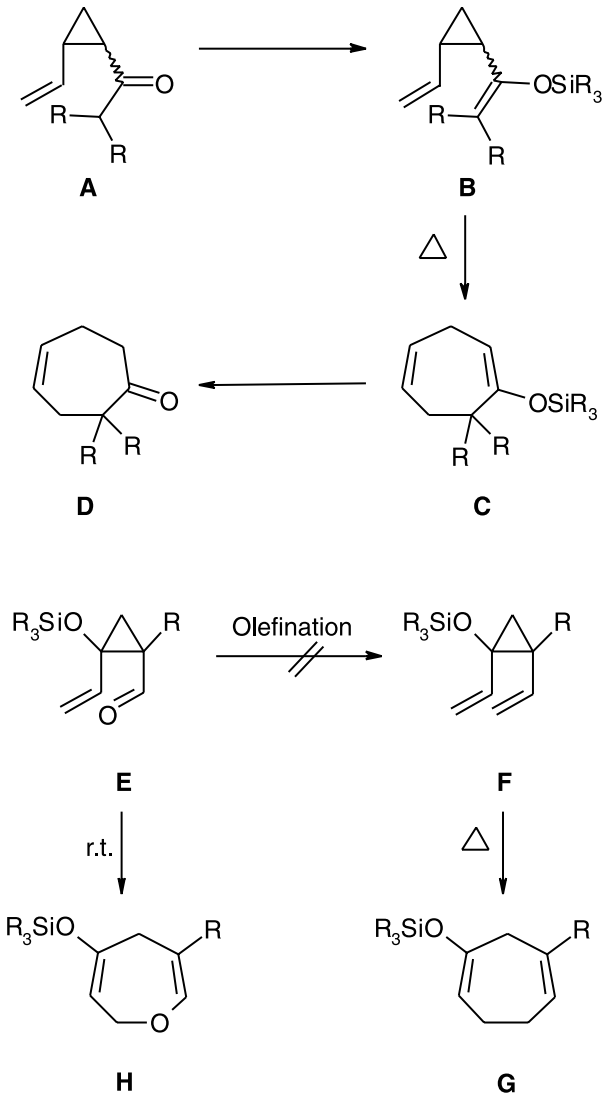
This surprising entry to seven-membered heterocycles prompted us to investigate the rearrangements of other compounds derived from easily available methyl 2-alkenyl-2-siloxycyclopropanecarboxylates. Among several systems examined (7) cyclopropyl isocyanates turned out to be the most interesting compounds. Although early examples of their rearrangement have been known since the pioneer study of Vogel et al. (8) in 1965, this pathway to azepinone derivatives was an almost forgotten reaction. Vogel found that heating of cis-substituted carbonyl azide **I** to 80 °C smoothly provided the 1,3-dihydroazepin-2-one **L**. Logical intermediates are isocyanate **J**, formed by Curtius reaction, which rearranged to 3,6-dihydroazepin-2-one **K** and a hydrogen shift finally furnished lactam L. Only heating to 350 °C caused rearrangement of the corresponding trans-substituted carbonyl azide. Meanwhile, just a few additional examples have been reported (9), although this approach to seven-membered heterocycles seems to be fairly flexible. In this report we want to disclose full details of our experiments, which involved siloxysubstituted cyclopropyl isocyanates and provided the corresponding functionalized 1,3-dihydroazepin-2-ones. For comparison, a few examples without siloxy group were included in this study (Scheme 2).

Results

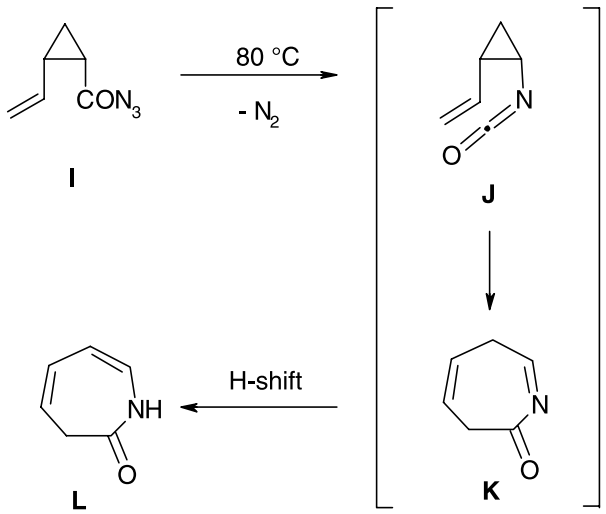
Although donor–acceptor substituted cyclopropanes are extremely versatile building blocks in organic synthesis (4), those with an additional 2-alkenyl group are even more useful. They open further pathways such as (formal) pericyclic processes involving the double bond or — after ring cleavage — Michael-type additions or Diels–Alder reactions of the intermediately generated enones. For the purpose of this study methyl 2-alkenyl-2-siloxycyclopropanecarboxylates **1**–**4** (10) with the less base labile *tert*-butyldimethylsilyl group were employed as starting materials. Compounds **1**–**4** are mixtures of cis/trans isomers, however, treatment with lithium diisopropylamide (LDA) followed by addition of an appropriate electrophile afforded C-1 substituted derivatives **5**–**9** in good yields and — most importantly — with the required cis arrangement of the alkenyl groups and the methoxycarbonyl group (11). We found many years ago that enolates derived from methyl siloxycyclopropanecarboxylates accept electrophiles with a surprising diastereoselectivity, which was interpreted as a stereoelectronic effect of the siloxy group (12) (Scheme 3).

Methyl esters **5**–**9** were easily converted into carboxylic acids **10**–**14** by treatment with potassium trimethylsilanolate — a mild method that has considerable advantages over standard saponification procedures (13). With carboxylic acid **13** we examined known literature methods for the conversion to the carbonyl azide. The Weinstock procedure (method A) (14), which employs ethyl chloroformate, triethylamine, and finally sodium azide in water, provided the desired cyclopropylcarbonyl azide **15** in 54% yield, whereas application of the commercially available diphenyl phosphorazidate (DPPA) in toluene at 0 °C (method B) (15) afforded **15** in 22% yield. Despite the lower yield in this example we gen-

Scheme 1.

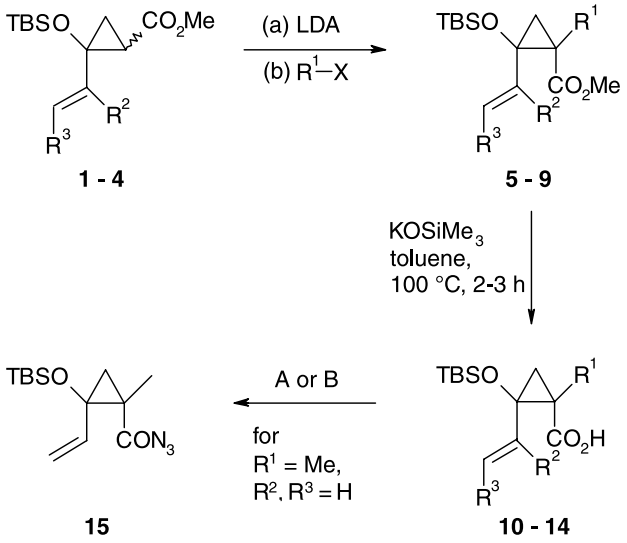


Scheme 2.



© 2004 NRC Canada

Scheme 3.



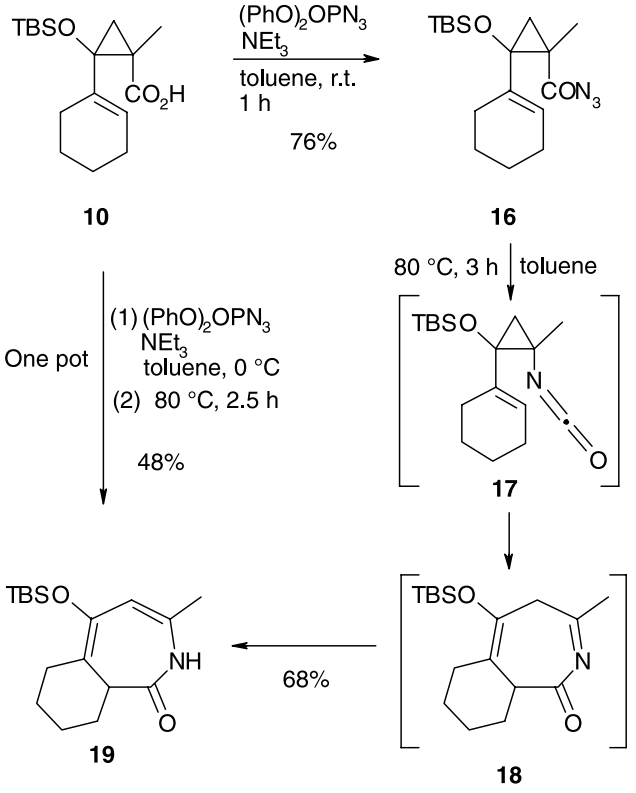
Method A: NaN_3, $ClCO_2Et$, NEt_3, acetone/H_2O, 0 °C, 2 h, 54%
Method B: DPPA, NEt_3, toluene, 0 °C, 1.5 h, 22%

Starting materials		R^1	R^2	R^3	Product	Yield (%)
1	5	Me	-$(CH_2)_4$-		10	96
2	6	Me	Ph	H	11	42
3	7	Me	Me	H	12	84
4	8	Me	H	H	13	70
4	9	Allyl	H	H	14	49

erally employed the latter method because it is easy to perform in organic solvents and the generated carbonyl azide can therefore be directly converted into the 1,3-dihydroazepin-2-ones by heating to 80 °C. To demonstrate this option carboxylic acid **10** was treated with DPPA at room temperature to furnish carbonyl azide **16** in 76% yield. Heating of this product to 80 °C for 3 h induced the Curtius rearrangement to cyclopropyl isocyanate **17**, which directly suffered the 3,3-sigmatropic ring-enlargement process, thus affording the expected bicyclic azepin-2-one derivative **19** in 68% yield via intermediate **18**. This sequence may be performed as a one-pot procedure without isolation of azide **16**; compound **19** was isolated in 48% yield, which is comparable to the two step procedure, but more convenient to perform (Scheme 4).

Having established the proper reaction conditions, we employed carboxylic acids **11**–**14** as starting materials. As expected, compounds **11** and **12** furnished seven-membered heterocycles **20** and **21** in good overall yield. The less-substituted carboxylic acid **13** led to rearranged product **22**, which is apparently more sensitive with respect to desilylation. Hydrolysis of the silyl enol ether unit of azepin-2-one **22** occurred probably during purification and produced 1*H*-

Scheme 4.



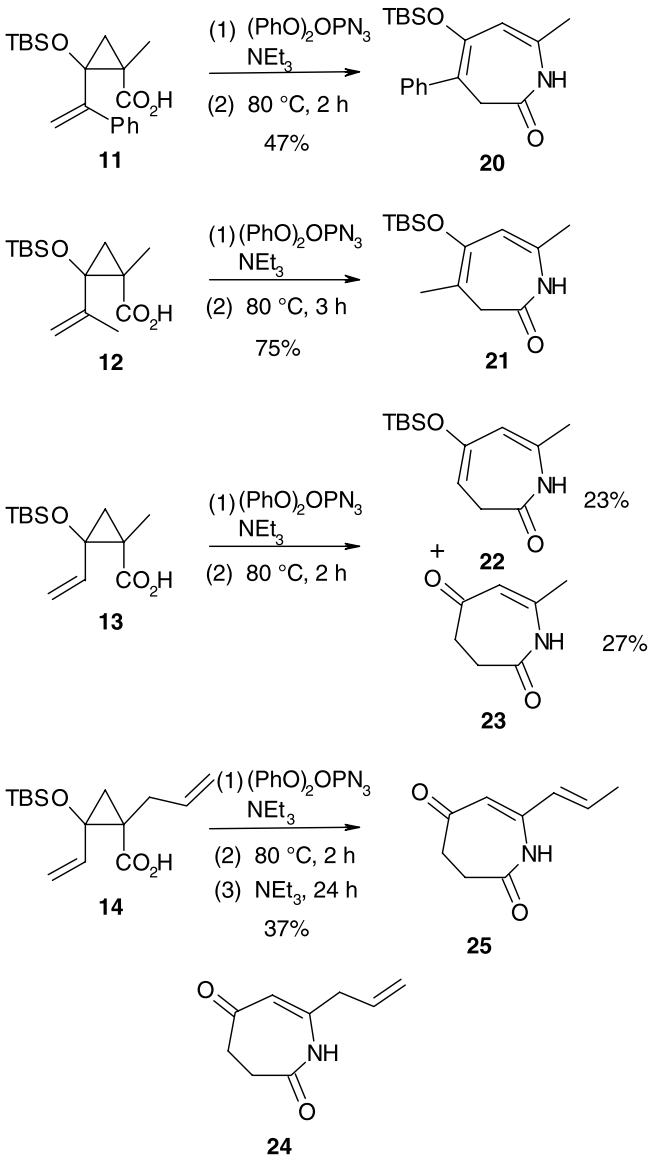
azepin-2,5-dione **23**. The rearrangement product obtained from carboxylic acid **14** seems to be even more labile. Here only 1*H*-azepin-2,5-dione derivatives **24** and **25** were isolated, primarily as a mixture with 7-(2-propenyl) and 7-(1-propenyl) substituents, but after treatment with triethylamine, compound **25** with conjugated double bonds was obtained exclusively in moderate yield. All reactions collected in Scheme 5 were not optimized, which should leave room for improvement of yields.

With carboxylic acid **13** we tried to trap the intermediate cyclopropyl isocyanate by performing the reaction sequence in *tert*-butanol instead of toluene. Surprisingly, only 1*H*-azepin-2,5-dione **23** was isolated in low yield (7). The expected urethane **26** could not be detected indicating that the rearrangement of the cyclopropyl isocycanate is considerably faster than the intermolecular reaction with *tert*-butanol. To gain additional insight into the reactivity of siloxy-substituted cyclopropyl azides we also studied phenyl-substituted derivative **28**, which was efficiently prepared from carboxylic acid **27** by the DPPA method. Curtius rearrangement of azide **28** occurred at 80 °C affording isocyanate **29** in excellent yield. Product **29** is the first siloxy-substituted cyclopropyl isocyanate that could be isolated. Unfortunately, this compound could not successfully be rearranged into a benzannulated azepine derivate. Finally, after a BF_3 etherate treatment of **29**, we isolated a little amount of a crystalline compound to which we assign structure **30** (16) (Scheme 6).

For comparison, we included *cis*-alkenylcyclopropanecarboxylic acids *without* a siloxy group into this study. The sequence to obtain the required cis-compounds is demonstrated for diphenyl-substituted compound **32**. Standard

© 2004 NRC Canada

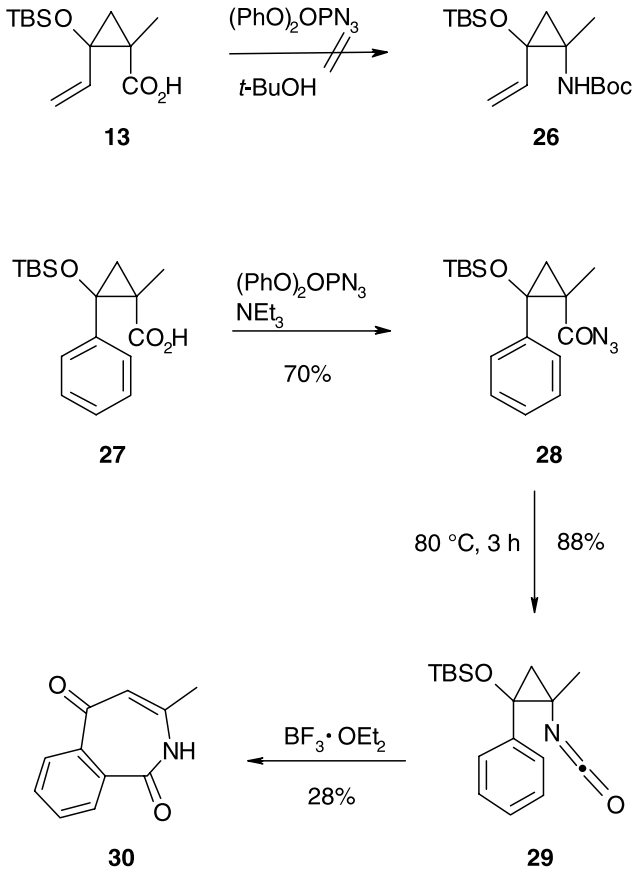
Scheme 5.



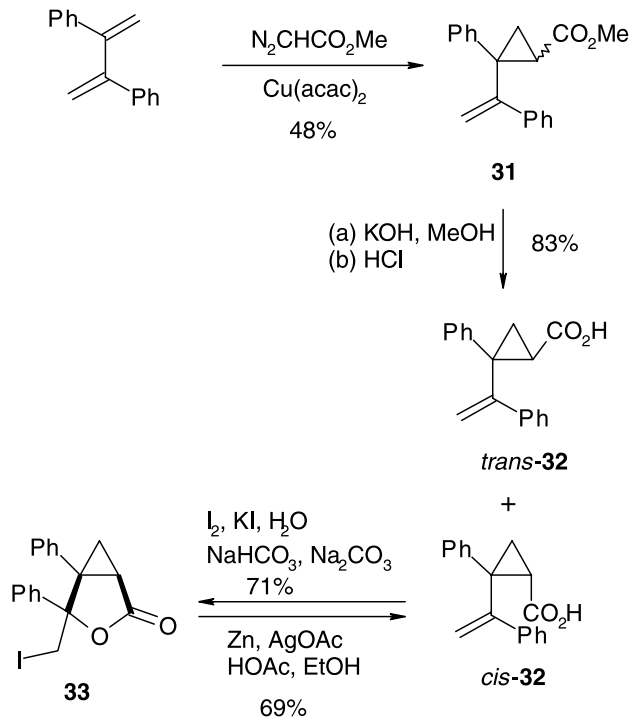
cyclopropanation of 2,3-diphenyl-1,3-butadiene with methyl diazoacetate provided the expected vinylcyclopropane derivative **31** in good yield and as a 57:43 mixture of diastereomers. The ester was saponified and the *cis*/*trans*-carboxylic acids **32** were subjected to iodolactonization (17), which provided a mixture of the iodolactone **33** (two diastereomers) derived from the cis-isomer and of unconsumed *trans*-**32**. Since the latter could easily be separated by extraction, the remaining iodolactone **33** was finally converted back to diastereomerically pure carboxylic acid *cis*-**32** by reduction with a zinc–silver couple in acetic acid (18). This chemical separation of diastereomers is fairly convenient and allowed the use of diastereomerically pure *cis*-cyclopropanecarboxylic acid **32**. Analogously, cis-compounds **34** and **35** were prepared from the corresponding alkenylcyclopropanes (Scheme 7).

Conversions of these three *cis*-alkenylcyclopropanecarboxylic acids **32**, **34**, and **35** into the corresponding azides by the DPPA method proceeded in good yields and subsequent thermal rearrangement of the purified azides smoothly

Scheme 6.



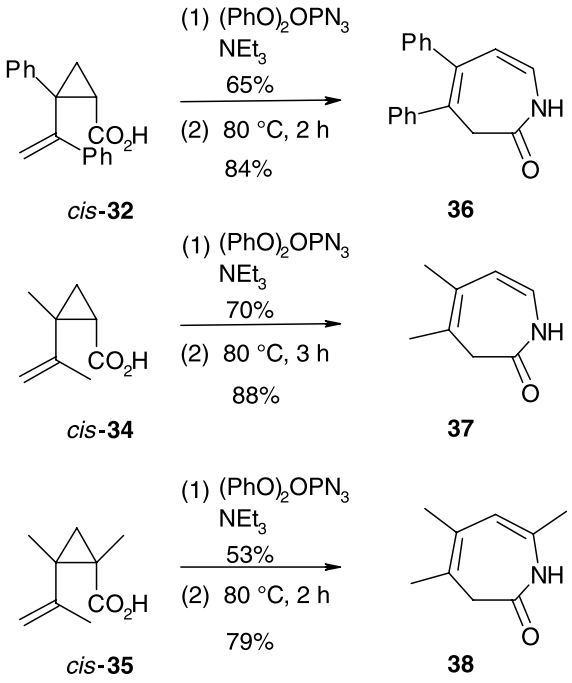
Scheme 7.



afforded the expected 1,3-dihydroazepin-2-ones **36**, **37**, and **38**, respectively, in moderate to good overall yields. No apparent difference in the reaction rates of the carbonyl azide

© 2004 NRC Canada

Scheme 8.



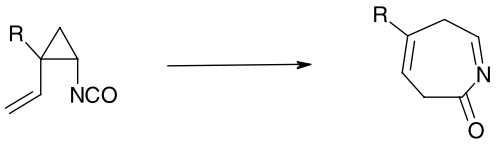
conversion or the rearrangement steps compared with siloxy-substituted compounds could be observed (Scheme 8).

Discussion

We found efficient methods to generate *cis*-alkenylcyclopropanecarboxylic acids (with or without a 2-siloxy group) and to convert these intermediates into the corresponding carbonyl azides. Individual examples of these azides were isolated. Their thermolysis at 80 °C afforded the desired 1,3-dihydroazepin-2-ones via alkenylcyclopropyl isocyanates. The Curtius rearrangement seems to be the rate-determining step of the sequence, since the isocyanate could only be isolated when a cis-located alkenyl group was absent (see compound **29**). For suitably cis-substituted compounds the subsequent [3,3]-sigmatropic ring-enlargement to the 3,6-dihydroazepin-2-one and the hydrogen shift to the final product are apparently much faster reactions (see Scheme 2).

For an estimation of the influence of the substitution pattern on the rate of the 3,3-sigmatropic rearrangement, Sperling (19)[4] performed DFT calculations (B3LYP/6-31G*) with two model systems **39** and **40**. The transformation of these compounds into 3,6-dihydroazepin-2-ones **41** and **42**, respectively, have to surpass only slightly different barriers that are in the order of 70 kJ/mol indicating that these rearrangements can occur at relatively low temperature — probably considerably lower than the applied 80 °C. In contrast, the reaction enthalpies are much more influenced by the substitution pattern: the cyclopropanol derivative **40** undergoes a much more exothermic reaction, which is likely due to the destabilization of the cyclopropane stage by this substituent and (or) the gain of conjugation in the product. These calculated energies suggest that the transition structures of the

Scheme 9.



	R	$\Delta H_o^{\ddagger}$(kJ/mol)	ΔH_o (kJ/mol)	
39	H	74.2	-44.2	**41**
40	OH	71.7	-61.7	**42**

Cope rearrangements are located early at the reaction coordinate, thus strongly resembling the starting materials and not the seven-membered products (Scheme 9).

Finally, we want to stress that the almost unexplored route to azepin-2-one derivatives via cyclopropyl isocyanates offers an interesting possibility for generating this type of heterocycle (20). The functionalized compounds presented in this report should be of interest for further synthetic use and can probably be employed in combinatorial chemistry.

Experimental section

All reactions were carried out under an argon atmosphere in flame-dried flasks, and the components were added by using syringes. All solvents were dried by standard methods. IR spectra were measured with a PerkinElmer FT-IR spectrometer Nicolet 5 SXC. ^{1}H and ^{13}C NMR spectra were recorded on Bruker instruments (AC 300, AC 500) in $CDCl_3$ solution. The chemical shifts are given relative to the TMS or to the $CDCl_3$ signal (δ_H = 7.27, δ_C = 77.0). The splitting patterns are designated as singulet (s), doublet (d), triplet (t), and multiplet (m). Higher order NMR spectra were approximately interpreted as first-order spectra if possible. CO_2H protons could not be identified for all carboxylic acids. Neutral alumina (activity III, Fa. Merck) was used for column chromatography. Melting points (uncorrected) were measured with an apparatus from Rapido.

Starting materials **1**–**4** and compounds **7**–**9** were prepared by literature procedures (21). Detailed procedures for synthesis of *cis*-**34** and *cis*-**35** are given in ref. 7. All other chemicals were commercially available and were used as received.

Methyl *t*-2-*tert*-butyldimethylsiloxy-*c*-2-(1-cyclohexenyl)-1-methyl-*r*-1-cyclopropanecarboxylate (5)

According to the general procedure described in ref. 21, 2-siloxycyclopropanecarboxylate **1** (2.68 g, 9.60 mmol) was deprotonated with LDA (14.4 mmol) and alkylated with methyliodide (7.04 g, 49.6 mmol) in THF (100 mL) at −78 °C for 17 h. Purification of the crude product (0.915 g) by Kugelrohr distillation (125 °C, 0.015 mbar (1 bar = 10^5 Pa) yielded 1.90 g (60%) of **6** as a colorless oil that slowly crystallized at room temperature (rt) (mp 38–42 °C). IR (cm^{-1}): 2935, 2855 (C-H), 1725 (C=O), 1250 (Si-C), 1305, 1150 (C-O). ^{1}H NMR ($CDCl_3$, 300 MHz) δ: 5.66 (m_c, 1H, 2′-H), 3.57 (s, 3H, CO_2Me), 2.25–1.99, 1.68–1.42 (2m, 8H, 3′-H to 6′-H), 1.88 (d, J = 5.8 Hz, 1H, 3-H_{trans}), 1.40 (s, 3H, 1-Me), 0.86 (s, 9H, *t*-Bu), 0.73 (d, J = 5.8 Hz, 1H, 3-H_{cis}),

[4] J. Fabian and D. Sperling. Unpublished results.

© 2004 NRC Canada

0.07, 0.06 (2s, 6H, $SiMe_2$). ^{13}C NMR ($CDCl_3$, 75.5 MHz) δ: 173.5, 51.6 (s, q, CO_2Me), 135.0 (s, C-1′), 125.8 (d, C-2′), 68.8 (s, C-2), 30.5 (s, C-1), 25.7, 18.1 (q, s, *t*-Bu), 25.0, 24.1, 22.6*,[5] 22.4 (4 t, C-3, C-3′ to C-6′), 15.1 (q, 1-Me), –3.9, –4.3 (2 q, $SiMe_2$). Anal. calcd. for $C_{18}H_{32}O_3Si$ (324.5): C 66.32, H 9.94; found: C 66.80, H 10.32.

Methyl *t*-2-*tert*-butyldimethylsiloxy-*c*-2-(1-phenylethenyl)-1-methyl-*r*-1-cyclopropanecarboxylate (6)

According to the general procedure described in ref. 21, 2-siloxycyclopropanecarboxylate **2** (0.922 g, 2.77 mmol) was deprotonated with LDA (4.00 mmol) and alkylated with methyliodide (1.09 g, 7.68 mmol) in THF (50 mL) at –78 °C for 19 h. Purification of the crude product (0.915 g) by column chromatography (heptane/EtOAc, 10:1) yielded 0.559 g (60%) of **6** as a colorless oil. ^1H NMR ($CDCl_3$, 300 MHz) δ: 7.40–7.07 (m, 5H, Ph), 5.55, 5.19 (2s, 1H each, 2′-H), 3.17 (s, 3H, CO_2Me), 1.96 (d, J = 5.9 Hz, 1H, 3-H_{trans}), 1.45 (s, 3H, 1-Me), 0.84 (d, J = 5.9 Hz, 1H, 3-H_{cis}), 0.64 (s, 9H, *t*-Bu), 0.00, –0.24 (2s, 6H, $SiMe_2$). ^{13}C NMR ($CDCl_3$, 75.5 MHz) δ: 172.6, 51.5 (s, q, CO_2Me), 145.5 (s, C-1′), 137.6, 127.8, 127.4, 126.9 (s, 3d, Ph), 115.0 (t, C-2′), 67.3 (s, C-2), 31.8 (s, C-1), 25.4, 18.0 (q, s, *t*-Bu), 24.3 (t, C-3), 15.0 (q, 1-Me), –4.0, –4.3 (2q, $SiMe_2$).

Saponification with $KOSiMe_3$ (general procedure 1)

To a solution of methyl cyclopropanecarboxylate (1 equiv.) in toluene (5 mL/mmol ester) was added $KOSiMe_3$ (3 equiv.) and the solution was heated (time and temperature are indicated in individual experiments). The mixture was cooled to room temperature, quenched with saturated aqueous ammonium chloride solution and the product was extracted with diethyl ether. The combined organic layers were dried over $MgSO_4$ and concentrated.

t-2-tert-*Butyldimethylsiloxy*-c-*2-(1-cyclohexenyl)-1-methyl*-r-*1-cyclopropanecarboxylic acid (10)*

According to *general procedure 1*, methyl cyclopropanecarboxylate **5** (1.86 g, 5.74 mmol) and $KOSiMe_3$ (2.21 g, 17.2 mmol) in toluene (60 mL) were heated for 3 h at 100 °C and yielded **10** (1.70 g, 96%) as a colorless solid, mp 115–120 °C. IR (cm^{-1}): 3400 (CO_2H), 2930, 2860 (C-H), 1690 (C=O), 1305, 1245 (Si-C). ^1H NMR ($CDCl_3$, 300 MHz) δ: 5.76 (m_c, 1H, 2′-H), 2.25–2.11 (m, 1H, 3′-H), 2.00 (br. s, 2H, 6′-H), 1.89 (d, J = 5.8 Hz, 1H, 3-H_{trans}), 1.72–1.60 (m, 1H, 3′-H), 1.53 (m_c, 4H, 4′-H, 5′-H), 1.40 (s, 3H, 1-Me), 0.87 (s, 9H, *t*-Bu), 0.79 (d, J = 5.8 Hz, 1H, 3-H_{cis}), 0.07, 0.06 (2s, 6H, $SiMe_2$). ^{13}C NMR ($CDCl_3$, 75.5 MHz) δ: 179.7 (s, CO_2H), 134.5 (s, C-1′), 126.5 (d, C-2′), 69.9 (s, C-2), 30.1 (s, C-1), 25.7, 18.1 (q, s, *t*-Bu), 25.2, 25.0, 22.6*,[5] 22.3 (4 t, C-3, C-3′ to C-6′), 14.8 (q, 1-Me), –3.8, –4.3 (2 q, $SiMe_2$). Anal. calcd. for $C_{17}H_{30}O_3Si$ (310.5): C 65.76, H 9.73; found: C 65.89, H 10.01.

t-2-tert-*Butyldimethylsiloxy*-c-*2-(1-phenylethenyl)-1-methyl*-r-*1-cyclopropanecarboxylic acid (11)*

According to *general procedure 1*, methyl cyclopropanecarboxylate **6** (0.492 g, 1.42 mmol) and $KOSiMe_3$ (0.528 g, 4.12 mmol) in toluene (14 mL) were heated for 2 h at 110 °C. Recrystallization of the crude product yielded **11** (0.196 g, 42%) as a colorless solid, mp 106–110 °C. IR (cm^{-1}): 3450 (CO_2H), 2960–2930 (CH), 1690 (C=O), 1260 (Si-C). ^1H NMR ($CDCl_3$, 300 MHz) δ: 7.35–7.08 (m, 5H, Ph), 5.46, 5.10 (2 s, 1H each, 2′-H), 1.93, (d, J = 5.9 Hz, 1H, 3-H_{trans}), 1.44 (s, 3H, 1-Me), 0.83 (d, J = 5.9 Hz, 1H, 3-H_{cis}), 0.63 (s, 9H, *t*-Bu), –0.04, –0.24 (2 s, 6H, $SiMe_2$). ^{13}C NMR ($CDCl_3$, 75.5 MHz) δ: 177.7 (s, CO_2H), 144.9 (s, C-1′), 137.7, 127.8, 127.4, 127.1 (s, 3d, Ph), 115.0 (t, C-2′), 67.9 (s, C-2), 31.9 (s, C-1), 25.6, 18.0 (q, s, *t*-Bu), 24.6 (t, C-3), 14.8 (q, 1-Me), –4.0, –4.3 (2q, $SiMe_2$). Anal. calcd. for $C_{19}H_{28}O_3Si$ (332.5): C 68.63, H 8.49; found: C 68.46, H 8.68.

t-2-tert-*Butyldimethylsiloxy*-c-*2-isopropenyl-1-methyl*-r-*1-cyclopropanecarboxylic acid (12)*

According to *general procedure 1*, methyl cyclopropanecarboxylate **7** (0.284 g, 1.00 mmol) and $KOSiMe_3$ (0.385 g, 3.00 mmol) in toluene (5 mL) were heated for 2 h at 100 °C and yielded **12** (0.225 g, 84%) as a colorless solid, mp 63–67 °C. IR (cm^{-1}): 3450 (OH), 2960–2830 (CH), 1700 (C=O), 1650 (C=C), 1260 (SiC). ^1H NMR ($CDCl_3$, 300 MHz) δ: 11.75 (br. s, 1H, CO_2H), 4.83, 4.80 (2 s, 1H each, 2′-H), 1.91 (d, J = 5.9 Hz, 1H, 3-H_{trans}), 1.70, 1.39 (2 s, 3H each, 1-Me, 1′-Me), 0.85 (s, 9H, *t*-Bu), 0.76 (d, J = 5.9 Hz, 1H, 3-H_{cis}), 0.06 (s, 6H, $SiMe_2$). ^{13}C NMR ($CDCl_3$, 75.5 MHz) δ: 179.5 (s, CO_2H), 141.7 (s, C-1′), 114.6 (t, C-2′), 69.4 (s, C-2), 30.8 (s, C-1), 25.6, 18.1 (q, s, *t*-Bu), 25.0 (t, C-3), 19.3 (q, 1′-Me), 14.7 (q, 1-Me), –4.2, –4.3 (2q, $SiMe_2$). Anal. calcd. for $C_{14}H_{24}O_3Si$ (268.4): C 62.18, H 9.01; found: C 62.40, H 9.26.

t-2-tert-*Butyldimethylsiloxy-1-methyl*-c-*2-vinyl*-r-*1-cyclopropanecarboxylic acid (13)*

According to *general procedure 1*, methyl cyclopropanecarboxylate **8** (0.270 g, 1.00 mmol) and $KOSiMe_3$ (0.385 g, 3.00 mmol) in toluene (5 mL) were heated for 2 h at 100 °C and yielded **13** (0.179 g, 70%) as a colorless solid, mp 55–57 °C. IR (cm^{-1}): 3450 (CO_2H), 2960, 2930 (CH), 1690 (C=O). ^1H NMR ($CDCl_3$, 300 MHz) δ: 5.78 (dd, J = 17.0, 10.7 Hz, 1H, 1′-H), 5.18 (dd J = 17.0, 1.5 Hz, 1H, 2′-H), 5.02 (dd, J = 10.7, 1.5 Hz, 1H, 2′-H), 1.73 (d, J = 6.1 Hz, 1H, 3-H_{trans}), 1.31 (s, 3H, 1-Me), 0.92 (d, J = 6.1 Hz, 1H, 3-H_{cis}), 0.79 (s, 3 H, *t*-Bu), 0.01, –0.03 (2 s, 6H, $SiMe_2$). ^{13}C NMR ($CDCl_3$, 75.5 MHz) δ: 178.1 (s, CO_2H), 136.4 (d, C-1′), 115.7 (t, C-2′), 65.8 (s, C-2), 32.4 (s, C-1), 26.4 (t, C-3), 25.8, 18.2 (q, s, *t*-Bu), 14.9 (q, 1-Me), –3.42, –3.56 (2q, $SiMe_2$). Anal. calcd. for $C_{13}H_{24}O_3Si$ (256.4): C 60.84, H 9.70; found: C 60.93, H 9.43.

1-Allyl*-c-*2*-tert-*butyldimethylsiloxy*-t-*2-vinyl*-r-*1-cyclopropanecarboxylic acid (14)

According to *general procedure 1*, methyl cyclopropanecarboxylate **9** (0.879 g, 2.96 mmol) and $KOSiMe_3$ (1.12 g, 8.73 mmol) in toluene (20 mL) were heated for 2 h at 110 °C. After extraction with diethyl ether, the combined organic layers were successively washed with 2 N HCl, satd. aq. $NaHCO_3$, and water. Yield: **14** (0.413 g, 49%) as a colorless solid, mp 65–70 °C. IR (cm^{-1}): 3450 (CO_2H), 2960–2930 (C-H), 1690 (C=O), 1650 (C=C), 1260 (Si-C). ^1H NMR ($CDCl_3$, 300 MHz) δ: 5.94–5.80 (m, 2H, 1′-H, 2″-H), 5.18 (dd, J = 17.2, 1.3 Hz, 1 H, 2′-H), 5.15 (dd, J = 10.7,

[5] * Indicates that the signal has double intensity.

© 2004 NRC Canada

1.3 Hz, 1 H, 2′-H), 5.10 (dd, J = 17.2, 1.7 Hz, 1H, 3′′-H), 5.02 (dd, J = 10.4, 1.7 Hz, 1H, 3′′-H), 2.90 (ddd, J = 15.6, 6.2, 1.3 Hz, 1H, 1′′-H), 2.27 (dd, J = 15.6, 6.8 Hz, 1H, 1′′-H), 1.85 (d, J = 6.3 Hz, 1H, 3-H_{trans}), 1.09 (d, J = 6.3 Hz, 1H, 3-H_{cis}), 0.91 (s, 9 H, *t*-Bu), 0.12, 0.09 (2 s, 6H, $SiMe_2$). ^{13}C NMR ($CDCl_3$, 75.5 MHz) δ: 177.7 (s, CO_2H), 136.1, 135.6 (2d, C-1′, C-2′′), 116.0 (t, C-3"), 115.9 (t, C-2′), 66.0 (s, C-2), 36.9 (s, C-1), 32.5 (t, C-1"), 25.8, 18.2 (q, s, *t*-Bu), 24.3 (t, C-3), –3.4, –3.6 (2q, $SiMe_2$). Anal. calcd. for $C_{15}H_{26}O_3Si$ (282.4): C 63.80, H 9.28; found: C 63.78, H 9.33.

Preparation of cyclopropanecarbonyl azide (general procedure 2)

To a solution of the cyclopropanecarboxylic acid (1 equiv.) in toluene (3–5 mL/mmol acid) was added NEt_3 (1.3–1.7 equiv.) and DPPA (1.1–1.7 equiv.). After stirring at 0 °C for 1–3 h the solvent was removed in vacuo and the residue was filtered (silica gel, diethyl ether/pentane).

One-pot procedure for synthesis of 1,3-dihydroazepin-2-ones (general procedure 3)

The corresponding cyclopropanecarboxylic acid (1 equiv.) was dissolved in toluene (10–30 mL/mmol acid) and cooled to 0 °C. After addition of NEt_3 (5.2–6 equiv.) and DPPA (1.8–3 equiv.) the mixture was allowed to warm up to room temperature. The solution was stirred for 2 to 3 h at this temperature and then heated to 80 °C for 2 to 3 h. Removal of the solvent in vacuo gave the crude product that was purified by column chromatography (silica gel, heptane/EtOAc, 2:1 to 0:1) or by recrystallization (heptane/EtOAc).

t-*2*-tert-*Butyldimethylsiloxy-1-methyl*-c-*2-vinyl*-r-*1-cyclopropanecarbonyl azide (15)*

Method A

To a solution of cyclopropanecarboxylic acid **13** (0.120 g, 0.503 mmol) in acetone (5 mL) NEt_3 (0.074 g, 0.73 mmol) and ethyl chloroformiate (0.084 g, 0.77 mmol) were slowly added at 0 °C. After 20 min at 0 °C, NaN_3 (0.060 g, 0.90 mmol) dissolved in water (5 mL) was added dropwise to the solution and stirred at this temperature for a further 2 h. The reaction mixture was poured into a mixture of ice/water and extracted with chloroform. The combined organic layers were washed with water and dried over Na_2SO_4. Removal of the solvent in vacuo gave 0.076 g (54%) of **15** as colorless oil.

Method B

According to *general procedure 2*, cyclopropanecarboxylic acid **13** (0.100 g, 0.39 mmol), NEt_3 (0.190 g, 1.88 mmol) and DPPA (0.266 g, 0.966 mmol) in toluene (5 mL) were stirred for 1.5 h at 0 °C. The resulting mixture was diluted with diethyl ether (25 mL) and water (5 mL) and the aqueous phase was extracted with diethyl ether (2 × 20 mL). The combined organic phases were washed with satd. aq. $NaHCO_3$ solution and brine (5 mL each) and dried over $MgSO_4$. Purification by flash chromatography (heptane/EtOAc, 2:1) gave 0.024 g (22%) of **15** as a yellow oil and 0.116 g (43%) of DPPA. Compound **15**: ^1H NMR ($CDCl_3$, 300 MHz) δ: 5.73 (dd, J = 17.0, 10.7 Hz, 1H, 1′-H), 5.17 (dd J = 17.0, 1.5 Hz, 1H, 2′-H), 5.04 (dd, J = 10.7, 1.5 Hz, 1H, 2′-H), 1.85 (d, J = 6.2 Hz, 1H, 3-H_{trans}), 1.29 (s, 3H, 1-Me), 0.95 (d, J = 6.2 Hz, 1H, 3-H_{cis}), 0.79 (s, H, *t*-Bu), 0.01, –0.03 (2s, 6H, $SiMe_2$). ^{13}C NMR ($CDCl_3$, 75.5 MHz) δ: 179.3 (s, C=O), 135.7 (d, C-1′), 116.0 (t, C-2′), 67.0 (s, C-2), 35.4 (s, C-1), 26.7 (t, C-3), 25.8, 18.2 (q, s, *t*-Bu), 14.9 (q, 1-Me), –3.5, –3.6 (2q, $SiMe_2$).

t-*2*-tert-*Butyldimethylsiloxy*-c-*2-(1-cyclohexenyl)-1-methyl*-r-*1-cyclopropanecarbonyl azide (16)*

According to *general procedure 2*, cyclopropanecarboxylic acid **10** (0.304 g, 0.979 mmol), NEt_3 (0.124 g, 1.22 mmol) and DPPA (0.299 g, 1.09 mmol) in toluene (3 mL) were stirred for 1 h at 0 °C. Filtration (diethyl ether/pentane, 10:1) of the crude product yielded 0.248 g (76%) **16** as colorless crystals, mp 37–39 °C. IR (cm^{-1}): 2950 (CH), 2135 (N_3), 1695 (C=O), 1640 (C=C), 1250 (Si-C). ^1H NMR ($CDCl_3$, 300 MHz) δ: 5.62 (m_c, 1H, 2′-H), 2.26–2.09 (m, 1H, 3′-H), 2.00 (m_c, 2H, 6′-H), 1.93 (d, J = 5.7 Hz, 1H, 3-H_{trans}), 1.59–1.47 (m, 5H, 3′-H, 4′-H, 5′-H), 1.37 (s, 3H, 1-Me), 0.79 (s, 9H, *t*Bu), 0.77 (d, J = 5.7 Hz, 1H, 3-H_{cis}), 0.07, 0.06 (2s, 6H, $SiMe_2$). ^{13}C NMR ($CDCl_3$, 75.5 MHz) δ: 179.3 (s, C=O), 134.1 (s, C-1′), 127.0 (d, C-2′), 71.3 (s, C-2), 33.4 (s, C-1), 25.6, 18.1 (q, s, *t*-Bu), 25.8, 25.0, 22.6, 22.3 (4t, C-3′ to C-6′), 14.9 (q, 1-Me), –3.9, –4.3 (2q, $SiMe_2$). Anal. calcd. for $C_{17}H_{29}N_3O_2Si$ (284.5): C 60.86, H 8.71, N 12.52; found: C 61.64, H 9.25, N 12.27. No better elemental analysis could be obtained.

2-Aza-1-oxo-3-methyl-5-tert-butyldimethylsiloxy-4,5-dihydrobicyclo[4.5.0]decane (19)

Carbonyl azide **16** (0.206 g, 0.614 mmol) was heated in toluene (5 mL) for 3 h to 80 °C under an argon atmosphere. Removal of the solvent in vacuo and purification of the resulting residue by recrystallization (heptane) gave 0.128 g (68%) of azepinone **19** as colorless crystals, mp 125–129 °C. IR (cm^{-1}): 3420 (NH), 2940–2850 (CH), 1670 (C=O), 1640 (C=C), 1260 (Si-C). ^1H NMR ($CDCl_3$, 300 MHz) δ: 7.88 (br. s, 1H, NH), 5.49 (s, 1H, 4-H), 2.82–2.78 (m, 1H, 9-H), 2.39 (d, J = 6.8 Hz, 1H, 9a-H), 2.24 (m_c, 1H, 8-H), 1.96 (s, 3H, 3-Me), 1.84 (m_c, 1H, 9-H), 1.71–1.61 (m, 3H, 7-H, 6-H), 1.51–1.44 (m, 1H, 8-H), 1.35–1.28 (m, 1H, 7-H), 0.92 (s, 9H, *t*-Bu), 0.07, 0.00 (2s, 6H, $SiMe_2$). ^{13}C NMR ($CDCl_3$, 75.5 MHz) δ: 172.8 (s, C=O), 143.8 (s, C-5), 133.6 (s, C-3), 112.5 (s, C-5a), 111.4 (d, C-4), 39.2 (d, C-9a), 25.8, 18.1 (q, s, *t*-Bu), 23.7 (t, C-9), 23.2 (t, C-8), 22.9 (t, C-7), 22.1 (t, C-6), 21.8 (q, 3-Me), –3.9, -4.3 (2q, $SiMe_2$). Anal. calcd. for $C_{17}H_{29}NO_2Si$ (307.5): C 66.41, H 9.51, N 4.56: found: C 66.84, H 9.73, N 4.51.

One-pot procedure

According to *general procedure 3*, cyclopropanecarboxylic acid **10** (0.312 g, 1.00 mmol), NEt_3 (0.526 g, 5.20 mmol) and DPPA (0.523 g, 1.90 mmol) in toluene (10 mL) were stirred for 1 h at 0 °C and then heated for 2.5 h to 80 °C. Purification by column chromatography (heptane/EtOAc, 2:1) yielded 0.147 g (48%) azepinone **19** as colorless crystals, mp 126–130 °C.

5-tert-*Butyldimethylsiloxy-7-methyl-4-phenyl-1,3-dihydroazepin-2-one (20)*

According to *general procedure 3*, cyclopropanecarboxylic acid **11** (0.064 g, 0.192 mmol), NEt_3 (0.112 g,

© 2004 NRC Canada

1.11 mmol), and DPPA (0.161 g, 0.585 mmol) in toluene (5 mL) were stirred for 1 h at 0 °C and then heated for 2 h to 80 °C. Purification by column chromatography (heptane/EtOAc, 2:1 to 0:1) yielded 0.030 g (47%) of azepinone **20** as a colorless solid. ^{1}H NMR ($CDCl_3$, 300 MHz) δ: 7.90 (br. s, 1H, NH), 7.68–7.28 (m, 5H, Ph), 5.78 (s, 1H, 6-H), 3.24 (s, 2H, 3-H), 2.21 (s, 3H, 7-Me), 0.93 (s, 9H, *t*-Bu), 0.15 (s, 6H, $SiMe_2$). ^{13}C NMR ($CDCl_3$, 75.5 MHz) δ: 169.8 (s, C=O), 145.2 (s, C-5), 139.5 (s, C-7), 134.7, 128.5, 127.7, 126.2 (s, 3d, Ph), 112.7 (d, C-6), 111.3 (s, C-4), 39.7 (t, C-3), 25.6, 18.0 (q, s, *t*-Bu), 22.2 (q, 7-Me), -4.3 (q, $SiMe_2$). Anal. calcd. for $C_{19}H_{27}NO_2Si$ (329.5): C 69.26, H 8.26, N 4.25; found: C 68.68, H 7.89, N 4.40.

5-tert-*Butyldimethylsiloxy-4,7-dimethyl-1,3-dihydroazepin-2-one (21)*

According to *general procedure 3*, cyclopropanecarboxylic acid **12** (0.600 g, 2.22 mmol), NEt_3 (1.35 g, 13.3 mmol), and DPPA (1.16 g, 4.13 mmol) in toluene (20 mL) were stirred for 1 h at 0 °C and then heated for 3 h to 80 °C. Purification by column chromatography (hexane/EtOAc, 4:1 to 1.1) yielded 0.445 g (75%) of azepinone **21** as colorless needles, mp 141–143 °C. IR (cm^{-1}): 3500 (NH), 1685 (C=O), 1650 (C=C), 1250 (Si-C), 1200 (C-O). ^{1}H NMR ($CDCl_3$, 300 MHz) δ: 7.45 (br. s, 1H, NH), 5.39 (s, 1H, 6-H), 2.61 (s, 2H, 3-H), 1.90, 1.75 (2 s, 3H each, 4-Me, 7-Me), 0.86 (s, 9H, *t*-Bu), 0.00 (s, 6H, $SiMe_2$). ^{13}C NMR ($CDCl_3$, 75.5 MHz) δ: 169.0 (s, C=O), 144.1 (s, C-5), 133.3 (s, C-7), 111.9 (d, C-6), 108.6 (s, C-4), 39.9 (t, C-3), 25.7, 18.1 (q, s, *t*-Bu), 21.9, 17.5 (2q, 4-Me, 7-Me), –4.1 (q, $SiMe_2$). Anal. calcd. for $C_{14}H_{25}NO_2Si$ (267.4): C 62.87, H 9.42, N 5.24; found: C 62.73, H 9.18, N 5.20.

5-tert-*Butyldimethylsiloxy-7-methyl-1,3-dihydroazepin-2-one (22) and 7-methyl-3,4-dihydro-1*H-*azepin-2,5-dione (23)*

According to *general procedure 3*, cyclopropanecarboxylic acid **13** (0.261 g, 1.02 mmol), NEt_3 (0.543 g, 5.47 mmol), and DPPA (0.502 g, 1.82 mmol) in toluene (30 mL) were stirred for 1 h at 0 °C and then heated for 2 h to 80 °C. Purification by column chromatography (heptane/EtOAc, 4:1 to 1:3) yielded 0.056 g (23%) of azepinone **22** as a colorless solid and 0.037 g (27%) of azepindione **23** as colorless crystals, mp 179–184 °C. Compound **22**: IR (cm^{-1}): 3400 (NH), 2950–2800 (CH), 1690 (C=O), 1640 (C=C), 1430 (C-O), 1235 (Si-C). ^{1}H NMR ($CDCl_3$, 300 MHz) δ: 8.26 (br. s, 1H, NH), 5.33 (s, 1H, 6-H), 4.66 (t, *J* = 7 Hz, 1H, 4-H), 2.59 (d, *J* = 7 Hz, 2H, 3-H), 1.87 (s, 3H, 7-Me), 0.79 (s, 9H, *t*-Bu), 0.00 (s, 6H, $SiMe_2$). ^{13}C NMR ($CDCl_3$, 75.5 MHz) δ: 170.0 (s, C=O), 151.3 (s, C-5), 135.5 (s, C-7), 111.0 (d, C-6), 97.8 (d, C-4), 33.1 (t, C-3), 25.7, 18.2 (q, s, *t*-Bu), 22.2 (q, 7-Me), –4.7, –4.9 (2q, $SiMe_2$). Anal. calcd. for $C_{13}H_{23}NO_2Si$ (253.4): C 61.61, H 9.15, N 5.53; found: C 59.13, H 9.00, N 9.88. No better elemental analysis could be obtained. Compound **23**: IR (cm^{-1}): 3400 (NH), 2950 (CH), 1700 (C=O), 1650, 1615 (C=C). ^{1}H NMR ($CDCl_3$, 300 MHz) δ: 8.23 (br. s, 1H, NH), 5.47 (s, 1H, 6-H), 2.72 (m_c, 4H, 3-H, 4-H), 2.07 (s, 3H, 7-Me). ^{13}C NMR ($CDCl_3$, 75.5 MHz) δ: 196.9 (s, C-5), 174.8 (s, C-2), 145.9 (s, C-7), 111.7 (d, C-6), 35.5, 30.3 (2t, C-3, C-4), 24.3 (q, 7-Me). Anal. calcd. for $C_7H_9NO_2$ (139.1): C 60.42, H 6.52, N 10.07; found: C 60.34, H 6.76, N 10.03.

*7-Allyl-3,4-dihydro-1*H-*azepin-2,5-dione (24) and 7-(*E*)-(1-propenyl)-3,4-dihydro-1*H-*azepin-2,5-dione (25)*

According to *general procedure 3*, cyclopropanecarboxylic acid **14** (22) (0.074 g, 0.262 mmol), NEt_3 (0.144 g, 1.42 mmol), and DPPA (0.161 g, 0.585 mmol) in toluene (5 mL) were stirred for 1 h at 0 °C and then heated for 2 h to 80 °C. Purification by by column chromatography (heptane/EtOAc, 1:1) yielded 0.018 g (42%) of a mixture of azepindiones **24** and **25** as a colorless solid (ratio of **24**:**25**, ca. 1:1.2). Signals assigned to compound **24**: ^{1}H NMR ($CDCl_3$, 500 MHz) δ: 7.80 (br. s, 1H, NH), 5.79 (m_c, 1H, 2′-H), 5.50 (s, 1H, 6-H), 5.26 (dd, *J* = 7.8, 1.3 Hz, 1H, 3′-H), 2.84–2.63 (m, 4H, 3-H, 4-H).

Isomerization of 24 to 25

The mixture of **24**/**25** (0.016 g, 0.097 mmol) was stirred with NEt_3 (5 drops) in dichloromethane (2 mL) at room temperature for 24 h. Removal of the solvent in vacuo and purification of the residue by column chromatography (heptane/EtOAc, 1:2) yielded 0.016 g (37% from **14**) of azepindione **25** as colorless crystals, mp 122–130 °C. ^{1}H NMR ($CDCl_3$, 500 MHz) δ: 7.64 (br. s, 1H, NH), 6.31 (dq, *J* = 15.7, 6.8 Hz, 1H, 2′-H), 5.94 (dd, *J* = 15.7, 1.6 Hz, H, 1′-H), 5.53 (s, 1H, 6-H), 2.73 (m_c, 2H, 3-H), 2.32 (m_c, 2H, 4-H), 1.89 (dd, *J* = 6.8, 1.6 Hz, 3H, 3′-H). ^{13}C NMR ($CDCl_3$, 126 MHz) δ: 197.7 (s, C-5), 174.1 (s, C-2), 142.8 (s, C-7), 133.9 (d, C-1′), 128.7 (d, C-2′), 112.0 (d, C-6), 36.3 (t, C-3), 30.6 (t, C-4), 18.5 (q, C-3′). Due to the small amount of **25** no further characterization was possible.

t-*2*-tert-*Butyldimethylsiloxy-1-methyl*-c-*2-phenyl*-r-*1-cyclopropanecarboxylic acid (27)*

According to *general procedure 1*, the corresponding methyl cyclopropanecarboxylate (0.173 g, 0.540 mmol) and $KOSiMe_3$ (0.209 g, 1.62 mmol) in toluene (5 mL) were heated for 2.5 h to 100 °C and yielded **27** (0.144 g, 83%) as light yellow crystals, mp 140–145 °C (recrystallization from heptane/EtOAc). IR (cm^{-1}): 3450 (CO_2H), 2960 (CH), 1690 (C=O), 1255 (SiC). ^{1}H NMR ($CDCl_3$, 300 MHz) δ: 7.32–7.21 (m, 5H, Ph), 2.16 (d, *J* = 6.0 Hz, 1H, 3-H_{trans}), 1.51 (s, 3H, 1-Me), 1.01 (d, *J* = 6.0 Hz, 1H, 3-H_{cis}), 0.83 (s, 9H, *t*-Bu), 0.00, –0.37 (2s, 6H, $SiMe_2$). ^{13}C NMR ($CDCl_3$, 75.5 MHz) δ: 178.4 (s, CO_2H), 138.8, 128.7, 127.7, 127.6 (s, 3d, Ph), 67.7 (s, C-2), 31.8 (s, C-1), 25.6, 18.0 (q, s, *t*-Bu), 24.8 (t, C-3), 14.8 (q, 1-Me), –4.2*[5] (q, $SiMe_2$). Anal. calcd. for $C_{17}H_{26}O_3Si$ (306.5): C 66.62, H 8.55; found: C 67.06, H 8.67.

t-*2*-tert-*Butyldimethylsiloxy-1-methyl*-c-*2-phenyl*-r-*1-cyclopropanecarbonyl azide (28)*

According to *general procedure 2*, cyclopropanecarboxylic acid **27** (0.301 g, 0.982 mmol), NEt_3 (0.158 g, 1.56 mmol), and DPPA (0.300 g, 1.09 mmol) in toluene (5 mL) were stirred for 1 h at 0 °C. Filtration (pentane/diethyl ether, 10:1) of the crude product yielded 0.226 g (70%) of **28** as colorless crystals, mp 40–42 °C. IR (cm^{-1}): 2900 (CH), 2145 (N_3), 1695 (C=O), 1255 (SiC). ^{1}H NMR ($CDCl_3$, 300 MHz) δ: 7.32–7.23 (m, 5H, Ph), 2.35 (d, *J* = 6.1 Hz, 1H, 3-H_{trans}), 1.56 (s, 3H, 1-Me), 1.11 (d, *J* = 6.1 Hz, 1H, 3-H_{cis}), 0.84 (s, 9H, *t*-Bu), 0.01, –0.36 (2 s, 6H, $SiMe_2$). ^{13}C NMR ($CDCl_3$, 75.5 MHz) δ: 179.2 (s, C=O), 138.3, 128.8, 128.0, 127.8 (s, 3d, Ph), 68.9 (s, C-2), 34.8 (s,

© 2004 NRC Canada

C-1), 25.5, 17.9 (q, s, *t*-Bu), 25.4 (t, C-3), 14.9 (q, 1-Me), –4.2 (q, $SiMe_2$). Anal. calcd. for $C_{17}H_{25}N_3O_2Si$ (331.5): C 61.60, H 7.60, N 12.68; found: C 62.08, H 7.54, N 12.40.

t-*2*-tert-*Butyldimethylsiloxy-1-methyl*-c-*2-phenyl*-r-*1-cyclopropylisocyanate (29)*

Carbonyl azide **28** (0.126 g, 0.380 mmol) was heated in toluene (3 mL) for 2 h at 80 °C under an argon atmosphere. Removal of the solvent in vacuo and purification of the resulting crude product by filtration (silica gel, diethyl ether/pentane) gave 0.102 g (88%) of isocyanate **29** as a reddish oil. IR (cm^{-1}): 3080–2880 (CH), 2235 (NCO). ^{1}H NMR ($CDCl_3$, 300 MHz) δ: 7.43–7.25 (m, 5H, Ph), 1.64 (s, 3H, 1-Me), 1.62 (d, J = 7.2 Hz, 1H, 3-H_{trans}), 1.03 (d, J = 7.2 Hz, 1H, 3-H_{cis}), 0.84 (s, 9H, *t*-Bu), 0.00, –0.31 (2s, 6H, $SiMe_2$). ^{13}C NMR ($CDCl_3$, 75.5 MHz) δ: 138.7, 128.6, 128.4, 128.3 (s, 3d, Ph), 120.4 (br. s, NCO), 65.1 (s, C-2), 41.6 (s, C-1), 25.4 (t, C-3), 25.6, 17.9 (q, s, *t*Bu), 19.8 (q, 1-Me), –3.7, –4.0 (2q, $SiMe_2$). Anal. calcd. for $C_{17}H_{25}NO_2Si$ (303.5): C 67.29, H 8.30, N 4.68; found: C 67.26, H 8.25, N 4.56.

*3-Methyl-2*H-*benzo[c]azepin-2,5-dione (30)*

Analogously to ref. 23, isocyanate **29** (0.058 g, 0.185 mmol) was treated with boron trifluoride etherate (1 mL, ≈0.8 mmol) at 0 °C for 2.5 h. The reaction mixture was allowed to warm to room temperature and was then quenched with water (2 mL). The aqueous phase was extracted several times with diethyl ether and the combined organic phases were dried over $MgSO_4$. Purification of the resulting crude product by column chromatography (chloroform/methanol, 60:1) yielded 10 mg (28%) of azepindione **30** as colorless needles, mp 150–155 °C (lit. (16) mp 120–122 °C). ^{1}H NMR ($CDCl_3$, 500 MHz) δ: 8.10–8.04 (m, 2H, Ar), 7.74–7.66 (m, 1H, Ar), 7.58–7.50 (m, 1H, Ar), 7.50 (br. s, 1H, NH), 6.57 (s, 1H, 6-H), 2.41 (s, 3H, 7-Me). ^{13}C NMR ($CDCl_3$, 126 MHz) δ: 192.5 (s, C-5), 182.9 (s, C-2), 135.4, 131.2, 129.2, 129.0, 128.9, 128.6, 128.3 (3s, 4d, Ar, C-7), 97.4 (d, C-6), 24.8 (q, 7-Me). Due to the low amount of **30** no further characterization could be performed.

Methyl t/c-*2-phenyl*-c/t-*2-(1-phenylethenyl)*-r-*1-cyclopropanecarboxylate (31)*

Cyclopropane **31** was prepared according to the general procedure described in the literature (21) by slow addition of methyl diazoacetate (2.88 g, 28.0 mmol) to a refluxing suspension of $Cu(acac)_2$ (0.131 g, 0.500 mmol) and 2,3-diphenyl-1,3-butadiene (5.15 g, 25.0 mmol) in EtOAc (80 mL) (reaction time: 19 h). Purification was achieved by column chromatography (silica gel, heptane/EtOAc (6:1)). Fraction 1: 1.98 g (39%) starting material; fraction 2: 3.38 g (48%) of **31** (ratio of isomers = 57:43) as a colorless oil. IR (cm^{-1}): 3090 (CH), 1735 (C=O), 1380, 1170 (C-O). ^{1}H NMR ($CDCl_3$, 300 MHz) major isomer δ: 7.42–7.14 (m, 10H, Ph), 5.46 (s, 2H, 2′-H), 3.41 (s, 3H, CO_2Me), 2.52 (dd, J = 8.2, 5.8 Hz, 1H, 1-H), 2.17 (dd, J = 6.1, 5.8 Hz, 1H, 3-H_{trans}), 1.46 (dd, J = 8.2, 6.1 Hz, 1H, 3-H_{cis}); minor isomer δ: 7.42–7.14 (m, 10H, Ph), 5.89, 5.49 (2s, 1H each, 2′-H), 3.37 (s, 3H, CO_2Me), 2.60 (dd, J = 8.1, 6.2 Hz, 1H, 1-H), 2.00 (dd, J = 6.2, 4.9 Hz, 1H, 3-H_{trans}), 1.54 (dd, J = 8.1, 4.9 Hz, 1H, 3-H_{cis}). ^{13}C NMR ($CDCl_3$, 75.5 MHz) major isomer, δ: 170.8, 51.5 (s, q, CO_2Me), 139.1 (s, C-1′), 145.5, 138.1, 128.3, 127.9, 127.8, 127.1, 126.5, 126.3 (2s, 6d, Ph), 114.9 (t, C-2′), 40.0 (s, C-2), 27.6 (d, C-1), 17.8 (t, C-3); minor isomer δ: 170.7, 51.5 (s, q, CO_2Me), 150.7, 143.1 (2s, Ph), 139.3 (s, C-1′), 129.4, 128.0, 127.7, 127.5, 127.3, 126.7 (6d, Ph), 118.0 (t, C-2′), 38.7 (s, C-2), 29.8 (d, C-1), 23.1 (t, C-3). Anal. calcd. for $C_{19}H_{18}O_2$ (278.4): C 81.98, H 6.52; found: C 81.68, H 6.66.

t/c-*2-Phenyl*-c/t-*2-(1-phenylethenyl)*-r-*1-cyclopropanecarboxylic acid (32)*

Methyl cyclopropanecarboxylate **31** (1.94 g, 6.95 mmol, ratio of isomers = 47:53) was added to a solution of KOH (1.52 g, 25.0 mmol) in methanol (30 mL) and heated for 5 h under reflux. After removal of the solvent in vacuo, water was added to the residue and extracted several times with diethyl ether. The aqueous layer was acidified with a 2 N HCl solution under ice cooling to pH 2 to 3, extracted with diethyl ether (5 times), and the combined organic layers were dried over Na_2SO_4. Purification of the crude product by recrystallization (methanol) gave **32** (1.52 g, 83%, cis:trans = 45:55) as a colorless solid, mp 154–156 °C. For analytical data of *cis*- and *trans*-**32** see the next section.

Iodolactonization of carboxylic acid cis-*32*

According to a procedure described in the literature (17) cyclopropanecarboxylic acid **32** (1.61 g, 6.09 mmol, cis:trans = 48:52) was dissolved in a 1:1 mixture of 1.6 mol/L $NaHCO_3$ and satd. aq. Na_2CO_3 solution (6 mL each) and cooled to 0 °C. To this mixture a 0.7 mol/L solution of I_2 in 2.5 mol/L KI solution (5.6 mL, 3.92 mmol) was added dropwise over a period of 3 h. After stirring for 30 min at this temperature the precipitate (iodolactone **33**) was filtered off and washed with water. The resulting filtrate was extracted twice with chloroform, acidified with a 2 N HCl solution, and finally extracted with diethyl ether. Both organic phases were combined and dried over $MgSO_4$ and the solvent was removed to provide *trans*-**32**. Yield: 0.798 g (34%, with respect to *cis*-**32**: 71%) of iodolactone **33** as a solid, mp 59–64 °C, and 0.466 g (29%, with respect to *trans*-**32**: 56%) of *trans*-**32** as a colorless oil.

4-Iodomethyl-4,5-diphenyl-3-oxa-bicyclo[3.1.0]hexan-2-one (33)

A 1:1 mixture of two diastereomers. IR (cm^{-1}): 1765 (C=O), 1445, 1185, 990, 965, 760. ^{1}H NMR ($CDCl_3$, 300 MHz) δ: 7.45–7.08 (m, 20H, Ph), 3.96, 3.86, 3.72, 3.53 (4 d, J = 11.4 Hz, 1H each, 4-CH_2), 2.53 (dd, J = 8.4, 4.2 Hz, 1H, 1-H*[6]), 2.47 (dd, J = 9.0, 3.1 Hz, 1H, 1-H*[6]), 1.75 (dd, J = 4.9, 3.1 Hz, 1H, 6-H*[6]), 1.37–1.30 (m, 3H, 6-H*[6]). ^{13}C NMR ($CDCl_3$, 75.5 MHz) δ: 174.3, 174.2 (2 s, C=O), 139.5, 139.4, 134.4, 134.2, 131.5, 130.7, 129.0, 128.7, 128.5, 128.4, 128.3, 128.3, 128.1, 127.9, 125.7, 125.0 (4s, 12d, Ph), 88.1, 86.5 (2s, C-5), 42.3, 40.4 (2s, C-4), 25.9*[5] (d, C-1), 19.2, 19.0 (2t, C-6), 14.3, 7.9 (2t, C-1′) HR-MS (80 eV) calcd. for $C_{18}H_{25}O_2I$: 390.0117; found: 390.0132.

[6] * Indicates that the assignment may be exchanged.

© 2004 NRC Canada

***c-2-Phenyl-t-2-(1-phenylethenyl)-r-1-cyclopropanecarboxylic acid* (trans-*32*)**

^{1}H NMR ($CDCl_3$, 300 MHz) δ: 7.44–7.09 (m, 10H, Ph), 6.90 (br. s, 1H, CO_2H), 5.44 (s, 2H, 2′-H), 2.47 (dd, J = 8.1, 5.8 Hz, 1H, 1-H), 2.11 (t, J = 5.5 Hz, 1H, 3-H_{trans}), 1.50 (dd, J = 8.1, 4.9 Hz, 1H, 3-H_{cis}). Anal. calcd. for $C_{18}H_{16}O_2$ (264.3): C 81.79, H 6.10; found: C 81.61, H 6.10.

***t-2-Phenyl-c-2-(1-phenylethenyl)-r-1-cyclopropanecarboxylic acid* (cis-*32*)**

According to a procedure described in the literature (18) zinc dust (0.395 g, 6.23 mmol) was added to a hot solution of AgOAc (0.0039 g, 0.0234 mmol) and glacial acid (15 drops) and stirred for 30 min. After removal of the glacial acid the residue was washed with diethyl ether (5 times). To the resulting Ag/Zn couple were added the iodolactone **33** (0.700 g, 1.79 mmol) dissolved in diethyl ether (15 mL), ethanol (4.25 mL), and few drops of glacial acid and the suspension was heated under reflux for 7 h. The cooled suspension was filtered and the filtrate was successively washed with satd. aq. $NaHCO_3$ solution and brine. Drying of the organic layer with $MgSO_4$ and removal of the solvent gave 0.146 g of the crude product, which was purified by column chromatography (heptane/EtOAc, 4:1). Yield: 0.327 g (69%) of *cis*-**32** as a colorless oil. IR (cm^{-1}): 3400 (CO_2H), 2925 (CH), 1700 (C=O), 1440, 1225. ^{1}H NMR ($CDCl_3$, 300 MHz) δ: 10.21 (br. s, 1H, CO_2H), 7.36–7.13 (m, 10H, Ph), 5.76, 5.42 (2s, 1H each, 2′-H), 2.52 (dd, J = 8.1, 6.1 Hz, 1H, 1-H), 1.90 (dd, J = 6.1, 5.0 Hz, 1H, 3-H_{trans}), 1.56 (dd, J = 8.1, 5.0 Hz, 1H, 3-H_{cis}). ^{13}C NMR ($CDCl_3$, 75.5 MHz) δ: 176.9 (s, C=O), 145.2 (s, C-1′), 142.9, 139.5, 128.4, 128.0, 127.6, 127.4, 126.7, 126.5 (2s, 6d, Ph), 118.1 (t, C-2′), 39.8 (s, C-2), 36.1 (d, C-1), 23.1 (t, C-3). HR-MS (80 eV) calcd.: 264.1150; found: 264.1163. Anal. calcd. for $C_{18}H_{16}O_2$ (264.3): C 81.79, H 6.10; found: C 80.93, H 6.17.

4,5-Diphenyl-1,3-dihydroazepin-2-one (36)

According to *general procedure 2*, cyclopropanecarboxylic acid *cis*-**32** (0.258 g, 0.976 mmol), NEt_3 (0.335 g, 3.32 mmol), and DPPA (0.170 g, 1.68 mmol) in toluene (20 mL) were stirred for 2 h at 0 °C. Filtration (diethyl ether/pentane, 20:1) of the crude product yielded 0.184 g (65%) of *t*-2-phenyl-*c*-2-(1-phenylethenyl)-*r*-1-cyclopropanecarbonyl azide as a colorless oil. IR (cm^{-1}): 3060, 2950 (CH), 2135 (N_3), 1710 (C=O), 1495 (CH). ^{1}H NMR ($CDCl_3$, 300 MHz) δ: 7.39–7.16 (m, 10H, Ph), 5.92, 5.50 (2 s, 1H each, 2′-H), 2.58 (dd, J = 8.0, 6.1 Hz, 1H, 1-H), 2.08 (dd, J = 6.1, 5.0 Hz, 1H, 3-H_{trans}), 1.64 (dd, J = 8.0, 5.0 Hz, 1H, 3-H_{cis}). ^{13}C NMR ($CDCl_3$, 75.5 MHz) δ: 176.5 (C=O), 144.6 (s, C-1′), 142.2, 139.0, 128.4, 128.0, 127.5, 126.7, 126.6, 126.3 (2s, 6d, Ph), 118.6 (t, C-2′), 41.5 (s, C-2), 32.3 (d, C-1), 24.4 (t, C-3). Anal. calcd. for $C_{18}H_{15}N_3O$ (298.3): C 74.72, H 5.22, N 14.52; found: C 74.46, H 5.13, N 13.86.

The azide (0.192 g, 0.446 mmol) was heated in toluene (10 mL) for 2 h to 100 °C under an argon atmosphere. Removal of the solvent in vacuo and purification of the resulting product by recrystallization (heptane/EtOAc) gave 0.098 g (84%) of azepinone **36** as colorless crystals, mp 181–183 °C. IR (cm^{-1}): 3205 (NH), 3080 (CH), 1675 (C=O), 1625 (C=C). ^{1}H NMR ($CDCl_3$, 300 MHz) δ: 9.18 (br. s, 1H, NH), 7.43–6.93 (m, 10H, 2 Ph), 6.36 (dd, J = 8.9, 4.7 Hz, 1H, 7-H), 5.96 (d, J = 8.9 Hz, 1H, 6-H), 3.38 (s, 2H, 3-H). ^{13}C NMR ($CDCl_3$, 75.5 MHz) δ: 168.1 (s, C-2), 140.8, 140.0, 135.8, 128.2 (4s, Ph, C-4, C-5), 130.1, 120.0, 127.9, 127.8, 127.0, 126.8, 125.6 (7d, Ph, C-7), 118.3 (d, C-6), 44.2 (t, C-3). Anal. calcd. for $C_{18}H_{15}NO$ (261.3): C 82.37, H 5.78, N 5.36; found: C 82.01, H 5.70, N 5.26.

4,5-Dimethyl-1,3-dihydro-azepin-2-one (37)

According to *general procedure 2*, cyclopropanecarboxylic acid *cis*-**34** (0.240 g, 1.71 mmol), NEt_3 (0.288 g, 2.85 mmol), and DPPA (0.554 g, 2.01 mmol) in toluene (5 mL) were stirred for 3 h at 0 °C. Filtration (diethyl ether/pentane 20:1) of the crude product yielded 0.194 g (70%) of *c*-2-isopropenyl-*t*-2-methyl-*r*-1-cyclopropanecarbonyl azide as a colorless oil. IR (cm^{-1}): 2975 (CH), 2160 (N_3), 1705 (C=O), 1650 (C=C), 1375, 1195. ^{1}H NMR ($CDCl_3$, 300 MHz) δ: 4.96 (q, J = 1.5 Hz, 1H, 2′-H), 4.91 (s, 1H, 2′-H), 1.73 (br. s, 3H, 1′-Me), 1.70–1.64 (m, 2H, 1-H, 3-H), 1.29 (s, 3H, 2-Me), 1.11–1.07 (m, 1H, 3-H). ^{13}C NMR ($CDCl_3$, 75.5 MHz) δ: 177.4 (s, C=O), 143.3 (s, C-1′), 114.3 (t, C-2′), 37.0 (s, C-2), 30.4, 25.1, 20.8 (d, 2q, C-1, 1′-Me, 2-Me), 22.3 (t, C-3). Anal. calcd. for $C_8H_{11}N_3O$ (165.2): C 58.17, H 6.71, N 25.44; found: C 57.39, H 6.61, N 23.42.

The crude product (0.042 g, 0.274 mmol) was heated in toluene (2 mL) for 2 h to 100 °C under an argon atmosphere. Removal of the solvent gave 0.033 g (88%) of azepinone **37** as a colorless solid. ^{1}H NMR ($CDCl_3$, 300 MHz) δ: 8.26 (br. s, 1H, NH), 6.09 (dd, J = 8.8, 4.4 Hz, 1H, 7-H), 5.73 (d, J = 8.8 Hz, 1H, 6-H), 2.78 (s, 2H, 3-H), 1.91, 1.80 (2s, 3H each, 4-Me, 5-Me). ^{13}C NMR ($CDCl_3$, 75.5 MHz) δ: 168.3 (s, C-2), 127.9, 124.4 (2d, C-6, C-7), 122.7, 111.9 (2s, C-4, C-5), 43.7 (t, C-3), 20.7, 17.9 (2q, 4-Me, 5-Me). Due to the low amount of **37** no elemental analysis could be performed.

4,5,7-Trimethyl-1,3-dihydroazepin-2-one (38)

According to *general procedure 2*, cyclopropanecarboxylic acid *cis*-**35** (0.254 g, 1.65 mmol), NEt_3 (0.231 g, 2.28 mmol), and DPPA (0.488 g, 1.77 mmol) in toluene (5 mL) were stirred for 1 h at 0 °C. Filtration (diethyl ether/pentane, 20:1) of the crude product yielded 0.159 g (53%) of *c*-2-isopropenyl-*t*-1,2-dimethyl-*r*-1-cyclopropanecarbonyl azide as a colorless oil. IR (cm^{-1}): 2970 (CH), 2135 (N_3), 1705 (C=O), 1680 (C=C). ^{1}H NMR ($CDCl_3$, 300 MHz) δ: 4.84, 4.01 (2m, 1H each, 2′-H), 1.90 (d, J = 4.8 Hz, 1H, 3-H_{trans}), 1.73 (br. s, 3H, 1′-Me), 1.40, 1.32 (2s, 3H each, 2-Me, 1-Me), 0.68 (d, J = 4.8 Hz, 1H, 3-H_{cis}). ^{13}C NMR ($CDCl_3$, 75.5 MHz) δ: 180.3 (s, C=O), 145.3 (s, C-1′), 113.3 (t, C-2′), 38.2 (s, C-2), 32.4 (s, C-1), 27.0 (t, C-3), 20.8, 20.7, 16.0 (3q, 2-Me, 1′-Me, 1-Me). Anal. calcd. for $C_9H_{13}N_3O$ (179.2): C 60.32, H 7.31, N 23.45; found: C 60.53, H 7.89, N 21.70.

The azide (0.068 g, 0.379 mmol) was heated in toluene (3 mL) for 2 h to 80 °C under an argon atmosphere. Removal of the solvent in vacuo and recrystallization (heptane/EtOAc) gave 0.045 g (79%) of azepinone **38** as colorless crystals, mp 130–132 °C. IR (cm^{-1}): 3500–3400 (NH) 3080, 2950–2850 (CH), 1650 (C=O), 1610 (C=C), 1380 (CH). ^{1}H NMR ($CDCl_3$, 300 MHz) δ: 8.36 (br. s, 1H, NH), 5.56 (s, 1H, 6-H), 2.76 (s, 2H, 3-H), 1.99, 1.87, 1.75 (3s, 3H each, 4-Me, 5-Me, 7-Me). ^{13}C NMR ($CDCl_3$, 75.5 MHz) δ: 167.7 (s, C-2), 131.7, 127.9, 122.2 (3s, C-4, C-5, C-7), 117.3 (d, C-6), 43.4 (t, C-3), 22.1, 20.4, 18.0 (3q, 4-Me, 5-Me, 7-

© 2004 NRC Canada

Me). Anal. calcd. for $C_9H_{13}NO \cdot 0.75\ H_2O$ (164.7): C 65.63, H 8.87, N 8.50; found: C 65.91, H 8.69, N 8.38.

Acknowledgements

Generous support of this work by the Deutsche Forschungsgemeinschaft (Struktur-Eigenschafts-Beziehungen bei Heterocyclen) and the Fonds der Chemischen Industrie is gratefully appreciated. We thank Ute Hain and Luise Schefzig for experimental assistance, Dr. Margit Gruner for measurements and help during interpretations of numerous NMR spectra and, in particular, Prof. Dr. Jürgen Fabian and Dr. Dirk Sperling for the DFT calculation and their interest in this and related types of cyclopropane rearrangements.

References

1. E. Piers. *In* Comprehensive organic synthesis. Vol. 5. *Edited by* B.M. Trost and I. Fleming. Pergamon Press, New York. 1991. p. 971.
2. (*a*) E. Piers and E.H. Ruediger. J. Org. Chem. **45**, 1725 (1980); (*b*) E. Piers, H.E. Morton, I. Nagakura, and R.W. Thies. Can. J. Chem. **61**, 1226 (1983); (*c*) E. Piers and E.H. Ruediger. Can. J. Chem. **61**, 1239 (1983); (*d*) E. Piers, G.L. Jung, and N. Moss. Tetrahedron Lett. **25**, 3959 (1984); (*e*) E. Piers and N. Moss. Tetrahedron Lett. **26**, 2735 (1985); (*f*) E. Piers, G.L. Jung, and E.H. Ruediger. Can. J. Chem. **65**, 670 (1987); (*g*) E. Piers and G.L. Jung. Can. J. Chem. **65**, 1668 (1987).
3. (*a*) E. Piers and H.-U. Reissig. Angew. Chem. **92**, 839 (1979); Angew. Chem. Int. Ed. Engl. **19**, 813 (1979); (*b*) E. Piers, M.S. Burmeister, and H.-U. Reissig. Can. J. Chem. **64**, 180 (1986).
4. Reviews: (*a*) H.-U. Reissig. Top. Curr. Chem. **144**, 73 (1988); (*b*) H.-U. Reissig and R. Zimmer. Chem. Rev. **103**, 1151 (2003).
5. (*a*) B. Hofmann and H.-U. Reissig. Synlett, 27 (1993); (*b*) B. Hofmann and H.-U. Reissig. Chem. Ber. **127**, 2327 (1994).
6. R.K. Boeckman, Jr., M.D. Shair, J.R. Vagas, and L.A. Stolz. J. Org. Chem. **58**, 1295 (1993).
7. G. Böttcher. Ph.D. Dissertation, Technische Universität Dresden, Dresden, Germany.1999.
8. E. Vogel, R. Erb, G. Lenz, and A.A. Bothner-By. Liebigs Ann. Chem. **682**, 1 (1965).
9. (*a*) T. Sasaki, S. Eguchi, and M. Ohno. J. Am. Chem. Soc. **92**, 466 (1970); (*b*) P. Müller and H. Imogai. Helv. Chim. Acta, **82**, 315 (1999); (*c*) T.T. Raj and M.R. Eftink. Synth. Commun. **28**, 3787 (1998); our preliminary communication: G. Böttcher and H.-U. Reissig. Synlett, 725 (2000).
10. E. Kunkel, I. Reichelt, and H.-U. Reissig. Liebigs Ann. Chem. 512 (1984).
11. I. Reichelt and H.-U. Reissig. Liebigs Ann. Chem. 531 (1984).
12. I. Böhm and H.-U. Reissig. J. Am. Chem. Soc. **104**, 1735 (1982); for more details see ref. 4*a*.
13. (*a*) E.D. Laganis and B.L. Chenard. Tetrahedron Lett. **25**, 5831 (1984); (*b*) J.E. Baldwin, R.M. Adlington, and M.B. Mitchell. Tetrahedron, **51**, 5193 (1995).
14. J. Weinstock. J. Org. Chem. **26**, 3511 (1961).
15. (*a*) P. Ohier, A. Daïch, and B. Duroix. Tetrahedron, **52**, 13547 (1996); (*b*) D.E. Hibbs, M.B. Hursthouse, I.G. Jones, W. Jones, K.M. Abdul Malik, and M. North. J. Org. Chem. **63**, 1496 (1998).
16. Y. Nagao, I.-Y. Jeong, and W.S. Lee. Tetrahedron Lett. **37**, 393 (1996).
17. K.H. Holm and L. Skattebøl. Acta Chem. Scand. Ser. B, **B39**, 549 (1985).
18. (*a*) J.M. Denis, C. Girard, and J.M. Conia. Synthesis, 549 (1972); (*b*) T. Tokoroyama, K. Matsuo, and R. Kanazawa. Bull. Chem. Soc. Jpn. **53**, 3383 (1980).
19. For details see: D. Sperling. Ph.D. Dissertation, Technische Universität Dresden, Dresden, Germany. 1998.
20. For a review concerning medium-sized ring lactams: U. Nubbemeyer. Top. Curr. Chem. **216**, 125 (2001).
21. B. Hofmann and H.-U. Reissig. Chem. Ber. **127**, 2315 (1994).
22. C. Brückner and H.-U. Reissig. Chem. Ber. **120**, 617 (1987).
23. L. Balázs, M. Nyerges, I. Kádas, and L. Töke. Synthesis, 1373 (1995).

© 2004 NRC Canada

An iterative approach to three fragments of ionomycin[1]

Claude Spino and Martin Allan

Abstract: The S_N2' displacement of menthone-derived allylic carbonates with cuprate reagents occurs with high diastereoselectivity. This method can be used in an iterative fashion to construct stereocenters bearing a 1,3-relationship in a carbon chain. Each iteration provides the adduct in greater than 99% de. The synthesis of three fragments of the polyether ionophore ionomycin is disclosed.

Key words: menthone, chiral auxiliary, S_N2' displacement, cuprate, iteration, ionomycin.

Résumé : La substitution S_N2' de carbonates allyliques dérivés de la menthone avec des cuprates se produit avec une grande diastéréosélectivité. On peut utiliser cette méthode de façon itérative pour construire des stéréocentres ayant une relation 1,3 dans une chaîne carbonée. Chaque itération fournit l'adduit avec un excès diastéréomérique plus grand que 99 %. On a réalisé la synthèse de trois fragments du polyéther ionophore de l'ionomycine.

Mots clés : menthone, auxiliaire chiral, substitution S_N2', cuprate, itération, ionomycine.

[Traduit par la Rédaction]

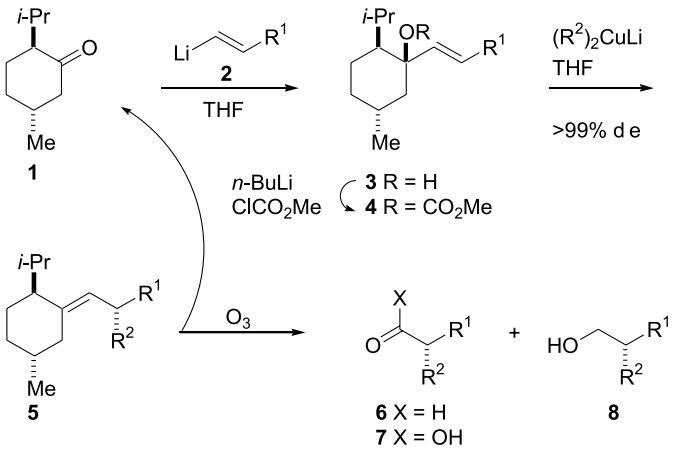
Introduction

We have developed in recent years a methodology equivalent to the alkylation of chiral enolates (1, 2). The key step in the strategy is the S_N2' displacement by cuprate reagents of a chiral allylic carbonate derived from (+)- or (–)-menthone **1** (Scheme 1). The transfer of chirality from carbonate **4** is generally high. Among the advantages of this strategy over the alkylation of chiral enolates is the higher diastereoselectivity generally achieved and the possible introduction of aryl and 2° or 3° alkyl groups.

Conceptually, the iterative alkylation of chiral enolates to form polyalkyl chains with a 1,3-relationship between the stereocenters is appealing. However, the relatively low reactivity of chiral enolates sometimes prohibits their reaction with β-branched alkyl halides or often requires that the electrophile be used in large excess. In addition, to be useful, any method used iteratively must provide products of high stereochemical purity at each iteration. For these reasons, examples of the use of enolates in an iterative approach to synthesis are scarce (3). The high diastereoselectivities and increased reactivity provided by our system prompted us to verify it's usefulness in an iterative approach to three fragments of the polyether ionophore ionomycin (Fig. 1) (4, 5).

We prepared a large quantity of **3** (R^1 = Me), the addition product of *trans*-propenyllithium to (–)-menthone (Scheme 1). The alcohol was isolated as a single diastereomer (1). We also prepared *ent*-**3** (R^1 = Me) starting from (+)-menthone. The corresponding carbonate **4** (R^1 = Me) was prepared immediately before its reaction with the cyanocuprate derived from *tert*-butyl methyl ether (6). Compound **9a** was then isolated in 92% yield (Scheme 2). Analysis by GC revealed the presence of essentially one diastereomer. For analysis purposes, the diastereomer **9b** was prepared from the same menthone, by addition of the cuprate derived from methyllithium on the carbonate of **13**, bearing the $CH_2O(t\text{-Bu})$ moiety (Scheme 3).

Scheme 1.



Ozonolysis of **9a** with a reductive work-up ($NaBH_4$) and conversion of the resulting alcohol **10** to the iodide **11** was achieved in high yield. In addition, some quantity of **10** was

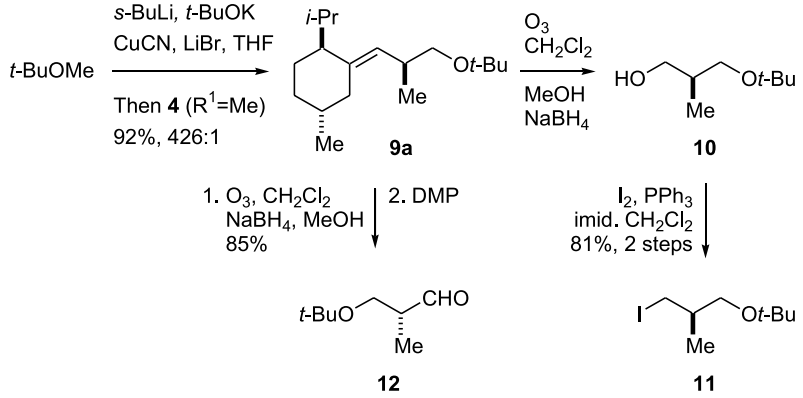
Received 1 July 2003. Published on the NRC Research Press Web site at http://canjchem.nrc.ca on 15 January 2004.

C. Spino[2] and M. Allan. Université de Sherbrooke, Département de Chimie, 2500 Boul. Université, Sherbrooke, QC J1K 2R1, Canada.

[1]This article is part of a Special Issue dedicated to Professor Ed Piers.
[2]Corresponding author (e-mail: e-mail: Claude.Spino@USherbrooke.ca).

 doi: 10.1139/V03-182 © 2004 NRC Canada

Scheme 2.



Scheme 3.

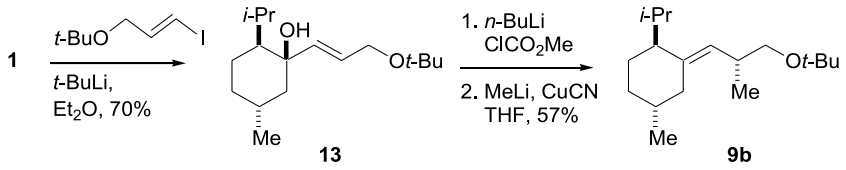
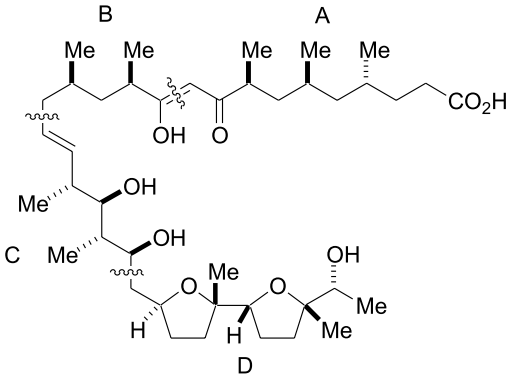


Fig. 1. Structure of ionomycin showing the three retrosynthetic disconnections.



oxidized to the aldehyde **12**, which is an intermediate to fragment C of ionomycin. This two-steps procedure for **12** was more efficient than the direct ozonolysis of **9a** in terms of yield and purity of the aldehyde, which was then used crude in the next step (vide infra).

The first iteration was tested with iodide **11**. Exchange of the iodine for lithium was accomplished with *t*-BuLi in diethyl ether and the monoalkylcyanocuprate derived from the resulting alkyllithium was added to carbonate **4** (R^1 = Me) with high diastereoselectivity to give **14** in 93% isolated yield (Scheme 4). Ozonolysis of **14** furnished syn alcohol **15**, which was shown to be >99% diastereomerically pure by comparison with an authentic sample of the diastereomeric *anti*-**15**, obtained by the same series of reaction starting from racemic **11**. A sufficient amount of **15** (precursor to fragment B of ionomycin) was set aside for its eventual coupling with fragments A and C. For that purpose, the free alcohol will be oxidized while the protected one will be converted to a primary iodide. The remainder of alcohol **15** was converted to iodide **16**, uneventfully. The latter suffered a lithium–iodine exchange under the same conditions as per **11** and further reaction with copper cyanide afforded the corresponding monoalkylcyanocuprate. Adding *ent*-**4** (R^1 = Me) to this mixture gave adduct **17a** in 87% yield. Ozonolysis gave alcohol **18a** as a 218:1 ratio of diastereomers, as shown by comparison with an authentic sample of its diastereomer **18b** (GC analysis). Alcohol **18b** was obtained by adding the same cyanocuprate made from **16** to carbonate **4** (R^1 = Me) followed by oxidative cleavage. Alcohol **18b** was also formed in >99% de. Any of the diastereomers of **18** can be prepared simply by choosing the appropriate carbonate (**4** or *ent*-**4** (R^1 = Me)) during the synthesis.

Fragment A of ionomycin was completed by a series of straightforward steps (Scheme 5). The auxiliary in **17a** was cleaved by ozonolysis and reductive work-up with triphenylphosphine gave an aldehyde. The latter was converted to the α,β-unsaturated methyl ester by a Wadsworth–Emmons reaction, which was further hydrogenated to give **19** in good overall yield. Deprotection of the *tert*-butyl ether with bromocatecholborane (7) gave the alcohol quantitatively, which was oxidized to aldehyde **20**. Conversion to fragment A (**21**) was performed using standard steps (4*a*).

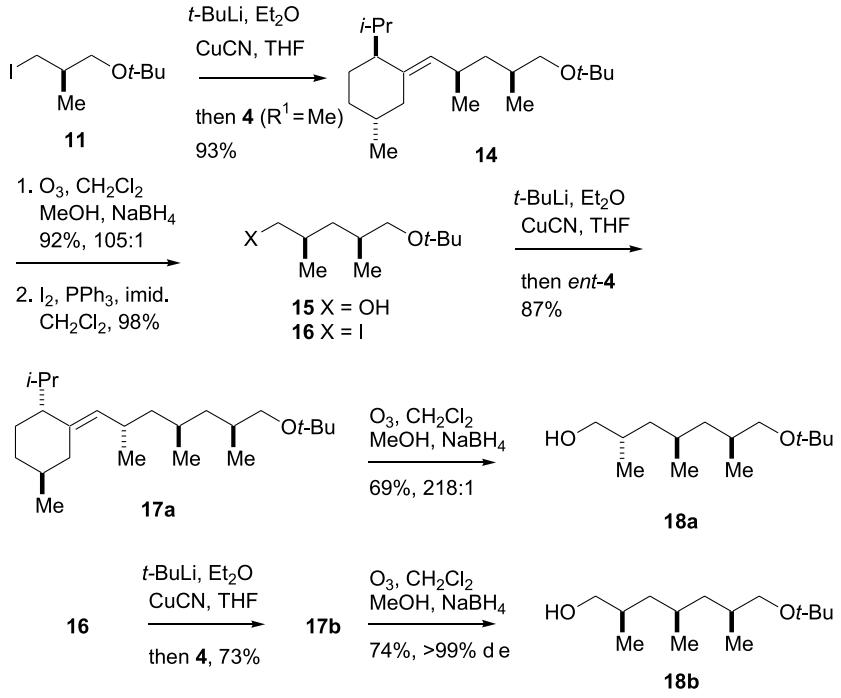
With fragments A and a precursor to fragment B in hand, we set out to prepare fragment C. Unpurified aldehyde **12** was reacted with Roush's (*E*)-crotyl boronate (8) to give alcohol **22** in 71% yield as a 82:18 ratio of diastereomers as determined by GC analysis (Scheme 6). The mixture was easily separated by column chromatography to yield 57% of pure alcohol **22**. Although the ratio was slightly lower than that obtained using the Brown protocol (9), the Roush method proved easier to use and provided a higher yield of pure **22**. After protection of the alcohol as it's triethylsilyl ether, the terminal double bond was cleaved to fragment C (**24**).

Conclusion

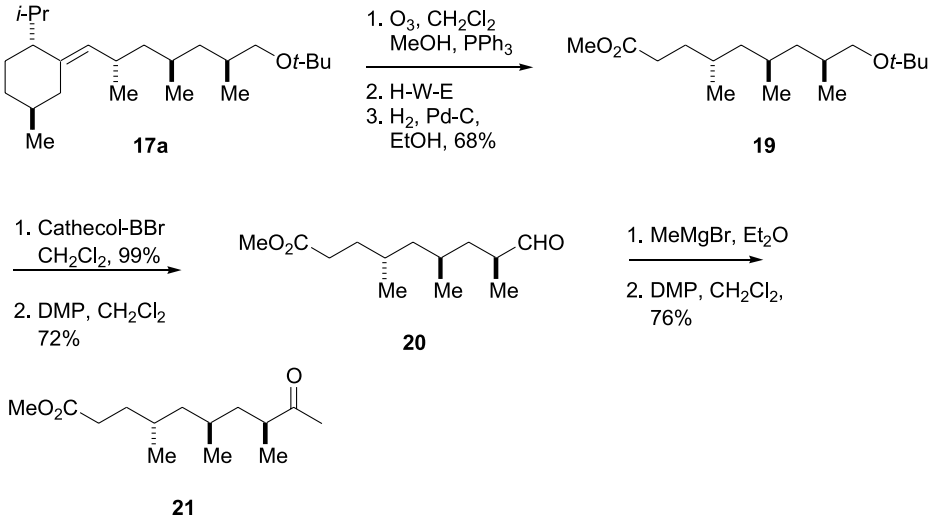
We have demonstrated the power of cyanoalkylcuprate displacement on menthone-derived carbonates as a synthetic

© 2004 NRC Canada

Scheme 4.



Scheme 5.



technology for the iterative preparation of 1,3-polymethyl-substituted carbon chains. Each iteration proceeded with >100:1 selectivity. A single intermediate **9** served to make fragments A, B, and C in 13, five, and five steps, respectively. It was itself prepared in three steps from (–)-menthone. This highly efficient strategy allowed us to make large quantities of each of these three fragments of ionomycin. The synthesis of fragment D is underway and the total synthesis of ionomycin will be reported in due course.

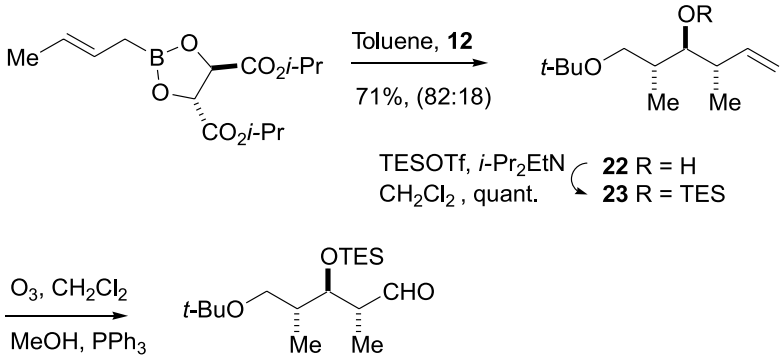
Experimental section

All reactions were carried out under an atmosphere of argon. Ethyl ether, toluene, and benzene were dried over metallic sodium using benzophenone as an indicator, while tetrahydrofuran was dried over both sodium and potassium using the same indicator. Methanol was distilled from magnesium. Dichloromethane, triethylamine, imidazole, diisopropylethylamine, and diisopropylamine were distilled over calcium hydride. Hexanes was purchased anhydrous from Aldrich. Copper cyanide was purchased from Aldrich and used as is. Thin layer chromatography was performed using 0.25 mm Silica Gel 60 F254 (EM Science-Merck) and flash chromatography using silica gel Kieselgel 60 (230–400 mesh ASTM).

All NMR spectra were taken in deuterated chloroform on a Brüker AC-300 (^{1}H (300 MHz), ^{13}C (75 MHz)). Chemical shifts are reported in parts per million (PPM) (δ) downfield from tetramethylsilane. The splitting patterns are designated as s (singlet), d (doublet), t (triplet), q (quartet), qi (quintet),

© 2004 NRC Canada

Scheme 6.



sx (sextet), sp (septet), oc (octuplet), m (multiplet). The IR spectra were determined on a PerkinElmer 1600 Fourier transform spectrometer. The IR spectra were determined neat, unless otherwise stated. The melting points were performed on a Mettler Toledo model 62. High- and low-resolution mass spectra (HR-MS and LR-MS) were obtained with a micromass spectrometer ZAB-1F model VG. GC analysis was performed using an Agilent series 6890 on a HP5 column (5% phenyl methyl siloxane) 30 m × 0.25 μM. All compounds were separated using a 100 °C for 2 min and 10 °C/min to 200 °C temperature program.

Alkene 9a

A solution of *tert*-butyl methyl ether (600 mL) and potassium *tert*-butoxide (18.33 g, 163 mmol) was cooled to –78 °C, then *s*-BuLi (117 mL of a 1.4 mol L^{-1} solution in hexanes, 163 mmol) was added dropwise. The resulting mixture was stirred for 2.5 h. In another flask, a solution of CuCN (14.63 g, 327 mmol) and LiBr (28.36g, 327 mmol) in THF (130 mL) was cooled to –78 °C. This solution was added dropwise to the first one by cannula, and stirring was continued for 1 h. The carbonate was dissolved in a minimum amount of THF, then added to the mixture dropwise. The mixture was allowed to warm gradually to room temperature while stirring for 18 h. The reaction was quenched by adding a satd. aq. NH_4Cl and NH_4OH (9:1) solution. The aqueous layer was separated and extracted with Et_2O three times. The combined organic extracts were washed with brine, then dried over anhyd $MgSO_4$, filtered, and concentrated in vacuo. Purification by flash chromatography on silica gel (hexanes) afforded the cuprate adduct (10.61 g, 92%) as a colourless oil. GC analysis showed a (426:1) diastereoisomer ratio. $[\alpha]_D$ = –2.82° ($CHCl_3$, *c* = 1.44). IR (cm^{-1}): 2970, 1461. ^1H NMR ($CDCl_3$) δ: 4.85 (d, 1H, *J* = 9.4 Hz), 3.23 (dd, 1H, *J* = 8.3 and 5.5 Hz), 3.03 (t, 1H, *J* = 8.5 Hz), 2.65–2.31 (m, 1H), 2.35 (dm, 1H, *J* = 16.5 Hz), 1.90 (sx, 1H, *J* = 6.8 Hz), 1.81–1.65 (m, 4H), 1.58–1.51 (m, 1H), 1.33-1.04 (m, 2H), 1.17 (s, 9H), 0.95–0.83 (m, 12H). ^{13}C NMR ($CDCl_3$) δ: 139.8 (s), 125.0 (d), 72.3 (s), 67.0 (t), 51.1 (d), 35.6 (t), 32.8 (d), 32.4 (d), 31.9 (t), 27.6 (q), 26.9 (t), 26.5 (d), 22.1 (q), 20.6 (q), 19.8 (q), 18.6 (q). LR-MS (*m*/*z* (relative intensity)): 266 (M^+, 5), 210 (35), 109 (100). HR-MS calcd. for $C_{18}H_{34}O$: 266.2610; found: 266.2614.

Alkene 9b

A solution of alcohol **13** (451 mg, 1.68 mmol) in THF (17 mL) was cooled to –78 °C. *n*-BuLi (1.26 mL of a 1.87 mol L^{-1} solution in hexanes, 2.36 mmol) was added dropwise, then stirring continued for 2 h. $ClCO_2Me$ (0.20 mL, 2.53 mmol) was added. The mixture was stirred for 2 h at –78 °C, then for 1 h while letting the reaction warm to 0 °C, and 1 h at 0 °C. The reaction was quenched by adding a satd. aq. NH_4Cl solution. The aqueous layer was separated and extracted with Et_2O three times. The combined organic extracts were washed with brine, then dried over anhyd $MgSO_4$, filtered, and concentrated in vacuo. The crude carbonate was used in the next step without further purification.

To a solution of CuCN (603 mg, 6.73 mmol) in THF (28 mL) cooled to –78 °C, MeLi (4.21 mL of a 1.6 mol L^{-1} solution in Et_2O, 6.73 mmol) was added slowly. This mixture was stirred for 1.5 h. The carbonate was dissolved in a minimum of THF, then added to the reaction mixture at –60 °C. Stirring was continued for 17 h, while the reaction was allowed to reach room temperature. The reaction was quenched by adding a satd. aq. NH_4Cl and NH_4OH (9:1) solution. The aqueous layer was separated and extracted with Et_2O three times. The combined organic extracts were washed with brine, then dried over anhyd $MgSO_4$, filtered, and concentrated in vacuo. Purification by flash chromatography on silica gel (hexanes) afforded cuprate adduct **9b** (256 mg, 57%) as a colourless oil. $[\alpha]_D$ = –48.9° ($CHCl_3$, *c* = 1.34). ^1H NMR ($CDCl_3$) δ: 4.83 (d, 1H, *J* = 9.4 Hz), 3.15 (dd, 1H, *J* = 8.8 and 6.1 Hz), 3.03 (t, 1H, *J* = 8.3 Hz), 2.66–2.54 (m, 1H), 2.35–2.29 (m, 1H), 1.91 (sx, 1H, *J* = 7.1 Hz), 1.81–1.64 (m, 4H), 1.58–1.52 (m, 1H), 1.33-1.24 (m, 1H), 1.16 (s, 9H), 1.14–1.06 (m, 1H), 0.95 (d, 3H, *J* = 6.6 Hz), 0.90 (d, 3H, *J* = 6.1 Hz), 0.87 (d, 3H, *J* = 6.6 Hz), 0.84 (d, 3H, *J* = 6.9 Hz). LR-MS (*m*/*z* (relative intensity)): 266 (M^+, 5), 210 (35), 123 (100). HR-MS calcd. for $C_{18}H_{34}O$: 266.2610; found: 266.2614.

General procedure for the ozonolysis of cuprate adducts to the corresponding alcohols

O_3 was bubbled through a stirred solution of cuprate adduct in CH_2Cl_2 and MeOH (4:1, 0.1 mol L^{-1}) at –78 °C until the appearance of a blue colour. Then argon was bubbled through this solution until the blue colour disappeared. $NaBH_4$ (5.0 equiv.) was added portion-wise. The mixture was allowed to warm to room temperature slowly while stirring for 16 h. The reaction was quenched by adding a satd. aq. NH_4Cl solution. The aqueous layer was separated and extracted with CH_2Cl_2 three times. The combined organic

© 2004 NRC Canada

extracts were washed with brine, then dried over anhyd $MgSO_4$, filtered, and concentrated in vacuo.

Alcohol 10

Prepared from **9a** (1.0 g, 3.75 mmol) according to the general procedure for the ozonolysis of cuprate adducts. Purified by flash chromatography on silica gel (hexanes–AcOEt, 30%) gave 467 mg of **10** (85%) as a colourless oil. $[\alpha]_D = -16.8°$ ($CHCl_3$, $c = 1.84$). IR (cm^{-1}): 3384. ^1H NMR ($CDCl_3$) δ: 3.66–3.50 (m, 3H), 3.28 (t, 1H, $J = 8.8$ Hz), 2.00 (m, 1H), 1.21 (s, 9H), 0.85 (d, 3H, $J = 7.15$ Hz). LR-MS (*m/z* (relative intensity)): 131 (M^+ – Me, 80), 89 (100), 87 (10). HR-MS calcd. for $C_7H_{14}O_2$: 131.1072; found: 131.1076.

Iodide 11

(A higher overall yield of iodide **11** from **9a** was obtained using crude alcohol **10**). To a solution of alcohol **10** (1.21 g, 8.30 mmol) in CH_2Cl_2 (165 mL) was added imidazole (3.39 g, 50.0 mmol), then Ph_3P (8.71 g, 33.3 mmol). After complete dissolution of PPh_3, the solution was protected from light, cooled to 0 °C, and I_2 (8.45 g, 33.3 mmol) was added. The mixture was warmed to room temperature and stirring was continued for 16 h. The reaction was quenched by adding a satd. aq. $Na_2S_2O_3$ solution. The aqueous layer was separated and extracted with EtOAc three times. The combined organic extracts were dried over anhyd $MgSO_4$, filtered, and concentrated in vacuo. The crude extract was triturated twice with hexanes to remove the remaining PPh_3. Purification by flash chromatography on silica gel (hexanes–EtOAc, 2%) afforded iodide **11** (1.71 g, 81% for two steps) as a slightly yellow oil. $[\alpha]_D = -12.4°$ ($CHCl_3$, $c = 1.46$). IR (cm^{-1}): 2973, 1479. ^1H NMR ($CDCl_3$) δ: 3.31 (d, 2H, J = 4.4 Hz), 3.23 (dd, 1H, J = 9.4, 5.5 Hz), 3.13 (t, 1H, J = 8.0 Hz), 1.66–1.55 (m, 1H), 1.18 (s, 9H), 0.96 (d, 3H, J = 6.6 Hz). ^{13}C NMR ($CDCl_3$) δ: 72.6 (s), 65.4 (t), 35.3 (t), 27.6 (s), 17.8 (q), 15.1 (q). LR-MS (*m/z* (relative intensity)): 256 (M^+, 10), 241 (25), 87 (100). HR-MS calcd. for $C_8H_{17}OI$: 256.0324; found: 256.0318.

Aldehyde 12

To a solution of alcohol (467 mg, 3.20 mmol) in wet CH_2Cl_2 (8.5 mL) was added Dess–Martin periodinane (1.628 g, 3.84 mmol). The mixture was stirred for 30 min. The reaction solution was evaporated in vacuo, then diluted with Et_2O, washed with a solution of satd. aq. $Na_2S_2O_3$, washed with a solution of satd. aq. $NaHCO_3$, and washed with brine. The combined aqueous extracts were extracted with Et_2O three times. The combined organic extracts were dried over anhyd $MgSO_4$, filtered, and concentrated in vacuo to afforded crude aldehyde, which was used without further purification in the next step.

Alcohol 13

A solution of 3-*tert*-butyloxy-1-iodo-1-propene (914 mg, 3,78 mmol) in Et_2O (11 mL) was cooled to –78 °C, then *t*-BuLi (6.05 mL of a 1.25 mol L^{-1} solution in Et_2O, 7.56 mmol) was added dropwise. The mixture was stirred for 1.6 h at –78 °C and 1.5 h at 0 °C, then cooled again at –78 °C. (–)-Menthone (0.44 mL, 2.52 mmol) was dissolved in a minimum of Et_2O, then added to the reaction. Stirring was continued for 21 h and the reaction was allowed to reach room temperature slowly during this time. The reaction was quenched by adding a satd. aq. NH_4Cl solution. The aqueous layer was separated and extracted with Et_2O three times. The combined organic extracts were washed with brine, then dried over anhyd $MgSO_4$, filtered, and concentrated in vacuo. Purification by flash chromatography on silica gel (10% EtOAc in hexanes) afforded alcohol **13** (472 mg, 70%) as a colourless oil. $[\alpha]_D = -19.1°$ ($CHCl_3$, $c = 1.98$). IR (cm^{-1}): 3466, 1468. ^1H NMR ($CDCl_3$) δ: 5.77 (dt, 1H, J = 15.9 and 5.0 Hz), 5.68 (d, 1H, J = 15.9 Hz), 3.95 (dd, 2H, J = 5.0 and 2.2 Hz), 2.02–1.90 (m, 1H), 1.80–1.67 (m, 2H), 1.54–1.43 (m, 4H), 1.21 (s, 9H), 1.23–1.11 (m, 2H), 0.94–0.83 (m, 10H). LR-MS (*m/z* (relative intensity)): 268 (M^+, 5), 212 (55), 127 (100). HR-MS calcd. for $C_{18}H_{34}O$: 268.2402; found: 268.2393.

General procedure for the addition of cuprates to allylic carbonates

A solution of the iodide (1.5 equiv.) in Et_2O (0.1 mol L^{-1}) was cooled to –78 °C. *t*-BuLi (3.0 equiv. of a solution in Et_2O) was added dropwise. The mixture was stirred for 30 min, then warmed to 0 °C for 1 h, and cooled again to –78 °C. In a different round-bottomed flask, CuCN (1.5 equiv.) in THF (0.2 mol L^{-1}) was degassed and purged with argon twice before being cooled to –78 °C. The organolithium solution was cannulated dropwise into the CuCN solution. The reaction was stirred for 2 h. The carbonate was dissolved in a minimum of THF, then added to the cuprate reaction mixture at –50 °C. While stirring, the temperature was allowed to reach 0 °C slowly over a 1 h period, then room temperature over a 16 h period. The reaction was quenched by adding a satd. aq. NH_4Cl and NH_4OH (9:1) solution. The aqueous layer was separated and extracted with Et_2O three times. The combined organic extracts were washed with brine, then dried over anhyd $MgSO_4$, filtered, and concentrated in vacuo.

Alkene 14

Prepared from **11** (6.40 g, 25.0 mmol) following the general procedure for the addition of cuprates to allylic carbonates. Flash column chromatography (hexanes) gave 4.77 g (93%) of **14** as a colourless oil. $[\alpha]_D = -30.8°$ ($CHCl_3$, c = 2.37). IR (cm^{-1}): 2864, 1478. ^1H NMR ($CDCl_3$) δ: 4.81 (d, 1H, J = 9.4 Hz), 3.19 (dd, 1H, J = 8.3 and 5.5 Hz), 3.02 (t, 2H, J = 7.7 Hz), 2.59–2.47 (m, 1H), 2.39–2.31 (m, 1H), 1.91 (sx, 1H, J = 7.1 Hz), 1.80–1.50 (m, 6H), 1.37–1.19 (m, 2H), 1.17 (s, 9H), 1.13–0.95 (m, 2H), 0.92–0.83 (m, 15H). ^{13}C NMR ($CDCl_3$) δ: 138.2 (s), 128.4 (d), 72.1 (s), 67.7 (q), 50.7 (t), 42.3 (t), 35.7 (t), 32.6 (d), 32.2 (t), 31.9 (d), 29.0 (d), 27.6 (q), 26.8 (t), 26.5 (d), 22.7 (q), 22.1 (q), 20.9 (q), 19.7 (q), 17.3 (q). LR-MS (*m/z* (relative intensity)): 308 (M^+, 5), 252 (70), 137 (100). $[\alpha]_D = -31.3°$ ($CHCl_3$, c = 1.33). IR (cm^{-1}): 2955, 1461. HR-MS calcd. for $C_{21}H_{40}O$: 308.3079; found: 308.3086. Minor isomer of alkene **14** (made by starting from racemic **11**): ^1H NMR ($CDCl_3$) δ: 4.87 (d, 1H, J = 9.1 Hz), 3.22 (dd, 1H, J = 8.1 and 5.2 Hz), 3.00 (t, 1H, J = 8.0 Hz), 2.55–2.48 (m, 1H), 2.37–2.32 (m, 1H), 1.91 (sx, 1H, J = 6.8 Hz), 1.80–1.50 (m, 6H), 1.37–1.19 (m, 2H), 1.17 (s, 9H), 1.14–0.96 (m, 2H), 0.92–0.83 (m, 15H). LR-MS (*m/z* (relative intensity)): 252 ($M^+ - C_4H_9$, 45), 177 (10), 99

© 2004 NRC Canada

(100). HR-MS calcd. for $C_{17}H_{31}O$: 252.2453; found: 252.2458.

Alcohol 15

Prepared from **14** (4.77 g, 15.5 mmol) according to the general procedure for the ozonolysis of cuprate adducts. Flash column chromatography on silica gel (hexanes–AcOEt, 30%) gave 2.68 g (92%) of **15** as a colourless oil. GC analysis showed a (105:1) diastereomer ratio. **15**: $[\alpha]_D$ = –0.2° ($CHCl_3$, *c* = 1.73). IR (cm^{-1}): 3341, 1479. ^1H NMR ($CDCl_3$) δ: 3.48 (d, 2H, *J* = 5.5 Hz), 3.18–3.09 (m, 2H), 1.72 (oc, 2H, *J* = 6.6 Hz), 1.50–1.40 (m, 1H), 1.18 (s, 9H), 1.00–0.90 (m, 1H), 0.93 (d, 3H, *J* = 6.6 Hz), 0.91 (d, 3H, *J* = 6.6 Hz). ^{13}C NMR ($CDCl_3$) δ: 72.5 (s), 67.8 (t), 67.2 (t), 38.0 (d), 33.5 (d), 31.4 (t), 27.4 (q), 18.4 (q), 18.0 (q). LR-MS (*m/z* (relative intensity)): 173 (M^+ – Me, 10), 143 (20), 97 (100). HR-MS calcd. for $C_{10}H_{21}O_2$: 173.1541; found: 173.1535. Minor isomer of alcohol **15** (made from the ozonolysis of the minor isomer of alkene **14**): $[\alpha]_D$ = +10.1° ($CHCl_3$, *c* = 1.43). IR (cm^{-1}): 3318, 1479. ^1H NMR ($CDCl_3$) δ: 3.45 (d, 2H, *J* = 6.6 Hz), 3.18–3.09 (m, 2H), 1.79 (oc, 2H, *J* = 6.6 Hz), 1.34–1.25 (m, 1H), 1.18 (s, 9H), 1.20–1.10 (m, 1H), 0.88 (d, 6H, *J* = 7.2 Hz). LR-MS (*m/z* (relative intensity)): 173 (M^+ – Me, 10), 143 (25), 83 (100). HR-MS calcd. for $C_{10}H_{21}O_2$: 173.1541; found: 173.1546.

Iodide 16

Prepared from **15** (2.68 g, 14.2 mmol) according to the same procedure as per iodide **11**. Flash chromatography on silica gel (hexanes–EtOAc, 10%) afforded iodide **16** (4.17 g, 98%) as a colourless oil. $[\alpha]_D$ = –1.4° ($CHCl_3$, *c* = 1.28). IR (cm^{-1}): 2974, 1479. ^1H NMR ($CDCl_3$) δ: 3.26 (dd, 1H, *J* = 9.9 and 4.4 Hz), 3.20 (dd, 1H, *J* = 8.3 and 5.0 Hz), 3.12 (dd, 1H, *J* = 9.4 and 6.0 Hz), 3.05 (dd, 1H, *J* = 8.3 and 6.6 Hz), 1.74–1.51 (m, 2H), 1.44–1.35 (m, 1H), 1.17 (s, 9H), 1.05–0.95 (m, 1H), 0.99 (d, 3H, *J* = 6.6 Hz), 0.90 (d, 3H, *J* = 6.6 Hz). ^{13}C NMR ($CDCl_3$) δ: 72.3 (s), 67.0 (t), 41.0 (t), 32.0 (d), 31.5 (d), 27.5 (t), 21.5 (q), 18.1 (q), 17.7 (q). LR-MS (*m/z* (relative intensity)): 283 (M^+ – Me, 20), 225 (30), 115 (100). HR-MS calcd. for $C_{10}H_{21}O_2$: 283.0559; found: 283.0563.

Alkene 17a

Prepared from **16** (1.12 g, 3.75 mmol) and carbonate *ent*-**8** following the general procedure for the addition of cuprates to allyl carbonates. Flash column chromatography (hexanes) gave 762 mg (87%) of **17a** as a colourless oil. $[\alpha]_D$ = +18.9° ($CHCl_3$, *c* = 2.07). IR (cm^{-1}): 2955, 1478. ^1H NMR ($CDCl_3$) δ: 4.85 (d, 1H, *J* = 9.1 Hz), 3.22 (dd, 1H, *J* = 8.7 and 4.7 Hz), 2.92 (t, 1H, *J* = 8.5 Hz), 2.53–2.43 (m, 1H), 2.39–2.31 (m, 1H), 1.91 (sx, 1H, *J* = 6.7 Hz), 1.80–1.47 (m, 6H), 1.28–1.17 (m, 2H), 1.16 (s, 9H), 1.15–0.96 (m, 3H), 0.92 (d, 3H, *J* = 6.3 Hz), 0.89 (d, 3H, *J* = 5.6 Hz), 0.87 (d, 6H, *J* = 5.8 Hz), 0.85 (d, 6H, *J* = 5.9 Hz). ^{13}C NMR ($CDCl_3$) δ: 137.4 (s), 129.0 (d), 72.1 (s), 67.2 (t), 50.9 (d), 45.4 (t), 42.1 (t), 35.9 (t), 32.7 (d), 32.3 (t), 31.3 (d), 28.9 (d), 27.9 (d), 27.6 (q), 27.1 (t), 26.5 (d), 22.1 (q), 21.3 (q), 21.0 (q), 20.7 (q), 19.7 (q), 18.3 (q). LR-MS (*m/z* (relative intensity)): 350 (M^+, 5), 294 (40), 99 (100). HR-MS calcd. for $C_{24}H_{36}O$: 350.3548; found: 350.3557.

Alkene 17b

Prepared from **16** (447 mg, 1.50 mmol) and carbonate **8** following the general procedure for the addition of cuprates to allyl carbonates. Flash column chromatography (hexanes) gave 255 mg (73%) of **17b** as a colourless oil. $[\alpha]_D$ = –28.8° ($CHCl_3$, *c* = 1.57). ^1H NMR ($CDCl_3$) δ: 4.77 (d, 1H, *J* = 9.4 Hz), 3.20 (dd, 1H, *J* = 8.8 and 5.5 Hz), 3.00 (t, 1H, *J* = 7.7 Hz), 2.56-2.46 (m, 1H), 2.40–2.32 (m, 1H), 1.89 (sx, 1H, *J* = 7.2 Hz), 1.80–1.61 (m, 5H), 1.54–1.43 (m, 1H), 1.31–1.06 (m, 4H), 1.16 (s, 9H), 0.99–0.88 (m, 3H), 0.92 (d, 3H, *J* = 6.1 Hz), 0.87 (d, 6H, *J* = 6.6 Hz), 0.85 (d, 6H, *J* = 6.1 Hz), 0.82 (d, 3H, *J* = 6.6 Hz). LR-MS (*m/z* (relative intensity)): 350 (M^+, 5), 293 (50), 141 (100). HR-MS calcd. for $C_{24}H_{46}O$: 350.3548; found: 350.3553.

Alcohol 18a

Prepared from **17a** (150 mg, 0.43 mmol) according to the general procedure for the ozonolysis of cuprate adducts. Flash chromatography on silica gel (hexanes–AcOEt, 20%) afforded 67 mg (69%) of alcohol **18a** as a colourless oil. GC analysis showed a (218:1) diastereoisomer ratio. $[\alpha]_D$ = –22.5° ($CHCl_3$, *c* = 1.13). IR (cm^{-1}): 3334, 1462. ^1H NMR ($CDCl_3$) δ: 3.48 (dd, 1H, *J* = 10.7 and 6.2 Hz), 3.40 (dd, 1H, *J* = 10.7 and 6.4 Hz), 3.18 (dd, 1H, *J* = 8.3 and 5.3 Hz), 3.04 (t, 1H, *J* = 8.4 Hz), 1.78–1.58 (m, 2H), 1.33–1.24 (m, 2H), 1.17 (s, 9H), 1.11–1.06 (m, 2H), 0.99–0.92 (m, 1H), 0.88 (d, 6H, *J* = 6.5 Hz), 0.86 (d, 3H, *J* = 6.4 Hz). LR-MS (*m/z* (relative intensity)): 230 (M^+, 5), 215 (10), 83 (100). HR-MS calcd. for $C_{13}H_{27}O_2$: 215.2011; found: 215.2003.

Alcohol 18b

Prepared from **17b** (234 mg, 0.67 mmol) according to the general procedure for the ozonolysis of cuprate adducts. The alcohol was purified by flash chromatography on silica gel (hexanes–AcOEt, 20%) to afford 113 mg (74%) of **18b** as a colourless oil. $[\alpha]_D$ = +8.7° ($CHCl_3$, *c* = 1.33). IR (cm^{-1}): 3351, 1480. ^1H NMR ($CDCl_3$) δ: 3.54 (dd, 1H, *J* = 11.0 and 5.5 Hz), 3.36 (dd, 1H *J* = 10.5 and 6.6 Hz), 3.21 (dd, 1H *J* = 8.8 and 5.0 Hz), 3.02 (t, 1H, *J* = 7.2 Hz), 1.79–1.54 (m, 2H), 1.31 (m, 2H) 1.16 (s, 9H), 0.93 (d, 3H, *J* = 6.6 Hz), 0.90–0.81 (m, 3H), 0.89 (d, 6H, *J* = 6.6 Hz). LR-MS (*m/z* (relative intensity)): 215 (M^+ – Me, 10), 173 (30), 83 (100). HR-MS calcd. for $C_{13}H_{27}O_2$: 215.2011; found: 215.2007.

Ester 19

Through a stirred solution of **17a** (800 mg, 2.28 mmol) in CH_2Cl_2 (19 mL) and MeOH (4 mL) at –78 °C was bubbled O_3 until the appearance of a blue colour. Then, argon gas was bubbled through the solution until the blue colour disappeared and Ph_3P (720 mg, 2.74 mmol) was added. The mixture was warmed to room temperature and stirred for 4 h. The reaction was concentrated in vacuo, then triturated twice with hexanes. The crude aldehyde was used in the next step without further purification. The crude aldehyde was dissolved in CH_2Cl_2 (27 mL), then $MeO_2CCH{=}PPh_3$ (1.723 g, 5.154 mmol) was added. The mixture was stirred and heated to reflux for 17.5 h. The reaction was cooled to room temperature, then concentrated in vacuo. Two triturations, first with Et_2O then with hexanes, were performed. Purification by flash chromatography on silica gel (5% EtOAc in hexanes) afforded only the trans alkene (490 mg, 76%) as a

© 2004 NRC Canada

colourless oil. $[\alpha]_D$ = +22.0° ($CHCl_3$, *c* = 1.82). IR (cm^{-1}): 1725, 1658. ^1H NMR ($CDCl_3$) δ: 6.88 (dd, 1H, *J* = 15.4 and 8.3 Hz), 5.78 (d, 1H *J* = 15.4 Hz), 3.72 (s, 3H), 3.18 (dd, 1H, *J* = 8.3 and 5.0 Hz), 2.99 (t, 1H, *J* = 8.0 Hz), 2.40 (sp, 1H, *J* = 7.2 Hz), 1.68 (oc, 1H, *J* = 5.5 Hz), 1.56 (oc, 1H, *J* = 6.6 Hz), 1.36–1.25 (m, 2H), 1.22–1.10 (m, 1H) 1.15 (s, 9H), 1.00 (d, 3H, *J* = 6.6 Hz), 0.94–0.85 (m, 1H), 0.88 (d, 3H, *J* = 6.6 Hz), 0.86 (d, 3H, *J* = 6.1 Hz). ^{13}C NMR ($CDCl_3$) δ: 167.1 (s), 155.2 (d), 118.7 (d), 72.0 (s), 66.7 (t), 51.1 (q), 43.3 (t), 41.6 (t), 33.8 (d), 31.1 (d), 27.6 (d), 27.3 (q), 20.3 (q), 19.0 (q), 18.2 (q). LR-MS (*m/z* (relative intensity)): 269 (M^+ – Me, 10), 227 (15), 127 (100). HR-MS calcd. for $C_{16}H_{29}O_3$: 269.2117; found: 269.2119.

To the α,β-unsaturated ester (426 mg, 1.50 mmol) dissolved in EtOH (15 mL) was added 5% Pd/C (75 mg). The reaction was degassed and flushed with argon 3 times, before being stirred for 2 h under 1 atm of H_2 (1 atm = 101.325 kPa). The mixture was filtered over a pad of Celite, then concentrated in vacuo. Purification by flash chromatography on silica gel (5% EtOAc in hexanes) afforded ester **19** (388 mg, 90%) as a colourless oil. $[\alpha]_D$ = –17.9° ($CHCl_3$, *c* = 0.88). IR (cm^{-1}): 1744, 1462. ^1H NMR ($CDCl_3$) δ: 3.66 (s, 3H), 3.19 (dd, 1H *J* = 8.8 and 5.5 Hz), 3.02 (t, 1H, *J* = 7.7 Hz), 2.37–2.25 (m, 2H), 1.69 (oc, 1H, *J* = 6.1 Hz), 1.62–1.42 (m, 4H), 1.37–1.18 (m, 1H), 1.17 (s, 9H), 1.16–1.06 (m, 1H), 1.02–0.90 (m, 2H), 0.87 (d, 3H, *J* = 6.6 Hz), 0.83 (d, 3H, *J* = 6.1 Hz), 0.82 (d, 3H, *J* = 6.6 Hz). LR-MS (*m/z* (relative intensity)): 271 (M^+ – Me, 5), 229 (20), 87 (100). HR-MS calcd. for $C_{16}H_{31}O_3$: 271.2273; found: 271.2265.

Aldehyde 20

To a solution of ester **19** (120 mg, 0.42 mmol) in CH_2Cl_2 (1.7 mL) was added slowly a solution of *B*-bromocatecholborane (167 mg, 0.84 mmol) in CH_2Cl_2 (2.0 mL). The reaction was stirred for 15 min, then H_2O (5 mL) was added. Stirring continued for 30 min. The aqueous layer was separated and extracted with CH_2Cl_2 3 times. The combined organic extracts were washed 3 times with a solution of satd. aq. Na_2CO_3, then dried over anhyd $MgSO_4$, filtered, and concentrated in vacuo. Purification by flash chromatography on silica gel (20% EtOAc in hexanes) afforded a primary alcohol (95 mg, 99%) as a colourless oil. $[\alpha]_D$ = –22.6° ($CHCl_3$, *c* = 1.46). IR (cm^{-1}): 3347, 1744, 1462. ^1H NMR ($CDCl_3$) δ: 3.66 (s, 3H), 3.50–3.39 (m, 2H), 2.38–2.24 (m, 2H), 1.77–1.36 (m, 6H), 1.34–1.25 (m, 1H), 1.15–0.87 (m, 3H), 0.92 (d, 3H, *J* = 6.6 Hz), 0.84 (d, 6H, *J* = 6.1 Hz). LR-MS (*m/z* (relative intensity)): 200 (M^+ – CH_2O, 20), 157 (20), 83 (100). HR-MS calcd. for $C_{12}H_{24}O_2$: 200.1776; found: 200.1782.

To a solution of this alcohol (157 mg, 0.69 mmol) in wet CH_2Cl_2 (3 mL) was added Dess–Martin's periodinane (349 mg, 0.82 mmol). The mixture was stirred for 30 min. The solution was then concentrated in vacuo, diluted with Et_2O, washed with a solution of satd. aq. $Na_2S_2O_3$, satd. aq. $NaHCO_3$, and with brine. The combined aqueous extracts were extracted with Et_2O 3 times. The combined organic extracts were dried over anhyd $MgSO_4$, filtered, and concentrated in vacuo. Purification by flash chromatography on silica gel (10% EtOAc in hexanes) afforded aldehyde **20** (113 mg, 72%) as a colourless oil. ^1H NMR ($CDCl_3$) δ: 9.59 (d, 1H, *J* = 2.2. Hz), 3.67 (s, 3H), 2.44 (dq, 1H, *J* = 7.2 and 2.8 Hz), 2.38–2.24 (m, 2H), 1.71–1.40 (m, 6H), 1.20–1.10 (m, 2H), 1.08 (d, 3H, *J* = 6.6 Hz), 0.86 (d, 3H, *J* = 6.0 Hz), 0.84 (d, 3H, *J* = 6.1 Hz). LR-MS (*m/z* (relative intensity)): 200 (M^+ – CO, 5), 197 (5), 87 (100). HR-MS calcd. for $C_{12}H_{24}O_2$: 200.1776; found: 200.1784.

Ketone 21

$[\alpha]_D$ = –14.1° ($CHCl_3$, *c* = 1.74) (lit. (4*b*) value –14.5°, CH_2Cl_2, *c* = 1.22). ^1H NMR ($CDCl_3$) δ: 3.66 (s, 3H), 2.61 (sx, 1H, *J* = 7.1 Hz), 2.40–2.23 (m, 2H), 2.13 (s, 3H), 1.66–1.39 (m, 5H), 1.15–1.02 (m, 5H), 1.07 (d, 3H, *J* = 6.6 Hz), 0.83 (d, 6H, *J* = 6.6 Hz). ^{13}C NMR ($CDCl_3$) δ: 212.9 (s), 174.4 (s), 51.4 (q), 44.7 (d), 44.1 (t), 41.1 (t), 32.7 (t), 31.8 (t), 29.6 (d), 27.9 (d), 19.5 (q), 18.8 (q), 16.9 (q). LR-MS (*m/z* (relative intensity)): 243 (MH^+, 5), 211 (20), 97 (100). HR-MS calcd. for $C_{14}H_{27}O_3$: 243.1960; found: 243.1953.

Alcohol 22

To a solution of Roush's crotyl borane (9.5 mL of a 0.51 mol L^{-1} solution in toluene, 4.81 mmol) was added 4 Å molecular sieves (60 mg). This mixture was stirred for 10 min, then cooled to –78 °C. Crude aldehyde **12** in toluene (2.5 mL) was added dropwise, then stirred for 4 h. $NaBH_4$ (40 mg, 1.05 mmol) in EtOH (1 mL) was added dropwise, then the reaction was warmed to 0 °C. NaOH (4 mL of a 2 N aqueous solution) was added and stirred for 1.5 h. The aqueous layer was separated and extracted with Et_2O 3 times. The combined organic extracts were dried over anhyd $MgSO_4$, filtered, and concentrated in vacuo. GC analysis of the crude product gave a (82:18) diastereoisomer ratio. Purification by flash chromatography on silica gel (2% EtOAc in hexanes) afforded the desired pure alcohol **22** (363 mg, 57%) as a colourless oil, and its diastereomer (88 mg, 14%) as a colourless oil. **22**: $[\alpha]_D$ = –29.3° ($CHCl_3$, *c* = 2.09). ^1H NMR ($CDCl_3$) δ: 6.01–5.89 (m, 1H), 5.07–5.02 (m, 2H), 4.37 (s, 1H), 3.49 (dd, 1H, *J* = 8.8 and 3.9 Hz), 3.37–3.31 (m, 2H), 2.37–2.31 (m, 1H), 1.89–1.77 (m, 1H), 1.20 (s, 9H), 1.10 (d, 3H, *J* = 6.6. Hz), 0.82 (d, 6H, *J* = 7.2 Hz). ^{13}C NMR ($CDCl_3$) δ: 139.9 (d), 114.7 (t), 80.8 (d), 76.5 (s), 67.7 (t), 41.1 (d), 36.2 (d), 27.2 (q), 17.8 (q), 13.5 (q). LR-MS (*m/z* (relative intensity)): 185 (M^+ – Me, 5), 145 (30), 84 (100). HR-MS calcd. for $C_{11}H_{21}O_2$: 185.1541; found: 185.1546. Minor isomer of alcohol **22**: $[\alpha]_D$ = +6.6° ($CHCl_3$, *c* = 3.72). ^1H NMR ($CDCl_3$) δ: 5.89-5.77 (m, 1H), 5.13–5.05 (m, 2H), 3.52–3.44 (m, 3H), 3.21 (d, 1H, *J* = 1.7 Hz), 2.26 (sx, 1H, *J* = 6.6 Hz), 1.90–1.80 (m, 1H), 1.18 (s, 9H), 0.97 (d, 3H, *J* = 7.2. Hz), 0.94 (d, 3H, *J* = 6.6 Hz). LR-MS (*m/z* (relative intensity)): 201 (MH^+, 100), 145 (50). HR-MS calcd. for $C_{12}H_{25}O_2$: 201.1854; found: 201.1858.

Silyl ether 23

To a solution of alcohol **22** (500 mg, 2.5 mmol) in CH_2Cl_2 (50 mL) at 0 °C was added *i*-Pr_2EtN (0.61 mL, 3.5 mmol) and TESOTf (0.68 mL, 3.0 mmol). The reaction was stirred for 30 min. The reaction was quenched by adding a satd. aq. $NaHCO_3$ solution. The aqueous layer was separated and extracted with Et_2O 3 times. The combined organic extracts were dried over anhyd $MgSO_4$, filtered, and concentrated in vacuo. Purification by flash chromatography on silica gel (2% EtOAc in hexanes) afforded the silyl ether **23** (784 mg, quantitative) as a colourless oil. $[\alpha]_D$ = +16.8° ($CHCl_3$, *c* =

© 2004 NRC Canada

1.98). ^{1}H NMR ($CDCl_3$) δ: 5.88 (ddd, 1H, *J* = 17.6, 10.4, and 8.2 Hz), 5.00–4.94 (m, 2H), 3.49–3.44 (m, 2H), 3.09 (t, 1H, *J* = 8.3. Hz), 2.43–2.31 (m, 1H), 1.84–1.71 (m, 1H), 1.16 (s, 9H), 1.02 (d, 3H, *J* = 7.2 Hz), 0.97 (t, 9H, *J* = 8.3 Hz), 0.89 (d, 3H, *J* = 6.6 Hz), 0.62 (q, 6H, *J* = 8.3 Hz). LR-MS (*m*/*z* (relative intensity)): 259 ($M^+ - C_4H_7$, 40), 229 (45), 173 (100). HR-MS calcd. for $C_{14}H_{31}O_2Si$: 259.2093; found: 259.2097.

Aldehyde 24

Through a stirred solution of silyl ether **23** (784 mg, 2.5 mmol) in CH_2Cl_2 (20 mL) and MeOH (5 mL) at –78 °C was bubbled O_3 until the appearance of a blue colour. Then argon was bubbled through the solution until the blue colour disappeared. Ph_3P (981 mg, 3.75 mmol) was added. The mixture was warmed to room temperature and stirred for 4 h. The reaction was concentrated in vacuo, then triturated twice with hexanes. The crude aldehyde was not purified further. ^{1}H NMR ($CDCl_3$) δ: 9.78 (d, 1H, *J* = 2.2 Hz), 3.95 (dd, 1H, *J* = 5.0 and 3.9 Hz), 3.38 (dd, 1H, *J* = 8.8 and 6.1 Hz), 3.17 (dd, 1H, *J* = 8.8 and 6.6 Hz), 2.63–.54 (m, 1H), 1.93 (sp, 1H, *J* = 6.1 Hz), 1.16 (s, 9H), 1.11 (d, 1H, *J* = 7.2 Hz), 0.96 (t, 9H, *J* = 7.7 Hz), 0.90 (d, 3H, *J* = 6.6 Hz), 0.62 (q, 6H, *J* = 7.7 Hz).[3]

Acknowledgements

We thank the Natural Sciences and Engineering Research Council of Canada (NSERC) and the Université de Sherbrooke for financial support.

References

1. C. Spino, C. Beaulieu, and J. Lafrenière. J. Org. Chem. **65**, 7091 (2000).
2. For a review on chiral enolate equivalents, see: C. Spino. Org. Prep. Proced. Int. **35**, 1 (2003).
3. (*a*) A.G. Myers, B.H. Yang, H. Chen, and D.J. Kopecky. Synlett, **5**, 457 1997; (*b*) J.D. White and A.T. Johnson. J. Org. Chem. **59**, 3347 (1994); (*c*) K.C. Nicolaou, E.W. Yue, S. La Greca, A. Nadin, Z. Yang, J.E. Leresche, T. Tsuri, Y. Naniwa, and F. De Riccardis. Chem. Eur. J. **1**, 467 (1995).
4. Ionomycin syntheses: (*a*) M. Lautens, J.T. Colucci, S. Hiebert, N.D. Smith, and G. Bouchain. Org. Lett. **4**, 1879 (2002); (*b*) D.A. Evans, R.L. Dow, T.L. Shih, J.M. Takacs, and R. Zahler. J. Am. Chem. Soc. **112**, 5290 (1990); (*c*) S. Hanessian, N.G. Cooke, B. DeHoff, and Y. Sakito. J. Am. Chem. Soc. **112**, 5276 (1990).
5. Ionomycin isolation and use: (*a*) C.-M. Liu and T.E. Hermann. J. Biol. Chem. **253**, 5892 (1978); (*b*) W.-C. Liu, D.S. Slusarchyk, G. Astle, W.H. Trejo, W. Brown, and X. Meyers. J. Antibiot. **31**, 815 (1978); (*c*) V. Parpura, T.A. Basrsky, F. Liu, K. Jeftinija, S. Jeftinija, and P.G. Haydon. Nature (London), **369**, 744 (1994).
6. E.J. Corey, and T.M. Eckrich. Tetrahedron. Lett. **24**, 3165 (1983).
7. R.K. Boeckman and J.C. Potenza. Tetrahedron Lett. **26**, 1411 (1985).
8. (*a*) W.R. Roush, K. Ando, D.B. Powers, A.D. Palkowitz, and R.L. Halterman. J. Am. Chem. Soc. **112**, 6339 (1990); (*b*) W.R. Roush, A.D. Palkowitz, and K. Ando. J. Am. Chem. Soc. **112**, 6348 (1990).
9. H.C. Brown, K.S. Bhat, and R.S. Randad. J. Org. Chem. **54**, 1570 (1989).

[3] Supplementary data may be purchased from the Directory of Unpublished Data, Document Delivery, CISTI, National Research Council Canada, Ottawa, ON K1A 0S2, Canada (http://www.nrc.ca/cisti/irm/unpub_e.shtml for information on ordering electronically).

© 2004 NRC Canada

Synthesis and conformations of phosphine- and phosphinite-derivatized resorcinarenes[1]

Dana J. Eisler and Richard J. Puddephatt

Abstract: The synthesis of resorcinarene derivatives with four or eight alkynyldiphenylphosphine or diphenylphosphinite functional groups is reported. The tetraphosphinite derivatives have effective C_{2v} symmetry and have the potential to adopt two different boat conformations in which the arene groups with phosphinite substituents are horizontal or vertical. A method for the determination of the solution-state conformation of the resorcinarene skeleton using correlated ^{1}H and ^{13}C NMR data is reported, and the boat conformation of one tetraphosphinite compound in the solid state has been determined crystallographically.

Key words: phosphine, phosphinite, resorcinarene, conformation.

Résumé : On a réalisé la synthèse de dérivés du résorcinarène portant quatre ou huit groupes fonctionnels alkynyldiphénylphosphine ou diphénylphosphinite. Les dérivés tétraphosphinites sont de symétrie effective C_{2v} et ils peuvent adopter deux conformations en bateau différentes dans lesquelles les groupes arènes portant les substituants phosphinites sont soit en position horizontale soit en position verticale. Faisant appel aux données de la RMN du ^{1}H et du ^{13}C, on a mis au point une méthode de déterminer la conformation en solution du squelette résorcinarène et on a fait appel à la diffraction des rayons X pour déterminer la conformation bateau d'un composé tétraphosphinite à l'état solide.

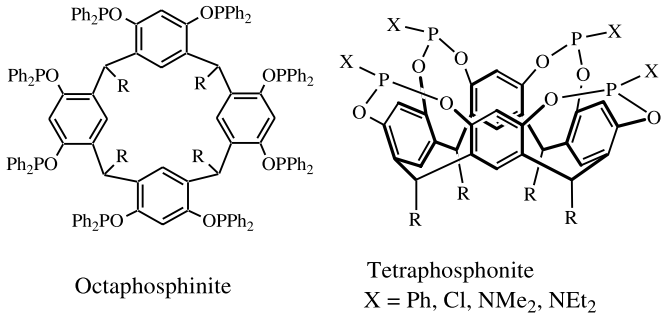
Mots clés : phosphine, phosphinite, résorcinarène, conformation.

[Traduit par la Rédaction]

Introduction

Resorcinarenes are macrocyclic octanols that provide a platform upon which multiple ligating groups can be arranged in an organized fashion (1–3). Thus, resorcinarenes can be used to arrange several metal centers in close proximity at the rim of the macrocyclic cavity, and there is then the potential for achieving size- and shape-selective catalysis and for establishing cooperativity between two or more metal centers in bond activation processes (3–5). While it is possible to bind early transition metals directly to the oxygen atoms of the resorcinol arene rings, it is better to incorporate soft donors, such as phosphorus donors, to develop the chemistry with the late transition metals (6). There are octaphosphinite and tetraphosphonite derivatives of resorcinarenes, as illustrated in Chart 1, but no octaphosphine or tetraphosphinite derivative appears to be known (7). This article reports the first examples of such compounds. They are derived from recently reported resorcinarenes in which two opposite arene rings are protected by acylation of the phenol groups (8, 9).

Chart 1.



Octaphosphinite

Tetraphosphonite
X = Ph, Cl, NMe_2, NEt_2

Results and discussion

Synthesis of octa(alkynyldiphenylphosphine) derivatives

The resorcinarene **1** (10) was converted to the octapropargyl resorcinarene (**2**) (11), and the new octa(propargyl carbonate) resorcinarene (**3**) as outlined in Scheme 1. Two new octa(alkynyldiphenylphosphine) resorcinarenes **4** and **5** were then synthesized by treatment of **2** or **3** with *n*-butyllithium followed by the addition of chlorodiphenylphosphine, as shown in Scheme 2. The alkynyldiphenylphosphine derivatives **4** and **5** are isolated as colourless solids. They are moderately air-sensitive, the decomposition being complete in hours in solution or weeks in the solid state.

Synthesis of tetra(diphenylphosphinite) derivatives

The tetraester resorcinarenes **6a**–**6e** were prepared as shown in Scheme 3, by a procedure similar to that described

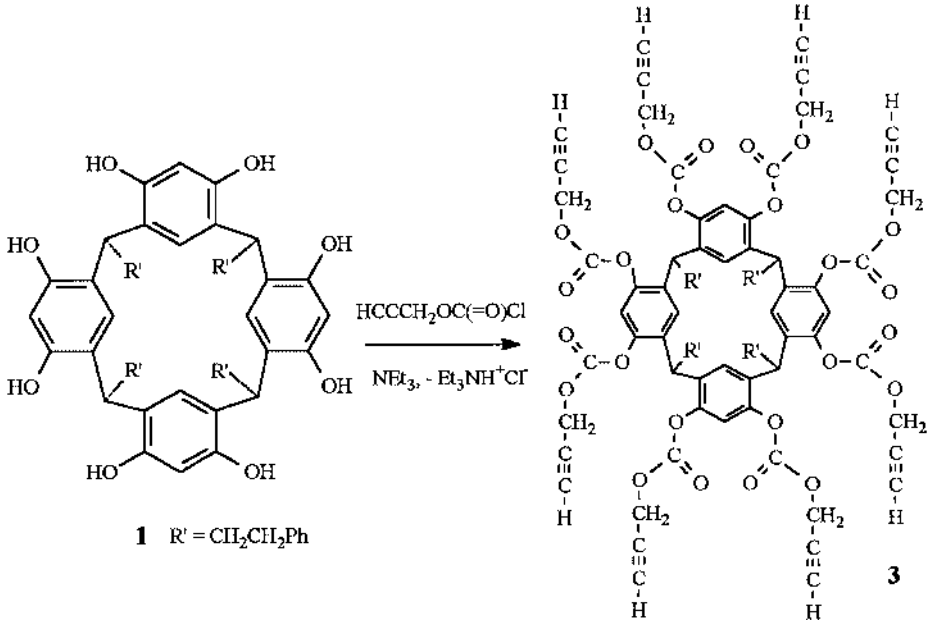
Received 4 May 2003. Published on the NRC Research Press Web site at http://canjchem.nrc.ca on 12 January 2004.

D.J. Eisler and R.J. Puddephatt.[2] Department of Chemistry, University of Western Ontario, London, ON N6A 5B7, Canada.

[1]This article is part of a Special Issue dedicated to Professor Ed Piers.
[2]Corresponding author (e-mail: pudd@uwo.ca).

 doi: 10.1139/V03-105 © 2004 NRC Canada

Scheme 1.



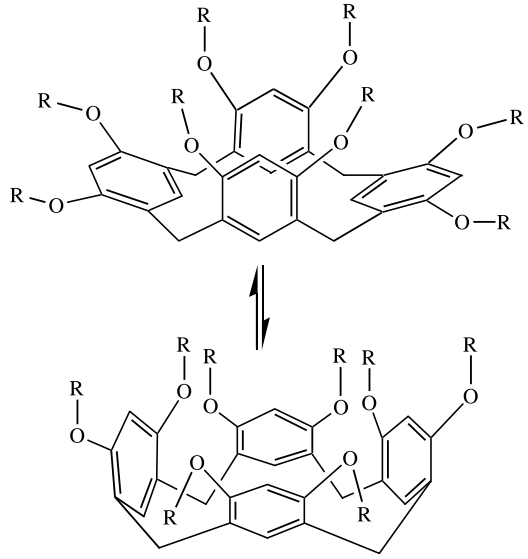
earlier for **6a** (8). The compounds **6a**–**6e** precipitate from the reaction solution with 2 equiv. of triethylammonium chloride incorporated, but pure samples, without triethylammonium chloride, were obtained by recrystallization. Further reaction of compounds **6a**–**6e** with chlorodiphenylphosphine, in the presence of triethylamine as base, gave the resorcinarenes **7a**–**7e** as outlined in Scheme 3. The new compounds **7a**–**7e** are colourless solids, which are air stable in the solid state but which decompose easily in solution on exposure to oxygen or moisture.

Characterization of the octa(alkyne) and octa(alkynyldiphenylphosphine) derivatives

The ^{1}H and ^{13}C NMR spectra of **2** and **3** at room temperature are indicative of effective C_{4v} symmetry. Thus, all propargyl groups and arene groups in resorcinarene **3** were equivalent by NMR. The methylene protons of the propargyl groups of **3** are diastereotopic, and so appeared as an AB multiplet ($J(H^aH^b)$ = 16 Hz in **3**), with further splitting by the acetylenic proton. The apparent symmetry of the NMR spectra could indicate a symmetrical bowl structure, but it is likely, based on several precedents (1, 6) that the compounds exist in a boat conformation with C_{2v} symmetry. Easy interconversion between equivalent boat conformations, each having C_{2v} symmetry, then leads to the apparent C_{4v} symmetry (eq. [1]). The NMR spectra of **3** were essentially unchanged down to –80 °C, indicating a low energy barrier to the fluxionality of eq. [1].

The ^{1}H, ^{13}C, and ^{31}P NMR spectra of the octa(diphenylphosphine) resorcinarene compounds **4** and **5** at room temperature were also consistent with C_{4v} symmetry. For example, only a single resonance was observed for each compound in the ^{31}P NMR spectrum, indicating effective equivalence of all diphenylphosphine groups. For compound **4** at –80 °C, the ^{1}H NMR spectrum resolved giving the spectrum expected for the boat conformation, with effective C_{2v} symmetry. For example, two sets of resonances were ob-

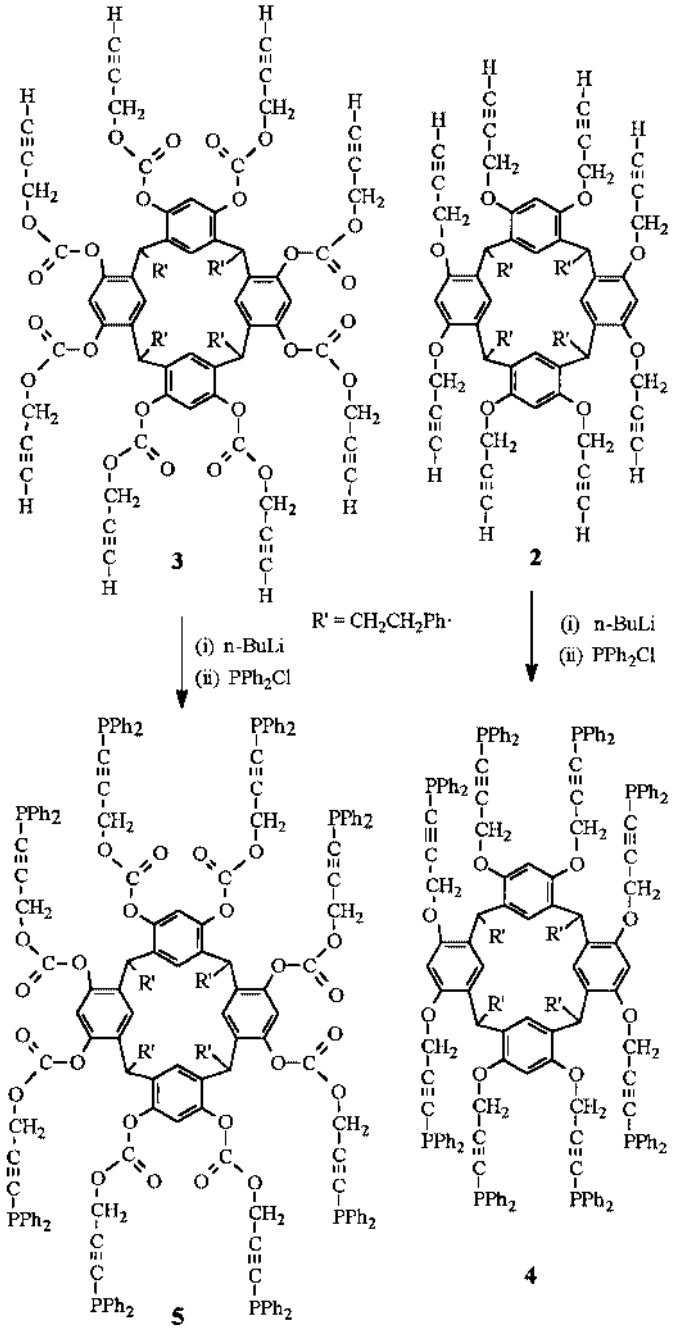
[1]



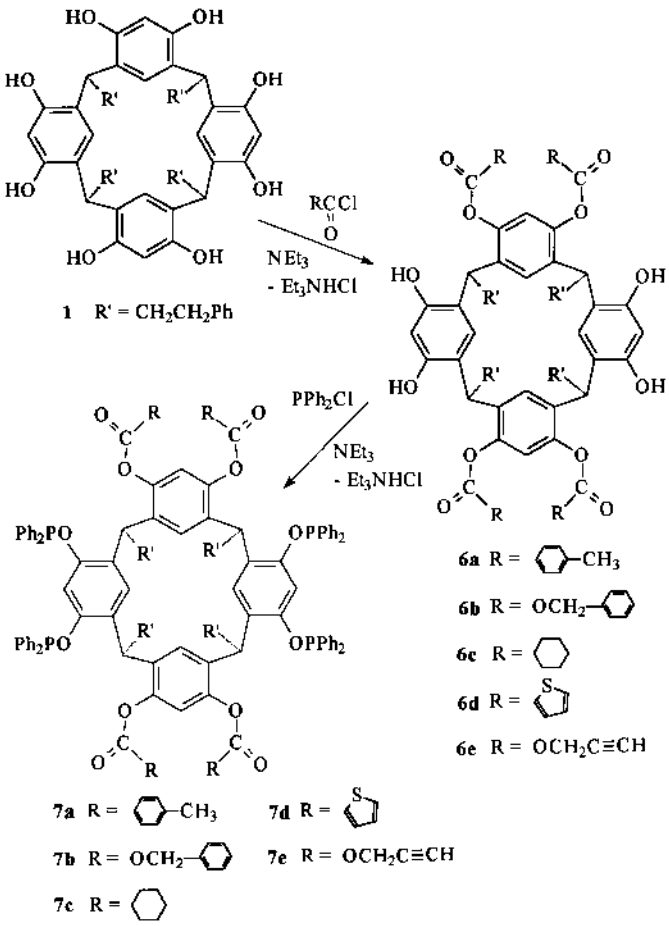
served for the methylene protons of the propargyl groups in the ^{1}H NMR spectrum at –80 °C, corresponding to substituents of the upright and flattened arene rings of the boat conformation. The resonances for each CH_2 group of the phenethyl substituents also split at –80 °C as these protons are diastereotopic in the boat conformation. The ^{31}P NMR spectrum of **4** at –80 °C resolved into two broad singlets (Fig. 1). The coalescence temperature was –50 °C for the methylene protons of the propargyl groups, giving through the Eyring equation the activation energy ΔG^* = 41(1) kJ mol^{-1} for the fluxionality according to eq. [1]. Thus, the addition of the bulky diphenylphosphine groups increases the energy barrier to the fluxionality of eq. [1] in **4** relative to the parent **2**, for which no fluxional behavior was observed (11). The ^{1}H and ^{31}P NMR spectra of compound **5** were broad at –80 °C but no splitting was observed, suggest-

© 2004 NRC Canada

Scheme 2.



Scheme 3.



ing a lower energy barrier to the fluxionality of eq. [1] in **5** compared to **4**.

Characterization of the tetra(diphenylphosphinite) derivatives

The tetra(diphenylphosphinite) derivatives **7** could exist in either boat conformation **A** or **B** (Chart 2), with the arene groups carrying the diphenylphosphinite groups in the upright or flattened positions, respectively. The structure of the tetra(benzyl carbonate) tetra(diphenylphosphinite) resorcinarene derivative **7b** in the solid state was determined crystallographically. The structure is shown in Fig. 1 and provides a benchmark for characterization of the series of tetraphosphinite derivatives. The resorcinarene skeleton of **7b** adopts a boat conformation, with the phosphinite-derivatized rings in a flattened position and the acylated rings in an upright position (conformation **B**, Chart 2). The upright resorcinol arene rings are near parallel, with the angle between the planes of the upright rings (fold angle) being 1°, while the flattened rings have a fold angle of 153°. There is little twisting distortion of the resorcinarene skeleton, as seen by the dihedral angles between opposing resorcinol arene rings of only 5° in each case. The molecule has crystallographically imposed C_2 symmetry. The boat conformation does not yield a large cavity between the upright arene rings of the resorcinarene but the four benzyl carbonate groups of **7b** extend the bowl structure, and there are two tetrahydrofuran molecules present as guest molecules in this region, as shown in Fig. 2.

The solution structures of **7** and of the precursor molecules **6** were probed by NMR spectroscopy. The ^{1}H and ^{13}C NMR spectra of the tetraester compounds **6a**–**6e** were consistent with effective C_{2v} symmetry, as described previously for **6a** (8), and the spectra remained essentially unchanged down to –80 °C. Hence, no information could be obtained about conformational switching between boat conformations (acylated rings up vs. acylated rings flattened, each having C_{2v} symmetry).

The ^{1}H, ^{13}C, and ^{31}P NMR spectra of compound **7b** will be described as an example of the series of compounds **7**.

© 2004 NRC Canada

Fig. 1. Variable temperature ^{31}P NMR spectra of the octaphosphine complex **4**, illustrating the boat to boat fluxionality.

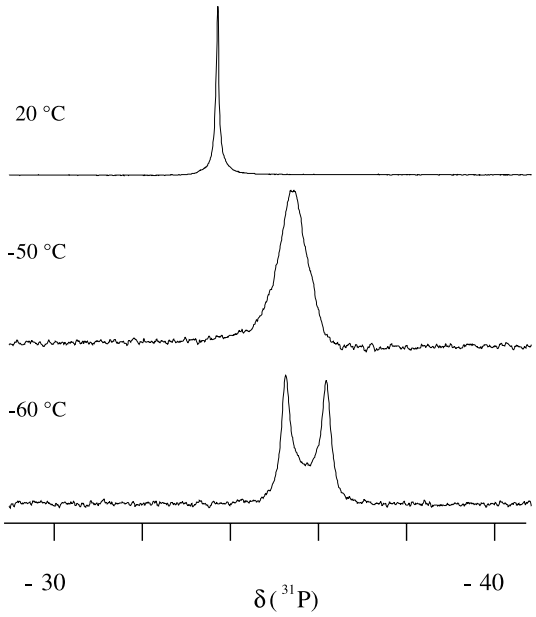
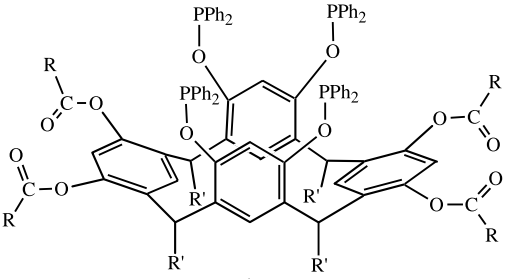
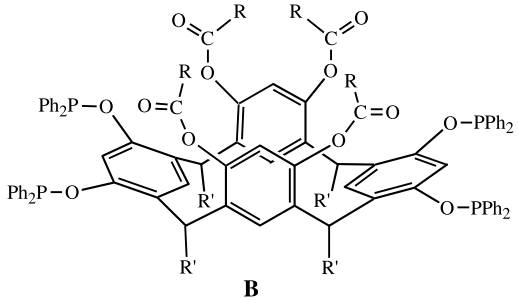


Chart 2.



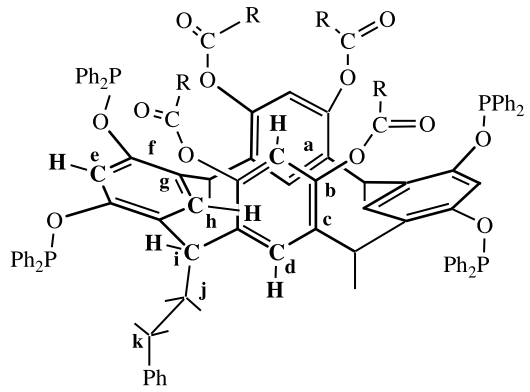
A



B

The NMR spectra at room temperature indicated effective C_{2v} symmetry. There were separate resonances for the aryl protons or carbon atoms of the acylated and phosphinite-derivatized resorcinol arene rings in the ^{1}H or ^{13}C NMR spectrum of **7b**, as expected for a single conformer with C_{2v} symmetry. A single resonance was observed in the ^{31}P NMR spectrum, as expected for C_{2v} symmetry. The low-temperature ^{1}H and ^{31}P NMR spectra of compounds **7a**–**7e** remained essentially unchanged, and so there was no evidence for fluxionality between the conformers of Chart 2. Relatively small motions are needed to convert the solid-state structure of **7b**, with C_2 symmetry, to a boat conformer with C_{2v} symmetry. However, a simple analysis of the spectra do not indicate if the same boat conformer, with the arene rings bearing the diphenylphosphinite substituents in the flattened position, is present in solution or if it can interconvert easily to the other conformer. A more detailed analysis of the 2D ^{1}H–^{13}C correlated NMR spectra (gHSQC and gHMBC) for compounds **6a**–**7e** makes it possible to establish which conformation is present in the solution state. For simplicity, the conformations will be assigned as **A**, acylated rings flattened, and **B**, acylated rings upright (Chart 2), and the assignment of conformation in solution is described below.

Chart 3.

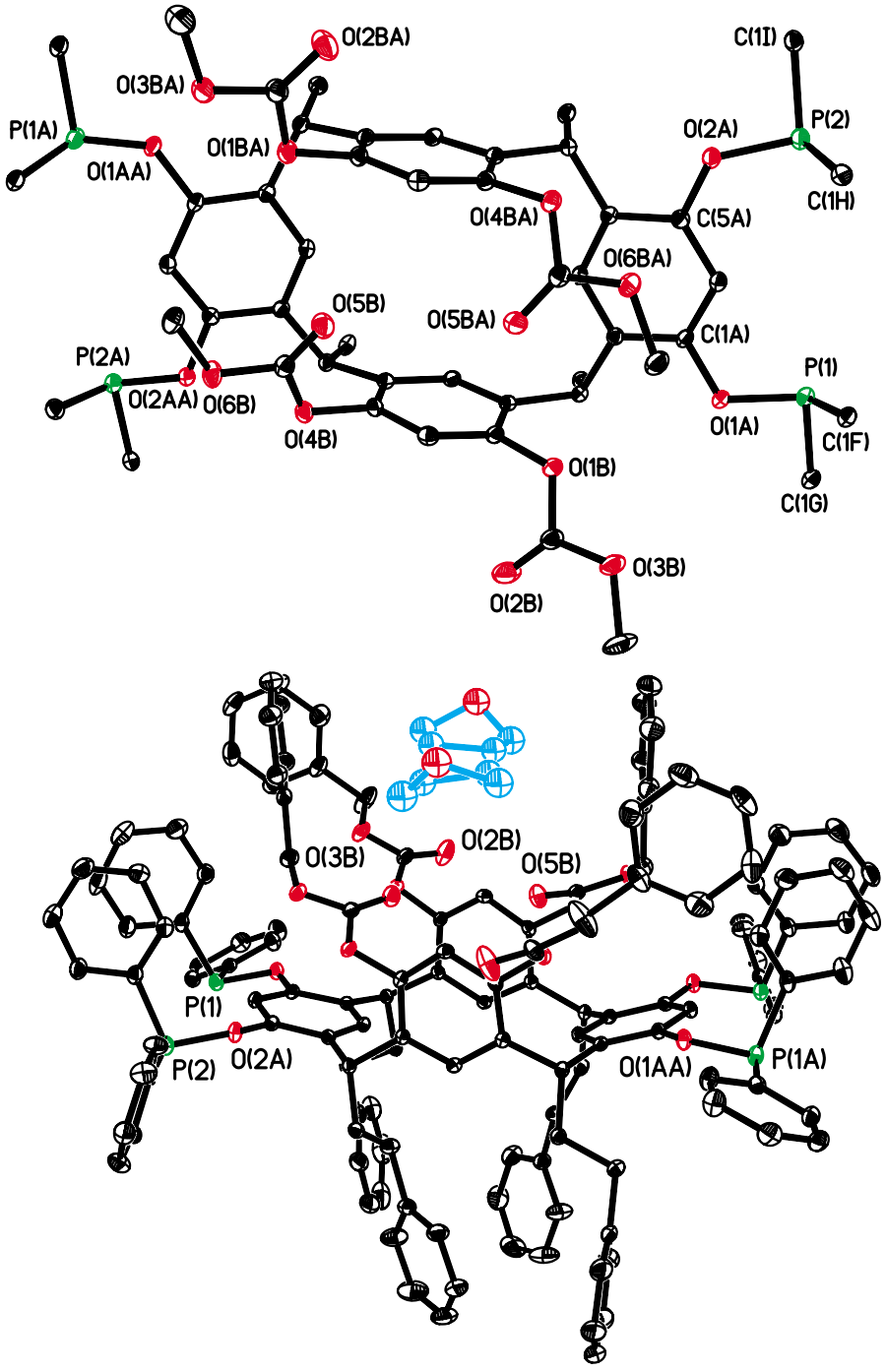


It has been established that the magnitude of the chemical shift separation of the resonances for H^{h} and H^{d} (Chart 3) can be taken as a measure of the distortion of the resorcinarene skeleton towards a boat conformation (8). Chemical shift differences of 0.3–0.6 ppm have recently been reported for a series of C_{2v} symmetrical tetraesters, which exist in a boat conformation in solution (8*b*). Furthermore, the resonance for the proton H^{h} on the flattened ring appears at higher field since it lies in the shielding zone of the upright rings (8, 12). Thus, if the resonances for H^{d} and H^{h} can be unambiguously assigned, it is possible to identify the conformation of the resorcinarene skeleton in solution.

For the series of tetraester resorcinarene compounds **6a**–**6e**, compound **6e** will serve as an example for how the skeletal atoms are assigned. The bridging methine carbon (C^{i} (Chart 3)) can be assigned from the gHSQC experiment, since the directly bonded proton H^{i} ($\delta = 4.58$) has a characteristic triplet appearance due to coupling with the two H^{j} protons. Further confirmation of the identification of this carbon atom comes from the observation of long-range couplings with H^{j} and H^{k} in the gHMBC experiment (Fig. 3). With the unambiguous assignment of C^{i} and H^{i} established, it is possible to assign the carbon atoms C^{b}, C^{c}, C^{d}, C^{f}, C^{g}, and C^{h} from the gHMBC data, as these all show long-range coupling to H^{i}. The protons H^{d} and H^{h} can be identified readily from the gHMBC experiment from the correlation with C^{i}, and the directly bonded carbon atoms C^{d} and C^{h} are then assigned from the gHSQC data. The two pairs of carbon atoms C^{b}, C^{c} and C^{f}, C^{g} were identified from their long-range couplings to H^{d} and H^{h}, respectively. The carbon atom C^{c} can be distinguished from C^{b} (and likewise, C^{g} from C^{f}) from the gHMBC data, since only C^{c} is correlated to the H^{j} protons. With the assignment of C^{b}, C^{c}, C^{f}, and C^{g} estab-

© 2004 NRC Canada

Fig. 2. Views of the structure of compound **7b**. Above: A top view, with only the ipso carbon atoms of the phenyl groups and α-carbon atoms of the phenethyl groups shown, for clarity. Below: A side view with all heavy atoms included, illustrating the position of the guest molecules of THF in the extended bowl defined by the benzyl carbonate substituents. Selected bond distances and angles: P1—O1A (1.659(1) Å), P2—O2A (1.665(2) Å), P1-O1A-C (119.6(1)°), P2-O2A-C (122.5(1)°).

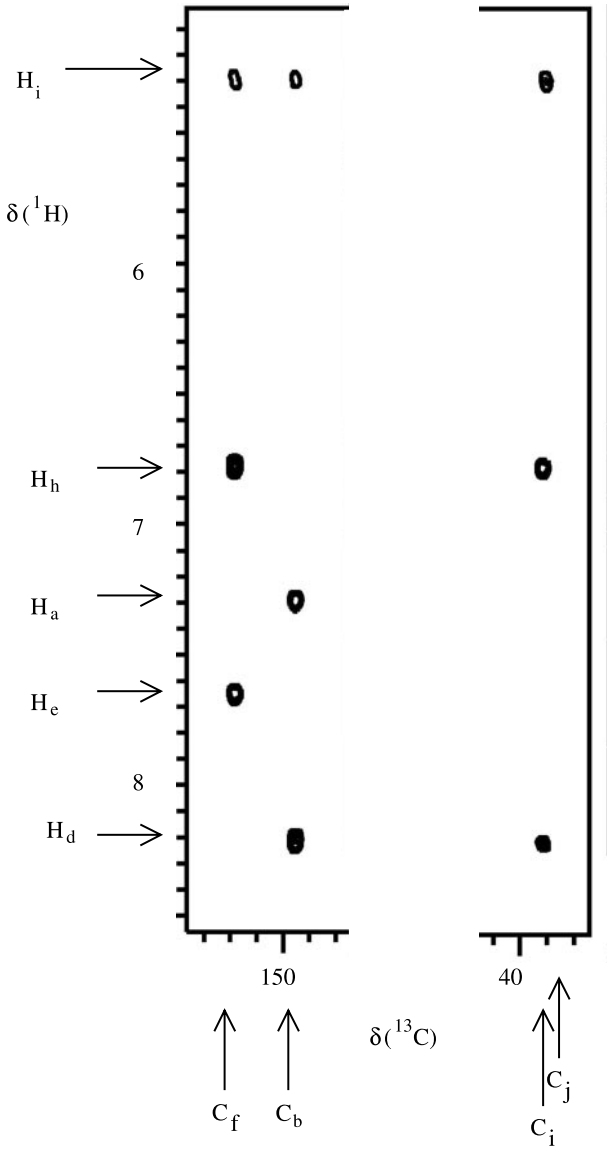


lished, it is possible to identify H^a and H^e, from long-range coupling in the gHMBC experiment. The gHSQC data then allows the assignment of C^a and C^e by correlation with H^a and H^e, thus, completing the full assignment of the resorcinarene skeletal atoms.

To determine which conformation is present in solution, it is necessary to be able to identify which ring is unsubstituted, and which ring contains the acyl substituents. This can be achieved from the observation that the addition of the acyl substituents results in a significant shift of the resonance for C^a in the ^{13}C NMR spectrum (8). In compound **1**, the resonance for C^a appears at δ = 103.44, which is slightly shifted with the addition of the propargyl groups in **3** to δ = 100.78. The addition of eight propargyl carbonate substituents in **2** however results in a shift to δ = 115.46. Final confirmation of the effect of the acyl substituents is obtained from compound **6e**, where the resonance for C^a (acylated rings) appears at δ = 115.76, whereas the resonance for C^e

© 2004 NRC Canada

Fig. 3. A section of the gHMBC ^{1}H–^{13}C correlated spectrum of compound **7c**, illustrating how the conformation is assigned. Similar spectra were obtained for all compounds **6** and **7**.



(unsubstituted) appears at δ = 103.42. Similar shifts are observed for the other tetra-acylated resorcinarene compounds **6a**–**6d**. Thus, with the identity of the rings established, comparison of the chemical shifts for the protons H^{d} and H^{h} allows the assignment of the conformation in solution. For compound **6e**, the resonance for H^{d} appears at δ = 6.94, while that for H^{h} is located at δ = 7.27 (Table 1). Hence, since H^{d} is the most shielded, this indicates that **6e** is present as conformation **A** (acylated rings in the flattened position) in solution. Similar treatment of the data for compounds **6a**–**6d** established that in each case, conformation **A** is present in solution. Conformation **A** has been established for compounds **6d** and **6e**, as the triethylammonium chloride and pyridinium chloride inclusion compounds, respectively, by preliminary X-ray structure determinations, so the preferred conformer is the same in both solution and solid states.

Table 1. ^{1}H NMR chemical shifts[a] (ppm) of skeletal ring hydrogen atoms.

Compound	a	d	e	h	Δδ (d,h)
6a	7.01	7.05	6.61	7.37	0.32
6b	6.94	7.00	6.06	7.28	0.28
6c	6.54	6.94	5.83	7.21	0.26
6d	6.88	7.17	6.11	7.30	0.13
6e	7.01	6.94	5.81	7.27	0.31
7a	7.00	7.71	6.78	6.25	1.46
7b	6.77	7.63	6.96	6.16	1.47
7c	6.63	7.52	6.99	6.11	1.41
7d	7.04	7.69	6.81	6.20	1.49
7e	6.87	7.51	6.90	6.05	1.46

[a]Not all resonances were directly observed in the ^{1}H NMR spectra, thus some chemical shifts were obtained from the 2D NMR data.

Assignment of the skeletal atoms for the tetraphosphinite compounds **7a**–**7e** is accomplished from the solution NMR data using the same technique outlined for compound **6e**. However, for the phosphinite derivatives, an additional confirmation is possible. In the carbon spectra of **7a**–**7e**, the phosphorus atoms of the diphenylphosphinite groups couple both to C^{f} and C^{e}. Hence, the resonance for C^{f} appears as a doublet, while the resonance for C^{e} appears as a multiplet, as it couples to both nearby diphenylphosphinite substituents. The skeletal carbon and hydrogen atom assignments are for **7a**–**7e** are summarized in Tables 1 and 2. In each case, it was established that, in solution, the phosphinite resorcinarene compounds adopt conformation **B** (phosphinite rings flattened), which is in accordance with the structure obtained for **7b**. The chemical shift separation of the resonances for H^{d} and H^{h} in the phosphinite derivatives is far greater than that observed for the parent tetraesters, ranging from 1.41 to 1.49 for the former compared with 0.13–0.31 in the latter (Table 1). The larger separation indicates a greater deformation towards a boat conformation in solution for the phosphinite derivatives compared to the parent tetraesters.

Conclusions

The resorcinarene compound **1** has been derivatized to give several new organophosphorus compounds. The octopus-like octa(alkynyldiphenylphosphine) compounds **4** and **5** have effective C_{4v} symmetry and have the potential to form highly metalated resorcinarene complexes. The tetra(diphenylphosphinite) derivatives **7a**–**7e** can potentially adopt two different boat conformations. If the boat conformation in which the phosphinite derivatized rings are in the upright position is adopted (**A**, Chart 1), the resorcinarene offers a platform of four coplanar phosphorus donors in relatively close proximity, suitable for forming cluster complexes. On the other hand, if the boat conformation in which the phosphinite-derivatized rings are in the flattened position is adopted (**B**, Chart 1), the overall resorcinarene architecture can be viewed as a bis(diphosphinite) ligand, with well-separated pairs of phosphorus donors. To develop this chemistry, a method for determining the preferred conformation of the tetraphosphinite compounds **7a**–**7e** in solution was needed and has been established by use of ^{1}H, ^{13}C, and ^{31}P NMR spectroscopic data.

© 2004 NRC Canada

Table 2. ^{13}C NMR chemical shifts[a] (ppm) of skeletal ring carbon atoms.

Compound	a	b	c	d	e	f	g	h
1	103.44	152.31	124.81	125.22	103.44	152.31	124.81	125.22
2	100.78	154.44	127.75	126.41	100.78	154.44	127.75	126.41
3	115.46	146.93	132.23	125.69	115.46	146.93	132.23	125.69
4	100.68	154.15	127.49	126.35	100.68	154.15	127.49	126.35
5	115.73	147.21	132.80	126.15	115.73	147.21	132.80	126.15
6a	116.05	145.56	135.56	127.11	102.97	153.70	118.88	124.16
6b	115.64	145.40	135.52	125.53	103.29	153.56	118.96	123.16
6c	115.64	145.20	134.82	127.86	103.24	153.55	118.76	123.23
6d	115.92	145.00	134.94	127.81	103.02	153.72	119.39	122.58
6e	115.76	144.89	135.71	126.12	103.42	153.79	119.82	122.30
7a	117.79	148.38	131.43	126.38	106.95(m)	153.10(d)	130.32	126.85
7b	117.66	148.36	132.32	126.69	106.23(m)	153.23(d)	129.18	127.50
7c	117.81	148.24	130.62	126.35	106.68(m)	152.85(d)	130.0	127.08
7d	117.76	148.02	131.85	126.62	106.86(m)	153.15(d)	130.29	126.89
7e	117.05	147.86	132.20	125.20	105.78(m)	153.10(d)	128.81	127.33

[a]Not all resonances were directly observed in the ^{13}C NMR spectra, thus some chemical shifts were obtained from the 2D NMR data.

Table 3. Crystallographic experimental details for **7b**·2THF.

Formula	$C_{140}H_{116}O_{16}P_4{\cdot}2(C_4H_8O)$
Formula weight	2322.42
Temperature (K)	200(2)
Wavelength (Å)	0.71073
Crystal size (mm)	0.38 × 0.35 × 0.30
Crystal system	Monoclinic
Space group	*C*2/*c*
a (Å)	35.2976(2)
b (Å)	16.8581(2)
c (Å)	25.4416(3)
β (°)	126.978(1)
Volume (Å^3)	12094.1(2)
Z	4
D_{calcd} (Mg/m^3)	1.275
Absorption coefficient (mm^{-1})	0.133
θ range (°)	1.96–27.48
Reflections collected	66 953
Independent reflections	13 863 (R_{int} = 0.059)
Completeness to θ (%)	99.9
Data / restraints / parameters	13 863 / 30 / 766
Goodness of fit on F^2	1.056
Final *R* indicies [I > 2σ(I)]	R_1 = 0.0557, wR_2 = 0.1364
R indices (all data)	R_1 = 0.1120, wR_2 = 0.1587
Largest diff. peak and hole	0.763 and -0.405

Experimental

The reactions, except for the preparation of the tetraester and octaester compounds, were carried out under a nitrogen atmosphere using standard Schlenk techniques. NMR and IR spectra were recorded using a Varian Inova 400 NMR or a Varian Mercury 400 NMR and a Perkin-Elmer FT-IR 2000 spectrometer, respectively. The resorcinarene compounds **1** (10), **2** (11), and **6a** (8) were prepared by literature methods. In the NMR assignments for compounds **6a**–**7e**, the skeletal carbon resonances are grouped according to the substituents on the resorcinol arene rings as follows: (Unsub.) = unsubstituted ring, (Acyl) = acylated ring, and (Phos.) = phosphinite-derivatized ring. The corresponding aryl protons are treated in a similar fashion.

Resorcinarene(OC(O)OCH$_2$C≡CH)$_8$ (3)

A solution of **1** (4.5 g, 4.97 mmol) in CH_2Cl_2 (20 mL) was treated with triethylamine (6.2 mL, 44.5 mmol) resulting in the immediate formation of a pink slurry. The mixture was stirred for 10 min and propargyl chloroformate (5.0 mL, 49.2 mmol) was added in 1.0 mL portions at 3 min intervals. The solution was stirred for 10 min, extracted with two 30 mL portions of water, and dried over $MgSO_4$. The solution was filtered and the product recrystallized from CH_2Cl_2–MeOH. White solid, mp 146–148 °C. Yield: 3.05 g, 39%. FT-IR (cm^{-1}): 2133 ν(C≡C). ^1H NMR ($CDCl_3$) δ: 2.19 (m, 8H, CHC*H*$_2$CH$_2$Ph), 2.53 (t, 8H, $^4J_{HH}$ = 2 Hz, OC(O)OCH$_2$C≡C*H*), 2.60 (m, 8H, CHCH$_2$C*H*$_2$Ph), 4.49 (t, 4H, $^3J_{HH}$ = 8 Hz, C*H*CH$_2$CH$_2$Ph), 4.74 (m, 16H, $^2J_{HH}$ = 16 Hz, $^4J_{HH}$ = 2 Hz, OC(O)OC*H*$_2$C≡CH), 6.85 (s, 4H, Ar-*H*, meta to O), 7.21 (s, 4H, Ar-*H*, ortho to O), 7.03, 7.15 (m, 20H, Ar-*H*, *Ph*). ^{13}C NMR δ: 33.96 (CHCH$_2$*C*H$_2$Ph), 36.05 (*C*HCH$_2$CH$_2$Ph), 36.80 (CH*C*H$_2$CH$_2$Ph), 56.04 (OC(O)O*C*H$_2$C≡CH), 76.10, 76.73 (OC(O)OCH$_2$*C*≡*C*H), 115.46 (Ar-*C*H, ortho to O), 125.69 (Ar-*C*H, meta to O), 125.79, 128.16, 128.30 (Ar-*C*, *Ph*), 132.23 (Ar-*C*C), 141.10 (ipso-*C*, *Ph*), 146.93 (Ar-*C*O), 151.81 (O*C*(O)OCH$_2$C≡CH). Anal. calcd. for $C_{92}H_{72}O_{24}$ (%): C 70.76, H 4.65; found: C 71.18, H 5.03.

Resorcinarene(OC(O)OCH$_2$C≡CPPh$_2$)$_8$ (5)

A solution of **3** (2.0 g, 1.28 mmol) in ether (140 mL) was cooled to –40 °C. To this was added a cold (–40 °C) solution of *n*-butyllithium (6.6 mL, 10.6 mmol) in ether (10 mL) via cannula over several min. The mixture was stirred for 1 h and a cold solution (–40 °C) of PPh_2Cl (2.0 mL, 10.6 mmol) in THF (15 mL) was added via cannula over 10 min. The mixture was then slowly warmed to room temperature and allowed to stir for 1.5 h. The solvent was removed under vacuum and the residue dissolved in CH_2Cl_2 (30 mL). The solution was filtered and a dark brown oil was precipitated

© 2004 NRC Canada

with pentane. The oil was washed with pentane (50 mL), redissolved in CH_2Cl_2, and precipitated with pentane followed by several washings with pentane (3 × 20 mL). The oil was dried under vacuum and a light brown solid was obtained: mp 71–73 °C. Yield: 2.38 g, 61%. FT-IR (cm^{-1}): 2194 ν(C≡C). ^{1}H NMR (CD_2Cl_2) δ: 2.26 (m, 8H, CHCH_2CH$_2$Ph), 2.58 (m, 8H, CHCH$_2$CH_2Ph), 4.49 (t, 4H, $^3J_{HH}$ = 8 Hz, CHCH$_2$CH$_2$Ph), 4.90 (m, 16H, $^2J_{HH}$ = 16 Hz, OC(O)OCH_2C≡CPPh$_2$), 6.97–7.59 (m, 108H, Ar-*H*, meta to O, *Ph*). ^{13}C NMR δ: 34.13 (CHCH$_2$*C*H$_2$Ph), 36.19 (*C*HCH$_2$CH$_2$Ph), 37.30 (CH*C*H$_2$CH$_2$Ph), 57.42 (O*C*H$_2$C≡CPPh$_2$), 85.84 (d, $^2J_{PC}$ = 13 Hz, OC(O)OCH$_2$*C*≡CPPh$_2$), 101.40 (OC(O)OCH$_2$C≡*C*PPh$_2$), 115.73 (Ar-*C*H ortho to O), 126.17 (Ar-*C*H meta to O), 125.91, 128.33–132.69 (Ar-*C*, *Ph*), 132.80 (Ar-*C*C), 135.26 (m, ipso-*C*, P*Ph*$_2$), 141.42 (ipso-*C*, *Ph*), 147.21 (Ar-*C*O), 152.10 (O*C*(O)OCH$_2$C≡CPPh$_2$).^{31}P NMR δ: –33.70 (s). Anal. calcd. for $C_{188}H_{144}O_{24}P_8$**:** C 74.40, H 4.78; found: C 73.80, H 4.95%.

Resorcinarene(OCH$_2$C≡CPPh$_2$)$_8$ (4)

This was prepared similarly from **2** (1.50 g, 1.24 mmol), *n*-butyllithium (6.60 mL, 10.6 mmol) and PPh$_2$Cl (2.00 mL, 10.6 mmol). Beige solid, mp 103–105 °C. Yield: 1.88 g, 73%. ^{1}H NMR (CD_2Cl_2) δ: 2.27 (m, 8H, CHCH_2CH$_2$Ph), 2.67 (m, 8H, CHCH$_2$CH_2Ph), 4.36 (m, 16H, $^2J_{HH}$ = 16 Hz, OCH_2C≡CPPh$_2$), 4.84 (t, 4H, $^3J_{HH}$ = 8 Hz, CHCH$_2$CH$_2$Ph), 6.62 (s, 4H, Ar-*H*, ortho to O), 7.05–7.60 (m, 104H, Ar-*H*, meta to O, *Ph*). ^{13}C NMR δ: 34.61 (CHCH$_2$*C*H$_2$Ph), 35.09 (*C*HCH$_2$CH$_2$Ph), 38.19 (CH*C*H$_2$CH$_2$Ph), 57.86 (O*C*H$_2$C≡CPPh$_2$), 84.28 (d, $^2J_{PC}$ = 11 Hz, OCH$_2$*C*≡CPPh$_2$), 100.68 (Ar-*C*H ortho to O), 104.55 (OCH$_2$C≡*C*PPh$_2$), 126.35 (Ar-*C*H meta to O), 127.49 (Ar-*C*C), 128.36–129.40 (Ar-*C*, *Ph*), 132.66 (m, Ar-*C*, P*Ph*$_2$), 135.91 (m, ipso-*C*, P*Ph*$_2$), 143.03 (ipso-*C*, *Ph*), 154.15 (Ar-*C*O). ^{31}P NMR δ: –33.73 (s). FT-IR (cm^{-1}): 2197 ν(C≡C). ^{1}H NMR (CD_2Cl_2, –80 °C) δ: 2.14, 2.18, 2.42, 2.69 (m, 16H, CHCH_2CH_2Ph), 3.73, 4.87 (m, 16H, OCH_2C≡CPPh$_2$), 4.71 (s, br, 4H, CHCH$_2$CH$_2$Ph), 5.78, 6.57 (s, 4H, Ar-*H*, ortho to O), 7.05–7.60 (m, 104H, Ar-*H*, meta to O, *Ph*). ^{31}P NMR δ: –35.65, –36.78 (s). Anal. calcd. for $C_{180}H_{144}O_8P_8$ (%): C 80.58, H 5.41; found: C 80.03, H 5.68.

Resorcinarene(OC(O)OCH$_2$Ph)$_4$(OH)$_4$ (6b)

A suspension of **1** (4.5 g, 4.97 mmol) in acetonitrile (70 mL) to which triethylamine (2.8 mL, 20.1 mmol) was added was stirred rapidly for 15 min, forming a pink slurry. To this was added benzyl chloroformate (3.0 mL, 20.0 mmol) in one portion with continued rapid stirring. The solution became homogenous with a white precipitate forming within 1 min. The solution was stirred for 16 h, filtered, and the white solid washed with acetonitrile (10 mL) and methanol (25 mL). The resulting product was complexed with 2 equiv. of NEt$_3$HCl. Pure samples of **6b** were obtained by recrystallization from CH_2Cl_2–MeOH; mp 101–103 °C. Yield: 3.21 g, 45%. ^{1}H NMR ($CDCl_3$) δ: 2.18, 2.34 (m, 8H, CHCH_2CH$_2$Ph), 2.37, 2.66 (m, 8H, CHCH$_2$CH_2Ph), 4.63 (t, 4H, $^3J_{HH}$ = 8 Hz, CHCH$_2$CH$_2$Ph), 5.08 (m, 8H, $^2J_{HH}$ = 12 Hz, OC(O)OCH_2Ph), 7.02–7.34 [m, 42H, Ar-*H*, *Ph*); Unsub.: 6.06 (s, 2H, Ar-*H*, ortho to O); Acyl: 6.94 (s, 2H, Ar-*H*, ortho to O), 7.00 (s, 2H, Ar-*H*, meta to O). ^{13}C NMR δ: 34.25 (*C*HCH$_2$CH$_2$Ph), 34.31 (CHCH$_2$*C*H$_2$Ph), 38.26 (CH*C*H$_2$CH$_2$Ph), 70.91 (OC(O)O*C*H$_2$Ph), 127.70–128.51 (Ar-*C*, *Ph*), 134.27 (ipso-*C*, OC(O)OCH$_2$*Ph*), 141.87 (ipso-*C*, CHCH$_2$CH$_2$*Ph*), 153.66 (O*C*(O)OCH$_2$Ph); Unsub.: 103.29 (Ar-*C*H, ortho to O), 118.96 (Ar-*C*C), 123.16 (Ar-*C*H, meta to O), 153.56 (Ar-*C*O); Acyl: 115.64 (Ar-*C*H, ortho to O), 125.53 (Ar-*C*H, meta to O), 135.52 (Ar-*C*C), 145.40 (Ar-*C*O). Anal. calcd. for $C_{92}H_{80}O_{16}$ (%): C 76.65, H 5.59; found: C 76.29, H 5.51.

Resorcinarene(OC(O)C$_6$H$_{11}$)$_4$(OH)$_4$ (6c)

This was prepared similarly from **1** (4.5 g, 4.97 mmol), triethylamine (2.8 mL, 20.1 mmol), and cyclohexanecarbonyl chloride (2.71 mL, 19.9 mmol). White solid. Yield: 2.42 g, 36%. ^{1}H NMR ($CDCl_3$) δ: 1.26–2.19 (m, 44H, CHCH_2CH$_2$Ph, C$_6H_{11}$), 2.33 (m, 4H, CHCH_2CH$_2$Ph), 2.48 (m, 8H, CHCH$_2$CH_2Ph, C$_6H_{11}$), 2.67 (m, 4H, CHCH$_2$CH_2Ph), 4.45 (t, 4H, $^3J_{HH}$ = 8 Hz, CHCH$_2$CH$_2$Ph), 6.44 (s, 4H, O*H*), 6.98 – 7.20 (m, 22H, *Ph*, Ar-*H*; Unsub.: 5.83 (s, 2H, Ar-*H*, ortho to O); Acyl: 6.54 (s, 2H, Ar-*H*, ortho to O), 6.94 (s, 2H, Ar-*H*, meta to O). ^{13}C NMR δ: 25.52, 25.77, 25.85, 28.70, 29.45, 44.10 (*C*$_6$H$_{11}$), 33.75 (*C*HCH$_2$CH$_2$Ph), 34.30 (CHCH$_2$*C*H$_2$Ph), 38.39 (CH*C*H$_2$CH$_2$Ph), 125.45, 128.12, 128.43 (Ar-*C*, *Ph*), 142.15 (ipso-*C*, *Ph*), 175.07 (*C*=O); Unsub.: 103.24 (Ar-*C*H, ortho to O), 118.76 (Ar-*C*C), 123.23 (Ar-*C*H, meta to O), 153.55 (Ar-*C*O); Acyl: 115.64 (Ar-*C*H, ortho to O), 127.86 (Ar-*C*H, meta to O), 134.82 (Ar-*C*C), 145.20 (Ar-*C*O). Anal. calcd. for $C_{88}H_{96}O_{12}$ (%): C 78.54, H 7.19; found: C 78.05, H 7.75.

Resorcinarene(OC(O)C$_4$H$_3$S)$_4$(OH)$_4$ (6d)

This was prepared similarly from **1** (4.5 g, 4.97 mmol), triethylamine (2.8 mL, 20.1 mmol), and 2-thiophenecarbonyl chloride (2.19 mL, 19.9 mmol). White solid. Yield: 2.54 g, 38%. ^{1}H NMR ($CDCl_3$) δ: 2.31, 2.38 (m, 8H, CHCH_2CH$_2$Ph), 2.49, 2.76 (m, 8H, CHCH$_2$CH_2Ph), 4.79 (t, 4H, $^3J_{HH}$ = 8 Hz, CHCH$_2$CH$_2$Ph), 6.66 (s, 4H, O*H*), 6.91–7.20 (m, 26H, *Ph*, Ar-*H*, C$_4H_3$S), 7.51 (m, 8H, C$_4H_3$S); Unsub.: 6.11 (s, 2H, Ar-*H*, ortho to O), 7.30 (s, 2H, Ar-*H*, meta to O); Acyl: 6.88 (s, 2H, Ar-*H*, ortho to O). ^{13}C NMR δ: 34.20 (*C*HCH$_2$CH$_2$Ph), 34.67 (CHCH$_2$*C*H$_2$Ph), 38.52 (CH*C*H$_2$CH$_2$Ph), 125.46, 128.24, 128.44, 132.76, 132.97, 134.41 (Ar-*C*, *Ph*, *C*$_4$H$_3$S), 142.38 (ipso-*C*, *Ph*), 161.40 (*C*=O). Unsub.: 103.02 (Ar-*C*H, ortho to O), 119.39 (Ar-*C*C), 122.58 (Ar-*C*H, meta to O), 153.72 (Ar-*C*O); Acyl: 115.92 (Ar-*C*H, ortho to O), 127.81 (Ar-*C*H, meta to O), 134.94 (Ar-*C*C), 145.00 (Ar-*C*O). Anal. calcd. for $C_{80}H_{64}O_{12}S_4$ (%): C 71.41, H 4.79; found: C 70.96, H 4.76.

Resorcinarene(OC(O)OCH$_2$C≡CH)$_4$(OH)$_4$ (6e)

This was prepared similarly from **1** (4.5 g, 4.97 mmol), triethylamine (2.8 mL, 20.1 mmol), and propargyl chloroformate (2.02 mL, 19.9 mmol). White solid. Yield: 1.82 g, 30%. ^{1}H NMR ($CDCl_3$) δ: 2.21, 2.34 (m, 8H, CHCH_2CH$_2$Ph), 2.44, 2.64 (m, 8H, CHCH$_2$CH_2Ph), 2.66 (t, 4H, $^4J_{HH}$ = 2 Hz, OC(O)OCH$_2$C≡C*H*), 4.58)(t, 4H, $^3J_{HH}$ = 8 Hz, CHCH$_2$CH$_2$Ph), 4.81 (m, 8H, $^2J_{HH}$ = 16 Hz, $^4J_{HH}$ = 2 Hz, OC(O)OCH_2C≡CH), 6.40 (s, 4H, O*H*), 7.07–7.22 (m, 22H, Ar-*H*, *Ph*); Unsub.: 5.81 (s, 2H, Ar-*H*, ortho to O); Acyl: 6.94 (s, 2H, Ar-*H*, meta to O), 7.01 (s, 2H, Ar-*H*, ortho to O). ^{13}C NMR δ: 33.59 (*C*HCH$_2$CH$_2$Ph), 34.10 (CHCH$_2$*C*H$_2$Ph), 37.88 (CH*C*H$_2$CH$_2$Ph), 57.14

© 2004 NRC Canada

(OC(O)O*C*H_2C≡CH), 78.12, 80.04 (OC(O)OCH$_2$*C*≡*C*H), 128.02, 128.11 (Ar-*C*, *Ph*), 142.02 (ipso-*C*, *Ph*), 152.18 (O*C*(O)OCH$_2$C≡CH); Unsub.: 103.42 (Ar-*C*H, ortho to O), 119.82 (Ar-*C*C), 122.30 (Ar-*C*H, meta to O), 153.79 (Ar-*C*O); Acyl: 115.76 (Ar-*C*H, ortho to O), 126.12 (Ar-*C*H, meta to O), 135.71 (Ar-*C*C), 144.89 (Ar-*C*O). Anal. calcd. for $C_{76}H_{64}O_{16}$ (%): C 74.01, H 5.23; found: C 73.83, H 5.49.

Resorcinarene(OC(O)C$_6$H$_4$CH$_3$)$_4$(OPPh$_2$)$_4$ (7a)

A solution of **6a** (1.0 g, 0.726 mmol) in THF (50 mL) was cooled to –40 °C and triethylamine (0.51 mL, 3.66 mmol) was added and the mixture was stirred for 15 min. Chlorodiphenylphosphine (0.69 mL, 3.65 mmol) in THF (15 mL) was added over several minutes via cannula. The reaction mixture was allowed to warm slowly to room temperature and stirred for an additional 2 h. The solution was filtered, and the solvent removed under vacuum. The oily residue was washed with methanol (30 mL) resulting in the formation of a white solid, which was washed with ether (50 mL), collected, and dried: mp 150–152 °C. Yield: 1.2 g, 78%. ^{1}H NMR (CD_2Cl_2) δ: 2.08 (m, 4H, CHC*H*$_2$CH$_2$Ph), 2.34 (m, 8H, CHC*H*$_2$C*H*$_2$Ph), 2.40, (s, 12H, OC(O)C$_6$H$_4$C*H*$_3$), 2.66 (m, 4H, CHCH$_2$C*H*$_2$Ph), 4.75 (m, 4H, C*H*CH$_2$CH$_2$Ph), 6.77–7.69 (m, 82H, Ar-*H*, *Ph*, OC(O)C$_6$*H*$_4$CH$_3$); Phos.: 6.25 (s, 2H, Ar-*H*, meta to O). ^{13}C NMR δ: 21.81 (C$_6$H$_4$*C*H$_3$), 34.78 (CHCH$_2$*C*H$_2$Ph), 37.14 (CH*C*H$_2$CH$_2$Ph), 37.91 (*C*HCH$_2$CH$_2$Ph), 125.67, 128.29–130.85 (Ar-*C*, *Ph*), 141.20 (d, $^1J_{PC}$ = 18 Hz, ipso-*C*, P*Ph*$_2$), 164.35 (*C*=O); Phos.: 106.95 (m, Ar-*C*H, ortho to O), 126.85 (Ar-*C*H, meta to O), 130.32 (Ar-*C*C), 153.10 (d, $^2J_{PC}$ = 10 Hz, Ar-*C*O); Acyl: 117.79 (Ar-*C*H, ortho to O), 126.38 (Ar-*C*H, meta to O), 131.43 (Ar-*C*C), 148.38 (Ar-*C*O). ^{31}P NMR δ: 109.64 (s). Anal. calcd. for $C_{140}H_{116}O_{12}P_4$ (%): C 79.53, H 5.53; found: C 79.41, H 5.91.

Resorcinarene(OC(O)OCH$_2$Ph)$_4$(OPPh$_2$)$_4$ (7b)

This was prepared similarly from **6b** (1.0 g, 0.694 mmol), triethylamine (0.48 mL, 3.47 mmol), and chlorodiphenylphosphine (0.66 mL, 3.47 mmol). White solid, mp 133–135 °C. Yield: 1.0 g, 66%. ^{1}H NMR (CD_2Cl_2) δ: 2.06, 2.27 (m, 8H, CHC*H*$_2$CH$_2$Ph), 2.38, 2.60 (m, 8H, CHCH$_2$C*H*$_2$Ph), 4.79 (t, 4H, $^3J_{HH}$ = 8 Hz, C*H*CH$_2$CH$_2$Ph), 4.80 (m, 8H, $^2J_{HH}$ = 12 Hz, OC(O)OC*H*$_2$Ph), 6.90–7.62 (m, 84H, Ar-*H*, *Ph*); Phos.: 6.16 (s, 2H, Ar-*H*, meta to O); Acyl: 6.77 (s, 2H, Ar-*H*, ortho to O). ^{13}C NMR δ: 34.46 (CHCH$_2$*C*H$_2$Ph), 36.68 (*C*HCH$_2$CH$_2$Ph), 37.93 (CH*C*H$_2$CH$_2$Ph), 70.10 (OC(O)O*C*H$_2$Ph), 125.50, 125.79, 128.34–131.10 (Ar-*C*, *Ph*), 135.38 (ipso-*C*, OCH$_2$*Ph*), 141.42 (d, $^1J_{PC}$ = 19 Hz, ipso-*C*, P*Ph*$_2$), 142.50 (ipso-*C*, CH$_2$CH$_2$*Ph*), 153.03 (O*C*(O)OCH$_2$Ph); Phos.: 106.23 (m, Ar-*C*H, ortho to O), 127.50 (Ar-*C*H, meta to O), 129.18 (Ar-*C*C), 153.23 (d, $^2J_{PC}$ = 10 Hz, Ar-*C*O); Acyl: 117.66 (Ar-*C*H, ortho to O), 125.50 (Ar-*C*H, meta to O), 132.32 (Ar-*C*C), 148.35 (Ar-*C*O). ^{31}P NMR δ: 109.69 (s). Anal. calcd. for $C_{140}H_{116}O_{16}P_4$ (%): C 77.19, H 5.37; found: C 76.84, H 5.76.

Resorcinarene(OC(O)C$_6$H$_{11}$)$_4$(OPPh$_2$)$_4$ (7c)

This was prepared similarly from **6c** (1.0 g, 0.743 mmol), triethylamine (0.52 mL, 3.73 mmol), and chlorodiphenylphosphine (0.70 mL, 3.70 mmol). White solid, mp 220–222 °C. Yield: 1.18 g, 76%. ^{1}H NMR (CD_2Cl_2) δ: 1.10–1.80 (m, 40H, C$_6$*H*$_{11}$), 2.11 (m, 4H, CHC*H*$_2$CH$_2$Ph), 2.27 (m, 12H, CHC*H*$_2$C*H*$_2$Ph, C$_6$*H*$_{11}$), 2.58 (m, 4H, CHCH$_2$C*H*$_2$Ph), 4.62 (m, 4H, C*H*CH$_2$CH$_2$Ph), 6.79–7.64 (m, 64H, Ar-*H*, *Ph*); Phos.: 6.11 (s, 2H, Ar-*H*, meta to O); Acyl: 6.63 (s, 2H, Ar-*H*, ortho to O). ^{13}C NMR δ: 25.85, 26.12, 29.09, 29.27, 42.97 (*C*$_6$H$_{11}$), 34.85 (CHCH$_2$*C*H$_2$Ph), 37.47 (CH*C*H$_2$CH$_2$Ph), 37.70 (*C*HCH$_2$CH$_2$Ph), 125.62, 128.21–131.07 ((Phos.) Ar-*C*C, Ar-*C*, *Ph*), 141.09 (m, ipso-*C*, P*Ph*$_2$), 142.25 (ipso-*C*, *Ph*), 173.39 (*C*=O); Phos.: 106.68 (m, Ar-*C*H, ortho to O), 127.08 (Ar-*C*H, meta to O), 152.84 (d, $^2J_{PC}$ = 10 Hz, Ar-*C*O); Acyl: 117.81 (Ar-*C*H, ortho to O), 126.35 (Ar-*C*H, meta to O), 130.62 (Ar-*C*C), 148.24 (Ar-*C*O). ^{31}P NMR δ: 110.46 (s). Anal. calcd. for $C_{136}H_{132}O_{12}P_4$ (%): C 78.44, H 6.39; found: C 78.36, H 6.62.

Resorcinarene(OC(O)C$_4$H$_3$S)$_4$(OPPh$_2$)$_4$ (7d)

This was prepared similarly from **6d** (1.0 g, 0.743 mmol), triethylamine (0.52 mL, 3.72 mmol), and chlorodiphenylphosphine (0.70 mL, 3.72 mmol). White solid, mp 249–251 °C. Yield: 1.25 g, 81%. ^{1}H NMR (CD_2Cl_2) δ: 2.10 (m, 4H, CHC*H*$_2$CH$_2$Ph), 2.34 (m, 8H, CHC*H*$_2$C*H*$_2$Ph), 2.68 (m, 4H, CHCH$_2$C*H*$_2$Ph), 4.77 (t, 4H, $^3J_{HH}$ = 8 Hz C*H*CH$_2$CH$_2$Ph), 6.20 (s, 2H, Ar-*H*), 6.80–7.61 (m, 76H, *Ph*, Ar-*H*, C$_4$*H*$_3$S); Phos.: 6.20 (s, 2H, Ar-*H*, meta to O); Acyl: 7.69 (s, 2H, Ar-*H*, meta to O). ^{13}C NMR δ: 34.79 (CHCH$_2$*C*H$_2$Ph), 37.20 (CH*C*H$_2$CH$_2$Ph), 37.86 (*C*HCH$_2$CH$_2$Ph), 125.81, 128.29–130.11, 130.81, 131.04, 133.07, 135.01 (Ar-*C*, *Ph*, *C*$_4$H$_3$S), 141.29 (m, ipso-*C*, P*Ph*$_2$), 142.42 (ipso-*C*, *Ph*), 159.92 (*C*=O); Phos.: 106.86 (m, Ar-*C*H, ortho to O), 126.89 (Ar-*C*H, meta to O), 130.29 (Ar-*C*C), 153.15 (d, $^2J_{PC}$ = 9 Hz, Ar-*C*O); Acyl: 117.76 (Ar-*C*H, ortho to O), 126.62 (Ar-*C*H, meta to O), 131.85 (Ar-*C*C), 148.02 (Ar-*C*O). ^{31}P NMR δ: 109.50 (s). Anal. calcd. for $C_{128}H_{100}O_{12}S_4P_4$ (%): C 73.83, H 4.84; found: C 74.41, H 5.07.

Resorcinarene(OC(O)OCH$_2$C≡CH)$_4$(OPPh$_2$)$_4$ (7e)

This was prepared similarly from **6e** (1.0 g, 0.811 mmol), triethylamine (0.57 mL, 4.05 mmol), and chlorodiphenylphosphine (0.77 mL, 4.07 mmol). White solid, mp 146–148 °C. Yield: 1.25 g, 78%. ^{1}H NMR (CD_2Cl_2) δ: 2.02, 2.23 (m, 8H, CHC*H*$_2$CH$_2$Ph), 2.37, 2.55 (m, 8H, CHCH$_2$C*H*$_2$Ph), 2.52 (t, 4H, $^4J_{HH}$ = 2 Hz, OC(O)OCH$_2$C≡C*H*), 4.36 (s, br, 8H, OC(O)OC*H*$_2$C≡CH), 4.72 (t, 4H, $^3J_{HH}$ = 8 Hz, C*H*CH$_2$CH$_2$Ph), 6.98–7.65 (m, 64H, Ar-*H*, *Ph*); Phos.: 6.05 (s, 2H, Ar-*H*, meta to O); Acyl: 7.51 (s, 2H, Ar-*H*, meta to O). ^{13}C NMR δ: 34.54 (CHCH$_2$*C*H$_2$Ph), 36.70 (*C*HCH$_2$CH$_2$Ph), 37.89 (CH*C*H$_2$CH$_2$Ph), 55.92 (OC(O)O*C*H$_2$C≡CH), 75.88, 77.35 (OC(O)OCH$_2$*C*≡*C*H), 125.75, 128.25–131.13 (Ar-*C*, *Ph*), 141.25 (m, ipso-*C*, P*Ph*$_2$), 142.35 (ipso-*C*, *Ph*), 152.15 (O*C*(O)OCH$_2$C≡CH); Phos.: 105.78 (m, Ar-*C*H, ortho to O), 127.33 (Ar-*C*H, meta to O), 128.81 (Ar-*C*C), 153.10 (d, $^2J_{PC}$ = 10 Hz, Ar-*C*O); Acyl: 117.05 (Ar-*C*H, ortho to O), 125.20 (Ar-*C*H, meta to O), 132.20 (Ar-*C*C), 147.86 (Ar-*C*O). ^{31}P NMR δ: 110.73 (s). Anal. calcd. for $C_{124}H_{100}O_{16}P_4$ (%): C 75.60, H 5.12; found: C 75.17, H 5.41.

X-ray structure determination

A crystal of **7b**·2THF, grown from a THF–pentane solution, was mounted on a glass fibre. Data were collected using a Nonius-Kappa CCD diffractometer using COLLECT

© 2004 NRC Canada

(13) software. The unit cell parameters were calculated and refined from the full data set. Crystal cell refinement and data reduction was carried out using the Nonius DENZO package. The data were scaled using SCALEPACK (14). The SHELXTL V5.1 (15) program package was used to solve and refine the structure. The centrosymmetric space group *C*2/*c* was chosen based on E-statistics and resulted in successful refinement of the data. The hydrogen atoms were calculated geometrically and were riding on their respective carbon atoms. The solvent of crystallization was disordered and was modeled as an isotropic 40:40:20 disordered mixture, with the carbon–carbon and carbon–oxygen distances fixed. Except as mentioned above, all non-hydrogen atoms were refined with anisotropic thermal parameters. Crystal data are summarized in Table 3.[3]

Acknowledgements

We thank the Natural Sciences and Engineering Research Council of Canada (NSERC) for financial support. RJP thanks the Government of Canada for a Canada Research Chair.

References

1. (*a*) C.D. Gutsche. Calixarenes. *In* Monographs in supramolecular chemistry. The Royal Society of Chemistry, Cambridge. 1989; (*b*) C.D. Gutsche. Calixarenes Revisited. *In* Monographs in supramolecular chemistry. The Royal Society of Chemistry, Cambridge. 1989; (*c*) V. Böhmer. Angew. Chem. Int. Ed. Engl. **35**, 713 (1995); (*d*) P. Timmerman, W. Verboom, and D.N. Reinhoudt. Tetrahedron, **52**, 2663 (1996).
2. (*a*) Y. Rondelez, G. Bertho, and O. Reinaud. Angew. Chem. Int. Ed. **41**, 1044 (2002); (*b*) R.G. Harrison, D.O. Fox, M.O. Meng, N.K. Dalley, and L.J. Barbour. Inorg. Chem. **41**, 838 (2002); (*c*) S.J. Park and J.-I. Hong. Chem. Commun. 1554 (2001); (*d*) D.O. Fox, N.K. Dalley, and R.G. Harrison. Inorg. Chem. **39**, 620 (2000); (*e*) P. Molenveld, S. Kapsabelis, J.F.J. Engbersen, and D.N. Reinhoudt. J. Am. Chem. Soc. **119**, 2948 (1997).
3. (*a*) C.B. Dieleman, C. Marsol, D. Matt, N. Kyritsakas, A. Harriman, and J.P. Kintzinger. J. Chem. Soc. Dalton Trans. 4139 (1999); (*b*) J. Gagnon, M. Vézina, M. Drouin, and P.D. Harvey. Can. J. Chem. **79**, 1439 (2001); (*c*) M. Stolmàr, C. Floriani, A. Chiesi-Villa, and C. Rizzoli. Inorg. Chem. **36**, 1694 (1997); (*d*) F.J. Parlevliet, C. Kiener, J. Fraanje, K. Goubitz, M. Lutz, A.L. Spek, P.C.J. Kamer, and P.W.N.M. van Leeuwen. J. Chem. Soc. Dalton Trans. 1113 (2000).
4. (*a*) C.B. Dieleman, D. Matt, and A. Harriman. Eur. J. Inorg. Chem. 831 (2000); (*b*) C. Loeber, D. Matt, P. Briard, and D. Grandjean. J. Chem. Soc. Dalton Trans. 513 (1996).
5. (*a*) M. Lejeune, C. Jeunesse, D. Matt, N. Kyritsakas, R. Welter, and J.-P. Kintzinger. J. Chem. Soc. Dalton Trans. 1642 (2002); (*b*) J. Gagnon, M. Drouin, and P.D. Harvey. Inorg. Chem. **40**, 6052 (2001); (*c*) T.N. Sorrell, C. Pigge, and P.S. White. Inorg. Chem. **33**, 632 (1994); (*d*) C. Wieser, D. Matt, J. Fischer, and A. Harriman. J. Chem. Soc. Dalton Trans. 2391 (1997); (*e*) X. Fang, B.L. Scott, J.G. Watkin, C.A.G. Carter, and G.J. Kubas. Inorg. Chim. Acta, **317**, 276 (2001).
6. C. Weiser, C.B. Dieleman, and D. Matt. Coord. Chem. Rev. **165**, 93 (1997).
7. (*a*) W. Xu, J.P. Rourke, J. Vittal, and R.J. Puddephatt. Inorg. Chem. **34**, 323 (1995); (*b*) W. Xu, J. Vittal, and R.J. Puddephatt. Inorg. Chem. **36**, 86 (1997); (*c*) W. Xu, J. Vittal, and R.J. Puddephatt. J. Am. Chem. Soc. **117**, 8362 (1995); (*d*) P. Sakhaii, I. Neda, M. Freytag, H. Thönnessen, P.G. Jones, and R. Schmutzler. Z. Anorg. Allg. Chem. **626**, 1246 (2000); (*e*) A. Vollbrecht, I. Neda, H. Thönnessen, P.G. Jones, R.K. Harris, L.A. Crowe, and R. Schmutzler. Chem. Ber. **130**, 1715, (1997); (*f*) I. Neda, A. Vollbrecht, J. Grunenberg, and R. Schmutzler. Heteroat. Chem. **9**, 553, (1998).
8. (*a*) A. Shivanyuk, E.F. Paulus, V. Böhmer, and W. Vogt. J. Org. Chem. **63**, 6448 (1998); (*b*) A. Shivanyuk, E.F. Paulus, K. Rissanen, E. Kolehmainen, and V. Böhmer. Chem. Eur. J. **7**, 1944 (2001); (*c*) A. Shivanyuk. Chem. Commun. 1472 (2001).
9. (*a*) A. Shivanyuk, C. Schmidt, V. Böhmer, E.F. Paulus, O. Lukin, and W. Vogt. J. Am. Chem. Soc. **120**, 4319 (1998); (*b*) O. Lukin, A. Shivanyuk, V.V. Pirozhenko, I.F. Tsymbal, and V. Kalechenko. J. Org. Chem. **63**, 9510 (1998); (*c*) M. Luostarinen, A. Shivanyuk, and K. Rissanen. Org. Lett. **3**, 4141 (2001); (*d*) A. Shivanyuk, A.R. Far, and J. Rebek, Jr. Org. Lett. **4**, 1555 (2002).
10. L.M. Punstad, J.A. Tucker, E. Dalcanale, J. Weiser, J.A. Bryant, J.C. Sherman, R.C. Helgeson, C.B. Knobler, and D.J. Cram. J. Org. Chem. **54**, 1305 (1989).
11. D. Eisler, W. Hong, M.C. Jennings, and R.J. Puddephatt. Organometallics, **21**, 3955 (2001).
12. (*a*) A.G.S. Högberg. J. Am. Chem. Soc. **102**, 6046 (1980); (*b*) A.G.S. Högberg. J. Org. Chem. **45**, 4498 (1980).
13. COLLECT [computer program]. Bruker Nonius B.V., Delft, The Netherlands. 1998.
14. SCALEPACK [computer program]. Bruker Nonius B.V., Delft, The Netherlands. 1998.
15. G.M. Sheldrick. SHELXTL. Version 5.1 [computer program]. Bruker AXS, Madison, Wis. 1997.

[3] Supplementary data may be purchased from the Directory of Unpublished Data, Document Delivery, CISTI, National Research Council Canada, Ottawa, ON K1A 0S2, Canada (http://www.nrc.ca/cisti/irm/unpub_e.shtml for information on ordering electronically). CCDC 195564 contains the crystallographic data for this manuscript (compound **7b**). These data can be obtained, free of charge, via www.ccdc.cam.ac.uk/conts/retrieving.html (or from the Cambridge Crystallographic Data Centre, 12 Union Road, Cambridge CB2 1EZ, U.K.; fax +44 1223 336033; or deposit@ccdc.cam.ac.uk).

© 2004 NRC Canada

Regiospecific synthesis of alkylphenanthrenes using a combined directed *ortho* and remote metalation – Suzuki–Miyaura cross coupling strategy[1]

Xiongwei Cai, Stephen Brown, Peter Hodson, and Victor Snieckus

Abstract: Using a combined directed *ortho* metalation (DoM) – Suzuki–Miyaura cross coupling – directed remote metalation (DreM) approach, the alkylphenanthrenes (APs) 1-methyl- (**5a**), 1,7-dimethyl- (**5b**), 2,7-dimethyl- (**5c**), 7-ethyl-1-methyl- (**15**), and 7-*tert*-butyl-1-methylphenanthrenes (**27**) have been synthesized in four to seven steps and 21%–36% overall yields. In contrast to classical protocols, this method, which may be scaled to gram quantities, provides single isomers of APs in high purity of value as analytical standards for environmental studies. Aminocarbonylation of triflates to *N*,*N*-diethylbenzamides (**9** → **10**) and anionic Fries rearrangement (**23** → **24**) provide other potential links to DoM chemistry.

Key words: phenanthrene, directed *ortho* metalation, Suzuki–Miyaura cross coupling, synthesis, polycyclic aromatic hydrocarbon, carbonylation.

Résumé : Faisant appel à une approche combinant une métallation orientée en ortho (MOo), un couplage croisé de Suzuki et Miyaura et une métallation orientée à distance (MOdi), on a réalisé des synthèses d'alkylphénanthrènes (AP), les 1-méthyl- (**5a**), 1,7-diméthyl- (**5b**), 2,7-diméthyl- (**5c**), 7-éthyl-1-méthyl- (**15**) et 7-*tert*-butyl-1-méthylphénanthrènes (**27**), qui impliquaient de quatre à sept étapes avec des rendements globaux allant de 21 % à 36 %. Par opposition avec les protocoles classiques, cette méthode être réalisée à des échelles du gramme et elle conduit à des isomères uniques d'AP, de grande pureté qui peuvent être utilisés comme références pour des études environnementales. L'aminocarbonylation de triflates de *N*,*N*-diéthylbenzamides (**9** → **10**) et le réarrangement anionique de Fries (**23** → **24**) fournissent d'autres liens vers la chimie de la MOo.

Mots clés : phénanthrène, métallation orienté en *ortho*, couplage croisé de Suzuki et Miyaura, hydrocarbure aromatique polycyclique, carbonylation.

[Traduit par la Rédaction]

Introduction

Alkylphenanthrenes (APs) represent a significant class of polycyclic aromatic hydrocarbons (PAHs) found in soil, sediment, and other aquatic sites, which constitute environmental pollutants with substantial levels of toxicity towards marine diatoms, gastropods, mussels, crustaceans, and especially fish (1–3). The key biological marker for toxicity, retene (7-isopropyl-1-methylphenanthrene) causes reductions in recruitment and growth and an increased prevalence of morphological abnormalities of laval pink salmon and Pacific herring (3, 4), effects which were observed in the 1989 Exxon Valdez oil spill in Alaska (1). Among the various PAH classes, the APs have been sparsely evaluated for toxicity effects, arguably because of lack of commercial sources of analytically pure compounds in sufficient quantity. Only a few APs are available, e.g., 1-methyl-, 1,7-dimethylphenanthrene, and retene at times of uncertain and insufficient isomer purity and inadequate quantity.[3] Among the few methods of phenanthrene synthesis, classical electrophilic substitution (5), Pschorr reaction (6), ring expansion (7), Mallory photocyclization (8), and recently, palladium-catalyzed trimerization (9) and radical cyclization (10), tactics have, to various degrees, been applied to AP preparation but suffer in length or produce mixtures of isomers. We report a combined metalation – Suzuki–Miyaura cross cou-

Received 29 July 2003. Published on the NRC Research Press Web site at http://canjchem.nrc.ca on 12 January 2004.

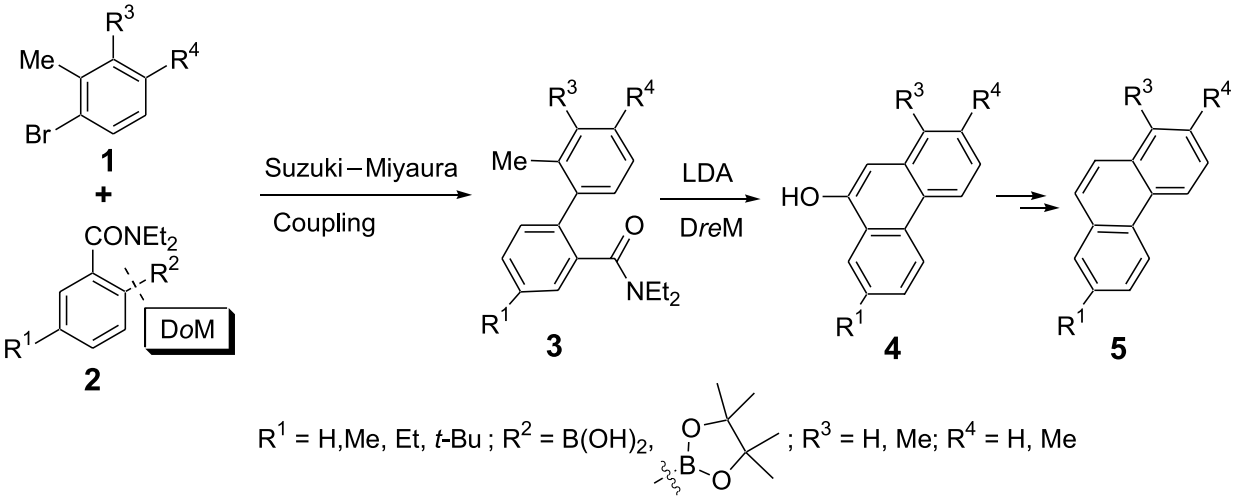
This manuscript is dedicated to Ed Piers for placing Canadian synthetic organic chemistry on the international map.

X. Cai, S. Brown, and V. Snieckus.[2] Department of Chemistry, Queen's University, Kingston, ON K7L 3N6, Canada.
Peter Hodson. School of Environmental Studies, Queen's University, Kingston ON K7L 3N6, Canada.

[1]This article is part of a Special Issue dedicated to Professor Ed Piers.
[2]Corresponding author (e-mail: snieckus@chem.queensu.ca).
[3]1,7-Dimethylphenanthrene and retene available from Chiron AS, Stiklestadveien 1, Trondheim, N-7041, Norway; 1-methylphenanthrene available from Absolute Standards, Inc., Hamdan, Conn. 06518, U.S.A.

 doi: 10.1139/V03-179 © 2004 NRC Canada

Scheme 1.



pling methodology involving both directed *ortho* (DoM) and remote metalation (DreM) reactions, **1** + **2** → **3** → **4** → **5** (Scheme 1) that provides short, efficient, and regioselective routes to APs **5a**, **5c**, **15**, and **27**. This general strategy provides the phenanthrene class of PAHs as single isomers in preparative quantities and contrasts with classical methods, which invariably involve harsh conditions, lack of regioselectivity, and considerable handling of potentially toxic materials (11). Recently, de Koning et al. has reported a general phenanthrene synthesis using *t*-BuOK-mediated cyclization of esters corresponding to **3** (12).

Synthesis of 1-methyl- (5a), 1,7-dimethyl- (5b), and 2,7-dimethyl- (5c) phenanthrenes

The synthesis of 1-methylphenanthrene (**5a**) (Scheme 2) was initiated from *N*,*N*-diethylbenzamide (**6a**) that upon metalation under standard conditions (*s*-BuLi / TMEDA / –78 °C / THF / 1 h) followed by quenching with trimethyl borate and acidic workup afforded the boronic acid **2a**. Without purification, **2a** was subjected, as the reactant in excess (1.4 equiv.), to the Suzuki–Miyaura cross coupling reaction with the commercially available 3-bromo-*o*-xylene to give the biaryl amide **3a** in good yield. Metalation–boronation of **6b**, the insecticide DEET® (13), at –98 °C proceeded smoothly to give the corresponding boronic acid, which was isolated and purified as the pinacol boronate **2b**. NMR analysis provided structural confirmation that DoM of **6b** occurred exclusively on C-6, a result differing with Beak and Brown's observation that metalation of **6b** under similar conditions but using MeOD quench yields C-6 and C-2 deuterated products in the ratio of 2:1 (Scheme 2) (14). The observed difference in regioselectivity using trimethyl borate as the electrophile may be due to its greater size. Boronate **2b** was subjected to Suzuki–Miyaura cross coupling with 3-bromo-*o*-xylene and 4-bromo-*m*-xylene to give biaryls **3b** and **3c**, respectively, in satisfactory yields.

Application of the standard DreM conditions (11*a*) to the biaryl amides **3a**–**3c** (2.5 equiv. of LDA / THF / 0 °C) resulted in smooth cyclization to the 9-phenanthrols **4a**–**4c**, which underwent oxidation slowly and changed colors in the air but were stable in sealed vials at –30 °C. The 9-phenanthrols **4a**–**4c** were then converted into their triflates **7a**–**7c** (15), which upon Pd-catalyzed hydrogenolysis in the presence of formic acid, afforded 1-methyl-phenanthrene (**5a**), 1,7-dimethylphenanthrene (**5b**), and 2,7-dimethylphenanthrene (**5c**) in modest to excellent yields. Overall yields (**5a** (29%), **5b** (27%), **5c** (45%), in four to six steps from commercial materials) cannot be compared with previous routes for lack of data with the exception of **6a**, which was obtained by Pschorr synthesis in 21% overall yield and four steps (16).

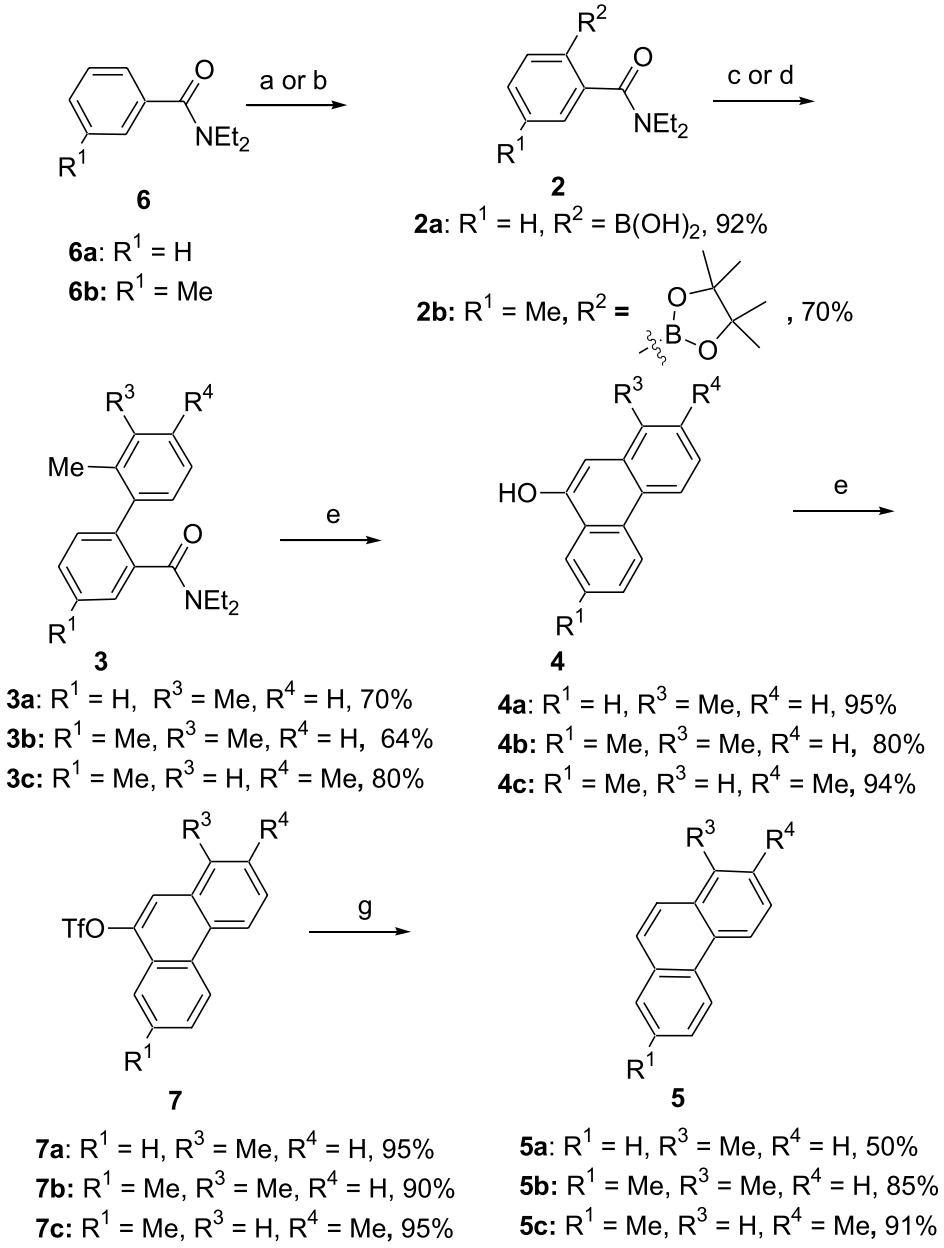
Synthesis of 7-ethyl-1-methylphenanthrene (15)

The synthesis of the homologous 7-ethyl-1-methylphanthrene (**15**) commenced from 3-ethylbenzamide (**10**), which was obtained by a aminocarbonylation protocol (Scheme 3). Thus, commercial 3-ethylphenol (**8**) was converted into the corresponding triflate **9** (15), which was subjected to aminocarbonylation conditions (17) using a number of phosphine ligands that included PPh_3, dppf, and dppp. In the case of PPh_3, rapid black precipitation was observed and the product **10** was obtained in low yield with the material balance being recovered starting material (72%). In contrast, the bidentate ligands dppp and dppf behaved well, leading to similar yields of **10** and completion of reactions with only trace amounts of starting material being detected by GC at the conclusion of the reaction. In this two-phase reaction, it is imperative to ensure good mixing, especially when the reaction is carried out on a large scale. Thus, using a balloon of CO led to poorer yields and longer completion times compared to bubbling CO into the solution for the duration of the reaction.

Metalation of 3-ethylbenzamide **10** (Scheme 4) under the low-temperature conditions used previously for **6b** (Scheme 2) followed by boronation and treatment with pinacol paralleled the reaction of **6b** in that it led to the formation of boronate **11**, the product of exclusive C-6 deprotonation. The isolated and purified boronate **11** was subjected to Suzuki–Miyaura cross coupling with 3-bromo-*o*-xylene under the previously defined conditions to afford the biaryl amide **12**, which, upon treatment with LDA, led cleanly to the 9-phenanthrol **13**. Analogous to the **4** → **7** reactions,

© 2004 NRC Canada

Scheme 2. Reagents and conditions: (*a*) (*i*) *s*-BuLi / TMEDA / THF / –78 °C; (*ii*) $B(OMe)_3$ / –78 °C; (*iii*) aq. NH_4Cl; (*b*) (*i*) *s*-BuLi / TMEDA / THF / –98 °C; (*ii*) $B(OMe)_3$ / –98 °C; (*iii*) aq. NH_4Cl; (*iv*) pinacol / $MgSO_4$ / CH_2Cl_2/ 0 °C; (*c*) $Pd(PPh_3)_4$ / DME / Na_2CO_3 / 6-bromo-*o*-xylene / reflux / 4 h; (*d*) $Pd(PPh_3)_4$ / DME / Na_2CO_3 / 6-bromo-*m*-xylene / reflux/ 4 h; (*e*) (*i*) LDA / THF / 0 °C; (*ii*) aq. NH_4Cl; (*f*) 2,6-lutidine / Tf_2O / CH_2Cl_2 / 30 min; (*g*) $Pd(OAc)_2$ / PPh_3 / Et_3N / HCO_2H / DMF / 60 °C / 20 min.



6

6a: R^1 = H
6b: R^1 = Me

2

2a: R^1 = H, R^2 = $B(OH)_2$, 92%
2b: R^1 = Me, R^2 = , 70%

3

3a: R^1 = H, R^3 = Me, R^4 = H, 70%
3b: R^1 = Me, R^3 = Me, R^4 = H, 64%
3c: R^1 = Me, R^3 = H, R^4 = Me, 80%

4

4a: R^1 = H, R^3 = Me, R^4 = H, 95%
4b: R^1 = Me, R^3 = Me, R^4 = H, 80%
4c: R^1 = Me, R^3 = H, R^4 = Me, 94%

7

7a: R^1 = H, R^3 = Me, R^4 = H, 95%
7b: R^1 = Me, R^3 = Me, R^4 = H, 90%
7c: R^1 = Me, R^3 = H, R^4 = Me, 95%

5

5a: R^1 = H, R^3 = Me, R^4 = H, 50%
5b: R^1 = Me, R^3 = Me, R^4 = H, 85%
5c: R^1 = Me, R^3 = H, R^4 = Me, 91%

conversion of **13** into its triflate **14** followed by Pd-catalyzed hydrogenolysis by the agency of formic acid furnished **15** in high yield and >98% purity (HPLC analysis). This concluded the synthesis of 7-ethyl-1-methylphenthrene (**15**) in six steps in an overall yield of 36%.

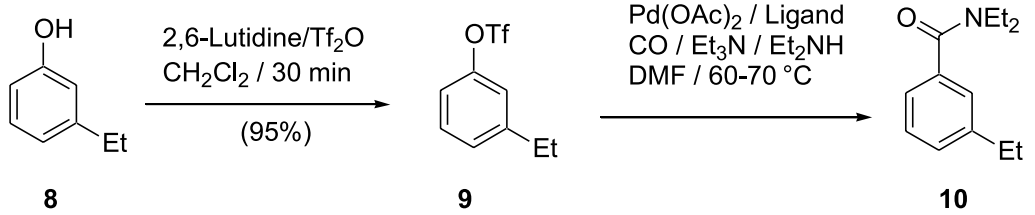
Synthesis of 7-*tert*-butyl-1-methylphenanthrene (27)

In pursuit of the same strategy (Scheme 3) for the synthesis of 7-*tert*-butyl-1-methyl-phenanthrene (**27**, Scheme 5), we envisaged the preparation of the requisite benzamide **18** by the amidocarbonylation of **17**, which, in turn, was available in high yield from the commercial phenol **16** (Scheme 6). However, modest exploration of conditions and bidentate phosphine ligands for the reaction **17** → **18**, as indicated in tabular form, gave unsatisfactory results.

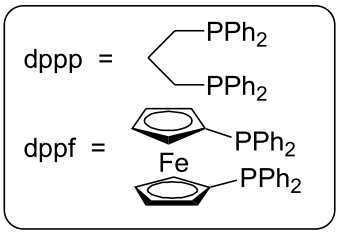
Therefore, a strategy involving the inversion of coupling partners in the Suzuki–Miyaura reaction **20** + **21** → **19** was pursued (Scheme 7). Thus, 4-*tert*-butylphenol **22** (Scheme 5) was quantitatively converted into the *O*-carbamate **23** that was subjected to conditions (*s*-BuLi / TMEDA / –78 °C) for the anionic Fries rearrangement (18) to give the salicylamide **24** in good yield. Conversion of **24** into triflate **20** using 2,6-lutidine proceeded in low yield (20%) compared to that achieved for previously prepared triflates. However, using pyridine as catalyst, **20** was obtained in good yield. In the key step, triflate **20** underwent Suzuki–Miyaura cross cou-

© 2004 NRC Canada

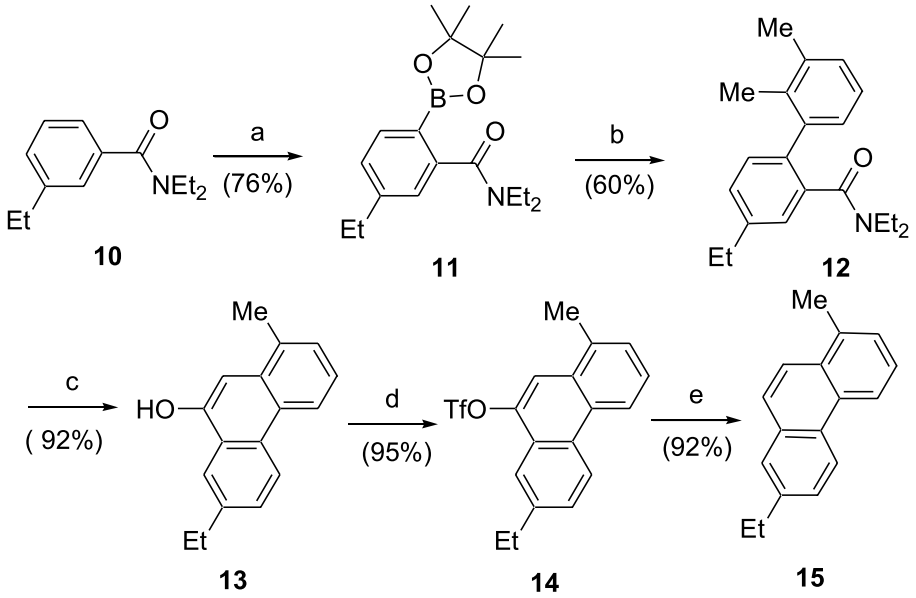
Scheme 3.



Ligand	Time (h)	Yld (%)
PPh_3	24	25
dppp	4	70
dppf	12	62



Scheme 4. Reagents and conditions: (*a*) (*i*) *s*-BuLi / TMEDA / THF / –98 °C; (*ii*) $B(OMe)_3$ / –98 °C, (*iii*) aq. NH_4Cl; (*iv*) pinacol / $MgSO_4$ / CH_2Cl_2 / 0 °C; (*b*) $Pd(PPh_3)_4$ / DME / Na_2CO_3 / 6-bromo-*o*-xylene / reflux / 4 h; (*c*) (*i*) LDA / THF / 0 °C; (*ii*) aq. NH_4Cl; (*d*) 2,6-lutidine / Tf_2O / CH_2Cl_2 / 30 min; (*e*) $Pd(OAc)_2$ / PPh_3 / Et_3N / HCO_2H / DMF / 60 °C / 20 min.



pling with the commercial boronic acid **21**, to form the biaryl amide **19** in very good yield. As before, LDA-mediated cyclization furnished, in excellent yield, the 9-phenanthrol **25** that was converted into its triflate **26** and thence into the target 7-*tert*-butyl-1-methylphenanthrene **27**. Thus, the synthesis of **27** was accomplished in seven steps in an overall yield of 21%.

Conclusion

This work constitutes a contribution for the convenient and efficient preparation of the phenanthrene class of PAHs that contrasts with classical methods in terms of regioselectivity, brevity, mildness of conditions, and necessity for considerable handling of potentially toxic materials. Thus, the alkylphenanthrenes (APs) 1-methyl- (**5a**), 1,7-dimethyl- (**5b**), 2,7-dimethyl- (**5c**), 7-ethyl-1-methyl- (**15**), and 7-*tert*-butyl-1-methyl (**27**) phenanthrenes have been synthesized by a combined D*o*M – Suzuki–Miyaura cross coupling – DreM methodology in overall yields of 29% (five steps), 27% (five steps), 45% (five steps), 36% (six steps), and 21% (seven steps), respectively. A general and effective methodology has been thereby provided that allows anticipated application for the synthesis of various APs as single isomers in high purity and in scales ranging from 1 to 4 g. As an adjunct, a representative aminocarbonylation method of readily available aryl triflates to *N*,*N*-diethylbenzamides has been briefly investigated (Scheme 3) based on which a further general link to D*o*M chemistry may be anticipated.

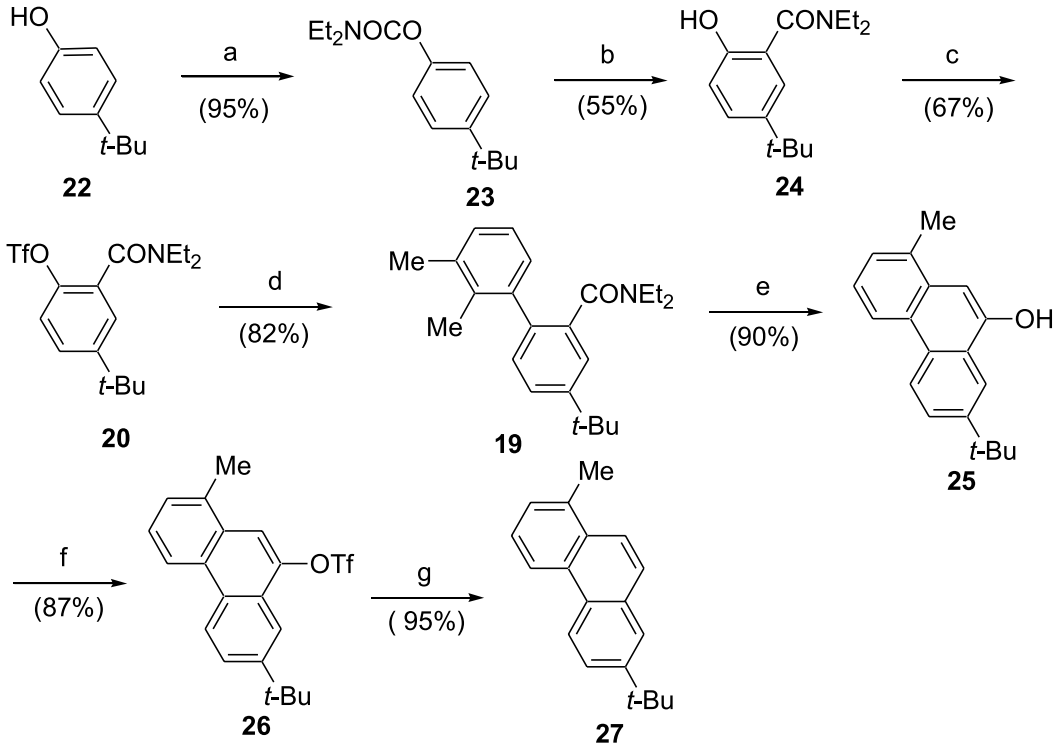
Experimental section

General methods

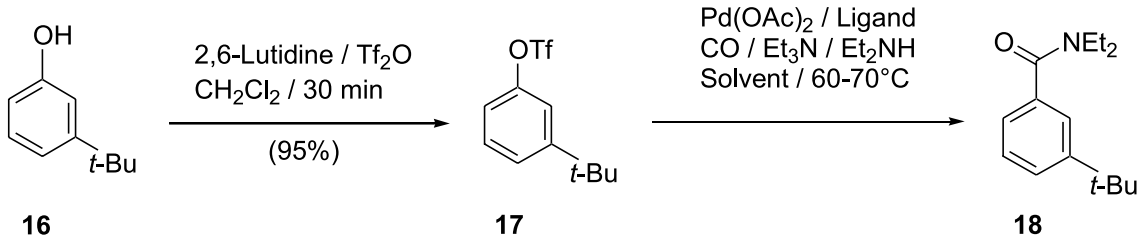
Melting points are uncorrected. IR spectra were recorded neat or as KBr discs using a BOMEM FT-IR spectrometer.

© 2004 NRC Canada

Scheme 5. Reagents and conditions: (*a*) (*i*) NaH / THF / 0 °C; (*ii*) $ClCONEt_2$; (*b*) (*i*) *s*-BuLi / TMEDA / THF / –78 °C to rt; (*ii*) aq. NH_4Cl; (*c*) Tf_2O / pyridine / CH_2Cl_2; (*d*) $Pd(PPh_3)_4$ / DME, Na_2CO_3 / **21** / reflux / 4 h; (*e*) LDA / THF / 0 °C; (*ii*) aq NH_4Cl; (*f*) 2,6-lutidine / Tf_2O / CH_2Cl_2 / 30 min; (*g*) $Pd(OAc)_2$ / PPh_3 / Et_3N / HCO_2H / DMF / 60 °C / 20 min.

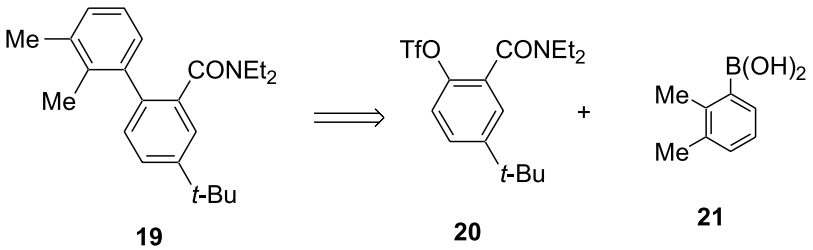


Scheme 6.



Ligand	Solvent	Time (h)	Yld (%)
dppp	DMF	24	20
dppf	DMF	24	22
dppp	DMSO	48	25
dppf	DMSO	48	27

Scheme 7.



© 2004 NRC Canada

^{1}H (300 MHz) and ^{13}C (75.43 MHz) NMR spectra were obtained in $CDCl_3$ using either TMS (for ^{1}H) or $CDCl_3$ (for ^{13}C) as the internal standard on a Bruker Avance-300 spectrometer. THF was freshly distilled from sodium benzophenone ketyl under nitrogen and CH_2Cl_2 and HN-*i*-Pr_2 were freshly distilled from CaH_2 under nitrogen. *n*-Butyllithium and *s*-butyllithium were purchased from Aldrich as solutions in hexanes, stored in resealable containers, and titrated periodically against *s*-butanol using 1,10-phenanthroline as the indicator (19). *N*,*N*-Diethyl benzamide (**6a**) was prepared from benzoyl chloride (20). *N*,*N*-Diethyl toluamide (DEET®) (**6b**), 6-bromo-*o*-xylene, 6-bromo-*m*-xylene, and 2,3-dimethylphenylboronic acid (**21**) were purchased from Aldrich Chemical Co. All experiments were carried out under argon in dried glassware, using syringe-septum cap techniques. The –78 °C and 0 °C external bath temperatures designated are approximate as achieved by a dry ice–acetone or ice–salt baths, respectively. Flash column chromatography was carried out using Merck Kieselgel 60 silica gel (particle size 32–63) with different ratios of EtOAc–hexane as eluents.

General procedures

A. Lithiation of benzamides

A solution of the benzamide (1.00 mmol) in anhyd THF (2 mL) was added dropwise to a stirred solution of *s*-BuLi–TMEDA (1:1, 1.20 mmol) complex in anhyd THF (3 mL) at –78 °C. The resulting mixture was stirred at –78 °C for 1 h, treated with an excess of $B(OMe)_3$ (2.40 mmol), and the mixture was warmed to ambient temperature over 8–12 h and quenched with a satd. aq. NH_4Cl solution (5 mL). The aqueous portion was extracted with Et_2O (3 × 5 mL), and the extract was dried (Na_2SO_4) and concentrated in vacuo. The residue was purified by flash column chromatography (EtOAc–hexanes) to afford the product.

B. Cross coupling reaction of arylboronic acids with aryl halides and aryl triflates

A mixture of $Pd(PPh_3)_4$ (0.04 mmol) and aryl halide or aryl triflate (1 mmol) in DME (3 mL) was stirred at room temperature (rt) for 10 min. The solution of aryl boronic acid (1.4 mmol) in a minimum amount of ethanol (1 mL) and DME (2 mL) mixture was added, followed by the addition of 2 mol L^{-1} aq. Na_2CO_3 solution (3 mL). The resulting mixture was heated at reflux for 12 h, cooled to rt, and extracted with Et_2O (3 × 5 mL). The organic extract was dried (Na_2SO_4) and concentrated in vacuo. The residue was purified by flash column chromatography (EtOAc–hexanes) to afford the product.

C. Synthesis of 9-phenanthrols

To a solution of LDA (2.50 mmol) in THF (8 mL) was added a solution of 2′-methyldiphenyl-2-carboxamide (1.00 mmol) in THF (2 mL) at 0 °C. The resulting mixture was stirred at rt for 30 min and quenched with a satd. aq. NH_4Cl solution (5 mL). The aqueous portion was extracted with Et_2O (3 × 5 mL) and the extract was dried (Na_2SO_4) and concentrated in vacuo. The residue was purified by flash column chromatography (EtOAc–hexanes) to afford the product.

D. Synthesis of triflates

A solution of the phenanthrol (1.00 mmol) and 2,6-lutidine or pyridine (1.2 mmol) in CH_2Cl_2 (10 mL) was stirred for 5 min at 0 °C followed by the addition of triflic anhydride (1.20 mmol). The resulting mixture was stirred at rt for 30 min and water was added (5 mL). The aqueous layer was separated and extracted with CH_2Cl_2 (3 × 10 mL). The combined extract was dried (Na_2SO_4) and concentrated in vacuo. The residue was purified by flash column chromatography (EtOAc–hexane) to afford the product.

2-(N,N-Diethylcarboxamido)phenylboronic acid (2a)

According to general procedure A, a solution of *N*,*N*-diethylbenzamide (1.77 g, 10.0 mmol), *s*-BuLi (9.60 mL of a 1.25 mol L^{-1} solution, 12.0 mmol), and TMEDA (1.07 mL, 1.39 g, 12.0 mmol) was treated with $B(OMe)_3$ (2.73 mL, 2.50 g, 24.0 mmol). Normal workup afforded 2.03 g (92%) of product as a viscous oil that was used in the cross coupling reactions without further purification.

N,N-*Diethyl 2′,3′-dimethyldiphenyl-2-carboxamide (3a)*

According to general procedure B, 1-bromo-2,3-dimethylbenzene (1.36 mL, 1.85 g, 10.0 mmol) was subjected to reaction with 2-(*N*,*N*-diethylcarboxamido)phenylboronic acid (3.09 g, 14 mmol) in the presence of $Pd(PPh_3)_4$ (0.185 g, 0.16 mmol). Normal workup followed by flash chromatography (EtOAc–hexanes, 1:5) afforded 2.30 g (82%) of **3a** as colorless crystals, mp 68 to 69 °C (EtOAc). IR (KBr) (cm^{-1}): 1632. ^{1}H NMR (300 MHz, $CDCl_3$) δ: 0.59 (br s, 3H), 0.80 (br s, 3H), 2.01 (s, 3H), 2.19 (s, 3H), 2.40–3.30 (br m, 3H), 3.65 (br s, 1H), 6.90–7.15 (m, 4H), 7.25 (s, 3H). ^{13}C NMR (75 MHz, $CDCl_3$) δ: 12.1, 14.0, 17.5, 20.9, 38.2, 42.8, 117.3, 118.9, 124.9, 127.5, 127.9, 128.6, 129.5, 130.1, 131.2, 135.0, 137.1, 137.6, 170.3. EI-MS *m*/*z* (rel. int.): 281 (M^+, 100), 209 (20), 181 (13), 165 (47), 74 (30). HR-MS *m*/*z* calcd. for $C_{19}H_{23}NO$: 281.1780; found: 281.1776.

1-Methyl-9-phenanthrol (4a)

According to general procedure C, treatment of a solution of *N*,*N*-diethyl 2′,3′-dimethylbiphenyl-2-carboxamide (2.81 g, 10 mmol) in THF (20 mL) with a solution of LDA (25.0 mmol) in THF (80 mL) followed by acidification, normal workup, and flash chromatography (hexane) afforded 1.98 g (95%) of **4a** as colorless crystals, mp 194–197 °C (CH_2Cl_2) (lit. (21) mp 199.5–200.5 °C (benzene)). IR (KBr) (cm^{-1}): 3307. ^{1}H NMR (300 MHz, DMSO-d_6) δ: 2.61 (s, 3H), 7.34 (t, *J* = 7.8 Hz, 1H), 7.39 (t, *J* = 6.8 Hz, 1H), 7.61–7.72 (m, 2H), 8.31 (d, *J* = 7.4 Hz, 1H), 8.53 (d, *J* = 7.8 Hz, 1H), 8.77 (d, *J* = 7.6 Hz, 1H), 10.39 (s, 1H). ^{13}C NMR (75 MHz, DMSO-d_6) δ: 20.5, 102.3, 121.7, 123.3, 123.9, 126.1, 128.0, 128.7, 132.2, 132.6, 132.9, 151.9. EI-MS *m*/*z* (rel. int.): 208 (M^+, 100), 178 (17), 165 (38), 152 (5), 89 (5), 76 (5).

1-Methylphenanthryl-9 trifluoromethanesulfonate (7a)

According to general procedure D, to a solution of 1-methyl-9-phenanthrol (**4a**) (1.04 g, 5.00 mmol) and 2,6-lutidine (0.69 mL, 0.64 g, 6.00 mmol) in CH_2Cl_2 was added triflic anhydride (1.01 mL, 1.69 g, 6.00 mmol). Normal workup followed by flash chromatography (hexane) afforded 1.62 g (95%) of **7a** as colorless crystals, mp 60 to 61 °C

© 2004 NRC Canada

(EtOAc). IR (KBr) (cm^{-1}): 1416, 1206, 1139. ^1H NMR (300 MHz, $CDCl_3$) δ: 2.72 (s, 3H), 7.49 (s, 1H), 7.57 (t, *J* = 7.2 Hz, 1H), 7.71–7.77 (m, 2H), 7.91 (s, 1H), 8.15–8.21 (m, 1H), 8.47 (d, *J* = 6.9 Hz, 1H), 8.63–8.68 (m, 1H). ^{13}C NMR (75 MHz, $CDCl_3$) δ: 20.0, 114.8, 119.5 (q, *J* = 323 Hz), 121.2, 121.9, 123.7, 125.4, 127.8, 128.0, 129.1, 129.8, 130.1, 132.6, 135.8, 144.7. EI-MS *m/z* (rel. int.): 340 (M^+, 55), 207 (49), 179 (100), 152 (5), 69 (8). HR-MS *m*/z calcd. for $C_{16}H_{11}F_3O_3S$: 340.0381; found: 340.0387.

1-Methylphenanthrene (5a)

A stirred mixture of 1-methylphenanthryl-9 trifluoromethanesulfonate (**7a**) (0.340 g, 1.00 mmol), $Pd(OAc)_2$ (4.5 mg, 0.02 mmol), PPh3, (10.5 mg, 0.04 mmol), Et_3N (0.303 g, 3.00 mmol), and HCO_2H (0.08 mL, 92 mg, 2.00 mmol) in DMF (10 mL) was heated at 60–70 °C for 30 min. The reaction mixture was cooled to rt, water was added, and the mixture was extracted with Et_2O. The combined organic layer was dried (Na_2SO_4), concentrated to dryness, and the residue was subjected to flash chromatography (hexane) to afford 96 mg (50%) of **6a** as colorless crystals, mp 118 to119 °C (hexane) (lit. (22) mp 120 to 121 °C (ethanol)). IR (KBr) (cm^{-1}): 1598. ^1H NMR (300 MHz, $CDCl_3$) δ: 2.87 (s, 3H), 7.56 (d, *J* = 7.2 Hz, 1H), 7.63–7.69 (m, 3H), 7.88 (d, *J* = 9.2 Hz, 1H), 8.01 (d, *J* = 9.2 Hz, 1H), 8.04 (t, *J* = 9.2 Hz, 1H), 8.69 (d, *J* = 8.1 Hz, 1H), 8.81 (d, *J* = 8.1 Hz, 1H). ^{13}C NMR (75 MHz, $CDCl_3$) δ: 20.5, 121.4, 123.4, 123.5, 126.7, 127.1, 127.2, 128.3, 129.0, 130.9, 131.3, 132.2, 135.4. EI-MS *m/z* (rel. int.): 192 (M^+, 100), 165 (23), 150 (4), 139 (4), 95 (28), 83 (24).

Pinacolo[2-(*N,N*-diethylcarboxamido)-4-methylphenyl]boronate (2b)

According to general procedure A, a solution of *N*,*N*-diethyl-3-methylbenzamide (1.91 g, 10.0 mmol), *s*-BuLi (9.60 mL of a 1.25 mol L^{-1} solution,12.0 mmol), and TMEDA (1.07 mL, 1.39 g, 12.0 mmol) was treated with $B(OMe)_3$ (2.73 mL, 2.50 g, 24.0 mmol). Normal workup afforded a thick oil that was stirred with pinacol (2.83 g, 24.0 mmol) and $MgSO_4$ in dry CH_2Cl_2 for 12 h. Filtration and concentration of the filtrate gave a residue that was purified by flash chromatography (EtOAc–hexanes, 1:3) to afford 2.21 g (70%) of **2b** as a colorless oil. IR (neat) (cm^{-1}): 1633, 1432, 1350. ^1H NMR (300 MHz, $CDCl_3$) δ: 0.88 (t, *J* = 7.2 Hz, 3H), 1.15 (s, 12H), 1.20 (t, *J* = 7.2 Hz, 3H), 2.20 (s, 3H), 3.02 (q, *J* = 7.2 Hz, 2H), 3.41 (q, *J* = 7.2 Hz, 2H), 6.90 (s, 1H), 7.02 (d, *J* = 8.1 Hz, 1H), 7.56 (d, *J* = 8.1 Hz, 1H). ^{13}C NMR (75 MHz, $CDCl_3$) δ: 14.2, 14.4, 22.3, 25.5, 38.8, 43.6, 84.2, 123.1, 126.8, 129.2, 136.2, 141.7, 144.1, 172.5. EI-MS *m/z* (rel. int.): 316 (M^+ – H, 25), 302 (13), 259 (100), 218 (18), 174 (18), 144 (18), 177 (18), 83 (7), 55 (4). HR-MS *m/z* calcd. for $C_{18}H_{27}BNO_3$ (M^+ – H): 316.2084; found: 316.2093.

N,N-*Diethyl 3,2′,3′-trimethyldiphenyl-2-carboxamide (3b)*

According to general procedure B, 1-bromo-2,3-dimethylbenzene (1.36 mL, 1.85 g, 10.0 mmol) was subjected to reaction with **2b** (3.16 g, 10 mmol) in the presence of $Pd(PPh_3)_4$ (0.185 g, 0.16 mmol). Normal workup followed by flash chromatography (EtOAc–hexane, 1:5) afforded 1.89 g (64%) of **3b** as colorless crystals, mp 66–68 °C (EtOAc). IR (KBr) (cm^{-1}): 1630. ^1H NMR (300 MHz, $CDCl_3$) δ: 0.65 (br, 3H), 0.75–1.00 (br, 3H), 2.28 (s, 3H), 2.48 (s, 3H), 2.50–3.30 (br, 4H), 3.65–3.85 (s, 1H), 6.98–7.23 (m, 6H). ^{13}C NMR (75 MHz, $CDCl_3$) δ: 12.0, 13.9, 17.4, 20.8, 21.3, 38.0, 42.7, 124.7, 127.4, 129.2, 130.0, 130.9, 131.6, 136.9, 137.1, 170.4. EI-MS *m/z* (rel. int.): 295 (M^+, 35), 222 (100), 177 (48), 180 (57), 165 (65), 74 (47). HR-MS *m/z* calcd. for $C_{20}H_{25}NO$: 295.1936; found: 295.1932.

1,7-Dimethyl-9-phenanthrol (4b)

According to general procedure C, treatment of a solution of **3b** (2.95 g, 10 mmol) in THF (20 mL) with a solution of LDA (25.0 mmol) in THF (80 mL) for 30 min followed by acidification, normal workup, and flash chromatography (hexane) afforded 1.78 g (80%) of **4b** as colorless crystals, mp 203–205 °C (CH_2Cl_2). IR (KBr) (cm^{-1}): 3351. ^1H NMR (300 MHz, $CDCl_3$) δ: 2.54 (s, 3H), 2.59 (s, 3H), 7.20 (s, 1H), 7.30–7.39 (m, 2H), 7.51 (d, *J* = 9.0 Hz, 1H), 8.07 (s, 1H), 8.49 (d, *J* = 9.0 Hz, 1H), 8.65 (d, *J* = 9.0 Hz, 1H), 10.30 (s, 1H). ^{13}C NMR (75 MHz, DMSO-d_6) δ: 20.9, 22.4, 102.5, 121.8, 123.1, 124.0, 124.2, 126.4, 126.8, 128.6, 129.9, 130.4, 132.4, 133.0, 136.6, 151.9. EI-MS *m/z* (rel. int.): 222 (M^+, 100), 207 (7), 194 (13), 179 (41), 110 (3), 89 (3). HR-MS *m/z* calcd. for $C_{16}H_{14}O$: 222.1045; found: 222.1040.

1,7-Dimethylphenanthryl-9-trifluoromethanesulfonate (7b)

According to general procedure D, a solution of **4b** (1.11 g, 5.00 mmol) and 2,6-lutidine (0.69 mL, 0.64 g, 6.00 mmol) in CH_2Cl_2 was treated with triflic anhydride (1.01 mL, 1.69 g, 6.00 mmol). Normal workup followed by flash chromatography (hexane) afforded 1.42 (90%) g of **7b** as colorless crystals, mp 74 to 75 °C (EtOAc). IR (KBr) (cm^{-1}): 1421, 1215, 1140. ^1H NMR (300 MHz, $CDCl_3$) δ: 2.64 (s, 3H), 2.75 (s, 3H), 7.49 (d, *J* = 7.2 Hz, 1H), 7.57–7.64 (m, 2H), 7.72 (s, 1H), 7.74 (s, 1H), 8.53 (d, *J* = 8.4 Hz, 1H), 8.63 (d, *J* = 8.4 Hz, 1H). ^{13}C NMR (75 MHz, $CDCl_3$) δ: 20.4, 22.5, 115.0, 119.5 (q, *J* = 315 Hz), 121.4, 121.7, 123.9, 125.8, 128.0, 128.9, 129.8, 130.6, 130.8, 136.0, 138.4, 144.9. EI-MS *m/z* (rel. int.): 354 (M^+, 38), 221 (39), 193 (100), 178 (20), 69 (7). H-MS *m/z* calcd. for $C_{17}H_{13}O_3F_3S$: 354.0538; found: 354.0545.

1,7-Dimethylphenanthrene (5b)

A stirred mixture of **7b** (0.354 g, 1.00 mmol), $Pd(OAc)_2$ (4.5 mg, 0.02 mmol), PPh_3 (10.5 mg, 0.04 mmol), Et_3N (0.303 g, 3.00 mmol), and HCO_2H (0.08 mL, 92 mg, 2.00 mmol) in DMF (10 mL) was heated at 60–70 °C for 30 min, cooled to rt, and treated with water (10 mL). The resulting aqueous solution was extracted with Et_2O (3 × 10 mL), the combined organic extract was dried (Na_2SO_4) and concentrated in vacuo, and the residue was subjected to flash chromatography (hexane) to afford 175 mg (85%) of **5b** as colorless crystals, mp 83 to 84 °C (hexane) (lit. (23) mp 86 °C (ethanol)). ^1H NMR (300 MHz, $CDCl_3$) δ: 2.59 (s, 3H), 2.78 (s, 3H), 7.43–7.58 (m, 3H), 7.71 (s, 1H), 7.75 (d, *J* = 9.1 Hz, 2H), 7.90 (d, *J* = 9.1 Hz, 1H), 8.70 (d, *J* = 8.4 Hz, 1H), 8.62 (d, *J* = 8.4 Hz, 1H). ^{13}C NMR (75 MHz, $CDCl_3$) δ: 20.4, 21.9, 121.2, 123.4, 126.5, 126.9, 127.8, 128.8, 129.0, 130.9, 131.0, 132.3, 135.3, 136.6. EI-MS *m/z* (rel. int.): 206 (M^+, 100), 192 (18), 179 96), 166 (6), 152 (5), 102 (6), 88 (5). HR-MS *m/z* calcd. for $C_{16}H_{14}$: 206.1096; found: 206.1090.

© 2004 NRC Canada

N,N-*Diethyl 4,2′,4′-trimethyldiphenyl-2-carboxamide (3c)*

According to general procedure B, 1-bromo-2,4-dimethylbenzene (0.27 mL, 0.37 g, 2.0 mmol) was subjected to reaction with pinacolo[2-(*N*,*N*-diethylcarboxamido)-4-methylphenyl]boronate (**2b**) (0.63 g, 2.0 mmol) in the presence of $Pd(PPh_3)_4$ (37 mg, 0.032 mmol). Normal workup followed by flash chromatography (EtOAc–hexane, 1:5) afforded 0.38 g (80%) of **3c** as a colorless oil. IR (neat) (cm^{-1}) 1633. ^1H NMR (300 MHz, $CDCl_3$) δ: 0.60–0.90 (m, 6H), 2.20 (s, 3H), 2.32 (s, 3H), 2.40 (s, 3H), 2.50–3.90 (br, 4H), 6.90–7.30 (m, 6H). ^{13}C NMR (75 MHz, $CDCl_3$) δ: 20.6, 21.5, 21.5, 126.2, 128.1, 128.6, 129.3, 130.1, 130.7, 131.2, 135.0, 135.1, 137.3, 137.4, 137.6, 170.8. EI-MS *m*/*z* (rel. int.): 294 (18), 265 (64), 74 (70). HR-MS *m*/*z* calcd. for $C_{20}H_{25}NO$: 295.1936; found: 295.1930.

2,7-Dimethyl-9-phenanthrol (4c)

According to general procedure C, treatment of a solution of (**3c**) (0.30 g, 1.0 mmol) in THF (10 mL) with a solution of LDA (2.5 mmol) in THF (10 mL) for 30 min followed by acidification, normal workup, and flash chromatography (hexane) afforded 0.21 g (94%) of **4c** as colorless crystals, mp 154 to 155 °C (CH_2Cl_2). IR (KBr) (cm^{-1}): 3545. ^1H NMR (500 MHz, $CDCl_3$) δ: 2.46 (s, 3H), 2.53 (s, 3H), 7.00 (s, 1H), 7.25 (dd, *J* = 8.5, 1.5 Hz, 1H), 7.49 (dd, *J* = 8.5, 1.5 Hz, 1H), 7.50 (s, 1H), 8.05 (s, 1H), 8.48 (d, *J* = 8.5 Hz, 1H), 8.58 (d, *J* = 8.5 Hz, 1H), 10.21 (s, 1H). ^{13}C NMR (125 MHz, DMSO-d_6) δ: 22.0, 22.1, 105.5, 122.9, 123.2, 124.2, 126.0, 126.7, 126.8, 129.5, 129.8, 133.6, 135.9, 136.5, 151.5. EI-MS *m*/*z* (rel. int.): 223 (100), 208 (30). HR-MS *m*/*z* calcd. for $C_{16}H_{14}O$: 222.1045; found: 222.1039.

2,7-Dimethylphenanthryl-9 trifluoromethanesulfonate (7c)

According to general procedure D, a solution of **4c** (0.11 g, 0.50 mmol) and 2,6-lutidine (0.07 mL, 0.064 g, 0.60 mmol) in CH_2Cl_2 was treated with triflic anhydride (0.10 mL, 0.17 g, 0.60 mmol). Normal workup followed by flash chromatography (hexane) afforded 0.17 g (95%) of **7c** as colorless crystals, mp 138 to 139 °C (hexane). IR (KBr) (cm^{-1}): 1430. ^1H NMR (500 MHz, $CDCl_3$) δ: 2.58 (s, 3H), 2.63 (s, 3H), 7.53 (dd, *J* = 8.5, 1.0 Hz, 1H), 7.58 (dd, *J* = 8.5, 1.0 Hz, 1H), 7.66 (s, 1H), 7.68 (s, 1H), 7.92 (s, 1H), 8.51 (*J* = 8.0 Hz, 1H), 8.56 (d, *J* = 8.0 Hz, 1H). ^{13}C NMR (125 MHz, $CDCl_3$) δ: 21.8, 22.2, 118.0, 119.2 (q, *J* = 318 Hz), 121.5, 122.9, 123.2, 125.5, 127.9, 128.9, 130.0, 130.3, 130.6, 137.6, 137.8, 144.71. EI-MS *m*/*z* (rel. int.): 354 (5), 221 (22), 193 (100), 178 (25), 69 (24). HR-MS *m*/*z* calcd. for $C_{17}H_{13}O_3F_3S$: 354.0538; found: 354.0540.

2,7-Dimethylphenanthrene (5c)

A stirred mixture of **7c** (0.035 g, 0.10 mmol), $Pd(OAc)_2$ (0.5 mg, 0.02 mmol), PPh_3 (1.0 mg, 0.004 mmol), Et_3N (0.030 g, 0.30 mmol), and HCO_2H (0.01 mL, 9 mg, 0.20 mmol) in DMF (2 mL) was heated at 60–70 °C for 30 min, cooled to rt, and treated with water (2 mL). The resulting aqueous solution was extracted with Et_2O (3 × 2 mL), the combined organic layer was dried (Na_2SO_4) and concentrated in vacuo, and the residue was subjected to flash chromatography (hexane) to afford 18 mg (91%) of **5c** as colorless crystals, mp 100 to 101 °C (hexane) (lit. (24*a*) mp 101 to 102 °C (ethanol); lit. (24*b*) mp 101 to 102 °C (methanol)). ^1H NMR (25) (500 MHz, $CDCl_3$) δ: 2.60 (s, 6H), 7.50 (dd, *J* = 8.5, 1.5 Hz, 2H), 7.69 (s, 2H), 7.70 (s, 2H), 8.58 (d, *J* = 8.5 Hz, 2H). ^{13}C NMR (125 MHz, $CDCl_3$) δ: 21.9, 122.8, 127.1, 128.5, 128.6, 128.7, 132.3, 136.2. EI-MS *m*/*z* (rel. int.): 206 (100), 191 (46), 189 (47), 178 (19), 69 (20).

3-Ethylphenyltrifluoromethanesulfonate (9)

According to method D, a solution of 3-ethylphenol (**8**) (1.22 g, 10.00 mmol) and 2,6-lutidine (1.40 mL, 1.28 g, 12.00 mmol) in CH_2Cl_2 (100 mL) was treated with triflic anhydride (2.01 mL, 3.38 g, 12.00 mmol). Normal workup followed by flash chromatography (hexane) afforded 2.28 g (90%) of **9** as a colorless oil. IR (neat) (cm^{-1}): 1424, 1214, 1143. ^1H NMR (300 MHz, $CDCl_3$) δ: 1.29 (t, *J* = 8.4 Hz, 3H), 2.73 (q, *J* = 8.4 Hz, 2H), 7.14 (s, 1H), 7.19–7.34 (m, 2H), 7.38 (t, *J* = 15.0 Hz, 1H). ^{13}C NMR (75 MHz, $CDCl_3$) δ: 15.4, 28.9, 118.8, 119.2 (q, *J* = 315 Hz), 121.0, 129.4, 130.4, 147.6, 150.1. EI-MS *m*/*z* (rel. int.): 254 (M^+, 100), 174 (75), 121 (47), 91 (90), 77 (22), 65 (8), which showed identical ^1H NMR, ^{13}C NMR, and MS spectra to those reported for authentic material (26).

N,N-*Diethyl 3-ethylbenzamide (10)*

A stirred mixture of **9** (0.254 g, 1.00 mmol), $Pd(OAc)_2$ (6.7 mg, 0.03 mmol), dppf (33 mg, 0.06 mmol), Et_3N (0.42 mL, 0.303 g, 2.00 mmol), and Et_2NH (2.06 mL, 1.46 g, 20.0 mmol) in DMF (10 mL) was heated at 60–70 °C for 12 h, cooled to rt, and treated with water (10 mL). The aqueous portion was extracted with Et_2O (3 × 10 mL) and the extract was dried (Na_2SO_4) and concentrated in vacuo. The residue was purified by flash column chromatography (EtOAc–hexane, 1:5) to afford 0.140 g (70%) of **10** as a yellow oil. IR (neat) (cm^{-1}): 1633. ^1H NMR (300 MHz, $CDCl_3$) δ: 1.00–1.20 (br, 6H), 1.17 (t, *J* = 7.2 Hz, 3H), 2.60 (q, *J* = 7.2 Hz, 2H), 3.17 (br s, 2H), 3.48 (br s, 2H), 7.08–7.27 (m, 4H). ^{13}C NMR (75 MHz, $CDCl_3$) δ: 13.2, 14.6, 15.7, 29.1, 39.5, 43.6, 123.7, 126.7, 128.9, 137.6, 144.7, 171.8. EI-MS *m*/*z* (rel. int.): 205 (M^+, 58), 176 (7), 133 (100), 105 (28), 77 (17). HR-MS *m*/*z* calcd. for $C_{13}H_{19}NO$: 205.1467; found: 205.1469.

Pinacolo[2-(*N,N*-diethylcarboxamido)-3-ethylphenyl]boronate (11)

According to general procedure A, a solution of **10** (2.05 g, 10.0 mmol), *s*-BuLi (9.60 mL of a 1.25 mol L^{-1} solution, 12.0 mmol), and TMEDA (1.07 mL, 1.39 g, 12.0 mmol) was treated with $B(OMe)_3$ (2.73 mL, 2.50 g, 24.0 mmol). Normal workup afforded a thick oil that was stirred with a solution of pinacol (2.83 g, 24.0 mmol) and anhyd $MgSO_4$ (5 g) in dry CH_2Cl_2 (20 mL). Filtration followed by concentration gave a residue that was purified by flash chromatography (EtOAc–hexane, 1:3) to afford 2.51 g (76%) of **11** as a colorless oil. IR (neat) (cm^{-1}): 1635, 1432, 1354. ^1H NMR (300 MHz, $CDCl_3$) δ: 1.01 (t, *J* = 7.5 Hz, 3H), 1.20 (t, *J* = 8.1 Hz, 3H), 1.25–1.30 (m, 15H), 2.63 (q, *J* = 7.5 Hz, 2H), 3.14 (q, *J* = 8.1 Hz, 2H), 3.55 (q, *J* = 8.1 Hz, 2H), 7.06 (s, 1H), 7.17 (d, *J* = 7.5 Hz, 1H), 7.72 (d, *J* = 7.5 Hz, 1H). ^{13}C NMR (75 MHz, $CDCl_3$) δ: 12.9, 14.1, 15.6, 25.2, 38.5, 43.3, 83.9, 125.4, 127.7, 135.9, 143.9, 149.9, 171.0. EI-MS *m*/*z* (rel. int.): 331 (M^+, 21), 273 (100), 232 (16), 188 (6), 158 (7), 105 (8), 55 (4). HR-MS *m*/*z* calcd. for $C_{19}H_{30}BNO_3$: 331.2319; found: 331.2321.

© 2004 NRC Canada

N,N-*Diethyl 3-ethyl-2′,3′-dimethylbiphenyl-2-carboxamide (12)*

According to general procedure B, 1-bromo-2,3-dimethylbenzene (1.36 mL, 1.85 g, 10.0 mmol) was subjected to reaction with **11** (3.31 g, 10 mmol) in the presence of $Pd(PPh_3)_4$ (0.185 g, 0.16 mmol). Normal workup followed by flash chromatography (EtOAc–hexane, 1:5) afforded 1.85 g (60%) of **12** as a viscous oil. IR (neat) (cm^{-1}): 1634. ^1H NMR (300 MHz, $CDCl_3$) δ: 0.68 (s, 3H), 0.75–1.04 (br, 3H), 1.28 (t, *J* = 7.8 Hz, 3H), 2.08 (s, 3H), 2.27 (s, 3H), 2.72 (q, *J* = 7.8 Hz, 2H), 2.75–3.30 (br, 4H), 3.73 (s, 1H), 6.96–7.25 (m, 6H). ^{13}C NMR (75 MHz, $CDCl_3$) δ: 12.1, 14.1, 15.6, 17.6, 20.9, 28.8, 38.2, 42.8, 125.4, 126.8, 128.0, 129.4, 130.1, 135.1, 137.2, 143.5, 170.8. EI-MS *m/z* (rel. int.): 309 (M^+, 100), 280 (13), 237 (15), 209 (8), 178 (18), 165 (15), 74 (35). HR-MS *m/z* calcd. for $C_{21}H_{27}NO$: 309.2093; found: 309.2086.

7-Ethyl-1-methyl-9-phenanthrol (13)

According to general procedure C, treatment of a solution of **12** (3.09 g, 10 mmol) in THL (20 mL) with a solution of LDA (25.0 mmol) in THF (80 mL) for 30 min followed by acidification, normal workup, and flash chromatography (hexane) afforded 2.24 g (95%) of **13** as colorless crystals, mp 192–195 °C (CH_2Cl_2). IR (KBr) (cm^{-1}): 3306. ^1H NMR (300 MHz, $CDCl_3$) δ: 1.28 (t, *J* = 8.1 Hz, 3H), 2.60 (s, 3H), 2.84 (q, *J* = 8.1 Hz, 2H), 7.25 (s, 1H), 7.28–7.38 (m, 2H), 7.51 (d, *J* = 8.4 Hz, 1H), 8.12 (s, 1H), 8.47 (d, *J* = 8.1 Hz, 1H), 8.63 (d, *J* = 8.1 Hz, 1H), 10.36 (s, 1H). ^{13}C NMR (75M Hz, $CDCl_3$) δ: 16.4, 20.5, 29.2, 102.1, 121.5, 123.7, 124.0, 126.1, 126.6, 127.4, 128.2, 128.4, 130.4, 132.2, 132.7, 142.5, 151.8. EI-MS *m/z* (rel. int.): 236 (M^+, 100), 221 (65), 207 (10), 193 (15), 179 (10), 165 (4), 89 (3). HR-MS *m/z* calcd. for $C_{17}H_{16}O$: 236.1201; found: 236.1206.

7-Ethyl-1-methylphenanthryl-9-trifluoromethanesulfonate (14)

According to general procedure D, a solution of **13** (1.18 g, 5.00 mmol) and 2,6-lutidine (0.69 mL, 0.64 g, 6.00 mmol) in CH_2Cl_2 (100 mL) was treated with triflic anhydride (1.01 mL, 1.69 g, 6.00 mmol). Normal workup followed by flash chromatography (hexane) afforded 1.20 g (95%) of **14** as colorless crystals, mp 61 to 62 °C (EtOAc). IR (KBr) (cm^{-1}): 1421, 1208, 1135. ^1H NMR (300 MHz, $CDCl_3$) δ: 1.41 (t, *J* = 7.5 Hz, 3H), 2.74 (s, 3H), 2.95 (q, *J* = 7.5 Hz, 2H), 7.48 (d, *J* = 7.2 Hz, 1H), 7.57–7.66 (m, 2H), 7.91 (s, 1H), 7.97 (s, 1H), 8.52 (d, *J* = 9.0 Hz, 1H), 8.64 (d, *J* = 9.0 Hz, 1H). ^{13}C NMR (75 MHz, $CDCl_3$) δ: 15.7, 20.1, 29.4, 114.7, 119.3 (q, *J* = 323 Hz), 120.1, 121.1, 123.7, 129.3, 129.5, 130.2, 130.7, 135.7, 144.3, 144.7. EI-MS *m/z* (rel. int.): 368 (M^+, 35), 235 (45), 207 (100), 192 (18), 165 (3), 69 (7). HR-MS *m/z* calcd. for $C_{18}H_{15}F_3O_3S$: 368.0684; found: 368.0689.

7-Ethyl-1-methylphenanthrene (15)

A stirred mixture of **14** (0.368 g, 1.00 mmol), $Pd(OAc)_2$ (4.5 mg, 0.02 mmol), PPh_3 (10.5 mg, 0.04 mmol), Et_3N (0.42 mL, 0.303 g, 3.00 mmol), and HCO_2H (0.08 mL, 92 mg, 2.00 mmol) in DMF (10 mL) was heated at 60–70 °C for 30 min. The reaction mixture was cooled to rt and water was added (10 mL). The aqueous layer was separated and extracted with Et_2O (3 × 10 mL), and the extract was dried (Na_2SO_4) and concentrated in vacuo. The residue was purified by flash column chromatography (hexane) to afford 202 mg (92%) of **15** as colorless crystals, mp 92 to 93 °C (hexane) (lit. (27) mp 87.5 °C (MeOH)). ^1H NMR (300 MHz, $CDCl_3$) δ: 1.47 (t, *J* = 7.5 Hz, 3H), 2.84 (s, 3H), 2.96 (q, *J* = 7.5 Hz, 2H), 7.48–7.65 (m, 3H), 7.78 (s, 1H), 7.81 (d, *J* = 9.0 Hz, 1H), 8.01 (d, *J* = 9.0 Hz, 1H), 8.63 (d, *J* = 9.0 Hz, 1H), 8.69 (d, *J* = 9.0 Hz, 1H). ^{13}C NMR (75 MHz, $CDCl_3$) δ: 16.1, 20.4, 29.2, 121.2, 123.2, 123.4, 126.5, 127.0, 127.2, 127.7, 127.8, 129.2, 130.8, 130.9, 132.3, 135.2, 142.9. EI-MS *m/z* (rel. int.): 220 (M^+, 100), 205 (73), 189 (15), 178 (3), 165 (3), 101 (4). HR-MS *m/z* calcd. for $C_{17}H_{16}$: 220.1252; found: 220.1255.

N,N-*Diethyl 4-*tert*-butylphenyl carbamate (23)*

To a suspension of sodium hydride (0.48 g, 60% in mineral oil, 12 mmol) in anhyd THF (20 mL) was added 4-*tert*-butylphenol (1.50 g, 10 mmol). After hydrogen evolution ceased (1 h), diethylcarbamoyl chloride (1.51 mL, 1.62 g, 12 mmol) was added and the reaction mixture was stirred at rt for 2 h, and treated with water (10 mL). The aqueous layer was separated and extracted with Et_2O (3 × 20 mL). The combined extract was dried (Na_2SO_4) and concentrated in vacuo to give a residue that was purified by flash column chromatography (EtOAc–hexane, 1:3) to afford 1.49 g (60%) of **23** as colorless crystals, mp 77 to 78 °C (CH_2Cl_2) (lit. (28) mp 86 °C (pentene)). IR (KBr) (cm^{-1}): 1706, 1480, 1402, 1277, 1211. ^1H NMR (300 MHz, $CDCl_3$) δ: 1.25 (s, 6H), 1.34 (s, 9H), 3.43 (s, 4H), 7.04–7.10 (m, 2H), 7.36–7.42 (m, 2H). ^{13}C NMR (75 MHz, $CDCl_3$) δ: 13.8, 14.6, 31.8, 34.7, 42.2, 42.6, 121.4, 126.4, 148.1, 149.6, 154.8. EI-MS *m/z* (rel. int.): 249 (M^+, 35), 163 (2), 146 (2), 135 (3), 100 (100), 72 (7). HR-MS *m/z* calcd. for $C_{15}H_{23}NO_2$: 249.1729; found: 249.1736.

N,N-*Diethyl 4-tert-butyl-2-hydroxybenzamide (24)*

A solution of **23** (2.49 g, 10.0 mmol) in anhyd THF (20 mL) was added dropwise to a solution of *s*-BuLi (9.6 mL of 1.25 mol L^{-1} solution, 12.0 mmol) and TMEDA (1.07 mL, 1.39 g, 12.0 mmol) in anhyd THF (30 mL) at –78 °C. The reaction mixture was stirred at –78 °C for 1 h, allowed to warm to rt over 12 h, and quenched with a satd. aq. NH_4Cl solution (10 mL). The aqueous layer was separated and extracted with Et_2O (3 × 20 mL), and the combined extract was dried (Na_2SO_4) and concentrated in vacuo. The resulting residue was purified by flash column chromatography (EtOAc–hexanes, 1:5) to afford 1.37 g (55%) of **24** as colorless crystals, mp 133 – 135 °C (CH_2Cl_2). IR (KBr) (cm^{-1}): 3142, 1595, 1268. ^1H NMR (300 MHz, $CDCl_3$) δ: 1.27–1.33 (m, 15H), 3.51 (q, *J* = 7.2 Hz, 4H), 6.92 (d, *J* = 17.1 Hz, 1H), 7.27 (d, *J* = 5.0 Hz, 1H) 7.34 (dd, *J* = 17.1, 5.0 Hz, 1H), 9.50 (s, 1H). $^{13}CNMR$ (75 MHz, $CDCl_3$) δ:13.8, 31.8, 34.4, 42.5, 117.6, 118.1, 124.3, 129.6, 141.4, 156.4, 172.2. EI-MS *m/z* (rel. int.): 249 (M^+, 31), 234 (72), 177 (76), 161 (100), 133 (16), 105 (20), 72 (38). HR-MS *m/z* calcd. for $C_{15}H_{23}NO_2$: 249.1729; found: 249.1719.

4*-tert-*Butyl-2-(*N,N-*diethylcarboxamido)phenyl trifluoromethanesulfonate (20)

According to general procedure D, a solution of **24** (2.49 g, 10.0 mmol) and pyridine (0.97 mL, 0.95 g, 12.0 mmol) in CH_2Cl_2 (100 mL) was treated with triflic an-

© 2004 NRC Canada

hydride (2.01 mL, 3.38 g, 12.0 mmol). Normal workup followed by flash chromatography (EtOAc–hexane, 1:5) afforded 2.48 g (65%) of **20** as a colorless oil. IR (neat) (cm^{-1}): 1645, 1426, 1215. ^1H NMR ($CDCl_3$) δ: 1.08 (t, J = 7.2 Hz, 3H), 1.17 (t, J = 7.2 Hz, 3H), 1.30 (s, 9H), 3.16 (q, J = 7.2 Hz, 2H), 3.40–3.70 (br, 2H), 7.23 (d, J = 8.6 Hz, 1H), 7.37 (d, J = 2.1 Hz, 1H), 7.40 (dd, J = 8.6, 2.1 Hz, 1H). ^{13}C NMR ($CDCl_3$) δ: 12.7, 14.2, 31.4, 35.1, 39.5, 43.3, 118.8 (q, J = 323 Hz), 121.5, 125.8, 128.0, 130.7, 143.3, 152.1, 166.2. EI-MS m/z (rel. int.): 382 (M^+, 71), 309 (100), 233 (38), 161 (73), 72 (69). HR-MS m/z calcd. for $C_{16}H_{22}F_3NO_4S$: 381.1222; found: 381.1234.

N,N-*Diethyl 3*-tert-*butyl-2′,3′-trimethyldiphenyl-2-carboxamide (19)*

According to general procedure B, 2,3-dimethylphenylboronic acid (1.50 g, 10.0 mmol) was subjected to reaction with **20** (3.82 g, 10 mmol) in the presence of $Pd(PPh_3)_4$ (0.185 g, 0.16 mmol). Normal workup followed by flash chromatography (EtOAc–hexane, 1:5) afforded 2.76 g (82%) of **19** as a viscous oil. IR (cm^{-1}): 1634. ^1H NMR ($CDCl_3$) δ: 0.69 (t, J = 7.2 Hz, 3H), 0.70–1.0 (br, 3H), 1.35 (s, 9H), 2.10 (s, 3H), 2.27 (s, 3H), 2.50–3.90 (br m, 4H), 6.80–7.43 (m, 6H). ^{13}C NMR ($CDCl_3$) δ: 12.2, 13.8, 24.1, 31.6, 34.9, 38.3, 124.4, 125.4, 126.5, 127.6, 128.4, 129.3, 134.7, 137.1, 142.6, 150.3, 151.6, 155.5, 171.1. EI-MS m/z (rel. int.): 337 (M^+, 97), 322 (7), 264 (100), 250 (37), 209 (40), 181 (12), 165 (17), 74 (32). HR-MS m/z calcd. for $C_{23}H_{31}NO$: 337.2406; found: 337.2398.

7*-tert-*Butyl-1-methyl-9-phenanthrol (25)

According to general procedure C, treatment of a solution of **19** (3.37 g, 10 mmol) in THF (20 mL) with a solution of LDA (25.0 mmol) in THF (80 mL) for 30 min followed by acidification, normal workup, and flash chromatography (hexane) afforded 2.38 g (90%) of **25** as a powder that gave colorless crystals, mp 165–168 °C (CH_2Cl_2). IR (KBr) (cm^{-1}): 3466. ^1H NMR ($CDCl_3$) δ: 1.53 (s, 9H), 2.63 (s, 3H), 5.81 (s, 1H), 7.20 (s, 1H), 7.38–7.45 (m, 2H), 7.81 (dd, J = 8.1, 2.1 Hz, 1H), 8.36 (d, J = 2.1 Hz, 1H), 8.49 (d, J = 8.1 Hz, 1H), 8.64 (d, J = 9.0 Hz, 1H). ^{13}C NMR ($CDCl_3$) δ 20.6, 31.1, 35.7, 103.4, 118.4, 121.3, 123.6, 124.3, 125.5, 126.2, 127.3, 128.2, 130.5, 131.9, 133.4, 149.9, 150.3. EI-MS m/z (rel. int.): 264 (M^+, 100), 250 (50), 232 (13), 221 (22), 194 (13), 179 (12), 165 (9), 11 (8). HR-MS m/z calcd. for $C_{19}H_{20}O$: 264.1514 (accurate data could not be obtained due to oxidation of the sample).

7*-tert-*Butyl-1-methylphenanthryl-9-trifluoromethanesulfonate (26)

According to general procedure D, to a solution of **25** (1.32 g, 5.00 mmol) and 2,6-lutidine (0.69 mL, 0.64 g, 6.00 mmol) in CH_2Cl_2 (100 mL) was added triflic anhydride (1.01 mL, 1.69 g, 6.00 mmol). Normal workup followed by flash chromatography (hexane) afforded 1.72 g (87%) of **26** as colorless crystals, mp 103 to 104 °C (EtOAc). IR (KBr) (cm^{-1}): 1423, 1207, 1139. ^1H NMR ($CDCl_3$) δ: 1.61 (s, 9H), 2.73 (s, 3H), 7.45 (d, J = 7.2 Hz, 1H), 7.56 (t, J = 8.4 Hz, 1H), 7.88 (dd, J = 9.0, 1.8 Hz, 1H), 7.93 (s, 1H), 8.27 (d, J = 1.8 Hz, 1H), 8.44 (d, J = 8.1 Hz, 1H), 8.66 (d, J = 9.0 Hz, 1H). ^{13}C NMR ($CDCl_3$) δ: 20.0, 31.6, 35.5, 114.7, 117.6, 119.4 (q, J = 323 Hz), 121.1, 123.6, 125.1, 126.9, 127.7, 128.7, 129.6, 130.1, 130.6, 135.6, 144.9, 151.2. EI-MS m/z (rel. int.): 396 (M^+, 68), 381 (14), 263 (100), 236 (75), 220 (32), 205 (16), 179 (8), 69 (11). HR-MS m/z calcd. for $C_{20}H_{19}F_3O_3S$: 396.1007; found: 396.1008.

7*-tert-*Butyl-1-methylphenanthrene (27)

A stirred mixture of **26** (0.396 g, 1.00 mmol), $Pd(OAc)_2$ (4.5 mg, 0.02 mmol), PPh_3 (10.5 mg, 0.04 mmol), Et_3N (0.42 mL, 0.303 g, 3.00 mmol), and HCO_2H (0.08 mL, 92 mg, 2.00 mmol) in DMF (10 mL) was heated at 60–70 °C for 30 min. The reaction mixture was cooled to rt, water (0 mL) was added, and the mixture was extracted with Et_2O (3 × 10 mL). The combined organic extract was dried (Na_2SO_4), concentrated to dryness, and the residue was subjected to flash chromatography (hexane) to afford 248 mg (95%) of **27** as colorless crystals, mp 126 to 127 °C (hexane). ^1H NMR ($CDCl_3$) δ: 1.74 (s, 9H), 2.96 (s, 3H), 7.64 (d, J = 7.4 Hz, 1H), 7.74 (t, J = 7.5 Hz, 1H), 7.93 (dd, J = 8.6, 1.8 Hz, 1H), 7.98 (d, J = 9.3 Hz, 1H), 8.12 (s, 1H), 8.14 (d, J = 9.2 Hz, 1H), 8.77 (d, J = 8.6 Hz, 1H), 8.82 (d, J = 8.8 Hz, 1H). ^{13}C NMR ($CDCl_3$) δ: 20.5, 32.0, 35.3, 121.7, 123.7, 125.8, 126.9, 127.9, 128.2, 129.4, 131.2, 131.5, 132.6, 135.6, 150.0. EI-MS m/z (rel. int.): 248 (M^+, 100), 234 (95), 218 (10), 205 (13), 189 (7), 178 (3). HR-MS m/z calcd. for $C_{19}H_{20}$: 248.1565; found: 248.1564.

Acknowledgements

We are grateful to Canadian Network of Toxicology Centers (CNTC) for support of this research program. XC is a recipient of a Queen's Graduate Award (QGA).

References

1. (*a*) R. Munoz, B. Guieysse, and B. Mattiasson. Appl. Microbiol. Biotechnol. **61**, 261 (2003); (*b*) R. van Herwijnen, P. Wattiau, L. Bastiaens, L. Daal, L. Jonker, D. Springael, H.A.J. Govers, and J.R. Parsons. Res. Microbiol. **154**, 199 (2003).
2. (*a*) A.C. Wertheimer and A.G. Celewycz. Am. Fish. Soc. Symp. **18**, 518 (1996); (*b*) W.R. Reeves, R. Barhoumi, R.C. Burgharat, S.L. Lemke, K. Mayura, T.T. McDonald, T.D. Philips, and K.C. Donnelly. Environ. Sci. Technol. **35**, 1630 (2001); (*c*) N. Basu, S. Billiard, N. Fragoso, A. Omoike, S. Tabash, S. Brown, and P. Hodson. Environ. Toxicol. Chem. **20**, 1244 (2001).
3. (*a*) S.M. Billard, K. Wuerbach, and P.V. Hodson. Env. Toxicol. Chem. **18**, 2070 (1999); (*b*) B.L. Boese, J.O. Lamberson, R.C. Swartz, R. Ozretich, and F. Cole. Arch. Environ. Contam. Toxicol. **34**, 235 (1998); (*c*) C.D. Metcalfe, T.L. Metcalfe, Y. Kiparissis, B.G. Koenig, C. Khan, R.J. Hughes, T.R. Croley, R.E. March, and T. Potter. Environ. Toxicol. Chem. **20**, 297 (2001).
4. (*a*) Y. Kiparissis, P.V. Hodson, Y. Blazeski, X. Cai, and V. Snieckus. Proceedings of the Society of Environmental Toxicology and Chemistry, 22nd Annual Meeting, Baltimore, Maryland, 11–15 Nov. 2001; (*b*) X. Cai, S. Brown, P. Hodson, and V. Snieckus. Canadian Network of Toxicology Centres (CNTC) Annual Symposium Report, Ottawa, Ontario, March 25 and March 26, 2003.
5. W. Krasodomski, M.K. Luczynski, J. Wilamowski, and J. Sepiol. Tetrahedron, **59**, 5677 (2003).

© 2004 NRC Canada

6. (*a*) P.H. Leake. Chem. Rev. **56**, 57 (1956); (*b*) P.E. Leake. Org. React. (N.Y.), **9**, 409 (1957); (*c*) P. Hanson, P.W. Lovenich, S.C. Rowell, P.H. Walton, and A.W. Timms. J. Chem. Soc. Perkin Trans. 2, 49 (1999); (*d*) F.W. Wassmundt and W.F. Kiesman. J. Org. Chem. **60**, 196 (1995); (*e*) R. Duclos, J.S. Tung, and H. Rapoport. J. Org. Chem. **49**, 5243 (1984); (*f*) B. Chauncy and E. Gellert. Austr. J. Chem. **22**, 993 (1969).
7. A.J. Floyd, S.F. Dyke, and S.E. Ward. Chem. Rev. **76**, 509 (1976).
8. (*a*) F.B. Mallory and C. Mallory. Org. React. (N.Y.), **30**, 1 (1984); (*b*) F.B. Mallory, M.J. Rudolph, and S.M. Oh. J. Org. Chem. **54**, 4619 (1989); (*c*) J.C. Estevez, M.C. Villaverde, R.J. Estevez, J.A. Seijas, and L. Castedo. Can. J. Chem. **68**, 964 (1990); (*d*) M.C. Pampin, J.C. Estévez, R.J. Estévez, M. Maestro, and L. Castedo. Tetrahedron, **59**, 7231 (2003); (*e*) A. Sugimoto, R. Hiraoka, H. Inoue, T. Adachi. J. Chem. Soc. Perkin Trans. 1, 1559 (1992); (*f*) M.K. Lakshman, P.L. Kole, S. Chaturvedi, J.H. Saugier, H.J.C. Yeh, J.P. Glusker, H.L. Carrell, A.K. Katz, C.E. Afshar, W. Dashwood, G. Kenniston, and W.M. Baird. J. Am. Chem. Soc. **122**, 12 629 (2000).
9. (*a*) G. Dyker, J. Korning, and F. Nerenz. Pure Appl. Chem. **68**, 323 (1996); (*b*) G. Dyker P. Siemsen, S. Sostmann, A. Wiegand, I. Dix, and P.G. Jones. Chem. Ber./Recl. **130**, 261 (1997); (*c*) G. Dyker. Eur. J. Inorg. Chem. **6**, 877 (1998); (*d*) K.V. Radhakrishnan, E. Yoshikawa, and Y. Yamamoto. Tetrahedron Lett. **40**, 7533 (1999); (*e*) E. Yoshikawa and Y. Yamamoto. Angew. Chem. Int. Ed. **39**, 173 (2000); (*d*) D. Pena, D. Perez, E. Guitian, and L. Castedo. J. Org. Chem. **65**, 6944 (2000); (*g*) D. Pena, D. Perez, E. Guitian, and L. Castedo. Synlett, 1061 (2000).
10. (*a*) J.C. Estevez, M.C. Villaverde, R.J. Estevez, and L. Castedo. Tetrahedron, **49**, 2783 (1993); (*b*) G.A. Kraus and N. Zhang. Tetrahedron Lett. **43**, 9597 (2002); (*b*) D.C. Harrowven, M.I.T. Nunn, and D.R. Fenwick. Tetrahedron Lett. **43**, 7345 (2002).
11. (*a*) For other recent application of DoM and DreM methodology see: J.-m. Fu and V. Snieckus. Can. J. Chem. **78**, 905 (2000); (*b*) A.V. Kalinin, M.A. Reed, B.H. Norman, and V. Snieckus. J. Org. Chem. **68**, 5992 (2003).
12. C.B. de Koning, A.L. Rousseau, and W.A.L. van Otterlo. Tetrahedron, **59**, 7 (2003).
13. R.P. Moody, D. Riedel, L. Ritter, and C.A. Franklin. J. Toxicol. Environ. Health, **22**, 471 (1987).
14. P. Beak and R.A. Brown. J. Org. Chem. **47**, 34 (1982).
15. P.J. Stang, M. Hanack, and L.R. Subramanian. Synthesis, **85** (1982).
16. R. Pschorr and H. Hofman. Chem. Ber. **39**, 3110 (1906).
17. (*a*) S. Cacchi and G. Ortar. Tetrahedron Lett. **27**, 3931 (1986); (*b*) R. Crettaz, J. Waser, and Y. Bessard. Org. Process Res. Dev. **5**, 572 (2001); (*c*) Y. Wan, M. Alterman, M. Larhed, and A. Hallberg. J. Org. Chem. **67**, 6232 (2002); (*d*) W. Mägerlein, A.F. Indolese, and M. Beller. Angew. Chem. Int. Ed. **40**, 2856 (2001).
18. M.P. Sibi and V. Snieckus. J. Org. Chem. **48**, 1935 (1983).
19. S.C. Watson and J.F. Eastham. J. Organomet. Chem. **9**, 165 (1967); (*b*) M. Gau and H.O. House. Org. Synth. Coll. VI, 121 (1988).
20. P. Beak and R.A. Brown. J. Org. Chem. **47**, 34 (1982).
21. T. Hasselstrom. J. Am. Chem. Soc. **63**, 2627 (1941).
22. W.E. Bachmann and A.L. Wilds. J. Am Chem. Soc. **60**, 624 (1938).
23. J.C. Bardham and D. Nasipuri. J. Chem. Soc. 350 (1956).
24. (*a*) M.S. Newman and K.C. Lilje. J. Org. Chem. **44**, 4944 (1979); (*b*) R.D. Haworth, C.R. Mavin, and G.J. Sheldrick. J. Chem. Soc. 454 (1934).
25. A. Helms, D. Heiler, and G. McLendon. J. Am. Chem. Soc. **114**, 6227 (1992).
26. H.M. Petrassi, T. Klabunde, J. Sacchettini, and J.W. Kelly. J. Am. Chem. Soc. **122**, 2178 (2000).
27. L. Ruzicka and St. Kaufman. Helv. Chim. Acta, **24**, 939 (1941).
28. R. Rips, C. Tilloy-Voillaume, J. Peyroux, and P. Rossignol. Chim. Ther. **5**, 418 (1970).

© 2004 NRC Canada

Comparison of the Suzuki cross-coupling reactions of 4,7-dichloroquinoline and 7-chloro-4-iodoquinoline with arylboronic acids using phosphine-free palladium catalysis in water[1]

Richard W. Friesen and Laird A. Trimble

Abstract: 4,7-Dichloroquinoline (**1a**) and 7-chloro-4-iodoquinoline (**1b**) undergo Suzuki cross-coupling reactions with arylboronic acids catalyzed by phosphine-free palladium acetate in boiling water. Using phenylboronic acid (**2**), the reaction of **1a** provides 7-chloro-4-phenylquinoline (**3**) (78%) together with diphenylquinoline (**4**) (12%), while **1b** reacts in a much more regioselective fashion and provides **3** in 98% isolated yield. Although **1b** undergoes a more regioselective Suzuki reaction than **1a**, additional important observations are that the overall reaction of **1b** with **2** is three times slower than **1a** and that the reaction occurs in the absence of tetrabutylammonium bromide. Using optimized reaction conditions, a variety of aryl and vinylboronic acids undergo regioselective Suzuki cross-coupling with **1b** to provide the products **7**, **10**, and **11** in good to excellent yield.

Key words: palladium, cross-coupling, regioselectivity, quinolines, boronic acids.

Résumé : La 4,7-dichloroquinoléine (**1a**) et la 7-chloro-4-iodoquinoléine (**1b**) subissent des réactions de couplage de Suzuki avec les acides arylboroniques qui sont catalysées par de l'acétate de palladium sans phosphine dans de l'eau bouillante. Avec l'acide phénylboronique (**2**), la réaction du composé **1a** fournit la 7-chloro-4-phénylquinoléine (**3**) (78%) aux côtés de diphénylquinoléine (**4**) (12%) alors que le composé **1b** réagit d'une façon beaucoup plus régiosélective et fournit le composé **3** avec un rendement de 98% en produit isolé. Même si le composé **1b** donne lieu à une réaction de Suzuki plus régiosélective que celle du composé **1a**, des observations importantes additionnelles sont que la vitesse globale du composé **1b** avec **2** est trois fois plus lente que celle du composé **1a** et que la réaction se produit en l'absence de bromure de tétrabutylammonium. Utilisant des conditions réactionnelles optimisées, une variété d'acides aryl- et vinylboroniques donnent lieu à des réactions régiosélectives de couplage croisé de Suzuki avec le composé **1b** et elles fournissent les produits **7**, **10** et **11** avec des rendements allant de bons à excellents.

Mots clés : palladium, couplage croisé, régiosélectivité, quinoléines, acides boroniques.

[Traduit par la Rédaction]

Introduction

The palladium-catalyzed cross-coupling of aryl halides with boronic acids, commonly referred to as the Suzuki reaction (1–5), is an exceptionally versatile and highly utilized reaction for the construction of carbon-carbon bonds and, in particular, for the preparation of heterobiaryls. The use of heteroaryl chlorides as one of the coupling partners has seen increasing utility (6–11) and is attractive since the starting materials are often more readily available than the corresponding bromides or iodides. We have recently described (12) the synthesis of 2,4,7-trisubstituted quinoline 5-lipoxygenase inhibitors using, as one of the key steps, the regioselective Suzuki cross-coupling reaction of 4,7-dichloroquinoline (**1a**) with arylboronic acids. As originally described by Mitchell and co-workers (6), the reaction of **1a** with 1.1 equiv. of phenylboronic acid (**2**) catalyzed by $Pd(Ph_3P)_4$ (3%) in refluxing aqueous ethanol – benzene and in the presence of Na_2CO_3 provided, after 48 h, 7-chloro-4-phenylquinoline (**3**) in 82% isolated yield (Scheme 1). It was not mentioned whether the bis-addition product 4,7-diphenylquinoline (**4**) or the regioisomeric mono-addition product 4-chloro-7-phenylquinoline (**5**) were observed in this reaction.

We have repeated this Suzuki cross-coupling reaction between **1a** and **2** in connection with our medicinal chemistry program. Dichloride **1a** was consumed in 6 h, and in addition to **3** (81%), a significant amount of bis-addition product **4** (10%) was obtained. Previous reports have demonstrated that 4,7-dichloroquinoline (**1a**) undergoes regioselective palladium-catalyzed Stille (13) and alkoxycarbonylation (14)

Received 7 July 2003. Published on the NRC Research Press Web site at http://canjchem.nrc.ca on 20 January 2004.

This paper is dedicated to Professor Ed Piers for his many contributions to synthetic organic chemistry and to the chemistry community in Canada.

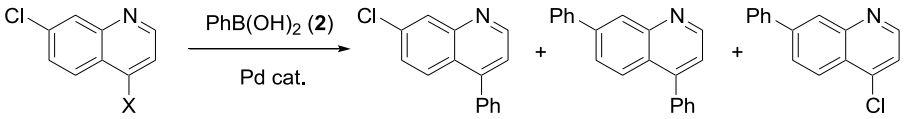
R.W. Friesen[2] and L.A. Trimble. Department of Medicinal Chemistry, Merck Frosst Centre for Therapeutic Research, 16711 Trans Canada Hwy., Kirkland, QC H9H 3L1, Canada.

[1]This article is part of a Special Issue dedicated to Professor Ed Piers.

[2]Corresponding author (e-mail: rick_friesen@merck.com).

 doi: 10.1139/V03-187 © 2004 NRC Canada

Scheme 1.



1a X = Cl
1b X = I

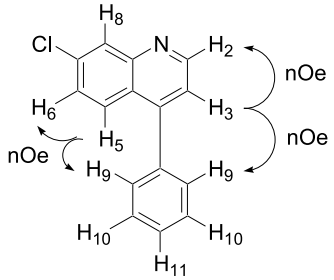
3 **4** **5**

reactions at the C4 position. However, in the latter reaction, alkoxycarbonylation at both C4 and C7 produces varying amounts of diester, depending on the reaction conditions used. Therefore, the observation of **4** in the reaction of **1a** and **2** was not completely unexpected. Since we required an efficient cross-coupling procedure that would bring about regioselective monofunctionalization of a quinoline (6, 7, 13–17), such as **1a**, without consuming more elaborate boronic acids by the production of bis-addition products, we undertook a more detailed study of the reactions of **1a** and the corresponding iodide **1b** to optimize the formation of **3**. The results of this study are presented here.

Results and discussion

Structural assignment

In their initial publication (6), Mitchell and co-workers assigned regioisomer **3** as the product of the Suzuki cross-coupling reaction between **1a** and **2**. This assignment was made without any structural verification, although one might reasonably expect **3** to be produced as the major regioisomer based on precedence with other reactions of **1a** (13, 14, 18). However, we felt that a rigorous structural assignment was warranted since the production of the bis-addition adduct **4** reveals that reactivity at both C4 and C7 is possible. ^{1}H NMR experiments ($CDCl_3$, 600 MHz) indicated that **3** is indeed the predominant mono-substituted regioisomer formed. Thus, proton resonance assignments (see Table 1) were made using a 2D-COSY experiment.[3] In a subsequent series of nuclear Overhauser enhancement (nOe) experiments, clear enhancements in resonance intensity were observed for H9 upon irradiation of H3 and H5, while irradiation of H8 did not result in nOe of any other resonance.



3

Reaction optimization studies

To optimize the reaction of **1a** for mono-substitution at C4, we rapidly surveyed many of the reaction conditions that are typically modified in the Suzuki cross-coupling reaction (1–5), including, for example, the palladium catalyst ($PdCl_2(Ph_3P)_2$, $Pd_2(dba)_3$ (with and without P(*t*-Bu)$_3$), Pd(dppf)Cl_2), solvents (DMF, THF, EtOH), aqueous base (Na_2CO_3, Cs_2CO_3), temperature, and the use of additives (KF). None of these changes substantially altered the yields of **3** and **4** that were observed upon reaction of **1a** with **2**. Several reports over the last decade have described the successful cross-coupling of arylboronic acids and aryl bromides, iodides, or triflates using phosphine-free palladium, such as $Pd(OAc)_2$, in aqueous–organic co-solvents (19, 20) or in water alone (21, 22). Employing reaction conditions optimized by Leadbeater and Marco (22), the reaction of **1a** with 1.1 equiv. of **2** in the presence of 1% $Pd(OAc)_2$ and 0.25 equiv. of nBu$_4$NBr in refluxing water (oil bath at 150 °C) under nitrogen atmosphere provided **3** (78%) and **4** (12%) upon consumption of **1a**. Although this reaction differed little from all the others we had surveyed in terms of the yields of the two products, it was complete within 30 min (Table 2, entry 1), while the majority of the others, including the original reaction described by Mitchell, required extended reaction times (6 h to 2 days). Since the rapidity of the reaction under these conditions was perceived as an advantage, we chose to further characterize the cross-coupling reaction of **1a** using phosphine-free palladium in water.

The results of the two experiments are informative. First, when the reaction between **1a** and **2** was stopped prior to consumption of **1a** (at 15 min), we observed the presence

Table 1. 7-Chloro-4-phenylquinoline (**3**): ^{1}H NMR spectrum and nOe experiments.

Proton[a]	Assignment[b]	nOe observed[c]
H_2	8.94 (d, J = 4.4 Hz)	H_3
H_3	7.34 (d, J = 4.4 Hz)	H_2, H_9
H_5	7.86 (d, J = 9.2 Hz)	H_6, H_9
H_6	7.45 (dd, J = 2.1 9.2 Hz)	
H_8	8.17 (d, J = 2.1 Hz)	None
H_9	7.48 (m)	
H_{10}, H_{11}	7.50–7.56 (m)	

Note: Spectra obtained in $CDCl_3$ at 600 MHz.
[a]See structure **3** for proton labeling.
[b]Resonances reported in ppm (δ) with multiplicity and coupling constants in parentheses.
[c]In an nOe experiment, irradiation of the resonance assigned to the proton in column 1 results in an enhancement in intensity of the listed proton resonances.

[3]This spectrum is available as supplementary material. Supplementary data may be purchased from the Depository of Unpublished Data, Document Delivery, CISTI, National Research Council Canada, Ottawa, ON K1A 0S2, Canada (http://www.nrc.ca/cisti/irm/unpub_e.shtml for information on ordering electronically).

© 2004 NRC Canada

Table 2. $Pd(OAc)_2$-catalyzed coupling reactions of **1a** and **1b** with phenylboronic acid **2**.

Entry	Substrate	equiv. $PhB(OH)_2$ (**2**)	Additive	Time (min)	Yield **3** (%)	Yield **4** (%)
1	**1a**	1.1	nBu$_4$NBr	30	78	12
2	**1a**	2.2	nBu$_4$NBr	60	72	24
3	**1b**	1.1	nBu$_4$NBr	90	98	0.2
4	**1b**	1.1	nBu$_4$NBr	180	85	12
5	**1a**	1.1	nBu$_4$NI	90	73	13
6	**1b**	1.1	None	30	97	Trace[a]
7	**1a**	1.1	None	10	83	10
8	**1b**	1.02	None	45	96	0.7
9[b]	**1b**	1.02	None	150	96	0.3
10[c]	**1b**	1.02	None	420	95	Trace[a]

Note: Reaction conditions: 1.0 equiv. **1**, 1.02–2.2 equiv. **2**, 1% $Pd(OAc)_2$, 0.25 equiv. additive, 1.0 equiv. Na_2CO_3, H_2O (1 mL/mmol **1**), bath temperature 150 °C.

[a]Observed by TLC but not isolated.

[b]0.1% $Pd(OAc)_2$.

[c]0.01% $Pd(OAc)_2$.

of minor amounts of the regioisomeric mono-addition product 4-chloro-7-phenylquinoline **5** (isolated as an inseparable mixture with **3** and identified by ^{1}H NMR spectroscopy). Second, using excess phenylboronic acid (2.2 equiv.), the yield of **4** could be increased to 24% (Table 2, entry 2). These observations suggest that although the aryl chloride at C4 is more reactive than the C7 aryl chloride, the latter is sufficiently reactive that the bis-addition product **4** can be derived from the initial reaction at either C4 or C7, followed by a second coupling, which is competitive with the first. Owing to the inherent reactivity of the two chlorides, it was expected that it would be difficult to identify reaction conditions for **1a** that would eliminate cross-coupling at C7 and provide **3** exclusively.

Thus, we turned our attention to the reactions of 7-chloro-4-iodoquinoline (**1b**) (15, 18). Since the order of reactivity of aryl halides in the Suzuki cross-coupling reaction is generally accepted to be I > Br >> Cl (1–5), it was thought that introduction of a C4-iodide might enhance the inherent C4 regioselectivity by virtue of the additional chemoselectivity that would be imparted by the more reactive iodide.

The difference in the reactivity of the two dihaloquinolines **1a** and **1b** was clearly seen upon monitoring the time course of their reactions with **2** (1.1 equiv. **2**, 0.25 equiv. nBu$_4$NBr, 1% $Pd(OAc)_2$, 1 equiv. Na_2CO_3, H_2O, reflux) by ^{1}H NMR spectroscopy. At suitable time points, aliquots of each reaction mixture were removed and analyzed for **1a** or **1b**, **3**, **4**, and **5** by the integration of characteristic and well-separated proton resonances (see Experimental section). The data are plotted in Figs. 1 and 2 for the reactions of **1a** and **1b**, respectively. In Fig. 1, it is clearly seen that **3**, **4**, and **5** were formed throughout the time-course of the reaction. When the starting material **1a** was consumed at 30 min, the reaction mixture was composed of **3** and **4** in a ratio of approximately 9:1. In contrast, the reaction of **1b** with **2** (Fig. 2) revealed that **3** was the only product formed until starting material was consumed (at 1.5 h), after which time the bis-addition product **4** was produced at the expense of **3**. The regioisomeric mono-adduct **5** was not observed in this latter reaction. Of note, and somewhat surprising, is the fact that the dramatic improvement in regioselectivity observed with **1b** (compared with **1a**) occurs at an overall reaction rate that is three times slower than that of **1a** (1.5 h vs. 30 min).

A subsequent reaction of **1b** with 1.1 equiv. of **2** under the conditions described above provided **3** (98%) and **4** (0.2%) upon consumption of **1b** at 1.5 h (Table 2, entry 3). However, if the reaction was allowed to progress for 3 h, the yield of **4** increased to 12% at the expense of **3** (85%) (Table 2, entry 4). These observations are consistent with the results shown in Fig. 2.

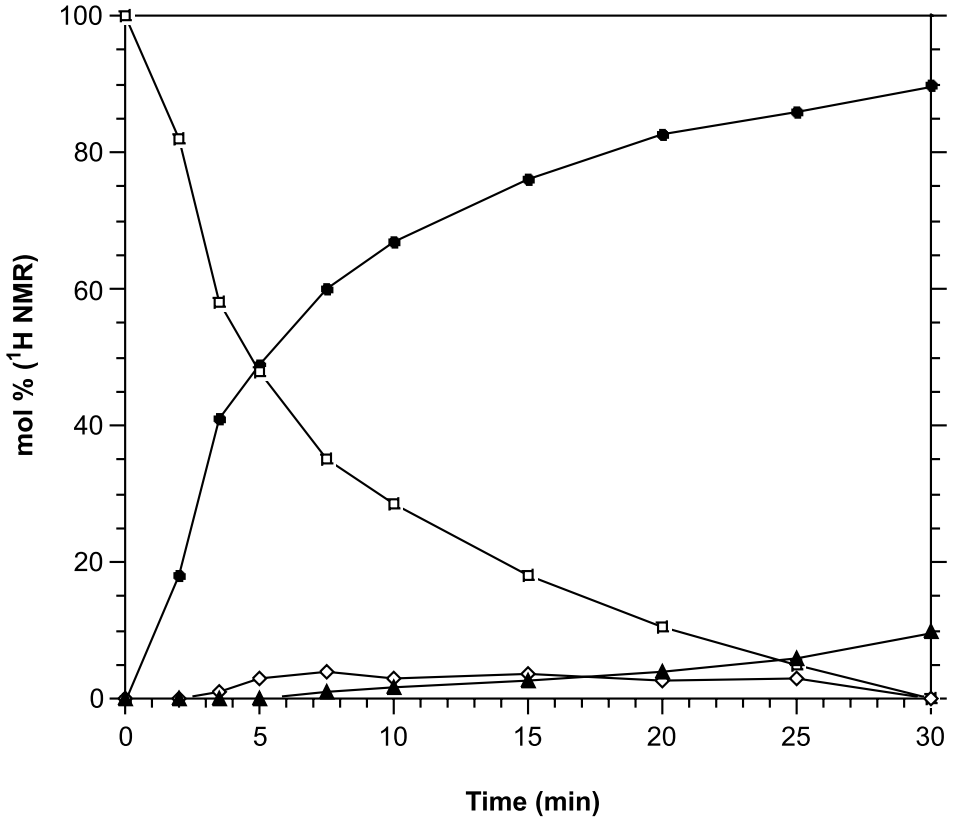
Subjection of **1b** and **2** to the reaction conditions originally described by Mitchell also provided **3** (93%) as the sole product upon consumption of **1b** (24 h), suggesting that the regioselectivity observed in the Suzuki reactions of **1b** is not limited to reactions catalyzed by phosphine-free palladium in water but is inherent to the reactivity of **1b**. Similarly, the overall rate of reaction of **1b** is approximately three times slower than that of **1a** under the Mitchell conditions (see introduction), suggesting that the solely aqueous conditions do not significantly impact the relative overall rates of reaction of **1a** and **1b**.

Thus, the cross-coupling reaction of the chloro-iodide **1b** catalyzed by phosphine-free $Pd(OAc)_2$ in water is slower but more regioselective than the dichloride **1a**. The difference in reactivity was further exemplified by the results obtained from conducting a competition experiment between **1a** and **1b** for phenylboronic acid (**2**) (1.0 equiv. of each of the quinolines and 1.02 equiv. of phenylboronic acid) using 1% $Pd(OAc)_2$ (Scheme 2). After 2 h, only the chloro-iodide **1b** was consumed to afford **3** (97%), and the dichloride **1a** was recovered in good yield (93%).

The differences that are observed in the reaction regioselectivity and overall reaction rate of **1a** and **1b** are readily rationalized. First, the regioselectivity of each reaction is reflective of the rate of irreversible oxidative addition of Pd(0) (generated from Pd(2+) and phenylboronic acid (19, 23)) to the C4 and C7 aryl halide bonds. In the case of dichloride **1a**, although the reactivity of the two chlorides is in the order C4—Cl > C7—Cl, the C7—Cl is of sufficient reactivity that the bis-addition product **4** derives from the initial reaction at either site, followed by a second coupling

© 2004 NRC Canada

Fig. 1. Time course of the $Pd(OAc)_2$-catalyzed coupling reaction of **1a** and **2**. The mol% of **1a** (□), **3** (●), **4** (▲), and **5** (◇), as measured by ^1H NMR spectroscopy (see Experimental section), are represented as a function of time.

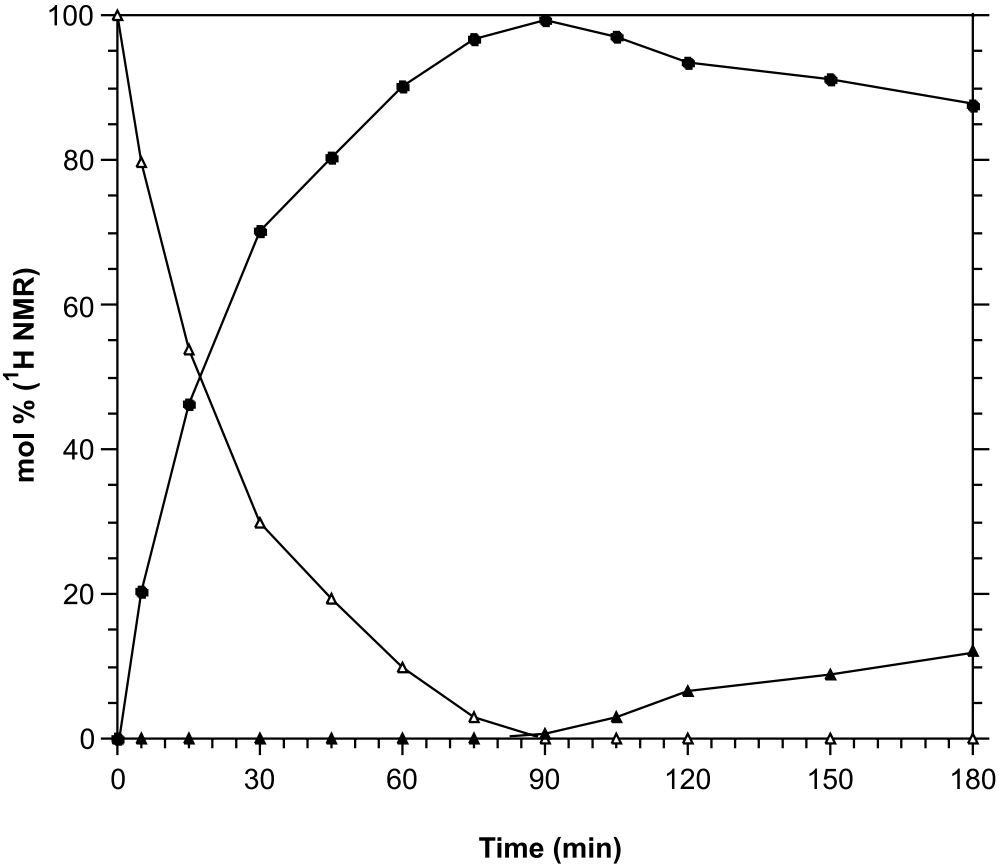


that is competitive with the first. For chloro-iodide **1b**, the difference in reactivity between C4—I and C7—Cl is > 100:1 (Table 2, entry 3). This chemoselectivity dictates that the bis-addition product **4** is produced only when the starting material is essentially completely consumed (see Fig. 2). Second, the more rapid overall reaction of **1a** compared with **1b** suggests that the oxidative addition step is not rate limiting in the overall catalytic cycle of **1b**. In contrast to those Suzuki reactions, in which the oxidative addition step is rate determining (leading to the typical ordering of overall reactivity I > Br >> Cl (1–5)), here transmetalation of the aryl-Pd-I species that is derived from **1b** appears to be rate determining. There are previous reports suggesting that transmetalation, rather than oxidative addition, can be rate determining in Suzuki cross-coupling reactions using both phosphine-free (21) and phosphine-ligated palladium catalysts (24, 25). Subtle differences in reaction conditions also have a dramatic impact on the mechanism since both oxidative addition (19) and transmetalation (21) steps have been found to be rate determining when using ligandless palladium catalysts. Thus, even though **1b** undergoes a rapid, irreversible, and chemoselective oxidative addition of Pd(0) to the aryl iodide bond at C4 (which results in very high regioselectivity compared with **1a**), the decreased rate of transmetalation results in the overall rate of reaction of chloro-iodide **1b** becoming slower than that of dichloride **1a** (note that the rate-determining step in the overall catalytic cycle of **1a** may be the oxidative addition or transmetalation steps). In addition, in spite of the fact that the overall rate of cross-coupling of **1a** is more rapid than **1b**, the highly chemoselective, rapid, and irreversible oxidative addition of Pd(0) to **1b** rationalizes the selective consumption of **1b** over that of **1a** in the competition experiment outlined in Scheme 2. Similar observations were made by Fu and co-workers (25) in their study of the Suzuki cross-coupling reactions catalyzed by $Pd_2(dba)_3$–$P(t\text{-}Bu)_3$. In these examples, the cross-couplings of aryl bromides with phenylboronic acid proceeded more rapidly than the corresponding aryl iodides, and in competition experiments analogous to those outlined in Scheme 2, only the aryl iodides underwent cross-coupling.

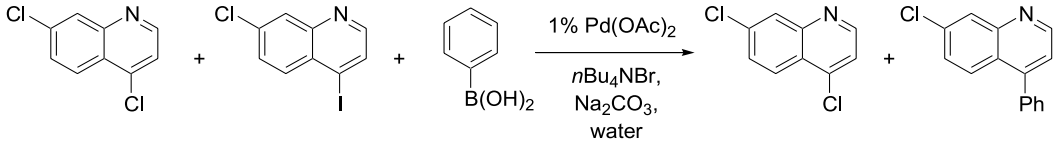
Another interesting observation was made when the cross-coupling reaction of **1a** and **2** was conducted in the presence of 0.25 equiv. $n\text{Bu}_4\text{NI}$ rather than $n\text{Bu}_4\text{NBr}$ (compare Table 2, entries 1 and 5). This modification had little effect on the isolated yield of **3** (73%) and **4** (13%), but the reaction now required 1.5 h to reach completion, similar to the rate that was observed using **1b** and $n\text{Bu}_4\text{NBr}$ (Table 2, entry 3). The presence of ammonium salts (21, 26) and the variation of halides (27–29) have been shown to have profound effects on the rate and mechanism of palladium-catalyzed processes in general. Although the reason behind this rate change is not completely understood, one can simplistically speculate that the aryl-Pd-Cl intermediate (formed upon reaction of **1a** with Pd(0)) is converted to aryl-Pd-I in the presence of $n\text{Bu}_4\text{NI}$ (the bond strength for palladium halides is Pd—Cl < Pd—Br < Pd—I (30, 31)). The reaction regioselectivity would still be governed by the relative rate of oxidative addi-

© 2004 NRC Canada

Fig. 2. Time course of the $Pd(OAc)_2$-catalyzed coupling reaction of **1b** and **2**. The mol% of **1b** (△), **3** (●), and **4** (▲), as measured by ^1H NMR spectroscopy (see Experimental section), are represented as a function of time.



Scheme 2.



1a (1.0 equiv.) **1b** (1.0 equiv.) **2** (1.02 equiv.) **1a** (93%) **3** (97%)

tion of Pd(0) to the aryl chlorides at C4 and (or) C7, but the overall rate would depend on the transmetalation of phenylboronic acid (**2**) to the aryl-Pd-I intermediate.

Since **1b** displays superb C4-regioselectivity and provides **3** in excellent yield upon reaction with **2**, we set out to further characterize the cross-coupling reactions of **1b** using **2** as substrate (Table 2, entries 6–10). Surprisingly, when the nBu$_4$NBr additive was removed (Table 2, entry 6), **1b** was consumed within 30 min, a threefold increase in overall rate. The yield of **3** (97%) was not affected. A similar observation of threefold rate enhancement in the absence of nBu$_4$NBr was made, using **1a** as substrate (Table 2, entry 7). These observations are surprising since they are in contrast to literature data (21), which suggest that nBu$_4$NBr is required for successful Suzuki cross-couplings using phosphine-free $Pd(OAc)_2$ in water. It may further imply a possible change in mechanism between the two reaction conditions (27, 28). The yield of **3** (96%) was not affected by decreasing the amount of phenylboronic acid (**2**) from 1.1 to 1.02 equiv. (Table 2, entry 8). This seemingly minor modification is important, since the reaction of **1b** still proceeds to completion, but monitoring for the disappearance of starting material **1b** becomes unnecessary. Recall that monitoring for the disappearance of starting material **1b** is necessary when using 1.1 equiv. of **2** since prolongation of the reaction after consumption of starting material (from 1.5 to 3 h) results in a significant increase in the formation of **4** (Table 2, entries 3 and 4). Finally, although the amount of $Pd(OAc)_2$ used can be decreased from 1% to 0.01%, this reduction in catalyst loading occurs with a corresponding increase in the time required for the reaction to reach completion (Table 2, entries 9 and 10).

Reaction scope

As illustrated in Scheme 3 and Table 3 (entries 1–14), reaction of **1b** using the optimized reaction conditions (A: 1.0 equiv. **1b**, 1.02 equiv. **6** or **8** or **9**, 1% $Pd(OAc)_2$, 1.0 equiv. Na_2CO_3, H_2O (1 mL/mmol **1b**), bath temperature 150 °C) with a variety of boronic acids afforded the expected products **7**, **10**, and **11** in good to excellent yields (84%–97%) without observation of the corresponding bis-addition prod-

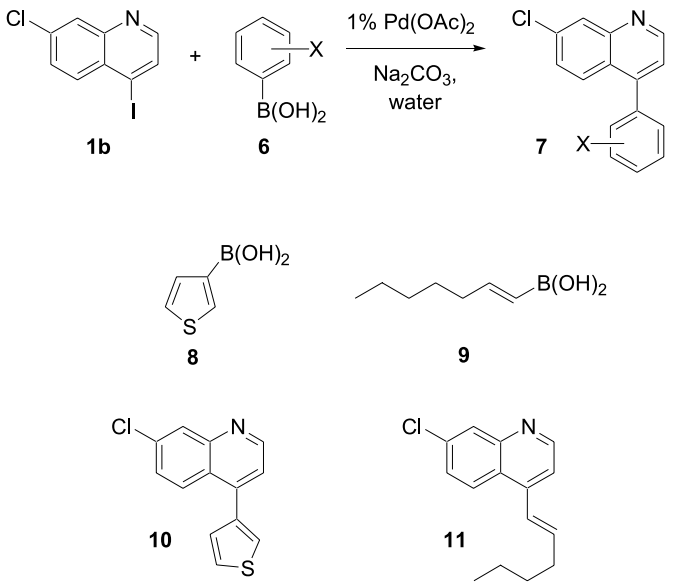
© 2004 NRC Canada

Table 3. Palladium-catalyzed coupling reactions of **1b** with arylboronic acids **6**, **8**, and **9**.

Entry	Boronic acid	X	Reaction conditions[a]	Time (min)	Product	Yield (%)[b]
1	**2**	—	A	45	**3**	96
2	**6a**	2-Me	A	15	**7a**	93
3	**6b**	2-OMe-5-Me	A	150	**7b**	91[c]
4	**6c**	2-Cl	A	150	**7c**	58 (85)
5	**6d**	3-F	A	35	**7d**	97
6	**6e**	3-NHAc	A	120	**7e**	76 (84)
7	**6f**	3-CN	A	150	**7f**	88[c]
8	**6g**	4-F	A	30	**7g**	96
9	**6h**	4-OMe	A	60	**7h**	97
10	**6i**	4-Ac	A	90	**7i**	89[c]
11	**6j**	3-F-4-OBn	A	60	**7j**	93
12	**6k**	2,6-diMe	A	120	**7k**	0
13	**8**		A	90	**10**	89[c]
14	**9**		A	15	**11**	95
15	**6c**	2-Cl	B	2880	**7c**	43 (79)
16	**6g**	4-F	B	1440	**7g**	94

[a]Reaction conditions. A: 1.0 equiv. **1b**, 1.02 equiv. **6** or **8** or **9**, 1% $Pd(OAc)_2$, 1.0 equiv. Na_2CO_3, H_2O (1 mL/mmol **1b**), bath temperature 150 °C. B: 1.0 equiv. **1b**, 1.1 equiv. **6**, 3% $Pd(Ph_3P)_4$, 1.5 equiv. aq Na_2CO_3 (2 mol/L), benzene (3 mL/mmol **1b**), ethanol (0.3 mL/mmol **1b**), reflux.
[b]Isolated yield of purified compound. Yield in parentheses based on unrecovered starting material **1b**.
[c]A trace of starting material observed by TLC.

Scheme 3.



ucts analogous to **4**. Degassing of the water (19, 21) is not required for a successful cross-coupling reaction.

The range of arylboronic acids **6** that serve as suitable coupling partners include those bearing electron donating and withdrawing substituents at the *ortho*-, *meta*-, and *para*-positions. 3-Thienylboronic acid **8** (Table 3, entry 13) and (*E*)-1-hexenylboronic acid **9** (Table 3, entry 14) are also suitable substrates. Typically, these reactions are complete within 1 h, but there are some exceptions. No reaction is observed after 2 h when using the sterically encumbered 2,6-dimethylphenylboronic acid (**6k**) (Table 3, entry 12). In several other examples, the reactions do not proceed to completion even after 2.5 h, as evidenced by the observation (TLC) or isolation of starting material **1b**. In each of these examples, the black precipitate that signals the completion of the reaction (and which is typically seen with those substrates that do consume all of **1b**) is not produced even if additional arylboronic acid or palladium catalyst is added. For several cases, the quantity of residual **1b** is minor (not isolated), and products **7** are obtained in yields over 88% (Table 3, entries 3, 7, 10, 13). In two cases (Table 3, entries 4 and 6), significant amounts of **1b** remain, although yields of **7** based on recovered starting material are still good. There does not appear to be any correlation between the steric or electronic nature of the substituent on the arylboronic acid and the extent of consumption of **1b**. Since these reactions are heterogeneous and take place in the absence of organic co-solvent, it is possible that the aqueous solubility or some other physical property of the boronic acid substrates may be responsible for these observed differences. However, this cannot be the sole explanation. Reactions of two representative arylboronic acids (**6c** and **6g**) with **1b** were conducted under the biphasic Mitchell reaction conditions ($Pd(Ph_3P)_4$, aqueous ethanol – toluene) for comparison purposes, and the reactivity patterns observed are similar to those observed under the phosphine-free palladium conditions in water (compare Table 3, entries 4 and 15, and 8 and 16, respectively). In the case of **6g**, **7g** was obtained in good yield (94%), but the reaction was complete after only 24 h. In the case of **6c**, a significant amount of starting material remained after an extended reaction time (2 days).

We have demonstrated that 7-chloro-4-iodoquinoline (**1b**) undergoes highly regioselective Suzuki cross-coupling reactions at C4 with a variety of boronic acids (aryl and vinyl), catalyzed by phosphine-free palladium in water solvent in the absence of nBu$_4$NBr. The regioselectivity that is observed is superior to that observed with the dichloride **1a**, but the overall reaction rate of **1b** is three times slower than **1a** (using phenylboronic acid). These results can be inter-

© 2004 NRC Canada

preted by considering that transmetalation of the intermediate aryl-Pd-I species, rather than the formation of this species by the rapid and chemoselective oxidative addition of Pd(0) to **1b**, is the rate-determining step in the overall catalytic cycle of **1b**.

Experimental section

All reagents were obtained from commercial suppliers except **1b**, which was prepared from **1a** and aqueous HI (57%) as described (15, 18). Melting points are uncorrected. FT-IR spectra were recorded as solutions in chloroform unless stated otherwise, and wavenumbers (ν) are reported in cm^{-1}. ^1H and ^{13}C NMR spectra were recorded as solutions in acetone-d_6, unless stated otherwise, at field strengths of 400 MHz (^1H) or 100 MHz (^{13}C). Chemical shifts are reported in parts per million (ppm) relative to the signals of residual protonated solvent as internal standard. ^{13}C NMR spectra were acquired with proton decoupling, and peak multiplicities refer to J_{CF}. Elemental analyses were performed at the Laboratoire d'Analyse Élémentaire in the Department of Chemistry, Université de Montréal, Montréal.

Reactions for Figs. 1 and 2

A mixture of **1a** (1.00 g, 5.04 mmol) (Fig. 1) or **1b** (1.46 g, 5.04 mmol) (Fig. 2), phenylboronic acid (**2**) (97%, 647 mg, 1.02 equiv.), nBu$_4$NBr (406 mg, 0.25 equiv.), $Pd(OAc)_2$ (11 mg, 0.01 equiv.), Na_2CO_3 (2.5 mL of a 2 mol/L solution, 1.0 equiv.), and water (2.5 mL) was placed in a 50 mL round-bottom flask under a nitrogen atmosphere and immersed in an oil bath at 150 °C. After the time intervals indicated in the figures, a small aliquot of the reaction mixture was removed and dissolved in ethyl acetate. The mixture was dried ($MgSO_4$), filtered, and concentrated. The crude residue was analyzed by ^1H NMR spectroscopy. One or more of the following characteristic resonances were integrated, and for each compound present, the mol% composition of the sample was calculated. **1a**: 7.74 (d, 1H), 7.78 (dd, 1H), 8.30 (d, 1H), 8.89 (d, 1H); **1b**: 7.75 (dd, 1H), 8.20 (d, 1H), 8.53 (d, 1H); **3**: 7.37 (d, 1H), 7.86 (d, 1H), 8.11 (d, 1H), 8.92 (d, 1H); **4**: 8.02 (d, 1H, J = 8.8 Hz), 8.39 (d, 1H), 8.99 (d, 1H); **5**: 8.34 (d, 1H), 8.36 (d, 1H), 8.87 (d, 1H). The resulting data were used to generate Figs. 1 and 2.

Competition experiment (Scheme 2)

A mixture of **1a** (1.00 g, 5.04 mmol), **1b** (1.46 g, 5.04 mmol), phenylboronic acid (**2**) (97%, 647 mg, 1.02 equiv.), nBu$_4$NBr (406 mg, 0.25 equiv.), $Pd(OAc)_2$ (11 mg, 0.01 equiv.), Na_2CO_3 (2.5 mL of a 2 mol/L solution, 1.0 equiv.), and water (2.5 mL) was placed in a 50 mL round-bottom flask under a nitrogen atmosphere and immersed in an oil bath at 150 °C. After stirring for 2 h, the mixture was cooled to room temperature; water (50 mL) was added, and the mixture was extracted twice with ethyl acetate (50 mL). The combined organics were washed with water (50 mL) and brine (50 mL), dried ($MgSO_4$), filtered, and concentrated. The residue was subjected to flash column chromatography (SiO_2, eluting with hexane–ether 4:1 volume fraction) to provide **1a** (927 mg, 93%) as a white solid and **3** (1.17 g, 97%) as a white solid.

Typical procedure (Table 3)

A mixture of **1b** (1.46 g, 5.04 mmol), phenylboronic acid **2** (97%, 647 mg, 1.02 equiv.), $Pd(OAc)_2$ (11 mg, 0.01 equiv.), Na_2CO_3 (2.5 mL of a 2 mol/L solution, 1.0 equiv.), and water (2.5 mL) was placed in a 50 mL round-bottom flask under a nitrogen atmosphere and immersed in an oil bath at 150 °C. After stirring for 45 min, the mixture was cooled to room temperature; water (50 mL) was added, and the mixture was extracted twice with ethyl acetate (50 mL). The combined organics were washed with water (50 mL) and brine (50 mL), dried ($MgSO_4$), filtered, and concentrated. The residue was subjected to flash column chromatography (SiO_2, eluting with hexane–ether 3:1 volume fraction) to provide **3** (1.16 g, 96%) as a white solid and **4** (9 mg, 0.7%) as a white solid (Table 2, entry 8 and Table 3, entry 1).

7-Chloro-4-phenylquinoline (3)

mp 73 to 74 °C (lit. (6) value mp 73.5–74.5 °C). ^1H NMR δ: 7.37 (d, 1H, J = 4.4 Hz), 7.47–7.58 (m, 6H), 7.86 (d, 1H, J = 9.0 Hz), 8.11 (d, 1H, J = 2.1 Hz), 8.92 (d, 1H, J = 4.4 Hz). ^{13}C NMR δ: 122.1, 125.4, 127.7, 127.9, 129.0, 129.1, 129.2, 129.9, 134.9, 137.8, 148.5, 149.6, 151.7.

4,7-Diphenylquinoline (4)

mp 128 to 129 °C. IR: 3023. ^1H NMR δ: 7.44 (d, 1H, J = 4.3 Hz), 7.48 (m, 1H), 7.54–7.63 (m, 7H), 7.88 (m, 2H), 7.93 (dd, 1H, J = 1.9, 8.8 Hz), 8.02 (d, 1H, J = 8.8 Hz), 8.39 (d, 1H, J = 1.8 Hz), 8.99 (d, 1H, J = 4.4 Hz). ^{13}C NMR δ: 122.1, 126.4, 126.8, 127.1, 128.1, 128.8, 129.3, 129.5, 129.9, 130.3, 138.8, 140.7, 142.4, 148.8, 150.1, 151.5. Anal. calcd. for $C_{21}H_{15}N$: C 89.65, H 5.37, N 4.98; found: C 89.47, H 5.38, N 4.99.

The remainder of the examples cited in Table 3 were prepared on the same scale in a manner similar to **3**, with reaction times as listed in the table. The eluting solvents used for column chromatography are indicated below.

7-Chloro-4-(2-methylphenyl)quinoline (7a)

Chromatography (hexane–ether 4:1 volume fraction) provided **7a** as a white solid (1.19 g, 93%), mp 86 to 87 °C. IR: 3017. ^1H NMR δ: 2.07 (s, 3H), 7.26 (d, 1H, J = 7.5 Hz), 7.36–7.49 (m, 5H), 7.55 (dd, 1H, J = 2.1, 9.0 Hz), 8.15 (d, 1H, J = 2.1 Hz), 9.00 (d, 1H, J = 4.3 Hz). ^{13}C NMR δ: 19.6, 122.4, 126.1, 126.4, 127.8, 128.1, 129.0, 129.1, 129.8, 130.7, 135.0, 136.1, 137.3, 148.5, 149.4, 151.9. Anal. calcd. for $C_{16}H_{12}ClN$: C 75.74, H 4.77, N 5.52; found: C 75.67, H 4.78, N 5.55.

7-Chloro-4-(2-methoxy-5-methylphenyl)quinoline (7b)

Chromatography (hexane – ethyl acetate 6:1 volume fraction) provided **7b** as a white solid (1.30 g, 91%), mp 133 to 134 °C. IR: 2961, 1502, 1250. ^1H NMR δ: 2.35 (s, 3H), 3.69 (s, 3H), 7.12 (m, 2H), 7.34 (dd, 1H, J = 1.8, 8.4 Hz), 7.39 (d, 1H, J = 4.4 Hz), 7.50 (dd, 1H, J = 2.2, 9.0 Hz), 7.62 (d, 1H, J = 9.0 Hz), 8.10 (d, 1H, J = 2.2 Hz), 8.95 (d, 1H, J = 4.4 Hz). ^{13}C NMR δ: 20.4, 55.8, 112.2, 123.3, 126.7, 127.6, 129.1, 129.3, 130.8, 131.5, 132.2, 135.0, 146.9, 149.7, 152.2, 155.6. Anal. calcd. for $C_{17}H_{14}ClNO$: C 71.96, H 4.97, N 4.94; found: C 71.96, H 5.04, N 4.86.

© 2004 NRC Canada

7-Chloro-4-(2-chlorophenyl)quinoline (7c)

Chromatography (hexane – ethyl acetate 6:1 volume fraction) provided **1b** (466 mg, 32%) and **7c** as a white solid (803 mg, 58%), mp 89 to 90 °C. IR: 2976. ^{1}H NMR δ: 7.43 (d, 1H, J = 4.4 Hz), 7.44 (dd, 1H, J = 1.8, 7.3 Hz), 7.49–7.59 (m, 4H), 7.64 (dd, 1H, J = 1.4, 7.8 Hz), 8.16 (d, 1H, J = 1.8 Hz), 9.02 (d, 1H, J = 4.4 Hz). ^{13}C NMR δ: 122.7, 125.6, 127.8, 128.0, 129.0, 130.2, 130.8, 131.9, 133.1, 135.1, 136.5, 146.0, 149.3, 151.8. Anal. calcd. for $C_{15}H_9Cl_2N$: C 65.72, H 3.31, N 5.11; found: C 65.67, H 3.24, N 5.08.

7-Chloro-4-(3-fluorophenyl)quinoline (7d)

Chromatography (hexane–ether 4:1 volume fraction) provided **7d** as a white solid (1.26 g, 97%), mp 88 to 89 °C. IR: 2979. ^{1}H NMR δ: 7.32–7.41 (m, 3H), 7.49 (d, 1H, J = 4.4 Hz), 7.59 (dd, 1H, J = 2.2, 9.0 Hz), 7.65 (br q, 1H, J = 7.8 Hz), 7.92 (d, 1H, J = 9.0 Hz), 8.13 (d, 1H, J = 2.1 Hz), 8.98 (d, 1H, J = 4.4 Hz). ^{13}C NMR δ: 115.9 (d, J_{CF} = 21.1 Hz), 116.8 (d, J_{CF} = 22.5 Hz), 122.2, 125.2, 126.0 (d, J_{CF} = 2.7 Hz), 127.8, 128.0, 129.0, 131.2 (d, J_{CF} = 8.5 Hz), 135.1, 140.1 (d, J_{CF} = 7.9 Hz), 147.1, 149.6, 151.8, 163.2 (d, J_{CF} = 245.6 Hz). Anal. calcd. for $C_{15}H_9ClFN$: C 69.91, H 3.52, N 5.44; found: C 69.70, H 3.50, N 5.45.

4-(3-Acetamidophenyl)-7-chloroquinoline (7e)

Chromatography (hexane – ethyl acetate 1:2 volume fraction) provided **1b** (142 mg, 10%) and **7e** as a white solid (1.14 g, 76%), mp 184 to 185 °C. IR: 3435, 3015, 1692. ^{1}H NMR ($CDCl_3$) δ: 2.23 (s, 3H), 7.22 (br d, 1H, J = 7.6 Hz), 7.33 (d, 1H, J = 4.4 Hz), 7.44–7.50 (m, 2H), 7.63–7.69 (m, 3H), 7.89 (d, 1H, J = 9.0 Hz), 8.17 (d, 1H, J = 2.0 Hz), 8.94 (d, 1H, J = 4.4 Hz). ^{13}C NMR ($CDCl_3$) δ: 24.6, 120.1, 120.8, 121.4, 125.1, 125.2, 127.3, 127.9, 128.1, 129.4, 135.7, 138.0, 138.5, 148.4, 148.7, 150.4, 168.7. Anal. calcd. for $C_{17}H_{13}ClN_2O$: C 68.81, H 4.42, N 9.44; found: C 68.86, H 4.49, N 9.12.

7-Chloro-4-(3-cyanophenyl)quinoline (7f)

Chromatography (hexane – ethyl acetate 3:1 volume fraction) provided **7f** as a white solid (1.18 g, 88%), mp 160 to 161 °C. IR: 2982, 2234. ^{1}H NMR ($CDCl_3$) δ: 7.26 (d, 1H, J = 4.4 Hz), 7.43 (dd, 1H, J = 2.1, 9.0 Hz), 7.62–7.78 (m, 5H), 8.11 (d, 1H, J = 2.1 Hz), 8.91 (d, 1H, J = 4.4 Hz). ^{13}C NMR ($CDCl_3$) δ: 113.1, 118.1, 121.3, 124.4, 126.3, 128.1, 128.8, 129.6, 132.1, 132.6, 133.6, 135.6, 138.6, 145.8, 148.9, 150.8. Anal. calcd. for $C_{16}H_9ClN_2$: C 72.60, H 3.43, N 10.58; found: C 72.50, H 3.39, N 10.55.

7-Chloro-4-(4-fluorophenyl)quinoline (7g)

Chromatography (hexane – ethyl acetate 4:1 volume fraction) provided **7g** as a white solid (1.25 g, 96%), mp 105 to 106 °C. IR: 2978. ^{1}H NMR δ: 7.39 (br t, 2H, J = 8.8 Hz), 7.47 (d, 1H, J = 4.4 Hz), 7.59 (dd, 1H, J = 2.2, 9.0 Hz), 7.61–7.66 (m, 2H), 7.92 (d, 1H, J = 9.0 Hz), 8.14 (d, 1H, J = 2.2 Hz), 8.98 (d, 1H, J = 4.4 Hz). ^{13}C NMR δ: 116.1 (d, $J_{C\text{-}F}$ = 21.8 Hz), 122.3, 125.4, 127.81, 127.85, 129.0, 132.0 (d, $J_{C\text{-}F}$ = 8.5 Hz), 134.0, 135.0, 147.5, 149.6, 151.8, 163.4 (d, $J_{C\text{-}F}$ = 246.5 Hz). Anal. calcd. for $C_{15}H_9ClFN$: C 69.91, H 3.52, N 5.44; found: C 69.73, H 3.40, N 5.44.

7-Chloro-4-(4-methoxyphenyl)quinoline (7h)

Chromatography (hexane – ethyl acetate 3:1 volume fraction) provided **7h** as a white solid (1.32 g, 97%), mp 90 to 91 °C. IR: 2963. ^{1}H NMR δ: 3.92 (s, 3H), 7.15 (br d, 2H, J = 8.7 Hz), 7.42 (d, 1H, J = 4.4 Hz), 7.50 (br d, 2H, J = 8.7 Hz), 7.56 (dd, 1H, J = 2.2, 9.0 Hz), 7.98 (d, 1H, J = 9.0 Hz), 8.11 (d, 1H, J = 2.2 Hz), 8.93 (d, 1H, J = 4.4 Hz). ^{13}C NMR δ: 55.3, 114.6, 122.0, 125.6, 127.5, 128.1, 128.9, 129.9, 131.2, 134.8, 148.3, 149.8, 151.8, 160.7. Anal. calcd. for $C_{16}H_{12}ClNO$: C 71.25, H 4.48, N 5.19; found: C 71.16, H 4.47, N 5.13.

4-(4-Acetylphenyl)-7-chloroquinoline (7i)

Chromatography (hexane – ethyl acetate 3:2 volume fraction) provided **7i** as a white solid (1.27 g, 89%), mp 143 to 144 °C. IR: 3015, 1688. ^{1}H NMR δ: 2.70 (s, 3H), 7.52 (d, 1H, J = 4.4 Hz), 7.61 (dd, 1H, J = 2.2, 9.0 Hz), 7.73 (d, 2H, J = 8.4 Hz), 7.91 (d, 1H, J = 9.0 Hz), 8.16 (d, 1H, J = 2.2 Hz), 8.21 (d, 2H, J = 8.4 Hz), 9.02 (d, 1H, J = 4.4 Hz). ^{13}C NMR δ: 26.4, 122.1, 125.1, 127.8, 128.0, 128.98, 129.01, 130.2, 135.1, 137.7, 142.2, 147.5, 149.6, 151.8, 197.1. Anal. calcd. for $C_{17}H_{12}ClNO$: C 72.47, H 4.29, N 4.97; found: C 72.36, H 4.34, N 4.90.

4-(4-Benzyloxy-3-fluorophenyl)-7-chloroquinoline (7j)

Chromatography (hexane – ethyl acetate 3:1 volume fraction) provided **7j** as a white solid (1.70 g, 93%), mp 150 to 151 °C. IR: 3014. ^{1}H NMR ($CDCl_3$) δ: 5.26 (s, 2H), 7.18 (m, 2H), 7.27 (br d, 1H, J = 11.5 Hz), 7.30 (d, 1H, J = 4.4 Hz), 7.39 (m, 1H), 7.43–7.53 (m, 5H), 7.89 (d, 1H, J = 9.0 Hz), 8.19 (d, 1H, J = 1.9 Hz), 8.93 (d, 1H, J = 4.4 Hz). ^{13}C NMR ($CDCl_3$) δ: 71.3, 115.5, 117.4, 117.6, 121.3, 125.0, 125.41, 125.45, 127.0, 127.4, 127.7, 128.3, 128.7, 130.5, 130.6, 135.4, 136.1, 147.0, 147.1, 147.3, 149.0, 150.8, 151.3, 153.8. Anal. calcd. for $C_{22}H_{15}ClFNO$: C 72.63, H 4.16, N 3.85; found: C 72.21, H 4.12, N 3.83.

7-Chloro-4-(3-thienyl)quinoline (10)

Chromatography (hexane – ethyl acetate 4:1 volume fraction) provided **10** as a white solid (1.10 g, 89%), mp 74 to 75 °C. IR: 2975. ^{1}H NMR δ: 7.43 (dd, 1H, J = 1.2, 4.9 Hz), 7.49 (d, 1H, J = 4.4 Hz), 7.56 (dd, 1H, J = 2.2, 9.1 Hz), 7.74 (dd, 1H, J = 3.0, 4.9 Hz), 7.80 (m, 1H), 8.10 (m, 2H), 8.92 (d, 1H, J = 4.4 Hz). ^{13}C NMR δ: 121.9, 125.4, 126.2, 127.3, 127.7, 128.0, 129.0, 129.2, 134.9, 138.2, 143.2, 149.7, 151.8. Anal. calcd. for $C_{13}H_8ClNS$: C 63.54, H 3.28, N 5.70; found: C 63.53, H 3.20, N 5.66.

(E)-7-Chloro-4-(1-hexenyl)quinoline (11)

Chromatography (hexane–ether 4:1 volume fraction) provided **11** as a colorless oil (1.05 g, 95%). IR (film): 2957, 2928, 1579. ^{1}H NMR δ: 0.95 (t, 3H, J = 7.3 Hz), 1.42 (m, 2H), 1.53 (m, 2H), 2.36 (br q, 2H, J = 7.0 Hz), 6.59 (dt, 1H, J = 15.6, 7.0 Hz), 7.15 (d, 1H, J = 15.6 Hz), 7.54 (m, 2H), 8.03 (d, 1H, J = 2.2 Hz), 8.21 (d, 1H, J = 9.0 Hz), 8.81 (d, 1H, J = 4.6 Hz). ^{13}C NMR δ: 13.8, 22.5, 31.4, 33.3, 117.7, 124.3, 125.0, 126.1, 127.1, 128.9, 134.7, 139.3, 143.7, 149.6, 151.8. Anal. calcd. for $C_{15}H_{16}ClN$: C 73.31, H 6.56, N 5.70; found: C 73.15, H 6.66, N 5.64.

© 2004 NRC Canada

References

1. N. Miyaura and A. Suzuki. Chem. Rev. **95**, 2457 (1995).
2. S.P. Stanforth. Tetrahedron, **54**, 263 (1998).
3. A. Suzuki. J. Organomet. Chem. **653**, 83 (2002).
4. J. Hassan, M. Sévignon, C. Gozzi, E. Schulz, and M. Lemaire. Chem. Rev. **102**, 1359 (2002).
5. N. Miyaura. Topics Curr. Chem. **219**, 5 (2002).
6. N.M. Ali, A. McKillop, M.B. Mitchell, R.A. Rebelo, and P.J. Wallbank. Tetrahedron, **48**, 8117 (1992).
7. M.A. Ciufolini, J.W. Mitchell, and F. Roschangar. Tetrahedron Lett. **37**, 8281 (1996).
8. O. Lohse, P. Thevenin, and E. Waldvogel. Synlett, 45 (1999).
9. Y. Gong and H.W. Pauls. Synlett, 829 (2000).
10. M. Allegretti, A. Arcadi, F. Marinelli, and L. Nicolini. Synlett, 609 (2001).
11. A.F. Littke and G.C. Fu. Angew. Chem. Int. Ed. **41**, 4176 (2002).
12. D. Dubé, M. Blouin, C. Brideau, C.-C. Chan, S. Desmarais, D. Ethier, J.-P. Falgueyret, R.W. Friesen, M. Girard, Y. Girard, J. Guay, D. Riendeau, P. Tagari, and R.N. Young. Bioorg. Med. Chem. Lett. **8**, 1255 (1998).
13. J.-Y. Legros, G. Primault, and J.-C. Fiaud. Tetrahedron, **57**, 2507 (2001).
14. D. Najiba, J.-F. Carpentier, Y. Castanet, C. Biot, J. Brocard, and A. Mortreux. Tetrahedron Lett. **40**, 3719 (1999).
15. A.S. Bhanu Prasad, T.M. Stevenson, J.R. Citineni, V. Nyzam, and P. Knochel. Tetrahedron, **53**, 7237 (1997).
16. T. Shiota and T. Yamamori. J. Org. Chem. **64**, 453 (1999).
17. J.M. Nolan and D.L. Comins. J. Org. Chem. **68**, 3736 (2003).
18. R.M. Peck, R.K. Preston, and H.J. Creech. J. Am. Chem. Soc. **81**, 3984 (1959).
19. T.I. Wallow and B.M. Novak. J. Org. Chem. **59**, 5034 (1994).
20. C.R. LeBlond, A.T. Andrews, Y. Sun, and J.R. Sowa, Jr. Org. Lett. **3**, 1555 (2001).
21. D. Badone, M. Baroni, R. Cardamone, A. Ielmini, and U. Guzzi. J. Org. Chem. **62**, 7170 (1997).
22. N.E. Leadbeater and M. Marco. J. Org. Chem. **68**, 888 (2003).
23. R.F. Heck. Palladium reagents in organic syntheses. Academic Press, London. 1985. p. 184.
24. G.B. Smith, G.C. Dezeny, D.L. Hughes, A.O. King, and T.R. Verhoeven. J. Org. Chem. **59**, 8151 (1994).
25. A.F. Littke, C. Dai, and G.C. Fu. J. Am. Chem. Soc. **122**, 4020 (2000).
26. A.-S. Castanet, F. Colobert, J.-R. Desmurs, and T. Schlama. J. Mol. Catalysis A Chem. **182–183**, 481 (2002).
27. C. Amatore and A. Jutand. J. Organomet. Chem. **576**, 254 (1999).
28. C. Amatore and A. Jutand. Acc. Chem. Res. **33**, 314 (2000).
29. K. Fagnou and M. Lautens. Angew. Chem. Int. Ed. **41**, 26 (2002).
30. P.M. Maitlis. The organic chemistry of palladium. Vol 1. Academic Press, New York. 1971. Chap 1.
31. S. Tasler and B.H. Lipshutz. J. Org. Chem. **68**, 1190 (2003).

© 2004 NRC Canada

Part 1: Efficient strategies for the construction of variably substituted bicyclo[5.3.1]undecenones (AB taxane ring systems)[1]

Alain Laurent, Nidia P. Villalva-Servín, Pat Forgione, Peter D. Wilson, David V. Smil, and Alex G. Fallis

Abstract: Strategies for the construction of cyclic molecules containing variably substituted bicyclo[5.3.1]undecenones (AB taxane ring systems) are described. These routes employ a multi-component coupling protocol that utilizes sequential magnesium-mediated carbometallation of propargyl alcohols and intramolecular Diels–Alder reactions (IMDA). The cycloaddition generates the key eight-membered taxane ring as a single diastereomer, induced by preferential Lewis acid (diethylaluminum chloride or boron trifluoride etherate) complexation with the cross-ring oxygens. Both the electronic nature of the dienophile and the neighbouring group non-bonded interactions contribute to the success of these cycloadditions.

Key words: magnesium chelate, Lewis acid, intramolecular Diels–Alder, cycloaddition.

Résumé : On décrit des stratégies permettant de construire des molécules cycliques contenant des bicyclo[5.3.1]undécénones (cycles AB du taxane). Ces routes font appel à un protocole de couplage à plusieurs composants qui utilise en séquence des réactions de carbométallation d'alcools propargyliques catalysées par le magnésium et des réactions de Diels–Alder intramoléculaires. La cycloaddition génère le cycle à huit chaînons du taxane sous la forme d'une seul diastéréomère en raison de la complexation préférentielle de l'acide de Lewis (chlorure de diéthylaluminium ou éthérate du trifluorure de bore) avec les atomes d'oxygène dans la partie opposée du cycle. La nature électronique du diénophile ainsi que les interactions non liées du groupe voisin jouent toutes les deux en faveur du succès de ces cycloadditions.

Mots clés : chélate magnésien, acide de Lewis, Diels–Alder intramoléculaire, cycloaddition.

[Traduit par la Rédaction]

Introduction

Taxol® (paclitaxel) and Taxotere® (docetaxel) are now established chemotherapeutic agents (selling more than $1 billion US each annually) for the treatment of ovarian and breast cancer. These drugs operate by a novel mechanism of action that differs from other spindle poisons such as vincristine. Based on a long tradition of natural products isolation and discovery, nature has provided a novel structure that represents a new chemotherapeutic lead. Thus, as previously demonstrated for penicillins and tetracyclines, modified taxoid structures have provided new understanding of the mode of action. Eventually novel compounds with improved water solubility and better therapeutic properties will be developed. We hope that eventually our own research will be able to contribute to this area with new, improved drugs. Paclitaxel **1** (Taxol®) and docetaxel **2** (Taxotere®) (Fig. 1) continue to receive increased medicinal attention because of their increased utility, particularly for mixed chemotherapy. These diterpenoids, classified as alkaloids (!), have elicited considerable interest over the last two decades, principally as a result of their proven chemotherapeutic utility and their attraction as highly challenging synthetic targets (1). The total synthesis of Taxol® has been surmounted by six different groups (2). However, new, efficient strategies for construction of the unique taxane tricyclo[9.3.1.$0^{3,8}$]pentadecane nu-

Received 26 June 2003. Published on the NRC Research Press Web site at http://canjchem.nrc.ca on 28 January 2004.

This paper is dedicated to Professor Edward Piers on the occasion of his 65th birthday. Presented with respect and gratitude for his contributions to organic chemistry and to our friendship.

A. Laurent,[2] N.P. Villalva-Servín, P. Forgione,[3] P.D. Wilson,[4] D.V. Smil,[5] and A.G. Fallis.[6] Centre for Research in Biopharmaceuticals, Department of Chemistry, University of Ottawa, 10 Marie Curie, Ottawa, ON K1N 6N5, Canada.

[1]This article is part of a Special Issue dedicated to Professor Ed Piers.
[2]Present address: Aegera Therapeutics, Inc., 810, chemin du Golf, Nun's Island, QC H3E 1A8, Canada.
[3]Present address: Boehringer-Ingelheim Ltd., Laval, QC H7S 2G5, Canada.
[4]Present address: Department of Chemistry, Simon Fraser University, 8888 University Drive, Burnaby, BC V5A 1A6, Canada.
[5]Present address: Methyl Gene Inc., 7220 Frederick Banting, Montreal, QC H4S 2A1, Canada.
[6]Corresponding author (e-mail: afallis@science.uottawa.ca).

 doi: 10.1139/V03-200 © 2004 NRC Canada

Scheme 1.

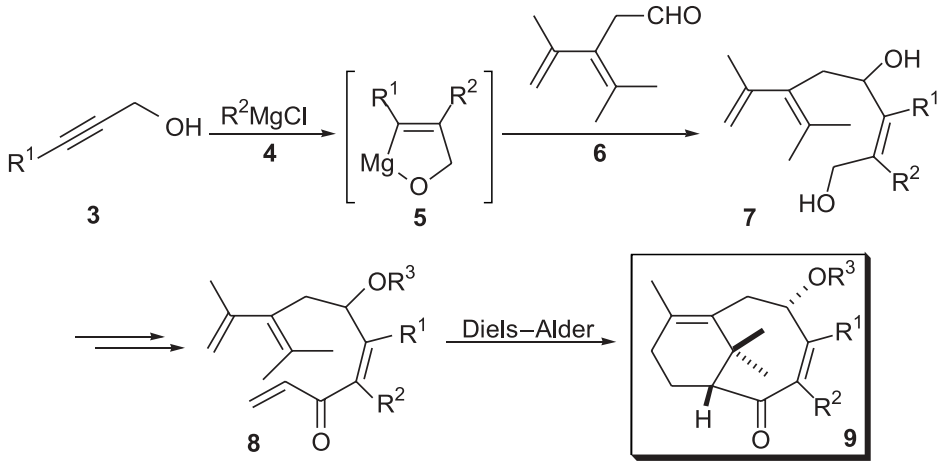
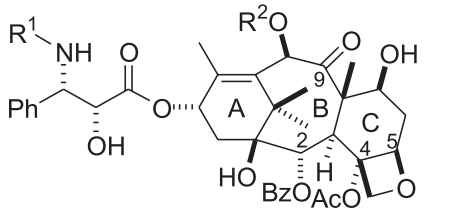


Fig. 1. Current taxoid drugs.



Paclitaxel **1** (Taxol®) R^1 = Bz, R^2 = Ac

Docetaxel **2** (Taxotere®) R^1 = Boc, R^2 = H

cleus are still required if we are to make new, improved analogues.

Carbometallation – intramolecular cycloaddition strategy

We have a long-standing interest in the area of taxane synthesis. We have examined different protocols, but particularly those that involve diverse strategies and that encompass intramolecular Diels–Alder sequences (3). We continue to develop more efficient and convergent routes for the preparation of the carbocyclic taxane skeleton via versatile approaches to the AB ring system. We wish to report the details of our recent progress, involving combinations of carbometallation reactions of propargyl alcohols and type II intramolecular Diels–Alder (IMDA) reactions (4) to generate eight-membered rings, induced by the presence of an endocyclic *cis*-akene (5). The following paper (6) describes further studies with related building blocks and their conversion to the tricyclic ABC taxane nucleus.

We have previously described the versatility of the magnesium-mediated carbometallation of propargyl alcohols for the assembly of several diverse structures generated in a single reaction. This three-component coupling strategy allows the direct regio- and stereocontrolled synthesis of halodienes, diene-diols, enediynes, tetraenes, tetrasubstituted alkenes, substituted furans, and 2(5*H*)-furanones (butenolides) with vinyl and related Grignard reagents (7).

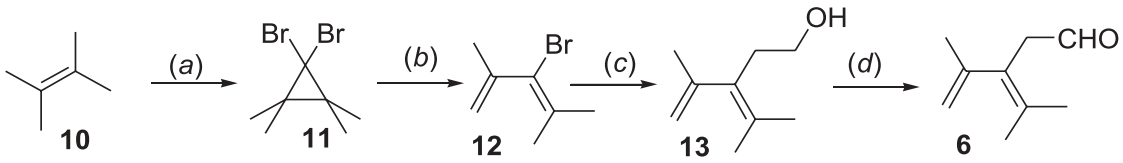
We have also established the beneficial influence of "planar" double bonds and aromatic rings in the side chain, to control the stereochemistry of IMDA reactions (8). For oxygenated targets, isopropylidene acetal tether control groups direct the enantioselectivity of the adducts, especially for *cis*-decalins (9). A related concept, namely the possibility of controlling the geometry of the side chain with a *cis* double bond, appeared attractive for the construction of the eight-membered ring embedded in the bicyclo[5.3.1]undecene AB skeleton of taxoids. We envisaged that a carbometallation strategy would allow efficient access to suitable cycloaddition precursors, which in turn would lead to the rapid assembly of variably functionalized taxane AB-ring systems.

This general strategy, via the magnesium chelate **5** and the cycloaddition precursor **8**, is outlined in Scheme 1 (5). We anticipated that the synthesis of key intermediate diols of type **7** could be conducted in one pot via the addition of Grignard reagents **4** to terminally substituted propargylic alcohols **3** and subsequent trapping of the putative magnesium chelate **5** with diene aldehyde **6**. Further elaboration would allow access to Diels–Alder precursors such as **8**. These cross-conjugated dienones were expected to readily undergo intramolecular cyclization to afford the desired bicyclo[5.3.1]undecenone skeletons **9** in the presence of a Lewis acid. Molecular modeling suggested that modest stereoselection might be achieved during the cycloaddition created by the preferential complexation between the cross-ring oxygens. In view of the flexibility available for the carbometallation partners, these cores could be constructed with sufficient functionality for the eventual attachment of the C-ring by annulation, cycloaddition, or ring-closing metathesis procedures.

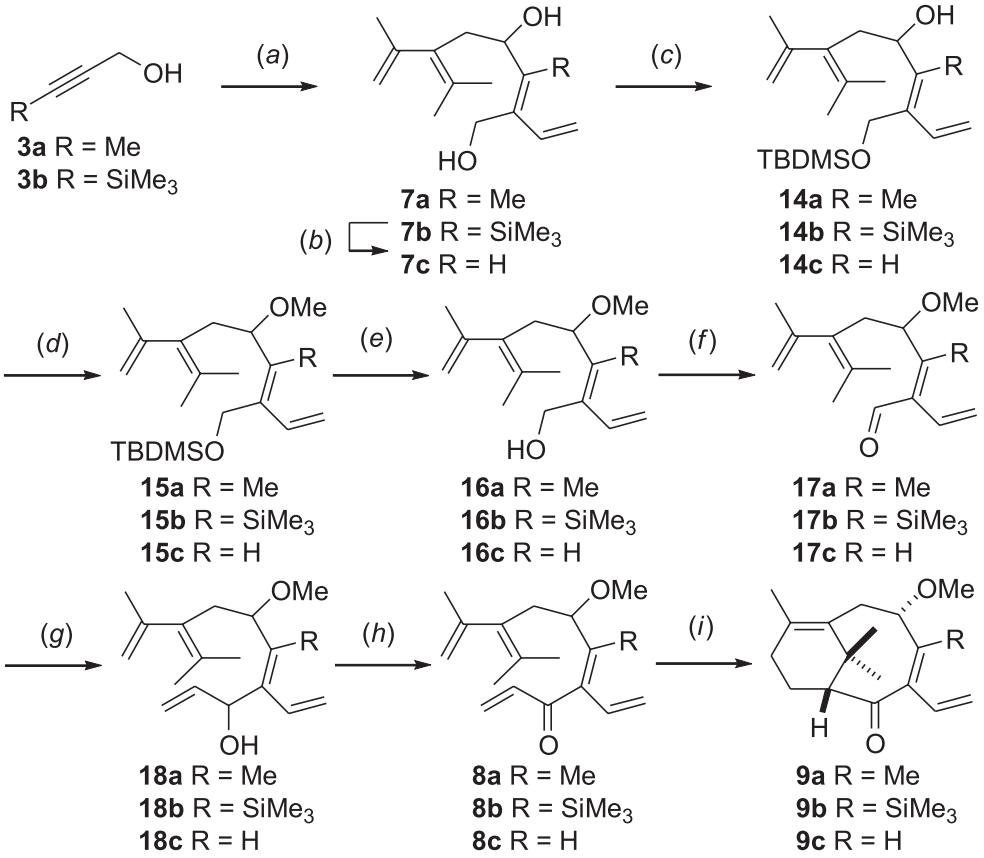
Current structure activity relationships (SAR) data for Taxol® have established that the C2 benzoate, the C4 acetate, and the oxetane or hydrogen bond acceptor on the "southern" perimeter of the molecule are crucial for activity. In contrast, the "northern" perimeter C7 hydroxyl and C10 acetate substituents can be omitted without compromising efficacy (1). Although not essential, the C9 hydroxyl increases activity slightly and acts as a useful handle for the formation of resolvable derivatives (10) or the introduction of solubilizing groups (11). We elected to employ diene aldehyde **6** as a source of the future C9 oxygen to take advantage of the rapid AB-ring assembly afforded by an IMDA

© 2004 NRC Canada

Scheme 2. Reagents and conditions: (*a*) *t*-BuOK, $HCBr_3$, pentane, 0 °C, 3 h, 71%; (*b*) 120–140 °C, 80%; (*c*) (*i*) *t*-BuLi, THF, –78 °C, 30 min; (*ii*) ethylene oxide, –78 °C to room temperature (rt) (22 °C), 2 h, 83%; (*d*) Dess–Martin periodinane, CH_2Cl_2, rt, 30 min, 95%.



Scheme 3. Reagents and conditions: (*a*) (*i*) CH_2=CHMgCl, cyclohexane–THF, rt (22 °C) to 70 °C, 20 h; (*ii*) **6**, –78 °C to rt, 3 h, 71%; (*b*) NaOMe, MeOH, rt to 80 °C, 2 h, 87%; (*c*) TBDMSCl, DMAP, CH_2Cl_2, rt, 18 h, 92%; (*f*) Dess–Martin periodinane, CH_2Cl_2, rt, 1 h, 89%; (*g*) CH_2=CHMgCl, Et_2O, –78 °C to 0 °C, 2 h, 97%; (*h*) Dess–Martin periodinane, CH_2Cl_2, rt, 1 h, 80%; (*i*) Et_2AlCl, CH_2Cl_2, –78 °C to 0 °C, 5 min, 72%.



strategy for **9**, while the propargylic alcohol **3** would contribute the requisite C2 oxygen.

Magnesium-mediated carbometallation – intramolecular Diels–Alder studies

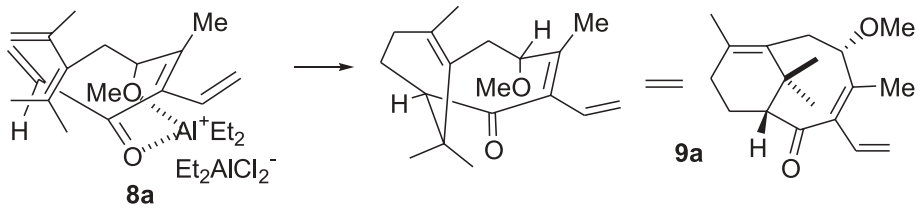
Diene aldehyde **6** was readily prepared in multigram quantities and 45% overall yield via our reported four-step sequence from 2,3-dimethyl-2-butene **10** (Scheme 2) (3*d*). Subsequent thermal rearrangement of the initially formed 1,1-dibromo-2,2,3,3-tetramethylcyclopropane **11** gave bromodiene **12**, and lithium–halogen exchange followed by alkylation with ethylene oxide afforded diene alcohol **13**. Diene aldehyde **6** was somewhat sensitive to prolonged storage, so it was prepared immediately prior to use by oxidation of diene alcohol **13** with Dess–Martin periodinane (12).

Our route for the preparation of the keto-pentaene **8a** began with the addition of vinylmagnesium chloride to 2-butynol (**3a**) and followed by quenching of the intermediate magnesium anion with diene aldehyde **6** (Scheme 3). Selective protection of the primary allylic alcohol, as silyl ether **14a**, permitted methylation of the secondary allylic alcohol in diol **7a** and subsequent fluoride-mediated desilylation of the methylated intermediate **15a** to afford alcohol **16a**. Swern, *o*-iodoxybenzoic acid (IBX), or Dess–Martin oxidation to aldehyde **17a** was followed by the addition of vinylmagnesium chloride and a second IBX or Dess–Martin oxidation of alcohol **18a** to give the Diels–Alder precursor **8a**.

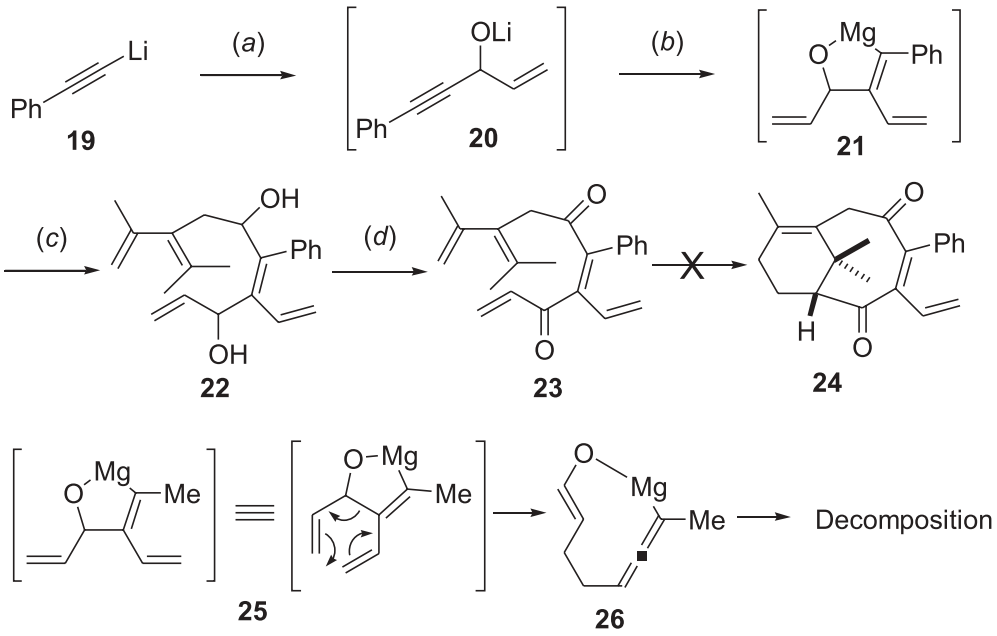
The Diels–Alder cycloaddition of substrate **8a** proceeded smoothly in the presence of Et_2AlCl to afford the taxane AB-ring building block **9a** as a single diastereomer (Scheme 3). The observed stereoselectivity, confirmed by X-

© 2004 NRC Canada

Fig. 2. Diastereoselective Lewis-acid complexation of **8a**.



Scheme 4. Reagents and conditions: (*a*) CH_2=CHCHO; (*b*) CH_2=CHMgCl; (*c*) **6**; (*d*) Dess–Martin periodinane, CH_2Cl_2, rt, 1 h, 80%.



ray crystallographic analysis (5), arose from chelation control provided by complexation of the Lewis acid between the C2 carbonyl and C9 methoxy substituents (Fig. 2). The geometry appears particularly favourable, created by the chair-like arrangement of the atoms involved. Related chelation effects have been shown to control the selectivity of both intermolecular (13) and intramolecular cycloadditions (14) mediated by Lewis acids.

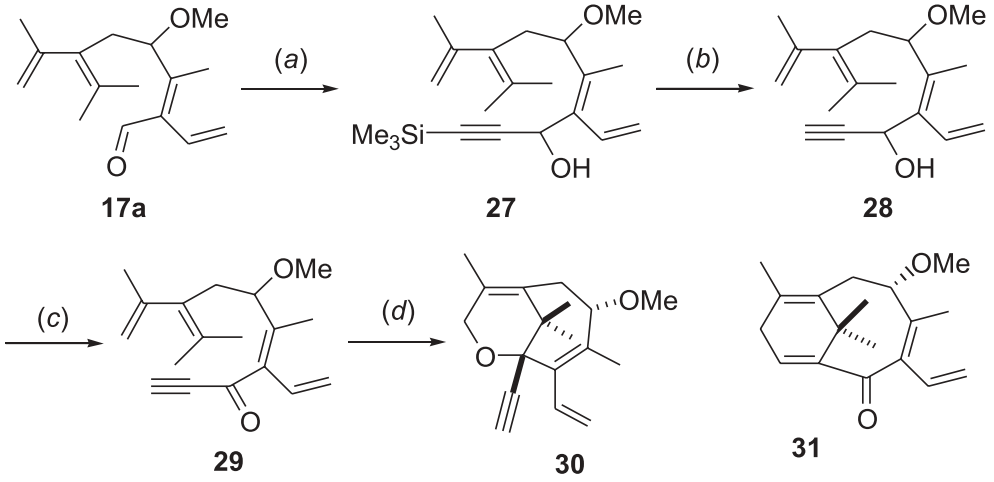
This direct route to the bicyclo[5.3.1]undecenone **9a** was also utilized to construct compounds **9b** and **9c** in a parallel fashion. Trimethylsilyl acetylene propargyl alcohol provided access to intermediate **7b**, from which the silyl group could be readily removed to afford the corresponding carbometallation product **7c**. This ultimately provided access to the bicyclo[5.3.1]undecenone **9c**, or alternatively, the silyl group could be retained until the adduct **9b**, to afford a second source of **9c**, as illustrated in Scheme 3.

An attempt to shorten this sequence, as we had done for our furan syntheses (7) with an acetylenic anion, gave variable results. The in situ generation of a secondary alkoxide by carbometallation to install the dienophilic olefin worked well with a phenyl substituent (Scheme 4). Thus the lithium salt of phenyl acetylene **19** was condensed with acrolein, treated with excess vinylmagnesium chloride, and quenched with diene aldehyde **6** to afford the phenyl pentadiene diol **22** directly. Subsequent oxidation of the allylic alcohols provided the diketone **23**. Unfortunately, this cross-conjugated diketone readily decomposed in the presence of Lewis acids. In addition, attempted thermal cycloadditions of **23** failed to give **24**. This appears to be a consequence of the reduced dienophilic character of **23** due to its extended conjugation, combined with the bulky phenyl group and the presence of a single methylene unit in the tether. This excessive planarity precluded the formation of the required Diels–Alder transition-state conformation. The phenyl acetylide was replaced with propynyllithium, and the sequence was repeated; however, a second complication was discovered. The modified electronic environment and reduced size of the methyl substituent in the chelate resulted in a rapid oxy-Cope rearrangement of the intermediate magnesium alkoxide **25**. The resulting allene aldehyde enolate **26** decomposed under the reaction conditions and necessitated the abandonment of this procedure.

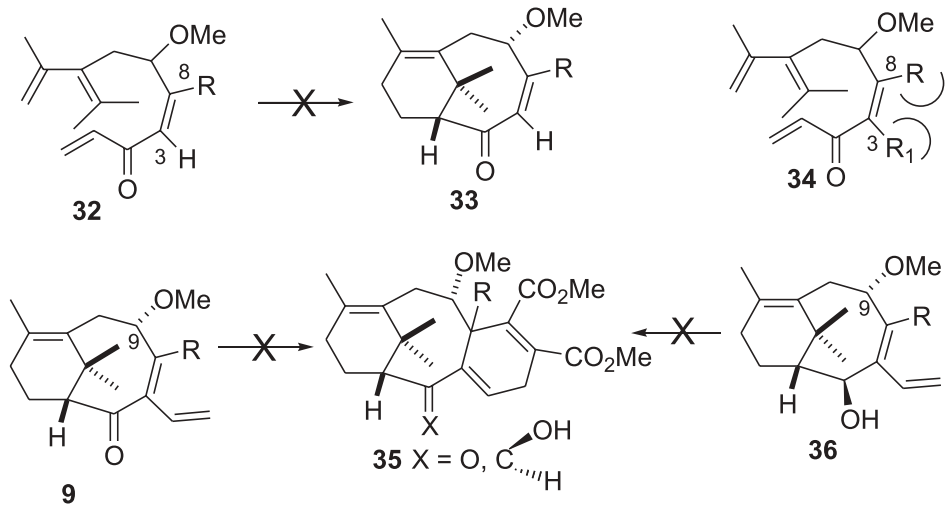
Another variation was investigated, based on related studies by Shea and co-workers (4) who incorporated an oxygen in the tether, to prepare an A-ring cycloheaxadiene. Ring systems of type **31** are desirable because of the increased potency of C14-substituted taxoids (1). The addition of trimethylsilylethynyl lithium to the unsaturated aldehyde **17a** was converted to the alternative Diels–Alder precursor **29**

© 2004 NRC Canada

Scheme 5. Reagents and conditions: (*a*) (*i*) TMS–acetylene, BuLi, THF, –78 °C, 30 min; (*ii*) **17a**, –78 °C, 1 h, 89%; (*b*) TBAF, THF, rt, 1 h, 85%; (*c*) Dess–Martin periodinane, CH_2Cl_2, rt, 1 h, 86%; (*d*) Et_2AlCl, CH_2Cl_2, –78 °C to 0 °C, 5 min, 62%.



Scheme 6.



with the intention of preparing **31**. Experimentally, the heterocyclic cycloaddition adduct **30**, containing a seven-membered ring, was formed exclusively (Scheme 5).

In the course of these investigations, several additional subtleties of these Diels–Alder precursors were uncovered. It was anticipated, in view of the success of the cyclization of **8** to **9**, that the cyclization of **32** under Lewis-acid conditions should also be straightforward. This would permit a "Robinson annulation"-type approach for the attachment of the C ring (Scheme 6). However, when members of the family represented by **32** in which the C3 substituent is hydrogen were investigated, they were completely inert under the cycloaddition reaction conditions above. These experiments revealed that an important nonbonded interaction played a key role in the success of these cycloadditions. A substituent at the C3 position (taxane numbering, **34**) is required to ensure the dienophile attains the required conformation. This interaction causes the enone to fold under the diene, to ensure the requisite transition state for the cycloaddition. The examples in Scheme 3 confirm this effect.

Additional examples with C3 allyl substituents are discussed in the following paper. Thus the vinyl methyl at C8 may be replaced by hydrogen (**8c**), but the group at C3 is more important than the substituent at C8.

It will be obvious that we intended to attach the C ring to the diene adducts **9** by a second Diels–Alder reaction of either an intermolecular or intramolecular variety, the latter via attachment of an ester dienophile to the C9 centre. However, a number of attempts to elaborate the ABC-ring core from **9** with a suitable C-ring dienophile via Diels–Alder protocols were unsuccessful (Scheme 6). Several activated dienophiles (maleic anhydride, *N*-phenylmaleimide) and even "relatively flat" diethyl acetylenedicarboxylate were investigated, but these reactions failed to yield significant amounts of the desired adducts. The stereochemical control available from an allylic hydroxyl or ether group in cycloadditions is well established (15). Reduction of the carbonyl in **9a** gave **36**, and protection afforded the *p*-methoxybenzyl ether (not illustrated). These compounds also failed to react with the same three dienophiles, although in these cases,

© 2004 NRC Canada

only the starting materials were recovered. Consequently, other variations were examined. These alternative protocols initially included modification of the vinyl silyl group present in **8b** (Scheme 3). Halodesilylation to afford the vinyl bromide in place of the C8 methyl substituent would have permitted subsequent palladium couplings for ring C appendages. Unfortunately, the desired transformation failed. However, an efficient method for attaching the C ring is described in the following paper.

Experimental section

Reagents, unless otherwise noted, were purchased from the Aldrich Chemical Company and used as received. Reaction solvents were distilled under a nitrogen atmosphere prior to use unless otherwise stated. Diethyl ether (Et_2O) and tetrahydrofuran (THF) were distilled from Na metal and benzophenone ketyl, while dichloromethane (CH_2Cl_2) was distilled from calcium hydride (CaH_2). All other solvents used were reagent grade.

All manipulations were carried out under a nitrogen atmosphere in flame-dried glassware. Analytical thin-layer chromatography (TLC) was performed on commercial aluminum sheets precoated (0.2 mm layer thickness) with silica gel 60 F_{254} (E. Merck), visualized with a UV_{254} lamp (Spectroline Longlife filter), and stained with 20% phosphomolybdic acid in ethanol (Aldrich Chemical Company). Column chromatography on silica gel (60 Å, 230–400 mesh, E. Merck) was performed with hexanes and ethyl acetate (EtOAc).

Melting points were determined in capillary tubes with a Thomas-Hoover unit-melt apparatus and are uncorrected. FT-IR spectra were recorded on a Bomem Michelson 100 FT-IR spectrometer, with samples loaded as neat films on NaCl plates. All ^{1}H and ^{13}C NMR spectra were obtained on a 500 MHz Brüker AMX500 or a 300 MHz Brüker AMX300 in $CDCl_3$ (referenced to the residual solvent signals at δ 7.24 and 77.00 ppm for ^{1}H and ^{13}C, respectively) or C_6D_6 (referenced to the residual solvent signals at δ 7.15 and 127.00 ppm for ^{1}H and ^{13}C, respectively). Features of peaks in the ^{1}H NMR spectra are labeled in brackets after each chemical shift in the following order: multiplicity (s = singlet, d = doublet, t = triplet, q = quartet, m = multiplet), coupling constant, and integration. Mass spectra (MS) were determined on a V.G. micromass 7070 HS instrument, using an ionization energy of 70 eV. Elemental analyses were conducted by M-H-W Laboratories (Phoenix, Arizona, U.S.A.). The purity of the title compounds were judged to be >95% pure, as determined by a combination of GC–MS, ^{1}H NMR, and ^{13}C NMR analysis.

1,1-Dibromo-2,2,3,3-tetramethyl-cyclopropane (11)

Bromoform (80.0 mL, 916 mmol) was added dropwise by means of an addition funnel to a stirred suspension of 2,3-dimethyl-2-butene **10** (50.0 mL, 421 mmol) and potassium *tert*-butoxide (86.4 g, 770 mmol) in pentane (150 mL) at 0 °C over a period of 1 h. After warming to 21 °C, stirring was continued for another 2 h prior to the addition of water (200 mL). The layers were separated, and the aqueous layer was extracted with hexanes (2 × 150 mL). The combined organic extracts were washed with brine (4 × 80 mL), dried ($MgSO_4$), filtered, and concentrated under reduced pressure. Cold methanol (100 mL) was added to the residue, and the solution was cooled to 0 °C. The resulting precipitate was then collected by filtration, washed with cold methanol (20 mL), and allowed to dry in air. The mother liquor was concentrated under reduced pressure, and the precipitation cycle was repeated to yield more of the white crystalline solid (75 g, 71%). mp = 77 to 78 °C. ^{1}H NMR ($CDCl_3$, 300 MHz) δ: 1.25 (s, 12H). ^{13}C NMR ($CDCl_3$, 75 MHz) δ: 18.4, 35.5, 58.7.

3-Bromo-2,4-dimethyl-penta-1,3-diene (12)

1,1-Dibromo-2,2,3,3-tetramethyl-cyclopropane **11** (28.7 g, 118 mmol) was slowly heated with a propane torch, and the resulting liquid was collected by distillation between 120–140 °C. The distillate was further purified by two additional distillations. The product was treated with NaOH pellets for 0.5 h and then filtered through glass wool to afford a colorless liquid (15.7 g, 80%). The product was stored at –20 °C over grains of NaOH. ^{1}H NMR ($CDCl_3$, 300 MHz) δ: 1.73 (s, 3H), 1.75 (s, 3H), 1.82 (s, 3H), 4.73–4.75 (m, 1H), 4.89–4.91 (m, 1H). ^{13}C NMR ($CDCl_3$, 75 MHz) δ: 17.0, 17.2, 19.8, 107.8, 111.9, 133.4, 145.7.

3-Isopropenyl-4-methyl-pent-3-en-1-ol (13)

A solution of 3-bromo-2,4-dimethylpenta-1,3-diene **12** (13.5 g, 77.0 mmol) in THF (235 mL) at –78 °C was added to a stirred solution of *tert*-butyllithium (100.0 mL, 170.0 mmol, 1.7 mol L^{-1} in pentane) cooled to –78 °C. After 0.5 h, ethylene oxide (39 mL) was added via a cannula. The resulting solution was subsequently stirred for 1 h at –78 °C and then for 1 h at 21 °C. Water (200 mL) was then added; the layers were separated, and the aqueous layer was extracted with ether (4 × 100 mL). The combined organic extracts were dried ($MgSO_4$), filtered, and concentrated under reduced pressure. Purification by flash chromatography (silica gel, ethyl acetate – hexanes) provided the title compound as a colorless liquid (9.0 g, 83%). IR (neat) (cm^{-1}) ν: 3357, 2923, 1623. ^{1}H NMR ($CDCl_3$, 300 MHz) δ: 0.90 (s, 1H), 1.67 (s, 3H), 1.69 (s, 3H), 1.75 (s, 3H), 2.37 (t, J = 6.7 Hz, 2H), 3.60 (t, J = 6.7 Hz, 2H), 4.54–4.56 (m, 1H), 4.93–4.95 (m, 1H). ^{13}C NMR ($CDCl_3$, 75 MHz) δ: 20.3, 22.2, 22.9, 34.2, 61.6, 113.9, 128.9, 132.9, 146.7. HR-MS (EI) *m*/*z* calcd. for $C_9H_{16}O$: 140.1201; found: 140.1213.

4-Methyl-3-vinyl-pent-3-enal (6)

Dess–Martin periodinane (8.30 g, 19.6 mmol) was added to a solution of 3-isopropenyl-4-methyl-pent-3-en-1-ol **13** (2.50 g, 17.8 mmol) in dichloromethane (30 mL) at 21 °C. The resulting solution was stirred for 0.5 h prior to dilution with a 10% aq. solution of NaOH (30 mL). The layers were separated, and the organic layer was extracted with dichloromethane (3 × 30 mL). The combined organic extracts were dried ($MgSO_4$), filtered, and concentrated under reduced pressure to afford the title compound as a colorless liquid (2.34 g, 95%). IR (neat) (cm^{-1}) ν: 2923, 1706, 1630. ^{1}H NMR ($CDCl_3$, 300 MHz) δ: 1.66 (s, 3H), 1.73 (s, 6H), 3.12 (d, J = 2.6 Hz, 2H), 4.62–4.64 (m, 1H), 4.93–4.96 (m, 1H), 9.52 (t, J = 2.6 Hz, 1H). ^{13}C NMR ($CDCl_3$, 75 MHz) δ: 20.5, 22.2, 22.5, 47.1, 114.6, 127.4, 131.9, 146.3, 200.3. HR-MS (EI) *m*/*z* calcd. for $C_9H_{14}O$: 138.1045; found: 138.1049.

© 2004 NRC Canada

3-Trimethylsilanyl-prop-2-yn-1-ol (3b)

Butyl lithium (189 mL, 434 mmol, 2.3 mol L^{-1} in hexane) was added to a solution of propargyl alcohol (11.0 mL, 189 mmol) in THF (300 mL) cooled to –78 °C. After 45 min, chlorotrimethylsilane (57.6 mL, 453 mmol) was added, and the solution was warmed to 21 °C for 3 h. After cooling to 0 °C, 10% aq. sulfuric acid (250 mL) was added; the layers were separated after 15 min, and the aqueous layer was extracted with ether (2 × 150 mL). The combined organic extracts were washed with brine (2 × 100 mL), dried ($MgSO_4$), filtered, and concentrated under reduced pressure. Purification by flash chromatography (silica gel, ether – petroleum ether) provided the title compound as a colorless oil (15.1 g, 62%). IR (neat) (cm^{-1}) ν: 3324, 2961, 2901, 2177. ^1H NMR ($CDCl_3$, 300 MHz) δ: 0.15 (s, 9H), 1.8 (s, 1H), 4.24 (s, 2H). ^{13}C NMR ($CDCl_3$, 75 MHz) δ: 0.13, 51.9, 91.0, 104.2. HR-MS (EI) *m/z* calcd. for $C_6H_{12}OSi$ ($[M]^+$): 128.0657; found: 128.0686.

General procedure for the carbometallation of the propargylic alcohols

Vinylmagnesium chloride (2.5 equiv.) was added to a solution of the propargylic alcohol (1.0 equiv.) in cyclohexane ([alcohol] = 1.0 mol L^{-1}) at 21 °C. The solution was heated at reflux for 20 h and cooled to –78 °C, and 4-methyl-3-vinyl-pent-3-enal **6** (0.5 equiv.) in ether ([aldehyde] = 0.3 mol L^{-1}) was added. The solution was stirred for 30 min at –78 °C, for 1 h at 0 °C, and for 1 h at 21 °C. The reaction was subsequently cooled to 0 °C, and a saturated aqueous solution of NH_4Cl added. The layers were separated, and the aqueous layer was extracted with dichloromethane. The combined organic extracts were washed with brine, dried ($MgSO_4$), filtered, and concentrated under reduced pressure. The crude material was purified by flash chromatography (silica gel, ether – petroleum ether).

6-Isopropenyl-3,7-dimethyl-2-vinyl-octa-2,6-diene-1,4-diol (7a)

71% from **3a**. IR (neat) (cm^{-1}) ν: 3355, 2964, 2917, 1630, 1442, 1374, 998, 900. ^1H NMR ($CDCl_3$, 500 MHz) δ: 1.65 (s, 3H), 1.66 (s, 3H), 1.73 (s, 3H), 1.82 (s, 3H), 2.19 (dd, *J* = 14.0, 5.2 Hz, 1H), 2.54 (s, 1H), 2.63 (dd, *J* = 14.0, 8.5 Hz, 1H), 4.24 (d, *J* = 11.9 Hz, 1H), 4.36 (d, *J* = 11.9 Hz, 1H), 4.67 (s, 1H), 4.85 (dd, *J* = 8.5, 5.2 Hz, 1H), 4.98 (s, 1H), 5.09 (dd, *J* = 11.1, 1.2 Hz, 1H), 5.42 (dd, *J* = 17.5, 1.2 Hz, 1H), 6.62 (dd, *J* = 17.5, 11.1 Hz, 1H). ^{13}C NMR ($CDCl_3$, 125 MHz) δ: 13.0, 20.2, 22.0, 22.6, 36.9, 57.5, 70.1, 114.1, 114.2, 129.0, 132.5, 133.4, 134.8, 141.0, 146.7. HR-MS (EI) *m/z* calcd. for $C_{15}H_{24}O_2$ ($[M]^+$): 236.1777; found: 236.1791.

6-Isopropenyl-7-methyl-3-trimethylsilanyl-2-vinyl-octa-2,6-diene-1,4-diol (7b)

56% from **3b**. IR (neat) (cm^{-1}) ν: 3408, 3075, 2958, 2913, 1631. ^1H NMR ($CDCl_3$, 500 MHz) δ: 0.21 (s, 9H), 1.72 (s, 3H), 1.76 (s, 3H), 1.79 (s, 3H), 2.06 (dd, *J* = 14.4, 2.8 Hz, 1H), 2.69 (dd, *J* = 14.4, 10.8 Hz, 1H), 4.25 (d, *J* = 11.7 Hz, 1H), 4.54 (d, *J* = 11.7 Hz, 1H), 4.62 (s, 1H), 4.67 (dd, *J* = 10.8, 2.8 Hz, 1H), 5.03 (s, 1H), 5.17 (dd, *J* = 11.0, 0.9 Hz, 1H), 5.47 (dd, *J* = 17.3, 0.9 Hz, 1H), 6.69 (dd, *J* = 17.3, 11.0 Hz, 1H). ^{13}C NMR ($CDCl_3$, 125 MHz) δ: 1.3, 20.2, 21.9, 23.3, 38.1, 58.6, 72.1, 114.3, 114.6, 130.2, 133.1, 138.0, 146.0, 146.6, 147.5. HR-MS (EI) *m/z* calcd. for $C_{17}H_{28}OSi$ ($[M^+ – H_2O]$): 276.1909; found: 276.1932.

6-Isopropenyl-7-methyl-2-vinyl-octa-2,6-diene-1,4-diol (7c)

Sodium methoxide (1.93 g, 34.0 mmol) was added to a solution of diol **7b** (2.50 g, 8.50 mmol) in methanol (40 mL) at 21 °C. The solution was heated at reflux for 2 h and then concentrated. A saturated aqueous solution of NH_4Cl (50 mL) was added; the layers were separated, and the aqueous layer was extracted with ether (2 × 40 mL). The combined organic extracts were washed with brine (2 × 50 mL), dried ($MgSO_4$), filtered, and concentrated under reduced pressure. Purification by flash chromatography (silica gel, ether – petroleum ether) provided the title compound as a colorless oil (1.64 g, 87%). IR (neat) (cm^{-1}) ν: 3308, 2908, 2859, 1630, 1606. ^1H NMR ($CDCl_3$, 500 MHz) δ: 1.69 (s, 3H), 1.70 (s, 3H), 1.76 (s, 3H), 2.27 (dd, *J* = 13.9, 5.1 Hz, 1H), 2.50 (dd, *J* = 13.9, 8.5 Hz, 1H), 4.27 (d, *J* = 12.1 Hz, 1H), 4.32 (d, *J* = 12.1 Hz, 1H), 4.35 (ddd, *J* = 8.5, 7.8, 5.1 Hz, 1H), 4.58 (s, 1H), 4.98 (s, 1H), 5.10 (d, *J* = 10.9 Hz, 1H), 5.38 (d, *J* = 17.6 Hz, 1H), 5.61 (d, *J* = 7.8 Hz, 1H), 6.25 (dd, *J* = 17.6, 10.9 Hz, 1H). ^{13}C NMR ($CDCl_3$, 125 MHz) δ: 20.2, 21.9, 22.4, 38.6, 57.2, 66.9, 114.0, 114.2, 129.8, 132.2, 136.3, 138.1, 139.5, 146.2. HR-MS (EI) *m/z* calcd. for $C_{14}H_{20}O$ ($[M^+ – H_2O]$): 204.1514; found: 204.1503.

General procedure for silylation of the primary alcohols

tert-Butyldimethylsilyl chloride (1.1 equiv.) and DMAP (1.1 equiv.) were sequentially added to a solution of the diol (1.0 equiv.) in dichloromethane ([diol] = 1.0 mol L^{-1}) at 0 °C, and the solution was stirred for 18 h at 21 °C. A saturated aqueous solution of $NaHCO_3$ was then added; the layers were separated, and the aqueous layer was extracted with ether. The combined organic extracts were washed with brine, dried ($MgSO_4$), filtered, and concentrated under reduced pressure. The crude material was purified by flash chromatography (silica gel, ether – petroleum ether).

3-(*tert*-Butyl-dimethyl-silanyloxymethyl)-7-isopropenyl-4,8-dimethyl-nona-1,3,7-trien-5-ol (14a)

92% from **7a**. IR (neat) (cm^{-1}) ν: 3469, 2941, 2858, 1631, 1472, 1377, 1254, 1053, 898, 776. ^1H NMR ($CDCl_3$, 500 MHz) δ: 0.10 (s, 6H), 0.96 (s, 9H), 1.66 (s, 6H), 1.77 (s, 3H), 1.86 (s, 3H), 2.12 (dd, *J* = 14.0, 3.1 Hz, 1H), 2.68 (dd, *J* = 14.0, 9.7 Hz, 1H), 4.35 (d, *J* = 11.4 Hz, 1H), 4.43 (d, *J* = 11.4 Hz, 1H), 4.71 (m, 1H), 4.95 (s, 1H), 5.03 (s, 1H), 5.16 (dd, *J* = 11.2, 1.4 Hz, 1H), 5.49 (dd, *J* = 17.5, 1.4 Hz, 1H), 6.69 (dd, *J* = 17.5, 11.2 Hz, 1H). ^{13}C NMR ($CDCl_3$, 125 MHz) δ: –5.1, 12.8, 18.4, 20.1, 22.0, 22.8, 26.1, 37.1, 58.4, 69.6, 114.0, 114.1, 129.3, 132.1, 133.3, 135.2, 140.8, 146.7. HR-MS (EI) *m/z* calcd. for $C_{21}H_{36}OSi$ ($[M^+ – H_2O]$): 332.2537; found: 332.2552. Anal calcd. for $C_{21}H_{38}O_2Si$ (%): C 71.95, H 10.65; found: C 71.86, H 10.65.

3-(*tert*-Butyl-dimethyl-silanyloxymethyl)-7-isopropenyl-8-methyl-4-trimethylsilanyl-nona-1,3,7-trien-5-ol (14b)

74% from **7b**. IR (neat) (cm^{-1}) ν: 3462, 2955, 2930, 2857. ^1H NMR ($CDCl_3$, 500 MHz) δ: 0.04 (s, 6H), 0.25 (s, 9H), 0.86 (s, 9H), 1.70 (s, 3H), 1.75 (s, 3H), 1.79 (s, 3H), 1.89 (s, 1H), 2.01 (dd, *J* = 14.2, 2.5 Hz, 1H), 2.66 (dd, *J* = 14.2,

© 2004 NRC Canada

10.7 Hz, 1H), 4.35 (d, *J* = 11.5 Hz, 1H), 4.39 (d, *J* = 11.5 Hz, 1H), 4.64 (s, 1H), 4.81 (dd, *J* = 10.7, 2.5 Hz, 1H), 5.01 (s, 1H), 5.13 (dd, *J* = 11.1, 1.1 Hz, 1H), 5.34 (dd, *J* = 17.3, 1.1 Hz, 1H), 6.62 (dd, *J* = 17.3, 11.1 Hz, 1H). ^{13}C NMR ($CDCl_3$, 125 MHz) δ: –5.2, 2.5, 18.2, 20.3, 21.9, 22.7, 25.9, 38.4, 58.8, 72.0, 114.1, 115.0, 128.9, 133.2, 137.9, 146.1, 146.2, 146.8. HR-MS (EI) *m/z* calcd. for $C_{23}H_{42}OSi$ ([$M^+ - H_2O$]): 390.2274; found: 390.2770.

3-(*tert*-Butyl-dimethyl-silanyloxymethyl)-7-isopropenyl-8-methyl-nona-1,3,7-trien-5-ol (14c)

78% from **7c**. IR (neat) (cm^{-1}) ν: 3432, 3075, 2954, 2929, 2857, 1631, 1607. ^{1}H NMR ($CDCl_3$, 500 MHz) δ: 0.06 (s, 3H), 0.07 (s, 3H), 0.87 (s, 9H), 1.69 (s, 3H), 1.72 (s, 3H), 1.77 (s, 3H), 2.24 (dd, *J* = 13.9, 5.3 Hz, 1H), 2.28 (s, 1H), 2.50 (dd, *J* = 13.9, 8.3 Hz, 1H), 4.25 (s, 2H), 4.57 (ddd, *J* = 8.3, 8.1, 5.3 Hz, 1H), 4.58 (s, 1H), 4.97 (s, 1H), 5.05 (d, *J* = 11.0 Hz, 1H), 5.31 (d, *J* = 17.6 Hz, 1H), 5.62 (d, *J* = 8.1 Hz, 1H), 6.24 (dd, *J* = 17.6, 11.0 Hz, 1H). ^{13}C NMR ($CDCl_3$, 125 MHz) δ: –5.4 (2), 18.2, 20.1, 21.8, 22.5, 25.8, 38.4, 58.1, 66.6, 113.6, 113.9, 129.2, 132.4, 136.4, 138.4, 146.2. HR-MS (EI) *m/z* calcd. for $C_{20}H_{34}OSi$ ([$M^+ - H_2O$]): 318.2379; found: 318.2383.

General procedure for methylation of the secondary alcohols

Sodium hydride (3.0 equiv., 60% dispersion in mineral oil) was added to a solution of the alcohol (1.0 equiv.) in THF ([alcohol] = 1.0 mol L^{-1}) at 0 °C. After 30 min, iodomethane (20.0 equiv.) was added, and the solution was stirred for 18 h at 21 °C. A saturated aqueous solution of NH_4Cl was subsequently added; the layers were separated, and the aqueous layer was extracted with dichloromethane. The combined organic extracts were washed with brine, dried ($MgSO_4$), filtered, and concentrated under reduced pressure. The crude material was purified by flash chromatography (silica gel, ether – petroleum ether).

3-(*tert*-Butyl-dimethyl-silanyloxymethyl)-7-isopropenyl-5-hydroxy-8-methyl-4-methyl-nona-1,3,7-triene (15a)

91% from **14a**. IR (neat) (cm^{-1}) ν: 2929, 2858, 1633, 1463, 1383, 1255, 1100, 1068, 898, 851, 837, 774. ^{1}H NMR ($CDCl_3$, 500 MHz) δ: 0.11 (s, 6H), 0.96 (s, 9H), 1.73 (s, 3H), 1.74 (s, 3H), 1.79 (s, 3H), 1.82 (s, 3H), 2.11 (dd, *J* = 14.2, 4.3 Hz, 1H), 2.79 (dd, *J* = 14.2, 8.9 Hz, 1H), 3.13 (s, 3H), 4.30 (d, *J* = 11.2 Hz, 1H), 4.48 (dd, *J* = 8.9, 4.3 Hz, 1H), 4.74 (d, *J* = 11.2 Hz, 1H), 4.81 (s, 1H), 5.09 (s, 1H), 5.16 (dd, *J* = 11.2, 1.1 Hz, 1H), 5.50 (dd, *J* = 17.5, 1.1 Hz, 1H), 6.69 (dd, *J* = 17.5, 11.2 Hz, 1H). ^{13}C NMR ($CDCl_3$, 125 MHz) δ: –5.2, 12.2, 18.5, 20.2, 22.1, 22.9, 26.1, 36.2, 56.3, 57.9, 79.1, 114.0, 127.6, 128.3, 133.5, 133.9, 135.0, 139.1, 147.0. HR-MS (EI) *m/z* calcd. for $C_{22}H_{40}O_2Si$ ([M]$^+$): 364.2799; found: 364.2801. Anal calcd. for $C_{22}H_{40}O_2Si$ (%): C 72.97, H 11.06; found: C 73.13, H 11.06.

3-(*tert*-Butyl-dimethyl-silanyloxymethyl)-7-isopropenyl-5-methoxy-8-methyl-4-trimethylsilanyl-nona-1,3,7-triene (15b)

95% from **14b**. IR (neat) (cm^{-1}) ν: 2956, 2858, 1630. ^{1}H NMR ($CDCl_3$, 500 MHz) δ: 0.10 (s, 3H), 0.11 (s, 3H), 0.38 (s, 9H), 0.95 (s, 9H), 1.74 (s, 3H), 1.79 (s, 3H), 1.83 (s, 3H), 2.09 (d, *J* = 14.4 Hz, 1H), 2.91 (dd, *J* = 14.4, 9.8 Hz, 1H), 3.20 (s, 3H), 4.35 (m, 1H), 4.49 (s, 2H), 4.83 (s, 1H), 5.12 (s, 1H), 5.13 (d, *J* = 11.1 Hz, 1H), 5.48 (d, *J* = 17.3 Hz, 1H), 6.83 (dd, *J* = 17.3, 11.1 Hz, 1H). ^{13}C NMR ($CDCl_3$, 125 MHz) δ: –5.1, 2.6, 18.4, 20.5, 22.1, 22.9, 26.1, 38.3, 57.1, 58.4, 81.9, 114.2, 114.9, 127.4, 127.9, 128.3, 134.0, 138.1, 146.9.

3-(*tert*-Butyl-dimethyl-silanyloxymethyl)-7-isopropenyl-5-methoxy-8-methylnona-1,3,7-triene (15c)

89% from **14c**. IR (neat) (cm^{-1}) ν: 2956, 2929, 2858, 1615. ^{1}H NMR ($CDCl_3$, 500 MHz) δ: 0.06 (s, 6H), 0.87 (s, 9H), 1.65 (s, 3H), 1.66 (s, 3H), 1.75 (s, 3H), 2.17 (dd, *J* = 14.1, 5.9 Hz, 1H), 2.51 (dd, *J* = 14.1, 7.4 Hz, 1H), 3.19 (s, 3H), 4.08 (ddd, *J* = 9.2, 7.4, 5.9 Hz, 1H), 4.22 (d, *J* = 11.3 Hz, 1H), 4.31 (d, *J* = 11.3 Hz, 1H), 4.56 (s, 1H), 4.95 (s, 1H), 5.06 (d, *J* = 11.0 Hz, 1H), 5.37 (d, *J* = 17.6 Hz, 1H), 5.41 (d, *J* = 9.2 Hz, 1H), 6.26 (dd, *J* = 17.6, 11.0 Hz, 1H). ^{13}C NMR ($CDCl_3$, 125 MHz) δ: –5.4, 18.3, 20.2, 21.9, 22.6, 25.9, 37.3, 56.3, 57.9, 75.8, 113.7, 113.9, 127.7, 132.5, 134.7, 138.3, 139.5, 146.4. HR-MS (EI) *m/z* calcd. for $C_{21}H_{38}O_2Si$ ([M]$^+$): 350.2641; found: 350.2642.

General procedure for deprotection of the primary alcohols

Tetrabutylammonium fluoride (1.5 equiv., 1.0 mol L^{-1} in THF) was added to a solution of silane (1.0 equiv.) in THF ([silane] = 1.0 mol L^{-1}) at 0 °C, and the resulting solution was stirred for 18 h at 21 °C. A saturated aqueous solution of NH_4Cl was then added; the layers were separated, and the aqueous layer was extracted with ether. The combined organic extracts were washed with brine, dried ($MgSO_4$), filtered, and concentrated under reduced pressure. The crude material was purified by flash chromatography (silica gel, ether – petroleum ether).

6-Isopropenyl-4-methoxy-3,7-dimethyl-2-vinyl-octa-2,6-dien-1-ol (16a)

99% from **15a**. IR (neat) (cm^{-1}) ν: 3445, 2922, 1629, 1444, 1364, 1099, 996, 898, 691, 630. ^{1}H NMR ($CDCl_3$, 500 MHz) δ: 1.65 (s, 6H), 1.66 (s, 3H), 1.72 (s, 3H), 2.18 (dd. *J* = 14.1, 5.9 Hz, 1H), 2.67 (dd, *J* = 14.1, 7.6 Hz, 1H), 3.00 (s, 3H), 4.29–4.40 (m, 3H), 4.72 (s, 1H), 4.99 (s, 1H), 5.10 (d, *J* = 11.1 Hz, 1H), 5.44 (d, *J* = 17.7 Hz, 1H), 6.59 (dd, *J* = 17.7, 11.1 Hz, 1H). ^{13}C NMR ($CDCl_3$, 125 MHz) δ: 12.2, 20.1, 22.0, 22.7, 36.0, 56.0, 57.4, 79.1, 114.1, 114.2, 128.5, 133.8, 134.5, 134.9, 139.3, 146.8. HR-MS (EI) *m/z* calcd. for $C_{16}H_{26}O_2$ ([M]$^+$): 250.1934; found: 250.1938.

6-Isopropenyl-4-methoxy-7-methyl-3-trimethylsilanyl-2-vinyl-octa-2,6-dien-1-ol (16b)

83% from **15b**. IR (neat) (cm^{-1}) ν: 3415, 2910, 2858, 2816, 1631. ^{1}H NMR ($CDCl_3$, 300 MHz) δ: 0.23 (s, 9H), 1.66 (s, 3H), 1.69 (s, 3H), 1.76 (s, 3H), 1.93 (dd, *J* = 7.6, 4.5 Hz, 1H), 2.07 (dd, *J* = 14.5, 4.5 Hz, 1H), 2.71 (dd, *J* = 14.5, 8.6 Hz, 1H), 3.17 (s, 3H), 4.22 (dd, *J* = 8.6, 4.5 Hz, 1H), 4.32 (dd, *J* = 12.1, 7.6 Hz, 1H), 4.45 (dd, *J* = 12.1, 4.5 Hz, 1H), 4.61–4.63 (m, 1H), 4.99–5.02 (m, 1H), 5.20 (dd, *J* = 11.1, 0.8 Hz, 1H), 5.43 (dd, *J* = 17.3, 0.8 Hz, 1H),

© 2004 NRC Canada

6.70 (dd, *J* = 17.3, 11.1 Hz, 1H). ^{13}C NMR ($CDCl_3$, 75 MHz) δ: 2.2, 20.6, 22.3, 23.1, 37.8, 57.5, 58.6, 82.0, 114.5, 115.1, 128.2, 133.8, 137.9, 146.6, 147.6, 147.8.

6-Isopropenyl-4-methoxy-7-methyl-2-vinyl-octa-2,6-dien-1-ol (16c)

90% from **15c**. IR (neat) (cm^{-1}) ν: 3438, 3076, 2925, 2820, 1630, 1606. ^{1}H NMR ($CDCl_3$, 500 MHz) δ: 1.65 (s, 3H), 1.66 (s, 3H), 1.76 (s, 3H), 2.29 (dd, *J* = 13.9, 7.6 Hz, 1H), 2.52 (dd, *J* = 13.9, 6.1 Hz, 1H), 3.23 (s, 3H), 4.07 (ddd, *J* = 8.9, 7.6, 6.1 Hz, 1H), 4.27 (s, 2H), 4.55 (s, 1H), 4.97 (s, 1H), 5.12 (d, *J* = 10.9 Hz, 1H), 5.39 (d, *J* = 17.6 Hz, 1H), 5.46 (d, *J* = 8.9 Hz, 1H), 6.27 (dd, *J* = 17.6, 10.9 Hz, 1H). ^{13}C NMR ($CDCl_3$, 125 MHz) δ: 20.2, 21.9, 22.6, 36.7, 56.2, 57.3, 76.1, 113.9, 114.0, 128.4, 132.4, 135.7, 138.1, 139.9, 146.2. HR-MS (EI) *m/z* calcd. for $C_{15}H_{24}O_2$ ($[M]^+$): 236.1776; found: 236.1786.

General procedures for oxidation of the primary alcohols

Oxalyl chloride (1.5 equiv.) was added to a solution of DMSO (3.0 equiv.) in dichloromethane ([oxalyl chloride] = 1.0 mol L^{-1}) at –78 °C. After 5 min, the alcohol (1.0 equiv.) was added, and the solution was stirred for 1 h at –78 °C. Triethylamine (7.0 equiv.) was added, and the solution was warmed to 0 °C for 1 h. A saturated aqueous solution of NH_4Cl was added; the layers were separated, and the aqueous layer was extracted with ether. The combined organic extracts were washed with brine, dried ($MgSO_4$), filtered, and concentrated under reduced pressure. The crude material was purified by flash chromatography (silica gel, ether – petroleum ether).

The alcohol (1.0 equiv.) in THF was added to a solution of IBX (1.5 equiv.) in DMSO ([alcohol] = 1.0 mol L^{-1}) at 0 °C. The resulting solution was stirred for 3 h at 21 °C prior to the addition of water. Following filtration, the solution was extracted with ether. The combined organic extracts were washed with brine, dried ($MgSO_4$), filtered, and concentrated. The crude material was purified by flash chromatography (silica gel, ether – petroleum ether).

6-Isopropenyl-4-methoxy-3,7-dimethyl-2-vinyl-octa-2,6-dienal (17a)

80% from **16a**. IR (neat) (cm^{-1}) ν: 3076, 2981, 2925, 2821, 1683, 1629. ^{1}H NMR ($CDCl_3$, 500 MHz) δ: 1.58 (s, 3H), 1.65 (s, 3H), 1.71 (s, 3H), 1.73 (s, 3H), 2.19 (dd, *J* = 14.1, 6.0 Hz, 1H), 2.63 (dd, *J* = 14.1, 7.5 Hz, 1H), 2.88 (s, 3H), 4.69 (dd, *J* = 7.5, 6.0 Hz, 1H), 4.68 (s, 1H), 4.98 (s, 1H), 5.26 (dd, *J* = 11.6, 1.7 Hz, 1H), 5.67 (dd, *J* = 17.8, 1.7 Hz, 1H), 6.34 (dd, *J* = 17.8, 11.6 Hz, 1H), 10.19 (s, 1H). ^{13}C NMR ($CDCl_3$, 125 MHz) δ: 14.3, 20.2, 22.0, 22.5, 35.9, 56.3, 77.6, 114.7, 119.8, 128.9, 130.4, 132.5, 136.5, 146.1, 154.8, 189.6. HR-MS (EI) *m/z* calcd. for $C_{16}H_{24}O_2$ ($[M]^+$): 248.1776; found: 248.1795.

6-Isopropenyl-4-methoxy-7-methyl-3-trimethylsilanyl-2-vinyl-octa-2,6-dienal (17b)

91% from **16b**. IR (neat) (cm^{-1}) ν: 3074, 2914, 2820, 2718, 1699, 1630. ^{1}H NMR ($CDCl_3$, 500 MHz) δ: 0.22 (s, 9H), 1.65 (s, 3H), 1.66 (s, 3H), 1.75 (s, 3H), 2.05 (dd, *J* = 14.8, 3.1 Hz, 1H), 2.64 (dd, *J* = 14.8, 9.9 Hz, 1H), 3.08 (s, 3H), 4.13 (dd, *J* = 9.9, 3.1 Hz, 1H), 4.57 (s, 1H), 4.98 (s, 1H), 5.27 (d, *J* = 11.2 Hz, 1H), 5.29 (d, *J* = 17.6 Hz, 1H), 6.52 (dd, *J* = 17.6, 11.2 Hz, 1H), 10.16 (s, 1H). ^{13}C NMR ($CDCl_3$, 125 MHz) δ: 0.6, 19.9, 21.8, 22.6, 37.4, 56.6, 81.4, 114.0, 118.7, 128.0, 132.3, 132.6, 145.8, 146.5, 195.5. HR-MS (EI) *m/z* calcd. for $C_{17}H_{27}O_2Si$ ($[M^+ – CH_3]$): 291.1780; found: 291.1732.

General procedure for vinyl Grignard addition to the aldehydes

Vinylmagnesium chloride (2.0 equiv., 1.60 mol L^{-1} in THF) was added to a solution of the aldehyde (1.0 equiv.) in ether ([aldehyde] = 1.0 mol L^{-1}) at –78 °C. The solution was stirred for 1 h at –78 °C and for 30 min at 0 °C. A saturated aqueous solution of NH_4Cl was then added; the layers were separated, and the aqueous layer was extracted with ether. The combined organic extracts were washed with brine, dried ($MgSO_4$), filtered, and concentrated under reduced pressure. The crude material was purified by flash chromatography (silica gel, ether – petroleum ether).

8-Isopropenyl-6-methoxy-5,9-dimethyl-4-vinyl-deca-1,4,8-trien-3-ol (18a)

72% from **17a**. IR (neat) (cm^{-1}) ν: 3458, 2923, 1629, 1445, 1100, 991, 919, 896, 638. ^{1}H NMR ($CDCl_3$, 500 MHz) δ: 1.60 (d, *J* = 5.1 Hz, 1H), 1.69 (s, 3H), 1.72 (s, 3H), 1.77 (s, 3H), 1.78 (s, 3H), 2.26 (dd, *J* = 14.1, 5.7 Hz, 1H), 2.67 (dd, *J* = 14.1, 7.7 Hz, 1H), 3.01 (s, 3H), 4.41 (dd, *J* = 7.7, 5.7 Hz, 1H), 4.83 (s, 1H), 5.02–5.06 (m, 2H), 5.17 (dd, *J* = 11.6, 1.9 Hz, 1H), 5.32–5.36 (m, 2H), 5.43 (dd, *J* = 17.9, 1.9 Hz, 1H), 6.04 (m, 1H), 6.36 (dd, *J* = 17.9, 11.6 Hz, 1H). ^{13}C NMR ($CDCl_3$, 125 MHz) δ: 13.7, 20.2, 22.1, 22.7, 36.0, 56.2, 70.4, 79.0, 114.1, 114.2, 117.9, 128.3, 133.4, 133.6, 136.5, 137.2, 140.4, 146.7. HR-MS (EI) *m/z* calcd. for $C_{18}H_{28}O_2$ ($[M]^+$): 276.2089; found: 276.2090.

8-Isopropenyl-6-methoxy-9-methyl-5-trimethylsilanyl-4-vinyl-deca-1,4,8-triene-3-ol (18b)

83% from **17b**. IR (neat) (cm^{-1}) ν: 3450, 3076, 2979, 1631. ^{1}H NMR ($CDCl_3$, 500 MHz) δ: 0.18 (s, 9H), 1.67 (s, 3H), 1.69 (s, 3H), 1.76 (s, 3H), 2.05 (dd, *J* = 14.7, 3.5 Hz, 1H), 2.77 (dd, *J* = 14.7, 9.7 Hz, 1H), 3.14 (s, 3H), 4.12 (dd, *J* = 9.7, 3.5 Hz, 1H), 4.61 (s, 1H), 5.00 (s, 1H), 5.11 (d, *J* = 10.5 Hz, 1H), 5.21 (dd, *J* = 11.5, 1.6 Hz, 1H), 5.25 (d, *J* = 17.3 Hz, 1H), 5.26 (d, *J* = 11.2 Hz, 1H), 5.32 (dd, *J* = 17.7, 1.6 Hz, 1H), 5.34 (s, 1H), 5.99 (ddd, *J* = 17.3, 11.2, 10.5 Hz, 1H), 6.47 (dd, *J* = 17.7, 11.5 Hz, 1H). ^{13}C NMR ($CDCl_3$, 125 MHz) δ: 2.3, 20.1, 21.8, 22.7, 37.3, 57.4, 71.6, 81.9, 113.7, 114.8, 118.2, 127.3, 133.3, 136.4, 139.6, 146.1, 146.2, 149.6.

8-Isopropenyl-6-methoxy-9-methyl-4-vinyl-deca-1,4,8-triene-3-ol (18c)

88% from **17c**. IR (neat) (cm^{-1}) ν: 3434, 3079, 2977, 2920, 1632. ^{1}H NMR ($CDCl_3$, 500 MHz) δ: 1.67 (s, 3H), 1.68 (s, 3H), 1.76 (s, 3H), 2.30 (dd, *J* = 13.9, 7.3 Hz, 1H), 2.40 (s, 1H), 2.53 (dd, *J* = 13.9, 6.3 Hz, 1H), 3.21 (s, 3H), 4.10 (ddd, *J* = 8.6, 7.3, 6.3 Hz, 1H), 4.59 (s, 1H), 4.98 (s, 1H), 5.02 (d, *J* = 4.8 Hz, 1H), 5.07 (d, *J* = 11.1 Hz, 1H),

© 2004 NRC Canada

5.14 (d, J = 10.5 Hz, 1H), 5.31 (d, J = 17.2 Hz, 1H), 5.40 (d, J = 17.6 Hz, 1H), 5.51 (d, J = 8.6 Hz, 1H), 5.95 (ddd, J = 17.2, 10.5, 4.8 Hz, 1H), 6.21 (dd, J = 17.6, 11.1 Hz, 1H). ^{13}C NMR ($CDCl_3$, 125 MHz) δ: 20.2, 21.9, 22.6, 36.6, 56.3, 69.9, 75.9, 113.9, 114.8, 115.2, 128.3, 132.3, 132.5, 136.2, 138.6, 141.5, 146.2. HR-MS (EI) m/z calcd. for $C_{17}H_{24}O$ ($[M^+ - H_2O]$): 244.1827; found: 244.1879.

General procedures for oxidation of the secondary alcohols

Oxalyl chloride (1.5 equiv.) was added to a solution of DMSO (3.0 equiv.) in dichloromethane ([oxalyl chloride] = 1.0 mol L^{-1}) at –78 °C. After 5 min, the alcohol (1.0 equiv.) was added, and the solution was stirred for 1 h at –78 °C. Triethylamine (7.0 equiv.) was added, and the solution was warmed to 0 °C for 1 h. A saturated aqueous solution of NH_4Cl was added; the layers were separated, and the aqueous layer was extracted with ether. The combined organic extracts were washed with brine, dried ($MgSO_4$), filtered, and concentrated under reduced pressure. The crude material was purified by flash chromatography (silica gel, ether – petroleum ether).

The alcohol (1.0 equiv.) in THF was added to a solution of IBX (1.5 equiv.) in DMSO ([alcohol] = 1.0 mol L^{-1}) at 0 °C. The resulting solution was stirred for 3 h at 21 °C prior to the addition of water. Following filtration, the solution was extracted with ether. The combined organic extracts were washed with brine, dried ($MgSO_4$), filtered, and concentrated. The crude material was purified by flash chromatography (silica gel, ether – petroleum ether).

8-Isopropenyl-6-methoxy-5,9-dimethyl-4-vinyl-deca-1,4,8-trien-3-one (8a)

82% from **18a**. IR (neat) (cm^{-1}) ν: 2970, 2925, 1738, 1444, 1366, 1228, 1217, 772, 686. ^{1}H NMR (C_6D_6, 500 MHz) δ: 1.67 (s, 3H), 1.70 (s, 3H), 1.71 (s, 3H), 1.79 (s, 3H), 2.09 (dd, J = 14.2, 3.7 Hz, 1H), 2.69 (dd, J = 14.2, 9.6 Hz, 1H), 3.01 (s, 3H), 3.91 (dd, J = 9.6, 3.7 Hz, 1H), 4.73 (s, 1H), 4.98–5.03 (m, 3H), 5.39 (dd, J = 10.4, 1.4 Hz, 1H), 5.95 (dd, J = 17.6, 1.4 Hz, 1H), 6.28 (dd, J = 17.6, 10.4 Hz, 1H), 6.47 (dd, J = 17.7, 11.0 Hz, 1H). ^{13}C NMR (C_6D_6, 125 MHz) δ: 20.2, 22.1, 22.7, 30.4, 35.5, 56.5, 80.6, 114.0, 117.2, 128.3, 129.7, 130.1, 131.6, 133.3, 137.8, 138.0, 139.1, 197.9. HR-MS (EI) m/z calcd. for $C_{18}H_{26}O_2$ ($[M]^+$): 274.1934; found: 274.1935. Anal calcd. for $C_{18}H_{26}O_2$ (%): C 78.79, H 9.55; found: C 78.88, H 9.41.

8-Isopropenyl-6-methoxy-9-methyl-5-trimethylsilanyl-4-vinyl-deca-1,4,8-trien-3-one (8b)

90% from **18b**. IR (neat) (cm^{-1}) ν: 2977, 2921, 2819, 1660, 1622, 1604. ^{1}H NMR (C_6D_6, 500 MHz) δ: 0.33 (s, 9H), 1.72 (s, 3H), 1.77 (s, 3H), 1.82 (s, 3H), 1.98 (dd, J = 14.5, 2.8 Hz, 1H), 2.89 (dd, J = 14.5, 10.6 Hz, 1H), 3.03 (s, 3H), 4.02 (dd, J = 10.6, 2.8 Hz, 1H), 4.74 (s, 1H), 5.01 (d, J = 10.9 Hz, 1H), 5.02 (s, 1H), 5.07 (d, J = 17.5 Hz, 1H), 5.38 (dd, J = 10.5, 1.2 Hz, 1H), 5.95 (dd, J = 17.6, 1.2 Hz, 1H), 6.27 (dd, J = 17.6, 10.5 Hz, 1H), 6.73 (dd, J = 17.5, 10.9 Hz, 1H). ^{13}C NMR (C_6D_6, 125 MHz) δ: 1.8, 20.4, 22.1, 22.7, 37.3, 57.2, 82.9, 114.1, 118.4, 127.5, 129.3, 133.8, 134.2, 137.8, 146.4, 146.6, 150.0, 198.8. Anal calcd. for $C_{20}H_{32}O_2Si_2$ (%): C 72.23, H 9.69; found: C 72.09, H 9.76.

8-Isopropenyl-6-methoxy-9-methyl-4-vinyl-deca-1,4,8-trien-3-one (8c)

84% from **18c**. IR (neat) (cm^{-1}) ν: 2978, 2925, 2822, 1670, 1631, 1606. ^{1}H NMR (C_6D_6, 500 MHz) δ: 1.68 (s, 3H), 1.70 (s, 3H), 1.77 (s, 3H), 2.23 (dd, J = 14.1, 5.6 Hz, 1H), 2.61 (dd, J = 14.1, 8.1 Hz, 1H), 3.11 (s, 3H), 3.89 (ddd, J = 8.8, 8.1, 5.6 Hz, 1H), 4.74 (s, 1H), 4.90 (d, J = 10.8 Hz, 1H), 5.05 (s, 1H), 5.01 (d, J = 17.6 Hz, 1H), 5.37 (d, J = 10.6 Hz, 1H), 5.51 (d, J = 8.8 Hz, 1H), 5.97 (d, J = 17.6 Hz, 1H), 6.12 (dd, J = 17.6, 10.8 Hz, 1H), 6.27 (dd, J = 17.6, 10.6 Hz, 1H). ^{13}C NMR (C_6D_6, 125 MHz) δ: 20.3, 22.1, 22.7, 37.3, 56.8, 77.4, 114.2, 116.8, 128.3, 130.3, 132.9, 135.8, 136.1, 137.5, 142.4, 146.7, 196.7. HR-MS (EI) m/z calcd. for $C_{17}H_{24}O_2$ ($[M]^+$): 260.1776; found: 260.1778.

8-Isopropenyl-6-methoxy-5,9-dimethyl-4-vinyl-deca-4,8-diene-1-yn-3-one (29)

86% from **28**. IR (neat) (cm^{-1}) ν: 3253, 3076, 2979, 2926, 2824, 2089, 1662, 1629. ^{1}H NMR (C_6D_6, 500 MHz) δ: 1.60 (s, 3H), 1.71 (s, 3H), 1.72 (s, 3H), 1.80 (s, 3H), 2.20 (dd, J = 14.2, 4.5 Hz, 1H), 2.47 (s, 1H), 2.72 (dd, J = 14.2, 8.9 Hz, 1H), 3.08 (s, 3H), 4.18 (dd, J = 8.9, 4.5 Hz, 1H), 4.79 (s, 1H), 5.04 (s, 1H), 5.07 (d, J = 11.1 Hz, 1H), 5.23 (d, J = 17.8 Hz, 1H), 6.34 (dd, J = 17.8, 11.1 Hz, 1H). ^{13}C NMR (C_6D_6, 75 MHz) δ: 12.7, 20.2, 22.2, 22.6, 35.7, 56.6, 78.9, 80.6, 83.5, 114.3, 118.0, 128.3, 130.4, 133.1, 138.1, 142.5, 146.4, 181.5. HR-MS (EI) calcd. for $C_{18}H_{24}O_2$ ($[M]^+$): 272.1776; found: 272.1768.

General procedures for Diels–Alder cyclizations

Diethylaluminum chloride (1.1 equiv., 1.0 mol L^{-1} in hexane) was added to a solution of ketone (1.0 equiv.) in dichloromethane ([ketone] = 1.0 mol L^{-1}) at –78 °C. The solution was slowly warmed to 0 °C and, after 5 min, cooled to –78 °C. A saturated aqueous solution of $NaHCO_3$ was added; the layers were separated, and the aqueous layer was extracted with ether. The combined organic extracts were washed with brine, dried ($MgSO_4$), filtered, and concentrated under reduced pressure. The crude material was purified by flash chromatography (silica gel, ether – petroleum ether).

Borontrifluoride etherate (1.0 equiv.) was added to a solution of ketone (1.0 equiv.) in dichloromethane (such that [ketone] = 1.0 mol L^{-1}) at –78 °C, and the solution was stirred for 2 h. A saturated aqueous solution of $NaHCO_3$ was then added; the layers were separated, and the aqueous layer was extracted with ether. The combined organic extracts were washed with brine, dried ($MgSO_4$), filtered, and concentrated under reduced pressure. The crude material was purified by flash chromatography (silica gel, ether – petroleum ether).

5-Methoxy-4,8,11,11-tetramethyl-3-vinyl-bicyclo[5.3.1]undeca-3,7-dien-2-one (9a)

76% from **8a**. mp = 76–81 °C. IR (neat) (cm^{-1}) ν: 2927, 1673, 1378, 1463, 911, 750. ^{1}H NMR (C_6D_6, 500 MHz) 0.92 (s, 3H), 1.26 (s, 3H), 1.36 (s, 3H), 1.64–1.66 (m, 1H), 1.66 (s, 3H), 1.79 (ddd, J = 18.3, 10.2, 3.6 Hz, 1H), 1.90–1.96 (m, 1H), 2.10–2.16 (m, 1H), 2.51–2.56 (m, 2H), 2.62 (dd, J = 12.5, 6.4, 2.5 Hz, 1H), 3.00 (s, 3H), 4.12 (dd, J = 11.1, 6.4 Hz, 1H), 4.92 (dd, J = 11.0, 0.5 Hz, 1H), 5.65 (dd, J =

© 2004 NRC Canada

17.5, 0.5 Hz, 1H), 6.42 (dd, *J* = 17.5, 11.0 Hz, 1H). ^{13}C NMR (C_6D_6, 125 MHz) δ: 12.1, 19.8, 21.6, 25.1, 28.1, 29.0, 35.4, 37.8, 57.6, 63.4, 82.3, 115.5, 131.6, 131.8, 134.5, 135.1, 141.3, 212.3. HR-MS (EI) *m/z* calcd. for $C_{18}H_{26}O_2$ ([M]$^+$): 274.1934; found: 274.1951. Anal calcd. for $C_{18}H_{26}O_2$ (%): C 78.79, H 9.55; found: C 78.65, H 9.50.

5-Methoxy-8,11,11-trimethyl-4-trimethylsilanyl-3-vinyl-bicyclo[5.3.1]undeca-3,7-dien-2-one (9b)

62% from **8b**. mp = 81 to 82 °C. IR (neat) (cm^{-1}) ν: 2898, 1672. ^{1}H NMR (C_6D_6, 500 MHz) δ: 0.35 (s, 9H), 0.95 (s, 3H), 1.26 (s, 3H), 1.49 (s, 3H), 1.60–1.69 (m, 1H), 1.74–1.82 (m, 1H), 1.88–1.93 (m, 1H), 2.14–2.20 (m, 1H), 2.40 (dd, *J* = 12.2, 11.4 Hz, 1H), 2.50 (d, *J* = 7.6 Hz, 1H), 2.64 (dd, *J* = 12.2, 5.8 Hz, 1H), 3.05 (s, 3H), 4.26 (dd, *J* = 11.4, 5.8 Hz, 1H), 4.96 (d, *J* = 11.0 Hz, 1H), 5.07 (d, *J* = 17.5 Hz, 1H), 6.73 (dd, *J* = 17.5, 11.0 Hz, 1H). ^{13}C NMR (C_6D_6, 125 MHz) δ: 3.4, 19.7, 22.4, 24.9, 28.5, 28.9, 35.8, 37.6, 57.5, 63.2, 86.0, 117.4, 132.6, 133.9, 134.3, 141.2, 153.4, 213.2. HR-MS (EI) *m/z* calcd. for $C_{20}H_{32}O_2Si$ ([M]$^+$): 332.2172; found: 332.2163. Anal calcd. for $C_{20}H_{32}O_2Si$ (%): C 72.23, H 9.69; found: C 71.37, H 9.51.

5-Methoxy-8,11,11-trimethyl-3-vinyl-bicyclo[5.3.1]undeca-3,7-dien-2one (9c)

53% from **8c**. mp = 62 to 63 °C. IR (neat) (cm^{-1}) ν: 2947, 2828, 1679. ^{1}H NMR (500 MHz) δ: 0.90 (s, 3H), 1.15 (s, 3H), 1.38 (s, 3H), 1.63–1.68 (m, 1H), 1.73–1.81 (m, 2H), 2.11–2.14 (m, 1H), 2.45 (dd, *J* = 12.6, 9.7 Hz, 1H), 2.51 (m, 1H), 2.69 (dd, *J* = 12.6, 7.6 Hz, 1H), 3.06 (s, 3H), 4.11 (ddd, *J* = 9.7, 7.6, 6.5 Hz, 1H), 4.78 (d, *J* = 10.7 Hz, 1H), 4.96 (d, *J* = 17.6 Hz, 1H), 5.36 (d, *J* = 6.5 Hz, 1H), 5.98 (dd, *J* = 17.6, 10.7 Hz, 1H). ^{13}C NMR (125 MHz) δ: 19.2, 21.6, 25.8, 27.9, 28.3, 36.4, 37.3, 57.1, 63.6, 80.5, 114.7, 131.7, 132.9, 134.0, 136.9, 145.4, 210.9. HR-MS (EI) *m/z* calcd. for $C_{17}H_{24}O_2$ ([M]$^+$): 260.1776; found: 260.1773.

8-Isopropenyl-6-methoxy-5,9-dimethyl-1-trimethylsilyl-4-vinyl-deca-4,8-dien-1-yn-3-ol (27)

Butyl lithium (7.93 mL, 19.1 mmol, 2.4 mol L^{-1} in hexane) was added to a solution of trimethylsilylacetylene (2.44 mL, 17.3 mmol) in THF (50 mL) cooled to –78 °C. After 30 min, aldehyde **17a** (2.15 g, 8.66 mmol) in THF (20 mL) was added, and the solution was then stirred for 1 h at –78 °C. A saturated aqueous solution of N_4Cl (100 mL) was then added; the layers were separated, and the aqueous layer was extracted with ether (2 × 100 mL). The combined organic extracts were washed with brine (2 × 100 mL), dried ($MgSO_4$), filtered, and concentrated under reduced pressure. Purification by flash chromatography (silica gel, ether – petroleum ether) provided the title compound as a colorless oil (2.66 g, 89%). IR (neat) (cm^{-1}) ν: 3334, 3075, 2930, 2165, 1625. ^{1}H NMR (C_6D_6, 300 MHz) δ: 0.12 (s, 9H), 1.73 (s, 3H), 1.74 (s, 3H), 1.77 (s, 3H), 1.86 (s, 3H), 2.29 (dd, *J* = 14.2, 4.8 Hz, 1H), 2.75 (dd, *J* = 14.2, 8.3 Hz, 1H), 3.11 (s, 3H), 4.57 (dd, *J* = 8.3, 4.8 Hz, 1H), 4.90 (s, 1H), 5.09 (s, 1H), 5.19 (dd, *J* = 11.6, 1.4 Hz, 1H), 5.63 (s, 1H), 5.66 (dd, *J* = 17.8, 1.4 Hz, 1H), 6.48 (dd, *J* = 17.8, 11.6 Hz, 1H). ^{13}C NMR (C_6D_6, 75 MHz) δ: –0.2, 13.6, 20.2, 22.2, 22.8, 35.8, 56.3, 59.8, 79.0, 89.4, 107.4, 114.2, 117.0, 128.3, 132.9, 133.5, 134.5, 139.0, 146.8. HR-MS (EI) *m/z* calcd. for $C_{21}H_{32}OSi$ ([M$^+$ – H_2O]): 328.2222; found: 328.2182.

8-Isopropenyl-6-methoxy-5,9-dimethyl-4-vinyl-deca-4,8-dien-1-yn-3-ol (28)

Tetrabutylammonium fluoride (6.35 mL, 6.35 mmol, 1.0 mol L^{-1} in THF) was added to a solution of silane **27** (1.10 g, 3.17 mmol) in THF (10 mL) at 0 °C, and the solution was stirred for 1 h at 21 °C. A saturated aqueous solution of NH_4Cl (30 mL) was then added; the layers were separated, and the aqueous layer was extracted with ether (2 × 40 mL). The combined organic extracts were washed with brine (2 × 40 mL), dried ($MgSO_4$), filtered, and concentrated under reduced pressure. Purification by flash chromatography (silica gel, ether – petroleum ether) provided the title compound as a colorless oil (0.738 g, 85%). IR (neat) (cm^{-1}) ν: 3421, 3307, 3076, 2929, 2821, 1630. ^{1}H NMR ($CDCl_3$, 300 MHz) δ: 1.66 (s, 6H), 1.74 (s, 3H), 1.76 (s, 3H), 2.22 (dd, *J* = 14.2, 6.2 Hz, 1H), 2.48 (d, *J* = 2.4 Hz, 1H), 2.51 (d, *J* = 6.4 Hz, 1H), 2.57 (dd, *J* = 14.2, 7.3 Hz, 1H), 3.15 (s, 3H), 4.09 (dd, *J* = 7.3, 6.2 Hz, 1H), 4.60 (s, 1H), 4.98 (s, 1H), 5.35 (dd, *J* = 11.7, 1.4 Hz, 1H), 5.52 (dd, *J* = 6.4, 2.4 Hz, 1H), 5.64 (dd, *J* = 17.9, 1.4 Hz, 1H), 6.47 (dd, *J* = 17.9, 11.6 Hz, 1H). ^{13}C NMR ($CDCl_3$, 75 MHz) δ: 14.9, 20.5, 22.3, 22.9, 35.6, 57.0, 59.6, 73.9, 79.9, 84.2, 114.5, 118.6, 128.8, 132.2, 133.0, 134.3, 137.9, 146.4. HR-MS (EI) *m/z* calcd. for $C_{18}H_{24}O$ ([M$^+$ – H_2O]): 256.1827; found: 256.1840.

6-Ethynyl-3-methoxy-4,9,10,10-tetramethyl-5-vinyl-7-oxa-bicyclo[4.3.1]deca-1(9),4-diene (30)

Diethylaluminium chloride (1.10 mL, 1.10 mmol, 1.0 mol L^{-1} in hexane) was added to a solution of ketone **29** (0.272 g, 1.00 mmol) in dichloromethane (20 mL) at –78 °C. The solution was slowly warmed to 0 °C and, after 5 min, cooled to –78 °C. A saturated aqueous solution of $NaHCO_3$ (20 mL) was added; the layers were separated, and the aqueous layer was extracted with ether (2 × 30 mL). The combined organic extracts were washed with brine (2 × 30 mL), dried ($MgSO_4$), filtered, and concentrated under reduced pressure. Purification by flash chromatography (silica gel, ether – petroleum ether) provided the title compound as a colorless oil (0.167 g, 62%). IR (neat) (cm^{-1}) ν: 3285, 2974, 2931, 2821, 1608, 1561. ^{1}H NMR (C_6D_6, 500 MHz) δ: 1.18 (d, *J* = 13.5 Hz, 1H), 1.36 (s, 3H), 1.37 (s, 3H), 1.44 (s, 3H), 1.51 (dd, *J* = 13.8, 10.2 Hz, 1H), 1.92 (d, *J* = 13.5 Hz, 1H), 2.01 (s, 3H), 2.72 (s, 1H), 2.85 (dd, *J* = 13.8, 7.0 Hz, 1H), 3.14 (s, 3H), 3.53 (dd, *J* = 10.2, 7.0 Hz, 1H), 5.10 (dd, *J* = 11.9, 1.5 Hz, 1H), 5.38 (dd, *J* = 18.0, 1.5 Hz, 1H), 6.89 (dd, *J* = 18.0, 11.9 Hz, 1H). ^{13}C NMR (C_6D_6, 75 MHz) δ: 21.5, 22.0, 22.2, 24.8, 30.7, 37.6, 44.2, 57.0, 77.6, 78.9, 79.7, 81.3, 113.9, 127.3, 129.2, 131.3, 133.0, 136.3. HR-MS (EI) *m/z* calcd. for $C_{18}H_{24}O_2$ ([M]$^+$): 272.1776; found: 272.1743.

Conclusion

We have successfully extended the magnesium-mediated carbometallation protocol developed in our laboratories to more complex systems and studied various aspects in more depth. In addition, the nuances of the *cis*-alkene tether controlled intramolecular Diels–Alder reactions to bicyclo-

© 2004 NRC Canada

[5.3.1]undecenones have been delineated. A key feature is the diastereoselectivity derived from Lewis acid complexation, which implies that enantioselective cycloaddition may eventually be feasible. A direct route to these taxane AB-ring building blocks has been established for future elaboration into the complete nucleus by different procedures. In total, these procedures provide direct access to functionalized molecules that may be employed for a variety of synthetic objectives.

Acknowledgements

We are grateful to the Natural Sciences and Engineering Research Council of Canada (NSERC) and the Canadian Breast Cancer Research Initiative (NCI, Canada) for financial support of this research. P. Forgione thanks Torcan Chemical Ltd. and the Government of Ontario for an OGSST Fellowship. N. P. Villalva-Servín thanks Consejo Nacional de Ciencia y Tecnología (CONACYT) Government of Mexico for a Graduate Scholarship.

References

1. (*a*) D.G.I. Kingston. J. Nat. Prod. **63**, 726 (2000); (*b*) D.G.I. Kingston. Chem. Commun. 867 (2001).
2. (*a*) R.A. Holton, C. Somoza, H.B. Kim, F. Liang, R.J. Biediger, P.D. Boatman, M. Shindo, C.C. Smith, S. Kim, H. Nadizadeh, Y. Suzuki, C. Tao, P. Vu, S. Tang, P. Zhang, K.K. Murthi, L.N. Gentile, and J.H. Liu. J. Am. Chem. Soc. **116**, 1597 (1994); **116**, 1599 (1994); (*b*) K.C. Nicolaou, Z. Yang, J.J. Liu, H. Ueno, P.G. Nantermet, R.K. Guy, C.F. Claiborne, J. Renaud, E.A. Couladouros, K. Paulvannan, and E.J. Sorensen. Nature (London), **367**, 630 (1994); (*c*) J.J. Masters, J.T. Link, L.B. Snyder, W.B. Young, and S.J. Danishefsky. Angew. Chem. Int. Ed. Engl. **34**, 1723 (1995); (*d*) P.A. Wender, N.F. Badham, S.P. Conway, P.E. Floreancig, T.E. Glass, J.B. Houze, N.E. Krauss, D. Lee, D.G. Marquess, P.L. McGrane, W. Meng, M.G. Natchus, A.J. Shuker, J.C. Sutton, and R.E.J. Taylor. J. Am. Chem. Soc. **119**, 2755 (1997); **119**, 2757 (1997); (*e*) T. Mukaiyama, I. Shiina, H. Iwadare, M. Saitoh, T. Nishimura, N. Ohkawa, H. Sakoh, K. Nishimura, Y.I. Tani, M. Hasegawa, K. Yamada, and K. Saitoh. Chem. Eur. J. **5**, 121 (1999); (*f*) H. Kusama, R. Hara, S. Kawahara, T. Nishimori, H. Kashima, N. Nakamura, K. Morihira, and I. Kuwajima. J. Am. Chem. Soc. **122**, 3811 (2000).
3. (*a*) Y.-F. Lu and A.G. Fallis. Tetrahedron Lett. **34**, 3367 (1993); (*b*) Y.-F. Lu, C.W. Harwig, and A.G. Fallis. J. Org. Chem. **58**, 4202 (1993); (*c*) T. Wong, M.A. Romero, and A.G. Fallis. J. Org. Chem. **59**, 5527 (1994); (*d*) M.W. Tjepkema, P.D. Wilson, T. Wong, M.A. Romero, H. Audrain, and A.G. Fallis. Tetrahedron Lett. **36**, 6039 (1995); (*e*) Y.-F. Lu and A.G. Fallis. Can. J. Chem. **73**, 2239 (1995); (*f*) Y.-F. Lu, C.W. Harwig, and A.G. Fallis. Can. J. Chem. **73**, 2253 (1995); (*g*) M.W. Tjepkema, P.D. Wilson, H. Audrain, and A.G. Fallis. Can. J. Chem. **75**, 1215 (1997); (*h*) A.G. Fallis. Pure Appl. Chem. **69**, 495 (1997); (*i*) A.G. Fallis. Acc. Chem. Res. **32**, 464 (1999); (*j*) A.G. Fallis. Can. J. Chem. **77**, 159 (1999).
4. For an excellent account of type II intramolecular Diels–Alder cycloadditions, see B.R. Bear, S.M. Sparks, and K.J. Shea. Angew. Chem. Int. Ed. **40**, 820 (2001).
5. P. Forgione, P.D. Wilson, G.P.A. Yap, and A.G. Fallis. Synthesis, 921 (2000).
6. N.P. Villalva-Servín, A. Laurent, and A.G. Fallis. Can. J. Chem. **82**, 227 (2004).
7. (*a*) T. Wong, M.W. Tjepkema, H. Audrain, P.D. Wilson, and A.G. Fallis. Tetrahedron Lett. **37**, 755 (1996); (*b*) P. Forgione and A.G. Fallis. Tetrahedron Lett. **41**, 11 (2000); (*c*) P. Forgione, P.D. Wilson, and A.G. Fallis. Tetrahedron Lett. **41**, 17 (2000); (*d*) A.G. Fallis and P. Forgione. Tetrahedron, **57**, 5899 (2001); (*e*) P.E. Tessier, A.J. Penwell, F.E.S. Souza, and A.G. Fallis. Org. Lett. **5**, 2989 (2003).
8. (*a*) S. Millan, T. Pham, J. Lavers, and A.G. Fallis. Tetrahedron Lett. **38**, 795 (1997); (*b*) C. Martin, N. Macintosh, N. Lamb, and A.G. Fallis. Org. Lett. **3**, 1021 (2001).
9. (*a*) T. Wong, P.D. Wilson, S. Woo, and A.G. Fallis. Tetrahedron Lett. **38**, 7045 (1997); (*b*) S. Woo, S. Legoupy, S. Parra, and A.G. Fallis. Org. Lett. **1**, 1013 (1999); (*c*) A. Melekov, P. Forgione, S. Legoupy, and A.G. Fallis. Org. Lett. **2**, 279 (2000).
10. S.-C. Kim, M.-S. Moon, and C.-S. Cheong. Bull. Korean Chem. Soc. **20**, 1389 (1999).
11. (*a*) K.C. Nicolaou, G. Zuccarello, Y. Ogawa, E.J. Schweiger, and T. Kumazawa. J. Am. Chem. Soc. **110**, 4866 (1988); (*b*) K.C. Nicolaou, G. Zuccarello, C. Riemer, V.A. Estevez, and W.-M. Dai. J. Am. Chem. Soc. **114**, 7360 (1992); (*c*) J.P. Snyder. J. Am. Chem. Soc. **112**, 5367 (1990).
12. (*a*) D.B. Dess and J.C. Martin. J. Org. Chem. **48**, 4155 (1983); (*b*) D.B. Dess and J.C. Martin. J. Am. Chem. Soc. **113**, 7277 (1991); (*c*) R.E. Ireland and L. Liu. J. Org. Chem. **58**, 2899 (1993).
13. (*a*) D.A. Evans, K.T. Chapman, and J. Bisaha. J. Am. Chem. Soc. **110**, 1238 (1988); (*b*) D.A. Evans, B.D. Allison, and M.G. Yang. Tetrahedron Lett. **49**, 4457 (1999); (*c*) S. Castellino and W.J. Dwight. J. Am. Chem. Soc. **115**, 2986 (1993).
14. (*a*) B. Frey, S. Hunig, M. Koch, and H.-U. Reissig. Synlett, 854 (1991); (*b*) J. Schnaubelt and H.-U. Reissig. Synlett, 452 (1995).
15. A.G. Fallis and Y.-F. Lu. Adv. Cycloadditions, **3**, 1 (1993).

© 2004 NRC Canada

Part 2: Efficient strategies for the construction of variably substituted bicyclo[5.3.1]undecenones (AB-taxane ring systems) and their conversion to tricyclo[9.3.1.0^{3,8}]pentadecenones (ABC taxane ring systems) and bicyclo[2.2.2]octanones[1]

Nidia P. Villalva-Servín, Alain Laurent, and Alex G. Fallis

Abstract: The extension of our strategies for the construction of cyclic molecules containing variably substituted bicyclo[5.3.1]undecenones (AB taxane ring systems) for the synthesis of the tricyclo[9.3.1.0^{3,8}]pentadecenone (ABC taxane ring system) and bicyclo[2.2.2]octanones are described. These routes employ a multi-component coupling protocol that employs sequential magnesium-mediated carbometallation of allyl-substituted propargyl alcohols followed by diastereoselective Lewis acid catalyzed intramolecular Diels–Alder reactions (IMDA). Subsequent ring-closing metathesis (RCM) afforded the ABC taxane core structure. Enone accelerated [3,3] sigmatropic rearrangements (Cope rearrangements) generated the bicyclo[2.2.2]octanone nucleus. In the presence of a Lewis acid, the dienophile precursor underwent a tandem reaction via the adduct directly to the bicyclo[2.2.2]octanones. This is the first example of a novel enone accelerated carbocycle Cope rearrangement and provides direct access to bicyclo[2.2.2]octanones by a new route that compliments the traditional cyclohexadiene cycloaddition approach.

Key words: magnesium chelate, Lewis acid, taxanes, Diels–Alder, sigmatropic rearrangement, oxy-Cope, ring-closing metathesis, bicyclo[2.2.2]octanone.

Résumé : On décrit une extension de nos stratégies développées pour la construction de molécules cycliques contenant des bicyclo[5.3.1]undécénones (noyaux AB du taxane) portant divers substituants à la synthèse d'un tricyclo[9.3.1.0^{3,8}]pentadécénone (noyaux ABC du taxane) et de bicyclo[2.2.2]octanones. Ces voies impliquent un protocole de couplage à plusieurs composants qui fait appel à des réactions séquentielles de carbométallation catalysée par le magnésium d'alcools propargyliques portant un substituant allyle et de réactions diastéréosélectives de Diels–Alder intramoléculaires catalysées par un acide de Lewis. La réaction subséquente de métathèse de fermeture de cycle conduit au noyau fondamental ABC du taxane. Des réarrangements sigmatropiques [3,3] accélérés de l'énone (réarrangements de Cope) génèrent le noyau bicyclo[2.2.2]octanone. En présence d'un acide de Lewis, le précurseur diénophile donne lieu à une réaction en tandem, par le biais de l'adduit, qui conduit directement à la bicyclo[2.2.2]octanone. Cette réaction correspond au premier exemple d'un nouveau réarrangement de carbocycle de Cope accéléré par une énone et elle permet d'accéder directement aux bicyclo[2.2.2]octanones par une nouvelle voie qui est un complément à l'approche traditionnelle des cycloadditions au cyclohexadiène.

Mots clés : chélate magnésien, acide de Lewis, taxanes, Diels–Alder, réarrangement sigmatropique, oxy-Cope, métathèse avec cyclisation, bicyclo[2.2.2]octanone.

[Traduit par la Rédaction]

Introduction

The preceding paper provides a brief introduction to the importance of Taxol® (**1**, paclitaxel) and Taxotere® (**2**, docetaxel). It outlines briefly their utility as cancer chemotherapeutic agents and the synthetic challenge they present to organic chemists. We also described our approach to the synthesis of key AB taxane building blocks possessing the

Received 25 June 2003. Published on the NRC Research Press Web site at http://canjchem.nrc.ca on 28 January 2004.

This paper is dedicated to Professor Edward Piers on the occasion of his 65th birthday. Presented with respect and gratitude for his contributions to organic chemistry and to our friendship.

N.P. Villalva-Servin, A. Laurent,[2] and A.G. Fallis.[3] Centre for Research in Biopharmaceuticals, Department of Chemistry, University of Ottawa, 10 Marie Curie, Ottawa, ON K1N 6N5, Canada.

[1]This article is part of a Special Issue dedicated to Professor Ed Piers.
[2]Present address: Aegera Therapeutics, Inc., 810, chemin du Golf, Nun's Island, QC H3E 1A8, Canada.
[3]Corresponding author (e-mail: afallis@science.uottawa.ca).

 doi: 10.1139/V03-201 © 2004 NRC Canada

bicyclo[5.3.1]undecenone skeleton. These investigations have been expanded to a synthesis of the carbocyclic ABC taxane core via a carbometallation–cycloaddition-ring-closing metathesis strategy. In addition, the Diels–Alder dienophile precursors may be converted in a tandem reaction to bicyclo[2.2.2]octanones (Fig. 1).

Carbometallation – intramolecular cycloaddition strategy

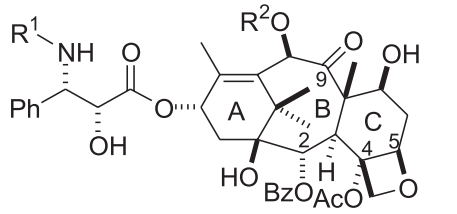
We have described our magnesium-mediated carbometallation of propargyl alcohols followed by diastereoselective Lewis acid catalyzed intramolecular Diels–Alder reactions for the preparation of bicyclo[5.3.1]undecenones (AB-taxane ring systems), as illustrated in Scheme 1. Unfortunately, as discussed in the preceding paper, the proposed [4 + 2] combinations with the family represented by **9** or **11** failed to give the desired adduct(s) **10**.

Cope rearrangements towards ring C taxanes and bicyclo[2.2.2]octanones

Clearly, a new approach was required to extend and build on this knowledge and capitalize on our ring assembly protocol. An efficient method was required to attach the C ring and assemble the complete ABC taxane nucleus. Two additional options appeared attractive, but both required repeating the synthesis from the beginning. Our initial plan was to prepare **14** from **9d**, as illustrated in Scheme 2. Based on previous studies, we have established that nucleophilic attack at the C2 carbonyl occurred from the underside of **9a**. Thus, it was anticipated that an anion-based [3,3] sigmatropic rearrangement would deliver the allyl group from the concave side of the molecule and thus establish, after protonation, the correct *trans* ring stereochemistry of the taxane natural products. Addition of allyl Grignard to **9d** should generate the bis-allyl secondary alcohol **12**. A subsequent oxy-Cope rearrangement could then be employed to install the allyl functionality in **13** for ring-closing metathesis to the tricyclic skeleton **14** (Scheme 2). However, this sequence had an inherent risk, owing to the very reactive nature of the ring A and ring B olefins. This complication affected our plans but also provided an unexpected, synthetically useful transformation, discovered earlier (1) and summarized below.

The existence of atropisomerism in taxane ring systems is well established (2, 3). Variable temperature ^{1}H NMR was investigated to determine the conformational bias in the bicyclo[5.3.1]undecene type synthon **9a**. It was anticipated that the details of the carbonyl-*exo* and carbonyl-*endo* conformers could be examined for their synthetic potential and stereochemical bias. However, rather than the conformational isomerization expected, the enone **9a** underwent a facile Cope rearrangement (commencing at ~60 °C), to give the bicyclo[2.2.2]octanone product **15a** (Scheme 3). Experimentally, this [3,3]-sigmatropic rearrangement afforded the same bicyclic ketone **15a** directly in 71% yield after 3 h in refluxing toluene (Scheme 3). The temperature required (110 °C) to effect this transformation is significantly lower than most carbocyclic rearrangements of this type (4). Consequently, this rearrangement provides an attractive method

Fig. 1. Current taxoid drugs.



Paclitaxel **1** (Taxol®) R^1 = Bz, R^2 = Ac

Docetaxel **2** (Taxotere®) R^1 = Boc, R^2 = H

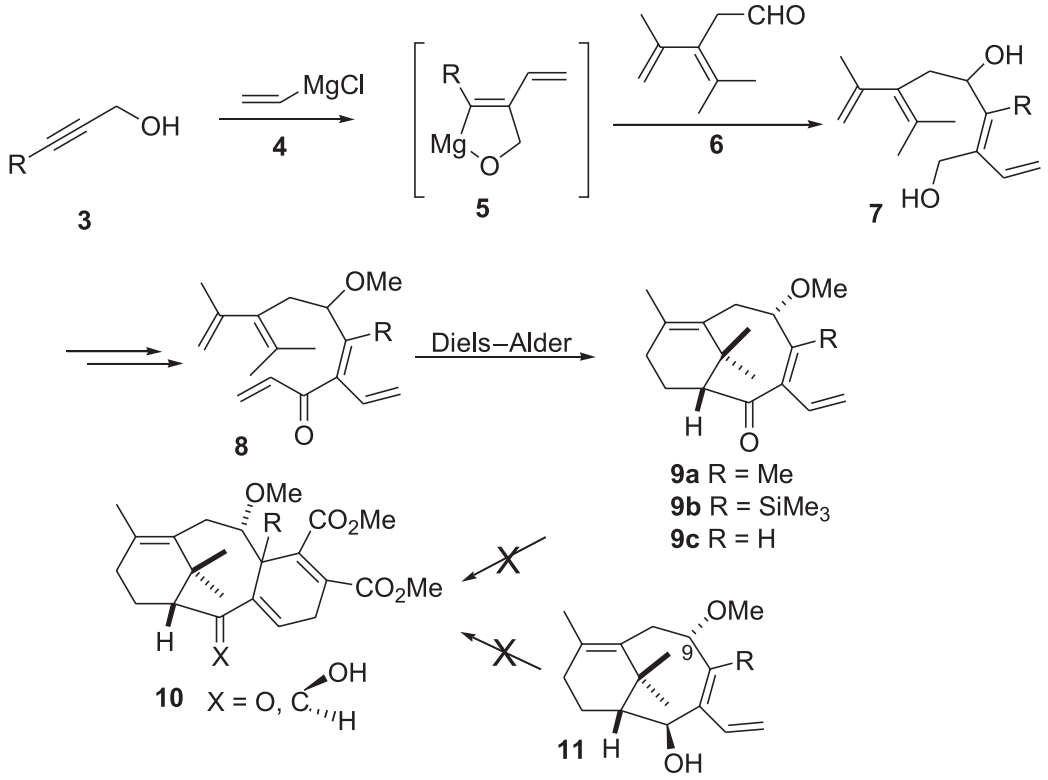
for the preparation of densely substituted bicyclooctenones **15**. The reverse transformation from an oxy-Cope bicyclo[2.2.2]octene precursor was employed in previous approaches to the taxane AB ring system (5). The ease of the rearrangement in **9a** is a consequence of the excellent alignment of the reactive diene units in a pre-organized chair-like conformation that mimics the required transition state. Our published X-ray analysis of **9a** (1) revealed that the C3—C8 separation is 3.13 Å, a separation less than the 3.2–3.3 Å c-d separation required for enediynes to undergo spontaneous cycloaromatization at room temperature (6, 7). However, an additional, beneficial influence from the carbonyl group is also implicated. Reduction of the carbonyl in **9a** to provide alcohol **11** (Scheme 1) and subsequent protection as the *p*-methoxybenzyl ether produced compound **16**, which was stable to prolonged reflux (20 h) in toluene, and none of **17** was observed (Scheme 3). Additional evidence for the importance of the conjugated carbonyl and its electronic influence was illustrated by the ease with which the tandem rearrangement **8** to **9** to **15** occurred at 0–22 °C in the presence of a catalytic amount of Lewis acid (Et_2AlCl, 70%–92%).

For subsequent synthetic applications this tandem conversion provides an attractive entry to highly functionalized bicyclo[2.2.2]octanones, which will complement the traditional route from cycloaddition of cyclohexadienes. These substitution patterns are difficult to achieve by traditional routes (for example, sorbiquinol, Fig. 2, (8)). This accelerating influence exerted by a conjugated carbonyl group in a carbocyclic [3,3] sigmatropic rearrangement does not appear to have been observed prior to our discovery. We are currently investigating the potential and generality of this interesting transformation.

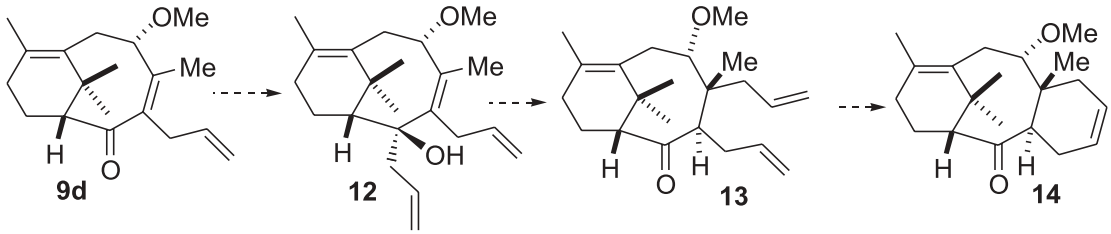
Based on the data above, it seemed reasonable to conclude that the anionic oxy-Cope rearrangement of a potassium salt should proceed at approximately 40–50 °C (9), and thus, the carbocyclic [3,3] rearrangement would not be competitive, as a consequence of the higher energy required. The adduct **9d** was synthesized in a parallel fashion to examine the validity of this assumption, as outlined in Scheme 4. Allylation of the ketone **9d** provided the allyl alcohol **13**. However, at room temperature the potassium salt derived from treatment with potassium *tert*-butoxide did not rearrange to the desired bis-allyl ketone **18** (Scheme 5) but followed a different pathway. Instead, the loss of the allyl substituent followed by double bond migration to **19** was observed. The use of potassium hydride provided no improvement and generated the isomeric ketone **20**. The failure of these mild conditions prompted a single experiment under more forcing conditions

© 2004 NRC Canada

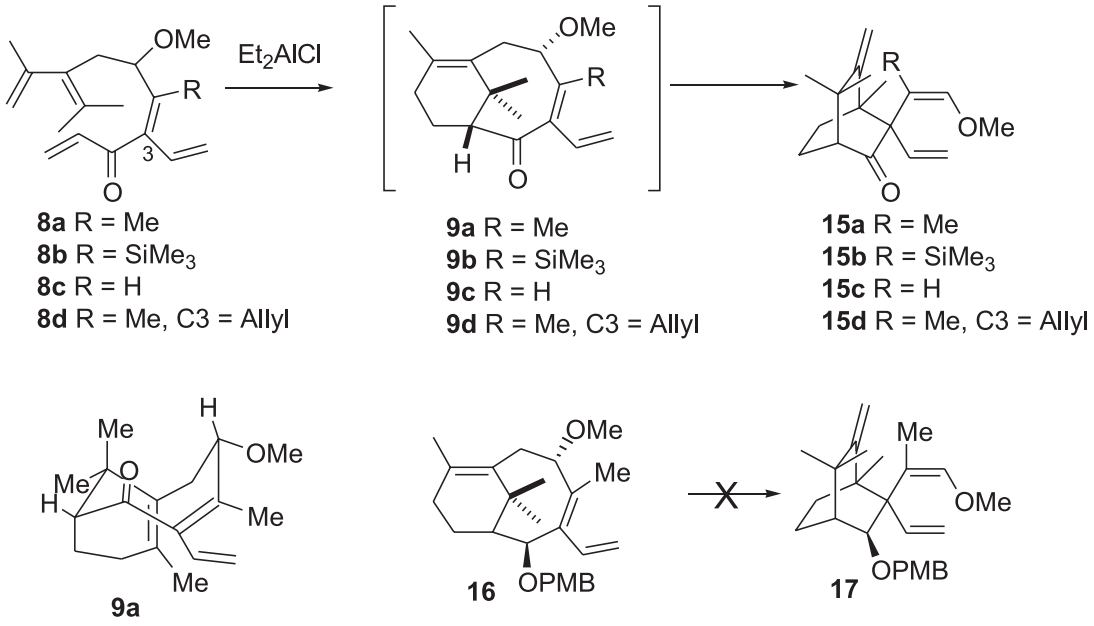
Scheme 1.



Scheme 2.



Scheme 3.



© 2004 NRC Canada

Scheme 4. Reagents and conditions: (*a*) (*i*) CH_2=$CHCH_2MgCl$, cyclohexane–THF, room temperature (rt) to 70 °C, 18 h; (*ii*) **6**, –78 °C to rt, 3 h, 40%; (*b*) TBDMSCl, DMAP, CH_2Cl_2, rt, 18 h, 81%; (*c*) NaH, MeI, THF, rt, 18 h, 89%; (*d*) TBAF, THF, rt, 2 h, 93%; (*e*) IBX, DMSO–THF, 0 °C to rt, 3 h, 86%; (*f*) CH_2=$CHMgCl$, Et_2O, –78 to 0 °C, 2 h, 50%; (*g*) IBX, DMSO–THF, 0 °C to rt, 3 h, 86%; (*h*) Et_2AlCl, CH_2Cl_2, –78 to 0 °C, 2 h, 70% or $BF_3{\cdot}(OEt)_2$, CH_2Cl_2, –78 to 10 °C, 2 h, 68%.

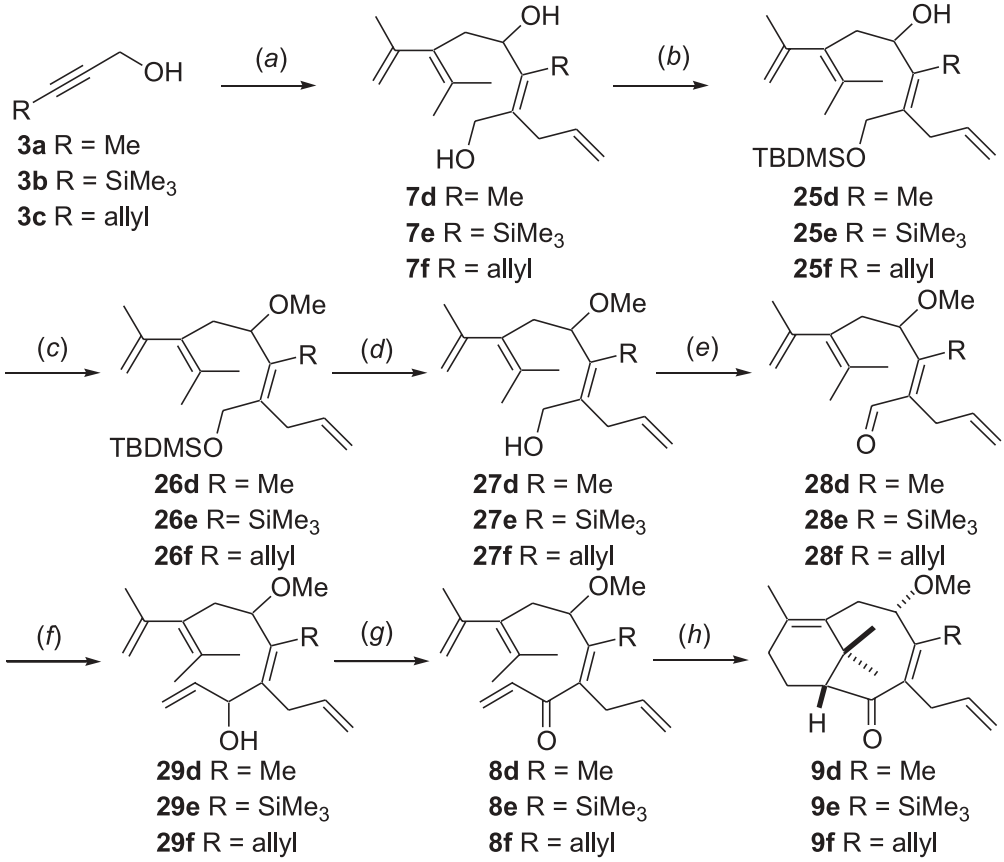
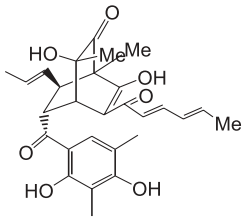


Fig. 2. Sorbiquinol.



in which treatment of **13** with 1,8-diazobiocyclo[5.4.0]undec-7-ene (DBU) under microwave irradiation also failed to produce the desired ring C precursor but gave instead the mixture of bicyclo[2.2.2]octenes **21** (7%), **22** (16%), and **23** (19%).

Ring-closing metathesis (RCM) for ring C

Despite the failure of the previous approach, the idea of installing the C ring by ring-closing metathesis was attractive. This variation for ring C is represented by the transformation **9f** to **24** in Scheme 6. One option was the introduction of a C3 allyl group by modification of the vinyl silyl group present in **9e** (Scheme 4). However, bromodesilylation failed and thus eliminated the possibility of direct palladium coupling from an advanced intermediate.

Consequently the strategy was modified (Scheme 6) to commence with an allyl-substituted propargyl alcohol **3c** followed by exposure to an allyl Grignard reagent for conversion to **8f**. Cycloaddition would generate the bicyclic ketone **9f** for conversion to the tricyclic compound **24**. The preparation of the desired Diels–Alder adduct **9f** and the precursor compounds is outlined in Scheme 4.

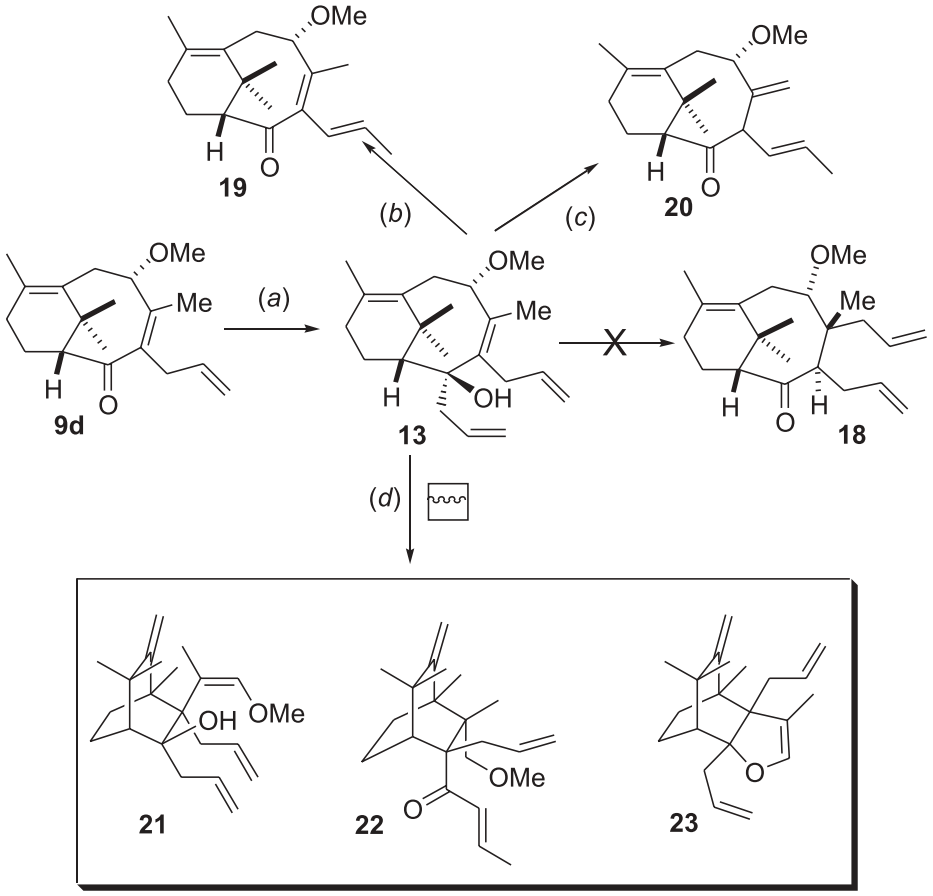
There appear to be two reports in which RCM approaches have been employed for the assembly of taxane AB (10) and BC (11) ring systems. However, the route in Scheme 6 for the construction of taxane ABC ring systems has not been explored. With the synthesis of the bicyclo[5.3.1]undecene **9f** completed it was anticipated that generation of the requisite cyclohexadiene **24** could be easily achieved. Indeed, treatment of **9f** with the second generation Grubbs' catalyst **30** ((4,5-dihydroIMES)(PCy_3)Cl_2Ru=CHPh) (12) gave rise to the desired tricyclo[$9.3.1.0^{3,8}$]pentadecane nucleus **24** in high yield (93%) (Scheme 7).

Experimental section

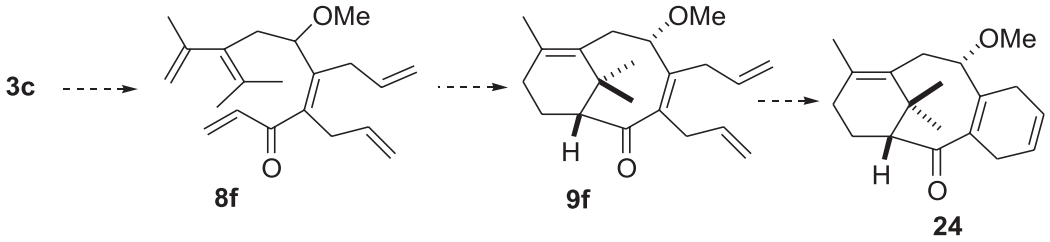
See preceding paper for general experimental details (13).

© 2004 NRC Canada

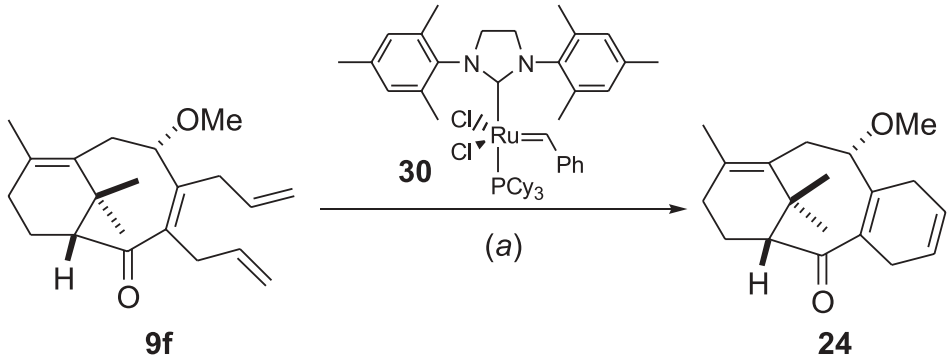
Scheme 5. Reagents and conditions: (*a*) CH_2=$CHCH_2MgCl$, Et_2O, –78 to 0 °C, 1 h, 59%; (*b*) . KO*t*Bu, DMF, 40 °C, 3 h, 51%; (*c*) KH, 18-crown-6, THF, rt, 1 h, 69%; (*d*) DBU, toluene, microwave, 220 °C, 1 h, **2**1 6%, **2**2 9%, **2**3 19%.



Scheme 6.



Scheme 7. Reagents and conditions: (*a*) **30**, CH_2Cl_2, 21 °C, 2 h, 93%.



© 2004 NRC Canada

3-Trimethylsilanyl-prop-2-yn-1-ol (3b)

Butyl lithium (189 mL, 434 mmol, 2.3 mol L^{-1} in hexane) was added to a solution of propargyl alcohol (11.0 mL, 189 mmol) in THF (300 mL) cooled to –78 °C. After 45 min, chlorotrimethylsilane (57.6 mL, 453 mmol) was added, and the solution was warmed to 21 °C for 3 h. After cooling to 0 °C, 10% aqueous sulfuric acid (250 mL) was added, and the layers were separated after 15 min, and the aqueous layer was extracted with ether (2 × 150 mL). The combined organic extracts were washed with brine (2 × 100 mL), dried ($MgSO_4$), filtered, and concentrated under reduced pressure. Purification by flash chromatography (silica gel, ether – petroleum ether) provided the title compound as a colorless oil (15.1 g, 62%). IR (neat) (cm^{-1}) ν: 3324, 2961, 2901, 2177. ^1H NMR ($CDCl_3$, 300 MHz) δ: 0.15 (s, 9H), 1.8 (s, 1H), 4.24 (s, 2H). ^{13}C NMR ($CDCl_3$, 75 MHz) δ: 0.13, 51.9, 91.0, 104.2. HR-MS (EI) *m/z* calcd. for $C_6H_{12}OSi$ ($[M]^+$): 128.0657; found: 128.0686.

3-Allyl-prop-2-yn-1-ol (3c) (14)

Propargyl alcohol (5.8 mL, 0.10 mol) was added to a stirred solution of acetone (400 mL), followed by allyl bromide (10.4 mL, 0.120 mol), potassium carbonate (27.6 g, 0.200 mol), sodium iodide (30 g, 0.20 mol), and copper iodide (19.0 g, 0.100 mol). The reaction was stirred under nitrogen at 21 °C for 5 h, quenched with 1 N HCl (120 mL), diluted with water (500 mL), and stirred for 10 min. The reaction mixture was subsequently filtered and extracted with diethyl ether (5 × 100 mL). The combined organic extracts were dried ($MgSO_4$), filtered, and concentrated under reduced pressure. The title compound was isolated as a colourless oil and purified by distillation (80–82 °C at 3 mmHg (1 mmHg = 133.322 Pa), 92%). IR (neat) (cm^{-1}) ν: 3351, 3086–2983, 2918–2872, 1420, 918, 780. ^1H NMR (C_6D_6, 300 MHz) δ: 2.33 (s, 1H), 2.94–2.98 (m, 2H), 4.24 (t, *J* = 2.2 Hz, 2H), 5.07 (ddd, *J* = 10.0, 3.3, 1.6 Hz, 1H), 5.27 (ddd, *J* = 17.0, 3.5, 1.7 Hz, 1H), 5.80 (dddd, *J* = 16.6, 10.6, 6.0, 5.6 Hz, 1H). ^{13}C NMR (C_6D_6, 75 MHz) δ: 23.2, 51.1, 81.9, 82.3, 116.1, 132.8. HR-MS (EI) *m/z* calcd. for C_6H_8O ($[M]^+$): 96.05752; found: 96.05597.

General procedure for the carbometallation of the propargylic alcohols

Vinyl- or allylmagnesium chloride (2.5 equiv.) was added to a solution of the propargylic alcohol (1.0 equiv.) in cyclohexane ([alcohol] = 1.0 mol L^{-1}) at 21 °C. The solution was heated at reflux for 20 h and cooled to –78 °C, and 4-methyl-3-vinyl-pent-3-enal **6** (0.5 equiv.) in ether ([aldehyde] = 0.3 mol L^{-1}) was added. The solution was stirred for 30 min at –78 °C, for 1 h at 0 °C, and for 1 h at 21 °C. The reaction was subsequently cooled to 0 °C, and a saturated aqueous solution of NH_4Cl added. The layers were separated, and the aqueous layer was extracted with dichloromethane. The combined organic extracts were washed with brine, dried ($MgSO_4$), filtered, and concentrated under reduced pressure. The crude material was purified by flash chromatography (silica gel, ether – petroleum ether).

2-Allyl-6-isopropenyl-3,7-dimethyl-octa-2,6-diene-1,4-diol (7d)

79% from **3a**. IR (neat) (cm^{-1}) ν: 3361, 3076, 2976, 2915, 1635, 1010, 996, 902. ^1H NMR (C_6D_6, 300 MHz) δ: 1.67 (s, 3H), 1.74 (s, 3H), 1.75 (s, 3H), 1.77 (s, 3H), 2.25 (dd, *J* = 13.9, 5.6 Hz, 1H), 2.6 (dd, *J* = 13.9, 8.1 Hz, 1H), 2.95 (d, *J* = 6.2 Hz, 2H), 3.00 (s, br, 2H), 3.93 (d, *J* = 11.6 Hz, 1H), 4.31 (d, *J* = 11.6 Hz, 1H), 4.69 (dd, *J* = 2.6, 0.8 Hz, 1H), 4.83 (dd, *J* = 8.1, 5.7 Hz, 1H), 4.99 (dd, *J* = 10.0, 2.0 Hz, 1H), 5.00 (d, 1H), 5.05 (dd, *J* = 17.1, 2.0 Hz, 1H), 5.78 (dddd, *J* = 16.9, 10.2, 6.4, 6.4 Hz, 1H). ^{13}C NMR (C_6D_6, 75 MHz) δ: 13.0, 20.3, 22.1, 22.6, 36.3, 37.2, 60.8, 69.6, 114.3, 115.2, 128.9, 132.5, 133.6, 136.1, 137.3, 146.7. HR-MS (EI) *m/z* calcd. for $C_{16}H_{24}O$ ($[M^+ – H_2O]$): 232.1827; found: 232.1829.

2-Allyl-6-isopropenyl-7-methyl-3-trimethylsilanyl-octa-2,6-diene-1,4-diol (7e)

43% from **3b**. IR (neat) (cm^{-1}) ν: 3386, 3077, 2962–2852, 1442, 1250, 1088–996, 838. ^1H NMR (C_6D_6, 500 MHz) δ: 0.31 (s, 9H), 1.66 (s, 3H), 1.69 (s, 3H), 1.73 (s, 3H), 2.10 (d, *J* = 14.2 Hz, 1H), 2.31 (s, br, 1H), 2.76 (dd, *J* = 14.2, 10.4 Hz, 2H), 3.04–3.14 (m, 2H), 4.14 (d, *J* = 11.8 Hz, 1H), 4.30 (d, *J* = 11.8 Hz, 1H), 4.65 (dd, *J* = 1.8, 0.7 Hz, 1H), 4.74 (dd, *J* = 10.4, 3.1 Hz, 1H), 4.98 (dd, *J* = 2.4, 1.4 Hz, 1H), 5.03 (ddd, *J* = 10.1, 3.0, 1.5 Hz, 1H), 5.08 (ddd, *J* = 17.1, 3.5, 1.7 Hz, 1H), 5.80 (dddd, *J* = 16.9, 10.4, 6.3, 6.3 Hz, 1H). ^{13}C NMR (C_6D_6, 125 MHz) δ: 2.2, 20.3, 22.0, 22.6, 39.0, 40.1, 61.7, 72.1, 114.2, 116.6, 129.2, 133.9, 137.1, 142.3, 146.7, 149.0. HR-MS (EI) *m/z* calcd. for $C_{18}H_{30}OSi$ ($[M^+ – H_2O]$): 290.2066; found: 290.2012.

2,3-Diallyl-6-isopropenyl-7-methyl-octa-2,6-diene-1,4-diol (7f)

64% from **3c**. IR (neat) (cm^{-1}) ν: 3303, 2955–2872, 1637, 1448, 1060, 993, 890. ^1H NMR (C_6D_6, 300 MHz) δ: 1.70 (s, 3H), 1.71 (s, 3H), 1.77 (d, 3H), 2.13 (d, br, *J* = 14.2 Hz, 2H), 2.18 (s, br, 1H), 2.62 (dd, *J* = 14.1, 10.2 Hz, 1H), 2.81 (dd, *J* = 15.6, 6.5 Hz, 1H), 2.88–2.96 (m, 3H), 4.03 (d, *J* = 11.8 Hz, 1H), 4.16 (d, *J* = 11.8 Hz, 1H), 4.54 (dd, *J* = 10.1, 3.5 Hz, 1H), 4.61 (t, br, 1H), 4.98–5.02 (m, 4H), 5.06 (dd, *J* = 5.1, 1.7 Hz, 1H), 5.70–5.87 (m, 2H). ^{13}C NMR (C_6D_6, 75 MHz) δ: 20.6, 22.4, 22.9, 33.5, 36.4, 37.7, 61.4, 71.1, 114.7, 115.7, 116.1, 130.3, 133.3, 135.4, 136.3, 137.3, 138.2, 146.4. HR-MS (EI) *m/z* calcd. for $C_{16}H_{26}O$ ($[M^+ – H_2O]$): 258.1984; found: 258.1978.

General procedure for silylation of the primary alcohols

tert-Butyldimethylsilyl chloride (1.1 equiv.) and DMAP (1.1 equiv.) were sequentially added to a solution of the diol (1.0 equiv.) in dichloromethane ([diol] = 1.0 mol L^{-1}) at 0 °C, and the solution was stirred for 18 h at 21 °C. A saturated aqueous solution of $NaHCO_3$ was then added; the layers were separated, and the aqueous layer was extracted with ether. The combined organic extracts were washed with brine, dried ($MgSO_4$), filtered, and concentrated under reduced pressure. The crude material was purified by flash chromatography (silica gel, ether – petroleum ether).

7-(*tert*-Butyl-dimethyl-silanyloxymethyl)-3-isopropylidene-2,6-dimethyl-deca-1,6,9-trien-5-ol (25d)

94% from **7d**. IR (neat) (cm^{-1}) ν: 3370, 3076, 2857, 1636, 1255, 1070, 837, 776. ^1H NMR ($CDCl_3$, 500 MHz) δ: 0.03

© 2004 NRC Canada

(s, 6H), 0.87 (s, 9H), 1.70 (s, 3H), 1.71 (s, 3H), 1.73 (s, br, 1H), 1.73 (s, 3H), 1.78 (s, 3H), 2.04 (dd, *J* = 14.0, 4.0 Hz, 1H), 2.59 (dd, *J* = 14.0, 9.6 Hz, 1H), 2.87 (dd, *J* = 14.4, 6.4 Hz, 2H), 4.02 (d, *J* = 11.4 Hz, 1H), 4.17 (d, *J* = 11.5 Hz, 1H), 4.61 (dd, *J* = 2.0, 0.8 Hz, 1H), 4.70 (dd, *J* = 9.6, 4.1 Hz, 1H), 4.95 (dd, *J* = 10.2, 1.6 Hz, 1H), 4.97 (dd, *J* = 17.4, 1.9 Hz, 1H), 4.96–4.99 (m, 1H), 5.73 (dddd, *J* = 17.2, 10.0, 6.5, 6.4 Hz, 1H). ^{13}C NMR ($CDCl_3$, 125 MHz) δ: –5.4, 12.4, 18.4, 20.1, 21.9, 22.6, 26.0, 34.8, 36.8, 60.7, 69.0, 114.0, 114.8, 129.2, 132.0, 133.0, 135.4, 135.8, 146.2. HR-MS (EI) *m/z* calcd. for $C_{22}H_{38}OSi$ ([$M^+ - H_2O$]): 346.2692; found: 346.2688.

7-(*tert*-Butyl-dimethyl-silanyloxymethyl)-3-isopropylidene-2-methyl-6-trimethylsilanyl-deca-1,6,9-trien-5-ol (25e)

71% from **7e**. IR (neat) (cm^{-1}) ν: 3371, 3043, 2956, 1433, 1259, 1084–990, 841. ^{1}H NMR ($CDCl_3$, 300 MHz) δ: 0.02 (s, 6H), 0.23 (s, 9H), 0.88 (s, 9H), 1.70 (s, 3H), 1.74 (s, 3H), 1.78 (s, 4H), 1.97 (d, *J* = 12.8 Hz, 1H), 2.65 (dd, *J* = 14.3, 10.7 Hz, 1H), 3.00 (dd, *J* = 14.1, 6.3 Hz, 1H), 3.12 (dd, *J* = 14.2, 6.5 Hz, 1H), 4.10 (d, *J* = 12.2 Hz, 1H), 4.32 (d, *J* = 12.2 Hz, 1H), 4.63 (dd, *J* = 2.4, 0.9 Hz, 1H), 4.69 (dd, *J* = 10.7, 2.9 Hz, 1H), 4.99–5.03 (m, 3H), 5.75 (dddd, *J* = 17.0, 10.1, 6.6, 6.6 Hz, 1H). ^{13}C NMR ($CDCl_3$, 75 MHz) δ: –5.4, 2.6, 18.3, 20.3, 21.9, 22.7, 25.9, 37.2, 38.6, 60.8, 71.6, 114.0, 115.8, 129.0, 133.5, 137.1, 140.3, 146.2, 148.1. Anal calcd. for $C_{24}H_{46}O_2Si_2$ (%): C 73.78, H 10.84; found: C 73.67, H 10.64.

6-Allyl-7-(*tert*-butyl-dimethyl-silanyloxymethyl)-3-isopropylidene-2-methyl-deca-1,6,9-trien-5-ol (25f)

81% from **7f**. IR (neat) (cm^{-1}) ν: 3298, 1643, 1412, 1095, 982, 885. ^{1}H NMR ($CDCl_3$, 300 MHz) δ: 0.02 (s, 6H), 0.86 (s, 9H), 1.70 (s, 3H), 1.71 (s, 3H), 1.78 (d, 3H), 1.81 (s, 1H), 1.98 (d, 1H), 2.60 (dd, *J* = 14.1, 10.3 Hz, 1H), 2.81–2.96 (m, 4H), 4.06 (d, *J* = 11.6 Hz, 1H), 4.19 (d, *J* = 11.6 Hz, 1H), 4.62 (d, 1H), 4.68 (dd, *J* = 10.3, 3.5 Hz, 1H), 4.94–5.09 (m, 5H), 5.74 (dddd, *J* = 16.9, 10.3, 6.4, 6.4 Hz, 1H), 5.86 (dddd, *J* = 16.9, 10.4, 6.2, 6.2 Hz, 1H). ^{13}C NMR ($CDCl_3$, 75 MHz) δ: –5.0, 18.7, 20.6, 22.3, 23.0, 26.3, 32.2, 34.8, 37.9, 60.7, 69.8, 114.4, 115.2, 115.6, 129.8, 133.3, 134.7, 136.6, 136.8, 138.1, 146.4. Anal calcd. for $C_{24}H_{42}O_2Si$ (%): C 73.78, H 10.84; found: C 73.67, H 10.64.

General procedure for methylation of the secondary alcohols

Sodium hydride (3.0 equiv., 60% dispersion in mineral oil) was added to a solution of the alcohol (1.0 equiv.) in THF ([alcohol] = 1.0 mol L^{-1}) at 0 °C. After 30 min, iodomethane (20.0 equiv.) was added, and the solution was stirred for 18 h at 21 °C. A saturated aqueous solution of NH_4Cl was subsequently added; the layers were separated, and the aqueous layer was extracted with dichloromethane. The combined organic extracts were washed with brine, dried ($MgSO_4$), filtered, and concentrated under reduced pressure. The crude material was purified by flash chromatography (silica gel, ether – petroleum ether).

(2-Allyl-6-isopropenyl-4-methoxy-3,7-dimethyl-octa-2,6-dienyloxy)-*tert*-butyl-dimethyl-silane (26d)

92% from **25d**. IR (neat) (cm^{-1}) ν: 3077, 2956–2820, 1255, 1100–1051, 837, 775. ^{1}H NMR ($CDCl_3$, 500 MHz) δ: 0.02 (s, 6H), 0.87 (s, 9H), 1.61 (s, 3H), 1.65 (s, 3H), 1.66 (s, 3H), 1.7 (s, 3H), 2.08 (dd, *J* = 14.3, 5.6 Hz, 1H), 2.52 (dd, *J* = 14.2, 7.8 Hz, 1H), 2.90 (d, br, 2H), 2.97 (s, 3H), 3.91 (d, *J* = 11.4 Hz, 1H), 4.17 (dd, *J* = 7.8, 5.7 Hz, 1H), 4.23 (d, *J* = 11.4 Hz, 1H), 4.56 (d, *J* = 2.7 Hz, 1H), 4.94 (dd, *J* = 16.9, 1.5 Hz, 1H), 4.95–4.96 (m, 1H), 4.97 (dd, *J* = 10.1, 1.7 Hz, 1H), 5.74 (dddd, *J* = 16.9, 10.4, 6.3, 6.3 Hz, 1H). ^{13}C NMR ($CDCl_3$, 125 MHz) δ: –5.3, –5.4, 11.9, 20.2, 21.9, 22.7, 25.9, 34.7, 35.7, 56.0, 60.3, 78.2, 113.7, 114.6, 127.3, 133.1, 133.2, 134.1, 135.9, 146.3. Anal calcd. for $C_{23}H_{42}O_2Si$ (%): C 72.95, H 11.18; found: C 73.16, H 11.12.

4-(*tert*-Butyl-dimethyl-silanyloxymethyl)-8-isopropenyl-6-methoxy-9-methyl-5-trimethylsilanyl-deca-1,4,8-triene (26e)

90% from **25e**. IR (neat) (cm^{-1}) ν: 3077–2814, 1255, 1102, 839, 775. ^{1}H NMR ($CDCl_3$, 300 MHz) δ: 0.02 (s, 6H), 0.21 (s, 9H), 0.88 (s, 9H), 1.66 (s, 3H), 1.69 (s, 3H), 1.76 (s, 3H), 1.95 (dd, *J* = 14.4, 3.2 Hz, 1H), 2.65 (dd, *J* = 14.5, 9.3 Hz, 1H), 3.04 (dd, br, 1H), 3.10 (dd, br, 1H), 3.12 (s, 3H), 3.99 (s, broad, 1H), 4.14 (d, *J* = 5.3 Hz, 1H), 4.35 (d, *J* = 11.8 Hz, 1H), 4.59 (q, 1H), 4.98 (q, 1H), 5.01 (d, *J* = 9.1 Hz, 1H), 5.02 (d, *J* = 17.9 Hz, 1H), 5.77 (dddd, *J* = 16.8, 10.5, 6.4, 6.4 Hz, 1H). ^{13}C NMR ($CDCl_3$, 75 MHz) δ: –5.5, 2.3, 18.2, 20.2, 21.9, 22.7, 25.9, 37.6, 37.7, 56.5, 60.3, 80.7, 113.6, 115.8, 126.8, 133.7, 136.9, 140.9, 146.3, 149.5.

4-(*tert*-Butyl-dimethyl-silanyloxymethyl)-8-isopropenyl-6-methoxy-9-methyl-5-allyl-deca-1,4,8-triene (26f)

89% from **25f**. IR (neat) (cm^{-1}) ν: 3077–2814, 1636, 1463, 1255, 1102–1069, 837, 775. ^{1}H NMR ($CDCl_3$, 300 MHz) δ: 0.03 (s, 6H), 0.87 (s, 9H), 1.66 (s, 6H), 1.75 (d, 3H), 1.99 (d, br, 1H), 2.60 (dd, *J* = 14.5, 9.3 Hz, 1H), 2.82–2.86 (m, br, 2H), 2.91 (dd, *J* = 6.2, 4.8 Hz, 2H), 3.09 (s, 3H), 4.02 (d, *J* = 11.4 Hz, 1H), 4.10 (dd, *J* = 9.3, 4.1 Hz, 1H), 4.25 (d, *J* = 11.4 Hz, 1H), 4.59 (d, br, 1H), 4.95–5.07 (m, 5H), 5.71–5.83 (m, 2H). ^{13}C NMR ($CDCl_3$, 75 MHz) δ: –5.0 (2), 18.7, 20.5, 22.3, 23.1, 26.3, 32.5, 34.7, 36.8, 57.0, 60.3, 79.3, 114.1, 115.4, 115.6, 127.5, 133.7, 135.2, 136.2, 136.8, 137.8, 146.6.

General procedure for deprotection of the primary alcohols

Tetrabutylammonium fluoride (1.5 equiv., 1.0 mol L^{-1} in THF) was added to a solution of silane (1.0 equiv.) in THF ([silane] = 1.0 mol L^{-1}) at 0 °C, and the resulting solution was stirred for 18 h at 21 °C. A saturated aqueous solution of NH_4Cl was then added; the layers were separated, and the aqueous layer was extracted with ether. The combined organic extracts were washed with brine, dried ($MgSO_4$), filtered, and concentrated under reduced pressure. The crude material was purified by flash chromatography (silica gel, ether – petroleum ether).

2-Allyl-6-isopropenyl-4-methoxy-3,7-dimethyl-octa-2,6-dien-1-ol (27d)

96% from **26d**. IR (neat) (cm^{-1}) ν: 3442, 3077, 2976, 2919, 2818, 1636, 1445, 1098, 996, 898. ^{1}H NMR ($CDCl_3$, 300 MHz) δ: 1.39 (s, br, 1H), 1.61 (s, 3H), 1.65 (s, 6H), 1.74 (s, 3H), 2.19 (dd, *J* = 14.0, 7.3 Hz, 1H), 2.50 (dd, *J* = 14.0,

© 2004 NRC Canada

6.4 Hz, 1H), 2.90 (t, 2H), 3.03 (s, 3H), 4.00 (d, *J* = 11.9 Hz, 1H), 4.09 (d, *J* = 11.9 Hz, 1H), 4.17 (d, *J* = 6.8 Hz, 1H), 4.56 (d, *J* = 2.0 Hz, 1H), 4.94–4.98 (m, 2H), 5.00 (ddd, *J* = 11.8, 3.3, 1.6 Hz, 1H), 5.77 (dddd, *J* = 16.7, 10.0, 6.6, 6.4 Hz, 1H). ^{13}C NMR ($CDCl_3$, 75 MHz) δ: 12.4, 20.5, 22.2, 23.0, 35.6, 36.3, 56.2, 61.2, 78.7, 114.2, 115.6, 128.6, 133.7, 134.9, 135.3, 135.9, 146.5. Anal calcd. for $C_{17}H_{28}O_2$ (%): C 77.22, H 10.67; found: C 77.36, H 10.51.

2-Allyl-6-isopropenyl-4-methoxy-7-methyl-3-trimethylsilanyl-octa-2,6-dien-1-ol (27e)

90% from **26e**. IR (neat) (cm^{-1}) ν: 3433, 3076, 2963–2814, 1636, 1443, 1250, 1100, 996, 838. ^{1}H NMR ($CDCl_3$, 300 MHz) δ: 0.19 (s, 9H), 1.65 (s, 3H), 1.68 (s, 3H), 1.75 (s, 3H), 2.04 (dd, *J* = 14.5, 3.8 Hz, 1H), 2.18 (s, br, 1H), 2.71 (dd, *J* = 14.5, 8.9 Hz, 1H), 3.04 (dd, *J* = 6.1, 1.1 Hz, 2H), 3.16 (s, 3H), 4.08 (d, *J* = 12.7 Hz, 1H), 4.11 (dd, *J* = 8.7, 4.4 Hz, 1H), 4.18 (d, *J* = 12.7 Hz, 1H), 4.60 (d, *J* = 1.9 Hz, 1H), 5.02 (d, br, *J* = 18.0 Hz, 1H), 5.05 (s, br, 1H), 5.08 (ddd, *J* = 11.0, 3.6, 1.6 Hz, 1H), 5.78 (dddd, *J* = 17.6, 9.6, 6.1, 6.1 Hz, 1H). ^{13}C NMR ($CDCl_3$, 75 MHz) δ: 2.2, 20.6, 22.3, 23.1, 37.9, 40.2, 57.2, 62.2, 81.6, 114.3, 117.1, 127.9, 134.0, 137.0, 141.2, 146.6, 149.7. Anal calcd. for $C_{19}H_{34}O_2Si$ (%): C 73.78, H 10.84; found: C 73.67, H 10.64.

2,3-Diallyl-6-isopropenyl-4-methoxy-7-methyl-octa-2,6-dien-1-ol (27f)

93% from **26f**. IR (neat) (cm^{-1}) ν: 3423, 3077, 2977–2814, 1635, 1446, 1100, 992, 909. ^{1}H NMR ($CDCl_3$, 300 MHz) δ: 1.63 (s, 6H), 1.79 (s, 3H), 1.88 (s, 1H), 2.12 (dd, *J* = 14.4, 4.6 Hz, 1H), 2.62 (dd, *J* = 14.3, 8.3 Hz, 1H), 2.74 (dd, *J* = 15.2, 7.1 Hz, 1H), 2.85 (d, *J* = 5.9 Hz, 1H), 2.90 (d, *J* = 6.0 Hz, 1H), 2.94 (d, *J* = 6.1 Hz, 1H), 3.17 (s, 3H), 4.03 (dd, *J* = 8.2, 5.0 Hz, 1H), 4.07 (d, *J* = 12.2 Hz, 1H), 4.16 (d, *J* = 12.2 Hz, 1H), 4.58 (s, 1H), 4.96–5.07 (m, 5H), 5.68–5.85 (m, 2H). ^{13}C NMR ($CDCl_3$, 75 MHz) δ: 20.5, 22.3, 23.0, 33.5, 36.1, 36.6, 57.2, 61.4, 80.2, 114.3, 115.8, 116.2, 128.2, 133.7, 136.1, 136.4, 136.9, 137.1, 146.6. Anal calcd. for $C_{19}H_{30}O_2$ (%): C 78.57, H 10.41; found: C 77.09, H 9.97.

General procedures for oxidation of the primary alcohols

Oxalyl chloride (1.5 equiv.) was added to a solution of DMSO (3.0 equiv.) in dichloromethane ([oxalyl chloride] = 1.0 mol L^{-1}) at –78 °C. After 5 min, the alcohol (1.0 equiv.) was added, and the solution was stirred for 1 h at –78 °C. Triethylamine (7.0 equiv.) was added, and the solution was warmed to 0 °C for 1 h. A saturated aqueous solution of NH_4Cl was added; the layers were separated, and the aqueous layer was extracted with ether. The combined organic extracts were washed with brine, dried ($MgSO_4$), filtered, and concentrated under reduced pressure. The crude material was purified by flash chromatography (silica gel, ether – petroleum ether).

The alcohol (1.0 equiv.) in THF was added to a solution of *o*-iodoxybenzoic acid (IBX) (1.5 equiv.) in DMSO (such that [alcohol] = 1.0 mol L^{-1}) at 0 °C. The resulting solution was stirred for 3 h at 21 °C prior to the addition of water. Following filtration, the solution was extracted with ether. The combined organic extracts were washed with brine, dried ($MgSO_4$), filtered, and concentrated. The crude material was purified by flash chromatography (silica gel, ether – petroleum ether).

2-Allyl-6-isopropenyl-4-methoxy-3,7-dimethyl-octa-2,6-dienal (28d)

90% from **27d**. IR (neat) (cm^{-1}) ν: 2924, 1671, 1443, 1100, 906. ^{1}H NMR ($CDCl_3$, 300 MHz) δ: 1.62 (s, 6H), 1.73 (s, 3H), 1.88 (s, 3H), 2.27 (dd, *J* = 14.2, 6.8 Hz, 1H), 2.60 (dd, *J* = 14.1, 7.8 Hz, 1H), 2.95 (dd, *J* = 15.1, 5.8 Hz, 1H), 3.08 (dd, *J* = 15.1, 5.8 Hz, 1H), 3.16 (s, 3H), 4.78 (t, *J* = 6.8 Hz, 1H), 4.89 (d, *J* = 17.8 Hz, 1H), 4.92 (d, *J* = 10.6 Hz, 1H), 4.97 (s, 1H), 5.67 (ddd, *J* = 16.6, 11.0, 6.0 Hz, 1H), 10.07 (s, 1H). ^{13}C NMR ($CDCl_3$, 75 MHz) δ: 14.7, 20.4, 22.3, 22.8, 30.4, 35.8, 56.9, 76.8, 115.3 (2), 129.5, 132.0, 134.8, 138.3, 145.7, 158.9, 189.4. HR-MS (EI) *m*/*z* calcd. for $C_{16}H_{23}O_2$ ($[M^+ - CH_3]$): 247.1698; found: 247.1721 or calcd. for $C_{16}H_{22}O$ ($[M^+ - CH_3OH]$): 230.1671; found: 230.1643.

2-Allyl-6-isopropenyl-4-methoxy-7-methyl-3-trimethylsilanyl-octa-2,6-dienal (28e)

73% from **27e**. IR (neat) (cm^{-1}) ν: 3077–2817, 1673, 1252, 1100, 905. ^{1}H NMR ($CDCl_3$, 300 MHz) δ: 0.24 (s, 9H), 1.65 (s, 3H), 1.66 (s, 3H), 1.74 (s, 3H), 2.14 (dd, *J* = 14.7, 3.2 Hz, 1H), 2.71 (dd, *J* = 14.7, 9.2 Hz, 1H), 3.15 (s, 3H), 3.11–3.17 (m, 2H), 4.48 (dd, *J* = 8.8, 3.2 Hz, 1H), 4.58 (d, *J* = 2.0 Hz, 1H), 4.92 (dd, *J* = 17.8, 1.6 Hz, 1H), 4.96 (s, 1H), 4.97 (dd, *J* = 10.8, 1.3 Hz, 1H), 5.77 (dddd, *J* = 16.9, 10.9, 5.6, 5.6 Hz, 1H), 10.19 (s, 1H). ^{13}C NMR ($CDCl_3$, 75 MHz) δ: 1.5, 20.6, 22.3, 23.0, 34.4, 38.7, 57.3, 80.4, 114.8, 116.2, 128.7, 132.9, 136.3, 146.1, 147.8, 193.5.

2,3-Diallyl-6-isopropenyl-4-methoxy-7-methyl-octa-2,6-dienal (28f)

93% from **27f**. .IR (neat) (cm^{-1}) ν: 3079–2821, 1671, 1446, 1101, 911. ^{1}H NMR (C_6D_6, 300 MHz) δ: 1.59 (s, 3H), 1.66 (s, 3H), 1.68 (s, 3H), 2.16 (dd, *J* = 14.4, 4.5 Hz, 1H), 2.73 (dd, *J* = 14.4, 8.6 Hz, 1H), 2.84 (dd, *J* = 14.3, 7.3 Hz, 1H), 2.91 (s, 3H), 2.99 (dd, *J* = 13.7, 5.1 Hz, 1H), 3.06 (dd, *J* = 14.3, 5.3 Hz, 1H), 3.24 (dd, *J* = 15.0, 6.2 Hz, 1H), 4.51 (dd, *J* = 8.5, 4.6 Hz, 1H), 4.66 (d, 1H), 4.95 (dd, br, 3H), 5.01 (dd, *J* = 16.7, 1.6 Hz, 2H), 5.66 (dddd, *J* = 16.8, 10.2, 6.5, 6.5 Hz, 1H), 5.82 (dddd, *J* = 16.9, 10.4, 6.3, 6.3 Hz, 1H), 10.49 (s, 1H). ^{13}C NMR (C_6D_6, 75 MHz) δ: 20.4, 22.2, 22.6, 30.6, 34.8, 37.5, 57.0, 79.0, 114.9, 115.4, 117.2, 128.8, 132.9, 134.9, 135.9, 138.3, 146.1, 157.1, 189.9. HR-MS (EI) *m*/*z* calcd. for $C_{18}H_{24}O$ ($[M^+ - CH_3OH]$): 256.1827; found: 256.1808.

General procedure for vinyl Grignard addition to the aldehydes

Vinylmagnesium chloride (2.0 equiv., 1.60 mol L^{-1} in THF) was added to a solution of the aldehyde (1.0 equiv.) in ether ([aldehyde] = 1.0 mol L^{-1}) at –78 °C. The solution was stirred for 1 h at –78 °C and for 30 min at 0 °C. A saturated aqueous solution of NH_4Cl was then added; the layers were separated, and the aqueous layer was extracted with ether. The combined organic extracts were washed with brine, dried ($MgSO_4$), filtered, and concentrated under reduced

© 2004 NRC Canada

pressure. The crude material was purified by flash chromatography (silica gel, ether – petroleum ether).

4-Allyl-8-isopropenyl-6-methoxy-5,9-dimethyl-deca-1,4,8-trien-3-ol (29d)

75% from **28d**. IR (neat) (cm^{-1}) ν: 3456, 3076, 2976, 2910, 2815, 1634, 1445, 1100, 992, 919.

Isomer A

65%. ^{1}H NMR (C_6D_6, 300 MHz) δ: 1.61 (s, br, 1H), 1.67 (s, 6H), 1.70 (s, 3H), 1.76 (s, 3H), 2.28 (dd, *J* = 14.1, 5.9 Hz, 1H), 2.71 (dd, *J* = 14.1, 7.4 Hz, 1H), 2.81 (dd, *J* = 15.7, 5.8 Hz, 1H), 2.92 (dd, *J* = 15.7, 6.0 Hz, 1H), 3.01 (s, 3H), 4.35 (t, *J* = 6.7 Hz, 1H), 4.78 (s, 1H), 4.97 (d, *J* = 10.2 Hz, 2H), 5.04 (d, *J* = 17.3 Hz, 2H), 5.26 (s, broad, 1H), 5.35 (d, *J* = 17.1 Hz, 1H), 5.82 (m, 2H). ^{13}C NMR (C_6D_6, 75 MHz) δ: 12.8, 20.4, 22.2, 22.8, 32.8, 36.2, 56.1, 71.1, 78.6, 114.2, 114.3, 114.9, 127.6, 133.9, 135.3, 135.4, 137.3, 139.5, 146.8.

Isomer B

10%. ^{1}H NMR (C_6D_6, 300 MHz) δ: 1.60 (d, br, 1H), 1.69 (s, 6H), 1.71 (s, 3H), 1.76 (s, 3H), 2.06 (dd, *J* = 14.1, 4.4 Hz, 1H), 2.76 (dd, *J* = 14.2, 8.6 Hz, 1H), 2.86 (d, *J* = 6.0 Hz, 2H), 3.06 (s, 3H), 4.38 (dd, *J* = 8.6, 4.6 Hz, 1H), 4.76 (d, *J* = 2.1 Hz, 1H), 4.96–5.03 (m, 3H), 5.07 (d, 1H), 5.29 (s, br, 1H), 5.36 (ddd, *J* = 17.1, 1.7, 1.7 Hz, 1H), 5.77 (ddd, *J* = 17.1, 10.5, 4.5 Hz, 1H), 5.84 (dddd, *J* = 16.9, 10.4, 6.3, 6.2 Hz, 1H). ^{13}C NMR (C_6D_6, 75 MHz) δ: 12.8, 20.3, 22.2, 22.9, 32.6, 36.0, 56.0, 70.8, 78.0, 114.0, 114.1, 114.9, 127.8, 133.6, 135.0, 135.5, 137.7, 139.8, 147.0. HR-MS (EI) *m/z* calcd. for $C_{19}H_{28}O$ ([M^+ – H_2O]): 272.2140; found: 272.2112.

4-Allyl-6-methoxy-9-methyl-5-trimethylsilanyl-8-vinyl-deca-1,4,8-trien-3-ol (29e)

57% from **28e**. IR (neat) (cm^{-1}) ν: 3445, 3076–2814, 1443, 1250, 1100, 851–839. ^{1}H NMR (C_6D_6, 300 MHz) δ: 0.31 (s, 9H), 1.73 (s, 3H), 1.80 (s, 6H), 2.17 (d, *J* = 14.0 Hz, 1H), 3.07 (s, 3H), 2.96–3.11 (m, 3H), 4.36 (s, br, 1H), 4.81 (d, *J* = 2.0 Hz, 1H), 4.98 (ddd, *J* = 10.2, 1.7 Hz, 1H), 5.04–5.12 (m, 3H), 5.37 (d, *J* = 17.1 Hz, 2H), 5.88 (dddd, *J* = 17.0, 10.5, 6.1, 6.1 Hz, 1H), 5.98 (ddd, *J* = 17.2, 10.4, 5.4 Hz, 1H). ^{13}C NMR (C_6D_6, 75 MHz) δ: 2.6, 20.5, 22.2, 23.0, 37.2, 38.3, 57.3, 73.6, 81.2, 114.3, 114.7, 116.2, 127.8, 128.1, 128.4, 134.2, 139.2, 140.1, 146.9.

4,5-Diallyl-8-isopropenyl-6-methoxy-9-methyl-deca-1,4,8-trien-3-ol (29f)

60% from **28f**. IR (neat) (cm^{-1}) ν: 3421, 3077–2819, 1636, 1444, 1100, 992, 909.

Isomer A

42%. ^{1}H NMR (C_6D_6, 300 MHz) δ: 1.73 (s, 3H), 1.74 (s, 3H), 1.79 (s, 3H), 1.93 (d, br, 1H), 2.22 (dd, *J* = 14.3, 3.1 Hz, 1H), 2.85 (s, 1H), 2.78–2.90 (m, 1H), 2.93–3.01 (m, 3H), 3.06 (s, 3H), 4.18 (dd, *J* = 9.3, 3.8 Hz, 1H), 4.78 (d, br, 1H), 4.99 (dd, *J* = 9.2, 1.8 Hz, 2H), 5.02–5.08 (m, 3H), 5.11 (dd, *J* = 11.9, 1.8 Hz, 1H), 5.32–5.39 (m, 2H), 5.74–5.84 (m, 2H), 5.90 (ddd, *J* = 17.2, 10.3, 4.7 Hz, 1H). ^{13}C NMR (C_6D_6, 75 MHz) δ: 20.4, 22.2, 22.9, 33.0, 34.1, 37.3, 57.1, 72.0, 80.3, 114.2, 114.4, 115.2, 115.8, 128.0, 134.0, 136.6, 136.8, 137.1, 137.9, 139.9, 146.9.

Isomer B

18%. ^{1}H NMR (C_6D_6, 300 MHz) δ: 1.38 (d, *J* = 3.6 Hz, 1H), 1.74 (s, 3H), 1.75 (s, 3H), 1.79 (s, 3H), 2.06 (d, *J* = 14.4 Hz, 1H), 2.92 (dd, *J* = 14.4, 10.0 Hz, 1H), 2.94–3.05 (m, 4H), 3.06 (s, 3H), 4.28 (dd, *J* = 10.0, 3.3 Hz, 1H), 4.79 (d, br, 1H), 4.95–5.06 (m, 5H), 5.35 (ddd, *J* = 18.0, 1.7, 1.7 Hz, 1H), 5.42 (s, br, 1H), 5.81 (ddd, *J* = 16.0, 10.3, 7.3 Hz, 2H), 5.90 (ddd, *J* = 16.7, 10.4, 6.1 Hz, 1H). ^{13}C NMR (C_6D_6, 75 MHz) δ: 20.3, 22.4, 22.9, 33.0, 34.1, 37.3, 57.1, 72.0, 80.3, 114.2, 114.4, 115.2, 115.8, 128.0, 134.0, 136.6, 136.8, 137.2, 137.9, 139.9, 146.9.

General procedures for oxidation of the secondary alcohols

Oxalyl chloride (1.5 equiv.) was added to a solution of DMSO (3.0 equiv.) in dichloromethane ([oxalyl chloride] = 1.0 mol L^{-1}) at –78 °C. After 5 min, the alcohol (1.0 equiv.) was added, and the solution was stirred for 1 h at –78 °C. Triethylamine (7.0 equiv.) was added, and the solution was warmed to 0 °C for 1 h. A saturated aqueous solution of NH_4Cl was added; the layers were separated, and the aqueous layer was extracted with ether. The combined organic extracts were washed with brine, dried ($MgSO_4$), filtered, and concentrated under reduced pressure. The crude material was purified by flash chromatography (silica gel, ether – petroleum ether).

The alcohol (1.0 equiv.) in THF was added to a solution of IBX (1.5 equiv.) in DMSO ([alcohol] = 1.0 mol L^{-1}) at 0 °C. The resulting solution was stirred for 3 h at 21 °C prior to the addition of water. Following filtration, the solution was extracted with ether. The combined organic extracts were washed with brine, dried ($MgSO_4$), filtered, and concentrated. The crude material was purified by flash chromatography (silica gel, ether – petroleum ether).

4-Allyl-8-isopropenyl-6-methoxy-5,9-dimethyl-deca-1,4,8-trien-3-one (8d)

97% from **29d**. IR (neat) (cm^{-1}) ν: 2978, 2923, 1660, 1638, 1443, 1399, 1099, 992. ^{1}H NMR (C_6D_6, 300 MHz) δ: 1.63 (s, 3H), 1.72 (s, 3H), 1.73 (s, 3H), 1.83 (s, 3H), 2.18 (dd, *J* = 14.1, 2.6 Hz, 1H), 2.72 (dd, *J* = 14.1, 9.3 Hz, 1H), 2.82 (d, *J* = 6.5 Hz, 2H), 3.05 (s, 3H), 4.10 (ddd, *J* = 9.2, 4.0, 1.6 Hz, 1H), 4.76 (d, 1H), 4.94 (dd, *J* = 10.1, 1.5 Hz, 1H), 5.01 (t, 1H), 5.03 (dd, *J* = 16.5, 1.0 Hz, 1H), 5.33 (dd, *J* = 10.4, 1.5 Hz, 1H), 5.66 (dddd, *J* = 16.8, 10.3, 6.4, 6.4 Hz, 1H), 5.95 (dd, *J* = 17.5, 1.5 Hz, 1H), 6.30 (dd, *J* = 17.5, 10.4 Hz, 1H). ^{13}C NMR (C_6D_6, 75 MHz) δ: 11.9, 20.3, 22.2, 22.8, 34.9, 35.8, 56.4, 80.3, 114.2, 116.2, 127.7, 129.0, 133.6, 134.5, 136.1, 137.3, 139.9, 146.7, 197.6. HR-MS (EI) *m/z* calcd. for $C_{19}H_{28}O_2$ ([$M]^+$): 288.2089; found: 288.2056 or calcd. for $C_{18}H_{24}O$ ([M^+ – CH_3OH]): 256.1827; found: 256.1837.

4-Allyl-8-isopropenyl-6-methoxy-9-methyl-5-trimethysilanyl-deca-1,4,8-trien-3-one (8e)

83% from **29e**. IR (neat) (cm^{-1}) ν: 3075–2821, 1664, 1251, 1102, 852–840. ^{1}H NMR (C_6D_6, 300 MHz) δ: 0.31 (s, 9H), 1.74 (s, 3H), 1.78 (s, 3H), 1.82 (s, 3H), 2.13 (d, *J* =

© 2004 NRC Canada

14.0 Hz, 1H), 2.88 (dd, *J* = 14.3, 10.5 Hz, 1H), 3.04 (s, 3H), 3.11 (d, br, 2H), 4.01 (dd, *J* = 10.4, 2.9 Hz, 1H), 4.75 (d, *J* = 2.3 Hz, 1H), 4.94–5.05 (m, 3H), 5.34 (dd, *J* = 10.4, 1.1 Hz, 1H), 5.69 (dddd, *J* = 16.9, 10.2, 6.7, 6.7 Hz, 1H), 5.91 (dd, *J* = 17.0, 1.1 Hz, 1H), 6.23 (dd, *J* = 17.6, 10.4 Hz, 1H). ^{13}C NMR (C_6D_6, 75 MHz) δ: 2.0, 20.5, 22.2, 22.9, 37.6, 38.7, 57.0, 83.0, 114.2, 117.5, 127.4, 128.9, 134.0, 134.7, 137.5, 142.5, 146.7, 150.3, 199.5.

4,5-Diallyl-8-isopropenyl-6-methoxy-9-methyl-deca-1,4,8-trien-3-one (8f)

72% from **29f**. IR (neat) (cm^{-1}) ν: 3077–2823, 1662, 1637, 1102, 991, 897. ^{1}H NMR (C_6D_6, 300 MHz) δ: 1.62 (s, 6H), 1.69 (s, 3H), 1.98 (d, *J* = 14.5 Hz, 1H), 2.59 (dd, *J* = 14.5, 10.0 Hz, 1H), 2.89 (d, *J* = 6.6 Hz, 2H), 3.03 (s, 3H), 2.90–3.10 (m, 2H), 3.73 (dd, *J* = 10.0, 3.1 Hz, 1H), 4.51 (d, *J* = 2.4 Hz, 1H), 4.91 (s, 1H), 4.99 (d, *J* = 9.6 Hz, 1H), 5.04 (d, *J* = 16.9 Hz, 1H), 5.05 (d, *J* = 9.8 Hz, 1H), 5.11 (d, *J* = 17.2 Hz, 1H), 5.69 (dddd, *J* = 17.1, 10.5, 6.9, 6.9 Hz, 1H), 5.93 (dddd, *J* = 17.1, 10.5, 6.7, 6.7 Hz, 1H), 5.89 (d, *J* = 10.4 Hz, 1H), 6.10 (d, *J* = 17.5 Hz, 1H), 6.38 (dd, *J* = 17.6, 10.4 Hz, 1H). ^{13}C NMR (C_6D_6, 75 MHz) δ: 20.4, 22.3, 22.9, 31.9, 35.3, 36.1, 57.3, 81.0, 114.2, 116.4, 117.2, 127.8, 130.2, 133.4, 134.5, 136.3, 137.3, 138.0, 139.5, 146.3, 199.9. HR-MS (EI) *m*/*z* calcd. for $C_{21}H_{30}O_2$ ($[M]^+$): 314.2246; found: 314.2261.

General procedures for Diels–Alder cyclizations

Diethylaluminum chloride (1.1 equiv., 1.0 mol L^{-1} in hexane) was added to a solution of ketone (1.0 equiv.) in dichloromethane ([ketone] = 1.0 mol L^{-1}) at –78 °C. The solution was slowly warmed to 0 °C and, after 5 min, cooled to –78 °C. A saturated aqueous solution of $NaHCO_3$ was added; the layers were separated, and the aqueous layer was extracted with ether. The combined organic extracts were washed with brine, dried ($MgSO_4$), filtered, and concentrated under reduced pressure. The crude material was purified by flash chromatography (silica gel, ether – petroleum ether).

Borontrifluoride etherate (1.0 equiv.) was added to a solution of ketone (1.0 equiv.) in dichloromethane (such that [ketone] = 1.0 mol L^{-1}) at –78 °C, and the solution was stirred for 2 h. A saturated aqueous solution of $NaHCO_3$ was then added; the layers were separated, and the aqueous layer was extracted with ether. The combined organic extracts were washed with brine, dried ($MgSO_4$), filtered, and concentrated under reduced pressure. The crude material was purified by flash chromatography (silica gel, ether – petroleum ether).

3-Allyl-5-methoxy-4,8,11,11-tetramethyl-bicyclo[5.3.1]-undeca-3,7-dien-2-one (9d)

72% from **8d**. IR (neat) (cm^{-1}) ν: 3077–2824, 1669, 1464, 1103. ^{1}H NMR (C_6D_6, 300 MHz) δ: 0.89 (s, 3H), 1.22 (s, 3H), 1.35 (s, 3H), 1.58 (s, 3H), 1.61–1.69 (m, 2H), 1.74–1.82 (m, 1H), 2.12–2.23 (m, 1H), 2.43–2.51 (m, 2H), 2.52–2.64 (m, 2H), 2.87 (dd, *J* = 15.8, 6.6 Hz, 1H), 3.06 (s, 3H), 4.05 (dd, *J* = 11.1, 6.3 Hz, 1H), 4.98 (ddd, *J* = 10.0, 3.3, 1.6 Hz, 1H), 5.06 (ddd, *J* = 17.0, 3.5, 1.7 Hz, 1H), 5.83 (dddd, *J* = 16.8, 10.2, 6.5, 6.5 Hz, 1H). ^{13}C NMR (C_6D_6, 75 MHz) δ: 12.1, 19.2, 21.6, 25.1, 28.5, 28.8, 35.6, 36.4, 37.9, 57.6, 63.0, 82.3, 115.8, 131.5, 132.2, 134.0, 135.2, 138.8, 213.4. HR-MS (EI) *m*/*z* calcd. for $C_{19}H_{28}O_2$ ($[M]^+$): 288.2089; found: 288.2078.

3-Allyl-5-methoxy-4,8,11,11-trimethyl-4-trimethylsilanyl-bicyclo[5.3.1]undeca-3,7-dien-2-one (9e)

65% from **8e**. IR (neat) (cm^{-1}) ν: 3074–2819, 1667, 1464, 1245, 1128–1095, 841. ^{1}H NMR (C_6D_6, 300 MHz) δ: 0.36 (s, 9H), 0.92 (s, 3H), 1.22 (s, 3H), 1.34 (s, br, 1H), 1.47 (s, 3H), 1.63–1.76 (m, 2H), 2.16–2.22 (m, 1H), 2.32 (t, *J* = 11.8 Hz, 1H), 2.43 (d, *J* = 5.9 Hz, 1H), 2.56–2.65 (m, 2H), 3.06 (s, 3H), 3.25 (dd, *J* = 16.1, 6.0 Hz, 1H), 4.15 (dd, *J* = 11.4, 5.7 Hz, 1H), 5.00 (ddd, *J* = 10.1, 3.2, 1.6 Hz, 1H), 5.09 (ddd, *J* = 17.1, 3.4, 1.7 Hz, 1H), 5.89 (dddd, *J* = 17.0, 10.1, 6.9, 6.9 Hz, 1H). ^{13}C NMR (C_6D_6, 75 MHz) δ: 3.4, 19.1, 22.4, 24.9, 28.7, 28.9, 35.8, 37.6, 38.4, 57.5, 63.0, 86.1, 116.4, 133.2, 133.4, 135.5, 136.2, 152.7, 213.8. HR-MS (EI) *m*/*z* calcd. for $C_{21}H_{34}O_2Si$ ($[M]^+$): 346.2328; found: 346.2339.

3,4-Diallyl-5-methoxy-8,11,11-trimethyl-bicyclo[5.3.1]-undeca-3,7-dien-2-one (9f)

68% from **8f**. IR (neat) (cm^{-1}) ν: 3076, 2934–2827, 1672, 1637, 1448, 1098, 911. ^{1}H NMR (C_6D_6, 300 MHz) δ: 0.89 (s, 3H), 1.21 (s, 3H), 1.34 (s, 3H), 1.67–1.75 (m, 2H), 1.80 (s, br, 1H), 2.13–2.20 (m, 1H), 2.35 (t, *J* = 11.8 Hz, 1H), 2.44 (d, *J* = 6.4 Hz, 1H), 2.59 (d, *J* = 6.8 Hz, 1H), 2.63 (d, *J* = 6.7 Hz, 1H), 2.70 (d, *J* = 6.0 Hz, 1H), 3.05–3.07 (m, 2H), 3.11 (s, 3H), 4.08 (dd, *J* = 11.0, 6.1 Hz, 1H), 4.97 (d, *J* = 10.5 Hz, 1H), 4.99–5.03 (d, br, 2H), 5.14 (d, *J* = 17.3 Hz, 1H), 5.81–5.98 (m, 2H). ^{13}C NMR (C_6D_6, 75 MHz) δ: 18.8, 21.6, 25.0, 28.6, 28.6, 31.7, 35.9, 36.3, 37.9, 58.6, 63.0, 82.2, 115.1, 116.4, 131.8, 132.4, 134.0, 135.7, 137.1, 141.0, 214.5. HR-MS (EI) *m*/z calcd. for $C_{21}H_{30}O_2$ ($[M]^+$): 314.2246; found: 314.2255.

5-Methoxy-4,8,11,11-tetramethyl-3-propenyl-bicyclo[5.3.1]undeca-3,7-dien-2-one (19)

Potassium *tert*-butoxide (0.042 g, 0.37 mmol) was added to a solution of **13** (0.081 g, 0.24 mmol) in DMF (10 mL) at 21 °C, and the solution was subsequently warmed to 40 °C. After stirring for 3 h, the suspension was filtered, neutralized, and extracted with ether (2 × 30 mL). The combined organic extracts were washed with brine (2 × 30 mL), dried ($MgSO_4$), filtered, and concentrated under reduced pressure. Purification by flash chromatography (silica gel, ether – petroleum) provided the title compound as a white solid (0.041 g, 51%). IR (neat) (cm^{-1}) ν: 3025–2819, 1663, 1456–1438, 1101, 961. ^{1}H NMR (C_6D_6, 300 MHz) δ: 0.94 (s, 3H), 1.29 (s, 3H), 1.40 (s, 3H), 1.51 (d, *J* = 6.5 Hz, 3H), 1.52 (s, 3H), 1.70 (s, 3H), 1.66–1.80 (m, 1H), 1.81–1.97 (m, 2H), 2.17 (t, br, 1H), 2.53–2.57 (m, 2H), 2.62 (dd, br, 1H), 3.04 (s, 3H), 4.15 (dd, *J* = 10.9, 6.6 Hz, 1H), 5.51 (dd, *J* = 15.8, 6.7 Hz, 1H), 6.24 (dd, *J* = 15.8, 1.7 Hz, 1H). ^{13}C NMR (C_6D_6, 75 MHz) δ: 12.2, 18.7, 19.9, 21.7, 25.2, 28.2, 29.2, 35.6, 38.0, 57.7, 63.3, 82.4, 126.7, 128.4, 131.8, 132.0, 134.5, 141.2, 212.8. HR-MS (EI) *m*/*z* calcd. for $C_{19}H_{28}O_2$ ($[M]^+$): 288.2089; found: 288.2076.

5-Methoxy-8,11,11-trimethyl-4-methylene-3-propenyl-bicyclo[5.3.1]undec-7-en-2-one (20)

Potassium hydride (0.240 g, 2.10 mmol, 35% in mineral

© 2004 NRC Canada

oil) was washed with pentane (3 × 1 mL) and suspended in THF (2 mL). The resultant mixture was treated with iodine (0.053 g, 0.21 mmol) in THF (0.5 mL). After 15 min, 18-crown-6 (0.554 g, 2.10 mmol) and alcohol **13** (0.120 g, 0.420 mmol) in THF (1 mL) were sequentially added, and the resultant mixture was stirred for 1 h at 21 °C. The reaction was then cooled to –78 °C and quenched with ethanol (2 mL). A saturated aqueous solution of NH_4Cl (10 mL) and ether (10 mL) were added; the layers were separated, and the aqueous layer was extracted with ether (2 × 30 mL). The combined organic extracts were washed with brine (2 × 30 mL), dried ($MgSO_4$), filtered, and concentrated under reduced pressure. Purification by flash chromatography (silica gel, petroleum ether – ether) provided the title compound as a colorless oil (0.083 g, 69%). IR (neat) (cm^{-1}) ν: 2950, 1705, 1640. ^1H NMR (C_6D_6, 300 MHz) δ: 0.95 (s, 3H), 1.11 (s, 3H), 1.52 (dd, *J* = 6.5, 1.6 Hz, 3H), 1.54–1.68 (m, 1H), 1.70–1.82 (m, 1H), 1.91 (dd, *J* = 9.3, 1.6 Hz, 1H), 1.97 (s, 3H), 2.35 (dd, *J* = 14.5, 5.2 Hz, 2H), 2.66 (dd, *J* = 9.8, 1.7 Hz, 1H), 2.91 (s, br, 1H), 2.95 (s, 3H), 3.50 (dd, *J* = 4.9, 1.6 Hz, 1H), 4.37 (d, *J* = 9.8 Hz, 1H), 4.88 (s, 1H), 5.27 (dddd, *J* = 14.5, 7.0, 7.0, 7.0 Hz, 1H), 5.47 (s 1H), 6.17 (ddd, *J* = 15.1, 9.9, 1.7 Hz, 1H). ^{13}C NMR (C_6D_6, 75 MHz) δ: 17.7, 19.2, 23.4, 28.9, 29.1, 29.3, 33.9, 37.2, 50.5, 56.0, 63.1, 87.3, 118.6, 124.2, 131.7, 133.6, 134.3, 148.9, 210.4. HR-MS (EI) *m/z* calcd. for $C_{19}H_{28}O_2$ ($[M]^+$): 288.2089; found: 288.2090.

Carbocyclic Cope rearrangements

A solution of trienone **9** in toluene ([trieneone] = 0.05 mol L^{-1}) was heated in a sealed tube at an external temperature of 110 °C for 3 h. Following removal of the solvent under reduced pressure, the residue was purified by flash chromatography (silica gel, ether – petroleum ether).

3-(2-Methoxy-1-methyl-vinyl)-4,6,6-trimethyl-5-methylene-3-vinyl-bicyclo[2.2.2]octan-2-one (15a)

71% from **9a**. IR (neat) (cm^{-1}) ν: 2959, 2930, 17016, 1660, 1461, 1382, 1229, 1131, 764, 750, 621. ^1H NMR (C_6D_6, 500 MHz) δ: 0.99 (s, 3H), 1.00 (s, 3H), 1.15 (s, 3H), 1.55–1.71 (m, 4H), 1.84 (d, *J* = 1.3 Hz, 3H), 2.03 (d, *J* = 2.2 Hz, 1H), 3.17 (s, 3H), 4.80 (s, 1H), 4.85 (s, 1H), 5.05 (dd, *J* = 10.8, 1.3 Hz, 1H), 5.35 (dd, *J* = 17.5, 1.3 Hz, 1H), 5.87 (dd, *J* = 17.5, 10.8 Hz, 1H), 5.94 (m, 1H). ^{13}C NMR (C_6D_6, 125 MHz) δ: 13.9, 18.2, 19.1, 29.8, 30.6, 31.0, 38.3, 45.4, 56.3, 58.9, 62.4, 106.9, 114.2, 116.7, 137.0, 148.9, 161.6, 212.1. HR-MS (EI) *m/z* calcd. for $C_{18}H_{26}O_2$ ($[M]^+$): 274.1934; found: 274.1945. Anal calcd. for $C_{18}H_{26}O_2$ (%): C 78.79, H 9.55; found: C 78.75, H 9.47.

3-(2-Methoxy-1-trimethylsilanyl-vinyl)-4,6,6-trimethyl-5-methylene-3-vinyl-bicyclo[2.2.2]octan-2-one (15b)

78% from **9b**. IR (neat) (cm^{-1}) ν: 2955, 2891, 1725. ^1H NMR (C_6D_6, 500 MHz) δ: 0.43 (s, 9H), 0.99 (s, 3H), 1.03 (s, 3H), 1.10 (s, 3H), 1.16–1.22 (m, 1H), 1.53–1.60 (m, 3H), 1.98 (s, 1H), 3.07 (s, 3H), 4.79 (s, 1H), 4.83 (s, 1H), 5.09 (d, *J* = 10.7 Hz, 1H), 5.39 (d, *J* = 17.3 Hz, 1H), 5.95 (dd, *J* = 17.3, 10.7 Hz, 1H), 6.45 (s, 1H). ^{13}C NMR (C_6D_6, 125 MHz) δ: 2.9, 18.2, 19.6, 29.8, 30.3, 30.4, 37.8, 46.5, 56.4, 58.8, 61.8, 106.6, 115.8, 118.2, 139.2, 159.4, 161.0, 213.8. HR-MS (EI) *m/z* calcd. for $C_{20}H_{32}O_2Si$ ($[M]^+$): 332.2172; found: 332.2179.

3-(2-Methoxy-vinyl)-4,6,6-trimethyl-5-methylene-3-vinyl-bicyclo[2.2.2]octan-2-one (15c)

92% from **9c**. IR (neat) (cm^{-1}) ν: 2966, 2830, 1722, 1642. ^1H NMR (C_6D_6, 500 MHz) δ: 0.89 (s, 3H), 0.96 (s, 3H), 1.03 (s, 3H), 1.17–1.22 (m, 1H), 1.51–1.70 (m, 3H), 2.00 (m, 1H), 3.11 (s, 3H), 4.68 (d, *J* = 12.7 Hz, 1H), 4.85 (s, 1H), 4.87 (s, 1H), 5.09 (dd, *J* = 10.7, 1.3 Hz, 1H), 5.32 (dd, *J* = 17.3, 1.3 Hz, 1H), 5.64 (dd, *J* = 17.5, 10.7 Hz, 1H), 6.62 (d, *J* = 12.7 Hz, 1H). ^{13}C NMR (C_6D_6, 125 MHz) δ: 17.7, 18.5, 28.3, 29.4, 30.6, 37.3, 45.2, 55.8, 55.9, 58.2, 102.5, 107.3, 117.1, 136.8, 153.1, 160.4, 212.3. HR-MS (EI) *m/z* calcd. for $C_{17}H_{24}O_2$ ($[M]^+$): 260.1776; found: 260.1771.

3-Allyl-3-(2-methoxy-1-methyl-vinyl)-4,6,6-trimethyl-5-methylene-bicyclo[2.2.2]octan-2one (15d)

79% from **9d**. IR (neat) (cm^{-1}) ν: 2923, 1718, 1637. ^1H NMR ($CDCl_3$, 500 MHz) δ: 0.93 (s, 3H), 0.96 (s, 3H), 1.12 (s, 3H), 1.17–1.23 (m, 1H), 1.48 (d, *J* = 9.3 Hz, 2H), 1.64 (dd, *J* = 12.2, 3.3 Hz, 1H), 1.78 (s, 3H), 1.99 (s, 1H), 2.35 (dd, *J* = 15.5, 5.4 Hz, 1H), 2.51 (dd, *J* = 15.6, 7.3 Hz, 1H), 3.16 (s, 3H), 4.79 (d, *J* = 6.5 Hz, 2H), 4.97 (d, *J* = 17.3 Hz, 1H), 5.04 (d, *J* = 10.1 Hz, 1H), 5.79 (s, 1H), 6.25–6.38 (m, 1H). ^{13}C NMR ($CDCl_3$, 125 MHz) δ: 13.7, 19.8, 20.3, 29.5, 29.7, 30.9, 36.6, 37.3, 46.6, 56.6, 58.7, 59.0, 106.8, 110.7, 115.8, 136.7, 149.9, 160.3, 214.5. HR-MS (EI) *m/z* calcd. for $C_{19}H_{28}O_2$ ($[M]^+$): 288.2089; found: 288.2089.

2,3-Diallyl-5-methoxy-4,8,11,11-tetramethyl-bicyclo[5.3.1]undeca-3,7-dien-2-ol (13)

Allylmagnesium chloride (1.3 mL, 2.6 mmol, 1.6 mol L^{-1} in THF) was added to a solution of ketone **9d** (0.376 g, 1.3 mmol) in ether (20 mL) at –78 °C. The solution was stirred for 1 h at –78 °C and for 30 min at 0 °C. A saturated aqueous solution of NH_4Cl (30 mL) was then added; the layers were separated, and the aqueous layer was extracted with ether (2 × 30 mL). The combined organic extracts were washed with brine (2 × 30 mL), dried ($MgSO_4$), filtered, and concentrated under reduced pressure. Purification by flash chromatography (silica gel, ether – petroleum ether) provided the title compound as a viscous oil (0.253 g, 59%). IR (neat) (cm^{-1}) ν: 3458, 3052–2814, 1640, 1463, 1093, 911. ^1H NMR (C_6D_6, 300 MHz) δ: 0.99 (s, 1H), 1.04 (s, 3H), 1.27–1.35 (m, 1H), 1.43 (s, 3H), 1.64 (s, 3H), 1.67–1.69 (m, 2H), 1.76 (s, 3H), 1.79–1.84 (m, 1H), 2.18 (dd, br, 1H), 2.33 (dd, *J* = 14.0, 6.2 Hz, 1H), 2.51 (dd, *J* = 17.3, 5.7 Hz, 1H), 2.58–2.70 (m, 2H), 2.74–2.90 (m, 2H), 3.30 (s, 3H), 4.99 (dd, *J* = 17.3 Hz, 2H), 5.05 (dd, *J* = 9.6 Hz, 2H), 5.73 (dddd, *J* = 16.7, 10.4, 6.1, 4.8 Hz, 1H), 5.87 (dddd, *J* = 17.2, 10.2, 7.6, 5.8 Hz, 1H), 5.93 (dd, *J* = 11.0, 6.3 Hz, 1H). ^{13}C NMR (C_6D_6, 75 MHz) δ: 15.0, 20.8, 21.3, 28.3, 29.3, 32.8, 36.5, 38.0, 39.9, 45.8, 52.3, 57.3, 81.1, 82.4, 115.1, 119.1, 131.2, 133.2, 135.6, 135.8, 137.7, 138.5. HR-MS (EI) *m/z* calcd. for $C_{22}H_{34}O_2$ ($[M]^+$): 330.2559; found: 330.2559.

Attempted oxy-Cope rearrangement

A solution of alcohol **13** (0.119 g, 0.360 mmol) and DBU (0.110 g, 0.720 mmol) in dry, deoxygenated toluene (10 mL) was heated in a quartz tube for 1 h at 220 °C. The solution

© 2004 NRC Canada

was then cooled to 21 °C, transferred to a round-bottom flask, and concentrated under reduced pressure. The residue was purified by flash chromatography (silica gel, ether – petroleum ether) to afford the compounds **21** (7%), **22** (16%), and **23** (19%) as a mixture of white solids.

2,3-Diallyl-3-(2-methoxy-1-methyl-vinyl)-4,6,6-trimethyl-5-methylene-bicyclo[2.2.2]octan-2-ol (21)

7% from **13**. IR (neat) (cm^{-1}) ν: 3559, 3076–2827, 1637, 1467, 1098, 998, 883. ^{1}H NMR ($CDCl_3$, 500 MHz) δ: 1.18 (s, 3H), 1.26 (s, br, 2H), 1.27 (s, 3H), 1.37 (s, 3H), 1.68 (s, 3H), 1.69–1.72 (m, 2H), 1.78–1.83 (m, 1H), 2.02 (s, 1H), 2.06–2.12 (m, 1H), 2.38 (ddd, *J* = 14.5, 7.4, 7.4 Hz, 1H), 2.41 (dd, *J* = 14.5, 8.1 Hz, 1H), 2.66 (dd, *J* = 14.6, 6.5 Hz, 1H), 3.19 (s, 3H), 4.70 (s, 1H), 4.80 (s, 1H), 5.01 (dd, *J* = 10.2, 1.1 Hz, 1H), 5.08 (dd, *J* = 17.1, 1.5 Hz, 1H), 5.17 (dd, *J* = 15.7, 5.6 Hz, 1H), 5.20 (d, *J* = 9.6 Hz, 1H), 5.22 (dd, *J* = 8.4, 5.5 Hz, 1H), 5.81 (dddd, *J* = 18.0, 10.3, 7.0, 7.0 Hz, 1H), 5.96 (dddd, *J* = 18.4, 8.8, 8.8, 6.5 Hz, 1H). ^{13}C NMR ($CDCl_3$, 125 MHz) δ: 13.7, 19.5, 25.6, 30.4, 33.6, 36.6, 38.6, 38.6, 44.1, 47.7, 49.5, 55.7, 78.1, 78.8, 101.5, 116.0, 119.4, 133.6, 134.5, 136.0, 144.6, 163.3. Anal calcd. for $C_{22}H_{34}O_2$ (%): C 79.95, H 10.37; found: C 76.62, H 9.57.

1-(2-Allyl-3-methoxymethyl-3,4,6,6-tetramethyl-5-methylene-bicyclo[2.2.2]oct-2-yl)-but-2-en-1-one (22)

16% from **13**. IR (neat) (cm^{-1}) ν: 3072–2813, 1690, 1660.7, 1625, 1442, 1095, 906. ^{1}H NMR ($CDCl_3$, 500 MHz) δ: 0.93 (s, 3H), 1.04 (dd, *J* = 13.9, 4.2 Hz, 1H), 1.14 (s, 3H), 1.29 (s, 3H), 1.48 (dd, *J* = 13.9, 3.6 Hz, 1H), 1.69 (s, 3H), 1.86 (dd, *J* = 6.9, 1.6 Hz, 3H), 2.07 (dd, *J* = 12.4, 3.4 Hz, 1H), 2.27 (dd, *J* = 14.5, 3.4 Hz, 1H), 2.57 (dd, *J* = 12.3, 3.7 Hz, 1H), 3.03 (dd, *J* = 15.9, 7.2 Hz, 1H), 3.12–3.16 (m, 1H), 3.24 (s, 3H), 3.90 (d, *J* = 10.7 Hz, 1H), 4.16 (d, *J* = 10.7 Hz, 1H), 4.99 (dd, *J* = 10.1, 1.3 Hz, 1H), 5.03 (dd, *J* = 17.2, 1.6 Hz, 1H), 5.09 (d, *J* = 6.5 Hz, 2H), 5.76 (dddd, *J* = 17.2, 10.1, 7.1, 5.4 Hz, 1H), 6.14 (dd, *J* = 15.6, 3.4, 1.6 Hz, 1H), 6.80 (ddd, *J* = 15.5, 13.8, 6.8 Hz, 1H). ^{13}C NMR ($CDCl_3$, 125 MHz) δ: 18.2, 18.8, 23.1, 23.9, 30.1, 32.0, 35.1, 40.3, 41.1, 46.2, 58.1, 58.9, 72.7, 108.4, 115.1, 130.9, 133.3, 137.9, 139.1, 141.9, 162.7, 202.3. HR-MS (EI) *m*/*z* calcd. for $C_{22}H_{34}O_2$ ($[M]^+$): 330.2559; found: 330.2555.

2,6-Diallyl-5,7,9,9-tetramethyl-8-methylene-3-oxa-tricyclo[5.2.2.0^{2,6}]undec-4-ene (23)

19% from **13**. IR (neat) (cm^{-1}) ν: 3068, 3032–2867, 1671, 1631, 1154, 1120, 1002, 921, 888, 859. ^{1}H NMR ($CDCl_3$, 500 MHz) δ: 1.07 (s, 3H), 1.10 (s, 3H), 1.28 (s, 3H), 1.21–1.32 (m, 1H), 1.42–1.47 (m, 1H), 1.50 (d, *J* = 1.5 Hz, 3H), 1.56–1.65 (m, 2H), 1.70–1.81 (m, 1H), 2.44 (dd, *J* = 16.3, 8.1 Hz, 2H), 2.55–2.60 (m, 1H), 2.62–2.64 (m, 1H), 4.78 (d, *J* = 8.3 Hz, 2H), 4.98 (d, *J* = 9.8 Hz, 1H), 5.00 (d, *J* = 15.9 Hz, 1H), 5.02 (d, *J* = 17.9 Hz, 1H), 5.08 (d, *J* = 8.8 Hz, 1H), 5.90 (d, *J* = 1.3 Hz, 1H), 5.80–5.94 (m, 2H). ^{13}C NMR ($CDCl_3$, 125 MHz) δ: 11.2, 19.1, 21.6, 28.8, 31.7, 32.7, 35.2, 37.4, 42.5, 43.7, 44.3, 57.6, 94.2, 103.8, 114.1, 115.3, 117.1, 135.9, 138.6, 140.3, 163.6. HR-MS (EI) *m*/*z* calcd. for $C_{21}H_{30}O$ ($[M]^+$): 298.2297; found: 298.2305.

9-Methoxy-12,15,15-trimethyl-tricyclo[9.3.1.0^{3,8}]pentadeca-3(8),5,11-trien-2-one (24)

Grubbs' catalyst **30** ((4,5-dihydroIMES)(PCy_3)Cl_2Ru=CHPh, 5 mol%) dissolved in dichloromethane (3 mL) was added to a solution of **9f** in dichloromethane ([**30**] = 0.02 mol L^{-1}). The solution was subsequently stirred at 21 °C for 2 h, at which point the solvent was removed under reduced pressure. The residue was purified by flash chromatography to afford the title compound as a white solid (93%), mp 90 to 91 °C. IR (neat) (cm^{-1}) ν: 3031–2822, 1665, 1465, 1103, 1072, 949. ^{1}H NMR (C_6D_6, 300 MHz) δ: 0.89 (s, 3H), 1.21(s, 3H), 1.42 (s, 3H), 1.54 (dd, *J* = 10.4, 3.2 Hz, 1H), 1.63–1.78 (m, 1H), 1.82 (dd, *J* = 10.3, 3.8 Hz, 1H), 2.14 (t, br, 1H), 2.42–2.50 (m, 3H), 2.63 (ddd, *J* = 12.4, 6.3, 2.1 Hz, 1H), 2.71–2.85 (m, 2H), 2.90 (dd, br, 1H), 3.03 (s, 3H), 4.07 (dd, *J* = 10.9, 6.4 Hz, 1H), 5.47 (dd, *J* = 9.8, 2.2 Hz, 1H), 5.58 (dd, *J* = 10.1, 2.9 Hz, 1H). ^{13}C NMR (C_6D_6, 75 MHz) δ: 20.3, 21.3, 24.9, 25.3, 28.1, 28.8, 30.6, 35.5, 37.6, 57.9, 63.3, 82.4, 123.4, 124.4, 127.5, 131.9, 134.6, 136.5, 214.5. HR-MS (EI) *m*/*z* calcd. for $C_{19}H_{26}O_2$ ($[M]^+$): 286.1933; found: 286.1906.

Conclusion

We have demonstrated the utility of bis-allylpropargyl alcohol in our magnesium-mediated carbometallation protocol for the synthesis of the AB taxane ring by a *cis*-alkene tether controlled intramolecular Diels–Alder reaction, followed by closing metathesis (RCM), to generate a substituted tricyclo[9.3.1.0^{3,8}]pentadecenone (ABC taxane) ring system. We have discovered the first example of an enone accelerated Cope rearrangement. This isomerization of conjugated bicyclo[5.3.1]undecadienes provides a rapid entry into bicyclo[2.2.2]octanone skeletons that complements the more traditional [4 + 2] cyclizations from cyclohexadienes. We are examining the generality of this conjugative effect. In total, the procedures described above provide direct access to a number of useful unsaturated compounds and bicyclic ring systems, which may be employed for a variety of synthetic objectives.

Acknowledgements

We are grateful to the Natural Sciences and Engineering Research Council of Canada (NSERC) and the Canadian Breast Cancer Research Initiative (NCI, Canada) for financial support of this research. N. P. Villalva-Servín thanks Consejo Nacional de Ciencia y Tecnología (CONACYT) Government of Mexico for a Graduate Scholarship.

References

1. P. Forgione, P.D. Wilson, G.P.A. Yap, and A.G. Fallis. Synthesis, 921 (2000).
2. (*a*) K.J. Shea and J.W. Gilman. Tetrahedron Lett. **25**, 2451 (1984); (*b*) K.J. Shea, J.W. Gilman, C.D. Haffner, and T.K. Dougherty. J. Am. Chem. Soc. **108**, 4953 (1986); (*c*) R.W. Jackson and K.J. Shea. Tetrahedron Lett. **35**, 1317 (1994).
3. (*a*) Y.-F. Lu and A.G. Fallis. Tetrahedron Lett. **34**, 3367 (1993); (*b*) Y.-F. Lu and A.G. Fallis. Can. J. Chem. **73**, 2239 (1995).

© 2004 NRC Canada

4. (*a*) R.K. Hill. *In* Comprehensive organic synthesis. Vol 5. *Edited by* B.M. Trost and I. Flemming. Pergamon Press, Oxford, 1991. Chap 7.1; (*b*) For oxy-Cope examples see L.A. Paquette. Tetrahedron, **53**, 13 971 (1997).
5. For oxy-Cope AB ring syntheses, see (*a*) F.S. Martin, J.B. White, and R. Wagner. J. Org. Chem. **47**, 3190 (1982); (*b*) M.G. Banwell, V.S. Bridges, J.R. Dupuche, S. Richards, and J.M. Walter. J. Org. Chem. **59**, 6338 (1994). For a related unsuccessful AB ring synthesis approach, see (*c*) P.A. Zucker and J.A. Lupia. Synlett, 729 (1990). For a different oxy-Cope route to Taxusin, see (*d*) L.A. Paquette and M. Zhao. J. Am. Chem. Soc. **120**, 5203 (1998).
6. (*a*) Y.-F. Lu, C.W. Harwig, and A.G. Fallis. J. Org. Chem. **58**, 4202 (1993); (*b*) Y.-F. Lu, C.W. Harwig, and A.G. Fallis. Can. J. Chem. **73**, 2253 (1995).
7. K.C. Nicolaou, C.F. Claiborne, P.G. Nantermet, E.A. Couladouros, and E.J. Sorensen. J. Am. Chem. Soc. **116**, 1591 (1994).
8. R. Andrade, W.A. Ayer, and L.S. Tifonov. Can. J. Chem. **74**, 371 (1996).
9. (*a*) G. Bérubé and A.G. Fallis. Tetrahedron Lett. **30**, 4045 (1989); (*b*) G. Bérubé and A.G. Fallis. Can. J. Chem. **69**, 77 (1991).
10. M. Wenz, D. Groβbach, M. Beitzel, and S. Blechert. Synthesis, 607 (1999)
11. D. Bourgeois, A. Pancrazi, S. Nolan, and J. Prunet. Synthesis, 869 (2000).
12. M. Scholl, Ch.S. Ding, W. Lee, and R.H. Grubbs. Org. Lett. **6**, 953 (1999).
13. A. Laurent, N.P. Villalva-Servín, P. Forgione, P.D. Wilson, D.V. Smil, and A.G. Fallis. Can. J. Chem. **82**, 215 (2004).
14. N. Bumagin, B. Ponomarev, and P. Beletskaya. Izv. Akad. Nauk SSSR Ser. Khim. **7**, 1565 (1987).

© 2004 NRC Canada

Photogeneration of 1,5-naphthoquinone methides via excited-state (formal) intramolecular proton transfer (ESIPT) and photodehydration of 1-naphthol derivatives in aqueous solution[1]

Matthew Lukeman, Duane Veale, Peter Wan, V. Ranjit N. Munasinghe, and John E.T. Corrie

Abstract: The photochemistry of naphthols **1**, **2**, **4**, **5** and **9**, and phenol **10** has been studied in aqueous solution with the primary aim of exploring the viability of such compounds for naphthoquinone and quinone methide photogeneration, along the lines already demonstrated by our group for phenol derivatives. 1-Naphthol (**1**) is known to be substantially more acidic than 2-naphthol (**2**) in the singlet excited state (pK_a^* = 0.4 and 2.8, respectively) and it was expected that this difference in excited-state acidity might be manifested in higher reactivity of 1-naphthol derivatives for photochemical reactions requiring excited-state naphtholate ions, such as quinone methide formation. Our results show that three types of naphthoquinone methides (**26a**, **26b**, and **27**) are readily photogenerated in aqueous solution by irradiation of 1-naphthols. Photolysis of the parent 1-naphthol (**1**) in neutral aqueous solution gave 1,5-naphthoquinone methide **26a** as well as the non-Kekulé 1,8-naphthoquinone methide **26b**, both via the process of excited-state (formal) intramolecular proton transfer (ESIPT), based on the observation of deuterium exchange at the 5- and 8-positions, respectively, on photolysis in D_2O–CH_3CN. A transient assignable to the 1,5-naphthoquinone methide **26a** was observed in laser flash photolysis experiments. The isomeric 2-naphthol (**2**) was unreactive under similar conditions. The more conjugated 1,5-naphthoquinone methide **27** was formed efficiently via photodehydroxylation of **4**; isomeric **5** was unreactive. The efficient photosolvolytic reaction observed for **4** opens the way to design related naphthol systems for application as photoreleasable protecting groups by virtue of the long-wavelength absorption of the naphthalene chromophore.

Key words: photosolvolysis, excited-state intramolecular proton transfer, quinone methide, photorelease, photoprotonation.

Résumé : Opérant en solution aqueuse, on a étudié la photochimie des naphtols **1**, **2**, **4**, **5** et **9** et du phénol **10** afin de déterminer la viabilité de tels composés pour la photogénération de méthides de naphtoquinone et de quinone suivant les voies déjà mises de l'avant par notre groupe pour les dérivés du phénol. Il est bien connu que, dans l'état excité singulet, le 1-naphtol (**1**) est beaucoup plus acide que le 2-naphtol (**2**) (pK_a^* de 0,4 et 2,8, respectivement) et on s'attendait à ce que cette différence d'acidité dans l'état excité pourrait se manifester par une plus grande réactivité des dérivés du 1-naphtol pour les réactions photochimiques impliquant des ions naphtanolates dans l'état excité, tel que la formation de méthide. Nos résultats démontrent que l'irradiation des 1-naphtols en solutions aqueuses conduit facilement à la formation de trois types de méthides de naphtoquinones (**26a**, **26b** et **27**). L'irradiation du 1-naphtol fondamental (**1**), en solutions aqueuses neutres, conduit au méthide de 1,5-naphtoquinone (**26a**) ainsi qu'au méthide de 1,8-naphtoquinone (**26b**), une structure qui ne répond pas aux normes de Kekulé; sur la base d'expériences de photolyse dans un mélange de D_2O–CH_3CN qui conduisent à un échange de deutérium dans les positions respectivement 5 et 8, ces deux méthides se produisent par un processus de transfert intramoléculaire de proton dans l'état excité (formel). Lors d'expériences de photolyse éclair au laser, on a observé une entité transitoire attribuable au méthide de la 1,5-naphtoquinone. Dans des conditions semblables, le 2-naphtol (**2**) isomère n'est pas réactif. Le méthide de la 1,5-naphtoquinone (**27**) qui est plus conjuguée se forme facilement par photodéhydroxylation du composé **4**; son isomère **5** n'est pas réactif. La réaction efficace de photosolvolyse du composé **4** ouvre la voie au développement de systèmes de naphtols qui pourraient être utilisés comme groupes protecteurs qui pourraient être éliminés photochimiquement en

Received 23 June 2003. Published on the NRC Research Press Web site at http://canjchem.nrc.ca on 30 January 2004.

M. Lukeman, D. Veale, and P. Wan.[2] Department of Chemistry, Box 3065, University of Victoria, Victoria, BC V8W 3V6, Canada.
V.R.N. Munasinghe and J.E.T. Corrie.[3] National Institute for Medical Research, The Ridgeway, Mill Hill, London, NW7 1AA, U.K.

[1]This article is part of a Special Issue dedicated to Professor Ed Piers.
[2]Corresponding author (e-mail: pwan@uvic.ca).
[3]Corresponding author (e-mail: jcorrie@nimr.mrc.ac.uk).

 doi: 10.1139/V03-184 © 2004 NRC Canada

vertu de la grande longueur d'onde de l'absorption du chromophore du naphtalène.

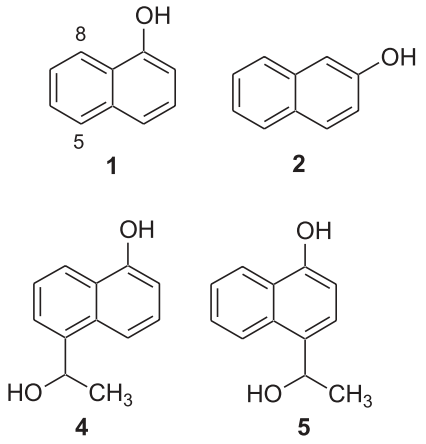
Mots clés : photosolvolyse, transfert intramoléculaire de proton dans l'état excité, méthide de quinone, photoélimination, photoprotonation.

[Traduit par la Rédaction]

Introduction

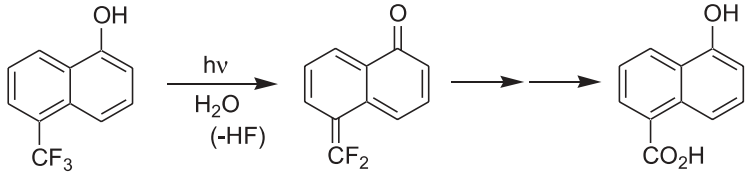
Quinone methides are reactive intermediates of general interest in organic chemistry (1–3). Recent studies from our laboratory (1, 2, 4, 5) have demonstrated that suitably designed simple phenol derivatives give rise to quinone methide-type intermediates efficiently on photolysis in aqueous solution. The substrates that we have investigated so far all possess a phenol and a benzylic-type alcohol or styryl moiety. The enhanced acidity of the phenol moiety in S_1 in these systems is essential for reaction, as previously described (1, 2, 4, 5). We have not investigated simple naphthol derivatives extensively except in some biaryl systems containing a 2-naphthol chromophore, where the quinone methides photogenerated are of the biaryl type (6).

Some time ago, Seiler and Wirz (7) reported the photohydrolysis (to the corresponding carboxylic acids) of a variety of trifluoromethyl-substituted 1-and 2-naphthols (as well as several phenols) and invoked the initial formation of naphthoquinone and quinone methides in their photohydrolysis mechanism (e.g., eq. [1]). Webb et al. (8) have reported a detailed study of the excited-state proton transfer dynamics of 1-naphthol (**1**) and have shown that it is a much stronger acid (in S_1) than 2-naphthol (**2**) (pK_a* values of 0.4 and 2.8, respectively). Moreover, it was shown that the 5- and 8-positions of **1** are much more basic in S_1, as evidenced by deuterium incorporation at these positions when **1** was irradiated in *acidic* D_2O. The formation of two isomeric naphthoquinone methide intermediates was proposed to account for the photoexchange but whether such intermediates were formed via a water-mediated excited-state (formal) intramolecular proton transfer (ESIPT) (from the naphthol OH to the carbon 5- or 8-position) was not explicitly addressed. We have recently reported (9) the first explicit example of an ESIPT from a phenolic OH to an aromatic ring carbon (on the ring not containing the phenolic OH) in 2-phenylphenol (**3**) (eq. [2]). This result led us to investigate whether such a process could operate in the naphthols (**1** and **2**), since naphthols are formally made up of two benzene rings, one of them containing a phenol moiety. Also addressed is whether suitably designed 1-naphthol derivatives **4** and **5** will react in an analogous manner as reported by us (1) for the parent hydroxy-substituted benzyl alcohols with respect to naphthoquinone methide formation. Seiler and Wirz's earlier results (7) suggest that this would indeed be possible.

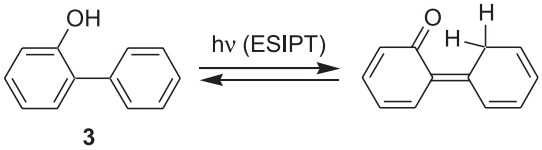


The photochemistry of phenols is also involved in the *p*-hydroxyphenacyl photodeprotection system reported by Givens and co-workers (10). An example designed to photorelease acetic acid from **6** is shown in eq. [3] (11). The essentials of the mechanism involve formation of a spiroketone intermediate **7** from photolysis of *p*-hydroxyphenacyl derivatives bearing good leaving groups, such as *p*-hydroxyphenacyl acetate **6**. Ring opening of **7** by water gives the observed product **8**. Release of the protected moiety (e.g., acetic acid from **6**) is believed to occur in the pri-

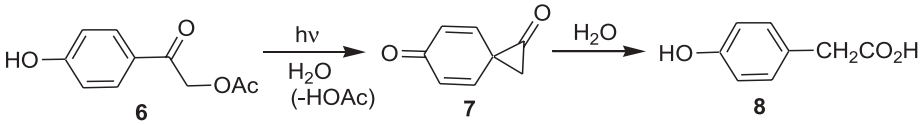
[1]



[2]

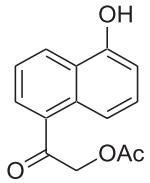


[3]

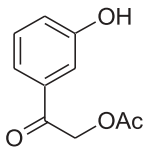


© 2004 NRC Canada

mary photochemical step. Although the question of triplet vs. singlet state reactivity (which might be dependent on the nature of the leaving group at the α-position) has been a topic of debate (10*c*, 11), the involvement of excited-state (singlet or triplet) deprotonation of the phenol moiety in the reaction sequence for formation of intermediate **7** seems likely. We felt that related substrates **9** and **10** might react similarly. The results of investigations of a variety of naphthols **1**,**2**,**4**, **5** and **9** (and phenol **10**) aimed at providing further insights to all of the above related photochemical reactions are reported herein.



9



10

Results and discussion

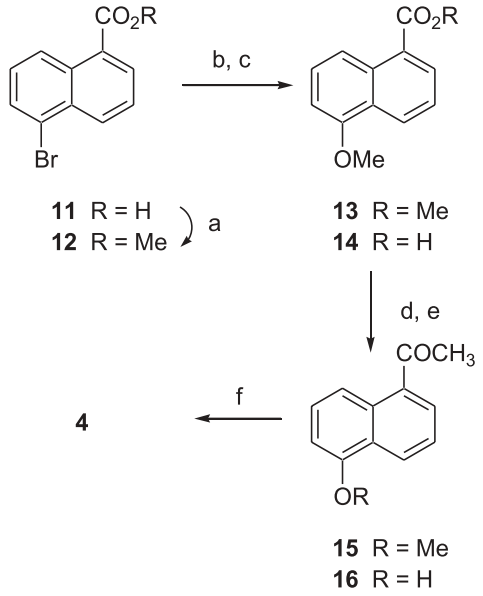
Materials

1- and 2-Naphthols (**1** and **2**) were purchased from Aldrich and were sublimed and recrystallized from hexanes prior to use. The hydroxyethylnaphthols **4** and **5** were synthesized as shown in Schemes 1 and 2. Although the corresponding hydroxyketones are both known compounds, the synthetic routes previously described were not particularly convenient or led to mixtures of regioisomers. The routes shown in the schemes were straightforward but, particularly for the 5-isomer, were only reached after some exploration of other published methods. For synthesis of the 5-isomer **4** (Scheme 1), the readily prepared 5-bromo-1-naphthoic acid **11** (12) was esterified and the 5-bromo group was displaced with methoxide in a copper(I)-catalyzed procedure (13). Further steps to the phenolic ketone **16** and its subsequent reduction readily gave the alcohol **4**. Note however that the work up procedure for the thiophenoxide-mediated demethylation of the methyl ether **15** (and of **17** in the route to the 4-hydroxy compound **5**), which used a literature procedure (14), was modified by addition of hydrogen peroxide to oxidize excess thiophenol, thereby minimizing the odour associated with the procedure. The route to the 4-isomer **5** (Scheme 2) requires no further comment, except to note that direct borohydride reduction of the phenolic ketone **18** gave only dark, uncharacterized material and it was found necessary to protect the phenol as its TBDMS ether **19** during this step. No attempts were made in this study at synthesizing derivatives of **1** with substituents at the 8-position, although these compounds would indeed be worthwhile to investigate in the future. The naphthacyl acetate **9** was prepared as shown in Scheme 3 and the 3-hydroxyphenacyl acetate **10** was made by a route similar to those for the corresponding 4-hydroxy esters previously described (11).

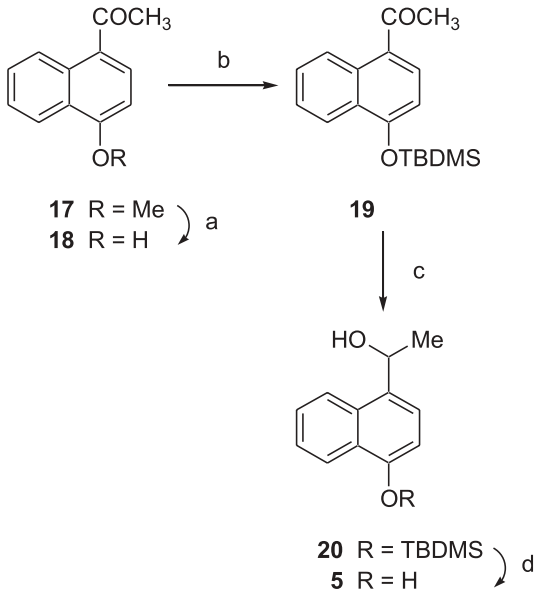
Deuterium exchange studies of 1 and 2

As noted in the *Introduction*, Webb et al. (8) have shown that 1-naphthol (**1**) is considerably more acidic than 2-naphthol (**2**) in S_1, due to the enhanced (localized) charge transfer character available for **1** but not for **2**, the latter

Scheme 1. Reagents: (*a*) MeOH, H_2SO_4, 74%; (*b*) NaOMe, CuBr, MeOH, 70%; (*c*) NaOH, MeOH–H_2O, 85%; (*d*) MeLi, THF–Et_2O, 78%; (*e*) PhSH, K_2CO_3, *N*-methylpyrrolidinone, 72%; (*f*) $NaBH_4$, EtOH, 55%.



Scheme 2. Reagents: (*a*) PhSH, K_2CO_3, *N*-methylpyrrolidinone, 59%; (*b*) TBDMS-Cl, imidazole, DMF, 80%; (*c*) $NaBH_4$, MeOH, 89%; (*d*) TBAF, THF, 88%.



compound having a more diffuse excited state electronic distribution. Moreover, charge transfer from the oxygen to the ring is localized at the 5- and 8-positions of **1**. To demonstrate the enhancement of basicity at these positions of **1**, they irradiated **1** in *acidic* D_2O–CH_3CN and showed that positions 5 and 8 were efficiently exchanged ($\Phi = 0.11$ in 99% D_2O, pD 3; Table 1) while similar irradiation of **2** resulted in no exchange. Photolysis in acidic solution raises the possibility that the exchange may be due to photoprotonation of **1** by hydronium ion, a process that is well known for 1-

© 2004 NRC Canada

Scheme 3. Reagents: (*a*) oxalyl chloride, DMF, CH_2Cl_2, 100%; (*b*) $TMSCHN_2$, CH_2Cl_2–THF–Et_3N, 74%; (*c*) aq. NH_3, THF–MeOH, 47%; (*d*) HCl, HOAc, 82%; (*e*) HOAc, DBU, toluene, 67%.

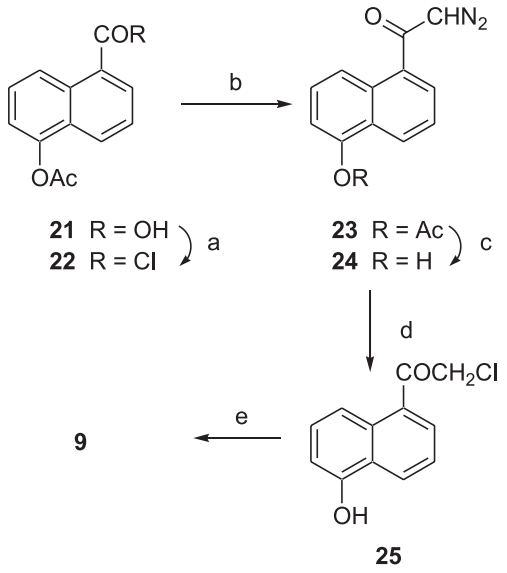


Table 1. Photophysical and photochemical parameters.

Compound	Φ_R	Φ_f[a]	τ[b] (ns)
1	0.11±0.05[c]	0.20 (0.174)	(10.6)
2	<0.001[c]	(0.27)	(13.3)
4	0.84[d]	0.17	5.4
5	<0.001[d]	0.23	5.9

[a]Fluorescence emission quantum yield in neat CH_3CN. Measured relative to the reported fluorescence quantum yield for 1-naphthol in cyclohexane (Φ_f = 0.174) (15) with correction to account for differences in the indices of refraction of the different solvents. Estimated error of ±10% of quoted value. Values in brackets are the fluorescence quantum yields in cyclohexane, from ref 15.

[b]Fluorescence lifetime in neat CH_3CN measured by single photon counting. Lifetimes measured in this way have an estimated error of ±0.2 ns. Values in brackets are the fluorescence lifetimes in cyclohexane from ref. 15.

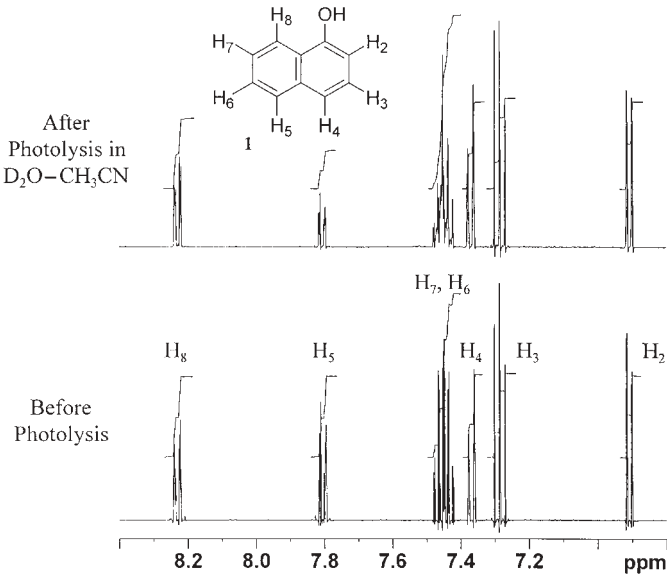
[c]Quantum yield of total deuterium exchange (of all ring positions) in 99% D_2O (pD 3) from ref. 8.

[d]Quantum yield of photomethanolysis in H_2O–CH_3OH (1:1). Estimated error ±10% of quoted value. Measured relative to the quantum yield for photomethanolysis of *o*-hydroxybenzhydrol in the same solvent (5).

methoxynaphthalene (16) and other aromatic compounds (17–19), but does not occur for 2-methoxynaphthalene (16). Therefore, we decided to study photochemical deuterium incorporation of **1** and **2** in aqueous solution, initially under neutral conditions and then over a wide pH range and as a function of water content. To our knowledge, this kind of study has not been previously reported for the naphthols. A similar study for **3** (eq. [2]) (9) resulted in the discovery of a new type of ESIPT (vide infra).

Irradiations of **1** and **2** were carried out in 1:1 D_2O–CH_3CN (~10^{-3} mol L^{-1}, pD 7, Rayonet photochemical reactor, 300 nm lamps, <30 min). Irradiation of **1** for 20 min resulted in efficient incorporation of deuterium at positions 5 (55%) and 8 (20%) to give **1-5D** and **1-8D**, respectively (eq. [4]). This was readily evident by examination of

Fig. 1. 500 MHz ^{1}H NMR spectra of **1** before (bottom), and after (top) 20 min irradiation at 300 nm in D_2O–CH_3CN (1:1), showing decreases in the integrated area of the peaks at 7.80 and 8.22 ppm assigned to ring protons at the 5- and 8-positions, respectively.



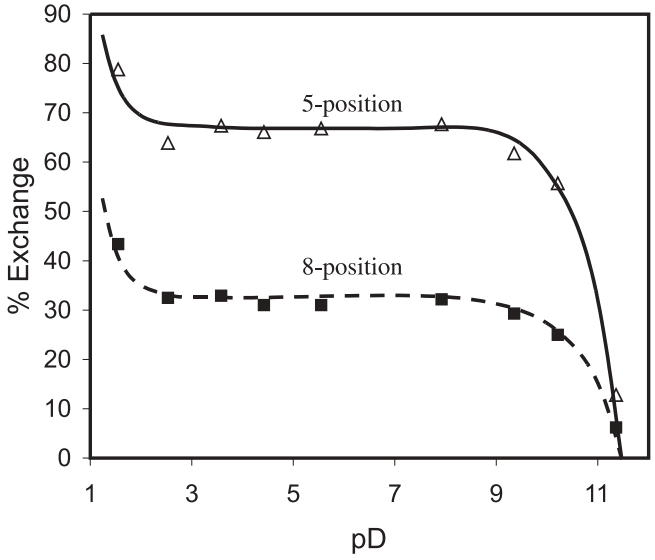
[4] **1** $\xrightarrow[D_2O-CH_3CN]{h\nu}$ **1-5D** + **1-8D**

500 MHz ^{1}H NMR spectra (Fig. 1); the areas of the peaks assigned to protons at the 5- and 8-positions (7.81 and 8.23 ppm, respectively) decreased smoothly with irradiation. The two overlapping triplets at 7.47 and 7.45 ppm assigned to the protons at the 6- and 7- ring positions exhibited changes consistent with diminished coupling to the adjacent protons at the 5- and 8-positions as they are replaced with deuterium. MS analysis of the photolyzed sample indicated an isotope distribution of 37% nondeuterated, 52% monodeuterated, and 11% dideuterated 1-naphthol, consistent with the overall deuterium incorporation measured by NMR. The observation of deuterium incorporation in neutral solution suggests that protonation by acid (D_3O^+) is not responsible for the observed reaction, and that the exchange might be due to an ESIPT process. Formation of **1-5D** and **1-8D** from an ESIPT to the 5- and 8-positions would necessarily proceed via quinone methides **26a-D** and **26b-D**, which have been previously proposed by Webb et al. (8). 2-Naphthol (**2**) did not undergo any observable exchange, even on prolonged irradiation, and the compound was completely recovered.

To better our understanding of the effect of acid on the deuterium incorporation reaction of **1**, photolyses were carried out in which the pD of the aqueous portion was varied over the pD range 1.5–11.4 (Fig. 2). While acid catalysis is observed at pD < 2.5, exchange efficiency was essentially constant from pD 2.5 through to pD 9. Since the hydronium ion concentration varies by many orders of magnitude over

© 2004 NRC Canada

Fig. 2. Plot of % deuterium exchange at the 5- (triangles) and 8- (squares) positions vs. pD (in D_2O–CH_3CN (1:1)) for **1**. Solutions (20 mg substrate in 40 mL solution) were irradiated at 254 nm (16 lamps) for 15 min.



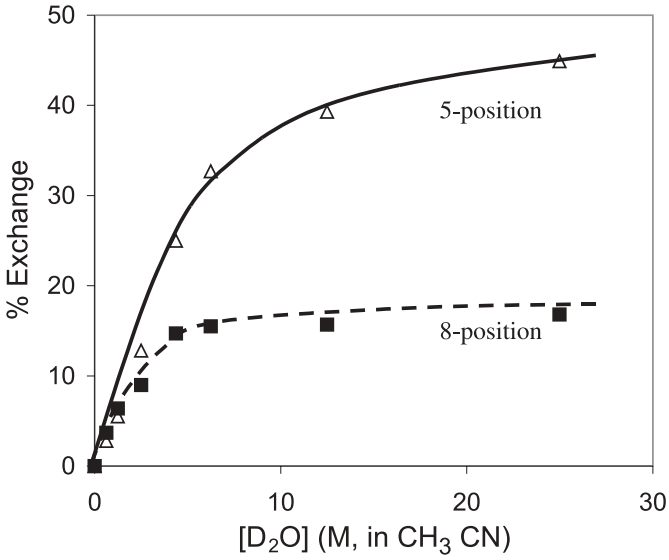
this pH range, it is very unlikely that the deuterium incorporation observed within this range results from protonation by D_3O^+ present in solution. The exchange efficiency decreases above pD 9, which corresponds with the ground state pK_a of **1** (pK_a = 9.2 (8)), indicating that the deprotonated form $\mathbf{1}^-$ does not undergo exchange. Consistent with this, no exchange was observed at high pD. This result rules out a stepwise mechanism in which **1** first undergoes excited-state proton transfer (ESPT) to give excited phenolate ($\mathbf{1}^-$*) that is protonated by D_2O in a subsequent step, since every excitation of $\mathbf{1}^-$ would necessarily lead to an excited phenolate. It is apparent that the naphthol OH is required for reaction, suggesting that an ESIPT might be taking place.

To investigate the role of solvent water in the ESIPT reaction of **1**, photolyses were performed in which the concentration of D_2O (in CH_3CN cosolvent) was varied (Fig. 3). The deuterium exchange efficiency for **1** was negligible at low D_2O concentrations, but increased dramatically as more D_2O was added. The enhancement of reaction efficiency appeared to reach saturation at about 1:1 D_2O–CH_3CN. The need for water to mediate the proton transfer indicates that the ESIPT is not intrinsic, in contrast to the ESIPT observed for **3**. This is probably because the distance between the acidic proton and both basic carbons is too large to allow ground state hydrogen bonding interactions, which are thought to be a prerequisite for intrinsic ESIPTs (9*b*). The efficiency for exchange at the 8-position plateaus at lower water concentrations than does exchange at the 5-position. This could be because the OH functionality is much closer to the 8-position, so less water is required to mediate the proton transfer.

Photodehydroxylation and photodehydration of 4 and 5

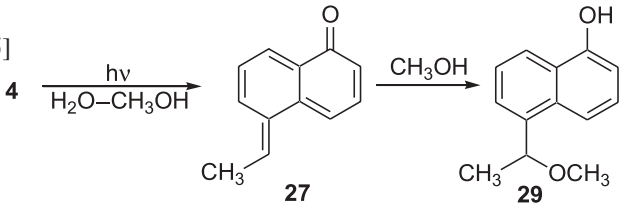
We have previously shown that the photolysis of phenols containing benzylic alcohol groups gives rise to *ortho*-, *meta*-, and *para*-quinone methides in high yield (1). In an attempt

Fig. 3. Plot of % deuterium exchange at 5- (triangles) and 8- (squares) positions vs. D_2O content (pD 7).



to apply this strategy to naphthoquinone methide generation, derivatives **4** and **5** were studied. The naphthoquinone methides produced by net photodehydration of **4** or **5** (**27** and **28**, respectively) were not expected to be sufficiently stable to isolate, so we instead sought to obtain indirect evidence of their presence by isolating their photosubstitution products arising from nucleophilic attack. For example, in methanol–water solutions, the expected photoproduct from **4** is methyl ether **29** (eq. [5]). Although formation of **29** is

[5]



consistent with the presence of **27** as an intermediate, reaction through a cationic intermediate would give the same product and cannot be excluded on the basis of product studies alone.

Irradiation of **4** in 1:1 H_2O–CH_3OH (~10^{-3} mol L^{-1}, Rayonet photochemical reactor, 300 nm lamps, 1 min) did indeed give **29** in 48% yield (eq. [5]), while solutions kept in the dark did not react. The photosubstitution is clean and has a remarkably high quantum yield for production of **29** from **4**, measured to be 0.84 ± 0.04 (Table 1). This value represents the highest reported quantum yield to date for photomethanolysis of benzyl alcohol derivatives. The high quantum yield for formation of **29** implies that attack by water on **27** to regenerate starting material must be very inefficient. This is in line with the known high nucleophilicity of methanol relative to that of water (20). Pure samples of **29** were obtained by chromatographic separation of the photolysate, and photolysis of these samples in 1:1 aqueous acetonitrile regenerated **4**. The methyl ether product can therefore also undergo photosubstitution, presumably through formal

© 2004 NRC Canada

loss of methanol to regenerate **27**. This result shows that ether and ester derivatives of **4** might prove useful as protecting groups for photorelease of alcohols and acids.

Results from the deuterium incorporation studies of **1** show that electron density in singlet excited 1-naphthols is primarily localized at the 5-position, and to a lesser extent at the 8-position. Naphthols **4** and **29** both react through the substituent located at the 5-position. In contrast to these examples, the substituent in **5** is located at the 4-position. No deuterium was incorporated at this position on irradiation of **1**, indicating that minimal charge is transferred to this position on excitation. When **5** was irradiated under similar conditions as **4**, no reaction was observed, showing that photodehydroxylation requires excited state charge transfer from the naphthol OH.

Photochemical studies of 9 and 10

The proposed mechanism for the photosolvolytic rearrangement of **6** (11) that leads to the release of acetic acid appears to require either ESPT to solvent water or an ESIPT from the phenol to the carbonyl oxygen mediated by water, to generate a reactive excited phenolate or a related enol species, respectively, prior to formation of spiroketone **7**. It was of interest to determine whether derivatives such as naphthol **9** and phenol **10** would show similar photosolvolysis. Since the parent 1-naphthol (**1**) has already been shown to undergo a water-mediated ESIPT to the 5- and 8-positions, it seemed reasonable to expect that a similar process could operate in **9**, with the difference that the proton transfer would end up at the carbonyl oxygen. This could activate the compound for release of acetic acid in a manner similar to the reactivity observed for **6**. In the case of phenol **10**, it is well known that there is substantial charge transfer through meta-positions on the benzene ring in S_1 that allows efficient formation of *m*-quinone methides (1, 2, 5). Such charge transfer would be expected to enhance ESIPT from the phenol to the carbonyl moiety of **10**, resulting in a reaction similar to that observed for **6**. To our surprise, both **9** and **10** were found to be completely unreactive in 1:1 H_2O–CH_3CN even on extended irradiation. Complete recovery of the substrates was achieved in all cases. What was surprising was the lack of photodecomposition even on extended photolysis, which leads us to suggest that ESPT or ESIPT processes are occurring for these compounds, but lead to no net chemistry. In the case of **10**, subsequent formation of the non-Kekulé spiroketone intermediate seems to be prohibitive as it would be a ground-state species. For **9**, formation of the requisite spiroketone would seem possible but on closer examination, such a reaction would result in loss of two aromatic rings *and* formation of a strained spiroketone. Moreover, the excited singlet or triplet energy of **9** (a 5-hydroxy-1-acetylnaphthalene) is expected to be substantially lower than that of **6** (a 4-hydroxyacetophenone). One of these factors probably explains the lack of reaction of **9**. No further studies of **9** and **10** were pursued due to their photoinertness in aqueous solution.

Fluorescence measurements

As the ESIPT reaction of **1** is strongly mediated by water, the fluorescence behaviour with respect to water concentration was studied to provide mechanistic insights. If the ESIPT reaction occurs from S_1, as do most ESPTs from phenols, addition of water to the solvent mixture should lead to quenching of the fluorescence intensity by enhancing the proton transfer pathways. Indeed, the fluorescence emission of **1** (in CH_3CN), after an initial red shift from λ_{max} 340 nm to λ_{max} 355 nm on addition of small amounts of water, was progressively quenched by added water, concomitant with a growth in fluorescence intensity at 460 nm. In pure water, the 355 nm band was completely quenched and only emission from the 460 nm band was observed. The band at 460 nm results from emission from the excited 1-naphtholate ion (**1**$^-$), which arises from ESPT from the OH proton of **1** to solvent (water), and is consistent with the previous assignment (8). Relatively large amounts of water were required for efficient formation of **1**$^-$, just as the ESIPT of **1** to give **1-5D** and **1-8D** required large amounts of D_2O. This correlation is not surprising as the two processes are closely related. Thus, quenching of the fluorescence emission of **1** in the presence of water arises from a combination of two competing pathways from S_1, namely ESPT to solvent water and water-mediated ESIPT to the 5- and 8-positions.

The fluorescence behaviour of **5** closely resembled that of **1**. Small amounts of water led to an initial red shift of the fluorescence emission band from λ_{max} 358 nm in neat CH_3CN to λ_{max} 375 nm (Fig. 4). Larger amounts of water led to quenching of this fluorescence band and to a growth in emission at 465 nm (from naphtholate ion **5**$^-$). This information suggests that there are no major pathways that deactivate the singlet excited state of **5** other than those available for **1**.

The fluorescence behaviour of **4** is quite different from that observed for **1** and **5**. Small amounts of water led to a red shift of the fluorescence emission band from λ_{max} 345 nm in neat CH_3CN to λ_{max} 360 nm, though significant quenching of this band was achieved with less water than required for **1** or **5** (Fig. 5). Naphtholate (**4**$^-$) emission (λ_{max} 460 nm) was observed only at high water concentrations and was much weaker than the observed emission of **1**$^-$ or **5**$^-$. Modified Stern–Volmer quenching plots of the emission intensity of **4** and **5** with added water are shown in Fig. 6. The enhanced quenching by water for **4** relative to **5** can be clearly seen. Since the pK_a values for **1**, **4**, and **5** are expected to be approximately equivalent, an additional water-dependent deactivation pathway must be operating for **4**. The net dehydration reaction to give **27** that is available for **4** but not for **1** or **5** can explain this additional quenching if deprotonation of the naphthol and dehydroxylation of the benzylic alcohol are concerted from S_1. This pathway would also compete with ESPT to solvent, explaining the weaker phenolate emission observed. Both Stern–Volmer plots exhibit a squared dependence on water concentration. Our group has previously reported nonlinear fluorescence quenching by water for related phenols, an effect attributable to involvement of water clusters in the ESPT (4).

Fluorescence quantum yields and lifetimes were measured for **4** and **5** in CH_3CN and are listed in Table 1, along with literature values for **1** and **2**. Both **4** and **5** exhibit similar photophysical behaviour to **1** in CH_3CN, indicating that no

© 2004 NRC Canada

Fig. 4. Representative fluorescence quenching traces of **5** by added water in CH_3CN (λ_{ex} 300 nm). Water concentrations are given in the legend. Naphtholate (**5**$^-$) emission grows in at λ_{em} 460 nm with increasing water content.

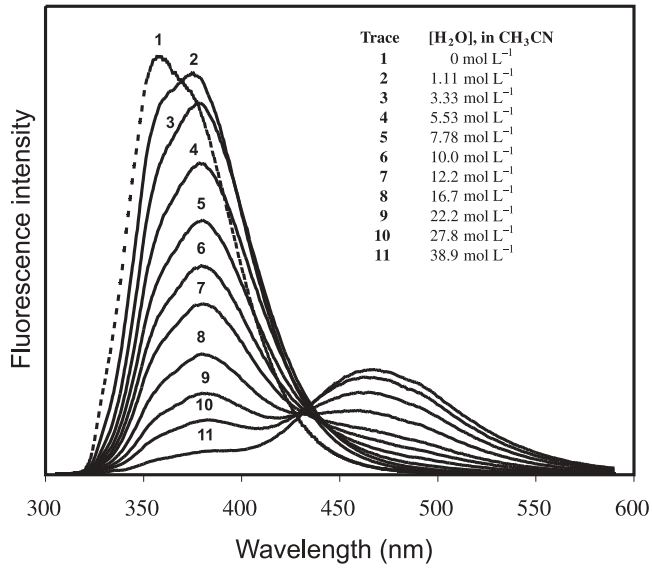
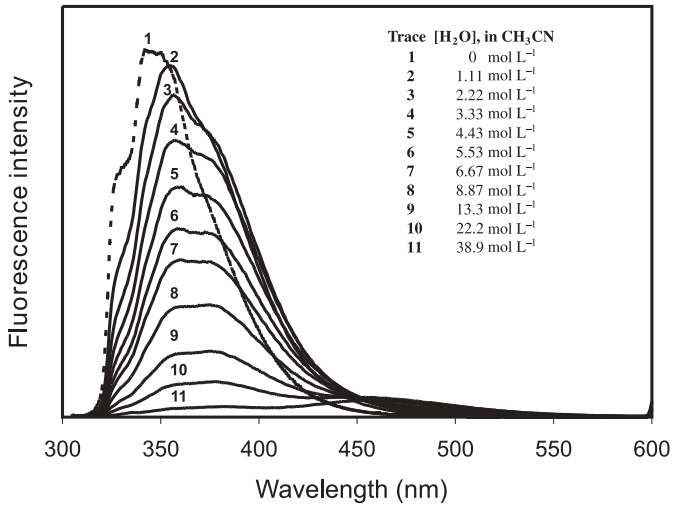


Fig. 5. Representative fluorescence quenching traces of **4** by added water in CH_3CN (λ_{ex} 300 nm). Water concentrations are given in the legend. Naphtholate (**4**$^-$) emission grows in at λ_{em} 465 nm with increasing water content.



major deactivation pathways open up on addition of the hydroxyethyl substituent to the 1-naphthol chromophore except when water is present.

Laser flash photolysis (LFP)

LFP experiments were performed for **1**, **4**, and **5** to gain direct evidence of the suspected naphthoquinone methide intermediates. The resulting data are summarized in Table 2. Mathivanan et al. (19*b*) previously studied 1-methoxynaphthalene by LFP in hexafluoroisopropyl alcohol (HFIP) and observed a transient with a broad absorption band at λ_{max} 550 nm and a second, more narrow band at

Fig. 6. Stern–Volmer plots for steady-state fluorescence quenching of **4** (triangles) and **5** (diamonds) by H_2O (in CH_3CN). The lines drawn are fits to $I_0/I = 1 + K_{SV}[H_2O]^2$.

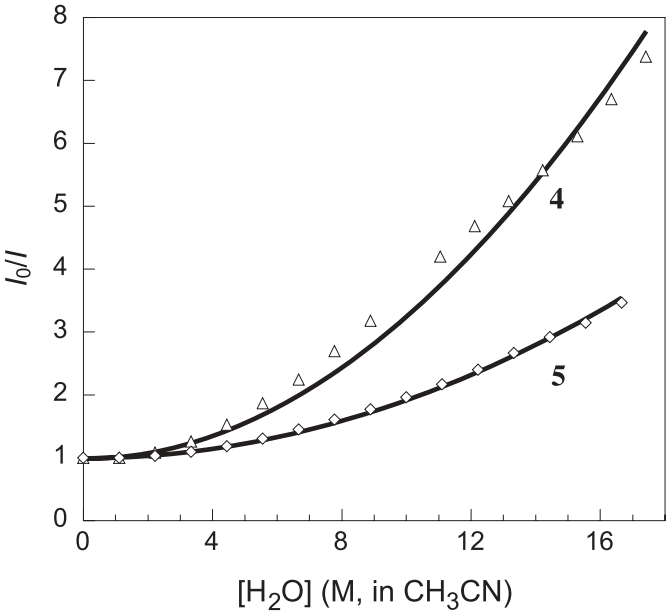


Table 2. Summary of laser flash photolysis transient data.[a]

Transient	λ_{max}[b] (nm)	τ[c] (μs)	k_q[d] (10^6 M^{-1} s^{-1})
26a	350, 530	17	0.90±0.10
27	410, 700	33	1.0±0.1
32	410, 700	1.7	>>50[e]
33	350, 530	45	Not determined

[a]LFP was performed on flowing solutions that were ~10^{-5} mol L^{-1} in the appropriate substrate. Excitation was achieved with an excimer laser (308 nm, ~ 10 ns, <30 mJ/pulse).

[b]Absorption maxima in H_2O–CH_3CN (1:1) solution.

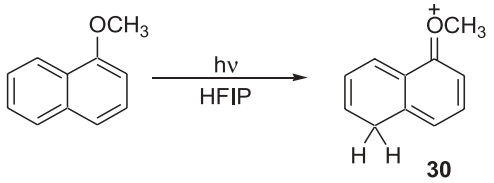
[c]Transient lifetime in H_2O–CH_3CN (1:1) solution, oxygen purged. The estimated error is ±10% of the reported value.

[d]Bimolecular quenching rate constant with added ethanolamine in H_2O–CH_3CN (1:1) solution, according to the following equation: $k_{obs} = k_0 + k_q[Q]$.

[e]Complete quenching was observed with 5.5 mol L^{-1} ethanolamine. Transients with lifetimes as short as 20 ns are readily detectable on the system used, so for complete quenching to be realized with 5.5 mol L^{-1} quencher, k_q must be at least 5×10^7 M^{-1} s^{-1}, and is probably at least an order of magnitude higher.

λ_{max} 360 nm, both of which were assigned to cation **30** obtained via photoprotonation (from HFIP) of 1-methoxynaphthalene at the 5-position (eq. [6]). This tran-

[6]

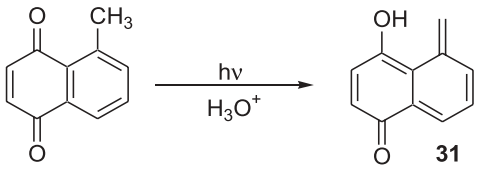


30

sient could not be detected in aqueous acid, which the authors proposed was because rapid reaction with water reduced the lifetime of the cation to a value shorter than their system could detect. This intermediate bears structural

© 2004 NRC Canada

resemblance to suspected naphthoquinone methide **26a** resulting from ESIPT to the 5-position in **1**. Chiang et al. (21) observed naphthoquinone methide **31** by LFP in dilute aqueous acid solution (generated by γ-hydrogen abstraction in 5-methyl-1,4-naphthoquinone (eq. [7])). This transient had a broad visible absorption band at λ_{max} 600 nm with a lifetime

[7] 

of ≈1 μs (lifetime shortened as pH was decreased), and is structurally related to **27** produced on photodehydration of **4**.

Nanosecond LFP of **1** in 1:1 H_2O–CH_3CN (O_2 saturated) resulted in the formation of a transient with a broad absorption band at 530 nm and a second, more narrow band at 340 nm (Fig. 7). Both peaks appeared immediately after the laser pulse (≈10 ns) and decayed to baseline. The decay kinetics of both peaks fit a monoexponential curve, giving a lifetime of 16 ± 2 μs. This transient spectrum is very similar to that assigned to **30** (19*b*), though blue-shifted by about 20 nm. We assign this absorption to be **26a** formed on ESIPT of **1**. The observed lifetime of 16 ± 2 μs in aqueous solution indicates that this transient is much less reactive with water than **30**, which is expected because of the greater electrophilic nature of **30**. Naphthoquinone methide **26b** is non-Kekulé and is expected to decay within the time of the laser pulse (10 ns). LFP of **1** in neat CH_3CN (O_2 purged) led to formation of a weaker transient (Fig. 7) with a broad visible band (λ_{max} 510 nm) and narrower bands with λ_{max} 390 and 350 nm. We assign this transient to the 1-naphthoxy radical based on the similarity of the observed absorption spectrum to that known for this species (22).

Nanosecond LFP of **4** in 1:1 H_2O-CH_3CN (O_2 saturated) resulted in the formation of a strongly absorbing transient immediately after the laser pulse, with peaks at 410 and 700 nm (Fig. 8). The decay kinetics gave a biexponential fit with a short-lived minor component (τ = 1.5 ± 0.5 μs) and a longer lived major component (τ = 34 ± 2 μs) that both decayed cleanly to baseline. This biphasic decay was observed at all wavelengths, demonstrating that the two decaying species have similar absorbance profiles. The position of the bands is consistent with what is expected for **27**: the red shift relative to **26a** results from the extra unit of conjugation and the extra methyl substituent. The long-wavelength band is similar to that reported for related naphthoquinone methide **31** by Chiang et al. (21). The major (long-lived) component of the observed absorption is assigned to **27** on this basis and on the results of the product studies. The shorter lived species can be assigned to cation **32** that would result from dehydroxylation without prior deprotonation of the phenol, a process well known for methoxy-substituted benzyl alcohols. This cation possesses a similar degree of conjugation as **27**, which would explain its similar absorbance characteristics. Its much shorter lifetime is consistent with the expected enhanced reactivity of a charged species relative to a neutral and closed-shell naphthoquinone methide. No strong transients were observed on LFP of **4** in neat CH_3CN (O_2 purged) in the absence of water. Instead, a weak transient was observed with a broad band at 580 nm, and with narrower bands at 400 and 350 nm (Fig. 8). This species closely resembles the transient observed for **1** in neat CH_3CN in the position, structure, and intensity of the absorption bands. This transient is therefore assigned to the 1-naphthoxy radical of **4**.

A strong transient was also observed on LFP of **5** (in H_2O–CH_3CN (1:1)), which exhibited a broad absorption

Fig. 7. Transient absorption observed on LFP of **1** in H_2O–CH_3CN (1:1) (triangles) and in neat CH_3CN (diamonds) (λ_{ex} 308 nm, O_2 purged for both). For both spectra, the decay trace was taken immediately after the laser pulse (~10 ns).

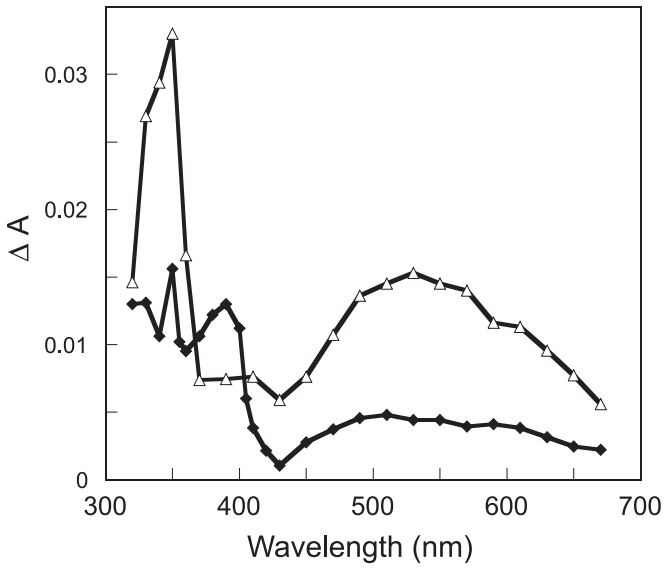
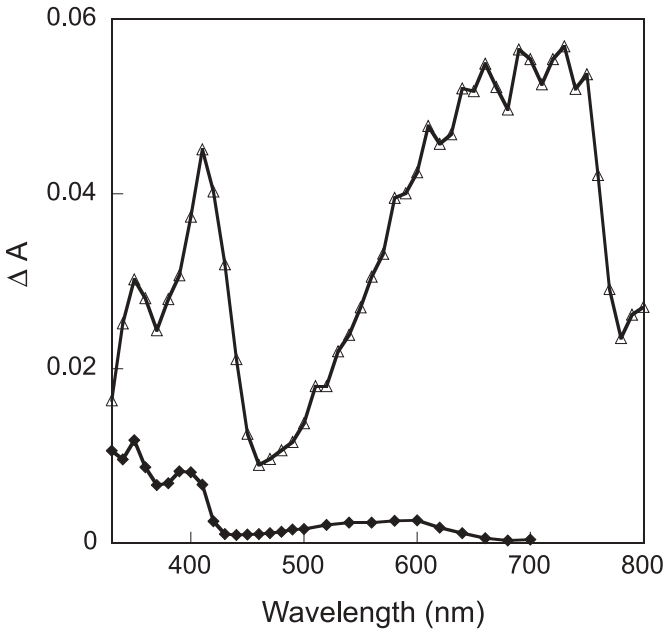


Fig. 8. Transient absorption observed on LFP of **5** in H_2O–CH_3CN (1:1) (triangles) and in neat CH_3CN (diamonds) (λ_{ex} = 308 nm, O_2 purged for both). The decay traces were taken immediately after the laser pulse (~10 ns).



© 2004 NRC Canada

band at 520 nm, a small band at 410 nm, and a strong narrow band at 350 nm. Again, all peaks displayed first-order decay kinetics, each with the same lifetime of 45 ± 2 μs. Product studies showed that **5** does not undergo photosubstitution; therefore, this transient is unlikely to be **28**. Nevertheless, the spectrum closely resembles that assigned to **26a**. Indeed, **5** should be able to form a similar naphthoquinone methide resulting from ESIPT to the 5-position of the naphthol ring. On this basis, we assign this absorption to naphthoquinone methide **33**. The enhanced lifetime of **33** relative to **26a** is probably due to steric shielding of the 5-position by the hydroxyethyl substituent that retards deprotonation at this site. LFP of **5** in neat CH_3CN shows formation of small amounts of the corresponding 1-naphthoxy radical.

Additional support for our assignment of the major transients observed for **1** and **4** as naphthoquinone methides was sought through quenching studies. We have recently shown (23) that ethanolamine can efficiently quench quinone methide intermediates. For **27** (or cation **32**), the expected quenching mechanism is nucleophilic attack at the benzylic position to furnish the ethanolamine adduct, while for quinone methide **26a**, the expected quenching mechanism is base-catalyzed tautomerization. Quenching analyses were first performed for the transients arising from LFP of **4** (Fig. 9). At the smallest ethanolamine concentration used (5.5 mM in H_2O–CH_3CN (1:1)), the short-lived component of the decay (assigned to **32**) was completely quenched, leaving only the longer lived component (assigned to **27**). As carbocations are known to react very rapidly with added nucleophiles, this observation supports our assignment of the short-lived component to **32**. The dynamic quenching of quinone methide **27** with added ethanolamine is plotted in Fig. 9 and a linear correlation was observed, giving a bimolecular quenching rate constant of $1.0 \pm 0.1 \times 10^6$ M^{-1} s^{-1}. A similar quenching analysis was performed for the transient formed on LFP of **1** (assigned to **26a**), and results are presented in Fig. 10. The decay of this transient was also accelerated with added ethanolamine, giving a good linear fit with k_q at $9.0 \pm 1.0 \times 10^5$ M^{-1} s^{-1}.

Fig. 9. Quenching plot showing the increase in the decay rate of **27** at 680 nm with added ethanolamine in H_2O–CH_3CN (1:1). Line is the least-squares fit to the data and gives $k_q = 1.0 \times 10^6$ M^{-1} s^{-1}. Estimated error is ±10%.

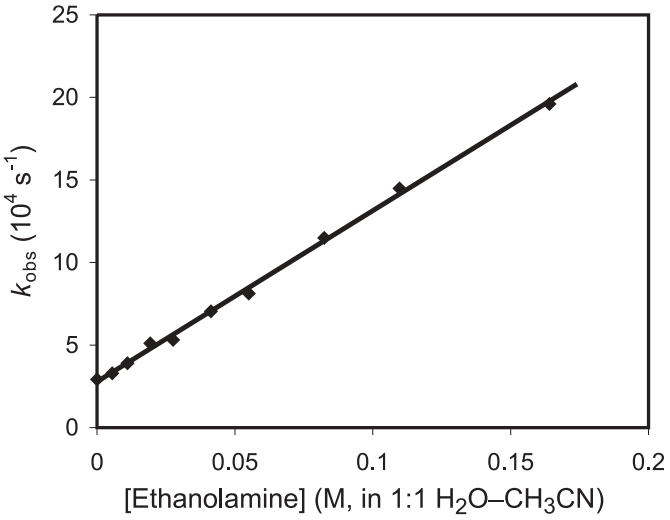
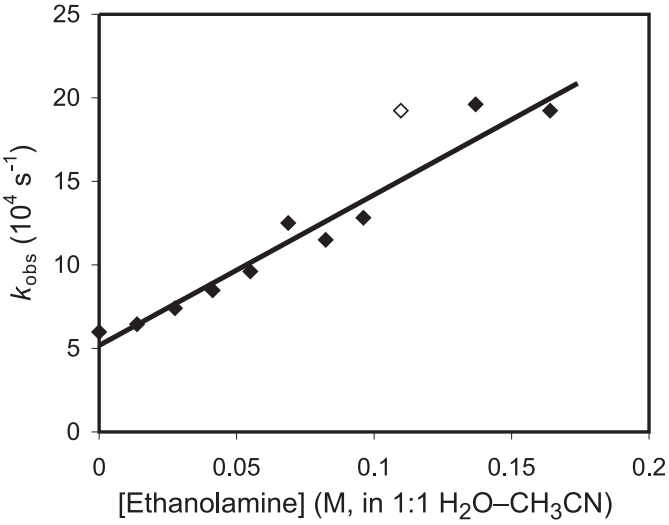


Fig. 10. Quenching plot showing the increase in the decay rate of **26a** at 530 nm with added ethanolamine in H_2O–CH_3CN (1:1). Line is the least-squares fit to the data and gives $k_q = 9.0 \times 10^5$ M^{-1} s^{-1}. Estimated error is ±15%. Outlined point was not included in the least-squares analysis.

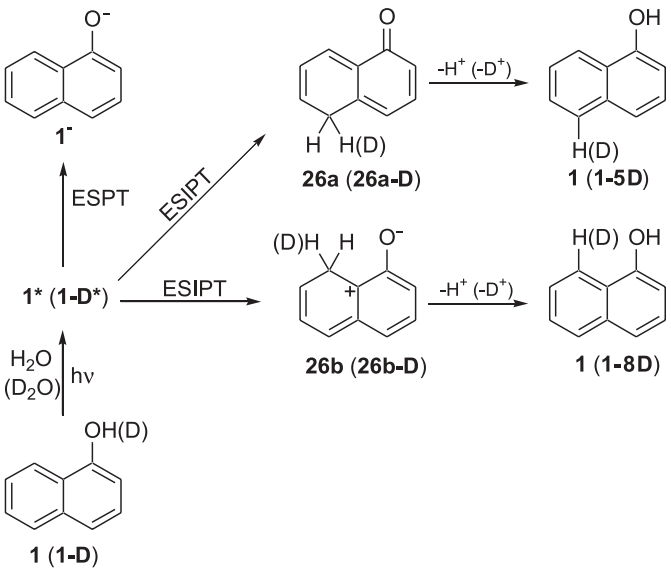


Mechanisms of reaction

The deuterium incorporation reaction of **1** on photolysis in D_2O–CH_3CN (1:1) is proposed to occur via a water-mediated ESIPT from the naphthol OH to the aromatic ring carbons at the 5- and 8-positions, to give naphthoquinone methide intermediates **26a** and **26b**, respectively, (Scheme 4). The enhanced acidity of the naphthol OH in the excited state ($pK_a^* = 0.4$) and the enhanced excited-state basicity of the 5- and 8-positions of 1-alkoxy- and 1-hydroxy-substituted naphthalenes suggest that an intramolecular acid–base reaction might be possible. The propensity of **1** to undergo excited-state proton transfer reactions in aqueous conditions is further demonstrated in fluorescence studies, with emission from (**1**$^-$)* observed on photolysis of **1** in aqueous conditions. The protonation of the 5- and 8-positions in the pH range 2.5–9 does not result from electrophilic attack by H_3O^+ (or D_3O^+) since the exchange efficiency is independent of pH (pD) throughout this large pH range. Solvent water alone cannot be acting as the acid, since no exchange was observed for irradiated (basic) solutions of **1**$^-$. Under basic conditions, the naphthalene still has a powerful electron-donating group at the 1-position, and the concentration of water is still very high. It is thus evident that the reaction requires the OH functionality, suggesting that the reaction proceeds through ESIPT from the OH to the ring carbons. The need for water to mediate the proton transfer was clearly borne out by the product studies, with efficient reaction only being observed at fairly high water concentrations. This is because the OH group is too far from the basic sites to allow any direct spatial interaction, so water is needed to "solvate" the proton as it is transferred. We have previously implicated water as mediating ESIPTs between remote sites in other phenols (4). Direct evidence for

© 2004 NRC Canada

Scheme 4.

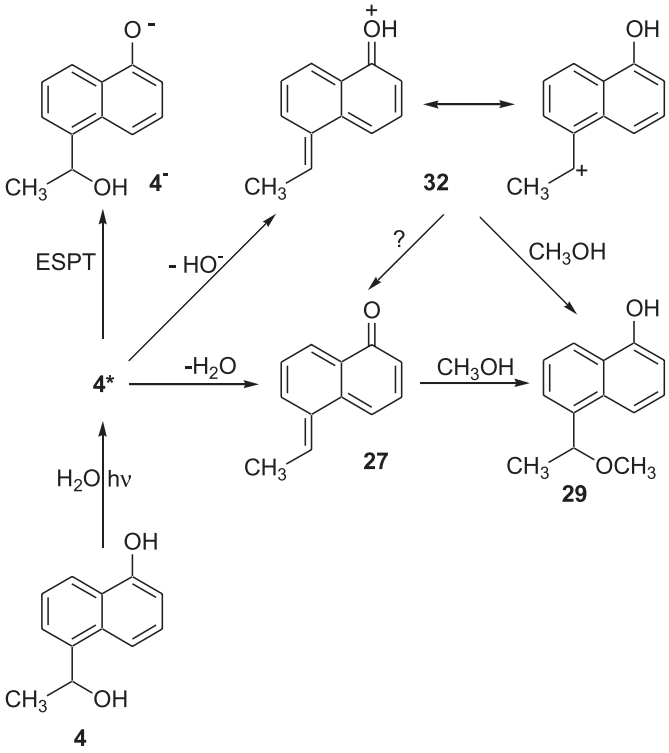


naphthoquinone methide intermediate **26a** that would arise from ESIPT to the 5-position was provided by LFP studies, lending further support to our mechanistic proposal.

An additional consideration of interest in the ESIPT of **1** is the possible presence of other intermediates prior to naphthoquinone methide formation. We recently reported an example of a simple hydroxybiaryl for which ESIPT to two aromatic carbon positions was observed (24). ESIPT to both positions was strongly water dependent, as is the ESIPT of **1** in the present work. Furthermore, the efficiency of exchange of the two positions had almost identical dependencies on water content, which is unlikely if the two routes are wholly independent. To account for this, we suggested that ESIPT first leads to a "proton – π complex", which can rearrange to either of the two possible quinone methides (24). The ESIPT in **1** appears not to occur through this route. Deuterium exchange efficiencies at the 5- and 8-positions appear to have different dependencies on water concentration, with exchange at the 8-position reaching saturation with less water than exchange at the 5-position. This observation favours a mechanistic picture where two separate ESIPTs are occuring that do not share a common intermediate prior to QM formation.

The photosubstitution reaction of **4** is mechanistically related to the ESIPT reaction of **1** in that it relies on excited-state charge transfer from the naphthol OH to the 5-position. The photochemical reactivity of **4** in aqueous solution can be explained as occuring through three different pathways (Scheme 5): (*i*) ESPT of the naphthol proton to solvent water to give $\mathbf{4}^{-}$; (*ii*) dehydroxylation of the benzylic alcohol moiety to give **32**; and (*iii*) photodehydration to form **27**. Evidence for the first pathway comes from the fluorescence studies: emission from $\mathbf{4}^{-*}$ was observed on excitation of **4** at high water concentrations, indicating that an adiabatic ESPT is occuring. As for the second pathway, a short-lived transient observed in LFP studies was assignable to the cation **32** that would result from simple dehydroxylation. Cation **32** might also undergo deprotonation to give **27**. The

Scheme 5.

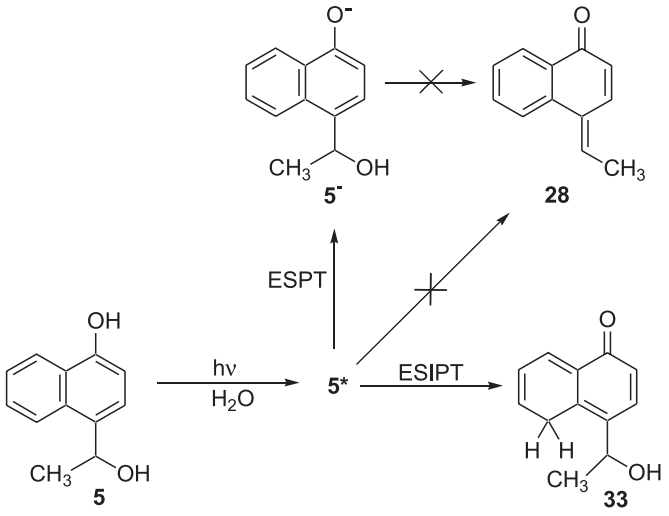


third and major pathway involves deprotonation of the naphthol OH concerted with dehydroxylation of the benzylic site to give **27** directly. The formation of the naphthoquinone methide intermediate **27** was inferred from the results of the product studies and the observation of a transient on LFP of **4** that was assignable to **27**. That the reaction to give **27** is concerted was inferred primarily from the fluorescence studies. The enhanced quenching of the fluoresence emission of **4** in aqueous solution by water over 1-naphthol derivatives **1** and **5** shows that an additional deactivation pathway is available for **4** that is not available for **1** or **5**, with this pathway being photodehydration to form **27**. If the ESPT to solvent preceded dehydroxylation of the benzylic alcohol, no enhanced quenching would be observed, since **1**, **4**, and **5** would be expected to have similar ESPT rates. The LFP quenching studies for **4** demonstrated that very small amounts of ethanolamine rapidly quenched the cation. If the cation was a precursor to **27**, the presence of ethanolamine would substantially reduce the amount of **27** that is observed, and that was not the case. Therefore, the only remaining option to explain the reactivity is via a concerted mechanism.

The reactivity of **5** (Scheme 6) is different from that of **4** in that no photosubstitution was observed in the product studies. Photodehydration to form naphthoquinone methide **28** therefore does not occur. The ESIPT in **1** and the photosubstitution reaction of **4** are both interpreted as arising from enhanced localized charge transfer from the naphtholic OH to the 5- and 8- ring positions. The failure of **5** to react through the 4-position confirms that this charge transfer is crucial for photodehydration. A strong transient was observed on LFP of **5** and was assigned to **33**, indicating that **5** reacts though an ESIPT pathway similar to that observed for

© 2004 NRC Canada

Scheme 6.



1. Despite containing a potentially reactive substituent at the 4-position, the chemistry is still dominated by the localized charge transfer to the 5- and 8-positions.

Experimental

General

^{1}H NMR spectra were obtained on Bruker AC300 (300 MHz), AM360 (360 MHz), AVANCE 500 (500 MHz), Varian AM400 (400 MHz), or JEOL FX90Q (90 MHz) instruments in $CDCl_3$ unless otherwise specified. Low-resolution mass spectra were obtained on a Finnigan 3300 (CI) and HR-MS were obtained on a Kratos Concept H (EI) instrument. UV–vis spectra were recorded on a Varian Cary 5 instrument. Acetonitrile (HPLC or spectral grade) used for fluorescence and LFP experiments was dried by distillation from calcium hydride. Organic extracts were dried over anhydrous magnesium sulfate and filtered. pD values were measured for the aqueous portion (prior to mixing with CH_3CN cosolvent) using a Fisher Accumet 915 pH meter and were not corrected for the deuterium isotope effect. Solutions were unbuffered with pD values adjusted with either NaOD (pD > 7) or D_2SO_4 (pD < 7).

Materials

5-(1-Hydroxyethyl)-1-naphthol (4)

A solution of 5-bromo-1-naphthoic acid **11** (12) (4.5 g, 17.9 mmol) and concentrated sulfuric acid (1.35 mL) in methanol (65 mL) was heated at reflux for 8 h, cooled, diluted with diethyl ether and washed with aqueous sodium hydrogen carbonate, water and brine, dried and evaporated under reduced pressure. The residue was crystallized from methanol to give methyl 5-bromo-1-naphthoate **12**. Yield: 3.5 g (74%); mp 66 to 67 °C (lit. (12) mp 66 to 67 °C).

A mixture of **12** (6.0 g, 22.6 mmol), CuBr (0.93 g, 6.5 mmol), ethyl acetate (1.77 mL, 18.1 mmol) and 25% sodium methoxide in methanol (Aldrich; 30.8 mL, 142.6 mmol) was heated under reflux for 3.5 h under nitrogen. The copper salts were filtered and the solid was washed with methanol. The combined filtrate was concentrated to about 5 mL, diluted with water and extracted with dichloromethane. The extracts were washed with brine, dried and evaporated, and crystallized from hexanes to give methyl 5-methoxy-1-naphthoate **13**. Yield 3.43 g (70%); mp 76–76.5 °C (lit. (25) mp 74.5–75.5 °C). This material (7.7 g) was saponified in aqueous methanolic sodium hydroxide to give 5-methoxy-1-naphthoic acid **14**. Yield: 6.1 g (85%); mp 225–227 °C (from ethanol) (lit. (26) mp 227–229 °C).

A solution of **14** (2.02 g, 10 mmol) stirred under nitrogen in anhyd THF (40 mL) was diluted with anhydrous diethyl ether (110 mL) and a 1.5 mol L^{-1} solution of methyl lithium in diethyl ether (16.7 mL, 25 mmol) was added over 20 min at room temperature. The mixture was stirred for 1.5 h and acetone (17 mL) was added. After 5 min, the solution was diluted with 2 mol L^{-1} aqueous hydrochloric acid and extracted with diethyl ether. The organic phase was washed with water, aqueous sodium hydrogen carbonate, water and brine, dried and evaporated under reduced pressure. The residue was crystallized from petroleum ether (bp 60–80 °C) to give 1-acetyl-5-methoxynaphthalene **15**. Yield: 1.56 g (78%), mp 85–87 °C (lit. (27) mp 88 to 89 °C).

Dry *N*-methyl-2-pyrrolidinone (10.5 mL) was added under nitrogen to a mixture of **15** (4.2 g, 21.0 mmol) and anhydrous potassium carbonate (0.145 g, 1.05 mmol) and the mixture was stirred for 5 min at room temperature. Thiophenol (3.23 mL, 31.5 mmol) was added and the mixture was heated at 190 °C for 45 min and cooled. Methanol (105 mL) and triethylamine (4.2 mL) were added, followed by 30% hydrogen peroxide (4.2 mL) in four equal portions over ~5 min. The solution was stirred for 10 min, then concentrated under vacuum to ~10 mL, diluted with 5% aqueous sodium hydroxide and extracted with diethyl ether. The aqueous layer was acidified to pH 2 with 6 mol L^{-1} hydrochloric acid and extracted with diethyl ether and the organic extract was washed with brine, dried and evaporated under reduced pressure. The residue was crystallized from EtOAc–hexanes to give 1-acetyl-5-hydroxynaphthalene **16** as pale yellow crystals. Yield: 2.82 g (72%); mp 173–174.5 °C (lit. (28) mp 172.5–173.5 °C). ^{1}H NMR (400 MHz, $CDCl_3$ – 10% CD_3OD) δ: 2.74 (s, 3H, CH_3), 6.90 (d, J = 7.6 Hz, 1H, Ar-H), 7.40 (m, 1H, Ar-H), 7.47 (m, 1H, Ar-H), 7.92 (d, J = 7.1 Hz, 1H, Ar-H), 8.14 (d, J = 8.6 Hz, 1H, Ar-H), 8.49 (d, J = 8.6 Hz, 1H, Ar-H).

A solution of **16** (1.60 g, 8.60 mmol) in EtOH (59 mL) was stirred at 0 °C and sodium borohydride (0.57 g, 15.1 mmol) was added. After 10 min, the solution was allowed to warm to room temperature and stirred for 1.5 h, then concentrated to ~10 mL. Unreacted borohydride was destroyed by dropwise addition of glacial acetic acid and the solution was diluted with water and extracted with ethyl acetate. The organic phase was washed with brine, dried and evaporated under reduced pressure. The residue was purified by flash chromatography (EtOAc–hexanes (3:7)) to give the title alcohol **4** as beige crystals. Yield: 0.89 g (55%); mp 167.5–169 °C (from EtOAc–hexanes). ^{1}H NMR (500 MHz, $CDCl_3$ – 10% CD_3OD) δ: 1.63 (d, J = 6.0 Hz, 3H, Me), 5.62 (q, J = 6.0 Hz, 1H, C*H*OH), 6.85 (d, J = 7.7 Hz, 1H, Ar-H), 7.33 (m, 1H, Ar-H), 7.45 (t, J = 7.7 Hz, 1H, Ar-H), 7.58 (d, J = 8.5 Hz, 1H, Ar-H), 7.68 (d, J = 6.8 Hz, 1H, Ar-H), 8.20 (d, J = 8.6 Hz, 1H, Ar-H). HR-MS calcd. for $C_{12}H_{12}O_2$: 188.0837; observed: 188.0838.

© 2004 NRC Canada

4-(1-Hydroxyethyl)-1-naphthol (5)

1-Acetyl-4-methoxynaphthalene **17** (29) was demethylated as described above for the 5-isomer **15** to give 1-acetyl-4-hydroxynaphthalene **18** as yellow crystals (from aqueous methanol), mp 198–199.5 °C (lit. (30) mp 197 °C).

A solution of **18** (2.0 g, 10.75 mmol) and TBDMS chloride (2.89 g, 19.2 mmol) in anhyd DMF (9.3 mL) was treated with imidazole (2.72 g, 40.0 mmol) and the mixture was stirred at room temperature for 2 h, then diluted with diethyl ether. The diluted solution was washed with 0.1 mol L^{-1} aqueous sodium carbonate and brine, dried and evaporated under reduced pressure to give crude 4-*tert*-butyldimethylsilyloxy-1-acetylnaphthalene **19** as a beige solid. Yield: 2.58 g (80%). This material was used without further purification. Thus, a solution of **19** (3.33 g, 11.1 mmol) in methanol (86 mL) was stirred at 10 °C and treated with sodium borohydride (0.42 g, 11.1 mmol) in three portions. The solution was stirred for 10 min at 10 °C and for 45 min at room temperature, then concentrated to ~30 mL and treated dropwise with glacial acetic acid (1.5 mL). The solution was diluted with water and extracted with ethyl acetate. The organic phase was washed with brine, dried and evaporated under reduced pressure to give crude 1-(4-*tert*-butyldimethylsilyloxy-1-naphthalenyl)ethanol **20** as a reddish brown viscous gum. Yield: 3.0 g (89%). This material was dissolved in THF (30.5 mL) and treated with 1 mol L^{-1} tetrabutylammonium fluoride in THF (10.93 mL). After 20 min at room temperature the solution was diluted with diethyl ether and washed with water and brine, dried and evaporated under reduced pressure. The residue was flash chromatographed (EtOAc-hexanes (3:7)) to give the title alcohol **5** as a brown solid. Yield: 1.64 g (88%). Crystallization from EtOAc–hexanes was accompanied by some decomposition in the mother liquor but gave the pure alcohol, mp 126–127.5 °C. ^{1}H NMR (500 MHz, $CDCl_3$ – 10% CD_3OD) δ: 1.63 (d, J = 6.5 Hz, 3H, CH_3), 5.57 (q, J = 6.5 Hz, 1H, C*H*OH), 6.83 (d, J = 7.7 Hz, 1H, Ar-H), 7.44–7.47 (m, 2H, Ar-H), 7.49–7.53 (m, 1H, Ar-H), 8.07 (d, J = 8.4 Hz, 1H, Ar-H), 8.27–8.29 (m, 1H, Ar-H). HR-MS calcd. for $C_{12}H_{12}O_2$: 188.0837; observed: 188.0837.

2-(5-Hydroxy-1-naphthalenyl)-2-oxoethyl acetate (9)

A stirred solution of 5-acetoxy-1-naphthoic acid **21** (31) (1.75 g, 7.6 mmol) in dry dichloromethane (30 mL) was treated at room temperature with oxalyl chloride (1.3 mL, 14.9 mmol) and dry DMF (65 μL). After 1 h, the solution was evaporated under reduced pressure and kept overnight under vacuum to leave the crude acid chloride **22**. Yield: 1.95 g (100%). This material (1.89 g, 7.6 mmol) was dissolved in a mixture of anhyd THF and acetonitrile (1:1; 15 mL) and treated with triethylamine (2.11 mL, 15.1 mmol). The solution was cooled in an ice bath and a 2 mol L^{-1} solution of trimethylsilyldiazomethane in hexane (Aldrich; 7.6 mL, 15.2 mmol) was added over 15 min. After 0.5 h, the solution was allowed to warm to room temperature and stirred overnight, then diluted with diethyl ether and washed with sat $NaHCO_3$, water, and brine, dried and evaporated under reduced pressure. The residue was triturated with diethyl ether to give crude diazoketone **23** as a brown solid. Yield: 1.43g (74%). ^{1}H NMR (90 MHz, $CDCl_3$ – 5% CD_3OD) δ: 2.42 (s, 3H, CH_3), 5.66 (s, 1H, CHN_2), 7.23–8.40 (m, 6H, Ar-H).

A solution of **23** (1.43 g, 5.36 mmol) in a mixture of THF and methanol (1:1; 28.6 mL) was treated with concentrated aqueous ammonia (4.77 mL). After 2 h at room temperature, the solution was diluted with ice water and adjusted to pH 8.0 with saturated aqueous oxalic acid. The aqueous layer was extracted with ethyl acetate and the organic extract was washed with water, dried and evaporated under reduced pressure. The residue was flash chromatographed (ethyl acetate – hexanes (3:7)) to give 2-diazo-1-(5-hydroxy-1-naphthalenyl)ethanone **24** as a yellow solid. Yield: 0.56 g (47%). ^{1}H NMR (90 MHz, $CDCl_3$ – 10% CD_3OD) δ: 5.73 (s, 1H, CHN_2), 6.80–8.44 (m, 6H, Ar-H). This material (0.47 g, 2.17 mmol) was added in portions over ~3 min to a stirred mixture of concentrated hydrochloric acid (0.44 mL) and glacial acetic acid (4.4 mL). After 0.5 h, the solution was diluted with water (22 mL) and stirred for 10 min. The precipitated solid was filtered, washed with cold water (3 mL), and dried under vacuum to give crude 1-chloroacetyl-5-hydroxynaphthalene **25** as a yellow powder. Yield: 0.39 g (82%). ^{1}H NMR (90 MHz, $CDCl_3$ – 5% CD_3OD) δ: 4.76 (s, 2H, CH_2Cl), 6.82–8.55 (m, 6H, Ar-H).

A stirred solution of **25** (0.39 g, 1.77 mmol) and glacial acetic acid (0.132 mL, 2.3 mmol) in dry toluene (23 mL) was cooled in ice and treated with DBU (0.344 mL, 2.3 mmol). The solution was stirred in the ice bath for 1 h, then at room temperature overnight. The solution was diluted with water, the aqueous layer was adjusted to pH 2 with 1 mol L^{-1} hydrochloric acid, and the mixture was extracted with diethyl ether. The organic layer was washed with water and brine, dried and evaporated under reduced pressure. The residue was dissolved in ethanol (7 mL), thiourea (0.15 g) was added and the solution was heated at reflux for 0.5 h to remove residual **25**, then concentrated under reduced pressure and partitioned between ethyl acetate and water. The organic phase was washed with water and brine, dried and evaporated and the residue was flash chromatographed (ethyl acetate – hexanes (3:7)). The recovered material was crystallized from toluene to give the title compound **9** as yellow plates. Yield: 0.29 g (50%); mp 99.5–101 °C. ^{1}H NMR (400 MHz) δ: 2.25 (s, 3H, CH_3), 5.31 (s, 2H, CH_2), 6.86 (d, J = 7.5 Hz, 1H, Ar-H), 7.39 (dd, J = 7.8 and 8.4 Hz, Ar-H), 7.48 (dd, J = 7.4 and 8.3 Hz, Ar-H), 7.83 (d, J = 7.0 Hz, Ar-H), 8.14 (d, J = 8.6 Hz, Ar-H), 8.44 (d, J = 8.4 Hz, Ar-H). Anal. calcd. for $C_{14}H_{12}O_4$: C 68.85, H 4.95; found: C 68.57, H 4.89.

2-(3-Hydroxyphenyl)-2-oxoethyl acetate (10)

A stirred solution of 3-hydroxyphenacyl bromide (32) (4.0 g, 18.6 mmol) and glacial acetic acid (2.45 mL, 42.8 mmol) in acetonitrile (63 mL) was cooled in an ice bath and treated dropwise with triethylamine (5.44 mL, 39.1 mmol). The solution was allowed to warm to room temperature and stirred for 2 h, then diluted with brine and extracted with diethyl ether. The extract was washed with 1 mol L^{-1} aq. HCl and brine, dried and evaporated under reduced pressure to give a brown gum (3.3 g) that was dissolved in boiling water, decolorized with charcoal, and extracted with diethyl ether. The extract was dried and evaporated and the residue was crystallized from ethyl acetate –

© 2004 NRC Canada

hexanes to give the title compound **10**. Yield: 0.9 g (25%); mp 94 °C. ^{1}H NMR (400 MHz, $CDCl_3$ – 10% CD_3OD) δ: 2.21 (s, 3H, CH_3), 5.30 (s, 2H, CH_2), 6.94–7.46 (m, 4H, Ar-H). Anal. calcd. for $C_{10}H_{10}O_4$: C 61.85, H 5.19; found: C 61.56, H 5.16.

Product studies

Preparative photolyses for **1**, **2**, **4**, and **5** were carried out with samples (10–20 mg) dissolved in the appropriate solvent (40–100 mL) and transferred to a quartz tube. The solution was irradiated in a RPR-100 photochemical reactor fitted with 254 or 300 nm lamps with continuous cooling (by a cold finger) and purging by a stream of argon for approximately 10 min before and continuously during irradiation (via a long stainless steel needle). Photolysis times ranged from 3 to 30 min, depending on the conversion desired, the efficiency of the reaction, and the size of the sample. After photolysis, aqueous samples were worked up by extraction with CH_2Cl_2 after addition of aq. NaCl. Direct evaporation of the organic solvent was used when samples were irradiated in wholly organic solvents. Typical experiments are described below. Analytical scale photolyses were employed for **9** and **10**, using NMR tubes, as described below.

Photolysis of 1

Photolysis of **1** (20 mg) in 1:1 D_2O–CH_3CN (v/v) (40 mL) with eight lamps (300 nm) for 20 min followed by standard workup gave starting material with deuterium incorporation at the 5-position (55%) and 8-position (19%) with no side products, as determined by 500 MHz ^{1}H NMR. MS analysis of the same sample indicated that it consisted of 37% non-deuterated, 52% monodeuterated, and 11% dideuterated substrate, giving the equivalent overall deuterium incorporation as measured by NMR.

Photolysis of 2

Photolysis of **2** (20 mg) in 1:1 D_2O–CH_3CN (v/v) (40 mL) with 16 lamps (300 nm) for 1 h followed by standard workup gave only starting material with no deuterium incorporation at any position, as determined by 500 MHz ^{1}H NMR. MS analysis of the same sample also indicated that no additional deuterium was incorporated in the sample following photolysis.

Photolysis of 4

Photolysis of **4** (50 mg) in 1:1 H_2O–CH_3OH (v/v) (100 mL) with four lamps (300 nm) for 1 min followed by standard workup gave methyl ether **29** in 48% conversion. Photolysis product **29** was chromatographically isolated on silica gel (10% EtOAc in CH_2Cl_2). ^{1}H NMR (300 MHz, $CDCl_3$) δ: 1.58 (d, 3H, CH_3), 3.30 (br s, 3H, OCH_3), 5.04 (q, 1H, ArC-H), 5.80 (br s, 1H, OH), 6.82 (d, 1H, Ar-H), 7.33 (t, 1H, Ar-H), 7.48 (t, 1H, Ar-H), 7.59 (d, 1H, Ar-H), 7.70 (d, 1H, Ar-H) 8.16 (d, 1H, Ar-H). HR-MS calcd. for $C_{13}H_{14}O_2$: 202.0994; observed: 202.0993.

Photolysis of 5

Photolysis of **5** (20 mg) in 1:1 H_2O–CH_3OH (v/v) (100 mL) containing $NaHCO_3$ (25 mg) with 16 lamps (300 nm) for 3 min followed by standard workup cleanly regenerated starting material with no reaction observable by 300 MHz ^{1}H NMR. A small amount of thermal decomposition was observed when $NaHCO_3$ was not added to the solution.

Photolysis of 9 and 10

In a typical procedure, 2–5 mg of substrate was dissolved in ~2 mL of D_2O–CD_3CN (1:1). The solution was transferred to an NMR tube and deoxygenated by purging with argon for 10 min. The tube was then placed in the middle of the Rayonet reactor (16 × 300 nm lamps) and irradiated for up to 30 min. ^{1}H NMR spectra were taken before and after photolysis without workup. Both **9** and **10** were found to be photochemically inert for up to 30 min photolysis. Under these conditions, **6** would have resulted in quantitative conversion to **8** in about 10 min of photolysis.

Quantum yields

The quantum yield for total deuterium incorporation in **1** has been previously reported (8) to be $\Phi_{H\text{-}D}$ = 0.11 in 99% D_2O, pD 3. Our results demonstrate that the exchange efficiency is the same at pD 7 and pD 3, and that the exchange efficiency appears to plateau around 1:1 H_2O–CH_3CN. Given these data, it is reasonable to assume that $\Phi_{H\text{-}D}$ in neutral 1:1 D_2O–CH_3CN solution should be approximately equal to 0.11 as previously measured. The quantum yield for the photosubstitution reaction of **4** was measured relative to the photomethanolysis reaction of *o*-hydroxybenzhydrol in H_2O–CH_3OH (1:1) (Φ = 0.46) (5). Preparative scale photoreactions (10^{-3} mol L^{-1}, 50 mL H_2O–CH_3OH (1:1), Ar purged, 2 × 254 nm lamps, 1–3 min) were performed for **4** and the reference compound, and the extent of reaction was measured by 300 MHz ^{1}H NMR. The reported value of Φ = 0.84 ± 0.04 is the average of three such runs.

Fluorescence measurements

Steady-state fluorescence measurements were conducted on a Photon Technology International A-1010 (PTI) QuantaMaster luminescence spectrometer. All solutions (absorbance ≈ 0.1 at λ_{ex} 300 nm) were purged with argon prior to excitation. Fluorescence lifetimes were measured on a PTI LS-1 instrument using time-correlated single-photon-counting techniques (10 000 counts, λ_{ex} 300 nm, λ_{em} 350 nm).

Laser flash photolysis (LFP)

A Spectra-Physics excimer laser (308 nm, ~10 ns, <30 mJ/pulse) was used for excitation and signals were digitized with a Tektronix TDS 520 recorder. Samples of OD ~ 0.3 at 308 nm were prepared and irradiated in quartz cells. Static cells were used for the kinetic studies of samples, otherwise flow cells were used for all other studies. Samples in flow cells were continuously purged with a stream of N_2 or O_2. Samples in static cells were purged with N_2 or O_2 then sealed prior to photolysis.

Acknowledgments

We thank the Natural Sciences and Engineering Research Council of Canada (NSERC) for continued support of this research, and for a post-graduate scholarship to one us

© 2004 NRC Canada

(ML). We thank Ms. Kai Zhang and Dr. Darryl W. Brousmiche for some initial experiments.

References

1. P. Wan, B. Barker, L. Diao, M. Fischer, Y. Shi, and C. Yang. Can. J. Chem. **71**, 465 (1996).
2. P. Wan, D.W. Brousmiche, C.Z. Chen, J. Cole, M. Lukeman, and M. Xu. Pure Appl. Chem. **73**, 529 (2001).
3. R.W. Van de Water and T.R.R. Pettus. Tetrahedron, **58**, 5367 (2002).
4. M. Fischer and P. Wan. J. Am. Chem. Soc. **121**, 4555 (1999).
5. L. Diao, C. Yang, and P. Wan. J. Am. Chem. Soc. **117**, 5369 (1995).
6. Y. Shi and P. Wan. J. Chem. Soc. Chem. Commun. 273 (1997).
7. P. Seiler and J. Wirz. Helv. Chim. Acta, **55**, 2693 (1972).
8. S.P. Webb, L.A. Philips, S.W. Yeh, L.M. Tolbert, and J.H. Clark. J. Phys. Chem. **90**, 5154 (1986).
9. (*a*) M. Lukeman and P. Wan. J. Chem. Soc. Chem. Commun. 1004 (2001); (*b*) M. Lukeman and P. Wan. J. Am. Chem. Soc. **124**, 9458 (2002).
10. (*a*) R.S. Givens, A. Jung, C.-H. Park, J. Weber, and W. Bartlett. J. Am. Chem. Soc. **119**, 8369 (1997); (*b*) R.S. Givens, P.S. Athey, B. Matuszewski, L.W. Kueper III, J.-y. Xue, and T. Fister. J. Am. Chem. Soc. **115**, 6001 (1993); (*c*) P.G. Conrad II, R.S. Givens, B. Hellrung, C.S. Rajesh, M. Ramseier, and J. Wirz. J. Am. Chem. Soc. **122**, 9346 (2000).
11. K. Zhang, J.E.T. Corrie, V.R.N. Munasinghe, and P. Wan. J. Am. Chem. Soc. **121**, 5625 (1999).
12. W.F. Short and H. Wang. J. Chem. Soc. 991 (1950).
13. S. Lee, S.P. Frescas, and D.E. Nichols. Synth. Commun. **25**, 2275 (1995).
14. M.K. Nayak and A.K. Chakraborti. Tetrahedron Lett. **38**, 8749 (1997).
15. J.B. Birks. Photophysics of aromatic molecules. Wiley-Interscience, New York. 1983. p. 123.
16. (*a*) H. Shizuka and S. Tobita. J. Am. Chem. Soc. **104**, 6919 (1982); (*b*) H. Shizuka. Acc. Chem. Res. **17**, 141 (1985).
17. R. Pollard, S. Wu, G. Zhang, and P. Wan. J. Org. Chem. **58**, 2605 (1993).
18. P. Wan and G. Zhang. Res. Chem. Intermed. **19**, 119 (1993).
19. (*a*) R.A. McClelland. Tetrahedron, **52**, 6823 (1996); (*b*) N. Mathivanan, F. Cozens, R.A. McClelland, and S. Steenken. J. Am. Chem. Soc. **114**, 2198 (1992).
20. D.N. Kevill and S.W. Anderson. J. Org. Chem. **56**, 1845 (1991).
21. Y. Chiang, A.J. Kresge, B. Hellrung, P. Schünemann, and J. Wirz. Helv. Chim. Acta, **80**, 1106 (1997).
22. H. Shizuka, H. Hagiwara, and M. Fukushima. J. Am. Chem. Soc. **107**, 7816 (1985).
23. D.W. Brousmiche and P. Wan. J. Photochem. Photobiol. A, **149**, 71 (2002).
24. M. Lukeman and P. Wan. J. Am. Chem. Soc. **125**, 1164 (2003).
25. H.J.E. Lowenthal and L. Gottlieb. J. Org. Chem. **57**, 2631 (1992).
26. A.I. Myers and K. Higashiyama. J. Org. Chem. **52**, 4592 (1987).
27. M. Sawada, T. Fujii, Y. Tairaka, and Y. Yukawa. Bull. Chem. Soc. Jpn. **48**, 3356 (1975).
28. T. Bisanz and M. Bukowska. Rocz. Chem. **48**, 777 (1974).
29. N.P. Buu-Hoi and P. Cagniant. Rec. Trav. Chim. Pays–Bas, **64**, 214 (1945).
30. W.H. Hunter, R.M. Quinton, P.H. Sherman, C.R. Worthing, and R.J. Boscott. J. Med. Chem. **7**, 167 (1964).
31. J. Cason. J. Am. Chem. Soc. **63**, 828 (1941).
32. S.J. Pasaribu and L.R. Williams. Aust. J. Chem. **26**, 1327 (1973).

© 2004 NRC Canada

Synthetic studies on cyathin diterpenes — Total synthesis of (±)-allocyathin B_3[1]

Dale E. Ward, Yuanzhu Gai, Qi Qiao, and Jianheng Shen

Abstract: The synthesis of racemic allocyathin B_3 from an advanced intermediate possessing the ring system and relative stereochemistry but lacking the isopropyl and hydroxymethyl groups is reported. The isopropyl group was introduced by radical cyclization of a methyl propargyl acetal of an α-bromoketone and the hydroxymethyl group was generated by Pd-catalyzed carbonylation of a vinyl triflate. The route provides functionalized intermediates that could allow access to more complex members of the cyathin family of diterpenes. Several modifications and improvements to the procedures previously described for the synthesis of the advanced intermediate have been achieved.

Key words: cyathin diterpenes, cyathanes, allocyathin B_3.

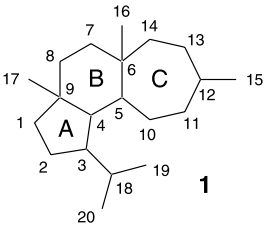
Résumé : On a complété la synthèse de l'allocyathine B_3 à partir d'un intermédiaire avancé comportant le système cyclique et la stéréochimie relative dans lequel il manquait les groupes isopropyle et hydroxyméthyle. Le groupe isopropyle a été introduit par une cyclisation radicalaire d'un cétal méthylique et propargylique d'une α-bromocétone et le groupe hydroxyméthyle a été généré par une carbonylation catalysée par le Pd d'un triflate de vinyle. Cette voie fournit des intermédiaires fonctionnalisés qui permettent d'accéder aux membres plus complexes de la famille de la cyathine des diterpènes. On a développé plusieurs modifications et améliorations aux méthodes décrites pour la synthèse de l'intermédiaire avancé.

Mots clés : diterpènes de la famille de la cyathine, cyathanes, allocyanthine B_3.

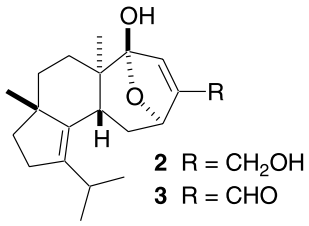
[Traduit par la Rédaction]

Introduction

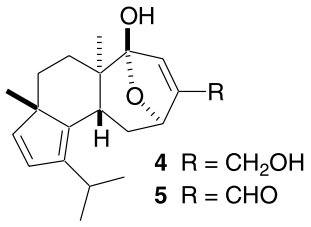
In the1970s, Ayer and co-workers described (1) a family of ca. 20 structurally related diterpenes, isolated from the culture broths of several species of bird's nest fungi of the genus *Cyathus*.[3] These so-called cyathins have the unique cyathane (**1**) (1*b*) carbon skeleton and were the first members of a then new diterpene family. All cyathins have an unfunctionalized B ring bearing trans methyl groups at C-6 and C-9 and, with the exception of allocyathin B_2 (**6**), possess a trans 6–7 ring fusion (cf. **2**–**5**); differences occur in the degree of oxidation and unsaturation around the five-membered and seven-membered rings. More recently, several cyathane diterpenoids with structures closely related to the cyathins have been isolated from a variety of fungi. For example, the striatins (from *C. striatus*) (2) and the erinacines (from *Hericium erinaceum*) (3) are carbohydrate conjugates of cyathins (e.g., **7**), the sarcodonins (from *Sarcodon scabrosus*) (4) are cyathins with a C-19 alcohol (e.g., **8**), and the scabronines (also from *S. scabrosus*) (5) are cyathins with a C-17 carboxylic acid.



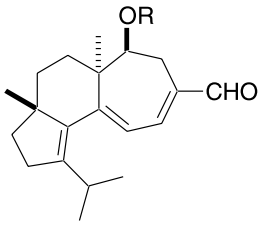
1



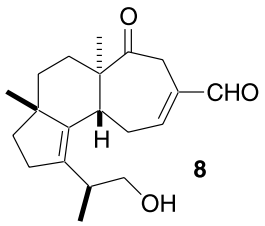
2 R = CH_2OH
3 R = CHO



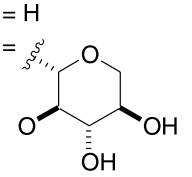
4 R = CH_2OH
5 R = CHO



6 R = H
7 R =



8



(1–β-D-xylopyranosyl)

Received 25 July 2003. Published on the NRC Research Press Web site at http://canjchem.nrc.ca on 2 February 2004.

This paper is dedicated to Professor Edward Piers for his numerous contributions to chemistry as a researcher, teacher, mentor, and colleague; a finer role model is hard to imagine.

D.E. Ward,[2] Y. Gai, Q. Qiao, and J. Shen. Department of Chemistry, University of Saskatchewan, 110 Science Place, Saskatoon SK S7N 5C9, Canada.

[1]This article is part of a Special Issue dedicated to Professor Ed Piers.

[2]Corresponding author (e-mail: Dale.Ward@usask.ca).

[3]These fungi belong to the family Nidulariaceae (derived from nidula, meaning little nest) and are so named because the fruit bodies that contain lentil-shaped spores resemble a miniature bird's nest.

 doi: 10.1139/V03-185 © 2004 NRC Canada

Many of the cyathins show strong antimicrobial activity (1*b*, 6) particularly the unsaturated aldehydes cyathin B_3 (**3**) and cyathin C_3 (**5**). The recent discovery that certain erinacines (3) and scarborines (5, 7) can stimulate the production of nerve growth factor (NGF) and thereby have potential therapeutic value in the treatment of neurodegenerative diseases has generated substantial interest in the synthesis of cyathane diterpenes (8). Although several strategies have successfully produced 5-6-7 tricyclic intermediates (9, 10), only four groups have achieved the total syntheses of a naturally occurring cyathane diterpene. Both Snider et al. (11) and Tori et al. (12) have reported syntheses of racemic allocyathin B_2 (**6**); Snider et al. also obtained (+)-erinacine A (**7**) by separation of the diastereomers resulting from glycosidation of (±)-**6** with D-xylose. The elegant synthesis of sarcodonin G (**8**) by Piers et al. (13) was the first of a cyathane with the characteristic trans 6–7 ring fusion. In this paper we report a full account of our work culminating in the total synthesis of racemic allocyathin B_3 (**4**) by a general route that should be applicable to many of the cyathane diterpenes (14).

Results and discussion

The biological activity and novel structure of the cyathins prompted Ayer et al. to initiate synthetic studies. Cyathin A_3 (**2**), the major metabolite isolated from *C. helenae*, can be easily transformed into several of the other members including **3**–**6** (1*d*, 1*f*) and was a logical synthetic target. The initial objective was a 5-6-6 tricyclic intermediate (15) and the feasibility of obtaining the desired seven-membered C ring by expansion of a six-membered cyclic ketone was demonstrated in a model study (15*c*). Approaches based on A + C → AC → ABC (15*b*) and on C → BC → ABC (15*c*) strategies failed to produce a tricyclic intermediate (15*a*).[4] In a conceptually different approach, the C ring of **2** was envisaged to arise from intramolecular aldol reaction of a 6-oxoheptanal derived by oxidative fragmentation of a 1-methylcyclohexene and a suitable 5-6-6 tricyclic intermediate (i.e., **13**) was efficiently prepared using a B → BC → ABC strategy (Scheme 1) (15*c*, 16).

Ward (9) successfully converted **13** into **19** (Scheme 1), an intermediate possessing the ring system and relative stereochemistry present in cyathin diterpenes (cf. **2**–**5**). In considering the conversion of **19** into a cyathin diterpene (e.g., **2**), strategies for introduction of an isopropyl group at C-3 (cyathane numbering) were not obvious. After considerable experimentation, a method was established to introduce a 3-carbon side chain based on radical cyclization of a propargyl α-bromoacetal (cf. **21** and **22** in Scheme 2); however, all attempts to unravel the resulting 3-methylenetetrahydrofuran in **22** to reveal the A ring present in one of the cyathins failed (17). Several years later, the significant interest in cyathane diterpenes as inducers of NGF production prompted us to reexamine this synthetic route (18).

Several modifications and improvements to the procedures previously described (9, 16) for the synthesis of the tricyclic intermediate **19** from **9** (Scheme 1) have been achieved resulting in an improved overall yield (10% → 12%). We found that the Diels–Alder reaction of **9** and **10** (a 1:1 mixture of *E*- and *Z*-isomers) was conveniently conducted in the absence of solvent at 120 °C to give the adduct **11** as a single stereoisomer in excellent yield after distillation. The relative configuration of **11** was assigned based on the observation of positive NOEs at HC-8a on irradiation of H_3CC-4a and at HC-3 on irradiation of H_3CC-5. The formation of **11** is consistent with an endo reaction of **9** and (*Z*)-**10** and the preferential reaction of (*Z*)-**10** was confirmed by the isolation of **10** enriched in the (*E*)-isomer from the Diels–Alder reaction mixture. Photochemical [2 + 2] addition of allene to **11** proceeded as reported (15*c*, 16) with the exception that trifluoroacetic acid (in place of Amberlyst-15) was used to hydrolyze the photoadducts to give a 4:1 mixture of **12a** and **12b**, respectively, in 85% yield after chromatography. Contrary to the previous report (16), pure **12a** could be obtained by fractional crystallization of this mixture, albeit in modest yield. More conveniently, the crude mixture of **12a** and **12b** (i.e., before chromatography) was subjected to the previously described protocol (9) to give **13** in 55% overall yield from **11**. It is noteworthy that crystalline **13** is obtained directly from the crude reaction mixture after this sequence and in only five operations from **9** in 50% yield without the need for chromatography.

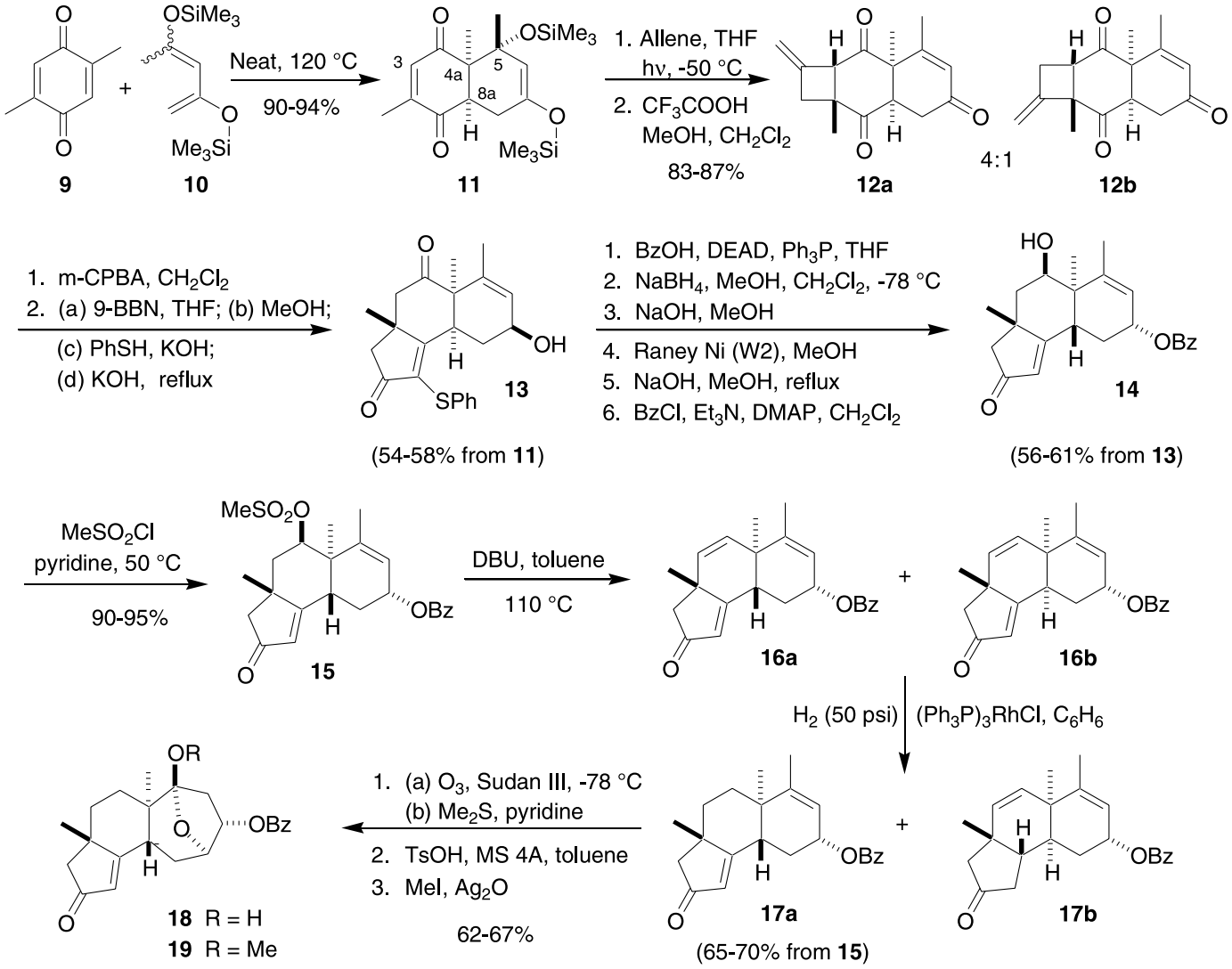
The reported (9) transformation of **13** into **14** (Scheme 1) required a tedious chromatographic purification step after Mitsunobu benzoylation to remove a large amount of by products. We found that this purification could be avoided because the subsequent chemoselective $NaBH_4$ reduction (19) of the C-5 ketone was tolerant of these contaminants and after base hydrolysis of this crude reaction mixture, aqueous work up removed most of the impurities other than Ph_3PO. The presence of Ph_3PO did not interfere with the ensuing Raney Ni desulfurization, base-catalyzed epimerization of the ring junction, and benzoylation thereby allowing the six-stage conversion of **13** into **14** to be carried out with unpurified intermediates in an overall yield comparable to that reported previously. Using the published (9) protocol, we were unable to reproduce the conversion of **14** into **16a**, the major difficulty being the formation of up to 25% of the inseparable epimerized isomer **16b** along with **16a**. Reduction of this mixture of **16a** and **16b** with H_2 and Wilkinson's catalyst gave a separable mixture of the desired **17a** and **17b**. Because **16b** was much less susceptible to reduction than **16a** under these conditions, pure **16b** could be isolated from incomplete reductions of the mixture. After much experimentation it was determined that the formation of **16b** was greatly attenuated (**16a**:**16b** > 20:1) if freshly distilled DBU was used to effect elimination of **15** and if the reaction time was strictly monitored. Although the reaction under these conditions could successfully be conducted with crude **15** (as reported) reproducible results were obtained only using purified materials. Reduction of **16a** as before (9) gave **17a** in 67% overall yield from **14**.

Considerable effort was directed at optimizing the conversion of **17a** to **19** (Scheme 1). Chemoselective ozonolysis of the cyclohexene-type olefin in **17a** was achieved in the pres-

[4] A, B, and C refer to the rings in **1** and the various synthetic strategies can be characterized by the sequence in which the rings are introduced.

© 2004 NRC Canada

Scheme 1.

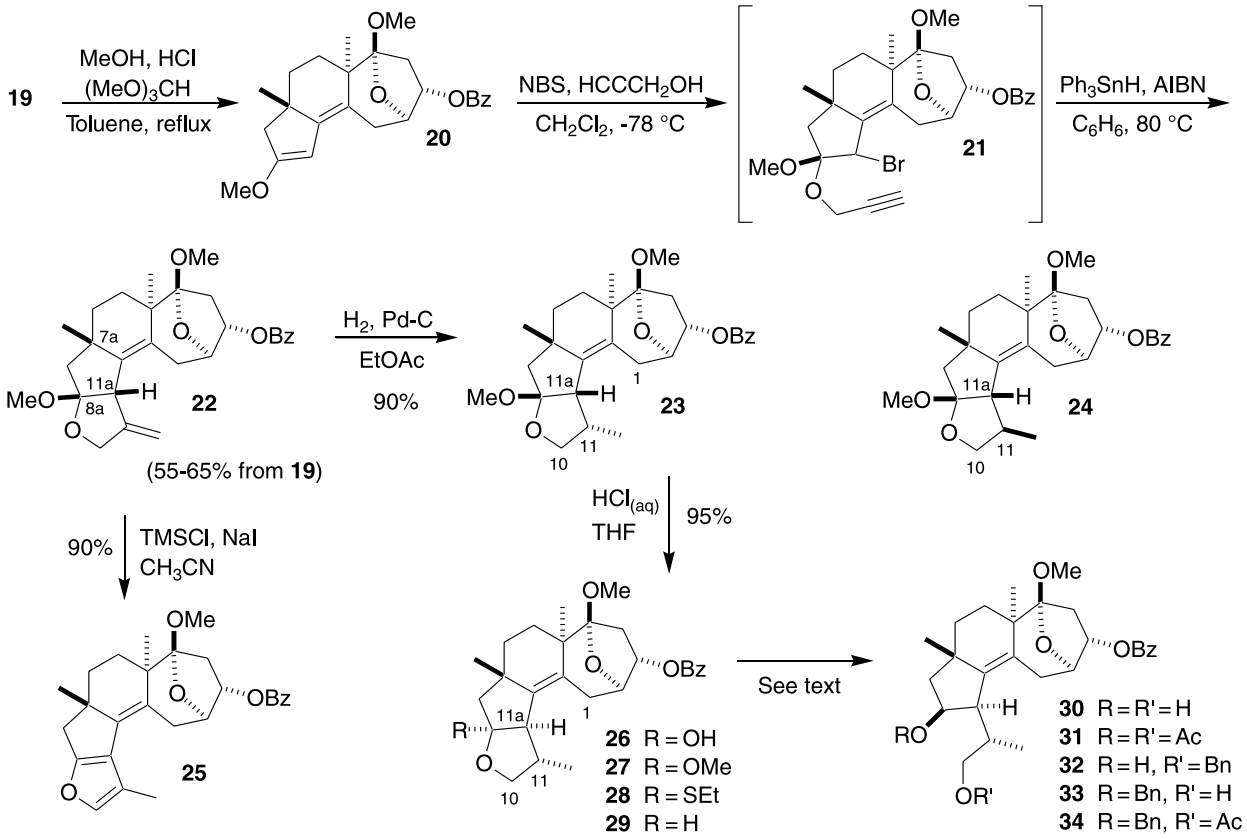


ence of Sudan III (20) to give the corresponding ketoaldehyde (9) (Scheme 1). In the presence of TsOH, the ketoaldehyde underwent aldol cyclization with concomitant 1,2-migration of the benzoyl group to give **18** along with significant quantities (3:1) of a side product derived from simple hydrolysis of the benzoate group in the ketoaldehyde (9). The cyclization reaction was very sensitive to the presence of water and various conditions (different acids, solvents, drying protocols) were attempted to improve the yield of **18**. Optimal results were obtained with the use of dry TsOH in dry toluene in the presence of 5 Å molecular sieves at 50 °C, which gave **18** in 80% yield and with very little of the hydrolysis side product (<5%). All of the above work was conducted using a rather old jar (>30 years) of $TsOH{\cdot}H_2O$ (slightly off-white flakes, Eastman); we were surprised to find that cyclization could not be effected using $TsOH{\cdot}H_2O$ from a "new" bottle (white crystals, Aldrich). Although the source of this discrepancy is uncertain, after much experimentation we were able to reproduce the cyclization using new $TsOH{\cdot}H_2O$ with 5% of H_2SO_4. We found that methylation of **18** with MeI to give **19** proceeded in higher yield and with fewer side products using freshly prepared Ag_2O rather than NaH (9) as the base.

Numerous attempts to introduce an isopropyl or other suitable functional group at the α-position of the cyclopentenone in **19** failed. It was noted that a product tentatively identified as the methyl dienol ether of **18** was isolated from an unsuccessful attempt to produce **19** from **18** by treatment with acidic MeOH and $(MeO)_3CH$ in refluxing toluene. Subjecting **19** to similar conditions gave **20** in near quantitative yield (Scheme 2). Our interest in the formation of a dienol ether such as **19** was inspired by the possibility of forming the desired C—C bond by radical cyclization of a derived α-bromoacetal as reported by the Ueno (21) and Stork (22) groups. For our purposes, cyclization of an allylic radical (23) would be required, which at that time (17) had not been demonstrated in the literature. Cohalogenation (24) of **20** with *N*-bromosuccinimide (NBS) and propargyl alcohol gave the somewhat unstable **21** as a single diastereomer (^1H NMR) which cyclized to **22** (60% overall yield from **19**) on treatment with Ph_3SnH and AIBN in refluxing benzene (25). Under the same conditions but replacing propargyl al-

© 2004 NRC Canada

Scheme 2.



cohol with allyl alcohol, **20** was converted into a 1:1 mixture of **23** and **24** in 45% yield.[5] Hydrogenation of **22** gave **23** as a single diastereomer in good yield. The relative configuration of **22** was established by NOE experiments; HC-11a and H_3CC-7a were enhanced on irradiation of the C-8a methoxy protons and the C-8a methoxy group was enhanced on irradiation of the C-7a methyl protons establishing the cis relationship among these three groups. The relative configuration of **23** was assigned based on the $^3J_{HH}$ coupling constants between HC-11 and H_2C-10 (4, <1 Hz) and HC-11a (6.5 Hz), which are consistent with the corresponding H-H dihedral angles (44°, –81°, and –28°, respectively) calculated for **23** by molecular mechanics;[6] the endo orientation of the C-11 methyl group accounts for its significant shielding by the alkene (δ_H 0.83) and is the expected result of hydrogenation from the sterically less-encumbered convex face of the fused ring system. It is noteworthy that the relative configuration at C-11 in **23** is the same as that in the sarcodonins A and G (4) and possibly in the cyathins A_4 and C_5 (1*d*). It was assumed that the relative configuration at C-7a and C-11a in **24** was the same as that in **22** and **23**. The exo orientation of the C-11 methyl group in **24** (δ_H 1.23) is consistent with the observed $^3J_{HH}$ coupling constants between HC-11 and H_2C-10 (6, 7 Hz) and HC-11a (3.5 Hz) as expected from the corresponding H-H dihedral angles (157°, 32°, and –137°, respectively) calculated for **24** by molecular mechanics.[6]

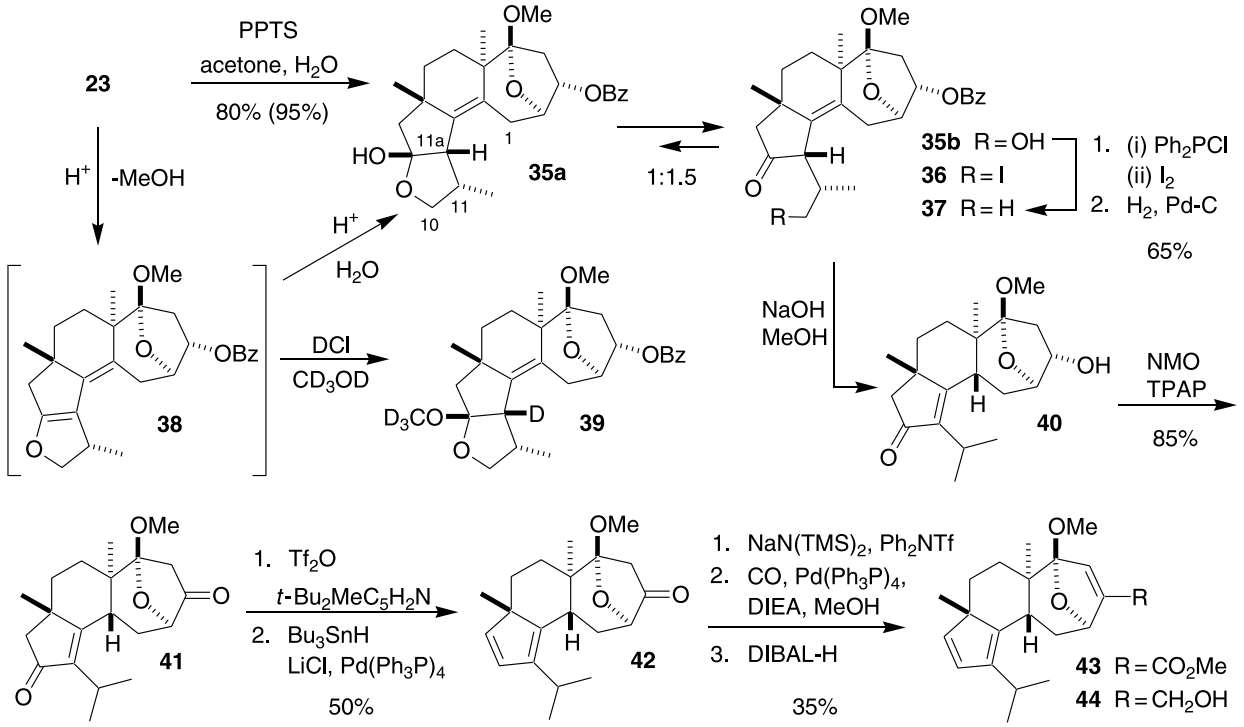
Unmasking the isopropyl group present in **22** proved to be difficult. Treatment with protic or Lewis acids led to loss of methanol and formation of the corresponding furan derivative as observed in related systems (26). For example, treatment of **22** with TMSI (prepared in situ) gave **25** in 90% yield (Scheme 2). Because of the facile formation of **25** from **22**, efforts were directed at unraveling the reduced derivative **23**. Exposure of **23** to 10% aq. HCl in THF slowly (ca. 14 h) produced the isomerized hemiacetal **26** without evidence of an intermediate (by TLC monitoring). The relative configuration of **26** was assigned based on the large changes in the $^3J_{HH}$ coupling constants between H_2C-10 and HC-11 (8, 10.5 Hz) and in the chemical shift of the C-11 methyl group (δ 1.32) compared to **23** (and **35a**, vide infra). These coupling constants are consistent with the corresponding H-H dihedral angles (–36°, –161°) for **26** calculated by molecular mechanics,[6] which also indicated that **26** was 1.3 kcal/mol more stable than **35a**.

Attempts to trap the hydroxy ketone tautomer of hemiacetal **26** by formation of acetate (Ac_2O, DMAP), xanthate ((*i*) CS_2, DBU; (*ii*) MeI), or dithioacetal (EtSH, H^+)[7] derivatives failed. Alternatively, reduction of **26** with $NaBH_4$ in ethanol gave the diol **30** in 70% yield (Scheme 2).

[5] This reaction was not optimized.
[6] CaChe, version 3.9.
[7] The cyclic thioacetal **28** was obtained under these conditions.

© 2004 NRC Canada

Scheme 3.



Deoxygenation of one or both hydroxy groups in **30** via a Barton-type process (27) was envisaged; however, attempted formation of a xanthate ((*i*) NaH, CS_2; (*ii*) MeI), thionocarbonate ($C_6F_5OC(S)Cl$, DMAP, pyridine) (28) or cyclic thionocarbonate (29) derivative surprisingly resulted in the formation of **29**. Similar cyclization of a sterically congested 1,4-diol on attempted derivatization has been observed previously (30). Acetylation of **30** (Ac_2O, DMAP, Et_3N) smoothly gave the diacetate **31** but benzylation of **30** (NaH, BnBr, Bu_4NI) gave a 1:1 mixture of the monobenzyl ethers **32** and **33** in 65% yield. Unfortunately, all efforts to deoxygenate the alcohol group in **32** or **33** were unsuccessful. For example, although acetylation of **33** (Ac_2O, Et_3N, DMAP) to give **34** was uneventful, attempted formation of a thionocarbonate ($C_6F_5OC(S)Cl$, DMAP, pyridine) from **33** unfortunately gave **29**.

A serendipitous observation was crucial to the eventual endgame (Scheme 3). On one occasion (31),[8] hydrogenation of **22** under the usual conditions unexpectedly gave **35** (25%) along with **23**. Importantly and in sharp contrast to **26**, **35** was a 1.5:1 mixture (by NMR in $CDCl_3$ solution) of the hydroxy ketone (**35b**) and hemiacetal (**35a**) tautomers, respectively, and esters of the hydroxy ketone tautomer **35b** could be prepared in good yield. A more detailed investigation of the hydrolysis of **23** was undertaken. On standing in $CDCl_3$ solution, **23** quantitatively isomerized into **27** within 3 days (presumably catalyzed by adventitious HCl); molecular mechanics[6] indicated that **27** was 2.1 kcal/mol more stable than **23** largely due to the decreased steric interaction between the C-11 methyl group with H_2C-1 in the former. Hydrolysis of **27** (10% aq. HCl in THF, 14 days) also gave **26** but much more slowly than hydrolysis of **23** (14 h) under the same conditions. Exposure of **23** to DCl in CD_3OD solution gave **39** at the same rate as the loss of **23** suggesting the formation of **38** as an intermediate. The formation of **39** indicated that hydrolysis of **23** without isomerization to **26** might be possible. After considerable experimentation, we found that reaction of **23** with pyridinium 4-methylbenzenesulfonate (PPTS) in aqueous acetone for 12 days gave **35** (80%) along with recovered **23** (15%) (Scheme 3).

Several methods for deoxygenation of the alcohol group in **35b** were attempted with varying success. The desired transformation was best accomplished by reaction of **35** with Ph_2PCl followed by I_2 (32) and reduction of the resulting iodide **36** with H_2 over Pd–C to give **37** (65% overall from **35**). At this stage, the amount of available material necessitated a direct route to the target with little opportunity for optimization. Treatment of **37** with NaOH in MeOH resulted in hydrolysis of the benzoate ester with concomitant isomerization of the double bond into the required position to give **40**. This isomerization reestablishes the desired trans 6–7 ring fusion, as expected; the presence of the transannular acetal within the seven-membered ring makes the cis-fused diastereomer impossibly strained. To avoid schemes requiring protection and deprotection steps, **40** was directly oxidized to diketone **41** with tetrapropylammonium perruthenate (TPAP) and *N*-methylmorpholine (NMO) (33). Selective deoxygenation of the cyclopentenone carbonyl was achieved by reaction of **40** with triflic anhydride (Tf_2O) in the presence of the hindered base 2,6-di-*tert*-butyl-4-methylpyridine (34) to chemoselectively give the dienol triflate, which was reduced to cyclopentadiene **41** by Pd-catalyzed reaction with Bu_3SnH (35, 36). Finally, introduction of the vinyl hydroxymethyl group was achieved by Pd-

[8] This outcome was presumably due to the presence of adventitious acid (31) but could not be reproduced despite numerous attempts.

© 2004 NRC Canada

catalyzed carbonylation (37) of the vinyl triflate derived from **42** followed by DIBAL-H reduction of the resulting methyl ester **43** to give (±)-**44**. Spectral data (^{1}H and ^{13}C NMR, UV, MS) for (±)-**44** closely matched that previously reported (1*b*, 38) for (–)-**44**. Hydrolysis of **44** to allocyathin B_3 (**4**; a mixture of hydroxy ketone and hemiacetal tautomers) proceeds readily in THF solution on exposure to aq. $HClO_4$ (1*d*).

In conclusion, the synthesis of racemic allocyathin B_3 (**4**) was achieved by introduction of the required isopropyl and vinyl hydroxymethyl groups onto an advanced intermediate (**19**) already possessing the correct ring system and relative stereochemistry. This is the first synthesis of a cyathin diterpene incorporating the trans 6–7 ring fusion and a fully functionalized seven–membered ring. The reported solution for introduction the isopropyl group (i.e., **19** → **40**; seven steps, 35% yield) provides intermediates with potentially useful functionality. For example, intermediate **35** has functionality that potentially can provide access to any of the various oxidation patterns present on the A (i.e., five-membered) ring of cyathin and related diterpenes. Indeed, simple modifications of the general route reported herein can be contemplated that might lead to *any* of the known cyathin diterpenes and several related natural products. Finally, this approach should be adaptable to asymmetric synthesis via an enantioselective Diels–Alder reaction of **9** and **10**. Our progress towards these objectives will be reported in due course.

Experimental

General methods

All solvents were distilled prior to use. Et_3N was distilled from CaH_2 and stored over KOH pellets. Anhydrous solvents were distilled under argon as follows: ether and tetrahydrofuran (THF) from benzophenone potassium ketyl; benzene, toluene, and CH_2Cl_2 from CaH_2 and stored over 4 Å molecular sieves; MeOH from $Mg(OMe)_2$. Unless otherwise noted, reactions were carried out under an atmosphere of argon and reaction temperatures refer to the bath. Concentration refers to removal of volatiles at water aspirator pressure on a rotary evaporator with final traces of solvent removed at high vacuum (ca. 1 mbar).

Preparative TLC (PTLC) was carried out on glass plates (20 × 20 cm) precoated (0.25 mm) with silica gel 60 F_{254}. Materials were detected by visualization under an ultraviolet lamp (254 nm) and (or) by treating a 1 cm vertical strip removed from the plate with a solution of phosphomolybdic acid (5%) containing a trace of ceric sulfate in aqueous sulfuric acid (5% v/v), followed by charring on a hot plate. Flash column chromatography (FCC) was performed according to Still et al. (39) with Merck Silica Gel 60 (40–63 μm). Dry FCC was performed according to Harwood (40). Medium pressure chromatography (MPC) was performed as described by Taber (41) using Silica Gel 60 (10–40 μm, type H). All mixed solvent eluents are reported as v/v solutions.

Spectral data

High resolution mass spectra (HR-MS) and low resolution mass spectra (LR-MS) were obtained on a VG 70E double focussing high resolution spectrometer; only partial data are reported. EI ionization was accomplished at 70 eV and CI at 50 eV with ammonia as the reagent gas; only partial data are reported. IR spectra were recorded on a Fourier transform interferometer using a diffuse reflectance cell (DRIFT); only diagnostic and (or) intense peaks are reported. Unless otherwise noted, NMR spectra were measured in $CDCl_3$ solution at 300 or 500 MHz for ^{1}H and 75 or 125 MHz for ^{13}C. For ^{1}H NMR, residual $CHCl_3$ in $CDCl_3$ was employed as the internal standard (δ 7.26); for ^{13}C NMR, $CDCl_3$ was employed (δ 77.2). The ^{1}H NMR chemical shifts and coupling constants were determined assuming first-order behavior. Multiplicity is indicated by one or more of the following: s (singlet), d (doublet), t (triplet), q (quartet), m (multiplet), br (broad), ap (apparent); the list of coupling constants (*J*) corresponds to the order of the multiplicity assignment. ^{1}H NMR spectra were normally obtained with a digital resolution of 0.2–0.3 Hz/pt and coupling constants are reported to the nearest 0.5 Hz. The ^{1}H NMR assignments were made on the basis of chemical shift and multiplicity and were confirmed, where necessary, by homonuclear decoupling and (or) NOE experiments. The multiplicity of ^{13}C NMR signals refers to the number of attached Hs (i.e., s = C, d = CH, t = CH_2, q = CH_3) and was determined by *J*-modulation (42).

Materials

Quinone **9** (43) and diene **10** (44) were prepared by known procedures. All other reagents were commercially available and, unless otherwise noted, were used as received.

*(4a*R*,5*R*,8a*R*)-rel-4a,5,8,8a-Tetrahydro-2,4a,5-trimethyl-5,7-bistrimethylsilyloxy-*p*-naphthoquinone (11)*

A suspension of **9** (10 g, 74 mmol) in **10** (85 g, 0.35 mol) was heated at 120 °C. After 42 h, excess **10** was removed by distillation (74–67 °C/1.7 mbar) and the residue was purified by bulb-to-bulb distillation (160–180 °C/0.2 mbar) to give **11** (16) as a viscous yellow oil (26 g, 93%).

*(2a*R*,3a*R*,7a*R*,8a*S*)-rel-1,2,2a,3,3a,4,5,7a,8,8a-Decahydro-2a,7,7a-trimethyl-1-methylenecyclobuta[b]naphthalen-3,5,8-trione (12a) and (2a*S*,3a*R*,7a*R*,8a*S*)-rel-1,2,2a,3,3a,4,5,7a,8,8a-decahydro-2a,7,7a-trimethyl-2-methylenecyclobuta[b]naphthalen-3,5,8-trione (12b)*

A solution of **11** (20 g, 53 mmol) and excess allene (150 mL) in dry THF (180 mL) was irradiated with a 1200 W mercury vapor lamp in a Pyrex vacuum-jacketed water-cooled immersion well while argon was bubbled through the solution. The entire apparatus was fitted with a dry ice condenser and was immersed in a dry ice – acetone bath that maintained an internal temperature of ca. –50 °C. After 12 h, the bath was removed and the excess allene was recovered (and could be reused) by passing the argon effluent through a dry ice condenser and the remaining reaction mixture was concentrated to afford the crude photoadducts as an oil (22 g). Trifluoroacetic acid (1 mL) was added to a stirred solution of the crude photoadducts (10 g) and MeOH (20 mL) in CH_2Cl_2 (180 mL). After 2 h, toluene (5 mL) was added and the mixture was concentrated to give crude **12** (6.8 g; **12a**:**12b** was 4:1 by ^{1}H NMR) that was purified by FCC (50% ethyl acetate in hexane) to give **12** as a 4:1 mixture of **12a** and **12b**, respectively, (5.3 g, 85% from **11**). Fractional crystallization of the mixture from ether–hexane gave pure **12a** (2.3 g; mp 120–124 °C, 136–138 °C (CCl_4)) and a second crop of highly enriched **12a** (0.4 g). Spectral data for

© 2004 NRC Canada

12a closely matched that reported previously (16). The mother liquor from the above crystallization (2.6 g) was a 1.1:1 mixture of **12a** and **12b**, respectively. NMR spectral data for **12b** was readily extracted from the spectra of the mixture. ^{1}H NMR (500 MHz, $CDCl_3$) δ: 5.90 (1H, q, J = 1.5 Hz, HC-6), 5.00 (1H, br s) and 5.00 (1H, br s) (exocyclic methylene Hs), 3.31 (1H, dddd, J = 2.5, 3, 10, 16 Hz, HC-1), 3.20 (1H, dd, J = 3.5, 4.5 Hz, HC-3a), 3.16 (1H, dd, J = 3.5, 17.5 Hz, HC-4), 3.04 (1H, dd, J = 5.5, 10 Hz, HC-8a), 2.99 (1H, dddd, J = 2, 2.5, 5.5, 16 Hz, HC-1), 2.54 (1H, dd, J = 4.5, 17.5 Hz, HC-4), 1.85 (3H, d, J = 1.5 Hz, H_3CC-7), 1.52 (3H, s, H_3C), 1.44 (3H, s, H_3C). ^{13}C NMR (75 MHz, $CDCl_3$) δ: 210.3 (s), 206.2 (s), 195.2 (s), 158.6 (s), 147.5 (s), 129.4 (d), 109.6 (t), 58.8 (s), 54,5 (s), 52.7 (d), 48.2 (d), 35.0, (t), 34.2 (t), 24.0 (q), 22.0 (q), 20.9 (q).

(3aS,5aR,8S,9aS)-rel-3a,4,5a,8,9,9a-Hexahydro-8-hydroxy-3a,5a,6-trimethyl-1-(phenylthio)-2H-benz[e]indene-2,5(3H)-dione (13)

Using the previously described procedure (9), a solution of crude **12** (1.78 g) (obtained as described above) and mCPBA (50%, 3.39 g, 9.92 mmol) in CH_2Cl_2 (200 mL) was stirred at room temperature for 48 h. $(CH_3)_2S$ (2 mL) was added and after 1 h, the reaction mixture was washed with satd. $NaHCO_3$, dried over Na_2SO_4, and concentrated to give the crude epoxides (1.85 g). 9-BBN (0.5 mol L^{-1} in THF, 24 mL, 12 mmol) was added to a stirred solution of the above crude epoxides (1.85 g) in THF (80 mL) at 0 °C under argon. The cooling bath was removed and after 5 h, MeOH (100 mL) was added. The solution was cooled to 0 °C and thiophenol (0.83 mL, 0.89 g, 8.1 mmol) and 2 N aq. KOH (0.31 mL, 0.62 mmol) were added. The solution was allowed to warm to room temperature and after 14 h, 2 N aq. KOH (8.5 mL, 1.2 mmol) was added and the resulting solution was heated under reflux for 2 h. The reaction mixture was concentrated, diluted with water, and extracted with CH_2Cl_2 (×3). The combined CH_2Cl_2 layers were washed with dilute aq. NaOH and with water, dried over Na_2SO_4, and concentrated to give an oil that on trituration with ether provided crystalline **13** (1.25 g, 54% from **11**; mp 209–211 °C). Spectral data for **13** closely matched that reported previously (16).

(3aS,5R,5aR,8R,9aR)-rel-8-(Benzoyloxy)-3,3a,4,5,5a,8,9,9a-octahydro-5-hydroxy-3a,5a,6-trimethyl-2H-benz[e]inden-2-one (14)

Using the previously described procedure (9), diethyl azodicarboxylate (0.23 mL, 0.25 mg, 1.5 mmol) was added dropwise over 5 min to a stirred solution of **13** (308 mg, 0.837 mmol), Ph_3P (309 mg, 1.18 mmol), and $PhCO_2H$ (155 mg, 1.27 mmol) in dry THF (36 mL) at 15–20 °C under argon. After 1 h, MeOH (5 mL) was added and the mixture was concentrated to give the crude benzoate **80** (1.09 g). $NaBH_4$ (128 mg, 3.38 mmol) was added to a solution of the above crude benzoate (1.09 g) in 1:1 CH_2Cl_2–MeOH (50 mL) at –78 °C. After standing at –78 °C for 14 h, acetic acid (2 mL) was added with stirring and the reaction mixture was allowed to warm to room temperature. Concentration from toluene (×2) provided the crude alcohol that was taken up in MeOH (100 mL) and 1 N NaOH (15 mL) was added and the reaction mixture was heated to 50 °C. After 16 h, the mixture was concentrated, diluted with water, and extracted with CH_2Cl_2 (×3). The combined CH_2Cl_2 layers were dried over Na_2SO_4, and concentrated to give the crude diol (650 mg; the major contaminant was Ph_3PO). W2 Raney Ni (1.6 mL) was added to a stirred solution of the above crude diol (650 mg) in MeOH (35 mL). After 2 h, the mixture was filtered through Celite and the combined filtrate and washings were concentrated to provide the crude desulfurized diol **82** (566 mg) that was taken up in MeOH (35 mL) and NaOH (545 mg, 13.6 mmol) was added and the resulting solution was heated under reflux for 5 days to effect epimerization of the ring junction. The reaction mixture was made slightly acidic (pH 6) by addition of 6 N HCl(aq) and $NaHCO_3$ (0.4 g) was added. The mixture was concentrated to dryness and the resulting solid was extracted with 30% MeOH in CH_2Cl_2 (×3). Concentration of the combined extracts provided a residue that was dissolved in CH_2Cl_2 (40 mL) and PhCOCl (0.28 mL, 0.34 g, 2.4 mmol), Et_3N (0.56 mL, 0.41 g, 4.0 mmol), and DMAP (20 mg, 0.16 mmol) were added. The reaction mixture was kept at 4 °C for 16 h and then MeOH (2 mL) was added. After 30 min, the solution was concentrated and the resulting oil was fractionated by MPC (eluting first with CH_2Cl_2 then with 75% ethyl acetate in hexane) to give **14** (171 mg, 56% overall yield from **13**). Spectral data for **14** closely matched that reported previously (9).

(3aS,5R,5aR,8R,9aR)-rel-8-(Benzoyloxy)-3,3a,4,5,5a,8,9,9a-octahydro-5-methanesulfonyloxy-3a,5a,6-trimethyl-2H-benz[e]inden-2-one (15)

Using the previously described procedure (9), methanesulfonyl chloride (0.90 mL, 1.3 g, 11 mmol) was added over 15 h using a syringe pump to a stirred solution of **14** (526 mg, 1.44 mmol) in dry pyridine (50 mL) at 50 °C under argon. The mixture was concentrated from toluene and then diluted with ethyl acetate, washed with dilute aq. HCl, satd. $NaHCO_3$ and brine, dried over Na_2SO_4, concentrated, and fractionated by FCC (25% ethyl acetate in hexane) to give **15** (580 mg, 91%). IR (KBr) ν_{max} (cm^{-1}): 2956, 1712, 1270, 1174, 918. ^{1}H NMR (300 MHz, $CDCl_3$) δ: 8.56 (2H, m, Ph), 7.59 (1H, m, Ph), 7.54 (2H, m, Ph), 5.85 (1H, d, J = 1.5 Hz, HC-1), 5.73 (1H, m, HC-8), 5.52 (1H, br s, HC-7), 5.07 (1H, dd, J = 2.5, 2.5 Hz, HC-5), 3.22 (1H, br d, J = 13 Hz, HC-9a), 3.08 (3H, s, H_3CSO_3), 2.59 (1H, dd, J = 2.5, 15.5 Hz, HC-4), 2.39 (1H, d, J = 18 Hz, HC-3), 2.35 (1H, m, HC-9), 2.26 (1H, d, J = 18 Hz, HC-3), 1.93 (1H, dd, J = 11, 13 Hz, HC-9), 1.91 (1H, dd, J = 2.5, 15.5 Hz, HC-4), 1.83 (3H, dd, J = 1.5, 1.5 Hz, H_3CC-6), 1.47 (3H, s, H_3C), 1.02 (3H, s, H_3C). ^{13}C NMR (75 MHz, $CDCl_3$) δ: 206.5 (s, C-4), 185.5 (s, C-2), 166.2 (s), 142.2 (s), 133.1 (d), 130.1 (s), 129.6 (d × 2), 128.3 (d × 2), 126.7 (d), 124.1 (d), 80.2 (d), 69.9 (d), 53.5 (t), 45.5 (s), 42.4 (s), 39.6 (q), 39.5 (t), 35.7 (d), 29.2 (q), 26.3 (t), 18.9 (q), 17.6 (q). LR-MS (EI), *m/z* (relative intensity): 348 ($[M - CH_3SO_3H]^+$, 11), 269 (16), 226 (22), 211 (28), 183 (12), 149 (36), 122 (20), 105 (100).

(3aR,5aR,8R,9aR)-rel-8-(Benzoyloxy)-3,3a,5a,8,9,9a-hexahydro-3a,5a,6-trimethyl-2H-benz[e]inden-2-one (16a)

Freshly distilled DBU (0.75 mL, 760 mg, 5.0 mmol) was added to a stirred solution of **15** (460 mg, 1.04 mmol) in toluene (30 mL) under argon and the mixture was heated under reflux. Reaction progress was monitored by TLC (50% ethyl acetate in hexane) and after 30–40 h, **15** was no longer

© 2004 NRC Canada

present. The mixture was diluted with ethyl acetate and washed with dilute aq. HCl, satd. $NaHCO_3$ and brine, dried over Na_2SO_4, concentrated, and fractionated by FCC (30% ethyl acetate in hexane) to give **16a** as a colorless oil (301 mg, 83%). Spectral data for **16a** closely matched that reported previously (9). Similar reactions using the DBU "as received" or with extended reaction times gave inseparable mixtures of **16a** with up to 25% of **16b** in lower yields (50%–75%).

(3aR,5aR,8R,9aS)-rel-8-(Benzoyloxy)-3,3a,5a,8,9,9a-hexahydro-3a,5a,6-trimethyl-2H-benz[e]inden-2-one (16b), (3aR,5aS,8S,9aR)-rel-8-(benzoyloxy)-3,3a,4,5,5a,8,9,9a-octahydro-3a,5a,6-trimethyl-2H-benz[e]inden-2-one (17a), and (3aR,5aR,8R,9aS,9bS)-rel-8-(benzoyloxy)-1,3,3a,5a,8,9,9a,9b-octahydro-3a,5a,6-trimethyl-2H-benz[e]inden-2-one (17b)

A solution of a 3:1 mixture of **16a** and **16b**, respectively (99 mg, 0.28 mmol), and $(Ph_3P)_3RhCl$ (25 mg, 0.027 mmol) in degassed benzene (12 mL) was stirred under a H_2 atmosphere (ca. 3 bar) for 72 h. The mixture was concentrated and fractionated by FCC (30% ethyl acetate in hexane) to give **17a** (68 mg, 68%), **17b** (23 mg, 23%), and **16b** (4.5 mg, 5%). Spectral data for **17a** closely matched that reported previously (9). Spectral data for **17b**: IR (KBr) ν_{max} (cm^{-1}): 2958, 2920, 1742, 1711, 1601, 1271, 1112. ^1H NMR (300 MHz, $CDCl_3$) δ: 8.06 (2H, m, Ph), 7.54 (1H, m, Ph), 7.44 (2H, m, Ph), 5.66 (2H, ap s, HC-4, HC-5), 5.44 (1H, m, HC-8), 5.38 (1H, br s, HC-7), 2.71 (1H, dd, J = 8.5, 19 Hz, HC-1), 2.43 (1H, d, J = 19 Hz, HC-1), 2.21 (1H, d, J = 18.5, HC-3), 2.10 (1H, d, J = 18.5 Hz, HC-3), 2.20–2.06 (3H, m, HC-9b, H_2C-9), 1.75 (3H, br s, H_3C), 1.60 (1H, ddd, J = 3.5, 3.5, 13 Hz, HC-9a), 1.31 (3H, s, H_3C), 1.06 (3H, s, H_3C). ^{13}C NMR (75 MHz, $CDCl_3$) δ: 218.1 (s), 166.5 (s), 144.3 (s), 133.2 (d), 132.9 (d, Ph), 132.5 (d), 130.6 (s), 129.6 (d × 2), 128.3 (d × 2), 119.7 (d), 68.9 (d), 49.9 (t), 42.1 (d), 41.4 (t), 40.7 (d), 39.6 (s), 38.8 (s), 28.4 (q), 28.3 (q), 26.3 (t), 19.6 (q). LR-MS (EI), *m/z* (relative intensity): 350 ($[M]^+$, 7), 228 (17), 213 (27), 171 (22), 162 (17), 143 (11), 119 (14), 105 (100). Spectral data for **16b**: IR (KBr) ν_{max} (cm^{-1}): 2965, 2927, 1712, 1616, 1267. ^1H NMR (300 MHz, $CDCl_3$) δ: 8.05 (2H, m, Ph), 7.58 (1H, m, Ph), 7.46 (2H, m, Ph), 6.03 (1H, s, HC-1), 5.82 (1H, d, J = 5.5 Hz, HC-7), 5.69 (1H, d, J = 10 Hz, HC-4 or HC-5), 5.62 (1H, d, J = 10 Hz, HC-4 or HC-5), 5.42 (1H, br s, HC-8), 3.17 (1H, br d, J = 13.5 Hz, HC-9a), 2.39 (2H, ap s, H_2C-3), 2.30 (1H, ddd, J = 3.5, 13.5, 13.5 Hz, HC-9), 2.08 (1H, br d, J = 13.5 Hz, HC-9), 1.87 (3H, s, H_3C), 1.38 (3H, s, H_3C), 1.09 (3H, s, H_3C). ^{13}C NMR (75 MHz, $CDCl_3$) δ: 218.1 (s), 166.5 (s), 144.3 (s), 133.2 (d), 132.9 (d, Ph), 132.5 (d), 130.5 (s), 129.6 (d × 2), 129.3 (d, C-3), 128.4 (d × 2), 119.7 (d), 68.9 (d), 49.9 (t), 40.6 (d), 39.6 (s), 38.7 (s), 28.4 (q), 28.3 (q), 26.3 (t), 19.6 (q). LR-MS (EI), *m/z* (relative intensity): 348 ($[M]^+$, 14), 243 (29), 226 (14), 211 (25), 183 (15), 149 (21), 105 (83), 84 (100). A similar reduction of pure **16a** (200 mg) under the above conditions gave **17a** (179 mg, 88%).

(3aR,5aS,6S,8R,9S,10aS)-rel-8-(Benzoyloxy)-3a,4,5,5a,6,7,8,9,10,10a-decahydro-6-methoxy-3a,5a-dimethyl-6,9-epoxycyclohept[e]inden-2(3H)-one (18)

A stream of ozone in air was bubbled through a solution of **17a** (295 mg, 0.84 mmol) and a small amount (1 to 2 mg) of Sudan III in 10% methanolic dichloromethane (40 mL) at –78 °C until the red color was discharged. Argon was bubbled through the solution for 20 min (to remove excess O_3) and then pyridine (0.1 mL) and dimethyl sulfide (0.5 mL) were added and the solution kept at 4 °C (refrigerator) for 16 h. The mixture was concentrated from xylene (to remove pyridine and dimethyl sulfoxide) to provide essentially homogeneous ketoaldehyde (320 mg, 99%). A solution of the ketaoaldehyde (320 mg, 0.84 mmol) in benzene (150 mL) was dried by concentration to a volume of ca. 100 mL via distillation under argon. Activated molecular sieves 5 Å (4.5 g; ca. 70 pellets) was added to this solution. A suspension of *p*-toluenesulfonic acid monohydrate (320 mg, 1.86 mmol) in toluene (80 mL) was heated under reflux in a modified Dean–Stark trap containing activated 5 Å molecular sieves. After 45 min, the resulting dry TsOH solution was allowed to cool to room temperature and then was added to the above solution of ketoaldehyde and the reaction mixture was heated to 50 °C. After 48 h, the mixture was allowed to cool to room temperature and $NaHCO_3$ (3 g) was added. After stirring for 20 min, the mixture was diluted with ethyl acetate (100 mL) and filtered. The combined filtrate and washings (20% MeOH in CH_2Cl_2) were concentrated and fractionated by FCC (30%–50% ethyl acetate in hexane) to give **18** (260 mg, 81%). Spectral data for **18** closely matched that reported previously (9).

(3aR,5aS,6S,8R,9S,10aS)-rel-8-(Benzoyloxy)-3a,4,5,5a,6,7,8,9,10,10a-decahydro-6-methoxy-3a,5a-dimethyl-6,9-epoxycyclohept[e]inden-2(3H)-one (19)

The acetal (166 mg, 0.434 mmol) was dissolved in MeI (5 mL); freshly prepared Ag_2O (100 mg, 0.43 mmol) was added in portions every 2 to 3 h for 24 h to a stirred solution of **18** (166 mg, 0.434 mmol) in MeI (5 mL). The reaction mixture was diluted with ethyl acetate and filtered through Celite. The combined filtrate and washings were concentrated and fractionated by FCC (20% ethyl acetate in hexane) to give **19** (138 mg, 83%). Spectral data for **19** closely matched that reported previously (9).

(3aS,5aR,6R,8S,9R)-rel-3,3a,4,5,5a,6,7,8,9,10-Decahydro-2,6-dimethoxy-3a,5a-dimethyl-6,9-epoxycyclohept[e]inden-8-yl benzoate (20)

A solution of 3% HCl in MeOH (0.45 mL) was added to a solution of **19** (18 mg, 0.045 mmol) and trimethyl orthoformate (0.6 mL) in toluene (3 mL). After 1 h, toluene (1 mL) was added and the reaction mixture was concentrated to a volume of ca. 1 mL by distillation of the solvent at atmospheric pressure. The reaction mixture was concentrated under reduced pressure to give **20** (19 mg) that was essentially homogeneous by TLC and was used in the next step without further purification. A sample purified by FCC (20% ethyl acetate in hexane) gave the following spectral characteristics: IR (cm^{-1}): 1716, 1608. ^1H NMR (300 MHz, C_6D_6) δ: 8.24 (2H, m, Ar-H), 7.10 (3H, m, Ar-H), 5.23 (1H, dd, J = 2, 7.5 Hz, HC-8), 5.01 (1H, br s, HC-1), 4.60 (1H, d, J = 4.5 Hz, HC-9), 3.48 (3H, s, H_3COC-6), 3.28 (3H, s, H_3COC-2), 2.54 (1H, dd, J = 4.5, 14 Hz, HC-10), 2.51 (1H, dd, J = 7.5, 14.5 Hz, HC-7), 2.38 (1H, d, J = 14.5 Hz, HC-3), 2.15 (1H, d, J = 14 Hz, HC-10), 2.14 (1H, dd, J = 2, 14.5 Hz, HC-7), 2.13 (1H, d, J = 14.5 Hz, HC-3), 1.55

© 2004 NRC Canada

(3H, s, H_3CC-3a), 1.24 (3H, s, H_3CC-5a). ^{13}C NMR (75 MHz, C_6D_6) δ: 165.9, 144.3, 132.7, 130.7, 129.6 (×2, Ph), 128.3 (×2, Ph), 119.6, 111.8, 96.2, 79.8, 78.7, 56.2, 49.1, 47.6, 45.1, 40.4, 32.8, 30.7, 30.0, 28.2, 28.1, 19.9. LR-MS (EI), *m/z* (relative intensity): 410 ($[M]^+$, 24), 305 (13), 289 (66), 249 (10), 221 (43), 105 (66), 100 (26), 99 (100).

(2*R*,3*S*,5*R*,5a*R*,7a*S*,8a*R*,11a*R*)-rel-1,2,3,4,5,5a,6,7,7a,8,8a,10,11,11a-Tetradecahydro-5,8a-dimethoxy-5a,7a-dimethyl-11-methylene-2,5-epoxycyclohept[6,7]indeno[2,1-b]furan-3-yl benzoate (22)

A solution of *N*-bromosuccinimide (recrystallized; 12 mg, 0.068 mmol) in CH_2Cl_2 (1.2 mL) was added to a stirred solution of the above crude **20** (19 mg) and distilled propargyl alcohol (0.12 mL, 115 mg, 2.0 mmol) in CH_2Cl_2 (0.8 mL) at –78 °C under argon. After 20 min, the reaction mixture was quenched by addition of 10% aq. $Na_2S_2O_3$ and the cooling bath was removed. The mixture was diluted with CH_2Cl_2 and washed with aq. $NaHCO_3$ and water, dried over Na_2SO_4, and concentrated to give the crude α-bromoacetal **21** (28 mg) that was somewhat unstable and was used immediately without further purification. Attempted fractionation of the crude by FCC (35% ethyl acetate in hexane) gave a sample (ca. 85% purity) with the following spectral characteristics: ^1H NMR (300 MHz, C_6D_6) δ: 8.22 (2H, m, Ph), 7.14 (3H, m, Ph), 5.43 (1H, dd, *J* = 2, 7 Hz, HC-8), 4.85 (1H, s, HC-1), 4.53 (1H, br d, *J* = 5 Hz, HC-9), 3.99 (2H, ap d, *J* = 2 Hz, H_2CO), 3.40 (3H, s, H_3COC-6), 3.11 (3H, s, H_3COC-2), 2.41 (1H, br d, *J* = 14 Hz, HC-10), 2.32 (1H, dd, *J* = 7, 15 Hz, HC-7), 2.19 (1H, dd, *J* = 5, 14 Hz, HC-10), 2.15–2.05 (2H, m, HC-3, HC-7), 2.04 (1H, t, *J* = 2 Hz, HC≡C), 1.70–1.30 (5H, m), 1.44 (3H, s, H_3C), 1.42 (3H, d, H_3C). Ph_3SnH (27 mg, 0.077 mmol) and AIBN, (1.6 mg, 0.01 mmol) were added to a solution of the above crude **21** (28 mg) in freshly distilled, degassed benzene (3 mL) under argon and the reaction mixture was immersed in an oil bath preheated to 80 °C. After 2 h, the mixture was concentrated and fractionated by MPC (10%–60% ethyl acetate in hexane) to give **22** (14 mg, 67% yield from **19**): IR (cm^{-1}): 1717. ^1H NMR (300 MHz, $CDCl_3$) δ: 8.03 (2H, m, Ph), 7.57 (1H, m, Ph), 7.45 (2H, m, Ph), 5.27 (1H, br s, HC=C), 5.20 (1H, br s, HC=C), 5.05 (1H, dd, *J* = 2, 7.5 Hz, HC-3), 4.37 (1H, br d, *J* = 5 Hz, HC-2), 4.34 (1H, br d, *J* = 11.5 Hz, HC-10), 4.28 (1H, br d, *J* = 11.5 Hz, HC-10), 3.76 (1H, br s, HC-11a), 3.40 (3H, s, H_3COC-5), 3.29 (3H, s, H_3COC-8a), 2.90 (1H, dd, *J* = 1, 15 Hz, HC-1), 2.36 (2H, m, HC-1, HC-4), 2.03 (2H, m, HC-8, HC-4), 1.83 (1H, d, *J* = 13.5 Hz, HC-8), 1.67–1.47 (4H, m, H_2C-6, H_2C-7), 1.18 (3H, s, H_3C), 1.15 (3H, s, H_3C). ^{13}C NMR (75 MHz, C_6D_6) δ: 166.5 (s), 148.9 (s), 140.5 (s), 132.8 (d), 130.9 (s), 130.6 (s), 129.6 (d × 2), 128.3 (d × 2), 117.6 (s), 111.0 (s), 110.3 (t), 78.9 (d), 78.3 (d), 71.0 (t), 56.0 (d), 50.4 (q), 49.6 (q), 49.0 (t), 45.9 (s), 43.0 (s), 33.0 (t), 32.6 (t), 29.4 (t), 28.3 (t), 27.8 (q), 20.1 (q). LR-MS (EI), *m/z* (relative intensity): 466 ($[M]^+$, 57), 435 (84), 313 (18), 231 (34), 197 (23), 171 (42), 157 (51), 105 (100).

(2R,3S,5R,5aR,7aS,8aR,11S,11aS)-rel-1,2,3,4,5,5a,6,7,7a,8,8a,10,11,11a-Tetradecahydro-5,8a-dimethoxy-5a,7a,11-trimethyl-2,5-epoxycyclohept[6,7]indeno[2,1-b]furan-3-yl benzoate (23)

A suspension of 5% Pd/C (15 mg) and **22** (20 mg, 0.043 mmol) in ethyl acetate (3 mL) was stirred under H_2 (50 psi, 1 psi = 6.894757 kPa). After 2 days, the mixture was filtered and the combined filtrate and benzene washings were concentrated and fractionated by FCC (20% ethyl acetate in hexane) to give **23** (18 mg, 90% yield). IR (cm^{-1}): 1717. ^1H NMR (300 MHz, $CDCl_3$) δ: 8.04 (2H, m, Ph), 7.58 (1H, m, Ph), 7.46 (2H, m, Ph), 4.96 (1H, dd, *J* = 2, 7.5 Hz, HC-3), 4.42 (1H, br d, *J* = 4.5 Hz, HC-2), 4.11 (1H, dd, *J* = 4, 8.5 Hz, H_2C-10), 3.73 (1H, d, *J* = 8.5 Hz, H_2C-10), 3.43 (3H, s, H_3COC-5), 3.32 (3H, s, H_3COC-8a), 3.30 (1H, dd, *J* = 2, 6.5 Hz, HC-11a), 2.56 (1H, ddd, *J* = 2, 4.5, 14 Hz, HC-1), 2.40 (1H, m, HC-11), 2.38 (1H, dd, *J* = 7.5, 14.5 Hz, HC-4), 2.24 (1H, dd, *J* = 1, 13 Hz, HC-8), 2.06 (2H, m, HC-13, HC-1), 180–1.46 (4H, m, H_2C-6, H_2C-8), 1.32 (1H, d, *J* = 13 Hz, HC-8), 1.23 (3H, s, H_3C), 1.22 (3H, s, H_3C), 0.83 (3H, d, *J* = 7 Hz, H_3CC-11). ^{13}C NMR (75 MHz, C_6D_6) δ: 165.9, 141.6, 132.7, 130.6, 129.6 (×2, Ph), 128.6, 128.3 (×2, Ph), 117.8, 111.5, 79.2, 78.4, 77.2, 57.0, 49.6, 49.0, 47.3, 45.7, 44.9, 37.1, 32.6, 32.0, 31.4, 27.6, 26.7, 20.3, 15.0. LR-MS (EI), *m/z* (relative intensity): 468 ($[M]^+$, 20), 427 (100), 436 (52), 331 (18), 315 (47), 213 (18), 157 (14), 105 (54).

(2*R*,3*S*,5*R*,5a*R*,7a*S*,8a*R*,11*R*,11a*S*)-rel-1,2,3,4,5,5a,6,7,7a,8,8a,10,11,11a-Tetradecahydro-5,8a-dimethoxy-5a,7a,11-trimethyl-2,5-epoxycyclohept[6,7]indeno[2,1-b]furan-3-yl benzoate (24)

A solution of *N*-bromosuccinimide (2.7 mg, 0.015 mmol) in CH_2Cl_2 (0.1 mL) was added to a stirred solution of crude dienol ether **20** (6.5 mg) (prepared from 19; 5.9 mg, 0.015 mmol) and allyl alcohol (0.025 mL, 21 mg, 0.37 mmol) in CH_2Cl_2 (1 mL) at –78 °C. After 5 min, the reaction mixture was filtered, and the precipitate was washed with hexane. The combined filtrate and washings were washed with aq. 5% KOH, dried over $MgSO_4$, and concentrated to give the crude bromoketal (7.8 mg) which was used without further purification. A solution of the above crude bromoketal 135 (7.8 mg), Bu_3SnH (4.2 μL, 4.5 mg, 0.015 mmol), and azobisisobutyronitrile (AIBN, 0.2 mg) in freshly distilled degassed benzene (1 mL) was heated for 2 h in an oil bath preheated to 80 °C. The reaction mixture was concentrated under reduced pressure to give a residue that contained a 1:1 mixture of **23** and **24** by ^1H NMR. Fractionation of the residue by MPC (20% ethyl acetate in hexane) gave **23** (1.2 mg) and **24** (2 mg) (45% total yield). ^1H NMR (300 MHz, $CDCl_3$) δ: 8.04 (2H, m, Ph), 7.58 (1H, m, Ph), 7.43 (2H, m, Ph), 4.99 (1H, dd, *J* = 2, 7.5 Hz, HC-3), 4.45 (1H, br d, *J* = 4.5 Hz, HC-2), 3.87 (1H, dd, *J* = 7, 8.5 Hz, HC-10), 3.59 (1H, dd, *J* = 6, 8.5 Hz, HC-10), 3.42 (3H, s, H_3COC-5), 3.33 (3H, s, H_3COC-8a), 2.84 (1H, dd, *J* = 3, 3.5 Hz, HC-11a), 2.65 (1H, ddd, *J* = 3, 5, 14 Hz, HC-1), 2.36 (1H, dd, *J* = 7.5, 14.5 Hz, HC-4), 2.18–2.00 (4H, m, HC-1, HC-4, HC-8, HC-11), 1.64–1.44 (4H, m, H_2C-6, H_2C-7, HC-8), 1.23 (3H, d, *J* = 6.5 Hz, H_3C), 1.19 (3H, s), and 1.16 (3H, s) (H_3C, 17). LR-MS (EI), *m/z* (relative intensity): 468 ($[M]^+$, 41), 437 (100), 436 (90), 331 (43), 315 (68), 289 (34), 217 (32), 105 (88).

(2*R*,3*S*,5*R*,5a*R*,7a*S*)-rel-1,2,3,4,5,5a,6,7,7a,8-Decahydro-5-methoxy-5a,7a,11-trimethyl-2,5-epoxycyclohept[6,7]indeno-[2,3-b]furan-3-yl benzoate (25)

Chlorotrimethylsilane (2 μL, 1.7 mg, 0.016 mmol) was

© 2004 NRC Canada

added to a solution of **22** (2.4 mg, 5.2 μmol) and sodium iodide (2.3 mg, 0.016 mmol) in acetonitrile (0.5 mL) under an argon atmosphere. After 5 min, the reaction was quenched by addition of water. The mixture was diluted with ethyl acetate, washed with aq. $Na_2S_2O_3$, dried over Na_2SO_4, concentrated under reduced pressure, and fractionated by MPC (20% ethyl acetate in hexane) to provide **25** (2.1 mg, 90%). ^{1}H NMR (300 MHz, $CDCl_3$) δ: 8.06 (2H, m, Ph), 7.58 (1H, m, Ph), 7.46 (2H, m, Ph), 7.13 (1H, br s, HC-10), 5.13 (1H, dd, *J* = 2, 7.5 Hz, HC-3), 4.49 (1H, br s, *J* = 1.5 Hz, HC-2), 3.44 (3H, s, H_3CO), 2.66 (1H, dd, *J* = 4, 14.5 Hz, HC-1), 2.59 (1H, m, *J* = 2, 14.5 Hz, HC-1), 2.58 (1H, d, *J* = 14.5 Hz, HC-8), 2.46 (1H, dd, *J* = 7.5 14.5 Hz, HC-4), 2.45 (1H, d, *J* = 14.5 Hz, HC-8), 2.19 (3H, br s, H_3C), 2.09 (1H, br d, *J* = 14.5 Hz, HC-4), 1.95–1.60 (4H, m, H_2C-6, H_2C-7), 1.28 (3H, s, H_3C) and 1.24 (3H, s, H_3C). HR-MS *m*/*z* calcd. for $C_{27}H_{30}O_5$: 434.2093; found: 434.2089 (EI).

*(2*R*,3*S*,5*R*,5a*R*,7a*S*,8a*S*,11S,11a*R*)-rel-1,2,3,4,5,5a,6,7,7a,8,8a,10,11,11a-Tetradecahydro-8a-hydroxy-5-methoxy-5a,7a,11-trimethyl-2,5-epoxycyclohept[6,7]indeno[2,1-*b*]furan-3-yl benzoate (26)*

HCl (10%, 0.5 mL) was added to a stirred solution of **23** (11 mg, 0.023 mmol) in THF (1.5 mL). After 14 h, the reaction mixture was diluted with CH_2Cl_2, washed with satd. $NaHCO_3$, dried over Na_2SO_4, concentrated, and fractionated by FCC (30% ethyl acetate in hexane) to give **26** (9 mg, 84%). ^{1}H NMR (300 MHz, $CDCl_3$) δ: 8.04 (2H, m, Ph), 7.56 (1H, m, Ph), 7.45 (2H, m, Ph), 4.95 (1H, dd, *J* = 2, 7.5 Hz, HC-3), 4.46 (1H, br d, *J* = 4 Hz, HC-2), 4.19 (1H, br dd, *J* = 8, 8.5 Hz, HC-10), 3.73 (1H, dd, *J* = 8.5, 10.5 Hz, HC-10), 3.43 (3H, s, CH_3O), 2.68 (1H, br d, *J* = 7 Hz, HC-11a), 2.53 (1H, dd, *J* = 4, 14 Hz, HC-1), 2.32 (1H, m, HC-11), 2.27 (1H, dd, *J* = 7, 14.5 Hz, HC-4), 2.23 (1H, dd, *J* = 1.5, 14 Hz, HC-1), 2.12 (1H, d, *J* = 12.5 Hz, HC-8), 2.06 (1H, br d, *J* = 14.5 Hz, HC-4), 1.63 (1H, d, *J* = 12.5 Hz, HC-8), 1.32 (3H, d, *J* = 6.5 Hz, H_3C), 1.24 (3H, s, H_3C), 1.19 (3H, s, H_3C). ^{13}C NMR (75 MHz, $CDCl_3$) δ: 166.4 (s), 144.0 (s), 133.1 (d), 130.1 (s, Ph), 129.6 (d × 2), 128.8 (s), 128.4 (d × 2), 116.6 (s), 111.8 (s), 79.5 (d), 78.0 (d), 75.4 (t), 60.5 (d), 53.1 (t), 49.6 (q), 45.4 (s), 44.2 (d), 42.8 (s), 34.2 (t), 32.2 (t), 30.5 (t), 27.5 (t), 26.3 (q), 19.0 (q), 17.4 (q). LR-MS (EI), *m*/*z* (relative intensity): 454 ([M]$^+$, 9), 436 (20), 395 (6), 332 (8), 315 (12), 199 (11), 105 (48), 69 (100). HR-MS *m*/*z* calcd. for $C_{27}H_{34}O_6$: 454.2355; found: 454.2353 (EI).

*(2*R*,3*S*,5*R*,5a*R*,7a*S*,8a*S*,11S,11a*R*)-rel-1,2,3,4,5,5a,6,7,7a,8,8a,10,11,11a-Tetradecahydro-5,8a-dimethoxy-5a,7a,11-trimethyl-2,5-epoxycyclohept[6,7]indeno[2,1-*b*]furan-3-yl benzoate (27)*

A solution of **23** (4.3 mg, 9.2 μmol) in $CDCl_3$ (1 mL) was sealed under vacuum in a 5 mm NMR tube. After 3 days at room temperature, ^{1}H NMR of the reaction mixture indicated that the **23** had completely epimerized to **27**. The tube was opened and the mixture was concentrated, and fractionated by MPC (1% methanol in dichloromethane) to give **27** (3.5 mg, 81%). IR (KBr) ν_{max} (cm^{-1}): 2962, 2939, 1717, 1271, 1105. ^{1}H NMR (300 MHz, $CDCl_3$) δ: 8.04 (2H, m, Ph), 7.58 (1H, m, Ph), 7.46 (2H, m, Ph), 4.95 (1H, dd, *J* = 2, 7 Hz, HC-3), 4.45 (1H, br d, *J* = 4 Hz, HC-2), 4.14 (1H, dd, *J* = 8, 8 Hz, HC-10), 3.58 (1H, dd, *J* = 8, 10.5 Hz, HC-10), 3.43 (3H, s, H_3COC-5), 3.26 (3H, s, H_3COC-8a), 2.64 (1H, d, *J* = 7 Hz, HC-11a), 2.51 (1H, dd, *J* = 4, 14 Hz, HC-1), 2.35 (1H, m, HC-11), 2.25 (1H, dd, *J* = 7, 14 Hz, HC-4), 2.24 (1H, dd, *J* = 1.5, 14 Hz, HC-1), 2.12 (1H, d, *J* = 12.5 Hz, HC-8), 2.05 (1H, d, *J* = 14 Hz, HC-4), 1.65–1.37 (5H, m, H_2C-6, H_2C-7, HC-8), 1.30 (3H, d, *J* = 6.5 Hz, H_3C), 1.24 (3H, s, H_3C), 1.18 (3H, s, H_3C). ^{13}C NMR (75 MHz, $CDCl_3$) δ: 166.4 (s), 143.5 (s), 133.1 (d), 130.3 (s), 129.5 (d × 2), 128.7 (s), 128.4 (d × 2), 119.5 (s), 111.8 (s), 79.5 (d), 78.0 (d), 75.1 (t), 60.7 (d), 49.9 (q), 49.6 (q), 48.9 (t), 45.4 (s), 43.8 (d), 42.3 (s), 34.3 (t), 32.1 (t), 30.4 (t), 27.5 (t), 26.4 (q), 18.9 (q), 17.2 (q). LR-MS (EI), *m*/*z* (relative intensity): 468 ([M]$^+$, 11), 437 (100), 331 (45), 315 (63), 275 (20), 199 (23), 157 (24), 105 (71).

*(2*R*,3*S*,5*R*,5a*R*,7a*S*,8a*R*,11S,11a*R*)-rel-1,2,3,4,5,5a,6,7, 7a, 8,8a,10,11,11a-Tetradecahydro-5-methoxy-5a,7a,11-trimethyl-8a-methylthio-2,5-epoxycyclohept[6,7]indeno[2,1-*b*]furan-3-yl benzoate (28)*

Amberlyst-15 (3 mg) was added to a stirred solution of **26** (0.8 mg, 2 μmol) in ethanethiol (0.3 mL). After 22 h, the mixture was filtered and the residue was washed with CH_2Cl_2. The combined filtrate and washings were concentrated and fractionated by MPC (10% ethyl acetate in hexane) to provide **28** (0.9 mg, quantitative). IR (KBr) ν_{max} (cm^{-1}): 2959, 2925, 1718, 1284, 1270, 1101, 1069, 1041. ^{1}H NMR (300 MHz, $CDCl_3$) δ: 8.03 (2H, m, Ph), 7.55 (1H, m, Ph), 7.45 (2H, m, Ph), 4.94 (1H, dd, *J* = 2, 7.5 Hz, HC-3), 4.46 (1H, br d, *J* = 4 Hz, HC-2), 4.13 (1H, br dd, *J* = 8, 9 Hz, HC-10), 3.68 (1H, dd, *J* = 9, 10.5 Hz, HC-10), 3.43 (3H, s, H_3CO), 2.69 (2H, ap q, *J* = 7.5 Hz, H_2CS), 2.61 (1H, d, *J* = 6.5 Hz, HC-11a), 2.53 (1H, dd, *J* = 4, 14.5 Hz, HC-1), 2.47 (1H, d, *J* = 13 Hz, HC-8), 2.29 (1H, m, HC-11), 2.27 (1H, dd, *J* = 7.5, 14.5 Hz, HC-4), 2.22 (1H, dd, *J* = 1, 14 Hz, HC-1), 2.07 (1H, br d, *J* = 14.5 Hz, HC-1), 1.85 (1H, d, *J* = 13 Hz, HC-8), 1.65–1–31 (4H, m), 1.30 (3H, d, *J* = 6.5 Hz, H_3C), 1.27 (3H, t, *J* = 7 Hz, H_3CCS), 1.25 (3H, s, H_3C), and 1.17 (3H, s, H_3C). LR-MS (EI), *m*/*z* (relative intensity): 498 ([M]$^+$, 10), 437 (100), 436 (13), 315 (71), 241 (28), 199 (14), 157 (17), 105 (65).

*(2*R*,3*S*,5*R*,5a*R*,7a*S*,8a*S*,11S,11a*R*)-rel-1,2,3,4,5,5a,6,7, 7a,8,8a,10,11,11a-Tetradecahydro-5-methoxy-5a,7a,11-trimethyl-2,5-epoxycyclohept[6,7]indeno[2,1-*b*]furan-3-yl benzoate (29)*

Pentafluorophenyl chlorothionoformate (4 μL, 7 mg, 0.02 mmol) was added dropwise to a stirred solution of **30** (3.4 mg, 0.0075 mmol), DMAP (1 mg, 0.008 mmol), and dry pyridine (5 μL, 5 mg, 0.06 mmol) in dry benzene (1 mL) under argon. After 1 h, the reaction mixture was filtered and the residue was washed with hexane. The combined filtrate and washings were washed with satd. $NaHCO_3$, dried over $MgSO_4$, concentrated, and fractionated by MPC (20% ethyl acetate in hexane) to give **29** (2.5 mg, 75%). IR (KBr) ν_{max} (cm^{-1}): 2952, 2922, 1718, 1270, 1102, 1069. ^{1}H NMR (300 MHz, $CDCl_3$) δ: 8.04 (2H, m, Ph), 7.58 (1H, m, Ph), 7.45 (2H, m, Ph), 4.99 (1H, dd, *J* = 2, 7.5 Hz, HC-3), 4.50 (1H, br dd, *J* = 7, 7 Hz, HC-8a), 4.47 (1H, m, HC-2), 4.16 (1H, br dd, *J* = 7, 9 Hz, HC-10), 3.44 (3H, s, H_3CO), 3.21 (1H, dd, *J* = 9, 10 Hz, HC-10), 2.76 (1H, br dd, *J* = 7, 7 Hz, HC-11a), 2.53 (1H, dd, *J* = 4.5, 14 Hz, HC-1), 2.34 (1H, dd, *J* = 1.5, 14 Hz, HC-1), 2.32–2.20 (1H, m, HC-11), 2.31 (1H,

© 2004 NRC Canada

dd, *J* = 7.5, 14.5 Hz, HC-4), 2.06 (1H, br d, *J* = 14.5 Hz, HC-4), 1.98 (1H, d, *J* = 13.5 Hz, HC-8), 1.70–1.25 (5H, m), 1.28 (3H, d, *J* = 7 Hz, H_3C), 1.27 (3H, s, H_3C), 1.16 (3H, s, H_3C). LR-MS (EI), *m*/*z* (relative intensity): 438 ($[M]^+$, 33), 396 (39), 333 (19), 316 (34), 301 (18), 159 (20), 145 (21), 129 (17), 105 (100).

*(1**S**,2**R**,3a**R**,5a**S**,6**S**,8**R**,9**S**)-rel-1,2,3,3a,4,5,5a,6,7,8,9,10-Dodecahydro-2-hydroxy-1-[(1**R**)-2-hydroxy-1-methylethyl]-6-methoxy-3a,5a-dimethyl-6,9-epoxycyclohept[**e**]indene-8-yl benzoate (30)*

$NaBH_4$ (3.5 mg, 0.093 mmol) was added to a stirred solution of **26** (5 mg, 1.1 μmol) in ethanol (1 mL) at room temperature. After 4 h, the reaction was quenched by addition of TFA (0.2 mL) (caution: H_2 evolution) and the mixture was concentrated from toluene. The residue was fractionated by MPC (65% ethyl acetate in hexane) to give **30** (3.5 mg, 70%). IR (KBr) ν_{max} (cm^{-1}): 3290, 2939, 1717, 1271, 1102, 1026. ^1H NMR (300 MHz, $CDCl_3$) δ: 8.03 (2H, m, Ph), 7.47 (1H, m, Ph), 7.45 (2H, m, Ph), 5.14 (1H, dd, *J* = 1.5, 7.5 Hz, HC-8), 4.43 (1H, br d, *J* = 4.5 Hz, HC-9), 4.20 (1H, ddd, *J* = 7, 7.5, 8 Hz, HC-2), 3.78 (1H, dd, *J* = 4, 10.5 Hz, H_2COH), 3.57 (1H, dd, *J* = 8, 10.5 Hz, H_2COH), 3.43 (3H, s, H_3CO), 2.68 (1H, br dd, *J* = 7.5, 8 Hz, HC-1), 2.50 (1H, dd, *J* = 4.5, 14.5 Hz, HC-10), 2.34 (1H, m, $HCCH_3$), 2.30 (1H, dd, *J* = 7.5, 14.5 Hz, HC-7), 2.22 (1H, dd, *J* = 1.5, 14.5 Hz, HC-10), 2.04 (1H, br d, *J* = 14.5 Hz, HC-7), 2.00 (variable) (2H, br s, HO), 1.88 (1H, dd, *J* = 8, 13 Hz, HC-3), 1.74 (1H, dd, *J* = 7.5, 13 Hz, HC-3), 1.60–1.45 (4H, m, H_2C-4, H_2C-5), 1.24 (3H, s, H_3C), 1.17 (3H, s, H_3C), 1.08 (3H, d, *J* = 7 Hz, H_3C). ^{13}C NMR (75 MHz, $CDCl_3$) δ: 166, 142.4, 133.2, 131.4, 130.0, 129.6, 128.4, 111.3, 79.4, 77.2, 53.0, 49.7, 48.2, 46.1, 38.7, 34.1, 32.2, 30.3, 29.4, 27.7, 19.9, 17.2. LR-MS (CI, NH_3), *m*/*z* (relative intensity): 455 ($[M - 1]^+$, 30), 439 (69), 438 (33), 437 (100), 412 (30), 397 (31), 136 (28), 105 (38).

*(1**S**,2**R**,3a**R**,5a**S**,6**S**,8**R**,9**S**)-rel-2-Acetoxy-1-[(1**R**)-2-acetoxy-1-methylethyl]-1,2,3,3a,4,5,5a,6,7,8,9,10-dodecahydro-6-methoxy-3a,5a-dimethyl-6,9-epoxycyclohept[**e**]indene-8-yl benzoate (31)*

A solution of acetic anhydride (0.1 mL, 0.1 g, 1 mmol), triethylamine (TEA, 0.2 mL, 0.14 g, 1.4 mmol), DMAP (0.2 mg), and diol **30** (0.6 mg, 0.0013 mmol) in CH_2Cl_2 (0.6 mL) was stirred at 0 °C for 1 h. MeOH (ca. 0.5 mL) was added and, after stirring for 15 min, the mixture was concentrated and fractionated by MPC (20% ethyl acetate in hexane) to give the diacetate **31** (0.6 mg, 78%). IR (KBr) ν_{max} (cm^{-1}): 2960, 2924, 1738, 1718, 1244. ^1H NMR (300 MHz, $CDCl_3$) δ: 8.03 (2H, m, Ph), 7.57 (1H, m, Ph), 7.45 (2H, m, Ph), 5.11 (1H, dd, *J* = 1.5, 7 Hz, HC-8), 5.06 (1H, ddd, *J* = 7, 7.5, 8 Hz, HC-2), 4.46 (1H, br d, *J* = 4 Hz, HC-9), 4.35 (1H, dd, *J* = 3, 10.5 Hz, H_2COAc), 3.95 (1H, dd, *J* = 7.5, 10.5 Hz, H_2COAc), 3.42 (3H, s, H_3CO), 2.75 (1H, dd, *J* = 7, 9.5 Hz, HC-1), 2.50 (1H, dd, *J* = 4, 14 Hz, HC-10), 2.37 (1H, m, $HCCH_3$), 2.30 (1H, dd, *J* = 7, 15 Hz, HC-7), 2.24 (1H, br d, *J* = 14 Hz, HC-10), 2.08 (3H, s, H_3CCO), 2.07 (3H, s, H_3CCO), 2.03 (1H, m, HC-7), 1.97 (1H, dd, *J* = 8, 13.5 Hz, HC-3), 1.74 (1H, dd, *J* = 7.5, 13.5 Hz, HC-3), 1.65–1.25 (4H, m, H_2C-4, H_2C-5), 1.25 (3H, s, H_3C), 1.17 (3H, s, H_3C), 1.14 (3H, d, *J* = 7 Hz, H_3C). LR-MS (EI), *m*/*z* (relative intensity): 540 ($[M]^+$, 23), 480 (17), 358 (22), 298 (24), 257 (31), 236 (25), 185 (38), 105 (100). HR-MS *m*/*z* calcd. for $C_{31}H_{40}O_8$: 540.2723; found: 540.2722.

*(1**S**,2**R**,3a**R**,5a**S**,6**S**,8**R**,9**S**)-rel-1,2,3,3a,4,5,5a,6,7,8,9,10-Dodecahydro-2-hydroxy-6-methoxy-3a,5a-dimethyl-1-[(1**R**)-2-phenylmethoxy-1-methylethyl]-6,9-epoxycyclohept[**e**]indene-8-yl benzoate (32) and (1**S**,2**R**,3a**R**,5a**S**,6**S**,8**R**,9**S**)-rel-1,2,3,3a,4,5,5a,6,7,8,9,10-dodecahydro-1-[(1**R**)-2-hydroxy-1-methylethyl]-6-methoxy-3a,5a-dimethyl-2-phenylmethoxy-6,9-epoxycyclohept[**e**]indene-8-yl benzoate (33)*

Tetrabutylammonium iodide (1 mg) and NaH (60% in oil, 4 mg, 0.1 mmol) were added to a stirred solution of diol **149** (4.3 mg, 0.0094 mmol) and benzyl bromide (2 μL, 3 mg, 0.01 mmol) in THF (2 mL) at 0 °C under argon. The ice bath was removed and, after 30 min, acetic acid (0.5 mL) was added (caution: H_2 evolution). The mixture was diluted with CH_2Cl_2, washed with satd. $NaHCO_3$, dried over Na_2SO_4, concentrated, and fractionated by MPC (30% ethyl acetate in hexane) to give **32** (1.6 mg, 32%) and **33** (1.7 mg, 33%). Spectral data for **32**: IR (KBr) ν_{max} (cm^{-1}): 3463, 2938, 1717, 1272, 1102. ^1H NMR (300 MHz, $CDCl_3$) δ: 8.02 (2H, m, Ph), 7.57 (1H, m, Ph), 7.43 (2H, m, Ph), 7.33 (5H, m, Ph), 5.16 (1H, dd, *J* = 1.5, 7 Hz, C-8), 4.56 (2H, ap s, H_2CPh), 4.42 (1H, br d, *J* = 4.5 Hz, HC-9), 4.15 (1H, ddd, *J* = 6.5, 7, 8.5 Hz, HC-2), 3.62 (1H, dd, *J* = 3.5, 8.5 Hz, H_2COBn), 3.43 (3H, s, H_3CO), 3.34 (1H, dd, *J* = 8.5, 9 Hz, H_2COBn), 2.63 (1H, dd, *J* = 7, 9 Hz, HC-1), 2.50 (1H, m, $HCCH_3$), 2.48 (1H, dd, *J* = 4.5, 14.5 Hz, HC-10), 2.29 (1H, dd, *J* = 7, 14.5 Hz, HC-7), 2.17 (1H, dd, *J* = 1, 14.5 Hz, HC-10), 2.05 (1H, br d, *J* = 14.5 Hz, HC-7), 1.85 (1H, dd, *J* = 8.5, 13.5 Hz, HC-3), 1.70 (1H, dd, *J* = 6.5, 13.5 Hz, HC-3), 1.61–1.20 (4H, m, H_2C-4, H_2C-5), 1.19 (3H, s, H_3C), 1.16 (3H, s, H_3C), 1.05 (3H, d, *J* = 7 Hz, H_3C). LR-MS (CI, NH_3), *m*/*z* (relative intensity): 545 ($[M - 1]^+$, 9), 439 (58), 425 (35), 317 (33), 279 (33), 122 (48), 105 (67), 91 (100). Spectral data for **33**: IR (KBr) ν_{max} (cm^{-1}): 3533, 3422, 2959, 1717, 1272, 1102. ^1H NMR (300 MHz, $CDCl_3$) δ: 8.02 (2H, m, Ph), 7.57 (1H, m, Ph), 7.44 (2H, m, Ph), 7.32 (5H, m, Ph), 5.12 (1H, dd, *J* = 1.5, 7.5 Hz, HC-8), 4.59 (1H, d, *J* = 11.5 Hz, H_2CPh), 4.46 (1H, d, *J* = 11.5 Hz, H_2CPh), 4.43 (1H, d, *J* = 3 Hz, HC-9), 3.85 (1H, ddd, *J* = 7, 7.5, 8 Hz, HC-2), 3.63 (2H, m, H_2COH), 3.42 (3H, s, H_3CO), 2.76 (1H, dd, *J* = 7.5, 9 Hz, HC-1), 2.48 (1H, dd, *J* = 4.5, 14.5 Hz, HC-10), 2.28 (2H, m, HC-7, HC-10), 2.04 (1H, d, *J* = 14.5 Hz, HC-7), 1.85 (2H, m, H_2C-1), 1.82–1.40 (5H, m, H_2C-4, H_2C-5, $HCCH_3$), 1.27 (3H, s, H_3C), 1.16 (3H, s, H_3C), 1.09 (3H, d, *J* = 7 Hz, H_3C). LR-MS (CI, NH_3), *m*/*z* (relative intensity): 547 ($[M + 1]^+$, 18), 529 (100), 439 (59), 437 (36), 333 (26), 317 (46), 105 (72), 91 (91).

*(1**S**,2**R**,3a**R**,5a**S**,6**S**,8**R**,9**S**)-rel-1-[(1**R**)-2-Acetoxy-1-methylethyl]-1,2,3,3a,4,5,5a,6,7,8,9,10-dodecahydro-6-methoxy-3a,5a-dimethyl-2-phenylmethoxy-6,9-epoxycyclohept[**e**]indene-8-yl benzoate (34)*

A solution of compound **33** (1.5 mg, 0.0027 mmol), acetic anhydride (0.1 mL, 0.1 g, 1 mmol), and TEA (0.2 mL, 0.1 g, 1 mmol) in CH_2Cl_2 (1 mL) was stirred at 0 °C for 30 min. MeOH (0.5 mL) was added and, after 15 min, the reaction mixture was concentrated and fractionated by MPC (20% ethyl acetate in hexane) to give **34** (1.7 mg, quantitative). IR

© 2004 NRC Canada

(KBr) ν_{max} (cm^{-1}): 2962, 2939, 1736, 1718, 1271, 1246, 1103, 1027. ^1H NMR (300 MHz, $CDCl_3$) δ: 8.03 (2H, m, Ph), 7.57 (1H, m, Ph), 7.43 (2H, m, Ph), 7.32 (5H, m, Ph), 5.12 (1H, dd, *J* = 1.5, 7 Hz, HC-8), 4.51 (1H, d, *J* = 12 Hz, HCPh), 4.43 (1H, d, *J* = 12 Hz, HCPh), 4.48–4.45 (2H, m, HC-9, HCOAc), 4.13 (1H, dd, *J* = 7.5, 10.5 Hz, HCOAc), 3.84 (1H, ddd, *J* = 7, 7.5, 8 Hz, HC-2), 3.42 (3H, s, H_3CO), 2.73 (1H, dd, *J* = 7, 10 Hz, HC-1), 2.50 (1H, dd, *J* = 4.5, 14.5 Hz, HC-10), 2.39 (1H, m, $HCCH_3$), 2.32 (1H, dd, *J* = 7, 15 Hz, HC-7), 2.27 (1H, br d, *J* = 14.5 Hz, HC-10), 2.06 (3H, s, H_3CCO), 2.03 (1H, br d, *J* = 15 Hz, HC-7), 1.84 (2H, ap d, *J* = 8 Hz, H_2C-3), 1.68–1.30 (4H, m, H_2C-4, H_2C-5), 1.25 (3H, s, H_3C), 1.16 (3H, s, H_3C), 1.13 (3H, d, *J* = 7 Hz, H_3C). LR-MS (EI), *m*/*z* (relative intensity): 588 ($[M]^+$, 3), 487 (19), 437 (54), 315 (14), 197 (10), 157 (13), 105 (66), 91 (100).

(2*R*,3*S*,5*R*,5a*R*,7a*S*,8a*R*,11*S*,11a*S*)-rel-1,2,3,4,5,5a,6,7,7a,8,8a,10,11,11a-Tetradecahydro-8a-hydroxy-5-methoxy-5a,7a,11-trimethyl-2,5-epoxycyclohept[6,7]indeno[2,1-b]furan-3-yl benzoate (35a) and (1*S*,3a*S*,5a*R*,6*R*,8*S*,9*R*)-rel-8-benzoyloxy-3,3a,4,5,5a,6,7,8,9,10-decahydro-1-[(1*S*)-2-hydroxy-1-methylethyl]-6-methoxy-3a,5a-dimethyl-6,9-epoxycyclohept[e]inden-2(1*H*)-one (35b)

A solution of **23** (16 mg, 0.034 mmol) and PPTS (36 mg, 0.14 mmol) in 7.5% aqueous acetone (2 mL) was allowed to stand at room temperature. After 12 days, the mixture was diluted with CH_2Cl_2, washed with satd. aq. $NaHCO_3$, dried over Na_2SO_4, concentrated, and fractionated by FCC (30% ethyl acetate in hexane) to provide recovered **23** (2.6 mg, 16%) and **35** (12.5 mg, 81%) as a 1:1.5 mixture of the ring-chain tautomers **35a** and **35b**, respectively. ^1H NMR (500 MHz, $CDCl_3$) δ (**35a**†, **35b***): 8.02 (2H, m, Ph), 7.56 (1H, m, Ph), 7.43 (2H, m, Ph), 4.97* (0.6 H, dd, *J* = 1.5, 7.5 Hz, HC-8) and 4.96† (0.4 H, dd, *J* = 1.5, 7 Hz, HC-3), 4.43* (0.6 H, br d, *J* = 4.5 Hz, HC-9) and 4.40† (0.4 H, br d, *J* = 4.5 Hz, HC-2), 4.19† (0.4 H, dd, *J* = 3.5, 8.5 Hz, HC-10), 3.64* (0.6 H, m, HCOH), 3.74† (0.4 H, d, *J* = 8.5 Hz, HC-10) and 3.57* (0.6 H, m, HCOH), 3.41*† (3H, s, H_3CO), 3.36* (0.6 H, br s, HC-1), 3.29† (0.4 H, d, *J* = 7 Hz, HC-11a), 2.70–1.45 (11H, m), 1.29† (1.2 H, s, H_3C), 1.26* (1.8 H, s, H_3C), 1.19† (1.2 H, s, H_3C), 1.06* (1.8 H, s, H_3C), 0.80† (1.2 H, d, *J* = 7 Hz, H_3C), 0.68* (1.8 H, d, *J* = 7 Hz, H_3C). ^{13}C NMR (125 MHz, $CDCl_3$) δ (**35a**†, **35b***): 219.0*, 166.4†, 166.2*, 142.1†, 139.9*, 133.22*, 133.17†, 130.6*, 129.92†, 129.83*, 129.55* (×2), 129.53† (×2), 128.8†, 128.43* (×2), 128.41† (×2), 114.8†, 111.5†, 110.9*, 79.1†, 78.5*, 78.1†, 77.8*, 77.2†, 65.7*, 57.1†, 56.6*, 54.7†, 50.0*, 49.55†, 49.51*, 45.7*, 45.4†, 45.1†, 39.4*, 37.6†, 35.9*, 32.5*, 32.4†, 31.9†, 31.42†, 31.47*, 31.2*, 28.3*, 27.4†, 27.2†, 27.1*, 20.5*, 20.0†, 14.9†, 12.2*. LR-MS (FAB), *m*/*z* (relative intensity): 455 ($[M + 1]^+$, 70), 437 (100), 395 (15), 315 (17), 105 (81). HR-MS *m*/*z* calcd. for $C_{27}H_{34}O_6$: 455.2434 (M + H); found: 455.2435 (FAB).

(1*S*,3a*S*,5a*R*,6*R*,8*S*,9*R*)-rel-8-(Benzoyloxy)-3,3a,4,5,5a,6,7,8,9,10-decahydro-6-methoxy-3a,5a-dimethyl-1-(1-methylethyl)-6,9-epoxycyclohept[e]inden-2(1*H*)-one (37)

Ph_2PCl (15 μL, 18 mg, 0.083 mmol) was added to a stirred solution of **35** (7.4 mg, 0.016 mmol) and pyridine (50 μL, 49 mg, 0.62 mmol) in dry toluene (1 mL) at room temperature under argon. After 2 h, a solution of iodine (21 mg, 0.083 mmol) in toluene (1 mL) was added. After 1 h, the reaction mixture was concentrated and the residue was fractionated by FCC (10% ethyl acetate in hexane) to give the iodide **36** (6.7 mg, 73%). ^1H NMR (300 MHz, $CDCl_3$) δ: 3.54 (1H, dd, *J* = 8, 10 Hz, CHI), 3.26 (1H, dd, *J* = 7, 10 Hz, CHI). HR-MS *m*/*z* calcd. for $C_{27}H_{33}IO_5$: 564.1373; found: 564.1366 (EI). A suspension of $BaCO_3$ (ca. 2 mg), Pd black (ca. 3 mg), and the above iodide (6.7 mg, 0.012 mmol) in C_6H_6 (1 mL) was stirred under H_2 (1 atm, 1 std atm = 101.325 kPa). After 7 h, the mixture was filtered through Celite and the combined filtrate and washings were concentrated to give **37** (4.6 mg, 88%). IR (cm^{-1}): 1741, 1718. ^1H NMR (500 MHz, $CDCl_3$) δ: 8.06 (2H, m, Ph), 7.61 (1H, m, Ph), 7.48 (2H, m, Ph), 5.02 (1H, br d, *J* = 7.5 Hz, HC-8), 4.46 (1H, br d, *J* = 5 Hz, HC-9), 3.46 (3H, s, H_3CO), 2.91 (1H, br s, HC-1), 2.69 (1H, ddd, *J* = 2.5, 5, 14.5 Hz, HC-10), 2.41 (1H, dd, *J* = 7.5, 15 Hz, HC-7), 2.31 (1H, m, HCC-1), 2.17 (2H, ap s, H_2C-3), 2.14 (1H, br d, *J* = 15 Hz, HC-7), 2.11 (1H, br d, *J* = 14.5 Hz, HC-10), 1.81–1.59 (4H, m, H_2C-4, H_2C-5), 1.29 (3H, s, H_3C), 1.13 (3H, d, *J* = 7 Hz, H_3C), 1.07 (3H, s, H_3C), 0.77 (3H, d, *J* = 7 Hz, H_3C). ^{13}C NMR (125 MHz, $CDCl_3$) δ: 217.8, 166.8, 133.7, 130.8, 130.3, 130.0 (×2), 128.9 (×2), 111.3, 79.1, 78.4, 56.8, 54.6, 50.0, 45.6, 39.5, 32.8, 32.0, 31.5, 29.6, 28.8, 27.6, 21.1, 20.9, 18.0. LR-MS (EI), *m*/*z* (relative intensity): 438 ($[M]^+$, 19), 395 (100), 316 (16), 273 (26), 216 (19), 199 (36), 105 (93), 77 (25). HR-MS *m*/*z* calcd. for $C_{27}H_{34}O_5$: 438.2406; found: 438.2410 (EI).

(2*R*,3*S*,5*R*,5a*R*,7a*S*,8a*R*,11*S*,11a*S*)-rel-11a-Deuterio-8a-trideuteriomethoxy-1,2,3,4,5,5a,6,7,7a,8,8a,10,11,11a-tetradecahydro-5-methoxy-5a,7a,11-trimethyl-2,5-epoxycyclohept[6,7]indeno[2,1-b]furan-3-yl benzoate (39)

A solution of **23** (1.2 mg, 0.0026 mmol) in CD_3OD containing 1% DCl was allowed to stand for 27 h. The mixture was concentrated and fractionated by MPC (20% ethyl acetate in hexane) to give **39** (1.2 mg, quantitative). ^1H NMR (300 MHz, $CDCl_3$) δ: 8.04 (2H, m, Ph), 7.58 (1H, m, Ph), 7.46 (2H, m, Ph), 4.96 (1H, dd, *J* = 2, 7.5 Hz, HC-3), 4.42 (1H, d, *J* = 4.5 Hz, HC-2), 4.11 (1H, dd, *J* = 4, 8.5 Hz, HC-10), 3.73 (1H, d, *J* = 8.5 Hz, HC-10), 3.43 (3H, s, H_3CO), 2.56 (1H, dd, *J* = 4.5, 14 Hz, HC-1), 2.40 (1H, m, HC-11), 2.38 (1H, dd, *J* = 7.5, 14.5 Hz, HC-4), 2.24 (1H, d, *J* = 13 Hz, HC-8), 2.06 (2H, m, HC-1, HC-4), 1.23 (3H, s, H_3C) and 1.22 (3H, s, H_3C) (H_3C-16), 0.83 (3H, d, *J* = 7 Hz, H_3C). LR-MS (EI), *m*/*z* (relative intensity): 472 ($[M]^+$, 11), 438 (69), 332 (20), 315 (88), 275 (17), 217 (21), 157 (19), 105 (100).

(1*S*,3a*S*,5a*R*,6*R*,8*S*,9*R*)-rel-3,3a,4,5,5a,6,7,8,9,10-Decahydro-8-(hydroxy)-6-methoxy-3a,5a-dimethyl-1-(1-methylethyl)-6,9-epoxycyclohept[e]inden-2(1*H*)-one (40)

Aqueous NaOH (1 mol L^{-1}, ca. 0.2 mL) was added to a solution of **37** (4.6 mg, 0.010 mmol) in MeOH (1.5 mL) and the mixture was heated under reflux. After 10 h, the mixture was diluted with CH_2Cl_2, washed with satd. $NaHCO_3$, dried over Na_2SO_4, concentrated to give **40** (3.5 mg), which was homogeneous by ^1H NMR and was used in the next step without further purification. ^1H NMR (300 MHz, $CDCl_3$) δ: 4.25 (1H, m, HC-9), 4.20 (1H, m, HC-8), 3.36 (3H, s, H_3CO), 2.94 (1H, sept, *J* = 7 Hz, HCC-1), 2.57 (1H, dd, *J* = 3, 13 Hz, HC-10a), 2.46 (1H, dd, *J* = 7.5, 15 Hz, HC-7),

© 2004 NRC Canada

2.31 (1H, ddd, *J* = 4, 13, 14 Hz, HC-10), 2.19 (1H, d, *J* = 18.5, HC-3), 2.11 (1H, d, *J* = 18.5, HC-3), 1.87 (1H, br d, *J* = 14 Hz, HC-10), 1.78–1.47 (5H, m, HC-7, H_2C-4, H_2C-5), 1.21 (3H, s, H_3C), 1.19 (3H, d, *J* = 7 Hz, H_3C), 1.18 (3H, d *J* = 7 Hz, H_3C), 0.96 (3H, s, H_3C).

(3aS,5aR,6R,9R,10aR)-rel-3,3a,4,5,5a,6,7,9,10,10a-Decahydro-6-methoxy-3a,5a-dimethyl-1-(1-methylethyl)-6,9-epoxycyclohept[e]indene-2,8-dione (41)

TPAP (5.3 mg, 0.015 mmol) was added to a stirred suspension of powdered 4 Å molecular sieves (20 mg), *N*-methylmorpholine oxide (3.8 mg, 0.032 mmol), and alcohol **40** (3.5 mg) in dry CH_3CN (0.8 mL). After 2 h, the mixture was concentrated and fractionated by FCC (20% ethyl acetate in hexane) to give **41** (3 mg, 85% from **37**). ^{1}H NMR (300 MHz, $CDCl_3$) δ: 4.32 (1H, br s, HC-9), 3.39 (3H, s, H_3CO), 2.91 (1H, sept, *J* = 7 Hz, HCC-1), 2.79–2.72 (2H, m, HC-7, HC-10a), 2.53 (1H, d, *J* = 18.5 Hz, HC-7), 2.44 (1H, ddd, *J* = 4, 13, 13 Hz, HC-10), 2.20 (1H, d, *J* = 18.5 Hz, HC-3), 2.12 (1H, d, *J* = 18.5 Hz, HC-3), 1.94 (1H, ddd, *J* = 2.5, 4, 13 Hz, HC-10), 1.78 (1H, m, HC-4 or HC-5), 1.55 (3H, m, HC-4, HC-5), 1.20 (3H, d, *J* = 7 Hz, H_3C), 1.17 (3H, s, H_3C), 1.16 (3H, d, *J* = 7 Hz, H_3C), 1.06 (3H, s, H_3C).

(3aS,5aR,6R,9R,10aR)-rel-4,5,5a,6,7,9,10,10a-Octahydro-6-methoxy-3a,5a-dimethyl-1-(1-methylethyl)-6,9-epoxycyclohept[e]inden-8(3aH)-one (42)

A solution of Tf_2O in CH_2Cl_2 (0.5 mol L^{-1}, 34 μL, 0.017 mmol) was added to a stirred solution of 2,6-di(*tert*-butyl)-4-methylpyridine (4.6 mg, 0.023 mmol) and **41** (3 mg, 9 μmol) in CH_2Cl_2 (0.8 mL) under argon and the mixture was heated under reflux. After 2 h, the mixture was concentrated and the residue taken up in pentane and filtered. The combined filtrate and washings were concentrated and fractionated by FCC (10% ethyl acetate in hexane) to give the enol triflate (3 mg). ^{1}H NMR (300 MHz, $CDCl_3$) δ: 6.09 (1H, s, HC=COTf). A solution of the above triflate (3 mg) in THF (0.3 mL) and a solution of Bu_3SnH in THF (0.4 mol L^{-1}, 40 μL) were sequentially added to a stirred solution of $Pd(Ph_3P)_4$ (3.8 mg, 0.0033 mmol) and dry LiCl (4 mg, 0.094 mmol) in dry THF (0.4 mL) under argon and the mixture was heated under reflux. After 1.5 h, the mixture was diluted with hexane and washed with 5% NH_4OH and brine, dried, concentrated, and fractionated by FCC (5% ethyl acetate in hexane) to give **42** (1.4 mg, 50%). ^{1}H NMR (300 MHz, $CDCl_3$) δ: 6.29 (1H, d, *J* = 5.5 Hz, HC-3 or HC-2), 6.23 (1H, d, *J* = 5.5 Hz, HC-3 or HC-2), 4.30 (1H, br s, HC-9), 3.38 (1H, s, H_3CO), 2.89 (1H, sept, *J* = 7 Hz, HCC-1), 2.72 (1H, d, *J* = 18.5 Hz, HC-7), 2.57 (1H, d, *J* = 18.5 Hz, HC-7), 2.49 (1H, dd, *J* = 2.5, 13.5 Hz, HC-10a), 2.39 (1H, ddd, *J* = 3.5, 12, 13.5 Hz, HC-10), 1.93 (1H, ddd, *J* = 2.5, 2.5, 12 Hz, HC-10), 1.68 (1H, ddd, *J* = 3, 3, 13 Hz, HC-4 or HC-5), 1.50–1.17 (3H, m, HC-4, HC-5), 1.09 (3H, d, *J* = 7 Hz, H_3C), 1.03 (3H, d, *J* = 7 Hz, H_3C), 0.95 (3H, s, H_3C-17), 0.88 (3H, s, H_3C-16).

Methyl (3aS,5aR,6R,9R,10aR)-rel-3a,4,5,5a,6,9,10,10a-Octahydro-6-methoxy-3a,5a-dimethyl-1-(1-methylethyl)-6,9-epoxycyclohept[e]indene-8-carboxylate (43)

$NaN(TMS)_2$ (1 mol L^{-1} in THF, 35 μL, 35 μmol) was added to a stirred solution of ketone **42** (1.4 mg, 4.4 μmol) and $PhN(Tf)_2$ (5.1 mg, 14 μmol) in THF (0.5 mL) at –78 °C under argon. After 30 min, the reaction was quenched by addition of water. The mixture was diluted with ethyl acetate, washed with brine, dried over Na_2SO_4, and concentrated to give a residue that contained a 3:1 mixture of the desired enol triflate and **42**, respectively. The residue was resubjected to triflation under the above conditions and the resulting crude product was fractionated by MPC (5% ethyl acetate in hexane) to give the enol triflate (1.3 mg). ^{1}H NMR (300 MHz, $CDCl_3$) δ: 6.08 (1H, s, HC=COTf). $Pd(Ph_3P)_4$ (3.1 mg, 2.7 μmol) and MeOH (50 μL) were sequentially added to a stirred solution of the above triflate (1.3 mg, 2.9 μmol) and *i*-Pr_2EtN (0.9 mg, 7 μmol) in CO-saturated THF (0.4 mL) at room temperature. The mixture was stirred under CO (1 atm, 1 std atm = 101.325 kPa) for 1 h and then was concentrated and fractionated by MPC (5% ethyl acetate in hexane) to give the ester **43** (0.9 mg, 50% from **42**). ^{1}H NMR (300 MHz, $CDCl_3$) δ: 7.13 (1H, s, HC-7), 6.30 (1H, d, *J* = 5.5 Hz, HC-3), 6.21 (1H, d, *J* = 5.5 Hz, HC-2), 5.08 (1H, dd, *J* = 2, 3 Hz, HC-9), 3.81 (3H, s, H_3COCO), 3.34 (3H, s, H_3COC-6), 2.96 (1H, sept, *J* = 7 Hz, HCC-1), 2.45–2.35 (2H, m, HC-10a, HC-10), 1.70–1.20 (5H, m, HC-10, H_2C-4, H_2C-5), 1.10 (3H, d, *J* = 7 Hz, H_3C), 1.03 (3H, d, *J* = 7 Hz, H_3C), 0.92 (3H, s, H_3C), 0.81 (3H, s, H_3C).

(±)-Allocyathin B_3 methyl acetal (44)

DIBAL-H (1.5 mol L^{-1} in toluene, 20 μL, 30 μmol) was added to a stirred solution of **43** (0.9 mg, 2.5 μmol) in dry ether (0.4 mL) under argon at –20 °C. After 30 min, the reaction was quenched by addition of MeOH (0.2 mL). After 1 h, the mixture was diluted with ether, washed with brine, dried over Na_2SO_4, concentrated, and fractionated by FCC (60% ethyl acetate in hexane) to give **44** (0.6 mg, 70%). UV λ_{max} (nm): 255 (CH_3CN–H_2O). ^{1}H NMR (500 MHz, $CDCl_3$) δ: 6.29 (1H, d, *J* = 5.5 Hz, HC-1), 6.20 (1H, d, *J* = 5.5 Hz, HC-2), 6.10 (1H, dd, *J* = 1.5, 2 Hz, HC-13), 4.80 (1H, dd, *J* = 2, 3 Hz, HC-11), 4.37 (1H, br d, *J* = 15 Hz, HC-15), 4.32 (1H, br d, *J* = 15 Hz, HC-15), 3.31 (3H, s, H_3CO), 2.95 (1H, sept, *J* = 7 Hz, HC-18), 2.52 (1H, dd, *J* = 4, 13 Hz, HC-5), 2.38 (1H, ddd, *J* = 3, 13, 13 Hz, HC-10), 1.70–1.40 (5H, m, HC-10, H_2C-8, H_2C-7), 1.09 (3H, d, *J* = 7 Hz, H_3CC-18), 1.03 (3H, d, *J* = 7 Hz, H_3CC-18), 0.92 (3H, s, H_3C-16 or -17), 0.79 (3H, s, H_3C-17 or -16). ^{13}C NMR (125 MHz, $CDCl_3$) δ: 148.3 (s, C-12), 144.5 (d, C-1), 142.7 (s, C-3), 141.1 (s, C-4), 128.0 (d, C-2), 124.3 (d, C-13), 114.6 (s, C-14), 78.5 (s, C-11), 59.3 (t, C-15), 54.3 (s, C-9), 51.1 (q, OCH_3), 44.7 (s, C-6), 39.5 (d, C-5), 31.5 (t, C-8), 29.2 (t, C-7), 26.0 (t, C-10), 25.9 (d, C-18), 22.9 (q, C-19), 22.8 (q, C-20), 20.9 (q, C-17), 12.0 (q, C-16). LR-MS (EI), *m/z* (relative intensity): 330 ($[M]^+$, 35), 312 (29), 299 (12), 297 (22), 187 (49), 173 (28), 141 (100). HR-MS *m/z* calcd. for $C_{21}H_{30}O_3$: 330.2195; found: 330.2195 (EI).

Acknowledgements

Financial support from the Natural Sciences and Engineering Research Council of Canada (NSERC) is gratefully acknowledged. We thank Professor W.A. Ayer for samples and spectra of cyathins.

© 2004 NRC Canada

References

1. (*a*) W.A. Ayer and H. Taube. Tetrahedron Lett. 1917 (1972); (*b*) W.A. Ayer and H. Taube. Can. J. Chem. **51**, 3842 (1973); (*c*) W.A. Ayer and L.L. Carstens. Can. J. Chem. **51**, 3157 (1973); (*d*) W.A. Ayer, L.M. Browne, J.R. Mercer, D.R. Taylor, and D.E. Ward. Can. J. Chem. **56**, 717 (1978); (*e*) W.A. Ayer, T. Yoshida, and D.M.J. Van Schie. Can. J. Chem. **56**, 2113 (1978); (*f*) W.A. Ayer and S.P. Lee. Can. J. Chem. **57**, 3332 (1979).
2. H.J. Hecht, G. Hoefle, W. Steglich, T. Anke, and F. Oberwinkler. J. Chem. Soc. Chem. Commun. 665 (1978).
3. (*a*) H. Kawagishi, A. Shimada, R. Shirai, K. Okamoto, F. Ojima, H. Sakamoto, Y. Ishiguro, and S. Furukawa. Tetrahedron Lett. **35**, 1569 (1994); (*b*) H. Kawagishi, A. Simada, K. Shizuki, H. Mori, K. Okamoto, H. Sakamoto, and S. Furukawa. Heterocycl. Commun. **2**, 51 (1996); (*c*) H. Kawagishi, A. Shimada, S. Hosokawa, H. Mori, H. Sakamoto, Y. Ishiguro, S. Sakemi, J. Bordner, N. Kojima, and S. Furukawa. Tetrahedron Lett. **37**, 7399 (1996); (*d*) H. Kenmoku, T. Sassa, and N. Kato. Tetrahedron Lett. **41**, 4389 (2000); (*e*) E.W. Lee, K. Shizuki, S. Hosokawa, M. Suzuki, H. Suganuma, T. Inakuma, J. Li, M. Ohnishi-Kameyama, T. Nagata, S. Furukawa, and H. Kawagishi. Biosci. Biotechnol. Biochem. **64**, 2402 (2000); (*f*) H. Kenmoku, N. Kato, M. Shimada, M. Omoto, A. Mori, W. Mitsuhashi, and T. Sassa. Tetrahedron Lett. **42**, 7439 (2001); (*g*) H. Kenmoku, T. Shimai, T. Toyomasu, N. Kato, and T. Sassa. Biosci. Biotechnol. Biochem. **66**, 571 (2002).
4. (*a*) H. Shibata, T. Tokunaga, D. Karasawa, A. Hirota, M. Nakayama, H. Nozaki, and T. Tada. Agric. Biol. Chem. **53**, 3373 (1989); (*b*) H. Shibata, A. Irie, and Y. Morita. Biosci. Biotechnol. Biochem. **62**, 2450 (1998).
5. (*a*) T. Ohta, T. Kita, N. Kobayashi, Y. Obara, N. Nakahata, Y. Ohizumi, Y. Takaya, and Y. Oshima. Tetrahedron Lett. **39**, 6229 (1998); (*b*) T. Kita, Y. Takaya, Y. Oshima, T. Ohta, K. Aizawa, T. Hirano, and T. Inakuma. Tetrahedron, **54**, 11 877 (1998).
6. A.D. Allbutt, W.A. Ayer, H.J. Brodie, B.N. Johri, and H. Taube. Can. J. Microbiol. **17**, 1401 (1971).
7. (*a*) Y. Obara, N. Nakahata, T. Kita, Y. Takaya, H. Kobayashi, S. Hosoi, F. Kiuchi, T. Ohta, Y. Oshima, and Y. Ohizumi. Eur. J. Pharmacol. **370**, 79 (1999); (*b*) Y. Obara, H. Kobayashi, T. Ohta, Y. Ohizumi, and N. Nakahata. Mol. Pharmacol. **59**, 1287 (2001).
8. Review: D.L. Wright and C.R. Whitehead. Org. Prep. Proced. Int. **32**, 307 (2000).
9. D.E. Ward. Can. J. Chem. **65**, 2380 (1987).
10. (*a*) K.R. Dahnke and L.A. Paquette. J. Org. Chem. **59**, 885 (1994); (*b*) P. Magnus and L. Shen. Tetrahedron, **55**, 3553 (1999); (*c*) D.L. Wright, C.R. Whitehead, E.H. Sessions, I. Ghiviriga, and D.A. Frey. Org. Lett. **1**, 1535 (1999); (*d*) K. Takeda, D. Nakane, and M. Takeda. Org. Lett. **2**, 1903 (2000); (*e*) P.A. Wender, F.C. Bi, M.A. Brodney, and F. Gosselin. Org. Lett. **3**, 2105 (2001); (*f*) C. Thominiaux, A. Chiaroni, and D. Desmaele. Tetrahedron Lett. **43**, 4107 (2002).
11. (*a*) B.B. Snider, N.H. Vo, S.V. O'Neil, and B.M. Foxman. J. Am. Chem. Soc. **118**, 7644 (1996); (*b*) B.B. Snider, N.H. Vo, and S.V. O'Neil. J. Org. Chem. **63**, 4732 (1998).
12. M. Tori, N. Toyoda, and M. Sono. J. Org. Chem. **63**, 306 (1998).
13. E. Piers, M. Gilbert, and K.L. Cook. Org. Lett. **2**, 1407 (2000).
14. Preliminary communication: D.E. Ward, Y. Gai, and Q. Qiao. Org. Lett. **2**, 2125 (2000).
15. (*a*) W.A. Ayer, L.M. Browne, S. Fernandez, D.E. Ward, and T. Yoshida. Rev. Latinoam. Quim. **9**, 177 (1978). (*b*) S. Fernadez. Ph.D. Thesis, University of Alberta, Edmonton, Alta., Canada, 1974; (*c*) D.E. Ward. Ph.D. Thesis, University of Alberta, Edmonton, Alta., Canada, 1979.
16. W.A. Ayer, D.E. Ward, L.M. Browne, L.T.J. Delbaere, and Y. Hoyano. Can. J. Chem. **59**, 2665 (1981).
17. D.E. Ward. 70th Canadian Chemical Conference and Exhibition, Quebec City, Que., Canada, 1987. Abstract No. ORG-71-G2.
18. Q. Qiao. M.Sc. Thesis, University of Saskatchewan, Saskatoon, Sask., Canada, 1996.
19. D.E. Ward and C.K. Rhee. Can. J. Chem. **67**, 1206 (1989).
20. T. Veysoglu, L.A. Mitscher, and J.K. Swayze. Synthesis, 807 (1980).
21. (*a*) Y. Ueno, K. Chino, M. Watanabe, O. Moriya, and M. Okawara. J. Am. Chem. Soc. **104**, 5564 (1982); (*b*) O. Moriya, M. Okawara, and Y. Ueno. Chem. Lett. 1437 (1984).
22. (*a*) G. Stork and R.J. Mook. J. Am. Chem. Soc. **105**, 3720 (1983); (*b*) G. Stork, R.J. Mook, S.A. Biller, and S.D. Rychnovsky. J. Am. Chem. Soc. **105**, 3741 (1983).
23. G. Stork and M.E. Reynolds. J. Am. Chem. Soc. **110**, 6911 (1988).
24. Review: J. Rodriguez and J.P. Dulcere. Synthesis, 1177 (1993).
25. B. Giese, B. Kopping, T. Gobel, J. Dickhaut, G. Thoma, K.J. Kulicke, and F. Trach. Org. React. (N.Y.), **48**, 301 (1996).
26. A. Srikrishna and K.C. Pullaiah. Tetrahedron Lett. **28**, 5203 (1987).
27. D.H.R. Barton and S.W. McCombie. J. Chem. Soc. Perkin Trans. 1, 1574 (1975).
28. D.H.R. Barton, P. Blundell, J. Dorchak, D.O. Jang, and J.C. Jaszberenyi. Tetrahedron, **47**, 8969 (1991).
29. (*a*) D.H.R. Barton and R. Subramanian. J. Chem. Soc. Perkin Trans. 1, 1718 (1977); (*b*) A.P. Kozikowski, T.R. Nieduzak, T. Konoike, and J.P. Springer. J. Am. Chem. Soc. **109**, 5167 (1987); (*c*) F.E. Ziegler and Z.L. Zheng. J. Org. Chem. **55**, 1416 (1990).
30. R.H. Schlessinger and J.A. Schultz. J. Org. Chem. **48**, 407 (1983).
31. H. Sajiki, T. Ikawa, and K. Hirota. Tetrahedron Lett. **44**, 7407 (2003).
32. B. Classon, Z. Liu, and B. Samuelsson. J. Org. Chem. **53**, 6126 (1988).
33. Review: S.V. Ley, J. Norman, W.P. Griffith, and S.P. Marsden. Synthesis, 639 (1994).
34. P.J. Stang and W. Treptow. Synthesis, 283 (1980).
35. W.J. Scott and J.K. Stille. J. Am. Chem. Soc. **108**, 3033 (1986).
36. Review: K. Ritter. Synthesis, 735 (1993).
37. S. Cacchi, E. Morera, and G. Ortar. Tetrahedron Lett. **26**, 1109 (1985).
38. W.A. Ayer, T.T. Nakashima, and D.E. Ward. Can. J. Chem. **56**, 2197 (1978).
39. W.C. Still, M. Kahn, and A. Mitra. J. Org. Chem. **43**, 2923 (1978).
40. L.M. Harwood. Aldrichimica Acta, **18**, 25 (1985).
41. D.F. Taber. J. Org. Chem. **47**, 1351 (1982).
42. D.W. Brown, T.T. Nakashima, and D.L. Rabenstein. J. Magn. Reson. **45**, 302 (1981).
43. M. Shimizu, H. Orita, T. Hayakawa, and K. Takehira. Tetrahedron Lett. **30**, 471 (1989).
44. T. Ibuka, Y. Ito, Y. Mori, T. Aoyama, and Y. Inubushi. Synth. Commun. **7**, 131 (1977).

© 2004 NRC Canada

Preparation and characterization of bicyclic amide acetals and monothioacetals[1]

J. Peter Guthrie, Roger T. Gallant, and Michael C. Jennings

Abstract: We have prepared and characterized new examples of 5-substituted-1-aza-4,6-dioxabicyclo[3.3.0]octanes (bicyclic amide acetals) and examples of the new heterocyclic system, 5-substituted-1-aza-4-oxa-6-thiabicyclo[3.3.0]octanes (bicyclic amide monothioacetals). Detailed analysis of NMR coupling constants and X-ray structure determination for an example of each class of compound established the stereochemistry and conformation of these ring systems.

Key words: bicyclic amide acetals, preparation, coupling constants, X-ray structure.

Résumé : On a préparé et caractérisé de nouveaux exemples de 1-aza-4,6-dioxabicyclo[3.3.0]octanes substitués en position 5 (amide acétals bicycliques) et des exemples du nouveau système hétérocyclique 1-aza-4-oxa-6-thiabicyclo[3.3.0]octanes substitués en position 5 (amide monothioacétals bicycliques). Une étude détaillée des constantes de couplage de la RMN et la détermination de la structure, par diffraction des rayons X, d'un exemple de chacune de ces classes de composés permet d'établir la stéréochimie et la conformation de ces composés cycliques.

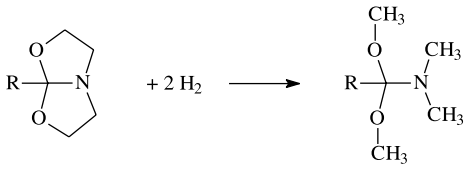
Mots clés : amide acétals bicycliques, préparation, constantes de couplage, structure par diffraction des rayons X.

[Traduit par la Rédaction]

Introduction

We have been interested in determining the energies of tetrahedral intermediates in acyl transfer reactions by an indirect thermochemical approach (1–7). Attempts to extend this approach from simple amides (2) to amides with various substituents on the α-carbon ran into frustrating problems of purification. Amide acetals could be made but could not be purified. In an attempt to overcome this problem we have turned to bicyclic versions of these compounds. Our plan is to determine the heats of hydrolysis and, thus, the heats of formation of the bicyclic acetals and monothioacetals and proceed from these to, first, the heats of formation of the acyclic acetals and monothioacetals, using computational methods to determine the heats of reaction for the hypothetical hydrogenations shown in reactions [1] and [2], and thence, to the free energies of formation of the analogous tetrahedral intermediates.

[1]



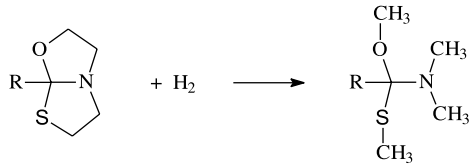
Received 9 July 2003. Published on the NRC Research Press Web site at http://canjchem.nrc.ca on 4 February 2004.

J.P. Guthrie,[2] R.T. Gallant, and M.C. Jennings.
Department of Chemistry, University of Western Ontario, London, ON N6A 5B7, Canada.

[1]This article is part of a Special Issue dedicated to Professor Ed Piers.

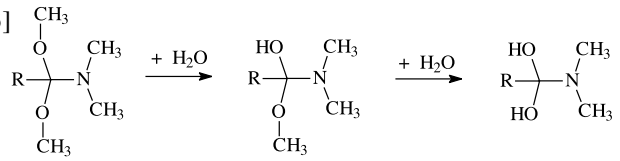
[2]Corresponding author (e-mail: peter.guthrie@uwo.ca).

[2]



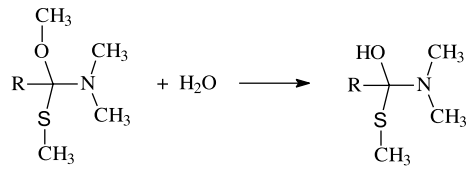
By methods that we have reported (8) and that involve a hypothetical hydrolysis, free energies of the acyclic amide acetals can be used to calculate the free energies of the corresponding amide hemiacetals and amide hydrates.

[3]



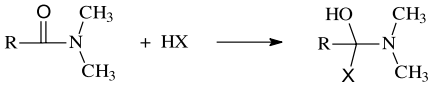
Similarly, the free energies of the acyclic amide monothioacetals can be used to calculate the free energies of the corresponding amide hemithioacetals.

[4]



The energies of these adducts can be combined with free energies of the amides to permit calculation of the free energy changes for addition reactions of amides, reactions that are quite unfavorable and difficult to determine experimentally.

 doi: 10.1139/V03-204 © 2004 NRC Canada

[5] 

X = OH, OCH_3, SCH_3.

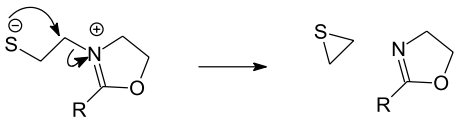
The first stage in this project was to prepare and characterize the bicyclic compounds, only a few of which were known. Calorimetric studies of these compounds are complete and computational studies to complement and in some cases to supplement them are nearly complete. The rest of our studies on these compounds will be reported in due course.

Results

The compounds examined in this work are shown in Scheme 1. The original plan had been to prepare compounds with a range of electron-withdrawing substituents, but difficulties were encountered in some of these attempted preparations, and then it became clear that the rate of hydrolysis was very sensitive to electron withdrawal, such that strong electron-withdrawing groups made hydrolysis too slow for the calorimetric measurements we planned to carry out.

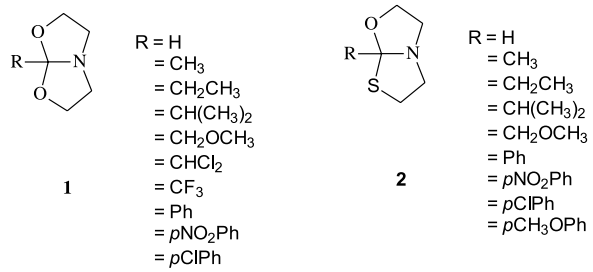
Although some of the bicyclic amide acetals are known compounds, most are novel, and preparations range from very easy to quite difficult.

The standard methods for preparation of compounds **1**, substituted 1-aza-4,6-dioxabicyclo[3.3.0]octanes, involve either reaction of diethanolamine with the corresponding nitrile, using a small amount of sodium as catalyst, or reaction of diethanolamine with the corresponding acyclic amide acetal. Similar methods allowed preparation of the novel compounds **2**, substituted 1-aza-4-oxa-6-thiabicyclo[3.3.0]octanes, by using 2-(2-mercaptoethyl)aminoethanol. The compounds **2** were thermally sensitive and could not be obtained by the standard reaction of a nitrile with 2-(2-mercaptoethyl)aminoethanol at 80 °C; such conditions led only to the oxazoline corresponding to the nitrile. Reaction at room temperature, though slow, led to the desired compounds. Attempted distillation of the crude 5-substituted-1-aza-4-oxa-6-thiabicyclo[3.3.0]octane at temperatures over 110 °C also led to breakdown to the corresponding oxazoline. A reasonable explanation is relatively facile cleavage of ethylene sulfide, e.g., by

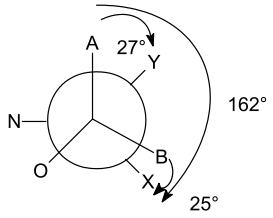


The 5-substituted-1-aza-4-oxa-6-thiabicyclo[3.3.0]octanes were higher boiling than the corresponding oxazolines and so purification by fractional distillation was possible if the temperature could be kept low enough to avoid thermal fragmentation. For the aryl-substituted compounds this was not possible, and pure product could be obtained only when the 5-substituted-1-aza-4-oxa-6-thiabicyclo[3.3.0]octane could be crystallized, as for **2** with R = phenyl and 4-nitrophenyl. In the case of **2** with R = 4-chlorophenyl and 4-methoxyphenyl, crystallization was not achieved, and the best samples were only 94% and 90% pure, with the remainder being the corresponding oxazoline. Details of these preparations and of the preparations of other compounds used in this work are found in the experimental section.

Scheme 1.



The oxazolidinooxazolidine system in the bicyclic amide acetals has two identical five-membered rings — each with four distinctive proton environments — leading to an ABXY pattern, with complicated splitting. The assignment of the methylene signals was based on the ^{1}H, ^{13}C, gCOSY, and gHSQC spectra. The proton NMR spectra of the 5-*R*-1-aza-4,6-dioxabicyclo[3.3.0]octanes are resolved well enough to allow a direct graphical calculation of the true chemical shifts and coupling constants. These calculated values were verified with the use of ACD Labs H NMR spin simulation software (9), as shown in Fig. 1. The worst deviation in chemical shift between the simulated and experimental spectra was approximately 0.002 parts per million (ppm). The chemical shifts and coupling constants resulting from this analysis are summarized in Tables 1 and 2. Analysis of the coupling constants by means of the Karplus–Conroy equation (10–12), using generic values of J° = 8.5 Hz and J^{180} = 9.5 Hz (as recommended when no better estimates are available (13)) led to the conclusion that the geometry of the ring systems for 5-(4-nitrophenyl)- 1-aza-4,6-dioxabicyclo[3.3.0]octane is as shown in



The logic of this assignment is as follows: (*i*) If the AB and XY protons were eclipsed (whether A with X and B with Y or A with Y and B with X), then $^3J_{AX} + {}^3J_{AY} = {}^3J_{BX} + {}^3J_{BY}$, but this is not the case; (*ii*) If the protons are staggered, then one of A and B will be *anti* to one of X and Y and gauche to the other, and the other of A and B will be gauche to both X and Y. Since *J* is largest for protons that are *anti*, the largest of the ^3J coupling constants must be for the pair of protons that are most nearly *anti*. This is $^3J_{AX}$; (*iii*) If A is approximately *anti* to X, then $^3J_{AY} \approx {}^3J_{BX}$, as is found; if instead A and Y were approximately *anti*, then $^3J_{AX} \approx {}^3J_{BY}$, which is not the case.

An X-ray structure was obtained for 5-(4-nitrophenyl)-1-

© 2004 NRC Canada

Fig. 1. Experimental and simulated ^{1}H NMR spectra for 5-isopropyl-1-aza-4,6-dioxabicyclo[3.3.0]octane.

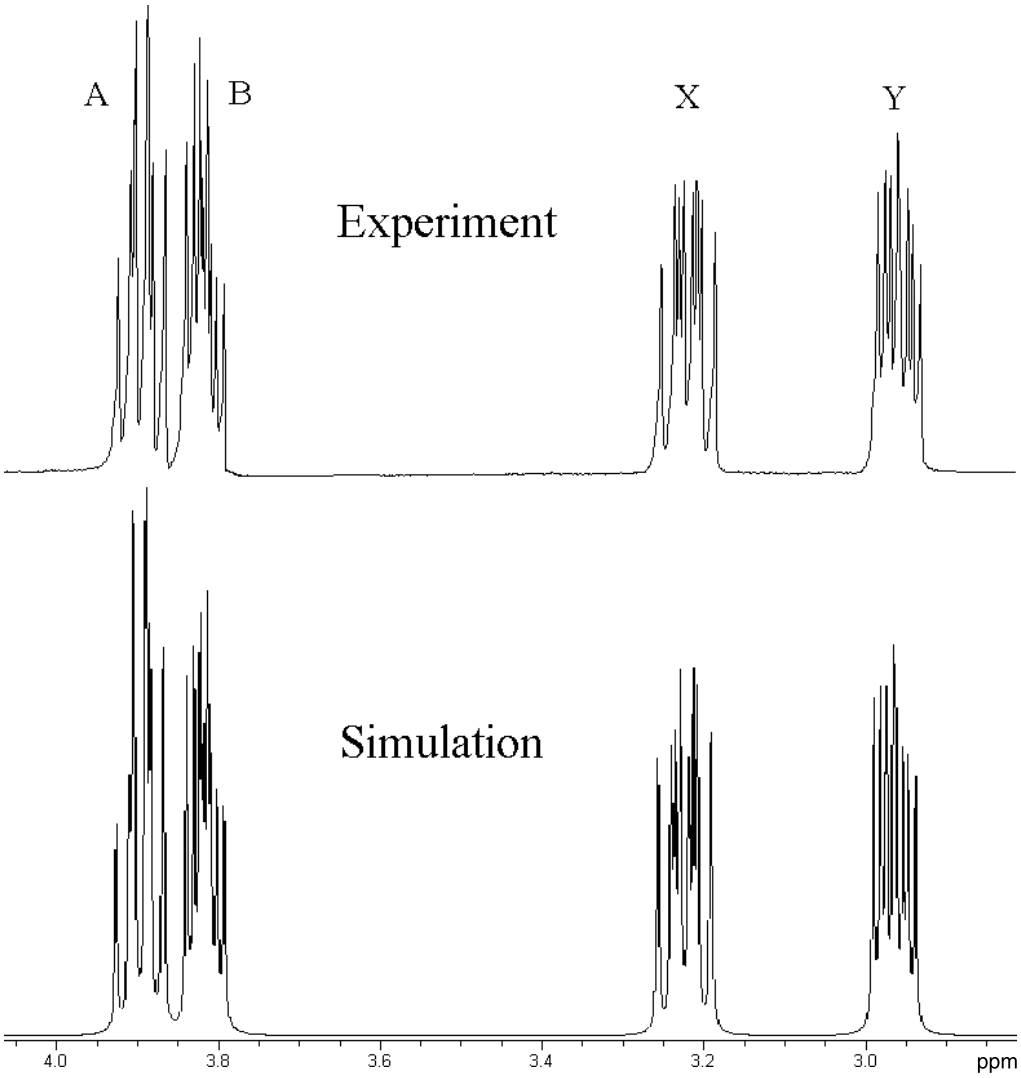


Table 1. Chemical shifts for the 5-*R*-1-aza-4,6-dioxabicyclo-[3.3.0]octanes in $CDCl_3$ (ppm) (Varian Mercury 400).

R	A	B	X	Y
H	3.838	3.796	3.199	2.924
Me	3.865	3.790	3.210	2.909
Et	3.904	3.813	3.219	2.947
i-Pr	3.895	3.816	3.219	2.959
$MeOCH_2$	3.949	3.870	3.275	2.966
Ph	4.119	3.998	3.358	3.094
p-NO_2-Ph	4.115	3.992	3.353	3.127
p-Cl-Ph	4.094	3.968	3.324	3.079
CF_3	4.093	4.012	3.339	3.028
Cl_2CH	4.095	4.055	3.468	3.062

Table 2. Coupling constants for the 5-*R*-1-aza-4,6-dioxabicyclo[3.3.0]octanes (Hz).

R	$^2J_{AB}$	$^3J_{AX}$	$^3J_{AY}$	$^3J_{BX}$	$^3J_{BY}$	$^2J_{XY}$
H	–8.20	8.40	6.04	6.83	4.30	–10.90
Me	–8.20	8.35	6.32	6.67	4.30	–10.95
Et	–8.10	8.25	6.28	6.77	4.10	–10.90
i-Pr	–8.30	8.70	6.28	6.63	3.55	–11.00
$MeOCH_2$	–8.00	7.85	6.24	6.50	4.55	–10.70
Ph	–8.15	8.00	6.56	6.90	4.35	–10.80
p-NO_2-Ph	–8.35	8.30	6.40	6.63	4.25	–11.00
p-Cl-Ph	–8.20	8.15	6.56	6.87	4.30	–11.05
CF_3	–7.95	7.13	6.60	6.50	5.85	–10.88
Cl_2CH	–8.10	7.65	6.54	6.80	4.73	–10.88

aza-4,6-dioxabicyclo[3.3.0]octane. This structure, Fig. 2, confirms that the bicyclic amide acetals have the five-membered rings *cis*-fused, as Anteunis et al. had concluded (14) based on analysis of the ^{1}H NMR spectra. The dihedral angles were close to, though not identical with, those deduced from the Karplus–Conroy analysis; the worst deviation was for the A–X dihedral, 146° rather than 162°. Examination of bond lengths in the X-ray structure showed no sign of an anomeric effect, which would be expected to cause a shortening of the quaternary carbon–nitrogen bond and a lengthening of at least one of the quaternary carbon–oxygen bonds.

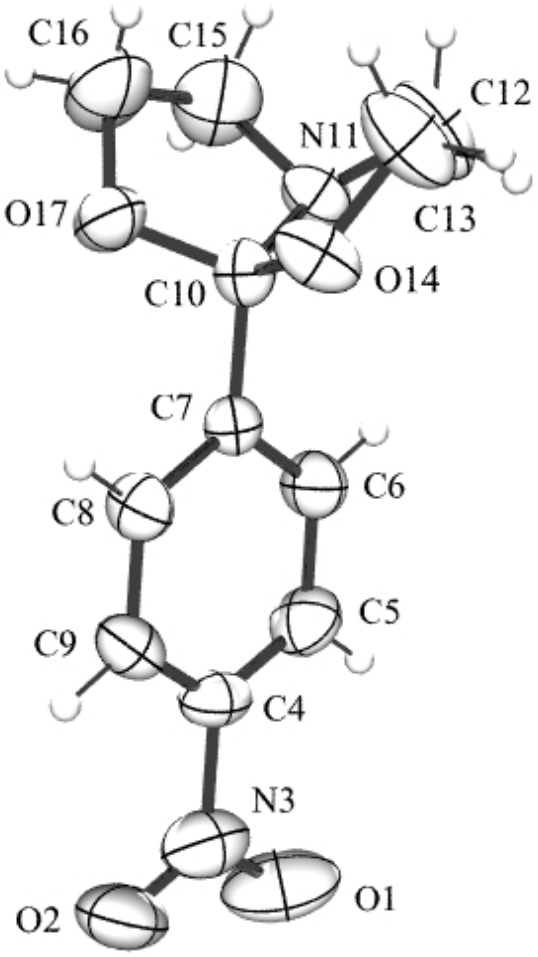
© 2004 NRC Canada

Table 3. MS peak listing of the 5-*R*-1-aza-4,6-dioxabicyclo[3.3.0]octanes.

R	$[M]^+$	$[M - R]^+$	$[M - CH_2O]^+$	$[RCO]^+$	$[C_3H_4NO]^+$	$[C_3H_6N]^+$
H	115(20)	114(8)	85(100)	—	70(3)	56(25)
Me	129(12)	114(12)	99(100)	—	70(12)	56(34)
Et	143(4)	114(100)	113(41)	57(52)	70(34)	56(20)
i-Pr	157(5)	114(16)	127(l)	71(26)	70(8)	56(17)
$MeOCH_2$	158(l)	114(100)	129(2)	—	70(30)	56(7)
CF_3	183(9)	114(100)	153(49)	97(3)	70(43)	56(60)
$C1_2CH$	197(l)	114(100)	167(4)	—	70(29)	—
Ph	191(12)	114(10)	161(61)	105(100)	70(6)	56(19)
p-NO_2-Ph	236(8)	114(8)	206(100)	150(67)	70(6)	—
p-Cl-Ph	225(8)	114(3)	195(37)	139(78)	70(3)	—

Note: Values in table are *m*/*z* (relative intensity (%)).

Fig. 2. Crystal structure of 5-(4-nitrophenyl)-1-aza-4,6-dioxabicyclo[3.3.0]octane.



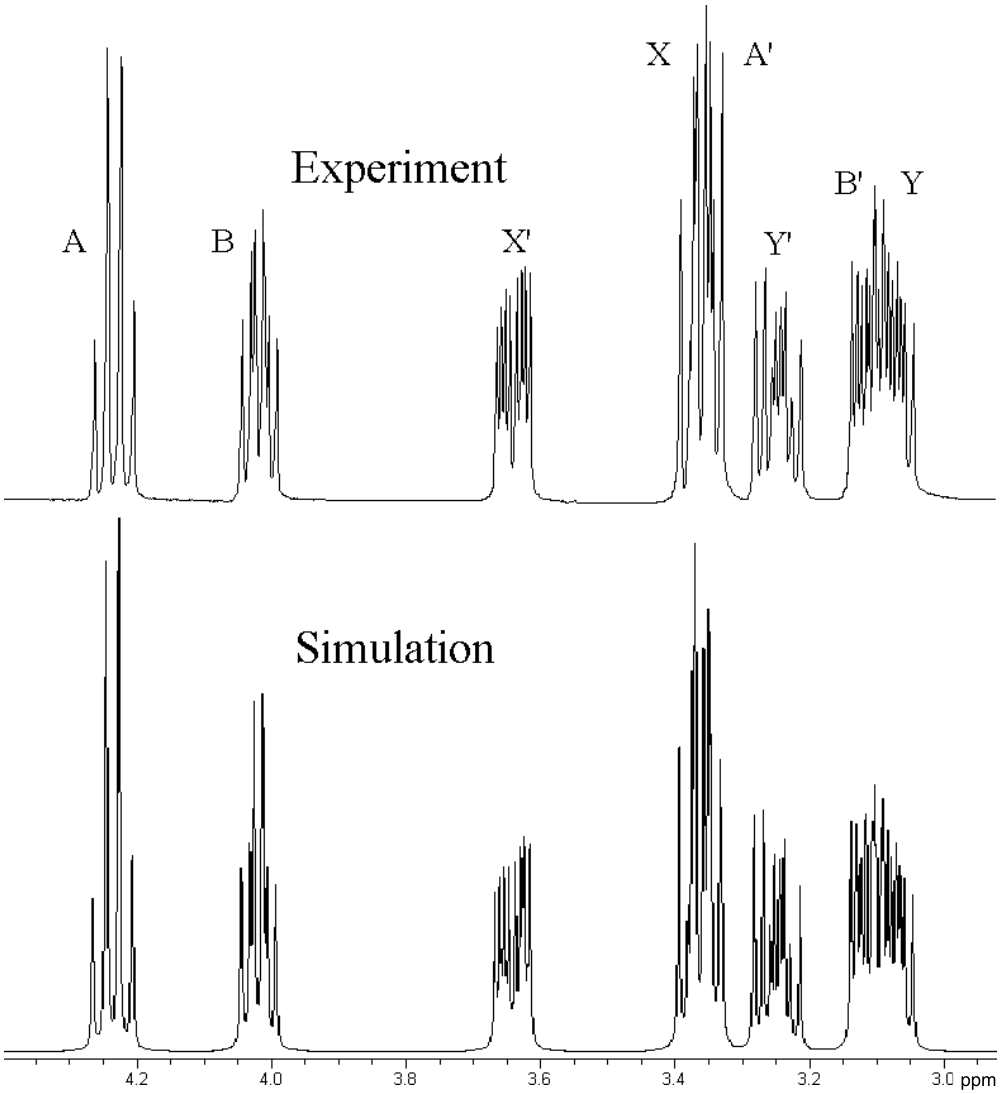
The mass spectra of these compounds were analyzed for characteristic fragmentation patterns. There were differences in fragmentation pattern for 5-aryl- vs. 5-alkyl-substituted 1-aza-4,6-dioxabicyclo[3.3.0]octanes. These results are collected in Table 3. The molecular ion peak for each bicyclic amide acetal was present with low relative intensity. Two primary fragmentation routes appear to be important based on the electron impact studies of these compounds, as follows: cleavage of the ring and elimination of the substituent. In the alkyl-substituted bicyclic amide acetals, the substituent elimination route appears to become more prevalent as R becomes larger. When the substituent was an aryl group, cleavage of the ring was favored, yielding dominant $[M - CH_2O]^+$ and acyl cation fragments.

The thiazolidinooxazolidine ring system has a more complicated ^{1}H NMR splitting pattern, with two overlapping ABXY patterns. The pattern for the thiazolidine ring will be labeled A′B′X′Y′; the primes are used to indicate the analogy with the unprimed peak in the oxazolidine ring. This is not the usual convention, where single primes are used to indicate protons that are chemically but not magnetically equivalent, which is not the case here. All the protons are different, and the pattern, though complicated, can be analyzed as in the oxazolidinooxazolidine case. The assignment of the methylene signals was based on the ^{1}H, ^{13}C, gCOSY, and gHSQC spectra. The ^{13}C signal for the methylene at lowest field was assigned to CH_2-O; the ^{13}C signal for the methylene at highest field was assigned to CH_2S. The combination of gCOSY and gHSQC spectra allowed the remaining assignments. Simulated spectra were in good agreement with the observed spectra, as shown in Fig. 3. The chemical shifts and coupling constants are found in Tables 4 and 5.

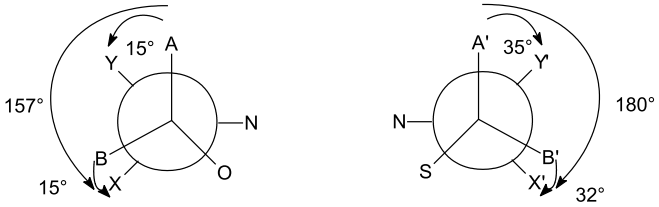
For most of the 5-substituted-1-aza-4-oxa-6-thiabicyclo-[3.3.0]octanes, the same logic as for the dioxa case can be used to deduce the dihedral angles for the oxazolidino ring from the Karplus–Conroy curve, but for three compounds (R = H, ethyl, and methoxymethyl), all four ^3J values are approximately equal, which leads to a contradiction. If $^3J_{AX} + {}^3J_{AY} \approx {}^3J_{BX} + {}^3J_{BY}$, then one might conclude that the hydrogens were eclipsed, but if so the dihedral angles would be 0° and 120°, leading to distinctly different coupling constants. We are forced to conclude that in fact the structure is partly staggered, and that the Karplus–Conroy curve, especially with generic parameter values, is only an approximate guide. The structures are, in all cases, likely to be staggered but closer to eclipsed than to fully staggered geometry. The approximate nature of the dihedral angles deduced from the Karplus–Conroy curve is shown by comparison with the X-ray structure for R = 4-nitrophenyl, where the AY and BX dihedrals are found to be 27.45° and 26.62°, respectively, and not 15° and 15°, as deduced from the coupling constants. Likewise the AX dihedral is 144.5°, according to the X-ray analysis, rather than 157°, as deduced from coupling constants. The Karplus–Conroy curve is a useful guide but is not exact. The coupling constants for the thiazolidino ring

© 2004 NRC Canada

Fig. 3. Experimental and simulated ^{1}H NMR spectra for 5-(4-nitrophenyl)-1-aza-4-oxa-6-thiabicyclo[3.3.0]octane.



were not all the same, and the logic used for the dioxa case led to a simpler analysis. Analysis of the coupling constants for 6-(4-nitrophenyl)-1-aza-6-thia-4-oxabicyclo[3.3.0]octane by the Karplus–Conroy equation leads to the geometries shown:



An X-ray structure was determined for 6-(4-nitrophenyl)-1-aza-6-thia-4-oxabicyclo[3.3.0]octane; see Fig. 4. Again, the five-membered rings are *cis*-fused, and the dihedral angles are in approximate, though not exact, agreement with the values from the Karplus–Conroy analysis.

The X-ray structure revealed an N-C-S anomeric effect; the quaternary carbon–nitrogen bond is shorter relative to the CH_2—N bonds (1.43 Å vs. 1.46 Å or 1.50 Å), and the quaternary carbon–sulfur bond is longer than the CH_2—S bond (1.93 Å vs. 1.80 Å). The X-ray crystal structure data are found in Tables S-1 to S-10.[3]

The mass spectra of the 5-substituted 1-aza-6-thia-4-oxabicyclo[3.3.0]octanes showed more complex fragmentation patterns, as one might expect for the less-symmetrical structures. Once again there were differences in preferred fragmentation pattern for 5-aryl- vs. 5-alkyl-substituted compounds. These results are found in Table 6. The molecular ion is present in greater amount in the sulfur-containing bicyclic acetals. As for the dioxa series, elimination of the

[3] Supplementary data may be purchased from the Depository of Unpublished Data, Document Delivery, CISTI, National Research Council Canada, Ottawa, ON K1A 0S2, Canada (http://www.nrc.ca/cisti/irm/unpub_e.shtml for information on ordering electronically). CCDC 214681 and 214682 contain the supplementary data for this paper. These data can be obtained, free of charge, via www.ccdc.cam.ac.uk/conts/retrieving.html (or from the Cambridge Crystallographic Data Centre, 12 Union Road, Cambridge, U.K.; fax +44 1223 336033; or deposit@ccdc.cam.ac.uk).

© 2004 NRC Canada

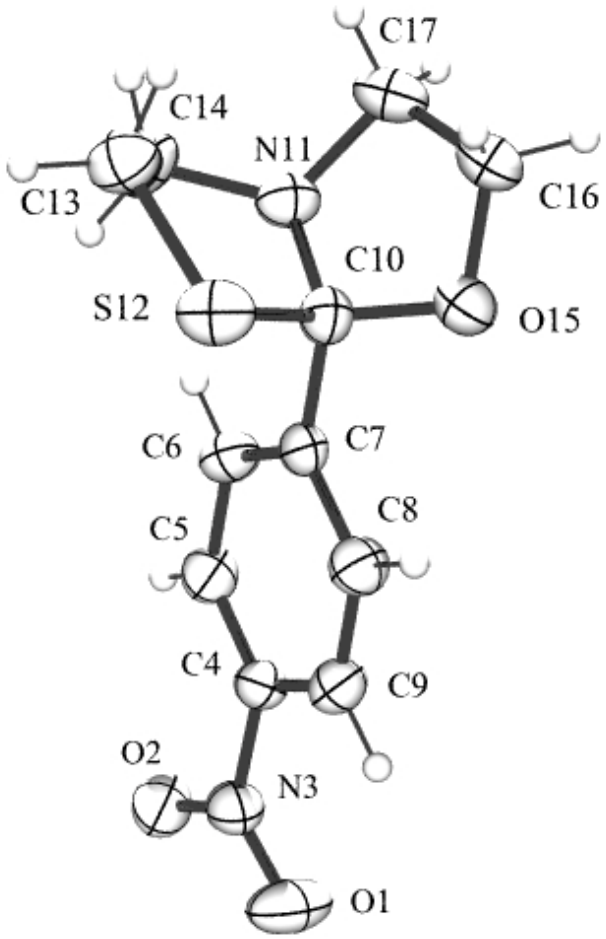
Table 4. Chemical shifts (ppm) for 5-*R*-1-aza-4-oxa-6-thiabicyclo[3.3.0]octanes in $CDCl_3$ (ppm) (Varian Inova 600).

R	A	B	X	Y	A′	B′	X′	Y′
H	4.104	3.947	3.176	2.798	3.122	2.830	3.500	3.054
Me	4.078	3.967	3.230	2.813	3.302	2.921	3.533	3.068
Et	4.053	3.918	3.200	2.816	3.233	2.824	3.509	3.013
i-Pr	4.026	3.884	3.206	2.832	3.183	2.802	3.505	3.026
$MeOCH_2$	4.026	3.930	3.186	2.777	3.137	2.745	3.466	3.002
Ph	4.225	4.029	3.353	3.030	3.346	3.070	3.589	3.211
p-NO_2-Ph	4.217	4.001	3.344	3.058	3.344	3.099	3.623	3.232
p-Cl-Ph	4.207	4.005	3.327	3.018	3.335	3.069	3.567	3.172
p-MeO-Ph	4.213	4.026	3.332	3.009	3.345	3.057	3.552	3.158

Table 5. Coupling constants for 5-*R*-1-aza-4-oxa-6-thiabicyclo [3.3.0] octanes (Hz).

R	$^2J_{AB}$	$^3J_{AX}$	$^3J_{AY}$	$^3J_{BX}$	$^3J_{BY}$	$^2J_{XY}$	$^2J_{A'B'}$	$^3J_{A'X'}$	$^3J_{A'Y'}$	$^3J_{B'X'}$	$^3J_{B'Y'}$	$^2J_{X'Y'}$
H	–7.80	7.58	6.45	6.69	7.65	–9.23	–10.20	4.89	10.20	2.35	5.60	–12.23
Me	–8.03	8.60	7.74	7.55	5.70	–9.15	–10.50	5.57	10.95	1.20	6.15	–12.90
Et	–7.13	7.43	7.56	7.15	7.50	–8.33	–10.20	5.76	10.95	0.00	5.80	–12.60
i-Pr	–7.65	7.35	7.50	7.25	5.57	–9.45	–10.43	5.23	10.88	1.20	5.55	–12.60
$MeOCH_2$	–7.73	7.35	6.60	7.00	7.32	–9.23	–10.43	5.40	10.88	1.28	6.00	–12.83
Ph	–7.73	7.58	7.74	7.60	5.31	–9.68	–10.13	5.49	9.98	2.50	5.90	–12.30
p-NO_2-Ph	–7.73	7.73	7.68	7.65	5.14	–9.98	–9.98	5.52	9.68	3.00	5.80	–12.45
p-Cl-Ph	–7.80	7.50	7.68	7.40	5.06	–9.90	–10.05	5.49	9.75	2.50	6.00	–12.15
p-MeO-Ph	–7.80	7.50	7.80	7.40	5.23	–9.60	–9.48	5.49	9.87	2.45	5.95	–12.83

Fig. 4. Crystal structure of 5-(4-nitrophenyl)-1-aza-4-oxa-6-thiabicyclo[3.3.0]octane.

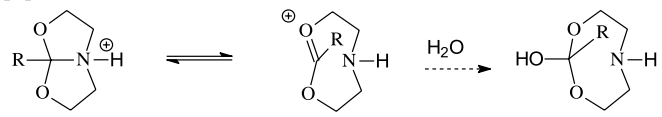


substituent R on C_5 becomes more important as R becomes larger, and ring cleavage is favored when R is an aryl group.

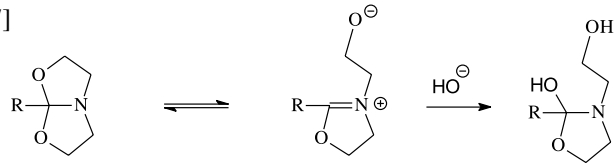
Discussion

As we had hoped, the bicyclic amide acetals and monothioacetals were much easier to purify than the acyclic amide dimethyl acetals and the amide dialkyl monothioacetals, although the bicyclic compounds are still rather sensitive. A range of these compounds has now been prepared, though it proved difficult to prepare even the bicyclic acetals of amides with electron-withdrawing substituents. Although no kinetics were carried out, it is clear that the rate of hydrolysis of these compounds is very sensitive to the nature of the substituent on the 5-carbon, as would be expected, given that this carbon becomes the carbon of an iminium ion during the hydrolysis. It is interesting that the hydrolysis is facile in basic solution, while the corresponding cations (from protonation or alkylation on nitrogen) can be studied in solution (14) or even recrystallized (15). We presume that this is a consequence of the facile reclosure of the cation, resulting from C–N cleavage and the more effective competition by hydroxide to trap the cation from C–O cleavage.

[6]



[7]



© 2004 NRC Canada

Table 6. MS peak listing of the 5-*R*-1-aza-4-oxa-6-thiabicyclo[3.3.0]octanes.

R	$[M]^+$	$[M - R]^+$	$[M - CH_2S]^+$	$[M - CH_3S]^+$	$[M - C_2H_3S]^+$	
H	131(66)	130(4)	85(70)	84(21)	72(68)	
Me	145(41)	130(6)	99(10)	98(3)	86(31)	
Et	173(49)	130(19)	113(12)	112(23)	100(46)	
i-Pr	173(100)	130(40)	127(4)	126(22)	114(87)	
$MeOCH_2$	175(68)	130(82)	129(l)	128(7)	116(20)	
Ph	207(13)	130(l)	161(3)	160(21)	148(10)	
p-NO_2-Ph	252(21)	130(2)	206(4)	205(20)	193(15)	
p-Cl-Ph	241(18)	130(l)	195(2)	194(12)	182(9)	
p-MeO-Ph	237(2)	130(l)	—	190(l)	178(l)	
R	$[M - C_2H_4S]^+$	$[M - C_2H_3SO]^+$	$[M - C_3H_6SO]^+$	$[RCO]^+$	$[C_3H_4NO]^+$	$[C_3H_6N]^+$
H	71(21)	56(100)	—	—	70(15)	56(100)
Me	85(13)	70(11)	55(36)	—	70(11)	56(100)
Et	99(14)	84(41)	69(21)	57(85)	70(19)	56(100)
i-Pr	113(13)	98(42)	83(10)	71(48)	70(29)	56(92)
$MeOCH_2$	115(3)	100(64)	85(9)	73(2)	70(1)	56(30)
Ph	147(12)	132(l)	117(32)	105(100)	70(2)	—
p-NO_2-Ph	192(8)	177(2)	162(15)	150(100)	70(3)	—
p-Cl-Ph	181(20)	166(l)	151(45)	139(100)	70(3)	—
p-MeO-Ph	177(94)	162(1)	147(100)	135(35)	70(1)	—

We have demonstrated by NMR and X-ray structure determination that both the 5-substituted 1-aza-4,6-dioxabicyclo[3.3.0]octanes and the 5-substituted 1-aza-6-thia-4-oxabicyclo[3.3.0]octanes are *cis* fused, with the ring methylene groups approximately staggered. Examination of the structure of 5-(4-nitrophenyl)-1-aza-4,6-dioxabicyclo[3.3.0]-octane showed no sign of changes in bond lengths attributable to an anomeric effect. All four C—O bonds were essentially the same length, 1.41, 1.41, 1.41, and 1.40 Å, as were all three C—N bonds, 1.47, 1.46, and 1.46 Å. Thus, the bonds that cannot be part of an anomeric effect are the same length as those that, in principle, might be. Consideration of the expected position of the nitrogen lone pair showed that this was not lined up to overlap with the σ* orbital of the C_5—O bond. Since the anomeric effect is attributed to this kind of overlap, the absence of bond length changes becomes reasonable. By contrast, the structure of 5-(4-nitrophenyl)-substituted 1-aza-6-thia-4-oxabicyclo[3.3.0]octane shows definite changes in bond length in the directions expected for an anomeric effect, namely, shortening of the C_5—N bond (1.43 Å vs. 1.46 Å or 1.50 Å) and lengthening of the C_5—S bond (1.80 Å vs. 1.93 Å). There is even a shortening of the C_5—O bond (1.40 Å vs. 1.44 Å). Examination of the structure suggests a dihedral angle between the N lone pair and the C—S bond of 140°. Apparently, this angle, though well short of 180°, is enough to allow for overlap of the lone pair and σ* antibonding orbitals. The longer C—S bonds, relative to C—O bonds, force a loss of symmetry in the bicyclic monothioacetal, and this allows partial overlap of the sort leading to an anomeric effect.

Experimental

General methods

Nuclear magnetic resonance spectra were recorded on a Varian Gemini 200 (^{1}H at 200.1 MHz, ^{13}C at 50.3 MHz), a Varian Gemini 300 (^{1}H at 299.9 MHz, ^{13}C at 75.4 MHz), a Varian Mercury 400 (^{1}H at 400.1 MHz, ^{13}C at 100.6 MHz), a Varian Inova 600 (^{1}H at 599.7 MHz), or a Bruker AMX-500 (University of Ottawa, Ont.) spectrometer (^{1}H at 500.1 MHz, ^{13}C at 125.8 MHz). Mass spectra were recorded on a Finnigan MAT 8200 high-resolution spectrometer. Melting points were recorded on a Gallenkamp melting point apparatus.

Data were collected on a Nonius Kappa-CCD diffractometer (either at the University of Western Ontario or the University of Toronto) using COLLECT software (16). For both compounds, the unit cell parameters were calculated and refined from the full data set. Crystal cell refinement and data reduction were carried out using the Nonius DENZO package (17). The data were scaled using SCALEPACK (18). The SHELXTL 5.1 (19) program package was used to solve the structure by direct methods, followed by successive difference Fouriers. The molecule was very well behaved. All non-hydrogen atoms were refined with anisotropic thermal parameters. The hydrogen atoms were calculated geometrically and were riding on their respective carbon atoms.

Crystals of 5-(*p*-nitrophenyl)-1-aza-4,6-dioxabicyclo-[3.3.0]octane were grown from diethyl ether. A colourless, thin plate was mounted on a glass fibre. Data were collected at low temperature (–73 °C). The crystal data and refinement parameters for $C_{11}H_{12}N_2O_4$ are listed in Table S-1.[3] Interatomic distances and angles are listed in Table S-3. The reflection data and systematic absences were consistent with the monoclinic space group $P2_1/c$. The largest residual electron density peak (0.155 e/A^3) was not associated with anything of significance. Full-matrix least-squares refinement on F^2 gave R_1 = 4.39 and wR_2 = 10.43 at convergence.

Crystals of 5-(*p*-nitrophenyl)-1-aza-4-oxa-6-thiabicyclo-[3.3.0]octane were grown from hexanes. A colourless, thin plate was mounted on a glass fibre and sent to the University

© 2004 NRC Canada

of Toronto. Data were collected at low temperature (–123 °C). The crystal data and refinement parameters for $C_{11}H_{12}N_2O_3S$ are listed in Table S-6. Interatomic distances and angles are listed in Table S-8. The reflection data were consistent with the triclinic space group $P\bar{1}$. The largest residual electron density peak (0.724 e/A^3) was not associated with anything of significance. Full-matrix least-squares refinement on F^2 gave R_1 = 7.94 and wR_2 = 16.88 at convergence.

Materials

1-Aza-4,6-dioxabicyclo [3.3.0] octane

1-Aza-4,6-dioxabicyclo [3.3.0] octane was prepared from diethanolamine (Caledon) and *N*,*N*-dimethylformamide dimethyl acetal (Aldrich) following Arnold and Kornilov (20) in 80.9% yield; bp 68 °C (7.0 torr (1 torr = 133.322 Pa)) (lit. (20) value bp 65 to 66 °C (5 torr)). ^{1}H NMR (400 MHz, $CDCl_3$)[4] δ: 2.90–2.96 (2H, m), 3.16–3.25 (2H, m), 3.77–3.87 (4H, m), 5.80 (1H, s). ^{13}C NMR (100 MHz, $CDCl_3$) δ: 52.53, 64.39, 114.91. Exact mass calcd. for $C_5H_9NO_2$: 115.0633; found: 115.0633.

In the same way were prepared the following two compounds.

1-Aza-4-oxa-6-thiabicyclo[3.3.0]octane

75.8% yield; bp 64 °C (0.050 torr). ^{1}H NMR (400 MHz, $CDCl_3$) δ: 2.78–2.85 (2H, m), 3.03–3.08 (1H, m), 3.10–3.14 (1H, m), 3.15–3.20 (1H, m), 3.48–3.52 (1H, m),.3.92–3.97 (1H,q), 4.08–4.13 (1H,q). ^{13}C NMR (100 MHz, $CDCl_3$) δ: 31.08, 49.59, 55.46, 65.37, 106.96. Exact mass calcd. for C_5H_9NOS: 131.0405; found: 131.0398.

5-Methyl-1-aza-4-oxa-6-thiabicyclo[3.3.0]octane

Prepared from from *N*,*N*-dimethylamide dimethyl acetal (21); 90.2% yield; bp 58 °C (0.025 torr). ^{1}H NMR (400 MHz, $CDCl_3$) δ: 1.81 (3H, s), 2.78–2.85 (1H, m), 2.90–2.95 (1H, m), 3.02–3.12 (1H, m), 3.20–3.35 (2H, m), 3.50–3.58 (1H, m), 3.92–4.02 (1H, q), 4.03–4.12 (1H, q). ^{13}C NMR (100 MHz, $CDCl_3$) δ: 31.0, 33.8, 50.5, 55.8, 65.7, 119.2. Exact mass calcd. for $C_6H_{11}NOS$: 145.0561; found: 145.0557.

General preparation of 5-substituted-1-aza-4,6-dioxabicyclo[3.3.0]octanes

Diethanolamine (Caledon) (25.0 g, 0.238 mol) and a sliver of sodium metal were placed in a two-necked, round-bottomed flask fitted with a condenser. The system was sealed with the use of septa. An exhaust needle was placed in the septum at the top of the condenser, while a stream of nitrogen was fed through the septum on the neck of the round-bottomed flask. A positive pressure of nitrogen was maintained throughout the remainder of the reaction. A magnetic stirrer and gentle heating with an oil bath (~50 °C) helped dissolve the sodium metal. Once the sodium had completely dissolved, the appropriate nitrile (0.239 mol) was added to the reaction flask with a syringe. The temperature of the oil bath was raised to 100 °C, and the reaction proceeded for 40 h at that temperature. Upon cooling, the reaction mixture was placed in a separatory funnel, and the product was extracted with multiple portions of hexanes. The hexanes were removed by rotary evaporation. The residue was doubly distilled at reduced pressure to give a clear colourless liquid.

In this way were prepared the following five compounds.

5-Methyl-1-aza-4,6-dioxabicyclo[3.3.0]octane

25.5% yield; bp 52 °C (5.0 torr) (lit. (15) value bp 65° (11 torr)). ^{1}H NMR (400 MHz, $CDCl_3$) δ: 1.49 (3H, s), 2.88–2.96 (2H, m), 3.18–3.26 (2H, m), 3.76–3.83 (2H, m), 3.83–3.90 (2H, m). ^{13}C NMR (100 MHz, $CDCl_3$) δ: 24.0, 53.0, 64.8, 123.1. Exact mass calcd. for $C_6H_{11}NO_2$: 129.0790; found: 129.0791.

5-Ethyl-1-aza-4,6-dioxabicyclo[3.3.0] octane

17.4% yield; bp 81 °C (9.5 torr) (lit. (15) value bp 72 °C (12 torr)). ^{1}H NMR (400 MHz, $CDCl_3$) δ: 0.96 (3H, t), 1.78 (2H, q), 2.92–3.00 (2H, m), 3.18–3.27 (2H, m), 3.78–3.85 (2H, m), 3.87–3.95 (2H, m). ^{13}C NMR (100 MHz, $CDCl_3$) δ: 8.7, 30.6, 53.6, 65.0, 125.1. Exact mass calcd. for $C_7H_{13}NO_2$: 143.0946; found: 143.0944.

5-Isopropyl-1-aza-4,6-dioxabicyclo[3.3.0] octane

31.2% yield; bp 86 °C (10 torr). ^{1}H NMR (400 MHz, $CDCl_3$) δ: 0.97 (3H, s), 0.98 (3H, s), 1.96 (1H, sept), 2.92–2.98 (2H, m), 3.17–3.25 (2H, m), 3.77–3.83 (2H, m), 3.85–3.92 (2H, m). ^{13}C NMR (100 MHz, $CDCl_3$) δ: 17.4, 35.8, 54.3, 65.2, 126.8. Exact mass calcd. for $C_8H_{15}NO_2$: 157.1103; found: 157.1098.

5-Methoxymethyl-1-aza-4,6-dioxabicyclo[3.3.0] octane

10.1% yield; bp 105 °C (8 torr). ^{1}H NMR (400 MHz, $CDCl_3$) δ: 2.94–3.00 (2H, m), 3.24–3.31 (2H, m), 3.41 (3H, s), 3.47 (2H, s), 3.84–3.90 (2H, m), 3.92–3.98 (2H, m). ^{13}C NMR (100 MHz, $CDCl_3$) δ: 53.0, 59.6, 65.2, 73.9, 122.1. Exact mass calcd. for $C_7H_{13}NO_3$: 159.0895; found: 159.0890.

5-Phenyl-1-aza-4,6-dioxabicyclo[3.3.0] octane

17.3% yield; bp 150 °C (5.0 torr) (lit. (15) value bp 79 to 80 °C (0.03 torr)). ^{1}H NMR (400 MHz, $CDCl_3$) δ: 3.05–3.13 (2H, m), 3.30–3.40 (2H, m), 3.96–4.03 (2H, m), 4.09–4.16 (2H, m), 7.32 (3H, t), 7.61 (2H, d). ^{13}C NMR (100 MHz, $CDCl_3$) δ: 53.0, 65.7, 123.2, 125.9, 128.1, 128.4, 140.1. Exact mass calcd. for $C_{11}H_{13}NO_2$: 191.0946; found: 191.0943.

5-(*p*-Nitrophenyl)-1-aza-4,6-dioxabicyclo[3.3.0]octane

The experimental procedure followed that of the synthesis of 5-methyl-1-aza-4,6-dioxabicyclo[3.3.0]octane with some modifications. A sliver of sodium metal was dissolved in warm diethanolamine (Caledon) (25.1 g, 0.238 mol), as usual. However, solid *p*-nitrobenzonitrile (Aldrich) (35.0 g, 0.236 mol) was dissolved in 1,4-dioxane (Caledon) prior to addition to the reaction flask. The reaction proceeded for 48 h at 80 °C. Upon removal of the 1,4-dioxane by rotary evaporation, a yellow solid precipitated. The solid was recrystallized from diethyl ether, giving shiny, pale yellow crystals (15.8 g, 28.3% yield); mp 90 to 91 °C. ^{1}H NMR (400 MHz, $CDCl_3$) δ: 3.08–3.14 (2H, m), 3.28–3.38 (2H, m), 3.95–4.00 (2H, m), 4.05–4.14 (2H, m), 7.77 (2H, d), 8.19 (2H, d). ^{13}C NMR (100 MHz, $CDCl_3$) δ: 53.8, 66.5, 122.4,

[4] Abbreviations used: m, multiplet; s, singlet, d, doublet; t, triplet; q, quartet.

© 2004 NRC Canada

123.9, 127.7, 147.5, 148.1. Exact mass calcd. for $C_{11}H_{12}N_2O_4$: 236.0797; found: 236.0807.

5-(*p*-Chlorophenyl)-1-aza-4,6-dioxabicyclo[3.3.0]octane

Solid *p*-chlorobenzonitrile (Aldrich) (20.0 g, 0.145 mol) was placed in a round-bottomed flask. Enough diethanolamine (Caledon) was added to the reaction flask to completely cover the nitrile. This excess of diethanolamine helped reduce the amount of *p*-chlorobenzonitrile that sublimed onto the upper walls of the reaction flask during the reaction. The round-bottorned flask was fitted with a condenser and kept under an N_2 atmosphere. The oil bath was heated to 50 °C and the reaction proceeded for 4 days. The reaction flask was allowed to cool before addition of hexanes to extract the title compound. Removal of hexanes by rotary evaporation resulted in a white solid that contained the target compound and unreacted nitrile. Recrystallization could not remove all of the nitrile. The white solid was placed in a sublimation apparatus, to take advantage of the willingness of the nitrile to sublime. Reduced pressure (0.025 torr) and very gentle heating removed the nitrile exclusively. The remaining solid was recrystallized in hexanes to give white crystals (2.9 g, 8.9% yield); mp 43–45 °C. ^{1}H NMR (400 MHz, $CDCl_3$) δ: 3.05–3.12 (2H, m), 3.29–3.37 (2H, m), 3.94–4.00 (2H, m), 4.06–4.13 (2H, m), 7.30 (2H, d), 7.53 (2H, d). ^{13}C NMR (100 MHz, $CDCl_3$) δ: 53.0, 65.8, 122.8, 127.6, 128.1, 134.3, 138.8. Exact mass calcd. for $C_{11}H_{12}NO_2Cl$: 225.0557; found: 225.0557.

5-Trifluoromethyl-1-aza-4,6-dioxabicyclo[3.3.0]octane

A sliver of sodium metal was dissolved in diethanolamine (Caledon) (28.7 g, 0.273 mol) and placed in a 300 cc Parr Instruments bomb. The bomb was placed into a dry ice – acetone bath to lower the temperature of the bomb and its contents to –78 °C. At that temperature, the contents of the bomb solidified. Freshly prepared, condensed trifluoroacetonitrile (prepared from trifluoroacetamide (22)) (~30 mL, ~0.316 mol) was poured into the chilled bomb. The bomb was then immediately sealed. Undoubtedly some trifluoroacetonitrile was lost during this crude transfer. The bomb was placed into its temperature controller and set to 70 °C. The temperature inside the bomb rose dramatically, requiring cooling of the bomb. Once the temperature was brought under control, the bomb was adjusted to 70 °C where it remained for 48 h. At the end of the reaction period, the bomb was flushed with nitrogen before opening to ensure removal of any remaining trifluoroacetonitrile. Inside the bomb was an orange viscous liquid that was mainly unreacted diethanolamine. Extraction with hexanes resulted in pure 5-trifluoromethyl-1-aza-4,6-dioxabicyclo[3.3.0]octane. The liquid crystallized on its own after sitting on the bench for 2 weeks. Recrystallization from hexanes resulted in translucent crystals (0.25 g, 0.5% yield). ^{1}H NMR (400 MHz, $CDCl_3$) δ: 3.01–3.09 (2H, m), 3.31–3.40 (2H, m), 3.99–4.06 (2H, m), 4.07–4.15 (2H, m). ^{19}F NMR (300 MHz, $CFCl_3$) δ: 83.0. ^{13}C NMR (100 MHz, $CDCl_3$) δ: 52.5, 66.7, 120.5, 123.3. Exact mass calcd. for $C_6H_8NO_2F_3$: 183.0505; found: 183.0503.

5-Dichloromethyl-1-aza-4,6-dioxabicyclo[3.3.0] octane

The experimental procedure followed that of the synthesis of 5-methyl-1-aza-4,6-dioxabicyclo[3.3.0]octane, with some modifications. Diethanolamine (Caledon) (12.5 g, 0.119 mol) and 75 mL of 1,4-dioxane (Caledon) were placed in the reaction flask with *no catalyst*. Caution: The standard reaction of 1:1 amine:nitrile with sodium catalyst in the absence of solvent resulted in an explosion. Dichloroacetonitrile (Aldrich) (10.0 mL, 0.125 mol) was added slowly to the reaction flask with a syringe. Once the nitrile was completely added, the oil bath was heated gently until it reached 50 °C. The evolution of ammonia appeared to be very rapid, so heating was stopped. The reaction continued at room temperature for 48 h. The 1,4-dioxane solvent was removed by rotary evaporation, leaving a thick residue. It was placed in a separatory funnel for extraction with hexanes. A white solid precipitated in the separatory funnel when hexanes were added. Recrystallization with hexanes resulted in white shiny flakes (5.65 g, 24.0% yield); mp 62 to 63 °C. ^{1}H NMR (400 MHz, $CDCl_3$) δ: 3.02–3.10 (2H, m), 3.42–3.51 (2H, m), 4.02–4.14 (4H, m), 5.75 (1H, s). ^{13}C NMR (100 MHz, $CDCl_3$) δ: 54.3, 67.2, 74.0, 123.4. Exact mass calcd. for $C_6H_9NO_2Cl_2$: 197.0009; found:. 197.0007.

5-Ethyl-1-aza-4-oxa-6-thiabicyclo[3.3.0]octane

With some heating, a sliver of sodium metal (Aldrich) was dissolved in freshly prepared 2-(2-mercaptoethyl)-aminoethanol (20.0 g, 0.165 mol) in a round-bottomed flask. Propionitrile (Aldrich) (25 mL, 0.328 mol) was added to the reaction flask and allowed to stir for 2 weeks at room temperature under an N_2 atmosphere. It was found that an excess of nitrile made the consistency of the final reaction mixture easier to handle. An extraction with diethyl ether removed the title compound and its corresponding oxazoline. The mixture was doubly distilled at reduced pressure to give a clear colorless fraction (3.5 g, 13.3% yield); bp 50 °C (0.025 torr). ^{1}H NMR (400 MHz, $CDCl_3$) δ: 1.05 (3H, t), 1.99 (2H, m), 2.80–2.88 (2H, m), 2.99–3.09 (1H, m), 3.19–3.29 (2H, m), 3.48–3.57 (1H, m), 3.92 (1H, q), 4.05 (1H, q). ^{13}C NMR (100 MHz, $CDCl_3$) δ: 9.9, 33.0, 37.0, 51.0, 56.0, 65.5, 123.3. Exact mass calcd. for $C_7H_{13}NOS$: 159.0718; found: 159.0717.

In the same way were prepared the following three compounds.

5-Isopropyl-1-aza-4-oxa-6-thiabicyclo[3.3.0]octane

14.3% yield; bp 53 °C (0.025 torr). ^{1}H NMR (400 MHz, $CDCl_3$) δ: 1.00 (3H, d), 1.10 (3H, d), 2.06 (1H, sept), 2.78–2.88 (2H, m), 2.98–3.08 (1H, m), 3.14–3.25 (2H, m), 3.47–3.55 (1H, m), 3.90 (1H, q), 4.03 (1H, q). ^{13}C NMR (100 MHz, $CDCl_3$) δ: 18.1, 18.5, 32.8, 40.2, 52.0, 56.9, 65.8, 126.4. Exact mass calcd. for $C_8H_{15}NOS$: 173.0874; found: 173.0878.

5-Methoxymethyl-1-aza-4-oxa-6-thiabicyclo[3.3.0]octane

19.0% yield; bp 73 °C (0.025 torr). ^{1}H NMR (400 MHz, $CDCl_3$) δ: 2.75–2.86 (2H, m), 3.00–3.12 (1H, m), 3.15–3.27 (2H, m), 3.40 (3H, s), 3.48–3.55 (1H, m), 3.58 (2H, s), 3.98 (1H, q), 4.08 (1H, q). ^{13}C NMR (100 MHz, $CDCl_3$) δ: 32.0, 51.0, 56.0, 60.0, 66.0, 76.5, 120.0. Exact mass calcd. for $C_7H_{13}NO_2S$: 175.0667; found: 175.0671.

5-Phenyl-1-aza-4-oxa-6-thiabicyclo[3.3.0]octane

The product mixture, after extraction, was distilled at reduced pressure only to remove the by-product, 2-phenyl-

© 2004 NRC Canada

oxazoline (~80 °C at 0.25 torr), leaving relatively pure bicyclic amide acetal in the still-pot. The contents of the still-pot were dissolved in diethyl ether and placed in a freezer. After 5 days, a solid had precipitated and was recrystallized, giving white shiny flakes (12.6% yield); mp 46–48 °C. ^{1}H NMR (500 MHz, $CDCl_3$) δ: 2.96–3.05 (2H, m), 3.14–3.20 (1H, m), 3.28–3.34 (2H, m), 3.53–3.57 (1H, m), 4.00 (1H, q), 4.19 (1H, q), 7.27 (1H, t), 7.32 (2H, t), 7.63 (2H, d). ^{13}C NMR (125 MHz, $CDCl_3$) δ: 33.74, 50.77, 56.37, 65.16, 120.00, 127.86, 142.92. Exact mass calcd. for $C_{11}H_{13}NOS$: 207.0718; found: 207.0723.

5-(*p*-Nitrophenyl)-1-aza-4-oxa-6-thiabicyclo[3.3.0]octane

With some heating, a sliver of sodium metal was dissolved in freshly prepared 2-(2-mercaptoethyl)-aminoethanol (20.0 g, 0.165 mol) in a round-bottomed flask. In a separate flask, solid *p*-nitrobenzonitrile (Aldrich) (24.5 g, 0.165 mol) was dissolved in 1,4-dioxane (Caledon). The nitrile solution was then added to the reaction flask. The reaction mixture was allowed to stir for 2 weeks at room temperature under an N_2 atmosphere. At the end of the reaction period, rotary evaporation was used to remove the 1,4-dioxane solvent. Diethyl ether was used to extract the title compound from the residue. The ethereal solution was placed in the freezer to facilitate crystallization. Within a short period of time, a yellow solid formed, which was collected and recrystallized from ether to give shiny, pale yellow flakes (5.4 g, 13.0% yield); mp 75 to 76 °C. ^{1}H NMR (400 MHz, $CDCl_3$) δ: 3.05–3.15 (2H, m), 3.20–3.29 (1H, m), 3.33–3.40 (2H, m), 3.61–3.68 (1H, m), 4.02 (1H, q), 4.23 (1H, q), 7.75 (2H, d), 8.18 (2H, d). ^{13}C NMR (100 MHz, $CDCl_3$) δ: 34.8, 51.8, 57.8, 65.8, 119.0, 124.0, 127.0, 147.9, 150.2. Exact mass calcd. for $C_{11}H_{12}N_2O_3S$: 252.0569; found: 252.0565.

5-(*p*-Chlorophenyl)-1-aza-4-oxa-6-thiabicyclo[3.3.0]octane

The experimental procedure followed that of the synthesis of 5-(*p*-nitrophenyl)-1-aza-4-oxa-6-thiabicyclo[3.3.0]octane, using freshly prepared 2-(2-mercaptoethyl)-aminoethanol (20.0 g, 0.165 mol) and *p*-chlorobenzonitrile (Aldrich) (25.1 g, 0.183 mol) dissolved in 1,4-dioxane. When the ethereal solution from the extraction was placed in the freezer, white needle-like crystals formed. These were later confirmed to be *p*-chlorophenyl-oxazoline. Several attempts at recrystallization successively removed less and less oxazoline. The product mixture still contained oxazoline. Since the oxazoline had a lower boiling point than the bicyclic amide monothioacetal, sublimation was used in a final attempt to remove the oxazoline. The sublimation was carried out under reduced pressure (0.025 torr) with very gentle heating. Before long, the cold finger of the sublimation apparatus was coated with a white solid. The remaining colorless liquid in the sublimation apparatus was determined to be 94% pure by NMR (4.2 g, 10.5% yield). Repeated attempts at sublimation provided no improvement in the purity of the title compound. ^{1}H NMR (400 MHz, $CDCl_3$) δ: 2.98–3.11 (2H, m), 3.14–3.22 (1H, m), 3.28–3.38 (2H, m), 3.54–3.61 (1H, m), 4.02 (1H, q), 4.21 (1H, q), 7.28 (2H, d), 7.55 (2H, d). ^{13}C NMR (100 MHz, $CDCl_3$) δ: 34.01, 51.0, 56.6, 65.5, 119.4, 127.2, 128.3, 133.8, 141.7. Exact mass calcd. for $C_{11}H_{12}ClNOS$: 241.0328; found: 241.0326.

5-(*p*-Methoxyphenyl)-1-aza-4-oxa-6-thiabicyclo[3.3.0]octane

The experimental procedure followed that of the synthesis of 5-(*p*-chlorophenyl)-1-aza-4-oxa-6-thiabicyclo[3.3.0]octane, using freshly prepared 2-(2-mercaptoethyl)-aminoethanol (22.5 g, 0.186 mol) and *p*-methoxybenzonitrile (Aldrich) (25.7 g, 0.193 mol). After sublimation of the product mixture, the remaining colorless liquid was determined to be 90% title compound and 10% *p*-methoxyphenyl-oxazoline (3.4 g, 7.7% yield). ^{1}H NMR (400 MHz, $CDCl_3$) δ: 2.96–3.07 (2H, m), 3.07–3.20 (1H, m), 3.27–3.37 (2H, m), 3.50–3.60 (1H, m), 3.78 (3H, s), 4.02 (1H, q), 4.20 (1H, q), 6.82 (2H, d), 7.55 (2H, d). ^{13}C NMR (100 MHz, $CDCl_3$) δ: 34.0, 51.5, 55.5, 56.5, 66.0, 120.4, 127.5, 130.0. Exact mass calcd. for $C_{12}H_{15}NO_2S$: 237.0824; found: 237.0825.

2-(2-Mercaptoethyl)aminoethanol

This procedure was based on a preparation of *N*-(2-methoxyethyl)-*N*-(2-mercaptoethyl)amine (23). Ethanolamine (Aldrich) (25.0 g, 0.409 mol) and 200 mL of 1,4-dioxane (Caledon) were added to a two-necked, round-bottomed flask. A condenser and a dropping funnel, containing roughly 25 mL of 1,4-dioxane, were connected to the round-bottomed flask. Septa were used to seal the system. An exhaust needle was placed in one septum, while nitrogen was introduced through the other. The contents were warmed to a temperature just below that at which refluxing occurred. At this point, ethylene sulfide (Aldrich) (25.0 g, 0.416 mol) was transferred with the use of a cannula to the dropping funnel that contained dioxane. Once transfer was completed, the dropping funnel was opened to allow the dioxane solution containing ethylene sulfide to be added dropwise. On completion of the addition, the reaction mixture was allowed to reflux for 6 h. The reaction mixture was allowed to cool before removal of the dioxane by rotary evaporation. The residue was immediately distilled under reduced pressure. If the residue was not distilled immediately (for instance, if it were distilled the following day), a noticeable reduction in yield was observed. The distillate collected was a clear, colorless liquid and, on occasion, a white solid when returned to atmospheric pressure (23.7 g, 47.8% yield); bp 50 °C (0.050 torr) (lit. (24) value bp 66–69 °C (0.03 torr)). ^{1}H NMR (400 MHz, $CDCl_3$) δ: 1.97 (3H, br s), 2.66 (2H, t), 2.76 (2H, t), 2.81 (2H, t), 3.63 (2H, t). ^{13}C NMR (100 MHz, $CDCl_3$) δ: 25.0, 50.4, 51.6, 60.9. Exact mass calcd. for $C_4H_{11}NOS$: 121.0561; found: 121.0558.

Acknowledgments

We thank the Natural Sciences and Engineering Research Council of Canada for financial support of this work.

References

1. J.P. Guthrie. J. Am. Chem. Soc. **95**, 6999 (1973).
2. J.P. Guthrie. J. Am. Chem. Soc. **96**, 3608 (1974).
3. J.P. Guthrie. Can. J. Chem. **54**, 202 (1976).
4. J.P. Guthrie. Can. J. Chem. **55**, 3562 (1977).
5. J.P. Guthrie. J. Am. Chem. Soc. **100**, 5892 (1978).
6. J.P. Guthrie and P.A. Cullimore. Can. J. Chem. **58**, 1281 (1980).

© 2004 NRC Canada

7. J.P. Guthrie, J. Barker, P.A. Cullimore, J. Lu, and D.C. Pike. Can. J. Chem. **71**, 2109 (1993).
8. J.P. Guthrie. Can. J. Chem. **53**, 898 (1975).
9. ACD Labs. H NMR spin simulation software [computer program]. Version 3.5. Advanced Chemistry Development, Inc., Toronto, Ont. 1998.
10. D.L. Pavia, G.M. Lampman, and G.S. Kriz. Introduction to spectroscopy. Saunders College Publishing, Orlando. 1996.
11. M. Karplus. J. Am. Chem. Soc. **85**, 2870 (1963).
12. H. Conroy. Adv. Org. Chem. **2**, 265 (1960).
13. D. Williams and I. Fleming. Spectroscopic methods in organic chemistry. Wiley, New York. 1989. p. 92.
14. M. Anteunis, J. Gelan, and R. Van Cauwenberghe. Org. Magn. Reson. **6**, 362 (1974).
15. R. Feinauer. Synthesis, 16 (1971).
16. Nonius. COLLECT software [computer program]. Delft, The Netherlands. 1998.
17. Nonius. DENZO package [computer program]. Delft, The Netherlands, 1997.
18. Nonius. SCALEPACK [computer program]. Delft, The Netherlands, 1997.
19. G.M. Sheldrick. SHELXTL 5.1. Bruker-Axn Inc., Madison, Wis. 1997.
20. Z. Arnold and M. Kornilov. Collect. Czech. Chem. Commun. **29**, 645 (1964).
21. S. Hanessian and E. Moralioglu. Can. J. Chem. **50**, 233 (1972).
22. H. Gilman and R. Jones. J. Am. Chem. Soc. **65**, 1458 (1943).
23. J. Haefele and R. Broge. Proc. Sci. Sect. Toilet Goods Assoc. **32**, 52 (1959).
24. R. Weinman, M. Gollis, J. James, and A. Pomponi. J. Org. Chem. **27**, 4222 (1962).

© 2004 NRC Canada

RZnI vs. R_2Zn in Pd(0)-catalyzed cross-coupling reactions with thioimidates[1]

William P. Roberts, Indranath Ghosh, and Peter A. Jacobi

Abstract: Thioimidates **1**-*Z* undergo facile cross-coupling with Pd(0)–RZnI but are inert to Pd(0)–R_2Zn. This difference is due to the lower Lewis acidity of R_2Zn, as opposed to lower nucleophilicity. Various sources of RZnI (R = Me, Et) and Pd(0) were evaluated for their convenience and reactivity.

Key words: thioimidates, cross-coupling, dialkylzincs, alkylzinc iodides.

Résumé : Les thioimidates (**1**-*Z*) donnent facilement des réactions de couplages croisés avec le Pd(0)–RZnI, mais ils sont inertes vis-à-vis du Pd(0)–R_2Zn. Cette différence est attribuée à l'acidité de Lewis plus faible du R_2Zn plutôt que d'un caractère nucléophile plus faible. On a évalué diverses sources de RZnI (R = Me, Et) pour leur facilité d'accès et leur réactivité.

Mots clés : thioimidates, couplage croisé, dialkylzinc, iodures d'alkylzinc.

[Traduit par la Rédaction]

Introduction

Recently we described an unusual reactivity pattern of *E*- and *Z*-thioimidates **1**-*E,Z*, which undergo Pd(0)-catalyzed cross-coupling with alkyl zinc iodides at markedly different rates (Scheme 1) (1). Thioimidates **1**-*Z* were cleanly converted to imines **3**-*Z* using Pd(0)–RZnI, while the geometric isomers **1**-*E* were inert (R = Me, Et). This difference was traced to a previously unrecognized activating effect of RZnI and other Lewis acids, which serve to polarize the thioimidate C—S bond by complexing with the imidate nitrogen. NMR studies showed that the reactive *Z*-isomers readily coordinate Zn(II), most likely as η^1- or η^5-chelates (cf. **2**-*Z*) (2*a*, 2*b*). In either geometry, oxidative addition to Pd(0) is facilitated by the increased electrophilicity of the C—S bond. In contrast, Zn(II) chelation is not possible with **1**-*E*, and simple imine complexes of type **2**-*E* are sterically disfavored.[3] In the absence of such activation, oxidative addition does not occur, even with stoichiometric Pd(0). Cross-coupling to afford **3**-*E* therefore fails. Interestingly, however, addition of the smaller (and harder) Lewis acid BF_3 efficiently catalyzed the conversion of **1**-*E* to **3**-*E* when B = H. These conditions were also effective with other systems previously regarded as unreactive (2*c*).

In ongoing studies we have evaluated a number of procedures for preparing RZnI (R = Me, Et) (3). One of the most widely employed methods involves transmetallation of Grignard reagents with ZnI_2 (eq. [1], R = Me, Et) (4).

$$[1] \qquad RMgBr + ZnI_2 \longrightarrow RZnI + MgBrI$$

However, in our hands this reaction gave RZnI of relatively low reactivity. For example, MeZnI prepared by this route reacted sluggishly with **1**-*Z* when E = CO_2t-Bu and not at all when E = CHO (in general, the formyl derivatives of **1**-*Z* are slightly less reactive toward cross-coupling).[4] More satisfactory results were obtained following eq. [2] (R = Me, Et), involving oxidative addition of RI to activated Zn (5).

$$[2] \qquad RI + Zn \longrightarrow RZnI$$

Both MeZnI and EtZnI prepared in this manner were consistently more reactive, regardless of the substitution pattern of **1**-*Z* (E = CO_2t-Bu, CHO; B = H, Me, Ph). However, we also experienced a number of drawbacks to this procedure, which requires activation of Zn with 1,2-dibromoethane and trimethylsilyl chloride (5*b*–5*d*). In addition, one has to guard against competitive Wurtz coupling, and the RZnI must be prepared fresh before every reaction. Equation [3] (R = Me, Et) takes advantage of the Schlenk equilibrium between

Received 23 October 2003. Published on the NRC Research Press Web site at http://canjchem.nrc.ca on 6 February 2004.

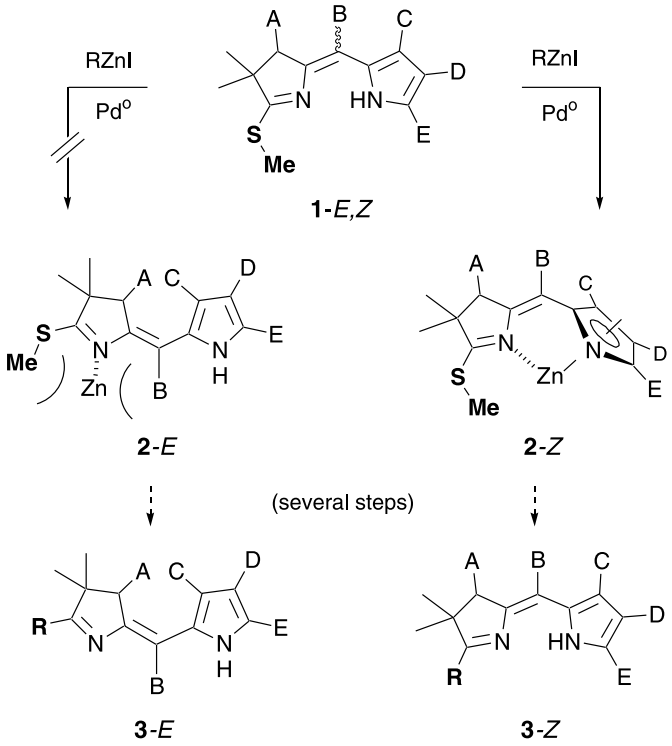
Dedicated to Professor Edward Piers, in appreciation of his seminal contributions to synthetic organic chemistry and chemical education.

W.P. Roberts, I. Ghosh, and P.A. Jacobi.[2] Department of Chemistry, 6128 Burke Laboratory, Dartmouth College, Hanover, NH 03755, U.S.A.

[1]This article is part of a Special Issue dedicated to Professor Ed Piers.
[2]Corresponding author (e-mail: p.jacobi@dartmouth.edu).
[3]Detailed NOE and X-ray studies showed that the imidate nitrogen in **1**-*E* is sterically shielded by the flanking S-Me and C-5-alkyl groups.
[4]Regardless of the method of preparation, we consistently found MeZnI to be less reactive than EtZnI.

 doi: 10.1139/V03-205 © 2004 NRC Canada

Scheme 1.



R_2Zn and ZnI_2, which Abraham and Rolfe (6) showed lies far to the right in polar solvents such as THF.

[3] $R_2Zn + ZnI_2 \rightleftharpoons 2RZnI$

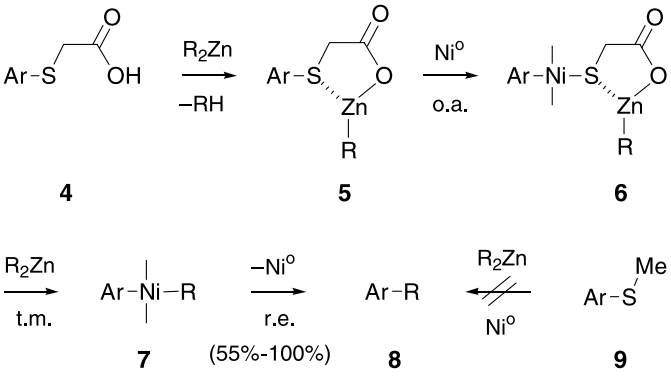
In general, this procedure worked well, but for reproducible results the ZnI_2 had to be freshly sublimed. By far the most convenient procedure for generating RZnI of uniform reactivity was the method of Charette and co-workers (eq. [4], R = Me, Et) (7).

[4] $R_2Zn + I_2 \longrightarrow RZnI + RI$

This method takes advantage of the nucleophilic character of R_2Zn and its ability to effect substitution on I_2. Among other advantages, displacement is carried out at –40 °C and is complete within minutes. Furthermore, both Me_2Zn and Et_2Zn are commercially available and relatively stable.

With a reliable means of preparing RZnI, we explored the effect of various Pd catalysts on converting **1**-*Z* to **3**-*Z* (cf. Scheme 1). Hayashi et al. (8) reported that dichloro[1.1′-bis-(diphenylphosphino)ferrocene]palladium(II) [($PdCl_2$(dppf)] was particularly effective in coupling *n*- and *sec*-BuZnCl with bromobenzene. The efficacy of $PdCl_2$(dppf) was ascribed to its large P-Pd-P bond angle, which presumably accelerates reductive elimination. In our case, however, we observed no significant advantage of $PdCl_2$(dppf) over a number of simpler homogeneous catalysts.[5] Perhaps the most convenient catalyst system tested was heterogeneous Pd–C, which has recently been employed in a number of related cross-coupling reactions (9). Although not quite as reactive as homogeneous PdL_4, Pd–C gave yields of imines **3**-*Z* in the range of 70%.

Scheme 2.



Given the ready availability of Me_2Zn and Et_2Zn (vide supra), it was of interest to examine the cross-coupling of these species with thioimidates **1**-*Z*. In contrast to the case with RZnI (5*c*), there are only scattered reports of transition-metal-catalyzed coupling of dialkylzincs R_2Zn with thioorganics. The most notable of these stem from the elegant studies of Liebeskind and co-workers (10),[6] who showed that thioglycolic acids **4** are excellent substrates for coupling with both RZnI and R_2Zn (Scheme 2). However, these examples represent a special case, since strong Zn-chelation assists both oxidative addition (o.a.) and subsequent transmetalation (t.m.). Under identical conditions, thiomethyl derivatives **9** are essentially inert.

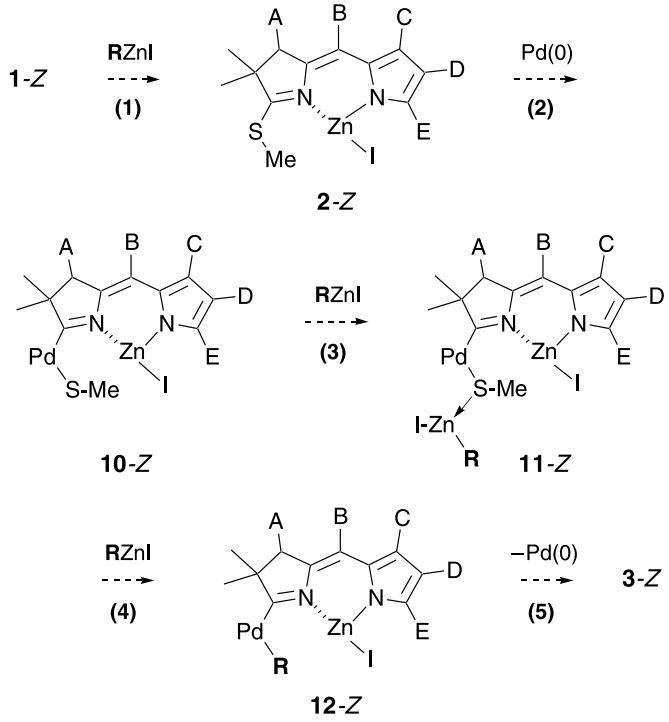
In the present work we observed a dramatic difference in reactivity between RZnI and R_2Zn (R = Me, Et). As noted above, Pd(0)-catalyzed cross-coupling of thioimidates **1**-*Z* with RZnI occurred readily to give high yields of the corresponding imines **3**-*Z* (Scheme 1). In contrast, salt-free Me_2Zn and Et_2Zn failed to react under Pd(0) catalysis[7] and gave only trace amounts of **3**-*Z* when more reactive Ni catalysts were used (10).[6] The reasons for this difference were unclear. Previously we showed that the conversion of thioimidate **1**-*Z* to imine **3**-*Z* using Pd(0)–RZnI requires five steps, involving a minimum of 3 equiv. of RZnI for complete cross-coupling (Fig. 1) (1). Two equivalents are taken up in complexation (steps **1** and **3**), while the third is the source of RZnI for intermolecular transmetalation (step **4**) (10*a*). It seemed unlikely that the rate of reductive elimination (step **5**) would be greatly effected by a change from EtZnI to Et_2Zn. Therefore, we focused our attention on steps **1**–**4**, substituting R_2Zn for RZnI.

It was tempting to attribute this failure to a difference in nucleophilicity between RZnI and R_2Zn, which could have a significant impact on transmetallation (step **4**). However, there is some indication that dialkylzincs are at least as reactive as alkylzinc halides toward simple electrophiles (4). In one experiment we compared the relative rates of addition of

[5] Including, among others, $PdCl_2(PPh_3)_4$, $Pd(PPh_3)_4$, and $Pd_2(dba)_3$–*tris*(2-furylphosphine).
[6] See ref. 5*c* for an additional example.
[7] Me_2Zn and Et_2Zn were purchased neat from Strem Chemicals, Inc., and as toluene solutions from Sigma-Aldrich Chemical Co.

© 2004 NRC Canada

Fig. 1. Steps involved in conversion of thioimidates **1**-*Z* to imines **3**-*Z* using RZnI–Pd(0): (**1**) N-complexation with Zn; (**2**) oxidative addition; (**3**) S-complexation with Zn; (**4**) transmetalation; (**5**) reductive elimination.

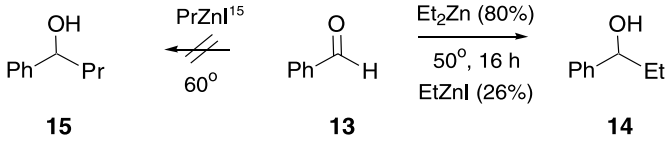


Et_2Zn and EtZnI to benzaldehyde. With Et_2Zn, GC analysis shows that the reaction is 80% complete after 16 h at 50 °C in THF–$PhCH_3$ (Scheme 3; see also Experimental section) (11).[8] During this same period, EtZnI reacts to the extent of 26%. Similar results have been found for PrZnI, which is reported to be unreactive at temperatures up to 60 °C (12).[9] In any event, both species are only weakly nucleophilic in the absence of added Lewis acids or bases (4).

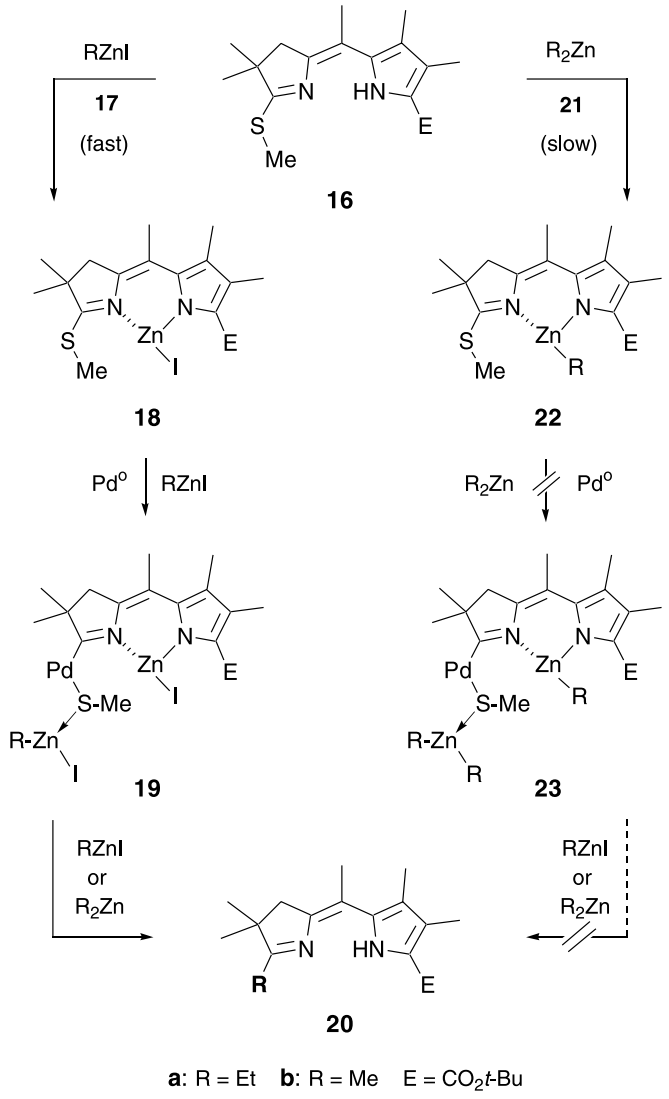
A more likely possibility was that dialkylzincs are less effective activators for oxidative addition (step **2**) and (or) transmetalation (step **4**). Both processes require strong complexation with Zn (1, 10*a*). This argument finds support in the fact that dialkylzincs are generally poorer acceptors than alkylzinc iodides (i.e., weaker Lewis acids) (4, 13, 14). In both species, Zn has a low-lying, filled 3*d* shell, and its coordination chemistry is influenced mainly by electrostatic effects (14*b*). In alkylzinc iodides, the metal center is covalently bonded to an electronegative iodine atom, which renders Zn more electron deficient (13). Consequently, there is a strong driving force for coordination between alkylzinc iodides and Lewis bases (EtZnI exists as a coordination polymer in the solid state) (13). In contrast, dialkylzincs are bonded to two R groups, and Zn is less electron deficient. This is reflected in the fact that dialkylzincs are less prone to undergo association or complexation and always occur as monomers (14).

NMR studies demonstrated the difference in the complexing abilities of RZnI and R_2Zn with thioimidates of type **1**-*Z*. With thioimidate **16**, for example, addition of ex-

Scheme 3.



Scheme 4.



cess EtZnI (**17a**) effects immediate loss of the N-H proton and concomitant liberation of ethane (Scheme 4). The resulting Zn complex **18** readily undergoes oxidative addition to Pd(0) to afford **19a** and, ultimately, imine **20a** following transmetallation and reductive elimination. Under identical conditions, but employing Et_2Zn (**21a**), deprotonation and complexation of **16** requires several hours. At the end of this period, the resultant complex **22a** was treated with Pd(0), but little or no oxidative addition could be detected. These experiments were carried out with 6 equiv. of **21a** and stoichiometric Pd(0), which returned only unchanged **16**

[8] See also ref. 4, p. 109.
[9] See also ref. 4.

© 2004 NRC Canada

upon quenching. It is worth noting that Zn complexes **18** and **22a** differ only in one ligand on Zn (I vs. Et). We believe it is the greater electron deficiency of Zn in **18** that provides the driving force for oxidative addition.

We performed a number of experiments to test this idea. Thioimidate **16** was first combined with 2 equiv. of Et_2Zn (**21a**) in THF–$PhCH_3$, and the resulting solution was allowed to stand at room temperature (RT) until complexation to give **22a** was complete. The reaction was then treated with catalytic Pd(0), and 1 equiv. of EtZnI (**17a**) was slowly added in the dark.[10] As expected based upon the pathway outlined in Scheme 4, we observed no formation of imine **20a**, since under these conditions oxidative addition to give **23a** does not occur. However, when this sequence was reversed the results were markedly different. Treatment of **16** with 2 equiv. of EtZnI (**17a**) and catalytic Pd(0), followed by 1 equiv. of *either* EtZnI (**17a**) *or* Et_2Zn (**21a**) led to formation of imine **20a** at approximately the same rate. This demonstrates that once oxidative addition *and S*-complexation with RZnI to give **19a** occurs, transmetalation and reductive elimination are equally facile with RZnI or R_2Zn. Next, we carried out a crossover experiment using MeZnI (**17b**) and Et_2Zn (**21a**). In this case, treatment of **16** with 2 equiv. of MeZnI – catalytic Pd(0), followed by slow addition of Et_2Zn, gave almost exclusively imine **20a** (R = Et). Interestingly, it was necessary to carry out this experiment with strict exclusion of light. Roughly equal amounts of **20a** and **20b** were obtained if this precaution was not taken.[11]

These experiments left unanswered the question of whether the lower complexing ability of R_2Zn also impacted on transmetallation. That is, do **19** and **23** undergo transmetallation at different rates? As shown by Liebeskind and co-workers (10*a*), this step requires considerable weakening of the Pd—S bond. Some indication that this was a problem could be inferred from our early experiments with Ni catalysts and R_2Zn (vide supra), which also produced little or no cross-coupling product **3**-*Z*. In these examples, however, oxidative addition to Ni almost certainly occurred (10).[6] To explore this issue further, we treated **16** with 0.9 equiv. of EtZnI, followed by catalytic Pd(0) and 2 equiv. of Et_2Zn. Our reasoning was that there should be sufficient EtZnI to produce complex **18**, which in turn is activated toward oxidative addition. At this point, however, there would be insufficient EtZnI to further activate the Pd—S bond to transmetalation.[12] Any such activation would have to come from Et_2Zn. Under these conditions we saw only very slow formation of imine **20a** (much slower than when employing 3 equiv. of EtZnI under otherwise identical conditions).

Finally, we briefly explored the possibility of in situ activation of both Et_2Zn and Me_2Zn toward Pd(0)-catalyzed cross-coupling. In this regard we were particularly drawn to the studies of Chastrette and Amouroux (15), who showed that the nucleophilic properties of linear dialkylzincs are markedly increased by tetra-*n*-butylammonium halides (Bu_4NX), while still maintaining the strong acceptor character of Zn (14*b*). Properties of this type might facilitate oxidative addition and (or) transmetallation. However, these modifications were only marginally successful in our case. Inclusion of either Bu_4NI or Bu_4NCl with Me_2Zn–Pd(0) had a modest effect in cross-coupling experiments with thioimidate **16**, raising the yield of imine **20b** from 0% to ~30% (cf. Scheme 4). It is possible, however, that more powerful donors might have a greater impact on accelerating these reactions, and this merits further investigation.

Experimental section

Melting points were determined in open capillaries and are uncorrected. ^{1}H NMR spectra were recorded at 300, 400, or 500 MHz and are expressed as parts per million (ppm) downfield from tetramethylsilane. All reactions were carried out in oven-dried glassware under an inert atmosphere of nitrogen or argon.

Formation of EtZnI

A flask containing 0.634 g (2.5 mmol) of iodine and 2.5 mL of THF was stirred at room temperature for 15 min to ensure that the iodine had completely dissolved. The solution was then cooled to –40 °C, and 2.5 mL (2.5 mmol, 1 equiv.) of 1 mol L^{-1} Et_2Zn in toluene was added in one portion. After an additional 5 min at –40 °C, the cold bath was removed, and the flask was allowed to warm to room temperature. This solution was then titrated against a freshly prepared 1 mol L^{-1} iodine-in-THF solution.

5-[1-(5-Ethyl-4,4-dimethyl-3,4-dihydro-pyrrol-2-ylidene)-ethyl]-3,4-dimethyl-1*H*-pyrrole-2-carboxylic acid *tert*-butyl ester (20a)

A solution of 25.0 mg (0.069 mmol) of thioimidate **16** and 4.8 mg (6.9 μmol, 0.1 equiv.) of $PdCl_2(PPh_3)_2$ in 1 mL of toluene was treated with 1.2 mL (0.414 mmol, 6 equiv.) of 0.4 mol L^{-1} EtZnI in THF–toluene (1:1) under argon. After stirring for 60 min at room temperature, the mixture was taken up in 5 mL of Et_2O, stirred for 10 min, and filtered through celite. To the filtrate was added 5 mL of saturated (sat'd) NH_4Cl, and the aqueous layer was extracted with Et_2O. The combined organic layers were washed with sat'd $NaHCO_3$, dried over Na_2SO_4, filtered, and concentrated to dryness under reduced pressure. The residue was purified by flash chromatography (silica gel, EtOAc:hexanes = 1:9 to 1:5) to give 16 mg (70%) of the imine **20a** as an off-white solid. R_f (1:4 EtOAc:hexanes) 0.54. ^{1}H NMR (500 MHz, $CDCl_3$): 1.18 (s, 6H), 1.33 (t, J = 7.32, 3H), 1.57 (s, 9H), 2.11 (s, 2H), 2.18 (s, 3H), 2.29 (s, 3H), 2.42 (q, J = 7.32, 2H), 2.58 (s, 2H), 11.69 (br s, 1H). ^{13}C NMR (500 MHz, $CDCl_3$): 189.5, 161.36, 149.10, 132.16, 127.36, 119.06, 118.38, 114.26, 79.86, 47.83, 44.44, 28.87, 26.40, 22.19, 18.47, 11.73, 11.67, 10.54. HR-MS (FAB) calcd. for $C_{21}H_{32}N_2O_2$: 344.2464; found: 344.2543 ([M + H]). Anal. calcd. for $C_{21}H_{32}N_2O_2$: C 73.22, H 9.36, N 8.13; found: C 73.20, H 9.44, N 8.08.

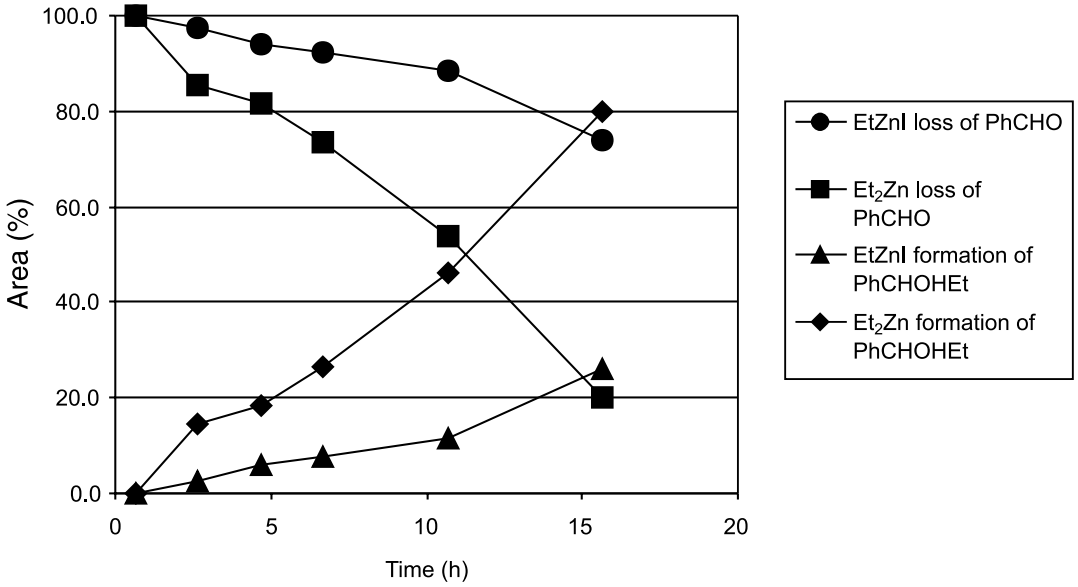
[10]Unless otherwise noted, the source of Pd(0) is $PdCl_2(PPh_3)_2$.

[11]The mechanism for this alkyl group exchange is unknown at present but may be related to the facile photoinduced synthesis of organozinc reagents recently described by Charette et al. (cf. ref. 7*b*).

[12]An alternative explanation is that oxidative addition to **18** requires activation by complexation of EtZnI at *both* the imidate N- and S-atoms. However, such a species would suffer prohibitive steric strain from the adjacent geminal dimethyl groups.

© 2004 NRC Canada

Fig. 2. The ratio of benzaldehyde to 1-phenyl-propan-1-ol.



Crossover experiment, 2 EtZnI + 1 Et_2Zn

A total of 10 mg (27.6 μmol) of thioimidate **16** was dissolved in 0.4 mL of toluene. To this was added 110 μL (55.2 μmol, 2 equiv.) of 0.5 mol L^{-1} EtZnI–THF, and the reaction was stirred at room temperature under argon. After stirring for 5 min, 2 mg (2.7 μmol, 0.1 equiv.) of $PdCl_2(PPh_3)_2$ was added, and the flask was purged with argon and wrapped in foil. After stirring for an additional 30 min, the reaction was checked by TLC, and no product was observed. At this time 28 μL (27.6 μmol, 1 equiv.) of 1 mol L^{-1} Et_2Zn in toluene was added dropwise over a period of 30 min. Monitoring of the reaction by TLC (1:9 EtOAc:hexanes) showed formation of **20a** after 30 min.

Crossover experiment, 2Et_2Zn + 1 EtZnI

A total of 10 mg (27.6 μmol) of thioimidate **16** was dissolved in 0.4 mL of toluene. To this was added 55 μL (55.2 μmol, 2 equiv.) of 1 mol L^{-1} Et_2Zn–THF, and the reaction was stirred at room temperature under argon. After stirring for 6 h to ensure complexation, 2 mg (2.7 μmol, 0.1 equiv.) of $PdCl_2(PPh_3)_2$ was added, and the flask was purged with argon and wrapped in foil. After an additional 30 min passed, the reaction was checked by TLC, and no products were observed. At this time, 55 μL (27.6 μmol, 1 equiv.) of 0.5 mol L^{-1} EtZnI in THF was added dropwise over 1 h. Monitoring of the reaction by TLC (1:9 EtOAc:hexanes) showed no formation of **20a**.

Crossover experiment, 2 MeZnI + 6Et_2Zn

A solution of 10 mg (27.6 μmol) of thioimidate **16** in 0.4 mL of toluene was treated with 110 μL (55.2 μmol, 2 equiv.) of 0.5 mol L^{-1} MeZnI–THF, and the resultant solution was stirred at room temperature under argon. After stirring for 5 min, 2 mg (2.7 μmol, 0.1 equiv.) of $PdCl_2(PPh_3)_2$ was added, and the flask was purged with argon and wrapped in foil. After stirring an additional 30 min, the reaction was checked by TLC, and no products were observed. At this time, 10 μL (10 μmol, 0.4 equiv.) of 1 mol L^{-1} Et_2Zn in toluene was added dropwise every 10 min for 2.5 h. Monitoring of the reaction by TLC (1:9 EtOAc:hexanes) showed formation of **20a** after 30 min, and at no point was **20b** observed. Upon completion of the addition of Et_2Zn, the reaction was allowed to stir for an additional 3 h and then worked up as in the synthesis of **20a** (vide supra). ^1H NMR confirmed that no **20b** was formed. If no foil was employed and (or) addition of Et_2Zn was completed too quickly, both **20a** and **20b** were observed.

Crossover experiment, 0.9 EtZnI + 2Et_2Zn

A solution of 10 mg (27.6 μmol) of thioimidate **16** in 0.4 mL of toluene was treated with 49 μL (25 μmol, 0.9 equiv.) of 0.5 mol L^{-1} EtZnI–THF, and the resultant solution was stirred at room temperature under argon. After stirring for 5 min, 2 mg (2.7 μmol, 0.1 equiv.) of $PdCl_2(PPh_3)_2$ was added, and the flask was purged with argon and wrapped in foil. After stirring an additional 30 min, the reaction was checked by TLC, and no products were observed. At this time, 55 μL (55 μmol, 2 equiv.) of 1 mol L^{-1} Et_2Zn in toluene was added dropwise over a period of 60 min. Monitoring of the reaction by TLC (1:9 EtOAc:hexanes) showed formation of **20a** after 50 min. The identical procedure employing 3 equiv. of EtZnI showed immediate formation of **20a**.

Addition of Et_2Zn to benzaldehyde

To 30 μL (3.3 mmol) benzaldehyde was added 1.2 mL of THF under argon. This solution was then treated with 1.0 mL (9.9 mmol, 3 equiv.) of 1 mol L^{-1} Et_2Zn–toluene, and the flask was immersed into an oil bath maintained at 50 °C. Using a 100 μL syringe, 50 μL aliquots were taken and quenched into 300 μL of MeOH. A 25 μL portion of each quenched aliquot was injected onto an HP 6890 GC, employing an HP-35 column (30 m × 0.25 mm × 0.25 μm film thickness). The temperature profile for the GC was as follows: 10 min at 60 °C, then an increase of 15 °C min^{-1} up to 220 °C, followed by 10 min at 220 °C. The ratio of benzaldehyde to 1-phenyl-propan-1-ol is plotted in Fig. 2 using Microsoft Excel 98®.

© 2004 NRC Canada

Addition of EtZnI to benzaldehyde

A solution consisting of 30 μL (3.3 mmol) of benzaldehyde and 2.2 mL (9.9 mmol, 3 equiv.) of 1 mol L^{-1} EtZnI in 1:1 THF:toluene was stirred in an oil bath maintained at 50 °C. The reaction progress was monitored and analyzed, as in the reaction employing Et_2Zn and benzaldehyde (see Fig. 2).

Acknowledgements

Financial support of this work by the National Institutes of Health, General Medical Sciences (NIGMS) Grant No. GM38913, is gratefully acknowledged.

References

1. I. Ghosh and P.A. Jacobi. J. Org. Chem, **67**, 9304 (2002).
2. F.C. March, D.A. Couch, K. Emerson, J.E. Fergusson, and W.T. Robinson. J. Chem. Soc. A, 440 (1971); (*b*) D.J. Burkey and Hanusa. J. Organomet. Chem. **512**, 165 (1996); (*c*) M.E. Angiolelli, A.L. Casalnuovo, and T.P. Selby. Synlett, **5**, 905 (2000).
3. For a general review for preparing organozinc reagents, see (*a*) P. Knochel and R.D. Singer. Chem. Rev. **93**, 2117 (1993); (*b*) P. Knochel and P. Jones (*Editors*). Organozinc reagents: A practical approach. Oxford University Press, New York. 1999.
4. E. Erdik. Organozinc reagents in organic synthesis. CRC Press, Boca Raton. 1996.
5. (*a*) A. Guijarro, D.M. Rosenberg, and R.D. Rieke. J. Am. Chem. Soc. **121**, 4155 (1999), and references cited therein; (*b*) C. Jubert and P. Knochel. J. Org. Chem. **57**, 5425 (1992); see also M.C.P. Yeh, H.G. Chen, and P. Knochel. Org. Synth. **70**, 195 (1991); (*c*) H. Tokuyama, S. Yokoshima, T. Yamashita, and T. Fukuyama. Tetrahedron Lett. **39**, 3189 (1998); ibid. J. Braz. Chem. Soc. **9**, 381 (1998); for an improved activation procedure, see (*d*) S. Huo. Organic Lett. **5**, 423 (2003).
6. M.H. Abraham and P.H. Rolfe. J. Organomet. Chem. **7**, 35 (1967).
7. (*a*) A.B. Charette and J.-F. Marcoux. J. Am. Chem. Soc. **118**, 4539 (1996); see also (*b*) A.B. Charette, A. Beauchemin, and J.-F. Marcoux. J. Am. Chem. Soc. **120**, 5114 (1998).
8. T. Hayashi, M. Konishi, Y. Kobori, M. Kumada, T. Higuci, and K. Hirotsu. J. Am. Chem. Soc. **106**, 158 (1984).
9. T. Shimizu and M. Seki. Tetrahedron Lett. **42**, 429 (2001), and references cited therein.
10. (*a*) J. Srogl, W. Liu, D. Marshall, and L.S. Liebeskind. J. Am. Chem. Soc. **121**, 9449 (1999); see also (*b*) C. Savarin, J. Srogl, and L.S. Liebeskind. Org. Lett. **2**, 3229 (2000); (*c*) L.S. Liebeskind and J. Srogl. J. Am. Chem. Soc. **122**, 11 260 (2000).
11. Marx reported a 40% yield for this reaction in diethyl ether: B. Marx. C.R. Hebd. Seances Acad. Sci. Ser. C, **266**, 1646 (1968).
12. Y. Tamaru, T. Nakamura, H. Sakaguchi, H. Ochiai, and Z-i Yoshida. J. Chem. Soc. Chem. Commun. 610 (1988).
13. N.A. Bell and P.T. Moseley. J. Organomet. Chem. **325**, 47 (1987).
14. (*a*) P.R. Markies, G. Schat, O.S. Akkerman, and F. Bickelhaupt. J. Organomet. Chem. **430**, 1 (1992); (*b*) J. Boersma. *In* Comprehensive organometallic chemistry. Vol. 2. *Edited by* G. Wilkinson, F.G.A. Stone, and E. Abel. Pergamon Press, Oxford. 1982. p. 823.
15. M. Chastrette and R. Amouroux. Tetrahedron Lett. **59**, 5165 (1970).

© 2004 NRC Canada

The solid-state molecular structure of $W(NO)_3Cl_3$ and the nature of its W—NO bonding[1]

Trevor W. Hayton, Brian O. Patrick, Peter Legzdins, and W. Stephen McNeil

Abstract: The monomeric trinitrosyl complex, $W(NO)_3Cl_3$, can be prepared by the treatment of WCl_6 in CH_2Cl_2 with NO gas, and its identity has been unambiguously confirmed by a single-crystal X-ray diffraction analysis. The complex crystallizes in the space group $Pmn2_1$ as a three-component twin (a = 10.4280(4) Å, b = 6.3289(2) Å, c = 5.6854(2) Å, Z = 2, R_1 = 0.065, wR_2 = 0.176). Its solid-state molecular structure consists of a tungsten centre bound to three chloride ligands and three linear nitrosyl ligands in a *fac*-octahedral stereochemistry. In addition, the structure contains a crystallographically imposed mirror plane. The two independent W—N linkages are 1.88(2) and 1.92(1) Å long, while the two corresponding N—O bond lengths are 1.13(2) and 1.16(2) Å. DFT calculations on *fac*-$W(NO)_3Cl_3$ at the B3LYP/LANL2DZ level of theory afford optimized intramolecular metrical parameters that match the X-ray crystallographically determined bond lengths and bond angles quite well. In addition, they provide a rationale for the nearly linear W-N-O linkages extant in the complex. Solutions of *fac*-$W(NO)_3Cl_3$ in CH_2Cl_2 lose ClNO under ambient conditions and deposit the well-known $[W(NO)_2Cl_2]_n$ polymer, and this conversion is fully reversible.

Key words: nitrosyl, tungsten, structure, bonding.

Résumé : On peut préparer le complexe trinitrosyle monomère, $W(NO)_3Cl_3$, en traitant du WCl_6 dans le CH_2Cl_2 avec du NO à l'état gazeux et on a confirmé d'une façon non ambigüe son identité par diffraction des rayons X. Le complexe cristallise dans le groupe d'espace $Pmn2_1$, sous la forme de jumeau à trois composant, avec a = 10,4280(4) Å, b = 6,3289(2) Å et c = 5,6854(2) Å, Z = 2, R_1 = 0,065 et wR_2 = 0,176. Sa structure moléculaire à l'état solide consiste en un atome de tungstène central lié à trois ligands chlorures et à trois ligands linéaires nitrosyles dans une stéréochimie *fac*-octaédrique. De plus, la structure comporte un plan miroir imposé par la cristallographie. Les deux liaisons W—N indépendantes sont égales à 1,88(2) et 1,92(1) Å respectivement alors que les longueurs des deux liaisons N—O correspondantes sont égales à 1,13(2) et 1,16(2) Å. Des calculs DFT sur le *fac*-$W(NO)_3Cl_3$ au niveau B3LYP/LANL2DZ de la théorie permettent d'obtenir des paramètres métriques intramoléculaires optimisés qui correspondent à ceux obtenus par diffraction des rayons X pour les longueurs et des angles de liaison. De plus, ils fournissent une explication pour l'arrangement pratiquement linéaire des liaisons W-N-O observés dans le complexe. En solution dans le CH_2Cl_2 dans les conditions ambiantes, le *fac*-$W(NO)_3Cl_3$ perd du ClNO, le polymère bien connu $[W(NO)_2Cl_2]_n$ se dépose et cette transformation est complètement réversible.

Mots clés : nitrosyle, tungstène, structure, liaison.

[Traduit par la Rédaction]

Introduction

The characteristic properties of metal–nitrosyl complexes are of fundamental importance and practical significance (1). An intriguing feature of metal nitrosyls is that, unlike their isoelectronic carbonyl analogues, polynitrosyl complexes (i.e., those containing three or more NO ligands per metal centre) are relatively rare (2). Thus, among the known coordination and organometallic metal–NO complexes, the only examples of species containing $M(NO)_3$ fragments are $[(\eta^5\text{-}C_5H_5)V(NO)_3][PF_6]$ (3), $[V(NO)_3Cl_2]_n$ (4, 5), $W(NO)_3Cl_3$ (6, 7), $[W(NO)_3Br_2]_2$ (8), $Mn(NO)_3L$ (L = neutral 2-electron donor) (9–18), $Fe(NO)_3X$ (X = halide or pseudohalide) (19–22), and $Co(NO)_3$ (23). Until recently, the only one of these complexes to have been characterized by X-ray crystallography was $Mn(NO)_3(PPh_3)$ (10). Given the rarity of metal–trinitrosyl complexes and the paucity of information currently available about them, we have begun to reinvestigate these systems. The first observations from our laboratory in this regard involved the $Fe(NO)_3X$ systems, which we found to exhibit a striking feature in their solid-state molecular structures (24). Specifically, the four such iron complexes that have now been structurally characterized possess Fe-N-O angles that are bent inward by about 15° in the so-called "*attracto*" conformation (2), in which the O-Fe-O angles are

Received September 30, 2003. Published on the NRC Research Press Web site at http://canjchem.nrc.ca on 4 February 2004.

This paper is dedicated to Professor Ed Piers, a valued colleague and a trusted friend.

T.W. Hayton, B.O. Patrick, and P. Legzdins.[2] Department of Chemistry, The University of British Columbia, 2036 Main Mall, Vancouver, BC V6T 1Z1, Canada.
W.S. McNeil. Department of Chemistry, Okanagan University College, 3333 College Way, Kelowna, BC V1V 1V7, Canada.

[1]This article is part of a Special Issue dedicated to Professor Ed Piers.
[2]Corresponding author (e-mail: legzdins@chem.ubc.ca).

 doi: 10.1139/V03-206 © 2004 NRC Canada

less than the N-Fe-N angles. This feature led us to wonder if other trinitrosyl complexes might also exhibit similar structural features. Consequently, for our next target in this class of compounds we decided to determine the solid-state molecular structure of $W(NO)_3Cl_3$.

Our interest in $W(NO)_3Cl_3$ dates back to 1984 when we reported its synthesis by the treatment of WCl_6 in CH_2Cl_2 with NO (7). Our original formulation of this material was based solely on elemental analyses and IR spectroscopic data, since we could not establish its solid-state molecular structure by X-ray crystallography at that time. However, other investigators, using similar preparative and characterization methods, had formulated this material at various times as a nitrosyl chloride adduct of $W(NO)_2Cl_2$, i.e., $W(NO)_2Cl_2{\cdot}ClNO$ (25), or as the seven-coordinate tetranitrosyl complex, $W(NO)_4Cl_3$ (26, 27). In other words, uncertainty about the true nature of this nitrosyl complex has existed for the past 19 years. We now wish to report that we have definitively determined the molecular structure of $W(NO)_3Cl_3$ in the solid state and in the process have established that it loses ClNO reversibly in CH_2Cl_2 solutions at room temperature. In this report we also present the results of DFT calculations that provide a rationale for the nearly linear W-N-O linkages extant in this molecule.

Results and discussion

Synthesis and structural characterization of $W(NO)_3Cl_3$

As we have described previously (7), $W(NO)_3Cl_3$ is conveniently synthesized by bubbling NO gas through a CH_2Cl_2 solution of WCl_6 (eq. [1]).

$$[1] \qquad WCl_6 + 6\ NO \rightarrow W(NO)_3Cl_3 + 3\ ClNO$$

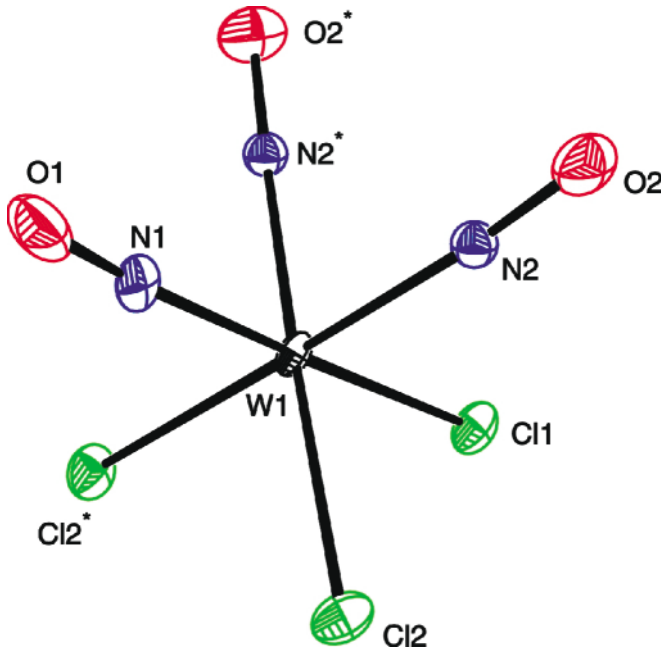
Prepared in this manner, the trinitrosyl complex is obtained as a bright green powder. The formation of single crystals of this complex requires the very slow addition of NO to the WCl_6 solution. This requirement can be met by connecting a glass-walled bomb filled with NO (1 atm (1 atm = 101.325 kPa)) via a bridge to a Schlenk tube containing a CH_2Cl_2 solution of WCl_6 and allowing the NO to diffuse slowly into the solution over the course of several weeks. In this manner, $W(NO)_3Cl_3$ can be obtained as small green crystals. As outlined in the Experimental section, the X-ray crystallographic analysis of these crystals has not been a straightforward matter, but eventual utilization of the TwinSolve software (28) to examine the raw diffraction data revealed that $W(NO)_3Cl_3$ crystallizes in the orthorhombic space group $Pmn2_1$ as a three-component twin. The intramolecular metrical parameters for $W(NO)_3Cl_3$ are collected in Table 1, and a plot of its solid-state molecular structure is shown in Fig. 1.

Although the extensive twinning does result in a structure of somewhat diminished quality, it is clear nevertheless that in the solid state $W(NO)_3Cl_3$ is monomeric, consisting of a tungsten centre bound to three chloride ligands and three nitrosyl ligands in a *fac*-octahedral stereochemistry. Furthermore, the structure contains a crystallographically imposed mirror plane. The two W—N bond lengths are 1.88(2) and 1.92(1) Å, while the corresponding N—O distances are 1.13(2) and 1.16(2) Å. The W—N bond lengths are comparable to those extant in related dinitrosyl species; for in-

Table 1. Selected interatomic distances (Å) and angles (°) for *fac*-$W(NO)_3Cl_3$, as determined by X-ray crystallography, and the fully optimized structure, as determined at the B3LYP/LANL2DZ level of theory.

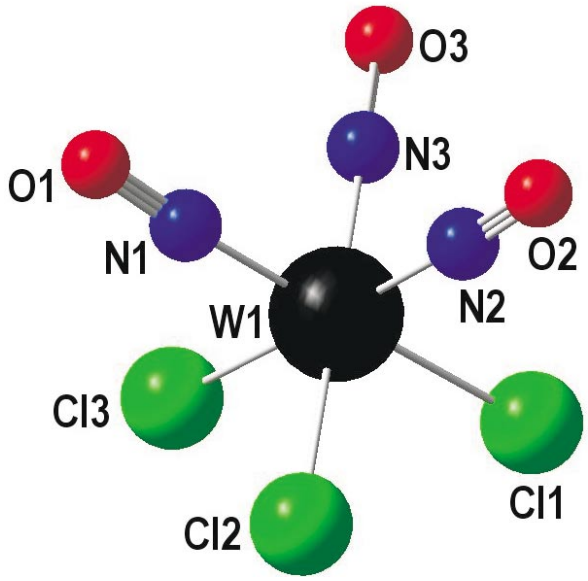
X-ray crystallography		B3LYP/LANL2DZ	
Bond lengths (Å)			
N1—O1	1.13(2)	N1—O1	1.189
N2—O2	1.16(2)	N2—O2	1.190
		N3—O3	1.189
N1—W1	1.88(2)	W1—N1	1.908
N2—W1	1.92(1)	W1—N2	1.908
		W1—N3	1.908
Cl1—W1	2.395(5)	W1—Cl2	2.435
Cl2—W1	2.369(3)	W1—Cl1	2.435
		W1—Cl3	2.436
Bond angles (°)			
O1-N1-W1	177(2)	W1-N1-O1	176.9
O2-N2-W1	175.7(9)	W1-N2-O2	176.6
		W1-N3-O3	176.9
N1-W1-N2	89.1(5)	N1-W1-N2	89.31
N2-W1-N2*	85.9(6)	N1-W1-N3	89.33
		N2-W1-N3	89.34
N2-W1-Cl2	92.3(3)	N1-W1-Cl2	89.76
N1-W1-Cl2	91.8(4)	N3-W1-Cl1	89.75
N2-W1-Cl1	89.7(3)	N1-W1-Cl3	89.70
		N2-W1-Cl2	89.92
		N2-W1-Cl1	89.83
		N3-W1-Cl3	89.59
N1-W1-Cl1	178.4(5)	N3-W1-Cl2	178.8
N2-W1-Cl2*	178.0(3)	N1-W1-Cl1	178.7
		N2-W1-Cl3	178.6
Cl2-W1-Cl2*	89.4(2)	Cl2-W1-Cl1	91.15
Cl2-W1-Cl1	89.3(1)	Cl2-W1-Cl3	91.13
		Cl1-W1-Cl3	91.15

Fig. 1. ORTEP diagram of the solid-state molecular structure of *fac*-$W(NO)_3Cl_3$ with 50% probability ellipsoids being shown.



© 2004 NRC Canada

Fig. 2. Fully optimized structure of *fac*-$W(NO)_3Cl_3$, as determined at the B3LYP/LANL2DZ level of theory.



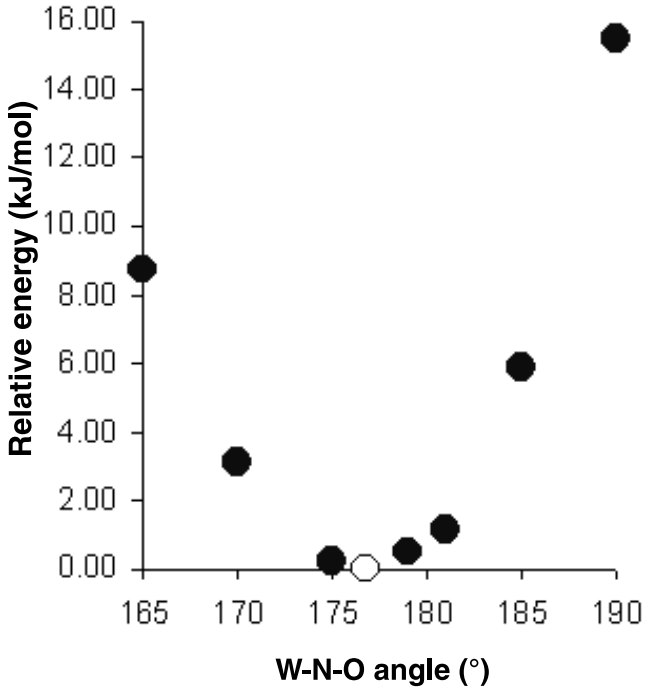
stance, $(\eta^5\text{-}C_5H_5)W(NO)_2Cl$ exhibits W—N distances of 1.832(9) and 1.819(8) Å (29), while the dimer $[WCl_3(NO)_2]_2^{2-}$ contains a W—N link of 1.85(1) Å (30). Most importantly, the two independent W-N-O linkages in $W(NO)_3Cl_3$ are essentially linear (W-N-O = 177(2)° and 175.7(9)°), unlike the Fe-N-O links in the recently characterized iron trinitrosyl complexes (24). The two W—Cl distances are 2.369(3) and 2.395(5) Å, and each interligand angle in *fac*-$W(NO)_3Cl_3$ is essentially 90° or 180° (Table 1).

Theoretical investigations of the W—NO bonding in *fac*-$W(NO)_3Cl_3$

In an effort to understand the differences between the solid-state structures of the $Fe(NO)_3X$ complexes and *fac*-$W(NO)_3Cl_3$, DFT calculations have been performed on *fac*-$W(NO)_3Cl_3$ using the B3LYP method and a LANL2DZ basis set. The resulting optimized geometry reproduces the key features of the experimentally determined structure remarkably well, including the approximate C_{3v} symmetry and the nearly linear nitrosyl ligands (Fig. 2). The optimized structure has W-N-O angles of 176.9°, 176.9°, and 176.6° in an "*attracto*" conformation, which is very similar to the experimental structure (W-N-O angles of 175.7(9)° and 177(2)°) (Table 1). Other metrical parameters also agree within experimental error, with the exception of the W—Cl bond lengths, which are calculated to be slightly longer (2.435, 2.435, and 2.436 Å) than those seen in the experimental structure (2.369(3) and 2.395(5) Å).

Lowest-energy structures have been determined with all three W-N-O angles contracted inward at identical values of 165°, 170°, 175°, and 179° and the NO groups bent outward at W-N-O angles of 181°, 185°, and 190°. The results are shown as solid circles in Fig. 3, which depicts the variation of the relative energy of *fac*-$W(NO)_3Cl_3$ as a function of the W-N-O angles. Variation of the W-N-O angle represents a fairly shallow energy well, with the calculated global energy minimum (open circle on Fig. 3, at an average W-N-O angle of 176.8°) being less than 1 kJ/mol below a structure with

Fig. 3. Relative energy of *fac*-$W(NO)_3Cl_3$ with changing W-N-O angles. In this representation, W-N-O angles less than 180° correspond to inward bending of the nitrosyl ligands to achieve the "*attracto*" configuration, and W-N-O angles greater than 180° correspond to outward bending of the nitrosyl ligands to achieve the "*repulso*" configuration. The open circle represents the energy of the fully optimized structure.



three perfectly linear nitrosyl linkages and less than 2 kJ/mol below a structure with the NO groups bent outward by an equivalent amount (i.e., W-N-O = 183.2°). Further bending of the NO ligands, either inward or outward, results in a much greater increase of energy, with an inward W-N-O angle of 165° representing an energy increase of over 8 kJ/mol. Two depictions of the calculated HOMO of the complex are shown in Fig. 4. Taking the molecular symmetry as C_{3v}, this orbital is best viewed as the symmetric a_1 π-backbonding combination of a tungsten d_{z^2} orbital with three NO π* orbitals. This is the highest-energy member of the three occupied orbitals that form the M-N-O backbonding interactions in *fac*-$W(NO)_3Cl_3$. The other two are of *e* symmetry and correspond roughly to the overlap of symmetric combinations of NO π* orbitals orthogonal to the *z* axis with appropriate metal-orbital combinations.

The linear W-N-O linkages of *fac*-$W(NO)_3Cl_3$ contrast to those exhibited by the series of structurally characterized iron–trinitrosyl complexes, $[(NO)_3FeX]^{n+}$ (n = 0, X = Cl, BF_4; n = 1, X = EtCN) (24). Like the tungsten compound, these iron complexes effectively possess C_{3v} symmetry, but unlike the tungsten complex, each iron species exhibits a distinctly "*attracto*" conformation of the three nitrosyl groups, with Fe-N-O angles ranging between 160° and 170°. At first glance, therefore, both the iron and tungsten complexes represent 18-electron C_{3v} symmetric trinitrosyl species, affording no immediately obvious electronic explanation for the difference in their M-N-O bond angles. However, the critical distinction between these systems lies in the

© 2004 NRC Canada

Fig. 4. Two pictorial representations of the HOMO in *fac*-$W(NO)_3Cl_3$.

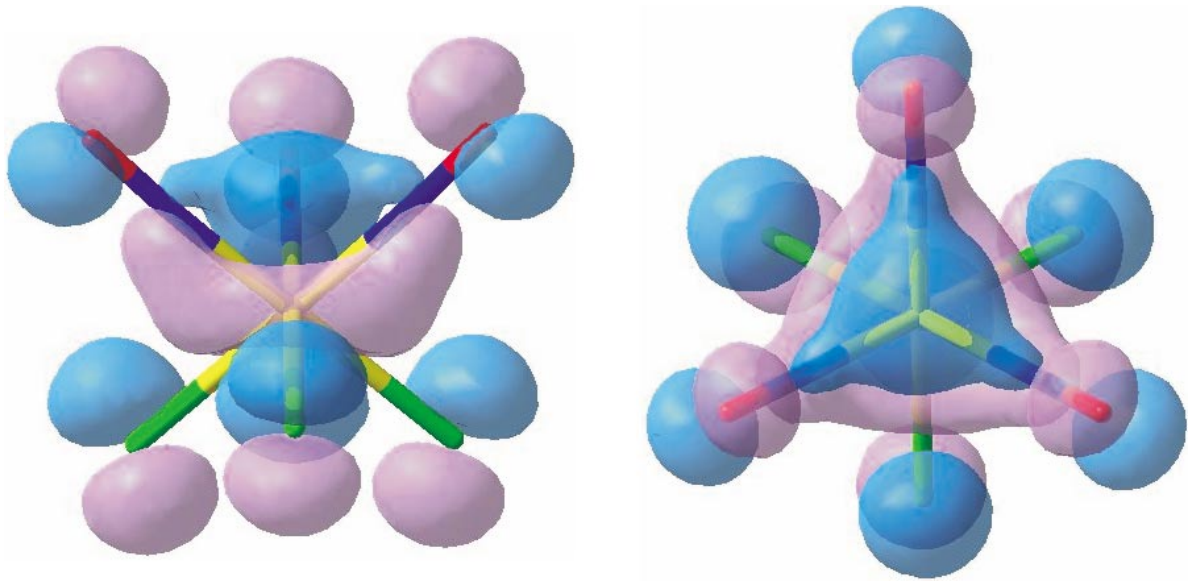
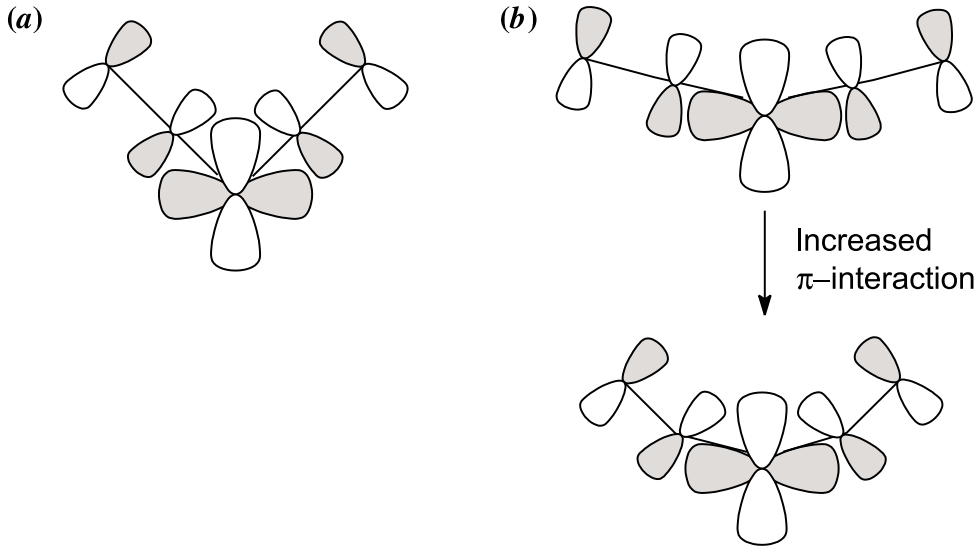


Fig. 5. (*a*) Qualitative pictorial representation of the π interaction between the metal and two orthogonal NO ligands; (*b*) Qualitative pictorial representation of the increased π interaction upon NO bending when the nitrosyl ligands are not orthogonal.



fact that the degree of bending observed in the metal–nitrosyl linkages is related to the N-M-N angles of the complex. Essentially, nonorthogonal nitrosyl groups, which share interactions with the same metal orbital(s) but are not perfectly oriented in the nodal planes of those orbitals, can enhance back-bonding from the metal by symmetrically adjusting the M-N-O angles (31, 32). This phenomenon is depicted pictorially in Fig. 5. In the tungsten complex, which exhibits orthogonal and effectively linear W-N-O groups, each nitrosyl ligand lies in the nodal plane of the metal-based orbital with which it forms a π interaction and does not need to bend to maximize this interaction (Fig. 5*a*). In contrast, the iron complexes exhibit N-Fe-N angles as great as 112°. Thus, each nitrosyl ligand does not lie in a nodal plane of the metal-based orbital with which it forms a π bond, and consequently, the nitrosyl ligand bends to maximize its π interaction (Fig. 5*b*).

These results are also consistent with previous theoretical considerations. In 1965 Kettle suggested (33) that any molecule of C_{3v} symmetry containing an $M(CO)_3$ or $M(NO)_3$ fragment must *necessarily* have bent M-E-O groups (E = C or N) resulting from inequivalent overlaps in the two sets of π-orbitals on each ligand, namely those parallel and perpendicular to the principal axis. Of course, the symmetry constraint does not guarantee that such bending will be large, or even detectable, and the observed angles of *fac*-$W(NO)_3Cl_3$ are sufficiently bent at 176° to satisfy this hypothesis. In any case, the restriction is relaxed somewhat if strict C_{3v} symmetry is lowered, and the experimentally determined structure of *fac*-$W(NO)_3Cl_3$ has a single crystallographic mirror plane that renders one NO and one Cl group very slightly inequivalent from the other two. Thus, the three NO ligands in *fac*-$W(NO)_3Cl_3$ remain essentially linear. A strong bending of the NO groups is neither favoured because of nonorthogonal

© 2004 NRC Canada

NO groups, as it is with the $Fe(NO)_3X$ compounds; nor enforced by a high electron count at the tungsten centre (31); nor dictated by strong symmetry constraints.

Solution and spectroscopic properties of *fac*-$W(NO)_3Cl_3$

As a solid, pure *fac*-$W(NO)_3Cl_3$ is thermally stable under ambient conditions. However, in CH_2Cl_2 solutions it readily loses ClNO, resulting in the precipitation of the well-known $[W(NO)_2Cl_2]_n$ polymer (eq. [2]) (7). We have now established that this conversion is fully reversible, since monitoring by IR spectroscopy confirms that the addition of excess ClNO to a CH_2Cl_2 suspension of independently prepared $[W(NO)_2Cl_2]_n$ (7) results in the formation of *fac*-$W(NO)_3Cl_3$.

$$[2] \qquad n\ fac\text{-}W(NO)_3Cl_3 \rightleftharpoons [W(NO)_2Cl_2]_n\downarrow + n\ ClNO$$

This reaction of ClNO with $[W(NO)_2Cl_2]_n$ (i.e., conversion 2 proceeding to the left) is similar to its reactions with other ML_n species to give $ML_{n-2}(NO)Cl$ (2). During these latter conversions, two ligands (L) contributing four electrons to the metal are displaced by a chloride and a nitrosyl group, while in $[W(NO)_2Cl_2]_n$ two bridging Cl→W dative interactions are broken to generate the trinitrosyl complex. To the best of our knowledge, though, the transformation summarized in eq. [2] is the first reported case in which its reversibility has been established.

Our determination of the solid-state molecular structure of *fac*-$W(NO)_3Cl_3$ establishes it as a trinitrosyl complex and not as the ClNO adduct of $W(NO)_2Cl_2$, i.e., $W(NO)_2Cl_2{\cdot}ClNO$, as had been proposed by some investigators (25). In addition, the IR spectra of *fac*-$W(NO)_3Cl_3$ indicate that it is probably a principal constituent of the material previously described in two reports (26, 27) as $W(NO)_4Cl_3$. Authentic *fac*-$W(NO)_3Cl_3$ as a Nujol mull exhibits three ν(NO) bands at 1773, 1794, and 1933 cm^{-1} in its IR spectrum. As a KBr pellet, it displays these IR bands at 1608, 1762, and 1934 cm^{-1}, similar to those attributed to the putative tetranitrosyl (27).[3] Furthermore, the material formulated as $W(NO)_4Cl_3$, like authentic *fac*-$W(NO)_3Cl_3$ (7), reacts with Lewis bases, L, to form either $W(NO)Cl_3L_2$ or $W(NO)_2Cl_2L_2$-type complexes. Hence, it is our view that the putative tetranitrosyl complex, $W(NO)_4Cl_3$, is really impure *fac*-$W(NO)_3Cl_3$.

Summary

In summary, we have confirmed the identity of *fac*-$W(NO)_3Cl_3$ and have established the intramolecular metrical parameters of this complex by a single-crystal X-ray diffraction analysis. DFT calculations on this complex have also allowed us to rationalize why this compound possesses essentially linear W-N-O linkages. Finally, we have demonstrated that the trinitrosyl complex reversibly eliminates ClNO when dissolved in CH_2Cl_2, the only chloronitrosyl complex yet known to exhibit this behaviour.

Experimental

General methods

All manipulations were performed under anaerobic and anhydrous conditions either under high vacuum or in an atmosphere of prepurified dinitrogen or argon. General procedures routinely employed in these laboratories have been described in detail previously (34). Dichloromethane was distilled from calcium hydride. WCl_6 was purchased from Strem chemicals; $W(CO)_6$ was purchased from Aldrich; and NO was purchased from Linde. All chemicals were used as received. $[W(NO)_2Cl_2]_n$ (7) and ClNO (35) were prepared by the published procedures.

Crystal growth of *fac*-$W(NO)_3Cl_3$

The preparation of powder samples of *fac*-$W(NO)_3Cl_3$ has been described previously (7). The preparation of crystalline samples of this complex was accomplished in the following manner: A deep-red CH_2Cl_2 (60 mL) solution of WCl_6 (0.331 g, 0.83 mmol) in a 100 mL Schlenk tube was connected via a glass bridge to a glass-walled bomb (500 mL) filled with NO (1 atm). The bridge and headspace above the CH_2Cl_2 solution were filled with Ar (1 atm), and the Kontes Rotoflo valve of the bomb was slowly opened. The apparatus was allowed to stand undisturbed at ambient temperatures for 1 month, after which time a mass of small green crystals (0.126 g, 40% yield) was isolated by removal of the supernatant solution by cannulation. IR (Nujol) (cm^{-1}): 1773 (s), 1794 (w), 1933 (w) IR (KBr) (cm^{-1}): 1608 (s br), 1762 (s br), 1934 (m). MS (EI, 100 °C) *m/z*: 351 ($[P^+ - NO]$).

Preparation of *fac*-$W(NO)_3Cl_3$ from $[W(NO)_2Cl_2]_n$

To a Schlenk tube charged with a powder sample of $[W(NO)_2Cl_2]_n$ (0.397 g, 1.26 mmol) at room temperature was added a solution of ClNO (0.26 mol/L solution in CH_2Cl_2, 15 mL, 3.9 mmol). The suspension was stirred for 30 min, during which time the olive-green powder characteristic of $[W(NO)_2Cl_2]_n$ was replaced by a bright green microcrystalline material. The supernatant solution was removed by filter cannula and discarded, and a further aliquot of ClNO (0.26 mol/L solution in CH_2Cl_2, 15 mL, 3.9 mmol) was added to the Schlenk tube. The mixture was stirred for a further 30 min, and the supernatant solution was then removed from the bright green powder by filter cannulation and discarded. The bright green powder was dried in vacuo (0.214 g, 47% yield). Infrared spectroscopy confirmed its identity as authentic *fac*-$W(NO)_3Cl_3$.

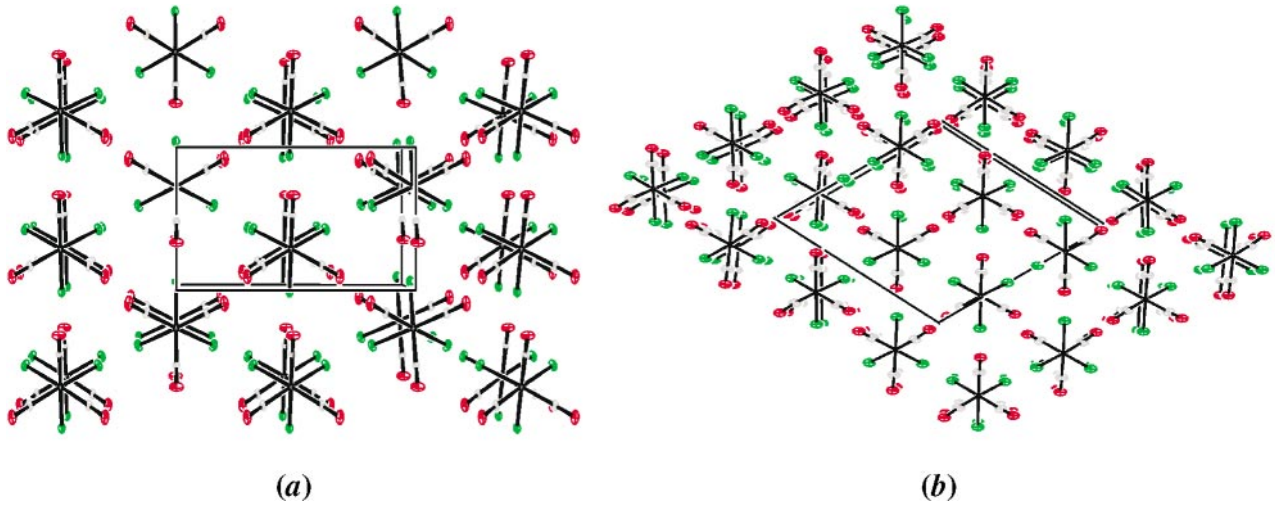
X-ray crystallography

Data collection for $W(NO)_3Cl_3$ was originally attempted in 1984 using an Enraf-Nonius CAD4-F diffractometer. However, attempts to index the unit cell were unsuccessful, and no data were ever collected. During the current investigation, data collection was carried out on a Rigaku/ADSC CCD diffractometer, where prior knowledge of the unit cell and its orientation was not required for data collection. The data were collected using graphite-monochromated Mo Kα radiation in 0.50° oscillations with 35 s exposures at

[3] The striking differences in the IR spectra of *fac*-$W(NO)_3Cl_3$ as a Nujol mull and as a KBr pellet suggest that it reacts in the solid state with KBr, possibly forming some $[WCl_2Br_2(NO)_2]^{2-}$. Thus, our KBr IR spectrum and that recorded by Taube and co-workers (ref. 27) is probably due to a mixture of nitrosyl compounds.

© 2004 NRC Canada

Fig. 6. ORTEP packing diagrams of (*a*) the correct orthorhombic cell viewed down the 5.69 Å *c*-axis and (*b*) the incorrect monoclinic cell viewed down the 5.68 Å *b*-axis.



–100 ± 1 °C. Preliminary treatment of the data using d*TREK (36) revealed a monoclinic unit cell with dimensions a = 12.174 Å, b = 5.676 Å, c = 12.177 Å, β = 117.49°, and V = 746.43 Å^3 (Fig. 6*b*). Integration was carried out to a maximum 2θ value of 59.5°. The internal consistency of the equivalent reflections was poor (R_{int} = 0.099); nevertheless, a reasonable preliminary solution was found in space group $P2_1/n$. Subsequent structure expansion and refinement revealed a significantly disordered structure, with three partially occupied nitrosyls interspersed between the three facial chlorides and three partially occupied chlorides interspersed between the three facial nitrosyls. Final residuals after anisotropic refinement were unsatisfactorily high (R_1 ~ 15%). An analysis of the crystal packing revealed several unreasonably short intermolecular contacts, including oxygen–oxygen contacts as short as 1.55 Å, chlorine–oxygen contacts as short as 1.88 Å, and chlorine–chlorine contacts as short as 2.18 Å. A re-examination of the raw data using TwinSolve (28) revealed an orthorhombic unit cell with dimensions a = 10.4280 Å, b = 6.3289 Å, and c = 5.6854 Å and with one-half the volume of the original cell (Fig. 6*a*). The internal consistency of the data was much better, with R_{int} = 0.04. This crystal formed with three twin components, where components 1 and 2 are related by a rotation of 180° around the axis normal to (–1, –1, 0), components 1 and 3 are related by a 180° rotation around the axis normal to (–1, 1, 0), and components 2 and 3 are related by a 123° rotation around the axis normal to (0, 0, 1). Data were integrated measuring all reflections, including those overlapped by reflections from other twin components. A Patterson (37) solution, using nonoverlapped data, was found in space group $Pmn2_1$, with the molecule residing on the mirror plane perpendicular to the *a*-axis. Figure 6 shows both the correct orthorhombic unit cell and the incorrect monoclinic unit cell and the evident similarities among their packing arrangements. Subsequent anisotropic refinement revealed no disorder and reasonable displacement parameters for all but one atom (N2). Refinement using all data (including overlapped reflections from the two minor components in HKLF5 format) gave final residuals of R_1 = 0.065 ($I > 2\sigma(I)$) and wR_2 = 0.176 (all data). Refinement of the batch scale factors associated with each twin component gave relative populations of 0.708, 0.217(1), and 0.075(1) for twin components 1, 2, and 3, respectively. N2 was refined isotropically while all other atoms were refined anisotropically. The absorption correction was performed along with batch scaling in a single step. The resulting transmission factors include contributions from absorption, detectable variations in beam intensity, and inhomogeneity of the detector surface. The final cycle of full-matrix, least-squares refinement was based on 2395 observed reflections and 49 parameters.

Neutral atom scattering factors were taken from Cromer and Waber (38). Anomalous dispersion effects were included in F_{calcd} (39); the values for $\Delta f'$ and $\Delta f''$ were those of Creagh and McAuley (40). The values for mass attenuation coefficients were those of Creagh and Hubbell (41). All calculations were performed using the CrystalClear software package of Rigaku/MSC, Inc. (42), which includes TwinSolve, or SHELXL-97 (43). X-ray crystallographic data are collected in Table 2, and full details of the crystallographic analysis are provided in the supplementary material.[4]

Theoretical DFT calculations

All theoretical calculations were performed using Gaussian03W (44). All calculations utilized a DFT method, using the three-parameter exchange functional of Becke (45) and the correlation functional of Lee, Yang, and Parr

[4] Supplementary material consists of full details of the crystallographic (CIF) and theoretical (PDF) analyses of *fac*-$W(NO)_3Cl_3$. Supplementary data may be purchased from the Depository of Unpublished Data, Document Delivery, CISTI, National Research Council Canada, Ottawa, ON K1A 0S2, Canada (http://www.nrc.ca/cisti/irm/unpub_e.shtml for information on ordering electronically). CSD 413576 contains the crystallographic data for this paper. These data can be obtained, free of charge, from the ICSD-Team/Crystal Structure Depot, Fachinformationszentrum (FIZ) Karlsruhe, Germany via CRYSDATA@FIZ-Karlsruhe.DE.

© 2004 NRC Canada

Table 2. X-ray crystallographic data for *fac*-$W(NO)_3Cl_3$.

Crystal data	
Empirical formula	$Cl_3N_3O_3W$
Crystal habit, color	Needle, green
Crystal size (mm)	0.20 × 0.07 × 0.03
Crystal system	Orthorhombic
Space group	$Pmn2_1$
Volume (Å^3)	375.22(2)
a (Å)[a]	10.4280(4)
b (Å)	6.3289(2)
c (Å)	5.6854(2)
Z	2
Formula weight (g/mol)	380.23
Density (calculated) (Mg/m^3)	3.365
Absorption coefficient (cm^{-1})	16.41
F_{000}	340
Radiation	Mo Kα, 0.71073 Å
Data refinement	
Final R indices[b]	R_1 = 0.065, wR_2 = 0.176
Goodness-of-fit on F^2 [c]	1.08
Largest diff. peak and hole (e Å^{-3})	3.49 and –3.14

[a]Cell dimensions based on 5205 reflections, $6.4° \le 2\theta \le 59.5°$.
[b]Number of observed reflections: 2190 ($I_o > 2\sigma I_o$), $R_1 = \Sigma \mid (|F_o| - |F_c|) \mid / \Sigma |F_o|$; $wR_2 = [\Sigma w(|F_o|^2 - |F_c|^2)^2 / \Sigma wF_o^4]^{1/2}$; $w = [\sigma^2(F_o^2) + (0.1374 \cdot P)^2 + 0.6000 \cdot P]^{-1}$, where $P = (\max(F_o^2, 0) + 2 \cdot F_c^2)/3$.
[c]GOF = [$\Sigma (w (|F_o| - |F_c|)^2)$ / degrees of freedom]$^{1/2}$.

(B3LYP) (46). The LANL2DZ basis set includes both Dunning and Hay's D95 sets for N and O (47) and the nonrelativistic electron core potential (ECP) sets of Hay and Wadt for Cl and Fe (48).

Geometry optimizations were performed in C_1 symmetry, and frequency calculations on optimized geometries established the absence of any imaginary frequencies. Energies are reported as the sum of electronic and zero-point energies. Metrical parameters and thermochemical data for of the optimized and partially optimized geometries of $W(NO)_3Cl_3$ are available as supplementary material.[4]

Acknowledgments

We are grateful to the Natural Sciences and Engineering Research Council of Canada for support of this work in the form of grants to P.L. and postgraduate scholarships to T.W.H. We also thank Dr. Lee Daniels of Rigaku/MSC, Inc., for invaluable assistance with the crystallographic analysis. P.L. is a Canada Council Killam Research Fellow.

References

1. T.W. Hayton, P. Legzdins, and W.B. Sharp. Chem. Rev. **102**, 935 (2002).
2. G.B. Richter-Addo and P. Legzdins. Metal nitrosyls. Oxford University Press, New York. 1992.
3. M. Herberhold, R. Klein, and P.D. Smith. Angew. Chem. Int. Ed. Engl. **18**, 220 (1979).
4. W. Beck, H.G. Fick, K. Lottes, and K.H. Schmidtner. Z. Anorg. Allg. Chem. **416**, 97 (1975).
5. W. Beck, K. Lottes, and K.H. Schmidtner. Angew. Chem. Int. Ed. Engl. **4**, 151 (1965).
6. R.D. Feltham, W. Silverthorn, and G. McPherson. Inorg. Chem. **8**, 344 (1969).
7. A.D. Hunter and P. Legzdins. Inorg. Chem. **23**, 4198 (1984).
8. A. Berg and K. Dehnicke. Z. Naturforsch. B Chem. Sci. **40**, 842 (1985).
9. H. Schumann and M. Meissner. Z. Naturforsch. B Chem. Sci. **35**, 863 (1980).
10. R.D. Wilson and R. Bau. J. Organomet. Chem. **191**, 123 (1980).
11. L. Hedberg, K. Hedberg, S.K. Satija, and B.I. Swanson. Inorg. Chem. **24**, 2766 (1985).
12. C.G. Barraclough and J. Lewis. J. Chem. Soc. 4842 (1960).
13. W. Hieber, W. Beck, and H. Tengler. Z. Naturforsch. B Chem. Sci. **15**, 411 (1960).
14. W. Hieber and H. Tengler. Z. Anorg. Allg. Chem. **318**, 136 (1962).
15. H. Wawersik and F. Basolo. J. Am. Chem. Soc. **89**, 4626 (1967).
16. R.B. King and T.F. Korenowski. J. Organomet. Chem. **17**, 95 (1969).
17. H.W. Chen and W.L. Jolly. Inorg. Chem. **18**, 2548 (1979).
18. D. Rehder, K. Ihmels, D. Wenke, and P. Oltmanns. Inorg. Chim. Acta **100**, L11 (1985).
19. W. Hieber and W. Beck. Z. Naturforsch. B Chem. Sci. **13**, 194 (1958).
20. W.P. Griffith, J. Lewis, and G. Wilkinson. J. Chem. Soc. 3993 (1958).
21. P. Legzdins and J.T. Malito. Inorg. Chem. **14**, 1875 (1975).
22. M. Herberhold, R. Klein, and H.G. Alt. Isr. J. Chem. **15**, 206 (1977).
23. I.H. Sabherwal and A.B. Burg. J. Chem. Soc. Chem. Commun. 1001 (1970)
24. T.W. Hayton, W.S. McNeil, B.O. Patrick, and P. Legzdins. J. Am. Chem. Soc. **125**, 12 935 (2003).
25. J. Kohan, S. Vastag, and L. Bencze. Inorg. Chim. Acta **14**, L1 (1975).
26. Y.A. Buslaev, N.A. Ovchinnikova, M.M. Ershova, and M.A. Glushkova. Izv. Akad. Nauk, Ser. Khim. **4**, 950 (1972).
27. K. Seyferth, K. Rosenthal, G. Kühn, and R. Taube. Z. Anorg. Allg. Chem. **513**, 57 (1984).
28. Rigaku/MSC Inc. and Prekat AB. TwinSolve: A program for the deconvolution and processing of rotation twins [computer program]. The Woodlands, Tex., U.S.A. 2002.
29. T.J. Greenhough, B.W.S. Kolthammer, P. Legzdins, and J. Trotter. Acta Crystallogr. Sect. B, **36**, 795 (1980).
30. A. Frankenau, W. Willing, U. Müller, and K. Dehnicke. Z. Anorg. Allg. Chem. **550**, 149 (1987).
31. J.H. Enemark and R.D. Feltham. Coord. Chem. Rev. **13**, 339 (1974).
32. R.H. Summerville and R. Hoffmann. J. Am. Chem. Soc. **98**, 7240 (1976).
33. S.F.A. Kettle. Inorg. Chem. **4**, 1661 (1965).
34. P. Legzdins, S.J. Rettig, K.J. Ross, R.J. Batchelor, and F.W.B. Einstein. Organometallics, **14**, 5579 (1995).
35. G. Pass and H. Sutcliffe. Practical inorganic chemistry. Chapman & Hall, London. 1968.
36. Molecular Structure Corp. d*TREK: Area detector software [computer program]. Version 8.0SSI. The Woodlands, Tex., U.S.A. 2003.
37. P.T. Beurskens, G. Admiraal, G. Beurskens, W.P. Bosman, S. Garcia-Granda, R.O. Gould, J.M.M. Smits, and C. Smykalla. PATTY: The DIRDIF program system: Technical report of the crystallography laboratory. University of Nijmegen, The Netherlands. 1992.
38. D.T. Cromer and J.T. Waber. International tables for X-ray crystallography. Vol. IV. Kynoch Press, Birmingham, U.K. 1974.
39. J.A. Ibers and W.C. Hamilton. Acta Crystallogr. **17**, 781 (1964).

© 2004 NRC Canada

40. D.C. Creagh and W.J. McAuley. International tables for X-ray crystallography. Vol. C. Kluwer Academic Publishers, Boston. 1992.
41. D.C. Creagh and J.H. Hubbell. International tables for X-ray crystallography. Vol. C. Kluwer Academic Publishers, Boston. 1992.
42. Molecular Structure Corp. CrystalClear [computer program]. Version 1.3.5b20. The Woodlands, Tex., U.S.A. 2002.
43. G.M. Sheldrick. SHELXL97 [computer program]. University of Göttingen, Germany. 1997.
44. M.J. Frisch. Gaussian 03 [computer program]. Revision B.01. Gaussian, Inc., Pittsburgh. 2003.
45. A. Becke. J. Chem. Phys. **98**, 5648 (1993).
46. C. Lee, W. Yang, and R.G. Parr. Phys. Rev. **B37**, 785 (1988).
47. T.H. Dunning and P.J. Hay. Modern theoretical chemistry. *Edited by* H.F. Schaefer III. Plenum Press, New York. 1976. pp. 1–28.
48. P.J. Hay and W.R. Wadt. J. Chem. Phys. **82**, 299 (1985).

© 2004 NRC Canada

Radio labelling of the gibberellin plant growth inhibitor 16,17-dihydro-GA_5[1]

Ellen J. Beck, Bruce Twitchin, and Lewis N. Mander

Abstract: An improved five-step procedure has been developed for the synthesis of the gibberellin plant growth inhibitor 16,17-dihydro-GA_5 from gibberellic acid. The 3-^{13}C and 3-^{14}C derivatives of this material have also been prepared by excising C-3 from the carbon skeleton (ozonolysis of a Δ^2-alkene derivative and subsequent retro-Claisen reaction) and then reassembling the A-ring by means of an intramolecular aldol reaction.

Key words: gibberellin, growth inhibitor, degradation, Radio labelling, Wittig reaction.

Résumé : On a développé une méthode améliorée en cinq étapes pour la synthèse, à partir de l'acide gibbérellique, du 16,17-dihydro-GA_5, un inhibiteur de la gibbérelline, une hormone de croissance des plantes. On a aussi préparé les dérivés 3-^{13}C et 3-^{14}C de ce produit en procédant à l'enlèvement du C-3 du squelette carboné (ozonolyse du dérivé Δ^2-alcène suivie d'une réaction subséquente de rétro-Claisen) et un réassemblage du noyau A par le biais d'une réaction intramoléculaire aldolique.

Mots clés : gibbérelline, inhibiteur de croissance, dégradation, marquage radioactif, réaction de Wittig.

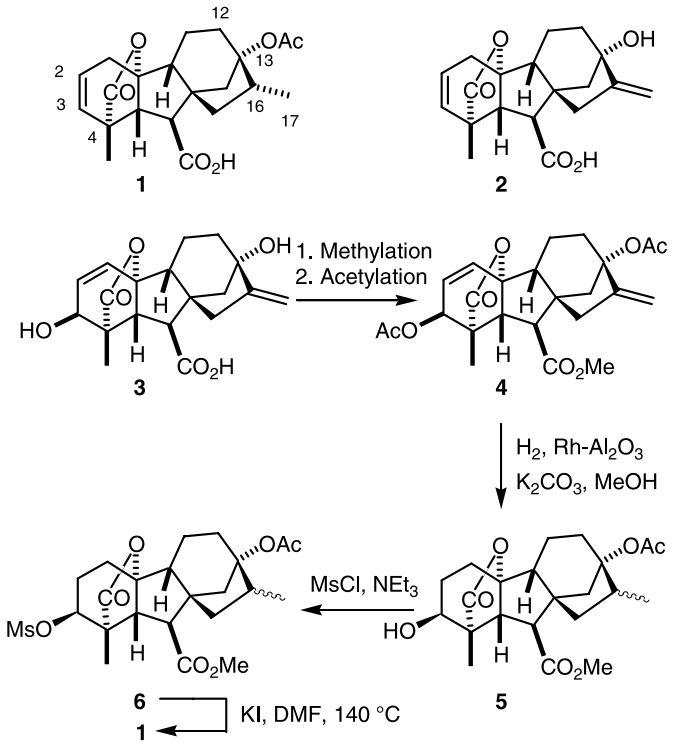
[Traduit par la Rédaction]

Introduction

The modified gibberellin *exo*-16,17-dihydro-GA_5-13-acetate (**1**) and related compounds are some of the most potent plant growth retardants presently known (1). Under greenhouse conditions, dosages of **1**, equivalent to 500 mg ha^{-1}, give distinct effects in wheat, barley, and many other graminaceous species. This substance has shown considerable promise for reducing the risk of lodging in cereal crops and, in field trials on wheat and barley, has been shown to be effective at application rates of ca. 25 g ha^{-1}. In contrast, rates of 200 or 1000 g ha^{-1} of prohexadione-Ca or chlormequat chloride, respectively, are required to produce an equivalent effect (2). Gibberellic acid (GA_3) (**3**) is readily available in tonne quantities from the fermentation of the fungus *Gibberella fujikuroi* and is relatively cheap, so there appeared to be reasonable prospects of producing **1** using **3** as a starting material. Several procedures for converting **3** into GA_5 (**2**) or its 16,17-dihydro derivatives have been reported (3), but none appeared sufficiently practical to produce **1** on a commercial basis. Of particular concern were the challenges of achieving a high overall yield, a minimization of steps, the use of cheap reagents, and the avoidance of chromatography. Assuming that these requirements could be addressed satisfactorily, the next phase of any commercialization and registration process would require isotopic labelling of **1** (desirably in a location that would not be lost through metabolism), to allow tracking and subsequent testing of metabolites for toxicity. In this paper we describe a high-yielding, five-step synthesis of **1** that meets the stated criteria, as well as derivatives of **1** that have been labelled with ^{13}C and ^{14}C at C-3.

Our first approach to the synthesis of **1** is outlined in Scheme 1 and involves simple hydrogenation of GA_3 deriva-

Scheme 1.



Received 15 October 2003. Published on the NRC Research Press Web site at http://canjchem.nrc.ca on 4 February 2004.

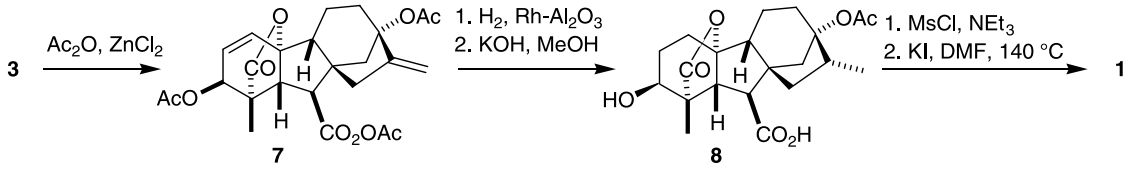
E.J. Beck, B. Twitchin, and L.N. Mander.[2] Research School of Chemistry, Australian National University, Canberra ACT 0200, Australia.

[1]This article is part of a Special Issue dedicated to Professor Ed Piers.

[2]Corresponding author (e-mail: mander@rsc.anu.edu.au).

 doi: 10.1139/V03-202 © 2004 NRC Canada

Scheme 2.



tives followed by dehydration of the 3-hydroxyl. Hydrogenation of GA_3 methyl ester over Pd- and Pt-based catalysts has been reported (4) to afford poor yields of a ca. 1:1 mixture of tetrahydro derivatives epimeric at C-16, since hydrogenolysis of the lactone function in the A-ring to give acidic products also occurs (ca. 30% with Pd–charcoal and 70% with PtO_2). Although hydrogenolysis is minimal with Rh–Al_2O_3, provided that the reduction is carried out in a non-polar solvent (acetone and ethyl acetate are suitable), a 2:1 mixture (*exo–endo*) of the 16-epimers is still obtained. The stereochemistry at C-16 (5) is established from the observation of mutual upfield shifts of the resonances from C-12 and C-17 in ^{13}C NMR spectra for the *endo* epimer (6), owing to the γ-gauche effect (7). Acylation of the 13-hydroxyl in the substrate, however, results in a minor degree of steric shielding of the *exo* face of the D-ring, favouring approach of the catalyst to the *endo* face of the 17-methylene group, such that the *exo*:*endo* ratio of 16-epimers from hydrogenation is improved. Thus, the diacetate **4** was reduced to give a 4:1 mixture of epimers in favor of the *exo*-isomer. Then, in preparation for the introduction of the Δ^2 alkene bond, the 3-acetate function was selectively hydrolyzed to give **5**. Although direct dehydration with, for example, $POCl_3$ (8) was feasible, our preferred procedure was based on preparation of the 3-mesylate **6** followed by DBU (1,8-diazabicyclo-[5.4.0]undec-7ene) induced elimination. Loss of the 13-acetate function could not be avoided during alkaline hydrolysis of the methyl ester, but treatment of **6** with KI in DMF at 140 °C effected both alkene formation and demethylation, with preservation of the acetate function to afford **1**.

Although this sequence was reasonably efficient, there appeared to be several opportunities for streamlining, including the elimination of the unnecessary "loop" of methylation (expensive) and demethylation of the carboxy function (modest yield). The changes are outlined in Scheme 2. Thus, GA_3 (**3**) was acetylated (acetic anhydride – $ZnCl_2$), and the resulting mixed anhydride **7** was hydrogenated in situ (after replacement of solvent with ethyl acetate), following which the solvent was removed, and the mixture was hydrolyzed in KOH–methanol to afford **8**. In this way, not only were the first three reactions carried out in "one pot", but the proportion of *exo* epimer was elevated to ca. 90%. Mesylation followed by elimination then led to the target compound **1** in 56% overall yield, with the amount of *endo* epimer being progressively reduced by successive recrystallizations.

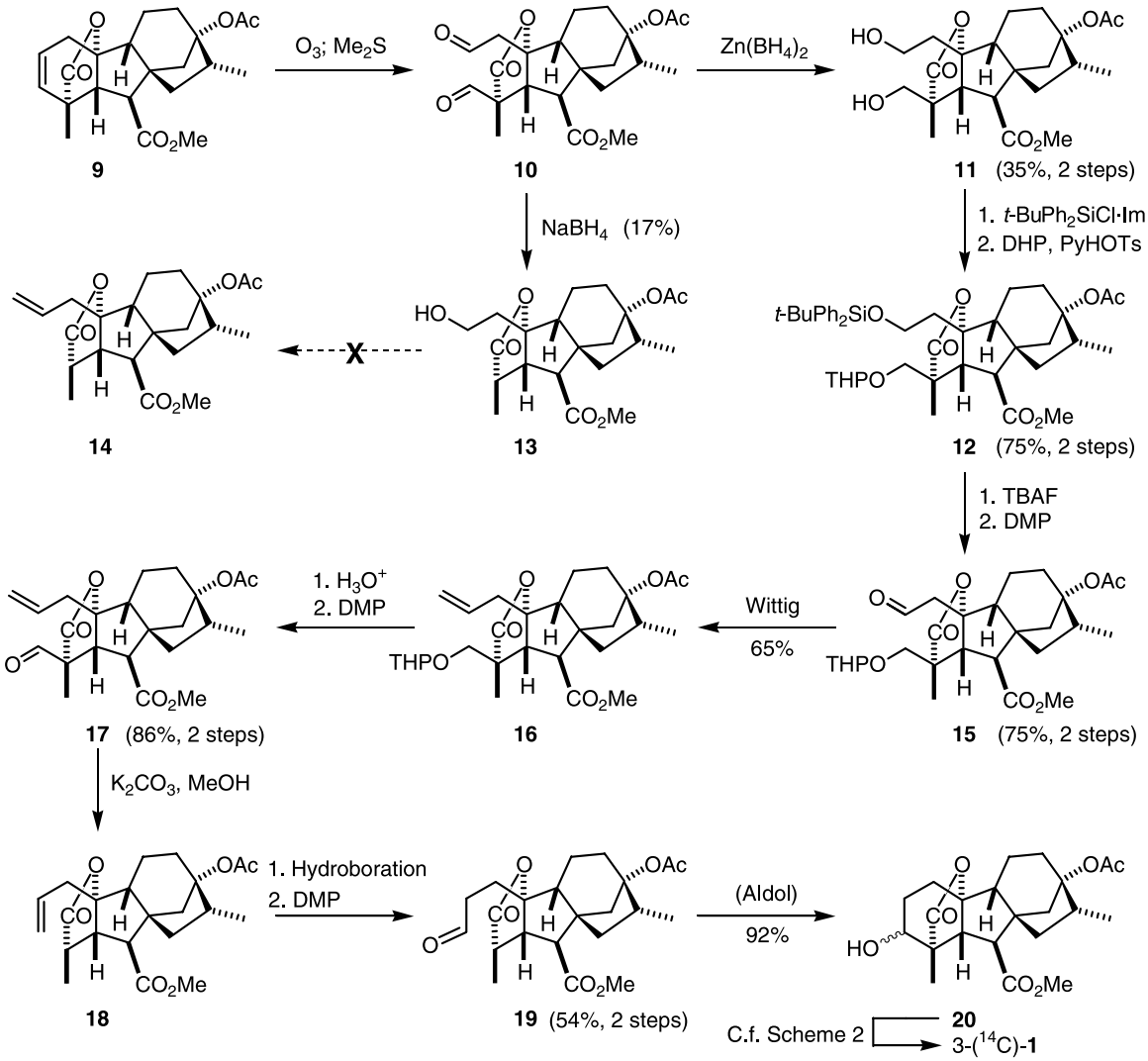
Next, we addressed the question of isotopic labelling. While the introduction of ^{14}C at C-17 in **1** would have been relatively straightforward, loss of this carbon by metabolic degradation was considered to be a possibility. Therefore, it was required that the label be located within the main skeleton. To achieve this aim, we elected to base our approach on the excision and restoration of C-3, the latter step being carried out by means of a Wittig methylenation, for which labelled reagents could be readily obtained. After a number of false starts we arrived at the sequence outlined in Scheme 3, in which the key steps are the removal of C-3 by a retrograde Claisen reaction (**17**→**18**) and the subsequent reconstitution of the gibberellin skeleton by means of an intramolecular aldol reaction (**19**→**20**) (for which there were several precedents) (9).

The dialdehyde **10** proved to be extremely labile and was therefore immediately reduced to diol **11** with zinc borohydride, as the more obvious reagent, sodium borohydride, afforded complex mixtures. We had originally planned to remove C-3 by means of a retrograde aldol process, given that an equivalent process is known to lead very readily to the inversion of stereochemistry in 3β-hydroxy gibberellins (10), but were surprised to find that **11** was stable to an extensive range of bases. Fortuitously, we had identified **13** as a minor component of the mixture obtained from the sodium borohydride treatment of dialdehyde **10** and, in a trial investigation, had oxidized it to the corresponding aldehyde and submitted it to a Wittig reaction. When we discovered that the desired alkene product **14** could not be obtained, possibly because of a competing aldol reaction between the lactone and aldehyde functions, we decided to postpone cleavage of the C-4 residue so that it could serve as a blocking group during the Wittig reaction. Thus, the C-2 carbinol function was selectively protected with *tert*-butyldiphenylsilyl chloride; then the C-3 hydroxyl was masked as a tetrahydropyranyl ether to furnish **12**. The silyl group was removed from C-2; the resulting alcohol was oxidized with the Dess–Martin periodinane (DMP) (11), and then the aldehyde product **15** was subjected to a series of Wittig reactions with a view to optimizing the yield of alkene while minimizing the amount of reagent used. The optimal stoichiometry proved to be 1.5 equiv. of ylide (generated from methyltriphenyl phosphonium iodide and potassium *tert*-butoxide), which afforded a 67% yield of **16** (based on substrate).

Following the hydrolysis of the THP function and oxidation, the resulting aldehyde **17** smoothly underwent a retro-Claisen reaction to give **18**, which was submitted to a number of hydroborating reagents, the most satisfactory of which proved to be disiamylborane. After oxidation to aldehyde **19**, the gibberellin skeleton was reassembled by an intramolecular aldol reaction to produce **20** as a 1:2 mixture of 3β:3α epimers. The mixture was then converted to **1**, using a similar protocol to the one employed in the latter part of Scheme 1. After repeating each of the eight steps from **15** to **1** at least three times and obtaining reproducible yields, aldehyde **15** was treated with ^{13}C- and ^{14}C-labelled phosphorane, and the sequence leading to 3-(^{14}C)–**1** was carried through in three batches, with a total yield of 40 mCi (1 Ci = 37 GBq) being obtained with the latter reagent.

© 2004 NRC Canada

Scheme 3.



Experimental

Melting points (°C) were recorded on a Reichert hot-stage apparatus and are uncorrected. Infrared spectra (ν_{max}, cm^{-1}) were recorded on a PerkinElmer 1800 Fourier Transform Infrared spectrometer. NMR spectra were recorded on a Varian Gemini 300 MHz instrument. For proton spectra recorded in chloroform, the residual peak of $CHCl_3$ was used as the internal reference (7.26 parts per million (ppm)), while the central peak of $CDCl_3$ (77.0 ppm) was used as the reference for ^{13}C spectra. Low- and high-resolution EI mass spectra (EI-MS, 70 eV) were recorded on a Fisons Autospec double focussing mass spectrometer. C, H, and N microanalyses were measured on a Carlo Erba EA 1106 CHN-O instrument and were carried out by the Australian National University Analytical Services Unit, Canberra. ^{14}C-methyltriphenylphosphonium iodide was supplied by Amersham Australia Pty Ltd., and the ^{13}C reagent was supplied by the Aldrich Chemical Co.

13-Acetoxy-3β-hydroxy-20-nor-16-*epi*-gibberellan-7-oic acid 19,10-lactone 8

To a suspension of GA_3 (10.8 g, 0.03 mol) in acetic anhydride (40 mL, 0.635 mol) was added zinc chloride (8.0 mg), and the mixture was left to stir overnight at room temperature (room temp) (15 h), by which time complete solution had occurred. The solvent was removed in vacuo and warmed to 60 °C. The residue was then redissolved in ethyl acetate, and the solution was reduced to a viscous oil. It is important to remove most of the solvent, since acetic acid promotes the opening of the A-ring lactone and slows the rate of reaction. This material was dissolved in ethyl acetate (100 mL); 5% rhodium on alumina (1 g) was added, and stirring was maintained under an atmosphere of hydrogen for 48 h. After purging with nitrogen, the solution was filtered through Celite (note that the catalyst may be reused several times), and the solvent was removed in vacuo to afford the crude product as a gum (17.4 g). IR (cm^{-1}): 1816, 1777, 1737. ^1H NMR δ: 0.87 (d, J = 6.9 Hz, 3H, H-17), 1.05 (s, 3H, H-18), 1.56–2.36 (m, 14H), 1.98 (s, 3H, OAc), 2.08 (s, 3H, OAc), 2.21 (s, 3H, OAc), 2.65 (d, J = 10.7 Hz, 1H, H-6), 3.11 (d, J = 10.9 Hz, 1H, H-5), 3.72, 4.92 (br s, 1H, H-3). ^{13}C NMR δ: 14.7, 17.2, 18.8, 21.0, 21.1, 22.3, 25.3, 27.5, 37.4, 38.8, 41.2, 44.8, 49.1, 49.1, 51.9, 52.2, 53.1, 54.9, 71.1, 84.8, 92.7 165.4, 167.8, 170.1, 170.3, 176.4.

The material prepared above was dissolved in methanol

© 2004 NRC Canada

(50 mL) and cooled to 5 °C initially; then 4 mol L^{-1} aq KOH (65 mL) was added slowly over 2 h, and the progress of the reaction was monitored by TLC. The pH of the reaction was then adjusted to pH 8 using 2 N HCl, and a volume of solvent equal to the amount of methanol (50 mL) was removed in vacuo. The reaction mixture was then diluted with water (60 mL), and any neutral material was extracted with ethyl acetate (2 × 50 mL). After the aqueous solution was cooled to 5 °C and the pH was adjusted to pH 3 with 4 mol L^{-1} HCl, the resulting precipitate was filtered and washed with water (2 × 50 mL). The crystalline product was dried under high vacuum at 60 °C to give the crude 16,17-dihydro-GA_1-13-acetate (**8**) (8.2 g, 76% yield). A sample was crystallized from ethyl acetate – petroleum ether, mp 179–181 °C. IR (cm^{-1}): 3506, 2951, 2877, 1772, 1734, 1438, 1370, 1272, 1243, 1198, 1173, 1101, 1059, 1038, 1020, 997, 972, 952, 928, 735. ^{1}H NMR δ: 0.88 (d, *J* = 6.9 Hz, 3H, H-17), 1.13 (s, 3H, H-18), 1.56–2.36 (m, 14H), 2.01 (s, 3H, OAc), 2.68 (d, *J* = 10.7 Hz, 1H, H-6), 3.19 (d, *J* = 10.9 Hz, 1H, H-5), 3.72 (s, 3H, CO_2CH_3), 3.83 (m, 1H, H-3). ^{13}C NMR δ: 14.9, 17.6, 19.1, 21.8, 27.6, 28.2, 37.8, 39.3, 41.3, 45.5, 49.2, 51.4, 52.0, 52.2, 54.6, 54.8, 70.3, 85.6, 93.8, 170.7, 173.1, 178.3. LR-MS *m/z* (relative intensity): 406 ([M^+], 7), 388 (16), 364 (100), 346 (65), 321 (85), 289 (47), 243 (26) 225 (20). HR-MS calcd. for $C_{22}H_{30}O_7$ ([M^+]): 406.1992; found: 406.1995. Anal. calcd. for $C_{22}H_{30}O_7$ (%): C 65.01, H 7.44; found: C 64.76, H 7.30.

13-Acetoxy-20-nor-16-*epi*-gibberell-2-en-7-oic acid 19,10-lactone 7-methyl ester 9

After 16,17-dihydro-GA_1 13-acetate (**8**) (406 mg, 1 mmol) was treated with diazomethane, excess reagent and solvent were removed; the residue was dissolved in dry pyridine (2.35 mL) at 0 °C under nitrogen, and methanesulfonyl chloride (194 μL, 2.5 mmol) was added with stirring. The reaction was allowed to warm to room temp, and stirring continued for 24 h. Ice chips were added to quench the reaction, and the product was extracted into ethyl acetate. After washing with dilute HCl and brine, the solution was dried and reduced to dryness. The crude product was dissolved in dry toluene (20 mL); DBU (0.5 mL) was added, and the mixture was heated under reflux for 20 h. The solution was decanted from a tarry residue, diluted with ether (50 mL), washed with dilute HCl and brine, and dried ($MgSO_4$). After removal of solvent, chromatography on silica gel (1:2 ethyl acetate : hexane) afforded the title compound as a colourless solid (298 mg, 77%). A sample was crystallized from ethyl acetate – petroleum ether, mp 110–112 °C. IR (cm^{-1}): 3033, 2954, 2875, 1775, 1734, 1437, 1368, 1242, 1198, 1168, 1100, 1030 939, 893, 735, 704. ^{1}H NMR δ: 0.88 (d, *J* = 6.9 Hz, 3H, H-17), 0.94 (dd, *J* = 6.0, 12.6 Hz, 1H), 1.21 (s, 3H, H-18), 1.60–2.40 (m, 11H), 2.01 (s, 3H, OAc), 2.56 (dq, *J* = 18.7, 1.8 Hz, 1H, H-1), 2.62 (dq, *J* = 18.7, 1.8 Hz, 1H, H-1), 2.65, 2.78 (2 × Abd, *J* = 9.3 Hz, 2 × 1H, H-5, H-6), 3.73 (s, 3H, OMe), 5.66 (d, *J* = 9.3 Hz, H-3), 5.80 (dt, *J* = 9.2, 3.2 Hz, H-2). ^{13}C NMR δ: 15.5, 17.7, 19.1, 21.8, 35.6, 37.5, 39.6, 41.0, 45.5, 48.3, 50.2, 52.0, 55.1, 52.3, 55.1, 55.3, 85.6, 91.9, 128.0, 132.4, 173.1, 177.9. LR-MS *m/z* (relative intensity): 388 ([M^+], 4), 357 (9), 344 (37), 284 (100), 259 (18), 241 (36), 225 (65). HR-MS calcd. for $C_{22}H_{28}O_6$ ([M^+]): 388.1885; found: 388.1879. Anal. calcd. for $C_{22}H_{28}O_6$ (%): C 68.02, H 7.26; found: C 68.22, H 7.35.

13-Acetoxy-20-nor-16-*epi*-gibberell-2-en-7-oic acid 19,10-lactone 1

To a solution of 16,17-dihydro-GA_1 13-acetate (**5**) (392 mg, 1 mmol) in dry pyridine (2.35 mL) at 0 °C under nitrogen was added mesyl chloride (194 μL, 2.5 mmol), with stirring. The reaction was allowed to warm to room temp, and stirring was continued for 24 h. To the residue was added DMF (5 mL) and KI (1.25 g), and the mixture was heated to 130 °C for 48 h and then cooled to room temp. The reaction was diluted with water (20 mL) and then acidified with 1 mol L^{-1} HCl (10 mL). The mixture was then extracted with dichloromethane (×5). The organic phase was washed with water, $Na_2S_2O_3$, and brine and dried ($MgSO_4$), and the solvent was evaporated in vacuo. The residue was crystallized from ethyl acetate – petroleum ether to give **1** (288 mg, 73%), mp 222–224 °C. When the methyl ester of **8** was used in place of the parent acid, purification was carried out by silica gel chromatography (3:1 hexane : ethyl acetate → 1:1 hexane : ethyl acetate with acetic acid (2 mL L^{-1})), furnishing the alkene acid **1** in 74% yield and its methyl ester in 14% yield. Similar results were obtained when the mixture of 3-epimers (obtained from the aldol reaction of aldehyde **19**) was employed. IR (cm^{-1}): 3532, 3180, 2959, 2925, 2853, 1772, 1732, 1455, 1370, 1246, 1226, 1172, 1143, 1101, 1029, 939, 736, 702. ^{1}H NMR δ: 0.89 (d, *J* = 6.9 Hz, 3H, H-17), 1.16 (dd, *J* = 6.0, 12.6 Hz, 1H), 1.27 (s, 3H, H-18), 1.60–2.40 (m, 11H), 2.02 (s, 3H, OAc), 2.18 (dq, *J* = 18.7, 1.8 Hz, 1H, H-1) 2.60 (dq, *J* = 18.7, 1.8 Hz, 1H, H′-1) 2.68, 2.74 (2 × Abd, *J* = 9.3 Hz, 2 × 1H, H-5, H-6), 5.68 (d, *J* = 9.3 Hz, H-3), 5.82 (dt, *J* = 9.2, 3.2 Hz, H-2). ^{13}C NMR δ: 15.6, 17.7, 19.1, 21.8, 35.6, 37.4, 39.7, 40.9, 45.2, 48.4, 50.2, 51.8, 55.1, 55.3, 85.6, 91.8, 128.0, 132.4, 170.8, 177.6, 177.8. LR-MS *m/z* (relative intensity): 374 ([M^+], 6), 332 (57), 330 (58), 314 (9), 289 (28), 270 (100), 241 (21), 225 (44). HR-MS calcd. for $C_{21}H_{26}O_6$ ([M^+]): 374.1729; found: 374.1724. Anal. calcd. for $C_{21}H_{26}O_6$ (%): C 67.36, H 7.00; found: C 67.39, H 7.36.

13-Acetoxy-2,3-dioxo-2,3-seco-20-nor-16-*epi*-gibberellan-7-oic acid 19,10-lactone 7-methyl ester 10

Ozone was bubbled through a solution of 13-acetoxy-16,17-dihydro-GA_5 methyl ester (**9**) (3.4 g, 8.8 mmol) in dichloromethane (150 mL) cooled to –78 °C, until a faint blue color appeared. Nitrogen was then bubbled through the solution for 15 min to remove the excess ozone. Methyl sulfide (3.2 mL, 43 mmol, 5 equiv.) was added, and the reaction was allowed to warm slowly in the cold bath for 1 h. The reaction was stirred at room temp overnight. The reaction mixture was then washed with water and brine and dried ($MgSO_4$), and the solvent was removed in vacuo. No further purification was attempted, owing to the instability of the dialdehyde. IR (cm^{-1}): 3439, 2949, 2872, 1770, 1730, 1436, 1369, 1241, 1205, 1173, 1112, 1039, 961, 734, 701. ^{1}H NMR δ: 0.91 (d, 3H, H-17), 1.0–2.0 (m), 1.4 (s, 3H, H-18), 2.00 (s, 3H, OAc), 2.2–2.6 (m), 2.73 (d, 1H, *J* = 1.1 Hz, H-6), 3.59 (s, 1H, H-5), 3.70 (s, 3H, CO_2CH_3), 9.62 (s, 1H, H-2), 9.69 (d, 1H, *J* = 0.7 Hz, H-3).

© 2004 NRC Canada

13-Acetoxy-2,3-dihydroxy-2,3-seco-20-nor-16-*epi*-gibberellan-7-oic acid 19,10-lactone 7-methyl ester 11

A solution of $Zn(BH_4)_2$ in DME (0.5 mol L^{-1} solution, 33 mL, 2 equiv.) was added to a solution of crude dialdehyde **10** (3.46 g, 8.2 mmol) in DME (60 mL) cooled to 0 °C, and the reaction was stirred for 1.5 h. The reaction was then quenched with acetone, and most of the DME was removed in vacuo. The residue was taken up in ethyl acetate and 10% HCl. The aqueous layer was extracted with ethyl acetate (×3). The combined organic extracts were washed with water and brine and dried ($MgSO_4$), and the solvent was removed in vacuo. Purification by silica gel chromatography (ethyl acetate) furnished the diol (1.25 g) in 35% over the two steps. IR (cm^{-1}): 3440, 2947, 2872, 1731, 1436, 1370, 1334, 1240, 1173, 1113, 1038, 957, 735. ^{1}H NMR δ: 0.92 (d, *J* = 6.9 Hz, 3H, H-17), 1.21 (s, 3H, H-18), 1.48–2.0 (m, 7H), 2.0 (s, 3H, OAc), 2.11–2.2 (m, 3H), 2.51 (m, 2H), 2.78 (d, *J* = 0.96 Hz, 1H, H-6), 3.17 (br, 2H, OH), 3.29 (d, *J* = 1.4 Hz, 1H, H-5), 3.63, 3.73 (2 × Abd, *J* = 10.9 Hz, 2H, H-3), 3.70 (s, 3H, CO_2CH_3), 3.88 (m, 2H, H-2). ^{13}C NMR δ: 18.1, 18.2, 19.2, 22.0, 33.1, 34.5, 39.6, 42.8, 43.3, 47.3, 50.4, 51.0, 51.5, 52.3, 52.9, 58.7, 69.8, 87.1, 95.6, 170.6, 176.0, 180.7. LR-MS *m/z* (relative intensity): 424 ([M^+], 7), 394 (10), 381 (50), 364 (52), 339 (100), 319 (30), 307 (34), 291 (36), 277 (28), 261 (55), 231 (50) 201 (35). HR-MS calcd. for $C_{22}H_{32}O_8$: 424.2097; found: 424.2089.

When this reaction was performed on a 235 mg scale with sodium borohydride in ethanol, a gross mixture was obtained, from which diol **11** (27 mg) and alcohol **13** (40 mg) were obtained. For the latter product: ^{1}H NMR δ: 0.91 (d, *J* = 6.9 Hz, 3H, H-17), 1.23 (d, 3H, *J* = 6.0 Hz H-18), 1.48–2.0 (m, 7H), 1.99 (s, 3H, OAc), 2.11–2.2 (m, 3H), 2.48 (m, 2H), 2.72 (d, *J* = 0.9 Hz, 1H, H-6), 3.15 (m, 1H, H-4), 3.29 (dd, *J* = 0.9, 10.7 Hz, 1H, H-5), 3.70 (s, 3H, CO_2CH_3), 3.81 (m, 4H, H-2 + H-3).

13-Acetoxy-2-*tert*-butyldiphenylsilyloxy-3-hydroxy-2,3-seco-20-nor-16-*epi*-gibberellan-7-oic acid 19,10-lactone 7-methyl ester

Triethylamine (0.51 mL, 3.7 mmol, 1.1 equiv.) and then TBDPS-Cl (0.95 mL, 3.7 mmol, 1.1 equiv.) were added to a cooled solution of the diol **11** (1.41 g, 3.3 mmol, 1 equiv.) and imidazole (0.05 g, 0.66 mmol, 0.2 equiv.) in DMF (75 mL), and the reaction was stirred overnight at room temp. The reaction was then poured into ethyl acetate and water, and the aqueous layer was extracted with ethyl acetate (×4). The combined organic extracts were washed with water and brine and dried ($MgSO_4$), and the solvent was removed in vacuo. Purification by silica gel chromatography (5:1 hexane : ethyl acetate → ethyl acetate) furnished the mono-protected diol in 86% yield. IR (cm^{-1}): 3454, 3071, 3050, 2934, 2859, 1760, 1732, 1589, 1471, 1461, 1428, 1369, 1334, 1239, 1169, 1112, 1086, 1038, 972, 958, 823, 738, 703. ^{1}H NMR δ: 0.89 (d, *J* = 6.8 Hz, 3H, H-17), 1.04 (s, 9H, $SiCCH_3$), 1.21 (s, 3H, H-18), 1.47 (dd, *J* = 5.9, 12.7 Hz, 1H), 1.58–1.73 (m, 5H), 1.87 (m, 1H), 1.98 (s, 3H, OAc), 2.12–2.24 (m, 3H), 2.44 (m, 2H), 2.73 (d, *J* = 1.5 Hz, 1H, H-6), 2.96 (d, *J* = 1.5 Hz, 1H, H-5), 3.56 (s, 2H, H-3), 3.62 (s, 3H, CO_2CH_3), 3.84–3.93 (m, 2H, H-2), 7.38–7.46 (m, 6H, Ar), 7.66–7.70 (m, 4H, Ar). ^{13}C NMR δ: 18.1, 18.4, 19.25, 19.3, 22.1, 27.1, 33.2. 34.5, 41.0, 42.9, 43.5, 47.9, 49.9, 51.0, 51.9, 52.6, 52.9, 60.2, 70.1, 87.2, 95.4, 127.99, 128.0, 130.02, 130.04, 133.55, 133.6, 135.8, 135.9, 170.6, 174.6, 180.5. Anal. calcd. for $C_{37}H_{47}O_7Si$ (%): C 68.85, H 7.60; found: C 68.67, H 7.51.

13-Acetoxy-2-*tert*-butyldiphenylsilyloxy-3-tetrahydropyranyloxy-2,3-seco-20-nor-16-*epi*-gibberellan-7-oic acid 19,10-lactone 7-methyl ester 12

Dihydropyran (0.03 mL, 0.38 mmol, 2 equiv.) and pyridinium *p*-toluenesulfonate (0.002 g, 0.006 mmol, 0.05 equiv.) were added to the silyl ether prepared above (0.127 g, 0.19 mmol, 1 equiv.) in dichloromethane (5 mL), and the reaction was stirred at room temp overnight. The reaction mixture was then washed with water and brine and dried ($MgSO_4$), and the solvent was removed in vacuo. Purification by silica gel chromatography (5:1 hexane : ethyl acetate → 3:1 hexane : ethyl acetate) furnished the protected compound **12** as a colorless gum in 87% yield. IR (cm^{-1}): 2942, 2859, 1764, 1732, 1453, 1428, 1367, 1254, 1238, 1167, 1112, 1077, 1036, 969, 904, 822, 740, 703. ^{1}H NMR δ: 0.88 (d, *J* = 7.0 Hz, 3H, H-17), 1.02 (s, 9H, CCH_3), 1.03 (s, 9H, CCH_3), 1.18 (s, 3H, H-18), 1.19 (s, 3H, H-18), 1.26–1.82 (m, 13H), 1.97 (s, 3H, OAc), 1.98 (s, 3H, OAc), 2.04 (d, *J* = 7.8 Hz, 0.5H), 2.09 (d, *J* = 7.8 Hz, 0.5H), 2.33–2.46 (m, 4H), 2.72 (br s, 1H), 3.04 (d, *J* = 9.2 Hz, 1H, H-5), 3.19 (d, *J* = 9.1 Hz, 1H), 3.47 (d, *J* = 9.3 Hz, 1H), 3.51 (m, 2H), 3.59 (s, 3H, CO_2CH_3), 3.60 (s, 3H, CO_2CH_3), 3.67–3.89 (m, 4H), 4.54 (m, 1H, THP H), 4.64 (m, 1H, THP H), 7.40 (m, 6H, phenyl), 7.67 (m, 4H, phenyl). Anal. calcd. for $C_{43}H_{58}O_9Si$ (%): C 69.14, H 7.83; found: C 69.40, H 7.95.

13-Acetoxy-2-hydroxy-3-tetrahydropyranyloxy-2,3-seco-20-nor-16-*epi*-gibberellan-7-oic acid 19,10-lactone 7-methyl ester

Tetrabutylammonium fluoride (2.0 mL, 2.0 mmol, 3 equiv.) was added to a solution of silyl ether **12** (0.501 g, 0.67 mmol, 1 equiv.) in THF (20 mL) and stirred at room temp for 4 to 5 h until reaction was complete. The reaction mixture was then poured into ethyl acetate and water. The aqueous phase was extracted with ethyl acetate (×3). The combined organic phases were washed with water and brine and dried ($MgSO_4$), and the solvent was removed in vacuo. Purification by silica gel chromatography (1:1 ethyl acetate : hexane → 2:1 ethyl acetate : hexane) furnished the deprotected compound as a colorless gum in 94% yield. IR (cm^{-1}): 3480, 2944, 2871, 1760, 1731, 1453, 1370, 1239, 1125, 1068, 1035, 958, 904. ^{1}H NMR δ: 0.93 (d, *J* = 7.0 Hz, 3H, H-17), 1.21 (s, 3H, H-18), 1.48–1.99 (m, 2H), 2.00 (s, 3H, OAc), 2.15–2.40 (m, 4H), 2.50 (m, 2H), 2.80 (m 1H), 3.24 (d, *J* = 9.1 Hz, 1H), 3.30 (d, *J* = 12.6 Hz, 1H), 3.52 (m, 2H), 3.71 (s, 3H, CO_2CH_3), 3.71–3.94 (m, 5H), 4.58 (m, 1H, THP), 4.67 (m, 1H, THP). Anal. calcd. for $C_{27}H_{40}O_9$ (%): C 63.76, H 7.93; found: C 63.47, H 7.47.

13-Acetoxy-2-oxo-3-tetrahydropyranyloxy-2,3-seco-20-nor-16-*epi*-gibberellan-7-oic acid 19,10-lactone 7-methyl ester 15

Dess–Martin periodinane (0.077 g, 0.20 mmol, 1.5 equiv.) was added to a solution of the alcohol prepared above (0.069 g, 0.14 mmol, 1 equiv.) in dichloromethane (2 mL) at room temp. The reaction was stirred for 1 h; then 1 mol L^{-1}

© 2004 NRC Canada

$Na_2S_2O_3$ (1 mL) and saturated $NaHCO_3$ (1 mL) solutions were added, and the mixture was stirred vigorously until both layers were clear. The aqueous phase was then extracted with dichloromethane (×3). The combined organic phases were washed with water and brine and dried ($MgSO_4$), and the solvent was removed in vacuo. Purification by silica gel chromatography (1:1 ethyl acetate : hexane) furnished aldehyde **15** as a colorless gum in 80% yield. IR (cm^{-1}): 2945, 2870, 1768, 1728, 1436, 1368, 1253, 1238, 1125, 1067, 1036, 962, 904. ^{1}H NMR δ: 0.91 (d, J = 7.0 Hz, 3H, H-17), 1.22 (s, 3H, H-18), 1.48–1.99 (m, 15H), 2.00 (s, 3H, OAc), 2.11 (m, 1H), 2.49 (m, 2H), 2.81 (m, 1H), 3.05 (m, 1H), 3.20 (m, 2H), 3.55 (m, 1H), 3.69 (s, 3H, CO_2CH_3), 3.68–3.82 (m, 1H), 3.97 (d, J = 8.9 Hz, 1H), 4.56 (m, 1H, THP), 4.68 (m, 1H, THP), 9.97 (m, 1H, CHO). Anal. calcd. for $C_{27}H_{38}O_9$ (%): C 64.02, H 7.56; found: C 63.73, H 7.60.

13-Acetoxy-4-tetrahydropyranyloxymethyl-3,4-seco-20-nor-16-*epi*-gibberell-2-en-7-oic acid 19,10-lactone 7-methyl ester 16

Potassium *tert*-butoxide (1.0 mol L^{-1} solution in THF, 3.4 mL, 3.4 mmol, 1.4 equiv.) was added to a suspension of methyl triphenylphosphine iodide (1.5 g, 3.7 mmol, 1.5 equiv.) in THF (30 mL) and stirred at room temp for 30 min. The stirring was then stopped, and the precipitate in the ylide solution was allowed to settle for at least 30 min. Aldehyde **14** (1.24 g, 2.4 mmol, 1 equiv.) was dissolved in THF (20 mL), and the supernatant ylide solution was cannulated into the aldehyde solution. The reaction was stirred for 1 h and then poured into ethyl acetate and water. The aqueous layer was extracted with ethyl acetate (×3). The combined organic layers were washed with water (×1) and brine and dried ($MgSO_4$), and the solvent was removed in vacuo. Purification by silica gel chromatography (2:1 hexane : ethyl acetate) furnished the olefin in 65% yield. IR (cm^{-1}): 2945, 2870, 1764, 1731, 1436, 1369, 1238, 1125, 1067, 1036, 970, 904. ^{1}H NMR δ: 0.91 (d, J = 6.9 Hz, 3H, H-17), 1.23 (s, 3H, H-18), 1.46–1.84 (m, 14H), 1.99 (s, 3H, OAc), 1.96–2.14 (m, 2H), 2.47 (m, 2H), 2.76 (m, 3H), 3.09 (d, J = 9.6 Hz, 1H), 3.23 (d, J = 9.1 Hz, 0.5H), 3.53 (d, part obscured, J = 9.5 Hz, 1.5H), 3.68 (s, 3H, CO_2Me), 3.68–3.86 (m, 1H), 3.93 (d, J = 9.1 Hz, 1H), 4.58, 4.66 (m, 1H, THP), 5.13 (m, 2H, H-3), 5.97 (m, 1H, H-2). Anal. calcd. for $C_{28}H_{40}O_8$ (%): C 66.65, H 7.99; found: C 66.31, H 7.96.

13-Acetoxy-4-hydroxymethyl-3,4-seco-20-nor-16-*epi*-gibberell-2-en-7-oic acid 19,10-lactone 7-methyl ester

A catalytic amount (10 mg) of *p*-toluenesulfonic acid was added to the THP-protected gibberellin **16** (0.151 g, 0.30 mmol) in methanol (10 mL) and stirred at room temp overnight. The methanol was then removed in vacuo, and the residue was taken up in ethyl acetate. The solution was washed with $NaHCO_3$, water, and brine and then dried ($MgSO_4$), and the solvent was removed in vacuo. The crude mixture was chromatographed (1:1 hexane : ethyl acetate) to furnish the alcohol (0.119 g) as a colorless gum in 94% yield. IR (cm^{-1}): 3455, 3076, 2946, 2871, 1760, 1732, 1435, 1369, 1238, 1169, 1037, 972. ^{1}H NMR δ: 0.93 (d, J = 6.9 Hz, 3H, H-17), 1.26 (s, 3H, H-18), 1.49 (dd, J = 6.3, 12.8 Hz, 1H), 1.56–1.84 (m, 7H), 1.96–2.1 (m, 3H), 1.99 (s, 3H, OAc), 2.46 (m, 2H), 2.68 (m, 2H), 2.76 (s, 1H, H-6), 2.89 (s, 1H, H-5), 3.68 (s, 3H, CO_2Me), 3.68 (s, 2H, H-3), 5.18 (m, 2H, H-3), 5.93 (m, 1H, H-2). ^{13}C NMR δ: 18.1, 18.3, 19.2, 22.1, 33.2, 34.6, 42.8, 43.5, 43.6, 47.8, 49.7, 51.0, 52.0, 52.3, 52.9, 69.6, 87.2, 95.9, 119.3, 133.1, 170.6, 174.8, 180.6. LR-MS *m*/*z* (relative intensity): 420, ([M^+], 5), 379 (97), 319 (100), 291 (60), 273 (43), 259 (64), 231 (55). HR-MS calcd. for $C_{23}H_{32}O_7$ ([M^+]): 420.2148; found: 420.2128.

13-Acetoxy-4-formyl-3,4-seco-20-nor-16-*epi*-gibberell-2-en-7-oic acid 19,10-lactone 7-methyl ester 17

Dess–Martin periodinane (0.16 g, 0.42 mmol, 1.5 equiv.) was added to a solution of the alcohol prepared above (0.119 g, 0.28 mmol, 1 equiv.) in dichloromethane (10 mL) and stirred at room temp for 1.5 h. The reaction was stirred for 1 h; then 1 mol L^{-1} $Na_2S_2O_3$ (5 mL) and saturated $NaHCO_3$ (5 mL) solutions were added, and the mixture was stirred vigorously until both layers were clear. The aqueous phase was then extracted with dichloromethane (×3). The combined organic phases were washed with water and brine and dried ($MgSO_4$), and the solvent was removed in vacuo. Purification by silica gel chromatography (2:1 hexane : ethyl acetate) furnished the aldehyde **17** (0.109 g) in 92% yield. IR (cm^{-1}): 2944, 2870, 1766, 1731, 1435, 1369, 1239, 1168, 1109, 1036, 917. ^{1}H NMR δ: 0.92 (d, J = 6.9 Hz, 3H, H-17), 1.40 (s, 3H, H-18), 1.49 (dd, J = 6.2, 12.9 Hz, 1H), 1.60–1.90 (m, 6H), 1.95 (d, J = 6.7 Hz, 1H), 2.00 (s, 3H, OAc), 2.11 (d, J = 8.7 Hz, 1H), 2.42–2.55 (m, 4H), 2.66 (d, J = 1.5 Hz, 1H, H-6), 3.56 (d, J = 1.7 Hz, 1H, H-5), 3.70 (s, 3H, CO_2Me), 5.16 (m, 2H, H-3), 5.72 (m, 1H, H-2), 9.47 (s, 1H, CHO). ^{13}C NMR δ: 17.1, 18.1, 19.2, 22.0, 33.1, 34.7, 42.3, 42.7, 43.3, 47.9, 48.1, 51.2, 52.2, 52.3, 60.9, 87.0, 96.5, 121.1, 131.9, 170.5, 174.4, 175.1, 195.2. LR-MS *m*/*z* (relative intensity): 418 ([M^+], 3), 377 (100), 359 (27), 349 (30), 333 (34), 317 (60), 289 (18), 257 (16), 231 (23). HR-MS calcd. for $C_{23}H_{30}O_7$ ([M^+]): 418.1992; found: 418.2000. Anal. calcd. for $C_{23}H_{30}O_7$ (%): C 66.01, H 7.23; found: C 65.57, H 6.63.

13-Acetoxy-3,4-seco-20-nor-16-*epi*-gibberell-2-en-7-oic acid 19,10-lactone 7-methyl ester 18

An aqueous solution of potassium carbonate (1 mol L^{-1}, 12.5 mL) was added to aldehyde **16** (0.714 g, 1.7 mmol, 1 equiv.) in methanol (50 mL) and stirred at room temp for 3 min. The reaction was then quenched with 1 mol L^{-1} HCl (10 mL) and poured into ethyl acetate and water. The aqueous phase was then extracted with ethyl acetate (×4). The combined organic phase was washed with water and brine and dried ($MgSO_4$), and the solvent was removed in vacuo. Purification by silica gel chromatography (2:1 hexane : ethyl acetate) furnished the deformylation product **18** (0.641 g) in 96% yield. IR (cm^{-1}): 2953, 2871, 1768, 1731, 1435, 1368, 1245, 1165, 1033, 960. ^{1}H NMR δ: 0.904 (d, J = 7.0 Hz, 3H, H-17), 1.20 (d, J = 7.4 Hz, 3H, H-18), 1.38 (dt, J = 13.1, 6.3 Hz 1H), 1.60–2.05 (m, 7H), 1.99 (s, 3H, OAc), 2.34 (dd, J = 8.2, 13.9 Hz, 1H), 2.45 (m, 2H), 2.67 (dd, J = 6.3, 14.0 Hz, 1H), 2.72 (d, J = 2.6 Hz, 1H, H-6), 2.91 (dq, J = 7.4, 10.9 Hz, 1H, H-4), 3.07 (dd, J = 2.6, 10.7 Hz, 1H, H-5), 3.69 (s, 3H, CO_2Me), 5.24 (m, 2H, H-3), 5.91 (m, J = 1H, H-2). ^{13}C NMR δ: 12.0, 18.3, 19.2, 22.0, 33.4, 35.2, 38.4, 42.0, 42.9, 43.1, 49.3, 49.9, 50.8, 51.0, 52.0, 87.0, 95.5,

© 2004 NRC Canada

120.6, 131.9, 170.6, 174.9, 179.6. LR-MS *m/z* (relative intensity): 390 ([M$^+$], 10), 349 (100), 330 (30), 305 (45), 289 (55), 275 (27), 261 (36), 233 (32), 201 (24), 173 (32). HR-MS calcd. for $C_{22}H_{30}O_6$ ([M$^+$]): 390.2042; found: 390.2044. Anal. calcd. for $C_{22}H_{30}O_6$ (%): C 67.67, H 7.74; found: C 67.52, H 7.82.

13-Acetoxy-3-hydroxy-3,4-seco-20-nor-16-*epi*-gibberellan-7-oic acid 19,10-lactone 7-methyl ester

2,3-Dimethyl-2-butene (0.36 mL, 3.0 mmol, 1.5 equiv.) was added to borane – dimethyl sulfide (2.0 mol L^{-1} solution in THF, 1.5 mL, 3.0 mmol, 1.5 equiv.) in THF (3 mL) at 0 °C. The reaction was stirred at 0 °C for 10 min and then at room temp for 1 h. The reaction was then cooled to 0 °C and alkene **18** (0.78 g, 2.0 mmol, 1 equiv.) was added in THF (10 mL). After stirring for 1.5 h, the reaction was quenched with ethanol (1 mL). Na_2HPO_4 (2 mol L^{-1} aqueous solution, 4 mL) and H_2O_2 (30%, 4 mL) were added simultaneously, and the reaction was stirred overnight at room temp. The reaction was poured into ethyl acetate and water. The aqueous phase was then extracted with ethyl acetate (×3). The combined organic phase was washed with water (×2) and brine and dried ($MgSO_4$), and the solvent was removed in vacuo. Purification by silica gel chromatography (2:1 hexane : ethyl acetate → ethyl acetate) furnished the primary alcohol (0.529 g) in 65% yield and the epimeric secondary alcohols (0.053 g) in 6% yield. IR (cm^{-1}): 3450, 2946, 2871, 1764, 1730, 1453, 1435, 1369, 1334, 1311, 1245, 1172, 1037, 960. ^{1}H NMR δ: 0.90 (d, *J* = 6.9 Hz, 3H, H-17), 1.22 (d, *J* = 7.0 Hz, 3H, H-18), 1.41 (m, 1H), 1.50–2.02 (m, 12H), 1.99 (s, 3H, OAc), 2.52 (m, 2H), 2.73 (d, *J* = 2.3 Hz, 1H, H-6), 3.01 (m, 2H, H-4), (dd, *J* = 2.3, 10.7 Hz, 1H, H-5), 3.67 (t, *J* = 6.0 Hz, 2H, H-3), 3.68 (s, 3H, CO_2Me). ^{13}C NMR δ: 12.1, 18.5, 19.2, 22.0, 27.3, 33.5, 34.2, 35.2, 38.4, 42.9, 43.2, 49.7, 49.9, 50.8, 51.1, 52.1, 62.8, 87.0, 96.0, 170.6, 174.9, 179.5. HR-MS calcd. for $C_{22}H_{32}O_7$: 408.2148; found: 408.2146.

13-Acetoxy-3-oxo-3,4-seco-20-nor-16-*epi*-gibberellan-7-oic acid 19,10-lactone 7-methyl ester 19

Dess–Martin periodinane (0.21 g, 0.55 mmol, 1.5 equiv.) was added to a solution of the alcohol prepared above (0.15 g, 0.37 mmol, 1 equiv.) in dichloromethane (15 mL). The reaction was stirred for 1 h; then 1 mol L^{-1} $Na_2S_2O_3$ (10 mL) and saturated $NaHCO_3$ (10 mL) solutions were added, and the mixture was stirred vigorously until both layers were clear. The aqueous phase was then extracted with dichloromethane (×3). The combined organic phases were washed with water and brine and dried ($MgSO_4$), and the solvent was removed in vacuo. Purification by silica gel chromatography (2:1 ethyl acetate : hexane) furnished the aldehyde **19** (0.124 g) in 83% yield. IR (cm^{-1}): 2945, 2870, 2728, 1766, 1727, 1453, 1436, 1368, 1245, 1191, 1174, 1036, 959. ^{1}H NMR δ: 0.91 (d, *J* = 6.9 Hz, 3H, H-17), 1.23 (d, *J* = 6.0 Hz, 3H, H-18), 1.43 (dd, *J* = 6.0, 13.1 Hz, 1H), 1.60–2.11 (m, 8H), 1.99 (s, 3H, OAc), 2.23 (m, 1H), 2.40–2.66 (m, 4H), 2.72 (d, *J* = 1.8 Hz, 1H, H-6), 2.98 (m, 2H, H-4, H-5), 3.69 (s, 3H, CO_2CH_3), 9.80 (t, *J* = 1.1 Hz, 1H, CHO). ^{13}C NMR δ: 12.0, 18.4, 19.2, 22.0, 29.6, 33.4, 35.1, 38.1, 38.9, 42.8, 43.1, 49.5, 49.6, 50.9, 51.0, 52.1, 86.8, 95.0, 170.5, 174.9, 179.0, 200.7. LR-MS *m/z* (relative intensity): 406 ([M$^+$], 27), 364 (81), 346 (65), 321 (100), 303 (35), 289 (89). HR-MS calcd. for $C_{22}H_{30}O_7$ ([M$^+$]): 406.1992; found: 406.1993.

13-Acetoxy-3α/3β-hydroxy-20-nor-16-*epi*-gibberellan-7-oic acid 19,10-lactone 7-methyl ester 20

Aqueous potassium carbonate (1 mol L^{-1}, 2.6 mL, 2.6 mmol, 5 equiv.) was added to aldehyde **18** (0.213 g, 0.52 mmol, 1 equiv.) in methanol (10.4 mL) and stirred at room temp for 3 h. The reaction was then quenched with excess 1 mol L^{-1} HCl (5 mL) and poured into ethyl acetate and water. The aqueous phase was then extracted with ethyl acetate (×4). The combined organic phase was washed with water and brine and dried ($MgSO_4$), and the solvent was removed in vacuo. Purification by silica gel chromatography (1:1 hexane : ethyl acetate → 2:1 ethyl acetate : hexane) furnished the epimeric alcohols **20** (0.195 g) in 92% yield. Data for the 3α-epimer have been provided above. 3α-OH epimer: mp 190 to 191 °C. IR (cm^{-1}): 3474, 2952, 2874, 1770, 1732, 1439, 1370, 1246, 1195, 1173, 1130, 1058, 1041, 1023, 950, 900, 735. ^{1}H NMR δ: 0.88 (d, *J* = 6.9 Hz, 3H, H 17), 1.16 (s, 3H, H-18), 1.40–2.36 (m, 14H), 2.01 (s, 3H, OAc), 2.54 (d, *J* = 10.3 Hz, 1H, H-6), 2.75 (d, *J* = 10.3 Hz, 1H, H-5), 3.68 (dd, 1H, *J* = 10.6, 5.9 Hz, 1H, H-3), 3.73 (s, 3H, CO_2CH_3). ^{13}C NMR δ: 13.1, 17.6, 19.1, 21.8, 29.7, 30.3, 37.6, 39.4, 41.1, 45.5, 50.3, 52.0, 52.3, 54.3, 54.7, 56.9, 73.0, 85.4, 92.6, 170.6, 173.0, 177.5. LR-MS *m/z* (relative intensity): 406 ([M$^+$], 7), 388 (16), 364 (100), 346 (65), 321 (85), 289 (47), 243 (26) 225 (20). HR-MS calcd. for $C_{22}H_{30}O_7$ ([M$^+$]): 406.1992; found: 406.1988. Anal. calcd. for $C_{22}H_{30}O_7$ (%): C 65.01, H 7.44; found: C 64.95, H 7.41.

Acknowledgement

We are grateful to Dr Wilhelm Rademacher for his support and encouragement with this project.

References

1. (*a*) L.T. Evans, R.W. King, L.N. Mander, R.P. Pharis, and K.A. Duncan. Planta, **193**, 107 (1994); (*b*) M. Takagi, D.W. Pearce, L.M. Janzen, and R.P. Pharis. Plant Growth Regul. **15**, 207 (1994); (*c*) L.N. Mander, D. Camp, L.T. Evans, R.W. King, R.P. Pharis, M. Sherburn, and B. Twitchin. Acta Hort. **394**, 45 (1995); (*d*) O. Junttila, R.W. King, A. Poole, G. Kretschmer, R.P. Pharis, and L.T. Evans. Aust. J. Plant Physiol. **24**, 359 (1997); (*e*) R.W. King, C. Blundell, L.T. Evans, L.N. Mander, and J.T. Wood. Crop Sci. **37**, 1878 (1997); (*f*) I.J. Lee, K.R. Foster, and P.W. Morgan. J. Plant Growth Regul. **17**, 185 (1998); (*g*) L.N. Mander, M. Sherburn, D. Camp, R.W. King, L.T. Evans, and R.P. Pharis. Phytochemistry, **49**, 2195 (1998).
2. (*a*) W. Rademacher, R.P. Pharis, and L.N. Mander. Jpn. J. Crop Sci. **68**, 362 (1999); (*b*) W. Rademacher. Ann. Rev. Plant Physiol. Plant Mol. Biol. **51**, 501 (2000).
3. (*a*) N. Takahashi and I Yamaguchi. *In* The biochemistry and physiology of gibberellins. Vol. 1. *Edited by* A. Crozier. Praeger, New York. 1983. pp. 457–484; (*b*) J.R. Hanson. Nat Prod. Rev. **7**, 41 (1990).
4. B.E. Cross. J. Chem. Soc. 3022 (1960).
5. K. Mori. Agr. Biol. Chem. **36**, 2519 (1972).

© 2004 NRC Canada

6. L.N. Mander, G. Adamson, V.K. Bhaskar, B. Twitchin, D. Camp, L.T. Evans, R.W. King, and R. P. Pharis. Phytochemistry, **49**, 1509 (1998).
7. D.K. Dalling and D.M. Grant. J. Am. Chem. Soc. **89**, 6122 (1967).
8. M.H. Beale, P. Gaskin, P.S. Kirkwood, and J. MacMillan. J. Chem. Soc. Perkin Trans. 1, 885 (1980).
9. (*a*) G. Adam and T.V. Sung. Tetrahedron Lett. 247 (1976); (*b*) L.J. Dolby and R.J. Milligan. J. Am. Chem. Soc. **88**, 4536 (1966); (*c*) G. Stork and J. Singh. J. Am. Chem. Soc. **101**, 7109 (1979); (*d*) L. Lombardo, L.N. Mander, and J.V. Turner. J. Am. Chem. Soc. **102**, 6626 (1980).
10. J. MacMillan and R.J. Pryce. J. Chem. Soc. 740 (1967).
11. D.B. Dess and J.C. Martin. J. Org. Chem. **48**, 4155 (1983).

© 2004 NRC Canada

The crystal structure of a simple enol formed in a single-crystal-to-single-crystal enolene rearrangement[1]

Kenneth C.W. Chong, Brian O. Patrick, and John R. Scheffer

Abstract: When crystals of 9-tricyclo[4.4.1.0]undecalyl-4-(carbomethoxy)phenyl ketone (**1**) were allowed to stand in the dark for extended periods of time at room temperature, the compound underwent a thermal reaction — the enolene rearrangement — to afford enol **2**. The crystals remained transparent and appeared unchanged in shape as the reaction proceeded. X-ray diffraction data were collected on single crystals containing 17%, 25%, 66%, and 100% of the enol. The crystal structure of a simple enol was obtained via this novel single-crystal-to-single-crystal enolene rearrangement.

Key words: single crystal, thermal, rearrangement, enol, enolene.

Résumé : Laissés à la température ambiante et à l'abri de la lumière pour des périodes prolongées, la 9-tricyclo-[4.4.1.0]undécalyl-4-(carbométhoxy)phényl cétone (**1**) subit une réaction thermique, le réarrangement énolène, qui conduit à la formation de l'énol **2**. Alors que la réaction se produit, les cristaux demeurent transparents et leur forme ne semble pas avoir changé. On a obtenu des données de diffraction des rayons X sur des échantillons contenant 17 %, 25 %, 66 % et 100 % d'énol. On a déterminé la structure cristalline d'un énol simple par le biais de ce nouveau réarrangement énolène d'un cristal unique à un cristal unique.

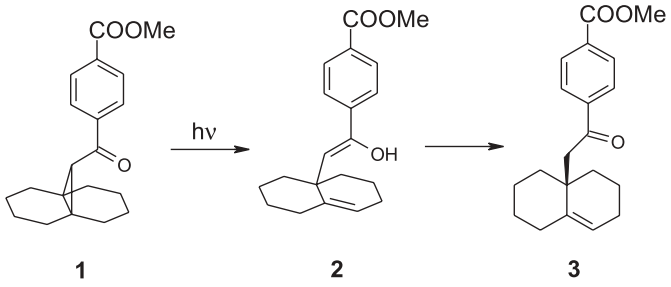
Mots clés : cristal unique, thermique, réarrangement, énol, énolène.

[Traduit par la Rédaction]

Introduction

The work reported in this paper is an outgrowth of our investigation into the photochemistry of ketones possessing the tricyclo[4.4.1.0]undecane ring system, e.g., **1** (Scheme 1) (1). Compounds of this type undergo photochemical Norrish type II cleavage in solution to afford chiral products (e.g., **3**), and the purpose of our original study was to explore methods of carrying out such transformations enantioselectively (2). During the course of this work, we had occasion to determine the X-ray crystal structure of ketone **1**, and the present paper reports the interesting results that were obtained in the process.

Scheme 1.



Results and discussion

The electron density maps obtained from single crystals of ketone **1** invariably contained residual peaks from a second component, and try as we might, we were never able to prepare a sample of ketone **1** completely free of this substance. The highest purity we were able to achieve was approximately 83%. After a series of control experiments ruled out the possibility that the impurity was ketone **3** formed by ambient light irradiation of ketone **1** during its preparation and storage, it became apparent that the unknown was being produced *thermally*. Thus, by simply allowing crystals of ketone **1** to stand in the dark for extended periods of time at room temperature, it was possible to prepare samples in which the unknown "impurity" was actually the major component. For example, after 5 days at room temperature, the extent of conversion to the unknown was 68%; after 12 days the conversion was 100%. Crystals that had been treated in this manner retained their integrity; that is, they remained transparent and appeared unchanged to the naked eye, suggesting the occurrence of a single-crystal-to-single-crystal reaction (3). Accordingly, X-ray diffraction data were col-

Received 9 July 2003. Published on the NRC Research Press Web site at http://canjchem.nrc.ca on 6 February 2004.

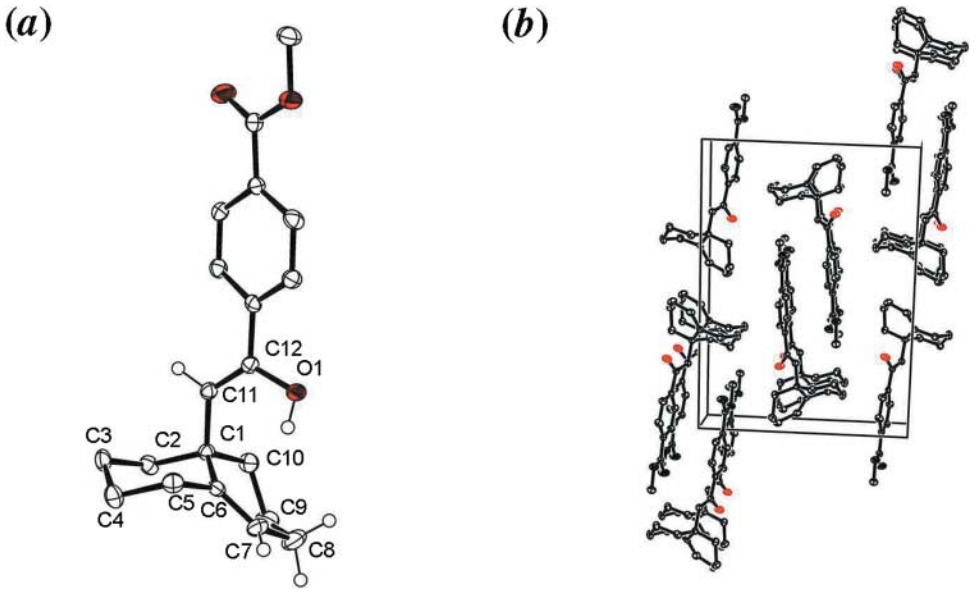
K.C.W. Chong, B.O. Patrick, and J.R. Scheffer.[2] Department of Chemistry, University of British Columbia, 2036 Main Mall, Vancouver, BC V6T 1Z1, Canada.

[1]This article is part of a Special Issue dedicated to Professor Ed Piers.

[2]Corresponding author (e-mail: scheffer@chem.ubc.ca).

 doi: 10.1139/V03-207 © 2004 NRC Canada

Fig. 1. (*a*) ORTEP drawing and (*b*) crystal packing diagram of enol **2**. The oxygen atoms of the enol groups are in red.



lected on single crystals containing 17%, 25%, 68%, and 100% of the unknown substance.

Solving the structure of these mixed crystals revealed that the unknown component was enol **2**, the tautomer of ketone **3** (Scheme 1). In agreement with this, conventional solution-phase workup of the mixed crystals gave mixtures of ketone **3** and unreacted **1**. By working quickly in anhydrous benzene-d_6, it was possible to measure the ^{1}H NMR spectrum of enol **2**, which showed three distinct signals at 4.81, 5.44, and 7.05 parts per million (ppm), corresponding to H11, H7, and the enolic hydrogen of enol **2**, respectively (Fig. 1*a*).

The thermal rearrangement of cyclopropyl ketone **1** to enol **2** is an example of the so-called enolene rearrangement, which interconverts γ-hydrogen-containing cyclopropyl ketones and enolizable γ,δ-unsaturated ketones (4). In the present instance the enol intermediate is isolable, since it is generated in the crystalline state, where the acid or base required for conversion to the keto form is lacking. Crystalline samples of enol **2** were stable for weeks at ambient temperatures under anhydrous conditions. As outlined in our original communication, enol **2** is also generated by irradiation of cyclopropyl ketone **1** in the crystalline state, a process that could be followed by solid-state infrared spectroscopy (1). In this case the reaction is not a single-crystal-to-single-crystal transformation. Photolysis of single crystals of ketone **1** caused them to become brittle and opaque, perhaps as a result of the reaction being less homogeneously distributed throughout the bulk of the crystal.

Table 1 shows the change in unit cell dimensions as a function of conversion for the thermal reaction. The data indicate a smooth transformation of ketone **1** into enol **2**. The space group remains $P2_1/n$, and the number of molecules in the unit cell is constant at $Z = 4$. There is a gradual increase in the length of the *a* and *c* axes, while there is a decrease in *b* in going from reactant to product. Overall, the unit cell volume increased by approximately 1.5%. Even though the increase in *c* (5.3%) seems rather large for a single-crystal-to-single-crystal reaction, other single-crystal-to-single-crystal reactions involving cell dimension changes of up to 5% have been reported (5).

Figure 2 provides ORTEP drawings of the molecular and crystal structures of cyclopropyl ketone **1**, and Fig. 1 does the same for enol **2**. Figure 3 depicts the superposition of these two structures in the mixed crystal containing 68% of enol **2** and 32% of ketone **1**. It is apparent from Fig. 3 that the correspondence between reactant **1** and product **2** is rather poor, indicating that significant motions take place during the rearrangement. This is not surprising when one considers the large relief of strain accompanying opening of the 3-membered ring. Based on the structure of the enol, the mechanism of the reaction is seen to involve transfer of hydrogen atom H_a to O1, accompanied by cleavage of the C6—C11 bond of the cyclopropane ring. The O1 to H_a distance is 2.23 Å, much shorter than the sum of the van der Waals radii for oxygen and hydrogen (2.72 Å) (6).[3] Interestingly, the distance between O1 and the other γ-hydrogen atom (H_b) is 2.37 Å, only 0.15 Å greater than the distance to H_a; yet, no H_b transfer occurs. A similar situation was encountered recently in a photochemical hydrogen atom abstraction reaction, where a difference in C=O···H distance of 0.27 Å (2.72 Å vs. 2.99 Å) led to exclusive abstraction of the nearer hydrogen (7).

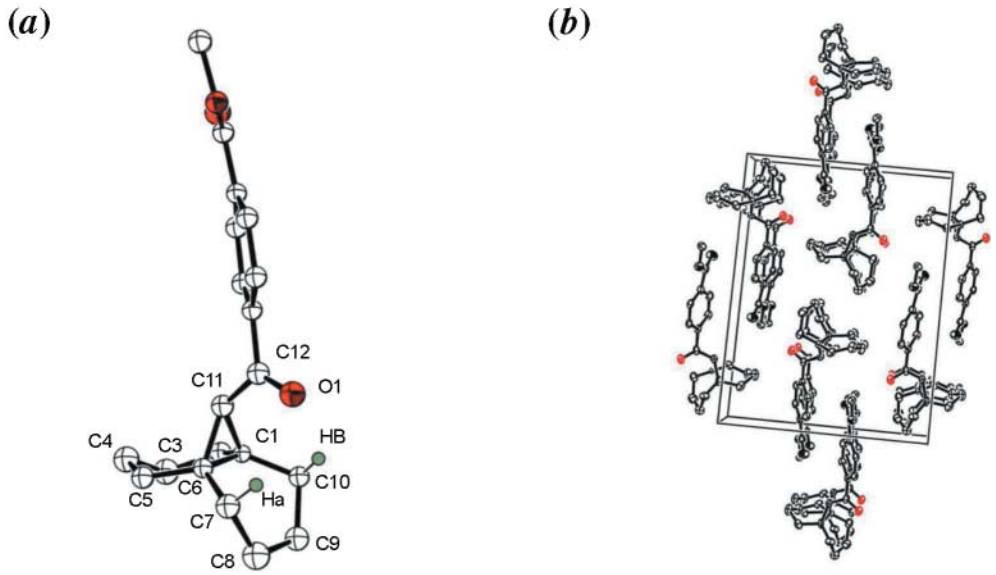
[3] Angular relationships are also important in γ-hydrogen transfer reactions. The value of the angle ω, defined as the degree to which the γ-hydrogen lies outside the mean plane of the carbonyl group, is 20° for H_a and 43° for H_b. The value of the angle Δ (the C=O···H angle) is 99° for H_a and 89° for H_b. The value of the angle θ (the C-H···O angle) is 136° for both H_a and H_b. Values of these parameters for a large number of photochemical hydrogen atom abstraction reactions have been reported and discussed. The present paper is the first instance in which such parameters have been determined for a thermal reaction involving γ-hydrogen transfer.

© 2004 NRC Canada

Table 1. Crystal data and structure refinement for crystals containing 17%, 25%, 68%, and 100% of enol **2**.

	17%	25%	68%	100%
Empirical formula	$C_{20}H_{24}O_3$			
M.W.	312.41			
Crystal system	Monoclinic			
Space group	$P2_1/n$			
β (°)	97.478 (5)	98.126(4)	101.976(6)	102.924(5)
a (Å)	6.2110(5)	6.2079(5)	6.2664(7)	6.2762(7)
b (Å)	14.239 (1)	14.227(1)	14.040(1)	13.811(2)
c (Å)	18.531(2)	18.651(2)	19.227(2)	19.528(3)
V (Å^3)	1625.0 (9)	1630.8(2)	1654.7(3)	1649.8(3)
Z	4	4	4	4
D_{calcd} (g cm^{-3})	1.277	1.272	1.254	1.258
Temperature (K)	173(2)			
μ (Mo Kα) (cm^{-1})	0.84	0.84	0.83	0.83
λ (Å)	0.71069			
$2\theta_{max}$	55.8	55.8	55.7	55.7
Residuals (F^2, all data): R; R_w	0.075; 0.118	0.077; 0.143	0.087; 1.76	0.067; 0.114
Residuals (F, $I > 2\sigma I$): R; R_w	0.046; 0.108	0.051; 0.131	0.060; 0.164	0.038; 0.052
GoF	0.991	1.01	1.11	1.05

Fig. 2. (*a*) ORTEP drawing and (*b*) crystal packing diagram of ketone **1**. The oxygen atoms of the keto groups are in red.



The structural changes involved in the transformation of ketone **1** to enol **2** are evidenced by the changes in bond angles and bond lengths given in Table 2. As the reaction proceeds, cleavage of the C6—C11 bond occurs, leading to an increase of the C6-C1-C11 bond angle from 60.1° in **1** to 110.7° in **2**. This causes a significant shift in the position of C11, C12, O1, and the aryl group. At the same time, the C11—C12 bond length decreases as it is transformed from a single to a double bond, and the C12—O1 bond length increases as it changes from a double to a single bond. While these motions are significantly greater than those accompanying other unimolecular single-crystal-to-single-crystal reactions (8), the overall packing arrangement remains constant, and as a result, the process can still occur in a topochemical fashion.

Attempts to recrystallize enol **2** to obtain a thermodynamically more stable crystal modification were unsuccessful, as tautomerization led exclusively to ketone **3**. However, molecular mechanics calculations showed that the minimum energy conformation of enol **2** is very similar to that determined by X-ray crystallography, a factor that might have facilitated the single-crystal-to-single-crystal transformation. Attempts were made to determine if the enol would undergo topochemical ketonization. However, tautomerization occurred only when crystals of enol **2** were heated above their melting point (82–84 °C).

© 2004 NRC Canada

Fig. 3. (*a*) ORTEP drawing of the 68% mixed crystal: blue = enol **2**; red = ketone **1**; (*b*) crystal packing diagram of the crystal. The oxygen atoms of the keto and enol groups are in red.

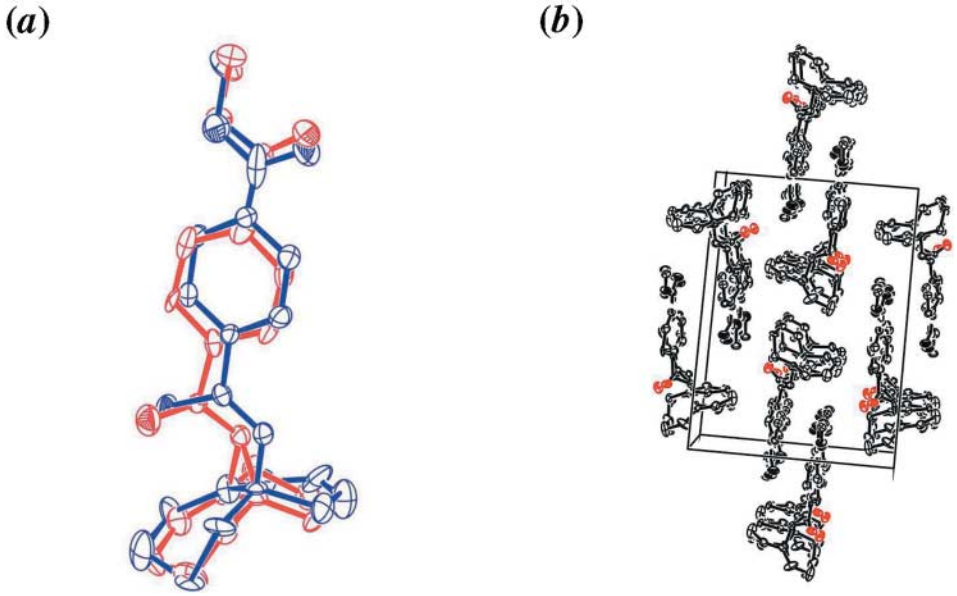


Table 2. Bond angles and lengths of selected atoms in ketone **1** and enol **2**.

Bond angles (°)	**1**	**2**	Bond lengths (Å)	**1**	**2**
C12-C11-H11	113.4	117.2	C12—O1	1.217(4)	1.376(1)
C6-C1-C11	61.4(3)	110.7(1)	C11—C12	1.487(4)	1.337(2)
C6-C7-H7[a]	110.0	117.6	C6—C7	1.475(1)	1.336(2)
			O1—H1	N/A	0.85(2)

[a]H7 is the "equatorial" hydrogen on C7. The axial hydrogen on this carbon is H_a, which is transferred in the reaction.

In summary, we have successfully obtained the crystal structure of a simple enol formed via a novel single-crystal-to-single-crystal enolene rearrangement. Simple enols are defined as species derived from the tautomerization of monofunctional aldehydes and ketones in which the enol is the only functional group present (9). In solution, simple enols ketonize rapidly unless kinetically stabilized by the presence of nearby bulky substituents. As a result, very few simple enols have been characterized crystallographically, since they tend to ketonize before they crystallize out (10). In the present instance, the enol is generated *in the crystalline state*, where it is protected from reagents that catalyze its ketonization. Under these conditions, the enol is stable over a period of weeks and can be fully characterized by a variety of techniques, including X-ray crystallography.

Experimental

General procedures

General procedures have been described in detail elsewhere (1).

Synthesis of ketone 1

The procedure for the preparation of this compound has been discussed in detail in the supporting information of ref. 1. X-ray quality crystals were grown by cooling a saturated hexanes solution at 4 °C; mp 68 to 69 °C. IR (KBr pellet) (cm^{-1}): 2927, 1720, 1666, 1445, 1278, 1224, 1109, 742. ^{1}H (400 MHz, $CDCl_3$) δ: 1.28–1.49 (10H, m), 1.97 (4H, m), 2.11 (1H, s), 3.93 (3H, s), 7.92 (2H, d, J = 8.9 Hz), 8.10 (2H, d, J = 8.9 Hz). ^{13}C (75 MHz, $CDCl_3$) δ: 199.95, 166.41, 143.00, 133.08, 129.73, 127.68, 52.36, 37.22, 33.60, 31.60, 28.16, 21.53, 20.82. HR-MS (ESI) calcd. mass for $C_{20}H_{25}O_3$: 313.25085; found: 313.25115. Anal calcd.: C 76.89, H 7.74; found: C 76.97, H 7.60.

Enol 2

mp 82–84 °C. ^{1}H (400 MHz, C_6D_6) δ: 1.12–2.22 (14H, m), 3.49 (3H, s), 4.81 (1H, s), 5.44 (1H, m), 7.05 (1H, s), 7.74 (2H, d, J = 8.2 Hz), 8.20 (2H, d, J = 8.2 Hz).

Ketone 3

mp 79 to 80 °C (ether – petroleum ether). IR (KBr pellet) (cm^{-1}): 2925, 1718, 1685, 1438, 1281, 1109, 957, 761, 666. ^{1}H (400 MHz, $CDCl_3$) δ: 8.08 (2H, d, J = 7.0 Hz), 7.95 (2H, d, J = 7.0 Hz), 5.40 (1H, m), 3.90 (3H, s), 3.23 (1H, d, J = 15.0 Hz), 3.13 (1H, d, J = 15.0 Hz), 2.23 (1H, m), 1.98–2.05 (1H, m), 1.87–1.92 (3 H, m), 1.76 (1H, m) 1.43–1.65 (4H, m), 1.14–1.31 (3H, m). ^{13}C (APT, 75 MHz, $CDCl_3$) δ: 200.50 (+), 166.28 (+), 142.39 (+), 142.26 (+), 133.43 (+),

© 2004 NRC Canada

129.76 (–), 127.81 (–), 121.40 (–), 52.40 (–), 41.67 (+), 39.07 (+), 38.23 (+), 35.71 (+), 32.67 (+), 28.24 (+), 25.55 (+), 22.34 (+), 18.92 (+). HR-MS (CI, NH_3) calcd. mass for $C_{20}H_{25}O_3$: 313.25085; found: 313.25115. Anal. calcd.: C 76.89, H 7.74; found: C 76.75, H 7.68.

Single-crystal-to-single-crystal reaction

X-ray diffraction data were collected for three different single crystals of ketone **1**. The first one showed the presence of 25% of enol **2**. The second showed a similar composition of the enol to the first, and the structure was not refined. This sample was allowed to stand at room temperature, and X-ray diffraction data were collected after 5 and 12 days, leading to the crystal structures containing 68% and 100% of enol **2**, respectively. The X-ray data of the third sample showed the presence of about 17% of the rearranged product.

X-ray crystallography

X-ray analyses were performed on a Rigaku/ADSC CCD diffractomer using Mo Kα irradiation at –100 °C. The structures were solved using the direct methods program SIR-97 (11), and full-matrix least-square refinement on F^2 were completed using the program SHELXL-97 (12).[4]

Acknowledgements

We thank the Natural Sciences and Engineering Research Council of Canada for financial support. KCWC would like to thank Mr. Carl Scott for his help in the X-ray crystal structure determination of the 83% pure sample.

References

1. K.C.W. Chong and J.R. Scheffer J. Am. Chem. Soc. **125**, 4040 (2003).
2. For a recent review outlining our general approach to asymmetric induction in organic photochemistry, see: J.R. Scheffer. Can. J. Chem. **79**, 349 (2001).
3. (*a*) S. Ohba and Y. Ito. Acta. Cryst. **B59**, 149 (2003); (*b*) T. Ohhara, S. Ikeda, H. Imura, H. Uekusa, Y. Ohashi, I. Tanaka, and N. Niimura. J. Am. Chem. Soc. **124**, 14 736 (2002); (*c*) V. Enkelmann, G. Wegner, K. Novak, and K.B. Wagner. J. Am. Chem. Soc. **115**, 10 390 (1993).
4. J.M. Watson, J.L. Irvine, and R.M. Roberts. J. Am. Chem. Soc. **95**, 3348 (1973).
5. W. Jones, H. Nakanishi, C.R. Theocharis, and J.M. Thomas. J. Chem. Soc. Chem. Commun. 610 (1980).
6. See H. Ihmels and J.R. Scheffer. Tetrahedron, **55**, 885 (1999).
7. T.J. Lewis, S.J. Rettig, J.R. Scheffer, and J. Trotter. Mol. Cryst. Liq. Cryst. Incorporating Nonlinear Opt. **219**, 17 (1992).
8. For an example of a unimolecular single-crystal-to-single-crystal photochemical reaction, see M. Leibovitch, G. Olovsson, J.R. Scheffer, and J. Trotter J. Am. Chem. Soc. **119**, 1462 (1997).
9. (*a*) A.J. Kresge. CHEMTECH, 250 (1986); (*b*) H. Hart. Chem. Rev. **79**, 515 (1979).
10. For an example of the crystal structure of a simple tetrasubstituted enol, see D.V. Pratt and P.B. Hopkins. J. Am. Chem. Soc. **109**, 5553 (1987).
11. A. Altomare, M.C. Buria, G. Cammalli, M. Cascarano, C. Giacovazzo, A. Guagliardi, A.G.G. Moliterni, G. Polidori, and A. Spagna. SIR-97 [computer program]. J. Appl. Cryst. **32**, 115 (1999).
12. G.M. Sheldrick. SHELXL-97 [computer program]. University of Goettingen, Germany. 1997.

[4] Crystallographic data (excluding structure factors) for the structures reported in this paper have been deposited as supplementary material. Supplementary data may be purchased from the Depository of Unpublished Data, Document Delivery, CISTI, National Research Council Canada, Ottawa, ON K1A 0S2, Canada (http://www.nrc.ca/cisti/irm/unpub_e.shtml for information on ordering electronically). CCDC 213933–213936 contain the supplementary data for this paper. These data can be obtained, free of charge, via www.ccdc.cam.ac.uk/conts/retrieving.html (or from the Cambridge Crystallographic Data Centre, 12 Union Road, Cambridge, U.K.; fax +44 1223 336033; or deposit@ccdc.cam.ac.uk).

© 2004 NRC Canada

Bifunctional bis(oxazolines) as potential ligands in catalytic asymmetric reactions[1]

Stephen Hanessian, Eric Jnoff, Noemy Bernstein, and Michel Simard

Abstract: C_2-symmetrical bis(oxazoline) ligands bearing pendant alkylthio ether groups were synthesized, and the structures of Cu complexes were determined by single crystal X-ray diffraction. The potential utility in catalysis was shown in the asymmetric addition of methyllithium to an aromatic aldimine, which resulted in a mixture of products with an enantiomeric excess of 68%.

Key words: two-center catalysis, bis(oxazoline), aldimine, imine alkylation.

Résumé : On a effectué la synthèse de ligands bis(oxazoline) à symétrie C_2 portant des groupes alkylthioéthers pendants et on a déterminé les structures de complexes de cuivre par diffraction des rayons X de cristaux uniques. Leur utilité potentielle en catalyse a été mise en évidence par l'addition asymétrique du méthyllithium sur une aldimine aromatique qui a conduit à la formation d'un mélange de produits avec un excès énantiomérique de 68%.

Mots clés : catalyse à deux centres, bis(oxazoline), aldimine, alkylation d'imine.

[Traduit par la Rédaction]

Introduction

Catalytic asymmetric reactions have assumed great importance in the realm of organic synthesis (1). In practice, a ligand possessing one or more elements of chirality is used in sub-stoichiometric amounts, with or without the presence of a metal (2). Among the more popular and synthetically useful ligands are the so-called C_2-symmetric bis(oxazolines) (3), which are easily prepared from naturally available amino acids by well-precedented chemical transformations (4). Fig. 1 depicts the structure of a typical 2,2′-bis(oxazolino)methane with appropriate stereodifferentiating appendages (*t*-Bu Box, **1**) (4). This ligand has been extensively used in conjunction with divalent metals as chiral Lewis acids in a number of catalytic reactions (3).

The use of bis(oxazoline) ligands that possess additional coordination sites leading to bifunctional catalysis has been less studied (5). Aggarwal et al. (6) prepared C_2-symmetric bis(oxazoline) ligands from cysteine and methionine and studied a catalytic version of an asymmetric sulfur ylide epoxidation of aldehydes mediated by Cu(II).

Recently, we described the catalytic asymmetric reduction of ketones by borane in the presence of thiazolidines derived from penicillamine (7). We report herein the synthesis and X-ray crystal structures of several novel C_2-symmetrical bis(oxazolino)methanes **2**–**5** and related structures with pendant ether and thioether appendages (Fig. 1). These ligands could have potentially interesting applications in catalysis. In this regard, we show an example of a catalytic asymmetric addition of MeLi to an aromatic aldimine (8).

Received 19 September 2003. Published on the NRC Research Press Web site at http://canjchem.nrc.ca on 6 February 2004.

Dedicated to Professor Ed Piers, wishing him the best in chemistry and in life.

S. Hanessian,[2] E. Jnoff, N. Bernstein, and M. Simard. Department of Chemistry, Université de Montréal, Montréal, QC H3C 3J7, Canada.

[1]This article is part of a Special Issue dedicated to Professor Ed Piers.

[2]Corresponding author (e-mail: stephen.hanessian@umontreal.ca).

Synthesis

The synthesis of bis(oxazoline) ligands **2**–**5** is shown in Scheme 1 and follows an established protocol for other alkyl-substituted analogues (4). Thus, the amino acids L-cysteine, D-penicillamine, and D-methionine were individually reduced to the corresponding amino alcohols, *S*-methylated in the case of L-cysteine and D-penicillamine, and then reacted with 2,2-dimethylmalonyl dichloride to afford the corresponding bis-amides. Treatment with TsCl and Et_3N effected cyclization to the respective ligands **2**–**4**. The L-serine analogue **5** was similarly prepared from the O-TBDPS ether.

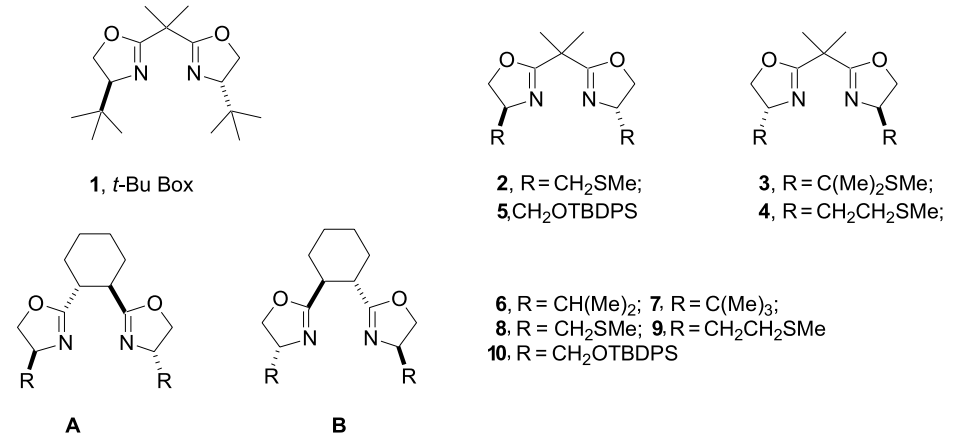
Another set of ligands representing a constrained scaffold (9) was prepared from 1,2-*trans*-cyclohexane dicarboxylic acid using the same protocol. Thus, treatment of the racemic diacid with *S*-methyl L-cysteine-ol, D-methionine-ol, L-valinol, O-TBDPS L-serinol, and L-*tert*-butylglycinol afforded mixtures of diastereomeric diamides that could be separated by chromatography. These were individually cyclized to the diastereomeric bis-(oxazoline) derivatives **6**–**10**. The identity of the major diastereomer was ascertained from the X-ray structure of the *tert*-butylglycinol product **7**, prepared from the resolved diacid as the quinine salt and inferred in the others.

X-ray structures of ligands and Cu(II) complexes

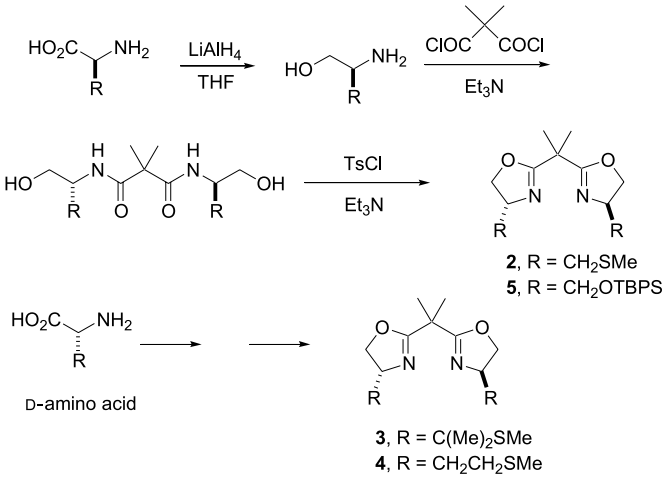
The ORTEP diagrams of selected ligands and their Cu(II) complexes are shown in Fig. 2, with corresponding bond

 doi: 10.1139/V03-198 © 2004 NRC Canada

Fig. 1. Structures of bis(oxazoline) ligands.



Scheme 1.



lengths and angles shown in Table 1.[3] Bis-(oxazoline)ditriflate **3a** formed monoclinic crystals in which Cu was pentacoordinated with the oxazoline nitrogens and the penicillamine methylthio groups, forming a trigonal bipyramid with N12 and S11 in the axial positions (164°–171°) (Fig. 2B). It is of interest that the two *S*-methyl groups occupy an *anti*-relationship in the complex. Only one triflate group was coordinated to copper.

Complex **4a** formed orthorhombic crystals with an unusual coordination around Cu (Fig. 3A, Table 2). The two oxazoline nitrogens and only one of the methionine sulfur atoms were coordinated to Cu in an axial orientation (N1-Cu-S2 angle = 172.3°), and two chlorines were in equatorial positions, forming a trigonal bipyramidal geometry. Curiously, the *S*-methyl group of the other methionine side-chain remained uncoordinated, thus adding an element of structural dissymmetry.

Ligand **4** also gave a crystalline complex **4b** with Cu(II)bis-triflate (Fig. 3B, Table 3). In this case an octahedral geometry was observed in which the two methionine sulfur atoms were engaged as equatorial coordination sites in two seven-membered rings. In contrast to complex **3a**, both axial sites were occupied by triflates. A strong Jahn–Teller effect was observed in this neutral complex, as evidenced by the shorter C4—N and Cu—S distances compared with Cu—OTf. The Cu atom was moved out of plane, by 0.2 Å, toward O31.

Table 1. Bond lengths and bond angles for ligand **3** and Cu(II) complex **3a**.

Bond lengths (Å)	
Cu(1)—N(11)	1.942(7)
Cu(1)—N(12)	1.934(6)
Cu(1)—O(13)	2.282(6)
Cu(1)—S(11)	2.337(2)
Cu(1)—S(12)	2.371(2)
Bond angles (°)	
N(11)-Cu(1)-N(12)	87.5
N(11)-Cu(1)-S(11)	85.21(19)
N(12)-Cu(1)-S(12)	85.3(2)
N(11)-Cu(1)-N(12)	143.2(2)
S(11)-Cu(1)-S(12)	104.66(8)
N(12)-Cu(1)-S(11)	170.0(2)

Ligand **7** crystallized with a molecule of water that was internally hydrogen-bonded in a bidentate fashion with the two oxazoline nitrogens (Fig. 4A, Table 4). The corresponding Cu(II) dichloride complex **7a** afforded monoclinic crystals with quasi-equidistant coordination sites, forming a distorted seven-membered ring (Fig. 4B).

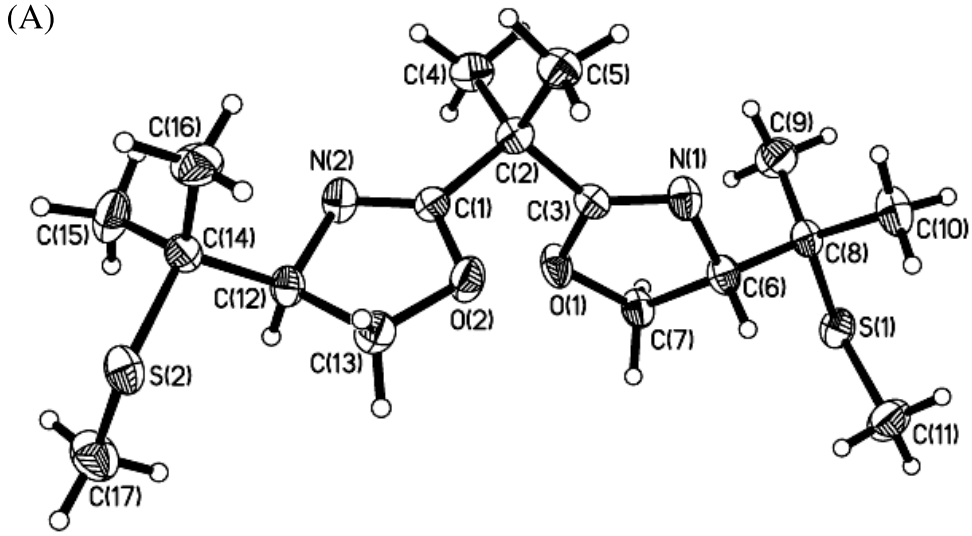
Catalytic asymmetric addition to an aldimine

The addition of organometallic reagents to aldimines is a method of synthesis of secondary amines (8). Although there are examples for the asymmetric synthesis of amines using stoichiometric amounts of external ligands (8, 10), by comparison there are fewer catalytic versions (11).

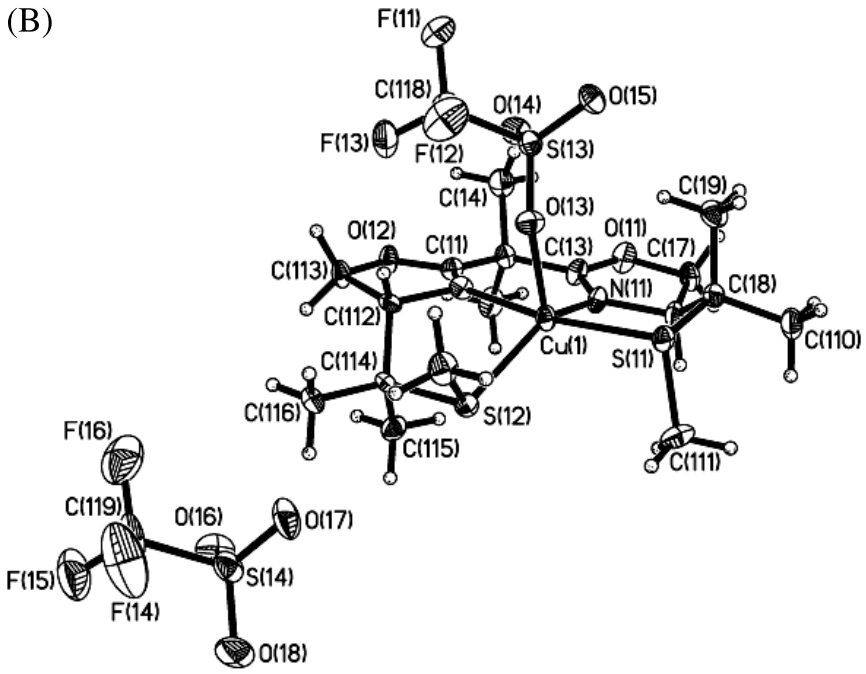
[3] Supplementary data may be purchased from the Depository of Unpublished Data, Document Delivery, CISTI, National Research Council Canada, Ottawa, ON K1A 0S2, Canada (http://www.nrc.ca/cisti/irm/unpub_e.shtml for information on ordering electronically). CCDC 229278–229283 contain the supplementary data for this paper. These data can be obtained, free of charge, via www.ccdc.cam.ac.uk/conts/retrieving.html (or from the Cambridge Crystallographic Data Centre, 12 Union Road, Cambridge, U.K.; fax +44 1223 336033; or deposit@ccdc.cam.ac.uk).

© 2004 NRC Canada

Fig. 2. ORTEP diagram for (A) ligand **3** and (B) Cu(II) complex **3a**.



3



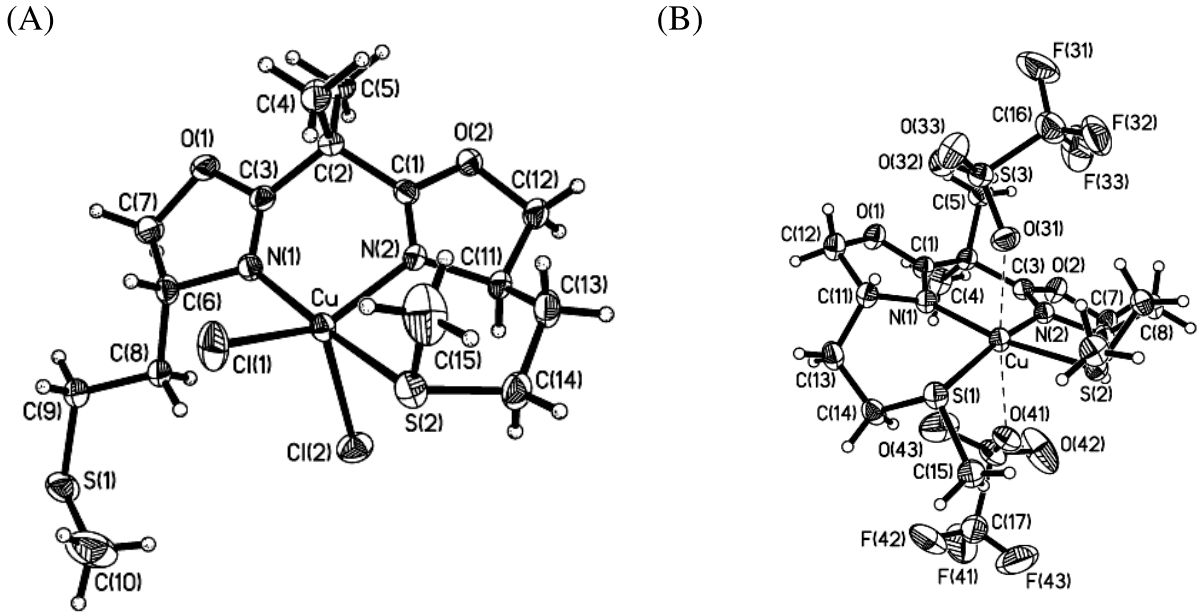
$Cu(OTf)_2$ complex **3a**

The groups of Tomioka and co-workers (12) and Denmark et al. (13) have reported on catalytic additions of alkyllithium reagents to *N*-arylaldimines in the presence of external ligands such as β-amino ethers, chiral amino alcohols, (–)-sparteine, and bis(oxazolines). The most promising ligands were (–)-sparteine and bis(oxazolines), giving ee values as high as 80% in some instances (13).

Initially, Denmark et al. (13) reported that *N*-arylaldimines were practically unreactive to MeLi at low temperature, unless ligands such as (–)-sparteine or *t*-Bu Box (**1**) were present in stoichiometric amounts. Catalytic versions with aryl *N*-*p*-methoxyphenylaldimines and arylalkyl analogues (possessing an enolizable α-hydrogen) with MeLi were reported with 0.1–0.2 equiv. of (–)-sparteine or *t*-Bu

© 2004 NRC Canada

Fig. 3. ORTEP diagram for Cu(II) complexes (A) **4a** and (B) **4b**.



$CuCl_2$ complex **4a**

$Cu(OTf_2)$ complex **4b**

Table 2. Bond lengths and bond angles for Cu(II) complex **4a**.

Bond lengths (Å)	
Cu—N(1)	2.016(2)
Cu—N(2)	2.023(3)
Cu—S(2)	2.354(9)
Cu—Cl(1)	2.278(8)
Cu—Cl(2)	2.450(9)
Bond angles (°)	
Ni(1)-Cu-N(2)	87.66(8)
N(1)-Cu-S(2)	172.32(6)
N(2)-Cu-S(2)	92.40(6)
N(2)-Cu-Cl(1)	90.97(6)
N(2)-Cu-Cl(2)	148.37(7)
N(1)-Cu-Cl(2)	102.96(6)
N(2)-Cu-Cl(2)	97.62(6)
C1(1)-CuCl(2)	113.43(4)
S(2)-Cu-Cl(2)	84.65(3)

Table 3. Bond lengths and bond angles for Cu(II) complex **4b**.

Bond lengths (Å)	
Cu—N(1)	1.961(3)
Cu—N(2)	1.965(3)
CU—S(1)	2.363(13)
Cu—S(2)	2.363(13)
Cu—O(41)	2.564(4)
Cu—O(31)	2.578(4)
Bond angles (°)	
N(1)-Cu-N(2)	89.80(13)
N(1)-Cu-S(2)	169.08(11)
N(2)-Cu-S(2)	89.41(10)
N(1)-Cu-S(1)	89.46(9)
N(2)-Cu-S(1)	166.43(10)
S(2)-Cu-S(1)	93.84(5)
N(1)-Cu-O(41)	104.28(14)
N(2)-Cu-O(41)	80.88(13)
S(1)-Cu-O(41)	86.18(9)
S(2)-Cu-O(41)	86.34(9)
N(1)-Cu-O(31)	83.89(13)
N(2)-Cu-O(31)	100.71(14)
S(1)-Cu-O(31)	92.69(10)
S(2)-Cu-O(31)	85.56(8)
O(31)-Cu-O(41)	171.73(1)

Box **1**, affording the corresponding secondary amines (Scheme 2) in excellent yields and enantiomeric excesses of 82% (for BuLi) and 68% (for MeLi), respectively. Denmark and Stiff (14) also studied the effect of ligand structure of the bis-(oxazoline) in the reaction of aryl *N*-*p*-methoxyphenyl aldimines with MeLi. They concluded that the ligand bite angle ϕ played a minor role and that the nature of the stereodifferentiating oxazoline substituents (e.g. *t*-Bu) had a dramatic effect on selectivity.

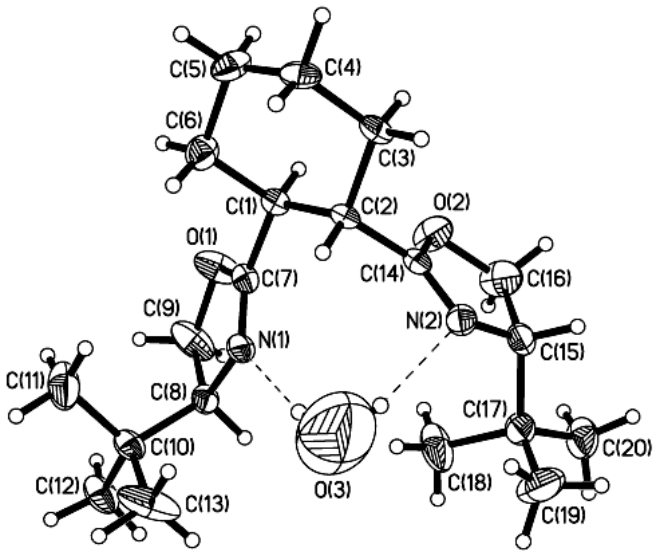
The catalytic asymmetric alkylation of *N*-*p*-methoxyphenyl benzaldehyde imine with MeLi was tried with ligands **2**–**4**, using the *t*-Bu Box catalyst **1** as a control (Scheme 2). The best ligand proved to be the one derived from D-penicillamine **3**, which gave an ee equal to **1**. In the presence of $Cu(OTf)_2$ or $Yb(OTf)_3$ in toluene, the ees for **1** and **4** were 48% and 33%, respectively, with either additive.

Structurally, the thioether appendage in ligand **3** is very similar to a *tert*-butyl group, except for the replacement of a *C*-methyl by an *S*-methyl group. While it can be assumed that the Li cation may be coordinated by the oxazoline nitrogens, there is no direct evidence that the thioether groups are

© 2004 NRC Canada

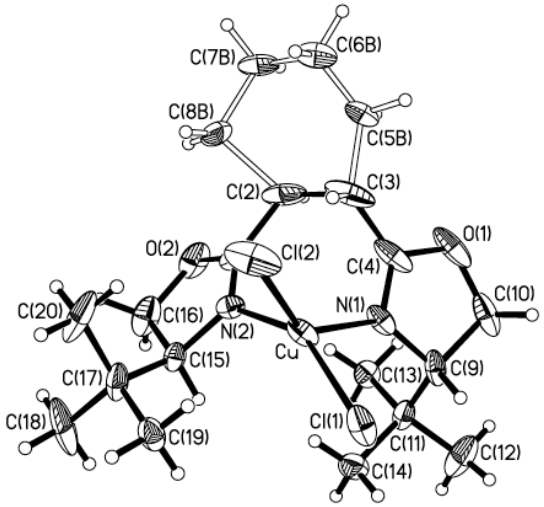
Fig. 4. ORTEP diagram for (A) ligand **7** monohydrate and (B) Cu(II) complex **7a**.

(A)



7 (hydrate)

(B)



$CuCl_2$ complex **7a**

also involved in a bidentate manner. Thus, it is not surprising that in the absence of such a tetracoordination (as observed for the Cu complexes), the extent of asymmetric induction was equal to the *t*-Bu Box ligand **1** (13).

The lower enantioselectivities shown in the case of **2** and **4** may be because of the smaller size of the thioether appendage compared with **3** and **1**, as observed by Denmark and Stiff for bis-(oxazolines) with different side-chains (14).

In spite of the interesting structural data available from the X-ray structures of the Cu complexes, especially **4a** with a tricoordinated geometry, we were not able to effectively utilize them as catalysts in a variety of representative model reactions.

Table 4. Bond lengths and bond angles for ligand **7** monohydrate and Cu(II) complex **7a**.

Bond lengths (Å)	
Cu—N(1)	1.993(3)
Cu—N(2)	2.003(3)
Cu—Cl(1)	2.221(13)
Cu—Cl(2)	2.240(14)
Bond angles (°)	
N(1)-Cu-N(2)	90.24(13)
N(1)-Cu-Cl(1)	95.48(11)
N(2)-Cu-Cl(1)	147.86(10)
N(1)-Cu-Cl(2)	134.88(11)
N(2)-Cu-Cl(2)	97.27(10)
Cl(1)-Cu-Cl(2)	100.78(6)

Thus, treatment of styrene with ethyl diazoacetate in the presence of **4** and CuOTf gave the corresponding cyclopropane in 40% ee for the *trans*-isomer (*cis*:*trans*, 1:2 by NMR) (15). Addition of methylmagnesium bromide to *p*-methoxybenzaldehyde in the presence of ligand **3** (10 mol%) gave the secondary alcohol in 10% ee. Using stoichiometric ligand raised the ee to 55% (HPLC). Applications to asymmetric reduction with BH_3·THF of acetophenone, allylation of benzaldehyde with allyltributylstannane, Michael addition to cyclohexenone, and Diels–Alder reaction with cyclopentadiene and *N*-acryloyloxazolidinone gave racemic products.

Future work will focus on exploiting other ligands with bidentate character in catalytic asymmetric reactions.

Experimental

General procedure

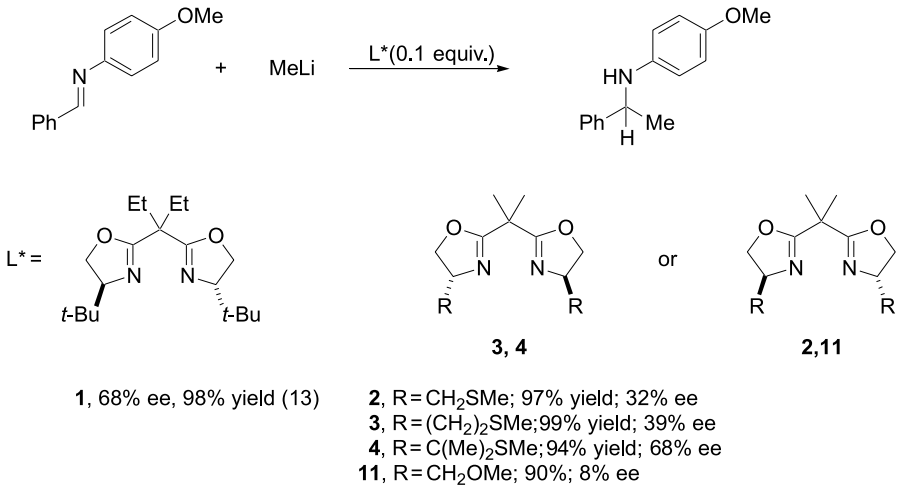
Flash chromatography was carried out using 230–400 mesh silica gel. Mixtures of ethyl acetate – hexanes were used as the eluents, unless otherwise specified. Analytical thin layer chromatography (TLC) was performed on glass plates coated with a 0.02 mm layer of silica gel 60 F-254. Melting points were uncorrected. IR spectra were recorded as films. ^{1}H and ^{13}C NMR spectra were recorded at 300 and 75 MHz, respectively, and the chemical shifts are reported in parts per million on the δ scale, with $CDCl_3$ as reference, unless otherwise specified. MS and HR-MS spectra were recorded using electron ionization or by the FAB technique. Optical rotations were measured in $CHCl_3$ at 23 °C. All reactions were carried out under nitrogen or argon unless otherwise specified. The –78 °C temperature is approximate, as achieved by a dry ice – acetone bath. The term "normal workup" means the addition of saturated aqueous NH_4Cl solution to the reaction mixture, followed by extraction with ethyl acetate, drying over Na_2SO_4, filtration, and evaporation of the filtrate in vacuo to afford the crude product.

Representative procedure for the bis-amide formation

To a solution of D-penicillaminol (0.20 g, 1.40 mmol) in dry CH_2Cl_2 (3 mL) was added Et_3N (0.5 mL, 3.6 mmol) at room temperature (r.t.), followed by dropwise addition of dimethylmalonyl chloride (0.10 g, 0.59 mmol) in dry CH_2Cl_2 (0.5 mL). A white precipitate began to form, and the mixture was stirred overnight, then concentrated in vacuo al-

© 2004 NRC Canada

Scheme 2.



1, 68% ee, 98% yield (13)

2, R = CH_2SMe; 97% yield; 32% ee
3, R = $(CH_2)_2SMe$; 99% yield; 39% ee
4, R = $C(Me)_2SMe$; 94% yield; 68% ee
11, R = CH_2OMe; 90%; 8% ee

most to dryness (without a warming bath), and the crude residue was dissolved in CH_2Cl_2, and several drops of MeOH were added. Chromatography, using 3% MeOH–CH_2Cl_2, yielded the desired bis-amide as a white solid (172 mg, 74% total). ^{1}H NMR (300 MHz) ($CDCl_3$): 6.92 (2H, d, J = 9.07, 2 × NH), 4.15 (2H, m, 2 × NHC*H*), 4.01 (2H, dd, J = 11.54, 3.57 2 × C*H*HOH), 3.73 (2H, dd, J = 11.54, 7.97, 2 × CH*H*OH), 2.14 (6H, s, 2 × SCH_3), 1.61 (6H, s, $C(CH_3)_2$), 1.41 and 1.37 (each 6H, s, $C(CH_3)_2SMe$). ^{13}C NMR (75 MHz) ($CDCl_3$): 174.81, 62.93, 58.96, 50.58, 46.67, 26.55, 26.19, 23.91, 11.68. HR-MS calcd. for $C_{17}H_{34}O_4N_2S_2$: 394.1960; found: 394.1979.

In the case of racemic 1,2-cyclohexanedicarboxylic acid, the diastereomeric bis-amides were separated and individually cyclized.

Representative procedure for bis-(oxazoline) formation

Ligand 3

To a solution of penicillaminol bis-amide (0.172 g, 0.436 mmol) in dry CH_2Cl_2 (4 mL) was added a catalytic amount of DMAP (spatula tip), followed by Et_3N (0.31 mL, 2.2 mmol) and tosyl chloride (0.30 g, 1.05 mmol) in one portion. The solution was stirred overnight at r.t., then the mixture was concentrated in vacuo (without a warming bath) and chromatographed on silica gel using 35% ethyl acetate – hexanes as eluant to give **3**, a viscous oil, which partly solidified (139 mg, 89%). $[\alpha]_D$ +46.2 (c 0.525, $CHCl_3$). ^{1}H NMR (400 MHz) ($CDCl_3$): 4.32 (2H, dd, J = 8.1, 6.7, 2 × NC*H*), 4.25–4.15 (4H, m, 2 × OCH_2CH), 2.03 (6H, s, 2 × SCH_3), 1.50 (6H, s, $C(CH_3)_2$), 1.38 and 1.10 (each 6H, s, 2 × $C(CH_3)_2$SMe). ^{13}C NMR (100 MHz) ($CDCl_3$): 169.65, 73.60, 69.65, 46.32, 38.77, 25.83, 24.13, 21.86, 10.65. HR-MS calcd. for $C_{17}H_{31}O_2N_2S_2$: 359.1827; found: 359.1833.

Ligand 2

Viscous oil (124 mg, 56%). $[\alpha]_D$ –37.8 (c 0.72, $CHCl_3$). ^{1}H NMR (400 MHz) ($CDCl_3$): 4.35–4.29 (4H, m, 2 × OCH_2CHN), 4.13 (2H, m, 2 × NC*H*), 2.81 (2H, dd, J = 13.5, 4.4, 2 × C*H*HSMe), 2.49 (2H, m, 2 × CH*H*SMe), 2.12 (6H, s, 2 × SCH_3), 1.49 (6H, s, $C(CH_3)_2$). ^{13}C NMR (100 MHz) ($CDCl_3$): 169.89, 72.22, 65.54, 38.78, 38.56, 24.12, 15.91. HR-MS calcd. for $C_{13}H_{23}O_2N_2S_2$: 303.1201; found: 303.1197.

Ligand 4

Viscous oil (145 mg, 52%). $[\alpha]_D$ +140.5 (c 0.76, $CHCl_3$). ^{1}H NMR (400 MHz) ($CDCl_3$): 4.31 (2H, dd, J = 9.5, 8.15, 2 × OC*H*HCHN), 4.20 (2H, m, 2 × NC*H*), 3.91 (2H, dd, J = 8.1, 7.0, 2 × OCH*H*CHN), 2.56–2.52 (4H, m, 2 × CH_2SMe), 2.08 (6H, s, 2 × SCH_3), 1.87 (2H, m, C*H*HCH_2SMe), 1.76 (2H, m, 2 × CH*H*CH_2SMe), 1.48 (6H, s, $C(CH_3)_2$. ^{13}C NMR (100 MHz) ($CDCl_3$): 169.03, 72.43, 64.95, 38.43, 34.97, 30.09, 24.19, 15.38. HR-MS calcd. for $C_{15}H_{27}O_2N_2S_2$: 331.1514; found: 331.1508.

Ligand 5

Viscous oil (115 mg, 87%). $[\alpha]_D$ –61 (c 0.57, $CHCl_3$). ^{1}H NMR (400 MHz) ($CDCl_3$): 7.70–7.65 (8H, m, ArH), 7.45–7.35 (12H, m, ArH), 4.40–4.29 (4H, m, 2 × OCH_2CHN), 4.27 (2H, m, 2 × NC*H*), 1.53 (6H, s, $C(CH_3)_2$), 1.06 (18H, s, 2 × $Si(Ph)_2C(CH_3)_3$. ^{13}C NMR (100 MHz) ($CDCl_3$): 170.26, 135.50, 135.46, 133.29, 133.18, 129.62, 129.54, 127.60, 127.56, 70.08, 67.35, 64.91, 38.56, 26.69, 24.39, 19.17. HR-MS calcd. for $C_{43}H_{55}O_4N_2Si_2$: 719.3701; found: 719.3723.

Ligand 6

Diastereomer A

Viscous oil (78 mg, 65%). $[\alpha]_D$ –23.4 (c 0.52, $CHCl_3$). ^{1}H NMR (400 MHz) ($CDCl_3$): 4.11 (2H, dd, J = 8.85, 7.55, NC*H*), 3.85–3.75 (4H, m, 2 × OCH_2CHN), 2.60 (2H, m, $CH_2CHCHCH_2$), 1.93 (2H, br, C*H*HCH_2CH_2C*H*H), 1.72–1.62 (4H, m, CH*H*CH_2CH_2CH*H* and 2 × C*H*$(Me)_2$), 1.48–1.42 and 1.32–1.21 (each 2H, m, $CH_2CH_2CH_2CH_2$), 0.89 and 0.80 (each 6H, d, J = 6.8, $CH(CH_3)_2$. ^{13}C NMR (100 MHz) ($CDCl_3$): 168.65, 71.75, 69.51, 39.75, 32.35, 29.89, 24.90, 18.79, 17.81. HR-MS calcd. for $C_{18}H_{31}O_2N_2$: 307.2386; found: 307.2377.

Diasteromer B

(90 mg, 70%). $[\alpha]_D$ –136.0 (c 0.55, $CHCl_3$). ^{1}H NMR (400 MHz) ($CDCl_3$): 4.12 (2H, dd, J = 9.4, 8.1, OC*H*HCHN), 3.89–3.77 (4H, m, 2 × OCH*H*CHN & NC*H*), 2.62 (2H, m, $CH_2CHCHCH_2$), 1.98–1.94 & 1.72–1.62 (each 2H, m, $CH_2CH_2CH_2CH_2$), 1.68 (2H, m, 2 × C*H*$(Me)_2$),

© 2004 NRC Canada

1.48–1.40 and 1.35–1.26 (each 2H, m, $CH_2CH_2CH_2CH_2$), 0.90 and 0.82 (each 6H, d, J = 6.8, $CH(CH_3)_2$). ^{13}C NMR (100 MHz) ($CDCl_3$): 168.80, 71.62, 69.51, 39.84, 32.39, 30.07, 25.00, 18.67, 17.80. HR-MS calcd. for $C_{18}H_{31}O_2N_2$: 307.2386; found: 307.2377.

Ligand 7

Diastereomer B

White solid (53 mg, 69%). ^1H NMR (400 MHz) ($CDCl_3$): 4.07 (2H, dd, J = 9.9, 8.8, 2 × OC*H*HCH), 3.94 (2H, t, J = 8.3, 2 × NC*H*), 3.76 (2H, dd, J = 10.1, 8.1, 2 × OCH*H*CH), 2.66 (2H, m, $CH_2CHCHCH_2$), 1.99 and 1.73 (each 2H, m, $CH_2(CH_2)_2CH_2$), 1.53–1.44 and 1.37–1.25 (each 2H, m, $CH_2CH_2CH_2CH_2$), 0.86 (18H, s, 2 × $C(CH_3)_3$). ^{13}C NMR (100 MHz) ($CDCl_3$): 168.86, 75.31, 68.22, 39.51, 33.36, 30.29, 25.71, 24.97. HR-MS calcd. for $C_{20}H_{35}O_2N_2$: 335.2699; found: 335.2713.

Ligand 8

Diastereomer A

Viscous oil (95 mg, 69%). $[\alpha]_D$ +23.8 (c 1.0, $CHCl_3$). ^1H NMR (400 MHz) ($CDCl_3$): 4.26–4.15 (4H, m, 2 × OCH_2CHN), 3.99 (2H, m, 2 × NC*H*CH_2), 2.75 (2H, dd, J = 13.3, 4.2, 2 × CHC*H*HSMe), 2.55 (2H, m, 2 × $CH_2CHCHCH_2$), 2.41 (2H, dd, J = 13.3, 8.1, 2 × CHCH*H*SMe), 2.09 (6H, s, 2 × SCH_3), 1.94 and 1.72 (each 2H, m, $CH_2CH_2CH_2CH_2$), 1.48–1.39 and 1.31–1.20 (each 2H, m, $CH_2CH_2CH_2CH_2$). ^{13}C NMR (100 MHz) ($CDCl_3$): 170.11, 71.53, 65.43, 39.68, 39.05, 29.66, 24.80, 15.84. HR-MS calcd. for $C_{16}H_{27}O_2N_2S_2$: 343.1514; found: 343.1520.

Diastereomer B

Viscous oil (70 mg, 70%). $[\alpha]_D$ –49 (c 0.51, $CHCl_3$). ^1H NMR (400 MHz) ($CDCl_3$): 4.26–4.16 (4H, m, 2 × OCH_2CHN), 4.00 (2H, m, 2 × NC*H*CH_2), 2.75 (2H, dd, J = 13.2, 4.3, 2 × CHC*H*HSMe), 2.54 (2H, m, 2 × $CH_2CHCHCH_2$), 2.37 (2H, dd, J = 13.3, 8.5, 2 × CHCH*H*SMe), 2.09 (6H, s, 2 × SCH_3), 1.94 and 1.74 (each 2H, m, $CH_2CH_2CH_2CH_2$), 1.43–1.38 and 1.31–1.21 (each 2H, m, $CH_2CH_2CH_2CH_2$). ^{13}C NMR (100 MHz) ($CDCl_3$): 170.26, 71.62, 65.38, 39.90, 39.04, 29.68, 24.89, 15.75. HR-MS calcd. for $C_{16}H_{27}O_2N_2S_2$: 343.1514; found: 343.1520.

Ligand 9

Diastereomer A

Viscous oil (7 mg, 71%). $[\alpha]_D$ +95.6 (c 1.5, $CHCl_3$). ^1H NMR (400 MHz) ($CDCl_3$): 4.23 (2H, dd, J = 9.4, 8.3, 2 × OC*H*HCHN), 4.10 (2H, m, 2 × NC*H*), 3.79 (2H, t, J = 7.6, 2 × OCH*H*CHN), 2.60–2.48 (6H, m, 2 × CH_2SMe and $CH_2CHCHCH_2$), 2.07 (6H, s, 2 × SCH_3), 1.95 (2H, m, CHC*H*H$(CH_2)_2$C*H*HCH), 1.82–1.65 (6H, m, CHCH*H*$(CH_2)_2$CH*H*CH and 2 × CH_2CH_2SMe), 1.44–1.37 and 1.30–1.25 (each 2H, m, $CH_2CH_2CH_2CH_2$). ^{13}C NMR (100 MHz) ($CDCl_3$): 169.37, 71.86, 64.88, 39.92, 35.36, 30.43, 29.87, 24.97, 15.39. HR-MS calcd. for $C_{18}H_{31}O_2N_2S_2$: 371.1827; found: 371.1821.

Diastereomer B

Viscous oil (140 mg, 54%). $[\alpha]_D$ +53° (c 0.5 $CHCl_3$). ^1H NMR (400 MHz) ($CDCl_3$): 4.21 (2H, dd, J = 9.5, 8.5, 2 × OC*H*HCHN), 4.09 (2H, m, 2 × NC*H*), 3.77 (2H, t, J = 7.9, 2 × OCH*H*CHN), 2.59–2.47 (6H, m, 2 × CH_2SMe and $CH_2CHCHCH_2$), 2.06 and 2.0595 (each 3H, s, SCH_3), 1.93 (2H, m, CHC*H*H$(CH_2)_2$C*H*HCH), 1.83–1.65 (6H, m, CHCH*H*$(CH_2)_2$CH*H*CH and 2 × CH_2CH_2SMe), 1.47–1.41 and 1.28–1.23 (each 2H, m, $CH_2CH_2CH_2CH_2$). ^{13}C NMR (100 MHz) ($CDCl_3$): 169.05, 71.87, 64.87, 39.80, 35.30, 30.42, 29.61, 24.84, 15.39. HR-MS calcd. for $C_{18}H_{31}O_2N_2S_2$: 371.1827; found: 371.1821.

Ligand 10

Diastereomers A and B could be separated after cyclization (59% total).

Diastereomer A

White solid (26 mg). $[\alpha]_D$ –58 (c 1.33, $CHCl_3$). ^1H NMR (400 MHz) ($CDCl_3$): 7.67–7.62 (8H, m, ArH), 7.43–7.31 (12H, m, ArH), 4.21–4.07 (6H, m, 2 × OCH_2CHN), 3.79 (2H, dd, J = 10.07, 3.51, 2 × C*H*HOTBDPS), 3.51 (2H, dd, J = 10.03, 6.68, 2 × CH*H*OTBDPS), 2.59 (2H, m, $CH(CH_2)_4CH$), 1.91, 1.73, 1.49 & 1.27 (each 2H, m, $CH_2CH_2CH_2CH_2$), 1.04 (18H, s, 2 × $C(CH_3)_3$). ^{13}C NMR (100 MHz) ($CDCl_3$): 170.16, 135.44, 133.27, 129.60, 129.55, 127.59, 69.97, 67.20, 65.58, 40.08, 29.29, 26.73, 24.79, 19.15. LR-MS: ([M + 1]) 740.

Diastereomer B

White solid (30 mg). $[\alpha]_D$ –21.9 (c 1.65, $CHCl_3$). ^1H NMR (400 MHz) ($CDCl_3$): 7.67–7.62 (8H, m, ArH), 7.44–7.35 (12H, m, ArH), 4.20–4.12 (6H, m, 2 × OCH_2CHN), 3.80–3.77 (2H, m, 2 × C*H*HOTBDPS), 3.56–3.52 (2H, m, 2 × CH*H*OTBDPS), 2.53 (2H, m, $CH(CH_2)_4CH$), 1.97, 1.72, 1.48 & 1.26 (each 2H, m, $CH_2CH_2CH_2CH_2$), 1.04 (18H, s, 2 × $C(CH_3)_3$). ^{13}C NMR (100 MHz) ($CDCl_3$): 170.62, 135.47, 133.27, 129.60, 129.54, 127.59, 127.55, 69.77, 67.29, 65.53, 39.82, 29.75, 26.69, 24.85, 19.14.

General procedure for ligand–Cu complexes

To a solution of the ligand (0.067 mmol) in anhydrous CH_2Cl_2 was added the copper salt (0.06 mmol). The mixture was stirred until it became homogeneous. Hexanes (0.3–0.5 mL) were added, and the solution was allowed to stand 2 days at room temperature and several days at 0 °C to afford the crystalline complexes.

Catalytic asymmetric addition of MeLi to an aldimine (13)

A solution of MeLi (2 equiv., 1.6 mol L^{-1} Et_2O) and ligand (0.1 equiv.) in toluene was stirred for 30 min at −41 °C. A solution of *N*-*p*-methoxyphenyl benzaldehyde imine in toluene was added over 10 min. After 60 min stirring at −41 °C, the mixture was quenched with 2 mL methanol. After dilution with water, the organic phase was extracted with ether and dried over Na_2SO_4. The product was purified by flash chromatography (hexanes:EtOAc 85:15). The enantiomeric excesses were measured by chiral HPLC analysis; OD, l: 210 nm; flow: 0.5 mL min^{-1}; hexanes:isopropanol 95:5; with elution times of 18.70 and 20.59 min for a racemic mixture.

© 2004 NRC Canada

Acknowledgments

We thank the Natural Sciences and Engineering Research Council of Canada (NSERC) for generous financial assistance through the Medicinal Chemistry Chair Program and the University of Louvain (fellowship to E.J.).

References

1. For recent authoritative reviews, see (*a*) E.N. Jacobsen, A. Pfaltz, and H. Yamamoto. (*Editors*). Comprehensive asymmetric catalysis. Vol. I–III. Springer, N.Y. 1999; (*b*) I. Ojima. (*Editor*). Catalytic asymmetric synthesis. VCH, Weinheim. 1993; (*c*) R. Noyori. *In* Asymmetric catalysis in organic synthesis. J. Wiley & Sons, N.Y. 1994.
2. For a recent review on metal-free catalysis, see (*a*) P.I. Dalko and L. Moisan. Angew. Chem. Int. Ed. **40**, 3726 (2001).
3. For recent reviews, see (*a*) J.S. Johnson and D.A. Evans. Acc. Chem. Res. **33**, 325 (2000); (*b*) K.A. Jorgensen, M. Johannsen, S. Yao, H. Audrain, and J. Thorhange. Acc. Chem. Res. **32**, 605 (1999); (*c*) A.K. Ghosh, P. Mathivanan, and J. Cappiello. Tetrahedron, **9**, 1 (1998); (*d*) A. Pfaltz. Acta Chem. Scand. **50**, 189 (1996); (*e*) A. Pfaltz. Acc. Chem. Res. **26**, 339 (1993); (*f*) A. Pfaltz. Chimia, **44**, 202 (1990).
4. See, for example: (*a*) E.J. Corey, N. Imai, and H.Y. Zhang. J. Am. Chem. Soc. **113**, 728 (1991); (*b*) D.A. Evans, K.A. Woerpel, M.M. Hinman, and M.M. Faul. J. Am. Chem. Soc. **113**, 726 (1991); (*c*) D.A. Evans, G.S. Peterson, J.S. Johnson, D.-M. Barnes, K.C. Campos, and K.A. Woerpel. J. Org. Chem. 6541 (1998); (*d*) S.E. Denmark, N. Nakajima, J.-C. Nicaise, A.-M. Faucher, and J.P. Edwards. J. Org. Chem. **60**, 4884 (1995).
5. For reviews on bimetallic and ambifunctional catalysis, see (*a*) G.J. Rowlands. Tetrahedron, **57**, 1865 (2001); (*b*) E.K. van den Beuken and B. Feringa. Tetrahedron, **54**, 12 985 (1998); (*c*) M. Shibasaki, H. Sasai, and T. Arai. Angew. Chem. Int. Ed. **36**, 1236 (1997); (*d*) H. Steinhagen and G. Helmchen. Angew. Chem. Int. Ed. **35**, 2339 (1996); see also (*e*) G. Vankoten. Pure Appl. Chem. **7**, 1455 (1994); (*f*) Q.-L. Zhou and A. Pfaltz. Tetrahedron, **50**, 4467 (1994).
6. V.K. Aggarwal, L. Bell, M.P. Coogan, and P.J. Jubault. J. Chem. Soc. Perkin Trans. 1, 2037 (1998).
7. S. Hanessian, A. Griffin, and E. Jnoff. Can. J. Chem. **80**, 885 (2002).
8. For reviews, see (*a*) S.E. Denmark and J.-C. Nicaise. *In* Comprehensive asymmetric catalysis. Vol. 2. *Edited by* E.N. Jacobsen, A. Pfaltz, and H. Yamamoto. Springer, Berlin. 1999. p. 923; (*b*) R. Bloch. Chem. Rev. **98**, 1407 (1998); (*c*) D. Enders and U. Reinhold. Tetrahedron Asymmetry, **8**, 895 (1997), and references cited therein.
9. See, for example: (*a*) J.M. Takacs, E.C. Lawson, M.J. Reno, M.A. Youngman, and D.A. Quincy. Tetrahedron Asymmetry, **8**, 3073 (1997); (*b*) J.M. Takacs, D.A. Quincy, W. Shay, B.E. Jones, and C.R. Ross III. Tetrahedron Asymmetry, **8**, 3079 (1997).
10. For examples of stoichiometric reactions, see (*a*) K. Tomioka, I. Inoue, M. Shindo, and K. Koga. Tetrahedron Lett. **31**, 6681 (1990); (*b*) I. Inoue, M. Shindo, K. Koka, and K. Tomioka. Tetrahedron Asymmetry, **4**, 4429 (1993); (*c*) K. Tomioka, M. Shindo, and K. Koga. J. Am. Chem. Soc. **111**, 8266 (1989); (*d*) S. Itsuno, H. Yanaka, C. Hachisuka, and K. Ito. J. Chem. Soc. Perkin Trans. 1, 1341 (1991); (*e*) S. Arrasate, E. Lete, and N. Sotomayor. Tetrahedron Asymmetry, **12**, 2077 (2001); (*f*) P. Anderson, F. Johansson, and D. Tanner. Tetrahedron, **54**, 11 549 (1998); for examples of allylation, see (*g*) M. Nakamura, A. Hirai, and E. Nakamura. J. Am. Chem. Soc. **118**, 8459 (1996); (*h*) S. Hanessian and R.-Yang. Tetrahedron Lett. **37**, 8997 (1996).
11. For some reviews, see (*a*) S. Kobayashi and H. Ishitani. Chem. Rev. **99**, 1069 (1999); (*b*) S.E. Denmark and O.J.-C. Nicaise. Chem. Comm. 999 (1996); (*c*) Y. Yamamoto and N. Asao. Chem. Rev. **93**, 2207 (1993); (*d*) R.A. Volkman. *In* Comprehensive organic synthesis, part I. Vol. 1. *Edited by* S.L. Schreiber. Pergamon, Oxford. 1991. p. 355; (*e*) E.F. Kleinman and R.A. Volkman. *In* Comprehensive organic synthesis, part II. Vol. 2. *Edited by* Ch. Heathcock. Pergamon, Oxford. 1991. p. 275.
12. (*a*) I. Inoue, M. Shindo, K. Koga, and K. Tomioka. Tetrahedron, **50**, 4429 (1994); (*b*) M. Shindo, K. Koga, M. Kanai, and K. Tomioka. Tetrahedron Asymmetry, **6**, 2527 (1995); (*c*) I. Inoue, M. Shindo; K. Koga, and K. Tomioka. Tetrahedron, **50**, 4429 (1994).
13. S.E. Denmark, N. Nakajima, and J.-C. Nicaise. J. Am. Chem. Soc. **116**, 8797 (1994).
14. S.E. Denmark and C.M. Stiff. J. Org. Chem. **65**, 5875 (2000).
15. For a recent review on asymmetric cyclopropanations, see H. Lebel, J.-F. Marcoux, C. Molinaro, and A.B. Charette. Chem. Rev. **103**, 977 (2003).

© 2004 NRC Canada

C_{19} quassinoid model studies: Preparation of *trans*-perhydroindans via a vinylogous Mukaiyama aldol – free-radical cyclization route[1]

Matthew G. Donahue and David J. Hart

Abstract: Aldehyde **9** was prepared in 5 steps from 3,5-dimethylbenzoic acid. Treatment of **9** with ketene acetals **10** and **19** and titanium tetrachloride gave free-radical cyclization substrates **11** and **20** in 67% and 51% yields, respectively. Tri-*n*-butylstannane-mediated cyclization of **11** and **20** gave *trans*-perhydroindans **14** and **21** in 60% and 63% yields, respectively. The relationship of these studies to an approach to C_{19} quassinoids is discussed.

Key words: vinylogous Mukaiyama aldol reaction, free-radical cyclization, *trans*-perhydroindans, C_{19} quassinoids, 1,2-asymmetric induction.

Résumé : L'aldéhyde **9** est préparé en 5 étapes à partir de l'acide 3,5-diméthylbenzoique. Le traitement de **9** avec les acetals de kétène **10** et **19** et le tetrachlorure de titane donne les substrats de cyclisation par radicaux libres **11** et **20** avec des rendements respectifs de 67% et 51%. La cyclisation de **11** et **20** par le tri-*n*-butylstanne donne les *trans*-perhydroindanes **14** et **21** avec des rendements respectifs de 60% et 63%. On discute la relation de ces études avec une approche vers les quassinoides en C_{19}.

Mots clés : réaction d'aldol vinylogue de Mukaiyama, cyclisation par radicaux libres, *trans*-perhydroindanes, quassinoides en C_{19}, induction asymétrique-1,2.

Introduction

The C_{19} quassinoids are a small family of terpenoids that have received less attention from the synthetic community than the corresponding C_{20} quassinoids (1). Indeed only the second synthesis of a C_{19} quassinoid was reported in 1999, when Grieco described a synthesis of (5*R*)-polyandrane (**1**) (2). We have been investigating a unified approach to selected C_{19} and C_{20} quassinoids that involves an extension of free-radical cyclization chemistry previously developed in our laboratories (3). The plan for the polyandranes (Fig. 1) involves preparation of *trans*-perhydroindans of type **2** via free-radical cyclization of substrates of type **3**. This communication reports preliminary results of this study.

Results and discussion

Our first objective was to prepare a substrate of type **3** where the incipient C_{11} hydroxyl group of the polyandranes is replaced with a methyl group and R_1 and R_2 are electron-withdrawing and methyl groups, respectively. The specific substrate selected for synthesis (**11**) was prepared as described in Schemes 1 and 2. 3,5-Dimethylbenzoic acid (**4**) was subjected to Birch reduction, according to an established procedure, to provide **5** (mp 113–115 °C) in 95% yield (4). Aldol condensation of the dianion derived from **5** with formaldehyde provided hydroxy acid **6** in 93% yield (5). Reduction of **6** using lithium aluminum hydride provided diol **7** (mp 99 to 100 °C) in 57% yield. Treatment of **7** with NBS in tetrahydrofuran gave cycloetherification product **8** (99%), and oxidation of the primary alcohol using Swern's conditions provided aldehyde **9** in 96% yield (6).

Reaction of **9** with dienol ether **10** (7) in the presence of titanium tetrachloride gave a 6:1 mixture of vinylogous Mukaiyama aldol products **11** (67%) and **12** (11%) (8).[3] We note that promotion of the vinylogous Mukaiyama aldol with boron trifluoride etherate provided **11** (mp 134 to 135 °C) and **12** (mp 83–85 °C) in 11% and 42% yields, respectively.

Received 16 September 2003. Published on the NRC Research Press Web site at http://canjchem.nrc.ca on 13 February 2004.

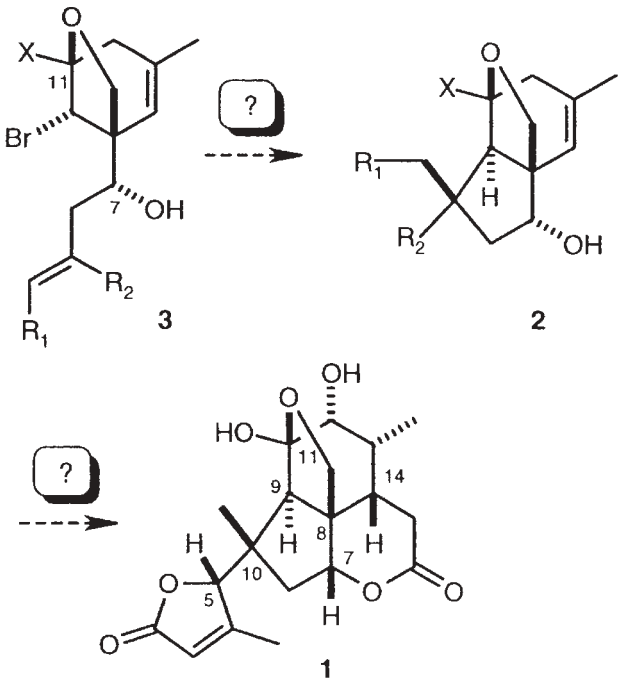
Dedicated to Professor Edward Piers whose commitment to science and education is admirable.

M.G. Donahue and D.J. Hart.[2] Department of Chemistry, The Ohio State University, 100 W. 18th Avenue, Columbus, OH 43210, U.S.A.

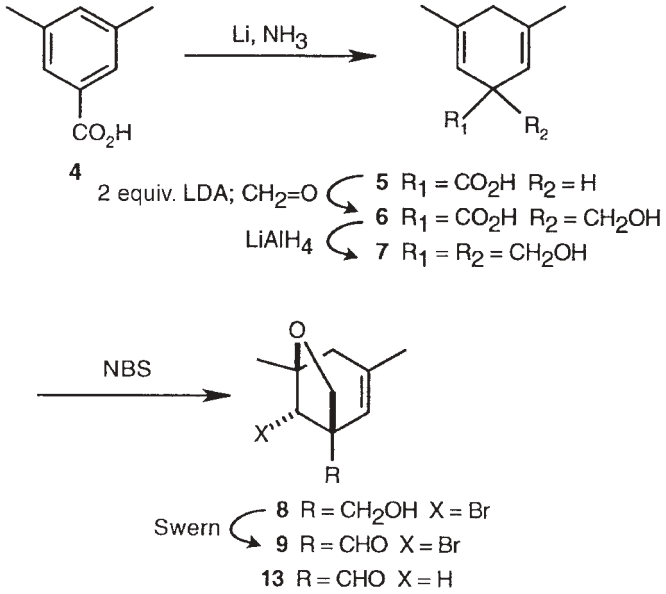
[1]This article is part of a Special Issue dedicated to Professor Ed Piers.
[2]Corresponding author (e-mail: hart@chemistry.ohio-state.edu).
[3]The stereochemical assignments at C_7 for **11** and **12** were based on NMR correlations with related compounds, including one for which an X-ray crystal structure was obtained. NMR studies on the cyclization products derived from **11** and **12** also clearly defined C_7 stereochemistry.

 doi: 10.1139/V03-197 © 2004 NRC Canada

Fig. 1. Synthetic plan.

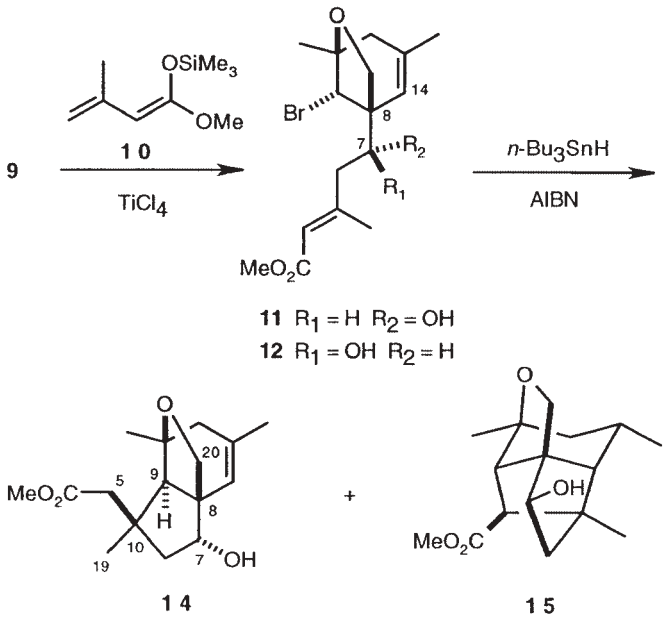


Scheme 1. Synthesis of aldehyde **9**.



In addition, titanium tetrachloride mediated reaction of *des*-bromo compound **13** with **10** gave a complex mixture of products that contained very little material resulting from a vinylogous aldol. Thus, the nature of the Lewis acid and the presence of a bromine atom in **9** play a central role in the observed diastereoselectivity. We speculate that the stereoselectivity observed with titanium tetrachloride is due to a combination of a chelation effect and principles for 1,2-asymmetric induction introduced by Felkin and co-workers

Scheme 2. Vinylogous Mukaiyama aldol – free-radical cyclization.



(9*a*) and Ahn and Eisenstein (9*b*). Thus, a complex between the Lewis acid and **9**, which involves bridging of the bromine and carbonyl oxygen with titanium, is conformationally constrained such that attack *anti* to the C_8—C_{14} bond should be stereoelectronically preferred, giving rise to **11** in a conformation in which substituents are staggered along the C_7—C_8 bond.

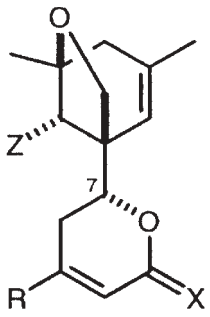
Treatment of **11** with tri-*n*-butylstannane in the presence of 2,2′-azobisisobutyronitrile (AIBN) provided cyclization products **14** (60%) and small amounts (less than 6%) of material suspected to be the C_{10} epimer of **14**. We note that a less than 1% yield of **15**, an interesting product derived from an initial 6-endo cyclization, was also isolated. The stereochemistry of **14** was established by difference NOE experiments, which confirmed a *cis*-relationship between the C_7 hydrogen and C_{20} methylene group, a *cis*-relationship between the C_{20} and C_5 methylene groups, and a *cis*-relationship between the C_9 hydrogen and C_{19} methyl group. This result established the viability of the proposed preparation of compounds of type **2** by free-radical cyclization of compounds of type **3**. It also demonstrated that this approach was unlikely to directly afford the required C_9–C_{10} stereochemical relationship.[4]

Two attempts to address the C_9–C_{10} stereochemical problem are described in Fig. 2 and Scheme 3. An examination of molecular models suggested that lactone **17** was constrained such that cyclization would provide the desired C_9–C_{10} stereochemistry. Treatment of **9** with 3-methyl-1-trimethylsiloxy-1,3-butadiene in the presence of potassium *tert*-butoxide followed by Jones oxidation of the resulting lactols **16** provided **17** in 33% overall yield (Fig. 2) (10). We were disappointed to find that attempts to cyclize **17** under a variety of conditions failed (11). For example, typical tri-*n*-

[4] Similar cyclization of **12** provided a 76% yield of the C_7 epimer. We note that derivatives of **11** and **12** lacking the impending C_{10} methyl group were prepared and cyclized with comparable results. In these cases compounds of type **14** (53%–72%) and the corresponding C_{10} epimer (15%–18%) were isolated, and the structures of all products were rigorously established.

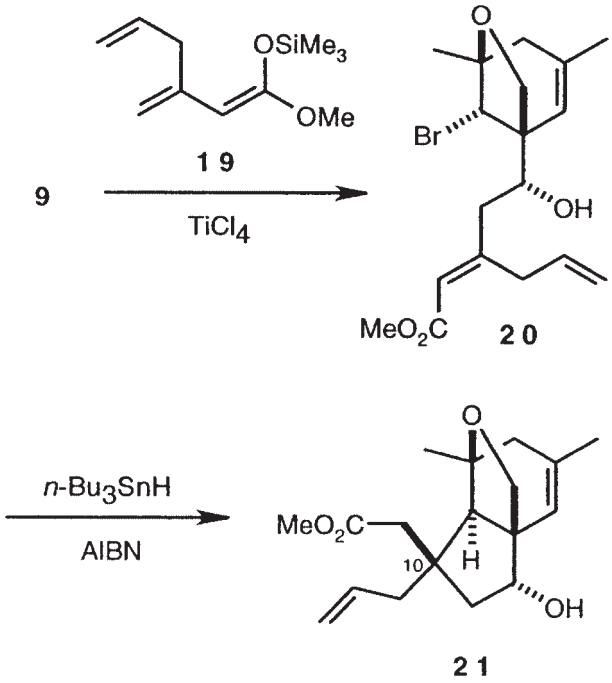
© 2004 NRC Canada

Fig. 2. Lactone substrates and products.



16 X = H, OH Z = Br R = Me
17 X = O Z = Br R = Me
18 X = O Z = H R = Me
22 X = O Z = Br R = $CH_2CH{=}CH_2$

Scheme 3. Synthesis and cyclization of **20**.



butylstannane conditions gave only reduction product **18** (mp 135 to 136 °C). Apparently, conformational constraints present in **17** severely retard radical cyclization rates relative to **11**. A potentially useful modification of the chemistry involved cyclization of **20**. This substrate was prepared in 51% yield by reaction of ketene acetal **19** with aldehyde **9** (12).[5,6] Free-radical cyclization of **20** provided **21** in 63% yield. We imagine the reductive decarboxylation of **21** will afford the required C_{10} methyl group.

Characterization data for compounds in synthesis of 21

^{13}C NMR multiplicities in parentheses determined by DEPT spectroscopy.

Hydroxy acid 6

mp 107–110 °C. IR (thin film) (cm^{-1}): 3334, 1707, 1694. ^1H NMR ($CDCl_3$, 400 MHz) δ: 1.73 (s, 6H), 2.47, 2.51 (AB q, J = 22.2 Hz, 2H), 3.61 (s, 2H), 5.43 (s, 2H); neither the acidic nor the alcoholic proton were recorded. ^{13}C NMR ($CDCl_3$, 100 MHz) δ: 23.4 (q), 36.5 (t), 53.2 (s), 69.1 (t), 118.3 (d), 136.5 (s), 179.8 (s). Exact mass calcd. for $C_{10}H_{14}O_3$ ($[M + Na]^+$) m/z: 205.0835; found: 205.0841. Anal. calcd. for $C_{10}H_{14}O_3$: C 65.90, H 7.75; found: C 65.84, H 7.73.

Diol 7

mp 99 to 100 °C. IR (thin film) (cm^{-1}): 3301 (br). ^1H NMR ($CDCl_3$, 400 MHz) δ: 1.40 (t, J = 6.0 Hz, 2H), 1.69 (s, 6H), 2.43 (s, 2H), 3.37 (d, J = 6.1 Hz, 4H), 5.16 (s, 2H). ^{13}C NMR ($CDCl_3$, 100 MHz) δ: 23.5 (q), 37.0 (t), 47.8 (s), 68.8 (t), 121.5 (d), 137.0 (s). Exact mass calcd. for $C_{10}H_{16}O_2$ ($[M + Na]^+$) m/z: 191.1043; found: 191.1045. Anal. calcd. for $C_{10}H_{16}O_2$: C 71.38, H 9.59; found: C 70.88, H 9.47.

Bromo ether 8

mp 49–51 °C. IR (neat) (cm^{-1}): 3419 (br). ^1H NMR ($CDCl_3$, 400 MHz) δ: 1.30 (s, 3H), 1.53 (s, 1H), 1.63 (s, 3H), 2.02 (d, J = 18.1 Hz, 1H), 2.34 (d, J = 18.1 Hz, 1H), 3.65, 3.67 (AB q, J = 11.2 Hz, 2H), 3.81, 3.90 (AB q, J = 6.8 Hz, 2H), 3.96 (s, 1H), 5.19 (s, 1H). ^{13}C NMR ($CDCl_3$, 100 MHz) δ: 22.3 (q), 23.6 (q), 44.3 (t), 50.1 (s), 55.8 (d), 63.0 (t), 76.4 (t), 81.5 (s), 122.8 (d), 135.9 (s). Exact mass calcd. for $C_{10}H_{15}BrO_2$ m/z: 246.0255; found: 246.0285. Anal. calcd. for $C_{10}H_{15}BrO_2$: C 48.74, H 6.14; found: C 48.45, H 6.19.

Aldehyde 9

mp 45–48 °C. IR (neat) (cm^{-1}): 2729, 1729. ^1H NMR ($CDCl_3$, 400 MHz) δ: 1.43 (s, 3H), 1.79 (s, 3H), 2.17 (d, J = 18.2 Hz, 1H), 2.45 (d, J = 18.3 Hz, 1H), 4.01, 4.10 (AB q, J = 7.1 Hz, 2H), 4.29 (s, 1H), 5.91 (s, 1H), 9.67 (s, 1H). ^{13}C NMR ($CDCl_3$, 100 MHz) δ: 20.9 (q), 21.6 (q), 42.7 (t), 52.0 (d), 58.8 (s), 74.3 (t), 81.2 (s), 117.4 (d), 135.7 (s), 197.4 (d). Exact mass calcd. for $C_{10}H_{13}BrO_2$ ($[M + Na]^+$) m/z: 266.9991; found: 267.0009. Anal. calcd. for $C_{10}H_{13}BrO_2$: C 49.18, H 5.37; found: C 49.02, H 5.42.

Ketene acetal 19

IR (neat) (cm^{-1}): 3078, 1650, 1605. ^1H NMR (C_6D_6, 500 MHz) δ: 0.17 (s, 9H), 3.04 (s, 3H), 3.14 (dd, J = 6.5, 1.2 Hz, 2H), 4.21 (s, 1H), 4.95 (d, J = 2.4 Hz, 1H), 5.05 (dd, J = 10.1, 2.1 Hz, 1H), 5.16 (dd, J = 17.1, 2.0 Hz, 1H), 5.31 (d, J = 2.5 Hz, 1H), 6.05 (dddd, J = 17.1, 10.2, 6.8, 6.6 Hz, 1H). ^{13}C NMR (C_6D_6, 125 MHz) δ: 0.47 (q), 42.4 (t), 54.6

[5] Ketene acetal **19** was prepared by deprotonation and silylation of methyl (*E*)-3-methylhexa-2,5-dienoate (12). The reaction of **9** with **19** also provided 6% of the C_7 diastereomer of **20** and several minor products (perhaps lactones) whose structures have yet to be determined.
[6] We note that reaction of **9** with a 1:1 mixture of **19** and its geometrical isomer provided lactones (stereochemistry at C_7 unknown) as the major products (Fig. 1). Thus, ketene acetal geometry influences the stereochemistry of this vinylogous Mukaiyama aldol.

© 2004 NRC Canada

(q), 80.1 (d), 108.6 (t), 115.2 (t), 138.3 (d), 142.0 (s), 157.8 (s). Exact mass calcd. for $C_{11}H_{20}O_2Si$ ($[M]^+$) *m/z*: 212.1227; found: 212.1222.

Dienone 20

mp 98 to 99 °C. ^{1}H NMR ($CDCl_3$, 500 MHz) δ: 1.37 (s, 3H), 1.73 (s, 3H), 1.95 (dd, *J* = 13.7, 11.1 Hz, 1H), 2.10 (d, *J* = 18.1 Hz, 1H), 2.25 (br s, 1H), 2.40 (d, *J* = 18.1 Hz, 1H), 2.66 (d, *J* = 13.9 Hz, 1H), 3.23 (dd, *J* = 13.7, 7.2 Hz, 1H), 3.72 (s, 3H), 3.74 (dd, *J* = 13.8, 6.0 Hz, 1H), 3.80 (d, *J* = 6.6 Hz, 1H), 3.88 (d, *J* = 10.8 Hz, 1H), 4.01 (d, *J* = 6.6 Hz, 1H), 4.24 (s, 1H), 5.13 (d, *J* = 10.0 Hz, 1H), 5.18 (dd, *J* = 17.2, 1.5 Hz, 1H), 5.30 (s, 1H), 5.8–5.9 (m, 1H), 5.86 (s, 1H). ^{13}C NMR ($CDCl_3$, 100 MHz) δ: 22.5 (q), 23.5 (q), 36.8 (t), 41.1 (t), 44.3 (t), 51.5 (q), 52.3 (s), 56.1 (d), 68.6 (d), 72.4 (t), 81.3 (s), 117.6 (t), 119.4 (d), 122.4 (d), 135.2 (d), 136.7 (s), 157.2 (s), 166.5 (s). Exact mass calcd. for $C_{18}H_{25}BrO_4$ ($[M + Na]^+$) *m/z*: 407.0828; found: 407.0802. Anal. calcd. for $C_{18}H_{25}BrO_4$: C 56.11, H 6.54; found: C 56.20, H 6.58.

Perhydroindan 21

IR (neat) (cm^{-1}): 3441, 3075, 3013, 1732, 1639. ^{1}H NMR ($CDCl_3$, 500 MHz) δ: 1.46 (s, 3H), 1.68 (s, 3H), 1.76 (s, 1H), 1.87 (d, *J* = 15.4 Hz, 1H), 2.13 (d, *J* = 17.8 Hz, 1H), 2.36 (d, *J* = 17.8 Hz, 1H), 2.35 (s, 1H), 2.42 (dd, *J* = 13.3, 7.5 Hz, 1H), 2.55 (dd, *J* = 15.4, 5.0 Hz, 1H), 2.66 (d, *J* = 14.5 Hz, 1H), 2.71 (dd, *J* = 13.6, 7.6 Hz, 1H), 2.88 (d, *J* = 14.5 Hz, 1H), 3.62 (d, *J* = 7.6 Hz, 1H), 3.69 (s, 3H), 3.92 (d, *J* = 7.7 Hz, 1H), 4.13 (d, *J* = 4.9 Hz, 1H), 5.17 (d, *J* = 4.2 Hz, 1H), 5.20 (s, 1H), 5.89–5.96 (m, 1H), 5.96 (s, 1H). ^{13}C NMR ($CDCl_3$, 125 MHz) δ: 22.2 (q), 23.4 (q), 40.4 (t), 45.3 (s), 47.8 (t), 48.4 (t), 51.7 (q), 52.6 (t), 61.7 (d), 62.3 (s), 73.2 (d), 79.2 (t), 85.4 (s), 119.1 (t), 128.2 (d), 135.6 (s), 135.8 (d), 173.3 (s). Exact mass calcd. for $C_{18}H_{26}O_4$ ($[M + Na]^+$) *m/z*: 329.1723; found: 329.1728.

Conclusions

In summary, a seven-step synthesis of **21** from 3,5-dimethylbenzoic acid has been developed. The chemistry extends the scope of a free-radical cyclization route to perhydroindans and reveals some interesting stereochemical features of the vinylogous Mukaiyama aldol condensation. Compound **21** is functionalized appropriately for the pursuit of the polyandranes at all positions except C_{11}. Modifications of this chemistry, incorporating more appropriate functionality at C_{11}, are being developed.

References

1. (*a*) K. Kawada, M. Kim, and D.S. Watt. Org. Prep. Proced. Int. **21**, 521 (1989); (*b*) J. Polonsky. Fortschr. Chem. Org. Naturst. **47**, 221 (1985); (*c*) J. Polonsky. *In* Chemistry and chemical taxonomy of the rutales. *Edited by* P.G. Waterman and M.F. Grundun. Academic Press, New York. 1983. pp. 247–266; (*d*) J. Polonsky. Fortschr. Chem. Org. Naturst. **30**, 101 (1973); (*e*) M. Kim, K. Kawada, R.S. Gross, and D.S. Watt. J. Org. Chem. **55**, 504 (1990); (*f*) H. Hirota, A. Yokoyama, K. Miyaji, T. Nakamura, M. Igarashi, and T. Takahashi. J. Org. Chem. **56**, 1119 (1991); (*g*) E.D. Moher, J.L. Collins, and P.A. Grieco. J. Am. Chem. Soc. **114**, 2764 (1992); (*h*) P.A. Grieco, J.L. Collins, E.D. Moher, T.J. Fleck, and R.S. Gross. J. Am. Chem. Soc. **115**, 6078 (1993); (*i*) J.M. VanderRoest and P.A. Grieco. J. Am. Chem. Soc. **115**, 5841 (1993); (*j*) P.A. Grieco, J.L. Collins, and J.C. Huffman. J. Org. Chem. **63**, 9576 (1998).
2. (*a*) P.A. Grieco and M.M. Piñeiro-Nuñez. J. Am. Chem. Soc. **116**, 7606 (1994); (*b*) D.P. Walker and P.A. Grieco. J. Am. Chem. Soc. **121**, 9891 (1999).
3. (*a*) C.P. Chuang and D.J. Hart. J. Org. Chem. **48**, 1782 (1983); (*b*) C.P. Chuang, J.C. Gallucci, and D.J. Hart. J. Org. Chem. **53**, 3210 (1988); (*c*) C.P. Chuang, J.C. Gallucci, D.J. Hart, and C. Hoffman. J. Org. Chem. **48**, 3218 (1988).
4. H. Van Bekkum, C.B. Van Den Bosch, G. Van Minnenpathius, J.C. De Mos, and A.M. Van Wijk. Recl. Trav. Chim. Pays-Bas. **90**, 137 (1971).
5. (*a*) B. Ganem, G.N. Holbert, L.B. Weiss, and K. Ishizumi. J. Am. Chem. Soc. **100**, 6483 (1978); (*b*) M. Schlosser, T. Jenny, and Y. Guggisberg. Synlett, 704 (1990).
6. A.J. Mancuso, S.L. Huang, and D. Swern. J. Org. Chem. **43**, 2480 (1978).
7. (*a*) C.P. Casey, C.R. Jones, and H. Tukada. J. Org. Chem. **46**, 2089 (1981); (*b*) D.W. Cameron, M.G. Looney, and J.A. Pattermann. Tetrahedron Lett. **41**, 7555 (1995).
8. (*a*) T. Mukaiyama, K. Banno, and K. Narasaka. J. Am. Chem. Soc. **96**, 7503 (1974); (*b*) T. Mukaiyama. Org. React. **28**, 203 (1982); (*c*) G. Casiraghi, F. Zanardi, G. Appendino, and G. Rassu. Chem. Rev. **100**, 1929 (2000).
9. (*a*) M. Chérest, H. Felkin, and N. Prudent. Tetrahedron Lett. **18**, 2199 (1968); (*b*) N.T. Ahn and O. Eisenstein. Tetrahedron Lett. **17**, 155 (1976).
10. P. Duhamel, D. Cahard, and J.M. Poirier. J. Chem. Soc. Perkin Trans. 1, 2509 (1993).
11. (*a*) D.J. Hart and F.L. Seely. J. Am. Chem. Soc. **110**, 1631 (1988); (*b*) M.P. Sibi, J. Ji, J.B. Sausker, and C.P. Jasperse. J. Am. Chem. Soc. **121**, 7517 (1999).
12. E.J. Corey, C.U. Kim, R.H.K. Chen, and M. Takeda. J. Am. Chem. Soc. **94**, 4395 (1972).

© 2004 NRC Canada

Diversity-oriented synthesis of enantiopure *N*-protected β,β-dialkylserines[1]

James E. Dettwiler and William D. Lubell

Abstract: A series of enantiomerically pure *N*-Boc-protected β,β-dialkylserines was synthesized by addition of the appropriate Grignard reagent to *N*-(Boc)serine methyl ester, followed by TEMPO-catalysed oxidation of the primary alcohol with sodium chlorite and sodium hypochlorite.

Key words: amino acid, serine, β,β-dialkylserines, ring-closing metathesis.

Résumé : Une série énantiomériquement pure de β,β-dialkylserines *N*-Boc protégées est synthétisée par addition du réactif de Grignard correspondant sur l'ester méthylique de la *N*-(Boc)serine suivie d'une oxydation catalysée de l'alcool primaire avec TEMPO, du chlorite de sodium et de l'hypochlorite de sodium.

Mots clés : acide aminé, sérine, β,β-dialkylserines, cyclisation par métathèse.

Introduction

β-Alkylserines are constituents of biologically active peptides, as well as starting materials for the synthesis of unusual amino acids and heterocycles (1–14). In peptides, the alkyl groups of β-substituted amino acids may exhibit steric interactions that can restrain χ-dihedral angle geometry and orient side-chains in particular conformations (1). They may also play roles that influence the interactions of the peptide with its environment and with its biological receptor. Alcohol activation and displacement may be used to convert β-alkylserines into aziridine-2-carboxylates (2–8), β-alkylcysteines (2, 3), and β-alkyltryptophans (4, 5), as well as amino acids possessing unnatural β-substituents like fluorine (6–8). Although many methods have been developed for the preparation of β-alkylserines, few approaches have been explored for the synthesis of the related, more substituted β,β-dialkylserines (10–14). The protection of serine as its OBO (2,6,7-trioxabicyclo[2.2.2]octyl) ester, followed by oxidation and addition of nucleophiles, such as Grignard reagents, at the β-carbon represents a notable means for stereoselectively synthesizing β,β-dialkylserines (10). Although diastereoselective condensations of aldehydes onto chiral glycine enolates have furnished a series of β-alkylserine analogs, the lower reactivity of ketones in this aldol approach limits its application for making β,β-dialkylserines (11–13). Recently, we have reported a two-step approach for synthesizing *N*-protected β-hydroxyvaline (β,β-dimethylserine), which involved treatment of *N*-protected serine methyl ester with methyl Grignard reagent followed by a selective oxidation of the resulting diol (14). When *N*-Boc-D-serine methyl ester was employed in this sequence, the corresponding *N*-Boc-L-β-hydroxyvaline (97% enantiomeric purity) was produced in 80% overall yield on a multi-gram scale. In light of this efficiency, we have investigated alternative Grignard reagents in this process and have now developed an effective diversity oriented synthesis of enantiopure *N*-Boc-β,β-dialkyl serines.

Received 8 October 2003. Published on the NRC Research Press Web site at http://canjchem.nrc.ca on 13 February 2004.

J.E. Dettwiler and W.D. Lubell.[2] Département de chimie, Université de Montréal, C.P. 6128, Succursale Centre Ville, Montréal, QC H3C 3J7, Canada.

[1]This article is part of a Special Issue dedicated to Professor Ed Piers.

[2]Corresponding author (e-mail: Lubell@chimie.umontreal.ca).

Results and discussion

For our investigation, a series of Grignard reagents were chosen, possessing primary and secondary alkyl, allyl, vinyl, benzyl, and aryl substitution. All of the Grignard reagents were obtained from commercial sources and used without further purification. Using conditions optimized with methyl magnesium bromide (14), the Grignard reagent was added to a solution of *N*-Boc-D-serine methyl ester at –78 °C in diethyl ether (THF in the case of vinyl magnesium bromide, Scheme 1). The desired diol **2** was typically obtained as the major product, contaminated with minor amounts of the corresponding ketone **3**. For example, diols **2a**–**2e** were isolated in 68%–83% yields after purification by silica gel column chromatography (Table 1). On the other hand, *iso*-propyl magnesium chloride reacted on *N*-Boc-D-serine methyl ester to provide diol **2g** in 38% yield along with the less substituted diol **4** (4:1 diastereomeric mixture) from reduction of the ketone intermediate **3g** (15). Reversing the addition of *N*-Boc-D-serine methyl ester by adding it to a solution of the *iso*-propyl Grignard reagent afforded the same result. Vinylmagnesium bromide reacted with the *N*-Boc-D-serine methyl ester to provide a 1:1 mixture of diol **2f** and homoallylic ketone **3h**, as measured by integration of the vinyl protons at 6.01 and 5.80 parts per million (ppm), respectively, in the ^{1}H NMR spectrum of the crude product in $CDCl_3$. Silica gel column chromatography was used to isolate diol **2f** and ketone **3h** in 25% and 35% respective yields, as well as a

 doi: 10.1139/V03-193 © 2004 NRC Canada

Scheme 1. Synthesis of β,β-dialkyl-*N*-(Boc)serines **1a**–**1g**.

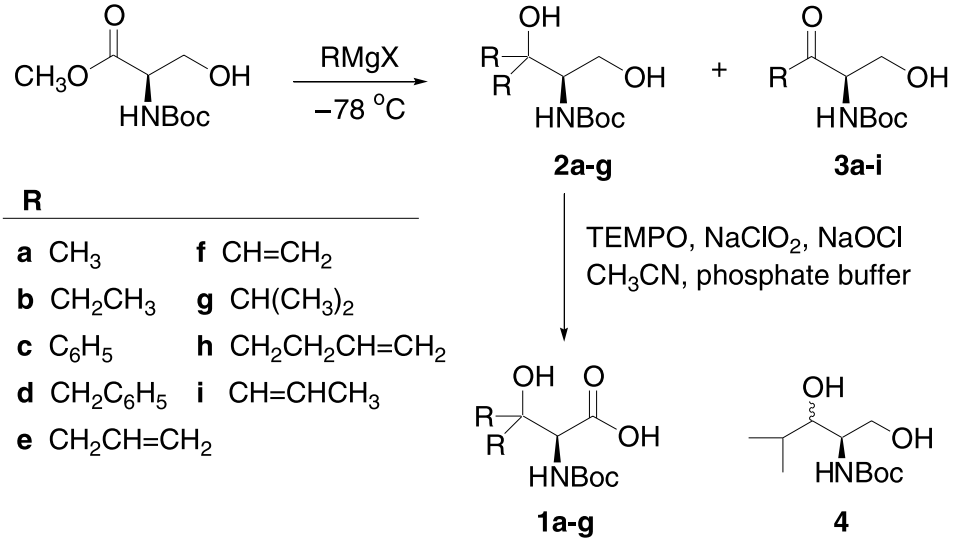


Table 1. Results of Grignard addition on *N*-(Boc)-L-serine methyl ester and oxidation of the resulting amino diol **2**.

		Yields (%)[a]		
Entry	RMgX	Amino diol **2**	Amino ketone **3**	Amino acid **1**
a	CH_3MgBr	83	2	96
b	CH_3CH_2MgBr	81	4	92
c	C_6H_5MgBr	79	4	76
d	$C_6H_5CH_2MgBr$	74	11	74
e	CH_2=CHCHMgBr	68	16[b]	78
f	CH_2=CHMgBr	25	35[c]	81
g	$(CH_3)_2CHMgCl$	38 (41)	19 (10)[d]	72

[a]Results obtained from inverse addition of *N*-Boc-L-serine methyl ester to *iso*-propyl Grignard reagent are reported in parentheses.

[b]*trans*-α,β-Unsaturated enone (2*R*)-2-[*N*-(Boc)amino]-1-hydroxy-hex-4-en-3-one **3i**.

[c](2*R*)-2-[*N*-(Boc)Amino]-1-hydroxy-hept-6-en-3-one **3h**; in addition, a 1:4 mixture of **3h** and (2*R*)-2-[*N*-(Boc)amino]-3-vinyl-pent-4-en-1,3-diol **2f** was isolated in 22% yield.

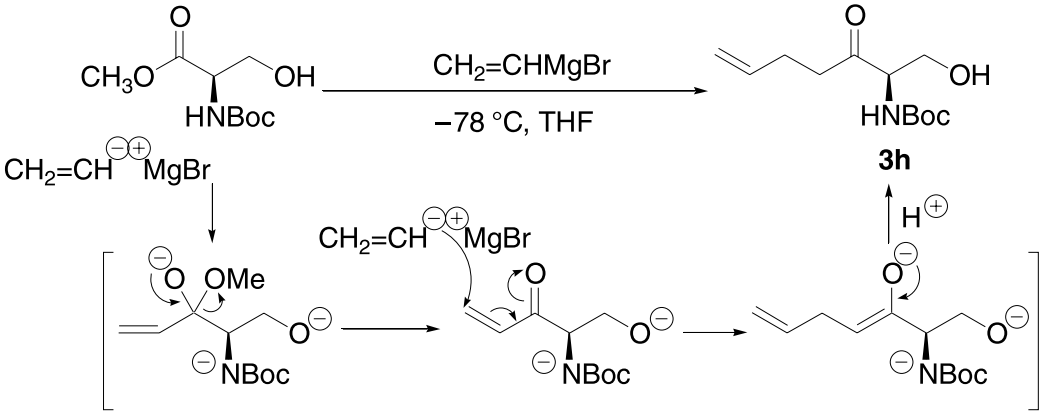
[d](2*R*)-2-[*N*-(Boc)Amino]-4-methyl-pentane-1,3-diol **4**, resulting from ketone reduction, was also isolated as a 4:1 diastereomeric mixture in 32% (41%) yield.

22% yield of a mixed fraction containing a 1:4 ratio of **3h** and **2f**. Addition of *N*-Boc-D-serine methyl ester to vinylmagnesium bromide gave a similar result. Homoallylic ketone **3h** was identified based on the presence of its carbonyl carbon at 207 ppm, as well as its COSY spectrum in $CDCl_3$, in which the vinyl protons (5.01 and 5.79 ppm) were shown to be coupled to allylic protons at 2.37 ppm. Apparently, attack of the ester followed by loss of methoxide ion provided the α,β-unsaturated ketone **3f**, which underwent conjugate addition to furnish the corresponding enolate and delivered **3h** after work-up (Scheme 2). Homoallylic ketone has been previously reported as the side product from addition of vinylmagnesium bromide to β-hydroxy ester derivatives in ether (16, 17). The addition of allyl magnesium chloride on *N*-Boc-D-serine methyl ester provided diol **2e** in 68% yield, as well as *trans*-α,β-unsaturated enone **3i** in 16% yield. Enone **3i** was likely formed from β,γ-unsubstituted ketone during quenching of the reaction with aqueous saturated NH_4Cl, which has previously been reported to effect conjugation (18).

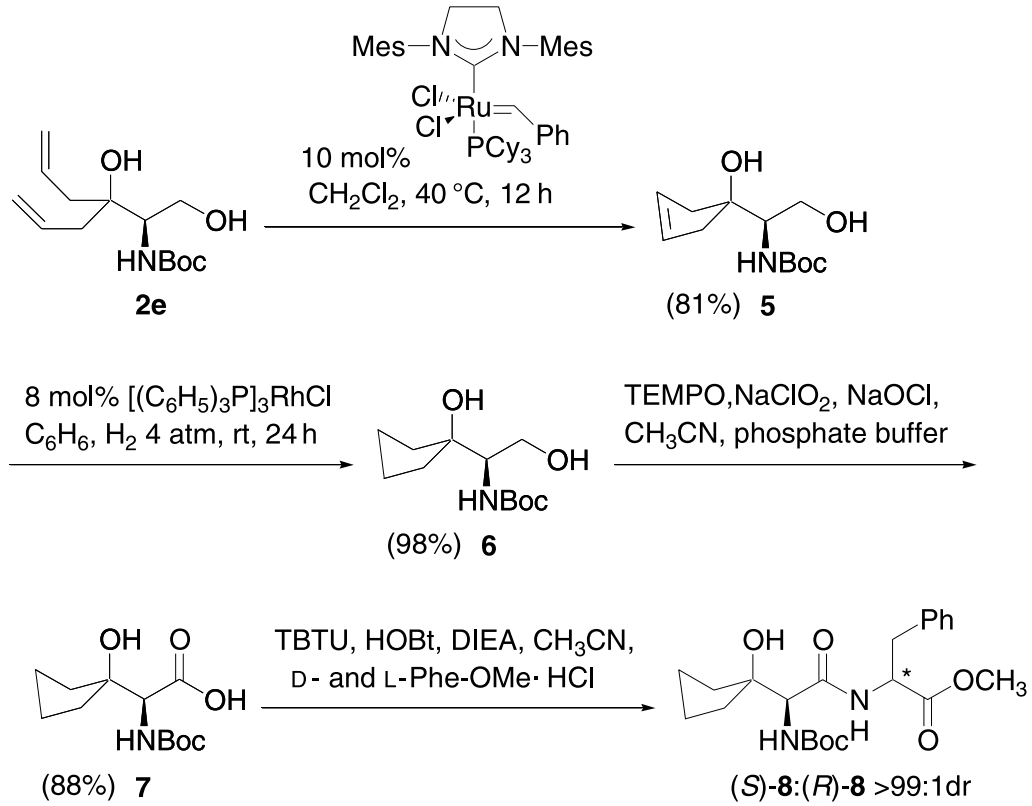
Cycloalkyl β-hydroxy α-amino acids, such as **7** in racemic form, have served as intermediates for preparation of novel β-lactam antibiotics (19–21). (*S*)-Cleonin, a component of the antitumor antibiotic cleorycin, is a cyclopropyl β-hydroxy α-amino acid that has recently been made by a route featuring the titanium(VI)-isopropoxide-catalysed addition of ethyl magnesium bromide to a fully protected serine methyl ester (22, 23). Cyclopentyl β-hydroxy α-amino acid has been introduced into the antimicrobial agent R-106 aureobasidin (24) by a route featuring a retro-aldol–aldol reaction, in which the β-hydroxy-*N*-methyl valine residue loses acetone and incorporates cyclopentanone into the native peptide (25, 26). The new aureobasidin analogue showed activity comparable with the native peptide R-106 (26). In light of such interest in cycloalkyl β-hydroxy α-amino acids, cyclopentenyl amino diol **5** was synthesized by ring-closure metathesis on bis-allyl amino diol **2e** (27–29). Exposure of amino diol **2e** to benzylidene[1,3-bis(mesitylene)-2-imidazolidinylidene]tricyclohexylphosphine ruthenium(IV) dichloride (10 mol%) in CH_2Cl_2 for 24 h at

© 2004 NRC Canada

Scheme 2. Mechanism for the formation of (2*R*)-2-[*N*-(Boc)amino]-1-hydroxy-hept-6-en-3-one **3h**.



Scheme 3. Synthesis and enantiomeric purity of cyclopentane amino acid **7**.



40 °C provided a dark brown, crude reaction product that was first passed through a silica gel column and then treated with activated carbon for 12 h at room temperature to yield **5** as a colorless oil in 81% yield (30). Reduction of the double bond in the five-membered ring of **5** was accomplished using Wilkinson's catalyst, which provided, after a similar chromatography – activated carbon purification, saturated product **6** in 98% yield (31, 32).

As in our synthesis of β-hydroxyvaline (14), selective primary alcohol oxidation was accomplished by treating diols **2a**–**2g** and **6** with TEMPO (2,2,6,6-tetramethyl-1-piperidinyloxy) free radical, sodium chlorite, and sodium hypochlorite in a sodium-phosphate-buffered acetonitrile solution (Scheme 1) (33). *N*-Boc-β,β-Dialkylserines **1a**–**1g** and **7** were obtained in 72%–96% yields after purification by silica gel column chromatography (Table 1).

To ascertain if racemization had occured during the synthesis of the various β,β-dialkylserines **1a**–**1f** and **7** from *N*-Boc-D-serine methyl ester, the enantiomeric purity of cyclopentane amino acid **7** was evaluated after conversion to diastereomeric dipeptide **8** (Scheme 3). Both (*S*)- and (*R*)-phenylalanine methyl ester hydrochloride were independently coupled with acid **7**, using benzotriazol-1-yl-1,1,3,3-tetramethyluronium tetrafluoroborate (TBTU) and 1-hydroxybenzotriazole (HOBt) in acetonitrile. Observation of the signals for the diastereotopic α-protons at 3.91 and 3.84 ppm in the 400 MHz ^{1}H NMR spectra of **8** (obtained after aqueous workup) during incremental additions of (*S*)-**8** in (*R*)-**8** in

© 2004 NRC Canada

$CDCl_3$, demonstrated dipeptide (*R*)-**8** to be of >98% diastereomeric purity. Protected diastereomer (*S*)-**8** and *N*-Boc-β,β-dialkylserines **1a**–**1g** and **7** are thus all presumed to be of similarly high enantiomeric purity.

Conclusion

The diversity oriented synthesis of enantiopure L-*N*-Boc-β,β-dialkylserines has been achieved in two practical steps from *N*-(Boc)-D-serine methyl ester as chiral educt. In light of applications of alkyl-branched serines in the study of biologically active peptides and the synthesis of other amino acids and heterocycles, this route provides a useful set of tools for peptide science and novel building blocks for diversity oriented synthesis.

Experimental section

General

Reagent and solvent purification, spectroscopic and spectrometric analyses, and chromatography — all were performed as described in the general section of the experimental that was presented in a previous work (14). The spectra for **1b**, **1f**, and **1g** were measured in D_2O with added NaOD, using dioxane (3.75 ppm, 67.19 ppm) as internal reference; in $CDCl_3$, the compounds were observed as conformational isomers. The synthesis and the analysis of (*S*)-β-hydroxy-*N*-(Boc)valine **1a** was performed as described previously (14). Minor reaction components were characterized by LC-MS using total ion chromatography (TIC).

General procedure for preparation of diol derivatives

A solution of *N*-(Boc)-L-serine methyl ester (548 mg, 2.5 mmol) in Et_2O at –78 °C was treated dropwise with a solution of the Grignard reagent (600 mol%, 15 mmol). The initial volume of Et_2O was adjusted to afford a 0.1 mol L^{-1} concentration of *N*-(Boc)-L-serine methyl ester after Grignard reagent addition. The dry ice bath was removed, and the reaction mixture was stirred for 2 h at room temperature, cooled to 0 °C, and treated dropwise with a solution of aqueous saturated NH_4Cl (20 mL). The phases were separated, and the aqueous layer was extracted with EtOAc (3 × 20 mL). The organic phases were combined, washed with brine, dried with $MgSO_4$, filtered, and evaporated to an oily residue, which was purified on silica gel.

(2*R*)-2-[*N*-(Boc)Amino]-3-ethyl-pentane-1,3-diol (2b)

Product from addition of ethyl magnesium bromide (3.0 mol L^{-1} in Et_2O) was purified on a silica gel column using a gradient of 5%–10% EtOAc in hexanes as eluant. First to elute was diol **2b,** a white solid (501 mg, 81%). TLC R_f = 0.30 (50% EtOAc in hexanes); mp 97 to 98 °C. $[\alpha]_D^{20}$ –29.0° (*c* 1.0, $CHCl_3$). ^{1}H NMR (400 MHz, $CDCl_3$) δ: 0.84 (t, 3H, *J* = 7.31), 0.90 (t, 3H, *J* = 7.38), 1.45 (s, 9H), 1.50–1.61 (m, 3H), 1.66–1.75 (m, 1H), 3.05 (s, 1H), 3.32 (s, 1H), 3.57 (d, 1H, *J* = 9.0), 3.78 (d, 1H, *J* = 4.7), 4.00 (d, 1H, *J* = 11.2), 5.50 (d, 1H, *J* = 8.9). ^{13}C NMR (100 MHz, $CDCl_3$) δ: 7.6, 7.9, 27.2, 28.2, 28.5, 54.4, 63.6, 78.2, 79.6, 156.5. HR-MS calcd. for $C_{12}H_{26}NO_4$ ($[MH]^+$): 248.1862; found: 248.1871. Anal. calcd. for $C_{12}H_{25}NO_4$: C 58.27, H 10.19, N 5.66; found: C 58.44, H 10.50, N 5.65.

Second to elute was (2*R*)-2-[*N*-(Boc)amino]-1-hydroxy-pentan-3-one (**3b**), an oil (22 mg, 4%): TLC R_f = 0.14 (50% EtOAc in hexanes). ^{1}H NMR (400 MHz, $CDCl_3$) δ: 0.97 (q, 3H, *J* = 7.6), 1.44 (s, 9H), 3.48–3.68 (m, 4H). MS (TIC) *m*/*z*: 219.8 ($[M + 2H]^+$).

(2*R*)-2-[*N*-(Boc)Amino]-1,1-diphenyl-propane-1,3-diol (2c)

Product from addition of phenyl magnesium bromide (3.0 mol L^{-1} in Et_2O) was purified on a silica gel column using a gradient of 10%–15% EtOAc in hexanes as eluant. First to elute was diol **2c**, a white solid (678 mg, 79%): TLC R_f = 0.48 (50% EtOAc in hexanes); mp 68 to 69 °C. $[\alpha]_D^{20}$ 65.6° (*c* 1.0, $CHCl_3$). ^{1}H NMR (400 MHz, $CDCl_3$) δ: 1.32 (s, 9H), 2.91 (s, 1H), 3.67 (d, 1H, *J* = 11.0), 3.77 (d, 1H, *J* = 10.7), 4.65 (d, 1H, *J* = 7.7), 4.86 (s, 1H), 5.53 (d, 1H, *J* = 8.4), 7.13–7.31 (m, 6H), 7.45–7.51 (m, 4H). ^{13}C NMR (100 MHz, $CDCl_3$) δ: 28.4, 55.5, 63.9, 79.9, 81.8, 125.2 (2C), 125.5 (2C), 126.9, 127.0, 128.3 (2C), 128.6 (2C), 144.7, 145.5, 156.2. HR-MS calcd. for $C_{20}H_{26}NO_4$ ($[MH]^+$): 344.1862; found: 344.1851.

Second to elute was (2*R*)-2-[*N*-(Boc)amino]-3-hydroxy-1-phenyl-propan-1-one (**3c**), an oil (27 mg, 4%): TLC R_f = 0.37 (50% EtOAc in hexanes). ^{1}H NMR (400 MHz, CD_3OD) δ: 1.45 (s, 9H), 3.80 (dd, 1H, *J* = 5.0, *J* = 11.4), 3.91 (dd, 1H, J_1 = 4.7, J_2 = 11.4), 5.23 (s, 1H), 7.00–7.53 (m, 2H), 7.54–7.66 (m, 1H), 8.01 (m, 2H). MS (TIC) *m*/*z*: 266.8 ($[MH]^+$).

(2*R*)-2-[*N*-(Boc)Amino]-3-benzyl-4-phenyl-butane-1,3-diol (2d)

Product from addition of benzyl magnesium bromide (3.0 mol L^{-1} in Et_2O) was purified on a silica gel column using a gradient of 10%–15% EtOAc in hexanes as eluant. First to elute was diol **2d**, a white solid (687 mg, 74%): TLC R_f = 0.49 (50% EtOAc in hexanes); mp 86 to 87 °C. $[\alpha]_D^{20}$ –13.6° (*c* 1.0, $CHCl_3$). ^{1}H NMR (400 MHz, $CDCl_3$) δ: 1.44 (s, 9H), 2.68–3.00 (m, 6H), 3.64 (br s, 1H), 3.92 (br s, 2H), 5.19 (br s, 1H), 7.19–7.33 (m, 10H). ^{13}C NMR (100 MHz, $CDCl_3$) δ: 28.1, 28.5, 42.6, 42.8, 57.0, 63.6, 80.0, 126.9 (2C), 128.5 (4C), 130.9 (4C), 136.4 136.6, 156.7. HR-MS calcd. for $C_{22}H_{30}NO_4$ (TOF EI): 372.2175; found: 372.2174. Anal. calcd. for $C_{22}H_{29}NO_4$+H_2O: C 67.84, H 8.02, N 3.60; found: C 67.91, H 8.11, N 3.65.

Second to elute was (2*R*)-3-[*N*-(Boc)amino]-4-hydroxy-1-phenyl-butan-2-one (**3d**), an oil (77 mg, 11%): TLC R_f = 0.39 (50% EtOAc in hexanes). ^{1}H NMR (400 MHz, CD_3OD) δ: 1.45 (s, 9H), 3.79 (d, 1H, *J* = 10.9), 3.89 (s, 2H), 3.90 (d, 1H, *J* = 10.9), 4.29 (s, 1H), 7.20–7.19 (m, 5H). MS (TIC) *m*/*z*: 280.8 ($[MH]^+$).

(2*R*)-2-[*N*-(Boc)Amino])-3-allyl-hex-5-ene-1,3-diol (2e)

Product from addition of allyl magnesium bromide (1.0 mol L^{-1} in Et_2O) was purified on a silica gel column using a gradient of 20%–25% EtOAc in hexanes as eluant. First to elute was diol **2e**, a white solid (485 mg, 68%): TLC R_f = 0.48 (50% EtOAc in hexanes); mp 69 to 70 °C. $[\alpha]_D^{20}$ –21.0° (*c* 1.0, $CHCl_3$). ^{1}H NMR (400 MHz, $CDCl_3$) δ: 1.45 (s, 9H), 2.30–2.36 (m, 3H), 2.45 (dd, 1H, J_1 = 6.4, J_2 = 14.0), 3.30–3.37 (m, 2H), 3.59 (d, 1H, *J* = 8.9), 3.80 (d, 1H, *J* = 10.5), 4.00 (d, 1H, *J* = 10.8), 5.10–5.18 (m, 4H), 5.51 (d,

© 2004 NRC Canada

1H, J = 9.0), 5.78–5.90 (m, 2H). ^{13}C NMR (100 MHz, $CDCl_3$) δ: 28.5, 40.47, 41.3, 54.9, 63.3, 77.0, 79.8, 119.2, 119,3, 132.8, 132.9, 156.3. HR-MS calcd. for $C_{14}H_{26}NO_4$ ($[MH]^+$): 272.1862; found: 272.1874. Anal. calcd. for $C_{14}H_{25}NO_4$: C 61.97, H 9.29, N 5.16; found: C 61.71, H 9.52, N 5.08.

Second to elute was (2*R*)-2-[*N*-(Boc)amino]-1-hydroxy-hex-4-en-3-one (**3i**), an oil (109 mg, 16%): TLC R_f = 0.44 (50% EtOAc in hexanes). ^{1}H NMR (400 MHz, $CDCl_3$) δ: 1.44 (s, 9H), 1.94 (d, 3H, J = 6.3), 3.76 (s, 1H), 3.88 (m, 2H), 6.31 (d, 1H, J = 15.6), 7.07 (m, 1H). MS (TIC) *m/z*: 230.8 ($[MH]^+$).

(2*R*)-2-[*N*-(Boc)Amino]-3-vinyl-pent-4-en-1,3-diol (2f)

A solution of *N*-Boc-L-serine methyl ester (1.1 g, 5.0 mmol) in THF (20 mL) at –78 °C was treated with a solution of vinyl magnesium bromide in THF (1.0 mol L^{-1}, 600 mol%, 30 mmol, 30 mL), and the reaction mixture was stirred, quenched, and purified as described in the general procedure. Chromatography was performed using a gradient of 25%–30% EtOAc in hexanes as eluant. First to elute was homoallylic ketone (2*R*)-2-[*N*-(Boc)amino]-1-hydroxy-hept-6-en-3-one **3h**, a white solid (429 mg), TLC R_f = 0.53 (50% EtOAc in hexanes); mp 57 to 58 °C. $[\alpha]_D^{20}$ –30.0° (*c* 1.0, $CHCl_3$). ^{1}H NMR (400 MHz, $CDCl_3$) δ: 1.45 (s, 9H), 2.36–2.39 (m, 2H), 2.65–2.75 (m, 3H), 3.90 (m, 1H), 3.96 (m, 1H), 4.33 (s, 1H), 5.01 (m, 2H), 5.76–5.81 (s, 1H), 5.79 (m, 1H). ^{13}C NMR (100 MHz, $CDCl_3$) δ: 28.1, 29.0, 39.8, 62.4, 63.8, 81.1, 116.3, 137.4, 158.0, 207.9. HR-MS calcd. for $C_{12}H_{22}NO_4$ ($[MH]^+$): 244.1549; found: 244.1551. Anal. calcd. for $C_{12}H_{21}NO_4$: C 59.24, H 8.70, N 5.76; found: C 59.29, H 8.80, N 5.59.

Then a 1:4 mixture of **3h** and diol **2f** was recovered (264 mg, 22%).

Last to elute was diol **2f**, a white solid (306 mg, 25%): TLC R_f = 0.48 (50% EtOAc in hexanes); mp 68 to 69 °C. $[\alpha]_D^{20}$ 35.7° (*c* 1.0, $CHCl_3$). ^{1}H NMR (400 MHz, $CDCl_3$) δ: 1.44 (s, 9H), 3.66 (br s, 1H), 3.75 (d, 1H, J = 3.1), 3.78 (d, 1H, J = 3.2), 3.96 (d, 1H, J = 16.9), 5.17 (d, 1H, J = 10.7), 5.25–5.34 (br m, 3H), 5.44 (d, 1H, J = 17.2), 5.89–6.02 (br m, 2H). ^{13}C NMR (100 MHz, $CDCl_3$) δ: 28.5, 56.1, 63.2, 79.7, 79.8, 114.2, 114.4, 139.9, 140.2, 156.5. HR-MS calcd. for $C_{12}H_{22}NO_4$ ($[MH]^+$): 244.1549; found: 244.1551. Anal. calcd. for $C_{12}H_{21}NO_4$: C 59.24, H 8.70, N 5.76; found: C 59.20, H 9.06, N 5.70.

(2*R*)-2-[*N*-(Boc)Amino]-3-isopropyl-4-methyl-pentane-1,3-diol (2g)

Product from addition of *iso*-propyl magnesium chloride (2.0 mol L^{-1} in Et_2O) was purified on a silica gel column using a gradient of 10%–15% EtOAc in hexanes as eluant. First to elute was diol **2g**, a white solid (262 mg, 38%): TLC R_f = 0.55 (50% EtOAc in hexanes); mp 84 to 85 °C. $[\alpha]_D^{20}$ –24.4° (*c* 1.0, $CHCl_3$). ^{1}H NMR (400 MHz, $CDCl_3$) δ: 1.01 (m, 12H), 1.45 (s, 9H), 2.06 (br s, 2H), 2.94 (s, 1H), 3.26 (br s, 1H), 3.83 (br s, 1H), 3.94 (br d, 2H, J = 7.7), 5.41 (br s, 1H). ^{13}C NMR (100 MHz, $CDCl_3$) δ: 17.9, 18.6, 18.7, 19.1, 28.5, 32.4, 34.9, 53.5, 64.8, 79.7, 80.0, 156.1. HR-MS calcd. for $C_{14}H_{30}NO_4$ ($[MH]^+$) 276.2175; found: 276.2179. Anal. calcd. for $C_{14}H_{29}NO_4$: C 61.06, H 10.61, N 5.09; found: C 61.48, H 10.78, N 5.08.

Second to elute was (2*R*)-2-[*N*-(Boc)amino]-1-hydroxy-4-methyl-pentan-3-one (**3g**), an oil (110 mg, 19%): R_f = 0.38 (50% EtOAc in hexanes). ^{1}H NMR (400 MHz, CD_3OD) δ: 1.07 (d, 3H, J = 6.8), 1.11 (d, 3H, J = 6.8), 1.45 (s, 9H), 2.96 (sept, 1H, J = 6.9), 3.75–3.86 (m, 2H), 1.45 (s, 9H), 4.79 (s, 1H). MS (TIC) *m/z*: 232.8 ($[MH]^+$).

Third to elute was (2*R*)-2-[*N*-(Boc)amino]-4-methyl-pentane-1,3-diol (**4**), a white solid (186 mg, 32%) containing a 4:1 diastereomeric mixture, as ascertained on measurement of the diastereotopic multiplets for the C_4 proton at 1.80 and 1.68 ppm. TLC R_f = 0.15 (50% EtOAc in hexanes). Signals for the major diastereomer: ^{1}H NMR (400 MHz, CD_3OD) δ: 0.92 (d, 3H, J = 6.6), 0.97 (d, 3H, J = 6.9), 1.78 (s, 9H), 1.80 (m, 1H), 3.31–3.53 (m, 1H), 3.53- 3.76 (m, 3H), 6.26 (d, 1H, J = 8.4).

Distinct signals for the minor isomer: ^{1}H NMR (400 MHz, CD_3OD) δ: 1.68 (m, 1H), 5.82 (d, 1H, J = 8.4). MS (TIC) *m/z*: 234.9 ($[MH]^+$).

General procedure for preparation of *N*-protected β,β-dialkyl-L-serines (1a–1g) and (7)

A mixture of diol **2b**–**2g** (1.5 mmol), sodium phosphate buffer (6.0 mL, 0.67 mol L^{-1}, pH = 6.7), and TEMPO (10 mol%, 0.15 mmol, 24 mg) in acetonitrile (7.5 mL) was heated to 35 °C and treated simultaneneously over 2 h (Caution! Do not mix bleach and sodium chlorite before adding to the reaction mixture) (33) with sodium chlorite (200 mol%, 3 mmol, 1.5 mL of solution: 5.71 g 80% mass fraction, 50.5 mmol in 25 mL of water) and diluted sodium hypochlorite (2 mol%, 0.03 mmol, 790 μL of solution: 0.66 mL commercial bleach 10.8% mass fraction in 25 mL of water). The mixture was stirred at 35 °C overnight, cooled to room temperature, treated with solid citric acid (pH = 3), and extracted with EtOAc (3 × 10 mL). The organic phases were combined, dried with $MgSO_4$, filtered, and evaporated. The solid residue, containing **1b**–**1g** and **7**, was purified by filtration through a pad of silica gel using, initially, 5% EtOAc in hexanes, followed by a solution of 1% AcOH in AcOEt. Evaporation of the collected filtrate gave *N*-protected β,β-dialkyl-L-serines **1b**–**1g** and **7**.

(2*R*)-2-[*N*-(Boc)Amino]-3-ethyl-3-hydroxy-pentanoic acid (1b)

Product was isolated as a white solid (361 mg, 92%): TLC R_f = 0.35 (89% $CHCl_3$, 10% MeOH, 1% CH_3CO_2H); mp 113 to 114 °C. $[\alpha]_D^{20}$ –9.5° (*c* 1.0, $CHCl_3$). ^{1}H NMR (300 MHz, D_2O, NaOD) δ: 0.80–0.91 (m, 6H), 1.43 (s, 9H), 1.46–1.66 (m, 4H), 3.98 (s, 1H). ^{13}C NMR (75 MHz, D_2O, NaOD) δ: 7.5, 7.7, 27.5, 28.3, 28.5, 60.6, 76.6, 81.8, 158.2, 178.9. HR-MS calcd. for $C_{12}H_{24}NO_5$ ($[MH]^+$): 262.1654; found: 262.1659. Anal. calcd. for $C_{12}H_{23}NO_5$: C 55.16, H 8.87, N 5.36; found: C 55.31, H 9.09, N 5.36.

(2*R*)-2-[*N*-(Boc)Amino]-3-hydroxy-3,3-diphenyl-propionic acid (1c)

Product was isolated as a white solid (407 mg, 76%): TLC R_f = 0.55 (89% $CHCl_3$, 10% MeOH, 1% CH_3CO_2H); mp 175 to 176 °C. $[\alpha]_D^{20}$ 29.9° (*c* 1.0, $CHCl_3$). ^{1}H NMR (400 MHz, CD_3OD) δ: 1.32 (s, 9H), 5.27 (s, 1H), 7.17 (m, 2H), 7.28 (m, 4H), 7.53 (m, 4H). ^{13}C NMR (100 MHz, $CDCl_3$) δ: 28.6, 60.6, 80.5, 80.8, 126.9 (2C), 127.2 (2C),

© 2004 NRC Canada

127.9, 128.0, 129.0 (4C), 145.7, 146.0, 157.5, 174.6. HR-MS calcd. for $C_{20}H_{24}NO_5$ ([MH]$^+$): 358.1654; found: 358.1645. Anal. calcd. for $C_{20}H_{23}NO_5$: C 67.21, H 6.49, N 3.92; found: C 67.05, H 6.66, N 4.00.

(2*R*)-2-[*N*-(Boc)Amino]-3-benzyl-3-hydroxy-4-phenyl-butyric acid (1d)

Product was isolated as a white solid (428 mg, 74%): TLC R_f = 0.48 (89% $CHCl_3$, 10% MeOH, 1% CH_3CO_2H); mp 76 to 77 °C. $[\alpha]_D^{20}$ –20.0° (*c* 1.0, MeOH). ^{1}H NMR (400 MHz, CD_3OD) δ: 1.46 (s, 9H), 2.66 (d, 1H, *J* = 14.1), 2.85–2.92 (m, 3H), 4.0 (s, 1H), 7.19–7.32 (m, 10H). ^{13}C NMR (100 MHz, CD_3OD) δ: 28.7, 43.2, 43.3, 60.4, 76.7, 80.8, 127.4, 127.5, 128.9, 129.0, 132.1 (2C), 138.0 (2C), 157.8, 175.4. HR-MS calcd. for $C_{22}H_{27}NO_5$ (TOF EI): 385.1877; found: 385.1889. Anal. calcd. for $C_{22}H_{27}NO_5$: C 68.55, H 7.06, N 3.63; found: C 68.10, H 7.17, N 3.68.

(2*R*)-2-[*N*-(Boc)Amino]-3-allyl-3-hydroxy-hex-5-enoic acid (1e)

Product was isolated as a yellow oil (334 mg, 78%): TLC R_f = 0.45 (89% $CHCl_3$, 10% MeOH, 1% CH_3COOH). $[\alpha]_D^{20}$ 14.4° (*c* 1.0, CH_3OH). ^{1}H NMR (400 MHz, CD_3OD) δ: 1.45 (s, 9H), 2.27–2.39 (m, 4H), 4.84 (s, 1H), 5.08–5.16 (m, 4H), 5.80–5.96 (m, 2H). ^{13}C NMR (100 MHz, CD_3OD) δ: 28.7, 41.4, 41.7, 60.4, 75.9, 80.8, 119.1, 119.3, 134.2, 134.4, 157.8, 174.3. HR-MS calcd. for $C_{14}H_{24}NO_5$ (TOF EI): 286.1654; found: 286.1660.

(2*R*)-2-[*N*-(Boc)Amino]-3-hydroxy-3-vinyl-pent-4-enoic acid (1f)

Product was isolated as yellow oil **1f** (313 mg, 81%): TLC R_f = 0.40 (89% $CHCl_3$, 10% MeOH, 1% CH_3CO_2H). $[\alpha]_D^{20}$ 17.9° (*c* 1.0, $CHCl_3$). ^{1}H NMR (300 MHz, D_2O, NaOD) δ: 1.42 (s, 9H), 4.02 (s, 1H), 5.23–5.36 (m, 4H), 5.96–6.08 (m, 2H). ^{13}C NMR (75 MHz, D_2O, NaOD) δ: 28.3, 62.8, 77.3, 81.9, 115.9, 116.0, 138.7, 139.2, 158.1, 177.0. HR-MS calcd. for $C_{12}H_{20}NO_5$ ([MH]$^+$): 258.1342; found: 258.1344.

(2*R*)-2-[*N*-(Boc)Amino]-3-hydroxy-3-isopropyl-4-methyl-pentanoic acid (1g)

Product was isolated as a white solid **1g** (313 mg, 72%): TLC R_f = 0.57 (89% $CHCl_3$, 10% MeOH, 1% CH_3CO_2H); mp 55 to 56 °C. $[\alpha]_D^{20}$ 18.0° (*c* 1.0, $CHCl_3$). ^{1}H NMR (300 MHz, D_2O, NaOD) δ: 0.84–1.01 (m, 12H), 1.44 (s, 9H), 1.88–1.98 (m, 1H), 2.03–2.14 (m, 1H), 4.19 (s, 1H). ^{13}C NMR (75 MHz, D_2O, NaOD) δ: 16.8, 17.6, 17.8, 31.5, 35.1, 55.1, 67.2, 79.5, 81.7, 158.1, 180.8. HR-MS calcd. for $C_{14}H_{28}NO_5$ (TOF EI): 290.1967; found: 290.1966.

(2*R*)-2-[1-*N*-(Boc)Amino-2-(1′-hydroxy-cyclopentyl]-acetic acid (7)

Product was isolated from TEMPO oxidation of diol **6** (39.6 mg, 0.161 mmol) as a yellow oil **7** (37 mg, 88%): TLC R_f = 0.40 (89% $CHCl_3$, 10% MeOH, 1% CH_3COOH). $[\alpha]_D^{20}$ –86.5° (*c* 1.5, $CHCl_3$). ^{1}H NMR (400 MHz, $CDCl_3$) δ: 1.45 (s, 9H), 1.61–1.85 (m, 8H), 4.25 (d, 1H, *J* = 8.5), 5.74 (d, 1H, *J* = 8.1). ^{13}C NMR (100 MHz, $CDCl_3$) δ: 23.3, 24.1, 28.4, 37.4, 38.0, 60.5, 80.7, 83.6, 156.5, 174.8. HR-MS calcd. for $C_{12}H_{22}NO_5$ ([MH]$^+$): 260.1498; found: 260.1510.

(1′*R*)-1-[1′-*N*-(Boc)Amino-2′-hydroxy-ethyl]-cyclopent-3-enol (5)

A solution of amino diol **2e** (68 mg, 0.25 mmol) in degassed CH_2Cl_2 (1 mL) was treated with benzylidene[1,3-bis(mesitylene)-2-imidazolidinylidene]tricyclohexylphosphine ruthenium(IV) dichloride (21 mg, 0.025 mmol) under an argon atmosphere, stirred overnight at 40 °C, and evaporated to a dark brown, oily residue, which was passed through a silica gel column using a 1:1 mixture of EtOAc in $CHCl_3$ as eluant. The colored product was stirred overnight with activated charcoal (50 mass equiv., 3.4 g) in CH_2Cl_2 (25 mL) to give, after filtration, cyclopentene **5** as a colorless oil (49 mg, 81%): TLC R_f = 0.39 (70% EtOAc in hexanes). $[\alpha]_D^{20}$ –10.5° (*c* 1.0, $CHCl_3$). ^{1}H NMR (300 MHz, $CDCl_3$) δ: 1.46 (s, 9H), 2.34–2.68 (m, 6H), 3.67 (m, 1H), 3.84 (dd, 1H, J_1 = 3.2, J_2 = 11.4), 3.99 (dd, 1H, J_1 = 3.0, J_2 = 11.4), 5.49 (d, 1H, *J* = 8.5), 5.73 (s, 2H). ^{13}C NMR (75 MHz, $CDCl_3$) δ: 28.5, 45.4, 46.1, 57.4, 64.4, 79.8, 84.8, 128.1, 128.8, 156.4. HR-MS calcd. for $C_{12}H_{22}NO_4$ ([MH]$^+$): 244.1549; found: 244.1552.

(1′*R*)-1-[1′-*N*-(Boc)Amino-2′-hydroxy-ethyl]-cyclopentanol (6)

A solution of cyclopentene **5** (60 mg, 0.25 mmol) in degassed benzene (3.1 mL) was treated with tris(triphenylphosphine)chlororhodium(I) (9.34 mol%, 0.01 mmol, 9.3 mg), heated at 60 °C under a hydrogen atmosphere (4 atm (1 atm = 101.325 kPa)) for 24 h, and evaporated to a dark brown residue, which was passed through a pad of silica gel using a 1:1 mixture of EtOAc in $CHCl_3$ as eluant. The colored product was stirred overnight with activated charcoal (50 mass equiv., 3.0 g) in $CHCl_3$ (25 mL) and filtered to give cyclopentane **6** as a white solid (59 mg, 98%): TLC R_f = 0.39 (70% EtOAc in hexanes); mp 88 to 89 °C. $[\alpha]_D^{20}$ –14.1° (*c* 1.0, $CHCl_3$). ^{1}H NMR (300 MHz, $CDCl_3$) δ: 1.45 (s, 9H), 1.52–1.95 (m, 8H), 3.27 (br s, 1H), 3.37 (br s, 1H), 3.49 (d, 1H, *J* = 8.9), 3.83 (d, 1H, *J* = 10.1), 3.97 (dd, 1H, J_1 = 2.8, J_2 = 11.2), 5.61 (d, 1H, *J* = 8.8). ^{13}C NMR (75 MHz, $CDCl_3$) δ: 23.5, 24.1, 28.5, 38.4, 38.5, 57.6, 64.5, 79.6, 85.6, 156.4. HR-MS calcd. for $C_{12}H_{24}NO_4$ ([MH]$^+$): 246.1705; found: 246.1712.

Enantiomeric purity of (2*R*)-2-[1-*N*-(Boc)amino-2-(1′-hydroxy-cyclopentyl)]-acetic acid (7)

A solution of **7** (15 mg, 0.058 mmol) in CH_3CN (0.5 mL) at 0 °C was treated with HOBt (100 mol%, 11 mg, 0.058 mmol) and TBTU (150 mol%, 28 mg, 0.087 mmol), stirred for 30 min, and treated with a premixed solution of (*S*)- or (*R*)-phenylalanine methyl ester hydrochloride (300 mol%, 37.5 mg, 0.174 mmol) and diisopropylethylamine (DIEA) (400 mol%, 30 mg, 0.232 mmol, 41 μL) in CH_3CN (0.5 mL) at 0 °C. The reaction mixture was stirred for 48 h at room temperature when TLC (EtOAc) showed complete disappearance of the starting acid **7**. The solvent was evaporated, and the solid residue was resuspended in CH_2Cl_2 (10 mL). The organic phase was washed with an aqueous saturated solution of $NaHCO_3$ (2 × 3 mL), 1 N NaH_2PO_4 (2 × 3 mL), and brine (3 mL); dried with $MgSO_4$; filtered; and evaporated to give a residue that was directly examined by 400 MHz ^{1}H NMR spectroscopy in $CDCl_3$. Observation of the 400 MHz ^{1}H NMR spectra during incremental addi-

© 2004 NRC Canada

tions of (*S*)-**8** in (*R*)-**8** in $CDCl_3$ and respective measurement of the signals for the diastereotopic α-protons at 3.91 and 3.84 ppm demonstrated dipeptide (*R*)-**8** to be of >98% diastereomeric purity.

(2*R*, 2′*S*)-*N*-2-[1-*N*-(Boc)Amino-2-(1′-hydroxy-cyclopentyl)]-acetyl phenylalanine methyl ester (8)

(S)-8

^{1}H NMR (400 MHz, $CDCl_3$) δ: 1.45 (s, 9H), 1.50–1.95 (m, 8H), 3.05 (dd, 1H, J_1 = 6.8, J_2 = 14.0), 3.14 (dd, 1H, J_1 = 5.5, J_2 = 13.8), 3.71 (s, 3H), 3.91 (d, 1H, J = 8.6), 4.83 (q, 1H, J_1 = 6.5, J_2 = 13.0), 5.55 (d, 1H, J = 8.3), 6.85 (d, 1H, J = 7.4), 7.14 (d, 2H, J = 7.4), 7.20–7.35 (m, 3H). MS (TIC) *m*/*z*: 421.1 ($[MH]^+$).

(R)-8

^{1}H NMR (400 MHz, $CDCl_3$) δ: 1.43 (s, 9H), 1.48–1.90 (m, 8H), 3.03 (dd, 1H, J_1 = 7.9, J_2 = 14.0), 3.17 (dd, 1H, J_1 = 5.4, J_2 = 13.9), 3.72 (s, 3H), 3.84 (d, 1H, J = 8.6), 4.83 (q, 1H, J_1 = 7.7, J_2 = 13.5), 5.53 (d, 1H, J = 8.4), 6.85 (d, 1H, J = 8.0), 7.14 (d, 2H, J = 7.2), 7.20–7.35 (m, 3H). MS (TIC) *m*/*z*: 421.1 ($[MH]^+$).

Acknowledgements

This research was supported in part by the Natural Sciences and Engineering Research Council of Canada (NSERC), the Ministère de l'Éducation du Québec, and Valorisation-Recherche Québec.

References

1. V.J. Hruby, G. Li, C. Haskell-Luevano, and M. Shenderovich. Biopolymers, **43**, 219 (1997).
2. T. Wakamiya, K. Shimbo, T. Shiba, K. Nakajima, M. Neya, and K. Okawa. Bull. Chem. Soc. Jpn. **55**, 3878 (1982).
3. C. Xiong, W. Wang, and V.J. Hruby. J. Org. Chem. **67**, 3514 (2002).
4. K. Sato and A.P. Kozikowski. Tetrahedron Lett. **30**, 4073 (1989).
5. B. Hofmann, P. Dauban, J.-P. Biron, P. Potier, and R.H. Dodd. Heterocycles, **46**, 473 (1997).
6. T.N. Wade, F. Gaymard, and R. Guedj. Tetrahedron Lett. **29**, 2681 (1979).
7. K. Nakajima, M. Neya, S. Yamada, and K. Okawa. Bull. Chem. Soc. Jpn. **55**, 3049 (1982).
8. J.E. Baldwin, R.M. Adlington, and N.G. Robinson. J. Chem. Soc. Chem. Commun. 153 (1987).
9. Recent synthesis of β-alkyl branched α-amino acids: M.J. O'Donnell, J.T. Cooper, and M.M. Mader. J. Am. Chem. Soc. **125**, 2370 (2003), and ref. 3 therein.
10. M.A. Blaskovich, G. Evindar, N.G.W. Rose, S. Wilkinson, Y. Luo, and G.A. Lajoie. J. Org. Chem. **63**, 3631 (1998), and ref. 11 therein.
11. U. Schöllkopf, W. Hartwig, K.-H. Pospischil, and H. Kehne. Synthesis, 966 (1981).
12. U. Schöllkopf, J. Nozulak, and U. Groth. Synthesis, 868 (1982).
13. Y.N. Belokon, K.A. Kochetkov, N.S. Ikonnikov, T.V. Strelkova, S.R. Harutyunyan, and A.S. Saghiyan. Tetrahedron Asymmetry, **12**, 481 (2001).
14. J.E. Dettwiler and W.D. Lubell. J. Org. Chem. **68**, 177 (2003).
15. E.P. Kohler and D. Thompson. J. Am. Chem. Soc. **55**, 3822 (1933).
16. B. Schmidt and H. Wildemann. Synlett, **10**, 1591 (1999).
17. B. Schmidt and H. Wildemann. J. Chem. Soc. Perkin Trans. 1, 2916 (2000).
18. C.G. Knudsen and H. Rapoport. J. Org. Chem. **48**, 2260 (1983).
19. V.F. Martynov and N.P. Sukhinin. Zh. Obshch. Khim. **28**, 2075 (1958).
20. K.A. Kochetkov, K.K. Babievskii, N.S. Garbalinskaya, and V.M. Belikov. Izv. Akad. Nauk Arm. SSR Ser. Khim. **11**, 2515 (1982).
21. J.E. Sundeen, W.H. Koster, and R. Zahler. U.S. Patent 4 638 060. 1987.
22. A. Esposito, P.P. Piras, D. Ramazzotti, and M. Taddei. Org. Lett. **3**, 3273 (2001).
23. L. Wessjohann, N. Krass, D. Yu, and A. de Meijere. Chem. Ber. **125**, 867 (1992).
24. Y. Yoshikawa, K. Ikai, Y. Umeda, A. Ogawa, K. Takesako, I. Kato, and H. Naganawa. J. Antibiot. **46**, 1347 (1993).
25. M.J. Rodriguez, M.J. Zweifel, and R.J. Loncharich. J. Org. Chem. **61**, 1564 (1996).
26. M.J. Rodriguez, M.J. Zweifel, J.D. Farmer, R.S. Gordee, and R.J. Loncharich. J. Antibiot. **49**, 386 (1996).
27. T.M. Trnka and R.H. Grubbs. Acc. Chem. Res. **34**, 18 (2001).
28. A. Fürstner. Angew. Chem. Int. Ed. **39**, 3012 (2000).
29. B.M. Trost and K. Dogra. J. Am. Chem. Soc. **124**, 7256 (2002).
30. J.H. Cho and B.M. Kim. Org. Lett. **5**, 531 (2003).
31. J.A. Osborn, F.H. Jardine, J.F. Young, and G. Wilkinson. J. Chem. Soc. A, 1711 (1966).
32. R.E. Harmon, J.L. Parsons, D.W. Cooke, S.K. Gupta, and J. Schoolenberg. J. Org. Chem. **34**, 3684 (1969).
33. M. Zhao, J. Li, E. Mano, Z. Song, D.M. Tschaen, E.J.J. Grabowski, and P.J. Reider. J. Org. Chem. **64**, 2564 (1999).

© 2004 NRC Canada

Reactions of phenyldimethylsilyllithium with β-*N*,*N*-dimethylaminoenones: A convenient synthesis of β-dimethyl(phenyl)silylacrylic acid and its derivatives[1]

Ian Fleming, Elena Marangon, Chiara Roni, Matthew G. Russell, and Sandra Taliansky Chamudis

Abstract: Phenyldimethylsilyllithium reacted with 5,5-dimethyl-3-(*N*,*N*-dimethylamino)cyclohex-2-enone (**7**), 3-(*E*)-*N*,*N*-dimethylaminopropenal (**11**), and 4-*N*,*N*-dimethylaminobut-3-en-2-one (**13**) to give the corresponding β-silyl-α,β-unsaturated carbonyl compounds **8**, **12**, and **14**, in which the dimethylamino group has been displaced by the phenyldimethylsilyl group. Phenyldimethylsilyllithium reacted with ethyl β-*N*,*N*-dimethylaminopropenoate (**15**) by conjugate addition, but, in contrast to the ketones **7** and **13** and the aldehyde **11**, the intermediate enolate **16** was *C*-protonated in the aqueous work-up to give ethyl 3-*N*,*N*-dimethylamino-3-dimethyl(phenyl)silylpropanoate (**17**). When the enolate **16** was instead given a mysteriously brief treatment with methyl iodide before work-up, the product was ethyl 3-(*E*)-dimethy(phenyl)silylpropenoate (**18**). Phenyllithium and methyllithium also added conjugatively to ethyl β-*N*,*N*-dimethylaminoacrylate (**15**) but, in contrast to the silyl case, the intermediate enolate **22** reacted unexceptionally with methyl iodide to give the products **25** and **26** of stereoselective *C*-methylation. This synthesis of the ester **18** was used to synthesize the Oppolzer sultam derivative **30**.

Key words: conjugate addition, elimination, substitution, silyllithium, silylenone.

Résumé : Le phényldiméthylsilyllithium réagit avec la 5,5-diméthyl-3-(*N*,*N*-diméthylamino)cyclohex-2-énone (**7**), le 3-(*E*)-*N*,*N*-diméthylaminopropénal (**11**) et la 4-*N*,*N*-diméthylaminobut-3-én-2-one (**13**) pour conduire à la formation des composés carbonylés β-silyl-α,β-insaturés correspondants, **8**, **12** et **14** dans lesquels le groupe diméthylamino a été remplacé par un groupe phényldiméthylsilyle. Avec le β-*N*,*N*-diméthylaminopropénoate d'éthyle (**15**), le phényldiméthylsilyllithium donne une réaction d'addition conjuguée, mais, par opposition avec ce qui a été observé avec les cétones **7** et **13** et l'aldéhyde **11**, l'intermédiaire énolique **16** la récupération aqueuse des produits provoque une *C*-alkylation qui conduit au 3-*N*,*N*-diméthylamino-3-diméthyl(phényl)silylpropénoate (**17**). Toutefois, lorsque l'énolate **16** est soumis à un mystérieusement court traitement par de l'iodure de méthyle avant la récupération des produits, le produit obtenu est alors le 3-(*E*)-diméthyl(phényl)silylpropénoate d'éthyle (**18**). Le phényllithium et le méthyllithium s'ajoutent aussi de façon conjugue au β-*N*,*N*-diméthylaminopropénoate d'éthyle (**15**) mais, par opposition à ce qui a été observé dans le cas silylé, l'intermédiaire énolique **22** réagit sans surprise avec l'iodure de méthyle pour conduire aux produits **25** et **26** de *C*-méthylation stéréosélective. Cette synthèse de l'ester **18** a été utilisée pour réaliser la synthèse du dérivé sultame d'Oppolzer **30**.

Mots clés : addition conjugue, élimination, substitution, silyllithium, silylénone.

[Traduit par la Rédaction]

Introduction

The phenyldimethylsilyllithium reagent (1) was first made and, along with its triphenylsilyl analogue, quite extensively studied by Gilman in the 1950s and 1960s (2), but it has been relatively little used except as a source of the corresponding cuprate reagent (3), which we introduced in 1978 (4). More recently, we have been engaged in further studies of the silyllithium reagent itself (5), and of its reactions with a number of substrates, including aromatic esters (6), α-silyloxy esters (7), saturated esters (8), amides (9, 10), thioamides (11), nitriles (12), sulfonamides (13), and acid chlorides (14). Most notably, tertiary amides have been a source of several remarkable reactions, which we have to a large

Received 12 September 2003. Published on the NRC Research Press Web site at http://canjchem.nrc.ca on 13 February 2004.

Dedicated with affection to Professor Ed Piers.

I. Fleming,[2] E. Marangon, C. Roni, M.G. Russell, and S. Taliansky Chamudis. Department of Chemistry, Lensfield Road, Cambridge CB2 1EW, U.K.

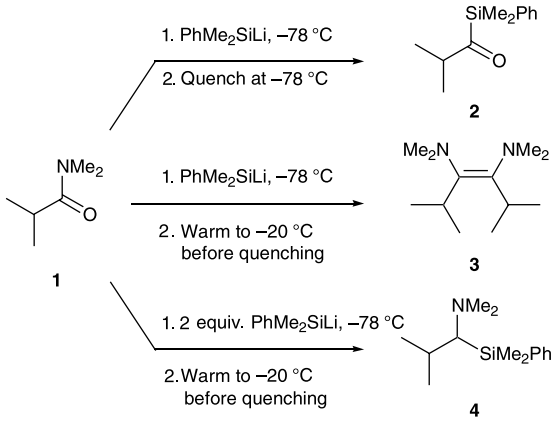
[1]This article is part of a Special Issue dedicated to Professor Ed Piers.
[2]Corresponding author (e-mail: if10000@cam.ac.uk).

 doi: 10.1139/V03-194 © 2004 NRC Canada

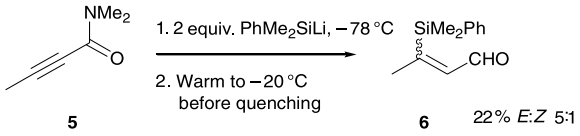
extent unravelled (9, 10). Most strikingly, the simple *N*,*N*-dimethylamide **1** could be induced to give in good yield any one of three distinct products (**2**, **3**, or **4**), depending upon the reaction conditions and (or) the stoichiometry (Scheme 1) (8, 9).

Almost every change we made to the structure of the starting amide led to other surprises, an experience Gilman was not immune to either. Thus, the reaction of the acetylenic amide **5** proved to be different from the saturated amide, not only because conjugate addition was now both possible and what occurred, but also because reduction took place as well, at least in the products **6** that we could recognise (Scheme 2). Conjugate addition is hardly surprising, since silyllithium and stannyllithium reagents can easily react in this way with unsaturated carbonyl compounds in THF (15), although the cuprates are usually rather better, but reduction to an aldehyde had not been a common outcome in our earlier work. The yield, however, was unimpressive, and we did not pursue this unpromising line. More interesting were the results of reactions with vinylogous amide systems, which we reported in a preliminary communication (16), and which we report in full here.

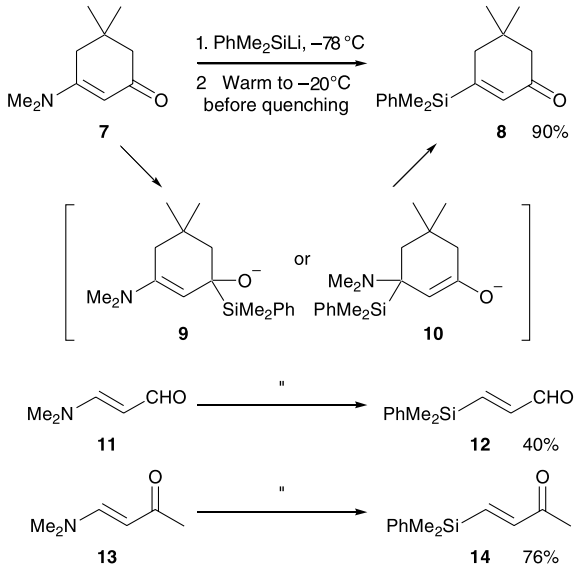
Scheme 1.



Scheme 2.



Scheme 3.



Results and discussion

The reaction of phenyldimethylsilyllithium with the enone **7** was unexceptional in giving the β-silylenone **8** in which the dimethylamino group has been replaced by the silyl group (Scheme 3). Two pathways might have been followed. In one, the silyllithium reagent attacked the carbonyl group directly to give the enamine **9**, hydrolysis of which, followed by elimination of water, would give the enone **8**. Alternatively, conjugate attack took place to give the enolate **10**, which underwent elimination of the dimethylamino group. A similar outcome was found for the enal **11** giving the enal **12**, in a less clean reaction with the same two possible pathways. The conjugate addition–elimination pathway is certainly followed in the reaction between the silyllithium reagent and the enone **13**, which gave the β-silylenone **14** in good yield. Furthermore, it is known that a β-amino group encourages conjugate addition by organolithium reagents (17), and trimethylsilyllithium is also known to give conjugate addition, rather than direct attack at the carbonyl group, with cyclohexenones in THF (15). Finally, it is not obvious why the pathway involving direct attack at the carbonyl group should not enter the carbene-forming sequence that we have seen is so accessible in the reactions described earlier, and involved, for example, in the formation of the enediamine **3** and the α-aminosilane **4** (9, 10). It seems likely that the conjugate addition–elimination pathway is followed in all of these reactions.

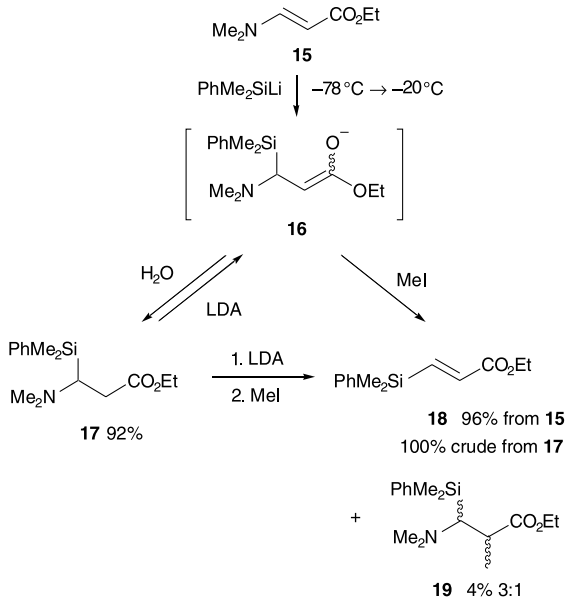
The products **8**, **12**, and **14** are easily made by other methods (18–20), and so we have not taken this investigation any further. Instead, we investigated the corresponding reaction with the vinylogous carbamate **15**, which gave us a curious result, and, incidentally, a better synthesis of the ester **18** than the one we had been using quite extensively hitherto in our synthetic work.

When we added the silyllithium reagent to the ester **15**, the only product after an aqueous quench was that of conjugate addition **17** (Scheme 4). While this is unsurprising in itself, it raised the first question: why was the dimethylamino group eliminated in the experiments in Scheme 3, and not here? One possibility is that the ketone and aldehyde enolates are kinetically protonated on oxygen. The resultant enols might then live long enough to expel the dimethylamino group in the aqueous medium before they underwent tautomerism to the ketones or the aldehyde. In contrast, it is possible that the ester enolate is protonated directly on carbon, and the dimethylamino group would not then be so easily lost.

However, this was not the most puzzling observation. If, instead of the aqueous quench, we added methyl iodide, and then worked up in the usual way, the major product was the β-silylester **18**. This was not the result that we expected, because the carbon atom of the enolate ion **16** ought to have

© 2004 NRC Canada

Scheme 4.

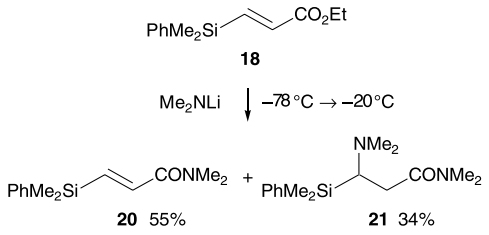


been more nucleophilic towards methyl iodide than the dimethylamino group. The product of enolate methylation **19** was detectable on one occasion, and then only in a small amount. Similarly, when we regenerated the enolate **16** from the ester **17** using LDA, and treated that enolate with methyl iodide, the same unsaturated ester **18** was formed.

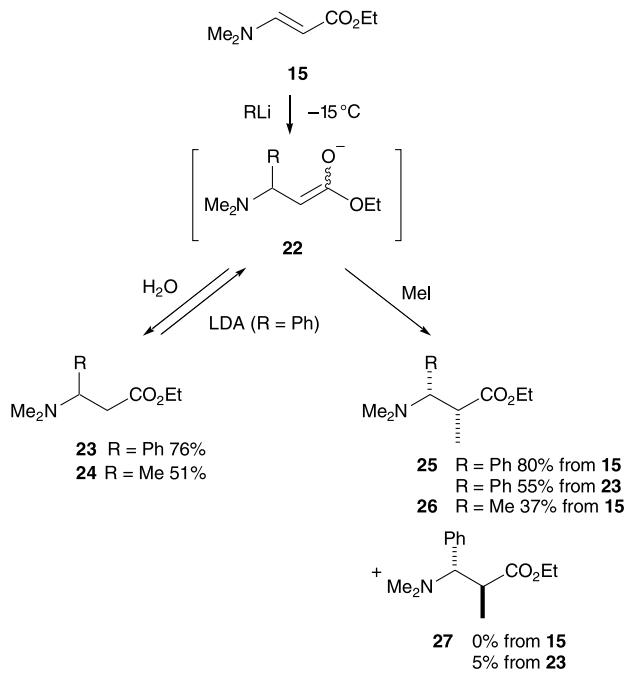
Additionally remarkable is that the elimination of dimethylamine **16** → **18** achieved by the treatment with methyl iodide took only a few minutes at –20 °C. In contrast, if we treated the amine **17** with methyl iodide in THF, little *N*-methylation took place over 18 h at room temperature — we recovered the amine **17** in 86% yield. Evidently, the α-silyl group does not on its own increase the nucleophilicity of the nitrogen lone pair (21) enough to suggest an exceptionally easy *N*-methylation. It seems improbable that coordination by the enolate oxygen to the silyl group could make the nitrogen lone pair more nucleophilic than the carbon atom of the enolate ion, and we have no convincing explanation for the ease with which the elimination took place. It is not specific to using methyl iodide, since benzyl bromide and allyl bromide had the same effect, although not in such good yield. The most obvious explanation would have been that the dimethylamide ion had already been expelled from the enolate **16** before the aqueous quench, and had added back during the aqueous quench giving the saturated ester **17**. The role of the methyl iodide in this scenario would have been to quench the dimethylamide ion, and prevent it from adding back. This is not the explanation, because the unsaturated ester **18**, which would have been the product of that elimination, reacted with lithium dimethylamide to give the amides **20** and **21** (Scheme 5). These products were not present in the reaction mixtures from Scheme 3. Furthermore, quenching the reaction mixture from the conjugate addition by injecting it directly into aqueous hydrochloric acid, which can be expected to protonate the amide ion rapidly, gave largely the ester **17** (67%) and only a little (9%) of the product of elimination **18**.

The easy elimination induced by methyl iodide has something to do with the presence of the silyl group. We repeated

Scheme 5.



Scheme 6.

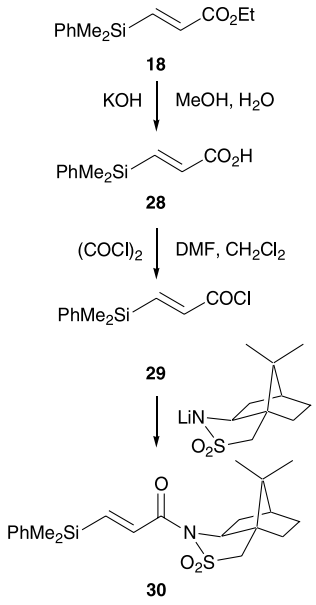


the reaction with the ester **15** using phenyllithium instead of phenyldimethylsilyllithium (Scheme 6). Conjugate addition took place to give the enolate **22** (R = Ph); quenching with ammonium chloride solution gave the amino ester **23**, but quenching with methyl iodide gave the expected enolate methylation, with the expected (22) high degree of diastereoselectivity in favour of the known (23) isomer **25**. Regeneration of the enolate **22** (R = Ph) from the ester **23** using LDA, followed by methylation with methyl iodide, gave the same result: *C*-methylation, this time with a detectable but small amount of the diastereoisomer **27** formed as well. In some rather lower yielding, but otherwise similar reactions, methyllithium also added in a conjugate manner, and the enolate **22** (R = Me) could be trapped with either protons or methyl iodide to give the esters **24** and **26**, respectively.

The ester **18** has usually been prepared most economically by hydrosilylation–dehydrogenation of ethyl acrylate (24), but in that otherwise excellent method it is always contaminated with the saturated analogue, no matter how much of an excess of ethyl acrylate is used to limit the amount of hydrosilylation. In our experience, the saturated analogue, although harmless to what we were doing, has frequently been difficult to remove, and we have found ourselves carrying it through the next few steps of our synthetic work until we found a stage at which it could be removed relatively easily.

© 2004 NRC Canada

Schcme 7.



The synthesis reported here is free of this problem. For further development, it was helpful to saponify the crude ester **18**, to separate acidic products from the inevitable silicon-containing by-products. The carboxylic acid was occasionally crystalline, but recrystallization, either of the acid or of various salts was not practical. Since we needed it attached to Oppolzer's sultam, as did he (25), we converted the acid into its acid chloride and joined it onto the auxiliary (Scheme 7), at which point we had a crystalline derivative **30** that could be purified by recrystallization. The overall yield of this useful compound from the amino ester **15** was 41%.

Experimental

^{13}C NMR data from attached proton tests (APT) are given in the form 133.6– when the C atom has an odd number of H atoms attached, and 167.2+ when it has an even number of H atoms attached.

(*E*)- and (*Z*)-3-Dimethyl(phenyl)silybut-2-enal (6)

But-2-ynoic acid *N*,*N*-dimethylamide (26) (0.22 g, 2.00 mmol) in THF (2 mL) was added dropwise to dimethyl-(phenyl)silyllithium (1, 7) (4.8 mL, 1 mol dm^{-3} in THF, 4.8 mmol) at –78 °C, and the mixture was kept at –20 °C for 1 h. Saturated aqueous sodium bicarbonate (5 mL) and diethylether (5 mL) were added. The aqueous portion was removed and the basic products extracted from the organic fraction with dilute hydrochloric acid (3 N). The aqueous layers were basified (10% NaOH) to pH 12 and then extracted with ether (3 × 20 mL), dried ($MgSO_4$) and evaporated under reduced pressure to give the crude products (0.24 g). Chromatography (SiO_2, CH_2Cl_2) gave the *aldehydes* (0.09 g, 22%) as an inseparable mixture (*E*:*Z*, 5:1). (*E*)-isomer: ^{1}H NMR (250 MHz, $CDCl_3$) δ: 10.1 (1H, d, *J* = 7.8, CHO), 7.5–7.4 (2H, m, Ph), 7.4–7.2 (3H, m, Ph), 6.3 (1H, dq, *J* = 7.8 and 1.7, C=CH), 2.2 (3H, d, *J* = 1.7, CMe), and 0.4 (6H, s, $SiMe_2$). ^{13}C NMR ($CDCl_3$) δ: 192.9–, 167.2+, 142.9–, 137.5+, 133.6–, 128.3–, 15.9– and –0.9– (1 signal missing). (*Z*)-isomer: ^{1}H NMR (250 MHz, $CDCl_3$) δ: 9.7 (1H, d, *J* = 8.5, CHO), 7.5–7.4 (2H, m, Ph), 7.4–7.2 (3H, m, Ph), 6.5 (1H, dq, *J* = 8.5 and 1.4, C=CH), 2.1 (3H, d, *J* = 1.4, CMe), and 0.5 (6H, s, $SiMe_2$). ^{13}C NMR (100 MHz, $CDCl_3$) δ: 190.2–, 163.9+, 137.8–, 135.4+, 134.0–, 129.7–, 128.1–, 26.8– and –0.4–.

5,5-Dimethyl-3-(dimethylphenylsilyl)cyclohex-2-enone (8)

Dimethyl(phenyl)silyllithium (2.4 mL, 1 mol dm^{-3} in THF, 2.4 mmol) was added dropwise to 5,5-dimethyl-3-(dimethylamino)cyclohex-2-enone (0.37 g, 2.20 mmol) in THF (2 mL) at –78 °C, the mixture stirred at –78 °C for 1 h, and then kept at –20 °C for 1 h. Saturated aqueous sodium bicarbonate solution (5 mL) and diethyl ether (5 mL) were added. The aqueous portion was removed and the basic products removed from the organic fraction with dilute hydrochloric acid. The organic layers were dried ($MgSO_4$) and evaporated under reduced pressure to give the crude neutral products (0.65 g) as a yellow oil. Chromatography (SiO_2, CH_2Cl_2) gave the ketone (18) (0.51 g, 90%) as an oil. R_f(CH_2Cl_2) 0.44. IR ν_{max} (film, cm^{-1}): 1675 (C=O), 1589 (C=C), 1249 (SiC), and 1112 (SiC). ^{1}H NMR (250 MHz, $CDCl_3$) δ: 7.5–7.45 (2H, m, Ph), 7.4–7.35 (3H, m, Ph), 6.30 (1H, t, *J* = 1.8, C=CH), 2.24 (2H, s, CH_2CO), 2.19 (2H, d, *J* = 1.8, CH_2C=C), 0.95 (6H, s, CMe_2), and 0.43 (6H, s, $SiMe_2$). ^{13}C NMR (100 MHz, $CDCl_3$) δ: 199.0+, 163.4+, 136.0–, 135.4–, 133.9–, 129.6–, 128.1–, 51.5+, 42.1+, 34.3+, 28.1– and –4.4–. MS *m*/*z* (EI): 259.1 (50%, MH$^+$), 243.1 (90, M – Me), and 137.0 (100) (found: M$^+$, 258.14402; $C_{16}H_{22}OSi$ requires M, 258.14398).

3-(*E*)-Dimethyl(phenyl)silylpropenal (12)

3-(*E*)-*N*,*N*-Dimethylaminopropenal (90%, 0.5 mL, 4.5 mmol) in THF (4.5 mL) was added dropwise to a solution of dimethyl(phenyl)silyllithium (0.9 mol dm^{-3} in THF, 5.5 mL, 4.95 mmol) under argon at –78 °C. The mixture was stirred for 1 h at this temperature and then at –15 °C for 1 h. Saturated aqueous sodium bicarbonate solution (5 mL) was added. The organic layer was washed with water (2 mL). The combined aqueous layers were extracted with ether (3 × 2 mL). The combined organic layers were washed with aqueous hydrochloric acid (3 N, 2 mL), brine (2 mL), dried ($MgSO_4$), and the solvent evaporated under reduced pressure. The residue was distilled to give the aldehyde (19) (0.342 g, 40%), bp 91 °C at 0.9 mmHg (1 mmHg = 133.322 Pa). R_f(CH_2Cl_2) 0.84. IR ν_{max} (film, cm^{-1}): 1693 (C=O), 1428 (C=C), 1251 (SiC), and 1117 (SiC). ^{1}H NMR (400 MHz, $CDCl_3$) δ: 9.53 (1H, d, *J* = 7.6, CHO) 7.52–7.50 (2H, m, Ph), 7.40–7.30 (4H, m, Ph and CHSi), 6.54 (1H, dd, *J* = 18.7 and 7.6, CHCO), and 0.47 (6H, s, Si*Me*$_2$). ^{13}C NMR (100 MHz, $CDCl_3$) δ: 194.5–, 156.4–, 145.1–, 135.7+, 133.7–, 129.8–, 128.1– and –3.4–. MS *m*/*z* (EI): found: M$^+$, 190.08271; $C_{11}H_{14}OSi$ requires M, 190.08132.

4-(*E*)-[Dimethyl(phenyl)silyl]but-3-en-2-one (14)

Dimethyl(phenyl)silyllithium (0.9 mol dm^{-3} in THF, 5.25 mL, 4.7 mmol) was added dropwise to a solution of 4-*N*,*N*-dimethylaminobut-3-en-2-one (0.5 mL, 4.3 mmol) in THF (5 mL) at –78 °C under argon. The mixture was stirred at this temperature for 1 h, and then at –10 °C for 1 h. Aque-

© 2004 NRC Canada

ous sodium bicarbonate (saturated, 5 mL) and ether (5 mL) were added and the layers separated. The aqueous layer was extracted with ether (2 × 3 mL). The combined organic layers were washed with dilute hydrochloric acid (3 N, 2 × 3 mL), brine (2 mL), dried ($MgSO_4$), and the solvent evaporated off under reduced pressure. The residue was chromatographed (SiO_2, light petroleum (bp 40–60 °C)) to give the ketone (20) (0.66 g, 76%). R_f(Et_2O) 0.87. IR ν_{max} (Nujol, cm^{-1}): 1678 (C=O), 1217 ($SiMe_2$), 1115 (SiPh), 735 (Ph), and 700 (Ph). ^1H NMR (400 MHz, $CDCl_3$) δ: 7.52–7.49 (2H, m, Ph), 7.40–7.36 (3H, m, Ph), 7.11 (1H, d, *J* = 19.2, SiCH), 6.48 (1H, d, *J* = 19.2, CHCO), 2.28 (3H, s, COMe), and 0.43 (6H, s, $SiMe_2$). ^{13}C NMR (100 MHz, $CDCl_3$) δ: 198.6+, 145.6–, 144.0–, 136.3+, 133.8–, 129.6–, 127.9–, 26.3–, –3.2–. MS *m*/*z* (ESI): 227 (100%, M^+Na) (found: MNa^+, 227.0871; $C_{12}H_{16}OSi$ requires M + Na, 227.0868).

Ethyl 3-*N*,*N*-dimethylamino-3-dimethyl(phenyl)silylpropanoate (17)

Dimethyl(phenyl)silyllithium (4.1 mL, 1 mol dm^{-3} in THF, 4.1 mmol) was added dropwise to (*E*)-ethyl 3-(dimethylamino)propenoate (0.53 g, 3.72 mmol) in THF (5 mL) at –78 °C. The mixture was stirred at –78 °C for 1 h then kept at –20 °C for 1 h. Saturated aqueous sodium bicarbonate (5 mL) and ether (5 mL) were added. The aqueous portion was removed and the basic products extracted from the organic fraction with dilute hydrochloric acid (3 N). The aqueous extract was basified (10% NaOH) to pH 12 and then extracted with ether (3 × 20 mL), dried ($MgSO_4$) and evaporated under reduced pressure to give the *ester* (1.17 g, 92%) as an oil. R_f(Et_2O) 0.95. IR ν_{max} (film, cm^{-1}): 1732 (C=O), 1249 (SiC), and 1111 (SiC), 836 (SiC), 734 (Ph), and 701 (Ph). ^1H NMR (250 MHz, $CDCl_3$) δ: 7.57–7.53 (2H, m, Ph), 7.36–7.26 (3H, m, Ph), 4.03 (2H, q, *J* = 7.2, OCH_2Me), 2.92 (1H, dd, *J* = 8.7 and 5.2, CHSiN), 2.56 (1H, dd, *J* = 15.2 and 8.8, CH_AH_BCO), 2.29 (6H, s, NMe_2), 2.26 (1H, dd, *J* = 14.7 and 5.1, CH_AH_BCO), 1.20 (3H, t, *J* 7.2, OCH_2Me), 0.42 (3H, s, $SiMe_AMe_B$), and 0.37 (3H, s, $SiMe_AMe_B$). ^{13}C NMR (100 MHz, $CDCl_3$) δ: 174.2+, 138.2+, 134.5–, 129.1–, 127.8–, 60.3+, 53.6–, 43.9–, 30.8+, 14.1–, 2.4– and –3.32–. LSI-MS m/*z*: found: MH^+, 280.1750; $C_{15}H_{25}NO_2Si$ requires M + H, 280.1727. In various runs, the neutral fraction gave small amounts of the conjugated ester **18** (typically 9%), identical (^1H NMR, ^{13}C NMR) with the sample described below.

A sample of the ester **17** was stirred overnight in iodomethane at room temperature. This gave, on work-up, recovered starting material (86%) and ethyl (*E*)-3-(dimethylphenylsilyl)-propenoate (14%).

Ethyl 3-(*E*)-dimethy(phenyl)silylpropenoate (18)

Method A

Ethyl 3-(*E*)-*N*,*N*-dimethylaminopropenoate (3 mL, 21 mmol) was added dropwise to a solution of dimethyl(phenyl)silyllithium (0.52 mol dm^{-3} in THF, 48 mL, 25 mmol) and toluene (25 mL) under argon at –15 °C keeping the temperature below –10 °C, and then kept at –15 °C for 15 min. Methyl iodide (3.9 mL, 63 mmol) was added dropwise keeping the temperature below –5 °C. The mixture was stirred at room temperature for 20 min and quenched with water (10 mL). The organic layer was washed with water (2 × 10 mL) and the combined aqueous layers extracted with ether (4 × 5 mL). The combined organic layers were washed with aqueous hydrochloric acid (3 N, 7 mL). The aqueous layer was then extracted with ether (4 × 2 mL). The combined organic layers were washed with brine (10 mL), dried ($MgSO_4$), filtered and the solvent evaporated under reduced pressure to give the crude ester (27) (9.9 g, 96%). Chromatography of an earlier run, with some losses, gave pure ester (67%). R_f(Et_2O:light petroleum (bp 40–60 °C), 50:50) 0.85. IR ν_{max} (film, cm^{-1}): 1727 (C=O), 732 (Ph), and 700 (Ph). ^1H NMR (400 MHz, $CDCl_3$) δ: 7.60–7.50 (2H, m, Ph), 7.40–7.32 (3H, m, Ph), 7.28 (1H, d, *J* = 19, CH=), 6.28 (1H, d, *J* = 19, CH=), 4.21 (2H, q, *J* = 7.1, OCH_2), 1.29 (3H, t, *J* = 7.1, CH_2Me), and 0.43 (6H, s, $SiMe_2$). ^1H NMR (100 MHz, $CDCl_3$) δ: 165.7+, 147.3–, 136.4+, 135.4–, 133.8–, 129.5–, 128.0–, 60.6+, 14.2– and –3.2–. MS *m*/*z* (EI): found: M^+, 234.1083; $C_{13}H_{18}O_2Si$ requires 234.1076). MS *m*/*z* (ESI): 257 (100%, Mna^+) (found: MNa^+, 257.0971; $C_{13}H_{18}O_2Si$ requires M + Na, 257.0974). In one run, the basic fraction gave ethyl 2-methyl-3-dimethylamino-3-dimethyl(phenyl)silylpropanoate (**19**) (4%) as an inseparable mixture of isomers (~3:1) characterized only by the definitive ^1H NMR spectrum: (250 MHz, $CDCl_3$) δ major isomer: 7.60–7.55 (2H, m, Ph), 7.35–7.30 (3H, m, Ph), 4.08 (2H, q, *J* = 7.4, CO_2CH_2Me), 2.90–2.70 (2H, m, CHN and C*H*Me), 2.40 (6H, s, NMe_2), 1.23 (3H, t, *J* = 7.1, CO_2CH_2Me), 0.97 (3H, d, *J* = 6.8, CH*Me*), and 0.42 (6H, s, $SiMe_2$); minor isomer: 7.60–7.55 (2H, m, Ph), 7.35–7.30 (3H, m, Ph), 3.91 (1H, q, *J* = 7.1, $CO_2CH_AH_BMe$), 3.91 (1H, q, *J* = 7.1, $CO_2CH_AH_BMe$), 2.90–2.70 (2H, m, CHN and C*H*Me), 2.37 (6H, s, NMe_2), 1.20 (3H, t, *J* = 7.1, CO_2CH_2Me), 0.97 (3H, d, *J* = 6.8, CH*Me*), and 0.41 (6H, s, $SiMe_2$).

Method B

n-Butyllithium (1.45 mol dm^{-3} in hexanes, 5.4 mL, 7.9 mmol) was added slowly to a stirred solution of distilled diisopropylamine (1.1 mL, 7.9 mmol) in dry THF (3.6 mL) at 0 °C under nitrogen. After 15 min, the solution was cooled to –78 °C and ethyl (*E*)-3-(*N*,*N*-dimethylamino)-3-dimethyl(phenyl)silylpropanoate (1.0 g, 3.6 mmol) in dry THF (4.5 mL) added by cannula, and the mixture was stirred for 1 h. Methyl iodide (1.5 mL, 25 mmol) was added slowly, and the mixture stirred for 1 h at –78 °C and warmed over 20 min to 0 °C. Saturated ammonium chloride solution was added, the layers separated, and the aqueous layers extracted with ether. The combined organic layers were washed with brine, dried ($MgSO_4$), and evaporated to give ethyl (*E*)-3-dimethyl(phenyl)silylpropenoate (0.88 g, >100%), identical (TLC, ^1H NMR) with the earlier sample. Basification of the aqueous layers (10% NaOH), and extraction with ether gave the basic products (25 mg), which were a complex mixture of several compounds (^1H NMR).

Method C

The procedure of Method A was followed, but benzyl bromide was used in place of methyl iodide. The products were the unsaturated ester **18** (43%) and the conjugate addition product **17** (38%). There was no sign of the product of *C*-benzylation.

© 2004 NRC Canada

Method D

The procedure of Method A was followed, but allyl bromide was used in place of methyl iodide. The products were the unsaturated ester **18** (67%) and the conjugate addition product **17** (3%). There was no sign of the product of *C*-allylation.

(*E*)-*N*,*N*-Dimethyl-3-dimethyl(phenyl)silylpropenamide (20) and *N*,*N*-dimethyl-3-dimethylamino-3-dimethyl(phenyl)silylpropionamide (21)

n-Butyllithium (1.5 mL of a 1.7 mol dm^{-3} solution in hexanes, 2.55 mmol) was added to dimethylamine (2.2 mL of a 1.7 mol dm^{-3} solution in THF, 3.7 mmol) at –78 °C and stirred at this temperature for 1 h to give a solution of lithium dimethylamide. (*E*)-Ethyl 3-dimethyl(phenyl)silylpropenoate (0.39 g, 1.68 mmol) in THF (2.0 mL) was added dropwise at –78 °C and stirred at this temperature for 30 min and then kept at –20 °C for 30 min. Saturated aqueous sodium bicarbonate (5 mL) and ether (5 mL) were added. The aqueous portion was removed and the basic products extracted from the organic fraction with hydrochloric acid (3 N). The organic layer was dried ($MgSO_4$) and evaporated under reduced pressure to give (E)-N,N- *dimethyl*-3-*dimethyl*(*phenyl*)*silylpropenamide* (0.215 g, 55%). R_f(Et_2O) 0.25. ^{1}H NMR (250 MHz, $CDCl_3$) δ: 7.55–7.52 (2H, m, Ph), 7.39–7.29 (3H, m, Ph), 7.25 (1H, d, *J* = 18.4, SiCH=C*H*), 6.29 (1H, d, *J* = 18.4, C*H*=CH), 3.04 (6H, br s, $CONMe_2$), and 0.39 (6H, s, $SiMe_2$). The aqueous extract was basified (10% NaOH) to pH 12, and then extracted with ether (3 × 20 mL), dried ($MgSO_4$), and evaporated under reduced pressure to give N,N-*dimethyl*-3-(*dimethylamino*)-3-*dimethyl*(*phenyl*)*silylpropionamide* (0.16 g, 34%). R_f(Et_2O) 0.36. ^{1}H NMR (250 MHz, $CDCl_3$) δ: 7.62–7.54 (2H, m, Ph), 7.36–7.32 (3H, m, Ph), 2.88 (3H, s, $CONMe_AMe_B$), 2.82 (3H, s, $CONMe_AMe_B$), 2.60 (1H, dd, *J* = 13.2 and 5.4, CHNSi), 2.35 (6H, s, $CHNMe_2$), 2.28–1.95 (2H, m, $COCH_2$), 0.40 (3H, s, $SiMe_AMe_B$), and 0.38 (3H, s, $SiMe_AMe_B$).

Ethyl 3-*N*,*N*-dimethylamino-3-phenylpropionate (23)

Phenyllithium (1.8 mol dm^{-3}, 12.5 mL, 22.4 mmol) was added slowly to a solution of ethyl (*E*)-3-*N*,*N*-dimethylaminopropenoate (1.84 g, 2 mL, 14 mmol) in dry ether (17 mL) under argon at –15 °C, keeping the temperature below –5 °C. The mixture was stirred at –10 °C for 0.5 h and at room temperature for 2.5 h. The mixture was quenched with aqueous ammonium chloride solution (25 mL, saturated). The aqueous layer was extracted with ether (3 × 10 mL). The combined organic layers were washed with aqueous hydrochloric acid (3 N, 65 mL). The aqueous layer was extracted with ether (3 × 10 mL), and then basified to pH 11 with sodium hydroxide solution (10%) using universal indicator paper, and the aqueous layer was extracted with ether (3 × 50 mL). The combined organic layers were washed with brine (1 × 30 mL), dried ($MgSO_4$), and evaporated under reduced pressure to give the amine (28) as an oil (2.4 g, 76%). IR ν_{max}(film, cm^{-1}): 1735 (C=O), 1371 (CHCO) and 700 (Ph). ^{1}H NMR (400 MHz, $CDCl_3$) δ: 7.33 (2H, m, Ph), 7.27–7.23 (3H, m, Ph), 4.06 (2H, q, *J* = 7.1, OCH_2), 3.86 (1H, dd, *J* = 6.9 and 8.2, C*H*Ph), 2.95 (1H, dd, *J* = 14.8 and 6.9, CH_ACH_B), 2.69 (1H, dd, *J* = 14.8 and 8.2, $CH_AC H_B$), 2.18 (6H, s, NMe_2), and 1.11 (3H, t, *J* = 7.1, CH_2Me). ^{13}C NMR (100 MHz, $CDCl_3$) δ: 171.7+, 138.8+, 128.4–, 128–, 127.4–, 68.7–, 66.4+, 42.2–, 38.6+, 14.0–. MS *m*/*z* (EI): 222 (100%, MH^+) (found: MH^+, 222.1493; $C_{13}H_{19}O_2N$ requires M + H, 222.1494); hydrochloride, mp 190 °C (from Me_2CO) (lit. (29) mp 192 °C).

Ethyl (2*SR*,3*RS*)-3-dimethylamino-2-methyl-3- phenylpropionate (25)

Method A

Phenyllithium (12.5 mL, 1.8 mol dm^{-3}, 22.4 mmol) was added slowly to a solution of ethyl (*E*)-*N*,*N*-dimethylaminopropenoate (2 g, 2 mL, 14 mmol) in dry ether (17 mL) under Ar at –15 °C, keeping the temperature below 0 °C. The mixture was stirred at –10 °C for 0.5 h and then kept at room temperature for 1 h. Methyl iodide (2.2 mL, 35 mmol) was added at –15 °C, and the solution kept at room temperature for 15 h. The reaction was quenched with ammonium chloride solution (40 mL). The aqueous layer was extracted with ether (3 × 10 mL). The combined organic layers were acidified with hydrochloric acid (3 N, 65 mL). The aqueous layer was washed with ether (2 × 15 mL), basified with sodium hydroxide solution (10%), and the basic product extracted with ether (4 × 40 mL). The organic layer was washed with brine, dried ($MgSO_4$), and the solvent evaporated under reduced pressure to give the amine (23) (2.52 g, 80%). R_f(Et_2O–light petroleum (bp 40–60 °C), 1:1) 0.55. IR ν_{max} (film, cm^{-1}): 1735 (C=O), 756 (Ph), and 705 (Ph). ^{13}C NMR (400 MHz, $CDCl_3$) δ: 7.36–7.26 (3H, m, Ph), 7.13–7.12 (2H, m, Ph), 4.20 (2H, qd, *J* = 1.9 and 7.1, OCH_2), 3.68 (1H, d, *J* 11.0, PhC*H*), 3.15 (1H, dq, *J* = 11.0 and 6.8, C*H*Me), 2.10 (6H, s, NMe_2), 1.28 (3H, t, *J* 7.1, CH_2Me), and 0.93 (3H, d, *J* 6.8, $CHMe$). ^{13}C NMR (100 MHz, $CDCl_3$) δ: 175.6+, 134.0–, 129.3–, 127.9–, 127.3–, 72.3–, 60.0+, 42.1–, 41.2–, 14.6– and 14.2–. MS *m*/*z* (EI): 236 (2%, MH^+), 191 (8, MH – OEt), and 160 (100, M – Ph) (found: M^+, 236.1649; $C_{14}H_{22}NO_2$ requires M, 236.1645).

Method B

Butyllithium (1.47 mol dm^{-3} in hexane, 50 mL, 1.44 mmol) was added to a solution of diisopropylamine (0.22 mL, 1.58 mmol) in dry THF (7.20 mL) under nitrogen at –78 °C and stirred for 15 min. Ethyl 3-dimethylamino-3-phenylpropionate (0.159 g, 0.718 mmol) was added at –78 °C, and the temperature maintained for 1 h. Methyl iodide (0.11 mL, 1.8 mmol) was added, the mixture stirred at –78 °C for 30 min and then allowed to come to room temperature and kept for 1 h. The reaction was quenched with ammonium chloride solution (10 mL). The aqueous layer was extracted with ether (3 × 3 mL). The combined organic layers were washed with brine, dried ($MgSO_4$), and the solvent was evaporated off under reduced pressure. The residue was dissolved in ether (20 mL) and washed with hydrochloric acid (3 N, 20 mL). The aqueous layer was washed with ether (3 × 6 mL) and basified with sodium hydroxide solution (10%), extracted with ether (4 × 10 mL), and the combined organic layers washed with brine, dried ($MgSO_4$), and evaporated under reduced pressure to give a mixture of the esters (0.117 g, 60%) in a ratio of 10:1. R_f(Et_2O–light petroleum (bp 40–60 °C), 1:1) 0.55. ^{1}H NMR (400 MHz, $CDCl_3$) δ (signals from the major isomer, identical to those reported

© 2004 NRC Canada

above, together with signals from the minor isomer **27**): 7.36–7.26 (3H, m, Ph), 7.13–7.12 (2H, m, Ph), 3.85 (2H, q, J = 7.1, OCH_2), 3.74 (1H, d, J = 11.0, PhC*H*), 3.10 (1H, dq, J = 11.0 and 6.85, C*H*Me), 2.10 (6H, s, NMe_2), 1.35 (3H, d, J = 6.85, CH*Me*), and 0.91 (3H, t, J = 7.1, OCH_2*Me*).

Ethyl 3-*N*,*N*-dimethylaminobutanoate (24)

Methyllithium (1.54 mol dm^{-3} in Et_2O, 18.5 mL, 28.5 mmol) was added to 3-(*E*)-*N*,*N*-dimethylaminopropenoate (2 g, 14 mmol) in dry ether (17 mL) at –15 °C under nitrogen, maintaining the temperature below 0 °C. The reaction was stirred at 0 °C for 30 min and then kept at room temperature for 1 h. The reaction was quenched with ammonium chloride solution (40 mL). The aqueous layer was extracted with ether (3 × 10 mL). The combined organic layers were washed with brine, dried ($MgSO_4$), and the solvent evaporated under reduced pressure to give the amine (30) (1.14g, 51%). IR ν_{max} (film, cm^{-1}): 1732 (C=O). ^{1}H NMR (400 MHz, $CDCl_3$) δ: 4.13 (2H, q, J = 7.1, OCH_2), 3.10 (1H, ddq, J = 8.5, 5.7, and 6.6, C*H*Me), 2.53 (1H, dd, J = 14.4 and 5.7, CH_ACH_BCO), 2.23 (6H, s, NMe_2), 2.18 (1H, dd, J = 14.4 and 8.5, CH_ACH_BCO), 1.24 (3H, t, J 7.1, OCH_2*Me*), and 1.03 (3H, d, J = 6.6, CH*Me*).

Ethyl 3-*N*,*N*-dimethylamino-2-methylbutanoate (26)

Methyllithium (1.54 mol dm^{-3} in Et_2O, 37 mL, 28.5 mmol)) was added to 3-(*E*)-*N*,*N*-dimethylaminopropenoate (4 g, 28 mmol) in dry ether (34 mL) at –15 °C under nitrogen, maintaining the temperature below 0 °C. The reaction was stirred at –15 °C for 30 min and then kept at room temperature for 16 h. The mixture was cooled to –15 °C, methyl iodide (2.2 mL, 35 mmol) was added, and the mixture kept at room temperature for 16 h. The reaction was quenched with ammonium chloride solution (15 mL) and water (10 mL). The aqueous layer was extracted with ether (3 × 10 mL). The combined organic layers were washed with brine and part of the solvent evaporated under reduced pressure. The organic layer was washed with hydrochloric acid solution (3 N), and the aqueous layer was washed with ether (3 × 8 mL). The aqueous layer was basified with sodium hydroxide solution (10%), and extracted with ether (5 × 17 mL). The organic layer was washed with brine, dried ($MgSO_4$), and the solvent evaporated off to give the *amine* (1.80 g, 37%) with only one diastereoisomer detectable, presumably the 2*RS*,3*RS* isomer by analogy with the formation of the known compound **25**. IR ν_{max} (film, cm^{-1}): 1735 (C=O) and 1155 (OC). ^{1}H NMR (400 MHz, $CDCl_3$) δ: 4.15 (2H, m, OCH_2), 2.75 (1H, dq, J = 9.6 and 6.6, NC*H*Me), 2.51 (1H, dq, J = 9.6 and 6.9, COC*H*Me), 2.19 (6H, s, NMe_2), 1.09 (3H, d, J = 6.9, COCH*Me*), and 0.89 (3H, d, J = 6.6, NCH*Me*). ^{13}C NMR (100 MHz, $CDCl_3$) δ: 176.1+, 61.8–, 59.8–, 44.6–, 40.6–, 14.2– and 8.5–. MS *m*/*z* (EI): 173 (30%, M^+), 158 (20, M – Me), 128 (13, M – EtO), 73 (39, CO_2Et), and 72 (100, Me_2N=CHMe) (found: M^+, 173.1411; $C_9H_{19}NO_2$ requires M, 173.1416).

3-(*E*)-Dimethyl(phenyl)silylpropenoic acid (28)

The crude ethyl 3-(*E*)-dimethy(phenyl)silylpropenoate (**15**) (9.9 g) in methanol (40 mL) and potassium hydroxide (10 g) in distilled water (9 mL) were stirred at room temperature for 1.5 h. The methanol and ethanol were evaporated off under reduced pressure, and the residue was taken up in distilled water (30 mL), washed with ether (4 × 10 mL), acidified to pH 1 with aqueous hydrochloric acid (3 N, ~50 mL), and extracted with ether (4 × 15 mL). The combined organic layers were washed with brine (15 mL), dried ($MgSO_4$), and the solvent evaporated off under reduced pressure to give the acid (19) (3.2 g, 75% over two steps) as an indeterminately low-melting solid. R_f(Et_2O:light petroleum (bp 40–60 °C), 50:50) 0.43. IR ν_{max} (film, cm^{-1}): 1694 (C=O), 1593 (C=C), 840 ($SiMe_2$), 732 (Ph), and 700 (Ph). ^{1}H NMR (400 MHz, $CDCl_3$) δ: 7.53–7.48 (2H, m, Ph), 7.51 (1H, d, J = 19, SiCH), 7.42–7.36 (3H, m, Ph), 6.29 (1H, d, J = 19, CHCO), and 0.45 (6H, s, $SiMe_2$). ^{13}C NMR (100 MHz, $CDCl_3$) δ: 170.9+, 150.8–, 136.0+, 134.5–, 133.8–, 130.4–, 128.0–, and –3.6–. MS *m*/*z* (ESI): 229 (10%, MNa^+). Anal. calcd. for $C_{11}H_{14}O_2Si$ (%): C 64.0, H 6.8; found: C 64.0 H 6.9. Benzylamine salt, mp 130 to 131 °C (from MeOH). N.B. Upon addition of ether to the basic aqueous solution, the formation of three layers was often observed. The dark-coloured middle layer, presumably the carboxylate salt, not completely soluble in the aqueous layer, was combined with the lower aqueous layer, and carried through in the acidification step. This problem was worse when sodium hydroxide was used to hydrolyze the ester, and largely avoided by using potassium hydroxide.

***N*-{*E*-3-[Dimethyl(phenyl)silyl]propenoyl-(7*R*)-2,10-camphorsultam (30)**

Oxalyl chloride (2 mL, 23 mmol), was added to 3-(*E*)-dimethyl(phenyl)silylpropenoic acid (3.2 g, 16 mmol) in dichloromethane (11 mL) under nitrogen at room temperature, followed by *N*,*N*-dimethylformamide (0.55 mL), and the mixture was stirred at this temperature until the bubbling ceased (~1 h). The solvent and the excess oxalyl chloride were evaporated off under reduced pressure at 50 °C and then at 2 mmHg (1 mmHg = 133.322 Pa) for 2 h to give the acid chloride **29**. Meanwhile, *n*-butyllithium (1.6 mol L^{-1}, ~10 mL) was added to (1*R*)-(+)-2,10-camphorsultam (31) (3.23 g, 15 mmol) in THF (15 mL) under nitrogen at –78 °C, using 1-pyreneacetic acid as the indicator. This solution was added by cannula to the solution of the acid chloride **29** in THF (20 mL) at –78 °C, and the mixture stirred at room temperature for 1 h. The mixture was filtered through a silica pad, washing through with ether (50 mL). This filtrate was washed with sodium bicarbonate (30 mL), dried ($MgSO_4$), filtered and the solvent evaporated off under reduced pressure to give the crude product (5.694 g, 90%), which was crystallized from ethanol (3.5 mL) to give a first crop of the *imide* (2.23 g, 35% from the acid) as pale yellow needles, mp 90 to 91 °C (from EtOH). The mother liquors were then evaporated to give a second crop (0.14 g, 2%), mp 88.5–89.5 °C. The mother liquors were chromatographed (SiO_2, light petroleum (bp 40–60 °C) – Et_2O, 9:1) to give a third crop (0.765 g, 12%), mp 89.5–90 °C, making the total yield (3.13 g, 49%). $[\alpha]_D^{20}$ +63.1 (*c* 1.04 in $CHCl_3$). R_f(Et_2O–light petroleum (bp 40–60 °C), 50:50) 0.47. IR ν_{max}(Nujol, cm^{-1}): 1672 (C=O), 1598 (C=C), 1166 (SO_2N), and 1117 (SiPh). ^{1}H NMR (250 MHz, $CDCl_3$) δ: 7.52–7.50 (2H, m, Ph), 7.48 (1H, d, J = 18.2, SiCH), 7.36–7.35 (3H, m, Ph), 7.01 (1H, d, J = 18.2, CHCO), 3.93 (1H, dd, J = 7.0 and 5.7, NCH), 3.50 (1H, d, J = 13.8, $SO_2CH_AH_B$),

© 2004 NRC Canada

3.44 (1H, d, J = 13.8, $SO_2CH_AH_B$), 2.20–2.03 (2H, m), 2.00–1.84 (3H, m), 1.48–1.32 (2H, m), 1.18 (3H, s, CMe_AMe_B), 0.98 (3H, s, CMe_AMe_B), and 0.44 (6H, s, $SiMe_2$). ^{13}C NMR (100 MHz, $CDCl_3$) δ: 163.5+, 148.7–, 136.4+, 134.2–, 133.9–, 129.5–, 128.0–, 65.2–. 53.1+, 48.6+, 47.8+, 44.7–, 38.5+, 32.9+, 26.5+, 20.9–, 19.9–, –3.2– and –3.3–. MS *m*/*z* (EI): 403 (47%, M^+), 267 (22, M – $PhMe_2SiH$), 189 (100, M – Me_2N), and 135 (46, $PhMe_2Si^+$) (found: M^+ 403.1640; $C_{21}H_{29}NO_3SSi$ requires M, 403.1637). Anal. calcd. for $C_{21}H_{29}NO_3SSi$(%): C 62.5, H 7.2, N 3.5; found: C 62.5, H 7.3, N 3.4. Although this compound has been described before (25), no mp, and no spectroscopic or analytical data were given.

Acknowledgements

This work was supported by research grant (RG/M17013) from the Engineering and Physical Sciences Research Council (EPSRC) (for MGR), and by the ERASMUS scheme (for ST), to both of which we are grateful. We also thank the Department of Pharmaceutical Sciences, University of Padua for arranging summer visits (for EM and CR). We thank Professor Barry Trost for a helpful discussion about the difference between the aqueous work-up reactions in Schemes 3 and 4, and David Barden for the full characterization of the sultam **30**.

References

1. M.V. George, D.J. Peterson, and H. Gilman. J. Am. Chem. Soc. **82**, 403 (1960); H. Gilman, R.A. Klein, and H.J.S. Winkler. J. Org. Chem. **26**, 2474 (1961).
2. D. Wittenberg and H. Gilman. Quart. Rev. **13**, 116 (1959).
3. I. Fleming. *In* Organocopper reagents: A practical approach. *Edited by* R.J.K. Taylor. OUP, Oxford. 1994. Chap 12. pp. 257–292; I. Fleming. *In* Encyclopaedia of reagents for organic synthesis. *Edited by* L.A. Paquette. Wiley, Chichester. 1995. pp. 3037–3040.
4. D.J. Ager and I. Fleming. J. Chem. Soc. Chem. Commun. 177 (1978).
5. I. Fleming, R.S. Roberts, and S.C. Smith. J. Chem. Soc. Perkin Trans. 1, 1209 (1998).
6. S. Saito, K. Shimada, H. Yamamoto, E. Martínez de Marigorta, and I. Fleming. Chem. Commun. 1299 (1997).
7. I. Fleming, R.S. Roberts, and S.C. Smith. J. Chem. Soc. Perkin Trans. 1, 1215 (1998).
8. I. Fleming and U. Ghosh. J. Chem. Soc. Perkin Trans. 1, 257 (1994); A. Chénedé, N. Abd. Rahman, and I. Fleming. Tetrahedron Lett. **38**, 2381 (1997); A. Chénedé, I. Fleming, R. Salmon, and M.C. West. J. Organomet. Chem. **686**, 84 (2003).
9. I. Fleming, U. Ghosh, S.R. Mack, and B.P. Clark. Chem. Commun. 711 (1998); I. Fleming, S.R. Mack, and B.P. Clark. Chem. Commun. 713 (1998).
10. I. Fleming, S.R. Mack, and B.P. Clark. Chem. Commun. 715 (1998); I. Fleming and M.G. Russell. Chem. Commun. 198 (2003); M. Buswell and I. Fleming. Chem. Commun. 202 (2003).
11. M. Buswell and I. Fleming. ARKIVOC, **vii**, 46 (2002).
12. I. Fleming, M. Solay, and F. Stolwijk. J. Organomet. Chem. **521**, 121 (1996).
13. I. Fleming, J. Frackenpohl, and H. Ila. J. Chem. Soc. Perkin Trans. 1, 1229 (1998).
14. I. Fleming, A.J. Lawrence, R.D. Richardson, D.S. Surry, and M.C. West. Helv. Chim. Acta, **85**, 3349 (2002).
15. W.C. Still. J. Org. Chem. **41**, 3063 (1976); W.C. Still. J. Am. Chem. Soc. **99**, 4836 (1977); W.C. Still and A. Mitra. Tetrahedron Lett. 2659 (1978); E. Piers, H.E. Morton, and J.M. Chong. Can. J. Chem. **65**, 78 (1987).
16. I. Fleming, E. Marangon, C. Roni, M.G. Russell, and S. Taliansky Chamudis. Chem. Commun. 200 (2003).
17. R.F. Abdulla and K.H. Fuhr. J. Org. Chem. **43**, 4248 (1978); T. Mukaiyama and T. Ohsumi. Chem. Lett. 875 (1983); C. Fontenas, H. Aït-Haddou, E. Bejan, and G.G.A. Balavoine. Synth. Commun. **28**, 1743 (1998).
18. I. Fleming and D.A. Perry. Tetrahedron, **37**, 4027 (1981).
19. I. Fleming and N.D. Kindon. J. Chem. Soc. Perkin Trans. 1, 303 (1995).
20. I. Fleming, T.W. Newton, V. Sabin, and F. Zammattio. Tetrahedron, **48**, 7793 (1992).
21. K.J. Shea, R. Gobeille, J. Braunblett, and E. Thompson. J. Am. Chem. Soc. **100**, 1611 (1978).
22. S.G. Davies and I.A.S. Walter. J. Chem. Soc. Perkin Trans. 1, 1129 (1994); S.G. Davies, O. Ichihara, and I.A.S. Walter. J. Chem. Soc. Perkin Trans. 1, 1141 (1994).
23. E. Graf and M. Graser. Arch. Pharm. (Weinheim, Ger.), **302**, 665 (1969).
24. K. Takeshita, Y. Seki, K. Kawamoto, S. Murai, and N. Sonoda. J. Org. Chem. **52**, 4864 (1987).
25. W. Oppolzer, R.J. Mills, W. Pachinger, and T. Stevenson. Helv. Chim. Acta, **69**, 1542 (1986); see also C. Palomo, J.M. Aizpurua, M. Iturburu, and R. Urchegui. J. Org. Chem. **59**, 240 (1994).
26. E. Piers and R.T. Skerlj. Can. J. Chem. **72**, 2468 (1994).
27. S.M. Sieburth and J. Lang. J. Org. Chem. **64**, 1780 (1999).
28. E. Graf and H. Boeddeker. Liebigs Ann. Chem. **613**, 111 (1958); E. Graf, M. Graser, and F. Sitsius. Arch. Pharm. (Weinheim), **302**, 561 (1969); S.G. Davies, J. Dupont, and R.J.C. Easton. Tetrahedron: Assymetry, **1**, 279 (1990).
29. V. Franzen and H. Kuntze. Liebigs Ann. Chem. **627**, 15 (1959).
30. K. Takagi, Y. Kasuya, and K. Hattori. J. Pharm. Soc. Jpn. **72**, 1592 (1952); Chem. Abstr. **47**, 9312c (1953); T.D. Perrine. J. Org. Chem. **18**, 898 (1953); A.H. Beckett and A.F. Casy. J. Chem. Soc. 900 (1955); I.N. Nazarov and R.I. Kruglikova. Zh. Obshch. Khim. **27**, 34 (1957); Chem. Abstr. **5**1 15 521i (1957).
31. M.C. Weismiller, J.C. Towson, and F.A. Davis. Org. Synth. Coll. **8**, 104 (1993); J.C. Towson, M.C. Weismiller, G.S. Lal, A.C. Sheppard, and F.A. Davis. Org. Synth. Coll. **8**, 110 (1993).

© 2004 NRC Canada

Studies directed toward the synthesis of reiswigin A: Total synthesis of (±)-*epi*-reiswigin A[1]

David I. MaGee and Dean E. Shannon

Abstract: As a testing ground for the practical application of asymmetric synthesis, (–)-reiswigin A, a potent antiviral agent, was chosen as a target for total synthesis. Initial studies were undertaken to prove the viability of the key asymmetric step, enantioselective deprotonation of an intermediate *meso*-bicyclic ketone, using a chiral lithium amide base. Enantiomeric excesses in the range of 90%–94% were routinely obtained, even on runs as large as 10 g. Unfortunately, conversion of this key enantio-enriched intermediate to the natural product proved unsuccessful. While these studies were enroute, a parallel synthesis using the racemic compound was transformed into (±)-*epi*-reiswigin A.

Key words: asymmetric deprotonation, synthesis, (±)-*epi*-reiswigin A.

Résumé : Comme méthode d'application pratique de synthèse asymétrique, la cible choisie a été la (–)-reiswigine A, un agent antiviral puissant. Les études initiales ont été entreprises pour montrer la viabilité de l'étape asymétrique clé, la déprotonation énantiosélective cétone *méso*-bicyclique intermédiaire à l'aide d'une base chirale, un amide de lithium. On a régulièrement obtenu des excès énantiomériques de l'ordre de 90 % à 94 %, même avec des lots allant jusqu'à 10 g. Malheureusement, de cet intermédiaire clé énantiomériquement enrichi en produit naturel n'a pu être réalisée. Alors que ces travaux progressaient, dans une synthèse parallèle il a été possible de transformer le produit racémique en (±)-*épi*-reiswigine A.

Mot clés : déprotonation asymétrique, synthèse, (±)-*épi*-reiswigine A.

[Traduit par la Rédaction]

Introduction

The development of methods for the preparation of carbocylic natural products with control of relative and absolute stereochemistries has been a longstanding challenge in organic synthesis. The problem of controlling the configuration of a stereogenic centre on a pendant side chain relative to the ring to which it is attached has been particularly troublesome. We report that enantioselective deprotonation can be used to help address this problem. As a testing ground for the practical application of this strategy, a biologically and structurally interesting natural product, (–)-reiswigin A (**1**) (Fig. 1), was chosen as a target for total synthesis.

Reiswigin A is a hydroazulenoid diterpene that was obtained from the deepwater marine sponge organism *Epipolasis reiswigi* collected by submersible at 330 m. Its isolation and characterization using mass spectrometry, IR, UV, and one- and two-dimensional NMR techniques was first reported by Koehn et al. (1). It was found to have intriguing biological properties, with complete inhibitory in vitro activity against herpes simplex type 1 virus (IC_{50} 2 mg) and vesicular stomatitis virus (IC_{50} 2 mg) and partial inhibition at 20 mg against murine A59 hepatitis virus. The absolute stereochemistry was not established until Snider et al. (2) developed an asymmetric synthesis of (–)-reiswigin A in 1990. A second synthesis by Kim et al. (3) in 1994 confirmed the assignments.

Retrosynthetically (Fig. 1), it was envisaged that reiswigin A could be generated from an intermediate such as **2** via some type of intramolecular condensation reaction, i.e., dithiane alkylation of **3** with a suitable electrophile derived from **2** and methylation of the thermodynamic enolate to install the angular ring methyl (C-11). Compound **2** could be conveniently generated by oxidative cleavage of the [3.2.1]-silyl enol ether produced by desymmetrization of the *meso* ketone **4** via enantioselective deprotonation (4). Bicyclic ketones like **4** are known and can be easily accessed by [4+3]-cycloaddition (5) between compounds like **5** and **6** (6).

Results and discussions

Construction of the [3.2.1]-bicyclic ketone became the first targeted intermediate. Starting with the known ketoaldehyde **8** (6), obtained as an inseparable 5:1 mixture of stereoisomers by acid catalyzed hydrolysis of [4+3]-cycloadduct **7**, Wittig reaction with acetonyltriphenylphosphorane (7) afforded, after separation of the *endo* and *exo* isomers, *E*- and *Z*-unsaturated diketone **9** in 73% combined yield (Scheme 1). The *E*- and *Z*-isomers of diketone **9** were then hydrogenated over 10% Pd–C to yield **4** in 95% yield. Selective ketalization provided ketone **10** in 81% yield. Complete

Received 20 June 2003. Published on the NRC Research Press Web site at http://canjchem.nrc.ca on 20 February 2004.

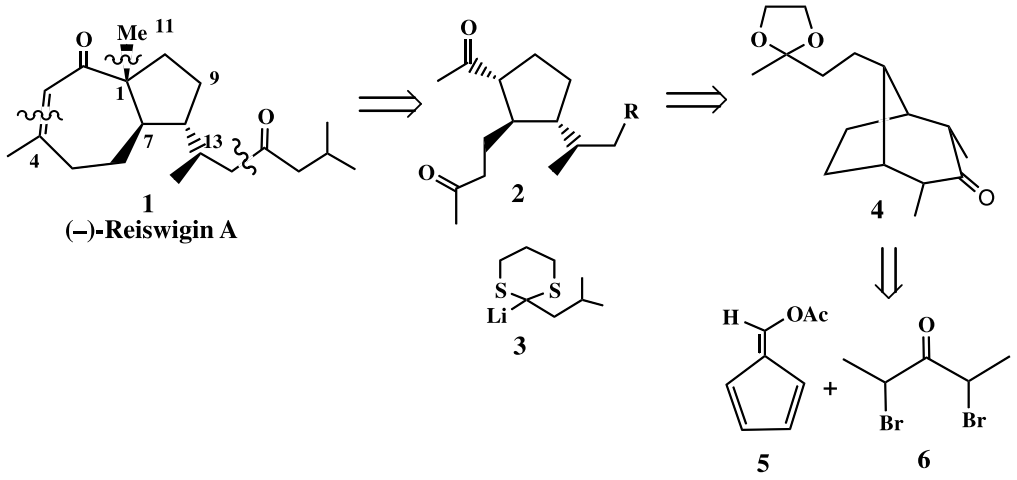
D.I. MaGee[2] and D.E. Shannon. Department of Chemistry, University of New Brunswick, P.O. Box 45222, Fredericton, NB E3B 6E2, Canada.

[1]This article is part of a Special Issue dedicated to Professor Ed Piers.

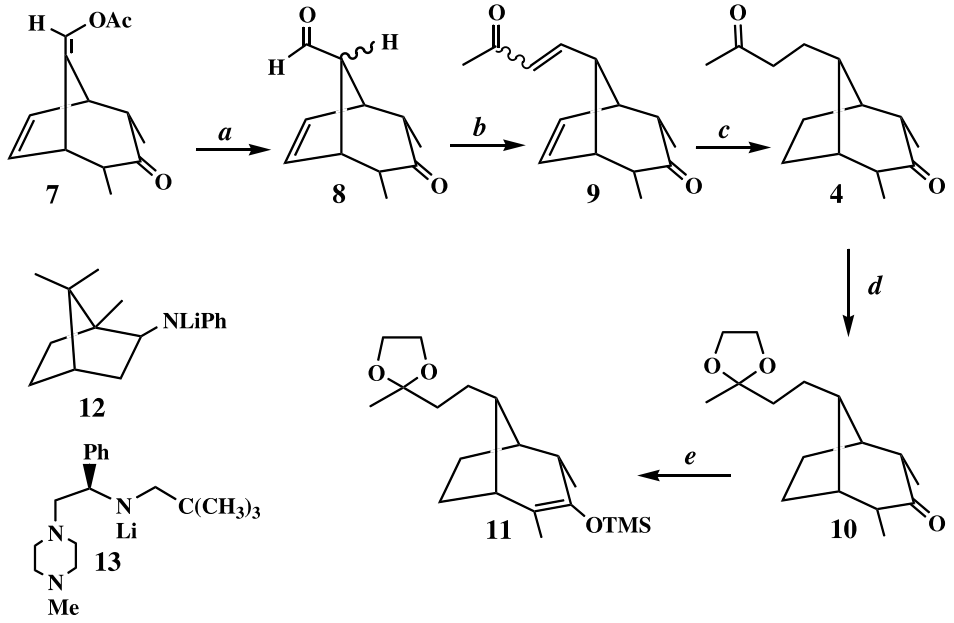
[2]Corresponding author (e-mail: dmagee@unb.ca).

 doi: 10.1139/V03-210 © 2004 NRC Canada

Fig. 1. Retrosynthetic analysis of (–)-reiswigin A.



Scheme 1. (*a*) 10% H_2SO_4, 1,4-dioxane, Δ; (*b*) acetonyltriphenylphosphorylidene, THF, Δ; (*c*) H_2, Pd–C, EtOAc; (*d*) ethylene glycol, $HC(OMe)_3$, pTSA, CH_2Cl_2; (*e*) (–)-**12**·hydrochloride salt, *n*-BuLi, TMSCl, THF, –30 °C to –100 °C.



and facile control of all the relative stereochemistries made this route very appealing.

Ketone **10** was deprotonated using chiral lithium amide base (CLAMB) **12** (8) and Corey's internal quench procedure to produce silyl enol ether **11** in 91% yield and 94% ee.[3]

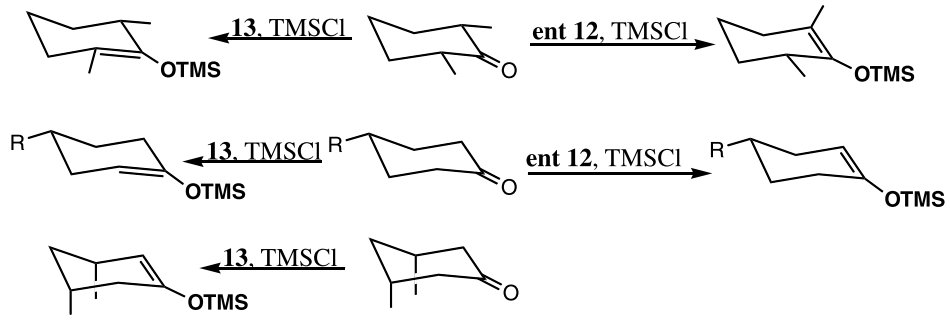
At this time the absolute stereochemistry and choice of base are worthy of comment. Although many studies had been undertaken on the desymmetrization of *meso* cyclic ketones, there had not been any previous studies on compounds that had substitution at all positions. However, examination of the studies on 2,6-dimethyl- (9), 3,5-dimethyl- (10), and 4-alkyl-cyclohexanones (11) suggested that Simpkins' base **12** (11)[4] and Koga's base **13** (12) give enantio-complimentary results, Fig. 2. Thus, it was believed that CLAMB **13** or CLAMB **12** would be the chiral base of choice, depending on which one was found to give the highest ee. Another consideration, however, was the fact that the synthesis of Simpkins' amine was considerably shorter and its recovery after reaction with the ketone much easier.

When CLAMBs **12** and **13** were used to deprotonate *meso*-ketone **10**, they were found to favour removal of the same enantiotopic proton (i.e., optical rotation of the resulting silyl enol ethers had the same sign). This supported the

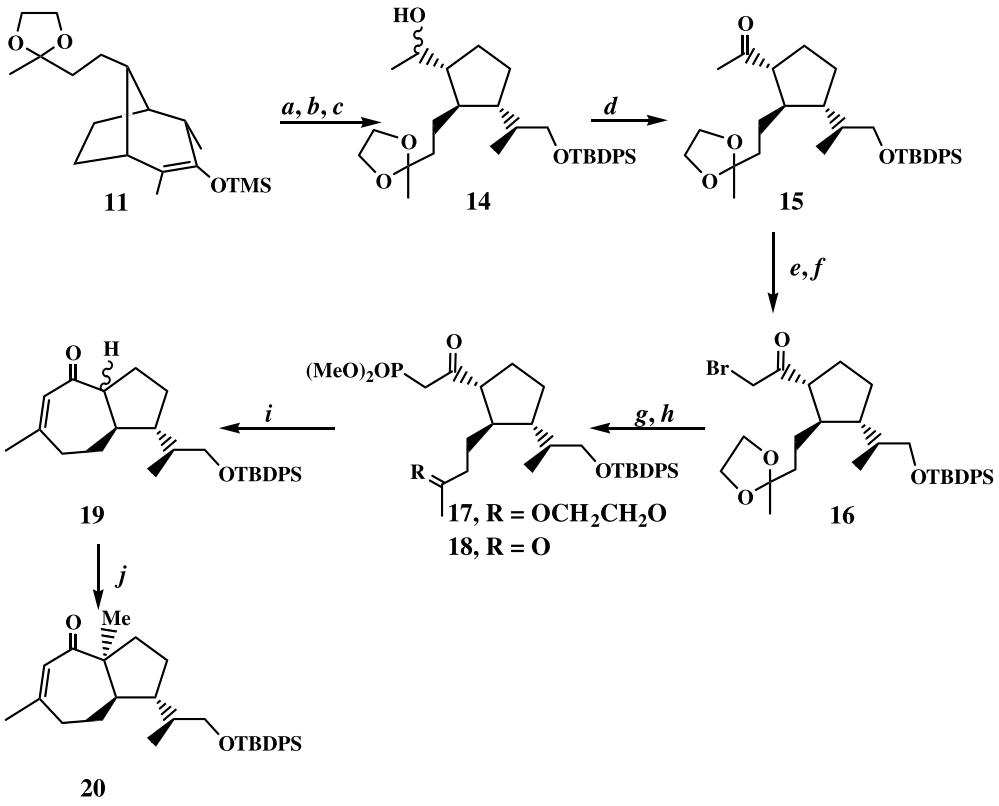
[3] The ee was determined via oxidation of the TMS – enol ether with DMDO, followed by use of chiral shift reagents. Complete separation of the methyl doublets was observed; integration of the ^{1}H NMR signals gave the enantiomeric ratio. This value was corroborated by conversion of another intermediate into its Mosher's ester, followed by integration of the ^{19}F and ^{1}H NMR signals of the diastereoisomers.
[4] Examples found in the literature used the enantiomer of **12**.

© 2004 NRC Canada

Fig. 2. Previous studies on asymmetric deprotonation of various substituted *meso*-cyclohexanones.



Scheme 2. (*a*) $NaIO_4$, $RuCl_3$, CCl_4, CH_3CN, H_2O, 15 °C; (*b*) $BH_3{\cdot}SMe_2$, THF, 0 °C; (*c*) TBDPSCI, DMAP, TEA, CH_2Cl_2; (*d*) $(COCl)_2$, DMSO, TEA, CH_2Cl_2, –60 °C; (*e*) LDA, TMSCl, THF, –78 °C; (*f*) NBS, THF, 0 °C; (*g*) $P(OMe)_3$, toluene, Δ; (*h*) PPTS, CH_3CN, Δ; (*i*) benzyltrimethylammonium methoxide, CH_3CN, 0 °C; (*j*) LDA, MeI, HMPA, THF, –78 °C to 0 °C.



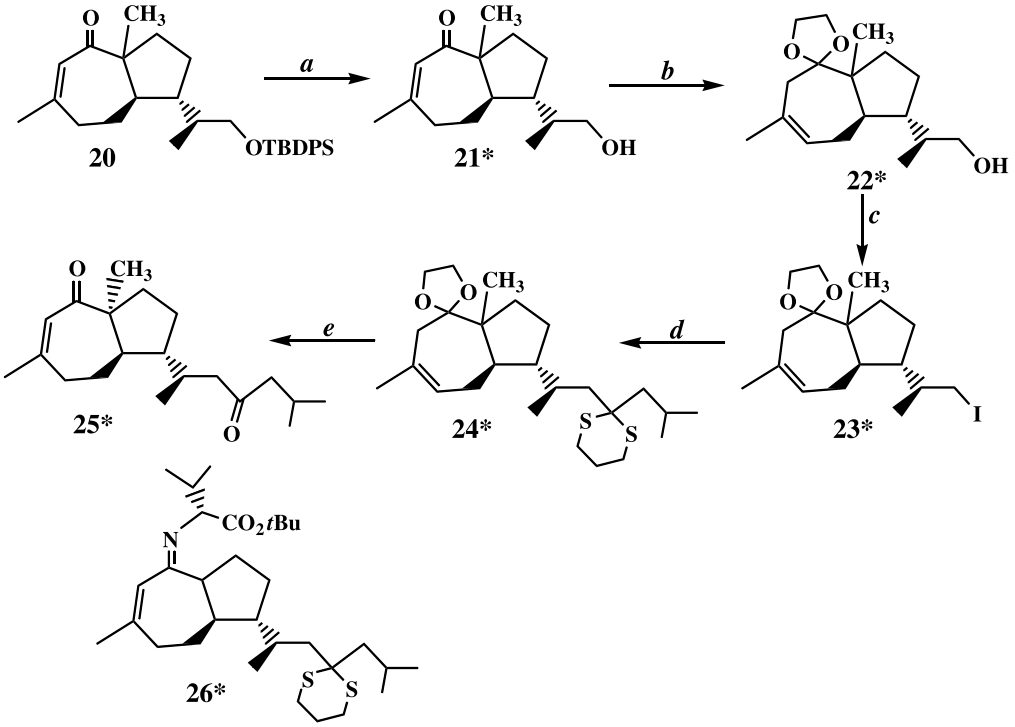
above conclusion and suggested that these chiral bases act on ketone **10** in a manner similar to the above-noted substituted cyclohexanones. The degree of stereoinduction and isolated yield were found to be higher using CLAMB **12** (90%–94% ee, 91% yield) than **13** (72%–75% ee, 84% yield). The high ees demonstrated the first known successful enantioselective deprotonation of a fully substituted *meso*-cyclohexanone and verified our earlier assumption that this technique would be useful for this substrate.[5]

With enantioenriched enol ether **11** in hand, the synthesis was continued (Scheme 2). Oxidative cleavage using Sharpless (13) conditions produced a highly unstable keto-acid, which was immediately reduced to the diol with $BH_3{\cdot}SMe_2$ (14) in 64% yield over the two steps. Several attempts at selective reduction of the acid functionality gave either only the starting acid or diol. Following standard conditions, the very polar diastereomeric alcohols were transformed to their *tert*-butyldiphenylsilyl ethers **14** via selective protection of the primary alcohol (15) followed by oxidation to ketone **15** using Swern conditions (16). It was hoped that protection of the primary alcohol with a very bulky group would help direct methylation at C-1; however, it was real-

[5] As a means of determining the absolute stereochemistry, attempts were made to obtain crystals that were suitable for X-ray analysis. Unfortunately all derivatives were found to be oils or failed to deliver suitable crystals. Therefore, all structures are shown with the stereochemistry inferred from the above analysis.

© 2004 NRC Canada

Scheme 3. (*a*) TBAF, THF; (*b*) ethylene glycol, $HC(OMe)_3$, pTSA, CH_2Cl_2; (*c*) PPh_3, I_2, imidazole, Et_2O, CH_3CN; (*d*) 2-isobutyl-1,3-dithiane, *n*-BuLi, THF, 0 °C to –90 °C; (*e*) $HgCl_2$, aq. CH_3CN, Δ.



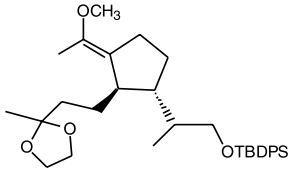
ized that 1,3-stereoinduction must override 1,2-stereoinduction in order for this to happen. Simple molecular modeling (MMFF92) on an analogue of **15** supported this speculation.[6] The six most stable conformers were found to be within 1.5 kcal of one another; of these, the four lowest energy conformations all had at least one phenyl group blocking the α-face. In fact, the first conformer that did not have this arrangement was 1.7 kcal higher in energy than the global minimum. To this end, valiant efforts were undertaken to methylate the thermodynamic enolate of ketone **15**; however, they were to no avail. The ineffectiveness of alkylation was primarily attributed to an inability to effect quantitative thermodynamic enolate formation.

To alleviate this difficulty, **15** was transformed into cycloheptenone **19** by the following sequence (Scheme 2): (*a*) bromination of the kinetic enolate with NBS (17) to give α-bromo-ketone **16**; (*b*) Arbuzov (18) reaction with trimethylphosphite to generate β-keto phosphonate **17**; (*c*) acid-catalyzed deprotection (19) of the dioxolane; and (*d*) intramolecular Horner–Emmons reaction. The intramolecular cyclization proved more difficult than expected. Following the traditional protocol of using DBU (20), very little desired product was obtained. Extended reaction times at room temperature or higher led to no improvement, while use of sodium hydride gave an unacceptable 34% yield. Fortunately, the use of benzyltrimethylammonium (BTMA) methoxide (21) led to the desired cycloheptenone in 75% yield, as an approximate 1:1 mixture of C-1 epimers, presumably because of the use of excess base. The epimeric mixture was of no concern, since the fate of that stereocenter was to be determined in the next step

Treatment of the epimeric cycloheptenones with LDA, followed by addition of MeI, gave a single alkylated product in 65% yield (Scheme 2). Extensive NMR investigation proved inconclusive in determining the structure of this alkylated product. Preliminary evidence,[7] however, suggested that C-11 was *trans* to C-5 and therefore the undesired product. It was reasoned that if the methylation were done before cyclization then perhaps the substrate would adopt a conformation that would allow for the desired stereochemical addition. Previous studies (22) on a ketone similar to compound **15** were unsuccessful in obtaining the thermodynamic methylation product. Ketophosphonate **17** (Scheme 2), on the other hand, had the potential to undergo a Weiler-type reaction (23). Treatment of **17** with NaH, followed by *n*-BuLi and then MeI gave no reaction. Furthermore, the use of lithium diethylamide as base yielded no improvement.

Although the nOe studies on compound **19** were disappointing, they were not conclusive. It was therefore decided

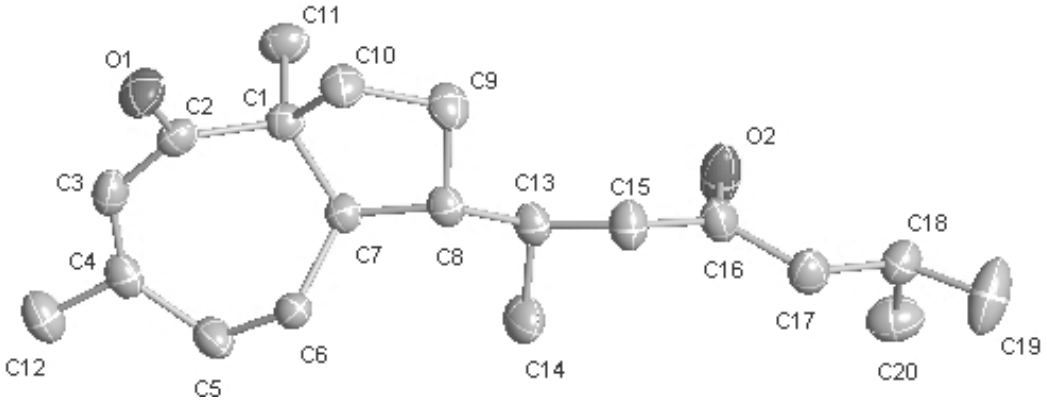
[6] The calculations were performed on the following structure:



[7] A small enhancement was seen in the nOesy experiment between H-11 and H-13, while no cross-peak was observed between H-11 and H-5.

© 2004 NRC Canada

Fig. 3. X-ray crystal structure of *epi*-reiswigin A.



that this compound should be carried on in an effort to finish the synthesis, thus allowing for the details of the isovaleraldehyde side-chain addition to be established. The spectra obtained from the final compound could then be compared to that of the natural product for definitive identification. This would unequivocally show whether or not the proper relative stereochemistry had been secured. In addition, owing to the lack of enantio-enriched material at this time, the synthesis was continued with racemic material.

To promote the desired substitution reaction, it was decided to protect the cyclic ketone as its ketal (Scheme 3). First, exposure of racemic ketone **19***[8] to TBAF (15) generated the primary alcohol **21***. When this alcohol was subjected to standard ketalization conditions, ketal-alcohol **22*** was obtained in only 58% yield with complete double-bond migration (24). Unexpectedly, however, a significant amount of ketal formate (30%) was produced. However, this was easily converted to the desired alcohol by exposure to aqueous base, therefore giving an overall yield of 88% for the ketalization. The alcohol was then converted to iodide **23*** in 62% yield, using conditions developed by Garegg and Samuelsson (25). When the iodide was treated with the anion of isobutyldithiane (26), dithioketal **24*** was produced in 81% yield. To achieve this yield, it was imperative to use HMPA and low temperatures; failure to do so resulted in significant elimination. Completion of the synthesis was accomplished by subjecting **24*** to $HgCl_2$ (27) in refluxing, aqueous CH_3CN to furnish **25*** in 67% yield (Scheme 3). Close examination of the ^1H and ^{13}C NMR data clearly indicated that our synthetic compound was not identical to the natural product reiswigin A. Furthermore, suitable crystals of **25** were obtained, and X-ray diffraction studies[9] unequivocally verified the earlier hypothesis; that is, the C-11 methyl group had unfortunately added incorrectly (Fig. 3), and this in fact meant that we had synthesized *epi*-reiswigin A.

Given that the configuration at C-1 was incorrect, efforts were directed towards finding a solution. It was felt that perhaps conversion of the cyclic ketone functionality into a chiral imine (2), similar to Snider's synthesis of (–)-reiswigin A, would force methylation from the desired face; see **26*** in Scheme 3. Unfortunately, when cycloheptenone **17*** was treated with *tert*-butyl L-valine ester (28) in refluxing toluene, only recovered starting material was obtained. Efforts to produce the imine using a variety of methods failed. Attempts to alter the stereochemical outcome of alkylation by using bulky chiral Lewis acids (29) also proved futile.

Given these results, it appears that it is unlikely that any nucleophilic-, electrophilic-, or radical-type additions to introduce the angular methyl group this late in the synthesis has any chance of success. Therefore, a revision of the synthetic route will have to be undertaken to account for this problem.

Summary

In conclusion, *epi*-reiswigin A was synthesized in 19 steps from the known keto-aldehyde **8** with an overall yield of 2.2%, with an average 82% yield per step. Efforts are currently underway to alter the strategy to allow for incorporation of the C-1 methyl group with the correct configuration. Although it was unfortunate that all endeavors to introduce the methyl group with the correct stereochemistry in the final stages of the synthesis failed, it was gratifying to see that the asymmetric deprotonation strategy worked as designed. Given the ease at which controlling the configuration of a stereogenic centre on a pendant side chain relative to the ring to which it is attached was accomplished, this approach should find use in the synthesis of similar cyclopentanoid compounds such as cereoplastol II (30) and albolic acid (31).

Experimental

All nonaqueous reactions were carried out in flame-dried round bottom flasks under an inert atmosphere (nitrogen or argon), unless stated otherwise. Temperatures indicated refer

[8] Racemic **19*** was generated as outlined in Schemes 1 and 2, except that deprotonation of **10** was performed with LDA.

[9] The crystallographic data for this compound has been deposited as supplementary data. Supplementary data may be purchased from the Depository of Unpublished Data, Document Delivery, CISTI, National Research Council Canada, Ottawa, ON K1A 0S2, Canada (http://www.nrc.ca/cisti/irm/unpub_e.shtml for information on ordering electronically). CCDC 227050 contain the supplementary data for this paper. These data can be obtained, free of charge, via www.ccdc.cam.ac.uk/conts/retrieving.html (or from the Cambridge Crystallographic Data Centre, 12 Union Road, Cambridge, U.K.; fax +44 1223 336033; or deposit@ccdc.cam.ac.uk).

© 2004 NRC Canada

to an external bath. All reactions were magnetically stirred. All organic solvents were distilled and dried following known procedures (32). Reagents were purchased from various commercial suppliers and used without further purification. Analytical thin layer chromatography (TLC) was performed using Merck 60 F-254 silica gel precoated glass plates (0.25 mm). Visualization was effected by short wave UV illumination and (or) $KMnO_4$ or PMA dip, followed by development on a hot plate. Flash column chromatography was performed using Fisher silica gel (32–63 particle size). Melting points were measured on a Gallenkamp melting point apparatus with uncorrected temperatures. Infrared spectra were recorded on either a PerkinElmer 598 IR spectrometer using NaCl cells and $CHCl_3$ as solvent or on a Bruker IFS 25 IR spectrometer using KBr discs and neat sample. Peaks are reported in wavenumbers (cm^{-1}). Nuclear magnetic resonance spectra[10] were recorded on a Varian Unity-400 (400 MHz) NMR spectrometer with $CDCl_3$ as solvent (unless stated otherwise). Chemical shifts were reported in parts per million (ppm) relative to $SiMe_4$ as internal standard, and coupling constants were reported in Hz. Low-and high-resolution electron impact mass spectra were recorded on a Kratos MS50TC mass spectrometer, with fragments reported as their m^+/z ratio. Optical rotations were measured on a PerkinElmer 241 polarimeter.

Synthesis of [3.2.1]-bicycloheptanone 7

To activated (33) copper powder (14.5 g, 228 mmol) and oven-dried sodium iodide (51.3 g, 342 mmol) was added 240 mL of CH_3CN. To the stirring mixture was slowly added 2,4-dibromo-3-pentanone **6** (41.7 g, 171 mmol) in 20 mL of CH_3CN and 6-acetoxyfulvene **5** (7.8 g, 57 mmol) in 20 mL of CH_3CN, simultaneously. The reaction mixture was stirred at room temperature for 16 h and then poured into 900 mL of a 1:1:1 mixture of ether, 30% NH_4OH, and H_2O. The layers were separated, and the aqueous layer was extracted with ether (3 × 180 mL). The combined organic layers were washed with H_2O (until the aqueous layer was neutral) and brine and then dried over $MgSO_4$, filtered, and concentrated in vacuo. The crude residue was first flash filtered through a pad of silica gel (8:1 hexanes (Hex) : EtOAc as eluant) and then more rigorously purified via SiO_2 column chromatography (14:1 Hex:EtOAc as eluant) to give 9.3 g (74% yield) of enol acetate **7** (4) as a colorless oil. IR (cm^{-1}): 2920, 1740, 1705, 1375, 1080. ^{1}H NMR δ: 1.07 (3H, d, J = 7.0), 1.11 (3H, d, J = 6.8), 2.18 (3H, s), 2.53–2.64 (2H, m), 3.16 (1H, br.s), 3.57 (1H, br.s), 6.16 (1H, dd, J = 2.6, 6.0), 6.22 (1H, dd, J = 2.67 6.1), 7.02 (1H, s). ^{13}C NMR δ: 13.8, 13.9, 20.7, 45.5, 47.8, 51.3, 52.9, 121.8, 134.4, 135.2, 135.3, 168.2, 211.2. HR-EI-MS: $C_{11}H_{14}O_2$ = 178.09909 ([$M^+ - C_2H_2O$]), $C_{11}H_{14}O_2$ = 178.09938 (calcd.).

Synthesis of ketoaldehyde 8

To enol acetate **7** (9.3 g, 42 mmol) was added 180 mL of 1,4-dioxane and 180 mL of 10% H_2SO_4. The reaction mixture was stirred at reflux for 6 h; the heat source was removed, and ice-cold saturated K_2CO_3 was immediately but carefully added until the mixture was neutral. It was then extracted with ether (5×), and the combined organic extracts were washed with H_2O and brine, dried over $MgSO_4$, and filtered. Concentration under reduced pressure gave crude ketoaldehyde **8** in a 5:1 ratio as a brown oil. All spectral data were identical to that reported by Hoffmann (6). This crude mixture was used directly in the next step.

Synthesis of unsaturated diketone 9

A crude mixture of aldehyde **8** (5.9 g, 33 mmol) in 15 mL of THF was added to a mixture of acetonyltriphenylphosphorane (12.7 g, 40 mmol) and 115 mL of THF. The reaction mixture was stirred at reflux for 2 days, cooled to room temperature, diluted with ether, and filtered through a pad of Celite, and the solvent was removed under reduced pressure. Purification by SiO_2 column chromatography (5:1 Hex:EtOAc as eluant) afforded 6.1 g of the *trans*-isomer and 0.61 g of the *cis*-isomer (73% combined yield over the two steps) as colorless oils.

trans-*Isomer*

IR (cm^{-1}): 2925, 1710, 1670, 1625, 1440, 1360. ^{1}H NMR δ: 1.06 (6H, d, J = 7.0), 2.23 (3H, s), 2.57 (2H, dq, J = 2.8, 6.9), 2.72 (2H, br. s), 3.02 (1H, d, J = 7.9), 6.07 (2H, dd, J = 0.9, 0.9), 6.13 (1H, dd, J = 16.0, 0.9), 6.78 (1H, dd, J = 16.1, 7.9). ^{13}C NMR δ: 13.9 (2C), 27.0, 50.3 (2C), 51.2 (2C), 57.9, 131.3, 133.9 (2C), 147.8, 198.5, 211.3. HR-EI-MS: $C_{14}H_{18}O_2$ = 218.13026 ([$M]^+$), $C_{14}H_{18}O_2$ = 218.13068 (calcd.).

cis-*Isomer*

IR (cm^{-1}): 2930, 1710, 1695, 1610, 1450, 1350, 1170. ^{1}H NMR δ: 1.03 (6H, d, J = 6.8), 2.24 (3H, s), 2.63 (2H, d, J = 0.9), 2.65–2.69 (2H, m), 4.00 (1H, d, J = 7.7), 6.06 (2H, dd, J = 1.5, 0.9), 6.07–6.18 (2H, m). ^{13}C NMR δ: 13.8 (2C), 31.7, 50.4 (2C), 52.2 (2C), 54.6, 126.9, 134.6 (2C), 150.1, 199.0, 212.2. HR-EI-MS: $C_{14}H_{18}O_2$ = 218.13002 ([$M]^+$), $C_{14}H_{18}O_2$ = 218.13068 (calcd.).

Synthesis of diketone 4

The unsaturated *E*- and *Z*-mixture of diketone **9** (10.0 g, 45.8 mmol) in 150 mL of EtOAc was placed in a Parr bottle, followed by a catalytic amount of 10% palladium on activated carbon (~1 g). The mixture was then shaken at room temperature on a Parr hydrogenation apparatus under H_2 atmosphere (~40 psi (1 psi = 6.894 kPa)) for 30 min. Celite was then added, and the reaction mixture was filtered, and the solvent was removed in vacuo. Purification by SiO_2 column chromatography (5:1 Hex:EtOAc as eluant) afforded 9.70 g (95% yield) of diketone **4** as a colorless oil. IR (cm^{-1}): 2930, 1710, 1360. ^{1}H NMR δ: 0.96 (6H, d, J = 6.7), 1.38 (2H, d, J = 8.9), 1.52–1.62 (4H, m), 2.02 (2H, br. d, J = 4.1), 2.17–2.21 (1H, m), 2.19 (3H, s), 2.47 (2H, m), 2.54 (2H, t, J = 7.5). ^{13}C NMR δ: 12.5 (2C), 21.9 (2C), 25.1, 29.9, 42.0, 47.0 (2C), 50.5 (2C), 52.3, 208.6, 213.3. HR-EI-MS: $C_{14}H_{28}O_2$ = 222.16047 ([$M]^+$), $C_{14}H_{28}O_2$ = 222.16199 (calcd.).

Synthesis of ketoketal 10

To a catalytic amount of pTSA in 70 mL of CH_2Cl_2 was added diketone **4** (5.7 g, 25.6 mmol) in 15 mL of CH_2Cl_2. To this stirring solution was added ethylene glycol (1.7 mL,

[10]Copies of ^{1}H and ^{13}C NMR spectra of all compounds are provided as supplemental material (see footnote 9).

© 2004 NRC Canada

30.7 mmol) and 98% trimethylorthoformate (3.4 mL, 30.7 mmol). The reaction mixture was stirred at room temperature for 5 h, diluted with saturated $NaHCO_3$, and extracted with CH_2Cl_2 (2×). The combined organics were washed with H_2O and brine and dried over $MgSO_4$. The solvent was removed under reduced pressure, and the residue was purified by SiO_2 column chromatography (5:1 Hex:EtOAc as eluant) to give 5.5 g (81% yield) of ketoketal **10** as a low-melting white solid. Further purification could be accomplished by recrystallization from hexane; mp 45.0–46.1 °C. IR (cm^{-1}): 2960, 1705, 1380, 1055. ^1H NMR δ: 0.96 (6H, d, J = 6.7), 1.33 (3H, s), 1.34–1.40 (4H, m), 1.58–1.62 (2H, m), 1.71–1.78 (2H, m), 2.04 (2H, br.d, J = 4.1), 2.18 (1H, t, J = 7.4), 2.47 (2H, dq, J = 1.6, 6.6), 3.91–3.99 (4H, m). ^{13}C NMR δ: 12.6 (2C), 22.0 (2C), 23.7, 25.6, 37.7, 47.2 (2C), 50.7 (2C), 53.3, 64.6 (2C), 109.9, 213.7. HR-EI-MS: $C_{16}H_{26}O_3$ = 266.18874 ($[M]^+$), $C_{16}H_{26}O_3$ = 266.18820 (calcd.).

Synthesis of silyl enol ether 11

To a mixture of Simpkins' (+) chiral amine HCl salt **12** (4.97 g, 18.7 mmol) and 90 mL of THF cooled to –30 °C was added a 2.5 mol L^{-1} solution of *n*-BuLi in hexane (14.5 mL, 36.3 mmol), dropwise. After complete addition, the mixture was stirred for an additional 20 min at –30 °C and then for 2 h at room temperature. It was cooled to –100 °C, and 98% chlorotrimethylsilane (5.7 mL, 44.0 mmol) was added quickly, followed immediately by slow dropwise addition of ketone **10** (2.93 g, 11.0 mmol) in 20 mL of THF. The reaction mixture was stirred at –100 °C for 1 h, and then triethylamine (9.2 mL, 66.0 mmol) was added, and stirring continued at –100 °C for 10 min. Ethyl acetate was added, and the mixture was concentrated under reduced pressure. The residue was diluted with ether and filtered through a pad of Celite, and the solvent was removed in vacuo. Purification by SiO_2 column chromatography (hexane followed by 20:1 Hex:EtOAc as eluant) afforded 3.39 g (91% yield) of silyl enol ether **11** as a colorless oil in 94% enantiomeric excess. $[\alpha]_D$ –20.5 (c = 1.27, CH_2Cl_2). IR (cm^{-1}): 2965, 1670, 1380, 1110, 1060, 885. ^1H NMR δ: 0.15 (9H, s), 0.97 (3H, d, J = 7.0), 1.20–1.26 (2H, m), 1.32 (3H, s), 1.47–1.56 (1H, m), 1.53, (3H, d, J = 2.2), 1.58–1.78 (6H, m), 1.88–1.91 (2H, m), 2.48–2.52 (1H, m), 3.90–3.98 (4H, m). ^{13}C NMR δ: 0.4 (3C), 15.2, 15.9, 20.7, 23.7, 26.2, 30.1, 37.5, 42.3, 44.2, 45.4, 49.4, 64.6 (2C), 110.1, 120.3, 144.7. HR-EI-MS: $C_{19}H_{34}SiO_3$ = 338.22751 ($[M]^+$), $C_{19}H_{34}SiO_3$ = 338.22772 (calcd.).

Synthesis of racemic silyl enol ether 11*

To a mixture of diisopropylamine (2.82 mL, 20 mmol) and 50 mL of THF cooled to –78 °C was added a 2.5 mol L^{-1} solution of *n*-BuLi in hexane (8.0 mL, 20 mmol), dropwise. After complete addition, the mixture was stirred for 5 min; then 98% chlorotrimethylsilane (2.85 mL, 22.0 mmol) was added, followed immediately by dropwise addition of ketone **10** (4.79 g, 18.0 mmol) in 20 mL of THF. The reaction mixture was stirred at –78 °C for 1 h, and then triethylamine (4.6 mL, 33.0 mmol) was added. After stirring for 10 min, the mixture was concentrated under reduced pressure. The residue was diluted with ether and filtered through a pad of Celite, and the solvent was removed in vacuo. Purification by SiO_2 column chromatography (hexane followed by 20:1 Hex:EtOAc as eluant) afforded 5.89 g (97% yield) of silyl enol ether **11*** as a colorless oil.

Synthesis of diastereomeric alcohols 14

A mixture of silyl enol ether **11** (2.49 g, 7.36 mmol), sodium metaperiodate (6.30 g, 29.44 mmol), a catalytic amount of ruthenium trichloride, and 52.5 mL of CCl_4:CH_3CN:H_2O (2:2:3) was vigorously stirred at ~5 °C for 10 min. It was then diluted with CH_2Cl_2 and just enough H_2O to dissolve the precipitate. The layers were separated, and the aqueous phase was extracted with CH_2Cl_2 (3×) and dried over Na_2SO_4. The combined organics were concentrated under reduced pressure, diluted with ether, and filtered through a pad of Celite. Concentration in vacuo afforded crude ketoacid as a black oil, which was unstable and therefore was used immediately for the subsequent reaction.

To a 2.0 mol L^{-1} THF solution of borane – dimethyl sulfide complex (19.9 mL, 39.72 mmol) was added 23 mL of THF. The solution was cooled to 0 °C, followed by dropwise addition of the crude ketoacid (1.98 g, 6.62 mmol) in 12 mL of THF. After complete addition, the ice-water bath was removed, and the reaction mixture was allowed to stir at room temperature for 2 h. Excess borane was then destroyed at 0 °C by slow dropwise addition of H_2O, followed by a few drops of 5% NaOH, and then stirring at room temperature for 15 min. The cloudy mixture was concentrated in vacuo, diluted with EtOAc, dried over $MgSO_4$, and filtered, and the solvent was removed under reduced pressure. The residue was taken up in ethyl acetate and filtered through a pad of SiO_2 (EtOAc as eluant) to afford 1.35 g of a 1:1 diastereomeric mixture of diols **14** as colorless oils. The diastereoisomeric diols **14** (1.80 g, 6.28 mmol) in 10 mL of CH_2Cl_2 were added quickly to a solution of 4-dimethylaminopyridine (100 mg), triethylamine (3.5 mL, 25.1 mmol), and 98% *tert*-butylchlorodiphenylsilane (1.83 mL, 6.91 mmol) in 20 mL of CH_2Cl_2. The reaction mixture was stirred at room temperature overnight, diluted with saturated $NaHCO_3$, and extracted with CH_2Cl_2 (2×). The combined organics were washed with H_2O and brine and dried over $MgSO_4$. It was then filtered, and the solvent was removed in vacuo. The product was purified by SiO_2 chromatography (2:1 Hex:EtOAc as eluant) to give 2.63 g of the diasteromeric silyl ethers as colorless oils.

Less polar diastereoisomer

$[\alpha]_D$ +6.4 (c = 1.02, CH_2Cl_2). IR (cm^{-1}): 3460, 3060, 2915, 1960, 1890, 1805, 1460, 1375, 1080. ^1H NMR δ: 1.02 (3H, d, J = 6.50), 1.05 (9H, s), 1.14 (3H, d, J = 6.3), 1.26–1.36 (1H, m), 1.30 (3H, s), 1.38–1.66 (12H, m), 3.43 (1H, dd, J = 7.0, 9.9), 3.56–3.62 (1H, m), 3.65 (1H, dd, J = 4.2, 10.0), 3.86–3.95 (4H, m), 7.34–7.43 (6H, m), 7.65–7.67 (4H, m). ^{13}C NMR δ: 16.7, 19.2, 22.1, 23.7, 26.0, 26.9 (3C), 28.3, 30.0, 37.1, 39.2, 43.9, 48.1, 52.6, 64.5, 64.5, 67.1, 69.3, 110.1, 127.5 (2C), 129.4 (2C), 134.0 (2C), 135.6 (4C), 135.6 (2C). HR-EI-MS: $C_{28}H_{41}SiO_2$ = 437.28564 ($[M^+ - C_4H_8O_2]$), $C_{28}H_{41}SiO_2$ = 437.28760 (calcd.).

More polar diasteroisomer

$[\alpha]_D$ +11.5 (c = 1.1, CH_2Cl_2). IR (cm^{-1}): 3460, 3080, 2915, 1960, 1890, 1825, 1460, 1375, 1090. ^1H NMR δ: 1.04 (3H, d, J = 6.8), 1.05 (9H, s), 1.11 (3H, d, J = 6.2), 1.24–

© 2004 NRC Canada

1.30 (2H, m), 1.30 (3H, s), 1.33–1.42 (1H, m), 1.45–1.57 (6H, m), 1.63–1.74 (4H, m), 3.42 (1H, dd, J = 7.0, 9.9), 3.46–3.50 (1H, m), 3.63 (1H, dd, J = 4.1, 9.9), 3.88–3.96 (4H, m), 7.35–7.44 (6H, m), 7.65–7.67 (4H, m). ^{13}C NMR δ: 16.7, 19.3, 21.6, 23.7, 26.9 (3C), 28.1, 28.9, 31.3, 37.0, 39.6, 44.4, 48.8, 53.0, 64.4, 64.6, 67.4, 71.4, 110.4, 127.6 (4C), 129.5 (2C), 134.0 (2C), 135.6 (2C), 135.6 (2C). HR-EI-MS: $C_{28}H_{41}SiO_2$ = 437.28546 ([M^+ – $C_4H_8O_2$]), $C_{28}H_{41}SiO_2$ = 437.28760 (calcd.).

Synthesis of ketone 15

To a stirring solution of 98% oxalyl chloride (0.51 mL, 5.68 mmol) in 8 mL of CH_2Cl_2 cooled to –60 °C was added dimethyl sulfoxide (0.84 mL, 11.82 mmol) in 8 mL of CH_2Cl_2, dropwise. This mixture was stirred at –60 °C for 15 min; then the alcohol (2.48 g, 4.73 mmol) in 14 mL of CH_2Cl_2 was slowly added. After stirring at –60 °C for 30 min, triethylamine (3.3 mL, 23.6 mmol) was added; the cold bath was removed, and stirring continued at room temperature for 10 min. The cloudy solution was diluted with saturated $NaHCO_3$ and extracted with CH_2Cl_2 (2×). The combined organics were washed with H_2O and brine and dried over $MgSO_4$ and filtered, and the solvent was evaporated in vacuo. Purification by SiO_2 column chromatography (3:1 Hex:EtOAc as eluant) afforded 2.25 g (91% yield) of ketone **15** as a colorless oil. $[\alpha]_D$ +5.6 (c = 1.10, CH_2Cl_2). IR (cm^{-1}): 3070, 2920, 1960, 1890, 1820, 1700, 1465, 1370, 1235. ^{1}H NMR δ: 1.03 (3H, d, J = 6.7), 1.05 (9H, s), 1.27–1.36 (2H, m), 1.29 (3H, s), 1.54–1.70 (7H, m), 1.72–1.76 (1H, m), 2.04–2.08 (1H, m), 2.11 (3H, s), 2.55 (1H, ddd, J = 5.9, 5.9, 8.3), 3.45 (1H, dd, J = 6.6, 10.0), 3.63 (1H, dd, J = 4.4, 9.9), 3.86–3.95 (4H, m), 7.35–7.43 (6H, m), 7.65–7.67 (4H, m). ^{13}C NMR δ: 16.4, 19.3, 23.8, 26.9 (3C), 28.8, 29.1, 29.3, 30.2, 37.4, 39.0, 43.7, 48.2, 58.5, 64.6 (2C), 67.1, 109.8, 127.5 (4C), 129.5 (2C), 133.9 (2C), 135.6 (4C), 210.9. HR-EI-MS: $C_{28}H_{37}SiO_4$ = 465.24595 ([M^+ – C_4H_9]), $C_{28}H_{37}SiO_4$ = 465.24612 (calcd.).

Synthesis of bromoketone 16

To a solution of diisopropylamine (0.84 mL, 6.38 mmol) in 14 mL of THF cooled to –78 °C was added a 2.5 mol L^{-1} solution of *n*-BuLi in hexane (2.4 mL, 6.06 mmol), dropwise. The mixture was stirred at –78 °C for 15 min; then 98% TMSCl (0.83 mL, 6.38 mmol) was added quickly, followed immediately by slow addition of a solution of ketone **15** (1.67 g, 3.19 mmol) in 14 mL of THF. The reaction mixture was stirred at –78 °C for 45 min and then at room temperature for 10 min. Triethylamine (1.3 mL, 9.57 mmol) was then added; the solution was stirred for 10 min, concentrated in vacuo, diluted with ether, and filtered through a pad of Celite. Solvent removal under reduced pressure afforded crude silyl enol ether as a pale yellow oil, which was used directly for the subsequent reaction.

To a mixture of *N*-bromosuccinimide (568 mg, 3.19 mmol) in 13 mL of THF cooled to 0 °C was added the silyl enol ether (1.90 g, 3.19 mmol) in 12 mL of THF. The reaction mixture was stirred for 2 h at 0 °C, diluted with ether, washed with saturated $NaHCO_3$ and brine, and dried over $MgSO_4$. The solvent was removed in vacuo, and purification via SiO_2 column chromatography (5:1 Hex:EtOAc as eluant) afforded 1.65 g (86% yield over the two steps) of α-bromoketone **16** as a colorless oil. $[\alpha]_D$ +6.4 (c = 1.3, CH_2Cl_2). IR (cm^{-1}): 3060, 2910, 1960, 1890, 1825, 1710, 1470, 1375, 1250, 1070, 945, 705. ^{1}H NMR δ: 1.02 (3H, d, J = 6.8), 1.05 (9H, s), 1.27–1.41 (3H, m), 1.28 (3H, s), 1.55–1.72 (6H, m), 1.79–1.85 (1H, m), 2.08–2.14 (1H, m), 2.91 (1H, ddd, J = 5.8, 5.8, 8.8), 3.46 (1H, dd, J = 6.4, 10.0), 3.62 (1H, dd, J = 4.5, 10.0), 3.86–3.94 (4H, m), 3.94 (2H, d, J = 0.9), 7.35–7.43 (6H, m), 7.65–7.67 (4H, m). ^{13}C NMR δ: 16.4, 19.3, 23.8, 26.9 (3C), 29.3, 29.9, 34.2, 37.2, 38.8, 44.4, 48.2, 54.6, 64.6 (3C), 67.0, 109.8, 127.6 (4C), 129.5 (2C), 133.8, 133.9, 135.6 (4C), 203.9. HR-EI-MS: $C_{16}H_{26}O_3{}^{79}Br$ = 345.10657 ([M^+ – $C_{16}H_{19}SiO$]), $C_{16}H_{26}O_3{}^{79}Br$ = 345.10654 (calcd.).

Synthesis of ketophosphonate 17

A mixture of α-bromoketone **16** (1.73 g, 2.88 mmol) and trimethylphosphite (1.4 mL, 11.5 mmol) in 29 mL of toluene was stirred at reflux overnight. After cooling to room temperature and concentration in vacuo, the residue was purified by SiO_2 column chromatography (1:3 Hex:EtOAc to EtOAc as eluant) to give 1.60 g (88% yield) of ketophosphonate **17** as a colorless oil. $[\alpha]_D$ +11.5 (c = 1.5, CH_2Cl_2). IR (cm^{-1}): 3060, 2910, 1960, 1895, 1835, 1710, 1460, 1375, 1265, 1050. ^{1}H NMR δ: 1.02 (3H, d, J = 6.7), 1.04 (9H, s), 1.27–1.36 (2H, m), 1.29 (3H, s), 1.55–1.73 (7H, m), 1.78–1.84 (1H, m), 2.08–2.14 (1H, m), 2.82 (1H, ddd, J = 5.4, 5.4, 8.6), 3.07 (1H, dd, J = 14.0, 22.6), 3.15 (1H, dd, J = 14.0, 22.6), 3.44 (1H, dd, J = 6.5, 9.9), 3.62 (1H, dd, J = 4.4, 10.0), 3.77 (6H, d, J = 11.3), 3.86–3.95 (4H, m), 7.35–7.43 (6H, m), 7.64–7.67 (4H, m). ^{13}C NMR δ: 16.3, 19.2, 23.7, 26.8 (3C), 28.9, 29.2, 30.0, 37.1, 39.0, 40.0 (d, J = 513.2), 43.3, 48.2, 52.9 (2C, d, J = 41.4), 58.5 (d, J = 6.4), 64.5 (2C), 67.1, 109.8, 127.5 (4C), 129.4 (2C), 133.9 (2C), 135.5 (4C), 203.8 (d, J = 25.6). HR-EI-MS: $C_{30}H_{42}PSiO_7$ = 573.24459 ([M^+ – C_4H_9]), $C_{30}H_{42}PSiO_7$ = 573.24377 (calcd.).

Synthesis of diketophosphonate 18

To ketophosphonate **17** (1.00 g, 1.59 mmol) in 10 mL of 20% aqueous acetonitrile was added a catalytic amount of pyridinium *p*-toluenesulfonate. The reaction mixture was stirred at reflux for 1 h, cooled to room temperature, and concentrated in vacuo. The residue was taken up in CH_2Cl_2 and washed with a small amount of H_2O. The aqueous phase was extracted with CH_2Cl_2 (2×), and the combined organics were washed with brine, dried over $MgSO_4$, and filtered, and the solvent was removed in vacuo. Purification via SiO_2 column chromatography (EtOAc as eluant) afforded 846 mg (91% yield) of diketophosphonate **18** as a colorless oil. $[\alpha]_D$ +10.4 (c = 1.3, CH_2Cl_2). IR (cm^{-1}): 3060, 2910, 1970, 1890, 1825, 1720, 1695, 1460, 1375, 1260, 1050. ^{1}H NMR δ: 1.03 (3H, d, J = 6.7), 1.05 (9H, s), 1.29–1.36 (1H, m), 1.40–1.50 (1H, m), 1.56–1.73 (4H, m), 1.74–1.88 (2H, m), 2.11 (3H, s), 2.11–2.17 (1H, m), 2.41 (2H, t, J = 7.7), 2.81 (1H, ddd, J = 5.8, 5.8, 9.1), 3.05 (1H, dd, J = 13.9, 22.5), 3.18 (1H, dd, J = 13.9, 22.6), 3.46 (1H, dd, J = 6.3, 10.1), 3.62 (1H, dd, J = 4.5, 10.0), 3.77 (3H, d, J = 11.3), 3.78 (3H, d, J = 11.3), 7.34–7.43 (6H, m), 7.64–7.67 (4H, m). ^{13}C NMR δ: 16.2, 19.1, 26.8 (3C), 28.9 (2C), 29.4, 29.8, 38.7, 39.9 (d, J = 513.2), 41.7, 42.1, 48.1, 52.8 (d, J = 38.2), 52.9 (d, J = 38.2), 58.6 (d, J = 6.4), 66.8, 127.5 (4C), 129.4 (2C), 133.7,

© 2004 NRC Canada

133.8, 135.4 (2C), 135.5 (2C), 203.5 (d, J = 25.6), 208.6. HR-EI-MS: $C_{28}H_{38}PSiO_6$ = 529.21589 ([$M^+ - C_4H_9$]), $C_{28}H_{38}PSiO_6$ = 529.21753 (calcd.).

Synthesis of heptenone 19

To a solution of diketophosphonate **18** (820 mg, 1.40 mmol) in 14 mL of CH_3CN cooled to 0 °C was added a solution of 40% by weight benzyltrimethylammonium methoxide in MeOH (1.2 mL, 2.80 mmol). The reaction mixture was stirred at 0 °C for 15 min and then at room temperature for 1.5 h. After neutralization with saturated NH_4Cl and extraction with ether (3×), the combined organics were washed with brine, dried over $MgSO_4$, and filtered, and the solvent was removed in vacuo. Purification via SiO_2 column chromatography (29:1 Hex:EtOAc as eluant) gave 482 mg (75% yield) of cycloheptenone **19** as a separable epimeric mixture (approximately 1:1) of colorless oils.

Less polar epimer

IR (cm^{-1}): 3060, 2910, 1960, 1890, 1825, 1660, 1640, 1465, 1375, 1200, 1100. ^1H NMR δ: 0.98 (3H, d, J = 6.8), 1.05 (9H, s), 1.16–1.23 (1H, m), 1.27–1.37 (1H, m), 1.45–1.53 (1H, m), 1.59–1.67 (1H, m), 1.69–1.79 (2H, m), 1.85–1.92 (1H, m), 1.87 (3H, s), 1.94–2.03 (1H, m), 2.12 (1H, dq, J = 3.9, 10.0), 2.26–2.30 (2H, m), 3.02 (1H, dt, J = 9.9, 7.2), 3.46 (1H, dd, J = 6.9, 10.0), 3.62 (1H, dd, J = 5.4, 10.0), 5.84 (1H, s), 7.35–7.44 (6H, m), 7.65–7.67 (4H, m). ^{13}C NMR δ: 16.3, 19.2, 25.9, 26.4, 26.8 (3C), 28.1, 31.9, 35.6, 38.1, 44.4, 48.6, 57.3, 66.7, 127.6 (4C), 128.6, 129.5 (2C), 133.8 (2C), 135.5 (2C), 135.6 (2C), 155.7, 204.4. HR-EI-MS: $C_{26}H_{31}SiO_2$ = 403.20886 ([$M^+ - C_4H_9$]), $C_{26}H_{31}SiO_2$ = 403.20932 (calcd.).

More polar epimer

$[\alpha]_D$ +11.2 (c = 0.25, CH_2Cl_2). IR (cm^{-1}): 3060, 2910, 1960, 1890, 1825, 1660, 1640, 1460, 1375, 1080. ^1H NMR δ: 0.94 (3H, d, J = 6.8), 1.03 (9H, s), 1.30–1.35 (2H, m), 1.52–1.59 (1H, m), 1.65–1.77 (5H, m), 1.91–2.07 (1H, m), 1.94 (3H, d, J = 1.0), 2.18 (1H, dt, J = 15.7, 5.0), 2.52–2.67 (2H, m), 3.44 (1H, dd, J = 6.5, 10.1), 3.58 (1H, dd, J = 5.5, 10.1), 5.91 (1H, d, J = 1.4), 7.35–7.44 (6H, m), 7.63–7.66 (4H, m). ^{13}C NMR δ: 16.0, 19.2, 24.2, 26.9 (3C), 27.5, 28.1, 29.5, 33.1, 37.8, 43.0, 50.0, 56.5, 66.8, 127.6 (4C), 129.3, 129.5 (2C), 133.8 (2C), 135.6 (4C), 156.3, 203.5. HR-EI-MS: $C_{26}H_{31}SiO_2$ = 403.20803 ([$M^+ - C_4H_9$]), $C_{26}H_{31}SiO_2$ = 403.20932 (calcd.).

Synthesis of methylated cycloheptenone 20

To a solution of diisopropylamine (0.157 mL, 1.20 mmol) in 3 mL of THF at –50 °C was added a 2.5 mol L^{-1} solution of *n*-BuLi in hexane (0.44 mL, 1.10 mmol), dropwise. The solution was stirred at –50 °C for 15 min and then cooled to –78 °C. A solution of cycloheptenone **19** (461 mg, 1.00 mmol, mixture of epimers) in 2 mL of THF was then added slowly, and stirring continued at –78 °C for 40 min. HMPA (0.5 mL) was then added, and the reaction mixture was warmed to 0 °C, followed by addition of iodomethane (0.189 mL, 3.00 mmol). The reaction mixture was allowed to warm gradually to room temperature and to stir for 6 h; it was diluted with ether; washed with saturated NH_4Cl, H_2O (2×), and brine; dried over $MgSO_4$; and filtered, and the solvent was removed in vacuo. Purification by SiO_2 column chromatography (29:1 Hex:EtOAc as eluant) afforded 308 mg (65% yield) of **20** as a colorless oil. $[\alpha]_D$ +9.2 (c = 0.25, CH_2Cl_2). IR (cm^{-1}): 3080, 2905, 1960, 1890, 1825, 1660, 1450, 1375, 1100. ^1H NMR δ: 1.02 (3H, d, J = 6.7), 1.06 (9H, s), 1.10 (3H, s), 1.17–1.26 (1H, m), 1.36–1.56 (4H, m), 1.61–1.67 (2H, m), 1.71–1.77 (1H, m), 1.83 (3H, d, J = 0.5), 2.04 (1H, dt, J = 6.5, 12.8), 2.15–2.33 (2H, m), 3.45 (1H, dd, J = 6.7, 9.9), 3.63 (1H, dd, J = 4.7, 10.0), 5.79 (1H, s), 7.35–7.45 (6H, m), 7.65–7.67 (4H, m). ^{13}C NMR δ: 16.5, 19.3, 25.6, 26.9 (3C), 27.3, 28.0, 32.7, 34.8, 36.6, 40.1, 50.4, 51.6, 61.4, 67.1, 126.6, 127.6 (4C), 129.6 (2C), 133.9 (2C), 135.6 (4C), 151.5, 208.5. HR-EI-MS: $C_{27}H_{33}SiO_2$ = 417.22515 ([$M^+ - C_4H_9$]), $C_{27}H_{33}SiO_2$ = 417.22498 (calcd.).

Synthesis of keto-alcohol 21*

To a solution of silyl ether **20***[11] (175 mg, 0.37 mmol) in 2.5 mL of THF was added a 1 mol L^{-1} solution of tetrabutylammonium fluoride in THF (0.56 mL, 0.56 mmol). The reaction mixture was stirred at room temperature for 2 h, diluted with EtOAc, and concentrated in vacuo. The residue was filtered quickly through a pad of silica gel using 1:1 Hex:EtOAc and concentrated in vacuo. A more rigorous purification via SiO_2 column chromatography (2:1 Hex:EtOAc as eluant) gave 82 mg (94% yield) of alcohol **21** as a colorless oil. IR (cm^{-1}): 3435, 2915, 1660, 1635, 1440, 1380, 1030. ^1H NMR δ: 1.03 (3H, d, J = 6.7), 1.17 (3H, s), 1.23–1.69 (7H, m), 1.73–1.81 (2H, m), 1.85 (3H, d, J = 0.5), 2.08 (1H, dt, J = 6.5, 12.8), 2.23–2.38 (2H, m), 3.45 (1H, dd, J = 7.2, 10.4), 3.68 (1H, dd, J = 4.4, 10.5), 5.81 (1H, s). ^{13}C NMR δ: 16.2, 25.5, 27.4, 28.0, 32.9, 34.8, 36.7, 40.3, 50.5, 51.7, 61.5, 66.4, 126.6, 151.5, 208.5. HR-EI-MS: $C_{15}H_{24}O_2$ = 236.17802 ([M^+]), $C_{15}H_{24}O_2$ = 236.17763 (calcd.).

Synthesis of ketal alcohol 22*

To a solution of cycloheptenone **21** (80 mg, 0.34 mmol) in 1.7 mL of CH_2Cl_2 was added pTSA (5 mg), ethylene glycol (38 mL, 0.68 mmol), and trimethylorthoformate (76 mL, 0.68 mmol). The reaction mixture was stirred at room temperature for 5 h, then diluted with NH_4OH, and stirred for an additional 30 min. After separation of the two layers, the aqueous phase was extracted with CH_2Cl_2 (2×). The combined organics were washed with H_2O and brine, dried over $MgSO_4$, and filtered. The solvent was removed in vacuo, and the residue was purified via SiO_2 column chromatography (5:1 Hex:EtOAc as eluant) to give 83 mg (88% yield) of ketal **22*** as a colorless oil. IR (cm^{-1}): 3380, 2925, 1720, 1690, 1450, 1370, 1285. ^1H NMR δ: 1.00 (3H, d, J = 6.8), 1.08 (3H, s), 1.22–1.38 (3H, m), 1.49–1.58 (2H, m), 1.59–1.71 (2H, m), 1.66 (3H, s), 1.82–1.90 (1H, m), 1.95–2.05 (1H, m), 2.22 (1H, AB quartet, J = 18.3), 2.37–2.47 (1H, m), 2.54 (1H, AB quartet, J = 17.9), 3.40 (1H, dd, J = 7.6, 10.5), 3.66 (1H, dd, J = 4.4, 10.5), 3.87–4.06 (4H, m), 5.45–5.49 (1H, m). ^{13}C NMR δ: 16.2, 25.8, 25.9, 27.1, 30.6, 33.1, 39.7, 40.8, 49.2, 51.6, 52.6, 64.0, 65.7, 66.4, 113.6,

[11]The synthesis was continued using racemic material. Racemic keto-alcohol **21*** was synthesized following the same steps as for optically pure **21**, with the exception that the deprotonation of **10** was done with LDA and not chiral lithium amide base **12**.

© 2004 NRC Canada

123.5, 132.6. HR-EI-MS: $C_{17}H_{28}O_3$ = 280.20383 ([M]$^+$), $C_{17}H_{28}O_3$ = 280.20386 (calcd.).

Synthesis of iodoketal 23*

To a solution of triphenylphosphine (37 mg, 0.14 mmol), imidazole (15 mg, 0.22 mmol), 2 mL of Et_2O, and 1 mL of CH_3CN was added iodine (33 mg, 0.13 mmol). After stirring for 10 min at room temperature, alcohol **22*** (30 mg, 0.11 mmol) in 1 mL of Et_2O was added. The reaction mixture was stirred at room temperature for 1 h, diluted with ether, and filtered through a pad of Celite, and then the solvent was removed under reduced pressure. Purification via SiO_2 column chromatography (29:1 Hex:EtOAc as eluant) afforded 27 mg (62% yield) of iodoketal **23*** as a colorless oil. IR (cm^{-1}): 2910, 1440, 1370, 1110, 835, 670. ^{1}H NMR δ: 1.06 (3H, d, *J* = 6.5), 1.08, (3H, s), 1.19–1.25 (1H, m), 1.26–1.34 (1H, m), 1.40–1.55 (3H, m), 1.66 (3H, s), 1.73 (1H, ddd, *J* = 6.5, 6.5, 11.9), 1.86–1.94 (2H, m), 2.18 (1H, AB quartet, *J* = 18.0), 2.39–2.48 (1H, m), 2.57 (1H, AB quartet, *J* = 18.1), 3.08 (1H, dd, *J* = 7.6, 9.5), 3.34 (1H, dd, *J* = 2.8, 9.5), 3.87–4.07 (4H, m), 5.46–5.48 (1H, m). ^{13}C NMR δ: 16.2, 20.1, 25.8, 25.9, 26.9, 31.0, 32.6, 40.0, 40.8, 51.8 (2C), 52.9, 63.9, 65.8, 113.3, 123.5, 132.6. HR-EI-MS: $C_{17}H_{27}IO_2$ = 390.10505 ([M]$^+$), $C_{17}H_{27}IO_2$ = 390.10559 (calcd.).

Synthesis of dithioketal 24*

To a solution of isobutyldithiane (32 mg, 0.18 mmol) in 0.5 mL of THF at 0 °C was added a 2.5 mol L^{-1} solution of *n*-BuLi in hexane (56 mL, 0.14 mmol), dropwise. The mixture was stirred at 0 °C for 1 h; then 100 µL of HMPA was added, and the solution was cooled to –90 °C. Iodoketal **23*** (14 mg, 0.036 mmol), cooled in a separate cooling bath to –50 °C, in 0.5 mL of THF was added via cannula to the reaction mixture. After stirring at –90 °C for 30 min, 2 mL of 0.3% oxalic acid was added, and the organic product was extracted with ether (2×). The combined organics were washed with H_2O (2×) and brine, dried over $MgSO_4$, and filtered, and the solvent was removed in vacuo. Purification via SiO_2 column chromatography (hexane to 29:1 Hex:EtOAc as eluant) gave 12.6 mg (81% yield) of dithioketal **24*** as a colorless oil. IR (cm^{-1}): 2920, 1465, 1370, 1100. ^{1}H NMR δ: 1.02 (3H, d, *J* = 6.7), 1.03 (3H, d, *J* = 6.7), 1.09 (3H, s), 1.10 (3H, d, *J* = 5.6), 1.20–1.32 (2H, m), 1.44–1.49 (1H, m), 1.53–1.65 (3H, m), 1.65 (3H, s), 1.79–1.98 (8H, m), 2.12–2.19 (1H, m), 2.29 (1H, AB quartet, *J* = 18.1), 2.30–2.41 (1H, m), 2.45 (1H, AB quartet, *J* = 18.0), 2.74–2.89 (4H, m), 3.86–4.06 (4H, m), 5.48 (1H, m). ^{13}C NMR δ: 22.1, 25.1, 25.2 (2C), 25.3, 25.6, 25.9, 26.3, 26.6 (2C), 28.8, 30.5, 33.7, 40.9, 43.3, 48.4, 50.7, 52.4, 53.6, 55.1, 64.3, 65.4, 114.0, 123.4, 132.4. HR-EI-MS: $C_{25}H_{42}S_2O_2$ = 438.26058 ([M]$^+$), $C_{25}H_{42}S_2O_2$ = 438.26263 (calcd.).

Synthesis of *epi*-reiswigin A 25*

To dithioketal **24*** (4.5 mg, 0.010 mmol) in 0.5 mL of 20% aqueous CH_3CN was added mercuric chloride (6.0 mg, 0.022 mmol), and the mixture was stirred at reflux for 2.5 h. It was then allowed to cool, diluted with ether, and filtered through a pad of Celite. The filtrate was washed with saturated $NaHCO_3$, H_2O, and brine and dried over $MgSO_4$ and filtered, and the solvent was removed in vacuo. Purification by SiO_2 preparative thin layer chromatography (8:1 Hex:EtOAc as eluant) afforded 2.0 mg (67% yield) of *epi*-reiswigin A **25***, as a low-melting white solid. Recrystallization from hexane provided crystals that were suitable for X-ray analysis; mp 35.9–36.8 °C. IR (cm^{-1}): 2915, 1710, 1660, 1450, 1370. ^{1}H NMR δ: 0.92 (3H, d, *J* = 6.7), 0.93 (6H, d, *J* = 6.7), 1.17 (3H, s), 1.20–1.29 (1H, m), 1.41–1.53 (4H, m), 1.67–1.73 (1H, m), 1.77–1.82 (1H, m), 1.85 (3H, s), 2.04–2.23 (5H, m), 2.26–2.33 (3H, m), 2.41 (1H, dd, *J* = 3.3, 16.1), 5.81 (1H, s). ^{13}C NMR δ: 19.7, 22.6, 22.7, 24.5, 25.6, 26.6, 28.3, 32.3, 32.4, 34.6, 36.6, 47.3, 52.0, 52.6, 53.5, 61.3, 126.6, 151.7, 208.2, 210.7. HR-EI-MS: $C_{20}H_{32}O_2$ = 304.24017 ([M]$^+$), $C_{20}H_{32}O_2$ = 304.24023 (calcd.).

Acknowledgments

Financial support from the Natural Sciences and Engineering Research Council of Canada (NSERC) and the University of New Brunswick (UNB) is gratefully acknowledged. We also wish to thank Gilles Vautour for recording all mass spectra, Dr. Andreas Decken for solving the X-ray crystal structure, and Dr. Larry Calhoun for helpful discussions on the interpretation of some of the NMR spectra. We thank the Harbor Branch Oceanographic Institute, Ft. Pierce, Fla., U.S.A., for kindly providing us with copies of ^{1}H and ^{13}C NMR spectra for (–)-reiswigin A.

References

1. F. Koehn, S. Cross, Y. Kashman, and S. Hirsch. Tetrahedron Lett. **28**, 5461 (1987).
2. B.B. Snider and K. Yang. J. Org. Chem. **55**, 4392 (1990).
3. D. Kim, K.J. Shin, I.Y. Kim, and S.W. Park. Tetrahedron Lett. **35**, 7957 (1994).
4. For recent reviews on enantioselective deprotonations, see: P.J. O'Brien. J. Chem. Soc. Perkin Trans. 1, 95 (2001); 14 (1998); see also: P. O'Brien (*Editor*). Recent developments in chiral lithium amide base chemistry. Tetrahedron, **58**, 4567 (2002).
5. M. Harmata. Acc. Chem. Res. **34**, 595 (2001); J. Cha and J. Oh. Curr. Org. Chem. **2**, 217 (1998); J.H. Rigby and F.C. Pigge. Org. React. **51**, 351 (1997).
6. D.I. Rawson, B.K. Carpenter, and H.M.R. Hoffmann. J. Am. Chem. Soc. **101**, 1786 (1979).
7. F. Ramirez and S. Dershowitz. J. Org. Chem. **22**, 41 (1957).
8. B.J. Bunn, P.J. Cox, and N.S. Simpkins. Tetrahedron, **49**, 207 (1993).
9. C.M. Cain, R.P.C. Cousins, G. Coumbarides, and N. Simpkins. Tetrahedron, **46**, 523 (1990).
10. H. Kim, R. Shirai, H. Kawasaki, M. Nakajima, and K. Koga. Heterocycles, **30**, 307 (1990).
11. N.S. Simpkins. J. Chem. Soc. Chem. Comm. 88 (1986).
12. R. Shirai, M. Tanaka, and K. Koga. J. Am. Chem. Soc. **108**, 543 (1986).
13. P.H.J. Carlsen, T. Katsuki, V.S. Martin, and K.B. Sharpless. J. Org. Chem. **46**, 3936 (1981).
14. N.M. Yoon, C.S. Pak, H.C. Brown, S. Krishnamurthy, and T.P. Stocky. J. Org. Chem. **38**, 2786 (1973).
15. S. Hanessian and P. Lavallee. Can. J. Chem. **53**, 2975 (1975).
16. For reviews, see: T.T. Tidwell. Synthesis, 857 (1990); T.T. Tidwell. Org. React. **39**, 297 (1990); A.J. Mancuso and D. Swern. Synthesis, 165 (181).
17. R.H. Reuss and A. Hassner. J. Org. Chem **39**, 1785 (1974).

© 2004 NRC Canada

18. A.K. Bhattacharya and G. Thyagarajan. Chem. Rev. **81**, 415 (1981).
19. H. Hagiwara and H. Uda. J. Chem. Soc. Chem. Commun. 1351 (1987).
20. A. Nangia, G. Prasuna, and P.B. Rao. Tetrahedron Lett. **35**, 3755 (1994).
21. Z. Valenta, D.I. MaGee, and S. Setiadji. J. Org. Chem. **61**, 9076 (1996).
22. D. Shannon. Ph.D. thesis. Studies directed towards the total synthesis of (–)-reiswigin A via enantioselective deprotonation. Department of Chemistry, University of New Brunswick, Fredericton, N.B. 2001.
23. P.A. Grieco and C.S. Pogonowski. J. Am. Chem. Soc. **95**, 3071 (1973).
24. J.W. Leeuw, E.R. DeWaard, T. Beetz, and H.O. Huisman. Recl. Trav. Chim Pays-Bas, **92**, 1047 (1973).
25. P.J. Garegg and B. Samuelsson. J. Chem. Soc. Chem. Commun. 978 (1979).
26. D. Seebach and E.J. Corey. J. Org. Chem. **40**, 231 (1975).
27. E.J. Corey and B.W. Erickson. J. Org. Chem. **36**, 3553 (1971).
28. K. Koga. *In* Organic synthetic modern trends. *Edited by* O. Chizhov. Blackwell Scientific Publishers, Oxford, U.K. 1987. p. 285.
29. K. Furuta, T. Maruyama, and H. Yamaomoto. J. Am. Chem. Soc. **113**, 1041 (1991).
30. T. Rios and L. Quijano. Tetrahedron Lett. 1371 (1969).
31. T. Rios and F. Gomez. Tetrahedron Lett. 2929 (1969).
32. W.L.F. Armarego and D.D. Perrin (*Editors*). Purification of laboratory chemicals. 4th ed. Butterworth-Heinemann, Cornwall, U.K. 1997.
33. E.C. Kleiderer and R. Adams. J. Am. Chem. Soc. **55**, 4225 (1933).

© 2004 NRC Canada

Biobleaching chemistry of laccase-mediator systems on high-lignin-content kraft pulps[1]

Fadi S. Chakar and Arthur J. Ragauskas

Abstract: A high-lignin-content softwood kraft pulp was reacted with laccase in the presence of 1-hydroxybenzotriazole (HBT), *N*-acetyl-*N*-phenylhydroxylamine (NHA), and violuric acid (VA). The biodelignification response with violuric acid was superior to both 1-hydroxybenzotriazole and *N*-acetyl-*N*-phenylhydroxylamine. NMR analysis of residual lignins isolated before and after the biobleaching treatments revealed that the latter material was highly oxidized and that the magnitude of structural changes was most pronounced with the laccase – violuric acid biobleaching system. An increase in the content of carboxylic acid groups and a decrease in methoxyl groups were noted with all three laccase-mediator systems. The oxidation biobleaching pathway is directed primarily towards noncondensed C5 phenolic lignin functional structures for all three laccase-mediated systems. The laccase – violuric acid system was also reactive towards C5-condensed phenolic lignin structures.

Key words: laccase, mediator, lignin, pulp, biobleaching, phenolics.

Résumé : On a soumis de la pulpe de papier kraft ayant un degré élevé de lignine à une réaction avec de la laccase en présence de 1-hydroxybenzotriazole (HBT), de *N*-acétyl-*N*-phénylhydroxylamine (NHA) et d'acide violurique (AV). La réponse de biodélignification avec de l'acide violurique est supérieure celle observée avec le 1-hydroxybenzotriazole ou la *N*-acétyl-*N*-phénylhydroxylamine. L'analyse RMN des lignines résiduelles isolées avant et après les traitements de bioblanchiment révèle que ces derniers matériaux sont fortement oxydés et que l'amplitude des changements structuraux est maximale avec le système de bioblanchiment avec de la laccase et de l'acide violurique. Avec chacun des systèmes utilisés, on a noté une augmentation de la teneur en groupes acides carboxyliques et une diminution en groupes méthoxyles. Pour les trois systèmes catalysés par la laccase, la voie d'oxydation de bioblanchiment est orientée principalement vers les structures fonctionnelles de la lignine phénolique en C5 non condensée. Le système de laccase – acide violurique est aussi réactif vis-à-vis des structures fonctionnelles de la lignine phénolique en C5 condensée.

Mots clés : laccase, médiateur, lignine, pulpe, bioblanchiment, phénoliques.

[Traduit par la Rédaction]

Introduction

The bleaching of kraft pulps is an integral component of manufacturing high-value products in the pulp and paper industry. Historically, removal of lignin from kraft pulps was accomplished primarily using chlorine or hypochlorous acid. However, because of environmental concerns, these chemical agents have been replaced with the use of chlorine dioxide, hydrogen peroxide, and oxygen (1). Nonetheless, each of these chemical agents has certain limitations, and research is ongoing for improved lignin removal treatments. One promising future strategy for bleaching kraft pulps involves the use of biological systems (2). Currently, several enzymatic technologies are being developed for pulp-bleaching operations, including manganese peroxidase, lignin peroxidase, and laccase (3, 4). Although all of these biobleaching technologies have advanced over the past decade, laccase biobleaching treatments have achieved some of the most notable results, yielding +50% delignification of low-lignin content kraft pulps with little oxidative degradation towards pulp carbohydrates (5–7). The high oxidative selectivity of a laccase biobleaching system towards lignin has been shown to provide distinct pulp-yield benefits when high-lignin-content kraft pulps are biodelignified (8–10).

It is now well established that laccase delignification of kraft pulps can only occur in the presence of a low-molecular-weight chemical mediator. This is commonly attributed to pulp fiber dimensions, which prevent the diffusion of laccase into the fiber to allow for lignin oxidation (11). Hence, laccase biobleaching of pulp fibers involves the oxidation of laccase by O_2, laccase oxidation of a mediator, and the diffusion of oxidized mediator into the fiber, which then oxidizes the lignin. The majority of the oxidized lignin is removed in a subsequent alkaline extraction stage.

The efficacy of a laccase-mediator system (LMS) for delignification is critically dependent on the type of mediator employed. The first reported mediator for LMS delignification was 2,2′-azinobis(3-ethylbenzothiazoline-6-sulfonate); its bleaching chemistry has been extensively Hexplored (12–14). Additional mediators have since been discovered that significantly improve the overall delignification effect of an LMS-stage (15). Many of these media-

Received 6 June 2003. Published on the NRC Research Press Web site at http://canjchem.nrc.ca on 23 February 2004.

F.S. Chakar and A.J. Ragauskas.[2] Institute of Paper Science and Technology, Atlanta, GA 30318, U.S.A.

[1]This article is part of a Special Issue dedicated to Professor Ed Piers.

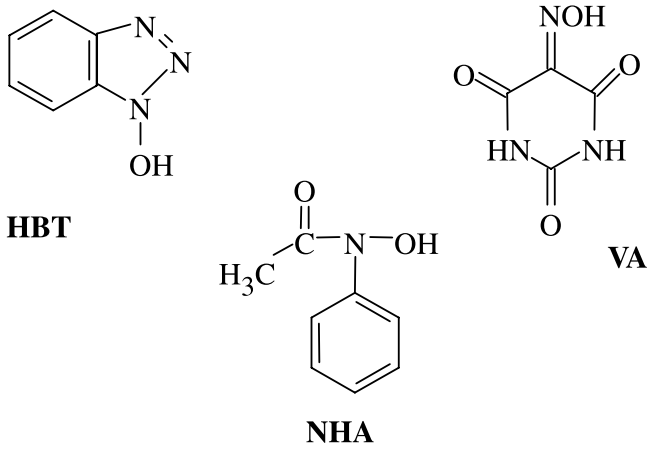
[2]Corresponding author (e-mail: arthur.ragauskas@ipst.edu).

 doi: 10.1139/V03-195 © 2004 NRC Canada

tors contain an *N*-hydroxy functionality, and the active delignification species is believed to be the nitroxyl radical (16). The first of these *N*-hydroxy mediators was 1-hydroxybenzotriazole (HBT). It was shown that with a laccase-HBT treatment delignification could be extended by 20%–30% over a laccase-2,2′-azinobis(3-ethylbenzothiazoline-6-sulfonate) treatment (17). LMS delignification chemistry using HBT with low-lignin-content kraft pulps or lignin model compounds has been extensively studied (18–22). Essential observations with respect to residual lignin structural changes after an LMS_{HBT} treatment are that the overall phenolic component of lignin is oxidatively decreased and carboxylic acid groups are introduced. Recently, *N*-acetyl-*N*-phenylhydroxylamine (NHA) and violuric acid (23) were introduced as improved *N*-hydroxy mediators (see Fig. 1) for LMS biobleaching treatments.

The delignification chemistry of LMS, employing violuric acid, vis-a-vis lignin structural changes remains largely unknown. To provide a fundamental basis from which new LMS bleaching technologies can be further advanced, this study examines the changes in lignin structure before and after an LMS treatment using violuric acid and compares these results against NHA and HBT.

Fig. 1. Chemical structure of NHA, HBT, and VA.



Experimental

Materials and methods

1-Hydroxybenzotriazole, violuric acid, and all other reagents and solvents were purchased from Aldrich, Milwaukee, Wis., and used as received, except for *p*-dioxane and *N*-acetyl-*N*-phenylhydroxylamine. *p*-Dioxane was freshly distilled over $NaBH_4$ before use. *N*-Acetyl-*N*-phenylhydroxylamine was synthesized in accordance with the Oxley et al. procedure (23). Laccase from *Trametes villosa* was donated by Novo Nordisk Biochem. A high-lignin-content southern softwood kraft pulp was prepared from *Pinus taeda* chips at Potlatch Corporation facilities in Cloquet, Minn. The pulp was thoroughly washed, screened, centrifuged, and stored at 4 °C. Prior to an LMS treatment the pulps were Soxhlet extracted with acetone and air dried.

Pulp characterization

The lignin content of the kraft pulps in this study was determined by a $KMnO_4$ titration of the pulp in accordance with TAPPI Standard Methods T236-cm85 (24). This procedure yields a value known as the kappa number, which is an indirect measurement of the lignin content in pulp: % mass lignin = 0.15 × kappa number. The kappa number of the Soxhlet-extracted starting kraft pulp was 71.4.

Enzyme assay

Laccase activity was measured by monitoring the rate of oxidation of syringaldazine (17). One unit of activity (U) was defined as the change in absorbance at 530 nm of 0.001 min^{-1} mL^{-1} of enzyme solution in a 100 mmol/L potassium phosphate buffer (2.20 mL) and 0.216 mmol/L syringaldazine in methanol (0.30 mL, pH 6.7). The procedure was carried out at 23 °C. The activity of the laccase was 1.87×10^6 U/mL of enzyme solution.

Laccase-mediator system (LMS) general procedure

A 2000 mL capacity 316 Parr reactor equipped with a stirrer, a pressure gauge, and a heating mantle and connected to a Parr 4842 temperature controller was charged with 60.00 g of pulp and distilled water (1137 mL). The pulp slurry was heated to 45.0 °C and was maintained at this temperature throughout the duration of the treatment. VA, NHA, or HBT (0.0206 mol) was then added to the heated slurry. (Note: (% mass mediator)/(mass pulp) was 5.4% VA; 4.6% HBT; 5.2% NHA) Subsequent to mixing the pulp slurry (approx. 5 min), the pH was adjusted to 4.5 with glacial acetic acid or saturated sodium bicarbonate solution. Laccase (93 500 U, 3 mL of enzyme solution) was added, and the reactor was sealed and pressurized with oxygen to 145 psi (1 psi = 6.894 757 kPa). After a reaction time of 2 h, stirring was halted, the reactor was depressurized, and the reacted pulp was removed from the reactor and thoroughly washed with distilled water (4800 mL). The treated pulp was then subjected to either an acidic dioxane extraction (see Isolation of residual lignins section below) or an alkaline extraction followed by an acidic dioxane extraction.

Alkaline extraction

Pulp fibers (60 g) were extracted with an aqueous 0.5 mol/L NaOH (75.00 mL) solution for 1 h at 80.0 °C with mixing. The fibers were then filtered and extensively washed until the filtrate was colorless and pH neutral. Prior studies with this pulp have shown that only 4% of the lignin present in the fiber is alkaline extractable without an LMS pretreatment (25).

Control bleaching experiments (MS)

The softwood kraft pulp was treated in accordance with the laccase-mediator delignification procedure described above, except no laccase was employed. Kappa number analysis of the pulp after a mediator system (MS), employing VA, HBT, or NHA, indicated no change in lignin content of the pulp.

Isolation of residual lignins

The isolation of residual lignins was carried out following standard literature methods (26, 27). In summary, a 5 L, three-necked round-bottom flask containing boiling chips

© 2004 NRC Canada

and fitted with a Friedrichs condenser was charged with 50 g of air-dried pulp. A solution of 0.10 mol/L HCl of 9:1 *p*-dioxane:water (1440 mL) was added to the pulp. The reaction mixture was refluxed for 2 h under an argon atmosphere before it was cooled and filtered through a 4 L capacity coarse fritted-glass Buchner funnel covered with filter paper. The resulting filtrate was passed through a fritted-glass Buchner funnel packed with celite to remove any pulp fines that may have been present. The lignin–water–dioxane mixture was then neutralized with an aqueous saturated solution of sodium bicarbonate to an apparent pH value of 5.0–5.5 and concentrated under reduced pressure to approximately 10% of the initial volume. Deionized water (approx. 400 mL) was added, and the mixture was concentrated again under reduced pressure to remove the last traces of *p*-dioxane. The resulting lignin–water mixture was transferred to a 1 L beaker, diluted with deionized water to a volume of approximately 800 mL, acidified to a pH of 2.0–2.5 with an aqueous 1 mol/L HCl solution, and centrifuged. The supernatant was siphoned and acidified with the addition of pH 2 aqueous HCl (200 mL). This step was repeated three times, each time reducing the volume of wash water by 30%. The lignin was then freeze dried and characterized by NMR. Lignin yields were calculated as follows: % lignin yield = ((mass of lignin isolated)/(initial kappa of brownstock) × 0.15) × 100. Lignin yields ranged from 45.4%–49.0%.

NMR characterization of residual lignins

The residual lignins isolated from the brownstock, MS, LMS, and LMS(E) were analyzed using a 400 MHz Bruker DMX spectrometer. Quantitative ^{13}C NMR spectra were acquired and analyzed in accordance with established literature methods (28). In brief, lignin (160–168 mg) was dissolved in 450 μL of DMSO-d_6, and the spectral data were acquired using an inverse gated decoupling sequence, 90° pulse angle, 14 s pulse delay, 23 000 Hz sweep, 10 000 – 12 000 transients, at 50.0 °C. The Fourier transformed spectra were integrated in accordance with reported chemical shifts for lignin functional groups. The integrals were normalized to the aromatic signals, which were assigned a value of six.

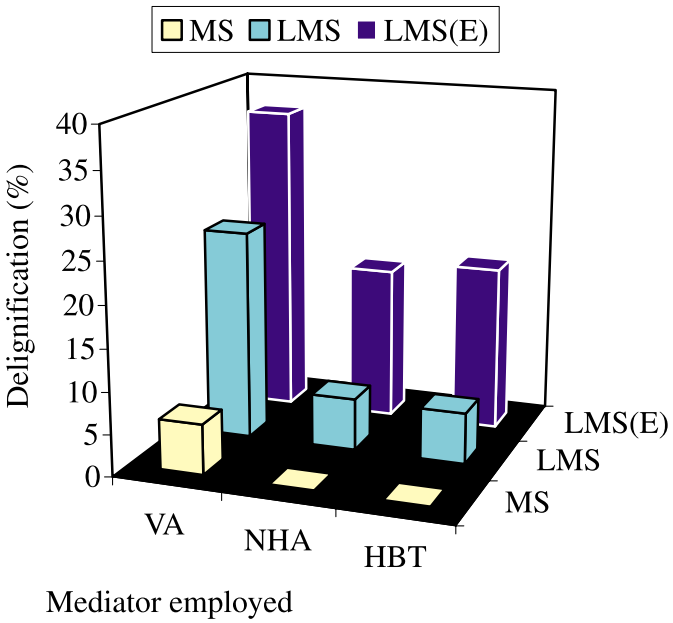
Lignin samples were also derivatized with 2-chloro-4,4,5,5-tetramethyl-1,3,2-dioxaphospholane and analyzed by ^{31}P NMR following literature methods (29). ^{31}P NMR spectra were recorded using an inverse gated decoupling sequence, 90° pulse angle, 25 s pulse delay, 13 000 Hz sweep, and 150 transients, at room temperature. NMR spectral acquisition and analysis were accomplished using Bruker's XWINNMR 2.1 software.

The lignin functional groups characterized by ^{13}C and ^{31}P NMR had standard errors of 2.0% and 1.2%, respectively. This was experimentally determined by three separate NMR measurements on three separately isolated lignin samples.

Results and discussion

Until recently, most LMS research activities have focused primarily on determining the delignification chemistry of low-lignin-content kraft pulps. Studies by Chakar and Ragauskas (25) have demonstrated that LMS delignification of high-lignin-content kraft pulps provides several distinct benefits, including improved pulp yields and simplification

Fig. 2. Extent of pulp delignification for MS, LMS, and LMS(E) treated kraft pulps using VA, NHA, and HBT as mediators, employing an SW kraft pulp with an initial kappa number 71.4.



of the overall bleaching process. This report examines the delignification chemistry of the newest generation of *N*-hydroxy mediators VA and NHA and compares these results against HBT employing a high-lignin-content softwood kraft pulp.

LMS delignification

The delignification response of LMS treatments employing NHA, HBT, and VA as mediators was established using an acetone-extracted softwood kraft pulp with an initial lignin content of 10.7% by mass. Furthermore, control experiments (MS) were carried out in accordance with the LMS procedure, except laccase was not used. The results shown in Fig. 2 clearly indicate that a treatment in the presence of a mediator and no laccase led to no delignification. This lack of activity has been reported on pulps treated solely with laccase and no mediator (4).

Based on the results summarized in Fig. 2, the delignification response of the LMS_{NHA} and LMS_{HBT} system was similar. The effectiveness of LMS_{VA} vis-à-vis delignification is evident as the LMS_{VA} system outperformed both the LMS_{HBT} and LMS_{NHA} treatments. Alkaline extraction of the LMS-treated pulps resulted in a further reduction in the lignin content of the pulp, to be expected since the alkaline conditions enhance the dissolution of oxidized lignin fragments.

Overall, the LMS treatment followed by an alkaline extraction removed 20%, 19%, and 37% lignin from the starting pulp, employing HBT, NHA, and VA as mediators, respectively. The improved efficiency of VA as a mediator for LMS is not limited to high-lignin-content pulps, as comparable results have been reported for low-lignin-content pulps (30). The biodelignification properties of LMS_{VA} have been shown to be accompanied by a darkening of the pulp due to the formation of quinoidal lignin structures (31), which can be oxidatively removed in subsequent bleaching

© 2004 NRC Canada

Fig. 3. Structural components of lignin.

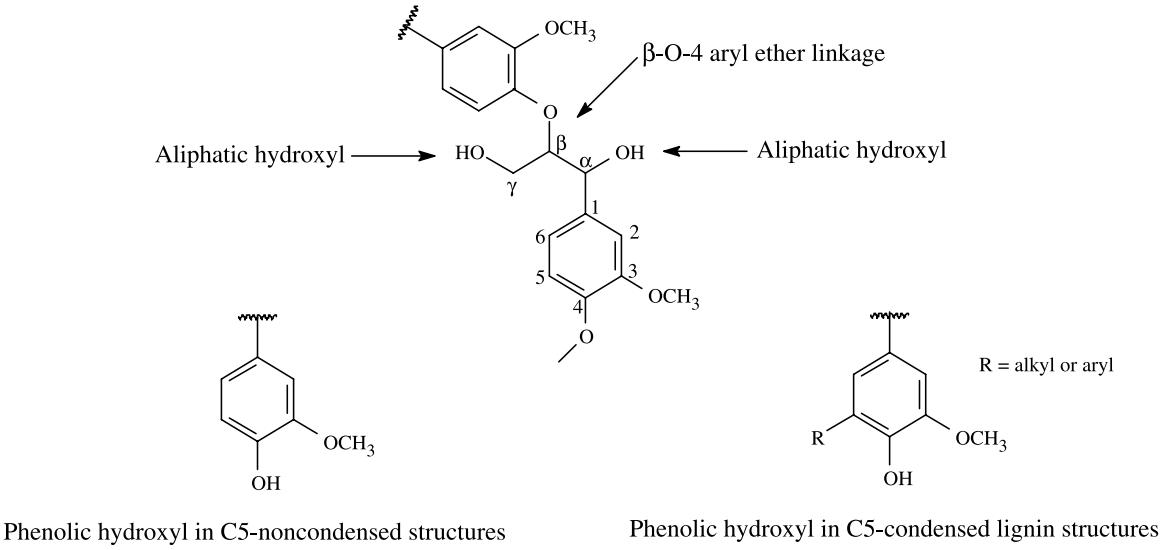


Fig. 4. ^{13}C NMR spectrum of residual lignin isolated from starting pulp.

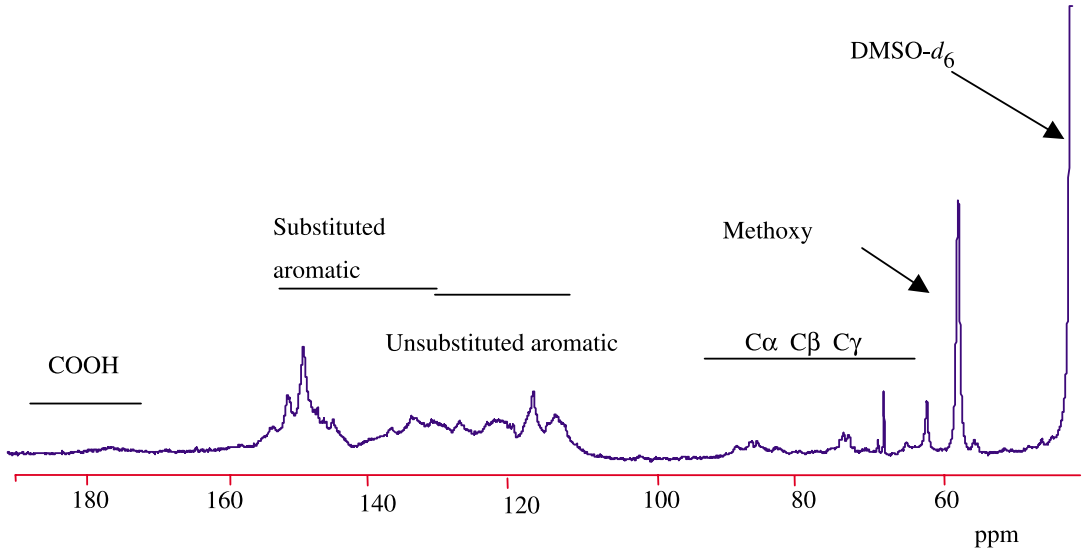
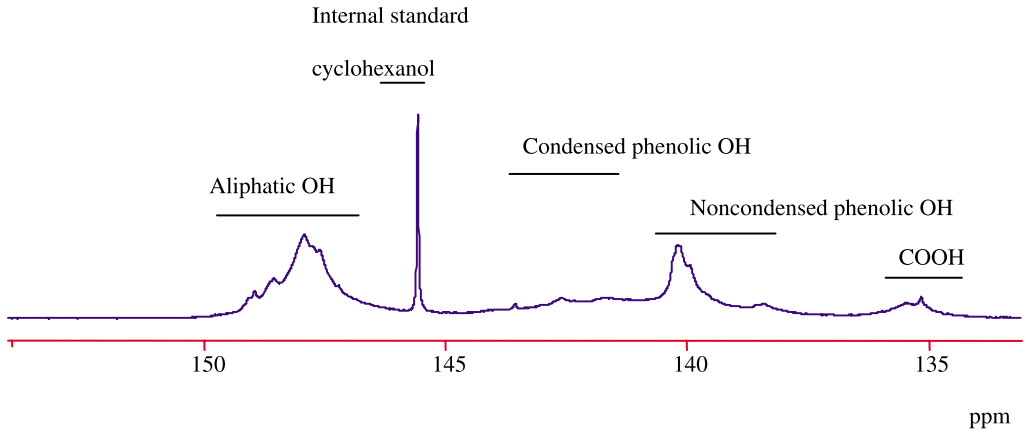


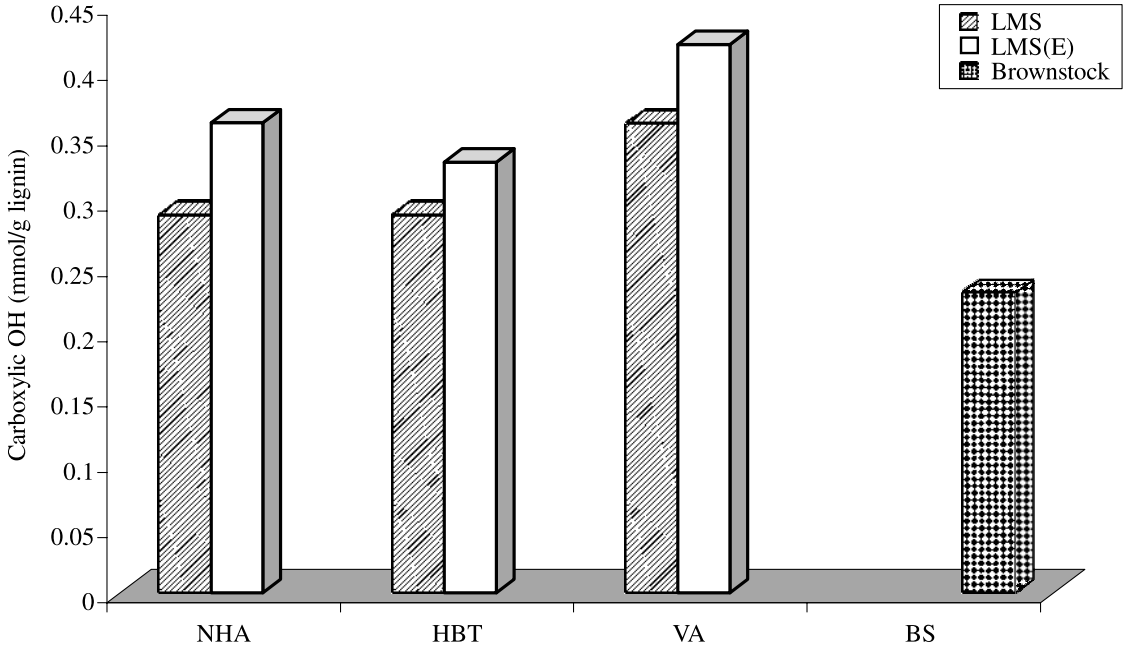
Fig. 5. ^{31}P NMR spectrum of residual lignin isolated from starting pulp.



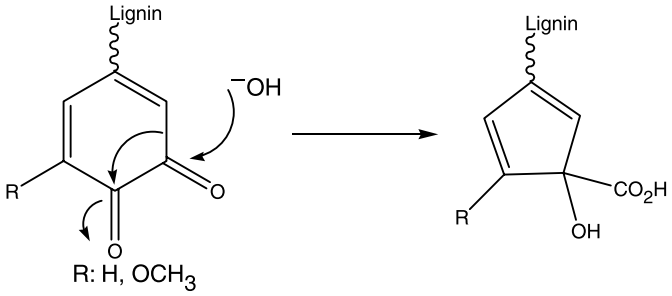
treatments. Several studies have attempted to correlate the biodelignification efficiency of mediators with isolated key parameters such as dissociation energies (19), radical half-lives (16), steric effects (32), and redox potentials (33). However, global correlations have been difficult to establish, although undoubtedly these parameters must be important

© 2004 NRC Canada

Fig. 6. ^{31}P NMR determination of carboxylic acid groups in residual lignins isolated from starting pulp, LMS, and LMS(E) treated pulps, employing NHA, HBT, and VA as mediators.



Scheme 1. Hydroxide addition and rearrangement of *ortho*-quinones.



factors. To further define the fundamentals of LMS delignification on the kraft pulp used in this study, the structure of residual lignins before and after the biobleaching treatments was examined.

NMR analysis

Residual lignins were isolated from the starting pulp, as well as the MS, LMS, and LMS(E) treated pulps, following literature methods (20). Figure 3 summarizes the lignin functional groups examined in this study. Quantification of these functional groups in lignin was determined using ^{13}C NMR and ^{31}P NMR after lignin phosphitylation.

NMR analysis of the residual lignin isolated from the MS_{VA}, MS_{HBT}, and MS_{NHA} treated pulps (i.e., pulps treated with mediator and no laccase) indicated no changes in the content of lignin functional groups with regards to the lignin isolated from starting pulp. This result was consistent with the results of the lignin content determinations of the MS treated pulps and supports the conclusion that laccase is a critical component in the overall LMS delignification process. Figures 4 and 5 summarize the ^{13}C and ^{31}P NMR spectral data acquired for the residual lignin isolated from starting softwood kraft pulp.

Of the various structural features of lignin, changes in carboxylic acid group content are often a strong indicative sign of oxidative degradation of lignin during pulp bleaching. The acid groups content of the residual lignin from the starting pulp, LMS, and LMS(E) treated pulps is summarized in Fig. 6. These results indicate the residual lignin after an LMS stage is enriched with acid groups. The increase in acid group content of the LMS_{HBT} and LMS_{NHA} treated pulps were comparable (26%), whereas the LMS_{VA} treated pulp had a 57% greater increase in acid groups. These results mirror the observed changes in delignification of the pulps after the LMS treatments. Interestingly, the acid group content for all LMS treated pulps increased slightly after the alkaline extraction stage. Since the extraction process removes oxidized lignin fractions, it seems unlikely that this effect is due solely to an enrichment process. Previous studies by our group have shown that LMS treated pulps are enriched with quinones, and these units are known to undergo a benzylic acid rearrangement upon exposure to base, as shown in Scheme 1.

These and other reactions presumably contribute to the increase in acid groups after an LMS(E) treatment. The oxidative formation of carboxyl groups in lignin during pulp bleaching is most frequently accompanied with oxidative degradation of phenoxy groups. The phenoxy content of the starting, LMS, and LMS(E) treated pulps is presented in Figs. 7 and 8. The results in Fig. 7 clearly demonstrate that all the residual lignins isolated after LMS treatments were depleted of C5-noncondensed phenolic hydroxyls. The LMS_{NHA} treatment removed 22% of noncondensed phenoxy, LMS_{HBT} removed 16%, and LMS_{VA} removed 44% with respect to the starting pulp. The improved delignification properties of LMS_{VA} were reflected in the increased degradation of C5-noncondensed phenolics. The minor increase in

© 2004 NRC Canada

Fig. 7. ^{31}P NMR determination of C5-noncondensed phenolic hydroxyls groups in residual lignin isolated from brownstock and LMS and LMS(E) treated pulps, employing NHA, HBT, and VA as mediators.

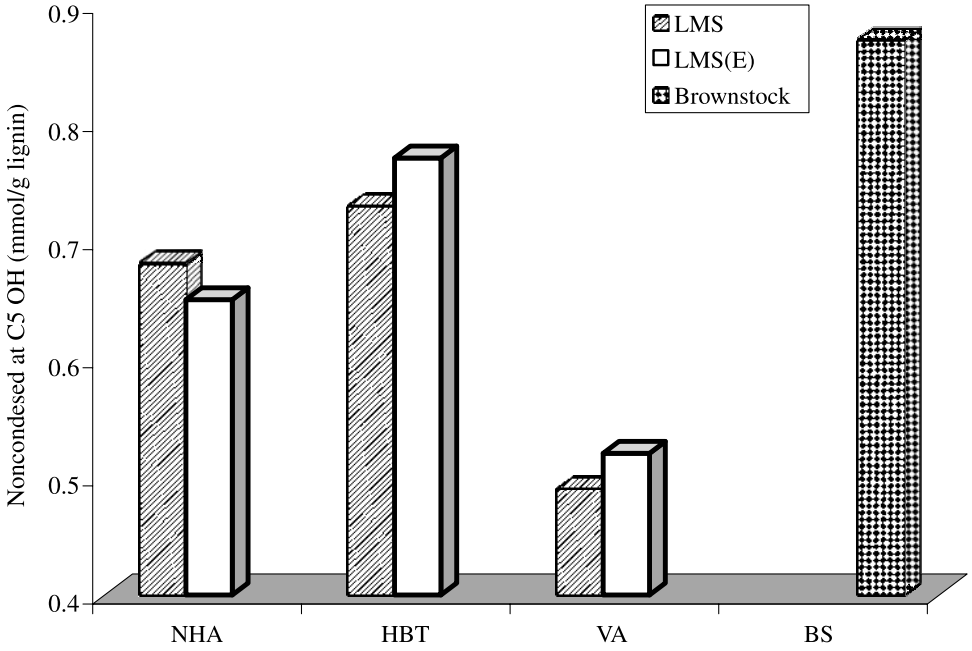
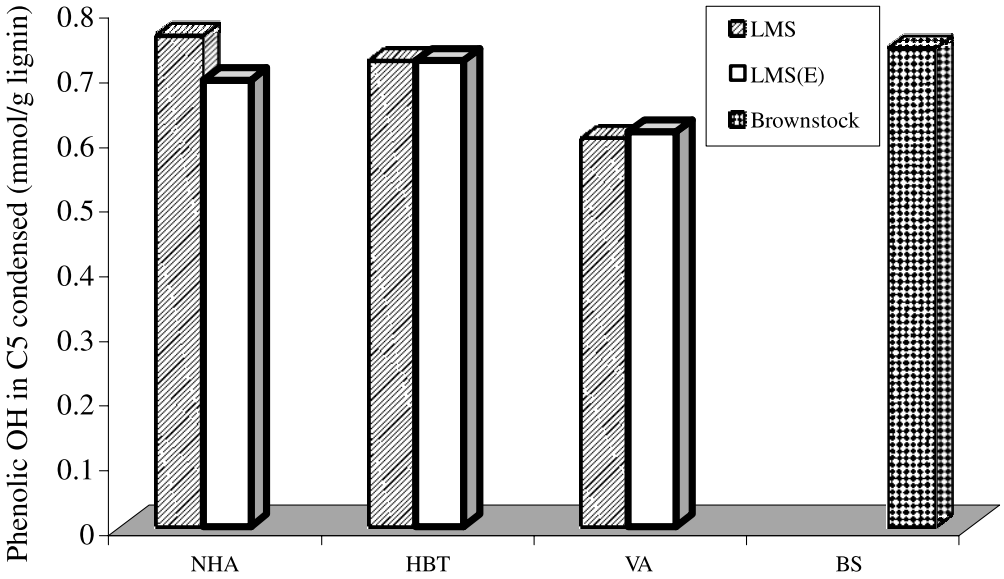


Fig. 8. ^{31}P NMR determination of C5-condensed phenolic hydroxyl groups in residual lignin isolated from brownstock and LMS and LMS(E) treated pulps, employing NHA, HBT, and VA as mediators.



phenolics after the LMS(E) stage suggests that the alkaline extraction is not causing further oxidative damage to phenolic lignin and is perhaps enriching the remaining lignin with phenolic units.

Figure 8 summarizes the changes in C5-condensed phenoxy groups after LMS and LMS(E) treatments. In general, bleaching chemistry of kraft pulps has shown that C5-noncondensed phenolics are resistant to assorted oxidative bleaching agents, including chlorine dioxide (34) and alkaline–oxygen conditions (35).

The biobleaching chemistry of an LMS_{VA} treatment was the only LMS process capable of significantly degrading C5-condensed phenolics in the pulp. These results suggest that this mediator exhibits an enhanced oxidative capability towards phenolic units in lignin. These data also clearly demonstrate that the LMS_{HBT} or LMS_{NHA} treatments do not oxidatively degrade C5-condensed phenolics in this high-kappa kraft pulp. This result differs from our previous studies employing low-lignin-content kraft pulps (i.e., pulps having <5% lignin content) in which we observed that an $LMS_{NHA\ or\ HBT}$ treatment would degrade both C5-condensed and noncondensed phenolic units with only a slight preference for C5-noncondensed lignin phenolic units (17). On this basis, the ^{31}P NMR results suggest that the oxidative

© 2004 NRC Canada

Fig. 9. ^{31}P NMR determination of aliphatic hydroxyl groups in residual lignin isolated from brownstock and LMS and LMS(E) treated pulps, employing NHA, HBT, and VA as mediators.

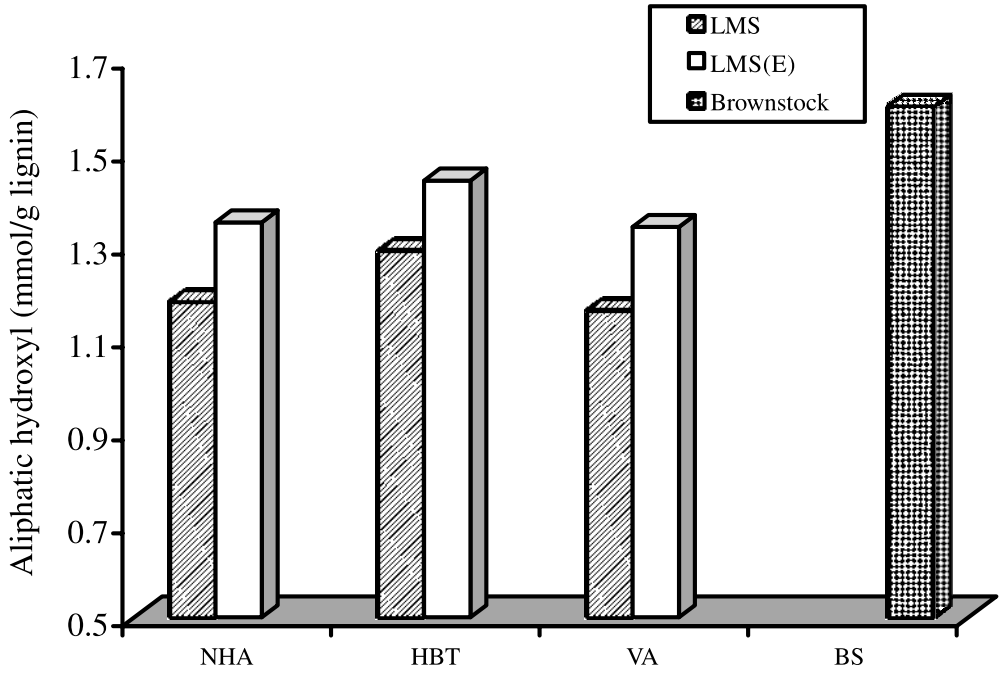


Table 1. Ratio of substituted to unsubstituted aromatic carbons in residual lignin samples, as determined by quantitative ^{13}C NMR.

Residual lignin isolated from	Ratio of substituted to unsubstituted aromatic carbons
Brownstock	1.67:1.00
LMS_{NHA}	2.07:1.00
LMS_{HBT}	1.92:1.00
LMS_{VA}	1.97:1.00
LMS_{NHA}(E)	1.96:1.00
LMS_{HBT}(E)	1.85:1.00
LMS_{VA}(E)	1.87:1.00

Note: Chemical shift distribution for substituted aromatic lignin is δ 154–123 parts per million (ppm), and for unsubstituted aromatic carbons, the frequency range is δ 123–106 ppm.

selectivity of the LMS_{VA} system is different than that of LMS_{HBT} and LMS_{NHA}. Nonetheless, the overall trend of these LMS systems indicates that the preferred site of phenolic oxidation is directed toward C5-noncondensed units in lignin.

Along with the oxidative degradation of phenolic units in lignin, side-chain oxidation of lignin has been proposed to occur to lignin during an LMS treatment. Figure 9 reveals that the content of aliphatic hydroxyl groups in residual lignins isolated after treatment with LMS_{NHA}, LMS_{HBT}, and LMS_{VA} is decreased by 11%–28% with respect to the brownstock lignin, with the greatest change occurring when VA and NHA were employed as mediators.

The lack of reactivity of C5-condensed phenolic structures suggests that the residual lignin after the LMS treatment on the high-lignin-content kraft pulps is of a condensed character. This claim was evaluated by measuring the ratio of substituted to unsubstituted aromatic carbon groups in the ^{13}C NMR spectra of the starting, LMS, and LMS(E) treated pulps. Table 1 summarizes the results of this investigation, and the data clearly support the hypothesis that after an LMS(E) treatment of a high-kappa kraft pulp, the lignin is further enriched in condensed lignin structures.

Figure 10 summarizes the changes in β-O-4 aryl ether content of the lignin structures before and after the LMS treatment, as determined by ^{13}C NMR. The results indicate that such structures are resistant to LMS treatments. Similar trends have been reported in previous LMS studies, using HBT as the mediator, on low-lignin-content kraft pulps (17). In contrast, reports on lignin model compound studies have indicated that such structures are reactive towards LMS (14). The factors contributing to this inactivity in kraft pulps remain unknown. However, it may be possible that this behavior is related to a selectivity phenomenon. Although a dimeric β-O-aryl ether lignin model compound may respond to an LMS treatment, a different scenario may be envisioned when dealing with the actual lignin macropolymer that contains an array of functional groups. On this basis, an LMS treatment may have a higher affinity towards other functional groups than β-O-aryl ether, and in turn, this may explain the resistance observed in this study and in the literature.

The results shown in Fig. 11 reveal a decrease in the content of methoxy groups. These results are consistent with previous LMS studies on low-lignin-content kraft pulps employing ABTS and HBT as mediators (36).

Conclusions

In summary, these results established that LMS_{VA} outperforms LMS_{HBT} and LMS_{NHA} with respect to delignification

© 2004 NRC Canada

Fig. 10. ^{13}C NMR determination of the content of β-O-aryl ether groups in residual lignins isolated from brownstock and LMS and LMS(E) treated pulps, employing NHA, HBT, and VA as mediators.

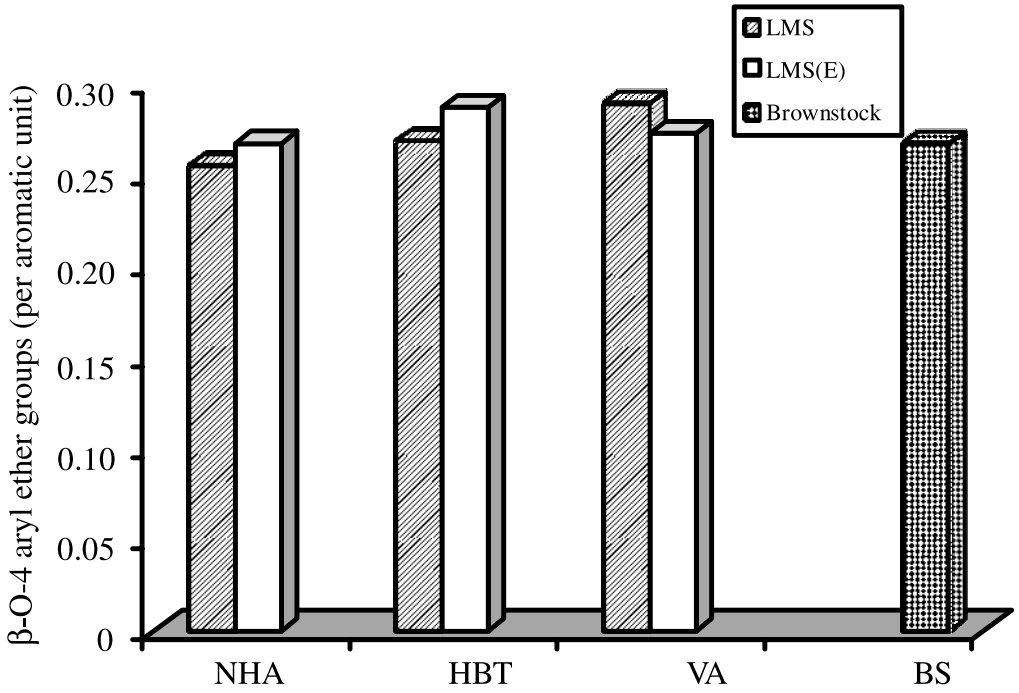
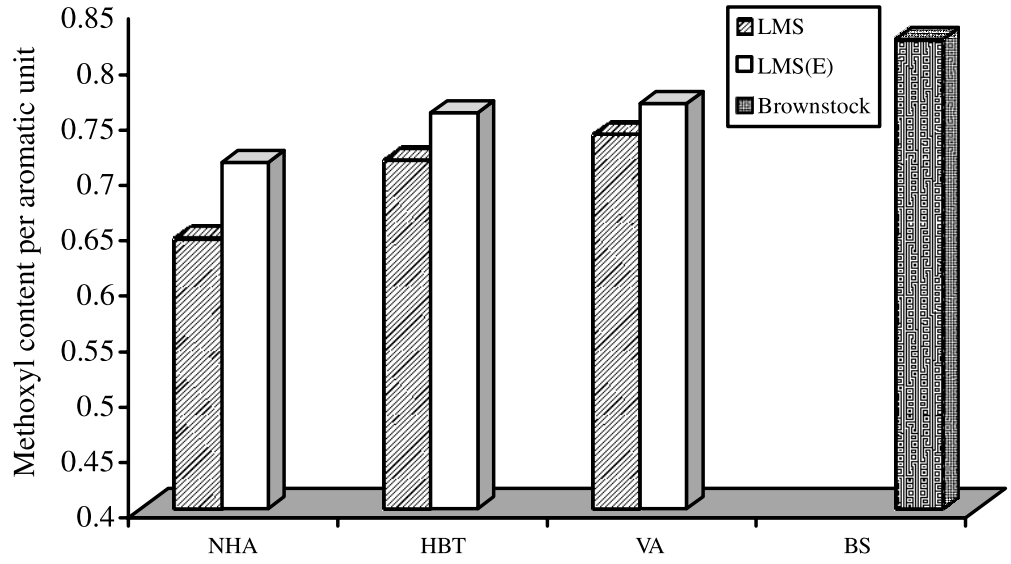


Fig. 11. Content of methoxy groups in residual lignins isolated from brownstock and LMS and LMS(E) treated pulps, employing NHA, HBT, and VA as mediators.



of high-lignin-content kraft pulps. The mediator effectiveness of VA was further supported by the magnitude of lignin structural changes with respect to NHA and HBT used as mediators for an LMS treatment. Spectral analyses of residual lignins isolated before and after LMS treatments, employing VA, NHA, and HBT as mediators, revealed that these mediators preferentially react with C5-noncondensed phenolic lignin structures, whereas C5-condensed phenolic lignin structures were to a large extent inactive. Nonetheless, in the presence of laccase and VA, our results indicate a decrease in the latter type of lignin functional groups, suggesting that the selectivity between these mediators may be different. These results are consistent with the studies reported by Pfaller et al. (37), which had reported that LMS_{VA} generally exhibited improved delignification over the use of either NHA or HBT.

It is now well established that HBT, VA, and NHA undergo degradation reactions during an LMS reaction (38). The results in this report further emphasis the sensitivity of an LMS stage to the structure of the mediator. The improved

© 2004 NRC Canada

delignification properties of LMS_{VA} are likely to be due, in part, to the unique properties of nitroxyl radical derived from the oxime, as opposed to a dialkyl *N*-hydroxy derivative. Further studies directed at exploring these issues are ongoing.

Acknowledgments

The authors would like to express their gratitude to Union Camp (now International Paper), Savannah, Georgia, for supplying the wood source; Potlatch Corporation for pulping the chips; and Novozyme, Inc. for furnishing the laccase needed for these studies. Portions of this work were used by F.S.C. as partial fulfillment of the requirements for the Ph.D. degree at the Institute of Paper Science and Technology. The authors also wish to acknowledge the financial assistance of the U.S. Department of Energy (DOE) (Cooperative Agreement No. DE-FC36-99GO10374) and USDA grant 98-35501-6911. However, any opinions, findings, conclusions, or recommendations expressed herein are those of the author(s) and do not necessarily reflect the views of the DOE or USDA. Finally, A.J.R. wishes to thank J.B. Stothers for his guidance, friendship, and help throughout his research career.

References

1. J. Rutkowski and K. Perlinska-Sipa. Przegl. Papier. **48**(7), 225 (1992).
2. A.J. Ragauskas. *In* Biotechnology in the pulp and paper industry: 8th ICBPPI meeting. Progress in biotechnology. Vol. 21. *Edited by* L. Viikari and R. Lantto. Elsevier, Amsterdam. 2002. Chap 21, p. 7.
3. H.P. Call and I. Mücke. J. Biotechn. **53**, 163 (1997).
4. M.G. Paice, R. Bourbonnais, I.D. Reid, F.S. Archibald, and L. Jurasek. J. Pulp Paper Sci. **21**, J280 (1995).
5. J.E. Sealey, T.M. Runge, and A.J. Ragauskas. TAPPI J. **83**, 66 (2000).
6. M.L. Niku-Paavola, T. Tamminen, B. Hortling, L. Viikari, and K. Poppius-Levlin. *In* Biotechnology in the Pulp and Paper Industry: 8th ICBPPI meeting. Progress in biotechnology. Vol. 21. *Edited by* L. Viikari and R. Lantto. Elsevier Science, Amsterdam. 2002. pp. 121–130.
7. R. Bourbonnais and M. Paice. TAPPI J. **79**, 199 (1996).
8. F.S. Chakar, A.J. Ragauskas, and N.-O. Nilvebrant. Pulping Conf. 1998, **1**, 109 (1998). pp. 109–118.
9. P. Nelson, J. Chin, W.J.Charles, L. Viikari, and M. Tenkanen. Appita J. **51**, 451 (1998).
10. R.P. Chandra, F.S. Chakar, L. Allison, D.H. Kim, A.J. Ragauskas, and T.J. Elder. *In* Biotechnology in the pulp and paper industry: 8th ICBPPI meeting. *Edited by* L. Viikari and R. Lantto. Elsevier, N.Y. 2002. p. 151.
11. L. Jurasek. J. Pulp Paper Sci. **21**, J274 (1995).
12. R. Bourbonnais and M. Paice. Appl. Microbiol. Biotechn. **36**, 823 (1992).
13. A. Muheim, A. Fiechter, P.J. Harvey, and H.E. Schoemaker. Holzforschung, **46**, 121 (1992).
14. R. Bourbonnais, M.G. Paice, B. Freiermuth, E. Bodie, and S. Borneman. Appl. Environ. Microbiol. **63**, 4267 (1997).
15. H.P. Call and I. Mucke. J. Biotechn. **53**(2,3), 163 (1997).
16. A. Potthast, H. Koch, K. Fischer. In Int. Symp. Wood Pulping Chem. 9th, F2-1–F2-4 (1997).
17. J. Sealey and A.J. Ragauskas. Enzyme Microb. Technol. **23**, 422 (1998).
18. K. Poppius-Levlin, W. Wang, T. Tamminen, B. Hortling, L. Viikari, and M.L. Niku-Paavola. J. Pulp Paper Sci. **25**, 90 (1999).
19. J. Sealey, A.J. Ragauskas, and T. Elder. Holzforschung, **53**, 498 (1999).
20. F.S. Chakar and A.J. Ragauskas. J. Wood Chem. Technol. **20**, 169 (2000).
21. A. Potthast, T. Rosenau, H. Koch, and K. Fischer. Holzforschung, **53**, 175 (1999).
22. C. Crestini and D. Argyropoulos. Bioorg. Med. Chem. **6**, 2161 (1998).
23. P.W. Oxley, B.M. Adger, M.J. Saase, and M.A. Forth. Org. Synth. **67**, 187 (1989).
24. TAPPI test methods T236-cm85. Tappi Press, Atlanta. 1998–1999.
25. F.S. Chakar and A.J. Ragauskas. Holzforschung, **54**, 647 (2000).
26. J.M. Pepper, P.E.T. Baylis, and E. Adler. Can. J. Chem. **37**, 1241 (1958).
27. P. Froass, A.J. Ragauskas, and J. Jiang. J. Wood Chem. Technol. **16**(4), 347 (1996).
28. D. Robert. Carbon-13 nuclear magnetic resonance spectrometry. *In* Methods in lignin chemistry. *Edited by* S. Lin and C. Dence. Springer-Verlag, New York. 1992. p. 250.
29. A. Granata and D.S. Argyropoulos. J. Agric. Food Chem. **43**, 1538 (1995).
30. F.S. Chakar, L. Allison, D.H. Kim, A.J. Ragauskas, and T. Elder. TAPPI Pulping/Process Prod. Qual. Conf. 2000, 938 (2000).
31. F.S. Chakar and A.J. Ragauskas. *In* Oxidative delignification chemistry: Fundamentals and catalysis. ACS symposium series. Vol. 785. *Edited by* D.S. Argyropoulos. Oxford Press, Washington. 2001. p. 444.
32. J. Freudenreich, M. Amann, E. Fritz-Langhals, and J. Stohrer. *In* Int. Pulp Bleaching Conf. 1998, **71** (1998).
33. F. X, K. Li, and T.J. Elder. *In* Biotechnology in the Pulp and Paper Industry: 8th ICBPPI meeting. Progress in biotechnology. Vol. 21. *Edited by* L. Viikari and R. Lantto. Elsevier Science B.B., Netherlands. 2002. pp. 89–104.
34. T.M. Runge and A.J. Ragauskas. Holzforschung, **53**, 623 (1999).
35. R. Yang, L. Lucia, H. Jameel, and A.J. Ragauskas. Ind. Eng. Chem. Res. **41**(24), 5941 (2002).
36. (*a*) R. Bourbonnais and M. Paice. Appl. Microbiol. Biotechnol. **36**, 823 (1992); (*b*) J. Sealey and A.J. Ragauskas. J. Wood Chem. Technol. **18**(4), 403 (1998).
37. R. Pfaller, M. Amann, and J. Freudenreich. Proc. Int. Conf. Biotech. Pulp Pap. Ind. 7th 1998, A99 (1998).
38. P. Baiocco, A.M. Barreca, M. Fabbrini, C. Galli, and P. Gentili. Org. Bio. Chem. **1**(1), 191 (2003).

© 2004 NRC Canada

Total synthesis of (–)-pateamine A, a novel immunosuppressive agent from *Mycale* sp[1]

Gerald Pattenden, Douglas J. Critcher, and Modesto Remuiñán

Abstract: A convergent synthesis of the unique thiazole-containing polyene bis-lactone pateamine A (**1**) isolated from the marine sponge *Mycale* sp is described. The synthesis features the ubiquitous Stille sp^2–sp^2 coupling reaction to elaborate the *E*,*Z*-diene macrolide core **23** and the all-*E* polyenamine side chain in the natural product. It also highlights the scope for enantiopure sulfinimine intermediates in the synthesis of chiral β-amino ester moieties in complex structures.

Key words: pateamine A, immunosuppressive agent from marine sponge *Mycale* sp, total synthesis, novel 19-membered bis-lactone, thiazole metabolite, polyenamine, Stille reaction, sulfinimines, chiral β-amino esters.

Résumé : On décrit une synthèse convergente de la patéamine A (**1**), une bis-lactone polyénique unique contenant un noyau thiazole isolée de l'éponge marine de l'espèce *Mycale*. La synthèse comprend une réaction omniprésente de couplage sp^2–sp^2 de Stille pour élaborer le macrolide *E*,*Z*-diénique fondamental **23** et la chaîne latérale polyénamine complètement *E* du produit naturel. Elle comporte aussi le moyen d'obtenir des intermédiaires sulfinimines énantiopurs dans la synthèse des portions esters β-aminés chiraux des structures complexes.

Mots clés : patéamine A, agent immunosuppressant de l'éponge marine de l'espèce *Mycale*, synthèse totale, nouvelle bis-lactone à 19 chaînons, métabolite thiazole, polyénamine, réaction de Stille, sulfinimines, esters β-aminés chiraux.

[Traduit par la Rédaction]

Introduction

Pateamine A (**1**) is a novel thiazole-containing 19-membered bis-lactone isolated by Munro and co-workers (1) from the marine sponge *Mycale* sp located off the coast of New Zealand. The natural product exhibits antifungal activity and also shows potent immunosuppresant properties with low cytotoxicity.[3] The bis-lactone core in pateamine accommodates an *E*,*Z*-1,3-diene unit together with a β-amino ester residue, and is substituted by an unusual polyenamine side chain. The absolute stereochemistry for pateamine A followed from degradation studies, in concert with synthetic work and NMR experiments (2). This stereochemical assignment was corroborated by a total synthesis of (–)-pateamine A presented by Romo et al. in 1998 (3). In an earlier publication from our laboratory (4) we layed the foundation for a total synthesis of pateamine A by describing a synthesis of the bis-lactone portion **2**, corresponding to deammoniated pateamine, based on an intramolecuar sp^2–sp^2 Stille coupling reaction (5, 6) to install the *E*,*Z*-1,3-diene unit as a key stratagem (7). To develop this strategy to pateamine A itself, we required a procedure for introducing the chiral β-amino ester moiety into the macrolide core, and methodology to elaborate the all-*E*-trienamine side chain in the natural product. In this paper we describe solutions to these issues, which have culminated in a new total synthesis of (–)- pateamine A (8).

Received 9 September 2003. Published on the NRC Research Press Web site at http://canjchem.nrc.ca on 20 February 2004.

This paper is dedicated to Professor E. Piers, who pioneered the development and application of the intramolecular Stille reaction in small ring synthesis, and made seminal contributions in target natural product synthesis.

G. Pattenden,[2] D.J. Critcher, and M. Remuiñán. School of Chemistry, The University of Nottingham, Nottingham, NG7 2RD, England.

[1]This article is part of a Special Issue dedicated to Professor Ed Piers.

[2]Corresponding author (e-mail: GP@Nottingham.ac.uk).

[3]G.T. Faircloth. PharmaMar Inc., M.A. Cambridge. Private communication to Professor D. Romo and quoted in ref. 3.

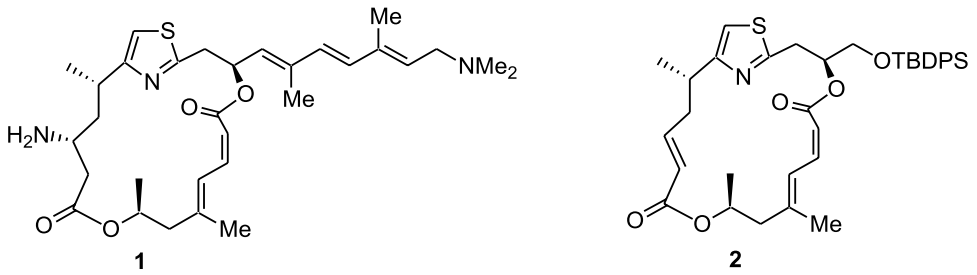
Synthetic strategy

Our overall synthetic strategy to pateamine A (**1**) was based on utilization of the ubiquitous Stille sp^2–sp^2 coupling reaction, firstly in an *intramolecular* manner to elaborate the *E*,*Z*-diene macrolide core **5** from the vinyl stannane-vinyl iodide precursor **6**, and secondly to produce the all-*E* polyene side chain using an *intermolecular* reaction between the vinyl iodide **4** and the dimethylaminostannane **3**. In turn, we planned to synthesize the stannane-iodide **6** from the 2,4-disubstituted thiazolepropanal **7** using nucleophilic addition of an appropriate carbanion to the corresponding chiral sulfinimine, as a key step (Scheme 1).

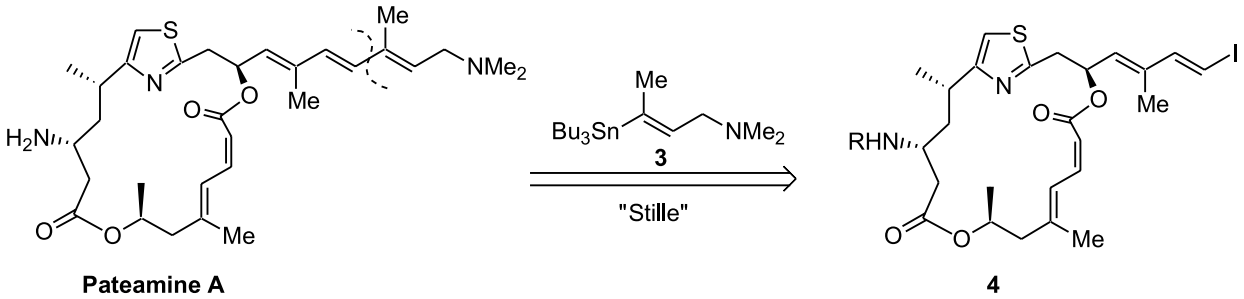
Synthesis of the thiazolepropanal 7

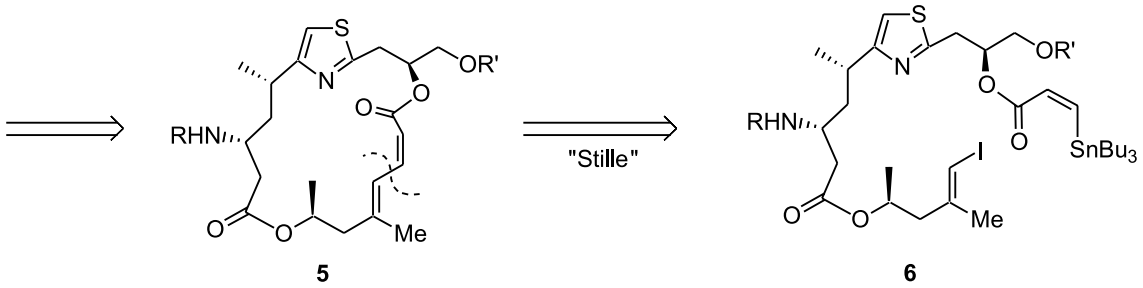
The thiazolepropanal intermediate **7** was smoothly synthesized starting from the chiral pool compounds dimethyl *L*-malate **8** and *S*-methyl 3-hydroxy-2-methylpropionate **13a**, and utilizing a modified Hantzch reaction between the thioamide **12** and the α-bromoketone **15b** as a key step. Thus, starting with commercially available dimethyl *L*-malate, the thioamide **12** was first elaborated in six straightforward steps

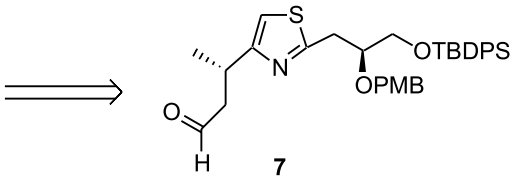
 doi: 10.1139/V03-199 © 2004 NRC Canada



Scheme 1. Retrosynthesis.







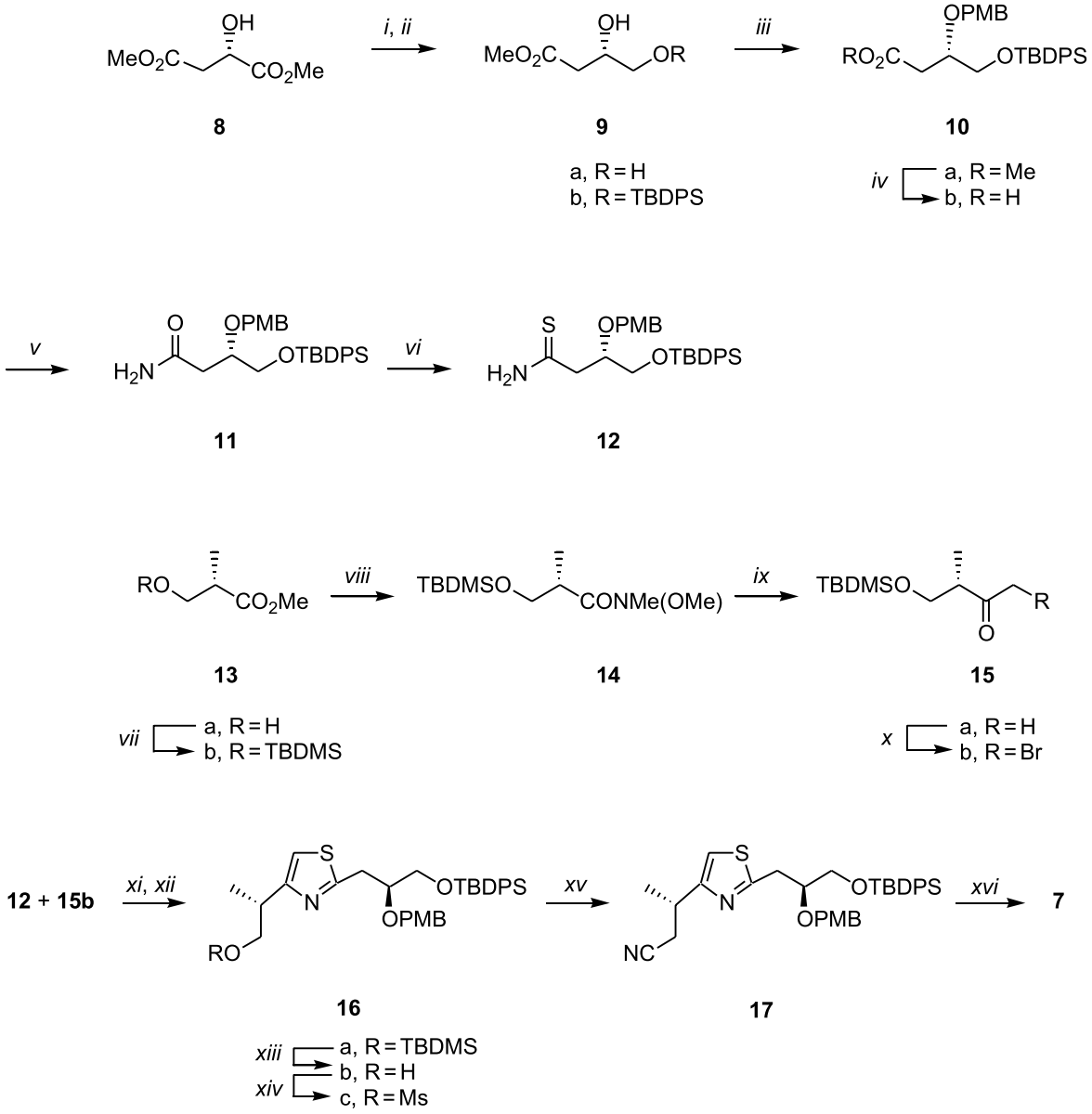
involving: (*i*) reduction using BH_3SMe_2–$NaBH_4$ and protection of the resulting primary alcohol **9a** as its TBDPS ether **9b**; (*ii*) protection of the secondary alcohol group in **9b** as its PMB ether **10a** followed by saponification of the resulting methyl ester to the corresponding carboxylic acid **10b**; and (*iii*) conversion of the acid **10b** into the thioamide **12** via the amide **11**. In a similar straightforward manner, commercially available *S*-methyl 3-hydroxy-2-methylpropionate **13a** was elaborated to the α-bromoketone **15b** following: (*i*) protection as the TBDMS ether **13b** followed by conversion into the Weinreb amide **14**; and (*ii*) addition of methylmagnesium bromide to **14**, and bromination of the resulting methyl ketone **15a** via its TMS enol ether using bromine at –78 °C. A modified Hantzsch reaction (9) between **12** and **15b** in the presence of 2,6-lutidine, followed by dehydration of the thiazoline intermediate using TFAA, then gave the 2,4-disubstituted thiazole **16a** in 64% overall yield. The thiazolepropanal intermediate **7** was then elaborated from the TBDMS ether **16a** in four straightforward steps using a one-carbon homologation and proceding via the alcohol **16b**, the mesylate **16c** and the nitrile **17** (Scheme 2).

Synthesis of the vinyl stannane – vinyl iodide 22 and elaboration to the macrolide 23

Our next objective was to elaborate the substituted vinyl iodide intermediate **22** from the thiazolepropanal **7**, by addition of the enolate produced from the chiral acetate **19** to the enantiopure sulfinimine **18** derived from **7** as a key and cru-

© 2004 NRC Canada

Scheme 2. Reagents and conditions: (*i*) $BH_3{\cdot}SMe_2$, $NaBH_4$, THF, 92%; (*ii*) TBDPSCl, Et_3N, DMAP, DCM, rt, 12 h, 93%; (*iii*) $PMBOC(=NH)CCl_3$, CSA, DCM, rt, 3 days, 76%; (*iv*) LiOH, H_2O–THF, rt, 12 h, 90%; (*v*) $ClCO_2Et$, Et_3N, NH_4OH, rt, 30 min, 93%; (*vi*) Lawesson's reagent, THF, rt, 30 min, 99%; (*vii*) TBDMSCl, Et_3N, DMAP, DCM, rt, 24 h, 95%; (*viii*) HNMeOMe·HCl, $AlMe_3$, DCM, Δ, 5 h, 61%; (*ix*) 1.5 equiv. MeMgBr, THF, 0 °C, 1 h, 94%; (*x*) LiHMDS, –78 °C, TMSCl, Br_2, 86%; (*xi*) 2,6-lutidine, DCM, rt, 12 h; (*xii*) $(CF_3CO)_2O$, Py, DCM, –30 °C, 30 min, 64% (two steps); (*xiii*) AcOH–THF–H_2O, rt, 12 h, 92%; (*xiv*) MsCl, Et_3N, DCM, 0 °C, 1 h; (*xv*) NaCN, DMSO, 60 °C, 6 h, 77% (two steps); (*xvi*) DIBAL, toluene, 0 °C, 2 h, 85%.



cial step. Thus, following a procedure described by Davis et al. (10), treatment of the thiazolepropanal **7** with (*R*)-*p*-toluenesulfinamide in the presence of titanium(IV) ethoxide at 50 °C first led to the chiral sulfinimine **18** in 64% yield. Much to our pleasure deprotonation of the ester **19** derived from the known corresponding chiral alcohol (11), using LiHMDS at –78 °C, followed by addition of the sulfinimine **18** to the resulting enolate, gave the substituted β-amino ester **20a** in 63% yield and approximately 90% diastereselectivity. The ρ-toluenesulfinyl group in **20a** was cleaved by treatment with TFA–methanol to provide the (3*R*)-amine **20b** whose configuration was established unambiguously using the NMR spectroscopic procedure reported by Riguera and co-workers (12), in concert with comparison of data with the corresponding (3*S*)-amine synthesized contemporaneously. We commend highly this straightforward and reproducible procedure for synthesizing reasonably complex chiral β-amino esters via sulfinimines, such as **18**. Hitherto, we had examined the scope for adding chiral amine nucleophiles to Michael acceptors, similar to **2**, and for chiral alcohol and azide precursors in preparing chiral β-amino ester precursors similar to **20**, but neither of these procedures gave encouraging results (Scheme 3). In their total synthesis of (–)-pateamine A, Romo et al. (3) used the ring open-

© 2004 NRC Canada

ing of a chiral β-lactam intermediate by an hydroxyl nucleophile, as a stratagem to elaborate the β-amino macrolide portion in the natural product.

With the chiral amine **20b** in hand, we were now poised to elaborate the key vinyl iodide – vinyl stannane intermediate **22** and study the critical intramolecular Stille reaction leading to the macrolide core **23** in pateamine A. Thus, the amine **20b** was first protected as the corresponding trichloro-*tert*-butoxycarbamate (TcBOC) **21a** and the PMB ether group was then cleaved leading to the secondary alcohol **21b**. Esterification of *Z*-3-tri-*n*-butylstannylpropenoic acid (13) with the alcohol **21b**, under Yamaguchi conditions (14), then led to the Stille reaction precursor **22**. Gratifyingly, when the stannane–iodide **22** was treated under Farina's conditions (15) with Ph_3As–Pd(O) dibenzylideneacetone in DMF at 55 °C for 1 h, it underwent smooth intramolecular sp^2–sp^2 coupling with complete preservation of the *E*- and *Z*-stereochemistries of the reacting partners and produced the *Z*,*E*-diene macrolide **23** in 65% yield (7, 16) (Scheme 4).

Introduction of the all-*E*-trienamine side chain and completion of (–)-pateamine A

We examined a range of olefination and coupling methods starting from the substituted bis-lactone **23** to install the all-*E* trienamine side chain in pateamine A, and ultimately elected to use a second (intermolecular) Stille reaction between the vinyl stannane **3** and the vinyl iododiene **26** derived from **23** as the key step. Thus, deprotection of the silyl ether group in **23**, followed by oxidation of the resulting alcohol **24a**, using a pyridine-buffered Dess–Martin periodinane procedure first gave the aldehyde **24b**. A Wittig reaction between **24b** and 2-(triphenylphosphoranylidene) propionaldehyde next gave the homologated *E*-unsaturated aldehyde **25**, which was then converted into the vinyl iodide **26** using a Takai reaction (17). A Stille coupling reaction between the vinyl iododiene **26** and the dimethylamino-substituted vinyl stannane **3**, using $Pd(CH_3CN)_2Cl_2$ in DMF at room temperature (18) then led to TcBOC-protected pateamine A (**27**) in an unoptimized yield of 36%. Finally, deprotection of **27** using a Cd–Pb couple in aq. NH_4OAc (19) gave (–)-pateamine A (**1**), which showed NMR spectroscopic and chiroptical data that were identical to those reported for the natural product isolated from *Mycale* sp.

In conclusion, a convergent total synthesis of the novel immunosuppressive agent, pateamine A, from the sponge *Mycale* sp has been achieved. The synthesis is concise, and features the Stille sp^2–sp^2 coupling reaction to elaborate key stereodefined polyene units in this novel structure.

Experimental

For general experimental details see ref. 20.

(*S*)-4-(*tert*-Butyldiphenylsilanyloxy)-3-(4-methoxybenzyloxy)butyric acid methyl ester (10a)

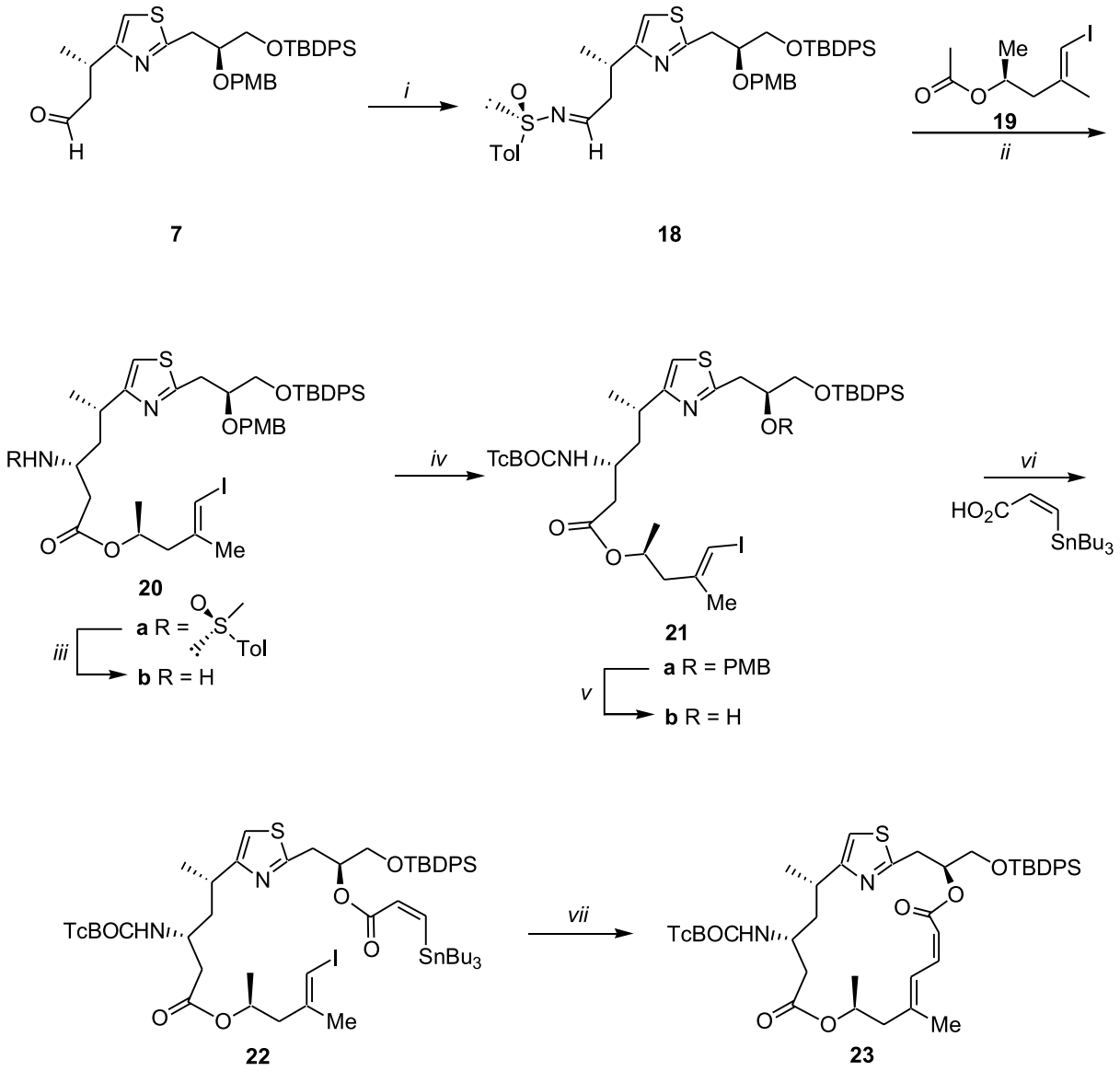
Camphorsulfonic acid (1.75 g, 7.5 mmol) was added in one portion to a stirred solution of the alcohol **9b** (21) (28 g, 75.26 mmol) and *p*-methoxybenzyltrichloroacetimidate (42.5 g, 150 mmol) in CH_2Cl_2 (250 mL) at 0 °C. The mixture was allowed to warm to room temperature, and stirred at this temperature for 3 days. The solvent was removed in vacuo, and the residue was dissolved in a mixture of CH_2Cl_2 (100 mL) and petroleum ether (bp 40–60 °C) (200 mL). The precipitated solids were filtered off and the filtrate was then concentrated in vacuo. The residue was purified by flash chromatography eluting with ethyl acetate:petroleum ether (bp 40–60 °C, 1:9 → 1:7) to give the *protected alcohol* (28.1 g, 76%) as a colourless oil. $[\alpha]_D^{24}$ –15.7 (*c* 1.35 in $CHCl_3$). IR ν_{max} (cm^{-1}, film): 2931, 1738, 1513, 1248, 1112, 703. ^1H NMR (360 MHz, $CDCl_3$) δ: 7.69–7.65 (4H, m, ArH), 7.46–7.36 (6H, m, ArH), 7.19 (2H, d, *J* = 8.7, MeOArH), 6.84 (2H, d, *J* = 8.7, MeOArH), 4.53 (1H, d, *J* = 11.1, CH_2Ar), 4.47 (1 H, d, *J* = 11.1, CH_2Ar), 4.04–4.00 (1H, m, CHOPMB), 3.80 (3H, s, OCH_3), 3.74 (1H, dd, *J* 5.2 and 10.5, CH_2OTPS), 3.67 (3H, s, OCH_3), 3.63 (1H, dd, *J* = 5.7 and 10.5, CH_2OTPS), 2.70 (1H, dd, *J* = 4.6 and 15.6, CH_2CO_2Me), 2.57 (1H, dd, *J* = 8.3 and 15.6, CH_2CO_2Me), 1.06 (9H, s, $((CH_3)_3CSi$). ^{13}C NMR (90.6 MHz, $CDCl_3$) δ: 171.8, 158.8, 135.2, 132.9, 132.8, 131.5, 130.2, 129.3, 129.0, 127.4, 113.4, 113.3, 75.9, 71.8, 64.8, 54.8, 51.2, 37.1, 26.4, 18.8. MS *m/z* (ES): 515.2203 (M + Na, $C_{29}H_{36}O_5SiNa$ requires 515.2230).

(*S*)-4-(*tert*-Butyldiphenylsilanyloxy)-3-(4-methoxybenzyloxy)butyramide (11)

A solution of lithium hydroxide (1.5 mol L^{-1}) in water (113 mL) was added to a solution of the ester **10a** (28 g, 56.9 mmol) in THF (250 mL) and MeOH (2 mL). The biphasic mixture was stirred at room temperature for 48 h and then acidified carefully with 2 N HCl (aq). The separated aqueous layer was extracted with ethyl acetate (3 × 200 mL) and the combined organic extracts were then dried ($MgSO_4$) and concentrated in vacuo. The residue was purified by flash chromatography, eluting with ethyl acetate:petroleum ether (bp 40–60 °C, 1:1) to give the corresponding carboxylic acid **10b** (25 g, 90%) as a colourless oil. Ethyl chloroformate (5.5 mL, 57.5 mmol) was added dropwise to a solution of the carboxylic acid (25 g, 52.3 mmol) and triethylamine (10.2 mL, 75.2 mmol) in THF (250 mL) at 0 °C. The mixture was allowed to warm to room temperature and stirred at this temperature for 30 min. Concentrated aqueous ammonia (75 mL) was added rapidly at 0 °C and the mixture was warmed to room temperature and then concentrated in vacuo. 2 N HCl was added until the mixture was acidic, and the aqueous layer was then extracted with ethyl acetate (3 × 150 mL). The combined organic extracts were dried ($MgSO_4$) and evaporated to dryness in vacuo. The residue was purified by flash chromatography, eluting with ethyl acetate:petroleum ether (bp 40–60 °C, 1:1 → 2:1) to give the *amide* (23 g, 93%) as a colourless oil. $[\alpha]_D^{24}$ –16.8 (*c* 0.19 in $CHCl_3$). IR ν_{max} (cm^{-1}, film): 3346, 3193, 2930, 1681, 1513, 1248, 1112, 703. ^1H NMR (360 MHz, $CDCl_3$) δ: 7.69–7.66 (4H, m, ArH), 7.47–7.36 (6H, m, ArH), 7.20 (2H, d, *J* = 8.7, MeOArH), 6.85 (2H, d, *J* = 8.7, MeOArH), 6.07 (1H, br s, NH), 5.26 (1H, br s, NH), 4.59 (1H, d, *J* = 11.0, CH_2Ar), 4.44 (1H, d, *J* = 11.0, CH_2Ar), 3.97–3.91 (1H, m, CHOPMB), 3.81 (3H, s, CH_3O), 3.76 (1H, dd, *J* = 5.1 and 10.7, CH_2OTPS), 3.70 (1H, dd, *J* = 5.2 and 10.7, CH_2OTPS), 2.58 (1H, dd, *J* = 3.8 and 15.1, CH_2CONH_2), 2.47 (1H, dd, *J* = 8.1 and 15.6, CH_2CONH_2), 1.07 (9H, s, $((CH_3)_3CSi$). ^{13} C NMR (90.6 MHz, $CDCl_3$) δ: 173.4, 159.2,

© 2004 NRC Canada

Scheme 3. Reagents and conditions: (*i*) (*R*)-tolylsulfinamide, $Ti(OEt)_4$, DCM, 50 °C, 4 h, 64%; (*ii*) LiHMDS, THF, –78 °C, 10 min, 63%; (*iii*) TFA, MeOH, rt, 4 h, 95%; (*iv*) TcBOCCl, Py, DCM, 0 °C, 2 h, 89%; (*v*) DDQ, DCM, H_2O, rt, 2 h, 87%; (*vi*) (*Z*)-3-tributylstannylpropenoic acid, 2,4,6-trichlorobenzoyl chloride, Et_3N, DMAP, toluene, –30 °C, 1 h, 67%; (*vii*) $Pd(dba)_2$, Ph_3As, DMF, 55 °C, 1 h, 65%.



135.5, 133.1, 133.0, 131.6, 130.0, 129.7, 127.7, 127.6, 113.8, 76.6, 65.1, 55.2, 51.2, 38.7, 26.7, 19.1. MS *m/z* (ES): 500.2255 (M + Na, $C_{28}H_{35}NO_4SiNa$ requires 500.2233).

(*S*)-4-(*tert*-Butyldiphenylsilanyloxy)-3-(4-methoxybenzyloxy)thiobutyramide (12)

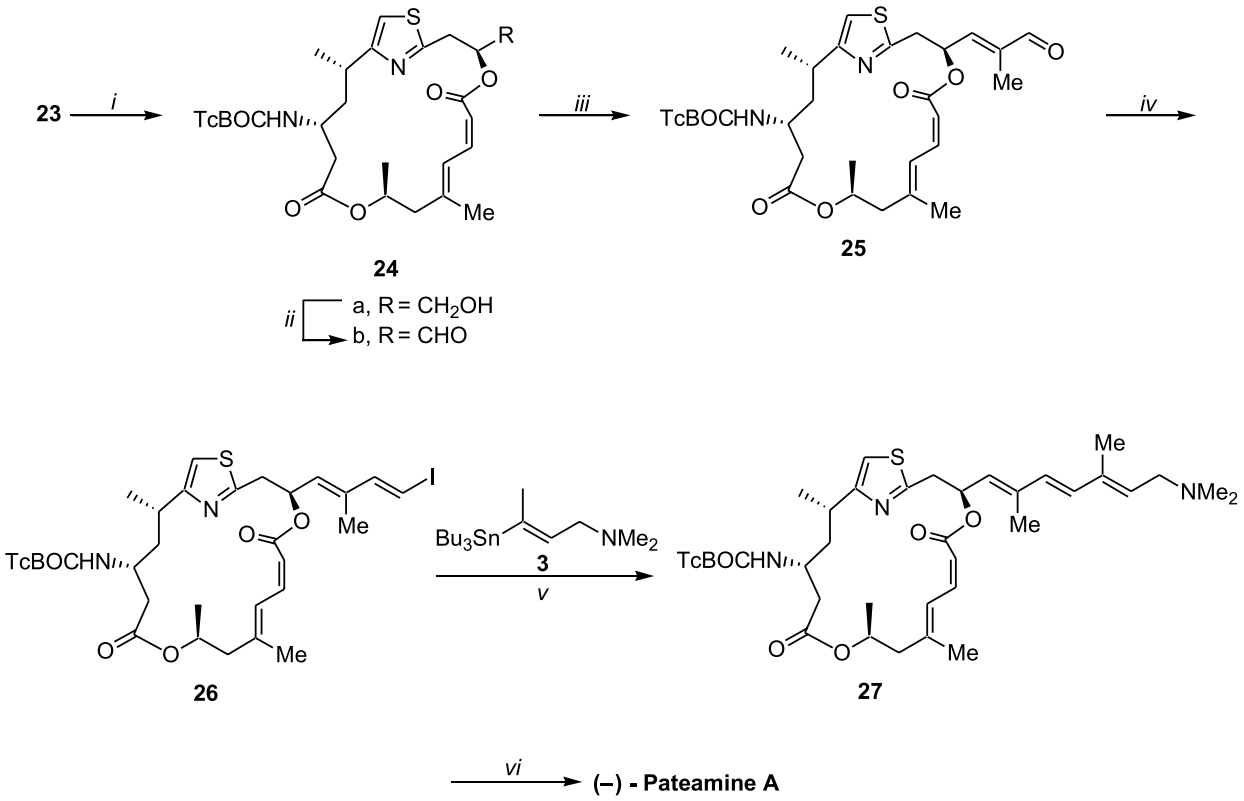
Lawesson's reagent (8.12 g, 20.0 mmol) was added in one portion to a stirred solution of the amide **11** (18.7 g, 39.4 mmol) in THF (250 mL) at room temperature and the mixture was stirred at this temperature for 30 min and then evaporated in vacuo. The residue was purified by flash chromatography, eluting with ethyl acetate:petroleum ether (bp 40–60 °C, 1:3 → 1:1) to give the *thioamide* (8.4 g, 99%) as a yellow oil. $[\alpha]_D^{25}$ –38.4 (*c* 0.50 in $CHCl_3$). IR ν_{max} (cm^{-1}, film): 3308, 3187, 2930, 1613, 1249, 1112, 702. ^1H NMR (360 MHz, $CDCl_3$) δ: 7.80 (1H, br s, NH), 7.70–7.66 (4H, m, ArH), 7.55 (1H, br s, NH), 7.47–7.36 (6H, m, ArH), 7.19 (2H, d, *J* = 8.7, MeOArH), 6.85 (2H, d, *J* = 8.7, MeOArH), 4.60 (1H, d, *J* = 10.9, CH_2Ar), 4.42 (1H, d, *J* = 10.9, CH_2Ar), 4.00–3.96 (1H, m, CHOPMB), 3.80 (3H, s, CH_3O), 3.75 (2H, d, *J* = 4.9, CH_2OTPS), 3.06 (1H, dd, *J* = 3.3 and 14.7, CH_2CSNH_2), 2.96 (1H, dd, *J* = 8.1 and 14.7, CH_2CSNH_2), 1.08 (9H, s, $((CH_3)_3CSi)$. ^{13}C NMR (90.6 MHz, $CDCl_3$) δ: 207.5, 159.3, 135.5, 135.4, 133.0, 132.9, 129.8, 129.7, 129.5, 127.7, 127.6, 113.9, 78.8, 72.3, 64.8, 55.2, 47.4, 26.7, 19.1. MS *m/z* (ES): 494.2007 (M + H, $C_{28}H_{36}NO_3SSi$ requires 494.2005).

(*S*)-3-(*tert*-Butyldimethylsilanyloxy)-*N*-methoxy-2,*N*-dimethylpropionamide (14)

A solution of trimethylaluminum (2.0 mol L^{-1}) in toluene (45 mL) was added dropwise over 45 min to a stirred solu-

© 2004 NRC Canada

Scheme 4. (*i*) TBAF, AcOH, THF, rt, 24 h, 78%; (*ii*) Dess–Martin, Py, DCM, 2 h, rt, 70%; (*iii*) 2-(triphenylphosphoralidene)propionaldehyde, 3 h, Δ, 73%; (*iv*) $CrCl_2$, CHI_3, THF, 1.5 h, rt, 68%; (*v*) $Pd(CH_3CN)_2Cl_2$, DMF, rt, 6 h, 36%; (*vi*) 10% Cd/Pb, 1 mol L^{-1} NH_4OAc, THF, rt, 5 h, 73%.



tion of *N*,*O*-dimethylhydroxylamine hydrochloride (8.8 g, 90.2 mmol) in CH_2Cl_2 (100 mL) at 0 °C. Once the gas evolution had ceased, the mixture was allowed to warm to room temperature and stirred at this temperature for 1 h. The solution was added dropwise via cannula to a stirred solution of the ester **13b** (10.44g, 45.1 mmol) in CH_2Cl_2 (30 mL) at room temperature. The mixture was heated under reflux for 5 h and then stirred at room temperature for 12 h. The mixture was poured cautiously into ice cold 2 N HCl, and the separated aqueous layer was then extracted with CH_2Cl_2 (4 × 60 mL). The combined organic extracts were washed with a saturated solution of $NaHCO_3$ and then dried ($MgSO_4$). The solvent was removed at reduced pressure, and the residue was purified by flash chromatography, eluting with ethyl acetate:petroleum ether (bp 40–60 °C, 1:3 → 1:1) to give the *amide* (7.1 g, 61%) as a colourless oil. $[\alpha]_D^{26}$ 21.1 (*c* 0.38 in $CHCl_3$). IR ν_{max} (cm^{-1}, film): 2930, 1667, 1103, 837. ^1H NMR (360 MHz, $CDCl_3$) δ: 3.84 (1H, dd, *J* = 8.2 and 9.4), 3.72 (3H, br s, OCH_3), 3.54 (1H, dd, *J* = 6.1 and 9.5), 3.20 (3H, br s, CH_3), 3.22–3.16 (1H, m, *CH*CH_3), 1.07 (3H, d, *J* = 6.9, C*H*$_3$CH), 0.88 (9H, s, $((CH_3)_3CSi)$, 0.05 (3H, s, CH_3Si), 0.04 (3H, s, CH_3Si). ^{13}C NMR (90.6 MHz, $CDCl_3$) δ: 176.1, 65.7, 65.1, 38.1, 29.7, 25.8, 18.2, 13.7, –5.45. MS *m*/*z* (ES): 284.1609 (M + Na, $C_{12}H_{27}NO_3SiNa$ requires 284.1658).

(*S*)-4-(*tert*-Butyldimethylsilanyloxy)-3-methylbutan-2-one (15a)

A solution of methylmagnesium bromide (3.0 mol L^{-1}) in ether (15 mL) was added dropwise via syringe to a stirred solution of the Weinreb amide **14** (6.8 g, 26.0 mmol) in diethyl ether at 0 °C. The mixture was stirred at 0 °C for 30 min, and then allowed to warm to room temperature. An ice cold saturated solution of NH_4Cl was added and the separated aqueous layer was then extracted with diethyl ether (3 × 50 mL). The combined organic extracts were washed with a saturated solution of $NaHCO_3$ and then dried ($MgSO_4$). The solvent was removed in vacuo and the crude methyl ketone (5.56 g, 94%) was used directly in the next step. $[\alpha]_D^{24}$ 23.9 (*c* 0.20 in $CHCl_3$). IR ν_{max} (cm^{-1}, film): 2930, 1717, 1092, 836. ^1H NMR (360 MHz, $CDCl_3$) δ: 3.73 (1H, dd, *J* = 7.2 and 9.8, CH_2O), 3.65 (1H, dd, *J* = 5.5 and 9.5, CH_2O), 2.77–2.71 (1H, m, C*H*CH_3), 2.18 (3H, s, CH_3CO), 1.05 (3H, d, *J* = 6.9, C*H*$_3$CH), 0.88 (9H, s, $((CH_3)_3CSi)$, 0.05 (3H, s, CH_3Si), 0.04 (3H, s, CH_3Si). ^{13}C NMR (90.6 MHz, $CDCl_3$) δ: 211.5, 65.1, 48.9, 29.1, 25.4, 17.8, 12.5, –5.9.

(*S*)-1-Bromo-4-(*tert*-butyldimethylsilanyloxy)-3-methylbutan-2-one (15b)

A solution of LiHMDS (1.0 mol L^{-1}) in THF (23 mL) was added dropwise over 30 min to a stirred solution of the ketone **15a** (4.7 g, 21.75 mmol) in THF (75 mL) at –78 °C under an atmosphere of nitrogen. The mixture was stirred at –78° for 1 h, then chlorotrimethylsilane (3.0 mL, 23.9 mmol) was added, and the solution was allowed to warm to 0 °C where it was stirred for 20 min. The solution was again cooled to –78 °C, and bromine (1.12 mL, 20.5 mmol) was

© 2004 NRC Canada

then injected rapidly. The orange solution was allowed to warm to room temperature and then poured cautiously into a mixture of a saturated solution of NH_4Cl and a solution of sodium thiosulfate. The mixture was shaken vigorously and the separated aqueous layer was extracted with ethyl acetate (3 × 30 mL). The combined organic extracts were dried ($MgSO_4$) and evaporated to dryness in vacuo. The residue was purified by flash chromatography, eluting with ethyl acetate:petroleum ether (bp 40–60 °C, 1:20 → 1:10) to give the *bromide* (5.5 g, 86%) as a colourless oil. $[\alpha]_D^{27}$ 99.9 (*c* 1.36 in $CHCl_3$). IR ν_{max} (cm^{-1}, film): 2930, 1718, 1095, 837. ^1H NMR (360 MHz, $CDCl_3$) δ: 4.11 (1H, d, *J* = 13.2, CH_2Br), 4.06 (1H, d, *J* = 13.2, CH_2Br), 3.73–3.70 (2H, m, CH_2O), 3.20–3.11 (1H, m, C*H*CH_3), 1.11 (3H, d, *J* = 6.9, C*H*$_3$CH), 0.91 (9H, s, $((CH_3)_3CSi)$, 0.08 (3H, s, CH_3Si), 0.06 (3H, s, CH_3Si). ^{13}C NMR(90.6 MHz, $CDCl_3$) δ: 204.4, 66.0, 45.9, 35.7, 25.7, 18.0, 12.9, –5.7.

4-[(*R*)-2-(*tert*-Butyldimethylsilanyloxy)-1-methylethyl]-2-[(*S*)-3-(*tert*-butyldiphenylsilanyloxy)-2-(4-methoxybenzyloxy)propyl]thiazole (16a)

A solution of the bromoketone **15b** (7.73 g, 26.2 mmol) in CH_2Cl_2 (60 mL) was added via cannula over 0.5 h to a stirred solution of thioamide **12** (11.75 g, 23.8 mmol) and 2,6-lutidine (4.16 mL, 35.7 mmol) in CH_2Cl_2 (150 mL) at 0 °C. The mixture was stirred at room temperature for 14 h and then the solvent was removed in vacuo. The residue was purified by flash chromatography, eluting with ethyl acetate:petroleum ether (bp 40–60 °C, 1:6 → 1:4) to give the corresponding thiazoline (12.25 g, 73%) as a colourless oil, which was used immediately in the next step.

Trifluoroacetic anhydride (7.43 mL, 52.6 mmol) was added dropwise over 20 min to a stirred solution of the thiazoline (9.3 g, 13.15 mmol) in CH_2Cl_2 (150 mL) at –30 °C. After 5 min, pyridine (7.43 mL, 52.7 mmol) was added and the mixture was stirred at –30 °C for 20 min. The mixture was quenched with brine (150 mL) and extracted with CH_2Cl_2 (2 × 150 mL). The combined organic extracts were dried ($MgSO_4$) and concentrated in vacuo. The residue was purified by flash chromatography, eluting with ethyl acetate:petroleum ether (bp 40–60 °C, 1:20 → 1:10) to give the *thiazole* (7.9 g, 87%) as a colourless oil. $[\alpha]_D^{24}$ –28.2 (*c* 0.88 in $CHCl_3$). IR ν_{max} (cm^{-1}, film): 2928, 1514, 1248, 1112, 836, 702. ^1H NMR (360 MHz, $CDCl_3$) δ: 7.70–7.67 (4H, m, ArH), 7.47–7.33 (6H, m, ArH), 7.16 (2H, d, *J* = 8.7, MeOArH), 6.83 (1H, s, ThzH), 6.81 (2H, d, *J* = 8.6, MeOArH), 4.54 (1H, d, *J* = 10.9, CH_2Ar), 4.43 (1H, d, *J* = 11.0, CH_2Ar), 3.95–3.88 (1H, m, CHOPMB), 3.87 (1H, dd, *J* = 5.6 and 9.7, CH_2OTPS), 3.80 (3H, s, CH_3O), 3.79–3.76 (2H, m, CH_2OTBS), 3.67 (1H, dd, *J* = 6.8 and 9.7, CH_2OTPS), 3.35 (1H, dd, *J* = 4.3 and 15.0, CH_2Thz), 3.20 (1H, dd, *J* = 8.1 and 15.1, CH_2Thz), 3.13–3.07 (1H, m, CHThz), 1.31 (3H, d, *J* = 7.0, C*H*$_3$CH), 1.07 (9H, s, $((CH_3)_3CSi)$, 0.86 (9H, s, $((CH_3)_3CSi)$, –0.02 (3H, s, CH_3Si), –0.03 (3H, s, CH_3Si). ^{13}C NMR (90.6 MHz, $CDCl_3$) δ: 166.5(s), 159.1(s), 158.9(s), 135.7(d), 135.6(d), 133.4(s), 133.3(s), 130.6(s), 129.7(d), 129.4(d), 127.7(d), 127.6(d), 113.7(d), 112.9(d), 79.5(d), 72.1(t), 67.5(t), 65.4(t), 55.3(t), 39.1(d), 36.0(t), 26.9(q), 25.9(q), 19.3(s), 18.3(s), 16.6(q), –5.3(q), –5.4(q). MS *m*/*z* (ES): 690.3519 (M + H, $C_{39}H_{56}NO_4SSi_2$ requires 690.3486).

(*R*)-2-{2-[(*S*)-3-(*tert*-Butyldiphenylsilanyloxy)-2-(4-methoxybenzyloxy)propyl]thiazol-4-yl}propan-1-ol (16b)

Acetic acid (120 mL) was added, in one portion to a biphasic solution of the thiazole **16a** (8 g, 10.6 mmol) in THF:H_2O (1:1, 120 mL), and the mixture was stirred at room temperature for 14 h and then evaporated to dryness in vacuo. The residue was dissolved in CH_2Cl_2 (200 mL), and the solution was washed with a saturated solution of $NaHCO_3$, then dried ($MgSO_4$) and evaporated in vacuo. The residue was filtered through a short pad of silica gel eluting with ethyl acetate:petroleum ether (bp 40–60 °C, 1:1) to give the *alcohol* (6.1 g, 92%) as a colourless oil. $[\alpha]_D^{24}$ –18.5 (*c* 0.26 in $CHCl_3$). IR ν_{max} (cm^{-1}, film): 3412, 2930, 1514, 1112, 823, 702. ^1H NMR (360 MHz, $CDCl_3$) δ: 7.69–7.66 (4H, m, ArH), 7.46–7.35 (6H, m, ArH), 7.13 (2H, d, *J* = 8.8, MeOArH), 6.84 (1H, s, ThzH), 6.81 (2H, d, *J* = 8.7, MeOArH), 4.52 (1H, d, *J* = 11.1, CH_2Ar), 4.39 (1H, d, *J* = 11.1, CH_2Ar), 3.92–3.86 (1H, m, CHOPMB), 3.80–3.67 (4H, m, CH_2OTPS and CH_2OH), 3.79 (3H, s, CH_3O), 3.36 (1H, dd, *J* = 4.1 and 15.0, CH_2Thz), 3.20 (1H, dd, *J* = 8.2 and 15.0, CH_2Thz), 3.13–3.08 (1H, m, CHThz), 1.30 (3H, d, *J* = 7.0, C*H*$_3$CH), 1.07 (9H, s, $((CH_3)_3CSi)$. ^{13}C NMR (90.6 MHz, $CDCl_3$) δ: 167.6, 159.3, 159.1, 135.6, 135.5, 133.3, 133.2, 130.3, 129.7, 129.6, 127.7, 113.6, 112.5, 78.9, 72.0, 67.7, 65.1, 55.2, 37.7, 35.9, 26.8, 19.2, 16.1. MS *m*/*z* (ES): 598.2403 (M + Na, $C_{33}H_{41}NO_4SSiNa$ requires 598.2423).

Methanesulfonic acid (*R*)-2-{2-[(*S*)-3-(*tert*-butyldiphenylsilanyloxy)-2-(4-methoxybenzyloxy)propyl]thiazol-4-yl}propyl ester (16c)

Methanesulfonyl chloride (0.98 mL, 12.7 mmol) was added to a solution of the alcohol **16b** (6.1 g, 10.6 mmol) and triethylamine (2.1 mL, 4.52 mmol) in CH_2Cl_2 (80 mL) at 0 °C and the resulting mixture was then stirred at 0 °C for 1 h. The solution was washed successively with brine (70 mL) and a saturated solution of $NaHCO_3$ (70 mL), and then evaporated to dryness in vacuo to leave the crude *mesylate* (96%), which was used directly in the next step. $[\alpha]_D^{24}$ –20.6 (*c* 0.63 in $CHCl_3$). IR ν_{max} (cm^{-1}, film): 2931, 1513, 1357, 823, 704. ^1H NMR (360 MHz, $CDCl_3$) δ: 7.72–7.69 (4H, m, ArH), 7.48–7.37 (6H, m, ArH), 7.16 (2H, d, *J* = 8.7, MeOArH), 6.94 (1H, s, ThzH), 6.84 (2H, d, *J* = 8.7, MeOArH), 4.56 (1H, d, *J* = 11.1, CH_2Ar), 4.50 (1H, dd, *J* = 6.1 and 9.6, CH_2OMs), 4.43 (1H, d, *J* = 11.1, CH_2Ar), 4.36 (1H, dd, *J* = 6.6 and 9.6, CH_2OMs), 3.95–3.90 (1H, m, CHOPMB), 3.83–3.75 (2H, m, CH_2OTPS), 3.81 (3H, s, CH_3O), 3.37 (1H, dd, *J* = 4.3 and 15.1, CH_2Thz), 3.37–3.34 (1H, m, CHThz), 3.23 (1H, dd, *J* = 8.1 and 15.1, CH_2Thz), 2.84 (3H, s, CH_3SO_2), 1.41 (3H, d, *J* = 7.0, C*H*$_3$CH), 1.10 (9H, s, $((CH_3)_3CSi)$. ^{13}C NMR (90.6 MHz, $CDCl_3$) δ: 167.5, 159.0, 155.8, 135.5, 135.5, 133.2, 133.1, 130.2, 129.7, 129.2, 127.7, 114.1, 113.6, 78.8, 73.4, 71.9, 65.1, 55.2, 36.9, 35.9, 35.8, 26.7, 19.2, 16.4. MS *m*/*z* (ES): 654.2328 (M + H, $C_{34}H_{44}NO_6S2Si$ requires 654.2379).

(*S*)-3-{2-[(*S*)-3-(*tert*-Butyldiphenylsilanyloxy)-2-(4-methoxybenzyloxy)propyl]thiazol-4-yl}butyronitrile (17)

Sodium cyanide (4 g, 82.5 mmol) was added in one portion to a stirred solution of the mesylate **16c** (4.9 g, 7.5 mmol) in DMSO (40 mL) at room temperature, and the

© 2004 NRC Canada

mixture was then stirred at 60 °C for 5 h. The cooled mixture was washed with water (75 mL) and the aqueous layer was then extracted with ethyl acetate (5 × 50 mL). The combined organic extracts were dried ($MgSO_4$) and concentrated in vacuo. The residue was purified by flash chromatography, eluting with ethyl acetate:petroleum ether (bp 40–60 °C, 1:4 → 1:3) to give the *nitrile* (3.54 g, 80%) as a colourless oil. $[\alpha]_D^{24}$ –32.1 (*c* 0.33 in $CHCl_3$). IR ν_{max} (cm^{-1}, film): 2930, 1513, 1248, 703. ^1H NMR (360 MHz, $CDCl_3$) δ: 7.71–7.68 (4H, m, ArH), 7.48–7.36 (6H, m, ArH), 7.15 (2H, d, *J* = 8.7, MeOArH), 6.93 (1H, s, ThzH), 6.83 (2H, d, *J* = 8.7, MeOArH), 4.56 (1H, d, *J* = 11.1, CH_2Ar), 4.43 (1H, d, *J* = 11.1, CH_2Ar), 3.95–3.89 (1H, m, CHOPMB), 3.82–3.74 (2H, m, CH_2OTPS), 3.80 (3H, s, CH_3O), 3.35 (1H, dd, *J* = 4.2 and 15.0, CH_2Thz), 3.34–3.28 (1H, m, CHThz), 3.21 (1H, dd, *J* = 8.1 and 15.0, CH_2Thz), 2.79 (1H, dd, *J* = 5.7 and 16.7, CH_2CN), 2.64 (1H, dd, *J* = 7.5 and 16.7, CH_2CN), 1.48 (3H, d, *J* = 7.0, C*H*$_3$CH), 1.09 (9H, s, $((CH_3)_3CSi)$. ^{13}C NMR (90.6 MHz, $CDCl_3$) δ: 167.9(s), 159.2(s), 157.2(s), 136.0(d), 135.7(d), 133.4(s), 133.3(s), 130.4(s), 129.8(d), 129.4(d), 127.8(d), 118.6(s), 113.7(d), 113.5(d), 78.9(d), 72.1(t), 65.3(t), 55.3(q), 36.0(t), 33.1(d), 27.0(q), 24.7(t), 19.3(s), 19.0(q). MS *m*/*z* (ES): 607.2463 (M + Na, $C_{34}H_{40}N_2O_3SSiNa$ requires 607.2427). Anal. calcd. for $C_{34}H_{40}N_2O_3SSi$ (%): C 69.8, H 6.9, N 4.8; found: C 70.15, H 6.7, N 4.8.

(*S*)-3-{2-[(*S*)-3-(*tert*-Butyldiphenylsilanyloxy)-2-(4-methoxybenzyloxy)propyl]thiazol-4-yl}butyraldehyde (7)

A solution of DIBAL-H (1.5 mol L^{-1}) in toluene (2.5 mL) was added dropwise over 20 min via syringe to a stirred solution of the nitrile **17** (1.85 g, 3.16 mmol) in toluene (16 mL) at –78 °C. The yellow solution was stirred at 0 °C for 3 h and then quenched by adding a half-saturated solution of $NaHSO_4$ (15 mL) dropwise. The biphasic mixture was stirred at room temperature for 20 min and then extracted with ethyl acetate (3 × 25 mL). The combined organic extracts were dried ($MgSO_4$) and concentrated in vacuo. The residue was filtered through a plug of silica gel, eluting with ethyl acetate:petroleum ether (bp 40–60 °C, 1:3) to give the *aldehyde* (1.57 g, 85%) as a colourless oil. $[\alpha]_D^{25}$ –14.9 (*c* 0.22 in CH_2Cl_2). IR ν_{max} (cm^{-1}, film): 2930, 1724, 1514, 1248, 1112, 823, 703. ^1H NMR (360 MHz, $CDCl_3$) δ: 9.76 (1H, t, *J* = 1.9, CHO), 7.70–7.68 (4H, m, ArH), 7.47–7.35 (6H, m, ArH), 7.15 (2H, d, *J* = 8.7, MeOArH), 6.82 (2H, d, *J* = 8.6, MeOArH), 6.81 (1H, s, ThzH), 4.56 (1H, d, *J* = 11.1, CH_2Ar), 4.42 (1H, d, *J* = 11.2, CH_2Ar), 3.96–3.90 (1H, m, CHOPMB), 3.81–3.75 (2H, m, CH_2OTPS), 3.80 (3H, s, CH_3O), 3.53 (1H, sextet, *J* = 6.9, CHThz), 3.34 (1H, dd, *J* = 4.3 and 15.0, CH_2Thz), 3.20 (1H, dd, *J* = 8.1 and 15.0, CH_2Thz), 2.91 (1H, ddd, *J* = 1.9, 6.5 and 16.8, C*H*$_2$CHO), 2.62 (1H, ddd, *J* = 2.1, 7.4 and 16.8, C*H*$_2$CHO), 1.37 (3H, d, *J* = 6.9, C*H*$_3$CH), 1.09 (9H, s, $((CH_3)_3CSi)$. ^{13}C NMR (90.6 MHz, $CDCl_3$) δ: 201.8(d), 167.3(s), 159.4(s), 159.0(s), 135.5(d), 135.5(d), 133.4(s), 133.2(s), 130.4(s), 129.6(d), 129.2(d), 127.6(d), 113.6(d), 112.2(d), 78.9(d), 71.9(t), 65.2(t), 55.2(q), 51.0(t), 35.9(t), 30.8(d), 26.8(q), 20.0(q), 19.2(s). MS *m*/*z* (ES): 588.2616 (M + H, $C_{34}H_{42}NO_4SSi$ requires 588.2604). Anal. calcd. for $C_{34}H_{41}NO_4Ssi$ (%): C 69.5,H 7.0,N 2.4; found: C 69.3, H 6.9, N 2.4.

The (*R*)-(–)-sulfinimine (18)

A solution of the aldehyde **7** (1.24 g, 2.11 mmol), (*R*)-(–)-*p*-toluenesulfinamide (0.32 g, 2.4 mmol) (11) and titanium ethoxide (2.21 mL, 10.5 mmol) in CH_2Cl_2 (30 mL) was heated under reflux in a nitrogen atmosphere for 4 h. The mixture was quenched at 0 °C by addition of H_2O (15 mL) and then stirred at 0 °C for 10 min. The white slurry was filtered through Celite, and the filter cake was washed with CH_2Cl_2 (2 × 30 mL). The aqueous layer was extracted with CH_2Cl_2 (30 mL) and the combined organic extracts were dried ($MgSO_4$) and concentrated in vacuo. The residue was purified by flash chromatography on silica gel, which had been treated previously with a few drops of Et_3N, eluting with ethyl acetate:petroleum ether (bp 40–60 °C, 1:4 → 1:2) to give the *sulfinimine* (0.96 g, 64%) as a colourless oil. $[\alpha]_D^{24}$ –99.9 (*c* 0.22 in CH_2Cl_2). IR ν_{max} (cm^{-1}, film): 2930, 1614, 1513, 1248, 1112, 703. ^1H NMR(360 MHz, $CDCl_3$) δ: 8.25 (1H, t, *J* = 5.0, CHN), 7.74–7.67 (4H, m, ArH), 7.54 (2H, d, *J* = 8.2, SOArH), 7.47–7.36 (6H, m, ArH), 7.30 (2H, d, *J* = 8.3, SOArH), 7.18 (2H, d, *J* = 8.6, MeOArH), 6.84 (2H, d, *J* = 8.6, MeOArH), 6.76 (1H, s, ThzH), 4.57 (1H, d, *J* = 11.1, CH_2Ar), 4.45 (1H, d, *J* = 11.2, CH_2Ar), 3.97–3.92 (1H, m, CHOPMB), 3.83–3.76 (2H, m, CH_2OTPS), 3.79 (3H, s, CH_3O), 3.39 (1H, sextet, *J* = 6.9, CHThz), 3.35 (1H, dd, *J* = 4.3 and 15.0, CH_2Thz), 3.22 (1H, dd, *J* = 8.0 and 15.0, CH_2Thz), 2.98 (1H, ddd, *J* = 4.8, 6.4 and 15.3, $CH_2C{=}N$), 2.75 (1H, ddd, *J* = 5.3, 7.5, and 15.3, $CH_2C{=}N$), 2.40 (3H, s, CH_3Ar), 1.34 (3H, d, *J* = 6.9, C*H*$_3$CH), 1.10 (9H, s, $((CH_3)_3CSi)$. ^{13}C NMR(90.6 MHz, $CDCl_3$) δ: 167.3, 165.9, 159.4, 159.0, 141.7, 141.6, 135.6, 135.5, 133.3, 133.2, 130.4, 129.7, 129.6, 129.3, 127.7, 124.5, 113.6, 112.2, 78.9, 72.0, 65.3, 55.2, 42.3, 35.9, 33.4, 26.8, 21.4, 20.0, 19.2. MS *m*/*z* (FAB): 725.2913 (M + H, $C_{41}H_{49}N_2O_4S_2Si$ requires 725.2903).

Acetic acid (*E*)-(*S*)-4-iodo-1,3-dimethylbut-3-enyl ester (19)

A solution of trimethylaluminium (2.0 mol L^{-1}) in toluene (27 mL) was added dropwise over 30 min to a stirred solution of bis(cyclopentadienyl)zirconium dichloride (3.92 g, 13.4 mmol) in CH_2Cl_2 (50 mL) at room temperature and the mixture was stirred for 15 min and then cooled to 0 °C. A solution of (*S*)-(+)-pent-4-yn-2-ol (22) (1.5 g, 17.9 mmol) in CH_2Cl_2 (5 mL) was added dropwise over 15 min and the resulting solution was then stirred in the dark at room temperature for 3 days. The solution was cooled to –40 °C and a solution of iodine (5.0 g, 19.7 mmol) in THF (25 mL) was then added dropwise via cannula over 20 min. The dark solution was placed in an ice bath and a saturated solution of NH_4Cl (20 mL) was then added cautiously and the mixture was stirred vigorously for 30 min. The precipitated solids were filtrated off and the residue was washed with copious amounts of CH_2Cl_2. The filtrate was washed with 2 N HCl (50 mL) and then dried ($MgSO_4$). The solvent was removed at reduced pressure and the residue was purified by flash chromatography, eluting with ethyl acetate:petroleum ether (bp 40–60 °C, 1:1) to give the *E*-(S)-iodo-4-methylpent-4-en-1-ol (11) (2.95 g, 73%) as a colourless oil. $[\alpha]_D^{24}$ 24.1 (*c* 0.34 in CH_2Cl_2). IR ν_{max} (cm^{-1}, film): 3356, 2966, 1273, 1118, 939. ^1H NMR (360 MHz, $CDCl_3$) δ: 6.02 (1H, c, *J* = 1.1, C=CH), 4.00–3.91 (1H, m, CH), 2.40–2.34 (2H, m,

© 2004 NRC Canada

CH_2), 1.88 (3H, d, J = 1.1, CH_3C=C), 1.20 (3H, d, J = 6.4 CH_3CH). ^{13}C NMR (90.6 MHz, $CDCl_3$) δ: 145.1, 62.3, 51.4, 49.3, 24.1, 23.0. Acetic anhydride (0.66 mL, 7.06 mmol) was added to a solution of the alcohol (1.52 g, 6.7 mmol) and triethylamine (1.03 mL, 7.4 mmol) in CH_2Cl_2 (30 mL) at 0 °C. After 5 min, 4,4-dimethylaminopyridine (0.7 mmol) was added in one portion and the mixture was stirred for 2 h at room temperature. The solution was poured into a 1 N HCl solution and extracted with CH_2Cl_2 (2 × 50 mL). The combined organic extracts were washed with a saturated solution of $NaHCO_3$ (50 mL), dried ($MgSO_4$) and concentrated at reduced pressure to give the *acetate* (1.63 g, 91%) as a yellow liquid. $[\alpha]_D^{24}$ –1.8 (*c* 0.34, $CHCl_3$). IR ν_{max} (cm^{-1}, film): 2976, 1737, 1242. ^{1}H NMR (360 MHz, $CDCl_3$) δ: 6.01 (1H, s, C=CH), 5.06 (1H, sextet, J = 6.2, CH), 2.51 (1H, dd, J = 7.4 and 13.7, CH_2), 2.32 (1H, dd, J = 5.6 and 13.7, CH_2), 2.04 (3H, s, CH_3CO), 1.87 (3H, s, CH_3C=C), 1.21 (3H, d, J = 6.1, CH_3CH). ^{13}C NMR (90.6 MHz, $CDCl_3$) δ: 170.3, 143.9, 77.5, 68.1, 45.6, 24.0, 21.2, 19.6. MS *m/z* (ES): 207.9751 (M – $C_2H_4O_2$ requires 207.9749).

The sulfinamine 20a

A solution of LiHMDS (1.0 mol L^{-1}) in THF (1.9 mL) was added dropwise to a solution of the acetate **19** (0.51 g, 1.9 mmol) in dry THF (13 mL) at –78 °C under a nitrogen atmosphere, and the yellow solution was stirred at –78 °C for 50 min. A solution of the sulfinimine **18** (1.15 g, 1.58 mmol) in THF (13 mL) was added dropwise via cannula over 20 min at –78 °C, and the mixture was stirred at –78 °C for 10 min and then quenched with a saturated solution of NH_4Cl (20 mL). The mixture was allowed to warm to room temperature and then diluted with ethyl acetate (25 mL) and washed with water (30 mL). The separated aqueous layer was extracted with ethyl acetate (2 × 30 mL) and the combined organic extracts were dried ($MgSO_4$) and then evaporated to dryness in vacuo. The residue was purified by flash chromatography, eluting with ethyl acetate:petroleum ether (bp 40–60 °C, 1:3 → 1:1) to give the *sulfinamine* (0.98 g, 63%) as a pale yellow oil. $[\alpha]_D^{24}$ –17.3 (*c* 1.78 in $CHCl_3$). IR ν_{max} (cm^{-1}, film): 2929, 1730, 1513, 1112, 702. ^{1}H NMR (360 MHz, $CDCl_3$) δ: 7.70–7.68 (4H, m, ArH), 7.62 (2H, d, J = 8.2, SOArH), 7.45–7.34 (6H, m, ArH), 7.29 (2H, d, J = 8.3, SOArH), 7.15 (2H, d, J = 8.7, MeOArH), 6.94 (1H, s, ThzH), 6.82 (2H, d, J = 8.7, MeOArH), 5.88 (1H, d, J = 1.0, C=CH), 5.06–5.03 (1H, m, CHOCO), 4.79 (1H, d, J = 9.3, NH), 4.53 (1H, d, J = 11.0, CH_2Ar), 4.42 (1H, d, J = 11.2, CH_2Ar), 3.97–3.91 (1H, m, CHOPMB), 3.79–3.75 (2H, m, CH_2OTPS), 3.78 (3H, s, CH_3O), 3.59–3.53 (1H, m, CHN), 3.35 (1H, dd, J = 4.3 and 15.2, CH_2Thz), 3.31–3.26 (1H, m, CHThz), 3.21 (1H, dd, J = 8.1 and 15.1, CH_2Thz), 2.60 (1H, dd, J = 5.7 and 16.0, CH_2CO_2), 2.53 (1H, dd, J = 5.0 and 16.0, CH_2CO_2), 2.45 (1H, dd, J 6.3 and 13.8, CH_2C=C), 2.39 (3H, s, CH_3Ar), 2.29 (1H, dd, J 5.6 and 13.2, CH_2C=C), 2.01–1.93 (1H, m, CH_2CHN), 1.89–1.83 (1H, m, CH_2CHN), 1.82 (3H, s, CH_3C=C), 1.33 (3H, d, J = 6.9, CH_3CH), 1.18 (3H, d, J = 6.7, CH_3CH), 1.08 (9H, s, ($(CH_3)_3$CSi). ^{13}C NMR (90.6 MHz, $CDCl_3$) δ: 170.9, 167.2, 160.0, 159.0, 143.8, 142.6, 141.1, 135.6, 135.5, 133.3, 133.2, 130.4, 129.6, 129.4, 129.2, 127.9, 127.6, 125.9, 125.4, 113.6, 112.7, 79.1, 77.6, 72.0, 68.5, 65.2, 55.2, 51.2, 45.7, 42.6, 41.4, 35.9, 32.8, 26.8, 24.0, 21.5, 21.3, 19.5, 19.1. MS *m/z* (FAB): 993.2885 (M + H, $C_{49}H_{62}N_2O_6S_2SiI$ requires 993.2863).

(3*R*,5*S*)-3-Amino-5-{2-[(*S*)-3-(*tert*-butyldiphenylsilanyloxy)-2-(4-methoxybenzyloxy)propyl]thiazol-4-yl}hexanoic acid (*E*)-(*S*)-4-iodo-1,3-dimethylbut-3-enyl ester (20b)

Trifluoroacetic acid (1.4 mL, 18.3 mmol) was added to a solution of the sulfinamine **20a** (0.91 g, 0.92 mmol) in dry methanol (20 mL) al 0 °C and the mixture was stirred at room temperature for 4 h and then concentrated at reduced pressure below 35 °C. The residue was dissolved in CH_2Cl_2 (25 mL), and the solution was washed with a saturated solution of $NaHCO_3$ (20 mL), and brine (20 mL), and then evaporated to dryness in vacuo. The residue was purified by flash chromatography on silica gel, eluting with ethyl acetate:petroleum ether (bp 40–60 °C, 1:3 → 1:0) to give the *amine* (0.74 g, 95%) as a colourless oil. $[\alpha]_D^{24}$ –3.9 (*c* 0.31 in $CHCl_3$). IR ν_{max} (cm^{-1}, film): 3340, 2929, 1728, 1112, 702. ^{1}H NMR (360 MHz, $CDCl_3$) δ: 7.70–7.67 (4H, m, ArH), 7.45–7.34 (6H, m, ArH), 7.16 (2H, d, J = 8.7, MeOArH), 6.82 (2H, d, J = 8.7, MeOArH), 6.81 (1H, s, ThzH), 5.94 (1H, s, C=CH), 5.07–5.04 (1H, m, CHOCO), 4.54 (1H, d, J = 11.0, CH_2Ar), 4.42 (1H, d, J = 11.2, CH_2Ar), 3.95–3.88 (1H, m, CHOPMB), 3.81–3.76 (2H, m, CH_2OTPS), 3.80 (3H, s, CH_3O), 3.36 (1H, dd, J = 4.2 and 15.1, CH_2Thz), 3.21 (1H, dd, J = 8.2 and 15.0, CH_2Thz), 3.17–3.11 (1H, m, CH), 3.07–3.02 (1H, m, CH), 2.48–2.21 (4H, m, CH_2CO_2 and CH_2C=C), 1.89–1.83 (1H, m, CH_2CHN), 1.82 (3H, s, CH_3C=C), 1.64–1.56 (1H, m, CH_2CHN), 1.31 (3H, d, J = 6.9, CH_3CH), 1.18 (3H, d, J = 6.7, CH_3CH), 1.08 (9H, s, ($(CH_3)_3$CSi). ^{13}C NMR (90.6 MHz, $CDCl_3$) δ: 171.7, 166.9, 160.6, 158.9, 143.9, 135.5, 135.5, 133.3, 133.2, 130.4, 129.6, 129.2, 127.9, 127.6, 117.8, 113.6, 111.9, 79.1, 77.7, 72.0, 68.1, 65.3, 55.2, 46.2, 45.7, 44.7, 42.9, 35.9, 33.0, 26.7, 25.0, 21.5, 19.8, 19.1. MS *m/z* (ES): 855.2663 (M + H, $C_{43}H_{56}N_2O_5SSiI$ requires 855.2724).

The amine was reacted with chiral α-methoxyphenylacetic acid (MPA), and the NMR spectrum of the resulting MPA amide, complexed with $Ba(ClO_4)_2$ was studied using the procedure developed by Riguera and co-workers (12). A similar NMR study was made with the enantiopure (3*S*)-amine prepared from the ester **19** and the enantiomeric sulfinimine corresponding to **18**. Inspection and comparison of relevant chemical shift data with the $Ba(ClO_4)_2$-complexed MPA amides confirmed the 3*R*-amine configuration in **20b**, and hence in **20a**.

(3*R*,5*S*)-5-{2-[(*S*)-3-(*tert*-Butyldiphenylsilanyloxy)-2-(4-methoxybenzyloxy)propyl]thiazol-4-yl}-3-(2,2,2-trichloro-1,1-dimethylethoxycarbonylamino)hexanoic acid (*E*)-(*S*)-4-iodo-1,3-dimethylbut-3-enyl ester (21a)

A solution of the amine **20b** (870 mg, 1 mmol) in CH_2Cl_2 (16 mL) was added dropwise over 30 min to a slurry of 1,1-dimethyl-2,2,2-trichloroethyl chloroformate (1.22 g, 5.1 mmol) in pyridine (12 mL) at 0 °C and the yellow suspension was stirred at 0 °C for 1.5 h and then evaporated to dryness in vacuo. The orange residue was purified by flash chromatography on silica gel, eluting with ethyl acetate:petroleum ether (bp 40–60 °C, 1:5 → 1:4) to give *the TcBOC-protected*

© 2004 NRC Canada

β-*aminoester* (950 mg, 89%) as a pale yellow oil. $[\alpha]_D^{24}$ –3.2 (*c* 0.31 in $CHCl_3$). IR ν_{max} (cm^{-1}, film): 3418, 2930, 1731, 1513, 1112, 703. ^1H NMR (360 MHz, $CDCl_3$) δ: 7.71–7.69 (4H, m, ArH), 7.47–7.35 (6H, m, ArH), 7.18 (2H, d, *J* = 8.6, MeOArH), 6.85 (1H, s, ThzH), 6.83 (2H, d, *J* = 8.7, MeOArH), 6.01 (1H, br s, C=CH), 5.44 (1H, d, *J* = 9.0, NH), 5.15–5.06 (1H, m, CHOCO), 4.57 (1H, d, *J* = 11.0, CH_2Ar), 4.44 (1H, d, *J* = 11.0, CH_2Ar), 4.00–3.92 (1H, m, CHOPMB), 3.90–3.85 (1H, m, CHN), 3.83–3.79 (2H, m, CH_2OTPS), 3.80 (3H, s, CH_3O), 3.37 (1H, dd, *J* = 3.9 and 15.1, CH_2Thz), 3.23 (1H, dd, *J* = 8.2 and 15.1, CH_2Thz), 3.09–3.00 (1H, m, CHThz), 2.54–2.43 (3H, m, CH_2CO_2 and CH_2C=C), 2.33 (1H, dd, *J* = 5.2 and 13.9, CH_2C=C), 2.00–1.96 (1H, m, CH_2CHN), 1.93 (3H, s, TcBOC), 1.92 (3H, s, TcBOC), 1.88–1.79 (1H, m, CH_2CHN), 1.86 (3H, s, CH_3C=C), 1.35 (3H, d, *J* = 6.9, CH_3CH), 1.20 (3H, d, *J* = 6.3, CH_3CH), 1.10 (9H, s, $((CH_3)_3CSi)$. ^{13}C NMR (90.6 MHz, $CDCl_3$) δ: 170.4(s), 167.0(s), 159.6(s), 158.7(s), 153.9(s), 143.8(s), 135.3(d), 135.3(d), 133.0(s), 132.9(s), 130.2(s), 129.4(d), 129.0(d), 127.7(d), 127.4(d), 113.3(d), 112.5(d), 106.3(s), 88.1(s), 78.8(d), 77.7(s), 77.5(d), 71.8(t), 68.1(d), 65.1(t), 54.9(q), 46.0(q), 45.5(t), 40.2(t), 39.8(t), 35.7(t), 32.8(d), 26.5(q), 23.7(q), 21.7(q), 20.9(q), 18.9(s). MS *m/z* (ES): 855.2663 (M + H, $C_{47}H_{62}N_2Cl_3O_7SSiI$ requires 855.2724).

(3*R*,5*S*)-5-{2-[(*S*)-3-(*tert*-Butyldiphenylsilanyloxy)-2-hydroxypropyl]thiazol-4-yl}-3-(2,2,2-trichloro-1,1-dimethylethoxycarbonylamino)hexanoic acid (*E*)-(*S*)-4-iodo-1,3-dimethylbut-3-enyl ester (21b)

2,3-Dichloro-5,6-dicyano-1,4-benzoquinone (300 mg, 1.45 mmol) was added, in one portion, to a rapidly stirred mixture of the *p*-methoxybenzylether **21a** (900 mg, 0.85 mmol) in CH_2Cl_2 (30 mL) and H_2O (1.2 mL) at room temperature. The mixture was stirred at 0 °C for 1.5 h, then at room temperature for 30 min, and quenched with satd. aq. $NaHCO_3$ (30 mL). The separated aqueous layer was extracted with CH_2Cl_2 (3 × 30 mL) and the combined organic extracts were dried ($MgSO_4$) and then evaporated to dryness in vacuo. The residue was purified by flash chromatography on silica gel, eluting with ethyl acetate:petroleum ether (bp 40–60 °C, 1:4 → 1:3) to give the *alcohol* (690 mg, 87%) as a colourless oil. $[\alpha]_D^{24}$ 1.65 (*c* 0.24 in $CHCl_3$). IR ν_{max} (cm^{-1}, film): 3428, 2930, 1714, 1112, 756. ^1H NMR (360 MHz, $CDCl_3$) δ: 7.69–7.66 (4H, m, ArH), 7.47–7.37 (6H, m, ArH), 6.85 (1H, s, ThzH), 6.01 (1H, br s, C=CH), 5.31 (1H, d, *J* = 9.2, NH), 5.12–5.06 (1H, m, CHOCO), 4.14 (1H, br s), 3.98 (1H, br s), 3.84–3.77 (1H, m, CHNH), 3.74 (1H, dd, *J* = 5.6 and 10.2, CH_2OTPS), 3.65 (1H, dd, *J* = 5.9 and 10.1, CH_2OTPS), 3.27 (1H, dd, *J* = 3.4 and 15.3, CH_2Thz), 3.12 (1H, dd, *J* = 8.2 and 15.4, CH_2Thz), 3.06–3.00 (1H, m, CHThz), 2.54–2.44 (3H, m, CH_2CO_2 and CH_2C=C), 2.33 (1H, dd, *J* = 5.1 and 13.7, CH_2C=C), 1.93–1.80 (2H, m, CH_2CHN), 1.91 (3H, s, TcBOC), 1.90 (3H, s, TcBOC), 1.85 (3H, s, CH_3C=C), 1.31 (3H, d, *J* = 7.2, CH_3CH), 1.19 (3H, d, *J* = 6.3, CH_3CH), 1.08 (9H, s, $((CH_3)_3CSi)$. ^{13}C NMR (90.6 MHz, $CDCl_3$) δ: 170.6, 167.6, 160.1, 153.3, 144.0, 135.5, 133.2, 132.9, 130.2, 129.7, 127.7, 112.4, 106.6, 87.8, 78.0, 77.7, 71.1, 68.5, 66.7, 46.1, 45.7, 40.7, 39.8, 39.5, 36.4, 32.9, 26.8, 23.9, 21.6, 20.5, 19.8, 19.2. MS *m/z* (ES): 937.1527 (M + H, $C_{39}H_{53}N_2O_6SCl_3SiI$ requires 937.1504).

(3*R*,5*S*)-5-{2-[(*S*)-3-(*tert*-Butyldiphenylsilanyloxy)-2-((*Z*)-3-tributylstannanylacryloyloxy)propyl]thiazol-4-yl}-3-(2,2,2-trichloro-1,1-dimethylethoxycarbonylamino)hexanoic acid (*E*)-(*S*)-4-iodo-1,3-dimethylbut-3-enyl ester (22)

Lithium hydroxide monohydrate (65.0 mg, 1.55 mmol) was added to a solution of (*Z*)-3-(tributylstannyl)propenoate (0.5 g, 1.29 mmol) (13) in a mixture of THF:H_2O (4:1) and MeOH (1.5 mL) at room temperature. The mixture was stirred at 60 °C for 48 h and then concentrated at reduced pressure. The residue was acidified carefully with 1 mol L^{-1} HCl and the aqueous solution was then extracted with ethyl acetate (3 × 15 mL). The combined organic extracts were dried ($MgSO_4$) and evaporated in vacuo to leave the *Z*-3-tributylstannane propenoic acid as a colourless oil. ^1H NMR (360 MHz, $CDCl_3$) δ: 7.40 (1H, d, *J* = 13.0, C=CH), 6.78 (1H, d, *J* = 13.0, C=CH), 1.52–1.46 (6H, m), 1.32–1.23 (6H, m), 1.00–0.96 (6H, m), 0.89 (9H, t, *J* = 7.3, CH_3CH_2). ^{13}C NMR (90.6 MHz, $CDCl_3$) δ: 171.5, 161.5, 134.1, 29.1, 27.2, 13.6, 11.0, which was used straightaway.

2,4,6-Trichlorobenzoyl chloride (0.24 mL, 1.57 mmol) was added to a solution of the stannylpropenoic acid (570 mg, 1.57 mmol) and triethylamine in THF (6 mL) at room temperature and the mixture was stirred at room temperature for 1 h. The volume of THF was reduced by evaporation in vacuo and then replaced by toluene (3 mL). The solution was cooled to –30 °C and then a solution of the alcohol **21b** (690 mg, 0.75 mmol) in toluene (4 mL) was added via cannula followed by DMAP (450 mg, 3.7 mmol). The mixture was stirred at –30 °C for 40 min and then quenched with 1 N HCl (10 mL). The separated aqueous extract was extracted with ethyl acetate (3 × 15 mL), and the combined organic extracts were then dried ($MgSO_4$) and evaporated to dryness in vacuo. The residue was purified by flash chromatography on silica gel, eluting with ethyl acetate:petroleum ether (bp 40–60 °C, 1:12 → 1:8) to give the *ester* (640 mg, 67%) as a colourless oil. $[\alpha]_D^{24}$ 1.21 (*c* 0.66 in $CHCl_3$). IR ν_{max} (cm^{-1}, film): 3426, 2955, 1714, 1199. ^1H NMR (360 MHz, $CDCl_3$) δ: 7.68–7.65 (4H, m, ArH), 7.47–7.34 (6H, m, ArH), 7.25 (1H, d, *J* = 12.7, C=CH), 6.87 (1H, s, ThzH), 6.78 (1H, d, *J* = 12.7, C=CH), 6.01 (1H, br s, C=CH), 5.43 (1H, d, *J* = 9.2, NH), 5.44–5.39 (1H, m, CHOCOC=C), 5.13–5.07 (1H, m, CHOCO), 3.90–3.83 (3H, m, CHNH and CH_2OTPS), 3.55 (1H, dd, *J* = 5.2 and 15.2, CH_2Thz), 3.43 (1H, dd, *J* = 7.6 and 15.1, CH_2Thz), 3.08–3.02 (1H, m, CHThz), 2.54–2.48 (3H, m, CH_2CO_2 and CH_2C=C), 2.33 (1H, dd, *J* = 5.2 and 13.8, CH_2C=C), 1.97–1.92 (1H, m, CH_2CHN), 1.92 (3H, s, TcBOC), 1.90 (3H, s, TcBOC), 1.86–1.79 (1H, m, CH_2CHN), 1.85 (3H, s, CH_3C=C), 1.54–1.48 (6H, m, Bu_3Sn), 1.32–1.23 (9H, m, CH_3CH and Bu_3Sn), 1.20 (3H, d, *J* = 6.3, CH_3CH), 1.07 (9H, s, $((CH_3)_3CSi)$, 0.95–0.90 (6H, m, Bu_3Sn), 0.89 (9H, t, *J* = 7.3, Bu_3Sn). ^{13}C NMR (90.6 MHz, $CDCl_3$) δ: 170.7, 166.8, 166.0, 159.9, 158.7, 153.3, 144.0, 135.5, 134.7, 133.1, 129.6, 127.8, 127.6, 113.1, 106.5, 87.8, 78.0, 73.1, 71.1, 68.4, 64.1, 46.2, 45.7, 40.4, 39.4, 34.2, 32.9, 29.1, 27.2, 26.7, 23.9, 21.6, 20.6, 19.7, 19.2, 13.7, 10.9.

© 2004 NRC Canada

[(6*Z*,8*E*)-(3*S*,11*S*,15*R*,17*S*)-3-(*tert*-Butyldiphenylsilanyloxymethyl)-9,11,17-trimethyl-5,13-dioxo-4,12-dioxa-20-thia-21-azabicyclo[16.2.1]henicosa-1(21),6,8,18-tetraen-15-yl]carbamic acid 2,2,2-trichloro-1,1-dimethylethyl ester (23)

A solution of the stannane-iodide **22** (641 mg, 0.5 mmol) in degassed DMF (60 mL) was added to a solution of Pd(0) bis-dibenzylidineacetone (46 mg, 0.05 mmol) and Ph_3As (107 mg, 0.35 mmol) in degassed DMF (60 mL), and the resulting yellow mixture was stirred at 60 °C for 1 h under argon. The solvent was evaporated in vacuo and the residue was purified by flash chromatography, eluting with ethyl acetate:petroleum ether (bp 40–60 °C, 1:5 → 1:3) to give the *diene macrolide* (278 mg, 65%) as a yellow oil. $[\alpha]_D^{24}$ –118.1 (*c* 0.17 in $CHCl_3$). IR ν_{max} (cm^{-1}, film): 3416, 2945, 1721, 1163. ^1H NMR (360 MHz, $CDCl_3$) δ: 7.70–7.66 (4H, m, ArH), 7.46–7.34 (6H, m, ArH), 7.07 (1H, d, *J* = 11.8, C=CH), 6.80 (1H, t, *J* = 11.5, C=CH), 6.80 (1H, s, ThzH), 5.56 (1H, d, *J* = 11.3, C=CH), 5.54–5.51 (1H, m, CHOCOC=C), 5.16–5.11 (1H, m, CHOCO), 4.84 (1H, d, *J* = 7.3, NH), 3.86–3.77 (2H, m, CH_2OTPS), 3.40–3.35 (1H, m, C*H*NH), 3.32 (1H, dd, *J* = 2.5 and 14.4, CH_2Thz), 3.21 (1H, dd, *J* = 11.0 and 14.2, CH_2Thz), 3.06–3.01 (1H, m, CHThz), 2.61 (1H, dd, *J* = 11.5 and 14.7), 2.39–2.34 (2H, m), 2.18 (1H, d, *J* = 13.4), 2.13–2.06 (1H, m, C*H*$_2$CHN), 1.96–1.90 (1H, m, C*H*$_2$CHN), 1.92 (6H, br s, TcBoc), 1.84 (3H, s, CH_3C=C), 1.25 (6H, d, *J* = 6.9, C*H*$_3$CH), 1.07 (9H, s, $((CH_3)_3CSi)$. ^{13}C NMR (90.6 MHz, $CDCl_3$) δ: 170.1(s), 166.0(s), 165.3(s), 160.9(s), 153.1(s), 145.8(s), 135.5(d), 133.8(d), 133.0(s), 129.8(d), 128.1(d), 127.7(d), 124.0(d), 115.5(d), 112.3(d), 106.7(s), 87.7(s), 72.4(d), 67.5(d), 64.4(t), 47.9(d), 47.6(t), 40.7(t), 39.1(t), 36.4(t), 33.5(d), 29.0(s), 26.7(q), 22.8(q), 21.5(q), 20.9(q), 19.2(s), 17.0(q). MS *m*/*z* (ES): 863.2452 (M + H, $C_{42}H_{54}N_2O_7Cl_3SSi$ requires 863.2487).

((6*Z*,8*E*)-(3*S*,11*S*,15*R*,17*S*)-3-Hydroxymethyl-9,11,17-trimethyl-5,13-dioxo-4,12-dioxa-20-thia-21-azabicyclo[16.2.1]henicosa-1(21),6,8,18-tetraen-15-yl)carbamic acid 2,2,2-trichloro-1,1-dimethylethyl ester (24a)

A solution on TBAF (1 mol L^{-1}) in THF (0.5 mL) was added to a mixture of the macrolide silyl ether **23** (211 mg, 0.24 mmol) and acetic acid (70 μL, 1.2 mmol) in THF (4.5 mL) at room temperature, and the mixture was stirred at this temperature for 20 h. The mixture was poured into a saturated solution of $NaHCO_3$ (5 mL) and then extracted with diethyl ether (3 × 10 mL). The combined organic extracts were dried ($MgSO_4$) and then evaporated to dryness in vacuo to leave a residue which was purified by flash chromatography, eluting with ethyl acetate:petroleum ether (bp 40–60 °C, 1:2 → 3:2) to give the *alcohol* (117 mg, 78%) as a colourless oil. $[\alpha]_D^{24}$ –137.5 (*c* 2.42 in $CHCl_3$). IR ν_{max} (cm^{-1}, film): 3431, 2947, 1714, 1163. ^1H NMR (360 MHz, $CDCl_3$) δ: 7.03 (1H, d, *J* = 11.9, C=CH), 6.83 (1H, t, *J* = 11.6, C=CH), 6.79 (1H, s, ThzH), 5.54 (1H, d, *J* = 11.3, C=CH), 5.52–5.48 (1H, m, CHOCOC=C), 5.14–5.06 (1H, m, CHOCO), 4.86 (1H, d, *J* = 6.9, NH), 3.85 (1H, dd, *J* = 4.0 and 11.9, CH_2OH), 3.79 (1H, dd, *J* = 5.3 and 11.9, CH_2OH), 3.43–3.33 (1H, m, C*H*NH), 3.30–3.20 (2H, m, CH_2Thz), 3.03–2.98 (1H, m, CHThz), 2.55 (1H, app t, *J* = 14.0), 2.33 (1H, dd, *J* = 11.0 and 13.3), 2.24 (1H, dd, *J* = 3.9 and 15.4), 2.16 (1H, d, *J* = 13.0), 2.10–2.03 (1H, m, CH_2CHN), 1.99–1.87 (1H, m, CH_2CHN), 1.90 (6H, br s, TcBoc), 1.82 (3H, s, CH_3C=C), 1.24 (6H, d, *J* = 6.7, CH_3CH). ^{13}C NMR (90.6 MHz, $CDCl_3$) δ: 170.2, 165.7, 165.1, 161.1, 153.1, 146.4, 141.2, 124.0, 115.0, 112.6, 106.7, 87.8, 72.8, 67.6, 64.6, 47.9, 47.7, 40.7, 39.2, 34.8, 33.6, 29.0, 22.7, 21.7, 16.9. MS *m*/*z* (ES): 625.1292 (M + H, $C_{26}H_{36}N_2O_7Cl_3S$ requires 625.1309).

((6*Z*,8*E*)-(3*S*,11*S*,15*R*,17*S*)-3-Formyl-9,11,17-trimethyl-5,13-dioxo-4,12-dioxa-20-thia-21-azabicyclo[16.2.1]henicosa-1(21),6,8,18-tetraen-15-yl)carbamic acid 2,2,2-trichloro-1,1-dimethylethyl ester (24b)

Dess–Martin periodinane (237 mg, 0.56 mmol) was added in one portion to a mixture of the alcohol **24a** (139 mg, 0.22 mmol) and pyridine (0.14 mL, 1.79 mmol) in CH_2Cl_2 (8 mL) at 0 °C. The white suspension was stirred at 0 °C for 30 min and then at room temperature for 3 h. The mixture was poured into ethyl acetate (8 mL) and a saturated solution of $NaHCO_3$ (8 mL), and the separated organic extract was then washed with 1 mol L^{-1} Na_2SO_3. The combined aqueous extracts were extracted with ethyl acetate (10 mL) and the combined organic extracts were dried ($MgSO_4$) and concentrated at reduced pressure. The residue was purified by flash chromatography, eluting with ethyl acetate:petroleum ether (bp 40–60 °C, 1:2 → 1:1) to give the *aldehyde* (88 mg, 70%) as a colourless oil. $[\alpha]_D^{26}$ –178.4 (*c* 0.56 in $CHCl_3$). IR ν_{max} (cm^{-1}, film): 3431, 2947, 1714, 1163. ^1H NMR (360 MHz, $CDCl_3$) δ: 9.70 (1H, s, CHO), 6.97 (1H, d, *J* = 11.9, C=CH), 6.88 (1H, t, *J* = 11.8, C=CH), 6.84–6.73 (1H, m, C*H*CHO), 6.82 (1H, s, ThzH), 5.51 (1H, d, *J* = 11.0, C=CHCO$_2$), 5.13–5.08 (1H, m, CHOCO), 4.88 (1H, d, *J* = 5.8, NH), 3.65 (1H, dd, *J* = 2.8 and 15.2, CH_2Thz), 3.49–3.40 (1H, m, C*H*NH), 3.19 (1H, dd, *J* = 10.5 and 15.2, CH_2Thz), 3.05–2.99 (1H, m, CHThz), 2.56–2.49 (1H, m), 2.32–2.22 (2H, m), 2.18 (1H, d, *J* = 11.8), 1.98–1.73 (2H, m, CH_2CHN), 1.89 (6H, br s, TcBoc), 1.84 (3H, s, CH_3C=C), 1.25 (6H, d, *J* = 6.9, CH_3CH). ^{13}C NMR (90.6 MHz, $CDCl_3$) δ: 198.0, 171.1, 164.8, 163.8, 161.4, 153.2, 147.1, 142.0, 124.0, 114.1, 112.9, 112.2, 106.6, 87.8, 75.8, 67.7, 47.6, 41.3, 39.3, 33.4, 33.0, 22.2, 21.6, 17.0. MS *m*/*z* (ES): 623.1178 (M + H, $C_{26}H_{33}N_2O_7Cl_3S$ requires 623.1152).

[(6*Z*,8*E*)-(3*S*,11*S*,15*R*,17*S*)-9,11,17-Trimethyl-3-((*E*)-2-methyl-3-oxopropenyl)-5,13-dioxo-4,12-dioxa-20-thia-21-azabicyclo[16.2.1]henicosa-1(21),6,8,18-tetraen-15-yl]carbamic acid 2,2,2-trichloro-1,1-dimethylethyl ester (25)

A solution of the aldehyde **24b** (89 mg, 0.14mmol) and 2-(triphenylphosphoranylidene)propionaldehyde (46 mg, 0.14 mmol) in benzene (7 mL) was heated under reflux for 3 h under a nitrogen atmosphere. The mixture was cooled to room temperature, quenched with water (7 mL), and then extracted with diethyl ether (2 × 10 mL). The combined organic extracts were dried ($MgSO_4$) and then evaporated to dryness in vacuo. The residue was purified by flash chromatography, eluting with ethyl acetate:petroleum ether (bp 40–60 °C, 1:2 → 1:1) to give the *unsaturated aldehyde* (70 mg,

© 2004 NRC Canada

73%) as a colourless oil. $[\alpha]_D^{28}$ –171.8 (*c* 0.17 in $CHCl_3$). IR ν_{max} (cm^{-1}, film): 3460, 2957, 1729, 1157. ^1H NMR (360 MHz, $CDCl_3$) δ: 9.48 (1H, s, CHO), 7.02 (1H, d, *J* = 11.9, C=CH), 6.83 (1H, s, ThzH), 6.81 (1H, t, *J* = 11.4, C=CH), 6.46 (1H, dd, *J* = 1.35 and 8.1,*H*C=C-CHO), 6.31 (1H, app c, J 7.5, CH-C=C), 5.52 (1H, d, *J* = 11.3, C=CHCO_2), 5.15–5.07 (1H, m, CHOCO), 4.84 (1H, d, *J* = 5.3, NH), 3.44–3.35 (1H, m, C*H*NH), 3.28–3.24 (2H, m, CH_2Thz), 3.06–2.99 (1H, m, CHThz), 2.54 (1H, dd, *J* = 11.3 and 15.4), 2.38–2.24 (2H, m), 2.17 (1H, d, *J* = 13.1), 1.98–1.75 (2H, m, CH_2CHN), 1.95 (3H, s, CH_3-C=C), 1.90 (6H, s, TcBOC), 1.83 (3H, s, CH_3C=C), 1.25 (6H, d, *J* = 6.7, CH_3CH). ^{13}C NMR (90.6 MHz, $CDCl_3$) δ: 194.4, 170.1, 164.4, 164.1, 161.2, 153.0, 147.6, 146.7, 141.5, 140.7, 123.8, 114.5, 113.0, 106.6, 87.8, 68.3, 67.5, 47.8, 47.7 40.8, 39.1, 37.5, 33.6, 22.6, 21.6, 21.0, 16.8, 9.9. MS *m*/*z* (ES): 663.1432 (M +H, $C_{26}H_{33}N_2O_7Cl_3S$ requires 623.1165).

[(6*Z*,8*E*)-(3*S*,11*S*,15*R*,17*S*)-3-((1*E*,3*E*)-4-Iodo-2-methylbuta-1,3-dienyl)-9,11,17-trimethyl-5,13-dioxo-4,12-dioxa-20-thia-21-azabicyclo[16.2.1]henicosa-1(21),6,8,18-tetraen-15-yl]carbamic acid 2,2,2-trichloro-1,1-dimethylethyl ester (26)

A solution of the unsaturated aldehyde **25** (70 mg, 0.1 mmol) and iodoform (250 mg, 0.63 mmol) in degassed THF (4 mL) was added dropwise over 15 min to a slurry of $CrCl_2$ (305 mg, 2.5 mmol) in degassed THF (3 mL) at 0 °C under an argon atmosphere. The mixture was stirred at room temperature for 1.5 h, then quenched with water (8 mL), and extracted with diethyl ether (2 × 10 mL). The combined organic extracts were dried ($MgSO_4$) and concentrated at reduced pressure. The yellow residue was purified by flash chromatography, eluting with ethyl acetate:petroleum ether (bp 40–60 °C, 1:4 → 1:3) to give the *vinyl iodide* (57 mg, 68%) as a pale yellow oil. $[\alpha]_D^{25}$ –271.6 (*c* 0.54 in $CHCl_3$). ^1H NMR (360 MHz, $CDCl_3$) δ: 7.07 (1H, d, *J* = 14.5, C=CHI), 7.03 (1H, d, *J* = 13.0, C=CH), 6.81 (1H, s, ThzH), 6.78 (1H, t, *J* = 11.7,HC=C), 6.46 (1H, d, *J* = 14.7, HC=CI), 6.16 (1H, app c, *J* = 7.8, CH-C=C), 5.52 (1H, d, *J* = 9.2, C=CH), 5.50 (1H, d, *J* = 11.5, C=CHCO_2), 5.15–5.07 (1H, m, CHOCO), 4.84 (1H, br s, NH), 3.44–3.38 (1H, m, C*H*NH), 3.23–3.17 (2H, m, CH_2Thz), 3.05–3.00 (1H, m, CHThz), 2.56 (1H, dd, *J* = 11.6 and 14.9), 2.34 (1H, dd, *J* = 11.2 and 13.3), 2.25 (1H, dd, *J* = 3.3 and 15.2), 2.16 (1H, d, *J* = 12.8), 2.10–2.04 (1H, m), 1.92 (3H, s, CH_3-C=C), 1.90 (7H, br s), 1.86 (3H, s, CH_3C=C), 1.24 (3H, d, *J* = 6.5, CH_3CH), 1.23 (3H, d, *J* = 6.5, CH_3CH). ^{13}C NMR (90.6 MHz, $CDCl_3$) δ: 170.1, 165.0, 164.6, 161.0, 153.0, 148.4, 145.9, 140.7, 137.9, 129.6, 123.9, 115.2, 112.6, 106.6, 87.7, 77.7, 68.4, 67.8, 47.9, 47.7, 40.5, 39.1, 38.6, 33.6, 22.7, 21.6, 20.9, 16.7, 12.7. MS *m*/*z* (ES): 809.0441 (M +H, $C_{26}H_{33}N_2O_7Cl_3S$ requires 809.0458).

TcBOC pateamine A (27)

Carbon tetrabromide (1.83 g, 5.54 mmol) was added in one portion to a solution of *E*-3-tributylstannanylbut-2-en-1-ol (23) (1 g, 2.77 mmol), 2,6-lutidine (64 μL, 0.55 mmol), and triphenylphosphine (1.45 g, 5.54 mmol) in acetonitrile (15 mL), and the mixture was stirred at room temperature for 1 h and then concentrated at reduced pressure. The residue was poured into brine (25 mL) and the solution was then extracted with diethyl ether (3 × 30 mL). The combined organic extracts were dried ($MgSO_4$) and concentrated at reduced pressure. The residue was purified by flash chromatography, eluting with petrol to give the corresponding allylic bromide (1.1 g, 90%) as a pale yellow oil. A solution of dimethylamine (1 mol L^{-1}) in THF) (10 mL) was added to a stirred solution of the bromide in THF (5 mL) at 0 °C. The mixture was stirred at 0 °C for 2 h, then concentrated in vacuo and poured into a mixture of 1 N NaOH (30 mL) and diethyl ether (40 mL). The separated organic extract was dried ($MgSO_4$) and evaporated to leave 3-methyl-((*E*)-3-tributylstannanylbut-2-enyl)amine **3** (0.63 g, 63%) as a pale yellow oil. ^1H NMR (360 MHz, $CDCl_3$) δ: 5.63 (1H, t, *J* = 7.0, C=CH), 3.23 (2H, d, *J* 6.8, CH_2N), 2.24 (6H, s, CH_3N), 1.97 (3H, s, CH_3-C=C), 1.52–1.46 (6H, m), 1.32–1.23 (6H, m), 1.00–0.96 (6H, m), 0.89 (9H, t, *J* = 7.3, CH_3CH_2).

bis-Acetonitrile palladium dichloride (2 mg) was added to a solution of the stannane **3** (28 mg, 0.0743 mmol) and the vinyl iodide **26** (29 mg, 0.037 mmol) in degassed DMF (1.5 mL), and the mixture was stirred at room temperature for 6 h and then concentrated in vacuo. The residue was purified by flash chromatography, eluting with ethyl acetate:pentane (1:8 → 1:4) to acetone:pentane (1:4 → 1:1) and triethylamine (1 drop per 10 mL) to give *TcBOC pateamine A* (9 mg, 36%) as a pale yellow oil. $[\alpha]_D^{24}$ –235.03 (*c* 0.1, $CHCl_3$). ^1H NMR (360 MHz, $CDCl_3$) δ: 7.03 (1H, d, *J* = 11.8, C=CH), 6.80 (1H, s, ThzH), 6.76 (1H, t, *J* = 11.6,HC=C), 6.37 (1H, d, *J* = 15.9, HC=C), 6.23 (1H, d, *J* = 15.9, HC=C), 6.27–6.17 (1H, m, CH-C=C), 5.65 (1H, t, *J* = 6.8, C=CH), 5.56 (1H, d, *J* = 8.8, C=CH), 5.51 (1H, d, *J* = 11.3, C=CHCO_2), 5.16–5.08 (1H, m, CHOCO), 4.84 (1H, d, *J* = 7.2, NH), 3.45–3.38 (1H, m, C*H*NH), 3.21 (2H, d, *J* 6.7, CH_2N), 3.08–2.98 (1H, m, CHThz), 3.06 (2H, app d, *J* = 7.0, CH_2Thz), 2.58–2.53 (1H, m), 2.38–2.05 (4H, m), 2.25 (6H, s, CH_3N), 1.97 (3H, s, CH_3-C=C), 1.96–1.81 (1H, m), 1.91 (6H, br s, TcBOC), 1.81 (6H, bs, CH_3C=C), 1.28–1.24 (6H, m, CH_3CH). ^{13}C NMR (125 MHz, $CDCl_3$) δ: 170.1, 165.0, 164.6, 161.0, 153.0, 145.9, 140.6, 138.2, 136.5, 134.5, 130.7, 130.2, 128.6, 124.1, 115.7, 112.6, 106.7, 87.9, 69.2, 67.6, 56.9, 47.9, 47.8, 44.8, 40.5, 39.1, 39.1, 33.7, 23.0, 21.7, 21.0, 16.7, 13.4, 12.8. MS *m*/*z* (ES): 760.2601 (M + H, $C_{26}H_{33}N_2O_7Cl_3S$ requires 760.2534).

Pateamine A (1)

A 10% Cd/Pd (40 mg) couple was added to a solution of the TcBOC pateamine **27** (8.5 mg, 0.011 mmol) in THF (1 mL) and aq. NH_4OAc (1 mol L^{-1}) (1 mL) at room temperature. The resulting slurry was stirred vigorously at room temperature for 3 h, then additional Cd/Pd (30 mg) was added and the mixture was stirred for a further 4 h. The mixture was filtered through cotton wool and the residue was washed with H_2O and diethyl ether. The filtrate was extracted with diethyl ether (2 × 2 mL), and the combined extracts were dried ($MgSO_4$) and then concentrated in vacuo. The residue was purified by chromatography on a Varian CBA cartridge eluting with 1% NH_4OH in MeOH to give *pateamine A* (4.5 mg, 73%) as an oil. $[\alpha]_D^{26}$ –302.8 (*c* 0.21 in MeOH). ^1H NMR (360 MHz, $CDCl_3$) δ: 7.00 (1H, d, *J* =

© 2004 NRC Canada

11.7, C=CH), 6.75 (1H, s, ThzH), 6.68 (1H, t, J = 11.5, HC=C), 6.38 (1H, d, J = 15.9, HC=C), 6.30–6.22 (1H, m, CH-C=C), 6.23 (1H, d, J = 15.8, HC=C), 5.65 (1H, t, J = 7.0, C=C*H*-CH_2), 5.53 (1H, d, J = 8.8, C=CH), 5.41 (1H, d, J = 11.4, C=$CHCO_2$), 5.18–5.09 (1H, m, CHOCO), 3.25–3.16 (2H, m), 3.14–3.05 (1H, m, CHThz), 3.10 (2H, d, J = 6.7), 2.55 (1H, app t, J = 10.6), 2.41 (1H, dd, J = 2.4 and 16.7), 2.36–2.26 (1H, m), 2.26 (6H, br s, CH_3N), 2.20–1.91 (3H, m), 2.02 (3H, s, CH_3-C=C), 1.84 (3H, s, CH_3-C=C), 1.82 (3H, s, CH_3-C=C), 1.80–1.65 (2H, br s), 1.39–1.26 (1H, m), 1.27 (3H, d, J = 7.8, CH_3CH), 1.25 (3H, d, J = 6.7, CH_3CH). ^{13}C NMR (125 MHz, $CDCl_3$) δ: 172.3, 165.5, 164.5, 161.2, 145.5, 140.6, 138.1, 135.9, 134.0, 130.7, 130.5, 128.5, 123.8, 115.1, 112.4, 69.2, 67.2, 57.2, 48.2, 45.4, 45.1, 42.9, 39.1, 33.3, 22.8, 21.1, 16.8, 13.4, 12.7. MS m/z (ES): 556.3246 (M + H, $C_{26}H_{33}N_2O_7Cl_3S$ requires 556.3209).

Acknowledgements

We thank the (EPSRC) (Fellowship to DJC) and the (EU) (Marie Curie Fellowship to MJR) for support of this research. We also thank Pfizer Ltd. and Zeneca Strategic Funding for financial support, and Dr. J.M. Clough (Zeneca Agrochemicals) for his interest in this program.

References

1. P.T. Northcote, J.W. Blunt, and M.H.G. Munro. Tetrahedron Lett. **32**, 6411 (1991).
2. R.M. Rzasa, D. Romo, D.J. Stirling, J.W. Blunt, and M.H.G. Munro. Tetrahedron Lett. **36**, 5307 (1995).
3. D. Romo, R.M. Rzasa, H.A. Shea, K. Park, J.M. Langenhan, L. Sun, A. Akhiezer, and J.O. Liu. J. Am. Chem. Soc. **120**, 12 237 (1998).
4. J.D. Critcher and G. Pattenden. Tetrahedron Lett. **37**, 9107 (1996).
5. E. Piers, R.W. Friesen, and B.A. Keay. J. Chem. Soc. Chem. Commun. 809 (1985); E. Piers, R.W. Friensen, and B.A. Keay. Tetrahedron, **47**, 4555 (1991); E. Piers, R.W. Friesen, and S.J. Rettig. Can. J. Chem. **70**, 1385 (1992).
6. E. Piers and R.W. Friesen. J. Org. Chem. **51**, 3405 (1986); E. Piers and R.W. Friesen. Can. J. Chem. **70**, 1204 (1992); E. Piers and Y.-F. Lu. J. Org. Chem. **31**, 926 (1988).
7. For a recent review of the Stille reaction see: M.A.J. Duncton and G. Pattenden. J. Chem. Soc. Perkin Trans. 1, 1235 (1999); For other illustrations of the scope for the intramolecular Stille reaction in target natural product synthesis from our laboratories see: G. Pattenden and D.J. Sinclair. J. Organomet. Chem. **653**, 261 (2002).
8. M.J. Remuiñán and G.Pattenden. Tetrahedron Lett. **41**, 7367 (2000).
9. (*a*) M.W. Brendenkamp, C.W. Holzapfel, and W.J. van Zyl. Synth. Commun. **22**, 3029 (1992); (*b*) E. Anguilar and A.I. Meyers. Tetrahedron Lett. **35**, 2473 (1994).
10. (*a*) G.A. Davis, Y. Zhang, Y. Andemichael, T. Fang, D.A. Fanelli, and H. Zhang. J. Org. Chem. **64**, 1403 (1999); (*b*) For a review of the chemistry of sulfinimines, see: F.A. Davis, P. Zhou, and B.C. Chen. Chem. Soc. Rev. **27**, 13 (1998).
11. C.L. Rand, D.E. Van Horn, M.W. Moore, and E. Negishi. J. Org. Chem. **46**, 4093 (1981); cf. ref. 2.
12. B. López, E. Quiñoá, and R. Riguera. J. Am. Chem. Soc. **121**, 9724 (1999).
13. Ethyl *Z*-3-(tributylstannyl)propenoate was prepared from ethyl propiolate, see: J.K. Stille and B.L. Broh. J. Am. Chem. Soc. **109**, 813 (1987); saponification of the ethyl ester with lithium hydroxide then gave *Z*-3-(tributylstannyl)propenoic acid.
14. J. Inanaga, K. Hirata, T. Katsuki, and M. Yamaguchi. Bull. Chem. Soc. Jpn. **52**, 1989. (1979).
15. V. Farina and B. Krishnan. J. Am. Chem. Soc. **113**, 9585 (1991).
16. For a comparison of the Heck reaction with the Stille reaction in elaborating the *Z*-2, *E*-4 – diene unit in the model compound **2** see: C. Câline and G. Pattenden. Synlett, 1661 (2000).
17. K. Takai, K. Nitta, and K. Utimoto. J. Am. Chem. Soc. **108**, 7408 (1986).
18. (*a*) D.E. Rudisill, L.A. Castonguay, and J.K. Stille. Tetrahedron Lett. **29**, 1509 (1988); (*b*) A.B. Smith, R.E. Maleczka, J.L. Leazer, J.W. Leahy, J.A. McCauley, and S.M. Condon. Tetrahedron Lett. **35**, 4911 (1994).
19. Q. Dong, C.E. Anderon, and M.A. Ciufolini. Tetrahedron Lett. **36**, 5681 (1995); this method was also used by Romo et al. in their synthesis of pateamine.
20. S.K. Chattopadhyay, J. Kempson, A. McNeil, M. Reader, D.E. Rippon, and D. Waite. J. Chem. Soc. Perkin Trans. 1, 2415 (2000).
21. S. Saito, T. Hasegawa, M. Inaba, R. Nishida, T. Fujii, S. Nomizu, and T. Moriwake. Chem. Lett. 1389 (1984); G. Guanti, L. Banti, and E. Narisano. Tetrahedron Lett. **40**, 5509 (1989).
22. R. Jacobsen, R.J. Taylor, H.J. Williams, and L.R. Smith. J. Org. Chem. **47**, 3140 (1982).
23. J.-F. Betzer, F. Delalogue, B. Muller, A. Pancrazi, and J. Prunet. J. Org. Chem. **62**, 7768 (1997); H. Miyake and K. Yamamura. Chem. Lett. 981 (1989).

© 2004 NRC Canada

Mono- and disubstitutions of (hepta-2,5-diyne-1,7-diol) bis(dicobalt) derivatives — Selectivity in Nicholas reactions[1]

Richard Guo, Romelo Gibe, and James R. Green

Abstract: Bis(hexacarbonyldicobalt) complexes of benzyl ether – methyl ether or benzyl ether – acetate derivatives of hepta-2,5-diyne-1,7-diols undergo selective Lewis-acid-mediated Nicholas reactions with enol silanes, silyl ketene acetals, and allylstannanes, preferentially replacing the methyl ether or acetate function. Hydride nucleophiles are similarly incorporated selectively using a benzyl ether – alcohol derivative. Subsequent Nicholas reaction at the benzyloxy-bearing site may be accomplished with an identical or a different nucleophile, affording skipped 1,4-diyne-$Co_4(CO)_{12}$ complexes. In instances of lower selectivity for monosubstitution reactions with benzyl ethers, reverting to the use of a menthyl ether – methyl ether complex gives much improved selectivity for methyl ether substitution.

Key words: cobalt alkyne complexes, Nicholas reaction, Lewis acids, 1,4-diynes.

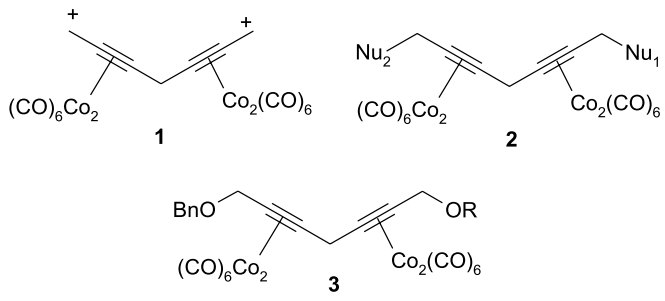
Résumé : Le bis(hexacarbonyldicobalt) forme des complexes avec des dérivés de l'hepta-2,5-diyne-1,7-diol portant un éther benzylique à une extrémité et un éther méthylique ou un acétate à l'autre extrémité qui donnent des réactions de Nicholas, catalysées par un acide de Lewis, avec des silanes énoliques, des acétals de cétènes silylés et des allylstannanes au cours desquelles il se produit un remplacement sélectif de l'éther méthylique ou de la fonction acétate. Les hydrures nucléophiles sont aussi incorporés d'une façon sélective en utilisant un dérivé portant à chaque extrémité un éther benzylique et un alcool. Une réaction de Nicholas subséquente au niveau du site portant le groupe benzyloxy-, réalisée avec un nucléophile identique ou différent, conduit des complexes 1,4-diyne-$Co_4(CO)_{12}$. Dans les cas où la sélectivité est plus faible lors des réactions de monosubstitution avec les éthers benzyliques, l'utilisation d'un complexe avec un dérivé portant un éther menthylique et un éther méthylique à chaque extrémité donne lieu à une sélectivité améliorée pour la substitution de l'éther méthylique.

Mots clés : complexes d'alcynes avec le cobalt, réaction de Nicholas, acides de Lewis, 1,4-diynes.

[Traduit par la Rédaction]

The chemistry of propargylhexacarbonyldicobalt cations, or the Nicholas reaction, has seen extensive use in organic synthesis (1). This interest stems from the predictable regiochemical and stereochemical aspects of the Nicholas reaction, and from the ability of cobalt alkyne complexes to protect the alkyne unit (2), to allow nonconventional alkyne geometries, to participate in synthetically useful cycloaddition reactions (3–5), and to alter the steric size of the formal alkyne function (6).

We have been interested in the use of tandem Nicholas reactions, both of derivatives of butyne-1,4-diol cobalt complexes, and of derivatives of bis(propargyl alcohol) complexes, for a number of synthetic purposes (7). The matter of selectivity where two sites for Nicholas reaction chemistry exist is an important issue, but this has been addressed only on rare occasion in butyne-1,4-diol-$Co_2(CO)_6$ derivatives (7*b*, 8), and not at all in the case of bis(propargyl alcohol)-$Co_4(CO)_{12}$ derivatives (9). Furthermore, substrates that would serve as synthons for skipped bis(propargyl) cations **1** selectively would give rise to 1,4-diyne complexes **2**, which are promising intermediates in the synthesis of compounds with skipped diene, diyne, or enyne functions, such as petrocortynes, petroformynes, and petrosiacetylenes (10), eicosanoids and oxoeicosanoids (11), including several of the leukotrienes (12). Consequently, we deemed the study of the selectivity in Nicholas reactions of **3** to be of importance; we have reported in preliminary form the substitution reactions of **3** and wish to more fully describe our efforts in this area (13).



Received 23 October 2003. Published on the NRC Research Press Web site at http://canjchem.nrc.ca on 24 February 2004.

Dedicated to Professor Ed Piers for his many contributions to terpene chemistry and the application of organometallic chemistry to organic synthesis.

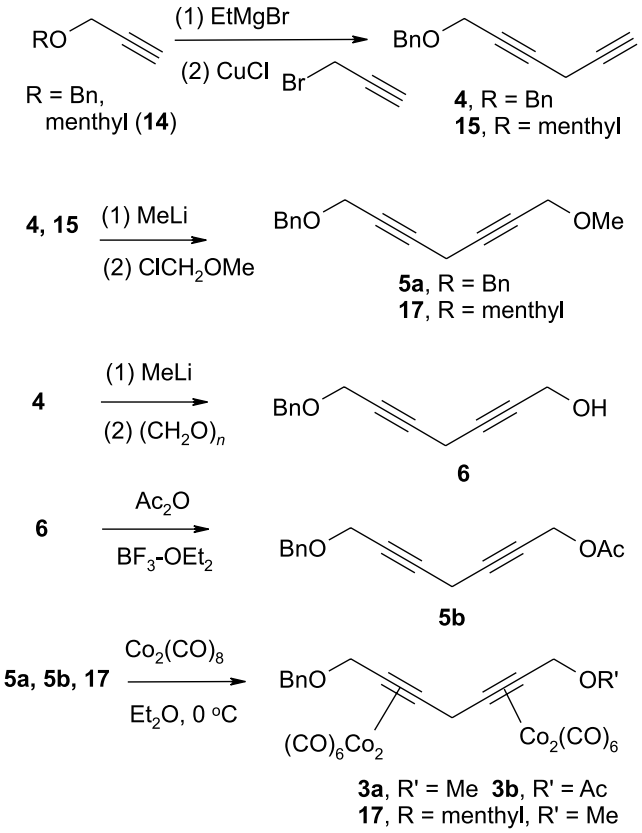
R. Guo, R. Gibe, and J.R. Green.[2] Department of Chemistry and Biochemistry, University of Windsor, Windsor, ON N9B 3P4, Canada.

[1]This article is part of a Special Issue dedicated to Professor Ed Piers.

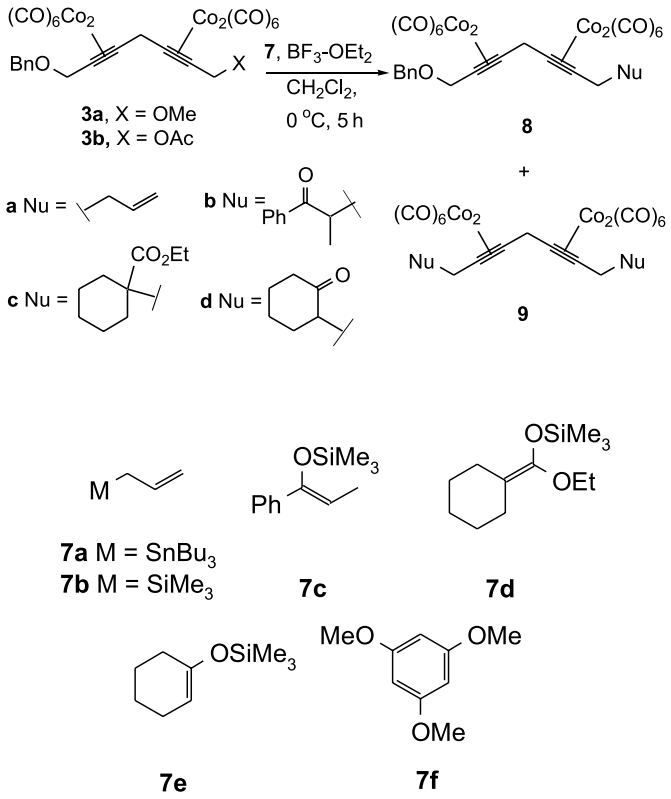
[2]Corresponding author (e-mail: jgreen@uwindsor.ca).

 doi: 10.1139/V03-209 © 2004 NRC Canada

Scheme 1.



Scheme 2.



The requisite heptyne-1,7-diol derivatives were prepared from benzyl propargyl ether (Scheme 1). Copper(I)-catalyzed coupling of the corresponding bromomagnesium acetylide with propargyl bromide afforded diyne **4** (78% yield), which was functionalized in two ways. Deprotonation of **4** with MeLi and exposure of the resultant acetylide to chloromethyl methyl ether gave benzyl methyl diether **5a** (59% yield). Alternatively, treatment of the same lithium acetylide with paraformaldehyde gave ether alcohol **6** (55% yield), and subsequent acetylation with acetic anhydride – BF_3-OEt_2 afforded the benzyl ether acetate **5b** (69% yield). The bis(hexacarbonyldicobalt) complexes of the diynediol derivatives were then prepared in a straightforward manner by subjecting **5a** and **5b** to excess $Co_2(CO)_8$, to give **3a** (77% yield) and **3b** (78% yield), respectively.

With two related substrates in hand, we investigated reactions of **3a** and **3b** with a series of representative nucleophiles, including the allylmetals allyltributylstannane (**7a**) and allyltrimethylsilane (**7b**), propiophenone trimethylsilyl enol ether (**7c**), ethyl cyclohexanecarboxylate trimethylsilyl ketene acetal (**7d**), and cyclohexanone trimethylsilyl enol ether (**7e**), all mediated by BF_3-OEt_2 (Scheme 2).

Allylation of **3a** or **3b** could be accomplished by either allyltributylstannane or allyltrimethylsilane; allyltributyltin, however, proved to be the significantly superior nucleophile for monosubstitution reactions. In the case of methyl ether **3a**, for example, reaction of 1.0 equiv. of BF_3-OEt_2 at 0 °C with 2.0 equiv. allyltrimethylsilane gave **8a** in a 39% yield (80% yield based on recovered starting material), and considerable recovered **3a**. Additional amounts of BF_3-OEt_2 caused greater conversion, but afforded significant amounts of diallylated **9a**. Conversely, allyltributyltin afforded a 63% yield of **8a** (82% based on recovered starting material (brsm) **3a**) in the presence of 2.0 equiv. of BF_3-OEt_2 (0 °C, 2 equiv. allyltributyltin) with more manageable amounts of unreacted **3a** (24%) and **9a** (7.5% yield). With acetate **3b**, reasonable results could be obtained with 1.5 equiv. BF_3-OEt_2 (0 °C, 1.5 equiv. allyltributyltin), giving **8a** (62% yield, 75% yield based on recovered starting **3b**), with 17% recovered **3b** (Table 1).

This necessity to optimize nucleophile – electrophile – Lewis acid stoichiometries in each case proved to be a general requirement with **3a** and **3b** and all nucleophiles, but allowed for satisfactory amounts of monosubstitution products in most cases, normally by stopping at the 80%–90% conversion range. The substitution of silyl enol ether **7c** with **3b** was found to be able to give **8b** in a 64% yield (70% brsm), while silyl ketene acetal **7d** with **3b** gave a 63% yield (70% brsm) of **8c**. Silyl enol ether **7e** proved somewhat less selective, and reactions were terminated at lower conversion levels (60%–70%) to minimize disubstitution. Under these circumstances, acetate **3b** afforded **8d** in 41% (70% brsm), while with methyl ether **3a**, **8d** could be obtained in 43% yield (76% brsm).

Intentional disubstitution reactions were attempted in two cases, using excess BF_3-OEt_2–nucleophile combinations (4 equiv. each). In the case of diallylation of **3a**, allyltributylstannane proved satisfactory, giving **9a** (73% yield) along with 12% of **8a**. Nevertheless, allyltrimethylsilane was superior in this regard, as complete consumption of **3a** occurred to give **9a** in 90% yield. Propiophenone trimethylsilyl enol ether **7c** also was amenable to giving disubstitution,

© 2004 NRC Canada

Table 1. BF_3-Et_2O mediated substitution of benzyl ether complexes.

Entry	Substrate	Nucleophile	Stoichiometry[a]	Product, yield (%)[b]	
1	**3b**	**7b**	1.0/1.5/1.5	**8a**, 62 (75)	
2	**3a**	**7b**	1.0/2.0/2.0	**8a,** 63 (82)	**9a**, 8
3	**3b**	**7c**	1.0/2.0/1.0	**8b**, 64 (70)	**9b**, 6
4	**3b**	**7d**	1.0/2.0/1.0	**8c,** 63 (70)	
5	**3b**	**7e**	1.0/1.2/1.5	**8d,** 41 (56)	
6	**3a**	**7e**	1.0/1.2/1.0	**8d**, 42 (76)	**9d**, 6
7	**3a**	**7a**	1.0/4.0/4.0		**9a**, 90
8	**3a**	**7b**	1.0/4.0/4.0	**8a**, 12	**9a**, 73
9	**3b**	**7c**	1.0/4.0/4.0		**9b**, 70
10	**8a**	**7f**	1.0/2.0/2.0		**10a**, 95
11	**8c**	**7a**	1.0/2.0/2.0		**10b**, 76
12	**11**	Ph_3SnH	1.0/1.5/1.0	**13**, 84	

[a]Ratio of diyne substrate/nucleophile/BF_3-OEt_2.
[b]Yields in parentheses are based on recovered starting material (brsm).

transforming **3b** to **9b** as a 1:1 diastereomeric mixture (70% yield).

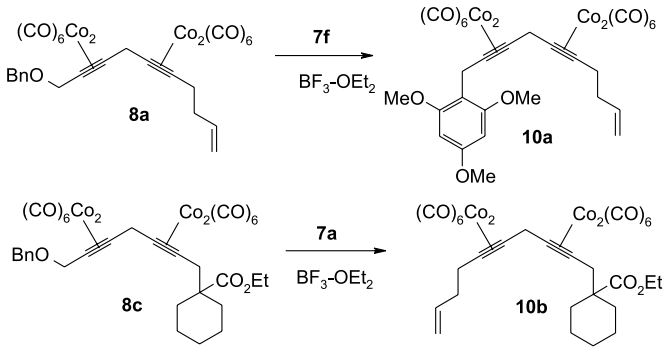
In addition to the persubstitution reactions described above, we wished to determine whether this framework possessed the ability to incorporate two different nucleophiles in disubstitution reactions. For this purpose, we chose allylation product **8a**, by virtue of the low reactivity of the isolated alkene function to many Lewis acid – nucleophile combinations. In the event, **8a** was subjected to reaction with BF_3-OEt_2 and 1,3,5-trimethoxybenzene (**7f**) (2 equiv. each, 0 °C). The benzyloxy function was replaced cleanly, and **10a** could be isolated in 95% yield. Ester-substituted **8c** also was successful in substitution by a second nucleophile, as allyltrimethylsilane and BF_3-OEt_2 (2.0 equiv. each, 0 °C) gave **10b** in 76% yield (Scheme 3).

As a final choice of nucleophile for Nicholas substitution reactions, we also chose to look at a stannane to induce an overall reduction. In this case, we selected substrate **11**, due to the *n*-pentyl group often being present as a (*Z*)-alkene substituent in leukotriene systems, and due to the fact that an alcohol function should be ionizable without destruction of the stannane nucleophile. This compound was prepared from **4**, by trapping of the lithium acetylide with pentanal, and reaction of unpurified alcohol **12** with $Co_2(CO)_8$ to form **11** (44% yield from **4**) (Scheme 4).

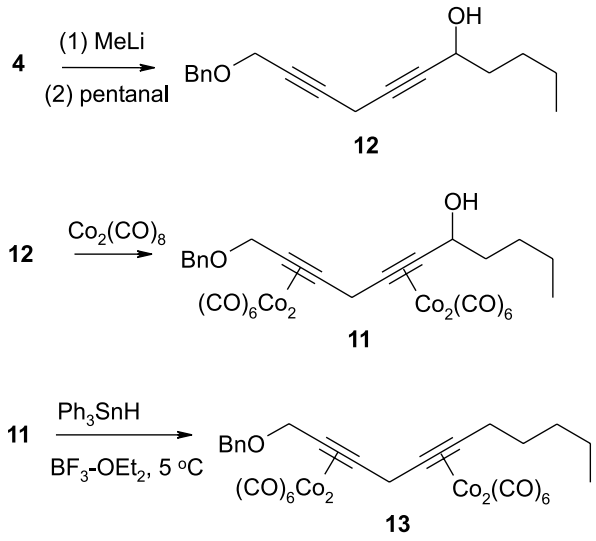
Reduction of **11** with BF_3-OEt_2 and a reactive stannane such as Bu_3SnH and Me_3SnH tended to be unselective, tending to give complete reduction of the alcohol and ether functions. Using the less reactive Ph_3SnH and BF_3-OEt_2 under carefully controlled conditions gave greater selectivity, however. At 5 °C, with 1.5 equiv. Ph_3SnH with 1.0 equiv. BF_3-OEt_2, total selectivity for reduction of the alcohol could be realized, and **13** (84% yield) was isolated as the sole product.

The results in Table 1 demonstrate that, in most cases, the benzyloxy function served as an acceptable potential leaving group which would be retained in monosubstitution reactions in deference to alcohol, methyl ether, or acetate functions. In the cases of allyltrimethylsilane (**7a**) and cyclohexanone silyl enol ether (**7e**) as the nucleophile, the reactions had to be terminated at relatively low levels of conversion and as a result the isolated yields of monosubstitution products **8a** and **8d** were limited. We deemed the selectivity in these cases insufficient, and chose to investigate alternatives that would give greater discrimination between oxygen functions, and hence, greater monosubstitution selectivity. We have observed selectivity in Nicholas reaction-based 4 + 3 cycloaddition chemistry by employing an isopropyl ether as the more slowly ionizing oxygen func-

Scheme 3.



Scheme 4.



© 2004 NRC Canada

tion (7*b*). Due to its straightforward preparation relative to isopropyl propargyl ether (14), we chose instead menthyloxy containing **14** (15) as a starting point. The bromomagnesium acetylide of this propargylic ether was coupled with propargyl bromide to afford diyne **15** (75% yield), which in turn was converted to the menthyl methyl diynyl diether bis(dicobalt) complex **16** by deprotonation and subsequent trapping with chloromethyl methyl ether, and exposure of unpurified intermediate **17** to $Co_2(CO)_8$ (72% yield overall from **15**) (Scheme 1).

With complex **16** in hand, we investigated its reactivity towards allyltrimethylsilane (**7a**) and cyclohexanone trimethylsilyl enol ether (**7e**). With allyltrimethylsilane, the use of near stoichiometric amounts of Lewis acid BF_3-OEt_2 resulted in the recovery of substantial amounts of starting **16**. For example, with even 2 equiv. of BF_3-OEt_2, allyltrimethylsilane (1.5 equiv., 12 h, –10 °C), 31% recovery of **16** was found in addition to **18a** (31%, 54% based on recovered **16**). The amount of conversion increased with further excess amounts of BF_3-OEt_2, and at 4 equiv., **16** was consumed completely and a 71% yield of **18a** was obtained (Scheme 5). Further increased amounts of Lewis acid gave a gradual degradation of product yield.

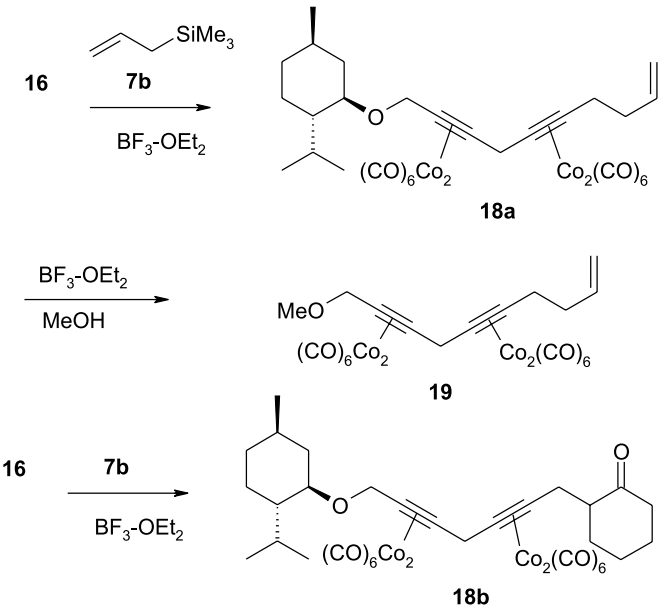
In the case of cyclohexanone trimethylsilyl enol ether (**7e**), an analogous trend was found with increasing amounts of BF_3-OEt_2, but modest amounts of starting material remained even at 4 equiv. (6% **16** recovery, 52% yield of **18b**, 60% yield brsm). In this case, switching the Lewis acid to Bu_2BOTf (1.2 equiv.), in addition to an excess (3 equiv.) of nucleophile gave an improved yield (71%) of **18b**, while greater excesses of this Lewis acid gave near-complete destruction of the product. In the case of **18b**, a new chiral centre was generated. An apparent doubling of the several of signals was apparent in both the ^1H and ^{13}C NMR spectra of **18b**, and integration of the signals showed that **18b** existed as a 1:1 diastereomeric mixture. This was most clearly apparent for ^1H NMR resonances for the diastereotopic propargyl methylene group α- to the ether oxygen, which resonated at 4.851 and 4.847 ppm, and 4.53 and 4.52 ppm for the two diastereomers. Due to the distance between the reacting centre and the nearest centre of chirality, this lack of asymmetric induction was not surprising.

We chose **18a** for study to determine whether the removal of the menthyloxy group was facile. Again, the substrate proved to be relatively sluggish in terms of reaction, but in the presence of 3 equiv. each of BF_3-OEt_2 and MeOH (0 °C, CH_2Cl_2), methoxy-substitution product **19** could be obtained in 65% yield (75% brsm).

A combination of these results with those of ref. 7*b* suggests the following approximate order in the kinetic ionization of oxygen-based functions in Nicholas reactions: OH > OMe, OAc > OBn > O-*i*-Pr, O-menthyl, OTBDMS. The dominant factor in this ordering is most likely steric accessibility to the oxygen atom, although it is likely that inductive effects in the benzyl ether plays some role in reducing its basicity. A lower basicity of the acetate function is also known (16, 17), but is offset by its innately better leaving group ability.

With respect to the nucleophiles concerned, no clear pattern of nucleophile reactivity vs. selectivity has emerged. For example, in the case of allylation, the more reactive allylstannane gives greater selectivity for monosubstitution; by contrast, a less reactive tin hydride (Ph_3SnH vs. Bu_3SnH or Me_3SnH) (18) is more productive in reductions. Nevertheless, by careful choice of conditions and nucleophile, synthetically useful amounts of selective monosubstitution products can be obtained in most cases using the benzyl substrates **3a** and **3b**. Disubstitution reactions of with either two identical or two different nucleophiles can also be accomplished in good to excellent yields. With the poorer cases for **3a** or **3b**, the menthyl ether complex **16** gives very good selectivity for monosubstitution; in fact, the menthoxy group is removed at all only sluggishly.

Scheme 5.



Experimental section

General methods

All solvents were used after distillation from the appropriate drying agent. Diethyl ether and THF were distilled from benzophenone ketyl immediately prior to use. Dichloromethane was distilled from CaH_2 immediately prior to use. Commercial BF_3-OEt_2 was distilled and stored under nitrogen. All reactions were performed under nitrogen unless otherwise noted. Flash chromatography was performed as described by Still et al. (19) using (230–240 mesh) silica gel 60.

NMR spectra were run at 500 MHz or 300 MHz for ^1H, and 125 MHz or 75 MHz for ^{13}C in $CDCl_3$; chemical shifts are given in ppm and coupling constants (*J*) are given in Hz. Mass spectra were run at the Chemistry and Biochemistry Mass Spectrometry Facility, University of Windsor, and the Mass Spectrometry Facility, Wayne State University.

6-Benzyloxy-1,4-hexadiyne (4)

To the freshly prepared EtMgBr (25 mmol) in dry THF (20 mL) was added 3-benzyloxy-1-propyne (3.000 g, 20.00 mmol) over 10 min. After several minutes, the THF began to reflux. When the exothermic reaction had subsided, the flask was warmed for 30 min at 55 °C. The solution was

© 2004 NRC Canada

then cooled to 30 °C and powdered CuCl (60 mg) was added. After 15 min, propargyl bromide (2.2 mL, 20 mmol) was added over 30 min. The mixture was warmed for 1 h to 60 °C. After cooling to room temperature, the reaction mixture was poured into a solution of NH_4Cl (3.0 g) and KCN (100 mg) in water (10 mL). After vigorous shaking, the reaction was subjected to a conventional workup. Flash chromatography (petroleum ether:diethyl ether, 10:1) followed by distillation afforded **4** (1.160 g, 78%); bp 116–120 °C/0.5 torr (1 torr = 133.322 Pa). IR (neat, NaCl) (cm^{-1}) ν_{max}: 3292, 3030, 2856, 1496. ^{1}H NMR δ: 7.35 (m, 5H), 4.62 (s, 2H), 4.20 (t, *J* = 3.4, 2H), 3.26 (m, 2H), 2.13 (t, *J* = 4.5, 1 H). ^{13}C NMR δ: 137.9, 128.8, 128.5, 128.3, 80.4, 78.2, 77.9, 72.0, 69.5, 57.9, 10.1. MS *m/e*: 184 (M^+). HR-MS *m/e* for $C_{13}H_{12}O$ calcd. (M^+): 184.0888; found: 184.0886.

7-Benzyloxy-2,5-heptadiyn-1-ol (6)

To **4** (1.000 g, 5.4 mmol) in dry Et_2O (10 mL) was added MeLi (1.5 mol L^{-1} in Et_2O, 3.6 mL, 5.4 mmol) at –78 °C over 20 min. Thereafter, the solution was warmed to –30 °C and paraformaldehyde (300 mg) was added. After 45 min, the mixture was heated under reflux for 3 h. After cooling to room temperature, the mixture was poured into ice water (10 mL), and a conventional workup performed. Flash chromatography (petroleum ether – diethyl ether, 1:1) followed by distillation afforded **6** (640 mg, 55%); bp 125–129 °C/0.5 torr (1 torr = 133.322 Pa). IR (neat, NaCl) (cm^{-1}) ν_{max}: 3402, 3030, 2914, 2282. ^{1}H NMR δ: 7.27–7.35 (m, 5H), 4.60 (s, 2H), 4.28 (s, 2H), 4.18 (t, *J* = 2.1, 2H), 3.29 (m, 2H), 1.62 (s, 1 H). ^{13}C NMR δ: 137.7, 128.8, 128.5, 128.3, 80.9, 79.8, 79.5, 77.1, 72.1, 57.9, 51.4, 10.4. MS *m/e*: 214 (M^+). HR-MS *m/e* for $C_{14}H_{14}O_2$ calcd. (M^+): 214.0994; found: 214.0990.

1-Acetoxy-7-benzyloxy-2,5-heptadiyne (5b)

To a mixture of compound **6** (1.200 g, 5.60 mmol) and Ac_2O (0.75 mL, 8.4 mmol) in THF (10 mL) was added an excess of BF_3-Et_2O at –78 °C over a period of 20 min. The reaction was warmed to 0 °C, and monitored by TLC. After 1.5 h, when the starting material had disappeared, the reaction mixture was poured into satd. $NaHCO_3$(aq). After a conventional workup, flash chromatography (petroleum ether:diethyl ether, 1:1) afforded product **5b** (985 mg, 69%); bp 108–110 °C/0.5 torr (1 torr = 133.322 Pa). IR (neat, NaCl) (cm^{-1}) ν_{max}: 3030, 2929, 2280, 1722, 1604, 1495. ^{1}H NMR δ: 7.27–7.40 (m, 5H), 4.68 (t, *J* = 2.1, 2H), 4.59 (s, 2H), 4.17 (t, *J* = 2.1, 2H), 3.29 (pentet, *J* = 2.1, 2H), 2.09 (s, 3H). ^{13}C NMR δ:170.0, 137.3, 128.3, 128.0, 127.8, 80.6, 79.8, 76.8, 74.6, 71.6, 57.4, 52.3, 20.6, 9.9. MS *m/e*: 256 (M^+). HR-MS *m/e* for $C_{16}H_{16}O_3$ calcd. (M^+): 256.1099; found: 256.1100.

Dodecacarbonyl[μ^4-(η,η,η,η)(1-acetoxy-7-benzyloxy-2,5-heptadiyne)]tetracobalt (2 Co-Co) (3b)

General procedure for complexation

To a solution of **5b** (1.000 g, 3.90 mmol) in anhyd. Et_2O (20 mL) at 0 °C was added an excess of dicobalt octacarbonyl. After 4 h, the reaction mixture was allowed to warm to room temperature. The resulting mixture was filtered through Celite® and the solvent was removed in vacuo. Flash chromatography (petroleum ether:diethyl ether, 15:1) afforded product **3b** (2.580 g, 78%). IR (neat, NaCl) (cm^{-1}) ν_{max}: 3031, 2922, 2860, 2087, 2034, 1742, 1626. ^{1}H NMR δ: 7.27–7.39 (m, 5H), 5.30 (s, 2H), 4.69 (s 2H), 4.66 (s, 2H), 4.61 (s, 2H), 2.09 (s, 3H). ^{13}C NMR δ: 199.4, 170.5, 137.7, 128.4, 127.7, 127.6, 92.8, 91.5, 91.1, 90.3, 73.1, 69.9, 64.3, 41.0, 20.3. MS (LSI-MS) *m/e*: 827 (M – 1)$^+$, 744 (M – 3CO)$^+$, 688 (M – 5CO)$^+$, 660 (M – 6CO)$^+$. Anal. calcd. for $C_{28}H_{16}Co_4O_{15}$ (%): C 40.61, H 1.95; found: C 40.49, H 1.88.

1-Benzyloxy-7-methoxy-2,5-heptadiyne (5a)

To a solution of compound **4** (480 mg, 2.60 mmol) in dry Et_2O (10 mL) was added MeLi (1.48 mol L^{-1} in Et_2O, 2.2 mL, 3.3 mmol) at –78 °C over 20 min. The mixture was stirred for 30 min at –78 °C. Chloromethyl methyl ether (0.20 mL, 2.60 mmol) was added dropwise over 20 min, and the temperature was then allowed to rise to room temperature. The reaction was kept at room temperature for 2 h. Thereafter, cold water was added and the mixture subjected to a conventional workup. Flash chromatography (petroleum ether:diethyl ether, 10:1) afforded product **5a** (330 mg, 59%); bp: 112–114 °C/0.5 torr (1 torr = 133.322 Pa). IR (neat, NaCl) (cm^{-1}) ν_{max}: 3031, 2929, 2280, 1604, 1495. ^{1}H NMR δ: 7.27–7.37 (m, 5H), 4.60 (s 2H), 4.18 (t, *J* = 2.0, 2H), 4.10 (t, *J* = 2.0, 2H), 3.38 (s, 3H), 3.30 (t, *J* = 2.0, 2H). ^{13}C NMR δ: 137.2, 128.1, 127.7, 127.5, 80.1, 80.0, 76.4, 76.3, 71.2, 59.6, 57.2, 57.1, 9.6. MS *m/e*: 228 (M^+). HR-MS *m/e* for $C_{15}H_{16}O$ calcd. (M^+): 228.1150; found: 228.1155.

Dodecacarbonyl[μ^4-(η,η,η,η)(1-benzyloxy-7-methoxy-2,5-heptadiyne)]tetracobalt (2 Co-Co) (3a)

Compound **5a** (300 mg, 1.32 mmol) was subjected to reaction with $Co_2(CO)_8$ via the general procedure. Flash chromatography (petroleum ether:diethyl ether, 20:1) afforded product **3a** (810 mg, 77%). IR (neat, NaCl) (cm^{-1}) ν_{max}: 3033, 2926, 2087, 2049, 2021. ^{1}H NMR δ: 7.27–7.39 (m, 5H), 4.73 (s, 2H), 4.69 (s, 2H), 4.65 (s, 2H), 4.57 (s, 2H), 3.44 (s, 3H). ^{13}C NMR δ: 199.6, 137.9, 128.4, 127.7, 127.5, 93.1, 92.7, 91.5, 91.2, 73.1, 72.6, 69.8, 58.8, 41.1. MS (EI) *m/e*: 744 (M – 2CO)$^+$, 716 (M – 3CO)$^+$. (LSI-MS) *m/e*: 799 (M – 1)$^+$, 716 (M – 3CO)$^+$, 632 (M – 6CO)$^+$.

Dodecacarbonyl[μ^4-(η,η,η,η)(1-benzyloxy-9-ene-2,5-decadiyne)]tetracobalt (2 Co-Co) (8a)

General procedure for substitution reactions

To a solution of compound **3b** (300 mg, 0.36 mmol) and nucleophile **7b** (179 mg, 0.54 mmol) in CH_2Cl_2 (15 mL) at 0 °C was added freshly distilled BF_3-Et_2O (77 mg, 0.54 mmol) dissolved in CH_2Cl_2 (5 mL) over 30 min. After 5 h, $NaHCO_3$(aq) was added. After a conventional workup, flash chromatography (petroleum ether:diethyl ether, 20:1) afforded product **8a** (183 mg, 62%); a subsequent fraction contained **3b** (50 mg, 16.7%). **8a**: IR (neat, NaCl) (cm^{-1}) ν_{max}: 3033, 2928, 2087, 2040, 1642. ^{1}H NMR δ: 7.27–7.39 (m, 5H), 5.89 (m, 1H), 5.14 (dd, *J* = 1.5, 15.6, 1H), 5.08 (dd, *J* = 1.5, 10.2, 1H), 4.72 (s, 2H), 4.68 (s, 2H), 4.64 (s, 2H), 2.95 (t, *J* = 8.0, 2H), 2.40 (m, 2H). ^{13}C NMR δ: 199.6, 137.8, 136.8, 128.4, 127.8, 127.5, 116.0, 93.8, 93.6, 93.5, 92.6, 73.1, 69.8, 41.2, 35.6, 32.8. MS (EI) *m/e*: 726 (M –

© 2004 NRC Canada

3CO)$^+$, 586 (M – 8CO)$^+$. MS (LSI-MS) *m/e*: 726 (M – 3CO)$^+$, 642 (M – 6CO)$^+$.

From **3a**: To a solution of complex **3a** (200 mg, 0.25 mmol) in CH_2C1_2 (15 mL) was condensed with nucleophile **7b** (166 mg, 0.50 mmol) in the presence of BF_3-Et_2O (71 mg, 0.50 mmol, 2 equiv.) according to the general procedure. After flash chromatography (petroleum ether:diethyl ether, 20:1), **8a** (127 mg, 63%) was obtained, followed by **3a** (47 mg, 23.5%).

From **3a** and **7a**: The reaction of the complex **3a** (200 mg, 0.25 mmol) with **7a** (79 µL, 57 mg, 0.50 mmol) in the presence of BF_3-Et_2O (36 mg, 0.25 mmol, 1 equiv.) according to the general procedure. After flash chromatography (petroleum ether:diethyl ether, 20:1), **8a** (79 mg, 39%) was obtained, followed by **3a** (102 mg, 51%).

Dodecacarbonyl[μ^4-(η,η,η,η)(1-benzyloxy-8-methyl-9-oxo-9-phenyl-2,5-nonadiyne)]tetracobalt (2 Co-Co) (8b)

Complex **3b** (300 mg, 0.36 mmol) was reacted with the nucleophile **7c** (150 mg, 0.72 mmol) in the presence of BF_3-Et_2O (51 mg, 0.36 mmol) via the general procedure. Flash chromatography (petroleum ether:diethyl ether, 10:1) afforded **8b** (208 mg, 64%). IR (neat, NaCl) (cm^{-1}) ν_{max}: 3033, 2934, 2085, 2063, 1990, 1683. ^{1}H NMR δ: 8.04 (d, *J* = 7.7, 2H), 7.27–7.59 (m, 8H), 4.76 (s, 2H), 4.75 (s, 2H), 4.58 (d, *J* = 4.8, 2H), 3.74 (m, 1H), 3.71 (1/2AB, *J* = 11.7, 1H), 2.93 (1/2AB, *J* = 11.7, 1H), 1.37 (d, *J* = 6.7, 3H). ^{13}C NMR δ: 201.7, 199.6, 137.9, 135.5, 133.3, 128.7, 128.3, 127.6, 127.5, 127.4, 97.3, 93.9, 93.0, 91.0, 73.0, 69.8, 43.1, 41.0, 36.1, 19.4. MS (EI) *m/e*: 818 (M – 3CO)$^+$, 762 (M –5CO)$^+$. (LSI-MS) *m/e*: 819 (M + 1 – 3CO)$^+$, 763 (M + 1 – 5CO)$^+$, 735 (M + 1 – 6CO)$^+$. A subsequent fraction contained **3b** (27 mg, 9%).

Dodecacarbonyl[μ^4-(η,η,η,η)(1-benzyloxy-7-(1-ethoxycarbonylcyclohexyl)-2,5-heptadiyne)]tetracobalt (2 Co-Co) (8c)

Compound **3b** was (300 mg, 0.36 mmol) reacted with nucleophile **7d** (150 mg, 0.72 mmol) in the presence of BF_3-Et_2O (51 mg, 0.36 mmol) according to the general procedure. Flash chromatography (petroleum ether:diethyl ether, 15:1) afforded product **8c** (210 mg, 63%). IR (neat, NaCl) (cm^{-1}) ν_{max}: 3033, 2935, 2094, 2086, 2022, 1730. ^{1}H NMR δ: 7.27–7.39 (m, 5H), 4.73 (s, 2H), 4.70 (s, 2H), 4.60 (s, 2H), 4.20 (q, *J* = 7.0, 2H), 3.23 (s, 2H), 1.25–2.17 (m, 13H). ^{13}C NMR δ: 199.7, 175.4, 137.8, 128.4, 127.7, 127.5, 95.2, 93.0, 92.9, 90.9, 73.0, 69.7, 60.6, 48.1, 41.0, 34.6, 25.5, 22.8, 14.0. MS (EI) *m/e*: 840 (M – 3CO)$^+$, 700 (M – 7CO)$^+$. (LSI-MS) *m/e*: 840 (M – 3CO)$^+$, 728 (M – 6CO)$^+$. A subsequent fraction contained **3b** (28 mg, 9%).

Dodecacarbonyl[μ^4-(η,η,η,η)(1-benzyloxy-7-(2-oxocyclohexyl)-2,5-heptadiyne)]tetracobalt (2 Co-Co) (8d)

Complex **3b** (200 mg, 0.24 mmol) was condensed with the nucleophile **7e** (86 mg, 0.29 mmol) in the presence of BF_3-Et_2O (51 mg, 0.36 mmol) via the general procedure. Flash chromatography (petroleum ether:diethyl ether, 10:1) afforded **8d** (85 mg, 41%). IR (neat, NaCl) (cm^{-1}) ν_{max}: 3033, 2933, 2085, 2022, 1716. ^{1}H NMR δ: 7.27–7.39 (m, 5H), 4.75 (s, 2H), 4.72 (s, 2H), 4.64 (s, 2H), 3.58 (m, 1 H), 1.49–2.60 (m, 10H). ^{13}C NMR δ: 210.9, 199.6, 137.9, 128.3, 127.6, 127.5, 98.1, 93.6, 92.9, 91.1, 73.0, 69.8, 53.4, 42.0, 41.2, 35.4, 32.8, 28.2, 25.3. MS (EI) *m/e*: 782 (M – 3CO)$^+$, 642 (M – 8CO)$^+$. (LSI-MS) *m/e*: 782 (M – 3CO)$^+$, 698 (M – 6CO)$^+$. A subsequent fraction contained **3b** (54 mg, 27%).

From **3a**: The complex **3a** (300 mg, 0.37 mmol) also reacted with the nucleophile **7e** (78 mg, 0.44 mmol) in the presence of BF_3-Et_2O (54 mg, 0.38 mmol) via the general procedure. Flash chromatography afforded **8d** (141 mg, 43%), followed by **3a** (130 mg, 43%).

Dodecacarbonyl[μ^4-(η,η,η,η)(trideca-1,12-diene-5,8-diyne)]tetracobalt (2 Co-Co) (9a)

Complex **3a** (200 mg, 0.25 mmol) was condensed with nucleophile **7b** (331 mg, 1.00 mmol) in the presence of BF_3-Et_2O (142 mg, 1.00 mmol) via the general procedure. Flash chromatography (petroleum ether:diethyl ether, 10:1) afforded **9a** (127 mg, 73%). IR (neat, NaCl) (cm^{-1}) ν_{max}: 3085, 2941, 2093, 2022, 1643. ^{1}H NMR δ: 5.94 (m, 2H), 5.17 (dd, *J* = 1.4 Hz, 17.2, 2H), 5.10 (dd, *J* = 1.4, 10.0, 2H), 4.65 (s, 4H), 2.99 (t, *J* = 7.9, 4H), 2.40 (m, 2H). ^{13}C NMR δ: 199.9, 136.8, 116.0, 98.5, 92.6, 41.4, 35.6, 32.8. MS (EI): 716 (M – 1CO)$^+$, 688 (M – 2CO)$^+$. (LSI-MS) *m/e*: 716 (M – 1CO)$^+$, 604 (M – 5CO)$^+$. A subsequent fraction contained **8b** (27.0 mg, 12%)

Under directly analogous conditions, the reaction of complex **3a** (200 mg, 0.25 mmol) with **7a** (0.16 mL, 1.0 mmol) and BF_3-OEt_2 (142 mg, 1.00 mmol) afforded product **9a** (170 mg, 90%).

Dodecacarbonyl[μ^4-(η,η,η,η)(2,10-dimethyl-1,11-diphenylundeca-4,7-diyne-1,11-dione)]tetracobalt (2 Co-Co) (9b)

Complex **3b** (75.1mg, 0.0907 mmol) was condensed with **7c** (74.9mg, 0.363 mmol) in the presence of BF_3-OEt_2 (46 µL, 0.36 mmol) via the general procedure. Flash chromatography (petroleum ether:diethyl ether, 10:1) gave **9b** (59.0 mg, 70%) as a 1:1 diastereomeric mixture. IR (neat, NaCl) (cm^{-1}) ν_{max}: 2093, 2084, 2051, 2017, 1683. ^{1}H NMR δ: 8.03 (d, *J* = 8.0, 4H), 7.57 (t, *J* = 7.6, 2H), 7.48 (apparent t, *J* = 7.7, 4H), 4.56 + 4.46 (AB, *J* = 18.1) and 4.52 (s) (2H), 3.73–3.81 (m, 4H), 2.91–3.03 (m, 2H), 1.41 (d, *J* = 6.5) and 1.39 (d, *J* = 6.5) (6H). ^{13}C NMR δ: 201.7, 199.9 and 199.5, 135.5, 133.29 and 133.28, 128.8, 128.4, 97.4 and 97.3, 93.9 and 93.8, 43.1, 41.0 and 40.9 36.0, 19.6 and 19.4. MS (EI) *m/e*: 844 (M – 3CO)$^+$, 648 (M – 10CO)$^+$. (LSI-MS) *m/e*: 929 (M + 1)$^+$, 844 (M – 3CO)$^+$.

Dodecacarbonyl[μ^4-(η,η,η,η)(1-(2,4,6-trimethoxyphenyl)dec-9-ene-2,5-diyne)]tetracobalt (2 Co-Co) (10a)

Compound **8a** (240 mg, 0.30 mmol) was condensed with 1,3,5-trimethoxybenzene (**7f**) (101 mg, 0.60 mmol) in the presence of BF_3-Et_2O (85 mg, 0.60 mmol) via the general procedure. Flash chromatography (petroleum ether:diethyl ether, 20:1) afforded **10a** (245 mg, 95%). IR (neat, NaCl) (cm^{-1}) ν_{max}: 3007, 2942, 2082, 2045, 2022, 1615. ^{1}H NMR δ: 6.14 (s, 2H), 5.95 (m, 1H), 5.18 (dd, *J* = 1.5, 17.0, 1H), 5.08 (dd, *J* = 1.5, 10.0, 1H), 4.59 (s, 2H), 4.17 (s, 2H), 3.81 (s, 3H), 3.77 (s, 6H), 3.06 (t, *J* = 8.1, 2H), 2.45 (m, 2H). ^{13}C NMR δ: 199.9, 160.5, 158.7, 136.9, 115.8, 108.2, 100.2, 98.4, 93.5, 92.8, 89.9, 55.3, 54.7, 41.2, 35.6, 32.8, 26.0. MS

© 2004 NRC Canada

(EI): 842 (M – 1CO)$^+$, 786 (M – 3CO)$^+$. (LSI-MS) *m/e* 767 (M – 3CO)$^+$, 730 (M – 5CO)$^+$.

Dodecacarbonyl[μ^4-(η,η,η,η)(1-(1-carboethoxycyclohexyl)dec-9-ene-2,5-diyne)]tetracobalt (2 Co-Co) (10b)

Compound **8c** (109.8 mg, 0.119 mmol) was reacted with allyltrimethylsilane (38 μL, 0.24 mmol) and BF_3-OEt_2 (30 μL, 0.24 mmol) via the standard procedure. Flash chromatography (petroleum ether:diethyl ether, 25:1) afforded **10b** (77.6 mg, 76%), as a red-brown oil. IR (neat, KBr) (cm^{-1}) ν_{max}: 2094, 2084, 2048, 2014, 1728. ^{1}H NMR δ: 5.95 (m, 1H), 5.17 (d, *J* = 17.1, 1H), 5.10 (d, *J* = 10.3, 1H), 4.60 (s, 2H), 4.21 (q, *J* = 7.1, 2H), 3.27 (s, 2H), 2.95–3.05 (m, 2H), 2.38–2.50 (m, 2H), 2.12–2.30 (m, 2H), 1.20–1.75 (m, 8H), 1.28 (t, *J* = 7.1, 3H). ^{13}C NMR δ: 199.9, 199.8, 175.4, 136.8, 115.8, 98.5, 95.2, 92.8, 92.6, 60.6, 48.1, 43.8, 41.2, 35.6, 34.6, 32.5, 29.7, 25.6, 22.8, 14.0. MS (EI): 774 (M – 3CO)$^+$, 718 (M – 5CO)$^+$. (LSI-MS) *m/e*: 774 (M – 3CO)$^+$, 718 (M – 5CO)$^+$, 690 (M – 6CO)$^+$.

Synthesis of dodecacarbonyl[μ^4-(η,η,η,η)(1-benzyloxy-7-hydroxy-2,5-undecadiyne)]tetracobalt (2 Co-Co) (11)

To a solution of freshly prepared 6-benzyloxy-1,4-hexadiyne (**4**) (56.4 mg, 3.06 mmol) in THF at –78 °C was added methyllithium (3.06 mL, 1.5 mol L^{-1}, 4.59 mmol). The mixture was stirred for 20 min and freshly distilled pentanal (651 μL, 6.12 mmol) was added dropwise. After stirring for 3 h, the reaction mixture diluted with cold water at 0 °C. Following a conventional workup, the crude product was diluted with diethyl ether and placed in an ice bath. An excess amount of cobalt carbonyl was added and the mixture stirred for 3.5 h. Following removal of the volatiles under reduced pressure, flash chromatography (petroleum ether:diethyl ether, 20:1) gave (**11**) (90.2 mg, 44%) as a red-brown oil. IR (neat) (cm^{-1}) ν_{max}: 3386, 2919, 2012. ^{1}H NMR δ: 7.32 (m, 5H), 4.68 (m, 7H), 2.79 (d, *J* = 5.2, 1H), 1.64 (m, 3H), 1.36 (m, 3H), 0.92 (t, *J* = 7.1, 3H). ^{13}C NMR δ: 199.6, 199.3, 137.0, 128.5, 128.1, 128.0, 102.4, 92.0, 91.3, 91.0, 73.4, 71.5, 70.1, 41.2, 39.2, 28.5, 22.4, 13.9. MS (EI) *m/e*: 758 (M – 3CO)$^+$, 618 (M – 8CO)$^+$. (LSI-MS) *m/e*: 757 (M – 1 – 3CO)$^+$, 617 (M – 1 – 8CO)$^+$.

Dodecacarbonyl[μ^4-(η,η,η,η)(1-benzyloxy-2,5-undecadiyne)]tetracobalt (2 Co-Co) (13)

To a solution of (**11**) (353 mg, 0.41 mmol) and Ph_3SnH (220 mg, 0.62 mmol) in CH_2Cl_2 (10 mL) at 5 °C was added BF_3-Et_2O (53 μL, 0.41 mmol). After stirring for 20 h with regular monitoring by TLC, the reaction mixture was diluted with water and subjected to conventional workup. Flash chromatography (petroleum ether:diethyl ether, 100:1) afforded (**13**) as a red-brown oil (290 mg, 84%). IR (neat) (cm^{-1}) ν_{max}: 2933, 2099. ^{1}H NMR δ: 7.35 (m, 5H), 4.74 (s, 2H), 4.70 (s, 2H), 4.65 (s, 2H), 2.84 (t, *J* = 8.0, 2H), 1.66 (m, 2H), 1.41 (m, 4H), 0.95 (t, *J* = 7.0, 3H). ^{13}C NMR δ: 200.0, 199.5, 137.8, 128.3, 127.7, 127.4, 99.7, 93.0, 92.5, 91.1, 73.0, 69.7, 41.2, 33.3, 31.6, 31.5, 22.3, 13.8. MS (EI) *m/e*: 742 (M – 3CO)$^+$, 658 (M – 6CO)$^+$. MS (ES–) *m/e*: 768.5 (M – 2CO-H)$^-$, 740.5 (M – 3CO-H)$^-$.

(1′*R*, 2′*S*, 5′*R*)- 1-Menthoxy-2,5-heptadiyne (15)

To a freshly prepared solution of EtMgBr (15.0 mmol) in dry THF (20 mL) was added 3-menthyloxy-1-propyne (**14**) (1.464 g, 7.53 mmol) in a cannula under a stream of nitrogen. The solution was heated for 30 min at 60 °C and cooled to room temperature. CuCl was added (74 mg, 0.75 mmol), followed by propargyl bromide (1.67 mL, 18.0 mmol). The solution was heated to reflux for 1 h. A conventional workup and subsequent flash chromatography (100% hexane) afforded (**15**) (1.313 g, 75%) as a colorless oil. $[\alpha]_D^{25}$ –66.9 (*c* 1.17 acetone). IR (neat) (cm^{-1}) ν_{max}: 3312, 2954, 2869. ^{1}H NMR δ: 4.16 (t of 1/2AB, *J* = 2.0, 15.5, 1H), 4.11 (t of 1/2AB, *J* = 1.9, 15.5, 1H), 3.16 (m, 3H), 2.18 (m, 1H), 2.03 (m, 1H), 1.57 (m, 2H), 1.57 (m, 1H), 1.34 (m,1H), 0.70–1.00 (m, 4H), 0.87 (d, *J* = 6.6, 3H), 0.84 (d, *J* = 7.1, 3H), 0.74 (d, *J* = 6.9, 3H). ^{13}C NMR δ: 78.5, 77.78, 77.74, 77.72, 68.8, 55.4, 48.0, 39.7, 34.3, 31.3, 25.2, 23.1, 22.2, 20.9, 16.0, 9.5. MS (EI) *m/e*: 232 (M)$^+$. HR-MS calcd. for $C_{16}H_{24}O$: 232.1827; found: 232.1826.

(1′*R*, 2′*S*, 5′*R*)- Dodecacarbonyl[μ^4-(η,η,η,η)(1-menthoxy-7-methoxy-2,5-heptadiyne)]tetracobalt (2 Co-Co) (16)

To a solution of **15** (1.75 g, 7.50 mmol) in diethyl ether (20 mL) at –78 °C was added MeLi (8.0 mL, 1.40 mol L^{-1}, 11.2 mmol). The solution was then stirred for 20 min, and chloromethyl methyl ether (1.13 mL, 15.0 mmol) was added. The reaction mixture was allowed to warm up to room temperature and stirred overnight. Following a conventional workup, the resulting crude product was dissolved in anhyd. Et_2O (20 mL) and cooled to 0 °C. An excess of cobalt carbonyl was added and the solution stirred for 3.5 h. The resulting crude product was filtered though Celite®, and the resulting filtrate was concentrated under reduced pressure. Flash chromatography (petroleum ether:diethyl ether, 50:1) gave **16** (3.946 g, 72%) as a red-brown oil. $[\alpha]_D^{22}$ +72 (*c* 0.036 acetone). IR (neat) (cm^{-1}) ν_{max}: 2923, 2052. ^{1}H NMR δ: 4.8 (d, *J* = 12.5, 1H), 4.6 (m, 4H), 4.51 (d, *J* = 12.5, 1H), 3.52 (s, 3H), 3.26 (apparent dt, *J* = 4.1, 10.5, 1H), 2.31 (m, 1H), 2.14 (d, *J* = 12.0, 1H), 1.67 (m, 2H), 1.41 (m, 1H), 1.31 (m, 1H), 0.88–1.10 (m, 3H), 0.96 (d, *J* = 6.0, 3H), 0.90 (d, *J* = 7.0, 3H), 0.80 (d, *J* = 6.9, 3H). ^{13}C NMR δ: 199.7, 94.7, 92.7, 91.6, 90.7, 79.3, 72.6, 67.8, 58.8, 48.2, 41.0, 40.3, 34.5, 31.6, 25.3, 23.1, 22.3, 20.8, 15.9. MS (EI) *m/e*: 820 (M – CO)$^+$, 596 (M – 9CO)$^+$. MS (ES+) *m/e*: 691 (M + K – 7CO)$^+$.

(1′*R*, 2′*S*, 5′*R*)- Dodecacarbonyl[μ^4-(η,η,η,η)(1-menthoxydec-9-ene-2,5-diyne)]tetracobalt (2 Co-Co) (18a)

To a solution of **16** (207 mg, 0.244 mmol) in CH_2Cl_2 (5 mL) at 0 °C was added BF_3·Et_2O (144 μL, 1.14 mmol). The solution stirred for 10 min; thereafter, allyltrimethysilane (67 μL, 0.42 mmol) was added and the reaction was continued until none of the starting **16** was detected in TLC analysis (12 h). A conventional workup and subsequent flash chromatography (100% petroleum ether) afforded **18a** (148 mg, 71%) as a red-brown oil. $[\alpha]_D^{22}$ +52 (*c* 0.079 acetone). IR (neat) (cm^{-1}) ν_{max}: 2924, 2085, 2049. ^{1}H NMR δ: 5.94 (m, 1H), 5.17 (d, *J* = 17.0, 1H), 5.10 (d, *J* = 12.1, 1H), 4.82 (d, *J* = 12.4, 1H), 4.65 (s, 2H), 4.50 (d, *J* = 12.4, 1H), 3.24 (apparent dt, *J* = 4.0, 10.5, 1H), 2.99 (m, 2H), 2.42 (m, 2H), 2.29 (m, 1H), 2.11 (br d, *J* = 12.1 1H), 1.63 (m, 2H), 1.30 (m, 1H), 1.28 (m, 1H), 0.85–1.17 (m, 3H), 0.95 (d, *J* = 6.4, 3H), 0.89 (d, *J* = 7.0, 3H), 0.78 (d, *J* = 7.0, 3H). ^{13}C

© 2004 NRC Canada

NMR δ: 199.7, 136.8, 115.9, 98.5, 94.6, 92.9, 90.5, 79.3, 67.8, 48.2, 41.2, 40.2, 35.5, 34.5, 32.8, 31.6, 25.4, 23.1, 22.3, 20.8, 15.9. MS (EI) *m/e*: 802 $(M - 2CO)^+$, 774 $(M - 3CO)^+$. MS (ES+) *m/e*: 795 $(M - 3CO + Na - H_2)^+$, 688 $(M - 6CO + Na - H_2)^+$.

(1′*R*, 2′*S*, 5′*R*)- Dodecacarbonyl[μ⁴-(η,η,η,η)(1-menthoxy-7-(2-oxocyclohexyl)-2,5-heptadiyne)]tetracobalt (2 Co-Co) (18b)

To a solution of **16** (90 mg, 0.12 mmol) and the trimethylsilyl enol ether of cyclohexenone **7e** (62 mg, 0.36 mmol) in CH_2Cl_2 (5 mL) at 0 °C was added Bu_2BOTf (73 μL, 1 mol L^{-1}). The solution was stirred for 3 h, and further Bu_2BOTf (74 μL, 1 mol L^{-1}) was added; stirring was continued until none of the starting **16** was detected in TLC analysis (12 h) (total amount of Bu_2BOTf used: 147 μL, 0.14 mmol). A conventional workup and subsequent flash chromatography (100% petroleum ether) afforded **18b** (70 mg, 71%, de = 0) as a red brown oil. IR (neat) (cm^{-1}) ν_{max}: 2929, 2869, 2085, 2053. ^1H NMR δ: 4.851 (d, *J* = 12.5) and 4.847 (d, *J* = 12.5) (1H), 4.61 (m, 2H), 4.53 (d, *J* = 12.5) and 4.52 (d, *J* = 12.5) (1H), 3.59 (dd, *J* = 6.5, 15.5, 1H), 3.24 (apparent dt, *J* = 4.1, 10.5, 1H), 2.59 (m, 2H), 2.45 (m, 1H), 2.38 (m, 1H), 2.27 (m, 2H), 2.12 (m, 2H), 1.92 (m, 1H), 1.65 (m, 6H), (m, 1H), 0.85–1.15 (m, 3H), 0.95 (d, *J* = 6.6, 3H), 0.88 (d, *J* = 6.9, 3H), 0.77 (d, *J* = 7.2, 3H). ^{13}C NMR δ: 211.0, 199.8, 98.0, 94.7, 94.6, 93.8, 90.4, 79.3, 79.2, 67.7,53.4, 48.2,42.1, 40.2, 35.6, 35.5, 34.5, 32.7, 31.6, 28.2, 25.4, 23.1, 22.3, 20.9, 15.9. MS (EI+) *m/e*: 830 $(M - 3CO)^+$, 718 $(M - 7\ CO)^+$. MS (ES+) *m/e*: 937 $(M + Na)^+$, 909 $(M + Na - CO)^+$.

Dodecacarbonyl[μ⁴-(η,η,η,η)(1-methoxydec-9-ene-2,5-diyne)]tetracobalt (2 Co-Co) (19)

To a solution of **18a** (122 mg, 0.16 mmol) in CH_2Cl_2 (5 mL) at 0 °C was added BF_3-Et_2O (83 μL, 0.65 mmol). The solution was stirred for 10 min, and MeOH (20 μL, 0.49 mmol) was added. After stirring for 12 h, the crude reaction mixture was subjected to conventional workup. Flash chromatography (100% petroleum ether) afforded **19** (66 mg, 65%, 74% yield based on recovered **18a**) as a red brown oil. IR (neat) (cm^{-1}) ν_{max}: 2922, 2085, 2049. ^1H NMR δ: 5.90 (m, 1H), 5.16 (d, *J* = 17.1, 1H), 5.10 (d, *J* = 10.7, 1H), 4.6 (d, *J* = 11.7, 4H), 3.5 (s, 3H), 2.9 (m, 2H), 2.42 (m, 2H). ^{13}C NMR δ: 199.8, 199.6, 136.8, 115.9, 98.6, 92.7, 92.6, 91.3, 72.6, 58.9, 41.2, 35.5, 32.7. MS (EI) *m/e*: 678 $(M - 2CO)^+$, 650 $(M - 3CO)^+$; (ES–) 733 $(M - H)^-$, 705 $(M - H - CO)^-$, 677 $(M - H - 2CO)^-$, 649 $(M - H - 3CO)^-$. HR-MS (ES–) *m/e* calcd. for $C_{23}H_{14}Co_4O_{13}$: $(M^+ - H - 2CO)$ 676.7786; found: 676.7767. A subsequent fraction contained the starting **18a** (14.8 mg, 12%).

Material on deposit

The ^1H NMR spectra of **4** and **5a** and the ^{13}C NMR spectra of **3a**–**3b**, **5a**–**5b**, **6**, **8a**–**8d**, **9a**–**9b**, **10a**–**10b**, **11**, **12**, **15**, **16**, **18a**–**18b**, and **19** have been deposited as supplementary material.[3]

Acknowledgements

We are grateful for the research support of the Natural Sciences and Engineering Research Council of Canada (NSERC) and the University of Windsor. We wish to thank Lew Hryhorczuk of the Wayne State University Mass Spectrometry Laboratory for the electrospray mass spectral work.

References

1. (*a*) J.R. Green. Curr. Org. Chem. **5**, 809 (2001); (*b*) T.J.J. Müller. Eur. J. Org. Chem. 2021 (2001); (*c*) B.J. Teobald. Tetrahedron, **58**, 4133 (2002).
2. D.G. Hamilton and J.K.M. Sanders. Chem. Commun. 1749 (1998), and refs. therein.
3. For recent reviews on hexacarbonyldicobalt alkyne complexes, see: (*a*) M.E. Welker. Curr. Org. Chem. **5**, 785 (2001); (*b*) M.J. Went. Adv. Organomet. Chem. **41**, 69 (1997).
4. (*a*) T. Sugihara, M. Yamaguchi, and M. Nishizawa. Chem. Eur. J. **7**, 1589 (2001); (*b*) K.M. Brummond and J.I. Kent. Tetrahedron, **56**, 3263 (2000); (*c*) Y.K. Chung. Coord. Chem. Rev. **188**, 297 (1999); (*c*) A.J. Fletcher and S.D.R. Christie. J. Chem. Soc. Perkin Trans. 1, 1657 (2000); (*d*) O. Geis and H.-G. Schmalz. Angew. Chem. Int. Ed. Engl. **37**, 911 (1998).
5. (*a*) T. Sugihara, A. Wakabayashi, H. Takao, H. Imagawa, and M. Nishizawa. Chem. Commun. 2456 (2001); (*b*) S.U. Son, Y.K. Chung, and S.-G. Lee. J. Org. Chem. **65**, 6142 (2000).
6. For example, see: (*a*) N.M. Deschamps, J.H. Kaldis, P.E. Lock, J.F. Britten, and M.J. McGlinchey. J. Org. Chem. **66**, 8585 (2001); (*b*) E.J. Corey and C.J. Helal. Tetrahedron Lett. **36,** 9153 (1995); (*c*) J. Bach, R. Berenguer, J. Garcia, T. Loscertales, and J. Vilarrasa. J. Org. Chem. **61**, 9021 (1996).
7. (*a*) J.R. Green. Chem. Commun. 1751 (1998). (*b*) M.M. Patel and J.R. Green. Chem. Commun. 509 (1999); (*c*) R. Guo and J.R. Green. Chem. Commun. 2503 (1999); (*d*) Y. Lu and J.R. Green. Synlett, 243 (2001); (*e*) R. Gibe and J.R. Green. Chem. Commun. 1550 (2002).
8. (*a*) J.M. Palazón and A.S. Martin. Tetrahedron Lett. **36**, 3549 (1995); (*b*) M. Takase, T. Morikawa, H. Abe, and M. Inouye. Org. Lett. **5**, 625 (2003); (*c*) For selective ionization of an acetal function, see: T.F. Jamison, S. Samayati, W.E. Crowe, and S.L. Schreiber. J. Am. Chem. Soc. **119**, 4353 (1997).
9. Nonselective disubstitution reactions of these complexes are known. For C-C forming reactions, see ref. 7*c* and: (*a*) G.G. Melikyan, M.A. Khan, and K.M. Nicholas. Organometallics, **14**, 2170 (1995); for C-X forming reactions, see: (*b*) L.J. Hope-Weeks, M.J. Mays, and A.D. Woods. J. Chem. Soc. Dalton Trans. 1812 (2002); (*c*) H. Amouri, C. Da Silva, B. Malézieux, R. Andrés, J. Vaissermann, and M. Gruselle. Inorg. Chem. **39**, 5053 (2000); (*d*) D. Díaz, T. Martín, and V.S. Martín. Org. Lett. **3**, 3289 (2001).
10. (*a*) J.S. Kim, Y.J. Lim, K.S. Im, C.J. Jung, C.O. Lee, J. Hong, and H. Lee. J. Nat. Prod. **62**, 554 (1999), and refs. therein; (*b*) Y. Seo, K.W. Cho, J.-R. Rho, J. Shin, and C.J. Sim. Tetrahedron, **54**, 447 (1998), and refs. therein; (*c*) J.S. Kim, K.S. Im, J.H. Jung, Y.-L. Kim, J. Kim, C.J. Shim, and C.-O. Lee. Tetrahedron, **54**, 3151 (1998), and refs. therein.
11. (*a*) G. Saha, M.K. Basu, S. Kim, Y.-J. Jung, Y. Adiyaman, M. Adiyaman, W.S. Powell, G. A. Fitzgerald, and J. Rokach. Tetrahedron Lett. **40**, 7179 (1999), and refs. therein; (*b*) A.F. Rowley, H. Kühn, and T. Schewe (*Editors*). Eicosanoids and

[3] Copies of materials on deposit may be purchased from the Depository of Unpublished Data, Document Delivery, CISTI, National Research Council of Canada, Ottawa, ON, K1A 0S2, Canada (http://www.nrc.ca/cisti/irm/unpub_e.shtml for information on ordering electronically).

© 2004 NRC Canada

related compounds in plants and animals. Princeton University, Princeton. 1998.
12. L.W. Chakrin and D.M. Bailey (*Editors*). The leukotrienes: Chemistry and biology. Academic, Orlando. 1984.
13. R. Guo and J.R. Green. Synlett, 746 (2000).
14. See, for example: T. Takahashi, T. Yokozawa, and T. Endo. Macromolecules, **28**, 866 (1995).
15. P. Rochet, J.-M. Vatèle, and J. Goré. Synthesis, 795 (1994).
16. (*a*) M. Berthelot, F. Besseau, and C. Laurence. Eur. J. Org. Chem. 925 (1998); (*b*) F. Besseau, C. Laurence, and M. Berthelot. J. Chem. Soc. Perkin Trans. 2, 485 (1994).
17. (*a*) P.-C. Maria and J.-F. Gal. J. Phys. Chem. **89**, 1296 (1985); (*b*) A. Rauk, I.R. Hunt, and B.A. Keay. J. Org. Chem. **59**, 6808 (1994).
18. H. Mayr and H. Patz. Angew Chem. Int. Ed. Engl. **33**, 938 (1994).
19. W.C. Still, M. Kahn, and A. Mitra. J. Org. Chem. **43**, 2923 (1978).

© 2004 NRC Canada

Efficient construction of benzohydrindenones from aryltrienones via domino Nazarov electrocyclization – electrophilic aromatic substitution[1]

Cindy C. Browder, Fredrik P. Marmsäter, and F.G. West

Abstract: 1,4-Dien-3-ones substituted with pendant arylethyl side chains attached at C-1 were readily prepared from substituted dihydrocinnamaldehydes. Treatment with $TiCl_4$ at low temperature effected domino Nazarov electrocyclization – arene trapping within 5 min to give racemic benzohydrindenones in near-quantitative yield and with complete diastereoselectivity.

Key words: domino process, electrophilic aromatic substitution, Lewis acid, Nazarov cyclization.

Résumé : Utilisant des dihydrocinnamaldéhydes substitués comme produits de départ, on a facilement préparé des 1,4-dién-3-ones substituées portant des chaînes latérales aryléthyles attachées en position C-1. Leur traitement par du $TiCl_4$ à basse température provoque en cinq minutes des réactions en chaîne d'électrocyclisation de Nazarov et de piégeage d'arène qui conduisent à la formation de benzohydrindénones avec un rendement pratiquement quantitatif et une diastéréosélectivité complète.

Mots clés : procédé domino, substitution aromatique électrophile, acide de Lewis, cyclisation de Nazarov.

[Traduit par la Rédaction]

Introduction

Domino processes have become important tools for organic synthesis, since they permit the one-stage construction of complex products from comparatively simple reactants (1). We have examined the use of the Nazarov reaction (2) of cross-conjugated dienones as a versatile initiating step for a variety of domino processes (3). The intermediate resulting from Lewis or Brønsted acid-catalyzed electrocyclic ring closure is a 2-oxido- or 2-hydroxycyclopentenyl cation (Scheme 1), which can potentially react as either a 2π partner in a [4 + 3]-cycloaddition (3*c*) or as an electrophile in a variety of intra- or intermolecular cation trapping processes (3*a*, 3*b*, 3*d*–3*f*).

In the latter category, we are particularly interested in developing routes to the hydrindan skeleton and benzannulated derivatives. These substructures are found within many natural and unnatural targets (4), including steroids (5), alkaloids (6) and the interesting hamigeran sponge metabolites, which have shown promising activity against polio and herpes viruses (7). Previous studies indicated that a suitably substituted butenyl group at C-1 of the dienone reactants **1** could participate in efficient 6-endo cation–olefin cyclization to furnish hydrindenyl cations **2** (Scheme 1) (3*d*). However, in most cases a mixture of products **3**–**5** ensued, resulting from the several available termination pathways available to this intermediate following 6-endo cyclization. In contrast, aryltrienones **6** underwent clean conversion to **7** in high yield via a cascade polycyclization process that began with a similar 6-endo cation–olefin cyclization (3*e*). We surmised that under the Nazarov conditions, cyclization via intermolecular electrophilic aromatic substitution could be an efficient and highly selective termination process. We therefore sought to explore the *direct* trapping of the Nazarov intermediate with pendant aryl groups (8). In this full account, we describe the convenient preparation of the necessary aryldienone substrates, and their high-yield and stereoselective conversion into benzohydrindenones.

Received 27 May 2003. Published on the NRC Research Press Web site at http://canjchem.nrc.ca on 20 February 2004.

Dedicated to Professor Ed Piers in recognition of his many important contributions to organic synthesis and Canadian science.

C.C. Browder, F.P. Marmsäter, and F.G. West.[2,3] Department of Chemistry, University of Utah, 315 S. 1400 East, Rm. 2020, Salt Lake City, UT 84112–0850, U.S.A.

[1]This article is part of a Special Issue dedicated to Professor Ed Piers.

[2]Current address: Department of Chemistry, University of Alberta, W5-67 Gunning–Lemieux Chemistry Centre, Edmonton, AB T6G 2G2, Canada.

[3]Corresponding author (e-mail: frederick.west@ualberta.ca).

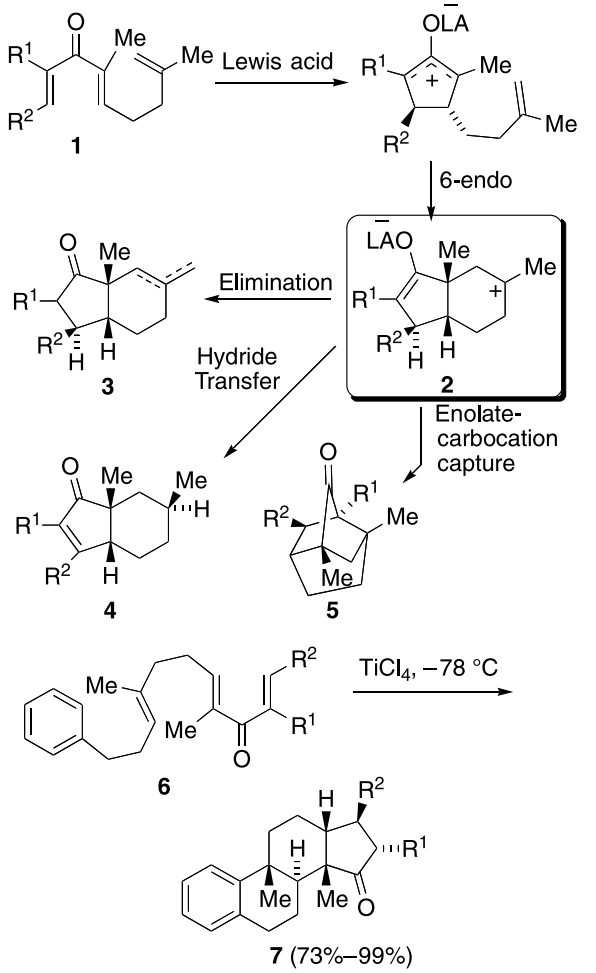
Results and discussion

Substrate synthesis

Several possible approaches to the aryldienone substrates needed to investigate the desired process were considered. The most flexible strategy involved addition of alkenyl anions **8** into enals **9** (prepared by Horner–Wadsworth–Emmons (HWE) olefination of readily available hydro-

 doi: 10.1139/V03-203 © 2004 NRC Canada

Scheme 1.



cinnamaldehydes **10**), followed by oxidation of the resulting dienols to dienones **11** (Scheme 2). Aldehydes **10b** and **10c** were prepared from the corresponding cinnamic acids, and together with the commercially available **10a** were subjected to olefination with triethyl phosphonopropionate under the modified Roush–Masamune conditions (9). Half-reduction to the enals **9a**–9**c** was most easily accomplished using a two-step reduction–oxidation sequence (excess DIBAL-H, then TPAP/NMO). Furan-containing enal **9d** was also prepared from (*E*)-3-furanacrylic acid using a similar sequence. This naturally occurring compound, perillenal, is a pheromone of the pine saw fly (10). Although it has been synthesized by a variety of methods, we have found that this route is quite convenient for the preparation of this compound in quantity (11).

With enals **9a**–**9d** in hand, conversion to the dienone substrates was readily effected by addition of 2-propenylmagnesium bromide, (*Z*)-3-lithio-3-hexene, or 1-lithiocyclohexene. The latter two were generated in situ from the trisylhydrazones of 3-hexanone and cyclohexanone under modified Shapiro conditions (12). Oxidation of the resulting dienols **12** was best accomplished using $BaMnO_4$ (13), providing dienones **11a**–**11h** in moderate to good yield.

Cyclization studies

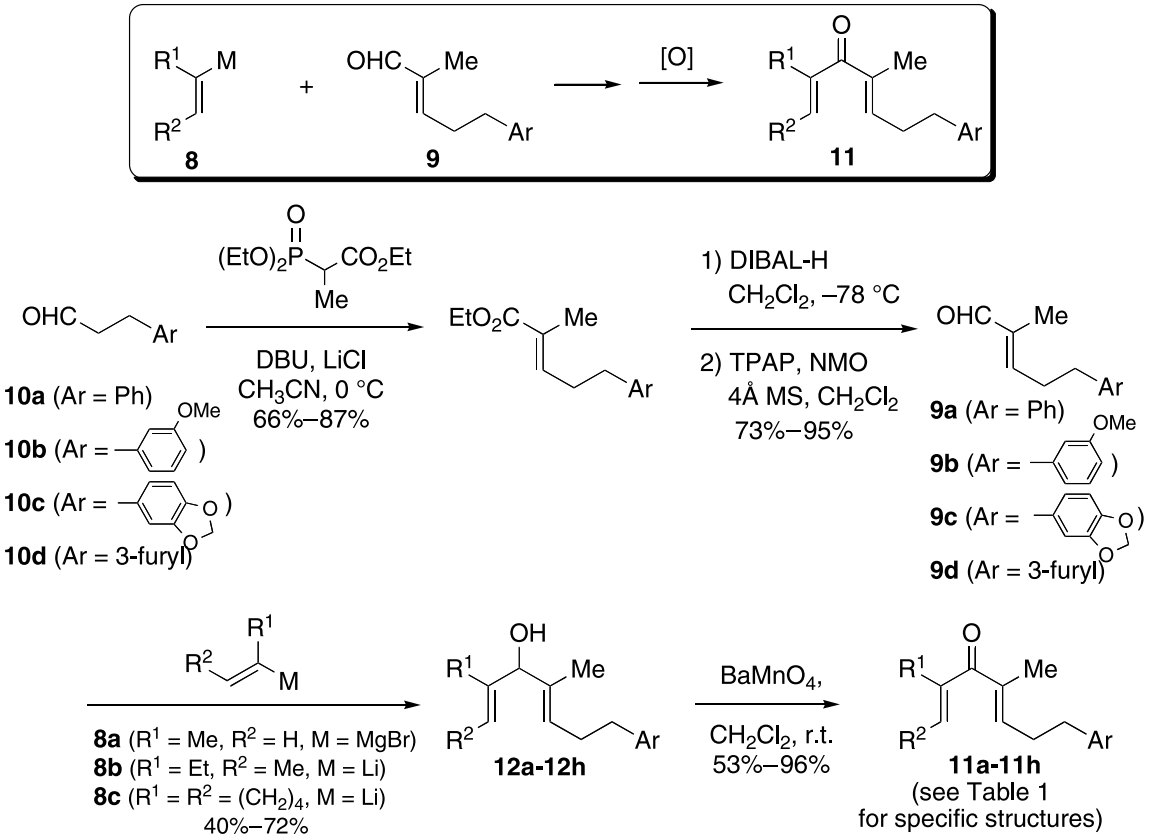
Initial attempts to effect the desired domino cyclization used the simplest substrate, **11a** (Scheme 3). In the event, we found that, although **11a** underwent the Nazarov electrocyclization upon treatment with $BF_3{\cdot}OEt_2$, subsequent electrophilic aromatic substitution did not occur. Instead, cyclopentenone **13a** was isolated in 69% yield. In the prior cascade polycyclization study, which also involved termination by cyclization onto a monosubstituted phenyl ring, $TiCl_4$ had been found to be superior to $BF_3{\cdot}OEt_2$, which furnished various quantities of truncated products resulting from incomplete cyclization of the polyene array (3*e*). However, in the case of **11a**, $TiCl_4$ gave a complex mixture of products containing neither **13a** nor any of the desired domino cyclization product **14a**. While disappointing, this result was not entirely unexpected. In earlier work involving attempted arene capture of photochemically generated 2-oxidocyclopentenyl cations, simple phenyl groups were found to be insufficiently nucleophilic to effectively trap the intermediate (e.g., **15** → **16**) in competition with other pathways (14). However, more electron-rich aryl groups had been effective, suggesting that substrates **11b**–**11h** would have a greater likelihood of undergoing the second cyclization event.

As with **11a**, treatment of **11b**–**11g** with $BF_3{\cdot}OEt_2$ gave cyclopentenone products derived from initial Nazarov cyclization and elimination rather than arene trapping. However, these products were admixed with cyclopentanone-containing products containing one fewer aryl protons in the ^{1}H NMR spectra than the starting dienones. These new compounds proved to be the desired benzohydrindenones derived from domino cyclization. In an effort to enhance this process at the expense of the monocyclization, we examined the use of the stronger Lewis acid, $TiCl_4$. The choice of Lewis acid indeed proved to be critical, as the desired products **14b**–**14g** were cleanly obtained in high yield within 5 min at –78 °C (Table 1). The arene substitution reaction occurred at the sterically less demanding position in all cases (para to the methoxy substituent rather than ortho for **11b**–**11d** and meta/para to the methylenedioxy group for **11e**–**11g**).[4] Furan-containing substrate **11h** was of interest, given the substantial precedent for the ability of pendant furans to participate in cationic cyclization processes (15), as well as the synthetic versatility of the furan nucleus in the resulting annulated products (16). In the event (entry 7), we found that this example proceeded in only 55% yield, and required warming to room temperature to fully consume the starting material. The remainder of the material appeared to be oligomeric by-products, presumably because of the higher temperature needed in this case. It is notable that simple Nazarov cyclization products analogous to **13a** were not isolated in any of these examples. The high efficiency of the electrophilic aromatic substitution process by **11b**–**11h** as compared with other possible termination pathways is striking. Examples of simple acyclic oxyallyl cations reacting with arenes to give a mixture of simple substitution products

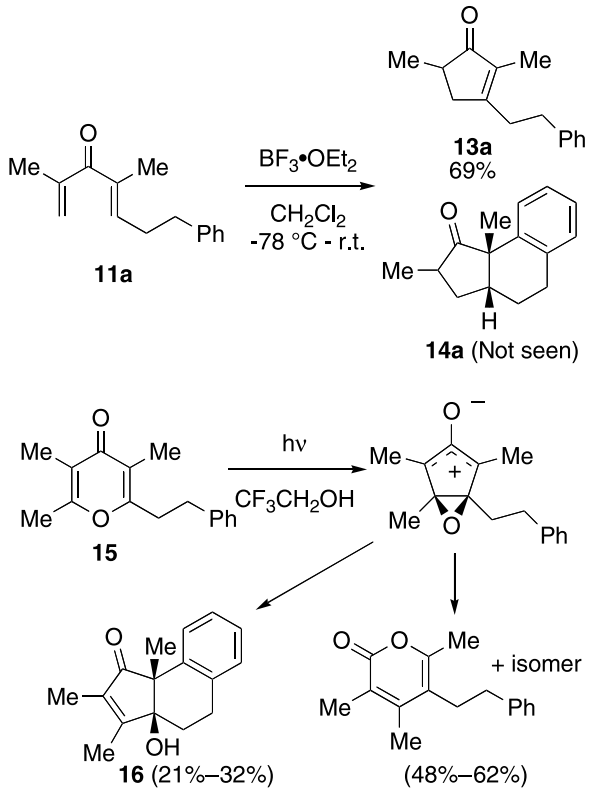
[4] Arene substitution patterns were readily discernable from the coupling patterns of the remaining aromatic protons in the ^{1}H NMR spectra of products **14b**–**4g**.

© 2004 NRC Canada

Scheme 2.



Scheme 3.



and [4 + 3]-adducts are known (17). A similar process in these intramolecular cases is unlikely, due to the substantial strain that would be encountered in the cycloaddition transition state; however, it is possible that products **14b**–**14h** may form through an abortive cycloaddition pathway in analogy to the intermolecular examples noted above.

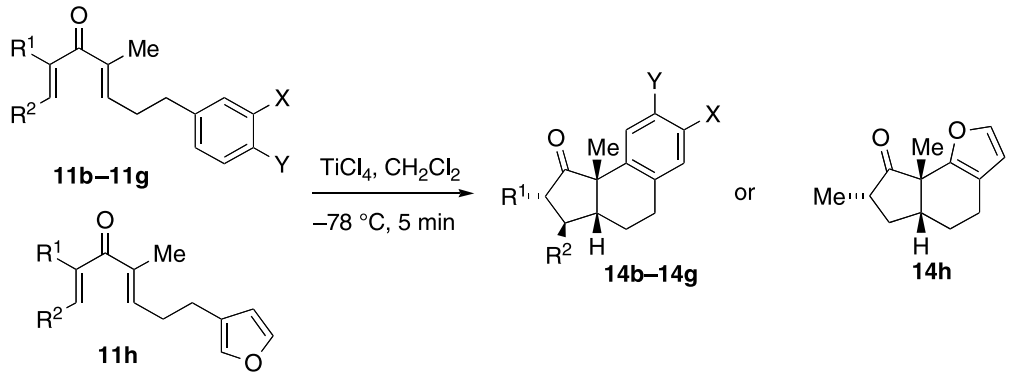
There are several important stereochemical considerations in these domino cyclizations. First, in cases employing tetrasubstituted dienones (i.e., $R^2 \neq H$; entries 2, 3, 5, and 6), orbital symmetry considerations demand a conrotatory electrocyclization (18), which ensures that R^2 will be cis to the neighbouring bridgehead proton (Scheme 4). Subsequent arene trapping of the racemic oxyallyl cation intermediate is presumed to proceed with approach of the aromatic ring from the same face as the side chain to which it is attached to give a *cis*-hydrindan ring fusion, in analogy to other Nazarov-initiated domino processes that involve 6-endo cyclizations (4*a*, 4*d*, 4*e*). Finally, the relative configuration at C-2 was assigned with R^1 trans to the hydrindan bridgehead substituents based on presumed protonation of the enolate precursor from the convex face, and following previous observations of this selectivity in related systems (4). These assignments were confirmed in the case of **14f** by single crystal X-ray diffraction analysis[5] and other examples were assigned by analogy.

We found that 1,4-dien-3-ones with pendant electron-rich aryl groups attached through C-1 can undergo efficient domino cyclization to give arene-fused hydrindenones with

[5] X-ray diffraction data for **14f** were previously published. See the *Supporting Information* for ref. 8.

© 2004 NRC Canada

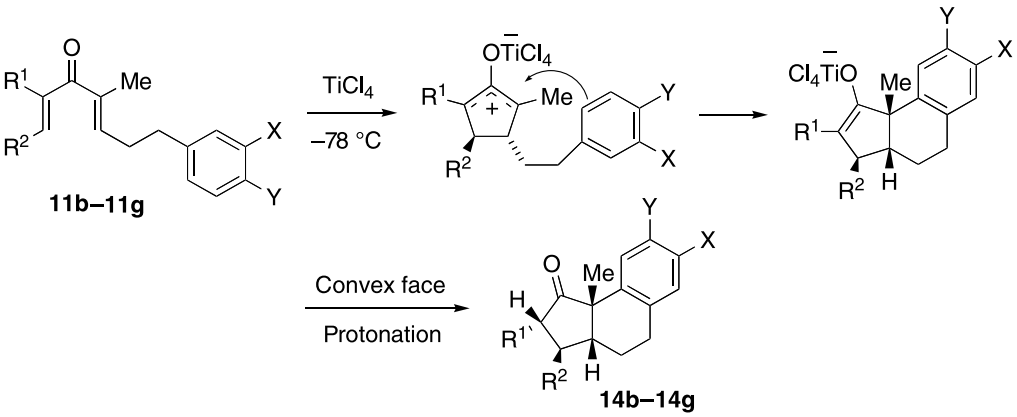
Table 1. $TiCl_4$-mediated domino cyclizations of **11** to produce benzohydrindenones **14**.



Entry	Substrate	R^1	R^2	X	Y	Yield **14** (%)[a]
1	**11b**	Me	H	OMe	H	90
2	**11c**	Et	Me	OMe	H	99
3	**11d**	$-(CH_2)_4-$		OMe	H	99
4	**11e**	Me	H	$-OCH_2O-$		99
5	**11f**	Et	Me	$-OCH_2O-$		99
6	**11g**	$-(CH_2)_4-$		$-OCH_2O-$		99
7	**11h**	Me	H	Not applicable		55[b]

[a]Isolated yields; products **14** were deemed homogeneous by TLC and NMR analysis.
[b]Warming to rt was required for complete consumption of substrate **11h**.

Scheme 4.



complete stereoselectively. Studies aimed at applying this methodology and related chemistry to targets containing this skeleton will be reported elsewhere in due course.

Experimental

General information

Reactions were conducted in oven-dried (120 °C) or flame-dried glassware under a positive nitrogen atmosphere unless otherwise stated. Transfer of anhydrous solvents or mixtures was accomplished with oven-dried syringes or cannulae. Solvents were distilled before use: dichloromethane from calcium hydride; diethyl ether and tetrahydrofuran from sodium benzophenone ketyl. Thin layer chromatography (TLC) was performed on plates of silica precoated with 0.25 mm Kieselgel 60 F_{254}. Flash chromatography columns were packed with 230–400 mesh silica gel. Where given, column dimensions include outer diameters. Radial chromatography was performed on plates of silica precoated with 1, 2, or 4 mm silica gel 60 PF_{254} containing gypsum. Barium manganate was purchased from Aldrich and was used without any prior activation or purification.

Proton nuclear magnetic resonance spectra (^1H NMR) were recorded on a 500 MHz Varian VXR NMR unless otherwise stated, and the chemical shifts are reported on the δ scale (ppm) downfield from tetramethylsilane. Coupling constants (*J*) are reported in Hz. Splitting patterns are designated as s (singlet), d (doublet), t (triplet), q (quartet), m (multiplet), br (broad), dd (doublet of doublets), etc. Carbon nuclear magnetic resonance spectra (^{13}C NMR) were obtained at 125 MHz and are reported (ppm) relative to the center line of a triplet at 77.23 ppm for deuterochloroform. Infrared (IR) spectra were measured with a Mattson Galaxy 3000 FT-IR or a Mattson Polaris FT-IR spectrophotometer.

© 2004 NRC Canada

Mass spectra were determined on a VG Micromass 7050E mass spectrometer equipped with a VG 2000 Data system. Elemental analyses were obtained from Altantic Microlabs Inc., Norcross, Ga.

Representative synthesis of hydrocinnamaldehydes 10

3-(3-Methoxyphenyl)propanal (10b)

General procedure for the LAH reduction

In a dry 50 mL round-bottomed flask fitted with a rubber septum and nitrogen inlet, a solution was made of 3-methoxycinnamic acid (5.139 g, 28.84 mmol) in THF (40 mL). A slurry of lithium aluminum hydride (LAH) (1.574 g, 41.47 mmol) in THF (250 mL) was prepared similarly in a dry 500 mL round-bottomed flask fitted with rubber septum, nitrogen inlet, and magnetic stirbar. The cinnamic acid solution was added slowly (1 to 2 h) via cannula to the LAH slurry at room temperature (rt). The mixture was stirred for 1 h after the end of the addition, then quenched by dropwise addition of MeOH (10 mL). 15 g of Celite/$NaSO_4$·$10H_2O$ (1:1) was added and the slurry was stirred for 15 h. Vacuum filtration and concentration provided 4.042 g (84%) 3-(3-methoxyphenyl)propanol as a pale yellow oil. ^{1}H NMR was in agreement with previously published data (19): R_f 0.36 (EtOAc/Hex, 1:1). IR (thin film, cm^{-1}): 3355 (br), 2939, 2863, 2835. ^{1}H NMR ($CDCl_3$) δ: 7.20 (t, J = 7.7 Hz, 1H), 6.90 (d, J = 7.6 Hz, 1H), 6.76–6.72 (m, 2H), 3.79 (s, 3H), 3.68 (t, J = 6.4 Hz, 2H), 2.69 (t, J = 7.7 Hz, 2H), 1.92–1.86 (m, 2H), 1.44 (br s, 1H). ^{13}C NMR ($CDCl_3$) δ: 129.6, 121.1, 114.5, 111.4, 111.1, 107.0, 62.5, 55.4, 34.3, 32.3.

3-(3-Methoxyphenyl)propanol 3.9a (1.037 g, 6.237 mmol) was treated with TPAP (0.076 g, 0.217 mmol, 3.5 mol %), NMO (0.887 g, 7.70 mmol), and crushed 4 Å molecular sieves (1.250 g) in CH_2Cl_2 (65 mL) as per the general procedure described for **9a** below. TLC showed the reaction was complete after 40 min. Column chromatography (silica gel, 235 mm × 35 mm, EtOAc/Hex, 1:1) provided 0.610 g (60%) 3-(3-methoxyphenyl)propanal 3.10a as a pale yellow oil: R_f 0.59 (EtOAc/Hex, 1:1). IR (thin film, cm^{-1}): 2955, 2921, 2849, 1709. ^{1}H NMR ($CDCl_3$) δ: 9.83 (t, J = 1.4 Hz, 1H), 7.22 (t, J = 7.9 Hz, 1H), 6.81–6.74 (m, 3H), 3.80 (s, 3H), 2.94 (t, J = 7.6 Hz, 2H), 2.79 (td, J = 7.6, 1.4 Hz, 2H). ^{13}C NMR ($CDCl_3$) δ: 201.8, 160.0, 142.2, 129.9, 120.8, 114.4, 111.8, 55.4, 45.4, 28.3.

3-(3,4-Methylenedioxyphenyl)propanol (10c)

(3,4-Methylenedioxy)cinnamic acid was treated with LAH in THF as per the procedure described for **10b**. The crude product provided 3-(3,4-methylenedioxyphenyl)propanol with a ^{1}H NMR spectrum in accordance with previously published data (20): R_f 0.29 (EtOAc/Hex, 1:1). ^{1}H NMR ($CDCl_3$) δ: 6.75–6.61 (m, 3H), 5.93 (s, 2H), 3.67 (t, J = 7.6 Hz, 2H), 2.64 (t, J = 7.6 Hz, 2H), 1.85 (tt, J = 7.6, 7.6 Hz, 2H), 1.26 (br s, 1H).

3-(3,4-Methylenedioxyphenyl)propanol (2.453 g, 13.61 mmol) was treated with TPAP (0.127 g, 0.362 mmol), NMO (1.882 g, 16.07 mmol), and crushed 4 Å sieves (2.883 g) in CH_2Cl_2 (150 mL) as per the general procedure described for **9a** below. Column chromatography (silica gel, 214 mm × 40 mm, EtOAc/Hex (1:4)) provided 3-(3,4-methylenedioxyphenyl)propanal (**10c**) (1.713 g, 71%) as a clear, colorless oil. ^{1}H NMR data were in accordance with previously published data (21): R_f 0.22 (EtOAc/Hex, 1:4). ^{1}H NMR ($CDCl_3$) δ: 9.80 (t, J = 1.4 Hz, 1H), 6.73 (d, J = 7.9 Hz, 1H), 6.68 (d, J = 2.2 Hz, 1H), 6.64 (dd, J = 7.9, 2.2 Hz, 1H), 5.92 (s, 2H), 2.88 (t, J = 7.4 Hz, 2H), 2.74 (td, J = 7.4, 1.2 Hz, 2H).

3-(3-Furyl)propanal (10d)

(*E*)-3-Furan acrylic acid (0.993 g, 7.19 mmol) was treated with LAH (0.571 g, 15.0 mmol) in THF (74 mL) as per the procedure described for **10b**. The crude product was redissolved in methanol (75 mL). Pd/C (0.268 g, 0.126 mmol) was introduced into the flask; the flask was evacuated and purged with nitrogen five times. The flask was evacuated again and then opened to a hydrogen balloon. After 30 min, the flask was evacuated and flushed with nitrogen. The slurry was then concentrated by rotary evaporation and filtered through a Celite plug. The crude product was concentrated and subjected to column chromatography (silica gel, 195 mm × 35 mm, EtOAc/Hex (0:1) and increased concentration to EtOAc/Hex (1:1)) to provide 3-(3-furyl)propanol (0.832 g, 60%) as a clear, pale yellow oil. ^{1}H and ^{13}C NMR and IR were consistent with previously published data (22): R_f 0.39 (EtOAc/Hex, 1:1). IR (thin film, cm^{-1}): 3333 (br), 2937, 2862. ^{1}H NMR ($CDCl_3$) δ: 7.36–7.35 (m, 1H), 7.24–7.23 (m, 1H), 6.28–6.27 (m, 1H), 3.68 (t, J = 6.4 Hz, 2H), 2.52 (t, J = 7.5 Hz, 2H), 1.83 (tt, J = 6.5, 6.5 Hz, 2H), 1.51 (br s, 1H). ^{13}C NMR ($CDCl_3$) δ: 143.1, 139.1, 124.6, 111.2, 62.5, 33.0, 21.2.

In a dry 25 mL round-bottomed flask fitted with a magnetic stirbar, a rubber septum, and a nitrogen inlet, oxalyl chloride (0.51 mL, 5.8 mmol) was dissolved in CH_2Cl_2 (9 mL) and cooled to –78 °C. A solution of DMSO (0.79 mL, 11 mmol) in CH_2Cl_2 (5 mL) was added dropwise via cannula. The mixture was stirred for 5 min before a solution of 3-(3-furyl)propanol (0.613 g, 4.86 mmol) in CH_2Cl_2 (2 mL) was added dropwise via cannula. After 15 min of additional stirring, triethylamine (3.4 mL, 24 mmol) was added dropwise via syringe. The reaction mixture was then allowed to warm slowly to rt, at which point it was quenched with water (15 mL). The layers were separated and the aqueous layer extracted with CH_2Cl_2 (3 × 5 mL). The combined organic portions were dried ($MgSO_4$) and concentrated to provide crude 3-(3-furyl)propanal as a brown oil, whose ^{1}H NMR spectrum was consistent with previously published data (23): R_f 0.56 (EtOAc/Hex, 1:1). ^{1}H NMR ($CDCl_3$) δ: 9.80 (t, J = 1.4 Hz, 1H), 7.37 (t, J = 1.7 Hz, 1H), 7.24–7.22 (m, 1H), 6.27–6.26 (m, 1H), 2.76 (br d, J = 6.7 Hz, 2H), 2.71 (td, J = 6.7, 1.2 Hz, 2H). ^{13}C NMR ($CDCl_3$) δ: 201.8, 143.3, 139.3, 123.5, 110.9, 44.2, 17.7.

Representative synthesis of aldehydes 9

(E)-2-Methyl-5-phenyl-2-pentenal (9a)

General procedure for the HWE olefination

In a dry 250 mL round-bottomed flask equipped with a rubber septum, a nitrogen inlet, and a magnetic stir bar, triethylphosphopropionate (2.097 g, 8.801 mmol), CH_3CN (60 mL), and LiCl (0.377 g, 8.90 mmol) were combined. 1,8-Diaza-bicyclo[5.4.0]undec-7-ene (DBU) (1.32 mL,

© 2004 NRC Canada

8.79 mmol) was added via syringe. The reaction mixture was allowed to stir at rt for 15 min, then cooled to 0 °C. Dihydrocinnamaldehyde **10a** (Aldrich; 0.77 mL, 5.9 mmol) in CH_3CN (5 mL) was then added dropwise via cannula and the reaction mixture was monitored by TLC. The reaction was complete within 30 min and was then quenched with satd. NH_4Cl (50 mL) and extracted with Et_2O (3 × 20 mL). Radial chromatography (silica gel, 4 mm plate, EtOAc/Hex (1:9)) provided ethyl (*E*)-2-methyl-5-phenyl-2-pentenoate (1.132 g, 89%) as a clear, colorless oil. ^1H and ^{13}C NMR and IR were in accordance with previously published data (24): R_f 0.53 (EtOAc/Hex, 1:4). IR (thin film, cm^{-1}): 3087, 3061, 3035, 3016, 1709. ^1H NMR ($CDCl_3$) δ: 7.37–7.27 (m, 2H), 7.23–7.18 (m, 3H), 6.80 (tq, *J* = 7.4, 1.5 Hz, 1H), 4.18 (q, *J* = 7.1 Hz, 2H), 2.75 (t, *J* = 7.8 Hz, 2H), 2.49 (dt, *J* = 7.8, 7.8 Hz, 2H), 1.78 (s, 3H), 1.29 (t, *J* = 7.1 Hz, 3H). ^{13}C NMR ($CDCl_3$) δ: 168.4, 141.5, 141.1, 128.6, 128.5, 126.3, 60.7, 35.0, 30.8, 14.5, 12.5 (two sp^2 carbon resonances overlapping).

General procedure for the DIBAL-H reduction

Ethyl (*E*)-2-methyl-5-phenyl-2-pentenoate (1.049 g, 4.803 mmol) was dissolved in CH_2Cl_2 (48 mL) in a dry 100 mL round-bottomed flask fitted with a rubber septum, a nitrogen inlet, and a magnetic stirbar. The solution was cooled to –78 °C and diisobutylaluminum hydride (DIBAL-H) (6.5 mL of a 1.5 mo L^{-1} solution, 9.8 mmol) was added dropwise via syringe. TLC indicated that the reaction was complete after 15 min. The reaction was quenched with saturated aqueous potassium sodium tartrate (10 mL) and stirred 5 h. The layers were separated and the aqueous layer extracted with CH_2Cl_2 (3 × 10 mL). The combined organic layers were dried ($MgSO_4$) and concentrated. Column chromatography (silica gel, 185 mm × 35 mm, EtOAc/Hex (1:4) and increased concentration to EtOAc/Hex (1:1)) provided (*E*)-2-methyl-5-phenyl-2-pentenol (0.792 g, 94%) as a clear, colorless oil. ^1H and ^{13}C NMR and IR are consistent with previously published data (25). R_f 0.42 (EtOAc/Hex, 1:1). IR (thin film, cm^{-1}): 3336 (br), 2923, 2855. ^1H NMR ($CDCl_3$) δ: 7.30–7.27 (m, 2H), 7.2–7.15 (m, 3H), 5.47 (tq, *J* = 7.1, 1.4 Hz, 1H), 4.00 (d, *J* = 5.2 Hz, 2H), 2.68 (t, *J* = 7.9 Hz, 2H), 2.37 (dt, *J* = 7.9, 7.9 Hz, 2H) overlapping with 2.36 (br s, 1H), 1.62 (s, 3H). ^{13}C NMR ($CDCl_3$) δ: 142.2, 135.6, 128.6, 128.5, 126.0, 125.4, 69.0, 35.9, 29.7, 13.8.

General procedure for the TPAP oxidation

(*E*)-2-Methyl-5-phenyl-2-pentenol (0.761 g, 4.32 mmol) was dissolved in CH_2Cl_2 (33 mL) in a dry 100 mL round-bottomed flask fitted with a rubber septum, a nitrogen inlet, and a magnetic stirbar. Crushed 4 Å molecular sieves (0.984 g) and 4-methylmorpholine-*N*-oxide (NMO) (0.597 g, 5.18 mmol) were added and stirred 5 min. Tetrapropylammonium perruthenate (TPAP) (0.074 g, 0.21 mmol, 3.5 mol %) was added slowly. TLC showed the reaction was complete after 30 min. The slurry was concentrated and eluted over silica with CH_2Cl_2 and EtOAc. The filtrate was concentrated under reduced pressure to yield crude (*E*)-2-methyl-5-phenyl-2-pentenal (**9a**) (0.652 g, 87%) as a brown oil, which was used without further purification. R_f 0.40 (EtOAc/Hex, 1:4). IR (thin film, cm^{-1}): 2915, 2857, 2823, 2760, 2713, 1683, 1646. ^1H NMR ($CDCl_3$) δ: 9.39 (s, 1H), 7.33–7.28 (m, 2H), 7.25–7.18 (m, 3H), 6.51 (dq, *J* = 7.3, 1.4 Hz, 1H), 2.83 (t, *J* = 7.7 Hz, 2H), 2.69 (dt, *J* = 7.7, 7.7 Hz, 2H), 1.69 (s, 3H). ^{13}C NMR ($CDCl_3$) δ: 195.4, 153.4, 140.8, 140.1, 128.8, 128.6, 126.5, 34.6, 30.9, 9.4.

(E)- 5-(3-Methoxyphenyl)-2-methyl-2-pentenal (9b)

The procedures described for **9a** were carried out using 3-methoxydihydrocinnamaldehyde (**10b**) in the initial HWE step.

Ethyl (*E*)-5-(3-methoxyphenyl)-2-methyl-2-pentenoate: colorless oil. R_f 0.65 (EtOAc/Hex, 1:1). IR (thin film, cm^{-1}): 2980, 2936, 1706. ^1H NMR ($CDCl_3$) δ: 7.21 (t, *J* = 7.6 Hz, 1H), 6.83–6.74 (m, 4H), 4.18 (q, *J* = 7.1 Hz, 2H), 3.80 (s, 3H), 2.73 (t, *J* = 7.8 Hz, 2H), 2.48 (dt, *J* = 7.8, 7.8 Hz, 2H), 1.80–1.79 (d, *J* = 1.3 Hz, 3H), 1.29 (t, *J* = 7.1 Hz, 3H). ^{13}C NMR ($CDCl_3$) δ: 168.4, 159.9, 143.1, 141.1, 129.7, 128.7, 121.0, 114.4, 111.6, 60.7, 55.4, 35.0, 30.7, 14.5, 12.5. Anal. calcd. for $C_{15}H_{20}O_3$: C 72.55, H 8.12; found: C 72.42, H 8.12.

(*E*)-5-(3-Methoxyphenyl)-2-methyl-2-pentenol: pale yellow oil. R_f 0.74 (EtOAc/Hex, 1:1). IR (thin film, cm^{-1}): 3358 (br), 2935, 2922, 2857, 2835. ^1H NMR ($CDCl_3$) δ: 7.23–7.19 (m, 1H), 6.81–6.78 (m, 1H), 6.76–6.73 (m, 2H), 5.47 (tq, *J* = 7.1, 1.3 Hz, 1H), 4.00 (s, 2H), 3.81 (s, 3H), 2.66 (t, *J* = 7.6 Hz, 2H), 2.36 (dt, *J* = 7.6, 7.6 Hz, 2H), 1.64 (s, 3H), 1.39 (br s, 1H). ^{13}C NMR ($CDCl_3$) δ: 159.8, 143.9, 135.7, 129.5, 125.5, 121.1, 114.5, 111.2, 69.1, 55.3, 35.9, 29.6, 13.9.

(*E*)-5-(3-Methoxyphenyl)-2-methyl-2-pentenal (**9b:**) pale yellow oil. R_f 0.67 (EtOAc/Hex, 1:1). IR (thin film, cm^{-1}): 2927, 2835, 2763, 2713, 1684. ^1H NMR ($CDCl_3$) δ: 9.39 (s, 1H), 7.23 (t, *J* = 7.8 Hz, 1H), 6.81–6.74 (m, 3H), 6.51 (tq, *J* = 7.2, 1.4 Hz, 1H), 3.81 (s, 3H), 2.81 (t, *J* = 7.6 Hz, 2H), 2.68 (dt, *J* = 7.6, 7.6 Hz, 2H), 1.71 (d, *J* = 1.3 Hz, 3H). ^{13}C NMR ($CDCl_3$) δ: 195.4, 160.0, 153.4, 142.4, 140.1, 129.8, 120.9, 114.5, 111.6, 55.4, 34.6, 30.7, 9.4.

(E)- 5-(3,4-Methylenedioxyphenyl)-2-methyl-2-pentenal (9c)

The procedures described above for **9a** were carried out using 3,4-methylenedioxydihydrocinnamaldehyde (**10c**) in the initial HWE step.

(*E*)-5-(3,4-Methylenedioxyphenyl)-2-methyl-2-pentenoate: pale yellow oil. R_f 0.69 (EtOAc/Hex, 1:1). IR (thin film, cm^{-1}): 2978, 2924, 2900, 1706. ^1H NMR ($CDCl_3$) δ: 6.77 (tq, *J* = 7.4, 1.4 Hz, 1H), 6.73 (d, *J* = 7.8 Hz, 1H), 6.68 (d, *J* = 1.7 Hz, 1H), 6.63 (dd, *J* = 7.9, 1.7 Hz, 1H), 5.92 (s, 2H), 4.18 (q, *J* = 7.1 Hz, 2H), 2.67 (t, *J* = 7.5 Hz, 2H), 2.44 (dt, *J* = 7.5, 7.5 Hz, 2H), 1.79 (d, *J* = 1.3 Hz, 3H), 1.29 (t, *J* = 7.1 Hz, 3H). ^{13}C NMR ($CDCl_3$) δ: 168.4, 147.8, 146.0, 141.0, 135.3, 128.7, 121.3, 109.0, 108.4, 101.0, 60.7, 34.7, 31.1, 14.5, 12.6. Anal. calcd. for $C_{15}H_{18}O_2$: C 68.68, H 6.92; found: C 68.85, H 6.86.

(*E*)-5-(3,4-Methylenedioxyphenyl)-2-methyl-2-pentenol: pale yellow oil. R_f 0.45 (EtOAc/Hex, 1:1). IR (thin film, cm^{-1}): 3226 (br), 2937, 2922. ^1H NMR ($CDCl_3$) δ: 6.72 (d, *J* = 7.9 Hz, 1H), 6.68 (d, *J* = 1.7 Hz, 1H), 6.63 (dd, *J* = 7.9, 1.7 Hz, 1H), 5.92 (s, 2H), 5.44 (tq, *J* = 7.0, 1.4 Hz, 1H), 3.99 (s, 2H), 2.59 (t, *J* = 7.5 Hz, 2H), 2.31 (dt, *J* = 7.5, 7.5 Hz, 2H), 1.63 (s, 3H). ^{13}C NMR ($CDCl_3$) δ: 147.7, 145.8, 136.1, 135.7, 125.3, 121.3, 109.1, 108.3, 101.0, 69.1, 35.6, 30.0, 13.9.

© 2004 NRC Canada

(*E*)-5-(3,4-methylenedioxyphenyl)-2-methyl-2-pentenal (**9c**): pale yellow oil. R_f 0.67 (EtOAc/Hex, 1:1). IR (thin film, cm^{-1}): 2924, 2857, 2777, 2715, 1683. ^1H NMR ($CDCl_3$) δ: 9.38 (s, 1H), 6.74 (d, *J* = 7.9 Hz, 1H), 6.68 (d, *J* = 1.8 Hz, 1H), 6.63 (dd, *J* = 7.8, 1.7 Hz, 1H)), 6.48 (tq, *J* = 7.2, 1.3 Hz, 1H), 5.94 (s, 2H), 2.74 (t, *J* = 7.6 Hz, 2H), 2.63 (dt, *J* = 7.6, 7.6 Hz, 2H), 1.69 (s, 3H). ^{13}C NMR ($CDCl_3$) δ: 195.4, 153.3, 147.9, 146.2, 140.1, 134.6, 121.4, 108.9, 108.5, 101.1, 34.4, 31.1, 9.4.

(E)-5-(3′-Furyl)-2-methyl-2-pentenal (perillenal) (9d)

The HWE – reduction – oxidation procedure described for **9a** was followed using 3-(3′-furyl)propanal (24).

Ethyl (*E*)-5-(3′-furyl)-2-methyl-2-pentenoate: pale yellow oil. R_f 0.67 (EtOAc/Hex, 1:1). IR (thin film, cm^{-1}): 2984, 2930, 2860, 1705. ^1H NMR ($CDCl_3$) δ: 7.36–7.34 (m, 1H), 7.26–7.24 (m, 1H), 6.77 (tq, *J* = 7.2, 1.4 Hz, 1H), 6.29–6.27 (m, 1H), 4.19 (q, *J* = 7.1 Hz, 2H), 2.57 (t, *J* = 7.4 Hz, 2H), 2.43 (dt, *J* = 7.4, 7.4 Hz, 2H), 1.81 (d, *J* = 1.3 Hz, 3H), 1.29 (t, *J* = 7.1 Hz, 3H). ^{13}C NMR ($CDCl_3$) δ: 168.3, 143.1, 141.1, 139.2, 128.7, 124.3, 111.1, 60.7, 29.4, 24.1, 14.5, 12.6.

(*E*)-5-(3′-Furyl)-2-methyl-2-pentenol: yellow oil. ^1H NMR consistent with previously published data (11*d*); R_f 0.43 (EtOAc/Hex, 1:1). ^1H NMR ($CDCl_3$) δ: 7.36–7.34 (m, 1H), 7.23–7.21 (m, 1H), 6.28–6.26 (m, 1H), 5.45 (tq, *J* = 7.0, 1.3 Hz, 1H), 4.00 (s, 2H), 2.49 (t, *J* = 7.6 Hz, 2H), 2.30 (dt, *J* = 7.6, 7.6 Hz, 2H), 1.66 (br s, 3H), 1.58 (br s, 1H). ^{13}C NMR ($CDCl_3$) δ: 142.9, 139.1, 135.7, 125.5, 124.9, 111.2, 69.1, 28.3, 24.9, 13.9.

(*E*)-5-(3-Furyl)-2-methyl-2-pentenal (**9d**): yellow oil. ^1H NMR consistent with previously published data (5, 11*c*); R_f 0.60 (EtOAc/Hex, 1:1). ^1H NMR ($CDCl_3$) δ: 9.39 (s, 1H), 7.36–7.37 (m, 1H), 7.25–7.24 (m, 1H), 6.49 (tq, *J* = 7.1, 1.3 Hz, 1H), 6.29–6.28 (m, 1H), 2.67–2.60 (m, 4H), 1.72 (br s, 3H). ^{13}C NMR ($CDCl_3$) δ: 195.3, 153.4, 143.3, 140.1, 139.3, 123.8, 110.9, 29.5, 23.8, 9.5.

Representative synthesis of dienones 11

(E)-2,4-Dimethyl-7-phenyl-1,4-heptadien-3-one (11a)

General procedure for the Grignard reaction

In a dry 10 mL round-bottomed flask equipped with a magnetic stir bar, a nitrogen inlet, a reflux condenser, and a rubber septum, magnesium powder (0.031 g, 1.3 mmol) was stirred with THF (2.0 mL). 2-Bromopropene (0.088 mL, 0.99 mmol) was added dropwise until exothermic reaction began, and then one drop at a time allowing the flask to cool between drops. When all of the bromide had been added, the Grignard reagent was cooled to 0 °C. (*E*)-2-Methyl-5-phenyl-2-pentenal **9a** (0.132 g, 0.760 mmol) was added to the Grignard reagent via cannula, and the reaction was monitored by TLC. The reaction was complete within 5 min and was quenched with satd. NH_4Cl (5 mL) and extracted with Et_2O (3 × 5 mL). The combined Et_2O layers were then dried ($MgSO_4$) and concentrated. Radial chromatography (silica gel, 2 mm plate, EtOAc/Hex (1:4)) provided (*E*)-2,4-dimethyl-7-phenyl-1,4-heptadien-3-ol **12a** (0.116 g, 71%) as a clear, pale yellow oil. R_f 0.32 (EtOAc/Hex, 1:4). IR (thin film, cm^{-1}): 3406 (br), 3027, 2856. ^1H NMR ($CDCl_3$) δ: 7.30–7.26 (m, 2H), 7.21–7.17 (m, 3H), 5.55 (tdq, *J* = 7.1, 1.1, 1.1 Hz, 1H), 5.05 (br s, 1H), 4.91 (dq, *J* = 1.5, 1.1 Hz, 1H), 4.19 (s, 1H), 2.70 (t, *J* = 7.7 Hz, 2H), 2.39 (dt, *J* = 7.7, 7.7 Hz, 2H), 1.57 (br s, 3H), 1.47 (br s, 3H). ^{13}C NMR ($CDCl_3$) δ: 145.5, 142.2, 135.8, 128.6, 128.5, 127.0, 126.0, 110.9, 80.9, 35.9, 29.8, 18.9, 11.6. Anal. calcd. for $C_{15}H_{20}O$: C 83.22, H 9.32; found: C 83.29, H 9.34.

General procedure for the barium manganate oxidation

In a dry 10 mL round-bottomed flask equipped with a magnetic stir bar, a nitrogen inlet, and a rubber septum, **12a** (0.111 g, 0.514 mmol) was dissolved in CH_2Cl_2 (5 mL) and combined with barium manganate (0.647 g, 2.69 mmol). After 5 days, TLC indicated that the dienol was consumed. The reaction mixture was concentrated, and the slurry was filtered over a pad of Celite on silica in CH_2Cl_2, followed by washing with EtOAc. The eluent was concentrated and radial chromatography (silica gel, 2 mm plate, EtOAc/Hex (1:9)) provided (*E*)-2,4-dimethyl-7-phenyl-1,4-heptadien-3-one **11a** (0.075 g, 68%) as a clear, pale yellow oil. R_f 0.50 (EtOAc/Hex, 1:4). IR (thin film, cm^{-1}): 2924, 2857, 1650. ^1H NMR ($CDCl_3$) δ: 7.32–7.28 (m, 2H), 7.23–7.18 (m, 3H), 6.39 (tq, *J* = 7.2, 1.3 Hz, 1H), 5.54 (dq, *J* = 1.6, 1.0 Hz, 1H), 5.33–5.32 (m, 1H), 2.78 (t, *J* = 7.6 Hz, 2H), 2.56 (dt, *J* = 7.6, 7.6 Hz, 2H), 1.92 (br s, 3H), 1.79 (br s, 3H). ^{13}C NMR ($CDCl_3$) δ: 200.8, 144.0, 143.2, 141.3, 136.6, 128.7, 128.6, 126.4, 123.1, 35.0, 30.9, 19.4, 12.5.

(E)-2,4-Dimethyl-7-(3-methoxyphenyl)-1,4-heptadien-3-one (11b)

The general procedures described for **11a** were followed using **9b** in place of **9a**.

(*E*)-7-(3-Methoxyphenyl)-2,4-dimethyl-1,4-heptadiene-3-ol (**12b**): colorless oil. R_f 0.66 (EtOAc/Hex, 1:1). IR (thin film, cm^{-1}): 3451 (br), 2937, 2921, 2856, 2830. ^1H NMR ($CDCl_3$) δ: 7.20 (td, *J* = 7.7, 1.3 Hz, 1H), 6.79 (d, *J* = 7.7 Hz, 1H), 6.75–6.72 (m, 2H), 5.54 (tdd, *J* = 7.1, 1.2, 1.2 Hz, 1H), 5.05 (s, 1H), 4.92–4.90 (m, 1H), 4.39 (s, 1H), 3.80 (s, 3H), 2.68 (t, *J* = 7.4, Hz, 2H), 2.38 (dt, *J* = 7.4, 7.4 Hz, 2H), 1.57 (s, 3H), 1.48 (s, 3H). ^{13}C NMR ($CDCl_3$) δ: 159.8, 145.5, 143.8, 135.8, 129.5, 127.0, 121.1, 114.5, 111.2, 110.9, 80.8, 55.4, 35.9, 29.7, 18.9, 11.6.

(*E*)-7-(3-Methoxyphenyl)-2,4-dimethyl-1,4-heptadiene-3-one (**11b**): pale yellow oil. R_f 0.47 (EtOAc/Hex, 1:4). IR (thin film, cm^{-1}): 2924, 2836, 1643. ^1H NMR ($CDCl_3$) δ: 7.21 (t, *J* = 7.8 Hz, 1H), 6.80–6.73 (m, 3H), 6.39 (tq, *J* = 7.2, 1.3 Hz, 1H), 5.54 (dq, *J* = 1.5, 1.5 Hz, 1H), 5.33 (s, 1H), 3.80 (s, 3H), 2.75 (t, *J* = 7.6 Hz, 2H), 2.56 (dt, *J* = 7.6, 7.6 Hz, 2H), 1.92 (br s, 3H), 1.80 (br s, 3H). ^{13}C NMR ($CDCl_3$) δ: 200.8, 159.9, 144.0, 143.2, 142.9, 136.6, 129.7, 123.1, 120.9, 114.4, 111.5, 55.4, 35.0, 30.8, 19.4, 12.5. Anal. calcd. for $C_{16}H_{20}O_2$: C 78.65, H 8.25; found: C 78.60, H 8.23.

(E,E′)-8-(3-Methoxyphenyl)-3-ethyl-5-methyl-2,5-octadien-4-one (11c)

General procedure for the Shapiro reaction

3-Pentanone trisyl hydrazone (0.489 g, 1.34 mmol) was dissolved in THF (13 mL) and cooled to –78 °C in a dry 50 mL round-bottomed flask fitted with arubber septum, a nitrogen inlet, and a magnetic stir bar. *sec*-BuLi (1.23 mol L^{-1} in hexane, 2.2 mL, 2.7 mmol) was added

© 2004 NRC Canada

dropwise by syringe and the mixture was allowed to stir at −78 °C for 1.5 h. Following this period, the reaction was placed in a 0 °C bath for 30 min or until nitrogen evolution ceased. After recooling to –78 °C, (*E*)-5-(3-methoxyphenyl)-2-methyl-2-pentenal (**9b**) (0.245 g, 1.28 mmol) was added via cannula in a solution with THF (2 mL). The reaction was monitored by TLC and quenched with satd. NH_4Cl (10 mL) upon consumption of aldehyde. The crude product was extracted with Et_2O (3 × 10 mL), dried ($MgSO_4$), concentrated, and purified by radial chromatography (silica gel, 2 mm plate, EtOAc/Hex (1:10 to 1:4)) to yield 0.165 g (47%) (*E*,*E*′)-8-(3-methoxyphenyl)-3-ethyl-5-methyl-2,5-octadien-4-ol (**12c**) as a clear, pale yellow oil. R_f 0.64 (EtOAc/Hex, 1:1). IR (thin film, cm^{-1}): 3453 (br), 2961, 2929, 2871, 2857. ^1H NMR ($CDCl_3$) δ: 7.20 (t, *J* = 8.0 Hz, 1H), 6.80 (d, *J* = 8.0 Hz, 1H), 6.76–6.73 (m, 2H), 5.57 (tdq, *J* = 7.1, 1.2, 1.2 Hz, 1H), 5.53 (q, *J* = 6.8 Hz, 1H), 4.40 (s, 1H), 3.81 (s, 3H), 2.68 (t, *J* = 7.6 Hz, 2H), 2.38 (dt, *J* = 7.6, 7.6 Hz, 2H), 2.04–1.97 (m, 1H), 1.91–1.83 (m, 1H), 1.65 (d, *J* = 6.8 Hz, 3H), 1.57 (br s, 1H), 1.46 (s, 3H), 0.92 (t, *J* = 7.6 Hz, 3H). ^{13}C NMR ($CDCl_3$) δ: 159.8, 144.0, 142.0, 136.4, 129.5, 125.8, 121.1, 120.3, 114.5, 111.2, 80.6, 55.4, 36.0, 29.8, 20.5, 13.7, 13.1, 12.4.

Dienol **12c** was oxidized with barium manganate per the procedure described for **11a** to give (*E*,*E*′)-8-(3-methoxyphenyl)-3-ethyl-5-methyl-2,5-octadien-4-one (**11c**) as a pale yellow oil. R_f 0.69 (EtOAc/Hex, 1:1). IR (thin film, cm^{-1}): 2962, 2931, 2836, 1634. ^1H NMR ($CDCl_3$) δ: 7.22 (t, *J* = 7.8 Hz, 1H), 6.79–6.73 (m, 3H), 6.12 (tq, *J* = 7.2, 1.5 Hz, 1H), 6.00 (q, *J* = 7.0 Hz, 1H), 3.80 (s, 3H), 2.74 (t, *J* = 7.6 Hz, 2H), 2.53 (dt, *J* = 7.6, 7.6 Hz, 2H), 2.34 (q, *J* = 7.6 Hz, 2H), 1.79 (br s, 3H), 1.76 (d, *J* = 7.0 Hz, 3H), 0.93 (t, *J* = 7.6 Hz, 3H). ^{13}C NMR ($CDCl_3$) δ: 201.5, 159.9, 143.4, 143.1, 140.8, 137.6, 135.8, 129.6, 121.0, 114.6, 111.4, 55.4, 35.1, 30.4, 20.2, 14.1, 13.2, 13.1.

*(*E*)-1-Cyclohexenyl-5-(3-methoxyphenyl)-2-methyl-2-penten-1-one (11d)*

The general procedures described for **11c** were followed using cyclohexanone trisyl hydrazone in place of 3-pentanone trisyl hydrazone.

(*E*)-1-Cyclohexenyl-5-(3-methoxyphenyl)-2-methyl-2-penten-1-ol (**12d**): pale yellow oil. R_f 0.26 (EtOAc/Hex, 1:4). IR (thin film, cm^{-1}): 3418 (br), 2924, 2855, 2835. ^1H NMR ($CDCl_3$) δ: 7.19 (t, *J* = 7.6 Hz, 1H), 6.79 (d, *J* = 7.6 Hz, 1H), 6.76–6.72 (m, 2H), 5.73 (dddd, *J* = 3.4, 3.4, 1.8, 1.8 Hz, 1H), 5.51 (tqd, *J* = 7.1, 1.2, 1.2 Hz, 1H), 4.30 (s, 1H), 3.80 (s, 3H), 2.67 (t, *J* = 7.6 Hz, 2H), 2.38 (dt, *J* = 7.6, 7.6 Hz, 2H), 2.07–2.02 (m, 2H), 1.80–1.67 (m, 2H), 1.62–1.51 (m, 5H), 1.46 (s, 3H). ^{13}C NMR ($CDCl_3$) δ: 159.8, 143.9, 138.0, 136.2, 129.4, 125.7, 122.8, 121.1, 114.5, 111.2, 80.9, 55.3, 36.0, 29.7, 25.2, 24.6, 22.9, 22.8, 12.3. Anal. calcd. for $C_{19}H_{26}O_2$: C 79.68, H 9.15; found C 79.41, H 9.12.

(*E*)-1-Cyclohexenyl-5-(3-methoxyphenyl)-2-methyl-2-penten-1-one (**11d**): pale yellow oil. R_f 0.38 (EtOAc/Hex, 1:4). IR (thin film, cm^{-1}): 2933, 2858, 2836, 1632. ^1H NMR ($CDCl_3$) δ: 7.22 (ddd, *J* = 7.6, 7.6, 1.0 Hz, 1H), 6.81–6.74 (m, 3H), 6.31 (ddd, *J* = 3.9, 2.2, 1.7 Hz, 1H), 6.12 (tq, *J* = 7.2, 1.5 Hz, 1H), 3.81 (s, 3H), 2.75 (t, *J* = 7.6 Hz, 2H), 2.54 (dt, *J* = 7.6, 7.6 Hz, 2H), 2.27–2.23 (m, 2H), 2.19–2.14 (m, 2H), 1.80 (d, *J* = 1.4 Hz, 3H), 1.69–1.57 (m, 4H). ^{13}C NMR ($CDCl_3$) δ: 200.9, 159.9, 143.2, 140.2, 140.0, 138.4, 136.6, 129.6, 121.0, 114.5, 111.4, 55.4, 35.1, 30.4, 25.9, 24.5, 22.3, 21.9, 13.2.

*(*E*)-7-(3,4-Methylenedioxyphenyl)-2,4-dimethyl-1,4-heptadien-3-one (11e)*

The general procedures described for **11a** were followed using **9c** in place of **9a**.

(*E*)-7-(3,4-Methylenedioxyphenyl)-2,4-dimethyl-1,4-heptadien-3-ol (**12e**): colorless oil. R_f 0.27 (EtOAc/Hex, 1:4). ^1H NMR ($CDCl_3$) δ: 6.72 (d, *J* = 7.9 Hz, 1H), 6.68 (d, *J* = 1.7 Hz, 1H), 6.63 (dd, *J* = 7.9, 1.7 Hz, 1H), 5.91 (s, 2H), 5.52 (tqd, *J* = 7.1, 1.2, 1.2 Hz, 1H), 5.05 (br s, 1H), 4.91 (br s, 1H), 4.39 (br s, 1H), 2.61 (t, *J* = 7.5 Hz, 2H), 2.34 (dt, *J* = 7.5, 7.5 Hz, 2H), 1.58 (br s, 1H) overlapping with 1.57 (br s, 3H), 1.48 (br s, 3H). ^{13}C NMR ($CDCl_3$) δ: 147.7, 145.8, 145.5, 136.0, 135.8, 126.8, 121.3, 110.9, 109.1, 108.3, 100.9, 80.8, 35.6, 30.1, 18.9, 11.6. Anal. calcd. for $C_{16}H_{20}O_3$: C 73.52, H 7.74; found: C 73.59, H 7.81.

(*E*)-7-(3,4-Methylenedioxyphenyl)-2,4-dimethyl-1,4-heptadien-3-one (**11e**): colorless oil. R_f 0.38 (EtOAc/Hex, 1:4). IR (thin film, cm^{-1}): 2922, 2863, 1652. ^1H NMR ($CDCl_3$) δ: 6.73 (d, *J* = 7.8 Hz, 1H), 6.67 (d, *J* = 1.7 Hz, 1H), 6.62 (dd, *J* = 7.8, 1.7 Hz, 1H), 6.37 (tq, *J* = 7.2, 1.3 Hz, 1H), 5.93 (s, 2H), 5.55 (dq, *J* = 1.5, 1.5 Hz, 1H), 5.34 (br s, 1H), 2.69 (t, *J* = 7.5 Hz, 2H), 2.51 (dt, *J* = 7.5, 7.5 Hz, 2H), 1.93 (br s, 3H), 1.79 (br s, 3H). ^{13}C NMR ($CDCl_3$) δ: 200.8, 147.9, 146.1, 144.0, 143.0, 136.6, 135.2, 123.0, 121.3, 108.9, 108.4, 101.1, 34.7, 31.1, 19.4, 12.5.

*(*E*,*E*′)-8-(3,4-Methylenedioxyphenyl)-3-ethyl-5-methyl-2,5-octadien-4-one (11f)*

The general procedures described for **11c** were followed using **9c** in place of **9b**.

(*E*,*E*′)-8-(3,4-Methylenedioxyphenyl)-3-ethyl-5-methyl-2,5-octadien-4-ol (**12f**): pale yellow oil. R_f 0.25 (EtOAc/Hex, 1:4). IR (thin film, cm^{-1}): 3438 (br), 2962, 2927, 2872. ^1H NMR ($CDCl_3$) δ: 6.72 (d, *J* = 7.9 Hz, 1H), 6.68 (d, *J* = 1.7 Hz, 1H), 6.63 (dd, *J* = 7.9, 1.7 Hz, 1H), 5.91 (s, 2H), 5.58–5.48 (m, 2H), 4.39 (br s, 1H), 2.61 (t, *J* = 7.6 Hz, 2H), 2.33 (dt, *J* = 7.6, 7.6 Hz, 2H), 2.06 (dq, *J* = 13.6, 7.4 Hz, 1H), 1.87 (dq, *J* = 13.0, 7.4 Hz, 1H), 1.65 (d, *J* = 6.7 Hz, 3H), 1.59 (br s, 1H), 1.45 (br s, 3H), 0.91 (t, *J* = 7.6 Hz, 3H). ^{13}C NMR ($CDCl_3$) δ: 147.7, 145.7, 141.9, 136.4, 136.2, 125.6, 121.3, 120.3, 109.1, 108.3, 100.9, 80.6, 35.7, 30.2, 20.6, 13.7, 13.2, 12.5.

(*E*,*E*′)-8-(3,4-Methylenedioxyphenyl)-3-ethyl-5-methyl-2,5-octadien-4-one (**11f**): colorless oil. R_f 0.40 (EtOAc/Hex, 1:4). ^1H NMR ($CDCl_3$) δ: 6.74 (d, *J* = 7.8 Hz, 1H), 6.68 (d, *J* = 1.5 Hz, 1H), 6.62 (dd, *J* = 7.8, 1.5 Hz, 1H), 6.11 (tq, *J* = 7.1, 1.3 Hz, 1H), 6.01 (q, *J* = 7.0 Hz, 1H), 5.93 (s, 2H), 2.68 (t, *J* = 7.4 Hz, 2H), 2.48 (dt, *J* = 7.4, 7.4 Hz, 2H), 2.34 (q, *J* = 7.5 Hz, 2H), 1.79 (d, *J* = 7.0 Hz, 3H),1.78 (s, 3H), 0.94 (t, *J* = 7.5 Hz, 3H). ^{13}C NMR ($CDCl_3$) δ: 201.5, 147.8, 146.0, 143.2, 140.8, 137.6, 135.7, 135.3, 121.4, 109.0, 108.3, 101.0, 34.8, 30.9, 20.2, 14.1, 13.2, 13.1. Anal. calcd. for $C_{18}H_{22}O_3$: C 75.50, H 7.74; found: C 75.52, H 7.73.

*(*E*)-1-Cyclohexenyl-5-(3,4-methylendioxyphenyl)-2-methyl-2-penten-1-one (11g)*

The general procedures described for **11d** were followed using **9c** in place of **9b**.

© 2004 NRC Canada

(*E*)-1-Cyclohexenyl-5-(3,4-methylendioxyphenyl)-2-methyl-2-penten-1-ol (**12g**): pale yellow oil. R_f 0.25 (EtOAc/Hex, 1:4). IR (thin film, cm^{-1}): 3360 (br), 2960, 2927, 2872. ^1H NMR ($CDCl_3$) δ: 6.71 (d, *J* = 7.9 Hz, 1H), 6.68 (d, *J* = 1.7 Hz, 1H), 6.63 (dd, *J* = 7.9, 1.7 Hz, 1H), 5.91 (s, 1H), 5.91 (s, 1H), 5.72 (dddd, *J* = 3.7, 3.7, 1.8, 1.5 Hz, 1H), 5.48 (tdq, *J* = 7.2, 1.2, 1.2 Hz, 1H), 4.29 (br s, 1H), 2.61 (t, *J* = 7.5 Hz, 2H), 2.33 (dt, *J* = 7.5, 7.5 Hz, 2H), 2.07–2.02 (m, 2H), 1.81–1.67 (m, 2H), 1.61–1.52 (m, 4H), 1.50 (br s, 1H), 1.45 (s, 3H). ^{13}C NMR ($CDCl_3$) δ: 147.7, 145.8, 138.0, 136.3, 136.2, 125.6, 122.9, 121.4, 109.1, 108.3, 100.9, 80.9, 35.7, 30.0, 25.2, 24.6, 22.9, 22.8, 12.3.

(*E*)-1-Cyclohexenyl-5-(3,4-methylendioxyphenyl)-2-methyl-2-penten-1-one (**11g**): pale yellow oil. R_f 0.39 (EtOAc/Hex, 1:4). ^1H NMR ($CDCl_3$) δ: 6.73 (d, *J* = 7.8 Hz, 1H), 6.68 (d, *J* = 1.7 Hz, 1H), 6.63 (dd, *J* = 7.8, 1.7 Hz, 1H), 6.31 (dddd, *J* = 3.7, 3.7, 2.2, 1.6 Hz, 1H), 6.10 (tq, *J* = 7.2, 1.4 Hz, 1H), 5.92 (s, 2H), 2.68 (t, *J* = 7.5 Hz, 2H), 2.48 (dt, *J* = 7.5, 7.5 Hz, 2H), 2.26–2.22 (m, 2H), 2.19–2.15 (m, 2H), 1.78 (d, *J* = 0.8 Hz, 3H), 1.68–1.58 (m, 4H). ^{13}C NMR ($CDCl_3$) δ: 200.9, 147.9, 146.0, 140.1, 139.9, 138.5, 136.7, 135.5, 121.4, 109.0, 108.4, 101.1, 34.9, 30.8, 25.9, 24.5, 22.3, 21.9, 13.2.

(E)-7-(3′-Furyl)-2,4-dimethyl-1,4-heptadien-3-one (11h)

The general procedures described for **11a** were followed using **9d** in place of **9a**.

(*E*)-7-(3′-Furyl)-2,4-dimethyl-1,4-heptadien-3-ol (**12h**): colorless oil. R_f 0.70 (EtOAc/Hex, 1:1). ^1H NMR ($CDCl_3$) δ: 7.35 (t, *J* = 1.6 Hz, 1H), 7.23–7.22 (m, 1H), 6.30–6.28 (m, 1H), 5.54 (tdq, *J* = 7.1, 1.2, 1.2 Hz, 1H), 5.07 (br s, 1H), 4.93 (dq, *J* = 4.0, 1.5 Hz, 1H), 4.41 (br s, 1H), 2.51 (t, *J* = 7.6 Hz, 2H), 2.33 (dt, *J* = 7.6, 7.6 Hz, 2H), 1.59 (br s, 3H), 1.57 (br s, 1H), 1.52 (s, 3H). ^{13}C NMR ($CDCl_3$) δ: 145.6, 142.9, 139.1, 135.8, 127.0, 124.9, 111.2, 111.0, 80.8, 28.4, 24.9, 28.8, 11.7.

(*E*)-7-(3′-Furyl)-2,4-dimethyl-1,4-heptadien-3-one (**11h**): colorless oil. R_f 0.63 (EtOAc/Hex, 1:1). ^1H NMR ($CDCl_3$) δ: 7.36 (t, *J* = 1.5 Hz, 1H), 7.23–7.22 (m, 1H), 6.37 (tq, *J* = 7.0, 1.3 Hz, 1H), 6.28–6.27 (m, 1H), 5.56 (dq, *J* = 1.5, 1.5 Hz, 1H), 5.36–5.35 (m, 1H), 2.59 (t, *J* = 7.0 Hz, 2H), 2.50 (dt, *J* = 7.0, 7.0 Hz, 2H), 1.93 (dd, *J* = 1.5, 1.0 Hz, 3H), 1.84–1.82 (m, 3H). ^{13}C NMR ($CDCl_3$) δ 200.8, 144.1, 143.2, 143.1, 139.2, 136.7, 124.2, 123.1, 111.0, 29.5, 24.1, 19.4, 12.6. Anal. calcd. for $C_{13}H_{16}O_2$: C 76.44, H 7.90; found: C 76.15, H 7.92.

Cyclization of 11a

2,5-Dimethyl-3-(2-phenylethyl)cyclopent-2-en-1-one (13a)

A solution of **11a** (0.073 g, 0.34 mmol) in CH_2Cl_2 (35 mL) in a 100 mL round-bottomed flask fitted with a magnetic stir bar, a nitrogen inlet, and a rubber septum, was cooled to –78 °C. $BF_3{\cdot}OEt_2$ (0.180 mL, 1.42 mmol) was added dropwise. The reaction was then allowed to warm slowly to rt, after which TLC indicated **11a** was consumed. The reaction was quenched with H_2O (20 mL), the layers separated, and the aqueous layer extracted with CH_2Cl_2. The combined organic layers were dried ($MgSO_4$), concentrated, and subjected to radial chromatography (silica gel, 2 mm plate, EtOAc/Hex (1:4)) to provide **13a** (0.036 g, 69%) as a clear, colorless oil. R_f 0.55 (EtOAc/Hex, 1:1). IR (thin film, cm^{-1}): 2962, 2924, 2861, 1697, 1649. ^1H NMR ($CDCl_3$) δ: 7.30–7.26 (m, 2H), 7.23–7.15 (m, 3H), 2.83 (t, *J* = 7.4 Hz, 2H), 2.75–2.68 (m, 3H), 2.34 (qdd, *J* = 7.2, 7.2, 2.4 Hz, 1H), 2.06 (br d, *J* = 18.4 Hz, 1H), 1.57 (t, *J* = 2.0 Hz, 3H), 1.14 (d, *J* = 7.4 Hz, 3H). ^{13}C NMR ($CDCl_3$) δ: 212.7, 170.7, 140.9, 135.7, 128.7, 128.4, 126.5, 39.6, 38.8, 33.5, 33.1, 16.8, 8.2.

Representative procedure for domino Nazarov cyclization – arene trapping of 11

Benzohydrindenone (14f)

Dienone **11f** (51 mg, 0.18 mmol) was dissolved in CH_2Cl_2 (18 mL) and cooled to –78 °C. A solution of $TiCl_4$ in CH_2Cl_2 (0.050 mL of a 3.51 mol L^{-1} solution, 0.18 mmol) was added dropwise, and after 5 min TLC showed complete consumption of the starting material. The reaction was quenched with water (5 mL) and allowed to warm to rt, then the layers were separated and the aqueous layer extracted with CH_2Cl_2 (3 × 5 mL). The combined organic layers were dried ($MgSO_4$) and concentrated to give 51 mg (99%) of **14f** as colorless crystals, deemed pure by TLC and NMR analysis: mp 71 to 72 °C. R_f 0.48 (EtOAc/hexanes, 1:4). IR (thin film, cm^{-1}): 2959, 2923, 2867, 1731. ^1H NMR ($CDCl_3$, 500 MHz) δ: 6.97 (s, 1H), 6.49 (s, 1H), 5.86 (s, 2H), 2.76 (ddd, *J* = 17.2, 13.0, 6.0 Hz, 1H), 2.63 (ddd, *J* = 17.1, 6.2, 1.6 Hz, 1H), 2.02 (dddd, *J* = 13.9, 5.2, 3.3, 1.8 Hz, 1H), 1.87 (dddd, *J* = 13.5, 13.5, 6.1, 3.7 Hz, 1H), 1.82–1.75 (m, 2H), 1.71–1.66 (m, 1H), 1.54–1.45 (m, 2H), 1.34 (s, 3H), 1.12 (d, *J* = 6.1 Hz, 3H), 0.65 (t, *J* = 7.5 Hz, 3H). ^{13}C NMR ($CDCl_3$, 125 MHz) δ: 221.6, 146.3, 146.3, 129.1, 128.4, 108.8, 108.4, 100.9, 56.6, 51.9, 48.8, 33.3, 27.2, 25.1, 21.9, 18.4, 17.7, 11.2.

The representative procedure described for the formation of **14f** was followed to give **14b**–**14e** and **14g**.

Benzohydrindenone **14b**: pale yellow oil; single regio- and diastereoisomer by ^1H and ^{13}C NMR analysis. R_f 0.39 (EtOAc/Hex, 1:4). IR (thin film, cm^{-1}): 2958, 2926, 2870, 1732. ^1H NMR ($CDCl_3$) δ: 7.42 (d, *J* = 8.8 Hz, 1H), 6.71 (dd, *J* = 8.8, 2.8 Hz, 1H), 6.58 (d, *J* = 2.8 Hz, 1H), 3.76 (s, 3H), 2.88 (ddd, *J* = 17.4, 12.0, 6.0 Hz, 1H), 2.72 (ddd, *J* = 17.4, 6.0, 2.0 Hz, 1H), 2.28 (ddq, *J* = 11.3, 8.2, 7.1 Hz, 1H), 2.19 (ddt, *J* = 12.0, 6.0, 3.5 Hz, 1H), 2.07 (ddd, *J* = 12.5, 8.3, 6.1 Hz, 1H), 2.00 (dddd, *J* = 12.5, 9.8, 6.1, 3.8 Hz, 1H), 1.92–1.85 (m, 2H), 1.36 (s, 3H), 0.99 (d, *J* = 7.1 Hz, 3H). ^{13}C NMR ($CDCl_3$) δ 222.6, 158.1, 136.9, 130.3, 127.7, 113.9, 112.8, 55.3, 50.7, 42.9, 41.5, 31.7, 27.2, 25.4, 21.3, 16.0.

Benzohydrindenone **14c**: colorless oil; single regio- and stereoisomer by ^1H and ^{13}C NMR analysis. R_f 0.70 (EtOAc/Hex, 1:1). IR (thin film, cm^{-1}): 2958, 2923, 2865, 1730. ^1H NMR ($CDCl_3$) δ: 7.37 (d, *J* = 8.7 Hz, 1H), 6.70 (dd, *J* = 8.6, 2.8 Hz, 1H), 6.57 (d, *J* = 2.8 Hz, 1H), 3.75 (s, 3H), 2.84 (ddd, *J* = 17.7, 13.0, 6.5 Hz, 1H), 2.71 (dd, *J* = 17.5, 5.0 Hz, 1H), 2.04 (dddd, *J* = 14.0, 5.1, 3.3, 1.8 Hz, 1H), 1.91 (dqd, *J* = 13.5, 6.2, 3.5 Hz, 1H), 1.83–1.75 (m, 2H), 1.73–1.68 (m, 1H), 1.54–1.42 (m, 2H), 1.35 (s, 3H), 1.12 (d, *J* = 6.1 Hz, 3H), 0.61 (t, *J* = 7.5 Hz, 3H). ^{13}C NMR ($CDCl_3$) δ: 221.6, 158.0, 137.0, 130.1, 127.5, 113.9, 112.7, 56.6, 55.3, 51.4, 48.9, 33.2, 27.1, 25.1, 21.9, 18.3, 17.7, 11.1.

© 2004 NRC Canada

Benzohydrindenone **14d**: colorless solid; single regio- and stereoisomer by ^{1}H and ^{13}C NMR analysis; mp 86–88 °C. R_f 0.40 (EtOAc/Hex, 1:4). IR (thin film, cm^{-1}) 2924, 2855, 1734. ^{1}H NMR ($CDCl_3$) δ: 7.66 (d, J = 8.8 Hz, 1H), 6.76 (dd, J = 8.8, 2.4 Hz, 1H), 6.57 (d, J = 2.8 Hz, 1H), 3.77 (s, 3H), 2.79 (ddd, J = 17.5, 13.2, 5.8 Hz, 1H), 2.67 (ddd, J = 17.5, 5.9, 2.4 Hz, 1H), 2.10–2.00 (m, 3H), 1.92–1.80 (m, 4H), 1.76 (ddd, J = 13.1, 11.4, 3.4 Hz, 1H), 1.49–1.40 (m, 1H), 1.42 (s, 3H), 1.29–1.08 (m, 3H), 1.04–0.96 (m, 1H). ^{13}C NMR ($CDCl_3$) δ: 219.6, 157.9, 137.1, 130.7, 128.9, 113.6, 112.8, 55.3, 54.3, 50.7, 48.2, 41.0, 30.6, 28.5, 26.4, 26.1, 25.8, 25.7, 19.1.

Benzohydrindenone **14e**: pale yellow oil; single regio- and diastereoisomer by ^{1}H and ^{13}C NMR analysis. R_f 0.39 (EtOAc/Hex, 1:4). IR (thin film, cm^{-1}): 2959, 2925, 2872, 1732. ^{1}H NMR ($CDCl_3$) δ: 7.01 (s, 1H), 6.50 (s, 1H), 5.88 (d, J = 1.5 Hz, 1H), 5.86 (d, J = 1.5 Hz, 1H), 2.80 (ddd, J = 17.0, 12.3, 5.9 Hz, 1H), 2.64 (ddd, J = 17.0, 5.9, 2.2 Hz, 1H), 2.28 (ddq, J = 15.4, 11.2, 7.2 Hz, 1H), 2.20–2.14 (m, 1H), 2.06 (ddd, J = 12.5, 8.3, 6.0 Hz, 1H), 1.96 (dddd, J = 12.5, 12.5, 6.0, 3.8, Hz, 1H), 1.90 (dd, J = 1.4, 1.4 Hz, 1H), 1.89–1.83 (m, 1H), 1.35 (s, 3H), 1.01 (d, J = 7.2 Hz, 3H). ^{13}C NMR ($CDCl_3$) δ: 146.4, 129.0, 128.5, 108.7, 100.9, 51.1, 42.8, 41.4, 31.6, 27.2, 25.4, 21.4, 16.0.

Benzohydrindenone **14g**: pale yellow solid; single regio- and stereoisomer by ^{1}H and ^{13}C NMR analysis; mp 124–126 °C. R_f 0.32 (EtOAc/Hex, 1:4). IR (thin film, cm^{-1}): 2924, 2856, 1735. ^{1}H NMR ($CDCl_3$) δ: 7.25 (s, 1H), 6.48 (s, 1H), 5.88 (d, J = 1.5 Hz, 1H), 5.84 (d, J = 1.5 Hz, 1H), 2.75–2.66 (m, 1H), 2.62–2.54 (m, 1H), 2.09–2.03 (m, 2H), 2.03–1.97 (m, 1H), 1.85–1.78 (m, 4H), 1.74 (ddd, J = 13.1, 11.2, 3.4 Hz, 1H), 1.47–1.39 (m, 1H), 1.39 (s, 3H), 1.24–1.07 (m, 3H), 1.05–0.97 (m, 1H). ^{13}C NMR ($CDCl_3$) δ: 219.4, 146.4, 146.2, 129.7, 129.1, 109.2, 108.5, 100.9, 54.2, 51.2, 48.1, 41.0, 30.6, 28.5, 26.4, 26.1, 25.7, 25.7, 19.2.

Cyclization of 3h furohydrindenone (14h)

(*E*)-7-(3-Furyl)-2,4-dimethyl-1,4-heptadien-3-one (**11h**) (0.042 g, 0.21 mmol) was dissolved in CH_2Cl_2 (20 mL) and cooled to –78 °C. $TiCl_4$ (0.060 mL of a 3.51 mol L^{-1} solution in CH_2Cl_2, 0.21 mmol) was added, and the reaction was allowed to warm to rt; after 15 min at rt, the reaction was quenched with H_2O (10 mL), and stirred overnight. The layers were separated, the aqueous layer was extracted with CH_2Cl_2 (3 × 10 mL), dried ($MgSO_4$), and concentrated. Radial chromatography (silica gel, 1 mm plate, EtOAc/Hex (1:4)) provided 0.024 g (56%) of the tricyclic ketone **14h** as a colorless oil and a single regio- and stereoisomer by ^{1}H and ^{13}C NMR analysis. R_f 0.70 (EtOAc/Hex, 1:1). ^{1}H NMR ($CDCl_3$) δ: 7.30 (d, J = 1.9 Hz, 1H), 6.15 (d, J = 1.9 Hz, 1H), 2.51–2.48 (m, 2H), 2.35–2.25 (m, 3H), 2.07 (ddd, J = 8.5, 6.3, 6.3 Hz, 1H), 1.91–1.86 (m, 2H), 1.39 (s, 3H), 1.05 (d, J = 7.1 Hz, 3H). ^{13}C NMR ($CDCl_3$) δ: 218.8, 147.9, 142.8, 117.4, 110.3, 49.8, 43.1, 42.8, 31.7, 29.9, 22.4, 18.8, 15.2. IR (thin film, cm^{-1}): 2960, 2924, 2853, 1739, 1456.

Acknowledgments

We thank U.S. National Institutes of Health (GM 44720) for support of this work, Dr. Atta Arif for assistance in obtaining the X-ray crystal structure of **14f**, and Ben Jessie for preliminary experiments in this study.

References

1. Reviews: (*a*) L.F. Tietze. Chem. Rev. **96**, 115 (1996); (*b*) G. Poli, G. Giambastiani, and A. Heumann. Tetrahedron, **56**, 5959 (2000); (*c*) L.F. Tietze and A. Modi. Med. Res. Rev. **20**, 304 (2000); (*d*) A. Padwa. Pure Appl. Chem. **75**, 47 (2003); (*e*) K.C. Nicolaou, T. Montagnon, and S.A. Snyder. Chem. Commun. 551 (2003).
2. Reviews: (*a*) K.L. Habermas, S.E. Denmark, and T.K. Jones. Org. React. (N.Y.), **45**, 1 (1994); (*b*) S.E. Denmark. *In* Comprehensive organic synthesis. Vol. 5. *Edited by* B.M. Trost and I. Fleming. Pergamon, Oxford. 1991. pp. 751–784.
3. (*a*) J.A. Bender, A.E. Blize, C.C. Browder, S. Giese, and F.G. West. J. Org. Chem., **63**, 2430 (1998); (*b*) S. Giese and F.G. West. Tetrahedron Lett. **39**, 8393 (1998); (*c*) Y. Wang, A.M. Arif, and F.G. West. J. Am. Chem. Soc. **121**, 876 (1999); (*d*) C.C. Browder and F.G. West. Synlett, 1363 (1999); (*e*) J.A. Bender, A.M. Arif, and F.G. West. J. Am. Chem. Soc. **121**, 7443 (1999); (*f*) S. Giese, L. Kastrup, D. Stiens, and F.G. West. Angew. Chem. Int. Ed. **39**, 1970 (2000); (*g*) Y. Wang, B.D. Schill, A.M. Arif, and F.G. West. Org. Lett. **5**, 2747 (2003).
4. C. Zeng, M. Han, and D.F. Covey. J. Org. Chem. **65**, 2264 (2000).
5. H. Nemoto, J. Miyata, M. Yoshida, N. Raku, and K. Fukumoto. J. Org. Chem. **62**, 7850 (1997).
6. M.E. Kopach, A.H. Fray, and A.I. Meyers. J. Am. Chem. Soc. **118**, 9876 (1996).
7. Isolation: (*a*) K.D. Wellington, R.C. Cambie, P.S. Rutledge, and P.R. Bergquist. J. Nat. Prod. **63**, 79 (2000); Synthesis: (*b*) K.C. Nicolaou, D. Gray, and J.S. Tae. Angew. Chem. Int. Ed. **40**, 3675 (2001); (*c*) K.C. Nicolaou, D. Gray, and J.S. Tae. Angew. Chem. Int. Ed. **40**, 3679 (2001).
8. For a preliminary report of this work, see: C.C. Browder, F.P. Marmsäter, and F.G. West. Org. Lett. **3**, 3033 (2001).
9. M.A. Blanchette, W. Choy, J.T. Davis, A.P. Essenfeld, S. Masamune, W.R. Roush, and T. Sakai. Tetrahedron Lett. **25**, 2183 (1984).
10. (*a*) G. Ahlgren, G. Bergstroem, J. Loefqvist, A. Jansson, and T. Norin. J. Chem. Ecol. **5**, 309 (1979); (*b*) A.B. Wassgren, O. Anderbrant, J. Loefqvist, B.S. Hansson, G. Bergstroem, E. Hedenstroem, and H.E. Hoegberg. J. Insect Physiol. **38**, 885 (1992).
11. Previous syntheses of **9d**: (*a*) P. Baeckstroem, S. Okecha, N. De Silva, D. Wijekoon, and T. Norin. Acta Chem. Scand. Ser. B, **B36**, 31 (1982); (*b*) R. Baker, N. Ekanayake, and S.A. Johnson. J. Chem. Res. Synop. 74 (1983); (*c*) S. Bernasconi, M. Colombo, G. Jommi, and M. Sisti. Gazz. Chim. Ital. **116**, 69 (1986); (*d*) I. Bock, H. Bornowski, A. Ranft, and H. Theis. Tetrahedron **46**, 1199 (1990); (*e*) M. Nishizawa, H. Takenaka, T. Kohno, H. Takao, and H. Yamada. Chem. Pharm. Bull. **41**, 791 (1993); (*f*) D.K. Barma, A. Kundu, R. Baati, C. Mioskowski, and J.R. Falck. Org. Lett. **4**, 1387 (2002).
12. Reviews: (*a*) R.H. Shapiro. Org. React. (N.Y.), **23**, 405 (1976); (*b*) R.M. Adlington and A.G.M. Barrett. Acc. Chem. Res. **16**, 55 (1983); Trisyl hydrazones: (*c*) N.J. Cusack, C.B. Reese, A.C. Risius, and B. Roozpeikar. Tetrahedron, **32**, 2157 (1976).
13. Barium manganate is a mild and effective oxidant for the conversion of dienols to dienones: (*a*) S.E. Denmark and G.A. Hite. Helv. Chim. Acta, **71**, 195 (1988); (*b*) H. Firouzabadi and E. Ghaderi. Tetrahedron Lett. 839 (1978).

© 2004 NRC Canada

14. F.G. West and D.W. Willoughby. J. Org. Chem. **58**, 3796 (1993).
15. (*a*) S.P. Tanis, M.V. Deaton, L.A. Dixon, M.C. McMills, J.W. Raggon, and M.A. Collins. J. Org. Chem. **63**, 6914 (1998); (*b*) S.P. Tanis, E.D. Robinson, M.C. McMills, and W. Watt. J. Am. Chem. Soc. **114**, 8349 (1992); (*c*) S.P. Tanis, M.C. McMills, T.A. Scahill, and D.A. Kloosterman. Tetrahedron Lett. **31**, 1977 (1990).
16. (*a*) G. Piancatelli, M. D'Auria, and F. Donofrio. Synthesis, 867 (1994); (*b*) J. Raczko and J. Jurczak. *In* Studies in natural product chemistry. Vol. 16. *Edited by* Atta-ur-Rahman. Elsevier, Amsterdam. 1995. pp. 639–685; (*c*) C.O. Kappe, S.S. Murphree, and A. Padwa. Tetrahedron, **53**, 14179 (1997); (*d*) X.L. Hou, H.Y. Cheung, T.Y. Hon, P.L. Kwan, T.H. Lo, S.Y. Tong, and H.N.C. Wong. Tetrahedron, **54**, 1955 (1998).
17. (*a*) A.E. Hill and H.M.R. Hoffmann. J. Am. Chem. Soc. **96**, 4597 (1974); (*b*) H. Shimizu, M. Tanaka, and Y. Tsuno J. Am. Chem. Soc. **104**, 1330 (1982).
18. (*a*) D.A. Smith and C.W. Ulmer. Tetrahedron Lett. **32**, 725 (1991); (*b*) D.A. Smith and C.W. Ulmer. J. Org. Chem. **58**, 4118 (1993).
19. (*a*) A.R. Bin Manas and R.A.J. Smith. Tetrahedron, **43**, 1847 (1987); (*b*) T. Horaguchi, E. Hasegawa, T. Shimizu, K. Tanemura, and T. Suzuki. J. Heterocycl. Chem. **26**, 365 (1989)
20. (*a*) J.W. Bode, M.P. Doyle, M.N. Protopopova, and Q. Zhou. J. Org. Chem. **61**, 9146 (1996); (*b*) J.X. de Araujo-Junior, E.J. Barriero, J.P. Parente, and C.A.M. Fraga. Synth. Commun. **29**, 263 (1999).
21. (*a*) J.M. Salvino, M. Mervic, H.J. Mason, T. Kiesow, D. Teager, J. Airey, and R. Labaudiniere. J. Org. Chem. **64**, 1823 (1999); (*b*) T. Sugahara and K. Ogasawara. Tetrahedron Lett. **37**, 7403 (1996).
22. J. Uenishi, R. Kawahama, and O. Yonemitsu. J. Org. Chem. **62**, 1691 (1997).
23. P. Weyerstahl, A. Schenk, and H. Marschall. Liebigs Ann. 1849 (1995).
24. Y.S. Hon and L. Lu. Tetrahedron, **51**, 7937 (1995).
25. (*a*) G.W. Daub, J.P. Edwards, C.R. Okada, J.W. Allen, C.T. Maxey, M.S. Wells, A.S. Goldstein, M.J. Dibley, C.J. Wang, D.P. Ostercamp, S. Chung, P.S. Cunningham, and M.A. Berliner. J. Org. Chem. **62**, 1976 (1997); (*b*) M.E. Jung and D.C. D'Amico. J. Am. Chem. Soc. **117**, 7379 (1995).

© 2004 NRC Canada

Molecular tectonics — Use of urethanes and ureas derived from tetraphenylmethane and tetraphenylsilane to build porous chiral hydrogen-bonded networks[1]

Dominic Laliberté, Thierry Maris, and James D. Wuest

Abstract: Tetraphenylmethane, tetraphenylsilane, and simple derivatives with substituents that do not engage in hydrogen bonding typically crystallize as close-packed structures with essentially no space available for the inclusion of guests. In contrast, derivatives with hydrogen-bonding groups are known to favor the formation of open networks that include significant amounts of guests. To explore this phenomenon, we synthesized six new derivatives **5a**–**5e** and **6a** of tetraphenylmethane and tetraphenylsilane with urethane and urea groups at the para positions, crystallized the compounds, and determined their structures by X-ray crystallography. As expected, all six compounds crystallize to form porous three-dimensional hydrogen-bonded networks. In the case of tetraurea **5e**, 66% of the volume of the crystals is accessible to guests, and guests can be exchanged in single crystals without loss of crystallinity. Of special note are: (*i*) the use of tetrakis(4-isocyanatophenyl)methane (**1f**) as a precursor for making enantiomerically pure tetraurethanes and tetraureas, including compounds **5b**, **5c**; and (*ii*) their subsequent crystallization to give porous chiral hydrogen-bonded networks. Such materials promise to include chiral guests enantioselectively and to be useful in the separation of racemates, asymmetric catalysis, and other applications.

Key words: crystal engineering, molecular tectonics, hydrogen bonding, networks, porosity, urethanes, ureas, tetraphenylmethane, tetraphenylsilane.

Résumé : Le tétraphénylméthane, le tétraphénylsilane et leurs dérivés simples ne portant pas de substituants pouvant participer à des liaisons hydrogène cristallisent généralement sous la forme de structures compactes dans lesquelles il n'y a pas de place disponible pour l'inclusion de molécules invitées. Par contraste, il est bien connu que les dérivés comportant des groupes pouvant donner lieu à des liaisons hydrogène favorisent la formation de réseaux ouverts qui peuvent inclure des quantités importantes de molécules invitées. Dans le but d'étudier ce phénomène, on a réalisé la synthèse de six nouveaux dérivés, **5a**–**5e** et **6a**, du tétraphénylméthane et du tétraphénylsilane portant des groupes uréthane et urée en position para qui ont été cristallisés et dont on a déterminé la structure par diffraction des rayons X. Tel que prévu, les six composés cristallisent en formant des réseaux poreux tridimensionnels reliés par des ponts hydrogène. Dans le cas de la tétraurée **5e**, 66 % du volume des cristaux est disponible pour des molécules invitées et les invités peuvent être échangés dans les cristaux uniques sans perte de cristallinité. Il est particulièrement important de noter: (*i*) qu'il est possible d'utiliser le tétrakis(4-isocyanatophényl)-méthane (**1f**) comme précurseur dans la synthèse de tétrauréthanes et de tétraurées énantiomèrement pures, y compris les composés **5b**, **5c** et (*ii*) qu'il est possible de les cristalliser subséquemment pour donner des réseaux chiraux poreux reliés par des ponts hydrogène. Des tels produits pourraient inclure énantiosélectivement des molécules invitées chirales et ainsi être utilisés dans la séparation de racémates, en catalyse asymétrique ou dans d'autres applications.

Mots clés : ingénierie cristalline, tectonique moléculaire, liaison hydrogène, réseaux, porosité, uréthanes, urées, tétraphénylméthane, tétraphénylsilane.

[Traduit par la Rédaction]

Introduction

No reliable method yet exists for predicting the detailed structure of molecular crystals (1–4), and the relationship between the structure of crystals and their physical properties remains poorly understood. For these reasons, attempts to control molecular crystallization and to engineer crystals for specific applications remain largely empirical activities.

Received 10 October 2003. Published on the NRC Research Press Web site at http://canjchem.nrc.ca on 4 March 2004.

Dedicated with respect and affection to Professor Ed Piers.

D. Laliberté, T. Maris, and J.D. Wuest.[2] Département de Chimie, Université de Montréal, Montréal, QC H3C 3J7, Canada.

[1]This article is part of a Special Issue dedicated to Professor Ed Piers.
[2]Corresponding author (e-mail: wuest@chimie.umontreal.ca).

 doi: 10.1139/V03-208 © 2004 NRC Canada

As a result, crystal engineering offers exceptional challenges and opportunities, and it has become one of the most exciting areas in contemporary science (5).

In a recent review (1), Dunitz identifies a strategy for directing molecular crystallization that has played a key role in bringing crystal engineering to the forefront of science: "…computational methods for predicting crystal structures of organic compounds cannot yet be regarded as reliable. From a more qualitative and descriptive viewpoint has come the notion that certain groupings in organic molecules exercise attractive intermolecular interactions and so guide the molecules into distinctive patterns in their crystal structures…This indeed has become one of the tenets of crystal engineering. The prime example of a structure directing interaction is, of course, the hydrogen bond."

This strategy can be used to design molecules to serve as subunits for the programmed construction of particular crystalline networks. This can be achieved by incorporating carefully oriented arrays of sticky sites that interact intermolecularly according to reliable motifs. Such molecules have been called tectons (6), a term derived from the Greek word for builder, and molecular tectonics refers to the strategy of building supramolecular structures from tectonic subunits (6, 7).

Tectons have arrays of sticky sites that direct intermolecular association, linked to cores that orient the sticky sites and introduce other desirable molecular features. In favorable cases, the oriented sticky sites play a dominant role in association and place each tecton in a predetermined position relative to its neighbors. Normally, tectons cannot form structures that pack efficiently and simultaneously obey the imperatives of strong directional interactions, so open molecular networks are favored, with significant space for the inclusion of guests. Many different sticky sites and cores can be used, giving molecular tectonics wide scope as a strategy for creating ordered materials with unique properties. In particular, we have recently made hydrogen-bonded molecular crystals that (*i*) can be engineered with sub-nanometric precision (8); (*ii*) use at least 75% of their volume to include guests, which can be exchanged without loss of crystallinity (9); (*iii*) can be deformed by at least 30% without loss of crystallinity (10); and (*iv*) react with external agents to give single crystals of new compounds with retention of the original crystalline architecture (11, 12).[3]

Invaluable basic information about molecular tectonics can be acquired through systematic comparison of structures built from tectons with a fixed core and variable sticky sites, or with fixed sticky sites and variable cores. In such studies, relatively rigid cores are beneficial because they facilitate comparison by minimizing polymorphism due to multiple conformations. The tetraphenylmethyl core (**1a**) and its tetraphenylsilyl analogue **2a** are particularly attractive choices, and various tectons with simple hydrogen-bonding sites attached to these cores have been used in crystal engineering (8, 13–16).

Tetraphenylmethane and tetraphenylsilane crystallize to form isomorphous close-packed structures held together by multiple phenyl–phenyl embraces (17, 18), and simple derivatives with substituents that do not engage in hydrogen bonding also typically form close-packed structures (19–29). In contrast, 4-substituted derivatives with simple hydrogen-bonding groups, including tetraphenols **1b** and **2b** (13), tetraboronic acids **1c** and **2c** (8), and other compounds (15, 16), are known to favor open networks that include significant amounts of guests. Even derivatives with substituents that form relatively weak C-H···O hydrogen bonds, such as tetrakis(4-nitrophenyl)methane (**1d**) (14), can form open networks.

To explore the scope of this phenomenon, help identify its origins, and test its potential for creating ordered materials with new properties, we have extended our study of tectons derived from tetraphenylmethane and tetraphenylsilane to include new 4-substituted derivatives bearing urethane and urea groups, which have been used previously in crystal engineering because they self-associate reliably in the solid state to form hydrogen-bonded chains **3** and **4** (30–37). In this paper, we show how such compounds can be made and used to generate networks that are both porous and chiral.

Results and discussion

Synthesis of urethanes and ureas derived from tetraphenylmethane and tetraphenylsilane

Tetrakis(4-nitrophenyl)methane (**1d**) (38) was reduced by an improved procedure (H_2/Pd/C, THF) to provide a 99% yield of the known tetrakis(4-aminophenyl)methane (**1e**) (16, 38, 39). Subsequent reaction of tetramine **1e** with triphosgene and triethylamine gave tetrakis(4-isocyanatophenyl)methane (**1f**) in 97% yield. The analogous isothiocyanate **1g** was obtained in 89% yield by the reaction of tetramine **1e** with thiophosgene and triethylamine. Heating tetra(isocyanate) **1f** with alcohols and amines then gave the corresponding urethanes and ureas. In this way, urethanes **5a**, **5b** and ureas **5c**, **5d** were prepared from ethanol, (*R*)-2-butanol, (*S*)-2-butylamine, and (*S*)-α-methylbenzylamine in yields of 83%, 78%, 99%, and 99%, respectively. Treatment of tetra(isocyanate) **1f** with aqueous ammonia at 25 °C gave simple urea **5e** in 92% yield. For comparison with tetraurethane **5a,** analogue **6a** with a tetraphenylsilyl core was prepared in 18% yield by Pd-catalyzed coupling of tetrakis(4-bromophenyl)silane (**2d**) (40) with ethyl carbamate (41).

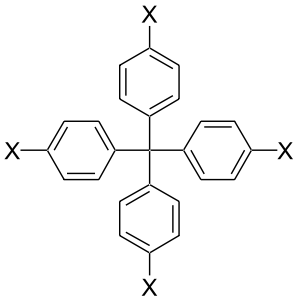
Structure of tetrakis(4-isothiocyanatophenyl)methane (1g)

Tetra(isothiocyanate) **1g** was crystallized from $CHCl_3$–hexane, and its structure was determined by X-ray diffraction (Table 1, Fig. 1).[4] Like most other simple derivatives of tetraphenylmethane and tetraphenylsilane (17–29), compound **1g** forms a close-packed structure without included guests. This observation confirms that molecules with a

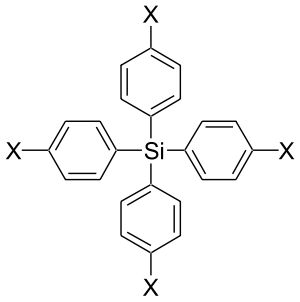
[3] For citations of other recent studies of the engineering of hydrogen-bonded molecular crystals, see refs. 8–12.

[4] Supplementary data may be purchased from the Directory of Unpublished Data, Document Delivery, CISTI, National Research Council Canada, Ottawa, ON K1A 0S2, Canada (http://www/nrc.ca/cisti/irm/unpub_e.shtml for information on ordering electronically). CCDC 221549–221554 contain the supplementary crystallographic data for this paper. These data can be obtained free of charge via www.ccdc.cam.ac.uk/conts/retrieving.html (or from the Cambridge Crystallographic Data Centre, 12 Union Road, Cambridge CB2 1EZ, U.K.; fax: +44 1223 336033; or e-mail: deposit@ccdc.cam.ac.uk).

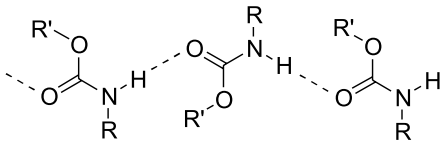
© 2004 NRC Canada



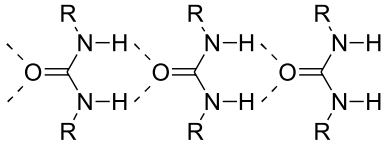
1a (X = H)
1b (X = OH)
1c (X = $B(OH)_2$)
1d (X = NO_2)
1e (X = NH_2)
1f (X = NCO)
1g (X = NCS)



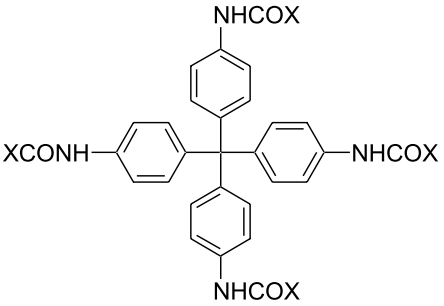
2a (X = H)
2b (X = OH)
2c (X = $B(OH)_2$)
2d (X = Br)



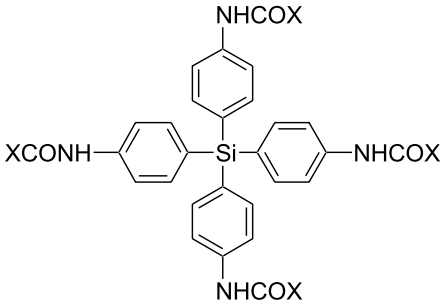
3



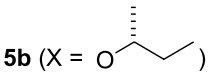
4



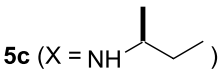
5a (X = OC_2H_5)



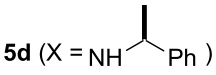
6a (X = OC_2H_5)



5b (X =)



5c (X =)



5d (X =)

5e (X = NH_2)

close structural relationship to tectons **5a**–**5e**, but without an ability to self-associate by hydrogen bonding, are not predisposed to form inclusion compounds.

Analysis of hydrogen-bonded networks formed by crystallization of tetraurethane 5a and the analogous silane 6a

Tecton **5a** crystallized from THF–pentane in the tetragonal space group *I*-4 as an inclusion compound of well-defined composition **5a**·2THF (Table 1).[4] The structure is shown in Figs. 2 and 3. The tectons can be divided into two equal populations (Fig. 2), one that donates single hydrogen bonds to four symmetrically oriented neighbors, and the other that accepts hydrogen bonds from four symmetrically oriented neighbors and simultaneously donates hydrogen bonds to four molecules of THF. Connecting the tetrahedral centers of hydrogen-bonded tectons defines a diamondoid network (42) with an alternating hydrogen bond donor–acceptor arrangement, in which each node is surrounded by four belonging to the other population. The network is held

© 2004 NRC Canada

Fig. 1. ORTEP drawing of the crystal structure of tetrakis(4-isothiocyanatophenyl)methane (**1g**). Ellipsoids are drawn at the 30% probability level, and hydrogen atoms are represented by a sphere of arbitrary size. One of the arms (N46) is disordered over two positions.

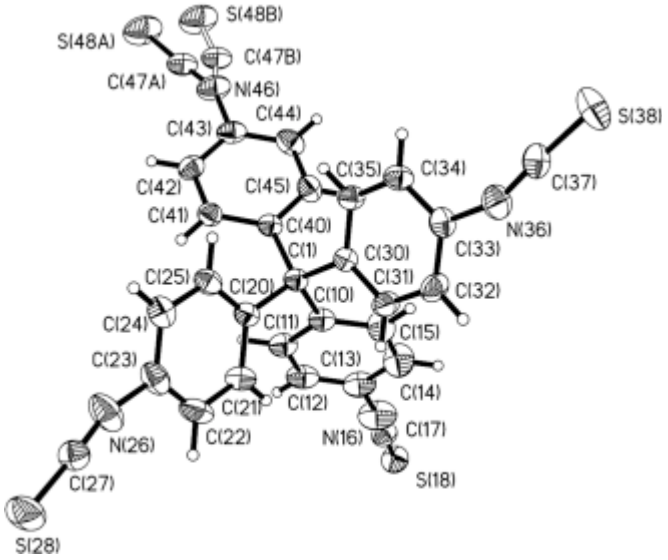
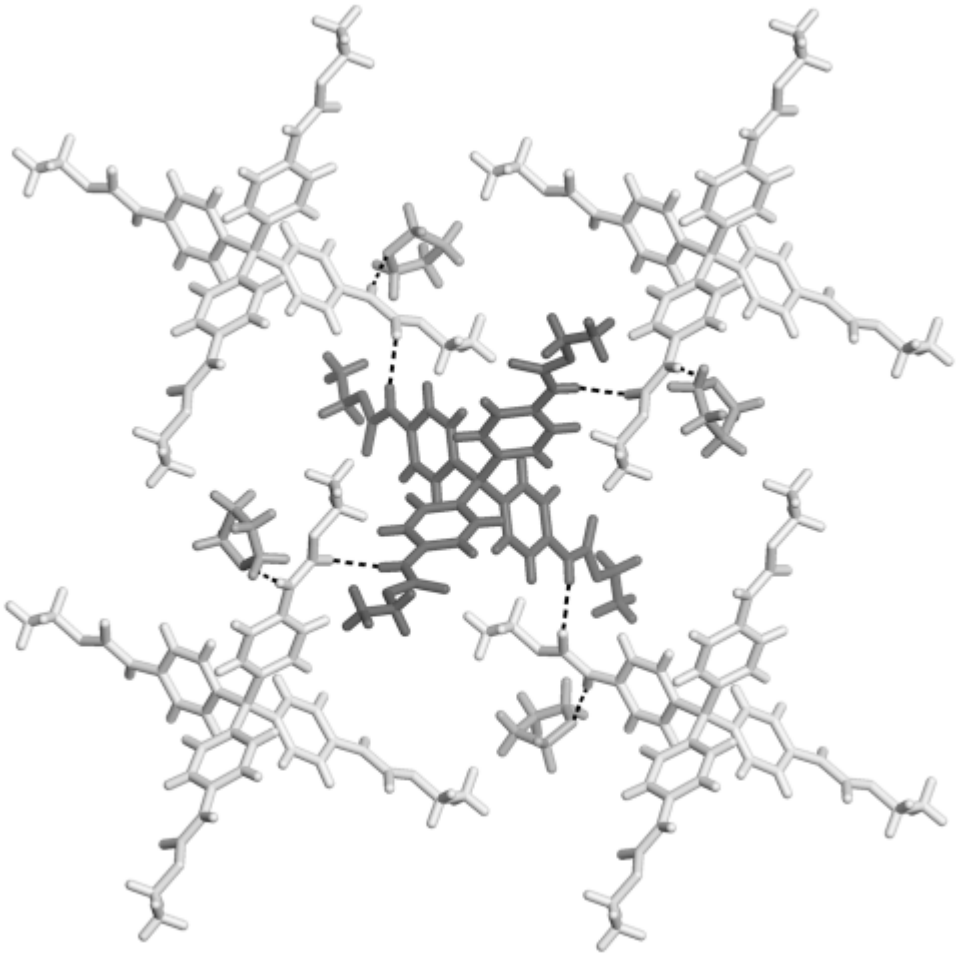


Table 1. Crystallographic data for compounds **1g**, **5a**·2THF, and **6a**·2dioxane.[4]

Compound	**1g**	**5a**·2THF	**6a**·2dioxane
Formula	$C_{29}H_{16}N_4S_4$	$C_{45}H_{56}N_4O_{10}$	$C_{44}H_{56}N_4O_{12}Si$
Fw	548.74	812.94	861.02
F(000)	1128	1736	916
Crystal system	Monoclinic	Tetragonal	Tetragonal
Space group	$P2_1/n$	$I\text{-}4$	$P4_2/n$
a (Å)	11.6490(1)	24.9135(8)	17.7781(2)
b (Å)	11.4547(1)	24.9135(8)	17.7781(2)
c (Å)	20.5132(1)	7.1597(2)	7.1904(1)
α (°)	90	90	90
β (°)	95.890(1)	90	90
γ (°)	90	90	90
Volume (Å^3)	2722.75(4)	4443.9(2)	2272.60(5)
Z	4	4	2
Density (g/cm^3)	1.339	1.215	1.258
Temperature (K)	293(2)	293(2)	293(2)
R_1	0.0609	0.0688	0.0724
wR_2	0.1810	0.1795	0.2160
GoF	1.056	1.008	1.024
Porosity (%)	0	29	0

Fig. 2. Representation of the structure of crystals of tetraurethane **5a** grown from THF–pentane, showing a central tecton (dark gray) that donates single hydrogen bonds to four neighboring tectons (light gray). Each neighbor accepts single hydrogen bonds from three other tectons and donates hydrogen bonds to the guests (THF). Hydrogen bonds appear as broken lines.



© 2004 NRC Canada

Fig. 3. View along the *c* axis of the network constructed from tetraurethane **5a** showing a 2 × 2 × 4 array of unit cells. Guests are omitted, and atoms are shown as spheres of van der Waals radii to reveal the cross sections of the channels. Atoms of hydrogen appear in white, atoms of carbon in light gray, atoms of oxygen in gray, and atoms of nitrogen in dark gray.

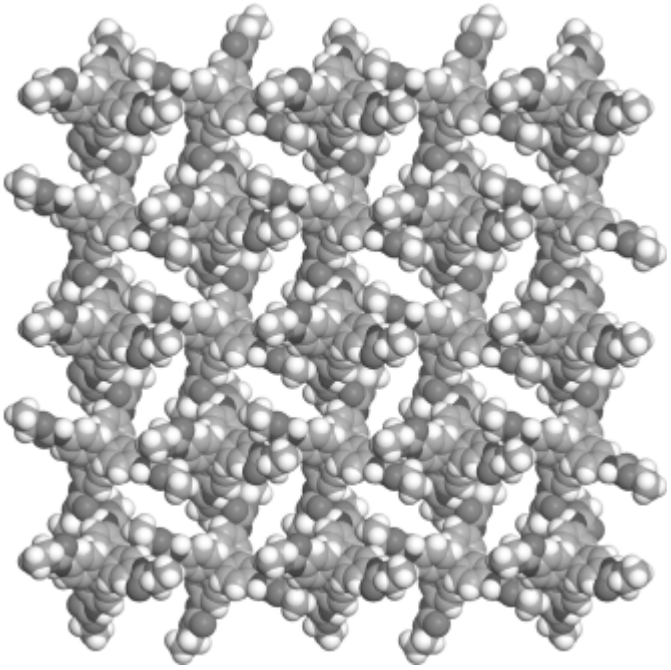
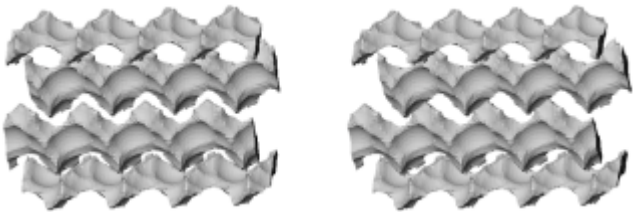


Fig. 4. Stereoscopic representation of the parallel helical channels defined by the network constructed from tetraurethane **5a**. The image shows a 1 × 1 × 4 array of unit cells viewed with the *c* axis horizontal. The outsides of the channels appear in light gray, and dark gray is used to show where the channels are cut by the boundaries of the array. The surface of the channels is defined by the possible loci of the centre of a sphere of diameter 3 Å as it rolls over the surface of the ordered network.[7]



together by only four hydrogen bonds per tecton. The average distance between the tetrahedral centers of hydrogen-bonded neighbors defines an intertectonic separation of 12.6 Å, which is too small to permit interpenetration (43, 44). Approximately 29% of the volume of crystals of tecton **5a** is available for including guests,[5] which occupy parallel channels that lie along the *c* axis and have cross sections measuring nearly 11 × 3 Å^2 (Fig. 3).[6] Close examination of the channels reveals that each is helical and chiral, with equal numbers of helices of opposite handedness (Fig. 4).[7]

Crystallization of tetraboronic acid **1c** and the analogous silane **2c** under similar conditions is known to produce isostructural hydrogen-bonded networks (8). Replacing the central C—C bonds in compound **1c** with longer Si—C bonds in analogue **2c** results in a rational expansion of the network, with predictable control of geometry on the sub-nanometric scale. To further test the ability of molecular tectonics to control crystallization with this degree of precision, we compared the structure of tetraurethane **5a** with that formed by the corresponding silane **6a**. Tecton **6a** crystallized from dioxane–pentane in the tetragonal space group $P4_2/n$ as an inclusion compound with the composition **6a**·2 dioxane (Table 1).[4] The structure is shown in Figs. 5 and 6. Each tecton donates four hydrogen bonds to four neighboring molecules of dioxane, and each molecule of dioxane accepts two hydrogen bonds from different tectons, thereby creating a diamondoid network (42) in which dioxane is an essential structural component (Fig. 5). The average Si···Si distance between closest pairs of tectons within the network is 16.6 Å, which is large enough to permit sixfold interpenetration (Fig. 6) (43, 44). This fills the available volume completely, giving a close-packed structure containing only tecton **6a** and molecules of dioxane that are an integral part of the network.

The observed structures of tectons **5a** and **6a** are largely consistent with the emerging principles of molecular tectonics. In particular, both compounds crystallize as expected to form open hydrogen-bonded diamondoid networks that incorporate solvent. Unexpectedly, the networks are not isostructural, but it is important to note that tecton **5a** was crystallized from THF–pentane and tecton **6a** from dioxane–hexane. We subsequently found that tecton **5a** can also be crystallized from dioxane and tecton **6a** from THF. However, we elected not to study these new structures further because those already solved did not show exceptional porosity.

Porous chiral hydrogen-bonded networks formed by crystallization of enantiomerically pure tetraurethane 5b and tetraurea 5c

Exciting opportunities for constructing new types of porous molecular networks are created by using enantiomerically pure tectons such as analogues **5b**–**5d** of tetraurethane **5a**. The principles of molecular tectonics suggest that crystallization of these analogues should produce porous hydrogen-bonded networks, as observed in the case of tecton **5a**. However, these new networks will be chiral and may therefore be able to include chiral guests enantio-

[5] The percentage of volume accessible to guests was estimated by the PLATON program (45, 46), using standard parameters (9, 13).

[6] The dimensions of a channel in a particular direction correspond to the cross section of an imaginary cylinder that could be passed through the hypothetical open network in the given direction in contact with the van der Waals surface. Such values are inherently conservative because (*i*) they measure the cross section at the most narrow constriction, and (*ii*) they systematically underestimate the sizes of channels that are not uniform and linear.

[7] Representations of channels were generated by the Cavities option in the programs ATOMS Version 5.1 (Shape Software, 521 Hidden Valley Road, Kingsport, TN 37663; www.shapesoftware.com). We are grateful to Eric Dowty of Shape Software for integrating this capacity in ATOMS at our suggestion.

© 2004 NRC Canada

Fig. 5. View of part of the structure of crystals of tetraurethane **6a** grown from dioxane–pentane, showing two tectons linked by hydrogen bonds donated to an intervening molecule of dioxane. Hydrogen bonds appear as broken lines.

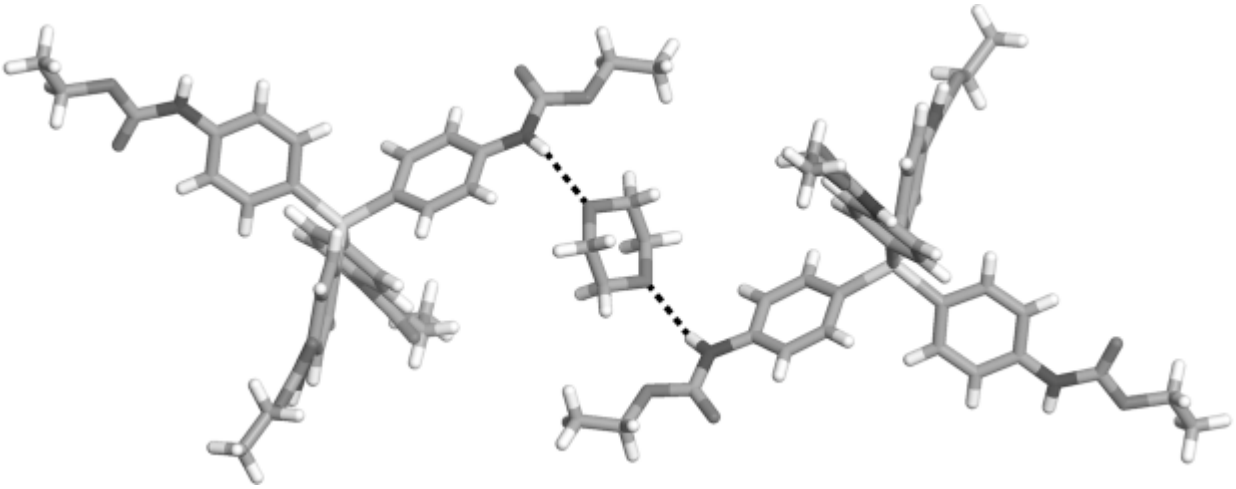
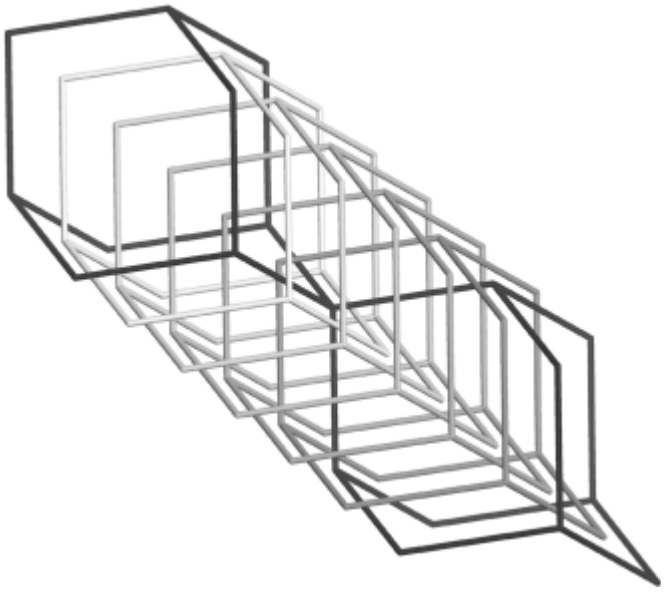


Fig. 6. Representation of the sixfold interpenetrated diamondoid networks generated by association of tetraurethane **6a** with dioxane. In this drawing, the central silicon atom of each tetraurethane lies at the intersection of solid lines that represent hydrogen bonding to four neighbors via intervening molecules of dioxane. Independent networks are shown in different shades of gray.



selectively. Such behavior would illustrate a key advantage of using molecules to make porous materials for applications in separation and catalysis, rather than using inorganic analogues such as zeolites. Specifically, creating asymmetric environments within supramolecular materials can be achieved by simple modifications of the individual molecular components, whereas very few zeolites are inherently chiral (47–49). As result, an important goal in crystal engineering is to devise molecules that form porous chiral hydrogen-bonded networks and then to use the resulting materials for the enantioselective inclusion and exchange of guests. However, few successes have been reported so far (50–58).

Enantiomerically pure tetraurethane **5b** crystallized from THF–pentane in the tetragonal space group $I4_1$ as an inclusion compound of approximate composition **5b**·2 pentane (Table 2).[4,8] As shown in Fig. 7, each tecton forms a total of eight hydrogen bonds with four symmetrically oriented neighbors, and each urethane group serves simultaneously as a donor and acceptor of hydrogen bonds. This defines a diamondoid network (42) in which the average intertectonic distance between the tetrahedral centers of neighbors is 9.73 Å. No interpenetration is observed (43, 44), and 16% of the volume remains available for including guests.[5] Despite intensive effort, we were unable to grow crystals of tecton **5b** suitable for X-ray diffraction when we used racemic solvents such as (±)-2-bromobutane, (±)-2-chloropentane, and (±)-2-methyltetrahydrofuran, so we were unable to examine the enantioselectivity of inclusion.

Crystals of the analogous enantiomerically pure tetraurea **5c** were obtained by allowing dioxane to diffuse into solutions in HCOOH. X-ray crystallography established that tecton **5c** crystallized under these conditions in the tetragonal space group $I4_1$ as an inclusion compound of well-defined composition **5c**·2HCOOH (Table 2).[4] Self-association of tetraurea **5c** produces a hydrogen-bonded diamondoid network (42) isostructural to the one generated by the analogous tetraurethane **5b** (Fig. 8). Each tecton forms a total of 16 hydrogen bonds with four symmetrically oriented neighbors, and each urea group serves simultaneously as a double donor and double acceptor of hydrogen bonds. No interpenetration is observed (43, 44), and 17% of the volume remains available for including guests.[5] Unfortunately, we were unable to grow crystals of tecton **5c** suitable for X-ray diffraction from racemic solvents, so we were not able to confirm that inclusion is enantioselective.

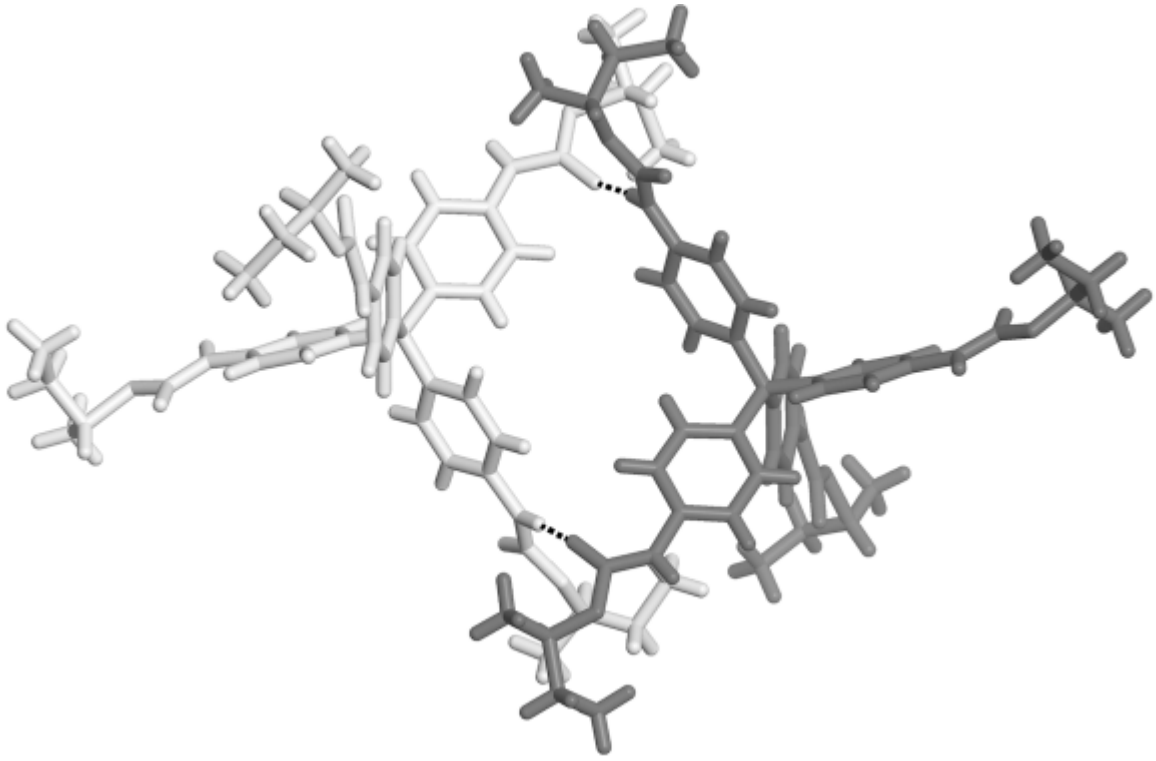
[8] The composition was estimated by X-ray crystallography and by ^{1}H NMR spectroscopy of dissolved samples. The amount of any H_2O included could not be determined accurately.

© 2004 NRC Canada

Table 2. Crystallographic data for compounds **5b**·2pentane, **5c**·2HCO_2H, **5e**·2DMSO·5dioxane, and **5e** after replacement of dioxane by THF.[4]

Compound	**5b**·2Pentane	**5c**·2HCO_2H	**5e**·2DMSO·5 dioxane	**5e**·2DMSO·5dioxane after exchange with THF
Formula	$C_{55}H_{80}N_4O_8$	$C_{47}H_{62}N_8O_{12}$	$C_{53}H_{80}N_8O_{16}S_2$	—
Fw	925.23	931.05	1149.37	—
F(000)	2008	1864	2456	
Crystal system	Tetragonal	Tetragonal	Tetragonal	Tetragonal
Space group	$I4_1$	$I4_1$	$P\text{-}42_1c$	$P\text{-}42_1c$
$a = b$ (Å)	17.7201(6)	17.2392(3)	17.281(2)	17.184(8)
c (Å)	16.0845(7)	17.3495(3)	20.591(2)	20.838(2)
Volume (Å^3)	5050.6(3)	5156.1(2)	6149(1)	6152(87)
Z	4	4	4	—
Density (g/cm^3)	1.217	1.12	1.242	—
Temperature (K)	293(2)	293(2)	223(2)	223(2)
R_1	0,1022	0,1089	0.0989	—
wR_2	0,2888	0.3059	0.2721	
GoF	1,038	1.265	1.249	—
Flack Parameter	0.1(18)	–0.2(3)	0.14(10)	—
Porosity (%)	16	17	66	—

Fig. 7. Representation of the structure of crystals of tetraurethane **5b** grown from THF–pentane, showing a tecton (dark gray) hydrogen-bonded to one of four neighbors (light gray). The illustrated neighbor is equivalent by symmetry to three others, which are omitted for clarity. Hydrogen bonds appear as broken lines, and guests are omitted for clarity. Each urethane group serves simultaneously as a donor and acceptor of hydrogen bonds.

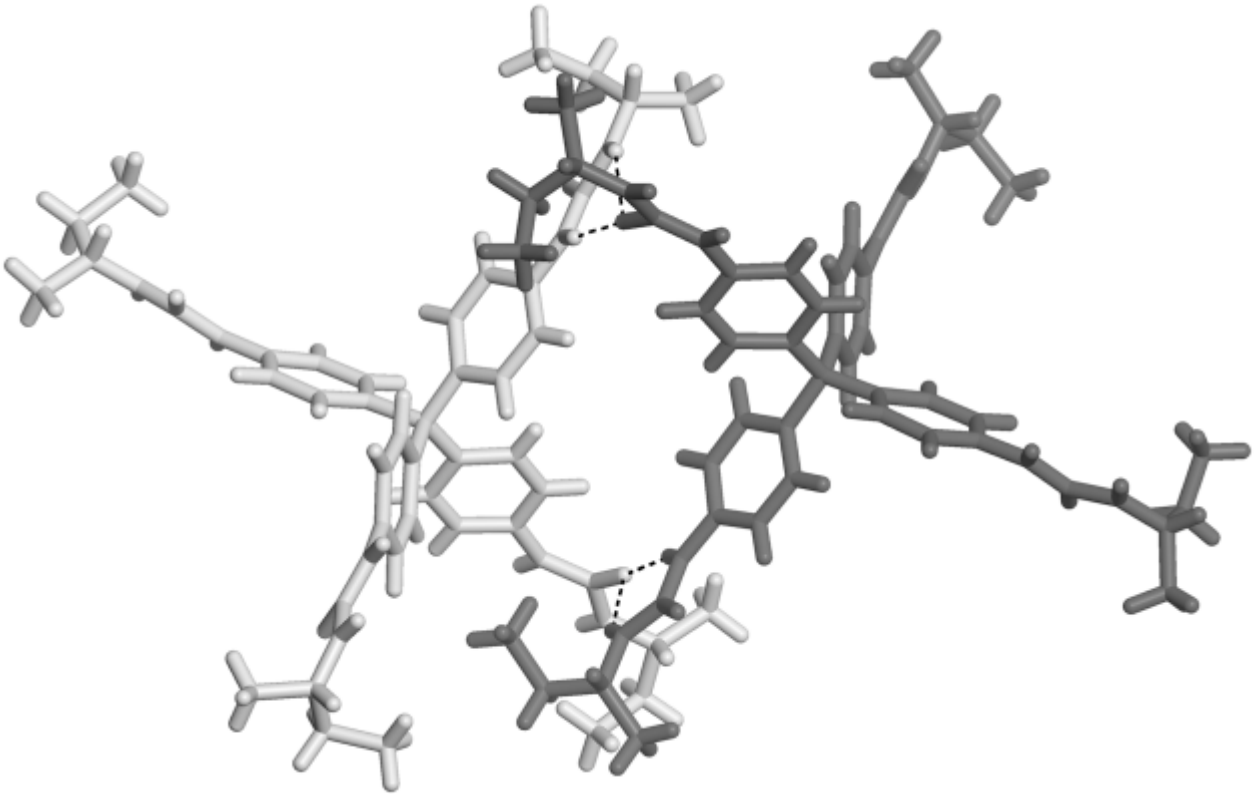


Porous hydrogen-bonded network formed by crystallization of tetraurea 5e

Tetraurea **5e** crystallized from DMSO–dioxane in the tetragonal space group $P\text{-}42_1c$ as an inclusion compound with the approximate composition **5e**·2DMSO·5dioxane (Table 2).[4,8] The composition of the crystals indicated immediately that a large fraction of the volume is accessible to guests. As shown in Fig. 9, each tecton forms hydrogen bonds with six neighboring tectons (Fig. 9*a*). Two neighbors that lie along the c axis on opposite sides of the central tecton are equivalent by symmetry, and each accepts four hydrogen bonds from the central tecton (Fig. 9*b*). The other four neighbors form a second symmetry-equivalent set, and each donates two hydrogen bonds to the central tecton

© 2004 NRC Canada

Fig. 8. Representation of the structure of crystals of tetraurea **5c** grown from HCOOH–dioxane, showing a tecton (dark gray) hydrogen-bonded to one of four neighbors (light gray). The illustrated neighbor is equivalent by symmetry to three others, which are not shown. Hydrogen bonds appear as broken lines, and guests are omitted for clarity. Each urea group serves simultaneously as a double donor and double acceptor of hydrogen bonds.



(Fig. 9*c*). In addition, part of the N—H bonds not used in intertectonic hydrogen bonding remain available for interacting with included DMSO. Each tecton therefore participates in a total of 16 hydrogen bonds with neighboring tectons. Joining the tetrahedral centers of the tectons defines the approximately octahedral 6-connected network shown in Fig. 9*d*. The average intertectonic distances are 10.30 Å in the *c* direction and 12.22 Å in the *a* and *b* directions.

No interpenetration is observed (43, 44), and approximately 66% of the volume of crystals of tecton **5e** remains available for the inclusion of guests,[5] which occupy interconnected channels. The porosity is unusually high, and it far exceeds the fraction of volume (normally about 30%) that is considered to remain unfilled in normal molecular crystals because of inefficient packing (59). The most significant channels are aligned with the *ab* diagonal and have cross sections measuring approximately 5.7 × 6.3 $Å^2$ at the narrowest points (Fig. 10).[6] The surface shown in Fig. 11 further defines the shape and complex interconnectivity of the channels.[7]

The network built from tecton **5e** is very porous, the interior of crystals is made accessible by significant interconnected channels, and high structural integrity is ensured by the formation of 16 hydrogen bonds per tecton. As a result, guests can be exchanged in single crystals without loss of crystallinity. For example, single crystals of estimated composition **5e**·2DMSO·5dioxane and approximate dimensions 1 mm × 1 mm × 5 mm were suspended in THF at 25 °C for 24 h. Subsequent analysis of recovered samples by ^{1}H NMR spectroscopy in solution showed complete replacement of dioxane by THF. The recovered samples remained transparent, showed no morphological changes visible by optical microscopy, and continued to diffract. Study of single exchanged crystals by X-ray diffraction showed little variation in the unit cell parameters (Table 2), suggesting that the network undergoes little distortion.

Conclusions

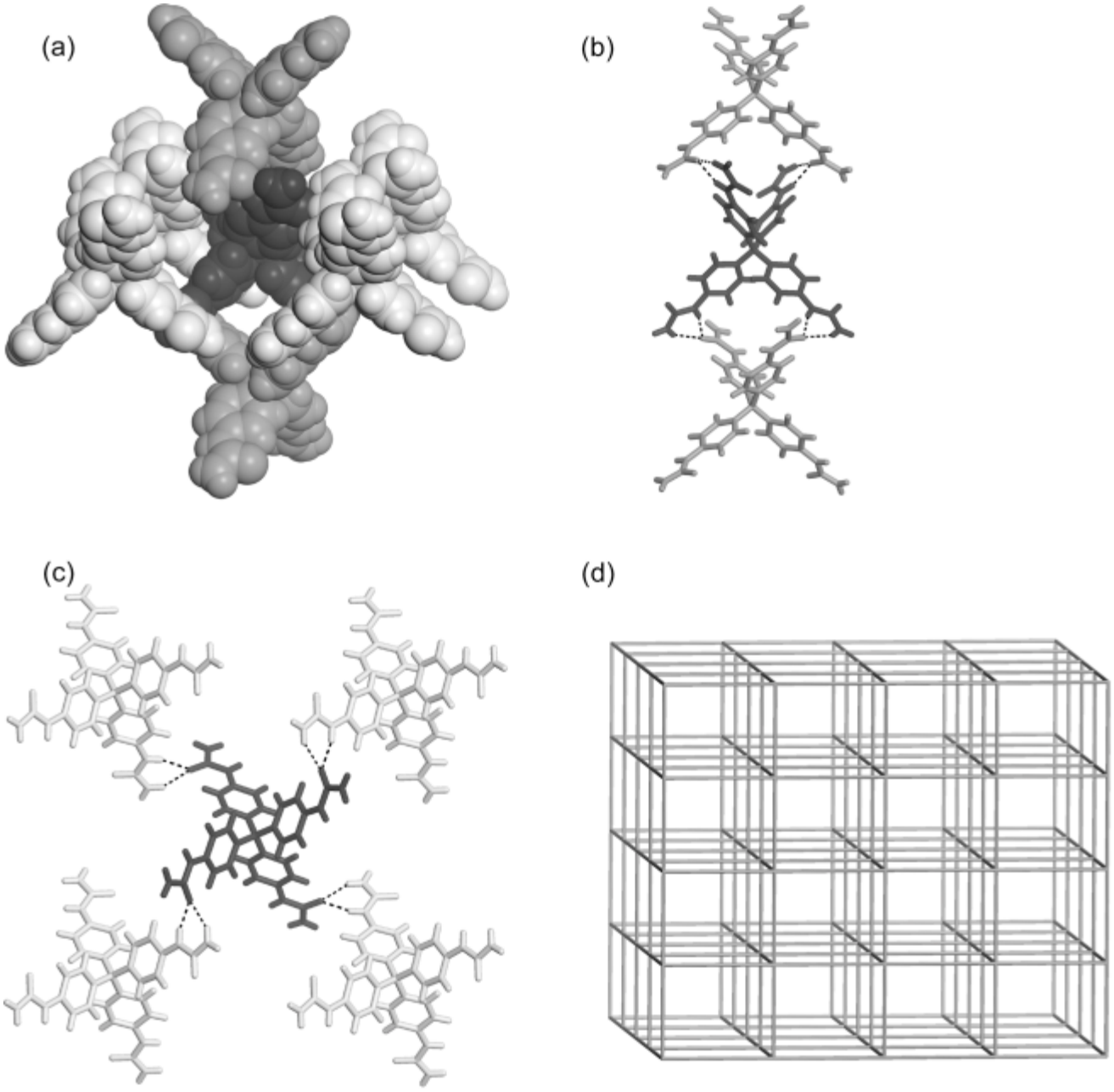
Our studies of tetraurethanes and tetraureas **5a**–**5e** and **6a** confirm that (*i*) tetraphenylmethane and tetraphenylsilane are effective cores for constructing molecules of value in crystal engineering, and (*ii*) substituting these cores with hydrogen-bonding groups produces tectons that crystallize predictably to give open three-dimensional networks that can include significant amounts of guests. Of special note is the observation that enantiomerically pure tectons such as tetraurethane **5b** and tetraurea **5c** can be made conveniently from tetra(isocyanate) **1f** and crystallize to give porous chiral networks. Such molecular materials have unique properties that promise to make them useful in enantioselective catalysis, the resolution of racemates, and other applications.

Experimental

Tetrahydrofuran (THF) was dried by distillation from the

© 2004 NRC Canada

Fig. 9. (*a*) View of the structure of crystals of tetraurea **5e** grown from DMSO–dioxane showing a central tecton (dark gray) and its six hydrogen-bonded neighbors. Four of the neighbors (light gray) define a set equivalent by symmetry, and two others (gray) define a second set. All atoms are shown as spheres of van der Waals radii, and guests are omitted for clarity. (*b*) Hydrogen bonding between the central tecton (dark gray) and the set of two symmetry-equivalent neighbors (gray). Hydrogen bonds appear as broken lines. (*c*) Hydrogen bonding between the central tecton (dark gray) and the set of four symmetry-equivalent neighbors (light gray). Hydrogen bonds appear as broken lines. (*d*) Representation of the 6-connected network defined by joining the central carbon atom of each tecton with the centres of the set of six neighbors shown in Fig. 1*a*.



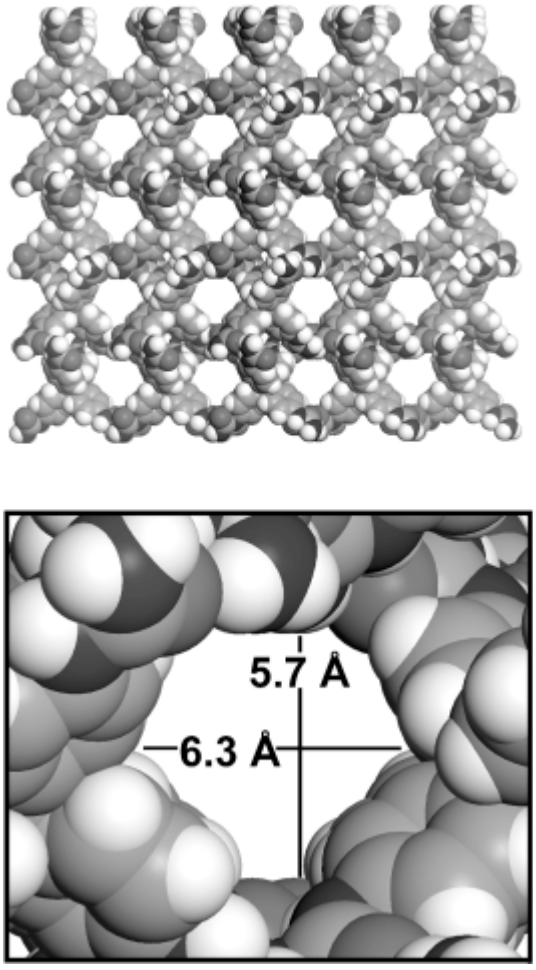
sodium ketyl of benzophenone. Xantphos (60) and tetrakis-(4-bromophenyl)silane (**2d**) (40) were synthesized according to known procedures. All other reagents were commercial products that were used without further purification.

Tetrakis(4-aminophenyl)methane (1e) (16, 38, 39)

A suspension of tetrakis(4-nitrophenyl)methane (**1d**, 4.10 g, 8.19 mmol) (38) and 10% Pd/C (410 mg) in THF (300 mL) was stirred for 70 h in a Parr reactor at 25 °C under H_2 (1200 kPa). The resulting mixture was filtered through Celite®, and volatiles were removed by evaporation under reduced pressure. The residue was triturated with $CHCl_3$ and washed with CH_3OH to afford tetrakis(4-aminophenyl)methane (**1e**, 3.09 g, 8.12 mmol, 99%) (16, 38, 39) as a colorless solid that was used without further purification. A sample of analytical purity was obtained by crystallization from ethanol–water to afford small colorless crystals; mp 319 °C (lit. (16) mp 331 °C, lit. (38) mp 319 to

© 2004 NRC Canada

Fig. 10. View along the *ab* diagonal of the network constructed from tetraurea **5e** showing a 2 × 2 × 2 array of unit cells. Guests are omitted, and atoms are shown as spheres of van der Waals radii to reveal the cross sections of the channels. Atoms of hydrogen appear in white, atoms of carbon in light gray, atoms of oxygen in gray, and atoms of nitrogen in dark gray.



320 °C, lit. (39) mp 318 °C). IR (KBr) (cm^{-1}): 3396, 3171, 3026, 1610, 1507, 1271, 1183, 860, 829, 813, 578. ^{1}H NMR (300 MHz, DMSO-d_6) δ: 6.69 (d, ^3J = 8.5 Hz, 8H), 6.40 (d, ^3J = 8.5 Hz, 8H), 4.86 (s, 8H). ^{13}C NMR (75 MHz, DMSO-d_6) δ: 145.7, 135.9, 131.4, 112.6, 61.1. MAB-HR-MS (N_2) calcd. for $C_{25}H_{24}N_4$ *m/e*: 380.200097; found: 380.200966. Anal. calcd. for $C_{25}H_{24}N_4$: C 78.92, H 6.36, N 14.73; found: C 78.65, H 6.33, N 14.23.

Tetrakis(4-isocyanatophenyl)methane (1f)

A solution of triphosgene (1.39 g, 4.68 mmol) in dry THF (10 mL) was added dropwise to a stirred solution of tetrakis-(4-aminophenyl)methane (**1e**, 1.19 g, 3.13 mmol) and triethylamine (3.49 mL, 25.0 mmol) in dry THF (60 mL) at –78 °C under N_2. The mixture was then warmed to 0 °C during 2 h, and insoluble solids were removed by filtration through Celite®. Volatiles were removed by evaporation under reduced pressure to give tetrakis(4-isocyanatophenyl) methane (**1f**, 1.48 g, 3.05 mmol, 97%) as a colorless solid that was used without further purification. A sample of analytical purity was obtained by sublimation (130 °C/0.1 mm Hg (1 mm Hg = 133.322 Pa)), mp 53 to 54 °C (softening). IR (KBr) (cm^{-1}): 2260, 1604, 1574, 1519, 1109, 1016, 822, 563. ^{1}H NMR (400 MHz, $CDCl_3$) δ: 7.10 (d, ^3J = 8.9 Hz, 8H), 7.00 (d, ^3J = 8.9 Hz, 8H). ^{13}C NMR (100 MHz, $CDCl_3$) δ: 143.6, 132.0, 131.8, 125.1, 124.4, 63.7. FAB-HR-MS (3-nitrobenzyl alcohol) calcd. for $C_{29}H_{16}N_4O_4$ *m/e*: 484.117155; found: 484.116508.

Tetrakis(4-isothiocyanatophenyl)methane (1g)

Thiophosgene (0.264 mL, 3.46 mmol) was added dropwise to a stirred solution of tetrakis(4-aminophenyl) methane (**1e**, 300 mg, 0.788 mmol) and triethylamine (0.880 mL, 6.31 mmol) in dry THF (25 mL) at –10 °C under N_2. The resulting mixture was then warmed to 25 °C during 1 h. Water was added, and the mixture was extracted twice with CH_2Cl_2. The combined organic extracts were dried over Na_2SO_4, and volatiles were removed by evaporation under reduced pressure. The residual solid was purified by flash chromatography (silica, CH_2Cl_2 (30%) – hexane (70%), R_f 0.59) to provide tetrakis(4-isothiocyanatophenyl) methane (**1g**, 386 mg, 0.703 mmol, 89%) as a colorless solid, mp 203 to 204 °C. IR (KBr) (cm^{-1}): 2200–2000 (bs), 1496, 932, 817. ^{1}H NMR (400 MHz, $CDCl_3$) δ: 7.15 (d, ^3J = 8.9 Hz, 8H), 7.10 (d, ^3J = 8.9 Hz, 8H). ^{13}C NMR (100 MHz, $CDCl_3$) δ: 144.4, 136.4, 131.8, 130.1, 125.6, 64.2. FAB-MS (3-nitrobenzyl alcohol) *m/e*: 548. Anal. calcd. for $C_{29}H_{16}N_4S_4$: C 63.48, H 2.94, N 10.21; found: C 63.33, H 2.81, N 10.05.

Tetraurethane 5a

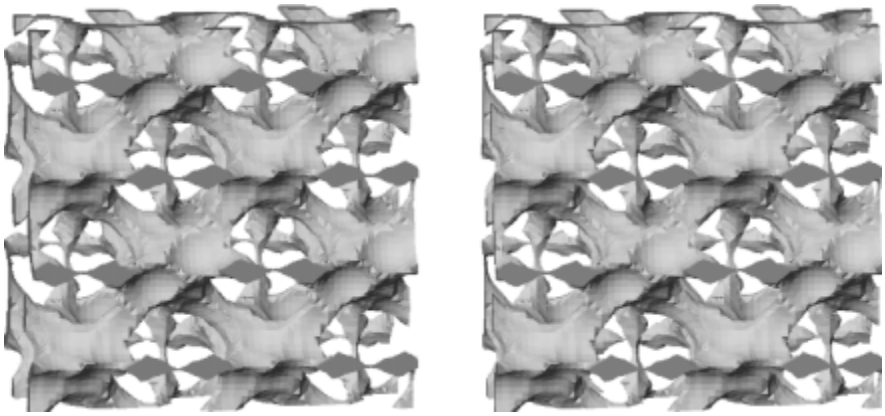
A solution of tetrakis(4-isocyanatophenyl)methane (**1f**, 315 mg, 0.650 mmol) in absolute ethanol (15 mL) was heated at reflux for 1 h. Volatiles were then removed by evaporation under reduced pressure, and the residual solid was purified by flash chromatography (silica, $CH_3COOC_2H_5$ (50%) – hexane (50%), R_f 0.50) to afford tetraurethane **5a** (360 mg, 0.538 mmol, 83%) as a colorless solid, mp 223 to 224 °C. IR (KBr) (cm^{-1}): 3292, 2980, 1729, 1597, 1535, 1412, 1317, 1297, 1221, 1113, 1063, 872, 811. ^{1}H NMR (300 MHz, DMSO-d_6) δ: 9.59 (s, 4H), 7.33 (d, ^3J = 8.4 Hz, 8H), 6.98 (d, ^3J = 8.4 Hz, 8H), 4.09 (q, ^3J = 6.5 Hz, 8H) 1.22 (t, ^3J = 6.5 Hz, 12H). ^{13}C NMR (100 MHz, DMSO-d_6) δ: 153.5, 140.7, 136.8, 130.5, 117.4, 62.3, 60.0, 14.4. FAB-HR-MS (3-nitrobenzyl alcohol) calcd. for $C_{37}H_{40}N_4O_8$ *m/e*: 668.28461; found: 668.28410. Anal. calcd. for $C_{37}H_{40}N_4O_8{\cdot}H_2O$: C 64.71, H 6.16, N 8.16; found: C 65.11, H 6.16, N 8.00.

Tetraurethane 5b

(*R*)-2-Butanol (0.66 mL, 7.2 mmol) was added to a stirred solution of tetrakis(4-isocyanatophenyl)methane (**1f**, 440 mg, 0.908 mmol) in dry THF (5 mL), and the mixture was heated at reflux for 1 h. Volatiles were then removed by evaporation under reduced pressure, and the residual solid was purified by flash chromatography (silica, $CH_3COOC_2H_5$ (30%) – hexane (70%), R_f 0.43) to provide tetraurethane **5b** (553 mg, 0.708 mmol, 78%) as a colorless solid, mp 273 °C. $[\alpha]_D$ = –21° (*c* 0.30 in ethanol). IR (KBr) (cm^{-1}): 3311, 2974, 2936, 2879, 1705, 1600, 1528, 1409, 1379, 1321, 1296, 1228, 1127, 1054, 826, 771, 530. ^{1}H NMR (400 MHz, $CDCl_3$) δ: 7.25 (d, ^3J = 8.7 Hz, 8H), 7.10 (d, ^3J = 8.7 Hz, 8H), 6.54 (s, 4H), 4.84 (m, 4H), 1.61 (m, 8H), 1.26 (d, ^3J =

© 2004 NRC Canada

Fig. 11. Stereoscopic representation of the interconnected channels within the network constructed from tetraurea **5e**. The image shows a 2 × 2 × 1 array of unit cells viewed along the *c* axis. The outsides of the channels appear in light gray, and dark gray is used to show where the channels are cut by the boundaries of the array. The surface of the channels is defined by the possible loci of the centre of a sphere of diameter 3.5 Å as it rolls over the surface of the ordered network.[7]



6.3 Hz, 12H), 0.94 (t, ^3J = 7.4 Hz, 12H). ^{13}C NMR (100 MHz, $CDCl_3$) δ: 153.7, 141.9, 136.2, 131.7, 117.7, 73.4, 63.1, 29.2, 19.9, 9.9. FAB-MS (3-nitrobenzyl alcohol) *m/e*: 780.1. Anal. calcd. for $C_{45}H_{56}N_4O_8$: C 69.21, H 7.23, N 7.17; found: C 69.21, H 7.31, N 7.18.

Tetraurea 5c

(*S*)-2-Butylamine (261 mg, 3.57 mmol) was added to a stirred solution of tetrakis(4-isocyanatophenyl)methane (**1f**, 392 mg, 0.809 mmol) in dry THF (20 mL), and the mixture was heated at reflux for 1 h. Hexane was then added, and the resulting precipitate was separated by filtration and washed with $CHCl_3$ and then hexane to afford tetraurea **5c** (622 mg, 0.800 mmol, 99%) as a beige solid. A sample of analytical purity was obtained by crystallization from HCOOH–dioxane to afford pale orange crystals, mp > 330 °C. $[\alpha]_D$ = +22° (*c* 1.00 in DMF). IR (KBr) (cm^{-1}): 3330, 2965, 2931, 2875, 1653, 1595, 1541, 1508, 1316, 1228, 816. ^{1}H NMR (400 MHz, DMSO-d_6) δ: 8.27 (s, 4H), 7.23 (d, ^3J = 8.8 Hz, 8H), 6.90 (d, ^3J = 8.8 Hz, 8H), 5.92 (d, ^3J = 8.1 Hz, 4H), 3.57 (m, 4H), 1.39 (m, 8H), 1.04 (d, ^3J = 6.6 Hz, 12H), 0.85 (t, ^3J = 7.4 Hz, 12H). ^{13}C NMR (100 MHz, DMSO-d_6) δ: 154.8, 139.6, 138.1, 130.6, 116.5, 62.0, 46.0, 29.3, 20.7, 10.2. FAB-HR-MS (3-nitrobenzyl alcohol) calcd. for $C_{45}H_{60}N_8O_4$ + H *m/e*: 777.481578; found: 777.484089. Anal. calcd. for $C_{45}H_{60}N_8O_4 \cdot 3.5H_2O$: C 64.34, H 8.04, N 13.34; found: C 64.22, H 7.84, N 13.73.

Tetraurea 5d

A procedure similar to the one used to synthesize tetraurea **5c** converted tetrakis(4-isocyanatophenyl)methane (**1f**, 125 mg, 0.258 mmol) and (*S*)-α-methylbenzylamine (0.166 mL, 1.30 mmol) into tetraurea **5d** (248 mg, 0.256 mmol, 99%), which was isolated as a colorless solid. A sample of analytical purity was obtained by crystallization from CH_3OH, mp 262 to 263 °C. $[\alpha]_D$ = –116° (*c* 0.30 in ethanol). IR (KBr) (cm^{-1}): 3400, 1677, 1596, 1506, 1407, 1319, 1292, 1238, 1115, 821. ^{1}H NMR (400 MHz, DMSO-d_6) δ: 8.36 (s, 4H), 7.31 (m, 16H), 7.22 (m, 12H), 6.88 (d, ^3J = 8.7 Hz, 8H), 6.56 (d, ^3J = 7.6 Hz, 4H), 4.79 (dq, ^3J = 7.6, 6.9 Hz, 4H), 1.36 (d, ^3J = 6.9 Hz, 12H). ^{13}C NMR (75 MHz, DMSO-d_6) δ: 154.4, 145.2, 139.7, 137.9, 130.7, 128.3, 126.6, 125.8, 116.6, 62.1, 48.6, 23.1. FAB-MS (3-nitrobenzyl alcohol) *m/e*: 969. Anal. calcd. for $C_{61}H_{60}N_8O_4$: C 75.60, H 6.24, N 11.56; found: C 75.26, H 6.37, N 11.39.

Tetraurea 5e

Aqueous NH_3 (28%, 5 mL) was added to a stirred solution of tetrakis(4-isocyanatophenyl)methane (**1f**, 480 mg, 0.991 mmol) in dry THF (20 mL), and the resulting mixture was stirred for 1 h. Volatiles were then removed by evaporation under reduced pressure, and the residual solid was washed with water and crystallized from 2-methoxyethanol–THF to provide tetraurea **5e** (501 mg, 0.907 mmol, 92%) as a colorless solid, mp > 330 °C. IR (KBr) (cm^{-1}): 3500–3000 (bs), 1666, 1588, 1532, 1509, 1410, 1344, 816. ^{1}H NMR (400 MHz, DMSO-d_6) δ: 8.49 (s, 4H), 7.26 (d, ^3J = 8.7 Hz, 8H), 6.93 (d, ^3J = 8.7 Hz, 8H), 5.80 (s, 8H). ^{13}C NMR (100 MHz, DMSO-d_6) δ: 156.1, 139.9, 138.1, 130.6, 116.9, 62.2. FAB-HR-MS (3-nitrobenzyl alcohol) calcd. for $C_{29}H_{28}N_8O_4$ *m/e*: 552.223352; found: 552.225072. Anal. calcd. for $C_{29}H_{28}N_8O_4 \cdot 1.5H_2O$: C 60.09, H 5.39; found: C 59.91, H 5.96.

Tetraurethane 6a

Deoxygenated dioxane (10 mL) was added to a deoxygenated mixture of tetrakis(4-bromophenyl)silane (**2d**, 652 mg, 1.00 mmol) (40), $Pd(OOCCH_3)_2$ (45.0 mg, 0.200 mmol), Xantphos (180 mg, 0.311 mmol) (60), Cs_2CO_3 (1.70 g, 5.22 mmol), and ethyl carbamate (392 mg, 4.40 mmol). The resulting mixture was stirred at reflux for 48 h under N_2 and then filtered through Celite®. Volatiles were removed by evaporation under reduced pressure, and the residual solid was purified by flash chromatography (silica, $CH_3COOC_2H_5$ (40%) – hexane (60%), R_f 0.25) to give tetraurethane **6a** (125 mg, 0.183 mmol, 18%) as a colorless solid, mp 138 to 139 °C. IR (KBr) (cm^{-1}): 3500–3300, 2980, 2928, 1707, 1596, 1519, 1396, 1319, 1222, 1062, 824, 685, 536. ^{1}H NMR (300 MHz, DMSO-d_6) δ: 9.74 (s, 4H), 7.49 (d, ^3J = 8.3 Hz, 8H), 7.33 (d, ^3J = 8.3 Hz, 8H), 4.12 (q, ^3J = 7.1 Hz, 8H), 1.24 (t, ^3J = 7.1 Hz, 12H). ^{13}C NMR (75 MHz, DMSO-d_6) δ: 153.5, 140.6, 136.4, 127.2, 117.7, 60.2, 14.5.

© 2004 NRC Canada

FAB-HR-MS (3-nitrobenzyl alcohol) calcd. for $C_{36}H_{40}N_4O_8Si$ *m/e*: 684.261543; found: 684.260943.

X-ray crystallographic studies

The structures were solved by direct methods using SHELXS-97 (61) and refined with SHELXL-97 (62). All non-hydrogen atoms were refined anisotropically, whereas hydrogen atoms were placed in ideal positions and refined as riding atoms.

Crystallization of compounds 1g, 5a–5e, and 6a

Single crystals of tetra(isothiocyanate) **1g** suitable for analysis by X-ray diffraction were grown from $CHCl_3$–hexane. Crystals of tetraurethanes **5a** and **6a** were obtained by slow diffusion of pentane into solutions in THF or dioxane at 25 °C. Crystals of tetraurethane **5b** were grown by slow diffusion of pentane into a solution in dioxane at 25 °C. Crystals of tetraurea **5c** were obtained by slow diffusion of dioxane into a solution in HCOOH at 25 °C. Crystals of tetraurea **5e** were grown by slow diffusion of dioxane into a solution in DMSO at 25 °C.

Acknowledgments

We are grateful to the Natural Sciences and Engineering Research Council of Canada (NSERC), the Ministère de l'Éducation du Québec, the Canada Foundation for Innovation, the Canada Research Chairs Program, and Merck Frosst for financial support. In addition, acknowledgment is made to the donors of the Petroleum Research Fund, administered by the American Chemical Society, for support of this research. Dominic Laliberté is grateful to Boehringer Ingelheim for a fellowship.

References

1. J.D. Dunitz. Chem. Commun. 545 (2003).
2. G.R. Desiraju. Nat. Mater. **1**, 77 (2002).
3. A. Gavezzotti. Acc. Chem. Res. **27**, 309 (1994).
4. J. Maddox. Nature (London), **335**, 201 (1988).
5. G.R. Desiraju. Crystal engineering: The design of organic solids. Elsevier, Amsterdam. 1989.
6. M. Simard, D. Su, and J.D. Wuest. J. Am. Chem. Soc. **113**, 4696 (1991).
7. S. Mann. Nature (London), **365**, 499 (1993).
8. J.-H. Fournier, T. Maris, J.D. Wuest, W. Guo, and E. Galoppini. J. Am. Chem. Soc. **125**, 1002 (2003).
9. J.-H. Fournier, T. Maris, and J. D. Wuest. J. Org. Chem. (2004). ASAP article [online]. DOI: 10.1021/jo0348118.
10. O. Saied, T. Maris, and J.D. Wuest. J. Am. Chem. Soc. **125**, 14 956 (2003).
11. P. Brunet, E. Demers, T. Maris, G.D. Enright, and J.D. Wuest. Angew. Chem. Int. Ed. **42**, 5303 (2003).
12. E. Le Fur, E. Demers, T. Maris, and J.D. Wuest. Chem. Commun. 2966 (2003). DOI: 10.1039/b308355a.
13. J.-H. Fournier, T. Maris, M. Simard, and J.D. Wuest. Cryst. Growth Des. **3**, 535 (2003).
14. R. Thaimattam, F. Xue, J.A.R.P. Sarma, T.C.W. Mak, and G.R. Desiraju. J. Am. Chem. Soc. **123**, 4432 (2001).
15. J.B. Lambert, Y. Zhao, and C.L. Stern. J. Phys. Org. Chem. **10**, 229 (1997).
16. G.P. Lorenzi, A.S. Manessis, N.C. Tirelli, and V. Gramlich. Struct. Chem. **8**, 435 (1997).
17. A. Robbins, G.A. Jeffrey, J.P. Chesick, J. Donohue, F.A. Cotton, B.A. Frenz, and C.A. Murillo. Acta Crystallogr. Sect. B, **B31**, 2395 (1975).
18. V. Gruhnert, A. Kirfel, G. Will, F. Wallrafen, and K. Recker. Z. Kristallogr. **163**, 53 (1983).
19. T.J. Zimmermann and T.J.J. Müller. Synthesis, 1157 (2002).
20. W. Guo, E. Galoppini, R. Gilardi, G.I. Rydja, and Y.-H. Chen. Cryst. Growth Des. **1**, 231 (2001).
21. R. Thaimattam, C.V.K. Sharma, A. Clearfield, and G.R. Desiraju. Cryst. Growth Des. **1**, 103 (2001).
22. E.C. Constable, O. Eich, D. Fenske, C.E. Housecroft, and L.A. Johnson. Chem. Eur. J. **6**, 4364 (2000).
23. E. Galoppini and R. Gilardi. Chem. Commun. 173 (1999).
24. W.J. Oldham, Jr., R.J. Lachicotte, and G.C. Bazan. J. Am. Chem. Soc. **120**, 2987 (1998).
25. R. Thaimattam, D.S. Reddy, F. Xue, T.C.W. Mak, A. Nangia, and G.R. Desiraju. New J. Chem. 143 (1998).
26. M.A. Lloyd and C.P. Brock. Acta Crystallogr. Sect. B, **B53**, 780 (1997).
27. D.S. Reddy, D.C. Craig, and G.R. Desiraju. J. Am. Chem. Soc. **118**, 4090 (1996).
28. M. Charissé, V. Gauthey, and M. Dräger. J. Organomet. Chem. **448**, 47 (1993).
29. M. Charissé, S. Roller, and M. Dräger. J. Organomet. Chem. **427**, 23 (1992).
30. T.L. Nguyen, F.W. Fowler, and J.W. Lauher. J. Am. Chem. Soc. **123**, 11 057 (2001).
31. M.C. Etter, Z. Urbañczyk-Lipkowska, M. Zia-Ebrahimi, and T.W. Panunto. J. Am. Chem. Soc. **112**, 8415 (1990).
32. B. Konig, T. Fricke, I. Dix, P.G. Jones, and I. Thondorf. Liebigs Ann. 2315 (1997).
33. S. Irie, M. Yamamoto, I. Iida, T. Nishio, K. Kishikawa, S. Kohmoto, and K. Yamada. J. Org. Chem. **59**, 935 (1994).
34. M. Bertault, J. Canceill, A. Collet, and L. Toupet. Chem. Commun. 163 (1988).
35. R.B. Wilson, E.N. Duesler, D.Y. Curtin, I.C. Paul, R.H. Baughman, and A.F. Preziosi. J. Am. Chem. Soc. **104**, 509 (1982).
36. K.H. Gardner and J. Blackwell. Acta Crystallogr. Sect. B, **B36**, 1972 (1980).
37. J.J. Beres and L.E. Alexander. Acta Crystallogr. Sect. B, **B32**, 2077 (1976).
38. F.A. Neugebauer, H. Fischer, and R. Bernhardt. Chem. Ber. **109**, 2389 (1976).
39. H. Langhals, C. Wagner, and R. Ismael. New J. Chem. **25**, 1047 (2001).
40. J.-H. Fournier, X. Wang, and J.D. Wuest. Can. J. Chem. **81**, 376 (2003).
41. J. Yin and S.L. Buchwald. Org. Lett. **2**, 1101 (2000).
42. M.J. Zaworotko. Chem. Soc. Rev. **23**, 283 (1994).
43. S.R. Batten. CrystEngComm. **18**, 1 (2001).
44. S.R. Batten and R. Robson. Angew. Chem. Int. Ed. **37**, 1460 (1998).
45. A.L. Spek. PLATON. A multipurpose crystallographic tool [computer program]. Utrecht University, Utrecht, The Netherlands. 2001.
46. P. van der Sluis, and A.L. Spek. Acta Crystallogr. Sect. A, **A46**, 194 (1990).
47. T.E. Gier, X. Bu, P. Feng, and G.D. Stucky. Nature (London), **395**, 154 (1998).
48. D.E. Akporiaye. Chem. Commun. 1711 (1994).
49. M.E. Davis. Acc. Chem. Res. **26**, 111 (1993).

© 2004 NRC Canada

50. R.G. Kostyanovsky, K.A. Lyssenko, D.A. Lenev, and I.A. Bronzova. Tetrahedron: Asymmetry, **13**, 2697 (2002).
51. S. Kim, R. Bishop, D.C. Craig, I.G. Dance, and M.L. Scudder. J. Org. Chem. **67**, 3221 (2002).
52. V. Bertolasi, O. Bortolini, G. Fantin, M. Fogagnolo, and A. Medici. Chem. Lett. 400 (2002).
53. F. Toda. Pure Appl. Chem. **73**, 1137 (2001).
54. M. Akazome, Y. Ueno, H. Ooiso, and K. Ogura. J. Org. Chem. **65**, 68 (2000).
55. S. Hanessian, R. Saladino, R. Margarita, and M. Simard. Chem. Eur. J. **5**, 2169 (1999).
56. M. Gdaniec, M.J. Milewska, and T. Połoński. Angew. Chem. Int. Ed. **38**, 392 (1999).
57. P. Holý, J. Závada, I. Císařová, and J. Podlaha. Angew. Chem. Int. Ed. **38**, 381 (1999).
58. K. Beketov, E. Weber, J. Seidel, K. Köhnke, K. Makhkamov, and B. Ibragimov. Chem. Commun. 91 (1999).
59. A.I. Kitaigorodskii. Organic chemical crystallography. Consultants Bureau, New York. 1961.
60. M. Kranenburg, Y.E.M. van der Burgt, P.C.J. Kamer, and P.W.N.M. van Leeuwen. Organometallics, **14**, 3081 (1995).
61. G.M. Sheldrick. SHELXS-97. Program for the solution of crystal structures [computer program]. Universität Göttingen, Göttingen, Germany. 1997.
62. G.M. Sheldrick. SHELXL-97. Program for the refinement of crystal structures [computer program]. Universität Göttingen, Göttingen, Germany. 1997.

© 2004 NRC Canada

Sequential olefin metathesis — Intramolecular asymmetric Heck reactions in the synthesis of polycycles[1]

Mark Lautens and Valentin Zunic

Abstract: Application of the intramolecular asymmetric Heck reaction in the desymmetrization of a novel class of symmetrical bicyclodienes, synthesized through a diastereoselective double ring-closing metathesis (DSRCM) reaction, was achieved with good yields (approximately 80%) and excellent enantioselectivities (up to 99% ee). Three contiguous stereocenters are established in a single desymmetrization reaction. The use of thallium carbonate as base in the asymmetric Heck reaction favours double bond migration in **13**. Cationic conditions delivered products with good to excellent enantioselectivities, surpassing the results under neutral conditions.

Key words: asymmetric, Heck, polycycles, metathesis, stereoselective, desymmetrization.

Résumé : L'application de la réaction asymétrique intramoléculaire de Heck pour la désymétrisation d'une nouvelle classe de bicyclodiènes symétriques, obtenus par une réaction de métathèse à double cyclisation diastéréosélective, a été réalisée avec de bons rendements (environ 80 %) et d'excellentes énantiosélectivités (jusqu'à 99 % ee). Les trois stéréocentres contigus ont été établis au cours d'une seule réaction de désymétrisation. L'utilization du carbonate de thallium comme base dans la réaction asymétrique de Heck favorise la migration de la double liaison dans le composé **13**. Les conditions cationiques ont permis de livrer des produits avec des énantiosélectivités allant de bonnes à excellentes qui étaient supérieures à celles obtenues dans des conditions neutres.

Mots clés : asymétrique, Heck, polycycles, métathèse, stéréosélective, désymétrisation.

[Traduit par la Rédaction]

Introduction

Heck reactions are among the most important and widely used carbopalladation reactions (1, 2). The effect of substrate, catalyst, ligand, and additives has been examined, resulting in highly selective Heck reactions. The enantioselective variant (3) of the Heck reaction has been successfully developed to the point where both tertiary and quaternary centers can be generated in excellent enantioselectivity and in good to excellent yields. The application of the asymmetric Heck reaction (AHR) has been most widely studied in its intermolecular variant, with ees >96% having been reported. For the intramolecular Heck reaction, the ee values are typically around 80%, with notable exceptions leading to >90% ee (3).

Since the initial reports in 1989 (4), many of the reported intramolecular AHRs involve the desymmetrization of prochiral alkene substrates (5).[3] This methodology has proven to be a powerful tool for the rapid construction of polycyclic compounds. The carbo- and heterocycles synthesized via the intramolecular AHR have been used as building blocks for complex natural products or as model compounds for pharmaceutically relevant substances (6).

We have reported the formation of *cis*- and *trans*-decalin systems, as well as *cis*-diquinanes, via a diastereoselective double ring-closing olefin metathesis reaction (DSRCM) (7) (see Fig. 1). These symmetrical bicyclodienes are ideal substrates in the area of alkene differentiation reactions. Desymmetrization of a symmetrical molecule to yield an enantiomerically enriched product is certainly a topic of great interest (8).

In this report we describe the intramolecular AHR on the bicyclodienes generated through the DSRCM methodology previously reported from our laboratories.

Results

Substrates used in our studies were conveniently prepared by appending appropriate aryl-halide tethers to the tertiary diallylic alcohol **1**. Thus, reaction of the tertiary alcohol **1**

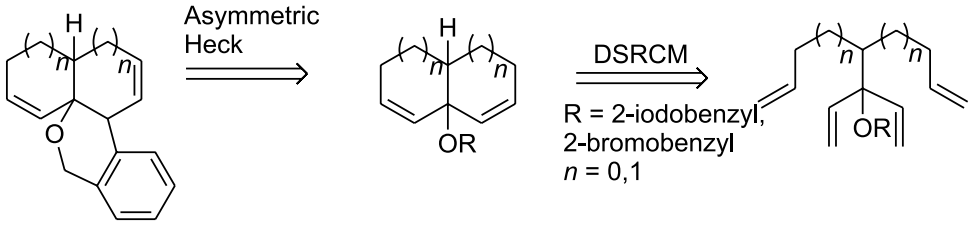
Received 26 June 2003. Published on the NRC Research Press Web site at http://canjchem.nrc.ca on 5 March 2004.

M. Lautens[2] and V. Zunic. Davenport Research Laboratories, Department of Chemistry, University of Toronto, 80 St. George Street, Toronto, ON M5H 3H6, Canada.

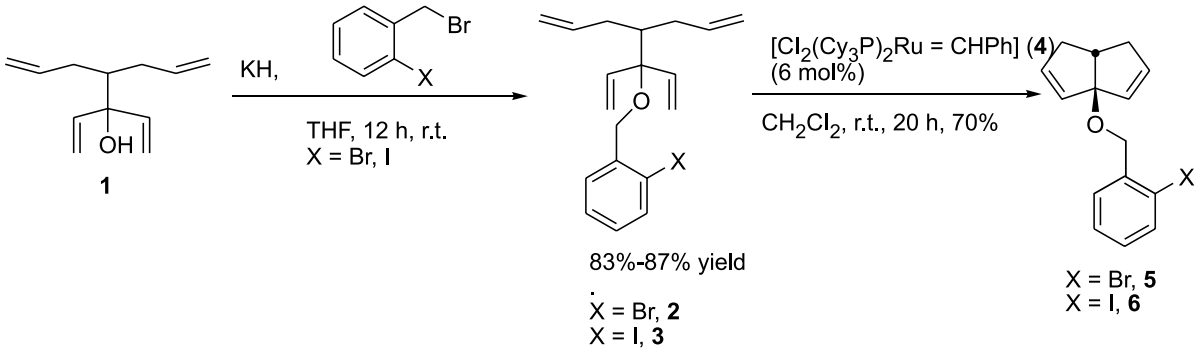
[1]This article is part of a Special Issue dedicated to Professor Ed Piers.
[2]Corresponding author (e-mail: mlautens@alchemy.chem.utoronto.ca).
[3]A highly enantioselective intramolecular Heck reaction with a monodentate ligand has recently been reported (ref. 5*d*).

 doi: 10.1139/V03-196 © 2004 NRC Canada

Fig. 1. Strategy for the synthesis of polycycles possessing three contiguous chiral centers.



Scheme 1. DSRCM in the synthesis of diquinane Heck reaction precursors.



with potassium hydride followed by 2-bromobenzyl bromide or 2-iodobenzyl bromide provided the coupled products **2** and **3** in >80% yield (Scheme 1).

Ring-closing metathesis of the haloaryl tetraenes **2** and **3** with Grubbs catalyst **4** provided the desired *cis*-fused bicyclo[3.3.0]octadienes **5** and **6** as the sole bicyclic products in good overall yields.

With a reliable and efficient route to the desired bicyclo[3.3.0]octadienes **5** and **6**, a detailed investigation into the AHR was then performed. Since oxidative addition with aryl iodides is much more facile than the analogous bromides (1), our initial investigations focused on the iodo-Heck precursors. Pd_2dba_3 was used as the palladium(0) source because of its ease of handling and its reported role in producing reproducible results (9) in asymmetric Heck reactions. The range of substrates that work well with BINAP (10) in asymmetric Heck reactions led us to initiate our studies using this ligand. The results from screening a variety of bases and solvents are shown in Table 1.

The results presented in Table 1 show that a variety of conditions are effective in promoting the asymmetric synthesis of **8**[4] It is generally accepted that cationic conditions, e.g., use of silver(I) salts to sequester a halide from palladium after the oxidative addition of the aryl halide, will generally lead to chiral products with higher enantiomeric ratios than those realized under neutral conditions (3, 9, 11).[5] However, under neutral conditions and in the presence of a tertiary amine base, similar levels of enantioselectivity to those seen under cationic conditions are obtained (Table 1, entry 2) (12).[6] The high enantiomeric excess obtained with the triflate substrate **7**[7] is the same as when an aryl iodide is used in the presence of a silver salt (cf. Table 1, entries 4 and 10). Triflate substrates can be used in lieu of the halide substrates with expensive silver salts.

Recent advances in the AHR have shown that a variety of other ligands mediate the reaction with equal levels of efficiency (3). A brief survey of other chiral ligands successfully used in the AHR is presented in Table 2.

Particularly noteworthy is the fact that the chiral phosphinooxazoline (PHOX) (13) ligand (*S*)-*t*-Bu-POX (14) does not efficiently mediate the asymmetric Heck reaction in this case (Table 2, entry 3). The use of *tol*-BINAP as ligand provides **8** with higher levels of enantioselectivity and yield than with BINAP. The use of cationic conditions with a more electron-rich bisphosphine will ensure a tighter binding of the bisphosphine throughout the catalytic cycle of the reaction.

Having explored the intramolecular AHR in the desymmetrization of bicyclo[3.3.0]octadienes, we focused our attention on applying the same transformation to the desymmetrization of bicyclo[4.4.0]decadienes. The synthesis of the required aryl-halide-tethered substrates was carried out in a similar manner to that discussed above for the preparation of diquinane substrates (Scheme 2). The DSRCM event

[4] The relative stereochemistry of **8** was proven by careful analysis of various 2D NMR experiments (COSY, ROESY, HMQC). The absolute stereochemistry of **8** has yet to be determined.

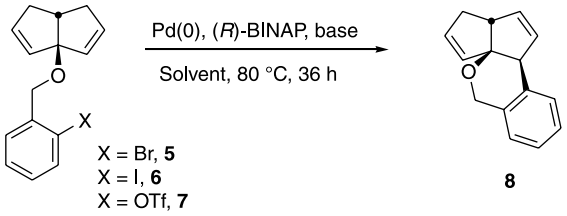
[5] Cationic conditions facilitate the binding of the chiral bidentate ligand, olefin, and aryl group in the square planar Pd(II) intermediate in the enantiodescriminating carbopalladation step.

[6] Overman (see ref. 12) in his studies in the use of asymmetric Heck reactions in the synthesis of chiral oxindoles noted a similar phenomenon. No conclusive argument was put forth in his studies, and results in our studies do not help to explain the highly effective role of tertiary amine bases in asymmetric Heck reactions. See ref. 9, as well as ref. 12.

[7] Substrate **7** was prepared in four steps, starting from **1** and 2-(*tert*-butyldimethylsilyloxy)benzylbromide. See experimental section for details.

© 2004 NRC Canada

Table 1. Effects of solvents and bases on the asymmetric synthesis of **8**.



Entry	Substrate	Pd source	Solvent	Base (2 equiv.)	Yield (%)	Enantiomeric excess (%)
1	**5**	$Pd(OAc)_2$	CH_3CN	Et_3N	43	93
2	**6**	Pd_2dba_3-$CHCl_3$	CH_3CN	Et_3N	52	98
3	**6**	Pd_2dba_3-$CHCl_3$	CH_3CN	K_2CO_3	60	83
4	**6**	Pd_2dba_3-$CHCl_3$	CH_3CN	Ag_2CO_3	80	97
5	**6**	Pd_2dba_3-$CHCl_3$	CH_3CN	Ag_3PO_4	37	97
6	**6**	Pd_2dba_3-$CHCl_3$	THF	Ag_3PO_4	73	94
7	**6**	Pd_2dba_3-$CHCl_3$	Toluene	Ag_3PO_4	77	99
8	**6**	Pd_2dba_3-$CHCl_3$	DMA	Ag_3PO_4	57	91
9	**6**	Pd_2dba_3-$CHCl_3$	NMP	Ag_3PO_4	60	63
10	**7**	Pd_2dba_3-$CHCl_3$	CH_3CN	K_2CO_3	53	97

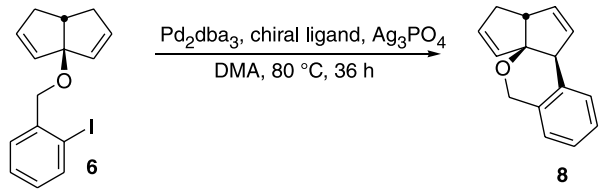
was carried out in a highly efficient process with the Grubbs second generation catalyst (4,5-dihydroIMES)$(PCy_3)Cl_2Ru$=CHPh (**9**). The reaction was efficient with catalyst loadings as low as 2 mol% (cf. 12 mol% of $[Cl_2(Cy_3P)_2Ru$=CHPh] (**4**)) (7) and was complete in 30 min in refluxing dichloromethane. A 4.5:1 mixture of diastereomeric bicyclo[4.4.0]decadienes was obtained, favouring the *cis*-fused decalin. The minor diastereomer was removed by stirring the reaction mixture with silica gel for ~15 min at room temperature followed by flash chromatography on silica gel.[8]

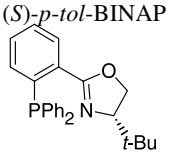
Application of the AHR to aryl iodide *cis*-**12** provided regioisomeric alkene products[9] in a 1:1 ratio and a combined 60% yield (Scheme 3). This system is more complex, since olefin isomerization is now a significant process. A β-hydride addition – elimination step involving **13** with a chiral hydridopalladium species, formed from the Heck reaction of *cis*-**12**, leads to the formation of **14**. Of note, the two regioisomeric products have different ee values (15).

Studies on the bicyclo[3.3.0]octadiene series revealed *p-tol*-BINAP to be the ligand that delivered products with the highest enantiomeric excess. Having obtained alkenes **13** and **14** in modest enantioselectivity, a brief study of chiral ligands was carried out to determine whether the alkene isomerization process could be controlled (Table 3).

Enantiomeric excesses in this series are lower, perhaps because of the elevated temperature used (100 °C versus 80 °C) for the desymmetrization of the bicyclo[4.4.0]decadiene **12**. The higher temperatures were required because of the sluggish nature of the Pd-PHOX catalysts with this substrate.[10] *p-tol*-BINAP is clearly the ligand that affords products with the highest enantiomeric ratios. Unlike palladium catalysts

Table 2. Effect of ligand in the asymmetric synthesis of **8**.



Entry	Ligand	Yield (%)	ee (%)
1	(*S*)-BINAP	57	91
2	(*S*)-*p-tol*-BINAP	87	99
3	 (*S*)-*t*-Bu-Pox	18	29

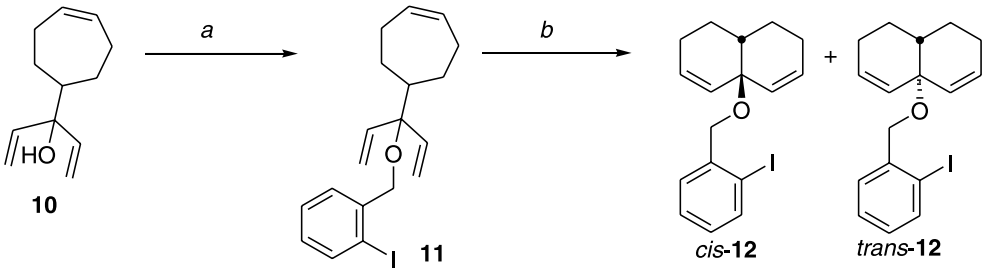
derived from BINAP, virtually no C=C double bond migration has been reported for Pd-PHOX catalysts. Yet, in the present system, the use of the (*S*)-*t*-Bu-POX and (*S*)-*i*-Pr-(*S*)-DIPOF (16) ligands resulted in a 1:2 ratio of the regioisomers **13** and **14**, respectively, with lower levels of enantioselectivity than seen with the BINAP catalysts (Table 3, entries 3 and 4).

The use of silver salts in the reactions of **12** did not seem to lead to any bias in the formation of the regioisomeric alkene products. However, the utilization of Tl_2CO_3 as base provided a 1:5.6 ratio of **13**:**14** (Scheme 4) with similar yields and levels of enantiomeric excesses as those seen with silver salts.

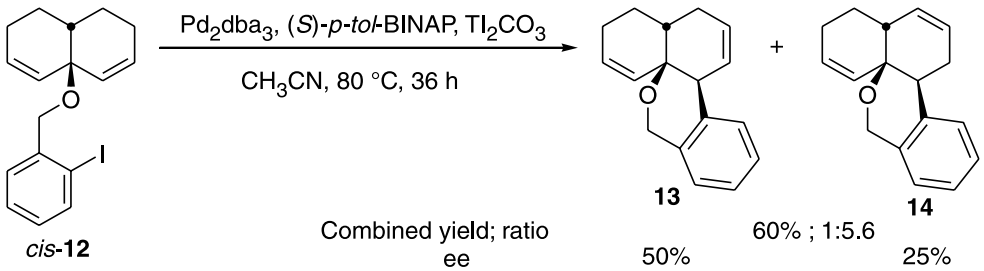
[8] Generally, the isolation of the bicyclodienes mentioned in this report required triethylamine-neutralized silica gel in the purification step.
[9] The relative stereochemistry of **13** and **14** are assumed to be as depicted, since 2D-NMR experiments (ROESY, NOESY) were unsuccessful at elucidating the relative stereochemistry assignment of **13** and **14**. To our knowledge, the intramolecular Heck reaction is a facile means to access *cis*-fused bicycles (see refs. 1–3). The absolute stereochemistry of **13** and **14** have yet to be determined.
[10] For the sake of consistency, the same temperature was used throughout the series in this ligand survey.

© 2004 NRC Canada

Scheme 2. Synthesis of bicyclo[4.4.0]decadienes for intramolecular Heck reactions. Conditions: (*a*) KH, 2-iodobenzyl bromide, THF, 23 °C, 12 h, 85%; (*b*) (4,5-dihydroIMES) $(PCy_3)Cl_2Ru$=CHPh (**9**) (2 mol%), CH_2Cl_2, reflux, 30 min, 4.5:1 (*cis*-**12**:*trans*-**12**), 100%.



Scheme 3. Desymmetrization of bicyclo[4.4.0]decadienes.



The exploration of the analogous aryl triflate substrate tethered to the bicyclo[4.4.0]decadienes was also undertaken in attempts to increase the enantiomeric excesses of the polycyclic products.[11] Subjecting triflate *cis*-**15** under AHR conditions provided the polycyclic products **13** and **14** in ~1:1 ratio but with significantly higher levels of asymmetric induction (Scheme 5). Attempts are now being directed at expanding the scope of this sequential olefin metathesis – intramolecular AHR sequence and highlighting the usefulness of the polycycles through further chemical transformations.

Summary

The stereoselective synthesis of tetracycles is made possible using a DSRCM and asymmetric Heck strategy. Cationic conditions in the asymmetric Heck reaction gave high enantioselectivities in the desymmetrization process in which three contiguous chiral centers are established with high enantioselectivities in a single step.

Experimental

The following experimental details apply to all subsequent experiments.

All reactions were carried out under an atmosphere of dry argon or nitrogen in oven- (overnight at 90 °C and then cooled under a stream of Ar or N_2) or flame-dried glassware. Solvents and solutions were transferred with syringes and cannulae, using standard inert atmosphere techniques.

^{1}H NMR spectra were recorded at 400 MHz, using a Varian XL400 spectrometer with $CDCl_3$ and TMS as reference standards (δ = 0.00 parts per million (ppm) or 7.26 ppm). ^{13}C NMR were recorded at 100 MHz using the same spectrometer with $CDCl_3$ as reference standard (δ = 77.16 ppm). IR spectra were obtained using a Nicolet DX FT-IR spectrometer as a neat film between KBr plates. High resolution mass spectra were obtained from a VG 70-250S (double focusing) mass spectrometer at 70 eV.

High performance liquid chromatography (HPLC) was performed on an Agilent 1100 Series HPLC using a CHIRACEL OD column. Column chromatography was performed as flash chromatography, as reported by Still et al. (17), using (200–400 mesh) Merck grade silica gel.

Toluene and THF were distilled from sodium–benzophenone. DMF was dried by prolonged standing over molecular sieves. CH_2Cl_2 was distilled from CaH_2.

Grubbs catalyst (**4**) was prepared according to the literature procedure (18) and triturated for 12–18 h in a 1:1 mixture of acetone and methanol. The absence of free tricyclohexyl phosphine and tricyclohexyl phosphine oxide was confirmed by ^{31}P NMR and was crucial for the double metathesis reactions to proceed. (DihydroIMES)(PCy_3)-Cl_2Ru=CHPh (**9**) was used as received from Strem. The following compounds were prepared as reported in the literature: 4-Allyl-3-vinyl-hepta-1,5-dien-3-ol (**1**) (7), 3-cyclohept-4-enyl-penta-1,4-dien-3-ol (**10**) (7), and 2-(*tert*-butyldimethylsilyloxy)benzyl bromide (19).

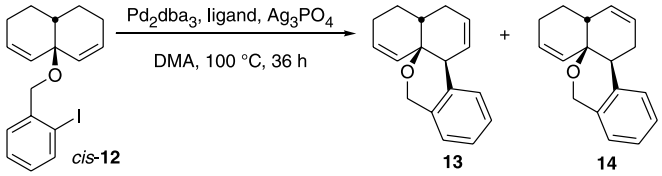
1-(2-Allyl-1,1-divinyl-pent-4-enyloxymethyl)-2-bromobenzene (2)

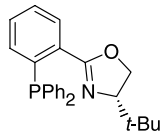
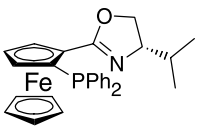
KH (35% dispersion in mineral oil, 1.0 g, 4 equiv.) was washed three times with pentane, dried under a stream of argon, and suspended in THF (10 mL). A solution of alcohol **1** in THF (5 mL) was added dropwise via cannula. After 15 min at room temperature, 2-bromobenzyl bromide was added all at once, and the resulting solution was stirred at

[11]Substrate *cis*-**15** was prepared in four steps, starting from **10** and 2-(*tert*-butyldimethylsilyloxy)benzylbromide. See experimental section for details.

© 2004 NRC Canada

Table 3. Effect of ligands in the asymmetric synthesis of **13** and **14**.



Entry	Ligand	**13**:**14**[a]	**13** ee (%)	**14** ee (%)	Combined yield (%)[b]
1	(*S*)-BINAP	1:1.1	11	30	50
2	(*S*)-*p-tol*-BINAP	1:1.5	50	35	44
3	 (*S*)-*t*-Bu-POX	~1:2	37	— [c]	40
4	 (*S*)-*i*-Pr-(*S*)-DIPOF	1:2.4	19	1.6	53

[a]Ratio was determined by integration of the singlet at 3.30 ppm (**13**) and the triplet at 2.83 ppm (**14**) in the ^{1}H NMR of the crude reaction mixture.
[b]Combined isolated yield.
[c]Undetermined.

room temperature for 2 h. The mixture was quenched by dropwise addition of water (25 mL) and then extracted with ether (3 × 30 mL). The organic layers were dried over Na_2SO_4, filtered, and concentrated. Flash chromatography (100% hexanes) on triethylamine-washed silica gel provided the product as a colourless oil (740 mg, 95%). IR (neat): 3074(m), 2978(m), 2922(m), 1914(w), 1869(w), 1831(w), 1638(m), 1439(m), 1269(w), 1091(s), 931(s), 910(s), 748(s), 667(w). ^{1}H NMR (400 MHz, $CDCl_3$) δ: 7.62 (1H, d, *J* = 8 Hz), 7.48 (1H, d, *J* = 8 Hz), 7.31 (1H, t, *J* = 7.6 Hz), 7.12–7.08 (1H, m), 5.93–5.86 (2H, m), 5.88–5.80 (2H, m), 5.38 (2H, dd, *J* = 11.2 Hz, 0.8 Hz), 5.31 (2H, dd, *J* = 17.6 Hz, 0.8 Hz), 5.01–4.93 (4H, m), 4.40 (2H, s), 2.48–2.42 (2H, m), 2.02–1.94 (2H, m), 1.84–1.90 (1H, m). ^{13}C NMR (100 MHz, $CDCl_3$) δ: 139.22, 138.78, 137.67, 132.22, 128.44, 128.27, 127.39, 121.89, 118.04, 115.41, 83.98, 64.97, 48.28, 34.56. HR-MS calcd. for $C_{19}H_{23}OBr$ ([M]$^+$): 345.2788; found: 345.2791.

3a-(2-Bromobenzyloxy)-1,3a,6,6a-tetrahydropentalene (5)

To a solution of **2** (930 mg, 2.67 mmol) in 50 mL of dichloromethane was added Grubbs catalyst **4** all at once. The reaction was stirred under a closed system for 20 h at room temperature. The solvent was removed in vacuo, and the residue was purified by flash chromatography (100% hexanes → 5% Et_2O–hexanes) on triethylamine-washed silica gel to provide the product (530 mg, 70%) as a colourless oil. IR (neat): 3047(s), 2918(s), 2851(s), 1619(w), 1467(m), 1350(s), 1218(m), 1097(m), 1070(m), 989(m), 750(s). ^{1}H NMR (400 MHz, $CDCl_3$) δ: 7.47–7.53 (2H, m), 7.30–7.24 (1H, m), 7.11–7.07 (1H, m), 5.94–5.91 (2H, m), 5.84–5.82 (2H, m), 4.46 (2H, s), 2.90–2.84 (3H, m), 2.14–2.08 (2H, m). ^{13}C NMR (100 MHz, $CDCl_3$) δ: 138.97, 134.67, 132.38, 132.35, 129.28, 128.58, 127.43, 122.52, 106.00, 65.13, 43.10, 40.79. HR-MS calcd. for $C_{15}H_{15}OBr$ ([M]$^+$): 290.0306; found: 290.0301.

1-(2-Allyl-1,1-divinyl-pent-4-enyloxymethyl)-2-iodobenzene (3)

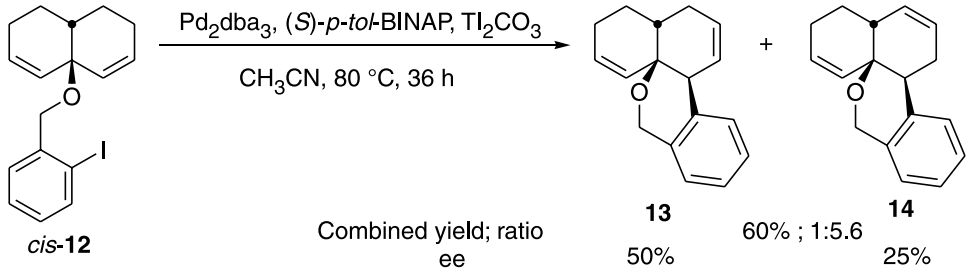
Following the the benzylation procedure to make **2**, alcohol **1** (1.15 g, 6.4 mmol) was reacted with 2-iodobenzylbromide (2.09 g, 7.06 mmol) to yield the product (2.08 g, 83%) as a colourless oil. IR (neat): 3073(m), 2911(m), 1952(w), 1908(w), 1864(w), 1627(s), 1440(s), 1085(s), 1012(s), 906(s), 752(s). ^{1}H NMR (400 MHz, $CDCl_3$) δ: 7.77 (1H, d, *J* = 7.6 Hz), 7.57 (1H, d, *J* = 7.6 Hz), 7.36 (1H, t, *J* = 8 Hz), 6.96 (1H, t, *J* = 8 Hz), 5.90 (2H, dd, *J* = 17.6 Hz, 10.8 Hz), 5.89–5.80 (2H, m), 5.39 (2H, dd, *J* = 11.2 Hz, 1.6 Hz), 5.31 (2H, dd, *J* = 17.6 Hz, 1.6 Hz), 5.02–4.94 (4H, m), 4.29 (2H, s), 2.49–2.43 (2H, m), 2.02–1.94 (2H, m), 1.90–1.84 (1H, m). ^{13}C NMR (100 MHz, $CDCl_3$) δ: 141.95, 138.84, 138.78, 137.63, 128.61, 128.23, 118.08, 115.43, 96.91, 83.99, 69.69, 48.26, 34.56. HR-MS calcd. for $C_{19}H_{23}OI$ ([M]$^+$): 393.0715; found: 393.0703.

3a-(2-Iodobenzyloxy)-1,3a,6,6a-tetrahydro-pentalene (6)

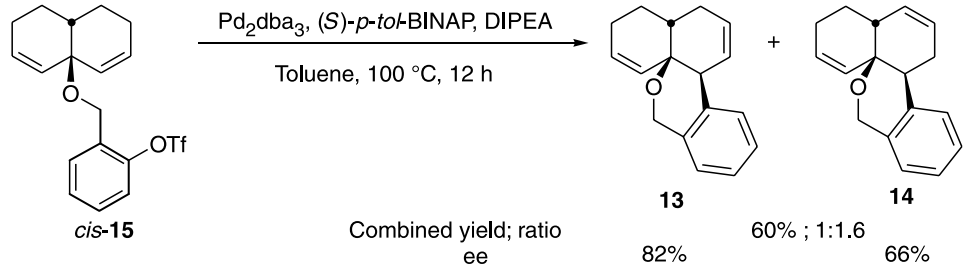
Following the procedure for RCM of tetraene **2**, iodobenzyl ether **3** (2.00 g, 5.08 mmol) was reacted with Grubbs catalyst **4** (250 mg, 6 mol%) in CH_2Cl_2 (50 mL) to provide the product (1.18 g, 70%) as a colourless oil after flash chromatography (5% Et_2O–hexanes) on triethylamine-washed silica gel. IR (neat): 3060(s), 2912(s), 1444(m), 1350(s), 1215(m), 1097(m), 1077(s), 1009(s), 942(w), 747(s). ^{1}H NMR (400 MHz, $CDCl_3$) δ: 7.87–7.76 (1H, m), 7.49–7.47 (1H, m), 7.34–7.30 (1H, m), 6.96–6.92 (1H, m), 5.94–5.92 (2H, m), 5.84 (2H, dt, *J* = 6 Hz, 1.6 Hz), 4.38 (2H, s), 2.91–2.84 (3H, m), 2.07–2.15 (2H, m). ^{13}C NMR

© 2004 NRC Canada

Scheme 4. Regiocontrol in the asymmetric Heck reaction using Tl salts.



Scheme 5. Asymmetric synthesis of **13** and **14** under cationic conditions.



(100 MHz, $CDCl_3$) δ: 141.80, 139.01, 134.71, 132.41, 128.99, 128.90, 128.30, 106.00, 97.70, 69.81, 43.21, 40.80. HR-MS calcd. for $C_{15}H_{13}OI$ ($[M]^+$): 338.0149; found: 338.0167.

Preparation of trifluoromethanesulfonic acid 2-(6,6a-dihydro-1*H*-pentalen-3a-yloxymethyl)-phenyl ester (7)

KH (35% dispersion in mineral oil, 1.0 g, 3 equiv.) was washed three times with pentane, dried under a stream of argon, and suspended in 10 mL of THF. Alcohol **1** in 5 mL of THF was added via cannula. The solution was heated to reflux for 10 min, cooled to room temperature, and a solution of 2-(*tert*-butyldimethylsilyloxy)benzyl bromide (19) in 5 mL of THF was added via cannula. The solution was stirred at reflux for 3 h, cooled to room temperature, quenched by dropwise addition of water (25 mL), extracted with ether (3 × 30 mL), dried over Na_2SO_4, filtered, and concentrated. Flash chromatography (100% hexanes) on triethylamine-washed silica gel provided 1-(2-allyl-1,1-divinyl-pent-4-enyloxymethyl)-2-(*tert*-butyldimethylsiloxy)-benzene (939 mg, 85%) as a colourless oil. IR (neat): 3088(s), 2919(s), 2855(s), 1634(m), 1579(m), 1491(s), 1250(s), 1070(m), 913(s), 832(s), 730(m). ^{1}H NMR (400 MHz, $CDCl_3$) δ: 7.57–7.55 (1H, m), 7.11 (1H, td, *J* = 7.6 Hz, 0.8 Hz), 6.98 (1H, td, *J* = 7.6 Hz, 0.8 Hz), 6.74 (1H, dd, *J* = 8 Hz, 0.8 Hz), 5.92–5.82 (4H, m), 5.35 (2H, dd, *J* = 10.8 Hz, 1.6 Hz), 5.29 (2H, dd, *J* = 17.8 Hz, 1.6 Hz), 5.02–4.94 (4H, m), 4.40 (2H, s), 2.51–2.44 (2H, m), 2.01–1.93 (2H, m), 0.97 (9H, s), 0.18 (6H, s). ^{13}C NMR (100 MHz, $CDCl_3$) δ: 152.21, 138.96, 137.91, 131.09, 131.46, 127.46, 127.25, 121.20, 118.03, 117.72, 115.28, 83.69, 61.07, 48.21, 34.57, 18.30, –4.11. HR-MS calcd. for $C_{21}H_{30}O_2Si$ ($[M - C_4H_9]^+$): 341.1936; found: 341.1934.

In a 10 mL round-bottom flask was added 1-(2-allyl-1,1-divinyl-pent-4-enyloxymethyl)-2-(*tert*-butyldimethylsiloxy)-benzene (300 mg, 0.75 mmol) and 3 mL of THF. To this solution was added TBAF (235 mg, 0.90 mmol) all at once at room temperature, and the reaction mixture was stirred at room temperature for 30 min. The reaction was diluted with water (10 mL) and extracted with ether (3 × 10 mL). The combined organic layers were dried over Na_2SO_4, filtered, and concentrated. The residue (2-(2-allyl-1,1-divinyl-pent-4-enyloxymethyl)-phenol) was then used in the next reaction without further purification. IR (neat): 3386(s), 3075(m), 2923(m), 1826(w), 1638(m), 1491(m), 1241(s), 1026(m), 912(s), 753(s). ^{1}H NMR (400 MHz, $CDCl_3$) δ: 7.75 (1H, br s), 7.18–7.14 (1H, m), 6.93–6.78 (3H, m), 5.91–5.75 (4H, m), 5.44–5.31 (4H, m), 5.02–4.95 (4H, m), 4.55 (2H, s), 2.39–2.32 (2H, m), 1.99–1.91 (2H, m), 1.87–1.82 (1H, m). ^{13}C NMR (100 MHz, $CDCl_3$) δ: 156.33, 138.01, 136.83, 128.98, 127.70, 123.56, 119.82, 118.77, 116.68, 115.92, 85.33, 65.69, 47.79, 34.42. HR-MS calcd. for $C_{19}H_{24}O_2$ ($[M]^+$): 284.1776; found: 284.1780.

In a 10 mL round-bottom flask was added 2-(2-allyl-1,1-divinyl-pent-4-enyloxymethyl)-phenol (215 mg, 0.75 mmol), CH_2Cl_2 (5 mL), and Et_3N (440 μL, 4 equiv.). The solution was then cooled to –78 °C and Tf_2O (254 μL, 2 equiv.) was added dropwise via syringe. The reaction mixture was stirred at –78 °C for 15 min, at which point water (5 mL) was added. The flask was warmed to room temperature and extracted with ether (3 × 15 mL), and the organic extracts were dried over Na_2SO_4, filtered, and concentrated. Flash chromatography (2% Et_2O–hexanes) on triethylamine-washed silica gel provided trifluoromethanesulfonic acid 2-(2-allyl-1,1-divinyl-pent-4-enyloxy methyl)-phenyl ester as a colourless oil (240 mg, 81%). IR (neat): 3074(s), 2903(m), 1918(w), 1863(w), 1634(m), 1487(m), 1413(s), 1210(s), 1099(s), 1066(s), 996(s), 896(s), 764(s), 605(m). ^{1}H NMR (400 MHz, $CDCl_3$) δ: 7.68 (1H, dd, *J* = 7.6 Hz, 0.8 Hz), 7.38 (1H, td, *J* = 7.6 Hz, 1.2 Hz), 7.32 (1H, td, *J* = 8.2 Hz, 2 Hz), 7.25–7.23 (1H, m), 5.87 (2H, dd, *J* = 17.6 Hz, 11.2 Hz), 5.86–5.78 (2H, m), 5.40 (2H, dd, *J* = 11.2 Hz, 1.2 Hz), 5.30 (2H, dd, *J* = 17.6 Hz, 1.6 Hz), 5.00–4.93 (4H, m), 4.46 (2H, s), 2.45–2.39 (2H, m), 1.99–1.92 (2H, m), 1.89–183

© 2004 NRC Canada

(1H, m). ^{13}C NMR (100 MHz, $CDCl_3$) δ: 146.89, 138.66, 137.32, 132.97, 129.77, 128.70, 128.47, 121.00, 120.31, 118.72 (q, J = 319.2 Hz), 118.33, 115.43, 84.27, 59.77, 48.24, 34.48. HR-MS calcd. for $C_{18}H_{20}O_4SF_3$ ([M – C_2H_3]$^+$): 389.1023; found: 389.1034.

In a 25 mL round-bottom flask was added trifluoromethanesulfonic acid 2-(2-allyl-1,1-divinyl-pent-4-enyloxy methyl)-phenyl ester (230 mg, 0.58 mmol) and 10 mL of CH_2Cl_2. Catalyst **4** (24 mg, 5 mol%) was added, and the solution was stirred under a closed atmosphere at room temperature for 12 h. The solvent was removed on the rotary evaporator to provide the crude product, which was purified by flash chromatography (100% hexanes → 5% Et_2O–hexanes) on triethylamine-washed silica gel. The yield of the title compound was 150 mg (75%). IR (neat): 3053(m), 2923(m), 2849(m), 1968(w), 1487(m), 1419(s), 1350(m), 1214(s), 1142(s), 1059(m), 992(m), 895(s), 764(m), 707(m), 597(m). ^{1}H NMR (400 MHz, $CDCl_3$) δ: 7.61–7.58 (m, 1H), 7.38–7.31 (m, 2H), 7.25–7.23 (m, 1H), 5.93 (2H, dt, J = 5.6 Hz, 2 Hz), 5.81 (2H, dt, J = 5.6 Hz, 2 Hz), 4.50 (2H, s), 2.92–2.83 (3H, m), 2.15–2.08 (2H, m). ^{13}C NMR (100 MHz, $CDCl_3$) δ: 147.37, 134.92, 132.74, 132.13, 130.13, 130.60, 129.10, 128.49, 121.11, 118.72 (J = 318.4 Hz), 106.30, 59.98, 42.99, 40.84. HR-MS calcd. for $C_{16}H_{15}O_4SF_3$ ([M]$^+$): 360.3530; found: 360.3538.

5-[1-(2-Iodobenzyloxy)-1-vinyl-allyl]-cycloheptene (11)

Following the benzylation procedure for **2** and **3**, alcohol **10** (1.15 g, 6.4 mmol) was reacted with 2-iodobenzyl bromide (2.09 g, 7.06 mmol) to yield the product (2.08 g, 83%) as a colourless oil. IR (neat): 3014(m), 2919(s), 1948(w), 1912(w), 1864(w), 1791(w), 1641(w), 1436(s), 1202(m), 1107(s), 928(s), 748(s), 748(s), 690(s). ^{1}H NMR (400 MHz, $CDCl_3$) δ: 7.78–7.76 (1H, m), 7.58–7.56 (1H, m), 7.38–7.32 (1H, m), 6.97–6.93 (1H, m), 5.87 (2H, dd, J = 17.6 Hz, 11.2 Hz), 5.79–5.77 (2H, m), 5.36 (2H, dd, J = 11.2 Hz, 1.6 Hz), 5.82 (2H, dd, J = 17.8 Hz, 1.6 Hz), 4.29 (2H, s), 2.32–2.25 (2H, m), 2.07–1.98 (4H, m), 1.82 (1H, tt, J = 10.8 Hz, 2.4 Hz), 1.71–1.04 (2H, m). ^{13}C NMR (100 MHz, $CDCl_3$) δ: 142.09, 138.83, 137.88, 132.04, 128.59, 128.23, 128.18, 117.74, 96.97, 83.95, 69.56, 28.18, 28.15. HR-MS calcd. for $C_{19}H_{23}OI$ ([M]$^+$): 394.0792; found: 394.0793.

4a-(2-Iodobenzyloxy)-1,2,4a,7,8,8a-hexahydro-napthalene (12)

In a 100 mL round-bottom flask was added 5-[1-(2-iodobenzyloxy)-1-vinyl-allyl]-cycloheptene (850 mg, 2.15 mmol) and 50 mL of CH_2Cl_2 under nitrogen. To this solution was added ruthenium catalyst **9** (35 mg, 0.04 mmol), and the solution was refluxed for 1 h, at which time all of the starting material had been consumed. ^{1}H NMR analysis showed a 4.5:1 mixture of diastereomers (integration of signals at 5.89 ppm (multiplet corresponding to all of the olefinic protons of the *trans* decalin plus half of the olefin protons of the *cis* decalin product) and 5.63 ppm (half of the olefin protons of the *cis* decalin)). Silica gel (~200 mg) was added, and the mixture was stirred at room temperature for 15 min. The solution was filtered, and the silica gel was washed with a copious amount of CH_2Cl_2. The solvent was removed in vacuo, and the residue was purified by flash chromatography (2% Et_2O–hexanes) to provide 520 mg (65%) of the *cis*-bicyclo[4.4.0]decadiene as a clear oil. IR (neat): 3011(m), 2922(s), 1952(w), 1911(w), 1826(w), 1871(w), 1650(w), 1562(m), 1434(s), 1371(m), 1265(m), 1202(m), 1110(m), 1066(s), 945(m), 747(s), 647(m). ^{1}H NMR (400 MHz, $CDCl_3$) δ: 7.76 (1H, d, J = 8 Hz), 7.52 (1H, d, J = 8 Hz), 7.32 (1H, t, J = 7.6 Hz), 6.93 (1H, t, J = 7.6 Hz), 5.89 (2H, dt, J = 9,9 Hz, 3.6 Hz), 5.63 (2H, dt, J = 9.9 Hz, 2.1 Hz), 4.42 (2H, s), 2.23–2.17 (1H, m), 2.14–2.01 (4H, m), 1.90–1.83 (2H, m), 1.51–1.59 (2H, m). ^{13}C NMR (100 MHz, $CDCl_3$) δ: 142.09, 138.92, 130.29, 129.93, 129.07, 128.81, 128.31, 97.70, 74.68, 68.79, 34.58, 24.51, 23.46. HR-MS calcd. for $C_{17}H_{19}OI$ ([M]$^+$): 366.0480; found: 366.0483.

Preparation of triflouromethanesulfonic acid 2-(1,7,8,8a-tetrahydro-2*H*-naphthalen-4a-yloxymethyl)-phenol ester (15)

KH (35% dispersion in mineral oil, 1.0 g, 3 equiv.) was washed three times with pentane, dried under a stream of argon, and suspended in 10 mL of THF. Alcohol **10** in 5 mL of THF was added via cannula. The solution was heated to reflux for 10 min, cooled to room temperature, and a solution of 2-(*tert*-butyldimethylsilyloxy)benzyl bromide (19) in 5 mL of THF was added via cannula. The solution was stirred at reflux for 3 h, cooled to room temperature, quenched by dropwise addition of water (25 mL), extracted with ether (3 × 30 mL), dried over Na_2SO_4, filtered, and concentrated. Flash chromatography (100% hexanes) on triethylamine-washed silica gel provided *tert*-butyl[2-(1-cyclohept-4-enyl-1-vinyl-allyloxymethyl)-phenoxy]-dimethylsilane (939 mg, 85%) as a colourless oil. IR (neat): 2929(s), 1858(w), 1602(m), 1584(m), 1489(s), 1378(m), 1252(s), 1114(m), 924(s), 838(s), 758(m), 692(m). ^{1}H NMR (400 MHz, $CDCl_3$) δ: 7.56–7.54 (1H, m), 7.13–7.09 (1H, m), 7.00–6.96 (1H, m), 6.75–6.73 (1H, m), 5.84 (2H, dd, J = 17.6 Hz, 11.2 Hz), 5.79–5.77 (2H, m), 5.33 (2H, dd, J = 10.8 Hz, 1.6 Hz), 5.26 (2H, dd, J = 17.6 Hz, 1.6 Hz), 4.39 (2H, s), 2.32–2.27 (2H, m), 2.08–1.97 (4H, m), 1.80 (1H, tt, J = 10.8 Hz, 2.4 Hz), 1.12–1.04 (2H, m), 0.97 (9H, s), 0.18 (6H, s). ^{13}C NMR (100 MHz, $CDCl_3$) δ: 152.29, 138.18, 132.12, 131.23, 127.48, 127.27, 121.23, 118.09, 117.41, 83.65, 60.92, 52.99, 28.19, 25.85, 18.31, –4.10. HR-MS calcd. for $C_{25}H_{38}O_2Si$ ([M]$^+$): 396.6448; found: 396.6451.

In a 10 mL round-bottom flask was added *tert*-butyl[2-(1-cyclohept-4-enyl-1-vinyl-allyloxymethyl)-phenoxy]-dimethylsilane (300 mg, 0.75 mmol) and 3 mL of THF. To this solution was added TBAF all at once at room temperature, and the reaction mixture was stirred at room temperature for 10 min. The reaction was diluted with water (10 mL) and extracted with ether (3 × 10 mL). The combined organic layers were dried over Na_2SO_4, filtered, and concentrated. The residue [2-(1-cyclohept-4-enyl-1-vinyl-allyloxymethyl)phenol] was then used in the next reaction without further purification. IR (neat): 3362(s), 3017(m), 2930(m), 1930(w), 1861(w), 1590(m), 1244(s), 1024(s), 845(w), 754(s), 692(w). ^{1}H NMR (400 MHz, $CDCl_3$) δ: 8.01 (1H, br s), 7.20–7.16 (1H, m), 6.95–6.80 (3H, m), 5.85 (2H, dd, J = 17.8 Hz, 11.2 Hz), 5.77–5.75 (2H, m), 5.42 (2H, d, J = 10.8 Hz), 5.32 (2H, d, J = 17.6 Hz), 4.59 (2H, s), 2.32–2.26 (2H, m), 2.03–1.92 (4H, m), 1.82 (1H, tt, J = 10.4 Hz, 2.4 Hz), 1.15–1.06 (2H, m). ^{13}C NMR (100 MHz, $CDCl_3$) δ:

© 2004 NRC Canada

156.37, 136.92, 131.74, 128.92, 127.60, 123.37, 119.80, 118.60, 116.64, 85.16, 65.74, 52.11, 28.07, 27.98. HR-MS calcd. for $C_{19}H_{24}O_2$ ([M]$^+$): 284.1776; found: 284.1778.

In a 10 mL round-bottom flask was added 2-(1-cyclohept-4-enyl-1-vinyl-allyloxymethyl)-phenol (215 mg, 0.75 mmol), CH_2Cl_2 (5 mL), and Et_3N (440 μL, 4 equiv.). The solution was then cooled to –78 °C and Tf_2O (254 μL, 2 equiv.) was added dropwise via syringe. The reaction mixture was stirred at –78 °C for 15 min, at which point water (5 mL) was added. The flask was warmed to room temperature and extracted with ether (3 × 15 mL), and the organic extracts were dried over Na_2SO_4, filtered, and concentrated. Flash chromatography (2% Et_2O–hexanes) on treithylamine-washed silica gel provided triflouromethanesulfonic acid 2-(1-cyclohept-4-enyl-1-vinyl-allyloxymethyl)-phenyl ester as a colourless oil (240 mg, 81%). IR (neat): 3018(w), 2928(w), 1866(w), 1422(s), 1214(s), 1143(s), 1093(m), 1003(w), 894(m), 767(m), 628(w). ^{1}H NMR (400 MHz, $CDCl_3$) δ: 7.68–7.66 (1H, m), 7.39–7.36 (1H, m), 7.33–7.29 (1H, m), 7.24–7.22 (1H, m), 5.83 (2H, dd, J = 17.8 Hz, 10.8 Hz), 5.87–5.75 (2H, m), 5.36–5.39 (2H, m), 5.29–5.24 (2H, m), 4.46 (2H, s), 2.30–2.23 (2H, m), 2.03–1.96 (4H, m), 1.83–1.77 (1H, m), 1.10–1.02 (2H, m). ^{13}C NMR (100 MHz, $CDCl_3$) δ: 147.00, 137.60, 133.10, 131.98, 131.98, 129.78, 128.69, 128.47, 120.99, 118.72 (q, J = 319.2 Hz), 117.96, 84.22, 59.71, 52.86, 28.11. HR-MS calcd. for $C_{20}H_{23}O_4SF_3$ ([M]$^+$): 416.1269; found: 416.1280.

In a 100 mL round-bottom flask was added triflouromethanesulfonic acid 2-(1-cyclohept-4-enyl-1-vinyl-allyloxymethyl)-phenyl ester (850 mg, 2.15 mmol) and 50 mL of CH_2Cl_2 under nitrogen. To this solution was added ruthenium catalyst **9** (35 mg, 0.04 mmol), and the solution was refluxed for 1 h, at which time all of the starting material had been consumed. ^{1}H NMR analysis showed a 4.5:1 mixture of diastereomers (integration of signals at 5.90 ppm (multiplet corresponding to all of the olefinic protons of the *trans* decalin plus half of the olefin protons of the *cis* decalin product) and 5.59 ppm (half of the olefin protons of the *cis* decalin)). Silica gel (~200 mg) was added, and the mixture was stirred at room temperature for 15 min. The solution was filtered, and the silica gel was washed with a copious amount of CH_2Cl_2. The solvent was removed in vacuo, and the residue was purified by flash chromatography (2% Et_2O–hexanes) to provide 520 mg (65%) of the *cis*-bicyclo-[4.4.0]decadiene (**15**) as a clear oil. IR (neat): 3029(m), 2941(s), 1487(m), 1454(m), 1418(s), 1330(w), 1209(s), 1143(s), 1056(m), 895(s), 763(m), 734(m), 602(m). ^{1}H NMR (400 MHz, $CDCl_3$) δ: 7.65–7.63 (1H, m), 7.37–7.22 (3H, m), 5.90 (2H, dt, J = 10.4 Hz, 3.6 Hz), 5.59 (2H, dt, J = 9.6 Hz, 2 Hz), 4.56 (2H, s), 2.20–2.00 (5H, m), 1.87–1.79 (2H, m), 1.50–1.59 (2H, m). ^{13}C NMR (100 MHz, $CDCl_3$) δ: 147.13, 133.09, 130.60, 130.50, 129.59, 128.86, 128.48, 120.95, 118.72 (q, J = 319.2 Hz), 74.97, 58.62, 34.44, 24.39, 23.40. HR-MS calcd. for $C_{18}H_{19}O_4SF_3$ ([M]$^+$): 388.0956; found: 388.0962.

General procedure for the asymmetric Heck reaction using $Pd(OAc)_2$

In a 10 mL round-bottom flask equipped with a stir bar and reflux condenser was added $Pd(OAc)_2$ (11.5 mg, 0.0513 mmol), (*R*)-BINAP (63.88 mg, 0.1025 mmol), Et_3N (74 μL, 0.513 mmol), and 2 mL of CH_3CN under an argon flush. The mixture was heated to 70 °C for 3 h and then the aryl halide (0.342 mmol) in 1 mL of CH_3CN was added via cannula. The reaction was stirred at 70 °C for 16 h. The reaction was cooled to room temperature, diluted with water (5 mL), and extracted with ether (3 × 10 mL). The organic layers were combined, dried over Na_2SO_4, filtered, and concentrated. Flash chromatography (2.5% Et_2O–hexanes → 5% Et_2O–hexanes) provided the product as an oil.

General procedure for the asymmetric Heck reaction using Pd_2dba_3

In a 10 mL round-bottom flask equipped with a stir bar and reflux condenser was added Pd_2dba_3 (8.15 mg, 0.0089 mmol), (*R*)-*tol*-BINAP (12.19 mg, 0.01958 mmol), and base (0.356 mmol) in solvent (1 mL) under an argon atmosphere. The solution was stirred at room temperature for 40 min, and then a solution of the aryl halide (0.178 mmol) in 1.5 mL of solvent was added via cannula under argon. The reaction was heated to 80 °C and stirred at this temperature for 36 h. The flask was cooled to room temperature, diluted with ether (20 mL), and washed with saturated aqueous $NaHCO_3$ (7 mL). The aqueous layer was further extracted with Et_2O (2 × 10 mL), and the combined organic extracts were washed with brine (7 mL) and dried over Na_2SO_4. Removal of the organic solvent followed by flash chromatography (5%–10% Et_2O–hexanes) provided the product as a colourless oil.

4b,6a,7,11-Tetrahydro-10-oxa-pentaleno[1,6a-a]naphthalene (8)

Following the general procedure for the asymmetric Heck reaction, the title compound was obtained as a colorless oil, which darkens upon storage at room temperature for prolonged time. The enantiomeric excess of the cyclized product was determined by HPLC analysis, as follows: CHIRACEL OD, 10% *i*-PrOH–hexanes, retention times for the enantiomers = 10.9 min, 11.5 min. (V_O = 0.5 ml/min, 23 °C, UV monitor: 254 nm.) $[\alpha]_D^{25}$ = +124.7 (c = 1.0, $CHCl_3$) (99% ee). ^{1}H NMR (400 MHz, $CDCl_3$) δ: 7.23 (1H, d, J = 7.2 Hz), 7.18 (1H, d, J = 7.2 Hz), 7.13 (1H, d, J = 7.2 Hz), 7.08 (1H, d, J = 7.2 Hz), 5.96 (1H, dt, J = 5.6 Hz, 2 Hz), 5.83 (1H, dt, J = 5.6 Hz, 2.8 Hz), 5.72 (1H, dt, J = 6.4 Hz, 2 Hz), 5.66 (1H, dt, J = 6 Hz, 1.6 Hz), 4.70 (1H, d, J = 14 Hz), 4.60 (1H, d, J = 14 Hz), 3.83 (1H, d, J = 2 Hz), 3.48 (1H, dt, J = 8.8 Hz, 2 Hz), 2.83 (1H, ddt, J = 17.2 Hz, 8.8 Hz, 2 Hz), 2.16 (1H, dd, J = 17.2 Hz, 2 Hz). ^{13}C NMR (100 MHz, $CDCl_3$) δ: 136.10, 135.13, 134.36, 134.14, 133.50, 132.65, 128.06, 127.58, 125.77, 125.13, 97.42, 64.18, 50.46, 50.31, 36.99. HR-MS calcd. for $C_{15}H_{13}O$ ([M]$^+$): 210.1042; found: 210.1044.

4b,7,7a,8,9,13-Hexahydrodibenzo[*c*,*i*]chromene (13) and 4b,5,7a,8,9,13-hexahydrodibenzo[*c*,*i*]chromene (14)

Following the general procedure for the asymmetric Heck reaction, the title compounds were obtained as colorless oils after flash chromatography (2% Et_2O–hexanes → 5% Et_2O–hexanes). Enantiomeric excesses of the cyclized products were determined by HPLC analysis, as follows: CHIRACEL OD, 10% *i*-PrOH–hexanes, retention times for the enantiomers: **13** = 4.02 min, 4.55 min; **14** = 4.43 min, 5.60 min.

© 2004 NRC Canada

(V_O = 1 ml/min, 23 °C, UV monitor: 220 nm.) **13** = $[\alpha]_D^{25}$ = –101.2 (c = 0.90, $CHCl_3$) (82% ee, using (*S*)-*tol*-BINAP); **14** = $[\alpha]_D^{25}$ = –88.9 (c = 0.85, $CHCl_3$) (66% ee, using (*S*)-*tol*-BINAP).

4b,7,7a,8,9,13-Hexahydrodibenzo[c,i]chromene (13)

IR (neat): 3405(m), 2927(s), 1717(s), 1603(w), 1457(m), 1271(m), 1082(m), 1032(w), 747(m). ^{1}H NMR (400 MHz, $CDCl_3$) δ: 7.22–7.15 (3H, m), 7.01 (1H, d, J = 7.6 Hz), 5.93–5.90 (1H, m), 5.70–5.66 (2H, m), 5.54–5.50 (1H, m), 4.98 (1H, d, J = 15.6 Hz), 4.83 (1H, d, J = 15.6 Hz), 3.30 (1H, s), 2.63–2.56 (1H, m), 2.65–2.08 (3H, m), 1.64–1.87 (3H, m). ^{13}C NMR (100 MHz, $CDCl_3$) δ: 136.01, 133.9, 129.42, 129.18, 129.18, 128.92, 127.48, 127.02, 126.16, 124.63, 124.12, 72.09, 62.37, 42.07, 36.59, 28.59, 26.16, 25.48. HR-MS calcd. for $C_{16}H_{18}O$ ($[M]^+$): 238.1357; found: 238.1359.

4b,5,7a,8,9,13-Hexahydrodibenzo[c,i]chromene (14)

IR (neat): 3419(m), 2924(m), 1713(s), 1603(m), 1458(w), 1299(m), 1278(m), 1108(w), 1072(w), 1018(w), 755(w), 734(m). ^{1}H NMR (400 MHz, $CDCl_3$) δ: 7.21–7.13 (3H, m), 7.04–7.02 (1H, m), 5.85 (1H, dt, J = 10.4 Hz, 3.6 Hz), 5.70–5.65 (2H, m), 5.55–5.52 (1H, m), 5.00 (1H, s), 2.83 (1H, t, J = 6.4 Hz), 2.41–2.26 (3H, m), 2.10–2.03 (2H, m), 1.96–1.89 (1H, m), 1.51–1.41 (1H, m). ^{13}C NMR (100 MHz, $CDCl_3$) δ: 138.00, 133.91, 131.28, 129.64, 128.63, 127.33, 126.60, 126.20, 124.40, 124.20, 71.89, 63.93, 39.15, 38.92, 30.78, 27.41, 24.48. HR-MS calcd. for $C_{16}H_{18}O$ ($[M]^+$): 238.1357; found: 238.1359.

Acknowledgment

We thank the University of Toronto, the Natural Sciences and Engineering Research Council of Canada (NSERC), and the Merck Frosst Centre for Therapeutic Research for financial support. V.Z. would like to thank NSERC and the Ontario Graduate Scholarship (OGS) for postgraduate scholarships.

References

1. (*a*) R.H. Crabtree. The organometallic chemistry of the transition metals. 2nd ed. John Wiley & Sons, Inc., New York. 1990; (*b*) A. de Meijere and F.E. Meyer. Angew. Chem. Int. Ed. Engl. **33**, 2379 (1994); (*c*) G.T. Crisp. Chem. Soc. Rev. **27**, 427 (1998).
2. For a review of cyclic carbopalladations, see: E. Negishi, C. Copéret, S. Ma, S. Liou, and F. Liu. Chem. Rev. **96**, 365 (1996).
3. For reviews on enantioselective Heck reactions, see (*a*) M. Shibasaki and E.M. Vogl. J. Organomet. Chem. **576**, 1 (1999); (*b*) M. Shibasaki. *In* Advances in metal-organic chemistry. *Edited by* L.S. Liebeskind. JAI, Greenwich. 1996. pp. 119–151; (*c*) M. Shibasaki, C.J.D. Boden, and A. Kojima. Tetrahedron, **53**, 7371 (1997).
4. (*a*) Y. Sato, M. Sodeoka, and M. Shibasaki. J. Org. Chem. **54**, 4738 (1989); (*b*) N.E. Carpenter, D.J. Kucera, and L.E. Overman. J. Org. Chem. **54**, 5846 (1989).
5. For example, see: (*a*) K. Kondo, M. Sodeoka, M. Mori, and M. Shibasaki. Tetrahedron Lett. **34**, 4219 (1993); (*b*) Y. Sato, S. Watanabe, and M. Shibasaki. Tetrahedron Lett. **35**, 2589 (1992); (*c*) Y. Sato, T. Honda, and M. Shibisaki. Tetrahedron Lett. **33**, 2593 (1992); (*d*) R. Imbos, A. Minnaard, and B.L. Feringa. J. Am. Chem. Soc. **124**, 184 (2002).
6. (*a*) Y. Sato, M. Mori, and M. Shibasaki. Tetrahedron Asymmetry, **6**, 757 (1995); (*b*) K. Kagechika and M. Shibisaki. J. Org. Chem. **56**, 4093 (1991); (*c*) S. Nukui, M. Sodeoka, H. Sasai, and M. Shibisaki. J.Org. Chem. **60**, 398 (1995); (*d*) T. Takemoto, M. Sodeoka, H. Sasai, and M. Shibisaki. J. Am. Chem. Soc. **115**, 8477 (1993); (*e*) A.B. Dounay, K. Hatanaka, J.J. Kodanko, M. Oestreich, L.E. Overman, L.A. Pfeifer, and M.W. Weiss. J. Am. Chem. Soc. **125**, 6261 (2003).
7. (*a*) M. Lautens and G. Hughes. Angew. Chem. Int. Ed. **38**, 129 (1999); (*b*) M. Lautens, G. Hughes, and V. Zunic. Can. J. Chem. **78**, 868 (2000).
8. (*a*) R.S. Ward. Chem. Soc. Rev. **19**, 1 (1990); (*b*) M.C. Willis. J. Chem. Soc. Perkin Trans. 1, 1765 (1999).
9. A. Ashimori, B. Bachand, L.E. Overman, and D.J. Poon. J. Am. Chem. Soc. **120**, 6477 (1998).
10. R. Noyori and H. Takaya. Acc. Chem. Res. **23**, 345 (1990).
11. (*a*) F. Ozawa, A. Kubo, and T. Hayashi. J. Am. Chem. Soc. **113**, 1417 (1991); (*b*) W. Cabri, I. Candiani, S. DeBernardinis, F. Francalanci, S. Penco, and R. Santi. J. Org. Chem. **56**, 5796, (1991); (*c*) W. Cabri and I. Candiani. Acc. Chem. Res. **28**, 2 (1995).
12. A. Ashimori, B. Bachand, M.A. Calter, S.P. Govek, L.E. Overman, and D.J. Poon. J. Am. Chem. Soc. **120**, 6488 (1998).
13. G. Helmchen and A. Pfaltz. Acc. Chem. Res. **33**, 336 (2000).
14. For the preparation and use of (4*S*)-2-(2-(diphenylphosphino)phenyl)-4-*tert*-butyl-1,3-oxazoline (abbreviated as (*S*)-*t*-Bu-POX), see: (*a*) J.M.J. Williams. Synlett, 705 (1996); (*b*) J. Spinz and G. Helmchen. Tetrahedron Lett. **34**, 1769 (1993).
15. (*a*) F. Ozawa, A. Kubo, Y. Matsumoto, and T. Hayashi. Organometallics, **12**, 4188 (1993); (*b*) L. Ripa and A. Hallberg. J. Org. Chem, **62**, 595 (1997).
16. For the synthesis of 2(*S*)-(diphenylphosphino)-1-[4(*S*)-isopropyl-l-2-oxazolin-2-yl]ferrocene (abbreviated as (*S*)-*i*-Pr-(*S*)-DIPOF), see: (*a*) C.J. Richards and A.J. Locke. Tetrahedron Asymmetry, **9**, 2377 (1998); (*b*) Y. Nishibayashi and S. Uemura. Synlett, 79 (1995).
17. W.C. Still, M. Kahn, and A. Mitra. J. Org. Chem. **43**, 2923 (1978).
18. P. Schwab, R.H. Grubbs, and J.W. Ziller. J. Am. Chem. Soc. **118**, 100 (1996).
19. J.C. Heslin and C.J. Moody. J.Chem. Soc. Perkin Trans. I, 1417 (1988).

© 2004 NRC Canada

TRIBUTE / HOMMAGE

This Special Issue of the *Canadian Journal of Chemistry* is dedicated to Professor Ed Piers for not only his outstanding contributions to the field of organic synthesis but also for his positive influence on more than 95 graduate students and postdoctoral fellows and his exemplary leadership to the profession of chemistry across Canada.

Edward Piers was born in the Province of Alberta, Canada, in 1938. He acquired his B.Sc. and Ph.D. degrees from the University of Alberta in 1959 and 1963, respectively. Following his Ph.D. studies, which were carried out under the supervision of Professor R.K. Brown, he spent two years as a postdoctoral fellow in the laboratory of Professor J.P. Kutney at the University of British Columbia. In 1965, Ed became a faculty member at UBC, where he is currently Professor of Chemistry.

Ed's research program has resulted in over 190 publications and focused mainly on studies involving (*a*) the development of new reagents and methods for organic synthesis, and (*b*) the total synthesis of biologically active and structurally challenging natural products utilizing these reagents and methods. Earlier in his career his research group focused on the utilization of cuprates in conjugate addition reactions as a means for introducing stereocentres into molecules. In addition, his group spent some time investigating the use and rearrangements of divinylcycloproapne systems and ultimately applied these reactions to the synthesis of complex natural products. In recent years, Ed and his research group have prepared and developed a number of new bifunctional and trifunctional reagents derived from organostannane and organogermane precursors. The use of these reagents in synthetic transformations usually required the addition of copper and (or) palladium reagents. Interestingly, the use of copper-based species has proven extremely beneficial for Ed's group over his entire career. During the course of these studies, a number of effective annulation methods were developed and they have played key roles in the total syntheses of several structurally complex natural products including aristolone, fukinone, α-cubebene, copacamphene, ylangocamphor, *cis*- and *trans*-sativenediol, isolongifolene, β-himachalene, 9-pupukeanone, triophamine, sinularene, quadrone, stemodin, palauolide, amijitrienol, $\Delta^{9(12)}$-capnellene, ambiliol B, stephalic acid, 8-epi-oplopanone, chiloscyphone, homalomentol A and B, crinipellin B, sarcodonin G, dysidiolide, africanol, and kelsoene.

His outstanding contributions to not only the field of organic chemistry but also as a teacher has resulted in Ed being the recipient of a number of awards, including an Alfred P. Sloan Fellowship (1970), the Chemical Institute of Canada (CIC) Merck, Sharpe and Dohme Award (1979), Killam Senior Fellowship (1984), the UBC Killam Research Prize (1989), the CSC Alfred Bader Award in Organic Chemistry (1994), the CSC R.U. Lemieux Award for Organic Chemistry (1996), and the ICI Montreal Medal (1999). In 1989, Ed was elected a Fellow of the Royal Society of Canada.

Ed has inspired many a student to pursue a career in the field of organic synthesis. His exemplary teaching skills resulted in him being awarded twice the C.I.C. Departmental Master Teaching Award (1972 and 1985). Ed's enthusiasm for synthesis, solving problems, and working out mechanisms was addictive and had an infectious effect on those working with him. These traits were not only seen when discussing research results with him, but also during his weekly

Ce numéro spécial de la *Revue canadienne de chimie* est consacré au professeur Ed Piers en hommage à ses contributions exceptionnelles dans le domaine de la synthèse organique, ainsi qu'en reconnaissance de l'influence positive qu'il a exercée sur plus de 95 doctorants et boursiers de perfectionnement postdoctoral et de son leadership exemplaire pour la profession de chimiste dans tout le Canada.

Edward Piers est né dans la province d'Alberta, au Canada, en 1938. Il a décroché son baccalauréat ès sciences et son doctorat de l'Université de l'Alberta en 1959 et en 1963 respectivement. Après ses études de doctorat, pour lesquelles il avait le professeur R.K. Brown comme directeur de thèse, il a passé deux ans comme boursier de perfectionnement postdoctoral dans le laboratoire du professeur J.P. Kutney à l'Université de la Colombie-Britannique. En 1965, Ed est devenu membre du corps enseignant de l'UBC, où il est actuellement professeur de chimie.

Le programme de recherche d'Ed a produit plus de 190 publications; il était axé principalement sur des études portant sur (*a*) la mise au point de nouveaux agents réactifs et méthodes pour la synthèse organique et (*b*) la synthèse intégrale de produits naturels biologiquement actifs et structuralement complexes au moyen de ces agents réactifs et méthodes. Au début de sa carrière, son groupe de recherche se concentrait sur l'utilisation de cuprates dans des réactions d'addition conjuguée pour introduire des stéréocentres dans des molécules. Par ailleurs, son groupe a consacré un certain temps à étudier l'utilisation et le réaménagement de systèmes divinylcyclopropanes et a fini par appliquer ces réactions à la synthèse de produits naturels complexes. Au cours des dernières années, Ed et son groupe de recherche ont préparé et mis au point un certain nombre de nouveaux agents bifonctionnels et trifonctionnels dérivés de précurseurs de l'organostannane et de l'organogermane. L'utilisation de ces agents dans des transformations synthétiques exige habituellement l'addition d'agents réactifs au cuivre ou au palladium. Il est intéressant de noter que l'utilisation d'espèces basées sur le cuivre s'est révélée extrêmement profitable pour le groupe d'Ed au cours de toute sa carrière. Pendant ces études, plusieurs méthodes d'annulation efficaces ont été mises au point et elles ont joué un rôle clé dans la synthèse intégrale de plusieurs produits naturels structuraux complexes, parmi lesquels ont trouve les suivants : aristolone, fukinone, α-cubebène, copacamphène, ylangocamphre, *cis*- et *trans*-sativénédiol, isolongifolène, β-himachalène, 9-pupukéanone, triophamine, sinularène, quadrone, stémodin, palauolide, amijitriénol, $\Delta^{9(12)}$-capnellène, ambiliol B, acide stéphalique, 8-*epi*-oplopanone, chiloscyphone, homalomenthol A et B, crinipellin B, sarcodonin G, dysidiolide, africanol et kelsoène.

Ses contributions exceptionnelles, non seulement dans le secteur de la chimie organique, mais également comme enseignant, ont mérité à Ed de nombreux prix, parmi lesquels une bourse de recherche Alfred P. Sloan (1970), le prix Marck, Sharpe et Dohme de l'Institut de chimie du Canada (ICC), une bourse de travail libre pour universitaire Killam (1989), et le prix de la recherche Killam de l'ICC (1989), le prix Alfred Bader de chimie organique de la Société canadienne de chimie (SCC) (1994), le prix R.U. Lemieux de chimie organique de la SCC (1996) et la Médaille de Montréal de l'ICC (1999). En 1989, Ed a été élu membre de la Société royale du Canada.

© 2004 NRC Canada

group meetings that focused on solving problems. Ed's respect for his co-workers, patience and never-ending willingness to discuss chemistry led those who worked with him to achieve high standards. His superb mentoring skills have resulted in many of the 65 graduate students (listed at the end of this tribute) and 33 postdoctoral fellows (also listed at the end of this tribute) ending up with excellent positions at universities, in the pharmaceutical industry, or in the chemical industry.

Ed has made significant contributions to the profession of chemistry in Canada. From 1982–1985, he was a member of the Natural Sciences and Engineering Research Council (NSERC) Chemistry Grants Selection Committee and was Chair of the Committee during 1984 to 1985. He has also been active in the Canadian Society for Chemistry (CSC). From 1990–1993 he was a member of the executive of the CSC Board of Directors, and he served as President of the CSC from 1991 to 1992. While he was Vice-President of this organization from 1990 to 1991, he was very actively involved with increasing the graduate student membership in the CSC. Ed has served the CSC by organizing or co-organizing national and international symposia at a variety of conferences. Ed also served three years (1993–1996) as a member of the Rutherford Medal (Chemistry) Selection Committee of the Royal Society of Canada and was Chair of this committee during 1995 to 1996. He was also a member of the RSC Academy of Science Council Fellowship Review Committee for 3 years (1992–1995). Ed has served on some national and international editorial and advisory boards. He has twice (1981–1984; 1990–1993) been a member of the Editorial Board of the *Canadian Journal of Chemistry,* he has served on the International Advisory Board of the *Encyclopedia of Reagents for Organic Synthesis* (1992–1995), and he is currently a member of the Advisory Editorial Board of Chemical Communications and the International Advisory Board of *J. Chem. Soc. Perkin Trans. 1*. Ed has also held Visiting Professorships at a number of universities, including UC Irvine, Western Ontario, and Sao Paulo.

Ed was born and raised in a small town in northern Alberta called Neerlandia (pop. 80), which lies a few kilometers north of Barrhead. He is married to Shirley and they have two sons, Warren and Kevin, who have Ph.Ds in inorganic chemistry and genetics, respectively.

The authors of this issue and the editors are pleased to present this special issue to Edward Piers as a token of our appreciation for his relentless passion and enthusiasm for chemistry and for his exemplary mentoring skills.

Brian A. Keay

Ed a été une source d'inspiration pour de nombreux étudiants qui ont choisi de faire carrière dans le domaine de la synthèse organique. Ses compétences exemplaires d'enseignant lui ont valu deux fois le prix Departmental Master Teaching de l'ICC (1972 et 1985). L'enthousiasme d'Ed pour la synthèse, la résolution de problème et la compréhension de mécanismes était comme une drogue et contagieux pour tous ceux qui travaillaient avec lui. Ces traits de caractère n'étaient pas seulement évidents lorsqu'on parlait de résultats de recherche avec lui, mais également pendant les réunions de groupe hebdomadaires qui se concentraient sur la résolution de problèmes. Le respect d'Ed pour ses collaborateurs, sa patience et son éternelle disponibilité à parler de chimie ont inspiré ceux qui travaillaient avec lui à atteindre des normes élevées. Ses superbes compétences en mentorat ont eu pour résultat que bon nombre des 65 doctorants (dont les noms figurent à la fin de cet hommage) et 33 boursiers de perfectionnement postdoctoral (dont les noms figurent également à la fin de cet hommage) qu'il a guidés ont obtenu d'excellents postes dans des universités, dans l'industrie pharmaceutique ou dans l'industrie chimique.

Ed a apporté une importante contribution à la profession de chimiste au Canada. Entre 1982 et 1985, il était membre du Comité de sélection des bourses en chimie du Conseil de recherches en sciences naturelles et en génie (CRSNG) et président de ce Comité de 1984 à 1985. Il s'est également impliqué dans la Société canadienne de chimie (SCC). Entre 1990 et 1993, il était membre du bureau du Conseil d'administration de la SCC et il a fait office de président de cet organisme de 1991 à 1992. Pendant qu'il était vice-président de la SCC, de 1990 à 1991, il s'est consacré très énergiquement à faire augmenter le nombre de doctorants membres de la SCC. Ed a aidé la SCC en organisant ou en co-organisant des symposiums nationaux et internationaux lors de diverses conférences. Il a également été pendant trois ans (1993–1996) membre du comité de sélection pour la Médaille Rutherford (chimie) de la Société royale du Canada et il était président de ce comité de 1995 à 1996. Il était également membre du Comité du Conseil des candidatures de l'Académie des sciences de la SRC pendant trois ans (1992–1995). Ed a également siégé au sein de plusieurs comités éditoriaux et consultatifs nationaux et internationaux. Il a été deux fois (1981–1984; 1990–1993) membre du comité éditorial de la *Revue canadienne de chimie*, membre du comité consultatif international de la *Encyclopedia of Reagents for Organic Synthesis* (1992–1995), et il est actuellement membre du Comité consultatif éditorial de *Chemical Communications* et du Comité consultatif international de *J. Chem. Soc. Perkin Trans. 1*. Ed a également été titulaire d'une chaire de professeur invité à plusieurs universités, notamment UC Irvine, Western Ontario et Sao Paulo.

Ed est né et a grandi dans une petite ville du nord de l'Alberta appelée Neerlandia (80 habitants) située à 15 kilomètres au nord de Barrhead. Il est marié à Shirley avec laquelle il a eu deux fils, Warren et Kevin, qui sont titulaires de doctorats en chimie inorganique et en génétique respectivement.

Les auteurs de ce numéro et la rédaction sont ravis de présenter ce numéro spécial à Edward Piers en gage de leur appréciation pour sa passion et son enthousiasme inextinguibles pour la chimie et pour ses compétences exemplaires en mentorat.

Brian A. Keay

© 2004 NRC Canada

Graduate students / Doctorants :

Abeysekera, Brian F.
Armbrust, Ralph
Boehringer, Eva M.
Boulet, Serge L.
Britton, Rob
Britton, Ronald W.
Burmeister, Max S.
Caillé, Sébastien
Cheng, Kin Fai
Chong, J. Michael
Coish, Philip D.
Cook, Katherine L.
De Waal, William
Dotse, Anthony K.
Dragojlovic, Veljko
Ellis, Keith A.
Fleming, Fraser F.
Friesen, Richard
Gavai, Ashvinikumar
Geraghty, M. Ber
Gilbert, Michael
Grierson, John R.
Hall, Tse-Wai (Eric)
Harrison, Cristian L.
Herbert, David J.
Jamieson, Pat R.
Jung, Grace L.
Kaller, Alan M.
Karunaratne, Veranja
Keziere, Robert J.
Lau, Cheuk Kun
Lemieux, René
Lu, Yee-Fung
Mar, Andrew
Marais, Pierre C.
Marrs, Peter S.
Maxwell, Anderson R.
McEachern, Ernest J.
Morton, Howard E.
Moss, Neil
Nadarajah, Sivakumar
Oballa, Renata M.
Orellana, Arturo
Price, Richard
Renaud, Johanne
Roberge, Jacques Y.
Romero, Miguel A.
Ruediger, Edward H.
Schindeler, Todd W.
Skerlj, Renato T.
Skupinska, Krystyna A.
Smillie, R. Dean
Story, Betty-Ann
Suckling, Ian D.
Tillyer, Richard D.
Tse, Hoi Lun Allan
Wai, John S.M.
Walker, Shawn D.
Winter, Manfred
Wong, Timothy
Worster, Paul M.
Yee, James G.K.
Yeung, Bik Wah Anissa
Zbozny, Michael

Postdoctoral Fellows / Boursiers de perfectionnement postdoctoral :

Andersen, Denise
Andrade, Romano
Banville, Jacques
Berger, Christian
Breau, Livain
Burns, Patricia
Chen, Gang
Gladstone, Patricia L.
Han, Yongxin
Harvey, Tommy
Isenring, Hans-Peter
Jean, Michel
Keay, Brian A.
Kido, Fusao
Lau, Stephen
Little, Dan
Llinas-Brunet, Montse
Marr, Peter
Nagakura, Isao
Nieman, Jim
Phillips-Johnson, Wynona M.
Plourde, Guy L.
Reissig, Hans-Ulrich
Ren, Li (Andy)
Rogers, Christine
Shaw, James E. (Jim)
Soucy, Marcel
Thies, Richard W.
Urech, Rudolf
Vanden Hoven, Bernard
Wallace, Debra J.
Yeh, Wen-Lung
Yu, Hong Ping
Zetina-Rocha, Carlo

© 2004 NRC Canada

This special issue is dedicated to

Professor Ed Piers

to honour his outstanding contributions to synthetic organic chemistry.

Associate Editors: Victor Snieckus and Brian Keay

Ce numéro spécial est dédié au

Professeur Ed Piers

en reconnaissance de ses inestimables contributions à la chimie des substances organique de synthèse.

Directeurs scientifiques associés : Victor Snieckus and Brian Keay

© 2004 NRC Canada



Professor Ed Piers

© 2004 NRC Canada

Role of trinuclear Zn(II) complexes in promoting the hydrolysis of 4-nitrophenyl acetate

Qing-Chun Ge, Yan-He Guo, Hai Lin, Dong-Zhao Gao, Hua-Kuan Lin, and Shou-Rong Zhu

Abstract: Potentiometric determination shows that trinuclear Zn(II) complexes of the four tripods 1,3,5-tri(2′,5′-diazahexyl)benzene (L1), 1,3,5-tri(2′,5′-diazaheptyl)benzene (L2), 1,3,5-tri(2′,5′-diazaoctyl)benzene (L3), and 1,3,5-tri(2′,5′-diazanonyl)benzene (L4) could be potential hydrolytic catalysts. CH_3CN solutions containing $[3Zn:L]^T$ (0.5~2 × 10^{-3} mol·dm^{-3}) with I = 0.10 mol·dm^{-3} of KNO_3 and Good's buffer (10% volume fraction) were studied for the catalyzing hydrolysis of *p*-nitrophenyl acetate (NA, 0.5~2 × 10^{-3} mol·dm^{-3}), at 298 K, in the 6.5–8.2 pH range. The observed rate constants, k_{obs}, fit the equilibrium equation $k_{obs} = k_{com}[3Zn:L]^T + k_{OH}[OH^-] + k_0$. The sigmoid pH~$k_{com}$ profiles for NA hydrolysis suggest that either the Zn(II)-bound hydroxyl or the Zn(II)-bound water forms of the catalysts can be the active species. The observed second-order rate constants are 0.0082, 0.011, 0.0059, and 0.0019 mol^{-1}·dm^3·s^{-1} for the four $Zn_3L–H_2O$ complexes (k_A) and 0.342, 0.257, 0.382, and 0.091 mol^{-1}·dm^3·s^{-1} for the four $Zn_3L–OH^-$ groups (k_B), respectively. However, under the condition that [NA] = 0.5 × 10^{-3} mol·dm^{-3} and $[3Zn:L1]^T$ = 2~4 × 10^{-2} mol·dm^{-3} at pH 7.6, the observed rate constants, k_{obs}, obey the equilibrium $k_{obs} = k_{com}[3Zn:L]^T/(1/K' + [3Zn:L]^T)$. This indicates that the 3:1 complex (or its deprotonated hydroxide form) mediates NA hydrolysis by nucleophilic attack of the carboxyl center with the pre-formation of a coordination bond between the carboxyl oxygen atom and the Zn(II) ion. Comparison with other models was made, and the reasons for the high catalytic efficiency of the tripodal complexes were given.

Key words: tripod, Zn(II), catalysis, NA hydrolysis, polynuclear.

Résumé : Des mesures potentiométriques ont montré que les complexes trinucléaires du Zn(II) de quatre bases en trépieds, le 1,3,5-tri(2′,5′-diazahexyl)benzène (L1), le 1,3,5-tri(2′,5′-diazaheptyl)benzène (L2), le 1,3,5-tri(2′,5′-diazaoctyl)benzène (L3) et le 1,3,5-tri(2′,5′-diazanonyl)benzène (L4) pourraient agir comme catalyseurs d'hydrolyse. On a étudié l'utilité de solutions contenant de 0,5 à 2 × 10^{-3} mol·dm^{-3} de $[3Zn:L]^T$ dans du CH_3CN à I = 0,10 mol·dm^{-3} de KNO_3 avec un tampon de Good à 10% (v/v) comme catalyseurs pour l'hydrolyse de l'acétate de *p*-nitrophényle (AN), à des concentrations de 0,5 à 2 × 10^{-3} mol·dm^{-3}, à 298 K et à des pH allant de 6,5 à 8,2. Les constantes de vitesse observées (k_{obs}) peuvent être ajustées par une équation d'équilibre de la forme $k_{obs} = k_{com}[3Zn:L]^T + k_{OH}[OH^-] + k_0$. Les profiles sigmoïdes du pK~k_{com} pour l'hydrolyse de l'AN suggèrent que les formes du catalyseur dans lesquelles le Zn(II) est lié à un hydroxyle et Zn(II) est lié à une molécule d'eau peuvent agir comme espèces actives. Les constantes de vitesse du deuxième ordre sont respectivement 0,0082, 0,011, 0,0059 et 0,0019 mol^{-1}·dm^3·s^{-1} pour les quatre complexes $Zn_3L–H_2O$ (k_A) et de 0,342, 0,257, 0,382 et 0,091 mol^{-1}·dm^3·s^{-1} pour les quatre complexes $Zn_3L–OH^-$ (k_B). Toutefois, dans les conditions où [AN] = 0,5 × 10^{-3} mol·dm^{-3} et que $[3Zn:L1]^T$ = 2~4 × 10^{-2} mol·dm^{-3}, à un pH de 7,6, les constantes de vitesses observées (k_{obs}) peuvent être ajustées par une équation d'équilibre de la forme $k_{obs} = k_{com}[3Zn:L]^T/(1/K' + [3Zn:L]^T)$. Ceci suggère que le complexe 3:1 (ou sa forme hydroxyde déprotonée) agit comme médiateur de l'hydrolyse de l'AN par l'attaque du nucléophile sur le centre carboxylique, avec la préformation d'une liaison de coordination entre l'atome d'oxygène du carboxyle et l'ion Zn(II). On a fait une comparaison avec d'autres modèles et on donne les raisons qui peuvent expliquer l'efficacité catalytique élevée des complexes en trépieds.

Mots clés : trépieds, Zn(II), catalyse, AN hydrolyse, polynucléaire.

Introduction

Zinc ion is biologically important and has been found in the active site of more than 200 types of enzymes such as carbonic anhydrase (1), carboxypeptidase (2), and alkaline phosphatase (3). In a protein environment, tetrahedral or penta-coordinate Zn^{2+} is ideally suited to activate a bound water, typically forming Zn^{2+}–OH as a nucleophile, which attacks the carbonyl carbon of a peptide bond, the carbon of carbon dioxide, or the phosphorus of a phosphate ester.

Recently, there have been many research efforts to design and synthesize model complexes for zinc enzymes, and detailed structural and mechanistic data are available. There is

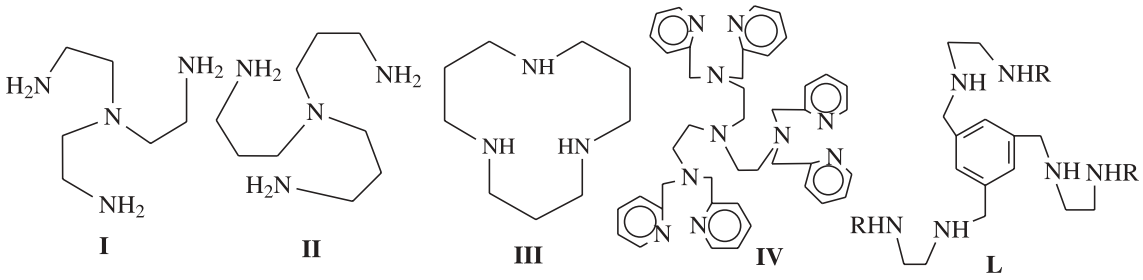
Received 5 January 2003. Published on the NRC Research Press Web site at http://canjchem.nrc.ca on 10 December 2003.

D.-Z. Gao, Q.-C. Ge, Y.-H. Guo, H.-K. Lin,[1] and S.-R. Zhu. Department of Chemistry of Nankai University, Tianjin, 300071, P.R. China.
H. Lin. State Key Laboratory of Functional Polymer Materials for Adsorption and Separation, Nankai University, Tianjin, 300071, P.R. China.

[1]Corresponding author (e-mail: hklin@nankai.edu.cn).

 doi: 10.1139/V03-190 © 2003 NRC Canada

Chart 1.



considerable interest in this field in developing rate increases and specificities similar to those of natural enzymes (4–10). Therefore, a large number of ligands, such as those in Chart 1, have been developed, which generate water-soluble and catalytic hydroxyl complexes (4–8). For example, the tris(3-aminopropyl)amine **II** complex of Co(III) increases the rate of hydrolysis of BNPP, bis(*p*-nitrophenyl)phosphate, by 10 times, with its rate maximum at pH 7 (5).

We have initiated a research program for development of novel dephosphorylation catalysts based on Zn(II) complexes of polyaza tripods. However, the hydrolysis of phosphate esters is fairly slow in neutral solution, so the substrate was changed to 4-nitrophenyl acetate (NA). NA is a very convenient substrate because hydrolysis can be followed easily and interactions with the good leaving groups are probably unimportant. We used the benzene-spaced tripods (L) because of the following factors: firstly, to increase the hydrophobicity around Zn(II); secondly, to widen the size of the semi-cavity formed by the tripod; and thirdly, to help with binding of aromatic substrates by π–π stacking interaction.

Another advantage of the use of tripods is attributed to the potential of these flexible ligands to form polynuclear complexes rather than mononuclear ones (11, 12), since it is reported that the reactivity of the center of enzymes depends on both the structure and the number of metal ions. For example, the elegant trinuclear zinc (II) complex of **IV** has been shown to hydrolyze RNA more efficiently than its dinuclear analog, and the maximum reactivity of **IV** was obtained when the ligand-to-metal ratio was 1:3 (7). Our purpose is to examine the catalytic effect of the mono-and trinuclear models on the rates of hydrolysis of NA, although we do not get into the relevance of an enzyme such as carbonic anhydrase (CA), where only one Zn(II) is present (2).

Experimental

Materials

All reagents and solvents used were of analytical grade. Acetonitrile (CH_3CN) was distilled over calcium hydride and stored in a dark bottle. 4-Nitrophenyl acetate (NA) was recrystallized from dry diethyl ether. 4-Nitrophenol (pK_a = 7.1), MES (2-(*N*-morpholino)-enthanesulfonic acid, pK_a = 6.39), MOPS (3-(morpholino)-proanesulfonic acid, pK_a = 7.2), HEPES (*N*-1-hydroxyethylpiperazine-*N*′-2-ethanesulfonic, pK_a = 7.5), and EPPS (*N*-2-hydroxyethylpiperazine-*N*′-3-propanesulfonic acid, pK_a = 8.0) were obtained from Aldrich Co.

Synthesis

The synthesis of 1,3,5-tri(2′,5′-diazahexyl)benzene (L1), 1,3,5-tri(2′,5′-diazaheptyl)benzene (L2), 1,3,5-tri(2′,5′-diazaoctyl)benzene (L3), and 1,3,5-tri(2′,5′-diazanonyl)benzene (L4) was neatly performed by condensation of 1,3,5-benzene-tricarboxaldehyde (13) with 3 equiv of *N*-R-ethylenediamine (R = methyl, ethyl, *n*-propyl, and *n*-butyl) and subsequent reduction with $NaBH_4$ (14). The synthesis of the L compounds and the formation of their complexes into the 3:1 Zn(II):L ratio are shown in Scheme 1.

Potentiometric measurements

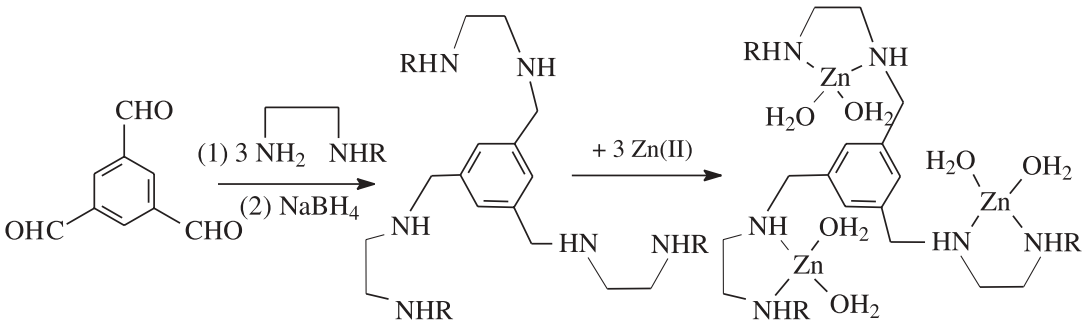
Potentiometric titrations were carried out with a Beckman auto-titrator of Model Φ71. The apparatus and procedure have been described before (14). The concentrations of the reagents are $[Zn^{2+}] = 3[L] = 3 \times 10^{-3}$ mol·dm^{-3}. Computation of equilibrium constants was made using the TITFIT (15) program.

Kinetics of 4-nitrophenyl acetate hydrolysis

A kinetic study was carried out by the UV spectral method using a Shimadzu UV-160A spectrophotometer equipped with a thermostated cell (298 K). The hydrolysis rate of 4-nitrophenyl acetate (NA) in aqueous solution was measured by an initial slope method, following the increase in 400 nm absorption of the released 4-nitrophenolate. The reaction solution was maintained at 298 K, and the ionic strength was adjusted to 0.10 mol·dm^{-3} with KNO_3. The concentrations of the 3:1 Zn(II):L complexes in the reaction solution, $[3Zn:L]^T$, were 0.5, 1.0, 1.5, and 2.0 × 10^{-3} mol·dm^{-3}, respectively (according to the concentration of L). The concentrations of NA were controlled at 0.5, 1.0, 1.5, and 2.0 × 10^{-3} mol·dm^{-3}, respectively. MES, MOPS, HEPES, and EPPS buffers (20 mmol·dm^{-3}) were used to maintain pH, and they do not coordinate with metal ions under these conditions (6). To increase the solubility of NA, 10% CH_3CN–H_2O solution was used. For the initial rate determination, the following typical procedure was employed: After 4-nitrophenyl acetate and the complexes (in 10% CH_3CN solution and at the appropriate pH) were mixed, the UV absorption increase was recorded immediately (the reference experiment did not contain the catalyst). The increase in concentration of nitrophenolate was measured every 5–60 s. The initial slope (<5% conversion) of a plot of measured absorbance vs. time was determined (correlation coefficient 0.99). All the experiments were run in triplicate, and the tabulated data represent the average of these experiments.

© 2003 NRC Canada

Scheme 1. Structure of complexes Zn_3L. The Zn(II)-bound water has the potential to deprotonate to give hydroxyl Zn_3L–OH.



R = Me, L1; Et, L2, *n*-Pr, L3; *n*-Bu, L4

Results and discussion

Active nucleophile in 3:1 Zn:L systems

The stability constants of various complexes of the four tripods (1×10^{-3} mol·dm^{-3}) with Zn(II) (3×10^{-3} mol·dm^{-3}) have been determined at 25 °C (I = 0.10 mol·dm^{-3} KNO_3 (11)), and the data are listed in Table 1. When in a 3:1 metal:ligand ratio, the system does prefer polynuclear complexes. As is seen from Fig. 1, there are four major complexes in solution, i.e., $ZnLH_4$ (114 (these values in parentheses stand for the stoichiometries of metal ion, ligand, and proton, respectively)), Zn_2LH_2 (212), Zn_3L (310), and Zn_3LH_{-1} (31–1), forming in turn with the increase of pH. The negative value (–1) means the release of a proton of Zn(II)-bound water. In the 3:1 Zn(II):L2 system (Fig. 1), the mononuclear protonated species $ZnLH_4$ (the charge is omitted for clarity) forms in the wide 3–6 pH range and becomes a major species at the 3.5~5 pH range. The diprotonated dinuclear complex Zn_2LH_2 starts to form at pH 4.0 and reaches the maximum concentration (>85%) at pH ca. 5.5. Subsequently, the trinuclear complexes Zn_3L and Zn_3LH_{-1} (Zn_3L–OH) start to form at pH 5 and 5.5, respectively, but the neutral species Zn_3L never becomes a predominant species, with its maximum concentration (<50%) at pH ca. 6.5. The action of other systems are similar to that of Zn(II):L2.

In the complex Zn_3L (Scheme 1), each branch of L coordinates with metal ions using two secondary nitrogen atoms, and the Zn(II)-bound water is easy to deprotonate to give the monohydroxyl M_3LH_{-1} (or M_3L–OH, 31–1). Seen from Table 1, all the pK_a values for the process $M_3L \rightarrow M_3LH_{-1} + H^+$, according to eq. [1], are in the 7.25~7.52 range. This indicates that the coordinated water molecules in the Zn_3L–H_2O complexes have low pK_as, similar to values for the hydrolytic Zn(II)-enzymes (16), facilitating the production of the nucleophilic Zn(II)-bound hydroxide species at physiological pH.

$$[1] \qquad pK_a = \log\beta_{310} - \log\beta_{31-1}$$

Hydrolysis rates

To determine whether the hydrolysis of NA is promoted by [Zn_3L] or [Zn_3L–OH^-], hydrolysis of NA (0.5, 1.0, 1.5, and 2.0 mmol·dm^{-3}) in a 10% CH_3CN (volume fraction) aqueous solution of the Zn(II) complexes (0.5, 1.0, 1.5, and 2.0 mmol·dm^{-3}; refers to the concentration of L) in the pH range 6.5~8.2 (Good's buffer, 20 mmol·dm^{-3}) at 25 °C and with I = 0.10 mol·dm^{-3} KNO_3 was carried out using a UV–vis spectrometer. The hydrolysis rate of 4-nitrophenyl acetate (NA) in aqueous solution was measured by an "initial rate" method, following the increased absorption of the released 4-nitrophenolate (NP^-) at 400 nm (6). The use of a buffer during the analysis was required, since the pH of the solution would cause changes in the concentration of the 4-nitrophenolate anion. The concentration of the released 4-nitrophenolate was calculated from the extinction coefficient at 400 nm (ε = 17 900 (mol·L^{-1})$^{-1}$·cm^{-1}).

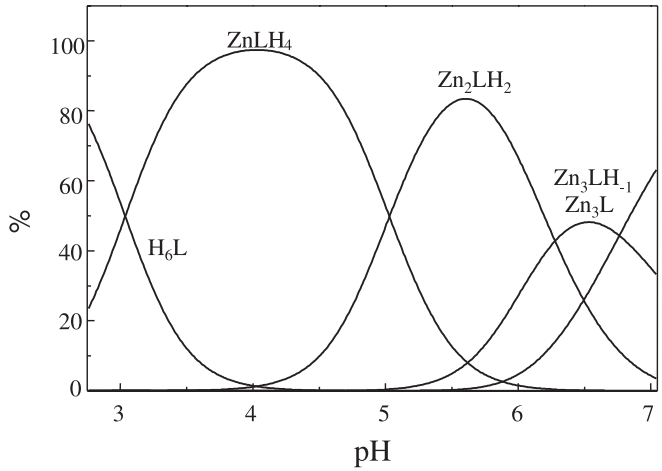
Table 1. The stability constants of complexes formed by L in the presence of Zn^{2+}.

Equilibria	L1	L2	L3	L4
$\log\beta_{114}$[a]	47.27±0.05	45.06±0.04	46.38±0.03	44.04±0.07
$\log\beta_{212}$	39.65±0.04	37.80±0.05	38.64±0.05	36.01±0.08
$\log\beta_{310}$	28.89±0.08	28.50±0.05	28.49±0.06	26.61±0.10
$\log\beta_{31-1}$	21.42±0.10	21.25±0.08	20.97±0.04	19.13±0.07

Note: Reaction conditions are 25 °C, I = 0.1 mol·dm^{-3} KNO_3, [L] = 1/3[Zn^{2+}] = 1×10^{-3} mol·dm^{-3} (14).

[a]The l, m, and n values of $\log\beta_{lmn}$ stand for the stoichiometries of metal ion, ligand, and proton, respectively. The negative value (–1) means the release of a proton of Zn(II)-bound water.

Fig. 1. Species distribution as a function of pH for the 3:1 Zn(II)–L2 complex; 25.0 ± 0.1 °C, I = 0.1 mol·dm^{-3} KNO_3, [L] = 1/3[Zn(II)] = 1×10^{-3} mol·dm^{-3}.



© 2003 NRC Canada

Table 2. The k_{obs} (10^{-5} (s^{-1})) values of NA hydrolysis catalyzed by Zn(II) complexes in a 3:1 metal:ligand ratio.

	pH						
Concentration ($\times 10^{-3}$ mol·L^{-1})	6.54	6.95	7.23	7.42	7.61	7.90	8.19
[3Zn:L1]							
0.5	0.53	2.45	6.35	10.08	16.67	22.91	30.09
1.0	0.93	3.27	10.41	17.93	26.28	34.08	43.27
1.5	1.48	4.44	13.60	25.80	38.55	52.14	66.54
2.0	2.14	5.59	15.52	34.83	52.37	71.31	83.15
[3Zn:L2]							
0.5	0.32	1.81	4.20	8.25	10.79	14.36	19.88
1.0	0.85	2.55	7.59	15.61	21.27	23.19	31.05
1.5	1.43	3.46	10.13	25.00	34.44	38.65	45.67
2.0	2.13	4.05	12.65	31.04	45.51	51.54	60.03
[3Zn:L3]							
0.5	1.04	4.51	9.96	16.32	26.48	40.77	52.75
1.0	1.89	5.78	15.89	24.35	36.21	59.63	69.20
1.5	2.54	7.22	22.63	33.68	49.36	77.25	85.84
2.0	3.23	8.64	27.32	44.62	63.75	93.39	106.52
[3Zn:L4]							
0.5	0.419	2.14	4.36	7.44	10.76	15.64	21.58
1.0	0.731	2.77	6.95	9.93	14.24	19.27	25.67
1.5	1.054	3.32	9.37	12.86	19.12	24.02	30.41
2.0	1.385	4.17	11.60	15.85	22.08	28.83	35.28

Note: $[3Zn:L]^T$ = 0.5, 1.0, 1.5, and 2.0 × 10^{-3} mol·L^{-1} (25.0 ± 0.1 °C, I = 0.1 mol·dm^{-3} KNO_3, 0.02 mol·dm^{-3} Good's buffer, 10% CH_3CN).

As shown in Fig. 2, the initial rate, v, can be obtained from the slope (<5% conversion) of a plot of the measured absorbance (A) vs. time (s). It is observed that the initial rate v increases linearly with the concentration of NA. Therefore, v is expressed as in the following (eq.[2]):

$$[2] \qquad v = d[NP]/dt = dA/\varepsilon b dt = k_{obs}[NA]$$

where b is the length of the cell, [NA] is the concentration of NA, and k_{obs} is the observed rate constant, respectively. The values of k_{obs}, obtained as the slopes of the plots of v vs. [NA] at different pH values, are listed in Table 2 for the different systems.

In solution, the following three factors are also involved: (*i*) k_{com}, the catalysis of metal complexes; (*ii*) k_{OH}, the catalysis of OH^-; and (*iii*) k_0, the effect of solution contribution to the hydrolysis rate of NA. Therefore, v should be represented by eq. [3].

$$[3] \qquad v = k_{obs}[NA] = (k_{com}[3Zn:L]^T + k_{OH}[OH^-] + k_0)[NA]$$

where $[3Zn:L]^T$ is the total concentration of the metal complexes.

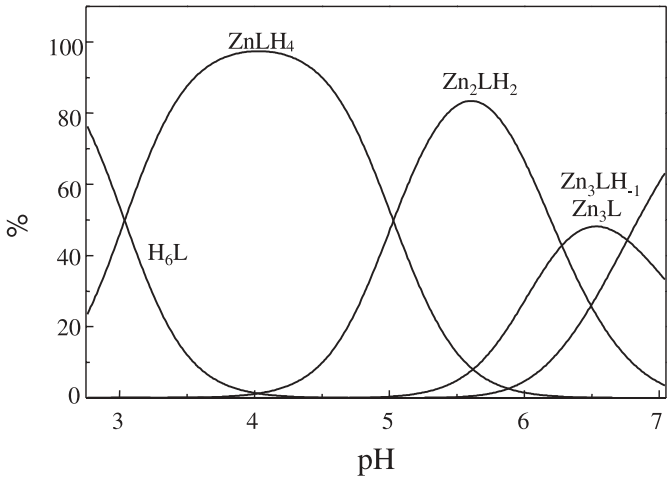
Plots of k_{obs} vs. $[3Zn:L]^T$ (Fig. 3) show that the rate of NA hydrolysis catalyzed by the Zn(II) complexes increases linearly with the concentration of the complexes, and the magnitude of the slope gradually decreases with decreasing pH. The slopes of the lines at different pH are the values of k_{com}, which are listed in Table 3.

It is interesting that NA hydrolysis does take place in the absence of complexes (Fig. 4). This indicates that OH^- and (or) solvent can catalyze NA hydrolysis. In the absence of Zn(II) complex, eq. [3] can be written in the form of eq. [3.1].

$$[3.1] \qquad v = k_{obs}[NA] = (k_{OH}[OH^-] + k_0)[NA]$$

A least-squares fit from a plot of reaction rate v vs. [NA] gives the following: k_{OH} = 13.27 $mol^{-1}\cdot dm^3\cdot s^{-1}$, k_0 = 4.33 × 10^{-7} s^{-1}, and γ = 0.998. The reported values are k_{OH} = 19.41 $mol^{-1}\cdot dm^3\cdot s^{-1}$, k_0 = 8.16 × 10^{-7} s^{-1}, and γ = 0.997 in the literature (17). The small value of k_0 is probably due to the solvolysis of NA (i.e., water attack on the ester).

Fig. 2. Dependence of absorbance (A) on time (s) for the hydrolysis of NA catalyzed by [3Zn:L1]; pH = 7.42, [NA] = 1.0 × 10^{-3} mol·dm^{-3}, 1/3[Zn^{2+}] = [L1] = 1.0 × 10^{-3} mol·dm^{-3}, 25.0 ± 0.1 °C, I = 0.1 mol·dm^{-3} KNO_3, λ = 400 nm.



© 2003 NRC Canada

Table 3. The k_{com} values ($mol^{-1}·dm^3·s^{-1}$) of the hydrolysis of NA catalyzed by 3:1 Zn–L complexes.

	pH						
Complex	6.54	6.95	7.23	7.42	7.61	7.90	8.19
[3Zn:L1]	0.011	0.0211	0.0628	0.162	0.235	0.327	0.334
[3Zn:L2]	0.012	0.0153	0.0566	0.155	0.239	0.254	0.270
[3Zn:L3]	0.014	0.0276	0.117	0.188	0.250	0.351	0.366
[3Zn:L4]	0.006	0.0133	0.0483	0.0564	0.0768	0.0805	0.0914

Fig. 3. Plots of k_{obs} vs. $[3Zn:L]^T$. The pH values from the bottom up are 6.54, 6.95, 7.23, 7.42, 7.61, 7.90, and 8.19, respectively.

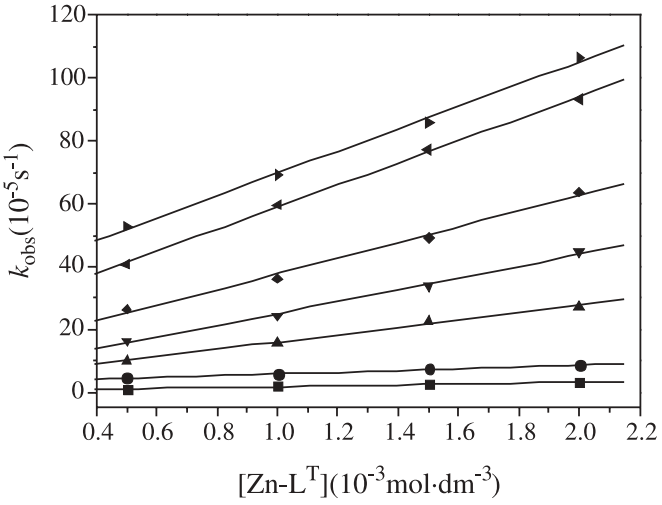
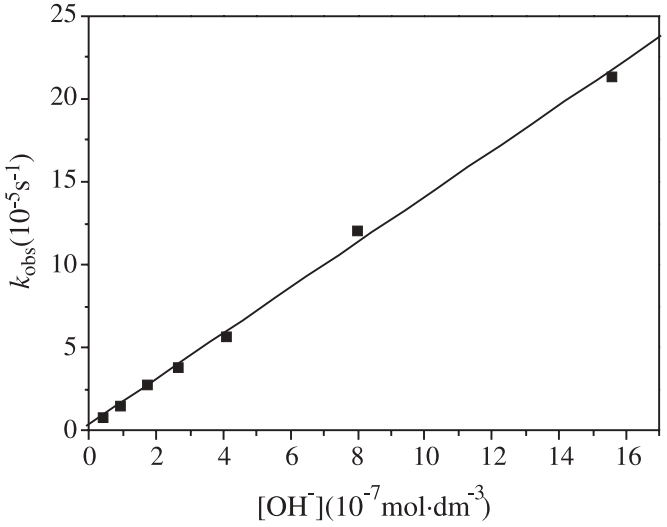


Fig. 4. The plot of k_{obs} vs. $[OH^-]$ in the absence of metal complexes (25.0 ± 0.1 °C, I = 0.1 mol·dm^{-3} KNO_3, 10% CH_3CN).



As discussed above, there is an equilibrium between the complexes Zn_3L and Zn_3LH_{-1} with a pK_a for the deprotonation of the Zn(II)-bound water in complex Zn_3L–H_2O (Scheme 1). The concentrations of Zn_3L and Zn_3LH_{-1} are expressed by eq. [4].

$$[4] \quad [Zn_3L] = [3Zn:L]^T[H^+]/(K_a + [H^+])$$

$$[Zn_3LH_{-1}] = [3Zn:L]^T\ K_a/(K_a + [H^+])$$

Since both the Zn(II) complexes with hydroxyl and water are the catalytic active species, eq. [5] is then obtained from the results of eqs. [3] and [4].

$$[5] \quad k_{com} = k_A[Zn_3L] + k_B[Zn_3LH_{-1}]$$

where k_A and k_B are the second-order rate constants of NA hydrolysis catalyzed by Zn_3L and Zn_3LH_{-1}, respectively.

Thus, when k_{com} is plotted vs. $[H^+]$, the values of k_A, k_B, and K_a can be obtained according to eq. [6].

$$[6] \quad k_{com} = (k_A[H^+] + k_BK_a)/([H^+] + K_a)$$

$$= k_A + (k_B - k_A)/(1 + [H^+]/K_a)$$

All reactions exhibited sigmoid pH–rate profiles when the observed rate constant k_{com} is plotted as a function of pH (Fig. 5), with inflection points at pH 7.46, 7.40, 7.44, and 7.38 for $[3Zn–L_x]$ (x = 1, 2, 3, 4), respectively. These results are in good agreement with pK_a values obtained from potentiometric pH-titrations. Such pH-profiles were observed in a number of phosphate or carboxyl ester hydrolyses promoted by Zn(II), Co(II), and Cu(II) complexes (6, 9, 18), and all presented with metal–hydroxyl species as the active catalysts. Analysis of k_{com} vs. $[H^+]$ (eq. [6]) gives the values of the second-order rate constants of NA hydrolysis catalyzed by complexes Zn_3L and Zn_3LH_{-1}, respectively; these are listed in Table 4.

Mechanisms

Based on the results mentioned above, referring to the catalytic mechanism of carbonic anhydrase, the catalytic mechanism for 3:1 Zn(II):L systems is proposed as shown in Scheme 2. The hydrolysis process involves the initial interaction of NA with the Zn(II)-coordinated water (**1**) or hydroxide group (**1′**) and then the slow dissociation of *p*-nitrophenolate and the binding of acetate by nucleophiles. The carboxylate oxygen of NA coordinates to the Zn(II) center, and the coordination conformation of the Zn(II) center changes to trigonal bipyramid, together with the nucleophilic attack of Zn(II)-water (**1**) or Zn(II)-hydroxide (**1′**) toward the carboxyl carbon. Subsequently, the acetate: nucleophile (**2** or **2′**) decomposes into acetate and Zn(II)-bound water or hydroxyl complex in aqueous solution at a fast rate, and thus, a catalytic cycle is completed. As shown in Table 1, poly-Zn(II) centers can activate a nucleophilic water molecule by decreasing its pK_a (nucleophilic catalysis) to form the stronger nucleophile Zn(II)-OH.

To determine the effect of free Zn(II) ion on the hydrolysis rate of NA (since the coordination of Zn(II) with the tripod is not 100% in the pH range studied), we also did control experiments, by replacing the Zn(II) complexes of L by equal molar Zn(II) ion alone. We found that Zn(II) has al-

© 2003 NRC Canada

Table 4. The second-order rate constants of NA hydrolysis catalyzed by complexes Zn_3L and Zn_3LH_{-1}, as well as the pK_a in different systems.

Catalysts	k_A	k_B	pK_a (calcd)	pK_a (titration)
[3Zn:L1]	0.0082±0.0009	0.34±0.04	7.46±0.05	7.47±(0.02~0.18)
[3Zn:L2]	0.011±0.005	0.26±0.02	7.40±0.07	7.25±(0.03~0.13)
[3Zn:L3]	0.0059±0.0003	0.38±0.07	7.44±0.09	7.52±(0.02~0.10)
[3Zn:L4]	0.0019±0.0004	0.091±0.006	7.28±0.04	7.38±(0.03~0.17)

Scheme 2. The proposed mechanism of the hydrolysis of NA catalyzed by Zn_3L and Zn_3LH_{-1}. The third arm of the tripod is omitted.

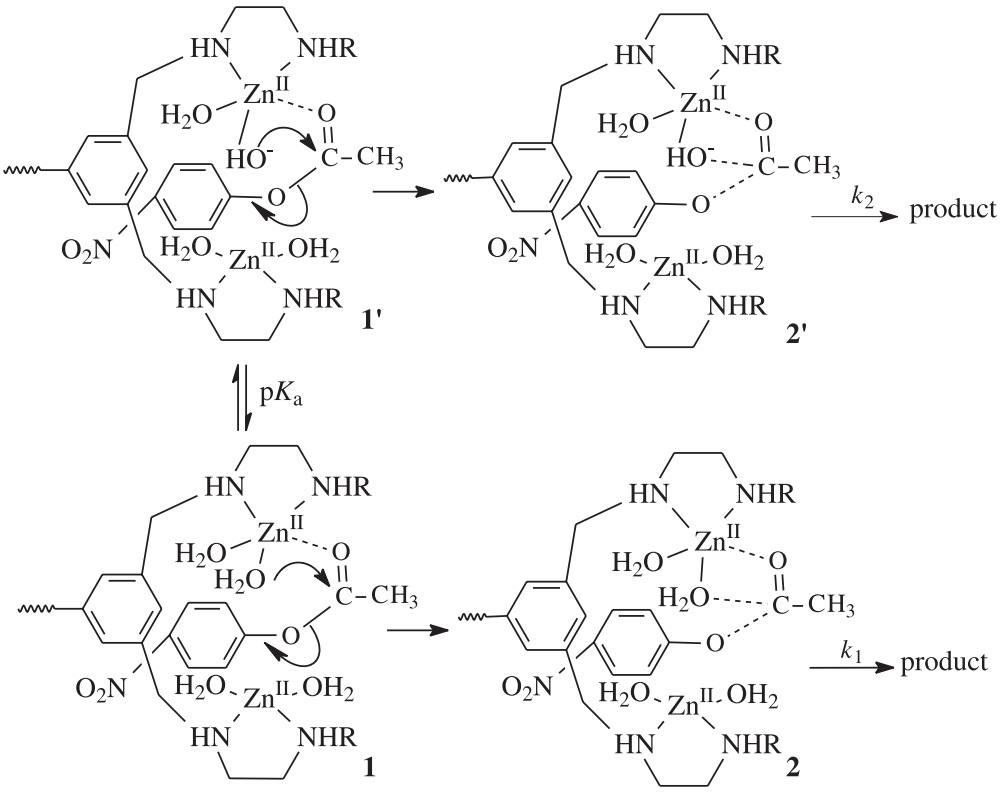
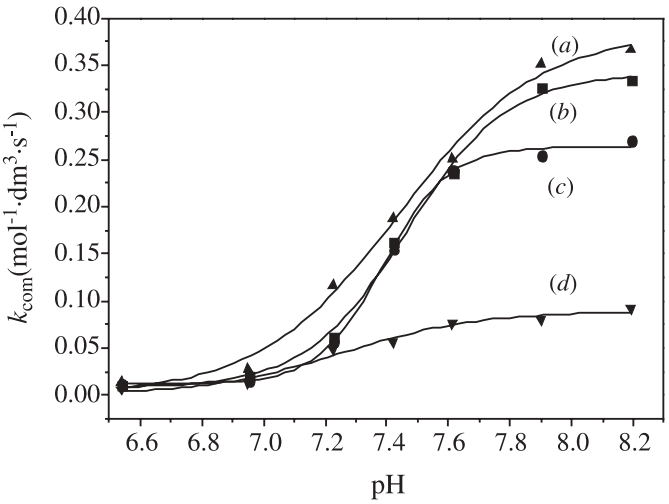


Fig. 5. The pH-rate profile for the rate of hydrolysis of NA at 25.0 °C, I = 0.1 mol·dm^{-3} KNO_3 in 10% CH_3CN (volume fraction) water solution: (*a*) Zn_3–L3, (*b*) Zn_3–L1, (*c*) Zn_3–L2, and (*d*) Zn_3–L4.



most no efficiency compared with that of Zn(II) complexes, so it is reasonable to ignore the influence of the Zn(II) ion.

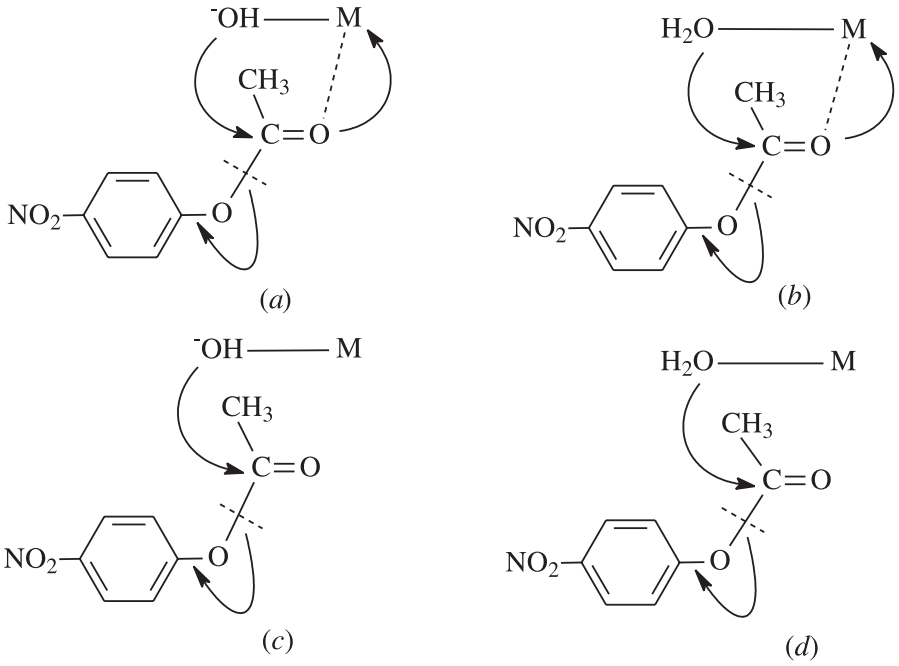
With carboxylate, the active center of metal-ion-catalyzed hydrolysis may involve the four forms shown in Scheme 3 (18). The first two methods are difunctional, and the metal ion frequently forms a stable intermediate by coordination to the carboxyl oxygen, which can neutralize the charge of carboxyl oxygen and assist departure of the leaving group (NP^-). The last two methods are the direct attack of metal-bound water or OH^- on the carboxyl carbon and cause the release of NP^-. In our systems, it is reasonable for the metal complexes to attack the carboxyl group by methods (*a*) and (*b*) (Scheme 3). If this occurs, there will exist a pre-equilibrium step (K) before the nucleophilic attack, and as a consequence, the k_{obs} will not increase linearly with the increase of the concentration of metal complexes, but will instead experience a hyperbola (eq. [7]).

$$[7] \qquad k_{obs} = k_{com}[3Zn:L]^T/(1/K' + [3Zn:L]^T)$$

However, this is in contrast to the results shown in Fig. 3, owing to the concentrations of the catalysts (these vary in the range of 0.5~2 × 10^{-3} mol·dm^{-3}). This range of concentrations is hardly enough to test for saturation. When the hy-

© 2003 NRC Canada

Scheme 3. The different paths that metal-bound water or hydroxyl can take when they act as a nucleophile.



drolysis reactions were made under the condition that [NA] = 0.5×10^{-3} mol·dm^{-3} and [3Zn:L1] = 2~4 × 10^{-2} mol·dm^{-3} at pH 7.61, the reciprocal of the observed rate constant, $(k_{obs})^{-1}$, increased linearly with $[3Zn:L1]^{-1}$. The k_{obs} values were found to be 0.0034, 0.0042, 0.0050, 0.0055, and 0.0067 mol^{-1}·dm^3·s^{-1} in the catalyst concentrations of 0.02, 0.025, 0.03, 0.035, and 0.04 mol·dm^{-3}, respectively. From a plot of $(k_{obs})^{-1}$ vs. $[3Zn:L1]^{-1}$, we obtained k_{com} = 0.229 mol^{-1}·dm^3·s^{-1} and K'= 0.74 dm^3·mol^{-1}. The value of k_{com} is almost the same as that obtained from hydrolysis in the lower catalyst concentrations (Table 3, 0.235 mol^{-1}·dm^3·s^{-1}). The results suggest that the catalyzed hydrolysis of NA occurs through the mechanisms (*a*) and (*b*), shown in Scheme 3, for the monohydroxyl and neutral complexes, respectively. During the formation of the nucleophile:NA complexes, the Zn(II) ion attains an increased opportunity to form a coordination bond with the carboxyl oxygen atom (Scheme 2, complexes **1** and **1′**). This pre-coordination between the Zn(II) ion and carboxyl group will decrease the negative electron density on carboxyl oxygen and will then weaken the repulsion between the hydroxide and carboxyl oxygen. For the nucleophile:NA complex, coordination bonding should constrain the acetate tightly and thus facilitate the expulsion of the leaving group.

On the other hand, the enhancement of the hydrolysis rate, observed for solutions containing 1:1 Zn(II) to L ratio, was not significant. In the 1:1 metal:ligand system, the Zn(II)-coordinated water is difficult to deprotonate to give the monohydroxide species (14) at neutral pH. The major complexes in neutral pH are ZnLH and ZnL (14), which have no or low catalytic activity at the pH range 6.5–8.2. For example, the k_{com} is 0.0012 and 0.334 mol^{-1}·dm^3·s^{-1} for the hydrolysis of NA catalyzed by 1:1 and 3:1 ZnL1 complexes at pH 8.2, respectively. The latter is about 278-fold greater than the former. The second-order rate constant of NA hydrolysis catalyzed by ZnL1 is only 0.021 mol^{-1}·dm^3·s^{-1}, which is also lower than that of Zn_3L1–OH, 0.34 mol^{-1}·dm^3·s^{-1}. Since the available site for coordination in ZnL1 is presumably fully occupied by amino groups, the formation of Zn(II)–OH$^-$ is difficult (pK_a = 9.6). Furthermore, a possible increase in the coordination number of zinc may radically change the conformation of the complex, thus making it difficult for the nucleophile to interact with the substrate. So, the Zn(II)-bound water molecule or hydroxyl can only take paths (*d*) or (*c*) (shown in Scheme 3) to attack the carboxyl group of the NA ester, respectively.

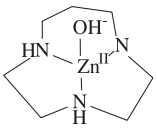
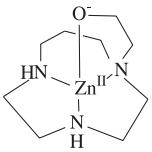
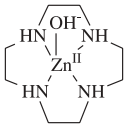
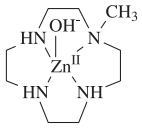
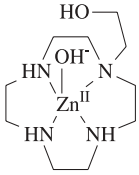
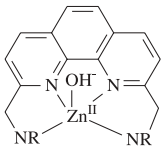
The pK_a of the Zn(II)-bound water plays an important role in the catalytic activity of these model complexes. As obtained from potentiometric titrations, the pK_a values for the process of $Zn_3L \rightarrow Zn_3LH_{-1}(Zn_3L–OH)$ are 7.47, 7.25, 7.52, and 7.38 for the four ligands, respectively. It was observed that the four pK_a values are almost identical, taking into account the calculation errors of the stability constants (Table 1). Thus, it is not reasonable to discuss the effects of the various substituents on the terminal nitrogen atoms (namely, Me, Et, *n*-Pr, and *n*-Bu for L1, L2, L3, and L4, respectively); these effects may include provision of space hindrance for the nucleophilic attack and a decrease the hydrophobicity of the active center of the complexes (Table 4). In general, the increasing size of the substituents will significantly hinder the interaction of the NA ester with metal complexes, resulting in a decrease in the metal–complex catalytic ability. On the other hand, the increased hydrophilicity of the metal center facilitates the stabilization of the NA ester. However, one should keep in mind that much lower pK_a values mean deprotonation at low pH and thus decrease the nucleophilicity of the coordinated nucleophiles, while a too bulky group can restrict the interaction of subject and metal catalysis. This subtle relationship is very important in the design of hydrolytic enzyme model complexes.

Comparison with the other systems

It was observed that all the axial deprotonated complexes Zn_3L–OH serve as good nucleophiles in the catalysis of NA hydrolysis. This observation was made by comparison of

© 2003 NRC Canada

Table 5. Comparison of the catalytic activity of selective model complexes.

Complexes		k_{NA}	pK_a	Ref.
	**1**	0.036	7.3	6
	**2**	0.14	7.4	6
	**3**	0.10	7.9	6
	**4**	0.047	7.7	6
	**5**	0.46	7.7	6
	[a]	0.14~0.93	8.6~8.9	17
Zn_3LH_{-1}		0.091~0.38	7.2~7.5	This paper

[a] L′ = phenanthroline-bridged di(2-*R*-ethylenediame) ligands: L = Me, **6**; Et, **7**; *n*-Pr, **8**; *n*-Bu, **9**; *i*-Pr, **10**; and *t*-Bu, **11** (17).

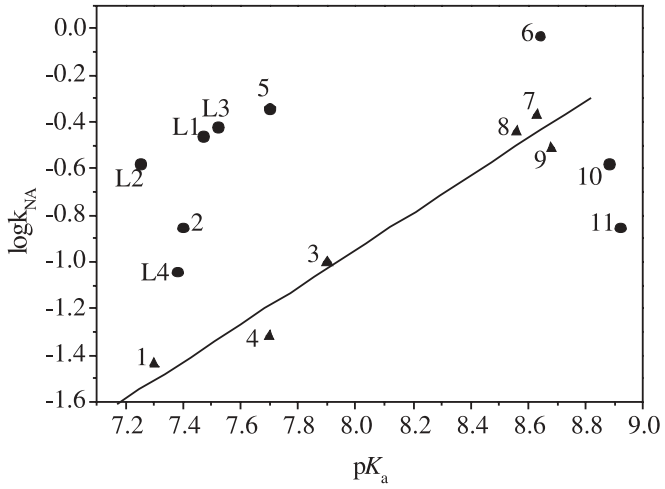
rates and by establishing the mechanism of other model complexes.

The Brönsted equation (eq. [8]) is usually used to compare the efficiency of different catalysts with different pK_a values.

$$[8] \qquad \log k_{NA} = C + \beta pK_a$$

where C is a constant and β is the Brönsted constant. On a plot of logk_{NA} vs. the pK_a values of various complexes, macrocyclic Zn(II) complexes **1**, **3**, and **4** (6) and Zn(II) complexes of linear phenanthroline-bridged polyamines **7**, **8**, and **9** (17) were found in the same line (Fig. 6). The following values were obtained: C = 7.34, Brönsted constant β = 8.80, and R = 0.98. The complexes **2** and **5** are above the line, owing to alkoxide, the more efficient nucleophile (Table 5). At the same time, the methyl-substituted phenanthroline-bridged polyamine **6** (Me) is also above the line, whereas its analogous complexes **10** and **11** are below the line because of the steric effects of the terminal *i*-Pr and *t*-Bu substituents on nucleophilic attack. It is interesting that all the four [3Zn:L] complexes are above the line; this is attributed to the following factors: (*i*) the low pK_a of Zn(II)-coordinated water facilitating the formation of nucleophile Zn(II)–OH^- at neutral pH; (*ii*) less steric effect than that in the 1:1 Zn–L system; and (*iii*) the formation of the coordination bond involving the carboxyl oxygen of NA and the Zn(II) ion, which grasps the CH_3COO^- group tightly and facilitates the release of NP^- to form the complex **2** or **2′** (Scheme 2).

Fig. 6. Comparison of the second-rate constants of NA hydrolysis catalyzed by [3Zn:L] complexes with other models. The numbers of the complexes are listed in Table 5.



Previous studies have reported the importance of multinuclear metal complexation for di- and triphosphates, which are relevant to the role of metal ions in biological phosphoryl transfer, as in the case of *Escherichia coli* alkaline phosphatase, where the active site of the enzyme contains a triplet of metal ions but only two are involved in the active center (18, 19). It is worth noting that it is not clear whether the real catalytic center of our models involve two or three metal ions, since the carboxyl group has only one site — carboxyl oxygen — for interaction with metal ions or others, restricting further investigation.

In summary, in the present paper we focus on the hydrolysis of a simple carboxylic monoester, 4-nitrophenyl acetate (NA), catalyzed by the Zn(II) complexes of tripods L1–L4 in a 3:1 metal:ligand ratio. The OH^- coordinates Zn(II) complexes of tripods that effectively catalyze the hydrolysis of 4-nitrophenyl acetate (NA). However, the pK_a values of our models are near to the physiological pH and, therefore, may have much practical use in mimicking enzyme behaviour, without taking into account the effect of the 10% CH_3CN–H_2O mixed solution on the pK_a values of the Zn_3L–H_2O complexes. To obtain further rate enhancements, one can vary the coordination number or change the microenvironment around the metal center from hydrophilic to hydrophobic. Work in this area is underway.

Acknowledgements

We gratefully acknowledge financial support from the National Natural Science Foundation of China (29971018) and the Natural Science Foundation of Tianjin (023605811).

© 2003 NRC Canada

References

1. (*a*) A.E. Eriksson, T.A. Jones, and A. Lilijas. Proteins, **4**, 274 (1988); (*b*) B.L. Vallee and D.S. Auld. Biochemistry, **29**, 5647 (1990).
2. W.N. Lipscomb. Acc. Chem. Res. **3**, 81 (1970).
3. E.E. Kim and H.W.J. Wyckoff. Mol. Biol. **218**, 449 (1991).
4. J.W. Canary, J. Xu, J.M. Castagnetto, D. Rentzeperis, and L.A. Marky. J. Am. Chem. Soc. **117**, 11 545 (1995).
5. J. Chin, M. Banaszczyk, V. Jubian, and X. Zou. J. Am. Chem. Soc. **111**, 186 (1989).
6. T. Koike, S. Kajitani, I. Nakamura, E. Kimura, and M. Shiro. J. Am. Chem. Soc. **117**, 1210 (1995).
7. M. Yashiro, A. lshikubo, and M. Komiyama. J. Chem. Soc. Chem. Commun. 83 (1997).
8. E. Kimura, Y. Kadama, T. Koike, and M. Shiro. J. Am. Chem. Soc. **117**, 8304 (1995).
9. A.M. Sargeson, J.M. Harrowfield, and V. Norris. J. Am. Chem. Soc. **98**, 7282 (1976).
10. M.J. Young, D. Wahnon, R.C. Hynes, and J. Chin. J. Am. Chem. Soc. **117**, 9441 (1995).
11. J.S. Seo, N.-D. Sung, R.C. Hynes, and J. Chin. Inorg. Chem. **35**, 7472 (1996).
12. Y. Bretonnière, M. Mazzanti, R. Wietzke, and J. Pécaut. J. Chem. Soc. Chem. Commun. 1543 (2000).
13. M. Li and N. Pan. HuaXue ShiJie, **5**, 168 (1985); Chem. Abs. **104**, 88 214 (1986).
14 Y.-H. Guo, Q.-C. Ge, H. Lin, H.-K. Lin, and S.-R. Zhu. Polyhedron, **21**, 1005 (2002).
15. S.A.A. Sajadi, B. Song, F. Gregan, and H. Sigel. Inorg. Chem. **38**, 439 (1999).
16. B.L. Vallee and H. Neurath. J. Am. Chem. Soc. **76**, 5006 (1954).
17. X.-C. Su, H.-W. Sun, Z.-F. Zhou, H.-K. Lin, L. Chen, Zh.-R. Zhu, and Y.-T. Chen. Polyhedron, **20**, 91 (2001).
18. D.E. Wilcox. Chem. Rev. **96**, 2435 (1996).
19. P. Hendry and A.M. Sargeson. Prog. lnorg. Chem. **38**, 201 (1990).

© 2003 NRC Canada

Conformational behaviour in *S*-methyl halothioacetates through NMR, FT-IR, and theoretical calculations

Ernani A. Basso, Barbara C. Fiorin, Cláudio F. Tormena, and Roberto Rittner

Abstract: This work presents an investigation of the conformational behaviour of *S*-methyl chlorothioacetate (MCTA), *S*-methyl bromothioacetate (MBTA), and *S*-methyl iodothioacetate (MITA) through NMR and IR spectroscopies and through theoretical calculations that apply DFT/B3LYP theory. The DFT calculations showed two stable rotamers in the vapour phase, *gauche* and *trans,* for all the compounds. The coupling constants, $^1J_{CH}$, were obtained from NMR spectroscopy; these were used in the solvation theory to calculate the vapour-phase energy difference, the coupling constants for each rotamer, the solution energy difference, and the rotamer population for each solvent. These data showed that for MCTA, the most stable rotamer is *trans*; however, for MBTA and MITA, the most stable rotamer is *gauche*, both in the vapour phase and in solution. The changes in rotamer stability are because of the preference in stereoelectronic interactions; in the MCTA case the interaction is mainly electrostatic, while for MBTA and MITA, it is because of the interaction between $n_{Br,I} \rightarrow \pi^*_{CO}$.

Key words: *S*-methyl halothioacetates, conformational analysis, theoretical calculations, NMR, solvation theory.

Résumé : Ce travail a été réalisé pour étudier le comportement conformationnel du chlorothioacétate de *S*-méthyle (CTAM), du bromothioacétate de *S*-méthyle (BTAM) et de l'iodothioacétate de *S*-méthyle (ITAM) par spectroscopies RMN et IR et par des calculs théoriques en se basant sur la théorie DFT/B3LYP. Les calculs DFT mettent en évidence, pour tous les composés, qu'il existe deux rotamères stables en phase vapeur, *gauche* et *trans*. Sur la base de la RMN, on a déterminé les constantes de couplage $^1J_{CH}$ qui ont été utilisées dans la théorie de la solvatation pour calculer la différence d'énergie libre en phase vapeur, les constantes de couplage de chaque rotamère, la différence d'énergie en solution et la population de chaque rotamère dans chaque solvant. Ces données montrent que dans le cas du CTAM, le rotamère le plus stable est le *trans* alors que pour les BTAM et ITAM le rotamère le plus stable est le *gauche*, tant en phase vapeur qu'en solution. Les changements dans la stabilité des rotamères sont dus à des préférences dans les interactions stéréoélectroniques qui, dans le cas du CTAM, sont principalement de nature électrostatique alors que, pour les BTAM et ITAM, elles sont principalement dues à l'interaction $n_{Br,I} \rightarrow \pi^*_{CO}$.

Mots clés : halothioacétates de *S*-méthyle, analyse conformationnelle, calculs théoriques, RMN, théorie de la solvatation.

[Traduit par la Rédaction]

Introduction

Geometric structure has a significant influence on the chemical, physical, and biological properties of a molecule (1). The geometrical parameter that is most important in establishing conformational properties is the torsional angle (dihedral angle) (1–5).

It is well known that fluorinated compounds are widely used in biochemistry, medicinal chemistry, and pharmacology (6). The substitution of hydrogen or hydroxyl by fluorine in pharmacologically active organic molecules can have an intense effect on their activity (7). This replacement causes a minor change in the functionality of the steric effect, unlike the significant effects it causes on the chemical properties, as well as on the stereoelectronic properties, which results in specific overall conformational change of the fluorinated nucleosides (6).

Fluorine substitution in the position α to a carbonyl group of small aliphatic compounds, as well as in α-fluoroaldehydes (8), α-fluoroketones (4–5), α-fluoroesters (2, 9), and α-fluoroamides (3, 10), gives only two conformers, *cis* and *trans*, except for fluoroamides, where the conformational equilibrium is between *cis* and *gauche* (3, 10).

An earlier study concerning the conformational behaviour of some *S*-ethyl-α-heterosubstituted molecules pointed out the existence of the *cis* and *gauche* rotamers (11). This study

Received 9 July 2003. Published on the NRC Research Press Web site at http://canjchem.nrc.ca on 16 December 2003.

E.A. Basso[1] and B.C. Fiorin. Departamento de Química, Universidade Estadual de Maringá, Av. Colombo 5790, 87020-900, Maringá, Paraná, Brazil.
C.F. Tormena and R. Rittner. Physical Organic Chemistry Laboratory, Instituto de Química, UNICAMP, Caixa Postal 6154, 13083-862 Campinas, São Paulo, Brazil.

[1]Corresponding author (e-mail: eabasso@uem.br).

 doi: 10.1139/V03-189 © 2003 NRC Canada

Table 1. Calculated geometries for MCTA, MBTA, and MITA at the B3LYP method with different basis sets.

	MCTA[a]		MBTA[a]		MITA[b]	
Parameter	*trans*	*gauche*	*trans*	*gauche*	*trans*	*gauche*
r (C=O)	1.206	1.202	1.207	1.203	1.207	1.204
r (C—S)	1.769	1.774	1.767	1.777	1.769	1.780
r (S—C_{Me})	1.812	1.810	1.813	1.811	1.813	1.810
r (C—C)	1.523	1.522	1.522	1.516	1.522	1.511
r (C—X[c])	1.790	1.798	1.958	1.968	2.157	2.168
r (C—H)	1.087	1.086	1.085	1.084	1.085	1.084
r (C_{Me}—H)	1.087	1.086	1.087	1.086	1.086	1.086
∠ X[c]-C-C	116.3	110.1	117.3	110.0	118.9	110.8
∠ C-C=O	118.6	122.9	117.9	122.9	118.0	123.3
∠ S-C=O	123.9	124.0	123.8	123.9	123.3	123.6
∠ C-S-C	98.3	99.7	98.4	99.7	98.5	99.7
ϕ X[c]-C-C=O	180.0	78.8	180.0	82.7	179.9	81.6
ϕ O=C-S-C	0.00	–1.53	–0.03	–2.03	0.03	–2.10
E[d]	–1051.014790	–1051.013108	–3164.934796	–3164.934811	–602.255016	–602.257225
E_{rel}[e]	0.00	1.05	0.01	0.00	1.39	0.00
Population[f]	75	25	33	67	5	95
Dipole moment[g]	0.82	2.44	0.90	2.26	0.90	2.00
$\nu_{C=O}$[h]	1671.42	1697.45	1664.67	1701.76	1661.78	1687.81

[a]Basis set for C, H, O, Cl, and Br: 6-311++g(d,p); S: 18s14p10d.
[b]Basis set for C, H, and O: 6-311++g(d,p); I: 9s9p4d and LANL2DZ pseudo-potential; S: 18s14p10d.
[c]For MCTA, X = Cl; for MBTA, X = Br; and for MITA, X = I.
[d]In units of hartrees (1 hartree = 4.359×10^{-18} J).
[e]In units of kcal mol^{-1}.
[f]In units of %.
[g]In units of Debye (1 Debye = 3.335641×10^{-30} C m).
[h]In units of cm^{-1}.

also concluded that the *gauche* rotamer predominates over the *cis* one for fluorine, chlorine, and bromine derivatives, while for iodine, only the *gauche* rotamer was assigned (11).

Theoretical calculations

The ab initio calculations were performed using the Gaussian 98 (12) program. The potential energy surfaces were obtained at the B3LYP/6-311+g(d,p) level. The geometries were optimized with the B3LYP method, using the 6-311++g(3df,3pd) basis set for carbon, hydrogen, oxygen, chlorine, and bromine atoms, with zero-point energy correction (ZPE). Since the sulphur atom has a more complicated electronic structure, a specific basis set (18s14p10d) developed for this atom has been applied (13). For the iodine atom, a special basis sets (9s9p4d) (14) was applied for the valence electrons and a pseudo-potential LAN2DZ was used for core electrons. The optimized geometries and energies of all the rotamers are given in Table 1.

Solvation theory

The solvation theory has been fully described elsewhere (2–5, 10, 15), and thus, only a brief description is given here. The solvation energy of any molecule in state A is the difference between the energy in the vapour phase (E_A^V) and in any solvent (E_A^S) within relative permittivity ε. This is given in terms of dipolar (k_A) and quadrupolar (q_A) reaction field terms in addition to a direct dipole–dipole term, which takes into account the breakdown of the Onsager reaction-field theory in very polar media (15). The input for the program is simply the dipole and quadrupole moments plus the solute radius and refractive index, the latter two calculated by the program. In state B, a similar equation is obtained, differing only in the values of dipole and quadrupole terms. The subtraction of the two equations ($E_A^S - E_B^S$) gives ΔE^S, the energy difference in any solvent within a relative permittivity, in terms of ΔE^V together with calculable parameters. An accurate value of the solvent dependence from a variety of conformational equilibria is obtained (2–5, 10).

It should be noted that the calculated energies correspond to the potential energy differences, while the experimental results refer to free energies (ΔG). However, the entropy value in the system is negligible, and thus, $\Delta G = \Delta E$. The calculations were performed by the MODELS program (15), using the geometries from Gaussian 98 (12) as input. The dipole and quadrupole moments of the molecules were calculated directly from their partial atomic charges, which were obtained from the CHARGE routine (16).

Experimental

The solvents were obtained commercially, stored over molecular sieves, and used without further purification.

^{1}H and ^{13}C NMR spectra were obtained on a Varian Mercury plus BB spectrometer operating at 300.059 MHz for proton and 75.457 MHz for carbon NMR. Spectra were of 0.65 mol L^{-1} solutions in a probe temperature of ca. 25 °C. Typical conditions for proton spectra were 48 transients,

© 2003 NRC Canada

Table 2. Chemical shifts (ppm) and coupling constants (Hz) for MCTA ($ClC^1H_2{}^1$-C^2(O)-S-$C^3H_3{}^2$).

Solvent	H^1	H^2	C^1	C^2	C^3	$^2J_{CH}$	$^3J_{CH}$	$^1J_{CH}{}^a$	$^1J_{CH}{}^b$
CCl_4	4.07	2.28	192.9	47.6	11.9	4.3	4.3	152.2	141.9
$CDCl_3$	4.20	2.37	194.5	47.8	12.1	4.2	4.2	152.4	142.3
CD_2Cl_2	4.20	2.33	194.5	48.3	12.2	4.2	4.2	152.7	142.3
Acetone-d_6	4.43	2.35	194.7	48.5	11.9	4.2	4.2	153.6	142.1
CD_3CN	4.31	2.32	195.4	48.9	12.3	4.2	4.2	153.6	142.3
DMSO-d_6	4.59	2.32	194.6	48.3	11.8	4.1	4.1	154.2	142.3
Pure compound	3.40	1.44	194.2	48.2	12.0	4.2	4.2	153.2	142.3

[a] CH_2.
[b] CH_3.

Table 3. Chemical shifts (ppm) and coupling constants (Hz) for MBTA ($BrC^1H_2{}^1$-C^2(O)-S-$C^3H_3{}^2$).

Solvent	H^1	H^2	C^1	C^2	C^3	$^2J_{CH}$	$^3J_{CH}$	$^1J_{CH}{}^a$	$^1J_{CH}{}^b$	$^4J_{CH}$
CCl_4	3.15	1.53	191.3	32.9	12.5	4.0	4.0	153.1	142.0	0.5
$CDCl_3$	4.05	2.38	193.0	33.2	12.6	4.0	4.0	153.4	142.3	0.5
CD_2Cl_2	4.05	2.35	193.2	33.8	12.8	4.0	4.0	153.6	142.4	0.5
Acetone-d_6	4.28	2.36	193.4	34.1	12.4	4.0	4.0	154.6	142.2	0.5
CD_3CN	4.15	2.33	194.2	34.6	12.9	4.0	4.0	154.6	142.4	0.5
DMSO-d_6	4.43	2.33	193.4	34.7	12.3	3.9	3.9	155.1	142.3	—
Pure compound	3.02	1.22	192.6	34.0	12.72	4.0	4.0	154.2	142.3	0.5

[a] CH_2.
[b] CH_3.

Table 4. Chemical shifts (ppm) and coupling constants (Hz) for MITA ($IC^1H_2{}^1$-C^2(O)-S-$C^3H_3{}^2$).

Solvent	H^1	H^2	C^1	C^2	C^3	$^1J_{CH}{}^a$	$^1J_{CH}{}^b$	$^4J_{CH}$
CCl_4	3.95	2.38	191.4	3.5	13.0	152.0	142.0	0.7
$CDCl_3$	4.01	2.39	193.2	3.8	12.8	152.3	142.3	0.7
CD_2Cl_2	4.01	2.35	193.4	4.5	13.0	152.5	142.3	0.7
Acetone-d_6	4.19	2.36	193.7	4.4	12.6	153.0	142.1	0.8
CD_3CN	4.08	2.33	194.5	5.2	13.0	153.2	142.3	0.7
DMSO-d_6	4.21	2.32	194.0	5.8	12.4	153.1	142.2	0.7
Pure compound	2.67	0.95	192.3	6.1	13.3	152.8	142.3	0.7

[a] CH_2.
[b] CH_3.

spectral width 3000 Hz with 32 k data points, and zero filled 128 k to reach a digital resolution of 0.04 Hz. Proton-coupled carbon spectra (gated decoupling) were obtained with 3000 transients, 2 s pulse delay, spectral width 15 000 Hz with 64 k data points, and zero filled 256 k for 0.1 Hz digital resolution. The spectra were all first-order, and the coupling constants and chemical shifts taken directly from them are shown in Tables 2–4.

The carbonyl stretching bands, both in the fundamental (1850–1600 cm^{-1}) and in the first overtone regions (3650–3300 cm^{-1}), were recorded in a Bomem FT-IR MB-100 spectrometer, from 0.03 mol L^{-1} solutions for all compounds studied, in solvents of varying polarity, using 0.5 mm sodium chloride matched cells for the fundamental region and 1.00 cm quartz matched cells for the overtone region. Deconvolution analyses were performed through the GRAMS program.

_S_-Methyl chloro- and bromothioacetate (17)

To a three-neck flask, equipped with magnetic stirrer and N_2 atmosphere, was added anhydrous THF (150 mL). The flask was cooled down to –60 °C with an $N_{2(l)}$–ethanol bath, and to this was added 5.0 mL of methanethiol (collected at –60 °C and dried over anhydrous magnesium sulphate), 5.1 mL (62.5 mmol) of pyridine, and 5.0 mL (62.5 mmol) of chloroacetyl chloride or 5.4 mL (62.5 mmol) of bromoacetyl chloride. The reaction mixture was stirred at –25 °C for 3 h and then poured into water (200 mL). The organic layer was separated, and the aqueous layer was extracted with ether (3 × 30 mL). The organic extracts were combined, washed with a 3% HCl solution (8 × 12 mL), and dried over anhydrous sodium sulphate. The solvent was evaporated under reduced pressure. The product obtained was distilled through a Vigreux column, yielding 4.6 g (bp 53–55 °C at 12 mmHg (1 mmHg = 133.322 Pa); 57%) of the *S*-methyl chloro-

© 2003 NRC Canada

Fig. 1. Potential energy surface at the B3LYP/6-311+g(d,p) level: (*a*) MCTA, (*b*) MBTA.

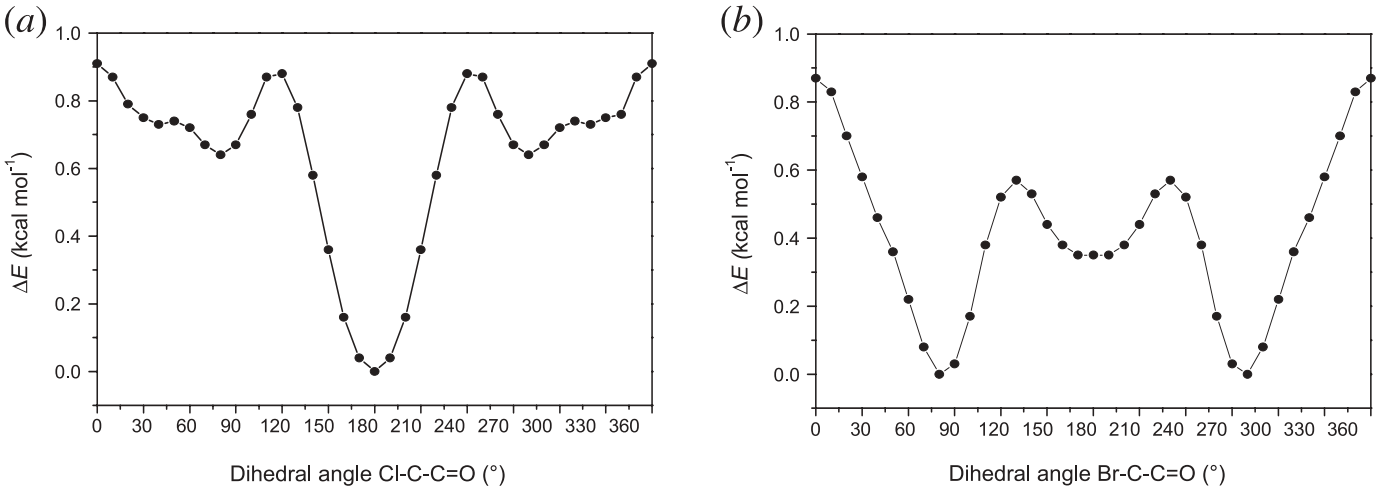


Fig. 2. Most stable rotamers for MCTA (X = Cl), MBTA (X = Br), and MITA (X = I).

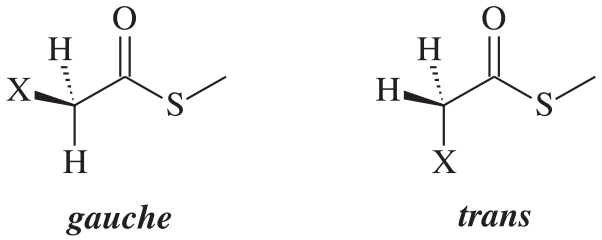
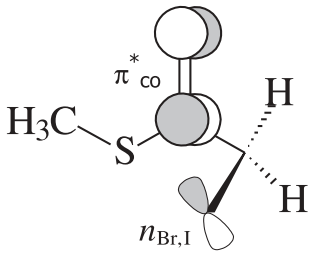


Fig. 3. The $n_{Br,I} \rightarrow \pi^*_{CO}$ orbital interaction.



thioacetate and 5.6 g (bp 63–64 °C at 7 mmHg; 51%) of the *S*-methyl bromothioacetate.

S-Methyl iodothioacetate (18)

Potassium iodide (15.28 g, 92 mmol) and acetone (10 mL) were placed into a 50 mL three-neck flask, which was equipped with magnetic stirrer, reflux condenser, and addition funnel. Soon after, *S*-methyl chlorothioacetate was added dropwise under stirring at room temperature. After the addition, the reaction mixture was stirred for 4 h. It was then filtered through a Büchner funnel; the solid was then washed with acetone, and the solution was concentrated under reduced pressure. The product was distilled through a Vigreux column, yielding pure *S*-methyl iodothioacetate (bp 79 °C at 6 mmHg; 9.30 g; 56%).

Results

The potential-energy surfaces were obtained, through DFT calculations, for MCTA and MBTA (see Fig. 1). Figures 1*a* and 1*b* show the *trans* and *gauche* rotamers (Fig. 2) as the most stable forms for all compounds. The geometries for the *gauche* and *trans* rotamers for each compound were optimized at special basis sets (see theoretical calculation section). The *trans* forms for MCTA, MBTA, and MITA were identified through the dihedral angles (X–C–C=O) of 180.0°, 180.0°, and 179.9°, respectively. The dihedral angles for the *gauche* rotamers were 78.8° for MCTA, 82.7° for MBTA, and 81.6° for MITA, as can be observed in Fig. 1 and Table 1.

In the case of MCTA, the *trans* rotamer is the most stable form in the vapour phase ($\Delta E_{gauche-trans}$ = 1.05 kcal mol^{-1}); for MBTA, the energy difference in the vapour phase is almost zero, but for MITA, the *gauche* form is more stable ($\Delta E_{trans-gauche}$ = 1.39 kcal mol^{-1}). This distinct behaviour is because of the different interactions. In chlorine derivatives, the electrostatic interaction between a chlorine atom and sulphur, in the *trans* form, is predominant in the vapour phase. On the other hand, for bromine and iodine derivatives, the electronic interaction between $n_{Br,I} \rightarrow \pi^*_{CO}$ is dominant in the *gauche* form (Fig. 3).

The ^{13}C NMR spectra of MCTA, MBTA, and MITA were recorded in solvents of varying polarity, and the coupling constant, $^1J_{CH}$, of the methylene carbon exhibited a dependence on the solvent (Tables 2–4).

Although the use of $^4J_{HF}$, $^1J_{CF}$, and $^2J_{CF}$ couplings in conformational investigations is well established (2–5), this is not the case for the $^1J_{CH}$ couplings measured in this work. Thus, it is of the first necessity to determine how much the observed variation in the couplings is because of changes in the conformer populations and how much is because of an intrinsic solvent dependence. Comparing the observed changes in $^1J_{CH}$ for methylene carbon (Tables 2–4) with those of the methyl group, in which all (methyl group) conformers are identical, the $^1J_{CH}$ couplings for methylene groups in MCTA, MBTA, and MITA are essentially independent from the solvent; thus, the noticed changes for these

© 2003 NRC Canada

Table 5. The individual coupling constants calculated and the energy differences between the rotamers in the vapour phase (ΔE^V).

Compound	Rotamer	$^1J_{CH}$ (Hz)	ΔE^V (kcal mol^{-1})
MCTA	*trans*	142.5	1.00
	gauche	176.0	
MBTA	*trans*	127.9	0.10
	gauche	162.4	
MITA	*trans*	113.7	0.65
	gauche	157.2	

couplings, in the methylene groups, may be reasonably attributed to changes in the conformer populations.

The $^1J_{CH}$ coupling constants were used to perform the solvation calculations, as shown in eq. [1], in which n is the molar fraction of the rotamer. Through this methodology, we compute the energy difference between the rotamers (ΔE^V), the individual coupling constants ($^1J_{CH(trans)}$ and $^1J_{CH(gauche)}$), the calculated coupling constants, and the population of the rotamers.

$$J_{obsd} = n_{gauche}J_{gauche} + n_{trans}J_{trans}$$

$$n_{trans} + n_{gauche} = 1$$

$$n_{trans}/n_{gauche} = (1/2)\exp^{(-\Delta E/RT)}$$

[1] $$\Delta E = E_{gauche} - E_{trans}$$

For the compounds MBTA and MITA, the ΔE value is given by $\Delta E = E_{trans} - E_{gauche}$; using this equation, the results are always positive. The energy differences between the rotamers in the vapour phase (ΔE^V) and the individual calculated coupling constants ($^1J_{CH(trans)}$ and $^1J_{CH(gauche)}$) are shown in Table 5. The energy differences between the rotamers in solution, the calculated coupling constants ($^1J_{CH(calcd)}$), and the rotamer population are shown in Table 6.

The IR spectra, using solvents of varying polarity, corroborate with the NMR data and show the carbonyl absorption as a double band for MCTA (Fig. 4). Through deconvolution analysis, it was possible to observe two resolved bands, which confirms the presence of the two rotamers. The same behaviour was observed for MBTA (Fig. 5) and for MCTA as well, except in the carbon tetrachloride solution where three bands were observed, both in the fundamental and the first overtone regions (Figs. 5*a* and 5*b*).

For MITA (Fig. 6), the IR spectra of the carbonyl absorption band appears as a single sharp band (except for the overtone region); however, the carbonyl band deconvolution showed two peaks (Fig. 7).

Discussion

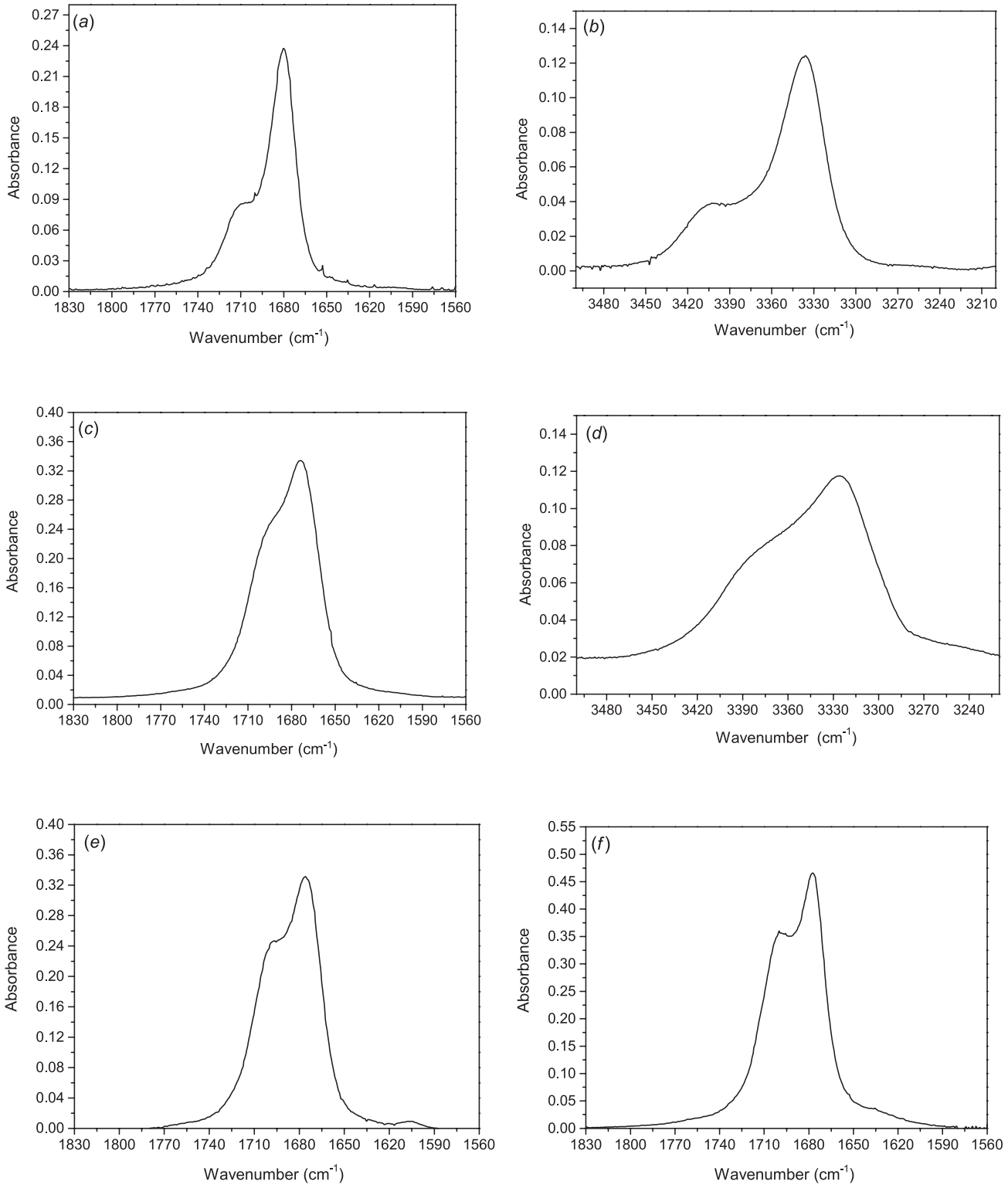
In this work, the DFT calculations allow us to observe (for MCTA, MBTA, and MITA) the presence of two rotamers, *gauche* and *trans* (Fig. 2), unlike in a previous study (11), in which it was concluded that the rotational isomerism for these compounds was between the *cis* and *gauche* forms. For MCTA, the *trans* rotamer predominates over the *gauche* form in the vapour phase, while for MBTA and MITA, the *gauche* rotamer is the most stable form. This behaviour can be explained by considering that in MCTA,

Table 6. Solution energy difference (kcal mol^{-1}), coupling constants observed and calculated (Hz), and the rotamers populations.

	MCTA				MBTA				MITA			
Solvent	$E_{gauche} - E_{trans}$	$^1J_{CH(calcd)}$	$^1J_{CH(obsd)}$	*gauche* (%)	$E_{trans} - E_{gauche}$	$^1J_{CH(calcd)}$	$^1J_{CH(obsd)}$	*gauche* (%)	$E_{trans} - E_{gauche}$	$^1J_{CH(calcd)}$	$^1J_{CH(obsd)}$	*gauche* (%)
CCl_4	0.98	151.8	152.2	28	0.15	152.7	153.1	72	0.73	151.7	152.0	87
$CDCl_3$	0.93	152.4	152.4	30	0.21	153.4	153.4	74	0.81	152.3	153.2	89
CD_2Cl_2	0.88	152.9	152.7	31	0.26	153.9	153.6	76	0.87	152.7	152.5	90
Acetone-d_6	0.84	153.5	153.6	33	0.31	154.5	154.6	77	0.93	153.1	153.0	91
CD_3CN	0.81	153.8	153.6	34	0.34	154.8	154.6	78	0.97	153.4	153.2	91
DMSO-d_6	0.80	154.0	154.2	34	0.35	154.9	155.1	78	0.98	153.4	153.1	91
Pure compound	0.85	153.4	153.2	32	0.30	154.3	154.2	77	0.93	153.1	152.8	91

© 2003 NRC Canada

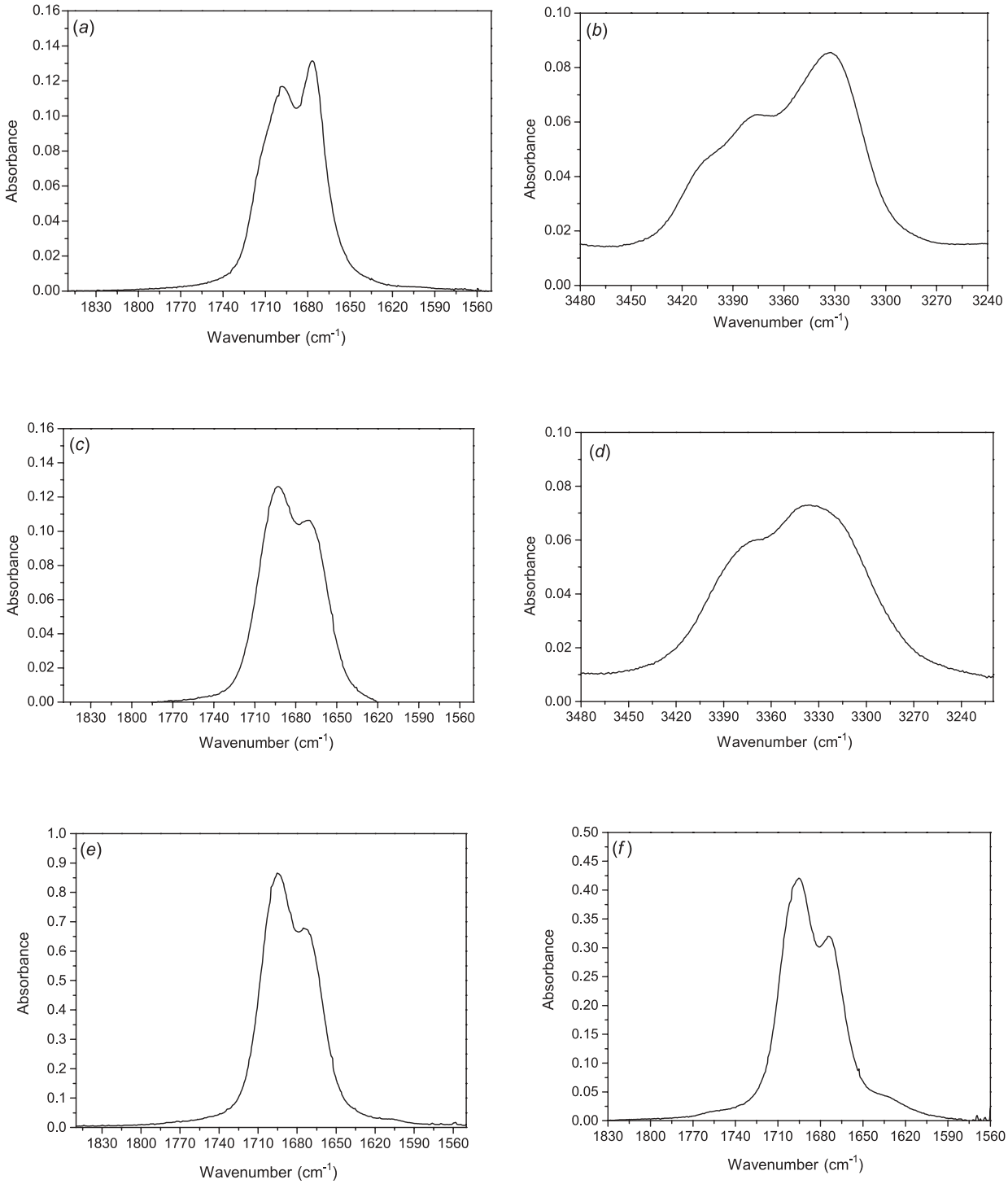
Fig. 4. The carbonyl absorption band in the IR spectrum of MCTA in (*a*) CCl_4, (*b*) CCl_4 in the first overtone, (*c*) $CHCl_3$, (*d*) $CHCl_3$ in the first overtone, (*e*) CH_2Cl_2, and (*f*) CH_3CN.



there is a strong Coulomb attraction between the positive charge on the sulphur atom (0.8026) and the negative charge on the chlorine atom (–0.2591). However, for the bromine and iodine derivatives, this attraction could be neglected because the bromine and iodine charges are –0.0816 and 0.608, respectively, giving support for the *gauche* rotamer preference. In addition, it should be expected that this behaviour could be related to the steric repulsion between the

© 2003 NRC Canada

Fig. 5. The carbonyl absorption band in the IR spectrum of MBTA in (*a*) CCl_4, (*b*) CCl_4 in the first overtone, (*c*) $CHCl_3$, (*d*) $CHCl_3$ in the first overtone, (*e*) CH_2Cl_2, and (*f*) CH_3CN.

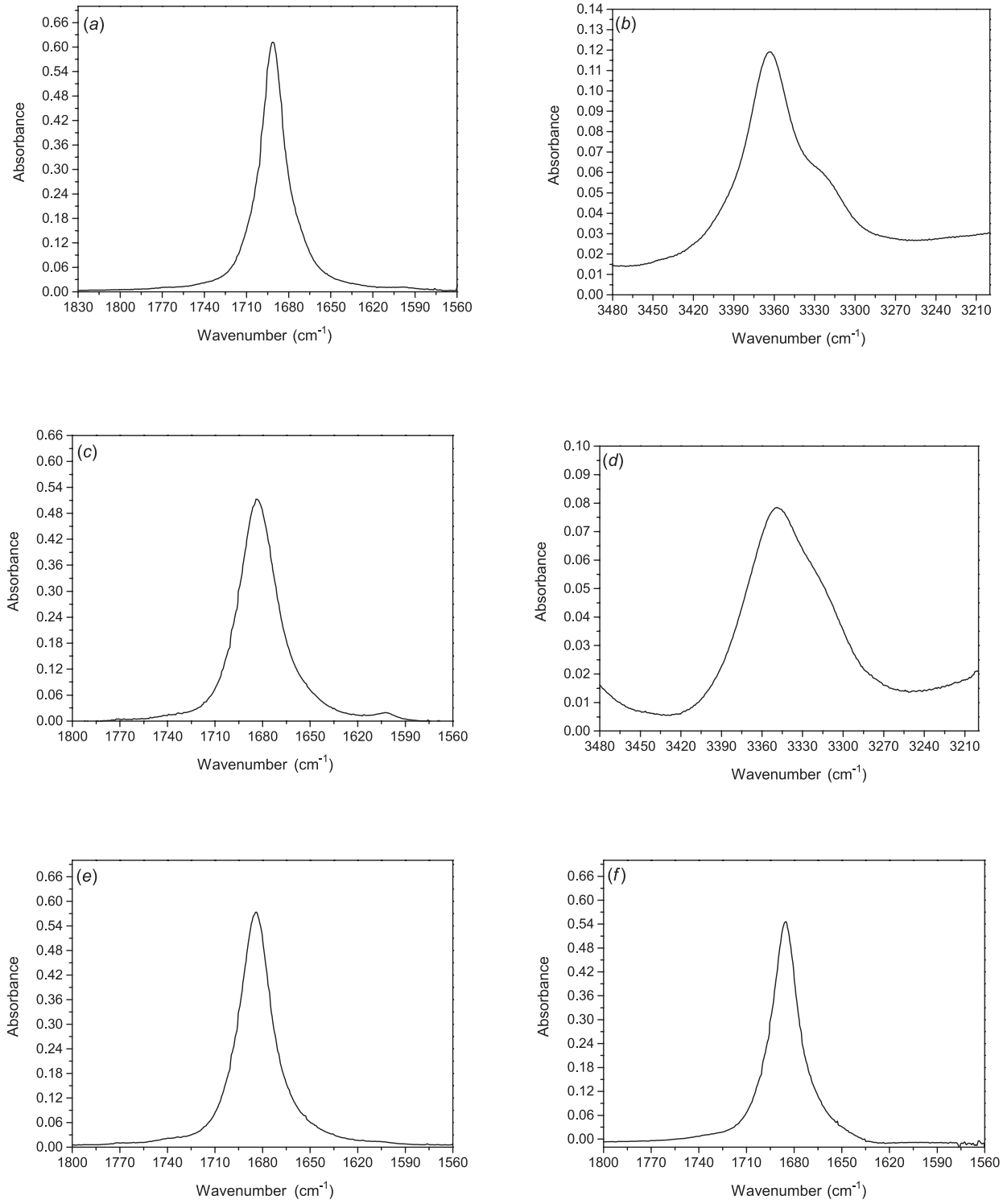


larger bromine and (or) iodine and sulphur atoms. The *gauche* rotamer stability in MBTA and MITA could also be due to attractive interaction between $n_{Br,I} \rightarrow \pi^*_{CO}$ (Fig. 3).

From the NMR data, it was observed that the coupling constant $^1J_{CH}$ shows dependence on solvent polarity, owing to the changes in rotamer population. The $^1J_{CH}$ for MCTA varied from 152.2 Hz in CCl_4 to 154.2 Hz in DMSO, producing a change in *trans* rotamer population from 72% to 66%, respectively. This result indicates that the most polar rotamer (*gauche*) is more favoured in polar solvents, but the *trans* form is the most stable overall in all the solvents employed. For MBTA and MITA, the *gauche* rotamer is the most stable one, and the $^1J_{CH}$ values varied from 153.1 and 152.0 Hz in CCl_4 to 155.1 and 153.1 Hz in DMSO, respec-

© 2003 NRC Canada

Fig. 6. The carbonyl absorption band in the IR spectrum of MITA in (*a*) CCl_4, (*b*) CCl_4 in the first overtone, (*c*) $CHCl_3$, (*d*) $CHCl_3$ in the first overtone, (*e*) CH_2Cl_2, and (*f*) CH_3CN.

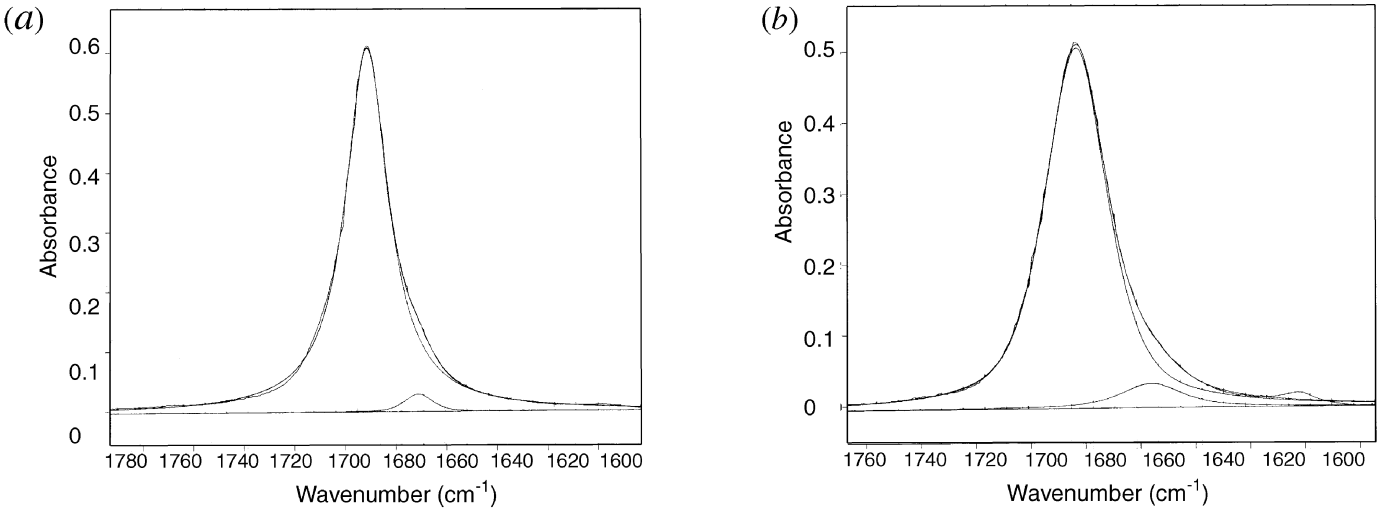


tively. The proportion of *gauche* rotamer for MBTA and MITA increased from 72% and 87% in CCl_4 to 78% and 91% in DMSO, respectively. All these data are compiled in Table 6. These results clearly show the preference for the *trans* rotamer for MCTA and the *gauche* form for MBTA and MITA. The rotational isomerism is affected by the solvent; as the solvent polarity increases, the population of the rotamer with the higher dipole moment also increases (Table 6).

The solvation theory, together with the NMR experiments, yields an excellent methodology for conformational analysis of these compounds. The FT-IR experiments for the three

© 2003 NRC Canada

Fig. 7. The carbonyl band deconvolution of MITA in (*a*) CCl_4 and (*b*) $CHCl_3$.



compounds showed one peak for each rotamer in the fundamental and the first overtone regions. After spectra deconvolution, the two bands were clearly observed. For MBTA in carbon tetrachloride solution, we observed a third band at a higher frequency. This third absorption is weak and may be the result of an overtone or combination frequency in Fermi resonance with the carbonyl stretching vibration. Studies explaining this behavior have not yet been done. Through theoretical calculations (Table 1), we have attributed the carbonyl bands for each rotamer of MCTA, MBTA, and MITA. In all compounds, the *trans* rotamer band absorbs in a lower frequency than the *gauche* one.

Acknowledgements

We acknowledge Fundação de Amparo à Pesquisa do Estado de São Paulo (FAPESP) for financial support (grant No. 2000/07692-5) and for a fellowship (to C.F.T.), Coordenação de Aperfeiçoamento de Pessoal de Nível Superior (CAPES) for a scholarship (to B.C.F.), and Conselho Nacional de Desenvolvimento Cientifico e Tecnológico (CNPq) for a fellowship (to R.R.).

References

1. S.E. Ulic, E.M. Coyanis, R.M. Romano, and C.O. Della Védova. Spectrochim. Acta A, **54**, 695 (1998).
2. R J. Abraham, C.F. Tormena, and R. Rittner. J. Chem. Soc. Perkin Trans. 2, 815 (2001).
3. C.F. Tormena, R. Rittner, R.J. Abraham, E.A. Basso, and R.M. Pontes. J. Chem. Soc. Perkin Trans. 2, 2054 (2000).
4. R.J. Abraham, C.F. Tormena, and R. Rittner. J. Chem. Soc. Perkin Trans. 2, 1663 (1999).
5. R.J. Abraham, A.D. Jones, M.A. Warne, R. Rittner, and C.F. Tormena. J. Chem. Soc. Perkin Trans. 2, 533 (1996).
6. C. Thibaudeau, J. Plavec, and J. Chattopadhyaya. J. Org. Chem. **63**, 4967 (1998).
7. P.E. Harrington, L. Li, and M.A. Tius. J. Org. Chem. **64**, 4025 (1999).
8. H.V. Phan and J.R. Durig. THEOCHEM, **209**, 333 (1990).
9. B.J. van der Veken, S. Truyen, W.A. Herrebout, and G. Watkins. J. Mol. Struct. **293**, 55 (1993).
10. C.F. Tormena, N.S. Amadeu, R. Rittner and R.J. Abraham. J. Chem. Soc. Perkin Trans. 2, 773 (2002).
11. P.R. Olivato, R. Nanartonis, and J.C.D. Lopes. Phosphorus Sulfur Silicon Relat. Elem. **71**, 107 (1992).
12. M.J. Frisch, G.W. Trucks, H.B. Schlegel, G.E. Scuseria, M.A. Robb, J.R. Cheeseman, V.G. Zakrzewski, J.A. Montgomery, R.E. Stratmann, J.C. Burant, S. Dapprich, J.M. Millam, A.D. Daniels, K.N. Kudin, M.C. Strain, O. Farkas, J. Tomasi, V. Barone, M. Cossi, R. Cammi, B. Mennucci, C. Pomeli, C. Adamo, S. Clifford, J. Ochterski, G.A. Petersson, P.Y. Ayala, Q. Cui, K. Morokuma, D.K. Malick, A.D. Rabuck, K. Raghavachari, J.B. Foresman, J. Cioslowski, J.V. Ortiz, B.B. Stefanov, G. Liu, A. Liashenko, P. Piskorz, I. Komaromi, R. Gomperts, R.L. Martin, D.J. Fox, T. Keith, M.A. Al-Laham, C.Y. Peng, A. Nanayakkara, C. Gonzalez, M. Challacombe, P.M.W. Gill, B.G. Johnson, W. Chen, M.W. Wong, J.L. Andres, M. Head-Gordon, E.S. Replogle, and J.A. Pople. Gaussian 98 [computer program]. Revision A.7. Gaussian Inc., Pittsburgh. 1998.
13. R. Custódio and J.D. Goddard. J. Mol. Struct. (THEOCHEM), **277**, 263 (1992).
14. M. Giordan, R. Custodio, and N.H. Morgon. Chem. Phys. Lett. **279**, 396 (1997).
15. R.J. Abraham and E. Bretschneider. *In* Internal rotation in molecules. *Edited by* W.J. Orville-Thomas. Wiley, London. 1974. Chap 13
16. R.J. Abraham. Prog. Nucl. Magn. Reson. Spectrosc. **35**, 85 (1999).
17. T. Wakui, H. Yamaguchi, and S. Motoki. Bull. Chem. Soc. Jpn. **50**, 1645 (1977).
18. A. Roedig. *In* Methoden der Organischen Chemie. Vol. 5. *Edited by* E. Muller. G. Thieme, Stuttgart. 1960. p. 601.

© 2003 NRC Canada

Neat reaction microwave technology for the synthesis of *N*-substituted-1,4-dihydropyridines

Mazaahir Kidwai and Richa Mohan

Abstract: Hantzsch synthesis of *N*-substituted-1,4-dihydropyridines (1,4-DHP) was carried out using an environmentally benign procedure. Neat reactants were subjected to microwave irradiation (MWI) to give the required products in excellent yield. Appreciable results were not obtained when conventional synthesis using neat reactants was carried out. The good yield and rate enhancement observed in the case of microwave irradiation is attributed to the uniform heating effect of microwaves.

Key words: 1,4-dihydropyridines (1,4-DHP), microwave irradiation (MWI), neat reaction, solid support.

Résumé : On a réalisé une synthèse de Hantzsch de 1,4-dihydropyridines (1,4-DHP) *N*-substituées en faisant appel à une méthode environnementalement bénigne. On a soumis les réactifs sans solvants à une irradiation par des microondes (IMO) qui a conduit à la formation des produits requis avec d'excellents rendements. On n'a pas obtenu de bons résultats lorsqu'on a effectué la synthèse conventionnelle avec des réactifs sans solvant. On attribue les excellents rendements et l'augmentation de la vitesse de la réaction observée avec une irradiation par des microondes à l'effet de chauffage uniforme des microondes.

Mots clés : 1,4-dihydropyridines (1,4-DHP), irradiation par des microondes (IMO), réaction sans solvant, support solide.

[Traduit par la Rédaction]

Introduction

Research on the 1,4-dihydropyridine (1,4-DHP) moiety is of current interest because of its recognition as a core structure in calcium antagonists (1). In the case of structure–activity relationships, the effect of substitution on the 1,4-DHP ring has been thoroughly studied (2). However, most of the studies have been devoted to the Hantzsch synthesis of *N*-unsubstituted dihydropyridines (3, 4), since the classical routes (5), yielding *N*-alkyl or *N*-aryl 1,4-DHP products, suffer from negative results (6) or very poor yields (7). Modified synthetic methodologies (8) for the above compounds reportedly provide improved yields but use expensive reagents and require longer reaction times. The drive for clean technology in the chemical industry requires a level of innovation. Thus, the eco-friendly goal of making organic compounds without using solvents has come several steps closer in recent years (9). With the development of microwave-assisted solid-phase synthesis (10), it has now become easier to perform reactions without solvents, as these high-yield protocols offer the benefits of enhanced reaction rates, greater selectivity, and experimental ease of manipulation (11).

In this communication, synthesis of *N*-substituted-1,4-DHP was carried out under conventional heating by refluxing 1 mol of aldehydes 1a–b, 2 mol of ethylacetoacetate, and 1 mol of amines 2a–d in acetic acid for several hours (Scheme 1). The products were obtained in low yield (Table 1), while the same reaction over acidic alumina[2] using microwave irradiation gave the desired products in good yield within a few minutes. The microwave reaction was also carried out over neutral alumina,[3] wherein appreciable yields were observed within the same reaction time. Although the microwave-assisted solid-support synthesis is a solventless technique, it requires the use of an appreciable amount of solvent at the pre- and post-reaction stages.

In our endeavour to develop an environmentally benign synthesis that eliminates the use of solvent, and in continuation to our earlier work on the neat Hantzsch synthesis (13) of 1,4-DHP, an attempt was made to synthesize *N*-substituted-1,4-DHP under neat reaction conditions. As a test case, 2 mol of ethylacetoacetate and 1 mol each of benzaldehyde and aniline were subjected to microwave irradiation. On completion of reaction, as monitored by TLC, the reaction mixture was cooled at 5 °C for 24 h, and the sticky solid obtained was titurated with a few drops of methanol to give the required product in excellent yield. The positive results obtained in the above case prompted us to synthesize some novel *N*-substituted-1,4-DHP using heterocyclic amines. The products were obtained in less time than with solid support and conventional methodology. A slight improvement in yield was also observed on moving from solid support to

Received 16 January 2003. Published on the NRC Research Press Web site at http://canjchem.nrc.ca on 12 December 2003.

M. Kidwai[1] and R. Mohan. Department of Chemistry, University of Delhi, Delhi-110007, India.

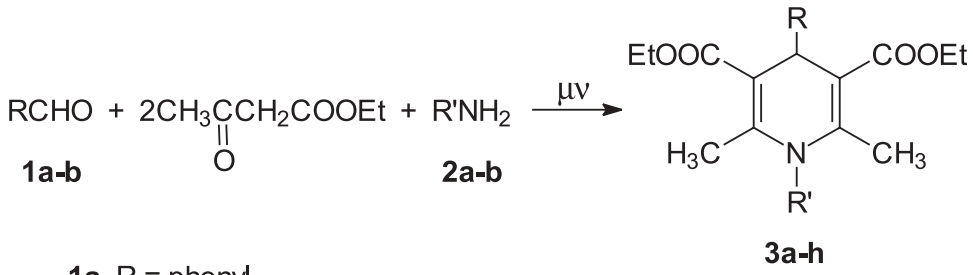
[1]Corresponding author (e-mail: mkidwai@mantraonline.com).

[2]Aluminium oxide, acidic, Brockmann I (~150 mesh; 58 Å; CAMAG 506-C-1; surface area 155 m^2/g).

[3]Aluminium oxide, neutral, Brockmann I (Aldrich Chem. Co., Cat. No., 19997-4; ~150 mesh; 58 Å; surface area 155 m^2/g).

 doi: 10.1139/V03-191 © 2003 NRC Canada

Scheme 1.



1a, R = phenyl
1b, R = 2-furyl
2a, R' = phenyl
2b, R' = 2-pyridyl
2c, R' = 2-furyl
2d, R' = 2-methyl-1,3,4-thiadiazolyl

Table 1. Comparison of the reaction times and yields for the compounds 3a–h.

				Solution phase (conventional)		Solid support (microwave)[a]		Neat (microwave)[a]	
Compd	R	R′	mp (°C)	Yield (%)	Time (h)	Yield (%)	Time (min)	Yield (%)	Time (min)
3a	Phenyl	Phenyl	159–160[b]	40	12	83	4.0	87	3.5
3b	Phenyl	2-Pyridyl	142–145	38	16	81	4.5	83	4.0
3c	Phenyl	2-Furyl	137–139	32	24	79	5.5	80	5.5
3d	Phenyl	2-Methyl-1,3,4-thiadiazolyl	155–157	18	>48	73	6.5	77	6.0
3e	Furyl	Phenyl	150–152	34	14	82	4.5	86	4.0
3f	Furyl	2-Pyridyl	195–198	30	18	80	5.0	81	5.0
3g	Furyl	2-Furyl	172–175	20	>48	75	7.0	76	6.5
3h	Furyl	2-Methyl-1,3,4-thiadiazolyl	240–242	15	>48	71	7.0	74	7.0

[a]Microwave heating (800 W, 100–110 °C, 1 min).
[b]Literature (12) value mp 158 °C.

neat reaction methodology (Table 1). The neat reaction was also carried out under conventional heating, keeping similar reaction conditions. Conventional neat synthesis took more time for completion and gave the products in moderate yield and, in certain cases, lead to charring.

Thus, we have developed an easier, practically convenient, and environmentally benign synthesis of bioactive *N*-substituted-1,4-DHP that proceeds under much milder reaction conditions than conventional means. Eliminating organic solvents in chemical synthesis is an important drive towards clean chemical technology. Although solventless reactions are more appropriate for small-scale production, these results may stimulate interest among researchers involved in the industrial scale-up of reactions.

Experimental section

Melting points were determined on a Thomas Hoover melting point apparatus and are uncorrected. IR spectra were recorded on a PerkinElmer FT-IR-1710 spectrophotometer. ^{1}H NMR spectra were recorded on an FT-NMR Hitachi R-600 (60 MHz) instrument using TMS as the internal reference. Microwave irradiation was carried out in a Kenstar microwave oven, Model No. OM9925E (2450 MHz, 800 W). Monitoring of the reaction was done through TLC, using silica-gel-coated Al plates (Merck). The reaction temperature was measured using an AZ minigun type non-contact IR thermometer (Model No. 8868).

General procedure for the synthesis of *N*-substituted diethyl 1,4-dihydro-2,6-dimethyl-4-furyl/phenyl-3,5-pyridinedicarboxylate (3a–h)

Solution phase (conventional)

A mixture of aldehyde 1a–b (0.01 mol), primary amine 2a–d (0.01 mol), and ethylacetoacetate (0.02 mol) in 30 mL acetic acid was refluxed for a specified time. On completion of the reaction, as monitored by TLC examination, the reaction mixture was cooled for 24 h; the solid obtained was filtered, washed with cold MeOH, dried, and recrystallized from ethanol.

Solid support (microwave)

To the solution of aldehyde 1a–b (0.01 mol), primary amine 2a–d (0.01 mol), and ethylacetoacetate (0.02 mol) in ethanol (15 mL), solid support (20 g) was added. The reaction mixture was dried in air, kept in an alumina bath, and subjected to MWI for a specified time (Table 1). On completion of the reaction, as examined by TLC (at an interval of 30 s), the product was extracted in ethanol (3 × 15 mL). Re-

© 2003 NRC Canada

covering the solvent under reduced pressure gave the required product, which was recrystallized from ethanol.

Neat synthesis (microwave)

A mixture of 0.01 mol of aldehyde 1a–b, 0.01 mol of primary amine 2a–d, and 0.02 mol of ethyl acetoacetate was taken in an Erlenmeyer flask and subjected to MWI. The progress of the reaction was monitored by TLC at an interval of 30 s. On completion of the reaction, the reaction mixture was cooled and titurated with a few drops of methanol, and the product was recrystallized from aqueous methanol.

Diethyl 1,4-dihydro-2,6-dimethyl-1,4-diphenyl-3,5-pyridinedicarboxylate (3a)

IR (cm^{-1}) ν_{max}: 2989.80, 1728.59, 1628.35, 1091.00. ^1H NMR (60 MHz, $CDCl_3$) δ_H: 1.1 (t, 3H, CH_3), 2.3 (s, 3H, CH_3), 4.2 (q, 2H, OCH_2), 5.0 (s, 1H, 4-H), 7.3–7.6 (m, 10H, Ar-H). Anal. calcd. for $C_{25}H_{27}NO_4$: C 74.07, H 6.66, N 3.45; found: C 74.09, H 6.70, N 3.42.

Diethyl 1,4-dihydro-2,6-dimethyl-4-phenyl-1-(2′-pyridyl)-3,5-pyridinedicarboxylate (3b)

IR (cm^{-1}) ν_{max}: 3115.56, 2965.64, 1689.18, 1635.22, 1042.22. ^1H NMR (60 MHz, DMSO-d_6) δ_H: 1.2 (t, 3H, CH_3), 2.5 (s, 3H, CH_3), 4.1 (q, 2H, OCH_2), 5.2 (s, 1H, 4-H), 7.2–8.1 (m, 9H, Ar-H & pyridine). Anal. calcd. for $C_{24}H_{26}N_2O_4$: C 70.93, H 6.40, N 6.89; found: C 70.91, H 6.43, N 6.91.

Diethyl 1,4-dihydro-2,6-dimethyl-1-(1′-furylmethyl)-4-phenyl-3,5-pyridinedicarboxylate (3c)

IR (cm^{-1}) ν_{max}: 3116.53, 2981.36, 1689.60, 1635.95, 1042.53. ^1H NMR (60 MHz, DMSO-d_6) δ_H: 1.2 (t, 3H, CH_3), 2.2 (s, 3H, CH_3), 3.1 (s, 2H, OCH_2), 4.2 (q, 2H, CH_2), 5.2 (s, 1H, 4-H), 6.2–6.4 (m, 3H, furan), 7.2–7.4 (m, 5H, Ar-H). Anal. calcd. for $C_{24}H_{27}NO_5$: C 70.41, H 6.60, N 3.42; found: C 70.43, H 6.62, N 3.45.

Diethyl 1,4-dihydro-2,6-dimethyl-4-phenyl-1-(5′-methyl-1,3,4-thiadiazolyl)-3,5-pyridinedicarboxylate (3d)

IR (cm^{-1}) ν_{max}: 2927.89, 1701.78, 1636.22, 1043.21. ^1H NMR (60 MHz, $CDCl_3$) δ_H: 1.3 (t, 3H, CH_3), 2.2 (s, 3H, CH_3), 2.6 (s, 3H, 5′-CH_3), 4.2 (q, 2H, OCH_2), 5.1 (s, 1H, 4-H), 7.2–7.4 (m, 5H, Ar-H). Anal. calcd. for $C_{22}H_{25}N_3O_4S$: C 61.82. H 5.85, N 9.83; found: C 61.83, H 5.81, N 9.82.

Diethyl 1,4-dihydro-2,6-dimethyl-4-furyl-1-phenyl-3,5-pyridinedicarboxylate (3e)

IR (cm^{-1}) ν_{max}: 2983.99, 1669.13, 1628.35, 1066.96. ^1H NMR (60 MHz, $CDCl_3$) δ_H: 1.2 (t, 3H, CH_3), 2.1 (s, 3H, CH_3), 4.2 (q, 2H, OCH_2), 5.3 (s, 1H, 4-H), 6.2–6.4 (m, 3H, furan), 7.3–7.7 (m, 5H, Ar-H). Anal. calcd. for $C_{23}H_{25}NO_5$: C 69.87, H 6.32, N 3.54; found: C 69.88, H 6.35, N 3.56.

Diethyl 1,4-dihydro-2,6-dimethyl-4-furyl-1-(2′-pyridyl)-3,5-pyridinedicarboxylate (3f)

IR (cm^{-1}) ν_{max}: 2989.92, 1692.50, 1635.58, 1035.98. ^1H NMR (60 MHz, DMSO-d_6) δ_H: 1.2 (t, 3H, CH_3), 2.4 (s, 3H, CH_3), 4.2 (q, 2H, OCH_2), 5.4 (s, 1H, 4-H), 6.2–6.4 (m, 3H, furan), 7.7–8.1 (m, 4H, pyridine). Anal. calcd. for $C_{22}H_{25}N_2O_5$: C 66.66, H 6.06, N 7.07; found: C 66.67, H 6.09, N 7.06.

Diethyl 1,4-dihydro-2,6-dimethyl-4-furyl-1-(1′-furyl methyl)-3,5-pyridinedicarboxylate (3g)

IR (cm^{-1}) ν_{max}: 3094.54, 1701.78, 1628.50, 1052.36. ^1H NMR (60 MHz, DMSO-d_6) δ_H: 1.3 (t, 6H, CH_3), 2.4 (s, 6H, CH_3), 3.2 (s, 2H, CH_2), 4.3 (q, 4H, OCH_2), 5.3 (s, 1H, 4-H), 6.4–7.0 (m, 6H, furan). Anal. calcd. for $C_{22}H_{25}NO_6$: C 66.16, H 6.26, N 3.50; found: C 66.14, H 6.23, N 3.52.

Diethyl 1,4-dihydro-2,6-dimethyl-4-furyl-1-(5′-methyl 1′,3′,4′-thiadiazolyl)-3,5-pyridinedicarboxylate (3h)

IR (cm^{-1}) ν_{max}: 3093.76, 1692.50, 1639.52, 1065.98. ^1H NMR (60 MHz, $CDCl_3$) δ_H: 1.2 (t, 3H, CH_3), 2.3 (s, 3H, CH_3), 2.7 (s, 3H, 5′-CH_3), 4.1 (q, 2H, OCH_2), 5.1 (s, 1H, 4-H), 6.2–6.4 (m, 3H, furan). Anal. calcd. for $C_{20}H_{23}N_3O_5S$: C 57.55, H 5.51, N 10.07; found: C 57.58, H 5.53, N 10.06.

References

1. (*a*) R.H. Bocker and F.P. Guengerich. J. Med. Chem. **28**, 1596 (1986); (*b*) A.C. Gaudio, A. Korolkovas, and Y. Takahata. J. Pharm. Sci. **83**, 1110 (1994).
2. (*a*) B.M. Khadilkar, H.G. Jaisinghani, M.N. Saraf, and S.K. Desai. Indian J. Chem. **40B**, 82 (2001); (*b*) F. Bossert, A. Heise, S. Kazda, E. Klauke, and K. Stoepal. Ger. Offen. 2753946. (1979); Chem. Abstr. **92**, 76 294 (1980).
3. (*a*) R. Alajarin, J.J. Vaquero, J.L. Garcia Navio, and J. Alvarez-Builla. Synlett, 297 (1992); (*b*) G. Penieres, O. Garcia, K. Franco, O. Hernandez, and C. Alvarez. Heterocycl. Commun. **2**(**4**), 359 (1996).
4. (*a*) J.G. Breitenbucher and G. Figliozzi. Tetrahedron Lett. **41**(22), 4311 (2000); (*b*) J.S. Yadav, B.V.S. Reddy, and K.B. Reddy. Synth. Commun. **31**(**3**), 425 (2001).
5. (*a*) M. Furdik and A. Gvozdjakova. Acta Fac. Rerum Nat. Univ. Comenianae Chim. **8**(**10**), 581 (1964); Chem. Abstr. **61**, 13 277 (1964); (*b*) F. Bossert and W. Vater. Ger. Offen. 1813436 (1970); Chem. Abstr. **74**, 22 702 (1971); (*c*) G. Duburs, B. Cekavicius, A. Sausins, R. Vitolina, and A. Kimenis. Ger. Offen. 2908738 (1979); Chem. Abstr. **92**, 58 623 (1980).
6. W. Traber and P. Karrer. Helv. Chim. Acta, **41**, 2066 (1958).
7. A. Hantzsch. Ber. **18**, 2580 (1885).
8. (*a*) B. Lachowicz. Monatsh. Chem. **17**, 343 (1896); (*b*) J.G. Erickson. J. Amer. Chem. Soc. **67**, 1382 (1945); (*c*) G.B. Gill, D.J. Harper, and A.W. Johnson. J. Chem. Soc. C, 1675 (1968); (*d*) J.-C.V. Eynde, A. Mayence, A. Maquestiau, and E. Anders. Synth. Commun. **22**(**22**), 3291 (1992).
9. D.C. Dittmer. Chem. Ind. (London), 779 (1997).
10. (*a*) M. Kidwai. Pure Appl. Chem. **73**(**1**), 147 (2001); (*b*) M. Kidwai, R. Venkataramanan, and B. Dave. Green Chem. **3**, 278 (2001).
11. R.S. Varma. Green Chem. **1**, 43 (1999).
12. Schiff. Ber. Dtsch. Chem. Ges. **31**, 604 (1898); Beilstein Abstract, **22**, 172 (1935).
13. M. Kidwai, S. Saxena, R. Mohan, and R. Venkataramanan. J. Chem. Soc. Perkin Trans. 1, **16**, 1845 (2002).

© 2003 NRC Canada

Kinetics and mechanism of the oxidation of L-α-amino-*n*-butyric acid in moderately concentrated sulfuric acid medium

Homayoon Bahrami and Mansour Zahedi

Abstract: The reaction kinetics of L-α-amino-*n*-butyric acid oxidation by permanganate ion have been investigated in moderately strong acid medium using a spectrophotometric technique. In all cases studied an autocatalytic effect, due to Mn^{+2} ions formed as a reaction product, was observed. Both catalytic and noncatalytic processes were determined to be first order with respect to the permanganate ion and the amino acid. The overall rate equation for this process may be written as:

$$-d[MnO_4^-]/dt = k'_1[MnO_4^-] + k'_2[MnO_4^-]\cdot[Mn^{+2}]$$

where k'_1 and k'_2 are pseudo-order rate constants for the noncatalytic and catalytic reactions, respectively. The influence of some factors such as temperature and reactant concentration on the rate constants has been studied, and the activation parameters have been calculated. Reaction mechanisms satisfying observations for both catalytic and noncatalytic routes have been presented.

Key words: L-α-amino-*n*-butyric acid, permanganate oxidation, concentrated acidic medium, autocatalysis, free radical intermediates.

Résumé : Faisant appel à une technique spectrophotométrique, on a étudié la cinétique de la réaction d'oxydation de l'acide L-α-aminobutyrique par l'ion permanganate dans un milieu acide relativement fort. Dans tous les cas étudiés, on a observé un effet autocatalytique par les ions Mn^{+2} qui se forment comme produit de la réaction. On a déterminé que les processus tant catalytique que non-catalytique sont tous les deux du premier ordre par rapport à l'ion permanganate et à l'acide aminé. L'équation globale de vitesse pour le processus est de la forme:

$$-d[MnO_4^-]/dt = k'_1[MnO_4^-] + k'_2[MnO_4^-]\cdot[Mn^{+2}]$$

dans laquelle k'_1 et k'_2 sont les constantes de vitesse du premier ordre des réactions respectivement non-catalytique et catalytique. On a étudié l'influence de quelques facteurs, tels que la température et la concentration, sur les constantes de vitesse étudiées et on a calculé les paramètres d'activation. On propose des mécanismes réactionnels pour les voies catalytique et non catalytique qui satisfont les résultats obtenus.

Mots clés : acide L-α-aminobutyrique, oxydation avec du permanganate, milieu acide concentré, autocatalyse, intermédiaires radicalaires.

[Traduit par la Rédaction]

Introduction

Owing to the biological importance of amino acids, the kinetics and mechanistic study of their oxidation has received considerable attention. The permanganate oxidation process of amino acids in strong acid media (1–14), in neutral and weak basic solutions (15–23), and in weak acid media (24–29) has been investigated. The occurrence of autocatalysis effects in weak acid media, neutral aqueous solution, and weak basic media has been extensive (15–29), whereas no rigorous evidence of such an effect has been reported in strong acid media. There have been just two reports (10, 14) of a "double-stage" process vaguely attributed to possible autocatalysis, with no thorough information as far as the autocatalysis effect is concerned.

In autocatalytic pathways in which Mn^{+2} ions have been determined to be responsible for the effect, a mechanism with no free radicals involved has been suggested (28, 29). In the present paper, distinct evidence of the autocatalytic influence of Mn^{+2} for the permanganate oxidation of L-α-amino-*n*-butyric acid in strong acid medium has been presented, and a free radical mechanism has been proposed.

Experimental

All the reagents were from Merck or Sigma. The solutions were prepared with triply distilled and deionized water. The

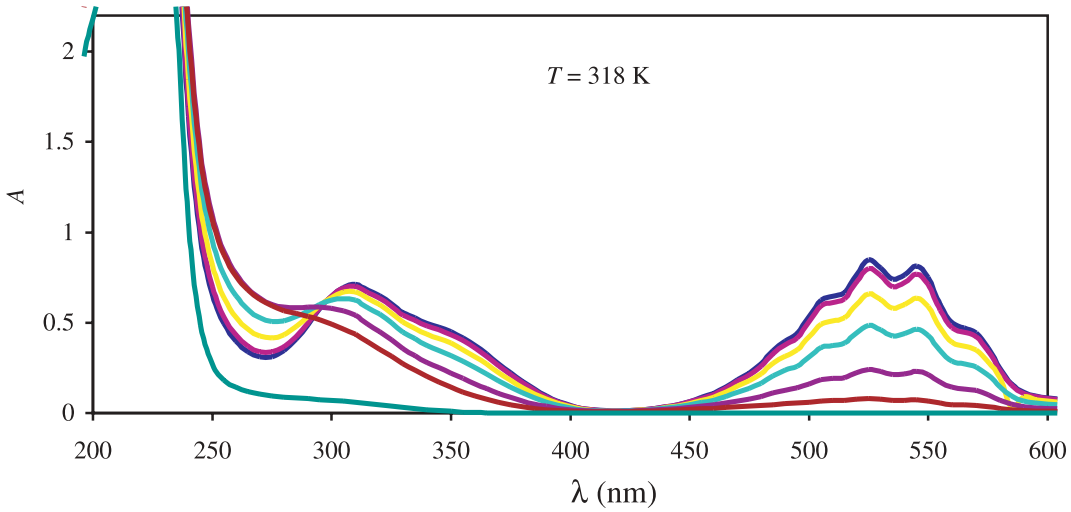
Received 18 June 2003. Published on the NRC Research Press Web site at http://canjchem.nrc.ca on 9 January 2004.

H. Bahrami and M. Zahedi.[1] Department of Chemistry, Faculty of Sciences, Shahid Beheshti University, Evin, Tehran 19839, Iran.

[1]Corresponding author (e-mail: m-zahedi@cc.sbu.ac.ir).

 doi: 10.1139/V03-181 © 2004 NRC Canada

Fig. 1. Spectral changes in the oxidation of L-α-amino-*n*-butyric acid by permanganate ion. [$KMnO_4$] = 4×10^{-4} mol dm^{-3}, [L-abu] = 0.1 mol dm^{-3}, [H_2SO_4] = 3.16 mol dm^{-3}, T = 318 K. Scanning time intervals = 6 min.



permanganate solutions were prepared and tested by the Vogle method (30). The kinetic progress of the reaction was followed by measuring the absorbance of the permanganate ions at 525 nm with a thermostated (Shimadzu TB-85 ± 0.1 K) Shimadzu (2100 Model) UV–vis spectrophotometer within the temperature range 25–45 °C. For the permanganate molar absorption coefficient at 525 nm and in strong acid solution, a value of 2.26×10^3 dm^3 mol^{-1} cm^{-1} was obtained.

In all the kinetic measurements, the amino acid was used in excess (250-fold) relative to permanganate, to insure pseudo-first-order kinetics (28, 29).

Results

Stoichiometry and product analysis

By employing spot tests (31, 32), the final reaction products were detected as ammonium ions and the corresponding aldehyde. For carbon dioxide detection, the standard Vogle method (33) was employed. As well, it is well known (4, 12, 34) that in the reduction process of permanganate ions in strong acid media (as long as the reducing species is in excess), Mn^{+2} ions are the final product.

Our reaction was performed in an excess of amino acid, and we used the procedure outlined below to study the stoichiometry of the reaction; the following equation is proposed as the reaction stoichiometry:

$$[1]\quad 2MnO_4^- + 5CH_3\text{-}CH_2\text{-}CH(NH_3)^+COO^- + 11H^+ \rightarrow 5CH_3\text{-}CH_2\text{-}CHO + 5NH_4^+ + 5CO_2 + 2Mn^{+2} + 3H_2O$$

Procedure

Equal concentrations of known amounts of permanganate and amino acid were mixed and kept at 45 °C temperature for 1 h. For the permanganate concentration determination, a known amount of reaction mixture was quenched by a standard iron(II) solution. The unreacted iron was subsequently titrated by a standard cerium(IV) solution. Aldehyde concentration was determined by a calorimetric procedure using chromotropic acid. We came to the final conclusion that 1 mol of permanganate generates 2.5 mol of aldehyde, as is indicated by the balanced equation, eq. [1] (1, 2, 8).

Rate equation

Figure 1 illustrates the permanganate absorption vs. wavelength curves obtained at 6 min intervals as the reaction proceeded. From previous studies (15–23), Mn(IV) ions absorb in the region 400–650 nm. Figure 1 shows the lack of spectral changes from 400–650 nm, which means that MnO_2 is not a reaction product. Furthermore, since no rise and fall in absorption is observed at 418 nm, it is concluded that Mn(IV) ions do not intervene as possible oxidizing agents unless they are short lived.

The absorbance–time plots are illustrated in Fig. 2. In all the experiments performed, curves with a sigmoid profile (Fig. 2*a*) were obtained. This characteristic suggests the existence of an autocatalytic mechanism. To demonstrate that Mn^{+2} is the species responsible for the autocatalytic effect, kinetic runs were carried out in the presence of the $MnSO_4$ species at the beginning of the reaction. As the initial concentration of Mn^{+2} ions increased, a notable increase in the reaction rate was seen (Fig. 2*b*). Further increases of initial Mn^{+2} concentration and maintaining the Mn^{+2} concentration equal to the permanganate ion concentration led to a complete disappearance of the sigmoid form (Fig. 2*c*). Taking the Mn^{+2} effect on the reaction rate into account, the following rate equation has been proposed:

$$[2]\quad d[MnO_4^-]/dt = k'_1[MnO_4^-] + k'_2[MnO_4^-]\cdot[Mn^{+2}]$$

where k'_1 and k'_2 are pseudo-order rate constants for the noncatalytic and catalytic processes, respectively. The amino acid concentration, which is always kept in large excess, and the constant acid concentration in each experiment are included in these pseudo-order rate constants.

The integrated form of this equation gives:

$$[3]\quad \ln[(k'_1/k'_2 + x)/(a - x)] = (k'_1 + k'_2a)t - \ln(k'_2a/k'_1)$$

© 2004 NRC Canada

Fig. 2. Effect of the added initial concentration of ions on the absorbance time plots. [$KMnO_4$] = 4×10^{-4} mol dm^{-3}, [L-abu] = 0.1 mol dm^{-3}, [H_2SO_4] = 3.16 mol dm^{-3}, T = 313 K. (*a*) [Mn^{+2}] = 0 mol dm^{-3}; (*b*) [Mn^{+2}] = 2×10^{-4} mol dm^{-3}; (*c*) [Mn^{+2}] = 4×10^{-4} mol dm^{-3}.

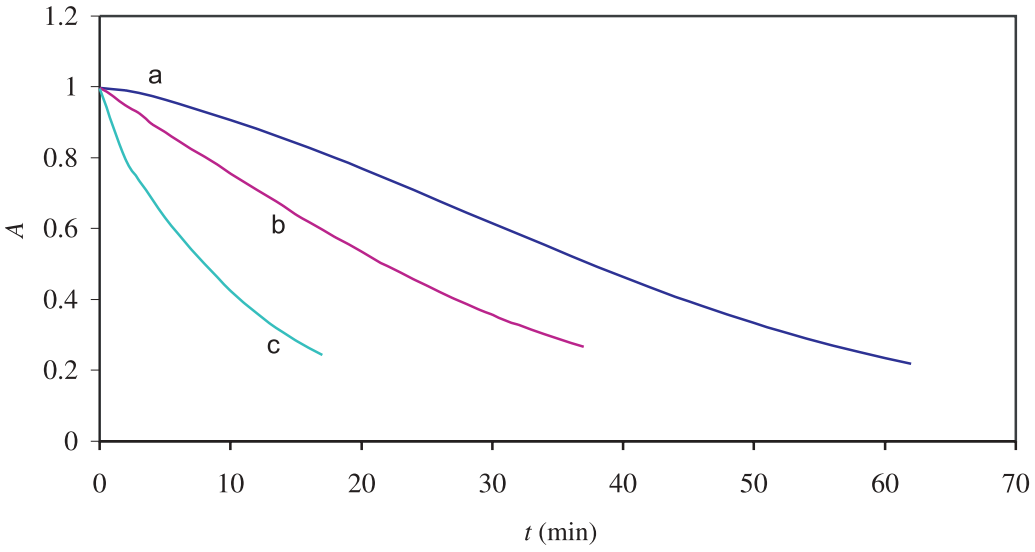
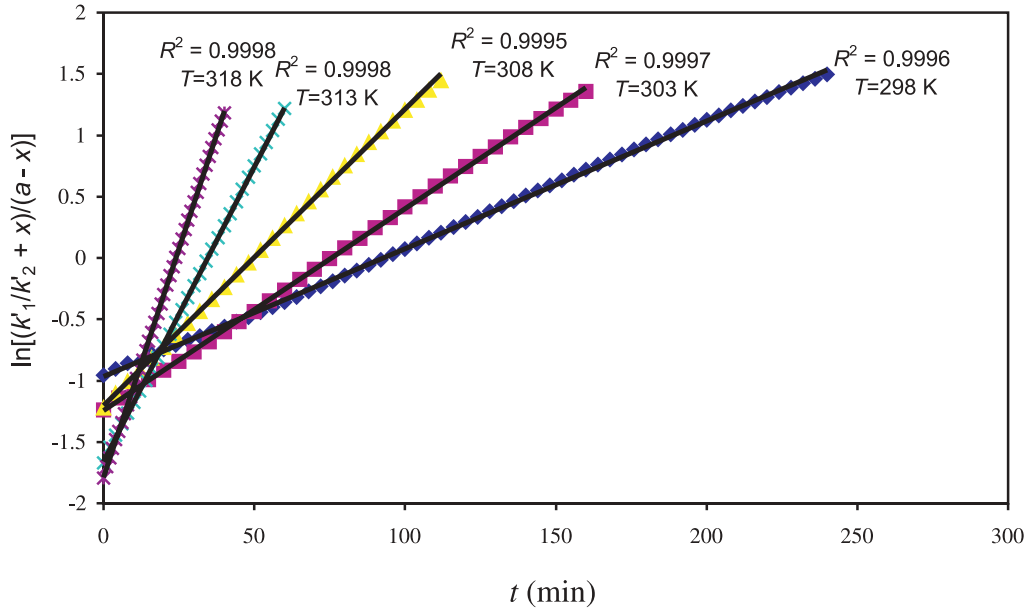


Fig. 3. Integrated rate-law plots for the oxidation of L-α-amino-*n*-butyric acid by potassium permanganate at various temperatures. [$KMnO_4$] = 4×10^{-4} mol dm^{-3}, [L-abu] = 0.1 mol dm^{-3}, [H_2SO_4] = 3.16 mol dm^{-3}.



where a represents the initial concentration of permanganate and x the amount of permanganate ion consumed up to time t.

For the correct determination of pseudo-constants k'_1 and k'_2, the following procedure has been employed. Because the reaction is slow and the initial Mn^{+2} concentration is sufficiently low, initial guesses of k'_1 values have been obtained by fitting the initial portion of the rate data to a first-order rate equation and assuming no catalytic effect in the early stages of the reaction. Moreover, our kinetic run in the presence of manganese sulfate(II) with a concentration equal to that of the permanganate ion satisfies the following rate equation:

$$[4] \qquad \ln[a(b + x)/b(a - x)] = k'_2 (a + b)t$$

where b refers to the initial concentration of manganese sulfate(II). The calculated rate constants under this condition have provided a reasonable initial guess for k'_2. Having previously determined preliminary values of k'_1 and k'_2, eq. [3] has then been used for the simultaneous determination of the kinetic data of the reaction by taking advantage of iterative methods (18, 24–29). Figure 3 demonstrates the results of the fitting process of rate data at various temperatures and under the same conditions.

Table 1 gives the final values for k'_1 and k'_2 at various temperatures. Almost perfect fits to the curves in Fig. 3 (R^2 values of 0.9995–0.9998) not only corroborate the validity of the applied kinetic method but also confirm the autocatalytic effect of the Mn^{+2} species.

© 2004 NRC Canada

Fig. 4. Effect of the amino acid concentration on the catalyzed and uncatalyzed pseudo-order rate constants. [$KMnO_4$] = 4 × 10^{-4} mol dm^{-3}, [H_2SO_4] = 3.16 mol dm^{-3}, T = 313 K.

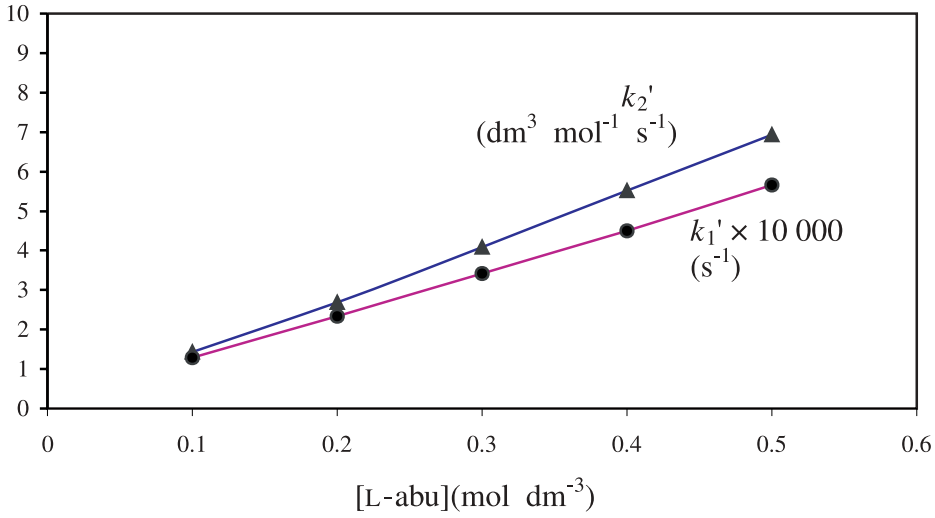


Table 1. Effect of temperature on k_1' and k_2'; [$KMnO_4$] = 4 × 10^{-4} mol dm^{-3}; [L-abu] = 0.1 mol dm^{-3}; [H_2SO_4] = 3.16 mol dm^{-3}.

T (K)	k_1'×10^5 (s^{-1})	k_2'×10^2 (dm^3 mol^{-1} s^{-1})
298	4.12 (±0.02)	27.72 (±0.05)
303	6.16 (±0.04)	49.98 (±0.11)
308	9.12 (±0.09)	81.05 (±0.19)
313	12.78 (±0.09)	142.24 (±0.2)
318	17.79 (±0.09)	239.8 (±0.2)

Note: Values in parenthesis are estimated errors on each of k_1' and k_2'.

Table 2. Variation of k_2' and k_1' vs. the concentration of butyric acid; [$KMnO_4$] = 4 × 10^{-4} mol dm^{-3}; [H_2SO_4] = 3.16 mol dm^{-3}; T = 313 K.

[L-abu] (mol dm^{-3})	k_2' (dm^3 mol^{-1} s^{-1})	k_1'×10^4 (s^{-1})
0.1	1.43	1.28
0.2	2.81	2.51
0.3	4.35	3.83
0.4	5.67	5.17
0.5	7.05	6.33

Dependence of the kinetic parameters

Dependence of reaction rate on [amino acid], [MnO_4^-], and [Mn^{2+}]

The pseudo-order rate constants obtained at various amino acid concentrations are summarized in Table 2. Figure 4 shows these results. The plots of $1/k_1'$ and $1/k_2'$ against 1/[L-abu] (L-abu = L-α-amino-*n*-butyric acid) (not shown) gave straight lines that both pass through the origin. These observations confirm first order with respect to the amino acid for both the noncatalytic and catalytic pathways (12).

To investigate the effect of permanganate concentration on the reaction rate, its concentration was varied from 4 × 10^{-4} to 6 × 10^{-4} mol dm^{-3} at 313 K, which caused k_1' and k_2' values to be decreased by 14% and 31%, respectively.

Table 3 summarizes the data that have been obtained for k_2' with increasing Mn^{+2} ion concentration. From these results it is evident that when Mn^{+2} concentration is raised, k_2' values decrease. This observation, and the fact that the very slow reaction of Mn^{+2} with MnO_4^- (35, 36) switches to a fast reaction when the amino acid is present, suggest that in the process of permanganate consumption some intermediate complex has probably been formed between Mn^{+2} and the amino acid (24–29).

Table 3. Effect of Mn(II) on k_2' at 313 K; [L-abu] = 0.1 mol dm^{-3}; [H_2SO_4] = 3.16 mol dm^{-3}; [$KMnO_4$] = 4 × 10^{-4} mol dm^{-3}.

[Mn(II)]	0	0.0002	0.0004	0.0006
k_2' (dm^3 mol^{-1} s^{-1})	1.43	1.41	1.34	1.19

Dependence of reaction rate on sulfuric acid concentration

The effect of [H^+] has been investigated by means of a series of experiments carried out at various sulfuric acid concentrations. As Fig. 5 indicates, k_1' increases when the acid concentration is raised, whereas k_2' initially decreases and then shows a sharp increase. The region of 3–4 mol dm^{-3} sulfuric acid shows the least variation for k_2'. Thus, this concentration region was determined to be the most appropriate region for the rest of our kinetic studies.

Determination of activation parameters

As a further justification of the method that has been applied to determine the pseudo-order rate constants k_1' and k_2' at various temperatures, calculated values of these parameters have been evaluated by the Eyring equation. Figure 6 demonstrates the agreement of both k_1' and k_2' with the Eyring equation. The thermodynamic activation parameters obtained, energy, enthalpy, and entropy, are reported in Table 4.

Acrylonitrile addition

The presence of free radicals as intermediates was con-

© 2004 NRC Canada

Fig. 5. Effect of the sulfuric acid concentration on the uncatalyzed and catalyzed pseudo-order rate constants. [$KMnO_4$] = 4 × 10^{-4} mol dm^{-3}, [L-abu] = 0.1 mol dm^{-3}, T = 313 K.

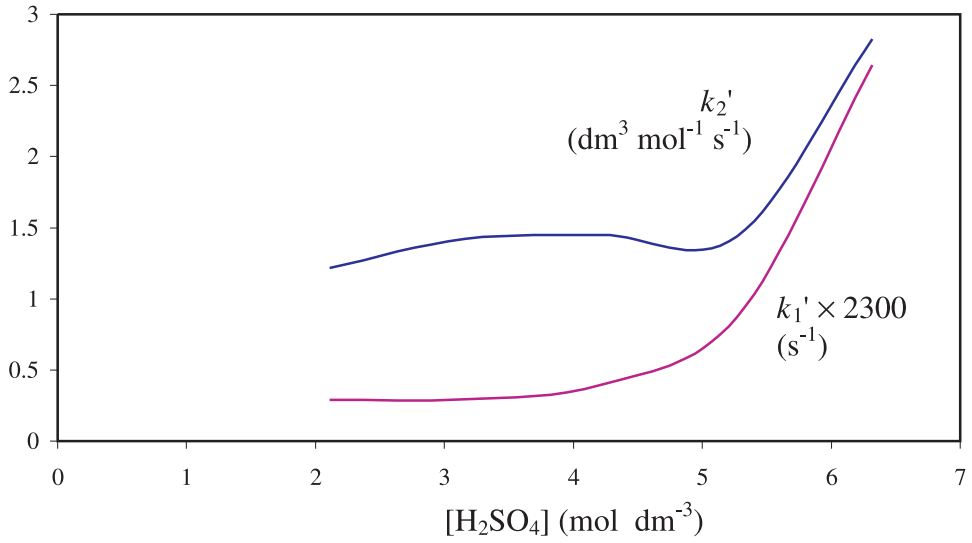


Fig. 6. Eyring plots for the uncatalyzed and catalyzed processes. [L-abu] = 0.1 mol dm^{-3}, [$KMnO_4$] = 4 × 10^{-4} mol dm^{-3}, [H_2SO_4] = 3.16 mol dm^{-3}.

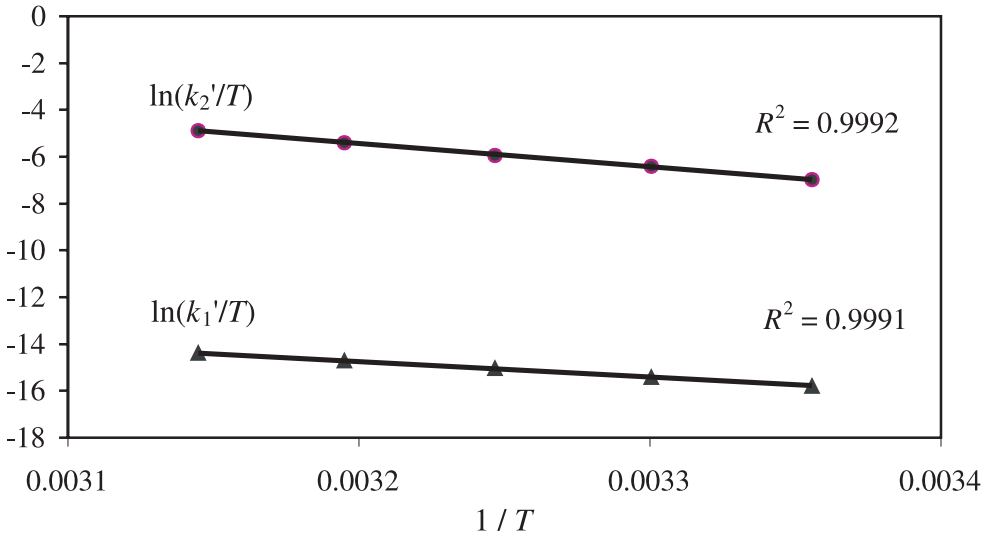


Table 4. Activation parameters; [$KMnO_4$] = 4 × 10^{-4} mol dm^{-3}; [L-abu] = 0.1 mol dm^{-3}; [H_2SO_4] = 3.16 mol dm^{-3}.

	Uncatalyzed process	Catalyzed process
$\Delta S^{\#}$ (J mol^{-1} K^{-1})	–144 (±3)	19 (±4)
$\Delta H^{\#}$ (kJ mol^{-1})	55 (±1)	82 (±1)
E_a (kJ mol^{-1})	58 (±1)	84 (±1)

Note: Values in parenthesis are estimated errors on each thermodynamical parameter.

firmed by addition of acrylonitrile, which led to polymerization, both in the presence and in the absence of manganese sulfate(II).

Discussion

In agreement with the experimental results that have been presented and taking into account the previous literature references, two separate mechanisms for the catalyzed and uncatalyzed pathways are proposed to describe the reaction pathway. Since the existence of intermediate free radicals was confirmed, their involvement in the reaction mechanism has also been considered.

Reaction mechanism for the uncatalyzed process

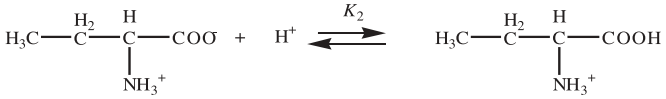
All the experiments were performed in strong acid media. With the evidence presented pointing to no involvement of other manganese oxidation states, Mn(VII) is the most probable reactive species. Reaction rate enhancement observed by increasing acid concentration suggests the formation of a more powerful oxidant, namely permanganic acid, by the following equilibrium:

[5] $$MnO_4^- + H^+ \underset{}{\overset{K_1}{\rightleftharpoons}} HMnO_4$$

© 2004 NRC Canada

At the high acid concentration used, protonation of the zwitterionic form of amino acid gives

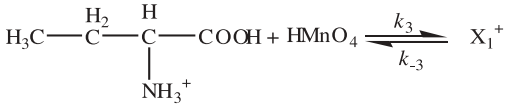
[6]



A mechanism consistent with the observed kinetic data includes the following steps.

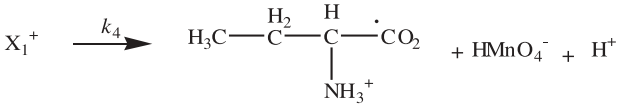
In agreement with the experimental results, the formation of an addition complex between the permanganic acid and the cationic form of the amino acid is proposed (11, 12, 28).

[7]



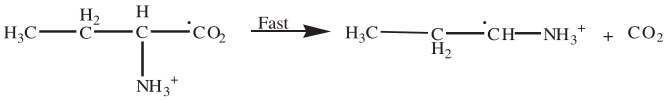
This complex may rupture according to the following equation:

[8]



Based on the radical involvement in the reaction mechanism, the iminium cation (24–29) is possibly formed via three steps

[9]



[10]

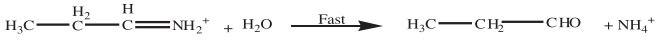


[11]



By hydrolysis of the iminium cation, the corresponding aldehyde is obtained (28)

[12]



Knowing the fact that the species Mn(V) is very unstable in strong acidic media, it will be converted into Mn(II) and Mn(VII) by means of a rapid disproportionation.

[13] $5HMnO_4^{2-} + 11H^+ \rightarrow 3MnO_4^- + 2Mn^{2+} + 3H_2O$

Multiplying eqs. [5], [6], [7], [8], [9], [10], [11], and [12] by a factor of five and then summing them with eq. [13] results in the overall reaction with the stiochiometry satisfied. In agreement with the above scheme, assuming a steady state approximation for X_1^+, the rate equation obtained for the uncatalyzed process is

[14] $-d[Mn(VII)]/dt = k_1'[MnO_4^-]$

[15] $$k_1' = \frac{\alpha_0[H^+]^2[\text{L-abu}]_t}{\beta_0(1+\beta_1[H^+]+\beta_2[H^+]^2)+\alpha_1[H^+]^2[MnO_4]}$$

where $[\text{L-abu}]_t$ represents the total concentration of amino acid; [Mn(VII)] represents the total concentration of permanganate; and where

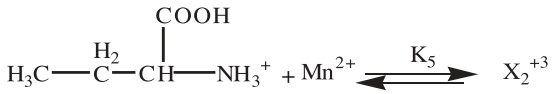
$$\alpha_0 = K_1K_2k_3k_4$$
$$\alpha_1 = K_1K_2k_3$$
$$\beta_0 = k_{-3} + k_4$$
$$\beta_1 = K_1 + K_2$$
$$\beta_2 = K_1K_2$$

The rate law obtained above corresponds to that mechanism explaining the observed experimental behavior: the first-order reaction with respect to both permanganate and amino acid and the change in k_1', the uncatalyzed pseudo-order rate constant, when the permanganate concentration varies.

Reaction mechanism for the catalyzed process

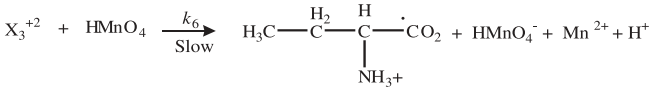
Addition of Mn^{+2} ions led to an increase in the reaction rate, while the evidence presented also suggests that an adduct might be formed between Mn^{+2} and the protonated L-α-amino-*n*-butyric acid in a fast step before it is oxidized by permanganic acid in a slow step (15, 16).

[16]



As the rate determining step, slow attack of permanganic acid on complexes has been proposed (28–29)

[17]



The remaining steps, leading to the final products, resemble those presented for the uncatalyzed pathway above. Again, multiplying eqs. [5], [6], [7], [16], [17], [9], [10], [11], and [12] by a factor of five and summing them up with eq. [12] results in the overall reaction with the correct stoichiometry. Assuming a steady-state approximation for the X_2^{3+} complex in the above mechanism, the following rate equation (28) is derived:

[18] $-d[Mn(VII)]/dt = k_2'[Mn^{2+}][MnO_4^-]$

© 2004 NRC Canada

$$[19] \quad k'_2 = \frac{\beta_0\delta_0[\text{L-abu}]_t[H^+]^2}{\beta_0(1+\beta_1[H^+]+\beta_2[H^+]^2)+\alpha_1[H^+][MnO_4^-]+\beta_0\delta_1[H^+][Mn^{+2}]+\beta_0\delta_2[H^+]^{2+}[Mn^{+2}]}$$

where the notation employed in eq. [14] is conserved, and in addition

$$\delta_0 = K_1K_2K_5k_6$$

$$\delta_1 = K_2K_5$$

$$\delta_2 = K_1K_2K_5$$

This rate law, along with the one proposed for the uncatalyzed process, is in accord with all experimental results presented in this article; namely, first-order dependence on Mn^{+2} ions, permanganate ions, and the amino acid and inverse dependence of k'_2 on permanganate and Mn^{+2} ion concentrations, as shown in the k'_2 expression.

Owing to the complexity of the proposed mechanism, evaluation of the values of the rate constants corresponding to the reaction rate-determining steps for both processes has not been possible. Thus, the activation parameters reported are associated with reaction pseudo-rate constants k'_1 and k'_2, and these values cannot be attributed to any particular reaction step.

Conclusions

The kinetics of the permanganate oxidation process of L-α-amino-*n*-butyric acid in strong acid media was investigated using a spectrophotometric technique. Addition of manganese sulfate(II) to the reaction mixture raised the reaction rate. The sigmoid profile observed for permanganate absorption variation at 525 nm vs. time was completely transformed to a linear one under conditions of $[KMnO_4] = [Mn(II)]$. In the presence of manganese sulfate(II), by increasing the amino acid concentration, the reaction rate was increased. Thus, we report the first conclusive evidence of an autocatalytic oxidation process of an amino acid in strong acid media in which Mn^{+2} species are responsible for the effect. The pseudo-order rate constants obtained for both the catalytic and noncatalytic pathways when the amino acid was in excess obeyed the Eyring relation. The presence of free radicals was confirmed, and mechanisms satisfying experimental observations for both catalytic and noncatalytic pathways were presented.

References

1. R.S. Verma, M.J. Reddy, and R. Shastry. J. Chem. Soc. Perkin Trans. **2**, 469 (1976).
2. A.A. Frost and R.G. Pearson. Kinetic and mechanisms. Wiley, New York. 1961. p. 152.
3. C.S. Ameta, P.N. Pande, H.L. Gupta, and H.C. Chowhhry. Acta Phys. Chem. **26**, 89 (1980).
4. C.S. Ameta, P.N. Pande, H.L. Gupta, and H.C. Chowhhry. Z. Phys. Chem. (Leipzig), **261**, 1222 (1980).
5. C.S. Ameta, P.N. Pande, H.L. Gupta, and H.C. Chowhhry. Z. Phys. Chem. (Leipzig), **261**, 802 (1980).
6. C.S. Ameta, P.N. Pande, H.L. Gupta, and H.C. Chowhhry. Acta. Chim. Acad. Sci. Hung. **110**, 7 (1982).
7. L.M. Bharadwaj and P.C. Nigam. Ind. J. Chem. Ser. A(8), **A**, 793 (1981).
8. V.S. Rao, B. Sethuram, and T.N. Rao. Int. J. Chem. Kinet. **11**, 165 (1979).
9. V.S. Rao, B. Sethuram, and T.N. Rao. Oxid. Commun. **9**, 11 (1986).
10. U.D. Mudaliar, V.R. Chourey, R.S. Verma, and V.R. Shastry. Ind. J. Chem. Soc. **60**, 561 (1983).
11. H.M. Girgis, R.M. Hassan, and A.S. El-Shahawy. Bull. Fac. Sci. Univ. **16**(1), 41 (1987).
12. R.M. Hassan, M.A. Mousa, and M.H. Wahdan., J. Chem. Soc. Dalton. Trans. **3**, 605 (1988).
13. H. Iloukani and H. Bahrami. Int. J. Chem. Kinet. **31**, 95 (1999).
14. B.R. Sahu, V.R. Chourey, S. Pandey, L.V. Shastry, and V.R. Shastry. Ind. J. Chem. Soc. **76**, 131 (2000).
15. F.J. Andrés Ordax, A. Arrizabalaga, and J.I. Martinez de Ilarduya. An. Quim. **80**, 531 (1984).
16. F.J. Andrés Ordax, A. Arrizabalaga, and R. Martinez Perez de mendiola. Studia Chemica, **11**, 303 (1986).
17. F.J. Andrés Ordax, A. Arrizabalaga, and K. Ortega. An. Quim. **85**, 218 (1989).
18. J.F. Perez Benito, F. Mata Perez, and E. Brillas. Can. J. Chem. **65**(10), 2329 (1987).
19. E. Brillas, J.A. Garrido, and J.F. Perez Benito. Collect. Czech. Chem. Comun. **53**, 479 (1988).
20. J.A. Garrido, J.F. Perez Benito, R.M. Rodrigouez, J. De Andrés, and E. Brillas. J. Chem. Res. **11**, 380 (1987).
21. J. De Andrés, E. Brillas, J.A. Garrido, and J.F. Perez Benito. J. Chem. Soc. Perkin Trans. **2**, 107 (1988).
22. R.M. Rodrigouez, J. De Andrés, E. Brillas, J.A. Garrido, and J.F. Perez Benito. New J. Chim. **2**(2–3), 143 (1988).
23. J. De Andrés, E. Brillas, J.A. Garrido, and J.F. Perez Benito. Gazz. Ital. **118**, 203 (1988).
24. F.J. Andrés Ordax, A. Arrizabalaga, J. Casado, and R. Peche. React. Kinet. Cattal. Lett. **44**, 293 (1991).
25. F.J. Andrés Ordax, A. Arrizabalaga, R. Peche, and M.A. Quintana. An. Quim. **87**, 828 (1992).
26. F.J. Andrés Ordax, A. Arrizabalaga, R. Peche, and M.A. Quintana. An. Quim. **88**, 440 (1992).
27. M.J. Insausti, F. Mata-pèrez, and M.P. Alvarez-macho. Int. J. Chem. Kinet. **27**, 507 (1995).
28. A. Arrizabalaga, F.J. Andrés Ordax, M.Y. Fernández Aránguiz, and R. Peche. Int. J. Chem. Kinet. **28**, 799 (1996).
29. A. Arrizabalaga, F.J. Andrés Ordax, M.Y. Fernández Aránguiz, and R. Peche. Int. J. Chem. Kinet. **29**, 181 (1997).
30. A.I. Vogel. Quimica analitica cuantitative. Vol. I. Kapelusz, Buenos Aires. 1960. p. 382.
31. F. Felig. Spot tests in inorganic analysis. Elsevier, Amsterdam.1972. p. 334.
32. F. Felig. Spot tests in inorganic analysis. Elsevier, Amsterdam.1976. p. 199.
33. A.I. Vogel. Quimica analitica cuantitative. Vol. I. Kapelusz, Buenos Aires. 1953. p. 250.
34. K.K. Banerji and P. Nath. Bull. Chem. Soc. Jap. **42**, 2038 (1969).
35. W.A. Waters. Q. Rev. Chem. Soc. **12**, 277 (1958).
36. P.S. Radhakrishnanurti and M.D. Rao. Indian J. Chem. Soc. A, **15**, 524 (1977).

© 2004 NRC Canada

A new family of N_xO_y pyridine-containing macrocycles: Synthesis and characterization of their Y(III), Ln(III), Zn(II), and Cd(II) coordination compounds

Carlos Lodeiro, Rufina Bastida, Emilia Bértolo, and Adolfo Rodríguez

Abstract: Reaction between 2,6-bis(2-formylphenoxymethyl)pyridine and *N*,*N*-bis(3-aminopropyl)methylamine or tris(2-aminoethyl)amine has been used as the starting point for the synthesis of seven oxa-aza macrocyclic ligands, five of them never reported previously. They all feature different pendant arms, which provide a wide range of coordination possibilities. The Schiff base macrocycles L^1 and L^4 and their reduced ligands L^2 and L^5 are derived from 2,6-bis(2-formylphenoxymethyl)pyridine and tris(2-aminoethyl)amine or *N*,*N*-bis(3-aminopropyl)methylamine, respectively. The reaction of L^1 with salicylaldehyde forms L^3, which features an imine bond in the pendant arm. The ligand L^5 has been the precursor for the pendant-armed L^6 and L^7, by alkylation of the free NH groups with methyl-imidazole or methyl-indole. By a template or a nontemplate approach, we have synthesized different mono- and dinuclear complexes with Y(III), Ln(III), Zn(II), and Cd(II) cations. Both the free macrocyclic ligands and their corresponding metal complexes have been characterized by microanalysis, IR, UV–vis, ^{1}H and ^{13}C NMR spectroscopy, FAB mass spectrometry, MS electrospray, and conductivity measurements.

Key words: Schiff-base macrocycle, template synthesis, macrocyclic ligand complexes, lanthanide(III) complexes.

Résumé : On a utilisé la réaction de la 2,6-bis(2-formylphénoxyméthyl)pyridine avec la *N*,*N*-bis(3-aminopropyl)méthylamine ou la tris(2-aminoéthyl)amine comme point de départ pour la synthèse de sept ligands oxa-aza macrocycliques, dont cinq n'avaient pas été rapportés antérieurement. Ils comportent tous des bras pendants différents qui peuvent donner lieu à des possibilités différentes de coordination. Les macrocycles à base de bases de Schiff, L^1 et L^4, ainsi que leurs ligands réduits, L^2 et L^5, sont dérivés respectivement de la 2,6-bis(2-formylphénoxyméthyl)pyridine et de la tris(2-aminoéthyl)amine ou de la *N*,*N*-bis(3-aminopropyl)méthylamine. La réaction du ligand L^1 avec le salicylaldéhyde conduit à la formation du ligand L^3 qui comporte une liaison imine dans le bras pendant. Le ligand L^5 est le précurseur des ligands L^6 et L^7 à bras pendant par l'alkylation des groupes NH libres à l'aide de méthyl-imidazole ou de méthyl-indole. Utilisant des approches avec ou sans gabarit, on a réalisé la synthèse de différents complexes mono- et dinucléaires comportant dans cations Y(III), Ln(III), Zn(II) et Cd(II). On a caractérisé les ligands macrocycliques libres ainsi que leurs complexes métalliques correspondants par microanalyse, spectroscopies IR, UV–vis et RMN du ^{1}H et du ^{13}C, par spectrométrie de masse par bombardement avec des atomes rapides (FAB) ou par ionisation par électronébulisation.

Mots clés : base de Schiff macrocyclique, synthèse à l'aide de gabarit, complexes de ligands macrocycliques, complexes de lanthanide(III).

[Traduit par la Rédaction]

Introduction

Pyridine-containing macrocycles have always attracted considerable interest because of their versatility. They can be used as building blocks that lead to more complicated structures, including systems with more than one cavity, three-dimensional cages, and ligands with additional functional groups attached to the macrocyclic skeleton (1–7). Some macrocycles involving *N*-methyl-pyridine, *N*-methyl-indole, or *N*-methyl-imidazole have been prepared and their coordination ability towards divalent and trivalent metal anions evaluated (8–11).

The synthesis of new receptors with pendant arms that have aromatic or aliphatic units is a fascinating area of research because of the importance of these receptors both in basic and applied chemistry. A subject of special interest is

Received 18 September 2003. Published on the NRC Research Press Web site at http://canjchem.nrc.ca on 16 February 2004.

C. Lodeiro,[1,2] R. Bastida, E. Bértolo, and A. Rodríguez. Departamento de Química Inorgánica. Universidad de Santiago de Compostela. Avda. das Ciencias s/n. 15782 Santiago de Compostela, Galicia, Spain.

[1]Present address: REQUIMTE-CQFB, Departamento de Química, Faculdade de Ciências e Tecnología, Universidade Nova de Lisboa, Quinta da Torre, 2829-516 Monte de Caparica, Portugal.
[2]Corresponding author (e-mail: lodeiro@dq.fct.unl.pt).

 doi: 10.1139/V03-214 © 2004 NRC Canada

the design of homo- or hetero-binuclear complexes for biomedical applications that require covalent attachment of the macrocycle system to a recognition site (12–16). Cytotoxic studies of transition metal ion concentrations (i.e., copper(II), zinc(II), and cadmium(II)) have also been carried out using macrocyclic ligands with pendant arms (17, 18). Lanthanide(III) ions have been employed as effective template agents (19, 20) in the synthesis of large macrocycles with pyridine head units.

In the present work, we describe the synthesis and characterization of a new group of oxa-aza macrocyclic ligands containing a pyridine head and phenyl lateral units (see Fig. 1). The heptadentate Schiff base macrocycle L^1 and its corresponding reduced ligand L^2 are derived from the reaction between 2,6-bis(2-formylphenoxymethyl)pyridine (**I**) and tris(2-aminoethyl)amine. Both macrocycles have a flexible amine pendant arm, with potential to form new macrocyclic ligands by condensation with different carbonylic species. Very recently we have reported a related compound of ligand L^1 (21). In those cases the stability of the complexes was increased by coordination of the flexible amine pendant arm to the metal ions. In this work, we present the reaction of L^1 with salicylaldehyde to form L^3, which features an imine bond. The Schiff base ligand L^4 has been obtained by reaction between 2,6-bis(2-formylphenoxymethyl)pyridine and *N*,*N*-bis(3-aminopropyl)methylamine and subsequently reduced to obtain L^5. The ligand L^5 has been the precursor for the pendant-armed macrocycles L^6 and L^7 by alkylation reaction of the NH groups with methylimidazole or methyl-indole. This thus covalently introduces a biological substrate in the macrocycle skeleton. We have studied the coordination capability of the macrocyclic ligands towards different metallic ions. We report the synthesis of the corresponding homodinuclear or mononuclear Y(III), Ln(III), Zn(II), and Cd(II) complexes, using nitrate or perchlorate as the counter ions. Both a direct route and a template approach have been used as required.

Experimental section

Methods

Elemental analyses were performed by the University of Santiago de Compostela Microanalytical Service in Carlo Erba 1108 and Leco CNHS-932 microanalysers. Infrared spectra were recorded as KBr discs or in CsCl windows, using a Mattson Cygnus 100 spectrophotometer. Proton and carbon NMR spectra were recorded using a Bruker WM-300. Positive ion FAB mass spectra were recorded on a Kratos MS50TC spectrometer, using 3-nitrobenzyl alcohol (MNBA), glycerol, or 2-hydroxyethyl disulfide matrixes. Electrospray mass spectra were recorded using acetonitrile and acetic acid mixture as solvent. Melting points were carried out using a BÜCHI melting point apparatus. Conductivity measurements were carried out in 10^{-3} mol dm^{-3} acetonitrile or DMF solutions at 25 °C using a WTW LF-3 conductivimeter. The electronic absorption spectra of some complexes and ligands (MeCN solutions) were measured in the 220–850 nm range using a PerkinElmer Lambda 6 spectrophotometer, and the fluorescence emission spectra of the Eu(III), Tb(III), and Zn(II) complexes were measured on a SPEX F111 Fluorolog spectrofluorometer.

Chemicals and starting materials

2,6-Bis(2-formylphenoxymethyl)pyridine was prepared according to the method reported by Fenton and co-workers (22). *N*,*N*-bis(3-aminopropyl)methylamine and tris(2-aminoethyl)amine, Y(III), Ln(III), Zn(II), and Cd(II) metal nitrates and perchlorates were commercial products from Alfa and Aldrich and were used without further purification. Salicylaldehyde was a commercial product from Carlo Erba. 5-Chloromethyl-4-methylimidazole hydrochloride and 3-chloromethylindole were synthesized according to the literature method (23). Solvents were of reagent grade and were purified by the usual methods. The synthesis of the free imine macrocyclic ligands L^1 and L^4 has been reported in a previous paper (24). Caution: Perchlorate salts are potentially explosive.

Synthesis of the reduced macrocycles L^2 and L^5

The two ligands were prepared by a modification of the method reported in refs. 22 and 25. The corresponding aliphatic polyamine (4.0 mmol) in warm solvent (100 cm^3) was slowly added to a solution of 2,6-bis(2-formylphenoxymethyl)pyridine (4.0 mmol) and $Ba(ClO_4)_2{\cdot}xH_2O$ (4.0 mmol) in warm solvent (300 cm^3). The reaction mixture was refluxed for 6 h, allowed to cool down, and then put in an ice bath. Solid $NaBH_4$ (55.0 mmol) was added carefully in solid incremental amounts, with stirring. After the effervescence stopped, a white precipitate was removed by filtration. The filtrate was reduced to dryness by rotary evaporation, and chloroform (150 cm^3) was added; the resulting solution was then stirred for ca. 72 h. A grey precipitate was removed by filtration; the filtrate was then dried over anhydrous sodium sulphate, and subsequently the sodium sulphate was removed by filtration. The filtrate was concentrated to ca. 10–15 cm^3 and diethyl ether was added, producing the product, which was filtrated (L^2) or decanted (L^5) and dried in vacuo.

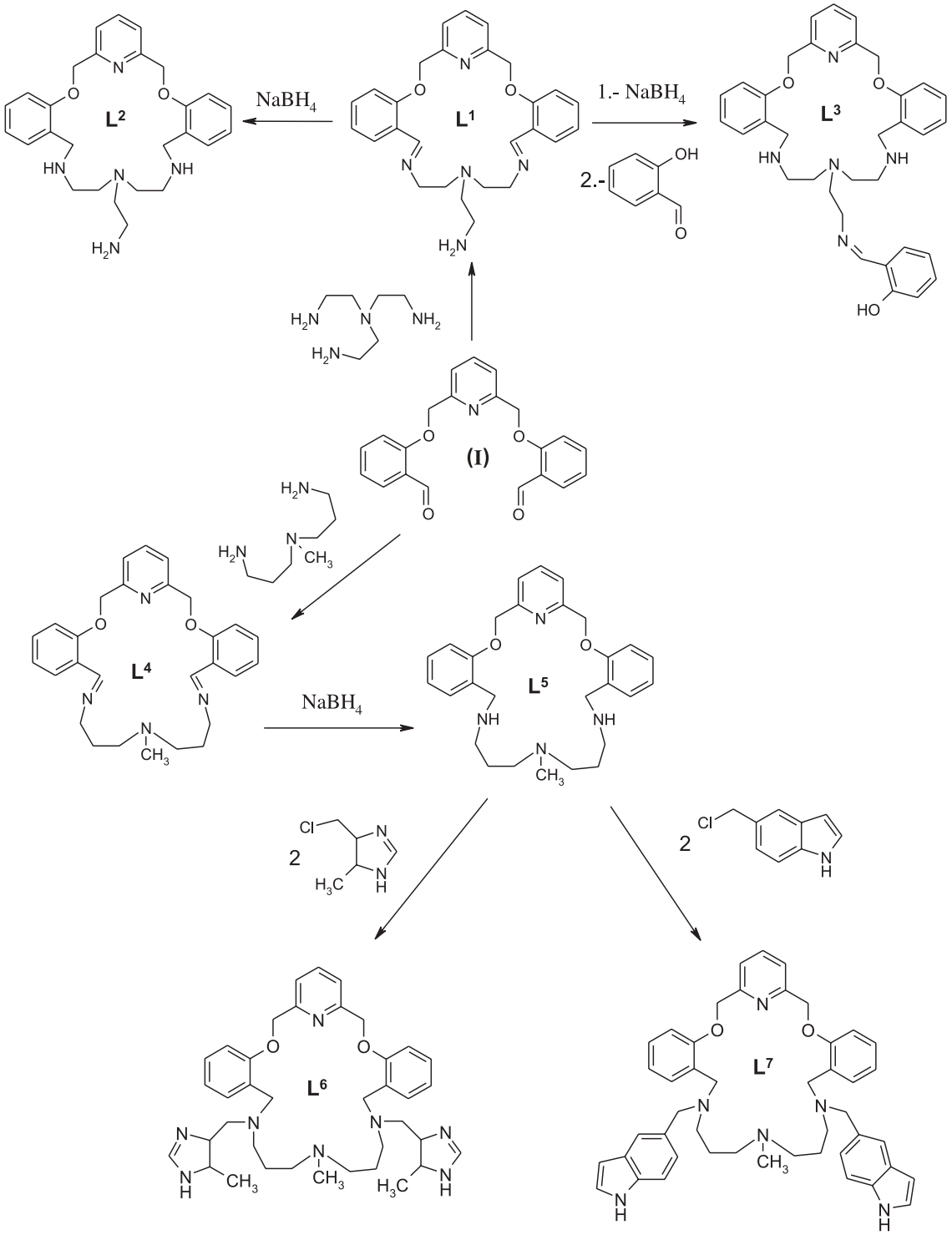
L^2

Yellow solid. Amine: tris(2-aminoethyl)amine. Solvent: methanol. Yield 64%. Melting point: 195–200 °C. IR (KBr disc) ν(NH) (cm^{-1}): 3200; ν(NH_2) (cm^{-1}): 3064, ν(C=C) and ν(C=N) (cm^{-1}): 1597, 1453. UV–vis spectrum (in CH_3CN) (λ(mn), ε((mol L^{-1})$^{-1}$·cm^{-1}): 269, 5344. ^{1}H NMR (CD_3CN) (ppm) δ: 8.6 (t), 1H, (Py); 8.3 (d), 2H, (Py); 7.6 (d) 2H, (C_6H_6); 7.5 (t), 2H, (C_6H_6); 7.3 (d), 2H, (C_6H_6); 7.1(t), 2H, (C_6H_6); 5.6(s), 4H, (Py-CH_2-O); 4.4(s), 4H, (Ph-CH_2-NH); 3.6–3.2(m), 12H, (-CH_2CH_2); 5.00(sw), (-N*H*). ^{13}C NMR (CD_3CN) (ppm) δ: 156.8, 156.0, 155.4, 137.6, 131.2, 130.3. 129.2, 128.7, 128.1, 127.7, 127.1, 126.1, 122.6, 121.9, 120.6, 112.7, 112.1, 97.1, 71.3, 61.7, 54.1, 53.3, 48.3, 47.8, 47.0, 45.6, 44.3. FAB-MS (positive-ion) *m*/*z*: 462 ([L^2 + H]$^+$). Anal. calcd. for $C_{27}H_{35}N_5O_2{\cdot}3.5H_2O$ (%): C 61.85, H 8.05, N 13.30; found: C 61.50, H 7.95, N 12.50.

The ligand is air stable and soluble in acetonitrile, absolute ethanol, chloroform, dimethylformamide, and dimethylsulfoxide; it is moderately soluble in dichloromethane and insoluble in diethyl ether, petroleum ether, and water.

© 2004 NRC Canada

Fig. 1. Schematic diagram showing the synthetic route to obtain the different ligands. **L[1]**: 2-[3.25-dioxa-11.14.17.31-tetrazatetracyclo-[25.3.1.O$^{4.9}$.O$^{19.24}$]hentriaconta-1(31).4(9).5.7.10.17.19(24).20.22.27.29-undecaen-14-yl]-1-ethanamine. **L[2]**: 2-[3.25-dioxa-11.14.17.31-tetrazatetracyclo[25.3.1.O$^{4.9}$.O$^{19.24}$]hentriaconta-1(31).4(9).5.7.10.17.19(24).20.22.27.29-nonaen-14-yl]-1-ethanamine. **L[3]**: 2-[({2-[3.25.dioxa-11.14.17.31-tetraazatetracyclo[25.3.1.O$^{4.9}$.O$^{19.24}$]hentriaconta-1(30).4(9).5.7.19(24).20.22.27(31).28-nonaen-14-yl]ethyl}imino)methyl]phenol. **L[4]**: 15-methyl-3.27-dioxa-11.15.19.33-tetraazatetracyclo[27.3.1.O$^{4.9}$.O$^{21.26}$]tritiaconta-1(32).4(9).5.7.10.19.21(26).22.24.29(33).30-undecane. **L[5]**: 15-methyl-3.27-dioxa-11.15.19.33-tetraazatetracyclo[27.3.1.O$^{4.9}$.O$^{21.26}$]tritiaconta-1(32).4(9).5.7.10.19.21(26).22.24.29(33).30-nonaene. **L[6]**: 15-methyl-11.19-di[(5-methyl-1*H*-4-imidazolyl)methyl]-3.27-dioxa-11.15.19.33-tetraazatetracyclo[27.3.1.O$^{4.9}$.O$^{21.26}$]tritiaconta-1(32).4(9).5.7.21(26).22.24.29(33).30-nonaene. **L[7]**: 11.19-di(1*H*-5-indolylmethyl)-15-methyl-3.27-dioxa-11.15.19.33-tetraazatetracyclo-[27.3.1.O$^{4.9}$.O$^{21.26}$]tritiaconta-1(32).4(9).5.7.21(26).22.24.29(33).30-nonaene.



© 2004 NRC Canada

L[5]

Pale yellow oil. Amine: *N*,*N*-bis(3-aminopropyl)methylamine. Solvent: absolute ethanol. Yield 58%. IR (CsCl windows) ν(NH) (cm^{-1}): 3290, ν(C=C) and ν(C=N) (cm^{-1}): 1595, 1454. UV–vis spectrum (in CH_3CN) (λ(mn), ε((mol $L^{-1})^{-1}\cdot cm^{-1}$)): 266, 3595. ^1H NMR ($CDCl_3$) (ppm) δ: 7.78 (t), 1H, (Py); 7.6 (d), 2H, (Py); 7.4–6.7 (m), 8H, (C_6H_6); 5.0 (s) 4H, (Py-CH_2-O); 3.7 (m) 4H, (Ph-CH_2-NH); 2.5 (t), 4H, (-C$H_2$$CH_2$$CH_2$); 2.3 (t), 4H, (-$CH_2$$CH_2CH_2$); 1.5 (m), 4H, (-$CH_2$$CH_2$$CH_2$); 1.7 (s), 3H, (-$CH_3$). ^{13}C NMR ($CDCl_3$) (ppm) δ: 155.2, 155.1, 154.8, 154.5, 135.9, 129.0, 128.2, 127.3, 127.1, 126.8, 126.4, 119.5, 119.2, 110.3, 109.8, 69.3, 55.0, 54.9, 54.5, 54.3, 54.0, 53.8, 49.2, 46.3, 40.6, 39.6, 38.9, 29.3. FAB-MS (positive-ion) *m*/*z* (%): 461 ([L^5 + H]$^+$, 100), 921 ([2 + 2]$^+$, 10). Anal. calcd. for $C_{28}H_{36}N_4O_2\cdot 3H_2O$ (%): C 65.35, H 9.05, N 10.90; found: C 65.65, H 9.20, N 10.60.

The ligand is air stable and soluble in acetonitrile, absolute ethanol, chloroform, dimethylformamide, and dimethylsulfoxide. It is moderately soluble in dichloromethane and benzene and is insoluble in diethyl ether, petroleum ether, *n*-hexane, and water.

Synthesis of the scorpionand macrocycle L[3]

A fresh solution of L^1 (yellow oil) in absolute ethanol (75 cm^3) was refluxed during 30 min; an ethanolic solution of salicylaldehyde (1.02 mmol) was then added dropwise. The resulting solution, with an intense yellow colour, was refluxed with magnetic stirring for ca. 4 h. After cooling over ice, it was filtered off and reduced to dryness by rotary evaporation. The intense yellow oil obtained was dried under vacuum for 2 h.

L[3]

Yield 80%. Intense yellow oil. IR (CsCl windows) ν(OH) (cm^{-1}): 3412, ν(NH) (cm^{-1}): 3292, $\nu(C{=}N)_{imi}$ (cm^{-1}): 1630, ν(C=C) and ν(C=N) (cm^{-1}): 1597, 1455. UV–vis spectrum (in CH_3CN) (λ(mn), ε((mol $L^{-1})^{-1}\cdot cm^{-1}$)): 257, 12 444, 317, 2121. ^1H NMR (CD_3CN) (ppm) δ: 8.0 (s), 1H, (*H*C=N_{imi}); 7.6–6.6 (m), 15H, (aromatics); 4.9 (s) 4H, (Py-CH_2-O); 4.8 (s), 4H, (Ph-CH_2-NH); 3.5–3.4 (m), 12H, (-CH_2CH_2); 4.5 (sw), (-N*H*). ^{13}C NMR (CD_3CN) (ppm) δ: 166.4, 161.0, 160.9, 156.4, 156.3, 155.3, 138.1, 136.5, 133.3, 132.07, 131.3, 130.8, 129.6, 129.1, 126.6, 123.7, 121.1, 120.9, 120.3, 119.5, 118.1, 117.0, 112.6, 97.6, 69.9, 61.6, 59.0, 56.6, 55.7, 55.5, 48.7, 46.7, 45.7, 17.5. ^{13}C NMR DEPT-135 (CD_3CN) (ppm) (CH, CH_3) δ: 167.2, 138.9, 137.4, 134.0, 132.8, 132.3, 132.1, 130.3, 129.9, 121.8, 121.1, 120.3, 117.96, 117.5, 113.5, 112.8, 97.9, (CH_2) 71.5, 71.0, 62.2, 61.8, 57.4, 56.6, 53.9, 52.9, 51.9, 47.4, 46.0. FAB-MS (positive-ion) *m*/*z* (%): 566 ([L^3 + H]$^+$, 100), 461 ([L^3 – $CH_2N{=}CH(C_6H_4OH)$], 33). Anal. calcd. for $C_{34}H_{39}N_5O_3\cdot 3.5H_2O$ (%): C 65.90, H 7.30, N 11.30; found: C 65.85, H 7.45, N 10.60.

Synthesis of the di-pendant-armed macrocycles L[6] and L[7]

Four millimoles of freshly prepared 5-chloromethyl-4-methylimidazole hydrochloride or 3-chloromethylindole were mixed with triethylamine in 50 cm^3 of dry acetonitrile under a nitrogen atmosphere. The mixture was refluxed during 1 h. After the effervescence disappeared, 2 mmol of L^5 dissolved in 50 cm^3 of dry acetonitrile was slowly added. The reaction was then kept at 50 °C in a silicone bath during 5 days, with vigorous stirring and under the nitrogen atmosphere. After 5 days, the solution was filtered, and the filtrate was reduced to dryness. The crude product was then dissolved in water–chloroform and extracted with 3 × 25 cm^3 of $CHCl_3$. The organic phase was washed twice with 2 × 40 cm^3 of water and dried with anhydrous Na_2SO_4. The solution was then filtered and reduced to give an oil.

L[6]

Orange-yellow oil. Yield 26%. IR (CsCl windows) $\nu(NH)_{imid}$ (cm^{-1}): 3331, ν(C=C) and ν(C=N) (cm^{-1}): 1597, 1456. ^1H NMR ($CDCl_3$) (ppm) δ: 7.70 (t), 1H, (Py); 7.3 (d), 1H, (NHC*H*Nimid); 7.5–6.8 (m), 10H, (*Py*+C_6H_6); 5.1 (d) 4H, (Py-CH_2-O); 3.9 (d) 4H, (Ph-CH_2-N); 3.6 (d), 4H, (CH_2Imi); 2.6 (m), 4H, (-C$H_2$$CH_2$$CH_2$); 2.3 (m), 4H, (-$CH_2$$CH_2CH_2$); 1.8 (m), 4H, (-$CH_2CH_2$$CH_2$); 1.9 (s), 3H, (-C$H_3$); 1.6 (s), 3H, (-C$H_3$), 1.2 (s), 3H, (-C$H_3$). ^{13}C NMR ($CDCl_3$) (ppm) δ: 157.4, 157.1, 156.8, 156.6, 156.0, 155.7, 155.3, 139.0, 132.5, 132.0, 131.8, 130.7, 128.4, 127.2, 126,5, 124.4, 123.8, 123.6, 122,6, 122.4, 121.6, 119.9, 119.8, 113.8, 77.5, 71.6, 55.9, 54.9, 53.9, 47.4, 46.3, 41.5, 40.4, 29.7, 22.9, 22.2, 9.8, 8.9. MS (electrospray) *m*/*z* (%): 650 ([L^6 + H]$^+$, 35), 555 ([L^6 – ($C_5H_6N_2$)]$^+$, 25), 461 ([L^6 – 2($C_5H_6N_2$)]$^+$, 65). Anal. calcd. for $C_{38}H_{48}N_8O_2\cdot 2H_2O$ (%): C 66.65, H 7.65, N 16.35; found: C 66.65, H 7.70, N 16.65.

L[7]

Dark yellow oil. Yield 31%. IR (CsCl windows) $\nu(NH)_{indol}$ (cm^{-1}): 3408; $\delta(NH)_{indol}$ (cm^{-1}): 3266, ν(C=C) and ν(C=N) (cm^{-1}): 1596, 1454. ^1H NMR ($CDCl_3$) (ppm) δ: 7.9–6.8 (t), 21H, (aromatics); 5.3 (d), 4H, (Py-CH_2-O); 4.9 (s) 4H, (Ph-CH_2-N); 3.9 (d) 4H, (CH_2 . -Indol); 2.6–1.6 (m), 15H, (Aliphatics). ^{13}C NMR (CD_3CN) (ppm) δ: 169.2, 168.8, 168.6, 168.2, 149.7, 148.7, 142.7, 140.7, 140.4, 139.9, 139.2, 136.3, 133.5, 133.3, 133.2, 132.9, 132.8, 131.0, 130.8, 128.8, 124.2, 123.8, 123.5, 123.4, 90.3, 90.0, 89.9, 89.8, 89.3, 82.5, 82.2, 76.7, 76.4, 68.9, 68.2, 67.7, 62.2, 59.4, 53.6, 52.8, 38.8, 38.3, 33.9, 30.0, 27.1, 12.0. MS (electrospray) *m*/*z* (%): 720 ([L^7 + H]$^+$, 25), 590 ([L^7 – (C_9H_8N)]$^+$, 10), 461 ([L^7 – 2(C_9H_8N)]$^+$, 65). Anal. calcd. for $C_{46}H_{50}N_6O_2\cdot 3H_2O$ (%): C 71.50, H 7.30, N 10.85; found: C 71.65, H 7.75, N 10.90.

The ligands are air stable and soluble in acetonitrile, absolute ethanol, chloroform, dimethylformamide, and dimethylsulfoxide. They are moderately soluble in dichloromethane and insoluble in diethyl ether, petroleum ether, *n*-hexane, and water.

Synthesis of the metal complexes

Template reaction of Schiff-base macrocycles L[1] and L[4] in the presence of metal ions: General procedure for [ML][X]$_n$ (X = ClO_4^- or NO_3^-)

2,6-Bis(2-formylphenoxymethyl)pyridine (1 mmol) and $MX_n\cdot xH_2O$ (1 mmol) (M = Y(III), Ln(III), Zn(II), or Cd(II)) were dissolved in hot methanol or absolute ethanol (30 cm^3). A solution of *N*,*N*-bis(3-aminopropyl)methylamine or tris(2-aminoethyl)amine (1 mmol) in methanol or absolute ethanol

© 2004 NRC Canada

Table 1. Analysis, yield, and molar conductance (in CH_3CN) data for the complexes $[M_mL^{1-2-3}][X]_n \cdot xH_2O$.

						Elemental analysis (%)[a]					
M	L	*m*	*n*	*x*	X	C	N	H	Yield (%)	Λ_M/Ω^{-1} ($cm^2 \cdot mol^{-1}$)	Colour
(L^1 = $C_{27}H_{31}N_5O_2$)											
La	L^1	1	3	10	ClO_4^-	30.70 (30.20)	6.95 (6.50)	5.25 (4.80)	34	295	Yellow
Zn	L^1	1	2	4	ClO_4^-	41.05 (40.85)	9.10 (8.80)	5.20 (4.95)	35	125	Orange-yellow
Cd	L1	2	4	5	ClO_4^-	27.40 (27.70)	5.50 (5.95)	3.75 (3.50)	18	238	Yellow
(L^2 = $C_{27}H_{35}N_5O_2$)											
Y	L^2	1	3	2	NO_3^-	42.35 (42.00)	14.75 (14.50)	5.25 (5.10)	43	119	Pale yellow
La	L^2	1	3	5	NO_3^-	37.45 (37.00)	12.95 (12.80)	4.50 (5.15)	18	123	Pale yellow
Sm	L^2	1	3	6	NO_3^-	35.55 (35.80)	12.30 (12.35)	4.95 (5.20)	59	121	Pale yellow
La	L^2	1	3	9	ClO_4^-	30.00 (30.55)	6.60 (6.60)	4.80 (5.05)	25	222	Yellow
Ce	L^2	1	3	2	ClO_4^-	35.00 (34.65)	7.00 (7.50)	4.35 (4.20)	63	236	Yellow-gold
Gd	L^2	1	3	8	ClO_4^-	30.45 (30.55)	6.75 (6.60)	4.60 (4.85)	42	247	Pale yellow
Er	L^2	1	3	5	ClO_4^-	32.30 (31.90)	6.25 (6.85)	4.20 (4.45)	44	285	Yellow-orange
(L^3 = $C_{34}H_{39}N_5O_3$)											
Eu	L^3	1	3	7	NO_3^-	39.50 (39.65)	10.70 (10.90)	5.35 (5.20)	52	137	Yellow
Tb	L^3	1	3	6	NO_3^-	39.80 (40.10)	10.25 (10.95)	4.85 (5.05)	46	127	Dark yellow
La	L^3	1	3	5	ClO_4^-	37.90 (37.35)	6.40 (6.40)	5.00 (4.55)	47	277	Yellow
Pr	L^3	2	6	5	ClO_4^-	27.00 (26.60)	5.15 (4.55)	3.20 (3.20)	46	369	Yellow
Sm	L^3	1	3	7	ClO_4^-	35.80 (35.80)	6.20 (6.15)	5.15 (4.70)	56	284	Yellow
Zn	L^3	2	4	4	ClO_4^-	35.45 (35.00)	6.45 (6.00)	4.15 (4.05)	30	265	Yellow

[a]Required values are given in parentheses.

(25 cm^3) was added dropwise; magnetic stirring and heating was maintained during the addition. The solution was refluxed for 3 to 4 h, allowed to cool to room temperature, and then concentrated to ca. 15 cm^3. The complexes precipitated directly or after addition of diethyl ether (15 cm^3); they were filtered off and dried in vacuo. Microanalytical data are given in Tables 1 and 2. The complexes are air stable and soluble in acetone, dimethylformamide, methanol, acetonitrile, and dichloromethane. They are moderately soluble in chloroform and insoluble in water and absolute ethanol.

Direct synthesis between L^2, L^3, L^5, L^6, and L^7 and divalent and trivalent metal ions: General procedure for $[ML][X]_n$ (X = ClO_4^- or NO_3^-)

The appropriate metal salt $MX_n \cdot xH_2O$ (Y(III), Ln(III), Zn(II), or Cd(II) and X = NO_3^- or ClO_4^-) (0.50 mmol) was dissolved in methanol (for L^2, L^3, L^5, and L^7) or absolute ethanol (for L^6) (20 cm^3) and added to a solution of the ligand (0.50 mmol) in methanol (L^2, L^3, and L^5) or chloroform (L^6 and L^7) (50 cm^3). The mixture was stirred during 24–72 h at room temperature and cooled. When a precipitate did not developed immediately, the solution was partially concentrated under vacuum to give a solid, although in some cases the precipitation was aided by addition of some diethyl ether (ca. 5–10 cm^3). The products were filtered off, washed with cold absolute ethanol or methanol, and dried in vacuo.

Microanalytical data are given in Tables 1, 2, and 3. The complexes are air stable and are soluble in acetone, methanol, acetonitrile, and dichloromethane. They are moderately soluble in dimethylformamide and insoluble in chloroform, water, and absolute ethanol.

Results and discussion

Synthesis of the free ligands

We have previously reported that direct reaction between (**I**) with aliphatic or aromatic amines in the absence of template agents is a valid method to obtain Schiff-base and oxa-aza macrocyclic ligands (2, 19, 24). We now present seven macrocyclic ligands derived from this dicarbonyl precursor and two aliphatic diamines (mentioned in the starting material section) and the study of the complexation capacity of these ligands with a range of trivalent and divalent metal ions. Ligands L^1 and L^4 were obtained by reaction of (**I**) with both aliphatic diamines. These two macrocycles have already been reported in a previous paper (24).

Using L^1 and L^4 as the starting point, we have prepared five new macrocyclic ligands with different donor atom arrays (see Fig. 1). L^2 was synthesized by reduction of L^1, formed in situ using barium perchlorate, with sodium borohydride. In a similar way, L^5 was obtained from L^4. The pendant-armed macrocycle L^3 was obtained by a Schiff-base reaction between L^2 and salicylaldehyde, with formation of an iminic bond in the pendant arm. The ligands L^6 and L^7 were obtained by reaction of L^5 with 5-chloromethyl-4-methylimidazole hydrochloride and 3-chloromethylindole, respectively, following the method described in the experimental section.

We have found that the template approach is more effective for the preparation of L^2 and L^5, with yields of 64% and 58%, respectively. In previous papers, we have reported the effectiveness of a direct approach in the synthesis of large macrocycles, in which the presence of aromatic groups in

© 2004 NRC Canada

Table 2. Analysis, yield, and molar conductance (in CH_3CN for L^4 or in DMF for L^5) data for the complexes $[M_mL^{4-5}][X]_n{\cdot}xH_2O$.

						Elemental analysis (%)[a]					
M	L	*m*	*n*	*x*	X	C	N	H	Yield (%)	Λ_M/Ω^{-1} ($cm^2{\cdot}mol^{-1}$)	Colour
(L^4 = $C_{28}H_{32}N_4O_2$)											
Y	L^4	1	3	5	NO_3^-	40.45 (40.95)	12.20 (11.95)	5.05 (5.15)	53	158	Orange
La	L^4	2	6	—	NO_3^-	30.05 (30.40)	12.30 (12.65)	2.90 (2.90)	58	264	Orange
Nd	L^4	1	3	0.5	NO_3^-	42.25 (42.25)	11.50 (12.30)	4.50 (4.20)	87	144	Orange
Eu	L^4	1	3	—	NO_3^-	42.75 (42.35)	11.90 (12.35)	3.90 (4.05)	57	124	Orange
Ho	L^4	1	3	4	NO_3^-	38.80 (38.25)	11.05 (11.15)	5.00 (4.60)	91	137	Orange
Lu	L^4	1	3	2	NO_3^-	40.06 (39.40)	11.05 (11.50)	4.05 (4.25)	51	147	Orange
La	L^4	1	3	4	ClO_4^-	34.90 (34.80)	6.25 (5.80)	4.55 (4.15)	77	247	Yellow
Ce	L^4	1	3	4	ClO_4^-	34.85 (34.80)	6.33 (5.80)	4.10 (4.20)	35	232	Yellow
Er	L^4	1	3	1	ClO_4^-	36.30 (35.75)	6.50 (5.95)	4.00 (3.65)	49	224	Yellow
Zn	L^4	2	4	2	ClO_4^-	32.20 (32.90)	5.20 (5.50)	3.00 (3.55)	46	220	Yellow
Cd	L^4	1	2	4	ClO_4^-	40.20 (40.05)	7.05 (6.70)	4.70 (4.80)	51	158	Yellow
(L^5 = $C_{28}H_{36}N_4O_2$)											
Y	L^5	2	6	3	NO_3^-	31.55 (31.60)	12.85 (13.15)	4.10 (4.00)	22	143	Pale yellow
Eu	L^5	1	3	5	NO_3^-	37.95 (37.85)	10.60 (11.00)	4.75 (5.20)	62	72	Yellow
Tb	L^5	1	3	6	NO_3^-	37.20 (36.80)	11.15 (10.70)	4.90 (5.30)	36	67	Pale yellow
La	L^5	1	3	6	ClO_4^-	33.15 (33.40)	5.90 (5.60)	4.60 (4.80)	68	172	Yellow
Gd	L^5	1	3	3	ClO_4^-	34.90 (34.65)	5.85 (5.80)	4.20 (4.35)	39	179	Pale yellow
Zn	L^5	1	2	0.5	ClO_4^-	46.00 (45.80)	7.65 (7.65)	4.80 (5.10)	68	79	Yellow
Cd	L^5	2	4	—	ClO_4^-	31.40 (31.05)	5.70 (5.20)	3.25 (3.35)	43	67	Yellow

[a]Required values are given in parentheses.

Table 3. Analysis, yield, and molar conductance (in DMF for L^6 or in CH_3CN for L^7) data for the complexes $[M_mL^{6-7}][X]_n{\cdot}xH_2O$.

						Elemental analysis (%)[a]					
M	L	*m*	*n*	*x*	X	C	N	H	Yield (%)	Λ_M/Ω^{-1} ($cm^2{\cdot}mol^{-1}$)	Colour
(L^6 = $C_{38}H_{48}N_8O_2$)											
Y	L^6	2	6	5	NO_3^-	35.35 (35.40)	15.30 (15.20)	4.55 (4.55)	22	236	Yellow
Gd	L^6	2	6	4	NO_3^-	32.40 (32.45)	13.90 (13.95)	4.50 (4.00)	26	274	Yellow
La	L^6	1	3	7	ClO_4^-	37.70 (37.65)	9.35 (9.25)	5.30 (5.15)	31	240	Yellow
(L^7 = $C_{46}H_{50}N_6O_2$)											
La	L^7	2	6	7	ClO_4^-	32.00 (32.15)	5.25 (4.90)	4.10 (3.75)	63	365	Yellow
Zn	L^7	2	4	—	ClO_4^-	44.75 (44.30)	7.15 (6.75)	3.60 (4.05)	32	273	Yellow

[a]Required values are given in parentheses.

both organic precursors helps to minimize the formation of acyclic structures (19, 20). However, when the direct route was used to prepare L^2 and L^5, the aliphatic nature of the amine precursors seemed to increase the formation of undesired acyclic compounds, and low yields were obtained for both macrocycles. A template approach was thus chosen, and we have found that the use of barium(II) as the template agent increased the yields of the two macrocycles.

The FAB mass spectra for L^2, L^3, and L^5, as well as the electrospray mass spectra for L^6 and L^7, show the highest molecular weight peaks at *m*/*z* 462 (L^2), 566 (L^3), 461 (L^5), 650 (L^6), and 720 (L^7), corresponding to ($[L + H]^+$). The IR spectra feature the secondary amine N–H stretching band at ca. 3200–3292 cm^{-1} (in L^2, L^3, and L^5) or $\delta(NH)_{pyrrolic}$ at ca. 3330–3400 cm^{-1} (in L^6 and L^7). The spectra for L^2 and L^5 do not show bands in the 1620–1640 cm^{-1} region, where imine stretches are expected. The spectrum for L^3 features a band at ca. 1630 cm^{-1}, owing to the imine group present in the pendant arm. For L^7 it is possible to observe a band at ca. 3266 cm^{-1}, attributable to δ(NH) of the indole group.

The ^1H NMR spectra in CD_3CN (for L^2 and L^3) and in $CDCl_3$ (for L^5, L^6, and L^7) confirm the integrity of the ligands in solution. The ^{13}C NMR spectra for L^2, L^5, L^6, and L^7 feature 27, 28, 38, and 46 signals, respectively, one for each C in the macrocyclic skeleton. This suggests that both the reduction of the imine bonds and the presence of the pendant arms lead to an increase in the ligand flexibility and unsymmetrical behaviour of the ligands. UV–vis spectra in acetonitrile were recorded for L^2, L^3, and L^5. The broad absorption bands observed at 269 nm for L^2, at 257 and 317 nm for L^3, and at 266 nm for L^5 can be attributed to the π–π* transitions of the pyridine and phenyl groups.

© 2004 NRC Canada

Metal complexes: Microanalytical and molar conductivity data

Yttrium and lanthanide trivalent metal ions and divalent zinc and cadmium have been used to explore the coordination behaviour of this new family of oxa-aza macrocycles. Condensation between 2,6-bis(2-formylphenoxymethyl)pyridine and tris(2-aminoethyl)amine (L^1) or *N*,*N*-bis(3-aminopropyl)methylamine (L^4) in the presence of the corresponding hydrated metal salt, in a 1:1:1 molar ratio, leads to the formation of mononuclear complexes formulated as $[LaL^1](ClO_4)_3 \cdot 10H_2O$, $[ZnL^1](ClO_4)_2 \cdot 4H_2O$, and $[ML^4](X)_n \cdot xH_2O$ (M = Y(III), Ce(III), Nd(III), Eu(III), Ho(III), Er(III), Lu(III), and Cd(II); X = NO_3^- or ClO_4^-) and dinuclear complexes formulated as $[Cd_2L^1](ClO_4)_4 \cdot 5H_2O$ and $[M_2L^4](X)_n \cdot xH_2O$ (M = La(III); X = NO_3^- and M = Zn(II); X = ClO_4^-). Microanalytical data for these complexes are shown in Table 1 (L^1) and Table 2 (L^4).

Only complexes with trivalent metal ions have been obtained with L^2, with the formula $[ML^2](X)_3 \cdot xH_2O$ (M = Y(III), La(III), Ce(III), Sm(III), Gd(III), and Er(III); X = ClO_4^- or NO_3^-). Reaction between L^5 and Y(III), La(III), Gd(III), Eu(III), Tb(III), Zn(II), and Cd(II) leads to the formation of mononuclear complexes, formulated as $[ML^5](X)_n \cdot xH_2O$ (M = La(III), Eu(III), Gd(III), Tb(III), and Zn(II); X = ClO_4^- or NO_3^-), as well as the dinuclear complexes $[M_2L^5](X)_n \cdot xH_2O$ (M = Y(III); X = NO_3^- and M = Cd(II); X = ClO_4^-). Microanalytical data for these complexes are shown in Table 1 (L^2) and Table 2 (L^5). The syntheses were also attempted with the perchlorates of Zn(II) and Cd(II) for L^2, as well as the nitrates of La(III) and the perchlorates of Ce(III) and Eu(III) for L^5; however, with these metals only species with unsatisfactory analytical data were obtained.

A direct method has been successfully used to synthesize complexes with L^3. Reaction of freshly prepared L^3 in the presence of the corresponding metal salt yielded mononuclear complexes of formula $[ML^3](X)_3 \cdot xH_2O$ (M = La(III) and Sm(III); X = ClO_4^-; M = Eu(III) and Tb(III); X = NO_3^-) (see Table 1) and the dinuclear complexes $[Pr_2L^3](ClO_4)_6 \cdot 5H_2O$ and $[Zn_2L^3](ClO_4)_4 \cdot 4H_2O$. Under the experimental conditions employed, it has been impossible to isolate the expected metal complexes with the nitrates of Y(III) and La(III) and with the perchlorate of Cd(II).

The reaction between equimolar amounts of freshly prepared L^6 and L^7 and the perchlorates of La(III) and Zn(II), as well as the nitrates of Y(III) and Gd(III), gave analytically pure products of formula $[LaL^6](ClO_4)_3 \cdot 7H_2O$, $[M_2L^6](NO_3)_6 \cdot xH_2O$ (M = Y(III) and Gd(III)), and $[M_2L^7](ClO_4)_n \cdot H_2O$ (M = La(III) and Zn(II)). The presence of extra donor atoms in the pendant arms leads to the formation of binuclear species with the majority of the metal ions employed. The syntheses were also attempted using the perchlorate of Cd(II) and the nitrates of Eu(III) and Tb(III), but only a mixture of unreacted metal salt and free ligand were recovered.

In the absence of crystal structures, which are decisive in the elucidation of the coordinative environment of the metal ions in these molecules, it is difficult to give an appropriate explanation for the formation, depending on the ligand and the metal ion, of di- or mononuclear complexes. Reaction with Cd(II) and Zn(II) yields dinuclear complexes in most cases, probably because of the small size of both ions when compared with the lanthanide(III) cations. It is also noteworthy that the increase in the flexibility and complexity of the ligands, from L^1 to L^3 and from L^4 to L^6 or L^7, does not appear to affect especially the formation of the corresponding complexes.

Molar conductivity data, measured at room temperature using DMF or acetonitrile solutions, show the ionic nature of all complexes in these solvents. The values are in accordance with those expected for 1:1 or 1:2 electrolytes (for complexes with L^1, L^2, L^3, L^4, and L^5) or for 1:2 or 1:3 electrolytes (L^6 and L^7 complexes) (26). The value for the complex $[Pr_2L^3](ClO_4)_6 \cdot 5H_2O$, measured in acetonitrile, falls between the ranges reported for 1:2 and 1:3 electrolytes. Data for the different complexes are given in Tables 1, 2, and 3. Molar conductivities were measured again 1 week after sample preparation for the complexes containing L^2, L^5, and L^6; a significant increase in the values was observed in some complexes, suggesting the displacement of counter ions from the coordination sphere by solvent molecules (26).

Metal complexes: FAB and electrospray mass spectra

All mass spectra feature peaks attributable to the corresponding macrocyclic ligand, confirming the stability of the seven macrocycles in their metal complexes. Moreover, the spectra show peaks at higher molecular weights, which in some cases have also been assigned. The spectra for the complexes with L^1 contain peaks attributable to $[ML^1]^+$ (M = La(III) and Cd(II)) and $[ZnL^1(ClO_4)]^+$. For the complexes with L^2, the spectra show peaks assignable to the fragments $[ML^2(ClO_4)]^+$ (M = La(III) and Ce(III)), and $[L^2(ClO_4)]^+$ and $[LaL^2(NO_3)]^+$ are present. In the case of the L^3 complexes, peaks assignable to the fragments $[ML^3(ClO_4)]^+$ (M = La(III), Pr(III), Sm(III) and Zn(II)), $[ML^3(NO_3)]^+$ (M = Eu(III)), and $[ML^3]^+$ (M = Eu(III) and Sm(III)) can be observed.

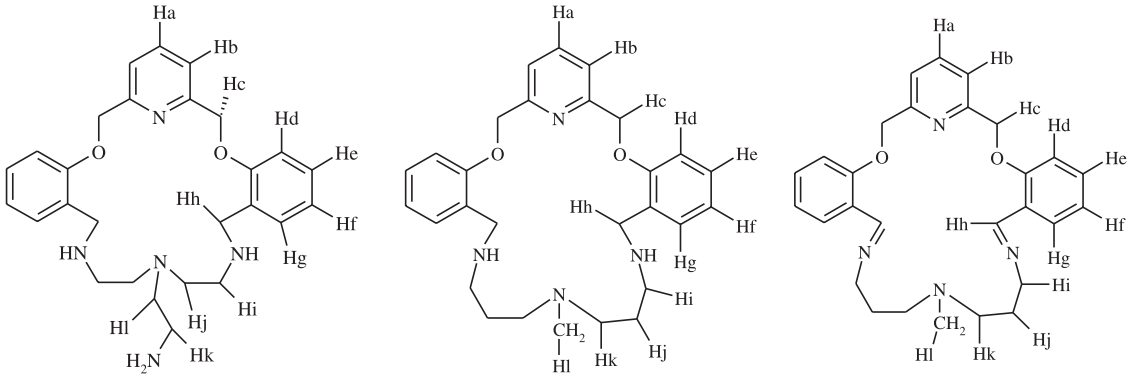
The spectrum of the dinuclear nitrate La(III) complex with L^4 contains peaks corresponding to the fragments $[La_2L^4(NO_3)_3]^+$ and $[LaL^4(H_2O)]^+$. The mononuclear Ce(III), La(III), and Nd(III) complexes exhibit peaks due to the species $[ML^4(ClO_4)_2]^+$ (M = La(III) and Ce(III)) and $[NdL^4(NO_3)]^+$, confirming the presence of the metal ions in the complexes. Peaks attributable to the fragment $[L^4(ClO_4)]^+$ are also present in the spectra of the complexes with Ce(III) and Cd(II). For the complexes with L^5, the mass spectra feature peaks assignable to the fragments $[ML^5(NO_3)_2]^+$ (M = Y(III), Eu(III), and Tb(III)), $[ML^5(ClO_4)]^+$ (M = La(III), Gd(III), Zn(II), and Cd(II)), and $[ML^5]^+$ (M = Y(III) and Zn(II)). The FAB mass spectra for the L^6 complexes show peaks assignable to the fragments $[ML^6]^+$ and $[L^6(NO_3)_2]^+$, while for the L^7 complexes, peaks corresponding to the fragments $[LaL^7]^+$ and $[ZnL^7(H_2O)]^+$ can be observed.

Infrared spectra

The IR spectra for the complexes with L^1, L^2, L^4, and L^5 confirm the cyclic nature of the ligands in their metal complexes. The spectra for the complexes with L^1 and L^4 show a band at ca. 1639–1660 cm^{-1}, attributable to the imine groups, and no bands due to ν(C=O) vibrations. In the Cd(II) complex with L^1, a band at ca. 3227 cm^{-1}, attributable to

© 2004 NRC Canada

Fig. 2. ^{1}H NMR data (300 MHz) for $[LaL^2](ClO_4)_3\cdot 9H_2O$ (in CD_3CN), $[LaL^5](ClO_4)_3\cdot 6H_2O$ (in $CDCl_3$), and $[La_2L^4](NO_3)_6$ (in DMSO-d_6).



L^2 **L^5** **L^4**

$\nu(NH_2)$, is also observed (27). The spectra exhibit medium to strong bands at ca. 1603–1597 and 1458 cm^{-1}, as expected for the $\nu(C{=}C)_{ar}$ and $\nu(C{=}N)_{py}$ ring vibrations (28). The $\nu(C{=}N)_{py}$ band, as well as those corresponding to the imine groups, are generally shifted to higher wave numbers when compared with those of the free ligands, suggesting coordination via nitrogen atoms (29, 30). The IR spectral results for the complexes with L^3 confirm that the imine group is present in the pendant arm of the ligand, showing an intense band at ca. 1630–1650 cm^{-1} that is attributable to $\nu(C{=}N)$ and no bands due to $\nu(C{=}O)$ and $\nu(NH_2)$ groups (27). The bands attributable to $\nu(NH)$ in the complexes of L^2, L^3, and L^5 cannot be observed because of the existence of a broad band at ca. 3380–3520 cm^{-1}, assignable to the stretching and bending modes of water (31). For the complexes with L^2 and L^5, the absence of bands at ca. 1620–1660 cm^{-1} in the spectra confirms the reduction of the iminic groups.

The IR spectra of the complexes with L^6 and L^7 also contain absorption bands characteristic of the ligand frameworks. The sharp absorption band occurring in the region 3340–3060 cm^{-1} is attributable to $\nu(NH)$ of the indole or imidazole groups. For the complexes of L^6, the band at ca. 1648 cm^{-1} can be assigned to the $\delta(NH)$ of the imidazole groups. Bands at ca. 1602 and 1458 cm^{-1}, corresponding to the aromatic ring vibrations, are also present. These bands are shifted to lower energy when compared with their position in the spectra of the free ligands, probably because of coordination to the metal ion.

The absorptions of the counter-ions provide some useful structural information. The IR spectra for all nitrate complexes show bands at ca. 1448–1460 (ν_5), 1300 (ν_1), and 1030 (ν_2) cm^{-1}, suggesting the existence of coordinated nitrate groups, as well as a band at ca. 1384 cm^{-1}, attributable to the presence of ionic NO_3^- (32, 33). Although the spectra do not allow a clear-cut difference between mono- and bidentate chelating nitrates, the separation between ν_5 and ν_1 (ca. 160 cm^{-1}) suggests the presence of nitrate groups acting as bidentate (34, 35). Regarding the perchlorate complexes, bands attributable to the asymmetric Cl–O stretching mode at ca. 1088 cm^{-1} (ν_3) and the asymmetric Cl–O bending mode (ν_4) at ca. 625 cm^{-1} can be observed. The highest energy band consists in three well-resolved maxima at ca. 1121, 1115, and 1088 cm^{-1}; the ν_4 band also shows splitting with maxima at ca. 636 and 626 cm^{-1} (36). The splitting of these bands is indicative of coordination of at least one perchlorate anion to the metal.

NMR spectra

The ^{1}H NMR spectra of some diamagnetic complexes with Y(III), La(III), and Zn(II) were recorded immediately after dissolution in CD_3CN, DMSO-d_6, or CD_3OD at room temperature. The spectra of the complexes $[LaL^1](ClO_4)_3\cdot 10H_2O$ and $[ZnL^1](ClO_4)_2\cdot 4H_2O$ (in CD_3CN) are complicated, showing more signals than expected. This may be indicative of the following: (*i*) the co-existence of additional processes in solution such as dimerization; (*ii*) the existence of demetallation processes in solution or geometric changes; and (or) (*iii*) the hydrolysis of the iminic groups. We ran the spectra at the following different temperatures: 298.15, 313.15, and 323.15 K. In all cases the number of signals never decreased notably, suggesting slow intersystem changes. The complexes $[LaL^2](ClO_4)_3\cdot 9H_2O$ and $[La_2L^4](NO_3)_6$ (in DMSO-d_6) and $[LaL^5](ClO_4)_3\cdot 6H_2O$ (in CD_3CN) gave the expected simple spectra, indicating the integrity of the complexes in those solvents (see Fig. 2, Table 4).

The spectra of the complexes $[LaL^3](ClO_4)_3\cdot 5H_2O$, $[YL^4](NO_3)_3\cdot 5H_2O$, $[Zn_2L^4](ClO_4)_4\cdot 2H_2O$, and $[LaL^4](ClO_4)_3\cdot 4H_2O$ (in CD_3CN) are complicated and show more signals than expected (complex and free ligand signals), which may be indicative of the existence of demetallation processes in solution or dimerization reactions in the dinuclear complexes. Nevertheless, clear peaks at δ 9.20, 8.60, 9.00, and 9.20 ppm, corresponding to the imine protons in the ligands, are present. The ^{1}H NMR spectra of $[Y_2L^6](NO_3)_6\cdot 5H_2O$ and $[LaL^6](ClO_4)_3\cdot 7H_2O$ (in DMSO-d_6) are also complicated, maybe because of the nonsymmetric topology of the ligand. Nevertheless, clear peaks at δ 7.8 and 8.8 ppm, corresponding to the aromatic imidazol protons of the pendant arms, as well as the signals attributable to aromatic rings of the macrocycle (37), confirm the integrity of the ligand L^6 in both metal complexes.

Electronic absorption spectra

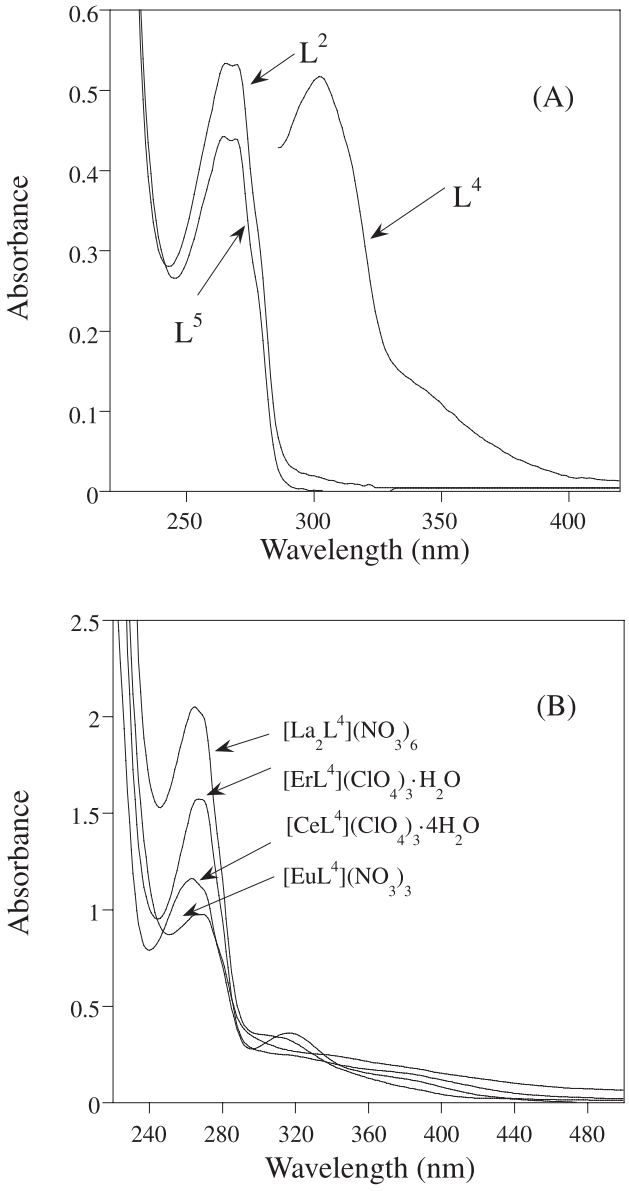
The electronic spectra for L^2, L^3, L^4, and L^5, as well as some of their corresponding metal complexes, were recorded at room

© 2004 NRC Canada

Table 4. ^{1}H NMR data for the complexes $[LaL^2](ClO_4)_3\cdot 9H_2O$ and $[La_2L^4](NO_3)_6$ (in DMSO-d_6) and $[LaL^5](ClO_4)_3\cdot 6H_2O$ (in CD_3CN).

	δ integration (ppm)		
Assignment	$[LaL^2](ClO_4)_3\cdot 9H_2O$	$[LaL^5](ClO_4)_3\cdot 6H_2O$	$[La_2L^4](NO_3)_6$
Ha	7.9 (t) — 1H	7.8 (t) — 1H	7.9 (t) — 1H
Hb, Hd–Hg	7.7–6.8 (m) — 10H	8.5–6.8 (m) — 10H	7.7–6.9 (m) — 10H
Hc	5.2 (s) — 4H	5.4 (s) — 4H	5.5 (s) — 4H
Hh	4.2 (s) — 4H	4.2 (s) — 4H	8.3 (s) — 2H
Hi, Hj, Hk, Hl	3.0–2.6 (m) — 12H	3.1–1.0 (m) — 15H	2.5–1.5 (m) — 15H

Fig. 3. Electronic spectra for L^2, L^4, and L^5 (A) and some ML^4 complexes (B) in acetonitrile solution. [L] = [ML] = 9.0 E^{-5} mol L^{-1}.



temperature in acetonitrile solutions. The spectra for the reduced ligands L^2 and L^5 present one band at ca. 269–266 nm (ε ≈ 5344 and 3595 $mol^{-1}\cdot L\cdot cm^{-1}$, respectively). The Schiff base ligands L^3 and L^4 exhibits two bands, at ca. 257 nm (ε ≈ 12 444 $mol^{-1}\cdot L\cdot cm^{-1}$) and ca. 317 nm (ε ≈ 2921 $mol^{-1}\cdot L\cdot cm^{-1}$) for L^3 and at ca. 303 nm (ε ≈ 16 066 $mol^{-1}\cdot L\cdot cm^{-1}$) and ca. 351 nm (ε ≈ 5930 $mol^{-1}\cdot L\cdot cm^{-1}$) for L^4. In all cases, these bands are associated with the π–π* and *n*–π* electronic transitions in the chromophores — pyridine and phenyl rings — that are present in the macrocyclic skeletons (38).

The UV–vis spectra for some Y(III), Ln(III), and Zn(II) nitrate and perchlorate complexes of L^2 and L^4 exhibit two or three absorption bands in the regions 262–270, 315–325, and 370–385 nm. The shift in the absorption maxima that is observed when it is compared with those of the free macrocycles may be due to the presence of the metal in the species and could be attributable to the π–π* and *n*–π* transitions of the coordinated macrocycles. In some cases, the intensity of the absorption bands changed slightly when the spectra were recorded after 1 and 2 weeks, suggesting the displacement of some coordinated anions or water molecules by acetonitrile molecules. The spectral data for the complexes are given in Table 5, and the electronic spectra for the free ligands L^2, L^4, and L^5 and some ML^4 metal complexes are shown in Fig. 3.

Fluorescence emission spectra

Room-temperature emission spectra were registered using 10^{-5}–10^{-6} mol L^{-1} acetonitrile solutions for the Eu(III), Tb(III), and Zn(II) complexes with L^3, L^4, and L^5. Unfortunately, no emission could be detected in these complexes, probably because of (*i*) the presence of water molecules in the complexes; (*ii*) the presence of free uncoordinated amines with the lone-pair unoccupied; and (*iii*) the coexistence of nonradiative mechanisms that quenched the emission, in a similar way to those reported for other macrocycle ligands derived from similar aliphatic or aromatic precursor (2, 19, 24, 39).

Conclusions

Seven [1+1] oxa-aza macrocyclic ligands, five of them new, have been prepared using 2,6-bis(2-formylphenoxymethyl)pyridine as the precursor. Treatment of the previously reported Schiff-base macrocycles L^1 and L^4 with $NaBH_4$, in the presence of Ba(II) as a template agent, gave the corresponding reduced macrocycles L^2 and L^5. The more sophisticated ligands L^3, L^6, and L^7, provided with pendant arms, have been synthesized by condensation or alkylation reactions with the amine groups present in L^2 and L^5. Complexes with these seven ligands have been prepared by template reaction or direct methods, using the nitrates and (or) perchlorates of Y(III), Ln(III), Cd(II), or Zn(II) ions.

The complexes are mono- or dinuclear, depending on the macrocyclic ligand and (or) metal salt employed. Although

© 2004 NRC Canada

Table 5. UV–vis spectral data for the complexes with L^2 and L^4 in acetonitrile solution at room temperature.

Complexes	λ (nm); ε ((mol L^{-1})$^{-1}$·cm^{-1})
$[YL^2](NO_3)_3·2H_2O$	264 (9071); 312(*sh*) (3065)
$[LaL^2](NO_3)_3·5H_2O$	266 (8528); 316(*sh*) (3113)
$[SmL^2](NO_3)_3·6H_2O$	266 (6778)
$[LaL^2](ClO_4)_3·9H_2O$	267 (6796)
$[CeL^2](ClO_4)_3·2H_2O$	268(11249); 322(*sh*) (2559)
$[GdL^2](ClO_4)_3·8H_2O$	268 (7770)
$[ErL^2](ClO_4)_3·5H_2O$	267 (7298)
$[YL^4](NO_3)_3·5H_2O$	266 (8468); 319(*sh*) (3257)
$[La_2L^4](NO_3)_6$	266 (5313); 313(*sh*) (1744)
$[EuL^4](NO_3)_3$	268 (4602); 339(*sh*) (999); 385(*sh*) (704)
$[LuL^4](NO_3)_3·2H_2O$	267 (9871); 323(*sh*) (2355)
$[LaL^4](ClO_4)_3·4H_2O$	256 (10940); 316 (4426); 384(*sh*) (1102)
$[CeL^4](ClO_4)_3·4H_2O$	268 (10202); 320(4862); 379(*sh*) (401)
$[ErL^4](ClO_4)_3·H_2O$	267 (5902); 324(4842); 379(*sh*) (527)
$[Zn_2L^4](ClO_4)_4·2H_2O$	269 (7282); 335(*sh*) (4347)

Note: [Complex] = 10^{-4}–10^{-6} mol L^{-1}; *sh* = shoulder.

it is not possible to establish any clear link between the formation of mono- or dinuclear species and the size of the cation employed, it is worth mentioning that reaction with Cd(II) and Zn(II) generally generates the dinuclear complex, suggesting that the macrocyclic cavity in L^1, L^3, L^4, and L^5 is large enough to accommodate two of these metal cations. The complexes obtained with L^6 and L^7, provided with two lateral pendant arms, are always dinuclear except in one case, suggesting that the increase in the number of donor atoms present in the macrocyclic skeleton facilitates the formation of dinuclear compounds and showing the ability of these two macrocycles to host two metal ions.

Acknowledgements

Work supported in part by Xunta de Galicia (PGIDT01PXI20901PR) (Spain) and the European Community's Human Potential Programme under contract HPRN-CT-2000-00029 (Molecular Level Devices and Machines). C.L. acknowledges the financial support provided through the European Community's Human Potential Programme under contract HPRN-CT-2000-00029 (Molecular Level Devices and Machines).

References

1. K. Campbell, R. McDonald, M.J. Fergusson, and R.R. Tykwinski. Organometallics, **22**(7), 1353 (2003).
2. C. Lodeiro, R. Bastida, E. Bértolo, A. Macías, and A. Rodríguez. Trans. Met. Chem. **28**, 388 (2003).
3. R.J.A. Janssen, L.F. Lindoy, O.A. Mattews, G.V. Meehan, A.N. Sobolev, and A.H. White. J. Chem. Soc. Chem. Commun. 735 (1995).
4. D.E. Fenton and B.A. Nájera. J. Coord. Chem. **54**, 239 (2001).
5. H. Adams, R. Bastida, D.E. Fenton, A. Macías, S.E. Spey, and L. Valencia. J. Chem. Soc. Dalton Trans. 4131 (1999).
6. L. Valencia, R. Bastida, M. López-Deber, A. Macías, A. Rodríguez, and M. Vicente. Z. Anorg. Allg. Chem. **629**(2), 268 (2003).
7. M. Kanesato, H. Houjou, Y. Nagawa, and K. Hiratani. Inorg. Chem. Commun. **5**(11), 984 (2002).
8. K.P. Balakrishnan, H.A.A. Omar, P. Moore, N.W. Alcok, and G.A. Pike. J. Chem. Soc. Dalton Trans. 2965 (1999).
9. S.J. Grant, P. Moore, H.A.A. Omar, and N.W. Alcock. J. Chem. Soc. Dalton Trans. 485 (1994).
10. K.R. Adam, L.F. Lindoy, B.W. Skelton, S.V. Smith, and A.H. White. J. Chem. Soc. Dalton Trans. 3361 (1994).
11. M. Raidt, M. Neuburger, and T.A. Kaden. Dalton Trans. **7**, 1292 (2003).
12. K.P. Wainwright. Applications of polyaza macrocycles with nitrogen-attached pendant arms. *In* Advances in inorganic chemistry. Vol. 52. *Edited by* A.G. Sykes. Academic Press, San Diego. 2001. p. 293.
13. S. Aime, E. Gianolio, D. Corpillo, C. Cavalloti, G. Palmisano, M. Sisti, G.B. Giovenzana, and R. Pagliarin. Helv. Chim. Acta, **86**(3), 615 (2003).
14. S.K. Sengupta, O.P. Pandey, A. Sinha, and S. Tripathi. Prog. Cryst. Growth Charact. Mater. **45**(1–2), 37 (2002).
15. F. Benetollo, G. Bombieri, A.M. Adeyga, K.K. Fonda, W.A. Gootee, K.M. Samaria, L.M. Vallarino. Polyhedron, **21**(4), 425 (2002).
16. J. Costamagna, G. Ferraudi, B. Matsuhiro, M. Campos-Vallette, J. Canales, M. Villagran, J. Vargas, and M.J. Aguirre. Coord. Chem. Rev. **196**, 125 (2000).
17. X. Chen, D.M. Du, and W.T. Hua. Tetrahedron Asymmetry, **14**(8), 999 (2003).
18. P.W. Smet, T.F. Pauwels, and P.J. Dierickx. Hum. Exp. Toxicol. **21**(8), 421 (2002).
19. C. Lodeiro, R. Bastida, A. De Blas, D.E. Fenton, A. Macías, A. Rodríguez, and T. Rodríguez-Blas. Inorg. Chim. Acta, **267**, 55 (1998).
20. M. Vicente, C. Lodeiro, H. Adams, R. Bastida, A. de Blas, D.E. Fenton, A. Macías, A. Rodríguez, and T. Rodríguez-Blas. Eur. J. Inorg. Chem. 1015 (2000).
21. M. Vicente, R. Bastida, C. Lodeiro, A. Macías, A.J. Parola, L. Valencia, and S.E. Spey. Inorg. Chem. **42**(21) 6768 (2003).
22. N.A. Bailey, D.E. Fenton, S.J. Kitchen, T.H. Lilley, M.G. Williams, P.A. Tasker, A.J. Tasker, and L.F. Lindoy. J. Chem. Soc. Dalton Trans. 627 (1991).
23. R. Turner, C.F. Huebner, and C.R. Scholz. J. Am. Chem. Soc. **71**, 2801 (1949).
24. C. Lodeiro, R. Bastida, E. Bértolo, A. Macías, and A. Rodríguez. Polyhedron, **22**, 1701 (2003).
25. P.G. Grimsley, L.F. Lindoy, H.C. Lip, R.J. Smith, and J.T. Baker. Aust. J. Chem. **30**(9), 2095 (1977).
26. W.J. Geary. Coord. Chem. Rev. **7**, 81 (1971)
27. S.C. Cummings and D.H. Bush. J. Am. Chem. Soc. **92**, 1924 (1970)
28. S.M. Peng, G.C. Gordon, and V.L. Goedken. Inorg. Chem. **17**(1), 119 (1970).
29. N.S. Gill, R.H. Nuttall, and D.E. Scaife. J. Inorg. Nucl. Chem. **18**, 79 (1961).
30. S. Aime, M. Botta, U. Casellato, S. Tamburini, and P.A. Vigato. Inorg. Chem. **34**(23), 5825 (1995).
31. K. Nakamoto. Infrared and raman spectra of inorganic and coordination compounds. 5th ed. Wiley Interscience, New York. 1997.
32. N.F. Curtis and Y.M. Curtis. Inorg. Chem. **4**(6), 804 (1965).
33. A.B.P. Lever, E. Mantovan, and B.S. Ramaswam. Can. J. Chem. **49**(11), 1956 (1971).
34. V.A.J. Aruma and V. Alexander. Inorg. Chim. Acta, **249**, 93 (1996).
35. W. Radecka-Paryzek. Inorg. Chim. Acta, **109**(3), L21 (1985).

© 2004 NRC Canada

36. L. Decola, D.L. Smailes, and L.M. Vallarino. Inorg. Chem. **25**, 1729 (1986).
37. M. Di Vaira, F. Mani, M. Menicatti, P. Stoppioni, and A. Vacca. J. Chem. Soc. Dalton Trans. 661 (1997).
38. E. Pretsch, T. Clerc, J. Seibl, and W. Simon. Tables of spectral data for structure determination of organic compounds. 2nd. ed. Springer-Verlag, Berlin-Heidelberg. 1989.
39. C. Bazzicalupi, A. Bencini, A. Bianchi, C. Giorgi, V. Fusi, B. Valtancoli, M.A. Bernardo, and F. Pina. Inorg. Chem. **38**(17), 3806 (1999).

© 2004 NRC Canada

1,2-Bis-(1-{3-pyridyl-}3-methyltriazen-3-yl)ethane: Synthesis and X-ray crystal structure

Keith Vaughan, Elizabeth Turner, and Hilary Jenkins

Abstract: 3-Aminopyridine is diazotized in the conventional manner and the diazonium salt coupled with *N*,*N*′-dimethylethylenediamine to afford the title compound (**1**), which is a potential antitumour agent. The compound has been characterized by spectroscopic methods. The ^{1}H NMR spectrum shows evidence of rotational conformerism, from the observation of broadening of the N-methyl signals in the room-temperature spectrum. Low-temperature NMR spectra (down to 223 K) show the presence of three distinct rotamers. The crystal structure of 1,2-bis-(1-{3-pyridyl-}3-methyltriazen-3-yl)ethane (**1**) has been determined by single crystal X-ray diffraction analysis. The bis-triazene (**1**) exists as the "staggered" conformation in the solid state, with an "*anti–anti*" configuration around the N—N bond of the triazene units. The crystal structure of **1** is compared with the closely related bis-triazene **2** and also compared with the simple mono-triazene **3**. Crystal data for **1**, $C_{14}H_{18}N_8$: orthorhombic, space group *Pbca*, a = 11.2550(8) Å, b = 8.8507(6) Å, c = 15.0069(10) Å, β = 90°, and V = 1494.91(18) Å^3, for Z = 4.

Key words: triazene, bis-triazene, pyridine, X-ray, VT NMR, diazonium coupling.

Résumé : On a réalisé la diazotation de la 3-aminopyridine de la façon conventionnelle et on a procédé au couplage du sel de diazonium avec le *N*,*N*′-diméthyléthylènediamine pour obtenir le produit mentionné dans le titre (**1**), un agent antitumoral potentiel. Le composé a été caractérisé par des méthodes spectroscopiques. L'élargissement des signaux du groupe N-méthyle dans le spectre RMN du ^{1}H à la température ambiante suggère l'existence de conformères rotationnels. Le spectre RMN à des températures allant jusqu'à 223 K met en évidence la présence de trois rotamères distincts. La structure cristalline du 1,2-bis-(1-{3-pyridyl-}-3-méthyltriazén-3-yl)éthane (**1**) a été déterminée par diffraction des rayons X sur un cristal unique. Dans l'état solide, le bis-(triazène) existe dans une conformation décalée dans laquelle on observe une configuration « *anti–anti* » autour de la liaison N—N des unités triazènes. On a comparé la structure cristalline du composé **1** avec celle du bis-triazène **2** qui lui est très apparentée ainsi qu'avec celle du monotriazène simple **3**. Les données cristallographiques pour **1**, $C_{14}H_{18}N_8$, sont: orthorhombique; groupe d'espace *Pbca*, a = 11,2550(8) Å, b = 8,8507(6) Å et c = 15,0069(10) Å, β = 90°, V = 1494,91(18) Å^3 et Z = 4.

Mots clés : triazène, bis-triazène, pyridine, rayons X, RMN à température variable, couplage de diazonium.

[Traduit par la Rédaction]

Introduction

In a previous study, a series of 1,2-bis-(1-aryl-3-alkyltriazen-3-yl)ethanes, e.g., **2**, was synthesized by diazonium coupling with *N*,*N*′-dimethylethylenediamine (1). Subsequently, two compounds in this series were characterized by X-ray crystallography (2), and the bis-triazene structure was confirmed. Heterocyclic modification to the benzene ring in these compounds may be seen as a way to evoke more enhanced antitumour activity. In this paper we report the first example of a bis-(pyridyltriazen-3-yl)ethane, compound **1**, with a complete X-ray crystal structure and a comparison of the structure with that of the bis-aryl triazenylethane, **2**, and of the 3,3-dimethyltriazene, **3** (3). The solution of the crystal structure of **1** is the first reported example of a 1-heteroaryl-3,3-dialkyltriazene crystal structure.

Synthesis

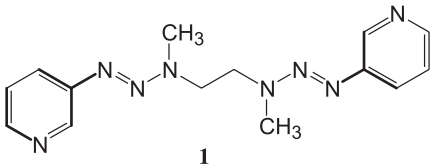
3-Aminopyridine (0.948 g, 0.010 mol) was dissolved in 2 mol L^{-1} hydrochloric acid (15 mL), and the solution was cooled to 0 °C. The cold solution was diazotized with aqueous sodium nitrite (0.827 g, 0.012 mol in 6.0 mL water) and then stirred in the cold for 0.5 h. The diazonium salt was treated gradually with a cold solution of *N*,*N*′-dimethylethylenediamine (0.450 g) in water (5.0 mL). The mixture was stirred cold for a further 0.5 h, and the solution was then basified with saturated sodium bicarbonate solution to pH 8. The solid precipitate was removed by vacuum filtration and dried to give the crude bis-triazene (1.062 g, 35% yield), which recrystallized from toluene to afford the crystal for X-ray study. mp 130–132 °C. ^{1}H NMR ($CDCl_3$) δ: 3.30 (6H, broad, N-Me), 4.14 (4H, s, N-CH_2), 7.26–8.41 (8H, m, aro-

Received 9 June 2003. Published on the NRC Research Press Web site at http://canjchem.nrc.ca on 11 February 2004.

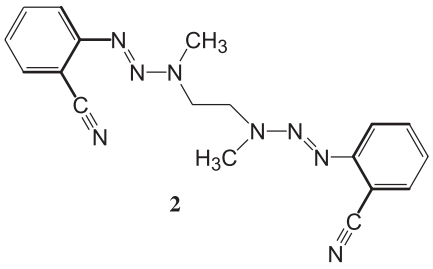
K. Vaughan,[1] E. Turner, and H. Jenkins. Department of Chemistry, Saint Mary's University, Halifax, NS B3H 3C3, Canada.

[1]Corresponding author (e-mail: keith.vaughan@smu.ca).

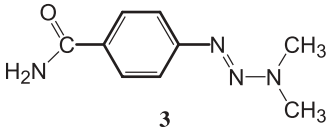
 doi: 10.1139/V03-213 © 2004 NRC Canada



1



2



3

matic). ^{13}C NMR ($CDCl_3$) δ: 34.72 (N-Me), 53.59 (N-CH_2), 123.72, 125.77, 142.80, and 146.09 (aromatic). Calcd. for $C_{14}H_{18}N_8$ (%): C 56.4, H 6.0, N 37.6; found: C 56.4, H 6.0, N 37.2.

Crystallography

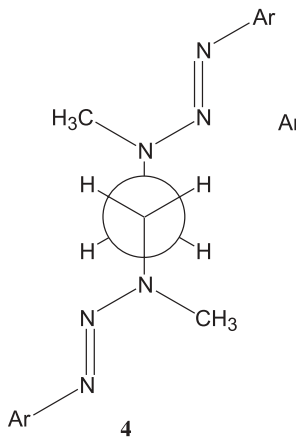
All X-ray diffraction data were collected on a Siemens SMART/CCD diffractometer equipped with an LT-II low temperature device.[2] Diffracted data were corrected for absorption corrections using the SADABS program (4). SHELXTL (5) was used for the structure solution, and refinement was based on F^2. All the nonhydrogen atoms were refined anisotropically. Hydrogen atoms were fixed in calculated positions and refined isotropically on the basis of corresponding C atoms (U(H) = 1.2 Ueq(C)). Structure refinement parameters for **1** are given in Table 1. Atomic coordinates and equivalent isotropic displacement parameters for **1** are provided in Table 2. Bond lengths and bond angles for compound **1** are given in Table 3.

Results and discussion

An ORTEP perspective view of the 1,2-bis-(1-{3-pyridyl-}3-methyltriazen-3-yl)ethane (**1**) is shown in Fig. 1. In the solid state, **1** adopts the "staggered" conformation with respect to the orientation around the C—C bond of the ethane unit and also has the *trans* configuration around each of the N=N azo groups in the triazene moieties. These geometries are pre-

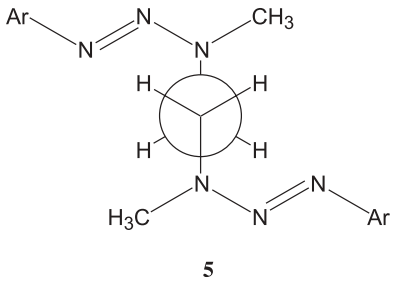
Table 1. Crystal data and structure refinement for **1**.

Empirical formula	$C_{14}H_{18}N_8$
Formula weight	298.36
Temperature (K)	223(2)
Wavelength (Å)	0.71073
Crystal system	Orthorhombic
Space group	*Pbca*
Unit cell dimensions	
a (Å)	11.2550(8)
b (Å)	8.8507(6)
c (Å)	15.0069(10)
α (°)	90
β (°)	90
γ (°)	90
Volume (Å^3)	1494.91(18)
Z	4
Density (calculated) (Mg·m^{-3})	1.326
Absorption coefficient (mm^{-1})	0.088
F(000)	632
Crystal size (mm^3)	0.3 × 0.4 × 0.4
Theta range for data collection (°)	2.71–23.27
Index ranges	$-12 \le h \le 11$, $-5 \le k \le 9$, $-16 \le l \le 16$
Reflections collected	6006
Independent reflections	1071 (*R*(int) = 0.0262)
Completeness to θ = 23.27° (%)	99.7
Absorption correction	None
Refinement method	Full-matrix least-squares on F^2
Data / restraints / parameters	1071 / 0 / 101
Goodness-of-fit on F^2	1.129
Final *R* indices [$I > 2\sigma(I)$]	R_1 = 0.0518, wR_2 = 0.1566
R indices (all data)	R_1 = 0.0545, wR_2 = 0.1588
Extinction coefficient	0.017(4)
Largest diff. peak and hole (e·Å^{-3})	0.488 and –0.479



4

(Ar = 3-pyridyl)



5

(Ar = *o*-cyanophenyl)

[2] Supplementary data may be purchased from the Depository of Unpublished Data, Document Delivery, CISTI, National Research Council Canada, Ottawa, ON K1A 0S2, Canada (http://www.nrc.ca/cisti/irm/unpub_e.shtml for information on ordering electronically). CCDC 218871 contain the supplementary data for this paper. These data can be obtained, free of charge, via www.ccdc.cam.ac.uk/conts/retrieving.html (or from the Cambridge Crystallographic Data Centre, 12 Union Road, Cambridge, U.K.; fax +44 1223 336033; or deposit@ccdc.cam.ac.uk).

© 2004 NRC Canada

Table 2. Atomic coordinates ($\times 10^4$) and equivalent isotropic displacement parameters ($Å^2 \times 10^3$) for **1**.

	x	*y*	*z*	U(eq)
N(1)	7087(2)	–1139(3)	2423(2)	43(1)
N(2)	6607(2)	1439(2)	4289(2)	34(1)
N(3)	5699(2)	2229(3)	4500(2)	34(1)
N(4)	5907(2)	3240(3)	5133(2)	37(1)
C(1)	6011(2)	–1761(3)	2335(2)	39(1)
C(2)	5064(3)	–1410(3)	2872(2)	39(1)
C(3)	5207(2)	–347(3)	3539(2)	37(1)
C(4)	6309(2)	340(3)	3634(2)	31(1)
C(5)	7215(2)	–114(3)	3068(2)	38(1)
C(6)	4950(3)	4301(3)	5296(2)	38(1)
C(7)	7068(3)	3421(3)	5535(2)	41(1)

Note: U(eq) is defined as one third of the trace of the orthogonalized U^{ij} tensor.

dictable, but the orientation of the triazene units around the N—N single bonds is more interesting. With respect to the orientation around the N—N bonds (N(3)—N(4) in Fig. 1), bis-triazene **1** adopts the "*syn–syn*" rotamer, as opposed to the "*anti–anti*" rotamer. (In this context, the terms *syn* and *anti* refer to the configuration of the C(7) methyl carbon and the N(2) nitrogen with respect to the N(3)—N(4) bond.) A Newman projection of this preferred structure is shown in structure **4**.

The comparable perspective of compound **2**, taken from the X-ray structure in ref. 2, looks like the Newman projection in structure **5**. The orientation around the C—C bond of the ethane unit is similarly staggered, but the triazene units adopt the "*anti–anti*" rotamer with respect to the N—N bond. Taken from the other perspective of the rotameric equilibrium shown below, it can be seen that the bis-pyridyltriazenylethane (1) prefers the "*syn–syn*" rotamer (**1B**), whereas the bisaryltriazenylethane (2) prefers the "*anti–anti*" rotamer (**1A**) (Scheme 1).

Previous NMR studies (1) of bis-triazenes of type **2** were very successful in elucidating the equilibrium behaviour in solution. The variable temperature NMR (VT NMR) spectra of the title compound **1** in $CDCl_3$ solution have been recorded down to 223 K (see Fig. 2), and it is apparent that there are three distinct species of this molecule in solution. The broad signal of the methylene protons at 4.14 parts per million (ppm) resolves into two signals of unequal intensity at 223 K, but the clearest picture comes from the separation of the N-methyl signal at 3.30 ppm. In the low-temperature spectrum, the three species visible are as follows: (*a*) the most abundant "*anti–anti*" species **1A**, with equivalent methyl signals at 3.10 ppm; (*b*) the least abundant "*syn–syn*" species **1B**, also with equivalent methyl signals at 3.43 ppm; and (*c*) the "*syn–anti*" species **1C**, with nonequivalent methyl signals at 3.16 and 3.40 ppm. These assignments are based on a comparison with the previously reported (1) NMR spectra of the benzenoid analogues of **1** and on the intuitive assumption that the *anti*-configuration is the most stable. From the relative intensities of the signals in the low-temperature NMR spectrum, the relative amounts of the three rotamers in the mixture at 223 K is 86% **1A**, 2% **1B**, and 12% **1C**. In this context, the terms "*syn*" and "*anti*" refer to the orientation of the CH_3 and Ar-N groups around the N3—N4 bond.

Table 3. Bond lengths (Å) and angles (°) for **1**.

Bond lengths (Å)	
N(1)—C(5)	1.334(4)
N(1)—C(1)	1.337(4)
N(2)—N(3)	1.278(3)
N(2)—C(4)	1.423(4)
N(3)—N(4)	1.326(3)
N(4)—C(7)	1.448(4)
N(4)—C(6)	1.451(3)
C(1)—C(2)	1.372(4)
C(2)—C(3)	1.384(4)
C(3)—C(4)	1.389(4)
C(4)—C(5)	1.386(4)
C(6)—C(6)#1	1.528(6)
Bond angles (°)	
C(5)-N(1)-C(1)	116.7(2)
N(3)-N(2)-C(4)	111.0(2)
N(2)-N(3)-N(4)	113.9(2)
N(3)-N(4)-C(7)	122.2(2)
N(3)-N(4)-C(6)	115.2(2)
C(7)-N(4)-C(6)	121.9(2)
N(1)-C(1)-C(2)	123.6(3)
C(1)-C(2)-C(3)	119.2(3)
C(2)-C(3)-C(4)	118.5(3)
C(5)-C(4)-C(3)	117.8(3)
C(5)-C(4)-N(2)	116.6(2)
C(3)-C(4)-N(2)	125.5(2)
N(1)-C(5)-C(4)	124.2(3)
N(4)-C(6)-C(6)#1	111.8(3)

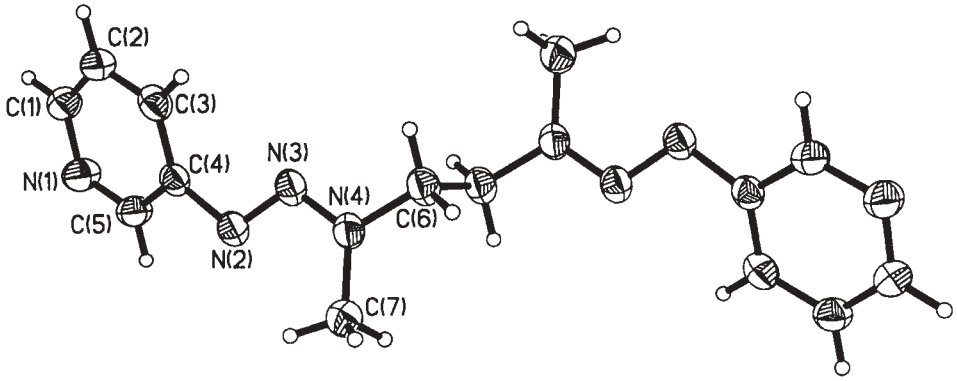
The bond lengths in structure **1** are comparable with previously reported (2, 3) results with similar triazenes. Table 4 shows a comparison of key bond lengths and bond angles for compounds **1**, **2**, and **3**. (It should be noted that the atom notations, e.g., N(2), N(3), N(4), etc., are the notations used in this structure for compound **1**; the atom notations used in refs. 2 and 3 may not be the same, but the bond lengths and angles listed in Table 4 have been cross-checked with meticulous attention to ensure that the analogous bonds are being compared.) The comparison of bond lengths in the three structures is remarkably close. The N=N azo linkages of the triazene moiety is observed at ca. 1.28 Å, whereas the N—N single bond of the triazene is consistently longer at ca. 1.32 Å but not as long as expected for an isolated N—N single bond, ca. 1.43 Å. This shortening of the N3—N4 bond in the triazene moiety is consistent with the resonance shown in Scheme 2, which gives the N3—N4 bond some double bond character.

The N-methyl bond length in the three structures is consistent at ca. 1.45 Å, as is the N2—aryl bond length at ca. 1.42 Å. The bond length of the C—C bond of the ethane spacer in **1** and **2** is very close at ca. 1.53 Å.

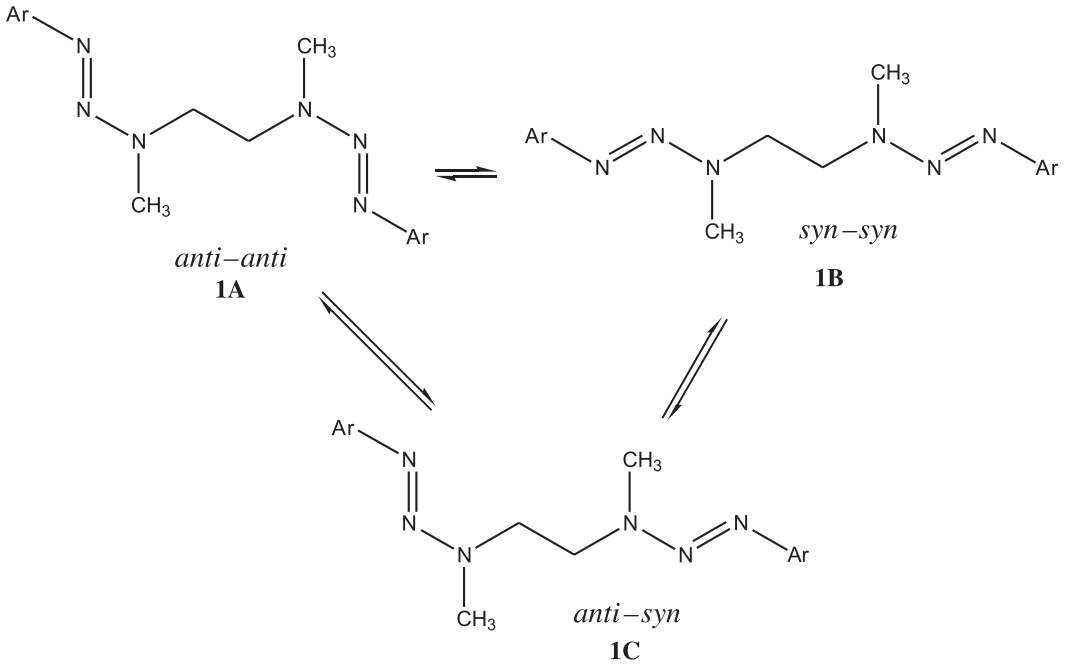
Bond angles in structure **1** indicate some distortion, arising from different interactions of N2 and N3 with neighbouring groups. Repulsion between the lone pair on N2 with the C7 methyl group causes the bond angle N3-N4-C7 to open up to 122.2°, with the concomitant compression of the

© 2004 NRC Canada

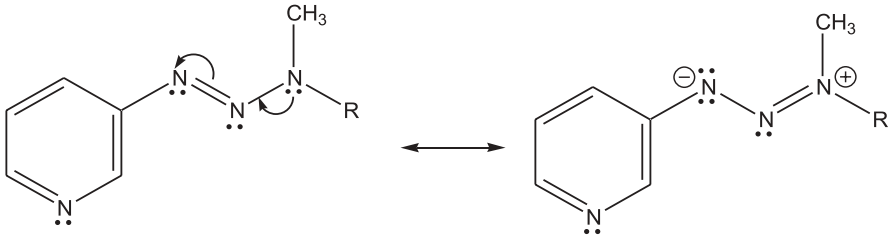
Fig. 1. ORTEP diagram of 1,2-bis-(1-{3-pyridyl-}3-methyltriazen-3-yl)ethane (**1**).



Scheme 1.



Scheme 2.



N3-N4-C6 bond angle to 115.2°. Similarly, steric crowding between N3 and the hydrogen attached at C3 causes the bond angle C3-C4-N2 to open up to 125.5°, with compression of C5-C4-N2 to 116.6°. The bond angle N4-C6-C6′ is found to be 111.8°, indicating slight distortion from tetrahedral geometry around C6.

The bond angle comparison of the three structures **1**, **2**, and **3** shows much similarity but also some real divergence. The major divergence in bond angles occurs in compounds **1** and **2** with respect to the bond angles around N4. The N-N-Me bond angle in structure **1** is 122.2(2)° compared with 115.9(3)° in structure **2**; the order of the N-N-CH_2 bond angles in **1** and **2** is predictably in the reverse order, 115.2(2)° in **1** compared with 123.4(3)° in **2**. The C-N-C angle at N4 is very close, 121.9(2)° vs. 120.6(3)°. This striking variation in bond angle appears to be consistent with the conformational preference of the two compounds described earlier. The crystal structure of **1** shows that this compound adopts the "*syn–syn*" structure (rotamer **1B**), which leads to repulsion between N(2) and C(7) (Fig. 1). This repulsion causes the bond angle N(3)-N(4)-C(7) to open up to 122.2(2)°, with a corresponding compression of the bond angle N(3)-N(4)-

© 2004 NRC Canada

Fig. 2. Variable temperature NMR stack plot of **1** in deuteriochloroform.

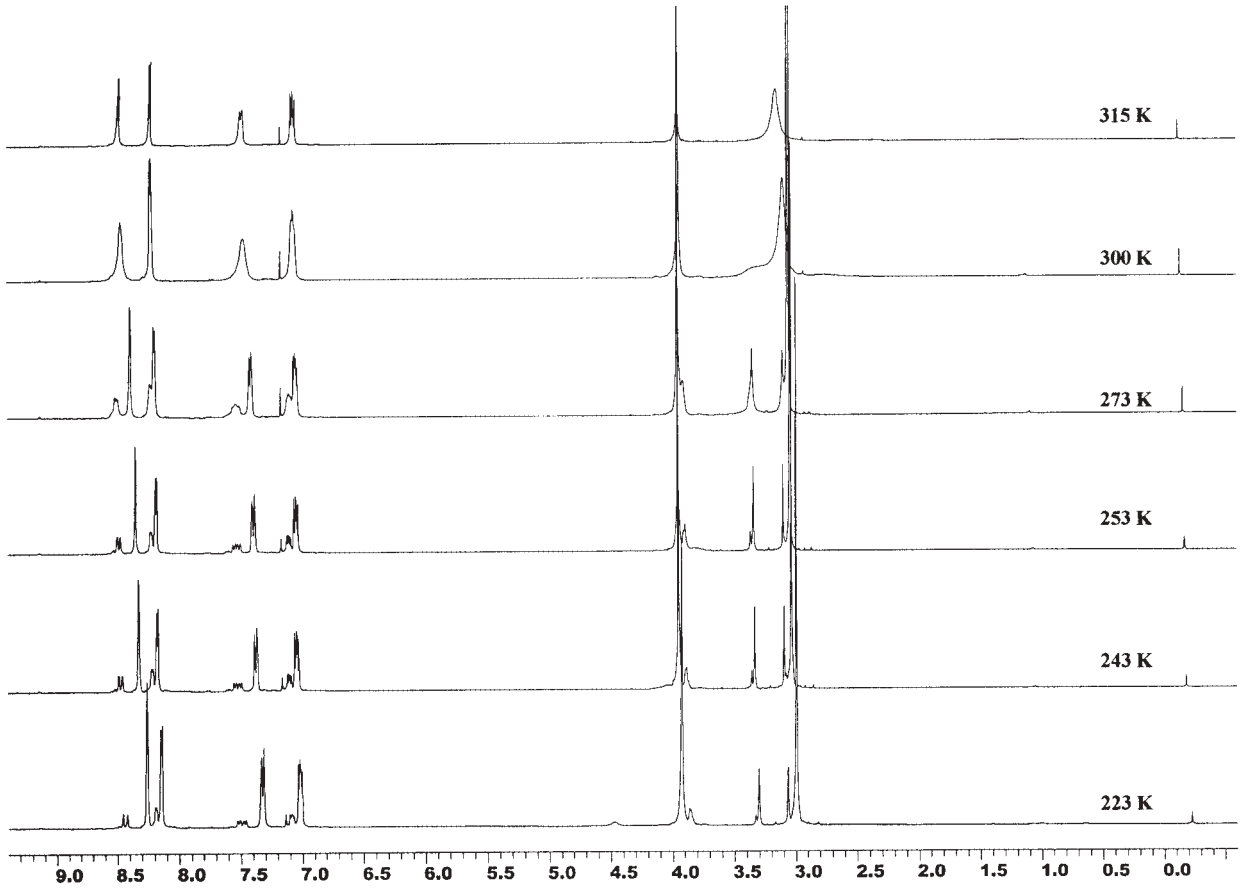
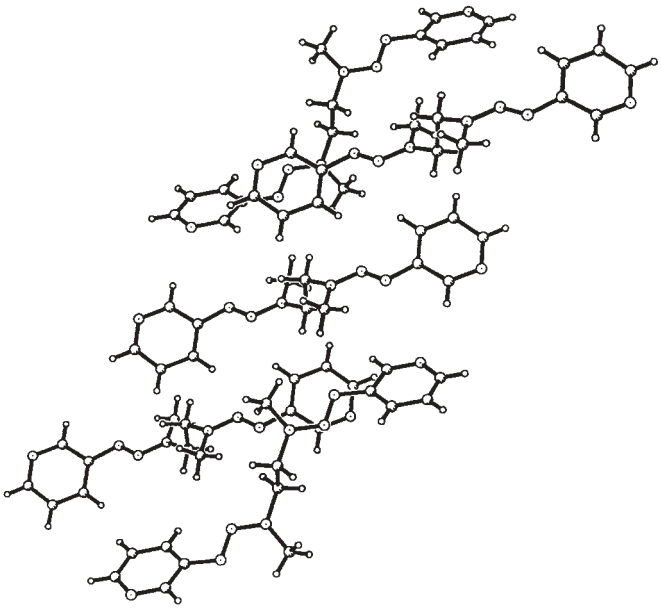


Table 4. Comparison of selected bond lengths and bond angles of compounds **1**, **2**, and **3**.

	1	**2**[a]	**3**[b]
Bond lengths (Å)			
N(2)—N(3)	1.278(3)	1.282(4)	1.282(8)
N(3)—N(4)	1.326(3)	1.316(4)	1.312(8)
N(4)—C(7)	1.448(4)	1.452(5)	1.466(8)
N(4)—C(6)	1.451(3)	1.459(5)	1.470(8)
N(2)—C(4)	1.423(4)	1.414(5)	1.433(8)
C(6)—C(6′)	1.528(6)	1.533(7)	—
Bond angles (°)			
C(3)-C(4)-N(2)	125.5(2)	125.7(3)	124.5(5)
C(4)-N(2)-N(3)	111.0(2)	111.5(3)	112.1(5)
N(2)-N(3)-N(4)	113.9(2)	113.8(3)	114.6(5)
N(3)-N(4)-C(7)	122.2(2)	115.9(3)	123.4(5)
N(3)-N(4)-C(6)	115.2(2)	123.4(3)	116.7(5)
N(4)-C(6)-C(6′)	111.8(3)	109.7(3)	—
C(6)-N(4)-C(7)	121.9(2)	120.6(3)	119.6(5)

[a]Reference 2.
[b]Reference 3.

Fig. 3. Stacking diagram of **1**.

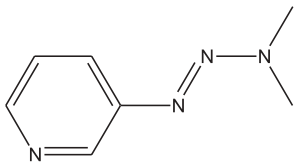


C(6) to 115.2(2)°. Compound **2** adopts the "*anti–anti*" structure (rotamer **2B**), leading to compression of the N(3)-N(4)-C(7) bond to 115.9(3)°.

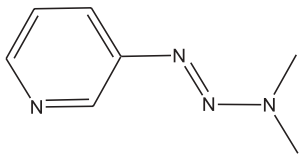
The comparison of bond lengths and bond angles in Table 4 shows that the presence of the heteroatom in the pyridyl ring has virtually no direct effect on the molecular parameters. However, there is one striking effect of the heteroatom, and that is the orientation of the triazene moiety with respect to the orientation of the pyridyl ring, as illustrated by structures **6** and **7**. The preferred structure of **1** in the solid state is that represented by **6**, i.e., with the triazene moiety angled away from the pyridyl nitrogen. There does not appear to be

© 2004 NRC Canada

any reason for this preference intrinsic to the molecule itself, and the reason for this preference may be something to do with the packing of molecules within the crystal.



6



7

A packing diagram of the crystal structure of **1** is shown in Fig. 3. There is no immediate indication of π-stacking between pyridyl rings of adjacent molecules. If anything, the plane of the pyridyl ring of one molecule is almost perpendicular to that of its neighbour. However, there is a close interaction between the pyridyl ring and the triazene nitrogen atoms of a neighbouring molecule. As shown in the packing diagram (Fig. 3), the structure is arranged to allow the lone pairs to face the partially positive 2- and 6-positions of the neighbouring pyridyl ring. The centre of the pyridine ring to N2 distance is the closest point of interaction at 4.060 Å; the next closest is N3 to the centre of pyridine at 4.587 Å.

Acknowledgements

The authors are grateful to the Natural Sciences and Engineering Research Council of Canada (NSERC) for a Discovery Grant (to K.V.). We are also grateful to the Atlantic Regional Magnetic Resonance Centre at Dalhousie University for providing NMR spectra.

References

1. D.L. Hooper, I.R. Pottie, M. Vacheresse, and K. Vaughan. Can. J. Chem. **76**, 125 (1998).
2. I.R. Pottie, C.V.K. Sharma, and K. Vaughan. J. Chem. Cryst. **28**, 5 (1998).
3. W.L. Bullerwell, L.R. MacGillivray, M.J. Zaworotko, K. Vaughan, and D.E.V. Wilman. Acta Crystallogr. **C51**, 2624 (1995).
4. G.M. Sheldrick. SADABS [computer program]. University of Göttingen, Germany. 1996.
5. G.M. Sheldrick. SHELXTL [computer program]. Release 5.03. Siemens Analytical X-ray Instruments Inc., Madison, Wis. 1994.

© 2004 NRC Canada

The synthesis of two novel neutral receptors and their anion binding properties

Zhen-Ya Zeng, Yong-Bing He, Lan-Hua Wei, Jin-Long Wu, Yan-Yan Huang, and Ling-Zhi Meng

Abstract: Two new neutral receptors (**1** and **2**) containing thiourea and amide groups were synthesized by simple steps in good yields. The binding properties of **1** and **2** with anions were examined by UV–vis, fluorescence, and ^{1}H NMR spectroscopy. Receptor **1** had a better AcO^-: $H_2PO_4^-$ selectivity in comparison with that for receptor **2**. The association constants of **1**·AcO^-, **2**·AcO^-, and **2**·$H_2PO_4^-$ were higher in comparison with those of other anions (Cl^-, Br^-, I^-, *p*-NO_2PhO^-, and *p*-$NO_2PhOPO_3^{2-}$). In particular, a clear color change was observed, from pale yellow to red-brown, upon addition of AcO^- to the solution of **1** in DMSO. The UV–vis and fluorescence data indicate that a 1:1 stoichiometry complex is formed between compound **1** or **2** and anions through hydrogen-bonding interactions.

Key words: neutral receptors, anion recognition, synthesis, hydrogen bonds.

Résumé : On a synthétisé les deux nouveaux récepteurs neutres (**1** et **2**) contenant des groupes thiourée et amide par des réactions simples et avec de bons rendements. On a évalué les propriétés de fixation des anions des composés **1** et **2** par le biais de leurs spectres UV–vis, de fluorescence et RMN du ^{1}H. Par rapport au récepteur **2**, le récepteur **1** présente une meilleure sélectivité AcO^-:$H_2PO_4^-$. Les constantes d'association des anions **1**·AcO^-, **2**·AcO^- et **2**·$H_2PO_4^-$ sont plus élevées que celles pour les autres anions (Cl^-, Br^-, I^-, *p*-NO_2PhO^- et *p*-$NO_2PhOPO_3^{2-}$). On a observé en particulier un changement remarquable de couleur de jaune pale à brun rouge lors de l'addition de AcO^- à une solution du composé **1** dans le DMSO. Les données de spectroscopie UV–vis et de fluorescence indiquent qu'il y a formation d'un complexe de stoechiométrie 1:1 entre les composés **1** ou **2** et les anions par le biais d'interactions de liaisons hydrogènes.

Mots clés : récepteurs neutres, reconnaissance d'anion, synthèse, liaisons hydrogènes.

[Traduit par la Rédaction]

Introduction

The development of anion receptors has attracted increasing interest in supramolecular chemistry, owing to potential applications in clinical diagnosis, environmental monitoring, and biological processes (1). In comparison with the large variety of ligands that have been described for cations (2), the development of selective artificial receptors for anions is still very limited because anions have a wide variety of geometry, comparatively large size, and low charge density. Additionally, anions may be sensitive to pH values for protonation at low pH and to losing their negative charge (3). The basic strategy for the construction of anion-binding receptors is to exploit the receptors that have electrostatic, hydrogen bonding, or Lewis acidic central interactions (4). For the purpose of lessening the dependence on pH values, considerable effort has recently been directed toward the development of synthetic neutral receptors that rely mainly on hydrogen-bonding interactions for anion recognition. These receptors have resulted in successful applications of ion sensors such as ion-selective electrodes (5). For the development of neutral anion receptors, the focus has been on urea or thiourea groups as anion binding sites, because the hydrogen bonding of these functional groups is directional in character and results in relatively strong complexes with biologically important anions such as carbonate, chloride, or phosphate (6).

Although some anion receptors have been reported in the last decades, neutral receptors containing, simultaneously, thiourea and amide binding units have seldom been reported. The cooperative act of two functional groups for the anion could effectively enhance selectivity in the recognition and stability of the complex. In this paper, we report the synthesis and binding properties of two new neutral anion receptors (**1** and **2**) containing thiourea and amide groups. The synthesis route is shown in Scheme 1. The anionic recognition of two compounds has been investigated by UV–vis, fluorescence, and ^{1}H NMR spectroscopy.

Results and discussion

Receptors **1** and **2**, which contain thiourea and amide groups, were synthesized by the reaction of the appropriate isothiocyanate and *N*,*N*′-di(aminoethylene)-2,6-pyridinedicarbonylamine (**3**) in good yields (Scheme 1). Receptor **1** could only dissolve very well in DMSO, as for most thiourea-type compounds, but the synthetic receptor **2** was

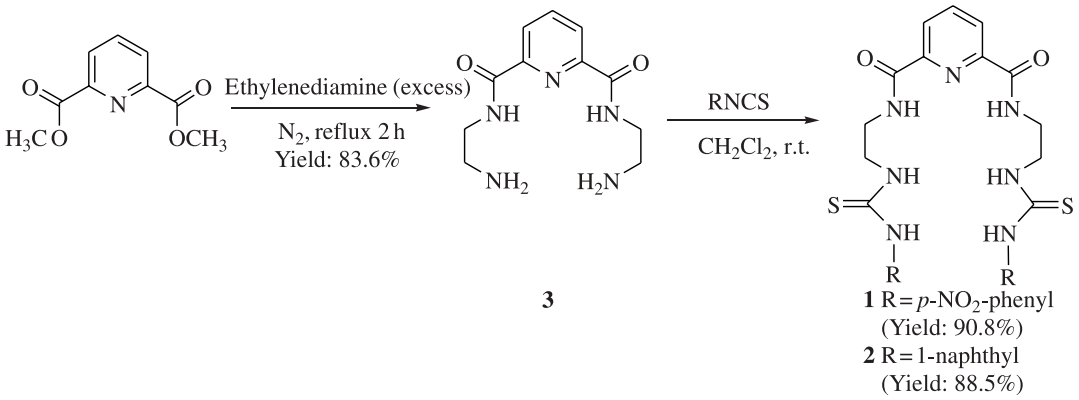
Received 29 July 2003. Published on the NRC Research Press Web site at http://canjchem.nrc.ca on 13 February 2004.

Z.-Y. Zeng, Y.-B. He,[1] L.-H. Wei, J.-L. Wu, Y.-Y. Huang, and L.-Z. Meng. Department of Chemistry, Wuhan University, Wuhan, Hubei 430072, P.R. China.

[1]Corresponding author (e-mail: ybhe@whu.edu.cn).

 doi: 10.1139/V03-212 © 2004 NRC Canada

Scheme 1.



readily dissolved in other organic solvents, such as CH_2Cl_2, $CHCl_3$, acetone, ethanol, methanol, etc.

Absorption and fluorescence spectra

Figure 1*a* shows the absorbance spectra of **1** (2.5×10^{-5} mol L^{-1}) with added dihydrogen phosphate anion in DMSO. Receptor **1** displayed a maximum absorption at 359 nm ($\varepsilon = 2.73 \times 10^4$ (mol $L^{-1})^{-1}$ cm^{-1}), which can be assigned as an intramolecular charge-transfer (CT) absorption band (7). Gradually adding $H_2PO_4^-$ produced a bathochromic shift in the absorption maxima (λ_{max}), from 359 to 370 nm, and a clear isosbestic point appeared at 352 nm. This observation indicated that **1** interacted with $H_2PO_4^-$, and non-linear curve fitting confirmed that **1** and $H_2PO_4^-$ formed a 1:1 complex.

Even after adding 100 equiv. of bromide or iodide anion, the absorption spectra of receptor **1** and **2** did not change at all. When chloride anion was added to a solution of **2**, a decrease of absorbance could be observed, but with receptor **1**, no decrease occured.

Remarkably, significant changes were observed when acetate anion was added to receptor **1** in DMSO. Upon gradually increasing the concentration of AcO^-, a new absorption band appeared with a maximum absorbance wavelength at 474 nm, as shown in Fig. 1*b*, and the color of the solution changed from pale yellow to red-brown, which could be observed by the naked eye. However, no similar color change was observed upon adding AcO^- to receptor **2**. In the supramolecular system, the electronic excitation was mostly accompanied by a charge transfer from the donor nitrogen of the thiourea to the acceptor substituents ($-NO_2$) of the chromophore. Introducing the electron-withdrawing substituents could enhance the acidity of the thiourea moiety, strongly stabilize the excited state, and result in a bathochromic shift in the absorption maxima, to produce a possible effective color change in aprotic media (8). Among all the anions that we studied, this phenomenon appeared only upon adding AcO^- to **1**.

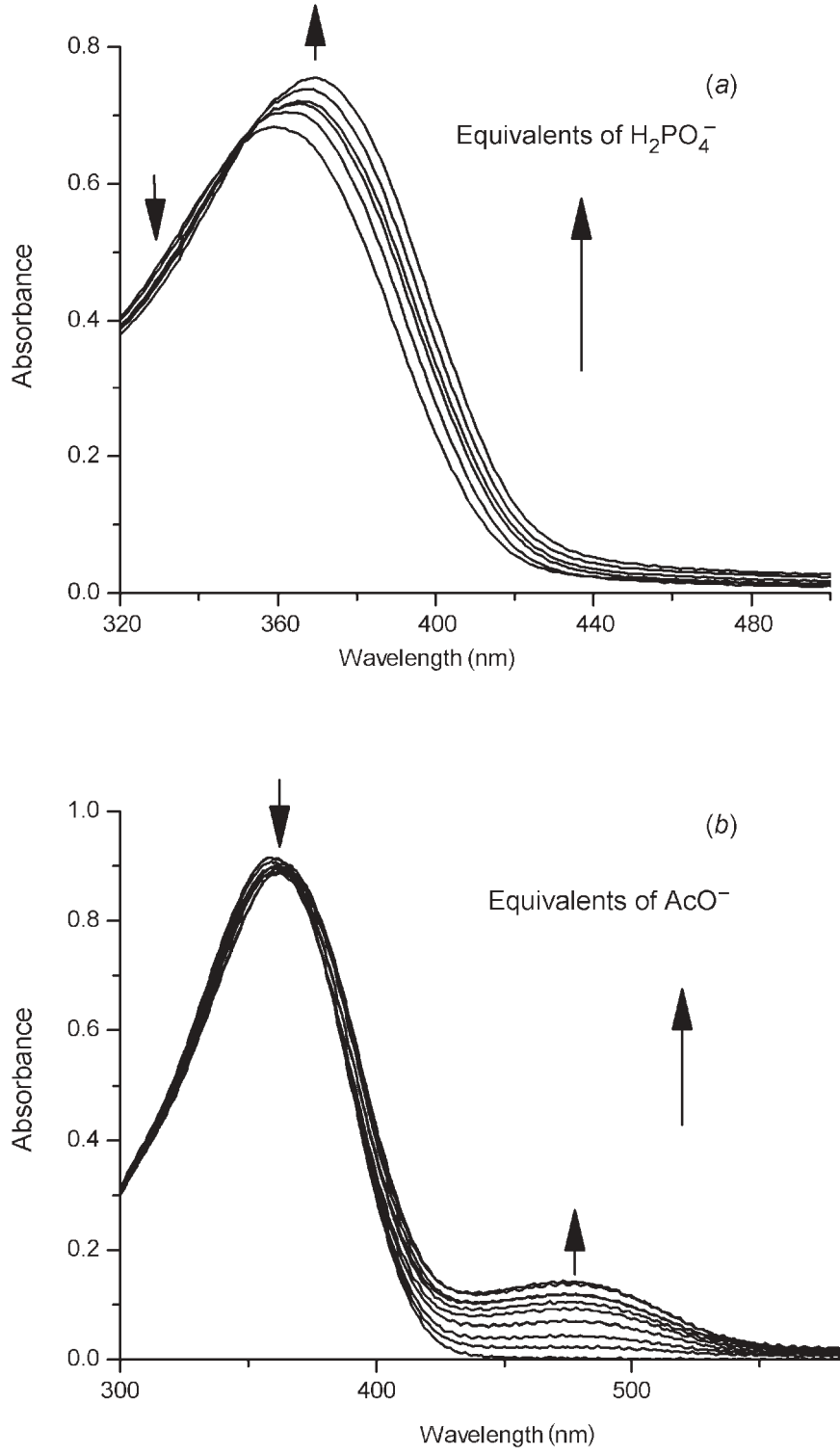
The binding property of **1** with AcO^- was further assessed by a UV–vis spectral titration. Because receptor **1** has many binding sites, a Job plot experiment was carried out to determine the complex ratio. Figure 2*a* illustrates that the absorption of the **1**–AcO^- complex approaches a maximum when the molar fraction of [**1**]/([**1**]+[AcO^-]) is about 0.5 (the total concentration of **1** and AcO^- was 0.1 mmol L^{-1}), meaning that a 1:1 complex of **1** and AcO^- is then formed. The satisfactory result (the correlation coefficient is over 0.99) of the nonlinear curve fitting (absorbance at 474 nm vs. equivalent amounts of anion) confirmed further the 1:1 ratio (Fig. 2*b*) (9).

The fluorescent spectral interactions of receptor **2** with anions were studied by gradual addition of the different substrates to a solution of receptor **2** (5×10^{-6} mol L^{-1}), and the results were analyzed by a non-linear least-squares fitting procedure. Figure 3 shows the changes of fluorescent emission intensity (excitation at 307 nm in $CHCl_3$) on complexation of the reaction of **2** with the AcO^- anion. The fluorescence intensity increased upon addition of AcO^-, with a slight red shift ($\Delta\lambda_{max} \approx 4$ nm) of the emission maximum at 376 nm, which is similar to the anion-induced fluorescence enhancement reported formerly (10). The fluorescence was enhanced with $H_2PO_4^-$ and Cl^-, too. In the absence of an anion, an electron-transfer process between naphthyl and weak electron-withdrawing thiono substituents might result in decreased fluorescence intensity. Upon the addition of anions (AcO^-, $H_2PO_4^-$, and Cl^-), the interaction of the anion with the receptor unit could diminish the PET progress to induce the fluorescence retrieval. Therefore, anion-induced fluorescence enhancement was observed (11). But the fluorescence of receptor **2** was quenched with the addition of 4-nitrophenol anion in $CHCl_3$. The anion-induced signal effects indicated that an efficient interaction happened between the receptor and the anion. In contrast to Cl^-, the fluorescent emission intensity of **2** did not change at all when anions (such as Br^- and I^-) with larger radii and the same spherical geometry were added. When 4-nitrophenylphosphate anion was introduced into a solution of receptor **2** in DMSO, the fluorescence intensity gradually decreased until it was almost completely quenched. The phenomenon was similar to the quenching induced by *p*-NO_2-PhO^-. When host **2** and a guest with a strong electron-withdrawing group (nitro-) interacted, it could be hypothesized that the fluorescence quenching was due to an electron-transfer process. The interaction between receptor **2** and *p*-NO_2-PhO^- (or *p*-$NO_2PhOPO_3^{2-}$) results in the nitro- group and the photoexcited naphthyl fragments being close enough that orbital overlap occurs, leading to efficient electron transfer (12).

Figure 4 shows the resulting fitted curves for the fluorescent emission intensity of receptor **2** at 375 nm when different concentrations of AcO^-, $H_2PO_4^-$, Cl^-, and *p*-NO_2-PhO^-,

© 2004 NRC Canada

Fig. 1. UV–vis absorption spectra of **1** in DMSO (2.5×10^{-5} mol L^{-1}) upon the addition of various amounts of anions; (*a*) equivalents of Bu_4N^+ ($H_2PO_4^-$): 0, 2, 3, 4, 6, and 20; (*b*) equivalents of Bu_4N^+ (AcO^-): 0, 0.2, 0.4, 0.8, 1, 1.6, 2, 3, 5, and 7.



respectively, were added to the solution of **2** in $CHCl_3$, or at 340 nm when different concentrations of *p*-$NO_2PhOPO_3^{2-}$ were added to the solution of **2** in DMSO. The fitted curves proved the formation of a 1:1 stoichiometry complex (9).

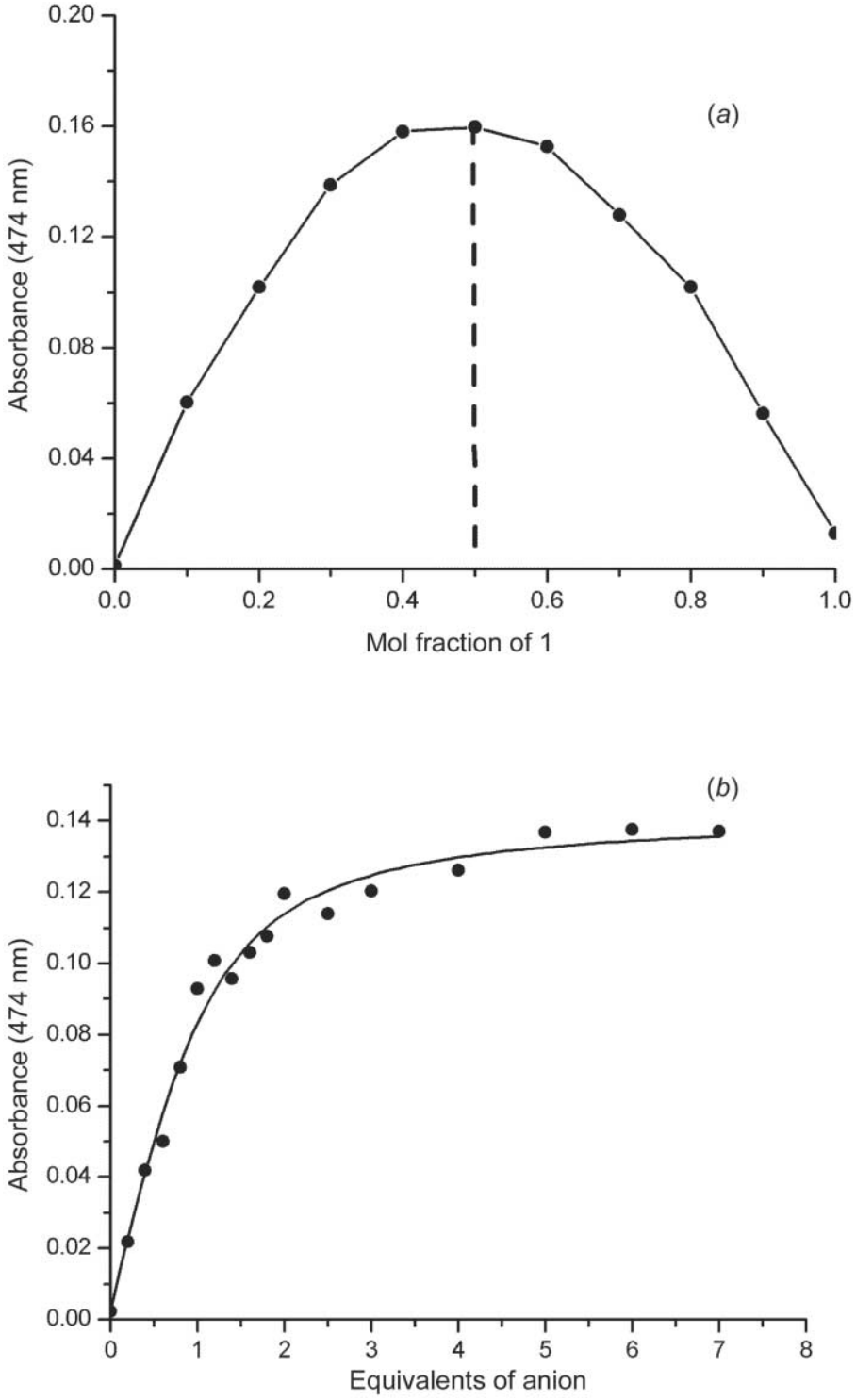
^{1}H NMR study

^{1}H NMR spectroscopy has been widely used to investigate receptor–substrate interactions, and it allows access to the details of the interaction between receptor and substrate.

Addition of anions to compound **1** or **2** caused all NH proton signals of the thiourea or amide groups to shift downfield, and the proton signals of pyridyl, phenyl, and N-CH_2 were changed too. Unfortunately, upon addition of the anions, some NH peaks of the thiourea or amide groups be-

© 2004 NRC Canada

Fig. 2. (*a*) Job plot of **1** and AcO^- at a total concentration of 0.1 mmol L^{-1} in DMSO; (*b*) the plot of the absorbance at 474 nm vs. equivalents of AcO^- in DMSO; [**1**] = 2.5×10^{-5} mol L^{-1}. The solid line is the fitting curve; the correlation coefficient is 0.9930.



came so broad that the peak changes of most receptor–anion systems couldn't be assigned properly. However, the complex of **1** with $H_2PO_4^-$ was assignable within the ^1H NMR spectrum, and the corresponding peak assignments are listed in Table 1. H_a (thiourea, adjacent to phenyl) showed a downfield shift from 10.26 to 12.06 parts per million (ppm); H_b (amide) shifted from 9.54 to 10.15 ppm; and H_c (thiourea, adjacent to methylene) shifted from 8.51 to 9.80 ppm. H_d (pyridyl) showed an upfield shift from 8.14~8.24 to 8.08~8.11 ppm. H_e ($CONCH_2$) at 3.76 ppm and H_f (NCH_2) at 3.61 ppm combined to form a singlet at 3.63 ppm. Compound **1** showed the signal corresponding to H_g (phenyl) as an AA′BB′ system, from 7.17 to 8.17 ppm. After adding $H_2PO_4^-$, H_g shifted to the extent of

© 2004 NRC Canada

Table 1. ^{1}H NMR chemical shifts (ppm) for receptor **1** (1.0×10^{-2} mol L^{-1} in DMSO-d_6) in the absence and the presence of dihydrogen phosphate anion (1:1).

Anion	H_a	H_b	H_c	H_d	H_e	H_f	H_g
None	10.26	9.54	8.51	8.14~8.24	3.76	3.61	7.17~8.17
$H_2PO_4^-$	12.06	10.15	9.80	8.08~8.11	3.63	3.63	8.00~8.05

Fig. 3. Emission spectra of **2** and complex of **2** with various amounts of AcO^- in $CHCl_3$; [**2**]: 5×10^{-6} mol L^{-1}, λ_{ex} = 307 nm. Equivalents of Bu_4N^+ (AcO^-): 0, 0.2, 0.4, 0.6, 0.8, and 1.

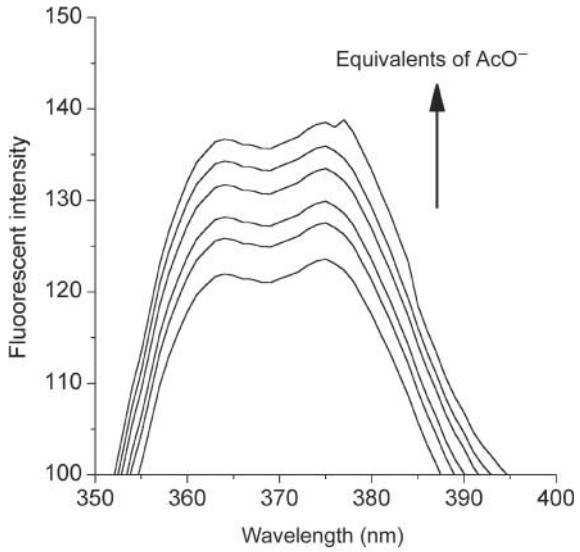
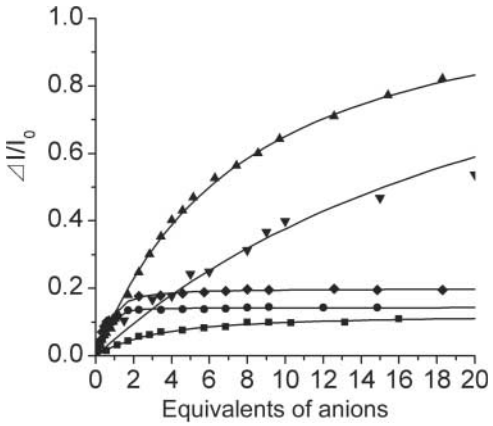


Fig. 4. Plots of fluorescence change vs. equivalents of anions added; [**2**]: 5×10^{-6} mol L^{-1}; the solid lines are the fitting curves (▲, *p*-NO_2-PhO^-; ▼, *p*-$NO_2PhOPO_3^{2-}$; ◆, $H_2PO_4^-$; ●, AcO^-; ■, Cl^-). For *p*-NO_2-PhO^- and *p*-$NO_2PhOPO_3^{2-}$, $\Delta I = I_0 - I$; for the other anions, $\Delta I = I - I_0$. The correlation coefficients are 0.9989, 0.9934, 0.9963, 0.9947, and 0.9958, respectively.



8.00~8.05 ppm. These results illustrate that the connection between receptor **1** and $H_2PO_4^-$ was by multiple hydrogen bonding interactions.

Determination of the association constants (K_{ass}) of the complexes

For a complex of 1:1 stoichiometry, the following relation can be derived easily, as reported formerly (13):

$$X = X_0 + 0.5\ \Delta\varepsilon\ \{c_H + c_G + 1/K_{ass} - [(c_H + c_G + 1/K_{ass})^2 - 4c_Hc_G]^{1/2}\}$$

where X is the absorption or the fluorescence intensity and c_H or c_G is the overall concentration of host or anion guest, correspondingly. The association constants, obtained by a nonlinear least-square analysis of X vs. c_H and c_G, are listed in Table 2. The data showed that both **1** and **2** recognize AcO^- with a high selectively over other anions and also with larger association constants than similar neutral receptors containing only amide groups, as reported formerly (14). This observation confirmed that the cooperative action of the thiourea and amide groups play important roles in bonding to the anion by multiple hydrogen bonding interactions. The interaction between receptor **1** and Cl^-, Br^-, or I^- was too weak to be detected. Receptor **2** bonds with Cl^- in a much weaker fashion than with AcO^- and $H_2PO_4^-$, but it does not bind Br^- or I^- at all. Receptors **1** and **2** bound anions with a similar selectivity, in the order $AcO^- > H_2PO_4^- >$ *p*-$NO_2PhO^- >$ *p*-$NO_2PhOPO_3^{2-}$ and $Cl^- >> Br^-$ and I^-. Receptor **1** had a better AcO^-:$H_2PO_4^-$ selectivity ($K_{ass}(AcO^-)/K_{ass}(H_2PO_4^-) \approx 9.0$~7.8) in comparison with that for receptor **2** ($K_{ass}(AcO^-)/K_{ass}(H_2PO_4^-) \approx 3.6$~3.2). The association constants of **1**·AcO^- ($K_{ass} = (1.3 \pm 0.2) \times 10^5$ (mol $L^{-1})^{-1}$), **2**·AcO^- ($K_{ass} = (3.4 \pm 0.6) \times 10^6$ (mol $L^{-1})^{-1}$), and **2**·$H_2PO_4^-$ ($K_{ass} = (1.0 \pm 0.2) \times 10^6$ (mol $L^{-1})^{-1}$) were higher than those for the other anions (Cl^-, Br^-, I^-, *p*-NO_2PhO^-, and *p*-$NO_2PhOPO_3^{2-}$).

Table 2. Association constants K_{ass} ((mol $L^{-1})^{-1}$) for receptors **1** or **2** with guest anions.

	Receptor **1**	Receptor **2**
Anion	K_{ass} ((mol $L^{-1})^{-1})^a$	K_{ass} ((mol $L^{-1})^{-1})^b$
AcO^- [c]	$(1.3\pm0.2)\times10^5$	$(3.4\pm0.6)\times10^6$
$H_2PO_4^-$ [c]	$(1.6\pm0.1)\times10^4$	$(1.0\pm0.2)\times10^6$
p-NO_2PhO^- [c]	$(1.1\pm0.3)\times10^4$	$(2.8\pm0.1)\times10^4$
p-$NO_2PhOPO_3^{2-}$ [d]	$(5.7\pm0.8)\times10^3$	$(8.1\pm0.7)\times10^3$
Cl^- [c]	[e]	$(8.2\pm0.8)\times10^3$

[a]The data were calculated from UV–vis titration in DMSO.
[b]The data were calculated from fluorescence titration in $CHCl_3$, except for *p*-$NO_2PhOPO_3^{2-}$, which was in DMSO.
[c]Anions were used as the tetrabutylammonium salts.
[d]Anions were used as the disodium salts.
[e]The changes in the spectra were too small to allow for calculation of the associated constants precisely.

Conclusion

The neutral receptors **1** and **2** were synthesized by an easy method in good yields. Both **1** and **2** form 1:1 complexes with anions by multiple hydrogen bonding. Receptor **1** had a better AcO^-:$H_2PO_4^-$ selectivity in comparison with that for receptor **2**. Receptors **1** and **2** bound anions with a similar

© 2004 NRC Canada

selectivity, in the order $AcO^- > H_2PO_4^- > p\text{-}NO_2PhO^- > p\text{-}NO_2PhOPO_3^{2-}$ and $Cl^- >> Br^-$ and I^-. The binding of receptor **1** with AcO^- produced a visible color change, which is promising for its use as an optical chemosensor for the acetate anion.

Experimental section

General methods

Melting points were measured on a Reichert 7905 melting-point apparatus (uncorrected). The infrared spectra were performed on a Nicolet 670 FT-IR spectrophotometer. The mass spectra were recorded on a ZAB-HF-3F spectrometer. Elemental analyses were determined by a PerkinElmer 204B elemental autoanalyzer. ^{1}H NMR spectra were recorded on a Varian Mercury VX-300MHz spectrometer. UV–vis spectra were taken on a TU-1901 spectrometer. Fluorescence spectra were obtained on a Schimadzu RF-5301 spectrometer.

Materials

Methanol was refluxed with magnesium and distilled before use, and CH_2Cl_2 was distilled after refluxing with CaH_2. All other commercially available reagents were used without further purification. The anionic substrates were used as the tetrabutylammonium salts, except $p\text{-}NO_2PhOPO_3^{2-}$, which was used as the disodium salt. Dimethyl 2,6-pyridinedicarboxylate was synthesized according to literature (15).

Synthesis

N,N′-*Di(aminoethylene)-2,6-pyridine-dicarbonylamine (3)*

Under a nitrogen atmosphere, ethylenediamine (4.49 g, 74.49 mmol) and dimethyl 2,6-pyridinedicarboxylate (2 g, 10.2 mmol) were dissolved in dry methanol (150 mL), and the reaction mixture was stirred at room temperature for 2 h. After filtration, the filtrate was collected, and then the solvent and the excess ethylenediamine were removed entirely by evaporation under reduced pressure to give **3** (2.24 g) as a white solid in 83.6% yield, which was used in the next step without further purification. mp 170–172 °C. FT-IR (KBr pellet) (cm^{-1}): 3488, 3405 (ν_{NH}), 1655 (ν_{CONH}). ^{1}H NMR (300 MHz, $CDCl_3$) δ: 2.87 (t, J = 5.4 Hz, 4H; NCH_2), 3.22 (b, 4H; NH_2, diminished after adding D_2O), 3.51 (t, J = 5.4 Hz, 4H; $CONCH_2$), 8.07~8.19 (m, 3H; PyH), 9.68 (s, 1H; CONH), 10.47 (s, 1H; CONH). Anal. calcd. for $C_{11}H_{17}N_5O_2$: C 52.56, H 6.83, N 27.87; found: C 52.45, H 7.02, N 27.62.

N,N′-*Di(*p-*NO_2-phenylthioureylene-ethylene)-2,6-pyridine-dicarbonylamine (1) (16)*

To a solution of *p*-nitrophenyl isothiocyanate (0.72 g, 4 mmol) in dry CH_2Cl_2 (25 mL), **3** (0.5 g, 2 mmol) in dry CH_2Cl_2 (25 mL) was added slowly at room temperature. After stirring overnight, the precipitate was filtered off, recrystallized from ethanol, washed with petroleum ether, and dried in vacuum to obtain pure **1** (1.11 g) as a pale yellow solid in 90.8% yield. mp 163 to 164 °C. IR (KBr pellet) (cm^{-1}): 1659 (ν_{CONH}), 1538 (ν_{NO2}), 1331 ($\nu_{N\text{-}CS\text{-}N}$), 851, 752 ($\nu_{Ar}$). ^{1}H NMR (300 MHz, DMSO-d_6) δ: 3.61 (s, 4H; NCH_2), 3.76 (s, 4H; $CONCH_2$), 7.77~8.17 (AA′BB′, 8H; ArH), 8.14~8.24 (m, 3H; PyH), 8.51 (s, 2H; NHCS), 9.54 (s, 2H; CONH), 10.26 (s, 2H; ArNHCS). MS (FAB) *m*/*z* (%): 611 (2, $[M]^+$). Anal. calcd. for $C_{25}H_{25}N_9O_6S_2$: C 49.08, H 4.13, N 20.61; found: C 49.15, H 4.22, N 20.44.

N,N′-*Di(1-naphthylthioureylene-ethylene)-2,6-pyridine-dicarbonylamine (2)*

To a solution of naphthylisothiocyanate (0.5 g, 2.7 mmol) in dry CH_2Cl_2 (10 mL), **3** (0.34 g, 1.35 mmol) in dry CH_2Cl_2 (20 mL) was added slowly at room temperature. After stirring overnight, the solvent was removed under reduced pressure to give a yellow oil. The crude product was purified by column chromatography using CH_2Cl_2–CH_3OH (100:1) as eluant on neutral alumina, to obtain **2** (0.73 g) as a white solid in 88.5% yield. mp 117 to 118 °C. FT-IR (KBr pellet) (cm^{-1}): 1664 (ν_{CONH}), 1269 ($\nu_{N\text{-}CS\text{-}N}$), 780, 752 ($\nu_{Ar}$). ^{1}H NMR (300 MHz, DMSO-d_6) δ: 3.61 (s, 4H; NCH_2), 4.30 (s, 4H; $CONCH_2$), 7.24~8.00 (m, 17H; ArH, PyH), 8.14 (s, 2H; NHCS), 8.29 (s, 2H; ArNHCS), 9.23 (s, 2H; CONH). MS (FAB) *m*/*z* (%): 621 (4, $[M]^+$). Anal. calcd. for $C_{33}H_{31}N_7O_2S_2$: C 63.74, H 5.04, N 15.77; found: C 63.68, H 5.09, N 15.61.

Binding studies

The studies on the binding properties of **1** were carried out in DMSO or DMSO-d_6. The studies on the binding properties of **2** were carried out in $CHCl_3$ or $CDCl_3$, except for $p\text{-}NO_2PhOPO_3^{2-}$, which were also in DMSO or DMSO-d_6. UV–vis spectral studies were carried out by addition of anions to a 2.5×10^{-5} mol L^{-1} solution of receptors, except that the receptors were first added to a solution of $p\text{-}NO_2PhOPO_3^{2-}$ or $p\text{-}NO_2PhO^-$ (2.5×10^{-5} mol L^{-1}). The fluorescence titration was performed with a series of 5×10^{-6} mol L^{-1} solutions of receptor **2** containing different amounts of anions (in $CHCl_3$, the excited wavelength was 307 nm, and the excitation and emission slit width were 5 nm and 10 nm, correspondingly, for AcO^-, $H_2PO_4^-$, Cl^-, Br^-, I^-, and $p\text{-}NO_2PhO^-$ anions; in DMSO, the excited wavelength was 293 nm, and the excitation and emission slit width were 5 nm for the $p\text{-}NO_2PhOPO_3^{2-}$ anion). The Job plot study was performed on a total concentration of 0.1 mmol L^{-1}. The ^{1}H NMR study was recorded by adding equivalent amounts of anions to the receptors (1.0×10^{-2} mol L^{-1}).

Acknowledgement

We thank the National Natural Science Foundation for financial support (grant No. 20072029).

References

1. (*a*) P.A. Gale. Coord. Chem. Rev. **213**, 79 (2001); (*b*) P.A. Gale. Coord. Chem. Rev. **199**, 181 (2000).
2. (*a*) G. McSkimming, J.H.R. Tucker, H. Bouas-Laurent, J.-P. Desvergne, S.J. Coles, M.B. Hursthouse, and M.E. Light. Chem. Eur. J. **8**, 3331 (2002); (*b*) J.S. Kim, O.J. Shon, J.A. Rim, S.K. Kim, and J. Yoon. J. Org. Chem. **67**, 2348 (2002); (*c*) J. Kang, M. Choi, J.Y. Kwon, E.Y. Lee, and J. Yoon. J. Org. Chem. **67**, 4384 (2002).
3. P.D. Beer and P.A. Gale. Angew. Chem. Int. Ed. Engl. **40**, 486 (2001).

© 2004 NRC Canada

4. (*a*) D.W. Yoon, H. Hwang, and C.H. Lee. Angew. Chem. Int. Ed. Engl. **41**, 1757 (2002); (*b*) H. Ihm, S. Yun, H.G. Kim, J.K. Kim, and K.S. Kim. Org. Lett. **4**, 2897 (2002); (*c*) M.J. Hynes, B. Maubert, V. McKee, R.M. Town, and J. Nelson. J. Chem. Soc. Dalton. Trans. 2853 (2000); (*d*) S. Aldridge, I.A. Fallis, and S.T. Howard. Chem. Commun. 231 (2001).
5. (*a*) M.M.G. Antonisse and D.N. Reinhoudt. Chem. Commun. 443 (1998); (*b*) P. Bühlmann, E. Pretsch, and E. Bakker. Chem. Rev. **98**, 1593 (1998); (*c*) M.A. Hossain, J.M. Llinares, D. Powell, and K. Bowman-James. Inorg. Chem. **40**, 2936 (2001).
6. (*a*) K. Shigemori, S. Nishizawa, T. Yokobori, T. Shioya, and N. Teramae. New J. Chem. **26**, 1102 (2002); (*b*) T. Gunnlaugsson, A.P. Davis, J.E. O'Brien, and M. Glynn. Org. Lett. **4**, 2449 (2002); (*c*) S. Sasaki, D. Citterio, S. Ozawa, and K. Suzuki. J. Chem. Soc. Perkin. Trans 2, 2309 (2001); (*d*) J.M. Benito, M. Gómez-García, J.L.J. Blanco, C.O. Mellet, and J.M.G. Fernández. J. Org. Chem. **66**, 1366 (2001).
7. R. Kato, S. Nishizawa, T. Hayashita, and N. Teramae. Tetrahedron Lett. **42**, 5053 (2001).
8. S. Nishizawa, R. Kato, T. Hayashita, and N. Teramae. Anal. Sci. **14**, 595 (1998).
9. J. Bourson, J. Pouget, and B. Valeur. J. Phys. Chem. **97**, 4552 (1993).
10. Y. Cubo, M. Tsukahara, S. Ishihara, and S. Tokita. Chem. Commun. 653 (2000).
11. (*a*) Y. Cubo, S. Ishihara, M. Tsukahara, and S. Tokita. J. Chem. Soc. Perkin Trans. 2, 1455 (2002); (*b*) P.D. Beer, V. Timoshenko, M. Maestri, P. Passaniti, and V. Balzani. Chem. Commun. 1755 (1999).
12. G. Santis, L. Fabbrizzi, M. Licchelli, A. Poggi, and A. Taglietti. Angew. Chem. Int. Ed. Engl. **35**, 202 (1996).
13. B. Valeur, J. Pouget, and J. Bourson. J. Phys. Chem. **96**, 6545 (1992).
14. A. Szumna and J. Jurczak. Eur. J. Org. Chem. 4031 (2001).
15. N. Ogata and K. Shimamura. Polymer J. **7**, 72 (1975).
16. R.J. Motekaitis and A.E. Martell. Inorg. Chem. **27**, 2718 (1988).

© 2004 NRC Canada

Concerning the mechanism of the Friedländer quinoline synthesis

Joseph M. Muchowski and Michael L. Maddox

Abstract: Detailed experiments regarding the mechanism of the Friedländer synthesis of quinolines from *o*-aminobenzaldehydes and simple aldehydes or ketones are described. Under the basic or acidic conditions commonly used in this reaction, it is concluded that the first step involves a slow intermolecular aldol condensation of the aldehyde or ketone with the *o*-aminobenzaldehyde. The aldol adduct **5** generated in this manner then undergoes very rapid cyclization to **4**, which subsequently loses water to produce the quinoline derivative **8**. Both **5** and **4** are too short lived to be detectable (TLC), even when deliberately generated by other means. It is also shown that *E*-enones corresponding to **6**, i.e., the aldol dehydration product, are converted into quinolines (e.g., **21a** and **21b** from **17a** and **17b**) under basic or acidic conditions. Such enones are not detected as intermediates in the base-induced Friedländer synthesis, even though certain congeners (**17b**) would be easily observable. Under acidic conditions these enones are too short lived to be detectable. Schiff bases derived from 2-aminobenzaldehyde (**18a**) and aldehydes or ketones can be generated under special conditions, but they show reactivity patterns different from those seen in the usual Friedländer condensations. Thus, the ytterbium-triflate-catalyzed reaction of aldehydes with **18a** at room temperature in toluene generates the *E*-Schiff bases (**33**, R^1 = H), from which isomeric mixtures of tetrahydroquinoline derivatives **26** are formed exclusively. At higher temperatures, the *E*-Schiff bases **33** are isomerized to the *Z*-Schiff bases **34**, from which the 3-substituted quinoline derivatives **24** are formed as the major products under appropriate conditions. Also, the ytterbium-triflate-catalyzed reaction of **18a** with the pyrrolidine enamines of the methyl-*n*-alkylketones **38a**,**b** produces mixtures in which the 2-monosubstituted kinetic products **37b**,**d** predominate over the 2,3-disubstituted thermodynamic products **21c**,**e** by a factor of 4:1 to 5:1. These results are opposite to those observed under the usual basic or acidic Friedländer reactions with methyl-*n*-alkylketones, where the thermodynamic products are usually strongly favored. The unusual kinetic:thermodynamic product ratios observed with **38a**,**b** are ascribed to the generation and rapid cyclization of mixtures of the Schiff bases **35** and **36**, in which the kinetic isomer **35** is highly predominant.

Key words: mechanism, Friedländer synthesis, quinolines, intramolecular aldol reactions, Schiff bases, tetrahydroquinolines, high kinetic:thermodynamic product ratios.

Résumé : On rapporte les détails d'expériences réalisées dans le but d'élucider le mécanisme de la synthèse des quinoléines de Friedländer à partir d'*o*-aminobenzaldéhydes et d'aldéhydes ou des cétones simples. On en déduit que, dans les conditions légèrement acides ou basiques utilisées pour cette réaction, la première étape implique une condensation aldolique intermoléculaire lente de l'aldéhyde ou de la cétone avec l'*o*-aminobenzaldéhyde. L'adduit aldolique ainsi généré, **5**, subit alors une cyclisation très rapide en **4** qui perd subséquemment de l'eau pour conduire au dérivé **8** de la quinoléine. Les temps de vie des intermédiaires **5** et **4** sont tous les deux beaucoup trop courts pour qu'on puisse les détecter (CCM), même lorsqu'on tente de les générer par d'autres méthodes. On a aussi montré que les *E*-énones correspondant à **6**, c'est-à-dire le produit de déshydratation de l'aldol, peuvent être transformées en quinoléines (par exemple, **21a** et **21b** à partir de **17a** et **17b**) dans des conditions acides ou basiques. Ce type d'énone n'est pas détecté comme intermédiaire dans la synthèse de Friedländer induite par les bases même si certains congénères (**17b**) seraient facilement observables. Dans des conditions acides, les temps de vie de ces énones sont trop courts pour qu'on puisse les détecter. Les bases de Schiff du 2-aminobenzaldéhyde (**18a**) avec les aldéhydes ou les cétones peuvent être générées dans des conditions spéciales, mais leurs patrons de réactivité sont différents de ceux observés dans les condensations de Friedländer habituelles. Ainsi, la réaction catalysée par le triflate d'ytterbium des aldéhydes avec **18a**, à la température ambiante et dans le toluène, conduit à la formation de bases de Schiff de stéréochimie *E*- (**33**, R^1 = H) à partir desquelles il se forme uniquement des mélanges isomères de dérivés tétrahydroquinoléines **26**. À des températures plus élevées, les bases de Schiff de stéréochimie *E*- (**33**) s'isomérisent en bases de stéréochimie *Z*- (**34**) à partir desquelles, dans des conditions appropriées, les produits qui se forment d'une façon prépondérante sont des dérivés de la quinoléine substitués en position 3 (**24**). De plus, la réaction catalysée par le triflate d'ytterbium du produit **18a** avec

Received 3 June 2003. Published on the NRC Research Press Web site at http://canjchem.nrc.ca on 27 February 2004.

Dedicated to Professor Victor Snieckus in recognition of his numerous fundamental contributions to heteroatom directed metalations.

J.M. Muchowski[1] and M.L. Maddox. Chemistry, Roche Palo Alto, 3431 Hillview Avenue, Palo Alto, CA 94304, U.S.A.

[1]Corresponding author (e-mail: joseph.muchowski@roche.com).

 doi: 10.1139/V03-211 © 2004 NRC Canada

des énamines formées par réaction de la pyrrolidine sur les méthylalkylcétones **38a,b** conduit à la formation de mélanges dans lesquels les produits cinétiques portant un substituant en position 2 (**37b,d**) prédominent par rapport aux produits thermodynamiques disubstitués en 2,3 (**21c,e**) par un facteur allant de 4:1 à 5:1. Ces résultats sont opposés à ceux observés dans les conditions usuelles des réactions de Friedländer acide ou basique des méthylalkylcétones dans lesquelles les produits thermodynamiques sont généralement fortement favorisés. Les rapports inhabituels de produits cinétiques et thermodynamiques observés avec les produits **38a,b** sont attribués à la génération et à la cyclisation rapide de mélanges des bases de Schiff **35** et **36** dans lesquels l'isomère cinétique **35** est fortement prédominant.

Mots clés : mécanisme, synthèse de Friedländer, quinoléines, réactions aldoliques intramoléculaires, bases de Schiff, tétrahydroquinoléines, rapport élevé des rapports de produits cinétiques et thermodynamiques.

[Traduit par la Rédaction]

Introduction

The formation of a quinoline derivative by the condensation of an aromatic *o*-aminoaldehyde or *o*-aminoketone with an aldehyde or a ketone containing a methylene group alpha to the carbonyl moiety, under basic or acidic conditions, is known as the Friedländer synthesis (1–5). The development of the heteroatom-directed *o*-metalation of aromatic systems (6), which has provided facile access to a variety of *o*-aminoaldehydes and *o*-aminoketones, has made the Friedländer reaction one of the most reliable of all quinoline syntheses. Basic reaction conditions are particularly efficient for the generation of quinoline derivatives from ketones and *o*-aminoaldehydes, whereas the condensation of ketones with *o*-aminoketones is best effected in acidic media. The most notable advantage of the Friedländer synthesis is that the positions of the substituents in the homocyclic ring are fixed by the structure of the *o*-aminocarbonyl component, and the regiochemistry of the substituents in the heterocyclic ring is predictable because nonsymmetrical ketones usually give rise to the quinoline derived from the thermodynamic enolate as the major or exclusive product.

Although the general features of the Friedländer synthesis are well understood, there is still a considerable degree of uncertainty regarding the mechanistic details of the process. Two distinctly different reaction pathways have been suggested (4, 5) to account for the facts. One involves the rate-determining formation of the Schiff base **3** (Scheme 1), followed by an intramolecular aldol-type condensation to the hydroxyimine **4** and subsequent loss of water therefrom to produce the quinoline **8**. In the other proposal, the rate-limiting step is the generation of the intermolecular aldol intermediate **5**, which proceeds to the quinoline via the above mentioned hydroxyimine **4**.

Evidence in support of each mechanistic proposal exists, but that for the intermolecular aldol process is very rare. Thus, a unique example of the isolation of the purported aldol adduct **9** (Scheme 2) in the piperidine-catalyzed, room temperature reaction of 2-aminonicotinaldehyde with 1,4-cyclohexanedione has been described (7). Although an NMR spectrum of **9** could not be obtained, analytical (CHN) and IR data and the nearly quantitative generation of the expected quinoline derivative on mere heating in toluene solution were consistent with the β-ketol structure. On the other hand, Schiff bases **10** bearing a stabilizing substituent in the β-position have been generated in several instances (8–10), although not under the usual Friedländer conditions (see below). These entities, which must exist in the vinylogously stabilized forms **11**, have been cyclized under both basic (8, 10) and acidic (9) conditions. No Schiff base derived from a simple aldehyde or ketone and an aromatic *o*-aminocarbonyl compound has ever been isolated.

Given the weight of the evidence cited above, the Friedländer synthesis is usually considered to occur via an intermediate Schiff base. The intermolecular aldol mechanism has also been considered improbable because of the expected facile formation of the conjugated unsaturated carbonyl compound **6** of *E*-geometry and the unlikely conversion of this species into the quinoline (via the *Z*-stereoisomer **7**) (5). Nevertheless, recently devised versions of the Friedländer synthesis show that neither **5** nor **6** can a priori be discounted as intermediates (11–14). Indeed, in a generally overlooked 1883 publication, Drewsen (15) reported that the nitroenone **12** was converted into 2-methylquinoline with stannous chloride in hydrochloric acid medium, although neither the exact conditions nor the yield were reported!

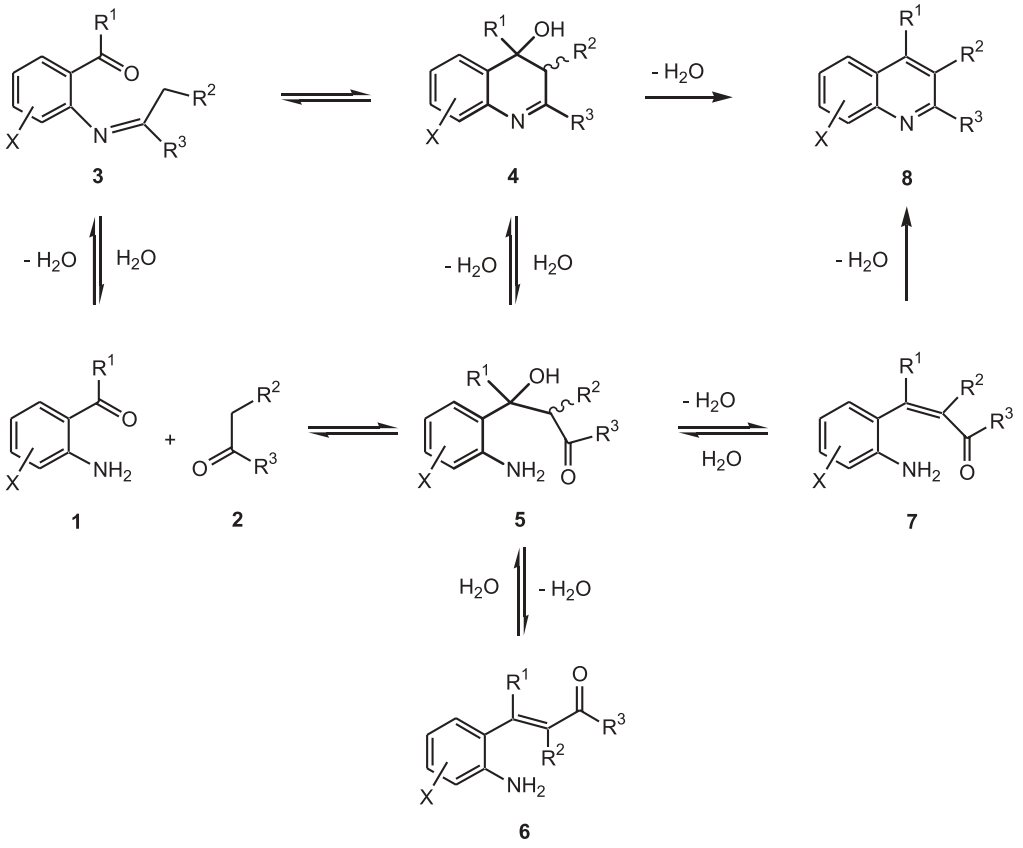
The putative generation of aldol intermediates corresponding to **5** (11, 12) and the isolation of enones (14) and the enals related to **6** (R^1, R^3 = H) (11) as *N*-acylated congeners, as well as the conversion of these species and **12** into quinolines, encouraged us to take another look at the mechanism(s) of the Friedländer synthesis. Herein are described our attempts to generate each of the intermediates shown in Scheme 1 and to establish the presence or absence thereof under conditions typically used in this synthesis.

Results and discussions

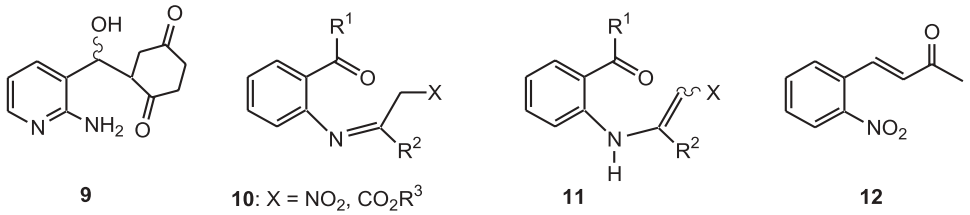
The starting materials required for this study were prepared as shown in Scheme 3. Thus, the sodium-hydroxide-promoted condensation of the aldehydes **13** with acetone or 2-butanone under conditions similar to or slightly modified from those of Baeyer and Drewsen (16) gave the β-ketols **14** as the major products. These were accompanied by minor amounts of the kinetic product **15**, from 2-butanone and **13a**, and the enone **16c**, from **13b** and acetone. The nitroenones **16a** and **16b**, obtained from the β-ketols **14a** and **14b** by dehydration with hot acetic anhydride, were converted into the amines **17a** and **17b** by reduction with iron powder and ammonium chloride in a two-phase system at room temperature (17, 18). The very unstable enal **17c** was prepared by this technique as well. This mild, chemospecific reducing system is also the preferred one for preparing 2-aminobenzaldehydes

© 2004 NRC Canada

Scheme 1. Possible mechanisms of the Friedländer quinoline synthesis.



Scheme 2.



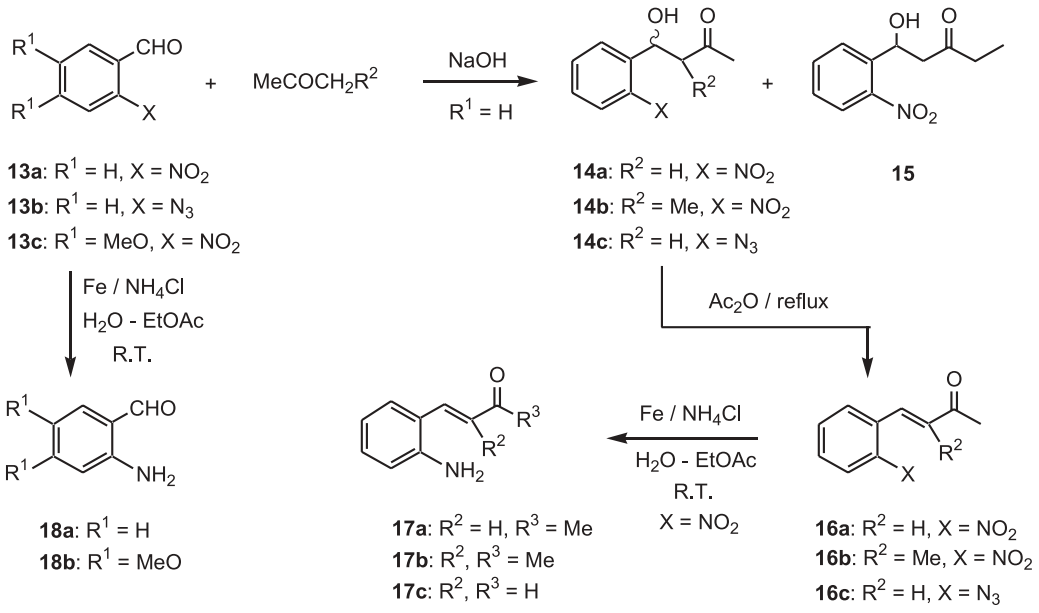
(**18**) from 2-nitrobenzaldehydes (**13a** and **13c**). Indeed, for the synthesis of 2-aminobenzaldehyde itself, it is far superior in terms of yield (86%–93%) and ease of workup than is the commonly used method (19) or its recent modification (20).

The generation of an aldol intermediate analogous to **5** (Scheme 1) was examined first. Reduction of the β-ketol **14a** with the iron – ammonium chloride system gave 2-methylquinoline-*N*-oxide (**20**, Scheme 4, Table 1) in 76% yield and a trace of 2-methylquinoline (**21a**). The *N*-oxide **20** is obviously produced by the cyclization of the very nucleophilic intermediate hydroxylamine **19a**. The nearly exclusive generation of **20** under these conditions is expected, since during the reduction of the nitro compounds **13a**, **16a**, and **16b** at least, the rapid formation of the intermediate hydroxylamines and the much slower appearance of the amines is easily seen by thin layer chromatography (TLC). In contrast, catalytic reduction of **14a** over Pd–C catalyst at atmospheric pressure gave a 4:1 mixture favoring the *N*-oxide. Somewhat similar results have been reported for the catalytic reduction of certain Baylis–Hillman (21) products derived from 2-nitrobenzaldehyde (13). Reduction of the azido compound **14c**, where the amine **19b** must be an intermediate, using the iron – ammonium chloride method gave **21a** exclusively in high yield. No intermediates were detectable by TLC in these reductions; therefore, the lifetime of both the aldol intermediate **19b** and the cyclization product **4** (Scheme 1) enroute to the quinoline must be quite short. This assumption was verified for the latter intermediate by reaction of the azido compound **14c** with triphenylphosphine. No intermediate, not even the iminophosphorane **22**, was detectable by TLC during the course of the reaction, even at room temperature.

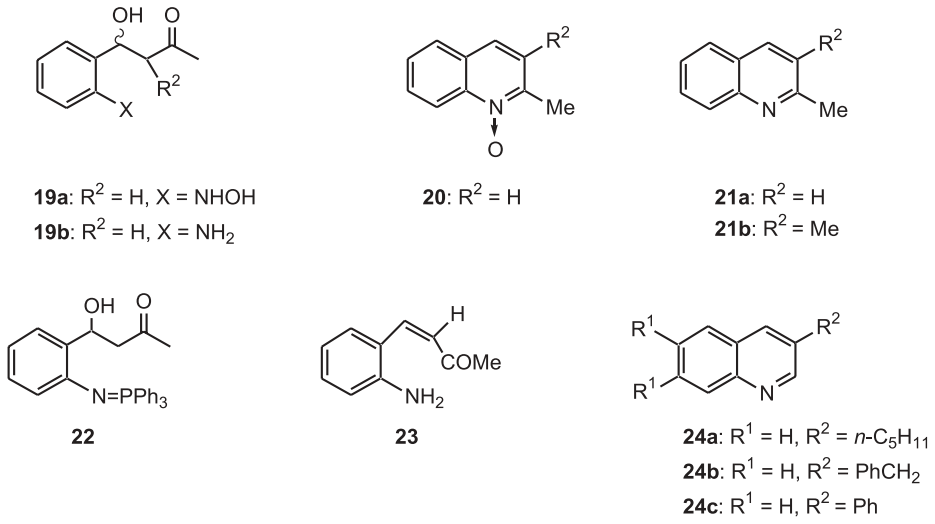
The *E*-enones **17a,b** were next studied as potential intermediates in the Friedländer synthesis. Under thermodynamic conditions, the base-catalyzed aldol condensation is reversible in all steps (22). For this reason, as well as because of

© 2004 NRC Canada

Scheme 3. Synthesis of the starting materials.



Scheme 4.



microscopic reversibility (23), it should be possible to convert the *E*-enones into the corresponding quinolines, possibly via the *Z*-enones **7** (see also ref. 24) under basic conditions. Indeed, when dissolved in aqueous ethanol containing 20 mol% sodium hydroxide, **17a** was cleanly converted into 2-methylquinoline (**21a**) after ca. 1 day at room temperature (Table 1). The reaction of 2-aminobenzaldehyde with excess acetone under very similar conditions produced **21a** more slowly but just as efficiently. These are the conditions described by Friedländer himself (2)! Even the aldehyde **17c** is very slowly transformed into quinoline with less than an equivalent of base at ambient temperature (entry 7). In contrast, the enone **17b** is stable under these conditions, but it is converted efficiently into 2,3-dimethylquinoline (**21b**) at reflux temperature using 3.3 equiv. of base. Excess sodium hydroxide is also required for the generation of **21b** from 2-aminobenzaldehyde and 2-butanone, but the reaction proceeds at room temperature (entry 9). It is noteworthy that the enone **17b** was not detectable during the course of the latter reaction, even though it would easily have been observable by TLC (intense yellow color on silica gel plates) had it been formed. Thus, although such enones clearly are viable intermediates, it is unlikely that they play a significant role in the alkali-induced version of the Friedländer quinolone synthesis. Hsaio et al. (14) have recently shown that the Horner–Emmons reaction of 2-aminonicotinaldehyde and β-ketophosphonates generated the expected naphthyridines via the *E*-enones, but they did not examine the corresponding Friedländer synthesis for these intermediates.

The question of a Schiff base intermediate **3** in the alkali-hydroxide-mediated version of the Friedländer synthesis can now be addressed with confidence. Under neutral conditions, 2-aminobenzaldehyde (**18a**) is remarkably resistant to reaction with ketones or aldehydes. For example, it can be recov-

© 2004 NRC Canada

Table 1. Formation of quinoline derivatives from putative Friedländer intermediates.

Entry	Starting materials	Conditions	Time (h)	Products (%)[a]
1	**14a**	Fe-NH_4Cl	1	**20** (76), **21a** (trace)[b]
2	**14a**	H_2, Pd–C	0.25	**20** (80)[c], **21a** (20)[c]
3	**14c**	Fe-NH_4Cl	12	**21a** (85)
4	**14c**	Ph_3P, Tol, Δ	2	**21a** (73)
5	**17a**	0.2 NaOH, EtOH-H_2O(3:1), RT	27	**21a** (83)
6	**18a** + Me_2CO	0.2 NaOH, EtOH-H_2O(4:3), RT	47	**21a** (80)
7	**17c**	0.8 NaOH, EtOH-H_2O(3:1), RT	75	Quinoline (63)
8	**17b**	3.3 NaOH, EtOH-H_2O(1:1), Δ	16	**21b** (83)
9	**18a** + MEK	3.3 NaOH, EtOH-H_2O(3:2), RT	7	**21b** (77)
10	**17c**	TFA, THF, RT	[d]	Tar
11	**17a**	1.5 mol L^{-1} HCl, Diox-H_2O(1:1), Δ	1	**21a** (82)
12	**17b**	1.5 mol L^{-1} HCl, Diox-H_2O(1:1), Δ	1	**21b** (87)
13	**18a** + Me_2CO	1.5 mol L^{-1} HCl, Diox-H_2O(1:1), Δ	2	**21a** (0)
14	**18a** + Me_2CO	cat. H_2SO_4-HOAc, Δ	18	**21a** (26)
15	**17a**	cat. H_2SO_4-HOAc, Δ	2	**21a** (35)
16	**17a**	hν, EtOH	16	**21a** (75)

Note: Tol = toluene; RT = room temperature; Diox = dioxan; cat. = catalytic H_2SO_4 in acetic acid..
[a]Yield of picrate except where indicated.
[b]TLC.
[c]Product ratio measured by NMR.
[d]Formation took place within seconds rather than hours.

ered unaltered after many hours at reflux temperature in acetone solution. Likewise, toluene solutions of **18a**, containing various aldehydes in excess, are stable at room temperature for long periods of time. Given the diminished reactivity of **18a** and its congeners toward aldehydes and ketones and the aqueous- and (or) alcohol-based media in which the alkaline hydroxide-mediated condensations are usually effected, a Schiff base intermediate in this version of the Friedländer synthesis is quite improbable.

The formation of quinoline derivatives from *N*-acylated congeners of **17c** in acidic media (11) and the relatively facile acid-induced isomerization of *Z*-enones to *E*-enones (24–28) augured well for the acid-promoted generation of quinolines from **17a-c**. The free enal **17c** was, however, rapidly destroyed, even under the mildly acidic conditions previously used (11) to cyclize the *N*-BOC congeners of **17c** (entry 10). By contrast, enones **17a**,**b** were converted into the quinolines **21a,b** in over 80% yields with 1.5 mol L^{-1} hydrochloric acid in 50% aqueous dioxane after only 1 h at reflux temperature. An attempt to prepare **21a** from 2-aminobenzaldehyde and acetone under these conditions resulted in the destruction of the starting materials. Quinoline **21a** was nevertheless slowly formed from these reactants, although only in 26% yield, when the reaction was carried out in acetic acid solution containing a catalytic amount of sulfuric acid (29) at reflux temperature. 2-Methylquinoline (**21a**) was also produced (35% yield) from the enone **17a** upon heating in the same reaction medium for 2 h. Although such enones could well be intermediates under those often-used acidic conditions, their short half-lives ensure that they would not be readily detectable, at least by TLC.

It was tacitly assumed that *Z*-enones were involved as tenuous intermediates in the conversion of the *E*-enones **17a,b** into the quinolines **21a,b**. Corroborative evidence that the *Z*-enones must indeed be very short lived was obtained by photolysis of **17a** in ethanolic solution. 2-Methylquinoline was produced as the sole product, but the presumed intermediate *Z*-enone **23** was undetectable by TLC.

Up to this point no convincing evidence for an intermediate Schiff base had been found under conditions commonly used in the Friedländer synthesis. It seemed reasonable, therefore, to attempt to generate such species from aldehydes and 2-aminobenzaldehyde (**18a**) under more classical conditions. Heating solutions of **18a** and 1.2 equiv. of *n*-heptanal, 3-phenylpropionaldehyde, or phenylacetaldehye, freshly generated from the corresponding bisulfite adducts, in toluene containing a catalytic amount (5 mol%) of *p*-toluenesulfonic acid monohydrate with separation of water, gave modest yields of 3-substituted quinolines **24a-c** (Table 2). These quinolines were formed extremely slowly, or not at all, at room temperature. The quinolines were also obtained under similar conditions and in comparable yields using ytterbium triflate (10 mol%) as the catalyst, except that the reaction periods were greatly reduced, and water separation was not necessary (Table 2, entries 2, 4, 6). In every case, independent of the catalyst used, TLC examination showed that several much less polar, yellow-colored, neutral substances were also formed, none of which was a Schiff base. *n*-Heptanal gave rise to one such material in relatively good yield (25%–43%, ytterbium triflate catalyst) as an oil with a mass spectral molecular weight of 416. This corresponds to the condensation of two molecules of heptanal and two molecules of **18a** with the loss of three molecules of water ($C_{28}H_{30}N_2O$). The IR spectrum showed absorptions at 3334, 2733, and 1659 cm^{-1}, consistent with the presence of aldehyde and NH groups strongly bonded to each other, and this was supported by the ^1H NMR spectrum (DMSO-d_6), with peaks at δ 9.80 and 8.91, respectively. In addition to

© 2004 NRC Canada

Table 2. Generation of quinolines from Schiff bases derived from RCH_2CHO (A) or $MeCOCH_2R$ (B) and **18a** or **18b**.

Entry	Starting material (R)	Catalyst	Time (h)	Products (%)[a]
1	**18a**; A(n-C_5H_{11})	TsOH	20	**24a** (34–36)[b]
2	**18a**; A(n-C_5H_{11})	$Yb(OTf)_3$	3 to 4	**24a** (29–47)[b]
3	**18a**; A($PhCH_2$)	TsOH	22	**24b** (28)[b]
4	**18a**; A($PhCH_2$)	$Yb(OTf)_3$	4	**24b** (28)[b]
5	**18a**; A(Ph)	TsOH	22	**24c** (31)[b]
6	**18a**; A(Ph)	$Yb(OTf)_3$	4	**24c** (44–53)[b]
7	**18a**; A(n-C_5H_{11})	$Yb(OTf)_3$	8(4)[c]	**24a** (47)[b]
8	**18b**; A(Ph)	$Yb(OTf)_3$	5(3)[c]	**24c** (80)
9	**18b**; A(n-C_5H_{11})	$Yb(OTf)_3$	6(3.75)[c]	**24d** (42)
10	**18b**; A(Ph)	$Yb(OTf)_3$	5(3)[c]	**24e** (78)
11	**18a**; B(Me)	$Yb(OTf)_3$	58(7)[d]	**21b** (48), **37a** (28)
12	**18a**; B(Et)	$Yb(OTf)_3$	48(7)[d]	**21c** (34.5), **37b** (41)
13	**18a**; B(Et)	NaOH	24	**21c** (66), **37b** (20)
14	**18a**; B(i-Pr)	$Yb(OTf)_3$	49(7)[d]	**21d** (4), **37c** (61)
15	**18a**; B(i-Pr)	NaOH	4	**21d** (5), **37c** (78)
16	**18a**; **38a**	$Yb(OTf)_3$	4.5[e]	**21c** (13), **37b** (62.5)
17	**18a**; **38a**	$Yb(OTf)_3$	1	**21c** (16), **37b** (77)
18	**18a**; **38b**	$Yb(OTf)_3$	6[e]	**21e** (14.5), **37d** (59)
19	**18a**; 1-heptyne	$HgCl_2$ – $Yb(OTf)_3$	72	**21e** (3.2), **37d** (0.8)

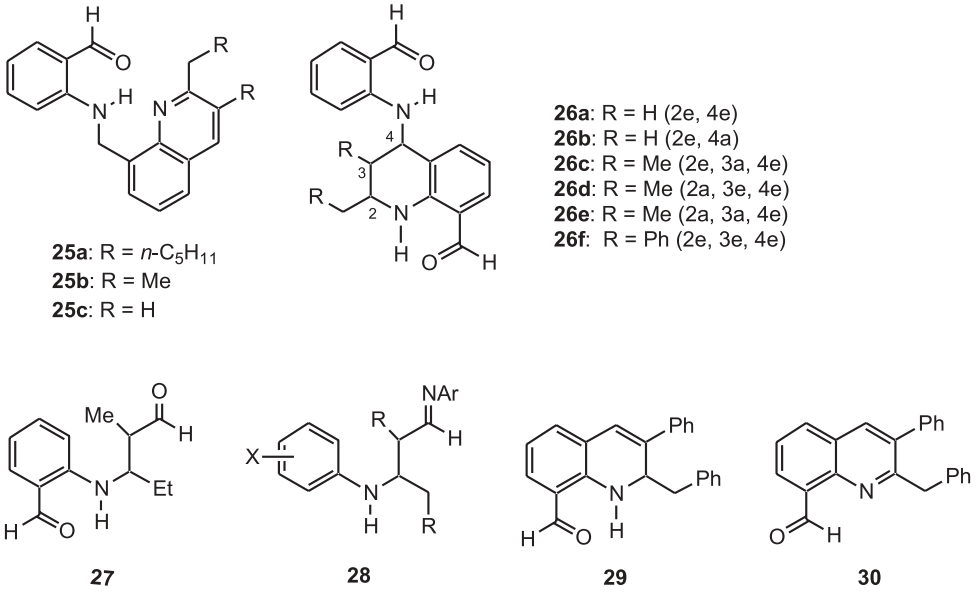
[a]Yield of free base unless otherwise indicated.
[b]Yield of picrate.
[c]Time of addition of reagents to catalyst; see Experimental.
[d]Parentheses, reflux time in toluene; no parentheses, time at 95 °C; see Experimental.
[e]Room temperature reaction.

other absorptions, the NMR spectrum possessed peaks for eight aromatic hydrogens and three methylene groups at δ 2.78, 2.98, and 5.04 (coupled to the NH by 6.2 Hz). Four of the aromatic hydrogens had a splitting pattern identical to and chemical shifts (δ 6.68 (t), 6.90 (d), 7.35 (dt), 7.58 (dd)) similar to those found in 2-aminobenzaldehyde (20). The chemical shifts of the remaining aromatic hydrogens (δ 7.43 (t), 7.63 (d), 7.78 (d), 8.05 (s)) were essentially identical to those reported for H-6, H-7, H-5, and H-4, respectively, of quinoline (30), and the multiplicities were concordant with those expected for a 2,3,8-trisubstituted derivative. This substitution pattern was strongly supported by a ROESY experiment, which showed that the δ 2.78 methylene group was vicinal to the hydrogen at δ 8.05, that the two upfield methylene groups were also vicinal, and that the low field (δ 5.04) methylene moiety was vicinal to the δ 7.63 hydrogen. The above information is fully accommodated by the quinoline derivative with structure **25a** (Scheme 5). In particular, the unusual chemical shift of the methylene group at C-8 stems from the strong deshielding effect of the peri lone electron pair of the quinoline nitrogen atom. The formation of this compound clearly requires the involvement of one or more Schiff base intermediates.

When the above reaction was attempted with propanal under similar conditions (sealed vessel), only a miniscule amount (ca. 1.5%) of **25b** was formed (crystalline). The major product in this complex reaction mixture was a structurally different yellow-colored oily substance (see below). A reaction with acetaldehyde (4 equiv.) at reflux temperature gave a complex mixture containing no major product and no trace of a material with an *Rf* expected for **25c**. It was assumed that the failure to generate significant amounts of **25b,c** was connected with the volatility of the aldehydes; therefore, the reactions were carried out at room temperature. After 2 to 3 days, acetaldehyde (4 equiv.) gave a major, new, yellow-colored oil (ca. 65% yield), but no quinoline. This material had a mass spectral molecular weight of 294, i.e., derived from the condensation of two molecules of acetaldehyde with two molecules of **18a** minus two molecules of water ($C_{18}H_{18}N_2O_2$). The NMR spectrum of this apparently homogeneous material (TLC) indicated, however, that it was a 4:1 mixture of isomers. The major component showed signals for two aldehyde moieties (δ 9.86 and 9.81), two NH groups (δ 8.67 and 8.40), seven aromatic hydrogens, multiplets corresponding to four mutually coupled aliphatic protons (δ 4.86, 3.38, 2.31, and 1.71), and a methyl group attached to a secondary carbon atom. The hydrogens at δ 4.86 and 3.83 were also coupled to the low-field NH and the methyl group, respectively. Deuteration of the NH hydrogens and decoupling of the methyl group permitted measurement of all the aliphatic hydrogen coupling constants (Table 3) and assignment of the *cis* 2,4-disubstituted tetrahydroquinoline structure **26a** to this substance, with the methyl and aniline moieties occupying equatorial sites in a half-chair system. Full decoupling studies were not carried out on the minor component, but the data in Table 3 indicate that it is the *trans* stereoisomer **26b** with the anilino group axial. When propanal was used in the room temperature reaction, a not-readily-separable 54:34:12 mixture of stereoisomers was obtained in about 50% yield. The high-temperature reaction

© 2004 NRC Canada

Scheme 5.



mentioned above gave mainly the major isomer, and the NMR spectral data in Table 3 establish that this is the 2,3,4-trisubstituted tetrahydroquinoline **26c**, analogous to **26a** but with a C-3 axial methyl group. The isomers of intermediate and least abundance have structures **26d** and **26e**, with the 2,3,4-substituents arranged a,e,e and a,a,e. In addition to the three tetrahydroquinolines, the acyclic dialdehyde **27** was isolated as a single isomer in ca. 40% yield. The room-temperature reaction of 2-aminobenzaldehyde and phenylacetaldehyde was not studied in detail, but a very insoluble, surprisingly high-melting (236 °C) yellow solid could be isolated in ca. 15% yield. The NMR spectral data (Table 3) unequivocally show that this is the all-equatorial isomer **26f**.

The formation of tetrahydroquinolines from anilines and aliphatic aldehydes has been known for some time (31, 32) and proceeds via an intermediate Schiff base dimer **28**, which sometimes can be isolated (e.g., for X = H, R = Et, Ar = Ph (31)). The dimer cyclization is acid catalyzed, high yielding, and takes place at room temperature. It is apparent that the dialdehyde **27** is the hydrolysis product of the intermediate enroute to the tetrahydroquinolines **26**. It is also worth noting that the tetrahydroquinolines and the dihydroquinoline described below are well-recognized intermediates in the Doebner–Miller quinoline synthesis (see ref. 5, pp. 102–104).

The high-temperature ytterbium-triflate-promoted reaction of phenylacetaldehyde with 2-aminobenzaldehyde gave, in addition to 3-phenylquinoline, a complicated neutral mixture from which a crystalline, yellow-colored, structurally unique monoaldehyde could be isolated (13%–29%). That this substance was the 1,2-dihydroquinoline **29** was evident from its NMR spectrum, which showed, among other signals, absorptions for an aldehyde hydrogen, an NH moiety, an olefinic hydrogen (singlet), a methine hydrogen, and a benzylic methylene group at δ 9.77, 8.38, 6.61, 5.03, and 2.82, respectively. The methine hydrogen was coupled to both the NH (J = 2.6 Hz) and the methylene hydrogens (J = 6.0 Hz).

Solutions of **29** underwent slow aerial oxidation to the corresponding quinoline **30**, which was obtained much more efficiently by oxidation with Fremy's salt (33). The aldehyde hydrogen of the latter compound is found at δ 11.46, nearly δ 2 downfield from that observed for **29**. The remarkably low-field position of this proton must be a consequence of an aldehyde conformation in which the hydrogen and oxygen are close to and remote from the lone pair of the quinoline nitrogen atom, which is a conformation that the aldehyde must adopt to avoid an unfavorable dipole–dipole interaction. The hydrogen of a series of quinoline-8-carboxaldehydes has been reported to resonate at δ 11.3–11.5 without comment (34).

The isolation of the dihydroquinoline **29** was of considerable significance, because it suggested a plausible mechanism for the formation of the quinoline containing dimers **25**. Specifically, fragmentation of the tetrahydroquinoline dimers **26** to 2-aminobenzaldehyde and the 1,2-dihydroquinoline **31**, followed by Schiff base formation from these fragments, would generate **32**, which could lead to **25** by an intramolecular redox process (Scheme 6). In fact, a boiling solution of the isomeric tetrahydroquinolines **26c**, **26d**, and **26e** in toluene containing 10 mol% of ytterbium triflate was slowly (15–21 h) converted into a mixture from which the previously described quinoline dimer **25b** could be isolated in ca. 25% yield. The tetrahydroquinoline mixture derived from acetaldehyde (**26a** and **26b**) was converted even more rapidly (4 h) and more efficiently (>45% yield) into the 2-methyl analog **25c**.

Why are the Schiff bases derived from aliphatic aldehydes and 2-aminobenzaldehyde converted exclusively into tetrahydroquinolines at room temperature and only give the expected 3-substituted quinolines at higher temperature? The answer must certainly be associated with the geometry of the Schiff base. At ambient temperature, the thermodynamically more stable *E*-isomer **33** (Scheme 7) must be generated essentially exclusively. This geometry cannot, however, lead to the 3-substituted quinoline; therefore, intermolecular aldolization to the Schiff base dimers followed by cyclization to the tetrahydroquinoline derivatives takes place. At higher temperature the *E*-isomer exists in equilibrium

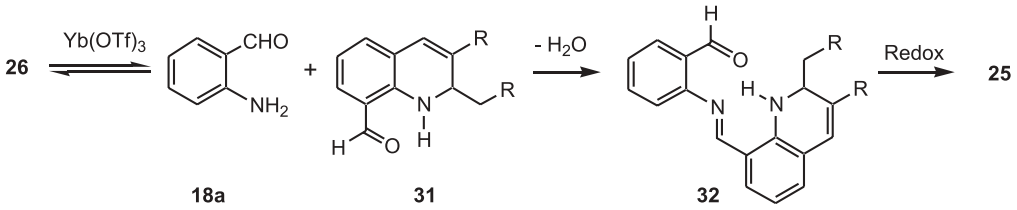
© 2004 NRC Canada

Table 3. NMR spectral data for tetrahydroquinolines **26** in CD_2Cl_2.

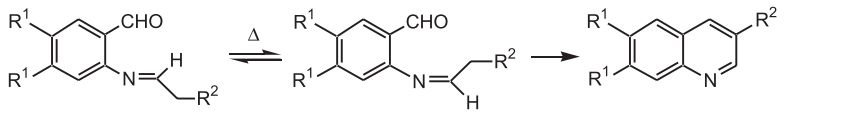
			δ (ppm) and *J* (Hz)											
Compound	R	Stereo	**1**-NH	**2**	**3a**	**3e**	**4**	**4**-NH	**2**-Me	**2**-$MeCH_2$	**2**-CH_2(A)	**2**-CH_2(B)	**3**-Me	CHO	CHO
26a	H	2e,4e	8.40	3.83 10.9 (2a,3a) 3.2 (2a,3e)	1.71 12.5 (3a,3e) 11.8 (3a,4a) 4.8 (3e,4a)	2.31	4.86 8.3 (4a,NH)	8.67	1.36 6.3 (2a,Me)					9.81	9.86 0.4
26b	H	2e,4a	8.37	3.60 10.1 (2a,3a) 3.1 (2a,3e)	1.65 13.1 (3a,3e) 3.6 (3a, 4e) 3.6 (3e, 4e)	2.17	4.74 7.2 (4e,NH)	8.48	1.33 6.5 (2a,Me)					9.78	9.84
26c	Me	2e,3a,4e	8.46	3.69 2.9 (2a,3e)		2.29 4.2 (3e,4a)	4.99 8.7 (4a,NH)	8.66		1.14 7.7	1.66 7.3 (2a,CH_2)		0.85 7.1	9.86	9.94
26d	Me	2a,3e,4e	8.56	3.30 3.4 (2e,3e)		1.91 10.4 (3a,4a)	4.45 9.2 (4a,NH)	8.64		1.07 7.6	1.60 14.1 (A,B) 3.4 (2e,CH_2)	1.86	1.06 7.0	9.87	9.92 0.8
26e	Me	2a,3a,4e	8.41	3.36 3.0 (2e,3e)	2.16 2.2 (3e,4a)		4.36 7.2 (4a,NH)	8.44		1.01 7.6	1.55 13.4 (A,B) 3.0 (2e,CH_2)	1.65	0.83 6.9	9.76 0.7	9.85
26f	Ph	2e,3e,4e	8.59	4.11 10.4 (2a,3a)	2.98 10.8 (3a,4a)		4.95 8.6 (4a,NH)	8.56			2.49 13.8 (A,B) 9.9 (2a,B) 3.0 (2a, A)	2.84		9.56 0.3	9.77

© 2004 NRC Canada

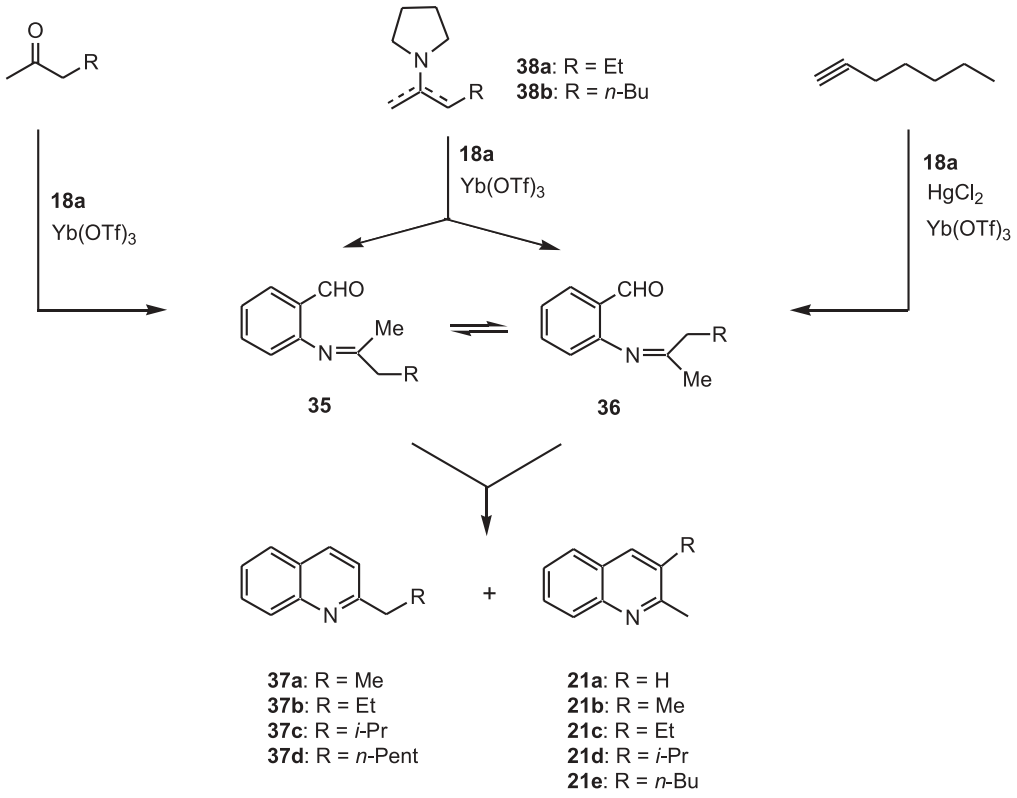
Scheme 6. Generation of quinolines **25** from tetrahydroquinolines **26**.



Scheme 7. Aldehyde Schiff base cyclization.



Scheme 8. Ketone Schiff base cyclization.



with *Z*-isomers **34**, which by an intramolecular aldolization can now produce the 3-alkylquinoline. The conversion of the tetrahydroquinoline derivatives **26** into the dimeric quinoline derivatives **25** must also involve higher energy processes, and thus, the temperature must be raised for this transformation to occur at a useful rate as well.

There are two important consequences of the above results. Firstly, given that the *Z*-Schiff base is a high-temperature intermediate, it should be possible to devise conditions that would favor its formation and thus increase the 3-alkylquinoline yield. Indeed, addition of a solution of the 2-aminobenzaldehydes **18a** or **18b** and a slight excess of *n*-heptanal or phenylacetaldehyde in toluene to a boiling suspension of ytterbium triflate in toluene over a 3 to 4 h period gave the expected 3-substituted quinolines in 40%–80% yields (Scheme 7 and Table 2, entries 7–10). Secondly, if Schiff bases of unsymmetrical ketones (e.g., methyl alkyl ketones) could be generated, and if *E–Z* equilibration did occur (e.g., **35** with **36**, Scheme 8), then mixtures of two quinolines (**21** and **37**) should be formed, and the 2-

© 2004 NRC Canada

substituted quinoline **37** might well predominate. This would be quite different from what occurs under the usual basic or acidic conditions of the Friedländer synthesis (see above). Schiff bases unfortunately do not form from ketones and 2-aminobenzaldehyde under the conditions described above for aldehydes. It was found, however, that heating a solution of **18a** in 2-butanone containing catalytic ytterbium triflate at 95 °C resulted in the very slow (>2 days) consumption of the aldehyde. Removal of the excess 2-butanone, followed by heating the residue in toluene at reflux temperature for 7 h, gave a 1.7:1 mixture of 2,3-dimethylquinoline (**21b**) and 2-ethylquinoline (**37a**, Scheme 8) in over 90% yield (Table 2, entry 11). In contrast, under alkaline conditions, 2,3-dimethylquinoline was the only product obtained (Table 1, entry 9). When 2-pentanone was used in the above reactions, 2-*n*-propylquinoline (**37b**) predominated over 2-methyl-3-ethylquinoline (**21c**) by a factor of 1.2 for ytterbium triflate, whereas the latter quinoline was the major product in the sodium-hydroxide-mediated reaction (**21c**:**37b** = 3.3:1, Table 2, entries 12 and 13). Hawes and Gorecki (35) also observed a slight predominance (factor of 1.1) of the kinetic over the thermodynamic product in the piperidine-catalyzed reaction of 4-aminonicotinaldehyde with neat 2-butanone. These results suggested that the kinetic product might be favored to an even greater extent for 4-methyl-2-pentanone, and a 15.3:1 **37c**:**21d** ratio supported this prediction. It was astonishing to find, however, that essentially the same product ratio (15.6:1) was observed for the sodium-hydroxide-promoted reaction, in which a Schiff base intermediate is unlikely based on the data described herein. Since the enolization of 4-methyl-2-pentanone occurs rapidly at both sites (deuteration complete in <5 min in perdeuteriomethanol containing a catalytic amount of the sodium derivative), it is probable that the highly selective formation of **37c** in the alkali-mediated condensation results from steric inhibition of aldolization at the methylene site. It is significant that analogous results have been reported for β-methyl substituted ketones both under acidic (36) and basic (37) conditions. Except for the case of 4-methyl-2-pentanone, the alterations in product ratios toward the kinetic one, although significant, are not so large that they are convincingly diagnostic of Schiff base intermediates. Since anhydrous conditions were not maintained in these reactions, it is quite possible that substantial amounts of the quinoline were formed by intermolecular aldol processes in both the piperidine- (35) and the ytterbium-triflate-catalyzed reactions. The facile acid-catalyzed transamination of enamines and Schiff bases (38–40) and the well-known water sensitivity of the latter prompted an examination of the reactivity of the pyrrolidine enamines of 2-pentanone (**38a**) and 2-heptanone (**38b**) towards 2-aminobenzaldehyde (Scheme 8). For example, a solution of **18a** in anhydrous toluene containing 2.4 equiv. of the enamine **38a** (1 equiv. of **38a** to ensure anhydrous conditions) and catalytic ytterbium triflate was rapidly and efficiently converted into a mixture of the expected quinolines **21c** and **37b**, both at reflux (<1 h) and room (4 h) temperature. The kinetic product **37b** was favored by a factor of ca. 5 in both cases (Table 2, entries 16 and 17). The kinetic product was also highly favored for the reaction of **18a** with the enamine **38b** at room temperature (**37d**:**21e** = 4:1). These are reasonable results if both the generation of the Schiff bases (mainly **35**) and the cyclization thereof to the quinolines are very fast processes.

Lastly, the room-temperature hydroarylamination of 1-heptyne with **18a** in the presence of an equimolar amount of mercuric chloride (41) and catalytic ytterbium triflate gave a mixture of **37d** and **21e** (4:1) in low, but reproducible yield (4%). In this case, the quinolines must be generated via Schiff base intermediates. The 4:1 kinetic:thermodynamic product ratio was identical to that observed for **38b** and strongly supports Schiff base intermediates in the enamine based reactions.

When this study was completed, Dormer et al. (37) reported that the kinetic product was dramatically favored when the methyl alkyl ketone was added slowly to a hot ethanolic solution of the 2-aminoarylaldehyde, a slight excess of various secondary amines, and a catalytic amount of sulfuric acid. Kinetic:thermodynamic product ratios as high as 24 were observed when the secondary amine was 1,3,3-trimethyl-6-azabicyclo[3.2.1]octane (TABO). The authors did not offer an explanation of these remarkable results. It is our contention that the reaction conditions reported by these investigators are precisely those that should result in the rapid formation and cyclization of the kinetic Schiff base, which arises by the fast transamination of an intermediate enamine.

In conclusion, the results described herein show that the generation of quinolines from simple aldehydes and 2-aminobenzaldehydes under the typically used acidic or basic conditions of the Friedländer synthesis takes place by a process in which an intermolecular aldol condensation is the first step. It is highly probable that the same mechanism is involved when 2-aminoarylketones are used to prepare quinolines. When Schiff bases are deliberately generated from aldehydes at room temperature, the kinetically formed *E*-isomer is diverted to nonFriedländer products. 3-Substituted quinolines are formed only at higher temperatures, which effect isomerization of the *E*-Schiff base to the *Z*-isomer, which then undergoes intramolecular aldolization to the heterocyclic aromatic product. When Schiff bases are generated from methyl alkyl ketones, the kinetically favored, less-hindered *Z*-Schiff base is formed preferentially and rapidly cyclizes to the 2-alkylquinoline derivative. Thus, the hallmark of such cyclizations is a high kinetic:thermodynamic product ratio, a result completely opposite to that observed when the usual acidic or basic reaction conditions are employed in the Friedländer quinoline synthesis. This result has obvious synthetic consequences, which have been convincingly demonstrated in the recently described study of Dormer et al. (37).

Experimental

General

The melting points are uncorrected. The NMR spectra (300 and 600 MHz) were recorded in deuteriochloroform unless indicated otherwise, and the chemical shifts are reported in parts per million (ppm) (δ) with internal tetramethylsilane as zero. The IR spectra were measured as dispersions in KBr for solids and as films for liquids. The UV spectra were taken in methanol solution. Reactions were followed by TLC on silica gel plates unless otherwise indi-

© 2004 NRC Canada

cated. Column chromatographic separations were effected using 230–400 mesh silica gel. The columns were packed dry, successively layered with the crude reaction mixture (absorbed onto silica gel) and a small amount of sand, and then eluted with the appropriate solvent system. The mixtures absorbed on silica gel were prepared by dissolving the reaction mixture in dichloromethane, adding this solution to silica gel, and then removing the solvent in vacuo.

The terms "worked up in the usual manner", "the usual workup", etc., signify that the extract was dried over anhydrous sodium sulfate, and the solvent was then removed in vacuo.

4-Hydroxy-4-(2-azidophenyl)-2-butanone (14c) and 4-(2-azidophenyl)-(3*E*)-buten-2-one (16c)

Aqueous sodium hydroxide (0.25 mol L^{-1}, 0.6 mL) was added dropwise at 15 °C to a stirred solution of 2-azidobenzaldehyde (**13b** (42)) (294 mg, 2 mmol) dissolved in a mixture of acetone (2.6 mL), water (2 mL), and ethanol (2 mL). One half hour after the addition was completed, the reaction mixture was poured into aqueous sodium chloride and extracted with dichloromethane. The extract was washed with water and then worked up as usual to give an oil (401 mg), which was taken up in a small amount of dichloromethane and added to silica gel (2 g), and the mixture was evaporated to dryness in vacuo. This material was layered onto a dry packed column (3.5 × 8.5 cm) of silica gel (40 g) covered with sand and eluted with hexane – ethyl acetate ((70:30), 20 mL fractions (F)). F 2–4 contained the enone **16c** (34 mg, 9.1%), and F 6–10 contained the β-ketol **14c** (324 mg, 78.9%), both of which were crystalline.

After crystallization from cyclohexane and drying in vacuo at 23 °C for 5 h with protection from light, the β-ketol **14c** had mp 69 to 70 °C. ^{1}H NMR δ: 2.20 (s, 3H), 2.72 (dd, 1H, *J* = 9.5, 17.6 Hz), 2.91 (dd, 1H, *J* = 2.7, 17.6 Hz), 3.47 (d, 1H, *J* = 3.1 Hz, exchanged with D_2O), 5.34 (m, 1H), 7.13 (dd, 1H, *J* = 1.0, 8.0 Hz), 7.17 (td, 1H, *J* = 1.1, 7.7 Hz), 7.32 (td, 1H, *J* = 1.7, 7.7 Hz), 7.54 (dd, 1H, *J* = 1.6, 7.7 Hz). ^{13}C NMR δ: 30.62, 50.45, 65.31, 117.87, 125.18, 128.65, 133.83, 136.05, 209.22. Anal. calcd. for $C_{10}H_{11}N_3O_2$: C 58.94, H 5.40, N 20.48; found: C 58.85, H 5.40, N 20.60.

After crystallization from cyclohexane and drying in vacuo (17 h), the enone **16c** had mp 107 to 108 °C. ^{1}H NMR δ: 2.39 (s, 3H), 6.70 (d, 1H, *J* = 16.5 Hz), 7.15 (d, 1H, *J* = 7.8 Hz), 7.20 (td, 1H, *J* = 1.0, 8.1 Hz), 7.43 (td, 1H, *J* = 1.5, 8.5 Hz), 7.6 (dd, 1H, *J* = 1.5, 7.8 Hz). ^{13}C NMR δ: 27.20, 118.82, 125.05, 126.11, 127.90, 128.71, 131.54, 137.62, 139.32, 198.57. Anal. calcd. for $C_{10}H_9N_3O$: C 64.16, H 4.85, N 22.45; found: C 64.54, H 4.89, N 22.33.

4-(2-Nitrophenyl)-3-methyl-(3*E*)-buten-2-one (16b)

Sodium hydroxide (0.25 mol L^{-1}) was added dropwise at 15 °C to a stirred solution of 2-nitrobenzaldehyde (**13a**, 3.022 g, 20 mmol) in a mixture of 2-butanone (32 mL, 25.7 g), ethanol (12 mL), and water (20 mL), until the solution was weakly alkaline (ca. 15 mL). After 1 h the solution was diluted with water, and the mixture was extracted with ether, washed with saturated NaCl solution, and then processed as usual to give a mixture of the β-ketols **14b** and **15** (4.42 g). This mixture was dissolved in acetic anhydride (10 mL); sodium acetate (1.64 g, 20 mmol) was added, and the mixture was heated at reflux temperature for 1 h. Water was added cautiously to the hot solution to decompose the excess acetic anhydride, and when the vigorous reaction was over, the mixture was poured into ice-water and extracted with dichloromethane. The extract was washed successively with 10 wt % sodium carbonate solution and water and then worked up as usual. The crude product (4.07 g) was absorbed onto silica gel (20 g), loaded onto a dry packed column (6 × 28 cm) of silica gel (380 g), and eluted with hexane – ethyl acetate (70:30, 50 mL fractions). F 13–16 contained the desired crystalline enone **16b** (2.66 g, 65.6%). Subsequent fractions contained a mixture of **16b** and 5-(2-nitrophenyl)-(4*E*)-penten-3-one. An analytical specimen of the desired enone was obtained by crystallization from hexane and had mp 59 to 60 °C after drying in vacuo (4 h). ^{1}H NMR δ: 1.83 (d, 3H, *J* = 1.4 Hz), 2.50 (s, 3H), 7.39 (d, 1H, *J* = 7.8 Hz), 7.54 (td, 1H, *J* = 1.2, 7.8 Hz), 7.69 (td, 1H, *J* = 1.2, 7.5 Hz), 7.81 (bs, 1H), 8.18 (dd, 1H, *J* = 1.3, 8.2 Hz). ^{13}C NMR δ: 13.25, 26.26, 125.38, 129.58, 131.68, 132.30, 133.83, 136.64, 139.22, 147.88, 200.14. Anal. calcd. for $C_{11}H_{11}NO_3$: C 64.38, H 5.40, N 6.83; found: C 64.52, H 5.33, N 6.95.

Reduction of nitro compounds with iron powder and ammonium chloride

The following is a typical reduction. A mixture of the nitro compound (10 mmol) dissolved in ethyl acetate (100 mL), water (60 mL), iron powder (2.1 g, 37.5 mmol (Fisher Scientific, electrolytic, <100 mesh; iron powder from other suppliers, e.g., Malinckrodt, gave similar results, but the reductions were slower.)), and ammonium chloride (3.34 g, 62.5 mmol) was stirred vigorously at room temperature for the time period shown below. The mixture was filtered through Celite, and the inorganic residue was washed well with ethyl acetate. The ethyl acetate phase was separated and combined with an ethyl acetate extract of the aqueous phase; the extract was washed with saturated NaCl solution and then worked up as usual. The crude product was then purified by column chromatography on silica gel as described below.

4-(2-Aminophenyl)-(3*E*)-buten-2-one (17a)

Reaction time, 17 h. A 4 mmol scale reaction product (absorbed on silica gel, 3 g) was purified by column (3.5 × 14 cm) chromatography on silica gel (67 g, 25 mL fractions). The product (0.516 g, 80.0%), present in F 3–5, was obtained as a yellow oil. ^{1}H NMR δ: 2.36 (s, 3H), 4.01 (bs, 2H), 6.53 (d, 1H, *J* = 16.0 Hz), 6.71 (dd, 1H, *J* = 1.3, 8.3 Hz), 6.77 (td, 1H, *J* = 1.0, 7.3 Hz), 7.18 (td, 1H, *J* = 1.5, 7.3 Hz), 7.39 (dd, 1H, *J* = 1.5, 8.0 Hz), 7.68 (d, 1H, *J* = 16.0 Hz). ^{13}C NMR δ: 28.47, 117.30, 119.48, 120.29, 127.16, 128.57, 131.96, 139.06, 146.32, 198.63. A sample of this material was converted into the pivalamide (59.9%) by the technique described below for **17b**. A sample on solution in hot toluene and dilution with an equal volume of hexane gave material with mp 119 to 120 °C (lit. (43) value mp 117 to 118 °C).

4-(2-Aminophenyl)-3-methyl-(3*E*)-buten-2-one (17b)

Reaction time, 20 h. The crude product from an 8.38 mmol reaction was absorbed onto silica gel (8 g) and

© 2004 NRC Canada

purified on a column (4 × 23 cm) of silica gel (152 g) using hexane – ethyl acetate (65:35, 50 mL fractions). The product was contained in F 10–15 as an oil (1.266 g, 83.8%). IR (film) (cm^{-1}): 3452, 3366, 3244, 1659, 1623. ^{1}H NMR δ: 1.95 (d, 1H, J = 1.4 Hz), 2.46 (s, 3H), 3.74 (bs, 2H), 6.74 (dd, 1H, J = 0.9, 8.0 Hz), 6.80 (dt, 1H, J = 1.0, 7.5 Hz), 7.12 (dd, 1H, J = 1.6, 7.6 Hz), 7.17 (dd, 1H, J = 1.5, 7.7 Hz), 7.45 (bs, 1H). ^{13}C NMR δ: 13.64, 26.38, 116.20, 118.77, 121.84, 130.02, 130.11, 136.19, 144.70, 200.55.

The pivalamide of this compound was prepared as follows. Trimethylacetyl chloride (0.25 mL, 245 mg, 2.03 mmol) was added all at once to a stirred solution of the above amino compound (269 mg, 1.49 mmol) in toluene (30 mL) containing triethylamine (0.3 mL, 218 mg, 2.15 mmol) and 4-dimethylaminopyridine (18 mg) at 0 °C. The cooling bath was removed, and the mixture was stirred at room temperature for 18 h. The mixture was washed successively with water, 1 mol L^{-1} HCl, 10 wt % sodium carbonate, and saturated NaCl solution. After the usual workup, the brown solid was taken up in hot toluene (3 mL) and diluted with hexane (9 mL) to give the pivalamide (127 mg, mp 111 to 112 °C). A second crop (31 mg, mp 110–111.5 °C, total yield, 158 mg, 40.9%) of product was obtained from the mother liquor. Recrystallization of the first crop gave the analytical specimen, which had mp 111.5–112 °C, after drying in vacuo (9 h at 40 °C). Anal. calcd. for $C_{16}H_{21}NO_2$: C 74.10, H 8.16, N 5.40; found: C 74.33, H 8.10, N 5.57.

2′-Aminocinnamaldehyde (17c)

Reaction time, 4 h. After washing the ethyl acetate solution of the crude product with saturated NaCl solution and drying over sodium sulfate, the solvent was removed in vacuo at room temperature or below and the amino compound (100% yield) was immediately dissolved in toluene. Toluene solutions of this material, which contains a trace of quinoline (TLC), can be kept for a few days without significant decomposition when stored at 5 °C with protection from light.

2-Aminobenzaldehyde (18a)

Reaction time, 5 h. The crude product from a 20 mmol reaction was purified by normal column (4.2 × 18 cm) chromatography on silica gel (125 g), using hexane – ethyl acetate (70:30, 50 mL fractions). F 5–8 contained the product (2.08–2.25 g, 86%–93%), which crystallized spontaneously and usually had mp 37 to 38 °C (lit. (19) value mp 38 to 39 °C) after drying in vacuo. It is indefinitely stable when stored at 5 °C.

2-Amino-4,5-dimethoxybenzaldehyde (18b)

Reaction time, 20 h. The crude product from a 10 mmol reaction was purified by normal column (3.5 × 19.5 cm) chromatography on silica gel (100 g) using hexane – ethyl acetate (1:1, 50 mL fractions). F 7–13 contained the product (1.395 g, 77%), which had mp 82–84 °C (lit.(44) value mp 86 °C) after drying in vacuo. ^{1}H NMR δ: 3.85 (s, 3H), 3.89 (s, 3H), 6.12 (s, 1H), 6.88 (s, 1H), 9.69 (d, 1H, J = 0.4 Hz). ^{13}C NMR δ: 56.36, 56.92, 98.82, 111.75, 116.43, 141.42, 147.67, 156.56, 191.78.

Preparation of 2-methylquinoline-*N*-oxide (20) and 2-methylquinoline (21a) from the β-ketol 14a

Iron – ammonium chloride reduction

This reduction was effected in the manner described above on a 1 mmol scale. Evaporation of the ethyl acetate phase in vacuo gave 92 mg of a crystalline solid. The aqueous phase was brought to pH 9 with solid sodium carbonate, then saturated with sodium chloride and extracted with ethyl acetate. The extract was processed as usual to give a further 42 mg of solid. The solid material was identical to authentic **20** (yield 75.6%) and contained only a trace of **21a** by TLC.

Catalytic reduction

A solution of **14a** (418 mg, 2 mmol) in ethanol (30 mL), containing 10% Pd–C (40 mg), was hydrogenated at room temperature and atmospheric pressure. After 25 min, hydrogen absorption (89% of theory) ceased, the mixture was filtered through Celite, and the solvent was removed in vacuo to give a residue (321 mg), which by ^{1}H NMR was an 80:20 mixture of **20** and **21a**. Crystallization from hot water gave the monohydrate of **20** (222 mg, 62.6%), which had mp 72.5–74 °C (lit. (45) value mp 77 to 78 °C).

Preparation of 2-methylquinoline (21a) from the azido compound 14c

Iron – ammonium chloride reduction

This reduction was carried out using the same reagent and solvent ratios as described above for the nitro compound reductions. Reaction time, 22 h. The ethyl acetate phase, containing **21a**, was extracted with 1 mol L^{-1} HCl; the acid extract was brought to pH 9 with solid sodium carbonate; the mixture was extracted with ethyl acetate, and the extract was washed with saturated NaCl solution. After the usual workup, the crude base (138 mg from a 1 mmol reaction) was converted into the picrate (317 mg, 85.1%) with picric acid (240 mg) in hot ethanol (10 mL). The picrate was identical to an authentic specimen by mmp, and the free base recovered therefrom was identical by NMR spectroscopy to authentic material.

Triphenylphosphine

A solution of the azido compound **14c** (61.5 mg, 0.3 mmol) in toluene (10 mL), containing triphenylphosphine (79 mg, 0.3 mmol), was stirred at room temperature. By 1 h, **21a** and triphenylphosphine oxide were clearly visible by TLC (20:80 ethyl acetate – hexane, UV), but no other new spots were present. After 2 h, the solution was heated at reflux temperature for 2 h; it was extracted with 1 mol L^{-1} HCl, and the acid extract was worked up exactly as described for the iron – ammonium chloride reduction. Crude **21a** (41 mg) was converted into the picrate (81.7 mg, 73.3%) with picric acid (70 mg) in hot ethanol (4 mL).

Preparation of the quinolines by isomerization of 17a-c

With sodium hydroxide

2-Methylquinoline (21a)

A solution of **17a** (100 mg, 0.62 mmol) in ethanol (3 mL), water (1 mL), and 1 mol L^{-1} NaOH (0.1 mL) was stirred at room temperature for 22 h. Water was added, and the mix-

© 2004 NRC Canada

ture was extracted with ethyl acetate; the extract was washed with saturated NaCl solution and worked up in the usual way. The crude base (96 mg) was converted into the picrate (192 mg, 83.4%) in the usual way.

Quinoline

A solution of the freshly prepared enal **17c** (147 mg, 1 mmol) in ethanol (6 mL), water (2 mL), and 1 mol L^{-1} NaOH (0.1 mL) was left at room temperature. Additional NaOH was added at 22 h (1 mol L^{-1}, 0.2 mL) and at 47 h (2.5 mol L^{-1}, 0.2 mL). After 75 h the ethanol was removed in vacuo, and the residue was made acidic with 1 mol L^{-1} HCl and washed with ethyl acetate. The acidic phase was then worked up, as described for the preparation of **21a** from **14c** above. The crude base was converted into quinoline picrate (224 mg, 62.5%).

2,3-Dimethylquinoline (21b)

A solution of the enone **17b** (120 mg, 0.67 mmol) in ethanol (3 mL), water (1 mL), and 1 mol L^{-1} NaOH (2.2 mL) was heated at reflux temperature for 16 h. The reaction mixture was worked up as described above for the preparation of **21a**. The crude base was converted into the picrate (213 mg, 82.8%). A sample of the picrate was stirred with excess 1 mol L^{-1} NaOH and toluene. The toluene phase was separated, washed with saturated NaCl solution, and worked up in the usual way to give 2,3-dimethylquinoline, mp 67–68.5 °C (lit. (46) value mp 68.2–69 °C).

Acid-mediated isomerization

2-Methylquinoline (21a): 1.5 mol L^{-1} HCl

A solution of **17a** (100 mg, 0.62 mmol) in dioxan (3 mL) and 3 mol L^{-1} HCl (3 mL) was heated at reflux temperature for 1 h. The cooled solution was diluted with water and made basic with solid sodium carbonate. The mixture was extracted with ethyl acetate; the extract was washed with saturated NaCl solution and worked up in the usual way to give the crude base (86 mg), from which was obtained the picrate (189 mg, 81.8%).

2-Methylquinoline (21b): Catalytic sulfuric acid in acetic acid

To a solution of the enone **17a** (315 mg, 1.95 mmol) in acetic acid (8 mL) was added a 0.18 mol L^{-1} solution of sulfuric acid in acetic acid (2 mL), and the blood-red reaction mixture was heated at reflux temperature for 2.25 h. Toluene was added, and the mixture was evaporated to a small volume in vacuo. The residue was diluted with water, made basic with sodium carbonate, and extracted with ethyl acetate. The extract was washed with 1 mol L^{-1} HCl, and the acid phase was made basic with solid sodium carbonate and extracted with ethyl acetate. The extract was washed with saturated NaCl solution and worked up as usual to give an oil (219 mg), which was absorbed onto silica gel (2.2 g) and purified by column (2.2 × 12 cm) chromatography on silica gel (23 g) using hexane – ethyl acetate (65:35, 10 mL fractions). F 6–9 contained the product (168 mg), which was converted into the picrate (251 mg, 34.6%).

2,3-Dimethylquinoline (21b): 1.5 mol L^{-1} HCl

The enone **17b** was converted into **21b** exactly as described above to give the picrate in 86.7% yield.

Preparation of the quinolines from 2-aminobenzaldehyde (18a) and ketones

Sodium-hydroxide-mediated condensations

2-Methylquinoline (21a)

A solution of **18a** (121 mg, 1 mmol) in ethanol (4 mL), water (4 mL), acetone (0.6 mL, 0.475 g, 8 mmol), and 1 mol L^{-1} NaOH (0.2 mL) was left at room temperature for 47 h. The reaction mixture was worked up exactly as described for the preparation of **21a** from **17a** under alkaline conditions to give the picrate (298 mg, 80.0%).

2,3-Dimethylquinoline (21b)

A solution of **18a** (121 mg, 1 mmol) in ethanol (6 mL) and 1 mol L^{-1} NaOH (3.5 mL) containing 2-butanone (108 mg, 1.5 mmol) was left at room temperature for 12 h and then worked up as described above for **17a**. The crystalline base was converted into the picrate (296 mg, 76.6%).

Acid-mediated condensation

2-Methylquinoline (21a)

To a solution of **18a** (61 mg, 0.5 mmol) and acetone (87 mg, 1.5 mmol) in acetic acid (4.5 mL) was added a 0.18 mol L^{-1} solution of sulfuric acid in acetic acid (0.5 mL), and the solution was heated at reflux temperature for 18 h. The reaction mixture was worked up exactly as described for the sulfuric-acid-catalyzed isomerization of **17a**. The crude product (43 mg) was absorbed onto silica gel (1 g) and purified by column (1.8 × 5.5 cm) chromatography on silica gel (9 g) using hexane – ethyl acetate (60:40, 10 mL fractions). F 2–4 contained the product (20 mg), which was converted into the picrate (49 mg, 26.2%).

2-Methylquinoline (21a) by photolysis of 17a

A solution of the enone **17a** (20 mg, 0.124 mmol) in ethanol (4 mL) in a pyrex test tube was placed next to a Pen-Ray Model PS-1 pencil light, and both were enveloped in aluminum foil. The solution was irradiated until TLC showed that **17a** was absent (24 h); the solvent was removed in vacuo, and the crude base was converted into the picrate (34.4 mg, 74.6%).

Preparation of 3-substituted quinolines 24a-c from 18a and aldehydes

p-Toluenesulfonic acid catalyst

A solution of **18a** (121 mg, 1 mmol) and the appropriate aldehyde (1.2 mmol, freshly liberated from the bisulfite adduct) in toluene (50 mL) containing *p*-toluenesulfonic acid monohydrate (10 mg) was heated at reflux temperature with separation of water in a Dean–Stark apparatus until **18a** was no longer present by TLC (see Table 2). The base was extracted into 1 mol L^{-1} HCl; the extract was made basic with solid sodium carbonate and extracted with ethyl acetate. After the usual processing the crude base was converted into the known picrate (See Table 2 for yields). The bases, liberated from the picrates, were also fully characterized by NMR spectroscopy.

© 2004 NRC Canada

Ytterbium triflate as catalyst

Normal conditions

A solution of **18a** (121 mg, 1 mmol) and the appropriate aldehyde (1.2–1.4 mmol, freshly liberated from the bisulfite adduct) in toluene (10 mL) containing suspended ytterbium triflate (62 mg, 0.1 mmol) was stirred at reflux temperature (argon atmosphere) for 4 h. The cooled mixture was vigorously stirred with 10 wt % sodium carbonate solution for 15 min, and the toluene phase was separated. The bases were extracted into 1 mol L^{-1} HCl and processed as described above. See Table 2 for picrate yields. When the product was 3-phenylquinoline, HCl extraction often caused the insoluble salt to crystallize and form an emulsion. In this case, it was necessary to alternatively extract with HCl and water, until all of the salt had been removed.

*Modified conditions: Preparation of quinolines **24a** and **24c-e***

A solution of **18a** or **18b** (2 mmol) and the aldehyde (2.4–2.5 mmol) in toluene (15 mL) was added dropwise (argon atmosphere) to a stirred suspension of ytterbium triflate (124 mg, 0.2 mmol) in toluene (15 mL) at reflux temperature over the time period indicated in Table 2 in parentheses. Heating at reflux temperature was then continued until the total elapsed time indicated in Table 2. The cooled mixture was vigorously stirred with 10 wt % sodium carbonate solution for 15 min, and the toluene phase was separated. The subsequent workup depended on the specific compound. For **24a** and **24c**, the bases were extracted with 1 mol L^{-1} HCl and liberated with sodium carbonate as described above. The yield of **24a** corresponds to that of the picrate, whereas that of **24c** refers to the free base. See below for **24d** and **24e**.

3-*n*-Pentyl-6,7-dimethoxyquinoline (24d)

The acid extract was made basic in the usual way and extracted with ethyl acetate. The extract was washed with saturated NaCl solution and then processed as usual to give the crude crystalline base (277 mg). This material was absorbed onto silica gel (1.5 g) and subjected to column (3.5 × 11.5 cm) chromatographic purification on silica gel (55.5 g) using 1:1 hexane – ethyl acetate (25 mL fractions). F 10–13 contained the solid product (217 mg, 41.8%). After two crystallizations from hexane and drying in vacuo for 24 h, it had mp 63.5–65 °C. ^{1}H NMR δ: 0.90 (t, 3H, J = 7.0 Hz), 1.29–1.40 (m, 4H), 1.65–1.75 (m, 2H), 2.74 (t, 2H, J = 7.6 Hz), 4.01 (s, 3H), 4.02 (s, 3H), 7.00 (s, 1H) 7.40 (s, 1H), 7.71 (d, 1H, J = 2.1 Hz), 8.57 (d, 1H, J = 2.1 Hz). ^{13}C NMR δ: 14.01, 22.51, 31.01, 31.37, 33.06, 56.00, 56.06, 104.78, 107.81, 123.72, 132.73, 133.68, 143.61, 149.58, 149.79, 151.71. Anal. calcd. for $C_{16}H_{21}NO_2$: C 74.10, H 8.16, N 5.40; found: C 74.25, H 8.16, N 5.56.

3-Phenyl-6,7-dimethoxyquinoline (24e)

The toluene solution containing the reaction mixture was not extracted with acid. Instead, after washing with saturated NaCl solution and the usual workup, the crude product from a 1 mmol reaction was absorbed onto silica gel (1.5 g) and subjected to column (2.2 × 20 cm) chromatographic purification on silica gel (35.5 g) using 1:1 hexane – ethyl acetate (20 mL fractions). F 9–18 contained the product (208 mg, 78.4%), the ^{1}H NMR spectrum of which was identical to that reported (47).

2-*n*-Hexyl-3-*n*-pentyl-8-(2-formyl)anilinomethylquinoline (25a)

A 2 mmol reaction was carried out as described in the section Normal conditions above, except that the acid extraction to remove **24a** was not carried out. The toluene solution of the product mixture was washed with saturated NaCl solution and then worked up as usual to give an oil (439 mg), which was absorbed onto silica gel (2.2 g) and subjected to column (3.5 × 17 cm) chromatography on silica gel (88 g) using hexane – ethyl acetate (90:10, 25 mL fractions). F 5–7 contained **25a** (104–179 mg, 25%–43%) as a yellow oil. IR: see Discussion section. UV (nm): 385 (ε 6520), 319.5 (ε 4620), 306.5 (ε 4330), 261.5 (ε 10 100), 229 (ε 57 700), 213 (ε 59 600). ^{1}H NMR: see Discussion section. ^{13}C NMR (CD_2Cl_2) δ: 14.58, 14.69, 23.34, 23.48, 28.93, 29.25, 30.20, 32.58, 32.71, 33.00, 36.12, 43.39, 112.23, 115.47, 119.49, 125.88, 126.85, 127.00, 127.92, 135.32, 136.27, 136.45, 137.31, 162.00, 194.50. MS m/z (%): 417 ([M + H]$^+$, 56), 312 (65), 296 (100), 212 (28), 198 (31), 171 (27). HR-FAB$^+$-MS m/z calcd. for $[C_{28}H_{36}N_2O]H^+$: 417.2897; found: 417.2895.

2-Ethyl-3-methyl-8-(2-formyl)anilinomethylquinoline (25b)

A mixture of the isomeric tetrahydroquinolines **26d-e** (227 mg, 0.704 mmol, see below for synthesis) in toluene (25 mL) containing suspended ytterbium triflate (48 mg, 0.077 mmol) was stirred at reflux temperature under argon for 22 h. The reaction mixture was stirred with sodium carbonate for 15 min, and then the toluene phase was processed as described above to give a solid residue (206 mg), which was absorbed onto silica gel (1.0 g) and purified by column (3.5 × 14 cm) chromatography on silica gel (69 g) using hexane – ethyl acetate (85:15, 20 mL fractions). F 3–5 contained the product (76 mg), and F 7 contained the product admixed with a slightly more polar material (8 mg). The major fraction on crystallization from cyclohexane gave the crystalline product in two crops, mp 145–147 °C (47 mg) and mp 144–146 °C (2 mg). The minor fraction gave an additional 2 mg of product, mp 144.5–145 °C, from cyclohexane. Total yields, 51 mg (23.8%). Recrystallization from cyclohexane gave an analytical specimen that had mp 147–148.5 °C after drying in vacuo (45 °C, 16 h). IR (KBr) (cm^{-1}): 3434, 3334, 2750, 1656. UV (nm): 386 (ε 6250), 318.5 (ε 3750), 304.5 (ε 3530), 263 (ε 9370), 228 (ε 51 600), 211 (ε 55 500). ^{1}H NMR (CD_2Cl_2) δ: 1.45 (t, 3H, J = 7.4 Hz), 2.48 (d, 3H, J = 0.9 Hz), 3.02 (q, 2H, J = 7.4 Hz), 5.16 (bs, 2H), 6.65 (td, 1H, J = 0.9, 6.7 Hz), 6.83 (d, 1H, J = 8.5 Hz), 7.30 (td, 1H, J = 1.7, 7.8 Hz), 7.37 (d, 1H, J = 7.1 Hz), 7.47 (dd, 1H, J = 1.7, 7.8 Hz), 7.57 (dd, 1H, J = <1, >6 Hz), 7.65 (dd, 1H, J = <1, 8.3 Hz), 7.85 (bs, 1H), 8.98 (bs, 1H, exchanged with D_2O), 9.83 (d, 1H, J = 0.6 Hz). ^{13}C NMR δ: 12.29, 19.40, 29.55, 43.22, 125.67, 126.39, 126.51, 127.59, 130.03, 135.82, 136.06, 137.02, 144.86, 151.47, 162.36, 194.25. Anal. calcd. for $C_{20}H_{20}N_2O$: C 78.92, H 6.62, N 9.20; found: C 79.25, H 6.58, N 9.35.

2-Methyl-8-(2-formyl)anilinomethylquinoline (25c)

A solution of a mixture of **26a** and **26b** (203 mg, 0.69 mmol, see below for synthesis) in toluene (20 mL) containing suspended ytterbium triflate (86 mg) was stirred at reflux temperature (argon atmosphere) for 4 h and then

© 2004 NRC Canada

worked up as described for **25b**. The crude product (177 mg) was absorbed onto silica gel (1 g) and subjected to column (3.5 × 11.5 cm) chromatographic purification on silica gel (54 g) using hexane – ethyl acetate (85:15, 20 mL fractions). F 5–10 contained the product (121 mg), which was crystallized from cyclohexane to give the desired material in two crops, mp 95–95.5 °C (85 mg) and mp 94.5–95 °C (10 mg). Thus the yield of **25c** was 95 mg (46.5%). Recrystallization of a sample from cyclohexane gave the analytical specimen, which had mp 94.5–95.5 °C after drying in vacuo (9.5 h). IR (KBr) (cm^{-1}): 3480 (bw), 3350, 2738, 1666. UV (nm): 383 (ε 6850), 317 (ε 3530), 304 (ε 3500), 267 (ε 9980), 224 (ε 52 900), 208 (ε 51 900), 206.5 (ε 52 500). ^{1}H NMR δ: 2.78 (s, 3H), 5.17 (d, 2H, *J* = 5.9 Hz), 6.65 (td, 1H, *J* = 0.8, 7.4 Hz), 6.76 (d, 1H, *J* = 8.5 Hz), 7.29 (td, 1H, *J* = 1.6, 8.6 Hz), 7.38 (t, 3H, *J* = 7.6 Hz), 7.47 (dd, 1H, *J* = 1.6, 7.7 Hz), 7.61 (dd, 1H, *J* = 1.0, 7.1 Hz), 7.66 (d, 1H, *J* = 8.1 Hz), 8.02 (d, 1H, *J* = 8.4 Hz), 9.02 (bs, 1H, exchanged with D_2O), 9.87 (s, 1H). ^{13}C NMR δ: 25.93, 43.21, 111.99, 115.19, 119.08, 122.37, 125.71, 126.82, 127.14, 127.42, 135.95, 136.09, 137.03, 146.30, 151.41, 158.68, 194.32. Anal. calcd. for $C_{18}H_{16}N_2O$: C 78.23, H 5.84, N 10.14; found C 78.50, H 5.89, N 10.22.

Synthesis of the tetrahydroquinolines 26

A solution of **18a** (242 mg, 2 mmol) and the appropriate aldehyde (8 mmol) in toluene (20 mL) containing suspended ytterbium triflate (124 mg, 0.2 mmol) was stirred at room temperature under argon for the time period indicated below. The reaction mixture was then vigorously stirred with excess 10 wt % sodium carbonate solution for 15 min; the toluene phase was separated, washed with saturated NaCl solution, and worked up as usual. The bases were purified as described below.

cis- And *trans*-2-methyl-4-(2-formyl)anilino-1,2,3,4-tetrahydroquinoline-8-carboxaldehydes 26a and 26b

The crude product from a 2 mmol reaction was absorbed onto silica gel (1.5 g) and purified by column (3.5 × 12.5 cm) chromatography on silica gel (63.5 g) using hexane – ethyl acetate (80:20, 25 mL fractions). F 4–7 contained the product as a TLC homogeneous oil (191–210 mg, 65%–72%), which by ^{1}H NMR spectroscopy was a 4:1 mixture of **26a** and **26b**. IR (film) (cm^{-1}): 3317, 2744, 1653. UV (nm): 388 (ε 12 000), 262.5 (ε 11 400) 237 (ε 33 800). ^{1}H NMR: see Table 3. ^{13}C NMR (*e*,*e*-isomer **26a**) δ: 22.51, 36.34, 46.93, 49.57, 111.39, 115.05, 115.84, 117.59, 118.99, 123.35, 132.40, 135.84, 136.48, 137.41, 147.93, 150.75, 193.96, 194.53. MS *m*/*z* (%): 294 (27), 279 (28), 174 (100). HR-FAB$^+$-MS *m*/*z* calcd. for $C_{18}H_{18}N_2O_2$: 294.1368; found: 294.1362.

2-Ethyl-3-methyl-4-(2-formyl)anilino-1,2,3,4-tetrahydroquinoline-8-carboxaldehydes (26c-e) and 2-methyl-3-(2-formyl)anilinopentanal (27)

A reaction effected in the usual manner was complete in 2 days. The mixture from a 2 mmol reaction was absorbed onto silica gel (2 g) and purified by column (4 × 21.5 cm) chromatography on silica gel (143 g) using hexane – ethyl acetate (85:15, 50 mL fractions). F 5–7 contained **26c-e** (135 mg); F 8,9 contained a 1:1 mixture of **26c-e** and **27**; and F 10–12 contained pure **27** (50 mg), all as oils. See Table 3 for the ^{1}H NMR spectra of **26c-e**. The aldehyde **27** was a single isomer. ^{1}H NMR (CD_2Cl_2) δ: 0.96 (t, 3H, *J* = 7.4 Hz), 1.19 (d, 3H, *J* = 7.2 Hz), 1.65 (m, 2H), 2.68 (m, 1H, *J* = 1.2, 4.6, 7.2 Hz), 3.96 (m, 1H), 6.69 (td, 1H, *J* = 0.9, 7.4 Hz), 6.79 (d, 1H, *J* = 8.6 Hz), 7.39 (td, 1H, *J* = 1.7, 7.9 Hz), 7.47 (dd, 1H, *J* = 1.7, 7.7 Hz), 8.41 (bd, 1H, *J* = 9.7 Hz, exchanged with D_2O), 9.69 (d, 1H, *J* = 1.2 Hz), 9.79 (d, 1H, *J* = 0.7 Hz). ^{13}C NMR (CD_2Cl_2) δ: 9.07, 11.05, 26.55, 50.01, 53.94, 111.51, 115.47, 119.01, 136.19, 137.30, 150.90, 194.46, 203.92. MS *m*/*z* (%): 219 (87), 190 (20), 161 (44), 162 (100), 144 (100), 132 (31), 122 (45), 118 (47), 93 (42). HR-FAB$^+$-MS *m*/*z* calcd. for $[C_{13}H_{17}NO_2]H^+$: 220.1337; found: 220.1341.

A reaction effected at 110 °C had a very different product spectrum. Thus, a 2 mmol reaction was carried out in toluene (40 mL) in a pressure bottle for 6 h. Workup as described above gave a mixture, which by TLC (hexane – ethyl acetate (85:15)) showed four major products with *Rf*s 0.88, 0.78, 0.72, and 0.67. The most polar material corresponded to **26c**. The mixture was absorbed onto silica gel (1.5 g) and subjected to column (3.5 × 12 cm) chromatography on silica gel (60 g) using hexane – ethyl acetate (85:15, 25 mL fractions). F 8–10 (112 mg) partially crystallized, and after slurrying with 95:5 hexane – ethyl acetate, crystalline **25b** (8.8 mg, 1.4%), mp 144 to 145 °C, was collected by filtration. F 11–13 (102 mg) contained impure **26c**. F 14,15 (11 mg) was pure **26c**. ^{1}H NMR: see Table 3. ^{13}C NMR (CD_2Cl_2) δ: 6.63, 10.96, 26.46, 54.21, 111.84, 115.36, 116.17, 117.53, 119.66, 122.58, 133.08, 135.78, 136.80, 135.78, 136.80, 137.70, 148.26, 151.17, 194.17, 194.94. MS *m*/*z* (%): 322 (32), 307 (13), 293 (34), 202 (100), 186 (55), 172 (29), 149 (47). HR-EI-MS *m*/*z* calcd. for $C_{20}H_{22}N_2O_2$: 322.1681; found: 322.1667.

trans,*trans*-2-Benzyl-3-phenyl-4-(2-formyl)anilino-1,2,3,4-tetrahydroquinoline-8-carboxaldehyde (26f)

Reaction was carried out in the usual manner, except that the ratio of phenylacetaldehyde to **18a** was 2 and the reaction time was 41 h. Removal of the toluene from a 2 mmol reaction gave a residue, which partially crystallized. The mixture was slurried with toluene; the insoluble solid was collected by filtration and dried to give **26f** (130.5 mg, 14.6%), mp 235–238 °C. A sample was dissolved in hot 1,2-dichloroethane, diluted with four volumes of hexane, and seeded to give material with mp 236–238 °C, after drying in vacuo (75 °C, 6 h). IR (KBr) (cm^{-1}): 3428, 3292, 2751, 2733, 1652. ^{1}H NMR: see Table 3. ^{13}C NMR (CD_2Cl_2) δ: 40.64, 49.56, 55.97, 58.06, 111.71, 115.04, 115.66, 118.07, 118.67, 124.25, 127.25, 127.67, 128.57, 128.79, 129.05, 129.17, 129.38, 129.88, 133.01, 135.77, 136.95, 137.86, 140.14, 146.85, 151.11, 193.68, 194.14. Anal. calcd. for $C_{30}H_{26}N_2O_2$: C 80.69, H 5.87, N 6.27; found: C 80.71, H 5.81, N 6.41.

1,2-Dihydro-2-benzyl-3-phenylquinoline-8-carboxaldehyde (29)

The reaction was carried out as described for the synthesis of **25a** except that the reaction time was 6 h, and the 3-phenylquinoline was removed by extraction with 1 mol L^{-1} HCl. The toluene phase containing **29** was then washed suc-

© 2004 NRC Canada

cessively with 10 wt % sodium carbonate and saturated NaCl solution and then worked up as usual. The crude product from a 2 mmol reaction was absorbed onto silica gel (2 g) and purified by column (4 × 17 cm) chromatography on silica gel (110 g) using hexane – 1,2-dichloroethane (35:65, 25 mL fractions). F 9–13 contained the product (52–115 mg, 13%–29% yield based on phenylacetaldehyde), which was crystalline. After two crystallizations from cyclohexane and drying in vacuo (7 h), it had mp 119.5–121.5 °C. IR (CCl_4) (cm^{-1}): 3313, 2737, 1663. UV (nm): 420.5 (ε 9330), 346.5 (ε 3940), 269 (ε 23 800), 234 (ε 18 600). ^{1}H NMR: see Discussion. ^{13}C NMR (CD_2Cl_2) δ: 43.28, 55.99, 115.99, 118.25, 122.20, 122.67, 125.75, 126.88, 128.36, 128.65, 130.08, 132.61, 135.22, 135.28, 137.66, 138.40, 146.29, 193.44. Anal. calcd. for $C_{23}H_{19}NO$: C 84.89, H 5.89, N 4.30; found: C 84.66, H 5.75, N 4.49.

2-Benzyl-3-phenylquinoline-8-carboxaldehyde (30)

A solution of potassium nitrosodisulfonate (Fremy's salt, 90 mg, 0.335 mmol) in 4 wt % aqueous sodium carbonate (6 mL) was added to a stirred solution of **29** (87 mg, 0.267 mmol) in acetonitrile (9 mL). This caused precipitation of some **29**, but after 1 h a clear solution was obtained. After 6 h, the solution was diluted with a large volume of water and extracted with ethyl acetate. The extract was washed with saturated NaCl solution and then worked up as usual. The crude product was absorbed onto silica gel (0.5 g) and subjected to column (2.2 × 15 cm) chromatographic purification on silica gel (27.5 g) using hexane – 1,2-dichloroethane (35:65, 15 mL fractions). F 4,5 contained the starting material (19 mg), and F 7–21 contained the product (46.5 mg, 66% yield based on starting material consumed). On crystallization from cyclohexane **29** was obtained in two crops, mp 131–132.5 °C (37.5 mg) and mp 126.5–129.5 °C (3.5 mg). Recrystallization of the first crop from cyclohexane gave pure **29**, which had mp 132–132.5 °C after drying in vacuo (6 h). IR (CCl_4) (cm^{-1}): 1692. ^{1}H NMR (CD_2Cl_2) δ: 4.35 (s, 3H), 7.04–7.07 (m, 2H), 7.12–7.20 (m, 3H), 7.31–7.34 (m, 2H), 7.43–7.48 (m, 3H), 7.65 (td, 1H, *J* = 0.7, 7.4 Hz), 8.06 (s, 1H), 8.09 (dd, 1H, *J* = 1.5, 8.1 Hz), 8.26 (dd, 1H, *J* = 1.5, 7.2 Hz), 11.46 (d, 1H, *J* = 0.7 Hz). ^{13}C NMR (CD_2Cl_2) δ: 43.15, 126.32, 126.48, 127.44, 128.28, 128.49, 128.82, 128.88, 129.58, 129.88, 131.69, 134.27, 136.94, 137.19, 139.51, 139.63, 146.84, 160.91, 193.11. Anal. calcd. for $C_{23}H_{17}NO$: C 85.42, H 5.30, N 4.33; found: C 85.62, H 5.28, N 4.50.

Synthesis of quinolines 21 and 37 from 2-aminobenzaldehyde (18a) and methyl alkyl ketones

Neat ketones

A solution of **18a** (121 mg, 1 mmol) in the neat ketone (10 mL) containing ytterbium triflate (62 mg, 0.1 mmol) was placed in an oil bath at 95 °C and stirred in an argon atmosphere for the time given in Table 2, and then the excess ketone was removed in vacuo. Toluene (20 mL) was added to the residue, and the mixture was stirred at reflux temperature in an argon atmosphere for 7 h. After the usual treatment with 10 wt % sodium carbonate solution, the toluene phase was extracted with 1 mol L^{-1} HCl; the extract was made basic with solid sodium carbonate, and the products were extracted into ethyl acetate. The extract was washed with saturated NaCl solution and then worked up as usual.

2,3-Dimethylquinoline (21b) and 2-ethylquinoline (37a)

The crude product was absorbed onto silica gel (1 g) and purified by column (3.5 × 10.5 cm) chromatography on silica gel (49 g) using hexane – ethyl acetate (80:20, 20 mL fractions). F 7–9 contained **37a** (54 mg, 28.2%, converted into the picrate, mp 147–149 °C, lit.(48) value mp 148 °C); F 11–19 contained crystalline **21b** (54 mg, 47.7%), mp 67–78 °C.

2-Methyl-3-ethylquinoline (21c) and 2-n-propylquinoline (37b)

Purified in exactly the same manner as described for **21b** and **37a**. F 2–5 contained **37b** (70 mg, 40.9%, identified by NMR), and F 8–12 contained **21c** (59 mg, 34.5%, mp 69.5–71.5 °C, lit.(49) value mp 74–74.5 °C).

2-Methyl-3-isopropylquinoline (21d) and 2-isobutylquinoline (37c)

Purified as described above. F 3–5 contained **37c** (112 mg, 60.5%, picrate mp 163–166 °C, lit.(50) value mp 163 to 164 °C), and F 8–12 contained **21d** (8 mg, 4.3%). See below for characterization.

From ketones under alkaline conditions

2-Methyl-3-ethylquinoline (21c) and 2-n-propylquinoline (37b)

A solution of **18a** (61 mg, 0.5 mmol) and 2-pentanone (71 mg, 0.82 mmol) in ethanol (3 mL) and 1 mol L^{-1} NaOH (1.75 mL) was left at room temperature for 24 h, diluted with water, and made acidic with 1 mol L^{-1} HCl. The acid solution was extracted with toluene, and then the acid phase was made basic with solid sodium carbonate. The products were extracted with toluene; the extract was washed with saturated NaCl solution and worked up as usual to give the mixture of bases (73 mg, 85.2%), which by ^{1}H NMR was shown to be a 77:23 mixture of **21c** and **37b**.

2-Methyl-3-isopropylquinoline (21d) and 2-isobutylquinoline (37c)

A solution of **18a** (121 mg, 1 mmol) and 4-methyl-2-pentanone (150 mg, 1.5 mmol) in ethanol (6 mL) and 1 mol L^{-1} NaOH (3.5 mL) was heated at reflux temperature under argon for 4 h. The reaction was worked up exactly as described above to give **37c** (144 mg, 77.7%) and **21d** (10 mg, 5.4%). Compound **21d** was an oil. ^{1}H NMR δ: 1.34 (d, 6H, *J* = 6.8 Hz), 2.78 (s, 3H), 3.26 (sept., 1H, *J* = 6.8 Hz), 7.45 (td, 1H, *J* = 1.1, 8.0 Hz), 7.61 (td, 1H, *J* = 1.5, 7.7 Hz), 7.74 (dd, 1H, *J* = 1.2, 81. Hz), 7.92 (s, 1H), 7.99 (d, 1H, *J* = 8.4 Hz). ^{13}C NMR δ: 23.52, 23.54, 29.75, 125.98, 127.49, 127.92, 128.63, 128.86, 131.56, 140.93, 146.51, 158.44. The base was converted into the picrate, mp 216–218 °C decomposition (dec), in hot ethanol. The mp was unchanged on recrystallization and drying in vacuo (60 °C, 14.5 h). Anal. calcd. for $C_{19}H_{18}N_4O_7$: C 55.07, H 4.38, N 13.52; found: C 55.12, H 4.43, N 13.49.

From pyrrolidine enamines 38

A solution of **18a** (121 mg, 1 mmol) and **38a** (51) or **38b** ((52), 2.4 mmol) in anhydrous toluene (10 mL) containing

© 2004 NRC Canada

ytterbium triflate (62 mg, 0.1 mmol) was either left at room temperature or heated at reflux temperature (see Table 2) in an argon atmosphere. HCl (1 mol L^{-1}, 10 mL) was added to the reaction mixture, which was stirred vigorously at room temperature for 15 min. The acidic aqueous phase was worked up as described above to give the crude mixture of bases. This mixture was spiked with hexamethylbenzene (internal standard) and analyzed by ^{1}H NMR.

By arylhydroamination of 1-heptyne

A solution of **18a** (121 mg, 1 mmol), mercuric chloride (472 mg, 1 mmol), and 1-hepytne (0.7 mL, 513 mg, 5.33 mmol) in anhydrous THF (15 mL) was stirred at room temperature for 18 h in an argon atmosphere. Ytterbium triflate (62 mg, 0.1 mmol) was added, and stirring was continued for a total time of 3 days. Even though **18a** was still present by TLC, the solvent was removed in vacuo, water and ethyl acetate were added, and the mixture was filtered through Celite. The organic phase was separated and extracted with 1 mol L^{-1} HCl. The acidic extract was worked up as in the section From pyrrolidine enamines 38 above; the crude mixture was spiked with hexamethylbenzene and analyzed by ^{1}H NMR.

Note added in proof

The Friedländer synthesis of quinolines from *o*-aminoarylketones and ketones also proceeds by a rate-determining aldol mechanism. This is strongly supported by the observation that heating a toluene solution (reflux, 17 h) of 2-hexanone (4 equiv.), *o*-aminoacetophenone (1 equiv.), and pyrrolidine (2 equiv.), containing suspended anhydrous magnesium sulfate (10 equiv., in situ generation of the pyrrolidine enamine of 2-hexanone (53)), and ytterbium triflate (0.1 equiv.), gave a 5.5:1 mixture (ca. 25% yield) of 2-*n*-butyl-4-methylquinoline (kinetic) and 2,4-dimethyl-3-*n*-propylquinoline (thermodynamic). In contrast, effecting the condensation of 2-hexanone and *o*-aminoacetophenone in acetic acid (reflux), containing catalytic sulfuric acid (29), gave a 1:1.7 kinetic to thermodynamic product ratio. Comparable results were obtained starting with 2-butanone and *o*-aminoacetophenone.[2]

References

1. P. Friedländer. Ber. **15**, 2572 (1882).
2. P. Friedländer and C.F. Gohring. Ber. **16**, 1833 (1883).
3. E. Reimann. *In* Houben-weyl. Methoden der organischen chemie. Hetarene II. Part 1. Vol. E7a. G. Thieme Verlag, Stuttgart. 1991. pp. 323–337.
4. C-C. Cheung and S-J. Yan. Org. React. **28**, 37 (1982).
5. G. Jones. *In* The chemistry of heterocylic compounds. Vol. 32. Quinolines. Part 1. *Edited by* G. Jones. John Wiley & Sons, New York. 1977. pp. 181–191.
6. V. Snieckus. Chem. Rev. **90**, 879 (1990).
7. T.G. Majewicz and P. Caluwe. J. Org. Chem. **40**, 3407 (1975).
8. K. Schofield and R.S. Theobald. J. Chem. Soc. 395 (1950).
9. E.A. Fehnel, J.A. Deyrup, and M.B. Davidson. J. Org. Chem. **23**, 1996 (1958).
10. Y. Tamura, T. Tsugoshi, S. Mohri, and Y. Kita. J. Org. Chem. **50**, 1542 (1985).
11. I-S. Cho, L. Gong, and J.M. Muchowski. J. Org. Chem. **56**, 7288 (1991).
12. J.I. Úbeda, M. Villacampa, and C. Avendaño. Synthesis, 1176 (1998).
13. O.B. Familoni, P.T. Kaye, and P.H. Klaas. Chem. Commun. 2563 (1998).
14. Y. Hsiao, N.R. Rivera, N. Yasuda, D.L. Hughes, and P.J. Reider. Org. Lett. **3**, 1101 (2001).
15. V.B. Drewsen. Ber. **16**, 1953 (1883).
16. A. Baeyer and V. Drewsen. Ber. **15**, 2854 (1882).
17. S-D. Cho, W-Y. Choi, S-G. Lee, Y-J. Yoon, and S.C. Shin. Tetrahedron Lett. **37**, 7059 (1996).
18. K. Ramadas and N. Srinivasan. Synth. Commun. **22**, 3189 (1992).
19. I.L. Smith and J.W. Opie. Org. Synth. Coll. Vol. 3, 56 (1955).
20. B.D. Foy, R.A. Smudde, and W.F. Wood. J. Chem. Educ. **7**0 322 (1993).
21. G.P. Black, F. Dimon, S. Fratucello, P.J. Murphy, M. Nielson, and H.L. Williams. Tetrahedron, **52**, 8001 (1996).
22. A.T. Nielsen and W.J. Houlihan. Org. Syn. **16**, 1 (1968).
23. M.B. Smith and J. March. *In* March's advanced organic chemistry. Reactions, mechanisms, structure. 5th ed. John Wiley & Sons, Inc. New York. 2002. pp. 285–286.
24. H.O. House and R.S. Ro. J. Am. Chem. Soc. **80**, 2428 (1958).
25. D.S. Noyce and M.J. Jorgensen. J. Am. Chem. Soc. **83**, 2525 (1961).
26. J.E. Dubois and M. Dubois. Compt. Rend. **256**, 715 (1963).
27. T. Vondrák and M. Procházka. Coll. Czech. Chem. Commun. **48**, 82 (1983).
28. D.M. Sammond and T. Sammakia. Tetrahedron Lett. **37**, 6065 (1996).
29. E.A. Fehnel. J. Org. Chem. **31**, 2899 (1966).
30. G. Barbieri, P. Lazzaretti, L. Schenetti and F. Taddei. Org. Magn. Res. **7**, 451 (1975).
31. M. Funabashi, M. Iwakawa, and J. Yoshimura. Bull. Chem. Soc. Jpn. **42**, 2885 (1969).
32. S. Talukdar, C-T. Chen, and J-M. Fang. J. Org. Chem. **65**, 3148 (2000).
33. P.A. Wehrli and B. Schaer. Synthesis, 288 (1974).
34. J.B. Wommack, T.G. Barbee, D.J. Thoennes, M.A. McDonald, and D.E. Pearson. J. Heterocycl. Chem. **6**, 243 (1969).
35. E.M. Hawes and D.K.J. Gorecki. J. Heterocycl. Chem. **11**, 151 (1974).
36. G. Kempter, P. Andratschke, D. Heilmann, H. Krausmann, and M. Mietasch. Chem. Ber. **97**, 16 (1964).
37. P.G. Dormer, K.K. Eng, R.N. Farr, G.R. Humphrey, J.C. McWilliams, P.J. Reider, J.W. Sager, and R.P. Volante. J. Org. Chem. **68**, 467 (2003).
38. P. Dalla Croce, P. Ferruti, and R. Stradi. Gazz. Chim. Ital. **97**, 589 (1967).
39. D. Pocar, G. Bianchetti, and P. Ferruti. Gazz. Chim. Ital. **97**, 597 (1967).
40. G.W. Fischer. J. Prakt. Chem. **330**, 981 (1988).
41. J. Barluenga, F. Aznar, R. Liz, and R. Rodes. J. Chem. Soc. Perkin Trans. 1, 2732 (1980).
42. A. Capperucci, A. Degl'Innocenti, M. Funicello, G. Mauriello, P. Scafato, and P. Spagnolo. J. Org. Chem. **60**, 2254 (1995).
43. H. Horina and N. Inoue. J. Org. Chem. **46**, 4416 (1981).
44. A. Rilliet. Helv. Chim. Acta, **5**, 547 (1922).

[2] J.M. Muchowski. Unpublished results.

© 2004 NRC Canada

45. J. Buckingham (*Editor*). Dictionary of organic compounds. Vol. 4. 5th ed. Chapman & Hall, London. 1982. p. 4053.
46. J.H. Markgraf, R.J. Katt, W.L. Scott, and R.N. Sherfin. J. Org. Chem. **34**, 4131 (1969).
47. M.P. Maguire, K.R. Sheets, K. McVety, A.P. Spada, and A. Ziberstein. J. Med. Chem. **37**, 2129 (1994).
48. R. Delaby and J. Hiron. Bull. Soc. Chim. Fr. **47**, 1395 (1930).
49. N. Satoshi. Yakugaku Zasshi. **81**, 479 (1961); Chem. Abstr. **55**, 105 853 (1961).
50. T. Higashino, K. Suzuki, and E. Hayashi. Chem. Pharm. Bull. **23**, 746 (1975).
51. R. Jacquier, C. Petrus, and F. Petrus. Bull. Soc. Chim. Fr. 2845 (1966).
52. J. Koyama, I. Toyokuni, and K. Tagahara. Chem. Pharm. Bull. **46**, 332 (1998).
53. P.A. Zoretic, F. Barcelos, and B. Branchaud. Org. Prep. Proced. Int. **8**, 211 (1976).

© 2004 NRC Canada

Packed-column supercritical fluid chromatography with splitless flame ionization detection

Kevin B. Thurbide and Shawn Gilbert

Abstract: The design and characterization of a flame ionization detector (FID) that is compatible with the high flow rates of packed-column supercritical fluid chromatography (pSFC) is presented. The modified FID uses a large quartz burner (4.0 mm i.d.) in place of the conventional burner (0.4 mm i.d.) and operates a stable flame in the presence of gas flows tested up to nearly 3000 mL/min. This modification allows the full flow of effluent from a pSFC column (i.e., splitless mode) to be directed into the FID. Results demonstrate that the modified FID yields response that is within a factor of 3 to that of a commercial FID. The attributes of the modified detector indicate that this approach could be a reliable and relatively simple means of achieving a splitless pSFC-FID system.

Key words: supercritical fluid chromatography, packed column, splitless, flame ionization detector.

Résumé : On a développé et caractérisé un détecteur à ionisation de flamme (DIF) qui est compatible avec les vitesses élevées d'écoulement d'une colonne à remplissage pour chromatographie fluide supercritique. Le DIF modifié utilise un grand brûleur en quartz (4,0 mm de diamètre intérieur) à la place du brûleur conventionnel (0,4 mm de diamètre intérieur) et il opère une flamme stable en présence d'écoulements de gaz allant jusqu'à environ 3000 mL/min. Cette modification permet de diriger tout l'effluent d'une colonne à remplissage (c'est-à-dire dans le mode sans division) vers le DIF. Les résultats démontrent que le DIF modifié fournit une réponse qui est à l'intérieur d'un facteur de trois par rapport à une DIF commercial. Les attributs du détecteur modifié indiquent que cette approche pourrait être une méthode fiable et relativement simple de développer un système sans division comme détecteur à ionisation de flamme pour chromatographie fluide supercritique avec colonne à remplissage.

Mots clés : chromatographie fluide supercritique, colonne à remplissage, sans division, détecteur à ionisation de flamme.

[Traduit par la Rédaction]

Introduction

In recent years there has been an increase in the use of packed-column supercritical fluid chromatography (pSFC) as a complimentary separation method to high-performance liquid chromatography (HPLC) and gas chromatography (GC) (1–3). This is attributed to the number of advantages that pSFC can offer, such as improved speed, selectivity, and resolving capability relative to HPLC and compatibility with a broader range of compounds relative to GC (4, 5). Additionally, the most common mobile phase in pSFC, carbon dioxide, provides a more environmentally compatible alternative to the conventional organic solvents used in HPLC (3). One of the greatest advantages offered by carbon dioxide as a mobile phase in pSFC is that it does not respond in the flame ionization detector (FID), which is widely used in GC for its large linear range and sensitive, universal response toward organic compounds (6). In this way, pSFC offers a beneficial means of combining HPLC-type separations with an informative GC detector.

Most commercial versions of the FID are compatible with conventional GC column flow rates on the order of 10–50 mL/min (7). Accordingly, since supercritical carbon dioxide expands about 500 times upon decompression, the FID can fully accept the typical microlitre per minute column flow rates used with capillary column supercritical fluid chromatography (8). However, pSFC commonly uses flow rates around 2 mL/min, similar to HPLC, which translates into about 1000 mL/min of carbon dioxide gas entering the FID burner. Such a large gas flow causes the flame to extinguish, and thus the FID can only be used in pSFC if the flow is split (usually after leaving the separation column), allowing only a portion of the effluent and analyte to enter the FID (9). While such methods allow a stable flame to be operated, a frequent concern reported for split-flow pSFC-FID interfaces is a variable split ratio that can lead to a nonuniform response factor (10). Still, this approach is common, and a successful split-flow interface adapted to operate with modern pSFC-FID instrumentation has been reported (7). In this method, the column flow was split twice before entering the FID, which provided a good detection limit of 50 pg for a mixture of *n*-alkanes. However, system plugging was reported to occur when injected amounts of sample exceeded 10 ng, which significantly limits the range of sample concentrations that can be directly investigated by the method.

Received 26 March 2003. Published on the NRC Research Press Web site at http://canjchem.nrc.ca on 2 March 2004.

K.B. Thurbide[1] and S. Gilbert. Department of Chemistry, University of Calgary, 2500 University Drive, NW, Calgary, AB T2N 1N4, Canada.

[1]Corresponding author (e-mail: thurbide@ucalgary.ca).

 doi: 10.1139/V04-008 © 2004 NRC Canada

Further, the use of an additional post-column solvent flow was advised to prevent plugging of the pressure regulation valve, which increases solvent usage relative to a pure carbon dioxide mobile phase. Thus, an FID method that has the ability to operate and maintain good detector performance in the presence of the full flow of column effluent in pSFC (i.e., splitless mode) is desirable.

This paper describes the design and characterization of an FID that has been modified to operate with pSFC in the splitless mode. Through systematically increasing the burner diameter, the FID can maintain a stable flame for flow rates of several liters per minute and yield comparable sensitivity with that of a conventional FID.

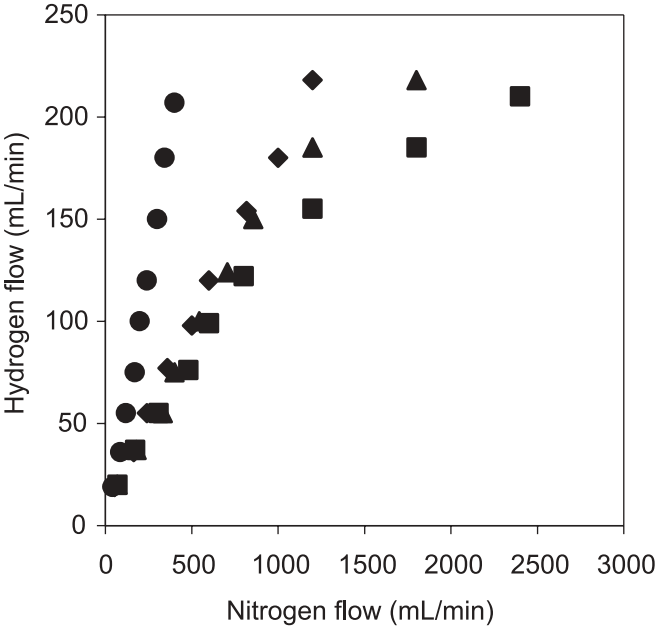
Experimental

The pSFC system was a Gilson series SF3 (Gilson, Villiers-le-Bel, France), which is comprised of a dual reciprocating pump – solvent delivery system (model 308 and 306), a column oven (model 831), a back pressure regulator (model 821), and a UV–vis variable wavelength detector (model 151). The separation column used was a 250 mm × 4.6 mm i.d. Econosil CN column packed with 5 µm diameter particles (Alltech, Deerfield, Ill., U.S.A.). The GC-FID system used for adaptation to the pSFC instrument was a Shimadzu model GC-9A (Shimadzu, Kyoto, Japan). Instrument-grade carbon dioxide and high-purity hydrogen, air, helium, and nitrogen were obtained from Praxair (Praxair, Calgary, Alta., Canada). Anthracene (99%) and octadecane (99%) were used as obtained from Aldrich (Aldrich, Oakville, Ont., Canada).

The FID is connected to the pSFC instrument directly downstream from the back pressure regulator, similar to a splitless interface described for an evaporative light-scattering detector (7). With the original outlet tubing removed, a 5 foot (1 foot = 0.3048 m) length of 1/16″ × 0.01″ (1″ = 25.4 mm) i.d. stainless steel tubing (Alltech) is instead used to guide the effluent from the back pressure regulator into the GC oven through a side port. Using a stainless steel zero dead volume union (Alltech), this tubing is connected to a 40 cm length of 0.10 mm i.d. deactivated, fused-silica restrictor tubing (Alltech), which extends into the detector base of the GC. The original Shimadzu FID burner was replaced by a length of quartz tubing (80 mm × 4.0 mm i.d. × 1 mm wall thickness), the last 25 mm of which tapers to 3.0 mm i.d. at the bottom to fit the threaded burner nut. The optimal restrictor position was 85 mm below the tip of the burner situated just below its base inside the stainless steel insert leading to the GC oven. The optimal position of the polarizer electrode was 2 mm below the tip of the burner, and the optimal separation between the polarizer and the collector electrode was found to be 25 mm. Optimal conditions for this transfer line were obtained when the GC oven was maintained at 250 °C and the FID was maintained at 350 °C.

Experiments in the conventional GC-FID mode employed an EC-5 ((5% phenyl)–95% methylpolysiloxane) megabore separation column (30 m × 0.53 mm i.d.; 1.00 µm thickness; Alltech). Typically, 8 mL/min of helium was used as the carrier gas and 30 mL/min of hydrogen and 400 mL/min of air provided optimum FID response. For GC-FID experiments using a 4.0 mm i.d. burner, the optimum hydrogen flow was 100 mL/min, and the optimum air flow was 1500 mL/min. Alternatively, ambient air could be entrained at the base of the detector housing with no change in the performance of the FID. For pSFC-FID experiments using a 4.0 mm i.d. burner, the optimum hydrogen flow was 340 mL/min, and all other conditions were the same. Also for this burner, a 300 mL/min flow of nitrogen added to the hydrogen flow was frequently found to improve the FID response by a factor of about 8. All other variations are outlined in the text.

Fig. 1. Stability of the FID flame at various gas flows using burners of 0.4 mm (●), 2.0 mm (◆), 3.0 mm (▲), and 4.0 mm (■) i.d. Each point on the graph represents the maximum amount of nitrogen flow that could be added to a given flow of hydrogen before the flame would extinguish.

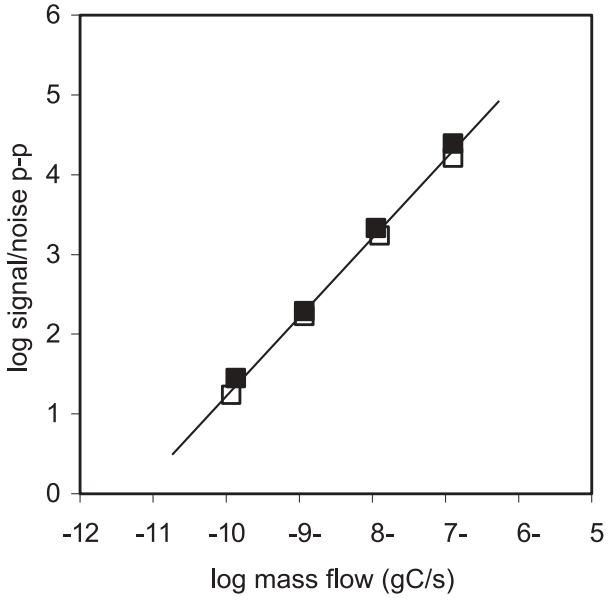


Results and discussion

Initial experiments were performed to evaluate how the flame stability is affected by varying the FID burner diameter and the gas flow directed through it. Figure 1 displays the results of flame stability tests conducted with the original FID burner (0.4 mm i.d.) and others tested up to an inside diameter of 4.0 mm. Nitrogen and hydrogen were used to estimate the maximum gas flow through the burner that the FID flame could withstand. Each point on the graph represents the amount of nitrogen required to extinguish the flame for a given flow of hydrogen. As can be seen in the figure, for a constant hydrogen flow, the corresponding amount of nitrogen that can be introduced into the FID flame increases with burner diameter. Also, for each burner, this parameter increases with an increase in the hydrogen flow. As an example, at 210 mL/min of hydrogen flow, the flame of the original burner can withstand up to about 400 mL/min of nitrogen, while, when using the 4.0 mm i.d. burner, about 2400 mL/min of nitrogen can be introduced into the FID before the flame extinguishes. This considerable difference in capacity is reasoned in terms of the linear

© 2004 NRC Canada

Fig. 2. GC-FID response toward anthracene, using the original low-flow 0.4 mm i.d. burner (■) and the modified high-flow 4.0 mm i.d. burner (□). See Experimental section for conditions.

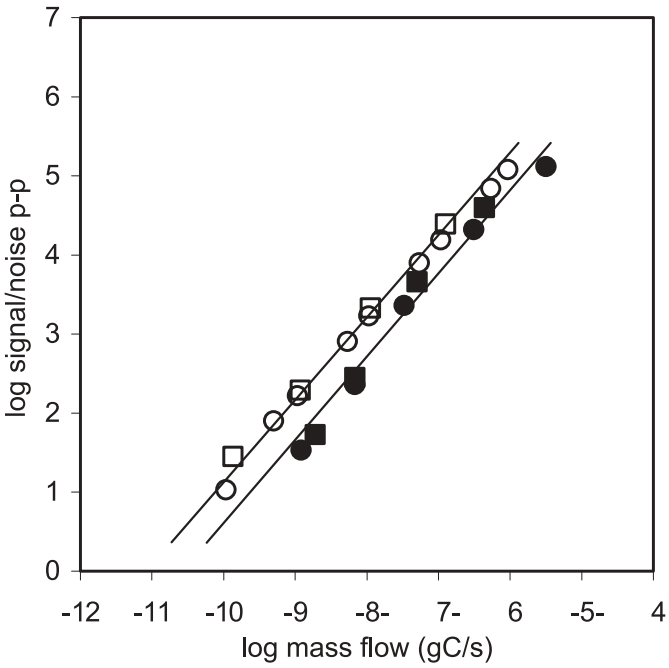


gas velocity travelling through the burner. For instance, the optimum gas flows of the original GC-FID instrument (i.e., 30 mL/min hydrogen and 8 mL/min helium) correspond to a linear gas velocity of about 500 cm/s through the burner. Using 210 mL/min of hydrogen and 400 mL/min of nitrogen, this value increases to about 8000 cm/s. By comparison, the maximum gas flow tested with the 4.0 mm i.d. burner (i.e., 210 mL/min hydrogen and 2400 mL/min nitrogen) corresponds to a linear gas velocity of about 360 cm/s through the burner. Thus, by reducing the linear gas velocity directed into the FID flame front, a stable flame can be maintained with larger gas flows, using burners with larger internal diameters.

To investigate the effect of using a larger flame in the FID on its response characteristics, experiments were conducted that compared the optimum FID performance of the original detector to that obtained using a larger burner. Figure 2 shows the results of calibrating anthracene in the GC mode using both the original FID burner and the 4.0 mm i.d. burner, each under optimized conditions. The figure clearly demonstrates that the response is practically identical between the two burners, and thus no deterioration in detector performance due to the usage of a larger burner in the FID is observed. The burner provided stable operation for several hours, with no change in performance, which correlates with visual observations of the larger flame that indicate it burns very smoothly with little turbulence compared with larger flows in the original burner.

Experiments were subsequently performed in the pSFC-FID mode using direct, splitless introduction of the decompressed carbon dioxide column flow into the modified detector. Several restrictor positions with respect to the burner tip were investigated. It was found that if the restrictor was too close to the flame front, then detector noise would increase. Increasing their separation improved this noise level; however, because of the large inner diameter of the burner and

Fig. 3. GC-FID response toward octadecane (○) and anthracene (□), using the original low-flow 0.4 mm i.d. burner, and the pSFC-FID response toward octadecane (●) and anthracene (■), using the modified high-flow 4.0 mm i.d. burner. The pSFC column pressure (isobaric) is 8.5 MPa for octadecane and 12 MPa for anthracene. The pSFC column flow rate is 1.0 mL/min. The pSFC oven temperature is 40 °C. All other conditions as outlined in the Experimental section.

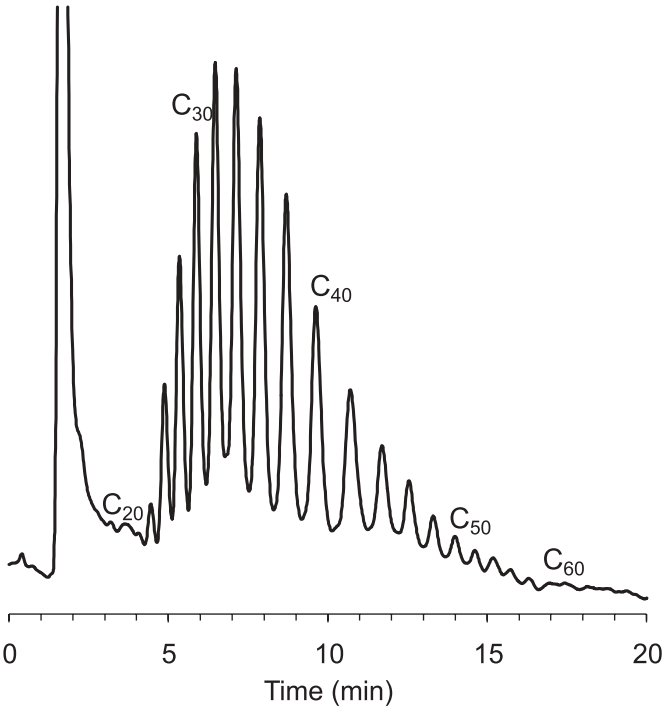


the relative cooling of the restrictor tip upon decompression, the restrictor would occasionally plug temporarily as solvent peaks eluted and froze. The optimum position for the restrictor was ultimately determined to be at the base of the burner, at a distance of about 85 mm from the flame front, where it was in contact with and resided inside the heated stainless steel enclosure leading to the GC column oven. Under these conditions, the flame response was very stable for extended periods of usage, and the restrictor no longer plugged in the presence of solvent peaks.

Using the 4.0 mm i.d. burner, the pSFC-FID flame remained stable toward increasing column flow rates of carbon dioxide tested up to 3.7 mL/min. This column flow rate translated into a decompressed flow of about 2200 mL/min of carbon dioxide gas entering the detector. Including the additional hydrogen and nitrogen flow through the burner under optimum pSFC-FID conditions, this amounts to nearly 3 L/min of gas flow being directed through the FID flame, which remained stable and did not extinguish. To investigate how the pSFC-FID system compares with the original GC-FID system in terms of response, two test analytes, anthracene and octadecane, were calibrated in each system under optimum conditions, and the results are shown in Fig. 3. As observed, the original GC-FID system yields a detection limit (i.e., signal/noise peak to peak equal to 2) of about 13 pg C/s, and a linear response over at least 5 orders of magnitude tested up to analyte mass flows of about 1 µg

© 2004 NRC Canada

Fig. 4. pSFC-FID chromatogram of a 10 μg sample of paraffin wax. Injection solvent is carbon disulfide. The pSFC oven temperature is 120 °C. Column flow rate is 1.5 mL/min. Pressure program is 20 MPa until 10 min, then increasing at 1 MPa/min for 5 min. All other conditions as outlined in the Experimental section.



C/s. These values are typical of those expected from a conventional FID and confirm that similar response is obtained from anthracene and octadecane in terms of carbon flow. By comparison, the pSFC-FID response, which is also similar between the two test analytes, yields a detection limit around 40 pg C/s. This compares quite well, differing within a factor of about 3 from the detection limit provided by the original GC-FID system. Additionally, the pSFC-FID system also provided linear response over the range investigated, which was tested up to analyte mass flows of about 3 μg C/s. Thus, the splitless pSFC-FID system is stable toward typical pSFC column flow rates and yields response that is similar to a conventional GC-FID system and similar to or better than other pSFC-FID systems operated in the split mode (7, 9). In daily operation, the splitless interface was routinely subjected to 10–100 μg quantities of test analyte, and plugging was not found to be a significant problem. Under regular usage, the restrictor tubing was usually replaced every 3 to 4 weeks.

Unlike earlier instruments, modern pSFC units independently control column pressure and flow (11). As such, a stable column flow and FID baseline can be maintained during changes in column pressure. The splitless pSFC-FID system was investigated at pressures up to 40 MPa (the maximum operating pressure of the instrument), and no adverse affects on the FID response or flame stability were observed. To illustrate this and demonstrate the pSFC-FID system response, Fig. 4 displays the separation of a 10 μg sample of paraffin wax using a basic pressure program. As shown, paraffins up to C_{60} are separated using a moderate pressure gradient up to 25 MPa and a typical column flow rate of 1.5 mL/min of carbon dioxide with no major changes in the detector baseline. The results of these experiments indicate that this approach may also be useful for coupling pSFC to other low-pressure, flame-based detection methods.

Acknowledgements

An operating grant in support of this research was provided by the Natural Sciences and Engineering Research Council of Canada (NSERC).

References

1. T.L. Chester, J.D. Pinkston, and D.E. Raynie. Anal. Chem. **70**, 301R (1998).
2. T.L. Chester and J.D. Pinkston. Anal. Chem. **74**, 2801 (2002).
3. F. Vérillon. Analusis, **27**, 671 (1999).
4. M.C. Ventura, W.P. Farrell, C.M. Aurigemma, and M.J. Greig. Anal. Chem. **71**, 2410 (1999).
5. M.C. Ventura, W.P. Farrell, C.M. Aurigemma, and M.J. Greig. Anal. Chem. **71**, 4223 (1999).
6. D.R.P. Thiébaut and E.C. Robert. Analusis, **27**, 681 (1999).
7. F. Vérillon and K. Coleman. *In* Supercritical fluid chromatography with packed columns: Techniques and applications. *Edited by* K. Anton and C. Berger. Marcel Dekker, New York. 1998. Chap 3.
8. T.A. Berger. J. Chromatogr. **785**, 3 (1997).
9. M.G. Rawdon. Anal. Chem. **56**, 831 (1984).
10. T.A. Berger and B.S. Todd. Chromatographia, **54**, 777 (2001).
11. H.E. Schwartz. J. Chromatogr. Sci. **26**, 275 (1988).

© 2004 NRC Canada

Syntheses, crystal structures, and magnetism of one-dimensional complexes generated from copper(II) and carbamyldicyanomethanide bridging ligand

Jing-Min Shi, Qing-Yun Liu, Wen Xu, Lin Meng, Peng Cheng, Bin Zhao, and Wen-Tao Yu

Abstract: Two one-dimensional chain complexes, $\{[Cu(cda)_2H_2O]\cdot H_2O\}_n$ (**1**) and $\{[Cu(cda)(H_2O)_2]\cdot(ClO_4)\cdot 3H_2O\}_n$ (**2**) (cda = carbamyldicyanomethanide anion) have been synthesized and their crystal structures determined by X-ray crystallography. The copper(II) ions in **1** are bridged by two $\mu_{1,5}$-cda bridging ligands, whereas in **2** the copper(II) ions are connected by a single $\mu_{1,5}$-cda ligand. Complex **1** is red while **2** is green. Variable-temperature magnetic susceptibility data indicate that there is a very weak antiferromagnetic interaction between the bridged copper(II) ions in both **1** and **2**.

Key words: synthesis, crystal structure, copper complex, polynitrile ligand, magnetism.

Résumé : On a synthétisé deux complexes en chaînes unidimensionnelles, $\{[Cu(cda)_2H_2O]\cdot H_2O\}_n$ (**1**) et $\{[Cu(cda)(H_2O)_2]\cdot(ClO_4)\cdot 3H_2O\}_n$ (**2**) (cda = anion carbamyldicyanométhanure) et on a déterminé leurs structures cristallines par diffraction des rayons X. Les ions cuivre(II) du composé **1** sont pontés par des ligands doublement pontants $\mu_{1,5}$-cda alors que les ions cuivre(II) du composé **2** sont reliés par une seule unité $\mu_{1,5}$-cda. La couleur du composé **1** est rouge alors que celle du composé **2** semble verte. L'analyse magnétique basée sur des données de susceptibilité magnétique à température variable indique qu'il existe une très faible interaction antiferromagnétique entre les ions de cuivre(II) pontés des composés **1** et **2**.

Mots clés : synthèse, structure cristalline, complexe du cuivre, ligand polynitrile, magnétisme.

[Traduit par la Rédaction]

Introduction

Recently, the field of molecular magnetism has attracted considerable attention, and major advances have been made in both the theoretical description and the application of molecular-based magnetic materials (1–4). Polynitrile compounds such as tricyanomethanide (5–7), dicyanamide (8–15), 7,7,8,8-tetracyanoquinodimethane (16–21), 1,2,4,5-tetracyanobenzene (22, 23), and tetracyanoethene (24–28) display versatile bridging modes, and many coordination compounds have been constructed from such polynitriles and metal ions, some of which exhibit distinctive magnetic properties (24). Although some complexes with the carbamyldicyanomethanide anion (cda) as ligand have been synthesized and their crystal structures determined by X-ray crystallography (29–32), no reports on the magnetic properties of cda-bridged complexes have been published. Here we report the crystal structures and the magnetic properties of the titled complexes $\{[Cu(cda)_2H_2O]\cdot H_2O\}_n$ (**1**) and $\{[Cu(cda)(H_2O)_2]\cdot(ClO_4)\cdot 3H_2O\}_n$ (**2**).

Experimental

Materials

Sodium carbamyldicyanomethanide (Na(cda)) was prepared according to a procedure reported in the literature (33). All other chemicals were analytical grade and used without further purification.

Physical measurements

IR spectra were recorded with a Shimadzu Corporation 408 IR spectrometer using KBr discs.The main bands (cm^{-1}) for **1** appear at 3250 (br, vs), 2225 (vs), 2175 (vs), 1630 (vs), 1565 (vs), and 1425 (vs) and for **2** at 2250 (vs), 2200 (vs), 1645 (vs), 1580 (vs), 1410 (vs), and 1100 (br, vs). C, H, and N elemental analyses were carried out on a PerkinElmer

Received 27 March 2003. Published on the NRC Research Press Web site at http://canjchem.nrc.ca on 3 March 2004.

J.-M. Shi,[1] Q.-Y. Liu, and L. Meng. Department of Chemistry, Shandong Normal University, Jinan, 250014, China.
W. Xu and W.-T. Yu. Institute of Materials, Shandong University, Jinan, 250010, China.
P. Cheng and B. Zhao. Department of Chemistry, Nankai University, Tianjin, 300071, China.

[1]Corresponding author (e-mail: shijingmin@beelink.com).

 doi: 10.1139/V04-006 © 2004 NRC Canada

Table 1. Crystallographic data and data collection parameters for complexes **1** and **2**.

	1	**2**
Chemical formula	$C_8H_8CuN_6O_4$	$C_4H_{12}ClCuN_3O_{10}$
Crystal system	Triclinic	Triclinic
Space group	$P\bar{1}$	$P\bar{1}$
a (Å)	7.1902(16)	7.499(2)
b (Å)	7.5288(17)	9.373(3)
c (Å)	11.562(3)	10.432(3)
α (°)	77.211(4)	102.561(4)
β (°)	80.432(4)	101.359(4)
γ (°)	74.070(4)	109.456(4)
V (Å^3)	583.2(2)	645.2(3)
D_{calcd} (g·cm^{-3})	1.798	1.859
Absorption coefficient (mm^{-1})	1.895	1.951
F(000)	318	366
Crystal dimensions (mm)	0.30×0.20×0.10	0.5×0.30×0.20
θ range for data collection (°)	1.82–25.02	2.09–25.03
Limiting indices	$-8 \le h \le 8$,	$-8 \le h \le 6$,
	$-8 \le k \le 8$,	$-10 \le k \le 11$,
	$-13 \le l \le 13$	$-12 \le l \le 11$,
Reflections collected/unique (R_{int})	2940/2027 (0.0237)	3428/2252 (0.0144)
Data/restraints/parameters	2027/9/204	2252/0/223
Final R indices [$I > 2\sigma(I)$]	$R_1 = 0.0464$,	$R_1 = 0.0380$,
	$wR_2 = 0.1108$	$wR_2 = 0.1036$
R indices (all data)	$R_1 = 0.0630$	$R_1 = 0.0468$
	$wR_2 = 0.1176$	$wR_2 = 0.1089$
Goodness of fit on F^2	0.969	1.096
Largest difference peak and hole (e·Å^{-3})	0.508 and –0.540	0.660 and –0.518

2400 elemental analyzer, and Cu content was measured on a Hitachi model Z-8000 atom absorption spectrophotometer. Thermogravimetric analysis was performed on a PerkinElmer TGA-7 thermogravimetric analyzer under flowing argon at a heating rate of 10 °C/min. The variable-temperature magnetic susceptibility of powder samples (0.10039 g for **1** and 0.06472 g for **2**) was measured under an applied magnetic field of 10 kOe in the approximate range 5–300 K with a SQUID magnetometer, and all the experimental data were corrected for the diamagnetic susceptibility of the samples by using Pascal constants.

X-ray crystallography

The determination of the crystal structures was carried out on a Bruker Smart-1000 CCD diffractometer using graphite-monochromated Mo Kα radiation (0.71073 Å). Data reduction and structure refinement were performed using the SHELXL-97 program system.[2] Crystal structure and data collection and refinement parameters are listed in Table 1. Selected bond lengths and angles are listed in Table 2, and the hydrogen bond lengths and angles are listed in Table 3.

Synthesis of $\{[Cu(cda)_2H_2O]\cdot H_2O\}_n$ (1)

Hydrated copper perchlorate (0.5521 g, 1.49 mmol) and Na(cda) (0.3506 g, 2.67 mmol) were each dissolved in 45 cm^3 H_2O, respectively. When the two solutions were mixed together, a yellowish green color appeared immediately. A well-formed deep-red single crystal suitable for X-ray determination was obtained after the mixed solution was kept at room temperature for about two weeks. Yield: 0.3794 g, 90%. Anal. calcd. for $C_8H_8CuN_6O_4$: C 30.43, H 2.55, N 26.62, Cu 20.13; found: C 30.12, H 2.41, N 24.26, Cu 20.52.

Synthesis of $\{[Cu(cda)(H_2O)_2]\cdot(ClO_4)\cdot 3H_2O\}_n$ (2)

Method 1

$Cu(ClO_4)_2\cdot 6H_2O$ (0.7256 g, 1.96 mmol) and Na(cda) (0.2510 g, 1.91 mmol) were each dissolved in ca. 80 cm^3 of H_2O, respectively, and the two solutions were mixed together. The resulting solution turned green when solid Na(cda) (4.9640 g, 0.0379 mol) was added in batches. Green single crystals were obtained after the green solution was kept at room temperature for ca. half a year. Anal. calcd. for $C_4H_{12}ClCuN_3O_{10}$: C 13.30, H 3.35, N 11.64, Cu 17.59; found: C 13.56, H 3.68, N 12.04, Cu 17.24.

Method 2

Hydrated copper perchlorate (0.6227 g, 1.68 mmol), Na(cda) (0.2224 g, 1.70 mmol), and $NaClO_4\cdot H_2O$ (4.0 g,

[2] Supplementary data (X-ray crystallographic files in CIF format) may be purchased from the Depository of Unpublished Data, Document Delivery, CISTI, National Research Council Canada, Ottawa, ON K1A 0S2, Canada (http://www.nrc.ca/cisti/irm/unpub_e.shtml for information on ordering electronically). CCDC 161875 and 161864 contain the supplementary data for for **1** and **2**, respectively. These data can be obtained, free of charge, via www.ccdc.cam.ac.uk/conts/retrieving.html (or from the Cambridge Crystallographic Data Centre, 12 Union Road, Cambridge, U.K.; fax +44 1223 336033; or deposit@ccdc.cam.ac.uk).

© 2004 NRC Canada

Table 2. Selected bond lengths (Å) and angles (°) for complexes **1** and **2**.

1		**2**	
Bond lengths			
Cu(1)—N(3B)	1.972(4)	Cu(1)—O(2)	1.950(3)
Cu(1)—N(2)	1.976(4)	Cu(1)—N(2)	1.960(3)
Cu(1)—N(5)	1.979(4)	Cu(2)—O(3)	1.934(3)
Cu(1)—N(6A)	1.984(4)	Cu(2)—N(3)	1.955(3)
Cu(1)—O(3)	2.323(4)		
Bond angles			
N(3B)-Cu(1)-N(2)	93.54(15)	O(2)-Cu(1)-O(2C)	180.0
N(3B)-Cu(1)-N(5)	85.93(16)	O(2)-Cu(1)-N(2)	90.13(14)
N(2)-Cu(1)-N(5)	177.43(17)	O(2C)-Cu(1)-N(2)	89.87(14)
N(3B)-Cu(1)-N(6A)	177.12(17)	O(2)-Cu(1)-N(2C)	89.87(14)
N(2)-Cu(1)-N(6A)	86.83(15)	O(2C)-Cu(1)-N(2C)	90.13(14)
N(5)-Cu(1)-N(6A)	93.57(15)	N(2)-Cu(1)-N(2C)	180.00(17)
N(3B)-Cu(1)-O(3)	93.52(16)	O(3)-Cu(2)-O(3B)	180.0
N(2)-Cu(1)-O(3)	94.24(15)	O(3)-Cu(2)-N(3)	90.14(14)
N(5)-Cu(1)-O(3)	88.31(17)	O(3B)-Cu(2)-N(3)	89.86(14)
N(6A)-Cu(1)-O(3)	89.29(16)	O(3)-Cu(2)-N(3B)	89.86(14)
		O(3B)-Cu(2)-N(3B)	90.14(14)
		N(3)-Cu(2)-N(3B)	180.0

Table 3. Hydrogen bond lengths (Å) and bond angles (°) for complexes **1** and **2**.

D—H	*l* (D—H)	*l* (H···A)	∠DHA	*l* (D···A)	A	ST
1						
N(1)—H(1)	0.969	2.115	161.84	3.050	O(2)	($x-1$, $y+1$, $z-1$)
N(4)—H(3)	0.967	1.861	158.41	2.783	O(4)	($x+1$, y, $z+1$)
N(4)—H(4)	0.963	2.031	153.85	2.926	O(1)	($x+1$, $y-1$, $z+1$)
O(3)—H(5)	0.968	1.888	148.45	2.760	O(1)	($-x+2$, $-y+2$, $-z+1$)
O(4)—H(7)	0.964	1.922	164.76	2.863	O(3)	($-x+2$, $-y+1$, $-z+1$)
O(4)—H(8)	0.968	1.954	141.79	2.780	O(2)	(x, y, $z-1$)
2						
O(2)—H(3)	0.841	1.793	172.99	2.630	O(9)	(x, y, $z-1$)
O(2)—H(4)	0.720	2.031	165.50	2.733	O(10)	($-x+1$, $-y+1$, $-z+1$)
O(3)—H(5)	0.640	2.091	168.01	2.721	O(8)	(x, $y-1$, z)
O(3)—H(6)	0.805	1.966	162.26	2.744	O(10)	
O(8)—H(7)	0.718	2.263	154.86	2.929	O(7)	($-x$, $-y+2$, $-z+1$)
O(8)—H(8)	0.668	2.162	156.23	2.787	O(9)	
O(9)—H(9)	0.671	2.138	149.07	2.736	O(1)	
O(9)—H(10)	0.797	2.098	155.46	2.842	O(8)	($-x+1$, $-y+2$, $-z+2$)
O(10)—H(11)	0.761	1.951	171.37	2.705	O(1)	

Note: D, donor atom; A, acceptor atom; *l*, length; ST, symmetry transformation for acceptor atom.

0.028 mol) were each dissolved in 10 cm^3 H_2O, respectively. When the three solutions were mixed together, a light-green color appeared immediately. When the mixed solution was kept at room temperature for about two weeks, a small amount of green single crystals and a large amount of red single crystals were obtained. The IR spectrum and elemental analysis indicated that the green single crystals were identical to those obtained by method 1.

Results and discussion

IR spectrum of $\{[Cu(cda)_2H_2O]\cdot H_2O\}_n$ (1)

In comparison with the bands of Na(cda), the characteristic -C≡N bands of compound **1** have shifted from 2160 and 2200 cm^{-1} to 2175 and 2225 cm^{-1}, respectively. The sharp peaks at 3220, 3320, and 3455 cm^{-1}, assigned to $\nu(NH_2)$, appear as a broad band between 3150 and 3350 cm^{-1}. The intense bands of the -$CONH_2$ group at 1440, 1560, and 1660 cm^{-1} are shifted to 1425, 1565, and 1630 cm^{-1} and are also broadened in the spectrum of complex **1**.

IR spectrum of $\{[Cu(cda)(H_2O)_2]\cdot(ClO_4)\cdot 3H_2O\}_n$ (2)

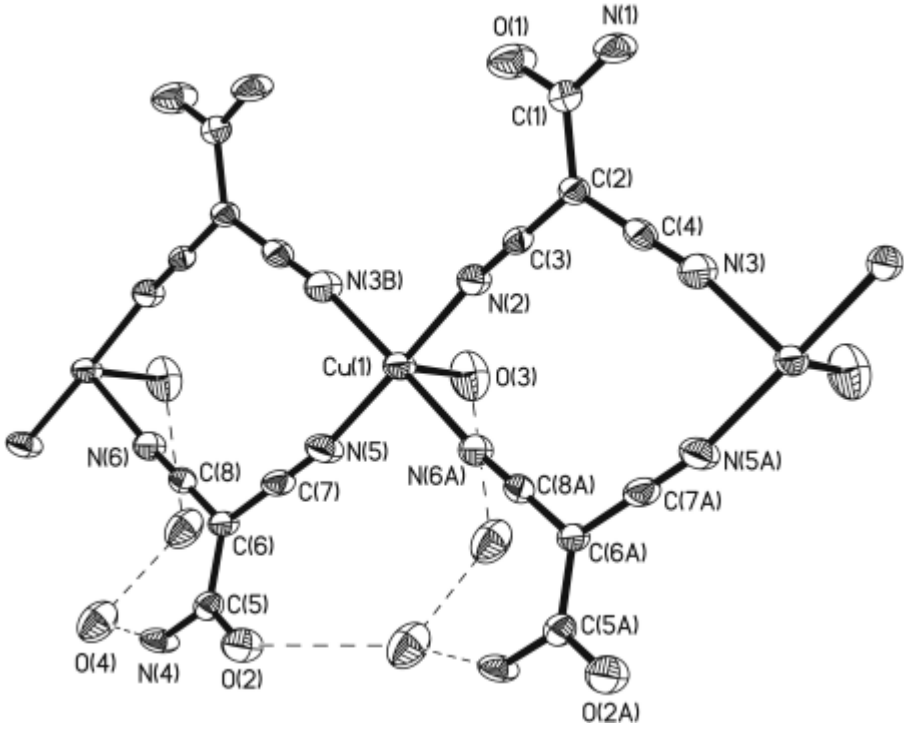
The characteristic -C≡N bands appear at 2250 and 2200 cm^{-1}. The strong and broad bands at 1645, 1580, and 1410 cm^{-1} may be attributed to ν(C=O), and the strong band near 1100 cm^{-1} may be assigned to the perchlorate ion.

Thermal stability of $\{[Cu(cda)_2H_2O]\cdot H_2O\}_n$ (1) and $\{[Cu(cda)(H_2O)_2]\cdot(ClO_4)\cdot 3H_2O\}_n$ (2)

The results of thermogravimetric analysis indicate that **1**

© 2004 NRC Canada

Fig. 1. The coordination and 1D chain diagram of **1** with the atom numbering scheme.



began to decompose distinctly at ca. 163 °C, and before 188 °C all the coordinated and uncoordinated H_2O had been lost, whereas **2** began to decompose distinctly at ca. 96 °C, and at ca. 209 °C all the coordinated and uncoordinated H_2O had been lost.

Crystal structure of $\{[Cu(cda)_2H_2O]\cdot H_2O\}_n$ (1)

Figure 1 shows the coordination diagram with the atom numbering scheme. In the crystal, each Cu(II) ion is coordinated to four $\mu_{1,5}$-cda ligands and capped by one H_2O ligand, and each $\mu_{1,5}$-cda ligand is coordinated to two copper(II) cations via two nitrile-nitrogen atoms. The Cu(1), N(2), N(5), N(3B), and N(6A) atoms lie in a plane, designated plane 1, such that a square-pyramidal polyhedron is formed around Cu(1), with O(3) located at the apex of the pyramid. Among copper(II) complexes with polynitriles as ligands, tetrahedral (22), square-planar (7), and octahedral coordination polyhedrons (6, 9–10, 14) have been observed, but no square-pyramidal polyhedron has been reported previously. The N(2), C(3), C(2), C(1), O(1), C(4), and N(3) atoms are located in a plane, designated plane 2, while the N(6A), C(8A), C(6A), C(5A), O(2A), C(7A), and N(5A) atoms lie in another plane, designated plane 3. The angles between planes 1 and 2, planes 1 and 3, and planes 2 and 3 are 13.2°, 18.6°, and 21.7°, respectively. The coordination mode of cda in this crystal is identical with that reported for a one-dimensional zinc(II) chain (31). Figure 2 shows the hydrogen bonding and also reveals that the two adjacent chains extensively interdigitate to form a parallelepiped block and that the blocks stack in a parallel fashion to form a three-dimensional structure.

Crystal structure of $\{[Cu(cda)(H_2O)_2]\cdot(ClO_4)\cdot 3H_2O\}_n$ (2)

Figure 3 shows the coordination diagram with the atom numbering scheme and the structure of the zigzag one-dimensional chain. In the crystal, the Cu(1) ion is coordinated by the O(2), O(2C), N(2), and N(2C) atoms, and the five atoms lie in a plane, which is designated plane 4. The bond lengths pertaining to the Cu(I) ion and the associated angles indicate that the coordination environment of the Cu(1) ion is slightly distorted from a square. The coordination geometry of the Cu(2) ion is almost identical with that of the Cu(1) ion, with the N(3), O(3), Cu(2), O(3B), and N(3B) atoms lying in a plane, designated plane 5. Obviously, the coordination geometry of **2** is different from that of **1**, and thus the splitting energy of the *d* orbitals in **1** and **2** is different, which leads to the difference in color. The N(2), C(3), C(2), C(1), O(1), C(4), and N(3) atoms of the cda bridging ligand are situated in another plane, designated plane 6. The angles between planes 4 and 6, planes 5 and 6, and planes 4 and 5 are 112.5°, 149.5°, and 59.0°, respectively. The bridging mode of cda is identical with that in **1**, but the neighboring Cu(II) ions are bridged by only a single $\mu_{1,5}$-cda bridging ligand. Figure 4 displays the unit cell and the locations of the chains, uncoordinated H_2O molecules, and the perchlorate counter anion in the crystal, as well as the hydrogen bonding between the cda anions, coordinated H_2O molecules, uncoordinated H_2O molecules, and the perchlorate ion.

Magnetic properties

The variable-temperature magnetic susceptibility data showed a small change of μ_{eff} from 300 to 50 K for the two complexes, and at 5 K the values of μ_{eff} are 1.64 and 1.81 for **1** and **2**, respectively. These values are close to the spin-only value for copper(II) and indicate that there is only very weak magnetic coupling between the bridged Cu(II) ions. To determine the extent of the magnetic coupling in **1** and **2**, the

© 2004 NRC Canada

Fig. 2. Unit cell of **1** and the location of the 1D chains viewed from the *a* axis.

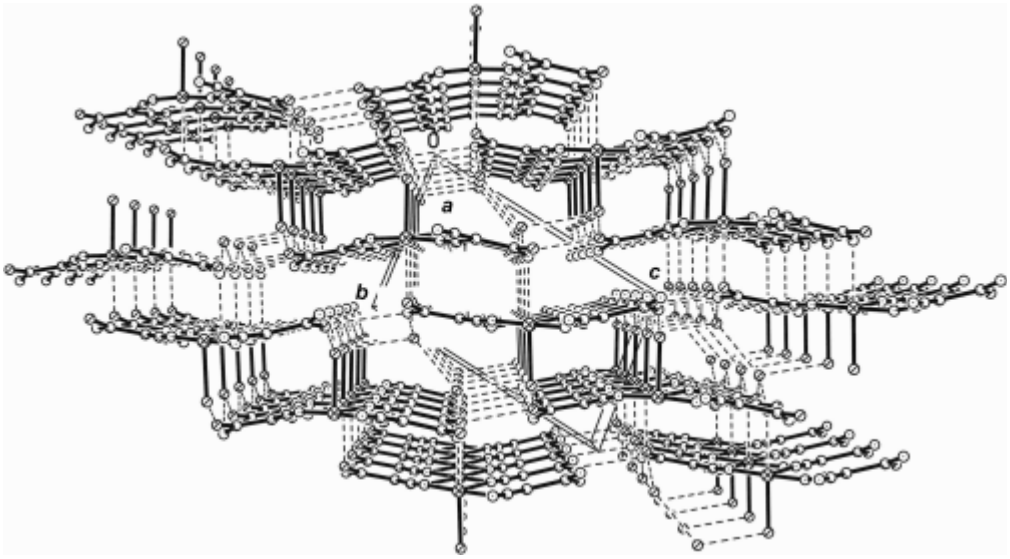


Fig. 3. The coordination and 1D chain diagram of **2** with the atom-numbering scheme.

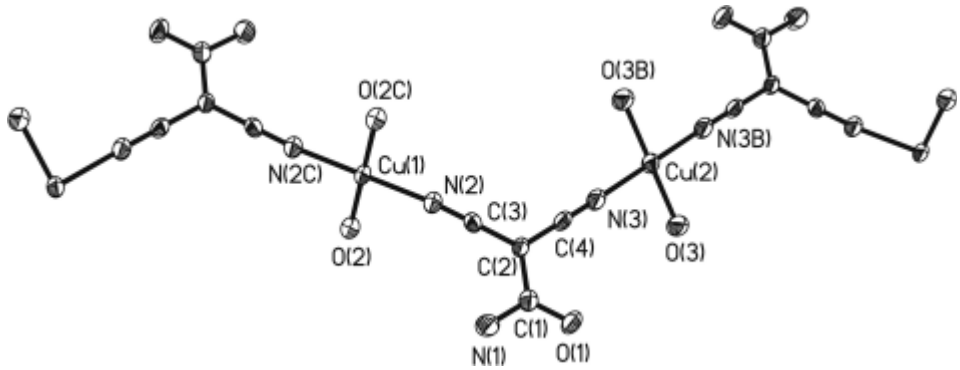
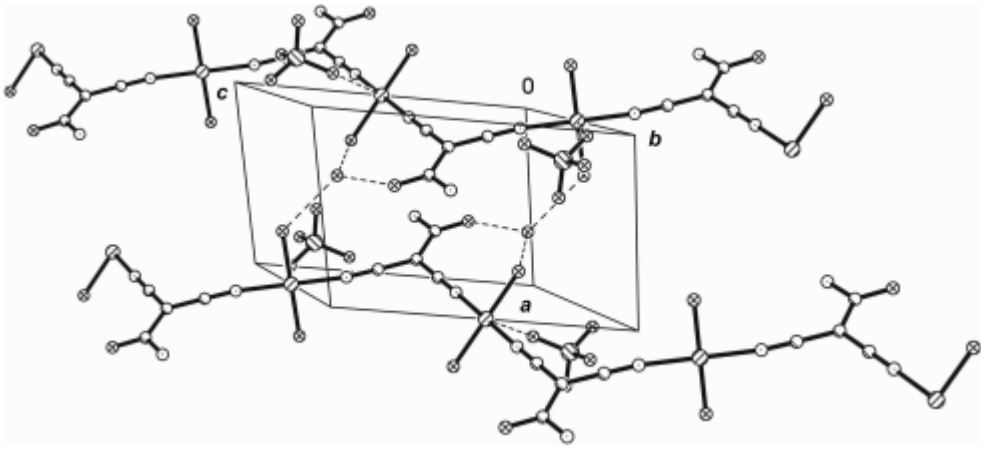


Fig. 4. Unit cell of **2** and the locations of the 1D chains, uncoordinated H_2O molecules, and the perchlorate counter ion.



following formula for the magnetic susceptibility of one-dimensional Cu(II) chain complexes (34) was used:

$$\chi_m = [Ng^2\beta^2/k(T - \theta)][0.2500 + 0.18297(J/kT)^2][1 + 1.5467(J/kT) + 3.4443(J/kT)^3]^{-1}$$

In the above equation, the symbols of J, θ, N, g, β, k, and T represent the magnetic coupling of intrachain, the magnetic coupling of interchains, the Avogadro constant, the lander g factor, Bohr magneton, the Boltzmann constant, and the absolute temperature, respectively. The plots of χ_m vs. T and $\chi_m T$ vs. T for **1** and **2** are shown in Figs. 5 and 6, respectively, and the formula fits the experimental data well. The

© 2004 NRC Canada

Fig. 5. Plots of temperature dependence of χ_M and $\chi_m T$ for **1**; (■) experimental data of χ_M; (○) experimental data of $\chi_m T$; (—) calcd. curve.

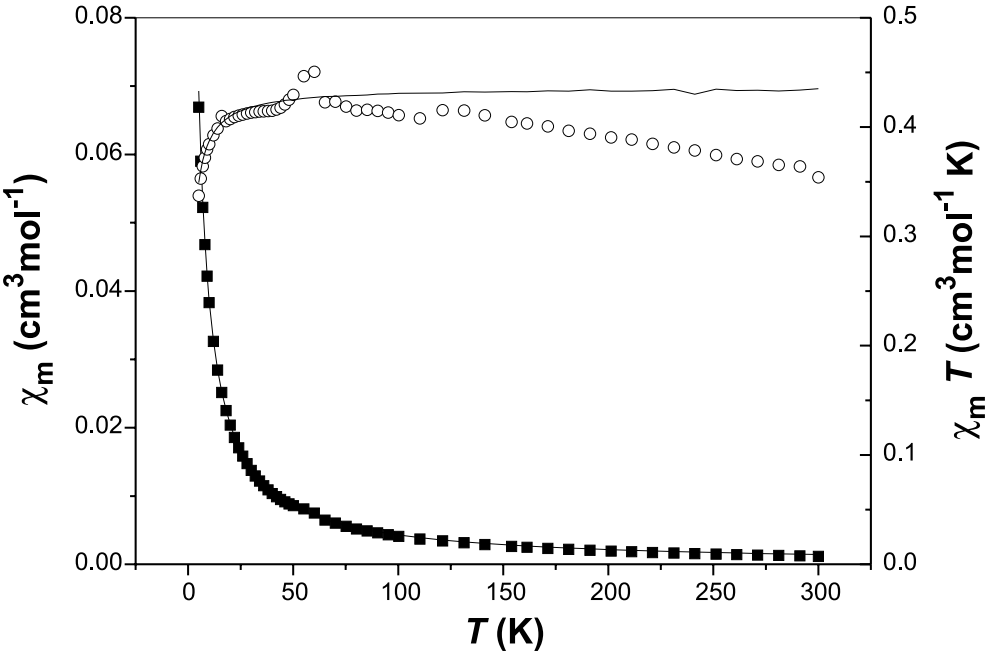
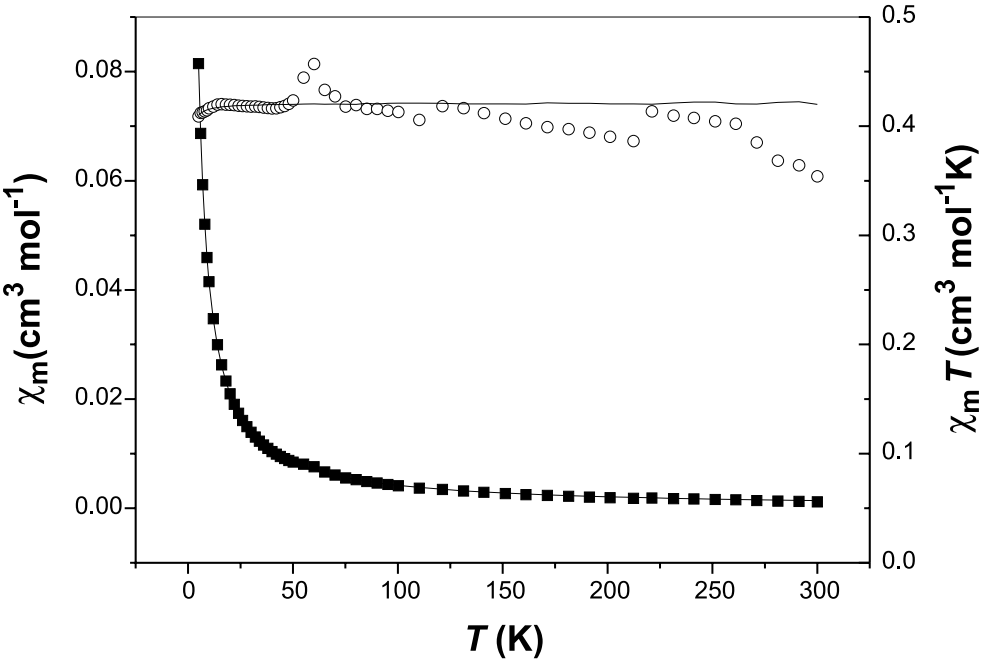


Fig. 6. Plots of temperature dependence of χ_M and $\chi_m T$ for **2**; (■) experimental data of χ_M; (○) experimental data of $\chi_m T$; (—) calcd. curve.



best-fit parameters are $J = -0.584$ cm^{-1}, $\theta = -0.003$ cm^{-1}, g = 2.16, and $F = [\Sigma(\chi_m)_{obsd} - \Sigma(\chi_m)_{calcd}]^2/\Sigma(\chi_m)^2_{obsd} = 1.41 \times 10^{-5}$ for **1**, and $J = -0.059$ cm^{-1}, $\theta = -0.006$ cm^{-1}, g = 2.12, and $F = 1.49 \times 10^{-6}$ for **2**. The very small J and θ values indicate that in both **1** and **2** there is a very weak antiferromagnetic interaction between the bridged Cu(II) ions and a very weak antiferromagnetic coupling in the interchains. The similar $\mu_{1,5}$-dicyanamide (dca)-bridged one-dimensional Cu(II) and one-dimensional Mn(II) complexes also exhibit very weak magnetic couplings (8, 9), and MO calculations confirm that the $\mu_{1,5}$-dicyanamide ligand is a very poor superexchange mediator (35). By comparing the bridging ligand cda to dca, with respect to its structure and coordination mode and the magnetic behavior of the complexes, it may be concluded that cda is also a very poor superexchange mediator. The difference in magnetic coupling between **1** and **2** may originate from coplanarity within their structures. Generally, in multiatom-bridged complexes the

© 2004 NRC Canada

magnetic interaction is propagated by a delocalized π orbital of the bridging ligand, and the coplanarity between the plane consisting of magnetic orbital atoms and the plane of bridging ligand atoms is one of the major factors that affect magnetic interaction (36). The higher the coplanarity is, the stronger the overlap of magnetic orbitals and hence the stronger the magnetic interaction. In **1** the angles between planes 1 and 2 and between planes 1 and 3 are 13.2° and 18.6°, respectively, whereas in **2** the angles between planes 4 and 6 and between planes 5 and 6 are 112.5° and 149.5°, respectively. Thus, planes 4 and 6 are almost perpendicular to each other and this severely limits electron delocalization, such that the magnetic coupling in **2** is weaker than in **1**.

Acknowledgements

This project was supported by the National Nature Science Foundation of China (No. 20271043) and the Natural Science Foundation of Shandong Province, China (No. Y2002B10).

References

1. J.R. Friedman, M.P. Sarachik, J. Tejada, and R. Ziolo. Phys. Rev. Lett. **76**, 3830 (1996).
2. W. Wernsdorfer and R. Sessoli. Science (Washington, D.C.), **284**, 133 (1999).
3. G.L.J.A. Rikken and E. Raupach. Nature (London), **405**, 932 (2000).
4. R. Lescouëzec, J. Vaissermann, C.R. Pérez, F. Lloret, R. Carrasco, M. Julve, M. Verdaguer, Y. Dromzee, D. Gatteschi, and W. Wernsdorfer. Angew. Chem. Int. Ed. **42**, 1483 (2003).
5. S.R. Batten, B.F. Hoskins, B. Moubaraki, K.S. Murray, and R. Robson. J. Chem. Soc. Dalton Trans. 2977 (1999).
6. S. Triki, F. Thetiot, J.S. Pala, S. Golhen, J.M. Clemente-Juan, C.J. Gomez-Garcia, and E. Coronado. J. Chem. Soc. Chem. Commun. 2172 (2001).
7. H. Hoshino, K. Iida, T. Kawamoto, and T. Mori. Inorg. Chem. **38**, 4229 (1999).
8. A. Claramunt, A. Escuer, F.A. Mautner, N. Sanz, and R. Vicente. J. Chem. Soc. Dalton Trans. 2627 (2000).
9. G.A. Albada, M.E. Quiroz-Castro, I. Mutikainen, U. Turpeinen, and J. Reedijk. Inorg. Chim. Acta, **298**, 221 (2000).
10. C. Kremer, C. Melian, J. Torres, M.P. Juanico, C. Lamas, H. Pezaroglo, E. Manta, H. Schumann, J. Pickardt, F. Girgsdies, O.N. Ventura, and F. Lloret. Inorg. Chim. Acta, **314**, 83 (2001).
11. P.M. Well, S.R. Batten, P. Jensen, B. Moubaraki, K.S. Murray, and E.H.-K. Tan. Polyhedron, **20**, 1129 (2001).
12. H. Miyasaka, R. Clerac, C.S. Campos-Fernandez, and K.R. Dunbar. Inorg. Chem. **40**, 1663 (2001).
13. P.M. Werff. S.R. Batten, P. Jensen, B. Moubaraki, and K.S. Murray. Inorg. Chem. **40**, 1718 (2001).
14. S. Martin, M.G. Barandika, J.I.R. Larramendi, R. Cortes, M. Font-Bardia, L. Lezama, Z.E. Serna, X. Solans, and T. Rojo. Inorg. Chem. **40**, 3687 (2001).
15. N. Moliner, A.B. Gaspar, M.C. Munoz, V. Niel, J. Cano, and J.A. Real. Inorg. Chem. **40**, 3986 (2001).
16. E. Waldhor, W. Kaim, M. Lawson, and J. Jordanov. Inorg. Chem. **36**, 3248 (1997).
17. B. Olvrich-Deussner, W. Kaim, and R. Gross-Lannert. Inorg. Chem, **28**, 3113 (1989).
18. C. Campanna, K.R. Dunbar, and X. Ouyang. J. Chem. Soc. Chem. Commun. 2427 (1996).
19. L. Shields. J. Chem. Soc. Faraday Trans. **81**, 21 (1985).
20. L. Ballester, A. Gutierrez, M.F. Perpinan, S. Rico, M.T. Azcondo, and C. Bellitto. Inorg. Chem. **38**, 4430 (1999).
21. H. Hartmann, W. Kaim, I. Hartenbach, T. Schleid, M. Wanner, and J. Fiedler. Angew. Chem. Int. Ed. **40**, 2842 (2001).
22. M. Mimalata. G.L. Ning, T. Kuroda-Sowa, M. Maekawa, Y. Suenaga, and T. Horino. Inorg. Chem. **37**, 5651 (1998).
23. F. Baumann, W. Kaim, J.A. Olabe, A.R. Parise, and J. Jordanov. J. Chem. Soc. Dalton Trans. 4455 (1997).
24. J.M. Manriquez, G.T. Yee, R.S. McLean, A.J. Epstein, and J.S. Miller. Science (Washington, D.C.), **252**, 1415 (1991).
25. W. Kaim and M. Moscherosch. Coord. Chem. Rev. **129**, 157 (1994).
26. D.K. Rittenberg and J.S. Miller. Inorg. Chem. **38**, 4838 (1999).
27. J.L. Wesemann and M.H. Chisholm. Inorg. Chem. **36**, 3528 (1997).
28. K. Falk, M. Balanda, Z. Tomkowicz, F. Mascarenhas, J. Schilling, P. Klavins, and W. Haase. Polyhedron, **20**, 1521 (2001).
29. J.M. Shi, S.C. Zhu, L.D. Liu, W.T. Yu, H.L. Yin, and J.L. Fan. Polish J. Chem. **75**, 1591 (2001).
30. J.M. Shi, W. Xu, Q.Y. Liu, F.L. Liu, Z.L. Huang, H. Lei, W.T. Yu, and Q. Fang, J. Chem. Soc. Chem. Commun. 756 (2002).
31. J.M. Shi, H.L. Yin, C.J. Wu, F.L. Liu, and W. Xu. Polyhedron, **22**, 493 (2003).
32. J.M. Shi, W. Xu, S.Q. Lu, C.J. Wu, J.C. Ge, and Z.D. Zhang. Chinese J. Struct. Chem. **21**, 640 (2002).
33. S. Trofimenko, Jr., E. L. Little, and H. F. Mower. J. Org. Chem. **27**, 433 (1962).
34. W. Hiller, J. Strahle, A. Datz, M. Hanack, W.E. Htfield, L.W. ter Haar, and P. Gutlich. J. Am. Chem. Soc. **106**, 329 (1984).
35. A. Escuer, F. A. Mautner, N. Sanz, and R. Vicente. Inorg. Chem. **39**, 1668 (2000).
36. O. Kahn. Angew. Chem. Int. Ed. **24**, 834 (1985).

© 2004 NRC Canada

Ionic liquids derived from trialkylsulfonium bromides: Physicochemical properties and potential applications

Li Xiao and Keith E. Johnson

Abstract: Several new ionic liquids were prepared from trialkylsulfonium bromides and $AlCl_3$ or HCl. They include both Lewis basic and acidic combinations of Et_3SBr with $AlCl_3$, which are liquid at ambient temperatures. Density, molarity, conductivity, NMR, infrared, and electrochemical data are presented. The sulfonium cations are not hydrogen bonding, are unattacked by hydride, provide NMR windows in the aromatic regions, and offer different solubility prospects from ionic liquids derived from aromatic cations.

Key words: ionic liquids, triethylsulfonium, haloaluminates, halohydrogenates, molarities, NMR, voltammetry, hydride.

Résumé : On a préparé plusieurs nouveaux liquides ioniques à partir des bromures de trialkylsulfonium et $AlCl_3$ ou HCl; ils incluent des combinaisons de Lewis tant basiques qu'acides de Et_3SBr avec $AlCl_3$, liquides à la température ambiante. On rapporte les données relatives à leur densité, molarité, conductivité, RMN, infrarouge et à leur propriétés électrochimiques. Les cations sulfonium ne forment pas de liaisons hydrogènes, ne sont pas attaqués par les hydrures, fournissent une fenêtre dans les régions aromatiques de la RMN et offrent des possibilités de solubilité différentes de celles associés aux liquides ioniques obtenus à partir de cations aromatiques.

Mots clés : liquides ioniques, triéthylsulfonium, haloaluminates, halohydrogénates, molarités, RMN, voltampérométrie, hydrure.

[Traduit par la Rédaction]

Introduction

There has been a steady increase in work on ambient-temperature ionic liquids since 1980. The early driving force for this was the development of an aluminum battery, so systems with wide electrochemical windows and involving chloroaluminates received much attention (1). Since $AlCl_3$ is well known for catalyzing Friedel–Crafts and other organic reactions (2), ionic liquids, as catalytic solvents, became a topic of research (3, 4). By now the variety of ionic liquids prepared is large, and electrochemical properties may be less significant than viscosities (5), NMR windows, and recovery and disposal limitations.

Although alkylammonium and alkylphosphonium salts have a long history, the favorite liquid semi-organic salts have become those of *N*,*N*′-dialkylimidazolium ions, especially 1-ethyl-3-methyl-1*H*-imidazolium ($[emim]^+$) (1) and now 1-butyl-3-methyl-1*H*-imidazolium ($[bmim]^+$) (6). *N*-Butylpryidinium salts also received attention, since some have low melting points (7), while simple pyridinium salts have been used for ether cleavage (8), although at higher temperature. In a study of the superacidity of liquids derived from an organic halide together with $AlCl_3$ or $AlBr_3$ plus HCl or HBr (9), we took advantage of the simple NMR spectrum of the salt $(CH_3)_3SBr$. However, ambient temperature liquidity does not extend to Lewis-basic compositions for these systems. We have synthesized, therefore, several asymmetric tri-alkylsulfonium bromides and their combinations with $AlCl_3$. The physiochemical characteristics of these liquids are reported with particular emphasis on the Et_3S–$AlCl_3$ system, which has a wider liquid composition range at ambient temperatures. We also discuss some halohydrogenate salts and the potential uses of these new liquids.[3]

Experimental

Materials

All manipulations involving aluminum chloride, semi-organic salts, and the ionic liquids derived therefrom were performed in a glovebox (Mbraun Labmaster 100) under an atmosphere of dry nitrogen. Aluminum chloride (Fluka AG,

Received 30 July 2003. Published on the NRC Research Press Web site at http://canjchem.nrc.ca on 4 March 2004.

L. Xiao[1] and K.E. Johnson.[2] Department of Chemistry & Biochemistry, University of Regina, Regina, SK S4S 0A2, Canada.

[1]Present address: TraceDetect Inc., 180 North Canal Street, Seattle, WA 98103, U.S.A.
[2]Corresponding author (e-mail: Keith.Johnson@uregina.ca).

[3]The organic bromides are easier to prepare than the chlorides, while AlC_3 and HCl are more readily available and somewhat easier to handle than $AlBr_3$ and HBr. While the physiochemical details would change for all-chloride or all-bromide systems and the cross-halogen ion equilibria would be eliminated, the primary conclusions regarding the sulfonium salts would be expected to hold for such systems, also.

 doi: 10.1139/V04-004 © 2004 NRC Canada

puriss) was purified by double vacuum sublimation, and trimethylsulfonium bromide was recrystallized twice with anhydrous ethanol (9) and vacuum dried at ~40 °C for 2 days. HCl gas (Mattheson) was electronic grade and ethene-free. Organic solvents were freshly distilled before use.

Ethyldimethylsulfonium bromide ($EtMe_2SBr$), diethylmethylsulfonium bromide (Et_2MeSBr), and triethylsulfonium bromide (Et_3SBr) were synthesized according to Saunders, Jr. and co-workers' method (10), with acetonitrile as the solvent and an alkyl halide : dialkyl sulfide ratio of 2. For Et_3SBr specifically, a yield of 25% was obtained after refluxing for 3 days; crystals were washed with ethanol and vacuum dried at 40 °C. The method of Islam and Leffek (11), employing excess sulfide, was unsuccessful.

1-Butyl-3-methyl-1*H*-imidazolium chloride (bmim Cl) was prepared under atmospheric pressure, as described by Rogers and co-workers (12). The yield was 90%.

Triethylsulfonium tetrafluoroborate and hexafluorophosphate were prepared by procedures akin to those for the $bmim^+$ salts, but since they had melting points close to 80 °C, they were not studied further.

Chloroaluminate ionic liquids were prepared by adding the required amount of $AlCl_3$ *slowly* with stirring to the solid organic salt so that a colorless or pale yellow liquid formed.

To reduce the proton level in such a liquid from the estimated 20 mmol L^{-1} level to <1 mmol L^{-1}, either $AlEtCl_2$ or CaH_2 was added in a roughly equivalent amount; any small excess of $AlEtCl_2$ does not affect the Lewis acidity.

Halohydrogenate(I) liquids were obtained by introducing HCl gas slowly through a needle valve into a preweighed, sealed vial containing solid organic salt. The added HCl was determined gravimetrically or by titration.

Physical measurements

Melting points were obtained with an Electrothermal 1A9100 series Digital Melting Point Apparatus. Densities of liquids were measured at 25 °C in the glovebox with 2 mL or 5 mL flasks calibrated with twice-distilled water. Viscosities were measured with a Cannon-Fenske viscometer 150 (constant of 0.04591 at 40 °C, 0.04570 at 100 °C). It was calibrated by the overlapping technique with aqueous glycerol solutions. Measurements were made in a thermostated paraffin oil bath in the glovebox, taking 10 min for equilibration and at least 120 s of flow time. Conductances were measured with a YSI Model 31 Conductivity Bridge (Yellow Spring Instrument Co.), using a commercial (1.0 cm^{-1} cell constant) or home-made cell (5.28 cm^{-1} cell constant) and 0.1 daL aqueous KCl at 25 °C as calibrant.

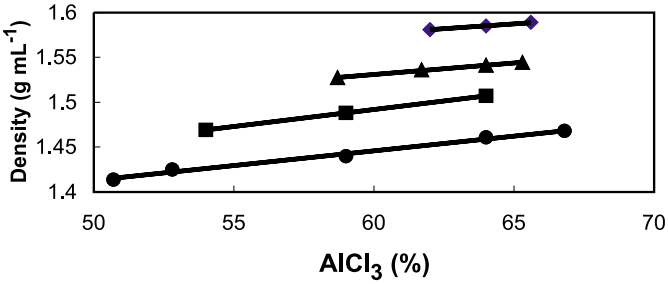
Fourier transform infrared (FTIR) spectra were obtained with a PerkinElmer instrument (range 400–2500 cm^{-1}) and KBr salt plates. Provided the plates were dry and the ionic liquid was placed between them in the glovebox, the film was sufficiently air stable.

NMR spectra were obtained with a Bruker AC-200 MHz spectrometer, using DMSO-d_6, D_2O, $CDCl_3$, and CD_3COCD_3 as locking solvents; they were sealed into capillaries and inserted into the 5 mm NMR tubes, which were loaded with ionic liquid samples and capped in the glovebox prior to measurements.

Table 1. Bromide content of trialykylsulfonium bromides.

Salt	Theoretical Br (%)	Experimental Br (%)	Deviation (%)
Me_2EtSBr	46.70	46.78	0.17
Et_2MeSBr	43.16	43.18	0.05
Et_3SBr	40.13	40.18	0.12

Fig. 1. Ambient temperature density of trialkylsulfonium ionic liquids at different compositions (25 °C): ◆ $AlCl_3$–Me_3SBr (R^2 = 0.9905); ▲ $AlCl_3$–Me_2EtSBr (R^2 = 1.000); ■ $AlCl_3$–Et_2MeSBr (R^2 = 0.9935); ● $AlCl_3$–Et_3SBr (R^2 = 0.9959).



Cyclic voltammetry was carried out with a BAS 100W system. A diamond-polished Pt working electrode, a Pt counter-electrode, and an Al – acidic chloroaluminate reference electrode were employed.

Results and discussion

Salt purity

The experimental (12) and theoretical bromide contents of the 3 trialkylsulfonium bromides synthesized are shown in Table 1.

Density

Figure 1 shows the density of trialkylsulfonium chloroaluminate ionic liquids at 25 °C at different $AlCl_3$ contents. The range of composition for which the systems are liquid at 25 °C increases with the total number of carbon atoms, reaching 23 mole % $AlCl_3$ for $AlCl_3$–Et_3SBr. An approximate phase diagram for $AlCl_3$–Et_3SBr shows a minimum at (46% $AlCl_3$, 10 °C) and a maximum at (50% $AlCl_3$, 40 °C) such that while a basic liquid is obtainable at 25 °C, a neutral one is a jelly. As the number of C atoms increases at constant $AlCl_3$ mole %, the density decreases linearly (R^2 = 0.9974), a trend noted for other ionic liquid groups (13). When the densities of several 64% $AlCl_3$ ionic liquids are compared, it is apparent that the trend is not a function of cation size but rather a question of packing (15), as follows: bmim Cl (1.3229 g L^{-1}) (5) < emim Cl (1.3747 g L^{-1}) (1) < Et_3SBr (1.4607 g L^{-1}) < PyHCl (1.4759 g L^{-1}) < Me_3SBr (1.5849 g L^{-1}) (9).

Molarities

Although it has been customary to express the acidity of haloaluminate ionic liquids in terms of the AlX_3 mole fraction, the molarity of the various species present in the system is determined by the density and average molecular

© 2004 NRC Canada

Table 2. Molarities of anions in different haloaluminate (R*x*–$AlCl_3$) ionic liquid systems.

R*x*	$AlCl_3$ (mole %)	Density (g cm^{-3})	MW	$X_{AlX_4^-}$ (mole fraction)	$M_{AlX_4^-}$	$X_{Al_2X_7^-}$	$M_{Al_2X_7^-}$	Ref.
emimCl (MW:145.5)	0.5000	1.2941	278.84	1.0000	4.64	0	0	1
	0.5499	1.3209	308.40	0.7783	3.33	0.2217	0.95	
	0.6001	1.3488	345.59	0.4994	1.95	0.5006	1.95	
	0.6666	1.3888	412.10	0	0	0.9976	3.37	
Me_3SCl (MW:112.5)	0.6666	1.40	378.78	0	0	0.9976	3.69	16
Me_3SBr (MW:157)	0.6666	1.59	423.28	0	0	0.9976	3.75	17
Et_3SBr (MW:199)	0.5000	1.4116	332.34	1.0000	4.25	0	0	This work
	0.5499	1.4286	361.97	0.7778	3.07	0.2217	0.88	
	0.6001	1.4455	399.01	0.4994	1.81	0.5006	1.81	
	0.64	1.4607	436.0	0.2222	0.74	0.7778	2.61	
	0.6666	1.4680	465.28	0	0	0.9976	3.15	
PyHCl (MW:115.46)	0.630[a]	1.4572	342.6	0.2973	1.26	0.7027	2.99	This work
	0.640[b]	1.4759	352.5	0.2222	0.93	0.7778	3.26	
bmimCl (MW:173.5)	0.640	1.3194	410.5	0.2222	0.71	0.7778	2.50	1

Note: $X_{AlX_4^-}$ represents the mole fraction of anion $AlCl_4^-$ or $AlCl_3Br^-$ and other halide-exchange species (when the organic salt is a bromide). Similarly, $M_{AlX_4^-}$ represents the molarity of the anion species, $AlCl_4^-$ or $AlCl_3Br^-$.
[a]Temperature of 50 °C.
[b]Temperature of 30 °C.

weight. Further, the ratio of the acid $Al_2X_7^-$ to the neutral AlX_4^- increases dramatically as the AlX_3 mole fraction approaches 2/3. Both of these effects are demonstrated by the data of Table 2.

Viscosity

The viscosities of the trialkylsulfonium haloaluminates (Table 3) decrease with the size of the sulfonium group (Fig. 2). The activation energy for viscous flow obtained from absolute viscosity – temperature plots is much smaller for $AlCl_3$–Et_3SBr (7.86 kJ mol^{-1}) than for AlC_3–Me_3SBr (12.75 kJ mol^{-1}), and for both sulfonium systems it is less than for $AlCl_3$–emimCl (19 kJ mol^{-1}). This is consistent with the denser packing of the Me_3SBr system and the presence of limited H bonding in the emim system (the H bonding in the acidic system is, however, much less than when free Cl^- is present).

Conductivity

The specific conductivities of 46% $AlCl_3$–Et_3SBr and 64% $AlCl_3$–Et_3SBr are 1.14 and 0.845 $mm^2\ s^{-1}\ cm^{-1}$ respectively. These values are of the same order as seen in $AlCl_3$–emimCl systems (1), but in the imidazolium systems the conductivity is higher for the acidic than the basic liquids, a situation readily ascribed to strong H bonding between Cl^- and $emim^+$ in basic liquids and no H bonding by Et_3S^+.

NMR spectra

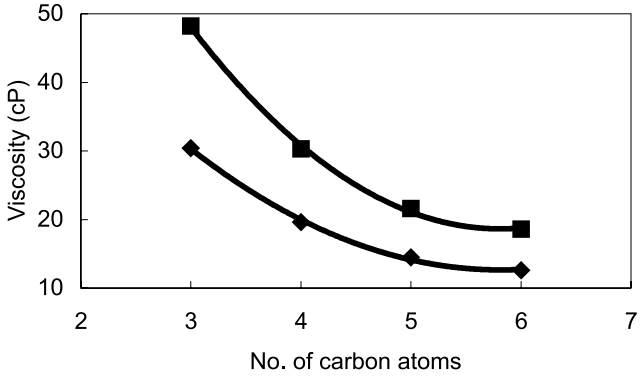
$R_1R_2R_3SBr$–$AlCl_3$ systems

The 64% $AlCl_3$–$R_1R_2R_3SBr$ systems show the anticipated ^1H NMR spectra ($R_1 = R_2 = R_3 = Me$ (8), $\delta = 0.9$ ppm; $R_1 = R_2 = R_3 = Et$, $\delta = 0.50$, 2.25 ppm; $R_1 = R_2 = Me$, $R_3 = Et$, $\delta = 0.4$, 2.15 ppm; $R_1 = Me$, $R_2 = R_3 = Et$, $\delta = 0.5$, 2.3 ppm). In contrast to the emimCl–$AlCl_3$ system (18), the chemical shift changes little with composition ($\delta = 0.55$, 2.35 for 51% $AlCl_3$).

Table 3. Trialkylsulfonium haloaluminate viscosities with 64% $AlCl_3$ at 25 °C.

Sulfonium salt	Salt mp (°C)	Kinematic viscosity ($mm^2\ s^{-1}$)	Absolute viscosity (Pa s)
Me_3SBr	193	30.4	0.0482
$EtMe_2SBr$	153	19.6	0.0302
Et_2MeSBr	83	14.4	0.0216
Et_3SBr	167	12.6	0.0185

Fig. 2. Relationship between absolute viscosity (cP (1 P = 0.1 Pa s)) and the number of carbon atoms in 64% $AlCl_3$–trialkyl sulfonium bromide ionic liquids: ■ absolute viscosity (cP) ($R^2 = 0.9988$ for polynomial relationship); ◆ kinematic viscosity (cSt (1 St = 100 $mm^2\ s^{-1}$) ($R^2 = 0.9984$ for polynomial relationship).

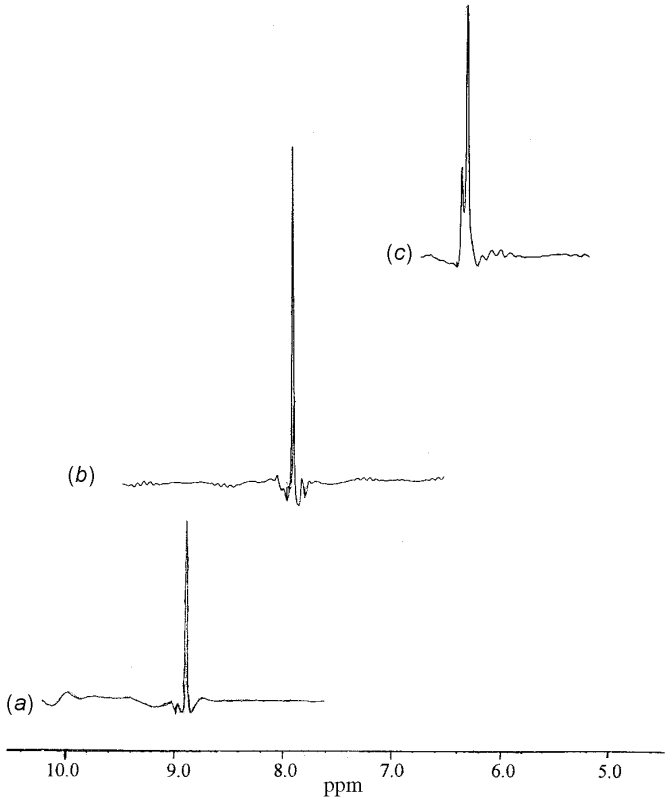


Et_3SBr–HCl and bmimCl–HCl systems

In the halohydrogenate(I) systems, the anionic species present change from X^- through HX_2^- to $H_2X_3^-$ and even $H_3X_4^-$ as the HX ratio is increased. For emimCl–HCl (19), the chemical shift of the acidic proton ranges from 13.5 ppm at 37 mole % HCl to 10.0 ppm at 60%, while for PyHCl–

© 2004 NRC Canada

Fig. 3. ^{1}H NMR spectra, at 24 °C, of Et_3SBr–HCl with (*a*) 52%, (*b*) 54%, (*c*) 68% HCl.



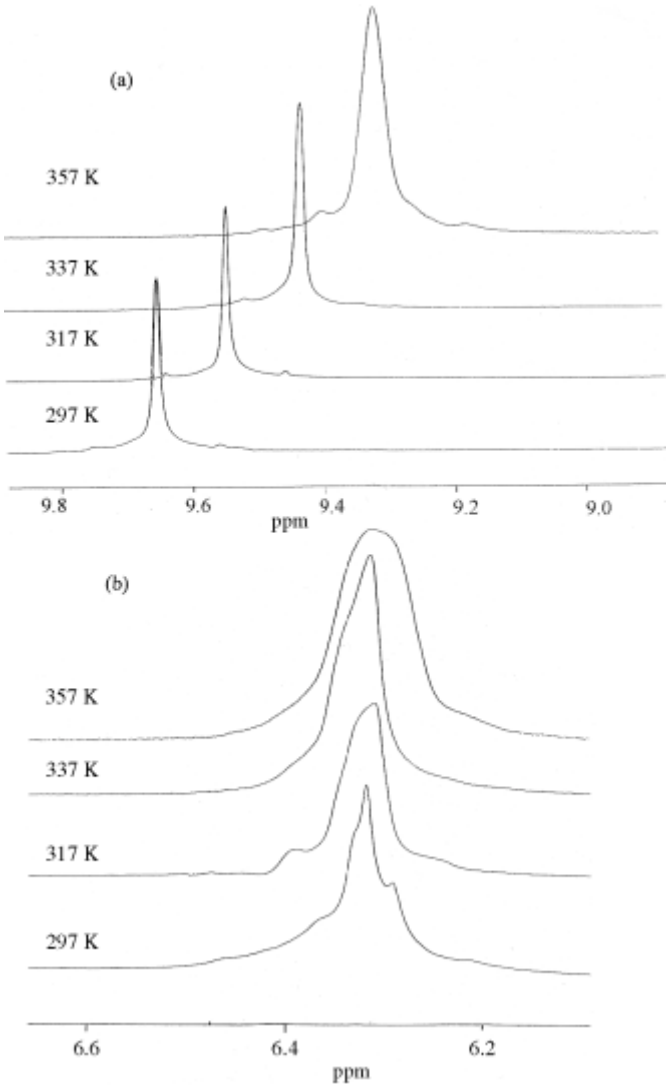
HCl (20), a shift from 13.3 ppm at 58% HCl to 3.0 ppm at 95% HCl was observed. In these systems, exchange gives rise to a single signal. In Et_3SBr–HCl, where halide exchange scrambles the halides X to all combinations of Cl and Br, we find the acidic proton shift moves from 8.85 ppm at 52% HCl to 6.30 ppm at 68% HCl. At the higher HCl composition, the signal splits at 24 °C (Fig. 3). This splitting is still discernible at 64 °C, and the peak at 84 °C is broad (Fig. 4*b*). For HCl:bmimCl, however, cooling to –6 °C is required to see any splitting; the signal at 84 °C is somewhat broad; and there is a shift upfield with temperature (Fig. 4*a*). At a constant HCl mole fraction of 0.58, the acidic proton signal for the series HCl:emimCl, HCl:bmimCl, and HCl:Et_3SBr moved from 10.7 to 9.97 to 7.85 ppm. Several effects are in play here, as follows: (*a*) the signal splitting at lower temperatures is due to the slowing down of exchange between protons in the different anions, and this is necessarily greater for bromide-containing species; (*b*) stronger H bonding in all-chloride anions (HCl_2^-, HCl_3^-, etc.) will lead to a downfield signal vs. that of the anions containing bromide; (*c*) further H bonding to $bmim^+$ by HCl_2^- would decrease with temperature and create the upfield shift not seen with the Et_3S^+ system.

Cyclic voltammetry

Et_3SBr–$AlCl_3$

The electrochemical window of a basic (46% $AlCl_3$) liquid is approximately 4 V, ranging from the reduction of Et_3S^+ to the oxidation of Br^- and $AlCl_3Br^-$. The protic impurity reduction and oxidation peaks were decreased by the addition of $EtAlCl_2$ (Fig. 5*a*). For an acidic (64% $AlCl_3$) system the window is closer to 2 V with the formation of Al metal being the limiting cathode reaction, as confirmed by the stripping peak at +0.1 V (Fig. 5*b*). Protic impurity peaks in this system were also decreased by $EtAlCl_2$ addition. When HCl was deliberately added to the (Lewis) acidic liquid, a composite peak developed in the 0.3–0.8 V region (Fig. 5*c*); this resembles the behavior of emimCl–$AlCl_3$–HCl (19), where the adducts $Al_2Cl_7{\cdot}HCl^-$ and $AlCl_4{\cdot}HCl^-$ show distinct reduction peaks ~0.7 V apart. The voltammograms also show the reduction (at 1.4 V) of anodically generated halogen.

Fig. 4. Variable temperature ^{1}H NMR spectra of (*a*) 60.5% HCl–bmimCl and (*b*) 68% HCl–Et_3SBr.

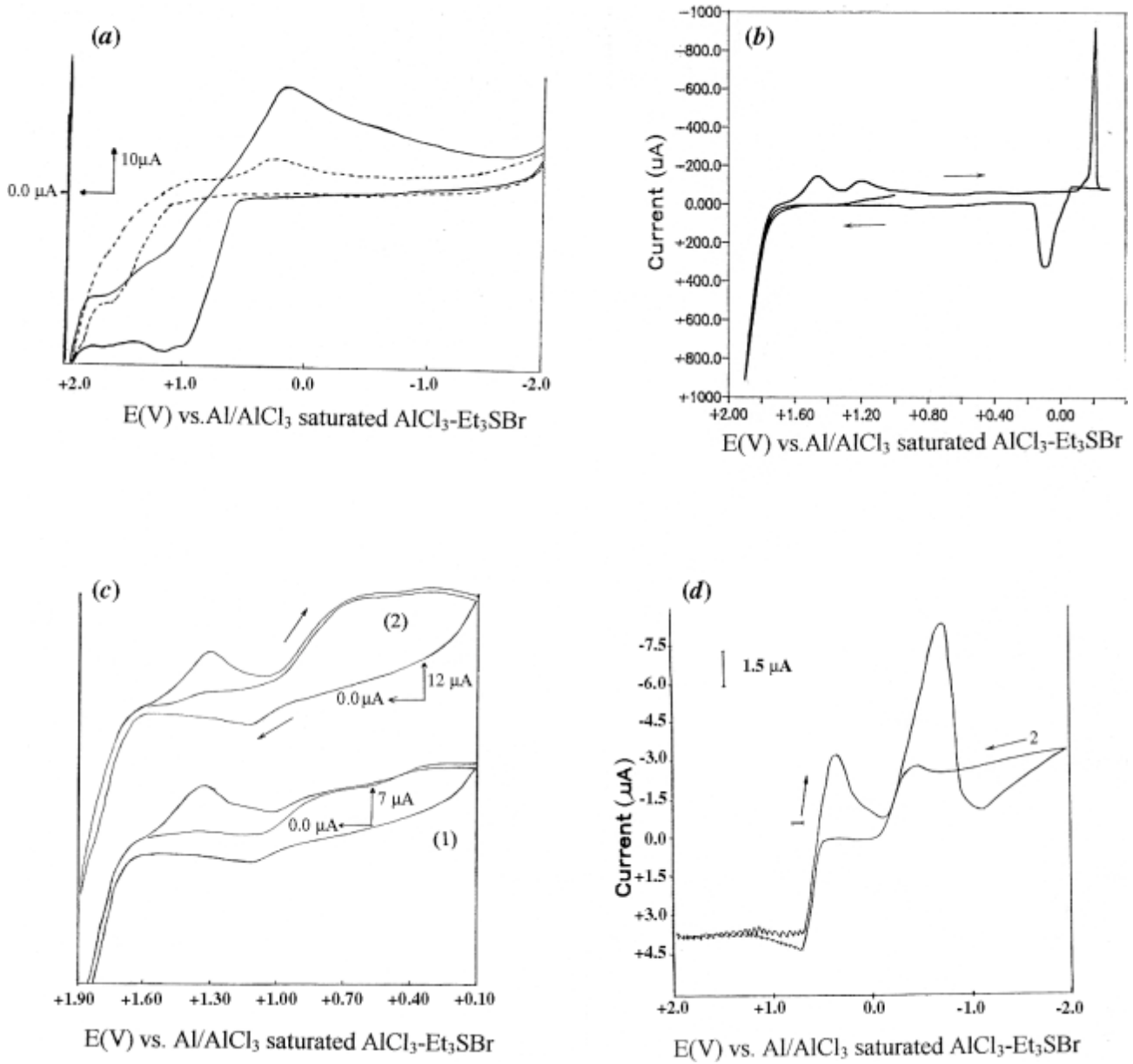


Et_3SBr–HCl

The cyclic voltammogram of 68% HCl–Et_3SBr shows well-separated reduction peaks at +0.3 V and –0.7 V (Fig. 5*d*). Since HCl_2^- and $H_2Cl_3^-$ reductions in an all-chloride system are separated by only 0.2 V, it appears that the expected $H_2Cl_2Br^-$ species disproportionates considerably to HBr_2^- (E_p +0.3 V) and $H_2Cl_3^-$ (E_p –0.7 V).

© 2004 NRC Canada

Fig. 5. Cyclic voltammograms of (*a*) basic (46%) $AlCl_3$–Et_3SBr before (——) and after (- - -) treatment with $EtAlCl_2$; (*b*) acidic (64%) $AlCl_3$–Et_3SBr; (*c*) acidic (64%) $AlCl_3$–Et_3SBr with increasing HCl added; (*d*) cyclic voltammogram of 68% HCl–Et_3SBr.



FTIR spectra

Table 4 shows the infrared spectrum of 52% HCl–Et_3SBr. The broad peak at 2060–1500 cm^{-1} can be assigned to the $HClBr^-$ and $H_2Cl_2Br^-$ species. This compares with the assignment of the 2200–1600 cm^{-1} absorption of HCl–emimCl (19) to the higher polymers $H_2Cl_3^-$ and $H_3Cl_4^-$. The broad band at 2200–1500 cm^{-1} in the HBr–Me_3SBr system (17) is probably due to $H_2Br_3^-$, not HBr.

Potential applications

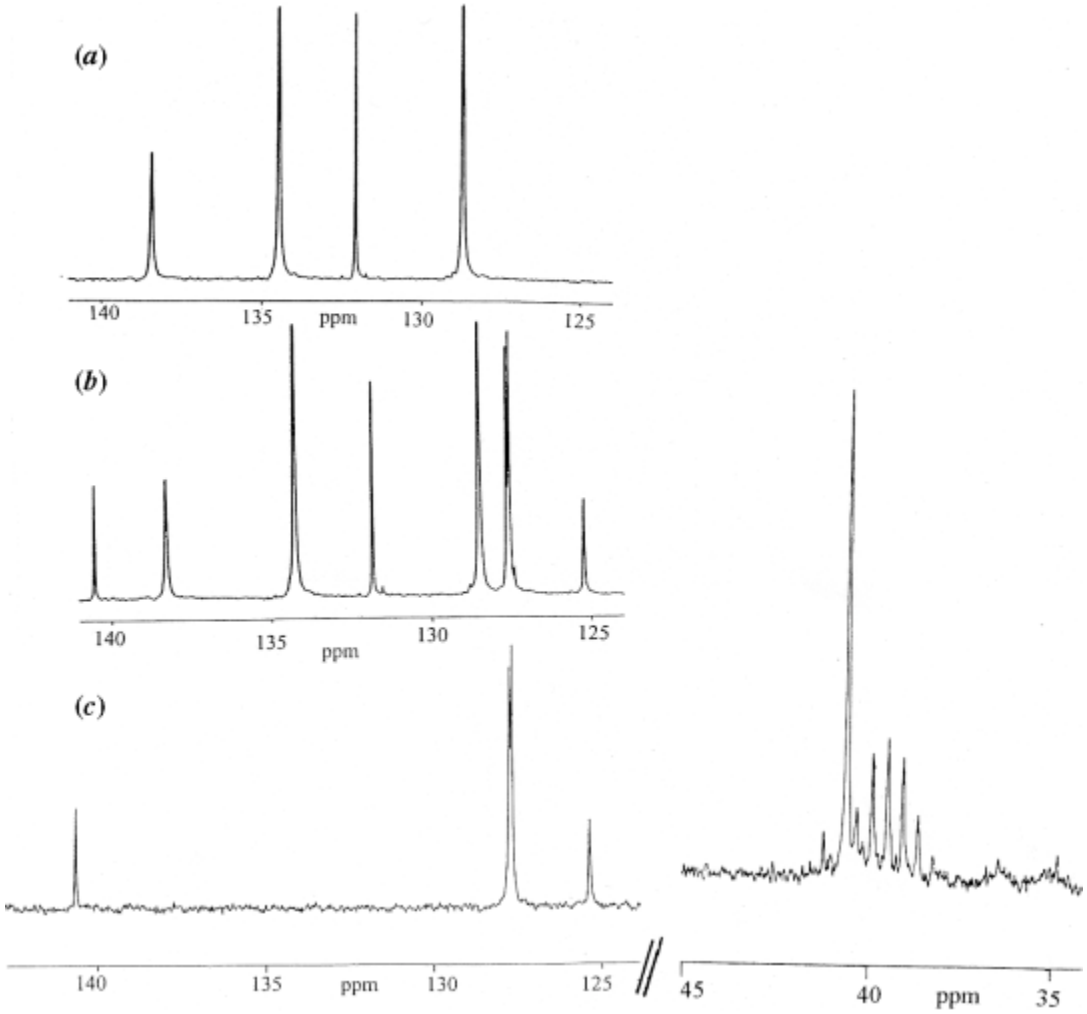
Hydride reactions

Under Lewis-basic conditions the hydrogen at the C-2 position of 1,3-disubstituted imidazolium salts reacts with hydride ions to produce hydrogen and carbenes, which can be used as a source of different salts or can form complexes with metals such as palladium (22, 23). Under Lewis-acidic conditions hydride does not attack the C-2 position of the imidazolium salts but rather the heptahaloaluminate, to form AlX_3H^- and substituted alanes (24).

CaH_2 is sparingly soluble in basic $AlCl_3$–Et_3SBr but does not react with either Et_3S^+ or $AlCl_3Br^-$. However, it reacts with the acidic $AlCl_3$–Et_3SBr, as shown by the IR band at 1904 cm^{-1} (Table 5). The IR and ^{13}C NMR spectra of benzophenone in this solvent were recorded (Tables 5 and 6), and their changes upon the addition of CaH_2 were found to be as follows: in the IR spectrum the Al-H band develops and the 1654 and 997 cm^{-1} bands are lost, while the five solute singlets in the ^{13}C NMR spectrum (Fig. 6*a*), including that due to C=O at 207.1 ppm (not shown), are replaced by five different singlets (Fig. 6*c*). The new peak at 40.6 ppm can be identified as arising from $–CHO^-$ (it is readily distinguish-

© 2004 NRC Canada

Fig. 6. ^{13}C NMR of 64% $AlCl_3$–Et_3SBr, containing (*a*) benzophenone; (*b*) benzophenone + CaH_2; (*c*) benzophenone + CaH_2 after a longer reaction time.



able from a weak DMSO locking solvent multiplet centred at 39.9 ppm) when compared with recent ^1C NMR spectra of liquid alkoxides (25). The addition of HCl to the product gives an IR spectrum with an O-H stretch at 3304 cm^{-1} and no Al-H band, consistent with the formation of the benzhydrol.

An aliphatic cation

Chemistry using ionic liquids at any temperature has tended to emphasize the anion of the salt. We have pointed out elsewhere (26) that the role of the cation is often much more than that of a spectator species. Sulfonium salts provide an aliphatic alternative to the aromatic imidazolium and pyridinium salts with different solubility prospects when complex reaction mixtures such as heavy oil – ionic liquid are considered (27). They also provide different NMR windows, are compatible with hydrides, and give different reduction products from imidazolium salts (not carbenes). The chirality of asymmetric sulfonium salts has long been known, and the possibility of developing a chiral solvent is intriguing.

Table 4. Infrared spectroscopy of 52% HCl–Et_3SBr ionic liquid.

Frequency	Intensity	Assignment
2968	s	Aliphatic C-H stretch
2939	s	Aliphatic C-H stretch
2879	s	Aliphatic C-H stretch
2060~1500	s,vb	$H_2Cl_2Br^-$; $H_3Cl_3Br^-$
1453	m	C-H bend
1420	m	C-H bend
1388	m	C-H bend
1273	m	
1147	m,b	$HClBr^-$, $H_2Cl_2Br^-$
1060	w	
1030	w	
977	w	
791	m	

Note: s, m, w, b, and vb stand for strong, medium, weak, broad, and very broad, respectively.

© 2004 NRC Canada

Table 5. FTIR of CaH_2-reduction of benzophenone in 51% $AlCl_3$–Et_3SBr ionic liquid.

$AlCl_3$–Et_3SBr (51%)	BzPh in 51% $AlCl_3$–Et_3SBr	CaH_2 in 51% $AlCl_3$–Et_3SBr	CaH_2 + BzPh in 51% $AlCl_3$–Et_3SBr	HCl + CaH_2+ BzPh in 51% $AlCl_3$–Et_3SBr	Mode of vibration
				3304	O-H stretch
2979	2979	2978	2978	2980	C-H stretch, asym (CH_3)
2941	2942	2942	2942	2942	C-H stretch, asym (CH_2)
2880	2880	2880	2880	2880	C-H stretch, asym (CH_3)
2836	2832	2832	2837	2834	C-H stretch, asym (CH_2)
		1904			A1-H stretch
	1654				C=O
	1593, 1581		1593, 1582	1593, 1582	} benzene ring
	1525, 1492		1519, 1493	1520, 1493	
1452	1452	1457	1450	1451	
1419	1419	1419	1418	1418	
1389	1389	1389	1389	1390	
	1346		1346	1346	
	1299		1298	1299	
1270	1278	1269	1269	1270	
	1181		1183	1183	
1081	1076	1081	1082	1082	
1038	1038	1038	1038	1039	
	997				
975	976	975	975	975	
789	784	792	788	788	
753	710	753	752	752	
			711	712	

Note: BzPh = benzophenone.

Table 6. ^{13}C NMR of hydridic reduction of benzophenone in 64% $AlCl_3$–Et_3SBr.

Sample name	^{13}C NMR chemical shifts (ppm)
Benzophenone in $CDCl_3$	196.8, 137.6, 132.5, 130.1, 128.3
Benzophenone in 64% $AlCl_3$–Et_3SBr	207.1, 138.4, 134.4, 132.0, 128.7, 31.6, 7.86
CaH_2 + benzophenone in 64% $AlCl_3$–Et_3SBr	140.6, 127.7, 127.6, 125.2, 40.6, 31.6, 7.86

References

1. J.S. Wilkes, J.A. Levisky, R.A. Wilson, and C.L Hussey. Inorg. Chem. **21**, 1263 (1982).
2. G.A. Olah. Friedel–Crafts and related reactions. Vol. 1. Wiley, New York. 1963. pp. 201–366, 853–888.
3. A.K. Abdul-Sada, M.P. Atkins, B. Ellis, P.K.G. Hodgson, M.L.M. Morgan, and K.R. Seddon. World Patent W095/21806, 1995.
4. P. Wasserscheid and T. Welton. (*Editors*). Ionic liquids in synthesis. Wiley-VCH, Weinheim. 2003.
5. K.R. Seddon, A. Stark, and M.-J. Torres. Pure Appl. Chem. **72**, 2275 (2000).
6. See, for example, many chapters in Ionic liquids: Industrial applications for green chemistry. ACS symposium series. Vol. 818. *Edited by* R.D. Rogers and K.R. Seddon. American Chemical Society, Washington, D.C. 2002.
7. R.J. Gale, B. Gilbert and R.A. Osteryoung. Inorg. Chem. **17**, 2728 (1978).
8. R.L. Burwell. Chem Rev. **54**, 615 (1954); R.M. Pagni. Adv. Molten Salt Chem. **6**, 211 (1987).
9. M. Ma and K.E. Johnson. Can. J. Chem. **73**, 593 (1995).
10. I.N. Feit, F. Schadt, J. Lubinkowski, and W.H. Saunders, Jr. J. Am. Chem. Soc. **93**, 6606 (1971).
11. M.N. Islam and K.T. Leffek. J. Chem. Soc. Perkins II, 952 (1977).
12. J.G. Huddleston, H.D. Willauer, R.P Swatloski, A.E. Visser, and R.D. Rogers. Chem. Commun, 1765 (1998).
13. W. Harris and B. Kratochvil. An introduction to chemical analysis. Saunders, Philadelphia. 1981. p. 201.
14. K.R Seddon, A. Stark, and M.-J. Torres. *In* Clean solvents: Alternative media for chemical reactions and processing. ACS symposium series. Vol. 819. *Edited by* L. Moens and M.A. Abraham. American Chemical Society, Washington, D.C. 2002.
15. L. Xiao, J.S. Wilkes, and K.E. Johnson. Proc. Electrochem. Soc. v.02-19, **13**, 964 (2002).
16. S.D. Jones and G.E. Blomgren. Proc. Electrochem. Soc. v.90-7, **7**, 273 (1990).
17. M. Ma. M.Sc. Thesis, Department of Chemistry, University of Regina, Sask. 1993.
18. P.A. Suarez, S. Einloft, J.E.L. Dullius, R.F. de Souza, and J. Dupont. J. Chim. Phys. **95**, 1626 (1998).
19. J.L.E. Campbell and K.E. Johnson. Inorg. Chem. **32**, 3809 (1993).
20. J.W. Shuppert and C.A. Angell. J. Phys. Chem. 3050 (1977).
21. J.L.E. Campbell and K.E. Johnson. J. Am. Chem. Soc. **117**, 7791 (1995).

© 2004 NRC Canada

22. L.-J. Xu, W.-P. Chen, and J.-P. Xiao. Organometallics, **19**, 1123 (2000).
23. C.J. Matthews, P.J. Smith, T. Welton, A.J.P. White, and D.J. Williams. Organometallics, **20**, 3848 (2001).
24. D.F. Wassell, K.E. Johnson, and L.J. Mihichuk. Proc. Electrochem. Soc. v.99-41, **12**, 132 (1999).
25. M. Earle and K.R. Seddon. World Patent WO 01/77081 A1, 2001.
26. K.E. Johnson, L. Xiao, and G. Driver. *In* Ionic liquids: Industrial applications for green chemistry. ACS symposium series. Vol. 818. *Edited by* R.D. Rogers and K.R. Seddon. American Chemical Society, Washington, D.C. 2002. p. 230.
27. D.W. Soveran, C.O. Jackson, K.E. Johnson, and Y. Patel. Using ionic liquids to upgrade heavy oil. SRC publication No. P-110-454-F-99. Saskatchewan Research Council, Regina. 1999.

© 2004 NRC Canada

Chemical transformations of *cis*-$W(CO)_4(C_5H_5N)_2$ in the ring-opening metathesis polymerization of norbornene

L. Bencze, N. Bíró, B. Szabó-Ravasz, and L. Mihichuk

Abstract: The six-coordinate W^0 complex *cis*-$W(CO)_4(C_5H_5N)_2$ has been found to be active in the in situ formation of a carbene species from norbornene, which generates a typical ring-opening metathesis product (ROMP). A proposed mechanism of initiation suggests that the reaction involves a 2,3-hydrogen shift in the coordinated norbornene ($\eta^2 \rightarrow \eta^1$). The initiating carbenoid group is identified from the products of the spontaneous carbene–CO coupling and Wittig reactions test. Formation of $W(CO)_3(\eta^6\text{-}C_6H_5CH_3)$ when toluene is the solvent, followed by reaction with the carbene, is blamed for catalyst deactivation.

Key words: bis-pyridine-tetracarbonyl-tungsten, ROMP, olefin metathesis, norbornene.

Résumé : On a trouvé que le complexe hexacoordiné du W^0, *cis*-$W(CO)_4(C_5H_5N)_2$, est actif dans la formation in situ d'une espèce carbénique dérivée du norbornène qui conduit à un produit résultant d'une ouverture typique de cycle avec métathèse. Un mécanisme d'initiation proposé suggère que la réaction implique un déplacement 2,3 d'hydrogène dans le norbornène pentacoordiné ($\eta^2 \rightarrow \eta^1$). Le groupe carbénoïde qui provoque l'initiation est identifié à partir des produits qui résultent d'un couplage spontané carbène–CO et de tests de réactions de Wittig. La formation de $W(CO)_3(\eta^6\text{-}C_6H_5CH_3)$, quand on utilize du toluène comme solvant et qu'on effectue ensuite la réaction avec le carbène, est attribuée à une désactivation du catalyseur.

Mots clés : bis-pyridine-tétracarbonyl-tungstène, produit d'ouverture de cycle avec métathèse, métathèse d'oléfine, norbornène.

[Traduit par la Rédaction]

Introduction

Olefin metathesis is of great value in organic and polymer synthesis. The reactions do not occur spontaneously, but all require the presence of a transition-metal carbene complex (*well defined catalyst*) or a *catalyst system* containing a transition-metal complex (precursor) in conjunction with a second compound, generally an organo main-group metal compound (co-catalyst), and sometimes a third compound (promoter) (1).

The transition-metal carbenes formed in these systems trigger the transalkylidenation (i.e., metathesis) of olefins (2, 3). Catalyst systems having neither a preformed metallocarbene nor an organometallic hydrocarbon group in any component represent a relatively minor class of metathesis initiators (4, 5).

Received 10 July 2003. Published on the NRC Research Press Web site at http://canjchem.nrc.ca on 10 March 2004.

L. Bencze, N. Bíró, B. Szabó-Ravasz, and L. Mihichuk.[1,2] Department of Organic Chemistry, Müller Laboratory, University of Veszprém, H-8201 Veszprém, POB 158, Hungary.

[1]Permanent address: Department of Chemistry and Biochemistry, University of Regina, Regina, SK S4S 0A2, Canada.

[2]Corresponding author (e-mail: Lynn.Mihichuk@uregina.ca).

We wish to report here the catalytic properties of *cis*-$W(CO)_4(C_5H_5N)_2$ (**1**) in the ring-opening metathesis polymerization (ROMP) of norbornene (NBE). This is the first six-coordinate W^0 noncarbenoid unimolecular catalyst that does not require a co-catalyst, a carrier, or light for activation. The aim of this work is to study the initiation reactions of a system in which the catalyst precursor contains the minimum number of ligands whose reactions might interfere with an olefin → carbene transformation and which involves no side reactions other than metathesis.

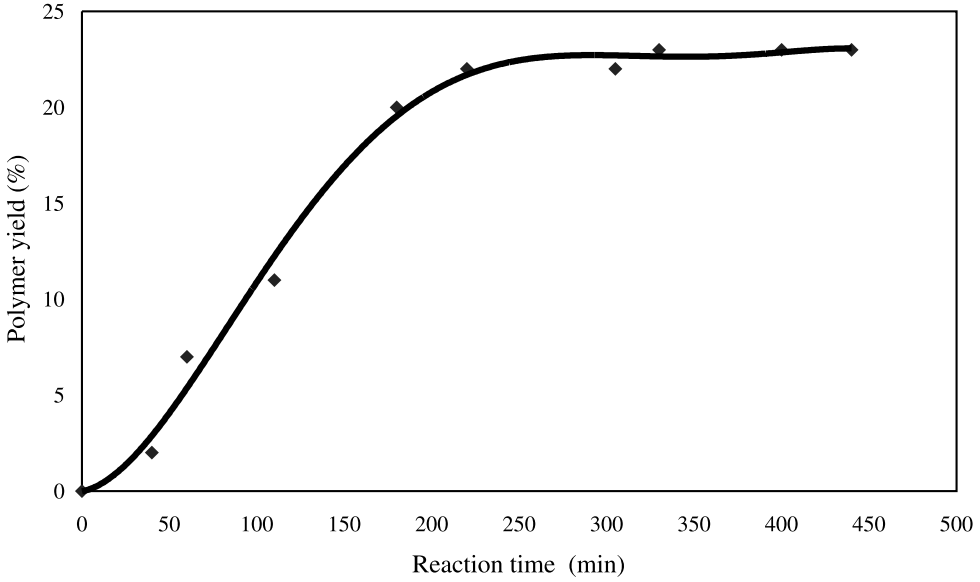
Experimental

cis-$W(CO)_4(C_5H_5N)_2$ (**1**) was prepared according to literature methods (6), with CO evolution being monitored until complete conversion of $W(CO)_6$ and formation of only the tetracarbonyl complex, as seen by infrared analysis. All experiments were conducted using standard Schlenk techniques under deoxygenated argon. Toluene was distilled from sodium and benzophenone, and NBE (Aldrich) was distilled from sodium before use. Tungsten hexacarbonyl (Aldrich) was used without further purification.

ROMP experiments were carried out in a reaction mixture composed of toluene (10 mL), olefin (0.52 mol/dm^3), and *cis*-$W(CO)_4(C_5H_5N)_2$ (4.4 mmol/dm^3). The reaction mixture was immersed in an oil bath heated to 116 °C and was stirred by a magnetic stirrer.

 doi: 10.1139/V04-007 © 2004 NRC Canada

Fig. 1. Norbornene polymer yield vs. reaction time. Each point represents the average of three experimental runs.



The NBE reaction mixture changed in time, from yellow to orange, to brown-orange, and then to a transparent golden brown color, with a gradual increase of viscosity. The reaction was quenched by the addition of ethanol (20 mL). The precipitated polymer was washed with ethanol, dried, and analyzed by $^{13}C\{^1H\}$ NMR spectroscopy. The spectra of the polymers were recorded in $CDCl_3$ solution at 125 MHz, using a GE GN Omega 500 spectrometer. The assignments of $^{13}C\{^1H\}$ NMR shifts were based on previous analysis, and the microstructural details of the polymers were calculated from the NMR integrals (7–10). GC–MS analyses were carried out on a Shimadzu QP5000, 70 eV instrument equipped with a 10 m × 0.20 mm HPI column at a flow rate of 2 mL/min. The identification of products from GC–MS analyses was carried out using an existing mass spectral library database. IR spectra were obtained using a SPECORD M80 spectrophotometer in CH_2Cl_2 solution, using KBr (0.065 mm) cells.

Results and discussion

The rate of polymer formation is rather slow, but nearly the same throughout the active period. The catalyst is poisoned or inactivated in some fashion within approximately 220 min. The maximum yield for the polymer is 25%, attainable after 220 min of reaction, as seen in Fig. 1.

The solubility of the polymer in $CDCl_3$ is satisfactory for NMR examination, but it is not free from some swollen gel. The $^{13}C\{^1H\}$ NMR analysis indicates a typical ROMP product of NBE. The assignments of $^{13}C\{^1H\}$ NMR shifts, based on previous analysis (7–10), were made as shown in Fig. 2, where a comparison of line intensity illustrates the high *cis* content (σ_c = 0.75–0.80) of the polymer. The distribution of the *cis* and *trans* double bonds in all cases is blocky ($r_c \cdot r_t$ ~ 9–14), consistent with the high *cis*- content of the polymers, as previously found (9–11).

The addition of benzaldehyde to the NBE–*cis*$W(CO)_4(C_5H_5N)_2$ system, followed by heating to 116 °C, inhibits the ROMP and leads to 2-benzylidenenorbornane (*m*/*z* (%): 184 (25, $[M]^+$), 155 (27), 130 (100), 115 (38), 77 (25)), the product of a Wittig-type carbene – aldehyde reaction, as illustrated in Scheme 1.

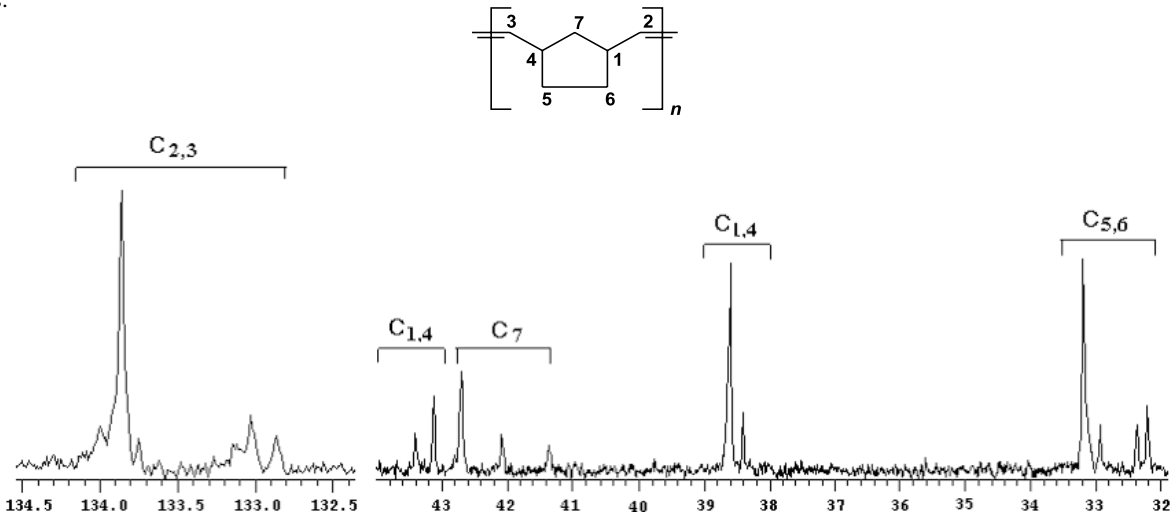
To elucidate the mechanism of carbene initiation, a GC–MS analysis was carried out on the low-molecular-weight fraction of the ethanol-quenched solution. The major products identified and mass spectral data are listed in Table 1. The first two entries (**5** and **6** in Scheme 2) are also consistent with a norbornylidene–carbene–ketene pathway, as found earlier for an NBE–$W(CO)_3Cl_2(AsPh_3)_2$ system, with the ketone being the major product formed (4*c*).

IR analysis of the quenched solution shows $W(CO)_5(C_5H_5N)$ (**2**) and $W(CO)_3$ (η^6-$C_6H_5CH_3$) (3) (besides traces of **1**) as the only complex-carbonyl-containing products identified by comparison of the ν_{CO} bands with literature values (6, 12) (Fig. 3). The GC–MS analysis of the quenched solution also provides evidence for the presence of the $W(CO)^3$ (η^6-$C_6H_5CH_3$) complex by a comparison of its mass spectrum with that of an authentic sample. The presence of the toluene-derived product, which was the second major product, seemed to be perplexing in a metathesis catalyst system; however, a separate experiment showed that it also forms from *cis*-$W(CO)_4(C_5H_5N)_2$ in refluxing toluene after a few hours, the result of a transformation pathway.

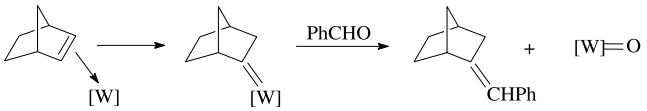
The transformation of the catalyst precursor is commenced by the loss of a pyridine ligand followed by the competition of CO, NBE, and toluene for the vacant coordination site (Scheme 2). The basis for this deduction is provided by the fact that $W(CO)_5(C_5H_5N)$ is the only product obtained when the above reaction is carried out *in the presence of CO*. The presence, in increasing quantity, of the penta- (**2**) and tricarbonyl (**3**) species at the beginning and by the end of the reaction helps to rule out their involvement as precursors in the formation of the active carbene species. Their presence does not maintain the catalytic activity. Owing to the rapid disappearance of *cis*-$W(CO)_4(C_5H_5N)_2$ and the quantity of the trapped primary alkylidene groups, it is

© 2004 NRC Canada

Fig. 2. Assignments of the ^{13}C NMR chemical shifts, illustrating the high *cis* content of the NBE polymer. Carbon signals are labeled as follows:



Scheme 1.

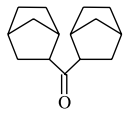
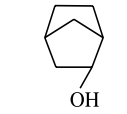
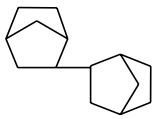
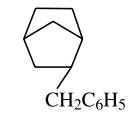


easily envisaged that the tetracarbonyl species is the precursor of the initiating carbene, and the latter forms soon after the reaction commences.

Thus, it appears that *cis*-$W(CO)_4(C_5H_5N)_2$ initiates the reaction at 116 °C through loss of one pyridine ligand followed by formation of a π-complex with NBE and rearrangement by a 2,3-hydrogen shift (4) to give the initiating carbene. Loss of the other pyridine ligand is followed by coordination of another NBE ligand in a π fashion, generating a metallacyclobutane intermediate (3), which then forms the coordinatively unsaturated ROMP propagator. The slow accumulation and the high molecular weight of the polymer product indicates that the primary carbene complex is relatively stable (13) and that the initiation is slow. Having no low-molecular-weight polymer fraction formed, living polymerization is assumed with little termination. The $^{13}C\{^1H\}$ NMR analysis of the polymer is indicative of only the repeating unit, as illustrated in the caption for Fig. 2, with no spectral lines associated with end groups, thereby suggesting no low-molecular-weight fraction.

The catalyst deactivation, leading to an approximate 25% polymer yield, is intriguing. The last entry in Table 1 is not a product derived from a norbornylidene–carbene–ketene pathway, as illustrated in Scheme 2, but may be indicative of an additional pathway involving the initiating carbene complex and the $W(CO)_3(\eta^6\text{-}C_6H_5CH_3)$ complex, leading to deactivation of the catalyst and the 25% maximum polymer yield. To gain further insight concerning this aspect, we are actively pursuing a detailed computational study of this reaction at the DFT level using the Gaussian 98 series of programs (14). It is interesting that although the olefin metathesis reaction is one of the most studied in organometallic chemistry, there have been few reports dealing with the modeling of this reaction and the ROMP reaction using quantum chemistry

Table 1. Low-molecular-weight products from the NBE–*cis*-$W(CO)_4(C_5H_5N)_2$ reaction.

Product	Mass spectral data (*m/z*, relative intensity (%))
	168 (2, $[M]^+$),139 (2), 123 (4), 95 (100)
	218 (23, $[M]^+$), 151 (69), 123 (70), 95 (100), 67 (88)
	112 (2, $[M]^+$), 94 (60), 79 (100), 67 (70)
	190 (18, $[M]^+$), 161 (18), 95 (96), 67 (100)
	186 (32, $[M]^+$), 95 (100), 91 (36), 77 (8), 67 (28)

tools (15–17). A future publication will deal with these computational results, as well as attempts to isolate the initiating carbene complex and an extension of these studies with the related norbornadiene substrate.

Conclusions

cis-$W(CO)_4(C_5H_5N)_2$ was found to be active in the in situ formation of a metathesis active carbene species from NBE substrate. The reactions follow the course of a 2,3-hydrogen shift in the coordinated olefin, and the initiating carbene could be identified from the products of the carbene–CO

© 2004 NRC Canada

Scheme 2.

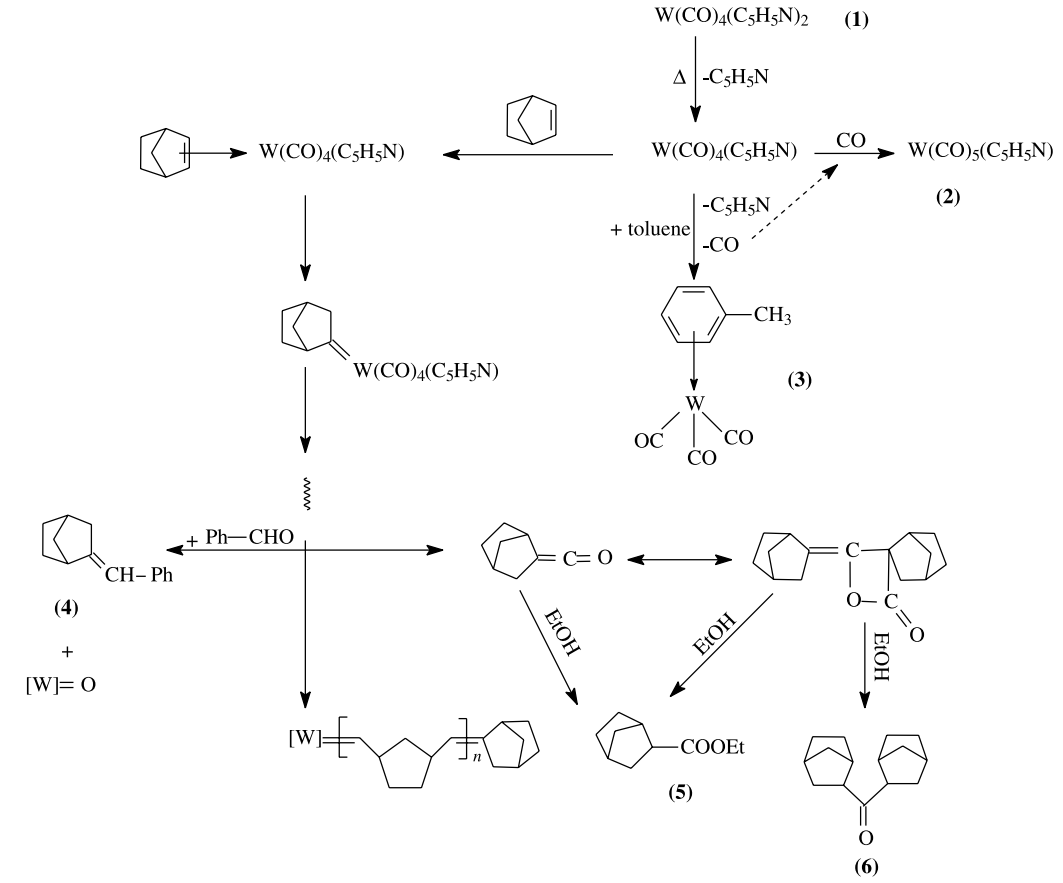
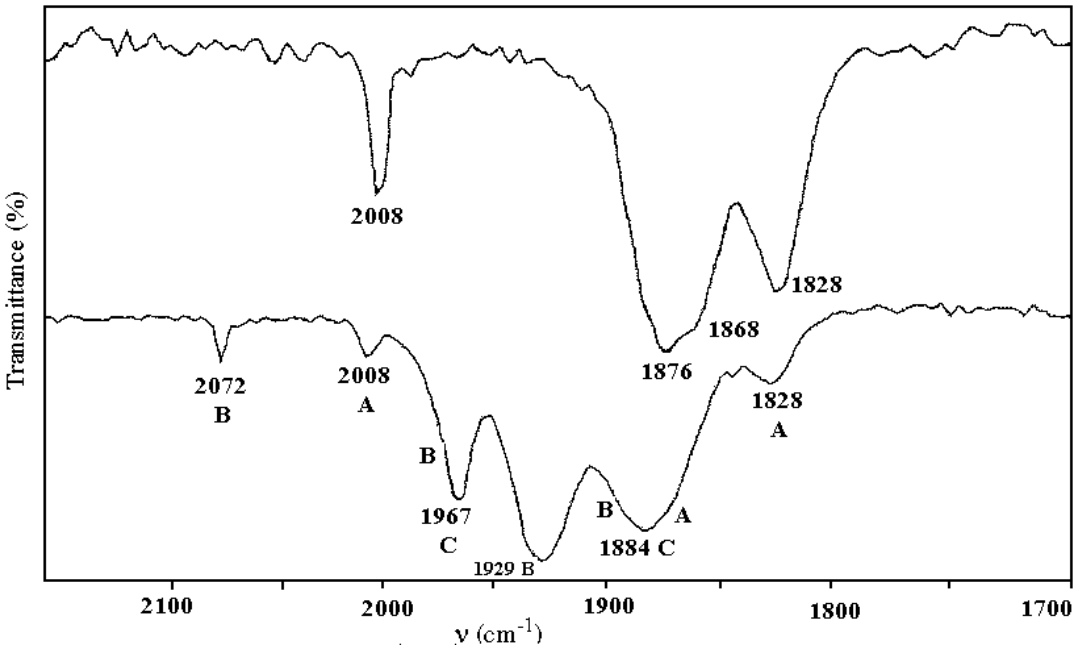


Fig. 3. Infrared spectra in the CO stretching region for $W(CO)_4(C_5H_5N)_2$ (upper trace) and a mixture of $W(CO)_4(C_5H_5N)_2$ (A), $W(CO)_5(C_5H_5N)$ (B), and $W(CO)_3(\eta^6\text{-}C_6H_5CH_3)$ (C) (bottom trace).



© 2004 NRC Canada

coupling reactions and Wittig reactions, as also seen in several seven-coordinate initiator systems.

This precatalyst (**1**) makes a unique single-component catalytic system, involving a six-coordinate W^0 species with no organophosphine or halide ligands involved.

Acknowledgments

This work was supported by the Hungarian Science Foundation under grants No. T35221 and T016326. L.M. thanks the Department of Chemistry and Biochemistry, University of Regina (Saskatchewan) for the granting of a sabbatical leave and the Department of Organic Chemistry, University of Veszprém (Hungary) for the invitation.

References

1. K.J. Ivin and J.C. Mol. Olefin metathesis and metathesis polymerization. Academic Press, London. 1997.
2. (*a*) J.L. Harrison and Y. Chauvin. Makromol. Chem. **141**, 161 (1970); (*b*) T.J. Katz, J. McGinnis, and C.J. Altus. J. Am. Chem. Soc. **98**, 606 (1976); (*c*) T.J. Katz and W.H. Hersh. Tetrahedron Lett. 585 (1977); (*d*) T.J. Katz, S.J. Lee, and M.A.J. Shippey. J. Mol. Catal. **8**, 219 (1980); (*e*) J. Kress, M. Wesolek, and J.A. Osborn. J. Chem. Soc. Chem. Commun. 514 (1982); (*f*) R.R. Schrock, S. Rocklage, J. Wengrovius, G. Rupprecht, and J. Fellman. J. Mol. Catal. **8**, 73 (1980).
3. R.H. Grubbs and S. Chang. Tetrahedron, **54**, 4413 (1998).
4. (*a*) D.T. Laverty, M.A. McKervey, J.J. Rooney, and A. Stewart. J. Chem. Soc. Chem. Commun. 193 (1976); (*b*) L. Bencze, K.J. Ivin, and J.J. Rooney. J. Chem. Soc. Chem. Commun. 834 (1980); (*c*) L. Bencze, A. Kraut-Vass, and L. Prokai. J. Chem. Soc. Chem Commun. 911 (1985).
5. (*a*) T. Szymanska-Buzar and T. Golowiak. J. Organometal. Chem. **489**, 207 (1995); (*b*) T. Szymanska-Buzar, T. Golowiak, and I. Czelusniak. Inorg. Chem. **3**, 102 (2000); (*c*) T. Szymanska-Buzar, T. Golowiak, and I. Czelusniak. J. Organometal. Chem. **640**, 72 (2001).
6. C.S. Kraihanzel and F.A. Cotton. Inorg. Chem. **2**, 533 (1963).
7. K.J. Ivin, D.T. Laverty, and T.J. Katz. Makromol. Chem. **178**, 1545 (1977).
8. K.J. Ivin, D.T. Laverty, and J.J. Rooney. Makromol. Chem. **179**, 253 (1978).
9. K.J. Ivin, D.T. Laverty, J.H. O'Donnel, J.J. Rooney, and C.D. Stewart. Makromol. Chem. **180**, 1989 (1979).
10. R.M.E. Greene, J.G. Hamilton, K.J. Ivin, and J.J. Rooney. Makromol. Chem. **187**, 619 (1986).
11. L. Bencze, G. Szalai, J.G. Hamilton, and J.J. Rooney. J. Mol. Catal. A Chem. **115**, 193 (1997).
12. V. Zanotti, V. Rutar, and R.J. Angelici. J. Organomet. Chem. **414**, 177 (1991).
13. L. Bencze and R.K. Szilágyi. J. Organometal. Chem. **505**, 81 (1995).
14. M.J. Frisch, G.W. Trucks, H.B. Schlegel, G.E. Scuseria, M.A. Robb, J.R. Cheeseman, V.G. Zakrzewski, J.A. Montgomery, Jr., R.E. Stratmann, J.C. Burant, S. Dapprich, J.M. Millam, A.D. Daniels, K.N. Kudin, M.C. Strain, O. Farkas, J. Tomasi, V. Barone, M. Cossi, R. Cammi, B. Mennucci, C. Pomelli, C. Adamo, S. Clifford, J. Ochterski, G.A. Petersson, P.Y. Ayala, Q. Cui, K. Morokuma, D.K. Malick, A.D. Rabuck, K. Raghavachari, J.B. Foresman, J. Cioslowski, J.V. Ortiz, A.G. Baboul, B.B. Stefanov, G. Liu, A. Liashenko, P. Piskorz, I. Komaromi, R. Gomperts, R.L. Martin, D.J. Fox, T. Keith, M.A. Al-Laham, C.Y. Peng, A. Nanayakkara, M. Challacombe, P.M.W. Gill, B. Johnson, W. Chen, M.W. Wong, J.L. Andres, C. Gonzalez, M. Head-Gordon, E.S. Replogle, and J.A. Pople. Gaussian 98 [computer program]. Revision A.9. Gaussian, Inc., Pittsburgh, Pa. 1998.
15. L.J. Cavallo. J. Am. Chem. Soc. **124**, 8965 (2002).
16. S. Fomine, S.M. Vargas, and M.A. Tlenkopatchev. Organometallics, **22**, 93 (2003).
17. F. Bernardi, A. Bottoni, and G.P. Miscione. Organometallics, **22**, 940 (2003).

© 2004 NRC Canada

The recognition and catalytic hydrolysis of ATP by protonated phenanthroline-bridged polyamine and (or) Ca(II), Mg(II), Zn(II), and La(III) ions

Yan-He Guo, Qing-Chun Ge, Hai Lin, Hua-Kuan Lin, and Shou-Rong Zhu

Abstract: The supramolecular interactions of 2,9-di(((2′-phenylamino)ethyleneamino)methyl)-1,10-phenanthroline (L) and (or) metal ions (M = Ca^{2+}, Mg^{2+}, Zn^{2+}, or La^{3+}) with nucleotides were investigated. Furthermore, the hydrolysis of ATP catalyzed by a protonated ligand and (or) a metal ion (M = Ca^{2+}, Mg^{2+}, Zn^{2+}, or La^{3+}) was studied at pH 7.6 using ^{31}P NMR spectra. Kinetics studies show that at pH 7.6 the protonated ligand, with a rate constant of 2.9×10^{-4} min^{-1}, does not significantly promote ATP hydrolysis. However, in the presence of Ca^{2+}, Mg^{2+}, Zn^{2+}, or La^{3+} ions, L can accelerate the hydrolysis of ATP, with corresponding rate constants of 5.73, 1.48, 6.76, and 31.7×10^{-3} min^{-1}, respectively, which are about 29-, 7.5-, 34-, and 159-fold faster than the hydrolysis rate of free ATP. By comparison with M–ATP (M = Ca^{2+}, Mg^{2+}, and La^{3+}) systems, the rates of M–L–ATP were also promoted. This has been achieved through the effective recognition of ATP and the availability of a good intramolecular nucleophile, i.e., a free amino nitrogen atom of L. Compared with the Zn^{2+}–ATP system, the decrease in the rate of the Zn^{2+}–L–ATP system at pH 7.6 may be attributed to the competition between the mixed ligands in binding Zn^{2+}. Similar to L–ATP, the hydrolysis reactions in the Zn^{2+}–L–ATP or M–L–ATP (M = Ca^{2+}, Mg^{2+}, and La^{3+}) systems occur through an addition–elimination type mechanism, in which phosphoramidate intermediates were observed at 2.88 and 4.06 parts per million (ppm) in the L–ATP and Mg^{2+}–L–ATP systems, respectively. Here, metal ions add control or regulation to the hydrolysis reaction.

Key words: recognition, ATP hydrolysis, metal ions, phenanthroline-bridged polyamine.

Résumé : On a étudié les interactions supramoléculaires de la 2,9-di((2′-phénylamino)éthylèneamino)méthyl-1,10-phénanthroline (L) et/ou de l'ion métallique (M = Ca^{2+}, Mg^{2+}, Zn^{2+} ou La^{3+}) avec des nucléotides. De plus, utilisant la spectroscopie RMN du ^{31}P, on a étudié l'hydrolyse de l'ATP, catalysée par un ligand protoné et/ou un ion métallique (M = Ca^{2+}, Mg^{2+}, Zn^{2+} ou La^{3+}), à un pH de 7,6. Les études cinétiques montrent que, à un pH de 7,6, le ligand protoné, avec une constante de vitesse de $2,9 \times 10^{-4}$ min^{-1}, n'active pas l'hydrolyse de l'ATP de façon significative. Toutefois, en présence des ions Ca^{2+}, Mg^{2+}, Zn^{2+} ou La^{3+}, le ligand L peut accélérer l'hydrolyse de l'ATP, avec des constantes de 5,73, 1,48, 6,76 et $31,7 \times 10^{-3}$ min^{-1} respectivement, soit 29, 7,5, 34 et 159 fois plus rapides que la vitesse d'hydrolyse de l'ATP libre. Par comparaison avec les systèmes M–ATP (M = Ca^{2+}, Mg^{2+}, Zn^{2+} ou La^{3+}), les vitesses d'hydrolyse sont aussi augmentées. Ce résultat a été obtenu par une reconnaissance effective de l'ATP et la disponibilité d'un bon nucléophile intramoléculaire, c'est-à-dire l'atome d'azote libre de l'amino du ligand L. Comparé au système Zn^{2+}–ATP, la diminution de la constante de vitesse dans le système Zn^{2+}–L–ATP, à un pH de 7,6, doit être attribuée à une compétition entre les ligands mixtes dans la fixation du Zn^{2+}. Semblable à celle observée dans le système L–ATP, la réaction d'hydrolyse dans les systèmes Zn^{2+}–L–ATP ou M–L–ATP (M = Ca^{2+}, Mg^{2+} ou La^{3+}) se produit par un mécanisme de type addition–élimination dans lequel les intermédiaires phosphoramidates sont observés à 2,88 et 4,06 ppm respectivement dans les systèmes L–ATP et Mg^{2+}–L–ATP. Dans ces cas, l'ion métallique contrôle ou régularise la réaction d'hydrolyse.

Mots clés : reconnaissance, hydrolyse de l'ATP, ions métalliques, polyamine pontée de la phénanthroline.

[Traduit par la Rédaction]

Introduction

The enzyme-catalytic transfers of nucleotidyl or phosphoryl groups of adenosine 5′-triphosphate (ATP) depend on the presence of divalent metal ions, which either play structural roles or may be one of the catalytic cofactors (1–7). In kinetic studies of ATP hydrolysis, the emphasis has been placed on the effect of transition metal ions, al-

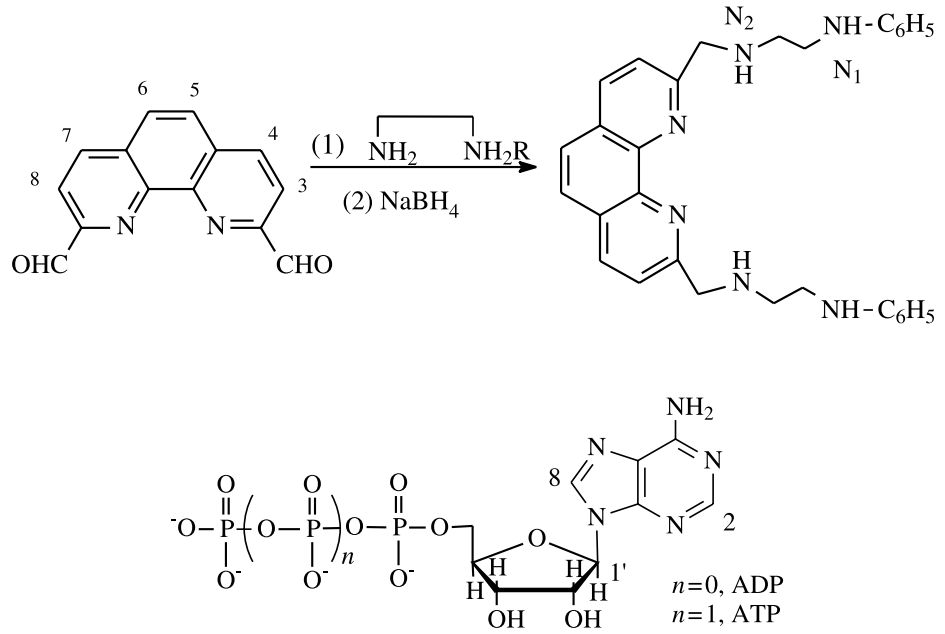
Received 4 January 2003. Published on the NRC Research Press Web site at http://canjchem.nrc.ca on 16 March 2004.

Y.-H. Guo, Q.-C. Ge, H.-K. Lin,[1] and S.-R. Zhu. Department of Chemistry of Nankai University, Tianjin, 300071, P.R. China.
H. Lin. State Kye Laboratory of Functional Polymer for Adsorption and Separation, Nankai University, Tianjin 300071, P.R. China.

[1]Corresponding author (e-mail: hklin@nankai.edu.cn).

 doi: 10.1139/V04-003 © 2004 NRC Canada

Scheme 1. Synthesis of L and structures of ATP and ADP.



though magnesium(II) and calcium(II) are reported as having the most biological significance (8). For example, studies of the binding interaction between highly biologically active Zn^{2+} and nucleotides have aroused intensive interest (9, 10), since the role zinc(II) plays in the active site of zinc-dependent enzymes can be conventionally studied with model zinc complexes (11). On the other hand, La(III) and its complexes, although not used directly by this type of enzyme for ATP hydrolysis, are by far the most efficient in promoting the hydrolysis of phosphate esters with good (12) or poor leaving groups (13).

Polyaza ligands in their protonated forms can bind to nucleotides strongly and selectively via electrostatic interactions, as well as by hydrogen bonding between the cationic binding sites (ammonium groups) of the receptor and the negatively charged polyphosphate groups of the substrates (14–17). On the other hand, recognition of the nucleobase residue may be achieved either by stacking with the nucleoside of nucleotides or by sites capable of forming complementary hydrogen-bonding patterns (15). It has been reported that polyammonium can promote the rate of ATP hydrolysis via an addition–elimination type mechanism, with the formation of a phosphoramidate intermediate (14–18).

Since metal ions influence the processes of recognition and nucleophilic attack of nucleotides, it is believed that metal ions with different properties — namely "hard" or "soft" metal ions — will exhibit unlike actions and differences in efficiency when assisting with ATP hydrolysis that is catalyzed by protonated polyaza receptors (19–21). In this paper, a multifunctional receptor L, containing phenanthroline and polyamines, has been used to achieve high molecular recognition and reaction selectivity in the dephosphorylation of ATP. The fact that ATP hydrolysis depends on the features of the Lewis acid (metal ions) provides insight into the supramolecular interactions between the receptor and the nucleotides and the catalytic hydrolysis of the physiologically important anions.

Experimental

Materials

All the experimental techniques and the standard IR, element analysis, and NMR equipment were the same as described previously (22). The compound 2,9-dicarboxaldehydro-1,10- phenanthroline (Phen) was synthesized according to the reported method (23), and *N*-phenylethylenediamine and sodium salts of ATP, ADP, and AMP were purchased from Aldrich Co. The synthesis of L is shown in Scheme 1.

Synthesis of 2,9-di(((*N*′-phenylamino)ethylene-amino)methylene)-1,10-phenanthroline (L)

To a suspension of 2,9-dicarboxaldehydro-1,10-phenanthroline (23) (0.8 g, 3.75 mmol) in anhydrous alcohol (50 cm^3), a solution of *N*′-phenylaminoethylenediamine hydrobromide (1.55 g, 8.0 mmol) and triethylamine (0.6 mL, 16 mmol) in 50 cm^3 alcohol was added slowly, and then the mixture was stirred under N_2 at 25 °C for 12 h. After filtration of the reaction mixture, $NaBH_4$ (0.15 g, 4.2 mmol) was added in small quantities, and the solution was stirred for another 12 h. The solvent was removed under reduced pressure, and NH_4OAC (4 g) in 20 cm^3 water was added to the white residue. The aqueous mixture was then extracted with chloroform (4 × 80 cm^3). The organic fractions were combined, washed with distilled water (3 × 30 cm^3), and then dried over $MgSO_4$. The solution was filtered, and the chloroform was removed on a rotary evaporator to give a yellow oil. The oil was dissolved in alcohol, and then concentrated HCl was added. The white-yellow precipitate formed was collected and dried on P_2O_5; 1.5 g was obtained, a yield of 42.64%. ^{1}H NMR (D_2O) δ: 6.51 (m, 6H, *m*-phenyl), 6.88 (m, 4H, *o*, *p*-phenyl), 3.49–3.58 (m, 8H, $NHCH_2CH_2NH$), 4.75 (s, 4H, Phen-CH_2), 7.86 (d, 2H Phen $H_{3,8}$), 7.98 (s, 2H, Phen $H_{5,6}$), 8.54 (d, 2H, Phen $H_{4,7}$). IR (KBr pellet): 3422 (ν_{N-H}); 693, 747 (Phen); 862, 1455, 1603 (Ar). Elemental analysis

© 2004 NRC Canada

calcd. for $C_{30}H_{32}N_6 \cdot 4HCl$ (%): H 5.83, C 57.89, N 13.50; found H 6.04, C 57.56, N 13.49.

Measurements

The potentiometric titrations (22), ^1H and ^{31}P NMR experiments, and the kinetic studies (^{31}P NMR spectra) were the same as those described previously (14).

Results and discussion

Protonation and metal complexes

The ligand L consists of a hexa-aza ligand with a Phen moiety and four amino groups. But potentiometric pH titration indicated that the ligand L has only four stepwise protonation constants, i.e., 10.16, 8.09, 6.64, and 2.50, respectively. The species distribution curves of the protonation of L are shown in Fig. 1*a*. Because of the electron repulsion of the already protonated ammonium ion(s) and the weaker basicity of 2,9-dimethyl-1,10-Phen compared with that of secondary amino groups (that is, $pK^{H}_{CH_3-Phen}$ = 5.85 vs. pK^{H}_{amine} = 9–11 (24)), the two nitrogen atoms of Phen are not involved in the protonation. This was proven by the ^1H NMR titration of L as a function of pH, which showed that the ^1H signals of Phen shift significantly only at pH < 2. Thus, the first two protonation steps involve the two benzylic N2 atoms, while the last two steps belong to the two terminal N1 atoms, since N1 is directly linked by an aromatic phenyl substituent.

[1] $\quad L + lH^+ = H_lL^{l+}$

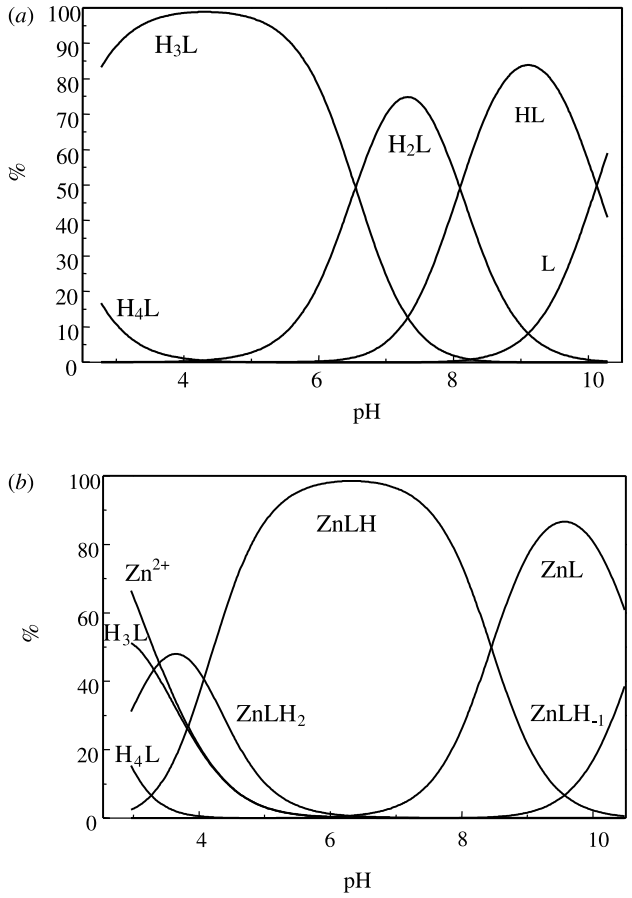
The ligands L that contain Phen and polyamines are good donors for Zn^{2+}. The stability constants of the species $ZnLH_2$, ZnLH, ZnL, and $ZnLH_{-1}$, formed in the Zn^{2+}–L system according to the equilibrium found in eq. [2], are listed in Table 1. Notwithstanding the existence of the strong donors of Phen and the four amino nitrogen atoms, the ligand cannot stabilize Zn^{2+} and three protons simultaneously because of the electrostatic repulsion effect. As is seen from Fig. 1*b*, species $ZnLH_2$, ZnLH, and ZnL (charge omitted for clarity) reach the maximum concentration at pH ca. 3.7, 6.2, and 9.6, respectively. The complex $ZnLH_2$ is formed at pH 2.7, and the structure has Phen and two terminal N1 atoms coordinated to Zn^{2+}, while the two benzylic N2 atoms are protonated. It is interesting to note that the complex ZnLH exists in a wide pH range (3–10) and is at almost 100% concentration at pH around 7, the physiological pH. The mono-hydroxyl compound $ZnLH_{-1}$ begins to form at pH 8.0 and becomes an important species at pH > 10; it is formed by deprotonation of the Zn(II)-bound water molecule. Although the highly charged species $ZnLH_3^{5+}$ was not involved in the calculations because of the pH range studied (2.5~10.5), we do accept the hypothesis of its existence in strongly acidic solution, and we make the assumption that the pK_a of the equation $ZnLH_3 = ZnLH_2 + H^+$ is 2.5.

[2] $\quad Zn^{2+} + L + mH^+ = ZnLH_m^{m+2}$

Protonated ligands interact with nucleotides

Protonated L forms five supramolecular complexes, $LNuH_m$ (Nu = ATP, ADP; m = 2, 3, 4, 5, and 6), with ATP or ADP in aqueous solution. The binding strength of protonated ligands with nucleotides, i.e., the log$K$ value of the equilibrium found in eq. [3], are listed in Table 1. The equilibrium in eq. [3] is obtained from eqs. [4], [5], and [5′], which represent the overall stability constants of molar complexes and the protonation constants of Nu, respectively. The protonation constants of Nu and the stability constants of their metal complexes were cited directly from the literature (25).

Fig. 1. Percentage distribution diagrams for the species present in solution of (*a*) 1×10^{-3} mol·dm^{-3} L; (*b*) 1×10^{-3} mol·dm^{-3} Zn^{2+} : 1×10^{-3} mol·dm^{-3} L at 25 °C and I = 0.1 mol·dm^{-3} KNO_3.



[3] $\quad H_lL^{l+} + H_nNu^{n-4\ (or\ 3)} = LNuH_{l+n}^{l+n-4\ (or\ 3)}$

[4] $\quad (l + n)H^+ + L + Nu^{-4\ (or\ 3)} = LNuH_{l+n}^{l+n-4\ (or\ 3)}$

[5] $\quad nH^{n+} + Nu^{-4\ (or\ 3)} = H_nNu^{n-4\ (or\ 3)}$

[5′] $\quad lH^+ + L = H_lL^+$

As seen from Fig. 2*a*, the supramolecular complexes form in the pH range in which the amine is protonated, while the nucleic acids are at least partly deprotonated. It is observed that the species $LATPH_3$ dominates at pH ca. 8, while $LATPH_6$, $LATPH_5$, $LATPH_4$, and $LATPH_2$ reach their maximum concentration at pH ca. 3, 5, 6.5, and 10, respectively.

The protonated ligands interact with the anion substrates via electrostatic interactions, as well as via hydrogen bonds formed between the polyammonium ions and the negatively charged oxygen atoms of the nucleotides. As shown in Table 1, the increasing degree of protonation of the ligand increases the binding strength between the supramolecular

© 2004 NRC Canada

Table 1. Stepwise protonation constants, stability constants, and binding strengths.

Equilibria	Constants	Equilibria	Constants
$H + L = HL$	10.16(5)	$Zn(II) + L = ZnLH_{-1} + H$	0.75(2)
$H + HL = H_2L$	8.09(6)	$Zn(II) + L = ZnL$	11.44(6)
$H + H_2L = H_3L$	6.64(4)	$Zn(II) + L + H = ZnLH$	20.91(5)
$H + H_3L = H_4L$	2.50(5)	$Zn(II) + L + 2H = ZnLH_2$	25.11(3)
$H_2L + ATP = H_2LATP$	6.28(3)	$ZnLH + ATP = ZnLATPH$	5.76(8)
$H_3L + ATP = H_3LATP$	10.93(1)	$ZnLH_2 + ATP = ZnLATPH_2$	10.40(9)
$H_3L + HATP = H_4LATP$	9.39(8)	$ZnLH_2 + HATP = ZnLATPH_3$	9.18(8)
$H_4L + HATP = H_5LATP$	14.79(2)	$ZnLH_2 + H_2ATP = ZnLATPH_4$	8.40(7)
$H_4L + H_2ATP = H_6LATP$	12.59(7)	$ZnLH_3 + H_2ATP = ZnLATPH_5$	10.34(9)
$H_2L + ADP = H_2LADP$	5.30(4)	$ZnLH + ADP = ZnLADPH$	3.98(6)
$H_3L + ADP = H_3LADP$	5.92(4)	$ZnLH_2 + ADP = ZnLADPH_2$	7.52(7)
$H_3L + HADP = H_4LADP$	5.09(6)	$ZnLH_2 + HADP = ZnLADPH_3$	6.56(5)
$H_4L + HADP = H_5LADP$	9.14(5)	$ZnLH_2 + H_2ADP = ZnLADPH_4$	6.03(5)
$H_4L + H_2ADP = H_6LADP$	8.07(4)	$ZnLH_3 + H_2ADP = ZnLADPH_5$	6.49 (4)

Note: Stepwise protonation constants of 1×10^{-3} mol·dm^{-3} L; stability constants of complexes present in the 1×10^{-3} mol·dm^{-3} Zn^{2+} : 1×10^{-3} mol·dm^{-3} L system; and binding strengths in 1×10^{-3} mol·dm^{-3} L : 1×10^{-3} mol·dm^{-3} ATP (ADP) and (or) 1×10^{-3} mol·dm^{-3} Zn^{2+} in water at 25 °C and I = 0.1 mol·dm^{-3} KNO_3. Charge is omitted for clarity.

Fig. 2. Percentage distribution diagrams for the species present in solution of the system (*a*) 1×10^{-3} mol·dm^{-3} L : 1×10^{-3} mol·dm^{-3} ATP; (*b*) 1×10^{-3} mol·dm^{-3} Zn^{2+} : 1×10^{-3} mol·dm^{-3} L : 1×10^{-3} mol·dm^{-3} ATP in water at 25 °C and I = 0.1 mol·dm^{-3} KNO_3.

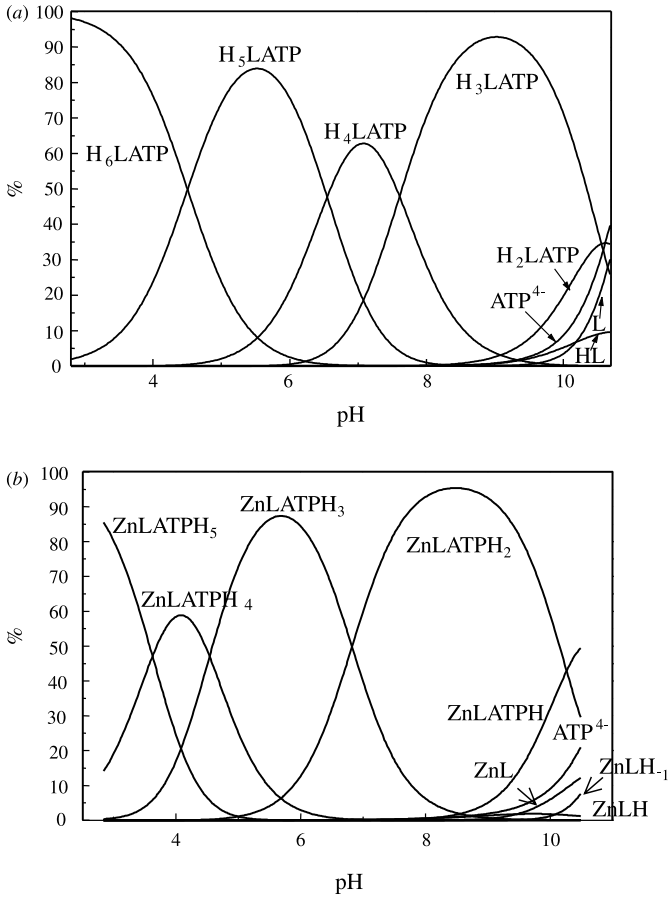


Table 2. ^{31}P NMR signal changes determined for ATP (0.01 mol·dm^{-3}) in the presence of L (0.01 mol·dm^{-3}) and (or) metal ions.

L	ATP	Metal	α	β	γ
–	+	Ca(II)	0.40	2.56	0.87
–	+	Mg(II)	0.43	2.85	0.94
–	+	Zn(II)	0.33	2.79	0.92
–	+	La(III)	–0.39	2.47	0.38
+	+	—	–0.05	0.32	1.42
+	+	Ca(II)	0.34	2.75	0.88
+	+	Mg(II)	0.33	2.80	0.87
+	+	Zn(II)	0.15	1.51	0.79
+	+	La(III)	–0.17	2.34	–0.08

Note: Metal ions: 0.01 mol·dm^{-3} Ca^{2+} (Mg^{2+}, Zn^{2+}, and La^{3+}) at pH 7.6 and at 25 °C. δATP: P_α, –15.54 ppm; P_β, –26.44 ppm, and P_γ, –11.92 ppm.

counterparts, owing to the increasing ability of the receptor to participate in Coulombic interactions and form H-bonds with the bound nucleotides. Because logK_1 (6.50 and 6.36 for ATP and ADP, respectively) (25) of the nucleotides is close to the third stepwise protonation constant of L (6.64) or higher than the last protonation constant of L (2.5), the highly protonated species formed at low pH might involve protonated HNu and H_2Nu (Nu = ATP and ADP). However, partial neutralization of the nucleotide will weaken the electrostatic interaction and decrease the number of H-bonds and then the binding strength. The orders of concentration $[H_3L][HATP] < [H_3L][ATP]$ and $[H_4L][H_2ATP] < [H_4L][HATP]$ are consistent with this result.

On the other hand, Table 2 shows that at pH 7.6, the ^{31}P NMR signals of P_β (0.32 ppm) and P_γ (1.42 ppm) shift downfield, whereas the P_α signal remains almost unchanged. This indicates that only the P_γ and P_β phosphorus centers are involved in the complexation. Moreover, the presence of Phen can indicate marked π-stacking interactions with the nucleoside of nucleotides, which has been proven by ^1H NMR spectra, as all the chemical resonances of $Phen_{3,8}$,

© 2004 NRC Canada

Table 3. ^{1}H NMR signal changes determined for the H-2, H-8, and H-1′ atoms of ATP and protons of the Phen of L in the absence or presence of Ca^{2+}(Mg^{2+}, Zn^{2+}, La^{3+}).

System	H-2	H-8	H-1′	$Phen_{3,8}$	$Phen_{4,7}$	$Phen_{5,6}$
ATP	(8.25)	(8.58)	(6.16)	—	—	—
Ca(II)–ATP	–0.14	–0.17	–0.13	—	—	—
Mg(II)–ATP	–0.09	–0.11	–0.04	—	—	—
Zn(II)–ATP	–0.14	–0.17	–0.13	—	—	—
La(III)–ATP	–0.18	–0.17	–0.16	—	—	—
L–ATP	–0.27	–0.32	–0.40	–0.13	0.01	–0.56
L–ADP	–0.42	–0.51	–0.69	–0.25	–0.18	–1.21
Ca(II)–L–ATP	–0.10	–0.35	–0.10	–0.24	–0.14	–0.64
Mg(II)–L–ATP	–0.07	–0.39	–0.06	–0.20	–0.08	–0.69
Zn(II)–L–ATP	–0.10	–0.29	–0.12	–0.10	–0.09	–0.66
La(III)–L–ATP	–0.06	–0.43	–0.06	–0.26	–0.02	–0.67
Zn(II)–L–ADP	–0.11	–0.27	–0.38	–0.13	–0.15	–0.69

Note: [ATP] = 0.01 mol·dm^{-3}; [L] = 0.01 mol·dm^{-3}; [Ca^{2+}] ([Mg^{2+}], [Zn^{2+}], [La^{3+}]) = 0.01 mol·dm^{-3}. Conditions: pH 7.6 and 25 °C.

$Phen_{5,6}$, and $Phen_{4,7}$ of L and those of H-2, H-8, and H-1′ of ATP shift upfield (see Table 3).

M–ATP systems (M = Zn^{2+}, Mg^{2+}, Ca^{2+}, and La^{3+})

Previously, studies have revealed that Zn^{2+}, Mg^{2+}, and Ca^{2+} can form 1:1 complexes with ATP in the 1:1 metal–ATP stoichiometry (26). Both the Ca^{2+} and Mg^{2+} complexes of ATP could be a mixture of α–β–γ tridentate and β–γ bidentate (ATP is mainly β–γ bidentate), whereas in the Zn^{2+}–ATP system, ATP uses only β and γ-phosphate to coordinate to Zn(II). With regard to the La^{3+}–ATP system, La(III) and ATP favor forming $La(ATP)_2$, and ATP is α–β–γ tridentate (27).

^{1}H NMR experiments indicated that the divalent metal ions Ca^{2+}, Mg^{2+}, Zn^{2+}, and Cd^{2+} can promote stacking of the purine bases (4). On the other hand, the hard metal ions have no tendency to interact with the N-7 of purine, while Zn^{2+} exhibits association with the N-7 of the adenosine ring (26). As shown in Table 2, ^{31}P NMR studies indicate a common trend for the binary metal–ATP systems, i.e., large downfield shifts for P_β (2.47–2.85 ppm) and P_γ (0.92–0.87 ppm) and small downfield shifts for P_α (0.33–0.43 ppm). The La^{3+} ion is an exception with a relatively small upfield shift for P_γ (–0.39 ppm) and a small downfield shift for P_α (0.38 ppm) (27).

The facilitation of ATP hydrolysis by Zn^{2+} was previously studied (26). The reaction occurs via a dimer, namely, $[Zn_2ATP]_2(OH^-)$. One Zn(II) ion coordinates to α- and β-phosphates, while another Zn^{2+} ion binds to the γ-phosphate of the ATP, with a large tendency to form a nucleophilic hydroxide complex. The other coordination side, involving two Zn^{2+} ions and one ATP molecule, is used only to stabilize the transition state of $[Zn_2ATP]_2(OH^-)$. At the same time, direct Zn(II)–N-7(purine) interaction occurs while the purine rings of different ATP molecules stack with each other. Because Mg^{2+} lacks metal ion – N-7 interaction and has a low tendency to form a nucleophilic Mg^{2+}–OH^- species at neutral pH (28), Mg^{2+} alone has a lower ability to accelerate ATP hydrolysis (4.5×10^{-4} min^{-1}) at neutral pH, whereas Ca^{2+} has a much higher catalytic rate constant (2.12×10^{-3} min^{-1}) because of the stronger affinity of Ca^{2+} (compared with that of Mg^{2+}) for the phosphate oxygens of ATP.

Recognition in the Zn(II)–L–ATP system

The interactions of Zn^{2+}–L complexes with nucleotides were determined by pH titrations and ^{31}P and ^{1}H NMR spectra. The binding strengths of the metal complexes with nucleotides, according to the equilibrium found in eq. [6], are listed in Table 1. The equilibrium in eq. [6] were obtained from eqs. [7], [2], and [5]. The species distribution curves are shown in Fig. 2*b*.

$$[6] \quad ZnLH_m^{m+2} + H_nNu^{n-4\ (or\ 3)} = ZnLNuH_{m+n}^{m+n-2\ (or\ 1)}$$

$$[7] \quad Zn^{2+} + L + (m+n)H^+ + Nu^{-4\ (or\ 3)} = ZnLNuH_{m+n}^{m+n-2\ (or\ 1)}$$

As is seen from Fig. 2*b*, there are five ternary species, from ZnLATPH to $ZnLATPH_5$, in the Zn^{2+}–L–ATP system. The increase in the binding strength of the Zn^{2+}–L–ATP system when compared with the L–ATP system should be attributed to the presence of noncovalent intramolecular interactions (29, 30). In the first approach, there are ion-pairing and H-bonding interactions between the polyammonium of L and the negatively charged phosphate chain of ATP; these were determined by comparison of the shifts of the ^{31}P signals of ATP before and after the addition of the metal ion to the L–ATP system. As shown in Table 2, the ^{31}P signals of α, β, and γ-phosphate of ATP in Zn^{2+}–L–ATP are upfield shifted by 0.15, 1.51, and 0.79 ppm, respectively, in comparison with those of free ATP, whereas the shifts of ATP in the Zn^{2+}–ATP system are 0.35, 2.79, and 0.92 ppm for α, β, and γ-phosphates, respectively. The results indicate that the mixed ligands compete to bind Zn^{2+} to some extent at neutral pH. On the other hand, all the signals of H-2, H-8, and H-1′ of ATP, as well as those of H-3,8, H-5,6, and H-4,7 of Phen in the Zn^{2+}–L–ATP system shift upfield, which indicates that the Phen has π-stacking interactions with the nucleobase residue of the substrate (Table 3). It is surprising that the Zn–L complexes mainly affect the chemical shifts of H-5,6 rather than the H-3,8 and H-4,7 of Phen; this is probably due to the fact that H-5,6 faces the nucleobase residue directly.

Taking into account the degree of protonation of the nucleotide and polyamine, it should be assumed that the species $ZnLATPH_3$ (which exists in the 4–8 pH range and binds

© 2004 NRC Canada

90% of the metal at pH ca. 5.5 (Fig. 2*b*)) can be considered a mixture of $[ZnLH_3][ATP]$ and $[ZnLH_2][HATP]$, since pK^{H}_{HATP} = 6.50 (25) is almost equal to $pK^{H}_{LH_3}$ = 6.64. For the same reason, the mixtures $[ZnLH_2][ATP]$ and [ZnLH][ATP] are reasonable assumptions for species $ZnLATPH_2$ and ZnLATPH, respectively. Because $pK^{H}_{H_2ATP}$ = 4.20 (25) and $pK^{H}_{LH_4}$ = 2.50, complex $ZnLATPH_4$ prefers the composition of $[ZnLH_2][H_2ATP]$. Because it is not easier for the nucleotide to be tri-protonated (pK_a < 1.7) (25) and because the ligand L can possibly bear one Zn^{2+} and three protons under the assisting coordination of the nucleotide, $[ZnLH_3][H_2ATP]$ is favorable for complex $ZnLATPH_5$. In a word, beside the coordination, ion-pairing, and H-bonding (^{31}P NMR) staking interactions (^{1}H NMR), there possibly exists cation–π-system, hydrophobic–hydrophilic, and even van der Waals interactions in the Zn^{2+}–L–ATP ternary system. These features are similar to those that occur in biosystems.

Supramolecular interactions in Ca(II), Mg(II), and La(III)–L–ATP systems

Since hard metal ions prefer oxygen atoms rather than nitrogen atoms, the competition between the mixed ligands disappears or decreases to some extent in the M–L–ATP systems (M = Ca^{2+}, Mg^{2+}, La^{3+}). Both the ^{31}P and ^{1}H NMR data indicate that Ca^{2+}, Mg^{2+}, and La^{3+} are strongly bound to the nucleotide ATP but not to L. As shown in Table 2, in the $Mg^{2+}(Ca^{2+})$–L–ATP system, the ^{31}P chemical shifts of α, β, and γ-phosphate of ATP are similar to those of the corresponding metal–ATP system. The La^{3+}–L–ATP system is an exception, with the upfield shift of P_α (–0.17 ppm) and P_γ (–0.08 ppm) (27). On the other hand, all the ^{1}H signals of the M–L–ATP systems (M = hard ions) upfield shift compared with those of free ATP and L, indicating that the nucleobase residue of ATP undergoes stacking interactions with the Phen moiety of L.

Owing to their high affinity for oxygen atoms, hard ions have the ability to "structure" ATP and facilitate the location of ATP in the polyammonium chain. The electron-withdrawing effect of positively charged metal ions bound to the substrate increases the susceptibility of the P_γ center and enhances its activity toward nucleophilic attack. If the recognition process occurs in such a sterically controlled way, the metal ion becomes a "messenger" between the receptor and the substrate.

ATP hydrolysis catalyzed by protonated L

Protonated L binds ATP strongly in the pH range of 3–10 (Fig. 1*b*). According to the binding strength of anions with the protonated ligands shown in Table 1, the catalytic conversion of ATP→ADP is reasonable. The product of this reaction, ADP, binds less strongly to protonated L than ATP does because of the shorter phosphate backbone of ADP, which has fewer oxygen atoms and, hence, weaker electrostatic interactions, as well as fewer hydrogen bonds.

The kinetics of ATP hydrolysis catalyzed by a protonated ligand as a function of time was studied at 70 °C using ^{31}P NMR spectra. Analysis of the ^{31}P NMR data shows that protonated L can accelerate the hydrolysis rate of ATP, with the observed rate constant $k_{obs} = 17.4 \times 10^{-3}$ min^{-1} at pH 2.5. But k_{obs} dropped acutely to a rate of 4.0×10^{-3} min^{-1} when the pH value was adjusted to 5.0. With an increase of pH, the k_{obs} decreased rapidly to small values of 2.9×10^{-4} min^{-1} and 3.1×10^{-5} min^{-1} at pH 7.6 and pH 10.1, respectively.

As shown in Scheme 2, the catalytic hydrolysis reaction involves an initial formation of the supramolecular complex (k_1), followed by intramolecular (by amine) or intermolecular nucleophilic attack (by water) of P_γ, leading to the formation of a phosphoramidate intermediate (k_2) and the release of ADP from the phosphorous center (k_3). Finally, the PO_3^{2-} of the intermediate captures a water molecule and gives HPO_4^{2-}, and the catalyst is regenerated and ready for another cycle. The ^{31}P signal observed at 2.55 ppm during the hydrolysis process of ATP should be considered a phosphoramidate intermediate. The same type of intermediate formed by phosphorylation of the amino nitrogen of the receptor has been found at 3–22 ppm (14–18). It is worth noting that the standard of ^{31}P signal in our studies was upfield shifted by 5.63 ppm in comparison with the reported values (14–18), so the ^{31}P shifts of the intermediate should be 8.18 ppm compared with other observations. For an efficient catalytic hydrolysis of ATP, strong binding of the substrate by the catalyst is required. The binding of ATP by protonated L has the following dual effects on the rate acceleration: neutralization of negative charge of the substrate and an increase in susceptibility of the phosphorus center.

ATP hydrolysis catalyzed by M–L complexes

The ^{31}P titration shows that the hydrolysis reactions in M–L–ATP systems favor 1:1:1 stoichiometry, which was demonstrated by the titration of [L–ATP] as a function of, for example, $[Zn^{2+}]$ (Fig. 3). The La^{3+}–L–ATP system also prefers a 1:1:1 stoichiometry in the control of 1:1:1 La^{3+}:L:ATP. As shown in Table 4, the ternary systems of Ca^{2+}, Mg^{2+}, Zn^{2+}, and La^{3+} possess the following rates: 5.73, 1.48, 6.76 and 31.7 × 10^{-3} min^{-1}, respectively, which are about 29-fold, 7.5-fold, 34-fold, and 159-fold as fast as the rate of free ATP (2×10^{-4} min^{-1}), respectively. By comparison with the rate of L–ATP (2.9×10^{-4} min^{-1}), the acceleration ratio is ca. 20-, 5-, 23-, and 109-fold, respectively. However, compared with M–ATP, the rate of the $La^{3+}(Ca^{2+}$, $Mg^{2+})$–L–ATP system is accelerated, while the Zn^{2+} ternary system is retarded.

The mechanisms proposed for the ATP hydrolysis catalyzed by L in the presence of Zn^{2+} and Mg^{2+} (or Ca^{2+} or La^{3+}) are shown in Scheme 3. Similar to Scheme 2, the first step is the formation of a supramolecular complex with a stability constant of K (k_1/k_{-1}). In the Zn^{2+}–L–ATP system, the coordination competition between L and ATP decreases the susceptibility of the P_γ group toward electrophilic attack, compared with that of the Zn^{2+}–ATP system. On the other hand, in the ternary system of Ca^{2+} (Mg^{2+} or La^{3+}), the "structuring" ATP, bound to hard metal ions, is more favored by the polyammonium chain.

Subsequently, the second step involves a nucleophilic attack on P_γ of ATP, the formation of an intermediate, and the release of ADP. In the $ZnLATPH_2$ complex, L coordinates with Zn^{2+} by one (or two) N1 atoms and (or) Phen (at pH > 7, the Zn^{2+}–Phen pair begins to dissociate), while two protonated N2 atoms interact with the phosphates of ATP via electrostatic and H-bonding interactions. Since it is difficult for the second N1 of L to bind Zn^{2+}, in view of its low ba-

© 2004 NRC Canada

Scheme 2. Proposed mechanism of ATP hydrolysis catalyzed by a protonated ligand. The model of supramolecular interactions, the H bonds, and the stacking interactions are consistent with those reported in literature (14).

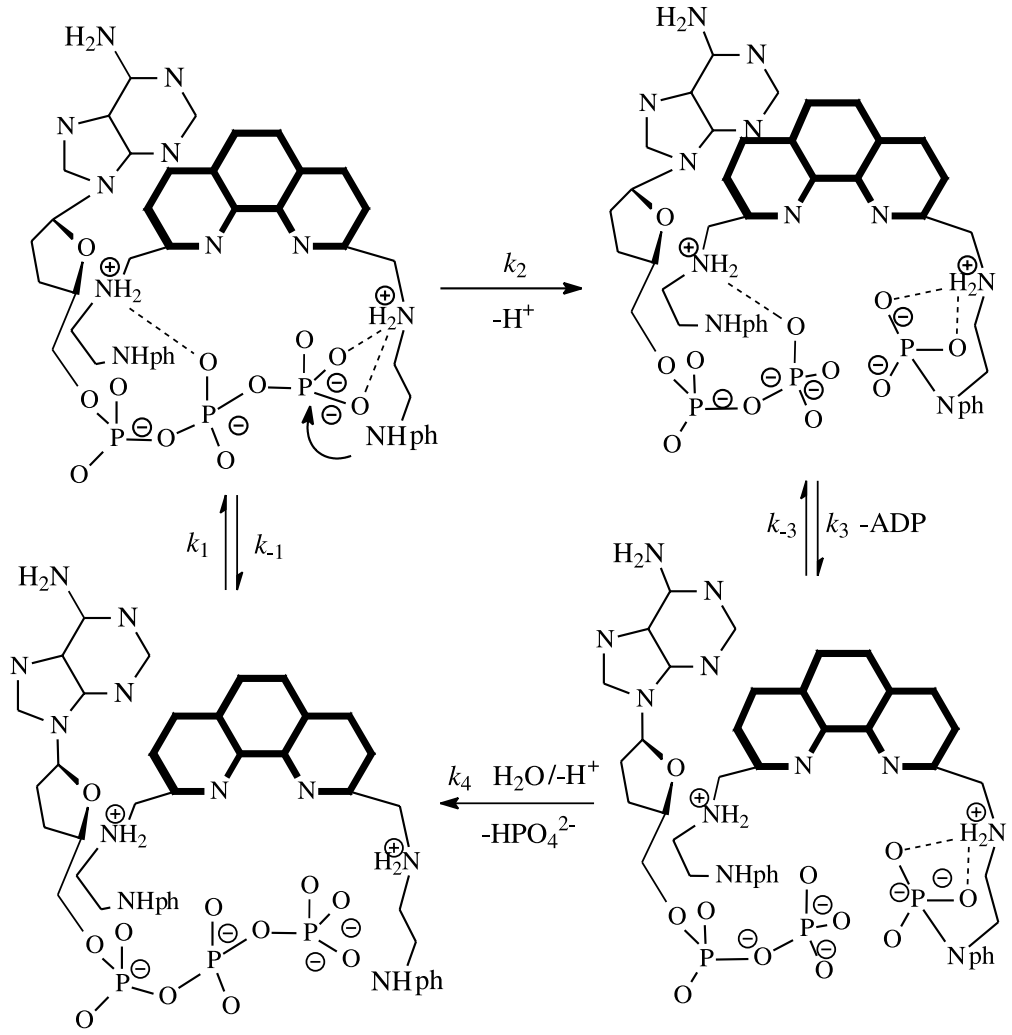


Fig. 3. ^{31}P titration of the binary tripod – ATP equimolar (0.01 mol·dm^{-3}) mixture with zinc(II) at pH 7.6; $\Delta = \delta_{Zn-L-ATP} - \delta_{ATP}$; δ_{ATP}: P_α (■), –15.54 ppm; P_β (●), –26.44 ppm, and P_γ (▲), –11.92 ppm.

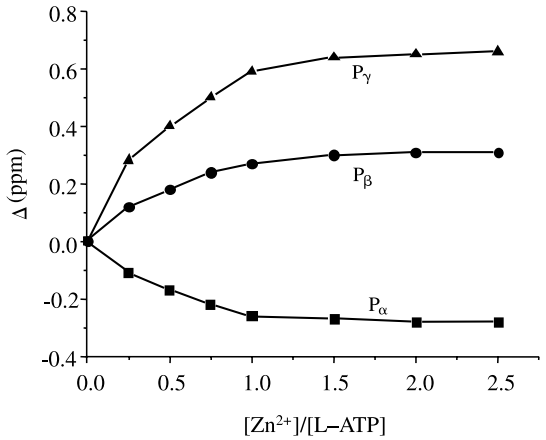


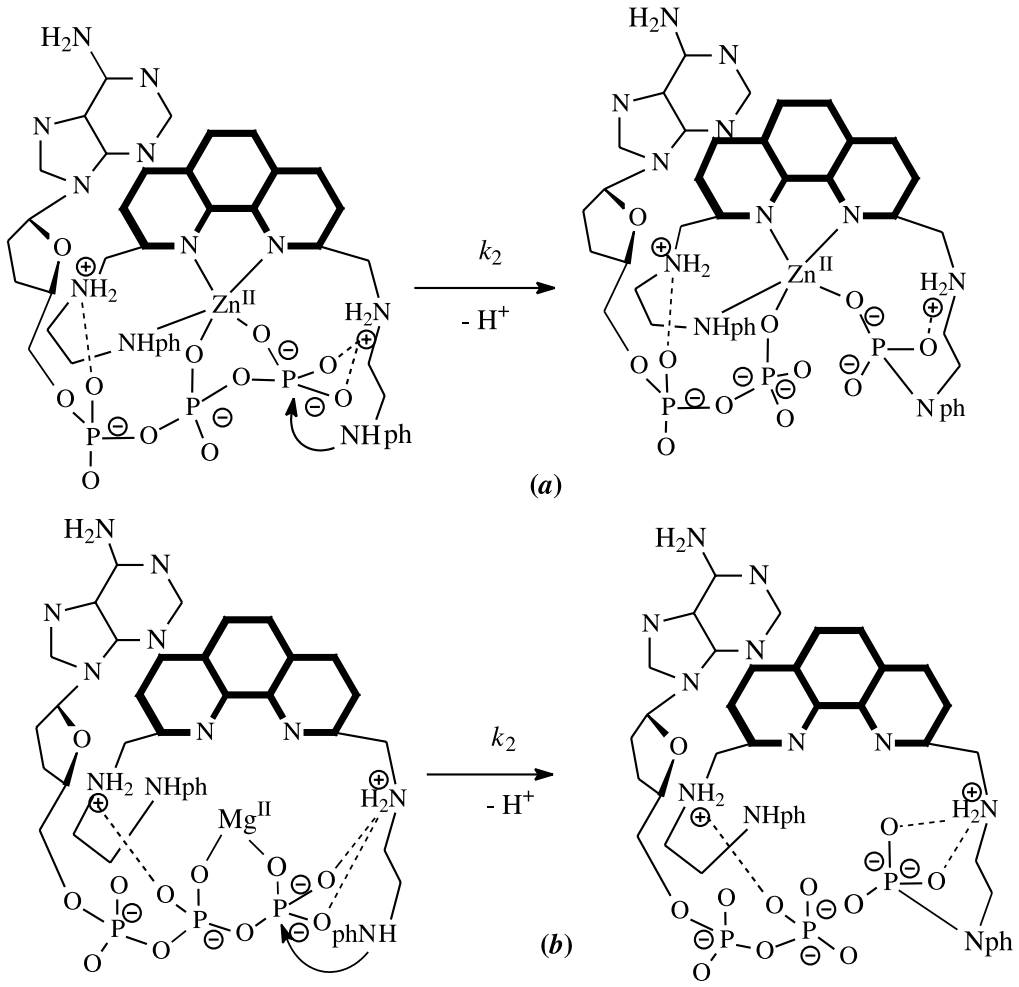
Table 4. First-order rates of ATP or ADP hydrolysis determined in the presence of ligand L and (or) various metal ions.

L	Metal	Substrate	k_{obs} (10^{-4} min^{-1})
–	—	ATP	2.0
–	—	ADP	1.5
–	Ca(II)	ATP	21.2
–	Mg(II)	ATP	4.5
–	Zn(II)	ATP	82.0
–	La(III)	ATP	27.2
+	—	ATP	2.9
+	—	ADP	1.7
+	Ca(II)	ATP	57.3
+	Mg(II)	ATP	14.8
+	Zn(II)	ATP	67.6
+	La(III)	ATP	317
+	Mg(II)	ADP	6.5
+	Zn(II)	ADP	15.3

Note: [ATP] = 0.01 mol·dm^{-3}; [ADP] = 0.01 mol·dm^{-3}; $k_{obs} = 10^{-4}$ min^{-1}; [L] = 0.01 mol·dm^{-3}; various metal ions: [Ca^{2+}] ([Mg^{2+}], [Zn^{2+}], and [La^{3+}]) = 0.01 mol·dm^{-3}. Conditions: pH 7.6 and 70 °C.

© 2004 NRC Canada

Scheme 3. Proposed mechanisms for the catalytic hydrolysis of ATP in the (*a*) Zn^{2+}–L–ATP; (*b*) Mg^{2+} (Ca^{2+}, La^{3+})–L–ATP systems.



sicity (pK_a = 2.5), it is reasonable for the free nitrogen atom to be an efficient nucleophile at neutral pH. Because Mg^{2+}, Ca^{2+}, and La^{3+} prefer phosphate oxygen atoms rather than the secondary amino nitrogen atoms of L, attack by uncharged amino groups is possible for these metal-ion-containing systems. It is worth noting that the ^{31}P signal of the phosphorylated intermediates (14–18) found at 2.88 and 4.06 ppm (should be added 5.63 ppm compared with other studies) in the hydrolysis process of ATP in the L–ATP and Mg^{2+}–L–ATP systems were not observed in the Ca^{2+}(Zn^{2+}, La^{3+})–L–ATP system, since the appearance of the phosporamidate intermediate is relative to several factors, such as pH, time, the concentration of ATP, and so on. Owing to the higher affinity of hard ions for the nucleotide, the release of ADP from the reaction center could be initially caused by a strong coordination of the metal ion to the negatively charged β- and γ-phosphates, leading to a release of metal–ADP in the M–L–ATP (M = hard metal ion) systems. With regard to the Zn^{2+}–L–ATP system, the products are the Zn–L complex and free ADP. The final step (k_4) of the mechanism at neutral pH is the breakdown of the intermediate, involving the capture of a water molecule by PO_3^{2-}, the release of HPO_4^{2-}, and the regeneration of the catalyst.

Thus, the broad range of the dephosphorylation rates, including retardation or acceleration (compared with M–ATP), depends on the metal ions. The metal ions play different roles in all the steps of the hydrolysis process in the Zn^{2+}–L–ATP system and M–L–ATP (M = Mg^{2+}, Ca^{2+}, and La^{3+}) systems, involving recognition of the substrate, nucleophilic attack of P_γ, stabilization of the negatively charged leaving group, and regeneration of the catalyst.

Table 4 shows that all the rate constants of the ternary systems are higher than those of L–ATP. This is because of the increased activity of the P-O-P group of the substrate, caused by the electron-withdrawing effect of metal ions towards the phosphate oxygens. However, the coordination of L to Zn^{2+} makes the positive charge density of Zn^{2+} shift to L, and it then decreases the power of attraction of the Zn^{2+} ion towards phosphates; thus the slower hydrolysis rate of ATP, compared with that of Zn^{2+}–ATP. On the other hand, the rate enhancements in Ca^{2+}, Mg^{2+}, and La^{3+} ternary systems, compared with the corresponding M–ATP systems, are attributed to the fact that metal ions "structure" ATP for a better recognition by the receptor. Owing to the neutralization of the negative charge of the intermediate oxygen atoms, the presence of Ca^{2+}, Mg^{2+}, or La^{3+} may be expected to increase the ability of ADP to release from the center of the intermediate. Moreover, the highest rate of La(III)–L–ATP might account for the tri-positive charge of La^{3+}, which favors the strongest electrostatic and acidic catalysis.

© 2004 NRC Canada

Conclusions

This paper reports the supramolecular interactions of nucleotides with Phen (phenanthroline) bridged polyamine and (or) metal ions (M = Zn^{2+}, Mg^{2+}, Ca^{2+}, and La^{3+}). Furthermore, the catalytic hydrolysis of ATP by L and (or) metal ions was also investigated. The results of ATP hydrolysis with different messengers, i.e., "critical" or "hard" metal ions, demonstrate the following two factors: (*i*) A highly facilitated reaction is connected with a very sensitive and delicate recognition; (*ii*) Metal ions play different roles in the process of the reaction mechanisms. Since the ternary complexes are viewed as the weak inter- or intramolecular interactions formed during biological self-assembly, they are "true" catalysts for ATP hydrolysis. To achieve more active molecular catalysts, ligands containing more amino groups or ligands bearing multi-ions are potentially useful (31).

Acknowledgements

The authors gratefully thank the National Science Foundation of P.R. China 20371028 and the National Science Foundation of Tianjin 023605811 for supporting this project.

References

1. A. Fersht. *In* Enzyme structure and mechanism. W.H. Freeman and Company, New York. 1985. p. 235
2. J. Weber and A.E. Senior. Biochim. Biophys. Acta, **1458**, 300 (2000).
3. H. Sigel. Chem. Soc. Rev. **22**, 255 (1993), and references therein.
4. H. Sigel, F. Hofstetter, R.B. Martin, R.M. Milburn, V. Scheller-Krattiger, and K.H. Scheller. J. Am. Chem. Soc. **106**, 7935 (1984).
5. D.J. Chanley and E. Feageson. J. Am. Chem. Soc. **85**, 1181 (1963).
6. P. Hendry and A.M. Sargeson. Inorg. Chem. **25**, 865 (1986).
7. B. Marciniec and H. Maciejewski. Coord. Chem. Rev. **223**, 301 (2001).
8. H. Sigel. J. Inorg. Nucl. Chem. **39**, 1903 (1977).
9. K.H. Scheller, F. Hofstetter, P. R. Mitchell, B. Prijs, and H. Sigel. J. Am. Chem. Soc. **103**, 247 (1981).
10. S.A.A. Sajadi, B. Song, F. Gregan, and H. Sigel. Inorg. Chem. **38**, 439 (1999).
11. A.L. Lehninger. Principles of biochemistry. Worth, New York. 1982.
12. J.R. Morrow and A.O. Chin. Inorg. Chem. **32**, 3357 (1993).
13. J.R. Morrow, L.A. Butrey, V.M. Shelton, and K.A. Berback. J. Am. Chem. Soc. **114**, 1903 (1992).
14. M.W. Hosseini, J.M. Lehn, L. Maggiora, K.B. Mertes, and M.P. Mertes. J. Am. Chem. Soc. **109**, 537 (1987).
15. G.F. Sweiegers and T.J. Malefetse. Chem. Rev. **100**, 3483 (2000).
16. E.M. Bianchi, S.A.A. Sajadi, B. Song, and H. Sigel. Inorgan. Chim. Acta, **300**–**302**, 487 (2000).
17. Q. Lu, R.I. Carroll, J.H. Reibenspies, A.E. Martell, and A. Clearfield. J. Mol. Struct. **470**, 121 (1998).
18. M.W. Hosseini, A.J. Blacker, and J.M. Lehn. J. Am. Chem. Soc. **112**, 3896 (1990).
19. I.O. Fritsky, R. Ott, and R. Krämer. Angew. Chem. Int. Ed. Engl. **39**, 3255 (2000).
20. T. Nabeshima. Coord. Chem. Rev. **148**, 151 (1996).
21. (*a*) G. Cathala, C.B. Brunel, D. Chappelet-Tordo, and M. Lazdunski. Biochemistry, **250**, 6046 (1975); (*b*) J.E. Murphy, T. Tibbits, and E.R. Kantrowitz. J. Mol. Biol. **253**, 604 (1995).
22. H. Sun, H. Lin, Z. Zhou, G. Zhao, X. Su, and Y. Chen. Indian J. Chem. **40A**, 763 (2001).
23. K. Madeja. J. Prakt. Chem. **17**, 97 (1962).
24. J.A. Dean. Lange's handbook of chemistry. Vol. 11. 1973. Chap 5, pp. 13–29.
25. R.M. Smith, A.E. Martell, and Y. Chen. Pure Appl. Chem. **63**, 1015 (1991).
26. K.H. Scheller, F. Hofstetter, P.R. Mitchell, B. Prijs, and H. Sigel. J. Am. Chem. Soc. **103**, 247 (1981).
27. Y.J. Shyy, T.C. Tsai, and M.D. Tsai. J. Am. Chem. Soc. **107**, 3478 (1985).
28. A.L. Miller and L.E. Orgel. The origins of life on the earth. Prentice-Hall, Englewood Cliffs, N.J. 1974. Chap 11.
29. P. Wang, R.M. Izatt, J.L. Oscarson, and S.E. Gllrdpoe. J. Phys. Chem. **100**, 9556 (1996).
30. J.M. Lehn. Angew. Chem. Int. Ed. Engl. **27**, 89 (1988).
31. I.O. Fritsky, R. Ott, and R. Krämer. Angew. Chem. Int. Ed. Engl. **39**, 3225 (2000).

© 2004 NRC Canada

Syntheses of novel modified acyclic purine and pyrimidine nucleosides as potential substrates of herpes simplex virus type-1 thymidine kinase for monitoring gene expression

Michaela Grote, Steffi Noll, Bernhard Noll, Bernd Johannsen, and Werner Kraus

Abstract: Suicide gene therapy with the herpes simplex virus type-1 thymidine kinase gene (HSV-1 tk) is considered to be a promising approach to the treatment of cancer. Making use of the lower specificity of the viral enzyme compared to human thymidine kinase, the therapy involves the administration of antiviral agents (e.g., ganciclovir) as prodrugs to induce enzymatic cell death in those cells that express the transferred gene. ^{18}F-labelled derivatives have been described for monitoring location, duration, and magnitude of the viral kinase enzyme activity by positron emission tomography (PET). Since an optimal radiotracer has not been developed, novel substances were synthesized for monitoring gene expression. A group of 13 nucleoside analogues were synthesized, among them N^1-methyl-9-[(1,3-dihydroxy-2-propoxy)methyl]guanine (**5**) and N^1-methyl-9-[(4-hydroxy)-3-hydroxymethylbutyl]guanine (**7**) as methyl analogues of ganciclovir and penciclovir and their related fluoro compounds (**6**, **8**). Further novel derivatives include N^6-methyl-9-[(1,3-dihydroxy-2-propoxy)methyl]-, N^6-methyl-9-[(4-hydroxy)-3-hydroxymethylbutyl]adenine (**9**, **10**), as well as the uracil derivatives 5-hydroxy-1-[(1,3-dihydroxy-2-propoxy)methyl]uracil (**11**), 6-methyl-1-[(1,3-dihydroxy-2-propoxy)-methyl]uracil (**12**), and its 3-fluoro-derivative (**13**).

Key words: fluorinated nucleoside analogues, gene therapy, PET, thymidine kinase.

Résumé : La thérapie à l'aide de gènes suicidaires dérivés du gène kinase de la thymidine du virus de type-1 de l'herpès simplex (HSV-1 tk) est considérée comme une approche intéressante au traitement du cancer. En utilisant une spécificité plus faible de l'enzyme viral par comparaison à celle de la kinase de la thymidine humaine, la thérapie implique l'administration d'agents antiviraux (par exemple le ganciclovir) comme prodrogues pouvant induire la mort de cellules enzymatiques dans les cellules qui expriment le gène transféré. Des dérivés marqués au ^{18}F ont été décrits pour la surveillance continue de la location, de la durée et du degré d'activité de l'enzyme kinase virale par tomographie à émission de positron (« PET »). Considérant qu'un marqueur isotopique optimal n'a pas encore été développé, de nouvelles substances ont été synthétisées pour la surveillance continue de l'expression génétique. On a synthétisé un groupe de 13 analogues de nucléosides, dont la N^1-méthyl-9-[(1,3-dihydroxy-2-propoxy)méthyl]guanine (**5**) et la N^1-méthyl-9-[(4-hydroxy)-3-hydroxyméthylbutyl]guanine (**7**) comme analogues méthylés du ganciclovir et du penciclovir et les composés fluorés apparentés (**6** et **8**). On a aussi synthétisé d'autres dérivés nouveaux, dont les N^6-méthyl-9-[(1,3-dihydroxy-2-propoxy)méthyl]- et N^6-9-[(4-hydroxy)-3-hydroxyméthylbutyl]adénine (**9** et **10**) ainsi que les dérivés uraciles 5-hydroxy-1-[(1,3-dihydroxy-2-propoxy)méthyl]uracile (**11**), 6-méthyl-1-[(1,3-dihydroxy-2-propoxy)méthyl]uracile (**12**) ainsi que son dérivé 3-fluoro (**13**).

Mots clés : analogues fluorés du nucléoside, thérapie génétique, « PET », kinase de la thymidine.

[Traduit par la Rédaction]

Introduction

Recently, transfer of genes for therapy has become more of reality for the treatment of human malignancies (1). One of the promising approaches is suicide gene therapy with the herpes simplex virus type-1 thymidine kinase gene (HSV-1 tk) (2, 3). This approach, which is also referred to as virus-directed enzyme–prodrug therapy (VDEPT) (4) involves gene delivery into replicating tumor cells, and after sufficient expression of the enzyme herpes simplex virus type-1

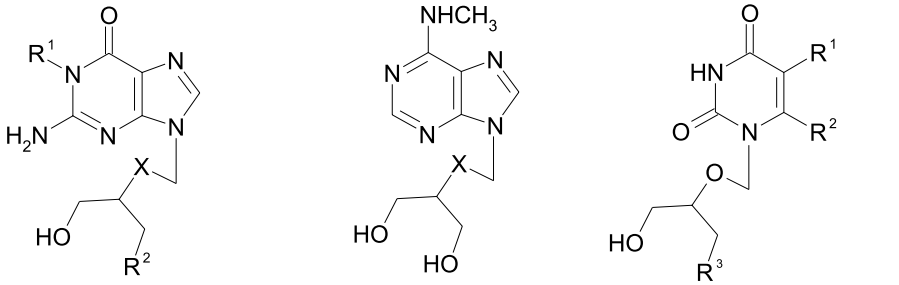
Received 20 February 2002. Published on the NRC Research Press Web site at http://canjchem.nrc.ca on 16 March 2004.

M. Grote,[1] S. Noll, B. Noll, and B. Johannsen. Forschungszentrum Rossendorf, Institut für Bioanorganische und Radiopharmazeutische Chemie, Postfach 510119, 01314 Dresden, Germany.
W. Kraus. Bundesanstalt für Materialforschung und -prüfung, Röntgenstruktur- und Phasenanalyse, Richard-Willstätter-Str. 11, 12489 Berlin, Germany.

[1]Corresponding author (e-mail: m.grote@fz-rossendorf.de)

 doi: 10.1139/V04-005 © 2004 NRC Canada

Fig. 1. Ganciclovir **1**, FHPG **2**, penciclovir **3**, FHBG **4**, and their related analogues **5**–**8**; acyclic derivatives of N^6-methyladenine **9**, **10** and the pyrimidines **11**–**13**.



1. R^1 = H, R^2 = OH, X = O
2. R^1 = H, R^2 = F*, X = O
3. R^1 = H, R^2 = OH, X = CH_2
4. R^1 = H, R^2 = F*, X = CH_2
5. R^1 = CH_3, R^2 = OH, X = O
6. R^1 = CH_3, R^2 = F*, X = O
7. R^1 = CH_3, R^2 = OH, X = CH_2
8. R^1 = CH_3, R^2 = F*, X = CH_2

9. X = O
10. X = CH_2

11. R^1 = OH, R^2 = H, R^3 = OH
12. R^1 = H, R^2 = CH_3, R^3 = OH
13. R^1 = H, R^2 = CH_3, R^3 = F*

F*: fluorine-18 or fluorine-19

thymidine kinase (HSV-1 TK), treatment with a prodrug, which is converted to a cell-toxic product by the viral enzyme.

Unlike the highly substrate-specific human TK, the viral enzyme (HSV-1 TK) accepts a diversity of pyrimidine- and purine-based nucleoside analogues, converting them into monophosphates. Subsequent phosphorylation by human (host) kinases leads to triphosphates that inhibit DNA polymerase and induce cell death. Inadequate site specific transfection and gene expression are some of the issues in gene therapy (5). Positron emission tomography (PET), a clinically valuable diagnostic modality for a noninvasive visualization of tissue functions in vivo, offers a possibility to monitor location and magnitude of gene expression, thereby helping to optimize protocols of gene and prodrug administration in humans. Fluorine-18, with a half-life of 110 min, is the most common isotope used for PET. Several nucleoside analogues labeled with ^{18}F for monitoring suicide gene therapy mediated by HSV-1 tk have been synthesized. They are usually derivatives of acyclonucleosides, which are selective anti-herpes agents, among them 9-[(3-[^{18}F]-fluoro-1-hydroxy-2-propoxy)methyl]guanine ([^{18}F]FHPG) **2**, derived from ganciclovir (GCV) **1**, and 9-[4-[^{18}F]-fluoro-3-hydroxymethylbutyl]guanine ([^{18}F]FHBG) **4**, derived from penciclovir **3** (6–11). Phosphorylation of these radioactive-labeled nucleoside analogues by virus-encoded thymidine kinase leads to metabolites trapped within the infected tumor cells, and the ensuing accumulation of radioactivity allows monitoring of the enzyme activity with PET (12).

In the search for improved PET radiotracers for gene therapy monitoring, we have synthesized and characterized a series of novel acyclic nucleosides.

Here we report on the synthesis of acyclic analogues of guanine (**5**–**8**) and adenine (**9**, **10**), as well as the related pyrimidines (**11**–**13**) (Fig. 1).

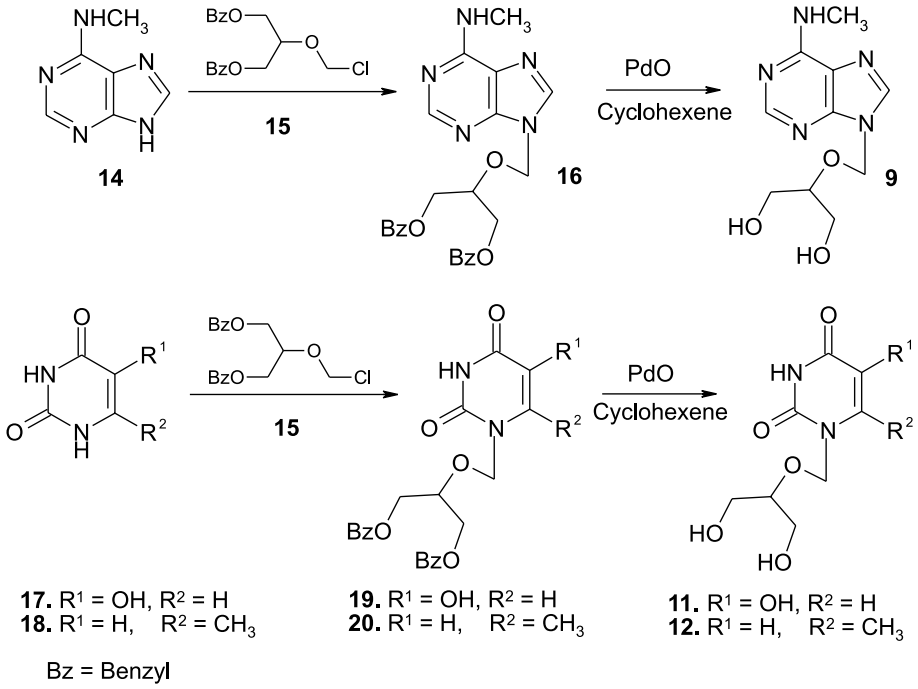
Guanine-based nucleoside analogues offer several possibilities to be labeled with ^{18}F, e.g., on the 8-position of the purine ring (13) or by replacement of a hydroxyl group in the side chain by fluorine (6, 10). Our strategy to replace fluorine for hydroxyl involves protection of one of the hydroxyl groups of the acyclic chain and, in the case of guanine derivatives, also the protection of the amino group in the 2-position, followed by introduction of a leaving group for the fluorination.

Chemistry

Many methods for the preparation of acyclic nucleoside analogues have been described. In most cases they involve synthesis of a suitably protected side chain, followed by coupling to the nucleobase and subsequent deprotection. For example, Martin et al. (14) started from epichlorohydrin to obtain GCV via condensation of 2-*O*-(acetoxymethyl)-1,3-di-*O*-benzylglycerol with N^2-9-diacetylguanine. We used 1,3-dichloro-2-propanol, sodium hydride, and benzyl alcohol to produce 1,3-dibenzyloxy-2-propanol, which was added to 1,2-dichloroethane followed by paraformaldehyde and hydrogen chloride gas, to obtain 1,3-dibenzyloxy-2-chloromethoxypropane (**15**) (15, 16). N^6-Methyladenine **14** was coupled to **15** in dry dimethyl formamide with triethyl amine. Compound **14** may react with **15** either at the 7-position or the 9-position of the purine ring, but additional heating of the reaction mixture afforded only **16**. Treatment with palladium oxide in cyclohexene removed the benzyl protection groups, yielding N^6-methyl-9-[(1,3-dihydroxy-2-propoxy)methyl]adenine (**9**) (15, 16). The structure of **9** was assigned by its ^1H NMR spectra as the 9-isomer. It was found that the chemical shifts resulting from the $H_2C(1')$ (5.64 ppm) and HC(8) (8.23 ppm) were in good agreement with the almost similar compound 9-[(2-hydroxyethoxy)methyl]adenine (5.67 and 8.27 ppm) (17); also the NH shift of **9** amounted to 7.73 ppm, which was also analogous to 9-[(2-hydroxyethoxy)methyl]adenine (~7.3 ppm), taking into account that the downfield shift is caused by a methyl group. Because our substance showed a weak downfield shift, we synthesized the 9-substituted guanine derivative. In contrast, the corresponding signals of 7-[(2-hydroxyethoxy)methyl]adenine showed a strong downfield

© 2004 NRC Canada

Scheme 1. Synthesis of compounds **9**, **11**, and **12**.



shift ($H_2C(1')$ = 5.79 ppm, HC(8) = 8.60 ppm, NH_2 = 9.2 ppm resp. 10.0 ppm) (17).

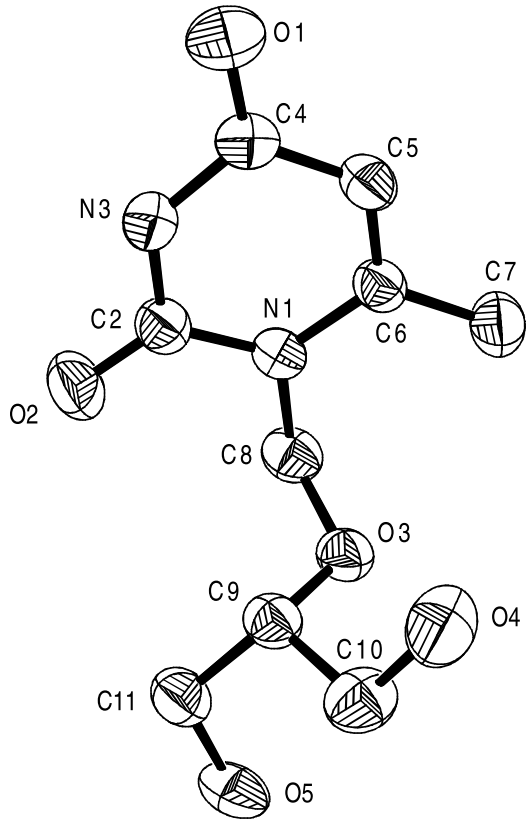
Nucleoside analogues can also be prepared by a coupling reaction of an activated base at the halogenated side chain (18). The pyrimidine derivatives were synthesized by direct condensation of the appropriate persilylated base with the chloromethyl ether **15** and tetra-*n*-butylammonium iodide as the catalyst to produce 5-hydroxy-1-[(1,3-dibenzyloxy-2-propoxy)methyl]uracil (**19**) and 6-methyl-1-[(1,3-dibenzyloxy-2-propoxy)methyl]uracil (**20**), respectively. Removal of the benzyl protection groups with palladium oxide resulted in 5-hydroxy-1-[(1,3-dihydroxy-2-propoxy)methyl]uracil (**11**) and 6-methyl-1-[(1,3-dihydroxy-2-propoxy)methyl]uracil) (**12**) (Scheme 1).

The molecular structure of **12** (Fig. 2) obtained by X-ray analysis proved that the acyclic chain has been coupled with the N^1-position of the pyrimidine ring.

The precursor 6-methyl-1-[[1-(*p*-anisyldiphenylmethoxy)-3-(*p*-toluenesulfonyloxy)-2-propoxy]methyl]uracil (**22**) was obtained from **12** by treatment with *p*-anisylchloro-diphenylmethane in dimethyl formamide and with traces of dimethylamino pyridine to produce 6-methyl-1-[[1-(*p*-anisyldiphenylmethoxy)-3-hydroxy-2-propoxy]methyl]uracil (**21**) in 47% yield, followed by tosylation with tosyl chloride in anhydrous pyridine (63%). Fluorination with potassium fluoride and Kryptofix® 2.2.2 in acetonitrile at 120 °C, afforded 6-methyl-1-[[1-(*p*-anisyldiphenylmethoxy)-3-fluoro-2-propoxy]methyl]uracil (**23**) in a yield of 23%. Finally, the protection group was removed, to give 63% of the fluorinated compound 6-methyl-1-[(3-fluoro-1-hydroxy-2-propoxy)methyl]uracil (**13**) (Scheme 2).

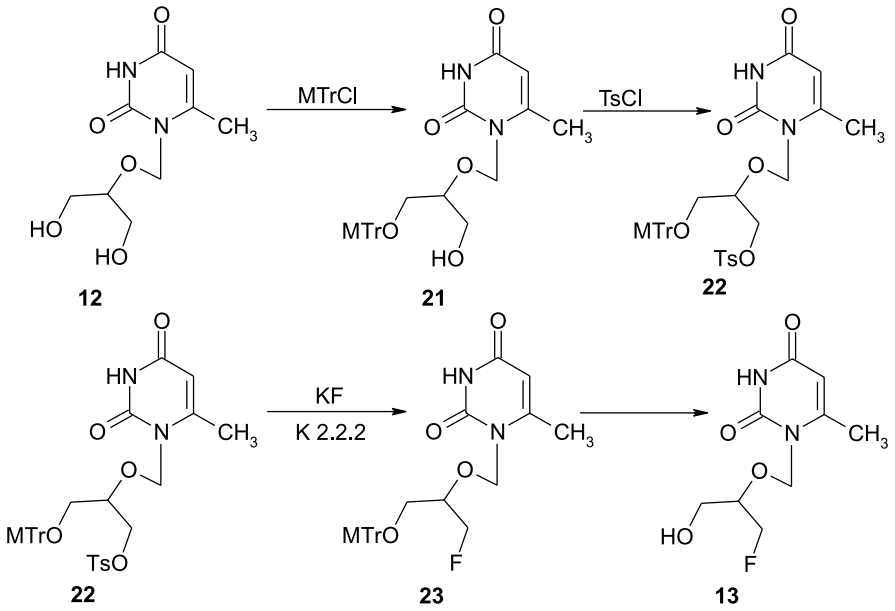
The carba-analogue of GCV (18, 19), penciclovir **3** can be prepared by several procedures. There are three steps, including the synthesis of a suitable side chain, coupling to a purine derivative that is able to undergo highly regioselective alkylation at the N-9 position, and transformation of the resulting alkylated purine derivative into the target compound. Some of the reported alkylating agents that

Fig. 2. X-ray structure of **12**.



© 2004 NRC Canada

Scheme 2. Protection, tosylation, and subsequent fluorination of **12** to obtain **13**.



Scheme 3. Synthesis of N^6-methyl-9-[(4-hydroxy)-3-hydroxymethylbutyl]adenine (**10**).

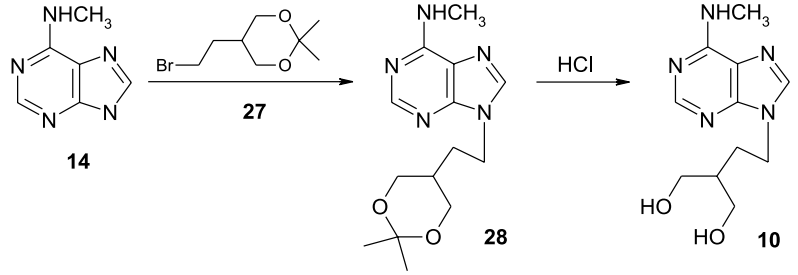
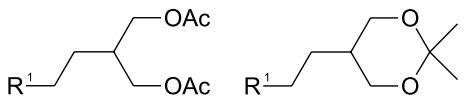


Fig. 3. Several alkylation agents used for the preparation of penciclovir.

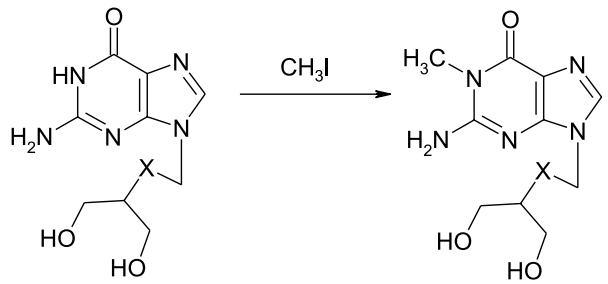


have been used are for instance, 4-acetoxy-3-acetoxymethyl-1-iodobutane (**24**) (20, 21), 4-acetoxy-3-(acetoxymethyl)butanol (**25**) (22), and 2,2-dimethyl-5-(2-*p*-toluenesulfonyloxyethyl)-1,3-dioxane (**26**) (23) (Fig. 3).

We used 5-(2-bromoethyl)-2,2-dimethyl-1,3-dioxane (**27**) to synthesize both penciclovir **3** (21, 24) and N^6-methyl-9-[(4-hydroxy)-3-hydroxymethylbutyl]adenine (**10**), using hydrochloric acid under refluxing conditions for deprotection (Scheme 3). The UV spectra of **10** and **9** were similar and suggested that it was the N-9 isomer.

We decided to modify the substrate properties of GCV and penciclovir by introducing a methyl group and therefore changing the lipophilicity of the molecule (Scheme 4). As

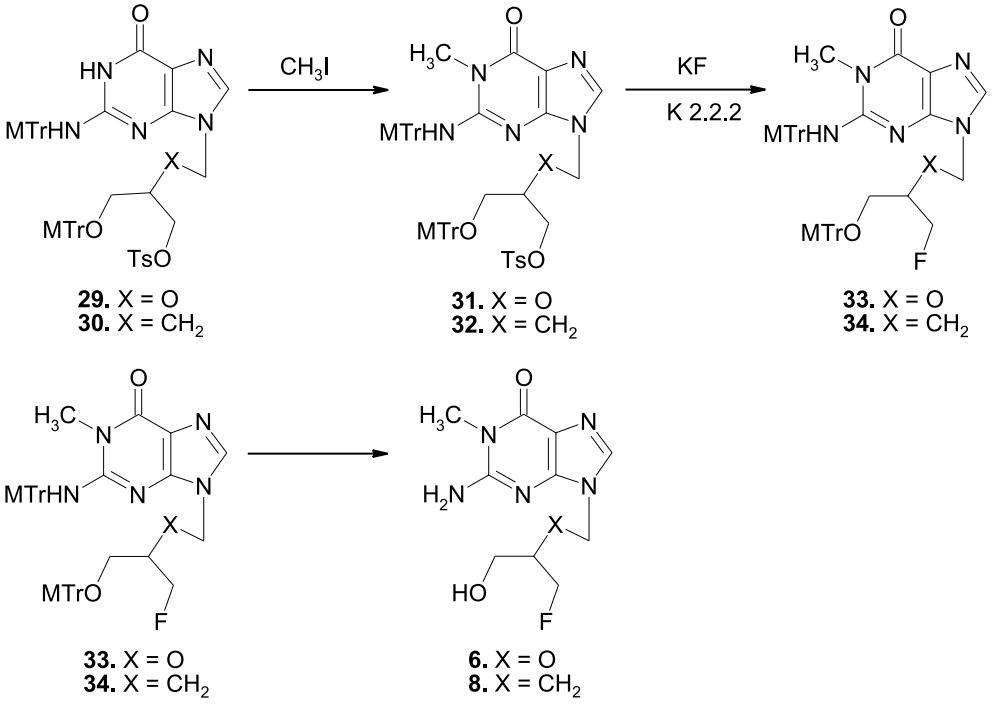
Scheme 4. Methylation of ganciclovir and penciclovir.



described for acyclovir (25, 26), introduction of a methyl group resulted in the alteration of the antiviral activities. The desired products **5** and **7** were obtained from GCV **1** and penciclovir **3** by treatment with methyl iodide in dimethyl formamide followed by extensive preparative column chromatography.

© 2004 NRC Canada

Scheme 5. Methylation, followed by fluorination and splitting off of the protection groups to obtain **6** and **8**.



To obtain N^1-methylated guanine derivatives **6** and **8**, we started from N^2-(*p*-anisyldiphenylmethyl)-9-[[1-(*p*-anisyldiphenylmethoxy)-3-(*p*-toluenesulfonyloxy)-2-prop-oxy]methyl]-guanine (**29**) or N^2-(*p*-anisyldiphenylmethyl)-9-[(4-(*p*-toluenesulfonyloxy))-3-*p*-anisyldiphenylmethoxy-methyl-butyl]guanine (**30**), prepared by modified literature procedures (6, 27). After reaction with methyl iodide yielding 44% of **31** and 29% of **32**, fluorination followed. After fluorination, the removal of the methoxytrityl group was carried out. Details of both sysnthesis steps were described above (Scheme 5).

All synthesized substances were characterized by elemental analysis and ^{1}H NMR spectroscopy, and derivatives containing fluorine were also determined by ^{19}F NMR. The UV spectra of the compounds **3**, **5**, **7**, and **9**–**13** are listed in Table 1.

Radiochemistry

To obtain [^{18}F]-labeled tracers the reaction conditions must consider the half-life of fluorine-18 (110 min). We synthesized the established [^{18}F]FHPG (**2**) and [^{18}F]FHBG (**4**) (6–11), as well as the new tracers [^{18}F]FMHPG (**6**) (N^1-methyl-9-[(3-[^{18}F]-fluoro-1-hydroxy-2-propoxy)methyl]guanine), [^{18}F]FMHBG (**8**) (N^1-methyl-9-(4-[^{18}F]-fluoro-3-hydroxymethyl-butyl)guanine), and [^{18}F]FMHPU (**13**) (6-methyl-1-[(3-[^{18}F]-fluoro-1-hydroxy-2-propoxy)methyl]-uracil. The tosylated and methoxytritylated precursors (**22**, **29**–**32**) were radiolabeled with a K[^{18}F]F/Kryptofix® 2.2.2 complex in acetonitrile, followed by splitting off the protection groups under acidic conditions. The labeled products were purified by HPLC. The synthesis time amounted to 90–110 min, the radiochemical purity was >98%, and an average specific activity of 19 GBq/μmol were determined.

Table 1. UV data for selected acyclic nucleosides.

No.	max nm (ε)	
1	258 (13 500)	(sh) 274 (9000)
3	253 (11 400)	(sh) 274 (8100)
5	254 (10 400)	(sh) 273 (7800)
7	255 (7 900)	(sh) 272 (6200)
9	265 (13 900)	
10	266 (13 600)	
11	278 (7 500)	
12	262 (11 200)	

Experimental

Instrumentation and reagents

^{1}H NMR spectra were obtained on a Varian Inova-400 (400 MHz) instrument with DMSO-d_6 as an internal standard. The chemical shifts are given as δ in ppm, the coupling constants as *J* in Hz. Fluorine ^{19}F NMR spectra were obtained on a Varian Inova-400 (376 MHz) with $CFCl_3$ as the internal standard. Elemental analyses were carried out with a LECO CHNS 932 elemental analyzer. Melting points were determined on a BOËTIUS melting point apparatus and are uncorrected. UV spectra were recorded on a Specord UV–vis S10 instrument (Zeiss) in aqueous solution.

The X-ray data were collected at room temperature (293 K) on a SMART-CCD diffractometer (Siemens), using graphite-monochromatized Mo-K_α radiation (λ = 0.71073 Å). A summary of the crystallographic data is given in Table 2. The structure was solved by direct methods. All hydrogen atoms were located by a difference Fourier synthesis and refined freely. Empirical absorption corrections were

© 2004 NRC Canada

Table 2. Crystallographic data for X-ray diffraction studies of 6-methyl-1-[(1,3-dihydroxy-2-propoxy)methyl]guanine (**12**).

	12
Formula	$C_9H_{14}N_2O_5 \cdot 2H_2O$
fw	230.22
Crystal system	Triclinic
Space group	*P*-1
a (Å)	6.867(2)
b (Å)	9.508(3)
c (Å)	10.493(4)
α (°)	101.593(7)
β (°)	107.857(6)
γ (°)	96.118(7)
V (Å^3)	626.3(4)
Z	2
Temperature (K)	293(2)
d (g/cm^3)	1.217
Absorption coefficient (mm^{-1})	0.100
F(000)	244
Wavelength (Å)	0.71073
Crystal size (mm^3)	1.5 × 0.6 × 0.4
2 θ Range (°)	2.10–25.00
Collection range	$-8 \le h \le 8$
	$-7 \le k \le 11$
	$-12 \le l \le 12$
Reflections collected	3100
Independent reflections	2186 (R_{int} = 0.0344)
GoF	0.984
R ($I > 2\sigma(I)$)	
R_1	0.0433
wR_2	0.1243
R (all data)	
R_1	0.0530
wR_2	0.1289

made using ψ scans. Most of the calculations were carried out in the SHELXTL system with some local modifications.

Position parameters and relevant bond lengths and angles are contained in Tables 3 and 4. Atomic positional and thermal parameters, full lists of bond lengths and angles, and F_o/F_c values have been deposited as supplementary material.[2]

Chromatographic purification was performed using either Silica gel 60 (Merck) or RP-18 material (LiChroprep™). Furthermore, a MPLC (middle pressure liquid chromatography) system (Knauer) with two columns (silica gel: Eurosil Baselect, 25 mm × 200 mm, from Merck; RP-18 material, 30 × 480, from Kronlab) was used with pressures ranging from 2 to 5 bar (1 bar = 100 kPa). HPLC analysis was performed on a system using a PerkinElmer LC binary pump 250, UV detector (absorbance detector model 759A, Applied Biosystems) operating at 254 nm, and a radioactivity detector using a semipreparative C-18-column (Eurospher, Knauer, 8 mm × 250 mm) and an analytical C-18-column (Eurospher, Knauer, 5 mm × 250 mm).

Table 3. Position parameters of 6-methyl-1-[(1,3-dihydroxy-2-propoxy)methyl]guanine (**12**) and the standard deviations.

	x	*y*	*z*	U_{eq}
N(3)	831(2)	7617(1)	3863(1)	38(1)
N(2)	3098(2)	9173(2)	5924(2)	41(1)
O(7)	572(2)	5521(1)	2088(1)	45(1)
C(3)	691(3)	8793(2)	3253(2)	37(1)
O(8)	2263(2)	6765(1)	5768(1)	57(1)
C(2)	2075(3)	7782(2)	5220(2)	40(1)
O(2)	1428(2)	2490(1)	1930(2)	55(1)
C(1)	2989(3)	10398(2)	5411(2)	41(1)
C(6)	–307(3)	6143(2)	3067(2)	45(1)
C(4)	1717(3)	10133(2)	4002(2)	42(1)
O(1)	3957(2)	11602(1)	6152(1)	60(1)
C(8)	2567(3)	5134(2)	2650(2)	41(1)
O(3)	4180(3)	6459(2)	1357(2)	64(1)
C(5)	–626(4)	8514(2)	1776(2)	52(1)
C(9)	2360(3)	3713(2)	3075(2)	50(1)
C(10)	3594(4)	5069(2)	1572(2)	53(1)
OW2	4161(2)	784(2)	1390(1)	51(1)
OW1	2722(2)	8028(2)	–511(2)	59(1)

Solvents and reagents were purchased from the following commercial sources and used without further purification: Sigma, Fluka, Lancaster, Aldrich, and Merck.

Ganciclovir **1** was obtained by neutralization of the sodium salt (Cymeven™) with 0.1 mol L^{-1} HCl and recrystallization from water; penciclovir **3** was synthesized according to a method of Harnden et al. (21). The precursors **29** and **30** were synthesized in modified procedures (10, 27).

Syntheses of potential substrate and fluorinated reference compounds

N^1-Methyl-9-[(1,3-dihydroxy-2-propoxy)methyl]guanine (5)

Ganciclovir (**1**, 214 mg, 0.838 mmol) and tetrabutylammonium hydroxide solution (1 mol L^{-1}, 0.88 mL, 0.88 mmol) were dissolved in 20 mL of dry DMF at room temperature. To this solution methyl iodide (120 µL, 1.93 mmol) in 1.2 mL DMF was slowly added and the mixture was stirred for an additional 45 min. The solvent was evaporated in vacuum and the crude product was purified by MPLC (RP-18, acetonitrile–water (1:9, v/v)) to afford **5** (136 mg, 61%), mp 198–200 °C. ^{1}H NMR (DMSO-d_6) δ: 7.79 (s, 1H, 8-CH), 7.04 (s, 2H, -NH_2), 5.43 (s, 2H, -H_2C(1′)), 4.58 (t, 2H, *J* = 5.4 Hz, -OH), 3.53–3.50 (m, 1H, -CH-O-), 3.44–3.38 (m, 2H, -CH_2-), 3.32 (s, 3H, -NCH_3), 3.29–3.24 (m, 2H, -CH_2-). Anal. calcd. for $C_{10}H_{15}N_5O_4$: C 44.61, H 5.62, N 26.01; found: C 44.35, H 5.58, N 25.92.

N^1-Methyl-9-[(3-fluoro-1-hydroxy-2-propoxy)methyl]guanine (6) (FMHPG)

N^1-Methyl-N^2-(*p*-anisyldiphenylmethyl)-9-[[1-(*p*-anisyldi-

[2] Supplementary data may be purchased from the Directory of Unpublished Data, Document Delivery, CISTI, National Research Council Canada, Ottawa, ON K1A 0S2, Canada (http://www.nrc.ca/cisti/irm/unpub_e.shtml for information on ordering electronically). CCDC 210605 contains the crystallographic data for this manuscript. These data can be obtained, free of charge, via www.ccdc.cam.ac.uk/conts/retrieving.html (or from the Cambridge Crystallographic Data Centre, 12 Union Road, Cambridge CB2 1EZ, U.K.; fax +44 1223 336033; or deposit@ccdc.cam.ac.uk).

© 2004 NRC Canada

Table 4. Bond lengths (Å) and angles for 6-methyl-1-[(1,3-dihydroxy-2-propoxy)-methyl]guanine (**12**).

Bond lengths (Å)	
N(3)—C(2)	1.384(2)
N(3)—C(3)	1.394(2)
N(3)—C(6)	1.473(2)
N(2)—C(2)	1.371(2)
N(2)—C(1)	1.378(2)
O(7)—C(6)	1.408(2)
O(7)—C(8)	1.435(2)
C(3)—C(4)	1.343(2)
C(3)—C(5)	1.488(3)
O(8)—C(2)	1.219(2)
O(2)—C(9)	1.420(2)
C(1)—O(1)	1.233(2)
C(1)—C(4)	1.422(3)
C(8)—C(10)	1.500(3)
C(8)—C(9)	1.511(3)
O(3)—C(10)	1.422(2)
Bond angles (°)	
C(2)-N(3)-C(3)	121.52(14)
C(2)-N(3)-C(6)	117.73(14)
C(3)-N(3)-C(6)	120.73(14)
C(2)-N(2)-C(1)	126.25(16)
C(6)-O(7)-C(8)	115.35(13)
C(4)-C(3)-N(3)	119.82(15)
C(4)-C(3)-C(5)	122.00(16)
N(3)-C(3)-C(5)	118.17(15)
O(8)-C(2)-N(2)	121.44(17)
O(8)-C(2)-N(3)	122.80(16)
N(2)-C(2)-N(3)	115.76(15)
O(1)-C(1)-N(2)	120.47(16)
O(1)-C(1)-C(4)	125.00(17)
N(2)-C(1)-C(4)	114.53(15)
O(7)-C(6)-N(3)	111.99(14)
C(3)-C(4)-C(1)	122.05(16)
O(7)-C(8)-C(10)	107.02(16)
O(7)-C(8)-C(9)	111.31(14)
C(10)-C(8)-C(9)	112.51(16)
O(2)-C(9)-C(8)	112.75(16)
O(3)-C(10)-C(8)	113.39(16)

phenylmethyl)-3-fluoro-2-propoxy]-methyl]guanine (**33**, 50 mg, 0.061 mmol) was heated under reflux in 5 mL methanol and 5 mL acetic acid (80%) for 4.5 h. The solvent was evaporated and the residue purified by MPLC (RP-18, acetonitrile–water (1:9, v/v)) to give **6** (13 mg, 78%), mp 216–219 °C. ^{1}H NMR (DMSO-d_6) δ: 7.81 (s, 1H, 8-CH), 7.08 (s, 2H, -NH_2), 5.43 (s, 2H, -H_2C(1′)), 4.89 (s, 1H, -OH), 4.54–4.27 (m, 2H, -CH_2-F), 3.85–3.77 (m, 1H, -CH-O-), 3.32 (m_c, 2H, -CH_2-), 3.30 (s, 3H, -NCH_3). ^{19}F NMR (DMSO-d_6) δ: –231.0. Anal. calcd. for $C_{10}H_{14}N_5O_3F$: C 44.28, H 5.20, N 25.82; found: C 44.17, H 5.34, N 25.70.

N^1-Methyl-9-[(4-hydroxy)-3-hydroxymethylbutyl]guanine (7)

Penciclovir (**3**, 231 mg, 0.841 mmol) and tetrabutylammonium hydroxide solution (1 mol L^{-1}, 0.88 mL, 0.88 mmol) were dissolved in 20 mL of dry DMF. A solution of methyl iodide (120 μL, 1.92 mmol) in 1.2 mL DMF was added under vigorous stirring at room temperature. After 2 h, the solvent was evaporated and the residue purified by MPLC (RP-18, acetonitrile–water (1:9, v/v)) to obtain **7** (48 mg, 21%), mp 221–227 °C. ^{1}H NMR (DMSO-d_6) δ: 7.68 (s, 1H, 8-CH), 6.97 (s, 2H, -NH_2), 4.42 (t, 2H, J = 5.2 Hz, -OH), 3.98 (t, 2H, J = 7.4 Hz, -H_2C(1′)), 3.44–3.38 (m, 4H, -CH_2(OH)), 3.29 (s, 3H, N-CH_3), 1.69 (m_c, 2H, -H_2C(2′)), 1.45–1.40 (m, 1H, -CH(3′)). Anal. calcd. for $C_{11}H_{17}N_5O_3$: C 49.43, H 6.41, N 26.20; found: C 49.35, H 6.30, N 26.12.

N^1-Methyl-9-[(4-fluoro)-3-hydroxymethylbutyl]guanine (8) (FMHBG)

N^1-Methyl-N^2-(*p*-anisyldiphenylmethyl)-9-[(4-fluoro)-3-*p*-anisyldiphenylmethoxy-methyl-butyl]guanine (**34**, 58 mg, 0.072 mmol) was heated under reflux with 5 mL methanol and 5 mL acetic acid (80%) for 4 h. The solvents were evaporated and the residue purified by MPLC (RP-18, acetonitrile–water (2:8, v/v)) to give **8** (17 mg, 88%), mp 135–138 °C. ^{1}H NMR (DMSO-d_6) δ: 7.70 (s, 1H, 8-CH), 6.98 (s, 2H, -NH_2), 4.68 (s, 1H, -OH), 4.55–4.34 (m, 2H, -CH_2-F), 4.01 (t, 2H, J = 7.2 Hz, -H_2C(1′)), 3.39 (d, 2H, J = 6.4 Hz, -CH_2(OH)), 3.29 (s, 3H, N^1CH_3), 1.78–1.67 (m, 2H, -H_2C(2′)), 1.65–1.61 (m, 1H, -HC(3′)). ^{19}F NMR (DMSO-d_6) δ: –227.4. Anal. calcd. for $C_{11}H_{16}N_5O_2F$: C 49.06, H 5.99, N 26.01; found: 49.01, H 5.78, N 25.88.

N^6-Methyl-9-[(1,3-dihydroxy-2-propoxy)methyl]adenine (9)

Freshly activated palladium oxide (495 mg) and 10 mL cyclohexene were added to a solution of N^6-methyl-9-[(1,3-dibenzyloxy-2-propoxy)methyl]adenine (**16**, 1.0 g, 2.3 mmol) in 20 mL ethanol and refluxed for 30 h. After that, the reaction mixture was filtered and the solvent evaporated. The residue was washed first with chloroform, then with diethyl ether and dried. The crude product was redissolved in hot water, ethanol was added, and the substance was allowed to precipitate when cooling down to give **9** (365 mg, 63%), mp 160 °C. ^{1}H NMR (DMSO-d_6) δ: 8.23 (s, 2H, 2-CH, 8-CH), 7.73 (s, 1H, -NH), 5.64 (s, 2H, -H_2C(1′)), 3.59 (t, 2H, J = 5.5 Hz, -OH), 3.59 (m_c, 1H, -CH-O), 3.44–3.38 (m, 2H, -CH_2(OH)), 3.31–2.94 (m, 2H, -CH_2(OH)), 2.94 (s, 3H, NCH_3). Anal. calcd. for $C_{10}H_{15}N_5O_3$: C 47.43, H 5.97, N 27.65; found: C 47.37, H 5.86, N 27.52.

N^6-Methyl-9-[(4-hydroxy)-3-hydroxymethylbutyl]adenine (10)

N^6-Methyl-9-[(2,2-dimethyl-1,3-dioxane-5-yl)ethyl]purine (**28**, 80 mg, 0.27 mmol) was dissolved in 1.5 mL methanol and 1.5 mL HCl (2 mol L^{-1}) and refluxed for 3 h. After cooling, the solvent was reduced and the precipitate filtered off. Crystallization from water gave **10** (23 mg, 34%), mp 134–136 °C. ^{1}H NMR (DMSO-d_6) δ: 8.22 (s, 1H, 8-CH), 8.14 (s, 1H, 2-CH), 7.73 (s, 1H, -NH-), 4.44 (s, 2H, -OH), 4.20 (t, 2H, J = 7.4 Hz, -H_2C(1′)), 3.39 (m_c, 4H, -CH_2(OH)), 2.94 (s, 3H, NCH_3), 1.78 (m_c, 2H, -H_2C(2′)), 1.44–1.40 (m, 1H, -HC(3′)). Anal. calcd. for $C_{11}H_{17}N_5O_2$: C 52.58, H 6.82, N 27.87; found: C 52.43, H 6.73, N 27.72.

5-Hydroxy-1-[(1,3-dihydroxy-2-propoxy)methyl]uracil (11)

5-Hydroxy-1-[(1,3-dibenzyloxy-2-propoxy)methyl]uracil (**19**, 412 mg, 1.0 mmol) was refluxed with 6 mL of ethanol, 2.4 mL of cyclohexene, and freshly activated palladium ox-

© 2004 NRC Canada

ide (170 mg, 1.40 mmol) for 17 h. The catalyst was filtered off and washed with ethanol and water. The solutions were collected and the solvents were removed. The residue was purified by crystallization from ethanol to give **11** (111 mg, 48%), mp 147 to 148 °C. ^{1}H NMR (DMSO-d_6) δ: 11.43 (s, 1H, -NH), 8.68 (s, 1H, 6-CH), 7.14 (s, 1H, -OH), 5.09 (s, 2H, -H_2C(1′)), 4.60 (s, 2H, -OH), 3.49 (m, 1H, -CH-), 3.45–3.29 (m, 4H, -CH_2(OH)). Anal. calcd. for $C_8H_{12}N_2O_6$: C 41.38, H 5.21, N 12.06; found: C 41.27, H 5.09, N 11.91.

6-Methyl-1-[(1,3-dihydroxy-2-propoxy)methyl]uracil (12)

6-Methyl-1-[(1,3-dibenzyloxy-2-propoxy)methyl]uracil (**20**, 6.17 g, 15 mmol) was dissolved in 64 mL ethanol and treated with freshly activated palladium oxide (2.0 g, 16.3 mmol), 20 mL cyclohexene, and stirred for 18 h at room temperature. Afterwards the mixture was refluxed for 90 min and the catalyst was filtered. Precipitation of the product proceeded when cooling and recrystallization from ethanol gave 2.4 g (70%) of **12**, mp 147–150 °C. ^{1}H NMR (DMSO-d_6) δ: 11.20 (s, 1H, -NH), 5.50 (s, 1H, 5-CH), 5.23 (s, 2H, -H_2C(1′)), 4.61 (t, 2H, J = 5.6 Hz, -OH), 3.51–3.47 (m, 1H, -CH-O), 3.45–3.39 (m, 2H, -CH_2(OH)), 3.35–3.30 (m, 2H, -CH_2(OH)), 2.29 (s, 3H, -CH_3). Anal. calcd. for $C_9H_{14}N_2O_5$: C 46.95, H 6.13, N 12.17; found: 46.77, H 6.09, N 12.07.

6-Methyl-1-[(3-fluoro-1-hydroxy-2-propoxy)methyl]uracil (13) (FMHPU)

6-Methyl-1-[[1-(*p*-anisyldiphenylmethoxy)-3-fluoro-2-propoxy]methyl]uracil (**23**, 55.0 mg, 0.109 mmol) was dissolved in 5 mL of ethanol and 5 mL of 80% acetic acid and refluxed for 1 h. The solvent was evaporated and the residue was dissolved in ethanol. Final purification was carried out with MPLC (RP-18, acetonitrile–water (1:4, v/v)) affording **13** (16.0 mg, 63%), mp 118–120 °C. ^{1}H NMR (DMSO-d_6) δ: 11.24 (s, 1H, -NH), 5.52 (s, 1H, 5-CH), 5.34 (d, 1H, J = 11.0 Hz, -H_2C(1′)), 5.30 (d, 1H, J = 11.0 Hz, -H_2C(1′)), 4.88 (s, 1H, -OH), 4.58–4.29 (m, 2H, -CH_2-F), 3.78 (m_c, 1H, -CH-O-), 3.41 (d, 2H, J = 5.6, -CH_2(OH)), 2.27 (s, 3H, 6-CH_3). ^{19}F NMR (DMSO-d_6) δ: –232.0. Anal. calcd. for $C_9H_{13}N_2O_4F$: C 46.55, H 5.65, N 12.06; found: C 46.42, H 5.59, N 12.02.

N^6-Methyl-9-[(1,3-dibenzyloxy-2-propoxy)methyl]adenine (16)

Triethylamine (3.8 mL) was added to N^6-methyladenine (**14**, 3.7 g, 24.8 mmol) dissolved in 20 mL of dry DMF under stirring. After addition of 1,3-dibenzyloxy-2-chloromethoxypropane (**15**, 8.0 g, 25.0 mmol) in 12.5 mL DMF, the solution was stirred for 1 h at room temperature and then heated for 3 h to 90 °C. The reaction mixture was cooled down and the precipitated triethylammonium chloride was removed. The solvent was evaporated and the residue purified by MPLC (RP-18, methanol–water (8:2, v/v)), yielding **16** (3.4 g, 31%), mp 91 °C. ^{1}H NMR (DMSO-d_6) δ: 8.25 (s, 2H, 2-CH, 8-CH), 7.75 (s, 1H, -NH), 7.31–7.16 (m, 10H, -CH(arom)), 5.66 (s, 2H, -H_2C(1′)), 4.37 (s, 4H, -CH_2(Bz)), 4.09 (m, 1H, -CH-O), 3.45–3.39 (m, 4H, -CH_2-(OBz)), 2.95 (s, 3H, NCH_3). Anal. calcd. for $C_{24}H_{27}N_5O_3$: C 66.50, H 6.28, N 16.15; found: C 66.25, H 6.08, N 16.06.

5-Hydroxy-1-[(1,3-dibenzyloxy-2-propoxy)methyl]uracil (19)

Isobarbituric acid (**17**, 384 mg, 3.0 mmol) was suspended in 17 mL of hexamethyldisilazane. Ammonium sulfate (225 mg, 1.70 mmol) was added and the mixture refluxed for 70 min. The solvent was evaporated and the residue suspended in 8 mL of dichloromethane, then tetra-*n*-butylammonium iodide (12.0 mg, 0.03 mmol) and 1,3-dibenzyloxy-2-chloro-methoxypropane (**15**, 1.44 g, 4.5 mmol) were added and the reaction mixture was refluxed for 90 min. After cooling, the solution was treated with 4 mL of methanol and 1 mL of water. The solvent was distilled off, the residue solved in CH_2Cl_2, washed with satd. NaCl solution and water. The organic layer was separated, dried, and the solvent was evaporated. The purification of the reaction product occurred by MPLC (silica gel, dichloromethane–methanol (25:1, v/v)) resulting in 853 mg (69%) of a yellowish viscous liquid of **19**. ^{1}H NMR (DMSO-d_6) δ: 11.47 (s, 1H, -NH), 8.72 (s, 1H, 6-CH), 7.32–7.22 (m, 10H, -CH(arom)), 7.17 (s, 1H, -OH), 5.14 (s, 2H, -H_2C(1′)), 4.45 (s, 4H, -CH_2(Bz)), 3.96 (m, 1H, -CH-O), 3.51–3.42 (m, 4H, -CH_2-(OBz)). Anal. calcd. for $C_{22}H_{24}N_2O_6$: C 64.07, H 5.87, N 6.79; found: C 63.81, H 5.92, N 6.66.

6-Methyl-1-[(1,3-dibenzyloxy-2-propoxy)methyl]uracil (20)

6-Methyluracil (**18**, 378 mg, 3.0 mmol) was refluxed with ammonium sulfate (150 mg, 1.14 mmol) and 11 mL of hexamethyldisilazane. The solvent was removed and the residue was dried. After dissolving the substance in CH_2Cl_2, it was treated with tetra-*n*-butylammonium iodide (12 mg, 0.03 mmol). 1,3-Dibenzyloxy-2-chloromethoxypropane (**15**, 1.44 g, 4.5 mmol) was added, followed by refluxing for 70 min. The reaction mixture was cooled, 1 mL of water and 4 mL of methanol were added and after stirring for 2 min, the solvent was removed. The residue was solved in CH_2Cl_2 and washed with satd. NaCl solution and water. The organic layer was separated, dried, and the solvent was removed. The reaction product was purified by column chromatography (silica gel, dichloromethane–methanol (25:1, v/v)) to afford **20** as yellow oil (426 mg, 35%). ^{1}H NMR (DMSO-d_6) δ: 11.24 (s, 1H, -NH), 7.34–7.25 (m, 10H, -CH(arom)), 5.49 (s, 1H, 5-CH), 5.34 (s, 2H, -H_2C(1′)), 4.45 (s, 4H, -CH_2(Bz)), 3.95–3.93 (m, 1H, -CH-O), 3.49–3.43 (m, 4H, -CH_2-(OBz)), 2.25 (s, 3H, -CH_3). Anal. calcd. for $C_{23}H_{26}N_2O_5$: C 67.30, H 6.38, N 6.82; found: C 66.98, H 6.34, N 6.51.

*6-Methyl-1-[[1-(*p*-anisyldiphenylmethoxy)-3-hydroxy-2-propoxy]methyl]uracil (21)*

6-Methyl-1-[(1,3-dihydroxy-2-propoxy)methyl]uracil (**12**, 460 mg, 2.00 mmol), *p*-anisylchloro-diphenylmethane (672 mg, 2.18 mmol), triethylethylamine (418 µL, 3.00 mmol), and DMAP (2.9 mg) in 7 mL DMF were stirred for 2 h at 50 °C. After removing the DMF, the residue was dissolved in ethyl acetate, washed with $NaHCO_3$ solution and water. The combined organic layers were dried, the solvent removed, and the crude product purified by chromatography (silica gel, dichloromethane–methanol (25:1, v/v)) to give **21** (468 mg, 47%), mp 83 °C. ^{1}H NMR (DMSO-d_6) δ:11.31 (s, 1H, -NH), 7.36–6.86 (m, 14H, CH(arom)), 5.56 (s, 1H, 5-CH), 5.50 (d, 1H, J = 12.3 Hz, -H_2C(1′)), 5.30 (d, 1H, J = 12.3 Hz, -H_2C(1′)), 4.71 (t, 1H, J = 5.5 Hz, -OH),

© 2004 NRC Canada

3.83 (m_c, 1H, -CH-O), 3.73 (s, 3H, -OCH_3), 3.36–3.30 (m, 2H, -CH_2(OH)), 3.00–2.92 (m, 2H, -CH_2-OMTr), 2.32 (s, 3H, -CH_3). Anal. calcd. for $C_{29}H_{30}N_2O_6$: C 69.31, H 6.02, N 5.57; found: C 69.55, H 6.13, N 5.30.

*6-Methyl-1-[[1-(*p*-anisyldiphenylmethoxy)-3-(*p*-toluenesulfonyloxy)-2-propoxy]methyl]-uracil (22)*

21 (508 mg, 1.01 mmol) and tosyl chloride (858 mg, 4.50 mmol) were suspended in 12 mL pyridine and left for 70 h at 30 °C. Subsequently, 2 mL of water were added and the reaction mixture was stirred for 2 h at 30 °C. The solvent was evaporated, the residue dissolved in ethyl acetate, and washed with water. The organic layer was dried, the solvent removed and the reaction mixture purified by chromatography (silica gel, dichloromethane–methanol (20:1, v/v)), yielding **22** (420 mg, 63%), mp 79 °C. ^{1}H NMR (DMSO-d_6) δ: 11.30 (s, 1H, -NH), 7.68 (d, 2H, J = 8.2 Hz, -CH, (m-Ts)), 7.41 (d, 2H, J = 8.2 Hz, -CH, (o-Ts)), 7.31–6.85 (m, 14H, -CH(arom)), 5.52 (s, 1H, 5-CH), 5.33 (d, 1H, J = 12.1 Hz, -H_2C(1′)), 5.21 (d, 1H, J = 12.1 Hz, -H_2C(1′)), 4.10–4.04 (m, 1H, -CH-O), 4.02–3.95 (m, 2H, -CH_2-OTs), 3.00–2.87 (m, 2H, -CH_2-OMTr), 2.38 (s, 3H, -CH_3, (Ts)), 2.21 (s, 3H, 6-CH_3). Anal. calcd. for $C_{36}H_{36}N_2O_8S$: C 65.84, H 5.53, N 4.27, S 4.88; found: C 65.87, H 5.21, N 4.26, S 4.72.

*6-Methyl-1-[[1-(*p*-anisyldiphenylmethoxy)-3-fluoro-2-propoxy]methyl]uracil (23)*

22 (180 mg, 0.274 mmol), Kryptofix® 2.2.2 (1.00 g, 2.66 mmol), potassium carbonate (125 mg, 0.904 mmol), and potassium fluoride (1.00 g, 17.2 mmol) were suspended in 20 mL of dry acetonitrile and heated for 15 min to 120 °C. The mixture was cooled down, the precipitated substances were filtered off, and the solvent was evaporated. The residue was purified by column chromatography (RP-18, acetonitrile–water (2:1, v/v)) to afford **23** (42.9 mg, 31%), mp 80 °C. ^{1}H NMR (DMSO-d_6) δ: 11.34 (s, 1H, -NH), 7.35–6.87 (m, 14H, -CH(arom)), 5.47 (d, 1H, J = 11.5 Hz, -H_2C(1′)), 5.32 (d, 1H, J = 11.5 Hz, -H_2C(1′)), 4.56–4.41 (m, 2H, -CH_2-F), 4.37–4.33 (m, 1H, -CH-O), 3.73 (s, 3H, -OCH_3), 3.07–2.97 (m, 2H, -CH_2-OMTr), 2.31 (s, 3H, 6-CH_3). ^{19}F NMR (DMSO-d_6) δ: –229.5. Anal. calcd. for $C_{29}H_{29}N_2O_4F$: C 69.03, H 5.79, N 5.55; found: C 68.95, H 5.72, N 5.49.

N^6-Methyl-9-[(2,2-dimethyl-1,3-dioxane-5-yl)ethyl]purine (28)

5-(2-Bromoethyl)-2,2-dimethyl-1,3-dioxane (**27**, 167 mg, 0.75 mmol) and potassium carbonate (138 mg, 1.00 mmol) were added to N^6-methyladenine (**14**, 113 mg, 0.75 mmol) suspended in 2 mL of dry DMF, and the mixture was stirred for 5 h at 20 °C. The mixture was then filtered to remove insoluble material. The combined filtrates were evaporated and the residue purified by MPLC (RP-18, water–acetonitrile (7:3, v/v)) yielding **28** (83 mg, 38%), mp 121–123 °C. ^{1}H NMR (DMSO-d_6) δ: 8.23 (s, 1H, 2-CH), 8.15 (s, 1H, 8-CH), 7.69 (s, 1H, -NH), 4.15 (t, 2H, J = 7.2 Hz, -H_2C(1′)), 3.76–3.72 (m, 2H, -CH_2-O-), 3.54–3.49 (m, 2H, -CH_2-O-), 2.93 (s, 3H, NCH_3), 1.77–1.73 (m, 2H, -H_2C(2′)), 1.55–1.54 (m, 1H, -HC(3′)), 1.30 (s, 3H, -CH_3), 1.23 (s, 3H, -CH_3). Anal. calcd. for $C_{14}H_{21}N_5O_2$: C 57.71, H 7.26, N 24.04; found: C 57.62, H 7.15, N 23.97.

*N^1-Methyl-N^2-(*p*-anisyldiphenylmethyl)-9-[[1-(*p*-anisyldiphenylmethoxy)-3-(*p*-toluene-sulfonyloxy)-2-propoxy]methyl] guanine (31)*

N^2-(*p*-Anisyldiphenylmethyl)-9-[[1-(*p*-anisyldiphenylmethoxy)-3-(*p*-toluenesulfonyloxy)-2-prop-oxy]methyl]guanine (**29**, 200 mg, 0.210 mmol), and tetrabutylammonium hydroxide solution (1 mol L^{-1}, 0.22 mL, 0.22 mmol) were dissolved in 20 mL of dry DMF. A solution of methyl iodide (30 µL, 0.48 mmol) in 0.30 mL DMF was added under vigorous stirring at room temperature. After 45 min, the solvent was evaporated and the residue purified by MPLC (silica gel, dichloromethane–methanol (25:1, v/v)) to afford **31** (89.0 mg, 44%), mp 160–162 °C. ^{1}H NMR (DMSO-d_6) δ: 7.81 (s, 1H, 8-CH), 7.67 (d, 2H, J = 8.4 Hz, -CH, (m-Ts)), 7.49 (d, 2H, J = 8.4 Hz, -CH, (o-Ts)), 7.32–6.66 (m, 29H, -NH, -CH(arom)), 5.08 (d, 1H, J = 11.7 Hz, -H_2C(1′)), 4.85 (d, 1H, J = 11.7 Hz, -H_2C(1′)), 3.75 (s, 3H, -OCH_3), 3.72 (s, 3H, -NCH_3), 3.54 (s, 3H, -OCH_3), 3.50–3.46 (m, 1H -CH-O-), 2.55–2.52 (m, 2H, -CH_2-OMTr), 2.43 (s, 3H, -CH_3, (Ts)), 2.37–2.34 (m, 2H, -CH_2-OTs). Anal. calcd. for $C_{57}H_{53}N_5O_8S$: C 70.72, H 5.52, N 7.23, S 3.31; found: C 70.28, H 5.42, N 7.15, S 3.19.

*N^1-Methyl-N^2-(*p*-anisyldiphenylmethyl)-9-[(4-(*p*-toluene-sulfonyloxy))-3-*p*-anisyldiphenylmethoxy-methylbutyl]guanine (32)*

N^2-(*p*-Anisyldiphenylmethyl)-9-[(4-(*p*-toluenesulfonyloxy))-3-*p*-anisyldiphenylmethoxy-methyl-butyl]guanine (**30**, 300 mg, 0.315 mmol) and tetrabutylammonium hydroxide solution (1 mol L^{-1}, 0.33 mL, 0.33 mmol) were dissolved in 7.5 mL of dry DMF. A solution of methyl iodide (45 µL, 0.72 mmol) in 0.45 mL DMF was added under vigorous stirring at room temperature. After 75 min, the solvent was evaporated and the residue purified by MPLC (silica gel, dichloromethane–methanol (25:1, v/v)) to obtain **32** (134 mg, 44%), mp 117 °C. ^{1}H NMR (DMSO-d_6) δ: 7.73 (d, 2H, J = 8.0 Hz, -CH, (m-Ts)), 7.46 (d, 2H, J = 8.0 Hz, -CH, (o-Ts)), 7.38 (s, 1H, 8-CH), 7.31–6.70 (m, 29H, N^2H, -CH(arom)), 3.73 (s, 3H, -OCH_3), 3.86–3.68 (m, 2H, -CH_2-OTs), 3.64 (s, 3H, N^1CH_3), 3.63 (s, 3H, -OCH_3), 3.29 (m_c, 2H, -H_2C(1′)), 2.72–2.51 (m, 2H, -CH_2-OMTr), 2.38 (s, 3H, -CH_3), 1.48 (m_c, 1H, -HC(3′)), 0.98–1.03 (m, 2H, -H_2C(2′)). Anal. calcd. for $C_{58}H_{55}N_5O_7S$: C 72.10, H 5.74, N 7.25, S 3.32; found: C 72.15, H 5.79, N 7.31, S 3.27.

*N^1-Methyl-N^2-(*p*-anisyldiphenylmethyl)-9-[[1-(*p*-anisyl-diphenylmethyl)-3-fluoro-2-propoxy]methyl]guanine (33)*

31 (200 mg, 0.207 mmol), potassium fluoride (182 mg, 3.13 mmol), potassium carbonate (125 mg, 0.904 mmol), and Kryptofix® 2.2.2 (500 mg, 1.32 mmol) in 20 mL acetonitrile were heated at 120 °C for 60 min. The mixture was cooled down, the precipitated substances were filtered off and the solvent was evaporated. The residue was purified by column chromatography (RP-18, acetonitrile–water (6:1, v/v)) to afford **33** (37 mg, 22%), mp 121–123 °C. ^{1}H NMR (DMSO-d_6) δ: 7.83 (s, 1H, 8-CH), 7.35–6.65 (m, 29H, -NH, -CH(arom)), 5.07 (d, 1H, J = 10.5 Hz, -H_2C(1′)), 4.95 (d, 1H, J = 10.5 Hz, -H_2C(1′)), 4.60–3.80 (m, 2H, -CH_2-F), 3.74 (s, 3H, -OCH_3), 3.72 (s, 3H, -NCH_3), 3.72–3.46 (m, 1H, -CH-O-), 3.56 (s, 3H, -OCH_3), 2.61–2.52 (m, 2H, -CH_2-OMTr). ^{19}F NMR (DMSO-d_6) δ: –229.5. Anal. calcd. for

© 2004 NRC Canada

Table 5. Syntheses times, HPLC conditions, and radiochemical yields of the radio-labelled compounds.

Tracer	Synthesis time (after EOB) (min)	HPLC conditions (water–ethanol)	R_t (min)	Radiochemical yield (d.c.) (%)
[^{18}F]FHPG (**2**)	90	95:5	8.0	15
[^{18}F]FHBG (**4**)	95	92:8	10.0	10
[^{18}F]FMHPG (**6**)	85	90:10	7.0	12
[^{18}F]FMHBG (**8**)	95	92:8	16.0	19
[^{18}F]FMHPU (**13**)	85	95:5	12.0	10

Note: EOB is the end of bombardement; d.c. is decay corrected.

$C_{50}H_{46}N_5O_5F$: C 73.60, H 5.68, N 8.58; found: C 73.37, H 5.33, N 8.38.

***N*^{1}-Methyl-*N*^{2}-(p-*anisyldiphenylmethyl)-9-[(4-fluoro)-3-*p*-anisyldiphenylmethoxy-methylbutyl]guanine (34)**

32 (190 mg, 0.197 mmol), potassium fluoride (333 mg, 5.73 mmol), potassium carbonate (125 mg, 0.904 mmol), and Kryptofix® 2.2.2 (500 mg, 1.32 mmol) were solved in 20 mL dry DMF and heated to 140 °C for 90 min. After cooling down, the precipitated substances were filtered off and washed well with DMF. The combined filtrates were evaporated and the residue purified by MPLC (RP-18, acetonitrile–water (9:1, v/v)) affording **34** (38.5 mg, 24%), mp 114–117 °C. ^{1}H NMR (DMSO-d_6) δ: 7.47 (s, 1H, 8-CH), 7.34–6.72 (m, 29H, N^2H, -CH(arom)), 4.34–4.11 (m, 2H, -CH_2-F), 3.73 (s, 3H, -OCH_3), 3.65 (s, 3H, N^1CH_3), 3.64 (s, 3H, -OCH_3), 3.45 (t, 2H, J = 7.1 Hz, -H_2C(1′)), 2.80–2.71 (m, 2H, -CH_2-OMTr), 1.60 (m_c, 1H, -HC(3′)), 1.22–1.07 (m, 2H, -H_2C(2′)). ^{19}F NMR (DMSO-d_6) δ: –225.8. Anal. calcd. for $C_{51}H_{48}N_5O_4F$: C 75.26, H 5.94, N 8.60; found: C 75.07, H 5.83, N 8.57.

General syntheses of the [^{18}F]-fluorinated compounds 2, 4, 6, 8, and 13

A solution of 0.5 mL of Kryptofix® 2.2.2 (45 mM), 20 µL potassium carbonate (1 mol L^{-1}), and aqueous [^{18}F]fluoride solution (0.5–1.0 mL, 0.5–5.0 GBq) was azeotropically evaporated with acetonitrile (3 mL) at 100 °C; 2 to 3 mg of the appropriate precursors **22**, **29**–**32** solved in dry acetonitrile (300 mg) were added to the dry K[^{18}F]F/Kryptofix® 2.2.2 complex. The reaction mixture was heated at 160 °C for 20 min. After cooling down to room temperature, the mixture was passed through a LiChrolut Si (500 mg) cartridge. ^{18}F-labelled compounds were eluted with 2 mL of dichloromethane–methanol (85:15). Methanolic hydrochloric acid (150 µL, 0.85 mol L^{-1}) was added to the eluate, the vial sealed and heated for 3 min at 120 °C, then the solvent was removed under a stream of nitrogen. A sodium hydroxide solution (400 µL, 0.2 mol L^{-1}) was added to the residue. The mixture was given to a LiChrolut RP-18 (200 mg) cartridge, the crude product eluted with 500 µL of a water–ethanol mixture (9:1) and subsequent purified by HPLC as described in Table 5 at a flow of 5 mL min^{-1}. The radiochemical purity and the identity of each probe with the reference standards was identified by analytical HPLC.

Acknowledgements

This study was supported by the Saxon Ministry of Science and Art (Grant 47531.50–03–844–98/2). The excellent technical assistance of B. Grosse is gratefully acknowledged.

References

1. W. Walther and U. Stein. Mol. Biotechnol. **13**, 21 (1999).
2. S.S. Gambhir, J.R. Barrio, H.R. Herschman, and M.E. Phelps. Nucl. Med. Biol. **26**, 481 (1999).
3. S.S. Gambhir, H.R. Herschman, S.R. Cherry, J.R. Barrio, N. Satyamurthy, T. Toyokuni, M.E. Phelps, S.M. Larson, J. Balatoni, R. Finn, S. Sadelain, J. Tjuvajev, and R. Blasberg. Neoplasia, **2**, 118 (2000).
4. B.E. Huber, C.A. Richards, and E.A. Austin. Ann. N.Y. Acad. Sci. 104 (1994).
5. F. Herrman. J. Mol. Med. **73**, 157 (1995).
6. M.M. Alauddin, P.S. Conti, S.M. Mazza, F.M. Hamzeh, and J.R. Lever. Nucl. Med. Biol. **23**, 787 (1996).
7. M.M. Alauddin, A. Shahinian, R.K. Kundu, E.M. Gordon, and P.S. Conti. Nucl. Med. Biol. **26**, 371 (1999).
8. G.G. Shiue, C.-Y. Shiue, R.L. Lee, D. MacDonald, R. Hustinx, S.L. Eck, and A.A. Alavi. Nucl. Med. Biol. **28**, 875 (2001).
9. P. Brust, R. Haubner, A. Friedrich, M. Scheunemann, M. Anton, O.-N. Koufaki, M. Hauses, St. Noll, B. Noll, U. Haberkorn, G. Schackert, H.K. Schackert, N. Avril, and B. Johannsen. Eur. J. Nucl. Med. **28**, 721 (2001).
10. M.M. Alauddin and P.S. Conti. Nucl. Med. Biol. **25**, 175 (1998).
11. M.M. Alauddin, A. Shahinian, E.M. Gordon, J.R. Bading, and P.S. Conti. J. Nucl. Med. **42**, 1682 (2001).
12. S. Yaghoubi, J.R. Barrio, M. Dahlbom, M. Iyer, M. Namavari, N. Satyamurthy, R. Goldman, H.R. Herschman, M.E. Phelps, and S.S. Gambhir. J. Nucl. Med. **42**, 1225 (2001).
13. M. Namavari, J.R. Barrio, T. Toyokuni, S.S. Gambhir, S.R. Cherry, H.R. Herschman, M.E. Phelps, and N. Satyamurthy. Nucl. Med. Biol. **27**, 157 (2000).
14. J.C. Martin, C.A. Dvorak, D.F. Smee, T.R. Matthews, and J.P.H. Verheyden. J. Med. Chem. **26**, 759 (1983).
15. K.K. Ogilvie, N. Nguyen-Ba, M.F. Gillen, B.K. Radatus, U.O. Cheriyan, and H.R. Hanna. Can. J. Chem. **62**, 241 (1984).
16. K.K. Ogilvie, R.G. Hamilton, M.F. Gillen, and B.K. Radatus. Can. J. Chem. **62**, 16 (1984).
17. G.H. Hakimelahi, T.W. Ly, A.A. Moosavi-Movahedi, M.L. Jain, M. Zakerinia, H. Davari, H.-C. Mei, T. Sambaiah, A.A. Mosfegh, and S. Hakimelahi. J. Med. Chem. **44**, 3710 (2001).
18. R.Z. Sterzycki, I. Ghazzouli, V. Brankovan, J.C. Martin, and M.M. Mansuri. J. Med. Chem. **33**, 2150 (1990).
19. H. Gao and A.K. Mitra. Synthesis, **3**, 329 (2000).
20. G.R. Geen, T.J. Grinter, P.M. Kincey, and R.L. Jarvest. Tetrahedron, **46**, 6903 (1990).
21. M.R. Harnden, R.L. Jarvest, T.H. Bacon, and M.R. Boyd. J. Med. Chem. **30**, 1636 (1987).
22. B. Brand, C.B. Reese, Q. Song, and C. Visintin. Tetrahedron, **55**, 5239 (1999).
23. J. Hannah, R.L. Tolman, J.D. Karkas, R. Liou, H.C. Perry, and A.K. Field. J. Heterocycl. Chem. **26**, 1261 (1989).

© 2004 NRC Canada

24. M.R. Harnden and R.L. Jarvest. Tetrahedron Lett. **26**, 4265 (1985).
25. A.A. Wilson, P.S. Conti, R.F. Dannals, H.T. Ravert, and H.N. Wagner. J. Labelled Compd. Radiopharm. **29**, 765 (1991).
26. J. Boryski, B. Golankiewicz, and E. De Clerq. J. Med. Chem. **31**, 1351 (1988).
27. J.C. Martin, D.P.C. McGee, G.A. Jeffrey, D.W. Hobbs, D.F. Smee, T.R. Matthews, and J.P.H. Verheyden. J. Med. Chem. **29**, 1384 (1986).

© 2004 NRC Canada

Synthesis, IR, and multinuclear NMR spectroscopic studies of complexes of the type *cis*- and *trans*-Pt(amine)$_2$(NO$_3$)$_2$

Fernande D. Rochon and Viorel Buculei

Abstract: Compounds of the types *cis*- and *trans*-Pt(amine)$_2$NO$_3$)$_2$ have been synthesized and characterized by IR and multinuclear (^{195}Pt, ^{13}C, and ^{1}H) NMR spectroscopies. The nitrato IR bands were compared for the two isomers. The ^{195}Pt NMR resonances of the trans complexes were observed at lower fields (avg. –1570 ppm for primary amines) than the cis analogues (avg. –1698 ppm) for an average $\Delta\delta$ value of 124 ppm. The complexes containing a secondary amine were observed at about the same field for the cis isomers (avg. –1682 ppm) and surprisingly at much higher fields for the trans compounds (avg. –1638 ppm). In ^{1}H NMR, the coupling constants $^{2}J(^{195}\text{Pt-}^{1}\text{HN})$ are larger for the cis isomers (avg. 67 Hz) than for the trans compounds (avg. 58 Hz). The $^{3}J(^{195}\text{Pt-}^{1}\text{H})$ are also larger for the cis complexes (avg. 40 vs. 33 Hz). In ^{13}C NMR, the coupling constants are also geometry dependent. The $^{3}J(^{195}\text{Pt-}^{13}\text{C})$ are larger for the cis isomers (avg. 37 Hz) than for the *trans* compounds (avg. 28 Hz). The $^{2}J(^{195}\text{Pt-}^{13}\text{C})$ are much smaller (avg. 18 Hz for the cis complexes and 16 Hz for the trans isomers).

Key words: platinum, amine, nitrato, NMR, IR.

Résumé : Des composés de types *cis*- et *trans*-Pt(amine)$_2$(NO$_3$)$_2$ ont été synthétisés et caractérisés par spectroscopies infrarouge et de résonance magnétique multinucléaire (^{195}Pt, ^{13}C et ^{1}H). Les vibrations des ligands nitrato ont été comparées dans les deux isomères. Les signaux en RMN du ^{195}Pt ont montré des résonances à plus hauts champs pour les composés cis (moy. –1698 ppm pour les amines primaires) que pour les analogues trans (moy. –1570 ppm). La valeur moyenne de $\Delta\delta$ est 124 ppm. Les complexes contenant des amines secondaires ont été observés à environ le même champ pour les isomères cis (moy. –1682 ppm) et à plus haut champ pour les composés trans (moy. –1638 ppm). En RMN du ^{1}H, les constantes de couplage $^{2}J(^{195}\text{Pt-}^{1}\text{HN})$ sont plus grandes pour les isomères cis (moy. 67 Hz) que pour les composés trans (moy. 58 Hz). Les couplages $^{3}J(^{195}\text{Pt-}^{1}\text{H})$ sont aussi plus importants pour les complexes cis (moy. 40 vs. 33 Hz). En RMN du ^{13}C, les constantes de couplage dépendent aussi de la géométrie. Les valeurs $^{3}J(^{195}\text{Pt-}^{13}\text{C})$ sont plus grandes pour les isomèrs cis (moy. 37 Hz) que pour les composés trans (moy. 28 Hz). Les constantes $^{2}J(^{195}\text{Pt-}^{13}\text{C})$ sont beaucoup plus petites (moy. 18 Hz pour les complexes cis et 16 Hz pour les isomères trans).

Mots clés : platine, amine, nitrato, IR, RMN.

Introduction

The antitumor compound *cisplatin* (*cis*-Pt(NH$_3$)$_2$Cl$_2$) is the most widely used anticancer drug today. Its mechanism of action involves its hydrolysis inside the cells, where the pH is neutral and the chloride ion concentration is low. In these conditions, *cis*-Pt(NH$_3$)$_2$Cl$_2$ becomes aquated, producing different ionic species that can bind to DNA (1) leading to the eventual destruction of the cell. One of these species is the diaqua complex *cis*-[Pt(NH$_3$)$_2$(OH$_2$)$_2$]$^{2+}$, which, because of the neutral pH inside the cells, will exist predominantly in the form *cis*-[Pt(NH$_3$)$_2$(OH)(OH$_2$)]$^{+}$ (2). The latter species has been shown in laboratories to produce different oligomeric species, which have been characterized by ^{195}Pt NMR (3–5) and by crystallographic methods (6–10). Some of these species are toxic and could be partially responsible for the toxicity of cisplatin in humans. Therefore, it is important to study the hydrolysis reactions of a complex before its development as an anticancer drug.

Platinum complexes with amines are potent antitumor agents. Some compounds have shown much better antitumor properties than *cis*-Pt(NH$_3$)$_2$Cl$_2$, but several are too insoluble to become useful drugs.

Our research group has undertaken a systematic study of complexes of the types *cis*- and *trans*-Pt(amine)$_2$I$_2$. The compounds have been studied by various spectroscopic techniques and by crystallography (11). We have characterized these products to study their hydrolysis reactions. However, the solubility of these complexes in water is very low. Substitution of the halides by nitrato ligands leads to a much greater solubility in water. A method for the synthesis of Pt(amine)$_2$(NO$_3$)$_2$ has been published for a few amines (12), but the complexes were characterized only by elemental analysis, IR spectroscopy, and by ^{1}H NMR.

Received 31 July 2003. Published on the NRC Research Press Web site at http://canjchem.nrc.ca on 25 March 2004.

F.D. Rochon[1] and V. Buculei. Département de chimie, Université du Québec à Montréal, C.P. 8888, Succ. Centre-ville, Montréal, QC H3C 3P8, Canada.

[1]Corresponding author (e-mail: rochon.fernande@uqam.ca).

 doi: 10.1139/V04-012 © 2004 NRC Canada

Several complexes of the types *cis*- and *trans*-$Pt(amine)_2(NO_3)_2$ have now been synthesized in our laboratories and the compounds were studied by IR and multinuclear NMR (^{195}Pt, ^1H, and ^{13}C) spectroscopies. The study of the hydrolysis and aquation reactions of these cis and trans dinitrato compounds is underway and the results will be published in a subsequent paper.

Experimental

Potassium tetrachloroplatinate(II) was purchased from Johnson Matthey and was recrystallized in water before use. The amine ligands were obtained from Aldrich, while silver nitrate was purchased from Anachemia. Deuterated acetone was acquired from CDN Isotopes.

The IR spectra were recorded between 4000 and 270 cm^{-1} as KBr pellets, on a PerkinElmer 783 grating spectrometer. The decomposition points were measured on a Fisher-Johns instrument. The NMR spectra were measured on a Varian Gemini 300BB in acetone. The fields were 300.075, 75.460, and 64.395 MHz for ^1H, ^{13}C, and ^{195}Pt, respectively. The acetone peaks were used as an internal standard for ^1H NMR (2.04 ppm) and ^{13}C NMR (29.8 ppm). For the ^{195}Pt spectra, $K_2[PtCl_4]$ (in D_2O with KCl, adjusted at –1628 ppm from $K_2[PtCl_6]$ whose δ(Pt) = 0 ppm) was the external standard.

Synthesis

The complexes $Pt(amine)_2I_2$ were synthesized as recently published (11). The dinitrato complexes were prepared according to a modified version of a published method described for other ligands (12). The complexes $Pt(amine)_2I_2$ (0.5 mmol) were dissolved in a minimum quantity of acetone (8 mL). A slight excess of $AgNO_3$ was added and the mixture was stirred in the dark and at lower temperature (5 °C) until a colorless solution (with a yellow precipitate) was obtained. The precipitate was filtered out and the solution was evaporated to dryness. The white residue was dissolved in 5 mL of acetone and filtered again to remove the last traces of AgI and $AgNO_3$. Diethyl ether was added and the mixture was cooled several hours until precipitation was complete. The precipitate was filtered, washed with diethylether, and dried under vacuum.

The notation of Nakamoto (13) was used for the IR assignments of the nitrato ligands.

***cis*-Pt($MeNH_2$)$_2$(NO_3)$_2$**

Yield: 75%; dec 132–150 °C. IR (cm^{-1}): ν(N-H) 3280s, 3255s, 3230s, ν(C-H) 2995w, 2950m, δ(N-H) 1603m, $\nu_4(NO_3)$ 1502s, δ(C-H) 1420w, 1395m, 1363m, $\nu_2(NO_3)$ 1261s, ν(C-N) 1103m, 1095s, $\nu_1(NO_3)$ 965s, $\nu_6(NO_3)$ 785m, $\nu_5(NO_3)$ 703m, ν(Pt-N) 535w, 515f, ν(Pt-O) 335m; other band: 990s, 755m. ^1H NMR (ppm) δ: NH 5.177s+d, $^2J(^{195}Pt\text{-}NH)$ = 69 Hz, H_1 2.466t+d, $^3J(^1H\text{-}^1H)$ = 6.3 Hz, $^3J(^{195}Pt\text{-}H_1)$ = 47 Hz. ^{13}C NMR (ppm) δ: C_1 34.460, $^2J(^{195}Pt\text{-}C_1)$ = 25 Hz. Anal. calcd. (%): C 6.30, H 2.64, N 14.70; found (%): C 6.47, H 2.78, N 14.73.

***cis*-Pt($EtNH_2$)$_2$(NO_3)$_2$**

Yield: 73%; dec 108–132 °C. IR (cm^{-1}): ν(N-H) 3260s, 3245s, 3150m, ν(C-H) 2965s, 2925m, 2865m, δ(N-H) 1585m, $\nu_4(NO_3)$ 1512s, δ(C-H) 1475m, 1455s, 1360w, $\nu_2(NO_3)$ 1263s, ν(C-N) 1112s, 1072m, $\nu_1(NO_3)$ 965F, $\nu_6(NO_3)$ 783s, $\nu_5(NO_3)$ 702m, ν(Pt-N) 530w, 460m, ν(Pt-O) 330m; other bands: 1335w, 1315w, 1045w, 996m, 742s. ^1H NMR (ppm) δ: NH 5.164s+d, $^2J(^{195}Pt\text{-}NH)$ = 68 Hz, H_1 2.763tq, $^3J(^1H\text{-}^1H)$ = 7.2 Hz and 6.6 Hz, H_2 1.308t, $^3J(^1H\text{-}^1H)$ = 6.9 Hz. ^{13}C NMR (ppm) δ: C_1 43.172, $^2J(^{195}Pt\text{-}C_1)$ = 24 Hz, C_2 15.776, $^3J(^{195}Pt\text{-}C_2)$ = 42 Hz.

***cis*-Pt(*n*-$PrNH_2$)$_2$(NO_3)$_2$**

Yield: 78%; dec 107–123 °C. IR (cm^{-1}): ν(N-H) 3260s, 3220s, ν(C-H) 2965s, 2925m, 2865w, δ(N-H) 1575m, $\nu_4(NO_3)$ 1515s, δ(C-H) 1465s, 1365s, $\nu_2(NO_3)$ 1270s, ν(C-N) 1160m, 1110m, 1080w, $\nu_1(NO_3)$ 962s, $\nu_6(NO_3)$ 783m, $\nu_5(NO_3)$ 702w, ν(Pt-N) 435m, ν(Pt-O) 332m; other bands: 1000s, 820s, 390w. ^1H NMR (ppm) δ: NH 5.160s+d, $^2J(^{195}Pt\text{-}NH)$ = 68 Hz, H_1 2.682tt, $^3J(^1H\text{-}^1H)$ = 7.5 Hz, 6.9 Hz, H_2 1.774tq, $^3J(^1H\text{-}^1H)$ = 7.5 Hz, 7.2 Hz, H_3 0.933t, $^3J(^1H\text{-}^1H)$ = 7.2 Hz. ^{13}C NMR (ppm) δ: C_1 50.017, $^2J(^{195}Pt\text{-}C_1)$ = 20 Hz, C_2 24.336, $^3J(^{195}Pt\text{-}C_2)$ = 40 Hz, C_3 11.177.

***cis*-Pt(*n*-$BuNH_2$)$_2$(NO_3)$_2$**

Yield: 72%; dec 99–110 °C. IR (cm^{-1}): ν(N-H) 3280s, 3245s, 3145m, ν(C-H) 2955s, 2925m, 2880w, δ(N-H) 1590m, $\nu_4(NO_3)$ 1513s, δ(C-H) 1480s, 1465s, 1395w, $\nu_2(NO_3)$ 1265s, ν(C-N) 1115m, 1075m, 1050m, $\nu_1(NO_3)$ 965s, $\nu_6(NO_3)$ 786m, $\nu_5(NO_3)$ 703w, ν(Pt-N) 530w, 465m, ν(Pt-O) 330m; other bands: 1000s, 900w, 885m, 745m. ^1H NMR (ppm) δ: NH 5.153s+d, $^2J(^{195}Pt\text{-}NH)$ = 66 Hz, H_1 2.719tt, $^3J(^1H\text{-}^1H)$ = 7.2 Hz, 6.6 Hz, H_2 1.745tt, $^3J(^1H\text{-}^1H)$ = 7.2 Hz, 6.9 Hz, H_3 1.376tq, $^3J(^1H\text{-}^1H)$ = 7.5 Hz, 7.2 Hz, H_4 0.900t, $^3J(^1H\text{-}^1H)$ = 7.2 Hz. ^{13}C NMR (ppm) δ: C_1 48.028, $^2J(^{195}Pt\text{-}C_1)$ = 21 Hz, C_2 33.199, $^3J(^{195}Pt\text{-}C_2)$ = 39 Hz, C_3 20.344, C_4 13.970.

***cis*-Pt(*i*-$PrNH_2$)$_2$(NO_3)$_2$**

Yield: 73%; dec 136–151 °C. IR (cm^{-1}): ν(N-H) 3260s, 3215s, 3150w, ν(C-H) 2965s, 2920m, 2870w, δ(N-H) 1580m, $\nu_4(NO_3)$ 1518s, δ(C-H) 1467s, 1395m, 1370m, $\nu_2(NO_3)$ 1270s, ν(C-N) 1155m, 1110s, 1085w, $\nu_1(NO_3)$ 960s, $\nu_6(NO_3)$ 782m, $\nu_5(NO_3)$ 702m, ν(Pt-N) 440m, ν(Pt-O) 330m; other bands: 1350w, 1000s, 820m, 392w. ^1H NMR (ppm) δ: NH 5.088s+d, $^2J(^{195}Pt\text{-}NH)$ = 67 Hz, H_1 2.993thept, $^3J(^1H\text{-}^1H)$ = 6.6 Hz, 6.3 Hz, $^3J(^{195}Pt\text{-}H_1)$ = 39 Hz, H_2 1.397d, $^3J(^1H\text{-}^1H)$ = 6.3 Hz. ^{13}C NMR (ppm) δ: C_1 50.123, $^2J(^{195}Pt\text{-}C_1)$ = 22 Hz, C_2 23.198, $^3J(^{195}Pt\text{-}C_2)$ = 30 Hz. Anal. calcd. (%): C 16.48, H 4.15, N 12.81; found (%): C 16.95, H 4.23, N 12.38.

***cis*-Pt(*i*-$BuNH_2$)$_2$(NO_3)$_2$**

Yield: 73%; dec 105–124 °C. IR (cm^{-1}): ν(N-H) 3280s, 3250m, 3230s, 3135w, ν(C-H) 2970m, 2930m, 2880w, δ(N-H) 1590m, $\nu_4(NO_3)$ 1503s, δ(C-H) 1460w, 1360m, $\nu_2(NO_3)$ 1263s, ν(C-N) 1100m, 1050w, $\nu_1(NO_3)$ 949s, $\nu_6(NO_3)$ 780m, $\nu_5(NO_3)$ 710s, ν(Pt-O) 335m; other bands: 1015w, 833w, 698m, 613w. ^1H NMR (ppm) δ: NH 5.157s+d, $^2J(^{195}Pt\text{-}NH)$ = 65 Hz, H_1 2.594td, $^3J(^1H\text{-}^1H)$ = 7.5 Hz, 6.9 Hz, $^3J(^{195}Pt\text{-}H_1)$ = 37 Hz, H_2 2.096thept, $^3J(^1H\text{-}^1H)$ = 6.9 Hz, 6.6 Hz, H_3 0.953d, $^3J(^1H\text{-}^1H)$ = 6.6 Hz. ^{13}C NMR (ppm) δ: C_1 55.693, $^2J(^{195}Pt\text{-}C_1)$ = 21 Hz, C_2 hidden by the solvent, C_3 20.101.

© 2004 NRC Canada

***cis*-Pt(*sec*-BuNH$_2$)$_2$(NO$_3$)$_2$**

Yield: 79%; dec 101–118 °C. IR (cm^{-1}): ν(N-H) 3225s, 3145m, ν(C-H) 2960s, 2915m, 2870w, δ(N-H) 1600m, ν_4(NO$_3$) 1509s, δ(C-H) 1470s, 1380s, ν_2(NO$_3$) 1278s, ν(C-N) 1140w, 1115m, 1075m, ν_1(NO$_3$) 965s, ν_6(NO$_3$) 788m, ν_5(NO$_3$) 702w, ν(Pt-N) 460w, 430w, ν(Pt-O) 335m; other bands: 1000m, 895w, 835w. ^{1}H NMR (ppm) δ: NH 5.117s+d, ^2J(^{195}Pt-NH) = 65 Hz, H$_1$ 2.712ttq, ^3J(^{1}H-^{1}H) = 7.2 Hz, 6.9 Hz, 6.6 Hz, ^3J(^{195}Pt-H$_1$) = 35 Hz, H$_2$ 1.543dq, ^3J(^{1}H-^{1}H) = 7.2 Hz, 6.6 Hz, H$_{2'}$ 1.404d, ^3J(^{1}H-^{1}H) = 6.6 Hz, H$_3$ 0.941t, ^3J(^{1}H-^{1}H) = 7.2 Hz. ^{13}C NMR (ppm) δ: C$_1$ 55.405, ^2J(^{195}Pt-C$_1$) = 20 Hz, C$_2$ hidden by the solvent, C$_{2'}$ 20.101, ^3J(^{195}Pt-C$_{2'}$) = 29 Hz, C$_3$ 10.631.

***cis*-Pt(Me$_2$NH)$_2$(NO$_3$)$_2$**

Yield: 72%; dec 121–147 °C. IR (cm^{-1}): ν(N-H) 3280s, 3225s, 3135w, ν(C-H) 2930s, 2865s, δ(N-H) 1585m, ν_4(NO$_3$) 1503s, δ(C-H) 1460m, 1370s, ν_2(NO$_3$) 1260s, ν(C-N) 1170m, 1125m, ν_1(NO$_3$) 949s, ν_6(NO$_3$) 780s, ν_5(NO$_3$) 710s, ν(Pt-N) 440w, 405w, ν(Pt-O) 342m; other bands: 1030m, 830w, 820w, 603w. ^{1}H NMR (ppm) δ: NH 5.998s+d, ^2J(^{195}Pt-NH) = 69 Hz, H$_1$ 2.650d+d, ^3J(^{1}H-^{1}H) = 5.7 Hz, ^3J(^{195}Pt-H$_1$) = 40 Hz. ^{13}C NMR (ppm): C$_1$ 44.553, ^2J(^{195}Pt-C$_1$) = 25 Hz.

***cis*-Pt(Et$_2$NH)$_2$(NO$_3$)$_2$**

This compound was not synthesized from *cis*-Pt(Et$_2$NH)$_2$I$_2$ as the other *cis*-dinitrato complexes. The compound *trans*-Pt(Et$_2$NH)$_2$I$_2$ contained about 30% of the cis isomer. A mixture of the cis and trans isomers of Pt(Et$_2$NH)$_2$(NO$_3$)$_2$ was obtained. ^{1}H NMR for the cis isomer (ppm) δ: NH 5.836s+d, ^2J(^{195}Pt-NH) = 67 Hz, H$_1$ 3.046tq, ^3J(^{1}H-^{1}H) = 7.2 Hz, 6.6 Hz, H$_2$ 1.368t, ^3J(^{1}H-^{1}H) = 6.6 Hz. ^{13}C NMR for the cis isomer: C$_1$ 51.350, ^2J(^{195}Pt-C$_1$) = 22 Hz, C$_2$ 15.220, ^3J(^{195}Pt-C$_2$) = 39 Hz.

***trans*-Pt(MeNH$_2$)$_2$(NO$_3$)$_2$**

Yield: 80%; dec 137–163 °C. IR (cm^{-1}): ν(N-H) 3260s, 3240s, 3150s, ν(C-H) 2985w, 2940m, 2890w, δ(N-H) 1595s, ν_4(NO$_3$) 1503s, δ(C-H) 1455m, 1420w, 1355m, ν_2(NO$_3$) 1251s, ν(C-N) 1095s, 1055s, ν_1(NO$_3$) 966s, ν_6(NO$_3$) 775s, ν_5(NO$_3$) 709s, ν(Pt-N) 505m, ν(Pt-O) 350m; other bands: 1020m. ^{1}H NMR (ppm) δ: NH 4.737s+d, ^2J(^{195}Pt-NH) = 57 Hz, H$_1$ 2.327 t+d, ^3J(^{1}H-^{1}H) = 6.6 Hz, ^3J(^{195}Pt-H$_1$) = 32 Hz. ^{13}C NMR (ppm) δ: C$_1$ 32.380, ^2J(^{195}Pt-C$_1$) = 20 Hz.

***trans*-Pt(EtNH$_2$)$_2$(NO$_3$)$_2$**

Yield: 83%; dec 120–157 °C. IR (cm^{-1}): ν(N-H) 3280s, 3240s, 3150m, ν(C-H) 2960m, 2930w, 2870w, δ(N-H) 1585s, ν_4(NO$_3$) 1512s, δ(C-H) 1485m, 1470m, 1380m, ν_2(NO$_3$) 1268s, ν(C-N) 1115m, 1075w, 1050w, ν_1(NO$_3$) 967s, ν_6(NO$_3$) 785w, ν_5(NO$_3$) 705w, ν(Pt-N) 465w, ν(Pt-O) 333m; other bands: 1000s, 885w, 740m. ^{1}H NMR (ppm) δ: NH 4.764s+d, ^2J(^{195}Pt-NH) = 59 Hz, H$_1$ 2.665tq, ^3J(^{1}H-^{1}H) = 7.5 Hz, 7.2 Hz, H$_2$ 1.321t, ^3J(^{1}H-^{1}H) = 7.2 Hz. ^{13}C NMR (ppm) δ: C$_1$ 41.229, ^2J(^{195}Pt-C$_1$) = 19 Hz, C$_2$ 15.487, ^3J(^{195}Pt-C$_2$) = 30 Hz. Anal. calcd. (%): C 11.74, H 3.45, N 13.69; found: C 11.69, H 3.32, N 13.06.

***trans*-Pt(*n*-PrNH$_2$)$_2$(NO$_3$)$_2$**

Yield: 79%; dec 138–152 °C. IR (cm^{-1}): ν(N-H) 3260s, 3230s, 3210s, ν(C-H) 2980s, 2930m, 2880w, δ(N-H) 1580m, ν_4(NO$_3$) 1508s, δ(C-H) 1430w, 1385s, ν_2(NO$_3$) 1261s, ν(C-N) 1100w, 1080m, 1055w, ν_1(NO$_3$), 965s, ν_6(NO$_3$) 785m, ν_5(NO$_3$) 700w, ν(Pt-N) 410w, ν(Pt-O) 338m; other bands: 1025m, 885w, 835w, 760w. ^{1}H NMR (ppm) δ: NH 4.759s+d, ^2J(^{195}Pt-NH) = 57 Hz, H$_1$ 2.584tt, ^3J(^{1}H-^{1}H) = 7.5 Hz, 6.9 Hz, H$_2$ 1.805 tq, ^3J(^{1}H-^{1}H) = 7.5 Hz, 7.2 Hz, H$_3$ 0.938t, ^3J(^{1}H-^{1}H) = 7.2 Hz. ^{13}C NMR (ppm) δ: C$_1$ 48.241, ^2J(^{195}Pt-C$_1$) = 16 Hz, C$_2$ 24.048, ^3J(^{195}Pt-C$_2$) = 29 Hz, C$_3$ 11.329.

***trans*-Pt(*n*-BuNH$_2$)$_2$(NO$_3$)$_2$**

Yield: 83%; dec 135–146 °C. IR (cm^{-1}): ν(N-H) 3240s, 3140m, ν(C-H) 2960s, 2930m, 2870m, δ(N-H) 1595s, ν_4(NO$_3$) 1510s, δ(C-H) 1480s, 1385s, ν_2(NO$_3$) 1260s, ν(C-N) 1150w, 1115w, 1075w, ν_1(NO$_3$) 962s, ν_6(NO$_3$) 788w, ν_5(NO$_3$) 702w, ν(Pt-N) 460w, ν(Pt-O) 337w; other bands: 1000s, 895w, 830w. ^{1}H NMR (ppm) δ: NH 4.746s+d, ^2J(^{195}Pt-NH) = 56 Hz, H$_1$ 2.622tt, ^3J(^{1}H-^{1}H) = 7.5 Hz, 6.9 Hz, H$_2$ 1.787tt, ^3J(^{1}H-^{1}H) = 7.5 Hz, 7.2 Hz, H$_3$ 1.385tq, ^3J(^{1}H-^{1}H) = 7.5 Hz, 7.2 Hz, H4 0.910t, ^3J(^{1}H-^{1}H) = 7.2 Hz. ^{13}C NMR (ppm) δ: C$_1$ 46.146, ^2J(^{195}Pt-C$_1$) = 16 Hz, C$_2$ 32.942, ^3J(^{195}Pt-C$_2$) = 26 Hz, C$_3$ 20.466, C4 14.030. Anal. calcd. (%): C 20.65, H 4.77, N 12.04; found: C 21.09, H 5.17, N 12.03.

***trans*-Pt(*i*-PrNH$_2$)$_2$(NO$_3$)$_2$**

Yield: 80%; dec 144–163 °C. IR (cm^{-1}): ν(N-H) 3305s, ν(C-H) 3080w, 3060w, 3010m, δ(N-H) 1575s, ν_4(NO$_3$) 1510s, δ(C-H) 1475w, 1450m, 1395w, ν_2(NO$_3$) 1266s, ν(C-N) 1170m, 1130s, 1090w, 1055s, ν_1(NO$_3$) 961s, ν_6(NO$_3$) 795m, ν_5(NO$_3$) 700w, ν(Pt-N) 550m, ν(Pt-O) 375m; other bands: 1000s, 930m, 750m. ^{1}H NMR (ppm) δ: NH 4.738s+d, ^2J(^{195}Pt-NH) = 59 Hz, H$_1$ 2.933thept, ^3J(^{1}H-^{1}H) = 7.2 Hz, 6.6 Hz, H$_2$ 1.380d, ^3J(^{1}H-^{1}H) = 6.6 Hz. ^{13}C NMR (ppm) δ: C$_1$ 48.514, ^2J(^{195}Pt-C$_1$) = 15 Hz, C$_2$ 23.076, ^3J(^{195}Pt-C$_2$) = 26 Hz.

***trans*-Pt(*i*-BuNH$_2$)$_2$(NO$_3$)$_2$**

Yield: 78%; dec 128–141 °C. IR (cm^{-1}): ν(N-H) 3280s, 3250s, 3150w, ν(C-H) 2970m, 2930m, 2880w, δ(N-H) 1585m, ν_4(NO$_3$) 1510s, δ(C-H) 1480m, 1465m, 1385s, ν_2(NO$_3$) 1266s, ν(C-N) 1115m, 1070w, ν_1(NO$_3$) 965m, ν_6(NO$_3$) 785w, ν_5(NO$_3$) 700w, ν(Pt-N) 470w, ν(Pt-O) 345m, other bands: 1045w, 1000s, 880w, 830w, 745m. ^{1}H NMR (ppm) δ: NH 4.714s+d, ^2J(^{195}Pt-NH) = 57 Hz, H$_1$ 2.481td, ^3J(^{1}H-^{1}H) = 6.9 Hz, 6.3 Hz, H$_2$ 2.131thept, ^3J(^{1}H-^{1}H) = 6.6 Hz, 6.3 Hz, H$_3$ 0.962d, ^3J(^{1}H-^{1}H) = 6.6 Hz. ^{13}C NMR (ppm) δ: C$_1$ 55.948, ^2J(^{195}Pt-C$_1$) = 15 Hz, C$_2$ hidden by the solvent, C$_3$ 20.223.

***trans*-Pt(*sec*-BuNH$_2$)$_2$(NO$_3$)$_2$**

Yield: 85%; dec 132–148 °C. IR (cm^{-1}): ν(N-H) 3260s, 3230s, 3160m, ν(C-H) 2960s, 2940m, 2870w, δ(N-H) 1600m, ν_4(NO$_3$) 1502s, δ(C-H) 1455m, 1370s, ν_2(NO$_3$) 1255s, ν(C-N) 1150w, 1122m, 1075m, ν_1(NO$_3$) 967s, ν_6(NO$_3$) 788w, ν_5(NO$_3$) 710w, ν(Pt-N) 470w, ν(Pt-O) 345m; other bands: 1035w, 900w, 830w. ^{1}H NMR (ppm) δ: NH 4.720s+d, ^2J(^{195}Pt-NH) = 58 Hz, H$_1$ 2.662ttq, ^3J(^{1}H-^{1}H) =

© 2004 NRC Canada

7.2 Hz, 6.6 Hz, 6.3 Hz, H_2 1.596dq, $^3J(^1H\text{-}^1H)$ = 6.9 Hz, 6.6 Hz, $H_{2'}$ 1.381d, $^3J(^1H\text{-}^1H)$ = 6,6 Hz, H_3 0.951t, $^3J(^1H\text{-}^1H)$ = 6.9 Hz. ^{13}C NMR (ppm) δ: C_1 54.008, $^2J(^{195}Pt\text{-}C_1)$ = 15 Hz, C_2 hidden by the solvent, $C_{2'}$ 20.041, $^3J(^{195}Pt\text{-}C_{2'})$ = 27 Hz, C_3 10.585.

***trans*-Pt(*t*-BuNH$_2$)$_2$(NO$_3$)$_2$**

Yield: 76%; dec 111–134 °C. IR (cm^{-1}): ν(N-H) 3270s, 3250s, 3170m, ν(C-H) 2980m, 2930w, 2880w, δ(N-H) 1600s, $\nu_4(NO_3)$ 1495s, δ(C-H) 1455w, 1380m, 1355m, $\nu_2(NO_3)$ 1265s, ν(C-N) 1080s, $\nu_1(NO_3)$ 970s, $\nu_6(NO_3)$ 783s, $\nu_5(NO_3)$ 710w, ν(Pt-O) 345m; other bands: 1030s, 880w, 740w, 605w. ^1H NMR (ppm) δ: NH 4.808s+d, $^2J(^{195}Pt\text{-}NH)$ = 59 Hz, H_2 1.385s, $^4J(^{195}Pt\text{-}H_2)$ = 15 Hz. ^{13}C NMR (ppm) δ: C_1 55.721, $^2J(^{195}Pt\text{-}C_1)$ = 11 Hz, C_2 31.763, $^3J(^{195}Pt\text{-}C_2)$ = 19 Hz.

***trans*-Pt(Me$_2$NH)$_2$(NO$_3$)$_2$**

Yield: 86%; dec 132–159 °C. IR (cm^{-1}): ν(N-H) 3225s, 3200s, ν(C-H) 2980w, 2940m, 2920m, δ(N-H) 1540m, $\nu_4(NO_3)$ 1512s, δ(C-H) 1465s, 1430w, 1395w, 1355s, $\nu_2(NO_3)$ 1260s, ν(C-N) 1140m, 1095s, 1080s, $\nu_1(NO_3)$ 960s, $\nu_6(NO_3)$ 778s, $\nu_5(NO_3)$ 703m, ν(Pt-N) 510m, ν(Pt-O) 347m; other bands: 1015s, 935s, 890s, 835w. ^1H NMR (ppm) δ: NH 5.500s+d, $^2J(^{195}Pt\text{-}NH)$ = 58 Hz, H_1 2.478d+d, $^3J(^1H\text{-}^1H)$ = 6.0 Hz, $^3J(^{195}Pt\text{-}H_1)$ = 33 Hz. ^{13}C NMR (ppm) δ: C_1 42.883, $^2J(^{195}Pt\text{-}C_1)$ = 18 Hz.

***trans*-Pt(Et$_2$NH)$_2$(NO$_3$)$_2$**

This compound was found to be a cis–trans mixture. Yield: 80%; dec 124–143 °C. IR (cm^{-1}): ν(N-H) 3280s, 3175m, ν(C-H) 2980m, 2885m, δ(N-H) 1575s, $\nu_4(NO_3)$ 1510s, δ(C-H) 1475m, 1455w, 1375m, $\nu_2(NO_3)$ 1267s, ν(C-N) 1210m, 1065w, $\nu_1(NO_3)$ 964s, $\nu_6(NO_3)$ 780w, $\nu_5(NO_3)$ 705w, other bands: 1005s, 865w, 755w. ^1H NMR of the trans isomer (ppm) δ: NH 5.519s+d, $^2J(^{195}Pt\text{-}NH)$ = 58 Hz, H_1 2.955tq, $^3J(^1H\text{-}^1H)$ = 7.5 Hz, 6.9 Hz, H_2 1.344t, $^3J(^1H\text{-}^1H)$ = 6.9 Hz. ^{13}C NMR of the trans isomer (ppm) δ: C_1 50.834, $^2J(^{195}Pt\text{-}C_1)$ = 14 Hz, C_2 15.099, $^3J(^{195}Pt\text{-}C_2)$ = 28 Hz.

Results and discussion

The dinitrato complexes were prepared by the reaction of the diiodo complexes with a slight excess (10%) of silver nitrate in acetone similar to a published method (12).

$$Pt(amine)_2I_2 + 2AgNO_3 \rightarrow Pt(amine)_2(NO_3)_2 + 2AgI\downarrow$$

The diiodo complexes dissolved in acetone resulting in a yellow solution. Silver nitrate is only slightly soluble in acetone. The reaction was performed in the dark and at a lower temperature in ice, to reduce decomposition. The published method (12), which was used for other ligands, required 5–20 min of stirring time. The reaction time for our ligands varied between a few hours to 2 days depending on the amine. After filtration and the purification process, the white dinitrato complexes were isolated and characterized. The cis or trans geometry was retained during the reaction. The cis and trans compounds with amine = methylamine ($MeNH_2$), ethylamine ($EtNH_2$), *n*-propylamine (*n*-$PrNH_2$), *n*-butylamine (*n*-$BuNH_2$), *iso*-propylamine (*i*-$PrNH_2$), *iso*-butylamine (*i*-$BuNH_2$), *sec*-butylamine (*sec*-$BuNH_2$), dimethylamine (Me_2NH), and trans compounds with *tert*-butylamine (*t*-$BuNH_2$) and diethylamine (Et_2NH) were synthesized.

The use of a slight excess of silver nitrate increased the yields. When the reactions were performed at room temperature, oily compounds were obtained and the products decomposed quite rapidly. The yields were also very low. Most dinitrato complexes are stable when kept in the dark and at lower temperature. Even in these conditions, a few compounds decomposed fairly rapidly to a black material. The complex *cis*-Pt(*i*-$BuNH_2)_2(NO_3)_2$ decomposed after a few hours. All the IR and NMR spectra were measured on fresh samples. The compound *trans*-$Pt(Et_2NH)_2(NO_3)_2$ was not pure, since two series of signals were observed in NMR (^1H, ^{13}C, and ^{195}Pt) spectroscopy. The second compound was assumed to be the cis analogue, since the starting material *trans*-$Pt(Et_2NH)_2I_2$ contained some cis isomers as described in a previous paper (11).

IR spectroscopy

The IR spectra of the complexes were recorded and are listed in the *Experimental* section. The notation of Nakamoto (13) was used for the bands involving the nitrato ligands.

The symmetry of the free nitrate ion is D_{3h}, with a bond order of 1 1/3. However, in the monodentate-coordinated nitrato ligand, the N—O(Pt) bond order is close to 1. The π electronic density is then delocalized on only two N—O bonds resulting in a bond order of 1 1/2 for the two bonds. The approximate symmetry of coordinated NO_3^- is C_{2v}. The reduction in the N—O(Pt) bond order is clearly observed by comparing the stretching band ν_1 (13) in free NO_3^- (1049 cm^{-1}) with the one observed in CH_3ONO_2 (854 cm^{-1}), a purely covalent compound (14). It has been suggested that the position of the ν_1 band gives important information on the covalent character of the Pt—O bond (15). Because of the reduction in symmetry of the coordinated nitrato ligand, some of the vibration modes, which were degenerate in the free ion, will be split. This is the case for the ν_3 stretching mode in D_{3h} (E), which will separate into the ν_2 (A_1) and ν_4 (B_2) stretching modes in C_{2v} symmetry (13). The energy difference between the two latter modes ($\Delta = \nu_4 - \nu_2$) should also give additional information on the covalent character of the Pt—O bond (14, 15). For ionic nitrate Δ is 0 cm^{-1}, while it is 385 cm^{-1} in CH_3ONO_2.

The values of Δ as well as the energy difference ($\Delta\nu_1$) between the ν_1 band for free nitrate and the coordinated nitrato ligands are shown in Table 1. The average value $\Delta(\nu_4 - \nu_2)$ is 243 cm^{-1} in the *cis* complexes and 246 cm^{-1} in the trans isomers. The difference is not significant. We have calculated this $\Delta(\nu_4 - \nu_2)$ value for a few dinitrato complexes reported in the literature. These values for *cis*-$PtA_2(NO_3)_2$ are 230 cm^{-1} for A = NH_3 (16), 227 cm^{-1} for NH_2CH_3 (12), 214 cm^{-1} for $NH_2(C_6H_{11})$ (12), 226 cm^{-1} for 4-hydroxymethylpyridine (12), and 238 cm^{-1} for $NH_2(CH_2Ph)$ (12), and 245 cm^{-1} for A_2 = bipy and 240 cm^{-1} for phen (14). These results are close to our values. In a study on *cis*- and *trans*-$Pt(Ypy)_2NO_3)_2$, (Ypy = pyridine derivative) the average value for $\Delta(\nu_4 - \nu_2)$ was found to be higher in the

© 2004 NRC Canada

Table 1. $\Delta(\upsilon_4 - \upsilon_2)$ and $\Delta\upsilon_1$ (cm^{-1}) (as defined in the text) of the complexes of $Pt(amine)_2(NO_3)_2$.

	cis-$Pt(amine)_2(NO_3)_2$		*trans*-$Pt(amine)_2(NO_3)_2$	
Amine	$\Delta(\upsilon_4 - \upsilon_2)$	$\Delta\upsilon_1$	$\Delta(\upsilon_4 - \upsilon_2)$	$\Delta\upsilon_1$
$MeNH_2$	241	84	252	83
$EtNH_2$	249	84	244	82
n-$PrNH_2$	245	87	247	84
n-$BuNH_2$	248	84	250	87
i-$PrNH_2$	248	89	244	88
i-$BuNH_2$	240	100	244	84
sec-$BuNH_2$	231	84	247	82
t-$BuNH_2$			230	79
Me_2NH	243	100	252	89

trans compounds (264 cm^{-1}) than in the cis isomers (233 cm^{-1}) (17).

The position of ν_1 for our compounds is also not very different in the two geometries (avg. $\Delta\upsilon_1$ 89 cm^{-1} for cis and 84 cm^{-1} for trans). For the compounds *cis*- and *trans*-$Pt(Ypy)_2NO_3)_2$, the ν_1 band was found to be less energetic in the trans complexes (avg. $\Delta\upsilon_1$ = 120 vs. 90 cm^{-1} for the cis isomers), suggesting a more covalent character for the Pt—O bonds in the trans geometry (17). Our results on the amine system seem to indicate that the covalency of the Pt—O bonds in the cis and trans compounds are not very different.

The stretching energy of a more covalent bond should increase and these results can be compared with the energies of the ν(Pt-O) vibrations. The skeletal symmetry around the platinum atom is C_{2v} for the cis complexes and D_{2h} for the trans isomers. Two ν(Pt-O) bands are expected for the cis compounds and one for the trans complexes, according to group theory. Our assignment of the υ(Pt-O) bonds was made according to some published works (17–19). These bands are shown in Table 2 along with the results published in the literature. Some of the published work on the cis complexes have shown two ν(Pt-O) absorption bands, while others have shown only one. We have observed only one band for both isomers. The position of the band is not very different for the different isomers, although it appears slightly larger for the trans compounds (avg. 346 vs. 333 cm^{-1}). These results seem to agree with our conclusion reached above from the study of the nitrato ν_1 band and $\Delta(\nu_4 - \nu_2)$ values. There seems to be no important difference between the two isomers. These ν(Pt-O) vibrations are not very energetic and are close to the ν(Pt-Cl) vibrations. They are difficult to assign with certainty, since they are quite weak. It is also possible that they are not pure and might couple with other vibrations.

The ν(Pt-N) bands were assigned based on some published works (13, 19–22). Two vibration modes are expected for the cis compounds and only one for the trans isomers. Our assignments are shown in Table 3. For most complexes, two bands were observed for the cis complexes while only one was shown by the trans isomers. The energies of these bands are slightly higher than those of the corresponding iodo complexes (11), suggesting that the covalency of the Pt—N bonds are greater in the dinitrato compounds than in the diiodo analogues. The reduced polarizability of the nitrato ligand compared to the iodo ligand could increase the energy of the ν(Pt-N) vibrations. The trans influence of the iodo ligand is larger than the one of the nitrato ligand, which should also increase the energy of the ν(Pt-N) vibrations in the *cis*-dinitrato complexes. The trans compounds with *tert*-butylamine and diethylamine and the *cis-iso*-butylamine compound did not show any band in the ν(Pt-N) region.

Table 2. ν(Pt-O) (cm^{-1}) vibrations in $Pt(amine)_2(NO_3)_2$ and some examples from the literature.

Amine	cis	trans	Reference
NH_3	330		18
$MeNH_2$	332		19
$C_6H_{11}NH_2$	334, 340	345	19
$PhCH_2NH_2$	350, 360		19
2,2′-Bipyridine	340, 350		19
4-Hydroxymethylpyridine	338, 346		19
Pyridine	341, 325	360	17
4-Picoline	338	350	19
	338	353	17
2-Picoline	340, 350	330	17
3-Picoline	330, 339	349	17
2,4-Lutidine	343	340	17
3,5-Lutidine	330, 337	351	17
$MeNH_2$	335	350	
$EtNH_2$	330	333	
n-$PrNH_2$	332	338	
n-$BuNH_2$	330	337	
i-$PrNH_2$	330	375	
i-$BuNH_2$	335	345	
sec-$BuNH_2$	335	345	
t-$BuNH_2$		345	
Me_2NH	342	347	
Et_2NH		340 (Mixture)	

^{195}Pt NMR spectroscopy

The ^{195}Pt NMR spectra of the dinitrato complexes were measured in acetone and the chemical shifts are listed in Table 4 as well as the pK_a of the protonated ligands (23) and the proton affinity of the amines (24–27). To determine if the nitrato ligands are partly dissociated in acetone, the conductivity of several cis and trans complexes were measured in acetone. The results have shown that there is no appreciable solvolysis of the compounds. The molar conductivity values varied between 0.03 and 0.06 S cm^2/mol. The corresponding values for several cesium salts were much larger. Therefore, the chemical shifts in Table 4 correspond to those of the dinitrato complexes.

The cis isomers were observed at higher fields than their trans analogues. The complex *trans*-$Pt(Et_2NH)_2(NO_3)_2$ contained a second compound, which we have assigned to the cis isomer, since the starting material *trans*-$Pt(Et_2NH)_2I_2$ was shown to contain some cis compound (11). The signal observed at higher field was assumed to be the cis compound as observed for the other ligands. The difference between the cis and trans isomers is larger for the primary amines (avg. 125 ppm) than for the secondary amines (avg.

© 2004 NRC Canada

Table 3. ν(Pt-N) (cm^{-1}) bands for the complexes of $Pt(amine)_2(NO_3)_2$.

Amine	cis		trans
	ν_s	ν_{as}	ν_{as}
NH_3 (28)	562	558	
$MeNH_2$	535	515	505
$EtNH_2$	530	460	465
n-$PrNH_2$		435	410
n-$BuNH_2$	530	465	460
i-$PrNH_2$		440	550
i-$BuNH_2$			470
sec-$BuNH_2$	460	430	470
Me_2NH	440	405	510

44 ppm). Our results are in agreement with those of the NH_3 complexes (28).

Surprisingly, the trans isomers of the complexes containing the secondary amines were observed at higher fields than the compounds containing the primary amines, while the cis compounds were observed at about the same fields. For square-planar complexes, the molecules of solvent can normally approach and weakly bind to the Pt atom on both sides of the coordination plane. For complexes containing more bulky ligands close to the binding site, the molecules of solvent cannot approach the Pt atom easily, resulting in a decrease of the electronic density around the Pt nucleus. This solvent factor is very important for solvents like water that can coordinate to platinum. However, the dinitrato complexes were measured in deuterated acetone, a solvent that could coordinate to Pt, but not as easily as water. Therefore the solvent effect should be considerably reduced. Furthermore, the reduced solvation for crowded ligands is less important in trans compounds, where the two ligands are far from each other.

Nitrato ligands are more bulky than iodo or chloro ligands. Therefore, the presence of the nitrato ligands should have an influence of the solvation of the Pt atom. There are two Pt NMR studies in the literature on dinitrato compounds. The results for the NH_3 (28) complexes are shown in Table 4. NH_3 complexes are usually observed at lower fields than amine complexes. The other published paper is on a series of pyridine complexes (17). In these compounds, the cis compounds were observed between –1485 and –1532 ppm, while the trans isomers were reported between –1402 and –1481 ppm, with Δδ (cis–trans) = –43 to –83 ppm. The compounds with ortho substituents were observed at lower fields than the others, probably because of reduced solvation around the Pt atom, due to a more limited rotation of the pyridine ligand around the Pt—N bond (17). The ortho substituents are mainly located on top of the Pt atom and prevent the approach of the molecules of solvent. Our results on the diamine complexes have shown values of Δδ (cis–trans) from –105 to –140 ppm for the primary amines. The difference is larger than those published for the pyridine complexes (17), but smaller than the one for the NH_3 compounds (28), where it is 179 ppm. Our values for the secondary amines (avg. 44 ppm) are closer to those reported for the pyridine system (17).

Table 4. δ(^{195}Pt) and $\Delta\delta = \delta_{cis} - \delta_{trans}$ (ppm) of the complexes of $Pt(amine)_2(NO_3)_2$. (PA = proton affinity, kJ/mole).

Amine	PA	pK_a	cis	trans	Δδ
NH_3 (DMF)	854	9.25	–1592 (28)	–1413 (28)	–179
$MeNH_2$	914	10.62	–1713	–1608	–105
$EtNH_2$	930	10.67	–1707	–1579	–128
n-$PrNH_2$	933	10.71	–1694	–1577	–117
n-$BuNH_2$	924	10.78	–1699	–1574	–125
i-$PrNH_2$		10.63	–1698	–1558	–140
i-$BuNH_2$		10.72	–1694	–1572	–122
sec-$BuNH_2$		10.56	–1683	–1548	–135
t-$BuNH_2$		10.68		–1540	
Me_2NH		10.73	–1696	–1675	–21
Et_2NH		11.04	–1668*	–1601	–67

Note: PA is the proton affinity (kJ/mol).
*Indicates an impurity in the trans compound (see text).

There seems to be a slight deshielding effect on the Pt atom as the bulkiness on the primary amine is increased. This is probably due to a reduction in the solvation of the metal centre. The difference in chemical shifts is smaller in the cis compounds (30 ppm) than in the trans isomers (68 ppm) for the complexes containing primary amines.

Attempts were made in the literature (29–31) to correlate the ^{195}Pt chemical shifts with the basicity of the amine ligands to study the nature of the Pt–amine bond. Contrary to pyridine, amines cannot accept π electron density from the metal. Therefore, in the formation of the σ(amine → Pt) bond, electron density is transferred from the amine ligand to the platinum nucleus, resulting in a shielding on the ^{195}Pt nucleus and a deshielding effect on the ligands (^{1}H and ^{13}C NMR signals). A weak relation between δ(^{195}Pt) and the basicity of the ligands was reported for complexes of the type *cis*- and *trans*-$Pt(Ypy)_2X_2$ (X = Cl^- or I^-) (29), but the dispersion around the straight line was fairly large. For pyridine derivatives, the ^{195}Pt chemical shifts seem to depend more on the position of the CH_3 substituents then on the basicity of the ligand. To verify the influence of the basicity of the amine on the δ(Pt) values, the latter were plotted vs. the pK_a of the protonated amines. No correlation could be observed for the cis or the trans compounds. The pK_a values were measured in a solvent (water or alcohol) and are influenced by the presence of the substituents on the protonated N atom. The errors on the pK_a values are not negligible, especially for the primary amines where the pK_a values do not vary very much (from 10.62 to 10.78). The proton affinity values of the amines that are measured in the gas phase, might represent better the basicity of the ligands. But these values are not as common as the pK_a values. Figure 1 shows the relation between the δ(Pt) and the published proton affinity of the amines (24–27) for the cis and trans complexes. The ^{195}Pt chemical shift seems to increase slightly as the proton affinity increases. But the difference is small, close to the experimental errors. More data are needed to reach a sound conclusion.

The δ(Pt) does not seem to be very influenced by the basicity of the ligands. Acetone is not an inert solvent for platinum, and solvation around the Pt atom is probably a more

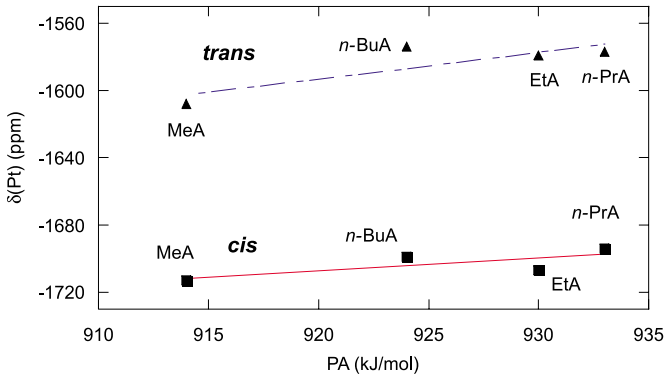
© 2004 NRC Canada

Table 5. δ(^{1}H) (ppm) and J(^{195}Pt-H$_1$) (Hz) of Pt(amine)$_2$(NO$_3$)$_2$ in CD$_3$COCD$_3$.

Amine		NH	H_1	H_2	H_3	H_4 or $H_{2'}$	^2J(^{195}Pt-NH)	^3J(^{195}Pt-H_1)
$MeNH_2$	cis	5.177	2.466				69	47
	trans	4.737	2.327				57	32
EtH_2	cis	5.164	2.763	1.308			68	
	trans	4.764	2.665	1.321			59	
n-$PrNH_2$	cis	5.160	2.682	1.774	0.933		68	
	*	4.600	2.700	1.700	0.940		65*	
	trans	4.759	2.584	1.805	0.938		57	
	*	3.850	2.700	1.750	0.960		65*	
n-$BuNH_2$	cis	5.153	2.719	1.745	1.376	0.900	66	
	trans	4.746	2.622	1.787	1.385	0.910	56	
i-$PrNH_2$	cis	5.088	2.993	1.397			67	
	trans	4.738	2.933	1.380			59	
i-$BuNH_2$	cis	5.157	2.594	2.096	0.953		65	37
	trans	4.714	2.481	2.131	0.962		57	
sec-$BuNH_2$	cis	5.117	2.712	1.543	0.941	1.404	65	35
	trans	4.720	2.662	1.596	0.951	1.381	58	
Me_2NH	cis	5.998	2.650				69	40
	trans	5.500	2.478				58	33
t-$BuNH_2$	trans	4.808		1.385			59	
Et_2NH	cis‡	5.836	3.046	1.368			67	
	trans	5.519	2.955	1.344			58	

*In $CDCl_3$ (32).
‡See text.

Fig. 1. δ(^{195}Pt) vs. proton affinity (PA) of the amine for the complexes of Pt(amine)$_2$(NO$_3$)$_2$.



important factor in determining the NMR chemical shifts. The trans complexes with secondary amines have shown resonances at higher fields than those with primary amines, but more complexes with secondary amines are needed before any conclusion can be reached.

^{1}H and ^{13}C NMR spectroscopy

The ^{1}H NMR chemical shifts are listed in Table 5 as well as the published values on Pt(*n*-$PrNH_2)_2(NO_3)_2$ measured in $CDCl_3$ (32). These authors have also measured their compounds in CD_3COCD_3, but only the -NH_2 are reported at 5.2 (cis) and 4.7 (trans) ppm (32). These values agree with ours. There are not many data in the literature on dinitrato amine complexes. The NH and H_1 chemical shifts of the cis compounds are more deshielded than the corresponding values for the trans isomers. These results are in agreement with the δ(Pt), where the cis compounds were observed at higher fields than the corresponding trans isomers. A larger reduction of electron density on the ligand in the cis compounds should be associated with a larger electron density on the platinum atom (δ(Pt) at higher fields). Therefore, the σ bonds seem stronger in the cis compounds than in the trans isomers.

For the chiral ligand, *sec*-butylamine, only one series of signals was observed in the ^{1}H NMR for both isomers. For the compound identified as *trans*-Pt($Et_2NH)_2(NO_3)_2$, two series of signals were observed as in ^{195}Pt NMR. The second series was assigned to the cis isomer as discussed above.

All the NH ^2J(^{195}Pt-^{1}H) coupling constants could be calculated. They are larger in the cis configuration where the average value is 67 Hz compared to 58 Hz (avg.) for the trans isomers. These values were found to be 67 Hz (cis) and 59 Hz (trans) for the corresponding diiodo complexes (11). The ^3J(^{195}Pt-^{1}H) coupling constants also depend on the geometry of the complex. They range between 35 and 47 Hz for the cis complexes and between 32 and 33 Hz for the trans compounds. These values are difficult to measure, since the signals are often multiplets of low intensity. These values agree with those reported for other similar complexes (11, 12, 17, 29, 33). One ^4J(^{195}Pt-$^1H_2$) coupling constant for *trans*-Pt(*t*-$BuNH_2)_2(NO_3)_2$ could be measured (15 Hz).

The ^{13}C NMR chemical shifts as well as the J(^{195}Pt-^{13}C) coupling constants are listed in Table 6. The ^{13}C NMR signals of C_1 and C_2 are more deshielded for the cis complexes than those of the trans analogues. This is consistent with the more upfield ^{195}Pt chemical shifts observed for the cis complexes and with the results obtained in ^{1}H NMR.

The ^2J(^{195}Pt-^{13}C) and ^3J(^{195}Pt-^{13}C) coupling constants are also dependent on the geometry of the compounds. For the

© 2004 NRC Canada

Table 6. $\delta(^{13}C)$ (ppm) and $J(^{195}Pt\text{-}^{13}C)$ (Hz) of $Pt(amine)_2(NO_3)_2$ in CD_3COCD_3.

Amine		C_1	C_2	C_3	C_4 or $C_{2'}$	$^2J(^{195}Pt\text{-}C_1)$	$^3J(^{195}Pt\text{-}C_2)$
$MeNH_2$	cis	34.460				25	
	trans	32.380				20	
$EtNH_2$	cis	43.172	15.776			24	42
	trans	41.229	15.487			19	30
n-$PrNH_2$	cis	50.017	24.336	11.177		20	40
	trans	48.241	24.084	11.329		16	29
n-$BuNH_2$	cis	48.028	33.199	20.344	13.970	21	39
	trans	46.146	32.942	20.466	14.030	16	26
i-$PrNH_2$	cis	50.123	23.198			22	30
	trans	48.514	23.076			15	26
i-$BuNH_2$	cis	55.693	*	20.101		21	
	trans	55.948		20.223		15	
sec-$BuNH_2$	cis	55.405	*	10.631	20.101	20	29
	trans	54.008		10.585	20.041	15	27
Me_2NH	cis	44.553				25	
	trans	42.883				18	
t-$BuNH_2$	trans	55.721	31.763			11	19
Et_2NH	cis‡	51.350	15.220			22	39
	trans	50.834	15.099			14	28

*Hidden by the solvent.
‡See text.

^3J the average value is 37 Hz for the cis complexes and 28 Hz for the trans isomers. The $^2J(^{195}Pt\text{-}^{13}C)$ coupling constants are smaller, probably because of inadequate orientation of the orbitals (30) as reported for other similar compounds. The average values are 18 Hz (cis) and 16 Hz (trans).

For the compound identified as *trans*-$Pt(Et_2NH)_2(NO_3)_2$, two series of signals were observed as in ^{195}Pt and ^1H NMR. The second series was assigned to the cis isomer as discussed above. For the chiral ligand, *sec*-butylamine, only one series of signals was observed in ^{13}C NMR for both isomers. For the diiodo analogues, some spectra with this ligand have shown two series of signals (11).

Acknowledgement

The authors are grateful to the Natural Sciences and Engineering Research Council of Canada (NSERC) for financial support of the project.

References

1. S.E. Miller and D.A. House. Inorg. Chim. Acta, **173**, 53 (1990).
2. M.J. Cleare and J.D. Hoeschele. Bioinorg. Chem. **2**, 187 (1974).
3. B. Rosenberg. Biochimie, **60**, 859 (1978).
4. B. Rosenberg. Cancer Chemother. Rep. **63**, 1433 (1979).
5. C.J. Boreham, J.A. Broomhead, and D.P. Fairlie. Aust. J. Chem. **34**, 659 (1981).
6. R. Faggiani, B. Lippert, C.J.L. Lock, and B. Rosenberg. J. Am. Chem. Soc. **99**, 777 (1977).
7. B. Lippert, C.J.L. Lock, B. Rosenberg, and M. Zvagulis. Inorg. Chem. **17**, 2971 (1978).
8. R. Faggiani, B. Lippert, C.J.L. Lock, and B. Rosenberg. Inorg. Chem. **16**, 1192 (1977).
9. R. Faggiani, B. Lippert, C.J.L. Lock, and B. Rosenberg. Inorg. Chem. **17**, 1941 (1978).
10. J.A. Stanko, L.S. Hollis, J.A. Schreifels, and J.D. Hoeschele. J. Clin. Hematol. Oncol. **7**, 138 (1977).
11. F.D. Rochon and V. Buculei. Inorg. Chim. Acta. In press.
12. J.-P. Souchard, F.L. Wimmer, T.B.T. Ha, and N.P. Johnson. J. Chem. Soc. Dalton Trans. 307 (1990).
13. K. Nakamoto. Infrared and Raman spectra of inorganic and coordination compounds. 5th Ed. John Wiley and Sons, New York. 1997.
14. S. Wimmer, P. Castan, F.L. Wimmer, and N.P. Johnson. J. Chem. Soc. Dalton Trans. 403 (1989).
15. J. R. Ferraro. J. Mol. Spectrosc. **4**, 99 (1960).
16. B. Lippert, C.J.L. Lock, B. Rosenberg, and M. Zvagulis. Inorg. Chem. **16**, 1525 (1977).
17. C. Tessier and F.D. Rochon. Inorg. Chim. Acta, **322**, 37 (2001).
18. T. Lind and H. Toftlund. Acta Chem. Scand. Ser. A, **A36**, 489 (1982).
19. T.B.T. Ha, F.L. Wimmer, J.P. Souchard, and N.P. Johnson. J. Chem. Soc. Dalton Trans. 1251 (1990).
20. G.B. Watt, B.B. Hutchinson, and D.S. Klett. J. Am. Chem. Soc. **89**, 2007 (1967).
21. J. Kritzenberger, F. Zimmerman, and A. Wokaun. Inorg. Chim. Acta, **210**, 47 (1993).
22. H.E. H.-Lock, C.J.L. Lock, G. Turner, and M. Zvagulis. Can. J. Chem. **59**, 2737 (1981).
23. D.D. Derrin. Dissociation constants of organic bases in aqueous solution. Butterworths, London. 1965. pp. 140–183.
24. J.P. Tollenaere and H. Moereels. Tetrahedron Lett. **15**, 1347 (1978).
25. A. Baeten, F. De Proft, and P. Geerlings. Chem. Phys. Lett. **235**, 17 (1995).
26. M.G. Hutchings and J. Gasteiger. Tetrahedron Lett. **24**, 2541 (1983).

© 2004 NRC Canada

27. K. Hiraoka. Can. J. Chem. **65**, 1258 (1987).
28. T.G. Appleton, A.J. Bailey, K.J. Barnham, and J.R. Hall. Inorg. Chem. **31**, 3077 (1992).
29. C. Tessier and F.D. Rochon. Inorg. Chim. Acta, **295**, 25 (1999).
30. F.D. Rochon, A.L. Beauchamp, and C. Bensimon. Can. J. Chem. **74**, 2121 (1996).
31. L.G. Marzilli, Y. Hayden, and M.D. Reily. Inorg. Chem. **25**, 974 (1986).
32. V. Cherchi, G. Faraglia, L. Sindellari, S. Sitran, A. Furlani, and V. Scarcia. Inorg. Chim. Acta, **155**, 267 (1989).
33. T.B.T. Ha, J.-P. Souchard, F.L. Wimmer, and N.P. Johnson. Polyhedron, **9**, 2647 (1990).

© 2004 NRC Canada

A new fluorous soluble Lewis acidic borane system

Horace Luong, Melanie D. Eelman, and Mark Stradiotto

Abstract: Treatment of trichlorovinylsilane with 3,3,4,4,5,5,6,6,7,7,8,8,8-tridecafluoro-1-octanol (3 equiv.) in the presence of excess triethylamine produces the fluorous vinylsilane, **1**, which can be isolated in 74% yield as an analytically pure oil. The addition of bis(pentafluorophenyl)borane to **1** produces the fluorous boranes, **2a**–**2b**, as an analytically pure, isomeric mixture of *anti*-Markovnikov and Markovnikov hydroboration products in 38% isolated yield. Compounds **2a**–**2b** are soluble in both arene solvents and perfluoro(methylcyclohexane). Treatment of **2a**–**2b** with excess trimethylphosphine generates a mixture of products, including the Lewis adduct, **3**, which can be isolated as an analytically pure oil in 15% yield. When exposed to either dimethylaminopyridine or piperidine at room temperature, the trimethylphosphine donor in **3** is cleanly displaced, based on in situ ^{31}P NMR studies; under similar conditions, triethylamine does not react with **3**. Addition of either dimethylaminopyridine or piperidine to **2a**–**2b**, followed by purification and subsequent treatment with an excess of either hydrogen chloride or *p*-toluenesulfonic acid, results in cleavage of the Si–O linkages and the regeneration of 3,3,4,4,5,5,6,6,7,7,8,8,8-tridecafluoro-1-octanol.

Key words: fluorous, borane, silane, Lewis acid.

Résumé : La réaction du trichlorovinylsilane avec du 3,3,4,4,5,5,6,6,7,7,8,8,8-tridécafluoroocatan-1-ol (3 équivalents), en présence d'un excès de triéthylamine, conduit à la formation du vinylsilane fluoré **1** qu'on peut isoler avec un rendement de 74 % sous la forme d'une huile analytiquement pure. L'addition de bis(pentafluorophényl)borane au composé **1** fournit les boranes fluorés **2a**–**2b**, analytiquement purs, qui correspondent au mélange d'isomère des produits d'hydroboration *anti*-Markovnikov et Markovnikov et qui sont obtenus avec un rendement de 38 % en produits isolés. Les produits **2a**–**2b** sont solubles tant dans les solvants aromatiques que dans le perfluoro(méthylcyclohexane). Le traitement du mélange des produits **2a**–**2b** à l'aide d'un excès de triméthylphosphine conduit à la formation d'un mélange de produits comportant le produit d'addition de Lewis, **3**, qui peut être isolé sous la forme d'une huile analytiquement pure, avec un rendement de 15 %. Sur la base d'études RMN du ^{31}P in situ, quand on le soumet à la température ambiante à de la diméthylaminopyridine ou à de la pipéridine, le donneur triméthylphosphine présent dans le composé **3** est complètement déplacé; dans des conditions semblables, la triéthylamine ne réagit pas avec le composé **3**. L'addition de diméthylaminopyridine ou de pipéridine au mélange **2a**–**2b**, suivie d'un traitement subséquent avec du chlorure d'hydrogène ou de l'acide *p*-toluènesulfonique conduit à un clivage des liaisons Si–O et à la régénération du 3,3,4,4,5,5,6,6,7,7,8,8,8-tridécafluoroocatan-1-ol.

Mots clés : fluoré, borane, silane, acide de Lewis.

[Traduit par la Rédaction]

Introduction

Since its introduction nearly a decade ago (1), fluorous biphasic catalysis (FBC) has emerged as a powerful and well-established methodology in synthetic chemistry (2). Under the standard FBC protocol, a perfluorocarbon or "fluorous" phase (containing an appropriately phase-labeled catalyst) is used in combination with an organic phase (containing the substrates and products). To sequester the catalytic agent to the fluorous phase, the catalyst must be phase-labeled with numerous perfluoroalkyl sidechains or "fluorous ponytails"; empirical studies indicate that at least 60% fluorine by weight is typically required to achieve *exclusive* fluorous solubility for a given molecule (3).[2] However, the efficient incorporation of such a large number of fluorinated chains into catalyst frameworks poses a considerable synthetic challenge, and virtually all of the FBC systems reported to date employ catalysts that have been permanently modified via covalent attachment of a fluorous phase-label. Though effective in providing a means of catalyst recovery, such an approach is inefficient in that unique labeling strategies must be developed for catalysts possessing different structural attributes.

In an effort to expand the utility and scope of fluorous biphasic techniques, we have recently initiated a research program directed towards the synthesis of new Lewis acidic

Received 3 November 2003. Published on the NRC Research Press Web site at http://canjchem@nrc.ca on 25 March 2004.

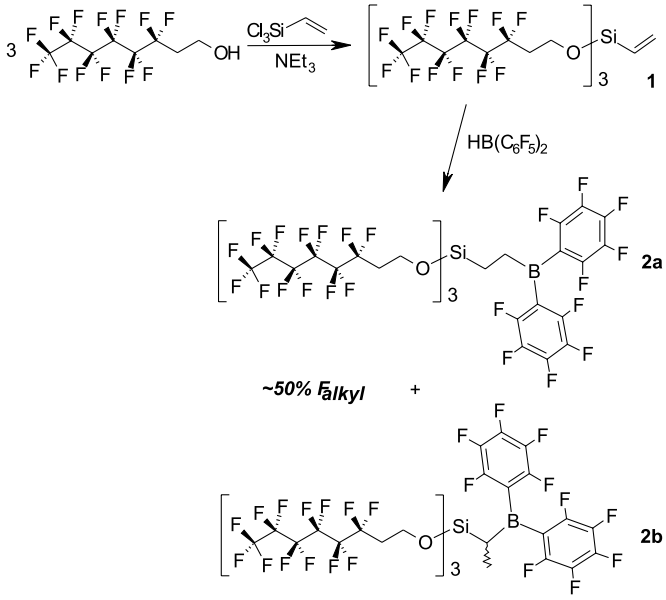
H. Luong, M.D. Eelman, and M. Stradiotto.[1] Department of Chemistry, Dalhousie University, Halifax, NS B3H 4J3, Canada.

[1]Corresponding author (e-mail: mark.stradiotto@dal.ca).

[2]It is worthy of mention that while the incorporation of extended perfluoroalkyl chains does impart fluorous solubility, fluorinated aryl groups do not; see ref. 2.

 doi: 10.1139/V04-018 © 2004 NRC Canada

Scheme 1. Hydroboration of the fluorous vinylsilane, **1**, producing **2a**–**2b**.



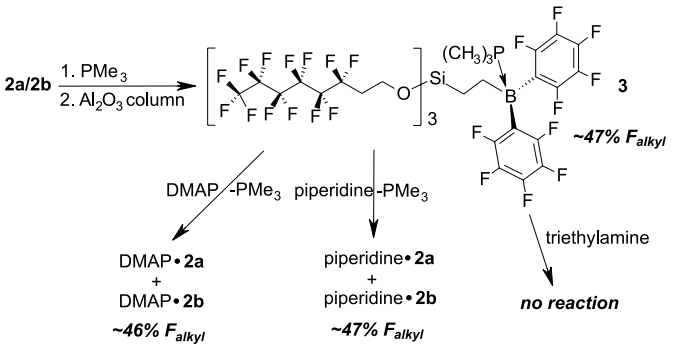
boranes, possessing chemical properties reminiscent of $B(C_6F_5)_3$, but that are compatible with a fluorous biphasic reaction system (4). In addition to the direct application of fluorous boranes as Lewis acid catalysts for organic transformations (5, 6) or as activators for transition-metal catalyst systems (7), we envision that Lewis acidic fluorous boranes may also function as a hitherto unknown class of fluorous phase-labels that could be reversibly attached to a Lewis basic pendant group (e.g., PR_2) built into the periphery of an appropriately designed transition metal catalyst (8). Herein we report our preliminary synthetic efforts in this area, including the synthesis and coordination chemistry of a new fluorous soluble, boron-centered Lewis acid system that is assembled via hydroboration.

Results and discussion

The synthesis of the target fluorous borane system (**2a**–**2b**) is summarized in Scheme 1 and begins with the dehydrohalogen coupling of 3,3,4,4,5,5,6,6,7,7,8,8,8-tridecafluoro-1-octanol with trichlorovinylsilane to yield the fluorous vinylsilane, **1**, in 74% isolated yield. Subsequent treatment of **1** in benzene with the bis(pentafluorophenyl)borane reagent developed by Piers and co-workers (9*a*) followed by biphasic extraction with perfluoro(methylcyclohexane) allowed for the isolation of an analytically pure mixture of *anti*-Markovnikov and Markovnikov hydroboration products (**2a**:**2b** ≈ 2:1, based on ^{1}H and ^{19}F NMR data) in 38% isolated yield. Examination of the combined benzene extracts revealed the presence of appreciable quantities of impure **2a**–**2b**, indicating that the perfluoroalkyl content (≈50% F_{alkyl} by weight) in this system is insufficient to promote exclusive fluorous solubility under biphasic conditions.

In contrast to the symmetrical nature of the terminal addition product, **2a**, the Markovnikov addition of $HB(C_6F_5)_2$ to **1** produces a stereogenic center that spans the boron and silicon fragments in **2b**. These structural differences are manifested in the observation of a symmetrical ^{1}H NMR resonance attributable to the OCH_2 linkage in **2a**, whereas in **2b** these hydrogen atoms are diastereotopic. The ^{11}B NMR resonance associated with **2a**–**2b** (42 parts per million (ppm)) is shifted to lower frequency relative to other $RB(C_6F_5)_2$ species (9*b*, 9*c*). Although we cannot rule out a dynamic process involving intramolecular coordination of oxygen and (or) fluorine atoms to the boron center, this chemical shift is not consistent with a typical four-coordinate adduct of the type $RB(C_6F_5)_2L$ (9, 10).

Scheme 2. Synthesis and phosphine displacement reactions involving **3**.



Piers and co-workers (9) have demonstrated that the initially formed hydroboration products generated when using $HB(C_6F_5)_2$ are often susceptible to thermal equilibration via retrohydroboration–hydroboration reaction sequences, leading to thermodynamic product mixtures. However, heating a mixture of **2a** and **2b** at 120 °C for several days resulted in no appreciable change in the ratio of these isomers, perhaps indicating that the energetic stability associated with the sterically less-congested isomer, **2a**, is somewhat offset by the stabilizing influence of the β-silyl fragment in **2b** (9*c*).

In an attempt to evaluate the feasibility of employing this new fluorous borane system as a reversibly bound fluorous phase-label (vide supra), the reactivity of **2a**–**2b** with Lewis bases was examined (Scheme 2). Treatment of **2a**–**2b** with excess trimethylphosphine in toluene initially produced a complex reaction mixture, from which the Lewis adduct, **3** (i.e., Me_3P·**2a**; ≈47% F_{alkyl} by weight), was isolated as an analytically pure oil in low yield (15%). Although we have been unable to characterize the side products formed in this reaction, it is conceivable that the addition of trimethylphosphine to **2a**–**2b** promotes retrohydroboration and (or) other unwanted reactions, leading to the degradation of **2a**–**2b** (9*b*).

The ability of nitrogen donors to displace the coordinated trimethylphosphine in **3** was examined. Treatment of **3** with a 30-fold excess of dimethylaminopyridine (DMAP) at room temperature resulted in the slow consumption of **3**, along with the clean production of free trimethylphosphine (^{31}P NMR). The displacement is approximately 30% complete after 6 h, and after 68 h the ^{31}P NMR resonance associated with **3** is no longer discernible. While similar results were obtained with piperidine, no reaction was observed between **3** and triethylamine after 68 h. Attempts to accelerate these displacement reactions by heating produced complex reaction mixtures. In the case of the DMAP and piperidine reactions, the ^{19}F NMR spectral data acquired from samples of the products generated upon completion of the displacement

© 2004 NRC Canada

were similar to those obtained from samples of **2a**–**2b** treated directly with amine. Unfortunately, we have not been able to isolate pure materials from these reactions. However, based on these observations we tentatively assign the displacement products formed upon treatment of either **2a**–**2b** or **3** with amines as a mixture composed primarily of LB·**2a** and LB·**2b** (LB = DMAP or piperidine). Attempts to regenerate **2a**–**2b** via protonolysis of the coordinated amine using an excess of either hydrogen chloride or *p*-toluenesulfonic acid were unsuccessful (11), resulting in the quantitative cleavage of the Si–O linkages, accompanied by the formation of free 3,3,4,4,5,5,6,6,7,7,8,8,8-tridecafluoro-1-octanol.

Summary

A "first-generation" fluorous borane system (**2a**–**2b**) that is comprised of approximately 50% F_{alkyl} by weight has been prepared by the addition of bis(pentafluorophenyl)borane to a new fluorous vinylsilane ponytail derived from commercially available 3,3,4,4,5,5,6,6,7,7,8,8,8-tridecafluoro-1-octanol. The Lewis acidic nature of **2a**–**2b** is evident in their ability to coordinate Lewis bases, which suggests that fluorous boranes of this type may ultimately find use as catalysts and (or) as reversibly bound phase-labels. However, while precise partition coefficients have not been measured, it is evident that **2a**–**2b** are sufficiently soluble in both organic and perfluorocarbon solvents so as to preclude their use within a strict FBC regime. In light of these preliminary results, we have undertaken the study of new and more robust classes of fluorous boranes that exceed 60% F_{alkyl} content by weight, which should exhibit exclusive solubility in fluorous media. Reports on these "second-generation" systems are forthcoming.

Experimental section

General considerations

All manipulations were conducted at room temperature in the absence of oxygen and water under an atmosphere of dinitrogen, either by using standard Schlenk methods or within an Innovative Technologies glove-box apparatus, and employed glassware that was oven dried (130 °C) and evacuated while hot prior to use. Unless otherwise stated, all materials were obtained from Aldrich and were used as received. Celite® was oven dried (130 °C) for 5 days and then evacuated for 24 h prior to use. Alumina (neutral, 150 mesh, activity Brockmann II) was degassed and dehydrated in vacuo for 48 h at temperatures between 200 and 300 °C and subsequently deactivated with 2% deionized water under argon prior to use. Solvents were dried and deoxygenated by refluxing for a minimum of 24 h under a flow of dinitrogen, in the presence of either sodium (for pentane, diethyl ether, and toluene) or potassium (for benzene). Benzophenone was added to the solvent – drying agent mixture to provide visual confirmation (i.e., the observed persistence of the benzophenone ketyl) that an appropriate level of purification had been achieved. The solvents used within the glove box were stored over activated 3 Å molecular sieves. Perfluoro(methylcyclohexane), 3,3,4,4,5,5,6,6,7,7,8,8,8-tridecafluoro-1-octanol, and C_6D_6 were degassed by three freeze-pump-thaw cycles and then dried over 3 Å molecular sieves for 24 h prior to use. Piperidine and $CDCl_3$ were each degassed by three freeze-pump-thaw cycles, dried over CaH_2 for 7 days, and distilled in vacuo. Triethylamine and trichlorovinylsilane were degassed by three freeze-pump-thaw cycles. Tris(pentafluorophenyl)borane, used in the preparation of bis(pentafluorophenyl)borane, was obtained from Boulder Scientific Company and was dried with chlorotrimethylsilane and purified by sublimation at 80 °C under dynamic vacuum; bis(pentafluorophenyl)borane in turn was prepared by using literature methods and was purified by washing with toluene (5 × 1 mL) at –30 °C and then was dried in vacuo for 18 h prior to use (9*b*). Unless otherwise stated, ^{1}H, ^{13}C, ^{19}F, and ^{31}P NMR data were collected at ambient temperature on a Bruker AC-250 spectrometer, at 250.1, 62.9, 235.3, and 101.3 MHz, respectively, while ^{11}B NMR spectra were recorded on an AVANCE 500-MHz NMR spectrometer at 160.5 MHz. Chemical shifts are reported in parts per million downfield of tetramethysilane (for ^{1}H and ^{13}C), BF_3 in diethyl ether (for ^{11}B, with peak width at half height in Hertz following the reported chemical shift), CCl_3F (for ^{19}F), and 85% H_3PO_4 in water (for ^{31}P). In some cases, fewer than expected independent ^{13}C NMR resonances were observed. Elemental analyses were performed by Desert Analytics (Tucson, Ariz.). Atmospheric pressure chemical ionization (APCI) mass spectra were obtained using a Finnigan LCQ Duo ion trap mass spectrometer. Samples were injected directly into the APCI source at a flow rate of 1.2 mL/h using toluene as the solvent with a source temperature of 473 K and collision energy of 0%. MS–MS spectra were obtained for the parent molecular ions using helium as the collision gas, and the collision energy was optimized for each sample.

CH_2=CHSi($OCH_2CH_2C_6F_{13}$)$_3$ (1)

Within a Schlenk flask containing a magnetic stir bar, 3,3,4,4,5,5,6,6,7,7,8,8,8-tridecafluoro-1-octanol (2.86 g, 7.86 mmol) was dissolved in 40 mL of diethyl ether. Triethylamine (2.0 mL, 14.3 mmol) was then added via syringe to the diethyl ether solution; the reaction flask was submersed within an ice bath, and the solution was stirred for 5 min. Trichlorovinylsilane (0.33 mL, 2.61 mmol) was then added dropwise via syringe over 5 min to the diethyl ether solution. Upon completion of the silane addition, the reaction mixture was allowed to warm to room temperature over 3 h while stirring. The solution was subsequently cannula filtered away from the precipitated white solid into a fresh Schlenk reaction flask. This reaction flask was then brought into the glove box, and the solution was filtered through a Pasteur pipette containing a Celite® plug. The resulting colorless solution was dried in vacuo for 24 h to yield **1** as a colorless oil (2.20 g, 1.92 mmol, 74%). ^{1}H NMR ($CDCl_3$) δ 6.26–5.77 (m, 3H, vinyl C*H*s), 4.08 (t, $^{3}J_{HH}$ = 6.6 Hz, 6H, $OCH_2CH_2CF_2$), 2.39 (t of t, $^{3}J_{HH}$ = 6.6 Hz, $^{3}J_{HF}$ = 18.5 Hz, 6H, $OCH_2CH_2CF_2$). $^{13}C\{^{1}H\}$ NMR ($CDCl_3$) δ 139.3 (vinyl *C*H), 126.9 (vinyl *C*H), 122.6–106.3 (m, CF_2s and CF_3), 55.7 ($OCH_2CH_2CF_2$), 33.9 (t, $^{2}J_{CF}$ = 21.2 Hz, $OCH_2CH_2CF_2$). $^{19}F\{^{1}H\}$ NMR (C_6D_6) δ –81.2 (s, CF_3), –113.8 (s, CF_2), –122.1 (s, CF_2), –123.1 (s, CF_2), –124.0 (s, CF_2), –126.5 (s, CF_2). APCI-MS *m*/*z* (*rel* intensity): 1144.9 (7, $[M]^+$). Anal. calcd. for $C_{26}H_{15}O_3F_{49}Si_1$ (%): C 27.29, H 1.32; found: C 27.56, H 1.51.

© 2004 NRC Canada

$(C_6F_5)_2BCH_2CH_2Si(OCH_2CH_2C_6F_{13})_3$ (2a) and $(C_6F_5)_2BCH(CH_3)Si(OCH_2CH_2C_6F_{13})_3$ (2b)

To a glass vial containing a stir bar, bis(pentafluorophenyl)borane (0.19 g, 0.55 mmol), and benzene (1 mL) was added a mixture of **1** (0.51 g, 0.45 mmol) in benzene (1 mL). The vial was then sealed with a PFTE-lined cap, and the solution was stirred for 2 h, after which the mixture was allowed to settle, forming a two-phase liquid–liquid system. The upper, benzene layer was then removed by using a Pasteur pipette. The remaining fluorous layer was washed with benzene (3 × 1 mL), and the volatiles in the remaining fluorous layer were removed in vacuo to yield an isomeric mixture of **2a** and **2b** (≈2:1 based on ^{1}H and ^{19}F NMR data) as a clear colorless oil (0.31 g, 0.21 mmol, 38%).

Data for 2a

^{1}H NMR (C_6D_6) δ 3.84 (t, $^3J_{HH}$ = 6.3 Hz, $OCH_2CH_2CF_2$), 2.31–1.82 (m, $OCH_2CH_2CF_2$), 1.66 (t, $^3J_{HH}$ = 7.6 Hz, $SiCH_2$ or BCH_2), 0.70 (t, $^3J_{HH}$ = 7.6 Hz, BCH_2 or $SiCH_2$). ^{19}F{^{1}H} NMR (C_6D_6) δ –82.1 (s, CF_3), –114.9 (s, CF_2), –123.0 (s, CF_2), –124.0 (s, CF_2), –124.8 (s, CF_2), –127.3 (s, CF_2), –133.7 (m, aryl C*F*), –153.4 (m, aryl C*F*), –163.0 (m, aryl C*F*).

Data for 2b

^{1}H NMR (C_6D_6) δ 4.24–3.75 (m, $OCH_2CH_2CF_2$), 2.63 (quart., $^3J_{HH}$ = 6.4 Hz, $CHCH_3$), 2.37–1.86 (m, $OCH_2CH_2CF_2$), 1.15 (d, $^3J_{HH}$ = 6.4 Hz, $CHCH_3$). ^{19}F{^{1}H} NMR (C_6D_6) δ –82.1 (s, CF_3), –114.5 (s, CF_2), –123.0 (s, CF_2), –124.0 (s, CF_2), –124.8 (s, CF_2), –127.3 (s, CF_2), –131.6 (m, aryl C*F*), –149.3 (m, aryl C*F*), –162.3 (m, aryl C*F*).

Data for 2a and 2b

^{13}C{^{1}H} NMR (C_6D_6) δ 150.2–135.1 (m, aryl *C*Fs), 121.1–107.4 (m, *C*F_2s and *C*F_3), 57.8–55.0 (m), 34.2–33.4 (m), 26.5, 15.4 (m), 12.2 (m), 8.1. ^{11}B{^{1}H} NMR (C_6D_6) δ 42 (310). APCI-MS *m/z* (*rel* intensity): 1490.6 (23, $[M]^+$). Anal. calcd. for $C_{38}H_{16}B_1O_3F_{49}Si_1$ (%): C 30.62, H 1.08; found: C 30.31, H 1.15.

$(CH_3)_3P\cdot(C_6F_5)_2BCH_2CH_2Si(OCH_2CH_2C_6F_{13})_3$ (3)

To a glass vial containing a magnetic stir bar and a freshly prepared sample of **2a**–**2b** (0.15 g, 0.10 mmol) was added excess trimethylphosphine (0.3 mL of a 1.0 mol L^{-1} toluene solution, 0.3 mmol) via syringe. The solution was stirred for 1 h and then dried in vacuo for 2 h to yield a colorless, opaque oil. ^{1}H NMR analysis of this crude oil indicated the formation of a complex reaction mixture. The crude product was then emulsified with pentane (3 mL) and passed through a Pasteur pipette alumina column (5 cm). Perfluoro(methylcyclohexane) (1 mL) was then added to the eluent collected in a fresh glass vial, and the resulting mixture was emulsified by using a Pasteur pipette before sealing the vial with a PFTE-lined cap and storing the vial at –30 °C for 10 min. The upper organic layer was separated from the lower fluorous layer by using a Pasteur pipette. The product-containing fluorous layer was then washed with benzene (3 × 1 mL), and the fluorous solvent and other volatiles in the residual fluorous layer were removed in vacuo to yield **3** as a transparent orange oil (0.061 g, 0.04 mmol, 15%). ^{1}H NMR (C_6D_6) δ 3.87 (t, $^3J_{HH}$ = 6.1 Hz, 6H, $Si(OCH_2CH_2C_6F_{13})_3$), 2.07 (t of t, $^3J_{HH}$ = 6.1 Hz, $^3J_{HF}$ = 18.6 Hz, 6H, $Si(OCH_2CH_2C_6F_{13})_3$), 1.24–1.05 (m, 2H, BCH_2 or $SiCH_2$), 0.63–0.45 (m, 2H, $SiCH_2$ or BCH_2), 0.53 (d, $^2J_{PH}$ = 11.0 Hz, 9H, $P(CH_3)_3$). ^{13}C{^{1}H} NMR (C_6D_6) δ 149.2–134.6 (m, aryl *C*Fs), 119.5–109.1 (m, *C*F_2s and *C*F_3), 55.8 ($OCH_2CH_2CF_2$), 34.0 (t, $^2J_{CF}$ = 21.1 Hz, $OCH_2CH_2CF_2$), 12.3 (m, BCH_2 or $SiCH_2$), 9.1 (d, $^1J_{PC}$ = 37.1 Hz, $P(CH_3)_3$), 6.8 (m, $SiCH_2$ or BCH_2). ^{19}F{^{1}H} NMR (C_6D_6) δ –82.2 (s, CF_3), –114.6 (s, CF_2), –123.0 (s, CF_2), –124.0 (s, CF_2), –124.8 (s, CF_2), –127.3 (s, CF_2), –131.8 (d, $^3J_{FF}$ = 24.0 Hz, CF_{ortho}), –158.1 (t, $^3J_{FF}$ = 20.7 Hz, CF_{para}), –163.9 (m, CF_{meta}). ^{31}P{^{1}H} NMR (C_6D_6) δ –9.6 (m). ^{11}B{^{1}H} NMR (C_6D_6) δ –13.1 (m, 320). APCI-MS *m/z* (*rel* intensity): 1565.7 (23, $[M]^+$). Anal. calcd. for $C_{41}H_{25}B_1O_3F_{49}Si_1P_1$ (%): C 22.25, H 1.61; found: C 22.01, H 1.79.

Treatment of 2a–2b with DMAP

A glass vial containing a magnetic stir bar was charged with **2a**–**2b** (0.35 g, 0.24 mmol) and a solution of DMAP (0.029 g, 0.24 mmol) in benzene (1 mL), followed by stirring for 24 h. Perfluoro(methylcyclohexane) (0.5 mL) was then added to the reaction mixture, and the biphasic mixture was emulsified for 1 min by using a Pasteur pipette. The mixture was then allowed to settle, and the upper benzene layer was removed by using a Pasteur pipette. The remaining fluorous material was again treated with benzene (2 × 0.5 mL) and emulsified, and the organic and fluorous layers were separated. Drying of the residual fluorous layer in vacuo for 6 h yielded a dark yellow oil (0.062 g), which we tentatively assign as a mixture of DMAP·**2a** and DMAP·**2b** (≈2:1 based on ^{1}H and ^{19}F NMR data). Drying of the combined organic extracts in vacuo for 6 h yielded a similar mixture of DMAP·**2a** and DMAP·**2b**, along with a small amount (<10%) of unreacted DMAP (0.134 g). Attempts to separate DMAP·**2a** and DMAP·**2b** by use of column chromatography on alumina were unsuccessful.

Data for DMAP·2a

^{1}H NMR (C_6D_6) δ 7.92 (m, aryl C*H*), 5.55 (m, aryl C*H*), 3.99 (t, $^3J_{HH}$ = 6.3 Hz, $OCH_2CH_2CF_2$), 2.14 (t of t, $^3J_{HH}$ = 6.3 Hz, $^3J_{HF}$ = 18.9 Hz, $OCH_2CH_2CF_2$), 1.87 (s, NCH_3), 1.70 (m, $SiCH_2$ or BCH_2), 0.69 (m, BCH_2 or $SiCH_2$). ^{19}F{^{1}H} NMR (C_6D_6) δ –82.1 (s, CF_3), –114.4 (s, CF_2), –122.9 (s, CF_2), –123.9 (s, CF_2), –124.7 (s, CF_2), –127.2 (s, CF_2), –133.5 (m, aryl C*F*), –159.3 (m, aryl C*F*), –164.6 (m, aryl C*F*).

Data for DMAP·2b

^{1}H NMR (C_6D_6) δ 7.92 (m, aryl C*H*), 5.55 (m, aryl C*H*), 3.85 (m, $OCH_2CH_2CF_2$), 2.03 (m, $OCH_2CH_2CF_2$), 1.93 (s, NCH_3), 1.13 (d, $^3J_{HH}$ = 7.0 Hz, $CHCH_3$). ^{19}F{^{1}H} NMR (C_6D_6) δ –82.1 (s, CF_3), –114.8 (s, CF_2), –122.9 (s, CF_2), –123.9 (s, CF_2), –124.7 (s, CF_2), –127.2 (s, CF_2), –131.9 (m, aryl C*F*), –160.1 (m, aryl C*F*), –165.1 (m, aryl C*F*).

Data for DMAP·2a and DMAP·2b

^{13}C{^{1}H} NMR (C_6D_6) δ 155.2, 151.1, 147.3, 144.6, 135.1–110.4 (m), 106.7, 106.4, 55.9, 38.4, 34.3 (t, $^1J_{CF}$ = 21.0 Hz), 33.9, 15.4 (m), 11.3, 5.9.

© 2004 NRC Canada

Treatment of 2a–2b with piperidine

To a Schlenk flask containing a magnetic stir bar, **2a**–**2b** (0.49 g, 0.33 mmol), and hexanes (3 mL) was added piperidine (0.04 mL, 0.40 mmol) dropwise via syringe. The mixture was stirred for 1 h, and then the volatiles were removed in vacuo over 2 h. The Schlenk flask containing the crude product was then sealed and transferred to the glovebox. Within the glovebox, the crude product was treated with perfluoro(methylcyclohexane) (1.5 mL) and toluene (1.5 mL), and the resulting biphasic mixture was transferred to a glass vial, which was sealed with a PFTE-lined cap, manually shaken for 1 min, and then stored at –30 °C for 20 min. The upper toluene layer was separated from the lower fluorous layer by using a Pasteur pipette. The remaining fluorous material was again treated with toluene (3 × 1 mL) and emulsified, and the organic and fluorous layers were separated. Drying of the residual fluorous layer in vacuo for 6 h yielded an orange oil (0.252 g), which we tentatively assign as a mixture of piperidine·**2a** and piperidine·**2b**; drying of the combined organic extracts in vacuo for 6 h yielded a similar mixture of piperidine·**2a** and piperidine·**2b** (0.059 g). Attempts to separate piperidine·**2a** and piperidine·**2b** by use of column chromatography on alumina were unsuccessful and resulted in decomposition.

Data for piperidine·2a and piperidine·2b

^{1}H NMR (C_6D_6) δ 4.39–3.60 (m), 3.36 (m), 3.11 (m), 2.77 (m), 1.84 (m), 1.63–0.21 (m). ^{13}C{^{1}H} NMR (perfluoro(methylcyclohexane), 125 MHz) δ 56.9–56.2 (m), 51.6–49.0 (m), 35.2–33.9 (m), 26.8–26.3 (m), 23.6, 9.8, 7.0–6.7 (m). ^{19}F{^{1}H} NMR (C_6D_6) δ –82.2 (s, CF_3, piperidine·**2a** and piperidine·**2b**), –114.6 (s, CF_2, piperidine·**2a** or piperidine·**2b**), –114.9 (s, CF_2, piperidine·**2b** or piperidine·**2a**), –123.0 (s, CF_2, piperidine·**2a** and piperidine·**2b**), –124.0 (s, CF_2, piperidine·**2a** and piperidine·**2b**), –124.8 (s, CF_2, piperidine·**2a** and piperidine·**2b**), –127.3 (s, CF_2, piperidine·**2a** and piperidine·**2b**), –133.5 (m, aryl C*F*, piperidine·**2a** and piperidine·**2b**), –158.0 (m, aryl C*F*, piperidine·**2a** and piperidine·**2b**), –163.7 (m, aryl C*F* piperidine·**2a** and piperidine·**2b**).

General procedure for displacement reactions involving 3 and nitrogen donors

Within a glass vial, a sample of **3** (≈0.03 g) dissolved in benzene (0.5 mL) was treated with a 30-fold excess of triethylamine, piperidine, or DMAP. The mixture was immediately transferred to a resealable NMR tube by using a Pasteur pipette, and the progress of the displacement reaction was monitored based on ^{19}F and ^{31}P NMR data. Prior to the acquisition of NMR data, the reaction mixture contained within the NMR tube was mixed vigorously for approximately 30 s.

General procedure for the treatment of LB·2a–LB·2b with acid (LB = DMAP or piperidine)

A Schlenk flask containing a magnetic stir bar was charged with either DMAP·**2a**–DMAP·**2b** or piperidine·**2a**–piperidine·**2b** (≈0.01 g, prepared by the addition of **2a**–**2b** to the nitrogen donor as described above), benzene (0.5 mL), and a 20-fold excess of either hydrogen chloride (from a 2.0 mol L^{-1} solution in diethyl ether) or *p*-toluenesulfonic acid. The reaction flask was then sealed, and the mixture was stirred for approximately 1 h, followed by removal of the solvent and other volatile materials in vacuo over 1 h to yield a white solid. This solid was then treated with C_6D_6 (1 mL), and the resulting suspension was filtered through a Pasteur pipette containing a Celite® plug and examined by use of ^{1}H NMR spectroscopic techniques.

Acknowledgements

This research was supported by an award from Research Corporation (RI0932), as well as the Natural Sciences and Engineering Research Council of Canada (NSERC), the Canada Foundation for Innovation, the Nova Scotia Research and Innovation Trust Fund, and Dalhousie University. M.D.E. thanks NSERC and MDS Sciex for an industrial postgraduate scholarship. We also thank Dr. Michael Lumsden and Dr. Bob Berno (Atlantic Region Magnetic Resonance Centre, Dalhousie University) for assistance in the acquisition of NMR data and the Dalhousie University Mass Spectrometry Centre for the use of instrumentation.

References

1. (*a*) I.T. Horváth and J. Rábai. Science (Washington, D.C.), **266**, 72 (1994); (*b*) J.A. Gladysz. Science (Washington, D.C.), **266**, 55 (1994).
2. (*a*) B. Cornils. Angew. Chem. Int. Ed. Engl. **36**, 2057 (1997); (*b*) I.T. Horváth. Acc. Chem. Res. **31**, 641 (1998); (*c*) E. de Wolf, G. van Koten, and B.-J. Deelman. Chem. Soc. Rev. **28**, 37 (1999); (*d*) L.P. Barthel-Rosa and J.A. Gladysz. Coord. Chem. Rev. **190–192**, 587 (1999); (*e*) D.J. Cole-Hamilton. Science (Washington, D.C.), **299**, 1702 (2003).
3. For a recent exception to the "60%" rule, see: M.L. Clarke. J. Organomet. Chem. **665**, 65 (2003).
4. Fluorous borates have been reported, see: J. van den Broeke, M. Stam, M. Lutz, H. Kooijman, A. L. Spek, B.-J. Deelman, and G. van Koten. Eur. J. Inorg. Chem. 2798 (2003), and refs. therein.
5. W.E. Piers and T. Chivers. Chem. Soc. Rev. 345 (1997).
6. For recent examples of transition-metal- and lanthanide-based fluorous Lewis acids, see: (*a*) K. Mikami, Y. Mikami, Y. Matsumoto, J. Nishikido, F. Yamamoto, and H. Nakajima. Tetrahedron Lett. **42**, 289 (2001); (*b*) Y. Nakamura, S. Takeuchi, K. Okumura, Y. Ohgo, and D.P. Curran. Tetrahedron, **58**, 3963 (2002); (*c*) A.G.M. Barrett, N. Bouloc, D.C. Braddock, D. Catterick, D. Chadwick, A.J.P. White, and D.J. Williams. Tetrahedron, **58**, 3835 (2002); for a recent example of a main group (Group 4) fluorous Lewis acid system, see: X. Hao, O. Yamazaki, A. Yoshida, and J. Nishikido. Tetrahedron Lett. **44**, 4977 (2003).
7. E. Y.-X. Chen and T.J. Marks. Chem. Rev. **100**, 1391 (2000).
8. The temporary incorporation of fluorous phase-labels that are covalently linked to organic substrates (not transition-metal catalysts) has been exploited by Curran and co-workers; for selected examples, see: (*a*) A. Studer, S. Hadida, R. Ferritto, S.Y. Kim, P. Jeger, P. Wipf, and D.P. Curran. Science (Washington, D.C.), **275**, 823 (1997); (*b*) D.P. Curran. Angew. Chem. Int. Ed. **37**, 1174 (1998); (*c*) Z. Luo, Q. Zhang, Y. Oderaotoshi, and D.P. Curran. Science (Washington, D.C.), **291**, 1766 (2001); (*d*) H. Nakamura, B. Linclau, and D.P. Curran. J. Am. Chem. Soc. **123**, 10 119 (2001).
9. (*a*) D.J. Parks, R.E. v H. Spence, and W.E. Piers. Angew. Chem. Int. Ed. Engl. **34**, 809 (1995); (*b*) D.J. Parks, W.E.

© 2004 NRC Canada

Piers, and G.A.P. Yap. Organometallics, **17**, 5492 (1998); (*c*) D.J. Parks and W.E. Piers. Tetrahedron, **54**, 15 469 (1998).
10. A.K. Dash and R.F. Jordan. Organometallics, **21**, 777 (2002).
11. K. Niedenzu and J.W. Dawson. *In* The chemistry of boron and its compounds. *Edited by* E.L. Muetterties. John Wiley & Sons, New York. 1976. Chap 7.

© 2004 NRC Canada

Diastereoselectivity in intramolecular ene cyclisation — A theoretical study

Nityagopal Mondal, Sannyasi Charan Mandal, and Gourab Kanti Das

Abstract: Diastereoselectivity in unactivated and activated ene cyclisation can be predicted using HF/6-31G(d) optimized geometry of the transition states. Relative energies of different conformations of the transition states, calculated using DFT, can be used for the prediction of product ratios. It was found that the dihedral angle around the forming carbon–carbon bond controls the cis–trans diastereoselectivity. A set of three model pericyclic transition structures has been proposed that mimics the activation process of ene cyclisation.

Key words: intramolecular ene reaction, ab initio, DFT.

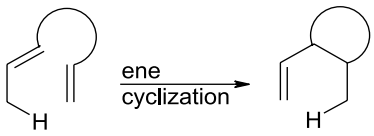
Résumé : Utilisant une géométrie optimisée au niveau HF/6-31G(d) des états de transition, il est possible de prédire la diastéréosélectivité des cyclisations ènes activées et non activées. Les énergies relatives des diverses conformations des états de transition, calculées à l'aide de la méthode DFT, peuvent être utilisées pour prédire les rapports de produits. On a trouvé que l'angle dièdre autour la liaison carbone–carbone qui se forme contrôle le diastéréosélectivité cis–trans. On propose un ensemble de trois structures de transition péricycliques modèles reflète bien le processus d'activation de la cyclisation ène.

Mots clés : réaction ène intramoléculaire, ab initio, DFT.

[Traduit par la Rédaction]

Introduction

Intramolecular ene cyclisation is a useful tool for the synthesis of five- or six-membered compounds in organic synthesis (1).



The presence of an activating substituent (electron-withdrawing group) in the reactant makes the reaction occur at low temperature (2). Various examples show that the diastereoselectivity depends on the nature of the activating group present in the reactant (3). Proper rationalization of the diastereoselectivity in this reaction is sometimes very difficult.

Theoretical work by Houk and co-workers (3, 4) revealed that the ratio of diastereomeric products in an unactivated ene cyclisation can be predicted nicely with the help of a rigid transition structure. The transition states (TSs) of various ene cyclisations were constructed by connecting a carbon tether to the transition structure of the basic ene reaction (4) in four possible ways (Fig. 1) (3).

The product ratios, obtained by a Boltzmann distribution of the TSs, were found to be in good agreement with the experimentally observed one. However, this approach fails to explain the variation of diastereoselectivity in the cyclisation process when an activating group is present in the reactant. The authors pointed out the fact that the presence of an activating group may deform the basic transition state, which was not considered in the rigid approximation.

Later on, our theoretical study (5) showed that the AM1 semiempirical approximation is, to some extent, capable of predicting the diastereoselectivity in an activated ene cyclisation. It also showed that the TSs obtained from binding modes (*1*), (*2*), and (*3*) (Fig. 1) are sufficient to predict the actual diastereoselectivity, without considering the TSs of the strained mode (*4*). However, the AM1 method is not accurate enough to predict the course of unactivated cyclisation using Houk's rigid model (3).

Meanwhile, another theoretical study (6) on the basic ene reaction revealed that the calculated activation energy, using density functional theory (DFT) on the HF/6-31G(d) optimized geometry, was in good agreement with the experimentally observed one.

In this report, it is shown that single point energies from DFT calculations on the HF/6-31G(d) optimized transition structures in ene cyclisation can be used for the prediction of diastereomeric product ratios in both unactivated and activated cyclisation processes. It is also shown that a small change of a particular dihedral angle in the basic transition structure (effected by a substituent) results in significant change in the diastereoselectivity of the corresponding ene

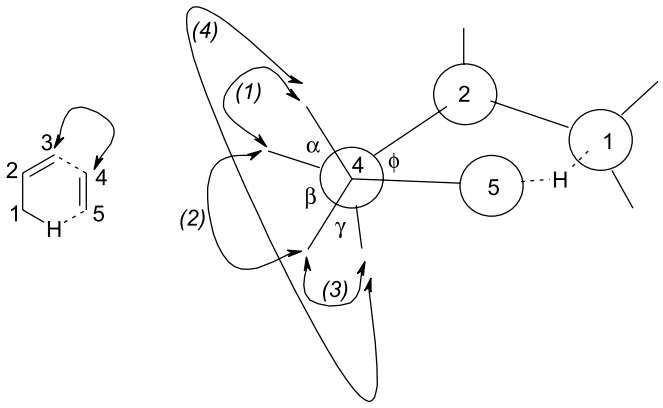
Received 25 July 2003. Published on the NRC Research Press Web site at http://canjchem.nrc.ca on 25 March 2004.

N. Mondal, S.C. Mandal, and G.K. Das.[1] Department of Chemistry, Visva-Bharati, Santiniketan-731235, West Bengal, India.

[1]Corresponding author (e-mail: bubuldas@hotmail.com).

 doi: 10.1139/V04-002 © 2004 NRC Canada

Fig. 1. Possible binding modes in the transition structure of the basic ene reaction to form the TSs of ene cyclisation.



cyclisation. Finally, some model pericyclic processes are proposed that mimic the variation in geometry of the TS and activation energy of the ene cyclisation.

Computational methods

All TSs were optimized at the HF/6-31G(d) level and single point energies were calculated by B3LYP/6-31G(d) DFT. GAMESS (7) software was used for optimization of the structure and calculation of energies. All structures were characterized by frequency analysis.

Results and discussion

Studies on the TSs of the ene cyclization

The reactions that we have studied are shown in Table 1. The generalized TSs (Fig. 2), produced from the reactants of Table 1, were constructed using binding modes (*1*), (*2*), and (*3*) of Fig. 1.

Energies and some relevant dihedral angles of the actual TSs are collected in Table 2. It is evident that TSs obtained from modes (*1*) and (*3*) give cis product while that from mode (*2*) gives trans product (Fig. 2). The product proportions were calculated, using a Boltzmann distribution, on the basis of the relative energies (Table 2) of the corresponding transition states and are shown in Table 1.

The first five entries in Tables 1 and 2 are the examples of ene cyclisation in unactivated molecules. Isomers (cis and trans) of 1,6-octadiene, its 7-methyl and 3,7-dimethyl derivatives are taken as reactants. Other entries represent the reactants with an activating group. We have inserted an aldehyde (entries 6, 8, 10, and 12) or a carboxylic acid group (entries 7, 9, 11, 13, 14, and 15) as an activating group at the enophile part of the reactant in cis or in trans orientation. The experimental results of the product ratios are shown in those cases where it is available in the literature (entries 1–5, 14, and 15 in Table 1). Although we have not found any actual experimental results in the literature for the reactions of entries 6–13, some similar reactions with similar configurations of reactants have been reported (1*f*, 1*g*). These observations support the fact that the cis product is exclusively formed from a reactant where the ene part is in the cis configuration (as in reactants of entries 10–13) and a mixture of cis and trans products is formed when the ene part in the reactant is in the trans configuration (as in reactants of entries 6–9). We have approximated the carbomethoxy group by the carboxylic group in our theoretical study (in entries 14 and 15).

Table 1 shows that only cis products are obtained experimentally in an unactivated reaction (entries 1–5), though theoretical results express the possibility of the formation of trans products in a very low percentage in some situations. The presence of an activating group in the reactant (entries 6–9, 14, 15) promotes cyclisation reactions to produce trans products in higher percentages (in 10–13, the formation of a TS with binding mode (*2*), which is necessary for the formation of a trans product, is not possible). This tendency increases when the activating group is placed in cis orientation in the reactant (entries 7 and 14). Comparison of product ratios in 7 and 14 and 9 and 15 clearly reveals that the presence of an extra methyl group in reactants 14 and 15 leads to the formation of the trans product in higher proportion.

A rough correlation may be observed between the variation of proportion of trans product for different reactants and the variation of the dihedral angle of the corresponding TS in binding mode (*2*) (ϕ) (Fig. 2). Table 2 shows that ϕ of the TS is always smaller in unactivated than in activated cyclisation. In unactivated cases a maximum value of ϕ is 53.6° (entry 1), whereas for activated reactions, the minimum value of the same is 53.9° (entry 6). The reactant, acquiring a maximum ϕ value in the TS (entry 14 in Table 2), also shows formation of a maximum percentage of trans product in a cyclisation reaction (entry 14 in Table 1). Comparison between the entries in 7 and 14 reveals that the presence of an extra methyl group in the ene part of the reactant R = CH_3) also shows a tendency to produce TSs with larger ϕ angles. However, this is not the case in entries 9 and 15.

It was pointed out by Houk and co-workers (3) that the formation of the trans product in higher proportion in activated cyclization is due to the deformation of the basic transition structure of the ene reaction, which results from the increased dihedral angle (ϕ) around the forming C—C bond. As ϕ increases the opposite angle (β) decreases (Fig. 1). As a result, the carbon tether in binding mode (*2*) suffers from less strain in the formation of the TS, which ultimately reduces its relative energy. This reduction of relative energy makes the TS more favorable and increases the possibility of the formation of the trans product.

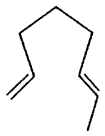
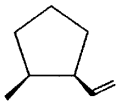
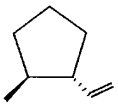
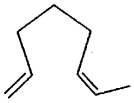
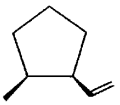
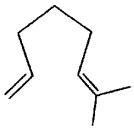
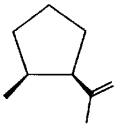
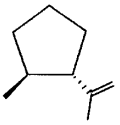
Studies on the TSs of the basic intermolecular ene process

To investigate the role of the dihedral angle in detail, we studied the basic TS with and without some activating groups and without binding any carbon tethers (Fig. 3).

Table 3 shows the dihedral angles ϕ, α, β, and γ for the basic transition structures. The activating groups selected are an aldehyde, a carboxylic acid, and a carbomethoxy group. Dihedral angles shown in parenthesis are for those TSs that contain a methyl group at the 2-position (R = CH_3). Comparison of the dihedral angles of entry 1 (unactivated TS) with others reveals that the presence of an activating substituent at the endo (R_2) or exo (R_1) position always increases ϕ, and consequently, the opposite dihedral angle β decreases. The change of ϕ after the insertion of a Me

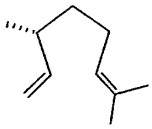
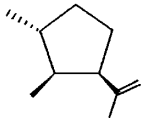
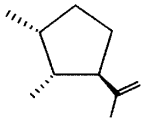
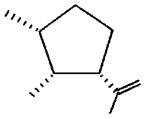
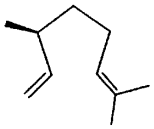
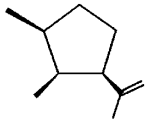
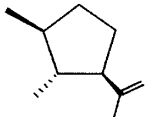
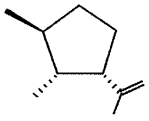
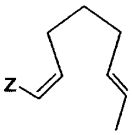
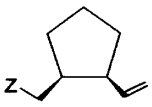
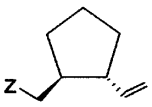
© 2004 NRC Canada

Table 1. Ene cyclisation of 1,6-diene with or without activating substituents.

	Reactant		Products		
			1	2	3
1		457°C			
		6-31G(d)	96%	4%	
		B3LYP	96%	4%	
		Exp (Ref. 8)	Only *cis*		
2		457°C			
		6-31G(d)	Only *cis*		
		B3LYP	Only *cis*		
		Exp (Ref. 8)	Only *cis*		
3		457°C			
		6-31G(d)	95%	5%	
		B3LYP	96%	4%	
		Exp (Ref. 8)	Only *cis*		

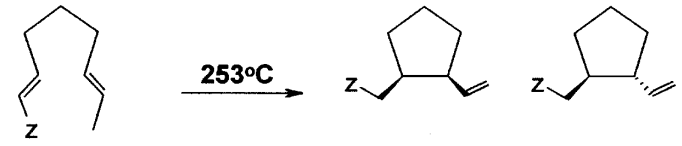
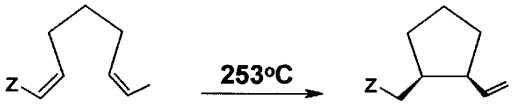
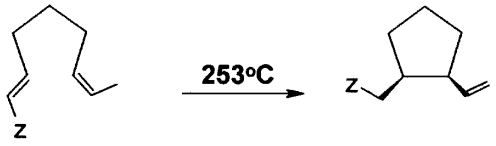
© 2004 NRC Canada

Table 1 (*continuing*).

	Reactant		Products		
			1	**2**	**3**
4		**480°C** →			
		6-31G(d)	~85%	~2%	~12%
		B3LYP	80%	3%	17%
		Exp (Ref. 9)	73%	-	27%
5		**450°C** →			
		6-31G(d)	6%	7%	87%
		B3LYP	9%	7%	85%
		Exp (Ref. 10)	25%	-	75%
		**253°C** →			
6	Z=CHO	6-31G(d)	95%	5%	
		B3LYP	91%	9%	
7	Z=COOH	6-31G(d)	87%	13%	
		B3LYP	74%	26%	

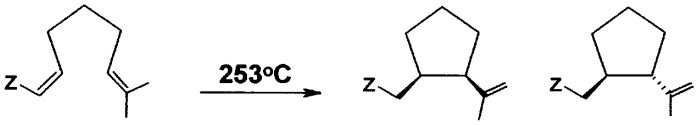
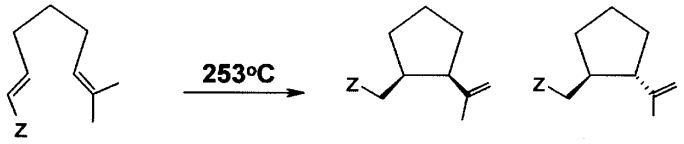
© 2004 NRC Canada

Table 1 (*continuing*).

	Reactant		Products		
			1	2	3
					
8	Z=CHO	6-31G(d)	95%	5%	
		B3LYP	90%	10%	
9	Z=COOH	6-31G(d)	95%	5%	
		B3LYP	94%	6%	
					
10	Z=CHO	6-31G(d)	Only *cis*		
		B3LYP	Only *cis*		
11	Z=COOH	6-31G(d)	Only *cis*		
		B3LYP	Only *cis*		
					
12	Z=CHO	6-31G(d)	Only *cis*		
		B3LYP	Only *cis*		
13	Z=COOH	6-31G(d)	Only *cis*		
		B3LYP	Only *cis*		

© 2004 NRC Canada

Table 1 (*concluded*).

	Reactant		Products		
			1	**2**	**3**
14					
	Z=COOH	6-31G(d)	63%	37%	
		B3LYP	58%	42%	
	Z=COOMe	Exp (Ref. 11)	43%	57%	
15					
	Z=COOH	6-31G(d)	76%	24%	
		B3LYP	79%	21%	
	Z=COOMe	Exp (Ref. 11)	76%	24%	

© 2004 NRC Canada

Fig. 2. Three transiton structures in three possible binding modes and the configuration of the cyclised products formed.

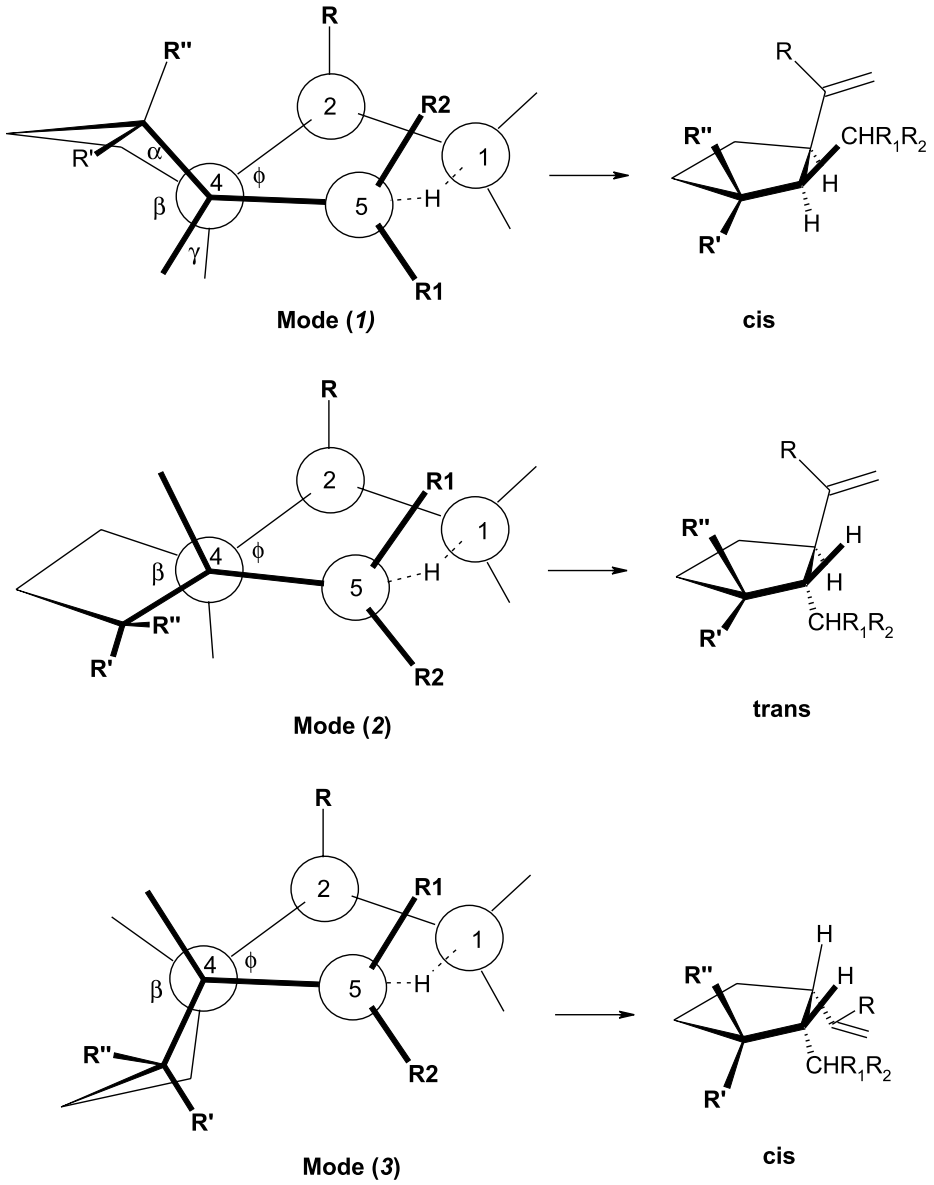
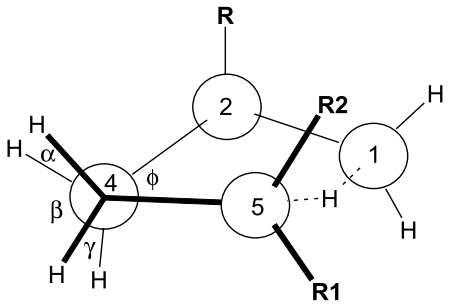


Fig. 3. TS of the basic ene reaction.



substituent at the 2-position of the TS is also interesting. For all activating substituents this change of ϕ value is about +1° to +3° except for entries 5 and 7. The presence of a carboxy (entry 5) or carbomethoxy (entry 7) group at the endo position causes a large increase of ϕ because of the incorporation of a methyl group at the 2-position (7.2° and 7.6° for entries 5 and 7, respectively). This clearly indicates that a strong steric repulsion develops between R and R_2 when R_2 is bulky (Fig. 3). Being a smaller substituent, the aldehyde group is unable to show this effect. We may put forward this idea to explain the formation of a higher proportion of trans products in cyclisation of the cis-carboxyl derivatives in Table 1 (entries 7 and 14). A steric effect between the carbon tether or methyl group (at the 2-position of the TS) and the activating group facilitates the increase in the relative stabilization of the TS of binding mode (*2*) and directs the formation of the product ratio to more of the trans isomer.

Model reactions mimic the activation process

A set of three ene-type pericyclic reactions (Scheme 1) showed a similar increase in the ϕ dihedral angle in their TSs.

© 2004 NRC Canada

Table 2. Energies and relevant dihedral angles of the TSs for ene cyclisation of the derivatives of 1,6-dienes with or without activating substituent (Table 1). Absolute energies are ZPE-uncorrected.

	Transition structure (Fig. 2)		HF/6-31G(d)		B3LYP/6-31G(d)//HF/6-31G(d)				
Entry	Binding mode	Substituents	Total energy (au)	Rel. energy (kcal mol^{-1})	Total energy (au)	Rel. energy (kcal mol^{-1})	ϕ (°)	β (°)	Products
1	(*1*)	R = R_1 = R_2 = R′ = R ″ = H[a]	–310.95398	0.00	–312.95649	0	20.6	97.1	**1**
	(*2*)		–310.94656	4.66	–312.94895	4.73	53.6	49.3	**2**
2	(*3*)	R = R_1 = R_2 = R′ = R ″ = H	–310.95191	—	–312.95472	—	18.3	99.4	**1**
3	(*1*)	R = Me; R_1 = R_2 = R′ = R ″ = H	–349.98796	0.68	–352.24196	0.43	19.2	95.6	**1**
	(*2*)		–349.98321	3.66	–352.23680	3.67	51.7	50.2	**2**
	(*3*)		–349.98904	0.00	–352.24265	0.00	19.6	98.4	**1**
4	(*1*)	R = Me; R_1 = R_2 = R′ = H, R ″ = Me	–389.02303	0.00	–391.52666	0.00	19.4	95.4	**1**
	(*2*)		–389.01448	5.36	–391.51885	4.90	49.8	49.0	**2**
	(*3*)		–389.01841	2.90	–391.52296	2.32	16.9	97.2	**3**
5	(*1*)	R = Me; R_1 = R_2 = R ″ = H, R′ = Me	–389.01791	3.85	–391.52264	3.29	15.2	98.8	**1**
	(*2*)		–389.01838	3.55	–391.52206	3.65	52.0	49.8	**2**
	(*3*)		–389.02404	0.00	–391.52788	0.00	19.4	98.2	**3**
6	(*1*)	R = R_1 = R′ = R ″ = H, R_2 = CHO	–423.68279	0.00	–426.22414	0.00	26.9	93.1	**1**
	(*2*)		–423.67792	3.06	–426.22021	2.47	53.9	47.2	**2**
7	(*1*)	R = R_1 = R′ = R ″ = H, R_2 = COOH	–498.57969	0.00	–501.44543	0.00	24.0	96.1	**1**
	(*2*)		–498.57653	1.98	–501.44373	1.07	57.7	44.8	**2**
8	(*1*)	R = R_2 = R′ = R ″= H, R_1 = CHO	–423.68716	0.00	–426.22829	0.00	21.8	95.9	**1**
	(*2*)		–423.68231	3.04	–426.22459	2.32	57.2	47.3	**2**
9	(*1*)	R = R_2 = R′ = R ″= H, R_1 = COOH	–498.58292	0.00	–501.44814	0.00	23.4	95.6	**1**
	(*2*)		–498.57802	3.07	–501.44342	2.96	55.6	48.8	**2**
10	(*3*)	R = R_1 = R′ = R ″ = H, R_2 = CHO	–423.67801	—	–426.22044	—	13.4	100	**1**
11	(*3*)	R = R_1 = R′ = R ″ = H, R_2 = COOH	–498.57398	—	–501.44133	—	25.3	87.9	**1**
12	(*3*)	R = R_1 = R′ = R ″ = H, R_2 = CHO	–432.68348	—	–426.22483	—	20.3	97.6	**1**
13	(*3*)	R = R_2 = R′ = R′′ = H, R_1 = COOH	–498.58069	—	–501.44620	—	19.3	98.8	**1**
14	(*1*)	R = Me, R_1 = R′ = R ″ = H, R_2 = COOH	–537.61579	0.00	–540.73347	0.00	24.1	93.3	**1**
	(*2*)		–537.61516	0.39	–540.73339	0.05	59.2	41.6	**2**
	(*3*)		–537.61292	1.80	–540.73144	1.28	30.3	83.2	**3**
15	(*1*)	R = Me, R_2 = R′ = R ″ = H, R_1 = COOH	–537.61860	0.21	–540.73528	0.40	21.9	94.0	**1**
	(*2*)		–537.61798	0.60	–540.73459	0.82	54.2	48.9	**2**
	(*3*)		–537.61893	0.00	–540.73591	0.00	22.3	96.1	**3**

[a]R indicates the substituents in Fig. 2 that form the corresponding TS.

Process (A) is the basic ene reaction. Process (B) is basically the mechanism of the oxyene reaction, while process (C) represents the pericyclic pathway of the aldol condensation. Table 4 shows the relevant dihedral angles around the forming C—C bond of the TSs (Fig. 4) of these reactions.

The progressive increase of dihedral angle ϕ and a corresponding decrease in β from reactions (A) to (C), as shown in Table 4, prompted us to use these three reactions as a model system for the activation process of the ene cyclization. As the activation was due to the one or two oxygen atom(s) alone, we may consider that there is no steric effect in these TSs because of a bulky activating group. The next step was to check the product proportions in the cyclisation processes using these three model reactions. As for our previous cases, we constructed the TSs using three binding modes (our results are shown in Tables 5 and 6). Table 5 shows the energies and relevant dihedral angles of the TSs obtained from the reactants shown. We considered

© 2004 NRC Canada

Table 3. Some relevant dihedral angles of the basic TSs of ene reactions with proper substituents (Fig. 3).

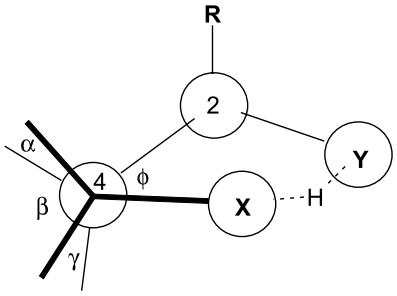
Entry	Substituents	ϕ (°)	α (°)	β (°)	γ (°)
1	R_1 = H, R_2 = H	37.3	37.2	77.1	38.8
		(38.5)[a]	(38.2)	(75.9)	(40.0)
2	R_1 = CHO, R_2 = H	39.9	38.5	74.9	41.4
		(41.8)	(40.1)	(72.9)	(43.6)
3	R_1 = H, R_2 = CHO	45.2	43.3	70.0	46.3
		(47.2)	(44.9)	(67.9)	(48.5)
4	R_1 = COOH, R_2 = H	46.0	43.8	70.4	46.2
		(48.6)	(45.9)	(67.9)	(48.9)
5	R_1 = H, R_2 = COOH	40.8	40.1	74.4	42.2
		(48.7)	(46.5)	(67.1)	(49.9)
6	R_1 = $COOCH_3$, R_2 = H	45.4	43.4	70.9	45.7
		(47.8)	(45.3)	(68.6)	(48.1)
7	R_1 = H, R_2 = $COOCH_3$	40.1	39.6	75.0	41.6
		(47.7)	(45.8)	(67.9)	(48.8)

[a]Angles shown in parentheses are for TS with R = CH_3.

Table 4. Relevant dihedral angles of the TSs of the model reactions (Scheme 1).

Reaction in Scheme 1	X and Y (Fig. 4)	ϕ (°)	α (°)	β (°)	γ (°)
(A)	X = Y = CH_2	37.3	37.2	77.1	38.8
(B)	X = O, Y = CH_2	44.1	40.9	72.7	45.8
(C)	X=O; Y=O	53.8	51.9	62.0	57.4

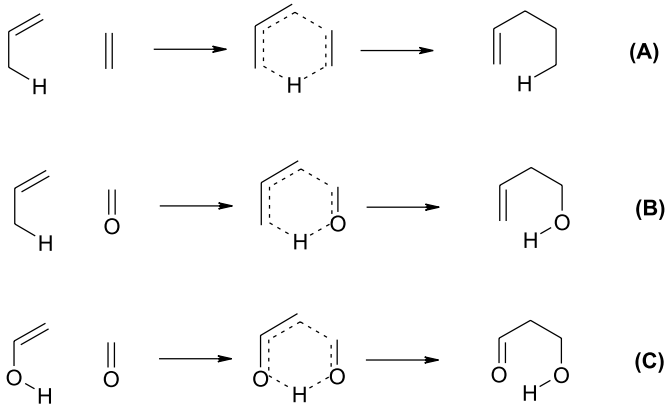
Fig. 4. TS for the model ene reaction.



only those reactant configurations that produced both cis and trans isomers. The product ratios (given in Table 6) were calculated at 253 °C (the temperature for activated cyclisation in some entries of Table 1). Reactants and the corresponding TSs in entries 4– 6 of Tables 5 and 6 contain an extra methyl group (R = Me in Fig. 4).

As expected, the proportion of the trans product steadily increases as we move from rxns. 1–3 (Table 6). The presence of a methyl substituent (entries 4–6 in Table 6) enhances this tendency. This suggests that the steric effect of other alkyl (e.g., methyl) substituents also plays a prominent role in determining the product proportions when there is no steric effect of the activating group (the steric effect produced by carbonyl oxygen is considered to be negligible). The dihedral angle, ϕ, (Table 5) also varies in accordance with the ratio of trans products.

Scheme 1.

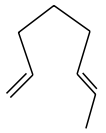
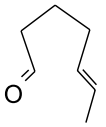
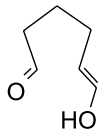
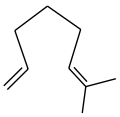
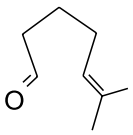
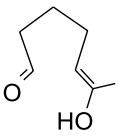


Conclusion

In a nutshell, it may be stated that activated ene cyclisation shows a tendency to produce more trans product than cis. This effect originates from the deformation of the basic transition structure owing to the presence of the activating group. The steric effect of this activating group, along with other substituents, plays a prominent role in controlling the proportion of the diastereomeric products. Proper consideration of the power of activation and bulkiness of substituents can lead a synthetic chemist to design a cyclization reaction that will produce the required diastereomer in high proportion according to his necessity.

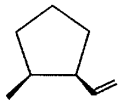
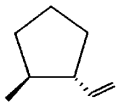
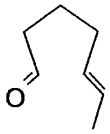
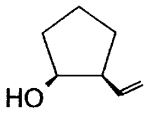
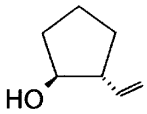
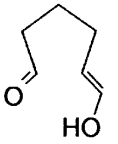
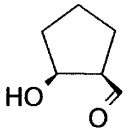
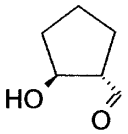
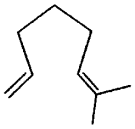
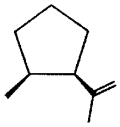
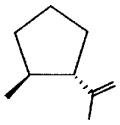
© 2004 NRC Canada

Table 5. Energies and relevant dihedral angles of the TSs for ene cyclisation using the model reactions of Scheme 1. Absolute energies are ZPE-uncorrected.

			HF/6-31G(d)		B3LYP/6-31G(d)//HF/6-31G(d)				
Entry	Reactant	Binding mode of TS	Total energy (au)	Rel. energy (kcal mol^{-1})	Total energy (au)	Rel. energy (kcal mol^{-1})	ϕ (°)	β (°)	Products
1		(*1*)	–310.95398	0.00	–312.95649	0.00	20.6	97.1	**1**
		(*2*)	–310.94656	4.66	–312.94895	4.73	53.6	49.3	**2**
2		(*1*)	–346.80388	0.00	–348.88073	0.00	22.8	94.6	**1**
		(*2*)	–346.79806	3.65	–348.87579	3.10	57.4	49.1	**2**
3		(*1*)	–382.65803	0.00	–384.80582	0.00	24.7	93.6	**1**
		(*2*)	–382.65522	1.77	–384.80333	1.56	64.7	41.1	**2**
4		(*1*)	–349.98796	0.68	–352.24196	0.43	19.2	95.6	**1**
		(*2*)	–349.98321	3.66	–352.23680	3.67	51.7	50.2	**2**
		(*3*)	–349.98904	0.00	–352.24265	0.00	19.6	98.4	**1**
5		(*1*)	–385.84077	0.71	–388.16854	0.72	20.5	92.7	**1**
		(*2*)	–385.83817	2.34	–388.16632	2.11	56.1	48.1	**2**
		(*3*)	–385.84190	0.00	–388.16968	0.00	22.3	98.0	**1**
6		(*1*)	–421.70143	0.00	–424.09947	0.00	22.4	90.8	**1**
		(*2*)	–421.70118	0.15	–424.09852	0.60	63.2	39.2	**2**

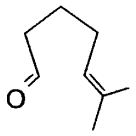
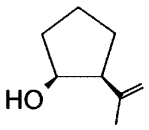
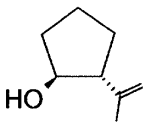
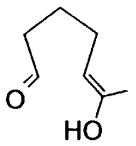
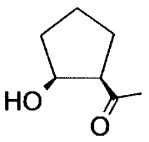
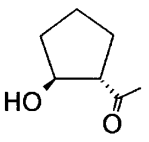
© 2004 NRC Canada

Table 6. Ene cyclisation using the model ene reactions of Scheme 1.

	Reactant		Products	
			1	**2**
1		**253°C** →		
		6-31G(d)	99%	1%
		B3LYP	99%	1%
2		**253°C** →		
		6-31G(d)	97%	3%
		B3LYP	95%	5%
3		**253°C** →		
		6-31G(d)	84%	16%
		B3LYP	82%	18%
4		**253°C** →		
		6-31G(d)	98%	2%
		B3LYP	98%	2%

© 2004 NRC Canada

Table 6 (*concluded*).

	Reactant		Products	
			1	**2**
5		**253°C** →		
		6-31G(d)	93%	7%
		B3LYP	92%	8%
6		**253°C** →		
		6-31G(d)	54%	46%
		B3LYP	64%	36%

Acknowledgement

The authors are thankful to the University Grants Commission (UGC), New Delhi, India for providing financial assistance for the research work.

References

1. (*a*) J.M. Conia and P. Le Perchec. Synthesis, 1 (1975); (*b*) W. Oppolzer and V. Snieckus. Angew. Chem. Int. Ed. Engl. **17**, 476 (1978); (*c*) K. Mikami and M. Shimizu. Chem. Rev. **92**, 1021 (1992); (*d*) T.K. Sarkar, B. Mukherjee, and S.K. Ghosh. Tetrahedron, **5**4, 3243 (1998); (*e*) D.L.J. Clive, X. He, M.H.D. Postema, and M.J. Mashimbye. J. Org. Chem. **64**, 4397 (1999); (*f*) K. Mikami, K. Takahashi, and T. Nakai. Tetahedron Lett. **30**, 357 (1989); (*g*) W. Oppolzer. Pure Appl. Chem. **53**, 1181 (1981).
2. (*a*) B.B. Snider. Acc. Chem. Res. **13**, 426 (1980); (*b*) K. Maruoka, Y. Hoshino, T. Shirasaka, and H. Yamato. Tetrahedron Lett. **29**, 3967 (1988).
3. B.E. Thomas, R.J. Loncharich, and K.N. Houk. J. Org. Chem. **57**, 1354 (1992).
4. R.J. Loncharich and K.N. Houk. J. Am. Chem. Soc. **109**, 6947 (1987).
5. G.K. Das. J. Chem. Soc. Perkin Trans. 2, 1779 (1999).
6. J. Pranata. Int. J. Quant. Chem. **62**, 509 (1997).
7. M.W. Schmidt, K.K. Baldridge, J.A. Boatz, S.T. Elbert, M.S. Gordon, J.J. Jensen, S. Koseki, N. Matsunaga, K.A. Nguyen, S. Su, T.L. Windus, M. Dupuis, and J.A. Montgomery. J. Comput. Chem. **14**, 1347 (1993).
8. W.D. Huntsman, V.C. Solomon, and D. Eros. J. Am. Chem. Soc. **80**, 5455 (1958).
9. J. Tanaka, T. Katagiri, and K. Ozawa. Bull. Chem. Soc. Jpn. **44**, 130 (1971).
10. W.D. Huntsman and T.H. Curry. J. Am. Chem. Soc. **80**, 2252 (1958).
11. S.K. Ghosh and T.K. Sarkar. Tetrahedron Lett. **27**, 525 (1986).

© 2004 NRC Canada

Azo-functionalized dendrimers

Kap-Soo Cheon, Peter M. Kazmaier, Sam-Rok Keum, Kuk-Tae Park, and Erwin Buncel

Abstract: We report the synthesis of azo-functionalized Starburst polyamidoamine (PAMAM) dendrimers. The following three systems of azo-functionalized PAMAM dendrimers were prepared by different synthetic routes: (*i*) phenylazo derivatives; (*ii*) naphthalimide azo derivatives; and (*iii*) phthalimide azo derivatives. Model compounds in each system were synthesized for spectroscopic comparison. Confirmation of structure was achieved using a combination of NMR and IR spectroscopy to ascertain the functional sites (i.e., the azo and the cyclic imides), while mass spectrometry and UV–vis spectrophotometry were employed to ascertain the extent of functionalization. Substitution by the azo pendent groups increased the thermal stability of PAMAM dendrimers (TGA weight loss of the naphthalimide azo-functionalized PAMAM dendrimers up to 300 °C, ca. 5%).

Key words: dendrimers, azo compounds, hydrazones, tautomerism, hydrogen bonding.

Résumé : On a réalisé la synthèse de dendrimères polyamidoamine (PAMAM) Starburst fonctionnalisés à l'azote. Faisant appel à diverses voies de synthèse, on a préparé trois systèmes de dendrimères PAMAM fonctionnalisés à l'azote, soit des dérivés phénylazo, des dérivés naphtalimideazo et des dérivés phtalamideazo. On a préparé des composés modèles de chaque système pour comparaison spectroscopique. La confirmation de la structure a été réalisée par une combinaison de spectroscopies RMN et IR qui ont permis de confirmer la présence des sites fonctionnels (par exemple, la fonction azo et les imides cycliques) alors que la spectrométrie de masse et la spectrophotométrie UV–vis a permis de déterminer le degré de fonctionnalisation. La substitution par des groupes azo pendants augmente la stabilité thermique des dendrimères PAMAM (lors de l'analyse thermogravimétrique jusqu'à 300 °C, la perte de poids des dendrimères PAMAM fonctionnalisés à l'azote par le naphtalimide est d'environ 5 %).

Mots clés : dendrimères, composés azo, hydrazones, tautomérie, liaison hydrogène.

[Traduit par la Rédaction]

Introduction

Starburst dendrimers are a new class of highly ordered and branched cascade molecules that have received a great deal of attention (1). Recently, functionalization of dendrimers has shown promising new applications in diverse areas, including materials sciences and life sciences, where applications in medical diagnostics have been proposed (2).

Azo functionalities have been inserted onto dendrimers both as inside linkers and as modifiers of the periphery (3). The resulting molecules have been utilized for their photoswitchable properties and investigated for applications in optical data storage systems, holographic gratings, and drug delivery systems as host molecules (3*e*).

Received 9 October 2003. Published on the NRC Research Press Web site at http://canjchem.nrc.ca on 26 March 2004.

K.-S. Cheon and E. Buncel.[1] Department of Chemistry, Queen's University, Kingston, ON K7L 3N6, Canada.
P.M. Kazmaier. Xerox Research Centre of Canada, 2660 Speakman Drive, Mississauga, ON L5K 2L1, Canada.
S.-R. Keum. Department of Chemistry, Graduate Studies of Korea University, Seoul, Korea 136-701.
K.-T. Park. Department of Chemical Education, Korea National University of Education, Chungbuk, Korea 363-791.

[1]Corresponding author (e-mail: buncele@chem.queensu.ca).

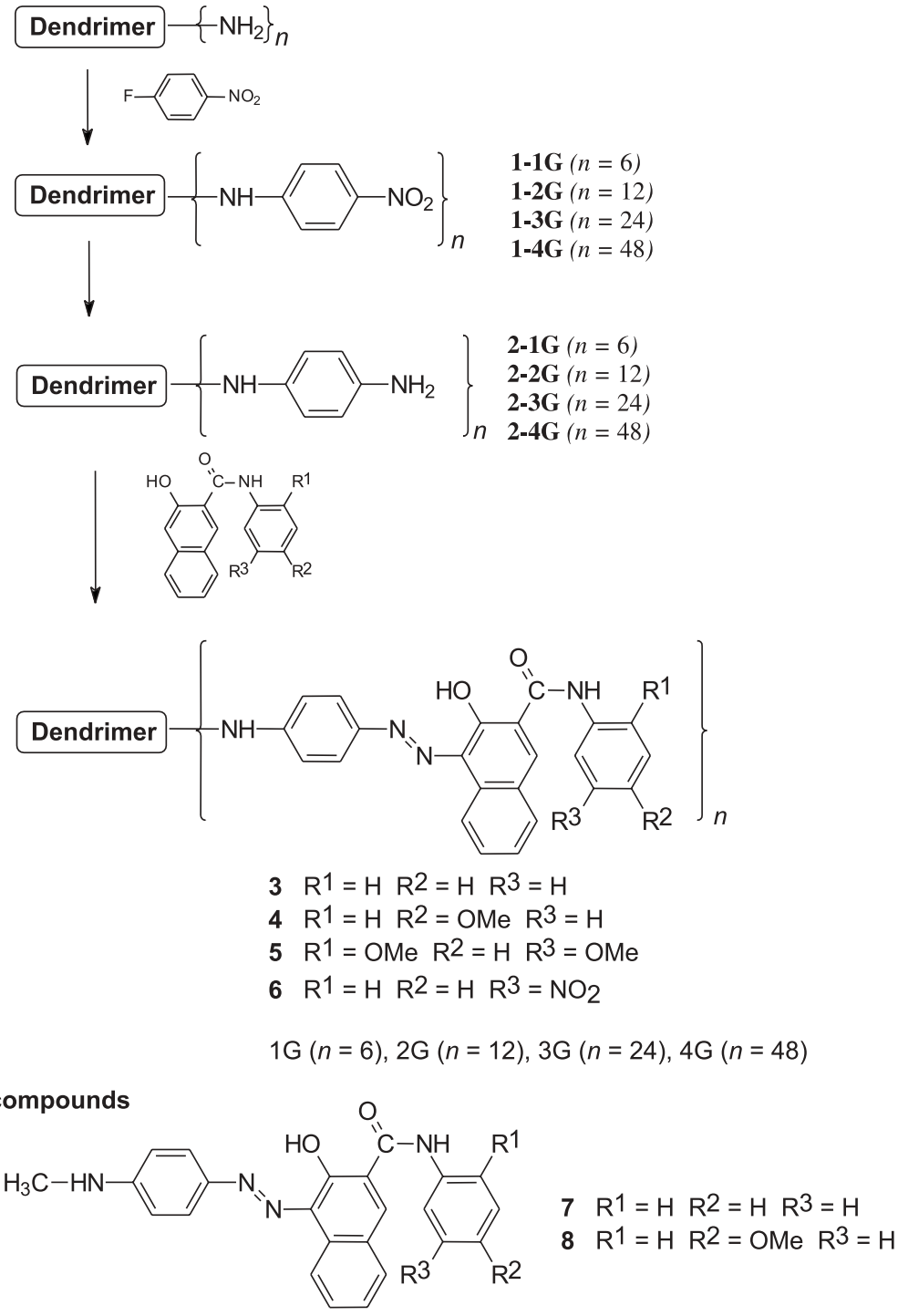
The photoconductive properties of azo compounds were discovered by Rau (4) in 1969, and several years later, the first commercial bisazo pigments (Chlorodiane Blue) for photogenerating pigments in bilayer xerographic devices appeared (5). Azo-functionalized linear polymers have shown promise in the development of electrographic imaging applications, particularly for photoreceptors in xerographic systems (6).

Photoconductivity in organic pigments proceeds primarily by the following two mechanisms: a so-called extrinsic and an intrinsic mechanism (7). The extrinsic mechanism takes advantage of sensitization at the pigment surface; that is to say, a hole-transporting molecule, such as a triarylamine, donates an electron to the exciton generated in the pigment to effect charge separation and hole injection. Surface-functionalized dendrimers have, potentially, a tremendous advantage, since the chromophores are arranged in a thin layer around an inert and impervious core. Thus, if photogeneration takes place in an azo-functionalized dendrimer, the exciton is confined to the surface and is constantly exposed to the hole-transporting sensitizer, and so very rapid and highly efficient hole injection should take place for these systems. We therefore undertook to synthesize a surface-functionalized dendrimer with azo couplers, which are known to have excellent photoimaging properties.

We report the functionalization of ethylenediamine-based Starburst dendrimers using mono-azo moieties. The reac-

 doi: 10.1139/V04-009 © 2004 NRC Canada

Scheme 1.



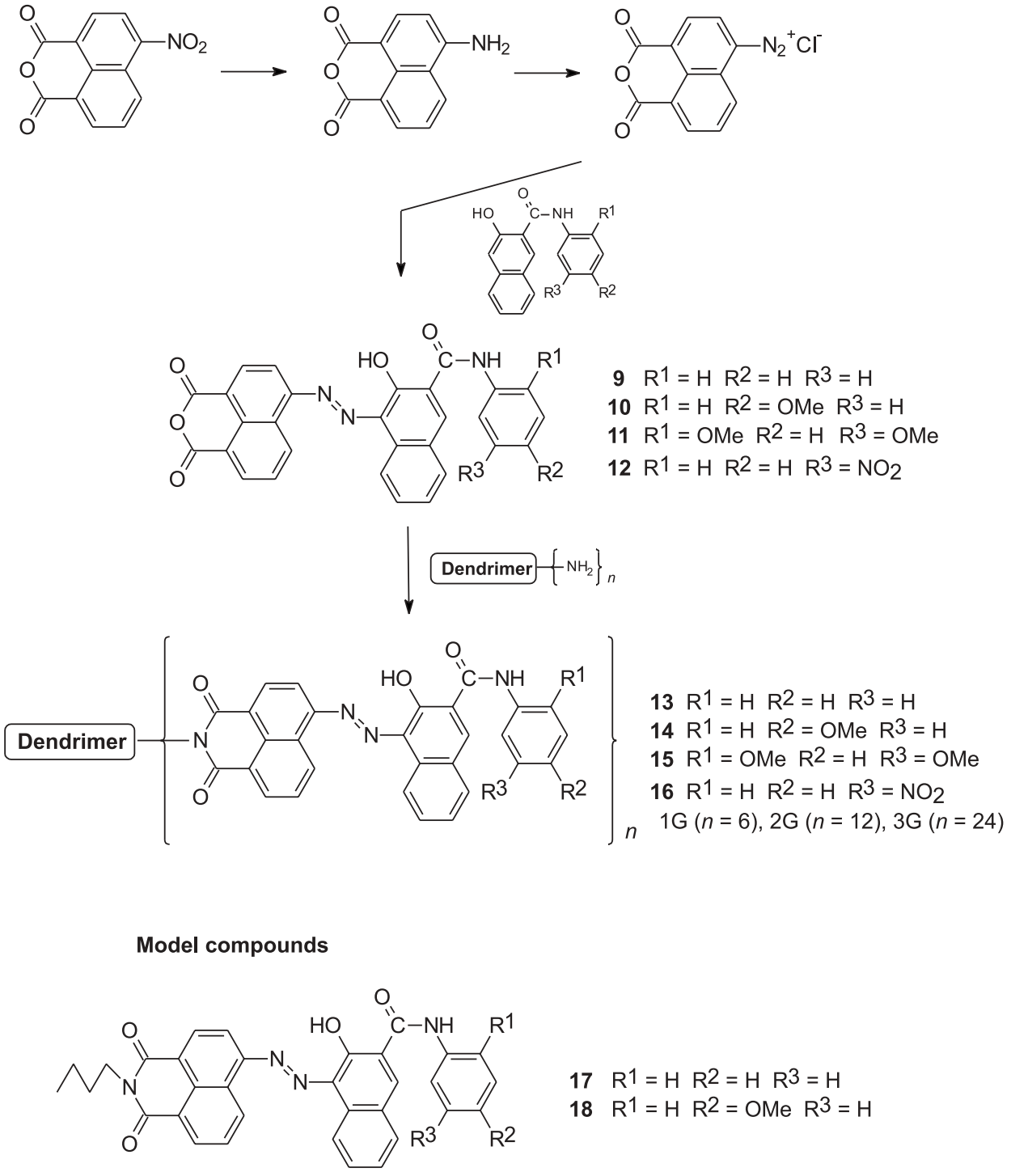
Model compounds

tions are shown in Schemes 1–3. A key feature of this chemistry is to select reaction conditions that take advantage of the water solubility of dendrimers and allow functionalization of the dendrimers under reaction conditions that do not lead to degradation of the dendrimer core. Polyamidoamine (PAMAM) dendrimers have been chosen for functionalization by azo dyes in this study because they are commercially available and have been well studied in terms of characterization and properties. The number of ending sites and molecular weights in each generation (G) of PAMAM dendrimers are as follows: 1st G (6 groups, 1043); 2nd G (12 groups, 2411); 3rd G (24 groups, 5147); 4th G (48 groups, 10 619). The present work encompasses up to the fourth generation of PAMAM dendrimers.

Since azo dyes and pigments containing the 2-naphthol-3-anilide moiety have shown high photoconductivity (low dark decay values; high photosensitivity) (8, 9), the derivatives of 2-naphthol-3-anilide were used as couplers for the synthesis of all azo-functionalized PAMAM dendrimers, as well as model compounds. The structure of the azo-modified gener-

© 2004 NRC Canada

Scheme 2.



ation 1 of PAMAM dendrimers synthesized and characterized in this study is exemplified in Fig. 1 (see also Schemes 1–3). Hereafter, the symbol Dendrimer will be used for the generic structure of the PAMAM dendrimer.

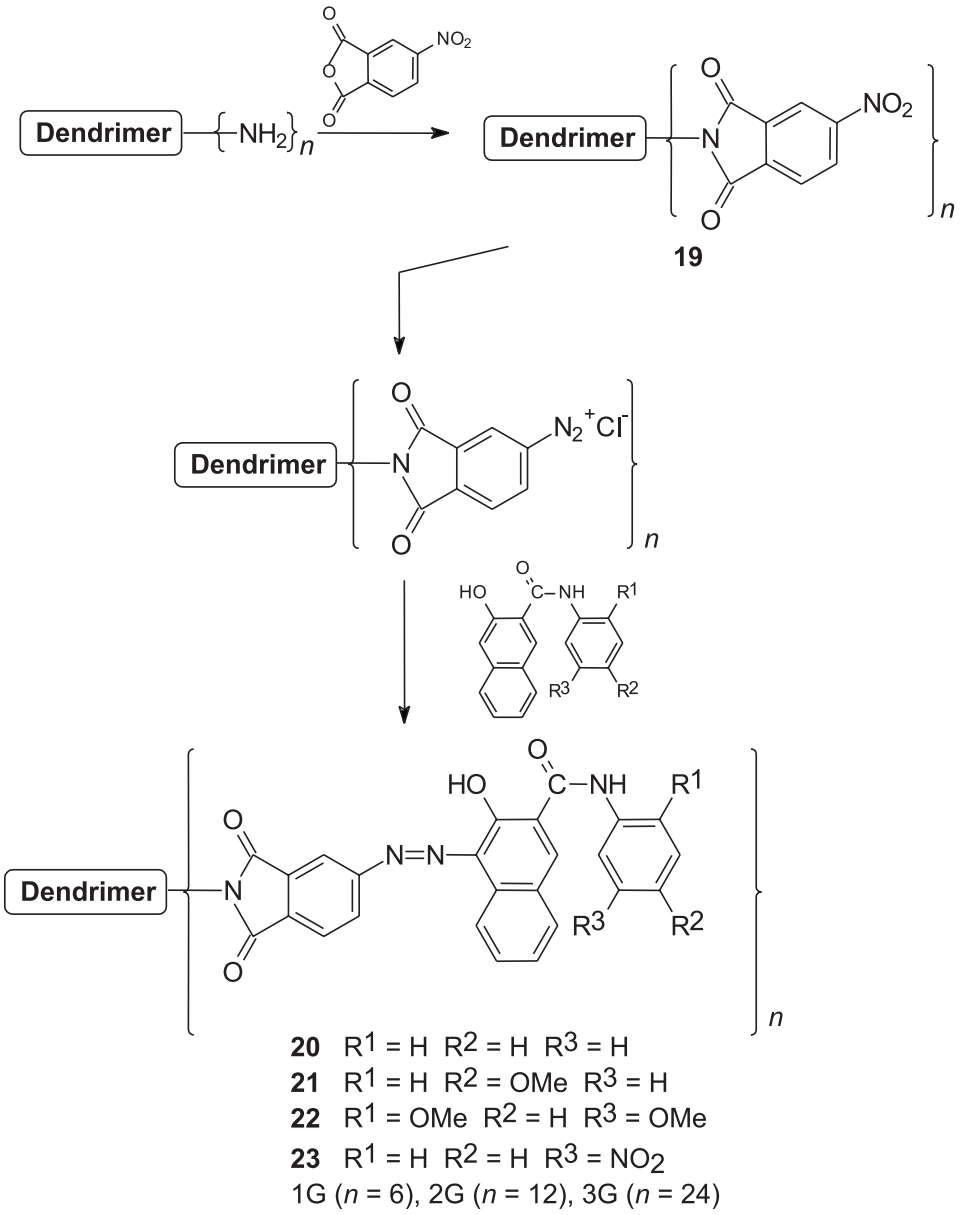
Results and discussion

The following three systems of azo-functionalized polyamidoamine (PAMAM) dendrimers were examined in this study: (*i*) phenylazo derivatives (Scheme 1); (*ii*) naphthalimide azo derivatives (Scheme 2); (*iii*) phthalimide azo derivatives (Scheme 3). Note that, since the three systems contain the same 2-naphthol-3-anilide moiety, for simplicity the naming of the three systems excludes the 2-naphthol-3-anilide portion. Several model compounds for the three systems were prepared in order to validate the synthetic methods. Furthermore, the spectroscopic characteristics of the model compounds were useful for identifying structures of the azo-functionalized dendrimers.

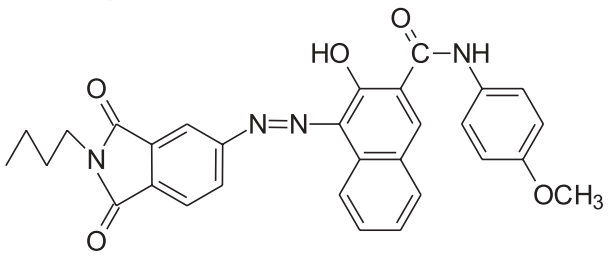
Structural confirmation and the determination of the de-

© 2004 NRC Canada

Scheme 3.



Model compound

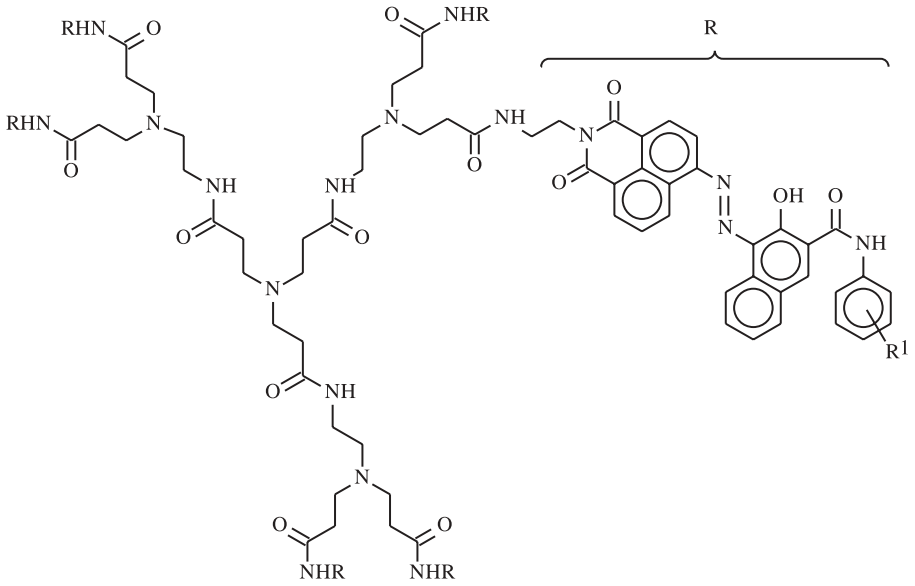


25

gree of functionalization were achieved using a combination of ^{1}H NMR, ^{13}C NMR, and IR spectroscopy to ascertain the site of azo coupling and the functional sites (i.e., the cyclic imides), while mass spectrometry and UV–vis spectrophotometry were employed to ascertain the extent of periphery substitution. UV–vis and ^{13}C NMR evidence revealed that the model compounds and dendrimers exist as equilibrium mixtures of azo and hydrazone tautomeric forms, with the

© 2004 NRC Canada

Fig. 1. Structure of naphthalimide azo-derivatized generation 1 PAMAM dendrimer.



R^1 = H (**13**), 4'-methoxy (**14**)
2', 5'-dimethoxy (**15**), 3'-nitro (**16**)

position of equilibrium being dependent on both structure and solvent medium.

Synthesis and characterization[2]

Phenylazo derivatives

The synthesis of phenylazo derivatives of polyamidoamine (PAMAM) dendrimers was achieved by the route shown in Scheme 1. Reactions of the various generations (from 1st G to 4th G) of PAMAM with *p*-fluoronitrobenzene provided the nitrophenyl moiety to the ending sites of the dendrimer. The structure of the nitrophenyl derivative **1** was identified by ^{1}H and ^{13}C NMR. Reduction of the pendent nitro group to the aromatic amine was accomplished by hydrogenation in the presence of Pd–C catalyst, giving almost quantitative yields of the amino compounds, **2**. ^{13}C NMR spectroscopy was used to verify complete reduction; the absence of a trace of carbon peaks corresponding to the nitro derivative indicated complete reduction. The resulting aminophenyl derivatives were used for formation of the diazonium salts, followed by the diazo-coupling reactions with 2-hydroxynaphthoic acid couplers, giving dendrimer compounds **3**–**6.** Model compounds **7** and **8** were synthesized by the same methods and fully characterized to facilitate the spectroscopic characterization of the resulting phenylazo derivatives of the dendrimer. The sites of azo coupling for the resulting azo-functionalized dendrimers were confirmed by ^{13}C NMR spectroscopy. The ^{13}C chemical shifts of the aromatic portion for the dendrimers are similar to those of the model compound **7**, which confirms the functionalization of the azo moiety at the surface of the dendrimer.

UV–vis spectroscopy was employed to determine the degree of functionalization. The molar extinction coefficient (ε) value at 384 nm of the nitrophenyl derivatives was taken as a measure of the degree of the functionalization by comparison with the corresponding ε value of *N*-methyl-4-nitroaniline (model compound). In other words, the ε value of the nitrophenyl derivative of the PAMAM dendrimer 1G, which has 6 reaction sites, should be 6 times that of the model compound if the reaction sites were fully functionalized. Adherence to the Beer–Lambert law was checked by measuring the absorbance *A* at different concentrations (from 1.04×10^{-5} to 1.51×10^{-4} mol L^{-1}) and plotting *A* vs. concentration. The degree of functionalization could be deduced from a comparison of the ε values of the dendrimer and the model compound, as summarized in Table 1.

According to the UV–vis results, the ending sites of the nitrophenyl-derivatized dendrimers **1**–**1G** to **1**–**4G** were not fully functionalized, i.e., the first generation of PAMAM, having 6 ending sites, was functionalized on 5 sites; for the 2nd G, 9 sites were functionalized; 17 sites and 30 sites were functionalized for the 3rd G and 4th G dendrimers, respectively. This lack of full functionalization with generation could be caused by reduced nucleophilicity of the ending amine moieties of the dendrimers with increasing generation because of crowdedness of the dendrimer surface.

Comparison of ε values between the azo-functionalized dendrimers **3** and the model compound **7** provided the de-

[2] Spectroscopic data of compounds synthesized are provided as supplementary material. Copies of material on deposit may be purchased from the Depository of Unpublished Data, Document Delivery, CISTI, National Research Council Canada, Ottawa, Canada K1A 0S2.

© 2004 NRC Canada

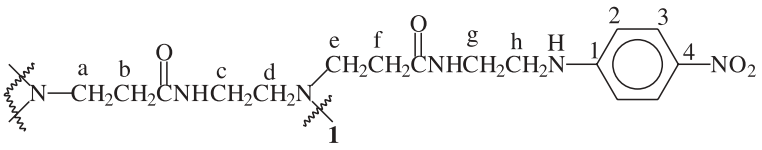
Table 1. Comparison of UV–vis data of *N*-methyl-4-nitroaniline (model compound) and nitrophenyl derivatives of PAMAM dendrimers.

Compounds	λ_{max} ($\varepsilon \times 10^4$)[a]	No. of ending sites	No. of functionalized sites[b]
N-Methyl-4-nitroaniline	384 (1.65)	1	1
p-Nitrophenyl deriv. (**1**–**1G**)	384 (8.65)	6	5.2
p-Nitrophenyl deriv. (**1**–**2G**)	384 (14.69)	12	8.9
p-Nitrophenyl deriv. (**1**–**3G**)	384 (27.74)	24	16.8
p-Nitrophenyl deriv. (**1**–**4G**)	384 (49.52)	48	30.0

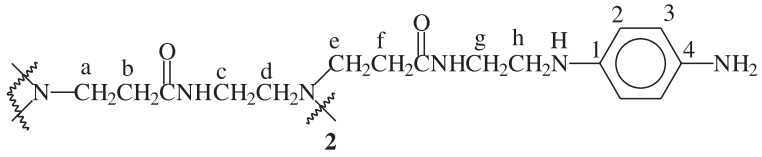
Note: deriv. = derivative.

[a]UV–vis data were obtained in EtOH.

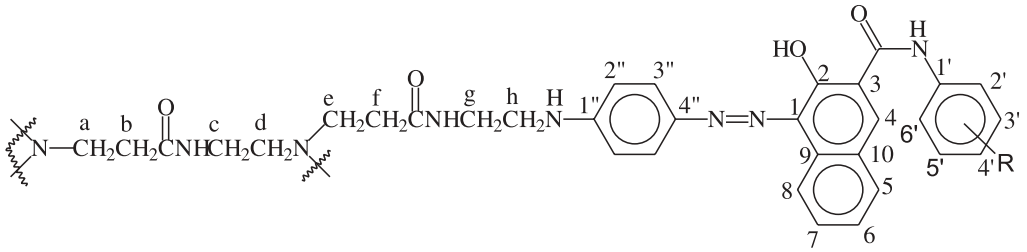
[b]These values were deduced from the comparison of ε values between the nitrophenyl derivatives and *N*-methyl-4-nitroaniline.



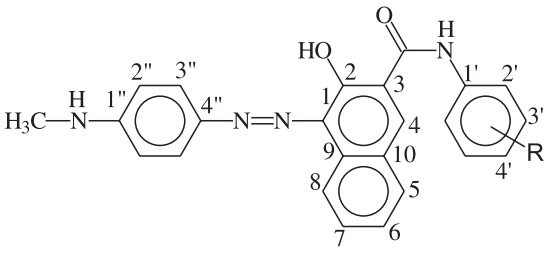
1



2



R = H (**3**), 4'-methoxy (**4**)
2', 5'-dimethoxy (**5**), 3'-nitro (**6**)



R = H (**7**),
4'-methoxy (**8**)

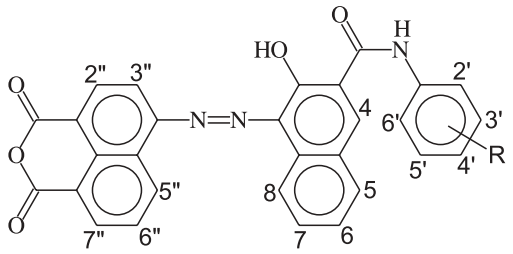
gree of functionalization summarized in Table 2. Though, in principle, the above method for evaluation of the number of azo pendent sites (i.e., loading) should be applicable, in the present system an uncertainty arises as a result of a solvent-dependent azo-hydrazone tautomerism, which is exhibited by both the model compounds and the dendrimers (vide infra) (10). In an attempt to circumvent this uncertainty, UV–vis measurements have been made in two solvents — toluene and 2,2,2-trifluoroethanol — these solvents having different polarities and H-bonding properties. The results presented in Table 2 show that there is fair agreement in the two sets of data, giving some credence to their validity. Both

© 2004 NRC Canada

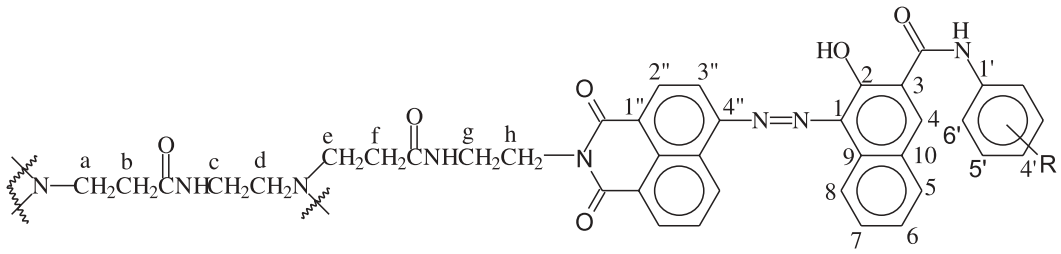
Table 2. Comparison of UV–vis data of model compound **7** with phenylazo derivatives of PAMAM dendrimers.

Compounds	No. of ending sites	*m/z* (ES) (calcd. MW)	TFE[a] λ_{max} ($\varepsilon\times10^4$)[b]	TFE[a] Calcd. No. azo pendent	Toluene λ_{max} ($\varepsilon\times10^4$)[b]	Toluene Calcd. No. azo pendent
Model (**7**)[c]	1	—	512 (1.42)	1	568 (1.50)	1
3–1G[c]	6	2979 (3237)	514 (7.23)	5.1	538 (6.96)	4.7
3–2G[d]	12	—	506 (10.4)	7.3	—	—
3–3G[d]	24	—	506 (21.0)	14.8	—	—
3–4G[d]	48	—	508 (31.5)	22.2	—	—

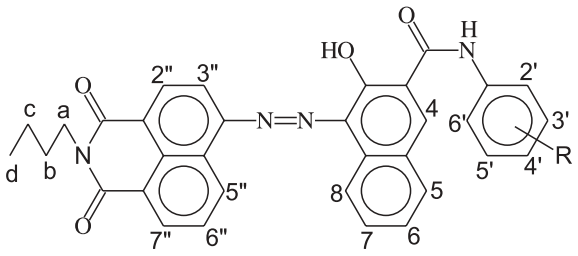
[a]2,2,2-Trifluoroethanol.
[b]These values were deduced from the comparison of ε values between dendrimers and the model compound.
[c]Stock solution was made in DMF.
[d]Stock solution was made in water.



R = H (**9**), 4'-methoxy (**10**)
2', 5'-dimethoxy (**11**), 3'-nitro (**12**)



R = H (**13**), 4'-methoxy (**14**)
2', 5'-dimethoxy (**15**), 3'-nitro (**16**)



R = H (**17**),
4'-methoxy (**18**)

sets show that there is incomplete functionalization. The number of azo pendent groups is similar to that for the *p*-nitrophenyl derivatives shown in Table 1, which indicates that the crucial step for this synthesis is the nucleophilic aromatic substitution reaction with *p*-fluoronitrobenzene.

The results of the degree of functionalization deduced from UV–vis data were comparable with those obtained from MS (ES) data. A series of multiply charged species (A_5–A_{10}) was recognized by the automated MS spectrometer. For example, in the case of dendrimer **3–1G**, multiply

© 2004 NRC Canada

Table 3. Comparison of UV–vis data of model compound **17** with naphthalimide azo derivatives of PAMAM dendrimers and MS (MALDI) data of dendrimers.

Compounds	No. of ending sites	*m/z* (MALDI) (calcd. MW)	Toluene		TFE	
			λ_{max} ($\varepsilon\times10^4$)	Calcd. No. azo pendent	λ_{max} ($\varepsilon\times10^4$)	Calcd. No. azo pendent
Model (**17**) [a]	1	—	536 (1.38)	1	530 (1.44)	1
(**13–1G**) [b]	6	3824 (3857)	518 (8.20)	5.9	504 (9.86)	6.8
(**14–1G**) [b]	6	3903 (4037)	528 (8.48)	6.1	502 (9.95)	6.9
(**15–1G**) [b]	6	4209 (4217)	512 (8.21)	6.0	498 (9.81)	6.8
(**16–1G**) [b]	6	4196 (4127)	512 (8.23)	6.0	502 (9.87)	6.9

[a]Stock solution was made in $CHCl_3$.
[b]Stock solution was made in DMSO.

charged peaks (A_8, A_7, etc.) yielded an average *m/z* 2978.53, which corresponds to the mass of a five-sites-functionalized dendrimer (Table 2). A series of multiply charged species originated from one species, while other series of multiply charged species were not found. Thus, the MS spectrum showed that dendrimer **3–1G** is the homogeneously five-sites-functionalized dendrimer by the azo moiety.

Naphthalimide azo derivatives

The synthetic method for the naphthalimide azo-functionalized dendrimers is described in Scheme 2. Initially, various azo dyes containing the naphthoic anhydride moiety were synthesized, using a standard diazo-coupling reaction. Then, the naphthoic anhydride moiety was attached to the ending sites of the dendrimers as the cyclic imides. The synthetic advantage of this method over the phenylazo system is that problems caused in purification of the modified PAMAM dendrimers formed in each step would be diminished, since attachment of the azo moiety to the dendrimer only occurred in the last step.

In the first step of the reaction sequence (Scheme 2), hydrogenation of the nitro group produced the amino compound, followed by a standard diazo coupling with the couplers to give the naphthoic anhydride azo compounds (**9–12**). These were coupled with PAMAM dendrimers by cyclic imide formation to give the azo-functionalized dendrimers (**13–16**). For the higher generations of PAMAM (2G and 3G), **9** was chosen for cyclic imide formation with the dendrimers. The model compounds (**17**, **18**) for this system were also synthesized. In the final step, *n*-$BuNH_2$ was used as the model compound for the PAMAM dendrimer, to determine the optimum reaction for the dendrimer synthesis and to compare its spectroscopic characteristics with those of the dendrimers. Two model compounds, **17** and **18**, were prepared.

The compounds **9–12** were fully characterized by NMR, IR, and CI mass spectroscopy. IR spectroscopy was specially useful for the characterization because the cyclic anhydride moiety shows two strong C=O stretching bands, resulting from asymmetrical and symmetrical C=O stretching modes; e.g., **9** (1773, 1734 cm^{-1}), **10** (1768, 1731 cm^{-1}), **11** (1771, 1734 cm^{-1}), and **12** (1773, 1736 cm^{-1}).

The model compounds (**17**, **18**) were first fully characterized. Formation of the cyclic imide linkage was indicated by the following: (*i*) ^1H NMR, the peak at 4.16 parts per million (ppm) being ascribed to the methylene protons attached to the cyclic imide nitrogen and (*ii*) IR C=O stretching bands for the naphthoic anhydrides, which shift to lower values because of the resonance effect of the imide linkage.

The naphthalimide azo-functionalized dendrimers (**13–16**) were insoluble in common organic solvents, making it difficult to obtain well-resolved ^1H and ^{13}C NMR spectra, even at a higher temperature and using a 10 mm NMR tube. Although complete NMR data of the dendrimers cannot be reported because of poor resolution of the spectra, peaks at 4.14 ppm and at ca. 6.9–8.6 ppm correspond to the characteristic methylene protons attached to the nitrogen of the cyclic imide and the protons of the azo moiety, respectively. Another characteristic for the dendrimers (**13–16**) is the shift of the C=O IR stretching frequencies to lower values, indicating formation of the cyclic imide linkage; e.g., 1658 and 1697 cm^{-1} for **13**, 1655 cm^{-1} for **14**, 1658 cm^{-1} for **15**, and 1696 and 1661 cm^{-1} for **16**.

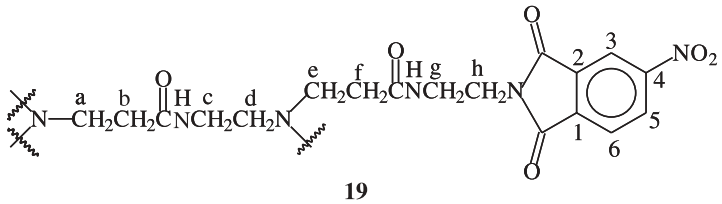
The degree of functionalization was determined through comparison of the UV data of dendrimers **13–16** with that of model compound **17**, measured in two solvents to lessen the uncertainty in interpretation of the results because of azo-hydrazone tautomerism. The results (Table 3) showed that the endings of the G1 dendrimers are fully functionalized by the azo naphthalimide fragment. Note that UV data for the higher generations of the dendrimers (**13–2G**, **13–3G**) could not be obtained because of their insolubility.

The molecular weights of the first generation of the azo-modified dendrimers were determined by MALDI (matrix-assisted laser desorption ionization) MS, Table 3 (MALDI results for the higher generations of the dendrimers (2nd G and 3rd G) could not be obtained because of their insolubility). The mass data of the dendrimers **13–1G** to **16–1G** are reasonably close to calculated values for the six-sites functionalized by the azo naphthalimide fragment, which places some confidence in the capacity of the UV method to allow for estimation of the degree of functionalization of the dendrimers.

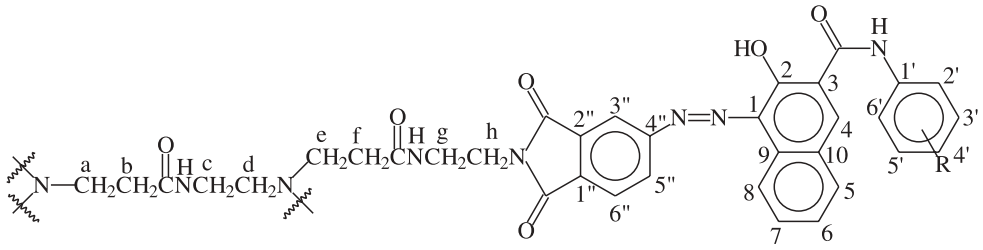
Phthalimide azo derivatives

The synthetic design toward phthalimide azo derivatives of the PAMAM dendrimers was initially similar to that of the naphthalimide system, as follows: preparation of azo compounds containing the phthalic anhydrides, followed by cyclic imide formation with PAMAM dendrimers. However, difficulty was encountered in formation of the cyclic imide linkage because of ring strain in the five-membered phthalimide ring, contrasting with the six-membered ring in the naphthalimide system. When more vigorous reaction

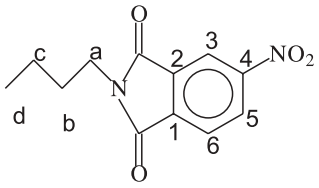
© 2004 NRC Canada



19



R = H (**20**), 4'-methoxy (**21**)
2',5'-dimethoxy (**22**), 3'-nitro (**23**)



24

conditions (i.e., high reaction temperature, 150–200 °C) were attempted (11), the azo chromophore was found to be unstable. Hence, an alternative synthetic strategy for this system was employed, as described in Scheme 3. The cyclic imide reaction between 4-nitrophthalic anhydride and the PAMAM dendrimers was first carried out at high temperature (130–150 °C), which was followed by catalytic hydrogenation to produce the corresponding amine derivatives and then diazo coupling with the couplers. For the synthesis of higher dendrimer generations (2nd G and 3rd G), naphthol AS-RL (**21** R^1 = H, R^2 = OMe, R^3 = H) was used as the coupler in the diazo coupling.

Formation of the cyclic imide linkage for dendrimer **19** was confirmed by ^{1}H and ^{13}C NMR, i.e., chemical shifts data for the CH_2 attached to the cyclic imide nitrogen (3.65 ppm in ^{1}H NMR and 36.57 ppm in ^{13}C NMR). The degree of functionalization in dendrimer **19** (G1, molecular weight 2093) was determined by MS (FAB+) ([M + 1]), which showed a peak at 2094, indicating full functionalization.

The model compound **25** was synthesized as an aid for structural verification of the phthalimide azo-functionalized dendrimers **20**–**23**. The ^{13}C NMR spectra (not shown) for the aromatic portion of **25** and of the dendrimer **21**–**1G** were compared. The similarity of the chemical shifts in the two ^{13}C NMR spectra provides confirmatory evidence for the structure of the dendrimer **21**. Another piece of information obtained from the ^{13}C NMR spectra (not shown) was that the peak corresponding to the CH_2 attached to the cyclic imide nitrogen appears at 36.82 ppm, in accord with the formation of the cyclic imide linkage. The cyclic imide linkage of the dendrimers (**20**–**23**) can be confirmed by the similar IR stretching frequency of the C=O group for the model and dendrimer compounds, e.g., 1770 and 1712 cm^{-1} for dendrimer **21** and 1769 and 1711 cm^{-1} for model compound **25**.

The UV data (measured in two solvents) of the phthalimide azo-functionalized dendrimers **20**–**23** are compared with that of the model compound **25** in Table 4. The results in 1,4-dioxane indicate that for 1G and 2G dendrimers, one site remains unfunctionalized, while for the 3G dendrimer, two sites are not functionalized by the phthalimide azo fragment. Note that the results in 2,2,2-trifluoroethanol (TFE) are slightly different from those in 1,4-dioxane, owing to an increase in the azo tautomer with dendrimer generations in TFE (10). Molecular weights of the dendrimers were also determined by MALDI MS and are summarized in Table 4. The MS data of the dendrimers (1G) are comparable to five-sites azo-functionalized dendrimers.

Thermal stability studies and xerographic properties

The thermal stability of the azo-functionalized dendrimers was evaluated by thermogravimetric analysis (TGA). The results of TGA weight-loss data obtained at 300 °C are summarized in Table 5. The TGA results of the azo-

© 2004 NRC Canada

Table 4. Comparison of UV–vis data of model compound (**25**) with phthalimide azo derivatives of PAMAM dendrimers and MS (MALDI) data of dendrimers.

Compounds	No. of ending sites	*m/z* (MALDI) (calcd. MW)	1,4-Dioxane λ_{max} ($\varepsilon\times10^4$)	1,4-Dioxane Calcd. No. azo pendent	TFE λ_{max} ($\varepsilon\times10^4$)	TFE Calcd. No. azo pendent
Model (**25**)[a]	1	—	500 (1.48)	1	498 (1.66)	1
(**20–1G**)[b]	6	3244 (3557)	498 (7.48)	5.1	486 (9.40)	5.7
(**21–1G**)[b]	6	3419 (3737)	498 (7.45)	5.0	486 (9.74)	5.9
(**22–1G**)[b]	6	3577 (3917)	498 (7.50)	5.1	486 (9.50)	5.7
(**23–1G**)[b]	6	3488 (3827)	498 (7.48)	5.1	490 (9.65)	5.8
(**21–2G**)[b]	12	—[c]	498 (15.8)	10.7	490 (19.5)	11.7
(**21–3G**)[b]	24	—[c]	498 (33.3)	22.5	488 (40.8)	24.6

[a]Stock solution was made in $CHCl_3$.
[b]Stock solution was made in DMSO.
[c]MALDI MS was attempted in order to obtain the molar mass of the higher generation of dendrimers, but this was not successful because of their insolubility.

Table 5. Summary of TGA (thermogravimetric analysis) weight-loss data of the azo-functionalized and non-functionalized dendrimers.

Compounds	TGA wt loss (%)[a]
PAMAM dendrimer	
1G	31.7
2G	28.7
3G	22.8
4G	22.1
Phenylazo derivatives	
Azo Na-AS deriv. (1G) **3**	17.7
Azo Na-RL deriv. (1G) **4**	8.3
Azo Na-BG deriv. (1G) **5**	22.6
Azo Na-BS deriv. (1G) **6**	20.5
Azo Na-AS deriv. (2G) **3–2G**	23.8
Azo Na-AS deriv. (3G) **3–3G**	23.9
Azo Na-AS deriv. (4G) **3–4G**	22.8
Naphthalimide azo derivatives	
Azo Na-AS deriv. (1G) **13**	4.6
Azo Na-RL deriv. (1G) **14**	5.6
Azo Na-BG deriv. (1G) **15**	6.1
Azo Na-BS deriv. (1G) **16**	6.0
Azo Na-AS deriv. (2G) **13–2G**	4.2
Azo Na-AS deriv. (3G) **13–3G**	4.0

[a]TGA wt loss data were obtained at 300 °C and with a heating rate of 20 °C/min under nitrogen.

functionalized dendrimers may be compared with those of the non-functionalized PAMAM dendrimers to investigate the effect of the azo moiety on thermal stability.

According to Table 5, the thermal stability of the azo-functionalized dendrimers shows no clear correlation with different substituents and with dendrimer generations. However, the azo-functionalized dendrimers are, in general, thermally more stable than the non-functionalized PAMAM dendrimers. The naphthalimide azo-functionalized dendrimers show especially good thermal stability (TGA wt loss ≈ 5% up to 300 °C). It can therefore be concluded that the thermal stability of the PAMAM dendrimers is increased through functionalization by the azo moiety.

Conclusions

In summary, three systems of the azo-functionalized PAMAM dendrimers were synthesized by different synthetic routes. The synthetic methods for the naphthalimide azo and the phthalimide azo systems were found to be more efficient than for the phenylazo system in terms of high yield, easy work-up, and high degree of functionalization. Significantly, formation of the six-membered cyclic imide in the naphthalimide azo system gave fully functionalized denderimers by the naphthalimide azo fragment. On the other hand, nucleophilic substitution involving *p*-fluoronitrobenzene and the dendrimeric amines employed for the phenylazo system revealed the limitation of the degree of functionalization with the higher dendrimer generations. ^1H and ^{13}C NMR and IR spectroscopy were employed to confirm structural identification of the dendrimers. Mass spectrometry (ES and MALDI) and UV–vis spectrophotometry (comparison of UV–vis data of the dendrimer compounds with those of the model compounds) were useful in the determination of the degree of functionalization. Thermogravimetric analysis showed that azo-functionalization increased the thermal stability of the PAMAM dendrimers.

Since one of the purposes of this study was to synthesize electronic materials that can show improved xerographic properties, and continuing with our investigations with dye and pigment molecules (e.g., azo (12), azoxy (13), spiropyran (14), and squaraine (15) dyes), the xerographic properties of the azo-modified dendrimers prepared will also be determined, via single-discharge measurements, surface potential vs. exposure (SPE) measurements, spectral sensitivity measurements, and xerographic cyclic stability measurements (16). The results of these studies will be reported in due course.

Experimental

Compounds synthesized were characterized by a combination of ^1H NMR, ^{13}C NMR, UV, IR, and mass spectroscopy and melting point and elemental analysis. ^1H and ^{13}C NMR spectra were obtained with a Bruker AM400 (^1H, 400.1 MHz; ^{13}C, 100.6 MHz) or Bruker AC - F 200 spectrometer (^1H, 200.1 MHz; ^{13}C, 50.3 MHz). Normally, $CDCl_3$

© 2004 NRC Canada

and DMSO-d_6 were used as the solvents and served as deuterium lock standards. Chemical shifts are reported in parts per million (ppm) relative to residual $CHCl_3$ (δ ^1H = 7.24 ppm, δ ^{13}C = 77 ppm) and DMSO (δ ^1H = 2.50 ppm, δ ^{13}C = 49 ppm) in the solvents. Infrared spectra were obtained using a Bomen MB - 120 spectrophotometer with samples prepared as KBr disks. The low-resolution MS results were recorded with a Fison's VG Quattro (Triple-Quadrople MS–MS). Several techniques were used, as follows: chemical ionization (CI), fast atom bombardment (FAB), and electrospray (ES). MALDI (matrix-assisted laser desorption ionization) technique was used for dendrimer compounds. MALDI MS results were recorded with a Kompact MALDI III by Kratos Analytical, with sinapinic acid as the matrix. High-resolution MS analyses were performed at either the University of Ottawa (Ontario) or the Scripps Research Institute of California. UV–vis absorption spectra were obtained using a Hewlett-Packard HP8452A Diode Array spectrophotometer fitted with a thermostated cell compartment. Melting points were measured using a Thomas Hoover apparatus and are uncorrected. Elemental analyses were performed by Canadian Microanalytical Service Ltd., Delta, B.C.

For UV–vis spectrophotometric studies, the solvents DMSO and EtOH were purified by distillation from calcium hydride and magnesium, respectively (17). Other organic solvents used in this study were the following: *N*,*N*-dimethylformamide (DMF), 2,2,2-trifluoroethanol (TFE), acetonitrile, toluene, chloroform, 1,4-dioxane, acetone, methanol, and hexane. These solvents were of spectroscopic grade and were purified, when necessary, according to literature procedures (17).

Stock solutions (0.1–1 mmol) of the dendrimer compounds were prepared by accurately weighing 1–10 mg and dissolving these in 1–5 mL of DMF or DMSO in volumetric flasks, which were wrapped in aluminum foil so as to prevent possible photochemical processes. Stock solutions (1–10 mmol) of the model compounds were prepared in $CHCl_3$ or DMF and were stored in the refrigerator. All UV–vis spectra in this study were obtained by injecting 20–50 µL of the stock solution into a 10 mm cell containing 2.5 mL of the solvent, followed by shaking the cell a few times and allowing a few seconds to pass to allow any air bubbles entrapped on mixing to escape, before taking the spectrum.

Compounds were purified by a combination of several techniques, as follows: thin layer and column chromatography, recrystallization, sonication, and ultrafiltration. Thin layer chromatography (TLC) was performed using silica gel 60 F_{254} plates (BDH) in various eluting solvent systems. Silica gel 60 (BDH, 230–400 mesh) was used for column chromatography. An Amicon ultrafiltration cell model 8400 was used for purification of high generations of the dendrimers. A Branson model 2200 sonication bath was used in all experiments requiring sonication.

The couplers (naphthol AS-RL, naphthol AS-BG, and naphthol AS-BS) for the diazo coupling reactions were supplied by Xerox Research Centre of Canada (XRCC). Various generations of polyamidoamine (PAMAM) dendrimers (1–4 G) were purchased from Michigan Molecular Institute, while the other starting materials were obtained from Aldrich Chemical Company.

Preparation of dye compounds

Phenylazo derivatives of the PAMAM dendrimers

*p-Nitrophenyl derivative of PAMAM dendrimer (**1**)*

The first generation polyamidoamine dendrimer (0.50 g, 0.48 mmol) was dissolved in 10 mL absolute ethanol, and to this was added 4-fluoronitrobenzene (0.41 g, 2.9 mmol), and the reaction mixture was refluxed for about 12 h. The solvent was removed in a rotary evaporator; the yellow oil was dissolved in 50 mL water, and the aqueous solution was washed four times with 50 mL portions of chloroform to remove any unreacted 4-fluoronitrobenzene. Removal of the water in a rotary evaporator gave 0.60 g of product (71% yield) as a yellow oil.

The synthetic method for the *p*-nitrophenylation of the 2nd, 3rd, and 4th generation (G) of PAMAM followed closely the above. The yields obtained were as follows: 2nd G (81%), 3rd G (85%), and 4th G (85%). The NMR characteristics of the *p*-nitrophenyl derivative of the PAMAM dendrimer 1G (**1**) are as follows:

1: ^1H NMR (DMSO-d_6) δ: 8.16 (outer amide NH, s), 7.96 (H_3, d), 7.86 (inner amide NH, s), 6.65 (H_2, d), 3.89 (NH, s), 3.08 (H_g, H_c, t), 2.79 (H_h, t), 2.63 (H_d, t), 2.42 (H_e, H_a, t), 2.20 (H_f, H_b, t). ^{13}C NMR (DMSO-d_6) δ: 171.88 (C=O-outer), 171.46 (C=O-inner), 154.46 (C_1), 135.70 (C_4), 126.22 (C_3), 110.75 (C_2), 52.11 (C_d), 49.59 (C_e, C_a), 41.87 (C_g), 37.71 (C_h), 36.90 (C_c), 33.23 (C_b, C_f).

*p-Aminophenyl derivative of polyamidoamine dendrimer (**2**)*

To a solution of dendrimer **1** (0.65 g, 0.37 mmol) in 150 mL of a 1:1 (volume fraction) mixture of water–ethanol in a glass Parr shaker bottle was added palladium on charcoal (100 mg of 5% Pd–C). The reaction mixture was pressurized to 45 psi (1 psi = 6.894 kPa) of hydrogen, and the Parr hydrogenation apparatus was shaken at room temperature for about 12 h. The reaction mixture was then filtered to remove the Pd–C, and the solvent was removed in vacuo to give the products **2–1G** (89% yield), **2–2G** (83%), **2–3G** (81%), and **2–4G** (34%).

2: ^1H NMR (DMSO-d_6) δ: 8.01 (outer amide NH, s), 7.83 (inner amide NH, s), 6.39 (H_2, H_3, m), 3.82 (NH_2, NH, s), 3.17 (H_g, H_c, t), 2.95 (H_h, t), 2.65 (H_d, t), 2.42 (H_e, H_a, t), 2.20 (H_f, H_b, t). ^{13}C NMR (DMSO-d_6) δ: 171.61 (C=O-outer), 171.19 (C=O-inner), 139.97 (C_4), 139.12 (C_1), 115.53 (C_2), 113.67 (C_3), 52.14 (C_d), 49.65 (C_e, C_a), 43.89 (C_g), 36.90 (C_h), 35.95 (C_c), 33.30 (C_b, C_f).

Phenylazo derivatives of PAMAM dendrimers

To a solution of the *p*-aminophenyl polyamidoamine dendrimer derivative **2–1G** (0.58 g, 0.37 mmol) in aqueous hydrochloric acid (0.64 mL concd HCl and 2 mL water) cooled below 2 °C in ice-water was added, slowly with stirring, a solution of sodium nitrite (0.15 g, 2.20 mmol) in 2 mL water. The resulting diazonium salt solution was coupled with various couplers (naphthol AS, naphthol AS-BG, naphthol AS-RL, and naphthol AS-BS). The diazo-coupling reaction with naphthol AS as the coupler is described below.

To the solution of the diazonium salt solution was added, slowly with stirring, naphthol AS (0.58 g, 2.2 mmol) in 6 mL *N*,*N*-dimethylformamide (DMF) and 1.8 mL 10%

© 2004 NRC Canada

aqueous sodium hydroxide solution, keeping the temperature below 2 °C, which gave a purplish-red precipitate. After all the diazonium salt solution had been added, the reaction mixture was allowed to stand in an ice bath for 1 h with stirring. The resulting precipitate was filtered and washed with cold water several times to remove residual DMF. The unreacted naphthol AS in the crude product was removed by soxhlet extraction with acetonitrile to give 0.48 g of pure product (39% yield, mp 216–218 °C).

The diazo-coupling reaction with other couplers (naphthol AS-RL, naphthol AS-BG, and naphthol AS-BS) was carried out by same method as above. Naphthol AS-RL azo derivative (**4**; 10% yield, mp > 250 °C); naphthol AS-BG azo derivative (**5**; 10% yield, mp 182–184 °C); naphthol AS-BS azo derivative (**6**; 14% yield, mp 188–190 °C). The diazo coupling reaction between higher generations of the aminophenyl derivative of the dendrimer (2G, 3G, and 4G) and naphthol AS was carried out by same method as above. 2G (20% yield, mp 178–180 °C); 3G (12% yield, mp 207–209 °C); 4G (14% yield, mp 211–213 °C). The characteristics of the phenylazo derivatives of the PAMAM dendrimers are as follows:

3–6

*R = H, **3–1G***: IR (KBr disk) (cm^{-1}): 3189, 2922, 2853, 1736, 1662, 1660, 1539, 1444, 1264, 1174, 1017, 808, 752, 692, 515. ^1H NMR (DMSO-d_6) δ: 12.4 (OH, s), 11.3 (amide NH, s), 8.6 ($H_{4,8}$, bs), 8.2 (H_5, amide NH, bs), 7.8 ($H_{3''}$, $H_{2'}$, H_7, inner amide NH, bt), 7.4 (H_6, $H_{3'}$, bt), 7.1 ($H_{4'}$, dd), 6.6 ($H_{2''}$, d), 3.8 (NH, bs), 3.2 (H_g, H_c, bs), 2.9 (H_h, bs), 2.7 (H_d, bs), 2.4 (H_e, H_a, bs), 2.1 (H_f, H_b, bs). ^{13}C NMR (DMSO-d_6) δ: 171.6 (C=O-outer), 170.9 (C=O-inner), 162.0 (C=O-phenyl), 161.5 (C_2), 150.4 ($C_{1''}$), 138.9 (C_4), 138.3 ($C_{1'}$), 138.1 ($C_{4''}$), 133.9 (C_1), 133.6 (C_{10}), 129.5 (C_5), 129.5 (C_7), 128.4 ($C_{3'}$), 125.5 (C_3, C_9), 124.6 (C_6), 123.3 ($C_{4'}$), 121.5 ($C_{3''}$), 120.3 (C_8), 119.7 ($C_{2''}$), 112.4 ($C_{2''}$), 52.0 (C_d), 49.5 (C_e), 49.3 (C_a), 43.4 (C_g), 42.3 (C_h), 36.8 (C_c), 33.2 (C_b, C_f). MS *m/z* (ES) calcd. for $C_{161}H_{167}N_{36}O_{19}$: 3234.4; found: 2978.5.

*Azo naphthol AS derivative of the PAMAM dendrimer -2G (**3–2G**)*: IR (KBr disk) (cm^{-1}): 3246, 2928, 1655, 1597, 1549, 1445, 1384, 1199.

*Azo naphthol AS derivative of the PAMAM dendrimer -3G (**3–3G**)*: IR (KBr disk) (cm^{-1}): 3253, 2927, 1654, 1596, 1550, 1384, 1199, 1147.

*Azo naphthol AS derivative of the PAMAM dendrimer -4G (**3–4G**)*: IR (KBr disk) (cm^{-1}): 3270, 2935, 1658, 1596, 1550, 1447, 1384, 1199.

*R = 4′-methoxy, **4–1G***: IR (KBr disk) (cm^{-1}): 3332, 3077, 2963, 1666, 1604, 1547, 1512, 1262, 1069, 806, 696, 462. ^1H NMR (DMSO-d_6) δ: 12.5 (OH, s), 11.4 (amide NH, s), 8.6 (H_4, H_8, bs), 8.3 (H_5, bs), 8.2 (outer amide NH, s), 7.9 ($H_{3''}$, bs), 7.8 ($H_{2'}$, H_7, bt), 7.2 (H_6, bt), 7.1 ($H_{3'}$, d), 6.7 ($H_{2''}$, d), 4.2 (NH, bs), 3.6 (OCH_3, s), 3.2 (H_g, H_c, bs), 2.9 (H_h, bs), 2.6 (H_d, H_e, H_a, bs), 2.2 (H_f, H_b, bs).

*R = 2′, 5′-dimethoxy, **5–1G***: IR (KBr disk) (cm^{-1}): 3323, 2964, 1657, 1603, 1539, 1449, 1263, 1069, 865, 808, 755, 700, 469. ^1H NMR (DMSO-d_6) δ: 12.4 (OH, s), 11.4 (amide NH, s), 8.5 ($H_{4,8}$, bs), 8.2 (H_5, bs), 8.1 (outer amide NH, s), 8.0 ($H_{6'}$, bs), 7.9 (inner amide NH), 7.8 ($H_{3''}$, bs), 7.7 (H_7, bt), 7.4 (H_6, bt), 7.2 ($H_{3'}$, d), 7.1 ($H_{4'}$, d), 6.9 ($H_{2''}$, bs), 4.1 (NH, bs), 3.8 (OCH_3, bs), 3.2 (H_g, H_c, bs), 3.0 (H_h, bs), 2.6 (H_d, bs), 2.4 (H_e, H_a, bs), 2.2 (H_f, H_b, bs). ^{13}C NMR (DMSO-d_6) δ: 172.0 (C=O-outer), 171.4 (C=O-inner), 162.0 (C=O-phenyl), 161.5 (C_2), 153.0 ($C_{5'}$), 148.8 ($C_{1''}$), 142.8 ($C_{2''}$), 139.7 ($C_{4''}$), 138.3 (C_4), 134.5 (C_1), 131.0 (C_5), 130.5 (C_7), 130.0 (C_{10}), 128.7 ($C_{1'}$), 125.7 (C_6), 125.6 (C_3), 125.6 (C_9), 122.4 ($C_{3''}$), 120.8 (C_8), 113.9 ($C_{2''}$), 11.4 ($C_{3'}$), 107.2 ($C_{4'}$), 106.9 ($C_{6'}$), 56.3 (OCH_3 at $C_{2'}$), 55.0 (OCH_3 at $C_{5'}$), 50.3 (C_d), 49.4 (C_a, C_e), 44.2 (C_g), 44.0 (C_h), 37.0 (C_c), 32.9 (C_b, C_f).

*R = 3′-nitro, **6–1G***: IR (KBr disk) (cm^{-1}): 3309, 2944, 1656, 1604, 1535, 1262, 1072, 806, 738, 464. ^1H NMR (DMSO-d_6) δ: 12.4 (OH, s), 11.4 (amide NH, s), 8.5 ($H_{4,8}$, broad s), 8.2 (H_5, broad s), 8.1 (outer amide NH, s), 8.0 ($H_{6'}$, bs), 7.9 (inner amide NH), 7.8 ($H_{3''}$, bs), 7.7 (H_7, bt), 7.4 (H_6, bt), 7.2 ($H_{3'}$, d), 7.1 ($H_{4'}$, d), 6.9 ($H_{2''}$, bs), 4.1 (NH, bs), 3.8 (OCH_3, bs), 3.2 (H_g, H_c, bs), 3.0 (H_h, bs), 2.6 (H_d, bs), 2.4 (H_e, H_a, bs), 2.2 (H_f, H_b, bs).

Model phenylazo derivatives of PAMAM dendrimers

The model compounds **7** and **8** were synthesized by the same method as that used for the dendrimer. **7** (29% yield, mp 224 to 225 °C); **8** (32% yield, mp 214 to 215 °C). The characteristics of the model compounds (**7** and **8**) are as follows:

7, 8

*R = H (**7**)*: IR (KBr disk) (cm^{-1}): 3343, 2922, 2853, 1736, 1662, 1660, 1539, 1444, 1264, 1174, 1017, 808, 752, 692, 515. ^1H NMR (DMSO-d_6) δ: 12.48 (OH, s, 1H), 11.30 (amide NH, s, 1H), 8.60 (H_4, d, 1H), 8.60 (H_8, d, 1H), 7.98 (H_5, d, 1H), 7.82 ($H_{3''}$, d, 2H), 7.80 ($H_{2'}$, d, 2H), 7.67 (H_7, t, 1H), 7.46 (H_6, t, 1H), 7.39 ($H_{3'}$ dd, 2H), 7.13 ($H_{4'}$, dd, 1H), 6.80 (NH, d, 1H), 6.73 ($H_{2''}$, d, 2H), 2.99 (CH_3, s, 3H). ^{13}C NMR (DMSO-d_6) δ: 162.7 (C=O), 161.8 (C_2), 152.0 ($C_{1''}$), 138.7 ($C_{1'}$), 138.4 (C_4), 134.3 ($C_{4''}$), 133.6 (C_{10}), 129.9 (C_7), 129.9 (C_5), 128.9 ($C_{3'}$), 128.6 (C_9), 125.9 (C_1), 125.9 (C_3), 125.0 (C_6), 123.7 ($C_{4'}$), 122.4 ($C_{3''}$), 120.8 (C_8), 119.8 ($C_{2'}$), 112.3 ($C_{2''}$), 29.14 (CH_3). MS *m/z* (ES+): 397. 3 ([M + 1]). MS *m/z* (high-resolution EI) calcd. for $C_{24}H_{20}N_4O_3$: 396.1586; found: 396.1598. Anal. calcd. for $C_{24}H_{20}N_4$ (MW 396.16): C 72.73, H 5.05, N 14.14; found: C 72.21, H 4.98, N 14.08.

*R = 4′-methoxy (**8**)*: IR (KBr disk) (cm^{-1}): 3340, 3021, 2879, 1735, 1660, 1658, 1540, 1450, 1258, 1170, 1015, 809, 690. ^1H NMR (DMSO-d_6) δ: 12.48 (OH, s, 1H), 11.12 (amide NH, s, 1H), 8.57 (H_8, d, 1H), 8.56 (H_4, s, 1H), 7.95 (H_5,d, 1H), 7.80 ($H_{3''}$, d, 2H), 7.70 ($H_{2'}$, d, 2H), 7.66 (H_7, t, 1H), 7.45 (H_6, t, 1H), 6.95 ($H_{3'}$, d, 2H), 6.78 (NH, d, 1H), 6.72 ($H_{2''}$, d, 2H), 3.76 (OCH_3, s, 3H), 2.80 (CH_3, d, 3H). ^{13}C NMR (DMSO-d_6) δ: 162.2 (C=O), 161.9 (C_2), 155.5 ($C_{4'}$), 152.0 ($C_{1''}$), 138.3 (C_4), 134.2 ($C_{4''}$), 133.5 (C_{10}), 131.8 ($C_{1'}$), 129.7 (C_5), 129.7 (C_7), 128.5 (C_9), 125.9 (C_1), 125.9 (C_3), 124.9(C_6), 122.3 ($C_{3''}$), 121.3 ($C_{2'}$), 120.7 (C_8), 114.0 ($C_{3'}$), 112.2 ($C_{2''}$), 55.1 (OCH_3), 29.4 (CH_3). MS *m/z* (CI+): 426.9 ([M + 1]). MS *m/z* (high-resolution EI) calcd. for $C_{25}H_{22}N_4$: 426.1692; found: 426.1673. Anal. calcd. for $C_{25}H_{22}N_4O_3$ (MW 426.17): C 70.40, H 5.20, N 13.14; found: C 69.86, H, 5.30, N 13.10.

© 2004 NRC Canada

Naphthalimide azo derivatives of the PAMAM dendrimers

4-Amino 1,8-naphthoic anhydride

This compound is commercially available but, because of its high cost, was instead synthesized in 97% yield by the hydrogenation (Pd–C catalyst) of 4-nitro 1,8-naphthoic anhydride.

Azo naphthoic anhydrides (9–12)

To a solution of 4-amino-1,8-naphthoic anhydride (0.82 g, 3.85 mmol) in 100 mL DMF and 10 mL water, cooled to 2 °C, was added concd. HCl (1.60 mL, 10.9 mmol), and to the cooled reaction mixture was added, slowly with stirring, a solution of sodium nitrite (0.37 g, 3.85 mmol) in 6 mL water. The resulting diazonium salt solution was coupled with various couplers (naphthol AS, naphthol AS-RL, naphthol AS-BG, and naphthol AS-BS). **9** (58% yield, mp > 250 °C); **10** (64% yield, mp > 250 °C); **11** (66% yield, mp > 250 °C); **12** (77% yield, mp > 250 °C).

The characteristics of the azo naphthoic anhydrides (**9**–**12**) are as follows:

9–12

*R = H (**9**)*: IR (KBr disk) (cm^{-1}): 3133, 1773, 1734, 1675, 1596, 1308, 1154, 1011, 817, 757, 693, 541. ^1H NMR (DMSO-d_6) δ: 13.39 (O-H, s, 1H), 9.27 (H_5, d, 1H), 9.20 ($H_{5''}$, d, 1H), 8.70 (H_4, s, 1H), 8.53 ($H_{7''}$, d, 1H), 8.49 ($H_{2''}$, d, 1H), 8.07 ($H_{3''}$, d, 1H), 7.96 ($H_{6''}$, t, 1H), 7.80 ($H_{2'}$, $H_{6'}$, d, 1H), 7.80 (H_8, d, 2H), 7.62 (H_6, t, 1H), 7.40 ($H_{3'}$, $H_{5'}$, t, 2H), 7.28 ($H_{4'}$, d, 1H), 7.10 (H_7, t, 1H). MS *m/z* (CI+): 488.4 ([M + 1]). MS *m/z* (high-resolution FAB+) calcd. for $C_{29}H_{18}N_3O_5$: 488.1246; found: 488.1256.

*R = 4′-methoxy (**10**)*: IR (KBr disk) (cm^{-1}): 3022, 1768, 1731, 1670, 1573, 1194, 1019, 757, 530. ^1H NMR (DMSO-d_6) δ: 13.54 (O-H, s, 1H), 9.40 (H_5, d, 1H), 9.36 ($H_{5''}$,d, 1H), 8.62 (H_4, s, 1H), 8.54 ($H_{7''}$, d, 1H), 8.49 ($H_{2''}$, d, 1H), 8.02 ($H_{3''}$, d, 1H), 7.94 ($H_{6''}$, t, 1H), 7.76 (H_8, d, 1H), 7.72 ($H_{2'}$, $H_{6'}$, d, 2H), 7.58 (H_6, t, 1H), 7.25 (H_7, t, 1H), 6.96 ($H_{3',5'}$, d, 2H), 3.79 (CH_3, s, 3H). MS *m/z* (CI+): 518.3 ([M + 1]). MS *m/z* (high-resolution EI) calcd. for $C_{30}H_{19}N_3O_6$: 517.1274; found: 517.1174.

*R = 2′, 5′-dimethoxy (**11**)*: IR (KBr disk) (cm^{-1}): 3214, 2929, 1771, 1734, 1671, 1570, 1153, 1017, 760, 701. ^1H NMR (DMSO-d_6) δ: 13.54 (O-H, s, 1H), 9.40 (H_5, d, 1H), 9.36 ($H_{5''}$, d, 1H), 8.63 (H_4, s, 1H), 8.54 ($H_{7''}$, d, 1H), 8.49 ($H_{2''}$, d, 1H), 8.30 ($H_{6'}$, d, 1H), 8.02 ($H_{3''}$, d, 1H), 7.94 ($H_{6''}$, t, 1H), 7.76 (H_8, d, 1H), 7.58 (H_6, t, 1H), 7.25 (H_7, t, 1H), 7.00 ($H_{3'}$, d, 1H), 3.92 (OCH_3 at $C_{2'}$, s, 3H), 3.73 (OCH_3 at $C_{5'}$, s, 3H). MS *m/z* (CI+): 548.3 ([M + 1]). MS *m/z* (high-resolution FAB+) calcd. for $C_{31}H_{22}N_3O_7$: 548.1458; found: 548.1446.

*R = 3′-nitro (**12**)*: IR (KBr disk) (cm^{-1}): 3120, 1773, 1736, 1678, 1593, 1013, 756. ^1H NMR (DMSO-d_6) δ: 13.50 (O-H, s, 1H), 9.40 (H_5, d, 1H), 9.20 ($H_{5''}$, d, 1H), 8.95 ($H_{2'}$, d, 2H), 8.63 (H_4, s, 1H), 8.54 ($H_{7''}$,d, 1H), 8.49 ($H_{2''}$, d, 1H), 8.02 ($H_{3''}$, d, 1H), 7.96 ($H_{6''}$, t, 1H), 7.95 ($H_{4'}$, d, 1H), 7.80 ($H_{6'}$, d, 1H), 7.76 (H_8, d, 1H), 7.68 ($H_{5'}$, t, 1H), 7.58 (H_6, t, 1H), 7.25 (H_7, t, 1H). MS *m/z* (CI+) calcd. for $C_{29}H_{17}N_4O_7$: 533.5; found: 534.5 ([M + 1]).

Naphthalimide azo derivatives of PAMAM dendrimers

The PAMAM 1G dendrimer (33.5 mg, 0.029 mmol) solution (8.8% in methanol) was evaporated to remove the methanol, and the residue was dissolved in 2 mL 1-methyl-2-pyrrolidinone (NMP). The resulting dendrimer solution was added to a solution of azo naphthol-AS naphthoic anhydride **9** (0.1 g, 0.21 mmol) and DABCO (39.4 mg, 0.35 mmol) in 5 mL, and the reaction mixture was stirred at 85 °C for 2 h. After cooling to room temperature, 200 mL of toluene was added, and the precipitate that formed was filtered, washed with toluene and petroleum ether, and dried at 80 °C for about 12 h. The crude product was sonicated in water for 10 min to remove protonated DABCO and unreacted PAMAM. After filtration, the solid was sonicated in acetone for 10 min to remove excess DABCO and unreacted azo starting compound. The solid obtained on filtration was checked by TLC using acetone as eluent; this showed the absence of starting materials and DABCO. The yields and mp are as follows: **13**–**1G** (81%, 242–244 °C); **13**–**2G** (68%, 234–236 °C); **13**–**3G** (69%, 241–243 °C); **14** (81%, >250 °C); **15** (50%, >250 °C); **16** (75%, 244–246 °C).

The characteristics of the azo naphthalimide deivatives of PAMAM dendrimers are as follows:

*Azo napthol AS derivative (1G), **13**–**1G***

IR (KBr disk) (cm^{-1}): 3376, 2892, 2361, 1941, 1697, 1658, 1589, 1546, 1011, 777, 755. ^1H NMR (DMSO-d_6) δ: 9.0–7.1 (aromatic protons, broad m), 4.2 (NH, s), 3.5 (H_g, H_c, bs), 2.9 (H_h, bs), 2.6 (H_d, bs), 2.4 (H_e, H_a, bs), 2.2 (H_f, H_b, bs). MS *m/z* (MALDI) calcd. for $C_{219}H_{183}N_{37}O_{33}$: 3858.4; found: 3824.3.

*Azo naphthol AS derivative (2G), **13**–**2G***

IR (KBr disk) (cm^{-1}): 3361, 2103, 1687, 1506, 1363, 1023, 777, 755.

*Azo naphthol AS derivative (3G), **13**–**3G***

IR (KBr disk) (cm^{-1}): 3440, 2880, 2115, 1934, 1698, 1662, 1542, 1492, 1359, 1009, 775, 754.

*Azo naphthol AS-RL derivative (1G), **14**–**1G***

IR (KBr disk) (cm^{-1}): 3059, 2925, 2832, 1655, 1566, 1511, 1441, 1403, 1354, 1239, 1024, 777, 752. ^1H NMR (DMSO-d_6) δ: 12.4 (OH, s), 11.3 (amide NH), 8.6–6.6 (aromatic protons, broad m), 4.1 (NH, s), 3.8 (OCH_3, s), 3.2 (H_g, H_c, bs), 2.9 (H_h, bs), 2.7 (H_d, bs), 2.4 (H_e, H_a, bs), 2.2 (H_f, H_b, bs). MS *m/z* (MALDI) calcd. for $C_{225}H_{195}N_{37}O_{39}$: 4038.4; found: 3902.9.

*Azo naphthol AS-BG derivative (1G), **15**–**1G***

IR (KBr disk) (cm^{-1}): 3241, 2933, 2832, 1658, 1584, 1373, 1227, 1043, 777, 756. ^1H NMR (DMSO-d_6) δ: 13.0 (OH, s), 11.2 (amide NH), 8.8–6.6 (aromatic protons, broad m), 4.0 (NH, s), 3.7 (OCH_3 at $C_{2'}$, $C_{5'}$, bs), 3.4 (H_g, H_c, bs), 3.0 (H_h, bs), 2.4 (H_d, H_e, H_a, bs), 2.2 (H_f, H_b, bs). MS *m/z* (MALDI) calcd. for $C_{231}H_{207}N_{37}O_{45}$: 4218.5; found: 4208.6.

*Azo naphthol AS-BS derivative (1G), **16**–**1G***

IR (KBr disk) (cm^{-1}): 3237, 2935, 2830, 1696, 1661, 1586, 1546, 1344, 1013, 777, 736. ^1H NMR (DMSO-d_6) δ: 12.4 (OH, s), 11.3 (amide NH), 8.6–6.6 (aromatic protons, broad m), 4.1 (NH, s), 3.2 (H_g, H_c, bs), 2.9 (H_h, bs), 2.7 (H_d,

© 2004 NRC Canada

bs), 2.4 (H_e, H_a, bs), 2.1 (H_f, H_b, bs). MS *m/z* (MALDI) calcd. for $C_{219}H_{177}N_{43}O_{45}$: 4128.3; found: 4196.3.

Model naphthalimide derivatives of PAMAM dendrimers

The reaction conditions for synthesis of the model compounds (**17**, **18**) were closely similar to those for the dendrimer compounds; *n*-$BuNH_2$ was used as a model amine for the PAMAM dendrimer. **17** (29% yield, mp > 250 °C); **18** (28% yield, mp > 250 °C).

The characteristics of the model naphthalimide derivatives of the PAMAM dendrimers (**17** and **18**) are as follows:

17, 18

R = H (17): IR (KBr disk) (cm^{-1}): 3215, 2933, 1697, 1659, 1588, 1547, 1353, 1008, 767, 750. ^{1}H NMR ($CDCl_3$) δ: 14.10 (O-H, s, 1H), 11.12 (amide NH, s, 1H), 8.93 (H_4, s, 1H), 8.66 ($H_{5''}$, d, 1H), 8.62 ($H_{2''}$, d, 1H), 8.44 ($H_{7''}$, d, 1H), 8.40 (H_5, d, 1H), 8.29 ($H_{3''}$, d, 1H), 7.93 ($H_{6''}$, t, 1H), 7.76 ($H_{2'}$, $H_{6'}$, d, 2H), 7.70 (H_8, d, 1H), 7.65 (H_6, t, 1H), 7.49 (H_7, t, 1H), 7.38 ($H_{3'}$, $H_{5'}$, t, 1H), 7.15 ($H_{4'}$, t, 1H), 4.16 (H_a, t, 2H), 1.71–1.36 (H_b, H_c, m, 4H), 0.99 (H_d, t, 3H). ^{13}C NMR ($CDCl_3$) δ: 179.53 (C_2), 163.18 (C=O amide), 162.65 (C=O at $C_{1''}$), 161.19 (C=O at $C_{8''}$), 150.57 (C_4), 141.84 ($C_{4''}$), 138.09 ($C_{1'}$), 134.50 (C_{10}), 133.11 ($C_{1''}$), 132.19 ($C_{2''}$), 131.73 (C_8), 131.70 ($C_{5''}$), 131.56 (C_6), 129.17 (C_9), 129.05 ($C_{3'}$), 128.24 (C_7), 127.74 ($C_{6''}$), 127.24 (C_3), 126.29 (C_1), 125.77 ($C_{7''}$), 124.60 ($C_{4'}$), 123.58 ($C_{8''}$), 122.53 (C_5), 121.57 ($C_{10''}$), 120.79 ($C_{2'}$), 119.88 ($C_{9''}$), 112.96 ($C_{3''}$), 40.39 (C_a), 30.24 (C_b), 20.42 (C_c), 13.84 (C_d). MS *m/z* (CI+): 543.4 ([M + 1]). MS *m/z* (high-resolution EI) calcd. for $C_{33}H_{26}N_4O_4$: 542.1954; found: 542.1969.

R = 4′-methoxy (18): IR (KBr disk) (cm^{-1}): 3038, 1694, 1655, 1592, 1308, 1008, 823, 760, 553. ^{1}H NMR ($CDCl_3$) δ: 14.06 (O-H, s, 1H), 11.01 (amide NH, s, 1H), 8.93 (H_4, s, 1H), 8.66 ($H_{5''}$, d, 1H), 8.62 ($H_{2''}$, d, 1H), 8.44 ($H_{7''}$, d, 1H), 8.40 (H_5, d, 1H), 8.30 ($H_{3''}$, d, 1H), 7.92 ($H_{6''}$, t, 1H), 7.68 (H_8, d, 1H), 7.65 ($H_{2'}$, $H_{6'}$, d, 2H), 7.61 (H_6, t, 1H), 7.50 (H_7, t, 1H), 6.90 ($H_{3'}$, $H_{5'}$, d, 2H), 4.16 (H_a, t, 2H), 3.82 (OCH_3, s, 3H), 1.71–1.36 (H_b, H_c, m, 4H), 0.98 (H_d, t, 3H). ^{13}C NMR ($CDCl_3$) δ: 179.81 (C_2), 164.91 (C=O amide), 164.68 (C=O at $C_{1''}$), 163.25 (C=O at $C_{8''}$), 157.79 ($C_{4'}$), 151.86 (C_4), 142.59 ($C_{4''}$), 134.60 (C_{10}), 133.42 ($C_{2''}$), 133.32 ($C_{1''}$), 133.06 (C_8), 132.80 ($C_{5''}$), 132.17 (C_6), 129.49 ($C_{1'}$), 129.23 (C_9), 128.80 (C_7), 128.04 ($C_{6''}$), 127.20 (C_3), 126.70 ($C_{7''}$), 124.57 (C_1), 124.14 ($C_{2'}$), 122.87 ($C_{8''}$), 122.79 (C_5), 121.42 ($C_{10''}$), 118.68 ($C_{9''}$), 114.70 ($C_{3'}$), 113.24 ($C_{3''}$), 55.75 (OCH_3), 41.11 (C_a), 30.08 (C_b), 20.29 (C_c), 13.66 (C_d). MS *m/z* (CI+): 573.3 ([M + 1]). MS *m/z* (high-resolution FAB+) calcd. for $C_{34}H_{29}N_4O_5$, 573.2138; found: 573.2126. Anal. calcd. for $C_{34}H_{28}N_4O_5$ (MW 573.21): C 71.33, H 4.90, N 9.79; found: C 70.77, H 4.88, N 9.49.

Phthalimide azo derivatives of the PAMAM dendrimers

Phthalimide azo derivatives of PAMAM dendrimers

Cyclic imide formation between the PAMAM dendrimer and 4-nitrophthalic anhydride was carried out as follows: To a solution of 4-nitrophthalic anhydride (1.25 g, 6.48 mmol) in 5 mL NMP was added a solution of PAMAM (0.97 g, 0.93 mmol) and DABCO (0.63 g, 5.55 mmol) dissolved in 5 mL NMP, and the reaction mixture was stirred at 130 °C for 40 min. After cooling to room temperature, 200 mL of toluene was added to give a white precipitate, which was washed with toluene and acetone several times to remove excess starting materials. Yield 78% (**19–1G**); 88% (**19–2G**); 90% (**19–3G**). The characteristics of compound **19** are as follows:

19

IR (KBr disk) (cm^{-1}): 3288, 3073, 2948, 1781, 1720. 1656, 1539, 1437, 1396, 1348, 1194, 1160, 1063, 720. ^{1}H NMR (DMSO-d_6) δ: 8.59 (H_5, dd), 8.47 (H_3, d), 8.10 (H_6, d), 8.02 (outer amide NH, s), 7.70 (inner amide NH, s), 3.65 (H_h, t), 3.30 (H_c, H_g, t), 2.61 (H_d, t), 2.36 (H_a, H_e, t), 2.29 (H_b, H_f, t). ^{13}C NMR (DMSO-d_6) δ: 171.63 (outer C=O), 171.02 (inner C=O), 166.31 (C=O at C_1), 166.03 (C=O at C_2), 151.31 (C_4), 136.38 (C_2), 133.11 (C_1), 129.47 (C_6), 124.46 (C_5), 117.68 (C_3), 52.01 (C_d), 48.47 (C_e, C_a), 44.38 (C_g), 36.57 (C_h), 32.94 (C_c), 30.09 (C_b, C_f). MS *m/z* (FAB^+) calcd. for $C_{93}H_{99}N_{25}O_{33}$: 2093.7; found: 2094.0 ([M + 1]).

The nitro compound (**19**) was reduced by hydrogenation in the presence of Pd–C catalyst to give the amino derivative used for the diazo coupling reaction with the couplers (naphthol AS, AS-RL, AS-BG, and AS-BS). The experimental procedure for the diazo coupling reaction followed standard reaction conditions and gave the following yields and mp: **20** (58%, 230–232 °C); **21** (63%, 218–220 °C); **21–2G** (31%, 218–221 °C); **21–3G** (38%, 225 to 226 °C); **22** (56%, 220–222 °C); **23** (55%, 231–233 °C).

The characteristics of azo phthalimide derivatives of PAMAM dendrimers are as follows:

20–23

R = H, 20–1G: IR (KBr disk) (cm^{-1}): 3248, 3054, 1770, 1712, 1667, 1545, 1443, 1380, 1259, 1200, 1158, 1012, 891, 817, 751, 539. ^{1}H NMR (DMSO-d_6) δ: 12.4 (OH,s), 11.3 (amide NH, s), 9.0 (H_4, bs), 8.4 (H_5, bs), 8.1 ($H_{3''}$, outer amide NH, bs), 7.9 ($H_{6''}$, inner amide NH, bs), 7.8 ($H_{2'}$, $H_{6'}$, $H_{5''}$, m), 7.7 (H_6, t), 7.6 (H_8, t), 7.4 ($H_{7,3',5'}$, m), 7.1 ($H_{4'}$, t), 3.8 (NH, bs), 3.4 (H_g, H_c, bs), 3.2 (H_h, bs), 2.8 (H_d, bs), 2.3 (H_f, H_b, H_e, H_a, bs). MS *m/z* (MALDI) calcd. for $C_{195}H_{171}N_{37}O_{33}$: 3558.3; found: 3243.9.

R = 4′-methoxy, 21–1G: IR (KBr disk) (cm^{-1}): 3245, 3053, 2791, 1770, 1713, 1667, 1532, 1390, 1246, 1022, 826, 747, 529. ^{1}H NMR (DMSO-d_6) δ: 12.8 (OH, s), 11.3 (amide NH, s), 8.9 (H_4, s), 8.6 (H_5, bs), 8.1 ($H_{3''}$, outer amide NH, bs), 7.9 ($H_{6''}$, inner amide NH, bs), 7.8 ($H_{5''}$, d), 7.7 ($H_{2'}$, d), 7.6 ($H_{6,8}$, bs), 7.3 (H_7, bt), 6.9 ($H_{3'}$, d), 3.8 (NH, s), 3.7 (OCH_3), 3.4 (H_g, H_c, bs), 3.1 (H_h, bs), 2.7 (H_d, bs), 2.4 ($H_{e,a}$, bs), 2.2 (H_f, H_b, bs). ^{13}C NMR (DMSO-d_6) δ: 177.14 (C_2), 169.64 (C=O outer), 167.34 (C=O at $C_{1''}$), 166.90 (C=O at $C_{2''}$), 166.57 (C=O inner), 160.42 (C=O at C_3), 155.51 ($C_{4'}$), 147.14 (C_4), 143.13 ($C_{4''}$), 133.81 ($C_{1'}$), 133.39 ($C_{2''}$), 131.99 (C_6), 131.22 (C_{10}), 131.09 (C_9), 130.58 (C_8), 129.82 ($C_{1''}$), 128.29 (C_7), 126.90 (C_3), 126.14 (C_1), 125.36 ($C_{6''}$), 122.20 (C_5), 121.11 ($C_{2'}$), 121.00 ($C_{5''}$), 113.77 ($C_{3'}$), 110.44 ($C_{3''}$), 54.96 (OCH_3), 52.59 (C_d), 51.59 (C_e, C_a), 37.03 (C_g), 36.82 (C_h), 34.41 (C_c), 30.13 (C_f), 30.02 (C_b). MS *m/z* (MALDI) calcd. for $C_{201}H_{183}N_{37}O_{39}$: 3738.3; found: 3419.4.

© 2004 NRC Canada

R = 4′-methoxy (2G), ***21–2G***: IR (KBr disk) (cm^{-1}): 3246, 3050, 2789, 1772, 1712, 1668, 1533, 1388, 1250, 1158, 1013, 834, 750, 540.

R = 4′-methoxy (3G), ***21–3G***: IR (KBr disk) (cm^{-1}): 3245, 3052, 2789, 1770, 1712, 1670, 1530, 1380, 1250, 1156, 1013, 880, 750, 541.

R = 2′,5′-dimethoxy, ***22–1G***: IR (KBr disk) (cm^{-1}): 3244, 3049, 2790, 1771, 1712, 1668, 1530, 1400, 1250, 1015, 880, 750, 538. ^{1}H NMR (DMSO-d_6) δ: 12.4 (OH, s), 11.3 (amide NH, s), 8.9 (H_4, s), 8.3 ($H_{6'}$, bs), 8.2 (H_5, outer amide NH, bs), 8.0 ($H_{3''}$, d), 7.9 ($H_{6''}$, inner amide NH, bs), 7.8 ($H_{5''}$, bs), 7.5 (H_6, bs), 7.4 ($H_{7,8}$, bs), 6.8 ($H_{3'}$, $_{4'}$ bs), 4.1 (NH, bs), 3.9 (OCH_3 at $C_{2'}$, s), 3.7 (OCH_3 at $C_{5'}$, s), 3.2 (H_g, H_c, bs), 2.9 (H_h, bs), 2.7 (H_d, bs), 2.4 (H_e, $_a$, bs), 2.2 (H_f, H_b, bs). ^{13}C NMR (DMSO-d_6) δ: 177.40 (C_2), 170.26 (C=O outer), 167.32 (C=O at $C_{1''}$), 166.94 (C=O at $C_{2''}$), 166.51 (C=O inner), 160.27 (C=O at C_3), 152.96 ($C_{5'}$), 147.46 (C_4), 142.80 ($C_{4''}$), 142.67 (C_4), 133.12 ($C_{2''}$), 132.29 ($C_{6''}$), 131.23 (C_6), 130.75 (C_8), 130.40 (C_{10}), 130.12 (C_9), 128.40 ($C_{1'}$), 128.25 ($C_{1''}$), 126.69 (C_7), 126.03 (C_3), 125.89 (C_1), 121.11 (C_5), 118.50 ($C_{5''}$), 117.98 ($C_{3''}$), 111.48 ($C_{3'}$), 107.59 ($C_{4'}$), 106.85 ($C_{6'}$), 56.39 (OCH_3 at $C_{5'}$), 55.17 (OCH_3 at $C_{2'}$), 51.67 (C_d), 49.17 (C_e, C_a), 37.02 (C_g), 36.81 (C_h), 34.40 (C_c), 30.13 (C_f), 30.01 (C_b). MS *m/z* (MALDI) calcd. for $C_{207}H_{195}N_{43}O_{45}$: 4002.3; found: 3577.4.

R = 3′-nitro, ***23–1G***: IR (KBr disk) (cm^{-1}): 3250, 3052, 1772, 1710, 1667, 1548, 1390, 1268, 1100, 1014, 890, 750, 540. ^{1}H NMR (DMSO-d_6) δ: 12.4 (OH, s), 11.3 (amide NH, s), 8.8–7.0 (aromatic protons, m), 3.8 (NH, bs), 3.2 (H_g, H_c, bs), 2.8 (H_h, bs), 2.7 (H_d, bs), 2.4 (H_e, $_a$, bs), 2.2 (H_f, H_b, bs). MS *m/z* (MALDI) calcd. for $C_{195}H_{165}N_{43}O_{45}$: 3828.2; found: 3488.2.

Model phthalimide derivatives of PAMAM dendrimers

The experimental procedure for the model azophthalimide derivatives of the PAMAM dendrimer was identical to that used for the dendrimers.

The cyclic imide reaction between 4-nitrophthalic anhydride and *n*-$BuNH_2$ was carried out according to literature procedure (18), to give **24** (81% yield). The NMR and IR characteristics of **24** are as follows:

24

IR (KBr disk) (cm^{-1}): 3111, 3055, 2948, 2870, 1771, 1702, 1623, 1536, 1439, 1402, 1347, 1069, 1051, 940, 866, 710, 603. ^{1}H NMR (DMSO-d_6) δ: 8.62 (H_5, dd, 1H), 8.48 (H_3, d, 1H), 8.11 (H_6, d, 1H), 3.61 (H_a, t, 2H), 1.62–1.26 (H_b, H_c, m, 4H), 0.90 (H_d, t, 3H). ^{13}C NMR (DMSO-d_6) δ: 166.30 (C=O at C_2), 166.03 (C=O at C_1), 151.30 (C_4), 136.31 (C_2), 133.04 (C_1), 129.48 (C_6), 124.40 (C_5), 117.69 (C_3), 37.66 (C_a), 29.80 (C_b), 19.43 (C_c), 13.43 (C_d).

Hydrogenation of the nitro compound **24** in the presence of Pd–C catalyst gave the amino compound (93% yield), which was used for the standard diazo coupling reaction with coupler (naphthol AS-RL), giving the model compound (**25**); 82% yield, mp 169 to 170 °C.

The characteristics of the model compound (**25**) are as follows:

IR (KBr disk) (cm^{-1}): 3246, 2940, 2867, 2863, 1769, 1711, 1672, 1608, 1544, 1499, 1445, 1382, 1245, 1199, 1158, 1010, 822, 748, 533. ^{1}H NMR ($CDCl_3$) δ: 14.94 (OH, s, 1H), 11.03 (amide NH, s, 1H), 8.84 (H_4, s, 1H), 8.31 (H_5, d, 1H), 8.02 ($H_{3''}$, d, 1H), 7.86 ($H_{6''}$, d, 1H), 7.75 ($H_{5''}$, dd, 1H), 7.63 ($H_{2'}$, d, 1H), 7.60 (H_6, t, 1H), 7.60 (H_8, d, 1H), 7.40 (H_7, t, 1H), 6.85 ($H_{3'}$, d, 1H), 3.79 (OCH_3, s, 3H), 3.69 (H_a, t, 2H), 1.68 (H_b, m, 2H), 1.40 (H_c, m, 2H), 0.97 (H_d, t, 3H). ^{13}C NMR ($CDCl_3$) δ: 178.42 (C_2), 167.22 (C=O at $C_{1''}$), 167.11 (C=O at $C_{2''}$), 159.83 (C=O at C_3), 155.82 ($C_{4'}$), 149.20 (C_4), 146.00 ($C_{4''}$), 134.06 ($C_{1'}$), 133.71 ($C_{2''}$), 131.48 (C_6), 131.17 (C_{10}), 130.82 (C_8), 130.52 (C_9), 128.31 ($C_{1''}$), 127.32 (C_7), 126.36 (C_3), 125.33 (C_1), 124.37 ($C_{6''}$), 121.92 (C_5), 121.04 ($C_{5''}$), 120.89 ($C_{2'}$), 113.60 ($C_{3'}$), 111.24 ($C_{3''}$), 55.15 (OCH_3), 37.86 (C_a), 30.53 (C_b), 20.05 (C_c), 13.59 (C_d). MS *m/z* (CI+): 523.3 ([M + 1]). MS *m/z* (high-resolution FAB+) calcd. for $C_{30}H_{27}O_5N_4$: 523.1981; found: 523.1970. Anal. calcd. for $C_{30}H_{26}N_4$ (MW 523.20): C 68.94, H 4.98, N 10.73; found: C 68.20, H 5.14, N 10.74.

Studies of thermal stability

Thermal analyses were performed under N_2 using a high-resolution TGA 2950 Thermogravimetric Analyzer at a heating rate of 20 °C/min.

Acknowledgments

Financial support of this research through a grant by the Natural Sciences and Engineering Research Council of Canada (NSERC) (to E.B.) is gratefully acknowledged.

References

1. (*a*) D.A. Tomalia and H.D. Durst. Top. Curr. Chem. **165**, 193 (1993); (*b*) G.R. Newkome, C.N. Moorefield, and F. Vögtle. Dendritic molecules. VCH, Weinheim. 1996; (*c*) J.M.J. Fréchet. Science (Washington, D.C.), **263**, 1710 (1994); (*d*) I. Gitsov and J.M.J. Fréchet. J. Am. Chem. Soc. **118**, 3785 (1996); (*e*) S.D. Hudson, H.T. Jung, V. Percec, W.D. Cho, G. Johansson, G. Ungar, and V.S.K. Balagurusamy. Science (Washington, D.C.), **278**, 449 (1997); (*f*) V. Percec, C.-H. Ahn, G. Ungar, D.J.P. Yeardley, M. Moller, and S.S. Sheiko. Nature (London), **391**, 161 (1998); (*g*) K.L. Wooley, C.A. Klug, K. Tasaki, and J. Schaefer. J. Am. Chem. Soc. **119**, 53 (1997); (*h*) S.C. Zimmerman, F. Zeng, D.E.C. Reichert, and S.V. Kolotuchin. Science (Washington, D.C.), **271**, 1095 (1996).
2. (*a*) J. Haenseler and F. Szoka. Bioconjugate Chem. **4**, 372 (1993); Chem. Abstr. **119**, 174952c (1993); (*b*) D. Meyer, and S. Le Greneur (S.A. Guerbet). France Patent 91 15037, 1991; Chem. Abstr. **120**, 72540v, 1993; (*c*) N.A. Peppas and A.B. Argade. Proc. Int. Symp. Controlled Release Bioact. Mater. 20th, 143 (1993); Chem. Abstr. **119**, 233759 (1993); (*d*) R.F. Barth, D.M. Adams, A.H. Soloway, F. Alam, and M.V. Darby. Bioconjugate Chem. **5**, 58 (1994); Chem. Abstr. **120**, 86391j (1994); (*e*) F.W. Winnik, A.R. Davidson, and M.P. Breton. U.S. Patent 5 098 475, 1992; Chem. Abstr. **117**, 133079p, 1992; (*f*) F.M. Winnik, J.W. Duff, G.G. Sacripante, and A.R. Davidson. U.S. Patent 5 256 516, 1993; Chem. Abstr. 90707j, 1993.
3. (*a*) D.M. Junge and D.V. McGrath. J. Chem. Soc. Chem. Commun. 857 (1997); (*b*) D.M. Junge and D.V. McGrath. J. Am. Chem. Soc. **121**, 4912 (1999); (*c*) D.V. McGrath and D.M. Junge. Macromol. Symp. **137**, 57 (1999); (*d*) A. Archut, F. Vögtle, L. De Cola, G.C. Azzellini, V. Balzani, P.S. Ramanujam, and R.H. Berg. Chem. Eur. J. **4**, 699 (1998);

© 2004 NRC Canada

(*e*) A. Archut, G.C. Azzellini, V. Balzani, and F. Vögtle. J. Am. Chem. Soc. **120**, 12 187 (1998); (*f*) A. Archut and F. Vögtle. Chem. Soc. Rev. **27**, 233 (1998).
4. H. Rau. Ber. Bunsen–Ges. **73**, 810 (1969).
5. R.B. Champ and M.D. Shattuck. U.S. Patent 3 898 084. 1975.
6. K.Y. Law. Chem. Rev. **93**, 449 (1993).
7. (*a*) Z.D. Popovic, A.M. Hor, and R.O. Loutfy. Chem. Phys. **127**, 451 (1988); (*b*) M. Sadrai, L. Hadel, R.R. Sauers, S. Husain, K. Krogh-Jespersen, J.D. Westbrook, and G.R. Bird. J. Phys. Chem. **96**, 7988 (1992).
8. K.Y. Law and I.W. Tarnawskyj. J. Imaging Sci. Technol. **37**, 22 (1993).
9. T. Yoshihara and T. Kimura. U.S. Patent 4 855 202. 1989.
10. K.S. Cheon, Y.S. Park, P.M. Kazmaier, and E. Buncel. Dyes Pigm. **53**, 3 (2002).
11. K.E. Uhrich and J.M.J. Fréchet. J. Chem. Soc. Perkin Trans. 1, 1623 (1992).
12. (*a*) K.S. Cheon, R.A. Cox, S.R. Keum, and E. Buncel. J. Chem. Soc. Perkin Trans. 2, 1231 (1998); (*b*) E. Buncel and K.S. Cheon. J. Chem. Soc. Perkin Trans. 2, 1241 (1998); (*c*) R.A. Cox, K.S. Cheon, S.R. Keum, and E. Buncel. Can. J. Chem. **76**, 896 (1998).
13. (*a*) E. Buncel and S. Rajagopal. J. Org. Chem. **54**, 798 (1989); (*b*) E. Buncel and S.R. Keum. Tetrahedron, **39**, 1091 (1983); (*c*) E. Buncel and S.R. Keum. J. Chem. Soc. Chem. Comm. 578 (1983).
14. (*a*) S.R. Keum, P.M. Kazmaier, K.S. Cheon, R.A. Manderville, and E. Buncel. Bull. Kor. Chem. Soc. **17**, 391 (1996); (*b*) S.R. Keum, K.B. Lee, P.M. Kazmaier, and E. Buncel. Tetrahedron Lett. **35**, 1015 (1994).
15. E. Buncel, A.J. McKerrow, and P.M. Kazmaier. J. Chem. Soc. Chem. Commun. 1242 (1992).
16. (*a*) P.M. Kazmaier, K.A. Moffat, M.K. Georges, R.P.N. Veregin, and G.K. Hamer. Macromolecules, **28**, 1841 (1995); (*b*) P.M. Kazmaier, K. Daimon, M.K. Georges, and G.K. Hamer. Polym. Prepr. Am. Chem. Soc. Div. Polym. Chem. **37**, 485 (1996).
17 (*a*) B.S. Furniss, A.J. Hannaford, P.W.G. Smith, and A.R. Tatchell. Vogel's textbook of practical organic chemistry. 5th ed. Longman Scientific & Technical, London. 1989; (*b*) D.D. Perrin and W.L.F. Armarego. Purification of laboratory chemicals. 3rd ed. Pergamon Press, London. 1989.
18. H. Tsubouchi, K. Tsuji, and H. Ishikawa. Syn. Lett. 63 (1994).

© 2004 NRC Canada

Regioselectivity in S_NH reactions of some 3-nitro-1,5-naphthyridines with chloromethyl phenyl sulfone

Maria Grzegożek and Barbara Szpakiewicz

Abstract: 3-Nitro-1,5-naphthyridine and its 2-substituted derivatives react with the carbanion of chloromethyl phenyl sulfone to give hydrogen-substitution products at position 4 in high yield. The intermediacy of 4-(phenylsulfonyl)-chloromethyl σ adducts of 2-R-3-nitro-1,5-naphthyridines (R = H, D, Cl, OC_2H_5, $NHCH_3$, OH) was established by ^1H NMR spectroscopy. A convenient synthesis of 2-*N*-methylamino-3-nitro-1,5-naphthyridine is reported.

Key words: 3-nitro-1,5-naphthyridines, anionic (phenylsulfonyl)chloromethyl σ adducts, vicarious nucleophilic substitution.

Résumé : La 3-nitro-1,5-naphtyridine et ses dérivés substitués en position 2 réagissent avec le carbanion de la chlorométhyl(phényl)sulfone pour conduire à la formation de produits de substitution de l'hydrogène en position 4, avec des rendements élevés. Faisant appel à la spectroscopie RMN du ^1H, on a établi que les adduits σ 4-(phénylsulfonyl)chlorométhyle des 2-R-3-nitro-1,5-naphtyridines (R = H, D, Cl, OC_2H_5, $NHCH_3$, OH) sont impliqués comme intermédiaires dans ces réactions. On rapporte une méthode pratique de synthèse de la 2-*N*-méthylamino-3-nitro-1,5-naphtyridine.

Mots clés : 3-nitro-1,5-naphtyridines, adduits anioniques σ du (phénylsulfonyl)chlorométhyle, substitution nucléophile indirecte.

[Traduit par la Rédaction]

Introduction

Our interest in the reactivity of nitronaphthyridines towards nucleophilic agents induced us to study the reaction of vicarious nucleophilic substitution of hydrogen (VNS), as described by Mąkosza (1). In a previous paper we reported that 3-nitro-1,8-naphthyridine and some of its 2-substituted derivatives undergo VNS reactions with chloromethyl phenyl sulfone to the corresponding 4-(phenylsulfonyl)methyl-3-nitro-1,8-naphthyridines (2).

Extending these studies, we investigated the VNS reactions of chloromethyl phenyl sulfone with 2-R-3-nitro-1,5-naphthyridines (R = H, D, Cl, OC_2H_5, $NHCH_3$, OH) (**1a**–**e**). Nitronaphthyridines, applied as substrates, were obtained according to literature procedures (3–6), except for 2-*N*-methylamino-3-nitro-1,5-naphthyridine (**1d**). The new compound **1d** was prepared by the reaction of 2-chloro-3-nitro-1,5-naphthyridine (**1b**) with a saturated methanol solution of methylamine (see Experimental section).

The S_NH reactions occur very selectively and give, exclusively, products of substitution at position 4. They were carried out in the following base–solvent system: sodium hydroxide – dimethyl sulfoxide.

The reaction process takes place between 3-nitro-1,5-naphthyridines (**1**) and the carbanion generated from chloromethyl phenyl sulfone (Scheme 1). In the first step, addition of the carbanion to the nitro compound **1** results in the formation of σ adduct **2**, which undergoes base-induced β-elimination of HCl to form a carbanion that is subsequently protonated during the workup procedure, giving product **3**.

3-Nitro-1,5-naphthyridine (**1a**) reacts with chloromethyl phenyl sulfone very easily to give, in high yield (87%), 3-nitro-4-(phenylsulfonyl)methyl-1,5-naphthyridine (**3a**). The structure of compound **3a** was proved by ^1H NMR spectroscopy. In the ^1H NMR spectrum of **3a**, besides the presence of double doublets of 6-H and 8-H, a multiplet (7-H) of the unsubstituted pyridine ring, the phenyl multiplet (δ 7.58–7.38), and a CH_2 singlet (δ 5.96), a singlet of 2-H in the region at δ 9.53 was observed. This observation showed that substitution had occurred in either the 2 or 4 position. To be able to distinguish between substitution at the 2 or 4 position, we synthesized 2-deuterio-3-nitro-1,5-naphthyridine (**1a′**, R = D) and found that in the ^1H NMR spectrum of the product (obtained after the reaction with chloromethyl phenyl sulfone), the singlet at δ 9.53 was absent. Since, in the ^1H NMR spectra of the compounds **3b**–**e**, no singlet in the range δ 9.25–8.46 is present, the conclusion that substitu-

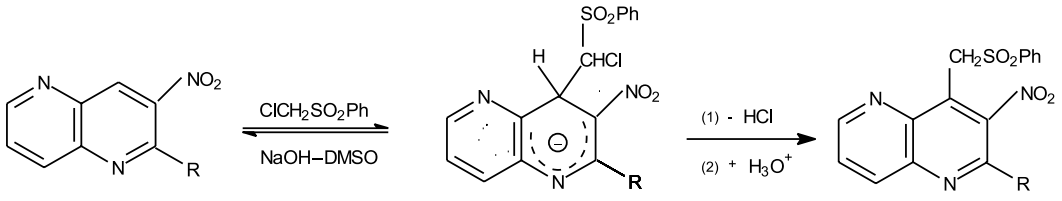
Received 4 July 2003. Published on the NRC Research Press Web site at http://canjchem@nrc.ca on 30 March 2004.

M. Grzegożek[1] and B. Szpakiewicz. Institute of Organic Chemistry and Technology, Cracow University of Technology, ul. Warszawska 24, PL-31155 Kraków, Poland.

[1]Corresponding author (e-mail: magre@indy.chemia.pk.edu.pl).

 doi: 10.1139/V04-001 © 2004 NRC Canada

Scheme 1.



1 σ adduct **2** **3**

1a R = H
1b R = Cl
1c R = OC_2H_5
1d R = $NHCH_3$
1e R = OH

3a R = H (87%)
3b R = Cl (73%)
3c R = OC_2H_5 (60%)
3d R = $NHCH_3$ (62%)
3e R = OH (83%)

Table 1. ^{1}H NMR data of some 3-nitro-1,5-naphthyridines (**1**) and their anionic σ adducts with chloromethyl phenyl sulfone.

		Chemical shifts (δ values)				
Compound	Solvent	2-H	4-H	6-H	7-H	8-H
3-Nitro-1,5-naphthyridine (**1a**)	DMSO-d_6	9.66	9.17	9.21	8.01	8.60
4-ClCH SO_2Ph σ adduct of **1a** (**2a**)	NaOD–DMSO-d_6	8.90	5.77	8.19	7.24	7.68
	Δδ	0.76	3.40	1.02	0.77	0.92
2-Chloro-3-nitro-1,5-naphthyridine (**1b**)	DMSO-d_6	—	9.25	9.19	8.02	8.52
4-ClCH SO_2Ph σ adduct of **1b** (**2b**)	NaOD–DMSO-d_6	—	5.86	8.21	7.21	7.40
	Δδ	—	3.39	0.98	0.81	1.12
2-Ethoxy-3-nitro-1,5-naphthyridine (**1c**)	DMSO-d_6	—	8.46	8.79	7.68	8.16
4-ClCH SO_2Ph σ adduct of **1c** (**2c**)	NaOD–DMSO-d_6	—	5.80			8.13
	Δδ	—	2.56	7.90 – 7.25[a]		0.03
2-*N*-Methylamino-3-nitro-1,5-naphthyridine (**1d**)	DMSO-d_6	—	8.87	8.70	7.68	8.08
4-ClCH SO_2Ph σ adduct of **1d** (**2d**)	NaOD–DMSO-d_6	—	5.42	8.08	7.00	7.61
	Δδ	—	3.47	0.62	0.68	0.47
2-Hydroxy-3-nitro-1,5-naphthyridine (**1e**)	DMSO-d_6	—	8.75	8.63	7.68	7.76
4-ClCH SO_2Ph σ adduct of **1e** (**2e**)	NaOD–DMSO-d_6	—	5.24	7.78	7.67	7.91
	Δδ	—	3.51	0.85	0.01	–0.15

[a]The signals of these protons form a complex multiplet and cannot be exactly assigned.

tion in **1b**–**e** has also occurred at the C-4 position is justified.

All experimental results show that for the 3-nitro-1,5-naphthyridines **1a**–**e**, the C-4 position is strongly favoured in the attack of the carbanion of chloromethyl phenyl sulfone (Scheme 1); likewise, in the reaction of 3-nitro-1,8-naphthyridines with chloromethyl phenyl sulfone (2).

To confirm that the intermediates in the above-mentioned reactions are detectable anionic σ adducts like **2**, we measured the ^{1}H NMR spectra of 3-nitronaphthyridines **1a**–**e** in a solution of NaOD in DMSO, containing 1.1 equiv. of chloromethyl phenyl sulfone. In the spectra, it was observed that nearly all signals are shifted upfield, particularly the signals of the protons at the carbon atoms that form σ adducts. Addition of the carbanion of chloromethyl phenyl sulfone to the sp^2 carbon atom of 3-nitronaphthyridines induces a change in its hybridization, from sp^2 to sp^3 (tetrahedral centre of σ adduct). This change is reflected in a considerable upfield shift of the signal of the hydrogen atom attached to that particular carbon atom. This rehybridization — sp^2 to sp^3 — is due to the σ adduct formation. The corresponding ^{1}H NMR data of 3-nitro-1,5-naphthyridines **1a**–**e** and their (phenylsulfonyl) chloromethyl σ adducts **2a**–**e** are compiled in Table 1.

The upfield shift, Δδ, of the signals of the C-4 hydrogen atom at the tetrahedral centre of the 4-(phenylsulfonyl)-chloromethyl σ adducts **2a**–**e** lie between 2.56–3.51 parts per million (ppm) and are in the same range as those found for the amino σ adducts of some 3-nitro-1,5-naphthyridines (Δδ, 2.55–3.81 ppm (2)) and for σ adducts of nitroquinolines with chloromethyl phenyl sulfone (Δδ, 2.90–4.11 ppm (7)). To explain whether we observed the first addition step in our study, we measured the ^{1}H NMR spectrum of 2-chloro-3-nitro-1,5-naphthyridine (**1b**) in a solution of NaOD in

© 2004 NRC Canada

DMSO, containing 1.1 equiv. of methyl phenyl sulfone instead of chloromethyl phenyl sulfone. In this case, if the first addition step takes place, the second stage of the reaction (elimination of HCl) cannot occur. It was observed that the value of the upfield shift ($\Delta\delta$) of the signal of the C-4 hydrogen atom that forms the σ adduct is the same ($\Delta\delta$ 3.39) as the case with chloromethyl phenyl sulfone (**2b**; Table 1). As shown by ^{1}H NMR spectroscopy, all of the compounds **1a–e** undergo covalent addition at C-4 when dissolved in a solution of NaOD in DMSO with chloromethyl phenyl sulfone, to give intermediate 4-(phenylsulfonyl)chloromethyl σ adducts **2a–e** (Table 1). In the case of **1a**, additional evidence that addition has taken place at C-4 and not at C-2 was provided by the ^{1}H NMR spectrum of 2-deuterio-3-nitro-1,5-naphthyridine, performed under the above-mentioned conditions. The spectrum showed the signal of the C-4 hydrogen at 5.77 ppm and its upfield shift $\Delta\delta$ 3.40 ppm. These values are identical to the 4-H of **2a** (Table 1).

Summary

In conclusion, all the results of the experimental data and the ^{1}H NMR study of the anionic intermediate (phenylsulfonyl)chloromethyl σ adducts indicate that the C-4 position in the 3-nitro-1,5-naphthyridines is strongly favoured for the attack of the carbanion of chloromethyl phenyl sulfone, and these results also confirm the regioselectivity of the studied *vicarious* S_NH reaction.

Experimental

Melting points (uncorrected) were determined on a Kofler plate. The ^{1}H NMR spectra were recorded on Mercury 300 varian (300 MHz) and Tesla BS-587A (80 MHz) spectrometers. The infrared spectra were recorded on a Bio-Rad FTS-175C spectrometer (in potassium bromide pellets). The mass spectra were recorded on an LKB GC–MS 9000 spectrometer.

Synthesis of starting and reference compounds

3-Nitro- (**1a** (3)), 2-deuterio-3-nitro- (**1a′** (4)), 2-chloro-3-nitro- (**1b** (4)), 2-ethoxy-3-nitro- (**1c** (5)), and 2-hydroxy-3-nitro-1,5-naphthyridine (**1e** (6)) were prepared according to the literature procedures. Chloromethyl phenyl sulfone was obtained from sodium benzenesulfinate and dichloroacetic acid (8). Methyl phenyl sulfone was prepared from tiophenol (9).

*2-*N*-Methylamino-3-nitro-1,5-naphthyridine 1d*

2-Chloro-3-nitro-1,5-naphthyridine (100 mg, 0.35 mmol) was dissolved in 8 mL of saturated methanol solution of methylamine at room temperature. A change of colour from light cream to red was observed. After 1 h, precipitated red needles were filtered off and washed with cold methanol to yield 50 mg of **1d**, mp 165–167 °C. The methanol filtrates were evaporated to 3 mL. Additionally, 6 mg of **1d** was obtained. Yield 58%. IR (ν_{max}) (cm^{-1}): 3436 (NH), 1526 (NO_2, as), 1399 (NO_2, s). ^{1}H NMR (DMSO) δ: 8.87 (s, 4-H), 8.70 (d, 6-H), 8.19 (br.s, NH), 7.99 (d, 8-H), 7.68 (q, 7-H), 3.06 (d, CH_3 NH), $J_{6,7}$ = 4.13 Hz, $J_{7,8}$ = 8.53 Hz, $J_{(CH_3,NH)}$ = 4,68 Hz. MS (70 eV) *m/z* (%): 204 (42, [M$^+$]) 187 (30, [M$^+$ – OH]), 130 (100). Anal. calcd. for $C_9H_8N_4O_2$ (204.19): C 52.94, H 3.95, N 27.44; found: C 53.32, H 4.06, N 27.08.

Reaction of 3-nitro-1,5-naphthyridines 1a–e with chloromethyl phenyl sulfone

General procedure

To a stirred suspension of powdered sodium hydroxide (100 mg, 2.5 mmol) in dimethyl sulfoxide (2 mL), a solution of the respective 3-nitro-1,5-naphthyridines **1a–e** (0.25 mmol) and chloromethyl phenyl sulfone (47 mg, 0.25 mmol) was added at room temperature (temp.). The reaction mixture was stirred for 2 h at room temp. Then the mixture was poured into 50 mL of a 5% aqueous solution of acetic acid. The crude products were filtered off, washed with water, dried, and crystallized from convent solvent, as described below.

3-Nitro-4(phenylsulfonyl)methyl-1,5-naphthyridine, 3a

Pale cream needles (71 mg, 87%) with mp 204 to 205 °C (*iso*-PrOH). IR (ν_{max})(cm^{-1}): 1532 (NO_2, as), 1349 (NO_2, s), 1318, 1163 (SO_2). ^{1}H NMR ($CDCl_3$) δ: 9.53 (s, 2H), 8.90 (d.d, 6-H), 8.46 (d.d, 8-H), 7.73 (m, 7-H), 7.58–7.38 (m, Ph), 5.96 (s, CH_2), $J_{6,7}$ = 3,8 Hz, $J_{6,8}$ = 1,6 Hz, $J_{7,8}$ = 8,67 Hz. MS (70 eV) *m/z* (%): 265 ([M$^+$ – SO_2]), 248 (64, [M$^+$ – SO_2 – OH]), 188 ([M$^+$ – SO_2Ph]). Anal. calcd. for $C_{15}H_{11}N_3O_4S$ (329.34): C 54.71, H 3.37, N 12.76; found: C 54.37, H 3.33, N 12.41.

2-Deuterio-3-nitro-4(phenylsulfonyl)methyl-1,5-naphthyridine, 3a′

This compound was obtained in an identical manner to the compound **3a**, starting from 2-deuterio-3-nitro-1,5-naphthyridine. The ^{1}H NMR analysis showed that the content of deuterium in position 2 was >95%.

2-Chloro-3-nitro-4-(phenylsulfonyl)methyl-1,5-naphthyridine, 3b

Light cream needles (66 mg, 73%), mp 211 °C (MeOH). IR (ν_{max})(cm^{-1}): 1542 (NO_2, as), 1324 (NO_2, s), 1295, 1166 (SO_2). ^{1}H NMR (DMSO) δ: 8.84 (d, 6-H), 8.55 (d, 8-H), 7.91 (q, 7-H), 7.77–7.65 (m, Ph), 5.57 (s, CH_2), $J_{6,7}$ = 3.9 Hz, $J_{7,8}$ = 8.01 Hz. MS (70 eV) *m/z* (%): 299–301([M$^+$ – SO_2]), 282–284 (56–17, [M$^+$ – SO_2 – OH]), 222–224 ([M$^+$ – SO_2Ph]). Anal. calcd. for $C_{15}H_{10}ClN_3O_4S$ (363.78): C 49.53, H 2.77, N 11.55; found: C 49.36, H 2.72, N 11.39.

2-Ethoxy-3-nitro-4-(phenylsulfonyl)methyl-1,5-naphthyridine, 3c

Light cream needles (56 mg, yield 60%), mp 185 to 186 °C (*iso*-PrOH). IR (ν_{max})(cm^{-1}): 1539 (NO_2, as), 1316 (NO_2, s),1332, 1145 (SO_2). ^{1}H NMR (DMSO) δ: 8.58 (d, 6-H), 8.19 (d, 8-H), 7.74 (q, 7-H), 7.78–7.58 (m, Ph), 5.41 (s, CH_2), 4.5 (q, CH_2), 1.40 (t, CH_3), $J_{6,7}$ = 3.02 Hz, $J_{7,8}$ = 6.90 Hz. MS (70 eV) *m/z* (%): 309 ([M$^+$ – SO_2]), 292 (100, [M$^+$ – SO_2 – OH]), 232 ([M$^+$ – SO_2Ph]). Anal. calcd. for $C_{17}H_{15}N_3O_5S$ (373.39): C 54.68, H 4.05, N 11.25; found: C 54.35, H 4.02, N 11.10.

© 2004 NRC Canada

2*-N-*Methylamino-3-nitro-4-(phenylsulfonyl)methyl-1,5-naphthyridine, 3d

Red needles (55 mg, yield 62%), mp 201 to 202 °C. IR (ν_{max})(cm^{-1}): 3454 (NH) 1514 (NO_2, as), 1331 (NO_2, s), 1311 (NH) 1390, 1166 (SO_2). ^{1}H NMR (DMSO) δ: 8.32 (dd, 6-H), 7.94 (dd, 8-H), 7.78–7.58 (m, 7-H, Ph), 5.48 (s, CH_2), 3.00 (d, CH_3, NH), $J_{6,7}$ = 3.91 Hz, $J_{7,8}$ = 8.50 Hz, $J_{(CH_3,NH)}$ = 4.80 Hz, $J_{6,8}$ = 1.70 Hz. MS (70 eV) *m*/*z* (%): 358 ([M^+]), 294 ([$M^+ - SO_2$]), 277 (100, [$M^+ - SO_2 - OH$]), 217 ([$M^+ - SO_2Ph$]). Anal. calcd. for $C_{16}H_{14}N_4O_4S$ (358.38): C 53.62, H 3.94, N 15.63; found: C 53.30, H 3.80, N 15.24.

2-Hydroxy-3-nitro-4(phenylsulfonyl)methyl-1,5-naphthyridine, 3e

Light yellow needles (71 mg, 83%), mp 286–288 °C (*iso*-PrOH). IR (ν_{max})(cm^{-1}): 1543 (NO_2, as), 1324 (NO_2, s), 1308, 1172 (SO_2). ^{1}H NMR (DMSO) δ: 8.33 (dd, 6-H), 7.94 (8-H), 7.69 (7-H), 7.90–7.53 (m, Ph), 5.58 (s, CH_2), $J_{6,7}$ = 3.91 Hz, $J_{6,8}$ = 1.71 Hz, $J_{7,8}$ = 8.30 Hz. MS (70 eV) *m*/*z* (%): 345 ([M^+]), 281 ([$M^+ - SO_2$]), 264 (30, [$M^+ - SO_2 - OH$]), 204 ([$M^+ - SO_2Ph$]). Anal. calcd. for $C_{15}H_{11}N_3O_5S$ (345.34): C 52.17, H 3.21, N 12.17; found: C 51.92, H 3.24, N 11.79.

Acknowledgements

The authors wish to thank Dr. E. Cholewka and Mr. M. Żylewski for measuring the ^{1}H NMR and IR spectra.

References

1. M. Mąkosza. Synthesis, 103 (1991); Pol. J. Chem. **66**, 3 (1992).
2. M. Grzegożek, M. Woźniak, A. Barański, and H.C. van der Plas. J. Heterocyclic Chem. **28**, 1075 (1991).
3. A. Albert and W.L.F. Armarego. J. Chem. Soc. 4237 (1963).
4. M. Woźniak, H.C. van der Plas, M. Tomula, and A. Van Veldhuizen. Recl. Trav. Chim. Pays–Bas, **102**, 511 (1983).
5. H.J.W. van den Haak and H.C. van der Plas. Recl. Trav. Chim. Pays–Bas, **99**, 83 (1980).
6. E.P. Hart. J. Chem. Soc. **I**, 212 (1956).
7. M.A. Grzegożek. Khim. Geterotsikl. Soedin. **420**, 786 (2002).
8. R. Otto. J. Prakt. Chem. **40**, 526 (1889).
9. C.M. Suter. The organic chemistry of sulphur. John Wiley, New York. 1944.

© 2004 NRC Canada

Cyclization of 2-(2-bromoethoxy)-acetophenones and 5-(ω-haloalkoxy)-1,5-dihydro-2*H*-pyrrol-2-ones — Formation of five- to eight-membered oxygen-containing heterocycles via intramolecular alkylation

Kirill V. Nikitin and Nonna P. Andryukhova

Abstract: Under basic conditions (lithium diisopropylamide or sodium hydride in THF) 2-(2-bromoethoxy)-acetophenones were transformed to 3,4-dihydro[1]benzoxepin-5(2*H*)-ones (homochromanones) in high yields. The preparation of novel tetrahydropyrano[2,3-*b*]pyrrol-6(2*H*)-ones and 3,4-dihydro-2*H*-pyrrolo[2,1-*b*][1,3]oxazin-6(8*aH*)-ones and spiro compounds was performed using similar cyclization in moderate to good yields.

Key words: cyclization, lithiation, spiro heterocycles.

Résumé : Dans des conditions basiques (diisopropylamidure de lithium ou hydrure de sodium dans le THF), les 2-(2-bromoéthoxy)-acétophénones se transforment en 3,4-dihydro[1]benzoxépin-5(2*H*)-ones (homochromanones) avec des rendements élevés. Utilizant une méthode de cyclisation semblable, on a aussi réalisé la préparation, avec des rendements allant de moyens à bons, de nouvelles tétrahydropyrano[2,3-*b*]pyrrol-6(2*H*)-ones et de 3,4-dihydro-2*H*-pyrrolo[2,1-*b*][1,3]oxazin-6(8*aH*)-ones ainsi que de composés spiro apparentés.

Mots clés : cyclisation, lithiation, composés spiro hétérocycliques.

[Traduit par la Rédaction]

Introduction

The cyclization via intramolecular enolate alkylation is a well-known route to the synthesis of carbocycles (1, 2). However that chemistry has rarely been used for the preparation of saturated heterocycles. We applied intramolecular enolate coupling to the formation of an oxygen-containing ring fused to an aromatic ring or to another heterocyclic ring.

As a model to find the optimum conditions for the cyclization, the 3,4-dihydro[1]benzoxepin-(2*H*)-ones (homochromanones) **2** were chosen as a family of potentially appealing synthetic targets (Scheme 1). Homochromanones **2** can be prepared by acid-catalyzed intramolecular acylation of γ-aryloxybutyric acids (3, 4). The cyclization of 2-(δ-bromoalkyl)-phenol under basic conditions (5) leads to homochromans. Similar heterocylclic systems are available (6). Noteworthy, compounds **2** were extensively studied particularly as potent diabetes remedies (7).

We also studied the cyclization of bromoalkoxy-1,5-dihydro-2*H*-pyrrol-2-ones (Scheme 2) to get biologically important partially saturated fused pyrano[2,3-*b*]pyrroles **10** (8, 9) and pyrrolo[2,1-*b*][1,3]oxazines **11** (10). Substituted 1,5-dihydro-2*H*-pyrrol-2-ones are attracting a growing interest in synthetic chemistry for pharmacological and pesticide activity (11). The compounds **10** and **11** are unknown to the best of our knowledge though they most probably indicate biological activity (12–15).

Received 11 July 2003. Published on the NRC Research Press Web site at http://canjchem.nrc.ca on 7 April 2004.

K.V. Nikitin.[1] Department of Chemistry, University College Dublin, Belfield, D4, Ireland.
N.P. Andryukhova. Department of Chemistry, Moscow State University, Moscow 119899, Russia.

[1]Corresponding author (e-mail: kirill.nikitin@ucd.ie).

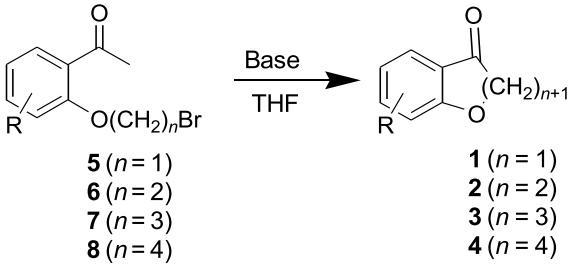
Results and discussion

The preparation of oxygen-containing heterocycles involved two steps. At the first step the carbonyl compound (hydroxylated ketone or pyrrolone) was conventionally converted into the corresponding ω-chloro- or bromoalkoxy derivative. At the second step the later derivative was cyclized in the presence of a strong base. That methodology has been successfully applied for the synthesis of **2** (Scheme 1), but limitations were found for the formation of eight- and nine-membered rings (**3**, **4**, respectively).

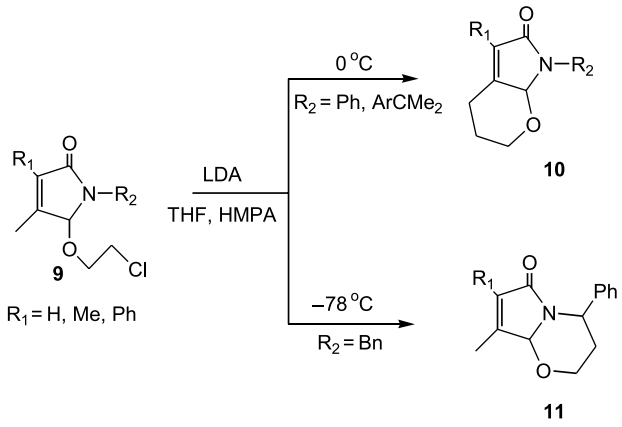
The availability of starting 2-(ω-bromoalkoxy)-ketones **5**–**8** depends upon the number *n* (Scheme 3). While the compounds **6a**–**6f** were obtained in good yields (52%–65%) along with considerable amount of corresponding bis(aryloxy)alkanes **13**, we failed to obtain 2-(bromomethoxy)acetophenone **5** ($n = 1$) by alkylation of 2-hydroxyacetophenone with methylene halides. Under phase transfer conditions (16) bis-(2-acetylphenoxy)methane **12** was solely produced. The attempts to use 1,2-dibromopropane and 2,3-dibromobutane as alkylating reagents were unsuccessful.

 doi: 10.1139/V04-011 © 2004 NRC Canada

Scheme 1. Cyclization of 2-(ω-bromoalkoxy)-acetophenones).



Scheme 2. Transformations of 5-(2-chloroethoxy)-pyrrol-2-ones.



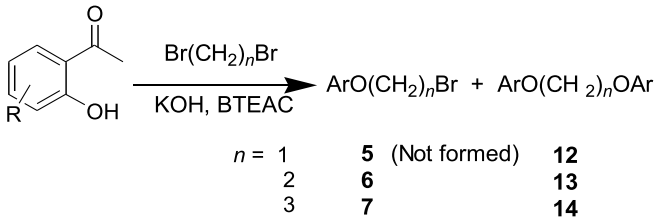
The cyclization of **6** to form **2** (Scheme 1) was performed in tetrahydrofuran (THF). In most cases (Table 1), the use of either lithium diisopropylamide (LDA) in the presence of hexamethylphosphoramide (HMPA) (conditions A, runs 1, 7, 9, 13, 15) or sodium hydride (conditions B, runs 2, 8, 10, 14, 16) allowed good yields of the cyclization product. The reaction with sodium hydride takes longer time but it is more convenient.

In the case of 2-(2-chloroethoxy)propiophenone **6f** no cyclization product was observed under either conditions A or B (Table 1, runs 11, 12). Instead, we found 2-hydroxypropiophenone as a sole product (run 11). It is likely that the abstraction of a proton from the -CH_2Cl group of **6f** is followed by formation of vinyl chloride and 2-propionylphenoxide anion.

The attempts to convert **7** and **8** into corresponding eight- and nine-membered heterocycles (Table 1, runs 3–6) showed that ω-halogenated hydrocarbon chains were prone to elimination or intermolecular alkylation rather than intramolecular cyclization process. The transformation of 2-(3-bromopropoxy)acetophenone **7a** in the presence of LDA led mainly to 2-allyloxyketone (Table 1, run 3) via elimination. In the presence of NaH (run 4), 2,3,4,5-tetrahydro[1]benzoxocin-6-one was still obtained though in poor yield (22%). The application of weaker bases was expected to minimize the contribution of the elimination pathway; nevertheless, only the elimination product was found in the presence of KOBu-*t*, while in the presence of NaOEt no reaction took place.

2-(4-Bromobutoxy)acetophenone **8a** in the presence of LDA (Table 1, run 5) furnishes an elimination product and intermolecular coupling products (Scheme 4). It is likely that the conformation of the ω-bromobutoxy chain of the respective enolate ion is unfavorable for intramolecular nucleophilic substitution. Under milder conditions in the presence of NaH (run 6) the concentration of enolate ion is lower and **8a** furnishes only the elimination product.

Scheme 3. Preparation of 2-(ω-bromoalkoxy)-acetophenones.



To apply the cyclization for the formation of a six-membered heterocyclic ring as a part of a fused heterocyclic system we studied the transformations of 5-chloroethoxy pyrrolones **9**. The starting materials **9** are directly available by etherification of the corresponding 5-hydroxy-1,5-dihydro-2*H*-pyrrol-2-ones (17).

We found that a ring fused to the pyrrolone ring could be successfully locked in the presence of a strong base (LDA) giving rise to **10** or **11** (Scheme 2) in moderate to good yields. Preliminary results obtained for the intramolecular cyclization of **9a** (R_1 = 2-FC_6H_4, R_2 = 3,5-$Cl_2C_6H_3CMe_2$) are summarized in Table 2. The use of HMPA drastically improved the cyclization yield (runs 1, 2). Since the dilution of the initial reaction mixture increased the yield (run 3), it is anticipated that an intermolecular process competed with the cyclization pathway.

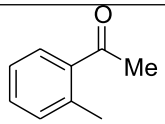
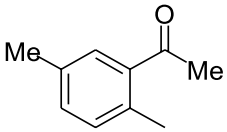
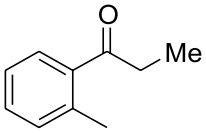
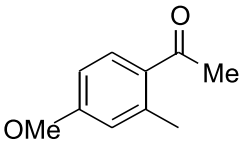
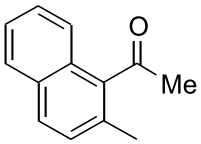
The syntheses of the compounds **10** and **11** (Table 3) were carried out under the optimum conditions found (Table 1, run 3). It is noteworthy that the formation of **10** proceeds relatively slow (1 h at 0 °C) and tolerates only phenyl or substituted α,α-dimethylbenzyl moieties at the nitrogen atom (Table 3, **10a**, **10b**). In the presence of a *tert*-butyl or an *iso*-propyl substituent at the nitrogen atom (Table 3, **10c**, **10d**) the cyclization fails.

The cyclization of **9**, containing a benzyl group at the nitrogen atom, led to **11** rather than **10** (Scheme 2). The process was unexpectedly fast compared to the formation of **10**. At –78 °C (Table 3, **11a**–**11c**), the reaction furnishes **11** from *N*-benzylated **9** (R_2 = $PhCH_2$). Rapid intramolecular alkylation of the benzyl carbon (formation of **11**) may account for the relatively high reactivity of the corresponding benzylic carbanion compared to the less reactive γ-anion of the α,β-unsaturated amide (formation of **10**). Nuclear Overhauser enhancement (NOE) measurements showed that irradiation of the proton at C8a in **11a** did not significantly enhance the signal of the proton at C4 (i.e., the benzylic position), compared to the considerable enhancement of the signal of the methyl protons. On the basis of NOE observations, we believe that the product **11a** has a 4,8a-*trans* configuration.

It appeared that the cyclization yield can be improved by the use of 2-bromoethoxy analogs of **9**. For example, the preparation of **10e** bearing base-susceptible 2-chloro-4-fluoro-5-hydroxyphenyl at the nitrogen is more successful (68% yield) when starting from the bromoethoxy compound (Table 3) than from the chloroethoxy derivative (20% yield).

© 2004 NRC Canada

Table 1. Cyclizations[a] of ketones $ArO(CH_2)_nBr$ (**6–8**) to fused heterocyclic ketones (**2–4**).

Entry	Starting ketone	*n*	Ar	Conditions[b]	Yield (%)
1	**6a**	2		A	80
2	**6a**	2		B	76
3	**7a**	3		A	0 (50)[c]
4	**7a**	3		B	22 (20)[c]
5	**8a**	4		A	0 (28)[d]
6	**8a**	4		B	0 (20)[d]
7	**6b**	2		A	78
8	**6b**	2		B	80
9	**6c**	2		A	40
10	**6c**	2		B	62
11	**6f**[e]	2		A	0
12	**6f**	2		B	0
13	**6d**	2		A	60
14	**6d**	2		B	58
15	**6e**	2		A	85
16	**6e**	2		B	87

[a]Reactions were carried out at 0.1 mol L^{-1} in the starting substrate.
[b]A: LDA (3 mmol), HMPA (3 mmol), 1.5 h at 0 °C; B: NaH (2 mmol), 80 h at 25 °C.
[c]The yield of 2-allyloxyacetophenone is given in parentheses.
[d]The yield of 2-homoallyloxyacetophenone is given in parentheses.
[e](2-Chloroethoxy)propiophenone was used as the substrate.

Table 2. Cyclization of **9a** into **10a** (R_1 = 2-FC_6H_4, R_2 = 3,5-$Cl_2C_6H_3CMe_2$, 0 °C, 1 mmol of **9a**, 2 mmol of LDA).

Run	Concentration (mol L^{-1})	HMPA (mmol)	Time (h)	Yield (%)
1	0.1	0	2	7
2	0.1	4	1	45
3	0.04	4	1	67

We applied the cyclization methodology to the formation of spiro heterocyclic compounds. The cyclization of 3-(3-bromopropoxy)-2-phenyl-2,3-dihydro-isoindol-1-one **15** in the presence of LDA (Scheme 5) furnished in good yield (50%) only one possible cyclization spiro product (**16**).

At the same time, the cyclization of an analogous pyrrolone derivative **17** (Scheme 5) resulted in the formation of two possible cyclization products (**18** and **19**) in moderate yields.

Conclusively, intramolecular cyclization of (2-bromoalkoxy) derivatives of aromatic ketones or 2,5-dihydro-2*H*-pyrrol-2-ones leads to the formation of a fused oxygen-containing heterocyclic system and can be efficiently applied for the preparation of homochromanones and several novel heterocyclic systems using a simple two-step protocol.

Experimental

Tetrahydrofuran was distilled from benzophenone–sodium under nitrogen. Melting points were measured with a Thomas–Hoover capillary melting point apparatus and are not corrected. ^{1}H NMR spectra were recorded on a Varian GEMINI-200 spectrometer. All chemical sifts are in ppm (δ),

© 2004 NRC Canada

Scheme 4. Transformations of 2-(4-bromobutoxy)-acetophenone.

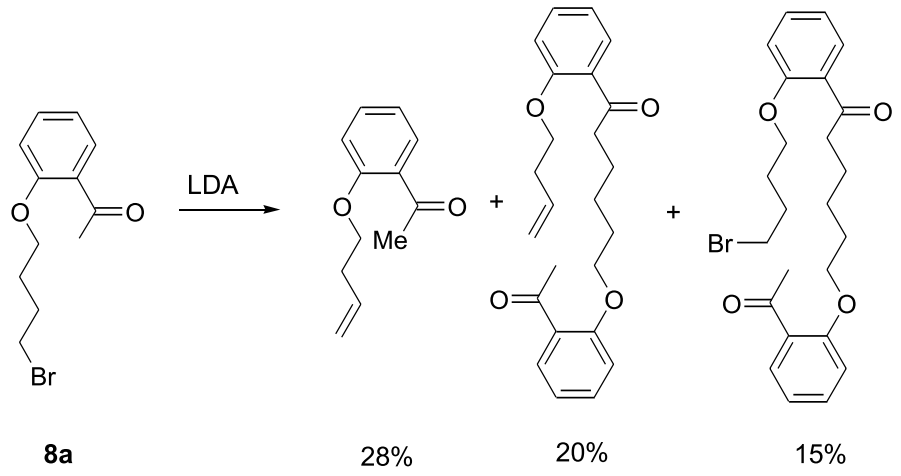
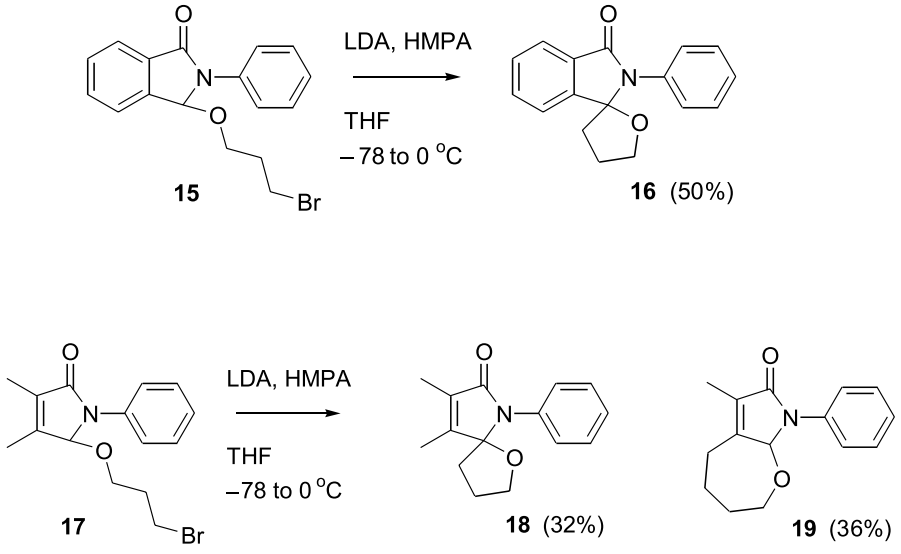


Table 3. Synthesis of **10** and **11** from **9** in THF using 2 equiv. of LDA and 4 equiv. of HMPA.

Starter	Product	R_1	R_2 (in **9** or **10**)	Temperature (°C)	Time (h)	Yield (%)
9a	(**10a**)	2-FC_6H_4	3,5-$Cl_2C_6H_3CMe_2$	0	1	67
9b	(**10b**)	Me	Ph	0	1	40
9c	(**10c**)	Me	*i*-Pr	0	0.5	0
9d	(**10d**)	Me	*t*-Bu	0	0.5	0
9e	(**10e**)	Me	2-Cl-4-F-5-OH	0	1	20
9f	(**10e**)[a]	Me	2-Cl-4-F-5-OH	0	0.5	68
9g	(**11a**)	H	$PhCH_2$	–78	1	40
9h	(**11b**)	Me	$PhCH_2$	–78	1	70
9i	(**11c**)	Ph	$PhCH_2$	–78	1	49

[a]The 5-(2-bromoethoxy) compound was used.

Scheme 5. Formation of spiro heterocyclic compounds via cyclization.



downfield tetramethylsilane and coupling constants are given in Hz. Mass spectra were recorded on a Shimadzu GC-MS-OP 1000 mass spectrometer. FT IR spectra were recorded on a Mattson Genesis II spectrophotometer. Chromatographic separations were carried out on a silica gel column (Merck, 60 μm).

General procedure for the synthesis of 2-(bromoalkoxy)-aromatic ketones (6–8)

A mixture of 2-hydroxyacetophenone (1.36 g, 10 mmol), 1,2-dibromoethane (11 g, 60 mmol), K_2CO_3 (2.76 g, 20 mmol), tetrabutylammonium bromide (0.322 g, 1 mmol), benzene (5 mL), and water (10 mL) was stirred under reflux

© 2004 NRC Canada

for 16 h, cooled, the organic layer was separated, washed with aq. NaOH, water, then dried ($MgSO_4$), evaported under reduced pressure, and subjected to column chtomatography separation (20% ethyl acetate – hexane) to afford 2-(2-bromoethoxy)-acetophenone (**6a**) (1.86 g, 65% yield) as a colorless solid; mp 45 °C. ^{1}H NMR (200 MHz, $CDCl_3$) δ: 2.68 (s, 3H), 3.70 (t, 2H, J = 5.8 Hz), 4.39 (t, 2H, J = 5.8 Hz), 6.8–7.8 (m, 4H). MS (70 eV) m/z: 242, 244 (M + 2); and 1,2-bis(2-acetylphenoxy)-ethane (**13a**) (0.31 g, 20% yield) as colorless solid; mp 125 °C. ^{1}H NMR (200 MHz, $CDCl_3$) δ: 2.59 (s, 6H), 4.50 (s, 4H), 6.9–7.1 (m, 4H), 7.5 (m, 2H), 7.7–7.8 (m, 2H). MS (70 eV) m/z: 298.

2-(3-Bromopropoxy)-acetophenone (**7a**) (1.5 g, 52% yield) was obtained from 2-hydroxyacetophenone (1.36 g) and 1,3-dibromopropane (**7g**) as a colorless liquid. ^{1}H NMR (200 MHz, $CDCl_3$) δ: 2.37 (tt, 2H, $J_1 = J_2$ = 6.3 Hz), 2.59 (s, 3H), 3.61 (t, 2H, J = 6.3 Hz), 4.22 (t, 2H, J = 6.3 Hz), 6.9–7.8 (m, 4H). MS (70 eV) m/z: 286, 288 (M + 2); along with 1,3-bis(2-acetylphenoxy)-propane (**14a**) (0.30 g, 18% yield) as colorless solid; mp 107 °C. ^{1}H NMR (200 MHz, $CDCl_3$) δ: 2.42 (quintet, 2H, J = 6.1 Hz), 2.62 (s, 6H), 4.30 (t, 4H, J = 6.1 Hz), 6.9–7.1 (m, 4H), 7.4–7.5 (m, 2H), 7.7–7.8 (m, 2H). MS (70 eV) m/z: 313 (M + 1).

2-(4-Bromobutoxy)-acetophenone (**8a**) (1.0 g, 33% yield) was obtained from 2-hydroxyacetophenone (1.36 g) and 1,4-dibromobutane (**8g**) as a colorless liquid. ^{1}H NMR (200 MHz, $CDCl_3$) δ: 1.9–2.2 (m, 4H), 2.62 (s, 3H), 3.49 (t, 2H, J = 5.8 Hz), 4.10 (t, 2H, J = 5.8 Hz), 6.9–7.1 (m, 2H), 7.4–7.5 (m, 1H), 7.7–7.8 (m, 1H). MS (70 eV) m/z: 300, 302 (M + 2).

2-Bromomethoxy-acetophenone (**5a**) was not obtained from 2-hydroxyacetophenone (1.36 g) and dibromomethane (**7g**) but only 1,1-bis(2-acetylphenoxy)-methane (**12a**) (1 g, 70% yield) was obtained as colorless solid; mp 97 °C. ^{1}H NMR (200 MHz, $CDCl_3$) δ: 2.59 (s, 6H), 5.93 (s, 2H), 7.0–7.75 (m, 8H). MS (70 eV) m/z: 149 (M – AcC_6H_4O).

2-(2-Bromoethoxy)-5-methylacetophenone (**6b**) (1.6 g, 62% yield) was obtained from 2-hydroxy-5-methylacetophenone (1.5 g) and 1,2-dibromoethane (**11g**) as a colorless solid; mp 66 °C. ^{1}H NMR (200 MHz, $CDCl_3$) δ: 2.30 (s, 3H), 2.67 (s, 3H), 3.70 (t, 2H, J = 5.8 Hz), 4.38 (t, 2H, J = 5.8 Hz), 6.8–7.1 (m, 2H), 7.4 (m, 1H), 7.7 (m, 1H). MS (70 eV) m/z: 256, 258 (M + 2); along with 1,2-bis(2-acetyl-4-methylphenoxy)ethane (**13b**) (0.2 g, 12% yield) as a colorless solid; mp 127 °C. ^{1}H NMR (200 MHz, $CDCl_3$) δ: 2.31 (s, 6H), 2.57 (s, 6H), 4.44 (s, 4H), 6.9 (m, 2H), 7.2–7.2 (m, 2H), 7.54 (s, 2H). MS (70 eV) m/z: 326.

2-(2-Bromoethoxy)-propiophenone (**6c**) (1.55 g, 60% yield) was obtained from 2-hydroxypropiophenone (1.5 g) and 1,2-dibromoethane (**11g**) as a colorless solid; mp 36 °C. ^{1}H NMR (200 MHz, $CDCl_3$) δ: 1.17 (t, 3H, J = 7.1 Hz), 3.05 (t, 2H, J = 7.1 Hz), 3.69 (s, 3H), 3.69 (t, 2H, J = 5.9 Hz), 4.37 (t, 2H, J = 5.9 Hz), 6.8–7.7 (m, 4H). MS (70 eV) m/z: 256, 258 (M + 2); along with 1,2-bis(2-propionylphenoxy)ethane (**13c**) (0.3 g, 18% yield) as a colorless solid; mp 97 °C. ^{1}H NMR (200 MHz, $CDCl_3$) δ: 1.08 (t, 6H, J = 7.3 Hz), 2.95 (quartet, 4H, J = 7.3 Hz), 4.45 (s, 4H), 7.0 (m, 4H), 7.4–7.6 (m, 2H), 7.7 (m, 2H). MS (70 eV) m/z: 326.

2-(2-Bromoethoxy)-4-methoxyacetophenone (**6d**) (1.65 g, 61% yield) was obtained from 2-hydroxy-4-methoxyacetophenone (1.66 g) and 1,2-dibromoethane (**11g**) as a colorless solid; mp 69 °C. ^{1}H NMR (200 MHz, $CDCl_3$) δ: 2.65 (s, 3H), 3.72 (t, 2H, J = 5.8 Hz), 3.85 (s, 3H), 4.38 (t, 2H, J = 5.8 Hz), 6.39 (d, 1H, J = 2.2 Hz), 6.46 (dd, 1H, J = 2.2 Hz, J = 8.8 Hz), 7.87 (d, 1H, J = 8.8 Hz). MS (70 eV) m/z: 272, 274 (M + 2).

2-(2-Bromoethoxy)-acetonaphthone (**6e**) (1.0 g, 63% yield) was obtained from 2-hydroxyacetonaphthone (1.0 g) and 1,2-dibromoethane (**11** g) as a colorless solid; mp 89 °C. ^{1}H NMR (200 MHz, $CDCl_3$) δ: 2.72 (s, 3H), 3.68 (t, 2H, J = 6 Hz), 4.48 (t, 2H, J = 6 Hz), 7.2–7.9 (m, 6H). MS (70 eV) m/z: 292, 294 (M + 2).

2-(2-Chloroethoxy)-propiophenone (**6f**) (1.32 g, 64% yield) was obtained from 2-hydroxypropiophenone (1.5 g) and 1,2-dichloroethane (**15** g) as a colorless solid; mp 56 °C. ^{1}H NMR (200 MHz, $CDCl_3$) δ: 1.17 (t, 3H, J = 7.2 Hz), 3.05 (t, 2H, J = 7.2 Hz), 3.86 (t, 2H, J = 5.5 Hz), 4.32 (t, 2H, J = 5.5 Hz), 6.8–7.1 (m, 2H), 7.4 (m, 1H), 7.7 (m, 1H). MS (70 eV) m/z: 212; along with **13c** (0.22 g, 14% yield).

Pyrrolones **9a**–**9i**, **15**, and **17** were prepared via the standard procedure including reduction of maleimides (17, 18).

1-(α,α-Dimethyl-3,5-dichlorobenzyl)-3-(2-fluorophenyl)-4-methyl-5-(2-chloroethoxy)-(2,5)-dihydro-2-pyrrolone (**9a**) as a colorless oil. ^{1}H NMR (200 MHz, $CDCl_3$) δ: 1.79 (s, 3H), 1.88 (s, 3H), 2.04 (s, 3H), 3.4–3.7 (m, 4H), 5.75 s (s, 1H), 7.0–7.4 (m, 7H).

1-Phenyl-3,4-dimethyl-5-(2-chloroethoxy)-(2,5)-dihydro-2-pyrrolone (**9b**) as a colorless oil. ^{1}H NMR (200 MHz, $CDCl_3$) δ: 1.90 (s, 3H), 2.03 (s, 3H), 3.2–3.5 (m, 4H), 5.79 (s, 1H), 7.1–7.8 (m, 5H).

1-Isopropyl-3,4-dimethyl-5-(2-chloroethoxy)-(2,5) dihydro-2-pyrrolone (**9c**) was obtained as a colorless oil. ^{1}H NMR (200 MHz, $CDCl_3$) δ: 1.22 (d, 6H, J = 7 Hz), 1.72 (s, 3H), 184 (s, 3H), 3.15 (m, 1H), 3.5 (m, 3H), 4.11 (m, 1H), 5.23 (s, 1H).

1-*tert*-Butyl-3,4-dimethyl-5-(2-chloroethoxy)-(2,5)-dihydro-2-pyrrolone (**9d**) was obtained as a colorless oil. ^{1}H NMR (200 MHz, $CDCl_3$) δ: 1.47 (s, 9H), 1.76 (s, 3H), 1.88 (s, 3H), 3.2 (m, 1H), 3.6 (m, 3H), 5.37 (s, 1H).

1-(2-Fluoro-4-chloro-5-hydroxyphenyl)-3,4-dimethyl-5-(2-chloroethoxy)-(2,5)-dihydro-2-pyrrolone (**9e**) was obtained as a solid; mp 148 °C. ^{1}H NMR (200 MHz, $CDCl_3$) δ: 1.92 (s, 3H), 2.05 (s, 3H), 3.3–3.7 (m, 4H), 5.75 (s, 1H), 6.79 (s, 1H), 7.0–7.3 (m, 2H).

1-(2-Fluoro-4-chloro-5-hydroxyphenyl)-3,4-dimethyl-5-(2-bromoethoxy)-(2,5)-dihydro-2-pyrrolone (**9f**) was obtained as a solid; mp 149 °C. ^{1}H NMR (200 MHz, $CDCl_3$) δ: 1.90 (s, 3H), 2.05 (s, 3H), 3.3–3.7 (m, 4H), 5.74 (s, 1H), 6.9–7.3 (m, 2H).

1-Benzyl-4-methyl-5-(2-chloroethoxy)-(2,5)-dihydro-2-pyrrolone (**9g**) was obtained as a colorless oil. ^{1}H NMR (200 MHz, $CDCl_3$) δ: 1.92 (s, 3H), 3.2–3.5 (m, 4H), 4.12 (d, 1H, J = 15 Hz), 4.8 (d, 1H, J = 15 Hz), 5.06 (s, 1H), 5.89 (s, 1H), 7.25 (s, 5H).

1-Benzyl-3,4-dimethyl-5-(2-chloroethoxy)-(2,5)-dihydro-2-pyrrolone (**9h**) as a colorless oil. ^{1}H NMR (200 MHz, $CDCl_3$) δ: 1.80 (s, 3H), 1.83 (s, 3H), 3.1–3.5 (m, 4H), 4.17 (d, 1H, J = 15 Hz), 4.83 (d, 1H, J = 15 Hz), 4.99 (s, 1H), 7.25 (s, 5H).

1-Benzyl-3-phenyl-4-methyl-5-(2-chloroethoxy)-(2,5)-dihydro-2-pyrrolone (**9i**) was obtained as a colorless oil. ^{1}H NMR (200 MHz, $CDCl_3$) δ: 2.11 (s, 3H), 3.3–3.6 (m, 4H),

© 2004 NRC Canada

Table 4. Characterization data for compounds **2** and **3**.

Product (Formula)	IR (KBr) ν (cm^{-1})	^1H NMR (200 MHz, $CDCl_3$–TMS) δ, *J* (Hz)	MS *m/z*
2a (19) ($C_{10}H_{10}O_2$)	1680 (CO)	2.20 (2H, tt, *J* = 6.9, *J* = 6.5), 2.88 (1H, t, *J* = 6.9), 4.23 (1H, t, *J* = 6.5), 7.08 (2H, m), 7.41 (1H, m), 7.76 (1H, d, *J* = 7)	162 (M^+)
2b (20) ($C_{11}H_{12}O_2$)	1685 (CO)	2.16 (2H, tt, *J* = 6.5, *J* = 6.9), 2.30 (3H, s), 2.86 (2H, t, *J* = 6.9), 4.18 (2H, t, *J* = 6.5), 6.94 (1H, d, *J* = 8.3), 7.22 (1H, d, *J* = 8.3), 7.55 (1H, s)	176 (M^+)
2c (21) ($C_{11}H_{12}O_2$)	1683 (CO)	1.22 (3H, d, *J* = 6.5 Hz), 1.6–1.8 (2H, m), 2.4–2.6 (1H, m), 3.1–3.3 (1H, m), 3.89 (1H, td, *J* = 5, 12.3), 4.4–4.6 (1H, m), 7.06 (2H, t, *J* = 7), 7.4 (1H, m), 7.76 (1H, d, *J* = 6)	176 (M^+)
2d (7*b*) ($C_{11}H_{12}O_3$)	1673 (CO)	2.17 (2H, tt, *J* = 6.6, *J* = 6.9), 2.85 (2H, t, *J* = 6.9), 3.82 (3H, s), 4.22 (2H, t, *J* = 6.6), 6.55 (1H, m), 6.63 (1H, d, *J* = 8.8), 7.22 (1H, d, *J* = 8.8)	192 (M^+)
2e (22) ($C_{14}H_{12}O_2$)	1705 (CO)	2.27 (2H, tt, *J* = 6.4, *J* = 6.9), 2.95 (2H, t, *J* = 6.9), 4.32 (2H, t, *J* = 6.4), 7.17 (1H, m), 7.43 (1H, m), 7.54 (1H, m), 7.8 (2H, m), 8.60 (1H, d, *J* = 8.6)	212 (M^+)
3a ($C_{11}H_{12}O_2$)	1673 (CO)	1.7 (2H, m), 1.95 (2H, m), 3.15 (2H, t, *J* = 6.7), 4.21 (2H, t, *J* = 6), 6.9–7.3 (2H, m), 7.5 (1H, m), 7.9 (1H, m)	176 (M^+)

4.30 (d, 1H, *J* = 14.5 Hz), 4.98 (d, 1H, *J* = 14.5 Hz), 5.22 (s, 1H), 7.2–7.6 (m, 10H).

3-(3-Bromopropoxy)-2-phenyl-2,3-dihydro-isoindol-1-one (**15**) was obtained as a solid; mp 107 °C. ^1H NMR (200 MHz, $CDCl_3$) δ: 1.8 (m, 2H), 3.03.3 (m, 4H), 6.42 (9s, 1H), 7.15 (t, 1H, *J* = 8 Hz), 7.37 (t, 2H, *J* = 8 Hz), 7.5 (m, 3H), 7.73 (d, 2H, *J* = 8 Hz), 7.84 (d, 1H, *J* = 8 Hz).

5-(3-Bromopropoxy)-3,4-dimethyl-2-phenyl-1,5-dihydro-4-methyl-2*H*-pyrrol-2-one (**17**) was obtained as a solid; mp 68 °C. ^1H NMR (200 MHz, $CDCl_3$) δ: 1.95 (s, 3H), 2.0 (m, 2H), 2.04 (s, 3H), 3.2–3.4 (m, 4H), 5.76 (s, 1H), 7.16 (t, 1H, *J* = 8 Hz), 7.40 (t, 2H, *J* = 8 Hz), 7.77 (d, 2H, *J* = 8 Hz).

3,4-Dihydro[1]benzoxepin-5(2*H*)-ones (2)

Method A

Into a nitrogen-purged flask equipped with a stirrer and cooled to –78 °C (dry ice acetone bath), THF (5 mL) and diisopropylamine (0.152 g, 1.5 mmol) were charged, then BuLi (1.5 mmol as 2.5 mol L^{-1} solution) was added. After 30 min a solution of **6** (0.5 mmol) in 5 mL of THF was added slowly followed by HMPA (0.3 mL, 1.5 mmol). The reaction mixture was stirred at –78 °C for 15 min and was warmed up to between 0–5 °C (ice bath). After 1.5 h a methanolic HCl (1 mL, 1 mol L^{-1}) was added. The mixture was concentrated, extracted with ethyl acetate, the extract washed with water, and dried ($MgSO_4$). Column chromatography gave **2**.

Method B

Into a nitrogen-purged flask equipped with a stirrer, NaH (0.100 g 60% dispersion in oil, 2 mmol) was charged, the mixture was cooled to 0 °C (ice bath) and a solution of **6** (1 mmol) in 5 mL THF was added. The mixture was warmed to 25 °C, kept for 80 h, and 1 mL of methanolic HCl was added. The mixture was concentrated, the residue was extracted with ethyl acetate, washed with water, and dried ($MgSO_4$). Column chromatography furnished **2**.

Characterization data for compounds **2** were in good accordance with the literature and are summarized in Table 4.

2,3,4,5-Tetrahydro-6*H*-1-benzoxocin-6-one (3a)

Method A

3a was not found. Only 2-allyloxyacetophenone was isolated as a colorless liquid. ^1H NMR ($CDCl_3$–TMS) δ: 2.64 (s, 3H), 4.63 (d, 2H, *J* = 5.3), 5.32 (d, 1H, *J* = 11), 5.45 (d, 1H, *J* = 17), 6.0–6.2 (m, 1H), 7.0 (m, 2H), 7.4 (m, 1H), 7.72 (d, 1H, *J* = 6). MS *m/z*: 176 (M^+).

Method B

3a was isolated as a colorless liquid and 2-allyloxyacetophenone (20% yield) was also obtained.

Attempted preparation of 3,4,5,6-tetrahydro-1-benzoxonin-7(2*H*)-one (4a)

Method A

4a was not found. The isolated products were: 2-(1-buten-4-yloxy)-acetophenone (28% yield) as a colorless liquid. ^1H NMR ($CDCl_3$–TMS) δ: 2.63 (s, 3H), 2.6 (m, 2H), 4.13 (t, 2H, *J* = 6.3), 5.2 (m, 2H), 5.95 (m, 1H), 6.9 (m, 2H), 7.4 (m, 1H), 7.7 (d, 1H, *J* = 8). MS *m/z*: 190 (M^+); 5-(2-acetylphenoxy)-pentyl-2′-(1-buten-4-yloxy)-phenyl ketone (20% yield) as a colorless liquid. ^1H NMR ($CDCl_3$–TMS) δ: 1.5–2.0 (m, 6H), 2.62 (m, 3H), 2.6 (m, 2H), 3.05 (d, 2H, *J* = 7), 4.0–4.2 (m, 4H), 5.2–5.3 (m, 2H), 5.8 (m, 1H), 6.9 (m, 4H), 7.4 (m, 2H), 7.7 (m, 2H). MS *m/z*: 381 (M + 1); 5-(2-acetylphenoxy)-pentyl-2′-(4-bromobutyloxy)phenyl ketone (15% yield) as a colorless liquid. ^1H NMR ($CDCl_3$–TMS) δ: 1.5–2.0 (m, 6H), 2.0 (m, 4H), 2.62 (s, 3H), 3.03 (t, 2H, *J* = 7), 3.47 (t, 2H, *J* = 7), 4.1 (m, 4H), 6.9 (m, 4H), 7.5 (m, 2H), 7.5–7.8 (m, 2H). MS *m/z*: 462, 464 (M + 2).

Method B

4a was not found. 2-(1-Buten-4-yloxy)-acetophenone (20% yield) was isolated.

3,4,7,7a-Tetrahydro-5-(2-fluorophenyl)-7-(α,α-dimethyl-3,5-dichloro-benzyl)-pyrano[2,3-*b*]pyrrol-6(2*H*)-one (10a)

All reactions were carried out under a nitrogen atmosphere. To a mixture of 2 mol L^{-1} LDA solution in hexane

© 2004 NRC Canada

(1 mL) and dry THF (12 mL) at –78 °C (a dry ice bath) a solution of 5-(2-chloroethoxy)-1-(α,α-dimethyl-3,5-dichlorobenzyl)-3-(2-fluorophenyl)-1,5-dihydro-4-methyl-2*H*-pyrrol-2-one (**9a**) (0.439 g, 0.96 mmol) in dry THF (12 mL) was added with vigorous stirring. Then dry HMPA (0.72 g, 4 mmol) was added dropwise and the mixture was stirred for 15 min at –78 °C. The mixture was allowed to warm to 0 °C and was stirred at this temperature for 1 h. The reaction mixture was quenched with 1 mol L^{-1} methanolic HCl (2 mL) and the solvent was evaporated to give an oily residue. The residue was separated by flash chromatography using silica and hexane – ethyl acetate (4:1) to give 0.269 g (67%) of **10a** as a colorless solid, mp 135 to 136 °C (ethyl acetate). ^{1}H NMR ($CDCl_3$) δ: 1.76 (s, 3H, CH_3), 1.78 (s, 3H, CH_3), 1.85 (m, 2H, CH_2), 2.5 (m, 1H), 2.8 (m, 1H), 3.75 (m, 1H, CH_2O), 4.1 (m, 1H, CH_2O), 5.25 (s, 1H, C_8-H), 7.0–7.5 (m, 7H, aryl protons). MS *m*/*z*: 419 (M^+, 8%), 233 (M^+ – CH_2=CMe-Ar, 16%). Anal. calcd. for $C_{22}H_{20}Cl_2FNO_2$: C 62.85, H 4.76, N 3.33; found: C 62.86, H 4.82, N 3.39.

3,4,7,7a-Tetrahydro-5-methyl-7-phenyl-pyrano[2,3-*b*]pyrrol-6(2*H*)-one (**10b**) was obtained as a colorless solid; mp 109 to 110 °C (ethyl acetate). ^{1}H NMR ($CDCl_3$) δ: 1.8 (m, 2H, CH_2), 1.84 (s, 3H, CH_3), 2.35 (m, 1H), 2.85 (m, 1H), 3.7 (m, 1H, CH_2O), 4.1 (m, 1H, CH_2O), 5.29 (s, 1H, C8-H), 7.11 (t, *J* = 8.3 Hz, 1H, Ph), 7.35 (t, *J* = 8.3 Hz, 2H, Ph), 7.72 (d, *J* = 8.3 Hz, 2H, Ph). ^{13}C NMR ($CDCl_3$) δ: 170.1, 148.0, 136.9, 128.7, 127.1, 122.6, 120.4, 91.5, 64.1, 30.3, 29.0, 9.1. MS *m*/*z*: 229 (M^+, 18%), 214 (M^+ – CH_3, 20%). Anal. calcd. for $C_{14}H_{15}NO_2$: C 73.36, H 6.55, N 6.11; found: C 73.31, H 6.65, N 6.11.

3,4,7,7a-Tetrahydro-5-methyl-7-(2-fluoro-4-chloro-5-hydroxyphenyl)-pyrano[2,3-*b*]pyrrol-6(2*H*)-one (**10e**) was obtained as a colorless solid; mp 158 °C (ethyl acetate). ^{1}H NMR ($CDCl_3$) δ: 1.88 (s, 3H), 1.6–2.0 (m, 2H, CH_2), 2.4 (m, 1H), 2.9 (m, 1H), 3.7 (m, 1H, CH_2O), 4.1 (m, 1H, CH_2O), 5.30 (s, 1H, C8-H), 7.1 (m, 2H, aryl). ^{13}C NMR ($CDCl_3$) δ: 169.7, 150.2, 149.0, 147.9, 124.6, 122.6, 118.2, 117.5, 110.6, 99.5, 65.1, 31.0, 30.2, 9.6. MS *m*/*z*: 297 (M^+, 17%). Anal. calcd. for $C_{14}H_{13}ClFNO_3$: C 56.48, H 4.40, N 4.70; found: C 56.70, H 4.27, N 4.92.

Spiro[2-phenyl-1-isoindolinone-2′-tetrahydrofuran] (16)

To a mixture of 2 mol L^{-1} LDA solution in hexane (1 mL) and dry THF (10 mL) at –78 °C (a dry ice bath), a solution of **15** (0.173 g, 0.5 mmol) in dry THF (1 mL) was added with vigorous stirring. Dry HMPA (0.18 g, 1 mmol) was then added dropwise and the mixture was allowed to warm to room temperature for 1 h. The reaction mixture was quenched by 1 mol L^{-1} HCl in methanol (2 mL), and the solvent was evaporated to give an oily residue. The residue was separated by flash chromatography to give **16** (0.067 g, 50%) as a colorless solid; mp 118 °C (ethyl acetate). ^{1}H NMR ($CDCl_3$) δ: 1.6 (m, 1H), 2.1 (m, 1H), 2.3 (m, 2H), 4.0–4.2 (m, 2H), 7.4–7.65 (m, 8H), 7.80 (d, 1H, *J* = 7.5 Hz). ^{13}C NMR ($CDCl_3$) δ: 166.90, 147.88, 135.97, 133.00, 130.96, 129.69, 129.51, 129.46, 128.35, 123.92, 121.75, 100.33, 70.38, 35.57, 26.58. MS *m*/*z*: 265 (M^+). Anal. calcd. for $C_{17}H_{15}NO_2$: C 76.96, H 5.70, N 5.28; found: C 76.56, H 5.64, N 5.07.

Spiro[5-(1-phenyl-3,4-dimethyl-1,5-dihydro-4-methyl-2*H*-pyrrol-2-one)-2′-tetrahydrofuran] (18) and 6-methyl-8-phenyl-2,3,4,5,8,8a-hexahydro-oxepino[2,3-*b*]pyrrol-7-one (19)

To a solution of **17** (0.162 g, 0.5 mmol) in dry THF (10 mL), 1.5 mol L^{-1} LDA solution in hexane (1 mL) at –78 °C (a dry ice bath) was added with vigorous stirring. Dry HMPA (0.18 g, 1 mmol) was then added dropwise and the mixture was allowed to warm to 0 °C for 1 h. The reaction mixture was quenched by a 1 mol L^{-1} HCl solution in methanol (2 mL), and the solvent was evaporated to give an oily residue. The residue was separated by chromatography to give **18** (0.039 g, 32%) and **19** (0.044 g, 36%). **18**: a colorless glassy solid. ^{1}H NMR ($CDCl_3$) δ: 1.6 (m, 1H), 1.88.(s, 3H), 1.94 (s, 3H), 2.1 (m, 1H), 2.3 (m, 2H), 4.0–4.2 (m, 2H), 7.4–7.65 (m, 8H), 7.80 (d, 1H, *J* = 7.5 Hz). ^{13}C NMR ($CDCl_3$) δ: 170.2, 150.5, 136.5, 129.3, 129.1, 128.3, 127.7, 101.4, 70.5, 32.5, 26.6, 10.3, 8.7. MS *m*/*z*: 243 (M^+, 8%), 228 (M – CH_3, 10%). Anal. calcd. for $C_{15}H_{17}NO_2$: C 74.06, H 7.04, N 5.76; found: C 73.90, H 7.16, N 5.56. **19**: a colorless glassy solid. ^{1}H NMR ($CDCl_3$) δ: 1.5 (m, 1H), 1.8 (m, 2H), 1.93 (s, 3H), 2.0 (m, 1H), 2.4 (m, 1H), 2.8 (m, 1H), 3.4–3.7 (m, 2H), 5.82 (s, 1H), 7.16 (t, 1H, *J* = 8Hz), 7.40 (t, 2H, *J* = 8 Hz)), 7.71 (d, 1H, *J* = 7 Hz). ^{13}C NMR ($CDCl_3$) δ: 170.5, 151.9, 138.1, 131.4, 129.2, 124.7, 121.0, 90.0, 64.9, 32.0, 27.2, 26.6, 8.6. MS *m*/*z*: 243 (M^+, 9%). Anal. calcd. for $C_{15}H_{17}NO_2$: C 74.06, H 7.04, N 5.76; found: C 73. 77, H 6.92, N 5.73.

3,4-Dihyro-8-methyl-4-phenyl-2*H*-pyrrolo[2,1-*b*][1,3]-oxazin-6(8a*H*)-one (11a)

All reactions were carried out under a nitrogen atmosphere. To the mixture of 2 mol L^{-1} LDA solution in hexane (1 mL) and dry THF (10 mL) at –78 °C (a dry ice bath) a solution of 1-benzyl-5-(2-chloroethoxy)-1,5-dihydro-4-methyl-2*H*-pyrrol-2-one (0.255 g, 0.96 mmol) in dry THF (5 mL) was added with vigorous stirring. Dry HMPA (0.90 g, 5 mmol) was then added dropwise and the mixture was stirred at –78 °C for 1 h. The reaction mixture was quenched by 1 mol L^{-1} methanolic HCl (2 mL), and the solvent was evaporated to give an oily residue. The residue was separated by flash chromatography to give 0.088 g (40%) of **11a** as a colorless solid; mp 114 to 115 °C (ethyl acetate). ^{1}H NMR ($CDCl_3$) δ: 2.02 (s, 3H, CH_3), 2.2 (m, 2H, C_3-CH_2), 3.74 (m, 1H, CH_2O), 4.0 (m, 1H, CH_2O), 5.05 (s, 1H, C8a-H), 5.54 (s, 1H, C4-H), 5.98 (s, 1H, =CH), 7.1–7.5 (m, 5H, Ph). MS *m*/*z*: 229 (M^+, 10%), 214 (M^+ – CH_3, 14%). Anal. calcd. for $C_{14}H_{15}NO_2$: C 73.36, H 6.55, N 6.11; found: C 73.32, H 6.63, N 6.17.

3,4-Dihydro-7,8-dimethyl-4-phenyl-2*H*-pyrrolo[2,1-*b*][1,3]-oxazin-6(8a*H*)-one (**11b**) was obtained as a colorless solid, mp 64 to 65 °C (ethyl acetate). ^{1}H NMR ($CDCl_3$) δ: 1.85 (s, 3H, CH_3), 1.92 (s, 3H, CH_3), 2.2 (m, 2H, C_3-CH_2), 3.7 (m, 1H, CH_2O), 4.0 (m, 1H, CH_2O), 4.97 (s, 1H, C8a-H), 5.52 (s, 1H, C_4-H), 7.2–7.4 (m, 5H, Ph). MS *m*/*z*: 243 (M^+, 11%), 228 (M^+ – CH_3, 10%). Anal. calcd. for $C_{15}H_{17}NO_2$: C 74.06, H 7.04, N 5.76; found: C 74.04, H 7.24, N 5.78.

3,4-Dihydro-8-methyl-4,7-diphenyl-2*H*-pyrrolo[2,1-*b*][1,3]-oxazin-6(8a*H*)-one (**11c**) was obtained as a colorless oil. ^{1}H NMR ($CDCl_3$) δ: 2.14 (s, 3H, CH_3), 2.2 (m, 2H, C_3-H), 3.85

© 2004 NRC Canada

(m, 1H, CH_2O), 4.1 (m, 1H, CH_2O), 5.14 (s, 1H, C8a-H), 5,64 (d, J = 4.5 Hz, 1H, C4-H), 7.2–7.5 (m, 10H, phenyls). MS m/z: 305 (M^+, 6%), 290 ($M^+ - CH_3$, 5%). Anal. calcd. for $C_{20}H_{19}NO_2$: C 78.68, H 6.23, N 4.59; found: C 78.43, H 6.48, N 4.57.

References

1. H.O. House, W.V. Phillips, T.S.B. Sayer, and C.-C. Yan. J. Org. Chem. **43**, 700 (1978).
2. Y. Morita, M. Suzuki, and R. Noyori. J. Org. Chem. **54**, 1785 (1989).
3. (*a*) O. Dann and W.D. Arndt. Ann. Chem. **587**, 38 (1954); (*b*) G. Fontaine and P. Maitte. Compt. Rend. Hebd. Seances. Acad. Sci. **258**, 4583 (1964).
4. J.Y. Nioche, J. Deceprit, and D. Festal. Eur. J. Med. Chem. **30**, 377 (1995).
5. M.S. Newman and A.B. Mekler. J. Org. Chem. **26**, 336 (1961).
6. (*a*) T. Nagamatsu, S. Tsurubayashi, K. Sasaki, and T. Hirota. Synthesis, **4**, 303 (1991); (*b*) B. El Ali, K. Okuro, G. Vasapollo, and H. Alper. J. Am. Chem. Soc. **118**, 4264 (1996); (*c*) J.-S. Shiue, C.-C. Lin, and J.-M. Fang. Tetrahedron Lett. **34**, 335 (1993).
7. (*a*) R.C. Tripathi, V.K. Tandon, J.M. Khanna, A.K. Saxena, and N. Anand. Ind. J. Chem. **28B**, 37 (1989); (*b*) A.N. Mandal, A. Ghosh, S. Bhattarcharyya, R. Patra, and A. Chatterjee. Indian J. Chem. Sect. B, **32B**, 1004 (1993); (*c*) T. Tatsuoka, M. Shibata, and M. Imoto. Jpn. Patent 4 178 381, 1992; Chem. Abstr. **118**, 101 953 (1993).
8. J.L. Krstenansky and B.L. Currie. US Patent 4 535 169, 1985; Chem. Abstr. **104**, 88 967v (1985).
9. J.H. Rigby, M. Qabar, G. Ahmed, and R.C. Hughes. Tetrahedron, **49**, 10 219 (1993).
10. P. Aeberli, J.H. Gogerty, W.H. Houlihah, and L.C. Iorio. J. Med. Chem. **19**, 436 (1976).
11. K. Moriyasu, H. Akieda, and H. Aoki. US Patent 5 409 886, 1995; Chem. Abstr. **124**, P86 808h (1995).
12. P. Tahtinen, R. Sillanpaa, G. Stajer, A.E. Szabo, and K. Pihlaja. J. Chem. Soc. Perkin Trans. 2, 597 (1997).
13. T.A. Narwid and A.I. Meyers. J. Org. Chem. **39**, 2572 (1974).
14. T. Eicher and D. Krause. Synthesis, **11**, 899 (1986).
15. G. Pandey, G. Kumaraswamy, and P.Y. Reddy. Tetrahedron, **48**, 8295 (1992).
16. (*a*) A. McKillop, J.-C. Fiaud, and R.P. Hug. Tetrahedron, **30**, 1379 (1974); (*b*) M. Motoi, K. Shimamura, S. Muramoto, S. Kanoh, and H. Suda. Bull. Chem. Soc. Jpn. **62**, 2553 (1989).
17. F. Farina, M.V. Martin, and M.C. Paredes. Heterocycles, **22**, 1733 (1984).
18. L. De Buyck, F. Ghelfi, I. Laureyn, E. Libertini, A. Mucci, K.V. Nikitin, U.M. Pagnoni, T.M. Rogge, and C.V. Stevens. Tetrahedron, **59**, 1147 (2003).
19. V.D. Orlov, E.I. Mikhed'kina, and V.F Lavrushin. J. Gen. Chem. USSR (Engl. Transl.), **54**, 148 (1984).
20. H. Christensen. Synth. Commun. **4**, 1 (1974).
21. S. Bhattacharya, A.N. Mandal, S.R.R. Chaudhuri, and A. Chatterjee. J. Chem. Soc. Perkin Trans.1, 5 (1984).
22. V.K. Tandon, R.B. Chhor, and G.K. Goswamy. Indian J. Chem. Sect. B, **37**, 1027 (1998).

© 2004 NRC Canada

3-Amino-1-hydroxyacetone

Nisar Ullah, Clara Nanfe Fali, and Ian D. Spenser

Abstract: 3-Amino-1-hydroxypropan-2-one (3-amino-1-hydroxyacetone) was prepared in an overall yield of 52% in 6 steps starting with *N*-phthaloylglycine. This synthesis is readily adaptable for the preparation of bond-labeled samples, i.e., samples that are labeled intramolecularly at contiguous sites.

Key words: 3-amino-1-hydroxyacetone, 3-amino-1-hydroxypropan-2-one.

Résumé : On a préparé la 3-amino-1-hydroxypropan-2-one (3-amino-1-hydroxyacétone), avec un rendement global de 52 %, en six étapes à partir de la *N*-phtaloylglycine. La synthèse peut facilement être adaptée à la préparation d'échantillons portant des marqueurs intramoléculaires sur des sites voisins.

Mots clés : 3-amino-1-hydroxyacétone, 3-amino-1-hydroxypropan-2-one.

[Traduit par la Rédaction]

Introduction

3-Amino-1-hydroxyacetone 1-O-phosphate (**2**), derived by oxidative decarboxylation of 4-hydroxy-L-threonine 4-O-phosphate (**1**), serves as a precursor of the C_3N unit, N-1,C-6,5,5′ of vitamin B_6 (**3**) in *Escherichia coli* (Scheme 1) (1).

In connection with our continuing investigations of the biosynthesis of vitamin B_6 in *E. coli* (2) and in yeast (3–5), we required a sample of aminohydroxyacetone that was intramolecularly contiguously $^{13}C,^{13}C$ or $^{15}N,^{13}C$ labeled, i.e., bond labeled. None of the reported syntheses of the compound (6–8) were readily adaptable to this purpose, since the starting materials employed in these synthetic sequences are not available in labeled form. The synthetic sequence here described starts from *N*-phthaloylglycine (**4**). Several syntheses of labeled samples of this compound, from commercially available labeled starting materials in almost quantitative yields, have been reported (see Scheme 2) in connection with the preparation of labeled samples of δ-aminolevulinic acid.

The preparation of the following singly and multiply labeled samples of *N*-phthaloylglycine (**4**) has been described: 1-^{14}C- (9–11), 1-^{13}C- (12–14), 2-^{13}C- (13–15), 1,2-$^{13}C_2$- (15), ^{15}N- (13, 14), 1-^{13}C,^{15}N- (16), 2-^{13}C,^{15}N- (16), and 1,2-$^{13}C_2$,^{15}N- (17). The corresponding acyl chloride (**5**), which was obtained quantitatively on treatment of the acid with thionyl chloride (9–17), was then converted into δ-aminolevulinic acid by several different routes.

In one of these routes, the labeled phthaloylglycyl chloride (**5**) was treated with diazomethane, an Arndt–Eistert reaction that was originally described by Balenović (18), yielding the correspondingly labeled 1-diazo-3-phthalimidopropan-2-one (**6**) (9, 10, 17), which was then used in the next step of the synthetic sequence, leading to labeled δ-aminolevulinic acid.

In the present preparation of aminohydroxyacetone, an acid-catalyzed decomposition of the diazo compound (**6**) (18) gave 1-hydroxy-3-phthalimidopropan-2-one (**7**), the *N*-phthaloyl derivative of the desired product. However, attempts to obtain (**10**) by hydrolytic removal of the phthaloyl group of (**7**) were unsuccessful.

The phthaloyl unit was removed by reaction with hydrazine. Before doing so, the keto group of (**7**) had to be protected. This was done by reaction with ethyleneglycol to yield 2-hydroxymethyl-2-phthalimidomethyl-1,3-dioxolane (**8**). This compound had been prepared previously by somewhat different reaction sequences (19, 20). Treatment of the ketal (**8**) with hydrazine, followed by dilute HCl, gave 2-hydroxymethyl-2-aminomethyl-1,3-dioxolane hydrochloride (**9**). For hydrolysis, the ketal was suspended in aqueous acetonitrile, and the mixture was refluxed in the presence of an ion-exchange resin, from which the product, 3-amino-1-hydroxyacetone hydrochloride (**10**), was eluted with 2 mol L^{-1} HCl and obtained in high yield.

When acetone, in place of acetonitrile, was employed as the solvent in the above procedure, the yield of product was less than 40%. Other methods used to carry out the deprotection of **9** were entirely unsuccessful. Attempted hydrolysis of **9** with HCl, with HCl in THF solution, or with CF_3CO_2H was unsuccessful, as was attempted hydrolysis with pyridinium *p*-toluenesulfonate (0.33, 0.66, 1.0, 1.5, and 2.0 g equiv.) and with *p*-toluenesulfonic acid in acetone at reflux temperature for 24 h. Hydrolysis with dilute sulfuric acid and cerium ammonium nitrate was successful, but the product could not be isolated since it could not be separated from the other water-soluble solids.

The unlabeled aminohydroxyacetone (**10**) was employed in two displacement experiments to test whether the compound serves as an intermediate in the biosynthesis of vitamin B_6 from glucose in yeast, as it does in *E. coli* (1).

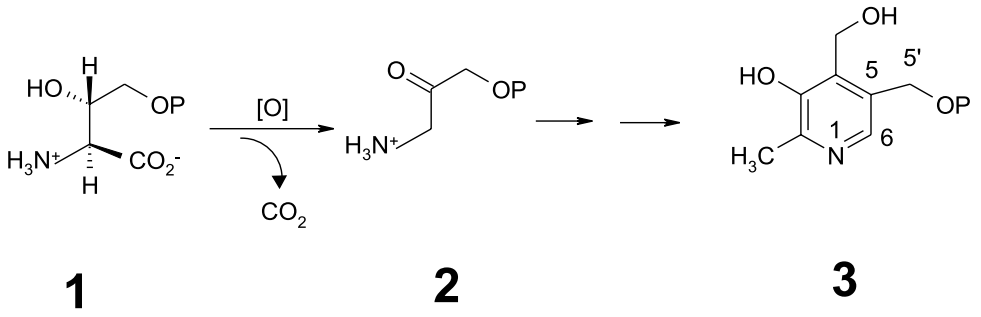
Received 15 September 2003. Published on the NRC Research Press Web site at http://canjchem.nrc.ca on 7 April 2004.

N. Ullah, C.N. Fali, and I.D. Spenser.[1] Department of Chemistry, McMaster University, Hamilton, ON L8S 4M1, Canada.

[1]Corresponding author (e-mail: spenser@mcmaster.ca).

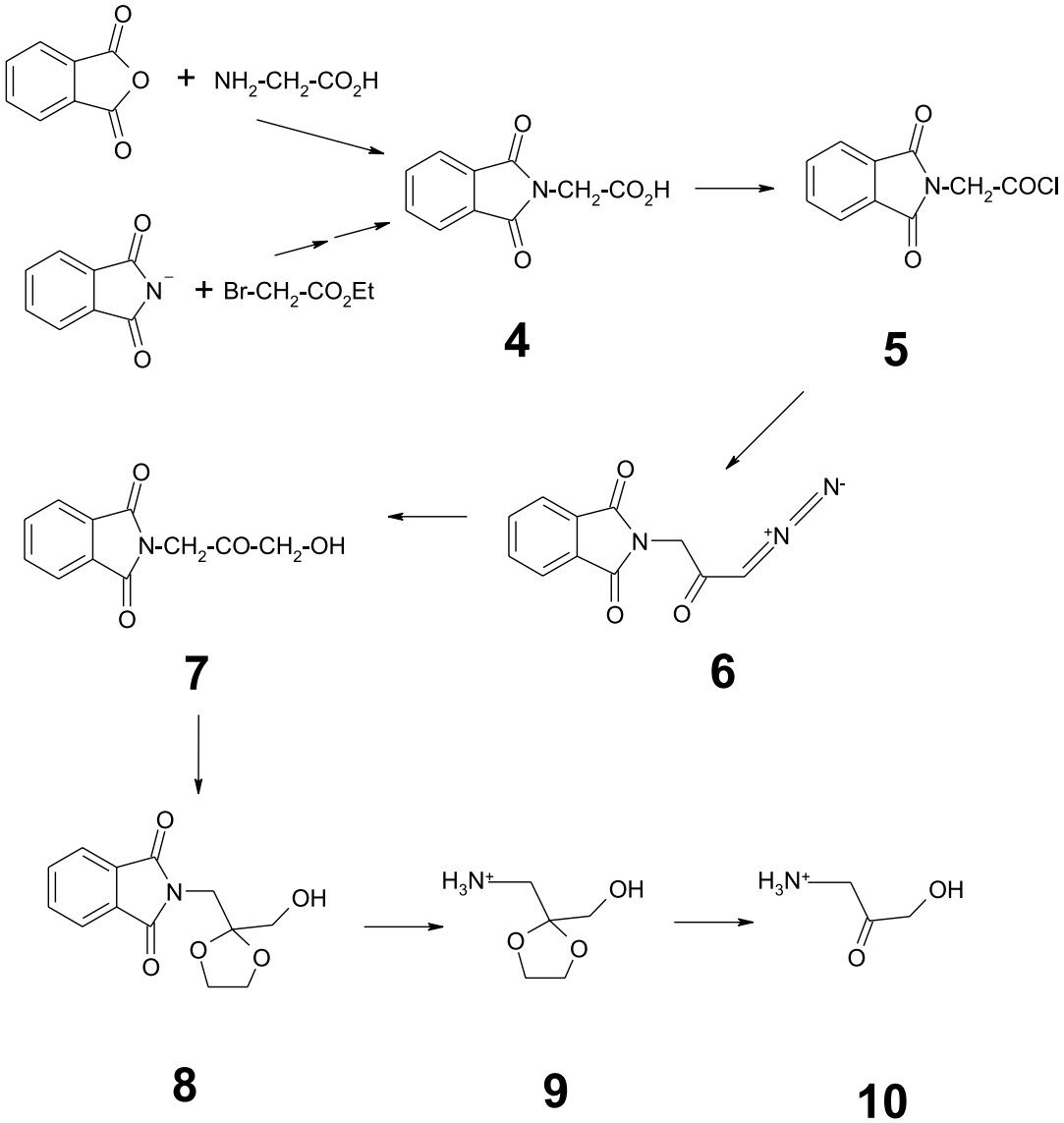
 doi: 10.1139/V04-010 © 2004 NRC Canada

Scheme 1. Biosynthetic origin, in *E. coli*, of the C_3N unit N-1,C-6,5,5′ of pyridoxine phosphate.



1 **2** **3**

Scheme 2. Synthesis of 3-amino-1-hydroxyacetone.



Incorporation of label from [$^{13}C_6$]glucose into pyridoxamine was not displaced by aminohydroxyacetone (**10**), either in *Saccharomyces cerevisiae* or in *Candida utilis* (5). This result made it unlikely that incorporation of a label from a sample of this compound into vitamin B_6 would be observed in these yeasts. The preparation of bond-labeled samples of aminohydroxyacetone was therefore not pursued.

Experimental

N-Phthaloylglycyl chloride (5) (18)

Phthaloylglycine (**4**) (15.4 g, 75 mmol) was suspended in thionyl chloride (21 mL, 40.2 g, 336 mmol), and the mixture was refluxed until a clear solution was obtained (ca. 35 min). Excess thionyl chloride was pumped off in vacuo,

© 2004 NRC Canada

and the residue solidified to yield the product (**5**) as a light yellow crystalline mass. mp 85 to 86 °C (lit. (18) value mp 84 to 85 °C). Yield 16.7 g, 99%. ^{1}H NMR (200 MHz, $CDCl_3$) δ: 7.93–7.89 (m, 2H), 7.80–7.76 (m, 2H), 4.82 (s, 2H). ^{13}C NMR (75.5 MHz) δ: 169.0, 166.6, 134.6, 131.5, 123.9, 47.5.

1-Diazo-3-phthalimidopropan-2-one (6) (18)

Phthaloylglycyl chloride (**5**) (10.7 g, 48 mmol) in 500 mL dry ether was treated with excess diazomethane (generated from 49 g methylnitronitrosoguanidine in 500 mL dry ether, adding 112 mL 40% KOH). The product crystallized from the ether solution after being kept at room temperature overnight. It was recrystallized from ethyl acetate. mp 163–165 °C (with decomposition (decomp.)) after sintering from 158 °C (lit. (18) value mp 168 °C (decomp.)). Yield 11.0 g (98%). IR (KBr pellet) (cm^{-1}) ν: 2128, 1774, 1733, 1629. ^{1}H NMR (200 MHz, $CDCl_3$) δ: 7.88–7.86 (m, 2H), 7.76–7.74 (m, 2H), 5.40 (s, 1H), 4.44 (s, 2H). ^{13}C NMR (75.5 MHz, $CDCl_3$) δ: 186.5, 167.6, 134.2, 132.0, 123.6, 53.8, 44.1. MS (CI, NH_3) *m/z* (%): 247 (70, [M + NH_4^+]), 202 (100, [M – N_2 + H^+]). MS (DEI) *m/z* (%): 201 (43, [M – N_2^+], 160 (15, [M – $COCHN_2^+$]).

1-Hydroxy-3-phthalimidopropan-2-one (7)

1-Diazo-3-phthalimidopropan-2-one (**6**) (10.9 g, 47.6 mmol) was suspended in dilute sulfuric acid (20% volume fraction) and stirred at 50 °C for 3 h until all the solid had gone into solution. The mixture was then extracted with ethyl acetate, and the solution was dried over $CaCl_2$. The solvent was removed, and the product was recrystallized from ethanol. Yield 9.3 g (82%). mp 119–121 °C (lit. (18) value mp 121 °C, rising to 142 °C on recrystallization). ^{1}H NMR (200 MHz, $CDCl_3$) δ: 7.91–7.87 (m, 2H), 7.78–7.76 (m, 2H), 4.59 (s, 2H), 4.45 (s, 2H), 2.50 (s, 1H). ^{13}C NMR (75.5 MHz, $CDCl_3$) δ: 202.4, 167.5, 134.4, 131.9, 123.7, 66.8, 43.5.

2-Hydroxymethyl-2-phthalimidomethyl-1,3-dioxolane (8)

To a soluton of (**7**) (8.5 g, 39 mmol) in 500 mL toluene was added ethylene glycol (19.5 g, 310 mmol) and *p*-toluenesulfonic acid monohydrate (0.28 g, 2 mmol). The mixture was refluxed using a Dean–Stark trap to remove water. After 5 h, the mixture was allowed to cool to room temperature and was then concentrated. Purification by flash column (diethyl ether, 100%) gave the product (**8**). Yield 7.9 g, 77%. mp 98–100 °C (lit. (20) value mp 114–117 °C). ^{1}H NMR (200 MHz, $CDCl_3$) δ: 7.84–7.80 (m, 2H), 7.72–7.67 (m, 2H), 4.13–3.97 (m, 4H), 3.85 (s, 2H), 3.49 (s, 2H), 2.98 (s, 1H, OH). ^{13}C NMR (75.5 MHz, $CDCl_3$) δ: 168.4, 134.1, 131.6, 123.4, 108.0, 65.3, 63.6, 38.8.

2-Hydroxymethyl-2-aminomethyl-1,3-dioxolane hydrochloride (9)

To a solution of the ketal (**8**) (7.5 g, 28.5 mmol) in 500 mL ethanol was added hydrazine monohydrate (3 mL) in ethanol (350 mL), and the mixture was allowed to stand at room temperature for 36 h. The mixture was then refluxed for 7 h, and the solvent was evaporated in vacuo to dryness. The residue was suspended in 1 mol L^{-1} HCl (300 mL), and the mixture was cooled to 0 °C, allowed to stand for 1 h, and filtered. The solid was washed with a little dilute HCl, and the filtrate was evaporated at 40 °C under reduced pressure to a thick syrup. Addition of methanol, followed by diethyl ether gave the product (**9**) as a crystalline solid. mp. 175–178 °C. Yield 4.2 g, 87%. ^{1}H NMR (200 MHz, D_2O) δ: 4.00 (s, 4H), 3.46 (s, 2H), 3.18 (s, 2H). ^{13}C NMR (75.5 MHz, D_2O) δ: 106.4, 65.8, 61.9, 41.5.

3-Amino-1-hydroxypropan-2-one (3-amino-1-hydroxyacetone) hydrochloride (10)

The ketal (**9**) (2.0 g, 12 mmol) (MW 169.5) was suspended in aqueous acetonitrile (5%, 100 mL). Dowex 50W-X8, 20–50 mesh (20 g) was added, and the mixture was refluxed for 5 h. The solvent was filtered off; the resin was applied to a column, and the column was eluted with 2 mol L^{-1} HCl. The eluate was evaporated in vacuo at 40 °C, and the residue was recrystallized from ethanol–ether to give the product. Yield 1.38 g, 93%. The procedure was repeated on a larger scale, when 3.3 g product (95%) was obtained from 4.85 g (29.1 mmol) ketal (**9**). mp 136 to 137 °C. (lit. (6) value mp 136 to 137 °C; lit. (8) value mp 134–136 °C; lit. (7) value mp 139 °C). ^{1}H NMR (200 MHz, D_2O) δ: 4.37 (s, 2H), 4.04 (s, 2H). ^{13}C NMR (75.5 MHz, D_2O) δ: 206.6, 65.7, 44.3.

Acknowledgments

This paper is dedicated to the memory of Dr. Clara Nanfe Fali (born 26 October 1960) (M.Sc., University of Jos, Nigeria; Ph.D., University of Florida), who initiated this investigation. Clara died unexpectedly and suddenly in May 2000 in Hamilton. She was a gifted organic chemist, a hard-working research associate, and a delighful person. She is sadly missed by the members of the McMaster Chemistry Department.

A research grant from the Natural Sciences and Engineering Research Council of Canada (NSERC) is gratefully acknowledged.

References

1. D.E. Cane, Y. Hsiung, J.A. Cornish, J.K. Robinson, and I.D. Spenser. J. Am. Chem. Soc. **120**, 1936 (1998).
2. R.E. Hill, K. Himmeldirk, I.A. Kennedy, R.M. Pauloski, B.G. Sayer, and I.D. Spenser. J. Biol. Chem. **271**, 30 426 (1996).
3. R.N. Gupta, T. Hemscheidt, B.G. Sayer, and I.D. Spenser. J. Am. Chem. Soc. **123**, 11 353 (2001).
4. J. Zeidler, N. Ullah, R.N. Gupta, R.M. Pauloski, B.G. Sayer, and I.D. Spenser. J. Am. Chem. Soc. **124**, 4542 (2002).
5. J. Zeidler, R.N. Gupta, B.G. Sayer, and I.D. Spenser. J. Org. Chem. **68**, 3486 (2003).
6. A.O. Jackson and C.S. Marvel. J. Biol. Chem. **103**, 191 (1933).
7. C. Tarnus, J.-M. Rémy, and H. d'Orchymont. Bioorg. Med. Chem. **4**, 1287 (1996).
8. E. Wolf, I.A. Kennedy, K. Himmeldirk, and I.D. Spenser. Can. J. Chem. **75**, 942 (1997).
9. L. Pichat and M. Herbert. Bull. Soc. Chim. Fr. 673 (1957).
10. A.E.A. Mitta, A.M. Ferramola, H.A. Sancovich, and M. Grinstein. J. Labelled Compd. **3**, 20 (1967).
11. J.B. Campbell and J.S. Johnston. J. Labelled Compd. Radiopharm. **27**, 1353 (1989).

© 2004 NRC Canada

12. K. Kurumaya, T. Okazaki, N. Seido, Y. Akasaka, Y. Kawajiri, M. Kajiwara, and M. Kondo. J. Labelled Compd. Radiopharm. **27**, 217 (1989).
13. R.A. Aitken, H.R. Cooper, and A.P. Mehotra. J. Chem. Soc. Perkin Trans 1, 475 (1996).
14. J. Wang and A.I. Scott. Tetrahedron Lett. **38**, 739 (1997); 2587 (1997).
15. K. Iida and M. Kajiwara. J. Labelled Compd. Radiopharm. **45**, 569 (2002).
16. K. Iida and M. Kajiwara. J. Labelled Compd. Rariopharm. **45**, 139 (2002).
17. B. Nitsche, H.-P. Köst, E. Cmiel, and S. Schneider. J. Labelled Compd. Radiopharm. **27**, 623 (1987).
18. K. Balenović, N. Bregant, D. Cerar, and M. Tkalčić. J. Org. Chem. **16**, 1308 (1951).
19. K. Kobayashi, H.S. Forrest, and M. El-Emary. Arch. Biochem. Biophys. **121**, 220 (1967).
20. M. Gall and B.V. Kamdar. J. Org. Chem. **46**, 1575 (1981).

© 2004 NRC Canada

A study of the electrochemical behaviour of cobalt in aqueous $H_2CO_3/HCO_3^-/CO_3^{2-}$ solutions at pH 7–9

Stéphan Simard and Danick Gallant

Abstract: The electrochemical behaviour of a cobalt rotating electrode in $H_2CO_3/HCO_3^-/CO_3^{2-}$ aqueous solutions was investigated in the pH region from 7 to 9. The effects of $H_2CO_3/HCO_3^-/CO_3^{2-}$ concentration, pH, and the presence of phosphates as inhibitors was explored using a rotating disc electrode at 1000 rpm. Some potentiodynamic experiments indicate that for pH 8.5 and higher, carbonate and bicarbonate species play a key role on the rate of electrooxidation of cobalt. For pH lower than 8.5, the electrochemical behaviour of cobalt changes drastically and very aggressive corrosion is observed. The involvement of carbonic acid must be considered in the corrosion process of cobalt in this pH region. The study of passive film potential decay under open circuit potential and galvanostatic reduction was performed on preanodized cobalt electrodes in solutions of various compositions. These experiments indicated the phenomena occurring at the electrode–solution interface during the corrosion process. A mechanism involving competitive adsorption of different species is suggested on the basis of the experimental evidence.

Key words: cobalt, bicarbonate, phosphate, carbonic acid, corrosion.

Résumé : Le comportement électrochimique d'une électrode tournante de cobalt dans des solutions aqueuses de $H_2CO_3/HCO_3^-/CO_3^{2-}$ a été étudié dans la zone de pH 7 à 9. L'effet de la concentration de $H_2CO_3/HCO_3^-/CO_3^{2-}$, du pH et de la présence de phosphates agissants comme inhibiteurs a été exploré à l'aide d'une électrode tournante à disque à 1000 rpm. Des expériences potentiodynamiques montrent que pour les pH supérieurs ou égaux à 8.5, les espèces carbonates et bicarbonates jouent un rôle déterminant sur le taux d'électrooxydation du cobalt. Pour les pH inférieurs à 8.5, le comportement électrochimique du cobalt change drastiquement et un phénomène agressif de corrosion est noté. L'implication de l'acide carbonique dans le processus de corrosion du cobalt dans cette zone de pH doit être considérée. Des mesures de potentiel en circuit ouvert et sous contrôle galvanostatique ont été effectuées sur des électrodes de cobalt préanodisées dans des solutions de diverses compositions. Ces expériences ont permis de déduire les phénomènes qui se produisent à l'interface métal–solution durant le processus de corrosion. Un mécanisme impliquant l'adsorption compétitive de différentes espèces est suggéré sur la base d'évidences expérimentales.

Mots clés : cobalt, bicarbonate, phosphate, acide carbonique, corrosion.

Introduction

Transition metals such as iron, nickel, and cobalt are often employed in industrial applications and the construction of transportation vehicles. Cobalt is a particularly useful material because its hardness allows its use under conditions leading to wear. Also, cobalt is often used as a metallic matrix for cemented carbide coatings which are good replacement materials for hard chrome plated coatings.

Despite the fact that many investigations on the corrosion of cobalt have been performed, its corrosion behaviour is not completely understood and different interpretations are often reported in the literature. Moreover, the corrosion behaviour of cobalt in highly dilute solutions at near-neutral pH has not been extensively studied.

In early studies, the passivation of cobalt in alkaline solutions was attributed to the formation of $Co(OH)_2$ films initiated by the reaction of adsorbed OH^- species on the metal surface (1). In other studies, the presence of CoO is preferred but the existence of $Co(OH)^+$ species is still identified as a precursor for the passive film formation (2). This anodic film formed in the potential range close to the active dissolution potential region is generally called the primary passive region. More recently, an investigation including X-ray photoelectron spectroscopy (XPS) surface analysis reported that the passive film previously formed on cobalt in alkaline solutions consists of an inner layer of α-$Co(OH)_2$ plus CoO and an outer layer consisting of the CoOOH species (3). Further oxidation of the passive film previously formed in the primary passive region occurs in a region called the secondary passive region. Another XPS study of passive films formed in similar solutions reveals that the composition of the primary passive film consists of a thick $Co(OH)_2$ layer and at a more anodic potential, i.e., in the secondary passive region, the film composition changes to Co_3O_4, CoOOH, and Co_2O_3 (4). Other early studies have been dedicated to

Received 12 November 2003. Published on the NRC Research Press Web site at http://canjchem@nrc.ca on 29 April 2004.

S. Simard[1] and D. Gallant. Département de biologie, chimie et sciences de la santé, Université du Québec à Rimouski, Rimouski QC G5L 3A1, Canada.

[1]Corresponding author (e-mail: stephan_simard@uqar.qc.ca).

 doi: 10.1139/V04-033 © 2004 NRC Canada

the understanding of the cobalt oxidation in neutral and alkaline buffered solutions. The passivation of cobalt by anodic polarization in borate solutions at pH ranging from 7 to 11 was described as beginning by the formation of a hydrous CoO layer. Polarization toward more anodic potentials generates further oxidation of the outer layer to obtain bilayered $CoO–Co_3O_4$ and finally a $CoO–Co_2O_3$ film (5).

The electrochemical behaviour of cobalt in slightly alkaline solutions, more precisely in borate and bicarbonate, has been investigated by Davies and Burstein (6). Their work was performed in solutions having an ionic strength around 0.8 mol L^{-1} and at pH 8.8. Under such conditions, they demonstrated that in bicarbonate solutions, HCO_3^- ionic species are aggressive toward cobalt and cobalt(II) oxides by promoting the dissolution of the bare metal and the primary passive film. It was reported that the primary passivation occurs through the formation of CoO or mainly $CoCO_3$(s) (6). It was then suggested that the dissolution of $CoCO_3$(s) occurs by the following equilibrium

$$[1] \quad CoCO_3(s) + HCO_3^-(aq) \rightleftharpoons Co(CO_3)_2^{2-}(aq) + H^+(aq)$$

and the dissolution of CoO can occur by a sequence of rxns. [2] and [1]

$$[2] \quad CoO(s) + HCO_3^-(aq) \rightarrow CoCO_3(s) + OH^-(aq)$$

Later, these dissolution pathways were supported by Gervasi et al. (7) and another process was suggested

$$[3] \quad Co(s) + H_2O \rightarrow Co(OH)(ad) + H^+(aq) + e^-$$

followed by

$$[4] \quad Co(OH)(ad) \rightarrow CoO(s) + H^+(aq) + e^-$$

or

$$[5] \quad Co(OH)(ad) + HCO_3^-(aq) + CO_3^{2-}(aq) \rightleftharpoons Co(CO_3)_2^{2-}(aq) + H_2O + e^-$$

In the region of higher anodic potentials (secondary passive region), the anodic dissolution process of cobalt is replaced by the formation of a more stable oxide film such as Co_3O_4 (7, 8). At higher pH values, where the concentration of HCO_3^- species in solution becomes less important, the formation of different oxides is directly promoted. A recent spectroelectrochemical study suggests that the formation of Co_3O_4 originates from a further oxidation of CoO species previously produced in parallel with active cobalt dissolution (9).

In carbonate–bicarbonate solutions at pH ranging from 8 to 10, it is clearly demonstrated that the solution composition in the vicinity of the metal is the determining factor for the dissolution and passivation of cobalt. However, the ionic composition of the H_2CO_3(aq)/HCO_3^-(aq)/CO_3^{2-}(aq) system changes strongly in the pH range from 7 to 9. Then, it can be deduced that the corrosion behaviour of cobalt can be largely affected by the pH in such a situation, or more accurately, by the nature of the dissolved species in aqueous media.

In natural environments such as marine media, the pH is slightly alkaline (usually $8.0 < pH < 8.2$) due to the presence of the H_2CO_3(aq)/HCO_3^-(aq)/CO_3^{2-}(aq) system at concentrations of a few mmol L^{-1} (10). Moreover, since the salinity of the marine environment (typically 35 (10)) is also an important parameter, another study on the influence of chlorides on cobalt corrosion is in progress in our laboratory. In the past, less attention has been paid to the corrosion behaviour of cobalt in low and intermediate bicarbonate concentrations and especially in media presenting a pH from 7 to 9. pH values lower than 8.3 are rarely considered in corrosion studies in the $H_2CO_3/HCO_3^-/CO_3^{2-}$ system and, to the best of our knowledge, no study has been performed at $pH < 8$. To understand the corrosion mechanisms of cobalt in such media, the present work is then dedicated to the study of the electrochemical behaviour of cobalt in bicarbonate solutions at pH ranging from ~7 to ~9. It will be demonstrated that the pH has a dramatic effect on the electrochemical behaviour of cobalt in this pH range. This is of primary importance considering that such media are omnipresent in the environment and that cobalt is an important component of several industrial alloys that are exposed to these conditions.

Experimental

The experiments were carried out with a rotating disc electrode at 1000 rpm to render mass transfer limitations marginal and to study the kinetics of the surface reactions. The working disc electrode was made with a cobalt disc from a cylindrical rod (99.95%) and had a surface area of 0.283 cm^2. The cobalt rod was set in a Kel-F holder sealed with epoxy resin. The auxiliary electrode was a platinized platinum sheet separated from the main compartment by a Nafion® membrane. The reference electrode was a saturated calomel electrode (SCE) connected to the cell by a bridge and a Luggin capillary. All potentials are referenced to this electrode. The volume of the electrochemical cell was 0.5 L or more, so that the concentration of dissolved cobalt in the bulk could be neglected. Aqueous solutions were prepared with ACS grade chemicals and deionized water. Solutions containing bicarbonate were deaerated by bubbling high-purity nitrogen or mixtures of nitrogen and carbon dioxide depending on the pH. The pH values under ~8.3 were reached by using an appropriate mixture of $N_2–CO_2$; pH values above ~8.3 were reached by using different $N_2–CO_2$ mixtures and (or) by addition of small volumes of concentrated NaOH solutions. For each experiment over the entire pH range, the pH was maintained at a stable value by bubbling an appropriate $N_2–CO_2$ mixture. Solutions not containing bicarbonate were deaerated by bubbling high-purity nitrogen before and during the course of the experiments. The electrode surface was ground successively with 600 and 1200 grit emery paper and mechanically polished with 5.0, 1.0, and 0.05 μm alumina suspensions before all immersions. At the beginning of each experiment, the electrode potential was held at –1.05 V for 4 min to produce a perceptible hydrogen evolution reaction. This preparation procedure ensured a mirror-like finish and oxide-free surface that gives reproducible results. All experiments were performed at room temperature.

© 2004 NRC Canada

The measurements on the rotating disc electrode were performed with a PAR 263-2A potentiostat controlled by a computer, and with a Pine Instrument Company bipotentiostat model AFCBP1, using a LabVIEW™ (National Instruments™) control software for signal acquisition. The electrode rotator was a Pine Instrument analytical rotator model AFSAR.

The composition of all buffer solutions used in the present work was linked to the pH through the following equilibria and equilibrium constants.

For $NaHCO_3$ (11):

[6] $H_2CO_3(aq) \rightleftharpoons HCO_3^-(aq) + H^+(aq)$

$$K_{a1} = 4.45 \times 10^{-7}$$

[7] $HCO_3^-(aq) \rightleftharpoons CO_3^{2-}(aq) + H^+(aq)$

$$K_{a2} = 4.69 \times 10^{-11}$$

For CO_2 dissolution (12):

[8] $CO_2(g) \rightleftharpoons CO_2(aq)$

$$K = \frac{[CO_2(aq)]}{P_{CO_2}} = 0.0334$$

[9] $CO_2(aq) + H_2O \rightleftharpoons H_2CO_3(aq)$

$$K = 1.3 \times 10^{-3}$$

For Na_2HPO_4 (11):

[10] $H_3PO_4(aq) \rightleftharpoons H_2PO_4^-(aq) + H^+(aq)$

$$K_{a1} = 7.11 \times 10^{-3}$$

[11] $H_2PO_4^-(aq) \rightleftharpoons HPO_4^{2-}(aq) + H^+(aq)$

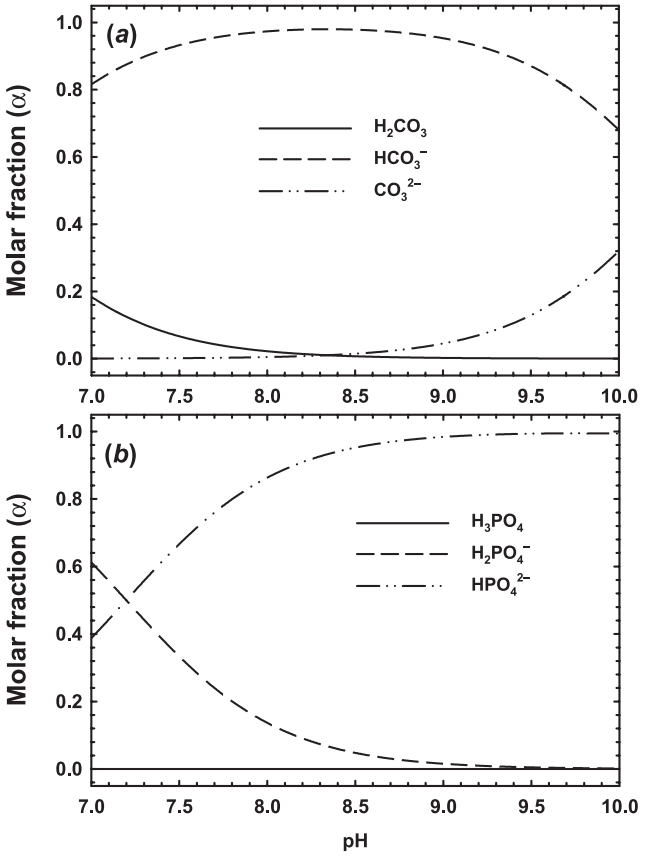
$$K_{a2} = 6.32 \times 10^{-8}$$

[12] $HPO_4^{2-}(aq) \rightleftharpoons PO_4^{3-}(aq) + H^+(aq)$

$$K_{a3} = 4.5 \times 10^{-13}$$

For both buffer systems ($NaHCO_3$ and Na_2HPO_4), the composition diagrams in the pH range of interest (i.e., pH 7–10) were calculated and are presented in Fig. 1.

Fig. 1. Calculated concentrations of dissolved species at various pH values for: (*a*) $H_2CO_3/HCO_3^-/CO_3^{2-}$; and (*b*) $H_3PO_4/H_2PO_4^-/HPO_4^{2-}/PO_4^{3-}$ buffer systems.



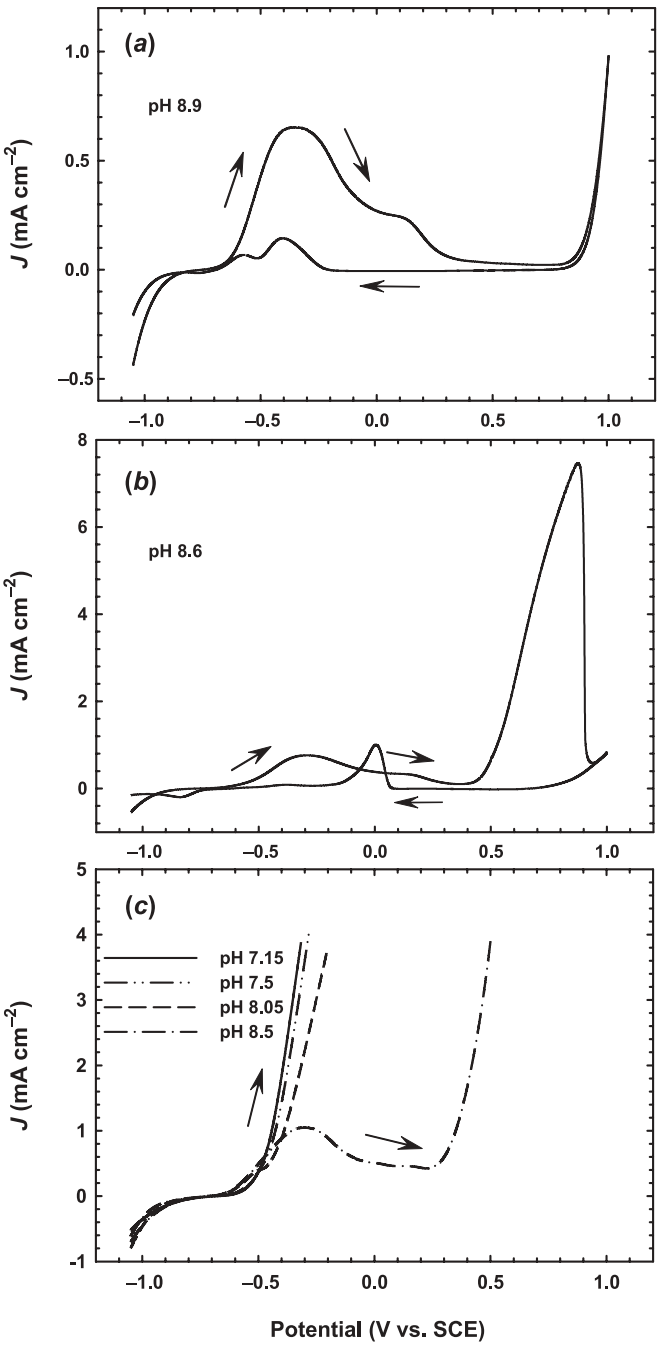
Results

The effect of pH on the electrochemical behaviour of cobalt is examined in $H_2CO_3/HCO_3^-/CO_3^{2-}$ solutions. Figure 2 displays the effect of different pH values on the potentiodynamic curves in a 0.1 mol L^{-1} $NaHCO_3$ buffer solution. At pH 8.9 (Fig. 2*a*), the voltammogram obtained from the potential sweep in the anodic direction displays a broad anodic peak located at –0.36 V followed by a smaller peak that produces a shoulder located at 0.10 V. Toward more anodic potentials, the anodic current diminishes and remains low until an increasing current is noted that corresponds to the solution oxidation wall. The low current region located between 0.30 and 0.85 V is attributed to the passive region. On the voltammogram obtained by the potential sweep in the cathodic direction, two reactivation current peaks are observed at –0.40 and –0.575 V. Figure 2*b* presents the resulting voltammogram obtained from the same triangular potentiodynamic program as at pH 8.9 in 0.1 mol L^{-1} $NaHCO_3$ solution except that the pH is lowered to 8.6. Within the anodic peak region, the shape of the anodic current trace is similar to the one observed at pH 8.9. However, the maximum peak current is slightly shifted toward a more positive potential and a higher peak current is recorded. Interestingly, it is observed that the electrochemical behaviour of cobalt in the passive region is significantly affected by the small pH difference. On the potentiodynamic curve obtained at pH 8.6, the passive region is strongly disturbed by the presence of an important asymmetric anodic current peak that starts to grow at 0.4 V and the current intensity culminates at 0.875 V. The strong anodic process stops at higher anodic potentials and the current falls abruptly. When the potential sweep is switched in the cathodic direction, the current remains small up to 0.075 V and a reactivation peak is observed at 0.00 V. A small reduction peak is also observed at –0.84 V.

The importance of the pH on the electrochemical behaviour of the cobalt electrode is also indicated by potentiodynamic curves obtained at pH 8.5 and lower as presented in Fig. 2*c*. Again, it is interesting to notice that only a slight pH change from 8.6 to 8.5 generates significant modification of the anodic processes. The intensity of the current peak located at ~ –0.36 V increases and, at a more anodic potential, the large asymmetric peak observed at pH 8.6 becomes, at pH 8.5, a nearly vertical current increase that starts at

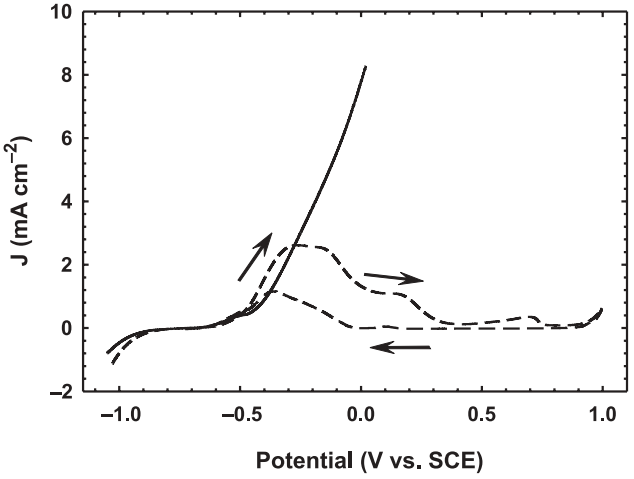
© 2004 NRC Canada

Fig. 2. Potentiodynamic curves for a cobalt electrode in 0.1 mol L^{-1} $NaHCO_3$ solution at: (*a*) pH 8.9; (*b*) pH 8.6; (*c*) pH 8.5, 8.05, 7.5, and 7.15. ω = 1000 rpm; d*E*/d*t* = 0.005 V s^{-1}.



+0.25 V. The current traces obtained by scanning potentials in the anodic direction in a 0.1 mol L^{-1} $NaHCO_3$ buffer solution at pH 8.05, 7.50, and 7.15 are overlaid in Fig. 2*c*. Their shape displays an essentially linear anodic current increase instead of a peak as observed near –0.36 V at pH ≥ 8.5. The lower the pH is, the larger the magnitude of the anodic process is and the passive region is no longer observed. For a constant pH of 8.05, the effect of the $H_2CO_3/HCO_3^-/CO_3^{2-}$ buffer concentration is presented in Fig. 3. It is observed that a higher buffer concentration (0.4 mol L^{-1} $NaHCO_3$) inhibits the vertical current increase that is observed in 0.1 mol L^{-1} $NaHCO_3$, and the peak shape of the anodic current at –0.36 V is recovered.

Fig. 3. Potentiodynamic curves for a cobalt electrode in 0.1 mol L^{-1} (——) and 0.4 mol L^{-1} (- - - -) $NaHCO_3$ aqueous solutions at pH 8.05. ω = 1000 rpm; d*E*/d*t* = 0.005 V s^{-1}.



The effect of buffer concentration on the anodic peaks and reactivation regions has been studied more extensively for $NaHCO_3$ buffer solutions at a constant pH of 8.9 (Fig. 4). The peak current located at –0.36 V increases linearly with the buffer concentration (Fig. 4*a*) and the same behaviour is observed for the reactivation peak located at –0.3 V in the cathodic part of the sweep (Fig. 4*b*).

Figure 5 displays the anodic traces obtained for selected pH values ranging from 7.85 to 9.20 for the cobalt electrode in 0.4 mol L^{-1} $NaHCO_3$ buffer solutions. It is observed that the current in the anodic peak region (from –0.6 to 0.3 V) increases as the pH drops. Also, an anodic current peak located at –0.14 V becomes more evident as the pH diminishes. At pH 9.2 and 8.7, the electrochemical behaviour of the cobalt electrode is similar to the behaviour observed in 0.1 mol L^{-1} $NaHCO_3$ solution at pH 8.9 (Fig. 2*a*) except that there is a larger magnitude for the anodic peak currents in the region from –0.6 to –0.3 V (Fig. 5*a*) and in the reactivation region (Fig. 5*b*).

For lower pH values, it is observed that lowering the pH in 0.4 mol L^{-1} $NaHCO_3$ solution generates more moderated changes on the voltammograms than in 0.1 mol L^{-1} $NaHCO_3$ solutions for the same pH value. The asymmetric anodic peak located at 0.66 V appears only as a small bump at pH 8.05 in 0.4 mol L^{-1} $NaHCO_3$ buffer solution, while an almost linear anodic current increase was observed in 0.1 mol L^{-1} solution at the same pH (Fig. 3). At pH values below 8.3 in 0.4 mol L^{-1} $NaHCO_3$ buffer solutions (Fig. 5*a*), the asymmetric anodic peak grows as the pH decreases. For potentials in the more anodic direction, a sudden current decrease is observed near 0.75 V. When the potential is scanned in the cathodic direction, the current remains very small until a sharp anodic current peak appears at 0.110 V (Fig. 5*b*). Toward more cathodic potentials from that sharp peak, the current trace has a similar shape to that observed at higher pH. Further measurements were performed at pH 7.70, 7.55, and 7.20 in 0.4 mol L^{-1} $NaHCO_3$ solution

© 2004 NRC Canada

Fig. 4. Voltammograms at various $NaHCO_3$ concentrations for: (*a*) the anodic part of the potential sweep; and (*b*) the cathodic part of the potential sweep at pH 8.9. ω = 1000 rpm; d*E*/d*t* = 0.005 V s^{-1}.

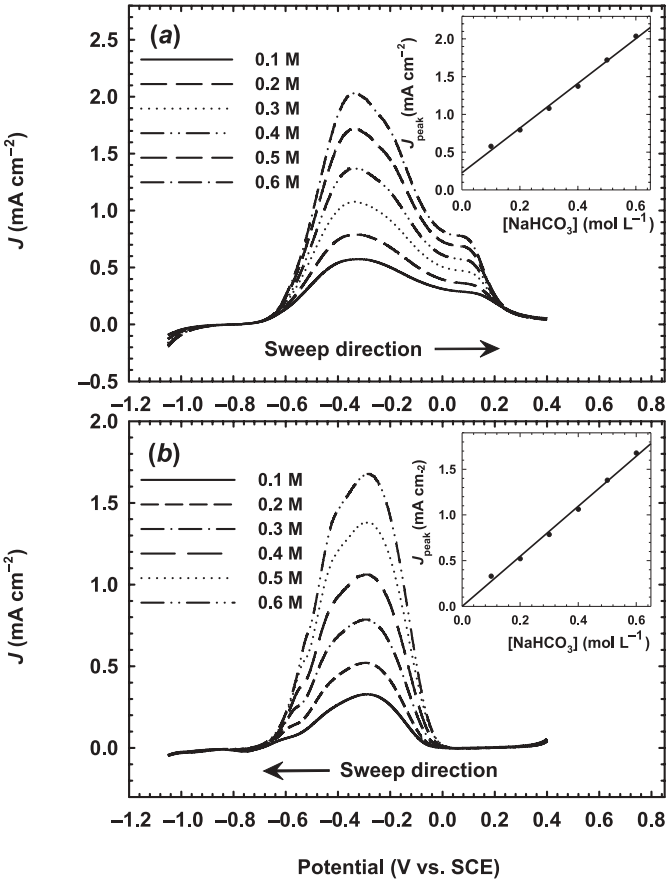
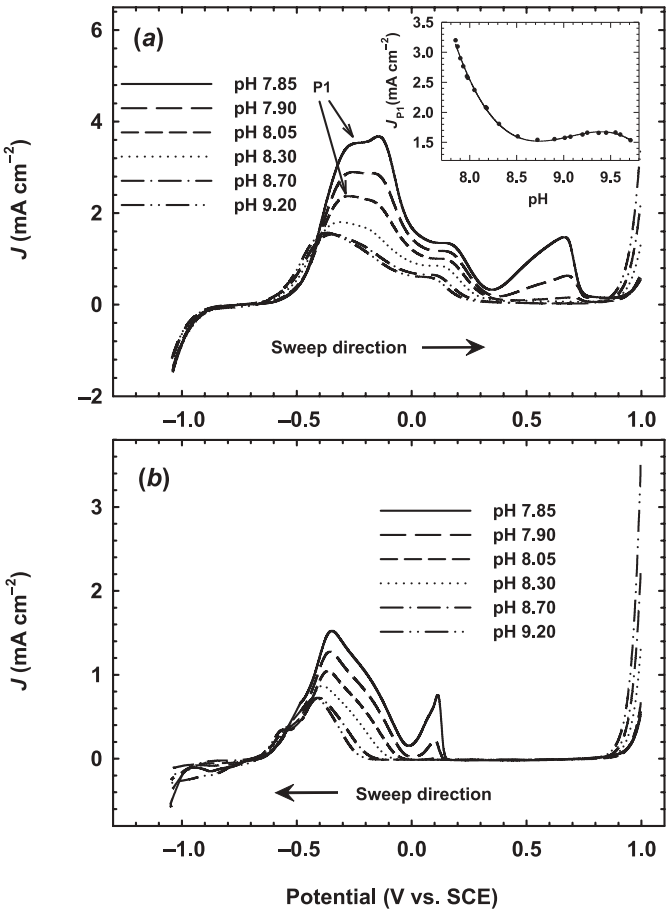


Fig. 5. Influence of pH (7.85–9.70) on: (*a*) the anodic portion; and (*b*) the cathodic portion of the potential sweep for a cobalt electrode in 0.4 mol L^{-1} $NaHCO_3$ solution. ω = 1000 rpm; d*E*/d*t* = 0.005 V s^{-1}.

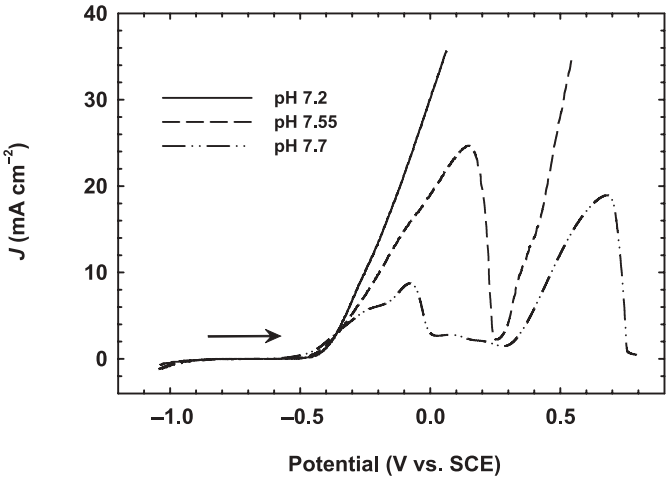


(Fig. 6). It is observed that an important anodic current starts to grow near –0.4 V for pH 7.55 and 7.2. At pH 7.2 the current increases almost linearly while a decreasing current is observed between 0.15 V and 0.25 V at pH 7.55. At pH 7.7, a potentiodynamic curve shape intermediate between those observed at pH 7.85 and 7.55 is obtained, which indicates a change in the dominant oxidation processes. All these data clearly demonstrate that changes in solution pH in the region from 7 to 8 in the $H_2CO_3/HCO_3^-/CO_3^{2-}$ system drastically affects the potentiodynamic behaviour of cobalt.

The effect of the hydrodynamic conditions on the electrochemical behaviour of cobalt in 0.4 mol L^{-1} $NaHCO_3$ buffer was studied at pH 7.9, where most of the individual electrochemical signals are noticeable. On the voltammograms in Fig. 7, four current peaks (P1–P4) are identified on the current trace of the anodic potential sweep (Fig. 7*a*) and two other major current peaks are identified on the current trace of the cathodic sweep (P5 and P6) (Fig. 7*b*). It is noted that only P1, P3, and P6 are clearly dependent on the rotation speed, while the other peaks do not show any obvious dependence on the hydrodynamic conditions.

Therefore, further experiments were carried out to understand the role played by the solution species on the electrochemical behaviour of cobalt, especially in the pH range from 7 to 8. One of the goals was to investigate whether the

Fig. 6. Effect of near-neutral pH on the potentiodynamic curve for a cobalt electrode. ω = 1000 rpm in 0.4 mol L^{-1} $NaHCO_3$ solution; d*E*/d*t* = 0.005 V s^{-1}.



effect of pH on the electrochemical behaviour of cobalt is linked only to the OH^- concentration, or if more complex considerations regarding changes in the concentrations of

© 2004 NRC Canada

Fig. 7. Potentiodynamic curves for: (*a*) the anodic portion; and (*b*) the cathodic portion of a potential sweep for a cobalt electrode at various rotation speeds (ω) in 0.4 mol L^{-1} $NaHCO_3$ solution at pH 7.9. d*E*/d*t* = 0.005 V s^{-1}.

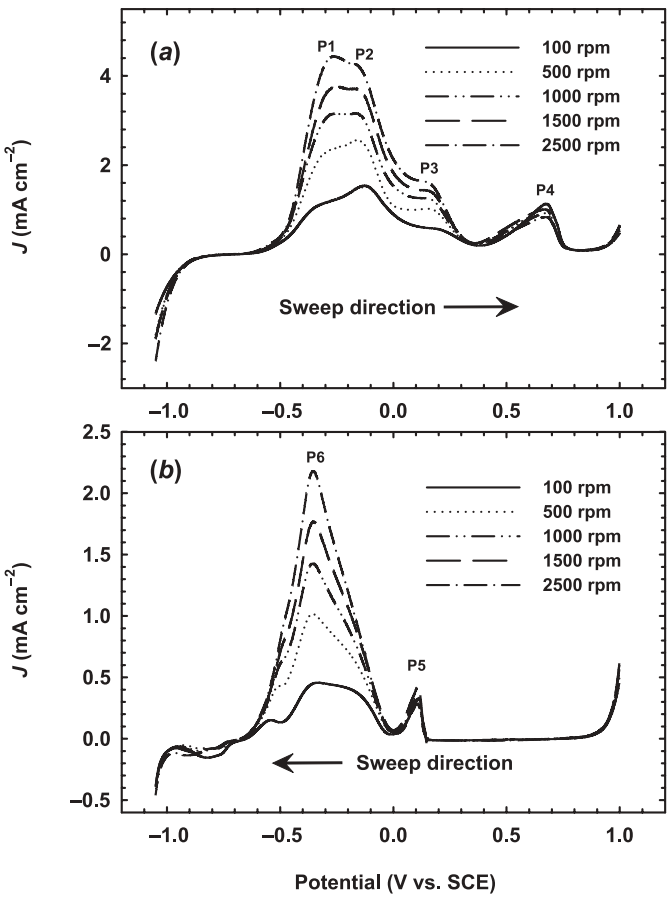
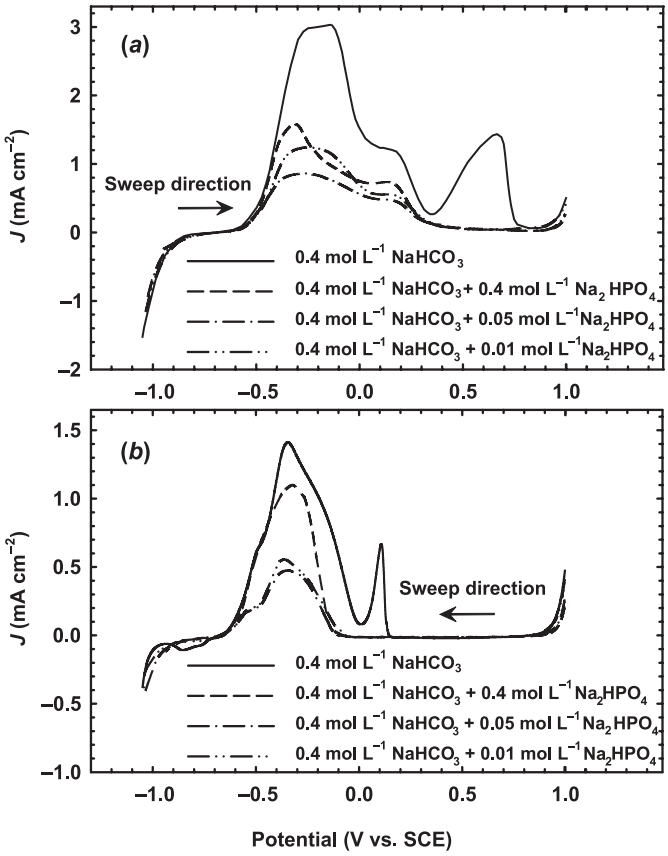


Fig. 8. Effect of Na_2HPO_4 concentration in 0.4 mol L^{-1} $NaHCO_3$ solution on: (*a*) the anodic portion; and (*b*) the cathodic portion of a potential sweep at pH 7.9. ω = 1000 rpm; d*E*/d*t* = 0.005 V s^{-1}.



dissolved species are more important factors. From these considerations, further experiments have been conducted in bicarbonate, bicarbonate–phosphate, and phosphate solutions at constant pH. Figure 8*a* displays the overlay of the anodic current traces obtained for the cobalt electrode in bicarbonate solution and in mixtures of bicarbonate–phosphate at pH 7.9. It is evident that an addition of only 0.01 mol L^{-1} phosphate (as Na_2HPO_4) in 0.4 mol L^{-1} $NaHCO_3$ solution decreases significantly the oxidation current in the anodic peak region located between –0.5 and 0.3 V. Moreover, the important asymmetric anodic current peak located between 0.2 and 0.8 V observed in 0.4 mol L^{-1} $NaHCO_3$ at pH 7.9 is totally inhibited by the presence of 0.01 mol L^{-1} Na_2HPO_4. For the portion of the voltammogram where the potential is swept in the cathodic direction (Fig. 8*b*), the sharp anodic peak observed in 0.4 mol L^{-1} $NaHCO_3$ solution at pH 7.9 and located at 0.1 V is completely inhibited by the presence of 0.01 mol L^{-1} Na_2HPO_4. The anodic current measured for the rest of the sweep is also significantly reduced. A higher Na_2HPO_4 concentration (0.05 mol L^{-1}) in 0.4 mol L^{-1} $NaHCO_3$ diminishes the anodic current for the whole voltammogram relative to 0.01 mol L^{-1} Na_2HPO_4 in 0.4 mol L^{-1} $NaHCO_3$. For 0.4 mol L^{-1} Na_2HPO_4 + 0.4 mol L^{-1} $NaHCO_3$ solutions, the shape of the anodic current trace is significantly modified and an anodic peak located at –0.315 V followed by a shoulder at 0.135 V are observed. Similar behaviour for the current trace obtained during the potential scan in the cathodic direction is noticed.

The comparison between the anodic traces obtained for phosphate solutions with and without bicarbonate at pH 7.9 is presented in Fig. 9*a*. It clearly demonstrates that for solutions equimolar in $NaHCO_3$ and Na_2HPO_4 at the same pH, the electrochemical signature is largely dominated by the presence of Na_2HPO_4. However, the presence of $NaHCO_3$ still contributes to the increase in the magnitude of the anodic current. Again, similar observations can be made for the current trace obtained during the potential scan in the cathodic direction (Fig. 9*b*).

The investigation of the effect of phosphate on the electrochemical behaviour of cobalt in $NaHCO_3$ solutions has been extended to pH 7.5 and 7.2 where strong corrosion was noted in bicarbonate solutions alone (Figs. 10 and 11). Figure 10 presents an overlay of the potentiodynamic curves recorded for 0.4 mol L^{-1} $NaHCO_3$ solutions with and without Na_2HPO_4 at pH 7.5 and 7.2. In 0.4 mol L^{-1} $NaHCO_3$ solutions at both pH values, the beginning of a very strong oxidation process starting near –0.4 V is evident. The presence of small amounts of Na_2HPO_4 in the $NaHCO_3$ solutions at these pH values is amazingly efficient at totally inhibiting

© 2004 NRC Canada

Fig. 9. Potentiodynamic curves for (*a*) the anodic portion, and (*b*) the cathodic portion of a potential sweep for cobalt electrode in 0.4 mol L^{-1} $NaHCO_3$ (———), 0.4 mol L^{-1} $NaHCO_3$ + 0.4 mol L^{-1} Na_2HPO_4 (··—··), and 0.4 mol L^{-1} Na_2HPO_4 (- - - -) at pH 7.9. ω = 1000 rpm; d*E*/d*t* = 0.005 V s^{-1}.

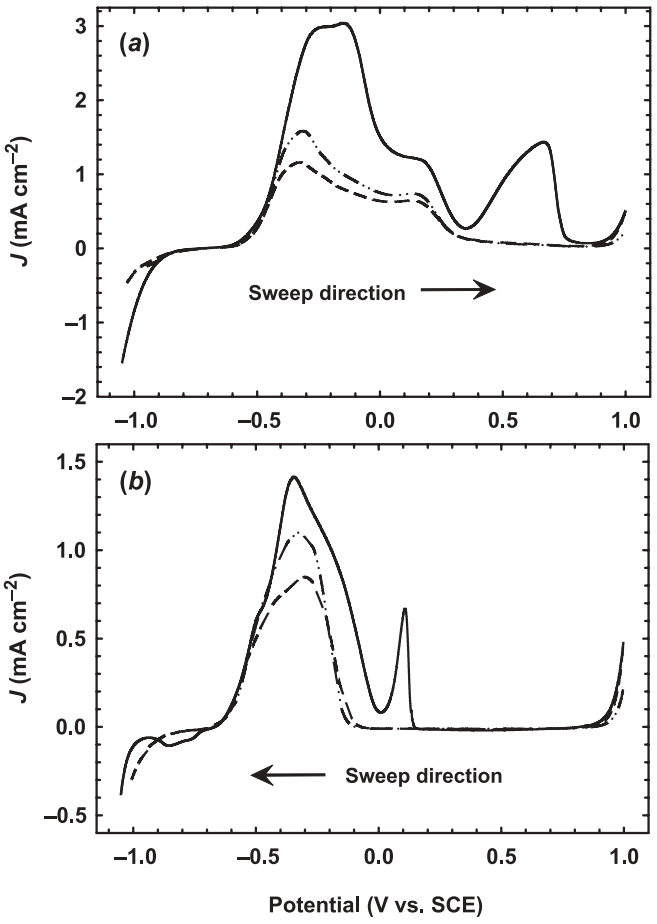


Fig. 10. Effect of Na_2HPO_4 concentration in 0.4 mol L^{-1} $NaHCO_3$ solution on potentiodynamic curves for a cobalt electrode at: (*a*) pH 7.5; (*b*) pH 7.2. ω = 1000 rpm; d*E*/d*t* = 0.005 V s^{-1}.

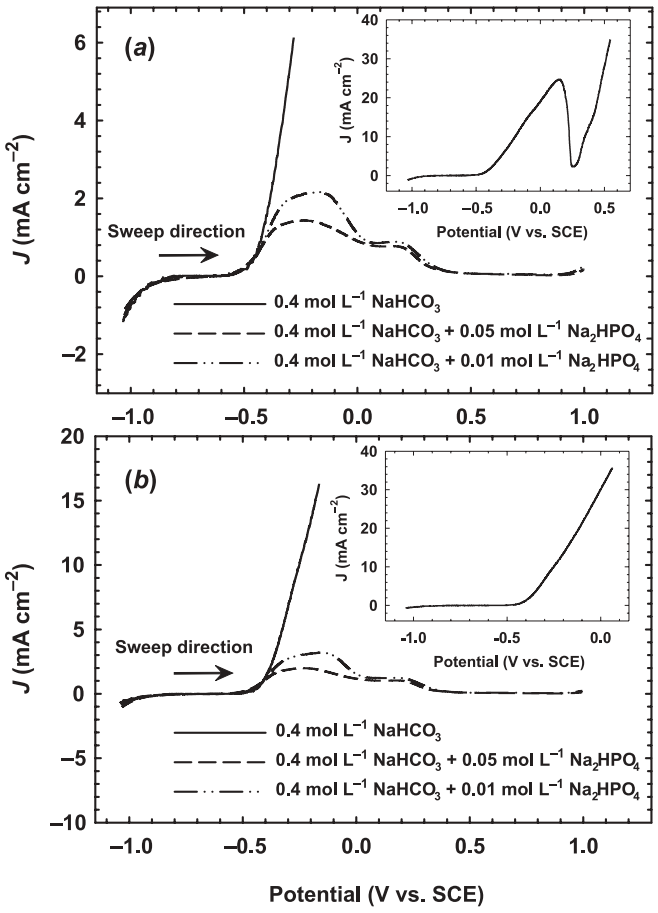
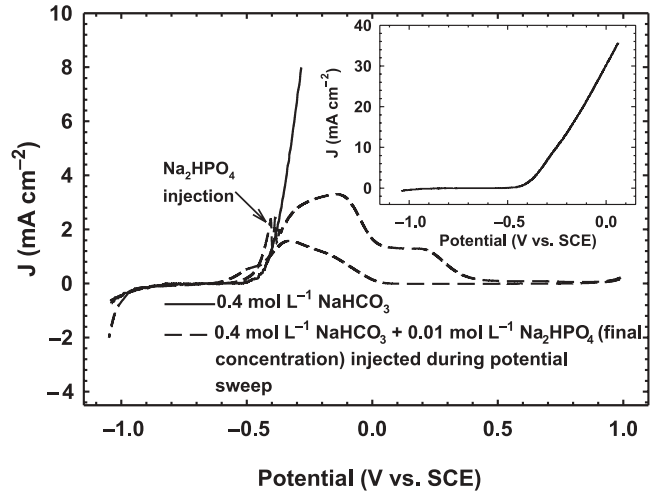


Fig. 11. Effect of Na_2HPO_4 addition (final Na_2HPO_4 concentration, 0.01 mol L^{-1}) in 0.4 mol L^{-1} $NaHCO_3$ solution during a potential sweep at pH 7.2. ω = 1000 rpm; d*E*/d*t* = 0.005 V s^{-1}.

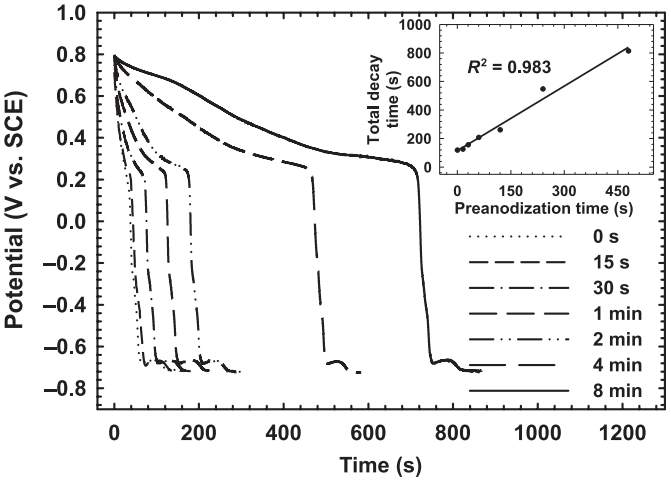


the oxidation process. Moreover, it is demonstrated in Fig. 11 that the strong oxidation process of cobalt (starting at –0.4 V) in 0.4 mol L^{-1} $NaHCO_3$ solution at pH 7.2 can be inhibited by the direct injection of a small volume of concd. Na_2HPO_4 solution (the resulting Na_2HPO_4 concentration is 0.01 mol L^{-1}) after the beginning of the process.

To understand the influence of pH on the cobalt passive film in $NaHCO_3$ solutions and to find out the inhibition mode of phosphate, the transient potential of prepassivated cobalt electrode was studied in bicarbonate solutions with and without phosphate. In all cases, the potential was swept in the anodic direction and held at 0.8 V, where passivation of cobalt is possible for all studied pH conditions. Thereafter, the open circuit potential (OCP) was measured until the potential of the bare cobalt electrode was reached. Figure 12 presents the potential decay curves for a preanodized cobalt electrode in 0.4 mol L^{-1} $NaHCO_3$ buffer solution at pH 7.9. It is possible to detect four arrest potential regions that are more evident after the 8 min preanodization. A first arrest potential region is located from 0.8 to 0.7 V, followed by a second dominant region between 0.7 and 0.3 V. The time corresponding to these two arrest potential regions are obviously dependent on the duration of the preanodization. When the potential reaches a value close to 0.3 V, it starts to change rapidly and a very small arrest potential region is observed from –0.2 to –0.4 V and another one at –0.675 V.

© 2004 NRC Canada

Fig. 12. Effect of preanodization time at +0.80 V on the open circuit potential curve in 0.4 mol L^{-1} $NaHCO_3$ at pH 7.9 for a cobalt electrode rotated at 1000 rpm. Potential swept from –1.05 to +0.80 V at 0.005 V s^{-1} and held at +0.80 V for the preanodization period.

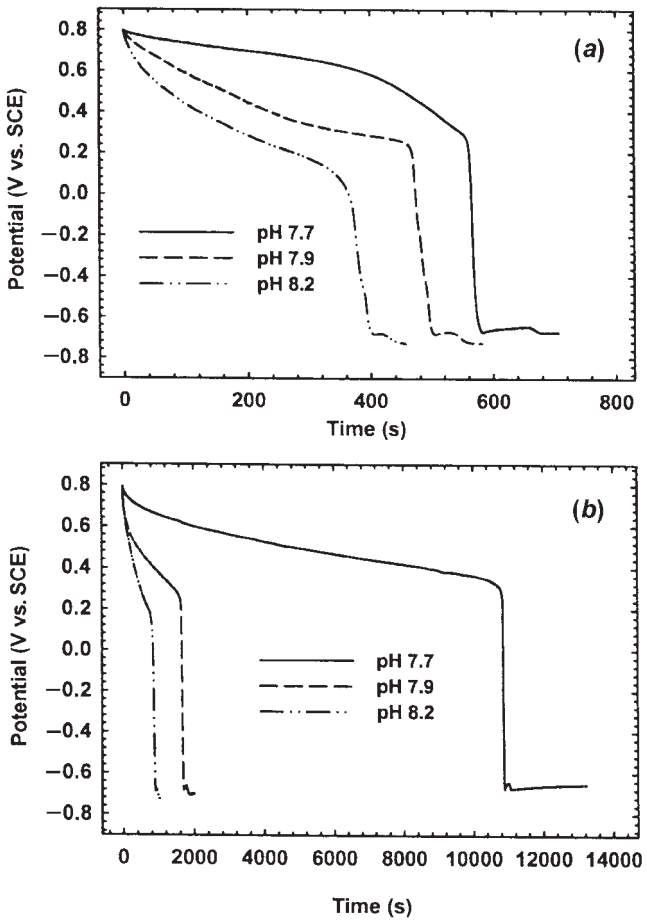


These last two potential arrest regions seem to be independent of the preanodization time. The total time elapsed to reach the potential of the bare metal in solution is directly proportional to the preanodization duration up to 8 min.

The effect of pH on the decay potential traces for the cobalt electrode was studied in 0.4 mol L^{-1} $NaHCO_3$ buffer solution at pH 7.7, 7.9, and 8.2 as presented in Fig. 13*a*. It was discovered that the higher the pH is, the shorter the decay time is. Moreover, it is observed that the first arrest potential region (0.8–0.7 V) becomes dominant at pH 7.7. The global amounts of oxide produced at pH 7.7 and pH 8.2 are similar since a galvanostatic reduction on the preanodized cobalt electrode gives a similar charge that is required to reduce the oxide films. Therefore, the study of the influence of solution composition was extended to the introduction of phosphate species in the bicarbonate buffer solution. Fig. 13*b* demonstrates that when 0.01 mol L^{-1} Na_2HPO_4 is added after the preanodization (just at the beginning of OCP measurement) in the 0.4 mol L^{-1} $NaHCO_3$ buffer solution at pH 8.2, 7.9, and 7.7, the decay time is significantly increased by a factor of 2, 3, and 20, respectively, relative to the decay time at the same pH in 0.4 mol L^{-1} $NaHCO_3$ solution (Fig. 13*a*). Another OCP measurement was performed in 0.4 mol L^{-1} $NaHCO_3$ buffer solution containing 0.01 mol L^{-1} Na_2HPO_4 during polarization (Fig. 14). It is very interesting to observe that the increase in the potential decay time observed in Fig. 13*b* is lost when phosphate is present in the solution during the preanodization and not only during the OCP measurement. A comparison of the open circuit potential curves obtained for 0.4 mol L^{-1} $NaHCO_3$ and for 0.4 mol L^{-1} Na_2HPO_4 buffer solutions at pH 7.7 and 8.2, demonstrates that the passive film electrogenerated on a cobalt in phosphate solution disappears more rapidly than in bicarbonate solutions (Fig. 15).

To estimate the amount of reducible oxides on the electrode surface, galvanostatic reduction experiments were performed and the transient potential curves are displayed in Fig. 16. It is found that at the same pH and nominal solution concentration, the charge required for the reduction of the electrogenerated passive film in the $NaHCO_3$ solution is 1.52 mC cm^{-2}, which is approximately twice the charge required to reduce the film electrogenerated in the Na_2HPO_4 solution, which is 0.80 mC cm^{-2}.

Fig. 13. Effect of pH on the open circuit potential for a cobalt electrode in (*a*) 0.4 mol L^{-1} $NaHCO_3$, and (*b*) 0.4 mol L^{-1} $NaHCO_3$ + 0.01 mol L^{-1} Na_2HPO_4 (added at the beginning of the OCP measurement) after a preanodization for 4 min at +0.80 V in 0.4 mol L^{-1} $NaHCO_3$. Potential swept from –1.05 to +0.80 V at 0.005 V s^{-1} and held at +0.80 V for preanodization. ω = 1000 rpm.



Discussion

Anodic dissolution region

In $NaHCO_3$ solutions near pH 9 (Figs. 2*a* and 5*a*), the anodic current peak located at –0.36 V is attributed to the dissolution of cobalt into a carbonato-complex as suggested in the literature (6, 7). The rate-determining species in the cobalt electrodissolution is identified as HCO_3^- following the reactions presented in eqs. [1] and [5] in the *Introduction*. However, a recent study reported that both bicarbonate and carbonate species can be important in the catalysis of cobalt dissolution in moderately alkaline solutions (9). The effect of ionic species on the dissolution rate of cobalt in bicarbonate buffer solution is confirmed in Fig. 4*a*, where a linear re-

© 2004 NRC Canada

Fig. 14. Open circuit potential curves for a cobalt electrode in 0.4 mol L^{-1} $NaHCO_3$ + 0.01 mol L^{-1} Na_2HPO_4 preanodized for 4 min at +0.80 V in: (*a*) 0.4 mol L^{-1} $NaHCO_3$ + 0.01 mol L^{-1} Na_2HPO_4 (- - - -); (*b*) 0.4 mol L^{-1} $NaHCO_3$ (——) (0.01 mol L^{-1} Na_2HPO_4 added to the 0.4 mol L^{-1} $NaHCO_3$ solution at the beginning of the open circuit potential measurement). Potential swept from –1.05 to +0.80 V at 0.005 V s^{-1} and held at +0.80 V for preanodization. ω = 1000 rpm; pH 7.9.

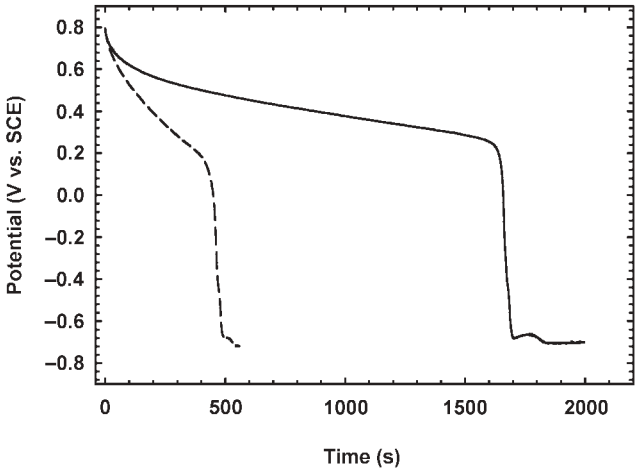
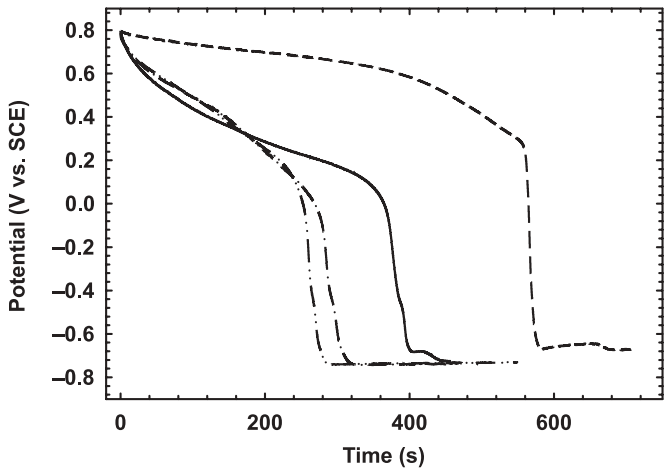


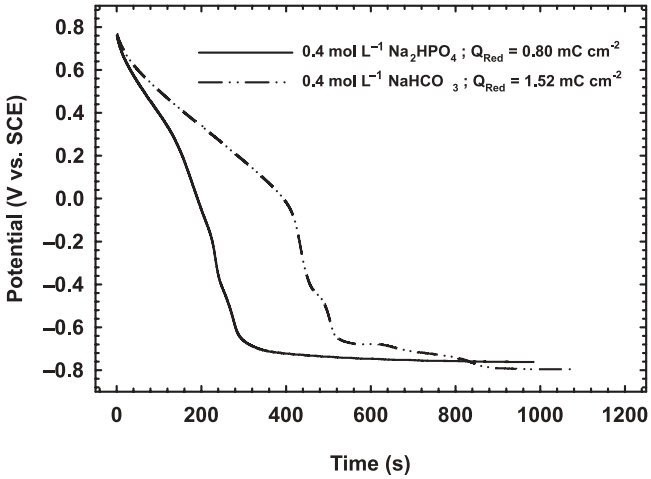
Fig. 15. Effect of pH and solution composition on the open circuit potential for a cobalt electrode preanodized for 4 min at +0.80 V in 0.4 mol L^{-1} $NaHCO_3$ solution at pH 8.2 (——), and pH 7.7 (- - - -); and in 0.4 mol L^{-1} Na_2HPO_4 solution at pH 8.2 (·—·), and 7.7 (··—··). Potential swept from –1.05 to +0.80 V at 0.005 V s^{-1} and held at +0.80 V for preanodization. ω = 1000 rpm.



lationship between the anodic peak current and the $NaHCO_3$ concentration is obtained. This behaviour is observed for both the anodic and cathodic parts of the potential sweep. These results are in good agreement with other results reported in the literature (6, 7, 9). When the potential reaches a sufficient anodic value, the dissolution process is being gradually replaced by a parallel passive film formation process.

As illustrated in Fig. 5*a* for a constant concentration of 0.4 mol L^{-1} $NaHCO_3$ buffer solution, the anodic peak current in the region from pH 8.5 to 9.7 is almost constant. As discussed above, the kinetics of cobalt electrodissolution in carbonate–bicarbonate solutions is catalyzed by both HCO_3^- and CO_3^{2-} ionic species (9). In this case, considering that Fig. 1*a* clearly demonstrates that $\alpha_{HCO_3^-} + \alpha_{CO_3^{2-}} \approx 1$ at pH values above 8.3, the cobalt electrodissolution rate should not be significantly influenced by pH. Therefore, it can be suggested that the cobalt electrodissolution process at pH > 8.5 is mainly influenced by the carbonate–bicarbonate solution concentration, and both ionic species (HCO_3^- and CO_3^{2-}) are most likely taking part in the process. Approaching the pH 9.7 region, the oxidation process becomes gradually dominated by the direct formation of cobalt oxide (7), which may explain why that the peak current is no longer constant.

Fig. 16. Effect of solution composition on chronopotentiometric curves recorded with a reduction current of 3.5 μA cm^{-2} preanodization for 20 min at +0.80 V. Potential swept from –1.05 to +0.80 V at 0.005 V s^{-1} and held at +0.80 V for preanodization. ω = 1000 rpm during potential sweep; ω = 0 rpm during galvanostatic reduction to minimize dissolution effect. pH 8.2.



At lower pH values in the region between pH 8.50 and 7.85, the anodic current peak increases exponentially as the pH is lowered (Fig. 5*a*). From Fig. 1*a*, it can be deduced that the CO_3^{2-} contribution to the anodic process must be negligible, or at least should diminish as the pH becomes lower. Moreover, the HCO_3^- concentration also decreases as the pH drops below 8.3 while, as mentioned above, the anodic peak current increases in this pH region. Consequently, the explanation based solely on the aggressiveness of the HCO_3^- and (or) CO_3^{2-} species becomes unrealistic for pH values lower than 8.3. In this pH range, therefore, the influence of dissolved species other than HCO_3^- and CO_3^{2-} must be considered to explain the anodic dissolution of cobalt. Examination of the pH-composition diagram for the $H_2CO_3/HCO_3^-/CO_3^{2-}$ system indicates that the H_2CO_3 fraction increases as the pH drops below 8.3. However, the trend of anodic peak current vs. the carbonic acid concentration does not fit with a linear relationship. It must be pointed out that as the pH diminishes, the anodic region from –0.6 to 0.3 V exhibits an overlap of few anodic peaks (Fig. 5*a*). In this case it can be deduced that the anodic behaviour of cobalt is not a unique process and several electrochemical processes may occur at

© 2004 NRC Canada

the same time but at different rates. It is reported in the literature that the anodic behaviour of cobalt in aq. $H_2CO_3/HCO_3^-/CO_3^{2-}$ solutions can be described by the coupling of two independent anodic processes sharing the electrode surface and generating a total current (9). One of the processes is independent of diffusion and the other one is under diffusion control. This behaviour is illustrated on Fig. 7, where the anodic peak region exhibits two components: the first one (P1) being under diffusion control and the second one (P2) being independent of hydrodynamic conditions. To clarify the anodic dissolution kinetics at pH < 8.5, the anodic peak current measured near –0.3 V was corrected by subtracting a current value estimated in the limit $[H_2CO_3] \rightarrow 0$. The logarithm of the value of the corrected current value was then plotted against the logarithm of the calculated H_2CO_3 concentration for each pH value, as shown on Fig. 17. It is especially interesting to see that a linear relationship is obtained with a slope close to 2 (1.95 with r^2 = 0.999). For pH values below 7.85, a linear relationship cannot be verified because the magnitude of the peak located near –0.15 V becomes predominant and inhibits an accurate determination of the peak current at ~ –0.3 V.

Considering the linearity of the log(corrected J_{P1}) vs. log$[H_2CO_3]$ plot, it can be suggested that cobalt dissolution for pH < 8.5 is mostly catalyzed by the presence of carbonic acid and the process could take place by the following overall reaction

$$[13] \quad Co + 2H_2CO_3(aq) \rightarrow Co(CO_3)_2^{2-}(aq) + 4H^+(aq) + 2e^-$$

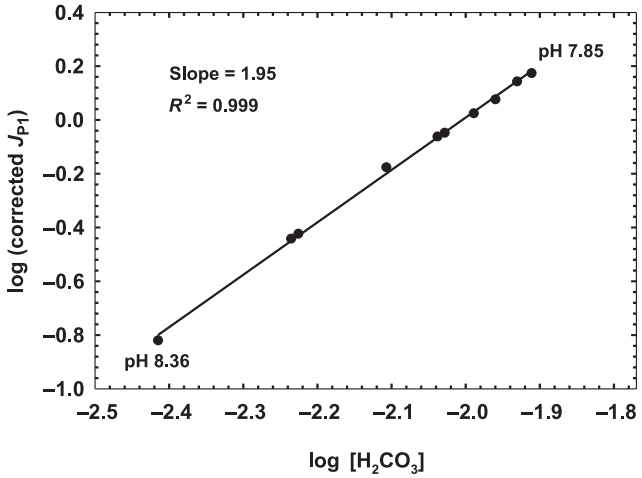
It is interesting to notice that for two different $NaHCO_3$ concentrations at the same pH (i.e., same ratio H_2CO_3/HCO_3^-), the electrochemical behaviour of cobalt is different (Fig. 3). At pH 8.05 in 0.1 mol L^{-1} $NaHCO_3$ buffer solution, the cobalt electrode is strongly oxidized without perceptible passivation while in the 0.4 mol L^{-1} solution, a passivation process is found adjacent to the active dissolution region. In that pH region, as discussed above, the mechanisms involving HCO_3^- and H_2CO_3 can occur competitively. Hence, it can be deduced that increasing the $NaHCO_3$ concentration at pH 8.05 or lower has an inhibitive effect on the attack of cobalt. This behaviour may be explained by a competitive adsorption between dissolved species in the environment. It is realistic to consider anion adsorption in the corrosion mechanism of cobalt because its zero charge potential (ZCP) is estimated to –0.550 V vs. SCE (13). As a result, when the electrode is polarized at higher potentials than the ZCP, adsorption of anions or polar molecules can occur (14).

The influence of competitive adsorption is well supported by the effect of a small amount of phosphate on the anodic dissolution of cobalt in bicarbonate buffer solutions. Figs. 8, 10, and 11 show that the presence of phosphate drastically diminishes the anodic dissolution intensity at pH 7.9 and also eliminates the aggressive attack at pH 7.2 and 7.5.

Passive region

In Figs. 2*a* and 2*b*, it is shown that the electrochemical behaviour of cobalt in the passive region is strongly affected by a small pH variation in 0.1 mol L^{-1} $NaHCO_3$ solutions.

Fig. 17. Plot of log(corrected J_{P1}) against log$[H_2CO_3]$ for a cobalt electrode in 0.4 mol L^{-1} $NaHCO_3$. ω = 1000 rpm; dE/dt = 0.005 V s^{-1}.



When the pH is changed from 8.9 to 8.6, a strong oxidation process takes place in the passive region observed at pH 8.9. In 0.4 mol L^{-1} $NaHCO_3$ buffer solutions, the passive region is preserved at pH values as low as 8.3. The important oxidation process, appearing gradually as the pH decreases, suggests strongly that the H_2CO_3 species is most likely aggressive toward the cobalt passive film. However, at highly anodic potentials (0.9 V in 0.1 mol L^{-1} $NaHCO_3$ and 0.7 V in 0.4 mol L^{-1} $NaHCO_3$), repassivation is taking place, which can be ascribed to the formation of Co(III) oxides, since no carbonato-complexes of Co(III) are known to exist (6). When the potential is swept in the cathodic direction, the cobalt(III) oxide is probably reduced to near 0.0 V in 0.1 mol L^{-1} $NaHCO_3$ (Fig. 2*b*) and 0.11 V in 0.4 mol L^{-1} $NaHCO_3$ (Fig. 5*b*), potentials at which a sharp anodic reactivation peak is recorded. This reactivation peak shows that the cobalt oxides formed at lower anodic potentials are not efficient at protecting cobalt from dissolution attack by bicarbonate ions, as previously reported (6).

It is also deduced that raising the $NaHCO_3$ buffer solution concentration at constant pH inhibits the passive film attack in the passive region. If one considers that the passive film attack is initiated by some adsorption phenomenon of the dissolved species on the electrode surface, it can be suggested that a competitive adsorption between H_2CO_3 and other species in solution reduces the access of H_2CO_3 to the surface. That competition effect may be less efficient at lower concentrations if the surface coverage from species in solution is possibly not complete. It is useful to point out that H_2CO_3 does not carry any charge and when the electrode is polarized at anodic potentials, the negatively charged species in solution should be adsorbed preferentially simply on an electrostatic basis. Also for that reason, catalysis efficiency of the passive film dissolution may be influenced by the pH of the solution. Considering that in the pH range from 8.2 to 7.7 the amount of HCO_3^- diminishes while H_2CO_3 increases, different rates of passive film dissolution should be expected. That is exactly what is indicated in Fig. 13*a*, since the OCP measurement at the solution pH corresponding to the highest amount of HCO_3^- (pH 8.2) pres-

© 2004 NRC Canada

ents the most rapid passive film dissolution. The effect of the amount of oxide cannot be taken into account to explain the different decay time since similar oxide amounts are found at pH 8.2 and 7.7. Nevertheless, at pH 7.7 the OCP curve suggests that a higher amount of Co(III) oxide is present since the potential remains in the region from 0.8 to 0.7 V, much longer than at more alkaline pH values. Considering that H_2CO_3 is not known to be aggressive toward this type of oxide, the passive film will take longer to disappear.

The explanation of the cobalt corrosion mechanism in $H_2CO_3/HCO_3^-/CO_3^{2-}$ solutions involving competitive adsorption is strengthened by experimental evidence obtained when phosphate is added to the system. Remarkably, it is observed that only a small addition of Na_2HPO_4 to the $NaHCO_3$ solution in a molar ratio of 1:40 has a great inhibitive effect on the corrosion of cobalt (Figs. 8, 10, and 11). From potentiodynamic experiments, it could be suggested that phosphate may improve the passive film quality as observed for iron in oxygenated phosphate solutions (see, for example, refs. 15 and 16). However, a different scenario must be considered for cobalt in phosphate solutions because the presence of phosphate diminishes the passive film decay time (Fig. 15) and the amount of film (Fig. 16) for OCP and galvanostatic measurements, respectively. Under these conditions, a specific adsorption of phosphate species on the cobalt electrode surface must be considered to be involved in the inhibition mechanism. Because the aggressive nature of $H_2CO_3/HCO_3^-/CO_3^{2-}$ solutions is explained by a catalysis effect on the cobalt passive film dissolution, the presence of phosphate species at the electrode surface will obstruct their access to the surface and then slow down considerably the passive film dissolution process. This explanation is supported by the influence of the presence of phosphate species during the OCP experiments for preanodized cobalt electrodes in 0.4 mol L^{-1} $NaHCO_3$ buffer solutions without added phosphate during preanodization. It is clearly demonstrated that the decay time of the anodic film is significantly increased by added phosphate at the beginning of the OCP measurement. The effect is enhanced at lower pH values. For example, dissolution is 20 times slower at pH 7.7 in the presence of phosphate species than in absence of these species (see Fig. 13). The enhancement of the inhibitive effect of phosphate observed when the pH is lower may be explained by the higher proportion of H_2CO_3 species in solution. Only on an electrostatic basis, this uncharged species is disadvantaged to compete adequately with the adsorption of charged phosphate species. Also, because the inhibitive effect of phosphate is enhanced when the pH is lowered from 8.2 to 7.7, it can be proposed, considering Fig. 1*b*, which $H_2PO_4^-$ is mainly adsorbed on the cobalt electrode and inhibits the dissolution of passive films previously formed in bicarbonate buffers. Al-Kharafi et al. (17) recently reported that phosphate ions are included in the passive film when a cobalt electrode is immersed in a phosphate buffer at pH 7. It can therefore be deduced that the nature of the passive film formed in a 0.4 mol L^{-1} $NaHCO_3$ solution and in the presence of a 0.4 mol L^{-1} $NaHCO_3$ + 0.01 mol L^{-1} Na_2HPO_4 solution is quite different, the last one containing phosphate. This can explain why the decay potential profiles during the OCP measurements of passive films formed in these two solutions are very different, even if both are dissolved in the same media (0.4 mol L^{-1} $NaHCO_3$ + 0.01 mol L^{-1} Na_2HPO_4). The passive film formed in 0.4 mol L^{-1} $NaHCO_3$ + 0.01 mol L^{-1} Na_2HPO_4 solutions dissolves more rapidly (Fig. 14) because phosphate salts included in passive films present preferential attack sites for aggressive species (17). This is consistent with the dissolution time observed for a preanodized electrode in $NaHCO_3$ solutions and Na_2HPO_4 solutions at the same pH and concentration (Fig. 15).

Conclusions

The potentiodynamic experiments on rotating cobalt electrodes in aq. $H_2CO_3/HCO_3^-/CO_3^{2-}$ solutions demonstrate that carbonate and bicarbonate species promote the anodic dissolution of cobalt in the pH range from 8.5 to 9.7. In this buffer system, the pH zone between 7 to 8 was studied for the first time and it is evident that for pH values below 8.5, the involvement of carbonic acid as a new aggressive species toward cobalt must be considered. Indeed, in this pH region where the H_2CO_3 concentration becomes important, the passivation of cobalt is completely inhibited.

The effect of solution composition on the cobalt passive film was studied on a prepassivated cobalt electrode using open circuit potential and galvanostatic measurements. It can be deduced that competitive adsorption mechanisms play a key role in the attack of passive films on cobalt. It was shown that the presence of a small amount of phosphate species in carbonic acid – bicarbonate – carbonate solutions is an efficient corrosion inhibitor, especially against the carbonic acid species. The inhibition mode of phosphate is most likely linked to a specific adsorption phenomenon since its beneficial contribution to the stability of passive films must be discarded.

Acknowledgments

This work was supported by a discovery grant from the Natural Sciences and Engineering Research Council of Canada (NSERC). The authors also thank Pr. Yves Paquin for useful discussions during the preparation of this paper.

References

1. R.D. Cowling and A.C. Riddiford. Electrochim. Acta, **14**, 981 (1969).
2. T.R. Jayaraman, V.K. Venkatesan, and H.V.K. Udupa. Electrochim. Acta, **20**, 209 (1975).
3. K.M. Ismail and W.A. Badawy. J. Appl. Electrochem. **30**, 1303 (2000).
4. A. Foelske and H.-H. Strehblow. Surf. Interface Anal. **34**, 125 (2002).
5. N. Sato and T. Ohtsuka. J. Electrochem. Soc. **125**, 1735 (1978).
6. D.H. Davies and G.T. Burstein. Corros. Sci. **20**, 973 (1980).
7. C.A. Gervasi, S.R. Biaggio, J.R. Vilche, and A.J. Arvia. Corros. Sci. **29**, 427 (1989).
8. C.A. Gervasi, S.R. Biaggio, J.R. Vilche, and A.J. Arvia. Electrochim. Acta, **36**, 2147 (1991).

© 2004 NRC Canada

9. J.A. Calderón, O.R. Mattos, O.E. Barcia, S.I. Córdoba de Torresi, and J.E. Pereira da Silva. Electrochim. Acta, **47**, 4351 (2002).
10. J. Brown, A. Colling, D. Park, J. Phillips, D. Rothery, and J. Wright. *In* Seawater: its composition, properties and behaviour. *Edited by* Pergamon Press, Oxford. 1989. p. 30; Chap. 6. p. 112.
11. D.A. Skoog, D.M. West, and F.J. Holler. *In* Fundamentals of analytical chemistry. *Edited by* Saunders College Publishing, Harcourt Brace College Publishers, New York. 1996. p. A-8.
12. D.M. Kern. J. Chem. Ed. **37**, 14 (1960).
13. S. Trasatti. J. Electroanal. Chem. **33**, 351 (1971).
14. R.W. Revie (*Editor*). Uhlig's corrosion handbook. John Wiley and Sons, New York. 2000. Chap. 59. p. 1094.
15. M.J. Pryor and M. Cohen. J. Electrochem. Soc. **98**, 263 (1951).
16. C.A. Melendres, N. Camillone III, and T. Tipton. Electrochim. Acta, **34**, 281 (1989).
17. F.M. Al-Kharafi, W.A. Badawy, and J.R. Al-Ajmi. Indian J. Chem. Technol. **6**, 194 (1999).

© 2004 NRC Canada

Telechelic poly(ε-caprolactones) with tethered mixed ligand ruthenium(II) chromophores

Abdiaziz A. Farah and William J. Pietro

Abstract: Well-characterized templates of polymer-forming ligands and their ruthenium tris(α,α′-diimine) initiators were utilized to divergently ring open an ε-caprolactone monomer. The same polymers were also obtained through the synthesis of quinoline and bipyridine diimine ligands incorporating poly(ε-caprolactone) (PCL) chains. These polymers contain vacant molecular recognition sites, enabling subsequent chelation of these macroligands to metal precursors. Both methods provided telechelic (ε-caprolactone) ruthenium(II)-centered polyesters of various hierarchy. Solution properties and thermal behaviour of such polyesters are described.

Key words: redox polymers, poly(ε-caprolactone), telechelics, metal–polymer complexes, macroligands, ring-opening polymerization (ROP).

Résumé : On a utilisé des gabarits bien caractérisés de ligands conduisant à la formation de polymères et leurs initiateurs ruthénium tris(α,α′-diimine) pour provoquer des ouvertures de cycle divergentes d'un monomère ε-caprolactone. On a pu aussi obtenir les mêmes polymères en effectuant la synthèse de ligands quinoléine ou bipyridine diimine incorporant des chaînes poly(ε-caprolactone) (PCL). Ces polymères contiennent des sites vacants de reconnaissance moléculaire qui permettent d'effectuer une chélation subséquente de ces macroligands sur des précurseurs métalliques. Les deux méthodes permettent d'obtenir des polyesters téléchéliques centrés sur le (ε-caprolactone)ruthénium(II). On décrit les propriétés en solution et le comportement thermique de tels polyesters.

Mots clés : polymères redox, poly(ε-caprolactone), téléchéliques, complexes métal–polymère, macroligands, polymérisation par ouverture de cycle (POC).

[Traduit par la Rédaction]

Introduction

The design and the study of functional polymers containing metal centers in their structure remains an area of growing interest (1). Such materials exhibit attractive electrical, electrochemical, magnetic, and optical properties associated with the metal (2). Inorganic and organometallic polymers are relatively underrepresented in the available literature concerning polymeric functional materials. Hence, the synthesis of analogous polymeric architecture with inorganic fragments would expand the structural features and properties of the resulting inorganic–organic hybrid materials. New applications in supramolecular chemistry and the need for new materials are the driving forces for the development of inorganic and organometallic polymeric systems. Owing to the lack of appropriate organic–inorganic hybrid monomers, along with poorly optimized reaction conditions that otherwise would ensure homogeneous and quantitative conversion of these monomers, the synthesis of long chains of inorganic elements becomes rather difficult if not impossible. Radical or ionic chain polymerization of unsaturated monomers proved to be possible only in some specific cases (3). Even the apparently easier step-growth polymerizations were also problematic because of the necessity of strict stoichiometric balance and monomer purity. Consequently, only low-molecular-weight products have been available in most cases (4).

Progress in inorganic polymer chemistry became possible when more specialized polymerization reactions were applied, such as ring-opening polymerization (ROP) (5) or transition-metal-catalyzed processes (6). These techniques, along with solubilizing side-chain moieties, provided a wide range of inorganic macromolecules with valuable properties. Four possible synthetic methods have been utilized for the incorporation of metal complexes into polymeric structures: binding via coordination site from a polymer-bound ligand (7); covalent attachment by reaction of a functionalized complex with a functionalized polymer (8); homopolymerization of metal-containing monomers incorporating polymerizable groups; and copolymerization of a complex bearing a polymerizable group with other selected monomers (9). Recently, Fraser and co-workers (10) have elegantly demonstrated that the combination of coordination chemistry with controlled polymerization methodologies would lead to a variety of functional materials. In contrast to the conventional way of synthesizing functional polymeric materials via post-polymer modification of end-reactive oligomers and polymeric precursors (11), this synthetic ap-

Received 21 April 2003. Published on the NRC Research Press Web site at http://canjchem.nrc.ca on 6 May 2004.

A.A. Farah[1] and W.J. Pietro.[2] Department of Chemistry, York University, 4700 Keele Street, Toronto, ON M3J 1P3, Canada.

[1]Present address: National Research Council Canada (NRC), Institute of Microstructural Science, Ottawa, ON K1A OR6, Canada.

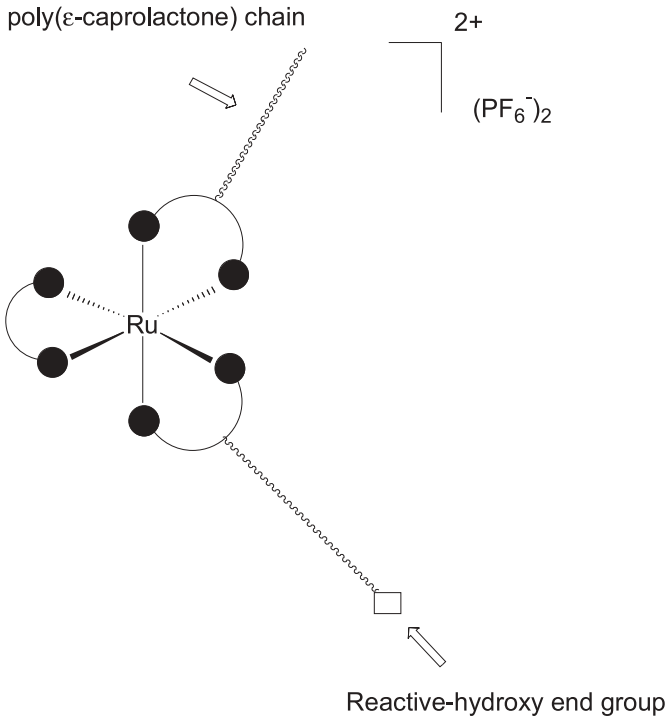
[2]Corresponding author (e-mail: pietro@yorku.ca).

 doi: 10.1139/V03-215 © 2004 NRC Canada

proach provides polymers of controlled molecular weights and, in particular, unique and well-defined spatial shapes. Almost none of these characteristics are found in conventional, mostly linear synthetic polymers. In turn, metal moieties in well-defined microdomains in the polymer chain allow the precise incorporation of functional groups, an indispensable feature in developing specific material functions with multi-dimensional environments.

In this contribution the synthesis and characterization of telechelic linear and multi-dimensional poly(ε-caprolactones) tagged with ruthenium(II)-centered chromophores of the general structure in Fig. 1 will be described. These polyesters have been prepared by two distinct approaches: macroligand-chelation and metalloinitiation. Both methods proceed under mild conditions and provide polymers with controlled properties, i.e., molecular weight and molecular-weight distributions.

Fig. 1. General structure of the telechelic ruthenium-centered poly(ε-caprolactones).



Experimental

Methods and materials

All reagents were obtained from Aldrich Chemicals Canada/Fluka and Alfa Aesar (Ward Hill, Mass). Reagent-grade solvents were obtained from Caledon and BDH Inc. Electrochemical solvents were freshly distilled over P_2O_5 under inert atmosphere, and electrolytes were twice recrystallized from absolute ethanol and dried in vacuum. All chemicals and solvents were purified where necessary, according to the conventional laboratory techniques (12), or were used as received. *cis*-$Ru(bpy)_2Cl_2 \cdot xH_2O$ (bpy = bipyridine) and metal complexes (**5**), (**6**), (**7**), (**8**), (**9**), and (**10**) were obtained as described in refs. 13 and 14, respectively. Analytical thin layer chromatography (TLC) was done on commercially prepared silica gel 60F 254 coated plastic sheets (Aldrich). Preparative TLC was performed on Aldrich silica gel 60F 254 precoated glass plates. For column chromatography, high-purity grade (70–230 mesh, 60 Å) silica gel and neutral standard grade (150 mesh, 58 Å) aluminum oxide were used. Melting points (mp) were recorded using a Laboratory Devices U.S.A. MEL-TEMP II and were uncorrected. Infrared spectra were recorded neat, as KBr pellets, or as solution-casted films with a Mattson 3000 Fourier transform infrared spectrophotometer. ^1H and ^{13}C NMR spectra were obtained on a Bruker ARX 400-MHz nuclear magnetic resonance spectrometer in an appropriate solvent, using tetramethylsilane as an internal standard. Electronic spectroscopy was performed using a Hewlett-Packard 8452 diode array spectrophotometer. Fluorimetry experiments were conducted in a Shimadzu RF 551 fluorimeter or a PerkinElmer LS-50B luminescence fluorimeter on argon or N_2 deaerated samples prior to recording. Electron impact (EI) mass spectrometry (positive mode) was carried out using a Kratos 902 mass spectrometer. Electrochemistry experiments were performed in a conventional three-electrode cell using a platinum working electrode, a platinum counter electrode, and an Ag/Ag^+ wire "quasi" reference electrode referenced to the ferrocenium–ferrocene couple (15). The solvent used was dimethylformamide (DMF), with tetrabutylammonium hexafluorophosphate ($TBAPF_6$) as the supporting electrolyte. A Princeton Applied Research Corp. 174 Potentiostat or an RDE3 potentiostat (Pine Instrument) with an *x*–*y* recorder or a computerized Cypress workstation was used for all electrochemical studies. All electroanalytical solutions were degassed with N_2 or argon for 20 min prior to each experiment. Molecular weights were determined by gel permeation chromatography (GPC) with a Waters Associates 2690 separation module accessoried inline solvent degasser, a high performance liquid chromatography (HPLC) pump, and an autosampler. The separation module was equipped with a Waters 410 differential refractometer as the concentration detector and was connected in parallel. A Viscotek T60A dual detector consisted of a right-angle laser light scattering detector with a laser source of 670 nm and a four-capillary differential viscometer. Software from Viscotek was used to analyze the data. Columns from Polymer Laboratories with pore sizes of 5×10^2, 1×10^4, and 1×10^5 Å were used with THF as the eluent at a flow rate of 1.0 mL/min. Polystyrene standards purchased from Aldrich and Viscotek were used for calibration. Absolute molecular weights were determined by low angle laser light scattering (LALLS) performed on a Chromatix KMX-6 instrument at a wavelength of 632.8 nm and a scattering angle of 6°–7°. Measurements were carried out at room temperature with a metal cell 4.93 mm long. Each solution was filtered three times through a MILEX filter with an average pore size of 0.2 μm before injection into the cell. The refractive index increment (dn/dc) of the polymer solution was obtained with a Chromatix KMX-16 differential refractometer, operating at a wavelength of 632.8 nm. The instrument was calibrated with NaCl solutions. A PerkinElmer DSC7 equipped with a TAC7 instrument controller or TA instrument DSC 2920 was used to study polymer thermal behavior. For differential scanning calorimetry (DSC) experiments, the instruments were calibrated with melting transitions of decane and indium, and

© 2004 NRC Canada

samples were heated under N_2 atmosphere at a heating rate of 10 °C/min. Reported thermal parameters were taken from the second heating cycle if not otherwise indicated. The glass transition (T_g) value was the mid-point of the heat capacity change, whereas the melting point (T_m) was the peak maximum. Thermogravimetric analyses (TGA) were also obtained on the same instrument, TGA7, and the temperature was calibrated with the transitions of Perkalloy and Nicoseal. Thermograms were obtained at a heating rate of 20 °C/min under an N_2 atmosphere.

2-(2-Pyridyl)-4-hydroxymethylquinoline (pq) ligand (1)

Lithium aluminum hydride (2.3 g, 52 mmol) was added into 200 mL of anhydrous diethyl ether under nitrogen. To this suspension was added 3.2 g (13 mmol) of 2-(2-pyridyl)-4-methylcarbonylquinoline (16) in 20 mL of dry THF over a period of 30 min at room temperature. The reaction mixture was allowed to reflux gently for 3 h and then cooled to room temperature. The excess lithium aluminum hydride was decomposed by gentle addition of 5% H_2SO_4, and the phases were separated. The organic phase was washed with 5% $NaHCO_3$ (3 × 30 mL) and water (2 × 30 mL) and then dried over Na_2SO_4. After removal of the solvent, the desired product was obtained as an orange crystalline solid. Yield 2.2 g (64%); mp 108 °C.

IR (KBr pellets, ν in cm^{-1}) ν: 3355 (s, broad, O-H str), 2924 (m, sharp, arom C-H str), 2859 (m, sharp, aliph C-H str), 1991–2058 (m, broad, arom overtone bands), 1602 (s, sharp, C=C ring str), 1310 (s, sharp, arom C-N str), 1260 (w, sharp, C-O-C str), 1037 (s, broad, C-H in-plane bend), 745 (s, sharp, arom C-H out-of-plane bend). ^{1}H NMR (DMSO-d_6, δ in ppm) δ: 9.08 (s, H3 of quinoline), 8.82 (d, H5 of quinoline, J = 9.6 Hz), 8.79 (d, H12 of pyridine, J = 12 Hz), 8.68 (d, H9 of pyridine, J = 8 Hz), 8.24 (d, H8 of quinoline, J = 8 Hz), 7.89 (dd, H10 of pyridine, J = 8 Hz), 7.79 (dd, H7 of quinoline, J = 7.5 Hz, J = 15 Hz), 7.67 (dd, H6 of quinoline, J = 7.5 Hz, J = 15 Hz), 7.38 (dd, H11 of pyridine, J = 8 Hz, J = 12 Hz), 5.23 (s, 2H, OCH_2), 3.72 (br. 1H, OH). EI-MS (*m*/*z*) (%): 236 (65), 205 (21), 178 (12).

4,4′-Dimethyl-2,2′-bipyridine (2)

4,4′-Dimethyl-2,2′ bipyridine (**2**) was prepared following the Sassi method (17), using 220 g (2.36 mol) of 4-picoline and 10 g of 10 wt % palladium on activated carbon. Yield 8.2 g (59%). (lit. (17) value 1.4 g/g of 10 wt % Pd–C). mp 174 °C (lit. (17) value mp 174–176 °C). IR (KBr pellets, ν in cm^{-1}) ν: 3037 (s, sharp, arom C-H str), 2967 (m, sharp, aliph C-H str), 2017–1677 (m, broad, arom overtone bands), 1598 (s, sharp, C=C ring str), 1369 (s, sharp, arom C-N str), 1119–1045 (m, sharp, aliph C-H in-plane bend), 725 (s, sharp, arom C-H out-of-plane bend). ^{1}H NMR ($CDCl_3$, δ in ppm) δ: 8.54 (s, 2H, H6, J = 4.9 Hz), 8.23 (d, 2H, H3, J = 1.7 Hz), 7.12 (d, 2H, H5, J = 4.7 Hz), 2.45 (s, 6H, CH_3). EI-MS (*m*/*z*) (%): 184 (100), 169 (14), 156 (11).

4-Methyl-2,2′-bipyridine-4′-carboxaldehyde (3)

A mixture of 5.27 g (28.6 mmol) of (**2**) and 3.48 g (31.4 mmol) of SeO_2 in 1,4-dioxane was refluxed for 24 h with vigorous stirring and hot filtered. The filtrate was cooled to room temperature, and the resulting light-brown precipitate was filtered and discarded. After the solvent was removed by rotary evaporation, the residue was partially dissolved in 450 mL of ethyl acetate and filtered to remove the insoluble fraction. The filtrate was extracted with 0.1 mol/L Na_2CO_3 (2 × 100 mL) and 0.3 mol/L $Na_2S_2O_5$ (2 × 100 mL). The combined aqueous extracts were adjusted to pH 10 with Na_2CO_3, extracted with dichloromethane (3 × 50 mL), and dried over Na_2SO_4. The solvent was removed under reduced pressure, affording an off-white solid. Yield 2.8 g (50%); mp 130 to 131 °C (lit. (18) value mp 130.9–131.7 °C).

IR (KBr pellets, ν in cm^{-1}) ν: 3061 (m, sharp, arom C-H str), 2961 (s, sharp, aliph C-H str), 2093–1817 (m, sharp, arom overtone bands), 1702 (s, sharp, C=O aldehyde str), 1593 (s, sharp, C=C ring str), 1350 (s, sharp, arom C-N str), 1090–1031 (m, sharp, aliph C-H in-plane bend), 754 (s, sharp, arom out-of-plane bend). ^{1}H NMR (DMSO-d_6, δ in ppm) δ: 10.18 (s, 1H, CHO), 8.93 (d, 1H, H6, J = 4.8 Hz), 8.76 (s, 1H, H3), 8.57 (d, 1H, H6′, J = 4.8 Hz), 8.23 (s, 1H, H3′), 7.81 (d, 1H, H5, J = 4.8 Hz, J = 1.3 Hz), 7.30 (d, 1H, H5′, J = 4.2 Hz), 2.47 (s, 3H, CH_3). ^{13}C NMR (DMSO-d_6, δ in ppm) δ: 193.46, 157.01, 154.15, 150.71, 149.28, 148.30, 142.68, 125.54, 121.40, 119.46, 20.73. EI-MS (*m*/*z*) (%): 198 (100), 170 (68), 169 (52).

4-Methyl-4′-hydroxymethyl-2,2′-bipyridine (4)

After 2.2 g (10 mmol) of (**3**) in 50 mL of ethanol were cooled in an ice-bath while stirring for 20 min, 1.9 g (50 mmol) of $NaBH_4$ dissolved in 20 mL of 0.2 mol/L NaOH (aq) was added. The reaction mixture was left reacting under vigorous stirring for 4 h. Excess $NaBH_4$ was destroyed by treatment with dilute H_2SO_4, and most of the ethanol was removed under reduced pressure. The remaining white slurry was diluted with water and extracted with chloroform (3 × 40 mL). The chloroform extracts were washed with $NaHCO_3$ (3 × 30 mL) and water (3 × 30 mL) and dried with Na_2SO_4. The desired product was obtained following removal of the solvent. Yield 1.6 g (78%); mp 122 °C.

IR (KBr pellets, ν in cm^{-1}) ν: 3470 (w, shoulder, O-H str), 3185 (s, sharp, arom str), 2833 (s, sharp, aliph str), 2064 (w, broad, arom overtone), 1586 (m, sharp, C=C ring str), 1454 (s, sharp, arom C-N str), 1247 (s, sharp, C-O str), 758 (s, sharp, C-H out-of-plane bend). ^{1}H NMR (DMSO-d_6, δ in ppm) δ: 8.50 (d, 1H, H6′, J = 3.4 Hz), 8.42 (d, 1H, H6, J = 5 Hz), 8.22 (s, 1H, H3′), 8.11 (s, 1H, H3), 7.20 (d, 1H, H5′, J = 4.9 Hz), 7.07 (d, 1H, H5, J = 4.9 Hz), 4.69 (s, 1H, CH_2O), 2.37 (s, 1H, CH_3). ^{13}C NMR (DMSO-d_6, δ in ppm) δ: 155.25, 152.74, 148.91, 148.88, 147.81, 124.82, 121.34, 121.27, 121.24, 117.87, 117.85, 61.85, 61.85, 20.68. EI-MS (*m*/*z*) (%): 200 (85), 169 (54), 154 (36).

Synthesis of ruthenium-centered polyesters via ring-opening polymerization of ε-caprolactone with ruthenium(II) metalloinitiators

Ru(bpy)$_2$(bpyPCL)(PF$_6$)$_2$ (11)

Initiator (**5**) (91 mg, 0.11 mmol) and 2.3 g (18 mmol) of ε-caprolactone were charged into an N_2-filled polymerization flask and immersed into a preheated oil at 110 °C for 20 min before addition of a catalytic amount (0.60 μL) of stannous octanoate ($Sn(Oct)_2$). The polymerization reaction mixture was then left reacting with stirring at 110 °C for

© 2004 NRC Canada

24 h. The resulting viscous product was diluted with THF while still warm and precipitated in cold MeOH. The polymer was further purified by precipitation twice from THF solution into MeOH. Yield 2.6 g (91%) of a red-orange polymeric product.

IR (KBr pellets, ν in cm^{-1}) ν: 3442 (s, broad, OH str), 2944 (m, sharp, arom C-H str), 2863 (m, sharp, aliph C-H str), 2195–1890 (m, broad, arom overtone bands), 1723 (s, sharp, C=O ester str), 1592 (s, sharp, C=C ring str), 1471 (m, sharp, arom C-N str), 1092 (s, broad, C-O-C str), 729 (s, sharp, arom out-of-plane bend). UV–vis (DMF) λ_{max}: 286 nm (ε = 78 500 $(mol/L)^{-1}$ cm^{-1}), 456 nm (ε = 12 700 $(mol/L)^{-1}$ cm^{-1}). ^1H NMR (DMSO-d_6, δ in ppm) δ: 4.05 (m, broad, CH_2O of PCL), 2.30 (m, broad, $OCCH_2$ of PCL), 1.64 (m, broad, CH_2 of PCL), 1.39 (m, broad, CH_2 of PCL). GPC (LALLS): M_w: 28 130; M_w/M_n: 1.26.

Ru(bpyPCL)$_2$(bpy)(PF$_6$)$_2$ (12)

The two-dimensional (**12**) polymer was synthesized by a similar experimental procedure to that described above for (**11**), using 45 mg (0.047 mmol) of (**6**), 2.4 g (18 mmol) of ε-caprolactone, and 0.63 μL of $Sn(Oct)_2$. Yield 1.6 g (52%) of a red-orange polymeric product.

IR (KBr pellets, ν in cm^{-1}) ν: 3445 (s, broad, OH str), 2945 (m, sharp, arom C-H str), 2863 (m, sharp, aliph C-H str), 2199–1891 (m, broad, arom overtone bands), 1721 (s, sharp, C=O ester str), 1592 (s, sharp, C=C ring str), 1479 (m, sharp, arom C-N str), 1090 (s, broad, C-O-C str), 743 (s, sharp, arom out-of-plane bend). UV–vis (DMF) λ_{max}: 289 nm (ε = 71 400 $(mol/L)^{-1}$ cm^{-1}), 452 nm (ε = 10 900 $(mol/L)^{-1}$ cm^{-1}). ^1H NMR (DMSO-d_6, δ in ppm) δ: 4.06 (m, broad, CH_2O of PCL), 2.37 (m, broad, $OCCH_2$ of PCL), 1.65 (m, broad, CH_2 of PCL), 1.40 (m, broad, CH_2 of PCL). GPC (LALLS): M_w: 47 300, M_w/M_n: 1.37.

Ru(bpyPCL)$_3$(PF$_6$)$_2$ (13)

The three-dimensional (**13**) was synthesized by a similar procedure to that described for (**11**), using 60 mg (0.060 mmol) of (**7**), 2.5 g (22 mmol) of ε-caprolactone, and 0.60 μL of $Sn(Oct)_2$. Yield 2.3 g (82%) of a red-orange polymeric product.

IR (KBr pellets, ν in cm^{-1}) ν: 3442 (s, broad, OH str), 2940 (m, sharp, arom C-H str), 2863 (m, sharp, aliph C-H str), 2191–1898 (m, broad, arom overtone bands), 1719 (s, sharp, C=O ester str), 1597 (s, sharp, C=C ring str), 1471 (m, sharp, arom C-N str), 1092 (s, broad, C-O-C str), 733 (s, sharp, arom out-of-plane bend). UV–vis (DMF) λ_{max}: 292 nm (ε = 79 300 $(mol/L)^{-1}$ cm^{-1}), 458 nm (ε = 12 800 $(mol/L)^{-1}$ cm^{-1}). ^1H NMR (DMSO-d_6, δ in ppm) δ: 4.03 (m, broad, CH_2O of PCL), 2.31 (m, broad, $OCCH_2$ of PCL), 1.69 (m, broad, CH_2 of PCL), 1.37 (m, broad, CH_2 of PCL). GPC (LALLS): M_w: 64 300, M_w/M_n: 1.45.

Ru(bpy)$_2$(pqPCL)(PF$_6$)$_2$ (17)

The one-dimensional (**17**) was synthesized by a similar procedure to that described for (**11**), using 74 mg (0.070 mmol) of (**8**), 2.3 g (18 mmol) of ε-caprolactone, and 0.54 μL of $Sn(Oct)_2$. Yield 1.1 g (82%) of a dark-red polymeric product.

IR (KBr pellets, ν in cm^{-1}) ν: 3440 (s, broad, OH str), 2951 (m, sharp, arom C-H str), 2857 (m, sharp, aliph C-H str), 2095–2019 (m, broad, arom overtone bands), 1730 (s, sharp, C=O ester str), 1595 (s, sharp, C=C ring str), 1471 (m, sharp, arom C-N str), 1100 (s, broad, C-O-C str), 842 (s, sharp, arom out-of-plane bend). UV–vis (DMF) λ_{max}: 290 nm (ε = 47 100 $(mol/L)^{-1}$ cm^{-1}), 500 nm (ε = 8 900 $(mol/L)^{-1}$ cm^{-1}). ^1H NMR (DMSO-d_6, δ in ppm) δ: 4.03 (m, broad, CH_2O of PCL), 2.39 (m, broad, $OCCH_2$ of PCL), 1.69 (m, broad, CH_2 of PCL), 1.31 (m, broad, CH_2 of PCL). GPC (LALLS): M_w: 19 150, M_w/M_n: 1.52.

Ru(pqPCL)$_2$(bpy)(PF$_6$)$_2$ (18)

The two-dimensional (**18**) was synthesized by a similar procedure to that described for (**11**), using 46 mg (0.045 mmol) of (**9**), 1.5 g (13 mmol) of ε-caprolactone, and 0.46 μL of $Sn(Oct)_2$. Yield 0.81g (62%) of a dark-red polymeric product.

IR (KBr pellets, ν in cm^{-1}) ν: 3442 (s, broad, OH str), 2939 (m, sharp, arom C-H str), 2857 (m, sharp, aliph C-H str), 2095–2019 (m, broad, arom overtone bands), 1721 (s, sharp, C=O ester str), 1591 (s, sharp, C=C ring str), 1475 (m, sharp, arom C-N str), 1100 (s, broad, C-O-C str), 842 (s, sharp, arom out-of-plane bend). UV–vis (DMF) λ_{max}: 300 nm (ε = 46 200 $(mol/L)^{-1}$ cm^{-1}), 486 nm (ε = 10 200 $(mol/L)^{-1}$ cm^{-1}). ^1H NMR (DMSO-d_6, δ in ppm) δ: 4.08 (m, broad, CH_2O of PCL), 2.41 (m, broad, $OCCH_2$ of PCL), 1.60 (m, broad, CH_2 of PCL), 1.39 (m, broad, CH_2 of PCL). GPC (LALLS): M_w: 28 500, M_w/M_n: 1.51.

Ru(pqPCL)$_3$(PF$_6$)$_2$ (19)

The three-dimensional (**19**) was synthesized by a similar procedure to that described for (**11**), using 40 mg (0.036 mmol) of (**10**), 1.5 g (13 mmol) of ε-caprolactone, and 0.60 μL of $Sn(Oct)_2$. Yield 0.98 g (79%) of a dark-red polymeric product.

IR (KBr pellets, ν in cm^{-1}) ν: 3449 (s, broad, OH str), 2951 (m, sharp, arom C-H str), 2857 (m, sharp, aliph C-H str), 2095–2019 (m, broad, arom overtone bands), 1725 (s, sharp, C=O ester str), 1594 (s, sharp, C=C ring str), 1471 (m, sharp, arom C-N str), 1100 (s, broad, C-O-C str), 842 (s, sharp, arom out-of-plane bend). UV–vis (DMF) λ_{max}: 311 nm (ε = 57 500 $(mol/L)^{-1}$ cm^{-1}), 480 nm (ε = 8 600 $(mol/L)^{-1}$ cm^{-1}). ^1H NMR (DMSO-d_6, δ in ppm) δ: 4.00 (m, broad, CH_2O of PCL), 2.31 (m, broad, $OCCH_2$ of PCL), 1.68 (m, broad, CH_2 of PCL), 1.29 (m, broad, CH_2 of PCL). GPC (LALLS): M_w: 34 540, M_w/M_n: 1.47

Synthesis of ruthenium-centered polyesters via macroligand–chelation approach

bpyPCL macroligand (23)

This macroligand was synthesized by a similar procedure to that described for (**11**), using 0.52 g (3.2 mmol) of (**4**) initiator, 33 g (289 mmol) of ε-caprolactone, and 16 μL of $Sn(Oct)_2$. Yield 35 g (94%) of a white polymeric product.

IR (KBr pellets, ν in cm^{-1}) ν: 3439 (s, broad, OH str), 2951 (m, sharp, arom C-H str), 2857 (m, sharp, aliph C-H str), 2095–2019 (m, broad, arom overtone bands), 1719 (s, sharp, C=O ester str), 1594 (s, sharp, C=C ring str), 1471 (m, sharp, arom C-N str), 1100 (s, broad, C-O-C str), 849 (s, sharp, arom out-of-plane bend). ^1H NMR (DMSO-d_6, δ in ppm) δ: 8.65 (d, broad, H6′ of bpy), 8.53 (d, broad, H6 of

© 2004 NRC Canada

bpy), 8.36 (s, broad, H3′ of bpy), 8.23 (s, broad, H3 of bpy), 7.13–7.18 (d, broad, H5′ & H5 of bpy), 5.20 (s, broad, CH_2O of bpy), 4.05 (m, broad, CH_2O of PCL), 2.30 (m, broad, $OCCH_2$ of PCL), 1.64 (m, broad, CH_2 of PCL), 1.39 (m, broad, CH_2 of PCL). GPC (LALLS): M_w: 27 900, M_w/M_n: 1.27.

Ru(bpy)$_2$(bpyPCL)(PF$_6$)$_2$ (14)

cis-Ru(bpy)$_2$Cl$_2$ (50 mg, 0.11 mmol) was dissolved in 20 mL of methanol; 43 mg (0.25 mmol) of $AgNO_3$ were added to the dissolved substrate, and the solution was left stirring for 2 h at room temperature. The resulting white precipitate was filtered off and evaporated to dryness, then redissolved in 30 mL of an acetonitrile–DME (1:1) mixture. To this was added 2.9 g (0.10 mmol) of (**23**) macroligand polymer, and the mixture was refluxed for 24 h with vigorous stirring. The solvent was then removed using a rotary evaporator, and the resulting red-orange product was purified by column chromatography (silica), using methylene chloride as the eluent. After reducing the solvent volume to 5–10 mL, the product was precipitated by addition with stirring to a methanolic potassium hexafluorophosphate solution. The product was then filtered, washed with ether, and vacuum dried. Yield 2.5 g (89%) of a red-orange polymeric product.

IR (KBr pellets, ν in cm^{-1}) ν: 3440 (s, broad, OH str), 2945 (m, sharp, arom C-H str), 2863 (m, sharp, aliph C-H str), 2195–1890 (m, broad, arom overtone bands), 1719 (s, sharp, C=O ester str), 1592 (s, sharp, C=C ring str), 1471 (m, sharp, arom C-N str), 1092 (s, broad, C-O-C str), 729 (s, sharp, arom out-of-plane bend). UV–vis (DMF) λ_{max}: 288 nm (ε = 79 600 $(mol/L)^{-1}$ cm^{-1}), 456 nm (ε = 12 900 $(mol/L)^{-1}$ cm^{-1}). ^{1}H NMR (DMSO-d_6, δ in ppm) δ: 7.63–8.66 (m, broad, bpy ArH), 5.33 (s, broad, CH_2O of bpy), 4.06 (m, broad, CH_2O of PCL), 2.37 (m, broad, $OCCH_2$ of PCL), 1.69 (m, broad, CH_2 of PCL), 1.41 (m, broad, CH_2 of PCL). GPC (LALLS): M_w: 28 430, M_w/M_n: 1.29.

Ru(bpyPCL)$_2$(bpy)(PF$_6$)$_2$ (15)

$RuCl_3 \cdot xH_2O$ (30 mg, 0.062 mmol), 3.5 g (0.13 mmol) of (**23**) macroligand polymer, and 2.1 g (50 mmol) of lithium chloride were dissolved in 30 mL of acetonitrile–DME (1:1) and refluxed overnight while stirring. The resulting intense dark-blue reaction product was evaporated to dryness, then dissolved in 10 mL of acetonitrile–DME (1:1) and reacted with 54 mg (0.32 mmol) of $AgNO_3$ under vigorous stirring for 6 h at room temperature. After filtering out the white AgCl precipitate through a Celite pad, 9.67 mg (0.063 mmol) of 2,2′-bipyridine was added to the filtrate and refluxed for 16 h. The desired polymer was then isolated from the reaction mixture by addition to a cold methanolic potassium hexafluorophosphate solution and filtered. It was further purified by column chromatography on silica and eluted with methylene chloride. Yield 2.7 g (70%) of an orange-red polymer.

IR (KBr pellets, ν in cm^{-1}) ν: 3449 (s, broad, OH str), 2945 (m, sharp, arom C-H str), 2866 (m, sharp, aliph C-H str), 2195–1890 (m, broad, arom overtone bands), 1722 (s, sharp, C=O ester str), 1598 (s, sharp, C=C ring str), 1471 (m, sharp, arom C-N str), 1092 (s, broad, C-O-C str), 756 (s, sharp, arom out-of-plane bend). UV–vis (DMF) λ_{max}: 290 nm (ε = 73 500 $(mol/L)^{-1}$ cm^{-1}), 456 nm (ε = 9 800 $(mol/L)^{-1}$ cm^{-1}). ^{1}H NMR (DMSO-d_6, δ in ppm) δ: 7.58–8.60 (m, broad, bpy ArH), 5.31 (s, broad CH_2O of bpy), 4.06 (m, broad, CH_2O of PCL), 2.33 (m, broad, $OCCH_2$ of PCL), 1.69 (m, broad, CH_2 of PCL), 1.45 (m, broad, CH_2 of PCL). GPC (LALLS): M_w: 29 870, M_w/M_n: 1.31.

Ru(bpyPCL)$_3$(PF$_6$)$_2$ (16)

This three-dimensional (**16**) polymer was obtained from 40 mg (0.082 mmol) of $RuCl_3 \cdot xH_2O$ and 6.9 g (0.33 mmol) of (**23**) macroligand polymer in 30 mL of acetonitrile–DME (20:80 volume fraction), using the procedure described for (**14**). Yield 5.1 g (61%).

IR (KBr pellets, ν in cm^{-1}) ν: 3455 (s, broad, OH str), 2942 (m, sharp, arom C-H str), 2866 (m, sharp, aliph C-H str), 2195–1890 (m, broad, arom overtone bands), 1729 (s, sharp, C=O ester str), 1602 (s, sharp, C=C ring str), 1471 (m, sharp, arom C-N str), 1098 (s, broad, C-O-C str), 756 (s, sharp, arom out-of-plane bend). UV–vis (DMF) λ_{max}: 286 (ε = 78 400 $(mol/L)^{-1}$ cm^{-1}), 456 (ε = 12 700 $(mol/L)^{-1}$ cm^{-1}). ^{1}H NMR (DMSO-d_6, δ in ppm) δ: 7.52–8.67 (m, broad, bpy ArH), 5.28 (s, broad CH_2O of bpy), 4.08 (m, broad, CH_2O of PCL), 2.31 (m, broad, $OCCH_2$ of PCL), 1.65 (m, broad, CH_2 of PCL), 1.42 (m, broad, CH_2 of PCL). GPC (LALLS): M_w: 53 370, M_w/M_n: 1.37.

pqPCL macroligand (24)

This macroligand polymer was synthesized by a similar procedure to that described for (**23**), using 0.59 g (2.5 mmol) of (**1**) initiator, 35 g (306 mmol) of ε-caprolactone, and 17 μL of Sn(Oct)$_2$. Yield 23 g (66%) of a white polymeric product.

IR (KBr pellets, ν in cm^{-1}) ν: 3356 (s, broad, O-H str), 2928 (m, sharp, arom C-H str), 2860 (m, sharp, aliph C-H str), 1991–2058 (m, broad, arom overtone bands), 1726 (s, sharp, C=O ester str), 1609 (s, sharp, C=C ring str), 1315 (s, sharp, arom C-N str), 1260 (w, sharp, C-O-C str), 1037 (s, broad, C-H in-plane bend), 749 (s, sharp, arom C-H out-of-plane bend). ^{1}H NMR (DMSO-d_6, δ in ppm) δ: 9.05 (s, broad, H3 of quinoline), 7.35–8.80 (m, complex, quinoline & bpy ArH), 5.27 (s, broad CH_2O of quinoline), 4.07 (m, broad, CH_2O of PCL), 2.32 (m, broad, $OCCH_2$ of PCL), 1.65 (m, broad, CH_2 of PCL), 1.43 (m, broad, CH_2 of PCL). GPC (LALLS): M_w: 19 800, M_w/M_n: 1.54.

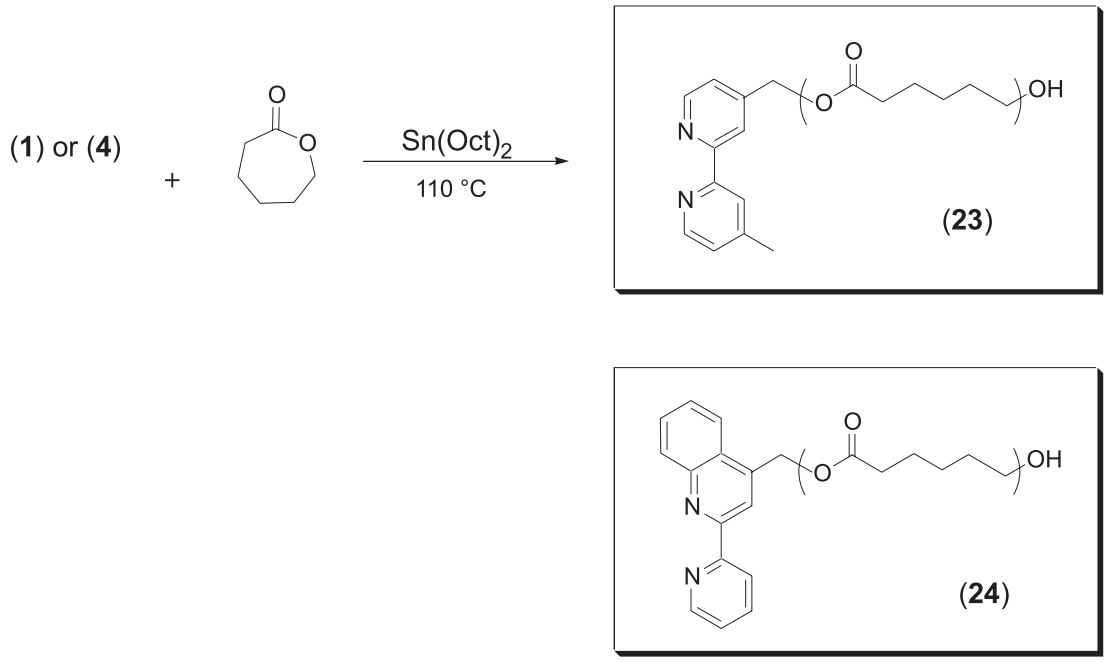
Ru(bpy)$_2$(pqPCL)(PF$_6$)$_2$ (20)

The one-dimensional polymer (**20**) was synthesized by a similar procedure to that described for (**14**), using 45 mg (0.093 mmol) of *cis*-Ru(bpy)$_2$Cl$_2$, 40 mg (0.23 mmol) of $AgNO_3$, and 2.7 g (0.091 mmol) of (**24**) macroligand polymer. Yield 1.7 g (90%) of a dark-red polymeric product.

IR (KBr pellets, ν in cm^{-1}) ν: 3356 (s, broad, O-H str), 2928 (m, sharp, arom C-H str), 2860 (m, sharp, aliph C-H str), 1991–2058 (m, broad, arom overtone bands), 1726 (s, sharp, C=O ester str), 1609 (s, sharp, C=C ring str), 1315 (s, sharp, arom C-N str), 1260 (w, sharp, C-O-C str), 1037 (s, broad, C-H in-plane bend), 749 (s, sharp, arom C-H out-of-plane bend). UV–vis (DMF) λ_{max}: 290 nm (ε = 41 200 $(mol/L)^{-1}$ cm^{-1}), 496 nm (ε = 8 900 $(mol/L)^{-1}$ cm^{-1}). ^{1}H NMR (DMSO-d_6, δ in ppm) δ: 8.87 (s, broad, H3 of quinoline), 7.35–8.97 (m, complex, quinoline & bpy ArH),

© 2004 NRC Canada

Scheme 1. Synthesis of macroligands (**23**) and (**24**) via ring-opening polymerization of (ε-caprolactone) monomer.



5.27 (s, broad CH_2O of quinoline), 4.07 (m, broad, CH_2O of PCL), 2.32 (m, broad, $OCCH_2$ of PCL), 1.65 (m, broad, CH_2 of PCL), 1.43 (m, broad, CH_2 of PCL). GPC (LALLS): M_w: 20 120, M_w/M_n: 1.58.

Ru(pqPCL)$_2$(bpy)(PF$_6$)$_2$ (21)

The two-dimensional polymer (**21**) was obtained by a similar procedure to that described for (**14**), using 35 mg (0.072 mmol) of $RuCl_3 \cdot xH_2O$, 5.1 g (0.18 mmol) of (**24**) macroligand polymer, 2.1 g (50 mmol) of lithium chloride, 31 mg (0.18 mmol) of $AgNO_3$, and 11 mg (0.071 mmol) of 2,2′-bipyridine. Yield 1.2 g (79%) of a dark-red polymeric product.

IR (KBr pellets, ν in cm^{-1}) ν: 3356 (s, broad, O-H str), 2928 (m, sharp, arom C-H str), 2860 (m, sharp, aliph C-H str), 1991–2058 (m, broad, arom overtone bands), 1726 (s, sharp, C=O ester str), 1609 (s, sharp, C=C ring str), 1315 (s, sharp, arom C-N str), 1260 (w, sharp, C-O-C str), 1037 (s, broad, C-H in-plane bend), 749 (s, sharp, arom C-H out-of-plane bend). UV–vis (DMF) λ_{max}: 294 nm (ε = 39 700 $(mol/L)^{-1}$ cm^{-1}), 494 nm (ε = 8 900 $(mol/L)^{-1}$ cm^{-1}). ^1H NMR (DMSO-d_6, δ in ppm) δ: 8.85 (s, broad, H3 of quinoline), 7.35–8.80 (m, complex, quinoline & bpy ArH), 5.27 (s, broad CH_2O of quinoline), 4.05 (m, broad, CH_2O of PCL), 2.31 (m, broad, $OCCH_2$ of PCL), 1.64 (m, broad, CH_2 of PCL), 1.43 (m, broad, CH_2 of PCL). GPC (LALLS): M_w: 20 840, M_w/M_n: 1.62.

Ru(pqPCL)$_3$(PF$_6$)$_2$ (22)

The three-dimensional polymer (**22**) was synthesized by a similar procedure to that described for (**16**), using 25 mg (0.052 mmol) of $RuCl_3 \cdot xH_2O$ and 4.7 g (0.17 mmol) of (**24**) macroligand polymer. Yield 1.1 g (69%) of a dark-red polymeric product.

IR (KBr pellets, ν in cm^{-1}) ν: 3338 (s, broad, O-H str), 2928 (m, sharp, arom C-H str), 2860 (m, sharp, aliph C-H str), 1991–2058 (m, broad, arom overtone bands), 1715 (s, sharp, C=O ester str), 1617 (s, sharp, C=C ring str), 1322 (s, sharp, arom C-N str), 1260 (w, sharp, C-O-C str), 1037 (s, broad, C-H in-plane bend), 762 (s, sharp, arom C-H out-of-plane bend). UV–vis (DMF) λ_{max}: 298 nm (ε = 51 300 $(mol/L)^{-1}$ cm^{-1}), 496 nm (ε = 9 700 $(mol/L)^{-1}$ cm^{-1}). ^1H NMR (DMSO-d_6, δ in ppm) δ: 8.83 (s, broad, H3 of quinoline), 7.35–8.80 (m, complex, quinoline & bpy ArH), 5.23 (s, broad CH_2O of quinoline), 4.01 (m, broad, CH_2O of PCL), 2.29 (m, broad, $OCCH_2$ of PCL), 1.65 (m, broad, CH_2 of PCL), 1.41 (m, broad, CH_2 of PCL). GPC (LALLS): M_w: 29 780, M_w/M_n: 1.67.

Results and discussion

Macroligand synthesis

Polymeric macroligands (**23**) and (**24**) of controlled molecular weight, bearing end-reactive functional groups, were prepared by insertion–coordination ring-opening polymerization of ε-caprolactone with high yield (19). The polymerization was initiated by 2-(2-pyridyl)-4-hydroxymethylquinoline ligand (**1**) and 4-methyl-4′-hydroxymethyl-2,2′-bipyridine (**4**) in the presence of stannous octanoate ($Sn(Oct)_2$) as a catalyst, as shown in Scheme 1. As expected, the resulting polymeric macroligands possess one chain terminated with a hydroxy group, active in post-polymerization reactions originating from the (ε-caprolactone) ring-opening polymerization reaction (19), and another terminus end-capped with an α,α′-diimine ligand, providing a free coordination site originating from the initiators. This synthetic approach has a notable advantage over the other conventional methods of synthesizing telechelic polymers, as it provides macromers with two distinct end functional groups per polymeric chain.

GPC, thermal, and electronic absorption data of these macroligands are collected in Table 1. UV–vis spectra of

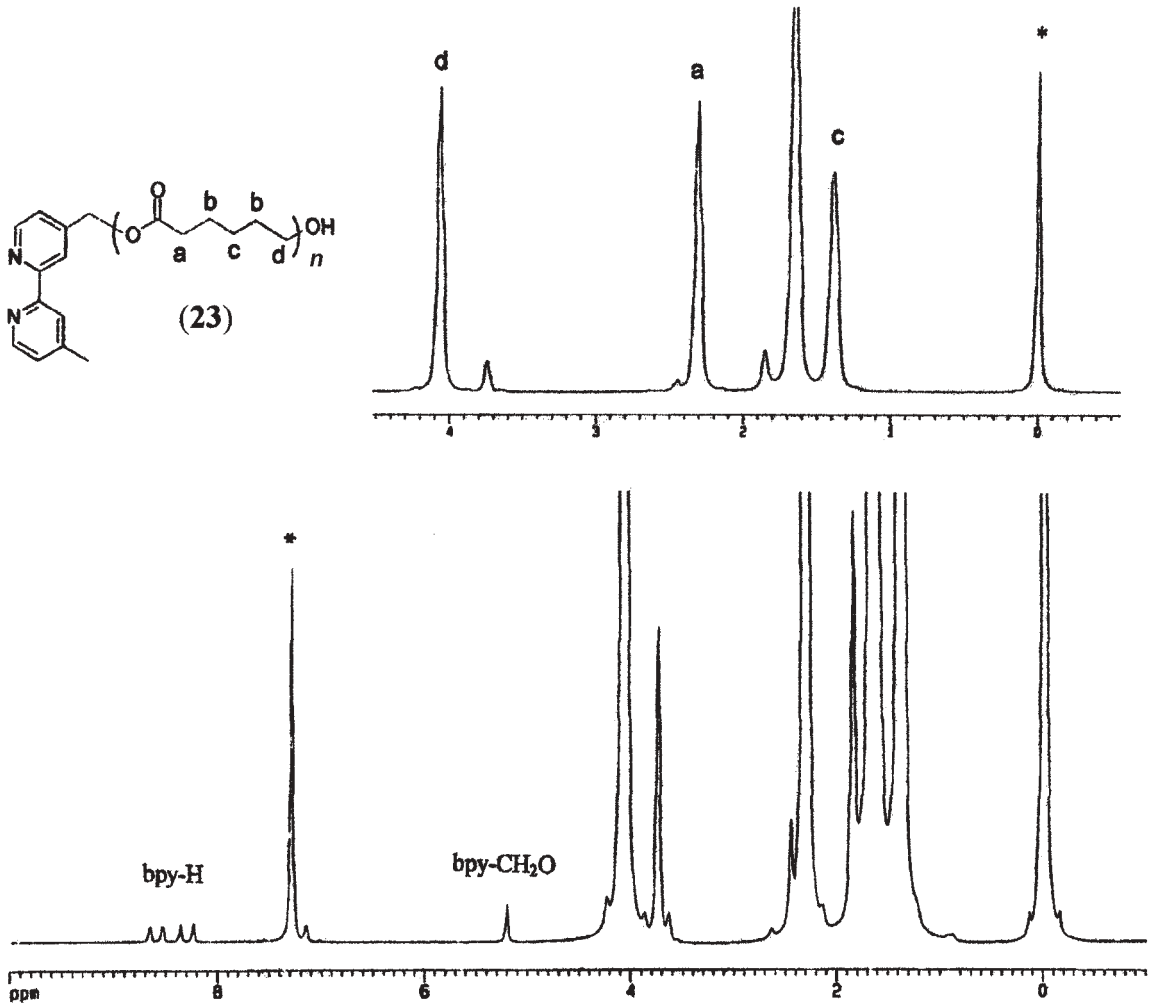
© 2004 NRC Canada

Table 1. Summary of data of macroligands (**23**) and (**24**) and their Ru(II)-containing polyesters obtained via macroligand–chelation.

Polymer	MW[a] (g/mol)	Polydispersity index	T_m[b] (°C)	ΔH_f[b] (J/g)	T_{dec}[c] (°C)	Absorbance (λ/nm)	Emission[d] (λ/nm)	Ch. eff.[e]
(**14**)	28 430	1.29	62	97	311	456	600	97
(**15**)	29 870	1.31	62	101	321	456	605	76
(**16**)	53 370	1.37	63	89	327	456	610	92
(**20**)	20 120	1.58	62	94	294	496	670	74
(**21**)	20 840	1.62	63	105	307	494	—[f]	73
(**22**)	29 782	1.67	67	112	311	496	—[f]	78
(**23**)	27 900	1.27	61	84	275	292		
(**24**)	19 800	1.54	62	87	281	340		

[a]Determined using LALLS–triple detector.
[b]DSC traces from second heating cycle.
[c]Thermogravimetric analysis (TGA); T_{dec} = decomposition temperature.
[d]In $CHCl_3$ degassed samples.
[e]Ch. eff. = estimated chelation efficiency; for example: εMLCT(**16**)$^{2+}$/εMLCT($[Ru(bpy)_3]^{2+}$). For εMLCT and λ_{max} values, refer to Experimental section.
[f]Non-emissive at room temperature.

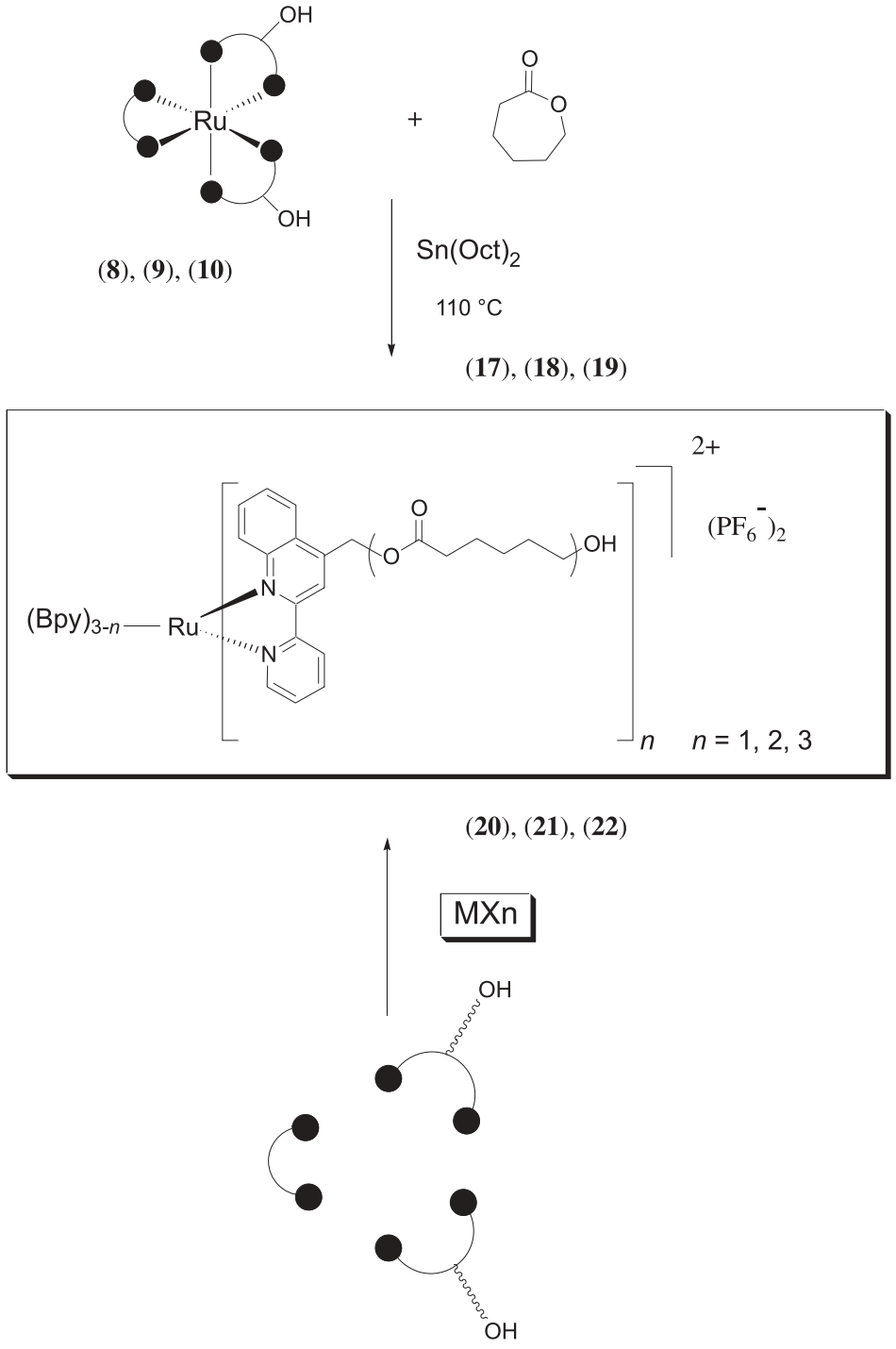
Fig. 2. ^{1}H NMR of macroligand (**23**) in $CDCl_3$.



(**23**) and (**24**) macroligands clearly revealed the presence of π–π* transitions typical of polypyridyl chromophores in the polymer chain. ^{1}H NMR analysis of these macroligands (macroligand (**23**), for example, is shown in Fig. 2) revealed well-resolved characteristic signals of the bipyridine units, as well as those of poly(ε-caprolactone). The ratios of integration between the bipyridine and quinoline ligand signals and the methylene units of the macroligand were approximately 1:1, suggesting that ligands (**1**) and (**4**) were the sole polymerization initiators. Although ^{1}H NMR spectroscopy has previously been utilized in determining the molecular weight of similar polymers with low monomer loading

© 2004 NRC Canada

Scheme 2. Synthesis of functionalized quinoline ligand based Ru(II) metal-centered polyesters.



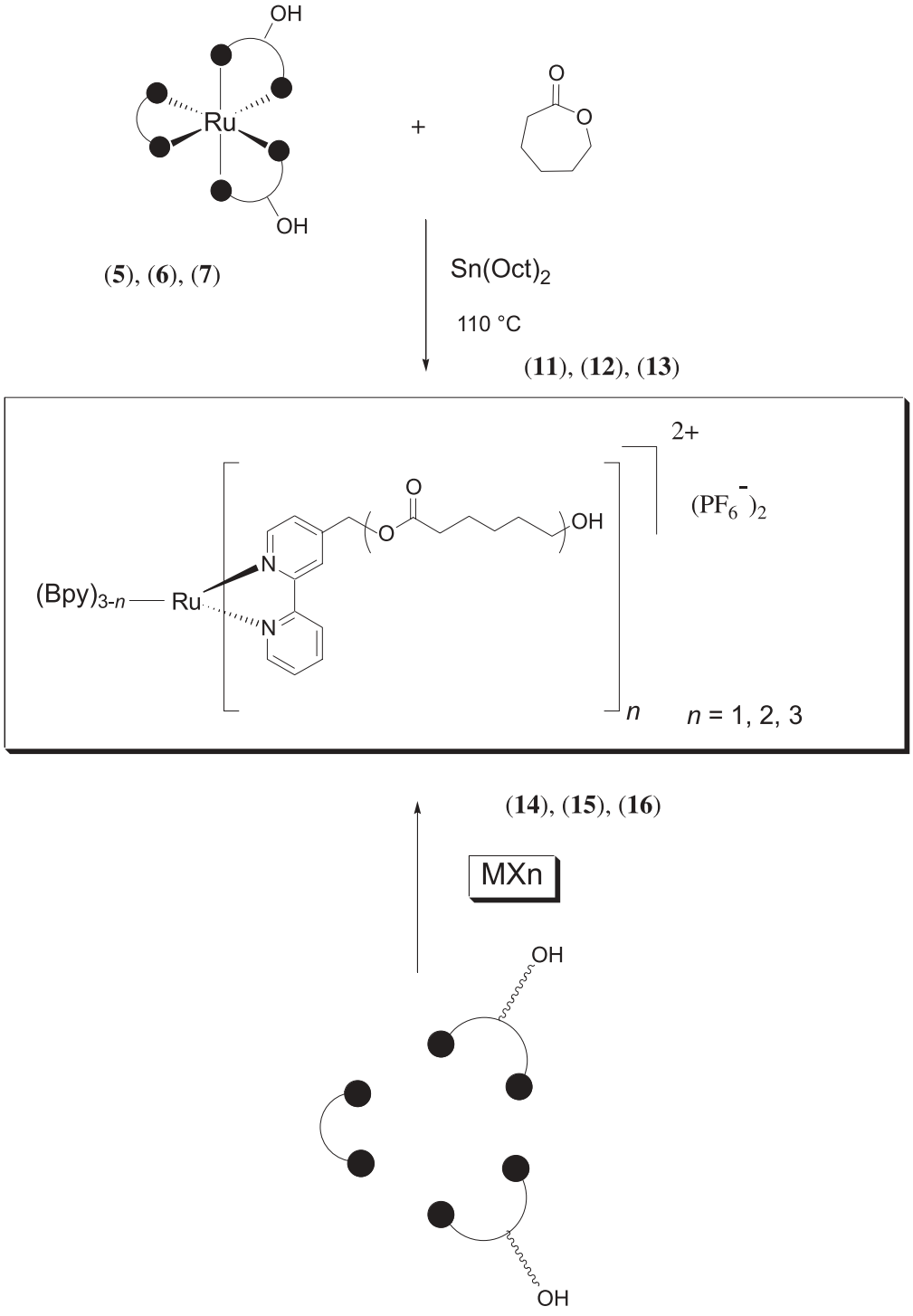
(10*b*), in our samples it would be difficult and inaccurate because of their relatively high molecular weight.

Metal complexes of polymeric ligands

The design and synthesis of our metal-containing polyesters was based principally on two different approaches (Schemes 2 and 3). The first, a metalloinitiation approach, uses appropriately functionalized heteroleptic Ru(II) complexes for the ring-opening polymerization of ε-caprolactone, producing multi-functional macromolecules with a well-defined transition-metal locus at the end of the polymer chain. The second approach, termed macroligand–chelation, involves the synthesis of polymeric macroligands that are subsequently chelated to metal ions or complex precursors through standard inorganic reactions. In the latter method, the reaction medium is modified to provide fully compatible reaction conditions between the metal precursors and the polymeric macroligands. With controlled experimental reaction settings and the use of an increasing number of polymeric macroligands, both methods generate linear and

© 2004 NRC Canada

Scheme 3. Synthesis of functionalized bipyridine ligand based Ru(II) metal-centered polyesters.



multi-dimensional ruthenium-centered polyesters. In the metalloinitiation approach, mixed ligand ruthenium(II) complexes (**5**), (**6**), (**7**), (**8**), (**9**), and (**10**), bearing peripheral OH groups, were utilized as initiating sites for further ring-opening polymerization of ε-caprolactone, employing similar procedures as those described in the preparation of the macroligands. Thus, metal complexes of polymeric ligands (**11**), (**12**), (**13**), (**17**), (**18**), and (**19**) were obtained in high yield in a one-pot synthesis, as red-orange products. In this method, chains propagate divergently outward and away from the congested metal center and can consequently provide materials of relatively high molecular weight. Very often the purification of the resulting polymeric metal complex is facile, as polymeric products can be separated from unreacted monomers by precipitation or by column chromatography. Metal complexes must be soluble in the polymerization conditions and be thermally stable so they do not decompose during the polymerization process. Ru(II)

© 2004 NRC Canada

Table 2. Summary of data of Ru(II)-containing polyesters obtained via metalloinitiation.

Polymer	[M]/[I][a]	MW[b] (g/mol)	Polydispersity index	T_m[c] (°C)	ΔH_f[c] (J/g)	T_{dec}[d] (°C)	Absorbance (λ/nm)	Emission[e] (λ/nm)
(**11**)	175	28 130	1.26	62	92	317	456	600
(**12**)	370	47 000	1.37	64	97	329	456	608
(**13**)	365	64 300	1.45	67	107	333	454	610
(**17**)	250	19 150	1.52	59	89	289	490	670
(**18**)	290	28 500	1.51	61	95	307	494	—[f]
(**19**)	290	34 540	1.47	63	102	317	498	—[f]

[a]Monomer to initiator loading.
[b]Determined using LALLS–triple detector.
[c]DSC traces from second heating cycle.
[d]Thermogravimetric analysis (TGA).
[e]In $CHCl_3$ degassed samples.
[f]Non-emissive at room temperature.

tris(bipyridine) complex initiators have been reported to be stable in various polymerization reactions (20). In our hands, bulk polymerization of ε-caprolactone with the aforementioned complexes under the conditions of our study provided homogenous monomer–metal complex initiator solutions with no evident metal residue upon reaction completion.

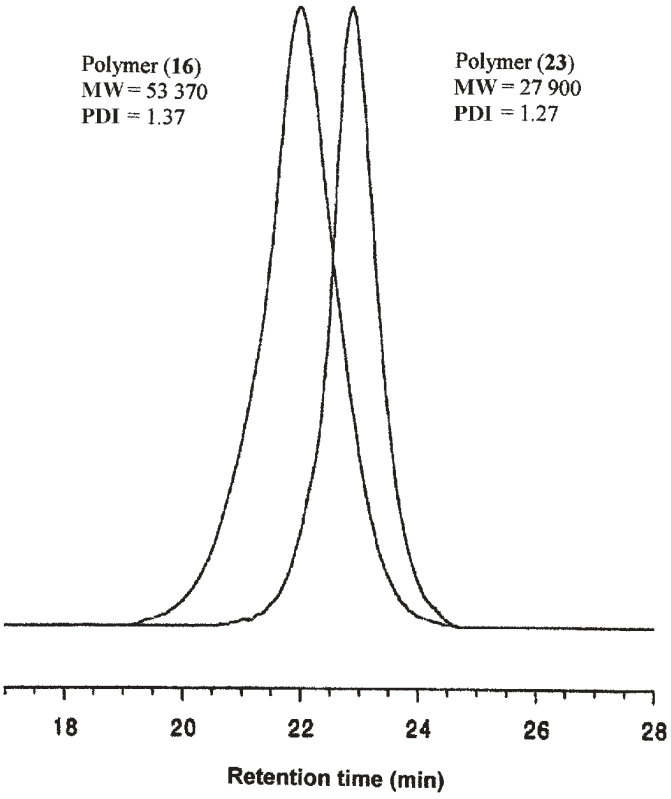
The macroligand–chelation approach is conceptually an extension of normal chelation reactions of small molecules and metal ion precursors in standard inorganic reactions (21). However, it is generally difficult to extrapolate chemistry from inorganic–organic synthesis to polymer reactions because the kinetics are usually different for each case. Polymer chain entanglement always limits the collision between active coordination sites in the polymer and metal ions. In the case of high-molecular-weight polymeric macroligands, additional reaction parameters have to be taken into account (22). The reaction medium must be capable of efficiently solubilizing both the metal ion precursors and the polymeric macroligand undergoing the substitution. More importantly, the solvent has to facilitate ligand substitution by solvating leaving groups or by providing labile metal ion solvent-coordinated intermediates, making the metal center sites prone to facile coordination. Macroligand solution phenomena, such as chain conformation and aggregation, have to be considered as well (23). Thus, in employing the macroligand–chelation method to prepare the mono-ligated metal complexes of polymeric ligands (**14**) and (**20**), *cis*-$Ru(bpy)_2Cl_2$ was first dehalogenated with $AgNO_3$ in methanol. After solvent removal, the resulting solvent-coordinated species $[Ru(bpy)_2(MeOH)_2]^{2+}$ was reacted with polymeric macroligands (**23**) and (**24**) in an acetonitrile–DME (1:1 volume fraction) mixed solvent medium to generate the desired polymers after column chromatography. The bis-ligated metal complexes of polymeric ligands (**15**) and (**21**) and also the tris-ligated metal complexes of polymeric ligands (**16**) and (**22**) were obtained with controlled combination of the metal source and the appropriate mole ratio of macroligands (**23**) and (**24**) in a polar reaction medium. For samples (**15**) and (**21**), for example, $RuCl_3{\cdot}xH_2O$ was heated with 2 equiv. of the desired macroligand in the presence of lithium chloride to prevent total substitution of the ligands around the coordination sphere of the metal center. This has provided dark, intense blue halogenated reaction intermediates of type $[Ru(\mathbf{23})_2Cl_2]$ or $[Ru(\mathbf{24})_2Cl_2]$. These intermediate species were then dehalogenated in situ with $AgNO_3$ and subsequently reacted with 2,2′-bipyridine to produce the desired red-orange bis-ligated metal complexes of polymeric ligands. In the case of tris-ligated metal complexes of polymeric ligands (**16**) and (**22**), $RuCl_3{\cdot}xH_2O$ was reacted with 3 equiv. of (**23**) and (**24**) macroligands in polar reaction medium for a longer time.

Summaries of molecular weight, thermal, electronic absorption, and emission analysis data for the ruthenium-centered polyesters prepared via macroligand–chelation and via metalloinitiation are presented in Tables 1 and 2, respectively. The presence of the ruthenium chromophore in the polymer chain was verified by ^1H NMR spectroscopy and electrochemical and UV–vis emission analysis. Metal-to-ligand charge-transfer (MLCT) bands around 460 nm, characteristic of $[Ru(bpy)_3]^{2+}$, and at 490 nm for $[Ru(pqX)_3]^{2+}$ (X = hydroxymethyl functionality) cores were observed. An emission band around 600–610 nm (excitation 400 nm) for all $[Ru(bpy)_3]^{2+}$-containing polymers was observed. For mixed quinoline ligand based ruthenium-centered polymers, mono-ligated metal complexes of polymeric ligands (**17**) and (**20**) were emissive at 670 nm (excitation 400 nm), while the rest of the series were either weakly emissive or not emissive at all. Molar absorptivities (ε) of the MLCT bands for all the polymers obtained via macroligand–chelation were determined using known masses and absolute molecular weights of the polymers. From these determinations, the estimated chelation efficiencies relative to the corresponding ruthenium complexes presented in Table 1 were obtained (24) to account for factors that might influence substitution reactions of macroligands of different molecular weights.

An overlay GPC trace of the tris-ligated metal complex of polymeric ligand (**16**) and the macroligand (**23**) from which it originated is shown in Fig. 3. As predicted, there was an increase in molecular weight for the formation of the metal-centered polymeric ligand (**16**), albeit lower than the theoretical calculated value. An increase in polydispersity index (PDI) of the target polymers and the existence of a shoulder in the GPC traces were also evident for the series of ruthenium-centered polymeric ligands, indicating the existence of small amounts of unreacted macroligands in our polymers. Although a small amount of uncomplexed macroligand does not affect the bulk properties of polymeric metal complexes or their usefulness in practical application, it can be removed by iterative column chromatography. In the ^1H NMR analysis of our polymers, the presence of characteristic signals of

© 2004 NRC Canada

Fig. 3. GPC traces of macroligand (**23**) and ruthenium-centered tris-ligated polyester (**16**).



the metal-complex core was observed, along with caprolactone resonances, for all polymers obtained via the macroligand approach. For polymers obtained via metalloinitiation, the situation was different. Only caprolactone peaks were observable in the ^{1}H NMR spectra. Similar observations were previously reported by McAlvin and Fraser (25) using hexafunctional tris(bipyridine) metalloinitiators for cationic polymerization of 2-ethyl-2-oxazolines.

The cyclic voltammogram of polymeric metal complex (**14**) is depicted in Fig. 4 as a representative example of the electrochemical behaviour of these series of polyesters. Half-wave potentials ($E_{1/2}$) in acetonitrile for all polymers obtained via the macroligand approach are collected in Table 3. For all metal-centered polymers, one reversible oxidation and two irreversible reduction waves were observed. Within each series, these electrochemical processes occur at nearly the same potential, regardless of the polymer dimensionality. Electrode passivation due to polymer film formation was also observed in equilibrium scans.

The macroligands and the ruthenium-centered polyesters were also analyzed by differential scanning calorimetry (DSC) and thermogravimetric analysis (TGA). There were no substantial differences in the melting points for the macroligands and the ruthenium-centered polyesters, regardless of molecular weight increase and polymer dimensionality or the metal presence in the polymer chain. As a typical example, an overlay DSC thermogram of macroligand (**23**) and the tris-ligated metal complex polymeric ligand (**16**) is shown in Fig. 5. Thermogravimetric analyses (TGA) of these series of ruthenium-centered polyesters show that they possess a high thermal stability under N_2 atmosphere. The

Fig. 4. Cyclic voltammogram of ruthenium-centered polyester (**14**) in acetonitrile–N_2, 0.1 mol/L $TBAPF_6$, scan rate 100 mV/s, Pt disc.

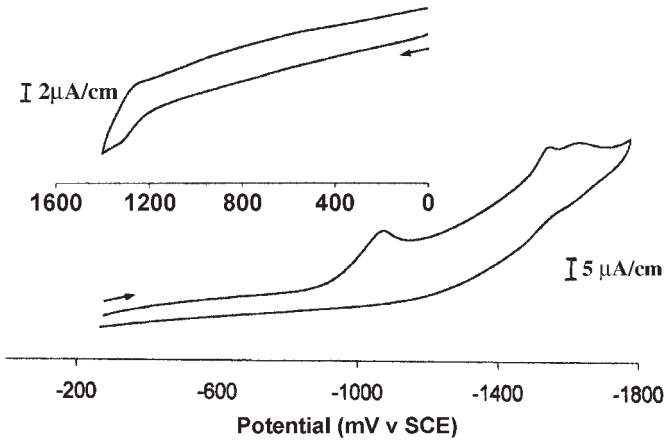


Table 3. Half-wave potentials for ruthenium-centered polymers obtained via macroligand approach.

Polymer	$E_{1/2}^{(ox)a}$	$E_{cath}^{(red)b}$	$E_{cath}^{(red)b}$
(**14**)	1.26	–1.25	–1.54
(**15**)	1.26	–1.33	–1.59
(**16**)	1.29	–1.31	–1.60
(**20**)	1.31	–1.32	–1.62
(**21**)	1.30	–1.30	–1.60
(**22**)	1.33	–1.21	–1.68

[a]Half-wave potential for Ru^{II} oxidation.
[b]Irreversible cathodic ligand reductions, all vs. SCE. Solutions were 0.1 mol/L in $TBAPF_6$, in acetonitrile, at room temperature.

onset of their thermal decomposition was high, as demonstrated in Fig. 6 for polyester (**16**), and varied from 275 to 350 °C. Moreover, the onset of decomposition temperature, as well as the apparent enthalpy of melting, increased slightly with the number of macroligands present around the metal center. This occurred with concomitant increase of molecular weight of the resulting polymeric metal complexes. This observation could be related to an increase of crystallinity of the metal-centered polymers due to the increasing content of semicrystalline poly(ε-caprolactone) macroligands coordinated to the metal ion.

Concluding remarks

Mixed ligand ruthenium-centered poly(ε-caprolactones) of various dimensionality were synthesized and characterized. These materials were obtained by preparing linear polymers with binding sites by ring-opening polymerization of ε-caprolactone, by using bpy or quinoline ligand initiators followed by chelation to metal ions. The same polymers were also obtained from ring-opening polymerization of ε-caprolactone via metal complexes with initiator sites in their ligand periphery. Both strategies produced polymers of relatively high molecular weight, possessing good filming properties and high thermal stability.

Selective end functionalization of macroligands, with the coordination site of the diimine ligands remaining intact, and the possibility for further functionalization of the metal-

© 2004 NRC Canada

Fig. 5. DSC thermogram of macroligand (**23**) and the tris-ligated ruthenium-centered polyester (**16**).

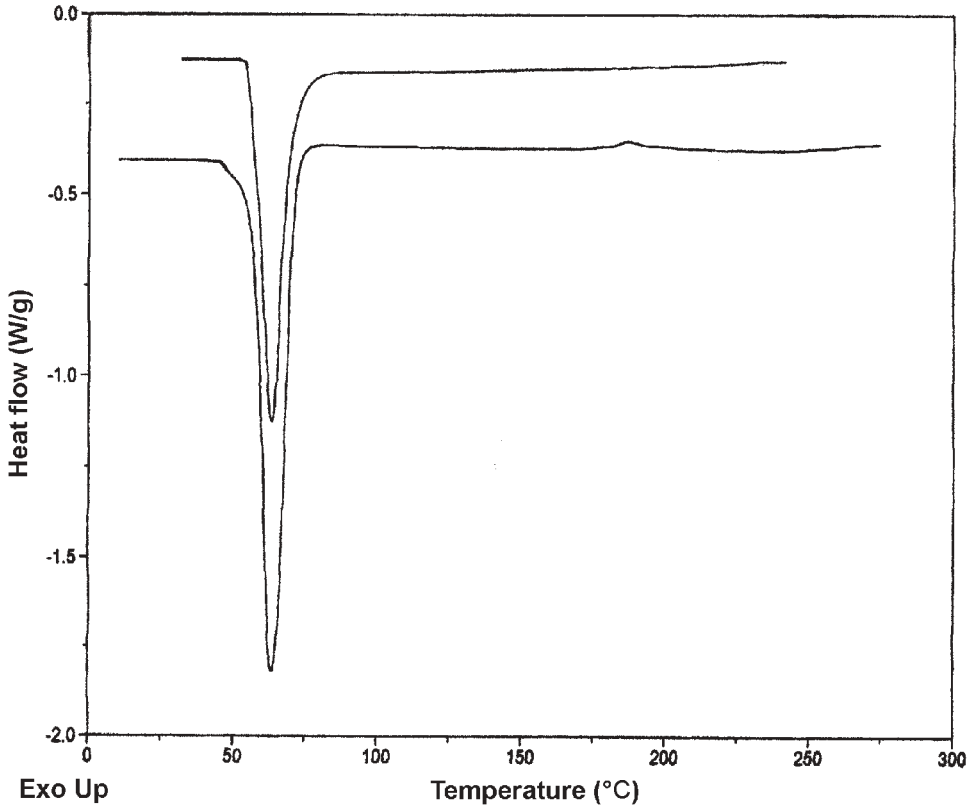
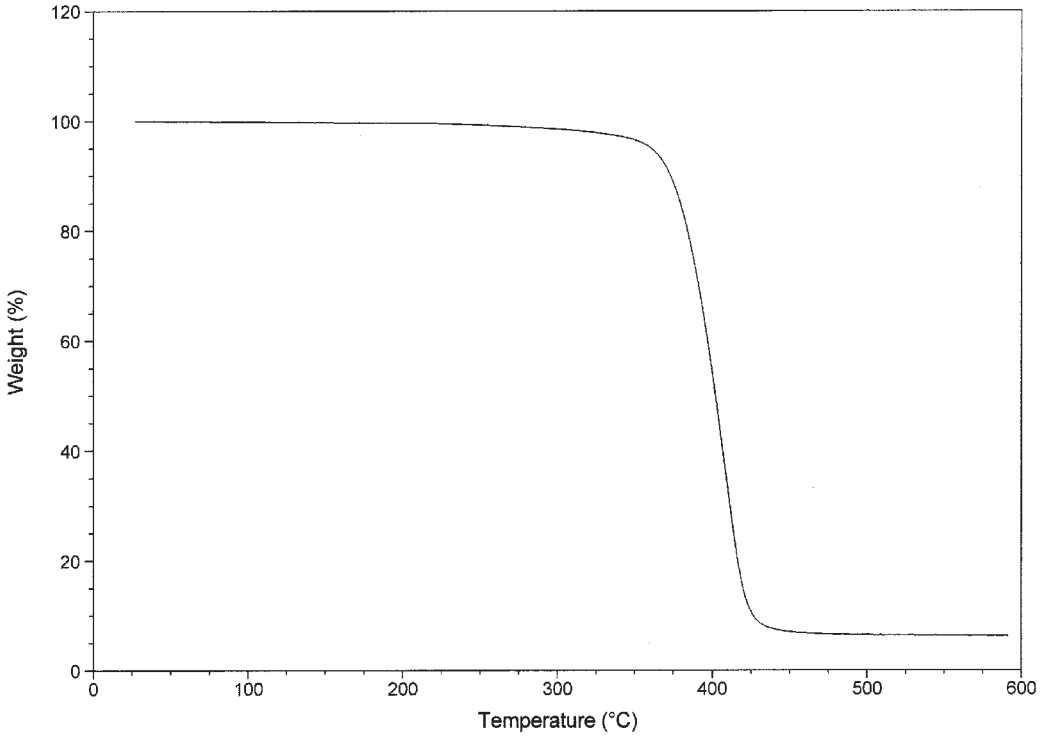


Fig. 6. TGA thermogram of ruthenium-centered tris-ligated polyester (**16**).



centered polyesters both merit further studies. They could potentially provide a wide of range of functionalized macromolecules of tailored properties. In turn, these polymers with luminescent chromophores in a well-defined location in the polymer chain have fulfilled our primary investigation in designing a new class of organic polymers with polypyridyl ruthenium(II) luminophores, a basis of transition-metal-mediated electroluminescent devices. A full account of such

© 2004 NRC Canada

an investigation will be the subject of a forthcoming publication.

Acknowledgements

We express our gratitude to Dr. I. Manners and his research groups for GPC assistance. The Natural Sciences and Engineering Research Council of Canada (NSERC) is also acknowledged for financial support.

References

1. For a general review of metal-containing polymers, see: (*a*) C.E. Carraher, Jr., J.E. Sheats, and C.U. Pittman, Jr. (*Editors*). Organometallic polymers. Academic Press, New York. 1978; (*b*) J.E. Sheats, C.E. Carraher, Jr., and C.U. Pittman (*Editors*). Metal containing polymeric systems. Plenum, New York. 1985; (*c*) J.E. Sheats, C.E. Carraher, Jr., C.P. Pittman, Jr., M. Zeldin, and B. Currel (*Editors*). Inorganic and metal-containing polymeric materials. Plenum, New York. 1985; (*d*) M. Zeldin, K.J. Wynne, and H.R. Allcock (*Editors*). Inorganic and organometallic polymers. ACS Symposium Series. Vol. 360. American Chemical Society, Washington, D.C. 1988; (*e*) B.M. Cullbertson and C.U. Pittman, Jr. New monomers and polymers. Plenum, New York. 1984; (*f*) E.W. Neuse and H Rosenberg. Metallocene polymers. Marcel-Dekker, New York. 1970; (*g*) J.E. Sheats. *In* Kirk-Othmer encyclopedia of chemical technology. 3rd ed. Vol. 15. John Wiley & Sons, New York. 1981; (*h*) I. Manners. Adv. Organomet. Chem. **37**, 131 (1995); (*i*) A.S. Abd-El-Aziz. Coord. Chem. Rev. **233**–**234**, 177 (2002); (*j*) I. Manners. J. Polym. Sci. Polym. Chem. **40**, 179 (2002); (*k*) K. Kulbaba and I. Manners. Macromol. Rapid Commun. **22**, 711 (2001).
2. Examples of metallo-polymers with specific properties: (*a*) Q. Wang, L. Wang, and L. Yu. J. Am. Chem. Soc. **120**, 12 860 (1998); (*b*) S.S. Zhu and T.M. Swager. Adv. Mater. **8**, 497 (1996); (*c*) C.M. Elliott, F. Pichot, C.J. Bloom, and L.S. Rider. J. Am. Chem. Soc. **120**, 6781 (1998); (*d*) C.H. Lyons, E.D. Abbas, J.K. Lee, and M.F. Rubner. J. Am. Chem. Soc. **120**, 12 100 (1998); (*e*) J.K. Lee, D.S. Yoo, E.S. Handy, and M.F. Rubner. Appl. Phys. Lett. **69**, 1686 (1996); (*f*) D.S. Yoo, A. Wu, J.K. Lee, and M.F. Rubner. Synth. Met. **85**, 1425 (1997); (*g*) W.Y. Ng, X. Gong, and W.K. Chan. Chem. Mater. **11**, 1165 (1999); (*h*) N. Najafi-Mohajeri and G.L. Nelson. Polymer, **42**, 7221 (2001); (*i*) P.G. Pickup. J. Mater. Chem. **9**, 1641 (1999); (*j*) Q. Wang, L. Liming, and L. Yu. Macromol. Rapid Commun. **21**, 723 (2000); (*k*) M. Sykora and T.J. Meyer. Chem. Mater. **11**, 1186 (1999).
3. (*a*) L.M. Dupray and T.J. Meyer. Inorg. Chem. **35**, 6299 (1996); (*b*) R.M. Leasure, T. Kajita, and T.J. Meyer. Inorg. Chem. **35**, 5962 (1996).
4. J.K. Lee, D Yoo, and M.F Rubner. Chem. Mater. **9**, 1710 (1997).
5. D.A. Foucher, B. Tang, and I. Manners. J. Am. Chem. Soc. **114**, 6246 (1992).
6. (*a*) S.J. Davies, B.F.G Johnson, M.S. Khan, and J. Lewis. J. Chem. Soc. Chem. Commun. 187 (1991); (*b*) H.B. Fyfe, M. Mlekuz, D. Zargarian, N.J. Taylor, and T.B. Marder. J. Chem. Soc. Chem. Commun. 188 (1991).
7. A.A. Farah and W.J. Pietro. Polym. Bull. **43**, 135 (1999).
8. A.A. Farah, J.G.C. Veinot, M. Najman, and W.J. Pietro. J. Macromol. Sci. Pure Appl. Chem. **A37**(11), 1507 (2000).
9. D.A. Friesen, T. Kajita, E. Danielson, and T.J. Meyer. Inorg. Chem. **37**, 2756 (1998).
10. (*a*) C.L. Fraser and A.P. Smith. J. Polym. Sci. Polym. Chem. **38**, 4707 (2000); (*b*) P.S. Corbin, M.P Webb, J.E. McAlvin, and C.L Fraser. Biomacromolecules, **2**, 223 (2001); (*c*) J.E. Collins and C.L. Fraser. Macromolecules, **31**, 6715 (1998); (*d*) A.P. Smith and C.L. Fraser. Macromolecules, **35**, 594 (2001)
11. (*a*) J.N. Younathan, S.F. McClanahan, and T.J. Meyer. Macromolecules, **22**, 1048 (1989); (*b*) G.F. Strouse, L.A. Worl, J.N. Younathan, and T.J. Meyer. J. Am. Chem. Soc. **111**, 9101 (1989); (*c*) L.A. Worl, G.F. Strouse, J.N. Younathan, S.M. Baxter, and T.J. Meyer. J. Am. Chem. Soc. **112**, 7571 (1990); (*d*) J.N. Younathan, W.E. Jones, Jr., and T.J. Meyer. J. Phys. Chem. **95**, 488 (1991); (*e*) S.M. Baxter, W.E. Jones, Jr., E. Danielson, L.A. Worl, G.F. Strouse, J.N. Younathan, and T.J. Meyer. Coord. Chem. Rev. **111**, 47 (1991); (*f*) W.E. Jones, Jr., S.M. Baxter, G.f. Strouse, and T.J. Meyer. J. Am. Chem. Soc. **115**, 7363 (1993); (*g*) T. Nakahira, Y. Inoue, K. Iwasaki, H. Tanigawa, Y. Kouda, S. Iwabuchi, and K. Kojima. Makromol. Chem. Rapid Commun. **9**, 13 (1988).
12. D.D Perrin, W.L.F. Armarego, and D.R. Perrin. Purification of laboratory chemicals. 2nd ed. Pergamon Press, Elmsford, New York. 1980.
13. B.P. Sullivan, D.J. Salmon, and T.J. Meyer. Inorg. Chem. **17**, 3334 (1978).
14. A.A. Farah and W.J. Pietro. Inorg. Chim. Acta. In press.
15. N.G. Connelly and W.E. Geiger. Chem. Rev. **96**, 877 (1996).
16. A.A. Farah, D.V. Stynes, and W.J. Pietro. Inorg. Chim. Acta, **343**, 295 (2003).
17. P.E. Rosevear and W.H.F. Sassi. J. Heterocycl. Chem. **8**, 483 (1971).
18. B.M. Peek, G.T. Ross, S.W. Edwards, G.J. Meyer, T.J. Meyer, and B.W. Erickson. Int. J. Pept. Protein Res. **38**, 114 (1991).
19. (*a*) T. Saegusa and E.J. Goethals. *In* Ring-opening polymerization. American Chemical Society, Washington, D.C. 1994. Chap 11; (*b*) A.J. Nijenhuis, D.W. Grijpma, and A.J. Pennings. Macromolecules, **25**, 6419 (1992).
20. (*a*) J.E. McAlvin and C.L. Fraser. Macromolecules, **32**, 1341 (1999); (*b*) J.J.S Lamba and C.L. Fraser. J. Am. Chem. Soc. **119**, 1801 (1997).
21. F.A. Cotton, G. Wilson, C.A. Murillo, and M. Bochmann. Advanced inorganic chemistry. 6th ed. John Wiley & Sons, New York. 1999.
22. (*a*) X. Wu and C.L. Fraser. Macromolecules, **33**, 7776 (2000); (*b*) X. Wu and C.L. Fraser. Macromolecules, **33**, 4053 (2000).
23. A. Heise, J.L. Hedrick, C.W. Frank, and R.D. Miller. J. Am. Chem. Soc. **21**, 8647 (1999).
24. S.J. Valenty, D.E. Behnken, and G.L. Gaines, Jr. Inorg. Chem. **18**, 2160 (1979).
25. J.E. McAlvin and C.L. Fraser. Macromolecules, **32**, 6925 (1999).

© 2004 NRC Canada

A new method of syntheses of 18-membered macrocyclic diphenyltin(IV) compounds and crystal structures of $\{Ph_2Sn[S(C_6H_3NO)O]\}_3 \cdot Y$ (Y = $2H_2O$ or $4C_6H_6$) and $\{Ph_3Sn[S(C_6H_3NO)O]SnPh_3(EtOH)\} \cdot [EtOH]$

Chunlin Ma, Qin Jiang, and Rufen Zhang

Abstract: Two diphenyltin(IV) compounds: $\{Ph_2Sn[S(C_6H_3NO)O]\}_3 \cdot Y$ (Y = $2H_2O$, **1**; $4C_6H_6$, **2**) have been unexpectedly obtained by the reactions of triphenyltin chloride with 2-mercaptonicotinic acid in the presence of Et_3N. However, by the reaction of the same reactants in the presence of EtONa, only a new triphenyltin(IV) compound ($\{Ph_3Sn[S(C_6H_3NO)O]SnPh_3(EtOH)\} \cdot [EtOH]$, **3**) was obtained. The X-ray analyses reveal that compounds **1** and **2** are trinuclear, 18-membered macrocyclic compounds while **3** is a dinuclear compound. Specially, π-π stacking interaction was recognized in crystals of compound **1**, which makes it a dimer. Co-crystallization was found in the crystals of all the three compounds **1**, **2**, and **3**, the co-crystallized solvent molecules are water, benzene, and ethanol molecules, respectively. A possible dephenylation mechanism of **1** and **2** was illustrated in detail.

Key words: triphenyltin, 2-mercaptonicotinic acid, dephenylation, macrocyclic, π-π stacking interaction, co-crystallization, crystal structure.

Résumé : Les réactions du chlorure de triphénylétain avec l'acide 2-mercaptonicotinique, en présence de Et_3N, conduisent à la formation inattendue de deux composés diphénylétain(IV): $\{Ph_2Sn[S(C_6H_3NO)O]\}_3 \cdot Y$ (Y = 2 H_2O, **1**; $4C_6H_6$, **2**). Toutefois, les mêmes réactifs en présence de EtONa ne conduisent qu'à la formation d'un seul nouveau composé triphénylétain(IV), le $\{Ph_3Sn[S(C_6H_3NO)O]SnPh_3(EtOH)\} \cdot [EtOH]$, **3**. Des études par diffraction des rayons X révèlent que les composés **1** et **2** sont des composés trinucléaires comportant des macrocycles à dix-huit chaînons alors que le composé **3** est un composé dinucléaire. On a particulièrement noté la présence d'une interaction d'empilement π-π dans les cristaux du composé, ce qui en fait un dimère. On a observé de la cocristallisation dans les cristaux de trois composés **1**, **2** et **3** dans lesquels les molécules de solvant cocristallisées sont respectivement des molécules d'eau, de benzène et d'éthanol. On a illustré en détail le mécanisme possible de la déphénylation des composés **1** et **2**.

Mots clés : triphénylétain, acide 2-mercaptonicotinique, déphénylation, macrocycles, interaction d'empilement π-π, cocristallisation, structure cristalline.

[Traduit par la Rédaction]

Introduction

Heterocyclic thiolates are ligands that contain at least one deprotonated heterocyclic thioamide group $(N\text{-}C\text{-}S)^-$. The aforementioned systems, which can act as monodentate, chelating, and bridging ligands, have been extensively studied in the field of coordination chemistry (1). In particular, many thionate-containing organotin complexes have been prepared and characterized due to their potential industrial applications and biological activities (2). Among them some exotic structures were obtained via self assembly determined by the types and geometries of the connecting ligands (3, 4), preference of tin atom for different donor atoms, as well as the competing specific intra- and intermolecular interactions such as H-bonds (5), π-π stacking interactions, and so on (6). The 2-mercaptonicotinic acid is an interesting ligand in this respect for its multiple coordination possibilities as well as its particular stereochemistry.

In our previous work, we studied the reactions of diphenyltin dichloride with the ligand and obtained two distinct trinuclear 18-membered macrocyclic compounds: $\{Ph_2Sn[S(C_6H_3NO)O]\}_3 \cdot 2.67H_2O$ and $\{Ph_2Sn[S(C_6H_3NO)O]\}_3 \cdot 4C_6H_6$ (7). To continue our investigation on organotin(IV) compounds, we carried out a series of reactions of triphenyltin chloride with the ligand to obtain some discrete triphenyltin(IV) compounds. To our surprise, we obtained three distinct compounds (**1**, **2**, and **3**) under different experimental conditions. Single crystal X-ray diffraction data reveal that **1** and **2** are trinuclear 18-membered macrocyclic diphenyltin(IV) compounds, while **3** is a dinuclear triphenyltin(IV) compound. Co-crystallization is found in crystals of all the three compounds **1**, **2**, and **3**, and the co-

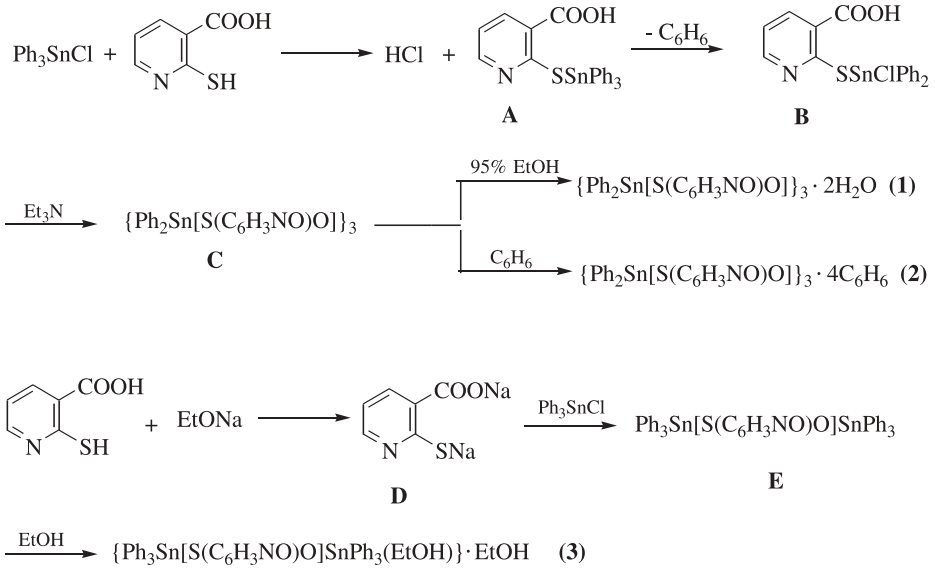
Received 4 October 2003. Published on the NRC Research Press Web site at http://canjchem@nrc.ca on 29 April 2004.

C. Ma.[1] Department of Chemistry, Liaocheng University, 34 Wenhua Road, Liaocheng, Shangdong 252059, P.R. China and Taishan University, Taian 271021, P.R. China.
Q. Jiang, and R. Zhang. Department of Chemistry, Liaocheng University, 34 Wenhua Road, Liaocheng, Shangdong 252059, P.R. China.

[1]Corresponding author (e-mail: macl@lctu.edu.cn).

 doi: 10.1139/V04-032 © 2004 NRC Canada

Scheme 1.



crystallized solvent molecules are water, benzene, and ethanol, respectively. It is worth noting that π-π stacking interaction was observed in crystals of compound **1**, which makes it a dimer. In this paper, we report the syntheses and characterizations of compounds **1**, **2**, and **3**. Crystal structures of the new compounds **1** and **3** are also given. The reaction procedure and possible dephenylation mechanism are shown in Scheme 1.

Experimental

Materials and measurements

Triphenyltin chloride and 2-mercaptonicotinic acid were commercially available, and they were used without further purification. The melting points were obtained with a Kofler micro melting point apparatus and are uncorrected. Infrared spectra were recorded on a Nicolet-460 spectrophotometer using KBr discs and sodium chloride optics. ^{1}H NMR spectra were obtained on a JEOL-FX-90Q NMR spectrometer, chemical shifts were given in ppm relative to Me_4Si in $CDCl_3$ solvent. Elemental analyses were performed with a PE-2400II apparatus.

Syntheses

Preparation of {Ph$_2$Sn[S(C$_6$H$_3$NO)O]}$_3$·2H$_2$O (1)

The reaction was carried out under a nitrogen atmosphere. Triphenyltin chloride (0.385 g, 1 mmol) and 2-mercaptonicotinic acid (0.155 g, 1 mmol) were added to the solution of absolute toluene (20 mL) in a Schlenk flask and stirred for 1.5 h at 90 °C. Then in the presence of triethyl amine (0.2 mL, 1mmol), the reaction mixture was stirred for 6 h at 110 °C, and then filtered. The filtrate was gradually removed by evaporation under vacuum until a solid product was obtained. The solid was then recrystallized from ethanol (95%) and the colorless block-like crystals of compound **1** were obtained.

Preparation of {Ph$_2$Sn[S(C$_6$H$_3$NO)O]}$_3$·4C$_6$H$_6$ (2)

The reaction was carried out under a nitrogen atmosphere. Triphenyltin dichloride (0.771 g, 2 mmol) and 2-mercaptonicotinic acid (0.155 g, 1 mmol) were added to the solution of absolute toluene (20 mL) in a Schlenk flask and stirred for 1.5 h at 90 °C. Then in the presence of triethyl amine (0.4 mL, 2 mmol), the reaction mixture was stirred for 6 h at 110 °C, and then filtered. The filtrate was gradually removed by evaporation under vacuum until a solid product was obtained. The solid was then recrystallized from benzene and the colorless block-like crystals of compound **2** were obtained.

Preparation of {Ph$_3$Sn[S(C$_6$H$_3$NO)O]SnPh$_3$(EtOH)}·[EtOH] (3)

2-Mercaptonicotinic acid (0.155g, 1 mmol) and sodium ethoxide (0.136 g, 2 mmol) were added to the solution of absolute benzene (20 mL) in a Schlenk flask and stirred for 0.5 h. After the triphenyltin chloride (0.771 g, 2 mmol) was added to the reactor, the reaction mixture was stirred for 20 h at 35 °C, and then filtered. The filtrate was gradually removed by evaporation under vacuum until a solid product was obtained. The solid was then recrystallized from ethanol. Colorless crystal compound **3** was formed.

Compound 1

mp > 200 °C (dec.). IR (KBr, cm^{-1}): υ(O-H) 3434, υ(C-H) 3066, υ_{as}(Sn-C) 270, υ_s(Sn-C) 232, υ(Sn-S) 290, υ(Sn-N) 448, υ(Sn-O) 587, υ(C=N) 1577, υ_{as}(COO) 1638, υ_s(COO) 1365. ^{1}H NMR ($CDCl_3$, ppm): 6.72–8.15 (m, 39H), 3.45 (s, 4H). Anal. calcd. for $C_{54}H_{43}N_3O_8S_3Sn_3$ (%): C 49.36, H 3.30, N 3.20, S 7.30; found: C 49.44, H 3.01, N 3.36, S 7.09.

Compound 2 (7)

mp > 200 °C (dec.). IR (KBr, cm^{-1}): υ(C-H) 3066, υ_{as}(Sn-C) 270, υ_s(Sn-C) 232, υ(Sn-S) 290, υ(Sn-N) 446, υ(Sn-O) 585, υ(C=N) 1577, υ_{as}(COO) 1638, υ_s(COO) 1365. ^{1}H NMR ($CDCl_3$, ppm): 6.74–8.10 (m, 63H). Anal. calcd. for

© 2004 NRC Canada

Table 1. Crystal data and structure refinement parameters for complexes **1** and **3**.

	Compound **1**	Compound **3**
Empirical formula	$C_{78}H_{63}N_3O_6S_3Sn_3$	$C_{46}H_{45}NO_4SSn_2$
Formula weight	1590.56	945.27
Crystal system	Triclinic	Monoclinic
Space group	*P*-1	*P*21/*n*
Unit cell dimensions		
a (Å)	9.770(6)	8.767(4)
b (Å)	18.68(3)	26.745(11)
c (Å)	20.80(3)	19.156(8)
α (°)	82.43 (3)	90
β (°)	81.65(3)	102.964(7)
γ (°)	75.25(2)	90
V (Å^3)	3614(10)	4377(3)
Z	2	4
D_c (g cm^{-3})	1.462	1.434
Crystal size (mm)	0.39 × 0.34 × 0.11	0.15 × 0.15 × 0.10
F(000)	1 596	1 904
Total reflections	18 324	25 550
Independent reflections	12 481	9 007
Data / restraints / parameters	12 481 / 0 / 826	9 007 / 2 / 432
Final *R* indices ($I > 2\sigma(I)$)	*R*1 = 0.0454	*R*1 = 0.0437
	*wR*2 = 0.0601	*wR*2 = 0.0637
R indices (all data)	*R*1 = 0.1113	*R*1 = 0.1394
	*wR*2 = 0.0715	*wR*2 = 0.0789
Goodness-of-fit	0.776	0.720
θ range for data colletion (°)	2.27–25.03	1.33–26.51
Absorption coefficient (mm^{-1})	1.163	1.230
Largest diff. peak and hole (e Å^{-3})	0.876 and –0.364	0.546 and –0.435

Table 2. Comparative structural data for **1** and **3** and related compounds.

	Bond distances (Å)				
Compounds	Sn—OR	O—Sn	C=O···Sn	C=O	Reference
$Me_3Sn(O_2CC_5H_4N)\cdot H_2O$	2.43(3)	2.18(2)			23
$(n\text{-}Bu)_3Sn$ (PMBP)$\cdot H_2O$	2.345(7)	2.224(6)		1.243(9)	24
$\{Ph_2Sn[S(C_6H_3NO)O]\}_3\cdot 2.67H_2O$		2.09[a]	3.22[a]	1.22[a]	7
$\{Ph_2Sn[S(C_6H_3NO)O]\}_3\cdot 4C_6H_6$		2.10[a]	3.19[a]	1.22[a]	7
$\{Ph_2Sn[S(C_6H_3NO)O]\}_3\cdot 2H_2O$ (**1**)		2.07[a]	3.17[a]	1.20[a]	This work
$\{Ph_3Sn[S(C_6H_3NO)O]SnPh_3(EtOH)\}_3\cdot[EtOH]$ (**3**)	2.468(4)	2.125(4)	3.107(4)	1.229(5)	This work

[a]Average data for all corresponding values.

$C_{78}H_{63}N_3O_6S_3Sn_3$ (%): C 58.90, H 3.99, N 2.64, S 6.04; found: C 59.04, H 3.71, N 2.80, S 5.84.

Compound 3

mp 80–82 °C. IR (KBr, cm^{-1}): υ(O-H) 3434, υ(C-H) 3063, υ(Sn-C) 630, 580, υ(Sn-S) 305, υ(Sn-N) 448, υ(Sn-O) 497, υ(C=N) 1575, υ_{as}(COO) 1635, υ_s(COO) 1366. ^{1}H NMR ($CDCl_3$, ppm): 6.70–8.10 (m, 33H), 3.21 (q, 4H), 1.10 (t, 6H). Anal. calcd. for $C_{46}H_{45}SnNO_4SSN_2$ (%): C 58.45, H 4.80, N 1.48, S 3.39; found: C 58.28, H 4.92, N 1.50, S 3.52.

X-ray structure determination

All X-ray crystallographic studies were done by using a Bruker Smart 1000 diffractometer fitted with graphite-monochromated MoKα radiation (λ = 0.71073 Å). The structure was solved by using direct methods and refined by a full-matrix least-squares procedure based on F^2 using the SHELXL-97 program system. All data were collected at a temperature of 298(2) K. Table 1 lists the crystal data and structure refinement parameters for complexes **1** and **3**. Table 2 lists the comparative structural data for **1** and **3** and related organotin(IV) compounds. The crystal structures and unit cells in the crystals of compounds **1** and **3** are shown in Fig. 1, Fig. 2, Fig. 3, and Fig. 4, respectively. Selected bond distances and angles are listed in Table 3 and Table 4, respectively.

Results and discussion

Syntheses aspects

It was surprising that we obtained three distinct products based on the same reactants under different conditions. When mixing triphenyltin chloride with 2-mercaptonicotinic

© 2004 NRC Canada

Fig. 1. Molecular structure of complex **1**.

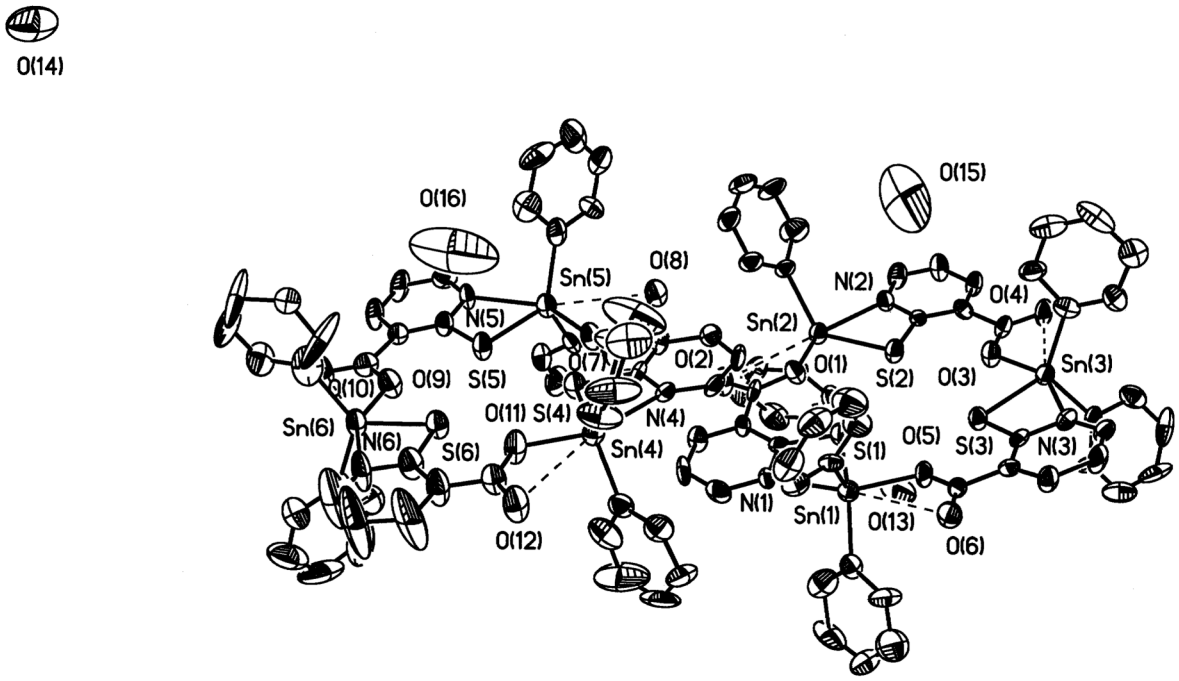
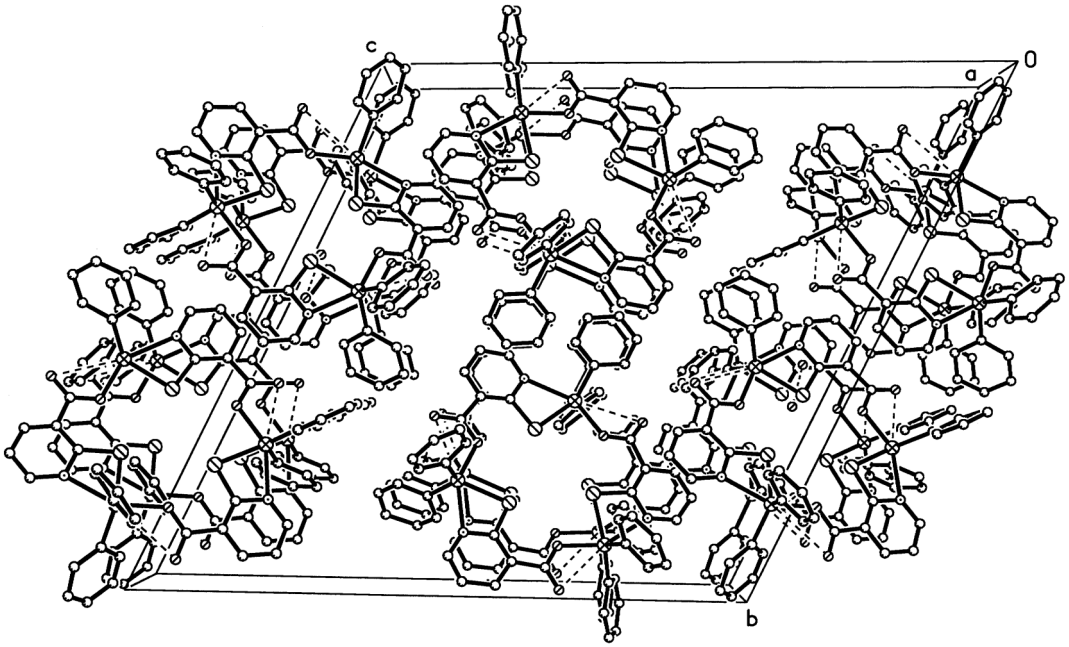


Fig. 2. Unit cell of complex **1**.



acid in the presence of Et_3N, we got two diphenyltin(IV) compounds: $\{Ph_2Sn[S(C_6H_3NO)O]\}_3 \cdot Y$ (Y = $2H_2O$ (**1**), $4C_6H_6$ (**2**)). However, by the reaction of the same reactants in the presence of EtONa, we got a triphenyltin(IV) compound: $\{Ph_3Sn[S(C_6H_3NO)O]SnPh_3(EtOH)\} \cdot [EtOH]$ (**3**).

According to the results of our experiments, together with those reported in the literature (8, 9), we can conclude that the reaction to produce compound **1** may undergo a three-step process as follows: first, the 2-mercaptonicotinic acid reacts with triphenyltin chloride to produce the triphenyltin complex **A**. Hydrogen chloride is the by-product from this reaction and more important is that it is the necessary reactant for dephenylation. Second, hydrogen chloride attacks the tin atom of **A** and makes one of the three Sn-C break, thus producing a diphenyltin chloride complex **B**. Third, in the presence of triethyl amine, molecules of complex **B** react with each other to produce a trinuclear 18-membered macrycyclic complex **C**. Complex **C** cannot exit discretely because of its weak interaction with solvent molecules. Therefore, when it is recrystallized from ethanol (95%), it co-crystallizes with double water molecules (**C**:H_2O) and produces compound **1**.

As far as compound **2** is concerned, the dephenylation is the same as that of **1**, what is different is its recrystallization.

© 2004 NRC Canada

Fig. 3. Molecular structure of complex **3**.

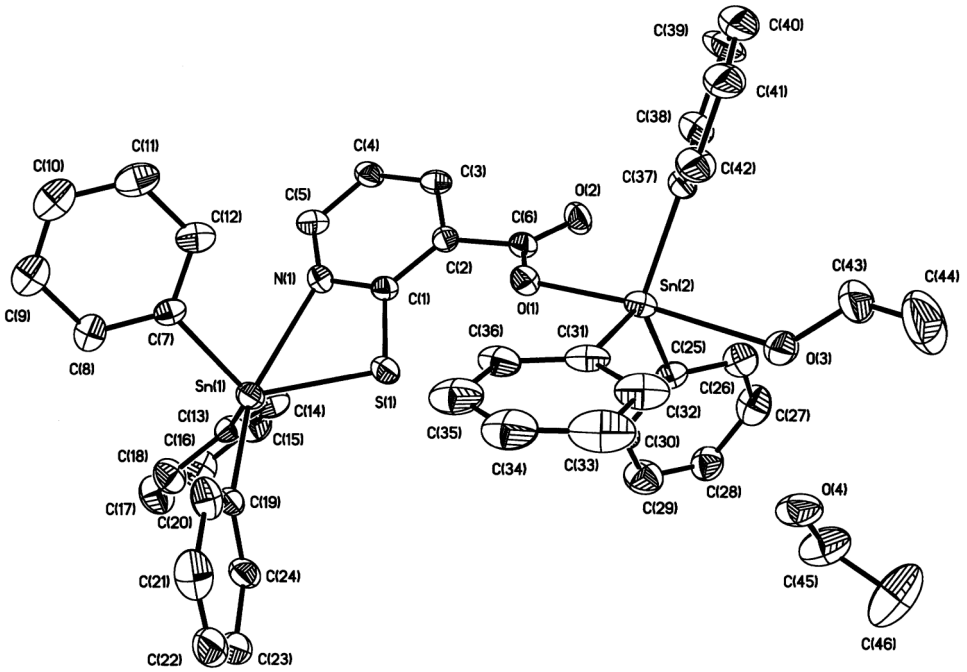
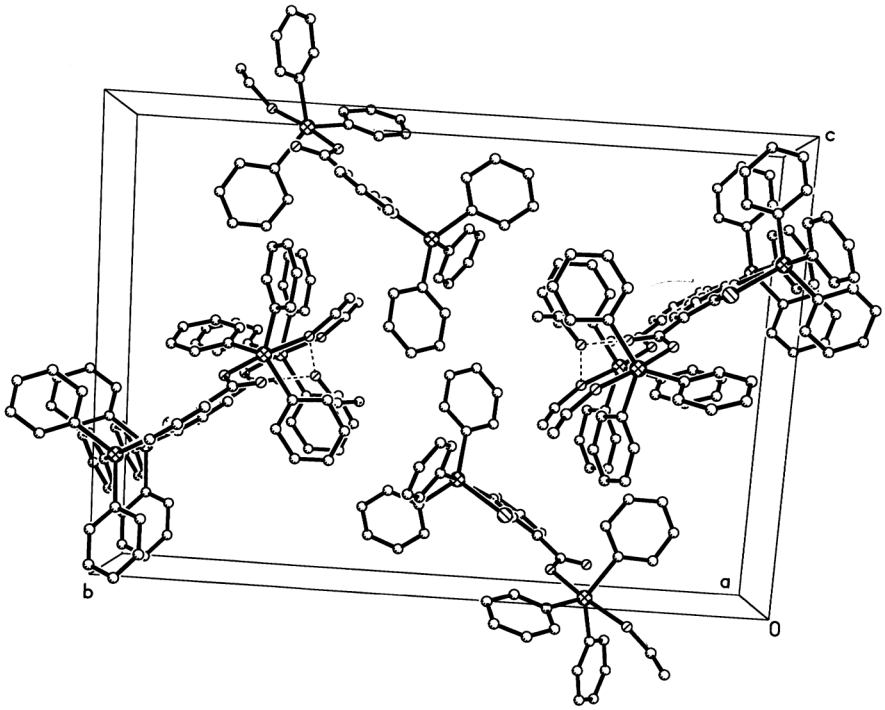


Fig. 4. Unit cell of complex **3**.



Compound **2** is recrystallized from benzene with four benzene molecules (**C**:C_6H_6) in each crystal unit. And as the X-ray data shows, complex **2** is the same compound as realized by the reaction of diphenyltin dichloride and 2-mercaptonicotinic acid (7).

Comparing the synthetic mechanism of **1** and **2**, we found that it does not matter what molar ratio of the ligand and triphenyltin chloride was applied, but the production of hydrogen chloride is crucial to break the Sn—C bond. A similar synthetic strategy has been used for preparation of mixed trialkyltin derivatives (9).

Concerning the reaction that affords compound **3**, a possible mechanism is presented in following description. In the presence of sodium ethoxide, 2-mercaptonicotinic acid converts into its sodium salt **D**, and then **D** reacts with triphenyltin chloride in the ratio of 1:2 to afford dinuclear triphenyltin complex **E**. When **E** recrystallizes from ethanol, because of the coordination between ethanol and one tin

© 2004 NRC Canada

Table 3. Selected bond lengths (Å) and angles (°) for compound 1.

Bond lengths	(Å)	Bond angles	(°)
Sn(1)—O(5)	2.079(7)	C(25)-Sn(1)-C(19)	124.5(5)
Sn(1)—C(19)	2.132(11)	C(25)-Sn(1)-S(1)	116.3(4)
Sn(1)—S(1)	2.448(3)	N(1)-Sn(1)-S(1)	63.8(2)
Sn(2)—C(37)	2.063(12)	C(37)-Sn(2)-C(31)	118.5(4)
Sn(2)—C(31)	2.124(10)	C(37)-Sn(2)-S(2)	116.8(4)
Sn(2)—N(2)	2.459(9)	C(43)-Sn(3)-C(49)	122.6(6)
Sn(3)—O(3)	2.064(7)	C(43)-Sn(3)-S(3)	117.0(4)
Sn(3)—C(49)	2.110(11)	S(3)-Sn(3)-N(3)	63.6(3)
Sn(3)—N(3)	2.464(8)	C(73)-Sn(4)-C(79)	123.5(5)
Sn(4)—O(11)	2.077(8)	C(73)-Sn(4)-S(4)	113.8(4)
Sn(4)—C(79)	2.103(13)	C(85)-Sn(5)-C(91)	126.6(5)
Sn(4)—S(4)	2.435(3)	C(85)-Sn(5)-S(5)	113.9(3)
Sn(5)—O(7)	2.098(7)	S(5)-Sn(5)-N(5)	64.0(2)
Sn(5)—C(91)	2.121(14)	C(97)-Sn(6)-C(103)	129.2(6)
Sn(5)—N(5)	2.447(9)	C(97)-Sn(6)-S(6)	114.3(4)
Sn(6)—O(9)	2.047(7)	O(5)-Sn(1)-N(1)	149.6(3)
Sn(6)—C(103)	2.168(12)	C(19)-Sn(1)-S(1)	116.8(3)
Sn(6)—N(6)	2.425(11)	S(2)-Sn(2)-N(2)	63.8(2)
Sn(1)—C(25)	2.100(13)	O(1)-Sn(2)-N(2)	144.9(3)
Sn(1)—N(1)	2.396(9)	C(31)-Sn(2)-S(2)	121.2(3)
Sn(1)—O(6)	3.258(8)	O(3)-Sn(3)-N(3)	146.5(3)
Sn(2)—O(1)	2.112(7)	C(49)-Sn(3)-S(3)	114.7(4)
Sn(2)—S(2)	2.417(4)	N(4)-Sn(4)-S(4)	64.2(2)
Sn(2)—O(2)	3.189(8)	O(11)-Sn(4)-N(4)	149.4(3)
Sn(3)—C(43)	2.109(12)	C(79)-Sn(4)-S(4)	118.7(4)
Sn(3)—S(3)	2.428(3)	O(7)-Sn(5)-N(5)	148.0(3)
Sn(3)—O(4)	3.021(7)	C(91)-Sn(5)-S(5)	117.4(4)
Sn(4)—C(73)	2.088(13)	S(6)-Sn(6)-N(6)	64.0(3)
Sn(4)—N(4)	2.432(9)	O(9)-Sn(6)-N(6)	149.5(4)
Sn(4)—O(12)	3.182(8)	C(103)-Sn(6)-S(6)	112.5(4)
Sn(5)—C(85)	2.099(12)		
Sn(5)—S(5)	2.426(3)		
Sn(5)—O(8)	3.212(9)		
Sn(6)—C(97)	2.058(17)		
Sn(6)—S(6)	2.420(4)		
Sn(6)—O(10)	3.143(9)		

Table 4. Selected bond lengths (Å) and angles (°) for complex **3**.

Bond lengths	(Å)	Bond angles	(°)
Sn(1)—C(7)	2.123(5)	C(7)-Sn(1)-C(13)	116.0(2)
Sn(1)—C(19)	2.160(5)	C(13)-Sn(1)-S(1)	118.49(17)
Sn(1)—N(1)	2.638(4)	C(19)-Sn(1)-N(1)	159.31(17)
Sn(2)—C(37)	2.116(6)	C(37)-Sn(2)-C(25)	128.8(2)
Sn(2)—O(1)	2.125(4)	C(25)-Sn(2)-C(31)	121.0(2)
Sn(2)—O(3)	2.468(4)	C(7)-Sn(1)-S(1)	111.96(18)
N(1)—C(5)	1.334(6)	C(19)-Sn(1)-S(1)	98.19(14)
O(4)—C(45)	1.405(8)	S(1)-Sn(1)-N(1)	61.13(11)
Sn(2)—O(2)	3.107(4)	C(37)-Sn(2)-C(31)	107.4(2)
O(4)—H(3)	1.76	O(1)-Sn(2)-O(3)	174.33(13)
O(4)—H(4)	0.82		
Sn(1)—C(13)	2.135(6)		
Sn(1)—S(1)	2.4389(17)		
Sn(2)—C(25)	2.123(6)		
Sn(2)—C(31)	2.125(6)		
N(1)—C(1)	1.337(6)		
O(1)—C(6)	1.284(6)		
O(2)—C(6)	1.229(5)		
O(3)—C(43)	1.369(8)		
O(3)—H(3)	0.93		
O(2)—H(4)	1.89		

atom of **E**, and also because of the hydrogen bonds between {$Ph_3Sn[S(C_6H_3NO)O]SnPh_3(EtOH)$} and EtOH, compound **3** was formed.

IR data

Comparing the IR spectra of the free ligands with compounds **1**, **2**, and **3**, several obvious differences are apparent. First, the band at 2642 cm^{-1}, which appears in the spectra of the free ligand as the ν(S-H) vibration, is absent in those of compounds **1**, **2**, and **3**, thus indicating metal–ligand bond formation through this site. Correspondingly, the strong absorptions at 290 cm^{-1} for both compounds **1** and **2**, and 305 cm^{-1} for compound **3**, which is absent in the spectrum of the ligand, are assigned to the Sn-S stretching mode of vibration, and all these values are consistent with that detected for a number of organotin(IV)-sulfur derivatives (10–12). Second, the ν(C=N) band, occurring at 1577 cm^{-1} for both compounds **1** and **2**, and at 1575 cm^{-1} for compound **3**, are considerably shifted towards a lower frequency with respect to that of the free ligand (1622 cm^{-1}), confirming the coordination of the heterocyclic N to the tin. The stretching frequency is lowered owing to the displacement of electron density from the N to Sn atom, thus resulting in the weakening of the C=N bond as reported in the literature (13). Therefore, the weak- or medium-intensity bands at 448, 446, and 448 cm^{-1} for compounds **1**, **2**, and **3**, respectively, can be assigned to Sn-N stretching vibrations. Third, the ν_{as}(COO) and ν_{as}(COO) occur at 1638 and 1365 cm^{-1} for both compounds **1** and **2** and at 1635 and 1366 cm^{-1} for compound **3**. The corresponding Δν values are 273, 273, and 269 cm^{-1}, meaning that the carboxyl groups in all three compounds are monodentate (14). Consequently, the new bands appearing at 585, 587, and 497cm^{-1} for compounds **1**, **2**, and **3**, respectively, have been assigned to Sn—O bond vibrations.

Also, the broad strong absorption at 3434 cm^{-1}, appearing in both spectras of compounds **1** and **3**, but absent in the spectra of compound **2**, has been assigned to ν(O-H) of H_2O and EtOH, respectively, which demonstrates the difference in their co-crystallized solvent molecules.

^{1}H NMR data

^{1}H NMR showed that the signal of the -SH proton in the spectrum of the ligand is absent in both compounds **1** and **3**, indicating the removal of the SH proton and the formation of Sn—S bonds. The signal of the -OH proton is also absent for the spectra of compound **2** but appears in both spectras of compounds **1** and **3**, which further proved the difference in their co-crystallized molecules. The information agrees well with what the IR data have revealed.

Molecular structures

Single crystal X-ray diffraction data revealed that **1** and **2** are trinuclear 18-membered macrocyclic compounds, while **3** is a dinuclear triphenyltin compound. Co-crystallization is

© 2004 NRC Canada

found in crystals of all the three compounds **1**, **2**, and **3**, which may be realized by face-to-face/edge-to-face π-π interactions and aromatic C-H···O (for benzene), or by C=O···H (for H_2O) weak hydrogen-bonding interactions as reported in the literature (15–17). It is worth noting that that the X-ray data revealed that compound **2** is the same compound as reported previously (7), thus in this paper, we only give some comparative structural data of compound **2**, together with those of **1** and **3** and related analogous compounds, which are shown in Table 2. Detailed discussion for the structures of compound **1** and **3** follows.

Structures $\{Ph_2Sn[S(C_6H_3NO)O]\}_3 \cdot 2H_2O$ (1)

As shown in Fig. 1, compound **1** contains a symmetrical trinuclear macrocyclic component with the deprotoned ligand 2-mercaptonicotinic acid bridging the adjacent tin atoms, which can be given the formula $\{Ph_2Sn[S(C_6H_3NO)O]\}_3$. The repeated unit is $Ph_2Sn[S(C_6H_3NO)O]$, in which the primary bondings of the ligand to tin occur through its sulfur atom and endocyclic carboxyl oxygen atom, while the nitrogen atom of the ligand is involved in a fifth weaker bonding interaction with tin. All the tin atoms have the same geometry as a distorted cis-trigonal bipyranid. The corresponding bond lengths and angles are listed in Table 3. All these values are consistent with those of analogous diphenyltin macrocycles, and are especially, similar to those of the compound $\{Ph_2Sn[S(C_6H_3NO)O]\}_3 \cdot 2.67H_2O$ (see Table 2).

It is worth noting that besides the difference in the number of co-crystallized water molecules, an obvious difference between the crystal structures of compound **1** and $\{Ph_2Sn[S(C_6H_3NO)O]\}_3 \cdot 2.67H_2O$ resides in that **1** is a dimer staked by a π-π staking interaction between heterocyclic rings from adjacent $\{Ph_2Sn[S(C_6H_3NO)O]\}_3$. Each pair of neighboring heterocyclic rings in the dimer are almost parallel with the dihedral angle being 4.9° (ring N(1), C(1)-C(5) and ring N(4), C(55)-C(59)), and separated by 3.49 vs. 3.58 Å (the distances between the ring centroids). The shortest distance of C(3) to ring C(55)-C(59) is 3.42 Å and that of C(56) to ring C(1)-C(5) is 3.41 Å. All theses values are consistent with that of the benzene polymer in theoretical studies (3.4 Å) (18) and approaches that of imidazole–imidazole (3.29–3.47 Å) (19, 20), indicating the presence of significant face-to-face π-π stacking interactions (21, 22).

Structure of $\{Ph_3Sn[S(C_6H_3NO)O]SnPh_3(EtOH)\} \cdot [EtOH]$ (3)

As Fig. 3 shows, compound **3** is a dinuclear triphenyltin(IV) co-crystallized compound with the formula $\{Ph_3Sn[S(C_6H_3NO)O]SnPh_3(EtOH)\} \cdot [EtOH]$. The co-crystallization is realized by hydrogen bonds between carboxyl oxygen and ethanol molecules. Both tin atoms (Sn(1) and Sn(2)) have the same geometry as a distorted cis-trigonal bipyramid but their environments are quite different.

For Sn(1), there are four primary bonds to the centered tin atom: three to the phenyl groups and one to the sulfur atom. In addition, there exists an interaction between the tin and the nitrogen atoms. The Sn(1)—N(1) bond length (2.638(4) Å) is a little longer than the sum of the covalent radii of the tin and nitrogen atoms, but much shorter than that of the van der Waals radii of the two atoms (2.15 and 3.75 Å, respectively) (23). Including the tin–nitrogen interaction, the geometry at Sn(1) becomes a distorted cis-trigonal bipyramid with one of the phenyl carbon (C(19)) and nitrogen (N(1)) atoms in the axial sites. Another two phenyl carbon (C(7) and C(13)) and sulfur (S(1)) atoms occupy the equatorial plane. The sum of the angles encircling the Sn(1) atom in the trigonal plane is 346.4°. The Sn(1) atom is 0.48 Å displaced out of the basal plane in the direction of C(19). Due to being part of a chelate ligand, the angle S(1)-Sn(1)-N(1) is not 90° but 61.13(11)°. Thus, the N(1) cannot occupy exactly the corresponding trans axial position of C(19) and the angle for C(19)-Sn(1)-N(1) is 159.31(17)°. The Sn(1)—S(1) bond length (2.4389(17) Å) lies in the range recently reported for triphenyltin thiolates (2.405–2.48 Å) (24–26), close to the sum of the covalent radii of the tin and sulfur atoms (2.42 Å) (27).

For Sn(2), the configuration about the tin atom is also a distorted cis-triagonal bipyramid but it is the three phenyl groups that occupy the equatorial sites. The valence extension is performed via the oxygen atom of ethanol (O(3)), which coordinats to tin along with the deprotonated oxygen of the monodentate carboxyl group of 2-mercaptonicotinic acid (O(1)). The Sn(2) atom is displaced from the C_3 plane for the phenyl carbon atom by only 0.08 Å, reflecting the strength of the bond between the metal and the solvent. The near linearity of the angle O(1)-Sn(2)-O(3) (174.33(13)°) also reflects the strength of coordination of the solvate molecule.

The two Sn—O bonds (Sn(2)-O(1) (2.125(4)) and Sn(2)-O(3) (2.468(4) Å)) are typical of their type (Table 3). In related diorganotin systems, the C-O distance increases upon coordination of the oxygen atom to the tin atom (28–30). However, in compound **3** the unique monodentate nature of the carboxyl group of the ligand means that the C(6)-O(2) distance of 1.229(5) Å has the lowest value yet observed among the relevant trialkyltin analogues.

The carboxyl oxygen atom O(2) is thus not involved in any intramolecular interactions involving tin. This fact may be partly explained on the basis of hydrogen bonding. Each coordinated ethanol atom serves as the acceptor of a hydrogen bond with an adjacent ethanol molecule, and this ethanol molecule also forms an acceptor of the hydrogen bond with the uncoordinated oxygen donor O(2) of the carboxyl group. The corresponding bond lengths for the hydrogen bonding are O(4)···H(4) = 0.82 Å, H(4)···O(2) = 1.89 Å, O(2)···O(4) = 2.70 Å, and O(3)···H(3) = 0.93 Å, H(3)···O(4) = 1.76 Å, O(3)···O(4) = 2.65 Å. Due to the existence of the two kinds of H-bond, the co-crystallized compound **3** was thus obtained at the ratio of 1:1 ($\{Ph_3Sn[S(C_6H_3NO)O]SnPh_3(EtOH)\}$:EtOH).

Supplementary material

Atomic coordinates, thermal parameters, and bond lengths and angles for complexes **1** and **3** may be purchased from the Directory of Unpublished Data, Document Delivery, CISTI, National Research Council Canada, Ottawa, ON K1A 0S2, Canada (http://www.nrc.ca/cisti/irm/unpub_e.shtml for information on ordering electronically). CCDC 216749 and 216173 contain the crystallographic data for this manuscript. These data can be obtained, free of charge, via www.ccdc.cam.ac.uk/conts/retrieving.html (or from the

© 2004 NRC Canada

Cambridge Crystallographic Data Centre, 12 Union Road, Cambridge CB2 1EZ, UK; fax +44 1223 336033; or deposit@ccdc.cam.ac.uk).

Acknowledgements

We thank the National Natural Foundation, P.R. China (20271025) and the National Natural Foundation of Shandong Province, P.R. China for financial support of this work.

References

1. E.S. Raper. Coord. Chem. Rev. **153**, 199 (1996).
2. S.K. Duboy and U. Roy. Appl. Organomet. Chem. **17**, 3 (2003).
3. C.L. Ma, F. Li, D.Q. Wang, and H.D. Yin. J. Organomet. Chem. **667**, 5 (2003).
4. R. Cea-Olivares, O. Jiménez-Sandoval, G. Espinosa-Pérez, and C. Silvestru. J. Organomet. Chem. **484**, 33 (1994).
5. A. Tarassoli, T. Sedaghat, B. Neumüller, and M. Ghassemzadeh. Inorg. Chim. Acta, **318**, 15 (2001).
6. C.L. Ma, Q. Jiang, and R.F. Zhang. Can. J. Chem. **81**, 825 (2003).
7. C.L. Ma, Q. Jiang, and R.F. Zhang. J. Organomet. Chem. **678**, 148 (2003).
8. X.Q. Song, A.L. Xie, and X.N. Fang. Chin. Chem. Lett. **9**, 977 (1998).
9. F. Yuan, Y. Huang, and O, Xie. Appl. Organomet. Chem. **16**, 660 (2002).
10. C.V.R. Moura, A.P.G. de Sousa, M.R. Silva, A.R. Abras, M. Horner, A.J. Bortoluzzi, C.A.L. Filgueiras, and J.L. Wardell. Polyhedron, **18**, 2961 (1999).
11. P.G. de Sousa, R.M. Silva, A. Cesar, J.L. Wardell, J.C. Huffman, and A. Abras. J. Organomet. Chem. **605**, 82 (2000).
12. R. Schmiedgen, F. Huber, H. Preut, G. Ruisi, and R. Barbieri. Appl. Organomet. Chem. **8**, 397 (1994).
13. C. Santini, M. Pellei, G.G. Lobbia, C. Pettinari, A. Drozdov, and S. Troyanov. Inorg. Chim. Acta, **325**, 20 (2001).
14. M. Ba, X.Z. He, Q.L. He, Z.J. Zhang, and B.D. Liu. Chem. J. Chin. Univ. **9**,1465 (1997).
15. F.M. Tabellion, S.R. Seidel, A.M. Arif, and P.J. Stang. J. Am. Chem. Soc. **123**, 11 982 (2001).
16. A.J. Blake, N.R. Champness, A.N. Khlobystov, D.A. Lemenovskii, W.-S. Li, and M. Schröder. Chem. Commun. 1339 (1997).
17. M.J. Calhorda. Chem. Commun. 801 (2000).
18. R.L. Jaffe and G.D. Smith. J. Chem. Phys. **105**, 2780 (1996).
19. N.W. Alcock, P.R. Barker, J.M. Haider, M.J. Hannon, C.L. Painting, Z. Pikramenou, E.A. Plummer, K. Rissanen, and P. Saarenketo. J. Chem. Soc. Dalton Trans. 1447 (2000).
20. M. Du, Z.L. Shang, X.B. Leng, and X.H. Bu. Polyhedron, **20**, 3065 (2001).
21. (*a*) T. Kuroda-Sowa, M. Munakata, H. Matsuda, S. Akiyama, and M. Maekawa. J. Chem. Soc. Dalton Trans. 2201 (1995); (*b*) J. Dai, M. Yamamoto, T. Kuroda-Sowa, M. Maekawa, Y. Suenaga, and M. Munakata. Inorg. Chem. **36**, 2688 (1997).
22. (*a*) M. Munakata, L.P. Wu, M. Yamamoto, T. Kuroda-Sowa, and M. Maekawa. J. Am. Chem. Soc. **118**, 3117 (1996); (*b*) T. Sugimori, N. Ohata, K. Koiwai, A. Odani, and O. Yamauchi. Inorg. Chem. **36**, 576 (1997).
23. P.J. Smith (*Editor*). Chemistry of tin. 2nd ed. Blackie, London. 1998.
24. J.S. Casas, A. Castineiros, E.G. Martinez, A.S. Gonzales, A. Sánchez, and J. Sordo. Polyhedron, **16**, 795 (1997).
25. B.D. James, R.F. Magee, W.C. Patalighug, B.W. Skelton, and A.H. White. J. Organomet. Chem. **467**, 51 (1994).
26. J. Bravo, M.B. Cordero, J.S. Casas, A. Sánchez, J. Sordo, E.E. Castellano, and J. Zukerman-Schpector. J. Organomet. Chem. **482**, 147 (1994).
27. J.E. Huheey. Inorganic chemistry: Principles of structure and reactivity. 3rd ed. Harper International SI Edition, Cambridge. 1983. p. 258.
28. T.S.B. Baul, S. Dhar, E. Rivarola, F.E. Smith, R. Butcher, X. Song, M. McCain, and G. Eng. Appl. Organomet. Chem. **17**, 261 (2003).
29. P.G. Harrison, R.C. Phillips, and F.A. Richards. J. Organomet. Chem. **182**, 37 (1979).
30. M.F. Mahon, K.C. Molloy, B.A. Omotowa, and M.A. Mesubi. J. Organomet. Chem. **511**, 227 (1996).

© 2004 NRC Canada

A novel self-complementary three-dimensional inorganic network organized by H-bond dimers of inorganic chains — Synthesis and crystal structure of $(C_6H_{16}N_2)[Zn(HPO_4)_2]$

Xian-Ming Zhang, Chan-Juan Bai, Yan-Li Zhang, and Hai-Shun Wu

Abstract: A novel organic-templated zincophosphate, namely $(C_6H_{16}N_2)[Zn(HPO_4)_2]$, was hydrothermally synthesized and X-ray single-crystal structural analysis reveals that the anions $[Zn(HPO_4)_2]^{2-}$, which have square-twisted chains containing corner-sharing four-rings of alternating ZnO_4 and PO_4 tetrahedra, are assemblied via self-complementary strong and symmetrical hydrogen-bonding $R_2^2(8)$ synthons between the phosphate groups into three-dimensional hydrogen bond frameworks featuring three-dimensional intersecting pseudochannels. The doubly protonated 2,5-dimethylpiperazinium cations are attached to the three-dimensional inorganic framework via N-H··O hydrogen bonds to strengthen the 3-D network.

Key words: hydrogen bond dimer, intersecting pseudochannel, linear chain.

Résumé : On a réalisé une synthèse hydrothermique d'un nouveau zincophosphate à patron organique, soit le $(C_6H_{16}N_2)[Zn(HPO_4)_2]$. Une étude par diffraction des rayons montre que les anions $[Zn(HPO_4)_2]^{2-}$ sont des chaînes carrées déformées comportant quatre cycles de tétraèdres de ZnO_4 et de PO_4 qui occupent les coins en alternance, qui sont reliées par de fortes liaisons hydrogènes symétriques et autocomplémentaires de synthons $R_2^2(8)$ entre les groupes phosphates et qui forment un squelette tridimensionnel de liaisons hydrogènes comportant des pseudocanaux tridimensionnels qui présentent des intersections. Les cations 2,5-diméthylpipérazinum doublement protonés sont attachés au squelette inorganique tridimensionnel par le biais de liaisons hydrogènes N-H··O qui renforcissent le réseau tridimensionnel.

Mots clés : dimère par liaison hydrogène, pseudocanal avec intersection, chaîne linéaire.

[Traduit par la Rédaction]

Introduction

Metal phosphates have been of intensive interest due to structural diversity and potential applications in catalysis, adsorption, and ion exchange (1–6). A subclass of metal phosphates is zinc phosphates, which are generally synthesized by hydrothermal method with organic amine as the structural directing agent (7–30). Although most zinc phosphates have layered or three-dimensional structures (7–24), several zinc phosphates with one-dimensional structures have also been investigated. The one-dimensional structures of zinc phosphates include linear chains formed by corner-shared four-membered rings (25–28) and ladders formed by edge-shared four-membered rings (29). Recently, the zero-dimensional monomer comprising the four-membered ring has also been isolated (25, 30). Despite the importance of layered and three-dimensional networks in practical applications, the zero-dimensional monomer and linear chains are more important from the hydrothermal mechanism point of view because the zero-dimensional monomer and linear chains are thought as possible primary and secondary building units (SBUs) for layered and three-dimensional networks (25, 30). In particular, Rao et al. (25, 30) prepared a layered zinc phosphate via mild heating of monomeric zinc phosphate containing only the four-membered ring as well as a family of zinc phosphates of different hierarchy containing piperazine template.

In the formation of zinc phosphate frameworks, the protonated organic amines play an important role. These amines could act as structure-directing agents, or merely fill the available voids and stabilize the structure through hydrogen bonding and other interactions. The charge, shape, and size of the organic amine cations have significant influences on the structures of the framework. One-dimensional simple linear zinc phosphate chains $[Zn(HPO_4)_2]^{2-}$ (25, 26, 28) possess corner-shared ZnO_4 and HPO_4 tetrahedra (Fig. 1*b* and Scheme 1) and are generally stabilized by van der Waals interactions or by strong hydrogen bonds with the organic templates. Each HPO_4^{2-} group in the $[Zn(HPO_4)_2]^{2-}$ chain has one pendent O-H and one pendent oxo that can be the potential donor and acceptor groups for the hydrogen bond

Received 16 November 2003. Published on the NRC Research Press Web site at http:canjchem@nrc.ca on 3 May 2004.

X.-M. Zhang,[1] C.-J. Bai, Y.-L. Zhang, and H.-S. Wu. School of Chemistry & Material Science, Shanxi Normal University, Linfen, Shanxi 041004, China.

[1]Corresponding author (e-mail: zhangxm@dns.sxtu.edu.cn).

 doi: 10.1139/V04-026 © 2004 NRC Canada

Scheme 1. Schematic view of the assembly of $[Zn(HPO_4)_2]^{2-}$ chains into a 3-D supramolecular inorganic open framework via strong and symmetrical hydrogen-bonding dimers.

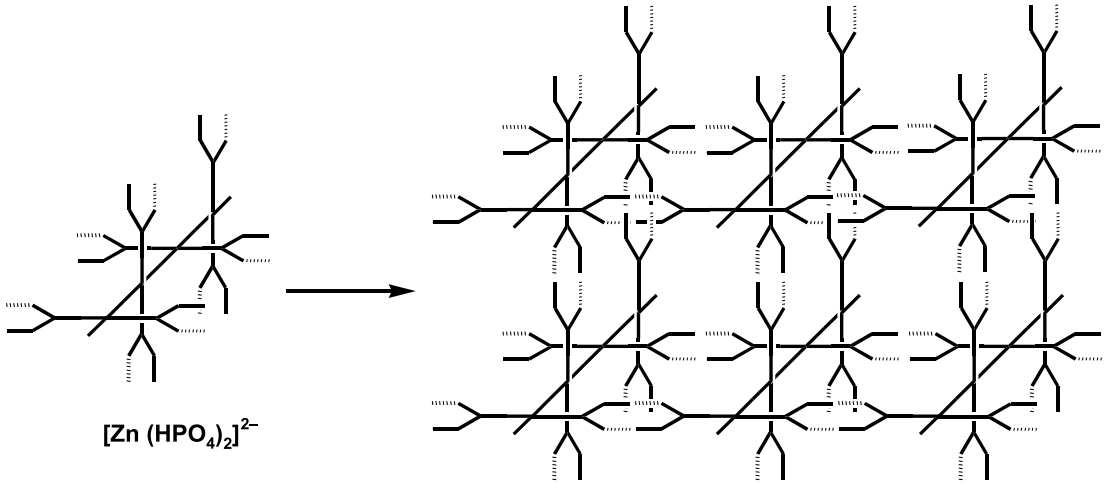
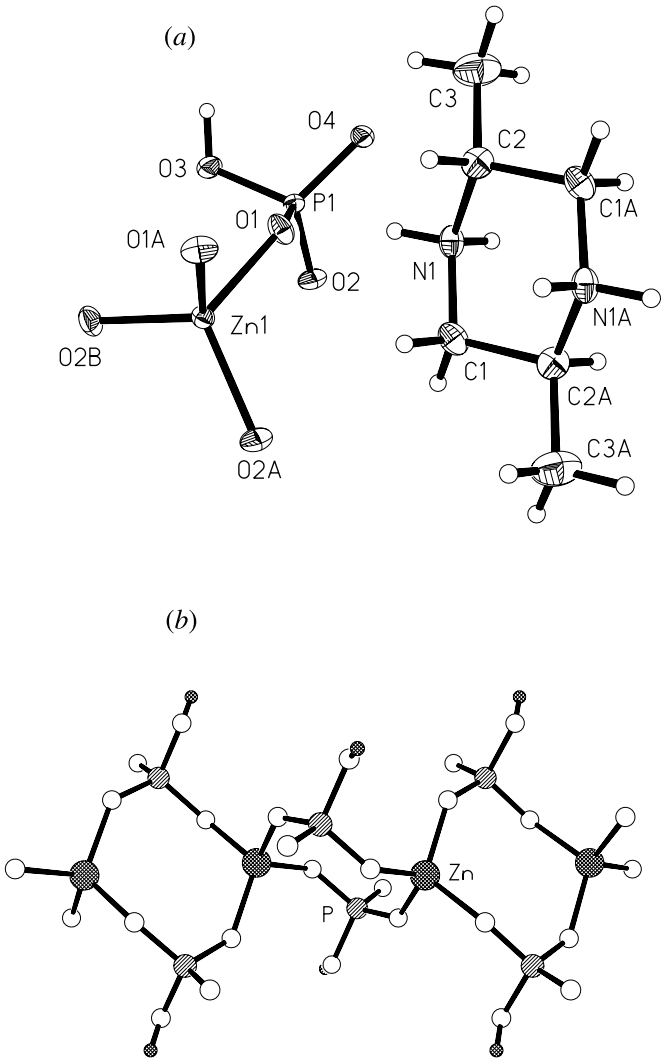


Fig. 1. Pespective views of atomic coordination environments showing the atom-labeling scheme and 35% thermal ellipsoids (*a*), and the chain-like structure (*b*) in **1**.



or the hydrogen dimer. Besides, the $[Zn(HPO_4)_2]^{2-}$ chain has a suitable geometry in which a pair of HPO_4^{2-} groups from each four-membered ring has the same orientation but is perpendicular to adjacent pairs of HPO_4^{2-} groups. Furthermore, Clearfield's studies on organo phosphonic acids demonstrated that deprotonated organo phosphonic acids having potential donor and acceptor groups for the hydrogen bond results in very strong and predictable structural aggregates through symmetrical O-H··O hydrogen dimers (31). Therefore, it occurred to us that we may be able to assemble $[Zn(HPO_4)_2]^{2-}$ chains into very stable three-dimensional inorganic networks (Scheme 1) by selecting a suitable template via strong hydrogen bond dimers. The expectation was realized in the synthesis of the 2,5-dimethylpiperazine templated compound $(C_6H_{16}N_2)[Zn(HPO_4)_2]$, which has a three-dimensional inorganic supramolecular network and three-dimensional pseudochannels occupied by organic guest cations.

Experimental

Synthesis of $(C_6H_{16}N_2)[Zn(HPO_4)_2]$ (1)

A mixture of $Zn(MeCO_2)_2{\cdot}2H_2O$ (0.220 g, 1 mmol), H_3PO_4 (0.2610 g, 85%, 2 mmol), 2,5-dimethylpiperazine (dmpip) (0.180 g, 1.5 mmol), and water (10 mL) in a molar ratio of 1:2:1.5:550 was stirred and transferred and sealed in a 23 mL teflon-lined stainless container that was heated to 150 °C for 120 h. After cooling to room temperature at the rate of 5 ° C/h, colourless needle-like crystals in a single phase were recovered in 60% yield. IR (KBr, cm^{-1}): 3433w, 3359m, 3224w, 2956m, 2603m, 1501m, 1395m, 1360s, 1307(w), 1085(s), 1008(s), 720(s), 643(w), 497(m). Anal. calcd. for $C_6H_{18}N_2O_8P_2Zn$ (**1**): C 19.29, H 4.86, N 7.50; found: C 19.19, H 4.94, N 7.46.

Physical measurements

Elemental analyses were performed on a PerkinElmer 240 elemental analyzer. The FT-IR spectra were recorded from KBr pellets in the range 400–4000 cm^{-1} on a Nicolet 5DX spectrometer.

© 2004 NRC Canada

Table 1. Crystal data and structure refinement for **1**.

Empirical formula	$C_6H_{18}N_2O_8P_2Zn$
Formula mass	373.54
Colour, habit	Colorless block
Crystal dimensions (mm)	0.41 × 0.25 × 0.20
Crystal system	Monoclinic
Space group	*C*2/*c*
Z	4
a (Å)	12.097(2)
b (Å)	13.685(3)
c (Å)	7.912(2)
β (°)	96.362(6)
Collection ranges	$-15 \le h \le 15$; $-17 \le k \le 11$; $-9 \le l \le 10$
T (K)	293(2)
V (Å^3)	1309.0(5)
D_m	Not measured
D_x (Mg m^{-3})	1.895
Radiation	Mo Kα (λ = 0.71073 Å)
μ (mm^{-1})	2.157
Absorption correction (T_{min}, T_{max})	0.6146, 0.8637
Intensity decay	None
Crystallization solvent	Water
θ_{max} (°)	27.10
Measured reflections	4028
Independent reflections	1429 (R_{int} = 0.019)
Reflections with $I > 2\sigma(I)$	1341
Parameters	88
Refinement on F^2	H atoms constrained
$R[F^2 > 2\sigma(F^2)]$	0.0207
$R[F^2$, all data]	0.0226
$wR(F^2)$	0.0525
$(\Delta/\sigma)_{max}$	0.000
Extinction coefficient	0.0040(3)
Largest diff. peak and hole ($\Delta\rho_{max}$, $\Delta\rho_{min}$) (e Å^{-3})	0.74, –0.295

Table 2. Selected bond lengths (Å) and angles (°) for **1**.

Bond lengths (Å)	
Zn(1)—O(2a)	1.9181(14)
Zn(1)—O(1)	1.9531(14)
P(1)—O(2)	1.5149(14)
P(1)—O(1)	1.5328(14)
O(2)—Zn(1b)	1.9181(14)
Zn(1)—O(2b)	1.9181(14)
Zn(1)—O(1c)	1.9531(14)
P(1)—O(4)	1.5183(14)
P(1)—O(3)	1.5753(14)
Bond angles (°)	
O(2a)-Zn(1)-O(2b)	112.50(9)
O(2b)-Zn(1)-O(1)	115.62(7)
O(2b)-Zn(1)-O(1c)	108.35(6)
O(2)-P(1)-O(4)	112.46(8)
O(4)-P(1)-O(1)	109.42(8)
O(4)-P(1)-O(3)	109.18(8)
P(1)-O(1)-Zn(1)	136.25(9)
O(2a)-Zn(1)-O(1)	108.35(6)
O(2a)-Zn(1)-O(1c)	115.62(7)
O(1)-Zn(1)-O(1c)	95.48(9)
O(2)-P(1)-O(1)	111.24(8)
O(2)-P(1)-O(3)	105.53(8)
O(1)-P(1)-O(3)	108.88(8)
P(1)-O(2)-Zn(1b)	135.28(9)

Note: Symmetry codes are: (*a*) *x*, –*y* + 1, *z* + 1/2; (*b*) –*x*, –*y* + 1, –*z*; (*c*) –*x*, *y*, –*z* + 1/2.

X-ray crystallography

Diffraction intensities were collected at 293 K on a Bruker Smart 1000 diffractometer (MoKα, l λ = 0.71073 Å). The structure was solved with the direct methods and refined with the full-matrix least-squares technique (SHELX-97) (32). Analytical expressions of neutral atom scattering factors were employed, and anomalous dispersion corrections were incorporated. All non-hydrogen atoms were refined anistropically and all hydrogen atoms were refined isotropically. Hydrogen atoms of organic ligands were geometrically placed; the hydrogen of phosphate was found from the difference Fourier map. The crystallographic data are listed in Table 1 and the selected interatomic distances and angles are given in Table 2.

Results and discussion

X-ray single crystal structural analysis revealed that the asymmetric unit contains one Zn(II) ion, one HPO_4^{2-} group, and 0.5 of a dimpip cation. As expected, the structure consists of a one-dimensional linear $[Zn(HPO_4)_2]^{2-}$ chain constructed from corner-shared four-membered rings and each of the four-membered rings is formed by two phosphate groups and two zinc ions via oxygen sharing. The Zn ion is tetrahedrally coordinated to four oxygen atoms from four HPO_4 tetrahedra with Zn—O bond lengths of 1.9181(14) and 1.9531(14) Å. The O-Zn-O bond angles are in the range of 95.48(9)–115.62(7)° (avg. for O-Zn-O is 109.3°). The phosphorus atom has P—O bond lengths in the range of 1.5149(14)–1.5753(14) Å. Each Zn atom in **1** is connected to four neighboring P atoms but each P atom is connected to two neighboring zinc atoms via Zn-O-P linkages (Zn-O-P, 136.25(9)° and 135.28(9)°). A framework structure of $Zn(PO_4)_2$ would result in a net framework charge of –4 and the presence of $[C_6N_2H_{16}]$ would account for the +2 charge arising from the diprotonation of dmpip. The excess negative charge of –2 is then balanced by the protonation of the PO_4 moieties, as given in the formula. Bond valence sum calculations (33) and a larger P(1)—O(3) bond distance of 1.5753(14) Å indicate that O(3) is attached by hydrogen (28). The hydrogen atom of -O(3)-H group was also found in the difference Fourier maps.

The most interesting feature of **1** is its 3-D supramolecular inorganic network constructed from the assembly of linear $[Zn(HPO_4)_2]^{2-}$ chains via strong and symmetrical hydrogen-bonded $R_2^2(8)$ dimers (19) between a pair of phosphate groups as shown in Fig. 2*a* and Table 3, which can be regarded as the supramolecular synthons. The terminal -O(3)-H and O(4) groups in PO_4 involve the formation of the

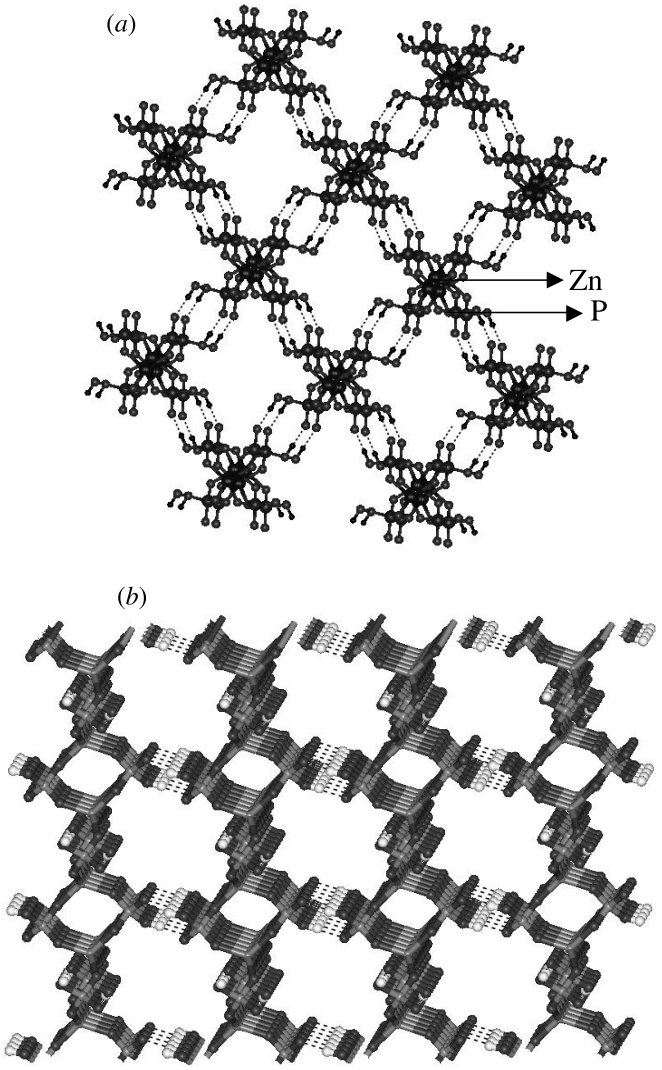
© 2004 NRC Canada

Table 3. Distances (Å) and angles (°) of possible hydrogen bond interactions in **1**.

Donor-H··acceptor	D-H (Å)	H··A (Å)	D··A (Å)	D-H··A (°)
N(1)-H(1C)··O(1)	0.900	1.875	2.768(2)	170.9
N(1)-H(1D)··O(4a)	0.900	1.816	2.708(2)	171.1
O(3)-H(1E)··O(4b)	0.850	1.710	2.605(2)	173.3

Note: Symmetry codes are: (*a*) –*x*, *y*, 1/2 – *z*; (*b*) 1/2 – *x*, *y*, –*z*.

Fig. 2. Pespective view of the self-complementary three-dimensional hydrogen bond framework without H_2dmpip molecules approximately running along the *c*-axis (*a*), and [110] direction (*b*). The balls from large to small represent Zn, P, O, and H atoms, respectively.



synthons with a short O(3)··O(4) distance (2.605 Å) and an approximately linear O(3-H··O(4) angle (173° based on restrained refinement of the hydrogen). These synthons extend the one-dimensional chains into a very rigid three-dimensional cooperative hydrogen-bonded network featuring three-dimensional intersecting pseudochannels. Two types of the pseudochannels run along the [110] and [–100] directions and have the same shape, whereas the third type runs along the *c*-axis direction. The organic dmpip cations occupy the pseudochannels and are attached to the three-dimensional inorganic framework via N-H··O hydrogen bonds to further strengthen the 3-D network (Fig. 3). Each nitrogen atom of dmpip is dually hydrogen bonded to the phosphate oxygen atoms with N(1)··O(1) and N(1)··O(4) distances of 2.767(2) and 2.708(2) Å, respectively. The strong symmetrical hydrogen bonds have stabilization energies up to 10 times greater than those of normally occurring hydrogen bonds (31). Hydrogen bonding synthons are important in the design of persistent supramolecular arrays because they have good strength, directionality, cooperativity, and complementarity (34). In **1**, the hydrogen bonding synthons play an important role in the stabilization of the three-dimensional network. The powder XRD pattern in combination with thermogravimetric analyses show compound **1** as a phase-ordered solid and is stable in air below 180 °C.

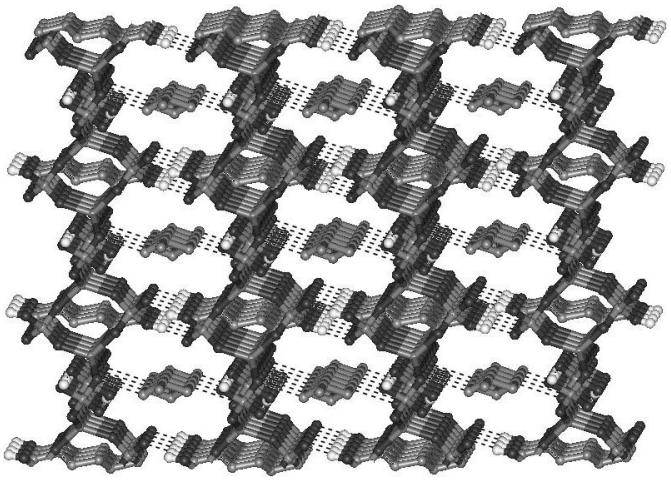
The overall structure of **1** is different than that of other linear zinc phosphates with *N*,*N*′-dimethylpiperazine, piperazine, and 2-methylpiperazine as templates, although they all have the same anionic $[Zn(HPO_4)_2]^{2-}$ chain (25–28). In other linear phosphates, HPO_4^{2-} groups only form the hydrogen bonds with organic amine and (or) lattice water molecules but no self-complementary hydrogen bond dimers exist between adjacent HPO_4^{2-} groups. Thus, the self-complementary three-dimensional inorganic network is a unique behavior of **1** among linear zinc phosphates.

The structure of **1** is also related to some piperazine-templated three-dimensional compounds ($[C_4N_2H_{12}][Zn_2(HPO_4)_3]$, $[C_4N_2H_{12}][Zn_2(PO_4)(H_{1.5}PO_4)_2]$, and $[C_4N_2H_{12}][Co_{0.14}Zn_{1.86}(PO_4)(H_{1.5}PO_4)_2]$) (25, 30, 35, 36) because they all contain square-twisted linear $[M(HPO_4)_2]^{2-}$ chains. In these piperazine-templated compounds, $[M(HPO_4)_2]^{2-}$ chains are linked by covalent bonds into a three-dimensional inorganic network. In contrast, $[Zn(HPO_4)_2]^{2-}$ chains are linked by hydrogen bond dimers (synthons) into a three-dimensional hydrogen bond network.

The linear chains are more important than layered and three-dimensional zincophosphate networks from the forming mechanism point of view because they are thought of as SBUs for layered and three-dimensional networks. Rao and et al. (25, 30) have recently isolated a monomeric zinc phosphate formulated as $[Zn_2(HPO_4)_2(H_2PO_4)_4]^{4-}$, which is the only known monomer of the zinc phosphate family containing only the four-membered ring and can transform into a layered structure on mild heating. The authors thought that the transformation of monomeric $[Zn_2(HPO_4)_2(H_2PO_4)_4]^{4-}$ into layers involves a simple chain $[Zn_2(HPO_4)_2(H_2PO_4)_2]^{2-}$, which is formed by losing the H_2PO_4 groups and the congregating of monomeric $[Zn_2(HPO_4)_2(H_2PO_4)_4]^{4-}$ units (30). Similarly, Oliver et al. (37) proposed a linear chain with corner-shared four-membered rings to be the fundamental building unit in the aluminophosphate framework solids. The difference between Rao and Oliver in the treatment of linear

© 2004 NRC Canada

Fig. 3. Pespective view of the self-complementary three-dimensional hydrogen bond framework approximately running along the [110] direction with H_2dmpip molecules.



chains only lies on secondary building units and fundamental building units. As for the formation of $[Zn(HPO_4)_2]^{2-}$ in the work, it may be the result of simply losing H_3PO_4 and the congregating of monomeric $[Zn_2(HPO_4)_2(H_2PO_4)_4]^{4-}$ units if the $[Zn_2(HPO_4)_2(H_2PO_4)_4]^{4-}$ units are universal primary building units in the formation of zinc phosphates.

$$n[Zn_2(HPO_4)_2(H_2PO_4)_4]^{4-} \xrightarrow{-2nH_3PO_4} [Zn(HPO_4)_2]_{2n}^{4n-}$$

It is also interesting to think about the further loss of H_2PO_4 groups and the congregating of the three-dimensional inorganic hydrogen bond network of **1**. If a pair of HPO_4^{2-} groups lose one $H_2PO_4^{2-}$ without destroying the symmetry of the network of **1**, which is accompanied by the further coordination of PO_4 groups, the network of **1** will transform into a fully four-connected and highly negatively charged three-dimensional network with analcime topology (38).

Supplementary data

Supplementary data may be purchased from the Directory of Unpublished Data, Document Delivery, CISTI, National Research Council Canada, Ottawa, ON K1A 0S2, Canada (http://www.nrc.ca/cisti/irm/unpub_e.shtml for information on ordering electronically). CCDC 215985 contains the crystallographic data for this manuscript. These data can be obtained, free of charge, via www.ccdc.cam.ac.uk/conts/retrieving.html (or from the Cambridge Crystallographic Data Centre, 12 Union Road, Cambridge CB2 1EZ, UK; fax +44 1223 336033; or deposit@ccdc.cam.ac.uk).

Acknowledgements

This work was financially supported by Shanxi Normal University.

References

1. A.K. Cheetham, G. Ferey, and T. Loiseau. Angew. Chem. Int. Ed. **38**, 3268 (1999).
2. S.-H. Feng and R.-R. Xu. Acc. Chem. Res. **34**, 239 (2001).
3. C.N.R. Rao, S. Natarajan, A. Choudhury, S. Neeraj, and A.A. Ayi. Acc. Chem. Res. **34**, 80 (2001).
4. R.H. Jones, J. Chen, G. Sankay, and J.M. Thomas. Zeolites and related microporous material: State of the art. Elsevier, New York. 1994.
5. W.M. Meier, D.H. Olson, and Ch. Baerlocher. Atlas of zeolite structure types. Elsevier, Boston. 1996.
6. P.Y. Feng, X. Bu, and G.D. Stucky. Nature (London), **388**, 735 (1997).
7. P. Feng, X. Bu, and G.D. Stucky. Angew. Chem. Int. Ed. Engl. **34**, 1745 (1995).
8. G.Y. Yang and S.C. Sevov. J. Am. Chem. Soc. **121**, 8389 (1999).
9. Y. Song, J. Yu, G. Li, Y. Li, Y. Wang, and R. Xu. Chem. Commun. 1720 (2002).
10. A. Choudhury, S. Natarajan, and C.N.R. Rao. J. Solid State Chem. **157**, 110 (2001).
11. W.T.A. Harrison, M.L.F. Phillips, W. Clegg, and S.J. Teat. J. Solid State Chem. **148**, 433 (1999).
12. R. Vaidyanathan, S. Natarajan, and C.N.R. Rao. J. Mater. Chem. **9**, 2789 (1999).
13. W.T.A. Harrison and M.L.F. Philips. Chem. Mater. **9**, 1837 (1997).
14. S. Neeraj, S. Natarajan, and C.N.R. Rao. New J. Chem. **23**, 303 (1999).
15. D. Chidambaram, S. Neeraj, S. Natarajan, and C.N.R. Rao. J. Solid State Chem. **147**, 154 (1999).
16. W.T.A. Harrison, Z. Bircsak, L. Hannooman, and Z. Zhang. J. Solid State Chem. **136**, 93 (1998).
17. A. Choudhury, S. Neeraj, S. Natarajan, and C.N.R. Rao. J. Mater. Chem. **11**, 1537 (2001).
18. P. Feng, X. Bu, and G.D. Stucky. J. Solid State Chem. **125**, 243 (1996).
19. R.W. Broach, R.L. Bedard, S.G. Song, J.J. Pluth, A. Bram, C. Riekel, and H.-P. Weber. Chem. Mater. **11**, 2076 (1999).
20. Y. Liu, L. Na, G. Zhu, F.-S. Xio, W. Pang, and R. Xu. J. Solid State Chem. **149**, 107 (2000).
21. S. Neeraj, S. Natarajan, and C.N.R. Rao. J. Solid State Chem. **150**, 417 (2000).
22. W.T.A. Harrison and M.L.F. Phillips. Chem. Commun. 2771 (1996).
23. S. Neeraj, S. Natarajan, and C.N.R. Rao. Chem. Commun. 165 (1999).
24. S. Neeraj, S. Natarajan, and C.N.R. Rao. Chem. Mater. **11**, 1390 (1999).
25. C.N.R. Rao, S. Natarajan, and S. Neeraj. J. Am. Chem. Soc. **122**, 2810 (2000).
26. A.N. Christensen, A. Bareges, R.B. Nielsen, R.G. Hazell, P. Norby, and J.C. Hanson. J. Chem. Soc. Dalton Trans. 1611 (2001).
27. W.T.A. Harrison, T.M. Nenoff, T.E. Cier, and G.D. Stucky. Inorg. Chem. **31**, 5395 (1992).
28. S. Fleith, L. Josien, A. Simon-Masseron, V. Gramlich, and J. Patarin. Solid State Sci. **4**, 135 (2002).
29. A. Choudhury, S. Natarajan, and C.N.R. Rao. Inorg. Chem. **39**, 4295 (2000).
30. C.N.R. Rao, S. Natarajan and S. Neeraj. J. Solid State Chem. **152**, 302 (2000).

© 2004 NRC Canada

31. C.V.K. Sharma and A. Clearfield. J. Am. Chem. Soc. **122**, 4394 (2000).
32. G.M. Sheldrick. SHELX-97 [computer program]. Göttingen University, Göttingen, Germany. 1997.
33. I.D. Brown and D. Aldermatt. Acta Crystallogr. Sect. B, **B41**, 244 (1984).
34. M.J. Krische and M.J. Lehn. Struct. Bonding (Berlin), **96**, 3 (2000).
35. X. Chen, Y. Zhao, R. Wang, M. Li, and Z. Mai. J. Chem. Soc. Dalton Trans. 3092 (2002).
36. M. Wiebcke. Microporous Mesoporous Mater. **54**, 331(2002).
37. S. Oliver, A. Kuperman, and G.A. Ozin. Angew. Chem. Int. Ed. **37**, 46 (1998).
38. J.V. Smith. Chem. Rev. **88**, 149 (1988).

© 2004 NRC Canada

Stereoselective synthesis of naturally occurring unsaturated amide alkaloids by a modified Ramberg–Bäcklund reaction

Yang Li, Yu Zhang, Zhi Huang, Xiaoping Cao, and Kun Gao

Abstract: A convenient and rapid approach for the synthesis of naturally occurring unsaturated amide alkaloids **1a**–**1n** by the recently developed one-flask Ramberg–Bäcklund reaction is described. The starting material was alcohol **3**, which was transformed into thiolacetate **4** using the Mitsunobu reaction. In situ cleavage of acetyl moiety of **4**, followed by alkylation of the resulting thiol with appropriate chloroacetamide **5**, provided the sulfide **6**. Oxidation of sulfide **6** gave the corresponding sulfone **2**. Treatment of the sulfone **2** with the dibromodifluoromethane in the presence of alumina-supported potassium hydroxide in dichloromethane solution afforded unsaturated amide alkaloids **1a**–**1n**. To the best of our knowledge, the synthesis of **1e** and **1i** was reported for the first time.

Key words: synthesis, unsaturated amide alkaloids, Ramberg–Bäcklund reaction.

Résumé : Faisant appel à la réaction de Ramberg–Bäcklund monotope développée récemment, on a mis au point une méthode pratique et rapide de réaliser la synthèse des alcaloïdes naturels **1a**–**1n** comportant une fonction amide non saturée. Le produit de départ est l'alcool **3** qui est transformé en thiolactate **4** à l'aide d'une réaction de Mitsunobu. Le clivage in situ de la portion acétyle du composé **4**, suivi d'une alkylation à l'aide du chloroacétamide **5** approprié du thiol qui en résulte conduit à la formation du sulfure **6**. L'oxydation du sulfure **6** fournit la sulfone **2**. Le traitement de la sulfone **2** à l'aide de dibromodifluorométhane, en présence d'hydroxyde de potassium supporté par de l'alumine dans le dichlorométhane, conduit à la formation des alcaloïdes recherches **1a**–**1n**. À notre connaissance, il s'agit des premières synthèses des composés **1e** et **1i**.

Mots clés : synthèse, alcaloïdes comportant une fonction amide non saturée, réaction de Ramberg–Bäcklund.

[Traduit par la Rédaction]

Introduction

Various unsaturated amide alkaloids bearing pyrrolidine, isobutyl, and piperidine moieties are interesting targets of numerous synthetic investigations, presumably because of their significant biological activities (1, 2). They are distributed widely in the plant kingdom. The series of compounds mostly isolated from the genus *Piper*, which is used in folk medicine, are amides of unsaturated alkanoic or arylalkanoic acids. These compounds display antiinflammatory, antidiarrheal, insecticidal, antifungal, antimalarial, as well as 5-lipoxygenase and cyclooxygenase-1 inhibitory activities (2). For example, piperine was the first amide to be isolated from the *Piper* species. Pharmacological studies reported that piperine had antipyretic, analgesic, and antiinflammatory activities (1*j*), and that it could also inhibit gastric emptying and gastrointestinal transit in rats and mice (2*c*). Sarmentine was isolated from *P. sarmentosum*, which showed larvicidal activity against second stage larva of *Toxocara canis* (1*a*). Recently, pellitorine and neopellitorine B were isolated from *Artemisia dracunculus*, which showed insectical activity against *Sitophilus oryzae* and *Rhyzopertha dominica* (1*i*). Pellitorine was also found as having antimalarial properties (2*a*), which can be explained by the tendency of the nucleic acids of the parasites to react with the α,β-unsaturated carbonyl moiety of pellitorine in a Michael addition fashion (2*a*). Pellitorine and piperine also exhibited antifungal activity against *Cladosporium sphaerospermum* (2*b*). Thus, it was concluded that the presence of a methylenedioxyphenyl and an unsaturated alkanoic amide group in the compounds may be crucial for high biological activity. The fact that unsaturated amide alkaloids occur naturally in very limited amounts in some rather inaccessible plant species has stressed the need for good synthetic methods. A perusal of numerous reviews on the chemistry of the unsaturated amide alkaloids reveals that the field is mainly dominated by two general strategies for the assembly of the unsaturated amide alkaloids skeleton units. One approach makes use of amidation with various amines of the stereochemically defined unsaturated acids or esters that are prepared by: (*a*) the

Received 29 October 2003. Published on the NRC Research Press Web site at http://canjchem@nrc.ca on 5 May 2004.

Y. Li, Y. Zhang, Z. Huang, X. Cao,[1] and K. Gao.[2] State Key Laboratory of Applied Organic Chemistry, College of Chemistry and Chemical Engineering, Lanzhou University, Lanzhou, 730000, P. R. China.

[1]Corresponding author (e-mail: caoxplzu@163.com).
[2]Corresponding author (e-mail: miaozm@lzu.edu.cn).

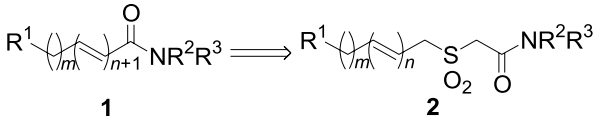
 doi: 10.1139/V04-028 © 2004 NRC Canada

Wittig type approaches (3*a*–3*d*); (*b*) Pummerer-type reaction intermediates (3*e*); (*c*) Still cross-coupling reactions (3*f*); (*d*) palladium-phase transfer co-catalyzed couplings of vinylic iodide and acrylate (3*g*); (*e*) allyl acetates eliminating the elements of acetic acid in the presence of *O*,*N*-bis(trimethylsilyl) acetamide and molybdenum hexacarbonyl (3*h*); (*f*) rearrangement of the corresponding 2-ynoic esters in the presence of Ph_3P (3*i*); and (*g*) addition of carbon nucleophiles to aldehyde tosylhydrazones of aromatic and heteroaromatic compounds (3*j*). Another method entails the anchoring of the amide unit to the end of a variable olefinic double bond that involves: (*a*) the Wittig methodology (4*a*); (*b*) Knoevenagel condensations (4*b*–4*c*); (*c*) thermal SO_2 extrusion from *cis*-2,5-disubstituted 2,5-dihydrothiofene-1,1-dioxides (4*d*); (*d*) a double elimination of β-acetoxy sulfones (4*e*); (*e*) further functionalization containing the sulfonyl and the cyano group (4*f*); (*f*) isomerization of 2-ynoic amides catalyzed by ruthenium or iridium complexes (4*g*); (*g*) hydrozirconation of the terminal acetylene using Schwartz's reagent ($Cp_2ZnCl(H)$) followed by Pd(0)-catalyzed coupling with the iodo-amide (4*h*–4*i*); (*h*) an easily accessible bifunctional dienyl compound based upon a double selective electrophilic substitution followed by coupling reaction (4*j*); and (*i*) the use of δ-tosyl dienamide as δ-acyldienyl cation equivalents (4*k*). Although numerous methods have been reported for the synthesis of unsaturated amide alkaloids, there still remains the necessity and urgency to discover milder and newer methods for the construction of the series of unsaturated amide alkaloids. We recently reported a new protocol of the Ramberg–Bäcklund reaction to effect the transformation of the α- and α′-hydrogen bearing sulfones directly into alkenes (5). From this investigation emerged the highly stereoselective generation of a new (*E*)-double bond with the retention of the configurations of the preexisting ones. We became interested in establishing a convenient and stereoselective new route to synthesize unsaturated amide alkaloids (**1**) (Scheme 1), without resorting to the prior preparation of the α-halosulfone precursors in a separate step (6). In this paper we extend this methodology to the synthesis of unsaturated amide alkaloids (**1**). The preparation of 13 natural products and one related analogue, as well as their full details are reported.

Results and discussion

Scheme 1 outlines the strategy we pursued in the quest for stereo-pure unsaturated amide alkaloids **1**. We wished to prepare it from functional sulfones **2**. The strategy shown in Scheme 1 was thought to be feasible because of the successful application of our procedure to the formation of conjugated trienes from diallylic sulfones (5*b*), conjugated tetraenes from allylic dienylic sulfones (5*d*), and linear and cyclic enediynes from dipropargylic sulfones (5*e*). Our synthetic method was also applied to the synthesis of natural products containing a triene unit such as galbanolenes. The procedure reported here started with a functional sulfones **2**, with the amide group and the functional carbon chain already in place and the new double bond to be realized by our modified Ramberg–Bäcklund procedure. This disconnection approach relied on the stereocontrolled synthesis of the functional sulfones **2**, which was in turn prepared by a

Scheme 1. Strategy of constructed unsaturated amide alkaloids **1**.



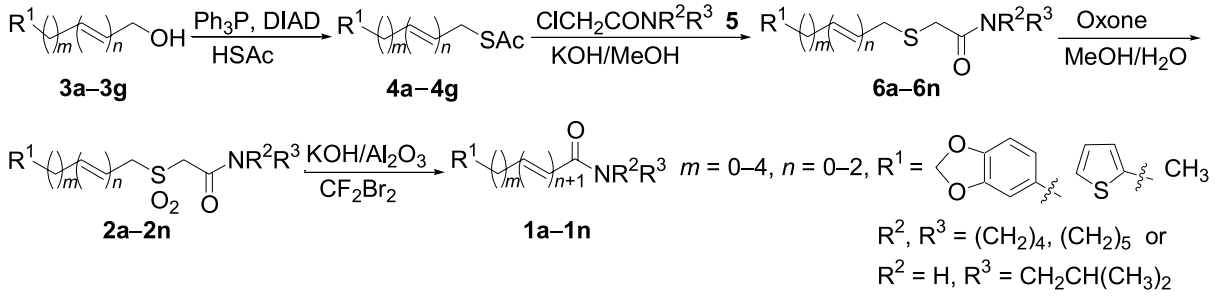
stereocontrolled preparation of alkenyl or alkyl thiolacetates **4** and chloroacetamides **5** (7). The coupling reaction between stereodefined thiolacetates **4** to pure chloroacetamides **5** assembled the sulfides **6**, from which the corresponding sulfones **2** could be obtained after oxidation. This procedure invariably demanded a stereoselective preparation of alcohols **3**, the common intermediate for the requisite thiolacetates **4** (Scheme 2). Several synthetic methods were tried. In the end, the alcohols **3** were secured by the Wittig reaction, and followed by reduction.

The alcohols **3** (R^1 = piperonyl, thienyl, or methyl) were prepared according to the Scheme 3. The commercially available aldehyde **7**, **8**, **9**, or **10** was used as a starting material for the preparation of the alcohols **3**. Treatment of **7**, **8**, or **10** with $Ph_3P{=}CHCO_2Et$ afforded an ester with good (*E*)-selectivity, which was followed by regioselective reduction of the ester moiety with aluminum hydride (AlH_3, from $LiAlH_4$:$AlCl_3$ = 3:1) to furnish the alcohols **3a**, **3e**, or **3g** (76%, 66%, 51%), respectively. The alcohol **3a** was hydrogenated, oxidized with pyridinium chlorochromate (PCC), then its carbon chain elongated by a Wittig reaction ($Ph_3P{=}CHCO_2Et$), and followed by a reduction of the resulting ester with aluminum hydride selectively to give the primary alcohol **3b** in 59% yield. On the other hand, treatment of aldehyde **7** or **9** with $Ph_3P{=}CHCH{=}CHCO_2Et$ followed by a reduction of the ester moiety with aluminum hydride gave alcohol **3c** or **3f** in 60% and 68% yield, respectively. Hydrogenation of **3c** afforded the saturated alcohol **3d** in nearly quantitative yield.

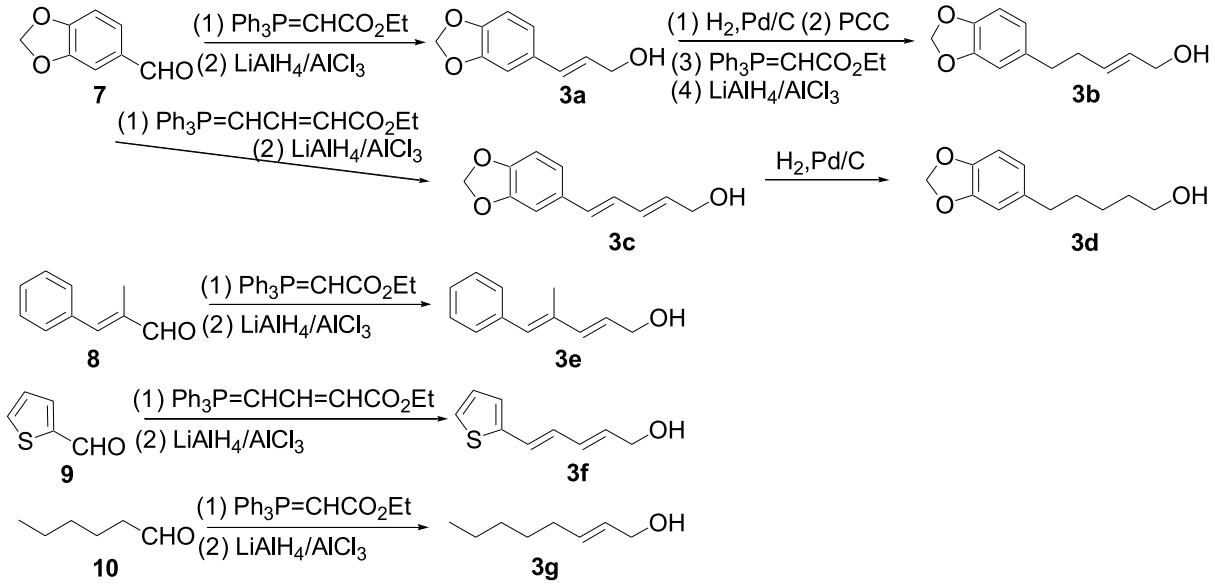
Alcohols **3a**–**3g** were transformed into the corresponding thiolacetates **4a**–**4g** using the Mitsunobu reaction with thiolacetic acid in the presence of triphenylphosphine and diisopropyl azodicarboxylate (DIAD) (8). In situ cleavage of acetyl moieties of **4a**–**4g** with potassium hydroxide in methanol, followed by alkylation of the resulting thiols with the appropriate chloroacetamides **5**, provided the sulfides **6a**–**6n** in good yields (Table 1) with no S_N2' substitution products. Oxidation of the sulfides **6** by oxone ($2KHSO_5{\cdot}KHSO_4{\cdot}K_2SO_4$) (9) in methanol–water (1:1) gave high yields of the corresponding sulfones **2** except **2j** and **2k** (Table 1). This is probably due to the side reaction of the heteroaromatic sulfides. As expected, stereochemistry of the double bonds was retained during these transformations. Subjecting the sulfones **2a**–**2n** to the modified Ramberg–Bäcklund reaction protocol (CBr_2F_2, KOH–Al_2O_3, CH_2Cl_2), previously described by us, invariably gave the geometrically defined unsaturated amide alkaloids **1a**–**1n** with the newly formed double bond that had the (*E*)-configuration in good yields (Table 2). The stereochemistry of the newly formed carbon–carbon bond in **1a**–**1n** was readily diagnosed by a typical coupling constant of 14.2–15.0 Hz for trans-olefinic protons. Examination of the ^{13}C NMR spectra of the products indicated the presence of one isomer in each case. Thus, the stereoselectivity of the reaction was >95%. All the compounds were characterized by IR, ^1H and ^{13}C NMR, and

© 2004 NRC Canada

Scheme 2. Synthesis of unsaturated amide alkaloids **1**. Piperylin (**1a**), piperlonguminine (**1b**), piperine (**1c**), pipercallosidine (**1d**), piperine S (**1e**), chingchengenamide A (**1f**), piperdardine (**1g**), piperettine (**1h**), *N*-isobutylotanthusic acid amide (**1j**), *N*-piperdineotanthusic acid amide (**1k**), sarmentine (**1l**), pellitorine (**1m**), neopellitorine B (**1n**).



Scheme 3. Synthesis of alcohols **3a**–**3g**.



high resolution mass spectra. The data of the natural unsaturated amide alkaloids **1a**–**1h**, **1j**–**1n** were in agreement with those reported in the literature (1). It is noteworthy that **1i** is not a natural alkaloid but one prepared for the first time with the readily available material in our laboratory. The synthesis of **1i** also relied on the functional sulfone **2i**, which could be prepared by the method similar to that used for the other sulfones (Scheme 4). To the best of our knowledge, **1e** and **1i** were synthesized for the first time.

Chloroacetamides **5** were prepared by acylation of various amines with chloroacetylchloride in high yields (7).

Conclusion

We have presented a rapid route with our protocol of the Ramberg–Bäcklund reaction as a key step to stereochemically defined naturally occurring unsaturated amide alkaloids. The synthetic transformation utilized readily available aldehydes as starting materials. The synthesis routes are facile, the yields are satisfactory, and the reactions can be performed in molar scales. We have also shown that the double bonds of stereochemically defined sulfone retain their stereochemistry and that the newly formed double bond has an (*E*)-configuration in our modified Ramberg–Bäcklund reaction. Investigation of the structure biological activity of these unsaturated amide alkaloids is in progress.

Experimental

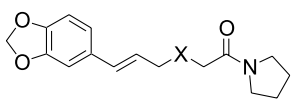
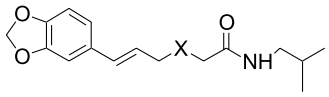
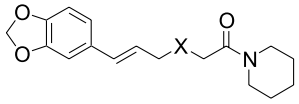
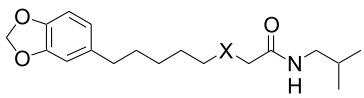
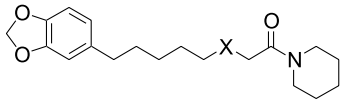
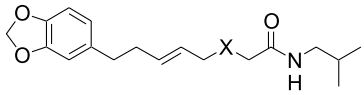
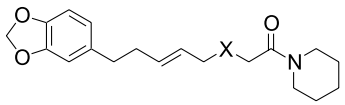
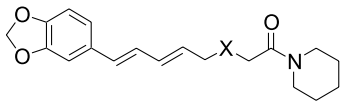
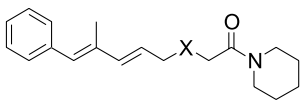
Melting points were measured on a Kofler apparatus and were uncorrected. IR spectra were recorded on a Nicolet NEXUS 670 FT-IR spectrophotometer, and reported in wave number (cm^{-1}). ^1H and ^{13}C NMR spectra were recorded on an Avance-200 or a Mercury Plus-300 spectrometer. The chemical shifts (δ) are reported in ppm and coupling constants (*J*) in Hz. Mass spectra (MS) were obtained on a HP-5988A mass spectrometer. High resolution mass spectra (HR-MS) were obtained on a Bruker Daltonics APEX II 47e mass spectrometer. Elemental analyses were performed on a Germany Varioel elemental instrument. Column chromatography was generally performed on silica gel (200–300 mesh), and TLC inspection on silica gel GF_{254} plates. All the aldehydes were purchased and used without further purification.

Alcohols 3

A solution of individual aldehyde **7** (50 mmol), **8** (50 mmol), **9** (50 mmol), or **10** (50 mmol) in benzene (25 mL) was added dropwise to a well-stirred solution of

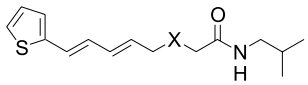
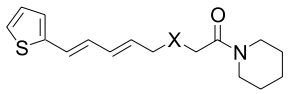
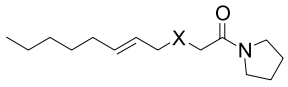
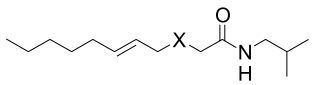
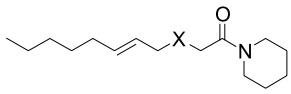
© 2004 NRC Canada

Table 1. The important data of sulfides **6** and sulfones **2**.

Entry[a]	Structure	Yield	δ_H and δ_C of CH_2XCH_2CO[b]	HR-MS
6a		68	3.19 (2 H, s) 32.5 3.50 (2 H, d, *J* = 7.5) 34.0	$C_{16}H_{20}NO_3S$ [M + H^+] 306.1158 requires 306.1158
2a		90	3.98 (2 H, s) 55.1 4.16 (2 H, d, *J* = 7.5) 57.2	$C_{16}H_{20}NO_5S$ [M + H^+] 338.1057 requires 338.1057
6b		68	3.21 (2 H, s) 34.7 3.29 (2 H, d, *J* = 7.5) 35.2	$C_{16}H_{22}NO_3S$ [M + H^+] 308.1315 requires 308.1315
2b		94	3.90 (2 H, s) 57.0 4.04 (2 H, d, *J* = 7.5) 57.4	$C_{16}H_{22}NO_5S$ [M + H^+] 340.1214 requires 340.1213
6c		85	3.28 (2 H, s) 31.7 3.39 (2 H, d, *J* = 7.5) 34.3	$C_{17}H_{22}NO_3S$ [M + H^+] 320.1316 requires 320.1315
2c		92	4.01 (2 H, s) 53.6 4.12 (2 H, d, *J* = 7.2) 57.3	$C_{17}H_{22}NO_5S$ [M + H^+] 352.1215 requires 352.1213
6d		73	2.52 (2 H, t, *J* = 6.9) 33.1 3.22 (2 H, s) 36.3	$C_{18}H_{28}NO_3S$ [M + H^+] 338.1784 requires 338.1784
2d		86	3.12–3.18 (2 H, m) 53.1 3.86 (2 H, s) 59.0	$C_{18}H_{28}NO_5S$ [M + H^+] 370.1683 requires 370.1683
6e		75	2.40–2.65 (2 H, m) 3.29 (2 H, s)	$C_{19}H_{28}NO_3S$ [M + H^+] 350.1791 requires 350.1784
2e		88	3.24 (2 H, t, *J* = 7.5) 53.4 4.06 (2 H, s) 56.1	$C_{19}H_{28}NO_5S$ [M + H^+] 382.1686 requires 382.1683
6f		65	3.10 (2 H, d, *J* = 7.5) 34.9 3.14 (2 H, s) 35.2	$C_{18}H_{26}NO_3S$ [M + H^+] 336.1628 requires 336.1628
2f		95	3.74 (2 H, s) 56.6 3.81 (2 H, d, *J* = 7.5) 57.0	$C_{18}H_{26}NO_5S$ [M + H^+] 368.1526 requires 368.1526
6g		82	3.20 (2 H, d, *J* = 7.5) 34.2 3.21 (2 H, s) 34.4	$C_{19}H_{26}NO_3S$ [M + H^+] 348.1632 requires 348.1628
2g		86	3.91 (2 H, d, *J* = 7.5) 53.5 3.95 (2 H, s) 57.2	$C_{19}H_{26}NO_5S$ [M + H^+] 380.1522 requires 380.1526
6h		78	3.25 (2 H, s) 31.8 3.32 (2 H, d, *J* = 7.6) 34.2	$C_{19}H_{24}NO_3S$ [M + H^+] 346.1478 requires 346.1471
2h		87	4.04 (2 H, s) 53.5 4.11 (2 H, d, *J* = 7.2) 57.2	$C_{19}H_{27}N_2O_5S$ [M + NH_4^+] 395.1643 requires 395.1635
6i		75	3.30 (2 H, s) 3.40 (2 H, d, *J* = 7.6)	$C_{19}H_{26}NOS$ [M + H^+] 316.1738 requires 316.1730
2i		87	4.07 (2 H, s) 53.7 4.12 (2 H, d, *J* = 7.6) 57.4	$C_{19}H_{26}NO_3S$ [M + H^+] 348.1632 requires 348.1628

© 2004 NRC Canada

Table 1 (*concluded*).

Entry[a]	Structure	Yield	δ_H and δ_C of CH_2XCH_2CO[b]	HR-MS
6j		88	3.20 (2 H, s) 34.8 3.24 (2 H, d, *J* = 7.5) 35.1	$C_{15}H_{22}NOS_2$ [M + H^+] 296.1136 requires 296.1137
2j		44	3.88 (2 H, s) 57.2 3.97 (2 H, d, *J* = 7.2) 57.4	$C_{15}H_{22}N_2O_3S_2$ [M + NH_4^+] 345.1306 requires 345.1301
6k		75	3.26 (2 H, s) 31.9 3.41 (2 H, d, *J* = 7.2) 34.2	$C_{16}H_{22}NOS_2$ [M + H^+] 308.1131 requires 308.1137
2k		34	4.05 (2 H, s) 53.7 4.06 (2 H, d, *J* = 7.5) 57.4	$C_{16}H_{22}NO_3S_2$ [M + H^+] 340.1036 requires 340.1036
6l		70	3.18 (2 H, s) 33.8 3.24 (2 H, d, *J* = 7.5) 34.4	$C_{14}H_{26}NOS$ [M + H^+] 256.1733 requires 256.1730
2l		98	3.96 (2 H, s) 55.0 3.97 (2H, d, *J* = 7.5) 56.9	$C_{14}H_{26}NO_3S$ [M + H^+] 288.1631 requires 288.1628
6m		78	3.19 (2 H, d, *J* = 7.5) 34.6 3.20 (2 H, s) 34.9	$C_{14}H_{28}NOS$ [M + H^+] 258.1888 requires 258.1886
2m		89	3.82 (2 H, d, *J* = 7.5) 56.7 3.84 (2 H, s) 57.2	$C_{14}H_{28}NO_3S$ [M + H^+] 290.1789 requires 290.1784
6n		62	3.20 (2 H, d, *J* = 7.2) 32.0 3.26 (2 H, s) 34.2	$C_{15}H_{28}NOS$ [M + H^+] 270.1891 requires 270.1886
2n		89	3.93 (2 H, d, *J* = 7.5) 53.4 4.04 (2 H, s) 57.0	$C_{15}H_{28}NO_3S$ [M + H^+] 302.1793 requires 302.1784

[a]X = S for entry **6** and X = SO_2 for entry **2**.
[b]^{1}H and ^{13}C NMR were recorded on an Avance-200 or a Mercury Plus-300 spectrometer; coupling constants (*J*) in Hz.

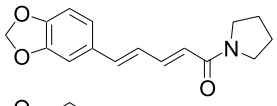
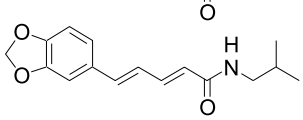
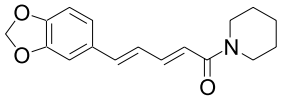
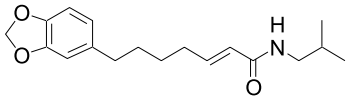
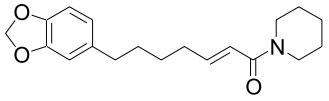
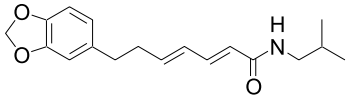
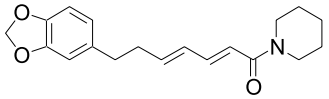
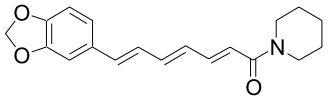
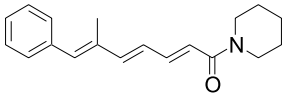
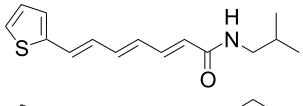
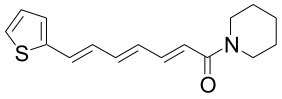
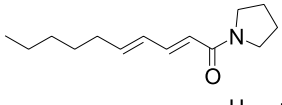
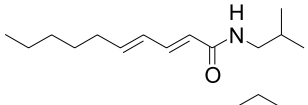
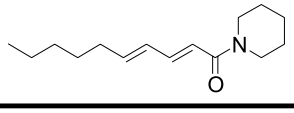
$Ph_3P{=}CH_2CO_2Et$ (60 mmol) in benzene (150 mL) or $Ph_3P{=}CHCH{=}CHCO_2Et$ (60 mmol) in benzene (200 mL). The reaction mixture was refluxed for 4 h and then the solvent was evaporated in vacuo. Flash chromatography of the residue over silica gel (petroleum ether (boiling range 60–90 °C) : ethyl acetate, 8:1) afforded the (*E*)-α,β-unsaturated esters or (*E*,*E*)-dienylesters. These esters (40 mmol) in THF (25 mL) were added dropwise to a well-stirred suspension of $LiAlH_4$ (120 mmol) and $AlCl_3$ (40 mmol) in THF (150 mL) at 0 °C, respectively. The reaction mixture was stirred at this temperature for 1 h and quenched by water (8 mL). The solid aluminates were removed by filtration. The combined filtrates were dried ($MgSO_4$) and concentrated in vacuo. Flash chromatography of the residue over silica gel (petroleum ether : ethyl acetate, 4:1) afforded alcohol **3a**, **3c**, **3e**, **3f**, or **3g** (76%, 60%, 66%, 68%, and 51% yield, respectively). The solution of **3a** (15 mmol) in EtOAc–EtOH (2:1, 60 mL) was hydrogenated under a hydrogen atmosphere (10% Pd–C, 10 mg) for 4 h to give the corresponding saturated alcohol. This saturated alcohol (15 mmol) in CH_2Cl_2 (10 mL) was added to a suspension of pyridinium chlorochromate (PCC) (18 mmol) in CH_2Cl_2 (60 mL). The reaction mixture was stirred at room temperature for 4 h and filtered, and the filtrate was concentrated in vacuo. Flash chromatography of the residue over silica gel (petroleum ether : ethyl acetate, 8:1) afforded the corresponding saturated aldehyde. After the treatment of this aldehyde with $Ph_3P{=}CH_2CO_2Et$, the resulting ester was reduced with $LiAlH_4$–$AlCl_3$ as above and alcohol **3b** was obtained in 59% yield. Alcohol **3c** was hydrogenated under a hydrogen atmosphere (10% Pd–C, 10 mg) to give saturated alcohol **3d** in nearly quantitative yield. All of these products were easily confirmed by their ^{1}H NMR and MS spectra. The focal methylene protons linked within the hydroxyl group of the unsaturated alcohols **3a**–**3c** and **3e**–**3g** have a chemical shift value of δ 3.94–4.59 ppm, and the chemical shift of methylene protons linked within the hydroxyl group of the saturated alcohol **3d** is 3.66 ppm (10).

Thiol acetates 4

A solution of DIAD (6 mmol) in dry C_6H_6 (5 mL) was added to a stirred solution of Ph_3P (6 mmol) in C_6H_6 (5 mL) at 0 °C. The resulting yellow solution was kept at 0 °C for 15 min and then a precooled mixture of the individual alcohols **3a**–**3g** (5 mmol) and CH_3COSH (6 mmol) in dry C_6H_6 (50 mL) was added in one portion. The mixture was stirred at room temperature for 1 h and the solvent was removed in vacuo. Flash chromatography of the residue over silica gel (petroleum ether : ethyl acetate, 10:1) afforded thiol acetate **4a**, **4b**, **4c**, **4d**, **4e**, **4f**, or **4g** in 83%, 95%, 93%, 85%, 88%,

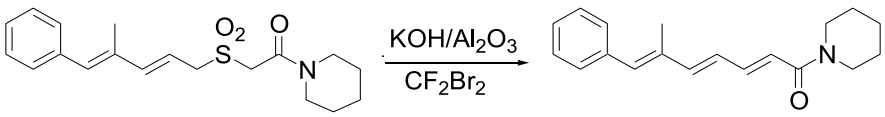
© 2004 NRC Canada

Table 2. The important data of unsaturated amide alkaloids **1**.

Entry	Structure	Yield	δ_H and J of C*H*=C*H*CO[a]	MS or HR-MS
1a		85	6.26 (1 H, d, *J* = 15.0) 7.43 (1 H, dd, *J* = 7.5 and 9.0)	271 (M^+, 32), 201 (100), 173 (38), 121 (53) and 115 (86)
1b		84	5.95 (1 H, d, *J* = 14.4) 7.36 (1 H, dd, *J* = 14.4 and 10.5)	273 (M^+, 37), 201 (100), 173 (71) and 115 (97)
1c		82	6.44 (1 H, d, *J* = 14.1) 7.41 (1 H, dd, *J* = 14.1 and 10.2)	285 (M^+, 36), 201 (100),173 (38), 115 (92) and 84 (42)
1d		68	5.74 (1 H, d, *J* = 15.0) 6.82 (1 H, dt, *J* = 15.0 and 7.5)	303 (M^+, 7), 203 (9), 168 (11) and 135 (100)
1e		65	6.23 (1 H, d, *J* = 15.0) 6.82 (1 H, dt, *J* = 15.0 and 7.4)	315 (M^+, 13), 202 (16), 180 (30), 166 (74) and 135 (100)
1f		78	5.76 (1 H, d, *J* = 15.0) 7.18 (1 H, dd, *J* = 15.0 and 10.0)	301 (M^+, 2), 229 (1), 201 (1), 161 (1) and 135 (100)
1g		80	6.26 (1 H, d, *J* = 15.0) 7.22 (1 H, dd, *J* = 15.0 and 10.2)	313 (M^+, 2), 201 (1), 178 (2), 164 (2) and 135 (100)
1h		83	6.38 (1 H, d, *J* = 14.7) 7.35 (1 H, dd, *J* = 14.7 and 11.4)	311 (M^+, 17), 226 (17), 199 (17), 135 (24) and 112 (100)
1i		83	6.44 (1 H, d, *J* = 14.1) 7.25 - 7.41(1 H, m)	$C_{19}H_{24}NO$ [M + H^+] 282.1854 requires 282.1852
1j		35	5.88 (1 H, d, *J* = 14.7) 7.30 (1 H, dd, *J* = 14.7 and 10.5)	261 (M^+, 40), 189 (34), 161 (92), 57 (99) and 43 (100)
1k		32	6.38 (1 H, d, *J* = 14.4) 7.34 (1 H, dd, *J* = 14.4 and 10.5)	273 (M^+, 61), 188 (38), 161 (88), 112 (98) and 84 (100)
1l		89	6.08 (1 H, d, *J* = 15.0) 7.27 (1 H, dd, *J* = 15.0 and 9.9)	221 (M^+, 22), 178 (12), 164 (15), 150 (100) and 81 (80)
1m		77	5.76 (1 H, d, *J* = 15.0) 7.20 (1 H, dd, *J* = 15.0 and 9.3)	223 (M^+, 24), 151 (100), 96 (62) and 81 (69)
1n		75	6.26 (1 H, d, *J* = 15.0) 7.24 (1 H, dd, *J* = 15.0 and 10.5)	235 (M^+, 3), 164 (8), 138 (100), 112 (8) and 84 (53)

[a]^{1}H NMR were recorded on an Avance-200 or a Mercury Plus-300 spectrometer; coupling constants (*J*) in Hz.

Scheme 4. Synthesis of 1-[(2*E*,4*E*,6*E*)-1-oxo-6-methyl-7-phenylheptatrienyl]piperidine (**1i**).



2i **1i**

© 2004 NRC Canada

82%, and 90% yield, respectively. These thiol acetates can be easily characterized by a comparison with their analogues (11). The focal methylene protons linked within the *S*-thioacetate group of the unsaturated thiol acetates **4a**–**4c** and **4e**–**4g** have a chemical shift value of δ 3.43–4.03 ppm, and the methylene protons of the saturated thiol acetate **4d** have a chemical shift of δ 3.00 ppm, whereas those of the corresponding thiol acetates experience a similar shift value to that of the alcohols.

Chloroacetamides 5

A solution of an appropriate amine (200 mmol) in anhyd THF (50 mL) was added to chloroacetylchloride (100 mmol) in anhyd THF (50 mL) under a nitrogen atmosphere. The reaction mixture was stirred for 10–12 h at room temperature. The side product ammonium chloride was filtered off and the solvent evaporated in vacuo to afford the chloroacetamides **5** in nearly quantitative yields. They were easily confirmed by their ^{1}H NMR and MS spectra (7).

General procedure for the preparation of sulfides 6

An individual solution of thiol acetates **4a**–**4g** (3 mmol) in MeOH (25 mL) was added to the solution of KOH (6 mmol) in MeOH (5 mL). After being stirred at 0 °C for 10 min, a solution of the appropriate chloroacetamide **5** (2.8 mmol) in MeOH (5 mL) was added to this well-stirred thiol solution and the stirring was continued for 1 h at 0 °C. The reaction mixture was poured into water (10 mL) and extracted with ethyl acetate (3 × 25 mL). The combined extract was washed with brine, dried with $MgSO_4$, filtered, and concentrated in vacuo. Flash chromatography of the residue over silica gel (petroleum ether : ethyl acetate, 5:1 gradient to 3:1) afforded the sulfides **6a**–**6n**. The important data for sulfides **6a**–**6n** are described in Table 1 and their full data are available as supplementary data.[3]

General procedure for the preparation of sulfones 2

The individual sulfide **6** (2 mmol) was added to a well-stirred solution of oxone (6 mmol) in MeOH–H_2O (1:1, 4 mL). The mixture was then stirred at 0 °C for 2–4 h. The reaction mixture was diluted with water (10 mL) and extracted with ethyl acetate (3 × 25 mL). The combined organic phase was washed with brine, dried with $MgSO_4$, filtered, and concentrated in vacuo. Flash chromatography of the residue over silica gel (petroleum ether : ethyl acetate : CH_2Cl_2, 4:1: 1 gradient to 2:1:1) afforded the sulfones **2**. The important data for sulfones **2a**–**2n** are described in Table 1 and their full data are available as supplementary data.[3]

General procedure for the preparation of unsaturated amide alkaloids 1

A solution of sulfone **2** (1 mmol) in dry CH_2Cl_2 (6 mL) was added to a stirred suspension of KOH–Al_2O_3 (10 mmol of KOH) in CBr_2F_2–CH_2Cl_2 (1:10, 10 mL). This mixture was then stirred for 1 h at room temperature, the KOH–Al_2O_3 was removed by filtering, and the filtrate was concentrated in vacuo. Flash chromatography of the residue over silica gel (petroleum ether : ethyl acetate : CH_2Cl_2, 5:1:1 gradient to 3:1:1) gave the unsaturated amide alkaloids **1a**–**1n**. The important data for unsaturated amide alkaloids **1a**–**1n** are described in Table 2 and their full data follows.

1-[(2*E*,4*E*)-1-Oxo-5-(3,4-methylenedioxyl)phenylpentadienyl]pyrrolidin (piperylin, 1a) (1*a*)

White needles, 85%; mp 147 to 148 °C (lit. (1*a*) 148 to 149 °C). IR ν_{max} (KBr disc) (cm^{-1}): 2876, 1636, 1420, 1249, 1037, 993, and 841. ^{1}H NMR (300 MHz, $CDCl_3$) δ: 1.86–2.05 (4H, m, 2 × CH_2), 3.45–3.55 (4H, m, 2 × CH_2N), 5.98 (2H, s, OCH_2O), 6.26 (1H, d, J = 15.0, 2-CH=), 6.74 (1H, d, J = 15.0, ArCH=), 6.75 (1H, d, J = 8.1, ArH), 6.76–6.99 (3H, m, 2ArH, CH=), and 7.43 (1H, dd, J = 15.0 and 9.0, CH=). ^{13}C NMR (75 MHz, $CDCl_3$) δ: 24.3, 26.1, 45.9, 46.4, 101.2, 105.6, 108.4, 121.4, 122.5, 125.1, 130.9, 138.6, 141.7, 148.1, 148.1 and 164.9. MS (EI) *m*/*z* (%): 271 (M$^+$, 32), 201 (100), 173 (38), 121 (53), and 115 (86).

(2*E*,4*E*)-N-Isobutyl-5-(3,4-methylenedioxyl)phenylpentadienamide (piperlonguminine, 1b) (1*b*)

White needles, 84%; mp 169 to 170 °C. IR ν_{max} (KBr disc) (cm^{-1}): 3463, 2985, 1741, 1374, 1245, 1046, 936, and 848. ^{1}H NMR (300 MHz, $CDCl_3$) δ: 0.94 (6H, d, J = 6.6, 2 × CH_3), 1.78–1.89 (1H, m, C*H*$(CH_3)_2$), 3.17–3.21 (2H, m, C*H*$_2$NH), 5.78 (1H, br s, NH), 5.95 (1H, d, J = 14.4, 2-CH=), 5.98 (2H, s, OCH_2O), 6.67 (1H, dd, J = 15.6 and 10.5, CH=), 6.76 (1H, d, J = 8.1, ArH), 6.77 (1H, d, J = 15.6, ArCH=), 6.88 (1H, d, J = 8.1, ArH), 6.96 (1 H, s, ArH), and 7.36 (1H, dd, J = 14.4 and 10.5, CH=). ^{13}C NMR (75 MHz, $CDCl_3$) δ: 20.1, 20.1, 28.6, 47.0, 101.3, 105.6, 108.4, 122.5, 123.2, 124.6, 130.8, 138.7, 140.9, 148.1, 148.1, and 166.2. MS (EI) *m*/*z* (%): 273 (M$^+$, 37), 201 (100), 173 (71), and 115 (97).

1-[(2*E*,4*E*)-1-Oxo-5-(3,4-methylenedioxyl)phenylpentadienyl]piperidine (piperine, 1c) (1*a*, 1*c*)

Yellow needles, 82%; mp 131 to 132 °C (lit. (1*a*) 132 to 133 °C). IR ν_{max} (KBr disc) (cm^{-1}): 2935, 1636, 1444, 1251, 1036, 929 and 854. ^{1}H NMR (300 MHz; $CDCl_3$) δ: 1.58–1.67 (6H, m, 3 × CH_2), 3.50–3.62 (4H, m, 2 × CH_2N), 5.97 (2H, s, OCH_2O), 6.44 (1H, d, J = 14.1, 2-CH=), 6.70 (1H, d, J = 15.9, ArCH=), 6.71–6.76 (1H, m, CH=), 6.78 (1H, d, J = 8.1, ArH), 6.90 (1H, d, J = 8.1, ArH), 6.99 (1H, s, ArH), and 7.41 (1H, dd, J = 14.1 and 10.2, CH=). ^{13}C NMR (75 MHz, $CDCl_3$) δ: 24.6, 25.6, 26.7, 43.2, 46.9, 101.3, 105.6, 108.5, 120.0, 122.5, 125.3, 130.9, 138.2, 142.5, 148.1, 148.1, and 165.4. MS (EI) *m*/*z* (%): 285 (M$^+$, 36), 201 (100), 173 (38), 115 (92), and 84 (42).

(2*E*)-N-Isobutyl-7-(3,4-methylenedioxyl)phenylheptenamide (pipercallosidine, 1d) (1*d*)

White needles, 68%; mp 79–81 °C (lit. (1*d*) 80–82 °C). IR ν_{max} (KBr disc) (cm^{-1}): 3302, 2926, 1629, 1494, 1248, 1039, 924, and 808. ^{1}H NMR (300 MHz, $CDCl_3$) δ: 0.92 (6H, d, J = 6.3, 2 × CH_3), 1.44–1.59 (4H, m, 2 × CH_2), 1.75–1.84 (1H, m, C*H*$(CH_3)_2$), 2.16 (2H, dd, J = 7.5 and 6.0, C*H*$_2$CH=), 2.53 (2H, t, J = 7.5, ArCH_2), 3.15 (2H, t, J = 6.2, C*H*$_2$NH), 5.48 (1H, br s, NH), 5.74 (1H, d, J = 15.0, 2-CH=), 5.92 (2H, s, OCH_2O), 6.61 (1H, dd, J = 8.1 and 1.5,

[3] Supplementary data may be purchased from the Directory of Unpublished Data, Document Delivery, CISTI, National Research Council Canada, Ottawa, ON K1A 0S2, Canada (http://www/nrc.ca/cisti/irm/unpub_e.shtml for information on ordering electronically).

© 2004 NRC Canada

ArH), 6.66 (1H, d, *J* = 1.5, ArH), 6.72 (1H, d, *J* = 8.1, ArH), and 6.82 (1H, dt, *J* = 15.0 and 7.5, CH=). ^{13}C NMR (75 MHz, $CDCl_3$) δ: 20.1, 20.1, 27.6, 28.6, 31.0, 31.9, 35.4, 46.8, 100.7, 108.0, 108.8, 121.0, 123.7, 136.2, 144.4, 145.5, 147.5, and 166.0. MS (EI) *m/z* (%): 303 (M^+, 7), 203 (9), 168 (11), and 135 (100).

1-[(2E)-1-Oxo-7-(3,4-methylenedioxyl)phenylheptenyl]piperidine (piperine S, 1e) (1e)

Yellow needles, 65%; mp 52 to 53 °C (lit. (1*e*) 52–54 °C). IR ν_{max} (KBr disc) (cm^{-1}): 2929, 1652, 1444, 1247, 1035, 930, and 809. ^{1}H NMR (200 MHz, $CDCl_3$) δ: 1.59–1.61 (10H, m, 5 × CH_2), 2.21 (2H, dd, *J* = 7.4 and 6.4, C*H*$_2$CH=), 2.54 (2H, t, *J* = 7.3, ArCH_2), 3.49–3.59 (4, m, 2 × CH_2N), 5.92 (2H, s, OCH_2O), 6.23 (1H, d, *J* = 15.0, 2-CH=), 6.64 (1H, d, *J* = 8.0, ArH), 6.57 (1H, s, ArH) 6.72 (1H, d, *J* = 8.0, ArH), and 6.82 (1H, dt, *J* = 15.0 and 7.4, CH=) ^{13}C NMR (75 MHz, $CDCl_3$) δ: 24.6, 25.6, 26.6, 27.9, 31.3, 32.4, 35.5, 43.1, 46.8, 100.7, 108.0, 108.8, 120.4, 121.0, 136.2, 145.5, 145.6, 147.4, and 165.5. MS (EI) *m/z* (%): 315 (M^+, 13), 202 (16), 180 (30), 166 (74), and 135 (100).

(2E,4E)-N-Isobutyl-7-(3,4-methylenedioxyl)phenylheptadienamide (chingchengenamide A, 1f) (1f)

White needles, 78%; mp 130–132 °C (lit. (1*f*) 126–128 °C). IR ν_{max} (KBr disc) (cm^{-1}): 3301, 2923, 1623, 1549, 1493, 1246, 1041, 996, and 811. ^{1}H NMR (300 MHz; $CDCl_3$) δ: 0.92 (6H, d, *J* = 6.6, 2 × CH_3), 1.76–1.84 (1H, m, C*H*$(CH_3)_2$), 2.42 (2H, dd, *J* = 7.2 and 6.9, C*H*$_2$CH=), 2.65 (2H, t, *J* = 7.2, ArCH_2), 3.14–3.18 (2H, m, C*H*$_2$NH), 5.54 (1H, br s, NH), 5.76 (1H, d, *J* = 15.0, 2-CH=), 5.92 (2H, s, OCH_2O), 6.06 (1H, dt, *J* = 15.3 and 6.9, CH=), 6.14 (1H, dd, *J* = 15.3 and 10.0, CH=), 6.61 (1H, d, *J* = 8.1, ArH), 6.66 (1H, s, ArH), 6.72 (1H, d, *J* = 8.1, ArH), and 7.18 (1H, dd, *J* = 15.0 and 10.0, CH=). ^{13}C NMR (75 MHz, $CDCl_3$) δ: 20.1, 20.1, 28.6, 34.9, 34.9, 46.9, 100.7, 108.1, 108.8, 121.1, 122.2, 128.8, 135.0, 141.0, 141.5, 145.7, 147.5, and 166.3. MS (EI) *m/z* (%): 301 (M^+, 2), 229 (1), 201 (1), 161 (1), and 135 (100).

1-[(2E,4E)-1-Oxo-7-(3,4-methylenedioxyl)phenylheptadienyl]piperidine (piperdardine, 1g) (1c, 12)

Pale yellow oil, 80%. IR ν_{max} (film) (cm^{-1}): 2925, 1713, 1362, 1223, 1093, 1039, and 906. ^{1}H NMR (300 MHz, $CDCl_3$) δ: 1.56–1.65 (6H, m, 3 CH_2), 2.42 (2H, dd, *J* = 7.5 and 6.9, C*H*$_2$CH=), 2.66 (2H, t, *J* = 7.5, ArCH_2), 3.49–3.62 (4H, m, 2 CH_2N), 5.92 (2H, s, OCH_2O), 6.05 (1H, dt, *J* = 15.0 and 6.9, CH=), 6.19 (1H, dd, *J* = 15.0 and 10.2, CH=), 6.26 (1H, d, *J* = 15.0, 2-CH=), 6.60 (1H, dd, *J* = 7.8 and 1.8, ArH), 6.66 (1H, d, *J* = 1.8, ArH), 6.72 (1H, d, *J* = 7.8, ArH), and 7.22 (1H, dd, *J* = 15.0 and 10.2, CH=). ^{13}C NMR (75 MHz, $CDCl_3$) δ: 24.6, 25.6 (br), 26.6 (br), 35.0, 35.0, 43.1 (br), 46.9 (br), 100.8, 108.1, 108.8, 119.1, 121.1, 129.5, 135.1, 140.8, 142.4, 145.7, 147.5, and 165.5. MS (EI) *m/z* (%): 313 (M^+, 2), 201 (1), 178 (2), 164 (2), and 135 (100).

1-[(2E,4E,6E)-1-Oxo-7-(3,4-methylenedioxyl)phenylheptatrienyl]piperidine (piperettine 1h) (1a, 1c, 12)

White needles, 83%; mp 146 to 147 °C (lit. (1*a*) 147–153 °C). IR ν_{max} (KBr disc) (cm^{-1}): 3390, 2932, 1635, 1446, 1252, 1036, 930, and 811. ^{1}H NMR (300 MHz, $CDCl_3$): 1.58–1.75 (6H, m, 3 × CH_2), 3.50–3.60 (4H, m, 2 CH_2N), 5.97 (2H, s, OCH_2O), 6.38 (1H, d, *J* = 14.7, 2-CH=), 6.41 (1H, dd, *J* = 14.7 and 11.4, CH=), 6.57–6.71 (3H, m, 3 CH=), 6.77 (1H, d, *J* = 8.1, ArH), 6.86 (1H, dd, *J* = 8.1 and 1.5, ArH), 6.96 (1H, d, *J* = 1.5, ArH), and 7.35 (1H, dd, *J* = 14.7 and 11.4, CH=). ^{13}C NMR (75 MHz, $CDCl_3$) δ: 24.6, 25.6 (br), 26.6 (br), 43.2 (br), 46.9 (br), 101.2, 105.5, 108.5, 120.0, 122.0, 126.7, 130.4, 131.5, 135.3, 139.1, 142.4, 147.8, 148.2, and 165.5. MS (EI) *m/z* (%): 311 (M^+, 17), 226 (17), 199 (17), 135 (24), and 112 (100).

1-[(2E,4E,6E)-1-Oxo-6-methyl-7-phenylheptatrienyl]piperidine (1i)

Yellow oil, 83%. IR ν_{max} (film) (cm^{-1}): 3385, 2935, 1733, 1628, 1448, 1251, 1019, and 703. ^{1}H NMR (200 MHz, $CDCl_3$) δ: 1.59–1.64 (6H, m, 3 × CH_2), 2.07 (3H, s, CH_3), 3.54–3.60 (4H, m, 2 × CH_2N), 6.44 (1H, d, *J* = 14.1, 2-CH=), 6.47 (1H, dd, *J* = 14.1 and 11.0, CH=), 6.67 (1H, s, ArCH=), 6.73 (1H, d, *J* = 15.2, CH=), and 7.25–7.41 (6H, m, 5 ArH, CH=). ^{13}C NMR (50 MHz, $CDCl_3$) δ: 13.8, 24.6, 25.6, 26.7, 43.2, 46.9, 120.0, 126.5, 127.0, 128.2, 128.2, 129.3, 129.3, 134.7, 135.4, 137.3, 142.8, 144.2, and 165.5. HR-MS (ESI) calcd. for $C_{19}H_{24}NO$: 282.1852; found: 282.1854 (M + H^+).

(2E,4E,6E)-N-Isobutyl-7-(2-thienyl)heptatrienamide (N-isobutylotanthusic acid amide, 1j) (1g, 4i)

Yellow solid, 35%; mp 186 to 187 °C (lit. (4*i*) 186 to 187 °C). IR ν_{max} (KBr disc) (cm^{-1}): 3297, 2924, 1645, 1544, and 995. ^{1}H NMR (300 MHz, $CDCl_3$) δ: 0.94 (6H, d, *J* = 6.6, 2 × CH_3), 1.79–1.84 (1H, m, C*H*$(CH_3)_2$), 3.18 (2H, t, *J* = 6.6, C*H*$_2$NH), 5.53 (1H, br s, NH), 5.88 (1H, d, *J* = 14.7, 2-CH=), 6.39 (1H, dd, *J* = 14.7 and 10.5, CH=), 6.58–6.70 (2H, m, 2 CH=), 6.83 (1H, d, *J* = 14.7, ArCH=), 6.97–7.02 (2H, m, 2 ArH), 7.21 (1H, d, *J* = 4.8, ArH), and 7.30 (1H, dd, *J* = 14.7 and 10.5, CH=). ^{13}C NMR (75 MHz, $CDCl_3$) δ: 20.1, 20.1, 28.6, 47.0, 123.5, 125.4, 127.0, 127.9, 127.9, 128.4, 130.2, 139.0, 140.7, 142.4, and 166.0. MS (EI) *m/z* (%): 261 (M^+, 40), 189 (34), 161 (92), 57 (99), and 43 (100).

1-[(2E,4E,6E)-1-Oxo-7-(2-thienyl)heptatrienyl]piperidine (N-piperidineotanthusic acid amide, 1k) (1g, 4i, 12)

Yellow solid, 32%; mp 113 to 114 °C (lit. (4*i*) 112.5–114 °C). IR ν_{max} (KBr disc) (cm^{-1}): 2930, 1632, 1443, 1261, 1004, and 852. ^{1}H NMR (300 MHz, $CDCl_3$) δ: 1.55–1.66 (6H, m, 3 × CH_2), 3.56–3.60 (4H, m, 2 × CH_2N), 6.38 (1H, d, *J* = 14.4, 2-CH=), 6.41 (1H, dd, *J* = 14.4 and 10.5, CH=), 6.60 (1H, dd, *J* = 14.4 and 10.5, CH=), 6.65 (1H, dd, *J* = 14.4 and 10.5, CH=), 6.82 (1H, d, *J* = 14.4, ArCH=), 6.98 (1H, dd, *J* = 5.4 and 3.6, ArH), 7.02 (1H, d, *J* = 3.6), 7.21 (1H, d, *J* = 5.4, ArH), and 7.34 (1H, dd, *J* = 14.4 and 10.5, CH=). ^{13}C NMR (75 MHz, $CDCl_3$) δ: 24.6, 25.6 (br), 26.7 (br), 43.3 (br), 46.9 (br), 120.3, 125.3, 126.9, 127.8, 128.0, 128.2, 130.9, 138.5, 142.2, 142.4, and 165.4. MS (EI) *m/z* (%): 273 (M^+, 61), 188 (38), 161 (88), 112 (98), and 84 (100).

1-[(2E,4E)-1-Oxo-decadienyl]pyrrolidin (Sarmentine, 1l) (1h)

Yellow oil, 89%. IR ν_{max} (film) (cm^{-1}): 3360, 2930, 1718, 1618, and 1447. ^{1}H NMR (300 MHz, $CDCl_3$) δ: 0.89 (3H, t, *J* = 6.3, CH_3), 1.26–1.47 (6H, m, 3 CH_2), 1.86–1.98 (4H, m, 2 CH_2), 2.15–2.17 (2H, m, C*H*$_2$CH=), 3.50–3.54 (4H, m,

© 2004 NRC Canada

2 CH_2N), 6.06 (1H, dt, J = 15.0 and 7.5, CH=), 6.08 (1H, d, J = 15.0, 2-CH=), 6.19 (1H, dd, J = 15.0 and 9.9, CH=), and 7.27 (1H, dd, J = 15.0 and 9.9, CH=). ^{13}C NMR (75 MHz, $CDCl_3$) δ: 14.0, 22.4, 24.3, 26.0, 28.4, 31.3, 32.9, 45.8, 46.4, 119.8, 128.6, 142.1, 143.1, and 165.2. MS (EI) *m*/*z* (%): 221 (M^+, 22), 178 (12), 164 (15), 150 (100), and 81 (80)

***(2E,4E)*-N-*Isobutyl-2,4-decadienamide (pellitorine, 1m)* (*1*h)**

White solid, 77%; mp 64 to 65 °C (lit. (1*h*) 66–68 °C). IR ν_{max} (KBr disc) (cm^{-1}): 3301, 2928, 1668, 1549, 1464, 1269, and 1161. ^{1}H NMR (300 MHz, $CDCl_3$) δ: 0.89 (3H, t, J = 7.2, CH_3), 0.93 (6H, d, J = 6.3, 2 CHCH_3), 1.26–1.47 (6H, m, 3 × CH_2), 1.76–1.87 (1H, m, CH(CH_3)$_2$), 2.14 (2H, dt, J = 7.2 and 6.6, CH_2CH=), 3.17 (2H, t, J = 6.0, CH_2NH), 5.52 (1H, br s, NH), 5.76 (1H, d, J = 15.0, 2-CH=), 6.04 (1H, dt, J = 15.0 and 7.2, CH=), 6.14 (1H, dd, J = 15.0 and 9.3, CH=), and 7.20 (1H, dd, J = 15.0 and 9.3, CH=). ^{13}C NMR (75 MHz, $CDCl_3$) δ: 14.0, 20.1, 20.1, 22.4, 28.4, 28.6, 31.3, 32.9, 46.9, 121.7, 128.1, 141.3, 143.2, and 166.4. MS (EI) *m*/*z* (%): 223 (M^+, 24), 151 (100), 96 (62), and 81 (69).

1-[(2E,4E)-1-Oxo-decadienyl]piperidine (neopellitorine B, 1n) (*1*i, 12)

Yellow oil, 75%. IR ν_{max} (film) (cm^{-1}): 3374, 2930, 1620, 1446, 1258, and 1019. ^{1}H NMR (300 MHz, $CDCl_3$) δ: 0.89 (3H, t, J = 6.6, CH_3), 1.26–1.47 (6H, m, 3 × CH_2), 1.53–1.68 (6H, m, 3 × CH_2), 2.14 (2H, dt, J = 7.2 and 7.2, CH_2CH=), 3.55–3.60 (4H, m, 2 × CH_2N), 6.06 (1H, dt, J = 15.0 and 7.2, CH=), 6.18 (1H, dd, J = 15.0 and 10.5, CH=), 6.26 (1H, d, J = 15.0, 2-CH=), and 7.24 (1H, dd, J = 15.0 and 10.5, CH=). ^{13}C NMR (75 MHz, $CDCl_3$) δ: 14.0, 22.4, 24.6, 26.3 (br), 28.5, 31.3, 32.9, 43.3 (br), 46.6 (br), 118.5, 128.8, 142.6, 142.8, and 165.7. MS (EI) *m*/*z* (%): 235 (M^+, 3), 164 (8), 138 (100), 112 (8), and 84 (53).

Acknowledgements

We are grateful to the National Natural Science Foundation of China (NSFC, QT program, No. 20021001) and the Natural Science Foundation of Gansu province (ZS011-A25-003-Z).

References

1. (*a*) F. Kiuchi, N. Nakamura, Y. Tsuda, K. Kondo, and H. Yoshimura. Chem. Pharm. Bull. **36**, 2452 (1988); (*b*) H. Achenbach, W. Fietz, J.Wörth, R. Waibel, and J. Portecop. Planta Med. **52**, 12 (1986); (*c*) J.X. Araujo, E.V.L. Da-Cunha, M.C.O. Chaves, and A.I. Gray. Phytochemistry, **44**, 559 (1997); (*d*) B.G. Pring. J. Chem. Soc. Perkin Trans. 1, 1493 (1982); (*e*) Q.L. Wu, Y.X. Feng, and J.S. Yang. Chin. Chem. Lett. **5**, 203 (1994); (*f*) Z.H. Ding, J.K. Ding, Z.L. Chen, P.Y. Bai, H. Nanao, and K. Hisashi. Phytochemistry, **30**, 3797 (1991); (*g*) F. Bohlmann, C. Zdero, and A. Suwita. Chem. Ber. **107**, 1038 (1974); (*h*) K. Likhitwitayawuid, N. Ruangrungsi, G.L. Lange, and C.P. Decicco. Tetrahedron, **43**, 3689 (1987); (*i*) B. Saadali, D. Boriky, M. Blaghen, M. Vanhaelen, and M. Talbi. Phytochemistry, **58**, 1083 (2001); (*j*) V.S. Parmar, S.C. Jain, K.S. Bisht, R. Jain, P. Taneja, A. Jha, O.D. Tyagi, A.K. Prasad, J. Wengel, C.E. Olsen, and P.M. Boll. Phytochemistry, **46**, 597 (1997).
2. (*a*) H. Weenen, M.H.H. Nkunya, D.H. Bray, L.B. Mwasumbi, L.S. Kinabo, V.A.E.B. Kilimali, and J.B.P.A. Wijnberg. Planta Med. **56**, 371 (1990); (*b*) M.D.N. Hosana, C.A. Alberto, J.K. Massuo, S.B. Vanderlan, C.M.Y. Maria, J.C. Alberto, and F. Maysa. Phytochemistry, **55**, 621 (2000); (*c*) S. Bajad, K.L. Bedi, A.K. Singla, and R.K. Johri. Planta Med. **67**, 176 (2001); (*d*) S. Tsukamoto, B.C. Cha, and T. Ohta. Tetrahedron, **58**, 1667 (2002).
3. (*a*) S.S. Bari, M.A. Sattar, R. Vig, A. Kumar, and N. Vasisht. J. Indian Chem. Soc. **67**, 995 (1990); (*b*) G.L. Kad, A.K. Arora, S. Singh, and J. Singh. Coll. Czech. Chem. Commun. **60**, 1050 (1995); (*c*) J.X. Araújo, C.M. Duarte, M.C.O. Chaves, J.P. Parente, C.A.M. Fraga, and E.J. Barreiro. Synth. Commun. **31**, 117 (2001), and refs. therein; (*d*) R. Schobert, S. Siegfried, and G.J. Gordon, J. Chem. Soc. Perkin Trans. 1, 2393 (2001); (*e*) W.S. Lin, H.M. Wang, and L.C. Chen. J. Chin. Chem. Soc. (Taipei), **45**, 159 (1998); **46**, 963 (1999); (*f*) M. Abarbri, J.L. Parrain, and A. Duchêne. Synth. Commun. **28**, 239 (1998), and refs. therein; (*g*) T. Jeffery. Synth. Commun. **18**, 77 (1988); (*h*) B.M. Trost, M. Lautens, and B. Peterson. Tetrahedron Lett. **24**, 4525 (1983); (*i*) G.M. Strunz and H.J. Finlay. Can. J. Chem. **74**, 419 (1996); (*j*) S. Chandrasekhar, M.V. Reddy, K.S. Reddy, and C. Ramaro. Tetrahedron Lett. **41**, 2667 (2000).
4. (*a*) F. Bohlmann and C. Hühn. Chem. Ber. **110**, 1183 (1977); (*b*) E.V. Dehmlow and A.R. Shamout. J. Chem. Res. Synop. 106 (1981); (*c*) J.E. Semple. Org. Prep. Proced. Int. **27**, 582 (1995); (*d*) R. Bloch and D. Hassan-Gonzales. Tetrahedron, **42**, 4975 (1986); (*e*) T. Mandai, T. Moriyama, K. Tsujimoto, M. Kawada, and J. Otera. Tetrahedron Lett. **27**, 603 (1986); (*f*) N.A. Plobeck and J.E. Bäckvall. J. Org. Chem. **56**, 4508 (1991); (*g*) D.W. Ma and X.Y. Lu. Tetrahedron, **46**, 3189 (1990); (*h*) L. Crombie and M.A. Horsham. Tetrahedron Lett. **28**, 4879 (1987), and refs. therein; (*i*) R. Rossi, A. Carpita, and V. Lippolis. Synth. Commun. **21**, 333 (1991); (*j*) F. Babudri, V. Fiandanese, F. Naso, and A. Punzi. Tetrahedron Lett. **35**, 2067 (1994); (*k*) M.C. Bernabeu, R. Chinchilla, and C. Nájera. Tetrahedron Lett. **36**, 3901 (1995).
5. (*a*) T.L. Chan, S. Fong, Y. Li, T.O. Man, and C.D. Poon. J. Chem. Soc. Chem. Commun. 1771 (1994); (*b*) X.P. Cao, T.L. Chan, H.F. Chow, and J. Tu. J. Chem. Soc. Chem. Commun. 1297 (1995); (*c*) X.P. Cao, T.L. Chan, and H.F. Chow. Tetrahedron Lett. **37**, 1049 (1996); (*d*) X.P. Cao. Tetrahedron, **58**, 1301 (2002); (*e*) X.P. Cao, Y.Y. Yang, and X.L. Wang. J. Chem. Soc. Perkin Trans. 1, 2485 (2002).
6. (*a*) C.Y. Meyers, A.M. Malte, and W.S. Matthews. J. Am. Chem. Soc. **91**, 7510 (1969); (*b*) J.M. Clough. *In* Comprehensive organic synthesis. *Edited by* B.M. Trost and I. Fleming. Pergamon Press, Oxford. 1991. p. 861; (*c*) G. Casy and R.J.K. Taylor. Org. React. **62**, 357 (2003)
7. H. Seguin, D. Gardette, M.F. Moreau, J.C. Madelmont, and J.C. Gramain. Synth. Commun. **28**, 4257 (1998).
8. O. Mitsunobu. Synthesis, 1 (1981).
9. B.M. Trost and D.P. Curran. Tetrahedron Lett. **22**, 1287 (1981).
10. (*a*) W.A. Donaldson, M.J. Jin, and P.T. Bell. Organometallics, **12**, 1174 (1993); (*b*) G. Maiti, S. Adhikari, and S.C. Roy. Tetrahedron Lett. **35**, 3985 (1994); (*c*) C. Bonini, C. Federici, L. Rossi, and G. Righi. J. Org. Chem. **60**, 4803 (1995).
11. (*a*) E. Juaristi and J.S. Cruz-Sánchez. J. Org. Chem. **53**, 3334 (1988). (*b*) K.N. Gurudutt, S. Rao, P. Srinivas, and S. Srinivas. Tetrahedron, **51**, 3045 (1995).
12. O. Hofer, H. Greger, W. Robien, and A. Werner. Tetrahedron, **42**, 2707 (1986).

© 2004 NRC Canada

The catalytic effect of boron substitution in MCM-41-type molecular sieves

V. Sundaramurthy, I. Eswaramoorthi, and N. Lingappan

Abstract: A series of B-MCM-41 samples has been synthesized with a wide range of boron content (SiO_2:B_2O_3 ratio from 20 to 200), using ethyl silicate ester-40 (ES-40) as the silica source and characterized by XRD, BET, FT-IR, ^{11}B-MAS NMR, SEM, pyridine adsorption, TPDA, and chemical analysis. The interplanar d_{100} spacing varies from 40 to 45 Å, depending on the Si:B ratio. On calcination, a significant amount of four-coordinated boron is converted into less stable three-coordinated boron, and some boron is removed from the framework. The degree of deboronation increases with an increase of boron content of the sample. The B substitution in the MCM-41 framework results in only weak and mild acid sites. The isomerization of 1-hexene is found to be influenced by the boron content in the framework. The isomerization leads to both a hydrogen shift and skeletal rearrangement. The selectivity ratios of *cis*-2-hexene to *trans*-2-hexene and 2-hexene to 3-hexene were found to decrease with an increase of temperature and a decrease of the SiO_2:B_2O_3 ratio of the catalysts. Skeletal isomerization starts at 250 °C, forming secondary products, and increases with an increase of temperature and an increase of boron content of the catalysts.

Key words: ES-40, B-MCM-41, deboronation, catalyst characterization, XRD, BET, FT-IR, ^{11}B-MAS NMR, SEM, 1-hexene isomerization, 2-hexene.

Résumé : Utilisant l'ester silicate d'éthyle-40 (ES-40) comme source de silicium, on a synthétisé une série d'échantillons B-MCM-41 comportant des quantités très variables de bore (rapport SiO_2:B_2O_3 allant de 20 à 200) qu'on a caractérisé par analyse chimique ainsi que par XRD, BET, FT-IR, RMN du ^{11}B-MAS, SEM, adsorption de la pyridine et TPDA. L'espace interplanaire d_{100} varie de 40 à 45 Å suivant la valeur du rapport Si:B. Par calcination, une quantité importante de bore tétracoordiné est transformée en bore tricoordiné et moins stable et une certaine quantité de bore est éliminée du squelette. Le degré de déboration augmente avec une augmentation dans la teneur en bore de l'échantillon. La substitution du bore dans les échantillons de MCM-41 ne conduit qu'à des sites acides faibles et doux. On a observé que l'isomérisation de l'hex-1-ène est influencée par la teneur en bore du squelette. L'isomérisation conduit à des migrations d'hydrogène et à des réarrangements du squelette. On a observé que les rapports de sélectivité *cis*-hex-2-ène:*trans*-hex-2-ène et de hex-2-ène:hex-3-ène diminuent avec une augmentation de la température et une diminution du rapport SiO_2:B_2O_3 des catalyseurs. L'isomérisation du squelette commence à 250 °C avec formation de produits secondaires et elle augmente avec la température et avec une augmentation dans la teneur en bore des catalyseurs.

Mots clés : ES-40, B-MCM-41, déboration, caractérisation du catalyseur, XRD, BET, FT-IR, RMN, ^{11}B-MAS, SEM, isomérisation du hex-1-ène, hex-2-ène.

[Traduit par la Rédaction]

Introduction

MCM-41 is a novel mesoporous material first described by Kresge et al. (1) in 1992. MCM-41 possesses unidirectional channel-like pores of uniform size, which are arranged in a regular hexagonal pattern. The pore diameters are adjustable in the range 15–100 Å, depending on the synthesis conditions, such as temperature, type, and size of the templating detergent cations. Current research on MCM-41 has two major aims. One is to find cheaper raw materials for synthesis. The other aim is to modify the framework of MCM-41, to generate catalytic sites needed for different types of reactions. Isomorphous substitution of Al (2–8), Ti (9, 10), Ga (11), and V (12, 13) in the MCM-41 framework has been described in the literature. The incorporation of boron in the MCM-41 structure has been claimed since 1994 (14). Definite evidence for boron in the MCM-41 framework position (14–23) and MCM-48 framework position (23) has been provided using various techniques. The growing interest in the synthesis of borosilicates is because they could be useful for synthesizing other metallosilicate analogues, which are sometimes difficult to synthesize by direct hydro-

Received 18 November 2002. Published on the NRC Research Press Web site at http://canjchem@nrc.ca on 6 May 2004.

V. Sundaramurthy,[1,2] I. Eswaramoorthi, and N. Lingappan. Department of Chemistry, Anna University, Chennai-25, India.

[1]Present address: Laboratoire Catalyse Spectrochime (LCS), UMR CNRS 6506, ENSICAEN, 6, boulevard Maréchal Juin, 14050, Caen CEDEX, France.
[2]Corresponding author (e-mail: sundaramurthyved@hotmail.com).

 doi: 10.1139/V04-017 © 2004 NRC Canada

thermal methods (24, 25). Mixtures of silica sources such as Cab-O-Sil M5 fumed silica, sodium silicate, and tetramethylammonium silicate (17), Cab-O-Sil M5 fumed silica and sodium silicate (19), and Ludox and sodium silicate (15) were used to synthesize B-MCM-41. Oberhagemann et al. (22) used a single silica source, tetramethoxysilane. The synthesis of B-MCM-41 using ethyl silicate-40 (ES-40) has not been studied so far. ES-40 is an oligomer silica with a molecular formula of $(C_2H_5O)_3Si\text{-}[O\text{-}Si(OC_2H_5)_2]_3\text{-}O\text{-}Si(OC_2H_5)_3$. It is a transparent liquid containing 40% silica (SiO_2) by mass. ES-40 is perfect for industrial use, considering the efficiency with which it supplies silica and its viscosity, specific gravity, stability when stored, and ease of handling during use. With its high silica content and cost, which has been kept low, ES-40 is widely used in industrial applications. We have already reported the synthesis of B-ZSM-5 using ES-40 as the silica source (26). Dongare and co-workers (27) and Mrowiec-Bialon and Jarzebski (28) reported synthesis of titanium silicalite-1 and sol–gel composites using ES-40.

The protonic form of borosilicate molecular sieves is less acidic than their aluminosilicate counterparts because of a lack of strong Brønsted acidity. Hence, the catalytic properties of borosilicate zeolites, especially B-ZSM-5, are being used for less acidity-demanding reactions such as double-bond migration in olefins (26, 29, 30), dehydration of aldehydes (31), *N*-methylaniline synthesis from aniline (32), and Beckmann rearrangement of cyclohexanone oxime to caprolactum (33). The weakly acidic sites in B-MCM-41 are reported to show high selectivity of isoprene by Prins condensation of isobutylene with formaldehyde (34). In the literature no report is available in detail on B-MCM-41 catalytic activity, particularly in hexene isomerization. Pines and Haag (35), Brouwer (36), and West et al. (37) used 1-hexene isomerization as a catalytic test for the evaluation of the relative acidity of alumina, silica alumina, and silica gel, respectively. The reports are available on 1-hexene isomerization over HY (38) and ZSM-5 zeolite (39, 40). Gati and Resofszki (41) and Paal et al. (42) studied double-bond isomerization over metal oxides and EUROPT-1, respectively. Zhiping and Changqing (43) studied the same reaction over phosphatotungstic acid catalyst. In this paper, we describe the synthesis of B-MCM-41 using ES-40, characterization of this molecular sieve by physico-chemical techniques, and its catalytic activity in 1-hexene isomerization. Further, the significant differences between the catalytic effects of B-MCM-41 and Al-MCM-41 were studied, and the ratio of selectivity of 2-hexenes was compared with those previously obtained (26) for B-ZSM-5 under similar conditions.

Experimental

Synthesis

Materials used were ethyl silicate-40 (ES-40, 40% SiO_2) (Mettur Chemicals, South India), sodium aluminate (AR), boric acid (Baker), cetyltrimethylammonium bromide (CTAB) (Ottokemi), sodium hydroxide (E. Merck), sulphuric acid (AR), and demineralized water.

A series of boron-containing MCM-41 samples were synthesized hydrothermally, using gel with the following molar composition: SiO_2 : 0.19 Na_2O : 0.25 CTAB : 63 H_2O : x B_2O_3.

The SiO_2:B_2O_3 ratio (i.e., 1:x) was varied from 20 to 200. The following is the experimental procedure adopted in the preparation of a sample with an SiO_2:B_2O_3 ratio of 50, as a typical case.

Diluted H_2SO_4 (30 mL water containing 0.5 mL concd. H_2SO_4) was added to ethyl silicate ester (20 g) and stirred mechanically. After 1 h, a solution of 12 g of CTAB in 50 mL of water was added to the previous silica–water slurry. After another 15 min, 20 mL of an aqueous solution containing 0.34 g of H_3BO_3 was added. Subsequently, a solution of sodium hydroxide (2 g in 50 mL water) was added carefully, to get a gel at pH 11. The gel obtained was transferred into a 300-mL stainless steel autoclave, and the sealed autoclave was heated statically in an air oven at 120 °C for 10 days. The crystallized mass was filtered, thoroughly washed, and then dried in static air at 120 °C. The solid product, which weighed about 7.0 g, constituted 87% yield on the basis of SiO_2. By varying the SiO_2:B_2O_3 ratio in the initial gel to 20, 50, 100, and 200, samples B-1, B-2, B-3, and B-4, respectively, were synthesized at 120 °C. The Al-MCM-41 (sample A-1) with gel SiO_2:Al_2O_3 = 20 was synthesized from a gel of molar composition SiO_2 : 0.19 Na_2O : 0.25 CTAB : 63 H_2O : 0.05 Al_2O_3, following the experimental procedure described above for B-MCM-41 but with H_3BO_3 replaced by sodium aluminate (2.4 g). Siliceous MCM-41 was crystallized using the same procedure but with no boron or aluminum. The organic cations in the channels were removed by calcination of samples under flowing dry nitrogen with a raise in temperature to 550 °C at a rate of 5 °C min^{-1}. The temperature was kept constant at 550 °C for 2 h before switching over slowly from N_2 to dry air. After an additional 4 h at 550 °C, the samples were cooled to room temperature under flowing air and stored in a desiccator. The calcinated samples were exchanged with a 1 mol L^{-1} solution of NH_4Cl (50 mL g^{-1} sample) at 80 °C for 10 h. The samples were filtered, washed with hot water, and dried at 120 °C. The procedure was repeated two more times to obtain maximum exchange. The acidic or protonated form of the catalyst was obtained by calcination of the NH_4 form of the sample at 550 °C, with a raise in temperature as described earlier.

Characterization

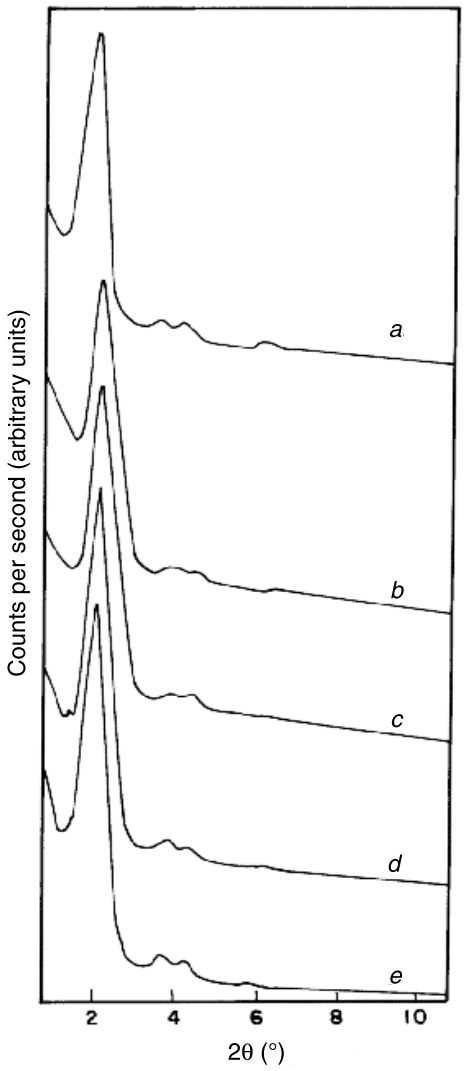
The powder X-ray diffraction patterns of samples were recorded on a Rigaku X-ray diffractometer in the scan range of 2θ between 1° and 10°, using Cu–Ni 40-kV/30-mA radiation. The unit cell parameter (a_o) was calculated using the formula $a_o = 2d_{100}/\sqrt{3}$. The IR spectra of the samples were recorded on a Testscan Shimadzu FT-IR 8000 series FT-IR spectrophotometer using KBr pellets. Each IR spectrum was recorded in the range 2000–250 cm^{-1}. Boron-11 magic angle spinning (MAS) NMR spectra were recorded on a Bruker Avance 400 spectrometer operating at 128.33 MHz. The zirconia rotor (7 mm o.d.) was spun at 6 kHz about the magic angle. The spectra were obtained with a π/2 pulse duration of 2.3 μs and a repetition time of 1.8 s. To prevent rehydration, the dehydrated protonated B-MCM-41 sample was transferred into the NMR rotor in a glove box under dry nitrogen gas. Chemical shifts were determined relative to

© 2004 NRC Canada

$BF_3{\cdot}O(C_2H_5)_2$. The morphology of samples was investigated using scanning electron microscopy (Leica, Stereoscan). The samples were suspended in acetone, and the specimen stub was dipped into the liquid and removed. The powder got deposited onto the surface of the stub evenly when the acetone evaporated. This specimen was coated with an Au–Pd evaporated film to prevent sample charging. Surface area measurements were carried out in a Sorptometric 1990 CE instrument following the BET procedure, using nitrogen as the adsorbent at liquid nitrogen temperatures. Prior to adsorption, the calcinated samples were degassed at 200 °C for 15 h under pressure. Helium was the carrier gas and a thermal conductivity detector was used. The molar compositions of the samples were obtained by wet chemical analysis. Silica in each sample was determined by taking the weight loss after treatment with hydrofluoric acid. Quantitative estimations of boron and sodium were done using inductively coupled plasma atomic emission spectrometry (ICPAES). The organic cation and water contents in the samples were determined by weight loss in TGA (Mettler TA 3000). FT-IR spectra of chemisorbed pyridine was recorded using a specially designed, all-silica, in situ controlled-environment cell. The samples were activated under vacuum (10^{-6} torr (1 torr = 133.322 Pa)) at 400 °C for 5 h and then cooled to 100 °C. Then the samples were allowed to adsorb pyridine for 1 h. Excess and physisorbed pyridine was removed by evacuation for 1 h before the spectra were recorded at 100 °C. Similarly, the pyridine-adsorbed samples were heated to 150, 200, and 250 °C successively under vacuum for 1 h at each temperature before the spectra were recorded. For the studies of temperature-programmed desorption of ammonia (TPDA), samples in H-form were activated at 500 °C for 1 h in a flow of He and then cooled to 120 °C in an He atmosphere; then, ammonia was sorbed at 120 °C. The He flow rate was increased to 40 mL min^{-1} for 1 h to remove the physically adsorbed ammonia. Thermal desorption was carried out in a stream of dry He at a heating rate of 10 °C min^{-1}. The desorbed amount of NH_3 was recorded continuously using a thermal conductivity cell.

The catalytic runs were carried out in a fixed-bed downflow reactor in the temperature range 200–350 °C. The H-form of the catalyst of particle size 20–40 mesh was kept in the middle of the reactor and was activated in pure dry air at 550 °C for 4 h, and the reaction temperature was brought down. The feed (1-hexene of 97.78% purity (Fluka)) was passed at a liquid hourly space velocity (LHSV) of 3 h^{-1}. The products were analyzed by a Hewlett-Packard 5890 A gas chromatograph. Identification of products was facilitated by use of a Finnigan MAT MS automated GC mass spectrometer. At the end of the reaction run, the reactor was flushed with nitrogen to remove the adsorbed hydrocarbons. A portion of the catalyst was removed, and the coke deposited on the catalyst was estimated from the weight loss in TGA (Mettler TA 3000). In this study, about 20–30 mg of the spent catalyst sample was subjected to temperature-programmed TGA (20 °C min^{-1}). The heating was done from ambient temperature to 800 °C in the presence of an air stream with a flow rate of 25 mL min^{-1}. A correction was made for weight loss due to moisture in the sample from the temperature profile (the weight loss from room temperature to 250 °C being ascribed to moisture). The low-temperature (250–500 °C) TGA weight loss corresponds to soft coke, whereas the high-temperature (500–800 °C) weight loss is attributed to hard coke molecules (44).

Fig. 1. X-ray diffraction patterns of the synthesized Al-MCM-41 and B-MCM-41: (*a*) A-1; (*b*) B-1; (*c*) B-2; (*d*) B-3; (*e*) B-4.



Results and discussion

X-ray diffraction

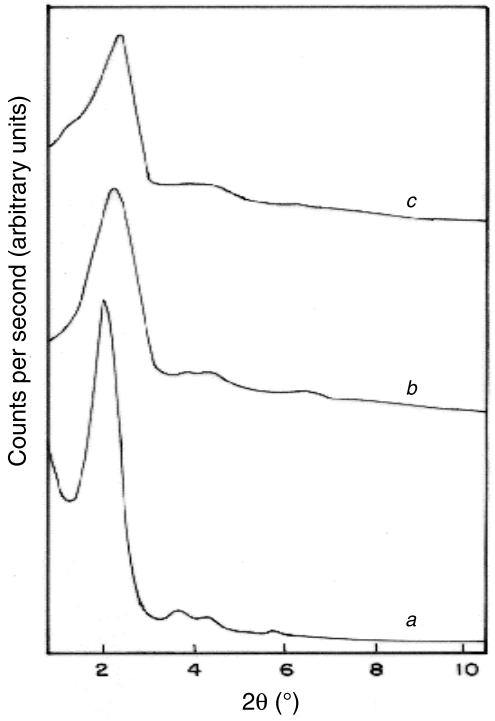
The X-ray diffraction patterns of the synthesized B-1 to B-4 and A-1 samples shown in Fig. 1 match well with that of the boron-free silicious MCM-41 and also with the patterns reported by Sayari et al. (17) and Oberhagemann et al. (14) for B-MCM-41 and that of Kresge et al. (2) for Al-MCM-41. One major peak, at $2\theta = 2.0°$, along with three peaks at $2\theta = 3.7°$, 4.2°, and 6.0° are observed for all the five samples. Beck et al. (3) indexed these peaks for a hexagonal unit cell. The unit cell parameter (a_o) and d_{100} spacing are given in Table 1. Thus, it is observed that the a_o and d_{100} spacing decrease with an increase of the boron content of the synthesized samples (B-4 to B-1). Further, the decrease in the a_o and d_{100} spacings of B-MCM-41, as compared with its pure silica analogue, is evidence for the boron in the sili-

© 2004 NRC Canada

Table 1. The unit cell parameter (a_o), d_{100} spacing, pore diameter, and pore volume of M-MCM-41 samples (M = B, Al, and Si).

Sample	d_{100} spacing (Å)	a_o (Å)	Pore diameter (Å)	Pore volume ($cm^3\ g^{-1}$)
B–1	40.5	46.7	29.2	1.02
B–2	42.3	48.8	30.3	1.16
B–3	43.8	50.6	31.0	1.06
B-4	44.7	51.6	31.6	0.92
Si-MCM-41	45.9	53.0	31.9	1.08
A-1	48.5	56.0	32.7	1.15

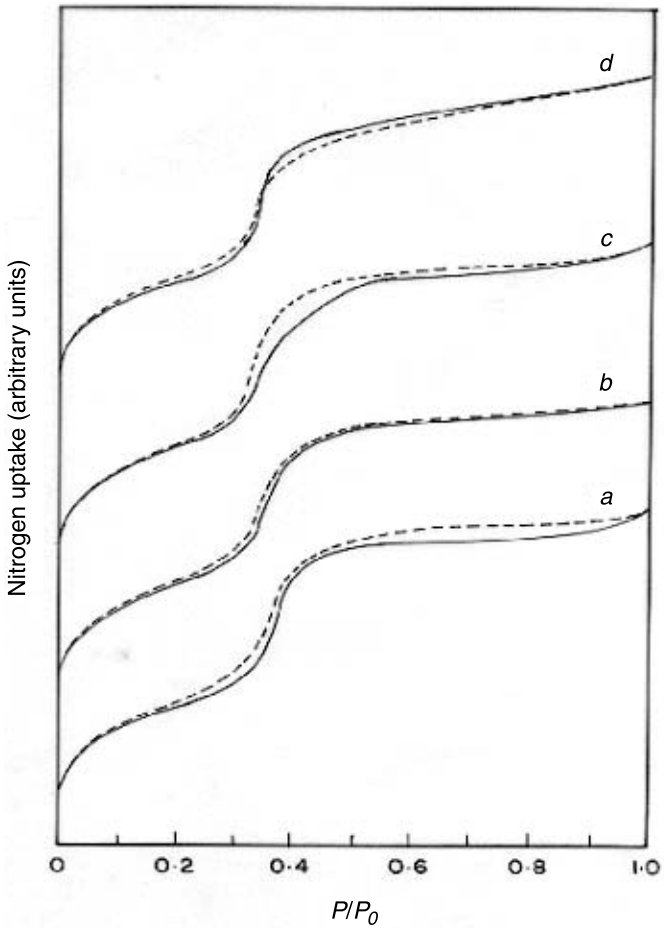
Fig. 2. X-ray diffraction patterns of the (*a*) synthesized, (*b*) calcinated Na-form, and (*c*) H-form of B-1.



cate framework. This is akin to the observation of Liu et al. (19) in their B-MCM-41 study, where a decrease in the d_{100} value with an increase of the boron content was observed. The increasing *d* spacing for the Al-MCM-41, compared, on similar lines, with Si-MCM-41, indicated that Al was incorporated into the framework.

The stability of the MCM-41 structure after removal of the template and conversion into the protonated form has also been studied using XRD. The X-ray diffraction patterns of the synthesized, calcinated, and protonated forms of a typical sample B-1 are shown in Fig. 2. On calcination (to remove the template), the peak at $2\theta = 2°$ becomes weaker and broader than that of the synthesized sample. On further conversion to the ammonium form and then to the hydrogen form, the intensity of the peak decreases slightly, and the peak becomes significantly broader than that of the calcinated form. The observed changes are attributed to the increasing formation of nonstructural B and the accompanying collapse of a portion of the borosilicate framework.

Fig. 3. N_2 isotherms of B-MCM-41 samples: (*a*) B-1; (*b*) B-2; (*c*) B-3; (*d*) B-4; (——) adsorption; (- - - -) desorption.



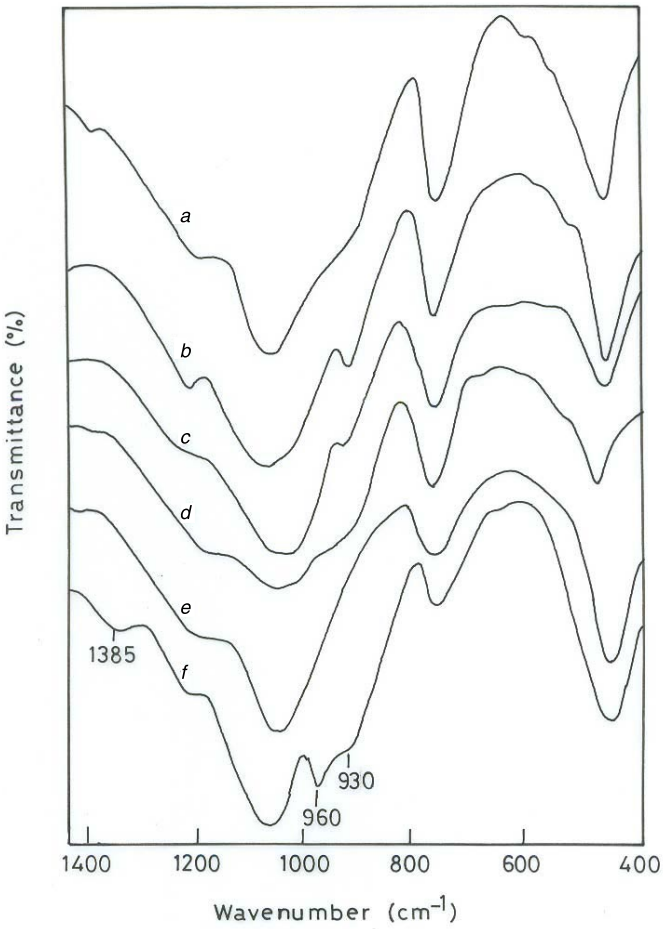
Samples B-1, B-2, B-3, B-4, and A-1 have a specific surface area of 920, 905, 935, 940, and 950 $m^2\ g^{-1}$, respectively, and exhibit type IV N_2 adsorption isotherms with the characteristic step at $P/P_0 = 0.4$ (Fig. 3). This further confirms the mesoporous nature of the samples (45, 46). The average pore diameters and specific pore volume for the B-MCM-41 samples are presented in Table 1. The average pore diameters decrease slightly with increasing B content of the sample. This may be because of the nature of the synthesis mixture, perhaps a salt effect.

Infrared spectroscopy of B-MCM-41

The IR spectra of the synthesized B-1, B-2, B-3, and B-4 samples exhibit a series of bands in the 1600–250 cm^{-1} region, which are characteristic of the SiO_2 tetrahedron unit and its modification by the introduction of boron into the framework (Fig. 4). The location of boron in the synthesized samples B-1 to B-4 is confirmed from the presence of an IR band at 930 cm^{-1}, which is characteristic of tetracoordinated boron in the MCM-41 framework (15). The intensity of this peak decreases as we go along from curves *b* to *e* in Fig. 4, and their decreasing trend is attributed to a decrease of boron content in the framework. The IR spectra of the Na-form and H-form of the typical sample B-1 are also shown in Fig. 4. The sample in its Na-form and dehydrated

© 2004 NRC Canada

Fig. 4. FT-IR spectra of the synthesized Al-MCM-41 and B-MCM-41 samples: (*a*) A-1; (*b*) B-1; (*c*) B-2; (*d*) B-3; (*e*) B-4; (*f*) H-form of B-1.

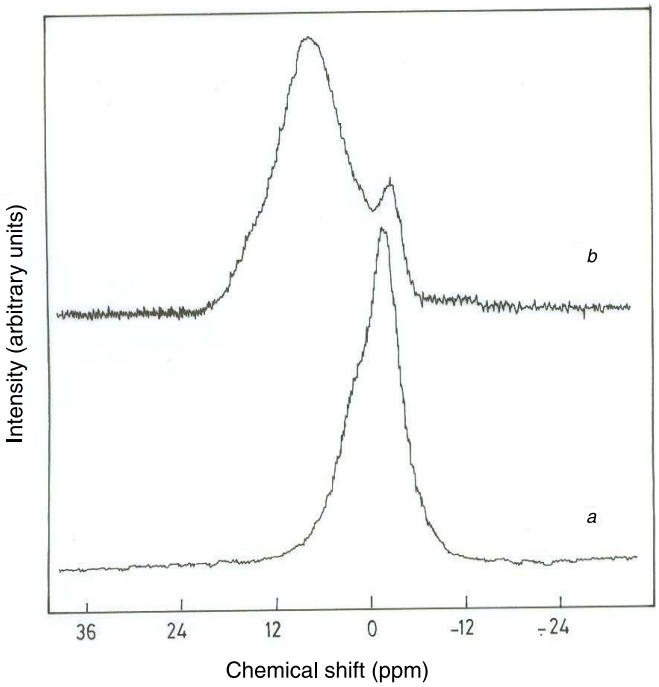


H-form exhibits weak bands at 930 and 1385 cm^{-1}, respectively, which are characteristic of tetra-coordinated boron and tri-coordinated boron in the MCM-41 framework, respectively (15). The fall in the IR band at 930 cm^{-1} and the appearance of a band at 1385 cm^{-1}, observed on the conversion of the Na-form of the sample to the H-form, show that, during the conversion, tetra-coordinated boron is converted to tri-coordinated boron. This observation was reported for both microporous (47, 48) and mesoporous borosilicates (15). This study shows that the tetra-coordinated boron is stable when sodium is counterbalancing the framework negative charge but unstable in the hydrogen form. The stability of these sites is caused by the formation of Na^+–$B(OSi)_4^-$ units, which are coordinatively saturated and stable to hydrolysis (49). The H-forms of the B-MCM-41 samples also exhibit a new band at 960 cm^{-1}. Sayari et al. (13) and Ruiter et al. (49) assigned this band to the Si–OH groups in the silanol nests.

^{11}B-MAS NMR spectroscopy

Boron-11 MAS NMR spectra of a typical B-1 sample are shown in Fig. 5. The synthesized sample has one signal at −2.3 ppm. A similar signal was reported earlier in studies dealing with boron-modified MCM-41 and is assigned to B

Fig. 5. ^{11}B-MAS NMR spectra of B-1: (*a*) synthesized; (*b*) H-form.



in the framework tetrahedral coordination (17–20). The ^{11}B-MAS NMR spectrum of dehydrated, protonated B-MCM-41 reveals that most of the tetrahedral-coordinated boron has undergone a change in coordination. In addition to a small signal at –2.3 ppm, a very broad signal appears, which is typical for trigonal boron species in the MCM-41 framework (17–20). The FT-IR studies also support these findings.

Scanning electron microscopy

Figure 6 represents the set of scanning electron micrographs of the B-MCM-41 samples. All B-MCM-41 samples have spherical particles. The size of these spheres is in the 500–1000 nm range. Small particles with size 100–300 nm with no distinct morphology also coexist with the spheres in all the samples. Among the samples, the change in morphology is small, and that change is only in size and not in the shape of the spheres.

Chemical composition

The molar compositions of the synthesized samples are shown in Table 2. The number of moles of Na_2O is lower than that of B_2O_3, suggesting that not only Na^+ ions but also cetyltrimethylammonium cations are involved in neutralizing the negative charges of the framework. Chemical analysis shows that boron is released from the MCM-41 framework during (*i*) thermal decomposition of the template and (*ii*) thermal conversion of the NH_4 form to the H-form.

In each of the above-mentioned processes, the released boron was found to come out as H_3BO_3 and to stay as the extra framework material and was extracted out of the channels by washing with distilled water at room temperature. The SiO_2:B_2O_3 ratio of the washed samples was analyzed by

© 2004 NRC Canada

Fig. 6. Scanning electron micrographs of B-MCM-41: (*a*) B-1; (*b*) B-2; (*c*) B-3; (*d*) B-4.

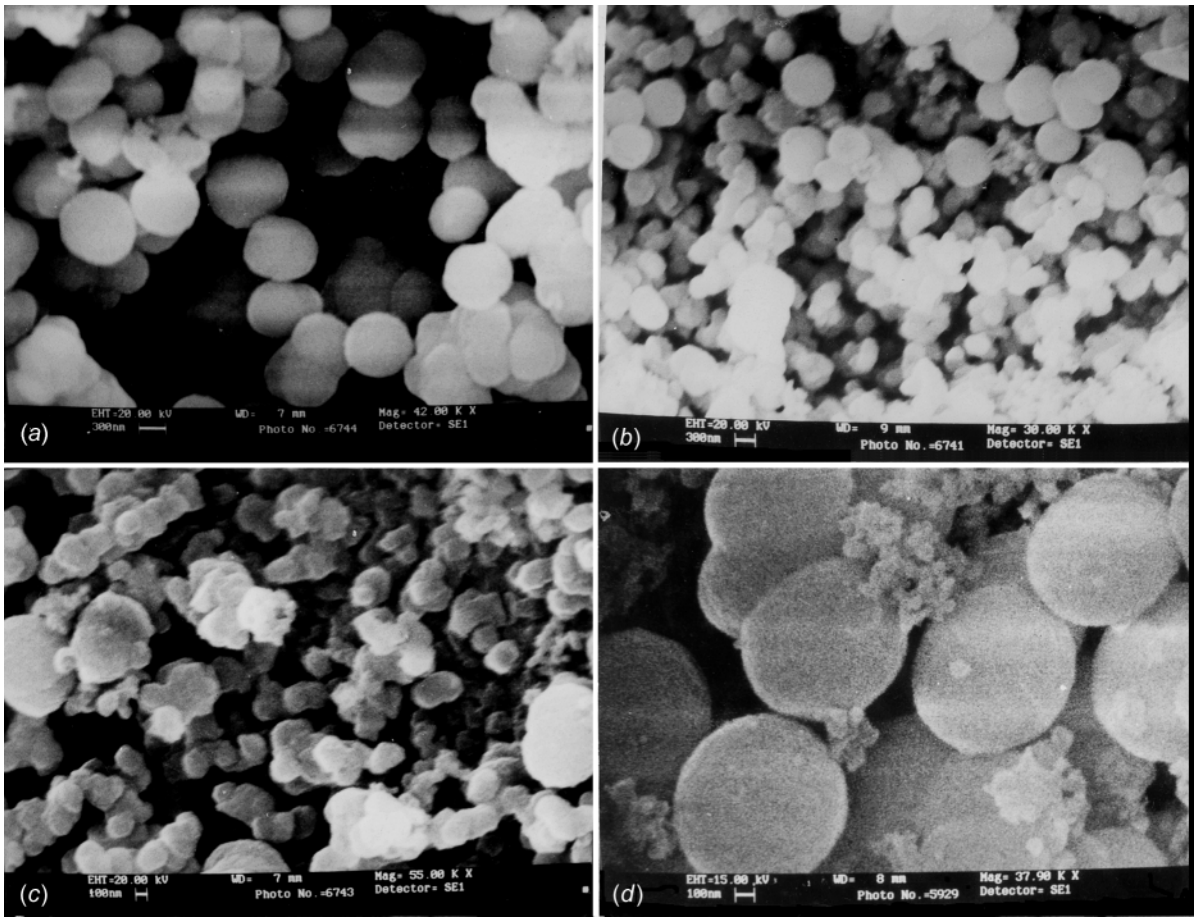


Table 2. Molar compositions of synthesized B-MCM-41 samples and % deboronation (β) of B-MCM-41 samples.

	Synthesized samples (moles per mole B_2O_3)				Deboronation (β) of B-MCM-41 (%)		
Sample	SiO_2	B_2O_3	Na_2O	CTAB	I[a]	II[b]	Total
B-1	50	1	0.62	2.1	21.5	23.2	44.7
B-2	84	1	0.59	1.9	18.0	21.4	39.4
B-3	145	1	0.60	2.0	15.2	17.7	32.9
B-4	270	1	0.68	2.3	13.3	14.3	27.6

[a]Deboronation during removal of template molecules.
[b]Deboronation during thermal decomposition of the NH_4 form of the sample.

chemical analysis. The extent of boron released is expressed in terms of % deboronation (β) and is given in Table 2.

$$\beta = (1 - n_{syn}/n) \times 100$$

where n_{syn} and n denote the molar SiO_2:B_2O_3 ratio of the synthesized B-MCM-41 and that of the modified B-MCM-41, respectively. Table 2 shows that the deboronation level (β) decreases with an increase of the SiO_2:B_2O_3 ratio in the samples. This leads to the conclusion that the more boron is found in the MCM-41 framework, the weaker it is bound, and it is more likely that it is released during heat treatment.

FT-IR spectra of chemisorbed pyridine

Figure 7 depicts the FT-IR spectra of pyridine adsorbed on a B-1 sample in the region 1600–1400 cm^{-1}. The sample exhibits IR bands at 1595, 1545, and 1445 cm^{-1}. The bands at 1595 and 1445 cm^{-1} are characteristic of physisorbed pyridine and hydrogen-bonded pyridine, respectively (15). The weak band at 1545 cm^{-1} is characteristic of Brønsted acid sites (15). The thermal stability of pyridine sorbed on the catalyst was measured by increasing the desorption temperature from 100 to 250 °C. These bands are decreased sharply upon evacuation at elevated temperatures and disappear at 250 °C. This shows that B-MCM-41 possesses only weak and mild acid sites.

TPDA of B-MCM-41 and Al-MCM-41

TPDA spectra of Al-MCM-41 and B-MCM-41 samples are shown in Fig. 8. The TPDA spectra of Al-MCM-41 exhibit three maxima, viz. at ca. 167, 340, and 500 °C. The low-temperature peak is caused by desorption of ammonia from weak Brønsted and Lewis acid sites (50). The weak Brønsted acid sites appear as a result of surface hydroxyl groups, whereas the structural weak Lewis acid sites may arise from tricoordinated metal ion in the framework (51). The medium-temperature peak at 340 °C is assigned to weak- to medium-acidic Brønsted sites. Such sites are well known from medium-pore zeolites (52) and have been detected in substituted MCM-48 (53). The high-temperature signal is caused by ammonia desorbed from strong Lewis

© 2004 NRC Canada

Fig. 7. FT-IR spectra of pyridine adsorbed on B-1 at desorption temperatures of (*a*) 100, (*b*) 150, (*c*) 200, and (*d*) 250 °C.

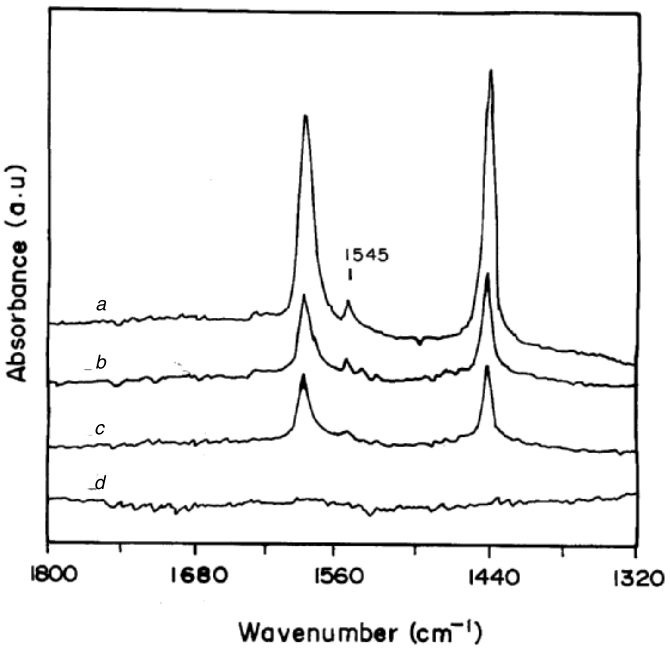
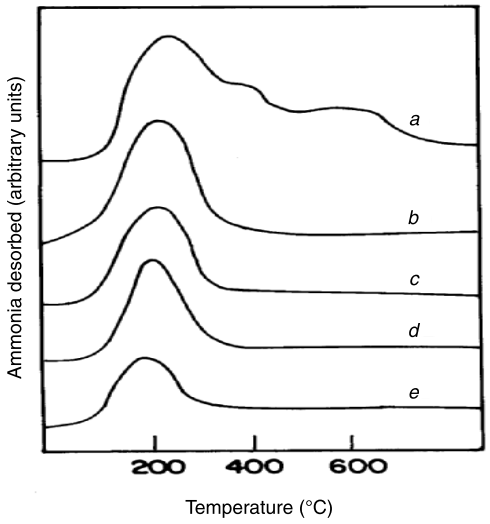


Fig. 8. TPDA of Al-MCM-41 and B-MCM-41: (*a*) A-1; (*b*) B-1; (*c*) B-2; (*d*) B-3; (*e*) B-4.



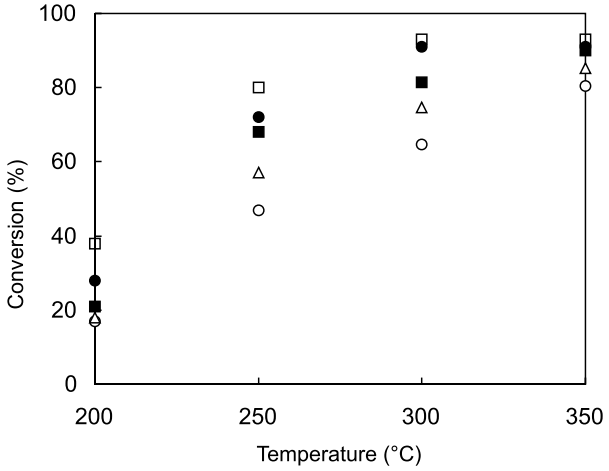
acid sites (53). The concentration of strong Lewis sites points to the dispersion of the extra framework aluminum species in the channels of MCM-41.

The major deviations observed in the TPD spectra on isomorphous substitution of B for Al are the absence of medium- and high-temperature signals and the presence of only low-temperature signals corresponding to weak Lewis and Brønsted acid sites. This study shows that boron substitution in the MCM-41 framework results in only weak acid sites like those of B-ZSM-5 samples (54, 55).

Catalytic studies

Isomerization of 1-hexene was carried out in the temperature range 200–350 °C and at a liquid hourly space velocity

Fig. 9. 1-Hexene conversion (wt %) at different temperatures, LHSV = 3 h^{-1}: (●) B-1; (■) B-2; (△) B-3; (○) B-4; (□) A-1.



(LHSV) of 3 h^{-1} over the H-form of catalysts B-1 to B-4 and A-1, all of which were activated at 500 °C. LHSV is the ratio of the weight of the liquid feed per hour (g h^{-1}) and the weight of the catalyst (g). The conversion of 1-hexene at different temperatures is presented in Fig. 9. At any given temperature, a decreasing trend of isomerization was observed with increasing SiO_2:B_2O_3 ratio of the catalyst, viz. 91%, 81.5%, 74.6%, and 64.7% conversions were obtained over catalysts B-1, B-2, B-3, and B-4, respectively, at 300 °C. The decrease in conversion is attributed to the decrease in the number of acid sites present in the catalyst as the SiO_2:B_2O_3 ratio increases. At all temperatures, higher conversion was obtained over the A-1 catalyst than over boron-substituted catalysts because of the presence of strong Brønsted acidic sites associated with the presence of Al^{3+}. As the temperature increased from 200 °C, the conversion of 1-hexene was found to increase for all the catalysts, and a maximum conversion (93%) of 1-hexene over the A-1 catalyst was observed at 300 °C, whereas for the B-1, B-2, B-3, and B-4 catalysts, the maximum conversions of 91%, 90%, 85.2%, and 80.5% were observed at 350 °C. Si-MCM-41 was also tested under similar conditions and was found to have no catalytic activity in the temperature range 200–350 °C.

Table 3 shows the product selectivity of 1-hexene isomerization at the following temperatures: 200, 250, 300, and 350 °C. The reaction products shown in the above-mentioned table are formed generally via double-bond shift, *cis–trans* isomerization, and skeletal rearrangement. The major isomerization products *trans*-2-hexene (t-2H), *cis*-2-hexene (c-2H), and (*cis*+*trans*)-3-hexene ((c+t)-3H) are formed by a 1–2 double-bond shift. For instance, at 300 °C *trans*-2-hexene, *cis*-2-hexene, and (*cis*+*trans*)-3-hexene constitute 95.9% of the total, from 88% conversion on B-1. This is comparable to the 94.75% double-bond shift at 54% conversion reported by Ko and Wojciechowski (38) on an HY catalyst at 200 °C and to that of 95% on ZSM-5 at 52% conversion reported by Abbot et al. (39) at 280 °C.

The increase of temperature from 200 to 350 °C shows a decrease in the selectivity of 2-hexene with a simultaneous increase in selectivity of 3-hexene. However, between the 2-hexenes, the selectivity of *trans*-2-hexene is not affected as

© 2004 NRC Canada

Table 3. Selectivity of 1-hexene isomerization products.

	Selectivity of products over different catalysts (wt %)				
Product	A-1	B-1	B-2	B-3	B-4
Selectivity of products at 200 °C					
t-2H	51.9	47.2	48	48.6	49
c-2H	38.1	44.6	45.4	46.4	47
(t+c)-3H	10	8.2	6.6	5	4
Selectivity of products at 250 °C					
t-2H	48.4	49	50	50.3	53.8
c-2H	29.9	32	33	34.2	36.2
(t+c)-3H	18.1	17	16	15.5	10.2
2M2P	3.6	2	1	—	—
Selectivity of products at 300 °C					
t-2H	41.8	48	49	50	51
c-2H	20.2	28	30	32	33.4
(t+c)-3H	15.5	19.9	17.8	16.1	14
2M2P	9.9	2.7	3.2	1.9	1.6
3M2P	4	1.3	—	—	—
4M2P	2.2	—	—	—	—
2M1P	3.2	—	—	—	—
3M1P	2.2	—	—	—	—
Selectivity of products at 350 °C					
t-2H	35.5	44.5	46.4	47.8	49.5
c-2H	13.8	24.7	28.1	29.9	31.5
(t+c)-3H	13.5	21.3	19.1	19.5	17
2M2P	13.4	5.8	4.2	2.8	2
3M2P	9.3	2.6	2.2	—	—
4M2P	3.8	1.1	—	—	—
2M1P	7.5	—	—	—	—
3M1P	3.2	—	—	—	—

Note: t-2H, *trans*-2-hexene; c-2H, *cis*-2-hexene; (c+t)-3H, (*cis*+*trans*)-3-hexene; 2M2P, 2-methyl-2-pentene; 3M2P, 3-methyl-2-pentene; 4M2P, 4-methyl-2-pentene; 2M1P, 2-methyl-1-pentene; 3M1P, 3-methyl-1-pentene.

much by temperature as that of *cis*-2-hexene. Over the A-1 catalyst, the selectivities of both t-2H and c-2H are affected similarly by a raise in temperature. Similarly, at any fixed temperature studied, an increase of boron content in the catalyst increases the selectivity of 3-hexenes and decreases that of 2-hexenes.

Skeletal isomerization products in considerable quantity are found to form on the A-1 catalyst as secondary products from 250 °C onwards, and they increase with an increase in temperature. They are 2-methyl-2-pentene (2M2P), 3-methyl-2-pentene (3M2P), 4-methyl-2-pentene (4M2P), 2-methyl-1-pentene (2M1P), and 3-methyl-1-pentene (3M1P). Among them, 2M2P and 3M2P are the major ones. At 250 °C and above, only small amounts of 2M2P and 3M2P are formed with each of the boron catalysts, as compared to the aluminum catalyst. For example, at 300 °C, the maximum skeletal isomerization product formed over B-1 amounts to 4.0% compared to 21.5% over A-1. Similarly, at any fixed temperature studied, selectivity of the skeletal isomerization products was found to increase with an increase of the boron content of the catalysts.

The mechanism of the reported double-bond shift (30) involves interaction of 1-hexene with the acid sites of the catalysts, leading to the formation of the C_6 carbenium ion. The carbenium ion can undergo deprotonation, hydrogen shift, cyclization, or oligomerization. The formation of 2-hexene is attributed to deprotonation and that of 3-hexene to a hydrogen shift. The large difference in the selectivity of 2-hexenes from that of 3-hexenes suggests that the rate of deprotonation from the carbenium ion is much faster than that of the hydrogen transfer from the C_6 carbenium ion. Skeletal isomerization products are formed by a sequence of hydrogen and methyl shifts. These are energy-demanding steps and, hence, register low selectivity over boron-substituted catalysts compared with the aluminum-substituted catalyst.

Ratios of selectivity of double-bond shift products of hexene (c-2H:t-2H and (c+t)-2H:(c+t)-3H) at four different temperatures over all the catalysts are shown in Table 4. The thermodynamic equilibrium ratios 0.39, 0.44, and 0.44 have been reported by Abbot et al. (39) for c-2H to t-2H at 200, 250, and 280 °C, respectively. Any different ratio of c-2H to t-2H than the above-mentioned ones is a clear indication that the reaction is kinetically controlled. Thus, ratios in Table 4 show that the reaction is kinetically controlled, with higher relative rates of production of *cis* isomers at all temperatures. Similar preferential formation of *cis* isomers has been reported by Abbot and Wojciechowski (40) over ZSM-5 and by Ko and Wojciechowski (38) over HY catalysts. We also observed and reported a similar result over B-ZSM-5 catalysts (26). The excess of the *cis* isomer with respect to the *cis*:*trans* equilibrium ratio is attributed to (*i*) steric effects on the C_6 carbenium ion leading to its preferential formation of c-2H (45) and (*ii*) the formation of a more stable intermediate π complex between the *cis* isomer and the proton on the Brønsted sites (38).

It is apparent from Table 4 that the c-2H:t-2H ratio decreases with an increase of temperature with all the catalysts. Similar results have been reported over the ZSM-5 catalyst (39). We have already reported the 1-hexene isomerization on B-ZSM-5 catalysts (26). The c-2H:t-2H ratio obtained with the B-ZSM-5 samples (26) is significantly lower than with the B-MCM-41 samples under similar conditions. This is probably a result of different pore structures and dimensions in the two molecular sieves. The elliptical channels in B-ZSM-5 have diameters (5 to 6 Å) in a range approaching the kinetic diameters of straight-chain olefins (4.3 Å). This property has led to a wide interest in the reactions (which are said to control shape selectivity) of hydrocarbons in this microporous molecular sieve. The reason for *cis*:*trans* ratios closer to equilibrium in B-ZSM-5 is associated with the initial spatial requirements of the transition state followed by equilibration encouraged by diffusional limitations. There is a high probability that a particular 2-hexene molecule, once formed, will undergo repeated collision with the channel walls before escaping from ZSM-5 channels. The above-mentioned equilibration is absent in B-MCM-41 because of the *meso* pore size, and it shows higher c-2H:t-2H ratios in relation to those of the B-ZSM-5 catalysts.

From the percentage of selectivity of c-2H, t-2H, and (c+t)-3H, values of the 2-hexenes:3-hexenes ratio, (c+t)-2H:(c+t)-3H, have been calculated and are presented in Table 4. At all temperatures, as the SiO_2:B_2O_3 ratio of catalysts

© 2004 NRC Canada

Table 4. Ratio of selectivity for isomerization of 1-hexene on the A-1 and B-1 to B-4 catalysts.

	c-2H:t-2H				(c+t)-2H:(c+t)-3H			
Catalyst	200 °C	250 °C	300 °C	350 °C	200 °C	250 °C	300 °C	350 °C
A-1	0.73	0.62	0.48	0.39	9	4.3	4	3.6
B-1	0.94	0.65	0.58	0.56	11.2	4.8	3.9	3.2
B-2	0.95	0.66	0.61	0.6	14.1	5.2	4.4	3.7
B-3	0.95	0.68	0.64	0.63	19	5.5	4.9	4.1
B-4	0.96	0.69	0.65	0.64	24	8.8	6	4.8
B-ZSM-5[a]	0.62	0.42	0.41	0.34	12.3	7.6	4.6	3.8
B-ZSM-5[b]	0.64	0.44	0.44	0.37	15.6	10.7	7.2	4.7

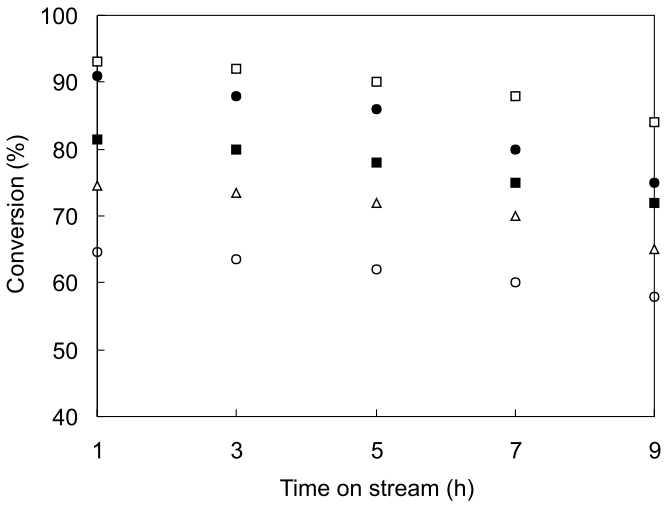
[a] SiO_2:B_2O_3 ratio = 180.
[b] SiO_2:B_2O_3 ratio = 350 (from ref. 26).

decreases, the (c+t)-2H:(c+t)-3H ratio decreases. This is ascribed to the increase in the number of acid sites of the catalyst with an increase of boron content in the framework, which in turn increases the rate of hydrogen shift from the 3- to the 2-carbon and enhances the formation of 3-hexene. Similarly, an increase of temperature from 200 to 350 °C increases the rate of hydrogen shift to form 3-hexene. A similar observation was also reported (39) over the ZSM-5 catalyst in the 1-hexene isomerization with an increase of reaction temperature.

The conversions of 1-hexene vs. time on stream over all the catalysts at 300 °C are shown in Fig. 10. The conversion of 1-hexene decreases steadily over all the catalysts with increasing time on stream, though the actual decrease is different for different catalysts. This is mainly because catalysts lose their activity steadily with time on stream. The activity loss is attributed to coke formation, which increases with time on stream, thereby poisoning the active acidic sites. The wt % coke formed is 7.4%, 6.9%, 6.6%, 6.1%, and 4.0% on the B-1, B-2, B-3, B-4, and A-1 catalysts, respectively, at the end of 9 h at 300 °C. It was observed that an increase of boron content in the framework slightly increases the coking and aging during time on stream. The amount of coke accumulation on boron-containing catalysts is greater than that on the corresponding aluminum-containing catalyst. Cornaro and Wojciechowski (30) also observed a greater amount of coke accumulation over the B-ZSM-5 catalyst than the Al-ZSM-5 catalyst in the 1-hexene isomerization. The difference in the coke content is a result of the difference in the acidity of the catalysts. Al-MCM-41 can crack off the precoke oligomer in the process of coke hardening because of the presence of a greater number of strong acidic sites, thus resulting in a lesser amount of coke. The boron catalysts, which have a mild acidity, are apparently not able to crack the precoke (26, 30) and, hence, accumulate a greater amount of coke.

FT-IR spectra of coke-deposited catalysts show the prominent IR band in the C-H deformation region around 1600 cm^{-1} (this figure is not shown). Eberly (56) ascribed this band to highly unsaturated carbonaceous residues, most likely adsorbed olefins. Abbot et al. (39) also observed the presence of mainly adsorbed olefins in the coke deposit on the ZSM-5 catalyst in the 1-hexene isomerization in the temperature range 200–350 °C. A TGA study of the coke formed on catalysts shows the formation of only soft coke molecules (TGA weight loss occurs between 300 and 500 °C) on the B-MCM-41 and the Al-MCM-41 catalysts in the above-mentioned reaction temperature range.

Fig. 10. Effect of time on stream on 1-hexene conversion at 300 °C, LHSV = 3 h^{-1}: (●) B-1; (■) B-2; (△) B-3; (○) B-4; (□) A-1.



Conclusion

The B-MCM-41 samples, with differing amounts of boron in the framework, were synthesized by a hydrothermal method using ES-40. Evidence for the presence of B in the silica network of MCM-41 was obtained by different characterization techniques. In the synthesized samples, boron was present in the four-coordinated state. Calcination and further conversion into the H-form converted a significant part of the boron into a three-coordinated state. The % deboronation of B-MCM-41 was found to be dependent on the concentration of boron in the silicate framework. Investigation of the acidity of B-MCM-41 revealed that the materials have only a weak acidity and a lower acidity than that of Al-MCM-41. The catalytic effect of framework boron, explored by means of 1-hexene isomerization, reveals that the extent of 1-hexene conversion changes with boron content and, hence, the acidity of the catalysts. The isomorphous substitution of B for Al in the MCM-41 framework changes both the conversion of 1-hexene and the selectivity of the products. The selectivity of the double-bond shift products is enhanced with the substitution of B for Al in the MCM-41 framework.

© 2004 NRC Canada

References

1. C.T. Kresge, M.E. Leonowicz, W.J. Roth, and J.C. Vartulli. U.S. Patent 5 098 684, 1992; U.S. Patent 5 102 643, 1992.
2. C.T. Kresge, M.E. Leonowicz, W.J. Roth, J.C. Vartulli, and J.S. Beck. Nature (London), **359**, 710 (1992).
3. J.S. Beek, J.C. Bartuli, W.J. Roth, M.E. Leonowicz, C.T. Kresge, K.D. Schmitt, C.T.-W. Chu, D.H. Olson, E.W. Sheppard, S.B. Mccullen, J.B. Higgins, and J.L. Schlenker. J. Am. Chem. Soc. **114**, 10 834 (1992).
4. A. Corma, V. Fornes, M.T. Navarro, and J. Perez-Pariente. J. Catal. **148**, 569 (1994).
5. R. Schmidt, D. Akporiaye, M. Stocker, and O.H. Ellested. J. Chem. Soc. Chem. Commun. 1493 (1994).
6. C.Y. Chen, H.X. Li, and M.E. Davis. Microporous Mater. **2**, 17 (1993).
7. C.Y. Chen, S.L. Burkett, H.X. Li, and M.E. Davis. Microporous Mater. **2**, 27 (1993).
8. Z. Luan, C-F. Cheng, W. Zhou, J. Klinowski, J.A. Sousa-Goncalves, and L.F. Gladden. J. Phys. Chem. **99**, 1018 (1995).
9. P.T. Tanev, M. Chibwe, and T.J. Pinnavaia. Nature (London), **368**, 321 (1994).
10. C.G. Wu and T. Bein. Science (Washington, D.C.), **264**, 1757 (1994).
11. C-F. Cheng, H. He, W. Zhou, and J. Klinowski. J. Phys. Chem. **100**, 390 (1996).
12. K.M. Reddy, I. Moudrakovski, and A. Sayari. J. Chem. Soc. Chem. Commun. 1059 (1994).
13. A. Sayari, K.M. Reddy, and I. Moudrakovski. Stud. Surf. Sci. Catal. **98**, 19 (1995).
14. U. Oberhagemann, I. Topalovic, B. Marler, and H. Gies. Stud. Surf. Sci. Catal. **98**, 17 (1995).
15. D. Trong On, P.N. Joshi, G. Lemay, and S. Kaliaguine. Stud. Surf. Sci. Catal. **97**, 543 (1995).
16. A. Sayari, C. Danumah, and I.L. Moudrakovski. Chem. Mater. **7**, 813 (1995).
17. A. Sayari, I. Moudrakovski, C. Danumah, C.I. Ratcliffe, J.A. Ripmeester, and K.F. Preston. J. Phys. Chem. **99**, 16 373 (1995).
18. D. Trong On, P.N. Joshi, and S. Kaliaguine. J. Phys. Chem. **100**, 6743 (1996).
19. S. Liu, H. He, Z. Luan, and J. Klinowski. J. Chem. Soc. Faraday Trans. **92**, 2011 (1996).
20. U. Oberhagemann, I. Kinski, I. Dierdorf, B. Marler, and H. Gies. J. Non–Cryst. Solids, **145**, 197 (1996).
21. S. Gontier and A. Tuel. Stud. Surf. Sci. Catal. **105**, 29 (1997).
22. U. Oberhagemann, M. Jeschke, and H. Papp. Microporous Mesoporous Mater. **33**, 165 (1999).
23. Z.Y. Yuan, Q. Luo, J.Q. Liu, T.H. Chen, J.Z. Wang, and H.X. Li. Microporous Mesoporous Mater. **42**, 289 (2001).
24. M.S. Rigutto, R. de Ruiter, J.P.M. Niederer, and H. Van Bekkum. Stud. Surf. Sci. Catal. **84**, 2245 (1994).
25. C.B. Dartt and M.E. Davis. Appl. Catal. **143**, 53 (1996).
26. V. Sundaramurthy and N. Lingappan. J. Mol. Catal. **160**, 367 (2000).
27. D.P. Sabde, S.G. Hegde, and M.K. Dongare. J. Mater. Chem. **10**, 1365 (2000).
28. J. Mrowiec-Bialon and A.B. Jarzebski. Langmuir, **17**, 626 (2001).
29. R. Fischer, W. Holderich, W.D. Mross, and H.M. Weitz. European Patent 0 167 021, 1986.
30. U. Cornaro and B.W. Wojciechowski. J. Catal. **120**, 182 (1989).
31. W. Holderich, F. Merger, W.D. Mross, and G. Fouguet. European Patent 0 162 385, 1985.
32. L.B. Pierella, O.A. Anunziata, and O.A. Orio. Lat. Am. Appl. Res. **25**, 223 (1995).
33. J. Roseler, G. Heitmann, and W.F. Holderich. Appl. Catal. **144**, 319 (1996).
34. E. Dumitriu, D. Trong On, and S. Kaliaguine. J. Catal. **170**, 150 (1997).
35. H. Pines and W.O. Haag. J. Am. Chem. Soc. **82**, 2471 (1960).
36. D.M. Brouwer. J. Catal. **1**, 22 (1962).
37. P.B. West, G.L. Haller, and R.L. Burwell. J. Catal. **29**, 486 (1973).
38. A.N. Ko and B.W. Wojciechowski. Int. J. Chem. Kinet. **15**, 1249 (1983).
39. J. Abbot, A. Corma, and B.W. Wojciechowski. J. Catal. **92**, 398 (1985).
40. J. Abbot and B.W. Wojciechowski. Can. J. Chem. Eng. **60**, 622 (1985).
41. G. Gati and G. Resofszki. Kem. Kozl. **72**, 86 (1991).
42. Z. Paal, M. Raeth, B. Brose, and W. Gomber. React. Kinet. Catal. Lett. **47**, 43 (1992).
43. D. Zhiping and X. Changqing. Riyoung Huaxue Gongye, **20**, 12 (1996).
44. F.A. Twaiq, N.A.M. Zabidi, and S. Bhatia. Ind. Eng. Chem. Res. **38**, 3230 (1999).
45. P.J.Branton, P.G. Hall, and K.S.W. Sing. J. Chem. Soc. Chem. Commun. 1257 (1993).
46. D. Franke, G. Schulz-Ekloff, and J. Rathousky. J. Chem Soc. Chem. Commun. 724 (1993).
47. G. Coudurier, A. Auroux, J.C. Vedrine, R.D. Farlee, L. Abrams, and R.D. Shannon. J. Catal. **108**, 1 (1987).
48. D. Trong On, M.P. Kapoor, L. Bonneviot, S. Kaliaguine, and Z. Gabelica. J. Chem. Soc. Faraday Trans. 1, **92**, 1031 (1996).
49. R.D. Ruiter, K. Pamin, A.P.M. Kentgens, J.C. Jansen, and H. Van Bekkum. Zeolites, **13**, 611 (1993).
50. H. Kosslick, G. Lischke, B. Parlitz, W. Storek, and R.Fricke. Appl. Catal. **184**, 49 (1999).
51. S.K. Badamali, A. Sakthivel, and P. Selvam. Catal. Lett. **65**, 153 (2000).
52. H.G. Karge, V. Dondur, and J. Weitkamp. J. Phys. Chem. **95**, 283 (1991).
53. H. Kosslick, G. Lischke, H. Landmesser, B. Parlitz, W. Storek, and R. Fricke. J. Catal. **176**, 102 (1998).
54. K.F.M.G.J. Scholle, A.P.M. Kentgens, W.S. Veeman, P. Frenken, and G.P.M. Van der Velden. J. Phys. Chem. **88**, 5 (1984).
55. M.W. Simon, S.S. Nam, W.-q. Xu, S.L. Suib, J.C. Edwards, and C.L. O'Young. J. Phys. Chem. **96**, 6381 (1992).
56. P.E. Eberly, Jr. J. Phys. Chem. **71**, 1717 (1967).

© 2004 NRC Canada

Experimental and computational investigation of the electrocatalytic hydrogenation of phenol in an electrochemical cell

A. Chagnes, F. Laplante, F. Kerdouss, P. Proulx, and H. Ménard

Abstract: The electrocatalytic hydrogenation (ECH) of phenol was carried out in aqueous media with a commercial Pd/Al_2O_3 (5% w/w) catalyst. A porous matrix of reticulated vitreous carbon (RVC) was used to study the porosity – stirring speed coupling (PSSC) effect on the phenol hydrogenation to form cyclohexanone and cyclohexanol. In accordance with the PSSC, the electrode can act as a fluidized bed electrode or as an agglomerated electrode. Fluidized bed electrodes develop for low porosity matrices (10–30 ppi, ppi = pores per inch) at high stirring speeds (>600 rpm), while agglomerated electrodes are obtained for high porosity matrices (60–100 ppi) with moderate stirring speeds under cathodic polarization. The distribution of the volume fraction of the particles and the agglomeration of the particles have been simulated by computational fluid dynamic (CFD) methods with FLUENT software. For the agglomerated electrode, the numerical simulations demonstrate the beneficial contribution of the cathodic polarization to the agglomeration process. However, at 650 rpm, for the fluidized bed electrode, the volume fraction of the particles in the RVC does not account for the distinction in the ECH efficiency between the 30 ppi matrix and the 100 ppi matrix. For a given amount of Pd/Al_2O_3 catalyst, it is observed that the ECH rates depend on the PSSC and increase in the following order: 100/650 < 30/650 < 100/200.

Key words: electrocatalytic hydrogenation (ECH), CFD, fluid mechanics, porous media, powder, porosity – stirring speed coupling (PSSC), reticulated vitreous carbon (RVC).

Résumé : On a effectué l'hydrogénation électrocatalytique (HEC) du phénol en milieu aqueux, à l'aide d'un catalyseur commercial de Pd/Al_2O_3 (5% p/p). Afin d'étudier l'effet de couplage de la vitesse d'agitation et de la porosité (CVAP) sur l'hydrogénation du phénol avec formation de cyclohexanone et de cyclohexanol, on a utilisé une matrice de charbon vitreux réticulé (CVR). Suivant le CVAP, l'électrode peut agir comme électrode à lit fluidisé ou comme électrode agglomérée. Les électrodes à lit fluidisé se développent avec des matrices de faibles porosités (10–30 ppi, ppi = pores per inch), à des vitesses élevées (>600 rpm) alors que les électrodes agglomérées sont obtenues avec des matrices de porosité élevée (60–100 ppi) et des vitesses d'agitation modérées, sous une polarisation cathodique. La distribution de la fraction volumique des particules et l'agglomération des particules ont été simulées par les méthodes de calculs dynamiques des fluides (CDF) à l'aide du logiciel FLUENT. Pour l'électrode agglomérée, les simulations numériques permettent de mettre en évidence la contribution bénéfique de la polarisation cathodique du processus d'agglomération. Toutefois, à 650 rpm, pour l'électrode à lit fluidisé, la fraction volumique des particules dans le CVR ne permet pas d'expliquer la distinction dans l'efficacité de l'HEC entre la matrice à 30 ppi et la matrice à 100 ppi. Pour une quantité donnée de catalyseur Pd/Al_2O_3, on a observé que les vitesses d'HEC dépendent du CVAP et qu'elles augmentent dans l'ordre 100/650 < 30/650 < 100/200.

Mots clés : hydrogénation électrocatalytique (HEC), CDF, mécanique des fluides, milieu poreux, poudre, couplage de la vitesse d'agitation et de la porosité (CVAP), carbone vitreux réticulé (CVR).

[Traduit par la Rédaction]

Introduction

The electrocatalytic hydrogenation (ECH) of phenol is a relevant electrochemical process used to produce cyclohexanone and cyclohexanol from phenol (1–3). The products can be used to produce solvents for varnishes, resins, dyes, or to produce "KA oil", a precursor of adipic acid (4). Computational simulation is an interesting tool to optimize the electrochemical cell design and the electrocatalytic hydrogenation conditions. To enhance the conversion rate of cyclohexanol obtained from hydrogenation of phenol, several studies have focused on the concept of optimized new cata-

Received 8 August 2003. Published on the NRC Research Press Web site at http://canjchem@nrc.ca on 7 May 2004.

A. Chagnes, F. Laplante, and H. Ménard.[1] Département de Chimie, Centre de Recherche en Electrochimie et Electrocatalyse, Université de Sherbrooke, Sherbrooke, QC J1K 2R1, Canada.
F. Kerdouss and P. Proulx. Département de Génie chimique, Centre de Recherche en Technologie des Plasmas, Université de Sherbrooke, Sherbrooke, QC J1K2R1, Canada.

[1]Corresponding author (e-mail: hugues.menard@usherbrooke.ca).

 doi: 10.1139/V04-019 © 2004 NRC Canada

lysts (5–7). ECH is another way to hydrogenate organic compounds with high efficiency. The more convenient approach is to carry out the hydrogenation process using electricity to generate in situ atomic hydrogen at room temperature and under normal pressure.

It is well established in the literature (8, 9) that the generation of atomic hydrogen (H_{ads}) and molecular hydrogen (H_2) on metal (M) in solutions can proceed through any of the following reactions:

[1] $H_2O + M + e^- \leftrightarrows MH_{ads} + OH^-$ (Volmer reaction)

[2] $H_2O + MH_{ads} + e^- \leftrightarrows M + H_2 + OH^-$ (Heyrovsky reaction)

[3] $2MH_{ads} \leftrightarrows 2M + H_2$ (Tafel reaction)

The efficiency of the electrocatalytic hydrogenation of phenol is determined by the preceding reactions, the adsorption and desorption power of the substrate toward the organic molecules, and other properties as well as the nature of the electrode, the current density, the pH, the solvent composition (6). Heyrovsky and Tafel reactions are competive reactions for the hydrogenation of organic compounds.

Recent developments in the preparation of catalytic electrode materials having high efficiency and long term stability have raised new interest in electrocatalytic hydrogenation (6, 7, 10–12). There are several methods to produce composite materials with a metallic matrix: powder metallurgy (13), metal plasma spraying (14), chemical and physical vapour deposition (15), liquid metal forging (15), and electrocodeposition (16).

In this paper, the effect of the porosity of the RVC foam vs. the stirring speed on the efficiency of commercial Pd/Al_2O3 5% catalysts for the hydrogenation of phenol was investigated. The experimental results were compared with a computer simulation of the hydrodynamic behaviour of catalyst particles for a RVC matrix of various porosity in the electrochemical cell described in a previous paper (17).

Experimental

The electrodes

The electrochemical cell used in this paper has been previously described (17) and is shown in Fig. 1. The electrode was made from the entrapment of catalytic powder particles in a piece of reticulated vitreous carbon (RVC) matrix. The RVC matrix was a piece of foam (25 mm × 20 mm × 6 mm, 30 pores per inch (ppi) or 100 ppi, Electrosynthesis Co.). The conducting matrix was mounted by inserting a glass rod (OD 5 ~ 6 mm, ID 3.5 mm) in the horizontal axis of a piece of RVC (20 mm × 40 mm × 6 mm). The excess RVC was then removed and a copper wire was inserted into the RVC to be further cemented with silver epoxy (Epoxy Technology). Finally, the electrical contact zone on the RVC matrix was glued to the glass rod with epoxy to isolate the electrical contact from the electroactive part of the electrode. The use of a nickel strip as a contact with the RVC electrode should be avoided because the nickel activity towards the electrocatalytic hydrogenation of ketone may affect the data (18).

The physical entrapment of the composite material in the RVC foam occurred under moderate stirring of the catholyte (~450 rpm), and the catalyst powder particles were trapped into the RVC matrix pores spontaneously. The catalytic powder remained in the pores of the RVC electrode cathodically polarized (j = 100 mA/dm²) for the electrohydrogenation process and was in electrical contact with the matrix (17). With such an RVC, the average diameter of the particle is 12.4 μm. The entrapment process is completed within 2 h, up to a charge of 50 C. The dimensions of the H-cell and those related to the other parts are described in a previous paper (17).

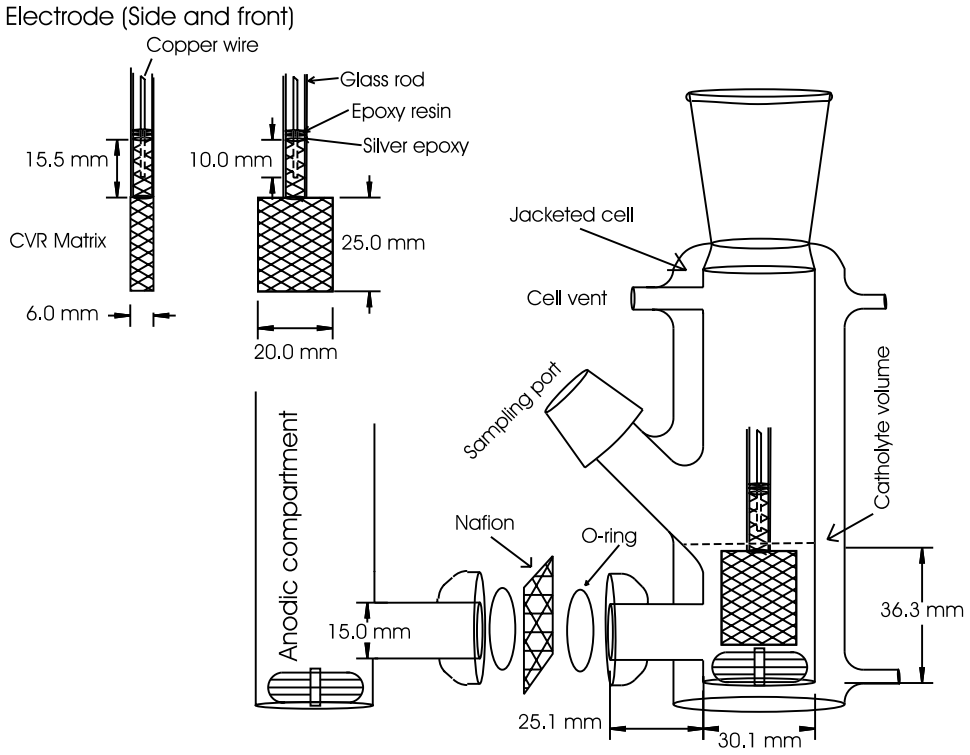
Electrolysis

The electrolysis was carried out in a two-compartment jacketed glass H-cell having a Nafion-117 (E.I. Dupont de Nemours and Co.) membrane as a separator. The cell temperature was fixed at 21 °C during the electrocatalytic hydrogenation process by a circulating thermostated bath (VWR 1160A). To prevent analyte evaporation, a water-cooled condenser was added to the top of the cell. Afterwards, the cathodic compartment was filled with a phosphate buffer (29 mL, 1 mol/L KH_2PO_4 + 1 mol/L NaOH) previously adjusted to pH 7 and 200 mg of the composite powder was added to the catholyte. The electrode was built-up in situ with the previously described technique. The anodic compartment was filled with a 1 mol/L NaOH solution (Fisher); the counter-electrode was a platinum mesh. Prior to the electrocatalytic hydrogenation process, 1 mL of a phenol solution in water (25 mg/mL) was added to the catholyte giving a total volume of 30 mL and a phenol concentration of 8.8×10^{-3} mol/L. The electrocatalytic hydrogenation was performed under galvanostatic control (j = 1 mA/cm²) using EG&G PAR model 273 for 25 h (450 C at 5 mA). The commercial powder catalyst considered in the present paper (Pd/Al_2O_3, 5%) was provided by Aldrich and used as received.

During the electrocatalytic hydrogenation process (ECH), aliquots of 500 μL were withdrawn from the catholyte, saturated with NaCl, and acidified to pH 1 with HCl (conc. HCl, 10 mol/L), and then extracted with 1 mL ethyl acetate and dried under sodium sulfate. After the completion of ECH, both the RVC electrode and the whole cell were rinsed with pure water. An internal standard (ISTD, 2-cyclohexen-1-one) was added to the cell solution; further, the extraction was carried out twice (2 × 20 mL) with distilled ethyl acetate. The organic layer was dried on sodium sulfate and filtered. The filtrate was collected in a 50 mL volumetric flask containing an external standard (ESTD, 3-methylcyclohexanol). The GC analyses were carried out using a Hewlett-Packard 6890 chromatograph equipped with a FID detector on a 30 m HP-5 column. The products were identified by comparison with the retention time of the authentic compound and the mass balance was obtained from the ISTD/ESTD ratio of the corrected peak surface area. In accordance to the ISTD/ESTD ratio, a recovery percentage greater than 85% was observed.

© 2004 NRC Canada

Fig. 1. Electrochemical cell used in the electrocatalytic hydrogenation of phenol.



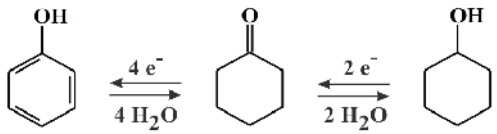
Computer simulation

The computer simulation of the hydrodynamic behaviour of the catalyst particles in the electrochemical cell was performed by the computational fluid dynamic method (CFD). The multiphase model, described in the computation simulation section of this paper, was solved using FLUENT version 6.0.1 with nonstructured mesh adapted to the geometry. The phase-coupled SIMPLE (PC-SIMPLE) algorithm was used for the pressure–velocity coupling. A first-order upwind discretization scheme was used for spatial derivatives and a first-order discretisation scheme was used for temporal derivatives. A time step of 10^{-4} s was used initially and augmented progressively to 10^{-2} s. A description of the mathematical techniques used in FLUENT is detailed in the computation simulation section of this paper.

Results and discussion

Electrochemical efficiency

During the electrohydrogenation of phenol, the chemisorbed hydrogen (MH_{ads} in eq. [1]) is generated in situ by electroreduction of water and reacts with the absorbed phenol substrate according to the following steps reported in the literature (19):

[4] 

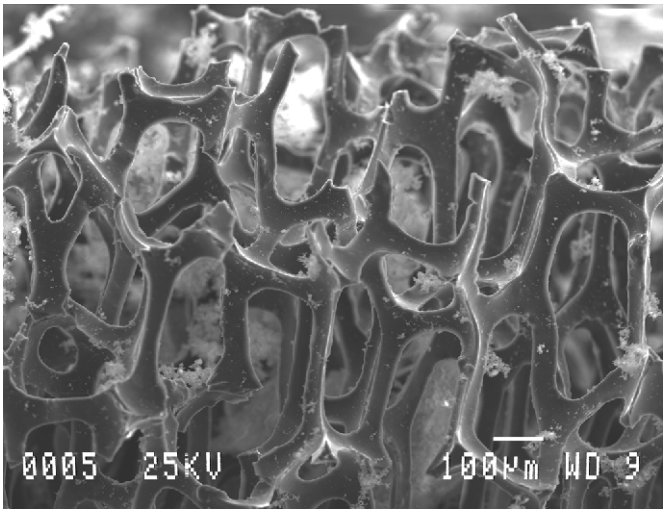
The electrochemical efficiency of the catalyst particles (Pd/Al_2O_3, 5% w/w) was investigated with an electrochemical cell described in a previous paper (17) (Fig. 1). Our work demonstrates that the stirring speed and the matrix porosity affect considerably the ECH process. According to the porosity – stirring speed coupling (PSSC–ppi/rpm), we determined that the RVC matrix can act as an agglomerated electrode or a fluidized bed electrode. First, for the high porosity electrode with moderate stirring, the electrode behaves as an agglomerated electrode, suggesting that the catalyst is entirely trapped inside the RVC pores and remains in electrical contact with the RVC matrix during the HEC process. With the high porosity matrix (60–100 ppi), the agglomeration must be complete prior to the ECH otherwise the hydrogenation of phenol is impossible (Fig. 2).

The second kind of electrode is inspired by fluidized bed systems. Fluidized bed systems are observed only with the low porosity matrix (between 30 and 10 ppi) at high stirring speeds (>600 rpm). With this type of porosity – stirring speed couple, there is no agglomeration of the catalyst powder in the matrix. For a PSSC of 30/650, the powder is free to circulate through the matrix and to establish brief electrical contacts with the RVC conductor. In such a way, the catalyst particles are charged with hydrogen and free to react with the phenol in solution.

The effects of the stirring speed (200 and 650 rpm) on the RVC porosity (30 and 100 ppi) on the electrocatalytic hydrogenation of phenol are displayed in Fig. 3. In accordance with the PSSC used, the ECH efficiency varies significantly. To study the electrohydrogenation efficiency at 200 rpm with the agglomerated electrodes, a new protocol was used: the particles were forced to agglomerate inside the electrode at 450 rpm during a charge of 50 C (I_{app} = 5 mA). When phenol was added, the stirring speed was lowered to 200 rpm and the electrocatalytic hydrogenation was studied. Results

© 2004 NRC Canada

Fig. 2. SEM picture of catalyst particles trapped in the porous RVC electrode (100 ppi).



obtained at 200 rpm with a porosity of 100 ppi (Fig. 3, curves a and a′) show improvement as compared with results obtained with a stirring speed of 650 rpm (Fig. 3, curves c and c′). The enhanced efficiency recorded at 200 rpm for the cyclohexanol production can be explained by the conservation of electrode integrity, which remains agglomerated during the entire process. Above 600 rpm, the agglomerated catalyst powder is washed out from the RVC matrix and the reagglomeration becomes impossible due to the turbulence of the fluid in the cell.

The PSSC of 30/650 (Fig. 3, curves b and b′) represents an alternate way to achieve HEC with non-agglomerating catalysts. The high void volume of the RVC foam permits the catalyst to penetrate into the RVC and to achieve brief electrical contacts with the matrix. These intermittent contacts cover the catalyst with electrosorbed hydrogen. The low porosity matrix should be employed at high stirring speed (>600 rpm) to optimize the uniformity of the distribution of the catalytic powder in the matrix.

In the preceding experiments, the hydrogenation was performed with convection. To investigate the impact of diffusion on the electrocatalytic hydrogenation, the stirring was stopped after trapping the particles into the RVC electrode, and the formation of cyclohexanol was studied during the electrolysis for different matrix porosities (between 60 and 100 ppi) (Fig. 4). Hydrogenation occurs with lower efficiencies but the porosity of the electrode does not influence the electrocatalytic hydrogenation in the absence of convective flow.

The optimal conditions for the ECH of phenol in the electrochemical cell can be deduced from Fig. 5, which shows the reaction map of the experimental results concerning the effect of the PSSC on the conversion efficiency. The electrocatalytic hydrogenation is quite dependent on the stirring and the porosity. The agglomerating electrodes (Fig. 5, sector A) have higher efficiency at high porosity with moderate stirring (PSSC 100/200), while the nonagglomerating electrodes (Fig. 5, sector B) reach their maximum efficiency for a PSSC of 30/650. The slight discrepancy observed between the experimental results (Fig. 4) and the graphical representation (Fig. 5) (between PSSC 60/0 and PSSC 100/0) is attributed to the smoothing process needed to plot the reaction map.

Fig. 3. Phenol depletion to cyclohexanol. Curve a and a′ (▲), 100 ppi at 200 rpm (catalyst Pd/alumina 5% previously trapped inside the RVC pores at 450 rpm); Curve b and b′ (■), 30 ppi at 650 rpm; and Curve c and c′ (●), 100 ppi at 650 rpm.

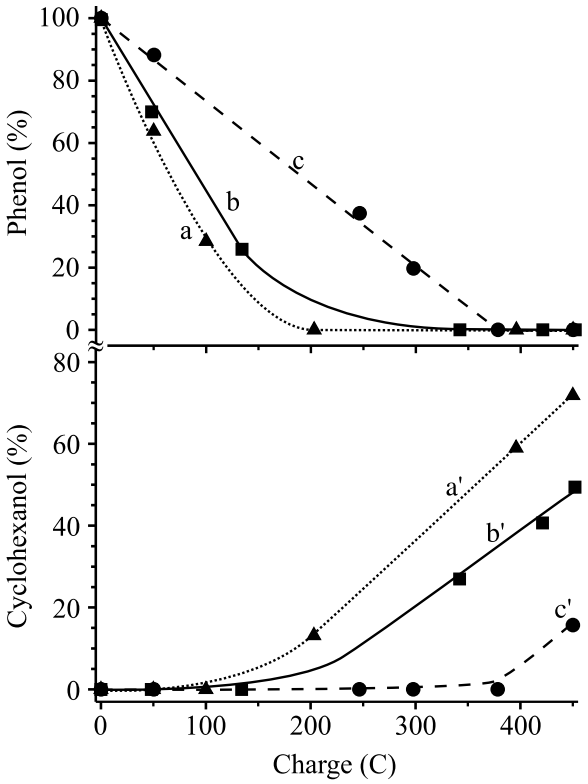
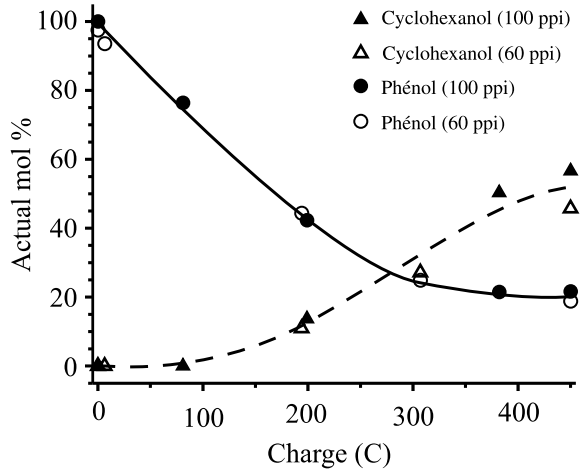


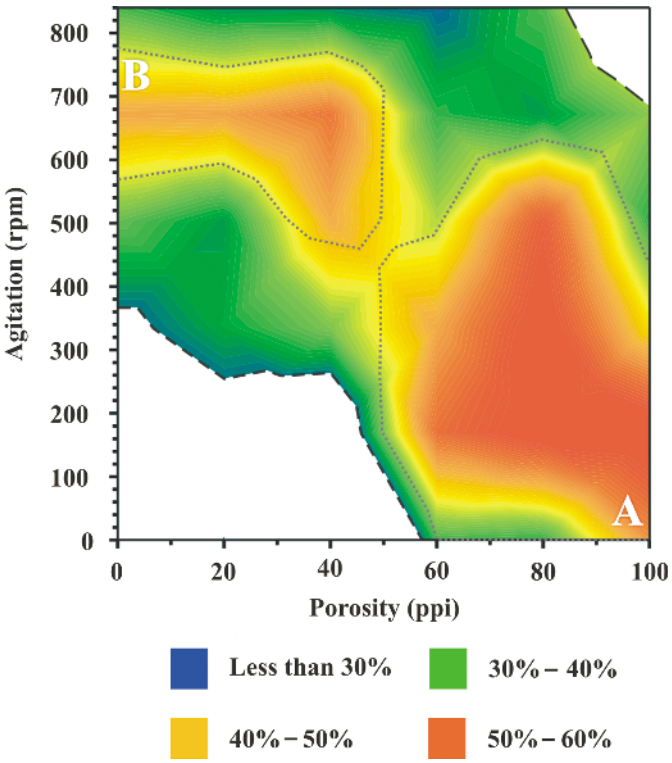
Fig. 4. Cyclohexanol yield from the ECH of phenol with Pd/alumina 5% (w/w) catalyst at 0 rpm after a complete trapping of the particles in the RVC electrode at 450 rpm.



To further investigate the roles of the porosity and the stirring on the electrohydrogenation efficiency, a CFD (computational fluid dynamic) simulation has been performed. Moreover, the CFD simulation was used to clarify the polarization effect on the agglomeration process.

© 2004 NRC Canada

Fig. 5. Experimental data for the evolution of the cyclohexanol yield during the hydrogenation of phenol with Pd/alumina 5% (w/w) in accordance with the PSSC.



CFD simulation

As previously stated, the hydrodynamic properties of the fluid in an electrochemical cell play important roles. A CFD simulation of the hydrodynamic behaviour of particles composed of alumina and palladium was realized by a CFD simulation using the commercial software package FLUENT. FLUENT uses finite volume mathematical procedures to solve the equations for fluid velocities, mass flow, pressure, temperature, species concentration, turbulence parameters, and fluid properties. Numerical techniques involve the subdivision of the domain into a finite set of neighbouring cells known as "control volumes" and applying discretized partial differential equations over each cell. This yields a large set of simultaneous algebraic equations that are highly nonlinear. These equations are in turn solved by iterative means until a converged solution is achieved.

The mathematical techniques are based on the solutions of Navier–Stokes equations for the Eulerian multiphase granular model along with the multiphase k–ε turbulence model. Multiple reference frame (MRF) and porous models are used, respectively, to account for the stirring and porous cathode in the cell.

The governing equations

The multiphase granular model was used to simulate monodispersed particles (S) in the electrolyte (L) (20). The mass conservation equation for each phase is written as

$$[5] \quad \frac{\partial}{\partial t}(\rho_q \alpha_q) + \nabla \cdot (\alpha_q \rho_q \vec{U}_q) = 0.0$$

where ρ_q, α_q, and $\vec{U}_q$ represent the density, volume fraction, and mean velocity, respectively, of phase q (L or S).

The momentum conservation equation for the liquid phase after Reynolds averaging is written as

$$[6] \quad \frac{\partial}{\partial t}(\alpha_L \rho_L \vec{U}_L) + \nabla \cdot (\alpha_L \rho_L \vec{U}_L \vec{U}_L) = -\alpha_L \nabla p + \nabla \cdot \bar{\bar{\tau}}_{\text{eff L}} + \vec{R}_{SL} + \alpha_L \rho_L \vec{g}$$

and for the dilute solid phase as

$$[7] \quad \frac{\partial}{\partial t}(\alpha_S \rho_S \vec{U}_S) + \nabla \cdot (\alpha_S \rho_S \vec{U}_S \vec{U}_S) = -\alpha_S \nabla p + \nabla p_S + \nabla \cdot \bar{\bar{\tau}}_{\text{eff S}} + \vec{R}_{LS} + \alpha_S \rho_S \vec{g} + \vec{F}_{\text{Selec}}$$

ρ is the pressure shared by the two phases, and p_s is the solid pressure modeled with the granular multiphase model (FLUENT) (19). $\vec{R}_{SL}$ represents the interfacial transfer term due to drag force. FLUENT uses a simple interaction term of the following form

$$[8] \quad \vec{R}_{SL} = -\vec{R}_{LS} = K_{SL}(\vec{U}_S - \vec{U}_L)$$

L_{SL} is the liquid–solid exchange coefficient calculated using the Syamlal–O'Brien model (21).

The external force due to the presence of an electrical field is written as

$$[9] \quad \vec{F}_{\text{Selec}} = q_s \cdot \vec{E}$$

where q_s is the solid particle charge, and $\vec{E}$ is the electrical field derived from the electrical potential (ϕ).

$$[10] \quad \vec{E} = -\nabla \phi$$

$\bar{\bar{\tau}}_{\text{eff L}}$ is the effective liquid phase stress–strain tensor defined as

$$[11] \quad \bar{\bar{\tau}}_{\text{eff L}} = -\frac{2}{3}\alpha_L(\rho_L k_L + (\mu_{\text{lam,L}} + \mu_{t,L})\nabla \cdot \vec{U}_L)\bar{\bar{I}} + \alpha_L(\mu_{\text{lam,L}} + \mu_{t,L})(\nabla \vec{U}_L + \nabla \vec{U}_L{}^T)$$

The liquid turbulent viscosity is written as

$$[12] \quad \mu_{t,L} = \rho_L C_\mu \frac{k_L^2}{\varepsilon_L}$$

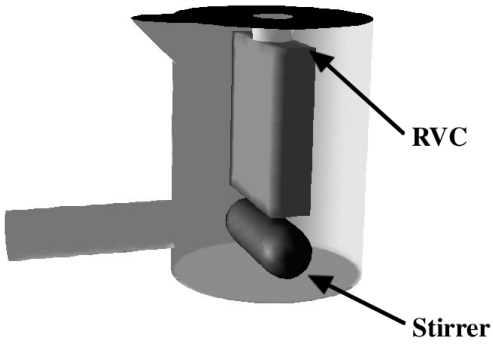
where k_L is turbulent kinetic energy, and ε_L is the turbulent energy dissipation rate in the liquid phase. The predictions are obtained from the modified standard k–ε model

$$[13] \quad \frac{\partial}{\partial t}(\alpha_L \rho_L k_L) + \nabla \cdot (\alpha_L \rho_L \vec{U}_L k_L) = \nabla \cdot \left(\alpha_L \frac{\mu_{t,L}}{\sigma_k} \nabla k_L\right) + \alpha_L G_{k,L} - \alpha_L \rho_L \varepsilon_L + \alpha_L \rho_L \Pi_{kL}$$

$$[14] \quad \frac{\partial}{\partial t}(\alpha_L \rho_L \varepsilon_L) + \nabla \cdot (\alpha_L \rho_L \vec{U}_L \varepsilon_L) = \nabla \cdot \left(\alpha_L \frac{\mu_{t,L}}{\sigma_\varepsilon} \nabla \varepsilon_L\right) + \alpha_L \frac{\varepsilon_L}{k_L}(C_{1\varepsilon} G_{k,L} - C_{2\varepsilon} \alpha_L \rho_L \varepsilon_L) + \alpha_L \rho_L \Pi_{\varepsilon L}$$

© 2004 NRC Canada

Fig. 6. Cathodic compartment used for the CFD simulation.



C_μ, $C_{1\varepsilon}$, $C_{2\varepsilon}$, σ_k, and σ_ε are parameters of the standard k–ε model used for single-phase flows (C_μ = 0.09, $C_{1\varepsilon}$ = 1.44, $C_{2\varepsilon}$ = 1.92, σ_k = 1.0, σ_ε = 1.3). G_{KL} is the production of turbulent kinetic energy based on single-phase flow. Π_{KL} and $\Pi_{\varepsilon L}$ represent the influence of the dispersed phase S on the continuous phase L. $\bar{\bar{\tau}}_{\text{eff S}}$ is the effective liquid phase stress–strain tensor defined as

$$[15]\quad \bar{\bar{\tau}}_{\text{eff S}} = \alpha_S\left(-\frac{2}{3}\rho_S k_S + \left(\lambda_S - \frac{2}{3}(\mu_{\text{lam,S}} + \mu_{t,S})\nabla\cdot\vec{U}_S\right)\right)\bar{\bar{I}} + \alpha_S(\mu_{\text{lam,S}} + \mu_{t,S})(\nabla\vec{U}_S + \nabla\vec{U}_S^{\,T})$$

The solid stress tensor contains the shear viscosity ($\mu_{\text{lam,S}}$) and the bulk viscosity (λ_S) arising from particle momentum exchange due to translation and collision. For the expression of $\mu_{\text{lam,S}}$ and λ_S, FLUENT uses the forms from Syamlal et al. (20) and Lun et al. (22), respectively. According to Simonin (23), FLUENT provides the turbulence quantities k_S and $\mu_{t,S}$.

The porous electrode was modelled by adding a momentum sink in the governing momentum equations. This sink term is nothing more than a viscous loss term representing the simple case of homogeneous porous media written as

$$[16]\quad \vec{S}_{\text{porous}} = -\frac{\mu_q}{\alpha}\vec{U}_q$$

where μ_q is the dynamic viscosity of phase q (L or S), $\vec{U}_q$ is the time-averaged velocity of phase q, and α is the porosity of the electrode.

The solution of flows in moving reference frames induced by the magnetic rotor requires the use of moving cell zones. This cell zone motion is interpreted as the motion of a reference frame to which the cell zone is attached. In this situation, the acceleration of the coordinate system is included in the equations of motion describing the flow. In FLUENT, multiple reference frame (MRF) is used including a rotating frame of reference attached to the magnetic rotor and a stationary frame of reference attached to the rest of the cell model.

Powder entrapment with no electric field

The CFD simulation was performed without an electric field, and the distribution of the volume fraction of the particles in the porous electrode was calculated for stirring speeds of 200 and 650 rpm for a given porosity of 100 ppi. The viscosity and the density of the electrolyte (60 mL of 1 mol/L KH_2PO_4 + 35 mL of 1 mol/L NaOH) are 0.001436 kg m^{-1} s^{-1} and 1069 kg m^{-3}, respectively, at 25 °C. The cathodic compartment of the electrochemical cell, used for CFD simulation, is presented at Fig. 6.

Fig. 7. Distribution of the particles in the RVC matrix for a porosity of 100 ppi at: (*a*) 200 rpm, and (*b*) 650 rpm.

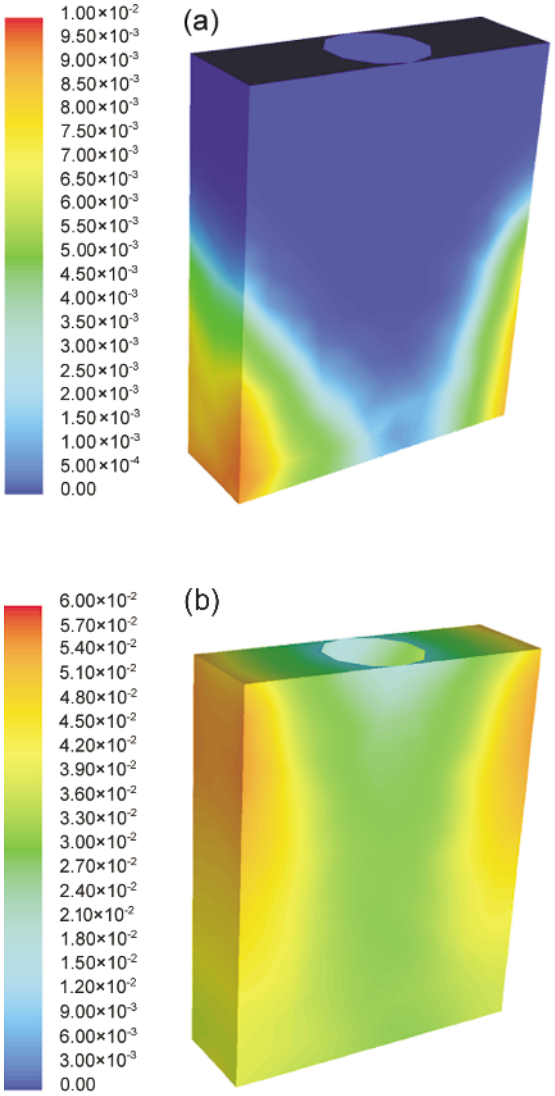


Figure 7 (A and B) displays the volume fraction of the particles for stirring speeds of 200 and 650 rpm in a RVC electrode (100 ppi). At 650 rpm, the particles are uniformly distributed in the porous electrode and the volume fraction is higher than the volume fraction at 200 rpm. The volume fraction of the particles in the RVC electrode at 200 rpm is not homogeneous. This difference of volume fraction and uniformity of the particles distribution may explain why no aggregation of particles in the porous electrode was observed at 200 rpm.

A similar study was realized at 650 rpm with a RVC porosity of 30 ppi to investigate the impact of the porosity on the distribution of the particles (Fig. 8). The porosity plays

© 2004 NRC Canada

Fig. 8. Distribution of the particles in the RVC matrix for a porosity of 30 ppi at 650 rpm.

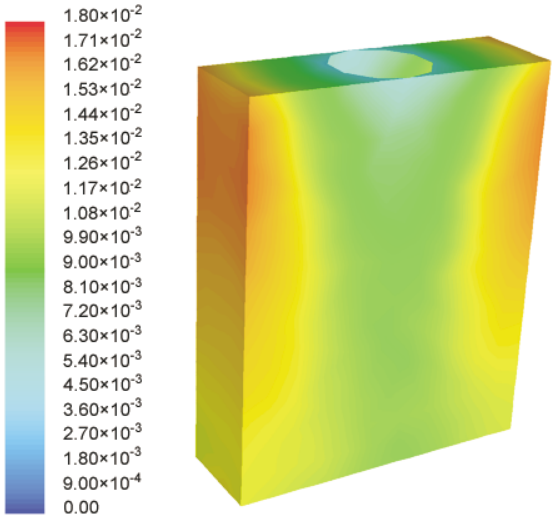
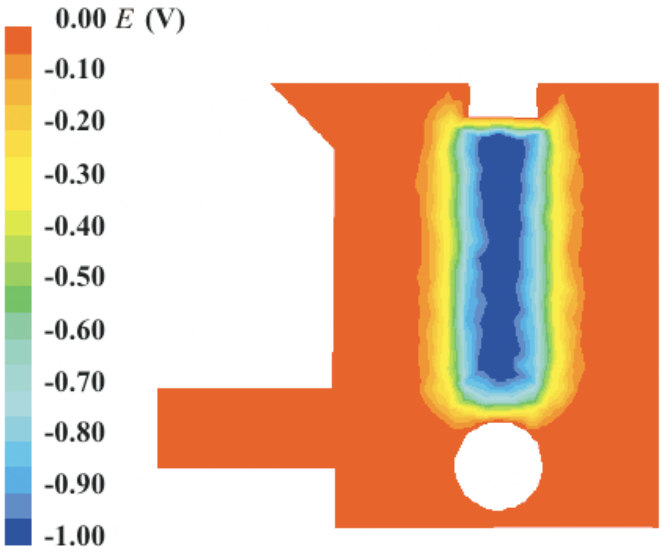


Fig. 9. Potential distribution in the electrochemical cell.



an important role concerning the distribution of the particles in the porous electrode as the volume fraction is divided by three when the electrode porosity is divided by three. However, the low hydrogenation efficiency obtained at 100 ppi (Fig. 3, curves c and c′) compared with 30 ppi (Fig. 3, curves b and b′) can not be explained by the volume fraction of catalyst particles in the RVC matrix. Assuming that the catalytic particles are in constant motion and free to travel through the matrix, it is reasonable to assume that the 30 ppi matrix has more electrical contact with the catalytic powder than the 100 ppi matrices.

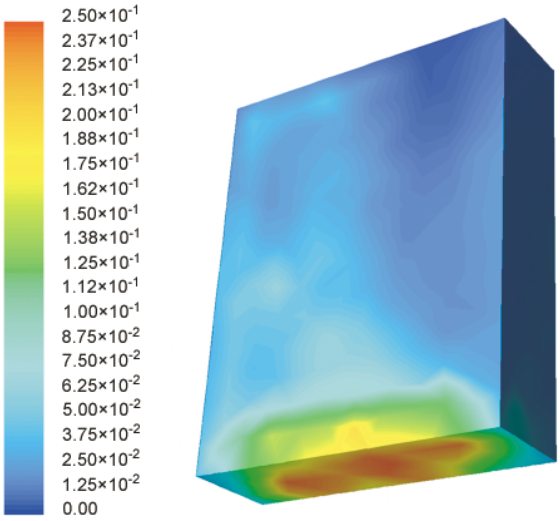
Powder entrapment in the presence of an electric field

Aggregation of the particles was only observed in the presence of an electric field in the electrochemical cell. The effect of the electric field on the volume fraction was studied by a CFD simulation to explain this experimental observation. The distribution of potential (ϕ) in the cell was calculated with eq. [5] and was implemented with a user-defined scalar in FLUENT version 6.0.1 with zero potential at the walls of the electrochemical cell and a negative potential (–1 V) in the RVC electrode (Fig. 9). The electric field in the cell was computed assuming that the potential distribution can be approximately described by Laplace's equation (i.e., reactions on the electrode do not significantly perturb the potential distribution (24)).

$$[17] \quad \frac{\partial^2 \phi}{\partial x^2} = 0$$

In this simulation, aggregation in the RVC electrode occurs only if the value of the charge on the particles (q) is larger than 5×10^{-7} C (Fig. 10).

Fig. 10. Distribution of the volume fraction of the particles in the presence of an electric field for $q = 5 \times 10^{-7}$ C.



Conclusion

The ECH efficiency of phenol depends on the electrode material but also on the electrochemical cell. In this study, the electrolysis was carried out in a two-compartment jacketed glass H-cell and it was demonstrated that the stirring and the porosity of the RVC electrode play important roles in determining the distribution of the particles in the porous electrode. The best hydrogenation efficiency was obtained with a high porosity electrode (between 60 and 100 ppi) with a moderate stirring speed. The CFD model used to describe the catalyst particle distribution in the RVC electrode when an electric field is applied confirms the catalyst entrapment phenomenon observed during the experiments. However, simulation does not allow us to show a direct correspondence between the volume fraction of the catalyst particles and the porosity of the reticulated vitreous electrode for the electrochemical hydrogenation of phenol.

Acknowledgements

We thank the Natural Sciences and Engineering Research Council of Canada (NSERC), le Fonds Québécois de la re-

© 2004 NRC Canada

cherche sur la nature et les technologies (FQRNT), and la Région Centre de France for financial support.

References

1. L.L. Miller and L. Christen. J. Org. Chem. **43**, 2059 (1978).
2. K. Sasaki, A. Kunai, J. Harada, and S. Nakabori. Electrochim. Acta, **28**, 671 (1983).
3. R.A. Misra and B.L. Sharma. Electrochim. Acta, **24**, 727 (1979).
4. D. Eckroth. *In* Encyclopedia of chemical technology. 3rd ed. Vol. 7. *Edited by* M. Grayson. John Wiley, New York. 1993. pp. 410–416.
5. G. Neri, A.M. Visco, A. Donato, C. Milone, M. Malentacchi, and G. Gubisota. Appl. Catal. A, **110**, 49 (1994).
6. A.M. Couper, D. Pletcher, and F.V. Walsh. Chem. Rev. **90**, 837 (1990).
7. P. Dubé, L. Brossard, and H. Ménard. Can. J. Chem. **80**, 345 (2002).
8. J.O'M. Bockris. *In* Comprehensive treatise of electrochemistry. Vol. 3. *Edited by* J.O'M. Bockris, E. Yeager, and R.E. White. Plenum Press, New York. 1981. pp. 1–505.
9. A. Lasia. *In* Handbook of fuel cells: Fundamentals, technology and applications. Vol. 2. *Edited by* W. Vielstich, A. Lamm, and H.A. Gasteiger. John Wiley and Sons, Ltd., New York. 2003. pp. 416–440.
10. A. Martel, B. Mahdavi, J. Lessard, L. Brossard, and H. Ménard. Can. J. Chem. **75**, 1862 (1997).
11. K. Amouzegar and O. Savadogo. Electrochim. Acta, **43**, 503 (1998).
12. P.I. Iotov and S.V. Kalcheva. J. Electroanal. Chem. **442**, 19 (1998).
13. F.V. Lenel. *In* Powder metallurgy principles and applications. Metal Powder Industries Federation, Princeton, N.J. 1980.
14. T.G. Coker and S.D. Agrade. US Patent 409 841, 1977.
15. K.K. Chawla. *In* Composite materials: Sciences and engineering. *Edited by* B. Ilschner and N.J. Grant. Springer-Verlag, New York. 1987. p. 102.
16. J. Lessard and G. Belot. US Patent 45 806, 1986.
17. F. Laplante, L. Brossard, and H. Ménard. Can. J. Chem. **81**, 258 (2003).
18. P. Dubé, F. Kerdouss, F. Laplante, P. Proulx, L. Brossard, and H. Ménard. J. Appl. Electrochem. **33**, 541 (2003).
19. K. Amouzegar and O. Savadogo. Electrochim. Acta, **39**, 557 (1994).
20. M. Syamlal, W. Rogers, and T.J. O'Brien. Theory guide. Vol. 1. National Technical Information Service, Springfield, Va. 1993.
21. M. Syamlal and T.J. O'Brien. AIChE Symp. Series, **85**, 22 (1989).
22. C.K.K. Lun, S.B. Savage, D.J. Jeffrey, and N. Chepurniy. J. Fluid Mech. **140**, 223 (1984).
23. C. Simonin and L. Viollet. *In* Proceedings of the American Society of Mechanical Engineers, Fluids Engineering Division, Toronto, June 1990. Vol. 91. ASME, New York. 1990.
24. F. Coeuret and A. Storck. *In* Éléments de génie électrochimique. Génie des procédés de l'école de Nancy (ENSIC). Technique & Documentation-Lavoisier, Paris. 1993. pp. 169–194.

© 2004 NRC Canada

Novel mixed-ligand Pt(II) complexes: Synthesis, multinuclear magnetic resonance, and crystal structures of *cis*- and *trans*-Pt(R_2SO)(pyrazine)Cl_2

Fernande D. Rochon and Julien R.L. Priqueler

Abstract: A new type of mixed-ligand Pt(II) complexes, Pt(R_2SO)(pyrazine)Cl_2, was synthesized from the aqueous reaction of K[Pt(R_2SO)Cl_3] with pyrazine. The compounds were characterized mainly by IR and multinuclear magnetic resonance spectroscopies (^{1}H, ^{13}C, and ^{195}Pt) and crystallography. Compounds with dimethylsulfoxide, tetramethylenesulfoxide, di-*n*-propylsulfoxide, di-*n*-butylsulfoxide, dibenzylsulfoxide, and diphenylsulfoxide were studied. IR spectroscopy suggested a cis geometry for the di-*n*-propylsulfoxide complex and trans geometry for the other compounds. The ^{195}Pt NMR resonances of the complexes were observed between –3042 and –3121 ppm, with that of the diphenylsulfoxide complex being at higher field than those of the others. The pyrazine $^3J(^{195}Pt\text{-}^1H)$ coupling constant was observed for the DMSO compound (33 Hz), suggesting a trans geometry. No $J(^{195}Pt\text{-}^{13}C)$ coupling could be detected. The crystal structures of *trans*-Pt(tetramethylenesulfoxide)(pyrazine)Cl_2 and of *cis*-Pt(di-*n*-propylsulfoxide)(pyrazine)Cl_2 were determined and confirmed the geometry suggested by IR and NMR spectroscopies. The compound with di-*n*-butylsulfoxide could not be isolated, because it rapidly formed the pyrazine-bridged dimer.

Key words: platinum, sulfoxide, pyrazine, crystal structure, NMR, IR.

Résumé : Un nouveau type de complexes du platine(II) contenant des ligands mixtes a été synthétisé lors de la réaction en milieu aqueux de K[Pt(R_2SO)Cl_3] avec la pyrazine. Les composés Pt(R_2SO)(pyrazine)Cl_2 ont été caractérisés par spectroscopie infrarouge, par résonance magnétique multinucléaire (^{1}H, ^{13}C et ^{195}Pt) et par cristallographie. Des complexes avec les ligands diméthylsulfoxyde, tétraméthylènesulfoxyde, di-*n*-propylsulfoxyde, di-*n*-butylsulfoxyde, dibenzylsulfoxyde et diphénylsulfoxyde ont été étudiés. La spectroscopie IR a suggéré une géométrie cis pour le composé contenant le ligand di-*n*-propylsulfoxyde et une isomérie trans pour les autres complexes. Les résonances en RMN du ^{195}Pt ont été observées entre –3042 et –3121 ppm. Le composé contenant diphénylsulfoxyde a été observé à plus haut champ que les autres. La constante de couplage de la pyrazine $^3J(^{195}Pt\text{-}^1H)$ a été observé pour le composé contenant le DMSO (33 Hz) suggérant une géométrie trans. Aucun couplage de type $J(^{195}Pt\text{-}^{13}C)$ n'a été détecté. Les structures cristallines des deux composés *trans*-Pt(tétraméthylènesulfoxyde)(pyrazine)Cl_2 et *cis*-Pt(di-*n*-propylsulfoxyde)-(pyrazine)Cl_2 ont été déterminées par diffraction des rayons-X et les résultats ont confirmé les géométries suggérées par les spectroscopies IR et RMN. Le composé avec le ligand di-*n*-butylsulfoxyde n'a pas été isolé, car le dimère à pont pyrazine se forme trop rapidement.

Mots clés : platine, sulfoxyde, pyrazine, structures cristallines, RMN, IR.

Introduction

The antitumor activity of Pt(II) complexes of the type *cis*-Pt(amine)$_2Cl_2$ is well known. Cisplatin (*cis*-Pt(NH_3)$_2Cl_2$) remains the most commonly used anticancer agent in chemotherapy (1, 2), even though it exhibits numerous and significant side effects, but the search for more specific and less toxic drugs is still continuing.

A few *trans* Pt(II) complexes with amine ligands have shown anticancer activity in specific organs (3). Compounds with neutral ligands containing other donor atoms such as S have also shown some antitumor properties (4). Several Pt(II) complexes of the types [Pt(R_2SO)(diamine)Cl]NO_3 (5) and *cis*- and *trans*-Pt(R_2SO)(quinoline)Cl_2 (6) have shown biological activity, depending on the sulfoxide chain. Recently, it was reported that the pyrazine–Pt(II) complex [*cis*-{Pt(NH_3)$_2$Cl}$_2$(μ-pz)]Cl_2 and its derivatives showed good potential as anticancer compounds, especially because they largely seem to overcome the cross-resistance of cisplatin (7). The compounds possess an appropriate flexibility to provide the cross-links with a minimal distortion of the DNA.

Our group has been involved in research on Pt–sulfoxide complexes for many years. Sulfoxides are interesting ligands because they can accept π electron density from the metallic center. For these types of ligands, the cis complexes are usually more stable than the trans compounds (contrary to the amine systems). We have recently reported a study on mixed-ligand Pt(II) complexes containing pyrimidine (pm)

Received 7 August 2003. Published on the NRC Research Press Web site at http://canjchem@nrc.ca on 7 May 2004.

F.D. Rochon[1] and J.R.L. Priqueler. Département de chimie, Université du Québec à Montréal, C. P. 8888, Succ. Centre-ville, Montréal, QC H3C 3P8, Canada.

[1]Corresponding author (e-mail: rochon.fernande@uqam.ca).

 doi: 10.1139/V04-020 © 2004 NRC Canada

and sulfoxide ligands (8, 9). Pyrimidine also has empty π antibonding orbitals that could accept electron density from Pt. The aqueous reaction of $K[Pt(R_2SO)Cl_3]$ with pyrimidine (1:1 ratio) produced first *trans*-$Pt(R_2SO)(pm)Cl_3$, which could then isomerize to the *cis* compound (8).

To determine the influence of the pyrimidine ligand in these reactions, we have started a new study with pyrazine (pz) instead of pyrimidine. Unlike the latter, pyrazine is a symmetric molecule, but it too has empty π* orbitals that could form π bonds with Pt. We have recently published the results of the first part of this study, on the pyrazine-bridged dinuclear compounds $\{Pt(R_2SO)Cl_2\}_2(\mu\text{-pz})$ (10), which were found to have the trans-trans geometry. Pyrazine can form bridges between two metallic centers quite easily, even when an excess of pyrazine is used. Most reported works in the literature involve pyrazine-bridged oligomers.

There is no reported research on Pt compounds containing both sulfoxides and pyrazine except our recent publication of the pyrazine-bridged dimers (10). Only four papers on Pt compounds with nonsubstituted pyrazine were found in the literature. Among them, only two papers involve Pt(II) monomeric compounds. Albinati et al. (11) synthesized and characterized *trans*-Pt(phosphine)$(pz)Cl_2$, while Siedle et al. (12) prepared *trans*-$Pt(C_2H_4)(pz)Cl_2$ and its derivatives and used them as catalysts in hydrosilation reactions. No cis mixed-ligand Pt monomeric compounds with pyrazine have been reported. The nature of the Pt–pyrazine bond has not been investigated yet.

In the present publication, we report the results of our study on the aqueous reactions of $K[Pt(R_2SO)Cl_3]$ with pyrazine. Six sulfoxides that differ in steric hindrance were studied: dimethylsulfoxide (DMSO), tetramethylenesulfoxide (TMSO), di-*n*-propylsulfoxide (DPrSO), di-*n*-butylsulfoxide (DBuSO), dibenzylsulfoxide (DBzSO), and diphenylsulfoxide (DPhSO). The products $Pt(R_2SO)(pz)Cl_2$ were characterized by IR and multinuclear magnetic resonance (^1H, ^{13}C, and ^{195}Pt) spectroscopies. The crystal structures of two compounds with different geometies were determined.

Experimental

$K_2[PtCl_4]$ was obtained from Johnson Matthey Inc. and was purified by recrystallization from water before use. $CDCl_3$ was purchased from CDN Isotopes. Pyrazine and the sulfoxide ligands were purchased from Aldrich except DMSO, which was bought from Anachemia Chemicals Ltd., and DPrSO, acquired from Phillips Petroleum Company. The latter was purified by distillation before use.

The decomposition points were measured on a Fischer-Johns instrument and were not corrected. The IR spectra were recorded in the solid state (KBr pellets) on a PerkinElmer 783 spectrometer between 4000 and 280 cm^{-1}. All NMR spectra were measured in $CDCl_3$ on a Varian Gemini 300BB spectrometer operating at 300.069, 75.460, and 64.326 MHz for ^1H, ^{13}C, and ^{195}Pt, respectively. The chloroform peaks were used as an internal standard for the ^1H (7.24 ppm) and ^{13}C (77.00 ppm) NMR spectra. For ^{195}Pt, the external reference was $K[Pt(DMSO)Cl_3]$ (in D_2O, adjusted to –2998 ppm from $K_2[PtCl_6]$). The ^{195}Pt NMR spectra were measured between –2500 and –4000 ppm.

The TMSO compound (crystal **I**) was crystallized from a dichloromethane–acetone (1:1) mixture, and the DPrSO crystal (crystal **II**) was obtained from a chloroform–acetone–methanol (3:1:1) solution. The crystallographic measurements were done on a Siemens P4 diffractometer using graphite-monochromatized Mo Kα (λ = 0.71073 Å (1 Å = 0.1 nm) radiation. The crystals were selected after examination under a polarizing microscope for homogeneity. The cell dimensions were determined at room temperature, from a least-squares refinement of the angles 2θ, ω, and χ obtained for well-centered reflections. The data collections were made by the 2θ/ω scan technique using the XSCANS (13) program. The coordinates of the Pt atoms were determined from Patterson map calculations. All the other non-hydrogen atoms were found by the usual Fourier methods. The refinement of the structures was done on F^2 by full matrix least-squares analysis. The hydrogen atoms were fixed in their calculated positions with U_{eq} = 1.2 x U_{eq} of the carbon to which they are bonded (or 1.5 x U_{eq} for methyl groups). Corrections were made for absorption (integration for *trans*-$Pt(TMSO)(pz)Cl_2$ and semiempirical for *cis*-$Pt(DPrSO)(pz)Cl_2$), Lorentz, and polarization effects. Crystal **II** did not diffract very well. It was also measured with Cu Kα radiation, but the results did not improve. Attempts to prepare crystals of better quality were not successful. The residual peaks were located in the close vicinity of the Pt atoms. The calculations were done using the Siemens SHELXTL (13) system. The pertinent crystal data and the experimental details are summarized in Table 1.

The $K[Pt(R_2SO)Cl_3]$ complexes were synthesized according to the method described by Kukushkin et al. (14). The DBzSO and DPhSO complexes were obtained in small quantities because of the aqueous insolubility of the ligands and the very favorable formation of the insoluble disubstituted compound $Pt(R_2SO)_2Cl_2$.

Preparation of *trans*-$Pt(R_2SO)(pz)Cl_2$

Pyrazine was dissolved in a minimum amount of water. The $K[Pt(R_2SO)Cl_3]$ compound, dissolved also in a minimum amount of water, was added gently to the pyrazine solution in a 1:1.1 proportion at room temperature. A pale yellow to yellow-orange precipitate appeared rapidly, but the stirring of the solution was continued until precipitation was complete. After filtration, the precipitate was dried, washed with ether, and dried in vacuum. For the DBzSO complex, the reaction was done in a 2:1 MeOH–H_2O mixture, while for the DPhSO complex, the reaction was done in a 3:1 EtOH–H_2O mixture.

trans-*Pt(DMSO)(pz)Cl₂*

Yield 89%; dec. 220–235 °C. IR (cm^{-1}): pz (vibration numbers assigned using the notation in ref. 15): 3117 m (ν_{13} (B_{1u})), 1417 s (ν_{19b} (B_{3u})), 1147 s (ν_{18a} (B_{1u})), 1112 w (ν_3 (B_{2g})), 1074 m (ν_{14} (B_{3u})), 1029 s (ν_1 (A_g)), 807 s (ν_{11} (B_{2u})); ν(S-O) 1122 w, ν(Pt-N) 517 m, ν(Pt-S) 444 s, ν(Pt-Cl) 350 s. ^1H NMR (ppm): H_{pz} 8.780 (d, 3.0), 8.770 (d, 3.0); H_α 3.48 (s+d, 23). ^{13}C NMR (ppm): C_{pz} 147.01, 145.33; C_α 44.46.

trans-*Pt(TMSO)(pz)Cl₂ (I)*

Yield 84%; dec. 156–195 °C. IR (cm^{-1}): pz (vibration

© 2004 NRC Canada

Table 1. Crystallographic data for the compounds $Pt(R_2SO)(pz)Cl_2$.

	I	II
Compound	*trans*-Pt(TMSO)(pz)Cl_2	*cis*-Pt(DPrSO)(pz)Cl_2
Chemical formula	$C_8H_{12}Cl_2N_2OPtS$	$C_{10}H_{18}Cl_2N_2OPtS$
MW	450.25	480.31
Space group	Orthorhombic, *Pbca*	Monoclinic, $P2_1/c$
a (Å)	11.931(3)	8.911(7)
b (Å)	10.434(2)	17.534(12)
c (Å)	20.490(4)	9.843(9)
β (°)		90.69(7)
Volume (Å^3)	2550.8(9)	1538(2)
Z	8	4
ρ_{calcd} (g cm^{-3})	2.345	2.075
μ(Mo Kα) (cm^{-1})	11.560	9.594
F(000)	1680	912
Measured reflections	18 659	10 597
Independent reflections	2506	2715
Obs. reflections ($I > 2\sigma(I)$)	1398	1543
R_1 ($F > 2\sigma(I)$)[a]	0.0494	0.0791
wR_2 (all data)[b]	0.1009	0.1358
S	1.052	1.059

[a] $R_1 = \Sigma (|F_o - F_c|) / \Sigma |F_o|$.
[b] $wR_2 = [\Sigma (w(F_o^2 - F_c^2)^2) / \Sigma (w(F_o^2)^2)]^{1/2}$.

numbers assigned using the notation in ref. 15): 3100 w (ν_{13} (B_{1u})), 1415 s (ν_{19b} (B_{3u})), 1394 w (ν_{19b} (B_{3u})), 1143 s (ν_{18a} (B_{1u})), 1119 s (ν_3 (B_{2g})), 1081 s (ν_{14} (B_{3u})), 1060 s (ν_1 (A_g)), 807 s (ν_{11} (B_{2u})); ν(S-O) 1160 m, ν(Pt-S) 479 m, ν(Pt-Cl) 348 s. ^{1}H NMR (ppm): H_{pz} 8.811 (dd, 3.0, 1.2), 8.764 (dd, 3.0, 1.2); H_α 4.00 (m), 3.65 (m); H_β 2.39 (m), 2.23 (m). ^{13}C NMR (ppm): C_{pz} 147.42, 145.70; C_α 57.05, C_β 24.67.

trans-*Pt(DBzSO)(pz)Cl$_2$*

Yield 89%; dec. 121–197 °C. IR (cm^{-1}): pz (vibration numbers assigned using the notation in ref. 15): 3123 w (ν_{13} (B_{1u})), 1495 m (ν_{19a} (B_{1u})), 1422 s (ν_{19b} (B_{3u})), 1381 m (ν_{19b} (B_{3u})), 1130 s (ν_{18a} (B_{1u})), 1114 s (ν_3 (B_{2g})), 1070 m (ν_{14} (B_{3u})), 1030 m (ν_1 (A_g)), 805 m (ν_{11} (B_{2u})); ν(S-O) 1167 s, ν(Pt-N) 516 vw, ν(Pt-S) 483 s, ν(Pt-Cl) 350 m.

trans-*Pt(DPhSO)(pz)Cl$_2$*:

Yield 85%; dec. 195–250 °C. IR (cm^{-1}): pz (vibration numbers assigned using the notation in ref. 15): 3094 w (ν_{13} (B_{1u})), 1470 w (ν_{19a} (B_{1u})), 1410 s (ν_{19b} (B_{3u})), 1381 w (ν_{19b} (B_{3u})), 1137 s (ν_{18a} (B_{1u})), 1112 m (ν_3 (B_{2g})), 1071 m (ν_{14} (B_{3u})), 1062 m (ν_1 (A_g)), 806 s (ν_{11} (B_{2u})); ν(S-O) 1153 m, ν(Pt-N) 507 vw, ν(Pt-S) 444 w, ν(Pt-Cl) 349 m. ^{1}H NMR (ppm): H_{pz} 8.896 (m); H_{ortho} 8.29 (t, 7.8), 7.93 (t, 7.4); $H_{meta,\ para}$ 7.58 (m). ^{13}C NMR (ppm): C_{pz} 147.32, 145.93; C_{phenyl} 138.42, 127.43, 128.76, 132.95.

Preparation of *cis*-Pt(DPrSO)(pz)Cl_2 (II)

Pyrazine was dissolved in a minimum amount of water. The K[Pt(R_2SO)Cl_3] compound, dissolved also in a minimum amount of water, was added gently to the pyrazine solution in a 1:1 proportion at room temperature. A yellow sticky paste formed immediately and stuck to the magnetic agitator. The paste was dissolved in chloroform and the solution evaporated to dryness. The residue was recrystallized in chloroform, filtered, washed with ether, and dried in vacuum.

Yield 68%; dec. 183–220 °C. IR (cm^{-1}): (vibration numbers assigned using the notation in ref. 15): 3086 w (ν_{13} (B_{1u})), 1457 m (ν_{19a} (B_{1u})), 1412 s (ν_{19b} (B_{3u})), 1379 m (ν_{19b} (B_{3u})), 1130 s (ν_{18a} (B_{1u})), 1111 w (ν_3 (B_{2g})), 1069 s (ν_{14} (B_{3u})), 807 m (ν_{11} (B_{2u})); ν(S-O) 1152 s, ν(Pt-N) 515 w, ν(Pt-S) 448 m, br, ν(Pt-Cl) 345 m, 341 m. ^{1}H NMR (ppm): H_{pz} 8.707 (d, 3.3), 8.685 (d, 3.3); H_α 3.76 (m), 3.12 (m); H_β 2.36 (m), 2.03 (m); H_γ 1.18 (t, 7.5). ^{13}C NMR (ppm): C_{pz} 147.59, 147.40; C_α 56.51, C_β 16.68, C_γ 12.75.

Results and discussion

Synthesis of the complexes

The aqueous reaction of K[Pt(R_2SO)Cl_3], where R_2SO = DMSO, TMSO, DBzSO, and DPhSO, with pyrazine in a 1:1.1 proportion produced the monomeric complexes *trans*-Pt(R_2SO)(pz)Cl_2 (eq. [1]). The K[Pt(R_2SO)Cl_3] solution must be added to the pyrazine solution to have an excess of pyrazine throughout the reaction because an excess of the Pt(II) salt will produce the pyrazine-bridged dimer recently reported (10), prepared by a similar reaction using a Pt:pz ratio of 2:1. For the DBzSO complex, the reaction was performed in a 1:2 water–methanol mixture, while a 1:3 water–ethanol solution was preferred for the DPhSO compound.

$$[1] \qquad K[Pt(R_2SO)Cl_3] + pz \rightarrow \textit{trans}\text{-}Pt(R_2SO)(pz)Cl_2 + KCl$$

A pale yellow to yellow-orange precipitate was formed. The time at which precipitation was observed varied with the bulkiness of the sulfoxide. The yields varied between 84% and 89%.

The characterization of the products has shown that these compounds have the trans configuration, as expected be-

© 2004 NRC Canada

cause of the large trans effect of sulfoxides. Sulfoxide complexes having the cis configuration are usually more stable than the trans compounds, because the π bonding is more effective in the cis configuration. For example, the aqueous reaction of $K[Pt(R_2SO)Cl_3]$ with R_2SO produces first the trans isomer, which rapidly isomerizes in water to the cis compound except in the case of very sterically demanding sulfoxides. Similarly, the reaction of $K[Pt(R_2SO)Cl_3]$ with pyrimidine produces first *trans*-$Pt(R_2SO)(pm)Cl_2$, which can isomerize to the cis compound (8). Since pyrazine is a very similar ligand to pyrimidine, both of them having empty π* orbitals that can accept electron density from Pt, the *trans*-$Pt(R_2SO)(pz)Cl_2$ compounds were expected to undergo isomerization, at least in organic solvents. However, several attempts in different solvents to isomerize the four *trans*-$Pt(R_2SO)(pz)Cl_2$ compounds were without success. Therefore, it appears that the reactivity of the R_2SO–pyrazine complexes is quite different from that of the R_2SO–pyrimidine compounds (8, 9). The pyrazine-bridged dimers recently published were identified as the trans-trans isomers (10), and various attempts to isomerize them were also not successful.

The aqueous reaction of $K[Pt(DPrSO)Cl_3]$ with pyrazine under the same conditions as for the other $K[Pt(R_2SO)Cl_3]$ complexes was quite different. With a Pt:pz ratio of 1:1 to 1:1.1, a bright yellow sticky paste formed immediately upon mixing. After the purification process in $CHCl_3$, the product was identified as the mononuclear complex *cis*-$Pt(DPrSO)(pz)Cl_2$.

[2] $K[Pt(DPrSO)Cl_3] + pz \rightarrow$ *cis*-$Pt(DPrSO)(pz)Cl_2 + KCl$

The lower yield of this reaction (68%) can be attributed to the oily nature of the product. When the Pt:pz ratio was greater than 1:1, the pyrazine-bridged dimeric species *trans*-$\{Pt(DPrSO)Cl_2\}_2(\mu\text{-pz})$ was formed as reported earlier. The fact that the final dinuclear product exhibits the trans-trans geometry (10) suggests that the mononuclear intermediate is *trans*-$Pt(DPrSO)(pz)Cl_2$. However, with a Pt:pz ratio of 1:1.1, the trans monomeric compound, which should first be produced, could not be isolated, suggesting that the compound *trans*-$Pt(DPrSO)(pz)Cl_2$ isomerized rapidly. This was quite surprising since all the complexes formed with the other ligands are believed to have the trans configuration and did not isomerize even upon heating in organic solvents.

The aqueous reaction of $K[Pt(DBuSO)Cl_3]$ with pyrazine under the same conditions (Pt:pz ratio of 1:1) produced the pyrazine-bridged dinuclear species *trans*-$\{Pt(DBuSO)Cl_2\}_2(\mu\text{-pz})$. No monomeric compound was obtained with the ligand DBuSO. The experimental conditions were varied (different solvents) and the Pt:pz ratio was varied from 1:1 to 1:15, but no monomeric mixed-ligand complex could be detected. It seems that in the case of $K[Pt(DBuSO)Cl_3]$, unlike the other $K[Pt(R_2SO)Cl_3]$ complexes, the binding of the first N atom of pyrazine to Pt activates the second N atom to react more rapidly than the first

All the mixed-ligand monomeric species were characterized by IR and multinuclear magnetic resonance spectroscopies. The low solubility of these complexes was a major problem in this project. The compound *trans*-$Pt(DBzSO)(pz)Cl_2$ could not be analyzed by NMR spectroscopy, being insoluble in all the solvents tested (H_2O, MeOH, EtOH, $CHCl_3$, CH_2Cl_2, CH_3COCH_3, and DMF).

The synthesized complexes were pure, since only one resonance was observed in their ^{195}Pt NMR spectra (confirmed by ^1H and ^{13}C NMR). The complexes *trans*-$Pt(TMSO)(pz)Cl_2$ and *cis*-$Pt(DPrSO)(pz)Cl_2$ were also studied by X-ray diffraction methods, which confirmed the geometry of the complexes.

IR spectroscopy

The IR spectrum of pyrazine has been reported (15), and our IR band assignments (Experimental section) are based on that study. The vibrations of coordinated pyrazine in the Pt complexes were observed at energies higher than or identical to those reported for the free ligand. The ν(S-O) vibrations absorb at higher energy than in the free sulfoxides (avg. +120 cm^{-1}), since the ligands are bonded to Pt by the S atom. The pπ–dπ bond is strengthened upon coordination in the complexes. The ν(S-O) energies (avg. 1151 cm^{-1}) are identical with those observed in the pyrazine-bridged dimeric compounds (avg. 1157 cm^{-1} (10)) and can be compared with the values reported for $Pt(DMSO)(NH_3)Cl_2$ and $Pt(DMSO)(2\text{-Me-py})Cl_2$ (1128 and 1138 cm^{-1}, respectively (16)).

For all the complexes except $Pt(DPrSO)(pz)Cl_2$, only one ν(Pt-Cl) vibration was observed, between 348 and 350 cm^{-1}. This suggests a trans geometry because, although two bands are predicted by group theory for both cis (C_s skeletal symmetry) and trans isomers (C_{2v}) of this type, two bands are usually observed for the cis compounds and only one band for the trans isomers (as reported, for example, for the complexes *cis*- and *trans*-$Pt(DMSO)(L)Cl_2$, where L = 2,6-lutidine and dimethylamine (17) and pyrimidine (8)). However, for $Pt(DPrSO)(pz)Cl_2$, two ν(Pt-Cl) bands located at 341 and 345 cm^{-1} were observed, suggesting a cis geometry.

An absorption band observed around 460 cm^{-1} was assigned to a ν(Pt-S) vibration as suggested in the literature (8–10, 16, 18–21), while a band around 515 cm^{-1} was assigned to the ν(Pt-N) vibration, based also on some published results (8–10, 22, 23).

^{195}Pt NMR spectroscopy

The ^{195}Pt NMR spectra of the monomeric compounds $Pt(R_2SO)(pz)Cl_2$ (except the DBzSO complex) were measured in $CDCl_3$, and the results were compared with those observed for the pyrimidine analogues $Pt(R_2SO)(pm)Cl_2$ (8) and for the pyrazine-bridged dimeric species *trans*-$\{Pt(R_2SO)Cl_2\}_2(\mu\text{-pz})$ (10). The chemical shifts are summarized in Table 2. All the synthesized complexes were pure as shown by multinuclear (^{195}Pt, ^1H, and ^{13}C) magnetic resonance spectroscopy. The compound containing a DBzSO ligand was found to be insoluble in all the classical organic solvents.

Except for the DPhSO complex, the ^{195}Pt NMR chemical shifts vary between –3042 and –3046 ppm. The $\delta(^{195}Pt)$ values of these monomers are very close to those determined for the pyrazine-bridged dimeric species (Table 2). In the pyrimidine series, the signals of the monomers were observed at slightly lower fields (avg. –3065 ppm) than those of the pyrimidine-bridged dimers (avg. –3075 ppm) (8, 9). Our re-

© 2004 NRC Canada

Table 2. ^{195}Pt chemical shifts (ppm) of the complexes $Pt(R_2SO)(pz)Cl_2$ (in $CDCl_3$) and related complexes in the literature.

R_2SO	Geometry	$Pt(R_2SO)(pz)Cl_2$	$\{Pt(R_2SO)Cl_2\}_2(\mu\text{-pz})$[a]	$Pt(R_2SO)(pm)Cl_2$[b]
DMSO	trans	–3045	–3049[c]	–3070
TMSO	trans	–3042	–3041	–3056
DPrSO	cis	–3046		–2951
	trans		–3048	–3059
DBuSO	trans	—[d]	–3051	–3060
DPhSO	trans	–3121	–3113	–3148

[a]Reference 10; in $CDCl_3$ except where otherwise indicated.
[b]Reference 8; in CD_2Cl_2.
[c]In DMF-d_7.
[d]Not prepared.

sults are also in agreement with the published work on analogues with phosphine ligands (11), where the ^{195}Pt NMR chemical shift of *trans*-$Pt(PR_3)(pz)Cl_2$ was reported at –3589 ppm, and that of the dinuclear coompound *trans*-$\{Pt(PR_3)Cl_2\}_2(\mu\text{-pz})$ at –3587 ppm. These results seem to indicate that the electron density on the Pt atom is the same in the monomers as in the pyrazine-bridged dimers.

The value of $\delta(^{195}Pt)$ for the *cis*-DPrSO complex was within the range observed for the trans monomers (except the DPhSO compound), which was not expected. In the pyrimidine series (8), the signals of the cis compounds were reported at much lower fields than those of the trans isomers (avg. $\Delta\delta$ ($\delta_{cis} - \delta_{trans}$) = 132 ppm). For sulfoxide Pt(II) complexes, the cis isomers are more stable than the trans compounds since the π(d-d) bonding is more efficient in the cis geometry, resulting in a lower electron density on the Pt center. The δ(Pt) are therefore observed at lower field for the cis isomers. For mixed-ligand complexes, the value of $\Delta\delta$ ($\delta_{cis} - \delta_{trans}$) will also depend on the second ligand. If the latter can form π bonds, the difference between the two isomers should increase, while an amine ligand should reduce the $\Delta\delta$ ($\delta_{cis} - \delta_{trans}$) values. In $Pt(DMSO)(NH_3)Cl_2$, the signal of the cis isomer was reported at –3045 ppm, whereas that of its trans analogue was observed at –3067 ppm (16, 24). In our R_2SO-pz compounds, only one cis compound (with DPrSO) was prepared, and its signal was observed at the same field as those of the trans isomers of the other R_2SO-pz compounds. We do not have enough data at the moment to reach a sound conclusion and will continue our attempts, which have not been successful up to now, to prepare other cis compounds and the trans DPrSO complex.

The ^{195}Pt NMR signal of the DPhSO complex was observed at much higher fields than those of the other compounds, as also reported for the other DPhSO complexes in Table 2 and for a series of compounds of the types $Pt(R_2SO)(R\text{-}CN)Cl_2$ (25) and $K[Pt(R_2SO)Cl_3]$ (25, 26). DPhSO is not only the most sterically hindered ligand, but also it is different from the other sulfoxides in that it contains aromatic groups directly attached to the sulfur atom. These groups are probably responsible for the different electronic effects observed for this compound. The electron density on the Pt atom is increased in the DPhSO complex compared to the complexes containing the other sulfoxide ligands. The shielded resonance is probably not caused by the bulkiness of the substituents on the sulfur, because the presence of bulky substituents on the atom bonded to Pt usually has a deshielding effect. For Pt–amine complexes, δ(Pt) was found at lower fields for amines having bulky substituents on the nitrogen atom (27, 28). For $K[Pt(R_2SO)Cl_3]$ (29) and the corresponding pyrazine-bridged dimeric complexes (10), we have suggested that the difference was caused by inverse polarization of the π electrons of the S=O bond, and this concept might be an interesting interpretation of our results in the present study as well. This phenomenon has been suggested in the literature to explain some ^{13}C NMR results for Pt–carbonyl (30) and Pt–carboxylato complexes (31). Such an effect would be present in all Pt–R_2SO complexes but would be more important for sulfoxide ligands containing electron-attracting aromatic groups attached directly to the S atom. This effect would increase the electron density on the atoms in close proximity to the S atom, especially the Pt atom, which would result in a higher field δ(Pt) signal.

^{1}H and ^{13}C NMR spectroscopies

The pyrazine signals of the complexes will first be discussed. Pyrazine is a symmetric molecule, and only a single resonance is observed in the ^{1}H and ^{13}C spectra at 8.59 and 145.07 ppm, respectively, in $CDCl_3$. When pyrazine is bonded to a metal, the molecule is no longer symmetric, as shown in Scheme 1. Two signals should now be observed for the coordinated molecule in the ^{1}H NMR (H_a and H_b) and ^{13}C NMR (C_a and C_b) spectra. The atoms H_a and C_a should be more affected by coordination to the metal than H_b and C_b.

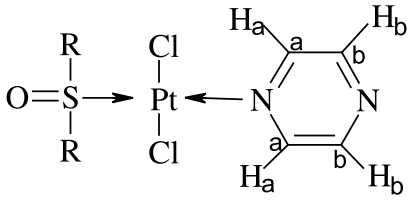
The chemical shifts and the coupling constants of the complexes are presented in the Experimental section, and the values $\Delta\delta$ ($\delta_{complex} - \delta_{pyrazine}$) are listed in Table 3. Coordination of pyrazine to the Pt atom causes a deshielding of all the pyrazine atoms. The chemical shifts of H_a and C_a are more deshielded than those of H_b and C_b as expected, resulting in larger $\Delta\delta$ values for H_a and C_a. For the DPhSO complex, the two multiplets were not separated. The reduction of electron density in bonded pyrazine is a consequence of the σ bond (N→Pt), which causes a deshielding effect in ^{1}H and ^{13}C NMR. In the literature, for a few complexes of the type *trans*-$Pt(PR_3)(pz)Cl_2$ (11), the reported $\Delta\delta_a$ values in ^{1}H NMR (avg. 0.38 ppm) were larger than ours, while their $\Delta\delta_b$ value was 0.15 ppm. The difference might be caused by the larger trans effect of phosphine ligands compared to that of sulfoxides (10). For the trans-trans pyrazine-bridged dimers $\{Pt(R_2SO)Cl_2\}_2(\mu\text{-pz})$ (in which the pyrazine is symmetric), the average $\Delta\delta$ value was around 0.52 ppm (10). It seems

© 2004 NRC Canada

Table 3. ^{1}H and ^{13}C NMR $\Delta\delta$ ($\delta_{complex} - \delta_{pyrazine}$) (ppm) of pyrazine resonances for the complexes $Pt(R_2SO)(pz)Cl_2$.

Compound	(^{1}H)$\Delta\delta_a$	(^{1}H)$\Delta\delta_b$	(^{13}C)$\Delta\delta_a$	(^{13}C)$\Delta\delta_b$
trans-Pt(DMSO)(pz)Cl_2	0.195	0.185	1.94	0.26
trans-Pt(TMSO)(pz)Cl_2	0.226	0.179	2.35	0.63
cis-Pt(DPrSO)(pz)Cl_2	0.122	0.100	2.52	2.33
trans-Pt(DPhSO)(pz)Cl_2	0.311	0.311	2.25	0.86

Scheme 1.



that the formation of two σ bonds (N→Pt) by pyrazine decreases further the electron density on pyrazine.

The ^{1}H $\Delta\delta$ values for *cis*-Pt(DPrSO)(pz)Cl_2 are smaller than those of the trans complexes (Table 3). These differences might be due to the different geometry, but more cis compounds are needed before a conclusion can be reached. Steric hindrance in the cis complex is an important factor that must be considered. In the trans compounds, the rotation around the Pt—N bond is not very restricted because the π component of the bond is probably not very important. For the cis isomers, the rotation of the pyrazine ring around the Pt—N bond is more hindered, and the planar ligand is probably close to being perpendicular to the Pt(II) coordination plane to reduce the steric hindrance. The rotation will be more restricted with more bulky sulfoxides.

The chemical shifts of the pyrazine protons in *trans*-Pt(DPhSO)(pz)Cl_2 were at lower fields ($\Delta\delta_{avg}$ = 0.311 ppm) than those of the other trans compounds ($\Delta\delta_{avg}$ = 0.20 ppm). This is in agreement with the observation of the ^{195}Pt NMR signal of this compound at higher field than those of the other complexes, since an increase of electron density on the Pt atom (upfield shift in ^{195}Pt NMR) corresponds to a reduction of electron density on the ligand (downfield shift in ^{1}H and ^{13}C NMR).

The coupling constants $^3J(^1H_a\text{-}^1H_b)$ are 3.0 Hz for *trans*-Pt(DMSO)(pz)Cl_2 and *trans*-Pt(TMSO)(pz)Cl_2 and 3.3 Hz for *cis*-Pt(DPrSO)(pz)Cl_2. A coupling constant with the Pt(II) nucleus, $^3J(^{195}\text{Pt-}^1\text{H})$ = 33 Hz, was also observed for the DMSO complex. This value is in agreement with the results in the literature reported for *trans*-Pt(DMSO)(Ypy)Cl_2 (Ypy = pyridine derivative) (32) and for *trans*-Pt(Ypy)$_2X_2$ (33). The coupling constants $^3J(^{195}\text{Pt-}^1\text{H})$ are usually smaller for trans isomers. For example, the values of $^3J(^{195}\text{Pt-}^1\text{H})$ for Pt(DMSO)(pm)Cl_2 are 31 and 44 Hz for the trans and cis compounds, respectively (8).

In ^{13}C NMR spectroscopy, similar results were observed. The two pyrazine signals in the spectra of the complexes were observed at lower fields than the single ^{13}C resonance of free pyrazine, with C_a being more affected ($\Delta\delta_a$ ~ 2 ppm) by coordination to the metal than C_b (Table 3). The formation of the N→Pt σ bond reduces the electron density on the pyrazine ligand. Surprisingly, $\Delta\delta$ for C_b is much larger for *cis*-Pt(DPrSO)(pz)Cl_2 ($\Delta\delta_b$ = 2.33 ppm) than for the other complexes ($\Delta\delta_b$ = 0.26–0.86 ppm). The difference is probably due to the cis geometry of the DPrSO compound. The latter ligand is very sterically demanding, and the rotation around the Pt—N bond is restricted. In solution, the pyrazine plane would probably be almost perpendicular to the Pt(II) coordination plane to reduce the steric hindrance to a minimum. The ^{13}C $\Delta\delta_{avg}$ of *cis*-Pt(DPrSO)(pz)Cl_2 is larger (2.44 ppm) than the corresponding values of the trans compounds (avg. 1.38 ppm). A similar observation was previously reported for $Pt(R_2SO)(pm)Cl_2$, where the value $\Delta\delta_{avg}$ was 2.13 ppm for the cis isomers and 1.51 ppm for the trans complexes (8). For *trans*-Pt(PR_3)(pz)Cl_2, the C_a and C_b signals were observed at 147.2 and 145.0 ppm, respectively (11). We have not observed any $J(^{195}\text{Pt-}^{13}\text{C})$ couplings for the pyrazine carbon atoms.

The chemical shifts and the coupling constants $J(^1\text{H-}^1\text{H})$ of the sulfoxide ligands are presented in the Experimental section, and the values of $\Delta\delta$ ($\delta_{complex} - \delta_{sulfoxide}$) are listed in Tables 4 (^{1}H NMR) and 5 (^{13}C NMR). In ^{1}H NMR, the $\Delta\delta$ values are positive, indicating that the sulfoxide protons are more deshielded in the ligands than in the free molecules. The protons located in positions α to the binding atom are the most affected by coordination to the metallic center. For the DMSO complex, only one signal at 3.48 ppm was observed; this chemical shift is close to that reported for *trans*-Pt(DMSO)(pm)Cl_2 (3.45 ppm (8)) and for *trans*-Pt(DMSO)(thiazole)Cl_2 (3.48 ppm (34)). For the other complexes, two series of signals were observed. For the TMSO complex, the two geminal protons of each CH_2 group are in different environments. Those closer to the O atom will be more deshielded than the others. For the other ligands, the two series of signals result from restricted rotation around the S—C bonds. The difference between the two series of resonances decreases as the distance from the S atom increases.

A coupling constant $^3J(^{195}\text{Pt-}^1\text{H})$ = 23 Hz was observed for *trans*-Pt(DMSO)(pz)Cl_2. This is in agreement with results reported for the similar trans complexes Pt(DMSO)(thiazole)Cl_2 (22 Hz) (34) and $Pt(R_2SO)(pm)Cl_2$ (22 Hz) (8). The other ligands gave low-intensity multiplets, and the coupling with ^{195}Pt could not be seen.

In ^{13}C NMR, the resonances of the C atoms in α positions were observed at lower fields than those of the corresponding atoms in the free sulfoxides ($\Delta_\alpha\delta$ = 2.31–3.76 ppm), except for the DPhSO complex (Table 5). These values are quite small compared to similar values for other types of ligands such as amines. Sulfoxides can accept electron density from the metal center, and the π (Pt→S) bond will increase the electron density on the sulfoxide ligand. Furthermore, the inverse polarization of the π electrons of the $^{\delta-}$S—O$^{\delta+}$

© 2004 NRC Canada

Table 4. ^{1}H NMR $\Delta\delta$ ($\delta_{complex} - \delta_{sulfoxide}$) (ppm) for the complexes $Pt(R_2SO)(pz)Cl_2$.

Complex	H_α	H_β	H_γ	H_δ
trans-$Pt(DMSO)(pz)Cl_2$	1.00			
	$J(^{195}Pt\text{-}^{1}H)$=23 Hz			
trans-$Pt(TMSO)(pz)Cl_2$	1.17, 0.82	0.25, –0.01		
cis-$Pt(DPrSO)(pz)Cl_2$	1.20, 0.56	0.62, 0.29	0.17	
trans-$Pt(DPhSO)(pz)Cl_2$		0.66, 0.30 (*ortho*)	0.14 (*meta*)	0.14 (*para*)

Note: H_α is located on the C atom closest to the S atom, H_β is on the second C from S, etc.

Table 5. ^{13}C NMR $\Delta\delta$ ($\delta_{complex} - \delta_{sulfoxide}$) (ppm) for the complexes $Pt(R_2SO)(pz)Cl_2$.

Complex	C_α	C_β	C_γ	C_δ
trans-$Pt(DMSO)(pz)Cl_2$	3.76			
trans-$Pt(TMSO)(pz)Cl_2$	2.66	–0.75		
cis-$Pt(DPrSO)(pz)Cl_2$	2.31	0.54	–0.52	
trans-$Pt(DPhSO)(pz)Cl_2$	–6.99	2.86 (*ortho*)	–0.34 (*meta*)	2.12 (*para*)

Note: C_α is the C atom closest to the S atom, C_β is the second C from S, etc.

bond would increase the electron density on the S atom and its neighbouring atoms, especially the α carbon atoms. This inverse polarization of the S—O π bond was first suggested by Cooper and Powell (30) to explain the ^{13}C NMR spectra of some Pt–carbonyl complexes and was later put forward in the interpretation of the ^{13}C NMR spectra of some Pt–carboxylate complexes (31). The chemical shifts in ^{13}C NMR spectroscopy are particularly dependent on such mesomeric effects.

For *trans*-$Pt(DPhSO)(pz)Cl_2$, the signals of the α carbon atoms were observed at much higher field than those of the free ligand ($\Delta_\alpha\delta$ = –6.99 ppm). Similar behavior was reported for the pyrazine-bridged dimer *trans*-$\{Pt(DPhSO)Cl_2\}_2(\mu\text{-pz})$, with $\Delta_\alpha\delta$ = –6.61 ppm (10). We suggest that the inverse polarization of the π electrons in the S=O bond would be greater in this ligand because of the presence of two strongly electron-attracting phenyl groups located directly on the S atom. This phenomenon would increase the electron density on the C atoms located in positions α to the S atom. The π component of the Pt—S bond (back-donation) might also be more important for this ligand because of the presence of the two electron-attracting groups on the ligand.

The NMR results for these complexes are very similar in general to those reported for the pyrazine-bridged dimers (10). This behavior is different from that reported for the R_2SO-pm complexes (8, 9). Since the two bridging atoms in pyrazine are far from each other, the presence of a second Pt atom does not influence the chemical shifts of the sulfoxides. There are seven bonds between C_α and the second Pt atom in the dinuclear species. In the pyrimidine series, the distances are shorter, and the influence of the second metal center is more important.

The results of this study seem to indicate that the Pt–pyrazine bond is more complicated than expected. Pyrazine has π^* orbitals that could form π bonds with Pt, but to a much reduced extent as compared to sulfoxides. Some published work on pyridine (33) and pyrimidine (8, 9) complexes seems to indicate the presence of some π bonding in the Pt—N bonds, although this is not easy to study.

Crystal structures

The crystal structures of one trans complex, $Pt(TMSO)(pz)Cl_2$ (**I**), and the one cis compound produced, $Pt(DPrSO)(pz)Cl_2$ (**II**), were studied by X-ray diffraction methods. The results confirmed the geometry of the complexes suggested by IR and NMR spectroscopies. Figures 1 and 2 show the labeled diagrams of the two complexes. The bond distances and angles are listed in Table 6. The CIF tables of the two crystal structure determinations have been deposited as supplementary material.[2]

The coordination around the Pt atoms is square planar as expected. The bond angles around the Pt atom are close to the ideal values. The largest deviation can be seen in the cis compound (**II**), where the N-Pt-Cl angle is reduced to 87.7(4)° while the N-Pt-S angle is increased to 92.0(4)°, to reduce the steric hindrance caused by the bulky sulfoxide ligand. In Pt–sulfoxide complexes, the O atom of the sulfoxide is often in the Pt coordination plane, which reduces the steric hindrance caused by the presence of the sulfoxide. In the cis compound (**II**), where this factor is very important, the O is almost in the coordination plane, with a deviation of 0.12(3) Å, while in the trans compound (**I**), the deviation is 1.41(1) Å.

The pyrazine ring is planar in both **I** and **II**. The dihedral angle between the pyrazine plane and the Pt coordination plane is 54.6(4)° and 60.3(5)° for the trans (**I**) and cis (**II**) complexes, respectively. This angle is usually larger in cis

[2] Supplementary data may be purchased from the Directory of Unpublished Data, Document Delivery, CISTI, National Research Council Canada, Ottawa, ON K1A 0S2, Canada (http://www.nrc.ca/cisti/irm/unpub_e.shtml for information on ordering electronically). CCDC 216747 and 216748 contain the crystallographic data for this manuscript. These data can be obtained, free of charge, via www.ccdc.cam.ac.uk/conts/retrieving.html (or from the Cambridge Crystallographic Data Centre, 12 Union Road, Cambridge CB2 1EZ, U.K.; fax +44 1223 336033; or deposit@ccdc.cam.ac.uk).

© 2004 NRC Canada

Fig. 1. Labeled diagram of *trans*-Pt(TMSO)(pz)Cl_2 (**I**). The ellipsoids correspond to 30% probability.

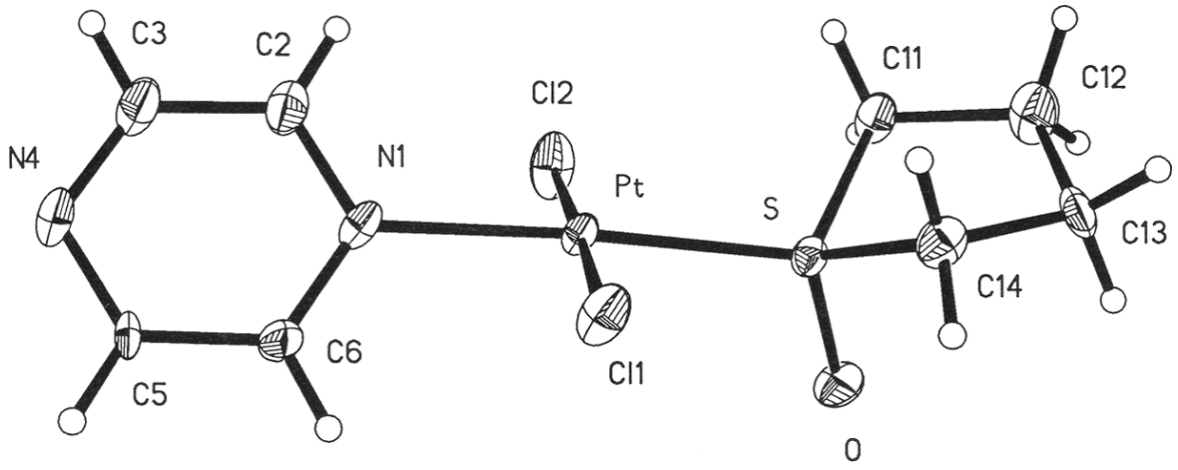
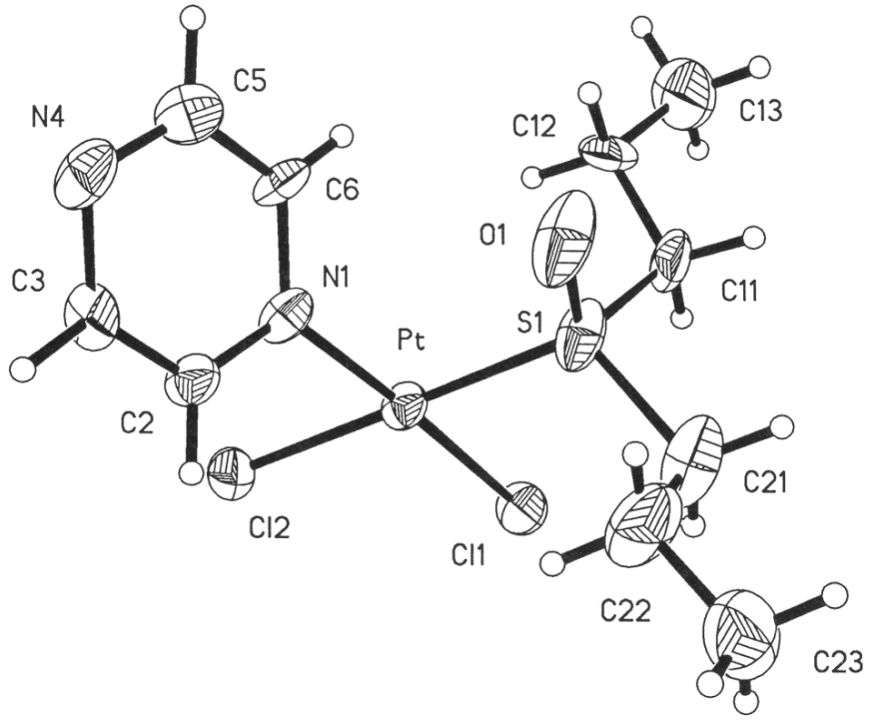


Fig. 2. Labeled diagram of *cis*-Pt(DPrSO)(pz)Cl_2 (**II**). The ellipsoids correspond to 25% probability.



compounds, where the bulkiness of the ligands is a more important factor.

The Pt—S bond lengths in the two structures are within the range reported for other Pt–sulfoxide complexes (8–10, 16, 34–36). In terms of trans influence, pyrazine and chloride are not very different, and the lengths of the Pt—S bonds do not seem to be very sensitive to the trans ligand. In *cis*-Pt(DPrSO)(pz)Cl_2, the Pt—Cl bond trans to the sulfoxide ligand is longer (2.316(5) Å) than the one trans to pyrazine (2.292(5) Å). The large trans influence of sulfoxides is well known. In crystal **I**, the Pt—Cl bonds are trans to each other, and their lengths (avg. 2.293(3) Å) are within the normal range. The lengths of Pt—N bonds are usually more sensitive to the trans ligands. In crystal **II**, where the trans ligand is a chloro ligand, the length of the Pt—N bond is 2.004(14) Å. In **I**, the Pt—N bond is trans to the sulfoxide and is significantly longer (2.053(11) Å). These results are close to those reported for similar compounds (8–10, 33, 34, 37, 38). All these data confirm that the trans influence of the sulfoxide ligand is clearly larger than that of the chloro ligand or pyrazine.

The bond distances and bond angles in the sulfoxide ligands are as expected and agree with published data on Pt–R_2SO complexes (8–10, 16, 39). As observed in other TMSO compounds, the C-S-C angle in *trans*-Pt(TMSO)(pz)Cl_2 is small (94.0(7)°) since the S atom is in a five-membered ring. The conformation of the TMSO ligand is of the envelope type, as seen in Fig. 1. The four C atoms are planar, and the S atom is 0.75(2) Å out of the plane. The dihedral angle between this plane and the Pt coordination plane is

© 2004 NRC Canada

Table 6. Bond distances and angles in crystals **I** and **II**.

	I, *trans*-Pt(TMSO)(pz)Cl_2	**II**, *cis*-Pt(DPrSO)(pz)Cl_2
Bond lengths (Å)		
Pt—Cl	2.290(3)	2.292(5)
	2.296(3)	2.316(5)[a]
Pt—S	2.217(3)	2.209(6)
Pt—N	2.053(11)	2.004(14)
S—O	1.488(10)	1.45(2)
S—C (avg.)	1.779(14)	1.78(2)
N—C (pz) (avg.)	1.34(2)	1.36(3)
C—C (pz) (avg.)	1.38(2)	1.36(3)
C—C (R_2SO) (avg.)	1.54(2)	1.47(3)
Bond angles (°)		
Cl-Pt-Cl	177.98(14)	90.3(2)
S-Pt-Cl	92.13(11)	90.0(2)
	89.89(12)	179.3(3)
N-Pt-Cl	89.0(3)	87.7(4)
	88.9(3)	177.2(5)
N-Pt-S	175.8(4)	92.0(4)
Pt-S-O	112.9(5)	115.5(7)
Pt-S-C (avg.)	115.7(5)	111.5(10)
Pt-N-C (avg.)	121.5(10)	122.3(13)
O-S-C (avg.)	108.5(7)	108.1(13)
C-S-C	94.0(7)	100.9(12)
C-N-C (pz) (avg.)	116.4(13)	115(2)
C-C-N (pz) (avg.)	122(2)	123(2)
S-C-C (R_2SO) (avg.)	104.1(11)	109(2)
C-C-C (R_2SO) (avg.)	109.1(12)	111(3)

[a]trans to DPrSO.

17.1(10)°. In *cis*-Pt(DPrSO)(pz)Cl_2, the C-S-C angle is smaller (100.9(12)°) than the other angles around the S atom, since the multiple S—O bond occupies more space than the single S—C bonds.

The average pyrazine C-N-C and C-C-N internal angles are 116.4(13)° and 122(2)°, respectively, for **I** and 115(2)° and 123(2)°, respectively, for **II**. For the free molecule, these angles were reported to be 115.1° and 122.4°, respectively (40). Therefore, the structure of pyrazine does not change upon coordination to Pt(II).

Acknowledgement

The authors are grateful to the Natural Sciences and Engineering Research Council of Canada for financial support of the project.

References

1. B. Rosenberg, L. Van Camp, and T. Krigas. Nature (London), **205**, 698 (1965).
2. B. Rosenberg, L. Van Camp, J.E. Trosko, and V.H. Mansour. Nature (London), **222**, 385 (1969).
3. M. Coluccia, A. Nassi, F. Loseto, A. Boccarelli, M.A. Mariggio, D. Giordano, F.D. Intini, P. Caputo, and G.J. Natile. J. Med. Chem. **36**, 510 (1993).
4. K.J. Barnham, M.I. Djuran, P.S. Murdoch, J.D. Ranford, and P.J. Sadler. Inorg. Chem. **35**, 1065 (1996).
5. N. Farrell, D.M. Kiley, W. Schmidt, and M.P. Hacker. Inorg. Chem. **29**, 397 (1990).
6. M. van Beusichem and N. Farrell. Inorg. Chem. **31**, 634 (1992).
7. S. Komeda, G.V. Kalayda, M. Lutz, A.L. Spek, Y. Yamanaka, T. Sato, M. Chikuma, and J. Reedjik. J. Med. Chem. **46**, 1210 (2003).
8. N. Nédélec and F.D. Rochon. Inorg. Chim. Acta, **319**, 95 (2001).
9. N. Nédélec and F.D. Rochon. Inorg. Chem. **40**, 5236 (2001).
10. J.R.L. Priqueler and F.D. Rochon. Inorg. Chim. Acta. **357**, 2165 (2004).
11. A. Albinati, F. Isaia, W. Kaufmann, C. Sorato, and L.M. Venanzi. Inorg. Chem. **28**, 1112 (1989).
12. A.R. Siedle, K.R. Mann, D.A. Bohling, G. Filipovich, P.E. Toren, F.J. Palensky, R.A. Newmark, R.W. Duerst, W.L. Stebbings, H.E. Mishmash, and K. Melancon. Inorg. Chem. **24**, 2216 (1985).
13. XSCANS and SHELXTL (PC, Version 5) [computer programs]. Bruker Analytical X-Ray Systems, Madison, Wis. 1995.
14. Y.N. Kukushkin, Y.E. Vyaz'menskii, and L.I. Zorina. Russ. J. Inorg. Chem. **13**, 1573 (1968).
15. J.D. Simmons and K.K. Innes. J. Mol. Spectrosc. **14**, 190 (1964).
16. V.Y. Kukushkin, V.K. Belsky, V.E. Konovalov, G.A. Kirakosyan, L.V. Konovalov, A.I. Moiseev, and V.M. Tkachuk. Inorg. Chim. Acta, **185**, 143 (1991).
17. V.N. Spevak, V.I. Lobadyuk, and D.M. Batueva. J. Gen. Chem. USSR, **60**, 1178 (1990).
18. J.H. Price, A.N. Williamson, R.F. Schramm, and B.B. Wayland. Inorg. Chem. **11**, 1280 (1972).

© 2004 NRC Canada

19. Y.N. Kukushkin and V.N. Spevak. Russ. J. Inorg. Chem. **18**, 240 (1973).
20. Y.N. Kukushkin and I.V. Pakhomova. Russ. J. Inorg. Chem. **16**, 336 (1971).
21. B.F.G. Johnson and R.A. Walton. Spectrochim. Acta, **22**, 1853 (1966).
22. Y.N. Kukushkin, N.V. Ivannikova, and K.A. Khokhryakov. Russ. J. Inorg. Chem. **15**, 1595 (1970).
23. K. Nakamoto, P.J. McCarthy, J. Fujita, R.A. Condrate, and G.T. Behnke. Inorg. Chem. **4**, 36 (1965).
24. S.J.S. Kerrison and P.J. Sadler. J. Chem. Soc. Chem. Commun., 861 (1977).
25. F.D. Rochon, S. Boutin, P.C. Kong, and R. Melanson. Inorg. Chim. Acta, **264**, 89 (1997).
26. F.D. Rochon, R. Boughzala, and R. Melanson. Can. J. Chem. **70**, 2476 (1992).
27. P.S. Pregosin. Coord. Chem. Rev. **44**, 247 (1982).
28. F.D. Rochon, M. Doyon, and I.S. Butler. Inorg. Chem. **32**, 2717 (1993).
29. C. Bensimon. M. Sc. thesis, Université du Québec à Montréal, Montréal, Que. 1986.
30. D.G. Cooper and J Powell. Inorg. Chem. **16**, 142 (1977).
31. F.D. Rochon and L. Gruia. Inorg. Chim. Acta, **306**, 193 (2000).
32. T.B.T. Ha, J.P. Souchard, F L. Wimmer, and N.P. Johnson. Polyhedron **9**, 2647 (1990).
33. C. Tessier and F.D. Rochon. Inorg. Chim. Acta, **295**, 25 (1999).
34. A. Cornia, A.C. Fabretti, M. Bonivento, and L. Cattalini. Inorg. Chim. Acta, **255**, 405 (1997).
35. R. Melanson and F. D. Rochon. Acta Crystallogr. Sect. C, **40**, 793 (1984).
36. K. Lövqvist and A. Oskarsson. Acta Crystallogr. Sect. C, **48**, 2073 (1992).
37. B. Viossat, P. Khodadad, and N. Rodier. Acta Crystallogr. Sect. C, **47**, 1316 (1991).
38. A.C. Albéniz, V. Calle, P. Espinet, and S. Gómez. Inorg. Chem. **40**, 4211 (2001).
39. R. Melanson and F. D. Rochon. Can. J. Chem. **53**, 2371 (1975).
40. P.J. Wheatley. Acta Crystallogr. **10**, 182 (1957).

© 2004 NRC Canada

Preparation of 4-anilino-6-aryl-2*H*-pyran-2-ones from trilithiated acetoacetanilides and aromatic esters

Jennifer R. Downs, Sally P. Grant, Jessica D. Townsend, Deborah A. Schady, Stefan J. Pastine, Mildred C. Embree, Clyde R. Metz, William T. Pennington, Rosa D. Bailey Walsch, and Charles F. Beam

Abstract: Acetoacetanilide and 4′-chloroacetoacetanilide were trilithiated with excess lithium diisopropylamide and condensed with several aromatic esters, followed by neutralization, separate acid cyclization, and rearrangements. After *C*-acylation of trilithiated acetoacetanilides and cyclization to 4*H*-pyran-4-ones, these compounds underwent multistep rearrangements to 4-anilino-6-aryl-2*H*-pyran-2-ones.

Key words: pyranones, trianions, Claisen-type condensations, rearrangements.

Résumé : L'acétoacétanilide et le 4′-chloroacétoacétanilide ont été trilithiés à l'aide d'un excès de diisopropylamidure de lithium et ces sels ont été soumis à une condensation avec plusieurs esters aromatiques, suivie d'une neutralisation, d'une cyclisation acide et de réarrangements. Après une *C*-acylation des acétoacétanilides trilithiés et une cyclisation en 4*H*-pyran-4-ones, ces composés donnent lieu à des réarrangements en plusieurs étapes qui conduisent à des 4-anilino-6-aryl-2*H*-pyran-2-ones.

Mots clés : pyranones, trianions, condensation du type de Claisen, réarrangements.

[Traduit par la Rédaction]

Introduction

The preparations, reactions, spectral studies, biological potential, and uses of 2*H*-pyran-2-ones **1** have been well documented (1). Strong base methods for preparing these compounds can involve the dianion of ethyl or methyl acetoacetate (2), which have had follow-up application studies (3). These dianions underwent a Claisen-type *C*-acylation with benzoate and related esters, and the resulting diketoester intermediates could undergo cyclization to 6-substituted 4-hydroxy-2*H*-pyran-2-ones **1** (R_4 = OH and R_6 = aryl, Fig. 1).

Related syntheses deal with 2,6-disubstituted 4*H*-pyran-4-ones **2** (R_2 and R_6 = aryl, Fig. 1) that were obtained by *C*-acylation of β-diketone dianions, such as dilithiated 1-benzoylacetone, with aromatic esters. This was then followed by acid cyclization of the resulting triketones to expected 2,6-disubstituted 4-pyranones **2** (R_2 and R_6 = aryl, Fig. 1) and other compounds (4, 5).

Of interest to this investigation is the rearrangement of 4-pyranones **2** (R_2 and R_6 = methyl or phenyl, Fig. 1) to 2-pyranones **1** (R_4 and R_5 = methyl or phenyl, Fig. 1) (6). For example, there are several select preparations of 4,5-disubstituted 2-pyranones **1** from 2,6-disubstituted 4-pyranones **2**, which involve an intramolecular multistep thermal or photochemical sequence containing several epoxide-type intermediates. Other 2-pyranones **1** have also undergone rearrangements to differently substituted 2-pyranones **1** (7). Several reports have dealt with the preparations of 4-amino-2*H*-pyran-2-ones **1** (R_4 = NH_2, *N*-alkyl or *N*,*N*-dialkyl), but 4-anilino-2*H*-pyran-2-ones **1** have not been reported. One of these recent syntheses deals with a selective *C*-acylation of enaminone lithium dianions followed by cyclization to 4-amino-2-pyranones **1** (R_4 = *N*-CH_3) (8*a*). Others have also involved related rearrangements of 4-alkylamino-2-pyranones **1** (8*b*–8*f*).

While the chemistry of β-ketones and β-ketoester dianions has been well investigated (9), there are limited studies reported concerning the use of β-ketoamide trianions (10–12) in syntheses. Their utilization has resulted in the preparations of chromone-2-acetamides (10) and chromone-2-thioacetamides (11), where the trianion-type intermediates were condensed–cyclized with anionic electrophiles, lithiated methyl salicylates, or lithiated methyl thiosalicylate.

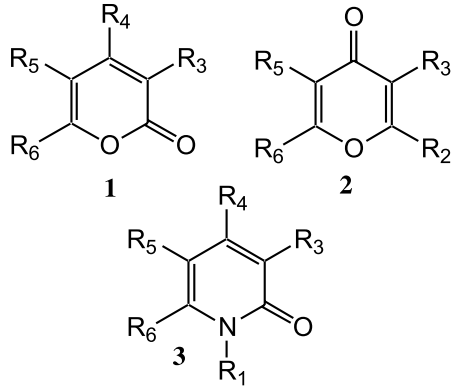
Received 7 August 2003. Published on the NRC Research Press Web site at http://canjchem@nrc.ca on 7 May 2004.

J.R. Downs, S.P. Grant, J.D. Townsend, D.A. Schady, S.J. Pastine, M.C. Embree, C.R. Metz,[1] and C.F. Beam.[2] Department of Chemistry and Biochemistry, College of Charleston, Charleston, SC 29424, USA.
W.T. Pennington and R.D. Bailey Walsch. Department of Chemistry, Clemson University, Clemson, SC 29634, USA.

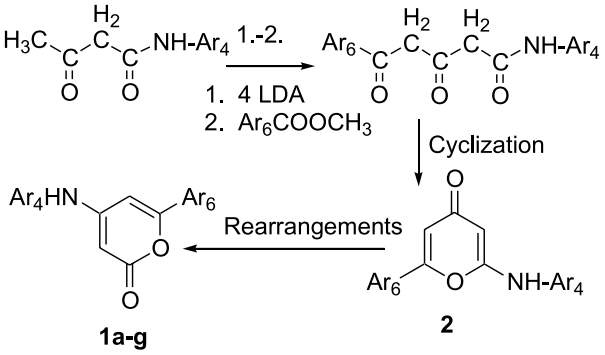
[1]Corresponding author (e-mail: metzc@cofc.edu).
[2]Corresponding author (e-mail: beamc@cofc.edu).

 doi: 10.1139/V04-029 © 2004 NRC Canada

Fig. 1. 2*H*-Pyran-2-ones (**1**); 4*H*-pyran-4-ones (**2**); 2(1*H*)-pyrid-2-ones (**3**).



Scheme 1. Preparation of 4-anilino-6-aryl-2*H*-pyran-2-ones (numbering Ar_4 and Ar_6 of products).



1a $Ar_4 = C_6H_5$; $Ar_6 = 4\text{-}ClC_6H_4$
1b $Ar_4 = C_6H_5$; $Ar_6 = 4\text{-}CH_3OC_6H_4$
1c $Ar_4 = C_6H_5$; $Ar_6 = 3,5\text{-}(CH_3O)_2C_6H_3$
1d $Ar_4 = 4\text{-}ClC_6H_4$; $Ar_6 = 4\text{-}ClC_6H_4$
1e $Ar_4 = 4\text{-}ClC_6H_4$; $Ar_6 = 4\text{-}CH_3OC_6H_4$
1f $Ar_4 = 4\text{-}ClC_6H_4$; $Ar_6 = 4\text{-}BrC_6H_4$
1g $Ar_4 = 4\text{-}ClC_6H_4$; $Ar_6 = 3,4\text{-}(CH_3O)_2C_6H_3$

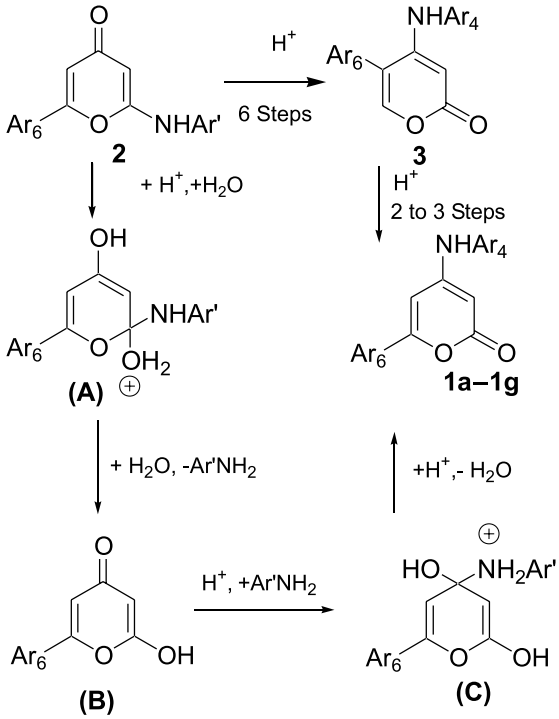
Results and discussion

What at first appeared to be a routine *C*-acylation of acetoacetanilide trianion with esters, such as methyl 4-methoxybenzoate or methyl 4-chlorobenzoate, with the potential to cyclize the 4*H*-pyran-4-ones **2** or 2(1*H*)-pyridones **3** (Fig. 1), gave, after several rearrangements, substituted 4-anilino-6-aryl-2*H*-pyranones **1** (Scheme 1; numbering of Ar_4 and Ar_6 in products used).

The two challenges that these results presented were the development of a reproducible experimental procedure, beyond a chance reaction or two, and the preparation of suitable crystals for X-ray crystal structure analysis. The initial study is now completed, and it has been extended to the current report.

Acetoacetanilide and 4′-chloroacetoacetanilide were trilithiated with excess lithium diisopropylamide (LDA), in tetrahydrofuran (THF) at 0 °C and condensed with several substituted benzoate esters, such as methyl 4-bromobenzoate, to give *C*-acylated intermediates that were not isolated. Attempts to isolate these compounds, or the possibility of

Scheme 2. Mechanistic details for the preparation of 4-anilino-6-aryl-2*H*-pyran-2-ones (**1a**–**1g**) (Ar_4 and Ar_6 numbering of products).



isolating a cyclized 4-pyranone **2** (or pyridone **3**, Fig. 1) only resulted in the eventual isolation of rearrangement products that were shown, primarily by X-ray crystal structural analysis, to be 4-anilino-6-aryl-2-pyranones **1a** and **1b**. The developing synthon indicated that additional examples of the polylithiation, condensation, cyclization, and rearrangements could be affected when the products from the initial condensation with the esters were not isolated, but separately acid cyclized with benzene or toluene using a water trap (see *Experimental*). The 2-pyranones, **1a**–**1g**, were obtained in 23%–68% yield without need of chromatographic purification.

The 1,6-diphenyl-4*H*-pyran-4-ones **2** (Fig. 1) can result from the cyclization of an expected *C*-acylated intermediate (Scheme 2) (2*a*). An acidic intermolecular pathway ((**A**) → (**B**) → (**C**)) is probable, and an intramolecular pathway (**2** → **3** → **1**) is overly complex, even though both may explain the formation of 4,6-disubstituted 2-pyranones **1**. The intermolecular pathway would involve the 1,4-addition of water–H^+ to anilinopyranone **2** to (**A**) with elimination of a substituted aniline to the 2-hydroxy-4-pyranone (**B**). This intermediate (**B**) would undergo a 1,2-addition of the substituted aniline to (**C**), followed by elimination of water, and give the 2-pyranones **1a**–**1g**, isolated. The less likely intramolecular path, usually representing a photochemical or thermal route, has seven steps involving several epoxide-type intermediates involving the rearrangement of a 1,6-disubstituted 4-pyranone **2** to a 4,5-disubstituted, 2-pyranone **1** (6). The remaining steps involve the rearrangement of a 4,5-disubstituted 2-pyranone **3** to a 4,6-disubstituted 2-pyranone **1** (7, 8*b*–8*f*, 13).

© 2004 NRC Canada

Fig. 2. Thermal ellipsoid plot (50% ellipsoids for non-hydrogen atoms) for **1a** ($C_{17}H_{12}ClNO_2$).

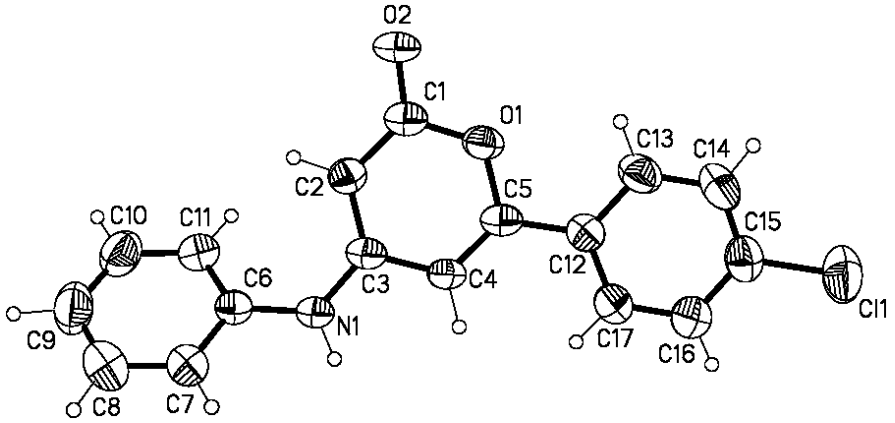
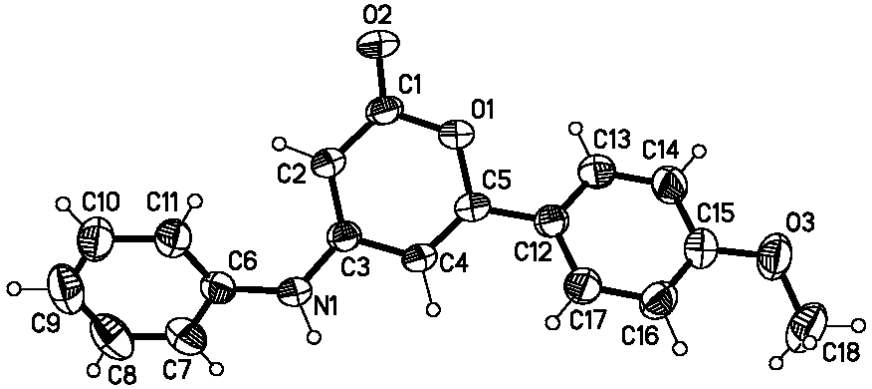


Fig. 3. Thermal ellipsoid plot (50% ellipsoids for non-hydrogen atoms) for **1b** ($C_{18}H_{15}NO_3$).



X-ray analysis for 2-pyranones **1a** and **1b** are shown in Figs. 2 and 3, respectively (14–17). Atomic positional parameters are listed in the *Supplementary material*,[3] and selected bond distances and angles are listed in the *Supplementary material*.[3] In 2-pyranone **1a**, the dihedral angles between the heterocycle ring and the phenyl ring containing C-6 is 46.2° and the phenyl ring containing C-12 is 8.4°, and in 2-pyranone **1b** the angles are 41.4° and 25.3°, respectively. Both compounds consist of hydrogen-bonded chains through the N-H group and the carbonyl oxygen atom. In 2-pyranone **1b**, adjacent molecules in the chain are related by translation, and in 2-pyranone **1a**, they are related by a *c*-glide.

Additional spectral data for 2-pyranones **1a**–**1g** were consistent with structural assignments with the following indicative absorptions: IR (cm^{-1}): NH, 3253–3275 and C=O, 1657–1673. ^{1}H NMR (ppm) δ: 5.32–5.37 (C_5-H) and 6.57–6.70 (C_3-H). ^{13}C NMR (ppm) δ: 162.3–163.5 (C=O). MS for 2-pyranone **1g**: [M + H] 360, 358, with loss of CO_2 at *m*/*z* 316 and 314.

Conclusions

This study demonstrates that trilithiated acetoacetanilides can undergo a Claisen-type condensation with benzoate esters, followed by an acid cyclization and several rearrangements to yield new 2-pyranones (**1a**–**1g**). The new synthesis of these 2-pyranones **1a**–**1g** has been developed utilizing strong-base multiple anion synthesis techniques that require an experimental set-up that is on the order of complexity required for standard Grignard syntheses, and the procedures can be reproduced by someone who is not necessarily experienced with these techniques. While the general procedure may not be under the optimal conditions for the preparation of a single compound, multigram quantities of products can be obtained, which is especially attractive for characterization, biological testing, and other uses. The syntheses are regioselective, and the products were readily purified by recrystallization from routine solvents.

Experimental section

Melting points were obtained with a Mel-Temp II melting point apparatus in open capillary tubes and are uncorrected. Fourier transform IR spectra were obtained with a Nicolet Impact 410 FT-IR or a Mattson Genesis II FT-IR with Specac Golden Gate Accessory. Proton and ^{13}C magnetic

[3] Supplementary data may be obtained from the Depository of Unpublished Data, Document Delivery, CISTI, National Research Council Canada, Ottawa ON K1A 0S2, Canada. CCDC 176993 (**1b**) and 176994 (**1a**) contain the supplementary data for this paper. These data can be obtained, free of charge, via www.ccdc.cam.au.uk/conts/retrieving.html (or from the Cambridge Crystallographic Data Centre, 12 Union Road, Cambridge, UK; fax +44 1223 336033; or deposit@ccdc.cam.ac.uk).

© 2004 NRC Canada

resonance spectra were obtained with a Varian Associates Mercury Oxford 300 MHz, NMR spectrometer, and chemical shifts are recorded in δ ppm downfield from an internal tetramethylsilane (TMS) standard. Combustion analyses were performed by Quantitative Technologies, Inc., P.O. Box 470, Whitehouse, N.J. 08888, USA. The mass spectrum for 2-pyranone **1g** was acquired by nanospray ionization on an LCQ Classic quadrupole ion trap mass spectrometer (ThermoFinnigan, San Jose, Calif.).

Single crystal X-ray measurements for crystals of 2-pyranone **1a** and 2-pyranone **1b** were collected on a Mercury CCD area detector coupled with a Rigaku AFC8 diffractometer with graphite monochromated Mo Kα (λ = 0.71073 Å) radiation. The data were collected at a temperature of 20 °C to a maximum 2θ value of 52.8°. Data for 2-pyranone **1a** were collected in 0.50° oscillations in ω with 45 s exposures (two identical scans were performed at each position to identify detector anomalies) and data for 2-pyranone **1b** were collected in 0.50° oscillations in ω with 5 s exposures. A sweep of data was done using ω oscillations from –90.0 to 90.0° at χ = 45.0° and ϕ = 0.0°; a second sweep was performed using ω oscillations from –30.0 to 30.0° at χ = 45.0° and ϕ = 90.0°. The crystal-to-detector distance was 26.92 mm. The detector swing angle was 0.00°. Cell parameters and additional details of the data collection are reported in the *Supplementary material*.[3]

Of the 14 171 reflections collected for 2-pyranone **1a**, 3058 were unique (R_{int} = 0.071), and of the 7022 reflections collected for 2-pyranone **1b**, 2962 were unique (R_{int} = 0.038); equivalent reflections were merged. Data was collected, processed, and corrected for Lorentz polarization and for absorption using CrystalClear (Rigaku) (14). The structures were solved by direct methods and expanded using Fourier techniques. The non-hydrogen atoms were refined anisotropically and hydrogen atoms were refined isotropically. The final cycle of full-matrix least-squares refinement on F^2 for 2-pyranone **1a** converged with R_1 = 0.0805 (2928 observed reflections ($I > 2.00\sigma(I)$), wR_2 = 0.1087 (all data). Likewise, for 2-pyranone **1b** the refinement converged with R_1 = 0.0528 (based on 2961 observed reflections ($I > 2.00\sigma(I)$), wR_2 = 0.1233 (all data). Structure solution, refinement, and the calculation of derived results were performed using the SHELXTL (15) package of computer programs. Neutral atom-scattering factors were those of Cromer and Waber (16), and the real and imaginary anomalous dispersion corrections were those of Cromer (17).

General procedure for preparation of 2*H*-pyran-2-ones (1a–1g)

(Ratio of reagents – acetoacetanilide or 4′-chloroacetoacetanilide: LDA: ester, 1:4:1)

In a typical reaction sequence, LDA (0.064 mol) was prepared by the addition of 40 mL of 1.6 mol L^{-1} *n*-butyllithium (0.064 mol) to a three-neck round-bottomed flask (e.g., 500 mL), equipped with a nitrogen inlet tube, a side-arm addition funnel (e.g., 125 mL), and a magnetic stir bar. The flask was cooled in an ice bath and 6.41 g (0.064 mol) of diisopropylamine (Aldrich Chem. Co., 99.5%), dissolved in 25–30 mL of dry tetrahydrofuran (THF) (sodium–benzophenone-ketyl), was added from the addition funnel at a fast dropwise rate during a 5 min period (0 °C, N_2). The solution was stirred at 0 °C for an additional 15–20 min, and then treated via the addition funnel with 2.67 g (0.0150 mol) acetoacetanilide (99.5%, Aldrich) or 3.24 g (0.0150 mol) of 4′-chloroacetoacetanilide (Aldrich, 98%) dissolved in 35–45 mL of THF. The addition time was 5 min. After 2.5 h of continuous stirring at 0 °C, 0.0158 mol of ester, dissolved in 25–35 mL of THF, was added to the trilithiated intermediate, and the solution was stirred for 1 h (0 °C, N_2). Then, 100 mL of 3 mol L^{-1} hydrochloric acid was added, and the two-phase mixture was poured into a large flask containing ice (ca., 100 g) followed by 100 mL of solvent grade ether. The mixture was then neutralized with solid sodium bicarbonate and the layers separated, extracted with ether (2 × 75 mL), and the organic layer was concentrated using a rotary evaporator. The crude material, usually solid, was cyclized using 150 mL of toluene, 15 drops of methanesulfonic acid (70%), and a water trap. The mixture, and then solution, was heated under reflux for 2 h with good stirring during the last step. The solution could then be transferred to a beaker and allowed to evaporate in a hood, or the toluene could be removed with a rotary evaporator.

*6-(4-Chlorophenyl)-4-(phenylamino)-2*H*-pyran-2-one (1a)*

Pyranone **1a** was prepared by the general polylithiation–condensation–cyclization–rearrangements procedure from trilithiated acetoacetanilide and methyl 4-chlorobenzoate, and yielded 3.20 g (68%), mp 305–307 °C (benzene–ethanol). IR (cm^{-1}): 3253, 3195, and 1658. ^{1}H NMR (DMSO-d_6) δ: 5.34 (s, 1H, C_5-H), 6.70 (s, 1H, C_3-H), 7.18–7.29, 7.41–7.46, 7.59–7.62, 7.77–7.80 (m, 9H, ArH), and 9.45 (s, 1H, NH). ^{13}C NMR (DMSO-d_6) δ: 83.1, 98.3, 123.3, 125.6, 127.7, 129.9, 130.2, 131.0, 136.0, 138.9, 156.0, 158.1, and 163.0. Anal. calcd. for $C_{17}H_{12}ClNO_2$: C 68.58, H 4.06, N 4.70; found: C 68.44, H 4.21, N 4.88.

*6-(4-Methoxyphenyl)-4-(phenylamino)-2*H*-pyran-2-one (1b)*

Pyranone **1b** was prepared by the general polylithiation–condensation–cyclization–rearrangements procedure from trilithiated acetoacetanilide and methyl 4-methoxybenzoate and yielded 1.76 g (40%), mp 238–240 °C (benzene–ethanol). IR (paraffin oil) (cm^{-1}): 3271, 3197, 1668. ^{1}H NMR (DMSO-d_6) δ: 3.81 (s, 3H, OCH_3), 5.27 (s, 1H, C_5-H), 6.57 (s, 1H, C_3-H), 7.06–7.27, 7.39–7.44, 7.68–7.71 (m, 9H, ArH), and 9.36 (s, 1H, NH). ^{13}C NMR (DMSO-d_6) δ: 56.1, 82.3, 96.2, 115.2, 123.2, 124.5, 125.5, 127.6, 130.2, 139.1, 156.3, 159.5, 161.9, and 163.5. Anal. calcd. for $C_{18}H_{15}NO_3$: C 73.71, H 5.15, N 4.78; found: C 73.37, H 5.13, N 4.58.

*4-(4-Chlorophenylamino)-6-(3,5-dimethoxyphenyl)-2*H*-pyran-2-one (1c)*

Pyranone **1c** was prepared by the general polylithiation–condensation–cyclization–rearrangements procedure from trilithiated 4′-chloroacetoacetanilide and methyl 3,4-dimethoxybenzoate and yielded 1.23 g (23%), mp 258–260 °C (benzene–ethanol). IR (paraffin oil) (cm^{-1}): 3263, 3188, 1667. ^{1}H NMR (DMSO-d_6) δ: 3.79 (s, 6H, OCH_3), 5.35 (s, 1H, C_5-H), 6.64 (s, 1H, C_3-H), 6.85 (s, 3H, ArH), 7.28 (d, 2H, ArH), and 7.45 (d, 2H, ArH), and 9.44 (s, 1H, NH). ^{13}C NMR (DMSO-d_6) δ: 56.2, 98.5, 103.4, 103.9, 121.9, 124.7, 130.1, 134.1, 138.1, 155.7, 159.1, 161.5, and

© 2004 NRC Canada

163.2. Anal. calcd. for $C_{19}H_{16}ClNO_4$: C 63.78, H 4.51, N 3.91; found: C 63.36, H 4.44, N 3.80.

*6-(4-Chlorophenyl)-4-(4-chlorophenylamino)-2*H*-pyran-2-one (1d)*

Pyranone **1d** was prepared by the general polylithiation–condensation–cyclization–rearrangements procedure from trilithiated 4′-chloroacetoacetanilide and methyl 4-chlorobenzoate and yielded 1.20 g (24%), mp 294–297 °C (benzene–ethanol). IR (paraffin oil) (cm^{-1}): 3263, 3181, 1673. ^{1}H NMR (DMSO-d_6) δ: 5.37 (s, 1H, C_5-H), 6.70 (s, 1H, C_3-H), 7.31 (d, 2H, ArH), 7.49 (d, 2H, ArH), 7.61 (d, 2H, ArH), 7.80 (d, 2H, ArH), and 9.50 (s, 1H, NH). ^{13}C NMR (DMSO-d_6) δ: 83.1, 97.5, 124.2, 127.1, 128.6, 129.3, 129.5, 130.2, 135.4, 137.4, 155.1, 157.6, and 162.3. Anal. calcd. for $C_{17}H_{11}Cl_2NO_2$: C 61.47, H 3.34, N 4.22; found: C 61.27, H 3.32, N 4.11.

*4-(4-Chlorophenylamino)-6-(4-methoxyphenyl)-2*H*-pyran-2-one (1e)*

Pyranone **1e** was prepared by the general polylithiation–condensation–cyclization–rearrangements procedure from trilithiated 4′-chloroacetoacetanilide and methyl 4-methoxybenzoate and yielded 2.46 g (50%), mp 282–285 °C (benzene–ethanol). IR (paraffin oil) (cm^{-1}): 3275, 3194, 1666. ^{1}H NMR (DMSO-d_6) δ: 3.83 (s, 3H, OCH_3), 5.32 (s, 1H, C_5-H), 6.58 (s, 1H, C_3-H), 7.08 (d, 2H, ArH), 7.31 (d, 2H, ArH), 7.47 (d, 2H, ArH), 7.72 (d, 2H, ArH), and 9.42 (s, 1H, NH). ^{13}C NMR (DMSO-d_6) δ: 55.4, 82.2, 95.4, 114.6, 123.7, 124.1, 126.9, 128.4, 129.4, 137.5, 155.4, 158.9, 161.2, and 162.6. Anal. calcd. for $C_{18}H_{14}ClNO_3$: C 65.96, H 4.31, N, 4.27; found: C 65.75, H 4.46, N 4.04.

*6-(4-Bromophenyl)-4-(4-chlorophenylamino)-2*H*-pyran-2-one (1f)*

Pyranone **1f** was prepared by the general polylithiation–condensation–cyclization–rearrangements procedure from trilithiated 4′-chloroacetoacetanilide and methyl 4-bromobenzoate and yielded 3.67 g (65%), mp 294–296° (benzene–ethanol). IR (cm^{-1}): 3261, 3183, 1658. ^{1}H NMR (DMSO-d_6) δ: 5.36 (s, 1H, C_5-H), 6.70 (s, 1H, C_3-H), 7.28–7.31, 7.45–7.48, 7.69–7.75 (m, 8H, ArH), and 9.48 (s, 1H, NH). ^{13}C NMR (DMSO-d_6) δ: 83.1, 97.5, 124.2, 124.3, 127.2, 128.7, 129.5, 130.6, 132.2, 137.4, 155.1, 157.7, and 162.3. Anal. calcd for $C_{17}H_{11}BrClNO_2$: C 54.21, H 2.94, N 3.72; found: C 54.05, H 3.09, N 3.60.

*4-(4-Chlorophenylamino)-6-(3,4-dimethoxyphenyl)-2*H*-pyran-2-one (1g)*

Pyranone **1g** was prepared by the general polylithiation–condensation–cyclization–rearrangements procedure from trilithiated 4′-chloroacetoacetanilide and methyl 3,4-dimethoxybenzoate and yielded 2.73 g (51%), mp 262–264 °C (benzene–ethanol). IR (cm^{-1}): 3264, 3188, and 1657. ^{1}H NMR (DMSO-d_6) δ: 3.81 (s, 3H, OCH_3), 3.83 (s, 3H, OCH_3), 5.32 (s, 1H, C_5-H), 6.59 (s, 1H, C_3-H), 7.09 (d, 2H, ArH), 7.24–7.46 (m, 5H, ArH), and 9.38 (s, 1H, NH). ^{13}C NMR (DMSO-d_6) δ: 56.3, 56.4, 82.9, 96.6, 108.9, 112.6, 119.3, 124.6, 124.7, 129.1, 130.1, 138.3, 149.6, 151.7, 156.0, 159.6, and 163.4. MS: [M + H] 360, 358, 316, 314; [M + H – 44 (CO_2)] 205, 157, 155. Anal. calcd. for $C_{19}H_{16}ClNO_4$: C 63.78, H 4.51, N 3.91; found: C 64.24, H 4.47, N 3.68.

Acknowledgements

We wish to thank the following sponsors: the National Science Foundation's Research at Undergraduate Institutions through grants CHE Nos. 9708014 and 0212699, the United States Department of Agriculture, NRICGP No. 2003-35504-12853, and the Donors of the Petroleum Research Fund, administered by the American Chemical Society. The acquisition of a 300 MHz NMR spectrometer was made possible through a National Science Foundation's Division of Undergraduate Education through grant DUE No. 9750721. The mass spectrum for **1g** was taken by Dr. Kevin L. Schey, Department of Pharmacology, Medical University of South Carolina, Charleston, S.C. 29425, USA. The assistance of Dr. Jason S. Overby is acknowledged with thanks.

References

1. (*a*) R. Livingstone. *In* Rodd's chemistry of carbon compounds. 2nd ed. *Edited by* M. Sainsbury. Elsevier, Amsterdam, The Netherlands. 1997. pp. 1–546; (*b*) J.D. Hepworth. *In* Comprehensive heterocyclic chemistry. *Edited by* A.R. Katritzky and C.W. Rees. Pergamon Press, New York. 1984. pp. 789–795.
2. (*a*) J.F. Wolfe, T.M. Harris, and C.R. Hauser. J. Org. Chem. **29**, 3249 (1964); (*b*) T.M. Harris, T.P. Murry, C.M. Harris, and M. Gumulka. J. Chem. Soc. Chem. Commun. 362 (1974); (*c*) S.N. Huckin and L. Weiler. Can. J. Chem. **52**, 1343 (1974); (*d*) S.N. Huckin and L. Weiler. Tetrahedron Lett. 2405 (1972).
3. (*a*) H. Stockinger and U. Schmidt. Justus Liebigs Ann. Chem. 1617 (1976); (*b*) M. Yamaguchi, K. Hasebe, M. Uchida, A. Irie, and T. Minami. Tetrahedron Lett. **28**, 2017 (1987); (*c*) M. Yamaguchi, K. Hasebe, and T. Minami. Tetrahedron Lett. **27**, 2401 (1986); (*d*) B. Lygo. Tetrahedron, **51**, 12 859 (1995); (*e*) M. Yamaguchi, K. Hasebe, K. Shibato, H. Nakashima, and T. Minami. Tetrahedron, **44**, 4767 (1988); (*f*) M. Yamaguchi, K. Shibato, and I Hirao. Chem. Lett. 1145 (1985).
4. C.R. Hauser and T.M. Harris. J. Am. Chem. Soc. **80**, 6360 (1958).
5. (*a*) A.J. Angel, D.R. Hurst, A.R. Williams, K.L. French, and C.F. Beam. Synth. Commun. **28**, 1547 (1998); (*b*) J.K. Cha, T.M. Harris, J.A. Ray, and H. Venkataraman. Tetrahedron Lett. **30**, 3508 (1989); (*c*) T.A. Oster and T.M. Harris. Tetrahedron Lett. **24**, 1851 (1983); (*d*) J.E. Hill and T.M. Harris. Synth. Commun. **12**, 621 (1982); (*e*) J.A. Ray and T.M. Harris. Tetrahedron Lett. **23**, 1971 (1982); (*f*) J. Brown, K.L Sides, T.D. Fulmer, and C.F. Beam. J. Heterocycl. Chem. **16**, 1669 (1979); (*g*) T.P. Murray and T.M. Harris. J. Am. Chem. Soc. **94**, 8253 (1972).
6. (*a*) J.A. Barltrop, A.C. Day, and C.J. Samuel. J. Am. Chem. Soc. **101**, 7521 (1979); (*b*) J.W. Pavlik and L.T. Pauliukonis. Tetrahedron Lett. 1939 (1976); (*c*) N. Ishibe, M. Sunami, and M. Odani. J. Am. Chem. Soc. **95**, 463 (1973); (*d*) N. Ishibe, M. Odani, and M. Sunami. J. Chem. Soc. Chem. Commun. 1034 (1971); (*e*) G.P. Ellis. *In* Comprehensive heterocyclic chemistry. *Edited by* A.R. Katritzky and C.W. Rees. Pergamon Press, New York. 1984. pp. 693–694.
7. (*a*) V.J. Ram and N. Agarwal. Tetrahedron Lett. **42**, 7127 (2001); (*b*) P. De March, M. Moreno-Manas, and I. Ripoll. Chem. Ber. **120**, 1413 (1987); (*c*) M. Eder, E. Ziegler, and E. Prewedourakis. Monatsh. Chem. **99**, 1395 (1968).

© 2004 NRC Canada

8. (*a*) C. Cimarelli, G. Palmieri, and M. Camalli. Tetrahedron, **53**, 6893 (1997); (*b*) Farhanullah, N. Agarwal, A. Goel, R. Atul, and V.J. Ram. J. Org. Chem. **68**, 2983 (2003); (*c*) V.J. Ram, N. Agarwal, A.S. Saxena, S. Abhishek, Farhanullah, A. Sharon, and P.R. Maulik. J. Chem. Soc. Perkin Trans. 1, 1426 (2002); (*d*) V.J. Ram and N. Agarwal. Tetrahedron Lett. **42**, 7127 (2001); (*e*) V.J. Ram, P. Srivastava, N. Agarwal, A. Sharon, and P.R. Maulik. J. Chem. Soc. Perkin Trans. 1, 1953 (2001); (*f*) V.J. Ram, M. Nath, P. Srivastava, S. Sarkhel, and P.R. Maulik. J. Chem. Soc. Perkin Trans. 1, 3719 (2000); (*g*) V.S. Parmar, S.C. Jain, A. Jha, N. Kumar, A. Kumar, A. Vats, H.N. Jha, S. Mukherjee, S.K. Singh, K.R. Jennings, S.G. Summerfield, W. Errington, and C.E. Olsen. Indian J. Chem. Sect. B, **36B**, 872 (1997).
9. (*a*) C.M. Thompson. *In* Dianion chemistry in organic synthesis. CRC Press, Boca Raton, Fl. 1994. pp. 27–44; (*b*) T.M. Harris and C.M. Harris. Org. React. (N.Y.), **17**, 155 (1969).
10. D.R. Hurst, K.L. French, A.J. Angel, A.R. Williams, M.E. Rampey, T.S. Guion, K.W. Chan, C.M. Kassis, S.L. Studer-Martinez, and C.F. Beam. J. Heterocycl. Chem. **35**, 1357 (1998).
11. A.J. Angel, A.E. Finefrock, K.L. French, D.R. Hurst, A.R. Williams, M.E. Rampey, S.L. Studer-Martinez, and C.F. Beam. Can. J. Chem. **77**, 94 (1999).
12. C.F. Beam, M.A. Hines, C.L. Mazat, D.C. Duncan, D.D. Beckman, R.J. Lachicotte, R.C. Tummons, and N.D. Heindel. Chem. Ind. (London), 727 (1989).
13. Molecular modeling calculations at the BB8-LYP/DZVP level indicate that the 4-anilino-6-phenyl-2*H*-pyran-2-one **1** is more stable than the 4-anilino-5-phenyl-2*H*-pyran-2-one **3** by 20 kJ mol^{-1}. See also: H. Wittmann, A. Wohlkoenig, H. Sterk, and E. Ziegler. Monatsh. Chem. **101**, 296 (1970).
14. R.A. Jacobson. CrystalClear [computer program]. Rigaku Corporation, the Woodlands, 1999; absorption correction used REQABS, version 1.1 [computer program]. Molecular Structure Corporation, Tex. 1998.
15. G.M. Sheldrick. SHELXTL version 5.1 [computer program]. Bruker Analytical X-ray systems, Madison, Wisconsin. 1997.
16. D.T. Cromer and J.T. Waber. International tables for X-ray crystallography. Vol. IV. the Kynoch Press, Birmingham, UK. 1974. Table 2.2B.
17. D.T. Cromer. International tables for X-ray crystallography. Vol. IV. Kynoch Press, Birmingham, UK. 1974. Table 2.3.1.

© 2004 NRC Canada

Gerhard Herzberg — A personal appreciation[1]

G. Winnewisser

Abstract: Some important contributions of Gerhard Herzberg to molecular astronomy and the study of free radicals are highlighted and placed in the context of the history of spectroscopy.

Key words: molecular spectroscopy, free radicals, methylene, interstellar lines.

Résumé : On met en relief quelques-unes des contributions de Gerhard Herzberg à l'astronomie moléculaire ainsi qu'à l'étude des radicaux et on les place dans le contexte de l'histoire de la spectroscopie.

Mots clés : spectroscopie moléculaire, radicaux libres, méthylène, raies interstellaires.

[Traduit par la Rédaction]

Introduction

The great contributions of Gerhard Herzberg to molecular science illustrate that spectroscopy advances quite often through significant, even monumental, individual achievements. Herzberg's long scientific life and his strong interaction with science demonstrate this in many ways.

It is most fitting to commemorate Gerhard Herzberg's 100th birthday in pausing for a moment and looking back to the very early beginnings of spectroscopy. Gerhard's birthday on Christmas Day 1904 happens to fall approximately half way between the 1814 recording of the first Fraunhofer lines in the solar spectrum, and the present time. Thus, it arbitrarily divides the nearly 200 years of spectroscopic science into two almost equal periods. The first time interval, approximately coincident with the 19th century, one might loosely call the pre-Herzberg era of spectroscopy.

The pre-Herzberg era

This era opened in southern Germany in 1814. In Bavaria, the talented young Joseph von Fraunhofer succeeded in manufacturing high quality lenses and constructed one of the finest refractory telescopes ever built (1). He invented a heliometer and a diffraction grating for measuring the wavelength of light precisely. In addition, he acquired great skill in the manufacture of homogenous glass prisms, which reached unparalleled quality. These technical achievements, in particular his uniquely homogeneous glass prisms, gave him the edge over all his predecessors and contemporaries in dispersing light. Pointing his refracting telescope together with his "self-built spectrograph" towards the sun and some of the close by stars, he discovered that the sun's spectrum, when sufficiently dispersed, was punctuated by a large number of fine dark lines, about 700 of which he studied in great detail. He collected an atlas of these lines, naming the strongest features consecutively A, B, C, D,….

Today a few of these catalogued lines are still known to spectroscopists by the famous Fraunhofer notation, such as the sodium D-lines. Fraunhofer found that the D feature consists of two lines, which he named $D_{1,2}$. We now know that the 3*p* level of Na displays an observable fine structure, so that the transition between the 3*s* and 3*p* levels appears as a closely spaced doublet. Thus, the two Fraunhofer lines correspond to the following transitions: $D_1 = {}^2P_{1/2} - {}^2S_{1/2}$ = 5895.940 Å and $D_2 = {}^2P_{3/2} - {}^2S_{1/2}$ = 5889.973 Å.

In retrospect, the discovery that the Sun and the stars are made up of the same chemical elements as the Earth is one of the earliest and greatest achievements of spectroscopy and its first application to astronomical objects. The identification of the Fraunhofer lines was begun in the years 1859–1861 by the new methods of spectral analysis introduced by R.W. Bunsen and G.R. Kirchhoff. This correlation marked the time and place of the establishment of spectroscopy as an analytical tool with an unparalleled power to study both physical and chemical processes in the laboratory and in cosmic dimensions. The power of this new tool "spectroscopy" and its potential for future applications were recognized by Kirchhoff and Bunsen, who stated that it would open "an entirely untrodden field, stretching far beyond the limits of the Earth, or even of our solar system" and who noted the "almost inconceivable" sensitivity of spectroscopy that would lead to the detection of hitherto unknown elements (2). Indeed many new elements, such as Cs, Rb, and He, were subsequently detected by their atomic spectra, in the laboratory and in stars. A detailed understanding of the spectra and their associated energy level diagrams had to await the advent of quantum mechanics in the 1920s. With

Received 1 March 2004. Published on the NRC Research Press Web site at http://canjchem.nrc.ca on 27 May 2004.

A Special Issue commemorating Gerhard Herzberg's 100th Birthday (December 25th 1904).

G. Winnewisser. Physikalisches Institut, Universität zu Köln, Zülpicher Str. 77, D-50937 Köln, Germany. (e-mail: herbst@mps.ohio-state.edu).

[1]This article is part of a Special Issue dedicated to the memory of Professor Gerhard Herzberg.

 doi: 10.1139/V04-067 © 2004 NRC Canada

this understanding, and subsequent technological development, the early predictions of Kirchoff and Bunsen have surely been surpassed.

The Herzberg era and nonterrestrial molecules

It would be impossible to describe the many achievements of Gerhard Herzberg in a short appreciation (3). Late in his life, as Guest of Honour at our 1st Zermatt Meeting in 1988, GH chose to talk about the start of interstellar spectroscopy and his major role in it: "I was, however, there in that prehistoric time at the very beginning of the study of molecules in the interstellar medium which occurred in 1937. Many years before that, molecules had been identified in comets and planetary atmospheres, and even in some stellar atmospheres. In 1937, Adams and Dunham had obtained the first high resolution spectra of O and B stars. They observed a number of very sharp absorption lines in the violet, some of which they could identify as interstellar lines of a number of atoms and ions while others they had to leave unidentified. It was Swings who discovered the very first interstellar molecule, CH" (4).

GH went on in his description of the situation at that time that "Soon after Swings and Rosenfeld, Andy McKellar at Victoria identified another electronic transition of CH and in addition the well-known CN lines near 3883 Å, also on the basis of Adams and Dunham's spectra. There was left a series of four lines at 4232, 3938, 3745, and 3579 Å in Adams and Dunham's spectra that remained unidentified for another two years. In June 1941, a few of us including Swings, Beutler, Mulliken, and Teller met at an informal meeting at Yerkes Observatory to discuss this question. The structure of the observed spectrum made it certain that it was molecular in origin. Mulliken suggested CH_2 ($^1B_1$–$^1A_1$); Teller and I suggested CH^+ because of the similarity to BH. In Saskatoon, where I worked at the time, Alex Douglas and I had an apparatus available that could be used to test the assumption. Within a few days we observed a new band system whose 0–0,1–0,2–0 bands were approximately at the place of the first three unidentified interstellar lines coming from the lowest rotational level ($J = 0$). It took some time to make certain that the new spectrum was due to CH^+ since there was no isotope shift observed. The discovery of the next interstellar molecule accomplished by radio astronomical methods took place 22 years later. As you all know, 5 years after that the floodgates were opened with the discovery of interstellar NH_3 and H_2O by C.H. Townes and his associates" (4).

Gerhard Herzberg and free radicals (especially CH_2)

Throughout his entire scientific life, Gerhard Herzberg pursued an abiding interest in free radicals. As a consequence of having an open outer shell of electrons, molecular species in this class are chemically rather unstable. The citation for his 1971 Nobel Prize in Chemistry reads: "for contribution to the knowledge of electronic structures and geometry of molecules, especially free radicals" and implies that the Prize had been awarded for a long series of studies extending virtually over his entire scientific life (5).

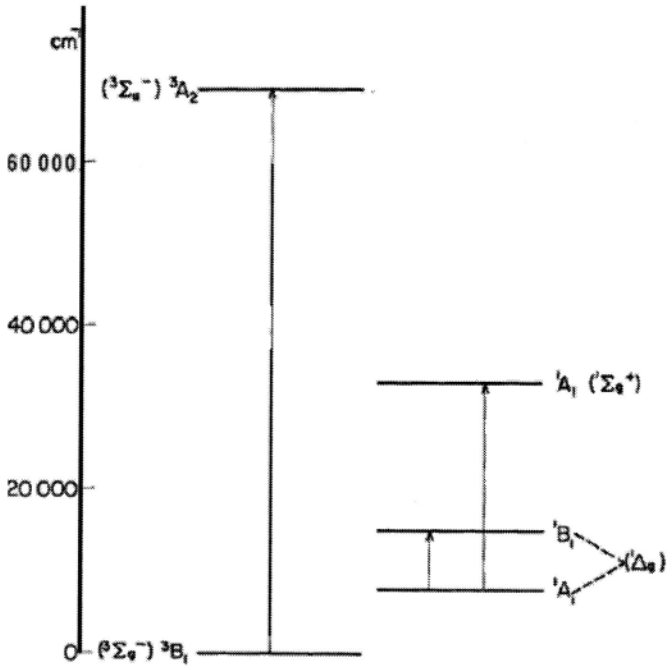
Due to one or more free electrons, molecular free radicals have a strong tendency to form more stable, larger molecules. In interstellar molecular clouds, gas-phase free-radicals are particularly abundant. In particular, the triatomic and very light methylene radical (CH_2) is a prime constituent in gas-phase chemical models of both diffuse and dense interstellar clouds, where it is produced early in the sequence of ion–molecule reactions. The appropriate processes have been summarized in our following paper (6) in this issue of *Can. J. Chem.*

The methylene radical was very early subjected to Gerhard's scrutiny: "While in Saskatoon I had tried to obtain the spectrum of CH_2" (7). In 1942, when he started to measure the electronic spectra of free radicals, he thought that he had produced methylene by discharging methane (CH_4). But the photographed UV-spectrum always fell short of showing traces of the CH_2 spectrum. One other experiment, intended to prove the presence of CH_2 in such a discharge, was to discharge fully deuterated methane (CD_4) and observe the CDH and CD_2 isotopomers with the appropriate isotope shifts. But this latter experiment produced the identical spectrum as did the CH_4 gas discharge. What a surprise! Since there was no isotope shift observed, Herzberg finally concluded that they had produced the radical C_3, which has recently been discovered in space and has been precisely measured in the laboratory. Indeed, the C_3 molecule is now considered to be essential in forming larger carbon chain species. Our KOSMA laboratory has produced various carbon chain clusters, such as C_{10} and others.

It became clear to Gerhard that the methylene spectrum would not reveal itself quickly. In reality, it took GH many more years than anticipated before he could overcome the substantial difficulties that beset the measurement of the methylene spectrum. But finally his determination and devotion prevailed. "It was ten years after I came to Ottawa and 17 years after the first experiments in Saskatoon that I finally observed the absorption spectrum of CH_2 in the vacuum ultraviolet. … Before CH_2 was found, the CH_3 radical was observed with much less difficulty" (7). It was Herzberg and Shoosmith (8) who found "the first true spectrum" of CH_2 as a prominent feature in the extreme UV region at 1415 Å. This spectral feature actually did shift when hydrogen was replaced by deuterium. Detailed analysis of the 1415 Å spectrum revealed the structural parameters of the CH_2 molecule. After initial uncertainty about whether the molecule was linear or bent, it was realized that it may be considered quasilinear, or just barely bent, and the electronic ground state was determined to be of $^3B_1$ symmetry. The geometrical structure is similar to water (H_2O) with a C—H bond distance of 1.071 Å but with a much wider HCH angle of about 140° (9). Indeed, the structure cannot be properly described independently of the electronic potential functions for the lowest electronic states. In his Nobel lecture (5) Gerhard discussed some of the details of finally securing beyond any doubt the unusual energy level diagram of the observed electronic states of CH_2. We reproduce his energy level diagram in Fig. 1 to honor the results, representing significant progress, which could only be achieved by tremenduous devotion and endurence. A problem that may

© 2004 NRC Canada

Fig. 1. Observed electronic states of CH_2.



look deceivingly simple from today's standpoint of knowledge may have posed a quite different challenge when faced for the first time. As Gerhard admitted in his Nobel lecture, "… of course the spectrum of CH_2 has given me a great deal of pleasure…".

The CH_2 radical turned out to be one of those molecular species that display spectra that are extremely difficult to analyze. And for methylene this holds true for all wavelength regions, from the UV through the visible spectrum clear down into the IR and on to the pure rotational spectrum. In the early eighties, the spectroscopy group at NRC Ottawa, led by Bunker and McKellar with support from Jensen (theoretical) and Sears (mainly experimental), pushed ahead with LMR techniques to detect and disentangle the hitherto unknown IR spectrum. We are presently investigating the last, rotational, part of the CH_2 spectrum, trying to measure it very precisely and understand it in detail. In our contribution to this volume, we describe our progress on the high-resolution rotational spectrum of CH_2 in its vibrational and electronic ground state. Based on technical developments at Cologne University (10, 11), it has now become possible with the introduction of terahertz techniques to measure the pure rotational transitions at Doppler resolution and thus with very high accuracy and sensitivity. These new data will give us further valuable information for understanding the dynamical idiosyncracies of this cosmically significant species to which GH persistently showed us the way.

A final word

Upon his return from Stockholm, as we picked him up at the Ottawa airport, I asked GH how he felt about receiving the Nobel Prize. After a short pause he answered, "I feel that my scientific life has been rewarding beyond anything that I deserve." The award did not change him at all; he remained, in his modest way, the world's foremost molecular spectroscopist and the leader in a research field of fundamental importance. His attitude to scientific work is best summarized by the following verse, written in stone over an archway at Cambridge University, and which I copied down as a young student:

Use every hour for time goes fast,
And what is now may soon be past,
A future time may never be,
The present is the time for thee!

References

1. J.v. Fraunhofer. Bestimmung des Brechungs- und Farbenzerstreuungs-Vermögens verschiedener Glasarten in Bezug auf die Vervollkommnung achromatischer Fernrohre. Denkschriften der Königlichen Akademie der Wissenschaften zu München, **5**, 193 (1814–1815).
2. G.R. Kirchhoff. Philos. Mag. **25**, 250 (1863).
3. B. Stoicheff. Gerhard Herzberg: An Illustrious Life in Science. NRC Research Press, Ottawa, Ontario, Canada. 2002.
4. G. Herzberg. *In* The physics and chemistry of interstellar molecular clouds. *Edited by* G. Winnewisser and J.T. Armstrong. (Lecture notes in Physics 331). Springer, Berlin. 1989. pp. 1–2.
5. G. Herzberg. Spectroscopic studies of molecular structure. Nobel lecture (1971). The Nobel Foundation. 1972.
6. S. Brünken, E.A. Michael, F. Lewen, Th. Giesen, H. Ozeki, G. Winnewisser, P. Jensen, and E. Herbst. Can. J. Chem. **82**, (2004). This issue.
7. G. Herzberg. Ann. Rev. Phys. Chem. **36**, 1 (1985).
8. G. Herzberg and J. Shoosmith. Nature (London), **183**, 1801 (1959).
9. G. Herzberg and J.W.C. Johns. J. Chem. Phys. **54**, 2276 (1971).
10. R. Gendriesch, F. Lewen, G. Winnewisser, and J. Hahn. J. Mol. Spectrosc. **203**, 205 (2000).
11. F. Lewen, R. Gendriesch, I. Pak, D.G. Paveliev, M. Hepp, R. Schieder, and G. Winnewisser. Rev. Sci. Instrum. **69**, 32 (1998).

© 2004 NRC Canada

High-resolution terahertz spectrum of CH_2 — Low *J* rotational transitions near 2 THz[1]

S. Brünken, E.A. Michael, F. Lewen, Th. Giesen, H. Ozeki, G. Winnewisser, P. Jensen, and E. Herbst

Abstract: The methylene radical (CH_2) was very important to Gerhard Herzberg. We have carried out high-resolution spectroscopic measurements on two energetically low-lying, pure rotational transitions of methylene in its ground vibrational–electronic state at frequencies near 2 THz. One of the transitions — the $N_{KaKc} = 2_{11} \leftarrow 2_{02}$ multiplet — belongs to *ortho*-CH_2 and is centered at 1.954 THz. The other rotational transition — the $N_{KaKc} = 1_{10} \leftarrow 1_{01}$ multiplet — belongs to *para*-CH_2 and is centered at 1.915 THz. Since the ground electronic state of methylene has $^3B_1$ symmetry, the rotational transitions are split into three fine-structure components, while the ortho transitions are split additionally by hyperfine structure. In total, we have measured 29 new lines, six for the para transition and the remainder for the ortho transition. The newly measured lines can be added to high-resolution spectral data obtained by ourselves and others at lower frequencies. Progress towards a global fit is discussed.

Key words: spectroscopy, THz frequencies, radicals, methylene, interstellar medium.

Résumé : Le radical méthylène (CH_2) a été très important pour Gerhard Herzberg. On a effectué des mesures spectroscopiques à haute résolution sur deux transitions de rotation pure, de basses énergies, du méthylène dans l'état électronique–vibrationnel fondamental, à des fréquences proches de 2 THz. L'une des transitions, celle du multiplet $N_{KaKc} = 2_{11} \leftarrow 2_{02}$, appartient au CH_2 ortho et elle est centrée à 1,954 THz. L'autre transition rotationnelle, celle du multiplet $N_{KaKc} = 1_{10} \leftarrow 1_{01}$, appartient au CH_2 para et elle est centrée à 1,915 THz. Puisque l'état électronique fondamental du méthylène est de symétrie $^3B_1$, les transitions rotationnelles sont dédoublées en une structure de trois composantes alors que les transitions ortho subissent un dédoublement additionnel par une structure hyperfine. Au total, on a mesuré 29 nouvelles raies, six pour la transition para et le reste pour la transition ortho. On peut ajouter les raies nouvellement mesurées aux données spectrales obtenues par nos soins et à celles obtenues à des fréquences plus faibles par d'autres. On discute des progrès réalisés dans le développement d'un ajustement global.

Mots clés : spectroscopie, fréquences THz, radicaux, méthylène, système interstellaire.

[Traduit par la Rédaction]

Introduction

Gerhard Herzberg and methylene

The methylene radical (CH_2) was of great interest to Gerhard Herzberg (1). The initial attempt to discover this species in the laboratory dates back to the year 1942, when Gerhard Herzberg was first trying to study the electronic spectra of free radicals. By discharging methane (CH_4), Herzberg thought very early on that he had produced the spectrum of the free radical CH_2. But in reality, it took many more years than anticipated before the methylene radical was finally discovered. This seminal event took place "seventeen years after Herzberg's first involvement with CH_2; proving his persistence and determination to finally solve this puzzle" (1). The discovery took place when Herzberg and Shoosmith (2) located a prominent new feature on their photographic plate in the extreme UV region at 1415 Å. Although Herzberg initially thought that methylene was linear in its ground state, detailed analyses of the spectra led eventually to the assignment of the ground state as one of $^3B_1$ symmetry with a nonlinear symmetrical structure, C–H bond distances of 1.071 Å, and an H-C-H angle of 140° (3), settling another long-standing problem. According to Herzberg's Nobel lecture (4), he had spent more than 20 years determining the nature of the electronic states of this difficult radical.

Gerhard Herzberg was so interested in improving our knowledge of methylene that after his successful assignment of the ground electronic state, he soon thought in terms of studying its rotational spectrum. One of us (G. Winnewisser) was a postdoctoral associate at NRC in Ottawa during the years 1968–1970. He had recently constructed a submillimeter-wave spectrometer for the NRC, so Herzberg asked him to attempt to study methylene. The request was then regretfully de-

Received 30 December 2003. Published on the NRC Research Press Web site at http://canjchem.nrc.ca on 26 May 2004.

S. Brünken, E.A. Michael, F. Lewen, G. Winnewisser, and Th. Giesen. Physikalisches Institut, Universität zu Köln, Zülpicher Str. 77, D-50937 Köln, Germany.
H. Ozeki. ISS Science Project Office, Japan Aerospace Exploration Agency, Tsukuba, 305-8505, Japan.
P. Jensen. Fachgruppe Chemie, Bergische Universität Wuppertal, D-42097 Wuppertal, Germany.
E. Herbst.[2] Departments of Physics, Chemistry, and Astronomy, The Ohio State University, Columbus, OH 43210.

[1]This article is part of a Special Issue dedicated to the memory of Professor Gerhard Herzberg.
[2]Corresponding author (e-mail: herbst@mps.ohio-state.edu).

 doi: 10.1139/V04-034 © 2004 NRC Canada

clined; Herzberg's requests for CH_2 microwave data were, just as the man himself, simply 25 years ahead of the time.

More than 10 years after Herzberg's success, work on methylene began anew. In the early eighties, there was a strong push within the spectroscopy group at NRC, led by P.R. Bunker and A.R.W. McKellar, and with the strong involvement of T.J. Sears and P. Jensen, to detect the IR spectrum of CH_2. The goal was to find vibration–rotation transitions of the ν_2 bending vibration of the radical in its $^3B_1$ electronic ground state. After much effort, the ν_2 bending vibration was finally detected using laser magnetic resonance (LMR) techniques in the wavenumber range 880–940 cm^{-1} (5). The present best numerical value for the bending frequency of CH_2 is 963 cm^{-1} (6). Although the symmetric and antisymmetric stretching vibrations (the ν_1 and ν_3 modes) remain undetected, reasonable estimates for these frequencies (2992 and 3213 cm^{-1}) are available from calculations based on the MORBID approach (6). Another push at NRC involved using the very sensitive LMR technique to study the rotational spectrum of methylene. Eventually, LMR was used to study the rotational spectrum through 6 THz in frequency (7, 8). In addition, diode laser spectroscopy was used to study five rotational transitions involving $K_a = 4 \leftarrow 3$ at frequencies near 12 THz (9).

Although the LMR technique possesses great frequency agility for the study of rotational spectra, it does not approach the accuracy of millimetre- and submillimetre-wave methods. But, the field-free rotational spectrum of methylene, a near-prolate asymmetric top with a dipole moment of 0.57 D along the intermediate *b* axis (10), has proved a difficult one to measure because of its wide-open structure due to the lightness of the radical, because of large amplitude motions, and because of both fine and hyperfine splittings. The wide spacings between most pairs of rotational levels mean that much of the rotational spectrum lies in the THz region.

The rotational energy levels of methylene are characterized by the quantum number N and the pseudo-quantum numbers K_a and K_c. The quantum number N refers to rigid-body angular momentum of the asymmetric top and replaces the normal symbol J, which is used here for the total nonnuclear angular momentum (rigid-body + electronic spin). The pseudo-quantum numbers K_a and K_c refer to the rigid-body angular momentum projection on the symmetry axes of the limiting prolate and oblate symmetric tops, respectively. Since the electronic spin quantum number $S = 1$ for CH_2 in its $^3B_1$ ground state, the values of J are N, $N + 1$, $N - 1$ for $N > 0$. Energy levels of the same N and differing J are split by fine-structure effects. In addition to the fine structure, N,J levels of *ortho*-CH_2, which possesses a total hydrogenic nuclear spin I_H of unity, are split by hyperfine effects into energy levels characterized by the total angular momentum quantum number $F = J$, $J + 1$, $J - 1$ for $J > 0$. On the other hand, the N,J levels of *para*-CH_2, where $I_H = 0$, are not split further by hyperfine effects. Given the splittings and the dipolar selection rules ($\Delta N = 0, \pm1$; $\Delta J = 0, \pm1$, $\Delta F = 0, \pm1$) rotational transitions of *ortho*- and *para*-CH_2 occur in multiplets of lines, with the components for the ortho form much more numerous and closely spaced. For *ortho*-CH_2, only rotational levels characterized by an even value for the sum $K_a + K_c$ are allowed (e.g., 4_{04} and 3_{13}), whereas for *para*-CH_2 levels, the sum must be odd. The allowed changes in these two pseudo-quantum numbers for *b*-type transitions are $\Delta K_a = \pm1, \pm3\ldots$, $\Delta K_c = \pm1, \pm3\ldots$.

Lovas et al. (11) were the first to study the high-resolution rotational spectrum; they measured the multiplet of lines in the 68–71 GHz range belonging to the rather high-lying $N_{KaKc} = 4_{04} \leftarrow 3_{13}$ transition of *ortho*-CH_2. These lines were later used to detect methylene in certain regions of dense interstellar clouds known as "hot cores" (12). The work of Lovas et al. (11) was followed by studies in the submillimeter-wave region by Ozeki and Saito (13), who measured the $N_{KaKc} = 2_{12} \leftarrow 3_{03}$ and $N_{KaKc} = 5_{05} \leftarrow 4_{14}$ multiplets of *para*-CH_2 at frequencies around 440–445 GHz and 592–594 GHz, respectively. Most recently, we studied the $N_{KaKc} = 1_{11} \leftarrow 2_{02}$ rotational transition of *ortho*-CH_2 in the 931–956 GHz range, inaugurating the study of its THz spectrum at high resolution (14). A global data set consisting of all of the high-resolution spectral transitions was fit to an asymmetric top, Watson-type Hamiltonian with additional fine-structure and hyperfine-structure terms.

In this paper, we report the measurement of two new rotational transitions of the methylene radical in its ground vibrational–electronic state at frequencies near 2 THz. One of the transitions — the $N_{KaKc} = 2_{11} \leftarrow 2_{02}$ multiplet of *ortho*-CH_2 — is centered at 1.954 GHz and consists of 23 detected components split by fine-structure and hyperfine effects. The other rotational transition is the $N_{KaKc} = 1_{10} \leftarrow 1_{01}$ multiplet of *para*-CH_2, which is split by fine-structure only, and is centered at 1.915 THz. Figure 1 shows the lowest lying rotational levels of methylene divided into ortho levels on the left and para levels on the right. Rotational transitions measured in the laboratory (including the present measurements) are depicted with arrows. The energy scale is in units of K, a convention favored by astronomers.

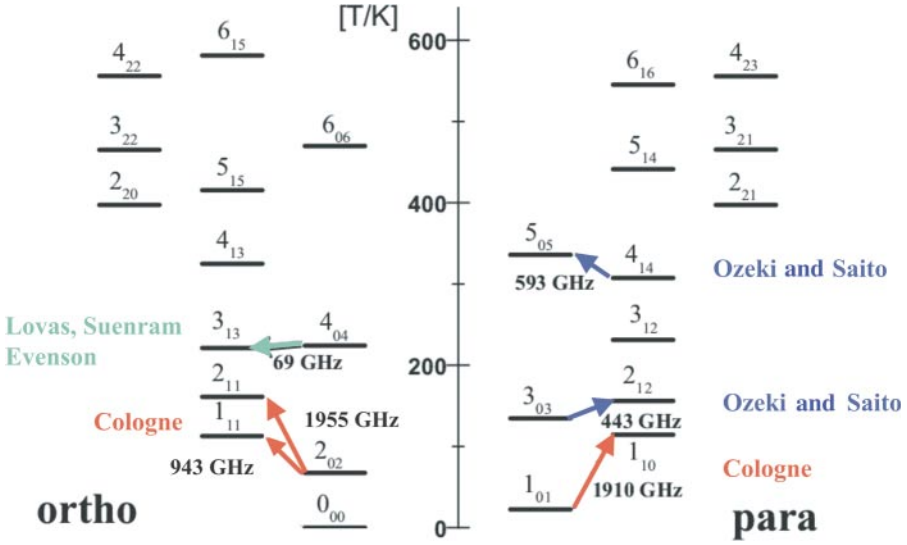
The remainder of this paper is divided as follows. First, we discuss the techniques used in the experimental measurements and show some of our spectral results. Then, we discuss the spectral assignments at 2 THz and our progress in fitting a global data set including the newly measured transitions to a standard Watson-type Hamiltonian with additional terms for fine-structure and hyperfine interactions. Progress has so far been partial only, and attempts with a nonrigid bender Hamiltonian will also be undertaken (6, 15). Afterwards, we discuss the role of methylene as an interstellar molecule. A discussion of current progress ends the paper.

Experimental measurements

For the reported measurements, the Cologne sideband spectrometer for Terahertz applications (COSSTA) was used. A detailed description of the experimental setup to generate frequencies in the range from 1.75 to 2.01 THz is given by Gendriesch et al. (16). Here we only give a short summary of the techniques employed. The basic idea of a sideband system is to mix the outputs of two sources of radiation by means of a nonlinear device such as a fast Schottky diode, and filter out the generated sum frequency, known as the upper sideband, for spectroscopy. In our laser sideband system, one radiation source is a frequency stabilized FIR laser operated at a fixed frequency. The second frequency source is a

© 2004 NRC Canada

Fig. 1. Rotational levels of *ortho*- and *para*-methylene through an energy of 600 K (1 K = 1.99 × 10^{-3} kcal mol^{-1}). Measured transitions to microwave accuracy are indicated by arrows with names of groups.



backward wave oscillator (BWO) with a tunable frequency output that is phase, and therefore, frequency stabilized (17).

A sketch of the experimental setup, found in Fig. 2, is divided into four parts: (*i*) the phase-locked BWO unit with its frequency synthesizers (left), (*ii*) the sideband mixer inside the evacuated optics box (center), (*iii*) the optically pumped difluoromethane FIR laser system (lower right), and (*iv*) the cooled discharge cell with the major components necessary for efficient methylene production (upper right). The laser system is stabilized to the 15th harmonic of a 108 GHz Gunn oscillator followed by a THz quasi-optical harmonic mixer. The resulting IF is processed with an analog frequency demodulator to derive a sensitive control signal for the CO_2 laser stabilization, and hence for the FIR laser.

Sideband radiation is generated by mixing the output radiation of a phase-stabilized BWO with frequency-stabilized radiation of the FIR ring laser on a whisker-contacted, low-capacitance Schottky diode. The FIR laser system operates at a fixed frequency of 1.626 THz. Since the BWOs used can be continuously tuned within a frequency range from ~130 to 390 GHz, the produced upper sideband radiation (at a frequency given by the sum of BWO and FIR-laser frequency) covers a frequency region from 1.75 to 2.01 THz. The frequency stability of the whole system is determined by the loop error of the AFC (automatic frequency control). The error was measured to be less than 5 kHz.

The CH_2 was generated in two steps. First, commercially available diketene was pyrolyzed through quartz wool at 650 °C over a length of 20 cm to form ketene. The pure ketene was then discharged in a DC glow discharge at 40 mA and 50–80 μbar (1 bar = 100 kPa). The active region was ~80 cm with a cell diameter of 10 cm and could be cooled down to 170 K by a LN2-flowing copper jacket.

As in our previous work (14), fast square-wave Zeeman modulation was used to detect the CH_2 lines; the technique was adapted for the first time with the Cologne sideband spectrometer. For this purpose, a copper wire coil, able to withstand 30 A current, was attached surrounding the glass cell over the whole discharge length. An axial magnetic field with B_{max} = 2 to 3 G and a modulation frequency of 4.3 kHz could then be applied.

To shield the background earth magnetic field of 300–500 mG, a box of high permeable mu-metal (1mm thick) was constructed to cover the entire discharge region of the absorption cell. The residual magnetic field was measured to be below 10 mG. Special attention was paid to minimize induced eddy currents inside the shielding box that arise from the Zeeman modulation and may cause field inhomogeneities.

Table 1 contains the measured frequencies of the newly studied lines in MHz along with their quantum assignments and the uncertainties (one standard deviation) in the measured frequencies. Assignments with asterisks next to them are to be regarded as doubtful. The measurement uncertainties are typically 200 kHz for the components of the 1_{10}–1_{01} transition of *para*-CH_2 and 200–500 kHz for the corresponding components of the 2_{11}–2_{02} transition of *ortho*-CH_2. The largest uncertainties arise from the weakness of some transitions and the overlapping of lines. These transitions were nonetheless included since the available rotational data for methylene are so sparse. Figure 3 shows the actual measured hyperfine structure for the $J = 3 \leftarrow 3$ fine-structure component of the 2_{11}–2_{02} transition in the region 1954.910–1954.930 GHz, while Fig. 4 shows a stick spectrum with the complete fine-structure, hyperfine pattern for this rotational transition, which occurs over a much wider region between 1943 and 1964 GHz. Note that the assorted hyperfine-structure multiplets are designated by the letter *G* and an appropriate subscript. Figure 5 shows both the $J = 2 \leftarrow 2$ and $1 \leftarrow 0$ fine-structure components of the 1_{10}–1_{01} transition, split by more than 8 GHz, while Fig. 6 shows both the actual $J = 2 \leftarrow 2$ component and a stick spectrum of all of the fine-structure components that extend over the region between 1902 and 1926 GHz.

Spectral analysis

In our previous work on methylene, it was possible to uti-

© 2004 NRC Canada

Fig. 2. Scheme of Cologne sideband spectrometer for Terahertz applications (COSSTA). See text for detailed description.

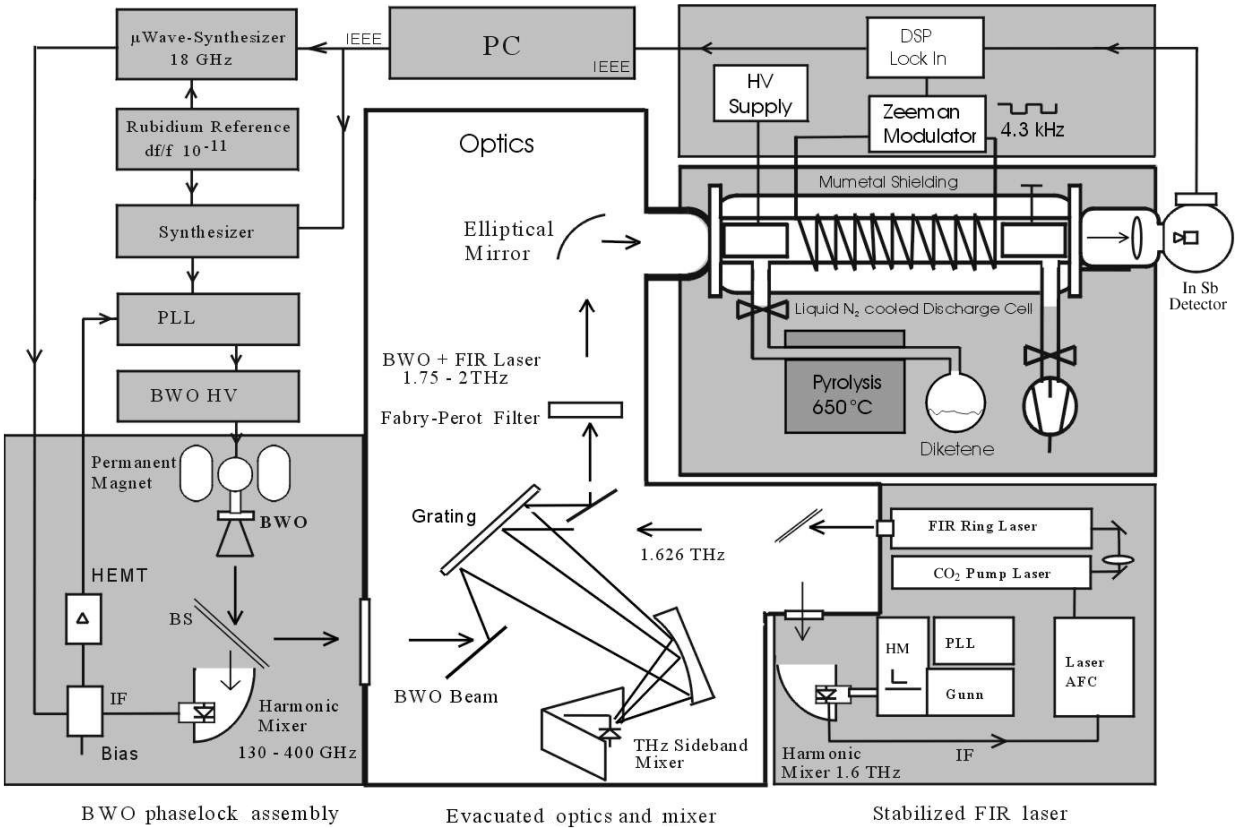
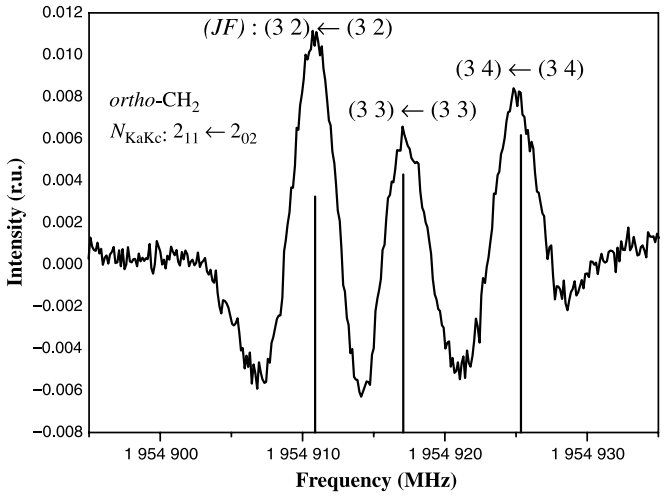


Fig. 3. Three newly measured spectral lines corresponding to the multiplet $J = 3 \leftarrow 3$ (G_4) of the rotational transition $2_{11} \leftarrow 2_{02}$ of *ortho*-CH_2 and split by hyperfine interactions.



lize a Watson-type Hamiltonian plus assorted fine-structure and hyperfine-structure terms to fit the then global rotational spectrum to experimental accuracy (14). A total of 23 lines were fit to a Hamiltonian with 15 variable parameters and seven parameters held fixed at values derived by previous authors. As can be seen, there is an unusually large number of parameters needed compared with the number of lines, a common problem for other small, light asymmetric tops such as water.

The previous fit to the spectrum of methylene (14) based on the augmented Watson Hamiltonian was used to predict the frequencies of the components for the two rotational transitions studied here to perhaps 10 MHz accuracy. A similar degree of accuracy comes from the predictions based on the LMR work of Sears et al. (8). The Hamiltonian H can be written as:

$$[1] \qquad H = H_{rot} + H_{spin-spin} + H_{spin-rot} + H_{hfs}$$

where the first term consists of the rigid-body and centrifugal distortion contributions (18), the second and third terms comprise the fine-structure interactions, and the last term represents the hyperfine contribution. For a light and floppy species such as CH_2, the centrifugal distortion is appreciably large and cannot be neglected. The fine-structure terms arise from the electron spin–spin interaction, and the interaction of the electron spin with the rigid-body rotation of the molecule. As with the fine structure, there are two contributions to the hyperfine term, both of which have to do with the interaction among the electronic and nuclear spins. One term represents the so-called Fermi-contact interaction, while the second represents the dipole–dipole interaction. Matrix elements were derived for the Hamiltonian in the coupling scheme $\mathbf{J} = \mathbf{N} + \mathbf{S}$, $\mathbf{F} = \mathbf{J} + \mathbf{I_H}$, $\mathbf{I_H} = \mathbf{I_{H(1)}} + \mathbf{I_{H(2)}}$. More detail on the various terms in the Hamiltonian and the procedure used to fit and predict the spectrum can be found in our previous publication (14).

A global data set comprising the previously measured transitions and those reported here was fit to the Hamiltonian discussed above. Based on this information, Figs. 7 and

© 2004 NRC Canada

Table 1. Newly measured spectral lines of CH_2 in its ground electronic–vibrational state.

$J',F'–J'',F''$	ν_{obs} (MHz)[a]
$1_{10}–1_{01}$	
1–1	1 902 654.362(200)
2–1	1 907 986.637(300)
1–2	1 912 328.935(200)
0–1	1 916 348.190(200)
2–2	1 917 661.094(100)
1–0	1 925 866.221(200)
$2_{11}–2_{02}$	
1,1–2,2	1 942 878.947(300)*
1,2–2,3	1 942 910.487(300)
3,4–2,3	1 944 411.017(300)
3,3–2,2	1 944 448.270(300)
3,2–2,1	1 944 476.330(500)
2,3–2,3	1 949 051.376(500)*
2,2–2,2	1 949 058.720(500)*
2,1–2,1	1 949 063.340(500)*
3,2–3,2	1 954 910.784(500)
3,3–3,3	1 954 917.270(500)
3,4–3,4	1 954 925.038(500)
3,2–3,3	1 954 943.129(500)*
3,3–3,4	1 954 959.111(500)*
1,1–1,2	1 958 077.452(500)
1,2–1,2	1 958 112.867(300)
1,0–1,1	1 958 112.867(300)*
1,1–1,1	1 958 130.100(500)*
1,1–1,0	1 958 156.446(500)
1,2–1,1	1 958 165.435(500)
2,1–3,2	1 959 496.844(300)
2,2–3,3	1 959 526.242(300)
2,3–3,4	1 959 564.919(200)
2,3–1,2	1 964 253.432(500)

Note: The asterisks represent lines for which the assignment is ambiguous.

[a]The numbers in parentheses represent experimental uncertainties (one standard deviation) in terms of the right-most significant figures.

8 summarize how the rotational levels for the $1_{10}–1_{01}$ transition are split and shifted by fine-structure interactions and for the $2_{11}–2_{02}$ transition by both fine- and hyperfine-structure interactions. Although the qualitative aspects of the figures are certainly correct, the detailed numbers must be taken with caution since they may not be accurate to the 1 MHz level depicted. The current status of the fit *as it pertains to the newly measured transitions* is that the individual components show observed – calculated deviations from a low of 0.1 MHz to a high of 8 MHz, the latter far greater than the experimental uncertainty. For the fine-structure components of the $1_{10}–1_{01}$ transition of *para*-CH_2, the separation is sufficiently great that the assignments are unambiguous. But, for the $2_{11}–2_{02}$ transition of *ortho*-CH_2, the hyperfine components of each group G_i of lines can lie sufficiently close together so as to leave the assignment ambiguous. For such lines, Table 1 contains an asterisk next to the measured frequency. Currently, eight out of the 23 measured components of this rotational transition lie in this category.

Interstellar importance

Almost four decades after its original detection in the laboratory, CH_2 was finally detected in emission in the interstellar medium by Hollis et al. (12), based on the *ortho*-CH_2 rotational transition $N_{KaKc} = 4_{04} \leftarrow 3_{13}$ at 68–71 GHz, previously studied in the laboratory in absorption by Lovas et al. (11). As can be seen in Fig. 1, the upper level of this rotational transition lies at an excitation of approximately 240 K, which means that for collisional excitation to populate it appreciably, the temperature of the medium has to be comparable. Dense interstellar clouds are mainly colder than this, with kinetic temperatures in the region 10–50 K, but exceptions are found in regions associated with star formation. When high-mass stars are formed, there is enough energy to heat surrounding regions to 300 K and even beyond. It is in two such regions, labelled hot cores by astronomers, that Hollis et al. found methylene.

According to chemical models of interstellar gas (19), however, the methylene radical should be an ubiquitous tracer of colder interstellar gas. To detect CH_2 in colder gas requires lower-lying upper states, which tend, however, to be associated with transitions that possess frequencies in the THz region of the spectrum. For example, the lowest-lying emitting level of *ortho*-CH_2 is the 1_{11} level, which lies at little over 100 K above the ground. This level can emit to either the 2_{02} level, at frequencies around 943 GHz, measured by us previously (13), or to the ground 0_{00} level, at frequencies around 2345 GHz (8). For *para*-CH_2, the lowest emitting level is the 1_{10} level, which also lies at an excitation of little more than 100 K. This level can emit to the ground state of *para*-CH_2 at the frequencies reported here, in the vicinity of 1910 GHz.

Transitions that occur at frequencies in the submillimeter-wave region cannot easily be measured from the ground because of the water vapor in the atmosphere of the earth. Although some ground-based facilities do exist for which strong transitions can be measured up to frequencies near 1 THz, the THz region is essentially inaccessible from the ground. For this and other reasons, astronomers have launched satellites and flown high-elevation airplanes to detect submillimeter-wave and shorter radiation from high up or above the atmosphere. Two future missions will be suited to study spectral transitions in the THz region. The project named SOFIA (http://sofia.arc.nasa.gov) will contain a telescope in a Boeing 747-SP aircraft and will have a high-resolution spectrometer in the region between 500 GHz and 4 THz. An even more sensitive telescope, named Herschel, is to be placed in orbit around the so-called L2 point of the earth–sun system (http://herschel.jpl.nasa.gov). The high-resolution THz spectrometer for Herschel, named HIFI, will operate in several bands through 1910 GHz. Detection of methylene with either of these telescopes should be achievable in cold regions of the interstellar medium if the current predictions of chemical models are accurate.

Discussion

We have chosen in part to study the molecular radical CH_2 because it played an important role in Gerhard Herzberg's scientific life. In addition, CH_2 appears to be one of the sim-

© 2004 NRC Canada

Fig. 4. A stick spectrum showing the frequencies and relative intensities of all lines of the rotational transition $2_{11} \leftarrow 2_{02}$ of *ortho*-CH_2. Each group of lines designed by G_i (i = 1–7) represents components belonging to a common fine-structure transition (N',$J' \leftarrow N''$,J'') but split by hyperfine effects. Asterisks indicate measured and assigned lines.

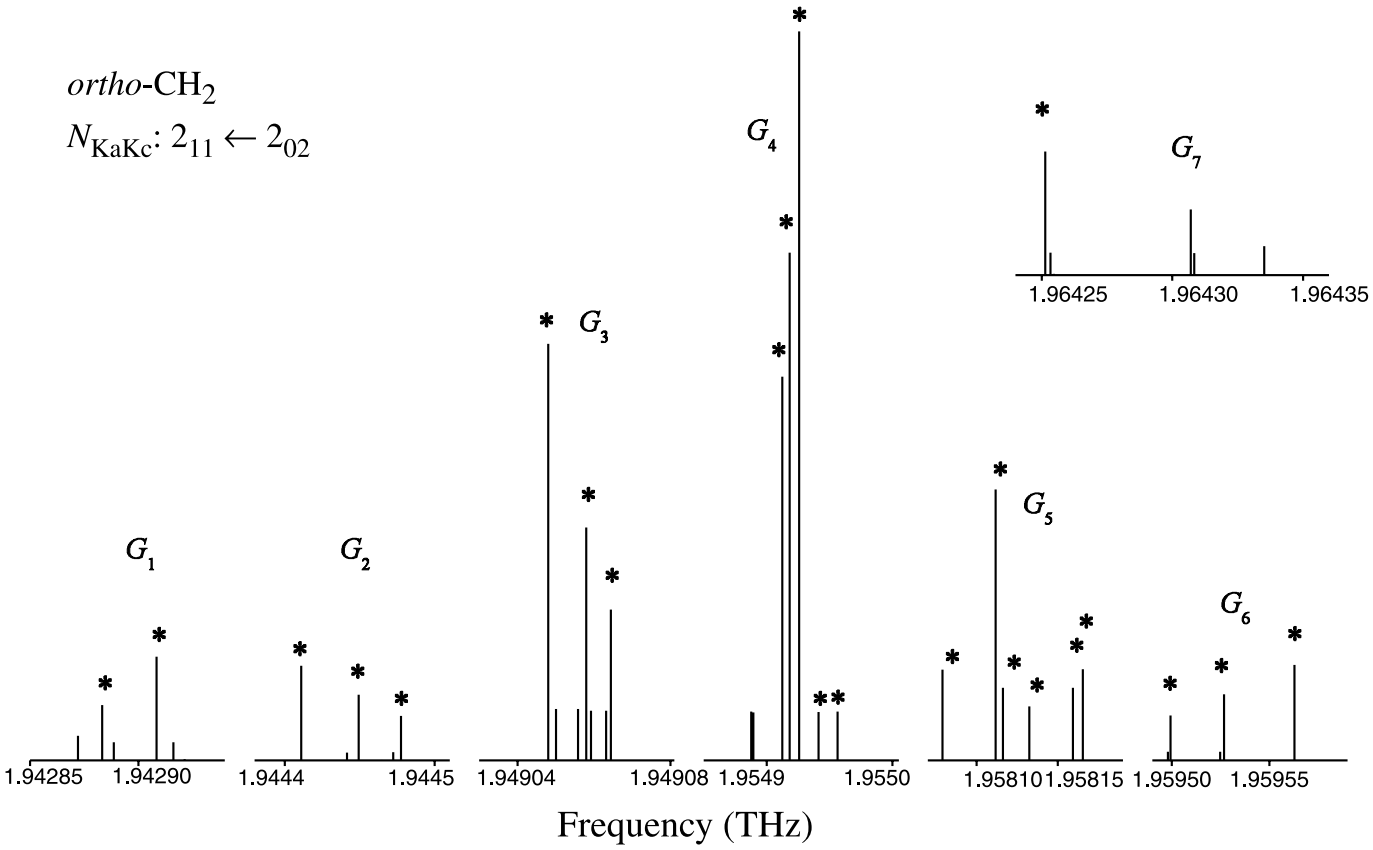


Fig. 5. Two newly measured fine-structure components of the $1_{10} \leftarrow 1_{01}$ rotational transition of *para*-CH_2. The sticks represent calculated frequencies and relative intensities.

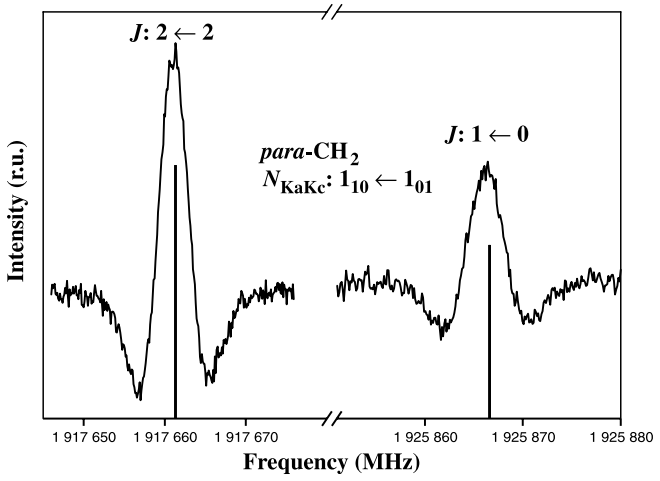
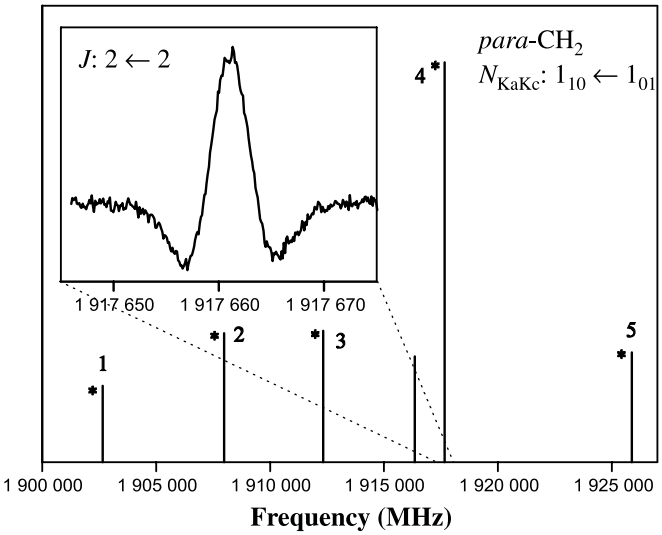


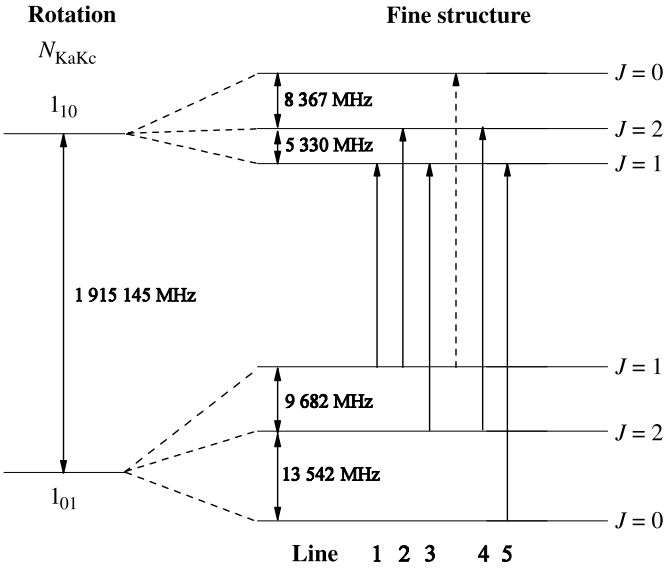
Fig. 6. A stick spectrum showing the frequencies and relative intensities of the six fine-structure components of the $1_{10} \leftarrow 1_{01}$ rotational transition of *para*-CH_2. All lines shown are measured and assigned. The actual measured spectral line designated by the number 4 (the $J = 2 \leftarrow 2$ component) is also shown.



plest free radicals in chemistry. But, the laboratory spectrum of CH_2 has proven difficult to study in all wavelength regions for a variety of reasons, including its lightness, and its intricate fine and hyperfine structure. For its rotational spectrum, CH_2 displays a perpendicular *b*-type spectrum, which is proving to be one of the most difficult to understand. One reason for the difficulty is the fact that the rotational spectrum is not confined to the rather standard microwave region, but ranges through the THz region into the far-IR! Perhaps the dominant reason for the difficulty is the fact that

© 2004 NRC Canada

Fig. 7. Energy level diagram of the 1_{10}–1_{01} rotational transition of *para*-CH_2. The splitting of the rotational levels by fine-structure interactions is shown. The six allowed rotational-fine structure transitions, all of which have been measured, are also shown. Actual numbers shown are uncertain due to the incomplete nature of the fit to the data.

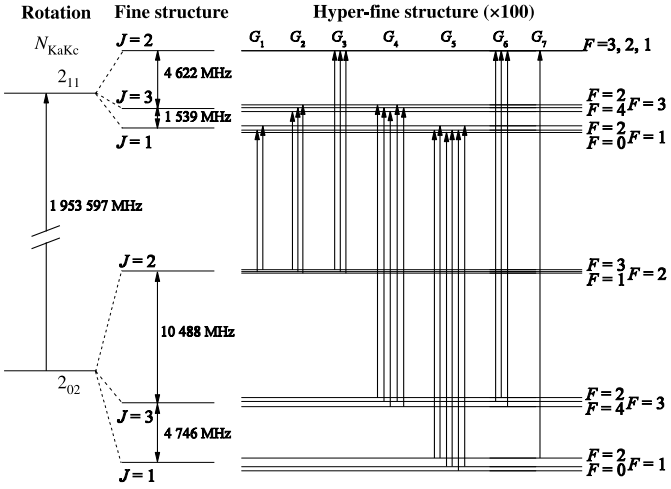


the molecule undergoes large amplitude motion so that the coordinates of the two hydrogen atoms and the carbon atom are not strictly defined. Indeed, the potential function along the appropriate coordinates is very shallow and fairly flat near the equilibrium position, lending the three atoms a restricted freedom to move around their equilibrium positions.

In the problem of large amplitude motions, methylene is not unique. The spectroscopic properties of other light asymmetric rotors such as H_2O, H_2S, NH_2 ($X\ ^2B_1$), and PH_2 ($X\ ^2B_1$), have been analyzed, in some cases with extreme difficulty, with the aid of the Watson Hamiltonian for asymmetric rotors (20–22). All of these triatomic molecules display large amplitude motions to various degrees, producing convergence problems of the angular momentum power representation for the Hamiltonian. For light molecules, higher order effects become appreciably large even at low rotational quantum numbers, because the rotational energies are already high. One is therefore forced to include into the rotational Hamiltonian high-order centrifugal distortion terms.

In this paper, we have reported our current state of progress on measuring, assigning, and fitting the pure rotational spectrum of the methylene radical (CH_2). Although we were able to fit a small number of fine- and hyperfine-split components of several rotational transitions in a previous investigation (14), addition of the newly measured lines reported here appears to exacerbate previous difficulties in fitting the global spectrum to a standard Watson-type effective Hamiltonian. At present, we can fit most of the newly measured lines that belong to the 1_{10}–1_{01} rotational transition of *para*-CH_2 at 1902–1926 GHz, and the 2_{11}–2_{02} rotational transition of *ortho*-CH_2 at 1943–1964 GHz, as part of a global fit to an accuracy good enough for assignment purposes. A significant minority of lines, however, especially those lying in closely spaced multiplets split by hyperfine effects, cannot be unambiguously assigned. Nor is the average deviation between the newly observed and calculated frequencies anywhere near experimental measurement accuracy. Indeed, some lines have observed–calculated frequencies as large as 8 MHz. The rotational, fine structure, and hyperfine structure constants obtained from fits that include our new data at 2 THz are distinctly not improved over our previous values (14).

Fig. 8. Energy level diagram of the 2_{11}–2_{02} rotational transition of *ortho*-CH_2. The splitting of the rotational levels by fine-structure and hyperfine interactions is depicted. The 23 measured components, divided into seven groups designated by G_i (i = 1–7) are also indicated. Actual numbers shown are uncertain due to the incomplete nature of the fit to the data.



To better our understanding of the spectrum, we are currently trying two alternative approaches to conventional spectroscopy. The first is the use of the Morse oscillator-rigid bender internal dynamics (MORBID) Hamiltonian (6, 15) to determine the rotational energy levels in place of the standard Watson-type Hamiltonian. The second is an Euler expansion of the rotational parameters to constrain the rotational structure, an approach that works nicely for water (23).

The MORBID approach is different from the Watsonian-type treatment of rotation–vibration states in that it provides an, in principle complete, solution of the rotation–vibration Schrödinger equation for the electronic state in question. Thus, it is possible to calculate the energies of a large number of rotation–vibration energies directly from the potential energy surface, which is represented by a parameterized analytical function, the parameter values of which are the input data for the calculation of this electronic state. Also, the potential energy parameters can be refined in fittings to experimental rotation–vibration data, as done by Jensen and Bunker (6), who used all extant rotation–vibration data for $\tilde{X}^3\ B_1\ CH_2$. MORBID is based on a theory first proposed by Hougen et al. (24) and designed so that it is applicable to both linear and bent triatomic molecules. Therefore, it describes well, for example, the dramatic change of the *A* rotational constant resulting from excitation of the bending vibration in the $\tilde{X}$-state of CH_2. Since *all* rotation–vibration energies of the electronic state are determined in terms of a rather small number of potential energy parameters (which

© 2004 NRC Canada

are the only parameters that can be adjusted in least-squares fittings to experimental data), the residuals observed in the fittings are generally larger by orders of magnitude than those obtained in fittings with Watsonian models. However, because of the shortcomings of the Watsonian model for light molecules with highly anharmonic potential energy surfaces, such as $\tilde{X}^3$ B_1 CH_2, the predictive power of MORBID is sometimes better than that of the Watsonian model.

Gerhard Herzberg said in his Nobel lecture "… of course the spectrum of CH_2 has given me a great deal of pleasure…" (4). His first attempts to savour it date back to 1942, and the story of its discovery is long, difficult, slow, and not yet finished. Now, more than 60 years later and despite much progress, the CH_2 problem remains with us.

Acknowledgments

GW thanks the Deutsche Forschungsgemeinschaft for its support via special grant SFB-494. He also thanks the Ministry of Science of the Land Nordrhein-Westfalen for special funding. EH wishes to acknowledge NASA for its support of the Ohio State program in laboratory astrophysics.

References

1. B. Stoicheff. Gerhard Herzberg: An Illustrious Life in Science. NRC Research Press, Ottawa. 2002.
2. G. Herzberg and J. Shoosmith. Nature (London), **183**, 1801 (1959).
3. G. Herzberg and J.W.C. Johns. J. Chem. Phys. **54**, 2276 (1971).
4. G. Herzberg. Nobel Lectures in Chemistry 1971–1980. *Edited by* S. Forsen. World Scientific, Singapore. 1993. pp. 9–46.
5. M.D. Marshall and A.R.W. McKellar. J. Chem. Phys. **85**, 3716 (1986).
6. P. Jensen and P.R. Bunker. J. Chem. Phys. **89**, 1327 (1988).
7. T.J. Sears, P.R. Bunker, A.R.W. McKellar, K.M. Evenson, D.A. Jennings, and J.M. Brown. J. Chem. Phys. **77**, 5348 (1982).
8. T.J. Sears, A.R.W. McKellar, P.R. Bunker, K.M. Evenson, and J.M. Brown. Astrophys. J. **276**, 399 (1984).
9. T.J. Sears. J. Chem. Phys. **85**, 3711 (1986).
10. P.R. Bunker and S.R. Langhoff. J. Mol. Spectrosc. **102**, 204 (1983).
11. F.J. Lovas, R.D. Suenram, and K.M. Evenson. Astrophys. J. **267**, L131 (1983).
12. J.M. Hollis, P.R. Jewel, and F.J. Lovas. Astrophys. J. **438**, 259 (1995).
13. H. Ozeki and S. Saito. Astrophys. J. **451**, L97 (1995).
14. E.A. Michael, F. Lewen, G. Winnewisser, H. Ozeki, H. Habara, and E. Herbst. Astrophys. J. **596**, 1356 (2003).
15. P. Jensen. J. Mol. Spectrosc. **128**, 478 (1988).
16. R. Gendriesch, F. Lewen, G. Winnewisser, and J. Hahn. J. Mol. Spectrosc. **203**, 205 (2000).
17. F. Lewen, R. Gendriesch, I. Pak, D.G. Paveliev, M. Hepp, R. Schieder, and G. Winnewisser. Rev. Sci. Instrum. **69**, 32 (1998).
18. W. Gordy and R.L. Cook. Microwave molecular spectroscopy. Wiley, New York. 1984.
19. H.H. Lee, R.P.A. Bettens, and E. Herbst. Astron. Astrophys. Suppl. Ser. **119**, 111 (1996).
20. A.H. Saleck, M. Tanimoto, S.P. Belov, T. Klaus, and G. Winnewisser. J. Mol. Spectrosc. **171**, 481 (1995).
21. R. Gendriesch, F. Lewen, G. Winnewisser, and H.S.P. Müller. J. Mol. Struct. **599**, 293 (2000).
22. L. Margulès, E. Herbst, V. Ahrens, F. Lewen, G. Winnewisser, and H.S.P. Müller. J. Mol. Spectrosc. **211**, 211 (2002).
23. H.M. Pickett and J.C. Pearson. Ohio State Univ. Int. Symp. Mol. Spectrosc. **57**, 108 (2001).
24. J.T. Hougen, P.R. Bunker, and J.W.C. Johns. J. Mol. Spectrosc. **34**, 136 (1970).

© 2004 NRC Canada

CH_2 revisited[1]

Apostolos Kalemos, Thom H. Dunning, Jr., Aristides Mavridis, and James F. Harrison

Abstract: The first four states of the CH_2 molecule ($\tilde{X}^3B_1$, $\tilde{a}^1A_1$, $\tilde{b}^1A_1$, and $\tilde{c}^1A_1$) are examined using state-of-the-art ab initio methods and basis sets. The construction of potential energy curves with respect to the C + H_2 and CH + H channels provides significant clues to understanding the geometric and electronic structure of the above states. All of our numerical findings are in excellent agreement with the existing experimental data.

Key words: CH_2, MRCI, potential curves, vbL icons.

Résumé : Les quatre premiers états électroniques de la molécule CH_2 ($\tilde{X}^3B_1$, $\tilde{a}^1A_1$, $\tilde{b}^1A_1$ et $\tilde{c}^1A_1$) ont été examinés en utilisant des méthodes ab initio et à l'aide des bases les plus étendues. Des courbes d'énergie potentielle par rapport aux C + H_2 et CH + H, nous donnent des renseignements importants pour la structure géométrique et électronique de ces états. Tous nos résultats sont en excellent accord avec les valeurs expérimentales.

Mots clés : CH_2, MRCI, courbes de potentiel, icônes vbL.

Introduction

The methylene molecule continues to be of interest to experimentalists and theoreticians alike (1–121) some 70 years after Mulliken's (1) pioneering theoretical work on its structure, and 60 years after Herzberg's (2) note on the 4050 group in cometary spectra. The reasons for this interest have been detailed in several reviews (8, 21, 27, 28, 65, 67, 70).

Methylene (CH_2) is: (*i*) the basic unit for divalent carbon chemistry, (*ii*) the smallest polyatomic radical with a ground triplet state and several low-lying singlets, (*iii*) a molecule with a remarkably complex electronic spectrum, and (*iv*) small enough to be studied by sophisticated ab initio methods. As discussed by Schaefer (70) the story of methylene is the story of the coming of age of computational quantum chemistry and, indeed, methylene has become a "paradigm for quantitative theoretical chemistry". We agree whole-heartedly with this assessment and in particular with the identification of the year 1970 as the origin of the coming of age (70). When one looks back on 1970 by citing the papers published during that year, one misses part of the excitement of the times, because much was going on in the background vis-à-vis preprints and personal communications. Some hint of this is found in the Herzberg and Johns 1971 paper (16) where the authors reinterpret the vacuum UV spectrum of methylene in terms of a bent structure of the radical. The acknowledgement in this paper reads "We are much indebted to Dr. Bernheim, Dr. Wasserman, Dr. Bender, and Dr. Harrison for sending us preprints of their papers." While both the Bernheim and Wasserman papers had appeared in print by the time the Herzberg and Johns paper was published, the referenced preprints of Bender and Harrison had not. From an historical perspective it is interesting to revisit the activities of 1970 by looking at the submission dates of the various CH_2-related papers.

The first of the 1970 papers was submitted in May by Bernheim et al. (10), and was the opening salvo that something might be wrong with the widely held belief that the ground triplet state of CH_2 was linear. On the basis of ESR measurements these authors suggested that the ground state of CH_2 was indeed a triplet and was slightly bent in a xenon matrix at 4.2 K.

A few weeks later the manuscript by Bender and Schaefer (9) was received and these authors explicitly challenged experiment, declaring that "... on the basis of the present and

Received 3 November 2003. Published on the NRC Research Press Web site at http://canjchem.nrc.ca on 14 June 2004.

A. Kalemos and T.H. Dunning, Jr.[2] Joint Institute for Computational Sciences, University of Tennessee, Oak Ridge National Laboratory, 1 Bethel Valley Road, Oak Ridge, TN 37831–6008, USA; Department of Chemistry, University of Tennessee, Knoxville, TN 37996–1600, USA; Computer Science and Mathematics Division, Oak Ridge National Laboratory, Oak Ridge, TN 37831–6008, USA.
A. Mavridis. Laboratory of Physical Chemistry, Department of Chemistry, National and Kapodistrian University of Athens, PO Box 64004, 157 10 Zografou, Athens, Greece.
J.F. Harrison. Department of Chemistry and Center for Fundamental Materials Research, Michigan State University, East Lansing, MI 48824–1322, USA.

[1]This article is part of a Special Issue dedicated to the memory of Professor Gerhard Herzberg.
[2]Corresponding author (e-mail: dunningthjr@ornl.gov).

 doi: 10.1139/V04-045 © 2004 NRC Canada

previous ab initio calculations and the stated numerical uncertainties, we conclude that the CH_2 ground state is nonlinear with a geometry close to r = 1.096 Å, θ = 135.1°." The previous ab initio calculations referred to were those of Foster and Boys (4) and Harrison and Allen (8).

In the ensuing month of July 1970, Harrison (13) submitted a manuscript describing an ab initio calculation of the angular dependence of the zero-field splitting (ZFS) parameters (D and E) of CH_2. If one could compare the computed D, and, in particular the E parameter, to the experimental, one could provide additional evidence for the CH_2 bond angle. In the course of these calculations the bond angle of CH_2 in the $\tilde{X}^3B_1$ state was computed to be 132.5°. Noting the disagreement with Herzberg and theoretical predictions, Harrison stated: "It seems that this persistent discrepancy between theory and experiment warrants a critical evaluation of the experimental data." This was the second formal challenge, following Bender and Schaefer (9), to the accepted view that CH_2 was linear.

August passed uneventfully and in September Wasserman et al. (11) submitted a manuscript in which they challenged the status quo by suggesting that CH_2 has a bond angle of 136°, in good agreement with the theoretical values (9, 13).

October saw two submissions. The first was a theoretical study by O'Neil et al. (20) in which they calculated potential energy surfaces for seven electronic states of CH_2, and an experimental ESR study of CH_2, CD_2, and CHD by Wasserman et al. (12), who concluded that the ground triplet state of CH_2 is bent with an angle of 136°.

In November, Harrison (14) submitted a second paper focused on the geometry and electronic structure of CH_2, CHF, and CF_2 and concluded again that the CH_2 $\tilde{X}^3B_1$ angle was 132.5°.

In the following month of December 1970, Herzberg and Johns (16) submitted their reinterpretation of the CH_2 angle and noted: "The considerations given here point strongly toward the bent structure of the triplet ground ($\tilde{X}^3B_1$) state of CH_2, as suggested by the electron-spin resonance work and the ab initio calculations."

Soon afterwards three important experimental ESR papers appeared. The first was titled "^{13}C Hyperfine Interactions in CD_2" by Bernheim et al. (17), (received on 11 January 1971), concluding that the CH_2 angle was 137.7°. The second was titled "^{13}C Hyperfine Interactions and Geometry of Methylene" by Wasserman et al. (18), (received in February 1971) concluding that the angle was 136 ± 5°. The third was also from the Wasserman group (19), "Zero-Field Parameters of Free CH_2; Spin-Orbit Contributions in Xenon" (received on 14 June 1971). This report concluded that the xenon matrix has a large effect on the observed zero-field parameters of CH_2 via intermolecular spin-orbit interactions and once this is accounted for, the experimental ZFS parameters were in good agreement with the calculations of Harrison (13).

The second problem of great importance with methylene was the singlet-triplet splitting ($\tilde{a}^1A_1 \leftarrow \tilde{X}^3B_1$) and this was resolved over a longer period of time and has been discussed in the excellent reviews of Shavitt (65), Goddard (67), and Schaefer (70).

In spite of the phenomenal interest in the CH_2 molecule, truly definitive calculations on other than the lowest $\tilde{X}^3B_1$ and $\tilde{a}^1A_1$ states are rare. It is our intention to study the electronic and geometric structure of the ground and excited states of CH_2 as accurately as conventional theory will permit. To this end, we report on the first four states of CH_2 ($\tilde{X}^3B_1$, $\tilde{a}^1A_1$, $\tilde{b}^1B_1$, and $\tilde{c}^1A_1$) employing all-electron variational multireference calculations in conjunction with very large basis sets. For all states above, potential energy profiles were constructed with respect to the HĈH (= θ) angle, and to the $CH_2 \rightarrow CH + H$ channel. We believe that our interpretation, coupled with our consistent numerical results, offers a fresh view in the conceptual saga of the CH_2 molecule.

Methodology and insights

For the C atom, the doubly augmented correlation consistent polarized core-valence basis set of sextuple quality (d-aug-cc-pCV6Z, 22*s*16*p*10*d*9*f*6*g*4*h*2*i*) of Dunning and coworkers (122) was employed. The core set was that of quintuple quality basis (i.e., 4*s*4*p*3*d*2*f*1*g*). For the H atom the plain sextuple cc-basis set (10*s*5*p*4*d*3*f*2*g*1*h*) was used (123).[3] Both were generally contracted to [13*s*12*p*10*d*8*f*6*g*4*h*2*i*/$_C$ 6*s*5*p*4*d*3*f*2*g*1*h*/$_H$] resulting in 461 spherical Gaussian functions. The spherically averaged SCF energy of the ^{3}P ground state of the C atom using the above basis set is –37.688 612 E_h, just 7 μE_h above the numerical value (124).

The method of choice followed in the present work is the standard internally contracted multireference CISD, based on a full valence (2*s* + 2*p* on C and 1*s* on Hs) complete active SCF zero order wave function (CASSCF). By distributing the six valence (active) electrons in the six orbitals, the CASSCF wave functions obtained contain 51, 56, 39, and 56 configuration functions (CF) for the $\tilde{X}^3B_1$, $\tilde{a}^1A_1$, $\tilde{b}^1A_1$, and $\tilde{c}^1A_1$ states, respectively.

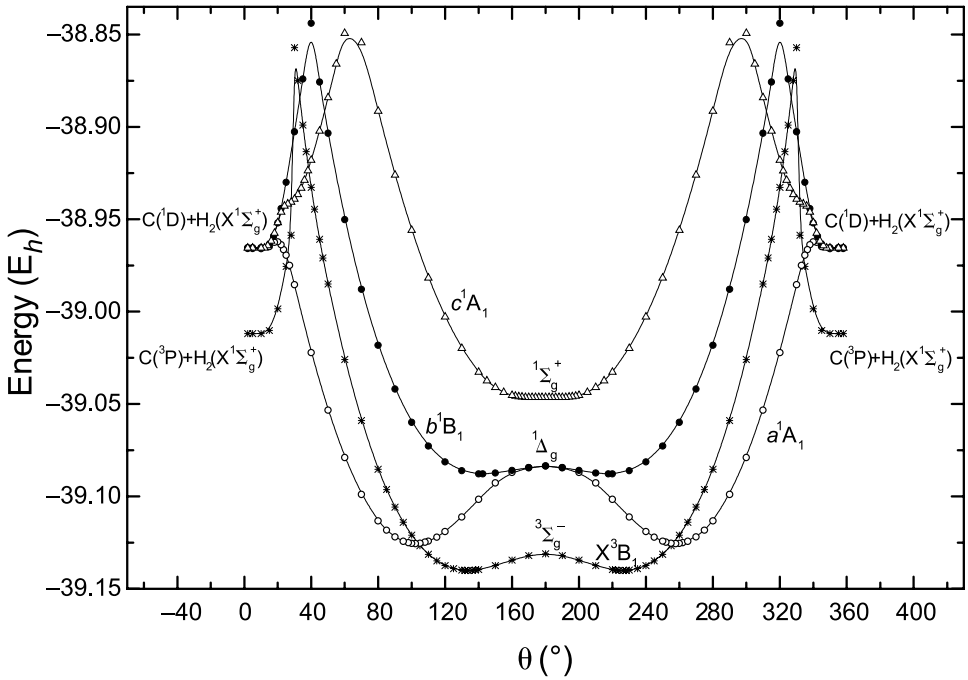
The CI expansion is generated by single and double replacements of all eight electrons (the ~$1s^2$ e^- of C included) out of the reference space (CASSCF(6e^-/6 orbitals) + 1 + 2 = MRCI(8e^-)) within the internally contracted ansatz as implemented in the MOLPRO package (125). The uncontracted MRCI expansions comprise 27.5 × 10^6 ($\tilde{X}^3B_1$), 18.3 × 10^6 ($\tilde{a}^1A_1$, $\tilde{c}^1A_1$), 15.9 × 10^6 ($\tilde{b}^1B_1$) CFs, reduced to about 1.3 × 10^6 CFs in the internally contracted approximation.

Due to the extended basis sets used no corrections for basis set superposition errors (BSSE) were considered. Size non-extensivity errors are reasonably small: at the MRCI level non-extensivity with respect to C(^{3}P; ^{1}D) + $H_2(X^1\sum_g^+)$ amounts to 1.59, 1.43, 1.42, and 1.42 mE_h for the $\tilde{X}^3B_1$,

[3] Basis sets were obtained from the Extensible computational chemistry environment basis set database, version 6/19/03, as developed and distributed by the Molecular Science Computing Facility, Environmental and Molecular Sciences Laboratory which is part of the Pacific Northwest Laboratory, PO Box 999, Richland, Washington 99352, USA, and funded by the US Department of Energy. The Pacific Northwest Laboratory is a multiprogram laboratory operated by Battelle Memorial Institute for the US Department of Energy under contract DE–AC06–76RLO 1830. Contact David Feller or Karen Schuchardt for further information.

© 2004 NRC Canada

Fig. 1. Potential energy profiles of the $\tilde{X}^3B_1$, $\tilde{a}^1A_1$, $\tilde{b}^1B_1$, and $\tilde{c}^1A_1$ CH_2 states at the all-electron MRCI level along the HĈH bending mode.



$\tilde{a}^1A_1$, $\tilde{b}^1B_1$, and $\tilde{c}^1A_1$ states, respectively. Restricted coupled cluster singles and doubles with perturbative triples computations (RCCSD(T)) were also performed for the $\tilde{X}^3B_1$ state around the equilibrium geometry.

For the first four states of the CH_2 molecule studied in the present work ($\tilde{X}^3B_1$, $\tilde{a}^1A_1$, $\tilde{b}^1B_1$, and $\tilde{c}^1A_1$) in ascending energy order, two obvious channels of formation can be considered, C + H_2 → CH_2 or H + CH → CH_2. In detail,

[1*a*] $CH_2(\tilde{X}^3B_1) \xrightarrow{C_{2v}} C(2p_z^1 2p_x^1; {}^3P) + H_2(X^1\Sigma_g^+)$

↓

[1*b*] $HCH(^3\Sigma_g^-) \xrightarrow{C_{\infty v}} CH(a^4\Sigma^-) + H(^2S)$

[2*a*] $HCH(^1\Delta_g) \xrightarrow{C_{2v}} CH_2(\tilde{a}^1A_1) \xrightarrow{C_{2v}}$

$C[1/\sqrt{2}(2p_z^2 - 2p_y^2); {}^1D] + H_2(X^1\Sigma_g^+) \xrightarrow{C_{2v}}$

$CH_2(\tilde{b}^1B_1) \xrightarrow{C_{2v}} C(2p_z^1 2\bar{p}_x^1; {}^1D) + H_2(X^1\Sigma_g^+)$

↓

[2*b*] $\xrightarrow{C_{\infty v}} CH(A^2\Delta) + H(^2S)$

[3*a*] $CH_2(\tilde{c}^1A_1) \xrightarrow{C_{2v}} C\{1/\sqrt{6}[2(2p_z^2) - 2p_x^2 - 2p_y^2]; {}^1D\} + H_2(X^1\Sigma_g^+)$

↓

[3*b*] $HCH(^1\Sigma_g^+) \xrightarrow{C_{\infty v}} CH(C^2\Sigma^+) + H(^2S)$

Two sets of fully optimized potential energy curves have been constructed at the all-electron MRCI level; one along the bending coordinate HĈH = θ (eqs. [1*a*], [2*a*], and [3*a*]), and a second one along the asymmetric CH + H dissociation mode (eqs. [1*b*], [2*b*], and [3*b*]) (Figs. 1 and 2). For the first set of curves, the C—H bond distance was optimized for each angle (HĈH); for the second set of curves HĈH = 180° and the C—H bond distances were optimized for each HC-H separation.

Results and discussion

Table 1 lists the most recent and reliable theoretical and experimental results of the literature on the first four states of the CH_2 carbene pertaining to the present work, while Tables 2 and 3 refer to this work. Figures 1 and 2 depict potential energy curves with respect to the HĈH = θ angle (eqs. [1*a*], [2*a*], and [3*a*]) and to the HCH → CH + H dissociation channel (eqs. [1*b*], [2*b*], and [3*b*]).

$\tilde{X}^3B_1$

The leading CASSCF configuration is

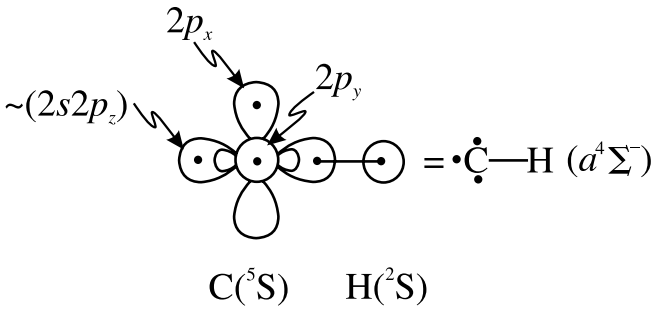
$$\left|\tilde{X}^3B_1\right\rangle \sim 0.99\left|1a_1^2\ 2a_1^2 3a_1^1\ 1b_1^1\ 1b_2^2\right\rangle$$

where $1a_1 \sim 1s_C$, $2a_1 \sim 0.79(2s)_C + 0.20(2p_z)_C + 0.73(1s_A + 1s_B)_H$, $3a_1 \sim 0.38(2s)_C - 0.85(2p_z)_C - 0.29(1s_A + 1s_B)_H$, $1b_1 \sim (2p_x)_C$, $1b_2 \sim 0.70(2p_y)_C + 0.93(1s_A - 1s_B)_H$ with corresponding CASSCF atomic Mulliken populations (C/H) ($1s^{2.0}2s^{1.38}2p_z^{0.90}2p_x^{0.98}2p_y^{1.03}/1s^{0.80}2p^{0.03}$).

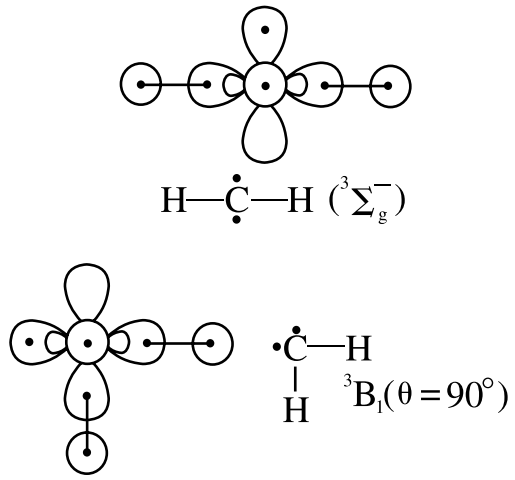
The analogous distributions of the $a^4\Sigma^-$ CH diatomic at the same level of theory are ($1s^{2.0}2s^{1.42}2p_z^{0.71}2p_x^{0.98}2p_y^{0.98}$/ $1s^{0.72}2p^{0.03}$), indicating clearly the common ancestry of both species to the $^5S(2s^12p^3)$ atomic state of carbon atom.

© 2004 NRC Canada

The valence-bond Lewis (vbL) diagram of the parental CH $a^4\Sigma^-$ state (see also ref. 126)



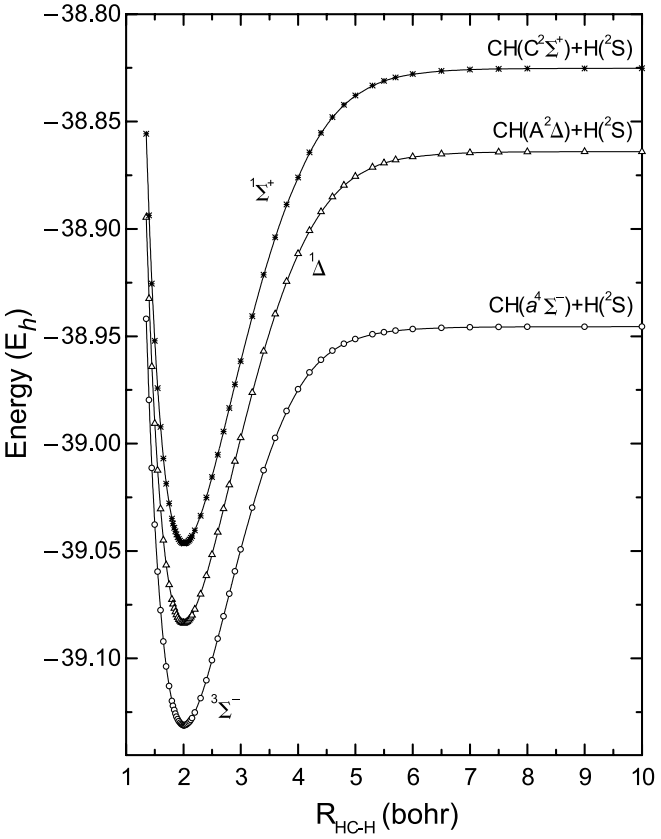
suggests two modes of attack of the second H(^{2}S) atom to form CH_2, linear and perpendicular, (i.e., along the z and x (or y) axes) predicting in turn a linear ($^3\Sigma_g^-$) or a bent ($^3B_1(\theta = 90°)$) CH_2 ground state, respectively. Diagrammatically,



The binding energy with respect to CH($a^4\Sigma^-$) + H(^{2}S) of the $^3\Sigma_g^-$ configuration is 116.5 kcal/mol (Fig. 2), 15.9 kcal/mol *higher* than that of the bent structure at θ = 90°. The equilibrium geometry is determined by the differences in energy between binding to the ($2s$–$\lambda 2p_z$) orbital and the $2p_x$ orbital, which favors a bond angle less than 180°, and the repulsion between the CH bond pairs, which favors a bond angle greater than 90°. This may also be viewed as the vibronic interaction of the two limiting $^3\Sigma_g^-$ and $^3B_1(\theta = 90°)$ structures through a pseudo Jahn–Teller effect. The result is a final bent geometry of θ_e = 133.66° (Table 2). Remarkably enough, the arithmetic average of the angles of the two limiting structures is (180° + 90°)/2 = 135°. This analysis supports a rather low inversion barrier, which, indeed, according to our calculations is just 1982.5 cm^{-1} (= 5.668 kcal/mol).

Our geometrical results (r_e, θ_e) are in complete agreement with the most recent theoretical results of Császár et al. (121), and in excellent agreement with existing experimental numbers (Tables 1 and 2) in both RCCSD(T) and MRCI methodologies. Our predicted atomization energy (AE_e) at the RCCSD(T)[MRCI+Q] level of theory is 190.06 [189.9] kcal/mol, as compared to a mixed experimental (AE_0) (127) plus theoretical (ZPE) (121) value of AE_e = AE_0 + ZPE = 180.043 + 10.683 = 190.73 kcal/mol.

Fig. 2. Potential energy profiles of the CH + H channel at the all-electron MRCI level.



$\tilde{a}^1A_1$

The two most important configurations of the $\tilde{a}^1A_1$ state (CASSCF) are

$$\left|\tilde{a}^1A_1\right\rangle \sim \left|1a_1^2\ 2a_1^2[0.97(3a_1^2) - 0.21(1b_1^2)]1b_2^2\right\rangle$$

where the "0.21" contribution is a symmetry dictated determinant (at the linear configuration). This configuration can also be viewed as a GVB angular correlation term arising from the $2s$–$2p$ near degeneracy in the carbon atom. At θ = 180° the $\tilde{a}^1A_1$ state of CH_2 correlates to the linear $^1\Delta_g$ symmetry (Fig. 1). Returning now to the low-lying states of the CH diatomic (126), it is observed that the linear $^1\Delta_g$ structure correlates to the CH($A^2\Delta$) + H(^{2}S) fragments (Fig. 2), while the bent structure ($^1A_1$) emanates from the $X^2\Pi$ state of CH, 67.46 kcal/mol *below* the $A^2\Delta$ state (Table 3). Pictorially, the two CH states can be represented as follows (126): Mutatis mutandis with the $\tilde{X}^3B_1$ discussion, a linear and perpendicular H attack on the $A^2\Delta$ and $X^2\Pi$ states of CH is pos-

© 2004 NRC Canada

Table 1. Recent ("best") theoretical and experimental results on the $\tilde{X}^3B_1$, $\tilde{a}^1A_1$, $\tilde{b}^1B_1$, and $\tilde{c}^1A_1$ states of CH_2.

$-E$ (hartree)	r_e (Å)	θ_e (°)	ZPE (cm^{-1})	T_e/T_0 (kcal/mol)	Reference (year)
$\tilde{X}^3B_1$					
39.0911477[a]	1.075981	133.8483		0.0	121 (2003)
39.1469003[b]	1.075981	133.8483	3736.4[c]	0.0	121 (2003)
39.089879[d]	1.0767	133.56		0.0	101 (1995)
39.145107[e]	1.0751	133.79		0.0	101 (1995)
39.086206[f]	1.0769	133.51		0.0	101 (1995)
39.139165[g]	1.0750	133.70		0.0	101 (1995)
39.0830835[h]	1.079441	133.576	3715	0.0	84 (1989)
Expt.[i]	1.07530	133.9308	3689	0.0	82 (1988)
$\tilde{a}^1A_1$					
39.0764083[a]	1.106907	102.1369		9.249	121 (2003)
39.1315040[b]	1.106907	102.1369	3612.0	9.661 (9.306)	121 (2003)
				9.327 (8.972)[j]	121 (2003)
	1.099[k]	104	3621	9.192	117 (2000)
39.061054[l]	1.1102	101.72	3639.55	10.007 (9.548)	110 (1997)
39.072067[f,m]	1.1083	102.02		8.872	101 (1995)
39.124334[g,m]	1.1061	102.18		9.307	101 (1995)
Expt.[n]	1.107±0.002	102.4±0.4			85 (1989)
Expt.[i]				(8.998±0.014)	82 (1988)
$\tilde{b}^1B_1$					
	1.062[k,o]	144	4034.034	31.897 (32.883)	117 (2000)
39.022514[l]	1.0754	142.60	3764.41	34.191 (34.089)	110 (1997)
				(32.911±0.014)[p]	82 (1998), 112 (1998)
Expt.[q]	1.086	139.3			81 (1988)
Expt.[q]	1.053	140±15			7 (1966)
$\tilde{c}^1A_1$					
39.981153[l]	1.0683	171.34	3676.97	60.146 (59.794)	110 (1997)
38.985644[r]	1.067616	172.70	3923.2	59.513	105 (1996)
38.979005[s]	1.1063897	171.62	3970.5	60.271	104 (1996)

Note: Total energies (E), bond distances (r_e), HĈH angles (θ_e), zero point energies (ZPE), and energy gaps (T_e/T_0).

[a]RCCSD(T)/aug–cc–pCV6Z//RCCSD(T)/aug–cc–pCVQZ (valence electron calculation).

[b]RCCSD(T)/aug–cc–pCV6Z//RCCSD(T)/aug–cc–pCVQZ (all electron calculation).

[c]RCCSD(T)/aug–cc–pCVQZ level employing the nonrigid – rotation – large – amplitude internal motion Hamiltonian (NRLH) and quartic force fields.

[d]RCCSD(T)/cc–pCV5Z (valence electron calculation).

[e]RCCSD(T)/cc–pCV5Z (all electron calculation).

[f]MRCI/cc–pCV5Z (valence electron calculation).

[g]MRCI/cc–pCV5Z (all electron calculation).

[h]MORBID analysis on a MRCI/[5*s*4*p*3*d*2*f*1*g*/3*s*2*p*1*d*] energy surface.

[i]MORBID analysis on experimental data. Inversion barrier ($^3\Sigma_g^- \leftarrow \tilde{X}^3B_1$), IB = 1952 cm^{-1} at r_{CH} = 1.064 Å.

[j]Based on a focal point analysis corrected for core-correlation, relativistic, and adiabatic effects; the exact numbers given in ref. 121 are $9.327^{+0.083}_{-0.046}$ ($8.972^{+0.097}_{-0.069}$) kcal/mol.

[k]MORBID analysis on an ab initio (ref. 84; MRCI/[5*s*4*p*3*d*2*f*1*g*/3*s*2*p*1*d*]) surface that takes into account the Renner–Teller effect, and refined by fitting to the experimentally available vibrational term values. Inversion barrier ($^1\Delta_g \leftarrow \tilde{a}^1A_1$), IB = 8666.1 cm^{-1} at r_{CH} = 1.051 Å.

[l]MRCI/[6*s*4*p*2*d*1*f*/4*s*2*p*1*d*] with the $1s^2$ e^- frozen and the corresponding virtual orbital deleted. ZPE based on harmonic frequencies.

[m]RCCSD(T) and all e^- RCCSD(T) energies, –39.075 244 and –39.129 825 E_h, respectively.

[n]IR – flash – kinetic spectroscopy.

[o]Inversion barrier ($^1\Delta_g \leftarrow \tilde{b}^1B_1$), IB = 725.1 cm^{-1}.

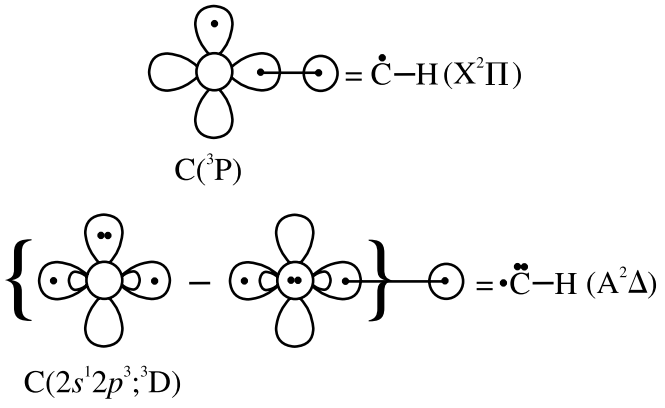
[p]Based on the $\tilde{a}^1A_1 \leftarrow \tilde{X}^3B_1$ T_0 = 8.998 ± 0.014 kcal/mol splitting (ref. 82) and the $\tilde{b}^1B_1 \leftarrow \tilde{a}^1A_1$ T_0 = 8363.8 cm^{-1} = 23.913 kcal/mol (ref. 107) according to the stretch-bender (SB) Hamiltonian.

[q]r_0 and θ_0 values.

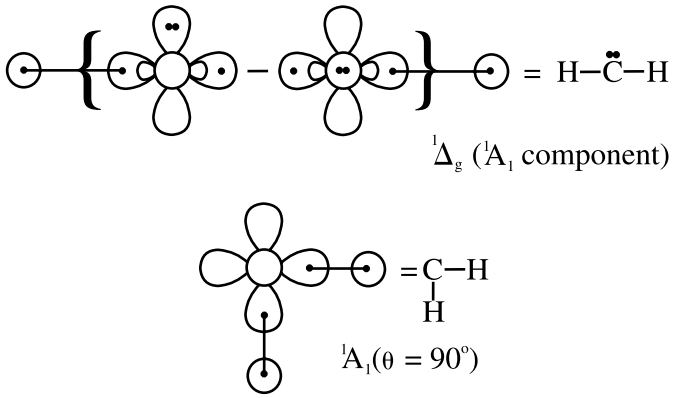
[r]MORBID analysis on a MRCI/[7*s*5*p*3*d*2*f*/5*s*3*p*2*d*] surface with the $1s^2$ e^- frozen and the corresponding virtual orbital removed. Inversion barrier ($^1\Sigma_g^+ \leftarrow \tilde{c}^1A_1$), IB = 6 cm^{-1}.

[s]MORBID analysis on a TC–CISD/[7*s*5*p*3*d*2*f*/5*s*3*p*2*d*] surface with the $1s^2$ e^- frozen and the corresponding virtual orbital removed. Inversion barrier ($^1\Sigma_g^+ \leftarrow \tilde{c}^1A_1$), IB = 12 cm^{-1}.

© 2004 NRC Canada



sible, resulting in the $^1\Delta_g$ and $^1A_1(\theta = 90°)$ symmetries of CH_2, or using the vbL iconal language,



The CH-H binding energies are 94.42 kcal/mol with respect to $CH(X^2\Pi) + H(^2S)$, and 137.77 kcal/mol with respect to $CH(A^2)) + H(^2S)$ for the $^1A_1(\theta = 90°)$ and $^1\Delta_g$ symmetries, respectively (Fig. 2). The linear $^1\Delta_g$ configuration is stabilized by 137.77 – T_e(CH; $A^2\Delta \leftarrow X^2\Pi$) = 137.77 – 67.46 = 70.31 kcal/mol with respect to the ground CH state. Therefore, the bent $^1A_1(\theta = 90°)$ structure of CH_2 is favoured by 94.42 – 70.31 = 24.11 kcal/mol and mildly "relaxed" to a final angle of 102.20° ($\tilde{a}^1A_1$); see Table 2. The high energy inversion barrier of this state corresponds to the energy difference of the two limiting structures ($^1\Delta_g$, $^1A_1(\theta = 90°)$) increased by the relaxation energy $^1A_1(\theta = 90°) \rightarrow \tilde{a}^1A_1$ (θ_e = 102.20°) or IB = 67.46 – 43.35 + 2.24 = 26.35 kcal/mol (Table 2).

The geometrical values (r_e, θ_e) of Table 2 are in complete agreement with the focal point analysis of ref. 121. The $\tilde{a}^1A_1 \leftarrow \tilde{X}^3B_1$ splitting corrected for ZPE from ref. 121 is 8.822 kcal/mol as contrasted to the most recent experimental value of 8.998 ± 0.014 kcal/mol (82).

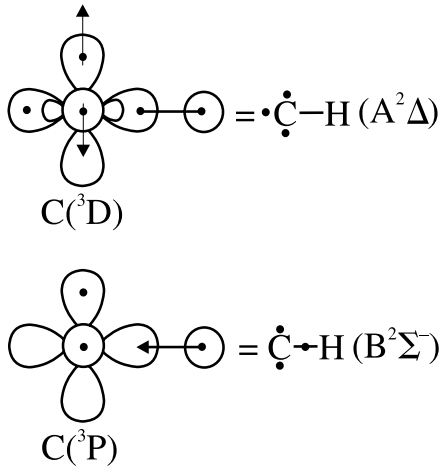
$\tilde{b}^1B_1$

The CASSCF main configuration for the $\tilde{b}^1B_1$ state is

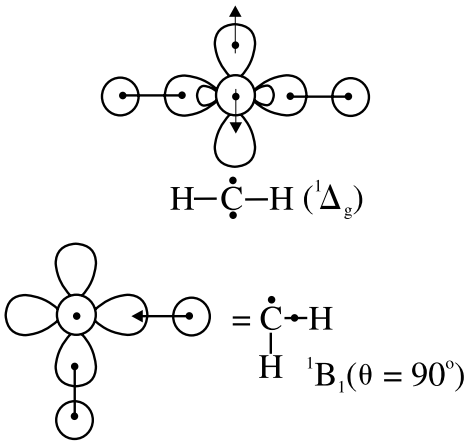
$$\left|\tilde{b}^1B_1\right\rangle \sim 0.99 \left|1a_1^2\, 2a_1^2 3a_1^1 1\bar{b}_1^1 1b_2^2\right\rangle$$

As can be seen, this state is the open-shell singlet analog of the $\tilde{X}^3B_1$ state. As expected, the $\tilde{b}^1B_1$ molecular orbitals and Mulliken atomic distributions are very similar to those of the ground state (vide supra).

At linearity the symmetry of this state is $^1\Delta_g$; it is the Renner–Teller companion of the previously discussed $\tilde{a}^1A_1$ state (Fig. 1). The $A^2\Delta$ and $B^2\Sigma^-$ states of the diatomic CH molecule, differing in energy by 7.21 kcal/mol (Table 3), can be considered as the parental states of the $CH^2\tilde{b}\,^1B_1$ state. This is clearly seen from the following vbL diagrams:



Two modes of H attack resulting in the formation of CH_2 are conceivable: a linear attack on the $A^2\Delta$ state of CH along the z axis and a perpendicular attack on the $B^2\Sigma^-$ state along the x (or y) axis, giving rise to $^1\Delta_g$ and $^1B_1(\theta = 90°)$ CH_2 symmetries, respectively. Diagrammatically,



The binding energies of the $^1\Delta_g$ and $^1B_1(\theta = 90°)$ CH_2 configurations with respect to $CH(A^2\Delta$ or $B^2\Sigma^-) + H(^2S)$ are 137.77 and 118.86 kcal/mol, respectively (Fig. 2, Table 3). Therefore, the $^1\Delta_g$ structure is *lower* in energy by 137.77 – 118.86 + 7.21 = 26.12 kcal/mol. The pseudo Jahn–Teller interaction between the two limiting cases ($^1\Delta_g$ and $^1B_1(\theta = 90°)$) results in the $\tilde{b}^1B_1$ state with a final θ_e angle of 142.44° (Table 2), again very close to (180° + 90°)/2 = 135°. It is clear by now that everything else being equal, the inversion barrier is strongly related to the energy separation of the CH states involved, i.e., the relative low IB = 2.72 kcal/mol (Table 2) of the $\tilde{b}^1B_1$ state is related to the small CH $A^2\Delta \leftarrow B^2\Sigma^-$ splitting.

Our predicted $\tilde{b}^1B_1 \leftarrow \tilde{X}^3B_1$ separation is T_e =

© 2004 NRC Canada

Table 2. Total energies (E), equilibrium bond distances (r_e), HĈH angles (θ_e), dipole moments (μ_e), inversion barriers (IB), atomization energies (AE_e), and energy gaps (T_e/T_0) of the $\tilde{X}^3B_1$, $\tilde{a}^1A_1$, $\tilde{b}^1B_1$, and $\tilde{c}^1A_1$ states of CH_2.

$-E$ (hartree)	r_e (Å)	θ_e (°)	μ_e[a] (Debye)	IB (cm^{-1})	AE_e (kcal/mol)	T_e/T_0 (kcal/mol)
$\tilde{X}^3B_1$						
39.140113[b]	1.0751	133.66	0.596	1982.5[c]	188.90[d]	0.0
39.146232[e]	1.0753	133.82			190.06[f]	0.0
$\tilde{a}^1A_1$						
39.125487[b,g]	1.1061	102.20	1.676	9217.7[h]	179.72[i]	9.178/8.822[j]
$\tilde{b}^1B_1$						
39.087831[b,k]	1.0723	142.44	0.664	953.2[h]	156.09[i]	32.807/33.658[l]
$\tilde{c}^1A_1$						
39.046391[b,m]	1.0657	171.92	0.193	10.3[n]	130.09[i]	58.811/59.345[o]

Note: For the present work.
[a]Calculated as expectation value.
[b]All electron MRCI/[13s12p10d8f6g4h2i/6s5p4d3f2g1h]. E (+Q = Davidson correction) = –39.1464 E_h.
[c]IB = 1982.5 cm^{-1} (= 5.668 kcal/mol) at $r_{CH}(^3\Sigma_g^-)$ = 1.0648 Å.
[d]AE_e = IB + D_e[HCH($^3\Sigma_g^-$) → CH($a^4\Sigma^-$) + H(^{2}S)] + D_e[CH($a^4\Sigma^-$)] = 5.668 + 116.47 + 66.76 = 188.90 kcal/mol. At the MRCI + Q level, AE = 189.9 kcal/mol.
[e]All electron RCCSD(T).
[f]AE_e[$CH_2(\tilde{X}^3B_1)$ → C(^{3}P) + 2H(^{2}S)] = (39.146232 – 37.843350 – (2 × 0.4999992)) × 627.51 = 190.06 kcal/mol.
[g]E(+Q) = –39.1321 E_h.
[h]IB to linearity at $r_{CH}(^1\Delta_g)$ = 1.0622 Å.
[i]With respect to C(^{3}P) + 2H(^{2}S).
[j]$T_0(\tilde{a}^1A_1) = T_e(\tilde{a}^1A_1)$ – [ZPE($\tilde{X}^3B_1$) – ZPE($\tilde{a}^1A_1$)], with ZPEs from ref. 121 (see Table 1).
[k]E(+Q) = –39.0958 E_h.
[l]$T_0(\tilde{b}^1B_1) = T_e(\tilde{b}^1B_1)$ – [ZPE($\tilde{X}^3B_1$) – ZPE($\tilde{b}^1B_1$)], with ZPE($\tilde{X}^3B_1$) and ZPE($\tilde{b}^1B_1$) from refs. 121 and 117, respectively (see Table 1).
[m]E(+Q) = –39.0550 E_h.
[n]IB to linearity at $r_{CH}(^1\Sigma_g^+)$ = 1.0650 Å.
[o]$T_0(\tilde{c}^1A_1) = T_e(\tilde{c}^1A_1)$ – [ZPE($\tilde{X}^3B_1$) – ZPE($\tilde{c}^1A_1$)], with ZPE($\tilde{X}^3B_1$) and ZPE($\tilde{c}^1A_1$) from refs. 121 and 105, respectively (see Table 1).

Table 3. Total energies (E), bond distances (r_e), and energy separations (T_e) of the first five CH states at the all-electron MRCI/(d–aug–cc–pCV6Z/cc–pV6Z) level.

State	$-E$ (hartree)	r_e (Å)	T_e (kcal/mol)
$X^2\Pi$	38.471454	1.1179	0
		(1.119786)	(0)
$a^4\Sigma^-$	38.445470	1.0857	16.31
		(1.0977)[a]	(17.11±0.18)[a]
$A^2\Delta$	38.363946	1.1027	67.46
		(1.1031)	(66.19)
$B^2\Sigma^-$	38.352464	1.1719	74.67
		(1.1640)	(74.51)
$C^2\Sigma^+$	38.325164	1.1129	91.80
		(1.1143)	(90.93)

Note: From the present work; experimental values in parentheses (taken from ref. 126).
[a]r_0 and T_0 values.

32.807 kcal/mol, in excellent agreement with the best available experimental/theoretical value of 32.911 ± 0.014 kcal/mol (Tables 1 and 2).

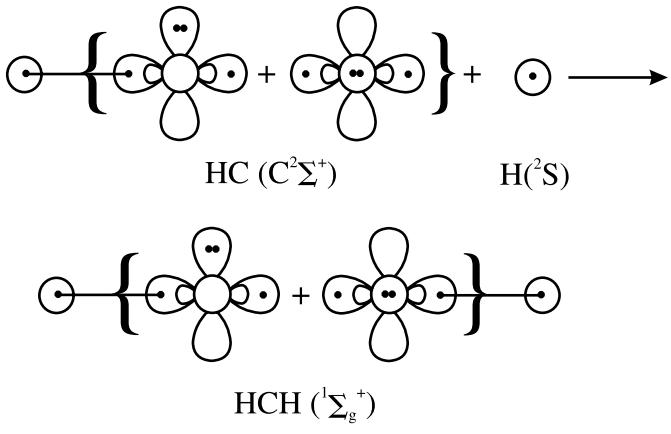
$\tilde{c}^1A_1$

This is the highest energy state examined in the present report with a $\tilde{c}^1A_1 \leftarrow \tilde{X}^3B_1$ splitting T_e (T_0) = 58.811 (59.345) kcal/mol at the MRCI level (Table 2). Unfortunately, there are no experimental results in the literature for this state. However, there is no reason to assume that our results for $\tilde{c}^1A_1$ are any less reliable than those for the other states. So, we believe they also are of experimental accuracy.

The leading CASSCF configurations for the $\tilde{c}^1A_1$ state are

$$\left|\tilde{c}^1A_1\right\rangle \sim \left|1a_1^2\,2a_1^2[0.67(3a_1^2) + 0.73(1b_1^2)]1b_2^2\right\rangle$$

The quasilinear character of this state (θ_e = 171.92°, IB = 10.3 cm^{-1}; Table 2) is its unique feature. This structure is easily rationalized after examining its linear limiting configuration ($^1\Sigma_g^+$), which correlates to CH($C^2\Sigma^+$) + H(^{2}S) (Fig. 2). The nature of this state becomes obvious upon considering the following diagram showing the unique way that $CH_2(^1\Sigma_g^+)$ is formed from CH + H:



© 2004 NRC Canada

With no other competitive CH state available (126) the final CH_2 state is, indeed, essentially vibrationally linear with an inversion energy barrier that is close to zero.

Conclusions

Using all electron multireference calculations and large basis sets we constructed potential energy curves along the HĈH and CH + H coordinates for the four lowest states of the CH_2 system, namely $\tilde{X}^3B_1$, $\tilde{a}^1A_1$, $\tilde{b}^1B_1$, and $\tilde{c}^1A_1$. Our geometrical results, binding energies, and energy separations are in excellent agreement with existing experimental values.

Taking into account the low-lying states of the CH diatomic molecule ($X^2\Pi$, $a^4\Sigma^-$, $A^2\Delta$, $B^2\Sigma^-$, and $C^2\Sigma^+$), we can rationalize the bonding schemes and geometrical characteristics of the four states of CH_2 examined in this paper. In particular, the large range of inversion barriers to linearity (5.668, 26.355, 2.725, 0.029 kcal/mol, respectively) can be comprehended in terms of the energy splittings among the related states of the CH fragment.

Acknowledgements

This work was performed in part at the Joint Institute for Computational Sciences, University of Tennessee–Oak Ridge National Laboratory. Support was provided by the Distinguished Scientist Program at the University of Tennessee and Oak Ridge National Laboratory. Oak Ridge National Laboratory is managed by UT–Battelle, LLC for the U.S. Department of Energy under Contract No. DE–AC05–00OR22725.

References

1. R.S. Mulliken. Phys. Rev. **41**, 751 (1932).
2. G. Herzberg. Astrophys. J. **96**, 314 (1942).
3. G. Herzberg and J. Shoosmith. Nature (London), **183**, 1801 (1959).
4. J.M. Foster and S.F. Boys. Rev. Mod. Phys. **32**, 305 (1960).
5. G. Herzberg. Proc. R. Soc. London A, **262**, 291 (1961).
6. G. Herzberg. Can J. Phys. **39**, 1511 (1961).
7. G. Herzberg and J.W.C. Johns. Proc. R. Soc. London A, **295**, 107 (1966).
8. J.F. Harrison and L.C. Allen. J. Am. Chem. Soc. **91**, 807 (1969).
9. C.F. Bender and H.F. Schaefer III. J. Am. Chem. Soc. **92**, 4984 (1970).
10. R.A. Bernheim, H.W. Bernard, P.S. Wang, L.S. Wood, and P.S. Skell. J. Chem. Phys. **53**, 1280 (1970).
11. E. Wasserman, W.A. Yager, and V.J. Kuck. Chem. Phys. Lett. **7**, 409 (1970).
12. E. Wasserman, V.J. Kuck, R.S. Hutton, and W.A. Yager. J. Am. Chem. Soc. **92**, 7491 (1970).
13. J.F. Harrison. J. Chem. Phys. **54**, 5413 (1971).
14. J.F. Harrison. J. Am. Chem. Soc. **93**, 4112 (1971).
15. J.F. Harrison. Int. J. Quantum Chem. **5**, 285 (1971).
16. G. Herzberg and J.W.C. Johns. J. Chem. Phys. **54**, 2276 (1971).
17. R.A. Bernheim, H.W. Bernard, P.S. Wang, L.S. Wood, and P.S. Skell. J. Chem. Phys. **54**, 3223 (1971).
18. E. Wasserman, V.J. Kuck, R.S. Hutton, E.D. Anderson, and W.A. Yager. J. Chem. Phys. **54**, 4120 (1971).
19. E. Wasserman, R.S. Hutton, V.J. Kuck, and W.A. Yager. J. Chem. Phys. **55**, 2593 (1971).
20. S.V. O'Neil, H.F. Schaefer III, and C.F. Bender. J. Chem. Phys. **55**, 162 (1971).
21. J.F. Harrison. *In* Carbene chemistry. *Edited by* W. Kirmse. Academic Press, Inc., New York and London. 1971.
22. P.J. Hay, W.J. Hunt, and W.A. Goddard III. Chem. Phys. Lett. **13**, 30 (1972).
23. C.F. Bender, H.F. Schaefer III, D.R. Franceschetti, and L.C. Allen. J. Am. Chem. Soc. **94**, 6888 (1972).
24. D.R. McLaughlin, H.F. Schaefer, and C.F. Bender. Theor. Chim. Acta, **25**, 352 (1972).
25. V. Staemmler. Theor. Chim. Acta, **31**, 49 (1973).
26. J.F. Harrison. J. Chem. Phys. **58**, 3106 (1973).
27. J.F. Harrison. Acc. Chem. Res. **7**, 378 (1974).
28. P.P. Gaspar and G.S. Hammond. *In* Carbenes. *Edited by* R.A. Moss and M. Jones. Wiley, New York. 1975.
29. J.F. Harrison and D.A. Wernette. J. Chem. Phys. **62**, 2918 (1975).
30. R.J. Blint and M.D. Newton. Chem. Phys. Lett. **32**, 178 (1975).
31. A.H. Pakiari and N.C. Handy. Theor. Chim. Acta, **40**, 17 (1975).
32. J.H. Meadows and H.F. Schaefer III. J. Am. Chem. Soc. **98**, 4383 (1976).
33. P.F. Zittel, G.B. Ellison, S.V. O'Neil, E. Herbst, W.C. Lineberger, and W.P. Reinhardt. J. Am. Chem. Soc. **98**, 3731 (1976).
34. R.A. Bernheim, T. Adl, H.W. Benard, A. Songco, P.S. Wang, R. Wang, L.S. Wood, and P.S. Skell. J. Chem. Phys. **64**, 2747 (1976).
35. L.B. Harding and W.A. Goddard III. J. Chem. Phys. **67**, 1777 (1977).
36. R.R. Lucchese and H.F. Schaefer III. J. Am. Chem. Soc. **99**, 6765 (1977).
37. C.W. Bauschlicher, Jr., H.F. Schaefer III, and P.S. Bagus. J. Am. Chem. Soc. **99**, 7106 (1977).
38. B.O. Roos and P.M. Siegbahn. J. Am. Chem. Soc. **99**, 7716 (1977).
39. S. Shih, S.D. Peyerimhoff, R.J. Buenker, and M. Peric. Chem. Phys. Lett. **55**, 206 (1978).
40. C.W. Bauschlicher, Jr. and I. Shavitt. J. Am. Chem. Soc. **100**, 739 (1978).
41. R.K. Lengel and R.N. Zare. J. Am. Chem. Soc. **100**, 7495 (1978).
42. C.W. Bauschlicher, Jr. and D.R. Yarkony. J. Chem. Phys. **69**, 3875 (1978).
43. L.B. Harding and W.A. Goddard III. Chem. Phys. Lett. **55**, 217 (1978).
44. W.T. Borden and E.R. Davidson. Ann. Rev. Phys. Chem. **30**, 125 (1979).
45. C.W. Bauschlicher, Jr. Chem. Phys. Lett. **74**, 273 (1980).
46. E.R. Davidson, D. Feller, and P. Phillips. Chem. Phys. Lett. **76**, 416 (1980).
47. J. Römelt, S.D. Peyerimhoff, and R.J. Buenker. Chem. Phys. **54**, 147 (1981).
48. P.C. Engelking, R.R. Corderman, J.J. Wendoloski, G.B. Ellison, S.V. O'Neil, and W.C. Lineberger. J. Chem. Phys. **74**, 5460 (1981).
49. P. Saxe, H.F. Schaefer III, and N.C. Handy. J. Phys. Chem. **85**, 745 (1981).
50. T.J. Sears, P.R. Bunker, and A.R.W. McKellar. J. Chem. Phys. **75**, 4731 (1981).

© 2004 NRC Canada

51. C.C. Hayden, D.M. Neumark, K. Shobatake, R.K. Sparks, and Y.T. Lee. J. Chem. Phys. **76**, 3607 (1982).
52. T.J. Sears, P.R. Bunker, A.R.W. McKellar, K.M. Evenson, D.A. Jennings, and J.M. Brown. J. Chem. Phys. **77**, 5348 (1982).
53. T.J. Sears, P.R. Bunker, and A.R.W. McKellar. J. Chem. Phys. **77**, 5363 (1982).
54. P. Jensen, P.R. Bunker, and A.R. Hoy. J. Chem. Phys. **77**, 5370 (1982).
55. L.B. Harding. J. Phys. Chem. **87**, 441 (1983).
56. P. Knowles, N.C. Handy, and S. Carter. Mol. Phys. **49**, 681 (1983).
57. H. Petek, D.J. Nesbitt, P.R. Ogilby, and C.B. Moore. J. Phys. Chem. **87**, 5367 (1983).
58. P.R. Bunker, T.J. Sears, A.R.W. McKellar, K.M. Evenson, and F.J. Lovas. J. Chem. Phys. **79**, 1211 (1983).
59. A.R.W. McKellar, C. Yamada, and E. Hirota. J. Chem. Phys. **79**, 1220 (1983).
60. P.R. Bunker and P. Jensen. J. Chem. Phys. **79**, 1224 (1983).
61. A.R.W. McKellar, P.R. Bunker, T.J. Sears, K.M. Evenson, R.J. Saykally, and S.R. Langhoff. J. Chem. Phys. **79**, 5251 (1983).
62. T.J. Sears and P.R. Bunker. J. Chem. Phys. **79**, 5265 (1983).
63. D.G. Leopold, K.K. Murray, and W.C. Lineberger. J. Chem. Phys. **81**, 1048 (1984).
64. S.J. Cole, G.D. Purvis III, and R.J. Bartlett. Chem. Phys. Lett. **113**, 271 (1985).
65. I. Shavitt. Tetrahedron, **41**, 1531 (1985).
66. P.R. Bunker. *In* Comparison of ab initio quantum chemistry with experiment for small molecules. *Edited by* R.J. Bartlett. D. Reidel Publishing Company, Dordrecht, The Netherlands. 1985.
67. W.A. Goddard III. Science (Washington, D.C.), **227**, 917 (1985).
68. D.G. Leopold, K.K. Murray, A.E.S. Miller, and W.C. Lineberger. J. Chem. Phys. **83**, 4849 (1985).
69. P.R. Bunker and T.J. Sears. J. Chem. Phys. **83**, 4866 (1985).
70. H.F. Schaefer III. Science (Washington, D.C.), **231**, 1100 (1986).
71. N.C. Handy, Y. Yamaguchi, and H.F. Schaefer III. J. Chem. Phys. **84**, 4481 (1986).
72. T.J. Sears. J. Chem. Phys. **85**, 3711 (1986).
73. M.D. Marshall and A.R.W. McKellar. J. Chem. Phys. **85**, 3716 (1986).
74. P.R. Bunker, P. Jensen, W.P. Kraemer, and R. Beardsworth. J. Chem. Phys. **85**, 3724 (1986).
75. C.W. Bauschlicher, Jr. and P.R. Taylor. J. Chem. Phys. **85**, 6510 (1986).
76. E.A. Carter and W.A. Goddard III. J. Chem. Phys. **86**, 862 (1987).
77. H. Petek, D.J. Nesbitt, D.C. Darwin, and C.B. Moore. J. Chem. Phys. **86**, 1172 (1987).
78. H. Petek, D.J. Nesbitt, C.B. Moore, F.W. Birss, and D.A. Ramsay. J. Chem. Phys. **86**, 1189 (1987).
79. C.W. Bauschlicher, Jr., S.R. Langhoff, and P.R. Taylor. J. Chem. Phys. **87**, 387 (1987).
80. A.D. McLean, P.R. Bunker, R.M. Escribano, and P. Jensen. J. Chem. Phys. **87**, 2166 (1987).
81. G. Duxbury and Ch. Jungen. Mol. Phys. **63**, 981 (1988).
82. P. Jensen and P.R. Bunker. J. Chem. Phys. **89**, 1327 (1988).
83. W. Xie, A. Ritter, C. Harkin, K. Kasturi, and H.-L. Dai. J. Chem. Phys. **89**, 7033 (1988).
84. D.C. Comeau, I. Shavitt, P. Jensen, and P.R. Bunker. J. Chem. Phys. **90**, 6491 (1989).
85. H. Petek, D.J. Nesbitt, D.C. Darwin, P.R. Ogilby, C.B. Moore, and D.A. Ramsay. J. Chem. Phys. **91**, 6566 (1989).
86. W. Xie, C. Harkin, and H.-L. Dai. J. Chem. Phys. **93**, 4615 (1990).
87. A. Alijah and G. Duxbury. Mol. Phys. **70**, 605 (1990).
88. W.H. Green, Jr., N.C. Handy, P.J. Knowles, and S. Carter. J. Chem. Phys. **94**, 118 (1990).
89. K.K. Irikura and J.W. Hudgens. J. Phys. Chem. **96**, 518 (1992).
90. K.K. Irikura, R.D. Johnson III, and J.W. Hudgens. J. Phys. Chem. **96**, 6131 (1992).
91. I. Garcia-Moreno, E.R. Lovejoy, C.B. Moore, and G. Duxbury. J. Chem. Phys. **98**, 873 (1993).
92. G.V. Hartland, D. Qin, and H.-L. Dai. J. Chem. Phys. **98**, 2469 (1993).
93. I. Garcia-Moreno and C.B. Moore. J. Chem. Phys. **99**, 6429 (1993).
94. L.B. Harding, R. Guadagnini, and G.C. Schatz. J. Phys. Chem. **97**, 5472 (1993).
95. V.J. Barclay, I.P. Hamilton, and P. Jensen. J. Chem. Phys. **99**, 9709 (1993).
96. B.-C. Chang, M. Wu, G.E. Hall, and T.J. Sears. J. Chem. Phys. **101**, 9236 (1994).
97. P. Piecuch, X. Li, and J. Paldus. Chem. Phys. Lett. **230**, 377 (1994).
98. A. Balková and R.J. Bartlett. J. Chem. Phys. **102**, 7116 (1995).
99. (*a*) R.A. Beärda, M.C. van Hemert, and E.F. van Dishoeck. J. Chem. Phys. **97**, 8240 (1992); (*b*) G.-J. Kroes, E.F. van Dishoeck, R.A. Beärda, and M.C. van Hemert. J. Chem. Phys. **99**, 228 (1993); (*c*) R.A. Beärda, G.-J. Kroes, M.C. van Hemert, B. Heumann, R. Schinke, and E.F. van Dishoeck. J. Chem. Phys. **100**, 1113 (1993); (*d*) G.-J. Kroes and M.C. van Hemert. J. Chem. Phys. **100**, 1128 (1994); (*e*) R.A. Beärda, M.C. van Hemert, and E.F. van Dishoeck. J. Chem. Phys. **102**, 8930 (1995).
100. G.V. Hartland, D. Qin, and H.-L. Dai. J. Chem. Phys. **102**, 6641 (1995).
101. D.E. Woon and T.H. Dunning, Jr. J. Chem. Phys. **103**, 4572 (1995).
102. D.R. Yarkony. J. Chem. Phys. **104**, 2932 (1996).
103. Y. Yamaguchi, C.D. Sherrill, and H.F. Schaefer III. J. Phys. Chem. **100**, 7911 (1996).
104. P.R. Bunker, P. Jensen, Y.Yamaguchi, and H.F. Schaefer III. J. Mol. Spectrosc. **179**, 263 (1996).
105. P.R. Bunker, P. Jensen, Y. Yamaguchi, and H.F. Schaefer III. J. Phys. Chem. **100**, 18 088 (1996).
106. Y. Yamaguchi and H.F. Schaefer III. J. Chem. Phys. **106**, 1819 (1997).
107. C.D. Sherrill, T.J. van Huis, Y. Yamaguchi, and H.F. Schaefer III. J. Mol. Struct.: THEOCHEM, **400**, 139 (1997).
108. K.A. Peterson and T.H. Dunning, Jr. J. Chem. Phys. **106**, 4119 (1997).
109. Y. Yamaguchi and H.F. Schaefer III. J. Chem. Phys. **106**, 8753 (1997).
110. Y. Yamaguchi and H.F. Schaefer III. Chem. Phys. **225**, 23 (1997).
111. C.D. Sherrill, M.L. Leininger, T.J. van Huis, and H.F. Schaefer III. J. Chem. Phys. **108**, 1040 (1998).
112. G. Duxbury, A. Alijah, B.D. McDonald, and C. Jungen. J. Chem. Phys. **108**, 2351 (1998).
113. G. Duxbury, B.D. McDonald, M. van Gogh, A. Alijah, C. Jungen, and H. Palivan. J. Chem. Phys. **108**, 2336 (1998).
114. C. Fockenberg, A.J. Marr, T.J. Sears, and B.-C. Chang. J. Mol. Spectrosc. **187**, 119 (1998).

© 2004 NRC Canada

115. A.J. Marr, T.J. Sears, and B.-C. Chang. J. Chem. Phys. **109**, 3431 (1998).
116. D.R. Yarkony. J. Chem. Phys. **109**, 7047 (1998).
117. J.-P. Gu, G. Hirsch, R.J. Buenker, M. Brumm, G. Osmann, P.R. Bunker, and P. Jensen. J. Mol. Struct. **517–518**, 247 (2000).
118. B. Bussery-Honvault, P. Honvault, and J.-M. Launay. J. Chem. Phys. **115**, 10 701 (2001).
119. L. Bañares, F.J. Aoiz, P. Honvault, B. Bussery-Honvault, and J.-M. Launay. J. Chem. Phys. **118**, 565 (2003).
120. J.-S.K. Yu, S.-Y. Chen, and C.-H. Yu. J. Chem. Phys. **118**, 582 (2003).
121. A.G. Császár, M.L. Leininger, and V. Szalay. J. Chem. Phys. **118**, 10 631 (2003).
122. T.H. Dunning, Jr. J. Chem. Phys. **90**, 1007 (1989); A.K. Wilson, T. van Mourik, and T.H. Dunning, Jr. J. Mol. Struct.: THEOCHEM, **388**, 339 (1997); D.E. Woon and T.H. Dunning, Jr. J. Chem. Phys. **100**, 2975 (1994); D.E. Woon and T.H. Dunning, Jr. J. Chem. Phys. **103**, 4572 (1995).
123. K.A. Peterson, D.E. Woon, and T.H. Dunning, Jr. J. Chem. Phys. **100**, 7410 (1994).
124. H. Partridge. J. Chem. Phys. **90**, 1043 (1989).
125. R.D. Amos, A. Bernhardsson, A. Berning, P. Celani, D.L. Cooper, M.J.O. Deegan, A.J. Dobbyn, F. Eckert, C. Hampel, G. Hetzer, P.J. Knowles, T. Korona, R. Lindh, A.W. Lloyd, S.J. McNicholas, F.R. Manby, W. Meyer, M.E. Mura, A. Nicklass, P. Palmieri, R. Pitzer, G. Rauhut, M. Schütz, U. Schumann, H. Stoll, A.J. Stone, R. Tarroni, T. Thorsteinsson, and H.-J. Werner. MOLPRO, version 2002.6 [computer program]. See www.molpro.net.
126. A. Kalemos, A. Mavridis, and A. Metropoulos. J. Chem. Phys. **111**, 9536 (1999).
127. R. Atkinson, D.L. Baulch, R.A. Cox, R.F. Hampson, Jr., J.A. Kerr, M.J. Rossi, and J. Troe. J. Phys. Chem. Ref. Data, **29**, 167 (2000).

© 2004 NRC Canada

The spectrum of singlet SiH_2[1]

S.N. Yurchenko, P.R. Bunker, W.P. Kraemer, and P. Jensen

Abstract: We report a theoretical study of the two lowest singlet electronic states ($\tilde{X}\,^1A_1$ and $\tilde{A}\,^1B_1$) of silylene SiH_2. These states become degenerate as a $^1\Delta_g$ state at linear configurations and are subject to the Renner effect. In ab initio calculations we have determined the potential energy and dipole moment surfaces for each state, and the transition moment surface between the states. Parameterized analytical functions have been fitted through the various sets of ab initio points, and the parameter values obtained for the potential energy surfaces have been further refined in fittings to experimental spectroscopic data. In these latter fittings, we use as input data experimentally derived energy differences together with ab initio points. In this manner, we achieve refined potential energy surfaces that behave reasonably also in regions of configuration space that are not sampled by the wavefunctions of the states for which experimentally derived energies are available. The calculation of rovibronic energies, the fittings to experimentally derived energies, and simulations of $\tilde{A}\,^1B_1 \rightarrow \tilde{X}\,^1A_1$ emission spectra of SiH_2 have been carried out with the RENNER program system. The higher excited vibrational states of $\tilde{X}\,^1A_1$ SiH_2 form polyads of heavily interacting states and many polyad states have been observed in dispersed fluorescence studies. The present theoretical work shows that owing to the heavy interaction between the states in the polyads, it is difficult to obtain unambiguous assignments for them.

Key words: silylene, RENNER, ab initio.

PACS Nos.: 31.15.Ar, 33.20.Wr, 33.20.Ea

Résumé : On a effectué une étude théorique des deux états électroniques singulets les plus faibles, $\tilde{X}\,^1A_1$ et $\tilde{A}\,^1B_1$ du silylène, SiH_2. Ces états deviennent dégénérés sous la forme d'un état $^1\Delta_g$ à configurations linéaires et ils sont sujets à l'effet de Renner. Dans les calculs ab initio, il a été possible de déterminer pour chaque état les surfaces de l'énergie potentielle et du moment dipolaire et la surface du moment de transition entre les états. Faisant appel à divers ensembles de points ab initio, on a ajusté des fonctions analytiques paramétrisées et on a mieux affiné les valeurs des paramètres obtenus pour les surfaces d'énergie potentielle en les ajustant aux données spectroscopiques expérimentales. Dans ces derniers ajustements, on a utilisé les données de base les différences d'énergie obtenues expérimentalement ainsi que les points *ab initio*. De cette façon, on a réussi à affiner les surfaces d'énergie potentielle de façon à ce qu'elles se comportent raisonnablement aussi dans des régions de l'espace de configuration qui ne sont pas soumises à l'échantillonnage des fonctions d'onde des états et pour lesquelles des énergies obtenues à partir de données expérimentales sont disponibles. Le calcul des énergies rovibroniques, les ajustements aux énergies obtenues à partir de données expérimentales et les simulations des spectres d'émission $\tilde{A}\,^1B_1 \rightarrow \tilde{X}\,^1A_1$ du SiH_2 ont été réalisés à l'aide du système de programme RENNER. L'état vibrationnel excité le plus élevé ($\tilde{X}\,^1A_1$) du SiH_2 forme des polyads d'états interagissant fortement et on a observé plusieurs états polyads dans le cadre d'études de fluorescence dispersée. Le présent travail théorique montre qu'en raison des fortes interactions entre les états des polyads, il est difficile d'obtenir des attributions non ambiguës pour eux.

Mots clés : silylène, RENNER, ab initio.

[Traduit par la Rédaction]

1. Introduction

Thin silicon films are essential for the industrial production of solar cells and semiconductor devices, and such films are produced by chemical vapour deposition following the decomposition of silane SiH_4. Silylene SiH_2 is a significant intermediate formed during decomposition reactions of SiH_4, and this paper is a contribution to the theoretical analysis of its spectra.

In contrast to the situation for methylene, the ground state of silylene is a singlet state: $\tilde{X}\,^1A_1$. The first excited state is the $\tilde{a}\,^3B_1$ state, and above that is the first excited singlet state $\tilde{A}\,^1B_1$. All these states are bent at equilibrium. At linearity the two singlet states become degenerate forming a $^1\Delta_g$ electronic state. As a result of this degeneracy at linearity there is a Renner effect interaction between the rovibronic levels of the $\tilde{X}$ and $\tilde{A}$

Received 2 October 2003. Published on the NRC Research Press Web site at http://canjchem.nrc.ca/ on 15 June 2004.

S.N. Yurchenko[2,3] and P.R. Bunker. Steacie Institute for Molecular Sciences, National Research Council of Canada, Ottawa ON K1A 0R6, Canada.
W.P. Kraemer. Max Planck Institute of Astrophysics, Karl-Schwarzschild-Strasse 1, Postfach 1523, D-85740 Garching, Germany.
P. Jensen. FB 9 - Theoretische Chemie, Bergische Universität, D-42097 Wuppertal, Germany.

[1]This article is part of a Special Issue dedicated to the memory of Professor Gerhard Herzberg.
[2]Present Address: Max-Planck-Institut für Kohlenforschung, Kaiser-Wilheim-Platz 1, D-45470 Mülheim an der Rurh, Germany.
[3]Corresponding author (e-mail: yurchenk@uni-wuppertal.de).

 doi: 10.1139/V04-030 © 2004 NRC Canada

electronic states. The theory of the Renner effect is reviewed, for example, in refs. 1 and 2. We report here a theoretical study of the spectra associated with the $\tilde{X}$ and $\tilde{A}$ singlet states of silylene.

The first observation of SiH_2 was made by Dubois et al. (3) who recorded the $\tilde{A}\,^1B_1 \leftarrow \tilde{X}\,^1A_1$ absorption spectrum in the visible region. Dubois and co-workers (4,5) subsequently rotationally analyzed the progression of bands $\tilde{A}\,^1B_1\ (0, v_2, 0) \leftarrow \tilde{X}\,^1A_1\ (0, 0, 0)$ with $v_2 = 1-6$ and Francisco et al. (6) obtained the vibrational energies of the $\tilde{A}\,^1B_1$ (0,7,0) and $\tilde{A}\,^1B_1$ (0,8,0) states. We use the notation $\tilde{X}\,^1A_1\ (v_1, v_2, v_3)$ or $\tilde{A}\,^1B_1\ (v_1, v_2, v_3)$ for the vibronic states, where v_2 is the vibrational quantum number appropriate for a bent molecule. Escribano and Campargue (7) observed and analyzed the $\tilde{A}\,^1B_1\ (0, 0, 0) \leftarrow \tilde{X}\,^1A_1\ (0, 0, 0)$ band in 1998 with significantly higher resolution than had been available in the earlier studies. Laser-induced fluorescence (LIF) studies of the $\tilde{A}$ state were reported by Ishikawa and Kajimoto (8). In 1989, Yamada et. al (9) used IR diode laser kinetic spectroscopy to observe the v_2 band of the $\tilde{X}$ state, and 2 years later Ishikawa and Kajimoto (10) obtained several $\tilde{X}$ state vibrational term values in a dispersed fluorescence experiment. This latter work was reanalyzed by Ishikawa and Kajimoto (11) and updated by Hirota and Ishikawa (12) in their analysis of the vibrational energy level structure of the $\tilde{X}$ state. LIF excitation and dispersed fluorescence studies of SiH_2 and SiD_2 were reported by Fukushima et al. (13) and Fukushima and Obi (14). Finally, in 2002 Ishikawa et al. (15) carried out an extensive stimulated emission pumping study of the $\tilde{A}$–$\tilde{X}$ system, obtaining a wealth of $\tilde{X}$-state vibrational term values (up to 9800 cm^{-1}above the $\tilde{X}$ vibrational ground state level) together with some information about the spin-orbit interaction between the $\tilde{X}\,^1A_1$ and the $\tilde{a}\,^3B_1$ electronic states.

On the theoretical side ab initio work involving limited dimensionality calculations of the potential energy surfaces have been performed, and the only full three-dimensional surfaces are those of the $\tilde{X}$ and $\tilde{a}$ states by Gabriel et. al (16) in a coupled-electron-pair-approach (CEPA) calculation (17). They calculated also rovibronic energies, spectroscopic constants, dipole moment parameters, and intensities. In 1993, Duxbury et. al (18) reanalyzed the available experimental data on $\tilde{X}$-state and $\tilde{A}$-state SiH_2 with a semiquantitative model incorporating the Renner interaction between the two states and the spin-orbit interaction with the $\tilde{a}\,^3B_1$ electronic state.

In the present study, we first made an ab initio calculation of the potential energy surfaces, and the dipole moment and transition moment surfaces, for the $\tilde{X}\,^1A_1$ and $\tilde{A}\,^1B_1$ states of SiH_2. Using the ab initio potential surfaces, we calculated rovibronic energies and compared them with experimental results. We then refined the potential energy surfaces in fittings to the large amount of experimentally derived rovibronic energy values available for the $\tilde{X}$ state of SiH_2, and to the energies available for the $\tilde{A}$ state. In these fittings, we used the ab initio information to constrain the potential energy surfaces so that they remained relatively close to the initial ab initio surfaces in regions of configuration space that are not sampled by the wavefunctions for the experimentally characterized states. We also present predictions for the energies of highly excited vibrational states calculated with the refined potential energy parameters, and we simulate the $\tilde{A}\,^1B_1 \rightarrow \tilde{X}\,^1A_1$ emission spectrum for comparison with the results of the stimulated emission pumping experiments of Ishikawa et al. (15). In some of these experiments, the molecules are pumped to the 0_{00} rotational level in either the $\tilde{A}(060)$ or $\tilde{A}(070)$ state, and the measured emission

Table 1. Potential energy parameters[a] for the $\tilde{X}\,^1A_1$ and $\tilde{A}\,^1B_1$ electronic states of SiH_2 (see eqs. [1]–[5] for the definitions of the parameters).

Parameter[b]	MCI ab initio[c]	Fitted
V_{ref}(hartree)	−290.075 28 (11)[d]	
$r_{12}^{(ref)}$ (Å)	1.489 089 13 (13)	1.489 089[e]
a_1 ($Å^{-1}$)	1.58[e]	1.58[e]
$f_{11}^{(0)}$	24 664 (207)	25 950 (22)
$f_{13}^{(0)}$	−372 (295)	−133 (22)
$f_{111}^{(0)}$	−2 592 (280)	−3 392 (77)
$f_{1111}^{(0)}$	1 293 (759)	2 941 (83)
$f_0^{(1,-)}$	−69 346 (387)	−68 962 (46)
$f_0^{(2,-)}$	103 276 (2034)	103 841 (81)
$f_0^{(3,-)}$	−106 731 (4539)	−108 072 (65)
$f_0^{(4,-)}$	73 767 (4951)	74 690 (12)
$f_0^{(5,-)}$	−27 365 (2601)	−27 783 (17)
$f_0^{(6,-)}$	4 406 (525)	4 549 (46)
$f_1^{(1,-)}$	−10 165 (183)	−10 095 (12)
$f_1^{(2,-)}$	17 448 (584)	17 340 (12)
$f_1^{(3,-)}$	−12 097 (599)	−12 320 (64)
$f_1^{(4,-)}$	2 333 (192)	2 585 (69)
$f_{11}^{(1,-)}$	4 265 (327)	2 650 (52)
$f_{11}^{(2,-)}$	−1 848 (204)	−1 662 (56)
$f_{111}^{(1,-)}$	10 836 (2129)	18 155 (115)
$f_{111}^{(2,-)}$	−7 878 (2062)	−13 534 (89)
$f_{113}^{(1,-)}$	−5 994 (1963)	−3 903 (219)
$f_0^{(1,+)}$	−44 077 (434)	−41 555 (58)
$f_0^{(2,+)}$	122 536 (3154)	112 569 (16)
$f_0^{(3,+)}$	−198 108 (9700)	−177 201 (18)
$f_0^{(4,+)}$	201 047 (14156)	177 276 (19)
$f_0^{(5,+)}$	−107 205 (9731)	−93 592 (24)
$f_0^{(6,+)}$	23 643 (2530)	20 587 (15)
$f_1^{(1,+)}$	4 818 (264)	3 663 (51)
$f_1^{(2,+)}$	−14 579 (1134)	−7 502 (148)
$f_1^{(3,+)}$	13 350 (1549)	1 524 (99)
$f_1^{(4,+)}$	−5 328 (669)	0
$f_{11}^{(1,+)}$	4 413 (452)	884 (98)
$f_{11}^{(3,+)}$	−4 873 (431)	−4 146 (127)
$f_{13}^{(2,+)}$	2 439 (969)	0

[a] Units are cm^{-1} unless otherwise indicated.
[b] Parameters for the $\tilde{X}$ state are denoted with a "−" in the superscript, and those for the $\tilde{A}$ state with a "+".
[c] After lowering the barrier to linearity by 150 cm^{-1} (see text).
[d] Quantities in parentheses are standard errors in units of the last digit quoted.
[e] Held fixed in the respective least-squares fittings.

© 2004 NRC Canada

Table 2. The ab initio dipole and transition moment parameters for the $\tilde{X}\,^1A_1$ and $\tilde{A}\,^1B_1$ electronic states of SiH_2 (see eqs. [9]–[13] for the definitions of the parameters).

$\widetilde{X}^1A_1$		$\widetilde{A}\,^1B_1$		$\widetilde{X}/\widetilde{A}$	
$q_0^{(0;-)}$ (D)	5.238(38)[a]	$q_0^{(0;+)}$ (D)	2.927(23)	$x_0^{(0;\pm)}$ (D)	−1.413(16)
$q_0^{(1;-)}$ (D)	−24.25(64)	$q_0^{(1;+)}$ (D)	−20.22(38)	$x_0^{(1;\pm)}$ (D)	0.548(50)
$q_0^{(2;-)}$ (D)	69.1(36)	$q_0^{(2;+)}$ (D)	64.4(21)	$x_0^{(5;\pm)}$ (D)	1.41(52)
$q_0^{(3;-)}$ (D)	−119.7(95)	$q_0^{(3;+)}$ (D)	−116.4(55)	$x_0^{(6;\pm)}$ (D)	−0.32(20)
$q_0^{(4;-)}$ (D)	117.4(123)	$q_0^{(4;+)}$ (D)	116.5(71)	$x_1^{(1;\pm)}$ (D Å^{-1})	0.906(23)
$q_0^{(5;-)}$ (D)	−60.1(77)	$q_0^{(5;+)}$ (D)	−60.4(45)	$x_{11}^{(0;\pm}$ (D Å^{-2})	0.123(78)
$q_0^{(6;-)}$ (D)	12.5(19)	$q_0^{(6;+)}$ (D)	12.6(11)	$x_{111}^{(0;\pm)}$ (D Å^{-3})	3.3(20)
$q_1^{(0;-)}$ (D Å^{-1})	−1.694(36)	$q_1^{(0;+)}$ (D Å^{-1})	−0.526(21)	$x_{113}^{(0;\pm)}$ (D Å^{-3})	−4.8(20)
$q_1^{(1;-)}$ (D Å^{-1})	0.123(31)	$q_1^{(1;+)}$ (D Å^{-1})	0.717(21)	Std. Dev.[b] (D)	0.023
$q_{11}^{(0;-)}$ (D Å^{-2})	−0.611(76)	$q_{13}^{(0;+)}$ (D Å^{-2})	−0.219(88)		
$q_{111}^{(0;-)}$ (D Å^{-3})	1.09(68)	$q_{111}^{(0;+)}$ (D Å^{-3})	−0.92(40)		
Std. Dev.[b](D)	0.076	Std. Dev.[b] (D)	0.012		
$p_1^{(0;-)}$ (D Å^{-1})	−0.240(46)	$p_1^{(0;+)}$ (D Å^{-1})	−0.253(25)		
$p_1^{(1;-)}$ (D Å^{-1})	12.35(61)	$p_1^{(1;+)}$ (D Å^{-1})	6.5(75)		
$p_1^{(2;-)}$ (D Å^{-1})	−27.0(21)	$p_1^{(2;+)}$ (D Å^{-1})	−16.4(29)		
$p_1^{(3;-)}$ (D Å^{-1})	24.0(25)	$p_1^{(3;+)}$ (D Å^{-1})	16.7(35)		
$p_1^{(4;-)}$ (D Å^{-1})	−7.39(93)	$p_1^{(4;+)}$ (D Å^{-1})	−5.6(14)		
$p_{111}^{(0;-)}$ (D Å^{-3})	4.5(16)	$p_{113}^{(0;+)}$ (D Å^{-3})	−4.3(26)		
$p_{113}^{(0;-)}$ (D Å^{-3})	−15.5(48)	$p_{1111}^{(0;+)}$ (D Å^{-4})	−5.2(26)		
		$p_{1111}^{(0;+)}$ (D Å^{-4})	11.2(99)		
Std. Dev.[b] (D)	0.0079	Std. Dev.[b] (D)	0.011		

[a]Quantities in parentheses are standard errors in units of the last digit quoted.
[b]Standard deviation of the fitting to the ab initio points.

spectra consist of the allowed $1_{10} \leftarrow 0_{00}$ rotational transition to vibrational levels of the $\tilde{X}$ state. In other experiments the $\tilde{A}(010)\ 1_{01}$ level is pumped and the spectra then consist of rotational transitions to both the 1_{11} and 2_{11} levels of vibrational levels of the $\tilde{X}$ state.

2. Ab initio calculations

Ab initio calculations of the potential energy surfaces were performed for the $\tilde{X}\,^1A_1$ and $\tilde{A}\,^1B_1$ singlet electronic states. The geometries involved a range of the HSiH bond angles (30°–160°) and SiH bond lengths (1.27–1.72 Å) including asymmetric bond stretches. The C_s point group symmetry was therefore used to classify the electronic wavefunctions.

General contraction type atomic natural orbital (ANO) bases were chosen to approximate the molecular orbitals. They consist for silicon of $17s$-, $12p$-, $5d$-, and $3f$-type functions contracted to $(7s6p4d3f)$-functions, and for the hydrogens of $8s$-, $4p$-, and $3d$-type functions contracted to $(6s4p3d)$-functions; in total 176 primitive functions contracted to 132 functions.

The energies were evaluated at the multireference configuration interaction (MR-CI) level of theory using molecular orbital bases that were optimized for each state separately by complete-active-space (CASSCF) calculations. The CASSCF partitioning scheme adopted here keeps the 10 electrons occupying the Si $1s$, $2s$, and $2p$ orbitals inactive and allows the remaining six valence electrons to be distributed among six active orbitals (4 a' orbitals and 2 a'' orbitals) in all possible ways consistent with the respective space and spin symmetries. In the MR-CI calculations these CASSCF wavefunctions (100 configuration state functions (CSFs) for the $\tilde{X}$ state and 80 CSFs for the $\tilde{A}$ state) are used as reference configurations from which all single and double excitations are generated. The total CI-expansions of the two states comprise 763 860 and 776 750 CSFs, respectively. The present calculations made use of the MOLCAS program system (19).

The equilibrium geometry parameters determined at this level of theory are close to the r_0 experimental parameters (4), and to those obtained recently in other high accuracy ab initio studies (16, 20, 21). For the strongly bent $\tilde{X}$ state the equilibrium bond angle is obtained as 92.4°, and the SiH bond length as $r_e = 1.5185$ Å. For the $\tilde{A}$ state, the equilibrium angle is 122.9° and the equilibrium bond length is found to be slightly shorter at $r_e = 1.4874$ Å. The equilibrium energy separation between the two singlet states is calculated as $T_e(\tilde{A}) = 15\,677\ cm^{-1}$, and from experiment (7) $T_0(\tilde{A}) = 15\ 547.773\ cm^{-1}$. Corresponding calculations that were also performed here for the excited $\tilde{a}^3B_1$ state of SiH_2 yield a singlet–triplet energy separation of

© 2004 NRC Canada

Table 3. Term values (in cm^{-1}) for the $\tilde{X}\,^1A_1$ electronic state of SiH_2.

$(v_1, v_2, v_3)^a$	$J_{K_aK_c}$	Observed[b]	O–C/MCI[c]	O–C/fitted[d]	Reference[e]
(0, 2, 0)	0_{00}	1978.153	9.629	1.316	(12)
(1, 0, 0)	0_{00}	2005.469	13.638	6.749	(12)
(1, 1, 0)	0_{00}	2952.7	13.6	3.0	(10)
(0, 3, 0)	0_{00}	2998.6	17.9	9.0	(10)
(1, 2, 0)	0_{00}	3907.4	24.4	−2.3	(10)
(2, 0, 0)	0_{00}	3923.3	20.1	−0.4	(10)
(0, 4, 0)	0_{00}	3976.8	18.5	4.6	(10)
(0, 0, 2)	0_{00}	3997.5	20.9	4.3	(10)
(0, 0, 1)	0_{00}	1992.816	1.541	−8.872	(12)
(0, 0, 0)	1_{10}	15.121	0.126	0.121	(12)
(0, 0, 0)	1_{01}	10.724	0.116	0.094	(12)
(0, 1, 0)	1_{01}	1009.42	2.64	1.20	(9)
(0, 0, 0)	1_{11}	11.801	0.066	0.078	(12)
(0, 1, 0)	1_{11}	1010.64	2.61	1.16	(9)
(3, 4, 0)	1_{11}	9487.14	61.08	−4.46	(15)
(1, 8, 0)	1_{11}	9522.23	63.21	−3.35	(15)
(2, 2, 2)	1_{11}	9592.28	47.80	−10.80	(15)
(0, 6, 2)	1_{11}	9612	44	−2	(15)
(0, 6, 2)	1_{11}	9641.18	44.32	−0.98	(15)
(1, 0, 4)	1_{11}	9670.99	63.58	−8.51	(15)
(0, 2, 4)	1_{11}	9696.98	50.84	7.95	(15)
(0,10, 0)	1_{11}	9735.38	34.26	13.29	(15)
(0, 0, 0)	2_{02}	29.700	0.261	0.231	(12)
(0, 0, 0)	2_{20}	45.564	0.354	0.354	(12)
(0, 1, 0)	2_{02}	1028.45	2.80	1.34	(9)
(0, 1, 0)	2_{00}	1045.42	2.93	1.46	(9)
(0, 0, 0)	2_{20}	29.930	0.239	0.223	(12)
(0, 1, 0)	2_{12}	1028.73	2.78	1.32	(9)
(0, 0, 0)	2_{21}	43.102	0.267	0.303	(12)
(0, 1, 0)	2_{21}	1042.87	2.85	1.38	(9)
(0, 0, 0)	2_{11}	39.879	0.418	0.352	(12)
(0, 1, 0)	2_{11}	1039.22	2.95	1.49	(9)
(3, 4, 0)	2_{11}	9517.72	62.16	−3.15	(15)
(1, 8, 0)	2_{11}	9553.58	68.83	−2.99	(15)
(2, 2, 2)	2_{11}	9623.17	50.35	−9.28	(15)
(0, 6, 2)	2_{11}	9642.23	44.09	−2.62	(15)
(0, 6, 2)	2_{11}	9671.18	44.75	−0.49	(15)
(1, 0, 4)	2_{11}	9698.96	65.52	−7.00	(15)
(0, 2, 4)	2_{11}	9725.16	49.65	−7.02	(15)
(0,10, 0)	2_{11}	9764.99	33.42	12.87	(15)

[a]The vibrational assignment of each state is that state which has the largest eigenvector coefficient from the output of the RENNER program using the fitted potentials.
[b]Experimentally derived term values.
[c]Residuals (observed–calculated) obtained using the MCI ab initio parameters from Table 1.
[d]Residuals (observed–calculated) obtained using the fitted parameters from Table 1.
[e]Reference for the experimentally derived ("Observed") term value.

$T_e(\tilde{a}) = 7140\ cm^{-1}$ (0.8852 eV). Experimentally (22), $T_0(\tilde{a})$ has been determined as being either 0.78 ± 0.03 eV or 0.91 ± 0.03 eV, and our result would suggest that the latter value is appropriate.

The two Renner states correlate with $Si(^1D) + H_2(\tilde{X}\,^1\Sigma_g^+)$ at dissociation (lowest dissociation channel) and hydrogen abstraction in the $\tilde{X}$ state leads to the higher dissociation channel: $SiH(\tilde{X}\,^2\Pi) + H(^2S)$. A wide variation in fluorescence lifetimes has been observed for individual rovibronic levels in the $\tilde{A}$ state that has been attributed to predissociation of these levels via random couplings to background levels of the $\tilde{a}\,^3B_1$ state (23). Some effort has been put recently into theoretical studies of the dissociation dynamics of the low-lying electronic states of SiH_2 including the triplet $\tilde{a}$ state (6). In these studies, both dissociation pathways of the ground electronic state have been found to be barrier free (without an energy maximum) whereas for the $\tilde{A}$

© 2004 NRC Canada

Table 4. Term values (in cm^{-1}) for the rotational level $J_{K_a K_c} = 1_{10}$ in various vibrational states of $\tilde{X}\,^1A_1$ SiH_2.

P^a	i^b	$(v_1, v_2, v_3)^c$	Observed[d]	O–C/MCI[e]	O–C/fitted[f]	P^a	i^b	$(v_1, v_2, v_3)^c$	Observed[d]	O-C/MCI[e]	O–C/fitted[f]
1	0	(0, 1, 0)	1014.14	2.66	1.22	8	8	(4, 0, 0)	(7578.04)	(7477.20)	(7578.49)
2	1	(0, 2, 0)	1993.62	9.93	1.47		7	(3, 2, 0)	7658.27	56.08	−4.17
	0	(1, 0, 0)	2020.82	13.59	6.83		6	(1, 6, 0)	7689.53	40.81	−1.02
3	1	(1, 1, 0)	2967.57	12.79	2.13		5	(2, 4, 0)	7753.27	44.77	0.91
	0	(0, 3, 0)	3014.28	17.86	9.00		4	(2, 0, 2)	7768.75	51.80	−5.06
4	3	(1, 2, 0)	3922.52	24.76	−2.64		3	(0, 4, 2)	7785.14	34.45	−4.63
	2	(2, 0, 0)	3939.45	20.36	0.64		2	(0, 8, 0)	7828.1	33.60	−0.53
	1	(0, 4, 0)	3991.33	17.28	3.16		1	(0, 0, 4)	7853.83	41.83	−1.06
	0	(0, 0, 2)	4011.73	20.22	3.85		0	(1, 6, 0)	7901.12	22.30	4.81
5	3	(1, 3, 0)	4877.49	26.13	−0.89	9	8	(4, 1, 0)	(8505.60)	(8401.54)	(8496.27)
	2	(2, 1, 0)	4904.98	25.71	0.91		7	(3, 3, 0)	8580.91	59.33	−2.53
	1	(0, 1, 2)	4956.74	18.01	−1.79		6	(1, 7, 0)	8612.59	46.95	−1.22
	0	(0, 1, 2)	4993.23	24.56	10.18		5	(0, 9, 0)	8682.95	47.99	−3.14
6	5	(3, 0, 0)	(5782.47)	(5729.31)	(5792.29)		4	(2, 1, 2)	8695.37	47.07	−2.96
	4	(1, 4, 0)	5823.36	30.77	0.14		3	(0, 5, 2)	8719.40	40.90	−1.85
	3	(2, 2, 0)	5863.23	30.55	2.15		2	(0, 1, 4)	8758.65	34.35	−9.30
	2	(1, 0, 2)	5905.36	30.78	−4.11		1	(0, 1, 4)	8798.85	38.04	10.02
	1	(1, 0, 2)	5931.12	32.90	8.84		0	(1, 7, 0)	8855.75	15.87	−1.95
	0	(1, 4, 0)	5970.53	27.50	12.32	10	11	(5, 0, 0)	9306.07	161.90	16.54
7	5	(3, 1, 0)	(6725.44)	(6671.64)	(6732.24)		10	(4, 2, 0)	(9424.55)	(9315.62)	(9406.03)
	4	(1, 5, 0)	6759.68	35.06	−0.75		9	(3, 4, 0)	9491.65	61.39	−4.10
	3	(2, 3, 0)	6812.43	34.00	1.98		8	(1, 8, 0)	9526.81	64.64	−3.33
	2	(1, 1, 2)	6845.77	28.76	−6.79		7	(3, 0, 2)	(9551.16)	(9475.72)	(9562.02)
	1	(1, 1, 2)	6887.15	33.00	8.48		6	(2, 2, 2)	9596.81	48.50	−10.43
	0	(1, 5, 0)	6939.03	25.87	9.41		5	(0, 6, 2)	9616.21	44.68	−2.86
							4	(0, 6, 2)	9644.74[g]	43.80	−1.48
							3	(1, 0, 4)	9675.08	64.57	−7.64
							2	(0, 2, 4)	9700.60	50.43	7.61
							1	(0,10, 0)	9739.40	33.97	13.14
							0	(1, 8, 0)	9800.78	4.58	−12.51

[a]Polyad quantum number $P = 2v_1 + v_2 + 2v_3$.
[b]Following ref. 15, we use i as a running number index within each polyad.
[c]The vibrational assignment of each state is that state which has the largest eigenvector coefficient from the output of the RENNER program using the fitted potentials.
[d]Experimentally derived term values from (15). The values in parentheses are calculated values from ref. 15.
[e]Residuals (observed–calculated) obtained using the MCI ab initio parameters from Table 1. For the levels that were not observed the MCI calculated value is placed here in parentheses.
[f]Residuals (observed–calculated) obtained using the fitted parameters from Table 1. For the levels that were not observed the calculated value obtained using the fitted potential is placed here in parentheses.
[g]Deperturbed from the triplet interaction (15).

state a very small energy maximum has been discovered in calculations at a medium accuracy level. To get reliable estimates of the basic energetics of these processes the relevant dissociation energies were calculated here at the theory level of the present study. For the two singlet states, the dissociation energies corresponding to the lower dissociation channel are 21 500 cm^{-1} and 5823 cm^{-1}, respectively, whereas for the higher dissociation channel of the $\tilde{X}$ state an energy of 27 545 cm^{-1} is obtained. The energy difference between the two dissociation limits of the $\tilde{X}$ state is thus 6045 cm^{-1}. This can be compared to the value of 6470 cm^{-1} that can be derived for this energy difference from the dissociation energies of H_2 and SiH, and the ^3P and ^1D term values for Si. Comparing the lower dissociation energies of the two singlet states with the corresponding energy barriers to linearity, we see that the barrier heights exceed the dissociation limits by several hundred wavenumbers.

The in-plane dipole moment components of the two singlet states were calculated relative to the molecular center of mass directly as expectation values from the previously iterated MR-CI wavefunctions for all different molecular geometries. The out-of-plane dipole transition moment was obtained at the CASSCF level from the individually optimized wavefunctions for each state, appying the restricted active space state interaction (RASSI) method of Malmqvist and Roos (24).

3. The potential energy and dipole moment surfaces

To calculate the rovibronic energies associated with the Renner-interacting $\tilde{X}\,^1A_1$ and $\tilde{A}\,^1B_1$ electronic states of SiH_2, we follow the approach described in refs. 25 and 26.

© 2004 NRC Canada

Table 5. Term values[h](in cm^{-1}) for the $\tilde{A}\,^1B_1$ state of SiH_2.

(v_1, v_2, v_3)	$J_{K_aK_c}$	Observed[b]	O–C/MCI[c]	O–C/fitted[d]	Reference[e]	(v_1, v_2, v_3)	$J_{K_aK_c}$	Observed[b]	O–C/MCI[c]	O–C/fitted[d]	Reference[e]
(0, 0, 0)	0_{00}	15 547.773	−1.304	−3.584	(7)	(0, 4, 0)	1_{10}	18 960.9	−72.5	−3.9	(18)
(0, 1, 0)	0_{00}	16 404.3	1.4	9.1	(18)	(0, 0, 0)	2_{11}	15 589.42	−1.76	−3.87	(7)
(0, 2, 0)	0_{00}	17 248.2	−17.7	2.9	(18)	(0, 1, 0)	2_{11}	16 447.8	−0.3	7.8	(18)
(0, 3, 0)	0_{00}	18 096.9	−33.1	1.9	(18)	(0, 2, 0)	2_{11}	17 297.5	−5.0	3.7	(18)
(0, 4, 0)	0_{00}	18 934.9	−55.6	−5.3	(18)	(0, 3, 0)	2_{11}	18 155.3	6.2	7.2	(18)
(0, 5, 0)	0_{00}	19 776	−69	−3	(18)	(0, 4, 0)	2_{11}	18 997.3	−55.0	−5.0	(18)
(0, 6, 0)	0_{00}	20 618.79	−77.24	4.06	(15)	(0, 5, 0)	2_{11}	19 852.1	−51.5	−4.0	(18)
(0, 7, 0)	0_{00}	21 467.89	−80.16	15.35	(15)	(0, 0, 0)	2_{21}	15 629.19	−3.61	−5.15	(7)
(0, 8, 0)	0_{00}	22 313	−97	26	(6)	(0, 1, 0)	2_{21}	16 492.1	−12.6	3.3	(18)
(1, 2, 0)	1_{10}	19 203.23	−49.91	−2.19	(8)	(0, 2, 0)	2_{21}	17 357.7	1.0	6.0	(18)
(1, 3, 0)	1_{10}	20 036.37	−64.49	2.56	(8)	(0, 3, 0)	2_{21}	18 227.2	−40.3	7.6	(18)
(1, 4, 0)	1_{10}	20 867.83	−76.54	9.85	(8)	(0, 4, 0)	2_{21}	19 097	−45	9	(18)
(1, 5, 0)	1_{10}	21 699.46	−82.51	23.26	(8)	(0, 0, 0)	2_{02}	15 573.7	−1.2	−3.4	(7)
(0, 0, 0)	1_{01}	15 556.44	−1.25	−3.53	(7)	(0, 0, 0)	2_{20}	15 629.26	−3.61	−5.15	(7)
(0, 1, 0)	1_{01}	16 412.4	0.8	8.6	(18)	(0, 1, 0)	2_{02}	16 428.7	−0.0	7.7	(18)
(0, 2, 0)	1_{01}	17 256.8	−17.7	2.9	(18)	(0, 1, 0)	2_{20}	16 492.3	−4.1	3.4	(18)
(0, 3, 0)	1_{01}	18 106.8	−31.8	3.2	(18)	(0, 2, 0)	2_{02}	17 274	−18	3	(18)
(0, 4, 0)	1_{01}	18 943.8	−55.3	−5.0	(18)	(0, 2, 0)	2_{20}	17 357.4	5.6	4.9	(18)
(0, 5, 0)	1_{01}	19 784.7	−69.2	−3.3	(18)	(0, 3, 0)	2_{02}	18 129.1	−26.8	8.4	(18)
(0, 6, 0)	1_{01}	20 629.6	−75.0	6.3	(18)	(0, 3, 0)	2_{20}	18 227.5	−40.0	10.8	(18)
(0, 0, 0)	1_{11}	15 569.83	−1.93	−3.96	(7)	(0, 4, 0)	2_{02}	18 960.9	−55.4	−5.0	(18)
(0, 1, 0)	1_{11}	16 429.6	1.1	9.2	(18)	(0, 4, 0)	2_{20}	19 096.9	−49.4	−7.6	(18)
(0, 2, 0)	1_{11}	17 277.6	−11.8	3.5	(18)	(0, 5, 0)	2_{02}	19 801.9	−69.7	−3.1	(18)
(0, 3, 0)	1_{11}	18 133.2	−3.3	4.4	(18)	(0, 6, 0)	2_{02}	20 644.7	−77.3	4.4	(18)
(0, 4, 0)	1_{11}	18 973.7	−62.9	3.3	(18)	(0, 0, 0)	2_{12}	15 586.03	−1.87	−3.91	(7)
(0, 5, 0)	1_{11}	19 832.7	−56.2	−7.6	(18)	(0, 1, 0)	2_{12}	16 443.2	−1.5	6.8	(18)
(0, 6, 0)	1_{11}	20 682.2	−52.7	7.7	(18)	(0, 2, 0)	2_{12}	17 293.9	−16.6	3.7	(18)
(0, 0, 0)	1_{10}	15 570.96	−1.89	−3.98	(7)	(0, 3, 0)	2_{12}	18 151.2	−14.0	5.4	(18)
(0, 1, 0)	1_{10}	16 430	0	8	(18)	(0, 4, 0)	2_{12}	18 992.5	−67.2	−2.5	(18)
(0, 2, 0)	1_{10}	17 278.1	−17.1	2.8	(18)	(0, 5, 0)	2_{12}	19 842.6	−73.0	−6.1	(18)
(0, 3, 0)	1_{10}	18 133.2	2.9	3.7	(18)	(0, 6, 0)	2_{12}	20 700.9	−63.9	0.5	(18)

[a]Term values are measured relative to the $(v_1, v_2, v_3)\,J_{K_aK_c} = (0, 0, 0)\,0_{00}$level of the $\tilde{X}\,^1A_1$ electronic state.
[b]Experimentally derived term values.
[c]Residuals (observed–calculated) obtained using the MCI ab initio parameters from Table 1.
[d]Residuals (observed–calculated) obtained using the fitted parameters from Table 1.
[e]Reference for the experimentally derived ("Observed") term value.

The rotational and vibrational motions in the two interacting Renner states are described in terms of a reference configuration with constant internuclear distances. This reference configuration is common for both electronic states and displacements due to stretching vibration are measured relative to it. As is customary (see (25–27)), since the two electronic surfaces are degenerate at linear configurations, we choose the bond lengths of the reference configuration to be those that minimize the electronic energy at linearity.

The Born–Oppenheimer potential energy function for the $\tilde{X}\,^1A_1$ electronic state is denoted by $V_-(\Delta r_{12}^{(\mathrm{ref})}, \Delta r_{32}^{(\mathrm{ref})}, \bar{\rho})$, and that for the $\tilde{A}\,^1B_1$ state is denoted $V_+(\Delta r_{12}^{(\mathrm{ref})}, \Delta r_{32}^{(\mathrm{ref})}, \bar{\rho})$, with

$$[1]\qquad V_{\pm}(\Delta r_{12}^{(\mathrm{ref})}, \Delta r_{32}^{(\mathrm{ref})}, \bar{\rho}) = V_{\mathrm{ref}} + V_0^{(\pm)}(\bar{\rho}) + \sum_j F_j^{(\pm)} y_j^{(\mathrm{ref})} + \sum_{j\le k} F_{jk}^{(\pm)} y_j^{(\mathrm{ref})} y_k^{(\mathrm{ref})} + \sum_{j\le k\le m} F_{jkm}^{(\pm)} y_j^{(\mathrm{ref})} y_k^{(\mathrm{ref})} y_m^{(\mathrm{ref})} + \sum_{j\le k\le m\le n} F_{jkmn}^{(\pm)} y_j^{(\mathrm{ref})} y_k^{(\mathrm{ref})} y_m^{(\mathrm{ref})} y_n^{(\mathrm{ref})} + \ldots$$

© 2004 NRC Canada

Table 6. Transition wavenumbers and band origins (in cm^{-1}) of the $\tilde{A} \rightarrow \tilde{X}$ transitions of SiD_2.

(v_1'', v_2'', v_3'')	(v_1', v_2', v_3')	Observed	O–C[c]
(0,0,0)	(0,0,0)	15 539.875[a]	−4.402
(0,1,0)	(0,0,0)	16 158.427[a]	1.735
(0,2,0)	(0,0,0)	16 774.440[a]	1.034
(0,3,0)	(0,0,0)	17 385[b]	−1
(0,4,0)	(0,0,0)	17 996[b]	−6
(0,5,0)	(0,0,0)	18 603[b]	−11
(0,6,0)	(0,0,0)	19 201[b]	−21
(0,7,0)	(0,0,0)	19 803[b]	−20
(0,8,0)	(0,0,0)	20 401[b]	−16
(0,9,0)	(0,0,0)	20 998[b]	−10
(0,10,0)	(0,0,0)	21 599[b]	−1
(0,1,0)	(0,1,0)	15 435.428[a]	−0.945
(0,2,0)	(0,2,0)	15 338.309[a]	1.006

[a]Experimentally derived band origins from ref. 14.
[b]Experimental transition wavenumbers for the rovibronic transitions $J_{K_a K_c} = 0_{00}(\tilde{A}) \rightarrow 1_{10}(\tilde{X})$ from ref. 13.
[c]Residuals (observed–calculated) obtained using the fitted parameters from Table 1.

where j, k, m, and n = 1 or 3. $V_-(\Delta r_{12}^{(\mathrm{ref})}, \Delta r_{32}^{(\mathrm{ref})}, \bar{\rho})$ and $V_+(\Delta r_{12}^{(\mathrm{ref})}, \Delta r_{32}^{(\mathrm{ref})}, \bar{\rho})$ depend on the stretching displacements

$$[2] \qquad \Delta r_{j2}^{(\mathrm{ref})} = r_{j2} - r_{j2}^{(\mathrm{ref})}$$

where r_{j2} is the instantaneous value of the distance between the proton labeled j (= 1 or 3) and the Si nucleus (labeled 2), and $r_{j2}^{(\mathrm{ref})}$ is the reference value of this quantity. As mentioned above, the $r_{j2}^{(\mathrm{ref})}$ are taken as the optimum bond lengths at linearity. In eq. [1],

$$[3] \qquad y_j^{(\mathrm{ref})} = 1 - \exp\left(-a\Delta r_{j2}^{(\mathrm{ref})}\right)$$

and $\bar{\rho} = \pi - \angle(\mathrm{HSiH})$, where $\angle(\mathrm{HSiH})$ is the instantaneous value of the bond angle. The functions $V_0^{\pm}(\bar{\rho})$ and $F_{jk\ldots}^{\pm}(\bar{\rho})$ are expressed as cosine series:

$$[4] \qquad V_0^{\pm}(\bar{\rho}) = \sum_{i=1}^{8} f_0^{(i,\pm)}(1 - \cos\bar{\rho})^i$$

and

$$[5] \qquad F_{jk\ldots}^{\pm}(\bar{\rho}) = f_{jk\ldots}^{(0)} + \sum_{i=1}^{N} f_{jk\ldots}^{(i,\pm)}(1 - \cos\bar{\rho})^i$$

where $f_0^{(i,\pm)}$, $f_{jk\ldots}^{(0)}$ and $f_{jk\ldots}^{(i,\pm)}$ are expansion coefficients. In eq. [5], the expression for $F_j^{\pm}(\bar{\rho})$ has $N = 4$, that for $F_{jk}^{\pm}(\bar{\rho})$ has $N = 3$, $F_{jkl}^{\pm}(\bar{\rho})$ has $N = 2$, and $F_{jklm}^{\pm}(\bar{\rho})$ has $N = 1$. Since the expansion coefficients $f_{jk\ldots}^{(0)}$ are chosen to be common for both electronic states, the potentials given by eq. [1] are degenerate for linear configurations; the term V_{ref} in eq. [1] is the energy for $\bar{\rho} = 0$, and $r_{12} = r_{32} = r_{12}^{(\mathrm{ref})}$, and it is also common for the two potential surfaces.

We describe the molecular dipole moment in terms of its components along three axes xqp (taken to form a right-handed axis system with origin in the nuclear center of mass) that are attached directly to the instantaneous nuclear configuration of the molecule (see Fig. 1 of ref. 28). For SiH_2, the q axis bisects the bond angle $\angle(\mathrm{HSiH})$ and is directed so that the q coordinates of the H nuclei 1 and 3 are positive. The p axis is perpendicular to the q axis and its direction is such that the p coordinate of nucleus 3 is positive, and the x axis is perpendicular to the molecular plane.

The expressions for the intensities of individual rovibronic transitions within the two Renner-degenerate electronic states are given in ref. 29. These intensities depend on electronic dipole moment and transition moment surfaces. We denote the electronic wavefunction for the $\tilde{X}\,^1A_1$ state as $\psi_{\mathrm{elec}}^{(-)}$, and that for the $\tilde{A}\,^1B_1$ state as $\psi_{\mathrm{elec}}^{(+)}$. In this notation we obtain the following non vanishing dipole and transition moments:

$$[6] \qquad \bar{\mu}_p^{(\sigma)}(\Delta r_{12}^{(\mathrm{ref})}, \Delta r_{32}^{(\mathrm{ref})}, \bar{\rho}) = \langle\psi_{\mathrm{elec}}^{(\sigma)}|\mu_p|\psi_{\mathrm{elec}}^{(\sigma)}\rangle_{\mathrm{el}}$$

$$[7] \qquad \bar{\mu}_q^{(\sigma)}(\Delta r_{12}^{(\mathrm{ref})}, \Delta r_{32}^{(\mathrm{ref})}, \bar{\rho}) = \langle\psi_{\mathrm{elec}}^{(\sigma)}|\mu_q|\psi_{\mathrm{elec}}^{(\sigma)}\rangle_{\mathrm{el}}$$

where, in eqs. [6] and [7], $\sigma = -$ or $+$, and

$$[8] \qquad \bar{\mu}_x^{(-+)}(\Delta r_{12}^{(\mathrm{ref})}, \Delta r_{32}^{(\mathrm{ref})}, \bar{\rho}) = \langle\psi_{\mathrm{elec}}^{(-)}|\mu_x|\psi_{\mathrm{elec}}^{(+)}\rangle_{\mathrm{el}}$$

where, in eqs. [6]–[8], the subscript "el" indicates that integration is over the electronic coordinates only.

The functions $\bar{\mu}_p^{(\sigma)}$ and $\bar{\mu}_q^{(\sigma)}$ are represented as (see ref. 28)

$$[9] \qquad \bar{\mu}_p^{(\sigma)}(\Delta r_{12}^{(\mathrm{ref})}, \Delta r_{32}^{(\mathrm{ref})}, \bar{\rho}) = \mu_0^{(p;\sigma)}(\bar{\rho}) + \sum_j \mu_j^{(p;\sigma)}(\bar{\rho})\Delta r_{j2}^{(\mathrm{ref})} + \sum_{j\le k} \mu_{jk}^{(p;\sigma)}(\bar{\rho})\Delta r_{j2}^{(\mathrm{ref})}\Delta r_{k2}^{(\mathrm{ref})} + \sum_{j\le k\le m} \mu_{jkm}^{(p;\sigma)}(\bar{\rho})\Delta r_{j2}^{(\mathrm{ref})}\Delta r_{k2}^{(\mathrm{ref})}\Delta r_{m2}^{(\mathrm{ref})} + \sum_{j\le k\le m\le n} \mu_{jkmn}^{(p;\sigma)}(\bar{\rho})\Delta r_{j2}^{(\mathrm{ref})}\Delta r_{k2}^{(\mathrm{ref})}\Delta r_{m2}^{(\mathrm{ref})}\Delta r_{n2}^{(\mathrm{ref})}$$

© 2004 NRC Canada

and

$$[10]\quad \bar{\mu}_q^{(\sigma)}(\Delta r_{12}^{(\mathrm{ref})}, \Delta r_{32}^{(\mathrm{ref})}, \bar{\rho}) = \sin\bar{\rho}\Bigg[\mu_0^{(q;\sigma)}(\bar{\rho}) + \sum_j \mu_j^{(q;\sigma)}(\bar{\rho})\Delta r_{j2}^{(\mathrm{ref})} + \sum_{j\le k} \mu_{jk}^{(q;\sigma)}(\bar{\rho})\Delta r_{j2}^{(\mathrm{ref})}\Delta r_{k2}^{(\mathrm{ref})} + \sum_{j\le k\le m} \mu_{jkm}^{(q;\sigma)}(\bar{\rho})\Delta r_{j2}^{(\mathrm{ref})}\Delta r_{k2}^{(\mathrm{ref})}\Delta r_{m2}^{(\mathrm{ref})} + \sum_{j\le k\le m\le n} \mu_{jkmn}^{(q;\sigma)}(\bar{\rho})\Delta r_{j2}^{(\mathrm{ref})}\Delta r_{k2}^{(\mathrm{ref})}\Delta r_{m2}^{(\mathrm{ref})}\Delta r_{n2}^{(\mathrm{ref})}\Bigg]$$

with $j, k, m, n = 1$ or 3. The angle-dependent coefficients are given by

$$[11]\quad \mu_{jk\ldots}^{(w;\sigma)}(\bar{\rho}) = \sum_{i=0}^{N} w_{jk\ldots}^{(i;\sigma)}(1-\cos\bar{\rho})^i$$

with $w = p$ or q. The function $\mu_0^{(w;\sigma)}(\bar{\rho})$ has $N = 8$, $\mu_j^{(w;\sigma)}(\bar{\rho})$ has $N = 4$, $\mu_{jk}^{(w;\sigma)}(\bar{\rho})$ has $N = 3$, $\mu_{jkm}^{(w;\sigma)}(\bar{\rho})$ has $N = 2$ and $\mu_{jkmn}^{(w;\sigma)}(\bar{\rho})$ has $N = 1$.

The function $\bar{\mu}_x^{(-+)}$ is parameterized as

$$[12]\quad \bar{\mu}_x^{(-+)}(\Delta r_{12}^{(\mathrm{ref})}, \Delta r_{32}^{(\mathrm{ref})}, \bar{\rho}) = \sin\bar{\rho}\Bigg[\mu_0^{(x;-+)}(\bar{\rho}) + \sum_j \mu_j^{(x;-+)}(\bar{\rho})\Delta r_{j2}^{(\mathrm{ref})} + \sum_{j\le k} \mu_{jk}^{(x;-+)}(\bar{\rho})\Delta r_{j2}^{(\mathrm{ref})}\Delta r_{k2}^{(\mathrm{ref})} + \sum_{j\le k\le m} \mu_{jkm}^{(x;-+)}(\bar{\rho})\Delta r_{j2}^{(\mathrm{ref})}\Delta r_{k2}^{(\mathrm{ref})}\Delta r_{m2}^{(\mathrm{ref})} + \sum_{j\le k\le m\le n} \mu_{jkmn}^{(x;-+)}(\bar{\rho})\Delta r_{j2}^{(\mathrm{ref})}\Delta r_{k2}^{(\mathrm{ref})}\Delta r_{m2}^{(\mathrm{ref})}\Delta r_{n2}^{(\mathrm{ref})}\Bigg]$$

with

$$[13]\quad \mu_{jk\ldots}^{(x;-+)}(\bar{\rho}) = \sum_{i=0}^{N} x_{jk\ldots}^{(i;-+)}(1-\cos\bar{\rho})^i$$

where the number of summation terms N is given exactly as for eq. [11].

For SiH_2, relations exist between the expansion coefficients in eqs. [11] and [13], so that the functions $\bar{\mu}_q^{(\sigma)}$ and $\bar{\mu}_x^{(-+)}$ are unchanged under the interchange of the two protons, whereas the function $\bar{\mu}_p^{(\sigma)}$ is antisymmetric under this operation.

4. Fitting to the ab initio points

The analytical expression for the potential energy function defined in eqs. [1]–[5] contains as adjustable parameters the coefficients $f_0^{(i,\pm)}$ in eq. [4], and $f_{jk\ldots}^{(0)}$ and $f_{jk\ldots}^{(i,\pm)}$ in eq. [5], and the parameters a in eq. [3] and V_{ref} in eq. [1]. We aim to determine values of these parameters in fittings to the MCI ab initio points. Since we define the reference bond length $r_{j2}^{(\mathrm{ref})}$ to be equal to the optimum bond length at linearity, this parameter can also be adjusted in the fittings.

Attempts to determine the parameter a in the fittings led to divergence of the least-squares-fitting procedure and so we had to constrain it. It was constrained to the value $a = 1.58$ Å^{-1} determined by fitting to the ab initio energies of the points with $r_{32} = r_{12}$ and $\bar{\rho} = 90°$ (close to the equilibrium value of $\bar{\rho}$ in the $\tilde{X}\,^1A_1$ electronic state). The energies in these points depend only on r_{12} and we fitted a Morse potential

$$[14]\quad V_{\mathrm{Morse}}(r_{12}) = V_{\mathrm{e}} + f_{11}^{(0)}\left[1 - e^{-a\Delta r_{12}^{(\mathrm{ref})}}\right]^2$$

through them, thus determining the value of a.

We carried out initial fittings to the ab initio points and used the resulting parameter values as input for the program RENNER (25, 26, 29), which calculates rovibronic energies and intensities for Renner-degenerate electronic states of triatomic molecules. This calculation produced values of the lowest $\tilde{A}\,^1B_1$ $(0, v_2, 0)$ energies that were consistently about 150 cm^{-1} higher than their respective experimental counterparts. This type of effect is often encountered in ab initio calculations of rovibronic energies associated with Renner-degenerate electronic states; it simply indicates that the $\tilde{A}$-state potential energy surface lies too high by 150 cm^{-1} relative to the $\tilde{X}$-state surfaces. To improve the agreement with experiment of the the rovibronic energies calculated from the ab initio results, we subtracted 150 cm^{-1} from all the $\tilde{A}$-state ab initio energies, and fitted the analytical expression for the potential energy function defined in eqs. [1]–[4] through these corrected $\tilde{A}$-state ab initio points and through the $\tilde{X}$-state points. The two analytical surfaces obtained in this fitting have barriers to linearity approximately 150 cm^{-1} lower than obtained in the initial fitting. In the final fitting, we used 250 ab initio points as input and we could usefully vary 34 potential parameters. The standard deviation was 20 cm. The optimized parameter values and their

© 2004 NRC Canada

Table 7. The composition (in percentage points[a]) of the rotational level $J_{K_aK_c} = 1_{10}$, in the polyad states with $P = 10$ of $\tilde{X}\,^1A_1$ SiH_2, in terms of vibrational basis functions (v_1, v_2, v_3).

$i = (v_1, v_2, v_3)$	0	1	2	3	4	5	6	7	8	9	10	11
(5,0,0)								6.8			1.5	85.8
(3,0,2)			2.4	31.2				54.0				6.5
(1,0,4)			3.2	56.1				34.8				1.1
(4,2,0)					1.2	4.4	4.4			1.7	63.0	
(2,2,2)		6.5	9.7		3.6	18.3	28.5			1.7	12.2	
(0,2,4)		14.4	39.6	8.4	14.2	8.2	1.1					
(3,4,0)		5.2			7.7		1.5		3.2	45.9		
(1,4,2)	1.5	13.7			9.9		23.6		17.4	6.7		
(2,6,0)	6.4	5.6	4.5			8.9	1.6		19.1	12.6		
(0,6,2)	5.5	4.5	8.9		35.7	20.0						
(1,8,0)	21.9					4.4	7.5		21.9	4.4		
(0,10,0)	20.3	15.9	10.7		1.7	7.7	9.7		7.8	1.1		
$\sum^b$	55.7	65.8	79.1	95.6	73.9	71.8	77.9	95.6	69.4	74.2	76.7	93.4

[a]Contributions that are less than 1% are omitted.
[b]Sum of percentage contributions for each state i within the polyad.

Table 8. The polyad composition (in percentage points[a]) of the rotational level $J_{K_aK_c} = 1_{10}$ in the polyad states with $P = 10$ of $\tilde{X}\,^1A_1$ SiH_2.

$i = P$	0	1	2	3	4	5	6	7	8	9	10	11
8									4.4	3.4		
9	18.0	12.1	3.0		7.1	6.4	3.8		5.4	4.3	8.6	2.6
10	55.7	65.8	79.1	95.6	73.9	71.8	77.9	95.6	69.4	74.2	76.7	93.4
11	5.4	2.3	3.1		2.9	1.8			1.7	2.3	4.6	1.7
12	9.1	4.1	2.5		3.5	5.1	6.0		9.3	7.2	3.8	
13	3.4										1.5	

[a]Contributions that are less than 1% are omitted.

standard errors are given in Table 1 under the heading "MCI ab initio".

The MCI ab initio fitted analytical potential functions (with the barrier to linearity lowered by 150 cm^{-1} as discussed above) are such that the equilibrium geometry (r_e, α_e) is (1.518 Å, 92.4°) for the $\tilde{X}$ state and (1.487 Å, 122.9°) for the $\tilde{A}$ state. The barrier heights at linearity in these functions are 22 139.2 and 6612.8 cm^{-1}, respectively, for the $\tilde{X}$ and $\tilde{A}$ states, so that $T_e(\tilde{A}) = 15\,526.4\ cm^{-1}$.

For the dipole moment and transition moment surfaces we obtain values for the $p^{(i;\sigma)}_{jk...}$, $q^{(i;\sigma)}_{jk...}$, and $x^{(i;-+)}_{jk...}$ parameters by fitting eqs. [9]–[13] through the ab initio dipole moment values. The results of the fittings (parameter values, standard errors, and the standard deviations of the fittings) are given in Table 2.

From the ab initio calculation we determine that the dipole moment for the $\tilde{X}$ state at its equilibrium configuration is 0.14 D, and for the $\tilde{A}$ state at its equilibrium configuration it is 0.01 D. The $\tilde{A} - \tilde{X}$ transition moment at the equilibrium geometry of the $\tilde{X}$ state is calculated to be 1.21 D.

5. Rovibronic energy calculations

In the RENNER calculations, the eigenvalues for the rovibronic Hamiltonian $\hat{H}_{Renner}$ were obtained by diagonalization of the matrix representation of $\hat{H}_{Renner}$ in the basis set $|v_2^{(\eta)}, K\rangle$ $|N_{vib}^{(\eta)}, \Gamma_{vib}^{(\eta)}\rangle$ $|\eta; NJSKM_J\tau\rangle$ defined in ref. 25. We used the 27 lowest bending basis functions $|v_2^{(\eta)}, K\rangle$ for both electronic states for every K block (where $K \leq J$). The $\tilde{X}\,^1A_1$ electronic state basis set included the $N_A = 20$ lowest stretching functions $|N_{vib}^{(\eta)}, A_1\rangle$ of A_1 symmetry and the $N_B = 15$ lowest stretching functions $|N_{vib}^{(\eta)}, B_2\rangle$ of of B_2 symmetry. For the $\tilde{A}\,^1B_1$ state we used $N_A = 15$ and $N_B = 10$ stretching functions. These stretching functions were constructed from Morse oscillator functions $|n_1\rangle$ $|n_3\rangle$ with $n_1 + n_3 \leq N_{stretch} = 17$.

Rovibronic energies calculated with the RENNER program from the ab initio parameters in Table 1 are compared with experimental values for SiH_2 in Tables 3–5 under the heading "O–C/MCI". In Table 3, the comparison is made for $J \leq 2$ term values for vibrational states in the $\tilde{X}\,^1A_1$ electronic state. In Table 4, the comparison is made for the extensive set of $\tilde{X}\,^1A_1$ term values (which all have $J_{K_aK_c} = 1_{10}$) obtained experimentally in the recent stimulated emission pumping study by Ishikawa et al. (15). The energies in Table 4 are labeled by the polyad quantum number

$$P = 2v_1 + v_2 + 2v_3.$$

Since, for $\tilde{X}\,^1A_1$ SiH_2, the three harmonic vibrational wavenumbers ω_1, ω_2, and ω_3 approximately satisfy the relation $\omega_1 =$

© 2004 NRC Canada

Table 9. Predicted term values T_{calc} (in cm^{-1}) for the rotational level $J_{K_aK_c} = 1_{10}$ in the polyad states with $P = 11$ and 12 of $\tilde{X}\,^1A_1$ SiH_2.

P	(v_1, v_2, v_3)	T_{calc}	P	(v_1, v_2, v_3)	T_{calc}
11	(5, 1, 0)	10 181.37	12	(6, 0, 0)	10 923.17
	(4, 3, 0)	10 307.98		(5, 2, 0)	11 067.05
	(3, 5, 0)	10 399.74		(4, 4, 0)	11 202.28
	(1, 5, 2)	10 439.36		(4, 0, 2)	11 273.94
	(3, 1, 2)	10 464.93		(3, 6, 0)	11 295.62
	(2, 3, 2)	10 515.08		(1, 6, 2)	11 341.27
	(0, 7, 2)	10 536.76		(3, 2, 2)	11 360.91
	(0, 7, 2)	10 564.67		(2, 4, 2)	11 414.06
	(1, 1, 4)	10 591.10		(0, 4, 4)	11 446.39
	(0, 3, 4)	10 611.07		(2, 0, 4)	11 474.45
	(0,11, 0)	10 661.68		(0, 8, 2)	11 477.20
	(1, 9, 0)	10 762.55		(1, 2, 4)	11 492.85
				(0, 4, 4)	11 525.16
				(0, 0, 6)	11 560.37
				(0,12, 0)	11 592.15
				(1,10, 0)	11 704.90

Table 10. Term values (in cm^{-1}) with K_a=J for $\tilde{A}\,^1B_1$ SiH_2.

(v_1, v_2, v_3)	$J_{K_aK_c}$	Observed[a]	O–C[b]
(0, 1, 0)	3_{31}	16 596.8	1.08
(0, 2, 0)	3_{31}	17 480.3	0.28
(0, 3, 0)	3_{31}	18 368.2	0.58
(0, 4, 0)	3_{31}	19 261.5	−6.43
(0, 1, 0)	4_{41}	16 739.3	−1.87
(0, 2, 0)	4_{41}	17 638.9	4.63
(0, 3, 0)	4_{41}	18 547.7	−5.08
(0, 4, 0)	4_{41}	19 462.3	−12.98
(0, 1, 0)	5_{51}	16 913.7	−6.38
(0, 2, 0)	5_{51}	17 832.1	−8.44
(0, 3, 0)	5_{51}	18 760.6	−8.31
(0, 4, 0)	5_{51}	19 697.9	0.37

[a]From ref. 15.
[b]Observed–calculated obtained using the fitted parameters from Table 1.

$2\omega_2 = \omega_3$, vibrational states with a common value of P will be close in energy and form polyads labeled by $P = 0, 1, 2, 3, \ldots$. Within each polyad the energies in Table 4 are labeled by the running number index i as in ref. 15. In Table 5, we make the comparison for $J \leq 2$ term values in the $\tilde{A}\,^1B_1$ state.

The energies calculated using RENNER with the ab initio parameters in Table 1 reproduce the experimental energies for SiH_2 in Tables 3–5 with a root-mean-square deviation of 41.7 cm^{-1}. It is noticeable that while the agreement between theory and experiment is fairly good for low-lying states, there are substantial deviations for the highly excited states, in particular for the $\tilde{X}\,^1A_1$ -levels characterized experimentally by Ishikawa et al. (15) in stimulated emission pumping experiments. To analyze theoretically these highly excited states and, hopefully, explain the intensities of the emission spectra observed by Ishikawa et al. (15), we have refined the potential energy surfaces of $\tilde{X}\,^1A_1$ and $\tilde{A}\,^1B_1$ SiH_2 in a least-squares fitting to the available low-J experimental data. This refinement is the subject of the following section.

Table 11. Term values (in cm^{-1}) for the rotational level $J_{K_aK_c} = 1_{10}$ in the polyad states with $P = 10$ of $\tilde{X}\,^1A_1$ SiH_2.

Observed (15)	i	Calculated term value[a]	i	Alternative term value[b]
9800.78	0	9813.29	0	9807.74
9739.40	1	9726.26	1	9731.52
9700.60	2	9692.99	2	9708.08
9675.08	3	9682.72	3	9673.94
9644.74	4	9646.22	4	9657.43
9616.21	5	9619.07	5	9621.92
9596.81	6	9607.24	6	9592.11
	7	9562.02	7	9551.47
9526.81	8	9530.14	8	9527.37
9491.65	9	9495.75	9	9494.86
	10	9406.03		
9306.07[c]	11	9289.53	10	9308.14
			11	9132.95

[a]Obtained using the fitted potentials with the parameters from Table 1.
[b]The result using the alternative potentials (see text).
[c]This would be assigned as $i = 11$ using our fitted potentials, but as $i = 10$ using the alternative potentials.

6. Refinement of the potentials

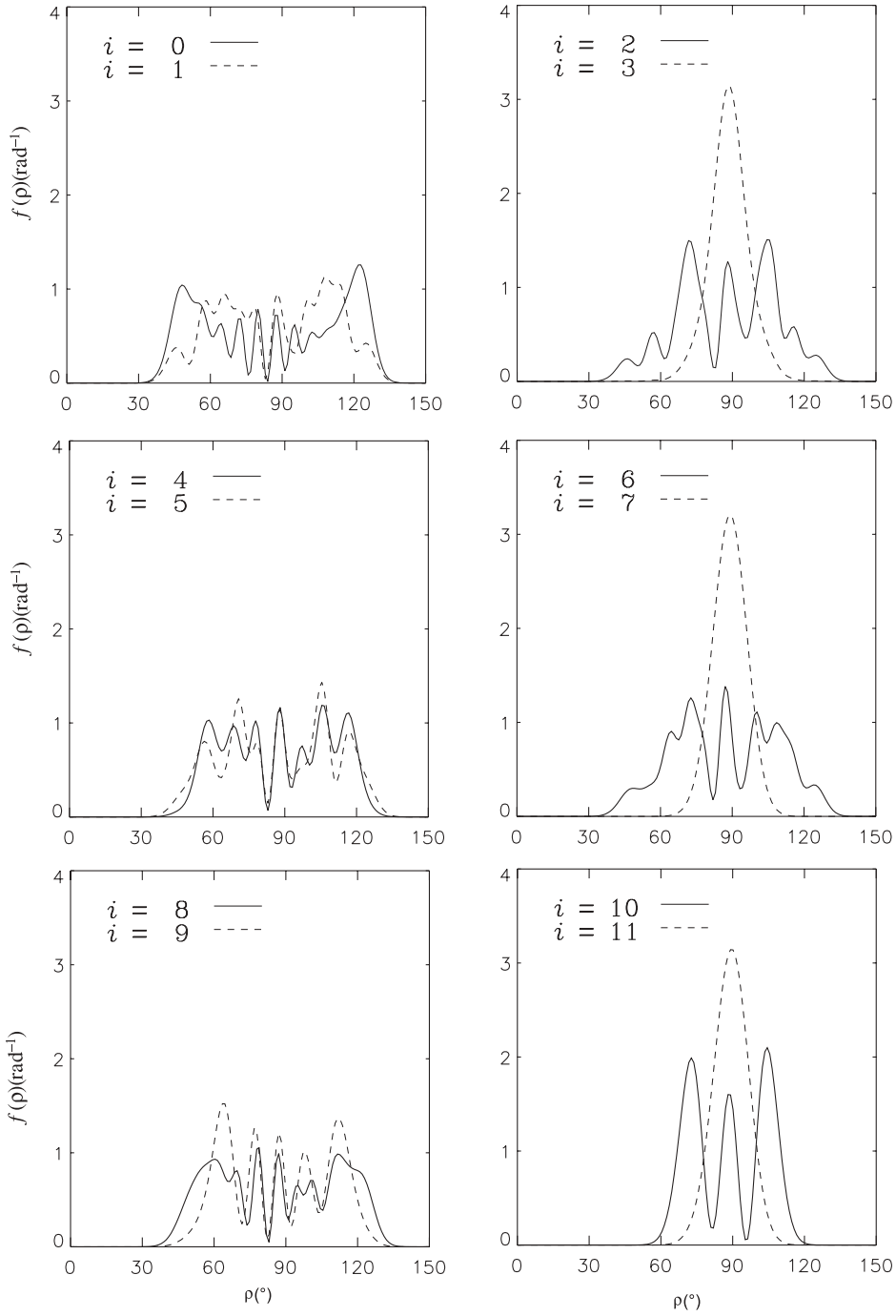
The adjustment of potential energy parameters in a fitting to experimental data can sometimes lead to an unrealistically shaped potential energy surface (PES). To constrain the shape of the PES during the fitting process we performed a simultaneous fitting of the potential parameters both to the observed data and to ab initio energies. By introducing the ab initio energies as input data for the fitting, we can constrain the fitted potential energy surface to be close to the initial ab initio one. This approach has been discussed in detail in ref. 30 and we give a brief outline here.

The ab initio parameters from Table 1 were first used to generate a grid of ab initio energy points that we used in the simultaneous fitting procedure. Some of these points involved extrapolation outside the region of the ab initio calculation and they were given low weight. In the simultaneous fitting procedure we must decide on a particular value for the ratio of the weights used for the experimental data (W_i^{exp}) to that used for the ab initio points (W_i^{points}), and in this work the weight for the data was taken to be 5.5 times larger than that on the ab initio points.

In the refinement we first fitted to levels with $J \leq 1$ for SiH_2 (excluding the levels from the 10th polyad (15) in the $\tilde{X}$ state). We added levels with $J = 2$, and levels for SiD_2 (see Table 6) as we achieved reasonable agreement with the experimental data. Finally, the energy levels of the $P = 10$ polyad were included; the vibrational assignments of these levels were very sensitive

© 2004 NRC Canada

Fig. 1. Probability distributions $f(\rho)$ for the rotational level $J_{K_aK_c} = 1_{10}$ in the polyad states with $P = 10$ of $\tilde{X}\,^1A_1$ SiH_2. The energies of these states are given in Table 11.



to any parameter change. The resultant parameters are listed in column three of Table 1, and the residuals "O–C/fitted" are given in Tables 3–6. The vibronic assignment of each state is that state which has the largest eigenvector coefficient from the output of the RENNER program. These assignments are of help in understanding the polyad structure of the vibrational levels in the ground electronic state. For example, one can learn from Table 4 that for the ground electronic state the highest level in every Pth polyad is the level $(v_1, v_2, v_3) = (1, P - 2, 0)$ for $P > 5$. In Table 7, we show the percentages of each (v_1,v_2,v_3) state that occurs in each of the $P = 10$ polyad states, and in Table 8, we show the percentages of neighboring polyads basis functions that are mixed into the $P = 10$ polyad states.

In Table 9 we give the predicted term values for the $J_{K_aK_c} = 1_{10}$ levels of the polyads having $P = 11$ and 12, and in Table 10 we compare calculated and observed $\tilde{A}$-state levels hav-

© 2004 NRC Canada

Fig. 2. Probability distributions $f(\rho)$ for the the rotational level $J_{K_aK_c} = 0_{00}$ in the $7\nu_2$ state of $\tilde{A}\,^1B_1$ SiH_2.

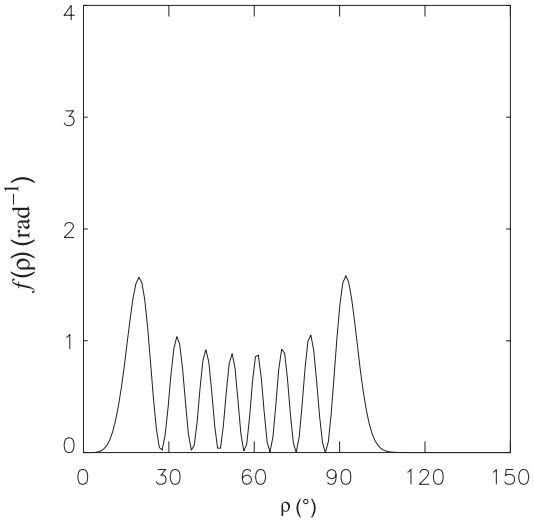


Fig. 3. Probability distributions $f(\rho)$ for the rotational level $J_{K_aK_c} = 0_{00}$ in the (*a*) ν_1 and (*b*) $2\nu_2$ states of $\tilde{X}\,^1A_1$ SiH_2.

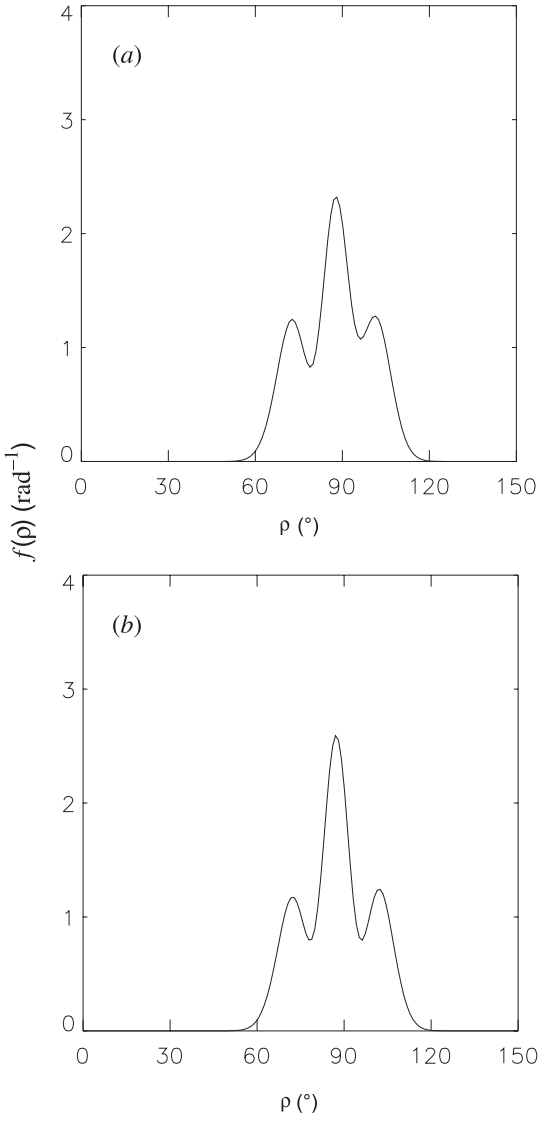


Fig. 4. The upper emission spectrum is the observed $P = 10$ spectrum (15) (see footnote 3), and the lower stick spectrum is the simulation using our fitted potentials and ab initio dipole moment and transition moment surfaces. The doublet in the observed spectrum at around 9645 cm^{-1} results from the presence of a triplet state perturber that we do not include in our simulation.

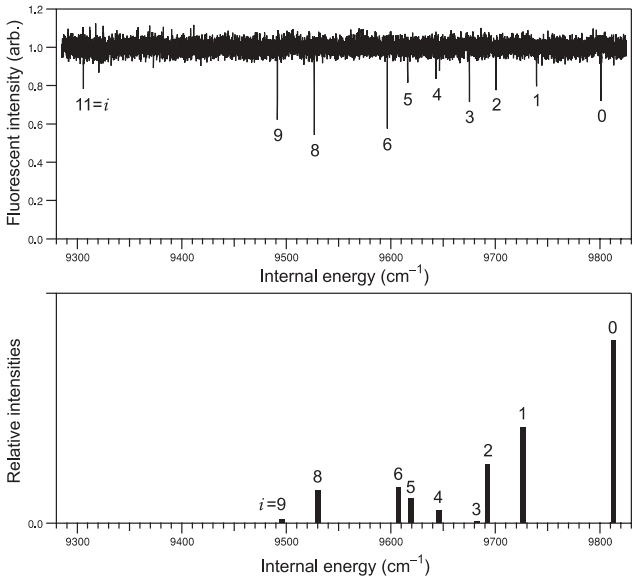
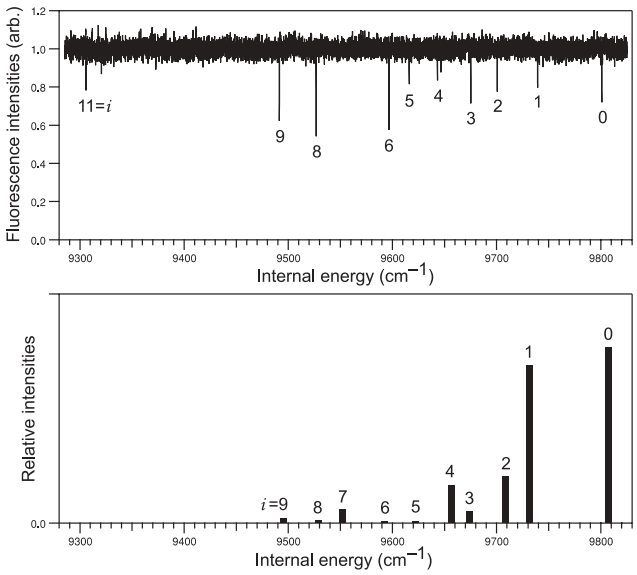


Fig. 5. The upper emission spectrum is the observed $P = 10$ spectrum (15) (see footnote 3), and the lower stick spectrum is the simulation using our alternative potentials (see text) with the ab initio dipole moment and transition moment surfaces. The reproduction of the intensities is worse than that in Fig. 4 and this leads us to discard the alternative potentials.



ing higher values of J and K_a. This latter comparison is a check that our calculation treats the Renner effect appropriately in higher angular momentum states.

The observed data, for $J = 0$, 1, and 2, are reproduced with a root-mean-square error of 5.8 cm^{-1} for the $\tilde{X}\,^1A_1$ state and

© 2004 NRC Canada

7.3 cm^{-1} for the $\tilde{A}\,^1B_1$ state. The energies of the ab initio points are reproduced with root-mean-square error of 30.0 cm^{-1} for the $\tilde{X}\,^1A_1$ state and 42.0 cm^{-1} for the $\tilde{A}\,^1B_1$ state.

The fitted potentials are such that the equilibrium geometry (r_e, α_e) is (1.518 Å, 92.4°) for the $\tilde{X}$ state and (1.486 Å, 123.0°) for the $\tilde{A}$ state. The barrier heights at linearity are obtained from the fitted potentials as 21 882.4 and 6340.6 cm^{-1}, respectively, for the $\tilde{X}$ and $\tilde{A}$ states, so that $T_e(\tilde{A})$ = 15 541.8 cm^{-1}.

7. Rovibronic wavefunctions and probability density functions

An eigenfunction obtained from the rovibronic RENNER calculation is given as a superposition of basis functions, and we can write it as

$$[15]\quad \psi_{\text{evr-ns}}^{(i,J,M_J,S,\Gamma_{\text{evr}};\tau)} = \Phi_{\text{ns}} \sum_{\eta=a,b} \sum_{N=|J-S|}^{J+S} \sum_{K=0}^{N} \sum_{v_2^{(\eta)},N_{\text{vib}}^{(\eta)},\Gamma_{\text{vib}}^{(\eta)}} c_{\eta,N,K,v_2^{(\eta)},N_{\text{vib}}^{(\eta)},\Gamma_{\text{vib}}^{(\eta)}}^{(i,J,M_J,S,\Gamma_{\text{evr}},\tau)} \times \Phi_{v_2^{(\eta)},K}(\rho)\, \Phi_{N_{\text{vib}}^{(\eta)},\Gamma_{\text{vib}}^{(\eta)}}(r_{12},r_{32})\, |\eta; NJSKM_J\tau\rangle$$

where the $c_{\eta,N,K,v_2^{(\eta)},N_{\text{vib}}^{(\eta)},\Gamma_{\text{vib}}^{(\eta)}}^{(i,J,M_J,S,\Gamma_{\text{evr}},\tau)}$ are expansion coefficients, and the functions $\Phi_{v_2^{(\eta)},K}(\rho)$ (called $|v_2^{(\eta)},K\rangle$ in ref. 25) and $\Phi_{N_{\text{vib}}^{(\eta)},\Gamma_{\text{vib}}^{(\eta)}}(r_{12},r_{32})$ (called $|N_{\text{vib}}^{(\eta)},\Gamma_{\text{vib}}^{(\eta)}\rangle$ in ref. 25) are basis functions describing the bending and stretching motions, respectively. $\Phi_{v_2^{(\eta)},K}(\rho)$ depends on the bending coordinate ρ which is almost, but not quite, equal to $\bar{\rho}$. The rigid-bender functions $\Phi_{v_2^{(\eta)},K}(\rho)$, and Morse oscillator stretching functions $\Phi_{N_{\text{vib}}^{(\eta)},\Gamma_{\text{vib}}^{(\eta)}}(r_{12},r_{32})$, are defined in ref. 25; $v_2^{(\eta)}$ is the bending quantum number appropriate for a bent molecule (See section 13.4.1 and eqs. [13]–[177] of ref. 1). $\Gamma_{\text{vib}}^{(\eta)}$ is the irreducible representation spanned by the function $\Phi_{N_{\text{vib}}^{(\eta)},\Gamma_{\text{vib}}^{(\eta)}}$ in the molecular symmetry group of the molecule and, $N_{\text{vib}}^{(\eta)}$ = 1, 2, 3, … numbers the functions with a given $\Gamma_{\text{vib}}^{(\eta)}$ in order of ascending energy. For SiH_2, the molecular symmetry group is C_{2v}(M) (1) and $\Gamma_{\text{vib}}^{(\eta)} = A_1$ or B_2. The basis functions $|\eta; NJSKM_J\tau\rangle$ describe the motion of the electrons, the electron spin, and the rotational motion (where $K = K_a$). These functions are given as

$$[16]\quad |a; NJSKM_J\tau\rangle = \cos\left[\gamma_K(\rho)\right] \Phi_{\text{elec}}^{(-)}\, |NJSKM_J\delta_{0\,\tau}\rangle + \sin\left[\gamma_K(\rho)\right]\, i\, \Phi_{\text{elec}}^{(+)}\, |NJSKM_J\tau\rangle$$

$$[17]\quad |b; NJSKM_J\tau\rangle = \cos\left[\gamma_K(\rho)\right]\, i\, \Phi_{\text{elec}}^{(+)}\, |NJSKM_J\tau\rangle - \sin\left[\gamma_K(\rho)\right] \Phi_{\text{elec}}^{(-)}\, |NJSKM_J\delta_{0\,\tau}\rangle$$

where $\Phi_{\text{elec}}^{(-)}$ is the electronic wavefunction for the lower Renner component $\tilde{X}\,^1A_1$, and $\Phi_{\text{elec}}^{(+)}$ is the electronic wavefunction for the upper component $\tilde{A}\,^1B_1$. In eqs. [16] and [17], $\delta_{0\,\tau}$ is a Kronecker Delta with $\delta_{00} = 1$ and $\delta_{01} = 0$. The angle $\gamma_K(\rho)$ determines, in a first approximation, the Renner interaction between these two electronic states. It is discussed in detail in section 15.4.2 of ref. 31. The rotation-spin basis functions $|NJSKM_J\tau\rangle$ (see refs. 25, 31) are symmetrized, simultaneous eigenfunctions of $\widehat{\mathbf{N}}^2$ [with eigenvalue $\hbar^2N(N+1)$], $\widehat{\mathbf{J}}^2$ [with eigenvalue $\hbar^2J(J+1)$], $\widehat{\mathbf{S}}^2$ [with eigenvalue $\hbar^2S(S+1)$], and $\widehat{J}_Z$, the component of $\mathbf{J}$ along the space-fixed quantization axis Z [with eigenvalue $\hbar M_J$] (see refs. 25, 31). Here, $\widehat{\mathbf{N}}$ is the total angular momentum of the molecule excluding spin, $\widehat{\mathbf{S}}$ is the electron spin, and $\widehat{\mathbf{J}} = \widehat{\mathbf{N}} + \widehat{\mathbf{S}}$. We assume that no electronic state other than the $\tilde{X}\,^1A_1$ – $\tilde{A}\,^1B_1$ pair of states contributes significantly to $\psi_{\text{evr-ns}}^{(i,J,M_J,S,\Gamma_{\text{evr}};\tau)}$. As indicated in eq. [15], the internal wavefunctions are labeled by the good quantum numbers J, M_J, S, and by Γ_{evr}, the irreducible representation spanned by $\psi_{\text{evr-ns}}^{(i,J,M_J,S,\Gamma_{\text{evr}};\tau)}$ in the molecular symmetry group C_{2v}(M) (1). The running index i numbers states with the same values of the good quantum numbers. This i is not to be confused with the i in Table 4. The parity of $\psi_{\text{evr-ns}}^{(i,J,M_J,S,\Gamma_{\text{evr}};\tau)}$ is $(-1)^\tau$, and $\tau = 0$ or 1. Φ_{ns} is an appropriate nuclear spin function.

The rovibronic wavefunctions given in eq. [15] are mathematically complicated, but they contain all accessible information about each rovibronic state. To obtain insight into the nature of the eigenfunctions, we have previously introduced and calculated the overall bending probability density function $f(\rho)$ of the states (32, 33). The quantity $\mathrm{d}p = f(\rho)\,\mathrm{d}\rho$ is the differential probability of finding the molecule with its bending angle between ρ and $\rho + \mathrm{d}\rho$. For the ith state $\psi_{\text{evr-ns}}^{(i,J,M_J,S,\Gamma_{\text{evr}};\tau)}$, having energy E_i, the normalized probability density function for the bending angle $f_i(\rho)$ is given by

$$[18]\quad f_i(\rho) = \int_0^\infty \mathrm{d}r_{12} \int_0^\infty \mathrm{d}r_{32} \int_{\text{rot,e,es,ns}} \mathrm{d}V\, |\psi_{\text{evr-ns}}^{(i,J,M_J,S,\Gamma_{\text{evr}};\tau)}|^2 = \sum_{\eta=a,b} \sum_{N=|J-S|}^{J+S} \sum_{K=0}^{N} \sum_{v_2^{(\eta)},v_2^{(\eta)\prime},N_{\text{vib}}^{(\eta)},\Gamma_{\text{vib}}^{(\eta)}} \left(c_{\eta,N,K,v_2^{(\eta)},N_{\text{vib}}^{(\eta)},\Gamma_{\text{vib}}^{(\eta)}}^{(i,J,M_J,S,\Gamma_{\text{evr}},\tau)}\right)^* \times c_{\eta,N,K,v_2^{(\eta)\prime},N_{\text{vib}}^{(\eta)},\Gamma_{\text{vib}}^{(\eta)}}^{(i,J,M_J,S,\Gamma_{\text{evr}},\tau)} \left(\Phi_{v_2^{(\eta)},K}(\rho)\right)^* \Phi_{v_2^{(\eta)\prime},K}(\rho)$$

© 2004 NRC Canada

where dV is the volume element associated with integration over the coordinates describing rotation, electronic orbital motion, electron spin, and nuclear spin.

In Fig. 1 we plot the bending probability distributions $f(\rho)$ for the the rotational level $J_{K_aK_c} = 1_{10}$ of the 12 members of the $P = 10$ polyad of the $\tilde{X}\,^1A_1$ state. In the following we shall be discussing emission transitions to these levels from the $J_{K_aK_c} = 0_{00}$ rotational level of the $7\nu_2$ state of $\tilde{A}\,^1B_1$ SiH_2; we plot the probability distribution of this level in Fig. 2.

A problem for $\tilde{X}\,^1A_1$ SiH_2 has been the assignment of the ν_1 and $2\nu_2$ states; these two states are in a strong Fermi resonance. The two $J = 0$ states of A_1 symmetry are observed at 1978.153 and 2005.469 cm^{-1}, respectively (12). Whereas Ishikawa and Kajimoto (10) initially assigned the highest level as $2\nu_2$ and the lowest level as ν_1, Hirota and Ishikawa (12) reversed these assignments. The wavefunction for the state at lower wavenumber has a 51.5% contribution from the $2\nu_2$ basis state and a 47.8% contribution from the ν_1 basis state. The state at higher wavenumber has a 51.7% contribution from ν_1 and a 46.7% contribution from $2\nu_2$. Consequently, as in ref. 12, we assign the lower state as $2\nu_2$ and the upper one as ν_1. The heavy mixing between the two states is also apparent in the probability distributions given in Fig. 3.

8. Simulation of spectra

To simulate spectra we use line positions obtained by calculating appropriate energy level differences, and intensities obtained from line strengths that are calculated from the square of the transition moment matrix elements involving the wavefunctions and ab initio transition moment surfaces given in eqs. [9]–[13]. The details of such a calculation are given in ref. 29. In Fig. 4 we show the result of simulating the emission spectrum from the 0_{00} rotational level of the $\tilde{A}$ (0,7,0) vibronic state to the 1_{10} levels of the $P = 10$ polyad of the $\tilde{X}$ state. For comparison we also show in this figure the observed spectrum from ref. 15[3] The relative intensities are extraordinarily sensitive to small changes in the potential energy functions and the agreement with experiment is not perfect; we underestimate the intensity of the transitions to the $i = 3$, 9, and 11 components. However, the weakness of the $i = 7$ and 10 components is correctly accounted for. The intensity distributions in our simulations of the emission spectra involving the other polyads are in broad agreement with the results in ref. 15, and all lines that could not be found experimentally are calculated as having low intensity relative to the observed lines. The strong transitions are generally those to states with high excitation of the bending mode. In such states, we get the highest vibronic transition moments with the initial state ($\tilde{A}\,^1B_1$ (0,7,0)), whose bending angle probability distribution is given in Fig. 2.

Initially in our fitting there seemed to be an interesting ambiguity in the assignment of the lowest two members ($i = 10$ and 11) of the polyad $P = 10$. In ref. 15 a level at 9306.07 cm^{-1} is observed and it is assigned as the $i = 11$ component of the $P = 10$ polyad; no level is assigned as the $i = 10$ component. Using the ab initio potential energy surfaces we find (see under the column headed "MCI Calc" in Table 4) that the $i = 10$ and 11 components of the $P = 10$ polyad are calculated at 9326.83 and 9151.24 cm^{-1}. Just looking at this result one would assign the 9306.07 observed term value as the $i = 10$ level rather than as the $i = 11$ level. However, the (obs–calc) deviations are large and negative for the lowest components of each polyad, and the assignment of the 9306.07 cm^{-1} level as $i = 11$, as done in ref. 15, is not unreasonable. Using this assignment we made the fitting to obtain the fitted potentials quoted here, and the simulation given in Fig. 4. We did try another fitting done just as above but with the single change of assigning the level at 9306.07 cm^{-1} as $i = 10$ in $P = 10$; the result for the $P = 10$ polyad is given in the column headed "Alternative" in Table 11, and the simulated $P = 10$ emission spectrum obtained using the alternative parameters is compared with the experimental spectrum[3] in Fig. 5. The relative intensities in the calculated spectrum using the alternative parameters are in very poor agreement with experiment, so although the fitting to the term values with the assignment of the 9306.07 cm^{-1} term value as $i = 10$ does not lead to unreasonable calculated term values it does lead to unreasonable calculated intensities. However, it is quite remarkable and alarming to us that with so much vibrational data there is still enough flexibility that it is possible to adjust the potential in a way that allows an alternative fitting to the same term value data but with a single level reassigned to have a substantial shift of about 100 cm^{-1}. We await with interest the results of further experiments to find more vibrational term values for singlet silylene.

[3] Reprinted from H. Ishikawa, Y. Muramoto, and N. Mikami. J. Mol. Spectrosc. **216**, 90 (2002). Copyright (2002) with permission from Elsevier.

Acknowledgments

We are very grateful to Professor Haruki Ishikawa for communicating his results to us before publication, and for some helpful correspondence. This work was initiated and supported under the auspices of a collaborative agreement between the National Research Council of Canada (NRC) and the National Science Council of Taiwan. The work of PJ was supported by the Deutsche Forschungsgemeinschaft and the Fonds der Chemischen Industrie. PJ is grateful to the Steacie Institute for Molecular Sciences for their hospitality.

References

1. P.R. Bunker and P. Jensen. Molecular symmetry and spectroscopy. 2nd ed. NRC Research Press, Ottawa, Ontario, Canada. 1998. See http://www.nrc.ca/cgi-bin/cisti/journals/rp/rp2_book_e?mlist1_90
2. P. Jensen and P.R. Bunker (*Editors*). Computational molecular spectroscopy. Wiley, Chichester, UK. 2000. See http://www.chem.uni-wuppertal.de/cms/
3. I. Dubois, G. Herzberg, and R.D. Verma. J. Chem. Phys. **47**, 4262 (1967).
4. I. Dubois. Can. J. Phys. **46**, 2485 (1968).
5. I. Dubois, G. Duxbury, and R.N. Dixon. J. Chem. Soc. Faraday Trans. 2, **71**, 799 (1975).
6. J.S. Francisco, R. Barnes, and J.W. Thoman. J. Chem. Phys. **88**, 2334 (1988).
7. R. Escribano and A. Campargue. J. Chem. Phys. **108**, 6249 (1998).
8. H. Ishikawa and O. Kajimoto. J. Mol. Spectrosc. **160**, 1 (1993).

© 2004 NRC Canada

9. C. Yamada, H. Kanamori, and E. Hirota. J. Chem. Phys. **91**, 4582 (1989).
10. H. Ishikawa and O. Kajimoto. J. Mol. Spectrosc. **150**, 610 (1991).
11. H. Ishikawa and O. Kajimoto. J. Mol. Spectrosc. **174**, 270 (1995).
12. E. Hirota and H. Ishikawa. J. Chem. Phys. **110**, 4254 (1999).
13. M. Fukushima, S. Mayama, and K. Obi. J. Chem. Phys. **96**, 44 (1992).
14. M. Fukushima and K. Obi. J. Chem. Phys. **100**, 6221 (1994)
15. H. Ishikawa, Y. Muramoto, and N. Mikami. J. Mol. Spectrosc. **216**, 90 (2002).
16. W. Gabriel, P. Rosmus, K. Yamashita, K. Morokuma, and P. Palmieri. Chem. Phys. **174**, 45 (1993).
17. W. Meyer. J. Chem. Phys. **58**, 1017 (1973).
18. G. Duxbury, A. Alijah, and R.R. Trieling. J. Chem. Phys. **98**, 811 (1993).
19. K. Andersson, M. Barysz, A. Bernhardsson, M.R.A. Blomberg, Y. Carissan, D.L. Cooper, T. Fleig, M.P. Fülscher, L. Gagliardi, C. de Graaf, B.A. Hess, G. Karlström, R. Lindh, P.-Å. Malmqvist, T. Nakajima, P. Neogrády, J. Olsen, B.O. Roos, B. Schimmelpfennig, M. Schütz, L. Seijo, L. Serrano-Andrés, P.E.M. Siegbahn, J. Stalring, T. Thorsteinsson, V. Veryazow, M. Wierzbowska, and P.-O. Widmark. MOLCAS. Version 5.2 [computer program]. Lund University, Sweden. 2001.
20. W.D. Allen and H.F. Schaefer. Chem. Phys. **108**, 243 (1986).
21. C.W. Bauschlicher, S.R. Langhoff, and P.R. Taylor. J. Chem. Phys. **87**, 387 (1987).
22. J. Berkowitz, J.P. Greene, H. Cho, and B. Ruščić, J. Chem. Phys. **86**, 1235 (1987).
23. J.W. Thoman, J.I. Steinfeld, R.I. McKay, and A.E.W. Knight. J. Chem. Phys. **86**, 5909 (1987).
24. P.-Å. Malmqvist and B.O. Roos. Chem. Phys. Lett. **155**, 189 (1989).
25. P. Jensen, M. Brumm, W.P. Kraemer, and P.R. Bunker. J. Mol. Spectrosc. **171**, 31 (1995).
26. M. Kolbuszewski, P.R. Bunker, W.P. Kraemer, G. Osmann, and P. Jensen, Mol. Phys. **88**, 105 (1996).
27. W.P. Kraemer, P. Jensen, and P.R. Bunker. Can. J. Phys. **72**, 871 (1994).
28. P. Jensen. J. Mol. Spectrosc. **132**, 429 (1988).
29. G. Osmann, P.R. Bunker, P. Jensen, and W.P. Kraemer. Chem. Phys. **225**, 33 (1997).
30. S.N. Yurchenko, M. Carvajal, P. Jensen, F. Herregodts, and T.R. Huet. Chem. Phys. **290**, 59 (2003).
31. P. Jensen, G. Osmann, and P.R. Bunker. *In* Computational molecular spectroscopy. *Edited by* P. Jensen and P.R. Bunker. Wiley, Chichester, UK. 2000.
32. G. Osmann, P.R. Bunker, W.P. Kraemer, and P. Jensen. Chem. Phys. Letters **309**, 299 (1999).
33. G. Osmann, P.R. Bunker, W.P. Kraemer, and P. Jensen. Chem. Phys. Lett. **318**, 597 (2000).

© 2004 NRC Canada

Collisions and reactions of ultracold molecules[1]

William C. Stwalley

Abstract: It is argued that collision dynamics of atoms and molecules at ultracold temperatures (below 1 mK) are not readily predictable from knowledge of collision dynamics above 100 K. In the case of elastic collisions, it is well known that the collision cross section is constant as $T \rightarrow 0$ K but mass and symmetry effects are dramatic. The cases of inelastic and reactive collisions are less studied, but a $T^{-1/2}$ dependence of the cross section as $T \rightarrow 0$ K is expected. It seems that extrapolations of high-temperature inelastic and reactive behavior normally greatly underestimate ultracold-temperature rates. The prospects for experimental observation of ultracold collision dynamics are rapidly improving.

Key words: ultracold molecules, collisions, reactions, hydrogen, scattering length.

Résumé : Dans cet article, on avance que la dynamique des collisions d'atomes et des molécules à des températures ultrafroides (en dessous de 1 mK) ne peut pas être prédite sur la base de nos connaissances de la dynamique des collisions à des températures supérieures à 100 K. Dans le cas des collisions élastiques, il est bien connu que la section droite de collision est constante lorsque la température tend vers 0 K, toutefois les effets de masse et de symétrie sont dramatiques. Les cas des collisions inélastiques ou réactives ont moins bien été étudiées, mais il est prévu que la section droite adoptera un comportement $T^{-1/2}$ lorsque la température tendra vers 0 K. Il semble que, d'une manière générale, les extrapolations du comportement inélastique ou réactif à température élevée sous-estiment grandement les vitesses à des températures ultrafroides. Les possibilités de pouvoir observer directement la dynamique de collisions à des températures ultrafroides augmentent rapidement.

Mots clés : molécules ultrafroides, collisions, réactions, hydrogène, longueur de diffusion.

[Traduit par la Rédaction]

Introduction

The study of chemical reactions and elastic and inelastic nonreactive collisions at ultracold (<1 mK) temperatures is a frontier in chemistry where many surprising results are expected. These collisions are sensitive to the details of atomic and molecular interactions such as small potential energy barriers (including centrifugal), fine and hyperfine structure, Stark shifts, and Zeeman shifts. They are highly quantum-mechanical, exhibiting large effects from resonances, tunneling, and identical particles. They are highly constrained by the precisely known energetics and by angular momentum barriers. Techniques for study of cold reactions include matrix isolation spectroscopy (since the 1950s), van der Waals photochemistry, low-temperature ion–molecule reactions, and, most recently, reactions in/on liquid helium (bulk or clusters) (1). A number of two-body and three-body ion–molecule reactions have been studied in the 0.3–1 K temperature range (2), but we are not aware of any neutral gas-phase reactions studied below 1 K and especially below 1 mK. However, ultracold photoassociation (PA) (the absorption of a photon by a colliding pair of atoms to produce an electronically excited molecule) has been studied extensively (3).

It is my contention here that ultracold (<1 mK) collision cross sections are basically independent of normal thermal ($\sim 10^2$–10^3 K) collision cross sections. This is true for elastic, inelastic, and reactive collisions. Moreover, the low-temperature cross sections, unlike those at normal thermal temperatures, depend strongly on the reduced mass of the collisions.

Elastic collisions

It is well known that two-body elastic collisions (as well as two-body bound states) are governed by the radial Schrödinger equation (RSE), here written in "reduced" form:

$$[1] \qquad \left[-\eta \frac{d^2}{dr^{*2}} + V^*(r^*)\right]\Psi(r^*) = E^*\Psi(r^*)$$

where $r^* = r/\sigma$ is the dimensionless reduced interatomic distance, $V^* = V/\varepsilon$ is the dimensionless reduced potential energy, $E^* = E/\varepsilon$ is the dimensionless reduced total energy, σ is the "hard sphere radius" where $V^*(\sigma) = 0$, ε is the potential-well depth, and $\eta = \hbar^2/2\mu\varepsilon\sigma^2$, where μ is the reduced mass (4).

Received 5 January 2004. Published on the NRC Research Press Web site at http://canjchem.nrc.ca on 4 June 2004.

W.C. Stwalley. Department of Physics, Unit-3046, University of Connecticut, Storrs, CT 06269–3046, USA. (e-mail: w.stwalley@uconn.edu).

[1]This article is part of a Special Issue dedicated to the memory of Professor Gerhard Herzberg.

 doi: 10.1139/V04-035 © 2004 NRC Canada

Table 1. Total elastic collision cross sections at 0 K for spin-polarized isotopic hydrogen atoms (5) and for isotopic helium atoms (4).

Species	a (a_0)	Q (a_0^2)
H + H	1.335	44.8[a]
H + D	–0.448	2.52
H + T	–1.597	32.0
D + D	6.907	0[b]
D + T	–15.53	3 031
T + T	–81.55	167 100[a]
^{3}He + ^{3}He	–13.19	0[b]
^{3}He + ^{4}He	–31.82	12 720
^{4}He + ^{4}He	231.0	1 341 000[a]

[a]Assuming identical boson spin states.
[b]Assuming identical fermion spin states (no s-wave scattering).

Of particular significance for this work is the solution of the RSE for small positive energy (ultracold temperatures below 1 mK). In particular as $T \rightarrow 0$ K, only "head-on" s-wave ($\ell = 0$) collisions penetrate to short "chemical" distances, all ($\ell \geq 1$) collisions being repelled by centrifugal barriers (3). The s-wave collisions are described by the s-wave phase shift δ_0, which in turn is conventionally related to the scattering length a and the effective range r_0 by the equation

$$[2] \qquad k \cot \delta_0 = -\frac{1}{a} + \frac{1}{2} r_0 k^2 + 0(k^4)$$

where $\hbar k$ is the momentum and the kinetic energy of collision $E_k = \hbar^2 k^2 / 2\mu$.

For two distinguishable particles, the low-temperature limit of the elastic scattering cross section Q is given by

$$[3] \qquad \lim_{T \rightarrow 0} Q^D = 4\pi a^2$$

For two indistinguishable bosons, this limit is

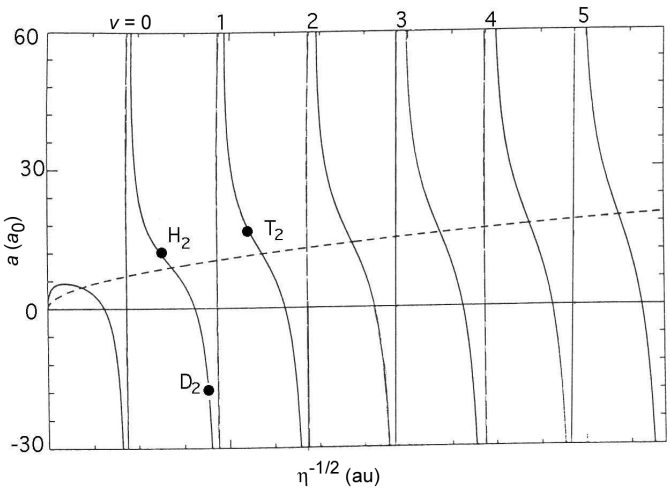
$$[4] \qquad \lim_{T \rightarrow 0} Q^{IB} = 8\pi a^2$$

while for two indistinguishable fermions, this limit is

$$[5] \qquad \lim_{T \rightarrow 0} Q^{IF} = 0$$

In this last case, "head-on" s-wave collisions are forbidden by symmetry and the p-wave collisions are suppressed by the $\ell = 1$ centrifugal barrier. Examples of scattering lengths and cross sections for nine light and weakly interacting systems are given in Table 1. Note the wide variation among systems that would have similar collision cross sections at room temperature. For two of the systems, the cross section is zero by symmetry (eq. [5]), but the cross sections of the others vary by 6 orders of magnitude! The largest is that for ^{4}He + ^{4}He, as this is the only case where there is a (barely) bound vibrational level ($v = 0$, $J = 0$) in the potential well. The cross section for the T + T case is also large (but the scattering length is opposite in sign) because there is not yet a bound level (a reduced mass of 1.62 amu (vs. 1.50 amu for T_2) would just give a bound level and an extremely large a approaching infinity). Remember that in the first six cases and in the last three cases in Table 1, the interactions are virtually identical; only the mass and symmetry are changing, but these have major dramatic effects.

Fig. 1. The scattering length for collisions of isotopic hydrogen molecules (all $J = 0$) based on spectroscopic experiments, collision experiments, and scattering calculations using ab initio potential surfaces (see text), plotted versus $\eta^{-1/2} = (2\mu\varepsilon\sigma^2/\hbar^2)^{1/2}$. Adapted from the work of Gribakin and Flambaum (13).



In general, molecule–molecule scattering lengths are unknown and hard to determine. We point out here an exception: the isotopic H_2 molecules ($v = 0$, $J = 0$). In particular, there is a variety of impressive experiments and calculations relating to the H_2–H_2 system. Early work by Watanabe and Welch on the $(H_2)_2$ van der Waals molecule (6) and by Bauer et al. on para-H_2 – para-H_2 scattering at low energies (7) highly constrained the molecule–molecule interaction. An excellent but now somewhat old review was published by Silvera (8). More recently, precise spectra of the $(H_2)_2$, $(HD)_2$, and $(D_2)_2$ van der Waals molecules were obtained by McKellar and others (see, e.g., refs. 9 and 10). Simultaneously, Schaefer and co-workers refined theoretical calculations of the interactions, cross sections, and bound states (see e.g., refs. 10–12). In particular, ref. 11 shows a low-energy limiting elastic H_2–H_2 cross section of ~3210 a_0^2, corresponding to a scattering length of +11.3 a_0 (which must be positive since it implies a value by simple mass scaling of –17 a_0 for D_2–D_2, consistent with the observation that the $(D_2)_2$ dimer has only a $v = 0$ level, and a value of +17 a_0 for T_2–T_2) as shown in Fig. 1. Thus, purely by accident, Q^{IB} for D_2–D_2 collisions and Q^{IB} for T_2–T_2 collisions are nearly identical as $T \rightarrow 0$ K (7800 a_0^2). Note that these limiting cross sections, as well as those in Table 1, can be much larger or much smaller (even zero) than room temperature cross sections.

Inelastic collisions

Wigner's work on threshold laws for excitation by collision (14) in combination with microscopic reversibility implies that de-excitation collision cross sections become infinite as the collision energy approaches zero (15). In particular, the inelastic nonreactive atom–molecule collisions of ^{4}He + I_2 ($v = 0$, $J = 0$) (15) and H + H_2 ($v = 0$, $J = 0$), ^{3}He + H_2 ($v = 0$, $J = 0$), and ^{4}He + H_2 ($v = 0$, $J = 0$) (16, 17) have

© 2004 NRC Canada

been studied theoretically down to $<10^{-3}$ K, where Wigner threshold law behavior is expected and found; the inelastic cross section increases as $T^{-1/2}$ as $T \rightarrow 0$ K, giving a constant relaxation rate at microKelvin temperatures and below. It is important to realize how erroneous any sort of extrapolation of results obtained for >100 K would be. For example, for vibrational relaxation of H_2 ($v = 1$, $J = 0$) by ^{3}He (17), the room temperature rate and the low-temperature ($T = 10^{-3}$ K) Wigner law rate are nearly identical ($\sim 3 \times 10^{-17}$ cm^3 molecule^{-1} s^{-1}). However, rough extrapolation of the 100–300 K results yields a ridiculously low rate of 10^{-29} cm^3 molecule^{-1} s^{-1} at 10^{-2} K and 10^{-40} cm^3 molecule^{-1} s^{-1} at 10^{-6} K, an error of >20 orders of magnitude!

Similar results are expected for other inelastic processes, for example, electronic and nuclear spin-flip collisions (18). One complication in the above picture, which can be written in terms of a complex scattering length (16), is the presence of resonances (15). If shape or Feshbach resonances occur in the $T < 10^{-3}$ K regime, where Wigner behavior is normally expected, the cross section will not show a simple $T^{-1/2}$ dependence. This becomes more of a problem as the masses of the atoms involved become heavier and the likelihood of sub-milliKelvin resonances becomes greater.

An interesting prediction was made many years ago that the rate of vibrational de-excitation might drop dramatically for the highest vibrational levels near dissociation (18). This is because the last level will have a very small average kinetic energy and the atoms will spend most of their time at much larger internuclear distances than in the next highest level; at room temperature, this would mean collision-induced dissociation would dominate over de-excitation. However, at the microKelvin temperatures, collision-induced dissociation is no longer possible, so such levels may be remarkably stable. This may be related to the exciting new announcements of Bose–Einstein condensation of "Cooper paired" molecules of $^6Li_2$ (19) and $^{40}K_2$ (20) in their last bound vibrational level.

Reactive collisions

It is useful to distinguish between reactions that are exoergic (e.g., $D + H_2 \rightarrow HD + H$) and those that are thermoneutral (e.g., $H + H_2 \rightarrow H_2 + H$), where the atoms and molecules are in their lowest energy states. In the former case, as for inelastic collisions (and for the same reason (14, 15)), the cross section increases like $T^{-1/2}$ as $T \rightarrow 0$, and the rate becomes constant. The latter case is not of practical importance here since it would not be "reaction" for truly indistinguishable particles. Since the isotopic variants of the $H + H_2$ reaction at thermal energies and above are well known and in excellent agreement with theory (21), it is appropriate to ask about them at ultracold temperatures (22). Rather surprisingly, careful calculations using variational transition-state theory with a transmission coefficient for tunneling (22) show a $T^{-1/2}$ dependence of the rate (T^{-1} dependence of the cross section) as $T \rightarrow 0$ K, in contrast to the expected constant rate and $T^{-1/2}$ dependence of the cross section. However, more recent close-coupling calculations by Simbotin and Côté show the predicted threshold behavior of constant rate and $T^{-1/2}$ dependence of the cross section (I. Simbotin and R. Côté, private communication, 2004). The tunneling transmission coefficients of ref. 22 do give far larger and far more reasonable rates at low temperatures than any simple extrapolation of the high-temperature results (21), but they do not give the correct Wigner behavior. Perhaps multiple traversals of the tunneling region could be contributing.

Again, the uppermost long-range molecular levels were discussed long ago (23), using the notation M_2^∞ to indicate that the radial extension was quite large (albeit not ∞). Such molecules, it was speculated, might selectively react

[6] $$A_2^\infty + B \rightarrow A + AB^\infty$$

even though the A_2 and AB bond strengths are different. Even more likely to be selective would be isotopic reactions, such as the one given in ref. 23:

[7] $$^6Li_2^\infty + {}^7Li \rightarrow {}^6Li^7Li^\infty + {}^6Li$$

The remarkable stability that the $^6Li_2$ and $^{40}K_2$ molecule Bose–Einstein condensates mentioned in the previous section show may be related in part to the above speculation.

Summary

We have argued that collisional behavior at very low "ultracold" temperatures (below 10^{-3} K), which are now becoming accessible experimentally, is dramatically different from that at room temperature. Elastic collision cross sections can be larger or smaller, depending more on the mass and symmetry than on the interaction. Inelastic and reactive collision rates are usually larger, often far larger, than any rates estimated from results obtained at $T > 100$ K. Thus, study of ultracold atomic and molecular collisions should be a rich and surprising field to study.

Acknowledgements

The beautiful low-temperature, rotationally limited spectra of molecular hydrogen obtained by Gerhard Herzberg (24) and his colleagues inspired my long-term interest in H_2 and its more laser-friendly analogues, the alkali-metal dimers. Their work also inspired my interest in detailed comparisons of experiment and theory, especially in diatomic molecules near dissociation where long-range interactions play a dominant role. The entire field of photoassociative spectroscopy of ultracold atoms (3) was in several ways brilliantly foreshadowed by the work of Herzberg and his colleagues (24).

Support of the National Science Foundation is gratefully acknowledged, as are helpful discussions with D. Truhlar, G. Scoles, A.R.W. McKellar, A. Dalgarno, R. Côté, and I. Simbotin.

References

1. J.T. Bahns, P.L. Gould, and W.C. Stwalley. Adv. At. Mol. Opt. Phys. **42**, 171 (2000).
2. M.A. Smith. *In* Unimolecular and bimolecular ion–molecule reaction dynamics. *Edited by* C.Y. Ng, T. Baier, and I. Powis. Wiley, New York. 1994. p. 183.
3. W.C. Stwalley and H. Wang. J. Mol. Spectrosc. **195**, 194 (1999).
4. Y.H. Uang and W.C. Stwalley. J. Chem. Phys. **76**, 5069 (1982).

© 2004 NRC Canada

5. Y.H. Uang and W.C. Stwalley. J. Phys. C, **41**, 7–33 (1980).
6. A. Watanabe and H.L. Welch. Phys. Rev. Lett. **13**, 810 (1964).
7. W. Bauer, B. Lantzsch, J.P. Toennies, and K. Walaschewski. Chem. Phys. **17**, 19 (1976).
8. I.F. Silvera. Rev. Mod. Phys. **52**, 393 (1980).
9. A.R.W. McKellar. J. Chem. Phys. **92**, 3261 (1990).
10. A.R.W. McKellar and J. Schaefer. J. Chem. Phys. **95**, 3081 (1991).
11. J. Schaefer and W. Meyer. J. Chem. Phys. **70**, 344 (1979).
12. J. Schaefer. Astron. Astrophys. **284**, 1015 (1994)
13. G.F. Gribakin and V.V. Flambaum. Phys. Rev. A, **48**, 546 (1993).
14. E.P. Wigner. Phys. Rev. **73**, 1002 (1948).
15. D.W. Schwenke and D.G. Truhlar. J. Chem. Phys. **83**, 3454 (1985).
16. N. Balakhrishnan, V. Kharchenko, R.C. Forrey, and A. Dalgarno. Chem. Phys. Lett. **280**, 5 (1997).
17. N. Balakhrishnan, R.C. Forrey, and A. Dalgarno. Phys. Rev. Lett. **80**, 3224 (1998).
18. W.C. Stwalley. *In* State-to-state chemistry. *Edited by* P.R. Brooks and E.F. Hayes. ACS Symposium Series No. 56. American Chemical Society, Washington, D.C. 1977. p. 247.
19. S. Jochim, M. Bartenstein, A. Altmeyer, G. Hendl, S. Reidl, C. Chin, J. Hecker Denschlag, and R. Grimm. Science **302**, 2101 (2003).
20. M. Greiner, C.A. Regal, and D.S. Jin. Nature **426**, 537 (2003).
21. S.L. Mielke, K.A. Peterson, D.W. Schwenke, B.C. Garrett, D.G. Truhlar, J.V. Michael, M.C. Su, and I.W. Sutherland. Phys. Rev. Lett **91**, 063 201 (2003).
22. G.C. Hancock, C.A. Mead, D.G. Truhlar, and A.J.C. Varandas. J. Chem. Phys. **91**, 3492 (1989).
23. W.C. Stwalley. Contemp. Phys. **19**, 65 (1978).
24. G. Herzberg. J. Mol. Spectrosc. **33**, 147 (1970).

© 2004 NRC Canada

Highly accurate transition frequencies in the H_2 Lyman and Werner absorption bands[1]

J. Philip, J.P. Sprengers, Th. Pielage, C.A. de Lange, W. Ubachs, and E. Reinhold

Abstract: The transition frequencies of low-J excitation lines in the $B^1\Sigma_u^+ - X^1\Sigma_g^+$, $(v', 0)$ Lyman bands have been measured for $v' = 2$–18 and in the $C^1\Pi_u - X^1\Sigma_g^+$, $(v', 0)$ Werner bands for $v' = 0$–4, using a narrow-band tunable extreme UV laser source at wavelengths $\lambda = 92$–105 nm in conjunction with the technique of $1 + 1'$ two-photon ionization. The measurements can be divided into three categories for which varying absolute accuracies were obtained. Special focus was on the B, $v' = 2$–5 bands, where an accuracy of 0.004 cm^{-1} or $\delta\nu/\nu = 4 \times 10^{-8}$ is achieved. For transitions to B, $v' \leq 13$ and C, $v' \leq 3$ states the accuracy is 0.005 cm^{-1} or $\delta\nu/\nu = 5 \times 10^{-8}$. Due to a different frequency mixing scheme uncertainties for B, $v' \geq 13$ and C, $v' = 4$ are at the level of 0.011 cm^{-1} or $\delta\nu/\nu = 1.1 \times 10^{-7}$. Inspection of combination differences between R(J) and P($J + 2$) lines shows that the accuracies are even better than estimated in the error budget. Based on the measurements of 138 spectral lines and the known combination differences, transition frequencies of 60 P-lines could be calculated as well, so that a data base of 198 accurately calibrated lines results for the Lyman and Werner bands of H_2.

Key words: vacuum UV, molecular spectroscopy, hydrogen, precision metrology.

Résumé : On a mesuré les fréquences de transition des raies d'excitation de faible J dans les bandes de Lyman $B^1\Sigma_u^+ - X^1\Sigma_g^+$, $(\nu', 0)$, pour des valeurs de ν' allant de 2 à 18 ainsi que dans les bandes de Werner $C^1\Pi_u - X^1\Sigma_g^+$, $(\nu', 0)$, pour des valeurs de ν' allant de 0 à 4 en faisant appel à une source laser UV extrême, ajustable et à bande mince, à des longueurs d'onde, λ, allant de 92 à 105 nm, utilisée de concert avec la technique d'ionisation à deux photons $1 + 1'$. Les mesures peuvent être divisées en trois catégories qui diffèrent entre elles par la précision des mesures obtenues. On a concentré nos efforts sur les bandes B, $\nu' = 2$–5, pour lesquelles la précision a été de 0,004 cm^{-1} ou $\delta\nu/\nu = 4 \times 10^{-8}$. Pour les transitions vers B, $\nu' \leq 13$ et C, $\nu' \leq 3$, la précision est de 0,005 cm^{-1} ou $\delta\nu/\nu = 5 \times 10^{-8}$. En raison d'une méthode différente de combinaison des fréquences, les incertitudes associées à B, $\nu' \geq 13$ et C, $\nu' = 4$, le niveau de précision est de 0,011 cm^{-1} ou $\delta\nu/\nu = 1{,}1 \times 10^{-7}$. Un examen des différences des combinaisons entre les raies R(J) et P($J + 2$) montre que les précisions sont meilleures que celles évaluées dans le budget des erreurs. Sur la base de mesures de 138 raies spectrales et de différences de combinaison connues, on a pu aussi calculer les fréquences de transition de 60 raies P et il en résulte qu'une base de données de 198 raies bien calibrées est disponible pour les bandes de Lyman et de Werner du H_2.

Mots clés : UV lointain, spectroscopie moléculaire, hydrogène, métrologie de précision.

[Traduit par la Rédaction]

1. Introduction

Molecular hydrogen is the smallest neutral molecule and the most abundant molecular species in the universe. The Lyman bands, corresponding to the $B^1\Sigma_u^+ - X^1\Sigma_g^+$ system, and the Werner bands, corresponding to the $C^1\Pi_u - X^1\Sigma_g^+$ system, connect the electronic ground state to the lowest excited states of singlet and *ungerade* symmetry in a dipole-allowed transition, making them the most prominent features in the H_2-spectrum. Both systems relate to the $1s$–$2p$ resonance line of the H_2 molecule in analogy to the Lyman-α line in the H atom. In case of the $B^1\Sigma_u^+$ state the electron is promoted to a $2p\sigma$ orbital, whereas for the $C^1\Pi_u$ state the electron is in $2p\pi$. In his pioneering studies on the vacuum UV emission spectrum, now a century ago, Lyman was the first to positively assign a spectrum to the H_2 molecule (1, 2): the $B^1\Sigma_u^+ - X^1\Sigma_g^+$ system. Later, in 1926, Werner was the first to assign spectral lines pertaining to the $C^1\Pi_u - X^1\Sigma_g^+$ system (3). Dr. Herzberg, to whom we dedicate the present study, devoted an appreciable part of his career to the study of the spectrum of molecular hydrogen. Among his pioneering breakthroughs we mention the observation of the IR quadrupole spectrum (4), his analysis of the Rydberg spectrum, with Jungen (5), laying the foundations for the application of quantum defect theory in molecules, the determination of the dissociation energy (6), and his work with Jungen, Dabrowski, and Vervloet (7) on the measurement of IR inter-Rydberg transitions, leading to a determination of the ionization potential. Also, for the Lyman and Werner bands Herzberg made cru-

Received 3 October 2003. Published on the NRC Research Press Web site at http://canjchem.nrc.ca/ on 10 June 2004.

J. Philip, J.P. Sprengers, Th. Pielage, C.A. de Lange, and W. Ubachs.[2] Laser Centre, Department of Physics and Astronomy, Vrije Universiteit, Amsterdam, Netherlands.
E. Reinhold. Laboratoire Aimé Cotton, Campus d'Orsay, Université Paris-Sud, Orsay, France.

[1]This article is part of a Special Issue dedicated to the memory of Professor Gerhard Herzberg.

[2]Corresponding author (e-mail: wimu@nat.vu.nl).

 doi: 10.1139/V04-042 © 2004 NRC Canada

cial contributions, with Howe (8) and with Dabrowski (9), on a full rotational analysis of the emission spectra. High resolution absorption spectra of the Lyman and Werner band systems, using classical grating spectrometers, were investigated by Namioka (10) and by Dabrowski (11). The classical studies culminated in a comprehensive study of the H_2 VUV-spectrum by scientists at the Meudon Observatory, which was published in the form of a high-resolution spectroscopic atlas (12).

Developments on the experimental side were, over the years, accompanied by theoretical studies, for which the H_2 molecule is a benchmark system. Ab initio calculations of the potential energy curves have been produced using the Born–Oppenheimer approximation and calculating separately the mass-dependent adiabatic corrections to the potential curves as well as the non-adiabatic corrections for determination of accurate level energies. Advanced calculations for the $X^1\Sigma_g^+$ electronic ground state are those of Wolniewicz (13). An accurate potential energy curve for the $B^1\Sigma_u^+$ state was reported by Cencek et al. (14) and for the $C^1\Pi_u$ state by Wolniewicz (15). For a calculation of level energies in the $B^1\Sigma_u^+$ and $C^1\Pi_u$ excited states the couplings between the $B^1\Sigma_u^+$, $B'^1\Sigma_u^+$, $C^1\Pi_u$, and $D^1\Pi_u$ states and the resulting interferences have to be treated, based upon the input of ab initio potentials. The Meudon group has calculated those coupling effects in a number of studies of increasing accuracy (16) finally resulting in tables of transition frequencies for the Lyman bands (17) and Werner bands (18). Based upon these studies, a vast amount of rotationally resolved lines of the H_2 atlas (12) could be assigned.

The first observation of molecular hydrogen in space was performed with a rocket-borne spectrometer detecting Lyman band absorption in the optical path toward ξ Persei (19). Since then various satellite-based telescopes including spectrometers in the vacuum UV range have been launched for the study of H_2 and other molecules. The *Copernicus* satellite telescope (20) was in operation for many years, while the better resolving instruments ORFEUS and IMAPS were flown aboard the Space Shuttle for limited periods. The Hubble Space Telescope yielded a greatly improved sensitivity combined with a good resolving power and absorption from H_2 vibrationally excited levels could even be recorded (21). The *Galileo* orbiter, equipped with an UV (113–432 nm) as well as an extreme-UV (54–128 nm) spectrometer, recorded the Lyman and other H_2 bands from the north and south polar regions of Jupiter (22). Since June 1999, the Far ultraviolet spectroscopic explorer (FUSE) is in flight and detecting hydrogen in space. It covers the wavelength range 90.5–118.7 nm, the range of the strong Lyman and Werner absorption bands, with high resolution (23) and with a 10^4 greater sensitivity than Copernicus.

The present paper reports on a high-resolution laser spectroscopic study of the Lyman and Werner bands. A narrow-band tunable extreme ultraviolet (XUV) laser source is used in a $1 + 1'$ resonance-enhanced multi-photon ionization (REMPI) scheme to determine transition frequencies of various low-J lines in $B^1\Sigma_u^+ - X^1\Sigma_g^+(v', 0)$ bands for $v' = 2$–18 and in $C^1\Pi_u - X^1\Sigma_g^+(v', 0)$ bands for $v' = 0$–4. In previous high-resolution studies by our group, a coherent laser-based XUV-source was also used, but now the resolution has been increased by an order of magnitude, while at the same time the methods for absolute calibration have been improved. Initially, in a pilot study, the $B–X(10, 0)$ band had been studied (24). This work was extended to a comprehensive laser excitation study of 291 lines in Lyman $B–X(v', 0)$ bands for $v' = 10$–19 and Werner $C–X(v', 0)$ bands for $v' = 0$–5 (25). Later, a further extension was performed for $B–X(v', 0)$ bands for $v' = 20, 22, 23, 25$–27, and $C–X(v', 0)$ bands for $v' = 6$–10 (26). The absolute accuracies on the transition frequencies in these laser-based measurements varied between 0.02 and 0.06 cm^{-1}. These accuracies have been improved now by almost an order of magnitude.

2. Experiment and assessment of error budget

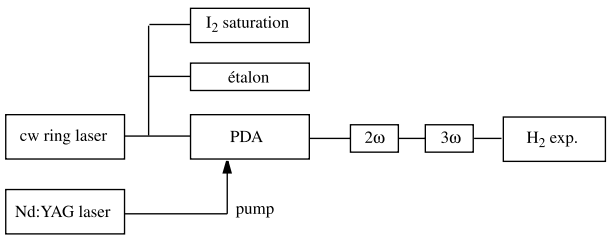
The Amsterdam narrow-band tunable XUV radiation source and its application in atomic (27) and molecular (28) spectroscopy have been described previously. A schematic layout of two slightly differing experimental setups, further referred to as schemes I and II, are displayed in Fig. 1. In short, the radiation source consists of a tunable ring-dye-laser delivering continuous wave (cw) radiation in the range 570–660 nm, a three-stage pulsed-dye amplifier (PDA) pumped by a pulsed Nd:YAG laser, a frequency-doubling crystal for converting the visible output of the PDA to the UV range, and a pulsed gas jet in which the pulsed UV radiation is frequency-tripled to cover the wavelength range 95–110 nm. The bandwidth of the XUV light in this range was previously estimated at 250–300 MHz, slightly below 0.01 cm^{-1} (see also ref. 28). The pulsed-XUV beam is crossed perpendicularly by a molecular beam obtained from a pulsed nozzle. In the interaction zone signal is generated by $1 + 1'$ photo-ionization, whenever the XUV radiation is tuned in resonance with a Lyman or Werner absorption line. In view of the cooling effect of the pulsed molecular beam, only transitions originating in the low rotational levels can be accessed. Spectral lines are recorded by scanning the cw laser system and monitoring the H_2^+-ion production in the interaction zone. The wavelength used in the ionizing step is the UV wavelength before tripling, corresponding to $\lambda_{UV} = 3\lambda_{XUV}$ at each H_2 resonance. For the $B–X(2, 0)$ band the total energy of the XUV and UV photons is not sufficient to produce H_2^+ ions directly. Nevertheless, this band could be recorded from the signal induced by a $1 + 2'$ process using the region of high Rydberg states for resonance enhancement. In this case, the H^+ signal was monitored, which originates from photo-dissociated H_2 molecules, producing $H(n = 2)$ atoms that are subsequently ionized. The $B–X$ (0,0) and (1,0) bands were not covered in this study because the saturation I_2 standard does not extend to these wavelengths for the fundamental (29, 30).

At the short wavelength limit (at $\lambda < 570$ nm), problems arose with the operation of the cw ring-dye laser, which was pumped by a Millennia 5W laser at 532 nm. Hence, the study was limited to $B(v' \leq 13)$ and $C(v' \leq 3)$ when using scheme I as displayed in Fig. 1. For this reason, wavelengths in the range $\lambda < 95$ nm were produced via an alternative frequency mixing scheme (shown as scheme II in Fig. 1). The green output of the Nd:YAG laser was used, both for pumping the PDA as well as for sum-frequency mixing with the output of the PDA, to reach shorter wavelengths. These methods have been described in more detail in a separate paper (31). Although the output frequency of the Nd:YAG laser is in principle fixed, temperature drifts caused slowly varying frequency excursions of several

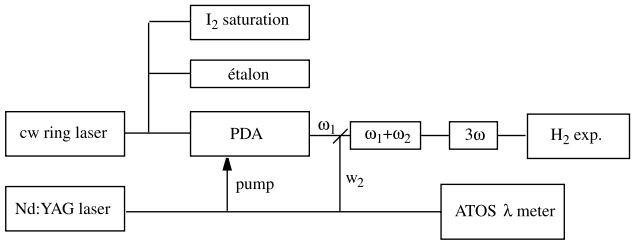
© 2004 NRC Canada

Fig. 1. Schematic layout of the experimental setup for both schemes used.

(*a*) Scheme I



(*b*) Scheme II



GHz during a measurement session. Its frequency was therefore monitored on-line by a four-étalon wavelength meter (ATOS), which was calibrated on an absolute scale by comparison to I_2 saturated lines, during each measurement session. This method yields an absolute accuracy of 100 MHz for the Nd:YAG output at 18 788 cm^{-1}.

The linewidths observed in the recording of the Lyman and Werner lines are ≈500 MHz, and slightly dependent on the measurement geometry and molecular beam conditions chosen. The bandwidth of the XUV laser source of ≈300 MHz (see refs. (27, 28)) is independent of the choice of scheme I or II. The upper $B^1\Sigma_u^+$ and $C^1\Pi_u$ states have lifetimes of 0.5–1 ns causing a Lorentzian type broadening of up to 300 MHz. For experimental geometries in which the nozzle–skimmer distance in the molecular beam was set at 15 cm (typical measurement conditions), the Doppler contribution was found to be negligible, particularly for molecular beams in which 25% H_2 was seeded in krypton gas to lower the average velocity of the molecules. Additional broadening was found if the nozzle–skimmer distance was lowered (i.e., when the signal intensity had to be increased). At very short nozzle–skimmer distances, we found increased population of high rotational states ($J = 4$ and $J = 5$), possibly due to glancing collisions at the conical skimmer surface. Detailed studies were performed comparing the transition frequencies and their Doppler shifts on the nearby lying transitions B–$X(12, 0)$ R(1) in H_2 and $4p^6\,{}^1S$–$5d_{1/2}(J = 1)$ in ^{84}Kr, at various beam conditions (i.e., beam velocities and nozzle–skimmer distances). From these measurements an estimate was made of the Doppler shift and of its effect on the uncertainty of the transition frequencies. The latter is included in the error budget for an amount of 60 MHz. For the set of measurements on B–$X(v', 0)$, $v' = 2$–5 lines an even more careful analysis of the Doppler shift, involving seeding H_2 gas in xenon, yields a maximal systematic error of only 40 MHz.

Calibration of the source was performed by reference measurements with the visible output of the cw ring-dye laser. Simultaneously with the H_2 spectrum, transmission fringes of a pressure- and temperature-stabilized étalon and the saturation spectrum of molecular iodine were recorded. The free spectral range (FSR) of the étalon was well calibrated at 148.9567 MHz and the t-hyperfine components of the I_2 saturation spectrum were calibrated in our laboratory with an absolute accuracy (2σ) of 2 MHz (29, 30). Hence, the XUV frequency scale can be obtained by multiplication of the scale for visible frequencies by a factor of six (i.e. for scheme I in Fig. 1), thus accounting for frequency doubling and subsequent frequency tripling. Estimates were made of the uncertainty caused by frequency drift of the pressure- and temperature-stabilized étalon. In the most unfortunate cases, when useful I_2 saturation lines were far away, continuous scans of ≈ 20 min duration had to be recorded, resulting in contributions to the error budget of 20 MHz (scheme I) or 10 MHz (scheme II). Special precautions were taken during measurements of the B–$X(v', 0)$ Lyman bands for $v' = 2$–5. During these recordings the étalon was actively stabilized with the aid of a HeNe laser, which was itself frequency-locked to an I_2 saturation line.

Two examples are presented of spectral recordings of the H_2 spectrum that elucidate the high-resolution capabilities of the setup. Fig. 2 shows the R(0) and R(1) lines in the C–$X(1, 0)$ Werner band, clearly separated by 1.09 cm^{-1}; in the classical absorption spectrum these lines were determined at a separation of 2 cm^{-1}, most likely because of partial overlap (9). A second spectrum, displayed in Fig. 3, shows the nearby lying P(3) line of the C–$X(1, 0)$ band and the R(0) line of the B–$X(9, 0)$ band, separated by only 0.16 cm^{-1}. Recordings of H_2^+ and H^+ signals show that excitation of Werner lines usually yields only parent ions, while excitation of Lyman lines also produces a H^+ signal. Absolute calibration is performed with respect to the t-component of the P(126) line of the B–$X(15, 2)$ band in iodine. Computerized fitting procedures to the spectral lineshapes aid in determining the line centers with high precision. The contribution of the uncertainty of the reference spectrum is minor (10 MHz). A statistical uncertainty in the determination of line centers is caused by the fitting of the observed line profiles. Slight variations in the central frequencies obtained in repeated scans of a transition are also treated as statistical uncertainty. The final value for a line position is obtained by the weighted mean deduced line centers from all scans, using the number of laser pulses per wavelength interval as a weight factor. In this procedure a final statistical uncertainty is derived. For ease of representation, and to take a conservative estimate, an upper limit of the statistical uncertainty in each of the measurement schemes is used, instead of slightly different values for each line. For the very weak lines, and the lines recorded under conditions of additional broadening, a higher estimate of the uncertainty is listed in the Tables. Most lines were recorded three times, except for the set of Lyman bands B–$X(v', 0)$ for $v' = 2$–5, where the lines were recorded 10 or more times. In cases where frequency-mixing scheme II was employed, the calibration uncertainty was dominated by the frequency measurement of the green output of the Nd:YAG laser. Since $\omega_{XUV} = 3\omega_{PDA} + 3\omega_{Nd:YAG}$, the uncertainty of this measurement comes into the error budget three times (i.e., 300 MHz).

The AC-Stark effect in the H_2 Lyman bands was investigated recently by Wetzig et al. (32). The intensity of the XUV beam

© 2004 NRC Canada

Fig. 2. Recording of the R(0) and R(1) lines of the $C–X(1, 0)$ Werner band separated by 1.09 cm^{-1}.

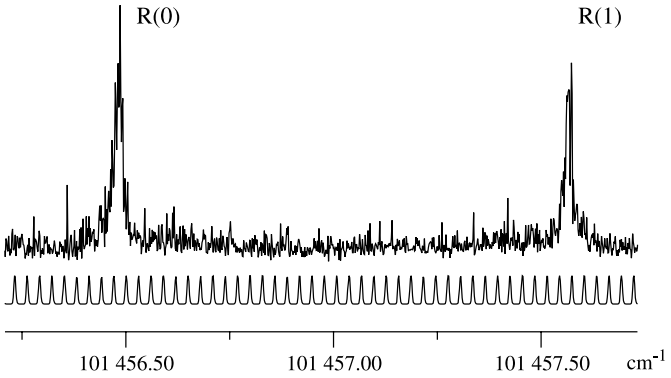
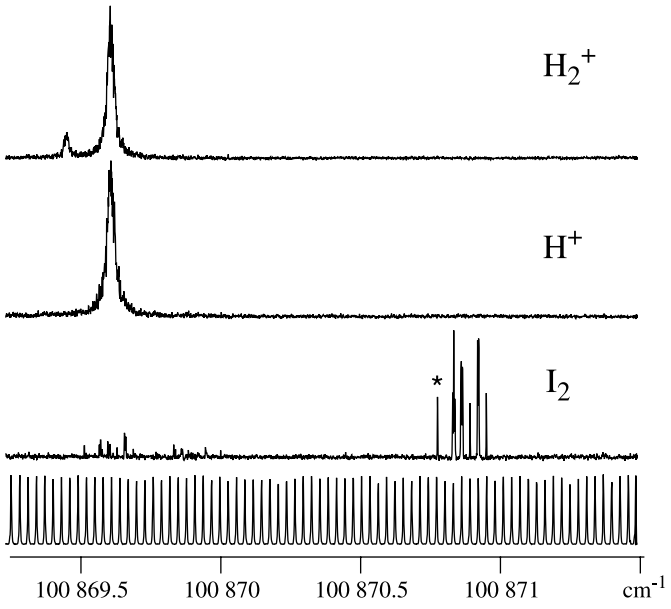


Fig. 3. Recording of the P(3) line of the $C–X(1, 0)$ Werner band and the R(0) line of the $B–X(9, 0)$ Lyman band of H_2 for both the H_2^+ and H^+ signals in the XUV domain. Below: simultaneous recordings of transmission fringes of the stabilized étalon and the saturation spectrum of molecular iodine at the fundamental frequency ($\nu_{XUV}/6$). The line marked with an asterisk denotes the P(126) line in the $B–X(15, 2)$ at 16 811.7958 cm^{-1}.



in the present experiment is so low (sub-nJ pulse energies in a diverging beam) that its AC-Stark inducing effects may be neglected, and the UV-ionizing laser in the $1 + 1'$ two-photon ionization process dominates the AC-Stark shifts. The maximum UV intensity in the interaction zone is 4 MW/cm^2 (20 mJ/pulse, 5 ns pulse duration, 1 cm^2 area) at the highest pulse energies used. By taking into account the quadratic Stark effect for $^1\Sigma$ states and the polarizabilities for the $B\,^1\Sigma_u^+$ state as calculated by Rychlewski et al. (33), as well as effective polarizabilities obtained from experimental data, they estimate for the case of $1 + 1'$ REMPI (UV intensities of $I = 10$ GW/cm^2 and parallel polarizations of XUV and UV beams, asymmetrically shaped lines with an intensity maximum shifted by -4.0 cm^{-1}, and a shift of the effective line center by -3.0 cm^{-1}. The polarizability of the $X\,^1\Sigma_g^+$ ground state is orders of magnitude smaller and can be neglected. With the estimated polarizability of ref. 32, this yields a shift of 0.0015 cm^{-1} or less for the line center at the highest pulse energies used in the present study. The work of Wetzig et al. (32), dealing with the $B\,^1\Sigma_u^+$, $v' = 3$ and $v' = 4$ levels, provides an exemplary case. If their analysis may be taken as a guidance, this would result in an upper limit of 50 MHz for the AC-Stark shift for spectral lines recorded at the highest laser pulse energies. In the case of frequency mixing scheme II, lower laser pulse energies (< 10 mJ/pulse) were produced, and hence limits to the AC-Stark shift could be relaxed accordingly. Eikema et al. (27) performed measurements on the $1 + 1'$ REMPI excitation mechanism via the $(2p)\,^1P$ state in He; such a scheme can be considered to represent the unified-atom limit to excitation via $(2p\sigma)$ and $(2p\pi)$ in the H_2 Lyman and Werner bands. From the study on He an AC-Stark shift of 2.5 MHz per MW/cm^2 can be deduced, confirming the estimate on an upper limit for the AC-Stark effect of less than 50 MHz.

In addition to these estimates, an experimental assessment was made of the AC-Stark effect. A large set of over 30 recordings was taken for the R(1) line of the $C–X(1, 0)$ Werner band in a pulse energy range of 2–15 mJ/pulse. From an analysis of these data it follows that a possible AC-Stark shift is smaller than the statistical spread in the data set; no intensity-dependent trend is observed. From these data we conclude that the estimated contribution of 50 MHz to the AC-Stark shift is conservative. In the study of the $B–X(v', 0)$ bands for $v' = 2$–5 another large data set was gathered focusing on laser intensity effects in the range of pulse energies 2–5 mJ/pulse. Even though the statistical error was smaller, no systematic trend that might possibly be attributed to an AC-Stark effect was found; for this particular data set the estimate of the error contribution by the AC-Stark effect is taken at the lower value of 30 MHz.

Two final remarks can be made on perturbing influences of the AC-Stark effect in the present absolute frequency measurements. If the total energy in the $1 + 1'$ REMPI scheme accidentally hits a resonance in the autoionization continuum, the AC-Stark effect may be enhanced, resulting in a possibly larger shift of the observed resonance in the Lyman or Werner bands. Such phenomena might be verified by using a wavelength-tunable ionization laser, but the procedures are too elaborate for addressing all lines in the present data set. Hence, it is not excluded that one or more of the lines undergoes an enhanced AC-Stark effect and the uncertainty in the transition frequency is then larger than specified. However, in the consistency checks (see next section) no such enhanced shifts were found. Secondly, AC-Stark effects on spectral lines induce asymmetric profiles (see e.g., ref. 32), due to splitting of m_J components. No such signatures were observed.

As was discussed in previous studies using the PDA-based narrow-band XUV source, frequency chirp (i.e., frequency excursions during the laser pulses of 5 ns duration as a result of time-dependent gain in the dye amplifiers) form a major limitation in precision studies involving pulsed lasers (27, 34). Although it was demonstrated that the chirp effect, giving rise to a net shift between the center frequency of the pulsed output of the PDA with respect to the cw-laser output (27), can be actively compensated, the procedures to do so are too cumbersome to apply in a study of 70 spectral lines. From the same studies it followed, however, that the chirp effect in a PDA-based XUV

© 2004 NRC Canada

Table 1. Error budget for the transition frequencies in the present high-precision 1 XUV + 1 UV two-photon ionization spectroscopic study in H_2.

Source	Scheme I	Ia	Scheme II
Doppler	60	40	60
AC Stark	50	30	30
Chirp	100	100	70
I_2 calibration	10	10	10
Etalon drift	20	—	10
Nd:YAG calibration	—	—	300
Statistical	80	30	80
Total	152	117	326

Note: The columns under scheme I and scheme II refer to the experimental configurations as shown in Fig. 1, where the data under Ia specifically denote transitions to the $B^1\Sigma_u^+$, $v' = 2$–5 states, where special care was taken to further reduce the uncertainties. All values are given in MHz.

source is limited to systematic shifts of 100 MHz, for the center frequency determined in a $1 + 1'$ two-photon ionization experiment. We adopt this value as an upper limit in the error budget (Table 1). It should be noted that, while this shift is systematic, there is a distribution of chirp shifts over the spectral lines measured in this study. As discussed in refs. 27 and 34, the systematic shift varies and changes sign when tuning a PDA over a single-dye curve; in the present study, full tuning curves of a number of different dyes and dye mixtures were used. For these reasons the chirp contribution to the error budget may be treated as a statistical summation of independent errors.

The contributions to the error budget are given in Table 1 for mixing schemes I and II. The separate column Ia relates to measurements of lines in B–$X(v', 0)$ Lyman bands for $v' = 2$–5, where special caution was taken to minimize some of the contributing causes of uncertainty, while using the measurement geometry of scheme I. For the major fraction of spectral lines this uncertainty was adopted in the list of resulting transition frequencies displayed in the tables. Some of the lines gave larger statistical uncertainties or were measured at unfavorable conditions (low intensity or very short nozzle–skimmer distance); the estimated uncertainties for these lines are indicated in the tables. Particularly in the wavelength range near 615 nm, problems were encountered in running the PDA laser system. As a result only weak signals could be observed in a geometrical configuration with a small nozzle–skimmer distance; the uncertainties in the transition frequencies are therefore higher.

In the measurements performed with scheme I, the frequency chirp in the PDA is the determining factor in the error budget, while in the measurements using scheme II, the uncertainty in the Nd:YAG frequency outweighs other error contributions. In the best case the uncertainty in the absolute frequency corresponds to 1/3 of the line width, while in the other cases it amounts to 2/3 of the line width of the observed resonances.

3. Results, discussion and conclusion

The data on the experimental transition frequencies are arranged in five tables. In Tables 2 and 3 transition frequencies in the H_2 Lyman bands for $v' = 2$–5 and $v' = 6$–13 as obtained with mixing scheme I are presented. Table 4 presents the Lyman lines for $v' = 14$–18, obtained with mixing scheme II. Finally, the transition frequencies of the Werner bands obtained in mixing schemes I and II are listed in Tables 5 and 6. The fact that the study is limited to transitions originating in low J levels is inherently connected to the use of a molecular beam, necessary to enter the regime of sub-Doppler accuracy.

Table 2. Observed transitions of the $B^1\Sigma_u^+ - X^1\Sigma_g^+(v', 0)$ Lyman bands in H_2 for $v' = 2$–5, obtained with frequency mixing scheme I.

J	P(J)	Δ_{o-m}	Band	R(J)	Δ_{o-m}
			(2,0)		
0				92 838.551(4)	−0.029
1	92 684.808(4)	−0.065		92 790.293(4)	−0.090
2				92 659.092(4)	0.075
			(3,0)		
0				94 083.809(4)	−0.011
1	93 931.518(4)	−0.055		94 032.673(4)	−0.070
2	93 729.437(4)	−0.010		93 897.171(4)	0.014
3				93 678.697(4)	−0.044
			(4,0)		
0				95 295.505(4)	−0.015
1	95 144.534(4)	−0.079		95 241.745(4)	−0.048
2				95 102.364(4)	0.017
3				94 878.812(4)	−0.069
			(5,0)		
0				96 474.270(4)	−0.010
1	96 324.532(4)	−0.031		96 418.076(4)	−0.087
2				96 275.091(4)	−0.016
3				96 046.817(4)	−0.054

Note: For this set of measurements the étalon was actively locked to a stabilized HeNe laser, while the Doppler effect was assessed through a number of experiments. The values between parentheses are the uncertainties of the last digits. The transition energies are compared with the experimental values by the Meudon group (Δ_{o-m}) (16).

A first comparison can be made with the classical data of Dabrowski and Herzberg (9), in which an accuracy of 0.15 cm^{-1} is claimed; we find that the data of ref. 9 are on average higher by 0.2 cm^{-1}, with a standard deviation of $\sigma = 0.4$ cm^{-1}. In the tables, the transition frequencies are compared with those of the most accurate values in the literature. On the one hand those are the values of the Meudon group, where we have not adopted the values obtained in direct measurements, as given in the Lyman (17) and Werner tables (18), but rather the experimentally deduced values of the level energies, which relate to an average over emission lines in various bands (16). We converted these values into transition frequencies of the Lyman and Werner bands by adding the most accurate values for the level energies of $X^1\Sigma_g^+$, $v" = 0$ rotational states (36). The transition frequencies of the Meudon analysis are found to be higher by 0.06 cm^{-1} on average, with some scatter that has a standard deviation of 0.047 cm^{-1}. Based on the latter one would expect that the average deviation of our entire data set from the Meudon data is on the order of 0.008 cm^{-1}. This implies that the difference of 0.06 cm^{-1} must be interpreted as a systematic shift. This is not disturbing since in the Meudon analysis an accuracy of 0.15 cm^{-1} is claimed, part of which may be systematic. In measurements of a classical spectrum, the calibration by reference lines is performed for the entire data set

© 2004 NRC Canada

Table 3. Observed transitions of the $B^1\Sigma_u^+ - X^1\Sigma_g^+(v',0)$ Lyman bands in H_2 for $v' = 6$–13, obtained with frequency mixing scheme I.

J	P(J)	Δ_{o-m}	Δ_{o-h}	Band	R(J)	Δ_{o-m}	Δ_{o-h}
				(6,0)			
0					97 620.600(8)	−0.050	
1	97 472.046(8)	−0.087			97 562.127(8)	−0.086	
				(7,0)			
0					98 734.907(5)	−0.003	
1	98 587.513(5)	−0.050			98 674.115(5)	−0.058	
2					98 524.415(6)	−0.012	
				(8,0)			
0					99 817.945(5)	−0.095	
1	99 671.421(5)	−0.122			99 755.390(5)	−0.123	
2	99 463.573(5)	−0.094			99 603.037(5)	−0.040	
3	99 168.359(6)	−0.122			99 362.672(6)	−0.119	
				(9,0)			
0					100 869.606(5)	−0.054	
1	100 724.240(5)	−0.043			100 804.788(5)	−0.075	
2					100 649.125(9)	−0.012	
3					100 404.350(20)	−0.061	
				(10,0)			
0					101 891.233(5)	−0.057	
1	101 746.444(5)	−0.149	-0.036		101 825.293(5)	−0.070	0.003
2	101 536.864(5)	−0.052			101 668.268(5)	0.022	−0.012
3	101 238.263(6)	−0.069			101 423.706(6)	−0.035	
				(11,0)			
0					102 882.115(5)	−0.045	−0.045
1	102 738.539(5)	−0.134	−0.011		102 813.729(5)	−0.074	−0.041
2	102 527.744(5)	−0.042			102 652.762(5)	−0.004	−0.078
3	102 226.698(6)	−0.073			102 401.014(6)	−0.067	
4					102 061.112(7)	−0.023	
5					101 636.453(7)	−0.137	
				(12,0)			
0					103 844.532(5)	−0.038	−0.088
1	103 701.023(5)	−0.120	−0.147		103 776.639(5)	−0.124	−0.111
2	103 490.154(5)	−0.042	−0.096		103 622.031(5)	0.005	−0.059
3	103 189.607(6)	−0.124	−0.103		103 340.273(6)	−0.118	−0.147
4					103 003.776(9)	−0.119	
5					102 576.045(9)	−0.105	
				(13,0)			
0					104 776.413(5)	−0.067	−0.077
1	104 634.440(5)	−0.113	−0.210		104 704.825(5)	−0.107	−0.045
2	104 422.041(5)	−0.065	−0.069		104 539.095(5)	−0.031	−0.035
3					104 281.088(6)	−0.123	−0.072
4	103 724.660(15)	−0.045			103 933.577(7)	−0.048	

Note: All values are given in cm^{-1}. The transition frequencies are compared with the experimental values by the Meudon group (Δ_{o-m}) (16) and by those of Hinnen et al. (Δ_{o-h}) (25).

and hence a systematic shift may be introduced.

A second accurate, but less extensive, data set is that of Hinnen et al. (25); wherever possible a comparison was made in the tables with those data as well. The previous laser-based data of Hinnen et al. (25) are found to be systematically higher by 0.07 cm^{-1}, where an experimental accuracy on the order of 0.05 cm^{-1} was estimated. A statistical analysis would again imply that there is a systematic off-set in the data of Hinnen et al. at the level of 1/4 of the line width in that experiment. We do not have an explanation for this phenomenon, other than that it may somehow be related to the procedures of comparison with the Doppler-broadened I_2-atlas (35) as a reference spectrum.

At the present level of accuracy it is not useful to attempt fitting procedures to derive effective molecular constants. A band-by-band analysis lacks sufficient data, while a global fit has to consider the non-adiabatic interactions, which cannot be dealt with at this level of accuracy. The present status of state-of-the-art close-coupling models are no better than 0.1 cm^{-1}. Calculations by the Meudon group (16–18) take into account non-adiabatic couplings between the four lowest electronic

© 2004 NRC Canada

Table 4. Observed transitions of the $B^1\Sigma_u^+ - X^1\Sigma_g^+(v',0)$ Lyman bands in H_2 for $v' = 14$–18, obtained with frequency mixing scheme II.

J	P(J)	Δ_{o-m}	Δ_{o-h}	Band	R(J)	Δ_{o-m}	Δ_{o-h}
				(14,0)			
0					105 689.330(11)	−0.020	−0.020
1	105 539.334(11)	−0.149	−0.056		105 598.807(11)	−0.036	−0.123
				(15,0)			
0					106 556.671(11)	−0.029	−0.019
1	106 416.181(11)	−0.082	−0.009		106 482.187(11)	−0.076	−0.030
				(16,0)			
0					107 404.159(11)	−0.001	−0.011
1	107 265.499(11)	−0.084	−0.001		107 326.898(11)	−0.065	−0.052
2					107 153.562(11)	−0.015	0.002
				(17,0)			
0					108 226.909(11)	−0.051	−0.111
1	108 087.714(11)	−0.029	−0.046		108 149.818(11)	−0.005	−0.122
				(18,0)			
0					109 021.296(11)	0.006	−0.124
1	108 883.440(11)	−0.133	−0.120		108 941.732(11)	−0.111	−0.078
2					108 764.439(11)	−0.048	−0.071

Note: All values are given in cm^{-1}. The transition energies are compared with the experimental values of the Meudon group (Δ_{o-m}) (16) and those of Hinnen et al. (Δ_{o-h}) (25).

Table 5. Observed transitions of the $C^1\Pi_u - X^1\Sigma_g^+(v',0)$ Werner bands in H_2 for $v' = 0$–3, obtained with frequency mixing scheme I.

J	P(J)	Δ_{o-m}	Δ_{o-h}	Q(J)	Δ_{o-m}	Δ_{o-h}	R(J)	Δ_{o-m}	Δ_{o-h}
(0-0) Band									
0							99 152.060(5)	−0.020	
1				99 032.367(5)	−0.186		99 157.343(5)	−0.090	
2	98 797.689(6)	−0.018		98 917.991(6)	0.044		99 105.580(6)	−0.047	
3	98 570.314(6)	−0.087		98 747.918(6)	−0.013		98 997.134(6)	0.013	
(1-0) Band									
0							101 457.569(5)	0.039	
1				101 337.862(5)	−0.221		101 456.482(5)	−0.091	
2	101 103.199(6)	0.042		101 217.192(6)	−0.015		101 394.780(6)	−0.047	
3	100 869.448(8)	−0.093		101 037.729(8)	−0.072		101 271.091(9)	−0.150	
(2-0) Band									
0							103 628.662(5)	−0.098	−0.088
1				103 509.373(5)	−0.110	−0.117	103 619.976(5)	−0.137	−0.064
2	103 274.289(6)	−0.098	−0.151	103 382.564(5)	−0.123	−0.086	103 541.589(6)	−0.098	−0.091
3	103 032.948(7)	−0.133		103 193.933(7)	−0.118	−0.107	103 436.111(7)	−0.110	−0.049
4	102 727.166(7)	−0.096		102 945.305(7)	−0.037				
5				102 639.037(8)	−0.134				
(3-0) Band									
0							105 660.712(5)	−0.028	−0.088
1				105 549.599(5)	−0.074	−0.131	105 665.270(5)	−0.083	−0.110
2	105 306.339(5)	−0.028	−0.061	105 416.752(5)	−0.015	−0.058	105 584.168(5)	−0.009	−0.092
3	105 078.236(6)	0.085	−0.104	105 219.106(6)	−0.135	−0.094	105 438.556(6)	−0.025	−0.084
4							105 228.227(6)	−0.055	

Note: All values are given in cm^{-1}. The values between parentheses are the uncertainties of the last digits. The transition energies are compared with the values of the Meudon group (Δ_{o-m}) (16) and those of Hinnen et al. (Δ_{o-h}) (25).

states of singlet character and u-symmetry. Such calculations have been refined since the publication of refs. 16, 17, but the improvements have not led to changes in level energies or transition frequencies, but rather in line strengths. We note here that the present study only produces accurate line positions. In a $1 + 1'$ photo-ionization study only relative intensities are measured that largely depend on the wavelength and intensity of the UV laser probing the ionization continuum. Hence, the ob-

© 2004 NRC Canada

Table 6. Observed transitions of the $C^1\Pi_u - X^1\Sigma_g^+(v', 0)$ Werner bands in H_2 for $v' = 4$, obtained with frequency mixing scheme II.

J	P(J)	Δ_{o-m}	Δ_{o-h}	Q(J)	Δ_{o-m}	Δ_{o-h}	R(J)	Δ_{o-m}	Δ_{o-h}
(4-0) Band									
0							107 580.936(11)	0.006	−0.014
1				107 460.201(11)	−0.072	−0.049	107 562.926(11)	−0.107	−0.064
2	107 226.569(11)	0.012	0.029	107 321.372(11)	−0.065	−0.068	107 475.203(11)	0.006	−0.037
3	106 975.891(12)	−0.142	−0.081	107 114.785(12)	−0.004	0.015	107 317.820(12)	−0.061	0.010

Note: All values are given in cm^{-1}. The values between parentheses are the uncertainties of the last digits. The transition frequencies are compared with those of the Meudon group (Δ_{o-m}) (16) and those of Hinnen et al. (Δ_{o-h}) (25).

served intensities do not give reliable information on the B–X line strengths.

A Dunham analysis was performed on a limited set of data with the aim of verifying the consistency of the data. In the region of excited energies below 99 000 cm^{-1}, the $B^1\Sigma_u^+$, $v' =$ 0–7 levels have no accidental perturbations with the $C^1\Pi$ state; interactions with higher lying states only cause small global shifts. Hence, in a Dunham analysis the data obtained for $B^1\Sigma_u^+$, $v' = 2$–7 were fitted to the functional form:

$$[1] \qquad E(v, J) = \sum_{k,j} Y_{k,j}(v + \frac{1}{2})^k [J(J+1)]^j$$

In total, 26 rotational states were observed in these bands as listed in Tables 2 and 3. Energies of the $v = 6$ band, which are measured with less accuracy, are used with reduced weight in the fit. Eleven Y_{kl} constants are determined and listed in Table 7, leaving 15 degrees of freedom for the fit. The constants have been chosen such that the sum of square deviations χ^2, divided by the number of degrees of freedom, is minimized; actually a small number of parameters could be added without a significant change, but none can be omitted. The main conclusion of this analysis is that the rovibrational structure of this part of the data set is smooth with an accuracy of 0.0135 cm^{-1}. There are no obvious drop-outs; the maximum deviation found is 0.030 cm^{-1} for $B^1\Sigma_u^+$, $v = 6$, $J = 2$, +0.023 cm^{-1} for $v = 7$, $J = 2$, and −0.021 cm^{-1} for $v = 7$, $J = 0$. We conclude further that the identification and use of specific I_2 saturation lines is unambiguous and correct for the bands in Tables 2 and 3.

Combination differences between P($J + 2$) and R(J) lines can further be verified with calculated ground state rotational splittings to test the accuracy and the internal consistency of the present data set. From the constants of Jennings et al. (36) the three lowest splittings can be calculated: 354.3734(2) cm^{-1}, 587.0325(2) cm^{-1}, and 814.4246(3) cm^{-1}. These splittings are consistent with the most accurate non-adiabatic calculations by Wolniewicz (13). The entire data set of Lyman and Werner band lines contains 11 measurements of the R(0)–P(2) energy splitting, of which the combination differences are plotted in Fig. 4. This shows the consistency of the data set involving these 22 spectral lines. The deviation of the combination differences from their average value amounts to much less than the typical uncertainties of 0.008 cm^{-1} (combined errors). This suggests that the determination of transition frequencies is more accurate than follows from the evaluation of the error budget for these pairs of lines. A statistical analysis yields a value for the combination difference of 354.3720(23) cm^{-1}, in agreement with the IR data (36). A similar procedure can be performed for the R(1)–P(3) combination differences where an average value of 587.031(3) cm^{-1} is derived from a set of nine pairs. The statistics are shown in Fig. 5. For the next combination difference, between R(2) and P(4) lines there are only two observations, in the B–X(13, 0) and C–X(2, 0) bands, yielding an average value of 814.426(8) cm^{-1}, which is in perfect agreement with the IR data (36).

Table 7. Dunham coefficients Y_{kl} representing the energies of observed rovibrational $B^1\Sigma_u^+$, $v = 2$–7 states, all values in cm^{-1}.

Y_{00}	89 533.70
Y_{10}	1352.907
Y_{20}	−18.4749
Y_{30}	0.1914
Y_{40}	−0.005075
Y_{01}	19.8673
Y_{11}	−1.0224
Y_{21}	0.06165
Y_{31}	−0.002808
Y_{02}	−0.01391
Y_{12}	0.000933

Note: The root mean square deviation of the representation from experimental energies is 0.0135 cm^{-1}.

On the basis of the ground state rotational energy splittings, accurately known from ref. 36, a number of transition frequencies for P-lines can be calculated, therewith extending the data set of Lyman and Werner bands spectral lines. Apart from the three lowest splittings cited above, we adopt values for higher lying combination differences: $\Delta_{53} = 1034.6703(1)$ cm^{-1}, $\Delta_{64} = 1246.098(1)$ cm^{-1}, and $\Delta_{75} = 1447.279(2)$ cm^{-1}. The calculated transition frequencies for the 60 P-lines and their estimated uncertainties are listed in Table 8.

The presently obtained data, measured at a greatly improved accuracy, provide a challenging test ground for future ab initio and close-coupling calculations. The accurately determined $B^1\Sigma_u^+$, v, J excited state level energies can be employed in multiple resonance studies to also determine accurate level energies of higher lying electronic states in H_2 as was demonstrated for some states of g symmetry by de Lange et al. (37). Also, the values can be incorporated in existing data sets on transitions between excited states to derive level energies of improved accuracy. One such example is that of the bound energy levels just below the $n = 2$ dissociation threshold in

© 2004 NRC Canada

Fig. 4. Combination differences between 11 sets of R(0) and P(2) lines measured in a number of Lyman and Werner bands. Indicated are the (weighted) average value from the 11 pairs and the resulting uncertainty: 354.3720(23) cm^{-1}.

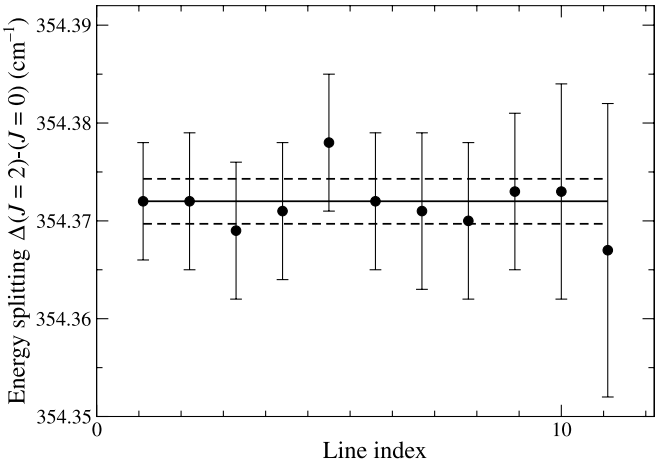
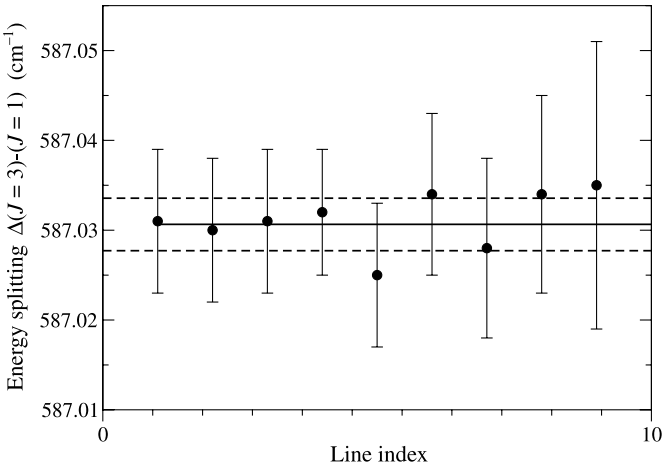


Fig. 5. Combination differences between nine sets of R(1) and P(3) lines measured in a number of Lyman and Werner bands. Indicated are the (weighted) average value and resulting uncertainty: 587.031(3) cm^{-1}.



H_2 (38). Combination with the present data on the $B^1\Sigma_u^+$, $v = 14$, $J = 0$ level energies yields improved values for level energies in the $II'^1\Pi_g$ potential: 118 361.202(13) cm^{-1} for the $II'^1\Pi_g$, $v = 2$, $J = 1(e)$ level, 118 373.169(13) cm^{-1} for the $II'^1\Pi_g$, $v = 3$, $J = 1(e)$ level, and 118 376.618(16) cm^{-1} for the $II'^1\Pi_g$, $v = 4$, $J = 1(e)$ level. The assignment of the latter two levels is tentative.

The accurate zero-velocity line centers form a set of lines for deducing accurate velocities of astrophysical objects, when ultra-high-resolution XUV spectrometers are used aboard satellites. At temperatures of 10 K the FWHM-Doppler width of the H_2 lines is 4.5 GHz; this may be compared with the width (0.55 GHz) and accuracy (<0.3 GHz) obtained in the present laboratory investigation. Finally, the present data may be implemented in improved comparisons between laboratory data and observed spectra from distant quasars, thus revealing possible cosmological variations of the proton-to-electron mass ratio (39–41).

Table 8. Calculated transition frequencies of some Lyman (L) and Werner (W) P-lines via the accurately known ground state energies.

Line	ν_0	Line	ν_0
L 2-0 P(2)	92 484.178 (4)	L 2-0 P(3)	92 203.261 (4)
L 2-0 P(4)	91 844.667 (4)	L 3-0 P(3)	93 445.641 (4)
L 3-0 P(4)	93 082.746 (4)	L 3-0 P(5)	93 644.027 (4)
L 4-0 P(2)	94 941.132 (4)	L 4-0 P(3)	94 654.713 (4)
L 4-0 P(4)	94 287.939 (4)	L 4-0 P(5)	93 844.142 (4)
L 5-0 P(2)	96 119.897 (4)	L 5-0 P(3)	95 831.044 (4)
L 5-0 P(4)	95 460.666 (4)	L 5-0 P(5)	95 012.147 (4)
L 6-0 P(2)	97 266.227 (8)	L 6-0 P(3)	96 975.095 (8)
L 7-0 P(2)	98 380.534 (5)	L 7-0 P(3)	98 087.083 (5)
L 7-0 P(4)	97 709.990 (6)	L 8-0 P(4)	98 788.612 (5)
L 8-0 P(5)	98 328.002 (6)	L 9-0 P(2)	100 515.233 (5)
L 9-0 P(3)	100 217.756 (5)	L 9-0 P(4)	99 834.700 (9)
L 9-0 P(5)	99 369.680 (20)	L 10-0 P(4)	100 853.843 (5)
L 10-0 P(5)	100 389.036 (6)	L 11-0 P(4)	101 838.337 (5)
L 11-0 P(5)	101 366.344 (6)	L 11-0 P(6)	100 815.014 (7)
L 11-0 P(7)	100 189.174 (7)	L 12-0 P(4)	102 807.606 (5)
L 12-0 P(5)	102 305.603 (6)	L 12-0 P(6)	101 757.678 (9)
L 12-0 P(7)	101 128.766 (9)	L 13-0 P(3)	104 117.793 (5)
L 13-0 P(5)	103 246.418 (6)	L 13-0 P(6)	102 687.479 (8)
L 14-0 P(2)	105 334.957 (11)	L 14-0 P(3)	105 011.775 (11)
L 15-0 P(2)	106 202.298 (11)	L 15-0 P(3)	105 895.155 (11)
L 16-0 P(2)	107 049.786 (11)	L 16-0 P(3)	106 739.866 (11)
L 16-0 P(4)	106 339.137 (11)	L 17-0 P(2)	107 872.536 (11)
L 17-0 P(3)	107 562.786 (11)	L 18-0 P(2)	108 666.923 (11)
L 18-0 P(3)	108 354.700 (11)	L 18-0 P(4)	107 950.014 (11)
W 0-0 P(4)	98 291.155 (6)	W 0-0 P(5)	97 962.464 (6)
W 1-0 P(4)	100 580.355 (6)	W 1-0 P(5)	100 236.421 (9)
W 2-0 P(5)	102 401.441 (7)	W 3-0 P(4)	104 769.743 (5)
W 3-0 P(5)	104 403.886 (6)	W 3-0 P(6)	103 982.129 (6)
W 4-0 P(4)	106 660.778 (11)	W 4-0 P(5)	106 283.150 (12)

Notes: Values in cm^{-1}.

Acknowledgments

The authors acknowledge the Netherlands Foundation for Fundamental Research of Matter (FOM) for financial support. The work was also supported by the European Union via the RTN network on Reactive Intermediates (HPRN-CT-2000-00006); ER acknowledges the EU for a Marie Curie individual fellowship (HPMF-CT-2000-00964). Additionally this work was supported by the European Community - Access to Research Infrastructures action of the Improving Human Potential Programme, Contract No. HPRI-CT-1999-00064.

References

1. T. Lyman. Astrophys. J. **19**, 263 (1904).
2. T. Lyman. Astrophys. J. **23**, 181 (1906).
3. S. Werner Proc. R. Soc. London Ser. A, **113**, 107 (1926).
4. G. Herzberg. Nature (London), **163**, 170 (1949).
5. G. Herzberg and Ch. Jungen. J. Mol. Spectrosc. **41**, 425 (1972).

© 2004 NRC Canada

6. G. Herzberg. J. Mol. Spectrosc. **33**, 147 (1970).
7. Ch. Jungen, I. Dabrowski, G. Herzberg, and M. Vervloet. J. Chem. Phys. **93**, 2289 (1990).
8. G. Herzberg and L.L. Howe. Can. J. Phys. **37**, 636 (1959).
9. I. Dabrowski and G. Herzberg. Can. J. Phys. **52**, 1110 (1974).
10. T. Namioka. J. Chem. Phys. **40**, 3154 (1964).
11. I. Dabrowski. Can. J. Phys. **62**, 1639 (1984).
12. J.-Y. Roncin and F. Launay. J. Phys. Chem. Ref. Data, Monograph 4 (1994).
13. L. Wolniewicz. J. Chem. Phys. **103**, 1792 (1995).
14. W. Cencek, J. Komasa, and J. Rychlewski. Chem. Phys. Lett. **246**, 417 (1995).
15. L. Wolniewicz. Chem. Phys. Lett. **233**, 644 (1995).
16. H. Abgrall, E. Roueff, F. Launay, J.-Y. Roncin, and J.-L. Subtil. J. Mol. Spectrosc. **157**, 512 (1993).
17. H. Abgrall, E. Roueff, F. Launay, J.-Y. Roncin, and J.-L. Subtil. Astron. Astrophys. Suppl. Ser. **101**, 273 (1993).
18. H. Abgrall, E. Roueff, F. Launay, J.-Y. Roncin, and J.-L. Subtil. Astron. Astrophys. Suppl. Ser. **101**, 323 (1993).
19. G.C. Carruthers. Astrophys. J. **161**, L81 (1970).
20. D.C. Morton and H.L. Dinerstein. Astrophys. J. **204**, 1 (1976).
21. S.R. Federman, J.A. Cardelli, E.F. van Dishoeck, D.L. Lambert, and J.H. Black. Astrophys. J. **445**, 325 (1995).
22. J. Ajello, D. Shemansky, W. Pryor, K. Tobiska, C. Hord, S. Stephens, I. Stewart, J. Clarke, K. Simmons, W. McClintock, C. Barth, J. Gebben, D. Miller, and B. Sandel. J. Geophys. Res. E, **103**, 20 125 (1998).
23. H.W. Moos, W.C. Cash, L.L. Cowie, A.F. Davidsen, A.K. Dupree, P.D. Feldman, S.D. Friedman, J.C. Green, R.F. Green, C. Gry, J.B. Hutchings, E.B. Jenkins, J.L. Linsky, R.F. Malina, A.G. Michalitsianos, B.D. Savage, J.M. Shull, O.H.W. Siegmund, T.P. Snow, G. Sonneborn, A. Vidal-Madjar, A.J. Willis, B.E. Woodgate, D.G. York, T.B. Ake, B.-G. Andersson, J.P. Andrews, R.H. Barkhouser, L. Bianchi, W.P. Blair, K.R. Brownsberger, A.N. Cha, P. Chayer, S.J. Conard, A.W. Fullerton, G.A. Gaines, R. Grange, M.A. Gummin, G. Hebrard, G.A. Kriss, J.W. Kruk, D. Mark, D.K. McCarthy, C.L. Morbey, R. Murowinski, E.M. Murphy, W.R. Oegerle, R.G. Ohl, C. Oliveira, S.N. Osterman, D.J. Sahnow, M. Saisse, K.R. Sembach, H.A. Weaver, B.Y. Welsh, E. Wilkinson, and W. Zheng. Astrophys. J. **538**, L1 (2000).
24. P.C. Hinnen, W. Hogervorst, S. Stolte, and W. Ubachs. Appl. Phys. B, **59**, 307 (1993).
25. P.C. Hinnen, W. Hogervorst, S. Stolte, and W. Ubachs. Can. J. Phys. **72**, 1032 (1994).
26. E. Reinhold, W. Hogervorst, and W. Ubachs J. Mol. Spectrosc. **180**, 156 (1996).
27. K.S.E. Eikema, W. Ubachs, W. Vassen, and W. Hogervorst. Phys. Rev. **A55**, 1866 (1997).
28. W. Ubachs, K.S.E. Eikema, W. Hogervorst, and P.C. Cacciani, J. Opt. Soc. Am. **B14**, 2469 (1997).
29. I. Velchev, R. van Dierendonck, W. Hogervorst, and W. Ubachs. J. Mol. Spectrosc. **187**, 21 (1998).
30. S.C. Xu, R. van Dierendonck, W. Hogervorst, and W. Ubachs, J. Mol. Spectrosc. **201**, 256 (2000).
31. J. Philip, J.P. Sprengers, P. Cacciani, C.A. de Lange, and W. Ubachs. Appl. Phys. B, **78**, 737 (2004).
32. D. Wetzig, A.D. Rudert, and H. Zacharias. Eur. J. Phys. D**17**, 181 (2001).
33. J. Rychlewski, J. Komasa, and W. Cencek. Phys. Rev. A , **41**, 5825 (1990).
34. S. Gangopadhyay, N. Melikechi, and E.E. Eyler. J. Opt. Soc. Am. B , **11**, 231 (1994).
35. S. Gerstenkorn and P. Luc Atlas du spectre d'absorption de la molecule de l'iode entre 14800-20000 cm^{-1}. Editions du CNRS, Paris. 1978.
36. D.E. Jennings, S.L. Bragg, and J.W. Brault. Astrophys. J. **282**, L85 (1984).
37. A. de Lange, E. Reinhold, and W. Ubachs. Phys. Rev. A , **65**, 064 501 (2002).
38. Th.G.P. Pielage, A. de Lange, F. Brandi, and W. Ubachs. Chem. Phys. Lett. **366**, 583 (2002).
39. D.A. Varshalovich and S.A. Levshakov. JETP Lett. **58**, 237 (1993).
40. A.Y. Pothekhin, A.V. Ivanchik, D.A. Varshalovich, K.M. Lanzetta, J.A. Baldwin, G.M. Williger, and R.F. Carswell. Astrophys. J. **505**, 523 (1998).
41. W. Ubachs and E. Reinhold. Phys. Rev. Lett. **92**, 101 302 (2004).

© 2004 NRC Canada

Line strength factors for E,F$^1\Sigma_g^+(v' = 0, J' = J'')$ – X$^1\Sigma_g^+$ (v'', J'') (2 + 1) REMPI transitions in molecular hydrogen[1]

Andrew E. Pomerantz, Florian Ausfelder, Richard N. Zare, and Winifred M. Huo

Abstract: Experimentally and theoretically determined line strengths are presented for E,F$^1\Sigma_g^+(v' = 0, J' = J'')$ – X$^1\Sigma_g^+$ (v'', J'') (2 + 1) REMPI transitions in H_2, HD, and D_2. The experimental technique employs a hot filament source of internally excited hydrogen that allows experimental determination of line strengths for the low rotational states of highly excited vibrational manifolds ($v'' \leq 4$). The line strengths are found to depend only weakly on J'' for the states measured here, and theoretical results indicate that the line strengths depend strongly on v''. These values are combined with previously measured and calculated line strengths for these transitions (K.-D. Rinnen, M.A. Buntine, D.A.V. Kliner, R.N. Zare, and W.M. Huo. J. Chem. Phys. **95**, 214 (1991)), resulting in a more complete compilation of REMPI line strengths for molecular hydrogen.

Key words: hydrogen, spectroscopy, REMPI, line strength, multiphoton.

Résumé : Nous avons déterminé théoriquement et expérimentalement les forces de raies pour les transitions REMPI E,F$^1\Sigma_g^+(v' = 0, J' = J'')$ – X$^1\Sigma_g^+(v'', J'')$ (2 + 1) de H_2, HD et D_2. La technique expérimentale, qui utilise un filament chauffé comme source d'hydrogène rovibrationnellement excité, permet de mesurer les forces de raies pour les états rotationnels bas des niveaux vibrationnels excités ($v'' \leq 4$). Nos mesures montrent que les forces de raies ne dépendent que faiblement de J'', et les résultats théoriques indiquent que les forces de raies dépendent fortement de v''. Ces valeurs sont combinées aux forces de raies mesurées et calculées antérieurement pour ces mêmes transitions (K.-D. Rinnen, M.A. Buntine, D.A.V. Kliner, R.N. Zare, and W.M. Huo. J. Chem. Phys. **95**, 214 (1991)), ce qui conduit à une compilation plus complète des forces de raies REMPI pour l'hydrogène moléculaire.

Mots clés : hydrogène, spectroscopie, REMPI, force de raie, multiphoton.

Introduction

The electronic spectroscopy of molecular hydrogen has been studied extensively over the past century, beginning with the measurement of emission spectra by Lyman (1) and Werner (2). The classic investigation by Herzberg and Howe (3) on the H_2 B–X system exemplified the richness of information that can be obtained from photographic spectroscopy. More recent work has employed laser-based techniques that sacrifice the ability to observe many transitions simultaneously while allowing quantitative measurements of quantum state selective molecular concentrations. In particular, rovibrational state selective populations of hydrogen molecules resulting from gas-phase chemical reactions (4–7) or gas-surface interactions (8–10) have been studied using resonant enhanced multiphoton ionization (REMPI). The interpretation of experimental data requires an understanding of the relationship between the measured signals (ion currents) and populations of rovibrational states. Accurate line strengths for these REMPI transitions are essential for performing this transformation.

Most previous attempts to measure state specific concentrations of molecular hydrogen using REMPI have employed Q-branch members of the E,F$^1\Sigma_g^+$ – X$^1\Sigma_g^+$ transitions. Pożgainer et al. (11) have measured line strengths for the (0,0) and (1,1) transitions by analyzing state distributions produced by a Knudsen source. Marinero et al. (4) have measured line strengths for the (0,1) and (0,2) transitions in HD by calibrating against a rotationally relaxed microwave discharge source. Rinnen et al. (12) have employed a hot nozzle source to measure line strengths for these (0,0), (0,1), and (0,2) transitions in H_2, HD, and D_2. They were able to measure line strengths for 102 rovibrational levels, typically including Q(0)–Q(15) for each molecule at each vibrational level, although they were unable to determine line strengths for the low J'' levels of the $v'' = 1, 2$ manifolds. Huo et al.

Received 19 December 2003. Published on the NRC Research Press Web site at http://canjchem.nrc.ca on 19 June 2004.

A.E. Pomerantz, F. Ausfelder, and R.N. Zare.[2] Department of Chemistry, Stanford University, Stanford, CA, 94305–5080 USA.
W.M. Huo. NASA Ames Research Center, Mail Stop T27B-1, Moffett Field, CA, 94035–1000 USA.

[1]This article is part of a Special Issue dedicated to the memory of Professor Gerhard Herzberg.
[2]Corresponding author (e-mail: zare@stanford.edu).

 doi: 10.1139/V04-074 © 2004 NRC Canada

(13) have performed calculations using adiabatic potentials and summing of 124 intermediate states to provide theoretical values for these same line strengths.

The conclusions of these studies were that experiment and theory agreed very well and that the line strengths depend strongly on v'' but only weakly on J''. For each isotope, the experimentally determined line strengths increase with v'' up to $v'' = 2$, but calculations predict the line strengths to decrease sharply for higher v''. Line strengths typically increase slowly with J'' (constant to within 10% for the first 10 J'' states) although there are some deviations starting at $J'' = 12$ for H_2, 17 for HD, and 24 for D_2, arising from resonant tunneling between the two wells of the E,F state at high J'' levels (14).

Here we present relative line strengths measured using a hot filament source and absolute values of the square of the two-photon transition moment calculated using previously described theoretical methods (13). The measurements are sensitive to line strengths for the low-lying rotational states of $v'' = 1$–4 in HD and D_2 and of $v'' = 1$–3 in H_2. For completeness, the previously determined line strengths are also presented.

Experimental methods

The line strength measurements require a source of internally excited hydrogen with two characteristics: there must be sufficiently high concentrations in internally excited states as to allow detection, and the relative concentrations of each excited state must be known. Relative line strengths are then determined by comparing the measured concentration to the concentration the source is known to produce; if the measured concentrations equal the known concentrations for a given set of states, then the line strengths are constant within the experimental error for transitions originating from those states. The source of internal excitation of hydrogen used in this measurement is a hot filament. This hot filament promotes recombination reactions that populate excited states of molecular hydrogen, and the excited products can be rotationally but not vibrationally relaxed by collisions before detection. This technique has been shown previously to produce high concentrations of vibrationally excited hydrogen that is rotationally thermalized to slightly above room temperature (15–18).

The filament used in this experiment is the tungsten filament of a nude ionization gauge (Granville Phillips 274-025 gauge with series 330 controller). The ion gauge is operated with an emission current of 10 mA, and the flow of hydrogen is metered with a dual-stage micrometer valve to maintain a nominal pressure of 9×10^{-5} to 10×10^{-5} torr (1 torr = 133.322 Pa) in the ion gauge during the course of an experiment. The chamber walls immediately surrounding the filament are water-cooled to approximately room temperature. The hydrogen excited by the filament flows through a collision cell en route to a high vacuum chamber evacuated with two turbopumps to a base pressure of 10^{-7} torr (1 torr = 133.322 Pa) when the hydrogen flow is stopped. The collision cell is a 3″ long piece of 3/4″ (1 inch = 25.4 mm) inner diameter stainless steel tubing with a 90° bend. The mean free path at this pressure is on the order of 10 cm, so most of the thermalizing collisions occur with the room temperature chamber walls; thus, the bend in the cell promotes collisions with the chamber walls, thereby promoting relaxation. Because the rotational levels are much more closely spaced than the vibrational levels ($2B \approx 100$ cm^{-1}, $\omega \approx 4000$ cm^{-1}), collisions can almost completely relax the rotational excitation while still leaving a measurably high concentration in vibrationally excited states.

The collision cell is connected to the main vacuum chamber near the ionization region of a Wiley–McLaren time-of-flight mass spectrometer (19). A pulsed, tunable UV laser (see below) is focused in the ionization region, and hydrogen molecules that intersect the laser focus are ionized via (2 + 1) REMPI on the $E,F\,^1\Sigma_g^+ - X\,^1\Sigma_g^+$ band of interest. The resulting photoions are detected with the mass spectrometer, and he signal is corrected for variation in laser power. Concen - trations are measured by recording the ion current as the laser is scanned over the Doppler profile and then integrating the spectral line. Line strengths are then extracted by comparing the measured concentrations to the expected concentrations.

Resonant ionization of these three different isotopes and four different vibrational manifolds requires pulsed, tunable UV light in the wavelength range 207–234 nm. Three different frequency-mixing schemes were implemented to cover this range. All schemes involved a dye laser pumped by the second or third harmonic of a Nd:YAG laser. For the reddest wavelength range (229–234 nm), corresponding to $H_2(v'' = 3)$ and $HD(v'' = 4)$, a frequency-doubling scheme was employed. For the bluest wavelength range (207–215 nm), corresponding to $H_2(v'' = 1)$, $HD(v'' = 1)$ and $D_2(v'' = 1, 2)$, a frequency-tripling scheme was used. For the intermediate range, a less common 355 nm mixing scheme was employed. In this technique, the Nd:YAG laser is frequency doubled and tripled, and the residual second harmonic pumps the dye laser. The dye laser fundamental is then frequency summed with the Nd:YAG third harmonic to produce UV light in the range 216–229 nm. These techniques all produce approximately 1 mJ of UV light in a 5 ns pulse.

Theoretical methods

The present study follows the same computational steps as described earlier. (13, 20, 21). The two-photon transition moment (M_{fo}) is given by

$$[1] \qquad M_{fo} = \sum_i \frac{\langle f|\bar{r}\cdot\hat{\varepsilon}|i\rangle\langle i|\bar{r}\cdot\hat{\varepsilon}|o\rangle}{(E_i - E_o - \hbar\omega)}$$

The summation is over all rovibrational states that can be coupled to the initial and final states by dipole-allowed transitions. In total, 124 intermediate states are used in the summation. For the four lowest electronic states that are dipole coupled to the ground state (i.e., the $B\,^1\Sigma_u^+$, $C\,^1\Pi_u$, $B'\,^1\Sigma_u^+$, and $D\,^1\Pi_u$ states) explicit summation is carried out over their vibrational levels. For the remainder, a nuclear sudden approximation (21) is used. The calculation of the vibrational wave functions of the X state is based on the adiabatic potential compiled by Schwartz and Le Roy (22). For the (E,F), B, C, B′, and D states, the calculations are based on the adiabatic potentials of Wolniewcz and Dressler (23, 24).

© 2004 NRC Canada

Fig. 1. Boltzmann plots of the measured concentrations in H_2. The rotational and nuclear spin degeneracies are represented by g_J and g_N, respectively.

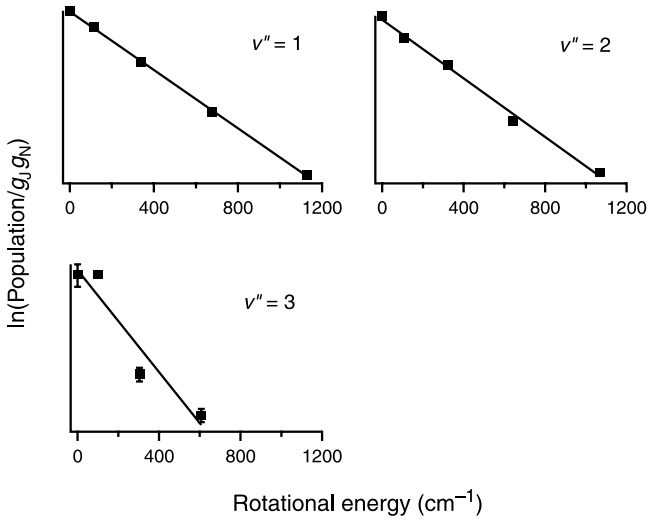
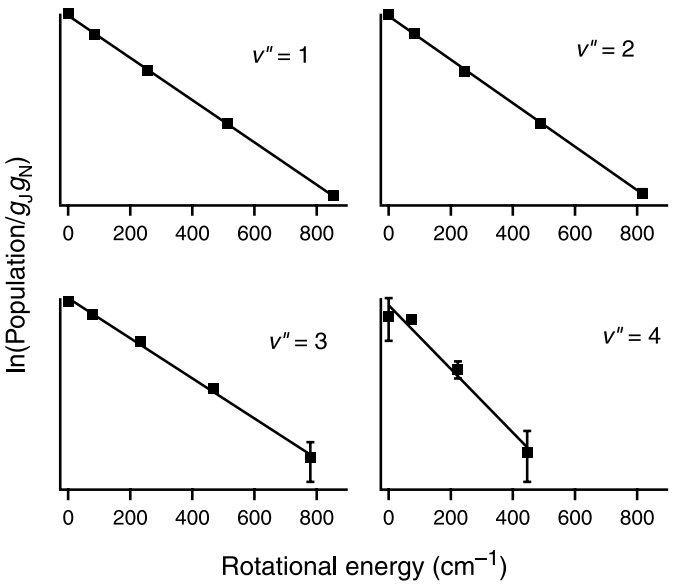


Fig. 2. Boltzmann plots of the measured concentrations in HD. The rotational and nuclear spin degeneracies are represented by g_J and g_N, respectively.



Results and discussion

Relative line strengths are extracted from the concentration measurements by comparing the measured concentrations to a Boltzmann distribution. This hot filament excitation technique is known to produce relative rotational concentrations that are well described by a Boltzmann distribution at slightly above room temperature (15–18). As the rotational line strengths are expected to be independent of J'', the experimentally determined concentrations are taken to be proportional to the area under the Doppler profile, without requiring a line strength correction. If this method of analysis returns an experimental distribution of concentrations that is well described by a Boltzmann distribution at slightly above room temperature then it represents experimental confirmation that the relative rotational line strengths are independent of J'' to within the experimental uncertainty. The experimental error is estimated to be approximately 10%. Further experimental determination of the relative rotational line strengths is impossible because the rotational temperature of the sample is not known precisely. Experimental determination of the v'' dependence of the line strengths is similarly impossible because the vibrational temperature of the sample is unknown.

It is important to note that the measured concentrations have been corrected for differences in the nuclear spin degeneracy. Because of these nuclear statistics, the concentration of $H_2(J'' = \text{odd})$ (*ortho*-hydrogen) is three times larger than the concentration of $H_2(J'' = \text{even})$ (*para*-hydrogen). To prepare the Boltzmann plots, the concentrations of $H_2(J'' = \text{odd})$ have been divided by three; similarly, the concentrations of $D_2(J'' = \text{even})$ have been divided by two. No correction is necessary for HD because the nuclei are not identical.

Boltzmann plots of the measured concentrations are presented in Figs. 1–3, and the resulting rotational temperatures are presented in Table 1. The Boltzmann plots present the natural logarithm of the population divided by the rotational degeneracy ($g_J = 2J''+1$) and the nuclear spin degeneracy

Fig. 3. Boltzmann plots of the measured concentrations in D_2. The rotational and nuclear spin degeneracies are represented by g_J and g_N, respectively.

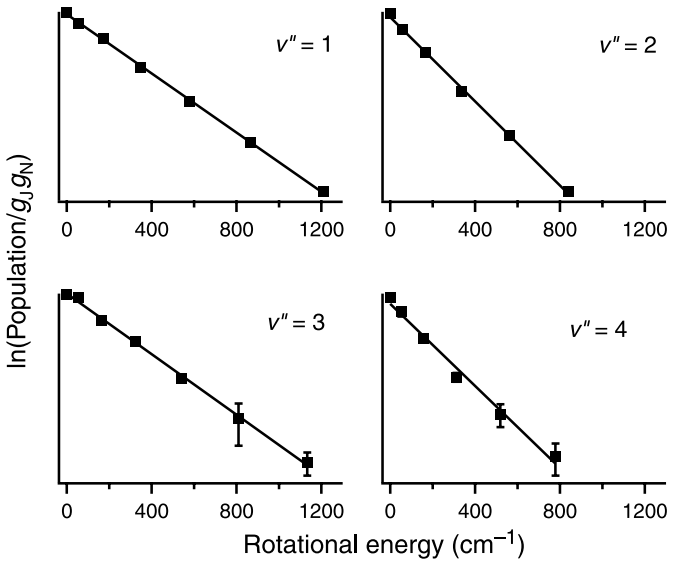


Table 1. Rotational temperatures (K) of each vibrational manifold.

v''	H_2	HD	D_2
1	317 (4)	308 (2)	312 (4)
2	323 (15)	314 (3)	308 (6)
3	342 (77)	302 (9)	316 (6)
4		340 (38)	323 (17)

Note: Uncertainties (one standard deviation) are listed in parentheses.

© 2004 NRC Canada

Table 2. Theoretical values of $|M_{fo}|^2$ for $E,F^1\Sigma_g^+(v' = 0, J' = J'') - X^1\Sigma_g^+(v'', J'')$ (2 + 1) REMPI transitions in H_2 (au).

J''	$v''=0$	$v''=1$	$v''=2$	$v''=3$	$v''=4$	$v''=5$	$v''=6$
0	**9.12**	**26.36**	**29.38**	**16.24**	4.73	0.71	0.07
1	9.15	**26.47**	**29.54**	**16.36**	4.78		
2	**9.20**	**26.61**	**29.71**	**16.45**	4.80		
3	**9.26**	**26.83**	**29.98**	**16.62**	4.85		
4	**9.34**	**27.12**	**30.36**	16.84	4.92		
5	9.44	**27.48**	**30.82**	17.13	5.01		
6	**9.56**	**27.91**	**31.39**	17.48	5.12		
7	**9.68**	**28.34**	**31.97**	17.85	5.24		
8	**9.85**	**28.97**	32.83	18.39	5.42		
9	**10.02**	**29.60**	33.70	18.91	5.66		
10	**10.18**	**30.28**	34.61	19.58	5.92		
11	**10.36**	**31.06**	35.73	20.38	6.16		
12	**9.66**	29.82	34.00	20.06	6.44		
13	**10.89**	**32.87**	38.17	22.03	6.92		
14	**8.77**	26.38	31.06	16.72	4.55		
15	**11.62**	35.47	41.38	23.93	7.79		
16	11.49	35.21	42.06	24.48	7.53		
17	11.65	37.00	42.15	25.84	10.20		
18	12.05	38.84	48.56	29.87	9.82		
19	9.26	31.62	39.00	22.53	5.52		
20	6.28	25.59	38.94	36.06	23.62		
21	8.63	33.58	49.84	39.62	16.72		

Note: Rotational line strengths that have been confirmed by the current or previous (12) experiment are listed in bold.

Table 3. Theoretical values of $|M_{fo}|^2$ for $E,F^1\Sigma_g^+(v' = 0, J' = J'') - X^1\Sigma_g^+(v'', J'')$ (2 + 1) REMPI transitions in HD (au).

J''	$v''=0$	$v''=1$	$v''=2$	$v''=3$	$v''=4$	$v''=5$	$v''=6$
0	**6.87**	**22.12**	**28.50**	**19.07**	**7.18**	1.53	0.18
1	**6.89**	**22.20**	**28.62**	**19.18**	**7.23**		
2	**6.91**	**22.28**	**28.74**	**19.26**	**7.26**		
3	**6.95**	**22.41**	**28.92**	**19.40**	**7.31**		
4	**6.99**	**22.59**	**29.19**	**19.60**	7.39		
5	**7.04**	**22.81**	**29.53**	19.84	7.48		
6	**7.11**	**23.07**	**29.92**	20.14	7.61		
7	**7.19**	**23.37**	**30.39**	20.49	7.74		
8	**7.27**	**23.72**	**30.92**	20.90	7.91		
9	**7.36**	**24.10**	31.53	21.37	8.10		
10	**7.45**	**24.51**	32.20	21.90	8.32		
11	**7.56**	**24.97**	32.93	22.49	8.60		
12	**7.66**	25.46	33.76	23.16	8.91		
13	**7.84**	26.04	34.53	23.59	9.28		
14	7.88	26.53	35.63	24.36	9.58		
15	7.93	27.10	36.41	25.56	10.07		
16	8.32	28.07	37.74	26.21	10.38		
17	3.92	14.93	19.61	14.83	6.88		
18	8.85	30.18	41.00	28.23	11.05		
19	8.65	30.65	41.49	29.12	11.65		
20	7.54	27.60	38.38	28.86	13.60		
21	9.08	33.11	47.47	34.67	14.17		
22	8.72	31.24	45.91	32.88	11.49		
23	5.10	18.91	33.76	34.97	21.59		
24	6.51	27.16	46.20	43.73	26.10		

Note: Rotational line strengths that have been confirmed by the current or previous (12) experiment are listed in bold.

Table 4. Theoretical values of $|M_{fo}|^2$ for $E,F^1\Sigma_g^+(v' = 0, J' = J'') - X^1\Sigma_g^+(v'', J'')$ (2 + 1) REMPI transitions in D_2 (au).

J''	$v''=0$	$v''=1$	$v''=2$	$v''=3$	$v''=4$	$v''=5$	$v''=6$
0	**4.25**	**16.33**	**25.48**	**22.15**	**11.49**	3.75	0.74
1	**4.29**	**16.23**	**25.63**	**22.17**	**11.55**		
2	**4.30**	**16.26**	**25.70**	**22.23**	**11.58**		
3	**4.31**	**16.32**	**25.81**	**22.33**	**11.63**		
4	**4.33**	**16.38**	**25.96**	**22.48**	**11.71**		
5	**4.35**	**16.48**	**26.15**	**22.66**	**11.81**		
6	**4.38**	**16.60**	**26.37**	**22.88**	11.94		
7	**4.41**	**16.77**	**26.64**	23.14	12.07		
8	**4.44**	**16.92**	**26.93**	23.44	12.25		
9	**4.47**	**17.10**	**27.27**	23.78	12.44		
10	**4.51**	**17.35**	**27.65**	24.16	12.66		
11	**4.55**	**17.50**	**28.06**	24.58	12.90		
12	**4.59**	**17.72**	28.51	25.04	13.18		
13	**4.64**	**17.96**	28.99	25.55	13.48		
14	**4.68**	**18.21**	29.52	26.10	13.81		
15	**4.72**	18.44	30.05	26.67	14.17		
16	**4.80**	18.79	30.63	27.30	14.47		
17	**4.79**	18.99	31.32	28.11	15.04		
18	4.86	19.32	31.95	28.81	15.54		
19	4.99	20.20	32.65	29.18	15.95		
20	5.02	20.07	33.39	30.31	16.58		
21	5.17	20.57	34.08	30.61	16.54		
22	5.21	21.03	35.25	32.04	17.58		
23	5.21	21.34	36.01	33.11	18.41		
24	4.97	20.82	36.12	33.65	18.72		
25	5.38	22.54	38.78	35.93	19.95		
26	5.82	26.10	43.56	40.66	21.38		
27	3.28	14.45	27.09	28.33	18.29		
28	5.27	24.56	47.57	51.92	34.37		
29	5.46	23.57	49.14	50.80	33.03		
30	4.71	19.57	39.98	41.56	22.77		

Note: Rotational line strengths that have been confirmed by the current or previous (12) experiment are listed in bold.

(g_N) as a function of rotational energy; they are fit to a straight line whose slope depends inversely on temperature. The measured rotational temperatures all lie in the expected range, indicating that the relative rotational line strengths are independent of J'' within the 10% experimental uncertainty for the rotational states measured here. This finding is confirmed by the theoretical values of the square of the two-photon transition moment $|M_{fo}|^2$, which are presented in Tables 2–4. For completeness, previously determined $|M_{fo}|^2$ are also presented in Tables 2–4 (12). The vibrational dependence of the line strengths is known theoretically, so the theoretical line strengths presented include the dependence on v''. Although the current experiment is insensitive to vibrational line strengths, a previous measurement of the vibrational line strengths is in good agreement with the theory for $v'' = 1, 2$ (12). Relative rotational line strengths that have been measured here or previously and shown to be in good agreement with theory are indicated in the tables. We find virtually no transitions in which experimental line strengths significantly disagree with the theoretical ones; the only exceptions occur at very high rotational levels ($J'' \sim 15$) of the lowest vibrational manifold. We note that the numbers presented here are line strengths, so concentrations should be

© 2004 NRC Canada

Table 5. Calculated values of frequencies for $E,F^1\Sigma_g^+(v' = 0, J' = J'') - X^1\Sigma_g^+$ (v'', J'') transitions in H_2 (cm^{-1}).

J''	$v'' = 0$	$v'' = 1$	$v'' = 2$	$v'' = 3$	$v'' = 4$	$v'' = 5$	$v'' = 6$
0	99 138.66	94 976.69	91 050.32	87 353.92	83 885.39	80 643.32	77 629.10
1	99 083.59	94 927.54	91 006.96	87 316.25	83 853.36		
2	98 974.02	94 829.76	90 920.72	87 241.36	83 789.76		
3	98 811.05	94 684.40	90 792.58	87 130.16	83 695.40		
4	98 596.29	94 492.94	90 623.93	86 983.96	83 571.52		
5	98 331.79	94 257.30	90 416.57	86 804.41	83 419.65		
6	98 019.96	93 979.73	90 172.58	86 593.47	83 241.62		
7	97 663.51	93 662.73	89 894.30	86 353.29	83 039.44		
8	97 265.46	93 309.12	89 584.34	86 086.30	82 815.36		
9	96 828.75	92 921.59	89 245.22	85 794.79	82 571.53		
10	96 356.68	92 503.20	88 879.78	85 481.40	82 310.40		
11	95 851.96	92 056.40	88 490.32	85 148.15	82 033.85		
12	95 316.32	91 582.67	88 078.05	84 796.11	81 742.80		
13	94 757.35	91 089.34	87 650.27	84 432.19	81 444.02		
14	94 185.04	90 586.18	87 215.12	84 065.80	81 146.82		
15	93 565.52	90 039.07	86 742.61	83 662.51	80 816.68		
16	92 947.40	89 496.42	86 276.01	83 270.13	80 501.33		
17	92 280.13	88 907.51	85 768.07	82 838.91	80 152.99		
18	91 637.43	88 345.91	85 289.69	82 440.65	79 840.66		
19	91 012.34	87 804.52	84 830.45	82 068.00	79 558.30		
20	90 200.23	87 078.66	84 192.28	81 518.58	79 103.63		
21	89 568.05	86 535.21	83 742.06	81 158.69	78 841.96		

Table 6. Calculated values of frequencies for $E,F^1\Sigma_g^+(v' = 0, J' = J'') - X^1\Sigma_g^+$ (v'', J'') transitions in HD (cm^{-1}).

J''	$v'' = 0$	$v'' = 1$	$v'' = 2$	$v'' = 3$	$v'' = 4$	$v'' = 5$	$v'' = 6$
0	99 303.14	95 670.43	92 215.25	88 933.81	85 824.09	82 884.45	80 114.85
1	99 261.70	95 632.85	92 181.45	88 903.73	85 797.70		
2	99 179.16	95 558.00	92 114.14	88 843.84	85 745.17		
3	99 056.11	95 446.45	92 013.86	88 754.66	85 667.00		
4	98 893.51	95 299.11	91 881.46	88 636.98	85 563.91		
5	98 692.52	95 117.05	91 717.97	88 491.77	85 436.85		
6	98 454.59	94 901.66	91 524.66	88 320.24	85 286.92		
7	98 181.34	94 654.45	91 302.97	88 123.73	85 115.40		
8	97 874.55	94 377.08	91 054.45	87 903.71	84 923.66		
9	97 536.15	94 071.36	90 780.80	87 661.76	84 713.18		
10	97 168.13	93 739.16	90 483.76	87 399.52	84 485.48		
11	96 772.55	93 382.39	90 165.12	87 118.64	84 242.16		
12	96 351.44	93 002.95	89 826.63	86 820.79	83 984.73		
13	95 906.80	92 602.69	89 470.03	86 507.56	83 714.72		
14	95 440.80	92 183.62	89 097.20	86 180.71	83 433.78		
15	94 954.91	91 747.06	88 709.35	85 841.34	83 142.93		
16	94 451.72	91 295.49	88 308.83	85 491.68	82 844.34		
17	93 921.18	90 818.72	87 885.34	85 121.34	82 527.55		
18	93 397.19	90 350.52	87 472.54	84 763.90	82 226.09		
19	92 852.79	89 863.82	87 043.30	84 392.17	81 912.70		
20	92 277.65	89 348.19	86 587.08	83 995.59	81 576.80		
21	91 715.55	88 847.34	86 147.53	83 617.77	81 262.02		
22	91 156.66	88 351.36	85 714.69	83 248.79	80 958.45		
23	90 469.91	87 729.13	85 157.39	82 757.48	80 535.06		
24	89 916.75	87 242.08	84 737.07	82 405.34	80 253.47		

obtained by dividing measured signal levels by these numbers. This convention was not followed in some previous publications in which inverse line strengths were reported (12).

Tables 5–7 present calculated frequencies for these transitions using the adiabatic potentials of the X state (22) and the (E,F) state (23). The transition frequencies for D_2 in Table 7 have been previously published (25). Due to the lack

© 2004 NRC Canada

Table 7. Calculated values of frequencies for $E,F^1\Sigma_g^+(v' = 0, J' = J'') - X^1\Sigma_g^+$ (v'', J'') transitions in D_2 (cm^{-1}).

J''	$v'' = 0$	$v'' = 1$	$v'' = 2$	$v'' = 3$	$v'' = 4$	$v'' = 5$	$v'' = 6$
0	99 460.11	96 466.56	93 592.10	90 834.67	88 192.60	85 664.71	83 250.28
1	99 432.38	96 440.94	93 568.56	90 813.16	88 173.11		
2	99 377.07	96 389.83	93 521.59	90 770.28	88 134.26		
3	99 294.45	96 313.52	93 451.47	90 706.26	88 076.28		
4	99 184.95	96 212.39	93 358.57	90 621.47	87 999.52		
5	99 049.10	96 086.96	93 243.38	90 516.37	87 904.41		
6	98 887.58	95 937.87	93 106.51	90 391.55	87 791.51		
7	98 701.14	95 765.83	92 948.64	90 247.65	87 661.44		
8	98 490.65	95 571.69	92 770.56	90 085.42	87 514.91		
9	98 257.06	95 356.32	92 573.12	89 905.67	87 352.68		
10	98 001.35	95 120.67	92 357.20	89 709.24	87 175.56		
11	97 724.60	94 865.76	92 123.78	89 497.04	86 984.40		
12	97 427.90	94 592.62	91 873.83	89 270.00	86 780.09		
13	97 112.36	94 302.29	91 608.33	89 029.05	86 563.51		
14	96 779.11	93 995.85	91 328.31	88 775.16	86 335.57		
15	96 429.29	93 674.37	91 034.76	88 509.27	86 097.16		
16	96 064.01	93 338.89	90 728.68	88 232.30	85 849.17		
17	95 684.37	92 990.45	90 411.04	87 945.20	85 592.46		
18	95 291.43	92 630.04	90 082.77	87 648.82	85 327.87		
19	94 886.25	92 258.65	89 744.81	87 344.07	85 056.25		
20	94 469.70	91 877.12	89 397.93	87 031.65	84 778.25		
21	94 043.03	91 486.60	89 043.26	86 712.65	84 494.94		
22	93 606.25	91 087.08	88 680.70	86 386.94	84 206.16		
23	93 161.66	90 680.80	88 312.46	86 056.69	83 914.04		
24	92 704.86	90 263.30	87 934.06	85 717.37	83 614.06		
25	92 245.48	89 844.18	87 555.05	85 378.52	83 315.73		
26	91 781.28	89 421.15	87 173.11	85 037.82	83 016.74		
27	91 276.13	88 958.06	86 752.06	84 659.05	82 680.91		
28	90 809.57	88 534.42	86 371.42	84 321.74	82 387.77		
29	90 337.70	88 106.30	85 987.22	83 981.95	82 093.46		
30	89 886.44	87 699.63	85 625.40	83 665.63	81 823.98		

of nonadiabatic and relativistic corrections, these frequencies are not of spectroscopic accuracy. For the X state, nonadiabatic corrections have been reported by Schwartz and Le Roy (22). However, similar calculations have not been done for the (E,F) state. To be consistent, the present calculation chooses to use the adiabatic approximation and does not incorporate nonadiabatic corrections for the X state. The calculated frequencies are expected to be of similar accuracy as the D_2 data where extensive comparisons with experiment have been made (25). Most differences are within a few cm^{-1}. The tabulated frequencies should be sufficiently accurate to allow determination of line positions in future experiments. We note that the simple appearance of these spectra (the spacing between rotational lines grows at a roughly constant rate in each vibrational manifold) will facilitate line identification. As the two-photon transition moments do not depend on the separation between the energy levels, any inaccuracies in the calculated line positions will not affect the accuracy of the line strength calculations.

Conclusions

Line strengths for many $E,F^1\Sigma_g^+(v' = 0, J' = J'') - X^1\Sigma_g^+$ (v'', J'') (2 + 1) REMPI transitions in H_2, HD, and D_2 are presented. Experimental and theoretical values for these line strengths show good agreement, and the line strengths are found to depend strongly on v'' but only weakly on J''. Knowledge of these line strengths should be useful whenever rovibrationally state resolved concentrations of molecular hydrogen are of interest, particularly in the study of the nascent populations of gas-phase or gas-surface interactions.

Acknowledgments

The work of the Stanford group is supported by the National Science Foundation under grant number 0242103.

References

1. T. Lyman. Astrophys. J. **23**, 181 (1906).
2. S. Werner. Proc. Roy. Soc. London Ser. A, **113**, 107 (1926).
3. G. Herzberg and L.L. Howe. Can. J. Phys. **37**, 636 (1959).
4. E.E. Marinero, C.T. Rettner, and R.N. Zare. J. Chem. Phys. **80**, 4142 (1984).
5. D.A.V. Kliner, K.-D. Rinnen, M.A. Buntine, D.E. Adelman, and R.N. Zare. J. Chem. Phys. **95**, 1663 (1991).
6. A.E. Pomerantz, F. Ausfelder, R.N. Zare, S.C. Althorpe, F.J. Aoiz, L. Bañares, and J.F. Castillo. J. Chem. Phys. **120**, 3244 (2004).
7. F. Ausfelder, A.E. Pomerantz, R.N. Zare, S.C. Althorpe, F.J. Aoiz, L. Bañares, and J.F. Castillo. J. Chem. Phys. **120**, 3255 (2004).

© 2004 NRC Canada

8. G. Požgainer, K.D. Rendulic, and A. Winkler. Surf. Sci. **307–309**, 344 (1994).
9. G. Eilmsteiner and A. Winkler. Surf. Sci. **366**, L750 (1996).
10. G.D. Kubiak, G.O. Sitz, and R.N. Zare. J. Chem. Phys. **83**, 2538 (1985).
11. G. Požgainer, L. Windholz, and A. Winkler. Meas. Sci. Technol. **5**, 947 (1994).
12. K.-D. Rinnen, M.A. Buntine, D.A.V. Kliner, R.N. Zare, and W.M. Huo. J. Chem. Phys. **95**, 214 (1991).
13. W.M. Huo, K.-D. Rinnen, and R.N. Zare. J. Chem. Phys. **95**, 205 (1991).
14. E.E. Marinero, R. Vasudev, and R.N. Zare. J. Chem. Phys. **78**, 692 (1983).
15. R.I. Hall, I. Cadež, M. Landau, F. Pichou, and C. Schermann. Phys. Rev. Lett. **60**, 337 (1988).
16. P.J. Eenshuistra, J.H.M. Bonnie, J. Los, and H.J. Hopman. Phys. Rev. Lett. **60**, 341 (1988).
17. D.C. Robie, L.E. Jusinski, and W.K. Bischel. Appl. Phys. Lett. **56**, 722 (1990).
18. F. Fernández-Alonso, B.D. Bean, J.D. Ayers, A.E. Pomerantz, and R.N. Zare. Z. Phys. Chem. (Muenchen), **214**, 1167 (2000).
19. W.C. Wiley and I.H. McLaren. Rev. Sci. Instrum. **26**, 1150 (1955).
20. W.M. Huo, and R.L. Jaffe. Chem. Phys. Lett. **101**, 463 (1983).
21. K.-D. Rinnen, D.A.V. Kliner, R.N. Zare, and W.M. Huo. Isr. J. Chem. **29**, 369 (1989).
22. C. Schwartz and R.J. Le Roy. J. Mol. Spectrosc. **121**, 420 (1987).
23. L. Wolniewicz and K. Dressler. J. Chem. Phys. **82**, 3292 (1985).
24. L. Wolniewicz and K. Dressler. J. Chem. Phys. **88**, 3861 (1988).
25. A.J. Heck, W.M. Huo, R.N. Zare, and D.W. Chandler. J. Mol. Spectrosc. **173**, 452 (1995).

© 2004 NRC Canada

CN spectroscopy and cosmic background radiation measurements[1]

Sydney Leach

Abstract: A source of possible error, not previously considered, in the determination of the cosmic background radiation (CBR) temperature T_γ(CN) from interstellar CN absorption is proposed. This concerns the intrinsic assumption of the validity of using Hönl–London rotational line intensity factors to determine the rotational components of the oscillator strengths of the R(0), R(1), and P(1) lines of the CN $B^2\Sigma^+$–$X^2\Sigma^+$ (0,0) transition. Published data on interstellar CN absorption shows that T_γ(CN) is slightly greater than the standard cosmological CBR temperature, T_γ(COBE) = 2.725 K, determined by the COBE satellite, even when local excitation effects of CN are taken into account. From this difference, an estimation was made of the maximum corrections, a few percent, to the ratio of the line strengths and to the ratio of the Hönl–London factors. Fluorescence lifetime data were shown to give similar values for the corrections as well as providing evidence for intramolecular coupling between the relevant $B^2\Sigma^+$ state rotational levels and close-lying levels of the $A^2\Pi$ state, this being responsible for rendering the standard Hönl–London factors invalid.

Key words: CN spectroscopy, cosmic background radiation, Hönl–London factors.

Résumé : La détermination de T_γ(CN), la température du rayonnement de fond cosmologique, à partir du spectre d'absorption de CN interstellaire pourrait être entachée d'une erreur qui n'avait jamais été envisagée jusqu'à présent. Il s'agit de l'hypothèse selon laquelle on peut utiliser les facteurs de Hönl–London pour déterminer les composantes rotationnelles des forces d'oscillateurs des raies R(0), R(1), and P(1) de la transition $B^2\Sigma^+$–$X^2\Sigma^+$ (0,0) du radical CN. Les données publiées sur le spectre d'absorption du CN interstellaire montrent que même en tenant compte des effets de l'excitation locale du CN, la valeur de T_γ(CN) est légèrement plus grande que celle du standard cosmologique, T_γ(COBE) = 2.725 K, mesurée par la satellite COBE. La différence entre T_γ(CN) et T_γ(COBE) a servi pour faire une estimation des corrections maximales, quelques pour cent, au rapport des forces de raies et au rapport des facteurs de Hönl–London. Des valeurs similaires pour ces corrections ont été obtenues à partir de données sur les durées de vie de fluorescence de CN. Ces données traduisent, d'autre part, l'existence de couplages intramoléculaires entre les niveaux rotationnels en jeu de l'état $B^2\Sigma^+$ et des niveaux voisins de l'état $A^2\Pi$, ces couplages étant responsables de la non-validité des facteurs Hönl–London classiques.

Mots clés : spectroscopie de CN, rayonnement de fond cosmologique, facteurs Hönl–London.

Introduction

Gerhard Herzberg's contributions to the application of molecular spectroscopy to astrophysics were very considerable during his long career, and his influence was profound in this respect. Herzberg was a pioneer in the electronic spectroscopy of the CN radical (1), and it is particularly fitting that the later use of interstellar CN absorption as a cosmic thermometer is of fundamental importance in studies of the cosmic background radiation (CBR) and its cosmological significance. The present work reviews the relevant spectroscopy and astrophysical observations of CN and discusses the validity of a hitherto unconsidered assumption in the spectroscopic derivation of CBR temperatures.

The first experimentally observed clear manifestation of CBR was through optical absorption spectroscopy of the CN radical in the interstellar medium (2–4), but its cosmological significance was not recognized at the time. The CN doublet at 3874 Å (1 Å = 0.1 nm) consists of the R(0) (3874.608 Å) and R(1) (3873.998 Å) lines of the $B^2\Sigma^+$–$X^2\Sigma^+$ (0,0) transition of CN (Fig. 1). The energy separation between the $N'' = 1$ and $N'' = 0$ levels (N = quantum number of angular momentum without spin) of the ground state is 3.94 cm^{-1}, which corresponds to a photon excitation wavelength of 2.64 mm. McKellar, in a paper written in 1941 (5), determined an excitation (rotational) temperature of 2.3 K, based on the (unpublished) estimation by Adams of the ratio of the relative intensities of the R(0) and R(1) lines, $I[R(0)]/I[R(1)] = 5$, in the spectrum observed in the line of sight of the star ξ Ophiuchi. The excitation mechanisms considered were those involving collisions with charged or neutral particles or the interstellar radiation field due to galactic stars. These mechanisms were later discussed by Field and Hitchcock (6) and by Thaddeus and Clauser (7).

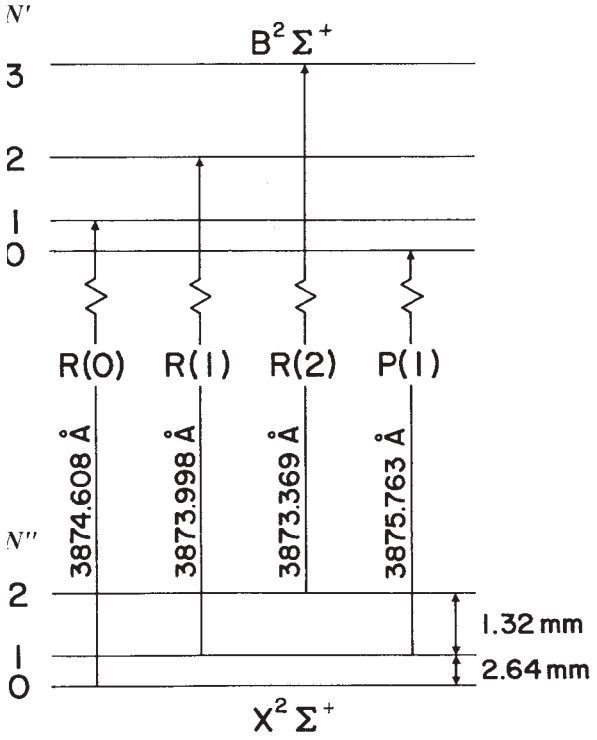
Received 25 November 2003. Published on the NRC Research Press Web site at http://canjchem.nrc.ca on 12 June 2004.

S. Leach. Laboratoire d'Etude du Rayonnement et de la Matière en Astrophysique, CNRS-UMR 8112, Observatoire de Paris-Meudon, 5 place Jules Janssen, 92195 Meudon, France. (e-mail: Sydney.Leach@obspm.fr).

[1]This article is part of a Special Issue dedicated to the memory of Professor Gerhard Herzberg.

 doi: 10.1139/V04-036 © 2004 NRC Canada

Fig. 1. Simplified energy level diagram illustrating rovibronic absorption transitions of the $B^2\Sigma^+$–$X^2\Sigma^+$ (0,0) band of CN observed in the interstellar medium.



Herzberg (8) considered the interstellar CN rotational temperature of 2.3 K to have "only a restricted meaning", which later turned out to be one of the great understatements in science. We now know that this temperature is an expression of the blackbody character of the CBR and that the quality of the Planck function, the degree of anisotropy of the radiation, its power spectrum, and the dependence of the CBR temperature on red shift restrict cosmological models (9, 10).

In 1965, Penzias and Wilson (11) observed cosmic microwave background radiation (CMBR) at $\lambda = 7.35$ cm and determined the temperature of the radiation field to be $T_\gamma = 3.5 \pm 1$ K. This brightness temperature was much more intense than that expected from extrapolation, to this wavelength region, of measurements of background radiation at wavelengths greater than 100 cm and smaller than 0.1 mm (12, 13). Dicke et al. (14) suggested that the origin of the $\lambda = 7.35$ cm radiation was related to the Big Bang, this radiation being a residue of the primeval fireball after expansion of the Universe.

The recognition that the CN observations were also manifestations of the CBR, i.e., that interstellar CN is in thermodynamic equilibrium with the CMBR at temperature T_γ, occurred in 1966, when it was shown (6, 7, 15) that the CN ground-state $N'' = 1$ rotational level could not be sufficiently populated by collisions or by transitions from higher levels but must be directly excited by photons of $\lambda = 2.64$ mm, which is close to the spectral peak of the CMBR flux. Since then, there have been many observations of interstellar CN absorption lines in a number of lines of sight, from which increasingly accurate (spectroscopic) values of T_γ have been obtained.

Determination of T_γ from CN absorption requires a number of corrections, in particular for line saturation and for eventual local electron collisional excitation (16). The present work considers a further possible source of error, not previously treated in this context. This concerns the intrinsic assumption, made in previous determinations of T_γ from CN absorption, of the validity of using Hönl–London rotational factors to express the rotational components of the transition oscillator strength values. The Hönl–London formulas are derived under the assumption of negligible interaction of rotation and electronic motion (8). Since the $v = 0$ and $v = 1$ levels of the $B^2\Sigma^+$ state of CN are affected by rotational perturbations (1, 17, 18), it is legitimate to question the validity of the assumption of negligible rotational coupling.

Direct measurements of T_γ have also been made by bolometer and radiometer techniques, which are not subject to the spectroscopic caveats, although they have other sources of error (13, 19–21). The values of T_γ obtained from these direct measurements are smaller than those deduced from CN absorption spectra. Up until now, the observed differences have been interpreted in terms of local excitation effects, mainly due to electron excitation of CN in the interstellar medium. It will be shown that even when local excitation effects are taken into account, there still exists an apparent small excess excitation temperature. The principal objective of the present investigation is to examine whether invalid Hönl–London factors can be responsible, at least in part, for the existence of an apparent difference between the T_γ values determined by these two types of measurement.

Discussion

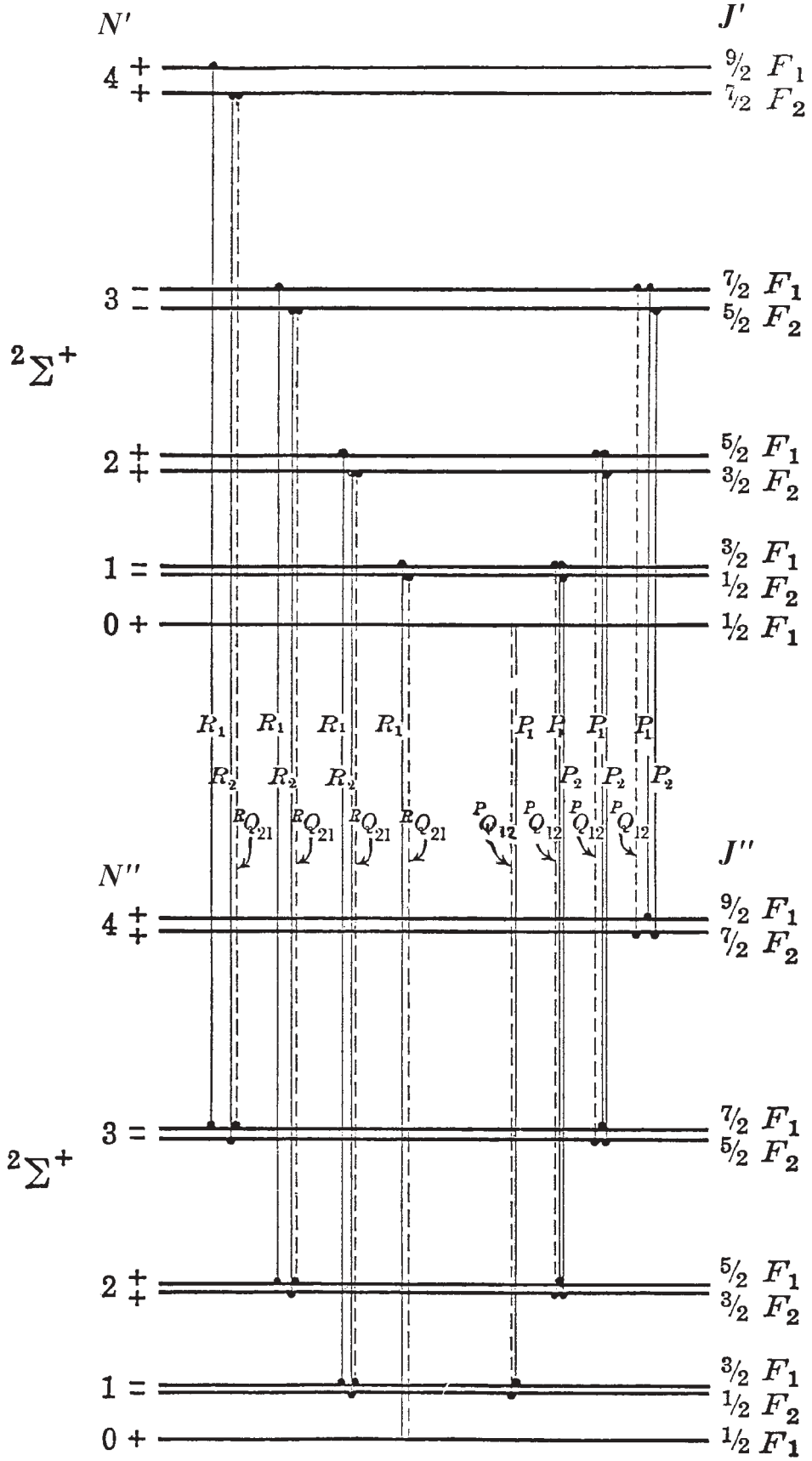
CN $B^2\Sigma^+$–$X^2\Sigma^+$ energy levels and transitions

Figure 1 presents the term diagram for the levels of most astrophysical concern in the (0,0) band of the CN $B^2\Sigma^+$–$X^2\Sigma^+$ electronic transition. Spin doubling (Fig. 2) and hyperfine structure have not been fully resolved in the optical observations of CN absorption in the interstellar medium. Therefore, the observed R(0), R(1), R(2), P(1), and P(2) lines have the following unresolved components, given in brackets: R(0) = $\{R_1(0), {}^RQ_{21}(0)\}$; R(1) = $\{R_1(1), {}^RQ_{21}(1), R_2(1)\}$; R(2) = $\{R_1(2), {}^RQ_{21}(2), R_2(2)\}$; P(1) = $\{P_1(1), {}^PQ_{12}(1)\}$; and P(2) = $\{P_1(2), {}^PQ_{12}(2), P_2(2)\}$.

From measurement of the strengths of the R(0), R(1), R(2), P(1), and P(2) absorption lines in a particular line of sight, the relative populations of CN molecules in the $N'' = 0$, 1, and 2 levels of the ground electronic state can be determined, enabling one to deduce the excitation temperatures corresponding to the $N'' = 0 \rightarrow N'' = 1$ and $N'' = 1 \rightarrow N'' = 2$ photon population processes at, respectively, $\lambda = 2.64$ mm and $\lambda = 1.32$ mm in the cosmic background blackbody radiation spectrum. As discussed later, rotational lines in the interstellar CN $B^2\Sigma^+$–$X^2\Sigma^+$ absorption transition have mainly been measured for the (0,0) band and, to a lesser extent, for the (1,0) band. The most precise data are from R(0), R(1), and P(1) lines of the (0,0) band, and these are exclusively discussed below.

© 2004 NRC Canada

Fig. 2. Energy level diagram for rotational lines of a $^2\Sigma^+$–$^2\Sigma^+$ transition (adapted from Herzberg (8)).



© 2004 NRC Canada

Determination of T_γ from CN observations

The relative populations of CN molecules in lower (″) and upper (′) rotational levels of the $v = 0$ level of the $X^2\Sigma^+$ electronic ground state are determined by the cosmic background radiation field temperature T_γ via an equation that rests on the assumption that the molecules are in thermal equilibrium and are therefore distributed in accordance with the Maxwell–Boltzmann law (8):

$$[1] \qquad N_c''/N_c' = (g''/g')\cdot\exp(h\nu/kT_\gamma)$$

where N_c'' and N_c' are the column densities of CN in lower and upper levels in the $X^2\Sigma^+$ electronic state, g' and g'' are statistical weights of the upper and lower levels, ν is the frequency difference between these levels (e.g., $\nu[(N'' = 1) - (N'' = 0)] = 1.134 \times 10^{11}$ Hz = 3.8 cm^{-1}, corresponding to the wavelength $\lambda[(N'' = 1) - (N'' = 0)] = 2.64$ mm (Fig. 1)), and k is Boltzmann's constant. If there are other sources of excitation, for example by collisions, the temperature derived from eq. [1] is an upper limit on T_γ.

The column densities, N_c, are obtained from measurement of the equivalent widths W_λ of the absorption lines (22, 23), via the following expression:

$$[2] \qquad N_c = (1.13 \times 10^{12}\ \text{cm}^{-1})(W_\lambda/\lambda^2 f)\ (\text{cm}^{-2})$$

where f is the oscillator strength of the absorption transition. The value of f for the CN $B^2\Sigma^+$–$X^2\Sigma^+$ transition is not known with very great precision (24–26), which can lead to uncertainties in column density determinations. The curve of growth (27) of W_λ as a function of a suitable parameter expressing the increasing amount of material traversed by the source photons is informative on the quality of the N_c determination.

The CBR temperature T_γ can be determined, for example, from the R(0) and R(1) absorption lines using the following equation:

$$[3] \qquad T_\gamma = (h\nu/k)/\ln[(f'/f'')(g'/g'')\{W_\lambda[\text{R}(0)]/W_\lambda[\text{R}(1)]\}]$$

with the approximation that the wavelengths of the R(0) and R(1) (and P(1)) lines are the same. In this equation, f' and f'' are the oscillator strengths of the rovibronic absorption transitions from the $X^2\Sigma^+$ ($v = 0$) ground state rotational levels $N'' = 1$ and $N'' = 0$, respectively, to specific rotational levels of the $B^2\Sigma^+$ excited state; i.e., in the case discussed here as an example, f' and f'' are, respectively, the R(1) and R(0) line transition strengths.

It should be noted that eq. [2] assumes unsaturated absorption lines, so that the temperature obtained from eq. [3] will be an upper limit on T_γ because correcting for line saturation would lead to an increase in the R(0)/R(1) intensity ratio, since the R(0) line is stronger than the R(1) line. Thus, corrections for line saturation are important. These require good knowledge of the true line profile. Very often, the assumption is made that the CN molecules have a Gaussian velocity dispersion and that the profile of the observed line corresponds to a convolution of the instrumental and intrinsic line profiles. Important in practice is the velocity width parameter b (Doppler parameter), which is related to the full width at half-maximum (fwhm) of the line profile, and its value should be consistent with the results of curve of growth studies. In all CN measurements discussed here, the observed line profiles were such that the separation between unresolved components is less than the Doppler width, so that the blend can be represented as a single line, to which is assigned an effective oscillator strength.

Interstellar CN absorption observations

The discovery of the CMBR by Penzias and Wilson in 1965 (11) soon led to a renewal of observations of interstellar CN. For 10 stars in various directions in the Galaxy, it was found that the observed CN interstellar absorption spectra were all consistent with an excitation temperature $T_{\text{rot}} \approx 2.8$ K, which showed, within experimental error, no significant difference among the different lines of sight (16). If collisions had played an important role in populating the excited rotational levels of the ground state, there should have resulted significantly different values of the CN rotational temperature in the various interstellar clouds, since physical conditions, and therefore collisional possibilities, vary from cloud to cloud. The possible contributions to CN ground-state rotational level excitation by the following four types of collision or other processes have been discussed and estimated for typical target lines of sight (16): (*i*) neutral particle impact, (*ii*) collisions with residual electrons, in HI regions, (*iii*) collisions with protons on an ionization front, and (*iv*) resonance fluorescence. Of these processes, the only one that usually has to be taken into account in CN spectroscopy determinations of T_γ is electron collisions, which generally contribute to only a very small fraction of the CN rotational temperature (16, 23, 28). A confirmation that this contribution is small is the absence of $N'' = 1 \rightarrow N'' = 0$ emission in the direction of the star BD +66° 1675, which has the highest concentration of CN in the 10 lines of sight mentioned above (29). A more recent measurement looked for CN emission towards ζ Oph, again with a null result (30). Even more recent emission measurements are discussed later.

The first measurements of the CBR temperature from optical CN observations were made on photographic plates (16). This has been found to introduce a number of errors in measurements of equivalent widths of the spectral lines (23). High-precision measurements became possible with the introduction of multichannel photoelectric detectors. Our further discussion will be based essentially on photoelectric detector measurements since 1984.

CN temperature measurements: 1984–86

The CN temperature measurements in the period 1984–86 showed increasing sophistication in dealing with the data analysis and corrections for saturation effects and collisional excitation. One of the first CN studies using photoelectric detection was that of Meyer and Jura (31), who measured CN lines at a signal-to-noise ratio (S/N) of 2000 in a molecular cloud in front of ζ Oph. After correction for saturation, the excitation temperatures were determined to be $T_{10} = 2.73 \pm 0.04$ K and $T_{21} = 2.8 \pm 0.3$ K. Electron collisional effects on the T_{10} temperature were estimated to be $T_e < 0.10$ K.

Federman et al. (24) observed the CN (0,0) band R(0), R(1), and P(1) lines along 15 lines of sight whose column density of H_2 is known. The spectral resolution R was 74 250 for 11 stars and 50 000 for 4 others. The observa-

© 2004 NRC Canada

tions were used for determining column densities for comparison with those of H_2. However, there was no discussion of T_γ, which was assumed to be 2.8 K in the calculation of CN column densities. The cosmochemistry of CN formation and destruction was the main issue in this study.

In a paper published in 1985 (23), Meyer and Jura measured CN lines in three lines of sight at $R \approx 60\,000$ and S/N » 1000. Various corrections to the raw data were discussed in detail. The sensitivity of the measurements revealed a weak broadened O_{II} line encompassing R(0) and R(1) in ζ Oph, which would have been lost in the spectral noise in the case of all previous measurements. The background continuum fit was therefore improved. Shifting photospheric lines in the spectrum of o Per (a spectroscopic binary) over 3 nights made possible measurement of CN line strengths with respect to different continua. Uncertainties in measured line strengths were due to (*i*) statistical channel-to-channel signal fluctuations, (*ii*) continuum placement errors due to noise in the continuum, (*iii*) the shape of the underlying photospheric structure, and (*iv*) the presence of weak telluric lines.

The excitation temperature T_{10} was determined with corrections for saturation, assuming Gaussian line profiles. These corrections are used to relate the observed equivalent widths to the relative rotational state populations. Taking into account the calculated correction to T_{10} for local excitation by electrons, based on a determination of the electron density in the three molecular clouds studied, the values of T_γ(CN) were as follows, where the 1σ errors were derived from equivalent width uncertainties: ζ Oph, T_γ(CN) = 2.663 ± 0.059 K; ζ Per, T_γ(CN) = 2.720 ± 0.049 K; o Per, T_γ(CN) = 2.698 ± 0.082 K. The weighted mean was T_γ(CN) = 2.70 ± 0.04 K (23).

CN temperature measurements since 1986

CN temperature measurements since 1986 are at higher spectral resolution and (or) at higher S/N than earlier measurements (28). Crane et al. (32) observed CN lines towards ζ Oph at $R = 156\,000$. They measured precise values of the equivalent widths of the (0,0) band R(0), R(1), and P(1) lines. They also detected the R(2) line uncontaminated by telluric lines. The linewidths were determined on the assumption that the interstellar cloud contains a single component with a Gaussian velocity spread. CN linewidths were narrower than those previously reported, which led to larger curve of growth corrections to the observed equivalent widths than in previous analyses. As a result, the measured equivalent widths of the R(0), R(1), and P(1) lines differ significantly from those of Meyer and Jura (23). In 1989, Crane et al. (30) reanalyzed their CN absorption data towards ζ Oph to provide even more accurate equivalent widths. To improve saturation corrections, they used new CO millimetre observations data to better understand the velocity structure of the interstellar clouds. They also searched for CN emission at 2.64 mm. From the null result, their analysis gives $T_e = 0.000(+0.031, -0.000)$ K for the electron collision component of the excitation temperature.

The nature of the possible errors on T_γ in this work is typical of all T_γ(CN) measurements. These errors and their estimated magnitudes (in parentheses) are (*i*) statistical error (±13.3 mK) in the equivalent widths; (*ii*) uncertainty due to possible scale error in the equivalent widths (±5 mK); (*iii*) error due to local excitation of CN (a maximum of −31 mK); and (*iv*) error introduced by uncertainty in the model for the saturation correction (–18 mK).

The final T_γ(CN) temperature values obtained are given in Table 1 separately for R(0)/R(1) and R(0)/P(1) measurements, as is done for all further T_γ(CN) measurements discussed in this work. These two sets of T_γ(CN) determinations involve different probes of the ground state $N = 1$ level population and therefore different f'/f'' values in eq. [3]. The significance of this distinction will be addressed later.

Meyer et al. (33) observed with high S/N the CN $B^2\Sigma^+$–$X^2\Sigma^+$ (1,0) 3580 Å and (0,0) 3874 Å lines towards HD 21483, providing very accurate measurements of the (0,0) band R(2) and P(2) and the (1,0) band R(0) lines. Measurement of the optically thin (1,0) band R(0) line allowed correction of CN lines for saturation and the determination of accurate $N'' = 0$ column densities. CN emission at 2.64 mm was searched for but not observed. Excitation temperatures were determined, with correction for saturation, and the resulting T_γ(CN) temperature values are listed in Table 1. It should be noted that other high-S/N observations of the CN $B^2\Sigma^+$–$X^2\Sigma^+$ (1,0) band R(0) line were made by Meyer and Roth, towards ζ Oph (34). Measurement of the equivalent width of the R(0) line provided column density values consistent with the earlier assumption of a single-component line profile, and this in spite of the complex velocity structure revealed by CO millimetre-wave observations in the ζ Oph line of sight. The data on a tentatively identified R(1) line in the (1,0) band were insufficient to determine a value of T_γ(CN) from this vibronic transition.

In 1990, Kaiser and Wright (35) published a study of the CN (0,0) band lines towards ζ Per at a high resolution, $R = 150\,000$–$170\,000$. They obtained a very accurate value of 1.25 ± 0.02 km s^{-1} for the R(0) linewidth parameter *b* along this line of sight. Kaiser and Wright consider that Meyer and Jura (23) did not have sufficient spectral resolution to determine *b* from their data along this same line of sight. Consequently, they believe that the uncertainty in the saturation corrections to the equivalent width measurements of Meyer and Jura was their dominant error along the line of sight to ζ Per. In determining T_γ, Kaiser and Wright adopted the collisional excitation correction determined for ζ Per by Meyer and Jura (23), $T_e = 0.04 \pm 0.02$ K. The T_γ values for the R(0)/R(1) and R(0)/P(1) measurements of Kaiser and Wright, separately averaged over four different nights of observation, are given in Table 1.

Measurements of CN towards HD 154368 were made by Palazzi et al. (36). This line of sight has a CN column density at least 7 times greater than that towards ζ Oph. Observation of weak CN emission at a wavelength of 2.64 mm enabled estimates to be made of the contribution of electron collisions to the excitation temperatures. After corrections for line saturation, the CN excitation temperatures obtained for HD 154368 were R(0)/R(1) $T_{10} = 2.849 \pm 0.037$ K and R(0)/P(1) $T_{10} = 2.889 \pm 0.037$ K, and the calculated correction to T_{10} for local excitation by electrons was $T_e = -0.035 \pm 0.009$ K. The ensuing T_γ values are given in Table 1.

This group of workers also observed the CN (0,0) band R(0), R(1), and P(1) lines in 10 other lines of sight (37) but

© 2004 NRC Canada

Table 1. Cosmic background radiation temperature T_γ from selected CN $B^2\Sigma^+$–$X^2\Sigma^+$ (0,0) band absorption observations.

		T_γ(CN) (K)	
Reference	Star	R(0)/R(1) measurements	R(0)/P(1) measurements
Crane et al. (30)	ζ Oph	2.796±0.016	2.797±0.025
Meyer et al. (33)	HD 21483	2.767±0.072	2.751±0.083
Kaiser and Wright (35)	ζ Per	2.792±0.025	2.707±0.045
Palazzi et al. (36)	HD 154368	2.814±0.035	2.854±0.037
Roth and Meyer (28)	ζ Oph	2.734±0.025	2.740±0.035

reported only the weighted averages of R(0)/R(1) and R(0)/P(1) values of the T_{10} excitation temperature, with quite large error bars. They also made a statistical analysis of all 35 (weighted average) excitation temperatures measured using interstellar CN, to which I will return later.

CN absorption of the (1,0) and (0,0) bands in lines of sight towards five diffuse interstellar clouds, ζ Oph, ζ Per, HD 27778, HD 21483, and HD 154368, was studied by Roth et al. (38) and by Roth and Meyer (28) at high S/N. The excitation temperatures they reported are weighted averages of R(0)/R(1) and R(0)/P(1) values of T_{10} and were corrected for estimated local collisional excitation processes. The best measurements are for the ζ Oph line of sight. From the column densities for the R(0), R(1), and P(1) lines reported by Roth and Meyer (28), and using their same local excitation correction, I determined T_γ for separate R(0)/R(1) and R(0)/P(1) measurements. The values obtained are reported in Table 1.

Direct bolometer and radiometer measurements of T_γ

Early radiometer measurements were made from the ground (39, 40) and from balloons with far-infrared (FIR) spectrometers. Measurements using rockets (COBRA (41)) and an orbiting observatory, the Cosmic Background Explorer (COBE) containing a Far IR Absolute Spectrophotometer (FIRAS) (42, 43), provided an initial value of T_γ = 2.726 ± 0.010 K. The best COBE value to date is T_γ(COBE) = 2.725 ± 0.001 K (9, 21, 43, 44). This is recognized as the standard value of T_γ for cosmological purposes (9).

Recent measurements of the CBR, in particular using the Wilkinson Microwave Anisotropy Probe (WMAP), have not provided new values of T_γ but have been concerned essentially with the CMB power spectrum, its analysis, and its cosmological implications (10).

Comparison between T_γ(COBE) and T_γ(CN)

Bolometer and radiometer measurements give local values of T_γ, i.e., at about 1 AU from the Sun, whereas T_γ measurements via CN absorption have provided values of interstellar T_γ in several clouds within 1 kpc. An analysis by Palazzi et al. (37) of 35 CN measurements of T_γ carried out by various authors, including some of their own measurements, during the period 1985–92, gave a weighted average value T_γ(CN) = 2.818 ± 0.018 K that is above the COBE value of 2.725 ± 0.001 K by 93 ± 19 mK. These authors examined all known mechanisms that could contribute to local rotational excitation of CN, in particular, electron and neutral particle collisions and radiative fields such as diffuse galactic starlight, stellar radiation beyond the molecular cloud, and radiation emanating from dust within the clouds. None of these mechanisms was found to account for the 93 ± 19 mK excess in the CN measurements.

Wright et al. (45) made a critique of the compilation of CN data by Palazzi et al. (37). They suggest that the local excitation corrections made by Palazzi et al. may not be justified and that there is a small statistical bias in the histogram technique used, the latter having been introduced previously by Palazzi and co-workers (46). This critique mainly stresses the difficulties, due to low optical depth, that are encountered in using CN millimetre emission to determine the extent of local excitation above the CBR temperature.

A more recent statistical study by Crane (47) is based on published CN data from a sample of the 13 most accurate measurements published during the period 1985–93. He used a common procedure to process the different data sets, i.e., for correcting the measured equivalent widths for saturation effects and for calculating the errors associated with the uncertainty in both the equivalent widths and the *b* values. In this way, he obtained a weighted average value T_γ(CN) = 2.762 ± 0.012 K from the CN data. The difference from the COBE value is 37 ± 13 mK, which is about 3 standard deviations.

I have also chosen to examine what I consider to be the 10 best measurements of T_γ(CN), including saturation corrections and electron excitation corrections, where the values determined from R(0)/R(1) and R(0)/P(1) intensity ratios are specified separately (Table 1). The average of the 10 CN measurements in Table 1 gives T_γ(CN) = 2.775 K. Since T_γ(COBE) = 2.725 K, it follows that T_γ(CN) - T_γ(COBE) = 50 mK. The statistical error of the weighed average of T_γ(CN) is of the order of 15 mK (47). I concur with a concluding remark of Crane (47) that this difference may be due to underestimated local excitation effects, but he also added that there could be a new effect, not previously considered, that could explain a difference between the COBE and CN values of T_γ. Invalid Hönl–London factors, as suggested in the present study, is indeed a "new effect" that I have considered as worth exploring.

The possible effects of intramolecular state mixing on the rotational component of the CN line oscillator strengths

Invalid Hönl–London factors are equivalent here to incorrect ratios f'/f'' of the oscillator strengths in eq. [3]. As

© 2004 NRC Canada

mentioned earlier, the $B^2\Sigma^+$–$X^2\Sigma^+$ transition oscillator strength f is not known with very great precision (24–26), and this leads to uncertainties in column density determinations. However, assuming the validity of the Born–Oppenheimer approximation, this oscillator strength can be factorized into three components, f_{el}, f_{vib}, and f_{rot}, which are, respectively, the purely electronic, the vibrational (Franck–Condon), and the rotational components. For a given vibronic transition, e.g., $B^2\Sigma^+$–$X^2\Sigma^+$ (0,0), and insofar as differential rovibronic effects on f are negligible, the binary product $f_{ev} = f_{el} \times f_{vib}$ would thus be the same for the upper ($N'' = 1$) and lower ($N'' = 0$) rotational levels of the $X^2\Sigma^+$ $v = 0$ ground state, so that the ratio f'/f'' is determined only by the rotational components, f'_{rot}/f''_{rot}. However, in all T_γ determinations from CN optical spectra, it was assumed that f_{rot} is given by Hönl–London factors, where these factors are summed for each unresolved component of each line.

Taking into account the blends of unresolved components in the rotational lines, the normalized Hönl–London factors $S_{J'J''}$ for the observed absorption lines of a CN $^2\Sigma$–$^2\Sigma$ transition are $S(R(0)) = 1$, $S(R(1)) = 2/3$, and $S(P(1)) = 1/3$. The normalization has been carried out according to the sum rule for $^2\Sigma^+ \rightarrow {}^2\Sigma^+$ transitions (48): $\sum S_{J'J''} = 2S(2J''+1)$, where the sum, over all J' values, covers the transitions R_1, R_2, $^RQ_{21}$, P_1, $^PQ_{12}$, and P_2 shown in Fig. 2. It follows that the Hönl–London factor ratios f'/f'' in eq. [3] have effective values for the CN ground state (24) of 2/3 for the R(1)/R(0) transitions and 1/3 for the P(1)/R(0) transitions.

As mentioned in the *Introduction*, the Hönl–London formulas are derived under the assumption of negligible interaction of rotation and electronic motion (8). However, it has been known since the pioneer study of Herzberg (1) that the $B^2\Sigma^+$ state of CN is affected by rotational perturbations. In particular, the $v' = 0$, $N' = 4$ rotational level is quite strongly coupled to the $N = 4$ rotational level of the $A^2\Pi$, $v = 10$ state of CN (18, 49). It is thus of interest to consider whether there exist intramolecular interstate coupling effects for lines involved in the CN interstellar absorption observations. In that case, the Hönl–London formulas would no longer be valid. Perturbation interactions between the $B^2\Sigma^+$ and $A^2\Pi$ states must obey Kronig's selection rules (8): $\Delta J = 0$; $\Delta S = 0$; $\Delta\Lambda = 0, \pm 1$, and interacting levels of the same parity, i.e., both + or both –, where the symbols are as defined by Herzberg (8).

Whether interstate coupling exists can be ascertained by observation of evident spectral perturbations or, possibly more sensitively, by determination of oscillator strengths, via lifetime measurements of fluorescence from the suspected rotational levels of the $B^2\Sigma^+$ state. The relevant information will be discussed later.

Comparison between T_γ(COBE) and T_γ(CN) values obtained from R(0)/R(1) and from R(0)/P(1) intensity ratios

R(0) is the only line that can effectively suffer from any saturation effects. Since R(0) is common to both sets of intensity ratios, the saturation correction uncertainty and local excitation uncertainty should be same for the R(0)/R(1) and R(0)/P(1) measurements. A comparison between the T_γ(CN) for the two sets of measurements should be independent of the absolute value of T_γ(CN), thereby permitting a test of whether there is a difference in their values.

The separate R(0)/R(1) and R(0)/P(1) data in Table 1 give average T_γ(CN) values: of 2.780 and 2.770 K, respectively. The COBE value of $T_\gamma = 2.725$ K is smaller than each of the two values of T_γ(CN): for R(0)/R(1), $T_\gamma(CN) - T_\gamma(COBE) = 55$ mK, and for R(0)/P(1), $T_\gamma(CN) - T_\gamma(COBE) = 45$ mK. The error bars on the weighted average values of T_γ(CN) are of the order of 15 mK (47), so that these results do not reveal a definite difference of the T_γ(CN) value in the two sets of measurements. However, they do corroborate previous findings (37, 47) that there is a significant difference between T_γ(CN) and T_γ(COBE) and that T_γ(CN) is greater than T_γ(COBE).

Following the discussion in the previous section, the existence of a difference between T_γ(CN) and T_γ(COBE) can be interpreted as indicating that in the CN $B^2\Sigma^+$ state, $v = 0$ level, the $N' = 2$ and $N' = 0$ rotational levels (i.e., the upper level of the R(1) and P(1) lines, respectively) are involved in intramolecular radiationless coupling between the $B^2\Sigma^+$ and the $A^2\Pi$ states of CN. As shown below, the effect would be to diminish the effective oscillator strength of these transitions, thus modifying the effective Hönl–London rotational line factors.

The oscillator strength of the $B^2\Sigma^+$–$X^2\Sigma^+$ transition is known to be much greater than that of the $A^2\Pi$–$X^2\Sigma^+$ transition (50). Therefore, intramolecular radiationless coupling between rovibronic levels of the $B^2\Sigma^+$ and $A^2\Pi$ states will lead to a decrease in the oscillator strengths of radiative transitions involving the rotational levels of the B state that are coupled to the A state levels (18). The $X^2\Sigma^+$ $v = 0$ ground state is not affected by intramolecular coupling. In the case of the R(1), R(0), and P(1) lines, the upper-state rotational levels have rotational quantum numbers $N' = 2$, $N' = 1$, and $N' = 0$, respectively. The f' value of eq. [3] refers to the R(1) and P(1) line transitions; i.e., the ground-state $N'' = 1$ level is probed by two lines, giving rise to two different f' values, while the f'' value is that of the R(0) line transition, which alone probes the $N'' = 0$ level (Fig. 1).

As mentioned above, interelectronic state coupling is certainly negligible for the $X^2\Sigma^+$ $v = 0$ level. Thus, if all other sources of error are equal, a comparison between T_γ values deduced from CN rotational level populations and the values of T_γ obtained from direct measurements, which are not subject to the spectroscopic caveats, can allow estimates to be made of the relative errors of the Hönl–London factor ratios in eq. [3] due to coupling between $B^2\Sigma^+$ and $A^2\Pi$ state rovibronic levels.

From eqs. [1]–[3], one obtains that the CN excitation temperature $T_\gamma(CN) \propto \beta[\ln \theta(f'/f'')]^{-1}$, where β and θ are constants whose values are specific to each line-of-sight measurement. Thus, the observational result $T_\gamma(CN) > T_\gamma(COBE)$ implies that the ratio f'/f'' must be increased to diminish T_γ(CN) so that it becomes equal to T_γ(COBE). In terms of Hönl–London factors, this implies that the standard Hönl–London factor ratios used in all previous determinations of T_γ(CN) from eq. [3] should be modified.

As an illustration, using eqs. [1]–[3], it is possible to estimate the values of these parameter modifications from the T_γ(CN) data discussed above. From the differences $T_\gamma(CN)$ –

© 2004 NRC Canada

Table 2. Radiative lifetimes of the $N' = 0$–4 rotational levels of the $B^2\Sigma^+$ state $v = 0$ vibrational level.

	Fluorescence lifetime (ns)	
Rotational level N'	Jackson (53)	Duric et al. (54)
0	65.1±0.8	66.7±1.4
1	66.9±0.5	64.8±1.4
2	64.8±0.6	65.8±1.4
3	65.0±0.6	68.0±1.4
4	71.3±0.3	72.9±0.6

T_γ(COBE) of 55 mK (R(0)/R(1) measurements) and 45 mK (R(0)/P(1) measurements), the correction should be an increase of 3.87% in the $f'(N' = 2)/f''(N' = 1)$ ratio and of 3.19% in the $f'(N' = 0)/f''(N' = 1)$ ratio. The corresponding Hönl–London factor ratios are then 0.6925 (instead of 0.6667) and 0.3440 (instead of 0.3333) for the R(0)/R(1) measurements and R(0)/P(1) measurements. respectively. These are order-of-magnitude values and can be refined by taking into account error estimates in T_γ(CN).

Is there spectroscopic or excited-state lifetime evidence for coupling between the CN $B^2\Sigma^+$, $v = 0$, $N' = 0$–2 rotational levels and the $A^2\Pi$ state?

Examination of the observed and calculated high-resolution spectral line position data for the (0,0) band of the CN $B^2\Sigma^+$–$X^2\Sigma^+$ transition, obtained by Prasad et al. (51) in two different laboratory emission sources, did not reveal any evident marked perturbation of the R(0), R(1), and P(1) lines. However, a weak line appears to exist close to the P(1) line in the published spectrum of the P branch (no spectrum of the R branch was published), obtained using a discharge source (51), and is possibly an extra-line which, if confirmed, is indicative of a perturbation of the $N' = 0$ level of the $B^2\Sigma^+$ $v = 0$ excited state.

Another test of intramolecular coupling between rotational levels of the $B^2\Sigma^+$ and $A^2\Pi$ states is possible from fluorescence lifetime measurements of individual rotational levels of the $B^2\Sigma^+$ $v = 0$ state, since there is an inverse relation between lifetime and oscillator strength (8, 52). Measurements of radiative lifetimes of up to 16 rotational states of the CN $B^2\Sigma^+$ $v = 0$ level have been carried out by Jackson (53) and by Duric et al. (54). The lifetimes of the individual rotational levels are sensitive to the degree of coupling between the $B^2\Sigma^+$ and $A^2\Pi$ states. For $v'' > 0$, only bandheads were measured. The method used by Jackson involved measuring the decay of CN $B^2\Sigma^+$ state fluorescence excited by a tunable dye laser, whereas Duric et al. used electron beam excitation coupled to the high-frequency deflection technique. It should be noted that the $B^2\Sigma^+$ state can also decay radiatively to the $A^2\Pi$ state (55). The B $\rightarrow$ A branching ratio for the $B^2\Sigma^+$ $v = 0$ level is of the order of 0.003 (56, 57) so that this radiative "leakage" has negligible effect on the lifetimes of the $N' = 0$–2 rovibronic levels of the $B^2\Sigma^+$ state.

Table 2 gives the values of the measured fluorescence lifetimes of the $N' = 0$–4 rotational levels. The measurements of Jackson (53) and Duric and al. (54) are generally in good agreement but differ significantly for the crucial $N' = 1$ rotational level. The error limits are 2σ in the case of Jackson's measurements and were not specified for those of Duric et al.

Because the oscillator strength is inversely proportional to the lifetime, a longer lifetime implies a smaller oscillator strength. In the case of the R(0)/R(1) measurements of T_γ(CN), the ratio f'/f'' is that of $f(N' = 2)/f(N' = 1)$, while for the R(0)/P(1) measurements, the ratio f'/f'' is that of $f(N' = 0)/f(N' = 1)$. The lifetime measurements of Jackson favour both $f(N' = 2) > f(N' = 1)$ and $f(N' = 0) > f(N' = 1)$. These results are consistent with the conclusion of the previous section that the ratio f'/f'' should be increased over that given by the standard Hönl–London factor ratios. The lifetime values of Duric et al., which are of lesser precision, and are possibly also subject to population cascade effects (54), also support $f(N' = 2) > f(N' = 1)$ but favour $f(N' = 0) < f(N' = 1)$. It is the different values of the $N' = 1$ lifetime in the two measurements that is responsible for this disagreement.

Quantitatively, the lifetime data of Jackson (53) indicate that for the determination of T_γ(CN) from R(0)/R(1) measurements, the f'/f'' ratio should be increased by 3.24% ± 1.7% and that of the R(0)/P(1) measurements by 2.76% ± 2.0%. These values are of the same order of magnitude as those deduced in the previous section (3.87% and 3.19%, respectively) from the T_γ(CN) – T_γ(COBE) data. The corresponding modifications of the Hönl–London factor ratios, from the mean values of the lifetimes, are 0.6883 (instead of 0.6667) and 0.3425 (instead of 0.3333) for the R(0)/R(1) and R(0)/P(1) measurements, respectively.

It should be noted that the lifetime of the $N' = 4$ state is markedly different from those of the other N' levels in Table 2. This longer lifetime results from the well-known perturbation of the $N' = 4$, $J' = 3.5$ rotational level of the $B^2\Sigma^+$ $v = 0$ state with an energetically quasi-degenerate rotational level, $N = 4$, $J = 4.5$, of the $v = 10$ vibrational level of the $A^2\Pi$ state (18), which shows up spectacularly in producing a strong extra-line in the CN absorption or emission spectrum (18, 49). The intrastate mixing coefficient can be estimated from the relative intensities of the main and extra-lines (18, 49) as well as from differences between the lifetimes of perturbed and unperturbed levels, as has been achieved for the $N' = 4$ level of the $B^2\Sigma^+$ $v = 0$ state (53, 54). For the $N' = 0$, 1, and 2 levels, the variation in the measured lifetimes, although real, is not large. This indicates that the coefficients of intrastate mixing of the $N' = 0$, 1, and 2 rovibronic levels with the appropriate $A^2\Pi$ state levels obeying the Kronig selection rules would be relatively small, thus making it difficult, in these cases, to observe any corresponding perturbations from spectral line positions.

Conclusion

Observations have been reviewed which indicate that the cosmic background radiation temperature T_γ determined from CN $B^2\Sigma^+$–$X^2\Sigma^+$ absorption line intensities is higher than that determined by direct methods such as from COBE satellite measurements. Even when CN local excitation processes have been taken into account, there still remains a small excess temperature. This excess temperature has been previously interpreted as due to insufficient corrections for electron excitation processes. This may indeed be the case,

© 2004 NRC Canada

since knowledge of electron densities n(e) in interstellar clouds is necessary for the determination of local excitation (16) but the estimation of n(e) by excitation modelling (37) or from CN emission measurements (45) is fraught with many difficulties and subtleties.

An alternative explanation of, or at least a contributory factor to, the excess temperature, given in the present study, is the use of invalid Hönl–London factor ratios in T_γ(CN) determinations from eq. [3], i.e., inadequate ratios of rotational line strengths. These inadequacies could arise from intramolecular coupling between the $B^2\Sigma^+$ state rotational levels involved in the R(0), R(1), and P(1) transitions and close-lying rotational levels of the $A^2\Pi$ state obeying the Kronig selection rules. Estimates of the necessary corrections to the f'/f''oscillator strength ratios and to the ratios of Hönl–London factors were made, assuming that the entire apparent excess temperature is due to invalid Hönl–London factor ratios. These corrections were determined from the differences between T_γCN) and T_γ(COBE) values obtained from R(0)/R(1) and R(0)/P(1) CN line intensity ratio measurements.

Similar correction values were obtained using values of the lifetimes of the $N' = 0$–2 rotational levels of the $B^2\Sigma^+$ $v = 0$ state. The lifetime measurements of Jackson (53) showed evidence for interstate coupling, but the mixing coefficients would be too small for these effects to show up as marked perturbations of the $N'= 0$–2 levels in the CN absorption or emission spectra.

Confirmation of the thesis of the present study, and determination of the extent of the contribution of invalid Hönl–London factors to the excess excitation temperature of CN, requires further studies: more precise interstellar CN measurements, better determinations of local excitation effects, and laboratory investigations, including both spectral and lifetime measurements, of possible interactions between the CN $A^2\Pi$ state and low-lying rotational levels of the $B^2\Sigma^+$ $v = 0$ state.

Acknowledgements

I thank Daniel Cossart, François Rostas, and Joelle Rostas for thoughtful remarks on the manuscript.

References

1. G. Herzberg. Z. Phys. **49**, 512 (1928); **52**, 815 (1929).
2. T. Dunham, Jr. Publ. Astron. Soc. Pac. **49**, 26 (1937).
3. A. McKellar. Publ. Astron. Soc. Pac. **52**, 187 (1940).
4. W.S. Adams. Astrophys. J. **93**, 11 (1941).
5. A. McKellar. Publ. Dom. Astrophys. Obs. Victoria, **7** [No.15, (1941)], 251 (1949).
6. G.B. Field and J.L. Hitchcock. Phys. Rev. Lett. **16**, 817 (1966).
7. P. Thaddeus and J.F. Clauser. Phys. Rev. Lett. **16**, 919 (1966).
8. G. Herzberg. Molecular spectra and molecular structure. I. Spectra of diatomic molecules. Van Nostrand, Princeton, N.J. 1950.
9. J.M. LoSecco, G.J. Mathews, and Y. Wang. Phys. Rev. D, **64**,123 002 (2001).
10. C.S. Frenk. Philos. Trans. R. Soc. London, Ser. A, **360**, 1277 (2002); J.R. Bond, C. Contaldi, and D. Pogosyan. Philos. Trans. R. Soc. London, Ser. A, **361**, 2435 (2003); J.A. Peacock, Philos. Trans. R. Soc. London, Ser. A, **361**, 2479 (2003).
11. A.A. Penzias and R.W. Wilson. Astrophys. J. **142**, 419 (1965).
12. M.S. Longair and R.A. Sunyaev. Sov. Phys. Usp. **105**, 41 (1971).
13. R. Weiss. Annu. Rev. Astron. Astrophys. **18**, 489 (1980).
14. R.H. Dicke, P.J.E. Peebles, P.G. Roll, and D.T. Wilkinson. Astrophys. J. **142**, 414 (1965).
15. I.S. Shklovsky. Astron. Circ. No. 364. Acad. Sci. USSR (1966).
16. P. Thaddeus. Annu. Rev. Astron. Astrophys. **10**, 305 (1972).
17. A.T. Wager. Phys. Rev. **64**, 18 (1943).
18. S. Leach. *In* Molecular energy transfer. *Edited by* R.D. Levine and J. Jortner. Halsted Press, New York. 1975. pp. 163–177.
19. R.Weiss. Annu. Rev. Astron. Astrophys. **18**, 489 (1980).
20. D.J. Fixsen, E.S. Cheng, D.A. Cottingham, R.E. Eplee, Jr., T. Hewagama, R.B. Isaacman, K.A. Jensen, J.C. Mather, D.L. Massa, S.S. Meyer, P.D. Noerdlinger, S.M. Read, L.P. Rosen, R.A. Shafer, A.R. Trenholme, R. Weiss, C.L. Bennett, N.W. Boggess, D.T. Wilkinson, and E.L. Wright. Astrophys. J. **420**, 457 (1994).
21. D.J. Fixsen, E.S. Cheng, J.M. Gales, J.C. Mather, R.A. Shafer, and E.L.Wright. Astrophys. J. **473**, 576 (1996).
22. L.Spitzer. Physical processes in the interstellar medium. Wiley, New York. 1978.
23. D.M. Meyer and M. Jura. Astrophys. J. **297**, 119 (1985).
24. S.R. Federman, A.C. Danks, and D.L. Lambert. Astrophys. J. **287**, 219 (1984).
25. S.P. Davis, D. Shortenhaus, G. Stark, R. Engleman, Jr., J.G. Phillips, and R.P. Hubbard. Astrophys. J. **303**, 892 (1986).
26. C.W. Bauschlicher, Jr., S.R. Langhoff, and P.R. Taylor. Astrophys. J. **332**, 531 (1988).
27. B. Strömgren. Astrophys. J. **108**, 242 (1948).
28. K.C. Roth and D.M. Meyer. Astrophys. J. **441**, 129 (1995).
29. A.A. Penzias, K.B. Jefferts, and R.W. Wilson. Phys. Rev. Lett. **28**, 772 (1972).
30. P. Crane, D.J. Hegyi, M.L. Kutner, and N. Mandolesi. Astrophys. J. **346**, 136 (1989).
31. D.M. Meyer and M. Jura. Astrophys. J. **276**, L1 (1984).
32. P. Crane, D.J. Hegyi, N. Mandolesi, and A.C. Danks. Astrophys. J. **309**, 822 (1986).
33. D.M. Meyer, K.C. Roth, and I. Hawkins. Astrophys. J. **343**, L1 (1989).
34. D.M. Meyer and K.C. Roth. Astrophys. J. **349**, 91 (1990).
35. M.E. Kaiser and E.L. Wright. Astrophys. J. **356**, L1 (1990).
36. E. Palazzi, N. Mandolesi, M.L. Kutner, P. Crane, J.C. Blades, and D.J. Hegyi. Astrophys. J. **357**, 14 (1990).
37. E. Palazzi, N. Mandolesi, and P. Crane. Astrophys. J. **398**, 53 (1992).
38. K.C. Roth, D.M. Meyer, and I. Hawkins. Astrophys. J. **413**, L67 (1993).
39. G.F. Smoot, M. Bensadoun, M. Bersanelli, G. De Amici, A. Kogut, S. Levin, and C. Witebsky. Astrophys. J. **317**, L45 (1987).
40. A. Kogut, M. Bensadoun, G. De Amici, S. Levin, and C. Witebsky. Astrophys. J. **335**, 102 (1990).
41. H.P. Gush, M. Halpern, and E.H. Wishnow. Phys. Rev. Lett. **65**, 537 (1990).
42. J.C. Mather, E.S. Cheng, R.E. Eplee, Jr., R.B. Isaacman, S.S. Meyer, R.A. Shafer, R. Weiss, E.L. Wright, C.L. Bennett, N.W. Boggess, E. Dwek, S. Gulkis, M.G. Hauser, M. Janssen, T. Kelsall, P.M. Lubin, S.H. Moseley, Jr., T.L. Murdock, R.F. Silverberg, G.F. Smoot, and D.T. Wilkinson. Astrophys. J. **354**, L37 (1990).
43. J.C. Mather, E.S. Cheng, D.A. Cottingham, R.E. Eplee, Jr., D.J. Fixsen, T. Hewagama, R.B. Isaacman, K.A. Jensen, S.S. Meyer, P.D. Noerdlinger, S.M. Read, L.P. Rosen,

© 2004 NRC Canada

R.A. Shafer, E.L. Wright, C.L. Bennett, N.W. Boggess, M.G. Hauser, T. Kelsall, S.H. Moseley, Jr., R.F. Silverberg, G.F. Smoot, R. Weiss, and D.T. Wilkinson. Astrophys. **420**, 439 (1994).
44. J.C. Mather, D.J. Fixsen, R.A. Shafer, C. Mosier, and D.T. Wilkinson. Astrophys. J. **512**, 511 (1999); D.J. Fixsen and J.C. Mather. Astrophys. J. **581**, 817 (2002).
45. E.L. Wright, J.C. Mather, D.J. Fixsen, A. Kogut, R.A. Shafer, C.L. Bennett, N.W. Boggess, E.S. Cheng, R.F. Silverberg, G.F. Smoot, and R. Weiss. Astrophys. J. **420**, 450 (1994).
46. E. Palazzi, N. Mandolesi, and P. Crane. Astrophys. J. **326**, 905 (1988).
47. P. Crane. Astrophys. Lett. Commun. **32**, 27 (1995).
48. E.E. Whiting, A. Schadee, J.B. Tatum, J.T. Hougen, and R.W. Nicholls. J. Mol. Spectrosc. **80**, 249 (1980).
49. H.E. Radford and H.P. Broida. J. Chem. Phys. **38**, 644 (1963).
50. S.P. Davis, D. Shortenhaus, G. Stark, R. Engleman, Jr., J.G. Phillips, and R.P. Hubbard. Astrophys. J. **303**, 892 (1986).
51. C.V.V. Prasad, P.F. Bernath, C. Frum, and R. Engleman, Jr. J. Mol. Spectrosc. **151**, 459 (1992).
52. M. Larsson. Astron. Astrophys. **128**, 291 (1983).
53. W.M. Jackson. J. Chem. Phys. **61**, 4177 (1974).
54. N. Duric, P. Erman, and M. Larsson. Phys. Scr. **18**, 39 ((1978).
55. F.J. Leblanc. J. Chem. Phys. **48**, 1841 (1968).
56. D.C. Cartwright and P.J. Hay. Astrophys. J. **257**, 383 (1982).
57. M. Larsson, P.E.M. Siegbahn, and H. Agren. Astrophys. J. **272**, 369 (1983).

© 2004 NRC Canada

SiO as a chemical signature of outflows from bright, compact sources in MSX IR-dark clouds[1]

P.A. Feldman, R.O. Redman, L.W. Avery, J. Di Francesco, J.D. Fiege, S.J. Carey, and F. Wyrowski

Abstract: The line profiles of dense cores in infrared-dark clouds indicate the presence of young stellar objects (YSOs), but the youth of the YSOs and the large distances to the clouds make it difficult to distinguish the outflows that normally accompany star formation from turbulence within the cloud. We report here the first unambiguous identification of a bipolar outflow from a young stellar object (YSO) in an infrared-dark cloud, using observations of SiO to distinguish the relatively small amounts of gas in the outflow from the rest of the ambient cloud.

Key words: infrared-dark clouds, star formation, bipolar outflows, SiO, G81.56+0.10.

Résumé : Les profils des raies des parties centrales denses de nuages infrarouges sombres signalent la présence de jeunes objets stellaires (JOS) ; toutefois, la jeunesse de ces objets et leur grande distance par rapport aux nuages fait qu'il est difficile de distinguer entre les écoulements vers l'extérieur qui accompagnent normalement la formation d'une étoile de la turbulence à l'intérieur du nuage. Dans ce travail, en utilisant des observations de SiO pour distinguer les quantités relativement faibles de gaz s'écoulant vers l'extérieur du reste du nuage ambiant, on rapporte la première identification non ambiguë d'un écoulement bipolaire à partir d'un jeune objet stellaire dans un nuage infrarouge sombre.

Mots clés : nuages infrarouges sombres, formation d'étoile, écoulement bipolaire, SiO, G81.56+0.10.

[Traduit par la Rédaction]

1. Introduction

Infrared-dark clouds (IRDCs) are a population of several thousand molecular clouds, which have been identified by their substantial mid-IR (8–25 μm) extinctions in MSX images (1). Egan et al. (1) concluded that the IRDCs possess hundreds of magnitudes of visual extinction and contain large column densities of cold dust. Spectral-line observations of several of these clouds by Carey et al. (2) revealed that much of the gas inside the IRDCs has $T_K \approx$ 10–15 K, $n(H_2) \gtrsim 10^6$ cm^{-3}, and $N(H_2) \lesssim 10^{23}$ cm^{-2}. Their kinematic distances range between 1 and 8.5 kpc.

Subsequent observations (3–6) found that the MSX IRDCs contain many bright, compact (<30″) submillimetre sources, which appear to be molecular cores in a variety of early stages of star formation. These objects have masses in the range $\approx$ 10–10^3 $M_\odot$, large enough for them to be pre-protocluster cores, the presumed precursors of ultra-compact H II regions and high-mass stars (5, 6), even if the star-forming efficiencies are low. Some of them show evidence of on-going star formation in the form of weak 8 μm emission sources, but most appear completely dark in the MSX 8 μm images. They may contain Class-0 protostars or may be stable, quiescent globules.

The presence of bipolar outflows would provide evidence of on-going star formation even if the protostars are too young or the clouds too opaque to allow IR radiation to escape. Our previous observations gave ambiguous evidence for bipolar outflows. The sources exhibited line profiles characteristic of outflow and (or) infall, but the outflow wings were unresolved and did not show bipolar structure. On the one hand, this is expected because of the large (0.5–5 kpc) distances of the IRDCs and the early state of their star formation. On the other hand, line profiles can be deceiving; the strong "blue wing" on the HCO^+ (3−2) line that we initially interpreted as evidence of infalling gas in G79.3+0.3 P1 proved on closer examination to be most likely due to the impact on the back of the cloud of the wind from a nearby Herbig Ae/Be star (6).

Our observations of H_2CO emission from several of these sources implied that the gas responsible for the line wings typically has temperatures in the range 40–60 K (see Fig. 1), using the calculations of Mangum and Wootten (7). Note that the gas responsible for the line wings is warmer than the bulk of the material in the IRDCs, which has temperatures in the range 15–30 K.

To provide more convincing evidence for the presence of bipolar outflows in the IRDCs, we decided to employ a chemical approach by searching for emission from SiO, a trace gas-phase species known to be enhanced behind the shocks driven by

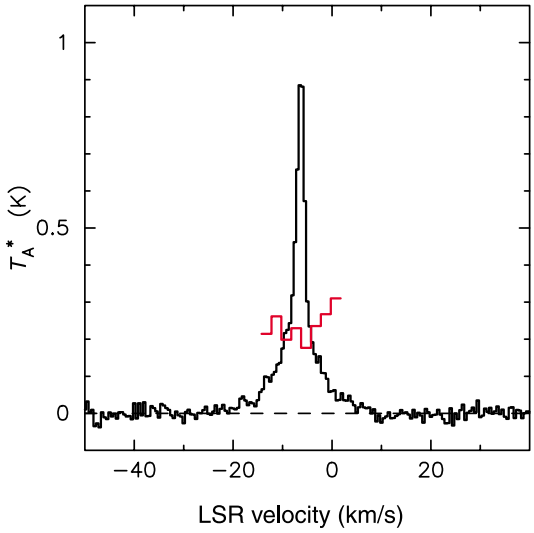
Received 27 February 2004. Published on the NRC Research Press Web site at http://canjchem.nrc.ca/ on 24 June 2004.

P.A. Feldman, R.O. Redman,[2] L.W. Avery, J. Di Francesco, and J.D. Fiege. National Research Council of Canada, 5071 West Saanich Road, Victoria, BC V9E 2E7, Canada.
S.J. Carey. IPAC, California Institute of Technology, 770 South Wilson Avenue, Pasadena, CA 91125, USA.
F. Wyrowski. Max-Planck-Institut-für-Radioastronomie, Auf den Hügel 69, Bonn, D-53125, Germany.

[1]This article is part of a Special Issue dedicated to Professor Gerhard Herzberg.
[2]Corresponding author (e-mail: Russell.Redman@nrc-cnrc.gc.ca).

 doi: 10.1139/V04-078 © 2004 NRC Canada

Fig. 1. Spectrum of H_2CO (3_{03}–2_{02}) with the ratio of the lines (3_{22}–2_{21})/(3_{03}–2_{02}) shown in red. The H_2CO (3_{03}–2_{02}) line intensity was reduced by a factor of 2 so that both graphs can use the same ordinate.



outflows. Enhancements of SiO by as much as a factor of 10^6 over its abundance in background gas have been observed (8,9). Desorption of SiO from grains and (or) sputtering of the grains themselves in the postshocked material behind the jet is believed to be the cause. This phenomenon is commonplace: Codella et al. (10) found that more than 50% of their survey sample of outflows were readily detected in SiO.

The H_2CO observations made us reasonably confident that the temperatures in the shocked gas would be high enough to excite SiO (6–5) emission. Furthermore, SiO emission in molecular outflows is more likely to be found from regions of high molecular density where shocks have succeeded in compressing gas to number densities of 10^{5-6} cm^{-3} (10), which are the gas densities deduced for the compact, bright sources in the IRDCs.

2. JCMT observations

In August 2003, we used the 15 m James Clerk Maxwell Telescope (JCMT) on Mauna Kea in Hawaii to observe nine bright, compact sources in six IRDCs using the SiO (6–5) transition at 260.518 GHz with the 18.3″ beam of receiver A3. We found that four of these objects clearly showed SiO emission. In Fig. 2 we show the brightest of these spectra, for the source G81.56+0.10 P1. Interestingly, all of these sources appear dark in the MSX images, with no obvious evidence of on-going star formation. Detecting the J = 6–5 line of SiO, which has an excitation temperature of 44 K, provides strong evidence for the presence of unresolved molecular outflows in cores large enough to form massive stars but that otherwise appear quiescent.

3. BIMA observations

To obtain higher spatial resolution images, we observed the SiO (2–1) transition at 86.847 GHz towards the bright, compact

Fig. 2. Spectrum of SiO (6–5) for G81.56+0.10 P1 taken with the JCMT.

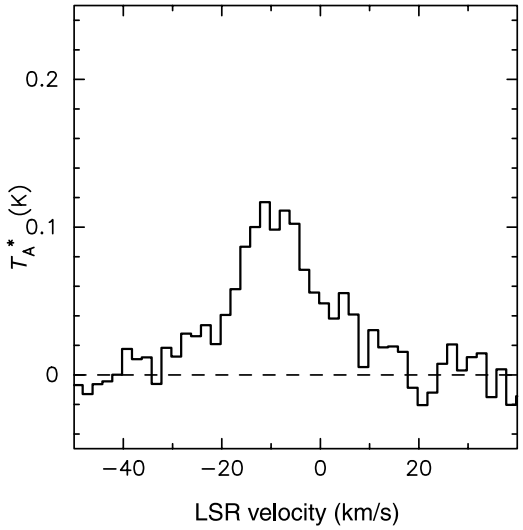
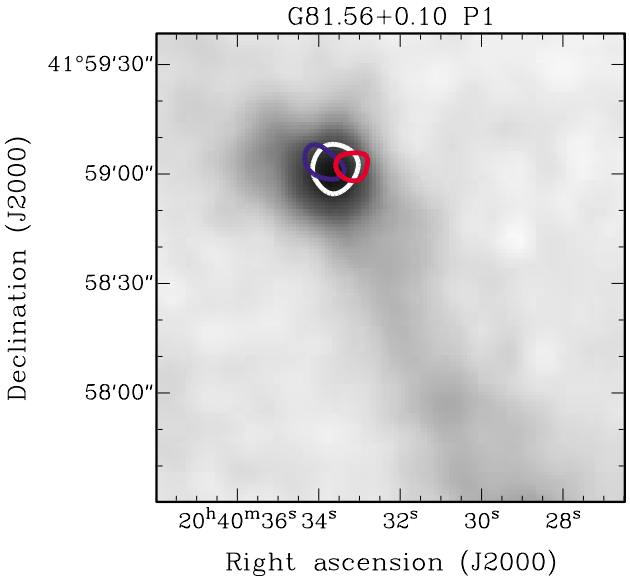


Fig. 3. SCUBA 850 μm image of G81.56+0.10 P1 made with the JCMT, with superimposed contours of integrated SiO (2–1) emission (blue and red) and 88.6 GHz dust continuum (white) made with BIMA. The contour parameters are: blue (velocity range [–26, –9] km s^{-1}, contour at 2.0 Jy/beam); red (velocity range [–3, 14] km s^{-1}, contour at 1.0 Jy/beam); white (contour at 0.01 Jy/beam).



source G81.56+0.10 P1 with the BIMA millimeter interferometer located at Hat Creek, California. The P1 object was observed for over 8 h on 29 September 2003 when the array was in its relatively compact "C" configuration. Clear evidence for a bipolar outflow was found (see Fig. 3).

The BIMA correlator was set such that a single 50 MHz window centered on SiO (2–1) would be sampled over 128 channels, yielding a velocity resolution of 1.25 km s^{-1}. In addition, eight 100 MHz correlator windows were also placed away from known line freqencies to sample continuum emission at an effective frequency of 88.592 GHz. The data were inverted with

© 2004 NRC Canada

uniform weighting of the visibilities to obtain a synthesized beam of size 7.5″ × 6.5″ FWHM (P.A. = 24.4°). The data cube was deconvolved using a standard Högbom CLEAN algorithm (see Cornwell and Braun (11) and refs. therein). The resulting (1 σ rms) sensitivity of the line data was δT_{mb} = 0.31 K and that of the continuum data was δS_ν = 1.6 mJy beam^{-1}.

4. Results

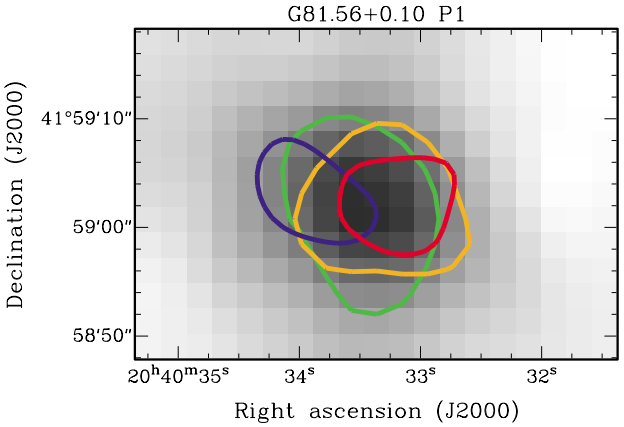
G81.56+0.10 is the filamentary IRDC that appears in Fig. 3 as the diagonal band of 850 μm emission. (We note in passing that this IRDC was formerly known as G81.50+0.14 due to the difficulty of distinguishing absorption patches from voids in this complicated region.) The bright, compact source G81.56+0.10 P1 is prominent at the northeast end of the filament. We have observed the P1 source in a variety of molecular tracers of high-density gas, such as HCO^+ (3–2), HCO^+ (4–3), and CS (7–6), all of which have line profiles qualitatively very similar to the H_2CO (3_{03}–2_{02}) line shown in Fig. 1. There is a tendency for the higher-excitation lines to have more prominent line wings relative to the line centers. The strong line wings suggested the presence of outflows from an embedded YSO, but we were unable to find convincing evidence for a bipolar outflow even in our HCO^+ (4–3) maps made with a 14″ beam and sampled on a 7″ grid.

Figure 2 shows the SiO (6–5) line from G81.56+0.10 P1. Notably, the narrow line core seen in the H_2CO (3_{03}–2_{02}) line, as well as all other high-density molecular-line tracers we have observed to date, is absent in the SiO line. Moreover, the SiO line wings are roughly twice as wide as, for example, the H_2CO (3_{03}–2_{02}) line. In fact, the center of the SiO line is shifted about 4 km s^{-1} to the blue of the mean velocity of the cloud.

The blue and red contours in Fig. 3, showing the integrated intensity of the line wings in SiO (2–1), provide the first unambiguous detection of a bipolar outflow from a YSO in an IRDC. The red and blue line wings peak about 8″ apart in the plane of the sky. At the (uncertain) kinematic distance quoted by Carey et al. (2) of 1.3 kpc, this corresponds to a physical separation of 0.05 pc. The blue lobe is substantially stronger than the red lobe, which explains the blue shift in the apparent line center of the JCMT SiO (6–5) line. There is good positional agreement between the peaks of the 88.6 GHz dust continuum and the midpoint of the bipolar outflow where we anticipate the YSO is located.

These results are consistent with the conclusions of previous observers (8–10) that the SiO abundance is greatly enhanced in the outflow over its normal value in the ambient cloud. By contrast, we find that the HCO^+ (4–3) emission is not significantly enhanced in the outflow. This can be seen in Fig. 4, which overlays the half-power contours of the blue-shifted and red-shifted line wings of HCO^+ (4–3) and SiO (2–1) on an image of the integrated emission of HCO^+ (4–3) in the line core of the ambient cloud. Note that the centers of the contours of the line wings of HCO^+ (4–3) are barely displaced, if at all, from the peak of the line core. If the HCO^+ (4–3) line wings had been enhanced and (or) displaced as much as the SiO (2–1) line wings, the separation of the green and orange contours in Fig. 4 would have been obvious. We suggest that the wings of the HCO^+ lines might come from a compact, turbulent region closer to the YSO. It is not clear what the relationship is between the outflow and the region of enhanced turbulence.

Fig. 4. JCMT image of G81.56+0.10 P1 showing the integrated emission of HCO^+ (4–3) in the velocity range [–9, –3] km s^{-1} of the line core, which arises in the ambient cloud. The super imposed contours show the integrated emission in the blue-shifted and red-shifted line wings of HCO^+ (4–3) (green and orange contours, respectively) and of SiO (2–1) (blue and red contours, respectively). The contour parameters are: green (velocity range [–19, –9] km s^{-1}, contour at 3.0 Jy/beam); orange (velocity range [–3, 7] km s^{-1}, contour at 1.5 Jy/beam); blue (velocity range [–26, –9] km s^{-1}, contour at 2.0 Jy/beam); red (velocity range [–3, 14] km s^{-1}, contour at 1.0 Jy/beam).



5. Conclusions

We have utilized SiO as a chemical tracer to make the first unambiguous identification of a bipolar outflow from a YSO in an IR-dark cloud. The enhanced abundance of SiO behind strong shocks in the outflow enabled us to detect a bipolar outflow in G81.56+0.10 P1 despite the presence of very large amounts of gas in the ambient cloud. We have also found evidence in the line wings of HCO^+ and H_2CO for what we suggest may be a compact, turbulent region in the dense ambient gas close to the YSO within G81.56+0.10 P1.

Acknowledgements

PAF and LWA wish to acknowledge the encouragement and help that Gerhard Herzberg gave us over two decades in using molecular probes to study the interstellar medium. The James Clerk Maxwell Telescope is operated by the Joint Astronomy Centre on behalf of the Particle Physics and Astronomy Research Council of the UK, the Netherlands Organisation for Scientific Research, and the National Research Council of Canada (NRC). The Berkeley-Illinois-Maryland Association (BIMA) is a consortium consisting of the Radio Astronomy Laboratory at the University of California (Berkeley), the Laboratory for Astronomical Imaging at the University pf Illinois (Urbana), and the Laboratory for Millimeter-Wave Astronomy at the University of Maryland (College Park), which operates a millimeter-wave radio interferometer at Hat Creek, California. The BIMA array is operated with support from the National

© 2004 NRC Canada

Science Foundation under grants AST-9981308, AST-9981363, and AST-9981289.

References

1. M.P. Egan, R.F. Shipman, S.D. Price, S.J. Carey, F.O. Clark, and M. Cohen. Astrophys. J. Lett. **494**, L199 (1998).
2. S.J. Carey, F.O. Clark, M.P. Egan, S.D. Price, R.F. Shipman, and T.A. Kuchar. Astrophys. J. **508**, 721 (1998).
3. S.J. Carey, P.A. Feldman, R.O. Redman, M.P. Egan, J.M. MacLeod, and S.D. Price. Astrophys. J. Lett. **543**, L157 (2000).
4. R.O. Redman, P.A. Feldman, S.J. Carey, and M.P. Egan. *In* Star formation from the small to the large scale. *Edited by* F. Favata, A.A. Kaas, and A. Wilson. ESA Special Publ. Ser. **445**, 449 (2000).
5. R.O. Redman, P.A. Feldman, S. Côté F. Wyrowski, S.J. Carey, and M.P. Egan. *In* The earliest phases of massive star birth. *Edited by* P. Crowther. A.S.P. Conf. Ser. **267**, 409 (2002).
6. R.O. Redman, P.A. Feldman, F. Wyrowski, S. Côté, S.J. Carey, and M.P. Egan. Astrophys. J. **586**, 1127 (2003).
7. J.G. Mangum and H.A. Wootten. Astrophys. J. Suppl. **89**, 123 (1993).
8. L.W. Avery and M. Chiao. Astrophys. J. **463**, 642 (1996).
9. A. Dutry, S. Guilloteau, and R. Bachiller. Astron. Astrophys. **325**, 758 (1997).
10. C. Codella, R. Bachiller, and B. Reipurth. Astron. Astrophys. **343**, 585 (1999).
11. T. Cornwell and R. Braun. *In* Synthesis imaging in radio astronomy. *Edited by* R.A. Perley, F.R. Schwab, and A.H. Bridle. PASP Conf. Ser. **6**, 167 (1994).

© 2004 NRC Canada

Photoionization dynamics in CS fragmented from CS_2 studied by high-resolution photoelectron spectroscopy[1]

Anouk M. Rijs, Ellen H.G. Backus, and Cornelis A. de Lange

Abstract: The photoionization dynamics of CS have been studied using high-resolution laser photoelectron spectroscopy. The photodissociation of CS_2 at ~308 nm results in highly rotationally excited CS in its $X^1\Sigma^+$ singlet ground state, as well as in rotationally cold CS in the excited $a^3\Pi$ triplet state. The ground-state CS fragments are formed together with sulfur in its ^3P, ^1D, and ^1S electronic states; triplet CS is produced in coincidence with ground-state sulfur (^3P). In both channels the photoelectron spectra are dominated by $\Delta v = 0$ propensity, but transitions involving $\Delta v = 1$ and 2 are also observed.

Key words: photoelectron spectroscopy, photoionization, photodissociation, excited states, reactive intermediates.

Résumé : On a étudié la dynamique de photoionisation du CS en faisant appel à la spectroscopie photoélectronique laser à haute résolution. La photodissociation du CS_2 à environ 308 nm conduit à la formation de CS fortement excité d'un point de vue rotationnel, dans son état fondamental singulet $X^1\Sigma^+$, ainsi que de CS rotationnellement froid dans un état triplet excité $a^3\Pi$. Les fragments CS dans l'état fondamental se forment en même temps que du soufre dans les états électroniques ^3P, ^1D et ^1S; les quantités de CS à l'état triplet se forment en coïncidence avec le soufre à l'état fondamental (^3P). Dans les deux voies, les spectres photoélectroniques sont dominés par la propensité $\Delta v = 0$, mais on observe aussi des transitions de $\Delta v = 1$ et 2.

Mots clés : spectroscopie photoélectronique, photoionisation, photodissociation, états excités, intermédiaires réactifs.

[Traduit par la Rédaction]

Introduction

Resonance-enhanced multiphoton ionization, in combination with kinetic energy resolved photoelectron spectroscopy (REMPI-PES), has proven to be an excellent and powerful method to study rotationally resolved photoionization and photodissociation dynamics of rotationally hot photofragments (1–3). In particular, with REMPI-PES, detailed information about the spectroscopy and photoionization dynamics of the intermediate state can be obtained. Fragments formed in a photofragmentation process are often generated with an appreciable degree of electronic, vibrational, and rotational excitation. With sufficient rotational excitation, even for fragments with small rotational constants, the spacings between excited rotational levels in the ion may exceed the energy resolution of the magnetic bottle electron spectrometer used, and rotationally resolved photoelectron spectra can be obtained. These rotationally resolved photoelectron spectra provide information on the photoionization dynamics.

In the present work the photodissociation of CS_2, resulting in CS photofragments, has been studied. The ionization energy of CS from its neutral ground state to the lowest $X^2\Sigma^+$ ionic state amounts to 11.33 eV (4). The rotational constant of CS^+ in its ionic ground state is only 0.857662 cm^{-1} (5). However, when the CS photofragments are formed with sufficient rotational excitation, rotational levels in the ion with high J^+ are accessed, and rotationally resolved PES can be observed.

Carbon disulphide (CS_2) has a structure and a photodissociation behavior similar to that of the previously studied N_2O and OCS (1–3). These molecules all possess a linear ground-state geometry with a 16 valence electron configuration. The absorption spectrum of CS_2 shows many absorption bands between ~100 and 400 nm (6). The photo-

Received 7 June 2003. Published on the NRC Research Press Web site at http://canjchem.nrc.ca on 25 June 2004.

A.M. Rijs. Laboratory for Physical Chemistry, University of Amsterdam, Nieuwe Achtergracht 127–129, 1018 WS Amsterdam, The Netherlands and Laser Centre and Department of Chemistry, Vrije Universiteit, De Boelelaan 1083, 1081 HV Amsterdam, The Netherlands.
E.H.G. Backus. Leiden Institute of Chemistry, Leiden University, Einsteinweg 55, P.O. Box 9502, 2300 RA Leiden, The Netherlands.
C.A. de Lange.[2] Laser Centre and Department of Physics, Vrije Universiteit, De Boelelaan 1081, 1081 HV Amsterdam, The Netherlands and Department of Chemistry, The University, Southampton SO17 1BJ, UK.

[1]This article is part of a Special Issue dedicated to the memory of Professor Gerhard Herzberg.
[2]Corresponding author (e-mail: delange@science.uva.nl).

 doi: 10.1139/V04-015 © 2004 NRC Canada

chemistry of CS_2 is strongly dependent on the wavelength of photolysis. Absorption of one photon of 193 nm results in the production of singlet CS ($X^1\Sigma^+$) fragments and sulfur atoms in the singlet or triplet state (^1D or ^3P) (7, 8). For photolysis wavelengths towards the ultraviolet, the production of triplet CS ($a^3\Pi$) becomes more important, and between 140 and 125 nm, the CS fragments are almost completely produced in the triplet state (9). CS_2 shows a strong absorption band around 340–290 nm. This band has been assigned to the $^1\tilde{B}_2 \leftarrow \tilde{X}^1\Sigma_g^+$ transition. This $^1\tilde{B}_2$ upper state is bent with an SCS angle of 131° and correlates to the $^1\Delta_u$ valence state in the linear configuration (10). One-photon excitation of CS_2 at ~308 nm (4.03 eV) correlates to the transition to the $^1\tilde{B}_2$ state. CS photofragments are formed by the sequential (1+1) absorption of two photons at ~308 nm (total energy 8.06 eV) via the $^1\tilde{B}_2$ intermediate state to a predissociative excited state lying near 150 nm (6). This state predissociates, yielding CS photofragments in combination with S atoms. There are several dissociation pathways in our energy region that can be accessed, producing singlet and triplet CS fragments (see Table 1), as follows:

[1] $CS_2 \rightarrow CS\ (X^1\Sigma^+) + S\ (^3P_J)$

[2] $CS_2 \rightarrow CS\ (X^1\Sigma^+) + S\ (^1D_2)$

[3] $CS_2 \rightarrow CS\ (X^1\Sigma^+) + S\ (^1S_0)$

[4] $CS_2 \rightarrow CS\ (a^3\Pi) + S\ (^3P_J)$

Dissociation pathways [2], [3], and [4] are spin-allowed processes from the optically prepared state. The first dissociation pathway [1] is a spin-forbidden process, which becomes weakly allowed by the spin–orbit interaction associated with the presence of the two sulfur atoms in CS_2.

The present paper is concerned with rotationally and vibrationally resolved laser photoelectron spectroscopy of CS fragments. At about 308 nm, the CS photofragments can be produced either in the singlet or the triplet state. The CS fragments formed in the $X^1\Sigma^+$ ground state are rotationally hot and are studied via a (2+1) ionization scheme using the intermediate $B^1\Sigma^+$ Rydberg state as a stepping-stone. The intermediate $B^1\Sigma^+$ Rydberg state represents the lowest member of a Rydberg series converging upon the $X^2\Sigma^+$ ionic ground state of CS^+ and is located at about 8.04 eV above the CS ($X^1\Sigma^+$) ground state (11). Together with the CS fragments formed in their singlet state, S atoms are also produced. These sulfur atoms can be formed via dissociation pathways [1], [2], and [3], resulting in ground- (^3P_J) and excited-state ($^1D_2$, $^1S_0$) S atoms. Various (2+1) ionization transitions of S (^3P_J, $^1S_0$) are used for calibration.

In addition to ground-state CS ($X^1\Sigma^+$) fragments, excited CS fragments can also be formed in the triplet state ($a^3\Pi$) via the dissociation route [4]. The electronically excited triplet CS ($a^3\Pi$) fragments, which possess low rotational excitation, are studied employing a (1+1) excitation step via the intermediate CS ($^3\Sigma^+$) state, resulting in CS^+ ($X^2\Sigma^+$) ionic fragments. With our photon energies, the CS ($a^3\Pi$) fragments can only be formed together with ground-state S (^3P_J) atoms. The appearance energy of the other dissociation channels of triplet CS ($a^3\Pi$) + S ($^1D_2$, $^1S_0$) lies above our two-photon dissociation energy.

Table 1. Threshold energies of the product states in the photodissociation of CS_2.

Pathway	CS channel	S channel	Energies (eV)
[1]	CS ($X^1\Sigma^+$)	S (^3P_J)	4.46
[2]	CS ($X^1\Sigma^+$)	S ($^1D_2$)	5.61
[3]	CS ($X^1\Sigma^+$)	S ($^1S_0$)	7.21
[4]	CS ($a^3\Pi$)	S (^3P_J)	7.88

Experimental

The experimental setup has been reported in great detail previously (1). Briefly, the laser system consists of an XeCl excimer laser (Lumonics HyperEx-460), producing pulsed radiation with a fixed wavelength of 308 nm and a pulse duration of ~10 ns. The laser pulses are generated with a repetition rate of 30 Hz and have an energy of 200 mJ pulse^{-1}. The excimer laser output is used to pump a dye laser (Lumonics HyperDye 500), operating on Rhodamine (bandwidth ~0.08 cm^{-1}). The dye laser output (about 615 nm) is frequency-doubled in a Lumonics HyperTrak 1000, using a KD*P crystal, resulting in 10-ns pulses with a maximum energy of about 15 mJ and a bandwidth of ~0.2 cm^{-1}. The laser light is focused into the ionization region of a magnetic bottle spectrometer by a quartz lens with a focal length of 25 mm. The laser pulse intensity is kept low enough to avoid nonresonant ionization of the parent compound CS_2. In the present experiments, the magnetic bottle spectrometer is used in the electron detection mode for both wavelength scans and photoelectron spectra and operates with a collection efficiency of ~50%. Since a time-of-flight method is used, time windows can be selected to achieve optimum resolution. Signal intensities are essentially independent of kinetic energies (1).

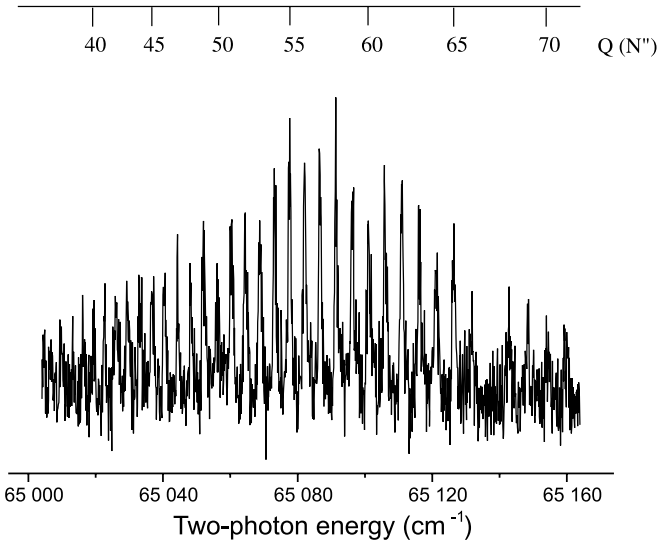
The CS photofragments are generated in situ by two-photon dissociation of CS_2 (Sigma-Aldrich, HPLC grade). The CS_2 gas sample is effusively introduced into the ionization chamber through a 13 mm outer diameter Pyrex flow tube, leading to a pressure in the ionization region of typically 10^{-3} mbar (1 bar = 100 kPa). The photodissociation of CS_2 and the subsequent ionization of the CS fragments are performed with the same laser photons of about 308 nm. For calibration of both the wavelength and the photoelectron kinetic energies, well-known resonances of sulfur atoms at two-photon energies of 64 889.0 and 66 741.6 cm^{-1} are used (12, 13).

Results and discussion

At 308 nm, the dissociation of CS_2 produces CS in the $X^1\Sigma^+$ ground state or in the $a^3\Pi$ triplet state. Figure 1 shows a two-photon excitation spectrum of CS fragments in the two-photon energy range 65 000 – 65 170 cm^{-1}. The spectrum was obtained by monitoring electrons with a kinetic energy of about 0.75 eV (flight time range of 2840–3000 ns). These photoelectrons arise from a (2+1) ionization process, starting from the $X^1\Sigma^+$ ($v'' = 1$; N'') electronic ground state via the intermediate $B^1\Sigma^+$ ($v' = 1$; N') Rydberg state to the $X^2\Sigma^+$ ($v^+ = 1$; N^+) ionic ground state. The rotationally resolved excitation spectrum shows the rotational distribution

© 2004 NRC Canada

Fig. 1. Rotationally resolved (2+1) REMPI excitation spectrum with electron detection of the Q branch of the $B^1\Sigma^+ \leftarrow\leftarrow X^1\Sigma^+$ transition of hot CS fragments in the two-photon energy range 65 000 – 65 170 cm^{-1} (vacuum energies).



of the Q branch ($\Delta N = 0$) of CS in the $B^1\Sigma^+$ ($v' = 1$) state, extending from $N' = 35$ up to $N' = 71$. The comb above the spectrum in Fig. 1 indicates the assignment of the N' rotational levels.

In the absorption step, only the transition from the $v'' = 1$ level of $X^1\Sigma^+$ to the $v' = 1$ level of $B^1\Sigma^+$ is observed. No transitions arising from $X^1\Sigma^+$ for $v'' \neq 1$ were observed. This unusual situation has to do with the properties of the vibrational levels associated with the $B^1\Sigma^+$ state. It is known from the literature (14) that the $B^1\Sigma^+$ Rydberg state predissociates, especially from the $v' = 0$ and the $v' = 2$ levels. Moreover, Sapers and Donaldson (15), who studied the rovibrational states of the CS $X^1\Sigma^+$ fragments formed in the CS_2 308-nm two-photon photolysis with laser-induced fluorescence detection, observed that CS was formed in its electronic ground state with a bimodal vibrational distribution that peaked at $v'' = 1$ with a secondary maximum at $v'' = 5$. In view of the fact that the CS $X^1\Sigma^+$ fragments are predominantly formed in their $v'' = 1$ vibrational state, and considering the significant predissociation of the $v' = 0$ and $v' = 2$ levels of the $B^1\Sigma^+$ Rydberg state, it is not surprising that we observe the CS $X^1\Sigma^+$ fragments only in their $v'' = 1$ vibrational state. The O and S branches associated with the $B^1\Sigma^+$ ($v' = 1$) $\leftarrow X^1\Sigma^+$ ($v'' = 1$) transition are not observed because of the great difference in line strengths between the Q and the O and S branches (16).

The assignment of the peaks in the excitation spectrum of Fig. 1 and the rotational analysis of the Q branch were performed by assigning the measured rotational lines in an iterative fashion. By using the published ground-state rotational constants (17), the $B^1\Sigma^+$ excited-state rotational constants B' were determined by fitting all the rotational energies of the Q branch to the following expression:

$$[5] \quad Q(N'') = \nu_{11} + (B_1' - B_1'')N''(N'' + 1) - (D_1' - D_1'')N''^2(N'' + 1)^2$$

Fig. 2. (*a*) Rotational fit of the measured line positions for the $B^1\Sigma^+$ ($v' = 1$) Rydberg state, based on the rotational constants of the $X^1\Sigma^+$ ground state of CS ($v'' = 1$) (17). Results are given in Table 2; (*b*) Residual plot, the difference between the experimental and calculated line positions.

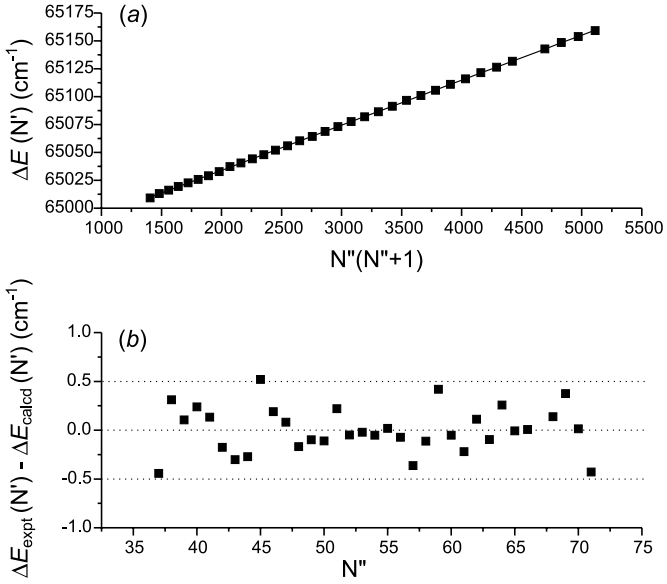


Table 2. Rotational constants (in cm^{-1}) for the $B^1\Sigma^+$ ($v' = 1$) Rydberg state of CS (left column), and a comparison with the literature (14) (central column).

	$B^1\Sigma^+$ ($v' = 1$)	$B^1\Sigma^+$	$X^1\Sigma^+$
ν_{11}	64 952.60(36)	—	—
B_1	0.85188(24)	0.8520	0.811163722
D_1	$1.3802(38)\times10^{-6}$	1.56×10^{-6}	1.337566×10^{-6}

Note: The ground-state rotational constants of CS ($X^1\Sigma^+$) (refs. 17 and 18) are presented in the right column.

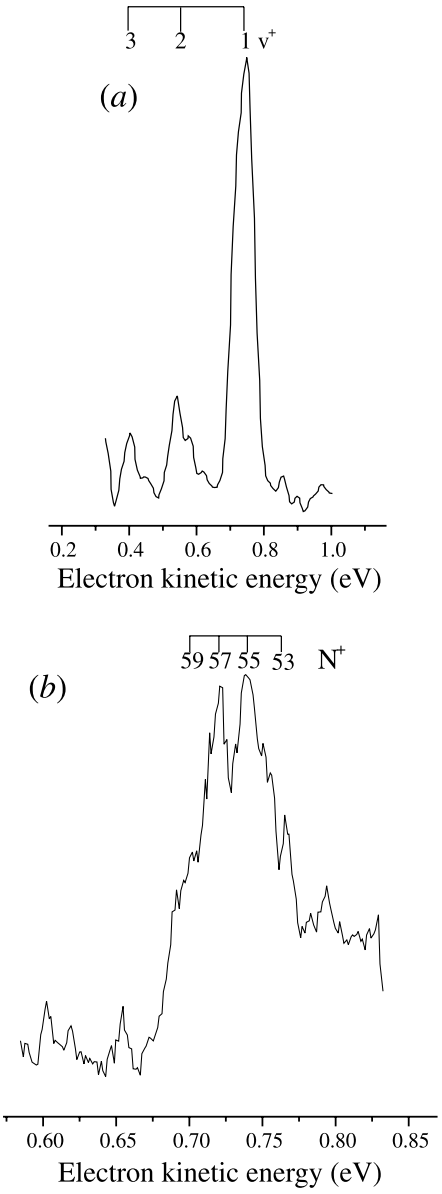
In our excitation spectrum of rotationally excited CS, we measured only high rotational levels, from $N' = 35$ up to $N' = 71$. Because we observe these high rotational levels, the centrifugal distortion constant D_1 of the $B^1\Sigma^+$ ($v' = 1$) state can be determined. The results of the rotational fit are shown in Fig. 2*a*, and the difference plot between the experimental and calculated line positions is presented in Fig. 2*b*. The improved rotational constants for the CS $B^1\Sigma^+$ ($v' = 1$) state are listed in Table 2 together with the CS $X^1\Sigma^+$ ground-state constants of refs. 17 and 18.

The two-photon dissociation of CS_2 at about 308 nm produces, in addition to CS fragments, S atoms in various states (see dissociation pathways [1], [2], and [3]). Several transitions of the S (^3P_J) and S ($^1S_0$) fragments are observed following (2+1) ionization. These well-known absorption lines are used for wavelength and kinetic-energy calibration. Dissociation resulting in S ($^1D_2$) (route [2]) is not observed because no transitions can be excited via a (2+1) ionization scheme with 308-nm photons. To observe S ($^1D_2$) atoms, the photon energy must be shifted to higher energies.

Photoelectron kinetic energy scans were obtained by one-photon ionization from the intermediate CS $B^1\Sigma^+$ ($v' = 1$; N') state into the continua of the ionic ground state $X^2\Sigma^+$ ($v^+ = 1$;

© 2004 NRC Canada

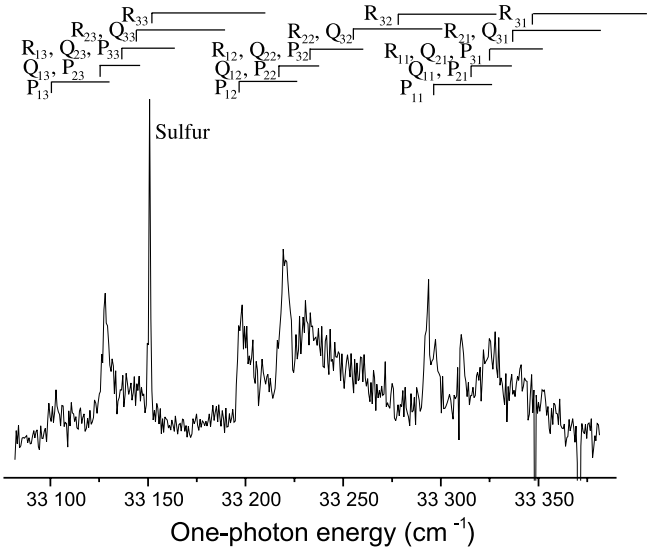
Fig. 3. Photoelectron spectrum of rotationally hot CS, produced in the two-photon dissociation of CS_2. The spectrum is obtained by (2+1) ionization, by employing the Q(55) transition via the $v' = 1$ level of the intermediate $B^1\Sigma^+$ Rydberg state. (*a*) In the spectrum, transitions to $X^2\Sigma^+$ ($v^+ = 1, 2, 3$) are shown; (*b*) more detailed scan for $\Delta v = 0$ ($v^+ = 1$), showing some rotational structure.



N^+). Figure 3*a* presents the photoelectron spectra associated with the Q(55) rotational transition at 65 077.6 cm^{-1} via $v' = 1$. The dominant peak at about 0.74 eV arises from the $\Delta v = 0$ transition. The smaller peaks can be assigned to the $\Delta v = (v^+ - v') = +1, +2$ transitions. The vibrational $\Delta v = 0$ propensity observed for this $X^2\Sigma^+ \leftarrow B^1\Sigma^+$ step is expected for one-photon ionization of a Rydberg state.

Despite the high rotational excitation of the CS fragment, the ionic spacings are not large enough to measure good-quality rotationally resolved photoelectron spectra. However, if we make a more detailed scan for the $\Delta v = 0$ transition at about 0.74 eV, some partially resolved rotational structure is

Fig. 4. (1+1) REMPI excitation spectrum with electron detection of the $^3\Sigma^+ \leftarrow a^3\Pi$ transition of CS photofragments in the one-photon energy range 33 075 – 33 400 cm^{-1} (vacuum energies).

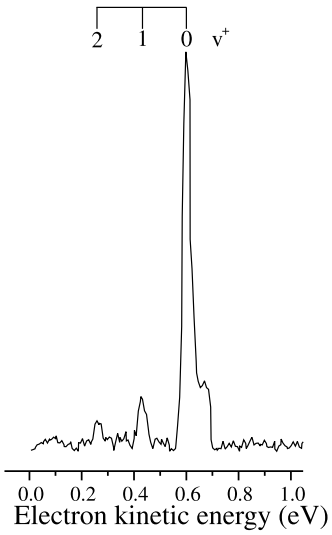


observed (see Fig. 3*b*). Besides the Q(55) ($\Delta N = 0$) feature, peaks are also observed at about 20–25 meV from the Q(55) peak. These peaks can be assigned to $\Delta N = \pm 2$ transitions. The rotational spacings between the $\Delta N = 0$ peak and the $\Delta N = +2$ and -2 peaks are expected to be $B^+(4N^+ + 6)$ (24 meV) and $B^+(4N^+ - 2)$ (23 meV), respectively. Here $B^+ = 0.857662$ cm^{-1} (5) is the ionic rotational constant, and N^+ is the rotational quantum number of CS^+. Higher order rotational contributions are neglected in this estimate. The rotational structure in the photoelectron spectra of CS is subject to selection rules. For one-photon ionization from the $B^1\Sigma^+$ (v') state, the selection rule $\Delta N + \ell = odd$ applies, where $\Delta N = N^+ - N'$ and ℓ is a partial wave component of the photoelectron (19, 20). In the present case, the CS Rydberg electron occupies a $3s\sigma$ molecular orbital. In an atomic-like picture, ionization of this $3s\sigma$ Rydberg electron is expected to lead to p ($\ell = 1$) partial waves, and, on this basis, strong $\Delta N = even$ transitions would be expected; $\Delta N = \pm 1$ transitions are forbidden on the basis of these selection rules. However, with the present quality of the rotationally resolved photoelectron spectra, no firm conclusions can be drawn.

Following two-photon dissociation of CS_2 at 308 nm, the CS photofragments can be formed in the triplet state, resulting in CS ($a^3\Pi$) + S (^3P_J). Figure 4 shows the one-photon excitation spectrum in the energy range 33 075 – 33 500 cm^{-1}, corresponding to the CS fragment produced in its $a^3\Pi$ state. The features observed belong to the $^3\Sigma^+$ ($v' = 0$) $\leftarrow a^3\Pi$ ($v'' = 2$) transition (21, 22). The origin (v_{00}) of this transition lies at 282 nm, whereas we excite with ~300 nm. Ono and Hardwick (21) observed three absorption bands at 282, 291, and 300 nm. These bands are assigned to the $^3\Sigma^+$ ($v' = 0$) $\leftarrow a^3\Pi$ ($v'' = 0, 1, 2$) transitions, respectively. In our experiment, we have studied only the $^3\Sigma^+$ ($v' = 0$) $\leftarrow a^3\Pi$ ($v'' = 2$) transition. Since the same photons are used for the photodissociation of CS_2 and for the spectroscopy of CS, the other transitions could not easily be accessed in a one-color experiment. Our rotational assignment is based on the results of

© 2004 NRC Canada

Fig. 5. Photoelectron spectrum of CS ($a^3\Pi$), resulting from the (1+1) photoionization via the $^3\Sigma^+$ Rydberg state.



Ono and Hardwick (21). The complexity of the rotational structure that is evident from Fig. 4 is typical for a $^3\Sigma^+ \leftarrow {}^3\Pi$ transition between the two states described in Hund's case (b) (23). Because of the high threshold energy of 7.88 eV for the formation of CS ($a^3\Pi$) (see Table 1) and the vibrational excitation (v''= 2), less energy is available for excitation of the internal degrees of freedom, resulting in rotationally cold (N''= 4–22) CS ($a^3\Pi$) (21). This situation is in sharp contrast to the formation of CS ($X^1\Sigma^+$) with significant rotational excitation. Since CS ($X^1\Sigma^+$) is produced in a (2+1) and CS ($a^3\Pi$) in a (1+1) REMPI experiment, the very different conditions do not allow any reliable conclusions about branching ratios between both channels.

Figure 5 presents the experimental photoelectron spectrum obtained for (1+1) photoionization of CS ($a^3\Pi$, v'' = 2) via the CS ($^3\Sigma^+$, v′ = 0) Rydberg state at 33 327.8 cm^{-1}, producing the $X^2\Sigma^+$ (v^+) ionic ground state of CS^+. The dominant peak in the photoelectron spectrum at about 0.60 eV is the Δv = 0 transition. The neighboring peaks at the left-hand side of the spectrum arise from Δv = +1, +2 transitions. No rotationally resolved features are observed in the photoelectron spectrum of CS ($a^3\Pi$, v'' = 2) because of the low rotational excitation and the small rotational B^+ constant. The shoulder on the right-hand side of the Δv = 0 peak is the result of nonresonant multiphoton ionization of ^{1}S sulfur atoms.

In summary, the photodissociation of CS_2 produces CS molecules both in the singlet ground state and in a triplet excited state. The ground state ($X^1\Sigma^+$, v'' = 1) formed is highly rotationally excited, while the triplet state ($a^3\Pi$, v'' = 2) generated is rotationally cold. Comparing the results of the photodissociation of CS_2 with previous studies of the photodissociation of the similar molecules N_2O (2) and OCS (3), the photodissociation of these molecules produced rotationally hot N_2 and CO photofragments and O and S atoms in their $^1D_2$ singlet excited states. In the photodissociation of CS_2 we observe both similarities and differences. In the case of photodissociation of N_2O and OCS, the N_2 and CO photofragments are only formed in their electronic ground states, and nearly all them are formed in their ground vibrational states (2, 3). The photodissociation of CS_2 produces both ground-state and excited-state CS fragments and results in vibrationally excited CS species, both in the singlet electronic $X^1\Sigma^+$ ground state and in the electronically excited triplet $a^3\Pi$ state. In the photodissociation process of OCS and N_2O, the C—O and the N—N fragments appear to act solely as spectators, while in CS_2 the nonbonding electrons of both S atoms contribute to the absorption and both C—S bonds are excited and stretched (24). Ultimately, if one C—S bond breaks, the other is strongly vibrationally excited.

The photoelectron spectra of ground-state CS photofragments are dominated by Δv = 0 propensity, as was the case with the photoelectron spectra of ground-state N_2 and CO. However, the photoelectron spectra of N_2 and CO could be measured with excellent rotational resolution, whereas in the case of CS it appears more difficult to obtain rotationally resolved photoelectron spectra. This is mostly because the rotational constant of the CS^+ ion is approximately half that of N_2^+ or CO^+.

Finally, the fact that our experiments on CS, both in its singlet and triplet electronic states, have been performed in the ~1 T field of a magnetic bottle spectrometer should not affect the observed dynamics. Systematic studies have shown that possible magnetic field effects in this type of spectrometer may only be significant for high Rydberg states close to the ionization threshold (25–27).

Conclusions

The photodissociation dynamics of CS_2 at about 308 nm encompasses a singlet and a triplet CS dissociation channel. The photodissociation via the singlet channel produces rotationally hot CS ($X^1\Sigma^+$) fragments in their first vibrationally excited level. A rotational distribution of CS extending from N' = 35 up to N' = 71 (with a maximum at N' = 58) has been observed and assigned. For the first time, a (2+1) high-resolution partly rotationally resolved excitation spectrum of CS ($X^1\Sigma^+$) via the Rydberg level $B^1\Sigma^+$ has been recorded. Improved spectroscopic rotational parameters have been obtained for the CS ($B^1\Sigma^+$) state. The other dissociation channel of CS_2 at 308 nm results in the production of CS ($a^3\Pi$) in its v'' = 2 vibrational level, with low rotational excitation. In both cases the photoelectron spectra were dominated by Δv = 0 propensity, with much weaker transitions involving Δv = 1 and 2.

Acknowledgements

AMR acknowledges the Holland Research School of Molecular Chemistry for a Ph.D. fellowship. CAdL acknowledges very useful discussions with Professor J.M. Dyke and members of his group during a stay in Southampton in the context of the EC Network on Reactive Intermediates.

References

1. A.M. Rijs, E.H.G. Backus, C.A. de Lange, N.P.C. Westwood, and M.H.M. Janssen. J. Electron Spectrosc. Relat. Phenom. **112**, 151 (2000).
2. A.M. Rijs, E.H.G. Backus, C.A. de Lange, M.H.M. Janssen, K. Wang, and V. McKoy. J. Chem. Phys. **114**, 9413 (2001).

© 2004 NRC Canada

3. A.M. Rijs, E.H.G. Backus, C.A. de Lange, M.H.M. Janssen, N.P.C. Westwood, K. Wang, and V. McKoy. J. Chem. Phys. **116**, 2776 (2002).
4. N. Jonathan, A. Morris, M. Okuda, K.J. Ross, and D.J. Smith. Faraday Discuss. Chem. Soc. **54**, 48 (1972).
5. D. Cossart. J. Mol. Spectrosc. **167**, 11 (1994).
6. J.W. Rabalais, J.M. McDonald, V. Scherr, and S.P. McGlynn. Chem. Rev. **71**, 73 (1971).
7. I.M. Waller and J.W. Hepburn. J. Chem. Phys. **87**, 3261 (1987).
8. Th.N. Kitsopoulos, Ch.R. Gebhardt, and T.P. Rakitzis. J. Chem. Phys. **115**, 9727 (2001).
9. G. Black, R.L. Sharpless, and T.G. Slanger. J. Chem. Phys. **66**, 2113 (1977).
10. Ch. Jungen, D.N. Malm, and A.J. Merer. Can. J. Phys. **51**, 1471 (1973).
11. E.K. Moltzen, K.J. Klabunde, and A. Senning. Chem. Rev. **88**, 391 (1988).
12. W.C. Martin, R. Zalubas, and A. Musgrave. J. Phys. Chem. Ref. Data, **19**, 821 (1990).
13. T.V. Venkitachalam and A.S. Rao. Appl. Phys. B, **52**, 102 (1991).
14. G. Stark, K. Yoshino, and P.L. Smith. J. Mol. Spectrosc. **124**, 420 (1987).
15. S.P. Sapers and D. J. Donaldson. Chem. Phys. Lett. **198**, 341 (1992).
16. R.G. Bray and R.M. Hochstrasser. Mol. Phys. **31**, 1199 (1976).
17. R.S. Ram, P.F. Bernath, and S.P. Davis. J. Mol. Spectrosc. **173**, 146 (1995).
18. J.B. Burkholder, E.R. Lovejoy, P.D. Hammer, and C.J. Howard. J. Mol. Spectrosc. **124**, 450 (1987).
19. J. Xie and R.N. Zare. J. Chem. Phys. **93**, 3033 (1990).
20. S.N. Dixit and V. McKoy. Chem. Phys. Lett. **128**, 49 (1986).
21. Y. Ono and J.L. Hardwick. J. Mol. Spectrosc. **119**, 107 (1986).
22. J.L. Hardwick, Y. Ono, and J.T. Moseley. J. Phys. Chem. **91**, 4506 (1987).
23. P.F. Bernath. Spectra of atoms and molecules. Oxford University Press, New York. 1995.
24. Y. Sato, Y. Matsumi, M. Kawasaki, K. Tsukiyama, and R. Bersohn. J. Phys. Chem. **99**, 16 307 (1995).
25. J.L. Dehmer, P.M. Dehmer, S.T. Pratt, F.S. Tomkins, and M.A. O'Halloran. J. Chem. Phys. **90**, 6243 (1989).
26. S.T. Pratt, E.F. McCormack, J.L. Dehmer, and P.M. Dehmer. J. Chem. Phys. **92**, 1831 (1990).
27. S. Guizard, N. Shafizadeh, M. Horani, and D. Gauyacq. J. Chem. Phys. **94**, 7046 (1991).

© 2004 NRC Canada

High-resolution vacuum ultraviolet laser spectroscopy of the C $0_u^+ \leftarrow$ X 0_g^+ transition of Xe_2[1]

A. Wüest, U. Hollenstein, K.G. de Bruin, and F. Merkt

Abstract: Rotationally resolved (1 + 1′), resonance-enhanced, two-photon ionization spectra of the C $0_u^+ \leftarrow$ X 0_g^+ transition of several isotopomers of Xe_2 have been recorded. Rotational constants have been determined for the $v' = 14$–26 levels of the C 0_u^+ Rydberg state and the $v'' = 0$ and 1 levels of the X 0_g^+ ground state, and band origins have been determined with an absolute accuracy of 0.015 cm^{-1} for the transitions to the $v' = 14$–26 levels of the C 0_u^+ state of the $^{129}Xe_2$, ^{129}Xe–^{132}Xe, and ^{131}Xe–^{136}Xe isotopomers. The equilibrium internuclear separation of the X 0_g^+ ground state ($R_e = 4.3773(49)$ Å) was determined from the rotational constants of the $v'' = 0$ and 1 levels. The analysis of the isotopic shifts of the band origins enabled the confirmation of the absolute numbering of the vibrational levels of the C 0_u^+ state determined by Lipson et al. (R.H. Lipson, P.E. Larocque, and B.P. Stoicheff. J. Chem. Phys. **82**, 4470 (1985)). A semiempirical interaction potential for the X 0_g^+ ground state was derived in a nonlinear fitting procedure using the present spectroscopic results, the positions of the $v'' = 2$–9 levels determined by Freeman et al. (D.E. Freeman, K. Yoshino, and Y. Tanaka. J. Chem. Phys. **61**, 4880 (1974)) and experimental values for the second virial coefficient. The interaction potential is similar to previous semiempirical potentials but the dissociation energy ($D_e = (196.1 \pm 1.1)$ cm^{-1}) differs from the value of 183.1 cm^{-1} determined in the latest ab initio calculation (P. Slavíček, R. Kalus, P. Paška, I. Odvárková, P. Hobza, and A. Malijevský. J. Chem. Phys. **119**, 2102 (2003)).

Key words: high-resolution vacuum ultraviolet laser spectroscopy, rare gas dimers and their cations, photoionisation, Xe_2, rotationally resolved electronic spectrum.

Résumé : On a enregistré les spectres d'ionisation biphotonique améliorés en résonance et résolus en rotation (1 + 1′) de la transition C $0_u^+ \leftarrow$ X 0_g^+ de plusieurs isotopomères de Xe_2. On a déterminé les constantes rotationnelles des niveaux $v' = 14$–26 de l'état de Rydberg C 0_u^+ et des niveaux $v'' = 0$ et 1 de l'état fondamental X 0_g^+ et on a déterminé les origines des bandes avec une précision absolue de 0,015 cm^{-1} pour les transitions des niveaux $v' = 14$–26 de l'état C 0_u^+ des isotopomères $^{129}Xe_2$, ^{129}Xe–^{132}Xe et ^{131}X–^{136}Xe. On a déterminé la séparation internucléaire à l'équilibre de l'état fondamental X 0_g^+ (R_e = 4,3773(49) Å) à partir des constantes rotationnelles des niveaux $v'' = 0$ et 1. L'analyse des déplacements isotopiques des origines des bandes a permis de confirmer la numérotation absolue des niveaux vibrationnels de l'état C 0_u^+ déterminée par Lipson et al. (R.H. Lipson, P.E. Larocque, et B.P. Stoicheff. J. Chem. Phys. **82**, 4470 (1985)). On a dérivé le potentiel d'interaction semi-empirique de l'état fondamental X 0_g^+ à l'aide de la méthode d'ajustement non linéaire en utilisant les données expérimentales obtenues dans ce travail ainsi que les positions des niveaux $v'' = 2$–9 déterminées par Freeman et al. (D.E. Freeman, K. Yoshino, et Y. Tanaka. J. Chem. Phys. **61**, 4880, 1974) et les valeurs expérimentales pour le deuxième coefficient viriel. Le potentiel d'interaction est semblable aux potentiels semi-empiriques obtenus antérieurement, mais l'énergie de dissociation (D_e = (196,1 ± 1,1) cm^{-1}) diffère de la valeur de 183,1 cm^{-1} déterminée dans le dernier calcul ab initio (P. Slavíček, R. Kalus, P. Paška, I. Odvárková, P. Hobza, et A. Malijevský. J. Chem. Phys. **119**, 2102 (2003)).

Mots clés : spectroscopie à haute résolution dans l'ultraviolet lointain, dimères de gaz rares et leurs cations, photoionisation, Xe_2, spectre électronique résolu en rotation.

[Traduit par la Rédaction]

1. Introduction

In their electronic ground state, the homonuclear rare gas dimers are bound solely by dispersion forces. They represent model systems to study van der Waals interactions, and considerable experimental and theoretical efforts have been invested to derive the interaction potentials of He_2, Ne_2, Ar_2, Kr_2, and Xe_2. The body of literature is so vast that it is impossible to cite all relevant contributions in a research article and the references cited in the following merely list the most recent contributions.

Received 5 December 2003. Published on the NRC Research Press Web site at http://canjchem.nrc.ca/ on 26 July 2004.

A. Wüest, U. Hollenstein, K.G. de Bruin, and F. Merkt.[2] Laboratorium für Physikalische Chemie, ETH Zürich, CH-8093 Zurich, Switzerland.

[1]This article is part of a Special Issue dedicated to the memory of Professor Gerhard Herzberg.

[2]Corresponding author (e-mail: feme@xuv.phys.chem.ethz.ch).

 doi: 10.1139/V04-073 © 2004 NRC Canada

The van der Waals interactions between the rare gas atoms are conveniently described by a one-dimensional interaction potential. Two approaches can be followed to derive the potential function: ab initio quantum chemistry and semiempirical methods.

Ab initio potentials of close to spectroscopic accuracy (± 1 cm^{-1}) have been reported for the lighter dimers He_2 and Ne_2 (1–3). The larger number of electrons and the growing importance of relativistic effects render ab initio calculations on the heavier dimers more demanding, and the determination of accurate interaction potentials for Kr_2 and Xe_2 by ab initio quantum chemistry remains a challenge (4).

High quality semiempirical potentials are currently known for all homonuclear rare gas dimers (5–9). The primary source of experimental data needed to derive such potentials are high-resolution spectra of dimers in the gas phase, atom–atom scattering cross sections, and physical properties in the condensed phases such as viscosity and diffusion coefficients, compressibilities, and lattice distances. A widely used model for the potential resulting from the van der Waals interaction was introduced by Tang and Toennies (5, 10)

$$[1] \qquad V(R) = V_{\text{repl}}(R) + V_{\text{attr}}(R) = A\,\mathrm{e}^{-bR} - \sum_{n=3}^{8} f_{2n}(R,b)\frac{C_{2n}}{R^{2n}}$$

and consists of a repulsive Born–Mayer term and a damped attractive dispersion series. In eq. [1], A and b are adjustable parameters, and $f_{2n}(R,b)$ and C_{2n} represent damping functions and dispersion coefficients of order $2n$, respectively. The damping functions prevent the R^{-2n} terms from dominating at short internuclear distances and have the form

$$[2] \qquad f_{2n}(R,b) = 1 - \mathrm{e}^{-bR}\sum_{k=0}^{2n}\frac{(bR)^k}{k!}$$

The dispersion coefficients are usually not adjusted to reproduce experimental data but are taken from atomic properties (either empirical or ab initio).

Spectroscopic data such as rotational constants B_v and vibrational energy intervals $\Delta G_{v+1/2}$ represent the most stringent tests of the quality of ab initio and semiempirical potentials. However, such information is not easily obtained for the homonuclear rare gas dimers because they lack a permanent dipole moment, and thus, do not have an electric dipole allowed rotational or vibrational spectrum. Rotational constants and vibrational intervals are determined in these systems from the rovibrational fine structure of electronic transitions from the ground neutral state to the lowest electronic states. These transitions all lie in the vacuum ultraviolet (VUV) region of the electromagnetic spectrum where high-resolution spectroscopic measurements are not as easy to carry out as in the microwave, IR, visible, or near-UV regions. For this reason, Xe_2 is one of the most important diatomic molecules for which no rotationally resolved spectroscopic information was available when Huber and Herzberg (11) published their classic reference work on the constants of diatomic molecules. For Ar_2 and Kr_2, rotationally resolved electronic spectra of excellent quality have been obtained in the pioneering investigations of Yoshino and co-workers (12, 13) and Stoicheff and co-workers (14, 15). The lowest excited electronic states of Ne_2 lie further in the VUV (beyond 16 eV) and fully rotationally resolved spectra have only been reported recently (6). The very small rotational constant of Xe_2 and the spectral congestion resulting from the large number of isotopomers have so far prevented the obtaining of rotationally resolved spectra. In this case, semiempirical potentials have primarily relied on isotopically averaged vibrational intervals for $v'' = 0$–9 from the work of Freeman et al. (16).

In this contribution, fully rotationally resolved spectra of the C $0_u^+ \leftarrow$ X 0_g^+ transition of selected isotopomers of Xe_2 are reported for the first time. The analysis of these spectra provides new information on the equilibrium internuclear distance and the first vibrational interval in the ground electronic state. This new measurement was combined with earlier spectroscopic and thermodynamical data to derive an improved semiempirical potential.

This article is structured as follows: the experimental procedure is described in Sect. 2. The analysis of the spectra of the C $0_u^+ \leftarrow$ X 0_g^+ transition carried out in terms of the standard expansion series for the term values is summarized in Sect. 3. Finally, Sect. 4 is devoted to the determination of a semiempirical potential for the ground electronic state of Xe_2 and to a comparison with earlier ab initio and semiempirical potentials.

2. Experimental

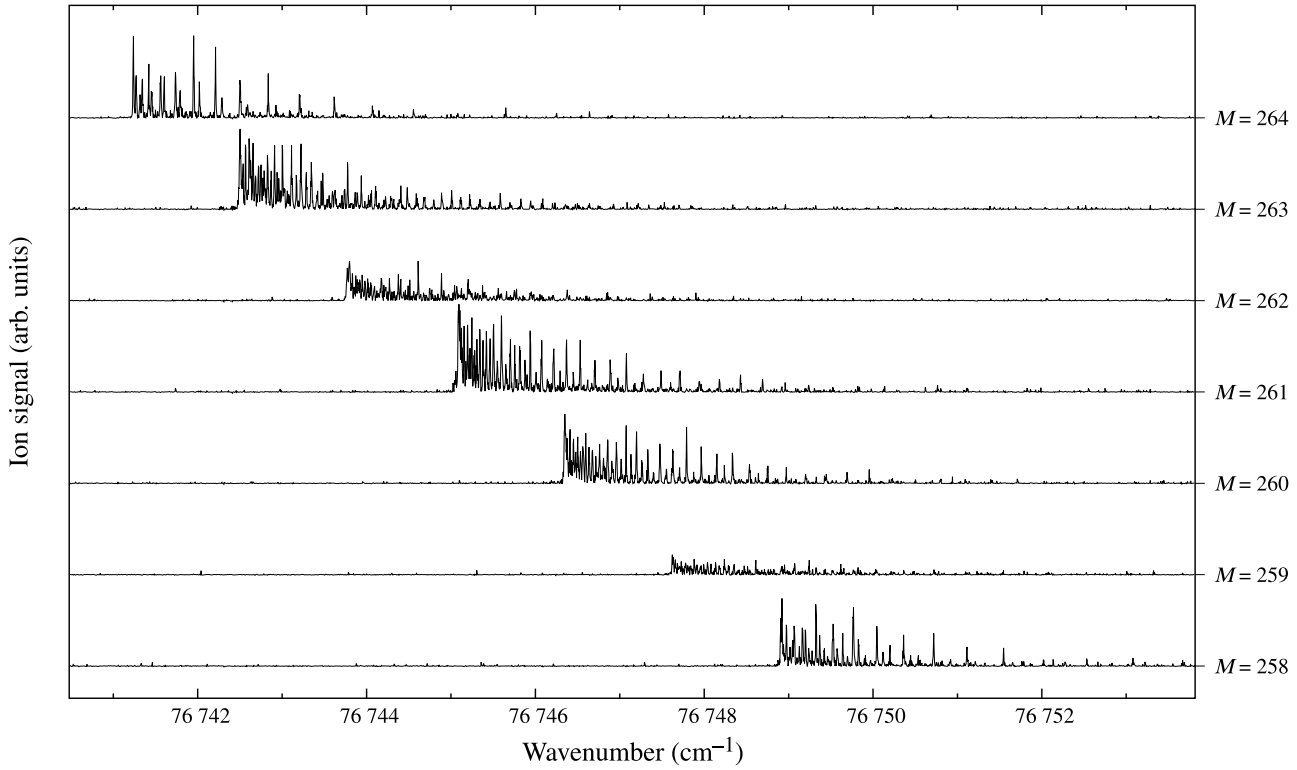
The spectra have been recorded using a narrow bandwidth (0.008 cm^{-1}), VUV laser system coupled to a time-of-flight mass spectrometer. The laser system and the procedure for the VUV wavenumber calibration have been described in detail earlier (17, 18), and only the aspects specific to the present study are summarized here.

Tunable VUV radiation in the range $\tilde{\nu}_{\text{VUV}} = 76\,000$ – $77\,000$ cm^{-1} was generated by resonance-enhanced, difference-frequency mixing ($\tilde{\nu}_{\text{VUV}} = 2\tilde{\nu}_1 - \tilde{\nu}_2$) in an atomic beam of krypton using two near-Fourier-transform-limited pulsed dye lasers. The dye laser pulses were produced by pulse amplifying the cw output of two single-mode ring dye lasers using chains of three dye amplification stages pumped transversally by the doubled output (532 nm) of an injection-seeded Nd:YAG laser. The resonance enhancement of the four-wave mixing process is achieved at the two-photon level by locking the wavenumber $\tilde{\nu}_1$ of the tripled output of the first pulsed dye laser to the position $2\tilde{\nu}_1 = 94\,092.906(9)$ cm^{-1} located close to the maximum of the $4p^5 5p[1/2]_0 \leftarrow {}^1S_0$ two-photon resonance of atomic krypton (18). The locking was achieved by stabilizing the fundamental frequency of the dye laser to a neighboring I_2 line according to the procedure described in ref. 19. The VUV wavenumber was tuned by scanning the wavenumber $\tilde{\nu}_2$ of the second pulsed dye laser. The wavenumber $\tilde{\nu}_2$ was calibrated by recording with each VUV spectrum several étalon spectra and a laser-induced fluorescence spectrum of I_2, and making reference to the iodine atlasses (20, 21).

The VUV wavenumber was determined with an absolute accuracy of 0.015 cm^{-1} from the wavenumbers $\tilde{\nu}_1$ and $\tilde{\nu}_2$ by building the difference $2\tilde{\nu}_1 - \tilde{\nu}_2$. The uncertainty of 0.015 cm^{-1} primarily originates from the chirp shifts arising in the pulse amplification and the nonlinear frequency upconversion processes (19). The difference-frequency VUV beam was separated

© 2004 NRC Canada

Fig. 1. $(1 + 1')$ Resonance-enhanced, two-photon ionization spectrum of the C 0_u^+ $(v' = 21) \leftarrow$ X 0_g^+ $(v'' = 0)$ transition of Xe_2. The different traces were recorded by collecting the ion signal corresponding to the mass numbers between $M = 258$ and 264. The spectra are rotationally resolved and display a P-branch band head on the low wavenumber side.



from the fundamental beams and beams generated in other nonlinear processes using a vacuum monochromator described in ref. 22.

The xenon dimers were formed in a pulsed supersonic expansion of pure xenon (Pan Gas, spectroscopic grade purity) using a nozzle stagnation pressure of 4 bar (1 bar = 100 kPa). The timing of the nozzle opening with respect to the Q-switch of the Nd:YAG laser was set so as to maximize the dimer production and minimize the formation of larger xenon clusters. The gas pulses entered the spectrometer through the 0.5 mm diameter orifice of a skimmer and crossed the VUV beam at a right angle in the middle of a set of cylindrical molybdenum plates designed for the application of homogeneous electric fields and used to extract the charged particles. Ionization of the xenon dimers after resonant VUV excitation was achieved in a $(1 + 1')$ two-photon ionization process using the 532 nm output of the Nd:YAG laser in the ionization step. The ions were extracted by applying pulsed voltages on the cylindrical plates and detected at the end of a 30 cm time-of-flight (TOF) tube using a microchannel plate (MCP) detector. The resolution of the TOF mass spectrometer was amply sufficient to fully separate ion peaks originating from xenon dimers differing by one mass unit.

The ion signals were transferred to a digital oscilloscope and spectra of the different isotopomers were recorded separately as a function of the VUV wavenumber by setting temporal gates on the TOF spectrum corresponding to the respective arrival times at the MCP detector. A slow drift of the TOF positions prevented measurements of more than typically 1 h. Under these conditions, the successive vibrational bands of the C–X transition had to be recorded in separate scans, thus preventing the determination of reliable relative vibrational band intensities. The relative rotational line intensities, on the other hand, could be measured reliably and indicated a rotational temperature of ≈ 4 K in the supersonic expansion. Only the lowest two vibrational levels of the ground state were sufficiently populated in the supersonic expansion to be detected in our measurements.

Of the nine natural isotopes of Xe, only two have a nonzero nuclear spin (^{129}Xe ($I = 1/2$) and ^{131}Xe ($I = 3/2$)). Forty-five dimers can be formed from these isotopes, 19 of which have a relative abundance of more than 1%. The most abundant dimers are ^{129}Xe–^{132}Xe (14.2%), ^{131}Xe–^{132}Xe (11.4%), and ^{129}Xe–^{131}Xe (11.2%). The resolution of our mass spectrometer being insufficient to distinguish between isotopomers of the same mass number, spectra obtained by collecting the ionization signal at a given mass peak typically corresponds to a superposition of contributions from several isotopomers. As an illustration of a typical measurement, Fig. 1 shows spectra of the C$(v' = 21) \leftarrow$ X$(v'' = 0)$ band recorded simultaneously by collecting the ionization signals at the times-of-flight corresponding to the mass numbers $M = 258$–264. The spectra recorded at $M = 258$, 260, and 261 are dominated by a single isotopomer ($^{129}Xe_2$, ^{129}Xe–^{131}Xe, and ^{129}Xe–^{132}Xe, respectively), and have a simpler and more regular structure than the other spectra to which several isotopomers contribute.

For the analysis, the isotopomers $^{129}Xe_2$, ^{129}Xe–^{132}Xe, and ^{131}Xe–^{136}Xe were chosen because: (*i*) they represent strongly dominant isotopomers at mass numbers 258, 261, and 267 (relative abundances of 96.9%, 89.1%, and 100%, respectively); (*ii*) the natural abundances (6.97%, 14.20%, and 3.77%, re-

© 2004 NRC Canada

spectively) are large enough for spectra of satisfactory signal-to-noise ratios to be recorded; and (*iii*) the large differences in reduced masses greatly facilitated the analysis of the isotopic shifts and the determination of the absolute vibrational numbering of the C state.

3. Results

The electronic states of Xe_2 are conveniently labeled using Hund's case c notation ($\Omega_{g/u}^{+/-}$) (23), which specifies the value of the quantum number Ω for the projection of the electronic angular momentum onto the internuclear axis, the gerade/ungerade (g/u) symmetry of the electronic wave function with respect to inversion of the electronic coordinates in the molecule fixed axis system, and the symmetry (+/−) of the electronic wave function with respect to a plane containing the internuclear axis (24). Because of the $\Delta J = \pm 1$ electric dipole selection rule accompanying $0_u^+ \leftrightarrow 0_g^+$ transitions, the rotational structure of each of the vibrational bands of the C $0_u^+ \leftarrow$ X 0_g^+ transition consists of a P- ($\Delta J = -1$) and an R-branch ($\Delta J = 1$). As examples, the rotational structures of the C($v' = 20$) $\leftarrow$ X($v'' = 0$) band of ^{129}Xe–^{132}Xe and of the C($v' = 16$) $\leftarrow$ X($v'' = 1$) band of ^{131}Xe–^{136}Xe are displayed in Figs. 2*a* and 2*b*, respectively. The C state of Xe_2 being more strongly bound than the X state, the rotational constants of most vibrational levels of the C state are larger than those of the lowest vibrational levels of the X state, and the P-branches display a band head at low J'' values. The rotational structure of each band is straightforward to analyze with the standard formula (25):

$$[3] \qquad \tilde{\nu} = \tilde{\nu}_{v'v''} + B_{v'}J'(J'+1) - D_{v'}J'^2(J'+1)^2 - B_{v''}J''(J''+1) + D_{v''}J''^2(J''+1)^2$$

At the low temperature of the supersonic expansion (4 K), only transitions out of J'' levels up to 40 of the $v'' = 0$ and 1 vibrational levels of the X state could be observed. Table 1 summarizes the positions of all rotational lines of the $v' = 16, 17 \leftarrow v'' = 0, 1$ bands of the ^{129}Xe–^{132}Xe isotopomer. Similar data were obtained for many other bands of ^{129}Xe–^{132}Xe and other isotopomers, and are available on request. Fully satisfactory simulations of the rotational structure of all bands could be obtained by fitting the band origins $\tilde{\nu}_{v'v''}$, the rotational constants $B_{v''}$ and $B_{v'}$, and the centrifugal distortion constants $D_{v''}$ and $D_{v'}$ to the experimental line positions. Unfortunately, because of the low rotational temperature and the strong correlation between the values of the centrifugal constants in the lower and upper levels, these constants could not be well determined from the experimental data.

Table 2 lists the origins and the rotational and centrifugal constants for all bands observed in the spectra of the three isotopomers $^{129}Xe_2$, ^{129}Xe–^{132}Xe, and ^{131}Xe–^{136}Xe. As expected, the vibrational intervals and the rotational constants decrease with increasing vibrational quantum number v'. The centrifugal distortion constants of the vibrational levels of the C state appear to increase with increasing vibrational excitation. However, given the large uncertainties, this trend may be fortuitous.

The first vibrational interval $\Delta G''_{1/2}$ could be measured to be 19.4060(41) cm^{-1} for ^{129}Xe–^{132}Xe and 19.206(13) cm^{-1} for ^{131}Xe–^{136}Xe. These values can be compared with the earlier result of 19.04 cm^{-1} for ^{129}Xe–^{132}Xe determined by Mao et al. (26). Several other values for $\Delta G''_{1/2}$ were determined from spectra in which the isotopic structure could not be resolved. Freeman et al. (16) reported an isotopically averaged value of 19.9 cm^{-1} determined from their emission spectrum. Tonkyn and White (27) determined values of $\Delta G''_{1/2}$ between 17.8 cm^{-1} and 21.6 cm^{-1} from the PFI-ZEKE photoelectron spectrum of the B $\leftarrow$ X photoionizing transition, and Dehmer et al. (28) reported values between 17.1 cm^{-1} and 19.8 cm^{-1} from measurements of dissociation thresholds.

To obtain satisfactory fits of the vibrational band origins using the standard expansion (25)

$$[4] \qquad \tilde{\nu}_{v'v''} = \tilde{\nu}_e + \left[\omega'_e\left(v'+1/2\right) - \omega_e x'_e(v'+1/2)^2 + \omega_e y'_e\left(v'+1/2\right)^3 - \ldots\right] - \left[\omega''_e\left(v''+1/2\right) - \omega_e x''_e\left(v''+1/2\right)^2 + \omega_e y''_e\left(v''+1/2\right)^3 - \ldots\right]$$

it was necessary to retain terms up to seventh order in $v'+1/2$. Moreover, the constants turned out to be correlated and to vary strongly with the number of terms retained in the expansion. The slow convergence of the expansions in eq. [4] is likely to originate from: (*i*) the *R*-dependent changes in the configurational mixing of the Rydberg state potential curve and of the ionic states to which the Rydberg series converge; and (*ii*) the fact that the vibrational levels probed experimentally ($v' = 14$–26) are located in a region where the contribution of the long-range dispersion interactions to the potential becomes substantial. The analysis of the isotopic shifts of the band origins using the well-known dependence of the vibrational constants on the reduced mass enabled the unambiguous determination of the absolute vibrational quantum number in the C state. The analysis confirmed the vibrational assignment made by Lipson et al. (29) and is indicated in Table 2. Further work on the lower vibrational levels of the C state would be desirable to obtain a more complete description of the potential curve of this state.

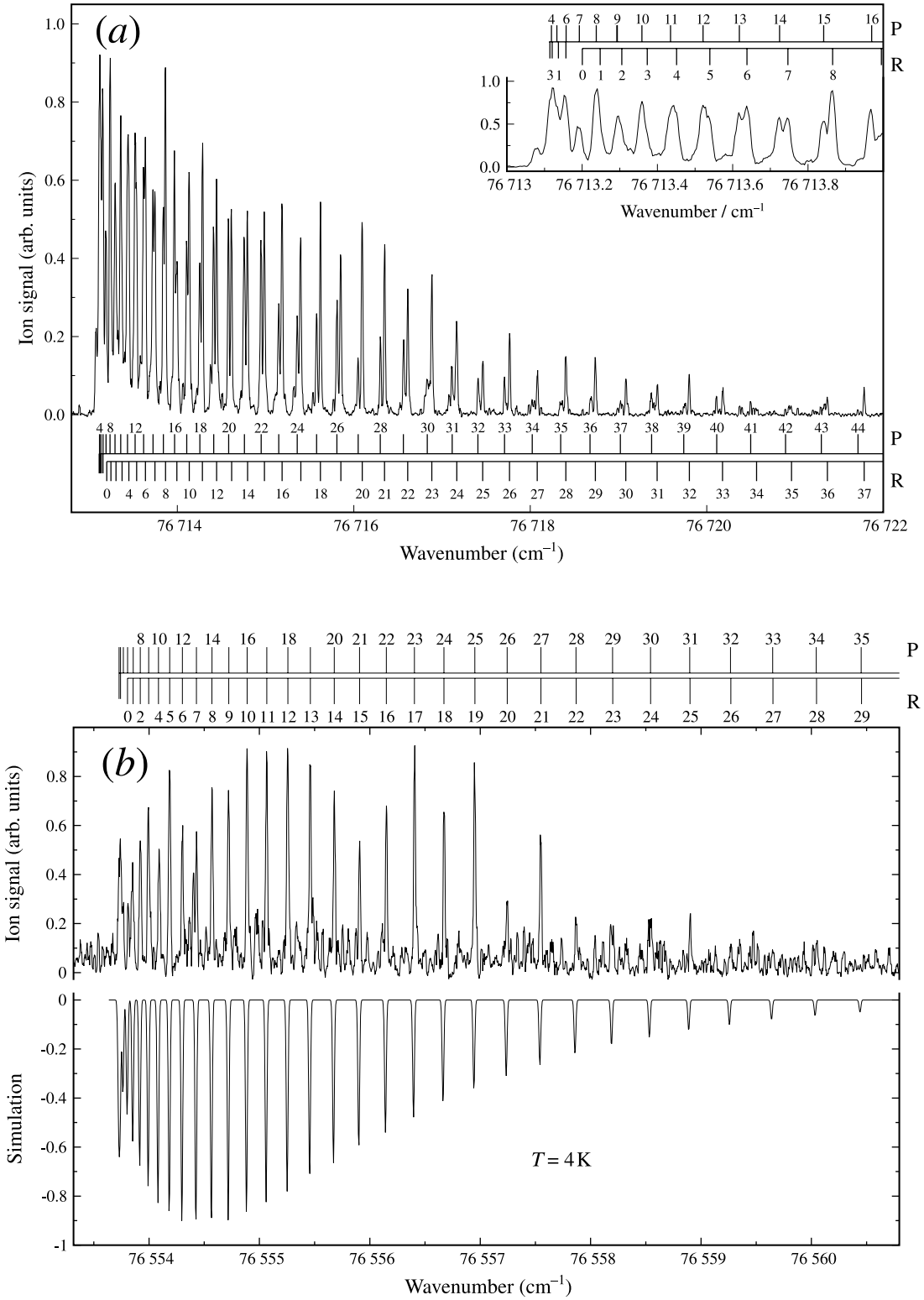
With the rotational constants B''_0 and B''_1 listed for ^{129}Xe–^{132}Xe in Table 2 and the relation

$$[5] \qquad B''_v = B''_e - \alpha''_e(v''+1/2)$$

B''_e and α''_e could be determined to be 0.013495(30) cm^{-1} and $3.02(33) \cdot 10^{-4}$ cm^{-1}, respectively. From the value of B''_e, the internuclear distance in the X ground state was estimated to

© 2004 NRC Canada

Fig. 2. (*a*) Rotational structure of the C 0_u^+ ($v' = 20$) ← X 0_g^+ ($v'' = 0$) transition measured by recording the ($1 + 1'$) resonance-enhanced, two-photon ionization signal corresponding to the mass number $M = 261$. The dominant contribution (89%) stems from the ^{129}Xe–^{132}Xe isotopomer. (*b*) Rotationally resolved spectrum (upper trace) of the C 0_u^+ ($v' = 16$) ← X 0_g^+ ($v'' = 1$) band of the ^{131}Xe–^{136}Xe isotopomer. The simulated spectrum (lower trace) was calculated assuming a rotational temperature of 4 K. The rotational branches are labeled by the branch index P ($\Delta J = -1$) or R ($\Delta J = 1$), and the value of J''.



© 2004 NRC Canada

Table 1. Wavenumbers of the rotational lines of the C 0_u^+ ($v' = 16, 17$) ← X 0_g^+ ($v'' = 0,\ 1$) bands of the ^{129}Xe–^{132}Xe isotopomer.

		P-branch			R-branch		
(v', v'')	J''	$\tilde{\nu}_{obs}$	$\Delta\tilde{\nu}^a$	$\Delta\tilde{\nu}^b$	$\tilde{\nu}_{obs}$	$\Delta\tilde{\nu}^a$	$\Delta\tilde{\nu}^b$
(16,0)	2				76 579.3518	−0.0005	−0.0010
	3				76 579.4209	0.0061	0.0055
	4				76 579.5106	0.0045	0.0038
	5	76 579.1844	0.0026	0.0028	76 579.6149	0.0004	−0.0003
	6	76 579.2182	0.0034	0.0037	76 579.7252	0.0028	0.0019
	7	76 579.2667	0.0019	0.0023	76 579.8492	0.0036	0.0027
	8	76 579.3241	0.0038	0.0042	76 579.9874	0.0025	0.0015
	9	76 579.3950	0.0044	0.0050	76 580.1361	0.0032	0.0022
	10	76 579.4784	0.0048	0.0055	76 580.2989	0.0021	0.0010
	11	76 579.5749	0.0044	0.0052	76 580.4726	0.0025	0.0013
	12	76 579.6876	0.0001	0.0010	76 580.6581	0.0033	0.0020
	13	76 579.8077	0.0008	0.0018	76 580.8596	0.0005	−0.0008
	14	76 579.9396	0.0020	0.0031	76 581.0712	−0.0002	−0.0016
	15	76 580.0878	−0.0008	0.0004	76 581.2948	−0.0004	−0.0019
	16	76 580.2460	−0.0013	−0.0000	76 581.5304	−0.0005	−0.0020
	17	76 580.4162	−0.0013	0.0001	76 581.7799	−0.0020	−0.0035
	18	76 580.5997	−0.0025	−0.0010	76 582.0408	−0.0025	−0.0041
	19	76 580.7926	−0.0005	0.0011	76 582.3131	−0.0022	−0.0039
	20	76 580.9989	0.0004	0.0021	76 582.5992	−0.0032	−0.0049
	21	76 581.2213	−0.0024	−0.0007	76 582.8995	−0.0060	−0.0078
	22	76 581.4529	−0.0020	−0.0001	76 583.2075	−0.0041	−0.0060
	23	76 581.6981	−0.0028	−0.0008	76 583.5300	−0.0043	−0.0063
	24	76 581.9557	−0.0036	−0.0015	76 583.8644	−0.0040	−0.0060
	25	76 582.2250	−0.0037	−0.0014	76 584.2081	−0.0005	−0.0026
	26	76 582.5063	−0.0031	−0.0008	76 584.5713	−0.0041	−0.0062
	27	76 582.8021	−0.0047	−0.0023	76 584.9483	−0.0089	−0.0111
	28	76 583.1067	−0.0027	−0.0002	76 585.3285	−0.0046	−0.0068
	29	76 583.4299	−0.0066	−0.0040	76 585.7278	−0.0068	−0.0091
	30	76 583.7592	−0.0042	−0.0015	76 586.1344	−0.0037	−0.0062
	31	76 584.1025	−0.0032	−0.0004	76 586.5538	−0.0010	−0.0035
	32	76 584.4609	−0.0048	−0.0018	76 586.9908	−0.0032	−0.0058
	33	76 584.8285	−0.0030	−0.0000	76 587.4404	−0.0055	−0.0081
	34	76 585.2062	0.0014	0.0045			
	35	76 585.6028	−0.0006	0.0026	76 588.3586	0.0087	0.0059
	36	76 586.0075	0.0019	0.0052	76 588.8501	0.0025	−0.0004
	37	76 586.4257	0.0037	0.0071	76 589.3406	0.0098	0.0068
	38				76 589.8458	0.0150	0.0120
	39	76 587.2939	0.0135	0.0172			
(17,0)	1				76 613.4403	0.0088	0.0086
	2				76 613.5058	0.0054	0.0050
	3				76 613.5811	0.0040	0.0035
	4				76 613.6667	0.0039	0.0034
	5	76 613.3383	0.0066	0.0070	76 613.7633	0.0047	0.0041
	6	76 613.3738	0.0034	0.0038	76 613.8730	0.0042	0.0035
	7	76 613.4146	0.0066	0.0071	76 613.9946	0.0036	0.0029
	8	76 613.4736	0.0036	0.0041	76 614.1269	0.0041	0.0033
	9	76 613.5406	0.0042	0.0049	76 614.2725	0.0031	0.0021
	10	76 613.6217	0.0026	0.0033	76 614.4290	0.0030	0.0020
	11	76 613.7138	0.0017	0.0026	76 614.5985	0.0018	0.0006
	12	76 613.8166	0.0021	0.0030	76 614.7788	0.0015	0.0003
	13	76 613.9318	0.0019	0.0030	76 614.9713	0.0009	−0.0004
	14	76 614.0595	0.0010	0.0021	76 615.1756	0.0002	−0.0011
	15	76 614.1978	0.0013	0.0025	76 615.3909	0.0005	−0.0009
	16	76 614.3493	0.0003	0.0016	76 615.6193	−0.0005	−0.0020

© 2004 NRC Canada

Table 1. (*continued*.)

		P-Branch			R-Branch		
(v', v'')	J''	$\tilde{\nu}_{obs}$	$\Delta\tilde{\nu}^a$	$\Delta\tilde{\nu}^b$	$\tilde{\nu}_{obs}$	$\Delta\tilde{\nu}^a$	$\Delta\tilde{\nu}^b$
	17	76 614.5122	−0.0003	0.0011	76 615.8598	−0.0016	−0.0032
	18	76 614.6862	−0.0001	0.0014	76 616.1114	−0.0021	−0.0037
	19	76 614.8730	−0.0007	0.0009	76 616.3739	−0.0016	−0.0033
	20	76 615.0740	−0.0036	−0.0020	76 616.6516	−0.0043	−0.0062
	21	76 615.2825	−0.0022	−0.0005	76 616.9389	−0.0048	−0.0067
	22	76 615.5016	0.0005	0.0023	76 617.2368	−0.0039	−0.0059
	23	76 615.7368	−0.0010	0.0009	76 617.5494	−0.0058	−0.0079
	24	76 615.9815	0.0001	0.0021	76 617.8701	−0.0039	−0.0061
	25	76 616.2444	−0.0052	−0.0030	76 618.2040	−0.0032	−0.0054
	26	76 616.5126	−0.0037	−0.0016	76 618.5528	−0.0053	−0.0077
	27	76 616.7873	0.0033	0.0055	76 618.9117	−0.0057	−0.0081
	28	76 617.0884	−0.0042	−0.0019	76 619.2803	−0.0037	−0.0063
	29	76 617.3919	−0.0020	0.0004	76 619.6692	−0.0100	−0.0126
	30	76 617.7119	−0.0043	−0.0018	76 620.0566	−0.0027	−0.0055
	31	76 618.0400	−0.0025	−0.0000	76 620.4641	−0.0035	−0.0063
	32	76 618.3796	−0.0003	0.0023			
	34	76 619.0986	0.0007	0.0034	76 621.7504	0.0028	−0.0004
	35				76 622.2096	−0.0012	−0.0045
	36	76 619.8670	0.0010	0.0038			
	37	76 620.2704	0.0001	0.0029			
	39	76 621.1060	0.0062	0.0091			
(16,1)	7	76 559.8838	−0.0075	−0.0067			
	8	76 559.9414	−0.0009	−0.0000			
	9	76 560.0163	0.0123	0.0133	76 560.7536	0.0040	0.0034
	10	76 560.1105	−0.0028	−0.0018	76 560.9236	0.0019	0.0012
	11	76 560.2103	0.0003	0.0015	76 561.1055	0.0009	0.0001
	12	76 560.3306	−0.0040	−0.0027	76 561.2977	0.0026	0.0017
	13	76 560.4586	−0.0032	−0.0018			
	14	76 560.5972	0.0001	0.0015	76 561.7225	0.0042	0.0032
	16				76 562.2067	−0.0017	−0.0029
	17				76 562.4657	−0.0020	−0.0033
	18				76 562.7360	−0.0007	−0.0020
	20				76 563.3155	0.0019	0.0005
(17,1)	9	76 594.1645	−0.0014	−0.0003			
	10	76 594.2471	0.0017	0.0029			
	11	76 594.3417	0.0052	0.0065			
	12				76 595.4230	−0.0039	−0.0047
	13				76 595.6243	−0.0052	−0.0061
	16				76 596.2917	0.0022	0.0010
	17				76 596.5507	−0.0068	−0.0081
	18	76 595.3795	0.0036	0.0054	76 596.8090	−0.0027	−0.0041
	19	76 595.5822	−0.0011	0.0008	76 597.0877	−0.0065	−0.0080
	20				76 597.3731	−0.0044	−0.0060
	21	76 596.0214	−0.0066	−0.0046			
	23	76 596.5026	−0.0040	−0.0018	76 598.3091	−0.0027	−0.0045
	24	76 596.7609	−0.0015	0.0007	76 598.6485	−0.0044	−0.0063
	25				76 598.9933	0.0012	−0.0010
	26	76 597.3250	−0.0062	−0.0038	76 599.3643	−0.0070	−0.0091
	28	76 597.9312	−0.0023	0.0001	76 600.1195	0.0017	−0.0007
	31	76 598.9423	−0.0035	−0.0008	76 601.3625	−0.0005	−0.0032
	32	76 599.3042	−0.0033	−0.0006	76 601.8040	−0.0030	−0.0058
	33	76 599.6794	−0.0036	−0.0009	76 602.2543	−0.0015	−0.0045
	34				76 602.7108	0.0065	0.0034

© 2004 NRC Canada

Table 1. (*concluded.*)

		P-Branch			R-Branch		
(v', v'')	J''	$\tilde{\nu}_{obs}$	$\Delta\tilde{\nu}^a$	$\Delta\tilde{\nu}^b$	$\tilde{\nu}_{obs}$	$\Delta\tilde{\nu}^a$	$\Delta\tilde{\nu}^b$
	35	76 600.4598	0.0040	0.0069			
	36	76 600.8698	0.0073	0.0101	76 603.6702	0.0146	0.0113
	38	76 601.7409	0.0012	0.0041	76 604.6870	0.0167	0.0131
	39	76 602.1837	0.0103	0.0132			

Note: The experimental uncertainties in the transition wavenumbers amount to 0.005 cm^{-1} (one standard deviation). The calculated transition wavenumbers were determined from the semiempirical potentials derived in Sect. 4. The deviations between calculated and experimental positions are listed for both potential fits as $\Delta\tilde{\nu} = \tilde{\nu}_{calc} - \tilde{\nu}_{exp}$.
[a]From spectroscopic data alone.
[b]From spectroscopic data and virial coefficients.

Table 2. Band origins, ground and excited rotational and centrifugal distortion constants of all measured bands of the C $0_u^+ \leftarrow$ X 0_g^+ transition of $^{129}Xe_2$, ^{129}Xe–^{132}Xe, and ^{131}Xe–^{136}Xe. The numbers in parentheses represent one standard deviation.

Isotopomer	v''	v'	$\tilde{\nu}_{v'',v'}$ / cm^{-1}	$B_{v''}$ / 10^{-2} cm^{-1}	$D_{v''}$ / 10^{-8} cm^{-1}	$B_{v'}$ / 10^{-2} cm^{-1}	$D_{v'}$ / 10^{-8} cm^{-1}
$^{129}Xe_2$	0	14	76 513.3291(59)	1.3491(21)	1.4(12)	2.0164(37)	−1.1(52)
	0	15	76 547.8180(26)			1.9934(23)	0.6(14)
	0	16	76 582.3706(17)			1.9702(22)	0.9(14)
	0	17	76 616.7014(22)			1.9467(27)	1.5(30)
	0	18	76 650.6538(27)			1.9198(23)	1.0(15)
	0	19	76 684.0924(57)			1.8938(38)	2.1(36)
	0	20	76 716.8958(28)			1.8654(22)	1.5(13)
	0	21	76 748.9608(20)			1.8364(22)	1.6(13)
	0	22	76 780.2025(42)			1.8074(24)	2.1(15)
	0	23	76 810.5545(31)			1.7758(24)	1.6(16)
	0	24	76 839.9469(73)			1.7448(41)	2.3(33)
	0	25	76 868.3373(62)			1.7124(38)	3.0(34)
^{129}Xe–^{132}Xe	0	14	76 510.5317(59)	1.3344(18)	2.15(97)	1.9972(85)	0.2(18)
	0	15	76 544.8255(25)			1.9740(22)	2.0(15)
	0	16	76 579.1930(21)			1.9503(20)	1.5(12)
	0	17	76 613.3547(17)			1.9263(20)	1.5(12)
	0	18	76 647.1579(22)			1.9014(20)	1.9(11)
	0	19	76 680.4679(51)			1.8753(22)	2.1(12)
	0	20	76 713.1635(26)			1.8478(21)	2.0(12)
	0	21	76 745.1390(18)			1.8198(18)	2.37(96)
	0	22	76 776.3089(32)			1.7911(21)	2.6(12)
	0	23	76 806.6077(36)			1.7612(25)	3.0(18)
	0	24	76 835.970(11)			1.7288(88)	1.0(140)
	0	25	76 864.3410(89)			1.6980(75)	2.0(120)
	0	26	76 891.680(14)			1.667(47)	−0.0(2400)
	1	16	76 559.7871(39)	1.3047(29)	3.0(17)		
	1	17	76 593.9509(72)				
^{131}Xe–^{136}Xe	0	14	76 505.0766(80)	1.3048(47)	1.3(37)	1.9549(79)	0.0(120)
	0	15	76 538.9863(65)			1.9326(55)	0.7(45)
	0	16	76 572.9735(64)			1.9101(84)	−0.10(150)
	0	17	76 606.7969(58)			1.8878(75)	0.0(130)
	0	18	76 640.3104(61)			1.8642(69)	1.0(89)
	0	19	76 673.3660(57)			1.8388(47)	1.4(35)
	0	20	76 705.8427(79)			1.8122(58)	0.7(49)
	0	21	76 737.6325(43)			1.7859(52)	1.4(42)
	0	22	76 768.6603(51)			1.7577(51)	1.2(40)
	0	23	76 798.8473(75)			1.7295(52)	2.0(39)
	0	24	76 828.1302(67)			1.7013(79)	5.0(120)
	0	25	76 856.468(17)			1.670(14)	3.0(210)
	1	16	76 553.767(11)	1.273(14)	−1.0(270)		

© 2004 NRC Canada

Table 3. Experimental values of the vibrational intervals $\Delta G''_{v''+1/2}$ in the ground electronic state of Xe_2 from the work of Freeman et al. (16) and the deviation $\Delta\left(\Delta G''_{v''+1/2}\right) = \Delta G''^{\,\mathrm{calc}}_{v''+1/2} - \Delta G''^{\,\mathrm{obs}}_{v''+1/2}$ with values calculated from the semiempirical potentials determined solely from spectroscopic data (third column) and from the spectroscopic data and the virial coefficients (fourth column).

v''	$\Delta G''^{\,\mathrm{obs}}_{v''+1/2}$ (cm^{-1})	$\Delta\left(\Delta G''_{v''+1/2}\right)^a$ (cm^{-1})	$\Delta\left(\Delta G''_{v''+1/2}\right)^b$ (cm^{-1})
1	18.55 ± 0.3	−0.38	−0.39
2	17.20 ± 0.3	−0.20	−0.21
3	16.17 ± 0.3	−0.33	−0.35
4	14.63 ± 0.3	0.06	0.03
5	13.70 ± 0.3	−0.15	−0.18
6	12.63 ± 0.3	−0.20	−0.24
7	11.33 ± 0.3	−0.01	−0.05
8	10.15 ± 0.3	0.09	0.04
9	8.95 ± 0.3	0.23	0.18

[a]From spectroscopic data alone.
[b]From spectroscopic data and second virial coefficients.

be 4.3773(49) Å by assuming that the reduced mass can be calculated using the atomic masses, an assumption that can be justified by the weakly bound nature of the ground electronic state of Xe_2. This internuclear equilibrium separation is in good agreement with the value of 4.37 Å of the semiempirical curve of Tang and Toennis (5).

4. Semiempirical potential for the X 0_g^+ ground state of Xe_2

In their determination of the semiempirical potential curve of the X 0_g^+ ground state of Xe_2, Dham et al. (9) optimized the potential parameters using, among other empirical data, the vibrational intervals determined by Freeman et al. (16). Consequently, their reported value for $\Delta G''_{1/2} = 19.61\ \mathrm{cm}^{-1}$ agrees within the uncertainty with the results of Freeman et al. (16), but differs by $\sim 0.3\ \mathrm{cm}^{-1}$ from our result (see Table 6).

To assess whether this discrepancy in the first vibrational interval has an effect on the interaction potential, the semiempirical potential parameters were fitted to a global empirical data set including: (*i*) the present set of line positions from Table 1, which contains implicitly a very accurate value of the first vibrational interval (see above); (*ii*) the vibrational intervals $\Delta G''_{v''+1/2}$ for $v'' = 1$–9 from the work of Freeman et al. (16) (the values are listed with their estimated uncertainties of 0.3 cm^{-1} in the second column of Table 3); and (*iii*) values of the second virial coefficient at several temperatures taken from a recent compilation (30) and listed with their uncertainties in the second column of Table 4.

A total of eight potential parameters were needed to describe our potential (see eqs. [1] and [2]): A, b, C_6, C_8, C_{10}, C_{12}, C_{14}, and C_{16}. Of these, only two were fitted to the experimental data, the long-range coefficients being kept fixed. The coefficient $C_6 = 285.9\ E_h a_0^6$ was taken from ref. 31, and the values of $C_8 = 12807\ E_h a_0^8$ and $C_{10} = 619840\ E_h a_0^{10}$ were adopted

Table 4. Comparison between experimental values of the second virial coefficient of Xe from ref. 30 and values calculated from the semiempirical potentials determined solely from spectroscopic data (third column) and from the spectroscopic data and the virial coefficients (fourth column).

T	$B_2^{\mathrm{exp}}(T)$	$B_2^{\mathrm{calc}}(T) - B_2^{\mathrm{exp}}(T)^a$	$B_2^{\mathrm{calc}}(T) - B_2^{\mathrm{exp}}(T)^b$
165	−403.3 ± 5.0	1.0	4.3
180	−341.6 ± 4.0	0.5	3.3
200	−279.7 ± 3.0	−0.6	1.7
220	−233.5 ± 3.0	−1.6	0.4
250	−183.3 ± 2.0	−2.3	−0.6
280	−147.5 ± 1.0	−2.6	−1.1
320	−113.5 ± 1.0	−2.4	−1.2
360	−89.0 ± 1.0	−2.2	−1.1
400	−70.6 ± 1.0	−1.9	−0.9
450	−53.2 ± 1.0	−1.6	−0.7
500	−39.8 ± 1.0	−1.5	−0.6
550	−29.2 ± 1.0	−1.4	−0.6
610	−19.1 ± 0.5	−1.5	−0.7
670	−10.9 ± 0.5	−1.7	−1.0
740	−3.2 ± 0.5	−2.0	−1.3
810	3.1 ± 0.5	−2.3	−1.7
890	9.0 ± 0.5	−2.8	−2.1
970	13.9 ± 0.5	−3.2	−2.6

Note: The temperatures are given in K and the second virial coefficients in $\mathrm{cm}^3\ \mathrm{mol}^{-1}$.
[a]From spectroscopic data alone.
[b]From spectroscopic data and second virial coefficients.

from ref. 32. The next three long-range coefficients (see Table 5) were determined from the values of C_6, C_8, and C_{10} using the recursion relation (33)

$$[6] \qquad C_{2n+4} = \Omega_n\, C_{2n-2} \left(\frac{C_{2n+2}}{C_{2n}}\right)^3$$

where Ω_n represents a factor that only slightly deviates from 1 and can be estimated using (33)

$$[7] \qquad \Omega_n \simeq \frac{(2n+1)\,(2n-3)\,n^3\,(n-2)\,(2^n-1)\left(2^{n-2}-1\right)^3}{(2n-1)^2\,(n+1)\,(n-1)^3\left(2^{n-3}-1\right)\left(2^{n-1}-1\right)^3} \quad \text{for } n \geq 4$$

Instead of fitting the parameters A and b, it turned out to be advantageous to use the boundary condition

$$[8] \qquad \left.\frac{\mathrm{d}V(R)}{\mathrm{d}R}\right|_{R=R_e} = 0$$

to express A as a function of R_e

$$[9] \qquad A = \frac{\mathrm{e}^{bR_e}}{b} \left.\frac{\mathrm{d}V_{\mathrm{attr}}(R)}{\mathrm{d}R}\right|_{R=R_e}$$

and to fit the parameters R_e and b.

To optimize the potential parameters on the basis of the $C(v' = 16, 17) \leftarrow X(v'' = 0, 1)$ transition wavenumbers

© 2004 NRC Canada

Table 5. Potential parameters for the X 0_g^+ ground state of Xe_2.

Parameter	Value[a]	Value[b]
R_e[c] / Å	4.378	4.385
A[d] / cm^{-1}	105 963 060	112 891 676
b / Å^{-1}	2.9654 ± 0.0002	2.9774 ± 0.0002
C_6[c] / (cm^{-1}Å^6)	1 377 861	1 377 861
C_8[c] / (cm^{-1}Å^8)	172 838 612	172 838 612
C_{10}[c] / (cm^{-1}Å^{10})	234 247 646	234 247 646
C_{12}[c] / (cm^{-1}Å^{12})	3 526 648 372	3 526 648 372
C_{14}[c] / (cm^{-1}Å^{14})	57 500 032 449	57 500 032 449
C_{16}[c] / (cm^{-1}Å^{16})	988 394 705 757	988 394 705 757
$\tilde{\nu}_{16,0}$ / cm^{-1}	76 579.1976 ± 0.0015	76 579.1974 ± 0.0019
$\tilde{\nu}_{17,0}$ / cm^{-1}	76 613.3604 ± 0.0015	76 613.3603 ± 0.0018
B_{16} / cm^{-1}	0.019473 ± 0.00002	0.019431 ± 0.00003
B_{17} / cm^{-1}	0.019231 ± 0.00002	0.019189 ± 0.00003

Note: The band origins of the C 0_u^+ ($v' = 16, 17$) ← X 0_g^+ ($v'' = 0$) transition of ^{129}Xe–^{132}Xe and the rotational constants of the C 0_u^+ ($v' = 16, 17$) levels were also refined during the fitting procedure. The uncertainties represent 95% confidence intervals.
[a]From spectroscopic data alone.
[b]From spectroscopic data and virial coefficients.
[c]Parameter kept fixed during the fit.
[d]Parameter calculated with eq. [9].

listed in Table 1, these wavenumbers were calculated using the expression

$$[10] \quad \tilde{\nu}_{v'J',v''J''} = \tilde{\nu}_{v',v''} + F_{v'}(J') - F_{v''}(J'')$$

where $\tilde{\nu}_{v',v''}$ represents the band origins. Because the contribution of the centrifugal distortion to the rotational term values was found to be negligible (see previous section), the rotational term values of the vibronic levels of the C state were calculated using the relation $F_{v'}(J') = B_{v'}\,J'(J'+1)$. The rotational term values of the vibronic levels of the X state $F_{v''}(J'') = \left[E_{v'',J''} - E_{v'',J''=0}\right]$ were determined by solving the radial Schrödinger equation

$$[11] \quad \left[-\frac{\hbar^2}{2\mu}\frac{\mathrm{d}^2}{\mathrm{d}R^2} + hc\,V_{J''}(R)\right]\psi_{v''J''}(R) = hc\,E_{v''J''}\,\psi_{v''J''}(R)$$

numerically using a discrete variable representation with 1001 equidistant points between 2 and 12 Å in a procedure analogous to that used in our previous determination of the ground state potential of Ne_2 (6). The effective potential $V_{J''}(R)$ in eq. [11] includes the centrifugal potential

$$[12] \quad V_{J''}(R) = V(R) + \frac{h}{8\pi^2\mu\,c}\frac{J''(J''+1)}{R^2}$$

Next to the two potential parameters R_e and b, four parameters ($\tilde{\nu}_{16,0}$, $\tilde{\nu}_{17,0}$, B'_{16}, and B'_{17}) had to be included in the fit procedure to account for the C state energy level structure.

To incorporate the vibrational intervals from the work of Freeman et al. (16) into the fitting procedure, the vibrational intervals were determined from the computed eigenvalues of eq. [11] using the relation

$$[13] \quad \Delta G''_{v''+1/2} = E_{v''+1,J''=0} - E_{v'',J''=0}$$

and then compared with the experimental values listed in Table 3. In this procedure, an average was built over all isotopomers because the isotopic structure was not resolved in the experimental spectra.

Finally, to include the values of the second virial coefficient into the fitting procedure, eqs. [14]–[18] were used, which express the various contributions to the second virial coefficients as a function of the potential function $V(R)$ (34–38):

$$[14] \quad B_2(T) = B_{\mathrm{cl}}(T) + \left(\frac{h^2}{m}\right)B_{\mathrm{I}}(T) + \left(\frac{h^2}{m}\right)^2 B_{\mathrm{II}}(T) + \cdots \mp \left(\frac{h^2}{m}\right)^{3/2} B_0(T) = B_{\mathrm{cl}}(T) + B^{\mathrm{I}}(T) + B^{\mathrm{II}}(T) + \cdots \mp B^0(T)$$

$$[15] \quad B_{\mathrm{cl}}(T) = -2\pi N_{\mathrm{A}}\int_0^\infty \left[\mathrm{e}^{-(V(R)/kT)} - 1\right]R^2\,\mathrm{d}R$$

$$[16] \quad B_{\mathrm{I}}(T) = +2\pi N_{\mathrm{A}}\frac{1}{48\pi^2k^3T^3}\int_0^\infty \mathrm{e}^{-(V(R)/kT)}\left(\frac{\mathrm{d}V(R)}{\mathrm{d}R}\right)^2 R^2\,\mathrm{d}R$$

$$[17] \quad B_{\mathrm{II}}(T) = -2\pi N_{\mathrm{A}}\frac{1}{1920\pi^4k^4T^4}\int_0^\infty \mathrm{e}^{-(V(R)/kT)}\left[\left(\frac{\mathrm{d}^2V(R)}{\mathrm{d}R^2}\right)^2 + \frac{2}{R^2}\left(\frac{\mathrm{d}V(R)}{\mathrm{d}R}\right)^2 + \frac{10}{9kT}\frac{1}{R}\left(\frac{\mathrm{d}V(R)}{\mathrm{d}R}\right)^3 - \frac{5}{36k^2T^2}\left(\frac{\mathrm{d}V(R)}{\mathrm{d}R}\right)^4\right]R^2\,\mathrm{d}R$$

© 2004 NRC Canada

Table 6. Dissociation energy (D_e), equilibrium internuclear distance (R_e), and first vibrational interval ($\Delta G''_{1/2}$) of the X 0^+_g ground electronic state of Xe_2.

D_e (cm^{-1})	R_e (Å)	$\Delta G''_{1/2}$ (cm^{-1})	Reference
196.1 ± 1.1	4.378 ± 0.009	19.3485 ± 0.0005[a]	This work[b]
195.3	4.385	19.3487[a]	This work[c]
—	4.3773(49)	—	(42)
195.54 ± 3.00	—	19.90 ± 0.3	(16)
196.56	4.366	19.61	(9)[d]
196.65	4.37	—	(5)
196.24	4.3634	19.61	(43)[e]
183.1	4.42	18.65	(4)[f]

[a]Values corresponding to an average over all isotopomers.
[b]From spectroscopic data alone.
[c]From spectroscopic data and second virial coefficients.
[d]HFD-B2 potential from the reference.
[e]X4 potential from the reference.
[f]Ab initio values (ECP+aug-cc-pVQZ+spdfg).

$$[18] \qquad B_0(T) = \frac{N_A}{2^{5/2}} \left(\frac{1}{2\pi kT} \right)^{3/2}$$

In these equations, h, N_A, and k are Planck's, Avogadro's, and Boltzmann's constants, respectively, and m represents the atomic mass of the gas particles. $B_{cl}(T)$ corresponds to the classical expression for the second virial coefficient; $B^{I}(T)$ and $B^{II}(T)$ represent the first and second quantum mechanical corrections; finally, $B^0(T) = (h^2/m)^{3/2} B_0(T)$ is the second virial coefficient for an ideal gas, whereby a plus sign has to be used in eq. [14] for fermions and a minus sign for bosons (39). The contribution of this last term to the second virial coefficient is negligible in the temperature range $T = 165$–970 K where experimental data are available.

To fit the potential parameters to the three very different sets of empirical data, a weighted nonlinear, least-squares fitting procedure was employed, the weights of each data point being determined from the corresponding experimental uncertainty. A fit was considered acceptable when the normalized root-mean-square (rms) deviation of the fit amounted to less than 1.

Two fits were performed, the first one relying solely on the spectroscopic data, i.e., the data set from the present work, and the vibrational intervals from the work of Freeman et al. (16), the second also including the second virial coefficients. Whereas it was possible to reach a rms deviation of less than one (rms = 0.891) in the former case, the rms deviation of the second fit amounted to 1.109. Table 5 lists the potential parameters determined in both fits, and Table 6 compares the dissociation energies (D_e), the equilibrium internuclear distances (R_e) and the calculated values of the first vibrational interval ($\Delta G''_{1/2}$) with earlier results. Both potentials are very similar to previously reported semiempirical potentials but lead to dissociation energies D_e that are significantly higher than predicted in the latest ab initio quantum chemical calculation.

Although both fits resulted in values of the internuclear distance and first vibrational interval that are compatible with the results of the spectroscopic analysis presented in the previous section, the results of the fit based on the spectroscopic data alone is in closer agreement. The rotational constants of the $v' = 16$ and 17 vibrational levels of the C state obtained from the fits are equal, within two standard deviations, to those determined in the fit to eq. [3]. This observation validates the procedure used to derive the X state potential parameters and also confirms that the effects of the centrifugal distortion can be neglected in good approximation.

For both fits, the deviations between experimental and calculated transition wavenumbers (see Table 1) and vibrational intervals (see Table 3) do not exceed two standard deviations. In contrast, the deviations between experimental and calculated second virial coefficients are often more than twice, at low temperatures even more than four times, larger than the experimental uncertainties given in ref. 30 (see Table 4). This behavior is not typical for the potentials determined here, but is also found (40) when calculating the second virial coefficients using the semiempirical potentials of refs. (5, 9, 41). It thus appears that the experimental uncertainties in the second virial coefficients may have been slightly underestimated, effectively leading to too large weights of these data in the fitting procedure and to an undesirable bias in the determination of the potential parameters. For this reason, the X state potential determined from the spectroscopic data alone, and which is described by the potential parameters listed in the second column of Table 5, is to be preferred. With this potential, the existence of 25 bound vibrational levels is predicted for the most abundant dimer ^{129}Xe–^{132}Xe.

5. Conclusions

When combined with mass spectrometry, high-resolution VUV laser spectroscopy can be successfully used to obtain rotationally resolved spectra of mass-selected species having small rotational constants. In the present investigation, this combination enabled the first experimental determination of the rotational structure of the ground electronic state of Xe_2 from a measurement of the rotational structure of the C $0^+_u \leftarrow$ X 0^+_g transition of several isotopomers of Xe_2. The analysis of the spectra led to the derivation of a set of rotational constants for the $v'' = 0$, 1 level of the X ground state, and the $v' = 14$–26 levels of the C state. The information contained in the rotational structure of the lowest two levels of the ground state of Xe_2 was combined with previous results on the vibrational intervals and on the second virial coefficients to determine an accurate semiempirical interaction potential for the X state. This potential differs only very slightly from earlier semiempirical potentials, and primarily in the fact that it leads to a smaller value for the first vibrational interval. The deviations between the equilibrium internuclear distance and dissociation energies of the X ground state ($R_e = 4.3773(49)$ Å, $D_e = 196.1 \pm 1$ cm^{-1}) determined here, and the results of the latest ab initio quantum chemical calculations ($R_e = 4.42$ Å, $D_e = 183.1 \pm 1$ cm^{-1}) (4) illustrate the difficulties that are still associated with the accurate theoretical treatment of molecules containing heavy atoms.

Acknowledgments

This work was supported financially by the Swiss National Science Foundation and the ETH Zürich.

© 2004 NRC Canada

References

1. R.J. Gdanitz. J. Chem. Phys. **113**, 5145 (2000).
2. S.M. Cybulski and R.R. Toczylowski. J. Chem. Phys. **111**, 10 520 (1999).
3. R.J. Gdanitz. Chem. Phys. Lett. **348**, 67 (2001).
4. P. Slavíček, R. Kalus, P. Paška, I. Odvárková, P. Hobza, and A. Malijevský. J. Chem. Phys. **119**, 2102 (2003).
5. K.T. Tang and J.P. Toennies. J. Chem. Phys. **118**, 4976 (2003).
6. A. Wüest and F. Merkt. J. Chem. Phys. **118**, 8807 (2003).
7. R.A. Aziz. J. Chem. Phys. **99**, 4518 (1993).
8. A.K. Dham, A.R. Allnatt, W.J. Meath, and R.A. Aziz. Mol. Phys. **67**, 1291 (1989).
9. A.K. Dham, W.J. Meath, A.R. Allnatt, R.A. Aziz, and M.J. Slaman. Chem. Phys. **142**, 173 (1990).
10. K.T. Tang and J.P. Toennies. J. Chem. Phys. **80**, 3726 (1984).
11. K.P. Huber and G. Herzberg. Constants of diatomic molecules. Van Nostrand Reinhold Company, New York. 1979.
12. Y. Tanaka and K. Yoshino. J. Chem. Phys. **53**, 2012 (1970).
13. Y. Tanaka, K. Yoshino, and D.E. Freeman. J. Chem. Phys. **59**, 5160 (1973).
14. P.R. Herman, P.E. LaRocque, and B.P. Stoicheff. J. Chem. Phys. **89**, 4535 (1988).
15. P.E. LaRocque, R.H. Lipson, P.R. Herman, and B.P. Stoicheff. J. Chem. Phys. **84**, 6627 (1986).
16. D.E. Freeman, K. Yoshino, and Y. Tanaka. J. Chem. Phys. **61**, 4880 (1974).
17. U. Hollenstein, H. Palm, and F. Merkt. Rev. Sci. Instrum. **71**, 4023 (2000).
18. R. Seiler, U. Hollenstein, G.M. Greetham, and F. Merkt. Chem. Phys. Lett. **346**, 201 (2001).
19. U. Hollenstein, R. Seiler, and F. Merkt. J. Phys. B: At. Mol. Opt. Phys. **36**, 893 (2003).
20. H. Katô, M. Baba, S. Kasahara, K. Ishikawa, M. Misono, Y. Kimura, J. O'Reilly, H. Kuwano, T. Shimamoto, T. Shinano, C. Fujiwara, M. Ikeuchi, N. Fujita, M.H. Kabir, M. Ushino, R. Takahashi, and Y. Matsunobu. Doppler-free high resolution spectral atlas of iodine molecule 15 000 to 19 000 cm^{-1}. Japan Society for the Promotion of Science, Tokyo. 2000.
21. S. Gerstenkorn and P. Luc. Atlas du spectre d'absorption de la molécule d'iode - 14 800–20 000 cm^{-1}. Laboratoire Aimé-Cotton CNRS II, Orsay, France. 1979.
22. F. Merkt, A. Osterwalder, R. Seiler, R. Signorell, H. Palm, H. Schmutz, and R. Gunzinger. J. Phys. B: At. Mol. Opt. Phys. **31**, 1705 (1998).
23. R.S. Mulliken. J. Chem. Phys. **52**, 5170 (1970).
24. J.T. Hougen. Nat. Bur. Stand. (US), Monogr. 115, (1970).
25. G. Herzberg. Molecular spectra and molecular structure. Vol. 1. 2nd ed. Krieger Publishing Company, Malabar, Florida. 1950.
26. D.M. Mao, X.K. Hu, S.S. Dimov, and R.H. Lipson. J. Mol. Spectrosc. **181**, 435 (1997).
27. R.G. Tonkyn and M.G. White. J. Chem. Phys. **95**, 5582 (1991).
28. P.M. Dehmer, S.T. Pratt, and J.L. Dehmer. J. Chem. Phys. **85**, 13 (1986).
29. R.H. Lipson, P.E. LaRocque, and B.P. Stoicheff. J. Chem. Phys. **82**, 4470 (1985).
30. J.H. Dymond, K.N. Marsh, R.C. Wilhoit, and K.C. Wong. *In* Landolt-Börnstein: Numerical data and functional relationships in science and technology, New series, Group IV: Physical chemistry. *Edited by* M. Frenkel and K.N. Marsh. Vol. 21. Springer-Verlag, Berlin. 2003.
31. A. Kumar and W.J. Meath. Mol. Phys. **54**, 823 (1985).
32. A.J. Thakkar, H. Hettema, and P.E.S. Wormer. J. Chem. Phys. **97**, 3252 (1992).
33. A.J. Thakkar. J. Chem. Phys. **89**, 2092 (1988).
34. G.E. Uhlenbeck and E. Beth. Physica, **3**, 729 (1936).
35. E. Beth and G.E. Uhlenbeck. Physica, **4**, 915 (1937).
36. L. Gropper. Phys. Rev. **50**, 963 (1936).
37. L. Gropper. Phys. Rev. **51**, 1108 (1937).
38. J.O. Hirschfelder and W.J. Meath. Adv. Chem. Phys. **12**, 3 (1967).
39. J.O. Hirschfelder, C.F. Curtiss, and R.B. Bird. Molecular theory of gases and liquids. John Wiley and Sons, New York. 1954.
40. A. Wüest. Spektroskopische strukturelle und dynamische Eigenschaften von Edelgasdimeren und deren Kationen. Ph.D. thesis, ETH Zürich, 2003, Diss. Nr. 15 310.
41. J.A. Barker, R.O. Watts, J.K. Lee, T.P. Schafer, and Y.T. Lee. J. Chem. Phys. **61**, 3081 (1974).
42. U. Hollenstein. Erzeugung und spektroskopische Anwendungen von schmalbandiger, kohärenter, vakuum-ultravioletter Strahlung. Ph.D. thesis, ETH Zürich, 2003, Diss. Nr. 15 237.
43. J.A. Barker, M.L. Klein, and M.V. Bobetic. IBM J. Re. Develop. **20**, 222 (1976).

© 2004 NRC Canada

Rydberg states of the rare gas dimers[1]

Marshall L. Ginter and J. Gary Eden

Abstract: This work is dedicated to Gerhard Herzberg and his prodigious contributions to molecular spectroscopy. Of particular relevance here is Herzberg's seminal 1987 article (Annu. Rev. Phys. Chem. **38**, 27 (1987)) in which he discussed the electronic structures of several groups of molecules he termed "Rydberg molecules". Among these are the rare gas dimers (Rg_2), a group whose study has benefited significantly from recent advances in laser excitation and synchrotron-based spectroscopies, as well as in theory. Following the spirit of Herzberg's 1987 article, this paper reviews some of the more prominent features of Rydberg states in the Rg_2 family as viewed from the current perspective.

Key words: rare gas dimers, rare gas dimer excited states, Rg_2 electronic structures, Rydberg states of He_2, Ne_2, Ar_2, Kr_2, and Xe_2, electronic states of He_2, Ne_2, Ar_2, Kr_2, and Xe_2.

Résumé : Ce travail est dédié à Gerhard Herzberg et à ses contributions exceptionnelles à la spectroscopie moléculaire, plus particulièrement à son important article de 1987 (Annu. Rev. Phys. Chem. **38**, 27 (1987)) dans lequel il a discuté des structures électroniques de plusieurs groupes de molécules appelées "molécules de Rydberg". Parmi ces groupes se trouvent les dimères de gaz rares (Rg_2), un groupe dont l'étude a bénéficié largement des récents progrès théoriques et des spectroscopies basées sur des excitations au synchrotron ou au laser. Dans l'esprit de l'article de Herzberg de 1987, ce travail passe en revue quelques-unes des caractéristiques principales des états de Rydberg dans la famille Rg_2, dans une optique contemporaire.

Mots clés : dimères de gaz rares, états excités des dimères de gaz rares, structures électroniques Rg_2, états de Rydberg de He_2, de Ne_2, de Ar_2, de Kr_2 et de Xe_2, états électroniques de He_2, de Ne_2, de Ar_2, de Kr_2 et de Xe_2.

[Traduit par la Rédaction]]

Introduction

In his classic 1987 paper in the *Annual Review of Physical Chemistry* (1), Gerhard Herzberg discussed several distinctive aspects of the spectroscopy and structure of three groups of molecules for which the electronic excited states were considered to be essentially Rydberg in character. As recounted by Stoicheff (2), the preface to this 1987 work (1) was Herzberg's search for H_3^+ and his subsequent discovery of emission spectra for H_3 and D_3 which he termed Rydberg molecules. In this molecular clasification, he "…included [the] dimers and hydrides of the rare gases and their respective ions" (2). Of special interest here are Herzberg's comments regarding prominent features in the Rydberg series for the rare gas (Rg_2) dimers, assessments based in part on the then recently reported (3, 4) Rydberg series spectra for Ne_2–Xe_2 and on spectral observations for He_2 (5) that extended back to the early 1900s.

This paper follows the spirit of ref. 1 by identifying and discussing key characteristics of a selected portion of the Rydberg electronic structures of the Rg_2 molecules and emphasizing Rydberg electronic structures that exist below, and converge on, the lowest ionization limit of the dimers, the $X^2\Sigma_u^+$ state of Rg_2^+. Thus, the following provides a brief discussion of specific aspects of the $X^2\Sigma_u^+$ core-based Rydberg structures in the Rg_2 family in toto and is not intended as a detailed review.

The remainder of the introduction is devoted mainly to definitions and nomenclature (Rydberg level energies, electronic state labels, molecular parameters, etc.). The article then proceeds with introductions to the Rydberg states built on ground-state $Rg^+ + Rg$ core structures, to spectroscopies utilized in characterizing Rg_2 Rydberg structures, to brief outlines of the known Rydberg structures and spectra for each dimer and, finally, to discussions of several issues involving the family as a whole that include a summary of suggested future work.

Rydberg electronic states for neutral molecules generally can be described in terms of series that converge on energy levels of the molecular ion core (5–7). The expression for the energy (E_n) of the nth member of a series is expressed:

$$[1] \qquad E_n = E_\infty - \Re/n^{*2} = E_\infty - \Re/(n - \delta)^2$$

where n is the principal quantum number (an integer), E_∞ is the series limit, $\Re$ is the mass-dependent Rydberg constant, δ is the quantum defect, and n^* is the effective quantum

Received 22 December 2003. Published on the NRC Research Press Web site at http://canjchem.nrc.ca on 26 August 2004.

M.L. Ginter. Institute for Physical Science and Technology, University of Maryland, College Park, MD 20742, USA.
J.G. Eden.[2] University of Illinois, Department of Electrical and Computer Engineering, 136 Everitt Laboratory, 1406 West Green Street, Urbana, IL 61801 USA.

[1]This article is part of a Special Issue dedicated to the memory of Professor Gerhard Herzberg.
[2]Corresponding author (e-mail: jgeden@uiuc.edu).

 doi: 10.1139/V04-089 © 2004 NRC Canada

number. Bonding in a Rydberg state is considered to reflect that of its core ion, while bonding in a valence state is determined by valence electron and configuration interactions. In some diatomic molecules, valence states interact so strongly with the Rydberg states that Rydberg – valence state distinctions tend to be less meaningful. However, the electronic excited states of the Rg_2 molecules built on their ground-state ionic cores are ideal for studying Rydberg character because they are seldom perturbed by valence levels or by Rydberg states built on excited ionic cores, at least for internuclear separations (R) in the vicinity of the equilibrium internuclear separation (R_e) of their $X^2\Sigma_u^+$ core.

The $^{2S+1}\Sigma_p^{p'}$ electronic state labels (term symbols) apply to the Λ,S coupling scheme (5) and include quantum numbers for the total electron spin (S), the component of electronic orbital angular momentum along the internuclear axis (Λ; $\Lambda = 0 \rightarrow \Sigma$, $\Lambda = 1 \rightarrow \Pi$, etc.), and the wave function's inversion parity ($p = g$ if even and u if odd) and reflection parity ($p' = +$ or $-$) in a plane containing the internuclear axis. States having $\Lambda = 0$ are either Σ_p^+ or Σ_p^-. Each state with $\Lambda_p > 0$ comprises two symmetry states (Λ_p^+ and Λ_p^-, sometimes referred to as lambda doublets), with the superscript + or – having the same meaning as that for the $\Lambda = 0$ states. Also associated with each Λ,S state are substates labeled by values of the quantum number Ω, which specifies the value of the total electronic angular momentum along the internuclear axis. For Λ,S coupling (5), Ω is the sum of Λ and the component of the total electron spin along the internuclear axis.

When considering electronic state behavior at large R or the structure of the heavier dimers Rg_2 or Rg_2^+, Λ,S representations break down because of spin–orbit and configuration interactions. However, in such instances, Ω-based representations, sometimes referred to as *case c* representations, remain valid (5). The Ω-based states are $\Omega_p^{p'}$ states, with both Ω_p^+ and Ω_p^- existing for $\Omega_p^{p'} > 0$ and with $\Omega_p^{p'}$ either 0_p^+ or 0_p^- for $\Omega = 0$. Thus, singlet and doublet sigma states map directly to their Ω values, such as $^1\Sigma_p^{p'} \rightarrow 0_p^{p'}$, $^1\Pi_p \rightarrow 1_p^{\pm}$, $^2\Sigma_p^{p'} \rightarrow 1/2_p^{p'}$, etc., while Λ,S-based triplet states can break down into collections of $\Omega_p^{p'}$ states, such as $^3\Sigma_p^+ \rightarrow 1_p^{\pm}$, 0_p^-, $^3\Pi_p \rightarrow 2_p^{\pm}$, $1_p^{\pm}$, $0_p^{\pm}$, $^3\Delta_p \rightarrow 3_p^{\pm}$, $2_p^{\pm}$, $1_p^{\pm}$, etc., where the $\Omega_p^{p'}$ states will generally have different energies.

Molecular parameters discussed here appear in polynomials representing the state energies (terms), $T(v,N)$, given by

$$[2] \quad T(v,N) = T(^{2S+1}\Lambda_p) + T_v^o + B_v N(N+1) - D_v[N(N+1)]^2 + H_v[N(N+1)]^3 + \ldots$$

where the T_v^o value is the energy for $N = 0$ (real, or extrapolated for $\Lambda > 0$) of vibrational level v, $T(^{2S+1}\Lambda_p)$ is the energy of the state being parameterized (in parentheses), defined relative to the zero energy reference employed (i.e., the energy of the $N = 0$, $v = 0$ level in the $a^3\Sigma_u^+$ state for He_2, etc.), and B_v, D_v, H_v,... are effective rotational and rotational distortion parameters (5). When several vibrational levels are observed, it is customary to parameterize T_v^o values and to reparameterize the rotational parameters in eq. [2] by fitting the following expressions (5):

$$[3] \quad T_v^o = \omega_e(v+1/2) - \omega_e x_e(v+1/2)^2 + \omega_e y_e(v+1/2)^3 + \ldots$$

Table 1. Representative values for the dissociation energy, the equilibrium internuclear separation (R_e), and other parameters for the weakly bound $X^1\Sigma_g^+$ states of Rg_2.

Rg_2	D_0 (cm^{-1})[a]	D_e (cm^{-1})[a]	R_e (Å)	ω_e (cm^{-1})	$\omega_e x_e$ (cm^{-1})
He_2		7.63[b]	2.97[b]	3.3[b]	
Ne_2	16.8[c]	29.4[c]	3.09[c]	28.6[c]	6.84[c]
Ar_2		99.2[d]	3.76[d]	30.7[d]	2.4[d]
Kr_2		138[e]	4.02[e]	23.53[e]	1.07[e]
Xe_2	186.0[f]	196.3[f]	4.37[f]	20.9[f]	

[a] D_0 and D_e are the dissociation energy relative to $v = 0$ and to the potential minimum (at R_e), respectively. These values are selected as being representative of values in the literature and demonstrate that the $X^1\Sigma_g^+$ potential energy curves are strongly repulsive except for shallow minima in the large-R van der Waals regions. When necessary, values of energy in hartrees, eV, or K were converted to cm^{-1} (1 hartree = 2.1947×10^5 cm^{-1}, 1 eV = 8065.54 cm^{-1}, 1 K = 0.6948 cm^{-1}) and R values in bohr to Å (1 bohr = 0.52917 Å). Values for D_0 and D_e are approximately related by $D_0 = D_e - 1/2\omega_e + 1/4\omega_e x_e$, while ω_e and $\omega_e x_e$ are defined in eq. [3].

[b] D_e value is from Anderson's Table I summary (ref. 8), while R_e and ω_e values are from ref. 9.

[c] The D_e and R_e values are from ref. 11 and are in agreement with refs. 9 and 13. Reference 9 provides $\omega_e = 28.6$ cm^{-1}, while ref. 10 lists $\omega_e = 31.3$ and $\omega_e x_e$ ($\equiv x\omega_e$) = 6.8 cm^{-1}.

[d] Values are from ref. 16 and are in agreement with refs. 9, 12, 14, and 15.

[e] Values are from refs. 17 and 18. Reference 14 gives $D_e = 139.9$ cm^{-1} and $R_e = 4.01$ Å, which agrees with ref. 21.

[f] Values are from refs. 19 and 20, with D_e and R_e in agreement with ref. 21. Reference 11 gives $D_e = 183$ cm^{-1} and $R_e = 4.42$ Å.

and

$$[4] \quad B_v = B_e - \alpha_e(v+1/2) + \beta_e(v+1/2)^2 + \gamma_e(v+1/2)^3 + \ldots$$

where ω_e, $\omega_e x_e$,... and B_e, α_e,... are referred to as equilibrium vibrational and rotational parameters, respectively. Finally, R_e is related (5) to B_e by the relation $B_e = \hbar(8\pi^2 c\mu R_e^2)^{-1}$, so that R_e determinations require either rotationally resolved experimental data or appropriate theoretical and (or) modeling calculations.

The potential energy curves for the $X^1\Sigma_g^+$ ground states, the principal and best determined of the valence states of the Rg_2 molecules, are repulsive except for a shallow van der Waals minimum at large R. This can be seen in part from the representative sample of D and R_e values in Table 1, where the dissociation energies (8–21) of the dimer ground states are low, ranging from 7.63 cm^{-1} (9.5×10^{-4} eV) for He_2 to 196 cm^{-1} (0.024 eV) for Xe_2. In addition, the R_e values for $X^1\Sigma_g^+$ are larger than the R_e values for their corresponding $X^2\Sigma_u^+$ ion cores (see Table 2). Finally, it should be noted that only these general properties of the R dependencies of the $X^1\Sigma_g^+$ potentials are important here.

Higher-lying (above X) valence states also tend to be unstable, and some states that are Rydberg in the vicinity of $R_e(Rg_2^+)$ have potential energies that exhibit "anomalies" at large R values, resulting from strong configuration interactions between the bound Rydberg states and dissociative valence states of the same symmetry. In an adiabatic picture, such strong interactions lead to noncrossings of the potential energy curves and to associated maxima and minima at large R.

© 2004 NRC Canada

Table 2. Representative values for the dissociation energy (D_0 (cm^{-1})) and R_e (Å) for the Rg_2^+ states derived from the ground separated atom limits.[a]

Rg_2^+	Ω	$X^2\Sigma^+_{1/2u}$	$A^2\Pi_{3/2g,1/2g}$	$B^2\Pi_{3/2u,1/2u}$	$C^2\Sigma^+_{1/2g}$
He_2^+	1/2	19 114 [1.081][b]	—	—	Repulsive
Ne_2^+	3/2		1174 [2.22][c]	96 [3.34][c]	
	1/2	10 856 [1.756][c]	670 [2.2][c]	261[c,d] [3.1][c]	63[c,d] [3.90][c]
Ar_2^+	3/2		1540 [≤2.99][f]	312 [3.80][g]	
			≥1509 [2.98][g]		
	1/2	10 604[e] [2.39][g]	686 [3.00][f]	≥616 [≤3.63][g]	625 [3.63][g]
			≥616 [≤2.98][g]		
Kr_2^+	3/2		1646[h] [6.33][h]	369[i] [7.77][h]	
	1/2	9 268[i] [2.75][i]	Repulsive[i]	1072[i]	609[i]
Xe_2^+	3/2		1793[j] [3.70][k]	437[j] [4.40][k]	
	1/2	7861[j] [3.11][k]	158[k] [5.77][k]	1447[j] [3.98][k]	842[j] [4.77][k]

[a]See footnote *a* to Table 1. The R_e values appear in square brackets. For He_2, the limit is $1s\ ^2S(He^+) + 1s^2\ ^1S(He)$. For the heavier members, the limit is $mp^5\ ^2P^o(Rg^+) + mp^6\ ^1S(Rg)$ with m = 2, 3, 4, and 5 for Ne, Ar, Kr, and Xe, respectively. The alphameric state designations follow the spectroscopic convention (22) of labeling the ground state X and excited states of the same multiplicity by alphabetic capitals in order of increasing energy rather than the labeling used for Xe_2 by Mulliken (23) in which X was labeled A, A was labeled B, and so forth. For members larger than Ne_2^+, *case c* designations for the A and B states become important. See text for discussion.

[b]Values from ref. 25, where D_e = 2.474 eV = 19 954 cm^{-1} has been changed to D_0 using the vibrational parameters for $X^2\Sigma^+_u$ in ref. 22. Reference 22 also lists R_e = 1.081 Å.

[c]Values from ref. 27. For $X^2\Sigma^+_{1/2u}$, ref. 28 gives D_0 = 10 410 cm^{-1}, which may be ~300 cm^{-1} low if the v numbering is increased by 1 as suggested by ref. 27. Reference 4 gives D_0 = 10 900 cm^{-1}.

[d]Values represent D_e.

[e]Values from ref. 26. For X, ref. 28 gives D_0 = 10 646 ± 40 cm^{-1}.

[f]Values from ref. 29.

[g]Values from ref. 24.

[h]Values from ref. 31.

[i]Values from ref. 30. Reference 28 gives D_0 = 9283 ± 25, 379, 1048, and 590 cm^{-1} for X, B(3/2), B(1/2), and C, respectively, and A(1/2) was designated repulsive.

[j]Values from refs. 28 and 33.

[k]Values from ref. 32, which also gives D_0 values of 7842, 1876, 582, 1577, and 359 cm^{-1}, for X, A(3/2), B(3/2), B(1/2), and C, respectively.

Rydberg configurations and associated electronic states

The rare gas dimer family He_2, Ne_2, Ar_2, Kr_2, Xe_2, and Rn_2 ranges from molecules among the lightest of the diatomics to nearly the largest dimers having stable or noninfinitesimally short half-life nucleoids. The ground states of the singly charged ions, the $X^2\Sigma^+_u$ states of Rg_2^+, are all stable (see Table 2). Consequently, the associated Rydberg states are also intrinsically stable although, for the dimers heavier than He_2, the lifetimes of the $X^2\Sigma^+_u$ ion core Rydberg-based states are often reduced drastically by predissociation.

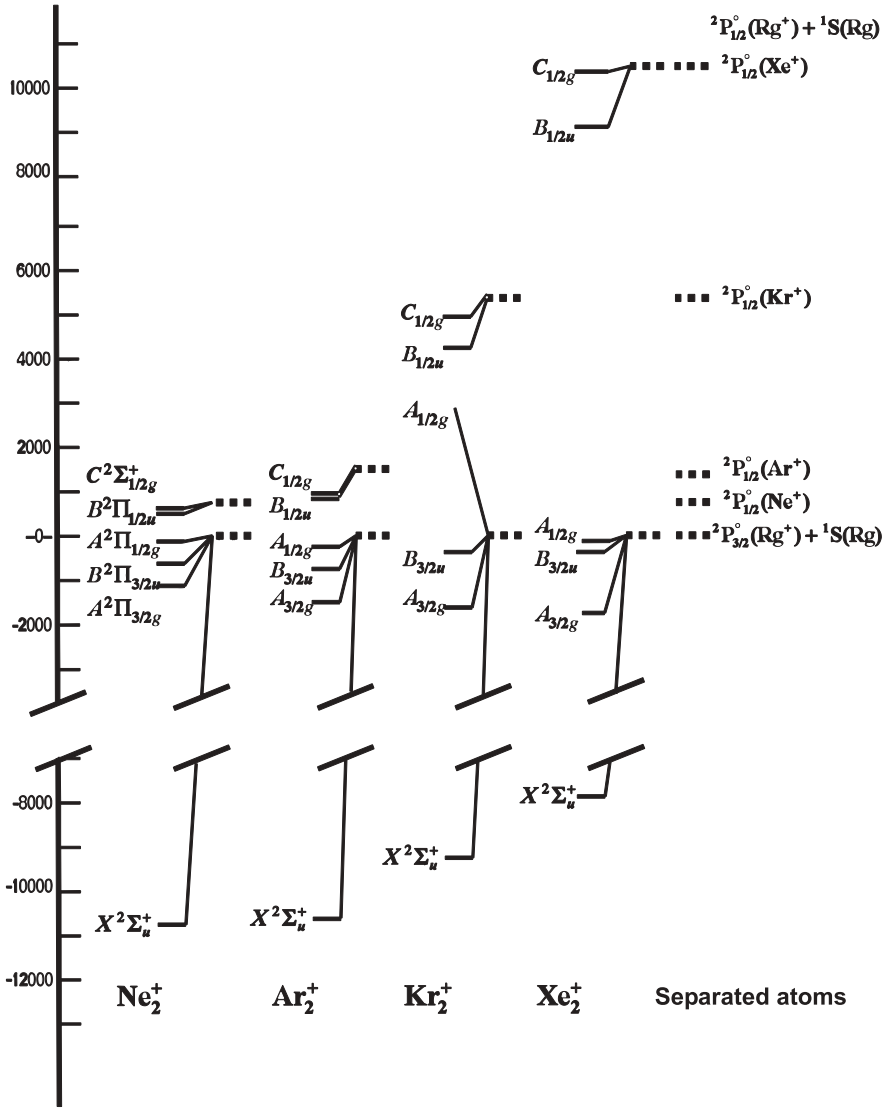
The Rydberg states built on the cores in Table 2 are associated with the configurations $[Rg_2^+]n\ell\lambda_p$, where $[Rg_2^+]$ represents the electronic configuration of the core and $n\ell\lambda_p$ designates the Rydberg electron in the united atom molecular orbital (UAMO) notation. UAMO designations are commonly adopted in place of $m\lambda_p$ orbital notation, valid for all values of R, or linear combination of atomic orbitals (LCAO) designations ($\pi_p n\ell$), generally applicable only for large R (5–7). The inversion parity (p) of the UAMO-based Rydberg orbital varies as $(-1)^\ell$, so that ℓ = 0, 2, 4,… (i.e., *s*, *d*, *g*,…) orbitals are *gerade* and ℓ = 1, 3, 5,… (i.e., *p*, *f*, *h*,…) orbitals are *ungerade*. Because the $X^2\Sigma^+_u$ cores are *ungerade*, the singlet and triplet states associated with ℓ even or odd will be *u* or *g*, respectively. It should be noted that, for clarity, all orbital and state symbols will be retained in the discussion to follow despite the risk of redundancies.

For He_2, the only possible ion core states associated with the ground-state $1s\ ^2S(He^+) + 1s^2\ ^1S(He)$ limit are the bound $X^2\Sigma^+_u$ and unbound $^2\Sigma^+_g$ states. The heavier dimer ions, however, have four electronic states correlated with their lowest energy atomic $mp^5\ ^2P^o(Rg^+) + mp^6\ ^1S(Rg)$ limits: $^2\Sigma^+_u$, $^2\Sigma^+_g$, $^2\Pi_u$, and $^2\Pi_g$. For rare gas atoms heavier than He, these states are $X^2\Sigma^+_u$ (strongly bound), $A^2\Pi_g$ (weakly to very weakly bound), $B^2\Pi_u$ (very weakly bound), and $C^2\Sigma^+_g$ (very weakly bound). Note that the standard practice for labeling electronic states (5, 22) is adopted here rather than a notation that originated with Mulliken's discussions (6, 23) of four *types* of Rg_2^+ core states, which he referred to as A through D. Subsequently, X, A, B, C state labels often have been denoted as A, B, C, D, respectively, in conflict with international convention.

Table 2 provides a representative sample for the dissociation energies, D_0 (defined relative to the v = 0 level), for the Rg_2^+ ion states associated with the ground $^2P^o(Rg^+) + {}^1S(Rg)$ limits (24–33). Also included in Table 2 are values of R_e expressed in Å and identified by square brackets. Finally, Fig. 1 provides a representation of the energies of the

© 2004 NRC Canada

Fig. 1. Relative energies of the electronic states of Rg_2^+ associated with the ground $mp^5\ ^2P^o_{3/2,1/2}(Rg^+) + mp^6\ ^1S(Rg)$ separated atom limits based on their $^2P^o_{3/2} + {}^1S$ limits. Level values were obtained from energy cycle calculations using values quoted in Tables 2 and 3. All energies are expressed in cm^{-1}.



$5p^5\ ^2P^o(Rg^+) + 5p^6\ ^1S(Rg)$-based Rg_2^+ core states in Table 2 with correlations to their appropriate dissociation limits.

Several other angular momentum coupling cases besides *case c* mentioned in the preceding section are encountered in the Rg_2 structures. Most important of these are *cases a*, *b*, *b′*, *d*, and *d′* (5, 34, 35). Often referred to as "Hund's cases", they describe the order and strength in which the angular momenta associated with a molecule are coupled. In *cases a* and *b*, for example, the electronic orbital angular momentum is strongly coupled to the internuclear axis, and Λ is considered well defined. *Cases a* and *b* differ in the strength of *electron spin* coupling with the internuclear axis, which is weak in *case b* but strong in *case a*. In both *cases a* and *b*, Ω is well defined, and multiplet spacings generally are not strongly affected by molecular rotation. Case *b′* is a subcase of *b* representing singlet or triplet states in which multiplet splittings are negligible. *Case d* describes the recoupling of *case a* or *b* states produced by molecular rotation and is associated with the phenomenon of ℓ-uncoupling (discussed below), while *case d′* is a subcase of *case d* for negligible multiplet splittings.

Electronic structures below and converging on the $[Rg_2^+, X^2\Sigma_u^+]$ limit

Introductory comments

The lowest-energy Rydberg states for Rg_2 are the $a^3\Sigma_u^+$ and $A^1\Sigma_u^+$ states associated with $[Rg_2^+, X^2\Sigma_u^+]ns\sigma_g$, with relative energy ordering being triplet below singlet and with n = 2, 3, 4,... for He_2, Ne_2, Ar_2,..., respectively. In addition to being the lowest-energy stable states, the $a^3\Sigma_u^+$ states are metastable (with respect to dipole-allowed transitions to $X^1\Sigma_g^+$) and have been exploited as "platform" states from which to optically pump higher-lying excited states. For He_2, the next states in order of increasing energy are the $b^3\Pi_g$ and $B^1\Pi_g$

© 2004 NRC Canada

Table 3. Ionization energies (cm^{-1}) for the Rg_2^+ states in Table 2 based on $v = 0$ in $a^3\Sigma_u^+$ states of Rg_2.[a]

Rg_2	Ω	IE ($X^2\Sigma_{1/2u}^+$)	IE ($A^2\Pi_{3/2g,1/2g}$)	IE ($B^2\Pi_{3/2u,1/2u}$)	IE ($C^2\Sigma_{1/2g}^+$)
He_2	1/2	34 302.2(1)[b]			Repulsive
Ne_2	3/2		44 091	45 169	
	1/2	34 409(2)[c]	44 595	45 786	45 984
Ar_2	3/2		38 437	39 665	
	1/2	29 373(3)[d]	39 291	40 793	40 784
Kr_2	3/2		36 106	37 383	
	1/2	28 484(5)[e]	Repulsive	42 051	42 514
Xe_2	3/2		32 198	33 554	
	1/2	26 130(20)[f]	33 833	43 081	43 686

[a]The values of the ionization energies (IE) for A, B, and C were obtained using the values for IE($X^2\Sigma_{1/2u}^+$), appropriate values from Table 2 (see Fig. 1 for limit correlations), and $mp^5\ ^2P_{3/2}^\circ - ^2P_{1/2}^\circ$ separations of 782, 1432, 5371, and 10 537 cm^{-1} from ref. 36 for Ne^+, Ar^+, Kr^+, and Xe^+, respectively (see the text for discussion). Reported experimental uncertainty estimates (in last places indicated) appear in parentheses.

[b]Reference 37.

[c]Reference 38.

[d]Reference 39.

[e]Reference 31.

[f]From the difference between the ionization potential for $X^2\Sigma_{1/2u}^+(1/2_u^+) \leftarrow X^1\Sigma_g^+$ photoionization in ref. 33 and the $T_0 = T_e + \omega_e - \omega_e x_e$ value (see the Xe_2 section in the text) for $a^3\Sigma_{1u}^+(1_u^\pm) \leftarrow X^1\Sigma_g^+$. Reference 4 reports 26 664(250) cm^{-1}.

states associated with $[Rg_2^+, X^2\Sigma_u^+]np\pi_u$ and the $c^3\Sigma_g^+$ and $C^1\Sigma_g^+$ states associated with $[Rg_2^+, X^2\Sigma_u^+]np\sigma_u$. Note that the $np\pi_u$ and $np\sigma_u$ energy ordering is reversed for the heavier Rg_2 molecules. For the Rg_2 family, the lowest n values for $np\pi_u$ are the same as those for $ns\sigma_u$, while the $np\sigma_u$ series is promoted (7, 23, 35). Consequently, the lowest value of n for the $np\sigma_u$ series is $n = 3$ for He_2. Additional states associated with $[Rg_2^+, X^2\Sigma_u^+]n\ell\lambda_p$ that have been observed experimentally (although not necessarily for all Rg_2 molecules) include $nd\lambda_g$ ($^{1,3}\Sigma_u^+$, $^{1,3}\Pi_u$, and $^{1,3}\Delta_u$ for $\lambda = \sigma$, π, and δ, respectively) and $nf\lambda_u$ ($^{1,3}\Sigma_g^+$, $^{1,3}\Pi_g$, $^{1,3}\Delta_g$, and $^{1,3}\Phi_g$ for $\lambda = \sigma$, π, δ, and ϕ, respectively), where for He_2 the lowest n values for d-type and f-type structures are 3 and 4, respectively.

At this point, a caveat is in order: occasionally one finds in the literature *different n* values attributed to the *same* electronic state. A root cause of such labeling differences is the fact that n, such as appears in eq. [1] or in the UAMO and LCAO orbital labels, is often not a valid quantum number, although it can serve as a useful sequential index label.

Table 3 summarizes the ionization energies (31, 33, 36–39) for Rydberg series that converge on the lowest-energy core states listed in Table 2. The value given for each series limit (E_∞) is based on the lowest stable state (the $a^3\Sigma_u^+$ state) in each Rg_2 molecule. The specific values for the A, B, and C states in Table 3 are obtained from the experimental value for the ionization energy for the $X^2\Sigma_{1/2u}^+$ state in Table 3, modified by adding the difference between the value of D_0 for X and D_0 for the upper state being considered (see Fig. 2 and Table 2), plus the $^2P_{3/2}^\circ$ and $^2P_{1/2}^\circ$ separation (see footnote *a* to Table 3) for the states dissociating to the $^2P_{1/2}^\circ + {}^1S_0$ limit (i.e., the $B^2\Pi_{1/2u}$ and $C^2\Sigma_g^+$ states). For example, in Ar_2, the ionization energy (IE) for $B^2\Pi_{3/2u}$ is 29 373 cm^{-1} + 10 604 cm^{-1} – 312 cm^{-1} = 39 665 cm^{-1}, while for $C^2\Sigma_g^+$, the IE is 29 373 cm^{-1} + 10 604 cm^{-1} – 625 cm^{-1} + 1432 cm^{-1} = 40 784 cm^{-1}. The values in the A through C columns of Table 2 can be obtained from other data, but the results are the same as those in Table 3 within experimental errors. For example, in Ar_2, the difference between the ionization potentials for $X^2\Sigma_{1/2u}^+$ and $B^2\Pi_{3/2u}$ from ref. 28 (synchrotron-based threshold photoelectron spectroscopy) is –116 547 ± 40 cm^{-1} + 126 879 ± 40 cm^{-1} = 10 332 ± 80 cm^{-1}, while from ref. 26 (laser-based ZEKE photoelectron spectroscopy) the $B^2\Pi_{3/2u} - X^2\Sigma_{1/2u}^+$ difference is 10 293 ± 10 cm^{-1}. The 10 332 ± 80 cm^{-1} and 10 293 ± 10 cm^{-1} values yield IE($B^2\Pi_{3/2u}$) = 39 705 ± 80 cm^{-1} and 39 666 ± 13 cm^{-1}, respectively, when combined with the 29 373 ± 3 cm^{-1} value for $X^2\Sigma_u^+$ in Table 3. Both are in agreement with the 39 665 cm^{-1} value for the IE of $B^2\Pi_{3/2u}$ in the table.

Table 4 lists a representative collection of energies (40–53) of the $v = 0$ levels for the first members of each $[X^2\Sigma_u^+]n\ell\lambda_p$ $^{1,3}\Lambda_{p'}$ Rydberg series with $\ell \leq 3$ and their associated n^* values. To be referenced in Table 4 implies the existence of specific spectral or theoretical assignments for the level listed. The n^* values in Table 4 were obtained using eq. [1], appropriate energies from Tables 3 and 4, and $\Re$ values of 109 729.800, 109 735.812, 109 736.565, 109 736.959, and 109 737.089 cm^{-1} for $^4He_2$, $^{20}Ne_2$, $^{40}Ar_2$, $^{84}Kr_2$, and $^{132}Xe_2$, respectively. These values were determined from the mass-dependent expression (54) for neutral molecules

$$[5] \qquad \Re = \Re_\infty/(1 + m/M)$$

where m and M are the masses of the electron and the charged core, respectively, and $\Re_\infty$ = 109 737.318 cm^{-1} is the Rydberg constant for infinite mass ($M = \infty$) (55).

Among other things, the data in Table 4 serve to introduce several general trends. For example, note that the n^* values for all the $a^3\Sigma_u^+$ states of Rg_2 are nearly the same (~1.9 ± 0.1). Thus, with n^* being approximately constant, the mutually compensating n and δ values successively increase by about 1 per molecular step as one progresses from He_2 to Xe_2. Comparable variations in n and δ are well known from Rydberg states in atomic, or other molecular, families. The past use of such observations in arguments attributing quantal significance to integral values of n in n^* and in state designations within a family should be considered questionable. Therefore, as mentioned above, in this work n will serve primarily as an index specifying ordering within a

© 2004 NRC Canada

Fig. 2. Typical laser excitation spectra (48) for the lowest n member of the $[X^2\Sigma_u^+]nf\lambda_u$ ($^3\Sigma_g^+$, $^3\Pi_g$) ← $a^3\Sigma_u^+$ (0–0) transition in $^{20}Ne_2$. This figure from ref. 48 demonstrated the effects of ℓ-uncoupling and f-complex formation in Ne_2. The index $n = 4$ in this figure would be 5 in the labeling scheme employed here (see text for discussion). Figure reprinted with permission of the American Institute of Physics.

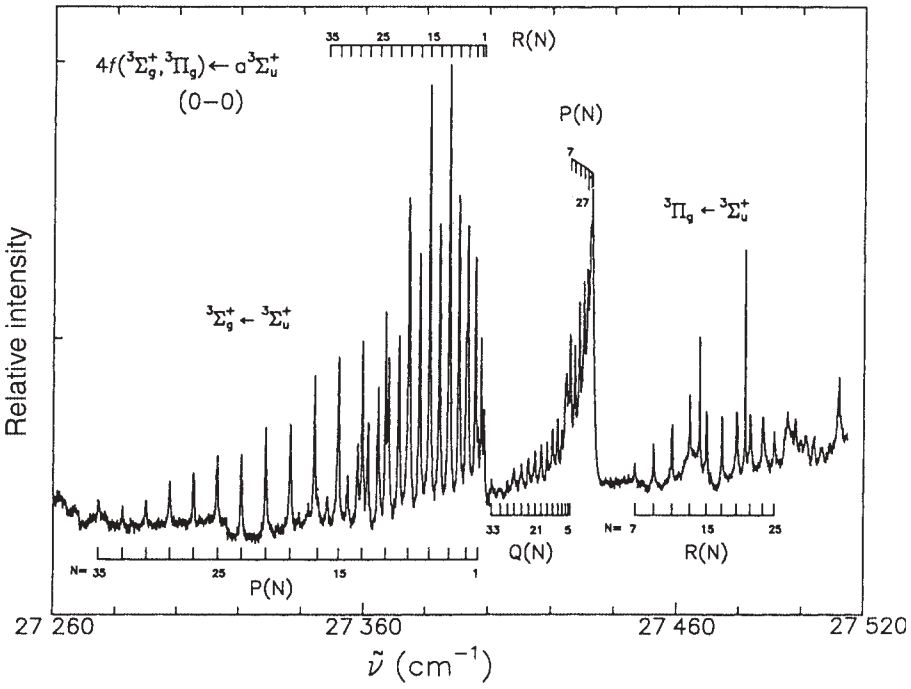


Table 4. Energies (cm^{-1}, vac) and n^* values for the $v = 0$ levels of the lowest energy $[Rg_2^+, X^2\Sigma_u^+]n\ell\lambda_p$ $^{1,3}\Lambda_p$ states.[a]

Orbital	State	He_2[b]	Ne_2[c]	Ar_2[d]	Kr_2	Xe_2
$2s\sigma_g$	$a^3\Sigma_u^+$	0.0	0.0	0.0	0.0	0.0
		1.7886	1.785	1.933	1.963	2.049
	$A^1\Sigma_u^+$	2343.91[b]	[700][c]	[870][e]	1100[f]	705.7[g]
		1.8530	1.804	1.962	2.001	2.078
$2p\pi_u$	$b^3\Pi_g$	4768.1454[h]	12 272[i]	10 120[j,k]	10 170[j]	9600[j]
		1.9275	2.226	2.387	2.447	2.576
	$B^1\Pi_g$	5845.71[l]	[12 372][c]	[10 500]	—[m]	—[n]
		1.9637	2.231	2.411		
$3p\sigma_u$	$c^3\Sigma_g^+$	10 889.472[h]	9090[o]	8500[j,p]	8000[j]	—[n]
		2.1649	2.082	2.293	2.314	
	$C^1\Sigma_g^+$	13 289.39[q]	[10 390][c]	[8980]	—[m]	—[n]
		2.2852	2.137	2.319		
$3d\sigma_g$	$f^3\Sigma_u^+$	21 548.81[r]	*	[15 090]	—[m]	—[n]
		2.9333		2.772		
	$F^1\Sigma_u^+$	21 682.97[r]	*	[15 530]	—[m]	—[n]
		2.9488		2.815		
$3d\pi_g$	$f^3\Pi_u$	21 754.0[r]	*	[16 630]	—[m]	—[n]
		2.9571		2.934		
	$F^1\Pi_u$	21 853.7[r]	*	[16 490]	—[m]	—[n]
		2.9690		2.918		
$3d\delta_g$	$f^3\Delta_u$	22 205.5[r]	*	[16 490]	—[m]	—[n]
		3.0118		2.918		
	$F^1\Delta_u$	22 206.3[r]	*	[16 490]	—[m]	—[n]
		3.0119		2.918		

© 2004 NRC Canada

Table 4 (*concluded*).

Orbital	State	He_2[b]	Ne_2[c]	Ar_2[d]	Kr_2	Xe_2
$4f\sigma_u$	$^3\Sigma_g^+$	27 398.3[s]	27 397.2[t]	22 012.3[u]	—[v]	
		3.9867	3.956	3.861		
	$^1\Sigma_g^+$	27 398.5[s]	*	[22 110]		
		3.9868		3.887		
$4f\pi_u$	$^3\Pi_g$	27 407.0[s]	27 428.0[t]	21 629.4[w]	—[v]	
		3.9892	3.965	3.764		
	$^1\Pi_g$	27 407.2[s]	*	[21 850]		
		3.9893		3.819		
$4f\delta_u$	$^3\Delta_g$	27432.7[s]	*	[22627]	—[v]	
		3.9967		4.033		
	$^1\Delta_g$	27 432.8[s]	*	[22 627]		
		3.9967		4.033		
$4f\phi_u$	$^{1,3}\Phi_g$	27 473.5[s]	*			
		4.0086				

[a]There are two entries for each electronic state listed. The top entry is the energy of $v = 0$, expressed in cm^{-1}. The bottom entry is the n^* value for the level in question. Values for n^* were obtained using eq. [1], the ionization energies in Table 3, and the mass-dependent Rydberg constant of eq. [5]. The n values ("Orbital" column) and state labels are those for He_2 (see text for discussion). Note that the b, B and c, C labeling would invert for molecules heavier than He_2.

[b]The singlet and triplet states are placed on the same basis, the $N = 0$, $v = 0$ level of $a^3\Sigma_u^+$ taken as the zero energy reference and 2343.91 cm^{-1} for the singlet–triplet separation (40).

[c]An asterisk (*) denotes an experimentally uncharacterized level. Energies in square brackets are based on theoretical calculations. Reference 44 calculates the singlet–triplet separations to be ~700, ~100, and 1300 cm^{-1} for the a–A, b–B, and c–C separations, respectively. Note that the b, B and c, C state labeling is reversed in going from He_2 to Ne_2 because of the energy inversion of the lowest $p\pi_u$- and $p\sigma_u$-based states (see text).

[d]Energy values in square brackets are theoretical energies for transitions originating at T_e of $(1)^3\Sigma_u^+$ (the $a^3\Sigma_u^+$ state here) from ref. 49.

[e]References 50 and 16 report T_e values for a and A from high v (see text) that imply the a–A separation is ~760 cm^{-1} with a high uncertainty. Also, a is designated as A, and A as B in the labeling scheme adopted in these references.

[f]References 16 and 50. In the labeling scheme adopted in these references, a is designated as A, and A as B.

[g]Reference 53.

[h]Reference 41.

[i]Data from ref. 45 assigned (46) as $2^3\Pi_g - 1^3\Sigma_u^+$ (0–0) based on theoretical calculations (47). Subsequently remeasured and extended. See text for discussion.

[j]References 45 and 46.

[k]Reference 49 predicts the $(1)^3\Pi_u$ state to be near [10 360 cm^{-1}].

[l]Reference 41 gives $T_0 = 3501.797$ cm^{-1}, based on $v = 0$, $N = 0$ of $A^1\Sigma_u^+$. See footnote *b*.

[m]Reference 52 presents theoretical results associated with these levels.

[n]Theoretical predictions exist for these levels. See text for discussion.

[o]Diffuse peak reported in ref. 45 and assigned in ref. 46 as $1^3\Sigma_g^+ - 1^3\Sigma_u^+$, based on the calculations of Iwata (47).

[p]Reference 49 predicts [8000 cm^{-1}].

[q]Reference 41 gives $T_0 = 10\,945.477$ cm^{-1}, based on $v = 0$, $N = 0$ of $A^1\Sigma_u^+$. See footnote *b*.

[r]Reference 42.

[s]Reference 43.

[t]Reference 48.

[u]Reference 51. Reference 49 predicts [22 082 cm^{-1}].

[v]Experimental assignment ambiguous. See text for discussion.

[w]Reference 51. Reference 49 predicts [21 850 cm^{-1}]. Assignment proposed in ref. 52 (see text for discussion).

particular Rydberg series, and secondarily as relating similar $n\ell\lambda_p$ series within a family to one another.

One might expect from Fig. 1 that some of the lower-energy members of Rg_2 Rydberg series associated with the excited core states in Table 3 would exist below the $X^2\Sigma_u^+$ limit. As will be discussed later, however, relatively few spectral features or Rydberg series perturbations have been attributable to excited core-based states. Thus, while perturbations between Rydberg states associated with different cores can exist, the significant differences in the shapes (see Table 2) of the X-based and A-, B-, and C-based potential energy curves should greatly reduce the strength of such interactions, especially in the R region around R_e for $X^2\Sigma_u^+$.

The Rydberg states built on the $A^2\Pi_g$ core would be associated with the $[Rg_2^+, A^2\Pi_g]n\ell\lambda_p$ configurations. The states associated with $ns\sigma_g$, $nd\sigma_g$, $ng\sigma_g$,... orbitals are $^{1,3}\Pi_g$; those with $np\sigma_u$, $nf\sigma_u$,... are $^{1,3}\Pi_u$; those with $np\pi_u$, $nf\pi_u$,... are $^{1,3}\Sigma_u^+$ and $^{1,3}\Delta_u$; and those with $nf\delta_u$, are $^{1,3}\Pi_u$ and $^{1,3}\Phi_u$. Rydberg states for $[Rg_2^+, B^2\Pi_u]n\ell\lambda_p$ would be similar to those for $[Rg_2^+, A^2\Pi_g]n\ell\lambda_p$, but with the u, g parities of the states reversed. Rydberg states for $[Rg_2^+, C^2\Sigma_g^+]n\ell\lambda_p$ would be similar to those for $[Rg_2^+, X^2\Sigma_u^+]n\ell\lambda_p$, but with the u, g parities of the states also reversed.

Electronic spectra — Emission, absorption, and laser excitation spectroscopy

The vacuum ultraviolet (VUV) continua produced by $A^1\Sigma_u^+ \rightarrow X^1\Sigma_g^+$ $(0_u^+ \rightarrow 0_g^+)$ transitions in the rare gas dimers have served for more than half a century as background sources for VUV absorption spectra (56, 57), as well as for excitation of photochemical processes or fluorescent devices (including, more recently, plasma display panel pixels).

© 2004 NRC Canada

These continua generally exhibit two intensity maxima, often referred to as the first (shorter λ) and second continua. For He_2, this emission band lies in the ~600–1000 Å region and is known as the Hopfield continuum (58). The Hopfield continuum exhibits a weak intensity maximum near 675 Å and a much stronger peak in the vicinity of 815 Å that are attributed to optical transitions from low vibrational levels of the $D^1\Sigma_u^+$ and $A^1\Sigma_u^+$ excited states (59), respectively, to a dissociative portion of the He_2 $X^1\Sigma_g^+$ state. Similar continua are also prominent in the heavier rare gas dimers and have long been of interest as gain media for VUV lasers. As the mass of the dimer is increased, both the first and second continua shift progressively to the red, with the well-known Xe_2 continuum peaking near 172 nm (1720 Å). An alternate explanation for the first continuum in the heavier dimers was proposed by Kiik et al. (60), who attributed the emission to transitions from high-lying vibrational levels of the $A^1\Sigma_u^+$ ($A0_u^+$) state rather than from low vibrational levels of a more highly excited electronic state.

Most, but not all, of the electronic structure of He_2 has been characterized from the analyses of extensive emission spectra observed in the ~2500 – 15 000 Å region, arising from transitions between hundreds of stable Rydberg states. However, relatively little information is available from emission spectra of the heavier Rg_2 molecules because most of the levels above the $a^3\Sigma_u^+(1_u^\pm, 0_u^-)$ and $A^1\Sigma_u^+(0_u^+)$ states are predissociated to various degrees. Thus, a marked disparity has existed between the experimental database available to characterize the excited electronic state structure of He_2 and those for the heavier dimers. Nevertheless, high-resolution synchrotron and laser spectroscopic techniques developed over the past two decades to examine the Rydberg states of Ne_2 through Xe_2, primarily by photoexcitation from $X^1\Sigma_g^+$ or $a^3\Sigma_u^+$, have revealed considerable detail regarding electronic structures in the heavier dimers. The following sections summarize key aspects of the structure of each dimer with emphasis on recent progress resulting from advances in both experiment and theory.

He_2

In addition to the VUV Hopfield continuum, absorption spectra are observed in He_2 in the region around 600 Å (61). This band-like absorption is attributed to transitions from $X^1\Sigma_g^+$ to excited vibrational levels in the $A^1\Sigma_u^+$ state of He_2. Known spectra and electronic structures of He_2 reported before 1970 and molecular parameters derived from data available before 1979 were summarized in refs. 62 and 22, respectively. No comprehensive reviews have been published subsequently.

The state designations and n^* values for the first members of the $[X^2\Sigma_u^+]n\ell\lambda_p$ $^{1,3}\Lambda$ states for $\ell \le 3$ are included in Table 4. The $\ell \le 2$ series have been observed to n members in the 15–20 range with vibrational development nominally in the $v = 0$ to $v = 2$–4 range observed for the lower n members. All of these characterizations are based on the analysis of rotationally resolved spectra, as are the $v = 0$ levels of the $4f\lambda_u$ $^{1,3}\Lambda_g$ states, the only $nf\lambda_u$ member observed experimentally to date (43). The reader is referred to refs. 41, 43, and 63–68 and the literature cited therein for spectral data published since the earlier reviews (22, 62).

At present, experimental observations of fully resolved multiplet splittings in the electronic states of He_2 are limited to $v = 0$–2 in the $a^3\Sigma_u^+$ state and a relatively few rotational levels in $v = 0$ and 1 of the $b^3\Pi_g$ state (see ref. 41 and refs. therein). The $[X^2\Sigma_u^+]4f\lambda_u$ $^{1,3}\Lambda_g$ states, the $[X^2\Sigma_u^+]nd\lambda_g$ $^{1,3}\Lambda_u$ states with $n \ge 3$, and the $[X^2\Sigma_u^+]np\lambda_u$ $^{1,3}\Sigma_g^+, ^{1,3}\Pi_g^+$ states for $n \ge 4$ are significantly ℓ-uncoupled, but the parameterizations for the lower n members can be corrected for this effect by using isolated complex models (37, 42, 43). The $[X^2\Sigma_u^+]np\lambda_u$ $^{1,3}\Pi_g^-$ states are relatively free from ℓ-uncoupling and other perturbations, and experimental data from these series are the basis for the determination of the He_2 ionization energy in Table 3.

Increased configuration interactions from outside the state set in an $n\ell$-complex decrease the applicability of isolated ℓ-complex models. The breakdown of these models occurs for $n \ge 6$ in the $[X^2\Sigma_u^+]np\lambda_u$ $^{1,3}\Lambda_g$ series and for $n \ge 4$ in the $[X^2\Sigma_u^+]ns\sigma_g, nd\sigma_g$ $^{1,3}\Lambda_u$ series, in which case the data are best treated using coupled-channel models. In such models, a channel corresponds to a Rydberg series of energy levels, all with the *same* angular momentum (N in this case because multiplet splittings are often unresolved) and parity, plus its associated continuum. Multichannel quantum defect theory (MQDT)-based models (69–71) have provided precise representations (66) of the energy levels determined from emission spectra for the $v = 0$ levels of $np\lambda_u$ $^3\Lambda_g$ (n = 3–20) with N values in the 1–19 range for $^3\Pi_g^-$ and in the 2–20 and 3–13 intervals for $^3\Pi_g^+$ and $^3\Sigma_g^+$, respectively. Energies for the $v = 0$ levels of the even-N channels in the 2–20 range associated with n = 3–14 for $nd\lambda_g(^3\Pi_u^-, ^3\Delta_u^-)$ and of the odd-N channels in the 1–17 range associated with n = 3–18 for $ns\lambda_g, nd\lambda_g(^3\Sigma_u^+, ^3\Sigma_u^+, ^3\Pi_u^+, ^3\Delta_u^+)$ were also precisely correlated (67) with a similar coupled-channel model. Because a full discussion of these coupled-channel results in He_2 is too extensive for presentation here, the reader is referred to the referenced articles for further details.

There are large R maxima in a number of the lower-energy Rydberg states of He_2, the most thoroughly studied being the maxima of the a, A, c, and C states. Mulliken (6) discussed reasons for the existence of such maxima and summarized the experimental evidence available as of the early 1960s. Subsequent refinements include contributions from both theory (72) and experiment (73, 74).

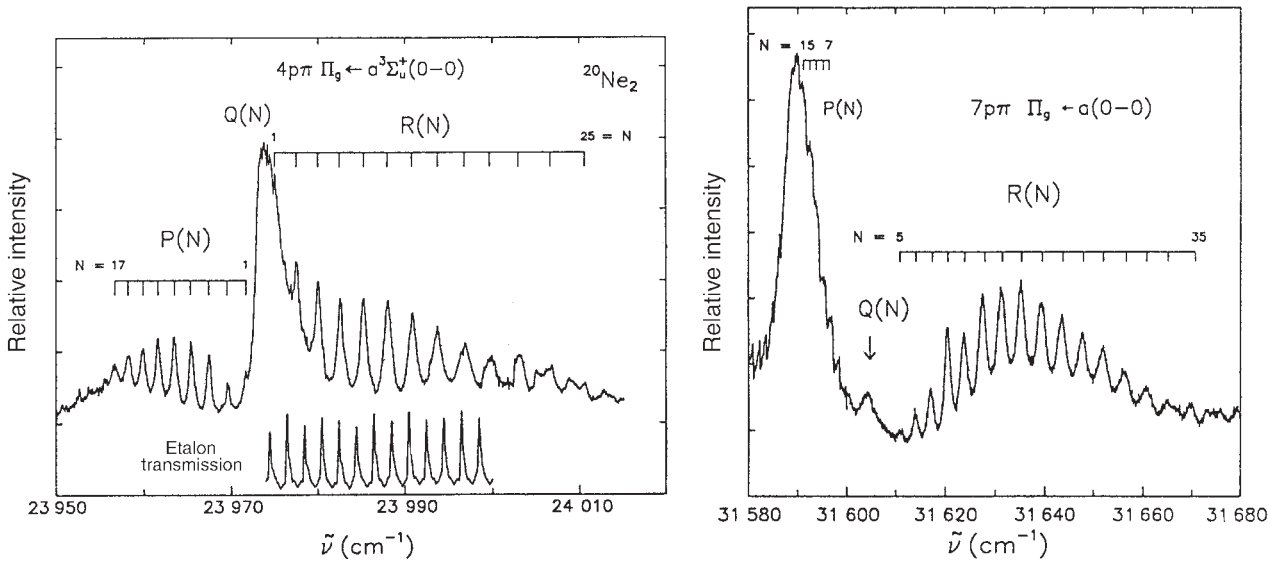
For He_2 there are no experimentally observed spectra attributed to transitions involving Rydberg states built on the unbound $^2\Sigma_g^+$ core (cf. Table 2). However, it should be noted that Mulliken (75) postulated the existence of at least a few $^2\Sigma_g^+$ ion core-based states as part of his explanation of the Hornbeck–Molnar effect, the process in which the collision of highly excited helium atoms with the ground state ($^1S_0$) species generates a He_2^+ ion.

Ne_2

In addition to the Ne_2 VUV emission continua mentioned previously, absorption spectral series have been observed (76) in the ~746–736 Å and ~660–600 Å regions and assigned to transitions between $X^1\Sigma_g^+$ and several excited electronic states. Analysis of the longer wavelength segment yielded $D_e = 30.2$ cm^{-1} and $\Delta G_{1/2} = 13$ cm^{-1} for $X^1\Sigma_g^+$, which compare favorably with the more recent values quoted in Table 1 and discussed below.

© 2004 NRC Canada

Fig. 3. Laser excitation spectra of $^{20}Ne_2$: (left) $4p\pi_u\ ^3\Pi_g \leftarrow a^3\Sigma_u^+$ (0–0) and (right) $7p\pi_u\ ^3\Pi_g \leftarrow a^3\Sigma_u^+$ (0–0) from ref. 80. Note the loss of the relative intensity of the Q(*N*) branches to the P(*N*) and R(*N*) branches with increasing *n* (see text for discussion). Figure reprinted with permission of the American Institute of Physics.



The state designations and *n** values for the first members of the $[X^2\Sigma_u^+]n\ell\lambda_p\ ^{1,3}\Lambda$ states for $\ell \leq 3$ were included in Table 4. Most of the rotationally resolved spectral data available for characterizing such Rydberg states have been obtained by laser excitation spectroscopy from the metastable $a^3\Sigma_u^+$ state (produced in the afterglow of pulsed electric discharges) or by single- or multiphoton absorption from the $X^1\Sigma_g^+$ state.

Based on the *n*-value labeling scheme mentioned above, the $np\sigma_u\ ^3\Sigma_g^+$ states for Ne_2 would begin with $n = 4$. The $np\sigma_u\ ^3\Sigma_g^+ - a^3\Sigma_u^+$ series has been observed in the $n = \sim 4$–22 range (38, 45), of which the first observed member (45) appears to be a diffuse band with a peak near 9090 cm^{-1} and assigned (46, 47) on the basis of theoretical calculations (47). The second member of the series, the lowest energy term observed by Kim et al. (38), occurs near 23 510 cm^{-1} and was labeled as $n = 6$ rather than with the index $n = 5$ employed here (see *Discussion*).

In 1989, Kane et al. (77) observed the rotationally resolved (0–0) band of the $4p\pi_u\ ^3\Pi_g \leftarrow a^3\Sigma_u^+$ system of $^{20}Ne_2$ and $^{22}Ne_2$. Giessl et al. (78) subsequently reported rotationally unresolved spectra for the principal sequence ($\Delta v = v' - v'' = 0$) of this system with $v'' = 0$–3. These earlier observations (77, 78) are superseded by more recent measurements (79) of rotationally resolved $4p\pi_u\ e^3\Pi_g \leftarrow a^3\Sigma_u^+(v' - v'')$ spectra in $^{20}Ne_2$ and $^{22}Ne_2$ that provide characterizations of the $v = 0$ through $v = 3$ levels in both states. The first member of the $np\pi_u\ ^3\Pi_g$ series is indexed $n = 3$ and has been assigned by Giessl et al. (78) from rotationally unresolved absorption spectra for the five principal sequence members (0–0) to (5–5). The four strongest members of this sequence had been reported previously (45, 46). The $np\pi_u\ ^3\Pi_g$ series has been recorded (38) to $n = 17$ in laser excitation spectra obtained by pumping $a^3\Sigma_u^+$ state.

Strongly ℓ-uncoupled $^3\Sigma_g^+$ and $^3\Pi_g$ components of the $v = 0$ levels in the $nf\lambda_u(^3\Sigma_g^+, ^3\Pi_g, ^3\Delta_g, ^3\Phi_g)$ complexes, labeled with $n = 4$, 5, and 6 in ref. 48, have been observed in transitions from $a^3\Sigma_u^+$, and a representative spectrum (reprinted from ref. 48) appears in Fig. 2. Also reported (48) were the $4f\lambda_u\ ^3\Sigma_g^+$ and $^3\Pi_g \leftarrow a(1–0)$ bands. Portions of $5f$ – a(1–0), $6f$ – a(1–0), and $7f$ – a(0–0) bands were observed at that time (48) but considered too fragmentary to warrant a full report. Subsequently, the spectra and analyses of the $5f\lambda_u\ ^3\Sigma_g^+, ^3\Pi_g \leftarrow a(1–0)$ bands were published (Table IV in ref. 80), and the involvement of the $5f$ states in a perturbation with the $N \sim 26$–28 levels of $6p\lambda_u\ ^3\Pi_g(v = 0)$ was identified. The $X^2\Sigma_u^+$ ionization energy for $^{20}Ne_2$ in Table 3 was determined with the aid of the $nf\lambda_u\ ^3\Sigma_g^+, ^3\Pi_g$ and $np\lambda_u\ ^3\Sigma_g^+, ^3\Pi_g$ data for $v = 0$ outlined above. The current series numbering scheme would label the first $nf\lambda_u$ as $5f\lambda_u$ rather than $4f\lambda_u$ as in refs. 48 and 80, which would increase all of the *n* values in this paragraph by +1. Altering the *n* labeling of the $nf\lambda_u$ orbital series does not affect any observable results presented in refs. 48 and 80.

Most of the $np\lambda_u\ ^3\Pi_g \leftarrow a^3\Sigma_u^+$ excitation spectra just discussed (38) were obtained by monitoring fluorescence from excited atoms produced by predissociation of the $^3\Pi_g$ states. These spectra present an intensity anomaly not fully rationalized at this time. As evident in Fig. 3*a*, low *n*-value members show normal Π–Σ branch intensities (5) with a strong Q-type branch. However, as *n* increases (Fig. 3*b*), the Q branch progressively weakens relative to the P and R branches, eventually disappearing altogether around $n = 10$. Such an effect is not consistent with intensity expectations in *cases b* or *d*, or ℓ-uncoupling intermediates, and does not appear to be produced by differences in the stabilities of the $^3\Pi_g^+$ and $^3\Pi_g^-$ components to predissociation (see section IV.B in ref. 80). Because most, but not all, of the higher *n* measurements were made monitoring the $3p(1/2)_1 - 3s(3/2)_2^o$ transition in Ne I, it is possible that as *n* increases the Π_g^- components predissociate to excited atoms that do not lead ultimately to $3p(1/2)_1$ production, but such a possibility is purely speculative.

One- and two-color laser excitation spectra have been observed (81) for transitions from $a^3\Sigma_u^+$ to the complex Ne_2 structures that exist between the $v = 0$ and 1, 1 and 2, and 2 and 3 levels in the $X^2\Sigma_{1/2u}^+$ state of the $^{20}Ne_2^+$ and $^{22}Ne_2^+$ dimer

© 2004 NRC Canada

ions. Analysis (81) indicates $\Delta G_{1/2}(X^2\Sigma^+_{1/2u}) = 575.2$ cm^{-1} and $\Delta G_{3/2}(X^2\Sigma^+_{1/2u}) = 564.4$ cm^{-1} for $^{20}Ne_2^+$, and $\Delta G_{3/2} = 539.70$ cm^{-1} for $^{22}Ne_2^+$, but a full coupled-channel treatment of these data has not been performed to date.

Rough estimates of energy structures built on excited cores imply that transitions involving such structures might be expected in the ~10 020, 13 000, and 25 600 cm^{-1} regions. The lowest-energy system could be a contributor to the broad, diffuse feature assigned (45) to the $4p\sigma_u\ ^3\Sigma^+_g - a$ system, but the higher energy estimates remain uncorrelated. In short, there are no spectral features observed below the $X^2\Sigma^+_u$ limit that are associated currently with Rydberg states built on excited ion core levels, although it is quite possible that several exist among weak, currently unassigned spectral features.

Ar_2

The state designations and n^* values for the first members of the $[X^2\Sigma^+_u]n\ell\lambda_p\ ^{1,3}\Lambda$ states for $\ell \leq 3$ are included in Table 4. As with Ne_2, much of the spectral data available for characterizing the Rydberg states in these series comes from laser excitation spectroscopies based on the $a^3\Sigma^+_u$ state, with additional information provided by single- or multiphoton absorption from the $X^1\Sigma^+_g$ state. For Ar_2, however, fewer assignments are supported by rotational analyses than is the case in Ne_2 because of decreased rotational level spacings. Rydberg series converging on the $X^2\Sigma^+_u$ core of the Ar_2 molecule were first observed in electron beam excitation experiments (3, 4) and discussed by Herzberg in ref. 1. An overview of the *laser* excitation spectrum of Ar_2 (39) in the 335–470 nm region, a spectrum of considerably higher resolution than that available in 1987, is presented in Fig. 4.

Triplet splitting is small and not resolved in most of the Ar_2 spectral data. An exception is data obtained recently by Herring et al. (82) for the transition labeled $7p\sigma_u\ ^3\Sigma^+_g - a^3\Sigma^+_u$. The (1–0) band for this system, shown in Fig. 5, provides an example of the spectra obtainable by laser excitation spectroscopy at moderate gas pressures (~30 torr Ar, 300 K). The n-indexing of the $np\sigma_u$-based states in refs. 39 and 82 is +3 higher than that for the $3p\sigma_u$ orbital of He_2. Doubts were expressed about this labeling scheme at the time (38) and it is no longer favored (see *Discussion*). Thus, $5p\sigma_u$ would be the first $np\sigma_u$ Rydberg indexing label for Ar_2 and the spectrum of Fig. 5 is assigned to the $6p\sigma_u\ ^3\Sigma^+_g - a^3\Sigma^+_u$ (1–0) band in the indexing scheme employed here.

In Λ,S notation, $np\sigma_u\ ^3\Sigma^+_g -$, $np\pi_u\ ^3\Pi_g -$, $nf\sigma_u\ ^3\Sigma^+_g -$, $nf\pi_u\ ^3\Pi_g -$, and $n\ell\lambda_g\ \Pi_g - a^3\Sigma^+_u$ series have been assigned by Kane et al. (39) for Rydberg levels with n^* values up to ~25.4, 25.4, 8.8, 8.0, and 8.5, respectively. The lowest-energy members of the $np\sigma_u\ ^3\Sigma^+_g$ and $np\pi_u\ ^3\Pi_g$ series ($5p\sigma_u$ and $4p\pi_u$) were not observed in ref. 39, but transitions from the a state to these levels had been observed and assigned previously (45, 46, 83, 84) to systems near 7900 and 10 120 cm^{-1}, respectively. Other possible contributors to spectra in the ~7000 – 11 000 cm^{-1} region are discussed by Dupláa and Spiegelmann (49), as are their predictions of Rydberg states associated with excited cores. However, as in Ne_2, no correlation of excited core-based Rydberg states to experimental observations seems to exist for Ar_2 at present.

The $n\ell\lambda\ \Pi_g - a$ and $nf\pi_u\ ^3\Pi_g - a$ series of ref. 39 subsequently were reassigned to $nf\pi_u\ ^3\Pi_g - a$ and $nf\delta_u\ ^3\Delta_g - a$ series, respectively, by Dupláa and Spiegelmann (49) based on their extensive theoretical calculations. Note that the reassignment inverts the relative energy order of $nf\sigma_u$ and $nf\pi_u$ from that observed in He_2 and Ne_2. In addition, rotational analyses of the reassigned $nf\sigma_u\ ^3\Sigma^+_g - a$ and $nf\pi_u\ ^3\Pi_g - a$ (0–0) bands (51) (see next paragraph) show that the upper states are not strongly affected by ℓ-uncoupling, raising additional questions about the mainly nf-based nature of these states that remain as yet unanswered (see ref. 51 for further discussion). Regardless of series labels, etc., the data (39) lead to an ionization energy for the $X^2\Sigma^+_u$ limit, relative to $v = 0$ in $a^3\Sigma^+_u$, of 29 373 ± 3 cm^{-1}.

The higher-resolution laser excitation spectra introduced above in connection with Fig. 5 provided rotationally resolved data for the $6p\sigma_u\ ^3\Sigma_g{}^+ - a^3\Sigma^+_u$ (0–0), (1–1), (1–0), and (0–1) bands (82), as well as the $5f\sigma_u\ ^3\Sigma^+_g - a^3\Sigma^+_u$ (0–0) and (0–1) and $5f\pi_u\ ^3\Pi_g - a^3\Sigma_u{}^+$ (0–0) and (0–1) bands (51), where the ℓ-labeling of the upper state of the $5f\pi_u\ ^3\Pi_g - a$ transition is that proposed by Dupláa and Spiegelmann (49). The numbering scheme employed here would label the first $nf\lambda_u$ as $6f\lambda_u$ rather than $5f\lambda_u$ as adopted in refs. 39, 51, and 82, with appropriate increases to the n label for other $nf\lambda_u$ orbitals in this paragraph. The rotationally resolved spectra of refs. 51 and 82 yield $\omega_e = 298$ cm^{-1}, $\omega_e x_e = 3.0$ cm^{-1}, and $R_e = 2.44$ Å for the $a^3\Sigma^+_u$ state, and, when combined with the high-v data from Herman et al. (16) (see the following), suggest $D_0 = 5700 \pm 200$ cm^{-1} and $D_e = 5850 \pm 200$ cm^{-1} for the $a^3\Sigma^+_u$ state. These values for the $a^3\Sigma^+_u$ state compare favorably with those calculated by Dupláa and Spiegelmann (49).

Herman et al. (16, 50) reported rotationally resolved VUV absorption spectra of Ar_2 cooled in a supersonic beam expansion and associated these spectra with transitions from $X^1\Sigma^+_g(0^+_g)$ to three excited electronic states designated in refs. 16 and 50 as $A1_u$, $B0^+_u$, and $C0^+_u$. The Al_u state is part, at least, of the $a^3\Sigma^+_u(1^\pm_u, 0^-_u)$ state, while the $B0^+_u$ state is the $A^1\Sigma^+_u(0^+_u)$ state of Table 4. Because of large differences in the shapes and positioning of the potential energy curves for X and the a and A states (see Tables 1 and 2), transitions were observed from $X^1\Sigma^+_g$ ($v = 0$) to excited-state vibrational levels in the $v \cong 20$–30 range in both upper states. Extrapolated origins and molecular parameters were determined to be (16) $T_e = 87\,458 \pm 500$ cm^{-1} for $a^3\Sigma^+_u$ and $T_e = 88\,210 \pm 400$ cm^{-1}, $\omega_e = 265$ cm^{-1}, $\omega_e x_e = 2.52$ cm^{-1}, and $\omega_e y_e = -0.0061$ cm^{-1} for $A^1\Sigma^+_u$. Spectra assigned to $C0_u{}^+ - X^1\Sigma^+_g$ (v–0) transitions were observed in the $v = 0$–9 range, indicating that the R_e values for X and C are similar, with effective parameters given (16) as $T_e = 95\,033.6$ cm^{-1}, $\omega_e = 68.16$ cm^{-1}, $\omega_e x_e = 4.63$ cm^{-1}, $\omega_e y_e = 0.049$ cm^{-1}, $\omega_e z_e = 0.007$ cm^{-1}, and $D_e = 466$ cm^{-1}. Subsequently, the $C0^+_u$ state was assigned (49) to a minimum at large R produced by the avoided crossing of an attractive $^1\Sigma^+_u(0^+_u)$ state, probably the second member of the $ns\sigma_g\ ^1\Sigma^+_u(0^+_u)$ series, and a repulsive $^3\Pi_g$ "valence" state. As with the lighter Rg_2 molecules, there are a number of other potential energy maxima besides the distinct peak in the $^1\Sigma^+_u(0^+_u)$ potential that arises from the other half of the avoided crossing described in the preceding sentence. The reader is referred to ref. 49 for further details.

There are predictions and observations of transitions to Rydberg states built on excited cores that bear mainly on questions relating to the large-R behavior of the Rydberg

© 2004 NRC Canada

Fig. 4. Panoramic view of the laser excitation spectrum of Ar_2 $a^3\Sigma_u^+$ in the 335–470 nm region. These data were obtained by D.J. Kane, S.B. Kim, and C.M. Herring in 1991 and published in sections in ref. 39.

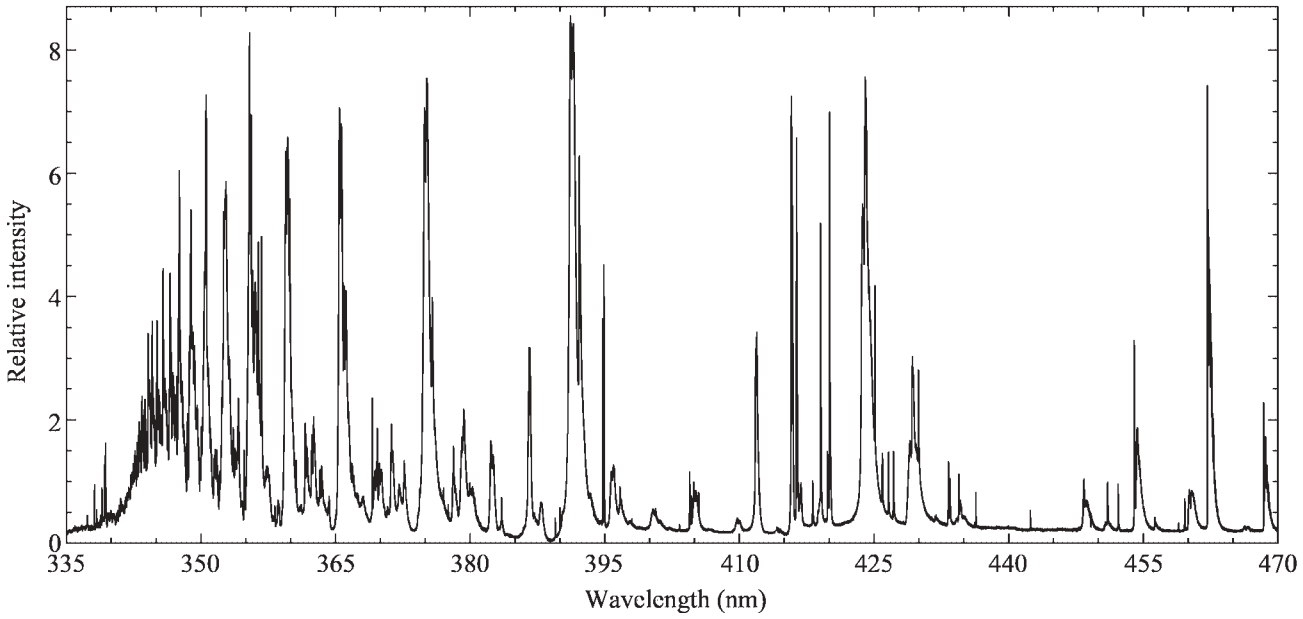
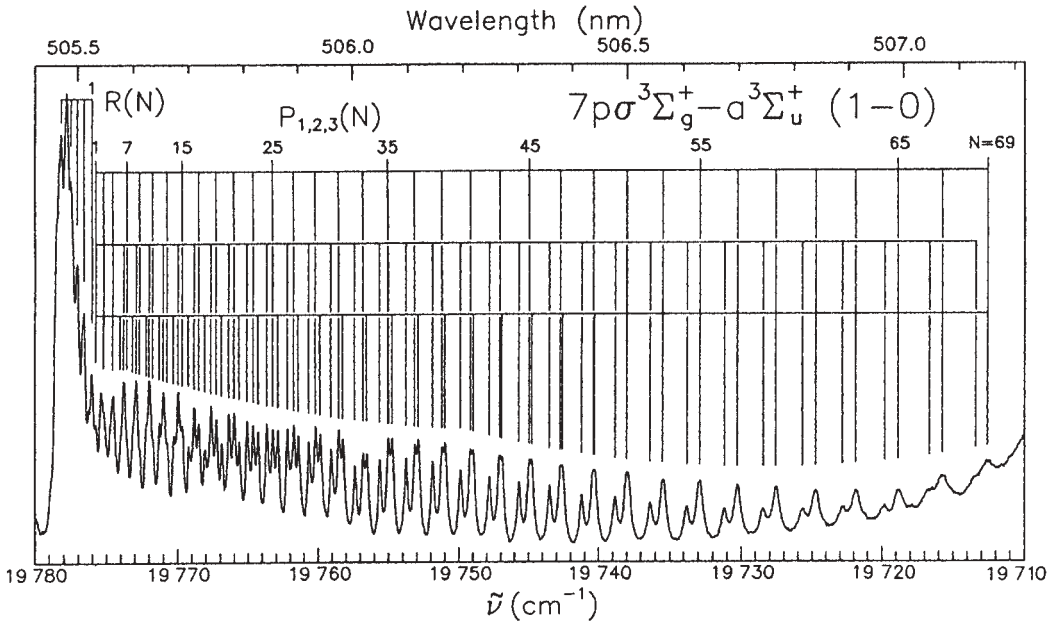


Fig. 5. Laser excitation spectrum of the $6p\sigma_u$ $^3\Sigma_g^+$ – $a^3\Sigma_u^+$ (1–0) band of Ar_2 with triplet splitting partially resolved (82). The label n = 7 in the reproduced figure is taken currently to be n = 6 (see text for discussion). Figure reproduced with permission of the American Institute of Physics.



states converging on the $X^2\Sigma_u^+(1/2_u^+)$ core, at least for the n^* ranges currently observed. The complexities resulting from increased configuration interactions of all types at large R are outside the scope of this article, and further discussion will be limited to brief commments in the following section dealing with excited core-based structures.

Kr_2

As was the case for Ne_2 and Ar_2, Rydberg series for Kr_2 converging on the $X^2\Sigma_{1/2u}^+(1/2_u^+)$ core were first observed in electron beam excitation experiments (3, 4). The first members of the $[X^2\Sigma_{1/2u}^+(1/2_u^+)]n\ell\lambda_p$ $^{1,3}\Lambda$ states for $\ell \leq 3$ are included in Table 4 and, again, much of the available spectral data comes from laser excitation and absorption spectroscopy of the $a^3\Sigma_u^+(1_u^\pm, 0_u^-)$ state, augmented by ground-state absorption experiments. Rotational structures generally have not been resolved for Kr_2, with notable exceptions including spectra associated with single-photon transitions from the ground state to three excited electronic states (17). Consequently, most assignments are not supported by rota-

© 2004 NRC Canada

tional analyses. Finally, it is most likely that $\Omega_p^{p'}$-type state (*case c*) designations are more appropriate for Kr_2, but the Λ,S -type labeling will also be retained to facilitate continuity.

LaRocque et al. (17) reported three rotationally resolved VUV absorption band systems (upper states A, B, and C) in jet-cooled Kr_2 that are analogous to the Ar_2 spectra (16, 50) discussed in the previous section. In the notation adopted here, the first two systems would be $a^3\Sigma_u^+(1_u^\pm, 0_u^-)$ – X and $A^1\Sigma_u^+(0_u^+)$ – X. The third system ($C0_u^+$ – X) might be considered analogous to the C – X transition in Ar_2, where the $C0_u^+$ state was assigned as a large-R minimum state produced by the avoided crossing of an attractive $^1\Sigma_u^+(0_u^+)$ state and a repulsive valence state. Transitions (17) to a and A from $v = 0$ in X involved bands in the $v' = 38$–32 and 38–30 ranges, respectively, observations that are consistent with substantial differences in the equilibrium internuclear separations (R_e) for the $X^1\Sigma_g^+(0_g^+)$ ground state and the a (and A) states. Thus, determinations of dissociation energies (D_0), equilibrium molecular parameters, and related constants involve long extrapolations in the upper-state vibrational quantum number v'. LaRocque et al. (17) reported $T_e = 74\,303.9$ cm^{-1}, $\omega_e = 244.6$ cm^{-1}, $\omega_e x_e = 2.60$ cm^{-1}, and $D_e = 5607$ cm^{-1} for $a^3\Sigma_u^+(1_u^\pm, 0_u^-)$, which gives $D_0(a) \cong 5475$ cm^{-1}. They (17) also reported $T_e = 75\,426.8$ cm^{-1}, $\omega_e = 219.5$ cm^{-1}, $\omega_e x_e = 2.23$ cm^{-1}, and $D_e = 5629$ cm^{-1} for $A^1\Sigma_u^+(0_u^+)$, which yields $D_0(A) \cong 5425$ cm^{-1}. In addition, the T_e- values cited in ref. 17 imply a separation between the $v = 0$ levels in $a^3\Sigma_u^+(1_u^\pm, 0_u^-)$ and $A^1\Sigma_u^+(0_u^+)$ of 1100 ± 10 cm^{-1}. Extrapolated values for B_e, α_e, and R_e are given (17) as 0.0817 cm^{-1}, 0.00128 cm^{-1}, and 2.214 Å, respectively, for $a^3\Sigma_u^+(1_u^\pm, 0_u^-)$; 0.06282 cm^{-1}, 0.00091 cm^{-1}, and 2.426 Å for $A^1\Sigma_u^+(0_u^+)$; and 0.02489 cm^{-1}, 0.0010 cm^{-1}, and 4.017 Å for $X^1\Sigma_g^+(0_g^+)$. LaRocque et al. (17) observed transitions from X to $v = 0$–5 in $C0_g^+$ and reported $T_e = 85\,520$ cm^{-1}, $\omega_e = 44$ cm^{-1}, $\omega_e x_e = 1.81$ cm^{-1}, and $D_e = 465$ cm^{-1} for the C state.

Infrared spectra observed (45, 46) near 7700 and 10 170 cm^{-1} were assigned (46), in terms of configuration and state designations employed here, to the first members of the $[X^2\Sigma_{u}^+(1/2_u^+)]mp\sigma_u\ ^3\Sigma_g^+(1_g^\pm, 0_g^-)$ – $a^3\Sigma_u^+(1_u^\pm, 0_u^-)$ and $[X^2\Sigma_{u}^+(1/2_u^+)]np\pi_u\ ^3\Pi_g\ (2_g^\pm, 1_g^\pm, 0_g^\pm)$ – a series, respectively, where $m = 6$ and $n = 5$ in the labeling system in present use. Kane et al. (85) reported nine absorption features, classified tentatively as vibronic structures of a $5p\pi_u\ ^{1,3}\Pi_g(1_g^\pm, 2_g^\pm, 1_g^\pm, 0_g^\pm)$ – $a^3\Sigma_u^+$ system, with (0–0) bands near 10 113 cm^{-1} $[^3\Pi_{0g}(0_g^\pm)]$, 10 167 cm^{-1} $[^3\Pi_{1g}(1_g^\pm)]$, 10 261 cm^{-1} $[^3\Pi_{2g}(2_g^\pm)]$, and 10 354 cm^{-1} $[^1\Pi_g(1_g^\pm)]$, with n^* values of 2.444, 2.448, 2.454, and 2.560, respectively. Alternatively, the 10 354 cm^{-1} band can be assigned as the (1–0) band of $5p\pi_u\ ^3\Pi_{1g}(1_g^\pm)$ – a rather than the $^1\Pi_g$ – a (0–0) band (85). These four bands comprise the 10 170 cm^{-1} system observed previously (45) and assigned (52) to the $\Omega_p^{p'}$ – a analogs of the transitions listed. To still lower energies are bands (45, 46) near 9488 cm^{-1} ($n^* = 2.403$) and 7692 cm^{-1} ($n^* = 2.297$), where the 7692 cm^{-1} feature was assigned as the lowest member of the $np\sigma$ series (46, 52). Kane et al. (85) proposed assigning the 7692 cm^{-1} feature as a transition from $a^3\Sigma_u^+(1_u^\pm, 0_u^-)$ to states associated with $[A^2\Pi_{3/2g}(3/2_g^+)]ns\sigma_g$ and the 9488 cm^{-1} feature as the lowest-energy member of the $[X^2\Sigma_{1/2u}^+(1/2_u^+)]np\sigma_u\ ^3\Sigma_g^+$ series, but unambiguous assignments are not possible from the present database.

Extensive spectra (85) involving transitions from the $a^3\Sigma_u^+(1_u^\pm, 0_u^-)$ levels to states energetically below the $[X^2\Sigma_{1/2u}^+(1/2_u^+)]$ limit were separable into four series. Figure 6 illustrates the variation of $(n^*)_{mod1}$ [$\equiv n^*|_{mod1}$] for the higher-n members of these series with n^* and ν (cm^{-1}) for the $v = 0$ levels. The data of Fig. 6 with $(n^*)_{mod1}$ near 0.8, 0.6, 0.4, and 0.2 were labeled series Y, Z, P, and X, respectively, with Y, Z, and P tentatively correlated with $nf\lambda$-, $n\ell\lambda$ Π-, and $np\lambda$-based series (85). Note that the ~7700 cm^{-1} and 10 170 cm^{-1} systems mentioned above could be lower members of the P series or possibly the P and the X series, depending on the variations of $(n^*)_{mod1}$ with n^* for these series.

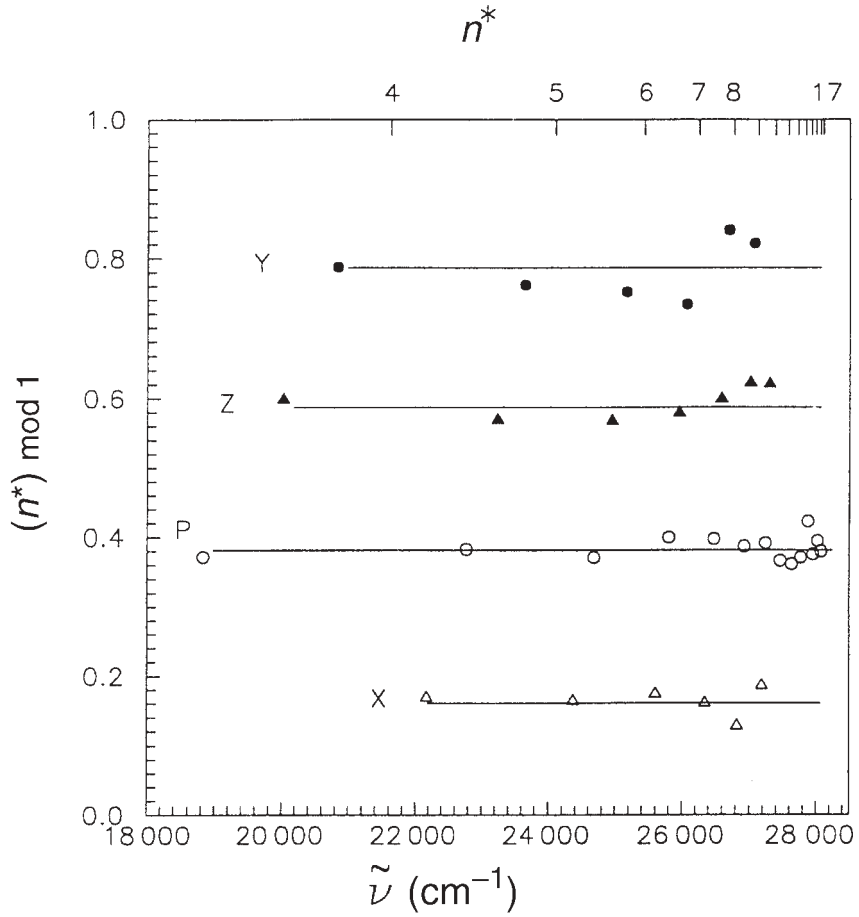
The strongest features among the four spectral series illustrated in Fig. 6 are those with $(n^*)_{mod1} \cong 0.40$, the P series. The first P member in Fig. 6 has a (0–0) band at 18 831 cm^{-1}, with the upper state being assigned as $[X^2\Sigma_u^+(1/2_u^+)]6p\sigma_u$ – $a^3\Sigma_u^+(1_u^\pm, 0_u^-)$ by Audouard and Spiegelmann (52) on the basis of theoretical calculations. This band system shows extensive vibrational development (85) and was designated P(2) with a tentative assignment of $8p\sigma_u\ ^3\Sigma_g^+$ – a (now $7p\sigma_u$). Audouard and Spiegelmann (52) also predicted a system near 19 200 cm^{-1}, arising from transitions to $[X^2\Sigma_u^+(1/2_u^+)]6p\pi_u\ ^{1,3}\Pi_g(1_g^\pm, 2_g^\pm, 1_g^\pm, 0_g^\pm)$, with singlet-triplet and multiplet splittings of ~80 and 40 cm^{-1}, respectively, and individual states described in a *case c* (Ω-state) distribution. Energetically, the nearest transition to these "$6p\pi_u$" predictions is the first member of series Z (ref. 85) in Fig. 6 at 20 022 cm^{-1}, a peak previously reported in refs. 3, 4, and 83 to be in the ~20 023 – 20 040 cm^{-1} spectral interval. The 18 831 and 20 022 cm^{-1} bands would have n^* values of 3.37 and 3.60, respectively, with the latter band being a member of the Kr_2 analog of an $n\ell\lambda\ \Pi_g$ series (85) assigned (52) to the $nf\pi_u\ ^3\Pi_g$ series in Ar_2.

The potential ambiguities in assignments discussed previously for the lower-energy states of Kr_2 propagate to higher energies. Thus, for example, it is not clear whether (*i*) the higher members of the P series are simply the $[X^2\Sigma_{1/2u}^+(1/2_u^+)]np\pi_u\ ^3\Pi_g\ (2_g^\pm, 1_g^\pm, 0_g^\pm)$ – a series, with a possible additional contribution from spin–orbit mixing allowed transitions to the associated $^1\Pi_g(1_g^\pm)$ states, or (*ii*) this series also includes transitions to the $[X^2\Sigma_u^+(1/2_u^+)]np\sigma_u\ ^{1,3}\Sigma_g^+(0_g^+, 1_g^\pm, 0_g^-)$ members energetically collapsed onto the $np\pi_u$ state manifold. If one adopts premise (*i*), then it is most likely that the X series is the $[X^2\Sigma_{1/2u}^+(1/2_u^+)]np\sigma_u\ ^3\Sigma_g^+(1_g^\pm, 0_g^-)$ – a series, with possible contributions from transitions to the "singlet" 0_g^+ states associated with $np\sigma_u$. Given that the X and P series can be assigned based on premise (*i*), there remains the Z series [$(n^*)_{mod1} \cong 0.6$] and the Y series [$(n^*)_{mod1} \cong 0.8$]. The Z and Y series might be associated with the $[X^2\Sigma_{1/2u}^+(1/2_u^+)]nf\pi_u\ ^{1,3}\Pi_g(1_g^\pm, 2_g^\pm, 1_g^\pm, 0_g^\pm)$ – a series and the $nf\sigma_u\ ^{1,3}\Sigma_g^+(0_g^+, 1_g^\pm, 0_g^-)$ – a series, respectively, but such assignments, along with their Ar_2 counterparts, remain tentative. Thus, because of inconsistencies, both observational and theoretical, a completely unambiguous description of the excited-state structures for Kr_2 must await improved data.

There can be additional complications in describing the states in Rydberg series converging on $[X^2\Sigma_{1/2u}^+(1/2_u^+)]$ produced by their interactions with states built on excited cores and with other large-R configuration interaction effects. As

© 2004 NRC Canada

Fig. 6. Plots of $(n^*)_{mod1}$ vs. n^* and $\tilde{\nu}$ (cm^{-1}) for the $v = 0$ levels of four Rydberg series observed (85) for Kr_2. See text for discussion. Figure reproduced with permission of the American Institute of Physics.



noted before, such complexities are beyond the scope of this article and will only be critiqued briefly in the following.

Xe_2

Experimental studies of the Xe_2 excimer extend back more than 50 years. Aside from fundamental interest in the dimer and its application as a VUV continuum light source, much of the recent experimental and theoretical work on this molecule has been motivated by its potential to produce a tunable laser in the second continuum (λ ~172 nm) region. Despite such continued activity, however, the Rydberg states of Xe_2 converging on $X^2\Sigma^+_{1/2u}(1/2^+_u)$ are the least well-characterized of the Rg_2 family, with the exception only of Rn_2. Rotationally resolved spectra have not yet been reported for Xe_2, but isotopically resolved vibronic spectra, photoexcitation of rotationally cold dimers produced in a supersonic jet, and transient absorption and laser excitation spectroscopic experiments have provided new insights into the structure of this molecule.

Lipson et al. (53) employed a coherent, tunable VUV source to observe absorption from Xe dimers produced in a supersonic jet. Vibrationally resolved spectra associated with transitions from $X^1\Sigma^+_g(0^+_g)$ to three low-lying *ungerade* excited states were reported for Xe_2, observations apparently analogous to those discussed previously for Ar_2 and Kr_2. Isotopic analyses revealed that the v' levels accessible within the Franck–Condon corridor were $v' = 36$–43 for $a^3\Sigma^+_u(1_u)$, $v' = 35$–46 for $A^1\Sigma^+_u(0^+_u)$, and $v' = 16$–27 for $C0^+_u$. Extrapolations of these data obtained at larger R yielded (53) the following "equilibrium" parameters: $T_e = 63\,089.9$ cm^{-1}, $\omega_e = 137.5$ cm^{-1}, $\omega_e x_e = 1.167$ cm^{-1}, and $D_e = 4174.$ cm^{-1} for $a^3\Sigma^+_u$; $T_e = 63\,795.6$ cm^{-1}, $\omega_e = 124.8$ cm^{-1}, $\omega_e x_e = 0.937$ cm^{-1}, and $D_e = 4446.$ cm^{-1} for $A^1\Sigma^+_u$; and $T_e = 75\,881.7$ cm^{-1}, $\omega_e = 49.7$ cm^{-1}, $\omega_e x_e = 0.422$ cm^{-1}, and $D_e = 1500.$ cm^{-1} for $C0^+_u$.

Kasama et al. (46) and Jonin et al. (86) observed a number of absorption features in the 9090–9800 cm^{-1} region that have been attributed by Jonin and Spiegelmann (87) on the basis of theoretical considerations to $[X^2\Sigma^+_{1/2u}(1/2^+_u)]6p\pi_u$ $^{1,3}\Pi_g$ $(1_g,2_g,1_g, 0^\pm_g)$ – $a^3\Sigma^+_u(1_u, 0^-_u)$ transitions, with ref. 86 using separated atom $\pi_u 6p$ notation. Jonin et al. (86) employed a fluorescence ($A \rightarrow X$) suppression approach to verify the existence of features reported by ref. 46 in the 9090–9800 cm^{-1} region and broad quasi-continua peaking at ~6780 and 7580 cm^{-1}. The former has been tentatively assigned (87) to transitions terminating on $[X^2\Sigma^+_{1/2u}(1/2^+_u)]0^-_g$ and 1_g states, and the latter to transitions terminating on the $[A^2\Pi_{3/2g}]1_g$ and 2_g states.

Two short Rydberg series were observed in absorption (4) in electron beam excited Xe and attributed to two members of the $np\sigma\ ^3\Sigma^+_g$ – a and four members of the $np\pi$ – a transitions. These series exhibited $n^*|_{mod1}$ values of ~0.7 and ~0.3, with first members tentatively assigned to $n = 8$ and 7,

© 2004 NRC Canada

respectively. Fluorescence suppression experiments (88) probed the structure superimposed onto a strong feature at ~549.4 nm previously assigned (4) to $[X]8p\sigma\ ^3\Sigma_g^+$ – a and assigned (86, 87) these structures to transitions from $a^3\Sigma_u^+(1_u,\ 0_u^-)$ to $[X^2\Sigma_{1/2u}^+(1/2_u^+)]7p\pi_g\ ^{1,3}\Pi_g(1_g,\ 2_g,\ 1_g,\ 0_g^\pm)$ in the notation employed here. In short, there is good reason to believe that states associated with at least the lowest two to four members of the $np\lambda_g$ series converging on $[X^2\Sigma_{1/2u}^+(1/2_u^+)]$ have been observed experimentally, although most of the members are not well characterized.

Reference 87 compares the meager experimental information available for $[X^2\Sigma_{1/2u}^+(1/2_u^+)]$ core-based Rydberg structures with their extensive theoretical calculations. Reference 87 also discusses lower-lying, excited core-based levels and other large-*R* phenomena. Some of these structures are relatively well characterized experimentally, but they are outside the principal area of emphasis of this work.

Heteronuclear rare gas diatomics

Theoretical and experimental investigation of the heteronuclear rare gas diatomics has also been considerable, particularly in the last decade. Although closely related, the structure of the RgRg′ molecular family is beyond the scope of this article, and the reader is referred to refs. 89 through 95, and references cited therein for an introduction to the subject. It should be noted that the preponderance of the recent experiments on RgRg′ electronic structures have involved one- or two-photon excitation of molecules, often produced in a supersonic jet, with subsequent photoionization of the diatomic species followed by analysis by mass spectrometry or photoelectron spectroscopy. Rydberg states built on a variety of molecular ion cores have been reported, and Lipson and Field (95) have proposed a model for interpreting the experimentally observed irregularities of the variation of interatomic potentials with *n**.

Diatomic Rn_2

At present, it appears that neither experimental nor theoretical studies of the excited electronic structure of Rn_2 has appeared in the literature. For the ground state $(X0_g^+(^1\Sigma_g^+))$, however, relativistic pseudopotential (96) and model potential (97) calculations have been reported. The former includes calculations for Xe_2 and RnXe, while the latter contains parameterizations of potentials for all of 21 possible Rg_2 and Rg′Rg molecules from Rg = He, Ne, Ar, Kr, Xe, and Rn.

Additional comments

There have been a number of experimental observations of electronic structures in the $R > R_e$ regions most easily accessible by absorption from the $X^1\Sigma_g^+(0_g^+)$ states. These observations fall mainly into two categories: transitions to the large-*R* portions of Rydberg states built on the $[X^2\Sigma_{1/2u}^+(1/2_u^+)]$ cores (as sometimes modified by interactions with valence states) and transitions to states built on the excited core states listed in Tables 2 and 3. The low-energy portions of states in the former category were encountered above in connection with observations of the C-state large-*R* minimum for Ar_2, Kr_2, and Xe_2. Few of the large-*R* observations of structures associated with more highly excited $[X^2\Sigma_{1/2u}^+(1/2_u^+)]n\ell\lambda_p\ ^{1,3}\Lambda_p$ levels have been correlated with electronic structures near the R_e of their core. At this time, such measurements at large *R* and observations of excited core-based states have not appeared as major contributors to the structures or perturbations of the $[X^2\Sigma_u^+(1/2_u^+)]$-based Rydberg states in the *R* regions near R_e for their core, nor to spectra associated with these states. However, such states certainly will be extremely important as the database is improved and to any future attempts to describe $[X^2\Sigma_u^+(1/2_u^+)]$-based Rydberg state behavior in the very complex region extending from $R > R_e$ to the dissociation limit. Thus, a few additional words seem appropriate even though they are outside the content bounds set forth in the *Introduction*.

Observations in the two categories listed in the preceding paragraph generally are associated with upper states labeled by the atomic limit to which the states dissociate (or are believed to dissociate). Early examples of this labeling appear in the Ne_2 work of ref. 10, where vibrationally resolved absorption spectra from $X^1\Sigma_g^+$ were grouped into 12 systems. The two lowest-energy systems were labeled (10) $I(0_u^+)$ (denoted here as the A state) dissociating to $2p^6\ ^1S + 2p^5\ 3s$ and $II(0_u^+)$ dissociating to $2p^6\ ^1S + 2p^5\ 3s'$, where $2p^5\ 3s$ is associated with $^3P_1$ and $2p^5\ 3s'$ with the more highly excited $^1P_1$ state of Ne. The remaining systems were then assigned (10) as transitions converging on *ns*,*ns*′ with *n* = 4 and 5 and *nd*,*nd*′ with *n* = 3 and 4. Thus, the upper-state labeling procedures follow the Rg atomic level labels in Moore (36) with subsequent correlations to levels built on the excited ion core states listed in Tables 2 and 3.

For Ar_2, spectra have been reported for transitions from X to states associated with $3p^5$ *ns*, *nd*, *ns*′, and *nd*′ for *n* values up to ~17, 15, 8, and 21, respectively, and the reader is referred to refs. 98–101 and references cited therein. For Kr_2, spectra have been reported for transitions from X to states associated with $4p^5$ *ns*, *np*, *np*′, *nd*, and *nd*′ for *n* values up to ~6, 4, 6, 5, and 9, respectively. For additional details concerning these experiments, the reader is referred to refs. 99, 102, and 103 and references cited therein.

The breadth of the experimental work reported for Xe_2 over the past several decades warrants an expanded discussion. In the 1970s and early 1980s, Castex and Damany (104, 105) and Castex (106) observed more than a dozen electronic states of Xe_2 by examining the temperature and pressure dependence of absorption by ground-state collision pairs in the VUV. Excited states correlated with Xe (6*s*, 6*s*′, 6*p*, 5*d*, 7*s*) + Xe $(5p^6\ ^1S_0)$ in the separated atom limit were reported (20, 104–106), while Dehmer and Pratt (99) reported observations of *nd*′ up to *n* = 10. Gornik et al. (107) subsequently introduced two-photon excitation spectroscopic techniques to detect stable Xe_2 excited states derived from Xe (6*p*, 5*d*).

More recently, two-photon excitation of dimers produced in a jet was combined with mass spectrometry and electrostatic energy analysis by Dehmer et al. (108, 109) to investigate the electronic states derived from Xe (6*p*, 5*d*) + Xe $(^1S_0)$. The states correlated with Xe $(6p[5/2]_2$, $6p[3/2]_2$, or $6p[1/2]_0)$ + Xe $(^1S_0)$ in the separated atom limits were found to be shallow ($D_0 \simeq$ 290–580 cm^{-1}) and were attributed to Rydberg states having the $B^2\Pi_{3/2g}$ or $C^2\Pi_{3/2u}$ ion cores. Similar results were reported for the observed states correlated with Xe (5*d*) + Xe $(^1S_0)$; except for a strongly bound state

© 2004 NRC Canada

associated with the Xe ($5d[7/2]_3$) + Xe ($^1S_0$) limit, most appeared to have dissociation energies of <600 cm^{-1} and $C^2\Pi_{3/2u}$ or $B^2\Pi_{3/2g}$ molecular ion cores. Resonantly enhanced multiphoton ionization (REMPI) combined with mass spectrometry were used by Dimov et al. (110) and Hu et al. (111, 112) in a series of experiments that observed and characterized more than 15 states correlated with the Xe ($6p$, $5d$, or $4f$) + Xe ($^1S_0$) separated atom limits. Again, the dissociation energies for most of the observed states were determined to be $\lesssim$1000 cm^{-1}. The exception was a strongly bound (D_e = 3470.4 cm^{-1}) state associated with the Xe ($6p[5/2]_2$) + Xe ($^1S_0$) limit.

Discussion

As already noted on several occasions, differing n and ℓ designations exist in the literature for the same Rydberg state. It also has been mentioned that the origin of these description differences is that n and ℓ are not meaningful quantum numbers for most of the Rg_2 Rydberg configurations. In the presence of configuration interactions, only Ω, p' and the $\Omega^{\pm}$ reflection parities are approximately valid state labels for all R and Rg_2 members, with spin–orbit effects also coupling states with $\Delta\Omega^{p''}_{p'} = 0$. However, molecular rotation couples states with $\Delta\Omega^{p''}_{p'} = \pm 1$ with identical values of p' but opposite values of p'' (i.e., $\Omega_p{}^+$ and $\Omega_p{}^-$) so that not even single $\Omega^{p''}_{p'}$ labels are valid state representations under some circumstances.

Values for n^* are a direct measure of the energy of the Rydberg state, given by eq. [1]. Fractional representations of n^*, such as $n^*|_{mod1}$ or $\delta|_{mod1} = (n - n^*)|_{mod1}$, indicate a relative phase shift of the wave function for a given Rydberg channel that arises from the interaction of the Rydberg electron with the ion core (69–71). These phase shifts can be determined semiempirically (see refs. 66, 67, and 113 and references cited therein) or from the polarization characteristics of the core (see ref. 43 and references cited therein) and are independent of any assumptions regarding the existence of n or ℓ, or the necessity of equating n^* to $n - \delta$. However, it is convenient to label successive members of a Rydberg series with an indexing number, and it has been the convention for presumptions regarding the lowest integer in eq. [1] to provide the initial value for an indexing protocol. Different presumptions invariably lead to different n labels for the same level. Although not currently in use, an approach to Rydberg series indexing that is more consistent with the $n^*|_{mod1}$ phase shift interpretation would be to adopt a labeling system similar to that for the all-R-valid $m\lambda_p$ orbital notation, in which the first member of a Rydberg $m\ell\lambda_p\ ^{2S+1}\Lambda_{p'}$ series would be designated m = 1 (as is the first $m\lambda_p$ orbital), and successive series members labeled by incrementing m by the appropriate integer. Such a labeling scheme would also be similar to the listing of excited electronic states associated with the same $^{2S+1}\Lambda_{p'}$ symmetries in order of ascending energies (i.e., $1^3\Pi_g$, $2^3\Pi_g$, $3^3\Pi_g$,... are the first, second, third,... $^3\Pi_g$ states in order of increasing energy), a practice employed by many theorists (see, for example, refs. 44, 47, 49, and 52). In any case, continuing to regard n as having integral quantal significance implies that the labeling of many molecular Rydberg series can be expected to be plagued by ambiguities and (or) inconsistencies.

The breakdown in the ability to interpret n as being semihydrogenic (i.e., the breakdown in the utilization of demi H_2^+ models (114)) occurs for even the lightest member of the Rg_2 series, He_2). In He_2, the breakdown manifests itself in the necessity of using coupled-channel methods to correlate quantitatively the higher n portions of much of the experimental database for the $[X^2\Sigma_u^+]n\ell\lambda_p\ ^{1,3}\Lambda_{p'}$ manifolds (see the *He_2* section). Even more extensive configuration interaction effects occur for the heavier Rg_2 members, but most of these effects have not been quantified experimentally because of the lack of rotationally resolved data for many of the Rydberg states in Ar_2, the majority of the Rydberg states in Kr_2, and all the Ryberg states of Xe_2.

Despite the progress of the last few decades in the observation and analysis of $[X^2\Sigma_u^+]$ core-based Rydberg series in the Rg_2 family, much of the observed structure of the heaviest of these molecules remains ambiguously characterized. Thus, the final comments in this article offer suggestions for steps to be taken to remove these ambiguities and to otherwise improve our understanding of the Rg_2 Rydberg structures.

For molecules heavier than He_2, there are two general areas involving the $[X^2\Sigma^+_{1/2u}(1/2^+_u)]n\ell\lambda_p$-based Rydberg states where new experimental data are of most immediate importance. Both areas require new spectra from the $a^3\Sigma_u^+(1_u^{\pm}, 0_u^-)$ state. The first involves obtaining two-photon spectra of sufficient quality to characterize excited Rydberg states of u symmetry, and the second pertains to obtaining one-photon spectra with increased vibrational band development. Results from both these areas are necessary to better understanding the Rydberg structures in the region of R near R_e of $Rg_2^+(X^2\Sigma_u^+)$ and to correlate these structures with observations in the larger-R regions leading eventually to dissociation.

There are two Ne_2 specific areas, outlined in the *Ne_2* section, that would clearly benefit from additional efforts. One involves determining the nature of the Q-branch intensity anomaly in the $np\pi\ ^3\Pi_g$ – a (0–0) series, while the other involves application of coupled-channel approaches to characterizing the complex spectral structures observed within a thousand or so wavenumbers on both sides of the $X^2\Sigma_u^+$, v = 0 ionization limit.

There are several areas for improvement outlined in the *Ar_2* section, but the one of most importance involves unequivocal assignment of the Rydberg series currently labeled as belonging to the $[X^2\Sigma_u^+(1/2_u^+)]nf\lambda_u$-based triplet series (see the *Ar_2* section). Obvious initial needs include new rotationally resolved spectra for the next higher members of the "$[X^2\Sigma_u^+(1/2_u^+)]nf\lambda_u\ ^3\Pi_g,\ ^3\Sigma_g^+$" ← $a^3\Sigma_u^+(1_u^{\pm}, 0_u^-)$ (0–0) transitions (n = 7 and 8 for the current n indexing system), as well as for the first member of the "$[X^2\Sigma_u^+(1/2_u^+)]6f\delta_u\ ^3\Delta_g$" ← a (0–0) transitions. The labels in quotations represent the theory-based labeling discussed in the *Ar_2* section.

For Kr_2, the most critical initial need is for the unequivocal assignment of the four series (Y, Z, P, X) tentatively assigned in the *Kr_2* section. This process will require rotationally resolved spectra for at least the most *easily accessible* low-n member of each of these series, which probably will prove to be transitions from the set $[X^2\Sigma_u^+(1/2_u^+)]np\lambda_u\ 3\Sigma_g{}^+(1_g^{\pm}, 0_g^-)$, $^3\Pi_g(2_g^{\pm}, 1_g^{\pm}, 0_g^{\pm})$ ← a (0–0)

© 2004 NRC Canada

and $nf\lambda_u$ $^3\Delta_g(2_g^{\pm})$, $^3\Pi_g(2_g^{\pm}, 1_g^{\pm}, 0_g^{\pm})$, $^3\Sigma_g^+(1_g^{\pm}, 0_g^-) \leftarrow$ a (0–0). This area of Kr_2 assignments will also benefit from unique assignments for several Rydberg series in Ar_2 discussed in the preceding paragraph.

As implied in the *Xe_2* section, a completely new, much more extensive database for transitions to states associated with $[X^2\Sigma_u^+(1/2_u^+)]np\lambda_p$ and $nf\lambda_p$ from the $a^3\Sigma_u^+(1_u^{\pm}, 0_u^-)$ state will be a starting point, to be followed by Xe_2 data of the types discussed previously which are representative of that necessary for all of the rare gas dimers heavier than He_2. In all cases, the highest practical resolution will be useful, and most Rydberg series assignments will likely rely on analogies with the lighter Rg_2 molecules as well as theoretical results.

Acknowledgements

The authors wish to thank Dr. D.S. Ginter for her invaluable assistance in the preparation of the manuscript and K. Collier and A.A. Senin for technical assistance. This work was supported in part by the National Science Foundation (PHY-9514413), the U S Air Force Office of Scientific Research (F49620-98-1-0030, F49620-99-1-0317, and F49620-00-1-0372), the University of Maryland (College Park), and the University of Illinois (Urbana-Champaign).

References

1. G. Herzberg. Annu. Rev. Phys. Chem. **38**, 27 (1987).
2. B. Stoicheff. Gerhard Herzberg: An illustrious life in science. NRC Research Press, Ottawa, Ont., Canada. 2002. pp. 361–366.
3. K.P. Killeen and J.G. Eden. J. Chem. Phys. **83**, 6209 (1985).
4. K.P. Killeen and J.G. Eden. J. Chem. Phys. **84**, 6048 (1986).
5. G. Herzberg. Molecular spectra and molecular structure I. Spectra of diatomic molecules. Van Nostrand Reinhold, Princeton, N.J. 1950.
6. R.S. Mulliken. J. Am. Chem. Soc. **86**, 3184 (1964).
7. R.S. Mulliken. J. Am. Chem. Soc. **88**, 1849 (1966).
8. J.B. Anderson. J. Chem. Phys. **115**, 4546 (2001).
9. T. van Mourik, A.K. Wilson, and T.H. Dunning, Jr. Mol. Phys. **96**, 529 (1999).
10. Y. Tanaka and K. Yoshino. J. Chem. Phys. **57**, 2964 (1972).
11. A. Wüest and F. Merkt. J. Chem. Phys. **118**, 8807 (2003).
12. P. Slavíček, R. Kalus, P. Paška, I. Odvárková, P. Hobza, and A. Malijevský. J. Chem. Phys. **119**, 2102 (2003).
13. R.A. Aziz and M.J. Slaman. Chem. Phys. **130**, 187 (1989).
14. R.A. Aziz. J. Chem. Phys. **99**, 4518 (1993).
15. E.A. Colbourn and A.E. Douglas. J. Chem. Phys. **65**, 1741 (1976).
16. P.R. Herman, P.E. LaRocque, and B.P. Stoicheff. J. Chem. Phys. **89**, 4535 (1988).
17. P.E. LaRocque, R.H. Lipson, P.R. Herman, and B.P. Stoicheff. J. Chem. Phys. **84**, 6627 (1986).
18. Y. Tanaka, K. Yoshino, and D.E. Freeman. J. Chem. Phys. **59**, 5160 (1973).
19. D.S. Green and S.C. Wallace. J. Chem. Phys. **100**, 6129 (1994).
20. D.E. Freeman, K. Yoshino, and Y. Tanaka. J. Chem. Phys. **61**, 4880 (1974).
21. K.T. Tang and J.P. Toennies. J. Chem. Phys. **118**, 4976 (2003).
22. K.P. Huber and G. Herzberg. Molecular spectra and molecular structure. IV. Constants of diatomic molecules. Van Nostrand Reinhold, New York. 1979.
23. R.S. Mulliken. J. Chem. Phys. **52**, 5170 (1970).
24. P. Rupper and F. Merkt. J. Chem. Phys. **117**, 4264 (2002).
25. W. Cencek and J. Rychlewski. J. Chem. Phys. **102**, 2533 (1995).
26. R. Signorell and F. Merkt. J. Chem. Phys. **109**, 9762 (1998).
27. A. Carrington, D.I. Gammie, J.C. Page, A.M. Shaw, and J.B. Hutson. J. Chem. Phys. **116**, 3662 (2002).
28. R.I. Hall, Y. Lu, T. Matsui, H. Yoshii, T. Hayaishi, and K. Ito. J. Phys. B, **28**, 2435 (1995).
29. E.C.M. Chen and E.S. Chen. Chem. Phys. Lett. **293**, 491 (1998).
30. R. Signorell, U. Hollenstein, and F. Merkt. J. Chem. Phys. **114**, 9840 (2001).
31. A. Wüest, P. Rupper, and F. Merkt. Mol. Phys. **99**, 1941 (2001).
32. I. Paidavová and F.X. Gadea. Chem. Phys. **274**, 1 (2001).
33. Y. Lu, Y. Morioka, T. Matsui, T. Tanaka, H. Yoshii, R.I. Hall, T. Hayaishi, and K. Ito. J. Chem. Phys. **102**, 1553 (1995).
34. R.S. Mulliken. Rev. Mod. Phys. **2**, 60 (1930).
35. R.S. Mulliken. Rev. Mod. Phys. **4**, 1 (1932).
36. C.E. Moore. Atomic energy levels. Vols. I, II, and III. US Government Printing Office, Washington, D.C. 1971.
37. M.L. Ginter and D.S. Ginter. J. Chem. Phys. **48**, 2284 (1968).
38. S.B. Kim, C.M. Herring, J.G. Eden, and M.L. Ginter. J. Chem. Phys. **96**, 1016 (1992).
39. D.J. Kane, S.B. Kim, D.C. Shannon, C.M. Herring, J.G. Eden, and M.L. Ginter. J. Chem. Phys. **96**, 6407 (1992).
40. T.A. Miller, R.S. Freund, B.R. Zegarski, R. Jost, M. Lombardi, and J. Derouard. J. Chem. Phys. **63**, 4042 (1975).
41. C. Focsa, P.F. Bernath, and R. Colin. J. Mol. Spectrosc. **191**, 209 (1998).
42. M.L. Ginter. J. Chem. Phys. **45**, 249 (1966).
43. G. Herzberg and Ch. Jungen. J. Chem. Phys. **84**, 1181 (1986).
44. F. Grein and S.D. Peyerimhoff. J. Chem. Phys. **87**, 4684 (1987).
45. S. Arai, T. Oka, M. Kogoma, and M. Imamura. J. Chem. Phys. **68**, 4595 (1978).
46. K. Kasama, T. Oka, S. Arai, H. Kurusu, and Y. Hama. J. Phys. Chem. **86**, 2035 (1982).
47. S. Iwata. Chem. Phys. **37**, 251 (1979).
48. S.B. Kim, D.J. Kane, J.G. Eden, and M.L. Ginter. J. Chem. Phys. **94**, 145 (1991).
49. P. Dupláa and F. Spiegelmann. J. Chem. Phys. **105**, 1500 (1996).
50. P.R. Herman, A.A. Madej, and B.P. Stoicheff. Chem. Phys. Lett. **134**, 209 (1987).
51. C.M. Herring, J.G. Eden, and M.L. Ginter. J. Chem. Phys. **108**, 5426 (1998).
52. E. Audouard and F. Spiegelmann. J. Chem. Phys. **94**, 6102 (1991).
53. R.H. Lipson, P.E. LaRocque, and B.P. Stoicheff. Opt. Lett. **9**, 402 (1984); J. Chem. Phys. **82**, 4470 (1985).
54. A. Dalgarno. *In* Rydberg states of atoms and molecules. *Edited by* R.F. Stebbings and F.B. Dunning. Cambridge University Press, New York. 1983.
55. H. Lefebvre-Brion and R.W. Field. Perturbations in the spectra of diatomic molecules. Academic Press, Orlando, Fla. 1986.
56. Y. Tanaka. J. Opt. Soc. Am. **45**, 710 (1955).
57. P.G. Wilkerson. Can. J. Phys. **45**, 1715 (1967).
58. J.J. Hopfield. Phys. Rev. **35**, 1133 (1930).

© 2004 NRC Canada

59. A.L. Smith and J.M. Meriwether, Jr. J. Chem. Phys. **42**, 2984 (1965).
60. M.J. Kiik, P. Dubé, and B.P. Stoicheff. J. Chem. Phys. **102**, 2351 (1995).
61. Y. Tanaka and K. Yoshino. J. Chem. Phys. **50**, 3087 (1969).
62. M.L. Ginter. *In* Spectroscopic data relative to diatomic molecules. *Edited by* R. Rosen. Pergamon Press, Oxford. 1970. pp. 193–202.
63. F.B. Orth and M.L. Ginter. J. Mol. Spectrosc. **61**, 282 (1976).
64. F.B. Orth and M.L. Ginter. J. Mol. Spectrosc. **64**, 223 (1977).
65. F.B. Orth, C.M. Brown, and M.L. Ginter. J. Mol. Spectrosc. **69**, 53 (1978).
66. D.S. Ginter, M.L. Ginter, and C.M. Brown. J. Chem. Phys. **81**, 6013 (1984).
67. D.S. Ginter and M.L. Ginter. J. Chem. Phys. **88**, 3761 (1988).
68. T.A. Miller and V.E. Bondybey. J. Mol. Spectrosc. **78**, 120 (1979).
69. M.J. Seaton. Proc. Phys. Soc. London, **88**, 801 (1966).
70. K.T. Lu and U. Fano. Phys. Rev. A, **2**, 81 (1970).
71. U. Fano. Phys. Rev. A, **2**, 353 (1970).
72. D.R. Yarkony. J. Chem. Phys. **90**, 7165 (1989).
73. D.C. Lorents, S. Keiding, and N. Bjerre. J. Chem. Phys. **90**, 3096 (1989).
74. I. Hazell, A. Nørregaard, and N. Bjerre. J. Mol. Spectrosc. **172**, 135 (1995).
75. R.S. Mulliken. Phys. Rev. **A136**, 962 (1964).
76. Y. Tanaka and K. Yoshino. J. Chem. Phys. **57**, 2964 (1972).
77. D.J. Kane, C.J. Zietkiewicz, and J.G. Eden. Phys. Rev. A, **39**, 4906 (1989).
78. W. Giessl, C. Völker, S. Czer, M. Zöger, and H. Langhoff. J. Phys. B, **24**, 4203 (1991).
79. J.A. Conway, F. Shen, C.M. Herring, J.G. Eden, and M.L. Ginter. J. Chem. Phys. **115**, 5126 (2001).
80. D.J. Kane, S.B. Kim, J.G. Eden, and M.L. Ginter. J. Chem. Phys. **95**, 3877 (1991).
81. S.B. Kim, D.J. Kane, and J.G. Eden. Phys. Rev. Lett. **68**, 1311 (1992).
82. C.M. Herring, S.B. Kim, J.G. Eden, and M.L. Ginter. J. Chem. Phys. **101**, 4561 (1994).
83. F. Spiegelmann and J.-P. Malrieu. Chem. Phys. Lett. **57**, 214 (1978).
84. R. Sauerbrey, H. Eizenhöfer, V. Schaller, and H. Langhoff. J. Phys. B, **19**, 2279 (1986).
85. D.J. Kane, C.C. Abele, R.D. Fraser, D.C. Shannon, J.G. Eden, and M.L. Ginter. J. Chem. Phys. **99**, 99 (1993).
86. C. Jonin, E. Descroix, P. Laporte, and F. Spiegelmann. Chem. Phys. Lett. **300**, 595 (2000).
87. C. Jonin and F. Spiegelmann. J. Chem. Phys. **117**, 3059 (2002).
88. C. Jonin, P. Laporte, and F. Spiegelmann. Chem. Phys. Lett. **30**8, 13 (1999).
89. T.P. Haley and S.M. Cybulski. J. Chem. Phys. **119**, 5487 (2003).
90. H. Yoshii, T. Hayaishi, T. Onuma, T. Aoto, Y. Morioka, and K. Ito. J. Chem. Phys. **116**, 7468 (2002).
91. I.D. Petsalakis, G. Theodorakopoulos, H.-P. Liebermann, and R.J. Buenker. J. Chem. Phys. **115**, 6365 (2001).
92. D.M. Mao, X.K. Hu, Y.J. Shi, and R.H. Lipson. J. Chem. Phys. **111**, 2985 (1999).
93. Y. Xu, W. Jäger, J. Djauhari, and M.C.L. Gerry. J. Chem. Phys. **103**, 2827 (1995).
94. N.Y. Du and C.H. Green. J. Chem. Phys. **90**, 6347 (1989).
95. R.H. Lipson and R.W. Field. J. Chem. Phys. **110**, 10 653 (1999).
96. N. Runeberg and P. Pyykkö. Int. J. Quantum Chem. **66**, 131 (1998).
97. K.T. Tang and J.P. Toennies. J. Chem. Phys. **118**, 4976 (2003).
98. P.M. Dehmer. J. Chem. Phys. **76**, 1263 (1982).
99. P.M. Dehmer and S.T. Pratt. J. Chem. Phys. **75**, 5265 (1981).
100. Y. Tanaka, W. Walker and K. Yoshino. J. Chem. Phys. **70**, 380 (1979).
101. Y. Tanaka and K. Yoshino. J. Chem. Phys. **53**, 2012 (1970).
102. D.M. Mao, X.K. Hu, Y.J. Shi, J.H. Leech, and R.H. Lipson. J. Chem. Phys. **114**, 4025 (2001).
103. R.H. Lipson, S.S. Dimov, J.Y. Cai, P. Wang, and H.A. Bascal. J. Chem. Phys. **102**, 5881 (1995).
104. M.-C. Castex and N. Damany. Chem. Phys. Lett. **13**, 158 (1972).
105. M.-C. Castex and N. Damany. Chem. Phys. Lett. **24**, 437 (1974).
106. M.-C. Castex. J. Chem. Phys. **74**, 759 (1981).
107. W. Gornik, S. Kindt, E. Mathias, and D. Schmidt. J. Chem. Phys. **75**, 4595 (1981).
108. P.M. Dehmer, S.T. Pratt, and J.L. Dehmer. J. Chem. Phys. **85**, 13 (1986).
109. P.M. Dehmer, S.T. Pratt, and J.L. Dehmer. J. Chem. Phys. **91**, 2593 (1987).
110. S.S. Dimov, J.Y. Cai, and R.H. Lipson. J. Chem. Phys. **101**, 10313 (1994).
111. X.K. Hu, D.M. Mao, S.S. Dimov, and R.H. Lipson. J. Chem. Phys. **106**, 9411 (1997).
112. X.K. Hu, D.M. Mao, Y.J. Shi, S.S. Dimov, and R.H. Lipson. J. Chem. Phys. **109**, 3944 (1998).
113. D.S. Ginter and M.L. Ginter. J. Chem. Phys. **86**, 1437 (1987).
114. R.S. Mulliken. J. Am. Chem. Soc. **91**, 4615 (1969).

© 2004 NRC Canada

A study of the $A^2\Pi/B^2\Sigma^+ - X^2\Sigma^+$ band systems of calcium monohydride (CaH) using a supersonic molecular beam source and laser-induced fluorescence detection[1]

T.C. Steimle, Jamie Gengler, and Jinhai Chen

Abstract: The high-resolution laser-induced fluorescence spectrum of a molecular beam sample of calcium monohydride (CaH) in the region of the strongly overlapped (1,0) $A^2\Pi - X^2\Sigma^+$ and (0,0) $B^2\Sigma^+ - X^2\Sigma^+$ band systems near 630 nm and the (0,0) $A^2\Pi - X^2\Sigma^+$ band system near 690 nm have been recorded and analyzed. The spectral features exhibit a small splitting that is attributed to proton magnetic hyperfine interaction in the $X^2\Sigma^+(v = 0)$ state. The energy levels of the $A^2\Pi(v = 0)$ vibronic state were modeled using a traditional "effective" Hamiltonian approach, whereas those for the interacting $A^2\Pi(v = 1)/B^2\Sigma^+(v = 0)$ vibronic levels were modeled by augmenting the traditional effective Hamiltonian with terms to account for local perturbations. An interpretation of the field-free parameters is presented.

Key words: calcium monohydride, molecular beam, fluorescence.

Résumé : On a enregistré et analysé le spectre de fluorescence induite au laser et à haute résolution d'un échantillon à l'état de faisceau moléculaire du monohydrure de calcium (CaH) dans la région de fort recouvrement des systèmes de bandes (1,0) $A^2\Pi - X^2\Sigma^+$ et (0,0) $B^2\Sigma^+ - X^2\Sigma^+$ près de 630 nm et du système de bande (0,0) $A^2\Pi - X^2\Sigma^+$ près de 690 nm. Les caractéristiques spectrales présentent un faible dédoublement qui a été attribué à l'interaction hyperfine magnétique du proton dans l'état $X^2\Sigma^+(v = 0)$. On a développé un modèle des niveaux d'énergie de l'état vibronique $A^2\Pi(v = 0)$ en utilisant une approche traditionnelle d'Hamiltonien effectif alors que ceux des niveaux vibroniques $A^2\Pi(v = 1)/B^2\Sigma^+(v = 0)$ ont été évalués à l'aide d'un modèle qui ajoute à l'Hamiltonien effectif des termes qui tiennent compte des perturbations locales. On présente une interprétation des paramètres à champ nul.

Mots clés : monohydrure de calcium, faisceau moléculaire, fluorescence.

[Traduit par la Rédaction]

Introduction

Dr. Herzberg was instrumental in the transformation of spectroscopy from a purely phenomenological endeavor to a discipline where high-resolution spectra are now routinely used both as a venue for extracting structure and serving as diagnostic probes of ambient environmental conditions such as temperature, velocity, and magnetic and electric fields. Simple free radical molecules such as calcium monohydride (CaH) are particularly useful molecular probes of ambient fields because of their intense visible transitions, which have readily resolved rotational structure, and because the electronic states involved in these transitions have sizable electric and magnetic dipole moments. The evolution of the understanding of the spectroscopy and associated quantum levels of CaH, which consist of three distinct periods, is a case study of this maturation of the discipline. The first period of this process began nearly a century ago with the identification of the visible and near-UV spectrum of CaH in the sun by Olmsted (1) and soon thereafter in the laboratory by Eagle (2). The unusual fine structure on the electronic band systems, which could readily be resolved with the spectrographs of the day, prompted notable spectroscopists to pursue the analysis of the near-UV $C^2\Sigma^+ - X^2\Sigma^+$ (3) and visible $A^2\Pi - X^2\Sigma^+$ and $B^2\Sigma^+ - X^2\Sigma^+$ band systems (4). The early developments of the theory associated with the rotational and spin-orbit mixing of electronic states (i.e., Born–Oppenheimer breakdown) in open shell molecules, most notably by Mulliken and Christy (5), were motivated in a large part by attempts to explain this fine structure. CaH is ideal for the development of this theory because to a first approximation the $A^2\Pi$ and $B^2\Sigma^+$ states are described by a single configuration that differs solely in the occupation of either a calcium centered $4p(\pi)$ or $4p(\sigma)$ orbital, respectively. The Born–Oppenheimer breakdown is manifested as a splitting of rotational energy levels in the $A^2\Pi$ state (i.e.,

Received 21 January 2004. Published on the NRC Research Press Web site at http://canjchem.nrc.ca on 26 August 2004.

T.C. Steimle,[2] J. Gengler, and J. Chen. Department of Chemistry and Biochemistry, Arizona State University, Tempe, AZ 85287–1604, USA.

[1]This article is part of a Special Issue dedicated to the memory of Professor Gerhard Herzberg.

[2]Corresponding author (e-mail: tsteimle@asu.edu).

 doi: 10.1139/V04-077 © 2004 NRC Canada

the Λ-doubling) and in the $B^2\Sigma^+$ state (i.e., the ρ-doubling). The Mulliken and Christy (5) formulas for the Λ- and ρ-doubling are the first application of the seminal theoretical work done by Hill and Van Vleck (6) and Van Vleck (7) on development of "effective" Hamiltonian methods, which are widely applied today in spectroscopy (8). Consequently, CaH is extensively used as a pedagogical example in Herzberg's 1939 monograph on diatomic molecules (9) because even at that early date in the history of spectroscopy the well-resolved visible and near-UV band systems had been subjected to more than 30 years of recording and modeling.

The second period of activity in the study of the visible spectrum of CaH began in the late 1960s. On the analysis front, Veseth (10, 11) extended Van Vleck's approach to fourth order and used the resulting expressions in an attempt to fit the previously recorded data. The derived analytical formulas were not satisfactory for modeling the spin splitting in the $A^2\Pi(v = 1)$ state. These formulas, as well as the previously derived lower-order formulas, are restricted to cases where the separation between the interacting $^2\Pi$ and $^2\Sigma$ states is large compared with the spin-orbit induced separation between the $^2\Pi_{1/2}$ and $^2\Pi_{3/2}$ components. The lowest rotational level of the $B^2\Sigma^+(v = 0)$ state is only approximately 20 cm^{-1} below the lowest rotational level of the $A^2\Pi_{3/2}(v = 1)$ state while the spin-orbit splitting between the $A^2\Pi_{1/2}$ and $A^2\Pi_{3/2}$ components is approximately 80 cm^{-1}, precluding the use of these expressions for the spectral analysis.

On the experimental front during this same period, high-resolution absorption spectra in the visible region were recorded (12–14). The Stockholm group (13, 14) made significant progress on the analysis of these spectra by abandoning the conventional effective Hamiltonian method and explicitly considering $A^2\Pi(v)/B^2\Sigma^+(v)$ and $A^2\Pi(v+1)/B^2\Sigma^+(v)$ interactions. A satisfactory modeling of the energy levels for the problematic $A^2\Pi(v = 1)$ and $B^2\Sigma^+(v = 0)$ states could only be achieved by excluding the low rotational levels ($J < 10.5$) (14). The first laser excitation spectroscopy measurements were performed during this period (15), which assisted in the assignment of the existing spectra. This period culminated in a grand analysis performed by Martin (16) in which new features in the earlier recorded absorption spectra were assigned and others reassigned based upon analysis of the polarization of laser-induced fluorescence signals. The modeling of the energy levels required more than 50 parameters to fit 655 term values for the $A^2\Pi(v = 0, 1, 2, 3)/B^2\Sigma^+(v = 0, 1, 2, 3) - X^2\Sigma^+(v = 0, 1, 2, 3)$ band systems. Numerous anomalies between the predicted and observed intensities were noted particularly for the (1,0) $A^2\Pi - X^2\Sigma^+$ and (0,0) $B^2\Sigma^+ - X^2\Sigma^+$ band systems where, for example, the R_2 branch features of the (1,0) $A^2\Pi - X^2\Sigma^+$ were missing.

The third and current period of the spectroscopy of CaH has been motivated in part by the desire to generate ultracold molecules (17, 18) as well as the speculation that CaH may be used as a probe of magnetic fields in astrophysical sources (19). In experiments by Dolye and co-workers (17, 18), CaH molecules were generated by laser ablation of solid CaH_2 and cooled by thermalizing collisions with a ^3He buffer gas at approximately 0.4 K and the low magnetic field seeking states were subsequently trapped. In all previous spectroscopic studies the CaH sample had been produced at temperatures of 900 °C or greater, which, for the most part, had precluded the observation of the spectral features associated with low rotational levels. On the contrary, the very low rotational temperature of the CaH sample in the magnetic trap reduced the overlapped (1,0) $A^2\Pi - X^2\Sigma^+$ and (0,0) $B^2\Sigma^+ - X^2\Sigma^+$ band systems to a few branch features associated with the very lowest rotational level of the $X^2\Sigma^+(v = 0)$ state. The Zeeman effect of the R_1 (0.5) branch feature in the intense (0,0) $B^2\Sigma^+ - X^2\Sigma^+$ band system was used as a diagnostic for determining the magnetic field in the trap. In modeling the Zeeman effect the interaction between the nearly degenerate $A^2\Pi(v = 1)$ and $B^2\Sigma^+(v = 0)$ states was accounted for explicitly in a fashion similar to Martin (16), but expanded to include the mixing due to the Zeeman operator. The orbital and spin gyromagnetic ratios (g_L and g_S, respectively) were held fixed to 1 and 2.0023. In reality, these values should be considered as adjustable parameters of the effective Hamiltonian operator and measurements of the magnetic induced shifts for additional branch features are required to fully determine the parameters of the Zeeman operator. An interesting result of the analysis was that the orbital angular momentum factor that describes mixing between the $A^2\Pi(v = 1)$ and $B^2\Sigma^+(v = 0)$ states, $\langle A^2\Pi \mid \hat{L}^+ \mid B^2\Sigma^+ \rangle$, was determined to be approximately a factor of two smaller than that predicted for a $4p(\pi)/4p(\sigma)$ "pure precession" pair of electronic states. A similar conclusion was reached in the analysis of the field-free spectrum (16). In support of the magnetically trapped measurements, interaction potentials for the He–CaH system has been calculated (20) and used for collision cross-section predictions (21). To access the accuracy of the interaction potentials the dipole moment at the equilibrium separation ($\mu(r_e)$) of the $X^2\Sigma^+$ state was calculated (= 0.9123 a.u.).

Recently, the first molecular beam study of CaH was reported (22). In this work on the (1 + 1′) resonance-enhanced multiphoton ionization (REMPI) spectrum, the (0,0) $A^2\Pi - X^2\Sigma^+$ and (1,0) $B^2\Sigma^+ - X^2\Sigma^+$ bands were recorded and analyzed. The overlapped and more problematic (1,0) $A^2\Pi - X^2\Sigma^+$ and (0,0) $B^2\Sigma^+ - X^2\Sigma^+$ bands were excluded. The beam was generated by skimming the free jet expansion output formed by a laser ablation of solid calcium in the presence of a helium–H_2 pulsed supersonic expansion. The spectral resolution of approximately 0.08 cm^{-1} was insufficient to resolve much of the fine and magnetic hyperfine structure. Inconsistencies with the measured transition frequencies and those obtained by Hulthén (4) for the (0,0) $A^2\Pi - X^2\Sigma^+$ band system and with those obtained by Berget al. (15) for the (1,0) $B^2\Sigma^+ - X^2\Sigma^+$ band system were noted.

Other spectroscopic studies relevant to the analysis performed here are the millimeter wave, pure rotational, spectroscopy of the $X^2\Sigma^+$ state (23, 24), the sub-Doppler optical spectroscopic study of the (0,0) $B^2\Sigma^+ - X^2\Sigma^+$ band system (25) and the FT-IR emission study of the vibrational transitions of the $X^2\Sigma^+$ state (26). A combined fit of all the data for the $X^2\Sigma^+$ state was performed by the University of Waterloo group and is presented in ref. 26 as is a more extensive review of the spectroscopy. Our ultimate goal is to fully characterize the optical Stark and Zeeman effects in the visible band systems of CaH. The resulting magnetic and electric dipole moments for the ground and excited electronic states are needed before CaH can be used as a probe

© 2004 NRC Canada

of fields both in electrostatic traps and astrophysical sources (27). A prerequisite for the Stark and Zeeman studies is the recording and analysis of the near natural line width limit, field-free, spectrum of a supersonic molecular beam sample of CaH and a subsequent understanding of the energy level pattern of the low rotational features. The vexing issue of modeling and interpreting the anomalous ρ-type and Λ-type doubling in the $B^2\Sigma^+(v = 0)$ and the nearly degenerate $A^2\Pi(v = 1)$ states, respectively, needs to be accomplished.

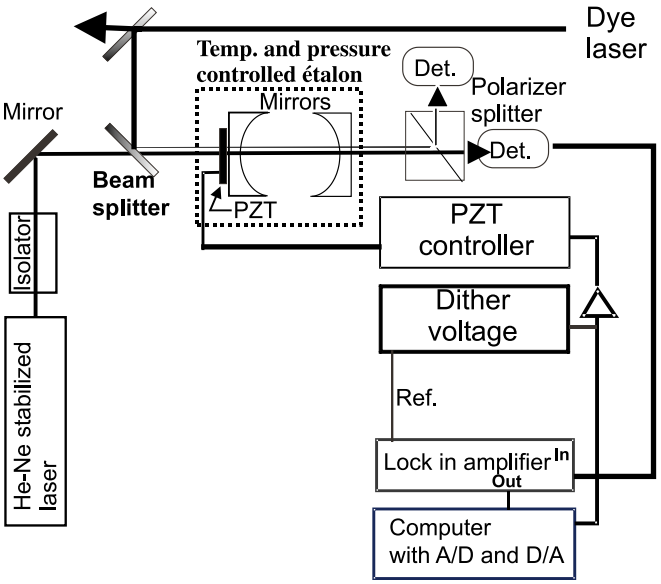
Experimental

A modified version of the laser ablation – supersonic expansion production scheme used in the REMPI measurement (22) was selected for sample preparation. A variable speed rotating Ca metal rod was irradiated by the third harmonic (355 nm) light originating from a Q-switched Nd:YAG laser operating at approximately 10 mJ/pulse. The 20 Hz pulses were focused onto the Ca sample with a 0.5 m focal length quartz lens. A commercial solenoid type valve was used to introduce an inert gas – H_2 mixture such as to entrain and react with the laser-vaporized metal. Initially a 5%–10% mixture of H_2 gas in Ar was employed, as done previously in our laboratory, but yielded very weak CaH LIF signals. Following the procedure of ref. 22, a H_2–He mixture was used. Although the production efficiency increases with the H_2:He ratio, the rotational temperature also increases. In most cases a 50:50 mixture with a backing pressure of approximately 2400 kPa was selected. A 5 mm diameter skimmer, situated approximately 15 cm downstream from the ablation source, separated the two compartments of the differentially pumped chambers of the molecular beam apparatus. Typical operating pressures of approximately 5×10^{-5} torr and 1×10^{-6} torr (1 torr = 133.322 Pa) for the source and detection chambers, respectively, were maintained. The gas pulses were variably timed relative to the Nd:YAG ablation pulses to optimize production of CaH.

Two types of spectra were recorded: (*i*) broad survey scans (>100 cm^{-1}) using a continuous wave, multilongitudinal mode, linear dye laser, which utilized a birefringent filter for wavelength tuning; (*ii*) narrow scans (<1 cm^{-1}) using a stabilized, single longitudinal mode, continuous wave ring dye laser. In both cases, the dye laser radiation intersected the molecular beam sample at a 90° angle 10 cm downstream from the skimmer. The bandwidths of the linear and ring dye laser systems are approximately 5 GHz and 10 KHz, respectively. The survey scans were recorded using powers of approximately 300 mW, whereas in the high-resolution scans the power was reduced to approximately 10 mW for the intense (0,0) $A^2\Pi - X^2\Sigma^+$ and (0,0) $B^2\Sigma^+ - X^2\Sigma^+$ band systems, and 50 mW for the weaker (1,0) $A^2\Pi - X^2\Sigma^+$ system to minimize power broadening.

The resulting laser-induced fluorescence was collected and collimated with a lens assembly and directed through a band-pass filter to minimize background light associated with the ablation plasma. The (1,0) $A^2\Pi - X^2\Sigma^+$ and (0,0) $B^2\Sigma^+ - X^2\Sigma^+$ bands both absorb near 637 nm, but while the (0,0) $B^2\Sigma^+ - X^2\Sigma^+$ system fluorescence is primarily at the absorbing wavelength, the (1,0) $A^2\Pi - X^2\Sigma^+$ band preferentially fluoresces at 690 nm corresponding to the (1,1) $A^2\Pi - X^2\Sigma^+$ system emission. The (0,0) $A^2\Pi - X^2\Sigma^+$ band system primarily fluoresces at the 690 nm excitation wavelength. Therefore, a ±10 nm filter centered either at 640 or 690 nm was used to process the signal. The filtered laser-induced fluorescence was detected via a cooled photomultiplier tube and processed using gated, single-photon, counting techniques.

Fig. 1. A block diagram of the actively stabilized confocal étalon used for extrapolation between I_2 wavelength calibration features.



The wavelength calibration of the broadband scans relied solely on a commercial wavemeter, which is accurate to ±0.01cm^{-1}. The single-frequency, high-resolution scans required simultaneous monitoring of the CaH LIF signal and the absorption spectrum of a heated gaseous I_2 cell for wavelength calibration (28, 29). The number of precisely measured I_2 features is relatively sparse in portions of the desired spectral range. Simultaneous recording of the transmission of two confocal étalons assisted the required long wavelength extrapolation from I_2 calibration lines to the CaH LIF features. One étalon, depicted in Fig. 1, was thermally stabilized, evacuated, and with 10 cm confocal optics whose mirror spacing was actively controlled by monitoring the transmission of a frequency stabilized He–Ne laser. Application of a variable voltage to a lead zirconate titanate (PZT) crystal attached to one of the confocal mirrors was used to adjust the spacing. A small, approximately 800 Hz, dithering voltage modulated the He–Ne laser transmission. The modulated transmission intensity was detected with a photodiode and used as input to a commercial lock-in amplifier. The output of the lock-in amplifier was monitored with a microcomputer and a correction voltage sent to the driving electronics of the PZT crystal to keep the He–Ne transmission intensity constant. The free spectral range (fsr) of this étalon (= 753.58 MHz) was very accurately determined by simultaneously recording the cw-dye laser transmission and the LIF signal from the $R_{11b}(J = 1)$ and $P_{11b}(J = 3)$ branch features of the (0,0) $B^3\Pi - X^3\Delta$ band system of TiO. The method for production of beams of TiO are described elsewhere (30). These two spectral features share the common $J = 2$ level in the $B^3\Pi(v = 0)$ state making the separation between the two spectral features the difference between the

© 2004 NRC Canada

Fig. 2. The low-resolution LIF spectrum of the (0,0) $A^2\Pi - X^2\Sigma^+$ band system of CaH. The fluorescence was filtered using a ±10 nm band pass filter centered at 690 nm. The prediction was obtained using the final optimized parameters (Table 4), a rotational temperature of 70 K, and a Lorentzian function having a FWHM line width of 15 GHz.

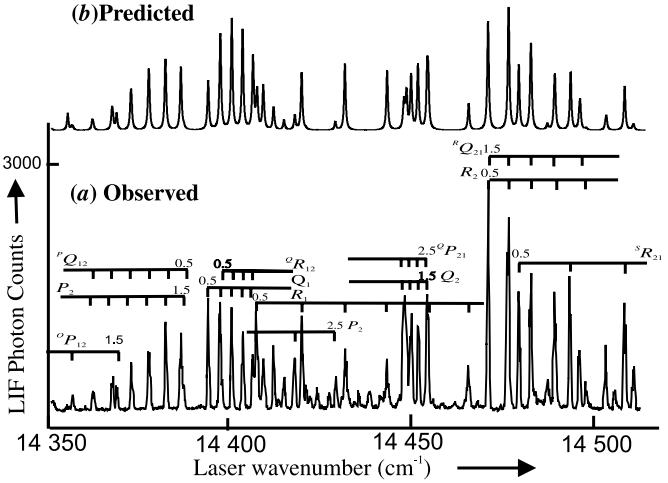
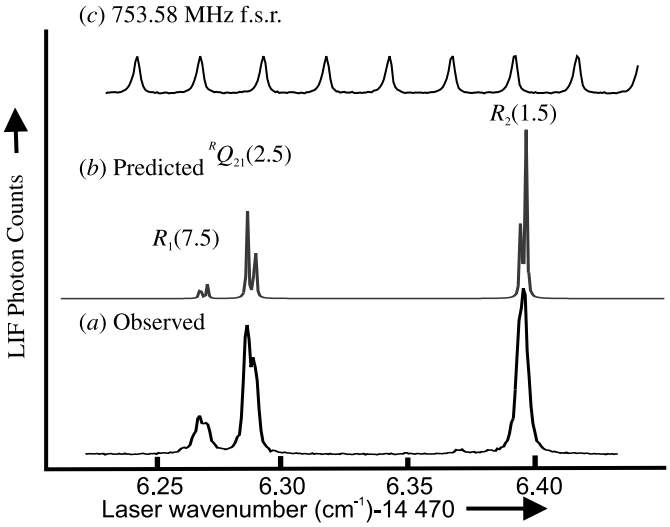


Fig. 3. A portion of the observed and calculated high-resolution LIF spectra of the (0,0) $A^2\Pi - X^2\Sigma^+$ band system of CaH in the region of the $R_2(1.5)$ and $^RQ_{21}(2.5)$ branch features. The predicted spectrum was obtained using the optimized set of spectroscopic parameters, a rotational temperature of 70 K, and a Lorentzian function having a FWHM line width of 40 MHz.



lower energy parity components of the $J = 1$ and $J = 3$ levels of the $X^3\Delta(v = 0)$ state. This spacing has been very precisely measured to be 158281.707(5) MHz (31). A second, unstabilized, 1 m confocal étalon (fsr = 74.5 MHz) was used to extrapolate between transmission peaks of the 10 cm, stabilized, confocal étalon.

Observations

A low-resolution LIF survey scan in the region of the (0,0) $A^2\Pi - X^2\Sigma^+$ band system is presented in Fig. 2. Twenty ablation pulses at a given excitation wavelength were co-added and a 25% H_2–He mixture employed. The low rotational energy levels of both the $X^2\Sigma^+(v = 0)$ and $A^2\Pi(v = 0)$ states exhibit a pattern typical of a molecule near the *case* $b_{\beta J}$ and *case* $a_{\beta J}$ coupling scheme limit, respectively, because in both states the proton hyperfine interaction is much smaller than that of fine structure and, in the case of the $A^2\Pi$ state, the spin-orbit interaction is much larger than the rotational spacing. The rotational levels of the $X^2\Sigma^+$ state, which has no electronic orbital angular momentum, are labeled by the approximately good quantum number N, associated angular momentum of the nuclear framework rotation. These levels are spilt into a pair (ρ-doubling) due to the coupling of the electronic spin and rotational angular momenta and are labeled by the intermediate quantum number J ($\equiv N \pm S$). By convention "F_i" indices are used to label the energy order of the various electron spin-split eigenvalues for a given J (9). In a doublet electronic state ($S = 1/2$), F_1 and F_2 label the lowest and highest energy levels for a given J, respectively, and each ρ-doublet consist of an F_1/F_2 pair. The rotational levels of the $A^2\Pi$ state separate into two widely spaced (≈80 cm^{-1}) groups due to the strong coupling of the electronic spin to the nuclear frame via spin-orbit interaction. The two groups are distinguished by the magnitude of the sum of the projection of electronic orbital angular momentum (Λ) and the spin angular momentum (Σ) designated with the subscript $|\Omega|(\equiv\Lambda \pm \Sigma)$. All the rotational levels of the $A^2\Pi_{1/2}$ group correspond to the coupling that produces values for J that correlate to $N + S$, whereas all the levels of the $A^2\Pi_{3/2}$ group correspond to the coupling that produces J values that correlate to $N - S$. The $A^2\Pi$ state has a positive spin-orbit coupling parameter making all the levels in the $A^2\Pi_{1/2}$ group have an F_1 index and those for the $A^2\Pi_{3/2}$ group an F_2 index.

The branch designation of Fig. 2 is the conventional labeling scheme of $^{\Delta N}\Delta J_{F_i' F_i''}$ (9) with the subscripts F_i taking on the corresponding "i" values of 1 or 2. There are 12 possible branch features: six branch features for the $A^2\Pi_{1/2} - X^2\Sigma^+$ sub-band corresponding to the $\Delta J = -1$, 0, and +1 with $F_i'' = 1,2 \rightarrow F_i' = 1$ transitions, and six branch features for the $A^2\Pi_{3/2} - X^2\Sigma^+$ sub-band corresponding to the $\Delta J = -1$, 0 and +1, $F_i'' = 1,2 \rightarrow F_i' = 2$ transitions. All 12 branches are readily identified in Fig. 2. Also presented in Fig. 2 is a prediction of the LIF spectrum for the (0,0) $A^2\Pi - X^2\Sigma^+$ band system, which agrees very well with the observation. The prediction was obtained using the final optimized parameters, a rotational temperature of 70 K, and a Lorentzian function having a full width half maximum (FWHM) line width of 15 GHz. Details of the prediction procedure are given in the next section. The relative intensities of the predicted spectral features show some deviation from the observation particularly for high-J branch features and are attributed to saturation effects associated with the relatively intense (>300 mW) excitation radiation.

The high-resolution scans of the low rotational features ($J'' < 6.5$) of the (0,0) $A^2\Pi - X^2\Sigma^+$ band system were recorded. Illustrated in Fig. 3 are the measured and predicted LIF spectra of the R_2 (1.5) and associated satellite $^RQ_{21}(2.5)$ branch features. The splitting between the R_2 (1.5) and $^RQ_{21}$ (2.5) branch features (≈3260 MHz) is due to the ρ-doubling in the $N = 2$ levels of the $X^2\Sigma^+(v = 0)$ state. The partially re-

© 2004 NRC Canada

Table 1. The observed and calculated transition wavenumbers (cm^{-1}) for the (0,0) $A^2\Pi - X^2\Sigma^+$ band system of CaH.

Branch	J''	F''	Observed[a]	Obs. – calcd.	Branch	J''	F''	Observed	Obs. – calcd.
$^QP_{21}$	2.5	3	14 453.7726	0.0066	Q_1	0.5	1	14 393.3674	–0.0004
		2	14 453.7772	0.0081			0	14 393.3749	0.0019
	3.5	4	14 451.1770	0.0052		1.5	2	14 396.7227	0.0051
		3	14 451.1795	0.0048			1	14 396.7260	0.0051
	4.5	5	14 447.9134	–0.0066		2.5	3	14 399.8558	–0.0029
		4	14 447.9167	–0.0061			2	14 399.8529	–0.0027
Q_2	1.5	2	14 453.8763	–0.0007		3.5	4	14 402.8376	–0.0043
	2.5	3	14 451.3191	–0.0072			5	14 402.8346	–0.0043
	3.5	4	14 449.4255	–0.0058		4.5	5	14 405.7252	0.0015
	4.5	5	14 448.1696	0.0084		5.5	6	14 408.5705	0.0087
	5.5	5	14 447.4739	0.0006			5	14 408.5723	0.0077
		6	14 447.4768	0.0011	$^QR_{12}$	0.5	1	14 396.7886	0.0039
$^SR_{21}$	0.5	1	14 479.1754	0.0004		1.5	2	14 399.9590	–0.0076
		0	14 479.1804	0.0001		2.5	3	14 402.9851	–0.0084
	1.5	2	14 493.4758	–0.0004		3.5	4	14 405.9148	–0.0068
		1	14 493.4790	–0.0006		4.5	5	14 408.8054	0.0024
	2.5	3	14 508.4047	–0.0063	R_1	0.5	1	14 406.8976	0.0016
		2	14 508.4076	–0.0065			0	14 406.9026	0.0066
	3.5	4	14 523.9352	–0.0045		1.5	2	14 419.1803	0.0010
	4.5	5	14 540.0168	0.0036		2.5	3	14 431.1283	–0.0045
$^RQ_{21}$	1.5	2	14 470.6319	0.0017		3.5	4	14 442.7817	–0.0003
		1	14 470.6339	0.0003		4.5	5	14 454.1573	–0.0044
	2.5	3	14 476.2882	–0.0009		5.5	6	14 465.3107	0.0002
		2	14 476.2902	–0.0020			5	14 465.3137	0.0004
	3.5	4	14 482.4246	–0.0003	P_1	1.5	2	14 385.7790	0.0030
		3	14 482.4266	–0.0006			1	14 385.7760	0.0000
	4.5	5	14 488.9735	–0.0008		2.5	3	14 381.4867	–0.0003
		4	14 488.9770	–0.0002			2	14 381.4906	0.0005
	5.5	6	14 495.8877	0.0057		3.5	4	14 376.8763	0.0014
R_2	0.5	1	14 470.6992	0.0018			3	14 376.8783	0.0005
	1.5	2	14 476.3977	–0.0033		4.5	5	14 371.9554	0.0002
	2.5	3	14 482.5775	–0.0013			4	14 371.9591	0.0011
	3.5	3	14 489.1692	–0.0007		5.5	6	14 366.7613	–0.0009
		4	14 489.1722	–0.0001	$^PQ_{12}$	0.5	1	14 385.8423	0.0025
	4.5	5	14 496.1275	0.0043		1.5	2	14 381.5968	–0.0012
P_2	2.5	3	14 428.4816	0.0013		2.5	3	14 377.0310	0.0016
	3.5	4	14 417.3098	0.0004		3.5	4	14 372.1532	0.0001
	4.5	5	14 406.6447	–0.0010		4.5	5	14 367.0026	–0.0008
					$^OP_{12}$	1.5	2	(14 368.0731)[b]	
						2.5	3	14 354.5641	–0.0035
						3.5	4	14 340.8740	–0.0019
	Std. dev. = 0.004 cm^{-1}					4.5	5	14 327.0586	–0.0018

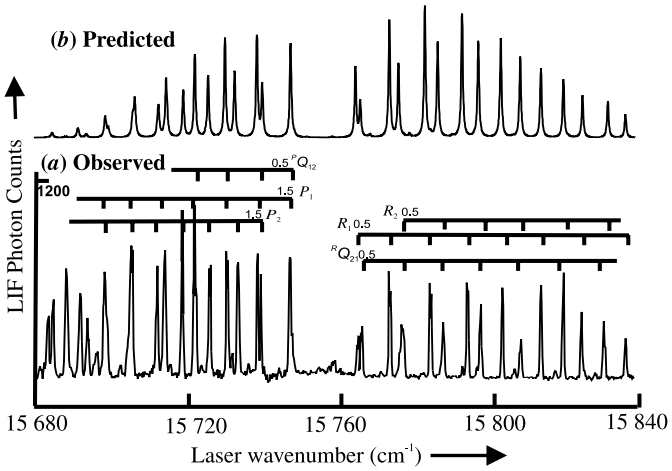
[a]The total angular momentum for the $A^2\Pi$ state (F') value was obtained from the $\Delta F = \Delta J$ relationship.
[b]Calculated value. Feature not measured.

solved splitting of the $^RQ_{21}(2.5)$ branch feature (≈50 MHz) and the broadening of the R_2 (1.5) feature are due to the proton magnetic hyperfine interaction in the F_1 and F_2 components, respectively, of the $N = 2$ rotational level in the $X^2\Sigma^+$ state. It was observed that the proton magnetic hyperfine interaction is larger in the F_1 levels than the F_2 levels and decreases with increasing N. The predicted spectrum of Fig. 3 was obtained using the optimized set of spectroscopic parameters, a rotational temperature of 70 K, and a FWHM line width of 40 MHz. The resulting complete set of measured transition frequencies, quantum number assignments, and deviation from predicted frequencies are given in Table 1. These values are in general agreement, but approximately 100 times more precisely determined, with those of refs. 13 and 16. Neither the branch assignments nor transition frequencies agree with those of the REMPI measurements of ref. 22.

The low-resolution LIF survey scan in the region of the intense (0,0) $B^2\Sigma^+ - X^2\Sigma^+$ band system is presented in Fig. 4. Features in all six possible branches are readily identified.

© 2004 NRC Canada

Fig. 4. The low-resolution LIF spectrum of the overlapped (0,0) $B^2\Sigma^+ - X^2\Sigma^+$ and (1,0) $A^2\Pi - X^2\Sigma^+$ band systems of CaH. The fluorescence was filtered using a ±10 nm band pass filter centered at 640 nm that selectively detects the fluorescence from the (0,0) $B^2\Sigma^+ - X^2\Sigma^+$ band system. The predicted spectrum was obtained using the final optimized parameters, a rotational temperature of 70 K, and a Lorentzian function having a FWHM line width of 15 GHz.



The predicted spectrum was obtained using the final optimized parameters, a rotational temperature of 70 K, and Lorentzian line width of 15 GHz (FWHM). The agreement between the predicted and observed spectra is not as good as in the case of the (0,0) $A^2\Pi - X^2\Sigma^+$ band system, particularly for the features at the low wavenumber end of the spectrum. This can be attributed in part to the fact that the transmission of the 640 ± 10 nm filter is centered at this portion of the spectrum. In addition, this portion of the spectrum may have some features from the overlapping (1,0) $A^2\Pi_{1/2} - X^2\Sigma^+$ band, which gain transition intensity due to mixing.

The observed and predicted high-resolution spectrum on the $R_1(0.5)$ spectral feature, which was used to probe the magnetic field in the trapping experiments (18), is presented in Fig. 5 along with the associated energy level. The approximate 155 MHz splitting of this spectral feature is due to the proton magnetic hyperfine splitting between the $F = 0$ and $F = 1$ (F = total angular momentum) of the $N = 0$, $J = 0.5$ level of the $X^2\Sigma^+(v = 0)$ state. This splitting was not resolved in the magnetic trap experiments. Both the frequency and intensity of the predicted spectrum (dashed line) are in good agreement with the observation. The measured and predicted high-resolution spectra of the $R_2(0.5)$ and associated satellite $^RQ_{21}(1.5)$ branch features of the (0,0) $B^2\Sigma^+ - X^2\Sigma^+$ band system are presented in Fig. 6. The splitting between the $R_2(0.5)$ and $^RQ_{21}(1.5)$ branch features (≈1950 MHz) is due to the ρ-doubling in the $N = 1$ levels of the $X^2\Sigma^+(v = 0)$ state. The partially resolved splitting of the $^RQ_{21}(1.5)$ branch feature (≈60 MHz) and the broadening of the $R_2(0.5)$ feature are due to the proton magnetic hyperfine interaction in the F_1 and F_2 components, respectively, of the $N = 1$ rotational level in the $X^2\Sigma^+$ state. The predicted spectra of Figs. 5 and 6 were obtained using the final optimized parameters, a rotational temperature of 70 K, and Lorentzian line width of 40 MHz (FWHM). The resulting complete set of measured

Fig. 5. A portion of the observed and predicted (dashed line) high-resolution LIF spectra of the $R_1(0.5)$ branch feature of the intense (0,0) $B^2\Sigma^+ - X^2\Sigma^+$ band system and associated energy levels. The energy level diagram was calculated using the parameters of ref. 23 for the $X^2\Sigma^+(v = 0)$ state and those of Table 5 for the interaction $B^2\Sigma^+(v = 0)/A^2\Pi(v = 1)$ systems.

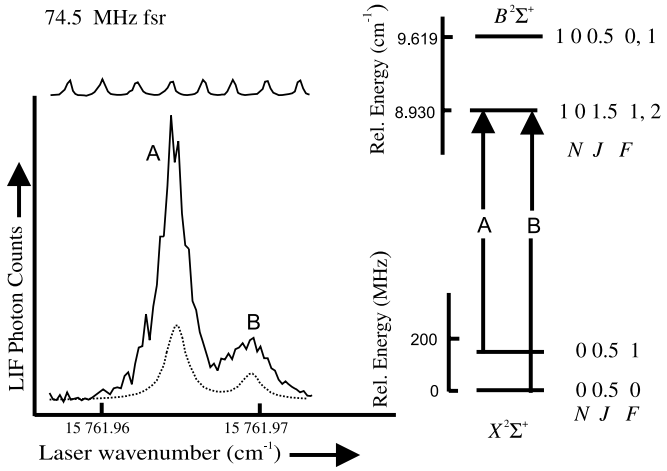
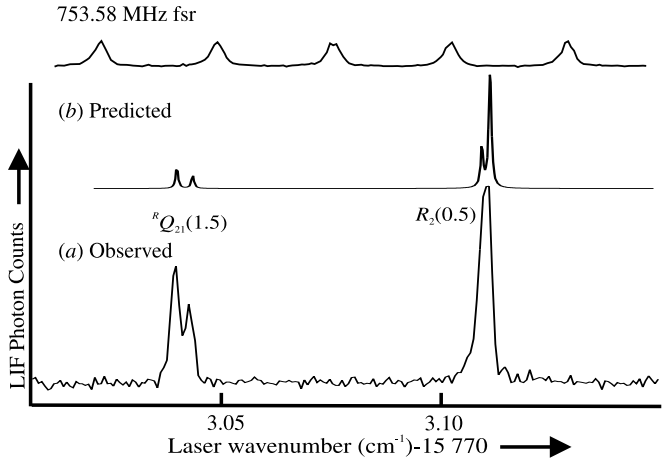


Fig. 6. The measured and predicted high-resolution spectra of the $R_2(0.5)$ and associated satellite $^RQ_{21}(1.5)$ branch features of the (0,0) $B^2\Sigma^+ - X^2\Sigma^+$ band system.



transition frequencies, quantum number assignments, and deviation from predicted frequencies for the (0,0) $B^2\Sigma^+ - X^2\Sigma^+$ band system is given in Table 2.

The low-resolution LIF survey scan in the region of the weak (1,0) $A^2\Pi - X^2\Sigma^+$ band is presented in Fig. 7. The Franck–Condon factor for this band is approximately a factor of 100 less than that of the (0,0) $B^2\Sigma^+ - X^2\Sigma^+$ band. Most of the 12 possible branch features can be identified. The measured and predicted LIF spectra of the $R_2(J'')$ and associated satellite $^RQ_{21}(J''+1)$ branch features of the weak (1,0) $A^2\Pi - X^2\Sigma^+$ band are presented Fig. 8. The predictions were done using the optimized parameters, a rotational temperature of 70 K, and Lorentzian line width of 50 MHz (FWHM). These two branch features can unambiguously be assigned because they are separated by the very accurately determined ρ-type doubling of the $X^2\Sigma^+(v = 0)$ state. Unlike the identical transitions for the (0,0) $A^2\Pi - X^2\Sigma^+$ band (see

© 2004 NRC Canada

Table 2. The observed and calculated transition wavenumbers (cm^{-1}) for the (0,0) $B^2\Sigma^+ - X^2\Sigma^+$ band system of CaH.

Branch	J''	F''	Observed[a]	Obs. – calcd.	Branch	J''	F''	Observed	Obs. – calcd.
R_1	0.5	1	15 761.9641	0.0002	$^PQ_{12}$	0.5	0	15 745.1824	0.0005
		0	15 761.9700	0.0009			1	15 745.1854	0.0017
	1.5	2	15 770.7402	0.0014		1.5	2	15 736.6619	–0.0018
		1	15 770.7436	0.0014			1	15 736.6642	–0.0017
	2.5	3	15 779.9338	0.0001		2.5	3	15 728.5924	0.0057
		2	15 779.9384	0.0016			2	15 728.5936	0.0047
	3.5	4	15 789.5448	0.0043	P_1	1.5	2	15 745.1174	0.0009
		3	15 789.5471	0.0037			1	15 745.1214	0.0015
	4.5	5	15 799.5469	–0.0031		2.5	3	15 736.5542	–0.0007
R_2	0.5	1	15 773.1087	0.0036			2	15 736.5572	–0.0008
	1.5	1	15 783.2508	–0.0003		3.5	4	15 728.4292	–0.0052
		2	15 783.2533	0.0001			3	15 728.4319	–0.0054
	2.5	2	15 793.7472	0.0006		4.5	5	15 720.7518	–0.0042
		3	15 793.7497	0.0009			4	15 720.7551	–0.0038
$^RQ_{21}$	0.5	1	15 763.2129	–0.0006	P_2	1.5	1	15 737.9129	–0.0005
		0	15 763.2184	–0.0004			2	15 737.9144	–0.0011
	1.5	2	15 773.0382	0.0004		2.5	2	15 730.8810	–0.0047
		1	15 773.0409	–0.0003			3	15 730.8826	–0.0053
	2.5	3	15 783.1507	0.0086		3.5	3	15 724.1577	–0.0025
		2	15 783.1537	0.0085			4	15 724.1599	–0.0026
	3.5	4	15 793.5951	0.0007		4.5	4	15 717.8099	–0.0035
		3	15 793.5972	–0.0001			5	15 717.8121	–0.0037

[a]The total angular momentum for the $B^2\Sigma^+$ state (F') value was obtained from the $\Delta F = \Delta J$ relationship.

Fig. 7. The low-resolution LIF spectrum of the overlapped (0,0) $B^2\Sigma^+ - X^2\Sigma^+$ and (1,0) $A^2\Pi - X^2\Sigma^+$ band systems of CaH. The fluorescence was filtered using a ±10 nm band pass filter centered at 690 nm that selectively detects the fluorescence from the (1,0) $A^2\Pi - X^2\Sigma^+$ band systems.

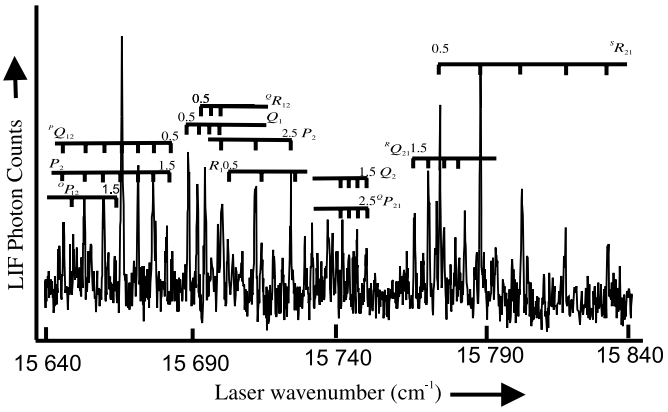


Fig. 3), the prediction does not reproduce the relative intensities. The transition frequency and the relative intensity of the overlapped hyperfine components that compose the R_2 branch features are reproduced, but the intensity of these features relative to the $^RQ_{21}$ (J'' + 1) and other branch features is not reproduced. The R_2 (0.5) feature was not detected and the higher branch features (J'' = 1.5–3.5) grow in intensity. None of the R_2 branch features had previously been identified in the high-temperature spectra (16) suggesting that for the still higher values of J'', where the previous data were most sensitive, the intensity of the R_2 branch becomes small. The resulting complete set of measured transition frequencies and quantum number assignments for the (1,0) $A^2\Pi - X^2\Sigma^+$ band system are given in Table 3.

Analysis

The analysis of the (0,0) $A^2\Pi - X^2\Sigma^+$ band system was straightforward. The energy levels of the $X^2\Sigma^+$ were modeled by including the rotation and its centrifugal distortion, the spin-rotation and the magnetic hyperfine interactions (8):

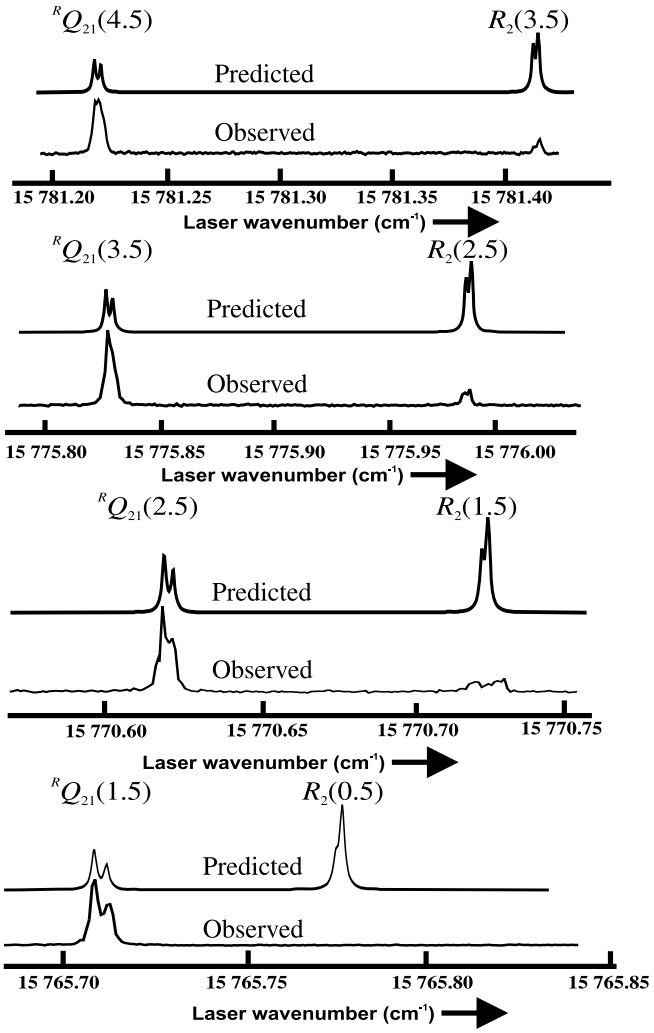
$$[1] \quad \mathbf{H}^{\mathbf{eff}}(^2\Sigma) = B\mathbf{N}^2 - D\mathbf{N}^4 + \gamma\mathbf{N}\cdot\mathbf{S} + b_F\mathbf{I}\cdot\mathbf{S} + c(\mathrm{I_zS_z} - 1/3\mathbf{I}\cdot\mathbf{S})$$

In eq. [1], **N** is the angular momentum operator excluding electronic and nuclear spin, **S** and **I**, respectively. The rotational fine structure parameters B (= 4.2286902 cm^{-1}), D (= 1.851405 × 10^{-4} cm^{-1}), and γ (= 4.3566 ×10^{-2} cm^{-1}) were held fixed to those of ref. 26 and the magnetic hyperfine parameters b_F (= 5.243 × 10^{-3} cm^{-1}) and c (= 1.39 × 10^{-4} cm^{-1}) to those of ref. 23. A 4 × 4 matrix representation, constructed using a *case* $a_{\beta J}$, nonparity basis set, $\Psi = |n\Lambda; S\Sigma;(\mathrm{JI})\mathrm{F}\Omega\mathrm{M_F}\rangle$, was numerically diagonalized to produce the eigenvalues and eigenvectors.

A check of the combination differences revealed that there was no evidence of magnetic hyperfine interaction in the excited $A^2\Pi(v = 0)$ state. The energies of this state were modeled by including the origin, spin-orbit interaction and associated centrifugal distortion correction, rotation and associated centrifugal distortion correction, and the Λ-doubling interaction terms (8):

© 2004 NRC Canada

Fig. 8. Portions of the observed and calculated high-resolution LIF spectra of the (1,0) $A^2\Pi - X^2\Sigma^+$ band system of CaH in the region of the $R_2(J'')$ and associated satellite ${}^RQ_{21}(J'' + 1)$ branch features. The predicted spectrum was obtained using the parameters of Table 5 to calculate the energies of the $A^2\Pi(v = 1)$ state. The anomalous intensity is an unsolved problem.



[2] $$\mathbf{H}^{\mathrm{eff}}(^2\Pi) = T_v + AL_zS_z + 1/2A_D[\mathbf{N}^2L_zS_z + L_zS_z\mathbf{N}^2] + B\mathbf{N}^2 - D(\mathbf{N}^2)^2 + 1/2(p + 2q)(e^{-2i\phi}J_+S_+ + e^{+2i\phi}J_-S_-) - 1/2q(J_+^2e^{-2i\phi} + J_-^2e^{2i\phi})$$

where $J_\pm$ are the shift operators of the total angular momentum in the absence of nuclear spin (**J**). Although the hyperfine splitting was not resolved in the $A^2\Pi(v = 0)$ state, a *case* $a_{\beta J}$, nonparity, basis set was still employed to facilitate intensity calculations. A 8 × 8 matrix representation was constructed and numerically diagonalized to produce the eigenvalues and eigenvectors.

A nonlinear least-squares fitting procedure program was written that used as input initial guesses of the $A^2\Pi(v = 0)$ state parameters, the observed transition frequencies of Table 1, and quantum number assignments of the associated levels. Initial guesses for the Λ-doubling fitting parameters ($p + 2q$ and q) were obtained using the approximate second-order perturbation expressions (32):

[3] $$p \approx 2\frac{\langle A^2\Pi(v = 0)|\,AL_+|B^2\Sigma(v = 0)\rangle\langle B^2\Sigma(v = 0)|BL_-|\,A^2\Pi(v = 0)\rangle}{E(A^2\Pi(v = 0)) - E(B^2\Sigma(v = 0))}$$

and

[4] $$q \approx 2\frac{\langle A^2\Pi(v = 0)\left|BL_+\right|B^2\Sigma(v = 0)\rangle^2}{E(A^2\Pi(v = 0)) - E(B^2\Sigma(v = 0))}$$

The $\langle A^2\Pi|\,AL_+|B^2\Sigma\rangle$ and $\langle A^2\Pi|\,BL_+|B^2\Sigma\rangle$ matrix elements were taken from Martin's paper (16) to be 73.6 cm^{-1} and 6.988 cm^{-1}, respectively. Using the term values of 15 725 cm^{-1} and 16 996 cm^{-1} for the $A^2\Pi(v = 0)$ and $B^2\Sigma^+(v = 0)$ levels results in estimates of $p \approx -0.81$ cm^{-1} and $q \approx -0.077$ cm^{-1}. The centrifugal distortion constant (D) was also held fixed to the value (= 1.896×10^{-4} cm^{-1}) given by Martin (16). The resulting optimized parameters, associated errors, and the correlation coefficients for the $A^2\Pi(v = 0)$ state are given in Table 4.

Modeling the energy levels of the $A^2\Pi(v = 1)/B^2\Sigma^+(v = 0)$ interacting vibronic levels was more complicated because of local perturbations. Based upon the analysis of the (0,0) $A^2\Pi - X^2\Sigma^+$ band system, the $B^2\Sigma^+(v = 0)$ state interacts strongly with the well-separated $A^2\Pi(v = 0)$ state in a predictable fashion. Similar to the treatment of the $A^2\Pi(v = 0)$ levels, this interaction in the $B^2\Sigma^+(v = 0)$ state was described using an effective Hamiltonian by the inclusion of the spin-rotation operator. The second-order perturbation expression predicts that (32):

[5] $$\gamma^{\mathrm{eff}}(B^2\Sigma^+(v = 0)) \approx -p(A^2\Pi(v = 0))$$

The $A^2\Pi(v = 1)$ state interacts strongly with the well-separated $B^2\Sigma^+(v = 1)$ levels and these interactions are accounted for by inclusion of the Λ-doubling interaction terms in the effective Hamiltonian.

The local perturbations arise from the $\langle A^2\Pi(v = 1)|AL_+|B^2\Sigma(v = 0)\rangle$ and $\langle A^2\Pi(v = 1)|BL_+|B^2\Sigma(v = 0)\rangle$ matrix elements, which are approximately a factor 100 and 10, respectively, smaller than the corresponding values for the $A^2\Pi(v = 0)/B^2\Sigma^+(v = 0)$ interaction (16). These interactions only become important because of the very near degeneracy of levels of the $A^2\Pi(v = 1)$ state with those of the $B^2\Sigma^+(v = 0)$ state that have the same total angular momentum and parity. To simultaneously account for local and remote interactions, a 12 × 12 Hamiltonain representation was constructed using the eight non-parity *case* $a_{\beta J}$ basis functions for a $^2\Pi$ state and the four non-parity *case* $a_{\beta J}$ for a $^2\Sigma$ state. The elements of the 4 × 4 block were constructed using the effective operator of eq. [1], and those of the 8 × 8 block constructed using the effective operator of eq. [2]. Matrix elements between the two sets of basis functions were taken from ref. 8 with the adjustable parameters being:

[6] $$M_1 \equiv \langle A^2\Pi(v = 1)\left|BL_+\right|B^2\Sigma(v = 0)\rangle$$

and

© 2004 NRC Canada

Table 3. The observed and calculated transition wavenumbers (cm^{-1}) for the (1,0) $A^2\Pi - X^2\Sigma^+$ band system of CaH.

Branch	J''	F''	Observed[a]	Obs. – calcd.	Branch	J''	F''	Observed	Obs. – calcd.
$^QP_{21}$	2.5	3	15 749.1734	–0.0016	Q_1	0.5	1	15 688.8756	–0.0012
		2	15 749.1770	–0.0011			0	15 688.8808	–0.0013
	3.5	4	15 746.0658	0.0004		1.5	2	15 691.9275	–0.0034
		3	15 746.0687	0.0004			1	15 691.9307	–0.0036
	4.5	5	15 743.3590	–0.0075		2.5	3	15 694.5883	0.0006
		4	15 743.3621	–0.0044			2	15 694.5917	0.0009
Q_2	1.5	1	15 749.2833	–0.0005		3.5	4	15 696.9046	0.0024
		2	15 749.2847	–0.0012			3	15 696.9079	0.0027
	2.5	2	15 746.2160	–0.0017	$^QR_{12}$	0.5	1	15 691.995	–0.0031
		3	15 746.2185	–0.0014		1.5	1	15 694.6973	0.0007
	3.5	3	15 743.5645	0.0052			2	15 694.699	0.0003
		4	15 743.5679	0.0063		2.5	3	15 697.0584	0.0016
	4.5	4	15 741.2855	–0.0020	R_1	0.5	1	15 702.1612	0.0033
		5	15 741.2880	–0.0019			0	15 702.1662	0.0030
$^SR_{21}$	0.5	1	15 774.5894	0.0054		1.5	2	15 713.9556	–0.0022
		0	15 774.5950	0.0058			1	15 713.9591	–0.0021
	1.5	2	15 788.3686	–0.0012		2.5	3	15 725.2095	–0.0023
		1	15 788.3731	–0.0001			2	15 725.2126	–0.0023
	2.5	3	15 802.5435	0.0021	P_1	1.5	2	15 681.3161	0.0047
		2	15 802.5464	0.0020			1	15 681.319	0.0042
	3.5	4	15 817.0681	–0.0004		2.5	3	15 676.7509	0.0020
		3	15 817.0705	–0.0009			2	15 676.7537	0.0017
$^RQ_{21}$	1.5	2	15 765.7085	0.0017		3.5	4	15 671.6545	0.0012
		1	15 765.7118	0.0016			3	15 671.6563	0
	2.5	3	15 770.6361	–0.0007		4.5	5	15 666.0331	–0.0010
		2	15 770.6394	–0.0005			4	15 666.0365	–0.0005
	3.5	4	15 775.8276	–0.0013		5.5	6	15 659.9191	0.0001
	4.5	5	15 781.2213	–0.0015			5	15 659.9216	–0.0002
		4	15 781.2228	–0.0029	$^PQ_{12}$	0.5	0	15 681.3774	0.0006
	5.5	6	15 786.7704	0.0026			1	15 681.3784	–0.0002
		5	15 786.7732	0.0026		1.5	1	15 676.8572	–0.0006
R_2	0.5		Not obs.				2	15 676.8588	–0.0011
	1.5	1	15 770.7391	–0.0065		2.5	2	15 671.8112	0.0056
		2	15 770.7483	0.0005			3	15 671.8131	0.0052
	2.5	2	15 775.9881	0.0071		3.5	3	15 666.2268	–0.0029
		3	15 775.9896	0.0063			4	15 666.2289	–0.0032
	3.5	3	15 781.4189	0.0005	$^OP_{12}$	1.5	1	15 663.5734	–0.0033
		4	15 781.4197	–0.0011			2	15 663.5763	–0.0025
	4.5	5	15 787.0080	–0.0009		2.5	2	15 649.7755	–0.0032
P_2	2.5	3	15 723.5517	–0.0052			3	15 649.7782	–0.0028
	3.5	3	15 711.6554	0.0007		3.5	3	15 635.6068	0.0011
		4	15 711.6572	0.0001			4	15 635.6085	0.0005
	4.5	4	15 700.0459	–0.0019		4.5	4	15 621.1219	0.0006
		5	15 700.0474	–0.0028			5	15 621.1236	–0.0001

[a]The total angular momentum for the $A^2\Pi$ state (F') value was obtained from the $\Delta F = \Delta J$ selection rule.

[7] $$M_2 \equiv \langle A^2\Pi(v = 1)|(A/2 + B)L_+|B^2\Sigma\rangle$$

In the end, the data were not sensitive enough to determine the M_2 parameter and it was constrained to zero. The centrifugal distortion constant (D) for the $A^2\Pi(v = 1)$ and $B^2\Sigma^+(v = 0)$ states were held fixed to the values of 1.901×10^{-4} cm^{-1} and 2.024×10^{-4} cm^{-1}, respectively, given by Martin (16). The resulting optimized parameters, associated errors, and the correlation coefficients for the $A^2\Pi(v = 1)/B^2\Sigma^+(v = 0)$ states are given in Table 5.

Modeling the spectra greatly assisted in the assignment of quantum numbers, particularly in the case of the overlapped (1,0) $A^2\Pi - X^2\Sigma^+$ and (0,0) $B^2\Sigma^+ - X^2\Sigma^+$ band systems. Either a 4×12 or 4×8 *case* $a_{\beta J}$ transition moment matrix for the $A^2\Pi(v = 1)/B^2\Sigma^+(v = 0) - X^2\Sigma^+$ and (0,0) $A^2\Pi - X^2\Sigma^+$ band system, respectively, was constructed. The transition moment was obtained by cross multiplication of the transition matrix by the *case* $a_{\beta J}$ eigenvectors for the $X^2\Sigma^+$ and *case* $a_{\beta J}$ eigenvectors for either the $A^2\Pi(v = 0)$ or the $A^2\Pi(v = 1)/B^2\Sigma^+(v = 0)$ vibronic state. The transition mo-

© 2004 NRC Canada

Table 4. The determined spectroscopic parameters from the analysis of the (0,0) $A^2\Pi - X^2\Sigma^+$ band system transition wavenumbers (Table 1).[a]

Parameters	Value[b]	Correlation matrix[c]					
$A^2\Pi(v = 0)$							
A	80.326(2)	1.000					
B	4.31223(6)	–0.143	1.000				
A_D	–0.04990(14)	–0.756	0.091	1.000			
$p + 2q$	–0.88336(69)	–0.049	0.040	0.085	1.000		
q	–0.06753(17)	–0.095	–0.025	0.190	0.602	1.000	
$T_0(A^2\Pi)$	14 429.6365(11)	0.112	–0.777	–0.049	–0.002	0.031	1.000

[a]All units in wavenumbers (cm^{-1}).
[b]Numbers in parentheses represent a 2σ error estimate in the last quoted decimal point. The centrifugal distortion constant (D) was also held fixed to the value (= 1.896×10^{-4} cm^{-1}) given by Martin (16).
[c]Elements of the correlation matrix given in the order in which the parameters are presented.

Table 5. The determined spectroscopic parameters from the analysis of the (1,0) $A^2\Pi - X^2\Sigma^+$ and overlapped (0,0) $B^2\Sigma^+ - X^2\Sigma^+$ band systems transition wavenumbers (Tables 2 and 3).[a]

Parameters	Value[b]	Correlation matrix[c]									
$B(B^2\Sigma^+)$	4.41263(14)	1.00									
$\gamma(B^2\Sigma^+)$	–0.7957(12)	–0.22	1.00								
$\gamma_D(B^2\Sigma^+)$	0.00023(7)	–0.05	–0.82	1.0							
$A(A^2\Pi)$	80.256(2)	–0.08	0.07	–0.02	1.00						
$B(A^2\Pi)$	4.21144(7)	–0.27	0.11	0.04	0.08	1.00					
$A_D(A^2\Pi)$	–0.05064(15)	–0.10	0.02	0.04	–0.73	–0.28	1.00				
$p+2q(A^2\Pi)$	–0.9141(6)	–0.38	0.20	0.05	0.17	0.21	–0.10	1.00			
$q(A^2\Pi)$	–0.0626(4)	–0.63	0.33	0.07	0.17	0.20	0.08	0.63	1.00		
M_1	0.69239(15)	–0.70	0.38	0.05	0.12	0.36	0.13	0.54	0.90	1.00	
$T_0(B^2\Pi^+)$[d]	753.5881(11)	–0.66	0.15	–0.04	0.01	0.09	0.04	0.11	0.18	0.19	1.00
$T_1(A^2\Pi)$[d]	725.2329(8)	–0.15	0.11	–0.01	0.12	–0.65	0.18	0.15	0.29	0.22	0.03

[a]All units in wavenumbers (cm^{-1}).
[b]Numbers in parentheses represent a 2σ error estimate in the last quoted decimal point. The centrifugal distortion constant (D) for the $A^2\Pi(v = 1)$ and $B^2\Sigma^+(v = 0)$ states were held fixed to the values of 1.901×10^{-4} and 2.024×10^{-4} cm^{-1}, respectively, given by Martin (16).
[c]Elements of the correlation matrix given in the order in which the parameters are presented.
[d]Origin = T_v + 15 000 cm^{-1}.

ment was squared, multiplied by a Boltzmann factor, and a Lorentzian line shape was superimposed on each spectral feature and co-added.

Discussion

The (0,0) $A^2\Pi - X^2\Sigma^+$ band system

The standard deviation of the fit (= 0.004 cm^{-1}) is commensurate with the measurement uncertainties, demonstrating that the effective Hamiltonian operator method is adequate for modeling both the transition frequencies and relative intensities of the low rotational levels of the (0,0) $A^2\Pi - X^2\Sigma^+$ band system. This is in contrast to the findings of refs. 14 and 16, which explicitly include interaction terms evidently because of the inclusion of higher rotational levels. There are no local perturbations in the range of J' (<6.5) investigated. The optimized set of spectroscopic parameters of Table 5 produce term values for the $A^2\Pi(v = 0)$ state that differ from those given in ref. 14 by up to 0.16 cm^{-1} over the range probed. There is no systematic trend in these deviations. The standard deviation of the fit (0.004 cm^{-1}) is a reflection of the standard deviation of the calculated energy levels $A^2\Pi(v = 0)$ state because the ground-state energy levels are very accurately determined.

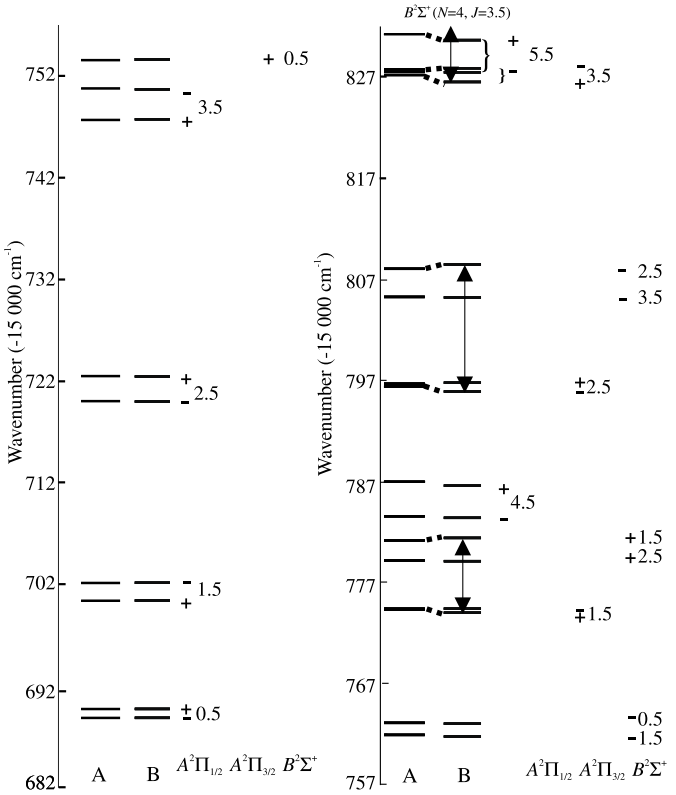
The Λ-doubling fitting parameters $p + 2q$ (= –0.88336(69) cm^{-1}) and q (= –0.06753(17) cm^{-1}) are in qualitative agreement of those predicted based upon second-order perturbation approximate expressions, which give –0.96 cm^{-1} and –0.077 cm^{-1}, respectively. The values of B and A from ref. 14 are (in cm^{-1}) 4.34769(4) and 79.01(2), which differ from those determined here of 4.31223(6) and 80.326(2), due presumably to the form of the effective Hamiltonian operator.

The overlapped (1,0) $A^2\Pi - X^2\Sigma^+$ and (0,0) $B^2\Sigma^+ - X^2\Sigma^+$ band systems

The standard deviation of the fit (= 0.003 cm^{-1}) is commensurate with the measurement uncertainties, indicating that the combination of using an effective Hamiltonian operator for the remote ($\Delta v = 0$) interactions and an inclusion of the explicit interaction terms for the local ($\Delta v = \pm 1$) interactions between $B^2\Sigma^+$ and $A^2\Pi$ vibronic levels is adequate for modeling the transition frequencies of the low rotational levels of the overlapped (1,0) $A^2\Pi - X^2\Sigma^+$ and (0,0) $B^2\Sigma^+ - X^2\Sigma^+$ band systems. The local perturbations are significant as

© 2004 NRC Canada

Fig. 9. The energy levels of the $B^2\Sigma^+(v = 0)$ and interacting $A^2\Pi(v = 1)$ vibronic states predicted using the optimized parameters of Table 5 without (*a*), and with (*b*), the inclusion of the M_1 term, which accounts for the local perturbations. The strong interactions are indicated by the double-headed arrows.



indicated in Fig. 9, where the predicted energy level diagram with and without the inclusion of the M_1 interaction term is presented. The strong interactions are indicated by double-headed arrows. The most marked effect of the $\Delta v = \pm 1$ interaction is an irregular Λ-doubling in the $A^2\Pi_{3/2}$ levels. A more subtle effect, which was noted by Martin (16), is the switching of the ordering of the Λ-doubling in the $A^2\Pi_{1/2}$ at about $J' = 9.5$.

There are many internal consistencies that demonstrate that the fitting parameters are physically meaningful. First, the Λ-doubling interactions for the $A^2\Pi(v = 1)$ state are very similar to those for the $A^2\Pi(v = 0)$ state, which lacks complication due to local perturbations. Second, the spin rotation parameter for the $B^2\Sigma^+(v = 0)$ follows the predicted relationship of eq. [5]. Finally, the change in the rotational constants for the $A^2\Pi(v = 1)$ and $A^2\Pi(v = 0)$ states is realistic.

Conclusions

After nearly a century since the first detection of CaH, the low rotational energy levels of the $A^2\Pi(v = 0$ and 1) state and the $B^2\Sigma^+(v = 0)$ states have been precisely (± 0.003 cm^{-1}) measured and modeled. The high-resolution LIF study of a molecular beam of CaH has been accomplished, which, along with the field-free frequencies, will facilitate optical Stark and Zeeman measurements that are currently in progress. Modeling of the $A^2\Pi(v = 0)$ state was successfully performed using a conventional effective Hamiltonian operator with a very limited number of terms. The determined spectroscopic parameters are physically meaningful. The energy levels of the $A^2\Pi(v = 1)/B^2\Sigma^+(v = 0)$ interacting system were successfully modeled using a hybrid approach of combining the effective Hamiltonian operator with explicit terms to account for local perturbations. The resulting parameters are consistent with those of the $A^2\Pi(v = 0)$ state. An interpretation of the anomalous intensity of the R_2 branch in the overlapped (1,0) $A^2\Pi - X^2\Sigma^+$ and (0,0) $B^2\Sigma^+ - X^2\Sigma^+$ band systems still needs to be made. This must be due to an intensity cancellation phenomena (33) and not predissociation or local perturbation by a yet to be identified state.

Acknowledgements

This work was supported by a grant from National Science Foundation-Experimental Physical Chemistry (CHE-0317130). The authors would like to thank Wilton Virgo and Professor John Brown (Oxford University) for their helpful discussion.

References

1. C.M. Olmsted. Astrophys. J. **27**, 66 (1908).
2. A. Eagle. Astrophys. J. **30**, 231 (1909).
3. R.S. Mulliken. Phys. Rev. **25**, 509 (1925).
4. E. Hulthén. Phys. Rev. **29**, 97(1927).
5. R.S. Mulliken and A. Christy. Phys. Rev. **38**, 87 (1931).
6. E.L. Hill and J.H. Van Vleck. Phys. Rev. **32**, 250 (1928).
7. J.H. Van Vleck. Phys. Rev. **33**, 467 (1929).
8. J. Brown and A. Carrington. Rotational spectroscopy of diatomic molecules. Cambridge University Press, Cambridge. 2003.
9. G. Herzberg. Spectra of diatomic molecules. Van Nostrand, Princeton. 1950.
10. L. Veseth. Mol. Phys. **20**, 1057 (1971).
11. L. Veseth. Mol. Phys. **21**, 287 (1971).
12. G. Liberale and S. Weniger. Physica, **41**, 27 (1969).
13. L.-E. Berg and L. Klynning. Astron. Astrophys. Suppl. Ser. **13**, 325 (1974).
14. L.-E. Berg and L. Klynning. Phys. Scr. **10**, 331 (1974).
15. L.-E. Berg, L. Klynning, and H. Martin. Opt. Commun. **17**, 320 (1976).
16. H. Martin. J. Mol. Spectrosc. **108**, 66 (1984).
17. J. Weinstein, R. deCarvalho, T. Guillet, B. Friedrich, and J.M. Doyle. Nature (London), **395**, 148 (1998).
18. B. Friedrich, J.D. Weinstein, R. deCarvalho, and J.M. Doyle. J. Chem. Phys. **110**, 2376 (1999).
19. S.V. Berdyugina and S.K. Solanki. Astron. Astrophys. **385**, 701 (2002).
20. G.C. Groenenboom and N. Balakrishnan. J. Chem. Phys. **118**, 7380 (2003).
21. N. Balakrishnan, G.C. Groenenboom, R.V. Krems, and A. Delagano. J. Chem. Phys **118**, 7386 (2003).
22. R. Pereira, S. Skowronek, A. González, Urana, A. Pardo, J.M.L. Poyato, and A.H. Pardo. J. Mol. Spectrosc. **212**, 17 (2002).
23. C.I. Frum, J.J. Oh, E.A. Cohen, and H.M. Pickett. Astrophys. J. **408**, L61 (1993).
24. W.L. Barclay, Jr., M.A. Anderson, and L.M. Zuirys. Astrophys. J. **408**, L65 (1993).

© 2004 NRC Canada

25. T.C. Steimle, T.P. Meyer, abnd Y. Al-Ramadin. J. Mol. Spectrosc. **125**, 225 (1987).
26. A. Shayesteh, K.A. Walker, I. Gordon, D.R.T. Appadoo, and P.F. Bernath. J. Mol. Structure, **695–696**, 23 (2004)
27. S.V. Berdyugina and S.K. Solanki. Astron. Astrophys. **385**, 701 (2002).
28. S. Gerstenkorn and P. Luc. Atlas du spectre d'absorption de la molécule de l'iode. Editions du C.N.R.S., Paris. 1978; Rev. Phys. Appl. **14**, 791 (1979).
29. S. Gerstenkorn, P. Luc, and R. Vetter. Rev. Phys. Appl. **16,** 529 (1981).
30. T.C. Steimle and W. Virgo. Chem. Phys. Lett. **381**, 30 (2003).
31. K. Namiki, S. Saito, J.C. Robinson, and T.C. Steimle. J. Mol. Spectrosc. **191**, 176 (1998).
32. H. Lefebvre-Brion and R.W. Field. Perturbations in diatomic molecules. Academic, Orlando, Fla. 1986.
33. A.J. Merer, U. Sassenberg, J.-L. Féménias, and G. Cheval. J. Chem. Phys. **86**, 1219 (1987).

© 2004 NRC Canada

"Spectrum-only" assignment of core-penetrating and core-nonpenetrating Rydberg states of calcium monofluoride[1]

Jeffrey J. Kay, Daniel S. Byun, Jason O. Clevenger, Xing Jiang, Vladimir S. Petrović, Robert Seiler, Jonathan R. Barchi, Anthony J. Merer, and Robert W. Field

Abstract: Rydberg states of calcium monofluoride in the n^* = 17–20 region have been observed by ionization-detected optical–optical double-resonance spectroscopy via the $D^2\Sigma^+$ v = 1 intermediate state. All members of the six core-penetrating Rydberg series in the n^* = 17–20 region and several components of the 17*f* and 17*g* core-nonpenetrating Rydberg states have been assigned. While the assignment of core-penetrating Rydberg states is straightforward without use of an effective Hamiltonian model, "spectrum-only" assignment of core-nonpenetrating states is complicated because strong ℓ-uncoupling causes the core-nonpenetrating states to evolve rapidly from Hund's case (b) to Hund's case (d) coupling. We describe "spectrum-only" assignment procedures, developed in the spirit of Gerhard Herzberg, that can be used to assign optical–optical double-resonance spectra of core-penetrating and core-nonpenetrating Rydberg states using only information contained in the spectrum rather than predictions derived from an effective Hamiltonian model. The ambiguities that arise in the assignment of each class of states are discussed in detail.

Key words: CaF, electric quadrupole moment, Rydberg states, laser spectroscopy.

Résumé : On a observé les états de Rydberg du monofluorure de calcium dans la région de n^* = 17–20, par le biais de l'état intermédiaire $D^2\Sigma^+$ v = 1, en faisant appel à spectroscopie de double résonance optique-optique détectée par ionisation. On a attribué tous les membres des six séries de Rydberg pénétrant le coeur, dans la région de n^* = 17–20, ainsi que plusieurs composants des états 17*f* et 17*g* de Rydberg ne pénétrant pas le coeur. Alors que l'attribution des états de Rydberg pénétrant le coeur peut se faire facilement sans avoir recours à l'utilisation d'un modèle à hamiltonien effectif, l'attribution uniquement sur la base du spectre des états ne pénétrant pas le coeur est compliquée par le fait que le fort découplage ℓ amène les états ne pénétrant pas le coeur à se transformer rapidement d'un couplage de Hund d'un type (b) à un type (d). On décrit une méthode d'attribution des états qui se fait sur la base uniquement du spectre, qui a été développée dans l'esprit de Gerhard Herzberg, qui peut être utilisée pour attribuer les spectres de double résonance optique-optique d'états de Rydberg pénétrant ou ne pénétrant pas le coeur et qui ne fait appel qu'aux informations contenues dans le spectre plutôt qu'aux prédictions obtenues à partir d'un modèle à hamiltonien effectif. On discute en détail des ambiguïtés rencontrées dans l'attribution de chacune des classes d'état.

Mots clés : CaF, moment quadripolaire électrique, états de Rydberg, spectroscopie laser.

[Traduit par la Rédaction]

Introduction

Characterization of the mechanisms of electron ↔ nuclear energy exchange is central to the development of global models of molecular electronic structure and intramolecular dynamics. Molecular Rydberg states are instructive because the orbital and precessional motions of a single electron are weakly coupled to the rotational and vibrational motions of the molecular ion core (1–18). Because of this weak coupling, and because the frequencies of electronic and rotational motions are systematically adjustable, it is possible to tune specific motions of these two molecular subsystems into resonance. Observation of resonances, through spectroscopic perturbations between electronic and nuclear motions, allows for measurement of the coupling strengths between molecular subsystems, namely the multipole moments and

Received 23 February 2004. Published on the NRC Research Press Web site at http://canjchem.nrc.ca on 25 August 2004.

J.J. Kay, D.S. Byun, J.O. Clevenger,[2] X. Jiang, V.S. Petrović, R. Seiler,[3] J.R. Barchi, and R.W. Field.[4] Department of Chemistry, Massachusetts Institute of Technology, Cambridge, MA 02139, USA.
A.J. Merer. Department of Chemistry, University of British Columbia, 2036 Main Mall, Vancouver, BC V6T 1Z1, Canada.

[1]This article is part of a Special Issue dedicated to the memory of Professor Gerhard Herzberg.
[2]Present address: Applied Materials, 3050 Bowers Avenue, Santa Clara, CA 95054, USA.
[3]Present address: ETH, Physical Chemistry Lab, CH-8093 Zurich, Switzerland.
[4]Corresponding author (e-mail: rwfield@mit.edu).

 doi: 10.1139/V04-071 © 2004 NRC Canada

polarizabilities of the ion core. These are the fundamental mechanisms by which electrons communicate with nuclei at long range.

The alkaline-earth monohalides (especially CaF, CaCl, and BaF) are important in the context of electron ↔ nuclear energy exchange because they have the largest multipole moments of any class of molecules studied to date (19, 20). Because the ion-core multipole moments are so large, the signatures of electron ↔ nuclear interactions are easily recognizable. However, the Rydberg states that appear in the spectra of these molecules are often severely intertwined, and many nominally allowed rotational transitions that terminate on these states are unexpectedly and systematically weak. Disentanglement of the spectra of these Rydberg states by rigorous spectral assignment procedures is a necessary prerequisite for the location of perturbations and comparison of experimental data with the predictions of theoretical models. Assignment of states based exclusively on information contained in the spectrum, as opposed to an assumed effective Hamiltonian model, minimizes possibilities for misidentification of states. "Spectrum-only" assignment also facilitates detection of tiny level shifts and splittings and circumvents some ambiguities associated with overly flexible effective Hamiltonian and multichannel quantum defect theory (MQDT) fit models. The Rydberg states of the alkaline-earth monohalides have been described (21–27) as simple two-body systems consisting of a single optically active electron weakly bound to a closed-shell $^1\Sigma^+$ molecular ion core. The electronic energies of each of the Rydberg states may be expressed by a modified Rydberg formula,

$$[1] \qquad E_{n^*,v^+,N^+} = \mathrm{IP}_{v^+,N^+} - \frac{RZ^2}{n^{*2}}$$

where n^* is the effective principal quantum number (given by $n^* = n - \delta$, where n is an integer and δ is the quantum defect), IP_{v^+,N^+} is the energy of the v^+, N^+ state of the ion core, E_{n^*,v^+,N^+} is the Rydberg energy, R is the Rydberg constant, and Z is the integer charge of the ion core. Molecular Rydberg orbitals may be divided into two classes: "core-penetrating" and "core-nonpenetrating". A Rydberg orbital may be classified as core-penetrating or core-nonpenetrating based on the location of the inner lobe of the Rydberg electron wave function relative to the spatial extent of the ion core r_{core}, defined as the distance from the molecular center of mass to the far side of the more distant atom (treated as a hard-sphere atomic ion) (28). The location of the inner lobe of the electronic wave function may be estimated by approximating the ion-core potential as a hydrogen atom effective radial potential:

$$[2] \qquad V_{\mathrm{eff}}(r) = -\frac{1}{r} + \frac{\ell(\ell+1)}{2r^2}$$

where ℓ is the electronic angular momentum quantum number and r is the distance between the Rydberg electron and the ion-core center of mass. The location of the inner lobe of the electronic wave function is determined by the inner turning point of $V_{\mathrm{eff}}(r)$. Rydberg orbitals are termed "core-penetrating" when the inner lobe of the electronic wave function lies within the spatial extent of the ion core, and "core-nonpenetrating" when the inner lobe is excluded from the core. For example, the inner turning point of $V_{\mathrm{eff}}(r)$ for $n = 3$, $\ell = 2$ occurs at approximately 3.8 au, whereas the inner turning point for $n = 4$, $\ell = 3$ occurs at approximately 8.0 au. For CaF^+, r_{core} is approximately 5.1 au. This indicates that CaF Rydberg orbitals derived from basis states with $\ell \leq 2$ will penetrate the core significantly. Owing to penetration of the core, these orbitals experience the nonspherical electric field of the ion core at short range, resulting in s~p~d mixed character. Orbitals derived from $\ell \geq 3$ basis states do not penetrate the core (with the exception of $f\sigma$) and therefore sample the ion-core electric field exclusively at long range. Core-nonpenetrating orbitals retain nearly pure ℓ character.

That these two classes of Rydberg states experience the ion core profoundly differently is reflected by their angular momentum coupling case, which in turn determines the rotational pattern exhibited by these states in a spectrum (29–32). The core-penetrating states, which include the energetically low-lying Rydberg terminus (or valence) states, are well described in the Hund's case (b) basis set, $|\lambda NSJ\rangle$, in which ℓ is not a good quantum number but λ, the projection of $\vec{\ell}$ along the internuclear axis, remains well defined, and N (total angular momentum apart from spin) is the rotational pattern-forming quantum number. The rotational energy of case (b) states is given by $E_{\mathrm{rot}} = BN(N+1) - \lambda^2$. In contrast, the core-nonpenetrating states are well described in the Hund's case (d) basis set, $|\ell NN^+SJ\rangle$, in which ℓ remains an approximately good quantum number, and N^+ (the total angular momentum of the ion core exclusive of spin) is the rotational pattern-forming quantum number.

Because the core-penetrating states are described in the Hund's case (b) basis and the valence intermediate states from which the Rydberg states are excited are described in either the case (a) or case (b) basis, the core-penetrating states appear in double-resonance spectra in rotational patterns that are relatively simple. Thus, the spectra may be assigned using the traditional method of lower-state rotational combination differences. The ability to assign core-penetrating states in double-resonance spectra by lower-state rotational combination differences is facilitated by the fact that Rydberg states are always excited from an a priori known rotational and e/f-symmetry level of the intermediate valence state. Rigorous assignment is frustrated only when multiple rotational transitions to a common upper state are unobservable because of systematic intensity effects.

The assignment of core-nonpenetrating states is complicated by the fact that the core-nonpenetrating states are better described in Hund's case (d) coupling case. In previous double-resonance studies (33) of the CaF ($n^* = 13$–14 and 17–18) Rydberg states, difficulties were encountered in the rotational assignments of the core-nonpenetrating states because the Rydberg states were excited from either the A or C intermediate state, both of which are case (a) $^2\Pi$ states. Often, the lowest rotational levels of the A and C states could not be accessed owing to spectral congestion, and many transitions terminating on core-nonpenetrating states are naturally weak because the $\Delta N = \Delta N^+$ propensity rule is not satisfied. To overcome this difficulty, we have recorded optical–optical double-resonance spectra of the Rydberg states of CaF in the $n^* = 17$–20 region using the case (b)

© 2004 NRC Canada

$D^2\Sigma^+$ state as the intermediate state. The present data set, which extends further in n^* and higher in rotation than previous data sets, also features factor of 3 improvements in spectral resolution and wavenumber precision and an increase in dynamic range. The increased precision and dynamic range afforded by the present data set has facilitated detection of numerous perturbations and long series of weak transitions that had previously been unobservable. This has led to reassignment of several components of the 17*f* and 17*g* nonpenetrating states.

Experimental

The experimental apparatus consists of a laser ablation/molecular beam source coupled to a time-of-flight mass spectrometer, housed in separate "source" and "detection" chambers. The source and detection chambers are separately pumped. A molecular beam of calcium monofluoride is produced in the source chamber by direct reaction of calcium vapor with fluoroform. A 350-μs pulse of 5% CHF_3 in He formed by a pulsed nozzle (General Valve Series 9, 0.5 mm orifice, 40 psi stagnation pressure, 20 Hz duty cycle) is synchronized with the pulsed production of a calcium plasma formed by laser ablation of a 1/4" diameter calcium rod by the third harmonic of a pulsed Nd:YAG laser (Spectra Physics GCR-130, 5–7 ns pulse, 7 mJ/pulse, 20 Hz repetition rate). The duration of the fluoroform pulse and the energy of the ablation laser are both adjusted to optimize the production of CaF and to reduce the amount of unreacted calcium. The dominant ions observed are Ca^+ (m/z = 40) and CaF^+ (m/z = 59), and no other ions with greater than 5% of the intensity of CaF^+ are observed. The rotational temperature of the molecular beam is ~30 K. The molecular beam is collimated by a 0.5-mm conical skimmer placed between the source and detection chambers, and again by a 3.0-mm skimmer prior to entering the excitation region of the detection chamber. Autoionizing Rydberg states are excited in the detection chamber by two collinear laser beams that intersect the molecular beam at a 90° angle. The CaF^+ ions that result from autoionization are accelerated down the 75-cm flight tube of the mass spectrometer by a 250-V electric field pulse that arrives 200 ns after the laser excitation pulse. Ions are detected by two microchannel plates (Burle Electro-optics, 10 μm channel diameter, 12 μm channel spacing) arranged in a chevron configuration. The ion signals are amplified by a low-noise voltage amplifier (FemtoAmp, 30 dB gain, 30 MHz low-pass filter) and averaged over 40 shots by a LeCroy 300-MHz digital oscilloscope. The ion extraction assembly is contained within a Ni-plated shroud to isolate the excitation region from stray electric fields.

Autoionizing CaF Rydberg series in the n^* = 17–20 region, converging to the v = 1 level of the ion core, were accessed by two-step excitation through the $D^2\Sigma^+$ intermediate state. Pump and probe laser pulses were produced by two pulsed dye lasers (Lambda Physik Scanmate 2E, <10 ns, 0.03 cm^{-1} fwhm) simultaneously pumped by the second harmonic of a single Nd:YAG laser (Spectra Physics GCR-290, 5–7 ns pulse, 2 × 80 mJ/pulse). The first dye laser, operating with DCM and equipped with a β-BBO frequency-doubling crystal, was tuned to a single rotational line of the $D^2\Sigma^+ \leftarrow X^2\Sigma^+$ transition. Due to unresolved spin structure, this apparently single rotational line terminates on two same-parity $J = N + 1/2$ and $J = N - 1/2$ levels. The second dye laser, operating with Rhodamine B, stimulates Rydberg $\leftarrow D^2\Sigma^+$ transitions and was swept in frequency across the n^* = 17–20 region. The two laser pulses were separated in time by approximately 10 ns to prevent undesired multiphoton transitions. The frequencies of the pump and probe laser pulses were calibrated by simultaneously recording high-temperature absorption and room-temperature fluorescence spectra of molecular iodine, respectively. The Rydberg states studied here have one quantum of ion-core vibration and lie above the $v^+ = 0$ ionization threshold, and transitions into these states are detected through CaF^+ ions produced by vibrational autoionization. Spectra in the n^* = 17, 18, and 20 regions were recorded using each of the N = 1–9 rotational levels of the $D^2\Sigma^+$ state as intermediates, and spectra in the n^* = 19 region were recorded using the N = 1–25 rotational levels of the $D^2\Sigma^+$ state as intermediates.

Results and discussion

Assignment of core-penetrating states

The $D^2\Sigma^+$ intermediate state and the six core-penetrating upper states are known from previous studies (6, 7) to be well described in terms of Hund's case (b) basis states, $|\lambda NSJ\rangle$. The case (b) – case (b) optical selection rules (34) are

$$[3] \qquad \Delta J = 0, \pm 1; \qquad \Delta\lambda = 0, \pm 1$$

A schematic energy level diagram with allowed $^2\Sigma^+ \leftarrow {}^2\Sigma^+$ and $^2\Pi \leftarrow {}^2\Sigma^+$ transitions is shown in Fig. 1. Branches are designated by $^{\Delta N}\Delta J$ (read "ΔN-form ΔJ"; e.g., "P-form Q"). Since the spin structure of the $D^2\Sigma^+ \leftarrow X^2\Sigma^+$ transitions is not resolvable, Rydberg states are simultaneously excited from both the $J = N + 1/2$ and $J = N - 1/2$ levels of the $D^2\Sigma^+$ state. Initial tests for partial resolution of spin splittings, involving excitation of Rydberg states from either the higher- or lower-energy side of a $D^2\Sigma^+ \leftarrow X^2\Sigma^+$ rotational line, failed to produce noticeable intensity effects in the spectra, and the Rydberg $\leftarrow D^2\Sigma^+$ spectra show no evidence of systematic spin-doubling. This unresolved spin structure of both the upper and lower states leads to the collapse of the $^{\Delta N}\Delta J$ branches into simple ΔN-form branches. Only the N, N^+ (not J) rotational structure of Rydberg states is resolvable (see Fig. 2). The observed term values for the n^* = 16 and n^* = 17 core-penetrating states of CaF are listed in Table 1.

Since each rotational level N' of $^2\Sigma^+$ and $^2\Pi$ core-penetrating states is nominally accessible from at least two rotational levels of the $D^2\Sigma^+$ state, it is reasonable to attempt rotational assignment of the core-penetrating states based exclusively on lower-state rotational combination differences. Lower-state combination differences are identified by plotting the spectra recorded from each of the rotational levels of the $D^2\Sigma^+$ intermediate state against their upper-state term values, which are the sum of the Rydberg $\leftarrow D^2\Sigma^+$ transition frequencies and the term value of the $D^2\Sigma^+$ rotational state from which they are recorded. The "term value" spectra are then stacked vertically, in order of increasing N'', and compared against each other to locate lines on separate spectra with identical term values. The observation of two or more lines with the same upper-state term value (the same

© 2004 NRC Canada

Fig. 1. Schematic energy level diagram showing allowed $^2\Sigma^+ \leftarrow {}^2\Sigma^+$ and $^2\Pi \leftarrow {}^2\Sigma^+$ transitions with resolved spin structure. Branches are labeled by $^{\Delta N}\Delta J$.

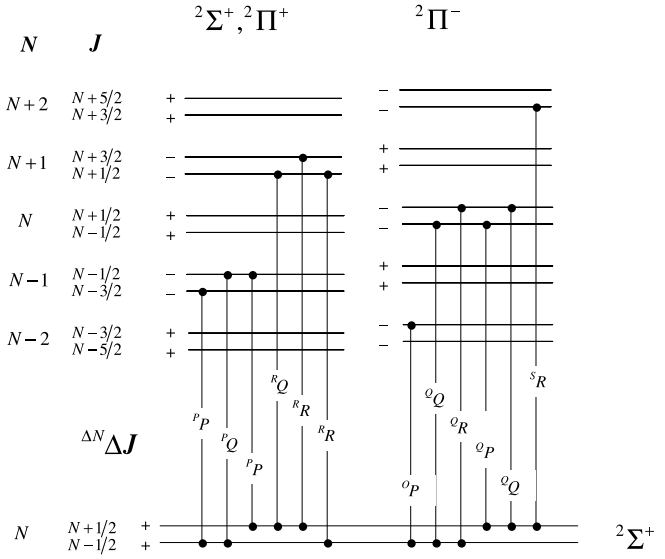
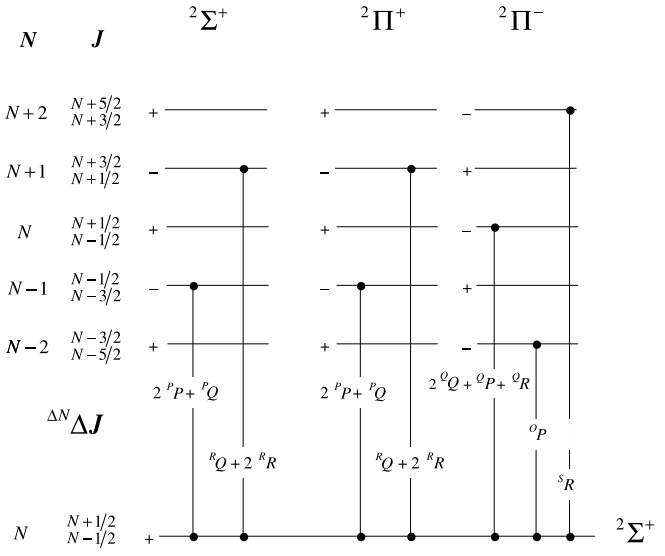


Fig. 2. Schematic energy level diagram showing allowed $^2\Sigma^+ \leftarrow {}^2\Sigma^+$ and $^2\Pi \leftarrow {}^2\Sigma^+$ transitions with unresolved spin structure.



vertical position on the term value stacked plot) suggests the occurrence of transitions from two or more $D^2\Sigma^+$ state rotational levels to a common upper state rotational level. Figure 3 shows the possible combination differences for $^2\Sigma^+ \leftarrow {}^2\Sigma^+$ and $^2\Pi \leftarrow {}^2\Sigma^+$ transitions. Rotational levels of $^2\Sigma^+$ and $^2\Pi^+$ core-penetrating states are each accessible from two rotational levels of the $D^2\Sigma^+$ state, and rotational levels of $^2\Pi^-$ core-penetrating states are accessible from three rotational levels of the $D^2\Sigma^+$ state. However, in our spectra, lower-state rotational combination differences are only observed between *at most* two states on N'' and $N''+2$ spectra (see Fig. 4), indicating that these states are populated by either O- and Q-, P- and R-, or Q- and S-form transitions. Many of the observed upper states do not exhibit lower-state

Table 1. Observed term values for the $n^* = 16$–17 core-penetrating states of CaF.

N	16.36 Π^+	16.36 Π^-	16.55 Σ^+	16.88 Σ^+	16.98 Π^+	16.98 Π^-	17.14 Δ^+	17.19 Σ^+	17.36 Π^+	17.36 Π^-	17.55 Σ^+
0				47 300.47							
1			47 285.20	47 301.18		47 306.94				47 321.68	47 330.32
2		47 275.94	47 286.09	47 302.46	47 307.89	47 308.01	47 314.15	47 315.70	47 324.51	47 323.34	47 331.68
3	47 278.22	47 277.55	47 287.51	47 304.31	47 309.93	47 309.81	47 316.58	47 318.09	47 327.40	47 325.74	47 334.17
4	47 281.38	47 279.86	47 289.81	47 306.90	47 312.43	47 312.36	47 319.73	47 320.99	47 331.76	47 328.91	47 337.33
5	47 285.56	47 283.02	47 292.91	47 309.82	47 315.67	47 315.84	47 323.58	47 324.85	47 336.77	47 332.97	47 341.38
6	47 290.05	47 287.01	47 296.71	47 313.53	47 319.67	47 319.82	47 328.46	47 329.51	47 342.62	47 337.72	47 345.83
7	47 295.72	47 291.76	47 301.33		47 324.29	47 324.66	47 333.90	47 334.75	47 348.98	47 343.29	47 351.49
8	47 302.19	47 297.13	47 306.49	47 322.93	47 329.74	47 330.07	47 340.15	47 340.87	47 355.79	47 349.71	
9	47 309.40	47 303.43	47 312.94	47 328.64		47 336.23	47 347.17	47 347.76		47 356.95	
10	47 317.19	47 310.53		47 335.00							

© 2004 NRC Canada

Fig. 3. Schematic energy level diagram showing transitions into $^2\Sigma^+$ and $^2\Pi$ states from different rotational levels of the $D^2\Sigma^+$ intermediate state.

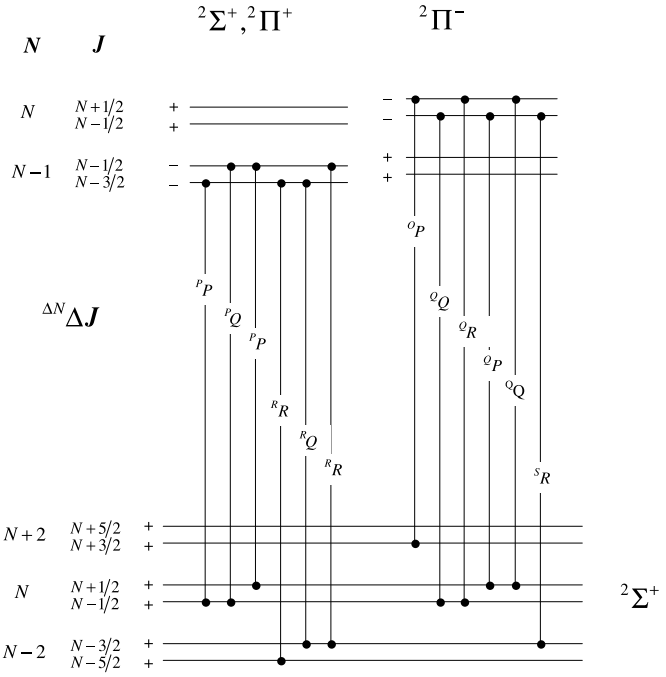


Fig. 4. "Term value" stacked plot: double-resonance spectrum plotted against upper-state term value. Combination differences are indicated with dashed lines.

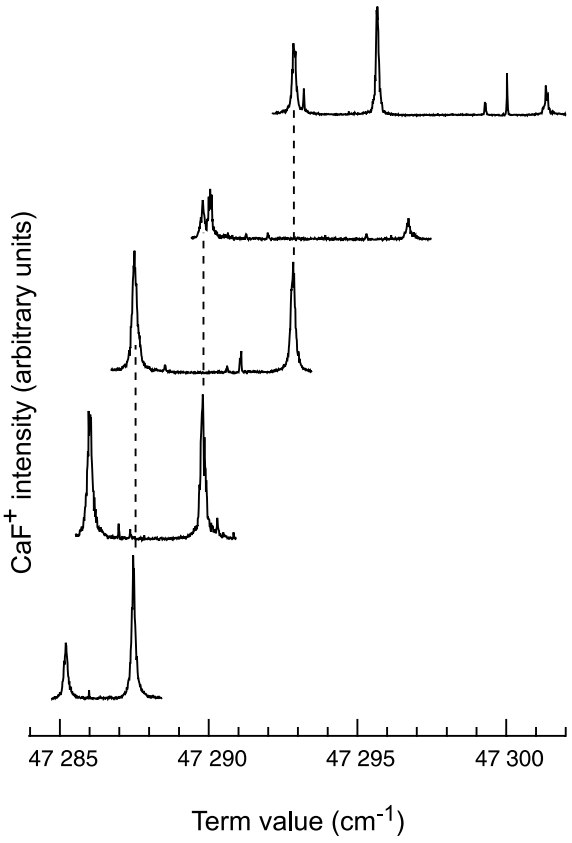
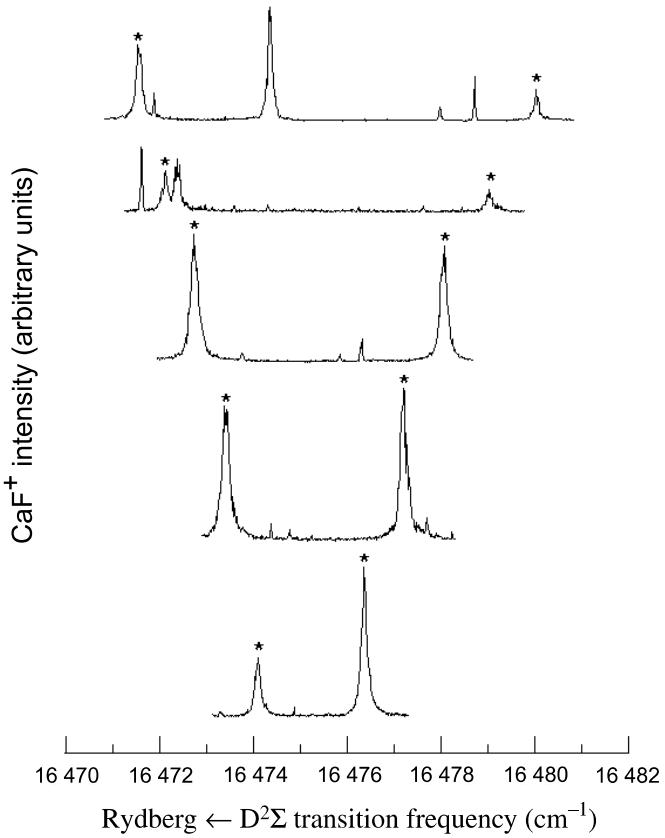


Fig. 5. "Raw spectrum" stacked plot: double-resonance spectrum plotted against Rydberg ← $D^2\Sigma^+$ transition frequency.



rotational combination differences. Rotational assignment is more secure for upper states that exhibit lower-state rotational combination differences, and these states are analyzed first.

Following identification of all bona fide combination differences, the spectra were replotted against the observed Rydberg ← $D^2\Sigma^+$ transition frequency and stacked vertically in order of increasing N'' to enable organization of the transitions into rotational branches (see Fig. 5). The transition frequencies of the members of the thus identified Rydberg ← $D^2\Sigma^+$ rotational branches were each fit to a polynomial in N'' to determine $\Delta N = N'' - N'$ for each branch. The difference $\Delta N = N'' - N'$ may be derived from the polynomial fit based on the difference in rotational energy between the $D^2\Sigma^+$ state and the core-penetrating states:

$$[4] \qquad \Delta E_{\text{rot}} = \nu_0 + B'\mathrm{N}'(N' + 1) - B''N''(N'' + 1)$$

The difference in rotational energies is related to the Rydberg ← $D^2\Sigma^+$ transition frequency through

$$[5] \qquad \Delta E_{\text{Rydberg}\leftarrow D^2\Sigma^+} = \Delta E_{\text{el}} + \Delta E_{\text{vib}} + \Delta E_{\text{rot}}$$

Hence

$$[6] \qquad \Delta E_{\text{Rydberg}\leftarrow D^2\Sigma^+} = \Delta E_{\text{rot}} + \text{const.}$$

where the constant on the right is independent of N. Substituting eq. [4] into eq. [6] and using the relation $N' = N'' + \Delta N$,

© 2004 NRC Canada

$$[7]\quad \Delta E_{\text{Rydberg}\leftarrow D^2\Sigma^+} = B'(N'' + \Delta N)(N'' + \Delta N + 1) - B'' N''(N'' + 1)$$

Expanding eq. [7],

$$[8]\quad \Delta E_{\text{Rydberg}\leftarrow D^2\Sigma^+} = N''^2(B' - B'') + N''(B'(2\Delta N + 1) - B'') + B'((\Delta N)^2 + \Delta N)$$

Since N'' is known a priori from the N-selectivity of the first step of the double-resonance excitation and B'' is known from previous rotational analyses of the $D^2\Sigma^+$ state (35), the linear term of eq. [8] yields the difference in rotational quantum number $\Delta N = N' - N''$ and the quadratic term yields the effective rotational constant, B', of the upper state. The rotationless upper-state quantum defects, δ, are then calculated from eq. [1] using the independently determined ionization thresholds of the $v^+ = 1$ or $v^+ = 2$ levels of the ion core (47 686 and 48 369 cm^{-1}, respectively) to establish membership in core-penetrating series converging to the $v^+ = 1$ and $v^+ = 2$ vibrational levels of the ion core. The calculated values of ΔN and B' and comparisons of the calculated rotationless quantum defects with the known quantum defects of the core-penetrating states allow many of the branches that are linked by lower-state rotational combination differences to be conclusively assigned as P- and R-form branches terminating on $v^+ = 1$ and $v^+ = 2$ core-penetrating states.

The fact that O-, Q-, and S-form branches were not observed to be linked to the assigned P- and R-form branches through lower-state combination differences reveals the presence of interactions that lift the degeneracy of the nominally near-degenerate positive and negative Kronig symmetry components. A systematic examination of the spectra of assigned core-penetrating states for evidence of nearby O-, Q-, or S-form branches showed additional branches consisting of strong, broad lines in the vicinity of the 0.36 $^2\Pi$ and 0.14 $^2\Delta$ states. A fit of the observed transition frequencies to the polynomial in eq. [8] indicated that these branches are Q-form branches, and extrapolation of the upper-state term values to $N = 0$ indicated that these branches terminate on the negative Kronig symmetry components of the 0.36 $^2\Pi$ and 0.14 $^2\Delta$ states. However, no O- or S-form branches terminating on the negative Kronig symmetry components of the 0.36 $^2\Pi$ or 0.14 $^2\Delta$ states could be located. This is likely due to the weakness of $\Delta N = 2$ case (b) – case (b) transitions, which are predicted to be weaker than $\Delta N = 1$ transitions (36). Although it was not possible to rigorously assign the negative Kronig symmetry components of the 0.36 $^2\Pi$ or 0.14 $^2\Delta$ states through lower-state rotational combination differences, the assignments are considered to be secure because no other rotational branches are expected to be present outside of the near-integer-n^* region. It has not been possible to securely assign any transitions as terminating on the negative Kronig symmetry components of the 0.98 $^2\Pi$ states as they lie very close to the integer-n^* region and likely overlap and (or) are perturbed by core-nonpenetrating states.

Assignment procedure for core-nonpenetrating states

Owing to strong ℓ-uncoupling interactions, the core-nonpenetrating states of CaF evolve rapidly from Hund's case (b) to Hund's case (d), and at even moderate N ($N = 8$), the core-nonpenetrating states are better described by Hund's case (d) basis states, $|\ell N^+ N \ell_R\rangle$. Core-nonpenetrating states are labeled by $n\ell(\ell_R)^{\pm}$ (e.g., $17f(-3)^+$), where ± refers to the σ_v reflection symmetry (Kronig symmetry) of the state and $\ell_R = N - N^+$. The case (d) – case (b) selection rules depend on the mechanism by which the core-nonpenetrating states are accessed from the $D^2\Sigma^+$ intermediate state. One mechanism by which core-nonpenetrating state $\leftarrow D^2\Sigma^+$ transitions are observed is based on the partial-ℓ composition of the $D^2\Sigma^+$ state. If the $D^2\Sigma^+$ state has significant $\ell = 2$ character, for example, it is possible to observe strong transitions to f states. In this case, the case (d) – case (b) selection rules are (37, 38)

$$[9]\quad \Delta N = 0, \pm 1;\quad N^{+\prime} = |\, N'' - \ell'' \,| \ldots |\, N'' + \ell'' \,|;\quad \pm \leftrightarrow \mp$$

Here, ℓ'' is the ℓ-value of the mixed-ℓ intermediate state that provides intensity for the transition into the core-nonpenetrating state, and ± is the overall parity of the molecular wave function, which in case (d) is $(-1)^{N^+ + \ell}$. Core-nonpenetrating states may also be excited due to intensity borrowing from nearby core-penetrating states. In this case, the selection rules are

$$[10]\quad \Delta N = 0, \pm 1; \qquad \pm \leftrightarrow \mp$$

All N^+ rotational states with $|\ell_R| = |\, N - N^+ \,| \leq \ell$ are accessible in this case, provided that the $\Delta N = 0$ core-penetrating ~ core-nonpenetrating interactions are strong enough to transfer significant intensity into the core-nonpenetrating state. A schematic energy level diagram is shown in Fig. 6. Owing to the selection rules on total parity outlined above, only odd (even) rotational levels of even-ℓ (odd-ℓ) states are accessible from odd (even) N levels of the $D^2\Sigma^+$ state. For example, the $N^+ = 3$ level of a g state is inaccessible from the $N = 3$ level of the $D^2\Sigma^+$ state. Because of this parity restriction, many rotational levels of a core-nonpenetrating state are accessible from only one rotational level of the $D^2\Sigma^+$ state, and not all core-penetrating rotational levels can be rigorously assigned through lower-state rotational combination differences. The observed term values for the $n^* = 17$ core-nonpenetrating states of CaF are listed in Table 2.

An attempt was made to determine the change in pattern-forming quantum number, $\Delta Q = N^{+\prime} - N''$, from a fit of the Rydberg $\leftarrow D^2\Sigma^+$ transition frequencies, just as was done for the core-penetrating states. Substituting $\Delta Q = N^{+\prime} - N''$ for $\Delta N = N' - N''$, one may derive an expression similar to eq. [8]:

$$[11]\quad \Delta E_{\text{Rydberg}} \leftarrow D^2\Sigma^+ = N''^2(B' - B'') + N''(B'(2\Delta Q + 1)) - B''((\Delta Q)^2 + \Delta Q)$$

However, for many of the branches, the calculated value of ΔQ turns out to be nearly half-integral. The reason for non-integer values of ΔQ is that ℓ-uncoupling is incomplete at low rotation. To demonstrate the effect of incomplete ℓ-uncoupling on the value of ΔQ obtained from a polynomial fit to eq. [11], an effective Hamiltonian was constructed. This Hamiltonian is identical to the effective Hamiltonian in

© 2004 NRC Canada

Fig. 6. Schematic energy level diagram showing allowed core-nonpenetrating state ← $D^2\Sigma^+$ transitions.

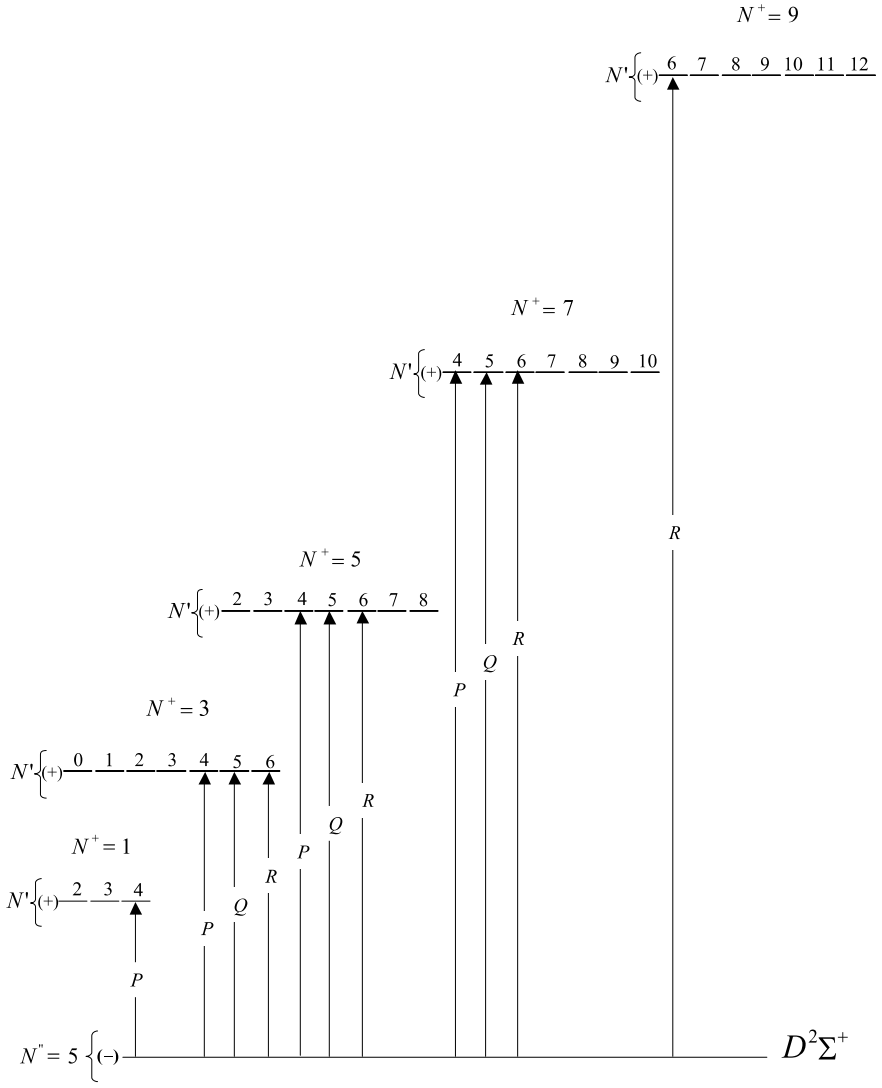


Table 2. Observed term values for n^* = 17 core-nonpenetrating series.

N	17f(0)	17f(–1)	17f(–2)	17f(–3)	17g(0)	17g(–1)	17g(–4)
1							
2	47 307.34	47 313.17		47 317.59			
3	47 309.24	47 316.36	47 317.68	47 320.20	47 313.18		47 323.15
4	47 311.95	47 320.43	47 321.74	47 323.67	47 316.71	47 317.39	47 328.50
5	47 315.53	47 325.36	47 326.78	47 328.15	47 321.07	47 322.02	47 334.23
6		47 330.97	47 332.42	47 333.29	47 326.04	47 327.03	47 340.57
7		47 337.31	47 338.87	47 339.16	47 332.10	47 332.83	47 347.27
8		47 344.32	47 345.94	47 345.59			
9			47 353.77	47 352.77			

ref. 6 and will only be discussed briefly here. The effective Hamiltonian is divided into diagonal and off-diagonal terms:

[12] $H = H^{(0)} + \mathrm{H}^{(1)}$

where

[13] $H^{(0)} = H_{\mathrm{el}} + H_{\mathrm{rot}}$

and

[14] $H^{(1)} = H_{\ell\text{-uncoupling}}$

Here, H_{el} is the electronic Hamiltonian and consists of the hydrogen-atom Hamiltonian and electric dipole and quadrupole interaction terms. Its eigenvalues are

© 2004 NRC Canada

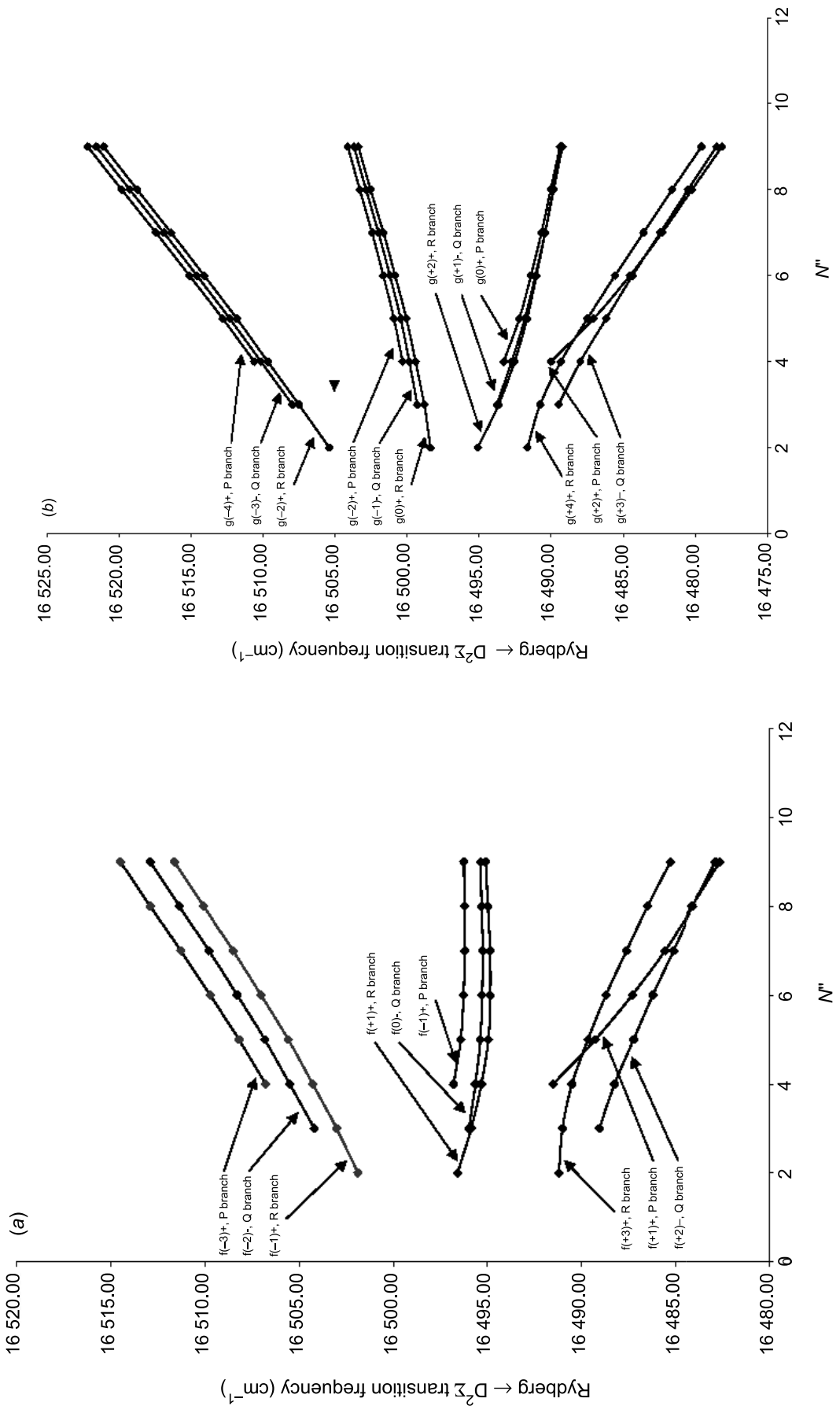
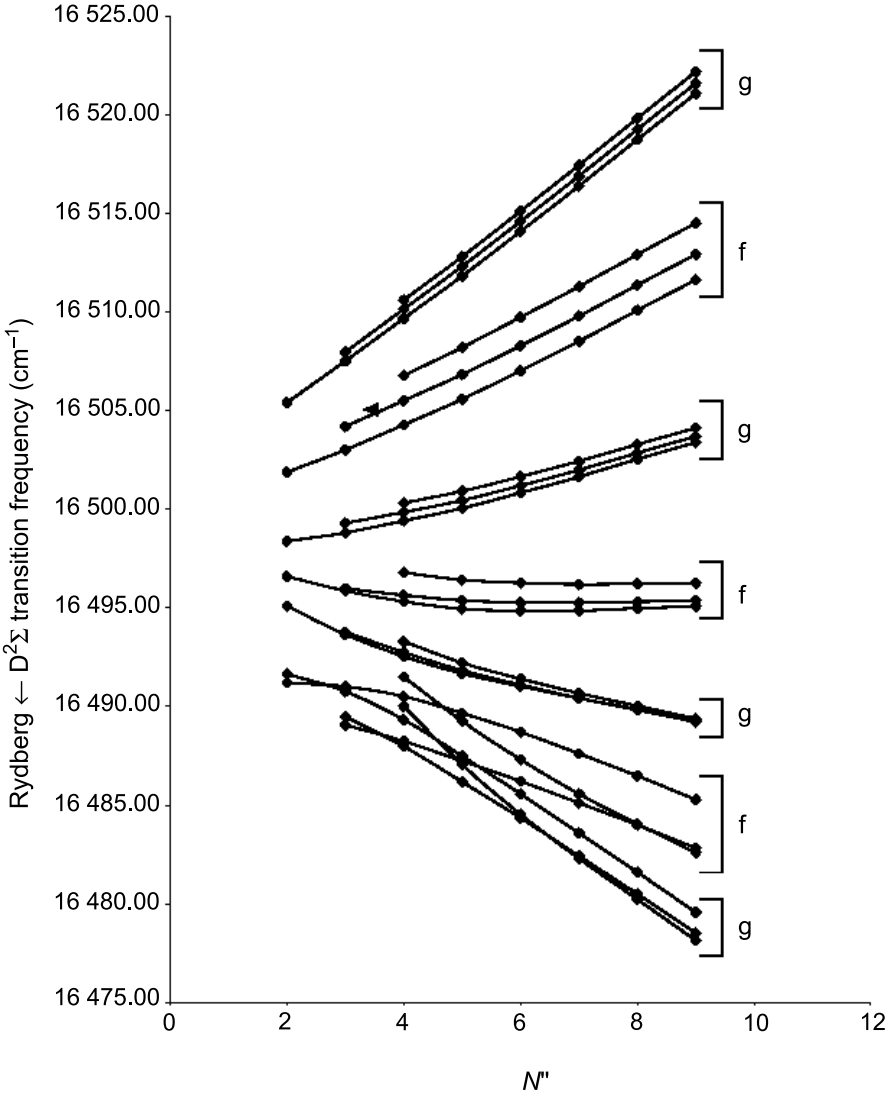


Fig. 7. Calculated Rydberg ← $D^2\Sigma^+$ transition frequencies plotted against N'': (*a*) $17f$ states; (*b*) $17g$ states.

© 2004 NRC Canada

Fig. 8. Superposition of $17f \leftarrow D^2\Sigma^+$ and $17g \leftarrow D^2\Sigma^+$ transitions. Note interleaving of opposite-parity N^+ clusters.



$$[15] \quad H_{\text{el}} = \left(\text{IP}_v - \frac{1}{n^2}\right) + \frac{2Z^2(\mu^2 - Q)(\ell(\ell+1) - 3\lambda^2)}{n^3(2\ell+3)(2\ell+1)(2\ell-1)\ell(\ell+1)}$$

The second term in eq. [13], H_{rot}, is the case (b) rotational Hamiltonian and has eigenvalues

$$[16] \quad H_{\text{rot}} = B(N(N+1) + \ell(\ell+1) - 2\lambda^2)$$

$H^{(1)}$ is the off-diagonal portion of the ℓ-uncoupling operator

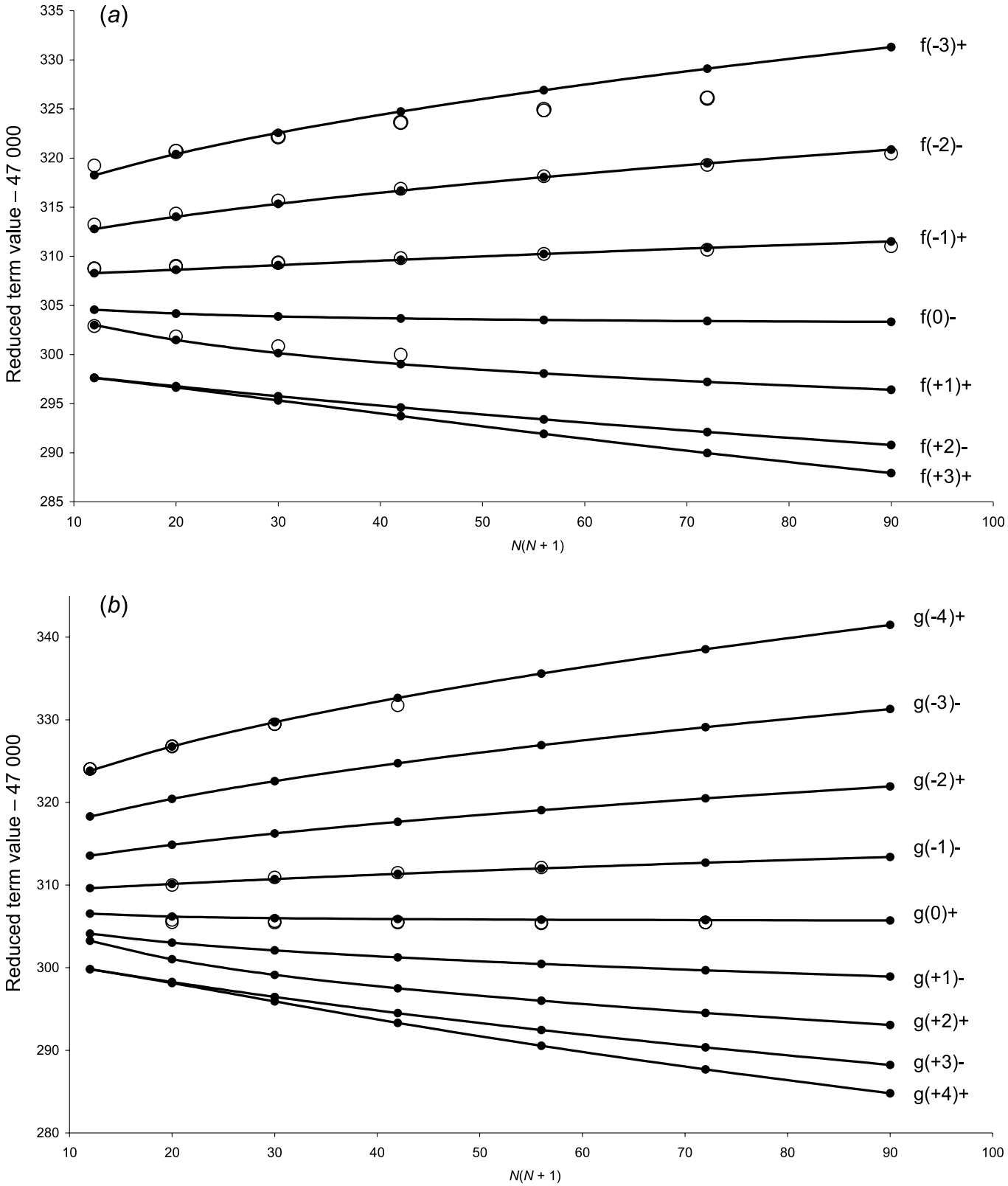
$$[17] \quad H_{\ell\text{-uncoupling}} = B(N^+\ell^- + N^-\ell^+)$$

This Hamiltonian matrix was diagonalized for each total angular momentum from $N = 3$ to $N = 9$ using the best-fit parameters of Gittins et al. (33) for both $17f$ and $17g$ states. The eigenvalues of this Hamiltonian were converted to transition frequencies by subtracting the term value of the rotational level of the $D^2\Sigma^+$ state from which each nonpenetrating state is accessible, and the calculated transition frequencies were fit to eq. [11]. Plots of the calculated transition frequencies vs. N'' are shown in Fig. 7.

As can be seen in Fig. 7, ℓ-uncoupling alters the calculated ΔQ values significantly and nonsystematically from their actual values, even for calculated data in which core-penetrating ~ core-nonpenetrating interactions are not treated explicitly. However, what is apparent from Fig. 7 is a clustering of branches in groups of three according to a common value of $N^{+\prime} - N$. This clustering of branches reflects the fact that N^+ is the rotational pattern-forming quantum number in case (d). In Fig. 7, the three groups of branches terminating on f states have $N^{+\prime} - N = 0, \pm 2$, and the four groups of branches terminating on g states have $N^{+\prime} - N = \pm 1, \pm 3$. By superimposing the $17f$ and $17g$ transition frequencies (see Fig. 8), it is seen that the transitions into the f and g states form a staggered pattern, reflecting the parity selection rules outlined above. The staggered pattern of f and g states in Fig. 8 is indeed observed in the double-resonance spectrum and allows branches terminating on core-nonpenetrating states to be organized into f and g $N^{+\prime} - N$ clusters. Six f (two $N^{+\prime} - N = 0$, three $N^{+\prime} - N = +2$, and one $N^{+\prime} - N = +4$) branches and five g (one $N^{+\prime} - N = -1$, two $N^{+\prime} - N = +1$, one $N^{+\prime} -$

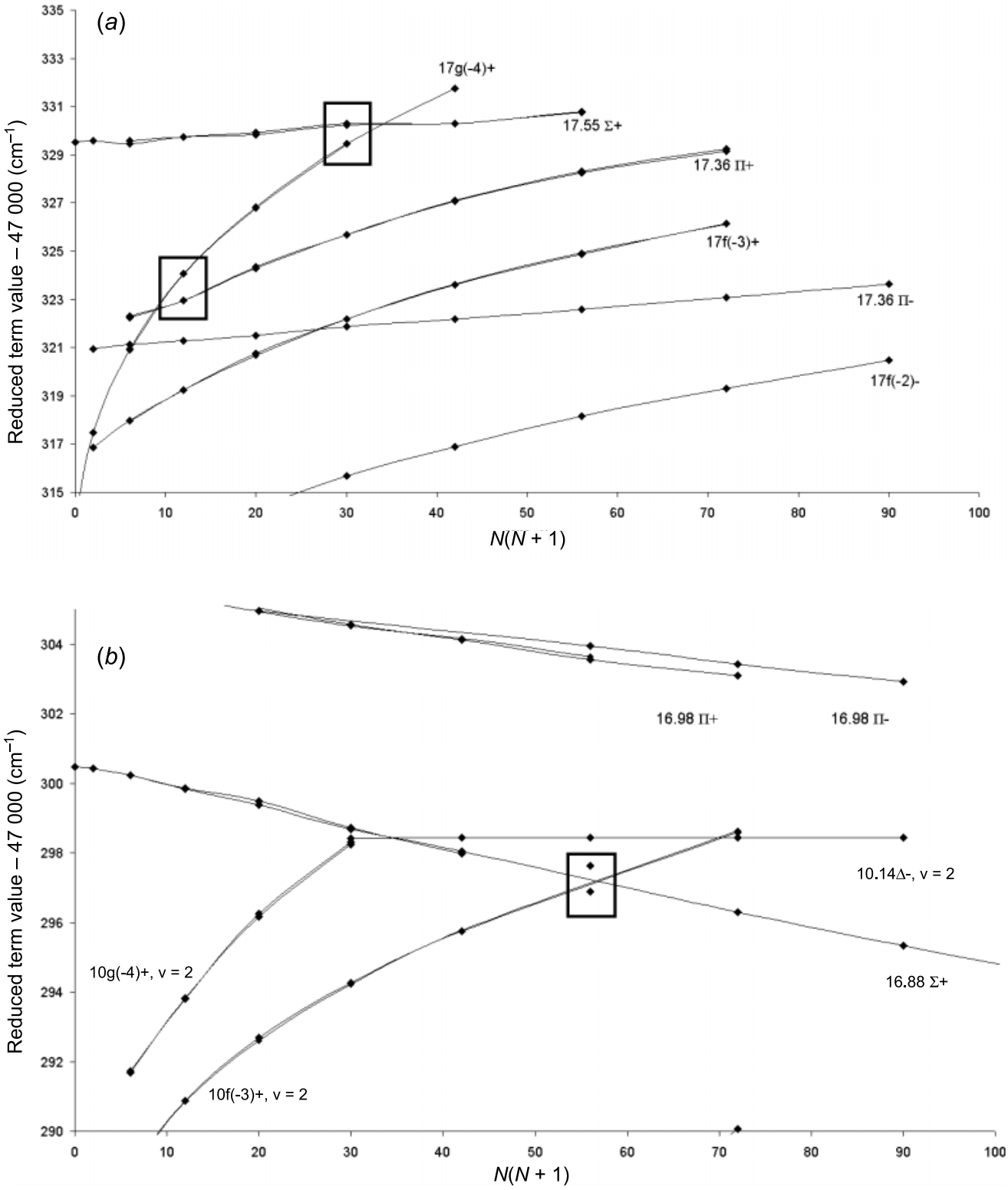
© 2004 NRC Canada

Fig. 9. Reduced term value plots of assigned core-nonpenetrating states: (*a*) 17*f* states; (*b*) 17*g* states. Observed and calculated values are represented by open and filled circles, respectively.



© 2004 NRC Canada

Fig. 10. Reduced term value plots of the n^* = 17 region showing (*a*) a relatively weak repulsion and (*b*) a relatively strong repulsion. Perturbations are enclosed in boxes.



N = +3, and one $N^{+\prime} - N$ = +5) branches are identified by inspection.

Following the identification of 17*f* and 17*g* components, a value of ℓ_R is assigned to each branch by the method of lower-state rotational combination differences outlined in the previous section. This allows rigorous assignment of the $f(-3)^+$, $f(-1)^+$, $g(-4)^+$, and $g(0)^+$ states. The assignment of $f(-3)^+$ and $f(-1)^+$ in the $N^{+\prime} - N$ = +2 cluster by lower-state

© 2004 NRC Canada

Table 3. Observed perturbations in the n^* = 16–17 region.

16.36 Π^+ ~ 16$g(-4)^+$
16.55 Σ^+ ~ 16$g(-4)^+$
16.88 Σ^+ ~ 10$f(-3)^+$, v = 2
17.36 Π^+ ~ 17$g(-4)^+$
16.55 Σ^+ ~ 17$g(-4)^+$

combination differences allows assignment of $f(-2)^+$ by process of elimination. An unpaired branch in the $N^{+\prime} - N$ = 0 cluster is securely assigned as $f(+1)^+$, as it is nearly coincident with transitions into the 0.98 Π^- state yet does not appear perturbed. A pair of intertwined branches that lie between the branches terminating in the $f(-1)^+$ and $f(+1)^+$ states are likely the 0.98 Π^- and $f(0)^-$ states and appear to exhibit strong mutual perturbations. An unpaired branch in the $N^{+\prime} - N$ = +1 g cluster is tentatively assigned as $g(-1)^-$. It is interesting to note that the observation of $N^{+\prime} - N$ = +4 f branches and $N^{+\prime} - N$ = +5 g branches, which violate the triangle rule condition in eq. [9], implies that the core-nonpenetrating states are accessible in our experiment through intensity borrowing from nearby penetrating states and not from the partial-ℓ characters of the $D^2\Sigma^+$ state. A comparison of observed and calculated term values is shown in Fig. 9.

Location of core-penetrating ~ core-nonpenetrating perturbations

Following assignment of all observed states in the n^* = 17 region, a reduced term value plot that includes all core-penetrating and core-nonpenetrating states was constructed. Reduced term value plots are constructed by subtracting the quantity $BN(N + 1)$ from the term value of each state and plotting the difference against $N(N + 1)$. All perturbations (excluding spin–orbit perturbations) have the selection rule $\Delta N = 0$ and act between states of identical Kronig symmetry. Hence, perturbations will be located in regions of the reduced term value plot where states of the same Kronig symmetry cross. Figure 10*a* shows an example of a weak level repulsion, while Fig. 10*b* depicts a case where the lines are dramatically split. Table 3 summarizes all of the observed perturbations in the n^* = 16–17 region of the double-resonance spectrum.

Conclusions

Rydberg states of calcium monofluoride in the n^* = 17–20 region have been observed by optical–optical double-resonance spectroscopy via the $D^3\Sigma^+$ intermediate state. While the assignment of core-nonpenetrating states in previous studies was complicated by many weak transitions and the inaccessibility of the lowest rotational levels of the $A^2\Pi$ and $C^2\Pi$ intermediate states, we have been able to assign all of the observable core-nonpenetrating states in the n^* = 17 region by excitation from the $D^2\Sigma^+$ state. The traditional assignment techniques presented here, fashioned in the style of Gerhard Herzberg, have allowed spectrum-only assignment of states and the location of numerous weak perturbations between core-penetrating and core-nonpenetrating states. The assignment of these states and the location of these perturbations by purely model-based predictions would be untenably complicated by the flexibility of model-based fits.

The assignment of states in the n^* = 18, 19, and 20 regions using these techniques is underway, and effective Hamiltonian and MQDT fits of states in all four regions will be performed. Analysis of the core-penetrating ~ core-nonpenetrating perturbations is in progress, and it is hoped that these perturbations between mixed-ℓ and pure-ℓ states will allow disentanglement of the polarizabilities and the dipole, quadrupole, and higher-order multipole moments of the ion core.

Acknowledgement

This research was supported by National Science Foundation grant CHE-0104197.

References

1. G. Herzberg and C. Jungen. J. Mol. Spectrosc. **41**, 425 (1972).
2. G. Herzberg and C. Jungen. J. Chem. Phys. **77**, 5876 (1982).
3. G. Herzberg and C. Jungen. J. Chem. Phys. **84**, 1181 (1986).
4. G. Herzberg. Annu. Rev. Phys. Chem. **38**, 27 (1987).
5. C. Jungen, I. Dabrowski, G. Herzberg, and D.J.W. Kendall. J. Chem. Phys. **91**, 3926 (1989).
6. A. Fujii and N. Morita. J. Chem. Phys. **97**, 327 (1992).
7. A. Fujii and N. Morita. J. Chem. Phys. **103**, 6029 (1995).
8. W.G. Sturrus, E.A. Hessels, and S.R. Lundeen. Phys. Rev. Lett. **57**, 1863 (1986).
9. W.G. Sturrus, P.E. Sobol, and S.R. Lundeen. Phys. Rev. Lett. **54**, 792 (1985).
10. E.E. Eyler, W.A. Chupka, S.D. Colson, and D.T. Biernacki. Chem. Phys. Lett. **119**, 177 (1985).
11. D.T. Biernacki, S.D. Colson, and E.E. Eyler. J. Chem. Phys. **88**, 2099 (1988).
12. E.E. Eyler and D.T. Biernacki. J. Chem. Phys. **88**, 2850 (1988).
13. E.E. Eyler, R.C. Short, and F.M. Pipkin. Phys. Rev. Lett. **56**, 2602 (1986).
14. F.X. Campos, Y. Jiang, and E.R. Grant. J. Chem. Phys. **94**, 5897 (1991).
15. F.X. Campos, Y. Jiang, and E.R. Grant. J. Chem. Phys. **93**, 2308 (1990).
16. S.T. Pratt. J. Chem. Phys. **108**, 7131 (1998).
17. E.F. McCormack, S.T. Pratt, J.L. Dehmer, and P.M. Dehmer. Phys. Rev. A, **44**, 3007 (1991).
18. S.T. Pratt, C. Jungen, and E. Miescher. J. Chem. Phys. **90**, 5971 (1989).
19. T. Toerring, W.E. Ernst, and J. Kaendler. J. Chem. Phys. **90**, 4927 (1989).
20. T. Toerring, W.E. Ernst, and S. Kindt. J. Chem. Phys. **81**, 4614 (1984).
21. J.E. Murphy, J.M. Berg, A.J. Merer, N.A. Harris, and R.W. Field. Phys. Rev. Lett. **65**, 1861 (1990).
22. J.M. Berg, J.E. Murphy, N.A. Harris, and R.W. Field. Phys. Rev. A, **48**, 3012 (1993).
23. M. Arif, C. Jungen, and A. L. Roche. J. Chem. Phys. **106**, 4102 (1997).
24. C. Jungen and A. L. Roche. Can. J. Phys. **79**, 287 (2001).
25. N.A. Harris and R.W. Field. J. Chem. Phys. **98**, 2642 (1993).
26. N.A. Harris and C. Jungen. Phys. Rev. Lett. **70**, 2549 (1993).
27. S.F. Rice, H. Martin, and R.W. Field. J. Chem. Phys. **82**, 5023 (1985).

© 2004 NRC Canada

28. Z.J. Jakubek, N.A. Harris, R.W. Field, J.A. Gardner, and E. Murad. J. Chem. Phys. **100**, 622 (1994).
29. H. Lefebvre-Brion and R.W. Field. Perturbations in the spectra of diatomic molecules. Academic Press, Orlando. 1986.
30. H. Lefebvre-Brion and R.W. Field. The spectra and dynamics of diatomic molecules. Elsevier, Amsterdam. 2004.
31. J.K.G. Watson. Mol. Phys. **81**, 277 (1994).
32. J.K.G. Watson. *In* Understanding chemical reactivity, Vol. 20: The role of Rydberg states in spectroscopy and photochemistry. *Edited by* C. Sándorfy. Kluwer, Dordrecht. 1999. p. 293.
33. C.M. Gittins, N.A. Harris, M. Hui, and R.W. Field. Can. J. Phys. **79**, 247 (2001).
34. G. Herzberg. Molecular spectra and molecular structure. I. Spectra of diatomic molecules. 2nd ed. Van Nostrand, New York. 1950.
35. C.M. Gittins, N.A. Harris, R.W. Field, J. Verges, C. Effantin, A. Bernard, J. d'Incan, W.E. Ernst, P. Bundgen, and B. Engels. J. Mol. Spectrosc. **161**, 303 (1993).
36. J.W.C. Johns and D.W. Lepard. J. Mol. Spectrosc. **55**, 374 (1975).
37. D. Gauyacq, M. Raoult, and N. Shafizadeh. *In* Understanding chemical reactivity, Vol. 20: The role of Rydberg states in spectroscopy and photochemistry. *Edited by* C. Sándorfy. Kluwer, Dordrecht. 1999. p. 393.
38. S. Guizard, N. Shafizadeh, M. Horani, and D. Gauyacq. J. Chem. Phys. **94**, 7046 (1991).

© 2004 NRC Canada

New applications of the genetic algorithm for the interpretation of high-resolution spectra[1]

W. Leo Meerts, Michael Schmitt, and Gerrit C. Groenenboom

Abstract: Rotationally resolved electronic spectroscopy yields a wealth of information on molecular structures in different electronic states. Unfortunately, for large molecules the spectra get rapidly very congested owing to close-lying vibronic bands, other isotopomers with similar zero-point energy shifts, or large-amplitude internal motions. A straightforward assignment of single rovibronic lines and, therefore, line position assigned fits are impossible. An alternative approach is unassigned fits of the spectra using genetic algorithms (GAs) with special cost functions for evaluation of the quality of the fit. This paper decribes the improvements we established on the GA method discussed before (J.A. Hageman, R. Wehrens, R. de Gelder, W.L. Meerts, and L.M.C. Buydens. J. Chem. Phys. **113**, 7955 (2000)). In particular, we succeeded in obtaining a dramatic reduction in computing time that made it possible to apply the GA process in a large number of cases. A completely automated fit of a rotationally resolved laser-induced fluorescence spectrum without any prior knowledge of the molecular parameters can now be performed in less than 1 h. We demonstrate the power of the method on a number of typical examples such as very dense rovibronic spectra of van der Waals clusters and overlapping spectra due to different isotopomers. The discussed results demonstrate the extreme power of the GA in automated fitting and assigning of complex spectra. It opens the road to the analysis of complex spectra of biomolecules and their building blocks.

Key words: high-resolution spectroscopy, genetic algorithm, biomolecules, structure, van der Waals clusters.

Résumé : La spectroscopie électronique résolue en fonction de la rotation fournit une profusion d'informations relatives aux structures moléculaires dans les différents états électroniques. Malheureusement, dans les cas de molécules de taille importante, les spectres deviennent rapidement très congestionnés en raison des bandes vibroniques adjacentes, d'autres isotopomères ayant des déplacements semblables de l'énergie du point zéro ou des mouvements internes de grandes amplitudes. Il est toutefois impossible de faire des attributions non ambiguës des raies rovibroniques simples et, par extension, des ajustements des positions de raies attribuées. Une autre méthode est de faire l'ajustement des raies non attribuées des spectres en faisant appel à des algorithmes génétiques (AG) et en appliquant des fonctions spéciales de coûts pour l'évaluation de la qualité des ajustements. Dans ce travail, on décrit les améliorations qu'on a apporté à la méthode des AG discutée antérieurement (J.A. Hageman, R. Wehrens, R. de Gelder, W.L. Meerts, et L.M.C. Buydens. J. Chem. Phys. **113**, 7955 (2000)). On a réussi, en particulier, à obtenir une diminution dramatique du temps de calcul nécessaire pour appliquer le processus d'AG à un grand nombre de cas. Il est maintenant possible de réaliser en moins d'une heure un ajustement complètement automatique d'un spectre de fluorescence induite au laser et résolue en fonction de la rotation, sans avoir recours à une connaissance préalable des paramètres moléculaires. On a démontré la puissance de la méthode sur un grand nombre d'exemples typiques, tels que les spectres rovibroniques très denses d'agrégats de van der Waals et les spectres comportant des recouvrements en raison d'isotopomères différents. Les résultats discutés démontrent la très grande puissance des AG dans l'ajustement automatique et l'attribution de spectres complexes. Ils ouvrent la voie à une analyse des spectres complexes de biomolécules et de leur composantes.

Mots clés : spectroscopie à haute résolution, algorithme génétique, biomolécules, structure, agrégats de van der Waals.

[Traduit par la Rédaction]

1. Introduction

Rotationally resolved electronic spectroscopy provides a valuable tool for determination of molecular structures in different electronic states. An implicit problem of this method is that for larger molecules the spectra rapidly get very congested. Additionally, overlapping bands due to (*i*) close-spaced vibronic bands, (*ii*) other isotopomers with similar zero-point energy

Received 3 November 2003. Published on the NRC Research Press Web site at http://canjchem.nrc.ca/ on 26 August 2004.

W.L. Meerts.[2] Department of Molecular and Laser Physics, NSRIM, University of Nijmegen, P.O. Box 9010, NL-6500 GL Nijmegen, The Netherlands.
M. Schmitt. Heinrich-Heine-Universität, Institut für Physikalische Chemie, D-40225 Düsseldorf, Germany.
G.C. Groenenboom. Institute of Theoretical Chemistry, NSRIM, University of Nijmegen, P.O. Box 9010, NL-6500 GL Nijmegen, The Netherlands (e-mail: gerritg@theochem.kun.nl).

[1]This article is part of a Special Issue dedicated to the memory of Professor Gerhard Herzberg.
[2]Corresponding author (e-mail: Leo.Meerts@sci.kun.nl).

 doi: 10.1139/V04-037 © 2004 NRC Canada

shifts, or (*iii*) split bands due to large-amplitude internal motions might complicate the experimental spectrum further. All these factors make a straightforward assignment of single rovibronic lines and, therefore, line position assigned fits impossible. In Neusser's group (1), a procedure has been developed that directly fits the experimental data without prior assignments. This method, which is called "correlation automated rotational fitting", was pioneered by Levy and co-workers (2–4) and uses the correlation between the experimental and the simulated spectrum as a measure of the quality of the fit. Unfortunately, the method still has limited applicability. An alternative approach is unassigned fits of the spectra using genetic algorithms (GAs) with special cost functions for evaluation of the level of the fit.

It has been shown by Hageman et al. (5) that a GA with a properly defined cost function was capable of performing automated fitting of spectra without any prior knowledge of the molecular parameters. The cost function used by Hageman et al. (5) is able to smooth the error landscape and, therefore, allows the GA to locate the global minimum. Unfortunately, this method is quite time-consuming, compared to other cost functions like simple least-squares or peak picking functions. The automated fitting of several overlapping bands requires, therefore, fast parallel processing and long computing times. In the present paper, we show how the computing time of the cost function can be reduced drastically, so that the automated fit of a rovibronic spectrum can be performed in less than 1 h using a standard desktop PC. The performance of the GA for spectral simulations has been described in detail elsewhere (5). A good introduction to the vocabulary and theory of GAs as a tool for solving optimization problems can be found in refs. 6 and 7.

In this paper, we extend the automated fit to the case of several overlapping spectra, i.e., the fitting of molecular parameters that belong to different molecular species or spectral components. The method is applied to a synthetic spectrum, which consists of two completely overlapping bands, to adapt the internal parameters for the GA fit. The refined method is then applied to a series of experimental rovibronic spectra of isotopomers of phenol and benzonitrile, and clusters thereof. The discussed results demonstrate the extreme power of the GA in automated fitting and assigning of complex spectra.

2. Experimental

The experimental setup for the rotational resolved laser-induced fluorescence (LIF) is described elsewhere (8). Briefly, it consists of a ring dye laser (Coherent 899-21) operated with Rhodamine 110, pumped with 6 W of the 514 nm line of an Ar^+-ion laser. The light is coupled into an external folded ring cavity (9) for second-harmonic generation (SHG). The molecular beam is formed by expanding the vaporized sample, seeded in 400−1000 mbar of argon (1 bar = 100 kPa), through a 70 μm hole into the vacuum. The molecular beam machine consists of three differentially pumped vacuum chambers that are linearly connected by skimmers (1 and 3 mm, respectively) to reduce the Doppler width. The molecular beam is crossed at right angles in the third chamber with the laser beam 360 mm downstream of the nozzle. The resulting fluorescence is collected perpendicular to the plane defined by the laser and molecular beam by an imaging optics setup consisting of a concave mirror and two plano-convex lenses. The resulting Doppler width in this setup is 25 MHz (fwhm). The integrated molecular fluorescence is detected by a photomultiplier tube, and the output is discriminated and digitized by a photon counter and transmitted to a PC for data recording and processing. The relative frequency is determined with a quasi-confocal Fabry−Perot interferometer with a free spectral range (FSR) of 149.9434(56) MHz. The FSR was calibrated using the combination differences of 111 transitions of indole for which the microwave transitions are known (10, 11). The absolute frequency was determined by recording the iodine absorption spectrum and comparing the transitions to the tabulated lines (12).

3. Theory

3.1. The Hamiltonian

For the simulation of the rovibronic spectra, a rigid asymmetric rotor Hamiltonian was employed (13):

$$[1] \qquad \widehat{H} = A P_a^2 + B P_b^2 + C P_c^2$$

Here, $P_g (g = a, b, c)$ are the components of the body-fixed angular momentum operator, and A, B, and C are the three rotational constants. The resulting Hamiltonian matrix is factorized into four submatrices using the Wang transformation (14). This enhances the computation speed because of the reduced dimension of the matrix to be diagonalized. The transition frequencies are determined by the rotational constants A, B, C in both electronic states and by the frequency of the origin ν_0 of the vibronic band. The line intensities depend on the rotational temperature, the orientation of the transition dipole moment with respect to the inertial axes, and, in some cases, the nuclear spin statistic. The temperature dependence of the intensities might be considered in a simple one-temperature model, which is sufficient for simulation of most of the rovibronic spectra, or in a more advanced two-temperature model, which should be applied in cases where line shape parameters are fitted (cf. Sect. 4.4.2). The orientation of the dipole moment vector is determined by the polar angle θ and the azimuthal angle ϕ.

3.2. The genetic algorithm

A description of the GA used in this investigation can be found in ref. 5. The GA library PGAPack version 1.0, which can run on parallel processors, was used (15). The calculations were performed on four processors of a SUN UltraSPARC 333 MHz and on a 2.6 GHz PC with two processors under Linux. The GA is basically a global optimizer, which uses concepts copied from natural reproduction and selection processes. For a detailed description of the GA, the reader is referred to the original literature (16–18). We introduce the elements of the GA that will be used in the following.

- Representation of the parameters: The molecular parameters are encoded binary or as real data type, each parameter representing a gene. A vector of all genes, which contains all molecular parameters, is called a chromosome. In an initial step the values for all parameters are set to random values between lower and upper limits, which have to be chosen by the user. No prior knowledge of the parameters is necessary. A total of 300−500 chromosomes are randomly generated, forming a population.

© 2004 NRC Canada

- The solutions (chromosomes) are evaluated by a fitness function (or cost function), which is a measure of the quality of the individual solution. The fitness function that is used here is described in Sect. 3.3.
- One optimization cycle, including evaluation of the cost of all chromosomes, is called a generation. Generally, convergence of the fit in our case is reached after 300−500 generations.
- Pairs of chromosomes are selected for reproduction, and their information is combined via a crossover process. This crossover might take place as a one-point, two-point, or uniform crossover. A crossover just combines information from the parent generations and basically explores the error landscape.
- The value of a small number of bits is changed randomly. This process is called mutation. Mutation can be viewed as exploration of the cost surface. The best solutions within a generation are excluded from mutation. This elitism prevents already good solutions from being degraded.

The performance of the GA depends on internal parameters like mutation probability, elitism, crossover probability, and population size, which therefore should also be optimized for a given problem. Fortunately, this meta-optimization results in similar parameters for quite different problems of optimization. The meta-optimization for some of the parameters is described in Sect. 4.2.

3.3. The fitness function

3.3.1. Definition

In the current paper we will use both the terms *fitness function* (F_{fg}) and *cost function* (C_{fg}), where $C_{fg} = 100(1 - F_{fg})$, to characterize the quality of a solution. The fitness function for the fit of the spectra with N points using the GA has been defined in eq. [5] of ref. 5 (in which C_{fg} is identical to F_{fg} in this paper) as:

$$[2] \qquad F_{fg} = \frac{\sum_{r=-l}^{l} w(r) \sum_{i=1}^{N} f(i)g(i+r)}{\sqrt{\sum_{r=-l}^{l} w(r) \sum_{i=1}^{N} f(i)f(i+r)}\sqrt{\sum_{r=-l}^{l} w(r) \sum_{i=1}^{N} g(i)g(i+r)}}$$

In this equation, f and g represent the experimental and calculated spectra, respectively. The function $w(r)$ determines the sensitivity of the fitness function for a shift of the two spectra relative to each other. This can be rewritten by interchanging the sums and substituting $i + r = j$ as

$$[3] \qquad F_{fg} = \frac{\sum_{i,j}^{N} f_i W_{ij} g_j}{\sqrt{\sum_{i,j}^{N} f_i W_{ij} f_j}\sqrt{\sum_{i,j}^{N} g_i W_{ij} g_j}}$$

where

$$[4] \qquad W_{ij} = w(|j - i|)$$

and $f_i = f(i)$ and $g_i = g(i)$.

F_{fg} in eq. [3] can be interpreted as the cosine of the "angle" between the experimental and the theoretical spectrum. With the column vectors

$$[5] \qquad \boldsymbol{f} = (f_1, f_2, ..f_N)^T$$
$$\boldsymbol{g} = (g_1, g_2, ..g_N)^T$$

and the symmetric matrix $\boldsymbol{W}$, which has the matrix elements W_{ij}, we can write:

$$[6] \qquad F_{fg} = \cos(\alpha) = \frac{(\boldsymbol{f}, \boldsymbol{g})}{\|\boldsymbol{f}\| \, \|\boldsymbol{g}\|}$$

Here the inner product $(\boldsymbol{f}, \boldsymbol{g})$ is defined with the metric $\boldsymbol{W}$ as:

$$[7] \qquad (\boldsymbol{f}, \boldsymbol{g}) = \boldsymbol{f}^T \boldsymbol{W} \boldsymbol{g}$$

and the norm of $\boldsymbol{f}$ as $\|\boldsymbol{f}\| = \sqrt{(\boldsymbol{f}, \boldsymbol{f})}$; similarly for $\boldsymbol{g}$. For $w(r)$ we used a triangle function (5) with a width the base of Δw:

$$[8] \qquad w(r) = \begin{cases} 1 - |r| \,/\, (1/2\Delta w) & \text{for } |r| \leqslant 1/2\Delta w \\ 0 & \text{otherwise} \end{cases}$$

In order for F_{fg} to serve as a good fitness function for the quality of the fit, it should have the property that it reaches its maximum value if and only if $\boldsymbol{f}$ and $\boldsymbol{g}$ are identical (apart from a normalization). This condition is fulfilled provided the matrix $\boldsymbol{W}$ is positive definite. In Appendix A, we show this holds if the Fourier transform of the function w is positive. The Fourier transform of $w(r)$ defined in eq. [8] is

$$[9] \qquad \tilde{w}(t) = \int_{-\infty}^{\infty} \mathrm{e}^{-2\pi i r t} w(r) \, \mathrm{d}r = \frac{\Delta w}{2} \, \mathrm{sinc}^2 \left(\frac{\Delta w}{2} \pi t \right)$$

where $\mathrm{sinc}\,(x) = \sin(x)/x$, so $\tilde{w}(t) \geqslant 0$.

3.3.2. Numerical evaluation of the fitness

Let us now consider the numerical evaluation of the fitness function F_{fg} from eq. [3] in its relation with the calculated spectrum. The calculated spectrum is obtained by a convolution of each calculated transition k with intensity s_k by the line shape function L:

$$[10] \qquad g_j = \sum_{k=1}^{N} L_{jk} s_k$$

© 2004 NRC Canada

with $L_{jk} = l(|j - k|)$. In matrix notation this can be rewritten as

[11] $$\boldsymbol{g} = \boldsymbol{L}\boldsymbol{s}$$

As it turned out, at least 50% of the computing time in ref. 5 was used to perform a straightforward calculation of F_{fg} from eq. [3]. For a typical GA fit, F_{fg} must be calculated 150 000 times. Hence, a considerable reduction in computing time can be obtained by a more efficient calculation of F_{fg}. We start with a rearrangement of the order of the evaluation of eq. [6] and using the properties of $\boldsymbol{W}$ and $\boldsymbol{L}$. The numerator of eq. [6] is evaluated first:

[12] $$(\boldsymbol{f}, \boldsymbol{L}\boldsymbol{s}) = \boldsymbol{f}^T\boldsymbol{W}\boldsymbol{L}\boldsymbol{s} = \tilde{\boldsymbol{f}}\boldsymbol{s}$$

[13] $$\tilde{\boldsymbol{f}} = \boldsymbol{f}^T\boldsymbol{W}\boldsymbol{L}$$

From eqs. [12] and [13] it is obvious that the effect of $w(r)$ can be interpreted as an effective line broadening of the experimental[3] spectrum. The use of the broadening function $w(r)$ results in a smoother error landscape, which allows an easier optimization of the GA process. It should be noted that the simple least-squares fitness function, where all spectral points have the same weight, is also described by F_{fg} for the limiting case that the width of $w(r)$ is zero and $\boldsymbol{W}$ becomes the identity matrix.

The transformed experimental spectrum from eq. [13] has to be evaluated only once. Formally, the sum on the right-hand side of eq. [12] runs over all N points of the spectrum. However, the stick spectrum array is a very sparse one: Typically, N is of the order of 60 000 − 250 000, while the number of sticks (nonzero values of s_k) is only about 1000−3000. Therefore, the use of eq. [12] strongly reduces the necessary computing time. The reduction of computing time is actually more dramatic since the double sum in the numerator of eq. [3] over N points is reduced to a single sum over a sparse array in eq. [12]. Furthermore, the theoretical spectrum itself $\{g_i\}$ does not have to be calculated anymore. The first term in the denominator of eq. [3] also has to be evaluated only once. The second term in this denominator has to be calculated every time a value of F_{fg} is needed in the process of the GA. Fortunately, this term can also be expressed in terms of the stick spectrum $\boldsymbol{s}(\{s_k\})$:

[14] $$\|\boldsymbol{g}\|^2 = \boldsymbol{s}^\dagger(\boldsymbol{L}^\dagger\boldsymbol{W}\boldsymbol{L})\boldsymbol{s}$$

Since $(\boldsymbol{L}^\dagger\boldsymbol{W}\boldsymbol{L})$ is a banded matrix, the evaluation of $\|\boldsymbol{g}\|^2$ from eq. [14] is in practice almost linear in the number of sticks rather than quadratic. Again, $(\boldsymbol{L}^\dagger\boldsymbol{W}\boldsymbol{L})$ has to be evaluated only once. It turned out that the effect of the above-discussed modifications of the calculation of F_{fg} was that its calculation time became negligible with respect to the total computing time.

The use of the stick spectrum, described in this section, is limited to applications in which the line shape parameters, like Gaussian or Lorentzian width in the Voigt profile, do not have to be fitted. Inclusion of the line width parameters in the fit requires the reevaluation of eq. [12] during the GA process, which in practice dramatically increases the computing time. Therefore, a line width fit should be performed after a determination of all other parameters in a separate fitting procedure. An example of this will be given in Sect. 4.4.2.

3.3.3. Further reduction of computing time

Further reduction of the computing time for the fitness function is made possible by setting the maximum J value in the evaluation of the simulated spectrum dynamically. In the first step of the evaluation, a maximum J value is taken, which is specified by the user. In the subsequent steps, the necessary $J_{\max}$ is computed from the temperature and the rotational constants using a cut-off factor of 0.001 for the intensities. In this way, the size of the matrices to be set up and diagonalized in the course of the computation of the simulated spectrum is minimized.

4. Results and discussion

4.1. Influence of the width (Δw) of the weight function *w(r)* on the convergence of the GA

The relative broadening of the spectra, introduced by the weight function $w(r)$, described in Sect. 3.3.2, critically determines the ability of the GA to converge to the global minimum and also the speed of convergence. The smoothing of the error landscape allows the sensing of regions far from the minimum. In the first step, the function $w(r)$ should be chosen relatively broad; $\Delta w \approx$ 15–20 times the line widths of an individual rovibronic line in the spectrum (Δ_{lw}). In this way, a first set of molecular parameters is obtained, which still has to be refined. This is done by decreasing Δw and narrowing the limits of the parameter space to be searched in the fit. Decreasing Δw improves the accuracy of the molecular parameters obtained from the fit, while narrowing the parameter space leads to an improved sampling in the region of the minimum. This of course is the critical step in the procedure. Too strong narrowing of the parameter space leads to premature convergence of the fit — with a high probability into a local minimum.

We performed a fit of a synthetic spectrum that consisted of two overlapping sub-spectra. It was generated using the molecular parameters from the "Best value" column in Table 1. A single-temperature model for the calculation of the intensities has been used. The maximum J value used in the computation of the cost function for this spectrum is 22. Table 2 lists the results of five GA calculations stopped after 500 generations, each started with a different randomly generated initial set of parameters. In Table 2, $\Delta w/\Delta_{lw} = 20$. This process has been repeated for different values of $\Delta w/\Delta_{lw}$. The convergence of the fit using different $\Delta w/\Delta_{lw}$ is shown in Fig. 1.

A ratio of $\Delta w/\Delta_{lw} = 20$ leads to convergence for all five initial seeds into the same minimum. Inspection of the parameters in Table 2 shows that the minimum found is the global one. Nevertheless, the deviations of the fitted parameters from the best values of Table 1 are quite large, owing to the large value of Δw, which leads to broad minima at the cost surface. As seen in Fig. 1, smaller values of Δw may lead to convergence into other (local) minima of the cost surface. With $\Delta w/\Delta_{lw}$ of 10, still three of the fits converge to the global minimum, with a ratio of 5, only one fit converges to the global minimum, and with 2.5, none of the fits converges to the global minimum.

[3] A different arrangement of the equations shows that $w(r)$ also can be interpreted as an effective broadening of the calculated spectum g. Actually, the experimental and the calculated spectra are broadened relative to each other.

© 2004 NRC Canada

Table 1. Input for the genetic algorithm (GA) fit of the synthetic spectrum.

Parameter	Best value	Lower limit	Upper limit	Coupling [a]
Parameters of the first spectrum				
A_1''	3 000.00	2 900.00	3 100.00	
B_1''	1 000.00	910.00	1 100.00	
C_1''	800.00	700.00	900.00	
T_1	2.00			
θ_1	54.74	0.00	90.00	
ϕ_2	45.00	0.00	90.00	
$\nu_0^{(1)}$	80 000.00	79 000.00	81 000.00	
ΔA_1	100.00	10.00	150.00	
ΔB_1	−50.00	−150.00	50.00	
ΔC_1	−50.00	−150.00	50.00	
Gaussian width	20.00			
Parameters of the second spectrum				
$A_2'' - A_1''$	10.00	5.00	15.00	D
$B_2'' - B_1''$	5.00	0.00	10.00	D
$C_2'' - C_1''$	−5.00	−10.00	0.00	D
T_1	2.00			C
θ_2	56.74			
ϕ_2	44.00			
$\Delta\nu_0^{(2)} - \Delta\nu_0^{(1)}$	500.00	0.00	1 000.00	D
$\Delta\Delta A$	2.00	−3.00	3.00	D
$\Delta\Delta B$	−1.00	−3.00	3.00	D
$\Delta\Delta C$	1.00	−3.00	3.00	D
Gaussian width	20.00		C	
Ratio scaling	1.00		R	

Note: All values are in MHz except T, which is in K, and θ and ϕ, which are in degrees. The Lorentzian contribution to the line width was sert to zero. $\Delta A_1 = A_1' - A_1''$; ΔB_1 and ΔC_1 correspondingly. $\Delta\Delta A = \Delta A_2 - \Delta A_1 = \left(A_2' - A_2''\right)\left(A_1' - A_1''\right)$; etc.

[a] C, parameters of spectrum 2 are taken the same as those of spectrum 1; D, parameters of spectrum 2 are those of spectrum 1 with the corresponding value in the table added; R, parameters of spectrum 2 are those of spectrum 1 multiplied by the corresponding value from the table.

In the next step, the fit has to be refined with a limited parameter space centered around the best fit (fit No. 4 in Table 2) and with successively smaller values of Δw. We could not establish a hard criterion for the reduction of the parameter space. A successfull reduction depends critically on the quality of the first series of fits. On the other hand, the parameter space cannot always be reduced by the same factor for each of the parameters. As a rule of thumb, we found that the parameter limits can be reduced to one-tenth of the initial range. This reduction depends on the quality (signal-to-noise (S/N)) of the spectrum and has to be checked carefully after each successive step. Table 3 gives the new input parameters for a refined fit, using a ratio $\Delta w/\Delta_{lw} = 5$, along with the result of the best of five fits with different starting populations.

As can be inferred from Table 3, the fit with the reduced line width ratio and the reduced parameter space is already quite close to the "real" values given in Table 1. It can further be improved by decreasing $\Delta w/\Delta_{lw}$ and the parameter search space in an iterative manner until convergence for the molecular parameters is reached.

To generate a more realistic spectrum, we added a randomly Gaussian-distributed noise to the synthetic spectrum, resulting in a S/N of 10:1 for the strongest lines. The GA performed equally well in this case, yielding the molecular parameters given in the last column of Table 3. The deviations of the parameters from the true values are similarly small as for the "perfect" spectrum without noise.

4.2. Meta-optimization of the internal GA parameters

The need to optimize the internal parameters of the GA (meta-optimization) for a given problem has been discussed to be a major drawback of this method (19). The speed and convergence of GAs depend on the data representation (binary or real), the crossover type (one-point, two-point, uniform), the size of the starting population, the rate of elitism, and the mutation probability. Several other factors that also influence the performance of the GA fit have been kept fixed. They will be discussed shortly. The crossover probability was chosen as 85%. Selection of the best solutions is performed via a tournament selection, which means that a random subset of the chromosomes is taken, and within each subset the chromosomes are selected by their cost. Duplicates within one generation are allowed for.

© 2004 NRC Canada

Table 2. Results of five successive GA evaluations of the synthetic spectrum from Table 1.

Parameter	Best value	Fit No. 1	Fit No. 2	Fit No. 3	Fit No. 4	Fit No. 5
Parameters of the first spectrum						
A_1''	3 000.00	2 996.19	2 998.14	2 998.53	3 000.68	2 996.38
B_1''	1 000.00	999.71	998.14	999.12	998.92	999.51
C_1''	800.00	801.49	799.90	797.95	800.88	800.68
θ_1	54.74	56.07	53.09	53.38	54.80	57.68
ϕ_2	45.00	45.17	44.68	45.42	45.71	42.29
$\nu_0^{(1)}$	8 0000.00	79 987.29	79 981.43	79 985.34	80 002.93	79 997.07
ΔA_1	100.00	101.61	101.81	101.42	99.46	101.81
ΔB_1	−50.00	−49.36	−48.58	−50.34	−49.17	−49.85
ΔC_1	−50.00	−49.95	−50.05	−49.27	−50.64	−50.34
Parameters of the second spectrum						
$A_2'' - A_1''$	10.00	13.53	11.22	11.93	9.52	15.07
$B_2'' - B_1''$	5.00	6.42	7.03	5.87	5.68	5.52
$C_2'' - C_1''$	−5.00	−5.31	−5.99	−2.45	−6.34	−6.29
θ_2	56.74	55.73	58.32	56.95	57.39	59.54
ϕ_2	44.00	47.03	42.68	43.56	44.34	42.09
$\Delta\nu_0^{(2)} - \Delta\nu_0^{(1)}$	500.00	505.38	520.04	509.29	488.76	501.47
$\Delta\Delta A$	2.00	0.49	0.71	0.54	2.92	−1.09
$\Delta\Delta B$	−1.00	−1.72	−2.44	−0.19	−2.00	−0.09
$\Delta\Delta C$	1.00	1.23	1.02	0.23	2.13	1.17
C_{fg}	0.000	0.394	0.526	0.397	0.279	0.571

Note: The starting set of parameters was generated randomly and the search limits are from Table 1, $\Delta w/\Delta_{lw} = 20$.

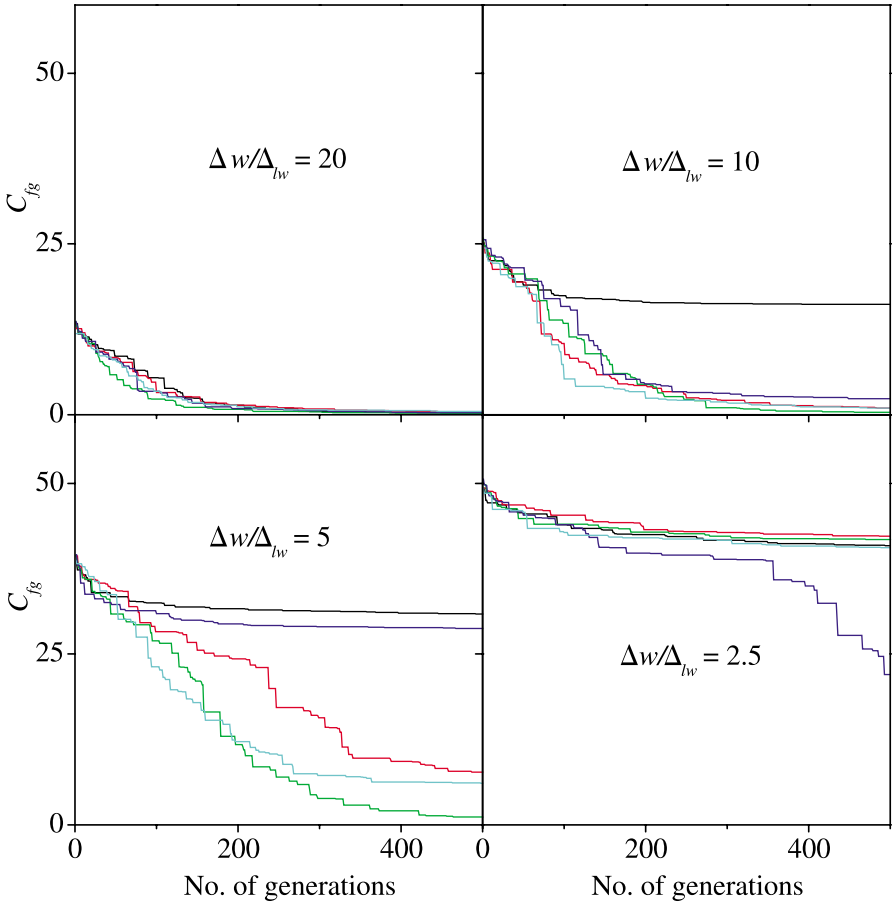
Table 3. Results of a GA evaluation of the synthetic spectrum of Table 1 with narrowed search regions and $\Delta w/\Delta_{lw} = 5$.

Parameter	Best fit	Lower limit	Upper limit	Best fit with noise
Parameters of the first spectrum				
A_1''	3 000.19	2 990.00	3 010.00	3 000.01
B_1''	1 000.22	990.00	1 010.00	1 000.01
C_1''	800.05	790.00	810.00	799.76
θ_1	55.11	40.00	60.00	53.74
ϕ_2	44.63	40.00	60.00	45.47
$\nu_0^{(1)}$	80 000.05	79 950.00	80 150.00	80 000.44
ΔA_1	100.11	90.00	110.00	99.91
ΔB_1	−50.12	−60.00	−30.00	−49.88
ΔC_1	−49.94	−60.00	−30.00	−50.12
Parameters of the second spectrum				
$A_2'' - A_1''$	9.66	5.00	15.00	10.44
$B_2'' - B_1''$	4.59	0.00	10.00	5.18
$C_2'' - C_1''$	−5.15	−10.00	0.00	−4.80
θ_2	56.99	40.00	60.00	56.30
ϕ_2	45.08	40.00	60.00	43.17
$\Delta\nu_0^{(2)} - \Delta\nu_0^{(1)}$	497.17	400.00	600.00	501.66
$\Delta\Delta A$	2.08	0.00	4.00	1.78
$\Delta\Delta B$	−0.85	−4.00	0.00	−1.17
$\Delta\Delta C$	0.97	0.00	4.00	1.15
C_{fg}	0.162	—	—	0.297

The "natural" choice for a genetic algorithm is a binary representation of the data. It has been discussed that a direct representation of the parameters as real-type data is advantageous if the type of data to be fitted is real. All tests performed with the data set given in Table 1 show that the binary encoding of the parameters leads to a smaller cost and converges more rapidly, compared to real-type representation. For the real-type data encoding, a number of runs do not even reach the global minimum.

© 2004 NRC Canada

Fig. 1. Dependence of the convergence of five fits of a synthetic spectrum that consists of two overlapping sub-spectra with different starting populations on the ratio $\Delta w/\Delta_{lw}$.



A change of the encryption depth for the binary representation from 10 bit to 20 bit virtually does not change the performance of the GA. A Gray code (20) is used throughout the present investigations in order to ensure a Hamming distance of one (21). Comparing uniform and two-point crossover, a clear advantage of the two-point crossover regarding speed of convergence and fitness of the solutions was found. Just in the case of real-type encoding, the uniform crossover forces more runs of the GA into the global minimum than the two-point.

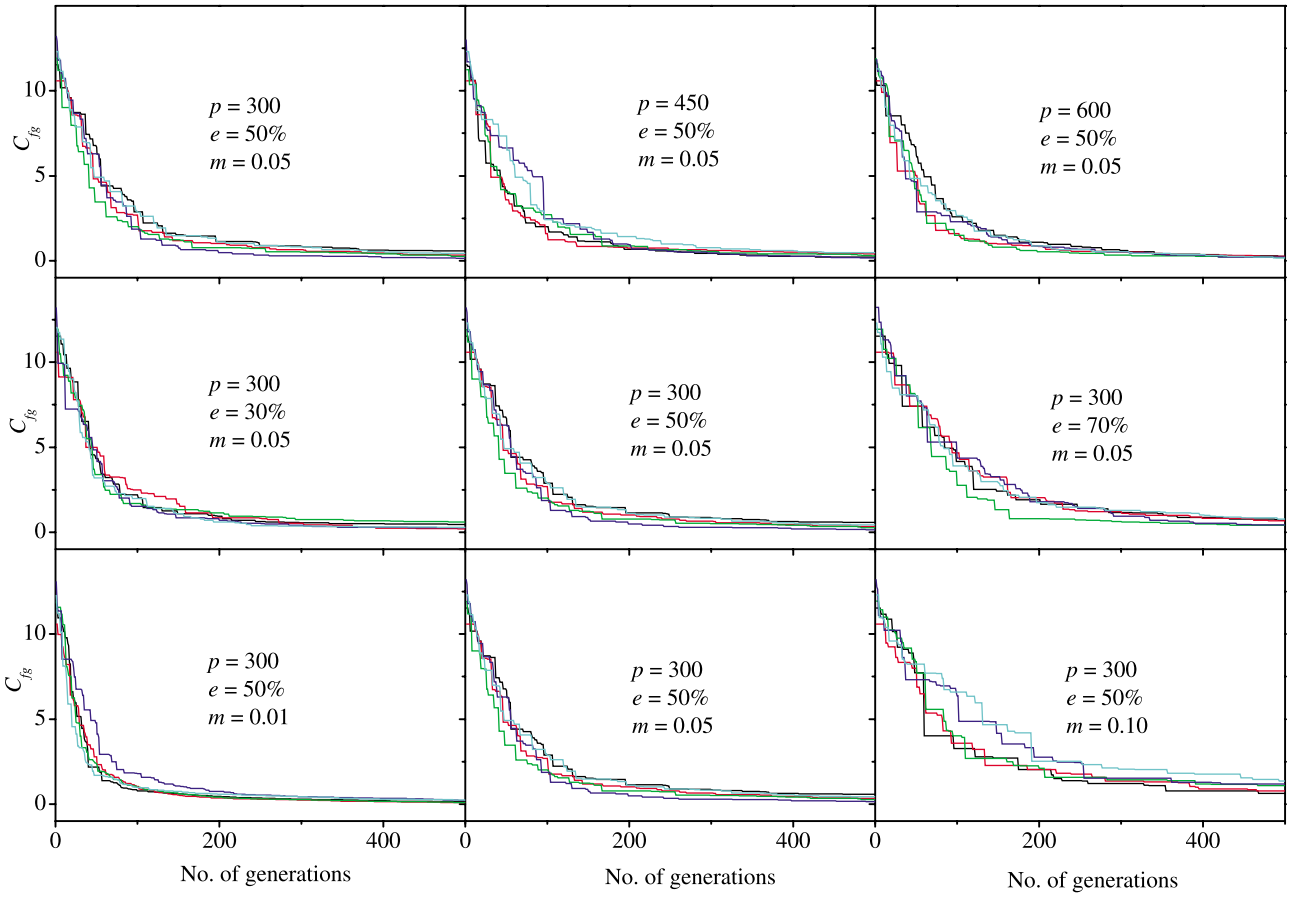
The first row of Fig. 2 shows the convergence of five fits with different starting populations as a function of the number of generations for different sizes of the starting population, using the parameters from Table 1 and $\Delta w/\Delta_{lw} = 20$ (cf. Sect. 4.1). The elitism was kept at 50% and mutation probability at 0.05 in these calculations. For a population of 300, the best value of the cost function was 0.15, the mean of five runs using different starting populations was 0.35, and the cost function dropped below 0.5 after 372 generations. The larger population of 450 had a slightly better mean of 0.30 and dropped below 0.5 after 324 generations. The largest population we investigated contained 600 chromosomes and resulted in a mean of the cost function of 0.21 and dropped below 0.5 after 278 generations. The better performance regarding the convergence as a function of the number of generations for the larger populations is more than compensated for by the increasing CPU time for increasing populations. One run for a population of 300 takes 21 min, for a population of 450 takes 43 min, and for 600, 52 min using four processors on a SUN UltraSPARC 333 MHz. All subsequent computing times are for this configuration. Almost the same computing time was attained on a dual processor PC with two Pentium 2.6 GHz processors.

The variation of elitism between 30% and 70% is shown in the second row of Fig. 2. The size of the population is kept fixed at 300 for these fits. An elitism of 30% means that the best 30% of one generation are passed unchanged to the next generation. Elitism helps to prevent good solutions from being lost from one generation to the next. As can be inferred from Fig. 2, a fit with an elitism of 30% converges more rapidly than one with 50% or 70%. Nevertheless, the mean cost function of five runs for an elitism of 50% is slightly better. For an elitism of 70%, the mean cost function never drops below 0.5 because too many bad solutions are kept. With regard to CPU time, an elitism of 30% is the most time-consuming (36 min) compared to 50% (21 min) and 70% (12 min).

The third row of Fig. 2 shows the variation of convergence with the mutation probability. Population size is kept fixed at 300 and elitism at 50%. Mutation is introduced to allow for a thorough exploration of the whole cost surface and prevents the algorithm from prematurely converging into a local minimum. With a mutation probability of 0.01, the mean value of the cost function is 0.15, and the cost function drops below 0.5 after 204 generations. With a mutation probability of 0.05, the

© 2004 NRC Canada

Fig. 2. Convergence of the GA as a function of population size (p), rate of elitism (e), and mutation probability (m). The cost function C_{fg} is plotted on the vertical axis.



mean of the cost function increases to 0.35 (drops below 0.5 after 372 generations), while for a mutation probability of 0.10, the mean cost function value is 1.00. Although all five runs converged to the same global minimum for mutation probabilities of 0.01, 0.05, and 0.10, the mutation probability of 0.01 performed best, considering mean cost function and speed of convergence. However, one has to be careful not to underestimate the risk of converging to a local minimum due to bad exploration of the cost surface. The CPU time as a function of the mutation probability virtually does not change (21 min for probabilities of 0.01, 0.05, and 0.10).

To conclude, the population size should not exceed 300 because of the bad time performance with larger populations, which is not compensated by a much better convergence of the algorithm. An elitism of 30% is advantageous regarding the convergence, but also very time-consuming. The best trade-off between time and convergence performance is found at 50% elitism. A mutation probability of only 0.01 leads to a very fast convergence, with very exactly determined parameters. Nevertheless, in cases where many local minima at the cost surface are present, such a low mutation probability might lead into a local minimum. Reduction of the value of this parameter has therefore to be performed with great care.

4.3. GA fit of very dense rovibronic spectra

In the following, we will present the automated-GA fits of some rovibronic spectra, which are very congested due to small rotational constants. These spectra normally do not represent a great difficulty for the GA, as will be shown in the next sections.

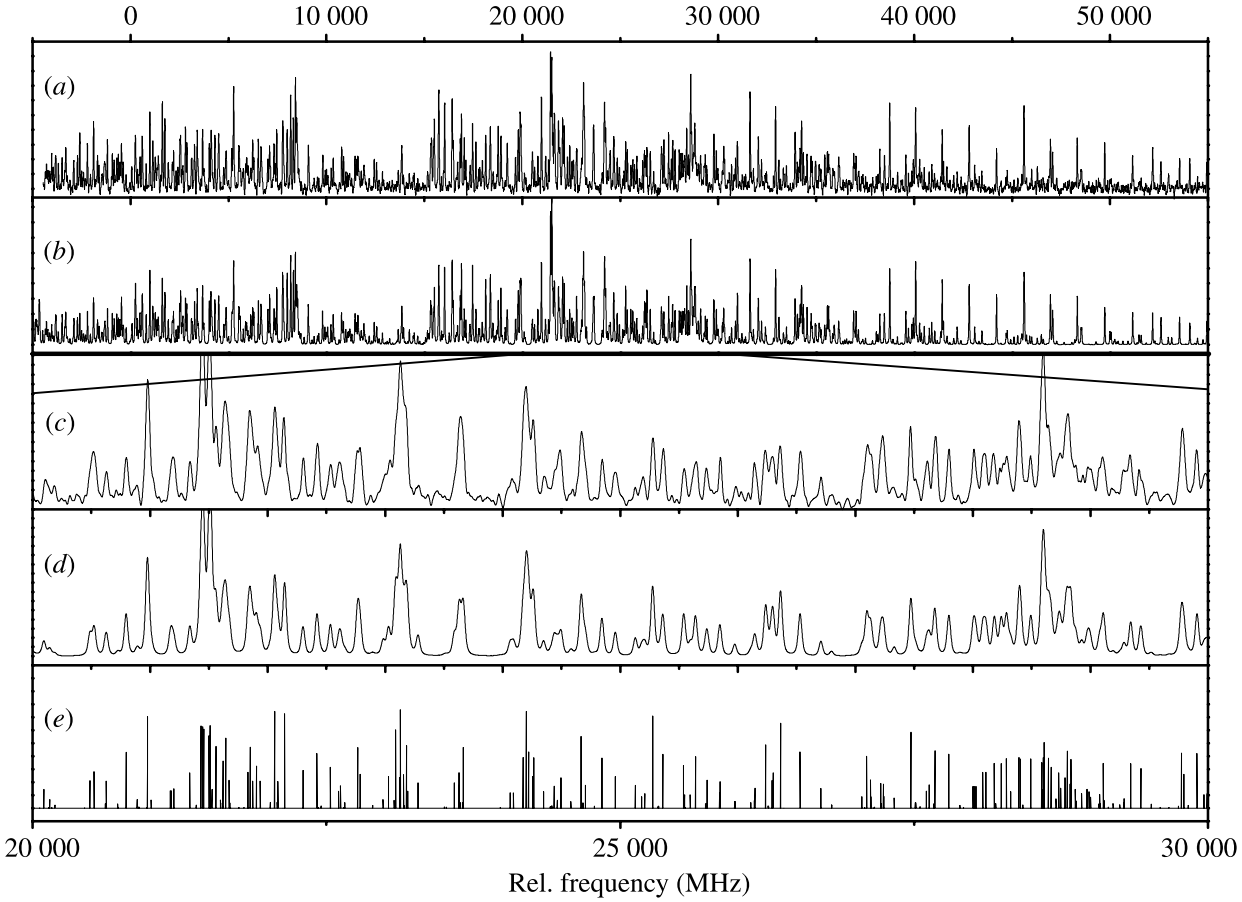
4.3.1. [7-D]Phenol–N_2

We recently performed a fit of the rovibronic spectra of several isotopomers of the phenol–nitrogen cluster (22). The nitrogen is located in the plane of the phenol, hydrogen bonded to the OH group with a bond length of 225.5 pm. In the following, we present the rovibronic spectra of different [7-D]phenol clusters. [7-D]Phenol means replacement of hydrogen by deuterium at the hydroxy group of phenol. The choice of [7-D]phenol instead of the normal isotopomer was made because of the longer lifetime of the deuterated isotopomers, yielding smaller line widths and, therefore, better signal-to-noise ratios. The rotationally resolved electronic spectrum of the electronic origin of [7-D]phenol–N_2 is shown in trace (*a*) of Fig. 3. The observed spectrum consists of about 400 clusters of lines, with only a few single rovibronic lines (cf. the simulated stick spectrum shown in trace (*e*) of Fig. 3).

An assigned fit for such a congested spectrum is very dif-

© 2004 NRC Canada

Fig. 3. (*a*) Experimental rotationally resolved electronic spectrum of the electronic origin of phenol−N_2. (*b*) Simulation, using the parameters given in Table 4. (*c*) Expanded view of trace (*a*). (*d*) Simulation in the same spectral range with Voigt-convoluted line shapes, using a Gaussian width of 26 MHz and a Lorentzian width of 39.4 MHz. (*e*) Stick spectrum in the given spectral range. Intensities are given in arbitrary units.



ficult because the shape changes considerably upon moderate changes of the molecular parameters. The initial search range for the parameters in the GA fit was obtained from a preliminary ab initio calculation. This calculation was based on a "hydrogen" structure as proposed by Ford et al. (23). The molecular parameters obtained from the GA fit with $\Delta w/\Delta_{lw} = 5$ are presented in the second column of Table 4. The values given and the quoted uncertainties are the result of statistics on 10 independent GA runs, with different initial seeds, i.e., different starting populations of the evolution. In a second step, we used the result of the GA calculation to assign quantum numbers to the individual transitions and clusters of lines. Because of the high quality of the GA fit, this was possible in spite of the large number of overlapping lines. With these line position assignments, a second fit to the parameters of the rigid rotor Hamiltonian of eq. [1] was performed. The latter fit yields better values, in particular for the uncertainties of the parameters. For most parameters, the values obtained from the assigned fit (Table 4, column 3) agree within their uncertainties to the corresponding GA results. This spectrum presents an example in which the rovibronic spectrum could be fitted by the GA in a single step, without further refinement of Δw.

Table 4. Comparison of the molecular parameters of the phenol−nitrogen cluster as obtained from an assigned fit and from the GA fit.

Parameter	GA fit	Assigned fit
A'' (MHz)	4071.06 (13)	4072.18(25)
B'' (MHz)	647.89(2)	648.01(4)
C'' (MHz)	559.13(2)	559.26(4)
T (K)	1.6(5)	2.0
θ (°)	62.53(7)	60.0
ΔA (MHz)	−140.99(6)	−141.560(91)
ΔB (MHz)	15.71(1)	15.708(13)
ΔC (MHz)	8.70 (1)	8.671(9)

The computation time for the GA fit of the spectrum with 12 parameters and the direct evaluation of F_{fg} by the full sum of all data points (eq. [3]) was 12 min. It could be reduced to 5 min using the sparse stick array. Thus, a very complex spectrum could be completely fit by the GA within 50 min of computation time.

© 2004 NRC Canada

Table 5. Molecular constants from a GA calculation and an assigned fit of the rovibronic spectrum of the electronic origin of phenol−Ar.

Parameter	GA fit	Assigned fit
A'' (MHz)	1779.04(46)	1779.23(13)
B'' (MHz)	1119.40(24)	1119.315(76)
C'' (MHz)	904.82(9)	904.672(193)
T (K)	1.33	1.5
θ (°)	18.24(7)	20
ϕ (°)	25.76(93)	30
ΔA (MHz)	−43.43(28)	−43.516(42)
ΔB (MHz)	25.15(13)	25.191(31)
ΔC (MHz)	23.24(6)	23.227(20)

4.3.2. [7-D]Phenol−Ar

The phenol−Ar cluster is an example of a weakly van der Waals-bonded molecular cluster. Owing to the weak binding forces, centrifugal distortion (24, 25) might play a role in the determination of the molecular parameters. We included the five quartic centrifugal distortion constants for each electronic state in the fit. Compared to an equivalent fit without centrifugal constants, no significant improvement of the fit could be obtained. We performed the GA fit, where the azimuthal and polar angles of the transition dipole moment were allowed to vary between 0° and 90°, i.e., within their complete definition range. Further parameters to be varied were the rotational constants of ground and excited state, the center frequency,[4] and a single temperature. We used $\Delta w/\Delta_{lw} = 10$. As in the case of the [7-D]phenol−N_2 spectrum, the spectrum could be fitted without refining Δw. The resulting molecular parameters from the GA and from an assigned fit are presented in Table 5. While the rovibronic spectrum of phenol is of pure *b*-type, the argon atom, which is located above the aromatic ring and shifted slightly towards the hydroxy group, switches the axes, so that the transition moment in the cluster is oriented nearly along the inertial *c*-axis. From the parameters given in Table 5, we calculated the perpendicular r_0-distance of the argon atom to the aromatic ring with the program pKrFit (26). In the electronic ground state this distance is found to be 352.1 pm, while in the electronically excited state the distance is slightly reduced to 350.3 pm. Both values are in good agreement with distances found for other aromatic − noble gas clusters.

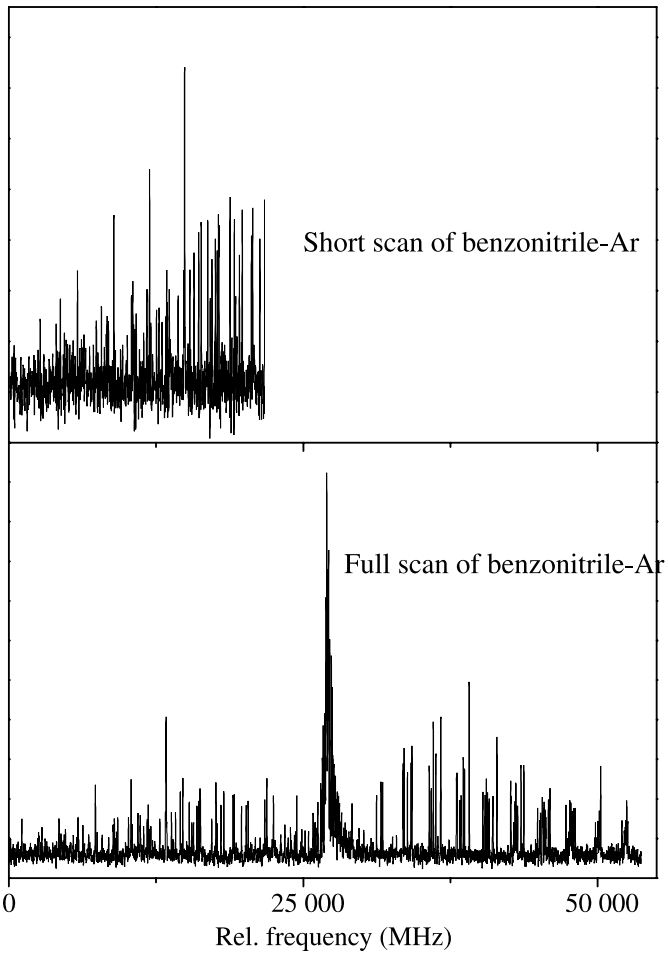
The GA fit of 10 molecular parameters was terminated in 6 min, using the sparse stick array implementation described in Sect. 3.3.2. Doubling of the dimension of the fitness surface by adding the 10 centrifugal distortion constants resulted in a computation time of 9 min. With the chosen ratio of $\Delta w/\Delta_{lw} = 10$, all five initial seeds converged to the same minimum within 500 generations.

4.3.3. Benzonitrile−Ar

If due to experimental limitations only the outermost parts of the *P*- or the *R*-branch can be recorded, and the electronic origin of a rovibronic band is missing, the task of performing an assigned fit gets tedious or even impossible. However, also in this difficult case the GA succeeds in finding the global minimum and assigning the spectrum properly. As an example we chose the spectrum of the electronic origin of benzonitrile−Ar, shown in the upper trace of Fig. 4. Obviously, the low-frequency side of the spectrum has been measured with a quite bad signal-to-noise ratio. Nevertheless, the GA was able to determine the molecular parameters. The result is given in the first column of Table 6. The computing time was the same as for a complete spectrum discussed in the previous section. The electronic origin is found by the GA to be 8000 MHz to the blue of the high-frequency end of the spectrum. A GA fit to the complete spectrum with good signal-to-noise (lower trace in Fig. 4) yields slightly different molecular parameters (second column of Table 6). Nevertheless, the quality of the parameters obtained from the fit to the partial spectrum is surprisingly good. The only parameters that have relatively large deviations are the polar and azimuthal angles of the transition dipole moment. This is obviously due to the fact that the band type cannot be determined accurately from a fit of a single branch only.

Results from previous studies on benzonitrile−Ar are also given in the last column of Table 6. The current results for the excited state are more accurate than those of Helm et al. (1) because of the substantially lower resolution of their experiment.

Fig. 4. Upper trace: low-frequency part of the spectrum of benzonitrile−Ar. Lower trace: complete rovibronic spectrum. Intensities are given in arbitrary units. For details see the text.



[4]The value for the center frequency is omitted in all tables, as it is a relative number.

© 2004 NRC Canada

Table 6. Molecular constants from GA assignments of the partial spectrum of the origin of benzonitrile–Ar and the complete spectrum and from an assigned fit.

Parameter	GA fit[a]	GA fit[b]	Assigned fit	Other work
A'' (MHz)	1343.80(150)	1347.32(19)	1347.58(18)	1347.789(12)[c]
B'' (MHz)	1002.55(121)	1004.99(4)	1004.98(14)	1006.020(9)[c]
C'' (MHz)	717.68(108)	718.99(4)	717.70(39)	719.817(2)[c]
θ (°)	22(3)	17.53(7)	20	
ϕ (°)	82(5)	70.05(2)	70	
T(K)	1.71(3)	1.68(3)	2	
ΔA (MHz)	−32.89(44)	−32.61(3)	−32.47(23)	−33.8(36)[d]
ΔB (MHz)	20.60(30)	21.08(16)	20.87(14)	21.4(27)[d]
ΔC (MHz)	6.25(15)	6.76(7)	6.80(34)	10.2(75)[d]

Note: See text for details.

[a]Fit to the spectrum in the upper trace of Fig. 4.

[b]Fit to the spectrum in the lower trace of Fig. 4.

[c]From ref. 27.

[d]From ref. 1.

Our ground-state values do not completely agree with the very accurate microwave results from Dreizler and co-workers (27). This is an indication that the uncertainties in our parameters, based on the statistical behavior of the GA fits, are slightly underestimated.

4.4. Simultaneous GA fit of two overlapping rovibronic spectra

A much more demanding task than a fit of a single rovibronic spectrum is the simultaneous fit of two (or more) overlapping spectra. First of all, the number of transitions within a spectral interval is doubled, leading to very dense and congested spectra. Secondly, the number of molecular parameters is also doubled, which generates quite a large parameter space.

Overlapping spectra occur in particular if several isotopic species are investigated. While mass resolution techniques like resonance two-photon ionization with time-of-flight mass spectroscopy are able to separate the isotopic species with a different mass, the technique normally lacks experimental resolution owing to the pulse-width-limited resolution used in these studies. On the other hand, mass selection cannot be combined with high-resolution LIF spectra. In the next sections, we show that the GA spectrum assignments are capable of handling overlapping spectra both from different isotopomers as well as from different conformers.

4.4.1. [7-D][^{18}O]Phenol and [7-D][^{16}O]phenol

Further tests of the GA were performed with experimental spectra consisting of two sub-spectra, which originate from two isotopomers. As a first example, we chose the rovibronic spectrum of [^{18}O][7-D]phenol/[^{16}O][7-D]phenol, which had been assigned and published before (26). The isotopic enrichment of the phenol sample resulted in an isotopic purity of about 50% for the oxygen isotopes and of 100% for hydrogen. Since the spectral shift of the two spectra is about 3 GHz, the spectra completely overlap within the rovibronic contour. Both sub-spectra are of pure b-type, and thus the polar and azimuthal angles θ and ϕ do not need to be fit in this case. The rovibronic lines have a Voigt profile with a Gaussian line width of 20 MHz and a Lorentzian contribution of 12 MHz because of the fluorescence lifetime of 12.5 ns. The maximum J value in the calculation of the cost function is 15. Due to the smaller number of lines in the calculated spectrum, the computation time for the cost function drops drastically, and throughout all calculations on the phenol system, a population of 600 could be employed. The method for the GA evaluation employed is the same as described in Sect. 4.1. An initial fit was performed with a large value of $\Delta w/\Delta_{lw} = 15$. Table 7 gives the results of a GA fit, the limits of the molecular parameters used in the fit, and the results of a previously published assigned fit for comparison. Four GA evaluations with different starting values all converge to the same global minimum. Thus, $\Delta w/\Delta_{lw}$ was chosen correctly in the first step of the analysis. The comparison with the results from an assigned fit nevertheless shows deviations of about 2 MHz for the inertial parameters and their changes upon electronic excitation.

A second fit is performed with $\Delta w/\Delta_{lw} = 4$. The limits for the rotational constants and ΔA were reduced by a factor of 5 compared to the fit with $\Delta w/\Delta_{lw} = 15$, while the limits for ΔB and ΔC, which were already quite small, were reduced only by a factor of approximately 2. The results given in Table 8 clearly show not only that the GA fit converged to the global minimum, which is determined unambiguously from the assigned fit, but that the values of the inertial parameters are reproduced within their experimental accuracies. Figure 5 shows the experimental spectrum, along with the simulated spectra, using the parameters from the GA fit and from the assigned fit.

One run of the GA calculation with a population size of 600, a mutation probability of 0.05, and an elitism of 50% takes only about 10 min. This is due to the small J_{max} in the calculation of the simulated spectrum. With an initial seed of five different starting populations and two successive fits with different line width ratios and parameter spaces, a complete automated assignment was performed in less than 2 h.

In summary, in a two-step fit the GA evaluation succeeded in determining all molecular parameters for both completely overlapping spectra of [^{18}O][7-D]phenol and [^{16}O][7-D]phenol. The accuracy is comparable to an assigned fit of individual

© 2004 NRC Canada

Table 7. Fit of the inertial parameters of [^{18}O][7-D]phenol/[^{16}O][7-D]phenol using the GA along with the limits of the parameters used in the fit and the previously published parameters from an assigned fit of the individual line positions.

Parameter	GA fit	Lower limit	Upper limit	Assigned fit (26)
[^{18}O][7-D]Phenol				
A''	5 610.70	5 550.00	5 650.00	5 607.181(200)
B''	2 408.55	2 350.00	2 450.00	2 407.924(66)
C''	1 685.87	1 650.00	1 700.00	1 684.810(71)
ν_0	14 326.49	14 000.00	15 000.00	14 322.24(10)
ΔA	−334.60	−400.00	−300.00	−332.77(290)
ΔB	3.33	−5.00	5.00	4.02(120)
ΔC	−29.13	−50.00	0.00	−28.77(100)
[^{16}O][7-D]Phenol				
A''	5 604.84	5 550.00	5 650.00	5 608.222(90)
B''	2 528.93	2 500.00	2 550.00	2 527.965(57)
C''	1 743.30	1 700.00	1 800.00	1 742.737(40)
ν_0	17 032.26	16 000.00	18 000.00	17 031.00(10)
ΔA	−331.09	−400.00	−300.00	−332.56(160)
ΔB	3.18	−5.00	5.00	2.55(90)
ΔC	−31.87	−50.00	0.00	−31.51(70)
C_{fg}	4.496	—	—	2.580

Note: All values are given in MHz except C_{fg}, which is dimensionless. $\Delta w/\Delta_{lw} = 15$.

Table 8. Fit of the inertial parameters of [^{18}O][7-D]phenol/[^{16}O][7-D]phenol where the parameter space is narrowed compared to Table 7.

Parameter	GA fit	Lower limit	Upper limit	Assigned fit (26)
[^{18}O][7-D]Phenol				
A''	5 606.22	5 595.00	5 615.00	5 607.181(200)
B''	2 407.88	2 400.00	2 420.00	2 407.924(66)
C''	1 684.45	1 676.00	1 696.00	1 684.810(71)
ν_0	14 321.54	14 300.00	14 340.00	14 322.24(10)
ΔA	−332.02	−340.00	−320.00	−332.77(290)
ΔB	3.83	0.00	5.00	4.02(120)
ΔC	−28.53	−50.00	−20.00	−28.77(100)
[^{16}O][7-D]Phenol				
A''	5 608.53	5 595.00	5 615.00	5 608.222(90)
B''	2 528.02	2 520.00	2 540.00	2 527.965(57)
C''	1 742.62	1 735.00	1 755.00	1 742.737(40)
ν_0	17 033.63	17 000.00	17 050.00	17 031.00(10)
ΔA	−332.81	−340.00	−320.00	−332.56(160)
ΔB	2.54	0.00	5.00	2.55(90)
ΔC	−31.41	−50.00	−20.00	−31.51(70)
C_{fg}	2.342	—	—	2.580

Note: All values are given in MHz except C_{fg}, which is dimensionless. $\Delta w/\Delta_{lw} = 4$.

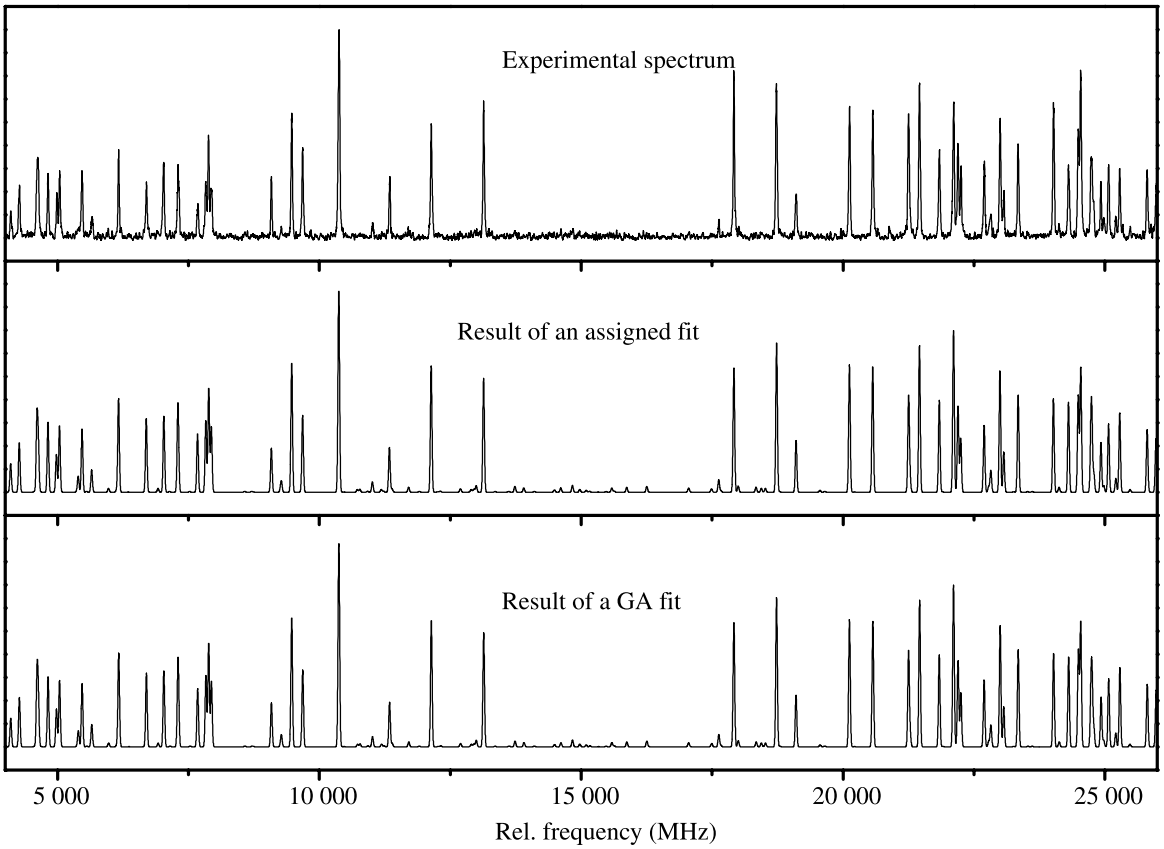
rovibronic transitions. This evaluation is performed in less than 2 h, without any prior knowledge of the molecular parameters.

4.4.2. [3-D][7-D]Phenol and [5-D][7-D]phenol

Another example of overlapping electronic origins of different isotopomers of phenol is the pair [3-D][7-D]phenol and [5-D][7-D]phenol. Here, we have to assign simultaneously two bands with different Lorentzian widths in the Voigt profiles. In a recent publication (26), the line widths of both isotopomers were obtained from a fit of some individual rovibronic lines of each species (26). Since the GA performs a line shape fit of the complete spectrum, it should yield more accurate values. In a first step, the inertial parameters were determined using the GA with $\Delta w/\Delta_{lw} = 5$. For the determination of the line

© 2004 NRC Canada

Fig. 5. Experimental rovibronic spectrum of [^{18}O][7-D]phenol/[^{16}O][7-D]phenol, along with the simulation using the parameters from an assigned fit and from a GA fit. Intensities are given in arbitrary units.



shape parameters, the parameter space for the inertial parameters was narrowed down to 1 MHz and the GA fit was performed with $\Delta w = 0$. The Gaussian width was fixed to the experimentally determined value of 25 MHz. The temperature dependence of the relative intensity n is described by a two-temperature model (28):

$$[15] \qquad n(T_1, T_2, w_T) = \mathrm{e}^{-E/kT_1} + w_T \mathrm{e}^{-E/kT_2}$$

Here, E is the energy of the lower state, w_T a weight factor, and T_1 and T_2 the two temperatures. The intensity ratio between the spectra is fit as well. This resulted in improved values for the Lorentzian component of the line width. The resulting parameters are presented in Table 9 and compared with the values of an assigned fit. While the inertial parameters all agree within their uncertainties, the line width parameters are quite different. From the Lorentzian widths, the S_1-state lifetimes could be determined to be 23.5 ns for [3-D][7-D]phenol and 18.5 ns for [5-D][7-D]phenol. These values differ considerably from 38.8 ns and 15.6 ns obtained from a line shape fit to individual transitions in the spectrum. We attribute this difference to the limited number of single rovibronic transitions that could be used in the analysis of the line shapes, given in ref. 26.

As discussed before, the sparse stick spectrum array cannot be used for a fit of a line shape parameter. Instead, the sum in eq. [3] runs over all 80 700 data points, compared to just 745 lines with an intensity of more than 0.001 in the stick spectrum. This of course slows down the calculation of the fitness function considerably. A fit using the sparse array was finished in only 4.5 min, while the calculation with all data points needed 12 min.

4.4.3. Benzonitrile–^{20}Ne and benzonitrile–^{22}Ne

In all the cases discussed so far, the relative intensity of the two spectra is approximately 1:1. The situation is much more complicated if both isotopomers have very different abundances.

We performed a fit of the rovibronic spectrum of the isotopomeric pair benzonitrile–^{20}Ne/benzonitrile–^{22}Ne in the natural abundance of ^{20}Ne/^{22}Ne (91:9). In this case, the GA has the much more difficult task of fitting quite a weak spectrum in the presence of a strong spectrum. The situation is further complicated by the fact that some of the lines present in the spectrum are due to benzonitrile monomer lines (the electronic origin of the monomer is shifted by about 4.3 cm^{-1} to higher frequency). Although the monomer origin has already been assigned (29), these monomer lines cannot be predicted with sufficient accuracy because they belong to very high J states.

The rovibronic spectrum of benzonitrile is of pure b-type. The neon atom is located above the aromatic ring, shifted slightly towards the cyano group. This structure gives rise to an axis switching. As a consequence, the transition moment in the cluster is oriented nearly along the inertial c-axis. For this molecular structure, an ac-hybrid is expected with strong c-type lines and much weaker a-type lines.

The results for the ac-hybrid type were checked against ab-, bc-, and abc-hybrid fits for consistency. The mean values for

© 2004 NRC Canada

Table 9. Molecular constants of [3-D][7-D]phenol and [5-D][7-D]phenol from the GA fit and an assigned fit (26) for comparison.

	[3-D][7-D]Phenol		[5-D][7-D]Phenol	
Parameter	GA	Assigned fit (26)	GA	Assigned fit (26)
A'' (MHz)	5337.98(79)	5338.161(166)	5349.82(8)	5349.789(175)
B'' (MHz)	2490.28(54)	2490.353(134)	2487.16(5)	2487.484(121)
C'' (MHz)	1698.58(31)	1698.567(65)	1697.98(4)	1698.088(76)
ΔA (MHz)	–309.32(8)	–309.42	–306.63(5)	–306.81
ΔB (MHz)	1.80(4)	1.69	0.31(5)	+0.08
ΔC (MHz)	–31.08(2)	–31.03	–31.26(3)	–31.13
T_1 (K)[a]	1.08	—	1.08	—
T_2 (K)[a]	2.81	—	2.81	—
w_T[a]	0.16	—	0.16	—
Ratio[b]	0.96	—	—	—
Δ_{Lorentz} (MHz)	8.57	10.2	6.77	4.1

[a]The assigned fit was performed with a one-temperature model.
[b]Ratio of intensities between the two spectra. No value given from the individual assigned fits.

Table 10. Results of a GA assignment and values of the inertial parameters of benzonitrile–^{20}Ne/benzonitrile–^{22}Ne.

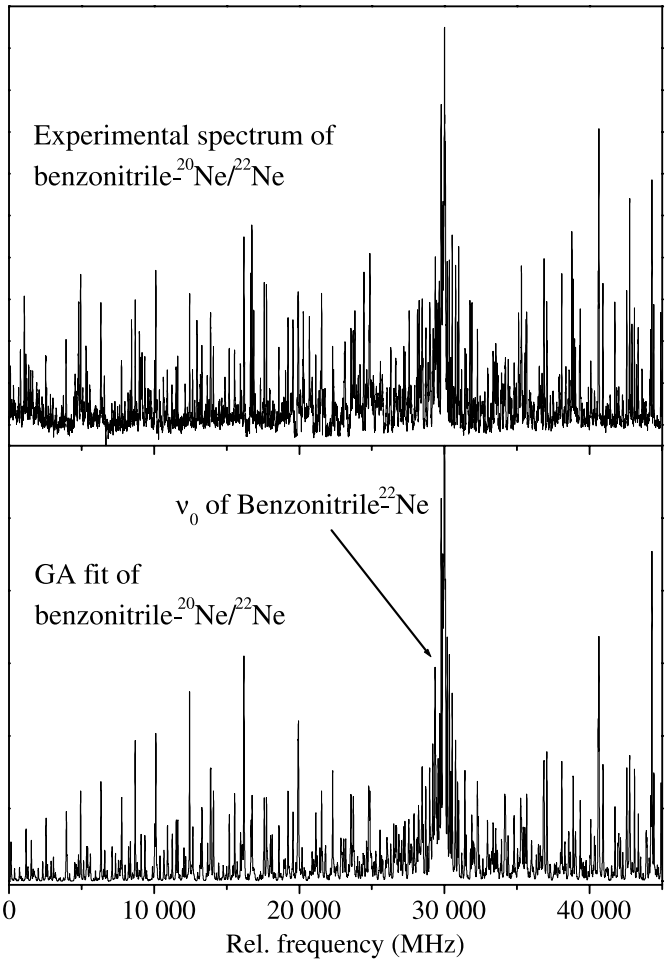
Parameter	Fit No. 1	Fit No. 2	Fit No. 3	Fit No. 4	Fit No. 5	Average
Benzonitrile–^{20}Ne						
A''	1 854.88	1 854.87	1 854.70	1 854.79	1 854.76	1 854.80
B''	1 193.99	1 193.80	1 194.06	1 194.11	1 194.02	1 193.99
C''	964.97	964.92	965.02	964.90	964.88	964.94
ν_0	30 327.45	30 328.14	30 325.94	30 325.97	30 328.11	30 327.12
ΔA	−2.83	−2.90	−2.78	−2.83	−2.88	−2.84
ΔB	−22.44	−22.41	−22.27	−22.32	−22.48	−22.39
ΔC	−22.44	−22.41	−22.27	−22.32	−22.48	−4.29
Benzonitrile–^{22}Ne						
A''	1 778.18	1 773.93	1 776.74	1 778.16	1 778.27	1 777.06
B''	1 178.15	1 178.14	1 165.85	1 178.86	1 177.87	1 175.77
C''	928.64	932.10	938.45	932.55	936.22	933.59
$\Delta\nu_0$	−1 454.95	−1 430.63	−1 450.33	−1 436.88	−1 461.91	−1 446.94
ΔA	25.75	26.28	26.13	24.93	25.40	25.70
ΔB	−16.05	−16.58	−13.43	−15.58	−13.59	−15.05
ΔC	−13.92	−14.35	−15.52	−14.43	−15.37	−14.72
C_{fg}	14.746	14.782	14.823	14.785	14.806	14.946

Note: All values are given in MHz except C_{fg}, which is dimensionles. $\Delta w/\Delta_{lw} = 1.5$. The five different fits were obtained with five different starting populations.

the cost functions are 7.95, 29.26, 9.27, and 7.18, respectively. Therefore, *ab*-hybrids can be discarded, which is in agreement with the geometry of the cluster. The *bc*-hybrid type fits slightly worse than the *ac*- type. However, the cost function differs only slightly because the spectrum is dominated by *c*-type lines. The *abc*-type did not improve the fit considerably. In conclusion, the initial assumption of the *ac*-hybrid type based on the approximate knowledge of the geometry was confirmed. Table 10 gives the molecular parameters obtained from a four-step GA fit. In the first step, $\Delta w/\Delta_{lw} = 10$ was employed. The search limits for the rotational constants were ±100 MHz for both isotopomers. The parameter limits were narrowed down to one-tenth that of the original size, centered around the best fit value of the first step. While the more abundant species (benzonitrile–^{20}Ne) presented no difficulties, the fit of the weaker component spectrum got trapped in a local minimum. This had two reasons: the intensity of the sub-spectrum of benzonitrile–^{22}Ne is only one-tenth that of the stronger component and the additional monomer lines have comparable intensities to the transitions of the stronger isotopic species. Thus, the parameter limits for the weaker sub-spectrum had to be reduced more slowly and in more steps. First, the parameter limits were reduced by only a factor of two, while $\Delta w/\Delta_{lw}$ was reduced to 7.5. In a subsequent step, $\Delta w/\Delta_{lw} = 5$ and limits of ±20 MHz for the rotational constants were employed. Finally, the molecular constants given in Table 10 were obtained for $\Delta w/\Delta_{lw} = 1.5$.

© 2004 NRC Canada

Fig. 6. Upper trace: experimental spectrum of benzonitrile–^{20}Ne/benzonitrile–^{22}Ne. Lower trace: simulation using the best parameters from Table 10. Intensities are given in arbitrary units.



In this case, the fit required some "fine tuning", which had to be done manually. Nevertheless, the results of the fit of the rovibronic spectrum of benzonitrile–^{20}Ne/benzonitrile–^{22}Ne (Fig. 6) show that even very congested spectra, with one spectral component much weaker than the other, can be assigned using the GA without any prior knowledge of geometry or molecular parameters.

5. Summary

In this paper we have shown that the GA is capable of treating a wide range of different spectra with complexity ranging from highly overlapping transitions to coinciding spectra of different isotopomers. Even if only a partial spectrum is available, the method is still successful. The GA succeeds in assigning the spectra and determines the molecular parameters without any prior knowledge of their values.

If the spectrum under study originates from a single vibronic transition, convergence could be reached in a one-step fit with a typical value for $\Delta w/\Delta_{lw}$ of 10. A great enhancement is obtained in the accuracy of the line shape and intensity parameters. While the assigned fit always uses the information from a few selected single rovibronic lines, the GA utilizes all transitions in the spectrum to adapt these parameters. In particular, the Lorentzian width (lifetime), the temperature, and the orientation of the transition dipole moment in the molecule or in the molecular cluster are determined more accurately from GA fits.

In cases in which the spectrum is composed of two subspectra, a more advanced strategy has to be followed. A preliminary fit with a relatively broad weight function was performed and subsequently refined with both smaller weight function widths and narrowed parameter search space. Using this technique, very complicated spectra of two overlapping bands could be fitted using the GA. Even a large difference in intensity between the overlapping band forms no obstacle.

The success of the GA procedure of automated fitting is based on the existence of a good model for the prediction of the spectra. This seems to be the only drawback until now. However, there are many cases for which a good model prediction exists, in particular in absorption, cavity ringdown, and laser-induced fluorescence spectra. We even expect that in the case of small and (or) local perturbations, the main spectral features that conform to the model can be extracted and hence the perturbations are isolated.

The examples discussed demonstrate the extreme power of the GA in automated fitting and assigning of very complex spectra, spectra that can hardly be assigned and analyzed with conventional methods. It has been shown that the evaluation of the fitness function can be made to a minor contribution in the computing time if the particular properties of F_{fg} are fully exploited. The computing power of modern PCs is more than adequate to perform the job in an acceptable time. This new technique opens the road to the analysis of the complex spectra of biomolecules and their building blocks.

Acknowledgements

We would like to thank Jos Hageman and Ron Wehrens for many helpful discussions. We thank Christian Ratzer for experimental help and Bert Groenenboom for giving the mathematical proof presented in Appendix A. The financial support of the Deutsche Forschungsgemeinschaft (SCHM 1043/9-4) is gratefully acknowledged. M.S. would like to thank the Nordrheinwestfälische Akademie der Wissenschaften for a grant, which made this work possible.

References

1. R.M. Helm, H.-P. Vogel, and H.J. Neusser. Chem. Phys. Lett. **270**, 285 (1997).
2. C.A. Haynam, D.V. Brumbaugh, and D.H. Levy. J. Chem. Phys. **81**, 2282 (1984).
3. L.A. Philips and D.H. Levy. J. Chem. Phys. **85**, 1327 (1986).
4. Y.R. Philips and D.H. Levy. J. Chem. Phys. **91**, 5278 (1989).
5. J.A. Hageman, R. Wehrens, R. de Gelder, W.L. Meerts, and L.M.C. Buydens. J. Chem. Phys. **113**, 7955 (2000).
6. R.E. Haupt and S.E. Haupt. Practical genetic algorithms. Wiley-Interscience, New York. 1988.
7. M. Mitchell. An introduction to genetic algorithms (complex adaptive systems). MIT Press, Cambridge, Mass. 1998.
8. M. Schmitt, J. Küpper, D. Spangenberg, and A. Westphal. Chem. Phys. **254**, 349 (2000).

© 2004 NRC Canada

9. M. Okruss, R. Müller, and A. Hese. J. Mol. Spectrosc. **193**, 293 (1999).
10. R.D. Suenram, F.J. Lovas, and G.T. Fraser. J. Mol. Spectrosc. **127**, 472 (1988).
11. W. Caminati and S. di Bernardo. J. Mol. Struct. **240**, 253 (1990).
12. S. Gerstenkorn and P. Luc. Atlas du spectre d'absoption de la molécule d'iode. CNRS, Paris. 1982.
13. H.C. Allen and P.C. Cross. Molecular vib-rotors. Wiley, New York. 1963.
14. S.C. Wang. Phys. Rev. **34**, 243 (1929).
15. D. Levine. PGAPack version 1.0 [computer program]. Available from ftp:ftp.mcs.anl.gov/pub/pgapck/pgapack.tar.z 1996.
16. J.H. Holland. Adaption in natural and artificial systems. MI: The University of Michigan Press, Ann-Arbor, Mich. 1975.
17. D.E. Goldberg. Genetic algorithms in search, optimisation and machine learning. Addison-Wesley, Reading, Mass. 1989.
18. I. Rechenberg. Evolutionsstrategie - Optimierung technischer Systeme nach Prinzipien der biologischen Evolution. Frommann-Holzboog, Stuttgart, Germany. 1973.
19. R. Wehrens, E. Pretsch, and L.M.C. Buydens. Anal. Chim. Acta, **388**, 265 (1999).
20. F. Gray. US Patent 2 632 058, 17 March 1953.
21. J. Schaffer, R. Caruana, L. Eshelman, and R. Das. *In* Proceedings of the third international conference on genetic algorithms. Morgan Kaufmann, San Mateo, Calif. 1989. p. 51.
22. M. Schmitt. C. Ratzer, and W.L. Meerts. J. Chem. Phys. **120**, 2752 (2004).
23. M.S. Ford, S.R. Haines, I. Pugliesi, C.E.H. Dessent, and K. Müller-Dethlefs. J. Electron Spectrosc. Relat. Phenom. **112**, 231 (2000).
24. J.K.G. Watson. J. Chem. Phys. **46**, 1935 (1967).
25. J.K.G. Watson. J. Chem. Phys. **48**, 4517 (1968).
26. C. Ratzer, J. Küpper, D. Spangenberg, and M. Schmitt. Chem. Phys. **283**, 153 (2002).
27. U. Dahmen, W. Stahl, and H. Dreizler. Ber. Bunsenges. Phys. Chem. **98**, 970 (1994).
28. Y.R. Wu and D.H. Levy. J. Chem. Phys. **91**, 5278 (1989).
29. D.R. Borst, T.M. Korter, and D.W. Pratt. Chem. Phys. Lett. **305**, 485 (2001).

Appendix A.

In this appendix we show that the real or complex matrix $\boldsymbol{W}$ with matrix elements $W_{ij} = w(r_i - r_j)$ is positive definite if $w(r)$ can be written as the inverse Fourier transform of a positive function $\tilde{w}(t)$. Let

$$[A.1] \quad w(r) = \int_{-\infty}^{\infty} \tilde{w}(t) e^{2\pi i r t} \mathrm{d}t$$

then

$$[A.2] \quad \boldsymbol{x}^{\dagger} \boldsymbol{W} \boldsymbol{x} = \sum_{i,j} x_i^* W_{ij} x_j$$

$$= \sum_{i,j} x_i^* \int_{-\infty}^{\infty} \tilde{w}(t) \exp\left[2\pi i (r_i - r_j) t\right] \mathrm{d}t \; x_j$$

$$= \int_{-\infty}^{\infty} \left| \sum_i x_i \exp\left[-2\pi i r_i t\right] \right|^2 \tilde{w}(t) \, \mathrm{d}t$$

Hence, if $\tilde{w}(t) > 0$ then $\boldsymbol{x}^{\dagger} \boldsymbol{W} \boldsymbol{x} > 0$ for any vector $\boldsymbol{x}$ and so $\boldsymbol{W}$ is positive definite. If $\tilde{w}(t)$ is zero for certain values of t, the integral is still positive. Note: one should read in eq. [4] $r_i = i$.

© 2004 NRC Canada

RKR-type inversion of the diatomic energy shifts due to breakdown of the Born–Oppenheimer approximation[1]

James K.G. Watson

Abstract: The principal effects of the breakdown of the Born–Oppenheimer approximation on the vibration–rotation energies of a diatomic molecule can be represented by the expectation values of terms to order (m_e/M_i) in the effective Hamiltonian, where m_e is the electron mass and M_i is the mass of atom i. This paper examines the possibility of inverting these expectation values to obtain the correction functions as functions of the internuclear distance r, using a generalization of the semiclassical Rydberg–Klein–Rees method. It is shown that the correction functions are not completely determinable from the inversion, and the form of the determinable combinations is obtained.

Key words: diatomic molecules, vibration–rotation energies, isotope effects, Born–Oppenheimer breakdown, Rydberg–Klein–Rees method.

Résumé : Les principaux effets de l'échec de l'approximation Born–Oppenheimer sur les énergies de vibration–rotation d'une molécule diatomique peuvent être représentés par les valeurs moyennes des termes d'ordre (m_e/M_i) de l'Hamiltonien effectif dans lequel m_e est la masse de l'électron et M_i est la masse de l'atome i. Dans ce travail, on a examiné la possibilité d'invertir ces valeurs moyennes afin d'obtenir les corrections comme fonctions de la distance internucléaire, r, en utilisant une généralisation de la méthode semi-classique Rydberg–Klein–Rees. On a démontré qu'il n'est pas possible de déterminer complètement les fonctions de correction à partir de l'inversion et on a obtenu la forme de combinaisons qui peuvent être déterminées.

Mots clés : molécules diatomiques, énergies de vibration–rotation, effets isotopiques, échec de l'approximation Born–Oppenheimer, méthode de Rydberg–Klein–Rees.

[Traduit par la Rédaction]

1. Introduction

The vibration–rotation energy levels of a set of isotopomers of a given diatomic molecule are frequently represented by the formula (1, 2)

$$[1] \qquad E_{vJ} = \sum_{kl} U_{kl} \left(1 + \sum_i \frac{m_e}{M_i} \Delta_{kl}^i\right) \times \left(\frac{v + 1/2}{\mu_C^{1/2}}\right)^k \left(\frac{J(J+1)}{\mu_C}\right)^l$$

where the coefficients U_{kl} and Δ_{kl}^i are isotope-independent. The coefficients U_{kl} come from a first-order semiclassical treatment (3) of the Born–Oppenheimer (BO) Hamiltonian for motion in the internuclear coordinate r,

$$[2] \qquad H_0 = \frac{1}{2\mu_C} p_r^2 + V_J(r)$$

Received 11 September 2003. Published on the NRC Research Press Web site at http://canjchem.nrc.ca/ on 26 August 2004.

J.K.G. Watson. Steacie Institute for Molecular Sciences, National Research Council of Canada, Ottawa, ON K1A 0R6, Canada. (e-mail: watson@hardy.sims.nrc.ca)

[1]This article is part of a Special Issue dedicated to the memory of Professor Gerhard Herzberg.

which contains the charge-modified reduced mass

$$[3] \qquad \mu_C = \frac{M_A M_B}{(M_A + M_B - C m_e)}$$

where C is the electric charge of the molecule AB in units of e, and

$$[4] \qquad V_J(r) = V(r) + \frac{\hbar^2 J(J+1)}{2\mu_C r^2}$$

is the effective potential energy. The correction terms in $U_{kl}\Delta_{kl}^i$ in eq. [1] are partly "Dunham corrections" from second-order semiclassical contributions (3) and partly contributions from H_1 due to Born–Oppenheimer breakdown (BOB) (2),

$$[5] \qquad H_1 = \sum_i (m_e/M_i) \left[\frac{1}{2\mu_C} p_r Q^i(r) p_r + \frac{\hbar^2}{2\mu_C r^2} R^i(r) J(J+1) + S^i(r)\right]$$

for a $^1\Sigma$ electronic state, where $Q^i(r)$, $R^i(r)$, and $S^i(r)$ are functions allowing for non-adiabatic and adiabatic electronic effects. The corrections $U_{kl}\Delta_{kl}^i$ in eq. [1] do not factorize naturally in this form (2, 4), and so there may occasionally seem to be anomalously large values of Δ_{kl}^i when U_{kl} is small. The remainder of the effective internuclear Hamiltonian,

$$[6] \qquad H = H_0 + H_1 + O\left(m_e^2/M_i^2\right)$$

 doi: 10.1139/V04-049 © 2004 NRC Canada

is usually regarded as negligible unless there is a near-degeneracy of electronic states.

The expectation value of H_1 over a radial wavefunction $|v, J\rangle$ is

$$[7] \qquad \langle v, J|H_1|v, J\rangle = \sum_i (m_e/M_i)\epsilon^i_{vJ}$$

where ϵ^i_{vJ} is the expectation value

$$[8] \qquad \begin{aligned}\epsilon^i_{vJ} &= \langle v, J|p_r Q^i(r) p_r/2\mu_C \\ &\quad + \hbar^2 J(J+1)R^i(r)/2\mu_C r^2 + S^i(r)|v, J\rangle \\ &= \sum_{kl} U_{kl}\left(\Delta^i_{kl} - \Delta^D_{kl}\right) \\ &\quad \times \left(\frac{v+1/2}{\mu_C^{1/2}}\right)^k \left(\frac{J(J+1)}{\mu_C}\right)^l\end{aligned}$$

where the Δ^D_{kl} are the Dunham corrections, which are the same for both atoms i, and can be calculated from the parameters of the BO potential (3).

Equation [8] raises the problem of the "inversion" of the ϵ^i_{vJ}, which can be regarded as observed quantities, to obtain, as far as possible, the functions $Q^i(r)$, $R^i(r)$, and $S^i(r)$. This is discussed here from a semiclassical point of view, as an extension of the familiar RKR (5–8) inversion of the BO energies. Previously, the inversion of the expectation values of a J-independent operator has been discussed (9, 10), but the fact that the present operator is J-dependent requires an extension of the theory.

2. Indeterminacy of $Q^{i(r)}$

The usual first-order semiclassical quantization condition is

$$[9] \qquad \int_{r^-_{vJ}}^{r^+_{vJ}} p_r\, dr = (h/2)(v+1/2)$$

where $r^\pm_{vJ}$ are the classical turning points in the effective potential $V_{\rm eff}$, which is taken in this section to be the full potential in $H_0 + H_1$. If we solve for p_r, the quantization condition gives

$$[10] \qquad \int_{r^-_{vJ}}^{r^+_{vJ}} (E_{vJ} - V_{\rm eff})^{1/2}\,(1+Q)^{-1/2}\, dr = \pi k(v+1/2)$$

where $Q = \sum_i (m_e/M_i)\, Q^i(r)$,

$$[11] \qquad \begin{aligned}V_{\rm eff}(r) &= V(r) + \frac{\hbar^2 J(J+1)}{2\mu_C r^2} + \sum_i (m_e/M_i) \\ &\quad \times \left[\frac{\hbar^2}{2\mu_C r^2} R^i(r) J(J+1) + S^i(r)\right]\end{aligned}$$

and

$$[12] \qquad k = \hbar/(2hc\mu_C)^{1/2}$$

if it assumed that the energies are in wavenumber units. Taking $(1+Q)^{-1/2} \approx 1 - \frac{1}{2}Q$, and then integrating the Q term by parts according to

$$[13] \qquad \begin{aligned}&-\frac{1}{2}\int_{r^-_{vJ}}^{r^+_{vJ}} [E_{vJ} - V_{\rm eff}(r)]^{1/2}\, Q(r)\, dr \\ &\quad = -\Big[[E_{vJ} - V_{\rm eff}(r)]^{1/2}\, A(r)\Big]_{r^-_{vJ}}^{r^+_{vJ}} \\ &\qquad - \frac{1}{2}\int_{r^-_{vJ}}^{r^+_{vj}} [E_{vJ} - V_{\rm eff}(r)]^{-1/2} V'_{\rm eff}(r) A(r)\, dr\end{aligned}$$

where

$$[14] \qquad A(r) = \frac{1}{2}\int_{r_0}^{r} Q(r')\, dr'$$

we find that the integrated part vanishes in eq. [13]. The second term on the right of eq. [13] can then be taken as the first correction term in a binomial expansion, to give the quantization condition

$$[15] \qquad \int_{r^-_{vJ}}^{r^+_{vJ}} [E_{vJ} - \tilde{V}_{\rm eff}(r)]^{1/2}\, dr = \pi k(v+1/2)$$

where

$$[16] \qquad \tilde{V}_{\rm eff}(r) = V_{\rm eff}(r) + V'_{\rm eff}(r)A(r)$$

The prime ($'$) here means differentiation with respect to r. Note that r_0 in the definition of $A(r)$ is arbitrary. This equivalence of the expectation value of a kinetic energy term to that of a potential energy term is a generalization of the virial theorem (11).

It is seen that the $Q^i(r)$ correction has the same effect on the energies as contributions from the $R^i(r)$ and $S^i(r)$ corrections. Thus, if we ignore higher-order terms by using $V_J(r)$ rather than $V_{\rm eff}(r)$, we see that the expectation value in eq. [8] is unchanged when $Q^i(r)$, $R^i(r)$, and $S^i(r)$ are replaced by

$$[17] \qquad \tilde{Q}^i(r) = 0$$

$$[18] \qquad \tilde{R}^i(r) = R^i(r) - 2A^i(r)/r$$

$$[19] \qquad \tilde{S}^i(r) = S^i(r) + V'(r)A^i(r)$$

where

$$[20] \qquad A^i(r) = A^i_0 + \frac{1}{2}\int_{r_e}^{r} Q^i(r')\, dr'$$

and $V(r)$ is the BO potential energy. The value of A^i_0 is arbitrary. The value of ϵ^i_{vJ} is therefore,

$$[21] \qquad \epsilon^i_{vJ} = \langle v, J|\tilde{S}^i(r) + \hbar^2 J(J+1)\tilde{R}^i(r)/2\mu_C r^2|v, J\rangle$$

and it is seen that $Q^i(r)$ is not separately determinable from the expectation values. At most, the combinations obtained from eqs. [18] and [19] by eliminating the arbitrary A^i_0 will be determinable.

© 2004 NRC Canada

3. Inversion of expectation values

The semiclassical expectation value of an operator $X_J(r)$ is (12)

$$[22] \qquad X_{vJ} = \frac{1}{\pi k}\frac{\partial}{\partial v}\int_{r_{vJ}^-}^{r_{vJ}^+} X_J(r)[E_{vJ} - V_J(r)]^{1/2}\,\mathrm{d}r$$

The classical turning points r_{vJ}^- and r_{vJ}^+ are the solutions of

$$[23] \qquad V_J(r_{vJ}^{\pm}) = E_{vJ}$$

A solution to this inversion problem for J-independent $X(r)$ has been given by Stwalley (9) and Watson (10). Here, we consider a more general version that is applied in Sect. 4 to the case of J-dependent $X_J(r)$. By changing v to v' in eq. [22], multiplying by $(E_{vJ} - E_{v'J})^{n-1/2}$, and integrating over v' from –1/2 to v, we find the master equation for inversion

$$[24] \qquad \int_{r_{vJ}^-}^{r_{vJ}^+} X_J(r)[E_{vJ} - V_J(r)]^n\,\mathrm{d}r = 2k\frac{2^{2n}(n!)^2}{(2n)!}\int_{-1/2}^{v} X_{v'J}(E_{vJ} - E_{v'J})^{n-1/2}\,\mathrm{d}v'$$

where the (now) left side has been evaluated by changing the order of integration. Note that for $n \geq 1$ the integrand on the left side of eq. [24] vanishes at both end points, and the integrand on the right vanishes at the upper end point.

The familiar RKR equations can be obtained by taking $X_J(r) \equiv 1$ in this equation. For the first RKR equation we take $n = 0$ and $J = 0$, to get

$$[25] \qquad r_v^+ - r_v^- = 2k\int_{-1/2}^{v}(E_v - E_{v'})^{-1/2}\,\mathrm{d}v'$$

The second RKR equation is obtained by taking $n = 1$, differentiating with respect to $J(J+1)$, putting $J = 0$, noting that $[\partial E_{vJ}/\partial J(J+1)]_{J=0} = B_v$, and using the first RKR equation. This procedure is simplified by introducing the operator

$$[26] \qquad D_j = \left[\frac{\partial}{\partial j} - \frac{\partial E_{vJ}/\partial j}{\partial E_{vJ}/\partial v}\frac{\partial}{\partial v}\right]$$

where j is defined as

$$[27] \qquad j = \hbar^2 J(J+1)/2hc\mu_C = k^2 J(J+1)$$

so that $V_J(r) = V(r) + j/r^2$. Then D_j commutes with E_{vJ}. If we operate with D_j on eq. [24] with $X_J(r) \equiv 1$ and $n = 1$ and then set $J = 0$, we get the second RKR equation

$$[28] \qquad \left[(r_v^+)^{-1} - (r_v^-)^{-1}\right] = -\frac{2}{k}\int_{-1/2}^{v} B_{v'}(E_v - E_{v'})^{-1/2}\,\mathrm{d}v'$$

because $D_j E_{v'J}|_{J=0} = B_{v'}/k^2$.

Let us now take $n = 0$ in eq. [24], and differentiate it with respect to v. For the derivatives of the turning points, we have from eq. [23]

$$[29] \qquad \frac{\partial r_{vJ}^{\pm}}{\partial v} = \frac{\omega_{vJ}}{V_J'(r_{vJ}^{\pm})}$$

where

$$[30] \qquad \omega_{vJ} = \partial E_{vJ}/\partial v$$

We, therefore, obtain

$$[31] \qquad \left[\frac{X_J(r)}{V_J'(r)}\right]_{r_{vJ}^-}^{r_{vJ}^+} = \frac{2k}{\omega_{vJ}}\frac{\partial}{\partial v}\int_{-1/2}^{v} X_{v'J}(E_{vJ} - E_{v'J})^{-1/2}\,\mathrm{d}v'$$

This is the first RKR-type equation for inverting expectation values. For $J = 0$, it is equivalent to eq. [15] of ref. 10.

The apparently singular terms on the right side of equations such as [31] can be avoided by integration by parts, which gives, for example,

$$[32] \qquad \int_{-1/2}^{v} X_{v'J}(E_{vJ} - E_{v'J})^{n-1/2}\,\mathrm{d}v' = -\frac{1}{(n+1/2)}\left[\frac{X_{v'J}}{\omega_{v'J}}(E_{vJ} - E_{v'J})^{n+1/2}\right]_{-1/2}^{v} + \frac{1}{(n+1/2)}\int_{-1/2}^{v}\frac{\partial}{\partial v'}\left(\frac{X_{v'J}}{\omega_{v'J}}\right) \times (E_{vJ} - E_{v'J})^{n+1/2}\,\mathrm{d}v' = \frac{1}{(n+1/2)}\left\{\frac{X_{eJ}}{\omega_{eJ}}(E_{vJ} - E_{eJ})^{n+1/2} + \int_{-1/2}^{v}\frac{\partial}{\partial v'}\left(\frac{X_{v'J}}{\omega_{v'J}}\right)(E_{vJ} - E_{v'J})^{n+1/2}\,\mathrm{d}v'\right\}$$

where e refers to equilibrium, $v = -1/2$. The right side can now be differentiated with respect to v, and gives an integrable singularity in the integrand. In the following equations, it is assumed that apparent singularities on the right sides have been removed by integrations by parts, repeatedly if necessary.

To obtain the second equation for inverting expectation values, we assume that $X_J(r)$ in eq. [24] is replaced by $X(r)$, independent of J, take $n = 1$, operate with D_j and then $\partial/\partial v$,

© 2004 NRC Canada

and put $J = 0$. The result is

$$[33]\quad \left[\frac{X(r)}{r^2V'(r)}\right]_{r_v^-}^{r_v^+} = \frac{2}{k\omega_v}\frac{\partial}{\partial v} \times \left\{\int_{-1/2}^{v} X_{v'}B_{v'}(E_v - E_{v'})^{-1/2}\,\mathrm{d}v' - 2\int_{-1/2}^{v} X_{Dv'}(E_v - E_{v'})^{1/2}\,\mathrm{d}v'\right\}$$

where $X_{Dv} = \partial X_{vJ}/\partial J(J+1)|_{J=0}$. Equation [33] is equivalent to eq. [16] of ref. 10.

The left sides of eqs. [31] and [33] can be solved for $X(r_v^{\pm})$ if the potential is known. Thus, there is in principle no indeterminacy in the solution for $X(r_v^{\pm})$.

4. RKR-type inversion of BOB functions

We now consider the J-dependent operator $X_J(r)$ given by

$$[34]\quad X_J(r) = \tilde{S}^i(r) + j\tilde{R}^i(r)/r^2$$

whose expectation values are the corrections ϵ^i_{vJ}.

To invert eq. [22] we want to evaluate both $\tilde{S}^i(r_v^{\pm})$ and $\tilde{R}^i(r_v^{\pm})$ at the classical turning points $r_v^{\pm}$. For each v we therefore need four equations. These are obtained by successive differentiations with respect to J, or equivalently with respect to j. For the first equation, we can use eq. [31] with this particular $X_J(r)$.

If we now take $n = 0$ in eq. [24] and operate with D_j, the left side gives

$$[35]\quad \int_{r_{vJ}^-}^{r_{vJ}^+} \frac{\partial X_J(r)}{\partial j}\,\mathrm{d}r - \left[\frac{X_J(r)}{r^2V_J'(r)}\right]_{r_{vJ}^-}^{r_{vJ}^+}$$

where

$$[36]\quad D_j r_{vJ}^{\pm} = -\frac{1}{(r_{vJ}^{\pm})^2 V_J'(r_{vJ}^{\pm})}$$

has been used. Then a differentiation by v gives

$$[37]\quad \left[\frac{1}{V_J'(r)}\left\{\frac{\partial X_J(r)}{\partial j} - \frac{\partial}{\partial r}\left(\frac{X_J(r)}{r^2V_J'(r)}\right)\right\}\right]_{r_{vJ}^-}^{r_{vJ}^+} = \frac{2k}{\omega_{vJ}}\frac{\partial}{\partial v}D_j\int_{-1/2}^{v} X_{v'J}(E_{vJ} - E_{v'J})^{-1/2}\,\mathrm{d}v'$$

This generalization of eq. [33] is the second RKR-type equation.

For the next equation, we take $n = 1$ in eq. [24] and operate twice with D_j and then once with $\partial/\partial v$. The result on the left side, using the fact that $X_J(r)$ is linear in j, is

$$[38]\quad -\left[\frac{\omega_{vJ}}{V_J'(r)}\left\{\frac{2}{r^2}\frac{\partial X_J(r)}{\partial j} - \frac{\partial}{\partial r}\left(\frac{X_J(r)}{r^4V_J'(r)}\right)\right\}\right]_{r_{vJ}^-}^{r_{vJ}^+}$$

Similarly, the fourth equation is obtained by taking $n = 2$, operating three times with D_j, and then differentiating with respect to v. The resulting left side is

$$[39]\quad \left[\frac{2\omega_{vJ}}{V_J'(r)}\left\{\frac{3}{r^4}\frac{\partial X_J(r)}{\partial j} - \frac{\partial}{\partial r}\left(\frac{X_J(r)}{r^6V_J'(r)}\right)\right\}\right]_{r_{vJ}^-}^{r_{vJ}^+}$$

Equations [31] and [37] and expressions [38] and [39] give the quantities obtained by inversion of the X_{vJ} values. Substituting eq. [34] into [31] and [37]–[39], letting $J \to 0$, and for convenience increasing n by 1, we see that the quantities determined are

$$[40]\quad \left[\frac{\tilde{S}^i(r)}{V'(r)}\right]_{r_v^-}^{r_v^+} = \frac{2k}{\omega_v}\frac{\partial}{\partial v}\int_{-1/2}^{v}\epsilon^i_{v'0}(E_v - E_{v'})^{-1/2}\,\mathrm{d}v'$$

and

$$[41]\quad \left[\frac{1}{V'(r)}\left\{\frac{n}{r^{2n}}\tilde{R}^i(r) - \frac{\mathrm{d}}{\mathrm{d}r}\left(\frac{\tilde{S}^i(r)}{r^{2n}V'(r)}\right)\right\}\right]_{r_v^-}^{r_v^+} = \left[\frac{n}{r^{2n}V'(r)}\left\{\tilde{R}^i(r) + \frac{2\tilde{S}^i(r)}{rV'(r)}\right\} - \frac{1}{r^{2n}V'(r)}\frac{\mathrm{d}}{\mathrm{d}r}\left(\frac{\tilde{S}^i(r)}{V'(r)}\right)\right]_{r_v^-}^{r_v^+} = (-1)^{n-1}\frac{2k}{\omega_{vJ}}\frac{2^{2n-2}(n-1)!}{(2n-2)!}\frac{\partial}{\partial v}D_j^n \times \int_{-1/2}^{v}\epsilon^i_{v'J}\,(E_{vJ} - E_{v'J})^{n-3/2}\,\mathrm{d}v'\Big|_{J=0}$$

with n= 1–3.

5. Solution of inversion equations

To discuss the solutions of these equations, we can first combine the three rotational equations corresponding to eq. [41] with n= 1–3 to eliminate $\tilde{R}^i(r_v^+)$ and $\tilde{R}^i(r_v^-)$ and produce a single equation for the quantity

$$[42]\quad 3\left[\frac{1}{r^2}\frac{\mathrm{d}}{\mathrm{d}V(r)}\left(\frac{\tilde{S}^i(r)}{V'(r)}\right)\right]_{r_v^-}^{r_v^+} - \left(r_v^+r_v^-\right)^2\left[\frac{1}{r^6}\frac{\mathrm{d}}{\mathrm{d}V(r)}\left(\frac{\tilde{S}^i(r)}{V'(r)}\right)\right]_{r_v^-}^{r_v^+}$$

© 2004 NRC Canada

We now have to consider the solution of eqs. [40] and [42] for $\tilde{S}^i(r_v^-)$ and $\tilde{S}^i(r_v^+)$.

The expansion of $\tilde{S}^i$ can be written

$$[43] \qquad \tilde{S}^i(r) = \tilde{S}^i_0 + \tilde{S}^i_1(r - r_e) + \tilde{S}^i_2(r - r_e)^2 + \ldots$$

Now, following Sandeman (13), we can expand the turning points in powers of the potential as

$$[44] \qquad r^{\pm} = \sum_{n=0} \alpha_n [V(r^{\pm})]^n \pm \sum_{n=0} \beta_n [V(r^{\pm})]^{n+1/2}$$

with $\alpha_0 = r_e$. This gives

$$[45] \qquad \frac{1}{V'(r^{\pm})} = \sum_{n=1} n\alpha_n [V(r^{\pm})]^{n-1} \pm \sum_{n=0} (n + 1/2)\beta_n [V(r^{\pm})]^{n-1/2}$$

Combining these equations, we get the expansion

$$[46] \qquad \frac{\tilde{S}^i(r^{\pm})}{V'(r^{\pm})} = \pm C^i(r^{\pm}) + D^i(r^{\pm})$$

$$[47] \qquad C^i(r^{\pm}) = \sum_{n=0}^{\infty} c^i_n [V(r^{\pm})]^{n-1/2}$$

$$[48] \qquad D^i(r^{\pm}) = \sum_{n=0}^{\infty} d^i_n [V(r^{\pm})]^n$$

where c^i_n and d^i_n are functions of the $\tilde{S}^i_n$, α_n, and β_n coefficients whose precise form is not required here. Expansions of this kind are also useful in evaluating RKR-type integrals (12). Here we get

$$[49] \qquad \left[\frac{\tilde{S}^i(r)}{V'(r)}\right]_{r_v^-}^{r_v^+} = 2C^i = 2\sum_{n=0}^{\infty} c^i_n E_v^{n-1/2}$$

and so, in principle, the c^i_n coefficients can be determined from eq. [40].

Substitution of eq. [46] in expression [42] gives, after some manipulation, the quantity

$$[50] \qquad \frac{\left[(r_v^+)^2 + (r_v^-)^2\right]\left[4(r_v^+ r_v^-)^2 - (r_v^+)^2 - (r_v^-)^2\right]}{(r_v^+ r_v^-)^4}\frac{dC^i}{dV} + \frac{\left[(r_v^+)^2 - (r_v^-)^2\right]^3}{(r_v^+ r_v^-)^4}\frac{dD^i}{dV}$$

As C^i is known from eq. [40], this allows the solution for dD^i/dV. Thus, all the d^i_n coefficients can be determined, in principle, except for d^i_0, which does not contribute to eq. [50].

From eqs. [46] and [48] it is seen that d^i_0 is the coefficient of $V'(r)$ in the expansion of $\tilde{S}^i(r)$. From eq. [19] this indeterminacy of d^i_0 therefore corresponds to the arbitrariness of A^i_0.

If $\tilde{S}^i(r)$ is known, it is then possible to determine $\tilde{R}^i(r) + 2\tilde{S}^i(r)/rV'(r)$ from eq. [41]. Thus, the only indeterminacy in $\tilde{R}^i(r)$ follows from the indeterminacy in A^i_0. In fact, the variation

$$[51] \qquad \delta\tilde{R}^i(r) = -2\delta A^i_0/r$$

$$[52] \qquad \delta\tilde{S}^i(r) = V'(r)\delta A^i_0$$

leaves eq. [41] invariant for all values of n, and so the indeterminacy cannot be resolved by using higher derivatives with respect to j.

These results show that there is only one degree of indeterminacy, corresponding to A^i_0, in the inversion of the ϵ^i_{vJ} data to give the functions $\tilde{R}^i(r)$ and $\tilde{S}^i(r)$. If these functions are combined to eliminate A^i_0, then the remaining combinations of parameters are determinable (14).

6. Discussion

There already exist a number of computer programs, such as those in refs. 15–22, to fit vibration–rotation frequencies of a range of isotopomers of a diatomic molecule, including the BOB terms, and there seems no reason for an additional program based on RKR-type inversion. However, it is valuable to consider such analytical approaches, because they help to distinguish between indeterminacies that are due to shortage of data and indeterminacies that are intrinsic to the Hamiltonian employed.

The present considerations show that there are intrinsic indeterminacies in the BOB Hamiltonian [5]. In the first place, the $Q^i(r)$ contribution is not distinguishable from those of $R^i(r)$ and $S^i(r)$. This leads to the problem of the inversion of eq. [21]. Since it is known (9, 10) that expectation values of J-independent operators can be inverted without indeterminacy, it may seem somewhat surprising that this does not apply to the expectation values ϵ^i_{vJ}. The reason is that there is a variation of the parameters given by eqs. [51] and [52], which is equivalent to

$$[53] \qquad \delta\tilde{S}^i(r) + j\delta\tilde{R}^i(r)/r^2 = \delta A^i_0 V'_J(r)$$

The expectation value [22] of this term involves the integral

$$[54] \qquad \int_{r_{vJ}^-}^{r_{vJ}^+} V'_J(r)\,[E_{vJ} - V_J(r)]^{1/2}\,dr = -\frac{2}{3}\left[\{E_{vJ} - V_J(r)\}^{3/2}\right]_{r_{vJ}^-}^{r_{vJ}^+} = 0$$

Thus, this variation of parameters does not affect the energy levels in first order. There is therefore a degree of indeterminacy in the values of the parameters. This possibility does not exist for a J-independent operator.

If we consider the expansion [43] and the similar expansion for $\tilde{R}^i(r)$, it is seen from eqs. [18] and [19] that

$$[55] \qquad \tilde{R}^i_0 = R^i_0 - \frac{2}{r_e}A^i_0$$

© 2004 NRC Canada

[56] $$\tilde{S}_1^i = S_1^i + V''(r_e)A_0^i$$

are not contaminated by terms from $Q^i(r)$. Only the combination $\tilde{R}_0^i + 2\tilde{S}_1^i/r_e V''(r_e)$ of these two parameters is independent of A_0^i and so is determinable. The way in which this indeterminacy affects actual fits is described in ref. 22. If we choose A_0^i to make $\tilde{S}_1^i = 0$, then

[57] $$\tilde{R}_0^i = R_0^i + 2S_1^i/r_e V''(r_e)$$

To break this indeterminacy requires additional data. The theoretical expression for the R^i function is (14)

[58] $$R^i = C_i - \sum_j \frac{C_j z_j^2}{r^2} + \frac{\mu_C g_J}{m_p}$$

where the C_j are effective charges on the atoms defined by

[59] $$\sum_j C_j = C, \qquad \sum_j C_j z_j = p/e$$

where p is the electric dipole moment, g_J is the rotational g-factor, m_p the proton mass, and z_j the coordinate of atom j referred to the nuclear centre of mass. While R^i and C_i are the same for all isotopomers, the second and third terms of eq. [58] are isotopomer-dependent. Thus, R^i can be calculated from measurements in electric and magnetic fields (or for several isotopomers in magnetic fields only). Constraining R_0^i to the equilibrium value is sufficient to remove the degree of indeterminacy represented by A_0^i, and allow a complete inversion to obtain $\tilde{R}^i(r)$ and $\tilde{S}^i(r)$.

References

1. A.H.M. Ross, R.S. Eng, and H. Kildal. Opt. Commun. **12**, 433 (1974).
2. J.K.G. Watson. J. Mol. Spectrosc. **80**, 411 (1980).
3. J.L. Dunham. Phys. Rev. **41**, 721 (1932).
4. R.J. Le Roy. J. Mol. Spectrosc. **194**, 189 (1999).
5. R. Rydberg. Z. Phys. **73**, 376 (1931).
6. O. Klein. Z. Phys. **76**, 226 (1932).
7. R. Rydberg. Z. Phys. **80**, 514 (1933).
8. A.L.G. Rees. Proc. Phys. Soc. **59**, 998 (1947).
9. W.C. Stwalley. Chem. Phys. Lett. **19**, 337 (1973).
10. J.K.G. Watson. J. Mol. Spectrosc. **74**, 319 (1979).
11. L.I. Schiff. Quantum Mechanics. 3rd ed. McGraw-Hill and Kōgakusha, New York and Tokyo. 1968.
12. S.M. Kirschner and J.K.G. Watson. J. Mol. Spectrosc. **47**, 234 (1973).
13. I. Sandeman. Proc. R. Soc. Edinburgh, **60**, 210 (1940).
14. J.K.G. Watson. J. Mol. Spectrosc. **217**, 157 (2003).
15. J.A. Coxon and P.G. Hajigeorgiou. J. Mol. Spectrosc. **203**, 49 (2000).
16. J.F. Ogilvie. J. Phys. B, **27**, 47 (1994).
17. H. Uehara. J. Mol. Spectrosc. **182**, 57 (1997).
18. M. Molski. J. Mol. Spectrosc. **185**, 256 (1997).
19. R.J. Le Roy and Y. Huang. J. Mol. Struct. (Theochem), **591**, 175 (2002).
20. M. Dulick, K.-Q. Zhang, B. Guo, and P.F. Bernath. J. Mol. Spectrosc. **188**, 14 (1998).
21. J.A. Coxon and M. Molski. PhysChemComm. **20**, 1 (2001).
22. J.K.G. Watson. J. Mol. Spectrosc. **223**, 39 (2004).

© 2004 NRC Canada

Can resonances occur in the photodissociation continuum of a diatomic molecule? The role of potential discontinuities[1]

Joel Tellinghuisen

Abstract: Continuum resonances are standard fare in the instructional literature for quantum mechanics, where they arise from the continuity conditions imposed on one-dimensional wavefunctions for piecewise-constant potential energy functions. Such resonance structure weakens progressively as the discontinuity in the potential is smoothed, showing that the structure is specifically attributable to the discontinuity. Since diatomic molecular potential energy curves seldom vary rapidly on the distance scale of the period of the wavefunction, such continuum resonances are not expected in absorption continua. A historically interesting prediction of such structure in the Schumann–Runge continuum ($B \leftarrow X$) of O_2 is attributed to the inadvertent incorporation of discontinuity in the B-state potential curve employed in the computations.

Key words: quantum mechanics, continuum resonance, diatomic absorption, photodissociation continuum, numerical methods.

Résumé : Les continuum de résonance sont des entités normales dans la littérature des étudiants de la mécanique quantique où elles découlent des conditions de continuité qui sont imposées aux fonctions d'ondes unidimensionnelles des fonctions d'énergie potentielle constantes. De telles structures de résonance perdent progressivement de l'importance lorsqu'on étale la discontinuité du potentiel, ce qui démontre que la structure peut être attribuée spécifiquement à la discontinuité. Comme les courbes d'énergie potentielle des molécules diatomiques varient rarement rapidement en fonction de l'échelle de distance de la période de la fonction d'onde, on ne s'attend pas à retrouver des tels continuum de résonances dans les continuum d'absorption. Une prédiction historiquement intéressante d'une telle structure dans le continuum de Schumann–Runge ($B \leftarrow X$) du dioxygène, O_2, est attribuée à l'incorporation accidentelle de la discontinuité dans la courbe de potentiel de l'état B utilisée dans les calculs.

Mots clés : mécanique quantique, continuum de résonance, absorption diatomique, continuum de photodissociation, méthodes numériques.

[Traduit par la Rédaction]

Introduction

The Schumann–Runge (SR) absorption transition of O_2 ($B^3\Sigma_u^- \leftarrow X^3\Sigma_g^-$) represents a prototypal diatomic photodissociation spectrum having an adjoining discrete spectrum. From a practical standpoint, this system is arguably the most important case of this type, since it largely accounts for the "vacuum" in "VUV". As such it received significant attention from Herzberg, especially in his landmark book on diatomics (1–3). Although the nature of the continuous absorption is now fairly well understood, it is only recently that it has arrived at this state (4–11). The absorption is essentially structureless in the region from the photodissociation limit at 175 nm to the peak near 143 nm. Structure does occur at shorter wavelengths, because of a strong *R*-dependence in the transition strength and a "ledge" in the adiabatic approximation of the B potential, resulting from interactions between the valence and Rydberg $^3\Sigma_u^-$ states that produce the adiabatic B and E states. However, an early attempt at quantitative analysis of the SR continuum predicted the occurrence of "wiggles" in the region of the strongest absorption, which were attributed to continuum resonances resulting from the presence of an attractive well in the potential (12). This result was never confirmed in subsequent treatments, but it was also never explained. A reexamination of the original treatment by Bixon et al. (12) has led me to conclude that the interesting structure in their computed spectrum was an artifact very likely stemming from an unphysical discontinuity inadvertently included in their B-state potential energy function. The present paper offers a more comprehensive look at the role of potential discontinuities in continuum resonances, with the conclusion that such structure must be very rare and weak in diatomic spectra, since realistic diatomic potentials are normally too smooth to support it.

To illustrate the last point first, consider the partial potential energy diagram for O_2 shown in Fig. 1 and the bound-free absorption spectra computed with these potentials in Fig 2. The two spectra in the latter figure are virtually identical, which implies that the B-state continuum wave-

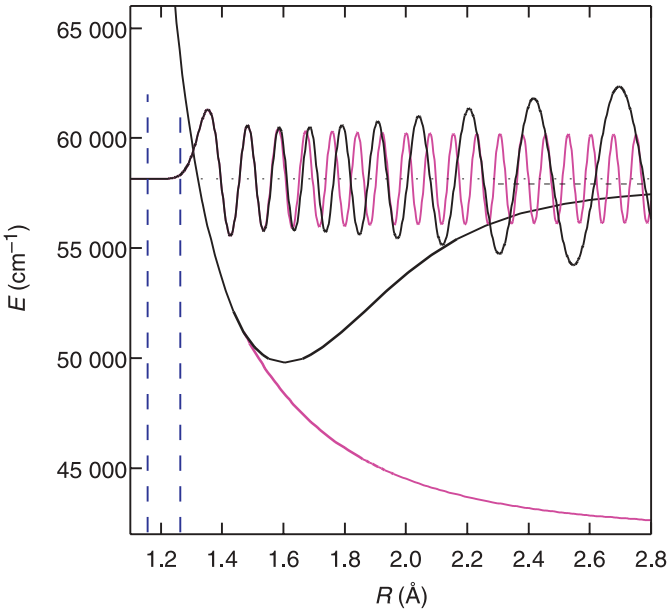
Received 17 December 2003. Published on the NRC Research Press Web site at http://canjchem.nrc.ca on 25 August 2004.

J. Tellinghuisen. Department of Chemistry, Vanderbilt University, Nashville, TN 37235, USA. (email: joel.tellinghuisen@vanderbilt.edu).

[1]This article is part of a Special Issue dedicated to the memory of Professor Gerhard Herzberg.

 doi: 10.1139/V04-047 © 2004 NRC Canada

Fig. 1. Potential curves and wavefunctions for the B state of O_2. The solid-black B curve consists of RKR turning points (13), extended at small R with an R^{-8} repulsion function. The magenta-coloured potential curve shares the same repulsive branch but dissociates to two ground state ^{3}P O atoms at 42 046 cm^{-1} above the ground-state minimum (cf. ^{3}P + ^{1}D at 57 914 cm^{-1} for the B state, marked by the lower dashed line segment to right). The dashed vertical lines denote the classical turning points for $v = 0$ in the X state. The wavefunctions are energy-normalized functions at an energy of 58 147 cm^{-1}, marked by the horizontal dotted line.



functions are identical where they overlap significantly with the X-state wavefunction. The energy-normalized wavefunctions shown in Fig. 1 indeed coincide at small R, in both shape and amplitude, and this in spite of their quite different nature where they diverge at larger R. This relationship has been illustrated before for a system in I_2 (14), and it is key to the realization that the Franck–Condon properties of such simple absorption spectra are determined solely by the shape of the final potential in the Franck–Condon region. This is true for the discrete region, too, in the case of a potential with a bound well, where the attractive branch of the potential serves just to "discretize" the spectrum (15, 16). From the standpoint of the continuum wavefunctions (ψ) themselves, which are obtained numerically in one pass by generating outward to large R and then normalizing (17), in a very real sense the ψs "know where they are going" right from the outset. So we might then ask, what could cause them to deviate from this course?

Figures 3 and 4 provide an answer to the question just posed: the ψs deviate when they encounter a sharp "bump", where sharp means abrupt on a distance scale comparable to the period of the wavefunction. However, even the small amount of smoothing illustrated by the dashed potential in Fig. 3 suffices to eliminate most of the resonance structure, the exception being the region very near threshold.

The properties exhibited for the wavefunctions in Fig. 3 can be seen also for the simple piecewise constant potentials used to illustrate continuum resonances in quantum mechan-

Fig. 2. Franck–Condon density (FCD) computed for absorption from $v = 0$ in the X state of O_2 to the two potentials illustrated in Fig. 1. The vertical line marks the photodissociation limit for the "real" potential, having the dashed spectrum.

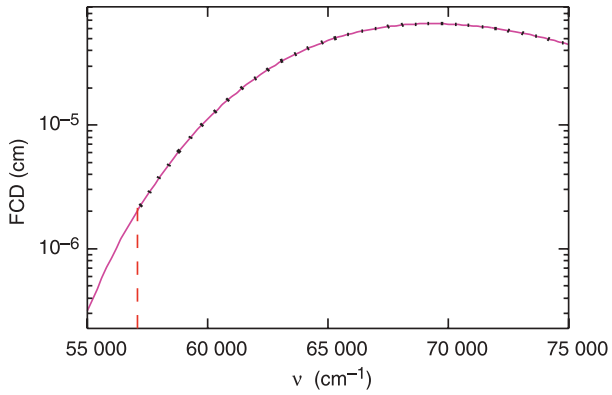
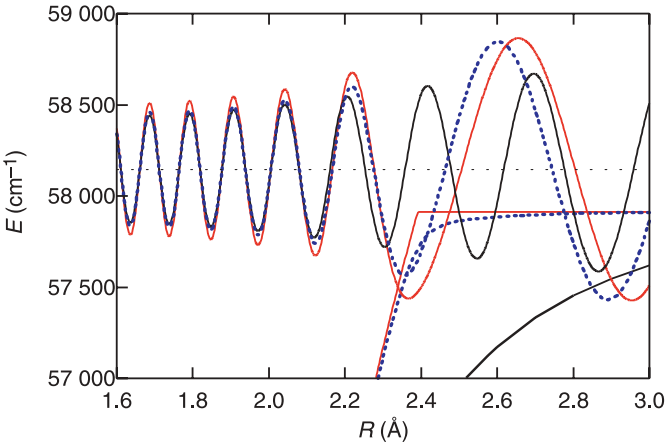


Fig. 3. Segment of RKR potential for B state (solid, lower right) and alternative extensions obtained by defining a Morse potential by ω_e and $\omega_e x_e$ for the B state (giving D_e = 11 800 cm^{-1}) and then chopping the attractive branch of the potential off at the true dissociation limit (D_e = 8121 cm^{-1}). The dashed potential curve was produced using an "avoided crossing" smoothing function. The wavefunctions were obtained for an energy of 58 147 cm^{-1} (dotted horizontal line), as in Fig. 1.



ics textbooks. Such examples prove both instructive and useful for checking computational procedures, so I turn my attention to them before returning to the O_2 historical puzzle.

Models and methods

The simplest model potential for a bound molecule is the piecewise constant potential illustrated in Fig. 5. The wavefunction in regions 1 and 2 can be taken as

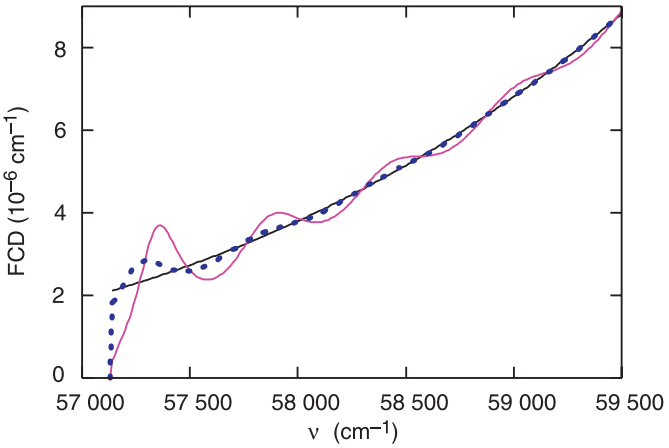
$$[1] \qquad \psi_1 = b_1 \sin k_1 x \text{ and } \psi_2 = b_2 \sin(k_2 x + \delta)$$

where k in each region is related to the kinetic energy ε in that region by

$$[2] \qquad k^2 = \frac{2\mu\varepsilon}{\hbar^2}$$

© 2004 NRC Canada

Fig. 4. FCD just above the photodissociation threshold, for potentials illustrated in Fig. 3. The continuum resonance at 57 360 cm^{-1} (magenta) corresponds to the energy used to generate the wavefunctions in Fig. 3. The three spectra are associated with the similarly depicted potential curves and wavefunctions in Fig. 3.



with μ the reduced mass and $\hbar$ Planck's constant divided by 2π. By making the wavefunction and its first derivative continuous at $x = a$, we obtain

$$[3] \qquad \left(\frac{b_1}{b_2}\right)^2 = \frac{\varepsilon_2}{\varepsilon_2 + (\varepsilon_1 - \varepsilon_2)\cos^2 k_1 a}$$

One of the two amplitudes is arbitrary until some normalization is chosen. In energy normalization, the amplitude is proportional to $\varepsilon^{-1/4}$ (17). Thus, if our wavefunction is normalized at large x, ${b_2}^2 \propto {\varepsilon_2}^{-1/2}$, and

$$[4] \qquad {b_1}^2 \propto \frac{{\varepsilon_2}^{1/2}}{\varepsilon_2 + (\varepsilon_1 - \varepsilon_2)\cos^2 k_1 a}$$

Alternatively, if ψ_1 were energy normalized in region 1 (e.g., for the dashed potential having $V = 0$ for all $x > 0$ in Fig. 5), it would have ${b_1}'^2 \propto {\varepsilon_1}^{-1/2}$. Any spectrum involving these wavefunctions would sense the square of the amplitude, so the ratio

$$[5] \qquad Q = \left(\frac{b_1}{b_1'}\right)^2 = \frac{(\varepsilon_1\varepsilon_2)^{1/2}}{\varepsilon_2 + (\varepsilon_1 - \varepsilon_2)\cos^2 k_1 a}$$

constitutes the continuum resonance spectrum. It shows specifically the effect of the potential step at $x = a$, and it varies between a maximum of $(\varepsilon_1/\varepsilon_2)^{1/2}$ and a minimum of $(\varepsilon_2/\varepsilon_1)^{1/2}$.

To investigate the effect of smoothing the discontinuity in $V(x)$ at $x = a$, we represent the potential by a hyperbolic tangent type function

$$[6] \qquad V(x) = \frac{V_0 y}{y + y^{-1}}, \qquad x > 0$$

where $y = \exp[p(x - a)]$. A large value of the parameter p gives a sharp step, while a small value yields a soft step.

All of the computations employed numerical methods like those described in ref. 17.

Fig. 5. Potential diagram for square well model. The energy goes to ∞ at $x = 0$. The subscripts on the kinetic energy ε designate regions 1 ($0 < x < a$) and 2 ($x \geq a$).

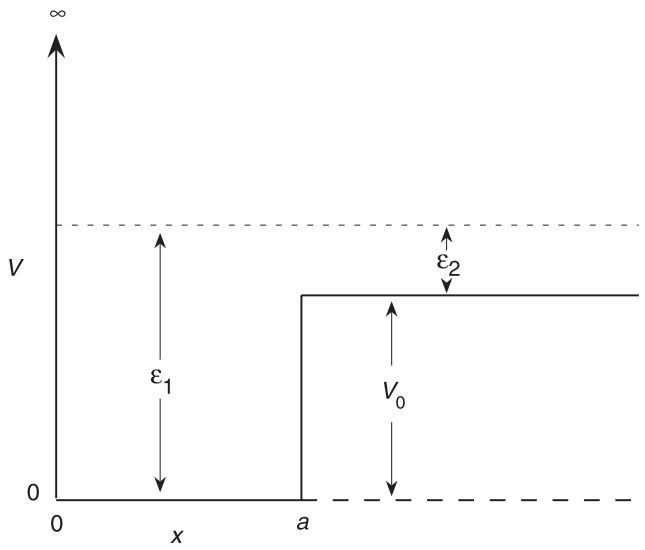
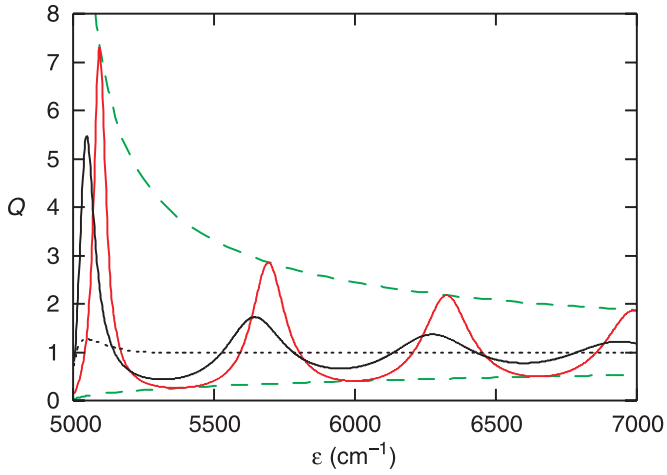


Fig. 6. Continuum resonance spectra for modified square well potential of eq. [6] having $V_0 = 5000$ cm^{-1}, $a = 1$ Å, μ = 10 amu, and $p = 1000$ $Å^{-1}$ (red), 50 $Å^{-1}$ (solid black), and 10 $Å^{-1}$ (fine dash). The broad dash lines delimit the extreme values of Q for $p = \infty$.



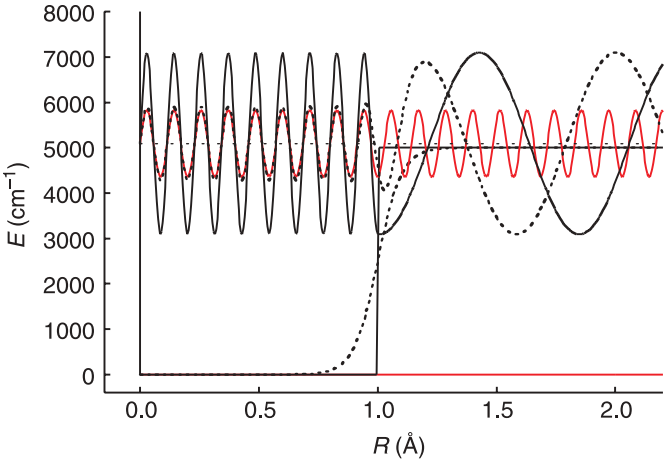
Results and discussion

Figure 6 illustrates continuum resonance spectra for the modified square well potential of eq. [6] with varying degrees of smoothing, while Fig. 7 shows the potentials and representative wavefunctions. The results for $p = 1000$ $Å^{-1}$ confirm the validity of the numerical methods, since a p this large gives essentially the original box potential. With $p =$ 10 $Å^{-1}$ (dashed potential in Fig. 7), the resonance structure is almost gone. Correspondingly, in region 1, the energy-normalized ψ at the energy of the strongest resonance is only slightly larger than that for $V_0 = 0$ (no well). (Of course, the dashed ψ matches the solid ψ in amplitude at large x, as it must.)

I return now to the O_2 puzzle that prompted this study. Bixon et al. (12) (BRJ) adjusted a linear repulsion potential

© 2004 NRC Canada

Fig. 7. Potential energy functions and wavefunctions relevant to Fig. 6 for p = 1000 (solid black) and 10 (dashed) Å^{-1}. Also shown (red) are $V(x)$ and $\psi(x)$ for V_0 = 0. Wavefunctions are centered at the energy ε_1 = 5094 cm^{-1} where they were generated (horizontal dashed line), corresponding to the first peak for p = 1000 Å^{-1} in Fig. 6.



in position and slope to achieve approximate agreement with the experimental B ← X data. When they attached a bound well to this potential at large R and repeated the computation, they obtained oscillations in the spectrum. For the well they used RKR points from Singh and Jain (18) and Richards and Barrow (19). Both of these show a great deal of scatter at high energy (Fig. 8), and BRJ did not explain how they dealt with this problem. Furthermore, the RKR curves and the derived linear potential are disjointed, suggesting that the BRJ working potential included an inadvertent discontinuity. I have checked this possibility by using the potential of Fig. 1 (with which the points of Richards and Barrow are reasonably consistent) at large R, and the linear potential of BRJ at small R, and repeating the computation of the spectrum for various assumed switchover distances. The two potential segments intersect near 1.29 Å with only a 20% slope discontinuity; when this distance is taken for switchover, the resulting spectrum agrees well with the spectrum of BRJ for the linear potential (Fig. 9). The spectrum obtained by jumping from the linear potential to the RKR curve at R = 1.326 Å (the minimum R of the Richards and Barrows points) agrees well in the positions of the wiggles but undershoots in their amplitudes. Moving the jump point to larger R increases the magnitude of the discontinuity and hence of the resonance structure; however, it also decreases the spacing of the peaks, so that for switchover at 1.365 Å, the structure more nearly matches that of BRJ in amplitude but includes an extra shoulder at low frequency.

Without detailed knowledge of how the RKR data were actually incorporated in the computations of BRJ, it is probably not possible to reproduce their results any better than shown in the solid spectrum of Fig. 9. For example, most commonly used algorithms for generating the wavefunctions (including the Numerov method used here and by BRJ) employ a working potential of points evenly spaced in R, which requires interpolation when RKR data are used to define the potential. The interpolators can perform badly on noisy data like those near dissociation in Fig. 8. To illustrate, if just the

Fig. 8. Repulsive branch of the O_2 B-state potential, from RKR calculations: ref. 18 (+), ref. 19 (○), ref. 20 (●) (cited by Richards and Barrow (19) for ν levels lower than those reported). The solid curve is that shown in Fig. 1, and the dashed line is as reported by Bixon et al. (12). Energies are relative to the minimum of the B potential.

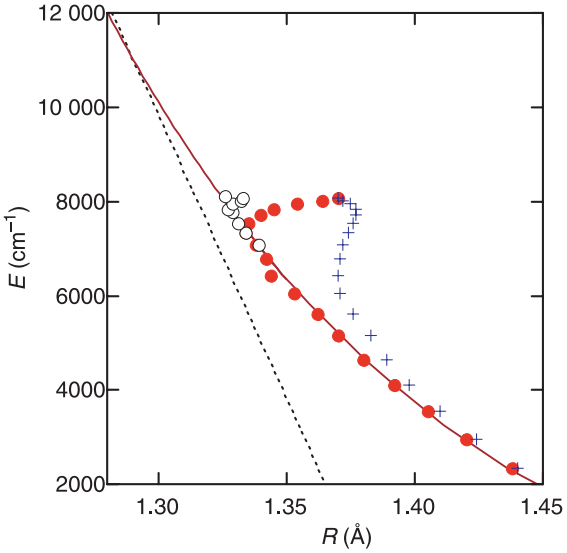
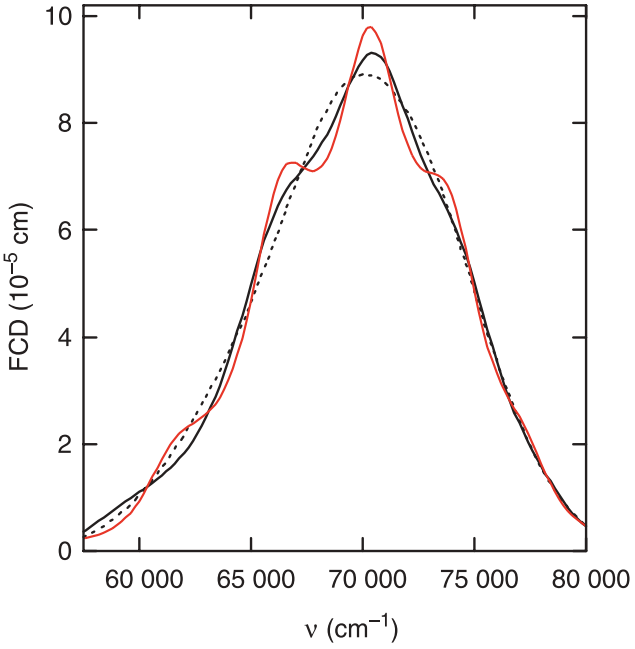


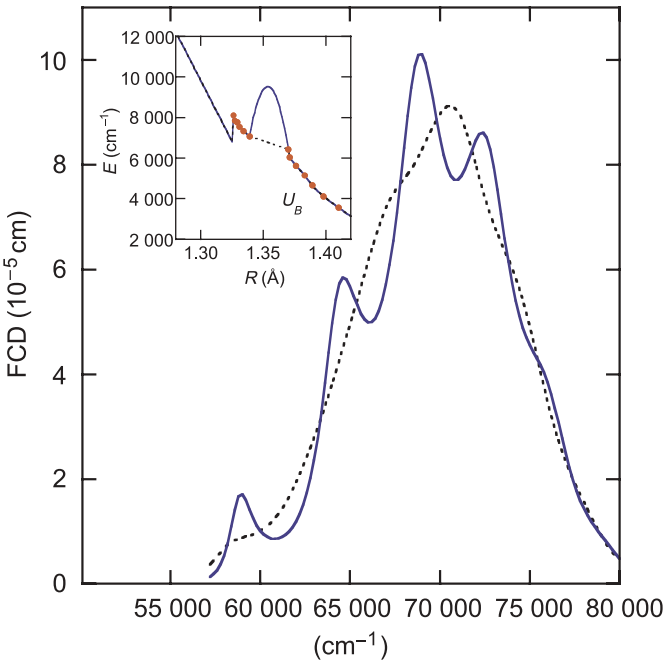
Fig. 9. O_2B ← X FCD computed for absorption from ν″ = 0 using linear potential from ref. 12 and Fig. 8 merged smoothly with potential of Fig. 1 at R = 1.29 Å (dashed), or discontinuously at 1.326 Å (solid black), and 1.365 Å (red).



monotonically varying (in R) data from refs. 18 and 19 are used to define the curve, even a quadratic Lagrangian interpolation can produce an anomalous bump in the potential at small R, which is sharp enough to act just like the other forms of discontinuity considered here, giving pronounced structure in the spectrum (Fig. 10). Thus, it seems likely that the computations reported in (12) were afflicted with artifactual potential errors of one or both of the types consid-

© 2004 NRC Canada

Fig. 10. O_2 B ← X FCD for v″ = 0 computed using linear potential from ref. 12 and selected, monotonically varying RKR points from refs. 18 and 19, with three-point (solid) and two-point (dashed) Lagrangian interpolation to produce the working potential. A segment of the latter is illustrated together with the relevant RKR points in the inset.



ered here; as concluded by others long ago, the resonance structure is not real.

A secondary moral of the present story is that in such molecular applications, one must take care to devise model potential energy functions that are realistic. Another illustration of this point comes from a study of the predissociation of the C state of N_2^+ by the B state. The C state is embedded in the continuum of the B state, with only very small Franck–Condon overlap between the two, making the computations very sensitive to the potentials (21, 22). When the B-state potential was represented by a cut-off Morse curve like that shown in Fig. 3 instead of by its RKR curve, the predicted C → B predissociation rates decreased by four orders of magnitude, causing earlier workers to dismiss this process as the major mode of C-state predissociative decay (21).

Conclusion

I return now to the question posed in the title. Most realistic potentials do not include the kinds of discontinuities and abrupt changes considered here, so we expect any actual continuum resonance structure to be subtle to the point of possibly escaping experimental detection. Since the requirement is a relatively rapid variation of the potential energy function on the distance scale of the wavefunction, the best chances for observation would seem to be in light molecules (small μ) at small kinetic energies, for example just above a barrier. Le Roy and Bernstein (23) computed several such resonances in the ground state of H_2 but noted that they were "too diffuse to be spectroscopically observable". Another qualifying example is the very narrow "hole" in the Franck–Condon density right at threshold, as noted by Allison and Dalgarno (15). In this case, as the kinetic energy approaches zero, the period of the wavefunction becomes infinite, so that even the very small variation in the potential energy function in the approach to dissociation might be viewed as significant on the distance scale of the wavefunction.

With the unintentional exception of the lowest frequencies in the highly structured spectrum in Fig. 10, I have specifically excluded from consideration here cases where the continuum levels are partially bound behind a potential barrier. Such shape resonances are certainly real and observable. The presence of a barrier can also affect the structure in the continuum. For example, if the model square well potential treated above and illustrated in Figs. 5 and 7 is altered to include a square barrier $V_1 > V_0$ in a region $a \le x \le a_1$, the continuity conditions on the wavefunction lead to a much richer interference-type structure in the pure continuum ($\varepsilon > V_1$). By using smoothing functions like eq. [6], one can "turn off" the structure associated with either the discontinuity at $x = a$ or that at $x = a_1$, or both.

References

1. J. Curry and G. Herzberg. Ann. Phys. **19**, 800 (1934).
2. G. Herzberg. Spectra of diatomic molecules. 2nd ed. Van Nostrand, Toronto. 1950.
3. P. Brix and G. Herzberg. Can. J. Phys. **32**, 110 (1954).
4. A.C. Allison, A. Dalgarno, and N.W. Pasachoff. Planet. Space Sci. **19**, 1463 (1971).
5. D.C. Cartwright, N.A. Fiamengo, W. Williams, and S. Trajmar. J. Phys. B, **9**, L419 (1976).
6. S.T. Gibson, H.P.F. Gies, A.J. Blake, D.G. McCoy, and P.J. Rogers. J. Quant. Spectrosc. Radiat. Transfer, **30**, 385 (1983).
7. A.C. Allison, S.L. Gubermann, and A. Dalgarno. J. Geophys. Res. **91**, 10 193 (1986).
8. J. Wang, D.G. McCoy, A.J. Blake, and L. Torop. J. Quant. Spectrosc. Radiat. Transfer, **38**, 19 (1987).
9. J.J. Lin, D.W. Hwang, Y.T. Lee, and X. Yang. J. Chem. Phys. **109**, 1758 (1998).
10. N. Balakrishnan, M.J. Jamieson, A. Dalgarno, Y. Li, and R.J. Buenker. J. Chem. Phys. **112**, 1255 (2000).
11. B.R. Lewis, S.T. Gibson, F.T. Hawes, and L.W. Torop. Phys. Chem. Earth Part C, **26**, 519 (2001).
12. M. Bixon, B. Raz, and J. Jortner. Mol. Phys. **17**, 593 (1969).
13. P.H. Krupenie. J. Phys. Chem. Ref. Data, **1**, 423 (1972).
14. J. Tellinghuisen. J. Chem. Phys. **80**, 5472 (1984).
15. A.C. Allison and A. Dalgarno. J. Chem. Phys. **55**, 4342 (1971).
16. J. Tellinghuisen. J. Chem. Phys. **59**, 849 (1973).
17. J. Tellinghuisen. Adv. Chem. Phys. **60**, 299 (1985).
18. N.L. Singh and D.C. Jain. Can. J. Phys. **40**, 520 (1962).
19. W.G. Richards and R.F. Barrow. Proc. Phys. Soc. London, **83**, 1045 (1964).
20. J.T. Vanderslice, E.A. Mason, and W.G. Maisch. J. Chem. Phys. **32**, 515 (1960).
21. J. Tellinghuisen and D.L. Albritton. Chem. Phys. Lett. **31**, 91 (1975).
22. A.L. Roche and J. Tellinghuisen. Mol. Phys. **38**, 129 (1979).
23. R.J. Le Roy and R.B. Bernstein. J. Chem. Phys. **54**, 5114 (1971).

© 2004 NRC Canada

Attosecond molecular spectroscopy — The one-electron H_2^+ system[1]

André D. Bandrauk and Hong Shon Nguyen

Abstract: Numerical solutions of the time-dependent Schrödinger equation for a 1-D model non-Born–Oppenheimer H_2^+ are used to illustrate the nonlinear, nonperturbative response of molecules to intense ($I \geq 10^{13}$ W/cm^2), ultrashort ($t < 10$ fs) laser pulses. Molecular high-order harmonic generation (MHOHG) is shown to be an example of such response, and the resulting nonlinear photon emission spectrum is shown to lead to the synthesis of single attosecond (10^{-18} s) pulses. Application of such ultrashort pulses to the H_2^+ system results in localized electron wave packets whose motion can be detected by asymmetry in the photoelectron spectrum generated by a subsequent probe attosecond pulse, thus leading to measurement of electron motion in molecules on an attosecond time scale.

Key words: attosecond spectroscopy, attosecond photoionization.

Résumé : On utilise des solutions numériques de l'équation de Schrödinger qui dépend du temps pour un modèle 1-D non-Born–Oppenheimer du H_2^+ pour illustrer la réponse non perturbante et non linéaire de molécules à d'intenses ($I \geq 10^{13}$ W/cm^2) et ultracourtes ($t < 10$ fs) pulsions laser. On montre que la génération d'harmonique moléculaire d'ordre élevée, « MHOHG », est un exemple d'une telle réponse et on montre aussi que le spectre d'émission photonique non linéaire qui en résulte conduit à la synthèse de pulsations attoseconde (10^{-18} s). L'application de telles pulsations ultracourtes au système H_2^+ conduit à des paquets d'onde électronique localisés dont on peut détecter le mouvement par asymétrie dans le spectre photoélectronique généré par une sonde subséquente de pulsation attoseconde qui conduit donc à la mesure du mouvement électronique dans les molécules à une échelle de temps de l'attoseconde.

Mots clés : spectroscopie attoseconde, photoionisation attoseconde.

[Traduit par la Rédaction]

Introduction

Advances in current laser technology allow experimentalists to have access to new laser sources for examining molecular structure and dynamics on the natural time scales for atomic (vibrational) motion, femtoseconds (1 fs = 10^{-15} s). These new sources are ultrashort ($t_p \leq 10$ fs) and intense ($I \geq 10^{14}$ W/cm^2) (1). Such pulses lead to a new regime of laser–matter interaction, the nonlinear, nonperturbative regime. Thus, since the atomic unit (au) of electric field strength $E_0 = e/a_0^2 = 5 \times 10^9$ V/cm ($a_0 = 1$ au $= 0.0529$ nm) corresponds to an au of intensity, $I_0 = cE_0^2/8\pi = 3.5 \times 10^{16}$ W/cm^2, laser intensities approaching I_0 have led to the discovery of new nonlinear phenomena in laser–atom experimental and theoretical studies (2), such as above–threshold ionization (ATI), the multiphoton equivalent of single-photon photoionization, and high-order harmonic generation (HOHG).

The study of interactions of intense, ultrashort laser pulses with molecules is a relatively new science (3) with the first discovery of nonlinear, nonperturbative laser–molecule interaction leading to a new concept, laser–induced molecular potentials (LIMPs), predicted as early as 1981 (4) and confirmed experimentally recently (5, 6). At the very high intensities now available ($I \geq 10^{14}$ W/cm^2), one now must consider dissociative ionization so that one must deal with bound–continuum transitions both in the electronic and nuclear Hilbert space. Multiphoton, nonperturbative transitions in the nonlinear Hilbert space describing photodissociation only via LIMPs can be treated adequately using a coupled-equations approach based on the dressed molecule representation (3). Inclusion of ionization involves treating numerically the complete field–electron–nuclear, non-Born–Oppenheimer problem, and this has been exactly solved recently for the 1-D H_2^+ system (7), leading to the first calculation of nonlinear molecular photoelectronic spectra or ATI (8), and the concomitant Coulomb explosion (CE) spectra (9, 10). This benchmark calculation has led to a new method of measuring nuclear wave functions by laser Coulomb explosion imaging (LCEI) (9, 10).

Electronic interaction with radiation in molecules differs from that of atoms due to the large delocalization of electrons in the former. As early as 1939, Mulliken explained intense absorption bands due to large transition moments in molecules (11). Thus, in H_2^+, the electronic transition moment between the HOMO ($1\sigma_g$) and LUMO ($1\sigma_u$) $\mu(R) = \langle 1\sigma_g|z|1\sigma_u\rangle = R/2$ leads to large nonperturbative radiative interactions at large distances ($V(R) = RE/2$) in a field of strength E. As an example, 1 au of field strength leads to 1 au = 27.2 eV of radiative interaction at the equilibrium dis-

Received 9 February 2004. Published on the NRC Research Press Web site at http://canjchem.nrc.ca/ on 26 August 2004.

A.D. Bandrauk[2,3] and H.S. Nguyen. Laboratoire de Chimie Théorique, Faculté des Sciences, Université de Sherbrooke, Sherbrooke, QC J1K 2R1, Canada.

[1]This article is part of a Special Issue dedicated to the memory of Professor Gerhard Herzberg.

[2]Corresponding author (e-mail: andre.bandrauk@usherbrooke.ca).

[3]Canada Research Chair in Computational Chemistry and Photonics.

 doi: 10.1139/V04-080 © 2004 NRC Canada

tance $R \simeq 2$ au in H_2^+. Thus, the combination of large electronic transition moments in symmetric molecules and current high laser intensities results readily in nonperturbative radiation–molecule interactions. Such effects lead to LIMPs (4–6) and charge resonant enhanced ionization (CREI), whereby molecular ionization rates can exceed that of atomic fragments by orders of magnitude at large critical internuclear distance $R_c \simeq 2R_e$, where R_e is the equilibrium distance (12–14). Quasi-static models of atom–laser field interaction (2) have been extended to nonperturbative laser–molecule interactions with the tunnelling ionization of Stark-displaced LUMOs leading to a simple, consistent explanation of CREI and CE in molecules for one- or odd-electron molecular systems (12–14).

Exact numerical solution of two-electron molecules H_2 (15, 16) and H_3^+ (17) in intense laser fields in the Born–Oppenheimer approximation (static nuclei) has shown the importance of the *ionic* states (e.g., H^+H^- in H_2), predicted by Herzberg to exist in the UV spectral region (18), as *doorway* states for CREI in these systems. Recently, the ionic state of O_2, O^+O^-, has been identified by ZEKE experiments (19). Such states have large dipole moments equal to the internuclear distance R and thus can lead to large radiative interactions $V(R) = ER$ exceeding molecular dissociation energies at current laser intensities. The study of molecules in the nonlinear, nonperturbative regime of molecule–radiation interaction is thus a new science requiring nonperturbative theories and numerical methods to treat laser control and manipulation of molecules in this regime (20, 21).

One of the seminal ideas emanating from simple quasi-static models of electron ionization in atoms is the possibility of *recollision* of the ionized electron with its parent ion (22). The returning energy of the electron at the nuclei can be shown to satisfy a simple law, which explains the maximum energy of harmonics emitted by such a recolliding electron,

$$[1] \qquad N_m \hbar\omega = I_p + 3.17U_p$$

where N_m is the maximum harmonic order, I_p is the ionization potential, and U_p is the ponderomotive or oscillatory energy of an electron of mass m in a pulse of frequency ω and intensity I,

$$[2] \qquad U_p(\text{au}) = I/4m\omega^2 = 3.4 \times 10^{21} I\,(\text{W/cm}^2)\lambda^2(\text{nm})$$

The corresponding field-induced displacement of such an ionized electron is given by the expression

$$[3] \qquad \alpha(\text{au}) = eE/m\omega^2 = 2.4 \times 10^{-12}\left[I\left(\text{W/cm}^2\right)\right]^{1/2}\lambda^2(\text{nm})$$

Thus, at an intensity $I = 10^{14}$ W/cm^2 and wavelength $\lambda = 1064$ nm, $U_p = 10.5$ eV and $\alpha = 1.2$ nm. We have shown that collision of ionized electrons with neighboring ions in molecules can lead to even larger harmonic orders with photon energies of $6U_p$ up to $12U_p$, thus extending the recollision energy cut-off law (eq. [1]) (23).

Using ultrashort pulses ($t \leq 5$ fs) results in continuum HOHG in the region of the cut-off law (eq. [1]) from which by selecting a slice of the spectrum one can synthesize *attosecond* (as) pulses. First experimental results on the production and measurement of a 650-as soft-X-ray pulse from high-intensity ionization of Ar atoms was reported in refs. 24 and 25. This opens up new possibilities for studying and controlling electron dynamics in atoms and molecules on attosecond time scales. We have recently shown that attosecond pulses can be used to measure the absolute electric field of few-cycle laser pulses (26) and to attain *attosecond control* of ionization and increase HOHG intensities, and thus create new single X-ray or UV pulses as short as 250 as (27). We illustrate, in the present paper, from numerical solutions of the time-dependent Schrödinger equation (TDSE) for a 1-D H_2^+ model with full electron–nuclear dynamics, i.e., from non-Born–Oppenheimer simulations, our proposed methodology for producing attosecond pulses from a molecular medium. Finally, we demonstrate from solutions of the TDSE how a pump–probe experiment of the photoionization of H_2^+ using attosecond pulses can allow one to study the evolution of the movement of localized electron wave packets, thus leading to a new attosecond molecular spectroscopy. Such experiments should now be feasible with the recent discovery of HOHG from ions themselves at high intensities (28).

A non-Born–Oppenheimer 1-D TDSE for H_2^+ in intense laser fields

The exact 1-D TDSE for H_2^+ is solved numerically, describing both coupled electron (Z-coordinate) and internuclear (R-coordinate) proton coordinates by the following equation in atomic units ($\hbar = m_e = e = 1$, $m_p/m_e = 1837$, $c = 137$; m_e and m_p are electron and proton masses) (7):

$$[4] \qquad i\frac{\partial\psi(Z,R,t)}{\partial t} = \hat{H}(Z,R,t)\psi(Z,R,t)$$

where

$$[5] \qquad \hat{H}(Z,R,t) = \hat{H}_R(R) + V_C(Z,R) + \hat{H}_Z(Z)$$

$$[6] \qquad \hat{H}_Z(Z) = -\beta\frac{\partial^2}{\partial Z^2} - \kappa E(t); \qquad \hat{H}_R(R) = -\frac{1}{m_p}\frac{\partial^2}{\partial R^2} + \frac{1}{R}$$

$$[7] \qquad \beta = \frac{2m_p + m_e}{4m_p + m_e}; \qquad \kappa = 1 + \frac{m_e}{2m_p + m_e}$$

$$[8] \qquad V_C(Z,R) = -\frac{1}{\left[a + (Z \pm R/2)^2\right]^{1/2}}$$

The Hamiltonian (eq. [5]) is the exact three-body Hamiltonian obtained after separation of the center-of-mass motion, since we are working in the dipole approximation ($r/\lambda \ll 1$), where the electric field is time-dependent only (3). The Coulomb potential now is a 1-D potential requiring a softening parameter a, which is set at $a = 1$ to obtain the correct I_p for H_2^+ near equilibrium. The corresponding I_p of a 1-D H atom with $a = 1$ is 0.67 au.

The softened V_C now contains no singularity so a high-order split-operator method (29) is used to propagate the total TDSE (eq. [4]) for a pulse length t_p. The integration step in space is $\delta z = 0.25$ au $\sim 10^{-2}$ nm, which means that grids with $3000^2 \simeq 10^7$ points are used. The temporal time step is $\delta t = 0.03$ au $= 0.7$ as, so that over a thousand time steps are required for a 10-fs pulse. The electric field $E(t)$ needs special care since pulse fields must have total area zero, a consequence of

© 2004 NRC Canada

Maxwell's equations (1). Thus, the electric field $E(t)$ is defined from the vector potential

$$[9] \qquad A(t) = -cE_0(t)\sin\left[\omega(t - t_m) + \phi\right]/\omega$$

$$[10] \qquad E(t) = -(1/c)\partial A(t)/\partial t$$

where $t_m = \tau/2$, i.e., half the pulse length. We generally used the pulse envelope $E_0(t)$ in the following form:

$$[11] \qquad E_0(t) = E_0 \sin^2(\pi t/\tau), \qquad 0 \le t \le \tau$$

With a pulse length $t_p = 4$ cycles $= 10.6$ fs for a 800 nm Ti:Sapphire laser, the pulse half-width (FWHM) is then given by $\tau_p = 0.3641 t_p \simeq 4$ fs. Our definition of $E(t)$ via $A(t)$ guarantees that $A(0) = A(\tau) = E(0) = E(\tau) = 0$.

The emitted radiation spectrum, constituting the HOHG spectrum in the presence of an intense laser field, can be obtained from the time-dependent acceleration for an electron in a potential $V(r)$ (29),

$$[12] \qquad a(t) = \frac{\mathrm{d}^2}{\mathrm{d}t^2}\langle r\rangle = \langle\psi(t)| - \partial V/\partial r|\psi(t)\rangle$$

The wave function $\psi(t)$ is the solution of the TDSE (eq. [4]). The Fourier transform of $a(t)$ — $a(\omega)$, from which one obtains the power spectrum of HOHG, $|a(\omega)|^2$ — is given by

$$[13] \qquad a(\omega) = i(2\pi)^{-1/2}\mathrm{e}^{-i\omega\tau}\dot{d}(\tau) + i\omega\mathrm{e}^{i\omega\tau}d(\tau) - \omega^2\int_0^\tau \mathrm{e}^{-i\omega t}d(t)\,\mathrm{d}t$$

The final integral in eq. [13] is the HOHG power spectrum using the dipole form $d(t) = \langle\psi(t)|r|\psi(t)\rangle$. Clearly, this is only valid if the transient $\dot{d}(\tau) = \frac{\mathrm{d}}{\mathrm{d}t}(d(t))|_{t=\tau}$ and $d(\tau)$ vanish at the end of the pulse. The acceleration form emphasizes maximum acceleration as in the case of a recolliding electron (22, 23). Since the energy E of such an electron is $3U_p \le E \le 10U_p$, where U_p is the ponderomotive energy (eq. [2]), at high intensities one has highly oscillatory electron wave functions so that solving the TDSE (eq. [4]) requires highly accurate numerical procedures (7, 29).

Attosecond pulse synthesis

As hinted in the *Introduction*, one of the great advances, if not breakthroughs, emanating from research on the nonlinear, nonperturbative response of atoms to short intense laser pulses has been the synthesis of attosecond pulses (24, 25). The source of attosecond radiation is HOHG by recollision of the ionized electron with its parent (22) or neighboring ions (23). Unfortunately, the efficiency of such spectra is low, as illustrated in Fig. 1. The dashed line represents the HOHG of H_2^+ with *moving* nuclei (i.e., non-Born–Oppenheimer) exposed to a single 10 fs, 800 nm pulse with peak intensity $I = 6 \times 10^{13}$ W/cm^2. Perusal of the spectrum shows the high inefficiency of the radiation coherently emitted owing to low ionization from tunnelling and the uncontrolled spreading of the ionized but returning (recolliding) electon wave packet (22, 23).

Fig. 1. HOHG power spectrum $|a(\omega)|^2$ (arbitrary units) for non-Born–Oppenheimer H_2^+ excited by an 800 nm, 10 fs, 6×10^{13} W/cm^2 IR pulse in combination with a 600 as (0.6 fs), 115 nm, UV probe at 2×10^{13} W/cm^2 and phase difference $\phi = \omega t = -0.2\pi$ (see inset). Solid line: fs + as pulse excitation. Dashed line: single fs pulse excitation.

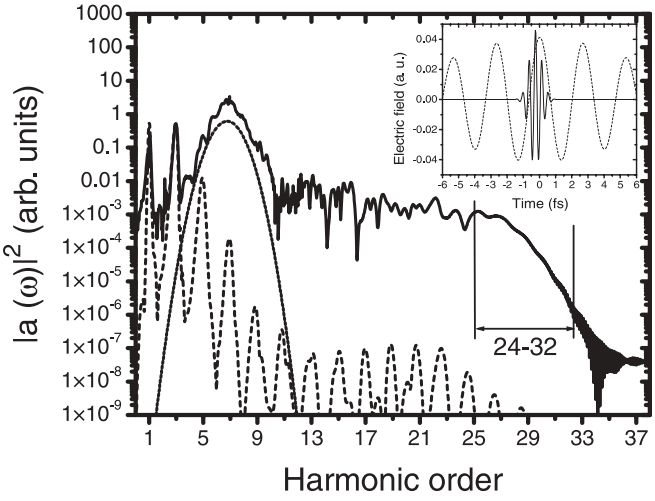
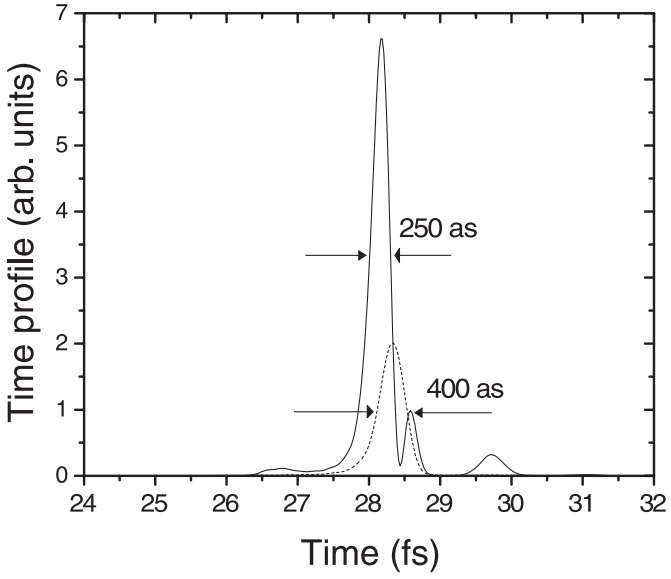


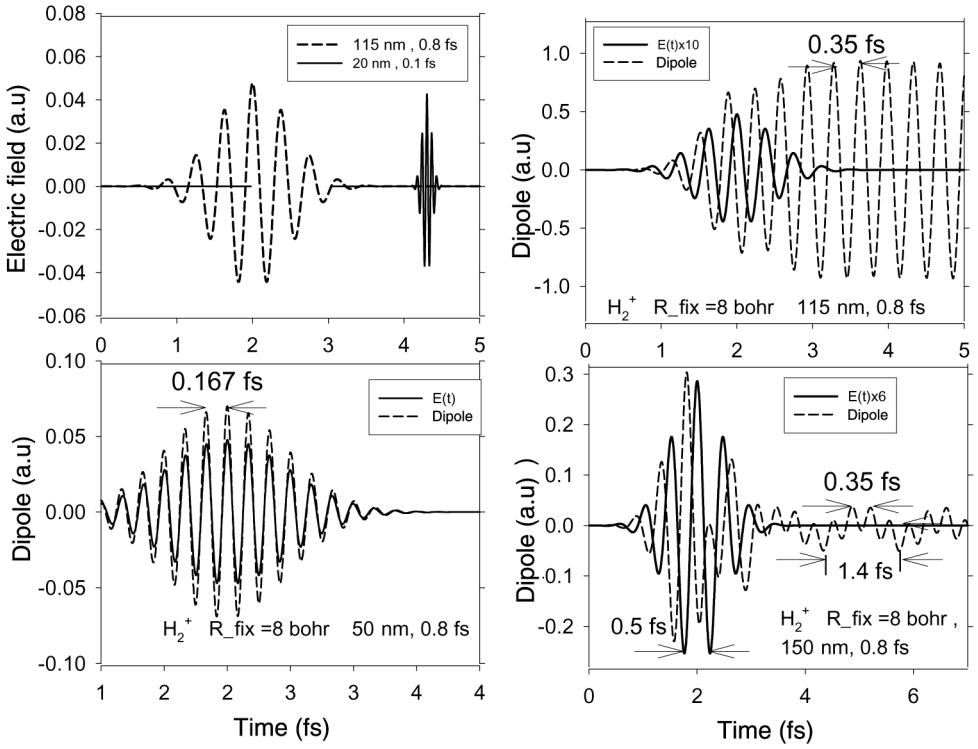
Fig. 2. Attosecond (as) pulses obtained from the continuous harmonics at relative phase $\phi = \omega t = -0.2\pi$ (inset Fig 1): 400 as from $24 < N < 32$; 250 as from $21 < N < 32$ (N is the order of the harmonic).



To enhance such low HOHG efficiencies, we originally suggested two-colour excitation to pre-ionize the electron by a high-frequency (3ω) field with subsequent control by an intense fundamental field (ω) (30). We have recently reformulated this idea by proposing a combination of an attosecond VUV pulse and an intense, short, 800 nm pulse (26). The advantage of this new approach is that the *pump* attosecond pulse has a large energy bandwidth and thus produces an initially narrow spatial electron wave packet, which is subsequently *controlled* by intense, short (fs) low-frequency pulses. As seen in Fig. 1, the

© 2004 NRC Canada

Fig. 3. Resulting induced dipoles (in atomic units) for H_2^+ at $R = 8$ au excited by 50 nm, 115 nm, and 150 nm 0.8 fs (800 as) pulses.



HOHG spectrum is now enhanced by several orders of magnitude. The spectrum is broad and quasi-continuous near the maximum order cut-off (N_m) predicted by eq. [1].

Such a spectrum can be used to synthesize new single UV pulses as short as 250 as, as illustrated in Fig. 2. This is obtained by combining continuous coherent radiation as an example for the order $24 \leq N \leq 32$, i.e.,

$$[14] \qquad a(t) = \int_{24\omega}^{32\omega} a(\omega) \mathrm{e}^{i\omega t} \mathrm{d}\omega$$

The end result is more intense attosecond pulses that are sensitive to the relative phase of the two colours (see inset of Fig. 1). Maximum enhancement of the new attosecond pulses is obtained at the relative phase $\phi = \omega t = -0.2\pi$, in contradiction to the atomic recollision model, which predicts the maximum order N_m for ionization at phase $\omega t = +0.1\pi$, with zero initial velocity due to tunnelling ionization (22,23). This phase sensitivity is an extension of *coherent control* of multiphoton processes (31) into the nonlinear, nonperturbative regime of laser–molecule interaction studied in the present paper.

Electron localization

In the previous section, we showed how the molecular ion H_2^+ can be used to create intense sub-femtosecond or, equivalently, attosecond pulses in the VUV frequency (wavelength) region. Thus, as shown in Figs. 1 and 2, combining harmonics by filtering techniques (2,3) between the 24th and 32nd will create sub-femtosecond pulses in the 30 nm region with considerable bandwidth. In the present section, we examine the broadband electronic excitation of H_2^+ at fixed internuclear distance $R = 8$ au, which is excited by an 800 as (0.8 fs), 115 nm *pump* pulse followed by a 100 as (0.1 fs), 20 nm *probe* pulse (Fig. 3). The latter induces direct one-photon ionization and we use the corresponding photoelectron spectrum to monitor the subsequent electron motion. All calculations were performed using the numerical code to solve the TDSE (eq. [4]) but with nuclei fixed at $R = 8$ au since the pulses are much shorter than the typical H atom motion time of ~10 fs. The TDSE thus yields the exact electronic wave function $\psi(Z, t)$, from which one can calculate the induced dipole moment $d(t) = \langle \psi(Z, t)|Z|\psi(Z, t)\rangle$.

Excitation at 50 nm shows that the induced dipole (Fig. 3) is completely in phase with the field $E(t)$, since such short wavelengths ionize the electron, which then follows the field. At 115 nm, which corresponds nearly to the H atom 1*s*–2*p* transition, one observes that the dipole is out of phase with the electric field $E(t)$ but shows a periodic oscillation of 0.35 fs or equivalently a photon energy at 105 nm ($\lambda = \tau c$). The dipole oscillations resulting from 800 as, 150 nm excitations are much more reduced in intensity. The obvious explanation is that at 115 nm excitation, one is exciting electronic states by transition to $2\sigma_u$ orbitals and others formed from 2*s* and (or) $2p\sigma$ atomic orbitals of H, whereas at 150 nm one is below such resonances and the induced dipole is much reduced. Thus, the resulting electronic wave function can be represented as the combination

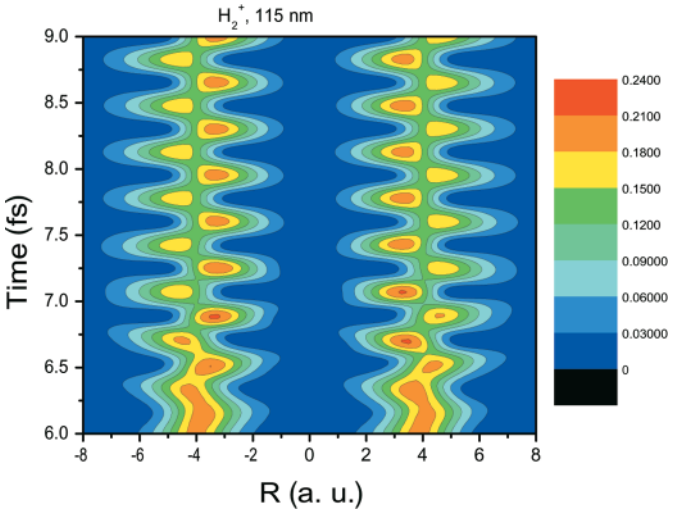
$$[15] \qquad \psi(t) = c_1(t)\psi_{1\sigma_g} + c_2(t)\psi_{2\sigma_u}$$

The corresponding induced dipole can be readily calculated to be

$$[16] \qquad d(t) = \langle \psi(t)|Z|\psi(t)\rangle = c_1(t)c_2^*(t)\langle 1\sigma_g|Z|2\sigma_u\rangle \, \mathrm{e}^{i(E_1 - E_2)t} + \text{c.c.}$$

© 2004 NRC Canada

Fig. 4. Electron probability $|\psi(Z,t)|^2$ at $R = 8$ au following excitation at 115 nm with a 0.8 fs pulse (see Fig. 3).



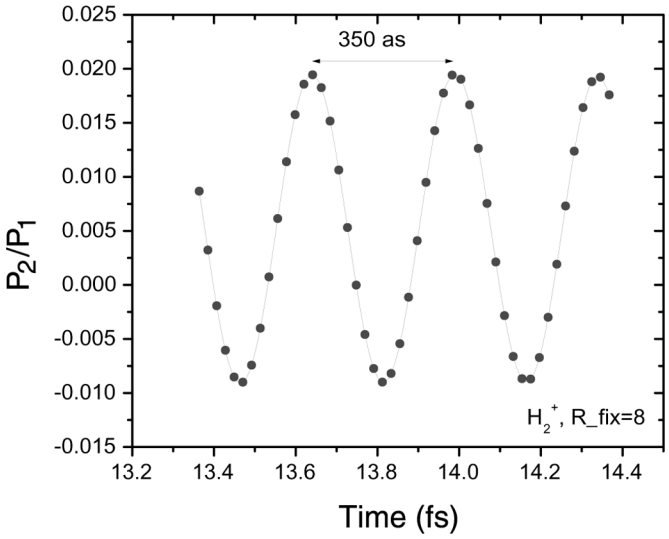
where c.c. is the complex conjugate. This induced dipole oscillates at the frequency corresponding to the energy difference $E_1 - E_2$ between the ground $1\sigma_g$ and excited $2\sigma_u$ molecular orbitals at $R = 8$ au. Furthermore, since $1\sigma_g \simeq (1/\sqrt{2})[1s_a + 1s_b]$ and $2\sigma_u \simeq (1/\sqrt{2})[2p\sigma_a - 2p\sigma_b]$ have the largest dipole $\langle 1\sigma_g|Z|2\sigma_u\rangle \simeq \langle 1s|Z|2p\sigma\rangle$, then the resulting time-dependent wave function $\psi(t)$ is an *sp* hybrid $(1s \pm 2p\sigma)$ situated on each proton. This laser-induced hybridization is clearly evident in Fig. 4, where we illustrate the electron density $|\psi(Z,t)|^2$ as a function of time. One observes initially that the electron is delocalized equally between the two protons at $Z = \pm 4$ au. After excitation with a 0.8 fs, 115 nm pulse, one sees the electron density polarized inside the molecular bond towards $Z = 0$, corresponding to a single *sp* hybrid (i.e, $s + p$), which oscillates between the two nuclei with the period of the energy difference $E_1 - E_2 = 0.35$ fs or 350 as. Since this oscillation is an induced dipole corresponding to oscillation from H^+H to HH^+ electronic configurations, emitted radiation will occur at the wavelength 105 nm. However, this will give no indication of the position of the electron.

We, therefore, propose herein a spectroscopic method of spatially locating the electron. This is based on the resulting ionization asymmetry predicted from ionization by intense, ultrashort pulses and used to measure the electric field phase profile of such pulses by attosecond probe pulses (26). Thus, as shown in Fig. 3, a 20 nm, 100 as pulse is used to ionize the *sp* hybrids prepared by the 115 nm, 800 as prepulse. As illustrated in Fig. 5, the resulting ionization asymmetry is defined as

$$[17] \qquad P_2/P_1 = \frac{P_- - P_+}{P_- + P_+}$$

where $P_{-(+)}$ is the left (right) ionization probability collected at opposing directions. This asymmetry pulsates precisely with the frequency corresponding to the energy difference $E_1 - E_2$ between the ground and excited states, which are coherently excited by the first (115 nm) attosecond pulse.

Fig. 5. Asymmetry in the ionization yield (P_2/P_1, eq. [17]) of the directional photoelectron spectrum of the electron distributions (Fig. 4) as a function of time delay between a 20 nm, 0.1 fs (100 as) ionization pulse and the pump probe.



Conclusion

We have shown from solution of the TDSE for H_2^+ that we can generate efficiently new ultrashort single attosecond pulses by the combination of a previously obtained attosecond probe with an intense, short IR pulse such as a 10 fs, 800 nm Ti:Sapphire pulse. Other methods have produced trains of attosecond pulses (33). Single attosecond pulses (as demonstrated) can be used to create localized electron wave packets in molecules that oscillate between nuclei on these attosecond time scales. Measuring the directional photoelectron spectrum of such wave packets or hybrids produces ionization asymmetries, which follow the electon position in the molecule on attosecond time scales.

Acknowledgements

We thank Paul Corkum (National Research Council (NRC), Ottawa) and Ferencz Krausz (Vienna) for "illuminating" discussions on attosecond pulse metrology.

References

1. T. Brabec and F. Krausz. Rev. Mod. Phys. **72**, 545 (2000).
2. M. Gavrila. Atoms in intense laser fields. Academic Press, New York. 1992.
3. A.D. Bandrauk. Molecules in laser fields. Marcel Dekker, New York. 1994.
4. A.D. Bandrauk and M.L. Sink. J. Chem. Phys. **74**, 1110 (1981); Chem. Phys. Lett. **57**, 569 (1978).
5. C. Wunderlich, E. Kohler, H. Figger, and T. Hansch. Phys. Rev. Lett. **78**, 2333 (1997).
6. D. Pavicic, H. Figger, and T. Hansch. Eur. Phys. J. **D26**, 39 (2003).
7. S. Chelkowski, C. Foisy, and A.D. Bandrauk. Phys. Rev. **A57**, 1156 (1998).
8. I. Kawata and A.D. Bandrauk. Phys. Rev. **A67**, 013 407 (2003).

© 2004 NRC Canada

9. S. Chelkowski, P.B. Corkum, and A.D. Bandrauk. Phys. Rev. Lett. **82**, 3416 (1999).
10. A.D. Bandrauk and S. Chelkowski. Phys. Rev. Lett. **87**, 273 004 (2002).
11. R.S. Mulliken. J. Chem. Phys. **7**, 20 (1939).
12. T. Zuo and A.D. Bandrauk. Phys. Rev. **A52**, 2511 (1995); **54**, 3254 (1996).
13. T. Seideman, M.Y. Ivanov, and P.B. Corkum. Phys. Rev. Lett. **75**, 2819 (1995).
14. S. Chelkowski and A.D. Bandrauk. J. Phys. **B28**, L723 (1995).
15. I. Kawata, H. Kono, and A.D. Bandrauk. Phys. Rev. **A62**, 031 401 (2000).
16. K. Harumiya, H. Kono, and A.D. Bandrauk. Phys. Rev. **A66**, 043 403 (2002).
17. I. Kawata, H. Kono, and A.D. Bandrauk. Phys. Rev. **A64**, 043 911 (2001).
18. G. Herzberg. Spectra of diatomic molecules. Van Nostrand, Amsterdam. 1951.
19. J.D. Martin and J.W. Hepburn. Phys. Rev. Lett. **79**, 3154 (1997).
20. A.D. Bandrauk, Y. Fujimura, and R.J. Gordon (*Editors*). Laser control and manipulation of molecules. ACS Symposium Series 821. American Chemical Society, Washington, D.C. 2002.
21. A.D. Bandrauk, M. Delfour, and C. LeBris (*Editors*). Quantum control. Lecture notes and proceedings. Vol. 33. Am. Math. Soc. Philadelphia, Pa. 2003.
22. P.B. Corkum. Phys. Rev. Lett. **71**, 1994 (1993).
23. A.D. Bandrauk and H. Yu. Phys. Rev. **A59**, 539 (1999); J. Phys. **B31**, 4243 (1998).
24. M. Hentschel, R. Kienberger, Ch. Spielmann, G.A. Reider, N. Milosevic, T. Brabec, P. Corkum, U. Heinzmann, M. Drescher, and F. Krauz. Nature (London), **414**, 509 (2001).
25. R. Kienberger, M. Hentschel, M. Uiberacker, Ch. Spielmann, M. Kitzler, A. Scrinzi, M. Wieland, Th. Westerwalbesloh, U. Kleineberg, U. Heinzmann, M. Drescher, and F. Krausz. Science, **297**, 1144 (2002).
26. A.D. Bandrauk, S. Chelkowski, and H.S. Nguyen. Phys. Rev. Lett. **89**, 283 903 (2002).
27. A.D. Bandrauk and H.S. Nguyen. Phys. Rev. **A66**, 031 401 (2002).
28. E.A. Gibson, A. Paul, N. Wagner, R. Tobey, S. Backus, I.P. Christov, M.M. Murnane, and H.C. Kapteyn. Phys. Rev. Lett. **92**, 033 001 (2004).
29. A.D. Bandrauk and H. Shen. J. Chem. Phys. **99**, 1185 (1993).
30. J.D. Jackson. Classical electrodynamics. John Wiley & Sons, New York. 1962.
31. A.D. Bandrauk, S. Chelkowski, H. Yu, and E. Constant. Phys. Rev. **A56**, 2357 (1997).
32. M. Shapiro and P. Brumer. Principles of the quantum control of molecular processes. Wiley Interscience, New York. 2002.
33. N.A. Papadogiannis, L.A.A. Nikolopoulos, D. Charalambidis, G.D. Tsakiris, P. Tzallas, and K. Witte. Phys. Rev. Lett. **90**, 133 902 (2003).

© 2004 NRC Canada

Spectroscopy of the XeC_2 molecule in xenon, argon, and krypton matrices[1]

Marcin Frankowski, Alice M. Smith-Gicklhorn, and Vladimir E. Bondybey

Abstract: A self-igniting DC-electric discharge of C_2H_2 in Xe (matrix gas) or C_2H_2 and Xe in Ar or Kr (matrix gas) is used to produce and study the XeC_2 molecule in these various rare gases at 12 K. Unlike in Ar and Kr, the well-known electronic spectra of C_2 is completely absent in a Xe matrix. This together with annealing experiments in Ar matrices indicate that ground state Xe and C_2 react uniquely and without a barrier to form the XeC_2 molecule. The IR-active C-C stretch of this compound is found to be close to the C-C stretching frequency of the C_2 anion, in excellent agreement with our density functional theoretical (DFT) calculations, which yield a XeCC singlet species bent by 148.6° and with substantial charge separation approaching $Xe^+C_2^-$ and a notably short (2.107 Å) Xe—C bond. The spectra of the Xe–^{13}C–^{12}C, Xe–^{12}C–^{13}C, and Xe–^{13}C–^{13}C species are also obtained and the isotopic shifts are in excellent agreement with the DFT predictions, although not sufficient to distinguish a bent from a linear structure. Numerous broad absorptions centered near 423 nm (in Xe) are observed, which are clearly due to the XeC_2 molecule. Laser-induced fluorescence studies reveal a near-IR emission likely due to XeC_2 but not yet understood. Infrared spectra in the Xe matrix reveal also formation of the HXeCCH molecule.

Key words: matrix-isolation spectroscopy, rare gas compounds, charge transfer compounds, xenon–carbon bonds.

Résumé : On a utilisé une décharge électrique, à courant direct et à auto-ignition, de C_2H_2 dans du Xe (matrice gazeuse) ou de C_2H_2 et Xe dans Ar ou Kr (matrice gazeuse) pour produire et pour étudier la molécule de XeC_2 dans ces divers gaz rares, à 12 K. Contrairement à ce qui est observé dans les gaz Ar ou Kr, le spectre électronique bien connu du C_2 est complètement absent dans une matrice de Xe. Ce résultat considéré à la lumière des expériences de recuisson dans les matrices de Ar indique que l'état fondamental du Xe et du C_2 réagissent d'une façon particulière, et sans barrière, pour former la molécule de XeC_2. L'élongation C-C de ce composé, active en infrarouge, se retrouve près de la fréquence d'élongation C-C de l'anion C_2^-, en excellent accord avec nos calculs théoriques de densité fonctionnelle (TDF) qui conduisent à une espèce XeCC singulet comportant un angle de 148,6°, une séparation de charge importante se rapprochant de $Xe^+C_2^-$ et une longueur de liaison Xe—C relativement courte, 2,107 Å. On a aussi obtenu les spectres des espèces Xe–^{13}C–^{12}C, Xe–^{12}C–^{13}C et Xe–^{13}C–^{13}C et les déplacements chimiques sont en excellent accord avec les prédictions faites sur la base de la TDF, même s'ils ne sont pas suffisants pour permettre de distinguer une structure linéaire ou repliée. On a aussi observé de nombreuses absorptions larges autour de 423 nm (dans le Xe) qui sont sans ambiguïtés dues à la molécule de XeC_2. Des études de fluorescence induite au laser révèlent l'existence d'une émission infrarouge probablement due à XeC_2, mais il est pour l'instant impossible de la comprendre. Les spectres infrarouges dans une matrice de Xe révèlent aussi la formation de la molécule de HXeCCH.

Mots clés : spectroscopie avec molécules isolées dans une matrice, composés des gaz rares, composés de transfert de charge, liaisons xénon–carbone.

[Traduit par la Rédaction]

Introduction

The C_2 molecule was observed as early as 1857 in the spectrum of flames (1). The numerous studies of its rich electronic spectrum, with many low-lying electronic states, have contributed significantly to the development of molecular spectroscopy (2–4). Investigations of C_2 in rare gas matrices have also made meaningful contributions (5). They also provided useful information about nonradiative relaxation processes in the solid medium and led to the first observation of stimulated emission in matrices (6). Up to recently, it was presumed that C_2 could be isolated and observed in all of the condensable noble gas matrices, but the literature shows that the spectrum of C_2, unlike that of C_2^-, (7, 8) has only been observed in Ne, Ar, and Kr, but never in a Xe matrix. The reason is, as we show here, the facile for-

Received 26 November 2003. Published on the NRC Research Press Web site at http://canjchem.nrc.ca on 26 August 2004.

M. Frankowski, A.M. Smith-Gicklhorn, and V.E. Bondybey.[2,3] Institute of Physical and Theoretical Chemistry, Technical University of Munich, Lichtenbergstr. 4, 85747 Garching, Germany.

[1]This article is part of a Special Issue dedicated to the memory of Professor Gerhard Herzberg.
[2]Corresponding author (e-mail: ve.bondybey@ch.tum.de).
[3]Second affiliation: Department of Chemistry, University of California, Irvine, CA 92697-2025, USA.

 doi: 10.1139/V04-054 © 2004 NRC Canada

mation of the XeC_2 molecule, whose bonding can be largely described as $Xe^+C_2^-$.

The list of rare gas compounds has increased dramatically since the pioneering work of Bartlet and co-workers in 1962 (9, 10). Although most compounds known today contain either a Xe—F or Xe—O bond, examples of Xe—Cl, Xe—Br, Xe—I, Xe—S, Xe—N, Xe—C, and Xe—B (tentatively) have also been found by now. Although many of these may be regarded as metastable species, several (such as XeF_2) salt-like compounds with a C—Xe bond in the cationic part, and recently a neutral C_6H_5XeF compound, are actually thermodynamically stable compounds used in preparative chemistry (11–13).

Another breakthrough in rare gas chemistry was the discovery of a new family of compounds, rare-gas hydrides HRgY (where Y is an electronegative fragment like F or other halogens, OH, SH, CN, etc.), prepared in xenon matrices using UV-laser photolysis of a HY precursor and subsequent mobilization of H atoms (14). Up to recently, since these Xe compounds were only observed in a Xe matrix, it was questionable whether these highly polar species could exist in a less-stabilizing environment. Lorenz et al. (15) have recently shown that these species, in particular HXeCl and HXeBr, can be formed with similar efficiencies in a highly dilute, weakly interacting neon matrix, and this, together with the results of extensive DFT calculations, suggests that they should be capable of independent existence as free molecules in the gas phase.

Nowadays, the rapid development of quantum chemistry is such that the predictions of stable compounds precede the experiments. A recently predicted family of Xe compounds involve C—H and O—H bond insertion products; from the computational viewpoint, species such as HXeCCH, $HXeC_6H_5$, $HXeOC_6H_5$, and even HXeCCXeH, etc., could exist (16). HXeOH was found in 1999 by the Räsänen group (17), and quite recently, by the same group (18), and independently by Feldman et al. (19), HXeCCH and HXeCCXeH were found.

The XeC_2 molecule was first discovered by Maier and Lautz (20) in 1998 through UV (193 or 248 nm) laser irradiation of C_2H_2:Xe matrices and identified via its IR-active C=C stretch. They found this species to be the sole contributor to the IR and UV–vis spectrum and that the intensity of the signal was insensitive to annealing (30 min at 38, 46, or 50 K), but decreased upon UV–vis irradiation ($\lambda \geq 254$ nm), with no new signals appearing. In contrast to this, Räsänen et al. (18) found that subsequent annealing of such samples led to the formation of HXeCC, HXeCCH, and even HXeCCXeH molecules. At the same time, Feldman et al. (19) bombarded C_2H_2:Xe matrices with high energy electrons (1 MeV) and found after subsequent annealing to 40–45 K, IR absorptions due to HXeCCH, with no mention of XeCC and the other related compounds.

Our work on XeC_2 also started with attempts at making HXeCCH in a pulsed DC discharge source of transients. In those experiments, a discharge of C_2H_2 diluted in the Xe matrix gas led to a very strong XeC_2 signal and a very weak HXeCCH signal, even after annealing to 50 K. Thus, we proceeded in the study of the XeC_2 molecule and its ^{13}C isotopic analogues, both experimentally and computationally. The Fourier-transform (FT) absorption spectra from 500–30 000 cm^{-1} and FT-emission spectra from 4000–30 000 cm^{-1} were recorded in an attempt to decipher the electronic spectra of this unusual molecule. By performing similar experiments with dilute mixtures of C_2H_2 and Xe with a large excess of argon or krypton, we were able to observe the spectra of the novel XeC_2 species in Ar and Kr matrices, and thus can address the important question of solvent effect on this highly polar, charge-transfer molecule.

Experimental section

The samples were generated by electric discharge through xenon gas doped with acetylene, as well as through gas mixtures with small amounts of acetylene and xenon diluted by Ar and Kr matrix gases. The products were deposited onto a KCl window cooled down to 12.5 K by a closed-cycle helium cryostat (APD Cryogenics, Berkshire, UK). The gas samples (C_2H_2 (99%), $^{13}C_2H_2$ (99%), C_2D_2 (99%), Xe (99.998%), Ar (99.999%), Kr (99.99%)) were mixed in various ratios, typically C_2H_2:Xe (1:800–1100), C_2H_2:Xe:Ar (1:1–5:1000), and C_2H_2:Xe:Kr (1:5:1000). Usually 8 mmol of the gaseous mixture was deposited for 2 h as estimated from the pressure drop and volume of the gas container and handling system. The self-igniting DC electric source with the pulsed gas inlet system has been already described in detail in refs. 21 and 22.

All absorption and emission spectra of the deposited samples were recorded using a Fourier transform Bruker IFS 120 HR spectrometer equipped with an Opus NT control and data acquisition system. Absorption spectra were measured in a wide spectral range from 400–31 000 cm^{-1} usually with a 0.06 cm^{-1} resolution in the IR and 1 cm^{-1} resolution in the UV–vis region. Although samples were always cooled down to 12.5 K after deposition, use of the broadband light sources caused an increase of the temperature up to 14 K at which all absorption measurements were performed.

Emission in the near-IR region was obtained by exciting the matrix samples using cw lasers, including intensity stabilized tunable dye lasers (Coherent 899-01 ring laser operated with stilbene 3; Coherent 599 standing wave laser with rhodamine 6G (Coherent, Palo Alto, CA, USA)). The dye lasers were optically pumped by Ar^+ ion lasers (Coherent) operating in multi-line UV (Coherent, Innova-200) and multiline visible (Coherent, Innova-70) modes. In some experiments, the Ar ion lasers were also used directly for the sample excitation. The Innova-70 laser operating in single line mode allowed for selection of discrete emission wavelengths between 514 and 466 nm. In all cases the laser beams were transmitted via fiber optics and focused onto the matrix sample.

Results and discussion

Infrared spectra

XeC_2 — Density functional theory calculations

The optimized geometry and vibrational frequencies of the XeC_2 molecule were calculated using the hybrid DFT technique as implemented in the Gaussian98 suite of programs (23) at the B3LYP level of theory. All electrons on the carbon atoms were explicitly treated with the 6-311++G(3df,3pd) basis set. For the rare gas atom, the quasi-

© 2004 NRC Canada

Table 1. Spectroscopic data for (*a*) the lowest singlet state of the XeC_2 molecule (in comparison to the ground states of C_2 and the C_2 anion) and (*b*) the lowest triplet state of the XeC_2 molecule (in comparison to the lowest triplet state of C_2).

(*a*) Data for the lowest singlet state of XeC_2

	Vibrational frequencies (cm^{-1}) {isotopic shifts}		
	B3LYP (intensities in km/mol)		
Molecule (electronic state)	Unscaled	Scaled with f = 0.96	Experimental
C_2, $^1\Sigma_g^+$	1872.9 (0)	1798.0	1828.0 (Gas)[a,b]
C_2^-, $^2\Sigma_g^+$	1841.9 (0)	1768.2	1779.7 (Ar)[a,c]
			1761.8 (Xe)[a,c]
			1757.9 (Gas)[a,c]
XeC_2 (singlet)			
Bending	87.4 (3)		
Xe-C stretching	325.1 (44)		
C-C stretching	[132-12-12][d] 1858.5 (20)	1784.2	1767.4 (Xe)[e], 1774.6 (Ar), 1770.6 (Kr)
	[132-13-12] 1820.8 (20)	1748.0 {36.2}	1732.8 (Xe) {34.6}
	[132-12-13] 1823.8 (19)	1750.8 {33.4}	1734.1 (Xe) {33.3}
	[132-13-13] 1785.3 (18)	1713.9 {70.3}	1698.8 (Xe)[f] {68.6}, 1705.2 (Ar) {69.4}
	[129-12-12] 1858.5 (20)	1784.2	

(*b*) Data for the lowest triplet state of XeC_2

	Vibrational frequencies (cm^{-1}) {isotopic shifts}		
	B3LYP (intensities in km/mol)		
Molecule (electronic state)	Unscaled	Scaled with f = 0.96	Experimental
C2, $^3\Pi_u$	1694 (0)	1626	1618.0 (Gas)[a,b]
XeC_2 (triplet)			
Bending	29.6 (0.2)		
Xe-C stretching	73.4(4.6)		
C-C stretching	[132-12-12] 1708.8 (19)	1640.4	
	[132-13-12] 1675.6 (18)	1608.6 {31.8}	
	[132-12-13] 1675.5 (18)	1608.5 {31.9}	
	[132-13-13] 1641.6 (17)	1575.9 {64.5}	
	[129-12-12] 1708.8 (19)	1640.4	

[a] $\omega_e - 2\omega_e x_e$.
[b] Value from ref. 26.
[c] Value from ref. 8.
[d] Isotopes [Xe-C-C].
[e] 1767.0 cm^{-1} as reported in ref. 20.
[f] 1698.6 cm^{-1} as reported in ref. 20.

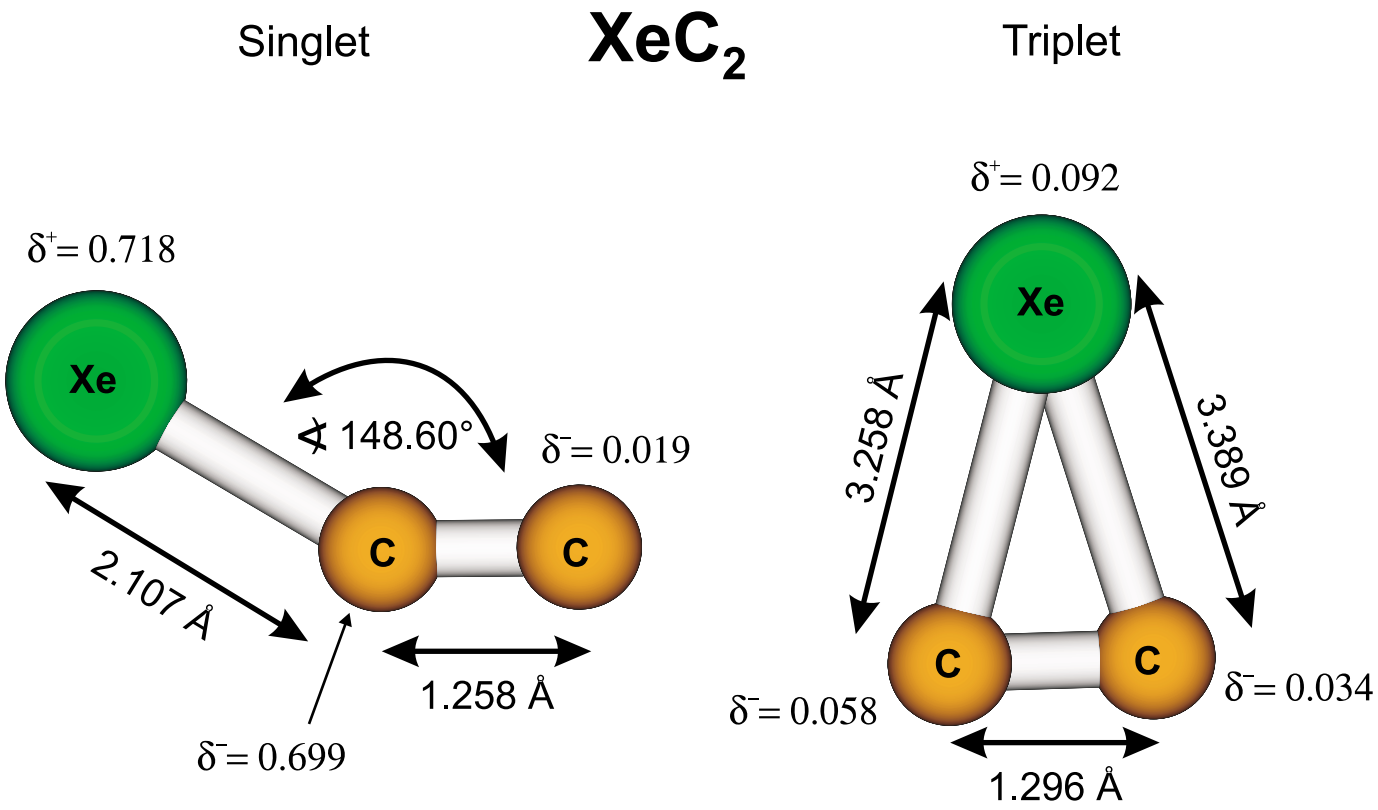
relativistic effective core potential SDD basis set was used (24). The lowest electronic singlet and triplet states of the C_2 are known experimentally to be very close in energy, with the triplet lying only 716 cm^{-1} above the ground state singlet. The theoretical results and experimental spectroscopic data for the lowest singlet and triplet states of XeC_2 are summarized in Tables 1*a* and 1*b*, respectively, with the data for C_2 and the C_2^- anion being also included for comparison. Corresponding geometries of the molecules are shown in Fig. 1. The binding in the singlet and triplet XeC_2 molecules is predicted to be considerably different in character. The singlet molecule was found to have a relatively strong, 82.4 kJ/mol bond and exhibit an appreciable (0.72 e^-) charge transfer from xenon to the C_2 unit. The triplet C_2, on the other hand, interacts with xenon more weakly (33 kJ/mol), with only 0.09 e^- being transferred. Particularly striking are the differences in geometry, with the linear (or nearly linear, see the next section) singlet XeC_2 molecule displaying a remarkably short, 2.107 Å Xe—C bond. The triangular triplet, on the other hand, exhibits much longer (3.26 and 3.39 Å) bonds to both the carbon atoms, and is probably best described as a weakly bound van der Waals complex.

This point of view is also confirmed by the computed vibrational frequencies. For the singlet, the computed C=C frequency decreases somewhat compared with free C_2, reflecting probably the fact that the corresponding mode in molecular XeC_2 involves also some motion of the heavy xenon atom. This is also consistent with the relatively high "skeletal" low frequency modes computed to be 325 and 87 cm^{-1}. On the other hand, in the triplet complex the C=C frequency is found to display a smaller shift in the opposite direction, and the "skeletal" distortion modes decrease to 73 and 30 cm^{-1}, respectively. Again, the results are consistent with the novel singlet species being best described as a discrete ionic $Xe^+C_2^-$ molecule (see Tables 1*a* and 1*b*), but the triplet being described as a weakly bound Xe···C_2 complex.

Returning to the structure of the singlet XeC_2 species, the optimizations converge smoothly to a linear Xe-C-C structure when the relatively primitive SDD basis set is used on all the atoms, including the carbons. On the other hand, with

© 2004 NRC Canada

Fig. 1. The calculated geometries of the XeC_2 molecule in singlet and triplet states with charge distribution obtained from natural population analysis.



the larger 6-311++G(3df,3pd) or similar basis set, including diffuse and polarization functions on the carbon atoms, the computation yields for the linear geometry imaginary frequencies. Allowing the symmetry to be lowered, the optimization converges to a slightly bent structure with all real frequencies. The computed dependence of the total energy of singlet XeC_2 molecule as a function of the Xe-C-C bending angle is shown in Fig. 2. It can be seen that the bending potential is very flat with the linear and bent (140°–180°) structures nearly isoenergetic, but the optimizations converge consistently to a bending angle around 148.6°. Some support for the bent structure can be also seen in the high intensity of the observed C=C stretching frequency for XeC_2. While for the linear arrangement the IR intensity predicted for this mode is extremely low (1 km/mol), the bent solutions give more than an order of magnitude higher IR intensities (20 km/mol) of the C=C stretch, more consistent with the experimental results to be discussed in the next section.

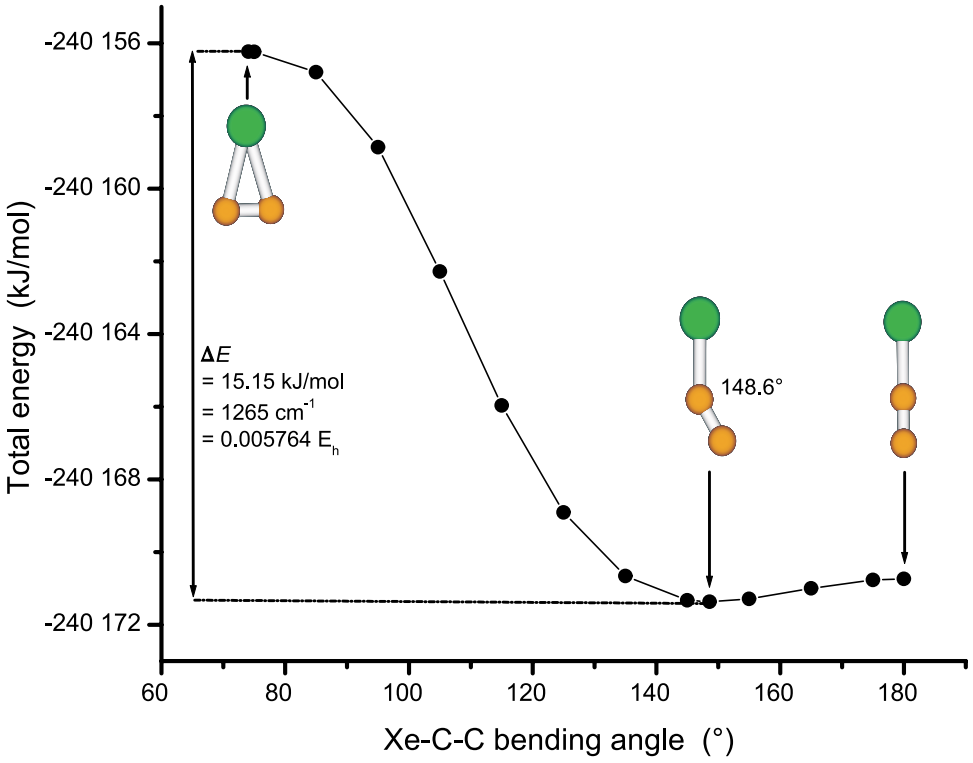
Besides computations on XeC_2, we have also explored the interaction of C_2 with more than one xenon atom. Starting from a linear, centrosymmetric $D_{\infty h}$ XeCCXe structure, the optimization with the all SDD basis set results in two relatively long (2.717 Å Xe—C bonds), and yields one rather high imaginary frequency. When the initial geometry is made slightly asymmetric ($C_{\infty h}$), the energy of the converged geometry drops substantially by nearly 22 kJ/mol, and the imaginary frequency disappears. The lengths of the two Xe—C bonds are now quite different, 2.139 and 4.063 Å, respectively. The converged structure is basically XeC_2, with essentially identical geometry and frequencies as in the three-atom computations, very weakly bound to the additional Xe atom. A very similar result is obtained for a linear Xe-Xe-CC arrangement, where the optimized geometry again yields a Xe atom weakly interacting with the Xe end of the unperturbed triatomic XeC_2, and with a Xe···Xe distance of 4.47 Å. As well, other geometries where the C_2 is forced to interact simultaneously with more than one xenon atom yield high energy optimized structures. For instance, a T-shaped C_{2v} Xe_2-C-C geometry where one of the carbon atoms interacts with two xenon atoms results in two long, 2.97 Å Xe—C bonds, and more than 45 kJ/mol above the asymmetric, linear global minimum.

Quite similar results were obtained with the larger, 6-311++G(3df,3pd) basis set on the carbon atoms. Again, trying to enforce a symmetric configuration results in a high energy structure with large imaginary frequencies, but allowing symmetry lowering, optimization converges to an XeC_2···Xe structure, with a bent XeC_2 structure essentially identical to that obtained in the three-atom computation, that is, with C=C and C-Xe distances of 1.258 and 2.107 Å, respectively, and a C-C-Xe bending angle of 146.8°, and with a weakly bound additional xenon atom at a large, 4.235 Å distance.

The conclusions of these computations seem therefore inescapable: XeC_2 is a well-defined, strongly bound discrete molecule, and the C_2 dimer prefers to interact with one, and only one, xenon atom. The presence of any additional ligand atoms has very little influence upon the geometry and vibrational frequencies of the XeC_2 molecule. When the starting geometry involves two equivalent xenon ligands (and similar

© 2004 NRC Canada

Fig. 2. The total energy of the XeC_2 molecule as a function of the Xe-C-C bending angle determined from density functional theory (DFT) calculations. Basis set: 6-311++G(3df,3pd) for carbon atoms and SDD for the rare gas atom.



results were obtained for Kr and Ar as well), one of these is in the optimization process tightly bound, while the other is pushed away. In other words, independent of the number of ligands used, there is a strong interaction with one. These results contradict a previous prediction of a T-shaped equilibrium structure of Ar_2C_2 (25), which is clearly not a global minimum in our calculations, both with the SDD and the 6-311++G(3df,3pd) basis sets.

Besides the calculations involving XeC_2, we have also carried out computations on a variety of related species, on similar molecules involving Kr or Ar, as well as on the $HXeC_2H$ molecule, acetylene with a Xe atom inserted into the C—H bond. The DFT calculations on all these species were performed at the same level of theory, and with the same basis sets as described for XeC_2 above.

XeC_2 in a xenon matrix

The IR spectra of a matrix obtained by discharging mixtures of acetylene and its ^{13}C isotopomer with xenon are presented in Fig. 3. Specific ratios of $^{12}C_2H_2$:Xe (1:870), $^{13}C_2H_2$:$^{12}C_2H_2$:Xe (1:1:1130), and $^{13}C_2H_2$:Xe (1:810) were used for the spectra in the top, middle, and bottom panel, respectively, and the measured vibrational frequencies are summarized in Table 1*a*. Analysis of the spectra and of the observed isotopic shifts, combined with the theoretical calculations described above, clearly identify 1767.4 cm^{-1} as the C=C stretch of the XeC_2 molecule, and confirm the previous assignment (20). The lack of any shift with deuterated $^{12}C_2D_2$ confirms the absence of hydrogen in the carrier, and the clearly resolved doublet of lines due to the mixed $Xe^{13}C^{12}C$ (1732.8 cm^{-1}) and $Xe^{12}C^{13}C$ (1734.1 cm^{-1}) species clearly demonstrates the presence of two inequivalent carbon atoms. Unfortunately, the frequencies cannot be used to distinguish between the linear or 148.6° bent configuration, since the effect of the angle is too small, and the agreement with the predicted isotopic shifts is good for both geometries.

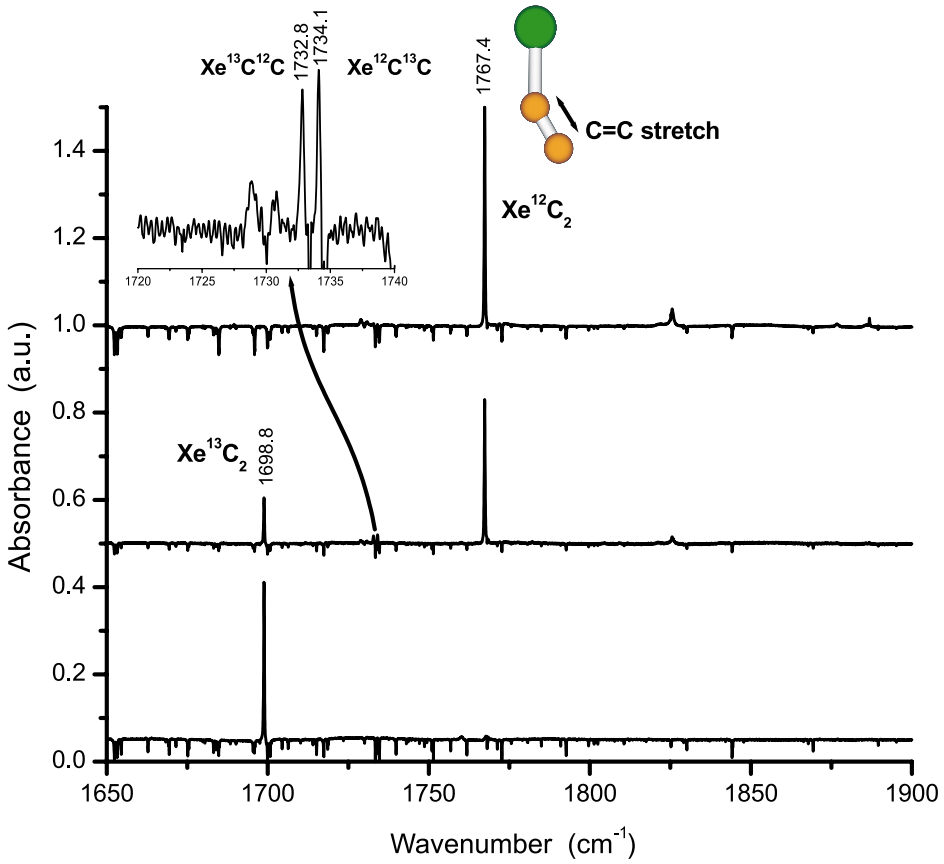
XeC_2 in argon and krypton matrices

Quite noteworthy is the absence of the so-called *Phillips bands* characteristic of C_2 in the visible absorption region. These are always prominent in matrices other than xenon, whenever acetylene or another unsaturated hydrocarbon is discharged, as also exemplified by Fig. 4, which compares the visible and near-IR spectra of discharged acetylene in argon, krypton, and xenon matrices. Apparently, the C_2 produced in the discharge reacts in the xenon matrix with the Xe atoms to produce "in situ" the XeC_2 molecules. This reaction must be nearly quantitative and proceed with essentially no activation barrier, since no trace of the Phillips bands is observed, and no further increase in the XeC_2 band absorption intensity can be detected when the xenon matrix is annealed to 40 K. It may be noted that we also did not observe the peak at 1852 cm^{-1} previously assigned to the ethynyl radical C_2H (19). A weak but unidentified feature appears at 1825.6 cm^{-1}.

Spectra obtained in experiments done under almost identical conditions, but using argon and krypton samples doubly doped with small amounts of Xe and acetylene, are presented in Figs. 4 and 5. The visible and near-IR spectra show, as noted previously, a prominent progression of absorptions due to the A–X C_2 transition in solid argon and

© 2004 NRC Canada

Fig. 3. Infrared spectra of the XeC_2 molecule and its isotopomers identified through its C=C stretching vibration. The spectra were recorded in a Xe matrix at 14 K after deposition at 30 K from discharge through $^{12}C_2H_2$:Xe (1:870), top; $^{13}C_2H_2$:$^{12}C_2H_2$:Xe (1:1:1130), middle; and $^{13}C_2H_2$:Xe (1:810), bottom. The expanded region shows C=C stretching at 1732.8 cm^{-1} of $Xe^{13}C^{12}C$ and 1734.1 cm^{-1} of $Xe^{12}C^{13}C$ isotopomers.



krypton, which is, however, quite absent in the xenon matrix. On the other hand, the strong band due to the origin of the Herzberg–Lagerqvist bands near 19 000 cm^{-1} (27) is present in all three matrices, indicating that C_2^-, unlike C_2 can be isolated in solid xenon also. Interestingly, the argon sample also shows a weak absorption due to the origin of the "Swan bands" of triplet neutral C_2.

Infrared spectra obtained with the doubly doped argon (C_2H_2:Xe:Ar = 1:5:1000) and krypton (C_2H_2:Xe:Kr = 1:5:960) samples are presented in Fig. 5. The presence of moderately intense, sharp bands at 1770.6 and 1774.6 cm^{-1} in solid krypton and argon, respectively, only moderately blue-shifted from the XeC_2 absorption at 1767.4 cm^{-1} in solid xenon, shows that the molecule can be isolated, alongside C_2, C_2^-, and other carbon cluster molecules, in solid Ar and Kr environments. The assignment of these bands to XeC_2 is further confirmed by their strong dependence on the concentrations of both Xe and acetylene. Using isotopically labeled acetylene, one obtains in solid argon a peak at 1705.2 cm^{-1}, which is clearly due to $Xe^{13}C_2$ (Table 1*a*). It may also be noted that the C=C stretching absorption band of this compound in solid Ar (1774.6 cm^{-1}) is just 5 cm^{-1} to the red from the vibrational frequency of the C_2^- anion, which is consistent with the appreciable charge separation predicted by the DFT results.

The three traces in the middle of Fig. 5 show the results of an annealing experiment, where the sample was deposited at 12 K, and then progressively warmed up for 30 min to 25 and 35 K respectively, recooling each time to 12 K before recording the spectrum. It can clearly be seen that the 1774.6 cm^{-1} band, which is rather weak in the original, at 12 K deposited sample (in the lowest trace), increases in intensity with each annealing step (the traces above it). The straightforward conclusion that can be drawn from this experiment is that during the annealing process and the resulting diffusion, the ground-state Xe atoms and C_2 can react essentially without the barrier to form the chemically bound XeC_2 molecule.

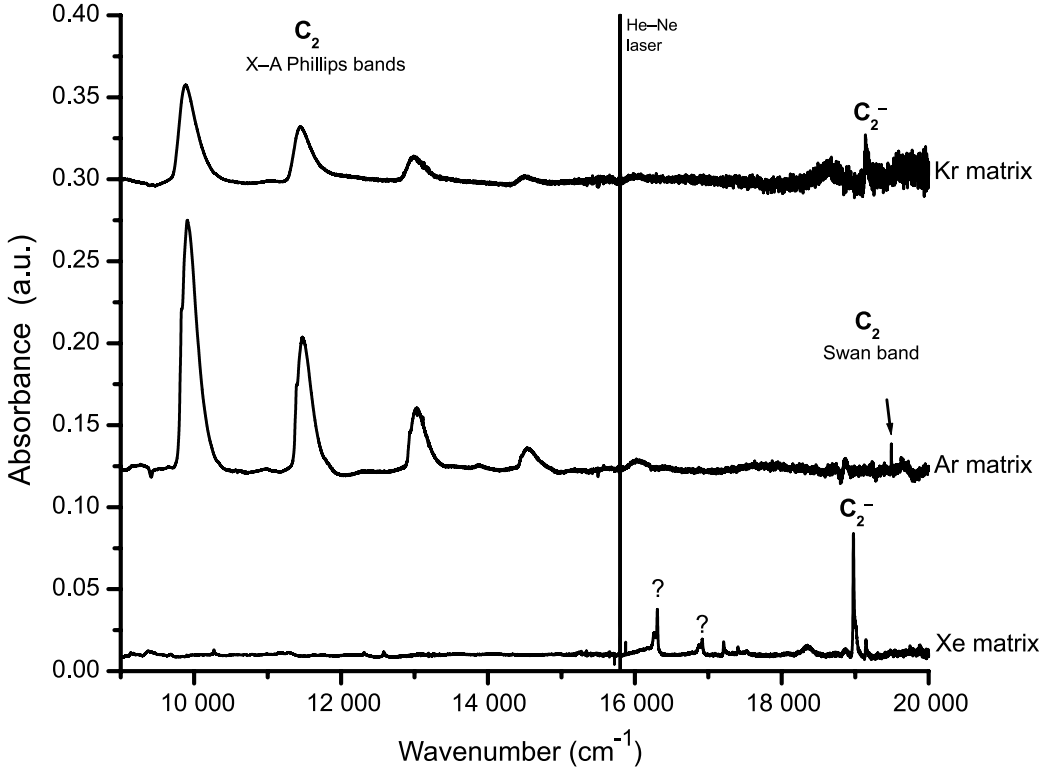
The results in the krypton and argon matrices are clearly in excellent agreement with the theoretical computations discussed in an earlier section. The diatomic C_2 prefers to react and interact strongly with a single xenon atom. Once this reaction occurs, and the molecular XeC_2 forms, its solvation by other atoms makes little difference. The vibrational frequencies, and presumably the structure of the molecule, are essentially independent of whether it is surrounded by additional xenon atoms, or whether it is isolated in solid krypton or argon matrices.

$HXeC_2H$ in a xenon matrix

Besides the recent observation of XeC_2 (20), the motivation for the present work was calculations done by Lundell et al. (16), which suggested that HXeCCH should exist as a stable molecule. Unfortunately, in contrast with the results

© 2004 NRC Canada

Fig. 4. Comparison of the spectra in the near-IR–vis absorption region of the C_2 molecule (Phillips band: $X^1\Sigma_g^+ \rightarrow A^1\Pi_u$ and Swan band: $a^3\Pi_u \rightarrow d^3\Pi_g$) for Xe, Ar, and Kr matrices. No C_2 bands are observed in Xe matrix.



recently reported by Khriachtchev et al. (18) and Feldman et al. (19) on this molecule in a xenon matrix, our experiments using a discharge source produce it in very small yields, and the very weak bands obtained in our early experiments unfortunately escaped detection. With the help of the previous assignments, these bands could, however, be identified in our spectra. Their analysis and the production of the molecule by a different technique provide some additional information and insights, complementary to the previous experimental work and earlier theoretical studies (16), and we will therefore discuss briefly our results here.

The experimental data, as well as the results of our DFT computations, are summarized in Table 2, where for the ease of comparison, the measured intensities given in parentheses are scaled to the computed intensity of the strongest band. With the help of the previous assignments (18, 19), the Xe-H and CH-stretching vibrations of HXeCCH at 1486.1 and 3273.5 cm^{-1}, respectively, can be easily identified. In similar experiments using deuterated or ^{13}C-substituted species, the corresponding vibrational modes of DXeCCD as well as the previously unknown vibrations of the $HXe^{13}C^{13}CH$ isotopomer could be established.

All the bands described above exhibit an interesting behavior upon photolysis and sample annealing, which is useful in confirming their assignment to the same carrier. The very weak absorption bands present right after sample deposition almost completely disappear when the matrix is irradiated by the visible light of a tungsten lamp for 2 to 3 h. When the sample is then annealed to 40–50 K, they reappear, and grow appreciably, undoubtedly due to reactions of the hydrogen atoms produced in the discharge. Unlike the photolysis experiments, however, which produce the H and C_2H pairs in close proximity, in our discharge setup the fragments are essentially randomly distributed through the matrix. In the former experiments, the two radical fragments have an appreciable probability of reacting with the same xenon atom to form the HXeCCH species, while in the random walk-like diffusion of the fragments in our discharge studies this probability is greatly reduced. We suspect that a substantial fraction of the hydrogen atoms produced by the discharge in our experiments recombine, during either the sample deposition or the diffusion, to form molecular H_2, and are thus from the point of observable product formation irretrievably lost.

Electronic spectra

While the interpretation of the XeC_2 IR absorption is rather straightforward, the corresponding electronic spectra are more difficult to understand. The absorption spectra observed in the visible and near-UV, which are presented in Fig. 6, exhibit a series of broad bands between 22 000 and 26 000 cm^{-1}, whose approximate frequencies are both for the $^{12}C_2H_2$–Xe and $^{13}C_2H_2$–Xe experiments summarized in Table 3. The excellent correlation between the intensity of these bands and that of the IR spectrum strongly suggests that they are also due to the XeC_2 molecule, as also suggested previously (20). When pure argon or krypton with no xenon is used, the broad bands are absent, but much sharper bands due to a well-known transition of C_3 appear approximately in this region. It seems, however, that C_3 can be safely excluded as a carrier of the broad bands.

In view of the width of the bands, and lack of spectral detail, a specific assignment or interpretation of these bands is difficult, in particular since no theoretical information on the

© 2004 NRC Canada

Fig. 5. Infrared absorption spectra of the XeC_2 molecule in Ar and Kr matrices. Spectra in Ar matrix show intensity changes upon two-step annealing for a sample deposited at 12 K (C_2H_2:Xe:Ar (1:1:1000), and for comparison at 20 K and higher Xe concentration (C_2H_2:Xe:Ar (1:5:1000)). Concentration for the Kr matrix deposited at 30 K was C_2H_2:Xe:Kr (1:5:960).

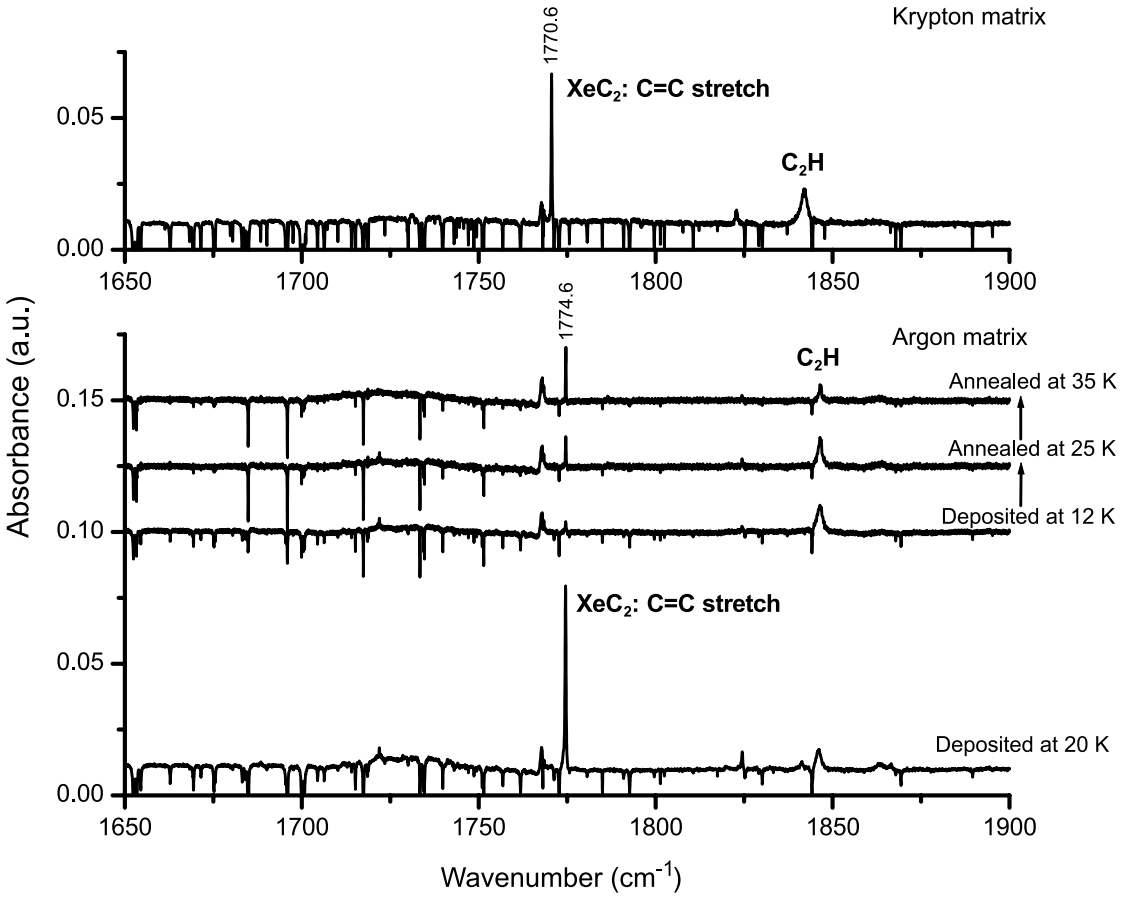


Table 2. DFT-computed (B3LYP (6-311++G(3df,3pd) on C and H atoms, SDD on Xe) harmonic and experimental frequencies measured in a Xe matrix for $HXe^{12}C^{12}CH$, $HXe^{13}C^{13}CH$, and $DXe^{12}C^{12}CD$ molecular vibrations.

	Vibrational frequencies (cm^{-1})		
Assignments	DFT calculations (intensities in km/mol)	Previous experiments	This work (relative intensities)
$HXe^{12}C^{12}CH$			
C-C-H bending	677.7 (50)	626	626 v. weak
Xe-H stretching	1627.4 (1131)	1486.0	1486.1 (1131)
C-H stretching	3443.5 (43)	3273	3273.5 (199)
$HXe^{13}C^{13}CH$			
C-C-H bending	672.1 (49)		
Xe-H stretching	1627.3 (1133)		1486
C-H stretching	3425.6 (41)		3257.3[a]
$DXe^{12}C^{12}CD$			
C-C-D bending	532.4 (18)	491.5	
Xe-D stretching	1154.9 (571)	1077.5	1077.5 (571)
C-D stretching	2663.1 (32)	2545	2544.9 (48)

Note: Experimental intensities were determined using Levenberg–Marquardt and local-least-squares fitting algorithms, then scaled to the maximal observed values and normalized to theoretical intensities for each experiment.

[a]Tentative assignment.

© 2004 NRC Canada

Fig. 6. The XeC_2 absorption region in the UV–vis spectral range for Xe and Ar matrices. For convenience, the frequency intervals are sketched for $Xe^{12}C_2$ and $Xe^{13}C_2$ bands (for band locations see Table 3). The spectrum recorded after $^{13}C_2H_2$:Ar discharge products deposition is shown for comparison.

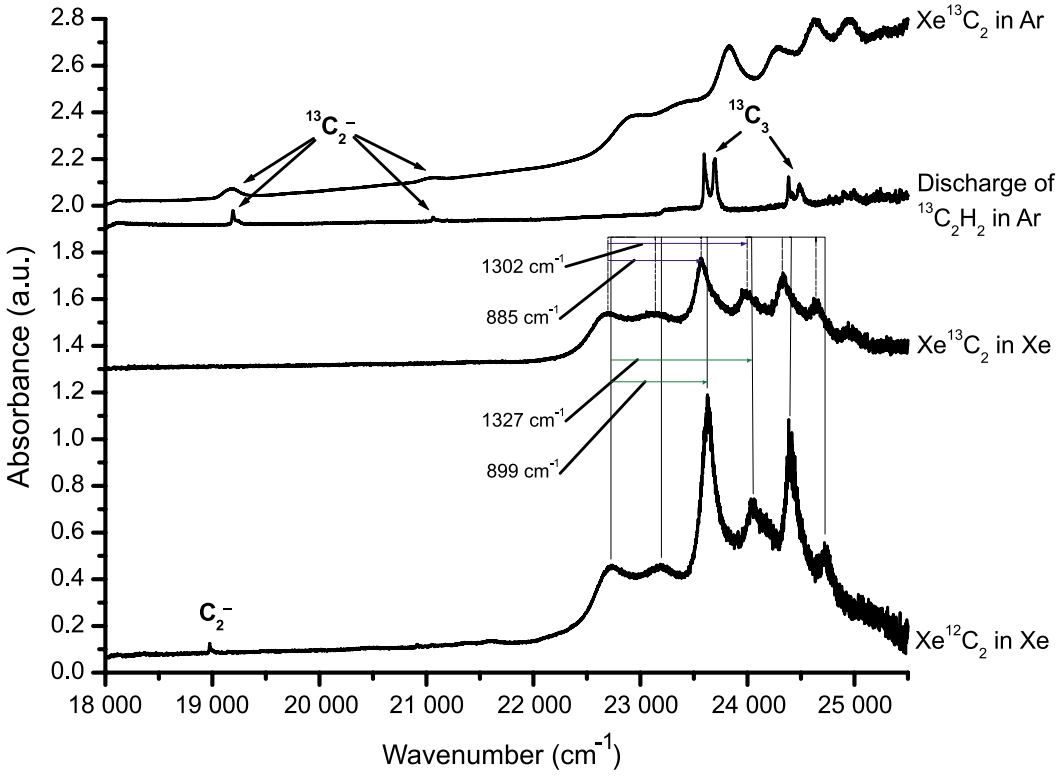


Table 3. Measured UV–vis absorption bands of $Xe^{12}C_2$ (1732.8 cm^{-1}) and $Xe^{13}C_2$ in Xe and Ar matrices, and near-IR emission observed from deposition of $^{12}C_2H_2$:Xe and $^{13}C_2H_2$:Xe discharge products.

UV–vis absorption (cm^{-1})			Near-IR emission (cm^{-1})	
$Xe^{12}C_2$–Xe	$Xe^{13}C_2$–Xe	$Xe^{13}C_2$–Ar	From $^{12}C_2H_2$:Xe discharge products	From $^{13}C_2H_2$:Xe discharge products
Very weak features in the region of 21 200 – 21 800		—	5 883	5 883
22 735	22 697	22 969	6 920	6 872
23 170	23 124	23 400	7 095	7 053
23 634	23 582	23 826	8 299	~8 230
24 062	23 999	24 283	8 494	8 403
24 414	24 341	24 628	8 703	8 599
24 711	24 634	24 967	~9 862 Very weak	9 740
Weak features around 25 000		~25 300	~10 104 Very weak	9 947

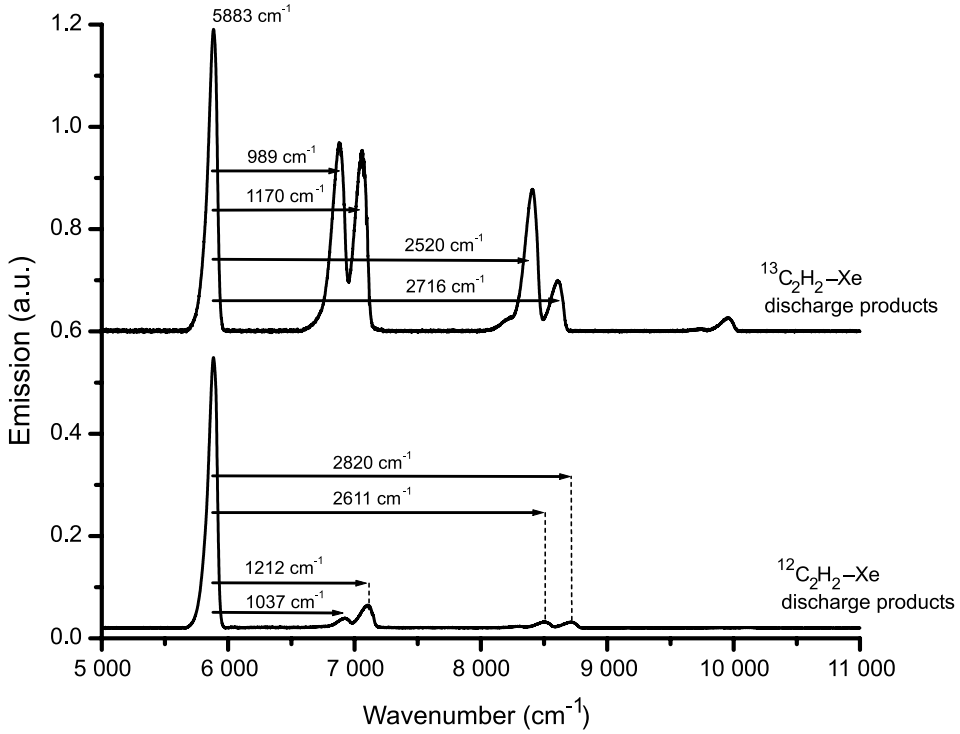
Note: The locations of the band centers were determined using the Levenberg–Marquardt fitting algorithm.

excited electronic states of XeC_2 is available. The spacing of the bands decreases in the ^{13}C experiment, with the approximate isotopic frequency ratio of $\rho \approx 0.97$ being relatively close to that expected for pure carbon motion (0.961). The spectrum appears relatively complex for a molecule as simple as XeC_2, and it is conceivable that overlapping progressions of two or more electronic states are present in this region.

If emission from the excited electronic state of the species of interest is observable, analysis of the fluorescence provides information complementary to the absorption spectrum, and often is of considerable help in untangling its structure. In the present case, however, even though an intense IR fluorescence is observed, it only serves to further deepen the mystery. Unfortunately, we do not have an excitation source capable of exciting the sample in the strongest absorption bands, and the two traces in Fig. 7 result from excitation of matrices obtained in $^{12}C_2H_2$:Xe and $^{13}C_2H_2$:Xe experiments, in each case near the low-energy end of the absorption, around 23 000 cm^{-1}. The emission bands are again relatively broad, and so the accuracy of their positions listed in Table 3 is probably not better than ±10 cm^{-1}. The bands exhibit distinct isotopic shifts, with their spacing reduced in the $^{13}C_2H_2$ experiment on the average by about a factor $\rho \approx 0.965$, very close to what would be expected, for instance, for diatomic XeC or C_2. The band at 5883 cm^{-1} shows es-

© 2004 NRC Canada

Fig. 7. Near-IR emission under excitation at 431 nm by means of stilbene 3 dye laser recorded after $^{12}C_2H_2$:Xe and $^{13}C_2H_2$:Xe discharge products deposition. The frequency intervals are shown with arrows and values (band locations are given in Table 3).



sentially no isotopic shift, and should therefore be the electronic origin. With this assignment, however, all the other observed bands occur at higher energies, suggesting that much of the emission would have to originate from vibrationally excited levels, which is rather unusual for polyatomic molecules. Furthermore, if this interpretation is accepted, the spectrum exhibits a strong negative anharmonicity, with the band spacing appearing to increase with increasing vibrational energy.

Also puzzling is the absence of any emission at energies below the 5883 cm^{-1} origin, which could be assigned to excited levels of the ground state. While part of the reason may be the sensitivity of the detector, which cuts off around 4000 cm^{-1}, but certainly some emission to the low ground state levels would be expected. In the absence of such emission, no information about the ground state is obtained. We must conclude that even though there appears to be strong evidence for assigning the electronic spectrum to the XeC_2 molecule, we have at this point little understanding of its structure. Clearly, additional experimental and, in particular, theoretical work would be desirable.

Summary

A self-igniting DC-electric discharge of C_2H_2 in Xe (matrix gas) produces no C_2, little C_2^-, and mainly the XeC_2 molecule, as revealed by its IR spectrum. The same molecule can be isolated in Ar and Kr matrices alongside C_2 and C_2^- and other carbon cluster molecules in discharges of C_2H_2:Xe diluted in Ar or Kr as the matrix gas. The IR-active C-C stretch of this compound is found just 5 cm^{-1} to the red (in Ar at 1774.6 cm^{-1}) from the C-C stretch of the C_2 anion, in excellent agreement with DFT calculations at the B3LYP level (basis sets 6-311++G(3df,3pd) on C, SDD on Xe), which yield a XeCC singlet species with substantial charge separation (natural charge populations of +0.72 e^- (Xe), –0.7 e^- (C), and –0.02 e^- (C)), and a remarkably short (2.107 Å) Xe—C bond. The spectra of the Xe–^{13}C–^{12}C, Xe–^{12}C–^{13}C, and Xe–^{13}C–^{13}C species are also obtained and the isotopic shifts are in excellent agreement with the DFT predictions, although not sufficient to distinguish a bent (a 148.6° structure is a shallow minimum) from a linear structure. More difficult to interpret are the broad electronic spectra of this species. Numerous broad absorptions centered near 423 nm (in xenon) are observed, which are clearly due to the XeC_2 molecule. Laser-induced fluorescence studies reveal a near-IR emission with origin at 5883 cm^{-1} likely due to XeC_2. The spectrum is rather unusual for a triatomic molecule and indicates a nonrelaxed vibrational emission.

The Xe matrix IR spectra reveal XeH and CH stretching vibrations of the HXeCCH molecule, observed also for its fully deuterated or all-^{13}C isotopomers. However, deposition from a gas discharge leads to a random distribution of radical fragments through the matrix and consequently its formation is fairly inefficient.

Acknowledgements

Research funding from Deutsche Forschungsgemeinschaft is gratefully acknowledged. We also thank the EU for financial support within the Reactive Intermediates Research Training Network.

© 2004 NRC Canada

References

1. W. Swan. Ann. Physik. Chem. **100**, 306 (1857).
2. S.R. Langhof, M.L. Sink, R.H. Pritchard, C.W. Kern, S.J. Strickler, and M.J. Boyd. J. Chem. Phys. **67**, 1051 (1977).
3. J.E. Bourlot and E. Roueff. J. Mol. Spectrosc. **120**, 157 (1986).
4. E.F. van Dishoeck and J.H. Black. Astrophys. J. **258**, 583 (1982).
5. G.M. Lask, J. Agreiter, R. Schlachta, and V.E. Bondybey. Chem. Phys. Lett. **205**, 31 (1993).
6. V.E. Bondybey. J. Chem. Phys. **65**, 2296 (1976).
7. V.E. Bondybey and L.E. Brus. J. Chem. Phys. **63**, 2223 (1975).
8. L.E. Brus and V.E. Bondybey. J. Chem. Phys. **63**, 3123 (1975).
9. N. Bartlett. Proc. Chem. Soc. London, 218 (1962).
10. F.O. Sladky, P.A. Bulliner, and N. Bartlett. J. Chem. Soc. A, 2179 (1969).
11. H.-J. Frohn, N. LeBlond, K. Lutar, and B. Zemva. Angew. Chem. Int. Ed. **39**, 391 (2000).
12. W. Tyrra and D. Naumann. In Inorganic chemistry highlights. *Edited by* G. Meyer, D. Naumann, and L. Wesemann. John Wiley and Sons, New York. 2002.
13. K.O. Christe. Angew. Chem. Int. Ed. **40**, 1419 (2001).
14. M. Pettersson, J. Lundell, and M. Räsänen. Eur. J. Inorg. Chem. 729 (1999).
15. M. Lorenz, M. Räsänen, and V.E. Bondybey. J. Phys. Chem. A, **104**, 3770 (2000).
16. J. Lundell, A. Cohen, and R.B. Gerber. J. Phys. Chem. A, **106**, 11 950 (2002).
17. M. Pettersson, L. Khriachtchev, J. Lundell, and M. Räsänen. J. Am. Chem. Soc. **121**, 11 904 (1999).
18. L. Khriachtchev, H. Tanskanen, J. Lundell, M. Pettersson, H. Kiljunen, and M. Räsänen. J. Am. Chem. Soc. **125**, 4696 (2003).
19. V.I. Feldman, F.F. Sukhov, A.Yu. Orlov, and I.V. Tyulpina. J. Am. Chem. Soc. **125**, 4698 (2003).
20. G. Maier and Ch. Lautz. Eur. J. Org. Chem. 769 (1998).
21. A. Thoma, B.E. Wurfel, R. Schlachta, G.M. Lask, and V.E. Bondybey. J. Phys. Chem. **96**, 7231 (1992).
22. A.M. Smith, J. Agreiter, M. Härtle, C. Engel, and V.E. Bondybey. Chem. Phys. **189**, 315 (1994).
23. M.J. Frisch, G.W. Trucks, H.B. Schlegel, G.E. Scuseria, M.A. Robb, J.R. Cheeseman, V.G. Zakrzewski, J.A. Montgomery, Jr., R.E. Stratmann, J.C. Burant, S. Dapprich, J.M. Millam, A.D. Daniels, K.N. Kudin, M.C. Strain, O. Farkas, J. Tomasi, V. Barone, M. Cossi, R. Cammi, B. Mennucci, C. Pomelli, C. Adamo, S. Clifford, J. Ochterski, G.A. Petersson, P.Y. Ayala, Q. Cui, K. Morokuma, P. Salvador, J.J. Dannenberg, D.K. Malick, A.D. Rabuck, K. Raghavachari, J.B. Foresman, J. Cioslowski, J.V. Ortiz, A.G. Baboul, B.B. Stefanov, G. Liu, A. Liashenko, P. Piskorz, I. Komaromi, R. Gomperts, R.L. Martin, D.J. Fox, T. Keith, M.A. Al-Laham, C.Y. Peng, A. Nanayakkara, M. Challacombe, P.M.W. Gill, B. Johnson, W. Chen, M.W. Wong, J.L. Andres, C. Gonzalez, M. Head-Gordon, E.S. Replogle, and J.A. Pople. Gaussian 98, Revision A.11. [computer program]. Gaussian, Inc., Pittsburgh, Pa. 2001.
24. A. Nicklass, M. Dolg, H. Stoll, and H. Preuss. J. Chem. Phys. **102**, 8942 (1995).
25. F.Y. Naumkin and F.R.W. McCourt. J. Chem. Phys. **107**, 1185 (1997).
26. K.P. Huber and G. Herzberg. Molecular spectra and molecular structure. Van Nostrand Reinhold, New York. 1979.
27. G. Herzberg and A. Lagerqvist. Can. J. Phys. **46**, 2363 (1968).

© 2004 NRC Canada

Electronic spectroscopy of the nonlinear carbon chains $C_4H_4^+$ and $C_8H_4^+$ [1]

Mitsunori Araki, Pawel Cias, Alexey Denisov, Jan Fulara, and John P. Maier

Abstract: The electronic spectrum of a nonlinear carbon chain radical $C_4H_4^+$ was observed after mass-selective deposition in a 6 K neon matrix. The corresponding gas-phase spectra of $C_4H_4^+$ and $C_4D_4^+$ have been observed in the 512 to 513 nm region and at 710 nm for $C_8H_4^+$. These were detected in direct absorption by cavity ringdown spectroscopy through a supersonic planar discharge. The electronic transition energies of these nonlinear carbon chain radicals correlate well with those of the polyacetylene cations HC_nH^+ (n = 4, 6, 8). The observed profiles are reproduced with rotational constants obtained by ab initio geometry optimizations and extrapolation between the ground and excited electronic states.

Key words: nonlinear carbon chain, carbon cation, electronic transition, diffuse interstellar bands, molecular structure.

Résumé : On a observé le spectre électronique d'un cation $C_4H_4^+$ correspondant à une chaîne carbonée non linéaire déposée par un procédé sélectif en fonction de la masse dans une matrice de néon, à 6 K. Les spectres correspondants en phase gazeuse des cations $C_4H_4^+$ et $C_4D_4^+$ ont été observés dans la région de 512–513 nm et à 710 nm dans le cas du $C_8H_4^+$. Ces spectres ont été détectés par absorption directe par la technique CRDS (« cavity ringdown spectroscopy ») grâce à une décharge supersonique planaire. Il existe une bonne corrélation entre les énergies de transition électronique de ces cations à chaîne carbonée non linéaire et celles des cations polyacétyléniques HC_nH^+ (n = 4, 6, 8). Les profils obtenus peuvent être reproduits à l'aide de constantes rotationnelles obtenues par des optimisations ab initio de géométrie et une extrapolation entre les états électroniques excités et fondamentaux.

Mots clés : chaîne carbonée non linéaire, cation carbone, transition électronique, bandes interstellaires diffuses, structure moléculaire.

[Traduit par la Rédaction]

Introduction

High-resolution spectroscopy of unsaturated carbon chain radicals is of interest in view of interstellar chemistry, as well as terrestrial discharge and flame processes. Electronic transitions of the polyacetylene cations HC_nH^+ (1–4) and radicals C_nH (5) with even number carbons have now been studied. Recently a nonlinear planar carbon chain radical $C_6H_4^+$, H-C≡C-C≡C-CH=CH_2^+, was detected in a supersonic planar discharge with cavity ring down spectroscopy in the 604 nm region (6). Therefore, the related $C_4H_4^+$ and $C_8H_4^+$ nonlinear chains were expected to be produced in the plasma discharge in a sufficient concentration for detection.

Hydrogenated nonlinear chains can exist in dark interstellar clouds as well as linear ones, e.g., the column densities of C_2O, H_2CCO, and CH_3CHO are of the same order of magnitude in Taurus Molecular Cloud-1 (7). However, the intensity of rotational transitions for a linear molecule with a smaller rotational partition function is stronger than for an asymmetric top, and thus, a long nonlinear carbon chain has not yet been detected by radio astronomy, even though the population may be comparable. In the case of electronic transitions, an asymmetric top molecule is not at a disadvantage compared with the linear one. Thus, the nonlinear chains can be considered as candidates, causing the diffuse interstellar band (DIB) absorptions in much the same way as the linear series (8).

The short nonlinear carbon chain H-C≡C-CH=CH_2 is predicted to be an intermediate between acetylene and polyaromatic hydrocarbons in the interstellar chemistry of circumstellar envelopes (9). Laboratory experiments indicate that photodissociation of aromatic molecules produces a nonlinear carbon chain (10). The potential energy surface for three C_4H_4 isomers is also of relevance in the fields of organic chemistry and reaction dynamics (11). Therefore, species and their ions having H-C_n-CH=CH_2 (n = 2, 4, 6,...) nonlinear chain structures are of interest, and information by high-resolution spectroscopy is needed.

The 604 nm origin of the $^2A''$–X^2A'' transition of $C_6H_4^+$ (6) is close to the 600 nm $^2\Pi_u$–$X^2\Pi_g$ one of HC_6H^+ (2). Both transitions involve the same $\pi \leftarrow \pi$ excitation. The transition energy difference in a homologous series should be comparable because $C_6H_4^+$ and HC_6H^+ are produced by an extension of the acetylene chain from $C_4H_4^+$ or HC_4H^+ (12). The

Received 11 September 2003. Published on the NRC Research Press Web site at http://canjchem.nrc.ca on 20 April 2004.

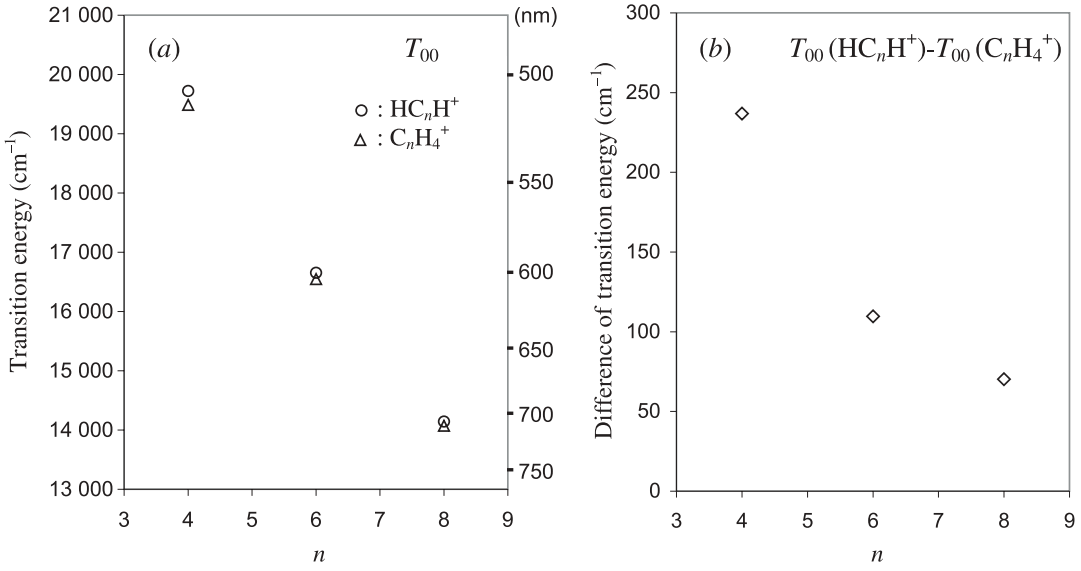
M. Araki, P. Cias, A. Denisov, J. Fulara,[2] and J.P. Maier.[3] Department of Chemistry, Klingelbergstrasse 80, CH-4056 Basel, Switzerland.

[1]This article is part of a Special Issue dedicated to the memory of Professor Gerhard Herzberg.

[2]Permanent address: Institute of Physics, Polish Academy of Science, Warsaw, Poland.
[3]Corresponding author (e-mail: J.P.Maier@unibas.ch).

 doi: 10.1139/V04-013 © 2004 NRC Canada

Fig. 1. (*a*) Energies of the origin bands in the $^2\Pi_u$–$X^2\Pi_g$ transition of HC_nH^+ and the $^2A''$–X^2A'' transition of $C_nH_4^+$. For HC_nH^+ (n = 4, 6, 8) and $C_6H_4^+$, those are the observed values reported in refs. 1–3 and 6, respectively. The transitions of $C_4H_4^+$ and $C_8H_4^+$ were estimated by shifting the HC_4H^+ and HC_8H^+ values down by the difference of HC_6H^+ to $C_6H_4^+$; (*b*) Observed transition-energy differences between HC_nH^+ and $C_nH_4^+$ with the same number of carbon atoms.



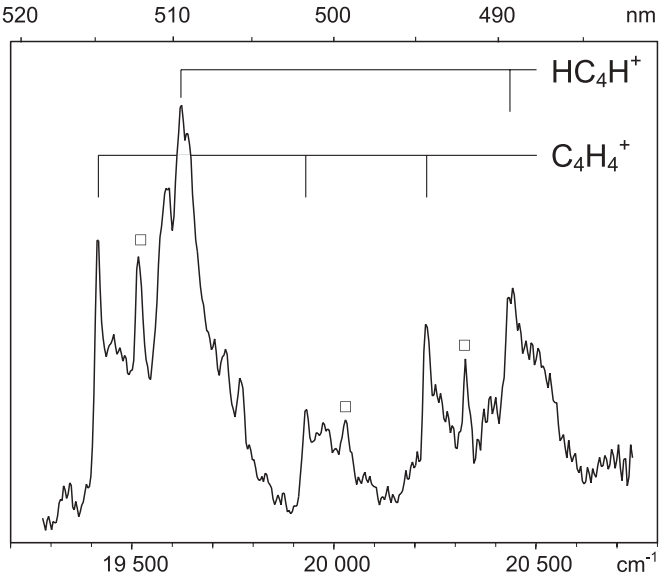
same argument may be applied to the six- and eight-carbon chain species. This trend is shown in Fig. 1*a*, and the transition energies of $C_4H_4^+$ and $C_8H_4^+$ are consequently estimated to lie near 510 and 712 nm, respectively.

The electronic transition of mass-selected $C_4H_4^+$ was subsequently observed in a neon matrix with origin band at 515 nm, in good agreement with the estimated value. Based on this, the gas-phase spectrum was searched for in a cavity ring down spectrometer, and the origin band was observed at 513 nm. Similarly the electronic transition of $C_8H_4^+$ was also detected in the gas phase in the expected 712 nm region. The observed rotational structure in the gas-phase spectra indicates that these are due to the nonlinear, planar carbon chains H-C≡C-CH=CH_2^+ and H-C≡C-C≡C-C≡C-CH=CH_2^+.

Experimental observations

To locate the electronic transition of $C_4H_4^+$, neon-matrix isolation spectroscopy in combination with mass selection was used at first. The $C_4H_4^+$ cation was produced from a benzene–helium mixture in a hot cathode discharge source. A 90° deflector and a quadrupole mass spectrometer were used to steer the ion beam onto the substrate, where the mass-selected ions were codeposited with excess of neon at 6 K (13). The absorption spectra were recorded by guiding monochromatized light (0.1 nm bandpass) through the matrix onto a photomultiplier. The observed spectrum is shown in Fig. 2. All bands observed in the absorption spectrum disappeared upon UV irradiation of the matrix, a test used to indicate that the species is a cation. Three bands of $C_4H_4^+$ were observed; the one at 19 416 cm^{-1} can be assigned to the origin of the electronic transition and the 19 931 and 20 229 cm^{-1} ones to transitions to excited levels in the upper electronic state corresponding to vibrational frequencies of 515 and 813 cm^{-1}, because the population of the species at 6 K is entirely in the lowest level of the ground state.

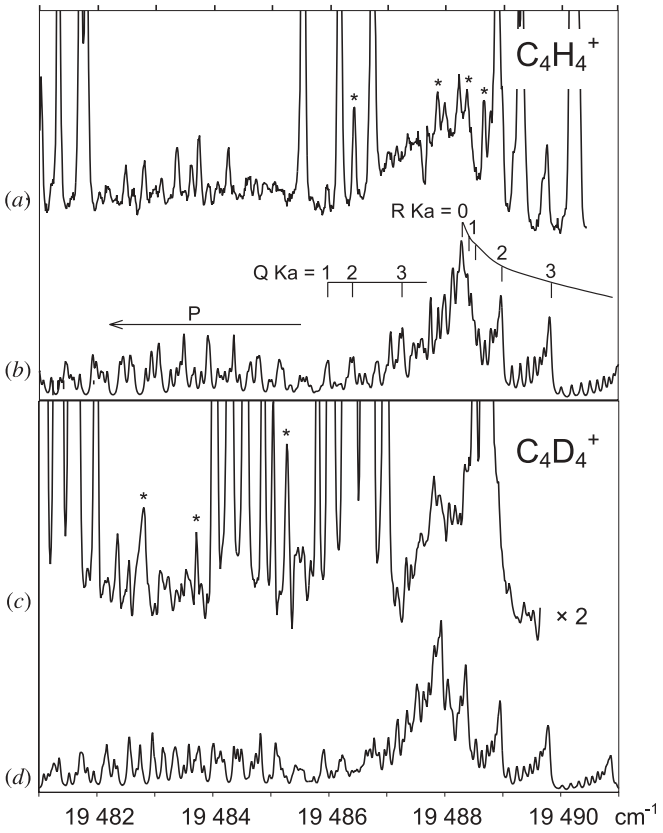
Fig. 2. The electronic absorption spectrum of $C_4H_4^+$, measured in a 6 K matrix after codeposition of mass-selected cations with excess of neon. The band at 19 416 cm^{-1} corresponds to the gas-phase spectrum shown in Fig. 3. The weaker bands at 19 931 and 20 229 cm^{-1} decrease at the same rate as the 19 416 cm^{-1} one upon UV radiation and are due to transitions to vibrationally excited levels in the upper $^2A''$ state. The three peaks (□) 100 cm^{-1} to the blue from the dominant ones are matrix artefacts, site structure. The bands at 19 630 and 20 440 cm^{-1} are due to the diacetylene cation HC_4H^+.



The gas-phase measurement used a cavity ring down spectrometer sampling a supersonic planar plasma (14). The latter was generated by a discharge through a gas pulse (30 Hz repetition rate) of a sample in a buffer gas mixture with a backing pressure of 1000 kPa in the throat of a 3 cm ×

© 2004 NRC Canada

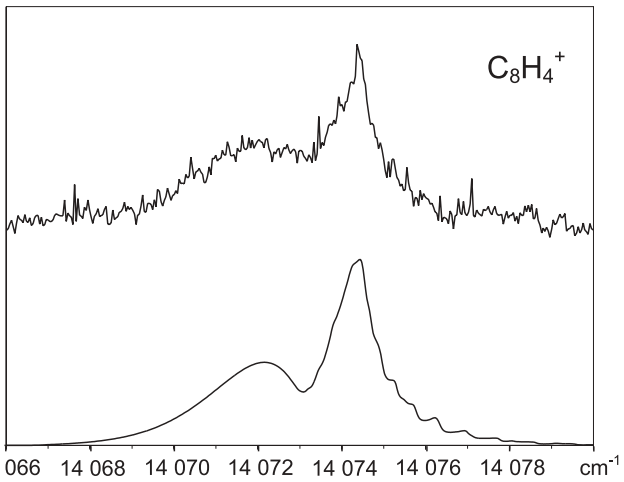
Fig. 3. The origin bands of the $^2A''$–X^2A'' electronic transition for $C_4H_4^+$ and $C_4D_4^+$ observed using cavity ring down spectroscopy through a supersonic planar plasma expansion. The rotational structure observed (traces *a* and *c*) can be simulated with a temperature of 30 K using constants derived from geometry optimization by ab initio calculation (traces *b* and *d*). Bands marked with * are due to another carrier. The peaks going off-scale are due to the Swan bands of C_2 and were used for the frequency calibration. The spectrum of $C_4D_4^+$ is shifted by –51.64 cm^{-1} for comparison with $C_4H_4^+$.



100 μm multilayer slit-nozzle geometry. Rotational temperatures of the order 30–50 K are routinely achieved. The nozzle was mounted in an optical cavity where the expansion was intersected ~2 mm downstream by the pulsed light of a tunable dye laser. The line width of the dye laser was 0.15 cm^{-1} when scanning with a grating and 0.04 cm^{-1} with an intracavity etalon. The light leaking out of the cavity was detected with a photodiode and was used as input for a standard ring down analysis (15). A spectrum was recorded by determining an averaged decay time as a function of the laser frequency.

The origin transition of $C_4H_4^+$ was searched for around the 19 416 cm^{-1} region, and a band having P- and R-branches was found at 19 486 cm^{-1}, as shown in Fig. 3*a*. When C_2D_2 was used as the sample gas, another band, having a similar profile, was detected around 19 537 cm^{-1} (Fig. 3*c*). The shift on deuteration is 51 cm^{-1}, which is comparable with the 67 cm^{-1} one for the $C_6H_4^+$–$C_6D_4^+$ pair (6). The 19 486 cm^{-1} band lies 70 cm^{-1} to the red in a neon matrix, comparable with the 79 cm^{-1} shift in HC_4H^+ (12). The optimized condition for the production of $C_4H_4^+$ used a mixture of 0.5% C_2H_2 in argon and a –700 V discharge while sampling 2 mm downstream from the discharge slit. The signals could not be detected when helium was used as the buffer gas. The behaviour of the HC_4H^+ absorption signals was similar.

Fig. 4. The $^2A''$–X^2A'' origin band in the electronic transition for $C_8H_4^+$ observed using cavity ring down spectroscopy through a supersonic planar plasma expansion. The rotational structure observed (upper trace) can be simulated (lower trace) using constants derived from geometry optimization by an ab initio calculation and a temperature of 50 K.



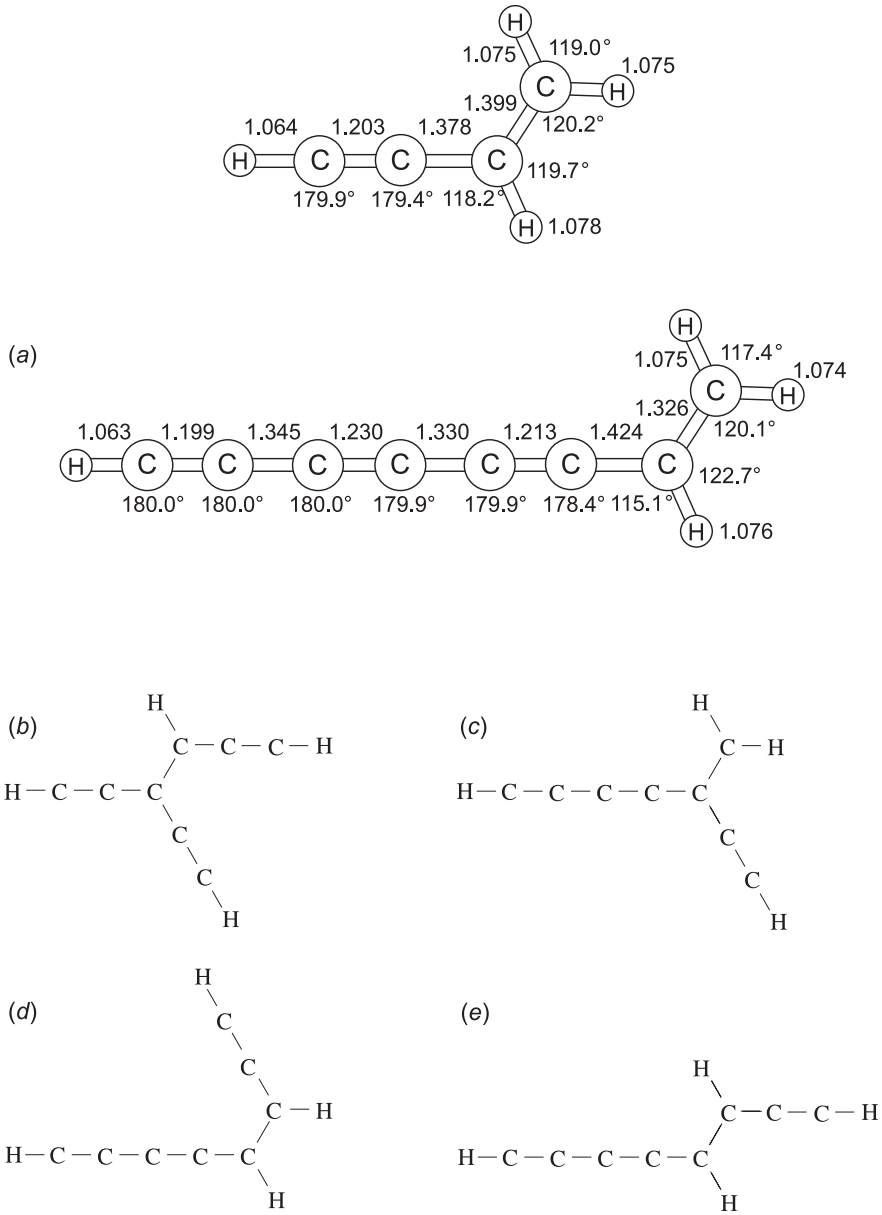
The energy of the electronic transition of $C_8H_4^+$ was expected around 14 030 cm^{-1} by reference to Fig. 1. One band was found in the gas phase at 14 073 cm^{-1}, as shown in Fig. 4. The optimized condition was quite similar to that for $C_6H_4^+$, a –300 V discharge through a mixture of 0.5% C_2H_2 in helium and with probing 1.5 mm downstream from the slit.

Results and discussion

The differences in frequency between the observed origin bands of $C_4H_4^+$, $C_6H_4^+$, and $C_8H_4^+$ and of the corresponding HC_nH^+ series (1–3) are 237, 110, and 70 cm^{-1}, as shown in Fig. 1*b*. The shifts decrease with increasing number of carbon atoms. This indicates that the contribution of the nonlinear part, -CH=CH_2, to the molecular orbital decreases on extension of the carbon chain. This trend in the two homologous series suggests that the observed bands can be assigned to $C_4H_4^+$ and $C_8H_4^+$ with the common chain structures. $C_8H_4^+$ has five isomers constructed by combination of ethylene and acetylene, as shown in Fig. 5. Structure (*b*) is intermediate between a prolate and an oblate top, but the observed spectrum has the profile of a typical near-prolate top and a-type transition. In the view of this, structure (*b*) is rejected as the carrier of the observed spectrum. Geometries (*b*) and (*c*) do not have eight carbons in a line but instead have a branching structure. Owing to the correlation of the transition energy of $C_nH_4^+$ and HC_nH^+ (Fig. 1), these should be π–π type electronic excitations in the conjugated system. Transition energies of the structures (*b*) and (*c*) would not show the correlation with the HC_nH^+ series. Structures (*d*) and (*e*) are cis and trans isomers, and both should have

© 2004 NRC Canada

Fig. 5. Optimized molecular structure in the ground state of $C_4H_4^+$ and $C_8H_4^+$ using ab initio calculations. The bond lengths are given in Å. Other isomers of $C_8H_4^+$ are indicated by simple pictures.



their electronic transition close to each other. No other signal could be detected within ±100 cm^{-1} from the observed band. Thus, the structures (*c*), (*d*), and (*e*) can be rejected as candidates for the observed spectrum. There remains structure (*a*), which would correlate with the HC_nH^+ series, and therefore this is the best candidate for the assignment. Consequently the symmetry of the electronic transitions observed for $C_4H_4^+$ and $C_8H_4^+$ is $^2A''$–X^2A''.

Determination of the rotational constants from the observed spectra is difficult because of overlap by the Swan bands of C_2 (16) in the case of $C_4H_4^+$ (Fig. 3) and the nonresolved rotational contour on $C_8H_4^+$ (Fig. 4). Thus, the rotational constants and molecular structure in the ground state of $C_4H_4^+$ and $C_8H_4^+$ were determined by ab initio calculations using GAMESS (17) with ROHF/6-31G**, the same method used in previous works (6, 18). The optimized bond lengths and angles are given in Fig. 5. From the latter, the rotational constants were calculated (Table 1).

In the case of the polyacetylene cations HC_nH^+, the ratio B''/B' of rotational constants between the ground and excited states decreases and approaches 1.0 on extension of the carbon chain (Fig. 6). The ratios B''/B' and C''/C' for the $C_nH_4^+$ series should follow the same trend and converge to the HC_nH^+ value for the long chains. Ratio A''/A' should increase and approach 1.0 on extension of the carbon chain. These trends were assumed in order to estimate the rotational constants in the excited states of $C_4H_4^+$ and $C_8H_4^+$ (Table 1). The profiles of the origin bands in the electronic transitions of $C_4H_4^+$ and $C_8H_4^+$ were then simulated using the ground-state rotational constants given by the ab initio calculation and the extrapolated excited-state values from the $C_6H_4^+$ data. The observed profiles are then well repro-

© 2004 NRC Canada

Table 1. Calculated rotational constants and assumed ratios between the ground and excited states.

	$C_4H_4^+$	$C_4D_4^+$	$C_6H_4^+$[a]	$C_8H_4^+$
A'' (cm^{-1})	1.562	1.075	1.217	1.220
B'' (cm^{-1})	0.162	0.138	0.0471	0.0193
C'' (cm^{-1})	0.147	0.122	0.0453	0.0190
A''/A'	0.91		0.94[b]	0.96
B''/B', C''/C'	1.06		1.03[b]	1.01

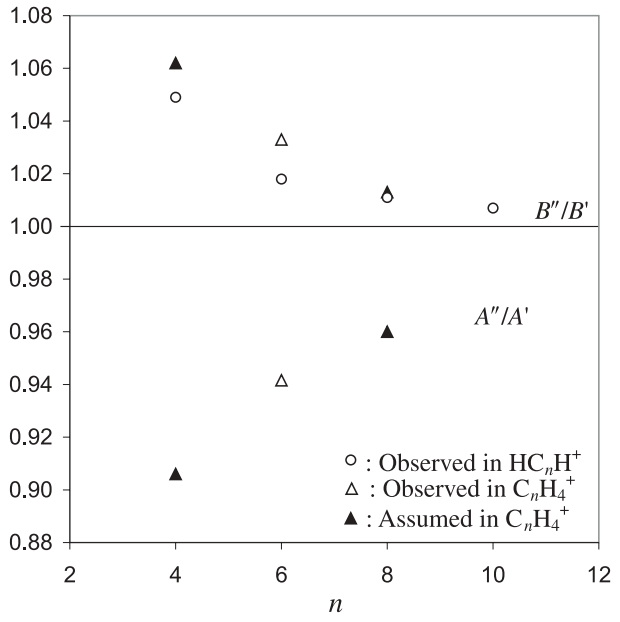
[a]Reference 6.
[b]Experimentally determined.

Table 2. Comparison of the origins (cm^{-1}) of the $^2A''$–X^2A'' electronic transition of $C_nH_4^+$ and $^2\Pi_u$–$X^2\Pi_g$ of HC_nH^+.

n	HC_nH^+	$C_nH_4^+$ ($C_nD_4^+$)	ΔT_{00}
4	19 722.61[a]	19 485.80 (19 537.45)	236.81
6	16 654.69[b]	16 544.98[c] (16 611.91)[c]	109.71
8	14 143.18[d]	14 073.00	70.18

[a]Reference 1.
[b]Reference 2.
[c]Reference 6.
[d]Reference 3.

Fig. 6. Ratios of rotational constants between the ground and excited states for HC_nH^+ and $C_nH_4^+$. A''/A' are <1.0 whereas B''/B' are >1.0, and it is assumed that $B''/B' = C''/C'$ in $C_nH_4^+$.



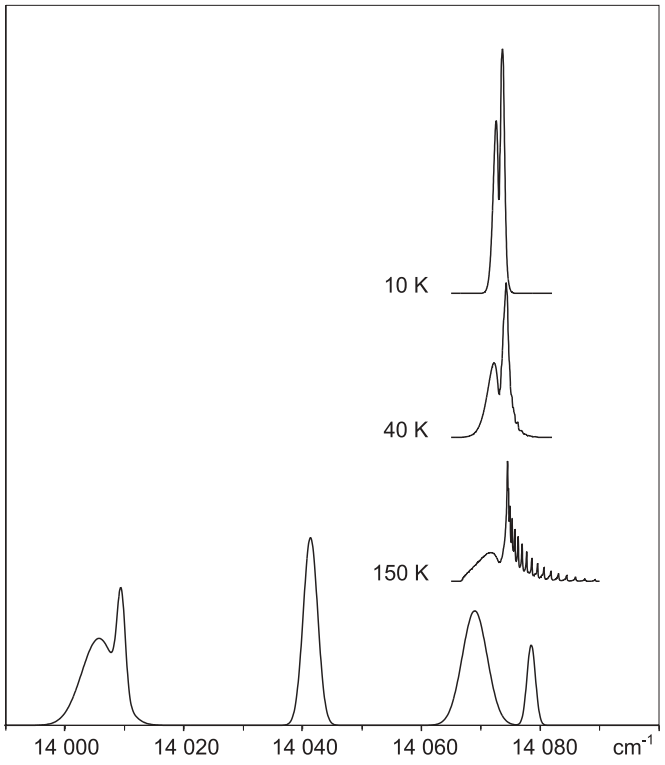
duced (Figs. 3 and 4) using the WANG program (19). By comparison of the simulated and observed spectra, the assignments were confirmed, and more accurate transition frequencies were inferred. These are given in Table 2.

Astrophysical relevance

The optical spectrum obtained for $C_8H_4^+$ allows a comparison with the available lists of DIB positions (20, 21). This shows that there is an overlap between the band observed around 14 073 cm^{-1} and two DIBs reported at 14 068.9 and 14 078.4 cm^{-1}. To check whether these differences in frequency might be due to a temperature effect, a comparison was made between an artificial DIB spectrum in the 709–714 nm range and the simulated $C_8H_4^+$ spectrum for low (10 K), intermediate (40 K), and high (150 K) temperature. This is shown in Fig. 7. From this it is clear that the absorption band of the nonlinear $C_8H_4^+$ does not fit the DIB absorption at any temperature.

A DIB having a double peak structure and similar rotational profile (with P- and R-branches) to that observed for $C_8H_4^+$ is located between 14 000 and 14 010 cm^{-1} (Fig. 7).

Fig. 7. Artificial diffuse interstellar band absorptions in the 709–714 nm range (lower trace reproduced from ref. 20) and the simulated $C_8H_4^+$ laboratory spectra at 10, 40, and 150 K (upper traces).



However, no absorption was detected in this region in the laboratory measurements. In the case of the $C_4H_4^+$ absorptions, there are no overlaps with DIBs.

An upper limit of the column density for the $C_nH_4^+$ series in diffuse clouds can be estimated by comparison of the laboratory and DIB data in a similar fashion to that used before (22). For this, it is assumed that the oscillator strengths of the 0–0 band in the $^2A''$–X^2A'' transition for $C_nH_4^+$ (n = 4, 6, 8) and $A^2\Pi_u$–$X^2\Pi_g$ for HC_nH^+ (22) are equal (i.e., 0.04, 0.06, and 0.08 for $C_4H_4^+$, $C_6H_4^+$, and $C_8H_4^+$) and that a signal-to-noise ratio of 5 is required for detection of a DIB absorption. The fwhm of the bands is about 2 Å, and the sensitivity limit for a DIB detection is 0.002 Å (20). This leads to upper limits for their column densities of 2×10^{12}, 1×10^{12}, and 0.6×10^{12} cm^{-2} for $C_4H_4^+$, $C_6H_4^+$, and $C_8H_4^+$, respectively.

© 2004 NRC Canada

Acknowledgement

This work has been supported by the Swiss National Science Foundation (project 200020-100019).

References

1. J. Lecoultre, J.P. Maier, and M. Rösslein. J. Chem. Phys. **89**, 6081 (1988).
2. W.E. Sinclair, D. Pfluger, H. Linnartz, and J.P. Maier. J. Chem. Phys. **110**, 296 (1999).
3. D. Pfluger, T. Motylewski, H. Linnartz, W.E. Sinclair, and J.P. Maier. Chem. Phys. Lett. **329**, 29 (2000).
4. P. Cias, O. Vaizert, A. Denisov, J. Mes, H. Linnartz, and J.P. Maier. J. Phys. Chem. A, **106**, 9890 (2002).
5. See for example: H. Linnartz, T. Motylewski, and J.P. Maier. J. Chem. Phys. **109**, 3819 (1998).
6. M. Araki, H. Linnartz, P. Cias, A. Denisov, J. Fulara, A. Batalov, I. Shnitko, and J.P. Maier. J. Chem. Phys. **118**, 10 561 (2003).
7. M. Ohishi, W.M. Irvine, and N. Kaifu. *In* Astrochemistry of cosmic phenomena. *Edited by* P.D. Singh. Kluwer, Dordrecht. 1992. pp. 171–177.
8. A.E. Douglas. Nature (London), **269,** 130 (1977).
9. M. Frenklach and E.D. Feigelson. Astrophys. J. **341**, 372 (1989).
10. See for example: W.J. van der Hart, E. Oosterveld, T.A. Molenaar-Langeveld, and N.M.M. Nibbering. Org. Mass Spectrom. **24**, 59 (1989).
11. R. Wrobel, W. Sander, D. Cremer, and E. Kraka. J. Phys. Chem. A, **104**, 3819 (2000).
12. J.P. Maier. Chem. Soc. Rev. **26**, 21 (1997).
13. P. Freivogel, J. Fulara, D. Lessen, D. Forney, and J.P. Maier. Chem. Phys. **189**, 335 (1994).
14. H. Linnartz, T. Motylewski, and J.P. Maier. J. Chem. Phys. **109**, 3819 (1998).
15. A. O'Keefe and D.A.G. Deacon. Rev. Sci. Instrum. **59**, 2544 (1988).
16. G.M. Lloyd and P. Ewart. J. Chem. Phys. **110**, 385 (1999).
17. M.W. Schmidt, K.K. Baldridge, J.A. Boatz, S.T. Elbert, M.S. Gordon, J.H. Jensen, S. Koseki, N. Matsunaga, K.A. Nguyen, S.J. Su, T.L. Windus, M. Dupuis, and J.A. Montgomery. J. Comput. Chem. **14**, 1347 (1993).
18. G. Koster and W.J. van der Hart. Int. J. Mass Spectrom. Ion Processes, **163**, 169 (1997).
19. D. Luckhaus and M. Quack. Mol. Phys. **63**, 745 (1989).
20. P. Jenniskens and F.-X. Désert. Astron. Astrophys. Suppl. Ser. **106**, 39 (1994).
21. S.Ó. Tuairisg, J. Cami, B.H. Foing, P. Sonnentrucker, and P. Ehrenfreund. Astron. Astrophys. Suppl. Ser. **142**, 225 (2000).
22. T. Motylewski, H. Linnartz, O. Vaizert, J.P. Maier, G.A. Galazutdinov, F.A. Musaev, J. Krełowski, G.A.H. Walker, and D.A. Bohlender. Astrophys. J. **531**, 312 (2000).

© 2004 NRC Canada

The rotationally resolved electronic spectra of several conformers of 1-hexoxy and 1-heptoxy[1]

Lily Zu, Jinjun Liu, Sandhya Gopalakrishnan, and Terry A. Miller

Abstract: Laser-induced fluorescence excitation spectra of five vibronic bands of 1-hexoxy and three bands of 1-heptoxy have been recorded in a jet-cooled environment. Experimental values of rotational constants for both the $\widetilde{X}$ and $\widetilde{B}$ states and components of the spin-rotational tensor for the $\widetilde{X}$ state were obtained by an analysis of the partially resolved rotational structure of the vibronic bands. Comparing these experimental results with quantum chemistry calculations, and using corresponding assignments of smaller alkoxy radicals as a guide, permitted unambiguous conformational assignments for the bands. The extension of similar assignments to larger alkoxy radicals is also discussed.

Key words: electronic spectroscopy, organic radicals, combustion, atmospheric chemistry.

Résumé : Les spectres de fluorescence induite par laser de cinq bandes vibroniques du 1-hexoxy et de trois bandes du 1-heptoxy ont été enregistrés en jet froid. Une analyse de la structure rotationnelle partiellement résolue des bandes vibroniques a permis d'obtenir les valeurs expérimentales des constantes rotationnelles des deux états $\widetilde{X}$ et $\widetilde{B}$, ainsi que les composantes tensorielles de spin-rotation de l'état $\widetilde{X}$. La comparaison des résultats expérimentaux avec des calculs de chimie quantique, ainsi qu'une utilisation des attributions correspondantes de plus petits radicaux alkoxy comme guide, a permis une attribution des conformères sans ambiguité possible pour chaque bande. L'extension d'attribution similaire à de plus gros radicaux de type alkoxy est discutée.

Mots clés : spectroscopie électronique, radicaux organiques, combustion, chimie de l'atmosphère.

[Traduit par la Rédaction]

1. Introduction

It is a privilege to contribute to this Gerhard Herzberg memorial issue. One of his abiding interests was the spectroscopy of free radicals (1). Arguably his electronic spectra of the simplest hydrocarbon free radicals (2–6) CH, CH_2, and CH_3, rank among the most significant achievements in his illustrious career.

In this spirit, this paper reports the electronic spectroscopy of some simple hydrocarbon-derived, oxygen-containing, free radicals, the alkoxies ($C_nH_{2n+1}O$). The importance of alkoxy radicals in atmospheric chemistry is well known (7). They are key intermediates in the oxidation of hydrocarbons. More than 100 studies have been published alone over the last 50 years on the spectroscopic studies of the smallest alkoxy radical, methoxy. Other small alkoxies like ethoxy (8, 9), C_2H_5O, and 2-propoxy (9, 10), $(CH_3)_2HCO$, have also been studied intensively.

The early laser magnetic resonance investigation of Radford and Russell (11) in the far-IR and the microwave studies of Endo et al. (12) yielded considerable information about the ground ^{2}E state of methoxy. Its electronic transition has long been known to be an excitation from the ground $\widetilde{X}^2$E state to the $\widetilde{A}^2$A state (13). When a hydrogen is substituted in methoxy, the C_{3v} symmetry of CH_3O is at least lowered to C_s; the excited $\widetilde{A}$ A_1 state of CH_3O correlates to a $\widetilde{B}$ A' state while the degenerate E ground state decomposes into $\widetilde{A}$ and $\widetilde{X}$ states, of A' and A'' symmetry assuming a plane of symmetry exists. Whether the $\widetilde{X}$ state is A' or A'' depends upon the radical. Tan et al. (14) determined the symmetry of the $\widetilde{X}$ and $\widetilde{A}$ electronic states of ethoxy, vinoxy, and isopropoxy, using the technique of laser-induced fluorescence (LIF) combined with supersonic jet cooling. The complete rotational analysis of the LIF spectrum of the ethoxy (14) $\widetilde{B} - \widetilde{X}$ transition further revealed a significant ground-state, spin-rotation splitting due to the close spacing of the low-lying $\widetilde{A}$ and $\widetilde{X}$ states. Within experimental resolution (≈200 MHz) no excited-state, spin-rotation splitting was observed.

While the smaller alkoxy radicals have drawn significant attention, the spectroscopic study of larger alkoxy radicals is much sparser. It was generally felt that the fluorescence quantum yield for the $\widetilde{B} - \widetilde{X}$ transition would rapidly decrease as non-radiative decay processes became dominant in the larger alkoxy radicals. That perception began to change when LIF spectra of *t*-pentoxy, 3-pentoxy, *t*-butoxy, and 2-butoxy were observed at near ambient temperature in 1999 (15, 16). However, the failed attempts to observe several other larger alkoxy radicals in the same LIF studies left the overall situation unclear. Clarification occurred when the LIF spectra of nearly 20 large alkoxy radicals containing 5–12 carbon atoms were reported by Carter et al. (17) in 2001. The studies showed that under

Received 13 April 2004. Published on the NRC Research Press Web site at http://canjchem.nrc.ca/ on 31 August 2004.

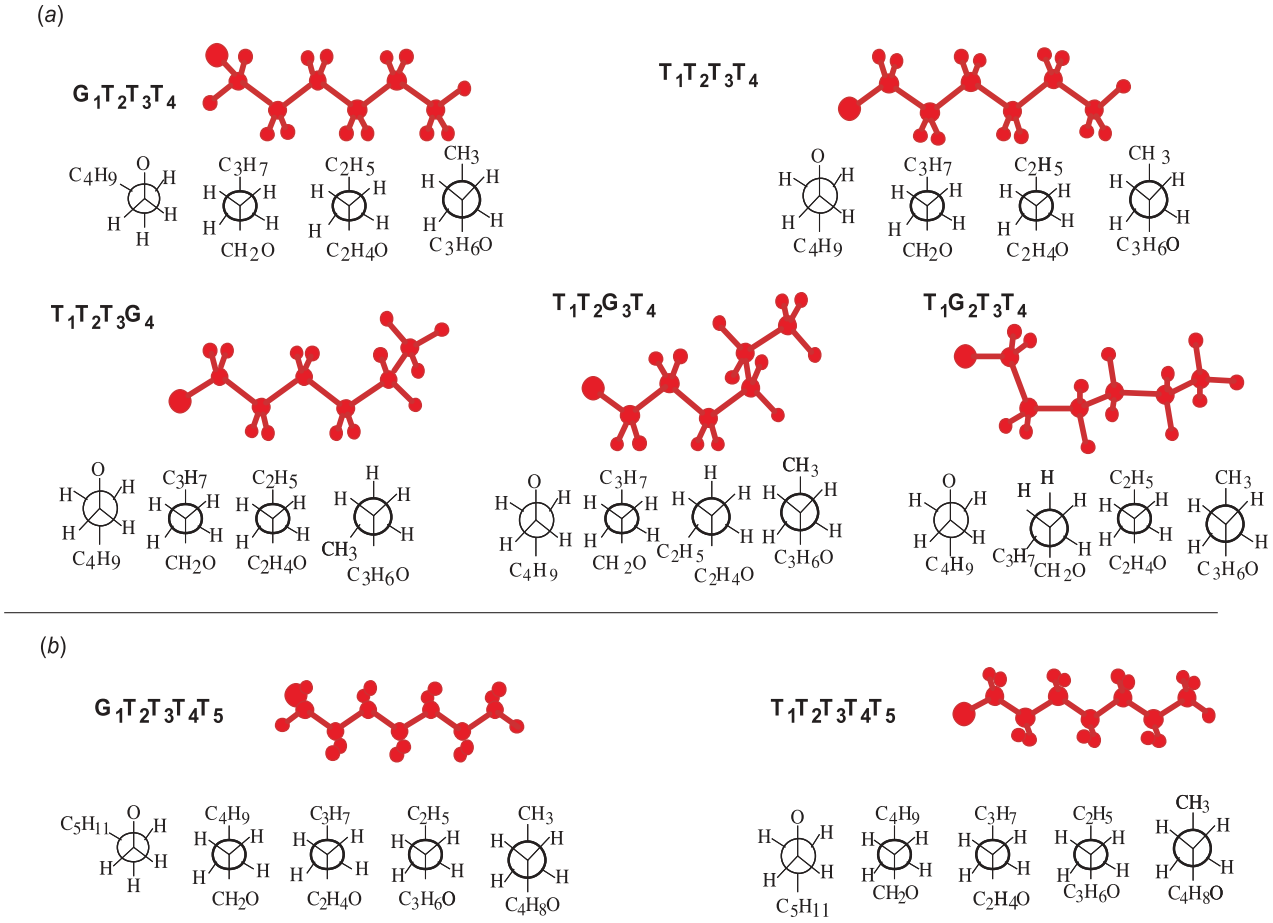
L. Zu, J. Liu, S. Gopalakrishnan, and T.A. Miller.[2] Laser Spectroscopy Facility, Department of Chemistry, The Ohio State University, 120 W. 18th Avenue, Columbus, OH 43210, USA.

[1]This article is part of a Special Issue dedicated to the memory of Professor Gerhard Herzberg.

[2]Corresponding author (e-mail: tamiller@chemistry.ohio-state.edu).

 doi: 10.1139/V04-056 © 2004 NRC Canada

Fig. 1. Structures of representative examples of the (*a*) 41 1-hexoxy conformers and (*b*) 122 1-heptoxy conformers. The corresponding Newman projections are also shown.



cold jet conditions, all of the alkoxy radicals exhibit sharp LIF excitation spectra with well-characterized vibrational structure. The S/N ratio of the spectra did become somewhat poorer as the number of carbon atoms (n) increased but not dramatically so, and the authors attributed the gradual reduction to the decreased vapor pressure of the higher molecular weight precursors.

Assignment of the observed spectral bands in the large alkoxy radicals has turned out to be very challenging. Unlike methoxy and ethoxy, larger alkoxy radicals have structural isomers, and the same structural isomer can exist in different conformations. Alkoxy conformers are typically labelled according to whether the non-H substituents are *gauche* (G) or *trans* (T) with respect to one another for each of the C—C bonds in the molecules, (with the C—C bond labelled 1 being the one that is closest to the O atom) (Fig. 1).

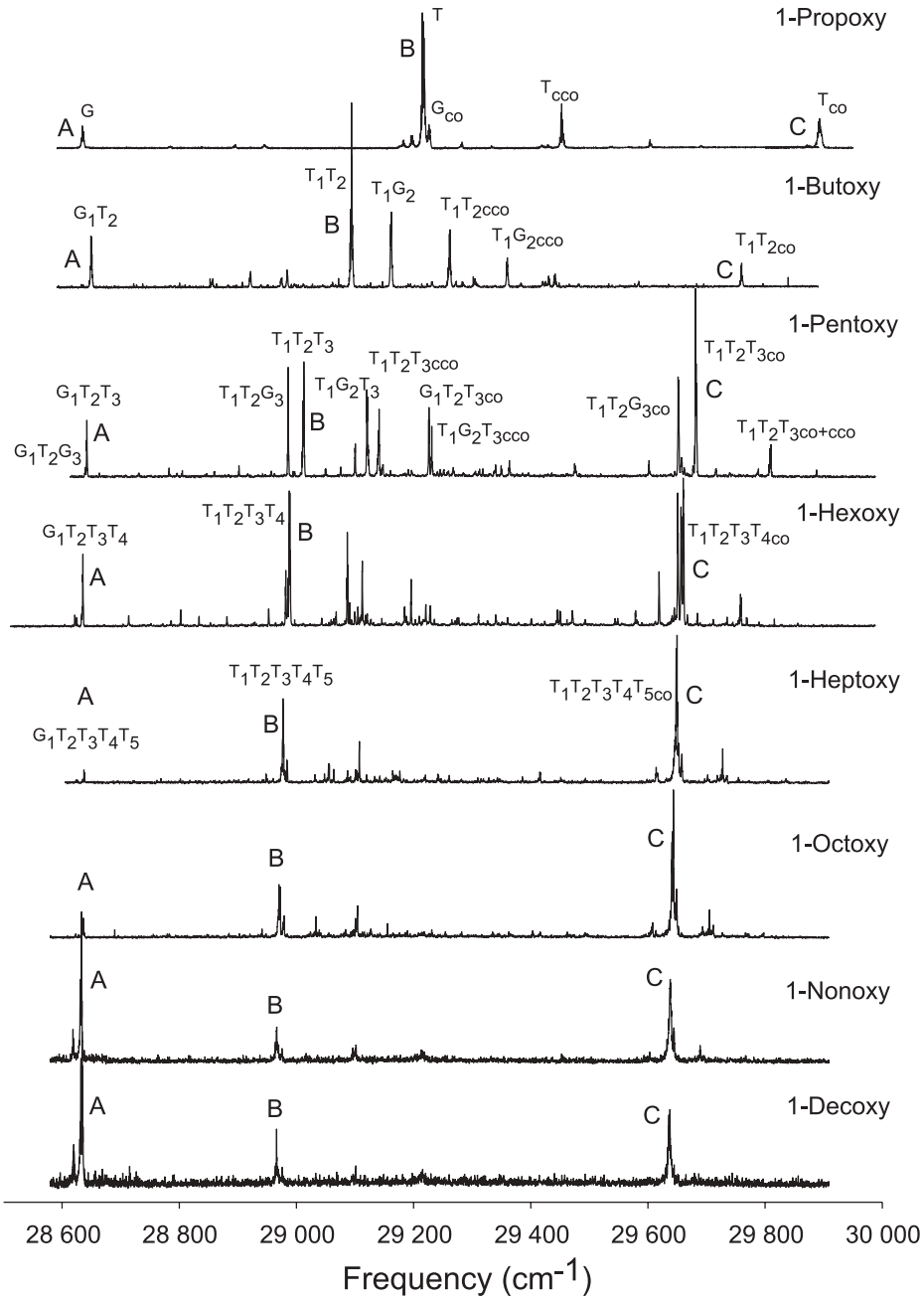
The spectral positions of structural isomers are usually well-separated but those of conformers are not. Indeed, closely-spaced vibronic bands can be expected from the various conformers, e.g., an origin band from one conformer can lie close to a C-O stretch band belonging to an entirely different conformer of the radical. Gopalakrishnan et al. (18) made significant progress analyzing the rotationally resolved $\tilde{B} - \tilde{X}$ LIF spectra of all the strong bands of 1-propoxy. Five vibronic bands were unambiguously assigned to two conformers (G and T). Experimental rotational constants for both $\tilde{X}$ and $\tilde{B}$ states as well as components of the electron spin-rotation tensor in the $\tilde{X}$ state were determined for each conformer. Similar rotational analyses (19) were recently published for 1-butoxy and 1-pentoxy, again correlating the strongest spectral lines with specific conformers.

The method used in the 1-propoxy, 1-butoxy, and 1-pentoxy analyses is computationally intensive (18, 19). It involves identifying all likely stable conformations using the systematic pseudo-Monte Carlo (SPMC) methods (20) available in MacroModel (21). This is followed by quantum chemistry calculations for both the $\tilde{X}$ and $\tilde{B}$ states, optimizing each of these geometries to predict rotational constants. Components of the ground-state electronic spin – molecular rotation tensor were also predicted by a semiempirical method using the experimentally observed spin-rotation tensor of ethoxy as a reference. Finally, comparisons between molecular constants obtained experimentally and those from the calculations are used to identify the carrier of a given band.

When one examines larger open-chain, primary alkoxies, the number (19) of conformers expected (41 for 1-hexoxy, 122 for 1-heptoxy) becomes so large that the computations described above become infeasible. In this paper, we suggest a new technique, which lets us select a candidate conformer for a given band based only upon a comparison of the given experimental spectra with those of smaller alkoxy radicals. Using this ap-

© 2004 NRC Canada

Fig. 2. LIF excitation spectra of the primary alkoxy radicals ($C_nH_{2n+1}O$) from $n = 3 - 10$. Persistent lines in the spectrum are marked A, B, and C. Conformationally assigned bands are labeled (G for gauche, T for trans) (18, 19) according to the various dihedral angle minima. Excited vibrational levels are indicated as subscripts by their approximate motion, e.g., CO (stretch), CCO (bend), etc.



proach, four conformers were assigned for five vibronic bands of 1-hexoxy and two conformers for three vibronic bands of 1-heptoxy. Extending the analysis to even larger alkoxy radicals is also discussed.

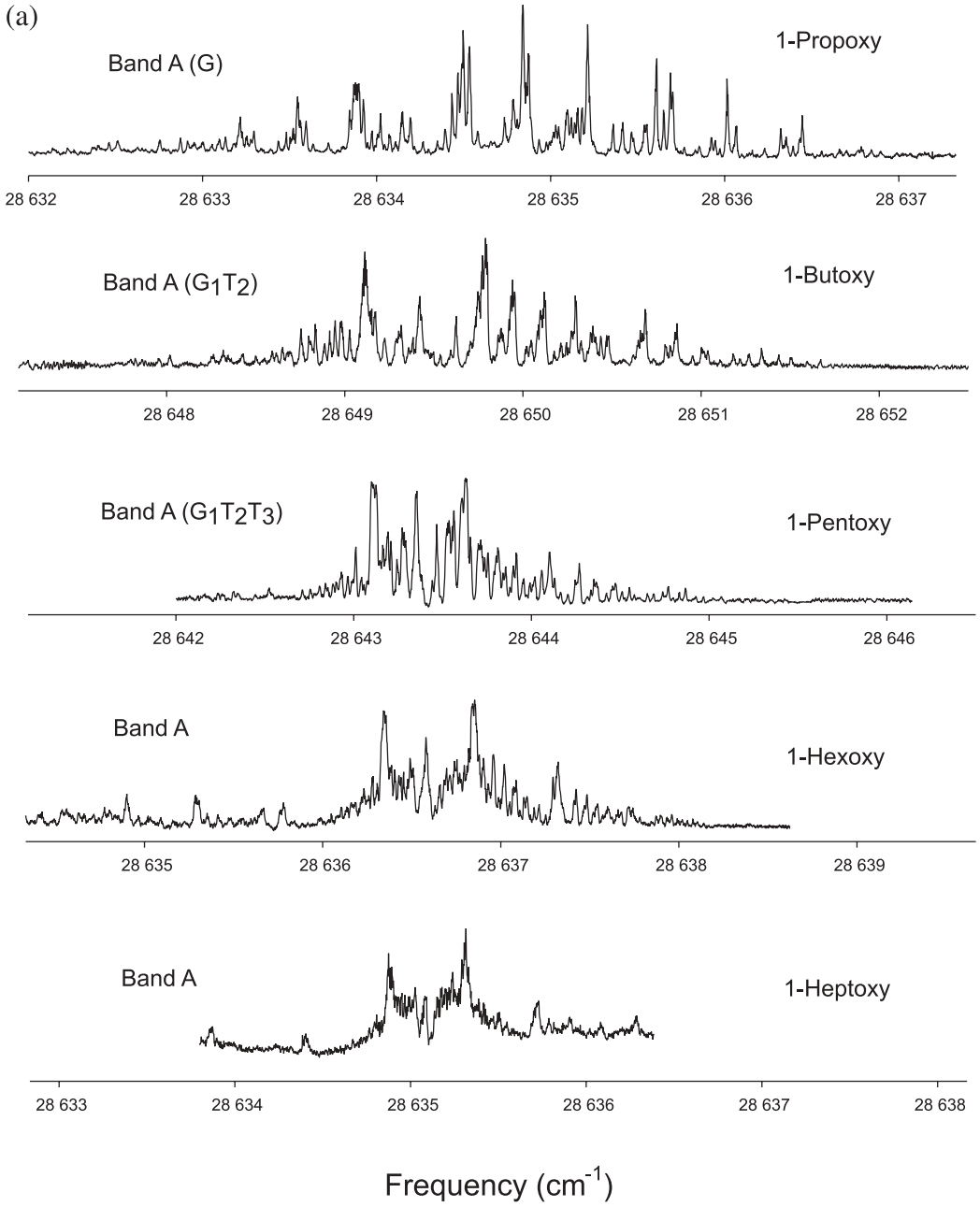
2. Experimental

The alkoxy radicals were generated in a supersonic free jet expansion by UV laser photolysis (XeF) of the corresponding alkyl nitrites at the base of a 0.5 mm circular nozzle. The alkyl nitrites were synthesized according to well-known procedures (22). A few torr (1 torr = 133.322 Pa) of the alkyl nitrite vapor was entrained into the jet flow by passing helium at 6 atm (1 std atm = 101.325 kPa) over the liquid contained in a steel bomb maintained at a suitable temperature depending upon the vapor pressure.

The rotationally resolved LIF spectra of the 1-alkoxy radicals were obtained on our high-resolution apparatus, which has been described elsewhere (23). Briefly, a cw ring dye laser (Coherent 899-29 Autoscan) pumped by an Ar^+ laser (Coherent Innova Sabre) was pulse amplified and frequency doubled using a KDP crystal to generate the UV radiation required to

© 2004 NRC Canada

Fig. 3. Rotationally resolved spectra of primary alkoxy radicals from 1-propoxy to 1-heptoxy: (*a*) band A, (*b*) band B, and (*c*) band C.



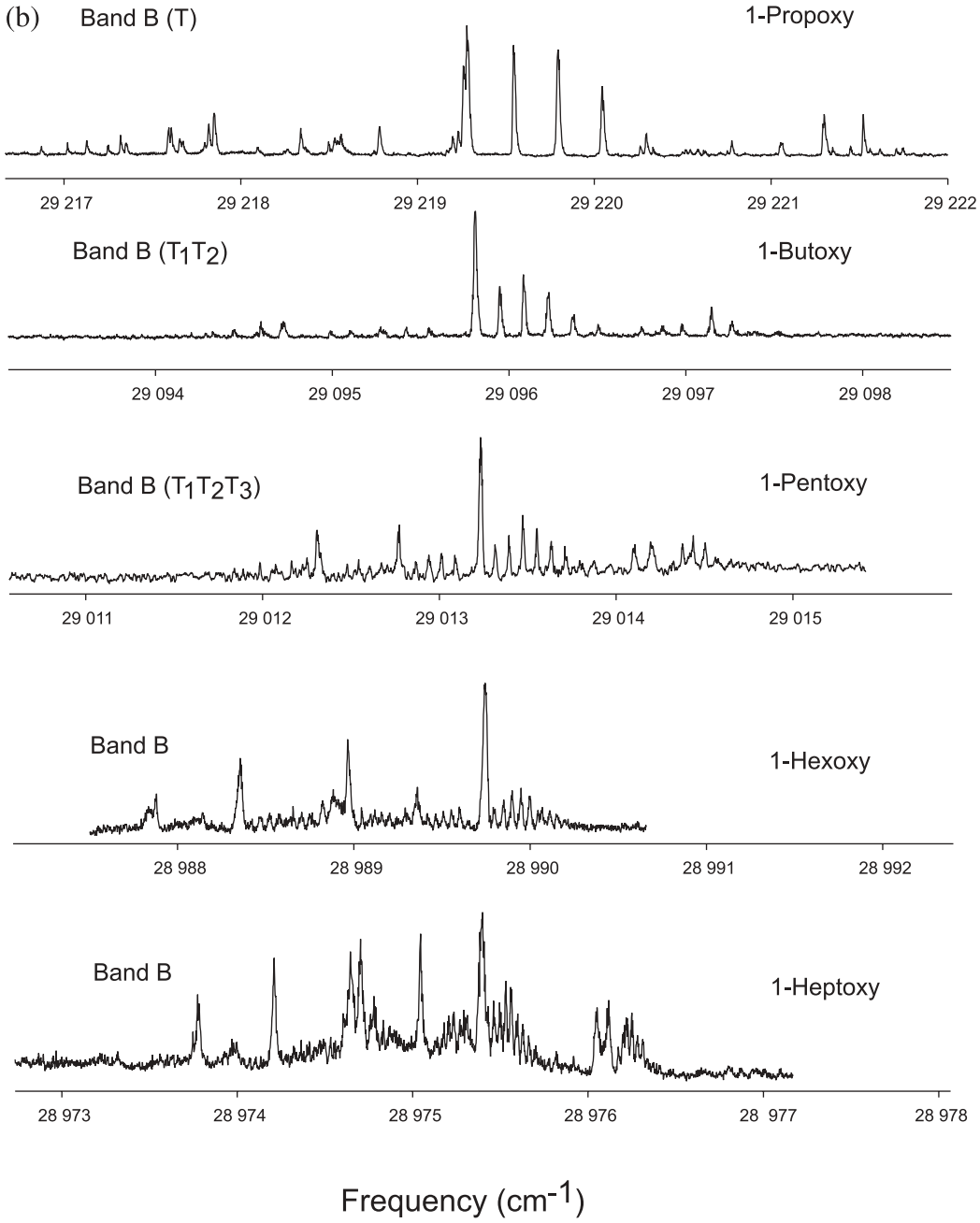
pump the $\widetilde{B} - \widetilde{X}$ transition of the alkoxy radicals. The pulse amplifier (Lambda Physik, FL 2003 model) was pumped by an excimer laser (XeCl, Lambda Physik, MSC 103 model) with a resulting line width of ≈100 MHz in the fundamental (200 MHz when doubled into the UV). This radiation was directed into a vacuum chamber ≈15 mm downstream of the nozzle orifice to excite the $\widetilde{B} - \widetilde{X}$ transition. The resulting fluorescence was collected perpendicular to the probe laser beam with a 2.5 cm f/1 lens. The light was then focused with a f/3 lens through an adjustable slit onto a photomultiplier tube (PMT). The slit can be adjusted to allow only the central portion of the fluorescence from the jet to be detected by the PMT, thereby reducing the Doppler width of the signal from off-axis velocity components in the jet expansion. This signal was then preamplified and sent to a boxcar averager (Stanford Research, SR250 boxcar) for integration. The amplified signal was then sent to the Coherent Autoscan unit for signal averaging and recording.

3. Theory

The theory upon which the analysis of the rotational structure of the bands is based is described in detail in ref. 18, hence only a brief description will be provided here. An asymmetric top Hamiltonian is used to model the rotational structure of the high-resolution electronic spectra of the primary alkoxy radicals. Because of the very low temperature in the jet, only

© 2004 NRC Canada

Fig. 3. (*continued*).



the lowest few rotational states are populated. Therefore, centrifugal terms in the rotational Hamiltonian ($\mathcal{H}_{Rot}$) may be neglected. However, the spin-rotation coupling certainly needs to be considered. Hence, the total Hamiltonian can be written:

[1] $$\mathcal{H} = \mathcal{H}_{Rot} + \mathcal{H}_{SR}$$

In which

[2] $$\mathcal{H}_{Rot} = AN_a^2 + BN_b^2 + CN_c^2$$

[3] $$\mathcal{H}_{SR} = \frac{1}{2}\sum_{\alpha\beta}\epsilon_{\alpha\beta}(N_\alpha S_\beta + S_\beta N_\alpha)$$

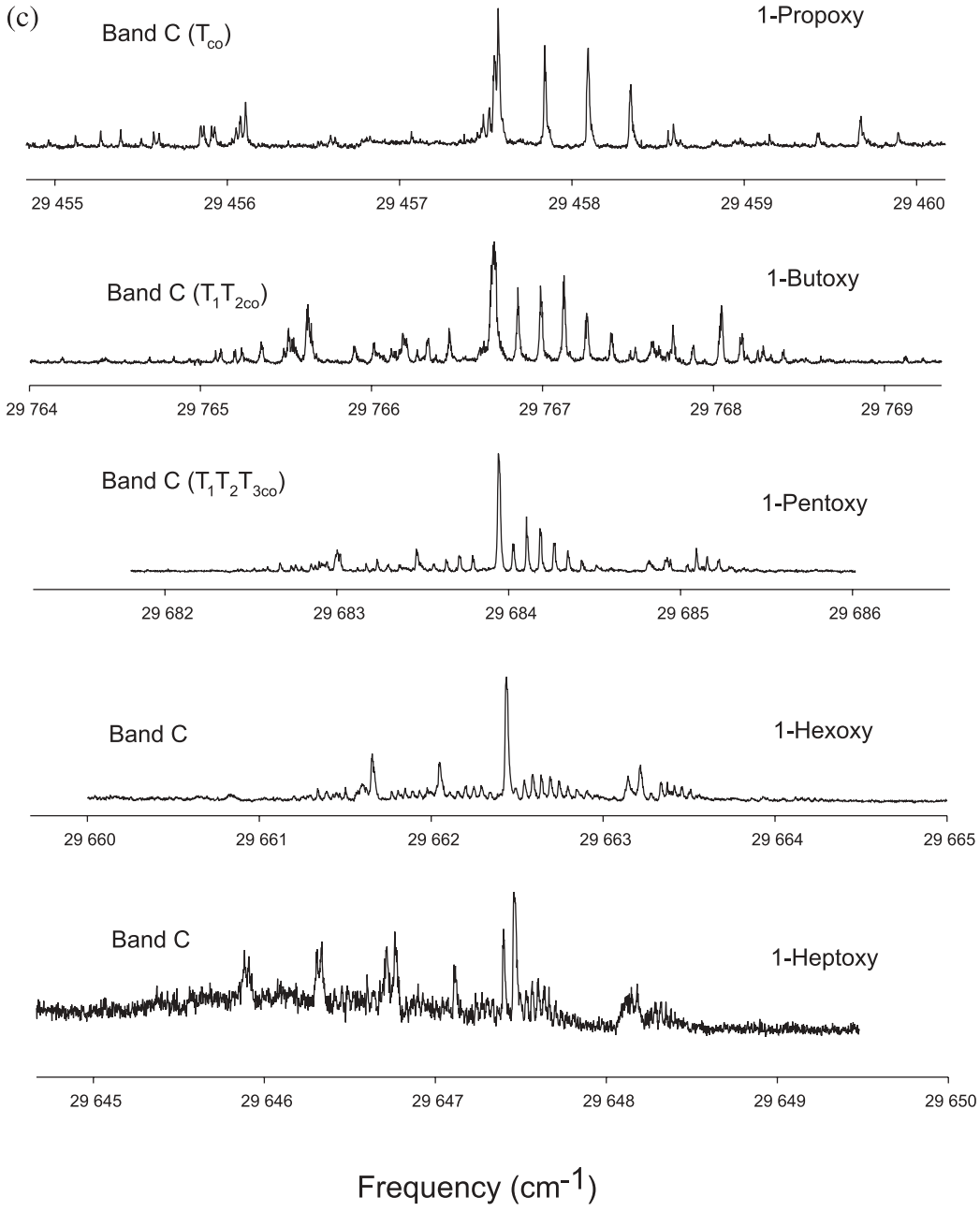
where **N** and **S** are the molecular rotational and electron spin angular momentum, respectively. A, B, and C are the rotational constants, and $\epsilon_{\alpha\beta}$ are the components of the spin-rotation tensor in the inertial axis system (*a, b, c*).

The matrix elements of the Hamiltonian of a nonrigid, nonlinear, polyatomic molecule in a multiplet electronic state have been derived by Raynes (24), and these were programmed into a graphical user interface program SpecView, which was developed in our laboratory (25) to model the spectra of the alkoxy radicals.

The six rotational constants, namely, A'', B'', and C'' in the ground state and A', B', and C' in the excited $\tilde{B}$ state, need to be fit to the spectra. For the spin-rotation interaction,

© 2004 NRC Canada

Fig. 3. (*concluded*).



only ground-state constants need to be fitted because the spin-rotation interaction in the excited state causes splittings unresolvable with the experimental resolution, as confirmed by the study of ethoxy (14). According to Brown et al. (26), six unique spin-rotation constants can be determined for molecules with C_1 symmetry, while only four can be determined for molecules with C_s symmetry. In the general case, the spin-rotation constants that can be determined for a single isotopic species are given below in terms of their relationship to the components of the reduced spin-rotation tensor $\tilde{\epsilon}$ introduced by Brown et al.:

$$T_0^0(\tilde{\varepsilon}) = (-1/\sqrt{3})(\tilde{\varepsilon}_{aa} + \tilde{\varepsilon}_{bb} + \tilde{\varepsilon}_{cc}) = \sqrt{3}a_0$$

$$T_0^1(\tilde{\varepsilon}) = (-1/\sqrt{2})i(\tilde{\varepsilon}_{cb} - \tilde{\varepsilon}_{bc}) = 0$$

$$T_{\pm1}^1(\tilde{\varepsilon}) = (1/2)[(\tilde{\varepsilon}_{ba} - \tilde{\varepsilon}_{ab}) \pm (\tilde{\varepsilon}_{ca} - \tilde{\varepsilon}_{ac})] = 0$$

$$T_0^2(\tilde{\varepsilon}) = (1/\sqrt{6})(2\tilde{\varepsilon}_{aa} - \tilde{\varepsilon}_{bb} - \tilde{\varepsilon}_{cc}) = \sqrt{6}a$$

$$T_{\pm1}^2(\tilde{\varepsilon}) = \pm(1/2)[(\tilde{\varepsilon}_{ba} + \tilde{\varepsilon}_{ab}) \pm (\tilde{\varepsilon}_{ca} + \tilde{\varepsilon}_{ac})] = \pm(d \pm ie)$$

$$T_{\pm2}^2(\tilde{\varepsilon}) = (1/2)[(\tilde{\varepsilon}_{bb} - \tilde{\varepsilon}_{cc}) \pm (\tilde{\varepsilon}_{bc} + \tilde{\varepsilon}_{cb})] = (b \mp ic)$$

© 2004 NRC Canada

Table 1. Experimentally determined and calculated (in brackets) values of molecular constants for several conformers of 1-hexoxy.

Constants (GHz)	Band A[a]	Band B[b]	Band C[c]	Band B_a[d]	Band C_b[e]
A''	8.884(3)[9.062]	12.817(13)[13.549]	13.633(8)[13.549]	7.741(19)[7.704]	8.322(23)[8.561]
B''	0.833(1)[0.818]	0.767(1)[0.728]	0.748(1)[0.728]	0.996(3)[0.853]	0.844(6)[0.825]
C''	0.770(1)[0.788]	0.697(1)[0.709]	0.722(1)[0.709]	0.909(3)[0.802]	0.830(6)[0.789]
$\widetilde{\epsilon}''_{aa}$	–0.34(1)[–0.41]	–3.41(6)[–3.82]	–4.08(4)[–3.82]	–0.33(6)[–1.44]	–3.14(30)[–2.70]
$\widetilde{\epsilon}''_{bb}$	–0.19(1)[–0.19]	–0.17(1)[–0.04]	–0.01(1)[–0.04]	–0.22(19)[–0.13]	–0.00(21)[0.01]
$\widetilde{\epsilon}''_{cc}$	–0.10(1)[–0.05]	0.02(0)[–0.00]	⋯ [–0.00]	⋯ [–0.01]	–0.07(21)[–0.01]
$\lvert\widetilde{\epsilon}''_{ab}\rvert = \lvert\widetilde{\epsilon}''_{ba}\rvert$	⋯ [0.50]	⋯ [1.00]	⋯ [1.00]	⋯ [0.72]	⋯ [0.35]
$\lvert\widetilde{\epsilon}''_{ac}\rvert = \lvert\widetilde{\epsilon}''_{ca}\rvert$	⋯ [0.27]	⋯ [0.04]	⋯ [0.04]	⋯ [0.19]	⋯ [0.34]
$\lvert\widetilde{\epsilon}''_{bc}\rvert = \lvert\widetilde{\epsilon}''_{cb}\rvert$	⋯ [0.10]	⋯ [0.00]	⋯ [0.00]	⋯ [0.03]	⋯ [0.01]
A'	8.142(2)[8.501]	12.974(8)[12.807]	12.474(3)[12.807]	7.149(9)[7.287]	8.193(11)[8.624]
B'	0.836(1)[0.837]	0.745(1)[0.738]	0.746(1)[0.738]	0.926(2)[0.869]	0.847(4)[0.827]
C'	0.792(1)[0.802]	0.715(1)[0.716]	0.729(1)[0.716]	0.966(2)[0.814]	0.815(5)[0.793]
T_0 (cm^{-1})	28 636.60(1)	28 989.34(1)	29 662.05(1)	28 983.21(1)	29 658.59(1)
Relative energies (cm^{-1})	⋯ [0.0]	⋯ [57]	⋯ [57]	⋯ [369]	⋯ [377]

[a]($G_1T_2T_3T_4$) 116 lines assigned, $\sigma = 43$ MHz.
[b]($T_1T_2T_3T_4$) 129 lines assigned, $\sigma = 121$ MHz.
[c]($T_1T_2T_3T_4$) 111 lines assigned, $\sigma = 35$ MHz.
[d]($T_1T_2G_3T_4$) 116 lines assigned, $\sigma = 194$ MHz.
[e]($T_1T_2T_3G_4$) 60 lines assigned, $\sigma = 91$ MHz.

Table 2. Experimentally determined and calculated (in brackets) values of molecular constants for several conformers of 1-heptoxy.

Constants (GHz)	Band A[a]	Band B[b]	Band C[c]
A''	7.496(6)[7.492]	11.674(32)[11.716]	11.738(26)[11.716]
B''	0.530(4)[0.542]	0.512(2)[0.489]	0.484(1)[0.489]
C''	0.518(4)[0.525]	0.492(3)[0.479]	0.489(1)[0.479]
$\widetilde{\epsilon}''_{aa}$	–0.08(4)[–0.35]	–3.79(4)[–3.47]	–3.49(5)[–3.47]
$\widetilde{\epsilon}''_{bb}$	–0.01(2)[–0.13]	0.00(9)[–0.03]	⋯ [–0.03]
$\widetilde{\epsilon}''_{cc}$	0.00(2)[–0.06]	–0.05(9)[0.00]	⋯ [0.00]
$\lvert\widetilde{\epsilon}''_{ab}\rvert = \lvert\widetilde{\epsilon}''_{ba\rvert}$	⋯ [0.41]	⋯ [0.85]	⋯ [0.85]
$\lvert\widetilde{\epsilon}''_{ac}\rvert = \lvert\widetilde{\epsilon}''_{ca}\rvert$	⋯ [0.22]	⋯ [0.03]	⋯ [0.03]
$\lvert\widetilde{\epsilon}''_{bc}\rvert = \lvert\widetilde{\epsilon}''_{cb}\rvert$	⋯ [0.07]	⋯ [0.00]	⋯ [0.00]
A'	6.872(4)[7.120]	11.085(9)[11.354]	11.124(9)[11.354]
B'	0.548(3)[0.554]	0.503(3)[0.495]	0.493(1)[0.495]
C'	0.526(3)[0.534]	0.502(3)[0.484]	0.491(1)[0.484]
T_0 (cm^{-1})	28 635.10(1)	28 975.04(1)	29 647.11(1)
Relative energies (cm^{-1})	⋯ [0.0]	⋯ [56]	⋯ [56]

[a]($G_1T_2T_3T_4T_5$) 109 lines assigned, $\sigma = 116$ MHz.
[b]($T_1T_2T_3T_4T_5$) 71 lines assigned, $\sigma = 66$ MHz.
[c]($T_1T_2T_3T_4T_5$) 69 lines assigned, $\sigma = 75$ MHz.

The parameters a_0, *a, b, c, d*, and *e* were defined by Raynes (24) and because of their notational convenience are used in our spectral analysis.

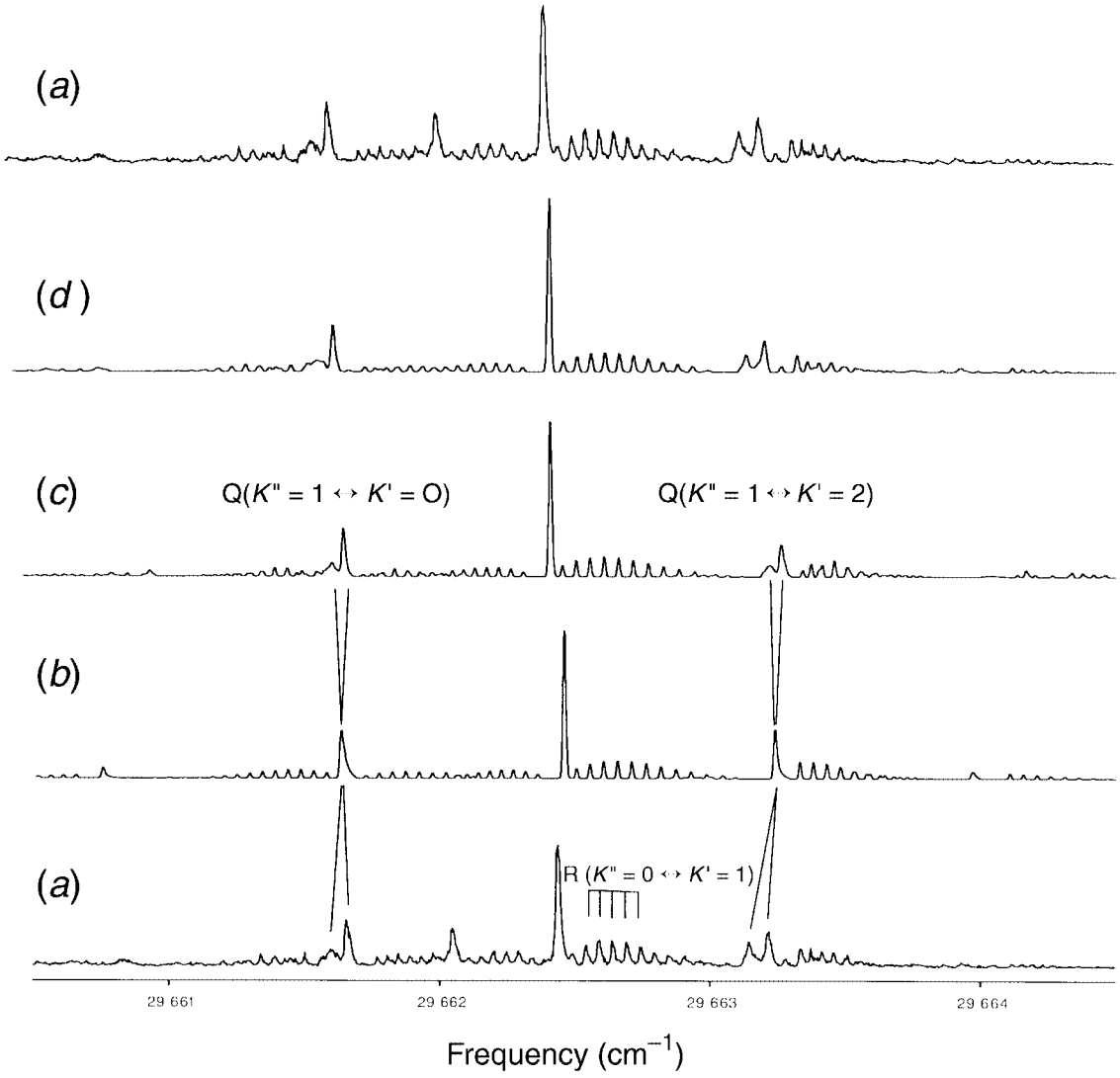
The prediction of rotational constants was performed via calculations using the Gaussian98 program (27) at the B3LYP/6-31+G* and the CIS/6-31+G* levels for the $\widetilde{X}$ and $\widetilde{B}$ states, respectively. As already mentioned in the *Introduction*, a semi-empirical approach based upon the knowledge of the experimentally determined spin-rotation constants of the ethoxy radical was used to estimate the spin-rotation constants (28).

4. Results

The number (N) of conformers grows rather dramatically according to the formula (19), $N = \frac{3^{n-2}-1}{2} + 1$, as the number ($n$) of carbon atoms in the alkoxy radical increases. However, the LIF excitation spectra (Fig. 2) show, if anything, fewer features with an increase of n instead of more congestion. Our approach to understanding these spectra builds upon corresponding analyses (18, 19) for 1-propoxy, 1-butoxy, and 1-pentoxy for which multiple conformers were "frozen out" in the jet. For these

© 2004 NRC Canada

Fig. 4. Rotationally resolved band C of 1-hexoxy: (*a*) experimental spectrum, (*b*) simulation using only calculated rotational constants of conformer $T_1T_2T_3T_4$, (*c*) simulation including spin-rotation component $a_0 + a/2$, and (*d*) spectrum simulated from fit constants of Table 1. The ratio of the electric dipole moments a:b:c for the simulation is 0:0:1. The rotational temperature is 1.2 K.



species, detailed spectroscopic analyses determined rotational and spin-rotation constants for two of two 1-propoxy conformers, three of a possible five 1-butoxy conformers, and five of 14 possible conformers of 1-pentoxy.

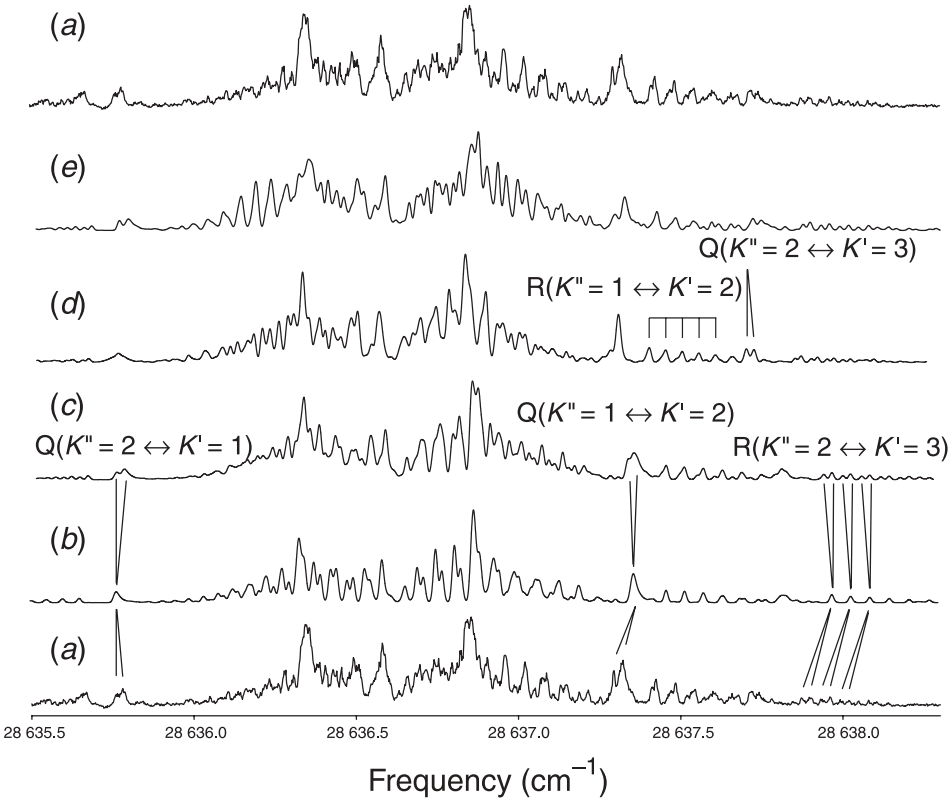
Figure 2 also shows that there are three bands that appear persistently for all the alkoxy radicals, labelled bands A, B, and C. Interestingly, for 1-propoxy, 1-butoxy, and 1-pentoxy, band B is always correlated with the all-trans conformer, which uniquely has C_s symmetry. Band B has been assigned as the origin band of the $T_1T_2...T_{n-2}$ conformer with all the bands C being assigned as the C-O stretch vibrational fundamental of the same conformer. Similarly, all A bands are assigned to the $G_1T_2...T_{n-2}$ conformer, which retains the C_s symmetry of the carbon chain but has the oxygen rotated 60° out of the carbon-chain plane. The structures of these conformations are illustrated in Fig. 1.

Figure 2 shows that nearly all the strong bands in the spectra of pentoxy and smaller alkoxy radicals have been assigned to specific conformers and their vibronic structure. Figure 3 compares the rotational structure for bands A, B, and C for the alkoxy radicals ($C_nH_{2n+1}O$) with $3 \leq n \leq 7$. Figure 3 shows, as expected, that the rotational structure becomes increasingly compressed as the molecule increases in size and its rotational constants concomitantly decrease. However, allowing for this compression, we see clearly a great deal of similarity in structure in each labelled band for all the alkoxy radicals. Previous detailed assignments for the propoxy, butoxy, and pentoxy radicals helped guide our present assignments. Based upon the absolute and relative positions of the lines relative to the smaller alkoxies, it seems very reasonable to assign bands B and C to the origin and first C-O stretch of the conformer with C_s symmetry (in 1-hexoxy and 1-heptoxy $T_1T_2T_3T_4$ and $T_1T_2T_3T_4T_5$, respectively), while band A is assigned to the origin of the conformer with the oxygen out of the C_s plane ($G_1T_2T_3T_4$ and $G_1T_2T_3T_4T_5$ for 1-hexoxy and 1-heptoxy, respectively).

Ab initio calculations were performed for these two conformers for both 1-hexoxy and 1-heptoxy, and the calculated molecular constants are given in Tables 1 and 2 and were used

© 2004 NRC Canada

Fig. 5. Trace of band A of 1-hexoxy: (*a*) experimental spectrum, (*b*) simulation using calculated rotational constants of conformer $G_1T_2T_3T_4$, (*c*) simulation including spin-rotation constants components, (*d*) pre-fit spectrum, and (*e*) spectrum simulated from fit constants of Table 1. The ratio of the electric dipole moment a:b:c is 3:1:0.5. The rotational temperature is 1.3 K.



as a starting point for a full rotational analysis. Details of the analysis are given below for bands A and C of 1-hexoxy. The assignments of other bands were performed in a similar manner.

Figure 4 shows the experimental trace of band C and the simulation of the $\widetilde{B} - \widetilde{X}$ transition using the rotational constants from the ab initio calculations of conformer $T_1T_2T_3T_4$ of 1-hexoxy. As the $T_1T_2T_3T_4$ conformer has C_s symmetry, only a *c*-type transition dipole is allowed, making the structure of band C (or B) rather simple. The simulation in Fig. 4*b* clearly resembles the experimental spectrum (trace *a*). The P and R branches of the $K'' = 0 \leftrightarrow K' = 1$ transition can be easily identified and assigned although there are clearly small discrepancies between the experimental and simulated structure. The positions of the Q branch for $K'' = 0 \leftrightarrow K' = 1$ as well as $K'' = 1 \leftrightarrow K' = 0$ and $K'' = 1 \leftrightarrow K' = 2$ can easily be located, but the latter two appear as doublets experimentally. At this stage, combinations of rotational constants, $(B + C)/2$ and $A - (B + C)/2$ of the ground state and $(B + C)/2$ of the excited $\widetilde{B}$ state, can be fitted.

The splitting between the doublets of the Q branches is about 2.2 GHz. It is close to the calculated splitting of 2.6 GHz $[3/2(a_0 + a/2)]$ for transitions involving $|K''| = 1$ and $N'' = 1$, due to the spin-rotation interaction in the ground $\widetilde{X}$ state. Smaller splittings are observed in the P($K'' = 0 \leftrightarrow K' = 1$) and R($K'' = 0 \leftrightarrow K' = 1$) branches (but not completely resolved); these observations are consistent with the calculated value of 0.06 GHz for transitions involving $K'' = 0$, which are split by the term $(N'' + 1/2)(a_0 - a)$.

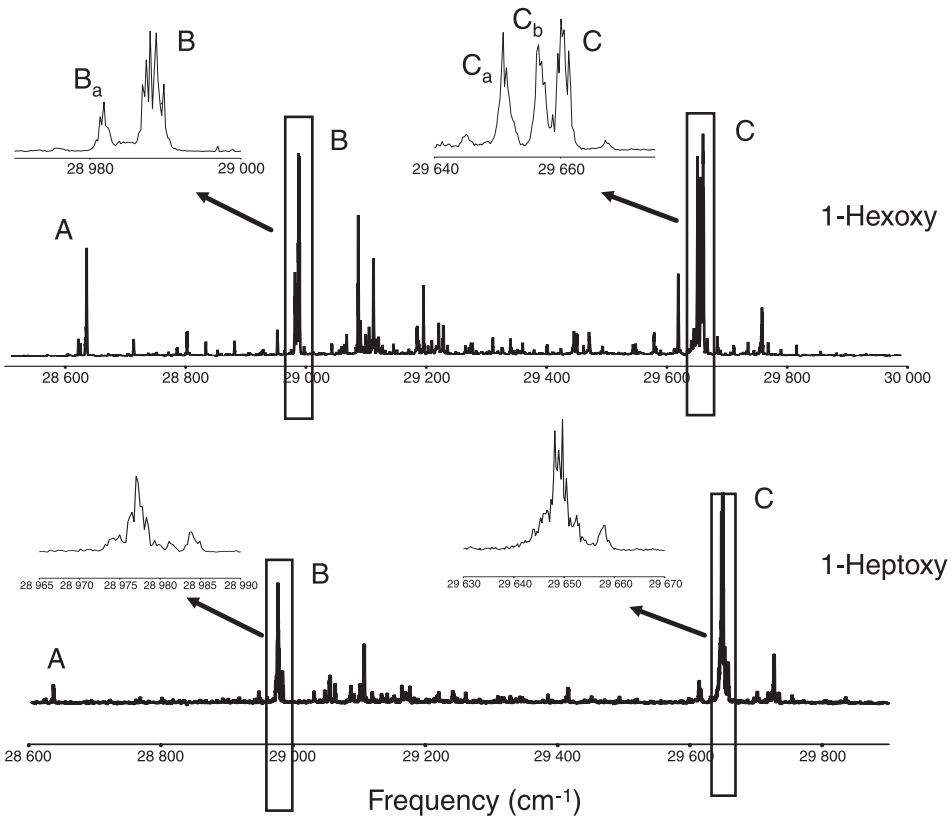
Simulations including the calculated spin-rotational component $a_0 + a/2$ (Fig. 4*c*) enabled us to assign most of the remaining experimental lines. At this point, least-square fits of 111 lines were used to determine the origin frequency, $\widetilde{X}$ and $\widetilde{B}$ state rotational constants, and the two most significant $\widetilde{X}$ state spin-rotation tensor components ($\widetilde{\epsilon}_{aa}, \widetilde{\epsilon}_{bb}$). The simulation based upon this fit is given in Fig. 4*d* and the corresponding molecular parameters are listed in Table 1. Good agreement is seen between the experimental results and values from the ab initio calculations. For the rotational constants, the values are within ±5% for both ground and excited states. For the spin-rotation constants, the values were within 7% for the larger component, $\widetilde{\epsilon}''_{aa}$. Several of the spin-rotation constants could not be determined experimentally because the effect they had on the spectrum was below the experimental resolution (≈200 MHz). In this case, those spin-rotation constants were fixed at zero in the fitting.

Band B was assigned according to the same procedure as described for band C. Its analysis was made after the assignment of band C because there was another band partially overlapping it (Fig. 3*b*). The overlap will be discussed later in this paper. In spite of the overlap, unambiguous assignments can still be made and the resulting parameters are listed in Table 1.

As noted in the beginning of this section, the likely assignment for band A is to conformer $G_1T_2T_3T_4$. The structure of band A appears more complicated than that of bands B and C because conformer $G_1T_2T_3T_4$ only has C_1 symmetry rather than

© 2004 NRC Canada

Fig. 6. Survey LIF spectra of 1-hexoxy and 1-heptoxy. Expanded views of the regions of bands B and C show additional lines in the 1-hexoxy spectrum, but not in the 1-heptoxy spectrum.



C_s symmetry as for the $T_1T_2T_3T_4$ conformer. There are now three nonzero components of the transition dipole rather than one. The increase in allowed transitions leads to increased spectral congestion, making the spectral analyses somewhat more difficult.

However, the analysis of bands B and C and other alkoxy bands in our previous work (18, 19) indicated that ab initio predictions of the molecular constants should be quite reliable. Indeed, the simulation using the calculated molecular constants of conformer $G_1T_2T_3T_4$ shows rather good agreement with the experimental spectrum of band A (Fig. 5*b*). Nonetheless, the spectral congestion makes it difficult to distinguish the rotational and spin-rotation splittings in the center of the band. The spin-rotation splitting is more easily discerned at the ends of the spectrum where higher N'', $|K''| > 0$ transitions lie. By including the calculated value of the spin-rotation constants $\widetilde{\epsilon}''_{aa}$ and $\widetilde{\epsilon}''_{bb}$ in the simulation, all the doublets at the ends of the experimental spectrum are accounted for in the simulation (Fig. 5*c*). Then assignments can be made for branches Q($K'' = 1 \leftrightarrow K' = 2$), R($K'' = 2 \leftrightarrow K' = 3$), and Q($K'' = 2 \leftrightarrow K' = 1$). Using these assignments, an initial fit can be made to obtain experimental rotational constants and spin-rotation components, and the resulting simulation is shown in Fig. 5*d*. At this stage, more lines in Q($K'' = 2 \leftrightarrow K' = 3$), R($K'' = 1 \leftrightarrow K' = 2$), P($K'' = 1 \leftrightarrow K' = 0$), and R($K'' = 0 \leftrightarrow K' = 1$) branches can be assigned. The final fit was then performed with all the off-diagonal spin-rotation components fixed at zero. The resulting simulation is shown in Fig. 5*e*, and the corresponding molecular constants are listed in Table 1.

For 1-heptoxy, band A is assigned to conformer $G_1T_2T_3T_4T_5$ despite the increasing congestion in the rotationally resolved spectrum. For bands B and C, overlap with an additional band makes the structure even more complicated. However, a reasonable fit can still be made for the $T_1T_2T_3T_4T_5$ conformer portion of the spectrum using the same approach as for the 1-hexoxy analysis. The results are given in Table 2.

Bands from additional conformers were identified in 1-butoxy and 1-pentoxy. The bands identified included the origin of the T_1G_2 conformer of 1-butoxy, the origin of the $T_1T_2G_3$ and $T_1G_2T_3$ conformers of 1-pentoxy, and the C-O stretch bands of the $T_1T_2G_3$ and $T_1T_2T_3$ conformers of the 1-pentoxy spectrum. In addition, low-frequency fundamentals and combination bands of these conformers appeared in the spectra. The additonal conformers observed in 1-butoxy and 1-pentoxy all have a nearly straight chain structure obtained by rotating one C-C-C dihedral angle of the C_s (all-trans) conformer. One expects that bands of this nature will shift closer to each other in 1-hexoxy as the difference between these conformers becomes less significant with the increasing length of the carbon chain. The expanded region in Fig. 6 of the 1-hexoxy LIF spectrum shows one extra band (B_a) close to band B and two extra bands (C_a and C_b) close to band C. From 1-heptoxy to 1-decoxy, there is no clear separation between these bands, implying they might completely overlap. An expanded view of the 1-heptoxy

© 2004 NRC Canada

Fig. 7. Simulations using the calculated constants of the $T_1T_2T_3G_4$, $T_1T_2G_3T_4$, and $T_1G_2T_3T_4$ conformers of 1-hexoxy, as well as rotationally resolved experimental spectra of additional bands of 1-hexoxy close to bands B and C.

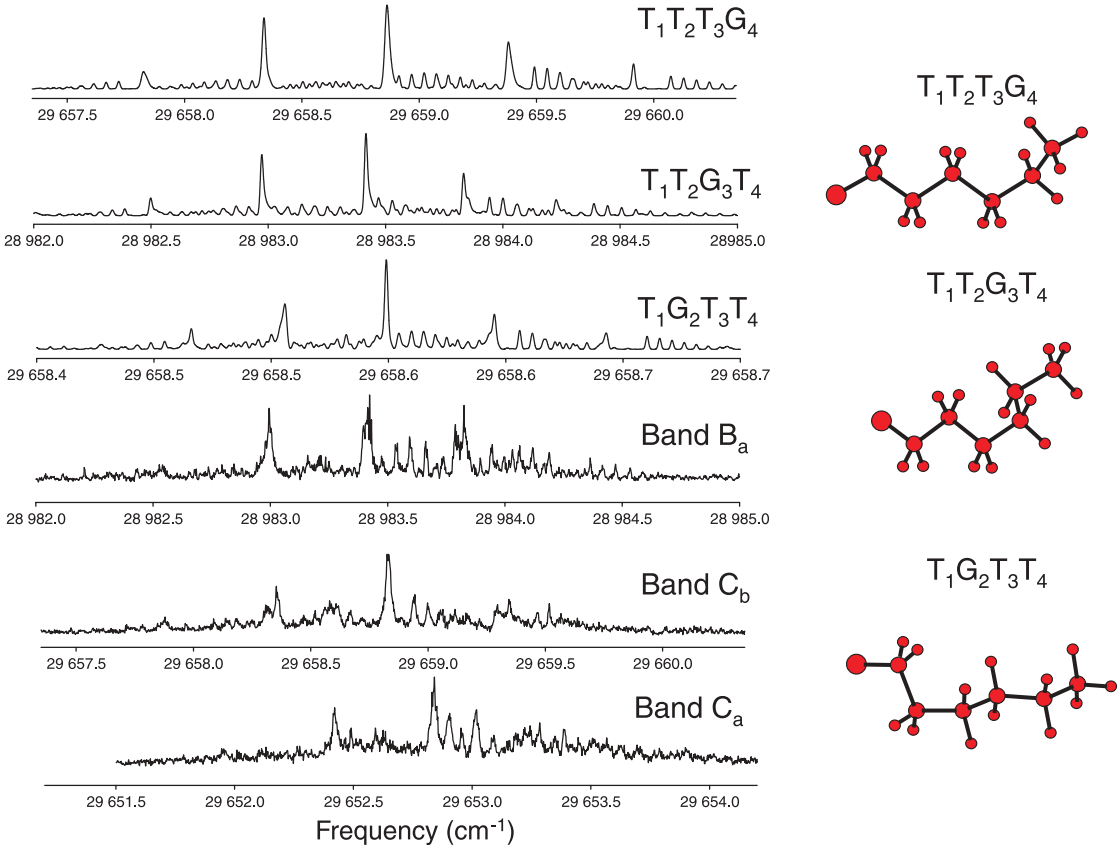
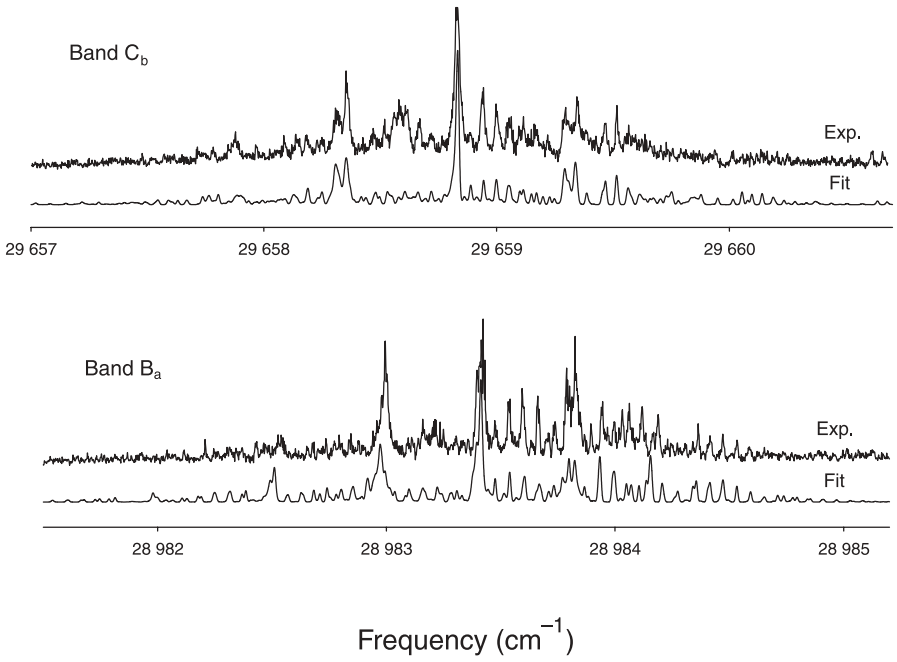


Fig. 8. Comparison of experimental rotationally resolved spectra of band C_b (top) and B_a (bottom) with their respective simulations using the constants from Table 1.



© 2004 NRC Canada

LIF spectrum in the band B and C region only shows a single band, but the rotationally resolved spectra of each band displays overlap with an additional transition.

High-resolution spectra of bands B_a, C_a, and C_b were obtained and are shown in Fig. 7. Of the 41 conformers of 1-hexoxy, there are three conformers derived from the all-trans T conformer by changing only one C-C-C dihedral angle, i.e., $T_1T_2T_3G_4$, $T_1T_2G_3T_4$, and $T_1G_2T_3T_4$. Simulations using the computed rotational constants (Fig. 7) indicated that the $T_1T_2T_3G_4$ conformer yields the closest match for band C_b, and the $T_1T_2G_3T_4$ conformer for B_a. Results of fits to these are given in Fig. 8 and Table 1. There is no obvious conformer assignment for band C_a.

Band B_a is assigned as the origin band of conformer $T_1T_2G_3T_4$, as no band with comparable intensity was assigned below this frequency. A definite vibrational assignment cannot be made for band C_b, although it appears in the C-O stretch frequency region. A band partially overlapped with band B appearing in the rotationally resolved spectrum might be the buried origin of the $T_1T_2T_3G_4$ conformer, but an unambiguous assignment cannot be made due to the low signal-to-noise ratio and the congestion.

With these results in hand, we can return to the spectra of 1-octoxy, 1-nonoxy, and 1-decoxy in Fig. 2. As with 1-hexoxy, 1-heptoxy, and the smaller alkoxies, it is easy to identify bands A, B, and C. We have not attempted to obtain rotationally resolved spectra of these bands to obtain a definitive conformational assignment. Nonetheless, we feel that the close analogy between the 1-octoxy to 1-decoxy spectra in Fig. 2 and the spectra of the smaller alkoxies leaves little doubt as to the conformational assignments. It appears highly probable that band A is the origin of the $G_1T_2...T_{n-2}$ conformer, while bands B and C are, respectively, the origin and CO stretch fundamental of conformer $T_1T_2...T_{n-2}$. One would also expect this pattern to continue in even larger alkoxy radicals.

5. Conclusions

Rotationally resolved spectra of six bands of 1-hexoxy and three bands of 1-heptoxy were obtained. A new strategy was used for the analysis of the 1-hexoxy and 1-heptoxy spectra and is applicable for larger primary alkoxy radicals. Using this approach, five bands of 1-hexoxy were assigned to four different conformers, i.e., band A to $G_1T_2T_3T_4$, bands B and C to $T_1T_2T_3T_4$, band B_a to $T_1T_2G_3T_4$, and band C_b to $T_1T_2T_3G_4$. For 1-heptoxy, band A was assigned to conformer $G_1T_2T_3T_4T_5$, while bands B and C were assigned to conformer $T_1T_2T_3T_4T_5$. Experimental molecular parameters were obtained from the rotational analyses, which are in rather good agreement with the values predicted for the given conformers by quantum chemistry calculations.

In earlier work (29, 30), probing a jet-cooled sample via microwave spectroscopy, it was suggested that little conformation relaxation takes place from the room-temperature conformer distribution. This work includes studies on 1-pentene and 1-hexene, which of course bear similarities to the presently studied alkoxies. However, with the alkoxy radicals there is an important difference in that they are created by photolysis in the jet.

Our earlier work on smaller alkoxies reached the conclusion (18,19) that multiple conformers exist in the cold-jet environment, i.e., the sample is not at thermal equilibrium with the rotational temperature — indeed the conformers do not appear to form an equilibrium distribution for any temperature. However, the conformers are not all populated. The bands assigned arise from all-trans conformers or conformers with at most one gauche linkage. Three bands, the $T_1T_2...T_{n-2}$ origin and CO stretch and the $G_1T_2...T_{n-2}$ origin, form the main "structure" of the LIF spectra of large primary alkoxy radicals. The origin, and occasionally the CO stretch fundamental bands from other nearly straight chain conformers, "decorate" the spectra and coalesce into the three dominant bands as the number of carbons in the radicals increases.

Acknowledgements

The authors wish to acknowledge György Tarczay for helpful discussions and the Chemical Sciences, Geosciences and Biosciences Division, Office of Basic Energy Sciences, Office of Science, US Department of Energy, via Grant DE-FG02-01ER15172.

References

1. G. Herzberg. The spectra and structures of simple free radicals: An introduction to molecular spectroscopy. Cornell University Press, Ithaca, N.Y. 1971.
2. G. Herzberg and J.W.C. Johns. Astrophys. J. **158**, 399 (1969).
3. G. Herzberg and J. Shoosmith. Can. J. Phys. **34**, 523 (1956).
4. G. Herzberg. Proc. R. Soc. A, **262**, 291 (1961).
5. G. Herzberg. Can. J. Phys. **39**, 1511 (1961).
6. G. Herzberg and J.W.C. Johns. Proc. R. Soc. A, **295**, 107 (1966).
7. W.P.L. Carter and R. Atkinson. J. Atmos. Chem. **3**, 377 (1985).
8. T.M. Ramond, G.E. Davico, R.L. Schwartz, and W.C. Lineberger. J. Chem. Phys. **112**, 1158 (2000).
9. J. Bai, H. Okabe, and J.B. Halpern. Chem. Phys. Lett. **149**, 37 (1988).
10. K. Ohbayashi, H. Akimoto, and I. Tanaka. J. Phys. Chem. **81**, 798 (1977).
11. H.E. Radford and D.K. Russell. J. Chem. Phys. **66**, 2222 (1977).
12. Y. Endo, S. Saito, and E. Hirota. J. Chem. Phys. **81**, 122 (1984).
13. S.C. Foster, Y.-C. Hsu, C.P. Damo, X. Liu, C.-Y. Kung, and T.A. Miller. J. Phys. Chem. **90**, 6766 (1986).
14. X.Q. Tan, J.M. Williamson, S.C. Foster, and T.A. Miller. J. Phys. Chem. **97**, 9311 (1993).
15. C. Wang, L.G. Shemesh, W. Deng, M.D. Lilien, and T.S. Dibble. J. Phys. Chem. A, **103**, 8207 (1999).
16. C. Wang, W. Deng, L. Shemesh, M.D. Lilien, D.R. Katz, and T.S. Dibble. J. Phys. Chem. A, **104** , 10 368 (2000).
17. C.C. Carter, S. Gopalakrishnan, J. Atwell, and T.A. Miller. J. Phys. Chem. A, **105**, 2925 (2001).
18. S. Gopalakrishnan, C.C. Carter, L. Zu, V. Stakhursky, G. Tarczay, and T.A. Miller. J. Chem. Phys. **118**, 4954 (2003).
19. S. Gopalakrishnan, L. Zu, and T.A. Miller. J. Phys. Chem. A, **107**, 5189 (2003).
20. J. Goodman and W.C. Still. J. Comput. Chem. **12**, 1110 (1991).

© 2004 NRC Canada

21. F. Mohamadi, N.G.J. Richards, W.C. Guida, R. Liskamp, M. Lipton, C. Caufield, G. Chang, T. Hendrickson, and W.C. Still. MacroModel — an Integrated Software System for Modeling Organic and Biorganic Molecules Using Molecular Mechanics. J. Comput. Chem. **11**, 440 (1990).
22. A.H. Blatt. Organic synthesis, collective volume. Wiley, New York. 1943.
23. X. Liu, S.C. Foster, J.M. Williamson, L. Yu, and T.A. Miller. Mol. Phys. **69**, 357 (1990).
24. W.T. Raynes. J. Chem. Phys. **41**, 3020 (1964).
25. V.L. Stakhursky and T.A. Miller. 56th OSU International Symposium on Molecular Spectroscopy (Ohio State University, Columbus, Ohio, 2001). Program available from http://molspect.mps.ohio-state.edu/goes/specview.html.
26. J.M. Brown, T.J. Sears, and J.K.G. Watson. Mol. Phys. **41**, 173 (1980).
27. M.J. Frisch, G.W. Trucks, H.B. Schlegel, G.E. Scuseria, M.A. Robb, J.R. Cheeseman, V.G. Zakrzewski, J.A. Montgomery, R.E. Stratmann, J.C. Burant, S. Dapprich, J.M. Millam, A.D. Daniels, K.N. Kudin, M.C. Strain, O. Farkas, J. Tomasi, V. Barone, M. Cossi, R. Cammi, B. Mennucci, C. Pomelli, C. Adamo, S. Clifford, J. Ochterski, G.A. Petersson, P.Y. Ayala, Q. Cui, K. Morokuma, D.K. Malick, A.D. Rabuck, K. Raghavachari, J.B. Foresman, J. Cioslowski, J.V. Ortiz, A.G. Baboul, B.B. Stefanov, G. Liu, A. Liashenko, P. Piskorz, I. Komaromi, R. Gomperts, R.L. Martin, D.J. Fox, T. Keith, M.A. Al-Laham, C.Y. Peng, A. Nanayakkara, C. Gonzalez, M. Challacombe, P.M.W. Gill, B. Johnson, W. Chen, M.W. Wong, J.L. Andres, C. Gonzalez, M. Head-Gordon, E.S. Replogle, and J.A. Pople. Gaussian 98. Revision A.7 [computer program]. Gaussian, Inc., Pittsburgh, Pa. 1998.
28. G. Tarczay, S. Gopalakrishnan, and T.A. Miller. J. Mol. Spectrosc. **220**, 276 (2003).
29. G. Fraser, R. Suenram, and C. Lugez. J. Phys. Chem. A, **104**, 1141 (2000).
30. G. Fraser, L. Xu, and R. Suenram. J. Chem. Phys. **112**, 6209 (2000).

© 2004 NRC Canada

Ultraviolet cavity ringdown spectra of 2-cyclohexen-1-one and its potential energy function and structure for the electronic ground state[1]

Emily J. Gilles, Jaebum Choo, Daniel Autrey, Mohamed Rishard, Stephen Drucker, and Jaan Laane

Abstract: The $S_1(n,\pi^*) \leftarrow S_0$ cavity ringdown spectrum of 2-cyclohexen-1-one vapor has been recorded in the vicinity of the 0_0^0 band, which is at 26 089.1 cm^{-1}. Observation of hot bands in the spectrum has permitted the determination of several low-frequency fundamentals and overtones in the ground electronic state. The lowest two excited quantum states for the inversion vibration (ν_{39}) were found to be at 99.0 and 197.0 cm^{-1}. Together with previously published far-IR spectra and vapor-phase Raman spectra, the fundamental frequencies for ν_{39}, ν_{38}, and ν_{37} have been determined. From observed ν_{39} levels, the barrier to inversion has been determined experimentally to be 1900 ± 300 cm^{-1}, which is very different from values of 935 and 3379 cm^{-1} previously reported from Raman and far-IR data, respectively. Density functional calculations carried out in this paper give a barrier value of 2090 cm^{-1} when the B3LYP/6-311+G(d,p) basis set is used.

Key words: cavity ringdown spectra, 2-cyclohexen-1-one, Raman spectra, potential energy function, inversion barrier.

Résumé : Faisant appel à la technique CRDS (« cavity ringdown spectroscopy »), on a étudié la transition $S_1(n,\pi^*) \leftarrow S_0$ de la cyclohex-2-èn-1-one en phase vapeur, aux environs de la bande 0_0^0 qui se trouve à 26 089,1 cm^{-1}. L'observation de bandes chaudes dans le spectre a permis de déterminer plusieurs bandes fondamentales et harmoniques de basse fréquence dans l'état électronique fondamental. Les deux états quantiques excités les plus bas pour la vibration d'inversion (ν_{39}) ont été observés à 99,0 et 197,0 cm^{-1}. Ces données utilisées de concert avec les spectres infrarouge lointain et les spectres Raman en phase gazeuse ont permis de déterminer les fréquences fondamentales ν_{39}, ν_{38} et ν_{37}. En se basant sur les niveaux ν_{39}, on a déterminé expérimentalement que la barrière à l'inversion est de 1900 ± 300 cm^{-1} et cette valeur est très différente des valeurs de 935 et 3379 cm^{-1} rapportées antérieurement sur la base respectivement de données Raman et infrarouge lointain. Les calculs de densité fonctionnelle effectués dans le cadre de ce travail en utilisant un ensemble de base B3LYP/6-311+G(d,p) conduisent à une valeur de 2090 cm^{-1} pour la barrière.

Mots clés : CRDS, cyclohex-2-èn-1-one, spectres Raman, fonction d'énergie potentielle, barrière à l'inversion.

[Traduit par la Rédaction]

Introduction

2-Cyclohexen-1-one (2CHO) is a non-planar, six-membered ring molecule for which conjugation between the C=O and C=C groups is expected to provide extra rigidity to the ring. Furthermore, the conjugation should make it possible to treat the ring inversion process using a one-dimensional potential energy function. In that sense, the inversion is similar to that of 1,3-cyclohexadiene (1) and 1,2-dihydronaphthalene (2), which we have recently studied using Raman and fluorescence spectroscopies as well as density functional (DFT) calculations. In 1970 Manley and Tyler (3) reported the microwave spectrum of 2CHO along with the rotational constants. They proposed a structure for which only the carbon atom in the 5 position was significantly out-of-plane. In 1979 Carreira et al. (4) published the low-frequency, vapor-phase Raman spectrum of 2CHO and concluded that the molecule had an inversion barrier of

Received 27 February 2004. Published on the NRC Research Press Web site at http://canjchem.nrc.ca on 26 August 2004.

E.J. Gilles and S. Drucker. Department of Chemistry, University of Wisconsin-Eau Claire, Eau Claire, WI 54702-4004, USA.
J. Choo. Department of Chemistry, Hanyang University, Ansan 425-791, South Korea.
D. Autrey. Department of Natural Sciences, Fayetteville State University, Fayetteville, NC 28301, USA and Department of Chemistry, Texas A&M University, College Station, TX 77843-3255, USA.
M. Rishard and J. Laane.[2] Department of Chemistry, Texas A&M University, College Station, TX 77843-3255, USA.

[1]This article is part of a Special Issue dedicated to the memory of Professor Gerhard Herzberg.
[2]Corresponding author (e-mail: laane@mail.chem.tamu.edu).

 doi: 10.1139/V04-070 © 2004 NRC Canada

935 cm^{-1} based on an assignment where the $0 \rightarrow 2/1 \rightarrow 3$ degenerate transitions for ν_{39}, the lowest frequency vibration, were at 248 cm^{-1}. One year later, Smithson and Wieser (5) analyzed the far-IR spectrum, which showed a series of Q branches in the 96.9–99.8 cm^{-1} range. From these, a potential function with a barrier of 3379 cm^{-1} was calculated. A type B band at 247 cm^{-1} was assigned to ν_{38}, the second-lowest frequency vibration.

To better understand the inversion process for this molecule, we have undertaken further spectroscopic work as well as DFT calculations. Here, we present the UV cavity ringdown spectra of 2CHO along with the vapor-phase Raman spectra and DFT computations, and then use these to determine the one-dimensional vibrational potential energy function for the ring inversion in the electronic ground state. In the future, we will also present data for the $S_1(n,\pi^*)$ and $T_2(n,\pi^*)$ electronic excited states. We have recently published the $T_1(n,\pi^*) \leftarrow S_0$ cavity ringdown spectra (6) and DFT calculations (7) for 2-cyclopenten-1-one (2CPO), and compared the potential energy functions for the S_0, S_1, and T_1 states. The experimental work and computations for the present paper were carried out in a similar manner.

Experimental and computational

2CHO was purchased from Acros and purified by vacuum transfer to the sample cells. The cavity ringdown spectra were recorded in a manner similar to that used for 2CPO (6). The details of the system have been presented elsewhere (8). The vapor-phase Raman spectra were recorded on a JY U-1000 instrument using a Coherent I-20 argon ion laser operating at 5145 Å with 2 W of laser power. Vapor cells previously described were also used (9). DFT calculations were carried out utilizing the same programs and methods previously described for 2CPO (7).

Results and discussion

Cavity ringdown (CRD) spectra

Figure 1 shows the CRD spectrum of 2CHO in the 400 to –400 cm^{-1} region relative to the 0_0^0 band for the S_1 state at 26 089.1 cm^{-1}. Figure 2 shows the difference band region in expanded form. A broader range of frequencies was examined but in the present paper we will only concentrate primarily on this region. Some of the more relevant transition frequencies for understanding the S_0 electronic ground state have been selected and are shown in Table 1. Most importantly, the ν_{39} inversion band ($\nu_I = 0 \rightarrow 2$ and $1 \rightarrow 3$) can be seen at –99.0 cm^{-1}. (The labeling scheme for inversion levels is indicated in Fig. 3.) The next band in the series corresponding to $0 \rightarrow 4$ and $1 \rightarrow 5$ occurs at –197.0 cm^{-1}, thus showing the next spacing (3 to 4) to be 98.0 cm^{-1}. There is also a weak band at –294.9 cm^{-1}, which seems to indicate that the 5 to 6 spacing is 97.9 cm^{-1}. A weak band also is present at –391.6 cm^{-1} indicating another possible spacing of 96.7 cm^{-1}. The reported far-IR spectrum (5) has bands listed at 99.85, 99.23, 98.63, 98.02, 97.48, and 96.87 cm^{-1}. Since these were recorded at 0.5 cm^{-1} resolution and the spectral points were probably calculated for each 0.25 cm^{-1}, the accuracy of these numbers can be taken to be ±0.3 cm^{-1}. It is not clear why they were reported to two-decimal place

Fig. 1. Cavity ringdown spectra of 2CHO relative to the $S_1\ 0_0^0$ band at 26 089.1 cm^{-1} in the 400 to –400 cm^{-1} region. The spectra were recorded using a 1 m cell.

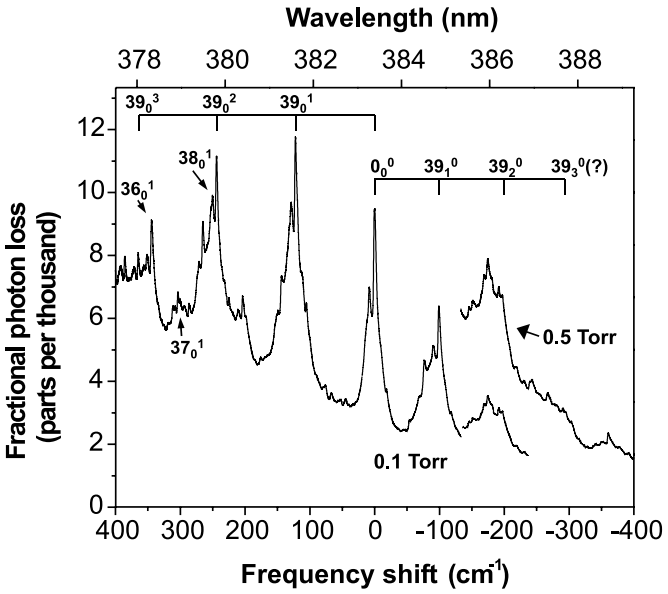
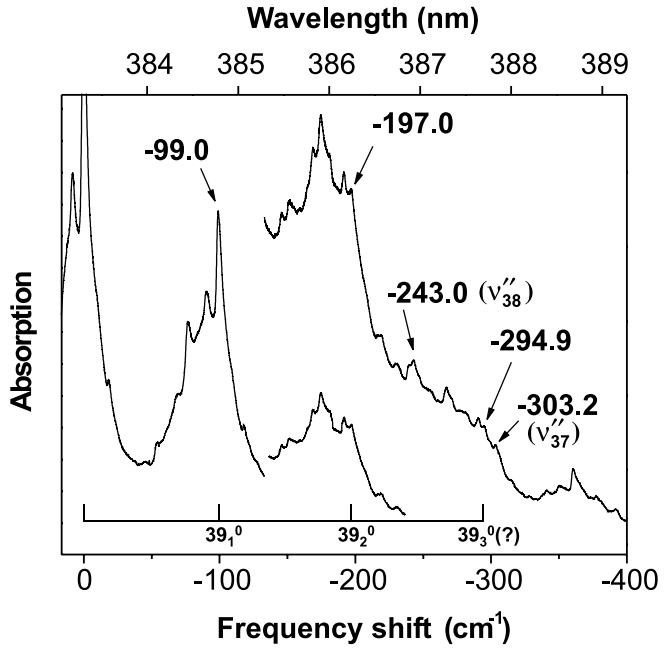


Fig. 2. Cavity ringdown spectra of 2CHO relative to the $S_1\ 0_0^0$ band at 26 089.1 cm^{-1} in the difference band region.



accuracy. In any case, since ν_{38} occurs at 243 cm^{-1} and since its excited vibrational state will be 30% as populated as the ground state at room temperature, a second superimposed series of ν_{39} bands can be expected in this region. The two strongest far-IR peaks occur at 99.2 and 98.0 cm^{-1}, so it seems apparent that these correspond to the first two spacings of 99.0 and 98.0 cm^{-1} obtained from the CRD spectra. The 99.8 and 98.6 cm^{-1} bands then arise within the ν_{38} excited state and not from the principal series as previously assumed. Moreover, the close spacing assumed by Smithson

© 2004 NRC Canada

Table 1. Selected assignments for the CRD spectrum (cm^{-1}) of 2-cyclohexen-1-one.

Observed	Calculated[a]	Inferred	Assignment	
–99.0	–103.0	–99.2[b]	39_1^0	
–197.0	—	–197.2[b]	39_2^0	
–294.9	—	–294.1[b]	39_3^0 (?)	
122.2	120.8	—	39_0^1	
244.0	—	—	39_0^2	
364.8	—	—	39_0^3	
–243.0	–240.8	–244[c]	38_1^0	
–303.2	–307.8	–304.1[b]	37_1^0	
250.1	249.9	—	38_0^1	
303.5	298.4	—	37_0^1	
344.1	341.9	—	36_0^1	
370.9	—	372.3	$38_0^1\,39_0^1$	250.1+122.2
143.7	—	145.0	39_1^2	244.0–99.0
265.1	—	265.8	39_1^3	364.8–99.0
150.3	—	151.1	$38_0^1\,39_1^0$	250.1–99.0
271.1	—	272.0	$38_0^1\,39_1^1$	371.0–99.0
244.0	—	245.1	$36_0^1\,39_1^0$	344.1–99.0
203.8	—	204.5	$37_0^1\,39_1^0$	303.5–99.0
–76.6	—	–74.8	39_2^1	122.2–197.0
44.9	—	47.0	39_2^2	244.0–197.0
52.7	—	53.1	$38_0^1\,39_2^0$	250.1–197.0
168.8	—	167.8	39_2^3	364.8–197.0

[a]From the B3LYP/6-311+G(d,p) calculation.
[b]Inferred from far-IR data (5).
[c]From the Raman spectrum.

and Wieser (5) led them to calculate an unreasonably high barrier to inversion of 3379 cm^{-1} (9.65 kcal/mol).

The remaining question then is whether the weak –294.9 and –391.6 bands in the CRD spectra arise from ν_{39} or from some other combinations. With the 39 vibrations of 2CHO there are many possibilities for combinations when various excited states are considered. If the –294.9 cm^{-1} CRD band is part of the ν_{39} series, then the 97.9 cm^{-1} spacing probably results from a small perturbation, since a value near 97 cm^{-1} is expected. Similarly, the 96.7 cm^{-1} inferred from the CRD spectrum for the following spacing seems to be almost 1 cm^{-1} too high. The presence of both spacings, however, would not conflict with the far-IR spectrum as the 98.0 and 97.9 cm^{-1} bands would be superimposed, and the 96.7 cm^{-1} CRD spacing would correspond to the 96.9 cm^{-1} far-IR band. Nonetheless, we prefer to assign the third spacing to the 96.9 cm^{-1} far-IR band and ascribe the two CRD bands in question to other combinations. For the computation of the potential energy function below, we utilize the energy levels and transitions in Fig. 3, where the energy levels are based on a combination of the CRD and far-IR spectra data for ν_{39}, ν_{38}, and ν_{37}. The –243.0 cm^{-1} band for ν_{38} can be seen in the CRD spectrum and was observed as a far-IR band of type B with a band center at 247 cm^{-1} (5). In the excited state of ν_{38}, the ring inversion (ν_{39}) bands can be seen in the far-IR at 99.8, 98.6, and 97.5 cm^{-1}, and as expected, on the whole, are somewhat weaker than the bands assigned as the principal series without ν_{38} excitation. For ν_{37}, the CRD spectra show

Fig. 3. Vibrational energy levels for the S_0 state of 2CHO for ν_{39} (inversion), ν_{38}, and ν_{37}. The ν_{39} levels are doubly degenerate. v_I represents the ν_{39} quantum number.

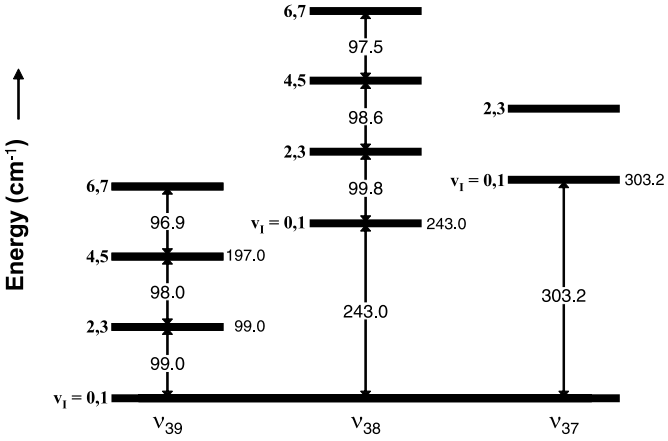
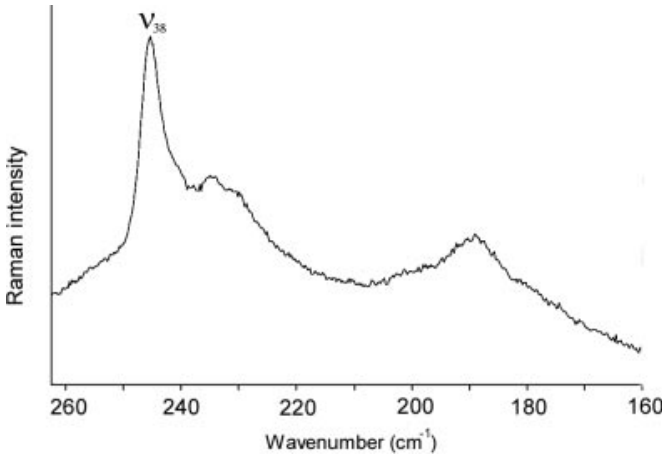


Fig. 4. Raman spectra of 2CHO vapor (0.6 atm, 1 std atm = 101.325 kPa) in the low-frequency region.



this level to be at 303.2 cm^{-1} as compared to 304.1 cm^{-1} in the far-IR.

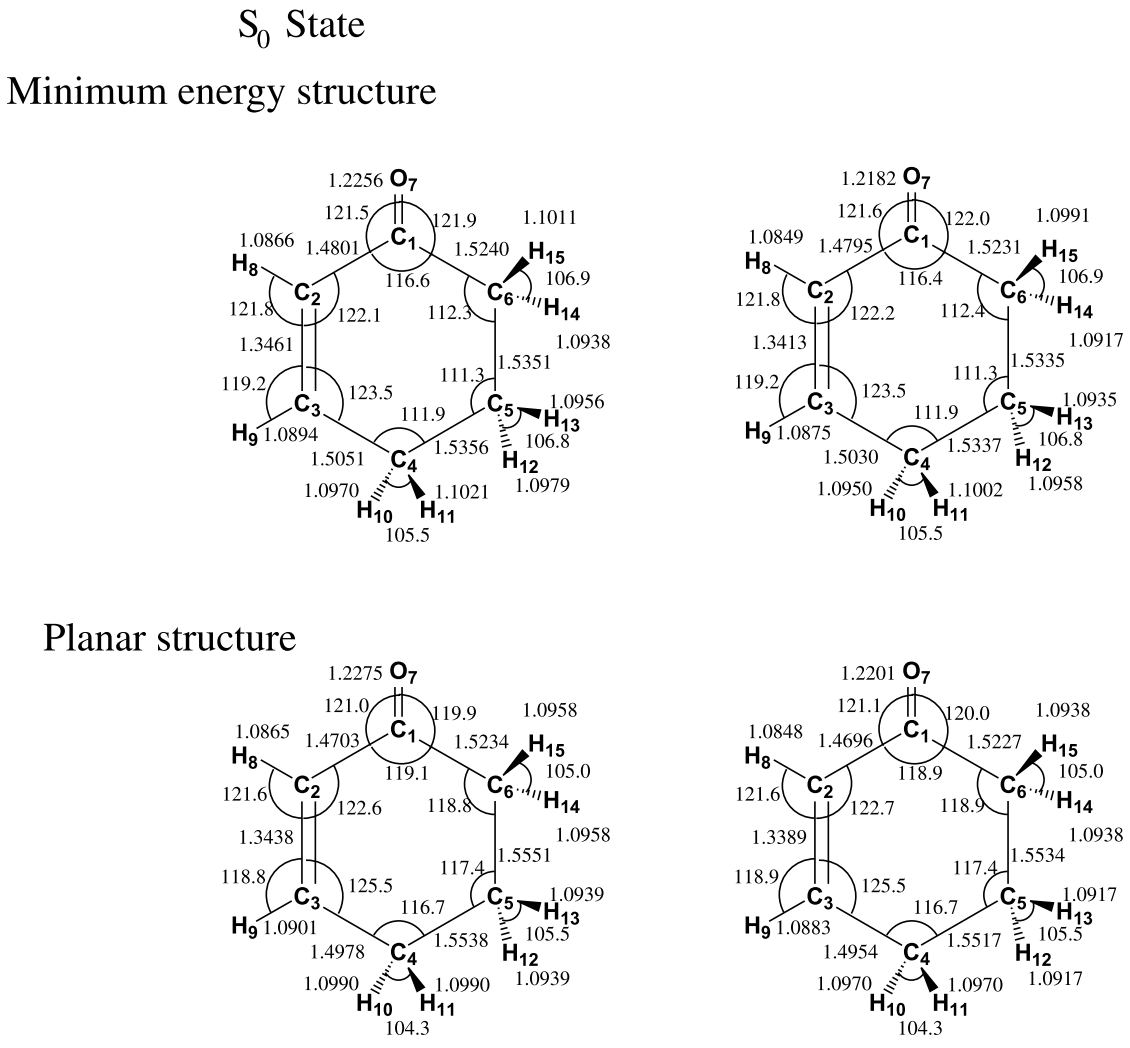
An important comment should be made about the band maxima listed in Table 1. The maxima themselves should be accurate to ±0.1 cm^{-1}. However, the maxima will not exactly correspond to the pure vibrational transitions, namely from $J = 0$ to $J = 0$ in the rotational quantum number. For the $S_1(n,\pi^*)$ state, several of the bond distances, notably for the C=O and C=C bonds, will be longer than for S_0. Hence, the moments of inertia will be larger for the S_1 state and the rotational constants will be smaller. This means that the rotationless Q branches actually will be on the high frequency extreme of each observed band in the spectrum. It also means that the combination bands listed in Table 1 cannot be expected to add up to yield the exact ground-state intervals since the band maxima are reported there. To a lesser extent, the rotational constants for the vibrational excited states of the inversion will, on the whole, also be smaller than for the $v_I = 0,1$ state.

Raman spectra

The low-frequency Raman spectrum of 2CHO vapor is shown in Fig. 4. This is similar to that reported previously

© 2004 NRC Canada

Fig. 5. Calculated structures for 2CHO using two different basis sets.



(4), except that the increased vapor pressure resulting from heating the sample to near its boiling point in a sealed cell results in high vapor pressure (0.6 atm, 1 std atm = 101.325 kPa) and a better signal-to-noise ratio. The band maximum for ν_{38} in the Raman spectrum is at 244 cm^{-1} and broad bands with maxima at 233 and 188 cm^{-1} can also be seen. Bands at 248, 230, 212, 165, and 145 cm^{-1} were previously reported (4), but we feel the last three of these are probably noise in the spectrum. A broad feature centered at about 190 cm^{-1} was also shown and this corresponds to our 188 cm^{-1} band. The origins of our 233 and 188 cm^{-1} bands are clearly not from any fundamentals, and this is supported by both the DFT calculations and the CRD spectra. The 233 cm^{-1} band could result from the $1 \rightarrow 2$ transition of ν_{38} but a shift of more than 10 cm^{-1} from the $0 \rightarrow 1$ band is larger than expected. Moreover, the band type appears to be broader than the 244 cm^{-1} band, and this would indicate it has a different assignment. A second possibility is that it may arise from ν_{36}–ν_{39} difference bands (from different inversion states), which are expected near 230 cm^{-1}. For example, the $\nu_{39}(v_I = 4,5) \rightarrow \nu_{36}(v_I = 0,1)$ band is expected at 228 cm^{-1}. The broad 188 cm^{-1} band is somewhat too low to correspond to $2\nu_{39}$ transitions expected in the 190–197 cm^{-1} region for the first several v_I states. Similarly, it is a bit higher than expected for the ν_{36}–ν_{38} bands, which should be near 182 cm^{-1}. However, the latter may be the best explanation. No Raman bands were detected between 90 and 100 cm^{-1} corresponding to ν_{39} as the rotational envelope for the molecule is still quite strong there.

DFT calculations

Several different basis sets were utilized to calculate the structure of 2CHO in its S_0 electronic ground state. Figure 5 shows the bond distances and angles calculated for the minimum energy structures and constrained planar structures using the B3LYP/6-31+G(d,p) and B3LYP/6-311+G(d,p) basis sets. The energy differences between the minimum energy structure and the planar structure were calculated to be 2098 and 2090 cm^{-1}, respectively. Table 2 shows the out-of-plane displacements for both calculations for the minimum energy

© 2004 NRC Canada

Table 2. Relative out-of-plane displacements of C1, C4, C5, and C6.

	B3LYP/6-31+G(d,p)	B3LYP/6-311+G(d,p)
C1	0.017 166	0.017 523
C4	0.133 595	0.130 933
C5	–0.340 025	–0.339 025
C6	0.267 045	0.269 044

Table 3. Rotational constants (GHz) of 2-cyclohexen-1-one.

	A (GHz)	B (GHz)	C (GHz)
Experiment (MW)[a]	4.770 4	2.543 20	1.758 29
Experiment (v = 4)[a]	4.717 85	2.557 09	1.770 78
B3LYP/6-31+G(d,p)	4.754 63	2.522 58	1.741 03
B3LYP/6311+G(d,p)	4.768 53	2.532 97	1.747 63
B3LYP/6-311+G(d,p) (planar)	4.659 82	2.486 08	1.669 94
MMPI[b]	4.763	2.557	1.769

[a]Reference 3.
[b]Reference 4.

structure for carbon atoms 1, 4, 5, and 6. The other atoms lie in the plane. Table 3 shows the rotational constants calculated for the two DFT theoretical structures and compares these to the experimental values from the microwave work (3). Also shown are the MMPI molecular mechanics results (4). It can be seen that the two DFT calculations, and especially that with the larger basis set, provide very good agreement with the microwave experiments. Table 3 also shows the rotational constants for the $v_I = 4$ quantum state of ν_{39} from the microwave study. These values have some relevance in helping us to better understand the band profiles in the far-IR and CRD spectra. The table also shows the rotational constants for the hypothetical planar structure; these values are sufficiently different from the microwave ones, confirming the non-planarity of the ring.

The S_0 vibrational frequencies were also calculated and the values for the low-frequency bands (ν_{39}, ν_{38}, and ν_{37}) are shown in Table 1 for the larger basis sets. A scaling factor of 0.9613 was used and the agreement with experiment is remarkably good, not only for these vibrations but for all of the others also.

Kinetic energy functions

We have previously described the calculation of the kinetic energy function (reciprocal reduced mass) for 1,2-dihydronaphthalene (2), and we have used the computer program for that molecule, with only slight modifications, to calculate the function for 2CHO. The vibrational model in the present work assumed that the inversion vibration labeled S follows the out-of-plane displacements according to those in Table 2. Hence, if the model is totally correct, the energy minima should correspond to an inversion coordinate value of $S = 1.0$ Å. The calculated function for which S is in Å for ν_{39} is

$$[1] \quad g_{44}(S) = 0.03119 - 0.04782S^2 - 0.1153S^4 + 0.1490S^6$$

Fig. 6. Ring-inversion potential energy function for 2CHO corresponding to eq. [2].

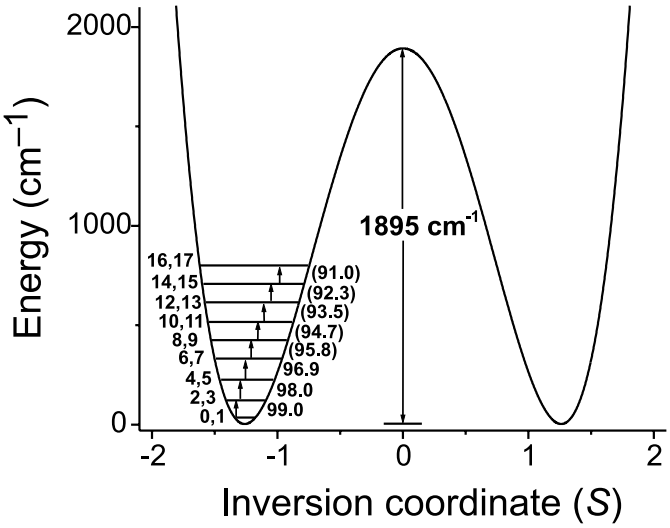


Table 4. Observed and calculated frequencies (cm^{-1}) for the ν_{39} vibration of 2-cyclohexen-1-one in its S_0 state.

	Frequency (cm^{-1})	
Separation	Experimental	Calculated
0–1	—	0.00
1–2	99.0	99.0
2–3	—	0.00
3–4	98.0	98.0
4–5	—	0.00
5–6	96.9[a]	96.9
6–7	—	0.00
7–8	—	95.8

[a]From reference 3.

The reciprocal of the first term, 32.06 in atomic units, corresponds to the reduced mass for the planar structure. The higher-order terms characterize the coordinate dependence of the function.

Ring-inversion potential energy function

As shown in Fig. 3, the first three levels of the ring-inversion vibration have been determined, the first two from the cavity ringdown spectra (±0.1 cm^{-1}), and all three from far-IR data (±0.3 cm^{-1}). These were used to determine the potential function

$$[2] \quad V = 7.459 \times 10^2 S^4 - 2.378 \times 10^3 S^2$$

based on the kinetic energy function in eq. [1]. The function is shown in Fig. 6, and it has a barrier of 1895 cm^{-1}, in very close agreement with the DFT results. However, it should be recognized that the observed levels only go up to about 340 cm^{-1} including the zero point energy, so the barrier is obtained by extrapolation. Moreover, if we changed the values for the spectral spacing even a small amount, large changes would be observed. For example, if the first transition is assumed to be 99.2 cm^{-1}, the barrier drops to

© 2004 NRC Canada

1687 cm^{-1} or 14% lower. Hence, the barrier is best stated to be 1900 ± 300 cm^{-1}. However, it is clearly very different from the values previously reported (3, 4). Table 4 compares the observed and calculated frequencies for ν_{39}, and the agreement is excellent.

Conclusions

The CRD spectra of 2CHO in the $S_1(n,\pi^*)$ region have allowed us to clarify the level spacings for the low-frequency vibrations (Fig. 3). Previous Raman and far-IR work had misinterpreted the spectra and resulted in incorrect values calculated for the inversion barrier. In this paper, we have experimentally determined the inversion barrier to be 1900 ± 300 cm^{-1}, with the large uncertainty arising from the need to extrapolate the potential energy function to values above the experimental data. Nonetheless, this barrier value is in excellent agreement with the DFT value of 2090 cm^{-1} from the B3LYP/6-311+G(d,p) calculation. The inversion model for the vibration, which does not affect the barrier height, was based on the out-of-plane displacements for the minimum energy structure obtained from the DFT computations. Using the kinetic energy function for this model produces an energy minimum occurring at 1.26 Å. Since S = 1.0 Å would indicate perfect correspondence with the DFT calculation, the minimum for our potential energy function shows the model to be quite reliable although the out-of-plane displacements of the atoms are likely to be somewhat larger than those calculated and shown in Table 2.

Work on this molecule is continuing so that we can determine the potential energy functions for the $S_1(n,\pi^*)$ and $T_2(n,\pi^*)$ states.

This manuscript is dedicated to the memory of Gerhard Herzberg and his many contributions to science.

> Gerhard Herzberg was indeed a giant,
> On his spectroscopy texts we are reliant,
> We find both theory and insight there.
> Such a man on this earth was surely rare [Jaan Laane, 2004].

Acknowledgements

Acknowledgement is made by S.D. to the donors of the Petroleum Research Fund (33947-GB6), administered by the American Chemical Society, for partial support of this research. S.D. also gratefully acknowledges funding from the Research Corporation (CC4938), the Camille and Henry Dreyfus Foundation, Inc. (Faculty Start-up Grant for Undergraduate Institutions), and the Office of Research and Sponsored Programs, as well as the McNair Postbaccalaureate Achievement Program of the University of Wisconsin-Eau Claire. J.C. thanks the Korean Science and Engineering Foundation (Grant Number R14-2002-004-01000) for financial support. J.L. thanks the National Science Foundation and the Robert A. Welch Foundation for financial support.

References

1. D. Autrey, J. Choo, and J. Laane. J. Phys. Chem. A, **105**, 10 230 (2001).
2. D. Autrey, Z. Arp, J. Choo, and J. Laane. J. Chem. Phys. **119**, 2557 (2003).
3. S.A. Manley and J.K. Tyler. Chem. Commun. 382 (1970).
4. L.A. Carreira, T.G. Towns, and T.B. Malloy, Jr. J. Chem. Phys. **70**, 2273 (1979).
5. T.L. Smithson and H. Wieser. J. Chem. Phys. **73**, 2518 (1980).
6. N.R. Pillsbury, J.B. Choo, J. Laane, and S. Drucker. J. Phys. Chem. A, **107**, 10 648 (2003).
7. J.B. Choo, S. Kim, S. Drucker, and J. Laane. J. Phys. Chem. A, **107**, 10 655 (2003).
8. S. Drucker, J.L. Van Zanten, N.D. Gagnon, E.J. Gilles, and N.R. Pillsbury. J. Mol. Struct. **692**, 1 (2004).
9. K. Haller, W.-Y. Chiang, A. del Rosario, and J. Laane. J. Mol. Struct. **379**, 19 (1996).

© 2004 NRC Canada

Configuration of ring-down spectrometers for maximum sensitivity[1]

Michael Jakubinek, Zhaoguo Tong, Sergei Manzhos, and Hans-Peter Loock

Abstract: Cavity ring-down (CRD) spectrometers used for analytical applications frequently have design requirements different from spectrometers used for gas-phase spectroscopic applications. A formalism that allows for maximization of the relative sensitivity by adapting the cavity length and absorption path through the sample is presented. These experimental configurations may not reduce the detection limit but do allow for a high sensitivity of the ring-down time measurement in the concentration range of interest. The formalism is applied to two common CRDS experimental configurations and to a fiber-loop ring-down experiment.

Key words: cavity ring-down (CRD), absorption, detector, fiber-loop, sensitivity, detection limit.

Résumé : Les spectromètres CRDS (utilisés pour la spectroscoie par temps de déclin d'une cavité optique) utilisés à des fins analytiques ont souvent des exigences de construction qui diffèrent de celles des spectromètres utilisés dans des applications spectroscopiques en phase gazeuse. On propose ici un formalisme qui permet de maximiser la sensibilité relative en adaptant la longueur de la cavité et celle d'absorption à travers l'échantillon. Bien que ces configurations expérimentales ne reduisent pas la limite de détection, elles permettent une grande sensibilité de la mesure du temps de declin dans le domaine operationnel de concentration. On a appliqué ce formalisme à deux configurations expérimentales courantes de CRDS et à une expérience en cavité impliquant une boucle en fibre.

Mots clés : spectromètre CRDS (spectroscopie par temps de déclin d'une cavité optique), absorption, détecteur, boucle en fibre, sensibilité, limite de détection.

[Traduit par la Rédaction]

Introduction

In recent years cavity ring-down laser absorption spectroscopy (CRDS or CRLAS) has been applied to a variety of gas-phase analytical measurement problems (1), ranging from the detection of trace gases in ambient air samples (2–4), to detection of stable or unstable compounds formed in a molecular beam environment (5, 6), or even in plasmas and flames (7). Recently our group and others have also developed detection techniques, based on CRD, that are capable of measuring absorption of liquid samples (8–11). In particular, it has been noted that CRDS is capable of identifying small amounts of absorbers in dilute solutions of picoliter-sized liquid samples (9, 12). It appears then that CRD has the potential to serve as an optical detection method suitable for microfluidic devices, capillary electrophoresis, or any other technique in which the absorption path is constrained by the instrumental architecture.

There exist a large number of implementations of CRD (*cw* laser and pulsed-laser light sources, phase-shift measurements, Fourier transform CRD, CRDS based on fiber optic cavities, etc.), and an equally large number of environments in which CRDS has been applied (13). For this report it is important to distinguish among CRDS devices in which the sample fills the entire cavity and those in which the sample fills only a fraction of the cavity. Further, we will only explicitly discuss the common scenario in which the individual round-trips are well-separated, i.e., the laser pulse width is short compared with the time for a cavity round-trip.

If the sample fills only part of the cavity, the experimenter frequently has the choice of adjusting the length of the cavity and the length of the sample's absorption path independently. This report is concerned with those values for each of these two lengths, which maximize the sensitivity of the concentration measurement. While our immediate interest lies in finding the optimum configuration for a fiber-loop ring-down spectroscopy (FLRDS) experiment, the formalism is applicable to many other CRDS problems.

Sensitivity issues have been addressed before. A general treatment of the use of CRDS as a quantitative absorption technique was given by Zalicki and Zare (14), and was later adapted to fiber-optic ring-down cavities (15). As was pointed out by many authors, the time it takes for a light pulse in a high finesse optical cavity to decay to *1/e* of its initial intensity is given to a very good approximation by

$$[1] \qquad \tau = \frac{t_r}{2[\alpha d - \ln R]}$$

This expression assumes the applicability of Lambert–Beer's law. Here the round-trip time in the cavity ($t_r = 2L/c_0$)

Received 28 November 2003. Published on the NRC Research Press Web site at http://canjchem.nrc.ca on 26 August 2004.

M. Jakubinek, Z. Tong, S. Manzhos, and H.-P. Loock.[2] Department of Chemistry, Queen's University, Kingston, ON K7L 3N6, Canada.

[1]This article is part of a Special Issue dedicated to the memory of Professor Gerhard Herzberg.

[2]Corresponding author (e-mail: hploock@chem.queensu.ca).

 doi: 10.1139/V04-038 © 2004 NRC Canada

depends on the length of the cavity (L), and the speed of light in the cavity medium (c_0). The reflectivities of the two mirrors are combined to $R = (R_1\ R_2)^{1/2}$ and the loss in the cavity medium is expressed by a product of the frequency dependent absorption coefficient (α), and the length of the sample's absorption path (d). For high reflectivities many workers set $-\ln R \approx (1 - R)$, but to keep general applicability we retain $\ln R$ in the following. As Zalicki and Zare (14) point out, the minimum absorbance that can be measured depends on both the quality of the mirrors that define the cavity and on the experimental accuracy with which ring-down times can be determined

$$[2] \qquad [\alpha d]_{\min} = -\ln R \frac{\Delta\tau}{\tau}$$

For a typical system the uncertainty of the time measurement is given by the laser jitter or temporal response of the data acquisition and is on the order a few nanoseconds — say $\Delta\tau = 3$ ns. With a reflectivity of $R = 99.9\%$ in a 1 m long cavity the ring-down time of the empty cavity is calculated as $\tau = 1.6$ μs and the minimum absorbance is about 1 to 2 ppm. Strictly speaking this number is a detection limit but not the sensitivity of the apparatus, since both $\Delta\tau$ and τ depend strongly on the concentration of the sample. Here it is demonstrated how one can optimize a ring-down apparatus for sensitivity as opposed to detection limit. The distinction is important since in analytical applications it may be more important to reliably measure a small increase of an otherwise large analyte concentration as opposed to a small absolute concentration on a "zero absorption" background.

Results

The sensitivity is usually defined as the derivative of the measurement variable, here the ring-down time (τ) with respect to concentration. If CRDS is used for absorption measurements on liquid samples, one can either fill the entire cavity with the sample solution or only a fraction. In the latter case, eq. [1] can be rewritten as

$$[3] \qquad \tau = \frac{L}{c_0[-\ln R + \varepsilon_A C_A d + \varepsilon_S C_S d + \alpha L]}$$

Here L and d are the lengths of the cavity and the absorption path, respectively. The frequency dependent absorption coefficients (ε) for the analyte and the solvent are given with respect to base-e and are multiplied by their respective concentrations. The frequency dependent absorption coefficient (α) accounts for the absorption of the cavity medium itself. If the length of the cavity (L) is comparable to the absorption path of the sample (d) one needs to replace L with L-d. Note that a very similar expression also holds for the fiber-loop ring-down experiments described in ref. 9. The derivative of eq. [3] is simply

$$[4] \qquad \frac{\partial\tau}{\partial C_A} = -\frac{L\varepsilon_A d}{c_0[-\ln R + \varepsilon_A C_A d + \varepsilon_S C_S d + \alpha L]^2}$$

From this expression it appears as if the highest sensitivity is achieved when d approaches L and the sample fills the entire cavity. In practice, this is true only if the absorptivities of the analyte and solvent are very small ($\varepsilon_A C_A \to 0$), since in all other cases the absorptivity of the sample will lead to a dramatic decrease in ring-down time and thereby to a large measurement uncertainty. Therefore, it appears reasonable to weight the above expression with the uncertainty in the ring-down time measurement $\delta\tau$, which in turn is a function of the concentration and the experimental parameters. Note that this expression for the sensitivity then has units of inverse concentration and therefore reflects the sensitivity of the measurement to an absolute concentration change. In a practical application it may be more convenient to use a dimensionless expression for the sensitivity obtained by multiplying the above expression with the analytes' concentration. This will produce the sensitivity of the measurement to a relative concentration change,

$$[5] \qquad S \equiv \left| \frac{\partial\tau / \partial C_A}{\delta\tau} \right| C_A$$

The difference between eqs. [4] and [5] is that the former is the sensitivity of only the observable and the second the dimensionless sensitivity of the measurement.

By adjusting the design parameters of the experiment one can now maximize the sensitivity of a concentration measurement in a particular concentration range. For example, being able to distinguish between a 1 mmol L^{-1} and 1.02 mmol L^{-1} solution (a 2% change) may require different experimental conditions than distinguishing between a 10 μmol L^{-1} and 30 μmol L^{-1} solution although the absolute concentration change is the same.

The uncertainty in the ring-down time, $\delta\tau$ in eq. [5], is the sum of the experimental time resolution and the uncertainty of the fit to the optical decay. A constant term, $\delta\tau_{exp}$, that accounts for the bandwidth of the data acquisition (arising from e.g., detector amplification circuitry, time-to-digital converters, pulse width of light source, etc.), has therefore been included in the sum, and the overall uncertainty is

$$[6] \qquad \delta\tau = T_{95}(N - M)\,\mathrm{RMS}\sqrt{V_{\tau\tau}} + \delta\tau_{exp}$$

where T_{95} is the Student 95% confidence t value, RMS is the fit error, N is the number of round trips, M is the number of parameters in the model (3 for a simple exponential decay), and $V_{\tau\tau}^{-1}$ is the correlation matrix:

$$[7] \qquad V_{\tau\tau}^{-1} = \sum_{i=1}^{N} \left(\frac{\delta I_i}{\delta\tau} \right)^2$$

where I_i is the intensity of the ith round-trip. The intensity in the cavity is assumed to decay exponentially with time

$$[8] \qquad \frac{\delta I_i}{\delta\tau} = I_0 \frac{t_i}{\tau^2} \exp\left(-\frac{t_i}{\tau} \right)$$

and consequently

$$[9] \qquad V_{\tau\tau}^{-1} = \frac{I_0^2}{\tau^4} \sum_{i=1}^{N} t_i^2 \exp\left(-\frac{2t_i}{\tau} \right)$$

Replacing the sum with an integral

© 2004 NRC Canada

$$[10] \quad V_{\tau\tau}^{-1} = \frac{I_0^2}{\tau^2}\int_0^\infty \frac{t^2}{\tau^2}\exp\left(-2\frac{t}{\tau}\right)\mathrm{d}\frac{t}{\tau} = \frac{I_0^2}{4\tau^2}$$

and substituting into eq. [6] yields

$$[11] \quad \delta\tau = T_{95}(N-M)\,\mathrm{RMS}\frac{2\tau}{I_0} + \delta\tau_{\mathrm{exp}}$$

Both the root mean square fit error of the ring-down time measurement

$$[12] \quad RMS = \sqrt{\frac{1}{N-M}\sum_{i=1}^{N}(I_i^{\mathrm{fit}} - I_i)^2} \equiv \sigma\sqrt{\frac{N}{N-M}}$$

and the Student T_{95} function depend on the number of points (N) used for obtaining the ring-down time and therefore on the dynamical range of detection.

The dynamical range of detection, which is assumed to be constant with respect to the above parameters, is determined by the minimum detectable relative intensity,

$$[13] \quad I_{\mathrm{min}}^{\mathrm{rel}} \equiv \frac{I_{\mathrm{min}}}{I_0} = \frac{3\sigma_{\mathrm{background}}}{I_0}$$

where $\sigma_{\mathrm{background}}$ is the standard deviation of the background noise. The intensity after n round-trips is given by

$$[14] \quad I_{\mathrm{rel}}(n) = R^{2n}e^{-2n\varepsilon_A C_A d}e^{-2n\varepsilon_S C_S d}e^{-2n\alpha L}, \qquad n = 0,1,2\ldots$$

and thus the number of rings observed, which is the total number of data points N that can be fitted to, is given by

$$[15] \quad N(d, L, C_A) = \frac{\ln I_{\mathrm{min}}^{\mathrm{rel}}}{2(\ln R - \varepsilon_A C_A d - \varepsilon_S C_S d - \alpha L)}$$

rounded down to the nearest integer. Ultimately, the minimum detectable relative intensity is an instrument function and may be on the order of 10^{-4} or less.

By combining eqs. [4], [5], [11], and [12], one obtains for the sensitivity

$$[16] \quad S(L, d|C_A) = \frac{\varepsilon_A C_A}{c_0}\left|\frac{\dfrac{Ld}{[-\ln R + \varepsilon_A C_A d + \varepsilon_S C_S d + \alpha L]^2}}{\delta\tau_{\mathrm{exp}} + \dfrac{2}{3}I_{\mathrm{rel}}^{\mathrm{min}}T_{95}(N(L,d)-M)\tau\sqrt{\dfrac{N(L,d)}{N(L,d)-M}}}\right|$$

and the optimal values of L and d are those that maximize this expression within the concentration range of interest. For the sample calculations presented here, the standard deviation of the data set in eq. [12] (σ) was approximated by the standard deviation of the background noise ($\sigma_{\mathrm{background}}$). This permits σ to be expressed in terms of the minimum detectable relative intensity, $I_{\mathrm{min}}^{\mathrm{rel}}$ (see eq. [13]). Equation [16] can be considered rather general: it also holds for fiber-loop ring-down spectroscopy and related techniques, and for devices in which the sample fills the entire cavity (i.e., $d = L$).

In the following sections, eq. [16] is applied to three problems of interest to researchers using CRDS for analytical measurements on liquid samples. The first two are related to a fictitious example of a liquid sample introduced into a "conventional" cavity defined by two high-reflectance mirrors. The third example is more closely related to experiments performed in our laboratory: the optimum configuration for a fiber-loop ring-down experiment.

Discussion

Example I: Liquid filled cavity

CRDS has found an interesting application in the sensing of trace gas species in a number of laboratory and industrial environments. Frequently, it is advantageous and practical to fill the entire cavity with the gas to be studied. The lower limit to the cavity length is determined by the reflectivity of the mirrors. As the cavity becomes very small the transmission and absorption losses at the mirrors dominate, thus decreasing the ring-down times and sensitivity. There also exists an upper limit to the desirable cavity size, since a very long cavity filled with a strong absorbing gas will return too few rings for an accurate exponential fit. Similar considerations also hold for liquid filled cavities, with the main difference being that in a dilute solution the solvent absorption and scattering may significantly contribute to the optical losses in the cavity. Other technical problems, such as changed optical properties of the mirrors can be overcome as recently demonstrated by Zare and co-workers (11).

Figure 1 illustrates that in the very low concentration range it is advantageous to use large cavities to obtain the highest relative sensitivity. As in all examples given below, the sample is assumed to consist of a solution of the strongly absorbing dye 1,1′-diethyl-4,4′-dicarbocyanide iodide (DDCI-4: $\varepsilon_{\mathrm{DDCI}}$ (825 nm) = 3.3×10^7 L mol^{-1} m^{-1}) in a fictitious solvent with absorptivity $\alpha = 10^{-2}$ m^{-1} and a refractive index of $n = 1.0$. Only when the solvent absorptivity or the analyte concentrations are large, will the decreased number of round-trips limit the optimum cavity length (not shown in Fig. 1). On the other hand, for many practical applications this upper limit is given by the necessity to align the cavity mirrors with high precision and stability. Disregarding this experimental aspect there exists an optimum length, which is a strong function of both the concentration and the absorption cross section of the sample and solvent.

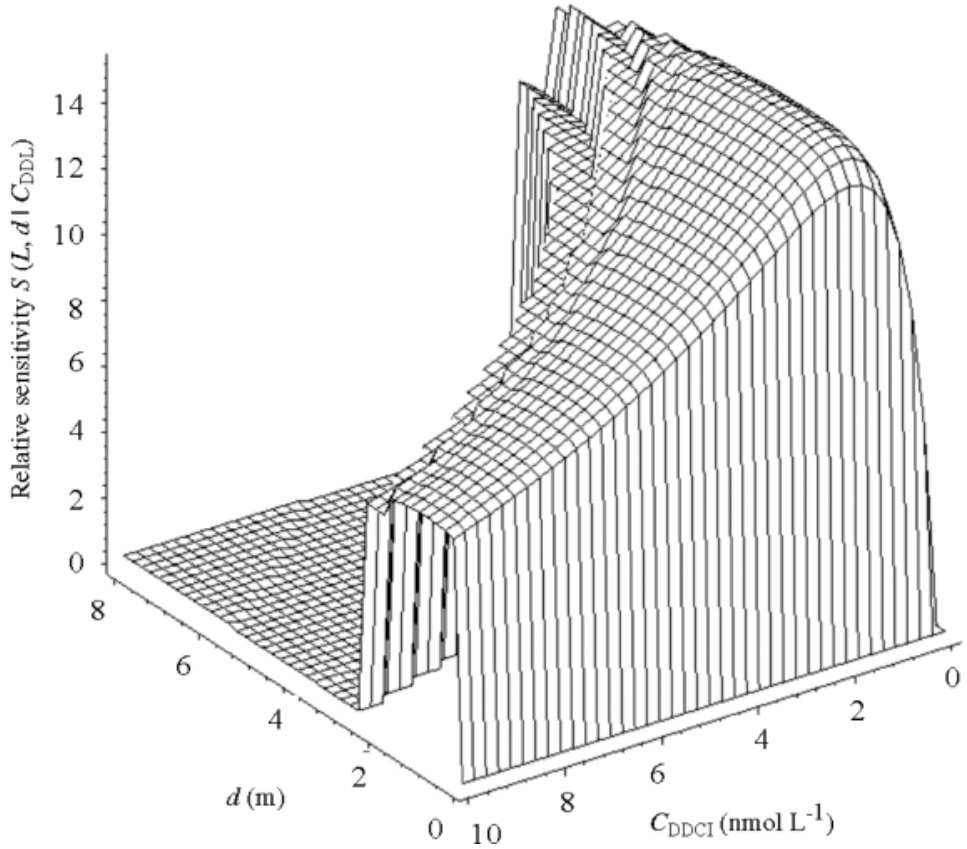
Example II: Cavity containing a small liquid sample

Recently, there has been interest in using CRDS as an absorption sensor in small flow channels (12, 16). One elegant way of implementing this idea is by introduction of a small flow channel on a transparent support medium into the cavity. Losses can further be minimized if the support is Brewster-angled with respect to the cavity axis. Since here the absorbing sample fills only a small fraction of the cavity — the absorption path is typically on the order of a few tens of microns — this arrangement resembles, at least conceptually, CRDS of a gas sample seeded in a molecular beam.

Figure 2*a* illustrates the strong dependence of the relative sensitivity on the concentration and absorption path of the

© 2004 NRC Canada

Fig. 1. Dimensionless relative sensitivity for a completely filled cavity. The absorptivity of the cavity medium was set to $\alpha_{cavity} = 5 \times 10^{-2}$ m^{-1}, $I_{min}^{rel} = 0.2\%$, $M = 3$, $\delta\tau_{exp} = 1$ ns, and the cavity losses were 0.1% so that $R = 0.999$. The maximum sensitivity is achieved for $L = d = 1.5$ m and $C_{DDCI} = 1.6 \times 10^{-9}$ mol L^{-1}. The stepwise reduction of the sensitivity with increasing concentration and increasing length of the cavity is due to the reduced number of available round-trips in the exponential fitting procedure.



sample solution. In the calculation it was assumed that the mirror losses and the scattering losses on the liquid–air interface add up to 0.1% per pass. Of course, the optimum path length (d) through the sample depends on its absorption coefficient. It is apparent that the highest sensitivity is achieved when $dC_{DDCI} = constant$. From Fig. 2*b* it is apparent that, if the cavity medium itself was not absorbing at all, there is no dependence of the measurement uncertainty on the distance between the mirrors, since the number of points being fitted to is the same for small or large mirror separation. It is therefore advisable to use a very large distance to reduce the contribution of the experimental uncertainty $\delta\tau_{exp}$ to the measurement. In practice, of course, there is an upper limit set by the difficulty to keep a large optical cavity well aligned. More interestingly, both figures show that for a given cavity length and concentration there is a strong dependence of the sensitivity on the absorption path (d) leading to a pronounced maximum.

Example III: Fiber-loop ring-down spectroscopy

In a fiber-loop ring-down experiment (Fig. 3), the experimenter is free to choose the length of the loop (L) and separation of the fiber ends (d). As such, it is desirable to choose values for those parameters so as to obtain maximum sensitivity to relative changes in the sample concentration. The following development considers the detection of a sample of DDCI in dimethyl sulfoxide (DMSO). Equation [3] may be rewritten as (9, 16)

$$[17] \qquad \tau = \frac{L}{c_0[-\ln T_{sp} + \varepsilon_{DDCI} C_{DDCI} d + \alpha_{DMSO} d + \alpha_{fiber} L]}$$

where ε_{DDCI} is the wavelength dependent absorption coefficient of DDCI in L mol^{-1} m^{-1}, α_{DMSO} is the absorption coefficient of DMSO in m^{-1}, α_{fiber} is the absorption coefficient of the fiber in m^{-1} and $c_0 = 2.07 \times 10^8$ m s^{-1} is the speed of light in the fiber.

In eq. [17] the transmittance of the fiber splice is expressed by T_{sp} and is a weak function of the distance between the fiber ends (i.e., the absorption path through the sample (d)). The transmission of the fiber–fiber connection can be approximated by (16)

$$[18] \qquad T_{sp} = T_0\left(1 - \frac{NA_0 d}{4 n_0 r}\right)$$

where r and n_0 are the radius and refractive index of the fiber core, NA_0 is the input numerical aperture, and T_0 is the experimentally determined transmission at zero separation (i.e., $d = 0$). Figure 4*a* shows that for our experimental conditions and a concentration of $C_{DDCI} = 1.5$ mmol L^{-1} the sensitivity is maximal when the length of the fiber loop is about

© 2004 NRC Canada

Fig. 2. Dimensionless relative sensitivity for a partially filled cavity. The absorptivity of the cavity medium was set to $\alpha_{cavity} = 5 \times 10^{-2}$ m^{-1}, $I_{min}^{rel} = 0.2\%$, $M = 3$, $\delta\tau_{exp} = 1$ ns, and the cavity losses were 0.1% so that $R = 0.999$. The sensitivity now depends on the length of the cavity (L) the absorption path (d), and the concentration (C_{DDCI}). (*a*) The length of the cavity was held constant at $L = 1$ m and the sensitivity is maximal for $dC_{DDCI} = 10^{-10}$ Mm. (*b*) The concentration was held constant at $C_{DDCI} = 4 \times 10^{-5}$ mol L^{-1} and there is a clear maximum sensitivity at about 2.5×10^{-6} m, largely independent of the cavity length.

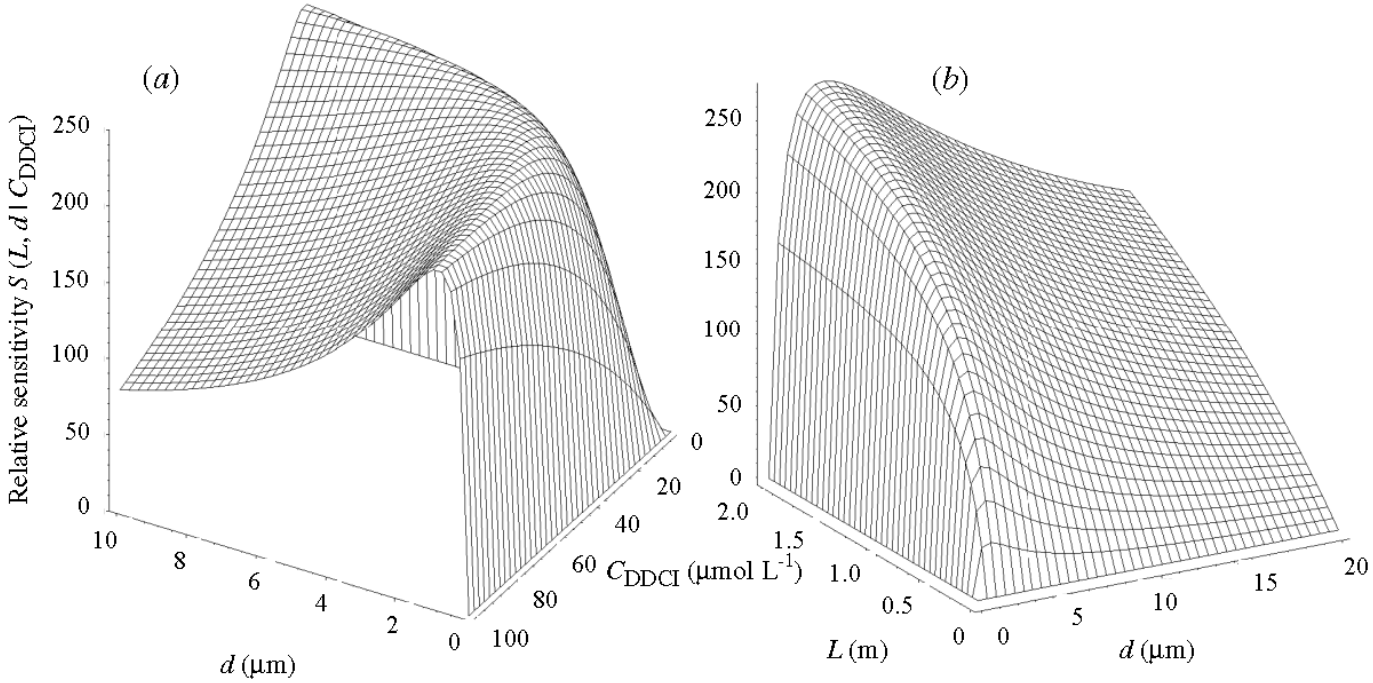
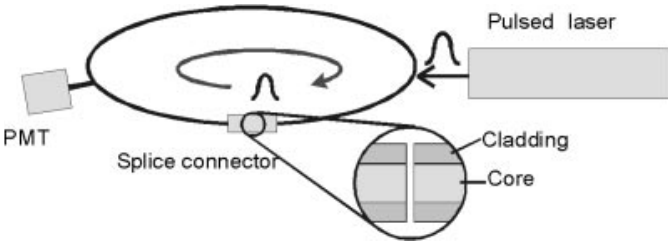


Fig. 3. Diagram of the fiber-loop ring-down experiment. A Nd:YAG pumped dye laser injects a ns pulse into a loop made of multimode optical fiber. A PMT detector monitors the intensity of each round-trip by detecting scattered light from the fiber core and cladding. After averaging a few thousand laser shots, a waveform is obtained that is then fitted using a bi-exponential decay function.



60 m and the distance between the fiber ends is 4 μm. If the absorption path is much larger, the ring-down time decreases and with it the number of data points (N) that can be used for fitting. The step-like appearance of that dependence is therefore due to the rounding to the nearest integer in eq. [15].

The minimal practical length of the fiber loop is given by the dramatic reduction in ring-down time as the transmission losses of the fiber splice begin to dominate the loss processes in eq. [17]. If those transmission losses were made very small, the lower limit is given by the macrobending losses, which increase dramatically as the radius of the loop approaches about 30 mm. The effect of macrobending losses is negligible for any loop with $L > 30$–40 cm and was ignored in this calculation. The upper practical limit of the loop length (L) depends on the number of round-trips necessary for a reliable fit to the ring-down time. It is ultimately limited when the optical losses in the fiber core begin to dominate the absorption losses in the sample.

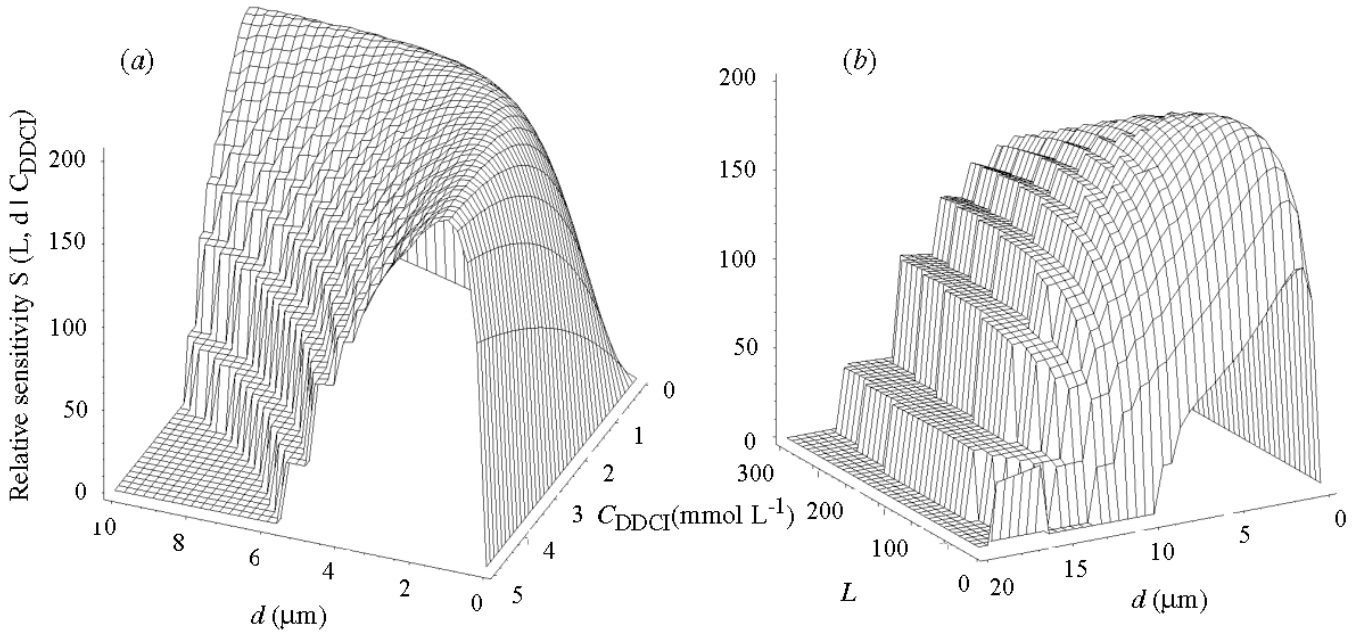
For a given L, the highest sensitivity is obtained when increasing d as the concentration is decreased (Fig. 4*b*). As in Fig. 2*a*, the relation for maximum relative sensitivity is very close to $dC_{DDCI} = constant$. However, eventually the sensitivity will decrease with very large d as in the FLRDS device the absorption path is limited by the fiber-to-fiber coupling losses described in eq. [18]. Figure 4*b* displays the dependence of the dimensionless sensitivity for a given length of the fiber loop ($L = 60$ m). It is clearly advantageous to use a short distance between the fiber ends ($d < 2$ μm) for all but the lowest concentrations. More importantly, it is possible to adjust the distance between the fiber ends in such a way that the same high relative sensitivity of about 200 (i.e., a detectable 0.5% change of the base concentration) can be obtained for a wide range of base concentrations, albeit in a concentration range about 100 times higher than the one for which a regular cavity with only 0.1% losses was optimized.

Conclusion

In the preceding paragraphs a simple formalism that allows for optimization of a ring-down spectrometer for particular analytical applications was derived. In particular it is apparent that a cavity ring-down spectrometer optimized for the highest detection limit may not give the highest sensitiv-

© 2004 NRC Canada

Fig. 4. Dimensionless relative sensitivity for a fiber-loop ring-down spectrometer. The absorptivity of the fiber core was set to $\alpha_{fiber} = 7 \times 10^{-4}$ m^{-1}, $c_0 = 2.07 \times 10^8$ m s^{-1}, $I_{min}^{rel} = 0.2\%$, $\delta\tau_{exp} = 1$ ns, the coupling losses were set to 3% so that $T_0 = 0.97$. Since both the fiber cladding and fiber core contribute to the exponential decay, five fitting parameters are needed and $M = 5$. The sensitivity depends on the length of the loop (L), the absorption path (d), and the concentration C_{DDCI}. (*a*) The length of the cavity was held constant at $L = 60$ m and the sensitivity is maximal for $dC_{DDCI} = 5 \times 10^{-9}$ Mm. (*b*) The concentration was held constant at $C_{DDCI} = 1.5 \times 10^{-5}$ mol L^{-1} and there is a clear maximum sensitivity at about 3.7×10^{-6} m, largely independent of the cavity length. The stepwise reduction with increasing concentration and increasing length of the loop is due to the reduced number of available round-trips in the exponential fitting procedure.



ity for large analyte concentrations and absorption cross sections. The formalism can easily be adapted to account for the effect of averaging (i.e., the time constant of the measurement) by including a functional dependence of the minimum relative detectable intensity on the number of laser shots sampled. The application of the formalism to the filled cavity shows no surprises and confirms what spectroscopists know by intuition, i.e., that the sensitivity is determined by a delicate balance between the length of the cavity and the absorptivity ($\alpha = Cd$) of the sample. For very weakly absorbing samples it is advisable to use the longest practical cavity, simply to increase the effective absorption path, whereas for more strongly absorbing species a very long cavity eventually reduces the accuracy of the measurement by reducing the number of data points that is available for the exponential fit.

Of more interest to analytical applications is the fact that when only part of the cavity is filled with sample there exists an optimum path length through the sample that depends on the concentration range over which a change should be measured. Again, this is known in molecular beam spectroscopy where the "concentration" of the sample is typically held constant but the absorptivity changes as a function of wavelength.

If the cavity medium itself contributes to the absorption losses, the sensitivity will more strongly depend on the length of the cavity or fiber-loop and the absorption path through the sample and the discretization of the sensitivity because of decreasing number of round-trips in the cavity becomes more apparent. These results are potentially useful not only for the FLRDS example that is given here but also for sensors and detectors based on fiber-Bragg gratings and even "conventional" optical cavities, when the cavity is filled with a medium that contributes considerably to background optical losses, such as in solvent-filled cavities. Of course, one can still obtain high sensitivity under those circumstances. Comparing the sensitivity in the conventional optical cavities with the FLRDS apparatus, a similar relative sensitivity of $S = 200$ is achieved (a detectable concentration change of 0.5%), although the transmission through the fiber splice with $T_0 = 97\%$ is considerably worse than common mirror reflectivities of $R = 99.9\%$ with base optical losses of 0.1% assumed for these cavities. FLRDS compensates the poor transmission per pass with a very long cavity ($L = 65$) and thereby allows for large ring-down times at comparably high sample absorptivities. Again it is important to distinguish between the dimensionless sensitivity that is discussed here, and the detection limit. The detection limit is rather high for FLRDS and is directly influenced by the poor transmission of the fiber–fiber joint.

Acknowledgements

The authors thank the Natural Sciences and Engineering Research Council of Canada (NSERC), Queen's University, and Photonics Research Ontario for financial support. HPL thanks Dr. Stephen Brown for bringing this problem to his attention.

© 2004 NRC Canada

References

1. D.B. Atkinson. Analyst (Cambridge, UK), **128**, 117 (2003).
2. S.S. Brown, H. Stark, and A.R. Ravishankara. Appl. Phys. B, **75**, 173 (2002).
3. R.T. Jongma, M.G.H. Boogaarts, I. Hollemann, and G. Meijer. Rev. Sci. Instrum. **66**, 2821 (1995).
4. B.L. Fawcett, A.M. Parkes, D.E. Shallcross, and A.J. Orr-Ewing. Phys. Chem. Chem. Phys. **4**, 5960 (2002).
5. A.J. Huneycutt, R.J. Stickland, F. Hellberg, and R.J. Saykally. Proc. SPIE Int. Soc. Opt. Eng. **4634**, 70 (2002).
6. J.B. Paul, C.P. Scherer, C.P. Collier, and R.J. Saykally. J. Chem. Phys. **104**, 2782 (1996).
7. L. Pillier, C. Moreau, X. Mercier, J.F. Pauwels, and P. Desgroux. Appl. Phys. B, **74**, 427 (2002).
8. S. Xu, G. Sha, and J. Xie. Rev. Sci. Instrum. **73**, 255 (2002).
9. R. Brown, I. Kozin, Z. Tong, R. Oleschuk, and H.-P. Loock. J. Chem. Phys. **119**, 10 444 (2002).
10. A.J. Hallock, E.S.F. Berman, and R.N. Zare. Appl. Spectrosc. **57**, 571 (2003).
11. A.J. Hallock, E.S.F. Berman, and R.N. Zare. Anal. Chem. **74**, 1741 (2002).
12. K. Snyder and R.N. Zare. Anal. Chem. **75**, 3086 (2003).
13. G. Berden, R. Peeters, and G. Meijer. Int. Rev. Phys. Chem. **19**, 565 (2000).
14. P. Zalicki and R.N. Zare. J. Chem. Phys. **102**, 2708 (1995).
15. T. von Lerber and M.W. Sigrist. Appl. Opt. **41**, 3567 (2002).
16. Z. Tong, M. Jakubinek, A. Wright, A. Gillies, and H.-P. Loock. Rev. Sci. Instrum. **74**, 4818 (2003).

© 2004 NRC Canada

Probing of the hot-band excitations in the photodissociation of OCS at 288 nm by DC slice imaging[1]

Myung Hwa Kim, Wen Li, Suk Kyoung Lee, and Arthur G. Suits

Abstract: The photodissociation dynamics of OCS at 288 nm has been investigated using the DC (direct current) slice imaging technique, which is a recently developed high-resolution "slicing" approach that directly measures the central slice of the photofragment distribution in imaging experiments. By analyzing a DC sliced image of $S(^1D_2)$ photofragments we observe dissociation originating from OCS molecules excited up to $v_2 = 4$ in the molecular beam. The measured translational energy distribution was used to determine the branching ratio for the contribution from each initial bending state ($0\ v_2\ 0$) of OCS and relative photodissociation cross section ratios compared to $v_2 = 1$. Large negative anisotropy parameters determined as a function of the $S(^1D_2)$ fragment recoil speed indicate that the photodissociation of OCS at 288 nm occurs exclusively from the $1^1A''(^1\Sigma^-)$ bending excited potential surface that can be accessed through a perpendicular transition.

Key words: DC slicing imaging, OCS, photodissociation, hot-band excitation.

Résumé : On a étudié la dynamique de la photodissociation du OCS à 288 nm en faisant appel à la technique de l'imagerie de raccordement à courant direct, une approche de « raccordement » à haute résolution développée récemment qui mesure directement le raccordement central de la distribution des photofragments dans des expériences d'imagerie. En analysant une image coupée en courant direct de photofragments de $S(^1D_2)$, on observe la photodissociation qui tire son origine dans les molécules de OCS excitées jusqu'au niveau $v_2 = 4$ dans un faisceau moléculaire. On a utilisé la distribution d'énergie de translation mesurée pour déterminer le rapport de bifurcation pour la contribution à partir de chaque état initial de déformation ($0\ v_2\ 0$) de OCS ainsi que les rapports de section droite de photodissociation relatifs comparés à $v_2 = 1$. Les valeurs très négatives des paramètres d'anisotropie qui ont été déterminées en fonction de la vitesse de recul de la fragment $S(^1D_2)$ indiquent que la photodissociation de OCS à 288 nm ne se produit qu'à partir de la surface potentielle excitée de déformation $1^1A''(^1\Sigma^-)$ à laquelle on peut accéder par une transition perpendiculaire.

Mots clés : imagerie de couplage en courant direct, OCS, photodissociation, excitation d'une bande chaude.

[Traduit par la Rédaction]

Introduction

Carbonyl sulfide (OCS) has been of considerable interest from a spectroscopic point of view (1–3) as a prototypical triatomic molecule, and in the earth's atmosphere as a primary source of sulfate for the stratospheric aerosol layer (4–6). Extensive studies have thus been performed to elucidate the photodissociation dynamics of OCS using laser-induced fluorescence (LIF) (7, 8), ion imaging (9–12), and photoelectron spectroscopy (13).

From these previous works (7–9), it is well known that photodissociation of $OCS(X^1\Sigma^+)$ in a range between 222 and 248 nm produces rotationally hot, but vibrationally cold $CO(X^1\Sigma^+)$ fragments along with $S(^1D_2)$ or $S(^3P_j)$ atoms in the branching ratio 95:5, through the $2^1A'(^1\Delta)$ and $1^1A''(^1\Sigma^-)$ excited states. Excitation of these excited states is weakly allowed in the bent geometry (C_s), but forbidden in the linear equilibrium geometry of the ground state molecule. Dissociation is thus strongly favored for the molecule in bent geometries on the ground electronic potential surface. The results obtained also show the bimodal distributions (7, 9, 11) for both the rotational levels of $CO(X^1\Sigma^+)$ and the translational energy of $S(^1D_2)$ because of two different dissociation pathways on the $2^1A'(^1\Delta)$ surface, which are ascribed to adiabatic and non-adiabatic processes. It is generally believed that the $2^1A'(^1\Delta)$ excited surface, corresponding to a parallel transition, is located higher in energy than the $1^1A''(^1\Sigma^-)$ excited surface corresponding to a perpendicular transition (7, 9). Katayanagi and Suzuki (11) reported that the transition probability of this non-adiabatic process is typically 0.35 at

Received 18 November 2003. Published on the NRC Research Press Web site at http://canjchem.nrc.ca on 26 August 2004.

M.H. Kim, W. Li, S.K. Lee, and A.G. Suits.[2] Department of Chemistry, SUNY Stony Brook, Stony Brook, NY 11794, USA. Department of Chemistry, Wayne State University, Detroit, MI 48202, USA. Chemistry Department, Brookhaven National Laboratory, Upton, NY 11973, USA.

[1]This article is part of a Special Issue dedicated to the memory of Professor Gerhard Herzberg.
[2]Corresponding author (e-mail: arthur.suits@sunysb.edu).

 doi: 10.1139/V04-072 © 2004 NRC Canada

230 nm from the rotational distribution of $CO(X^1\Sigma^+)$ and the $S(^1D_2)$ image obtained by using conventional velocity map ion imaging technique (14).

One particularly interesting result from the recent work (9–12) is that, owing to the fact that the transition is forbidden from the linear geometry, bent geometries, and in particular vibrational bending excitation of OCS, can play an important role in the excitation and dissociation dynamics even if the molecular beam is translationally and rotationally very cold. This is also true for the isoelectronic N_2O molecule. These studies have largely been performed in the vicinity of the local maximum in the absorption around 230 nm, where both the $2^1A'(^1\Delta)$ and $1^1A''(^1\Sigma^-)$ may contribute. Both surfaces cross repulsive $^1\Pi$ states in the linear geometry, but these crossings are avoided (and become conical intersections) for the bent molecule. Very recently, the presence of vibrationally excited OCS molecules in a cold molecular beam was experimentally reported from only the rotational state selection of $CO(X^1\Sigma^+)$ at 230 nm in velocity map ion imaging by Sugita et al. (10), Katayanagi and Suzuki (11), and Janssen and co-workers (12), independently. Janssen and co-workers used the hexapole state selection technique (12) to study the state-resolved angular recoil distribution of $CO(X^1\Sigma^+; v = 0|J)$ from the photodissociation of $OCS(\nu_2 = 0|JM = 10)$ and $OCS(\nu_2 = 1|JlM = 111)$. Here, we present a study of OCS photodissociation via hot-band absorption in the very long wavelength tail of the absorption at 288 nm.

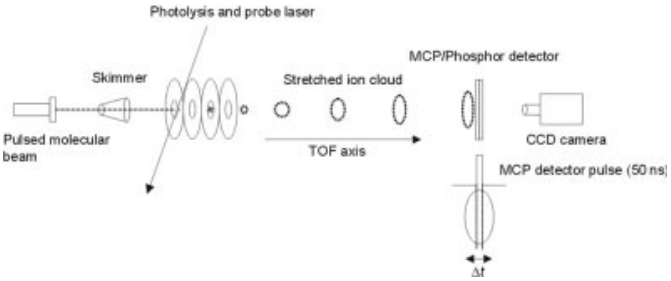
As shown in our previous papers (15, 16), DC (direct current) slice imaging techniques, refined from the original slicing approach (17), can measure directly the center slice of the photofragment distribution and can be effectively used to resolve more clearly some of the structures in the kinetic energy release or velocity distribution for any molecule without the need for numerical reconstruction methods. We achieved this by employing a low voltage, multilens velocity mapping assembly that eliminates the need for pulsed electric fields and grids, and therefore, considerably enhances the experimental resolution attainable. Also, this slicing approach is a highly sensitive and widely applicable technique for the study of orbital polarization (16, 17).

In the present study, we apply the high-resolution DC slice imaging technique to detection of the $S(^1D_2)$ photofragments following excitation of OCS at 288 nm. Even though this photolysis wavelength is placed far away from the weak absorption maximum of OCS around 230 nm, and the photoabsorption cross section is very small (4, 5), the yield of photodissociation is still sufficient to get meaningful information about the dissociation dynamics related to the vibrationally excited states of the parent molecules.

Experimental

The DC slice imaging apparatus used in this study, shown in Fig. 1, has been described in more detail elsewhere in our previous work (15) and only a brief description will be given here. A pulsed supersonic molecular beam of OCS is formed by expanding OCS molecules diluted about 30% with Ar gas into the source chamber of our differentially pumped apparatus at a backing pressure of 3 bar (1 bar = 100 kPa). After passing through a skimmer and collimator, the molecular beam enters into a velocity mapping ion optics assembly

Fig. 1. Experimental schematic showing the slice imaging approach.



consisting of four electrodes. The beam is perpendicularly intersected with a laser beam tuned to a two-photon resonant excitation of $S(^1D_2)$. The operating pressures were ~2.5×10^{-5} in the source chamber and ~5×10^{-7} torr (1 torr = 133.322 4 Pa) in the main chamber.

The wavelength of laser light in the present study was produced by frequency doubling the output of a dye laser (Continuum Jaguar, R590/R610 dyes) pumped by a Nd:YAG system (Quanta Ray GCR-5). The vertical polarization of the laser beam in the laboratory frame was achieved using a Soleil-Babinet compensator (Special Optics) with its optical axis set at 45° with respect to the horizontal polarization vector of the laser beam and was then focused with a lens (f = 30 cm) into the interaction volume with the pulsed molecular beam of OCS diluted in Ar. This linearly polarized laser beam was used for both photolysis of OCS and ionization of S atoms in a one-color experiment. Typical output power for the doubled dye laser beam entering the chamber was 2 mJ/pulse and accurate wavelength calibration was achieved using a wavemeter (Coherent WaveMaster). The $S(^1D_2)$ photofragments were ionized by using the following (2 + 1) resonance enhanced multiphoton ionization (REMPI) scheme:

$$S\ 3p^4(^1D_2) \xrightarrow{2h\nu} S\ 3p^3 4p(^1F_3) \xrightarrow{h\nu} S^+$$

at 288.18 nm

and then accelerated through the multilens velocity mapping assembly optimized for DC slicing of the ion cloud.

After flying through the field free flight path, ions were impacted on a position-sensitive dual MCP/phosphor screen detector of 120 mm diameter (Burle electro-optics). The flight path was extended up to 192.5 cm from the interaction region to the front face of the MCP to improve the velocity resolution. In addition, a repeller voltage was set at +500 V, keeping the optimized velocity mapping condition to stretch the photofragment ion cloud along the time-of-flight axis to the order of about 400 ns. We applied a narrow time gate (effectively 50 ns) at the detector to select the central section of the distribution. The fact that the slice is a finite fraction of the recoil velocity distribution, and in fact this fraction is itself speed dependent, might suggest that the accurate speed dependence will not be faithfully reproduced by the slicing technique. However, extensive Monte Carlo simulations have shown that the speed dependence of the distribution is remarkably faithful over all recoil speeds, although the velocity resolution does suffer for the poorly sliced slow fragments. The reasons for this are subtle and nonintuitive,

© 2004 NRC Canada

and beyond the scope of the current paper. However, a detailed treatment of these issues is in preparation. The velocity resolution of the experiment is largely determined by the S^+ recoil owing to excess energy in the ionization step. This is about 18 m/s, (implying an energy resolution of ~60 cm^{-1} at the $v = 2$ peak) and is large enough that neighboring rotational levels will not be resolved.

The image was accumulated for 5.4×10^5 laser shots. In this case, it was not necessary to scan the probe laser wavelength owing to the small Doppler width of the transition and the relatively broad laser line width. The image magnification factor (1.157) was obtained from Simion simulations of the ion optics. These simulations were also found to give accurate reproduction of the focusing conditions and ion time-of-flight.

Results and discussion

Figure 2 shows a DC sliced image of the $S(^1D_2)$ photofragments from the photodissociation of OCS at 288 nm. The electric vector of the photolysis light is parallel to the vertical direction in the plane of the image. As can be seen in Fig. 2, four distinct rings are clearly visible with different intensities. All of the rings exhibit strong anisotropic angular distributions corresponding to a perpendicular transition, in which the transition dipole moment is perpendicular to the recoil direction. Thus, it is immediately apparent that the contribution from the $1^1A''(^1\Sigma^-)$ state, which is accessed through a perpendicular transition, is predominant. According to previous results by Suzuki and co-workers (9, 11), this observation can be interpreted more clearly from the result that the image of fast $S(^1D_2)$ photofragments changes from rather isotropic distribution ($\beta \sim 0$) to the anisotropic distribution ($\beta < 0$) corresponding to a perpendicular transition with changing photoexcitation wavelength from 223 to 248 nm. This implies that the contribution from the $2^1A'(^1\Delta)$ excited state in a mixed transition (9, 18) attributed to both $2^1A'(^1\Delta)$ and $1^1A''(^1\Sigma^-)$ excited states relatively decreases for decreasing excitation energy. In addition, although the bimodal distribution is still shown at 248 nm in the previous works, the contribution of the slow component corresponding to a non-adiabatic process through only the $2^1A'(^1\Delta)$ excited surface is considerably reduced due to the lowering of the excitation energy. These previous experimental investigations strongly suggest that the $2^1A'(^1\Delta)$ excited surface cannot be reached with a 288 nm photolysis wavelength because of insufficient energy. Our observed image is also consistent with this expectation, showing a predominantly perpendicular transition related to the exclusive excitation of the $1^1A''(^1\Sigma^-)$ excited state.

The available energy for our system is 151 cm^{-1} from energy conservation using the dissociation energy D_0 (0 K) of 25 311 ± 72 cm^{-1} recently reported by Janssen and co-workers (12), (this gave better results than scaling the NIST values (19) to 0 K), the spin-orbit energy of $S(^1D_2)$ (9239 cm^{-1}) (20) with respect to the ground state $S(^3P_2)$, and the photon energy at 288.18 nm. There is insufficient energy for vibrational excitation of $CO(X^1\Sigma^+)$ photofragments following dissociation at 288 nm. Given the low recoil energy and the rotationally cold starting sample, angular momentum considerations predict modest rotational excitation in the CO photoproduct, discussed further in the next section.

Fig. 2. DC sliced image of the $S(^1D_2)$ from the photodissociation of OCS at 288 nm. The probe laser polarization is aligned vertically in the plane of the image.

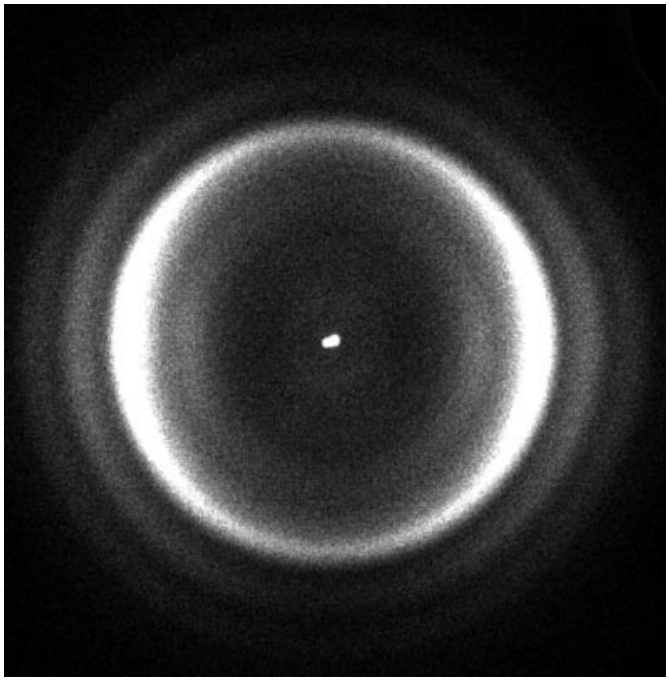


Figure 3(*a*) gives the translational energy distribution determined from the sliced image. The peaks in the distribution clearly correspond to a hot-band bending progression in the parent molecule, showing a maximum at two quanta initial excitation. If we assume no rotational excitation in the parent molecule, then the translational energy origins for the hot bands should be 151, 671, 1198, 1724, and 2257 cm^{-1} for $v_2 = 0$–4, respectively (21). The deviations of the peak maxima from these positions may be used to estimate (albeit crudely) the level of rotational excitation in the CO product. On this basis, we find the most probable J values for the CO product to be 8, 12, 13, and 14 for $v_2 = 1$–4, respectively. For the most intense peak ($v_2 = 2$), this implies an exit impact parameter of 0.43 Å. By way of comparison, Suzuki et al.'s results at 248 nm (9), show the product CO rotational distribution peaking at a roughly $J = 32$, corresponding to an exit impact parameter of 0.52 Å, in quite reasonable agreement with our determination. The increasing rotational excitation we observe with increasing hot-band excitation is a natural consequence of the increasing product orbital angular momentum (i.e., the increasing relative velocity between the photofragments).

These results show for the first time the contribution of the hot-band excitations up to $v_2 = 4$ in photodissociation originating from the different bending excited states of OCS parent molecules in a cold molecular beam. As seen in Table 1, the branching ratios for the contribution from the initial vibrational bending state of OCS were determined by the integration of each contribution obtained in Gaussian fits to the peaks, a somewhat arbitrary choice that nevertheless gave good fits to the resolved peaks. Our results clearly show that the absorption cross section for bend-excited OCS

© 2004 NRC Canada

Fig. 3. The solid line represents the translational energy distribution for the $S(^1D_2)$ photofragments derived from DC sliced image in Fig. 2. This was fitted to a sum of five Gaussians to generate the data in Table 1. The dotted line shows the speed dependence of the anisotropy parameter (β) for the $S(^1D_2)$ photofragments.

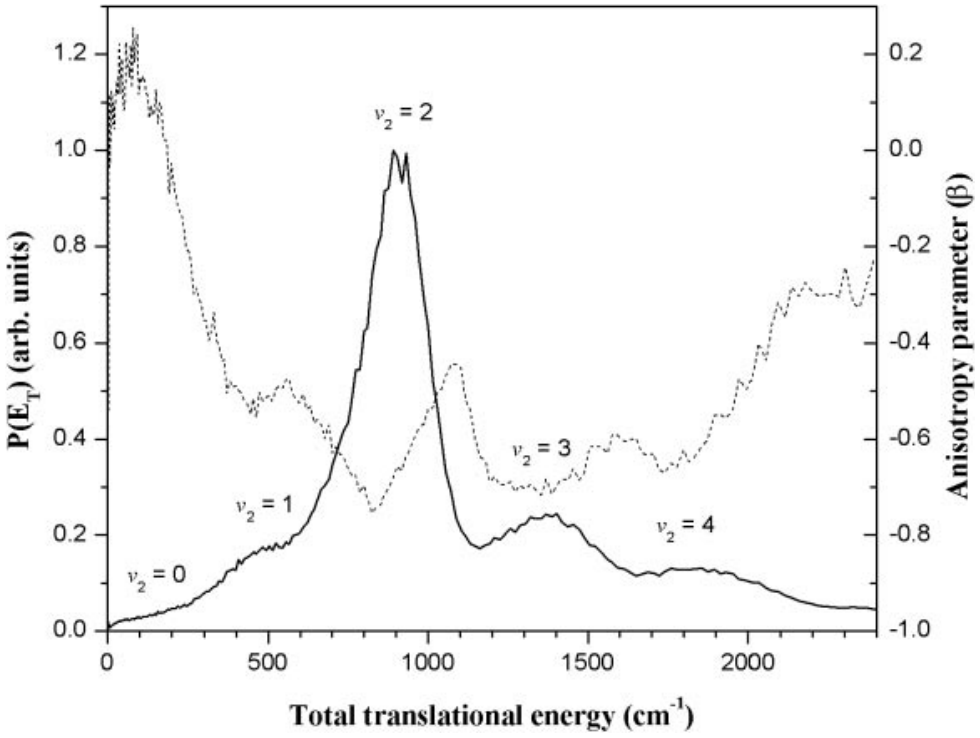


Table 1. Contributions and relative photodissociation cross section ratios at 288 nm for different initial states of OCS.

		Relative thermal population		Relative cross section ratio ($\sigma(0\ v_2\ 0)/\sigma(0\ 1\ 0)$)	
OCS vibrational state ($0\ v_2\ 0$)	Branching ratio	298 K	200 K	298 K	200 K
(0 0 0)	≤0.01*	1	1	na	na
(0 1 0)	0.15	8.11×10^{-2}	2.37×10^{-2}	1	1
(0 2 0)	0.52	6.37×10^{-3}	5.35×10^{-4}	44	1.5×10^{2}
(0 3 0)	0.20	5.02×10^{-4}	1.21×10^{-5}	2.2×10^{2}	2.6×10^{3}
(0 4 0)	0.13	3.84×10^{-5}	2.64×10^{-7}	1.8×10^{3}	7.8×10^{4}

Note: na, not available.
*Indicates a very small or negligible contribution to the kinetic energy release.

to the $1^1A''(^1\Sigma^-)$ surface at 288 nm is greatly enhanced relative to the vibrationless molecule. If we assume a Boltzmann distribution to calculate the relative thermal populations for each excited vibrational bending state relative to ground state of OCS parent molecules at 298 K and 200 K (the actual vibrational temperature of the beam is not well known), the relative cross section ratio compared to the $v_2 = 1$ vibrational bending state can be simply estimated as given in Table 1. It should be noted that since the vibrational temperature is possibly much lower than the values used to calculate the relative thermal populations in this study, the relative cross section ratios here are a lower limit. Since the vibrational origin gives a negligible contribution to the translational energy release, we only indicate an upper bound for its relative population. In comparison, even though Katayanagi and Suzuki (11) reported the photodissociation cross section for $v_2 = 1$ is at least 7 times larger than that of $v_2 = 0$ at 230 nm excitation, our results indicate that the cross sections of hot bands from bending excited states of OCS are significantly enhanced at 288 nm excitation relative to that at 230 nm. It is likely owing to several key factors: the transition moment increases, as shown theoretically by Suzuki et al. (9); the energy gap between the two surfaces drops dramatically with the bend angle; and because the bending excitations of OCS parent molecules considerably increase Franck–Condon overlaps between the ground electronic state and excited states at the lower excitation energy region (10–12).

Also shown in Fig. 3 is the recoil speed dependence of the anisotropy parameter (β) for the $S(^1D_2)$ photofragments extracted by least-squares fit of the angular distribution with respect to recoil velocity with the following equation:

© 2004 NRC Canada

$$I(\theta) = \left(\frac{1}{4\pi}\right)[1 + \beta P_2(\cos\theta)]$$

where θ is the recoil angle relative to the electric vector of the dissociating laser beam, and P_2 is the second-order Legendre polynomial ($P_2(\cos\theta) = (3\cos^2\theta - 1)/2$). Although there is a possibility for orbital alignment in the $S(^1D_2)$ product to modulate the signals and add additional terms, in this "one-laser" experiment we cannot directly probe this phenomenon. However, inasmuch as our angular distributions fit quite well with these contributions omitted, we feel confident in neglecting this effect. The β values correlated with each ring of the sliced image are approximately in the range between –0.55 and –0.75, indicating a predominantly perpendicular transition. However, the magnitude of the anisotropy parameters are close to, but slightly lower than the theoretical limiting value of $\beta = -1$ anticipated for the case of a pure perpendicular transition. This kind of behavior may be rationalized in terms of the breakdown of the axial recoil approximation for near-threshold photodissociation (10, 22) or the partial contribution from the higher $2^1A'(^1\Delta)$ excited surface (11, 12). The latter can likely be ruled out from the previous result (12) that if both the $2^1A'(^1\Delta)$ and $1^1A''(^1\Sigma^-)$ excited states are simultaneously involved in dissociation, the β value should be largely dependent on the vibrational bending excitation of OCS because of the difference of the angle dependence of the transition dipole moment between two surfaces. According to the calculations of Suzuki et al. (9), the transition dipole moment of the $2^1A'(^1\Delta)$ state increases more steeply than that of the $1^1A''(^1\Sigma^-)$ state for the bending angle of OCS. In the most recent work (12), the average β values were 0.24 for $v_2 = 0$ and 0.71 for $v_2 = 1$ at 230 nm. The data presented here show that the β values do not change dramatically with each initial bending excitation for the 288 nm excitation. This provides further evidence that the photodissociation of OCS at 288 nm purely occurs from the $1^1A''(^1\Sigma^-)$ excited potential energy surface.

Conclusions

We have studied the photodissociation dynamics of OCS at 288 nm by applying the high-resolution DC slice imaging technique. The results obtained clearly showed that there are progressions up to $v_2 = 4$ in dissociation starting from the bend-excited vibrational states of OCS parent molecules in a cold molecular beam. Large negative anisotropy parameters suggest that the photodissociation of OCS at 288 nm purely occurs on the $1^1A''(^1\Sigma^-)$ bending excited potential surface that can be accessed through a perpendicular transition. DC slice imaging has been shown as a highly sensitive probe technique able to give more detailed information about the photodissociation dynamics.

Acknowledgements

The authors would like to acknowledge Dr. D. Townsend and M.P. Minitti for their help. This work was supported by the National Science Foundation under award number CHE-0102174.

References

1. W.R. Breckenridge and H. Taube. J. Chem. Phys. **52**, 1713 (1970).
2. J.W. Rabalais, J.M. McDonald, V. Scherr, and S.P. McGlynn. Chem. Rev. **71**, 73 (1971).
3. C. Cossart-Magos, M. Jungen, R. Xu, and F. Launay. J. Chem. Phys. **119**, 3219 (2003).
4. L.T. Molina, J.J. Lamb, and M.J. Molina. Geophys. Res. Lett. **8**, 1008 (1981).
5. R.N. Rudolph and E.C.Y. Inn. J. Geophys. Res. **86**, 9891 (1981).
6. C.Y.R. Wu, F.Z. Chen, and D.L. Judge. J. Quant. Spectrosc. Radiat. Transfer, **61**, 265 (1999).
7. N. Sivakumar, G.E. Hall, P.L. Houston, J.W. Hepburn, and I. Burak. J. Chem. Phys. **88**, 3692 (1988).
8. G. Nan, I. Burak, and P.L. Houston. Chem. Phys. Lett. **209**, 383 (1993).
9. T. Suzuki, H. Katayanagi, S. Nanbu, and M. Aoyagi. J. Chem. Phys. **109**, 5778 (1998).
10. A. Sugita, M. Mashino, M. Kawasaki, Y. Matsumi, R. Bersohn, G. Trott-Kriegeskorte, and K.-H. Gericke. J. Chem. Phys. **112**, 7095 (2000).
11. H. Katayanagi and T. Suzuki. Chem. Phys. Lett. **360**, 104 (2002).
12. A.J. van den Brom, T.P. Rakitzis, J. van Heyst, T.N. Kitsopoulos, S.R. Jezowski, and M.H.M. Janssen. J. Chem. Phys. **117**, 4255 (2002).
13. A.M. Rijs, E.H.G. Backus, C.A. de Lange, N.P.C. Westwood, K. Wang, and V. McKoy. J. Chem. Phys. **116**, 2776 (2002).
14. A.T.J.B. Eppink and D. H. Parker. Rev. Sci. Instrum. **63**, 3477 (1997).
15. D. Townsend, M.P. Minitti, and A.G. Suits. Rev. Sci. Instrum. **74**, 2530 (2003).
16. D. Townsend, S.K. Lee, and A.G. Suits. Chem. Phys. **301**, 197 (2004).
17. C.R. Gebhart, T.P. Rakitzis, P.C. Samartzis, V. Ladopoulos, and T.N. Kitsopoulos. Rev. Sci. Instrum. **72**, 3848 (2001).
18. Z.H. Kim, A.J. Alexander, and R.N. Zare. J. Phys. Chem. A, **103**, 10 144 (1999).
19. H.Y. Afeefy, J.F. Liebman, and S.E. Stein. NIST Standard reference database 69: NIST chemistry webbook [online]. Available from http://www.ChemWeb.com/databases/. 2003.
20. W.C. Martin, J.R. Fuhr, and D.E. Kelleher. NIST atomic spectra database. Version 2.0 [online]. Available from http://physics.nist.gov/cgi-bin/AtData/spass.ksh?@/PhysRefData/AtData/html/contents.html. 2002.
21. A. Foord, J.G. Smith, and D.H. Whiffen. Mol. Phys. **29**, 1685 (1975).
22. E. Wrede, S. Laubach, S. Schulenburg, A.J. Orr-Ewing, and M.N.R. Ashfold. Chem. Phys. Lett. **326**, 22 (2000).

© 2004 NRC Canada

Measurement of the autoionization lifetime of the superexcited atomic sulfur S($3s^2 3p^3(^2D^o)4d$) state using tunable vacuum ultraviolet (VUV) radiation[1]

Jianhua Huang, Dadong Xu, Alexei Stuchebrukhov, and William M. Jackson

Abstract: A new method is described that combines a tunable coherent vacuum ultraviolet (VUV) radiation source and an ion velocity imaging apparatus to study the autoionization of superexcited sulfur atoms. The photolysis of CS_2 at 193 nm is used to produce metastable sulfur atoms in the $^1D_2$ state. The S($^1D_2$) atom is then directly excited to the neutral superexcited state $3s^2 3p^3(^2D^o)4d$ ($^1D_2^o$) at 11.317 eV with a tunable VUV photon at ~121.896 nm. This excited state then undergoes autoionization into the first ionization continuum state of $S^+(^4S_{3/2}^o) + e^-$, which is not directly accessible from the S($^1D_2$) state through optical transition. By monitoring the S^+ signal in the time-of-flight mass spectrometer while scanning the excitation wavelength, the line profile of the $3s^2 3p^3 4d\ ^1D_2^o \leftarrow 3s^2 3p^4\ ^1D_2$ transition is recorded and found to have a full width at half maximum (FWHM) of 0.9 cm^{-1}. This has been used to determine an autoionization lifetime of the neutral superexcited $3s^2 3p^3 4d\ ^1D_2^o$ state of 5.9 ps. The accurate measurement of the autoionization lifetime provides a benchmark for testing fundamental theoretical models of processes occurring in excited states of atoms.

Key words: autoionization, atomic sulfur, vacuum ultraviolet (VUV), full width at half maximum (FWHM).

Résumé : On décrit une nouvelle méthode qui combine une source cohérente et réglable de rayonnement ultraviolet du vide avec un appareil d'imagerie de la vitesse des ions pour étudier l'autoionisation d'atomes de soufre surexcités. On a utilisé la photolyse du CS_2 à 193 nm pour produire des atomes de soufre métastables dans l'état $^1D_2$. L'atome S($^1D_2$) est alors directement excité à l'état surexcité neutre $3s^2 3p^3(^2D^o)4d$ ($^1D_2^o$), à 11,317 V, à l'aide d'un photon VUV réglable à ~121,896 nm. Cet état excité subit alors une autoionisation dans le premier état d'ionisation continue du $S^+(^4S_{3/2}^o) + e^-$ qui n'est pas directement accessible à partir de l'état S($^1D_2$) par le biais d'une transition optique. En suivant le signal du S^+ dans un spectromètre de masse à temps d'envol alors qu'on balaye la longueur d'onde d'excitation, on a enregistré le profil de la raie de la transition $3s^2 3p^3 4d\ ^1D_2^o \leftarrow 3s^2 3p^4\ ^1D_2$ et on a trouvé que la largeur totale à demi-hauteur maximale (« FWHM ») est de 0,9 cm^{-1}. Cette valeur a été utilisée pour déterminer que le temps de vie de l'autoionisation de l'état surexcité neutre $3s^2 3p^3 4d(^1D_2^o)$ est de 5,9 ps. La mesure précise du temps de vie d'autoionisation fournit une référence pour évaluer les modèles théoriques fondamentaux des processus se produisant dans les états excités d'atomes.

Mots clés : autoionisation, soufre atomique, ultraviolet du vide, largeur totale à demi-hauteur maximale.

[Traduit par la Rédaction]

Introduction

The study of the photoionization of sulfur is of great interest because of its applications in astrophysics. Spectroscopic measurements indicate that sulfur and oxygen dominate the torus plasma of the Jupiter satellite Io (1, 2). Furthermore, the study of the photoabsorption spectrum of sulfur is interesting because it is an open-shell heavy atom where spin–orbit coupling can be large and correlation effects in determining the properties of the excited state can be important. The electronic configuration of atomic sulfur is $1s^2 2s^2 2p^6 3s^2 3p^4$, which gives rise to the $^3P_{2,1,0}$, $^1D_2$, and $^1S_0$ terms. The ground state is the $^3P_2$ state. The photoionization of ground-state sulfur ($^3P_2$) has been extensively studied in the past. The absolute values of the cross sections were reported by Tondello (3) for photon energies from the ionization threshold at 119.67 to 90 nm using the flash pyrolysis method. Sarma and Joshi (4) did the same work but made more detailed analysis in the region between 109 and 100 nm. Berkowitz and co-workers (5) observed the photoionization spectrum of sulfur in the region between the first ionization threshold and 92.5 nm. They assigned many of the autoionization states that converge on the $^4S^o$, $^2D^o$, $^2P^o$ states of the S^+ ion originating from the ground state of sulfur ($^3P_2$). They also showed that the autoionization features of the $3p^3(^2D^o)nd\ ^3D^o$ levels are broad, while those of the $3p^3(^2D^o)nd\ ^3S^o, ^3P^o$ levels are narrow. However, surprisingly, we failed to find previous measurements of the lifetimes

Received 7 Novenber 2003. Published on the NRC Research Press Web site at http://canjchem.nrc.ca on 26 August 2004.

J. Huang, D. Xu, A. Stuchebrukhov, and W.M. Jackson.[2] Department of Chemistry, University of California, Davis, One Shields Ave., Davis, CA 95616, USA.

[1]This article is part of a Special Issue dedicated to the memory of Professor Gerhard Herzberg.

[2]Corresponding author (email: wmjackson@ucdavis.edu).

 doi: 10.1139/V04-039 © 2004 NRC Canada

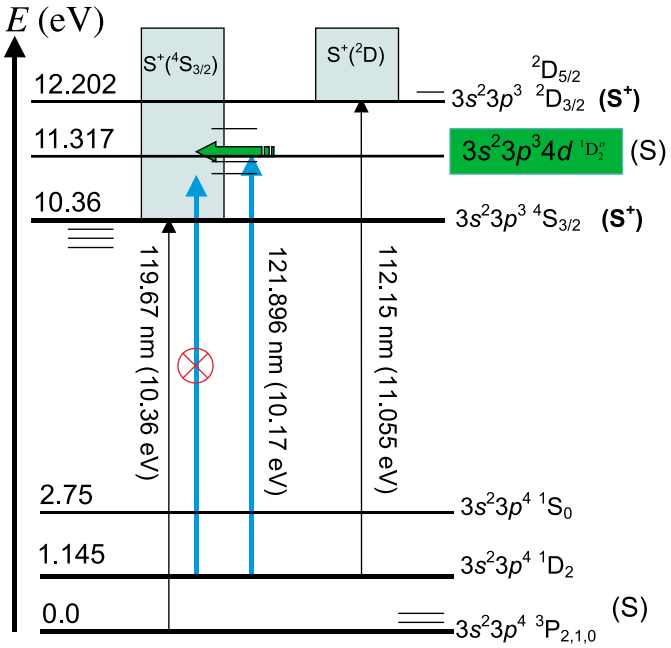
from these line widths for atomic sulfur. For atomic oxygen, with the similar electronic configuration $1s^2 2s^2 2p^4$, Smith and co-workers (6, 7) measured the autoionizing lifetimes originating from the ^{3}P state by a variety of techniques including Rabi oscillation. All of their measurements were based on multiphoton ionization of atomic oxygen (6, 7). Some lifetime measurements of weakly autoionizing states in O I in the region of 75–125 nm were also done by observing the decay rate of emitted photons (8). Fewer studies have been carried out on the superexcited singlet states of oxygen atoms compared to the triplet states, most likely because of the difficulty of producing a high density of atoms in the lower singlet state, from which optical excitation originates. We will show that this limitation can be overcome by using laser photolysis of the proper precursor for the metastable atom in a pulsed molecular beam along with a tunable coherent vacuum ultraviolet (VUV) source to excite the atom to the autoionization state. Strong signals can be obtained for the autoionizing state because the lasers cross the molecular beam at the point in both space and time at which the atom density is at a maximum, as well as because of the high sensitivity of the ion velocity imaging system.

The photodissociation dynamics of CS_2 at 193 nm has been extensively studied (9–14). It is well known that the photolysis of CS_2 gives rise to sulfur atoms in both the ground ($^3P_{2,1,0}$) and excited ($^1D_2$) states. The S($^1D_2$) in the beam is then excited using a single VUV photon at 121.896 nm (10.17 eV) to the $3s^2 3p^3(^2D^o)4d\ ^1D_2^o$ neutral state at 11.317 eV, which is above the first ionization threshold of the sulfur atom. This superexcited state then undergoes autoionization into the first ionization continuum of $S^+(^4S_{3/2}) + e^-$, with its threshold at 10.36 eV. The energy of the photon (10.17 eV) is not high enough to ionize the ground state S($^3P_2$). The relevant energy level diagram of the sulfur atom and ion is shown in Fig. 1. The $3s^2 3p^3(^2D^o)4d\ ^1D_2^o \leftarrow 3s^2 3p^4\ ^1D_2$ transition line profile is then recorded by monitoring the S^+ signal in the time-of-flight mass spectrometer (TOF-MS), while scanning the excitation wavelength.

Experimental

The measurements were performed using an ion velocity imaging apparatus, which has been described in detail elsewhere (15). It consists of three stainless steel chambers that are all pumped with separate turbo-molecular pumps. The first chamber is the molecular beam source chamber, which houses a piezoelectric pulsed valve with a nozzle having a diameter of 0.25 mm. The molecular beam is skimmed twice before it interacts with the laser beams. The second chamber is the reaction chamber where the skimmed molecular beam crosses the laser beams. During the experiments, the typical pressure in this chamber was 4×10^{-5} Pa. The laser beams enter the reaction chamber in a direction that is perpendicular to the molecular beam and intercept the molecular beam in the center of the ion optics of the TOF-MS. The ion optics of the TOF-MS consists of three plates, a repeller, an accelerator, and a ground plate, the last of which is the entrance to the flight tube for the mass spectrometer. High voltages with the appropriate ratio for ion velocity imaging are applied to the repeller and accelerator to focus the ions into the flight tube that is perpendicular to the plane defined by the laser and the molecular beams. The typical voltage ratio in our experiment was 1500 V/1042 V. To avoid any field effects on the line width measurement, the voltages on the ion optics were applied 300 ns after the arrival of the VUV light in the ionization region. The pressure in the flight tube during an experiment was about 8×10^{-7} Pa. This is low enough so that the ion cloud can fly for 62 cm without a collision in a field-free region before it strikes the detector. The detector assembly consists of two microchannel plates and a fast P47 phosphor screen. A CCD camera and a photomultiplier tube are mounted behind the screen to collect images and TOF spectra, respectively.

Fig. 1. Energy level diagram of the sulfur atom and ion.



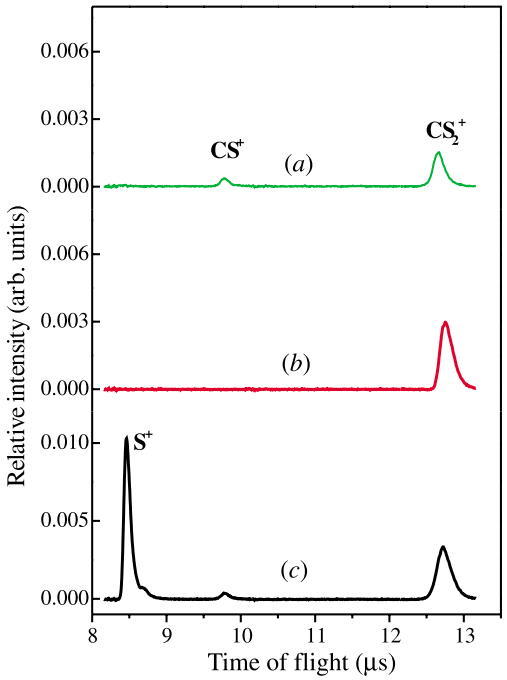
The CS_2 molecular beam is crossed with a 193 nm laser beam, which is produced by a GAM laser (EX5). The S($^1D_2$) atom is ionized by a coherent VUV radiation beam that is obtained by frequency tripling. A Scanmate 2 (or FL2002) dye laser operating with the Pyridine 2 dye is pumped by the 532 nm output of an Nd:YAG laser (Spectra-Physics, Pro-230–30). The wavelength of the dye laser is calibrated by a wavelength meter (COHERENT WaveMaster^{TM}). The dye laser output is frequency doubled in an Inrad auto-track unit, which keeps the intensity of the UV output the same while the wavelength is scanned. The UV beam is separated from its fundamental with a prism and is focused with a quartz lens into a gas cell, which contains Kr gas that is used for generating the VUV radiation. The focal length of the quartz lens is 15 cm, and the UV light is focused about 6.5 cm in front of a LiF lens with a 6.5 cm focal length at the VUV wavelength so that the VUV light is nearly collimated through the reaction chamber.

Results

Figure 2 shows a series of mass spectra that were obtained under different excitation conditions. A pure CS_2 beam with 50 torr (1 torr = 133.322 Pa) backing pressure was used for

© 2004 NRC Canada

Fig. 2. Time-of-flight mass spectra of CS_2: (*a*) beam + 193 nm light; (*b*) beam + 121.896 nm light; (*c*) beam + 193 nm light + 121.896 nm light (121.896 nm light arrives 20 ns later relative to 193 nm light).



these experiments. The timing for the pulse valve opening was carefully adjusted so that no clusters were observed in the TOF spectra. Figure 2*a* shows that CS_2^+ and CS^+ ions are produced by multiphoton ionization even though the 193 nm laser fluence is very low (~1 mJ/cm^2) (16). This is because the single and multiphoton absorption cross sections of CS_2 are very large. Figure 2*b* is the TOF spectrum taken when only the VUV light at 121.896 nm (10.17 eV) was present. The CS_2^+ signal is the result of single-photon ionization of the CS_2 molecule whose ionization energy is 10.07 eV. Figure 2*c* shows the TOF mass spectrum when both lasers were present. The 121.896 nm light is delayed 20 ns with respect to the 193 nm laser. A strong S^+ signal is now seen in the TOF mass spectrum as expected. The S^+ ion comes from the VUV ionization of the S($^1D_2$) atom that is produced by the photodissociation of CS_2 at 193 nm. The S^+ ion signal disappears when the Kr gas is evacuated from the VUV cell.

The S^+ ion signal as a function of ionization wavelength was recorded using a Stanford Research Boxcar Averager (SR 250). Figure 3 shows the line profiles obtained when the wavelength of the ionization laser was scanned through the $3s^23p^3(^2D^o)4d\ ^1D_2^o \leftarrow 3s^23p^4\ ^1D_2$ transition using different gas pressures in the four-wave mixing cell with Scanmate 2 and FL2002 dye lasers. Different conversion efficiencies occur at these different pressures for frequency tripling that result in different VUV intensities. The absolute intensities at different Kr pressures vary by more than one order of magnitude. Figure 3 shows that the line profile does not change as the Kr pressure changes, which indicates that it is free from power broadening. The FWHM is a little different for the two dye lasers because of the different bandwidths of the lasers. The natural line width can be determined from these scans by assuming the dye lasers have Gaussian profiles, which have to be convoluted with the expected Lorentzian profile to produce the measured line shape. Figure 4 shows the fits obtained for the experimental line profiles using this convolution. The FWHM of the Lorentzian profiles obtained by these convolutions was 0.90 cm^{-1} for scans using both Scanmate 2 and FL2002 dye lasers. Different Gaussian bandwidths of 0.5 and 0.9 cm^{-1} have to be used in the convolution for the measurements using the Scanmate 2 and FL2002 dye lasers, respectively. The fits are excellent, and they yield a FWHM of 0.90 ± 0.05 cm^{-1} for the natural line width in both cases, which corresponds to an autoionization lifetime of 5.90 ± 0.31 ps. The bandwidths of the fundamentals of the two dye lasers are 0.09 and 0.16 cm^{-1} for the Scanmate 2 and the FL2002, respectively. The VUV bandwidths obtained by tripling the doubling output of the dye lasers should be at most 6 times those for the fundamentals, which turn out to be 0.54 and 0.96 cm^{-1}, respectively. However, during the fitting it was found that the width of the Gaussian function for the FL2002 could be chosen between 0.9 and 1.2 cm^{-1} to obtain a reasonable fit, with 0.9 cm^{-1} producing the best fit. Similarly, the width of the Gaussian function for the Scanmate 2 could be chosen between 0.4 and 0.6 cm^{-1}, with 0.5 cm^{-1} producing the best fit. The identical results for the natural line width from measurements using different dye lasers indicate the results are reliable.

Discussion

When an electron combines with the $3s^23p^3$ ion-core states of the sulfur atom, Rydberg series are formed whose energies converge to the associated $^4S^o$, $^2D^o$, or $^2P^o$ ion states. The $^4S^o$ core forms a series of triplet and quintet S, P Rydberg states, while $^2D^o$ forms singlet and triplet P, D, F Rydberg states, and $^2P^o$ forms singlet and triplet S, P, D Rydberg states. Photoabsorption and photoionization spectra of sulfur have been studied extensively in this region (3–5). Berkowitz and co-workers (5) reported the photoionization spectrum of sulfur in detail between the first ionization threshold and 92.5 nm. They assigned many of the autoionization states that converge to the $^4S^o$, $^2D^o$, $^2P^o$ states of the S^+ ion originating from the ground state of sulfur ($^3P_2$) (5).

Even though there have been many studies on the photoionization of sulfur atoms and the autoionization levels for these sulfur atoms have been previously assigned, to our knowledge no autoionization lifetime measurements have been reported. On the other hand, there are measurements on the autoionization lifetimes for atomic oxygen. The O ($^2D^o$)$3p\ ^1P_1$ and $^1F_3$ levels were first observed in the emission studies by Edlen and Sven (17) and by Eriksson and Isberg (18). The transitions involving the $^1P_1$ level were broadened by approximately 0.2 cm^{-1} with an autoionization lifetime of 3×10^{-11} s to the $^4S^o_{3/2}$ continuum; the transitions involving the $^1F_3$ level were sharper, and hence the lifetimes were longer (18). Instances of forbidden autoionization in atomic oxygen have been discussed by Huffman et al. (19) and Dehmer and co-workers (20–22) for Rydberg states excited from the ^3P, $^1D_2$, and $^1S_0$ lower states. Recently, Pratt et al. (23) reported the autoionization of O ($^2D^o$)$3p\ ^1P_1$ and

© 2004 NRC Canada

Fig. 3. The line profiles obtained under different Kr pressures in the VUV cell (indicated on the figure in torr (1 torr = 133.322 Pa)) and using different dye lasers. The curves are individually normalized to 1 at the highest point. The absolute intensities differ by more than one order of magnitude at different pressures.

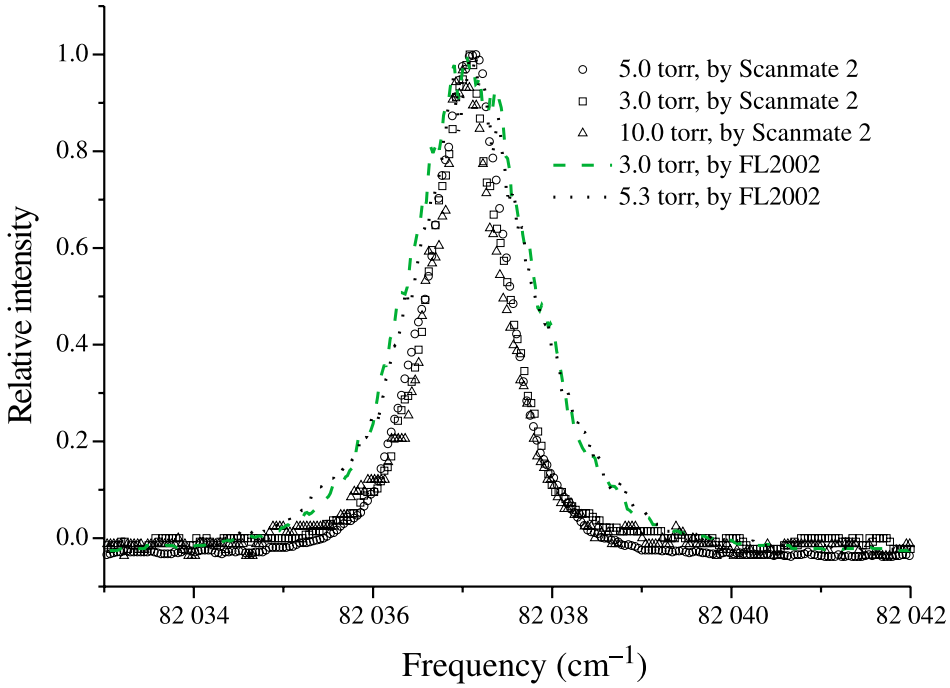
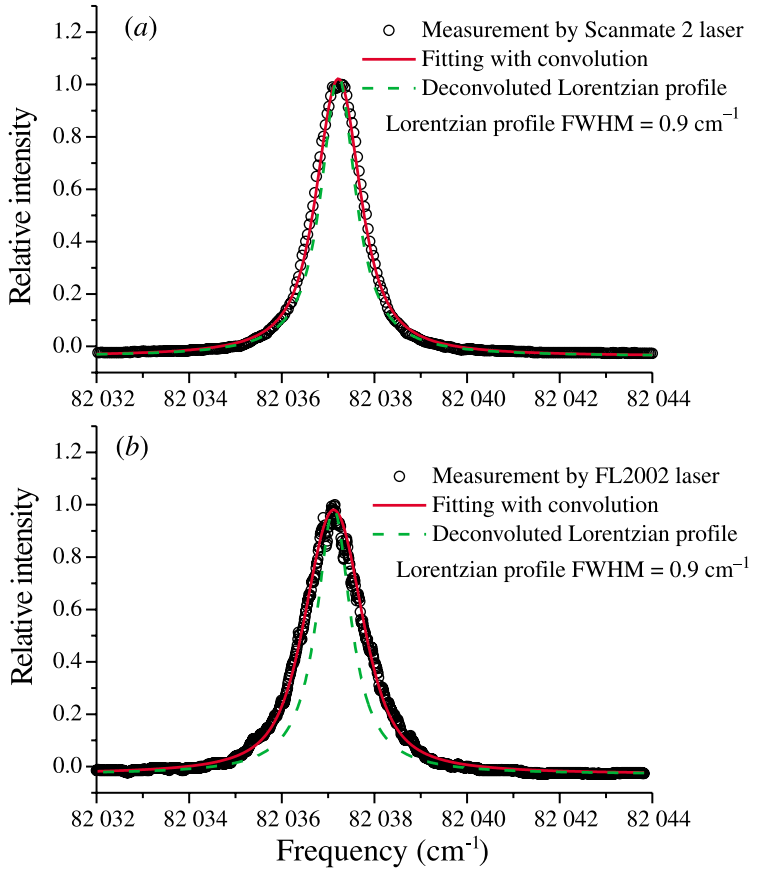


Fig. 4. The convolution fits of the experimental line profiles and the deconvoluted Lorentzian profile with a FWHM of 0.9 cm^{-1} in both cases: (*a*) for measurements with the Scanmate 2 dye laser, whose fundamental bandwidth is 0.09 cm^{-1}, and (*b*) for measurements with the FL2002 dye laser, whose fundamental bandwidth is 0.16 cm^{-1}.



© 2004 NRC Canada

$^1F_3$ levels excited from the O($^1D_2$) state by two-photon absorption. They evaluated the autoionization lifetimes of the $^1P_1$ and $^1F_3$ levels and found that they were longer than 3×10^{-10} and 5.8×10^{-10} s, respectively. Smith and co-workers (6, 7) have done a considerable amount of work on the autoionizing states of atomic oxygen. They measured the autoionization lifetimes for the ($^2D^o$)3p ^{1,3}P and ($^2D^o$)3p ^{3}D, ^{3}F states by measuring the Rabi oscillations that were induced when the atoms were excited from the $^3P_2$ ground state by the multiphoton process. The autoionization lifetimes are on the order of 10^{-10} s for all the states except the ($^2D^o$)3p ^{3}P state, which has a 6-fs lifetime (7). More recently, single-photon ionization of atomic singlet oxygen O ($^1D_2$) was investigated by Flesch et al. (24). The photoionization efficiency spectrum was recorded between the onset of the first ($^4S^o$) and the second ($^2D^o$) ionization thresholds. However, no lifetimes were reported in this paper.

Within the *LS* coupling approximation, direct photoionization to the $^4S^o + e^-$ state between the first and the second ionization threshold (to ($^2D^o$)) is optically forbidden from the singlet states of the atom, since it violates the spin conservation rule. Thus, the only way these states can be ionized is via autoionization to $^4S^o$ as a result of spin–orbit, spin–spin, or other possible weaker interactions that couple atomic states with different spins (25–27). As discussed above, the lifetimes of the singlet states for atomic oxygen were found to be of the order of 10^{-10} s. In the current measurements for singlet atomic sulfur $^1D_2^o$, the lifetime was determined as 5.9 ps. This much faster autoionization rate for sulfur $^1D_2^o$ compared with singlet oxygen atoms can be understood in terms of spin–orbit and spin–spin interactions. The mass of the sulfur atom is much greater than that of the oxygen atom; one would therefore expect that spin–orbit interaction in the heavier sulfur atom would be much stronger than in the oxygen atom. This is seen in the spin–orbit splittings that are observed in the $^3P_{2,1,0}$ ground state of the sulfur atom, which are 396 and 177 cm^{-1} for $^3P_1$–$^3P_2$ and $^3P_0$–$^3P_1$, respectively, whereas they are only 158 and 69 cm^{-1} for the oxygen atom (28). The spin–spin interaction can also play an important role in the autoionization process. In the highly excited states, mixing between states with different spin is expected because of spin–spin interaction. The existence of state mixing between the very rapidly ionizing triplet state and the singlet state could promote the autoionizing rate of the singlet state.

The rate of autoionization, and the corresponding lifetime, can be estimated by the Golden Rule formula,

$$[1] \qquad k = \frac{2\pi}{\hbar}\left|V_{if}\right|^2 \rho_f$$

where V_{if} is the transition matrix element and ρ_f is the density of the final states. The zeroth-order initial and final states are described in a SCF Breit–Pauli approximation (29) by neglecting spin–spin and spin–orbit interactions. In the initial state $3s^2 3p^3(^2D^o)4d$ ($^1D_2^o$), prepared by single-photon excitation, one electron occupies a 4d orbital, and the rest form an ionic core, whose electronic configuration, $3s^2 3p^3(^2D^o)$, corresponds to an excited state of the S^+ ion. In the absence of spin–spin and spin–orbit interactions, the excited state is stable, with one 4d electron moving in a Coulomb field of the ionic core. The additional interaction between this electron and the core results in their energy exchange, a process in which the 4d electron is excited to an unbound state with kinetic energy sufficient to escape the Coulomb cage of the core, while the ionic core itself relaxes to its ground state of $^4S_{3/2}$. In the latter process, one of the electrons in the doubly occupied p orbital of the $3s^2 3p^3(^2D^o)$ configuration is transferred to an empty p orbital, simultaneously changing its spin, so that in the final state of the core all three electrons occupy three different p orbitals and have parallel spins, yielding $3s^2 3p^3$ $S^+(^4S^o_{3/2})$. Owing to the exchange effects, the same final state can be obtained by a transfer of the 4d electron to an empty orbital of the 3p shell, while one of the paired electrons from the 3p shell of the core is promoted to an unbound state and ejected from the atom. However, the contributions of the exchange effects in the latter type of interactions are typically small (29). The exact evaluation of the rate of the described process requires rather sophisticated computational work as, e.g., in ref. 30. However even a rough estimate described in the *Appendix* gives FWHM values in the range 10–40 cm^{-1}, which is about an order of magnitude higher than the experimental measurements.

Conclusion

For the first time, we are able to record the $3s^2 3p^3 4d$ $^1D_2^o \leftarrow 3s^2 3p^4$ $^1D_2$ transition line width of atomic sulfur using single VUV photon excitation by monitoring the S^+ signal in a TOF-MS while scanning the excitation wavelength. The deconvolution of the measured excitation line shape with the finite laser bandwidth yields a natural line width (FWHM) of 0.90 ± 0.05 cm^{-1}, from which the autoionization lifetime of the neutral superexcited state $3s^2 3p^3 4d$ $^1D_2^o$ is found to be 5.90 ± 0.30 ps. These results show that this is a general method to measure the lifetimes of atomic autoionization states with strong spin–orbit and spin–spin interactions.

Acknowledgements

This work was supported by the National Science Foundation (NSF) (grant No. CHE-0100965) and NASA (grant No. NAG5–12124).

References

1. A.L. Broadfoot, B.R Sandel, D.E. Shamansky, J.C. McConnell, G.R. Smith, J.B. Holberg, S.K. Atreya, T.M. Donahue, D.F. Strobel, and J.L. Bertaux. Geophys. Res. **86**, 8259 (1981).
2. D.E. Shemansky and G.R. Smith. Geophys. Res. **86**, 9179 (1981).
3. G. Tondello. Astophys. J. **172**, 771 (1972).
4. V.N. Sarma and Y.N. Joshi. Physica C, **123**, 349 (1984).
5. S.T. Gibson, J.P. Greene, B. Ruščić, and J. Berkowitz. J. Phys. B, **19**, 2825 (1986).
6. A.V. Smith and T.D. Raymond. Opt. Lett. **16**, 267 (1991).
7. A.V. Smith, T.D. Raymond, and M.E. Riley. Phys. Rev. A, **45**, 4688 (1992).
8. E.J. Knystautas, M. Brochu, and R. Drouin. Can. J. Spectrosc. **18**, 143 (1973).
9. S.C. Yang, A. Freedman, M. Kawasaki, and R. Bersohn. J. Chem. Phys. **72**, 4058 (1980).

© 2004 NRC Canada

10. V.R. McCrary, R. Lu, D. Zakheim, J.A. Russell, J.B. Halpern, and W.M. Jackson. J. Chem. Phys. **83**, 3481 (1985).
11. W.-B. Tzeng, H.-M. Yin, W.-Y. Leung, J.-Y. Lou, S. Nourbakhsh, G.D. Flesch, and C.Y. Ng. J. Chem. Phys. **88**, 1658 (1988).
12. J.G. Frey and P. Felder. Chem. Phys. **202**, 397 (1996).
13. W.S. McGivern, O. Sokhabi, A.H. Rivi, A.G. Suits, and S.W. North. J. Chem. Phys. **112**, 5301 (2000).
14. T.N. Kitopoulos, C.R. Gebhardt, and T.P. Rakitzis. J. Chem. Phys. **115**, 9727 (2001).
15. J. Huang, D. Xu, J.S. Francisco, and W.M. Jackson. J. Chem. Phys. **119**, 3661 (2003), and refs. cited therein.
16. J.W. Rabalais, J.M. McDonald, V. Scherr, and S.P. McGlynn. Chem. Rev. **71**, 73 (1971).
17. B. Edlen and K. Sven. Vetenskapsakad. Handl. **20**, 10 (1943).
18. K.B.S. Eriksson and H.B.S. Isberg. Ark. Fys. **37**, 221 (1968).
19. R.E. Huffman, J.C. Larrabee, and Y. Tanaka. J. Chem. Phys. **47**, 4462 (1967).
20. P.M. Dehmer, J. Berkowitz, and W.A. Chupka. J. Chem. Phys. **59**, 5777 (1973).
21. P.M. Dehmer and W.A. Chupka. J. Chem. Phys. **62**, 584 (1975).
22. P.M. Dehmer, W.L. Luken, and W.A. Chupka. J. Chem. Phys. **67**, 195 (1977).
23. S.T. Pratt, P.M. Dehmer, and J.L. Dehmer. Phys. Rev. A, **43**, 282 (1991).
24. R. Flesch, M.C. Schurmann, J. Plenge, H. Meiss, J. Hunnekuhl, and E. Ruhl. Phys. Rev. A, **62**, 52 723 (2000).
25. E.U. Condon and G.H. Shortley. The theory of atomic spectra. Cambridge University Press, Cambridge, UK. 1979.
26. P. Feldman and R. Novick. Phys. Rev. **160**, 143 (1967).
27. M.E. Rudd and K. Smith. Phys. Rev. **169**, 79 (1968).
28. NIST atomic spectra database data [online]. Available from http://physics.nist.gov [accessed 24 February 2004].
29. H.A. Bethe and E.E. Salpeter. Quantum mechanics of one and two electron atoms. Plenum, New York. 1977.
30. H.P. Saha and D. Lin. Phys. Rev. A, **63**, 042 701 (2001).

Appendix A

Here, we estimate the order of magnitude of the autoionization rate of the process described in the text, using experimental data for typical spin–orbit interactions in sulfur. The rate is given by the Golden Rule formula,

$$[A1] \quad k = \frac{2\pi}{\hbar}\left|V_{\mathrm{if}}\right|^2 \rho_{\mathrm{f}}$$

where V_{if} is the transition matrix element, and ρ_{f} is the density of the final states. The final states result from the ionized electron moving in the field of the ionic core. The number of such states is given by the usual expression:

$$[A2] \quad \mathrm{d}n = V\frac{\mathrm{d}\vec{p}}{(2\pi\hbar)^3}$$

where V is the volume of the system, and $\vec{p}$ is the momentum of the ejected electron. Integration over all directions gives the density of states,

$$[A3] \quad \rho = V\frac{m}{\pi^2\hbar^3}\sqrt{\frac{mE}{2}}$$

where E is the kinetic energy of the ejected electron ($E(^1\mathrm{D}^{\mathrm{o}}_2)$ – IP; about 1 eV). The exit state of the ejected electron should be described by a wave function of an electron moving in the field of the ionic core. For a rough estimate, however, we will take

$$[A4] \quad \left|\vec{p}\right\rangle = \frac{1}{\sqrt{V}}\exp\left(\frac{i\vec{p}\vec{r}}{\hbar}\right)$$

For an estimate of the matrix element, we can then write

$$[A5] \quad V_{\mathrm{if}} = \left\langle \varphi^{\downarrow}_{3px}(1)\,\varphi^{\uparrow}_{4d}(2)\left|\hat{V}(1,2)\right|\varphi^{\uparrow}_{3pz}(1)\vec{p}(2)\right\rangle \approx \overline{V}_{12}\frac{a_{4d}^{3/2}}{\sqrt{V}}$$

where a_{4d} is the radius of the 4*d* orbital, and $\overline{V}_{12}$ is the average spin–spin and spin–orbit interactions between the 4*d* electron and electrons of the 3*p* shell of the core. The exchange effects should not change the order of magnitude of the above estimate. Here, we neglect factor $2\sqrt{2}/\pi$, which is on the order of unity. Thus, for the rate we roughly have

$$[A6] \quad k \approx \frac{\overline{V}_{12}^2}{2\hbar}\frac{a_{4d}^2 m}{\hbar^2}\frac{a_{4d}\sqrt{mE}}{\hbar}$$

The last term in the above expression is roughly the angular momentum of the ejected electron; since the kinetic energy of the electron is about 1 eV, the last term gives a factor close to 4. The second term is the inverse kinetic energy of the 4*d* electron, the order of magnitude of which is also 1 eV. A typical value of spin–orbit interaction in the sulfur atom can be estimated from the splittings of the $^3\mathrm{P}_2$–$^3\mathrm{P}_1$ (396 cm^{-1}) and $^3\mathrm{P}_1$–$^3\mathrm{P}_0$ (177 cm^{-1}) energy levels of the ground state (A1). For $\overline{V}_{12}$ = 200 cm^{-1}, the FWHM is estimated to be 10 cm^{-1}; for $\overline{V}_{12}$ = 400 cm^{-1}, FWHM = 40 cm^{-1}. Given the crude nature of the estimate, it is not surprising that the estimation is an order of magnitude higher than the observed value. Note that the term $\overline{V}_{12}$ in eq. [A5] should be the interaction between the 4*d* Rydberg electron and the 3*p* core electrons. Considering the large diameter of the Rydberg orbital, the interaction $\overline{V}_{12}$ should be much weaker than that in the ground state S(^{3}P). Using the measured line width of 0.9 cm^{-1}, we can estimate $\overline{V}_{12}$ to be 60 cm^{-1}.

References

A1. NIST atomic spectra database data [online]. Available from http://physics.nist.gov [accessed 24 February 2004].

© 2004 NRC Canada

Transition state dynamics and a QM/MM model for the $Cl^- + C_2H_5Cl$ S_N2 reaction[1]

Lipeng Sun, Eunkyung Chang, Kihyung Song, and William L. Hase

Abstract: A MP2/6-31G* direct dynamics simulation is used to study the dynamics of the central barrier $[Cl\text{-}C_2H_5\text{-}Cl]^-$ for the $Cl^- + C_2H_5$ S_N2 reaction. The majority of the trajectories move off the central barrier to form the Cl^-–C_2H_5Cl complex and appear to undergo efficient IVR as assumed by RRKM theory. However, some of the trajectories move directly to products without forming the complex, a non-RRKM result. A hydrogen atom link-atom QM/MM model is described for studying the dynamics of $[X\text{-}CH_2R\text{-}Y]^-$ central barriers with the -R substituent. The model is used to calculate vibrational frequencies for the $[Cl\text{-}C_2H_5\text{-}Cl]^-$ central barrier.

Key words: S_N2 reaction dynamics, RRKM theory, QM/MM model, central barrier dynamics, direct dynamics classical trajectories.

Résumé : On utilise une simulation dynamique directe MP2/6-31G* pour étudier la dynamique de la barrière centrale $[Cl\text{-}C_2H_5\text{-}Cl]^-$ de la réaction S_N2 $Cl^- + C_2H_5$. La majorité des trajectoires se déplacent à partir de la barrière centrale pour former le complexe $Cl^$–C_2H_5Cl et elles semblent subir un « IVR » efficace, tel que suggéré par la théorie « RRKM ». Toutefois, certaines de ces trajectoires se déplacent directement vers les produits sans former de complexe, ce qui est un résultat qui ne correspond pas à la théorie de RRKM. On décrit un modèle QM/MM d'atome d'hydrogène agissant comme atome liant pour étudier la dynamique de $[X\text{-}CH_2R\text{-}Y]^-$ comportant un substituant -R. On a utilisé le modèle pour calculer les fréquences vibrationnelles de la barrière centrale de $[Cl\text{-}C_2H_5\text{-}Cl]^-$.

Mots clés : dynamique d'une réaction S_N2, théorie de RRKM, modèle QM/MM, dynamique de la barrière centrale, trajectoires classiques.

[Traduit par la Rédaction]

Introduction

Bimolecular nucleophilic substitution (S_N2) reactions of the type

[1] $$X^- + CH_3Y \rightarrow XCH_3 + Y^-$$

are of central importance in gas-phase ion chemistry (1–4) and organic reaction mechanisms (5). Extensive investigations, both computational–theoretical (6–19) and experimental (20–32), have been carried out to understand the energies and dynamics of these reactions. Given the prominence of statistical theories in chemical reaction dynamics and kinetics (33), it was natural to use these theories to model S_N2 reaction rates (1). However, recent detailed examinations of S_N2 reactions of the type in eq. [1] have discovered a range of important nonstatistical attributes (7, 8, 11–18, 27–32) arising from weak couplings between the X^--CH_3Y intermolecular and CH_3Y intramolecular modes. Trajectories calculated for the $Cl^- + CH_3Cl$ and $Cl^- + CH_3Br$ S_N2 reactions become trapped in the central barrier region of the potential energy surface, with concomitant recrossing of the barrier (8, 11, 15). The former suggests that vibrational states prepared in the central barrier region may be sufficiently long-lived to resolve their spectra (34), while the latter indicates that crossing the central barrier may not be the rate-controlling step, as assumed by statistical theories for many S_N2 reactions (1, 10).

In a previous classical trajectory study (15) of the $Cl^- + CH_3Cl$ reaction, 10 trajectories were calculated by sampling 300 K Boltzmann distributions at the $[Cl\text{-}CH_3\text{-}Cl]^-$ central barrier for the reaction coordinate, the 11 orthogonal normal modes of vibration, and the three external rotational degrees of freedom. The Born–Oppenheimer direct dynamics method (35) was used to calculate the trajectories, with the potential energy and its gradient obtained directly from the MP2/6-31G* level of theory. Each of the 10 trajectories initiated at the central barrier was integrated for 3 ps in both forward and backward directions off the barrier. The RRKM statistical theory of chemical kinetics (36) assumes the trajectories move off the barrier and form a Cl^-–CH_3Cl com-

Received 3 November 2003. Published on the NRC Research Press Web site at http://canjchem.nrc.ca on 26 August 2004.

L. Sun. Department of Chemistry, Northwestern University, Evanston, IL 60208–3113, USA.
E. Chang and K. Song. Department of Chemistry, Korea National University of Education, Chongwon, Chungbuk 363–791 Korea.
W.L. Hase.[2] Department of Chemistry and Biochemistry, Texas Tech University, Lubbock, TX 79409–1061, USA.

[1]This article is part of a Special Issue dedicated to the memory of Professor Gerhard Herzberg.
[2]Corresponding author: (e-mail: bill.hase@ttu.edu).

 doi: 10.1139/V04-082 © 2004 NRC Canada

plex with an average lifetime (τ) equal to the anharmonic RRKM value of 4 ps. For the integration time (t) of 3 ps, RRKM predicts that 50% (i.e., $\exp(-t/\tau)$) of these complexes should form Cl^- + CH_3Cl products. In contrast to this prediction, not one of the twenty 3 ps forward and backward trajectories off the central barrier formed products. Instead, five of the 10 trajectories initiated at the central barrier started in one Cl^-–CH_3Cl complex and ended in another, while the remaining five trajectories started and ended in the same complex. Many of the trajectories exhibited a regular type motion, with well-defined frequencies and extensive recrossings of the central barrier. The barrier recrossing dynamics observed for these direct dynamics trajectories is very similar to that found for trajectories calculated on an analytic potential energy function fit to HF/6-31G* calculations (11).

A total of 29 central barrier crossings occurred for the 10 direct dynamics trajectories, a result much different than the predictions of the RRKM and transition state (TST) theories. Because of the higher potential energy at the central barrier in comparison to that for the products (i.e., ~3 kcal/mol) (37) and the much tighter transition state at the central barrier compared to that for dissociation, RRKM theory predicts that the Cl^-–CH_3Cl complex preferentially dissociates to Cl^- + CH_3Cl with negligible recrossing of the central barrier. Thus, crossing the central barrier is predicted to be the rate-controlling step of the S_N2 reaction, as assumed by TST.

In the first part of this article, the $[Cl\text{-}C_2H_5\text{-}Cl]^-$ central barrier dynamics of the Cl^- + C_2H_5Cl S_N2 reaction was studied for comparison with the above $[Cl\text{-}CH_3\text{-}Cl]^-$ central barrier dynamics. MP2/6-31G* direct dynamics was also used for this study. It is of interest to determine the effect of replacing one of the structureless H-atoms in $[Cl\text{-}CH_3\text{-}Cl]^-$ with a $-CH_3$ group. This changes the symmetry of the system, which influences the dynamics. In addition, the $-CH_3$ group may serve as an energy bath during the course of the reaction, which may also affect the reaction dynamics. This study of the $[Cl\text{-}C_2H_5\text{-}Cl]^-$ central barrier dynamics will lead to a deeper understanding of the effect of a -R side chain on the dynamics of Cl^- + CH_2RCl S_N2 reactions. It is noteworthy that Brauman and co-workers (38) found that the kinetics for the Cl^- + $ClCH_2CN$ S_N2 reaction, with the -CN substituent, agrees with the RRKM theory.

Direct dynamics simulations often require a prohibitive amount of computer time as the number of atoms in the chemical reaction increases (35). An approach to treat such large systems by direct dynamics is to represent the atoms most intimately involved in the chemical reaction by a quantum mechanical (QM) electronic structure theory and the remaining atoms by a molecular mechanical (MM) analytic potential energy function. This QM/MM model (39) may be used to replace one or more of the H-atoms of the CH_3Y reactant in eq. [1] with -R substituents, by using the MM component of the model to represent the potential energy of the substituents. In this manner, a direct dynamics simulation may be used to study how a S_N2 reaction's central barrier dynamics is affected by the number and type of substituents on the CH_3Y reactant. In the second part of this paper, a link-atom QM/MM model is presented and its application to the Cl^- + C_2H_5Cl S_N2 reaction, with $-CH_3$ represented by a MM potential, is described.

Transition state dynamics for the Cl^- + C_2H_5Cl reaction

Computational procedure

Electronic structure theory

The MP2/6-31G* level of theory was used to calculate the direct dynamics trajectories. In previous work (40, 41), MP2/6-31G* and other ab initio theories (e.g., MP2, MP3, and MP4 with 6-311+G(2d) and 6-31+G* basis sets) (40) were compared for the Cl^- + $C_2H_5Cl^-$ reaction. The MP2/6-31G* geometries and energies for stationary points on the potential energy surface are in good agreement with experiment and the higher-level ab initio calculations (40). Though MP2/6-31G* has not been compared with CCSD(T)/large basis set calculations for the Cl^- + C_2H_5Cl reaction, they have been compared for Cl^- + CH_3Cl (15). For the latter reaction, the MP2/6-31G* classical potential energy barrier of 4.54 kcal/mol is in good agreement with the CCSD(T) value of 3.16 kcal/mol (37). For this reaction, MP2/6-31G* also gave a structure and vibrational frequencies for the $[Cl\text{-}CH_3\text{-}Cl]^-$ central barrier (15) in excellent agreement with the CCSD(T) values (37) (i.e., the Cl—C bond lengths of the two theories agree to within 0.005 Å and the symmetric Cl-C and C-H stretch frequencies differ by only 6 and 65 cm^{-1}, respectively).

The MP2/6-31G* classical barrier for the Cl^- + C_2H_5Cl reaction is 8.39 kcal/mol (i.e., 3.85 kcal/mol higher than the Cl^- + CH_3Cl barrier). The MP2, MP3, and MP4 theories with the 6-311+G(2d) basis set gave 3.0–3.4 kcal/mol for this barrier difference (40). Though there are no definitive values for the Cl^- + CH_3Cl and Cl^- + C_2H_5Cl barrier heights, experimental values in the range of 1.1–3.4 kcal/mol have been reported (23, 24, 42) for the difference in the barrier heights for the similar reactions Cl^- + CH_3Br and Cl^- + C_2H_5Br. The MP2/6-31G* value for the Cl^- + $C_2H_5Cl \rightarrow Cl^-\text{-}C_2H_5Cl$ complexation energy is 12.3 kcal/mol, very similar to the 11.0 kcal/mol value for Cl^- + CH_3Cl. The MP2, MP3, and MP4 theories with the 6-311+G(2d) basis set (40) give 11.5–11.8 kcal/mol for the Cl^- + C_2H_5Cl complexation energy.

At the MP2/6-31G* level of theory, the Cl^- + $C_2H_5Cl^-$ central barrier has an asymmetric structure (40) with C—Cl bonds that have slightly different lengths of 2.342 and 2.369 Å. One of the C—H bonds of the $-CH_3$ group eclipses one of the C—Cl bonds. However, apparently there is no strong preference for a specific internal rotation orientation of the $-CH_3$ group. Rotating the $-CH_3$ group by 30° so that the central barrier has a plane of symmetry, which includes the two carbon atoms, the two hydrogens on the reacting carbon, and one hydrogen on $-CH_3$, forms a second-order saddle point only 0.11 kcal/mol higher in energy (40).

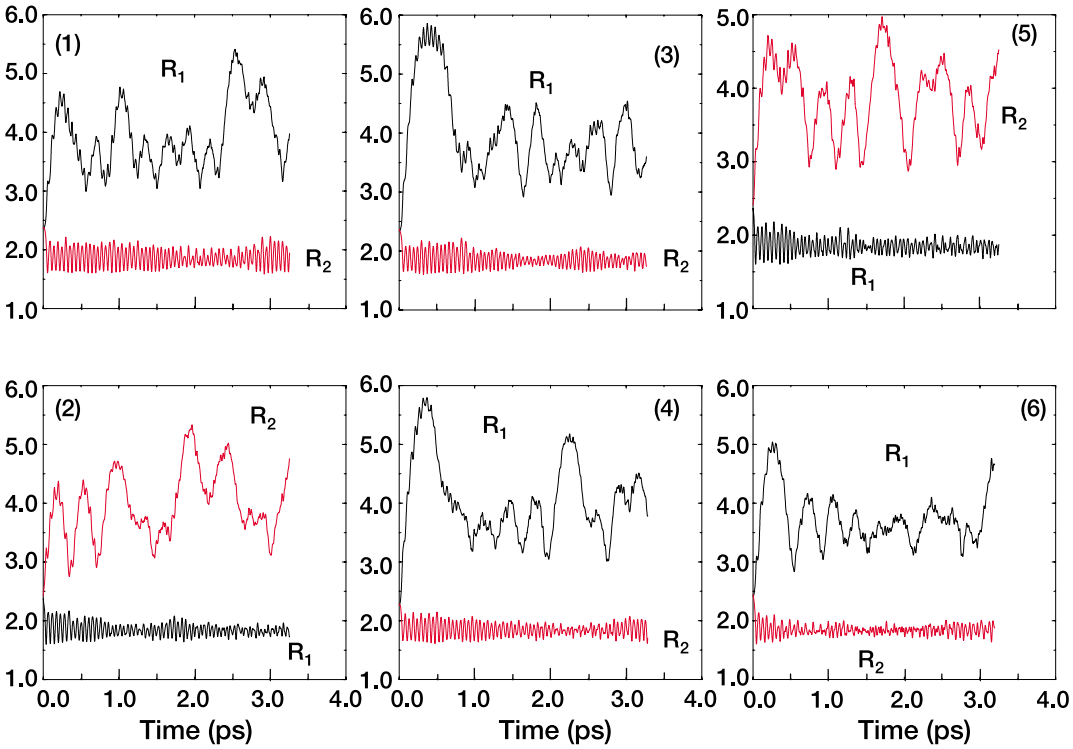
The conclusion reached from the above comparisons between MP2/6-31G* and other electronic structure theories and experiment, for the Cl^- + $C_2H_5Cl^-$ reaction and related S_N2 reactions, is that MP2/6-31G* theory gives a good representation of the Cl^- + $C_2H_5Cl^-$ potential energy surface and is a practical approach for performing a direct dynamics simulation of the $[Cl\text{-}C_2H_5\text{-}Cl]^-$ central barrier dynamics.

Trajectory initial conditions and calculations

The direct dynamics $[Cl\text{-}C_2H_5\text{-}Cl]^-$ barrier excitation tra-

© 2004 NRC Canada

Fig. 1. The two C—Cl bond lengths (R_1 and R_2) in Å vs. time (ps) for six of the [Cl-C_2H_5-Cl]$^-$ barrier excitation trajectories.



jectories were calculated by interfacing (43) the VENUS96 (44) chemical dynamics and GAUSSIAN98 (45) electronic structure programs. Hessian updating (46) and an efficient predictor–corrector algorithm (47) were used to numerically integrate the classical equations of motion. Energy conservation at the end of the integration varied from 0.03–0.17 kcal/mol, out of a total energy of 45–48 kcal/mol.

Quasiclassical sampling (48), which includes zero-point energy, was used to select initial conditions for 68 trajectories from the 300 K Boltzmann energy distributions at the central barrier for the reaction coordinate, the 11 orthogonal normal modes of vibration, and the three external rotation degrees of freedom. The sign (i.e., positive or negative) of the reaction coordinate momentum was chosen randomly so that initially the trajectory could move towards either Cl^-–C_2H_5Cl potential energy well. The trajectories were integrated for 3.2–3.4 ps or until the Cl^- + C_2H_5Cl separation reached 16 Å for a dissociation event. It required about 140 CPU-hours to integrate a trajectory for 3.2 ps on a Pentium IV/1.9 GHz single processor.

Direct dynamics results

Plots of the Cl—Cl bond lengths vs. time for the first 10 [Cl-C_2H_5-Cl]$^-$ barrier excitation trajectories, which were calculated, are given in Figs. 1 and 2. Eight of the trajectories became immediately trapped in the ion-dipole well of the Cl^-–C_2H_5Cl complex as they moved off the central barrier. One of the trajectories directly dissociates to products, within 1.2 ps, without being trapped in the ion-dipole potential energy well. For another trajectory, the Cl^- ion leaves C_2H_5Cl and reaches a center of mass separation of 12 Å and then returns to the potential energy well.

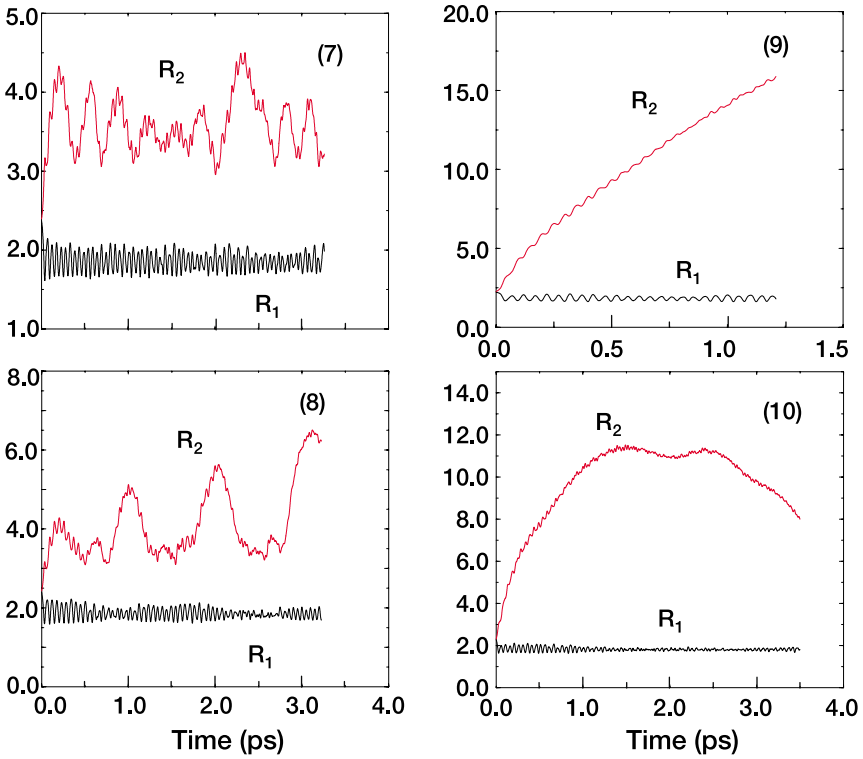
The dynamics illustrated in Figs. 1 and 2 are representative of those for the complete batch of 68 trajectories. Sixty-two of the trajectories moved off the barrier and became immediately trapped in one of the Cl^-–C_2H_5Cl complexes. One of these trajectories dissociated with a lifetime of 3.3 ps and two had large Cl^- + C_2H_5Cl center-of-mass separations of 14.5 and 15.3 Å when they were terminated. As discussed above, another trajectory became trapped in a Cl^-–C_2H_5Cl complex and did not dissociate, but initially moved directly towards products, attaining a center-of-mass separation of 12 Å. Three trajectories directly formed products with lifetimes of 1.2 ps or less, without forming a Cl^-–C_2H_5Cl complex. Two trajectories had a single barrier recrossing and remained trapped in a Cl^-–C_2H_5Cl complex. For one of these, the center-of-mass separation between the reaction products was 11.8 Å when the trajectory was terminated.

The [Cl-C_2H_5-Cl]$^-$ barrier excitation trajectories do not exhibit the regular type motion observed for the [Cl-CH_3-Cl]$^-$ system. The former trajectories do not remain locked in a nonstatistical motion giving rise to extensive recrossings of the central barrier. For the 62 trajectories that leave the central barrier and immediately form the Cl^-–C_2H_5Cl complex, the intermolecular Cl^--C and intramolecular Cl-C stretch modes undergo irregular motion as a result of energy transfer to and from these modes. Such efficient energy transfer is consistent with the RRKM theory of unimolecular dynamics, which assumes the vibrational states of the energized species are populated in a statistical way (36).

Though the Cl^-–C_2H_5Cl complexes exhibit statistical type behavior, strong evidence remains for a nonstatistical component in the Cl^- + C_2H_5Cl S_N2 reaction. Four of the 68 trajectories are inconsistent with the RRKM model of unimolecular kinetics, which assumes the Cl^-–C_2H_5Cl complex should be formed as the trajectory moves off the central barrier as a result of strong coupling between the reaction coordinate motion and the system's other degrees of freedom.

© 2004 NRC Canada

Fig. 2. Same as for Fig. 1, but for the remaining four trajectories.



For these four trajectories, this initial coupling is weak. Three trajectories go directly to products without forming a complex, as depicted by trajectory (9) in Fig. 2. Though another trajectory, i.e., number (10) in Fig. 2, returns to the ion-dipole complex, initially a sufficient amount of translational energy remains in the Cl^--C stretch motion to extend this bond to about 12 Å. The implication from these trajectories is that for the 300 K temperature considered here a fraction of the $Cl^- + C_2H_5Cl$ reaction will occur with trajectories moving directly from the $[Cl\text{-}C_2H_5Cl]^-$ central barrier to $Cl^- + C_2H_5Cl^-$ products without becoming trapped in the exit channel $Cl^–C_2H_5Cl$ ion-dipole complex. This fraction is expected to increase as the temperature or energy of the reactive system is increased (2, 4). In addition, two trajectories recross the high central barrier, a result inconsistent with both RRKM and TST (15).

A link-atom QM/MM model for S_N2 reactions

A QM/MM model for a chemical reaction or molecule partitions the system into one part whose potential energy is represented by a quantum mechanical (QM) electronic structure theory and the remainder by a molecular mechanical (MM) analytic potential energy function (39). Often the QM/MM boundary cuts through one or more chemical bonds. To illustrate, one might construct a QM/MM model for *n*-hexane (C_6H_{14}) with the C_2H_5· moiety represented by QM and C_4H_9· by MM. The QM/MM boundary is a C—C bond and it is necessary to saturate the valency of C_2H_5·. One way to accomplish this is to use the "link-atom" method (49–51), in which an unphysical atom is added to the boundary QM atom. Typically a hydrogen atom is chosen as the link atom since the broken bond is usually a σ bond (e.g., a C—C bond). The link atom is invisible to the MM atoms, since there are no interactions between the link and MM atoms. MM potentials are used to connect the QM and MM atoms at the boundary. For the above C_2H_5· and C_4H_9· QM and MM components, a stretching potential is added to connect the two C atoms, and bending and torsional analytic functions are used to represent the angular and internal rotational potentials at the QM/MM boundary.

In this work, an H atom link-atom model is described for a QM/MM boundary at a C—C bond. This C—C bond is constrained to lie along the C—H bond of the link atom, with the C—C bond length constrained to equal the length of this C—H bond plus a constant additional length. As a result of the similarity between both stretching and bending force constants for C—C and C—H bonds (52), only small forces must be added, or minor scaling of the force constants performed, (53) to obtain accurate vibrational frequencies for the complete QM/MM system.

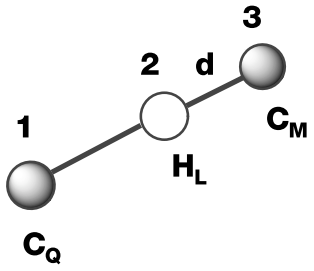
Details of the model

The link-atom model described here for a QM/MM boundary that cuts through a C—C covalent single bond is depicted in Fig. 3. To avoid introducing additional degrees of freedom, the link hydrogen atom H_L was constrained on the C—C bond. The distance between H_L and the MM carbon C_M was kept fixed. Therefore, the motion of H_L and C_M was synchronized. The relationship between the force on H_L and C_M were derived and shown in the next section.

Let $\vec{r}_1$, $\vec{r}_2$, $\vec{r}_3$ denote the positions of the QM carbon C_Q, H_L, and C_M, respectively. The C_Q—H_L and H_L—C_M bonds

© 2004 NRC Canada

Fig. 3. A H-atom link-atom model for a QM/MM boundary that cuts through a C—C bond.



are then $\vec{r}_{12} = \vec{r}_2 - \vec{r}_1$ and $\vec{r}_{23} = \vec{r}_3 - \vec{r}_2 = \vec{d}$. Their components on the x-axis are

$$[2] \quad x_3 - x_2 = d\ \sin\theta\ \cos\phi$$

$$[3] \quad x_2 - x_1 = r_{12}\ \sin\theta\ \cos\phi$$

where θ and ϕ are the polar angles that determine the orientation of C_Q-H_L-C_M. The first- and second-order time derivatives of eqs. [2] and [3] are

$$[4] \quad \dot{x}_3 - \dot{x}_2 = d(\cos\theta\cos\phi\dot{\theta} - \sin\phi\sin\theta\dot{\phi})$$

$$[5] \quad \ddot{x}_3 - \ddot{x}_2 = d[\cos\theta\cos\phi\ddot{\theta} - \sin\phi\sin\theta\ddot{\phi} - \sin\theta\cos\phi(\dot{\theta}^2 + \dot{\phi}^2) - 2\sin\phi\cos\theta\dot{\theta}\dot{\phi}]$$

$$[6] \quad \dot{x}_2 - \dot{x}_1 = r_{12}\sin\theta\cos\phi + r_{12}(\cos\theta\cos\phi\dot{\theta} - \sin\phi\sin\theta\dot{\phi})$$

$$[7] \quad \ddot{x}_3 - \ddot{x}_2 = r_{12}[\cos\theta\cos\phi\ddot{\theta} - \sin\phi\sin\theta\ddot{\phi} - \sin\theta\cos\phi(\dot{\theta}^2 + \dot{\phi}^2) - 2\sin\phi\cos\theta\dot{\theta}\dot{\phi}] + \ddot{r}_{12}\sin\theta\cos\theta + \cos\theta(\sin\phi + \cos\phi)\dot{r}_{12}\dot{\theta}_{12} - \sin\theta(\sin\phi + \cos\phi)\dot{r}_{12}\dot{\phi}$$

Combining eqs. [4]–[7] one obtains

$$[8] \quad \ddot{x}_2 - \ddot{x}_1 = \ddot{r}_{12}\sin\theta\cos\phi + \cos\theta(\sin\phi + \cos\phi)\dot{r}_{12}\dot{\theta} - \sin\theta(\sin\phi + \cos\phi)\dot{r}\dot{\phi} + \frac{r_{12}}{d}(\ddot{x}_3 - \ddot{x}_2)$$

from which the x-component of the force on C_M can be obtained as

$$[9] \quad -\frac{\partial V}{\partial x_3} = \frac{(d + r_{12})}{r_{12}}\frac{m}{M}\left(-\frac{\partial V}{\partial x_2}\right) - \frac{d}{r_{12}}\left(\frac{\partial V}{\partial x_1}\right) + \frac{d}{r_{12}}m\,(\ddot{r}_{12}\sin\theta\cos\phi + 2\cos\phi\cos\theta\dot{r}\dot{\theta} + 2\sin\theta\sin\phi\dot{r}\dot{\phi})$$

where the m and M are the atomic masses of carbon and hydrogen. Similarly, the force component of C_M on the y-axis and z-axis can be derived, i.e.,

$$[10] \quad -\frac{\partial V}{\partial y_3} = \frac{(d + r_{12})}{r_{12}}\frac{m}{M}\left(-\frac{\partial V}{\partial y_2}\right) - \frac{d}{r_{12}}\left(\frac{\partial V}{\partial y_1}\right) + \frac{d}{r_{12}}m\,(\ddot{r}_{12}\sin\theta\sin\phi + 2\sin\phi\cos\theta\dot{r}\dot{\theta} + 2\sin\theta\cos\phi\dot{r}_{12}\dot{\phi})$$

$$[11] \quad -\frac{\partial V}{\partial z_3} = \frac{(d + r_{12})}{r_{12}}\frac{m}{M}\left(-\frac{\partial V}{\partial z_2}\right) - \frac{d}{r_{12}}\left(\frac{\partial V}{\partial z_1}\right) + \frac{d}{r_{12}}m\,(\ddot{r}_{12}\cos\theta - 2\sin\theta\dot{r}_{12}\dot{\theta})$$

In most cases the classical trajectory is integrated in a Cartesian coordinate system. Therefore, the internal coordinates variables in eqs. [9]–[11] must be transformed into Cartesian coordinates. The transformations of $\vec{r}_1$, $\vec{r}_2$, $\vec{r}_3$ are straightforward. Transformation of their first derivatives is written as

$$[12] \quad \begin{pmatrix} \dot{x}_2 - \dot{x}_1 \\ \dot{y}_2 - \dot{y}_1 \\ \dot{z}_2 - \dot{z}_1 \end{pmatrix} = \begin{pmatrix} \sin\theta\cos\phi & \cos\theta\cos\phi & -\sin\phi \\ \sin\theta\sin\phi & \cos\theta\sin\phi & \cos\phi \\ \cos\theta & \sin\theta & 0 \end{pmatrix} \begin{pmatrix} \dot{r}_{12} \\ r_{12}\dot{\theta} \\ r\sin\theta\,\dot{\phi} \end{pmatrix}$$

Since the 3 × 3 matrix is unitary, the transformation is just the interchange of the off-diagonal elements. Therefore, $\dot{r}$, $\dot{\theta}$, $\dot{\phi}$ are derived directly. Once the forces for C_Q and H_L are calculated from the QM potential, the force on C_M is determined from eqs. [9]–[12].

In the QM/MM classical direct dynamics calculation, the quantum mechanical program calculates the QM part, which includes the H_L atom. The forces on H_L and C_Q are then transformed to C_M according to eqs. [9]–[12]. Together with the force for the MM part, the trajectory is integrated for one step for every atom in the system except the H_L atom to find the new coordinates and momenta. The position of H_L is then updated by $|\vec{r}_{C_M} - \vec{d}|$. A new QM and MM force calculation with an update of H_L is then carried out for the next integration step. Such a procedure repeats until the trajectory reaches one of its stopping criteria.

Tests and (or) applications of the model

Collinear three-atom model

With the H_L and C_M distances fixed, holding the atoms collinear is equivalent to making the C_Q-H_L-C_M bending and H_L-C_M stretch forces very high (i.e., making these vibrations stiff). It is straightforward to show that, if the H_L-C_M distance is fixed, the vibrational frequency for the collinear system is

$$[13] \quad \nu = \frac{1}{2\pi}\sqrt{\frac{k_1}{\mu}}$$

© 2004 NRC Canada

$$\mu = \frac{(M+m)m}{M+2m}$$

where m is the mass of the carbon atoms and M is that of H_L. Equation [13] means that C_M and H_L behave as a single atom with mass $M + m$.

To show that eq. [13] is also the result for the stiff model, first assume that the C_Q-H_L interaction can be described by a harmonic oscillator with a force constant k_1. Similarly, the H_L-C_M potential is given by a harmonic oscillator with force constant k_2. The potential can be written as

$$[14] \quad V = \frac{1}{2}k_1(x_2 - x_1)^2 + \frac{1}{2}k_2(x_3 - x_2)^2$$

where x_1, x_2, and x_3 are the deviations of C_Q, H_L, and C_M from their equilibrium positions. Following the standard procedure for a normal mode analysis, the force constant matrix is constructed as

$$[15] \quad \begin{vmatrix} \frac{k_1}{m} - \lambda & -\frac{k_1}{\sqrt{mM}} & 0 \\ -\frac{k_1}{\sqrt{mM}} & \frac{k_1+k_2}{M} - \lambda & -\frac{k_2}{\sqrt{mM}} \\ 0 & -\frac{k_2}{\sqrt{mM}} & \frac{k_2}{m} - \lambda \end{vmatrix} = 0$$

Diagonalization of the above equation involves solving

$$[16] \quad \lambda^2 - (k_1 - k_2)\left(\frac{1}{m} + \frac{1}{M}\right)\lambda + \left(\frac{2k_1k_2}{Mm} + \frac{k_1k_2}{m^2}\right) = 0$$

When $k_2 \to \infty$, which is the stiff model, eq. [16] becomes

$$[17] \quad \lambda^2 - \left[k_1\left(\frac{1}{m} + \frac{1}{M+m}\right) + k_2\left(\frac{1}{m} + \frac{1}{M}\right)\right]\lambda + \left(\frac{2k_1k_2}{Mm} + \frac{k_1k_2}{m^2}\right) = 0$$

Therefore, $\lambda_1 = k_1/\mu_1$, where $\mu_1 = (M+m)m/(M+2m)$, $\lambda_2 = k_2/\mu_2$, and $\mu_2 = 1/M + 1/m$. The eigenvalue λ_1 gives the same frequency as eq. [13].

[Cl-C_2H_5-Cl]$^-$ central barrier

It is of interest to test the QM/MM model described here by using the [Cl-C_2H_5-Cl]$^-$ central barrier as an example. If the model correctly describes the properties of [Cl-C_2H_5-Cl]$^-$, it is expected that it can be used to study how adding -R substituents to the [Cl-CH_3-Cl]$^-$ system affects the S_N2 reaction dynamics. For [Cl-C_2H_5-Cl]$^-$ the -CH_3 group is -R.

This QM/MM model was used to calculate vibrational frequencies for the [Cl-C_2H_5-Cl]$^-$ central barrier. Force constants for the [Cl-CH_3-Cl]$^-$ QM part of the model were calculated at the MP2/6-31G* level of theory. The -CH_3 MM force field consists of three C_M-H stretches and three H-C_M-H bends. Three C_Q-C_M-H bends are added for the QM/MM boundary. The -CH_3 torsion is treated as a free rotor (see previous discussion) and nondiagonal force constants were neglected in the MM force field. The MM force constants are the same as the MP2/6-31G* values for the [Cl-C_2H_5-Cl]$^-$ central barrier. The C_Q-C_M stretching and H-C_Q-C_M bending force constants associated with the C_Q-C_M interaction are the same as those for the C_Q-H_L interaction.

Table 1. Vibrational frequencies (cm^{-1}) for the [Cl-C_2H_5-Cl]$^-$ central barrier.

Ab inito[a]	QM/MM[b]	QM/MM[c]	Stiff[d]
191.1	164.3	164.2	164.9
225.1	203.1	203.1	201.3
242.0	230.9	231.1	207.3
326.5	231.4	231.4	231.4
849.0	841.9	867.1	855.0
1006	963.2	1015	1015
1045	1015	1045	1045
1088	1056	1073	1073
1102	1071	1114	1079
1245	1102	1127	1099
1450	1414	1474	1474
1522	1426	1555	1554
1546	1438	1563	1563
1556	1582	1647	1618
3135	3128	3128	3127
3226	3237	3238	3240
3232	3247	3248	3250
3345	3357	3357	3356
3473	3489	3490	3489

[a]MP2/6-31G* frequencies for the [Cl-C_2H_5-Cl]$^-$ stationary point.
[b]QM/MM model with the MM force constants obtained from the ab initio calculation in footnote *a*.
[c]The same QM/MM model with the MM force constants increased to get better overall agreement with the ab initio calculated frequencies.
[d]The same QM component and MM force field as used in footnote *c*, except the C_Q-H_L-C_M bending and H_L-C_M force constants are set to 15.0 mdyn Å/rad^2 and 50.0 mdyn/Å, respectively.

Since the QM part of the model is [Cl-CH_3-Cl]$^-$, the Cl—C bond lengths and Cl-C-Cl angle for the [Cl-C_2H_5-Cl]$^-$ central barrier are the values for [Cl-CH_3-Cl]$^-$. The latter has a symmetric structure with bond lengths of 2.307 Å and the Cl-C-Cl angle is 180°. The structure of [Cl-C_2H_5-Cl]$^-$ is slightly asymmetric with Cl—C bond lengths of 2.342 and 2.369 Å and a Cl-C-Cl angle of 165.3°.

The ab initio and QM/MM vibrational frequencies for the [Cl-C_2H_5-Cl]$^-$ central barrier are compared in Table 1. The first two colums in the table are the ab initio frequencies and the QM/MM frequencies with the force constants described previously. There is overall good agreement between the two sets of frequencies, with the difference usually much less than 10%. However, the difference is much larger for some of the frequencies in the 200–300 and 1100–1500 cm^{-1} ranges. There are two sources for this difference. As described below, there are differences between the force field for [Cl-CH_3-Cl]$^-$ and the force field for the Cl-CH_2-Cl component of [Cl-C_2H_5-Cl]$^-$, particularly for the low-frequency vibrations. Second, because the MM force constants are only taken from the diagonal elements of the ab initio force constant matrix for [Cl-C_2H_5-Cl]$^-$, inaccuracies in the frequencies may also result from neglecting the nondiagonal elements.

The third column in Table 1 illustrates the effect of making minor adjustments to the MM force field by increasing the H-C_M-H and C_Q-C_M-H bending force constants by scaling factors in the range of 1.17–1.23. Comparing columns

© 2004 NRC Canada

1–3 in the table shows that increasing the MM force constants results in much better agreement between the ab initio and QM/MM frequencies in the 1440–1600 cm^{-1} range. As expected, the low vibrational frequencies, which are for motions involving the Cl-atoms, are independent of these changes in the MM force field. The factor of 1.41 difference between the 326.5 and 231.4 frequencies is the largest difference between the ab initio and QM/MM vibrational frequencies. This mode is analogous to the CH_3 out-of-plane bend for the $[Cl\text{-}CH_3\text{-}Cl]^-$ central barrier and apparently it is not well described by the Cl-C-H and Cl-C-Cl force constants of the $[Cl\text{-}CH_3\text{-}Cl]^-$ QM component of the QM/MM model. These force constants could be scaled to bring the ab initio and QM/MM frequencies for this mode into better agreement.

The fourth column in Table 1 illustrates the effect of replacing the QM/MM link-atom model with a constrained collinear $C_Q\text{-}H_L\text{-}C_M$ geometry and a fixed H_L-C distance by a force field with large $C_Q\text{-}H_L\text{-}C_M$ and $H_L\text{-}C_M$ bending and stretching force constants of 15.0 mdyn-Å/rad^2 and 50.0 mdyn/Å, respectively. If larger force constants were used, calculating the force constant matrix from the gradient of the potential by finite difference becomes numerically unstable. However, even with these force constants, the comparison between the third and fourth columns of Table 1 shows excellent agreement between the QM/MM link-atom and equivalent stiff-force constant model. If it were possible to calculate analytic second derivatives of the potential from VENUS (i.e., they are not programmed), it would be possible to show by numerical means that the two approaches are equivalent.

Summary

The 300 K central barrier dynamics for $[Cl\text{-}C_2H_5\text{-}Cl]^-$ is strikingly different than that for $[Cl\text{-}CH_3\text{-}Cl]^-$. Trajectories initiated at the central barrier for the latter system show extensive recrossings of the central barrier and no dissociation to the Cl^- + CH_3Cl products on a 3 ps timescale. In contrast, RRKM theory predicts no recrossing and approximately 50% dissociation. For the $[Cl\text{-}C_2H_5\text{-}Cl]^-$ system, the majority of the 68 trajectories calculated form Cl^-–C_2H_5Cl complexes, which appear to undergo efficient IVR. Only two barrier recrossings occur. However, some trajectories leave the barrier and go directly to Cl^- + C_2H_5 products without first becoming trapped in the Cl^-–C_2H_5Cl complex, an important non-RRKM property. Recrossing the high central barrier is also a non-RRKM result.

The origin of the remarkable difference in the $[Cl\text{-}CH_3\text{-}Cl]^-$ and $[Cl\text{-}C_2H_5\text{-}Cl]^-$ intramolecular and unimolecular dynamics is unclear and needs to be probed in detail in future studies. Previous studies (54–58) have shown that the presence of a -CH_3 rotor, as is the case for $[Cl\text{-}C_2H_5\text{-}Cl]^-$, often enhances IVR because of coupling between the rotor and the molecule's low frequency vibrations. This may explain why central barrier recrossing is unimportant for the $[Cl\text{-}C_2H_5\text{-}Cl]^-$ system and why this system tends to form a complex as it moves off the central barrier. However, this coupling with the rotor does not keep some of the $[Cl\text{-}C_2H_5\text{-}Cl]^-$ trajectories from dissociating directly without forming a complex.

A QM/MM link-atom model is described for studying the central barrier dynamics of S_N2 reactions. In the model, the C_Q—C_M bond of the QM/MM boundary is constrained to lie along the C_Q—H_L bond of the hydrogen link atom, with the $H_L\text{-}C_M$ separation held fixed so that $C_Q\text{-}C_M$ distance represents that for a C—C bond. Because of the similarity in stretching and bending force constants for C-C and C-H interactions, bending and stretching force constants for $C_Q\text{-}H_L$ are good models for those of $C_Q\text{-}C_M$. Better agreement may be obtained with only minor scaling of the $C_Q\text{-}H_L$ forces.

This QM/MM model is used to calculate vibrational frequencies for the $[Cl\text{-}C_2H_5\text{-}Cl]^-$ central barrier, with a QM/MM boundary at the C—C bond. Excellent agreement is found between the QM/MM and ab initio frequencies except for one mode that involves Cl-C-C bending, which is not well-described by the $[Cl\text{-}CH_3\text{-}Cl]^-$ QM component of the model. This problem may be rectified by scaling this bending force constant or using the larger QM/MM model $[Cl\text{-}CH_2(CH_2)_nCH_3\text{-}Cl]^-$ with the QM/MM boundary at the CH_2—$(CH_2)_nCH_3$ bond. With this model, one could investigate the change in the central barrier dynamics as the $-(CH_2)_nCH_3$ chain length is increased. RRKM theory predicts a significant increase in the lifetime of the Cl^-–$ClCH_2(CH_2)_nCH_3$ complex as the chain length is increased and it will be of interest to study the actual dynamics by direct dynamics simulations with this QM/MM model.

Acknowlegement

This material is based upon work supported by the National Science Foundation under Grant Nos. 0078558 and 0412677.

References

1. C.R. Moylan and J.I. Brauman. *In* Advances in classical trajectory methods. Vol. 2. *Edited by* W.L. Hase. JAI Press, New York. pp. 95–114. 1994.
2. W.L. Hase. Science (Washington, D.C.), **266**, 998 (1994).
3. M.L. Chabinyc, S.L. Craig, C.K. Regan, and J.I. Brauman. Science (Washington, D.C.), **279**, 1882 (1998).
4. W.L. Hase, H. Wang, and G.H. Peslherbe. *In* Advances in gas phase ion chemistry. Vol. 3. *Edited by* N.G. Adams and L.M. Babcock. JAI Press, New York. pp. 125–156. 1998.
5. S.S. Shaik, H.B. Schlegel, and S. Wolfe. Theoretical aspects of physical organic chemistry: The S_N2 mechanism. Wiley, New York. 1992.
6. V.M. Ryaboy. *In* Advances in classical trajectory methods. Vol. 12. *Edited by* W.L. Hase. JAI Press, New York. pp. 115–145. 1994.
7. S.R. Vande Linde and W.L. Hase. J. Chem. Phys. **93**, 7962 (1990); W.L. Hase and Y.J. Cho. J. Chem. Phys. **98**, 8626 (1993); G.H. Peslherbe, H. Wang, and W.L. Hase. J. Chem. Phys. **102**, 5625 (1995); D.J. Mann and W.L. Hase. J. Phys. Chem. A, **102**, 6208 (1998).
8. Y.J. Cho, S.R. Vande Linde, L. Zhu, and W.L. Hase. J. Chem. Phys. **96**, 8275 (1992).
9. S.C. Tucker and D.G. Truhlar. J. Am. Chem. Soc. **112**, 3338 (1990); A.A. Viggiano, J.S. Paschkewitz, R.A. Morris, J.F. Paulson, A. Gonzalez-Lafont, and D.G. Truhlar. J. Am. Chem.

© 2004 NRC Canada

Soc. **113**, 9404 (1991); W.-P. Hu and D.G. Truhlar. J. Am. Chem. Soc. **117**, 10 726 (1995).
10. H. Wang, L. Zhu, and W.L. Hase. J. Phys. Chem. **98**, 1608 (1994); H. Wang and W.L. Hase. J. Am. Chem. Soc. **117**, 9347 (1995); J.V. Seeley, R.A. Morris, and W.L. Hase. J. Am. Chem. Soc. **119**, 577 (1997); H. Wang and W.L. Hase. J. Am. Chem. Soc. **119**, 3093 (1997).
11. H. Wang, G.H. Peslherbe, and W.L. Hase. J. Am. Chem. Soc. **116**, 9644 (1994).
12. H. Wang and W.L. Hase. Chem. Phys. **212**, 247 (1996); H. Wang and W.L. Hase. Int. J. Mass Spectrom. Ion Processes, **166**, 573 (1996); H. Wang, E.M. Goldfield, and W.L. Hase. J. Chem. Soc. Faraday Trans. **93**, 737 (1997); T. Su, H. Wang, and W.L. Hase. J. Phys. Chem. A, **102**, 9819 (1998); Y. Wang, W.L. Hase, and H. Wang. J. Chem. Phys. **118**, 2688 (2003).
13. M. Igarashi and H. Tachikawa. Int. J. Mass Spectrum. Ion Processes, **181**, 151 (1998); H. Tachikawa and M. Igarashi. Chem. Phys. Lett. **303**, 81 (1999); H. Tachikawa. J. Phys. Chem. A, **104**, 497 (2000); H. Tachikawa. J. Phys. Chem. A, **105**, 1260 (2001).
14. G.H. Peslherbe, H. Wang, and W.L. Hase. J. Am. Chem. Soc. **118**, 2257 (1996); G. Li and W.L. Hase. J. Am. Chem. Soc. **121**, 7124 (1999).
15. L. Sun, W.L. Hase, and K. Song. J. Am. Chem. Soc. **123**, 5753 (2001).
16. L. Sun, K. Song, and W.L. Hase. Science (Washington, D.C.), **296**, 875 (2002).
17. D.C. Clary and J. Palma. J. Chem. Phys. **106**, 575 (1997); S. Schmatz and D.C. Clary. J. Chem. Phys. **109**, 8200 (1998); S. Schmatz and D.C. Clary. J. Chem. Phys. **110**, 9483 (1999); S. Schmatz. Chem. Phys. Lett. **330**,188 (2000).
18. S. Schmatz, P. Botschwina, J. Hauschildt, and R. Schinke. J. Chem. Phys. **114**, 5233 (2001); J. Hauschildt, R. Schinke, S. Schmatz, and P. Botschwina. Phys. Chem. Chem. Phys. **3**, 2275 (2001). S. Schmatz and J. Hauschildt. J. Chem. Phys. **118**, 4499 (2003).
19. P. Botschwina, M. Horn, S. Seeger, and R. Oswald. Ber. Bunsen-Ges. Phys. Chem. **101**, 387 (1997).
20. W.E. Farneth and J.I. Brauman. J. Am. Chem. Soc. **98**, 7891 (1978).
21. C.H. DePuy, S. Gronert, A. Mullin, and V.M. Bierbaum. J. Am. Chem. Soc. **112**, 8650 (1990).
22. T. Su, R.A. Morris, A.A. Viggiano, and J.F. Paulson. J. Phys. Chem. **94**, 8426 (1990).
23. W.B. Knighton, J.A. Bognar, P.M. O'Connor, and E.P. Grimsrud. J. Am. Chem. Soc. **115**, 12 079 (1993).
24. C. Li, P. Ross, J.E. Szulejko, and T.B. McMahon. J. Am. Chem. Soc. **118**, 9360 (1996).
25. S.L. Graig and J.I. Brauman. J. Phys. Chem. A, **101**, 4745 (1997).
26. L.A. Angel and K.M. Ervin. J. Phys. Chem. A, **105**, 4042 (2001).
27. S.T. Graul and M.T. Bowers. J. Am. Chem. Soc. **116**, 3875 (1994).
28. A.A. Viggiano, R.A. Morris, J.S. Paschkewitz, and J.F. Paulson. J. Am. Chem. Soc. **114**, 10 477 (1994).
29. V.F. DeTuri, P.A. Hintz, and K.M. Ervin. J. Phys. Chem. A, **101**, 5969 (1997).
30. D.S. Tonner and T. McMahon. J. Am. Chem. Soc. **122**, 8783 (2000).
31. S. Kato, G.E. Davico, H.S. Lee, C.H. DePuy, and V.M. Bierbaum. Int. J. Mass Spectrom. **210**, 223 (2001).
32. L.A. Angel and K.M. Ervin. J. Am. Chem. Soc. **125**, 1014 (2003).
33. J.I. Steinfeld, J.S. Francisco, and W.L. Hase. Chemical kinetics and dynamics. 2nd ed. Prentice-Hall, Upper Saddle River, N.J. 1999.
34. D.E. Manopoulos, K. Stark, H.-J. Werner, D.W. Arnold, S.E. Bradforth, and D.M. Neumark. Science (Washington, D.C.), **262**, 1852 (1993).
35. K. Bolton, W.L. Hase, and G.H. Peslherbe. *In* Modern methods for multidimensional dynamics computations in chemistry. *Edited by* D.L. Thompson. World Scientific, London pp. 143–189. 1998.
36. T. Baer and W.L. Hase. Unimolecular reaction dynamics: Theory and Experiments. Oxford University Press, New York. 1996.
37. P. Botschwina. Theor. Chem. Acc. **99**, 426 (1998). The CCSD(T) calculations used a basis set of 367 cGTOs and briefly described as *spdfg* (av5z) for chlorine, *spdfg* (v5z) for carbon, and *spd* (vqz) for hydrogen.
38. A.A. Viggiano, R.A. Morris, T. Su, B.D. Wladkowski, S.L. Craig, M. Zhang, and J.I. Brauman. J. Am. Chem. Soc. **116**, 2213 (1994).
39. A. Warshel and M. Levitt. J. Mol. Biol. **103**, 227 (1976); I. Anthes and W. Thiel. J. Phys. Chem. A, **103**, 9290 (1999).
40. F. Jensen. Chem. Phys. Lett. **196**, 368 (1992).
41. B.L. Kormos and C.J. Cramer. J. Phys. Org. Chem. **15**, 712 (2002).
42. G. Caldwell, T.F. Magnera, and P. Kebarle. J. Am. Chem. Soc. **106**, 959 (1984).
43. K. Bolton, H.B. Schlegel, W.L. Hase, and K. Song. Phys. Chem. Chem. Phys. **1**, 999 (1999).
44. W.L. Hase, R.J. Duchovic, X. Hu, A. Komornicki, K.F. Lim, D.-h. Lu, G.H. Peslherbe, K.N. Swamy, S.R. Vande Linde, A. Varandas, H. Wang, and R.J. Wolf. Quantum Chemistry Program Exchange (QCPE) Bulletin, **16**, 671 (1996).
45. M.J. Frisch, G.W. Trucks, H.B. Schlegel, G.E. Scuseria, M.A. Robb, J.R. Cheeseman, V.G. Zakrzewski, J.A. Jr. Montgomery, R.E. Stratmann, J.C. Burant, S. Dapprich, J.M. Millam, A.D. Daniels, K.N. Kudin, M.C. Strain, O. Farkas, J. Tomasi, V. Barone, M. Cossi, R. Cammi, B. Mennucci, C. Pomelli, C. Adamo, S. Clifford, J. Ochterski, G.A. Petersson, P.Y. Ayala, Q. Cui, K. Morokuma, D.K. Malick, A.D. Rabuck, K. Raghavachari, J.B. Foresman, J. Cioslowski, J.V. Ortiz, B.B. Stefanov, G. Liu, A. Liashenko, P. Piskorz, I. Komaromi, R. Gomperts, R.L. Martin, D.J. Fox, T. Keither, M.A. Al-Laham, C.Y. Peng, A. Nanayakkara, C. Gonzalez, M. Challacoombe, P.M.W. Gille, B. Johnson, W. Chen, M.W. Wong, J.L. Andres, C. Gonzalez, M. Head-Gordon, E.S. Replogle, and J.A. Pople. Gaussian98 [computer program]. Gaussian, Inc. Pittsburgh, Penn. 1998.
46. V. Bakken, J.M. Millam, and H.B. Schlegel. J. Chem. Phys. **111**, 8773 (1999).
47. J.M. Millam, V. Bakken, W. Chen, W.L. Hase, and H.B. Schlegel. J. Chem. Phys. **111**, 3800 (1999).
48. G.H. Peslherbe, H. Wang, and W.L. Hase. *In* Advances in chemical physics Vol. 105. *Edited by* D.M. Ferguson, J.I. Siepmann, and D.G. Truhlar. Wiley, New York. pp. 171–201. 1999.
49. J. Gao and M.A. Thompson. Combined quantum mechanical and molecular mechanical methods, ACS Symposium Series 712. American Chemical Society, Washington, D.C. 1998.
50. J. Gao and D.G. Truhlar. Annu. Rev. Phys. Chem. **53**, 467 (2002).
51. G. Li, S.B.M. Bosio, and W.L. Hase. J. Mol. Struct. **556**, 43 (2000).
52. S. Califano. Vibrational states. John Wiley and Sons, New York. 1976.

© 2004 NRC Canada

53. M. Eichinger, P. Tavan, J. Hutter, and M. Parrinello. J. Chem. Phys. **110**, 10 452 (1999).
54. D.B. Moss and C.S. Parmenter. J. Chem. Phys. **98**, 6897 (1993).
55. H.J. Elston, B.D. Gilbert, C.S. Parmenter, H.-K. Oh, T.A. Stone, M.-C. Su, and Z.-Q. Zhao. *In* Proceedings of the 6th International Conference on Time Resolved Vibrational Spectroscopy. *Edited by* A. Lau. Springer-Verlag, Heidelberg. pp. 14–17. 1994.
56. P.J. Timbers, C.S. Parmenter, and D.B. Moss. J. Chem. Phys. **100**, 1028 (1994).
57. Q. Ju, C.S. Parmenter, T.A. Stone, and Z.-Q. Zhao. Isr. J. Chem. **37**, 379 (1997).
58. C.C. Martens and W.P. Reinhardt. J. Chem. Phys. **93**, 5621 (1990).

© 2004 NRC Canada

Methods for calculating vibrational energy levels[1]

Tucker Carrington, Jr.

Abstract: This article reviews new methods for computing vibrational energy levels of small polyatomic molecules. The principal impediment to the calculation of energy levels is the size of the required basis set. If one uses a product basis the Hamiltonian matrix for a four-atom molecule is too large to store in core memory. We discuss iterative methods that enable one to use a product basis to compute energy levels (and spectra) without storing a Hamiltonian matrix. Despite the advantages of iterative methods it is not possible, using product basis functions, to calculate vibrational spectra of molecules with more than four atoms. A very recent method combining contracted basis functions and the Lanczos algorithm with which vibrational energy levels of methane have been computed is described. New ideas, based on exploiting preconditioning, for reducing the number of matrix-vector products required to converge energy levels of interest are also summarized.

Key words: vibrational energy levels, kinetic energy operators, Lanczos algorithm, contracted basis functions, preconditioning.

Résumé: Dans ce travail, on passe en revue de nouvelles méthodes de calculs des niveaux d'énergie vibrationnelle de petites molécules polyatomiques. Le principal obstacle au calcul des niveaux d'énergie est la taille requise de l'ensemble de base. Si on utilise une base produite, la matrice de l'hamiltonien pour une molécule contenant quatre atomes est trop grosse pour être placée dans la mémoire active. On discute de méthodes itératives qui permettent d'utiliser une base produite pour calculer les niveaux d'énergie (et les spectres) sans garder une matrice d'hamiltonien en mémoire. Malgré les avantages des méthodes itératives, il n'est pas possible, en utilisant fonctions de base produites, de calculer les spectres vibrationnels de molécules contenant plus de quatre atomes. On décrit une méthode très récente, combinant des fonctions de base contractées et l'algorithme de Lanczos, à l'aide de laquelle il a été possible de calculer les niveaux d'énergie du spectre vibrationnel du méthane. On résume aussi de nouvelles idées, basées sur l'exploitation du préconditionnement, pour réduire le nombre de produits matrice–vecteur nécessaire pour faire converger les niveaux d'énergie qui présentent de l'intérêt.

Mots clés : niveaux d'énergie vibrationnelle, opérateurs d'énergie cinétique, algorithme de Lanczos, fonctions de base contractées, préconditionnement.

[Traduit par la Rédaction]

1. Introduction

The methods of spectroscopic analysis thoroughly and carefully presented in Herzberg's books enable one to understand spectra of semi-rigid molecules (1, 2). Using these methods one can disentangle the spectrum of a molecule to extract, for example, its equilibrium geometry and information about its Born–Oppenheimer potential. Standard methods of spectroscopic analysis are based on the use of normal coordinates (to describe the shape of the molecule), Eckart axes (to describe its orientation), and perturbation theory (to calculate energy levels) (3). When vibrations are of small amplitude, normal coordinates are appropriate and perturbation theory converges well. Normal coordinates and standard perturbative methods are, however, not suitable if vibrations are of large amplitude. To analyse in detail the spectra of molecules for which large amplitude motion is important, one must choose geometrically defined curvilinear coordinates to describe the shape of the molecule, derive a kinetic energy operator (KEO) in terms of the curvilinear coordinates, and calculate transition energies and intensities from eigenvalues and eigenvectors of a matrix that represents the Hamiltonian operator in a basis (5–10). This numerical approach is difficult for three reasons: (*i*) for the potential energy $\hat{V}$, one must calculate electronic energies at a large number of points and either fit a functional form to them or employ an interpolation scheme; (*ii*) for the kinetic energy T, one must derive an operator in advantageous coordinates; (*iii*) to determine energy levels and wavefunctions, one must choose basis functions, construct a matrix representation of the Hamiltonian operator, and compute eigenvalues and eigenvectors of the (typically) very large matrix **H**. New methods are being developed in all of these areas. In this article we focus on (*ii*) and (*iii*).

New methods for the calculation of energy levels and wavefunctions have evolved with the ability of quantum chemists to calculate reasonably accurate potential energy surfaces and the ability of experimentalists to measure highly resolved rovi-

Received 19 December 2002. Published on the NRC Research Press Web site at http://canjchem.nrc.ca/ on 17 September 2004.

T. Carrington, Jr. Département de chimie, University of Montréal, C.P. 6128, succursale Centre-ville, Montréal, QC H3C 3J7, Canada. (e-mail: tucker.carrington@umontreal.ca).

[1]This article is part of a Special Issue dedicated to the memory of Professor Gerhard Herzberg.

 doi: 10.1139/V04-014 © 2004 NRC Canada

brational spectra of small polyatomic molecules. A method for calculating energy levels (and intensities) is the link between the potential surface and the spectrum. If a potential energy surface is known, one can analyse experimental spectra and sometimes predict unobserved spectral features. Alternatively, knowing the spectrum and having a method to calculate spectra, one can learn a lot about a molecule's potential energy surface. Potential energy surfaces are extremely important in chemistry. They determine not only spectra but also everything from properties of clusters to reaction dynamics. Because there is no direct, general approach for determining potentials of polyatomic molecules from experimental spectroscopic information, the best way to test and refine a potential is to calculate its spectrum and to adjust the potential to minimize the difference between the calculated and observed spectra.

In this article I shall discuss the calculation of vibrational spectra. To calculate rovibrational energy levels, one must choose not only internal coordinates, to describe the shape of the molecule, but also define a molecule-fixed axis system (that rotates with the molecule). The Hamiltonian matrix is also larger than for the vibrational ($J = 0$) case (one must calculate eigenvalues of matrices approximately $JN_v \times JN_v$, where N_v is the size of the vibrational basis).

2. Deriving the kinetic energy operator

If motions of large amplitude have an important effect on the spectrum, it is frequently best not to use normal coordinates but instead to use geometrically defined internal coordinates that describe the shape of the molecule. Geometrically defined internal coordinates have the advantage that even if motion is of large amplitude, each point in configuration space is described by only one set of coordinate values. Of the $3N$ coordinates required to specify the configuration of the N nuclei of an N-atom molecule, $3N - 6$ coordinates describe its shape. What criteria should one consider when choosing vibrational (shape) coordinates? (*i*) Vibrational coordinates (and their domains) must be chosen so that there is a one-to-one correspondence between a geometry of the molecule and a set of coordinate values. If two sets of coordinate values describe the same molecular geometry, the coordinates are not acceptable. It is also essential that a single set of coordinate values not correspond to more than one molecular geometry. (*ii*) Because basis functions are usually chosen as functions of the coordinates in terms of which the kinetic energy operator is written, choosing coordinates influences the quality of the basis functions. It is advantageous to choose coordinates to minimize coupling and therefore facilitate choosing good basis functions. If the basis functions are good, the size of the matrix required to converge the energy levels of interest will be smaller. (*iii*) Coordinates should also be chosen to allow one to take advantage of symmetry. (*iv*) It is often helpful to choose coordinates to simplify the kinetic energy operator. (*v*) If potential integrals are evaluated by Gauss quadrature (11), the number of points required to converge the integrals depends on the degree of the polynomial of largest degree in a polynomial expansion of the potential (even if the potential is not explicitly expanded) and it is, therefore, good to choose coordinates so that the potential, when expanded in terms of polynomials of the coordinates, converges quickly.

Most methods of deriving KEOs follow one of two routes: (*i*) obtain the classical kinetic energy expression and then quantize it (usually using the procedure of Podolsky (12)), or (*ii*) use the chain rule to transform a known quantum mechanical KEO (usually the space-fixed Cartesian KEO) to derive a new KEO. Chapuisat and co-workers (13–18) have advocated the first route. Sutcliffe and Tennyson and co-workers (19–23) and Handy (24) were early proponents of the second route. In recent articles, Mladenović (25, 26) has also used the chain rule route. Lukka (27) has greatly simplified the derivation of KEOs in bond coordinates by suggesting the use of infinitesimal rotation angles. In recent years, several groups have noticed that it is easy to write a compact rovibrational KEO in terms of angular momenta operators for $N - 1$ vectors, which specify the shape and orientation of a molecule in the centre of mass frame. Chapuisat and Iung (16) were perhaps the first to adopt this sort of approach, which was also used recently in refs. 17, 18, 25, and 26.

2.1. Kinetic energy operators from vectors

For any set of $N - 1$ vectors, the KEO has the general form

$$[1] \qquad K = \frac{-1}{2} \sum_{i,j=1}^{N-1} \frac{1}{\mu_{ij}} \nabla(\vec{t}_i) \nabla(\vec{t}_j)$$

This general form is discussed and expressions for μ_{ij} are given in refs. 20 and 25. Note that in ref. 25, $\frac{1}{\mu_{ij}}$ is denoted by F_{ij}.

If $\frac{1}{\mu_{ij}} = 0$ when $i \neq j$, then there are no cross terms in the previous equation, and one says that the vectors are orthogonal. There are different ways of choosing the $\vec{t}_i$ so that they are orthogonal. To obtain a useful KEO from eq. [1], it is necessary to transform it to write the KEO in terms of orientational and shape coordinates. The orientational coordinates are usually the Euler angles that specify the orientation of a molecule-fixed axis system with respect to a space-fixed axis system. The shape coordinates are any coordinates derived from the $N - 1$ $\vec{t}_i$ vectors that describe the shape of the molecule. Chapuisat and Iung (16) pointed out that if one uses coordinates they denoted polyspherical coordinates and chooses the molecule-fixed z axis so that it is parallel to one of the $\vec{t}_i$ vectors it is possible to derive, from eq. [1], a general and rather simple KEO for an N-atom molecule. Polyspherical coordinates are the lengths of the $N - 1$ $\vec{t}_i$ vectors, $N-2$ angles between pairs of $\vec{t}_i$ vectors, and $N-3$ dihedral angles between two vectors around a third. Chapuisat and Iung (16) defined the molecule-fixed frame so that the molecule-fixed z axis is along $\vec{t}_1$ and the molecule-fixed xz plane is the plane defined by $\vec{t}_1$ and $\vec{t}_2$. Using this molecule-fixed frame and $N - 2$ polar polyspherical angles that are the angles between $\vec{t}_1$ and the other $\vec{t}_j$ ($j = 2, 3, \cdots, N-1$) and $N-3$ dihedral polyspherical angles that are the dihedral angles between the planes $(\vec{t}_1\ \vec{t}_2)$ and $(\vec{t}_1\ \vec{t}_j)$, they derived a general and compact KEO by first obtaining a classical kinetic energy expression and then quantizing it. They and their co-workers derived KEOs both for orthogonal (17) and non-orthogonal vectors (18). Recently, Mladenović (25, 26) obtained a compact KEO in terms of the same set of polyspherical coordinates and in the same molecule-fixed axis system. She obtains a general and useful KEO from the chain rule: she does not proceed via a classical expression. Bramley and Carrington (28) transformed the KEO of eq. [1], for four-atom molecules, using the chain rule to obtain a $J = 0$ KEO in terms of polyspherical coordinates. They demonstrated

© 2004 NRC Canada

that one obtains the same four-atom KEO regardless of the set of orthogonal (Jacobi, Radau, hybrid Radau–Jacobi, orthogonal satellite) vectors from which the polyspherical coordinates are defined.

An important advantage of the KEO in polyspherical coordinates and in a molecule-fixed frame whose z axis is along one of the $N-1$ vectors from which the polyspherical coordinates are defined is its generality: one can write a general KEO for a molecule with N atoms. A disadvantage of a polyspherical vector-embedded KEO is its lack of flexibility. If one uses the polyspherical vector-embedded KEO, one must place the molecule-fixed z axis along one of the $\vec{t}_i$ vectors and one must choose as vibrational coordinates polyspherical coordinates obtained from the $N-1$ $\vec{t}_i$ vectors.

If the $\vec{t}_j (j = 3, \cdots, N-1)$ vectors are orthogonal to the two embedding vectors, then a useful (and more flexible) molecule-fixed KEO can be derived from the KEO of eq. [1] as follows (29). (*i*) Rewrite it as

$$[2] \qquad K = -\frac{1}{2\mu_1}\frac{\partial^2}{\partial \vec{t}_1^{\,2}} - \frac{1}{2\mu_2}\frac{\partial^2}{\partial \vec{t}_2^{\,2}} - \frac{1}{\mu_{12}}\frac{\partial}{\partial \vec{t}_1}\frac{\partial}{\partial \vec{t}_2} - \frac{1}{2}\sum_{i,j=3}^{N-1}\frac{1}{\mu_{ij}}\frac{\partial}{\partial \vec{t}_i}\frac{\partial}{\partial \vec{t}_j}$$

(*ii*) From the first three terms in eq. [2], derive a rovibrational KEO for a triatomic-like system in terms of vibrational coordinates q_1, q_2, and q_3 and in (*any*) molecule-fixed frame attached to the two embedding vectors $\vec{t}_1$ and $\vec{t}_2$. (*iii*) Substitute $\vec{J} - \vec{l}$ for $\vec{J}$ in the triatomic-like KEO. This yields

$$[3] \qquad K = K_{\text{tri}}(q_1, q_2, q_3, \vec{J} - \vec{l}) - \frac{1}{2}\sum_{i,j=3}^{N-1}\frac{1}{\mu_{ij}}\frac{\partial}{\partial \vec{z}_i}\frac{\partial}{\partial \vec{z}_j}$$

where the $\vec{z}_i$ are Cartesian coordinates in the molecule-fixed frame. (*iv*) Transform from the z_{ia} coordinates to some non-Cartesian coordinates that describe the length and orientation of the $N-3$ $\vec{z}_j$ vectors with respect to the molecule-fixed frame attached to $\vec{t}_1$ and $\vec{t}_2$. Here, $\vec{l}$ is the total angular momenta of the non-embedding vectors in the molecule-fixed frame. This recipe enables one to obtain a KEO for an N-atom molecule from the KEOs of smaller molecules. This procedure works only because the $\vec{t}_j (j = 3, \cdots, N-1)$ vectors are orthogonal to the two embedding vectors (29).

This KEO is simple and general despite the fact that we do not require that the z axis be placed along one of the $\vec{t}_i$ vectors. This is important because either to reduce rovibrational coupling or to facilitate exploiting symmetry it is sometimes better not to have the z axis along a $\vec{t}_i$ vector.

3. Basis functions

To define a matrix representation of the Hamiltonian (composed of the KEO and the potential energy surface), one must choose basis functions.

3.1. Product basis functions

A product basis is a basis each of whose functions is a product of functions of a single coordinate. If each of the single coordinate functions is labelled by a single index, the basis is a direct product basis and each function may be written

$$[4] \qquad \Phi_{i_1,i_2,\cdots,i_f} = \phi_{i_1}(q_1)\phi_{i_2}(q_2)\cdots\phi_{i_f}(q_f)$$

where f is the number of vibrational degrees of freedom. Direct product basis sets are simple to work with because if the Hamiltonian is factorizable, i.e., if it can be written in the form

$$[5] \qquad \hat{H} = \sum_{l=1}^{g}\prod_{k=1}^{f}\hat{h}^{(k,l)}(q_k)$$

as a sum of g terms each with f factors (for a single term at most two of the factors involve derivative operators), then matrix elements of each term can be written as products of matrix elements of the factors. If one chooses basis functions of the form $\phi_{i_k}(z_k) = h_{i_k}^{-1/2}[w(z_k)]^{1/2}p_{i_k}(z_k)$ where $p_{i_k}(z_k)$ is a classical polynomial, $w(z_k)$ is the corresponding weight function, $z_k = f(q_k)$, and h_{i_k} is a normalization factor, then matrix elements of the kinetic energy factors are usually known in closed form. Matrix elements of potential factors can be computed by evaluating one-dimensional quadratures. To perform the quadrature it is actually not necessary that the potential be factorizable, or even known, as a function of the coordinates in terms of which the kinetic energy operator and the basis functions are written (30). Direct product basis sets have the advantage of simplicity, but to calculate highly excited states of triatomic molecules, or more than a few levels for four-atom molecules, one requires an enormous number of direct product basis functions and it becomes impossible to use conventional diagonalization methods to calculate eigenvalues. As a crude rule of thumb, one requires about 10 basis functions per degree of freedom, and hence about 10^f product-basis functions to calculate vibrational energy levels and wavefunctions of a molecule with f vibrational degrees of freedom. For a triatomic molecule, the product-basis Hamiltonian matrix is only about $1\,000 \times 1\,000$, but for a four-atom molecule the product-basis Hamiltonian matrix is about $1\,000\,000 \times 1\,000\,000$, which cannot be stored in the main memory of any computer.

3.2. Single coordinate basis functions

If the $\phi_{i_k}(q_k)$ functions are of the form $h_{i_k}^{-1/2}[w(f(q_k))]^{1/2} \times p_{i_k}(f(q_k))$ and potential integrals are evaluated with the Gauss quadrature scheme appropriate for the $p_{i_k}(f(q_k))$ polynomials with as many points as there are $\phi_{i_k}(q_k)$ functions, one obtains what is called the finite basis representation (FBR) (31). Instead, it is often advantageous to choose the $\phi_{i_k}(q_k)$ functions to be discrete variable representation (DVR) (31,32) functions. DVR functions are (orthogonal) finite basis approximations to Dirac delta functions. DVR functions are linear combinations of functions of the form $h_{i_k}^{-1/2}[w(f(q_k))]^{1/2}p_{i_k}(f(q_k))$ chosen so that DVR and FBR matrices are unitarily equivalent and so that the DVR matrix for $f(q_k)$ is diagonal. DVR functions are usually obtained by diagonalizing the FBR matrix, which represents $f(q_k)$. DVRs are useful because potential and multiplicative operators in the kinetic energy operator are diagonal in the DVR and hence easy to construct (no integrals are computed) and use.

Whether or not one uses DVR functions, one begins by choosing polynomial basis functions. When choosing polynomials

© 2004 NRC Canada

for the single coordinate functions of q_k, one must consider the domain of the coordinate and the behaviour of wavefunctions near limiting values of the coordinates. For an angle coordinate θ, which assumes values between 0 and $+\pi$, one might choose Legendre or Jacobi polynomials of $\cos(\theta)$ (31). For a stretch coordinate r, which assumes values between 0 and ∞, it is best to take Laguerre polynomials of $Ke^{-a(r-r_e)}$, where K and a are defined in ref. 33, and r_e is the equilibrium value of r. It is possible to choose the parameters of the Laguerre basis so that N_e basis functions exactly span the space spanned by N_e solutions of a Morse oscillator (see ref. 33).

It is of course possible to use single coordinate functions that are not of the form $h_{i_k}^{-1/2}[w(f(q_k))]^{1/2}p_{i_k}(f(q_k))$, either directly or to construct DVR functions. DVR functions obtained by diagonalizing a function of the coordinate operator in a basis of selected eigenfunctions of a one-dimensional Hamiltonian whose potential is derived from the f-dimensional potential are called potential optimized discrete variable (PO–DVR) functions (33, 34).

3.3. Contracted basis functions

Product basis functions would be good basis functions if coupling were unimportant, but because coupling is important the number of product basis functions required to converge even a modest number of energy levels of a four-atom molecule is enormous. Contracted basis functions represent wavefunctions more compactly. They are chosen to reduce the number of basis functions required to obtain converged energy levels. It has been clearly demonstrated that contracted basis functions are powerful tools for computing vibrational energy levels (32,35). Contracted basis functions are usually obtained by diagonalizing reduced-dimension Hamiltonian matrices. There are at least two ways to define effective reduced-dimension Hamiltonian matrices: (*i*) one diagonalizes blocks of the full Hamiltonian matrix in a product basis representation; (*ii*) one diagonalizes matrices that represent the Hamiltonian with one or more coordinates fixed. The first route leads to nondirect product basis functions (32, 36–42). The second route leads to basis functions that are direct products of functions of different coordinates or groups of coordinates (35,43). An example should make this clearer. For a triatomic molecule, a contraction scheme of type 1 is obtained by diagonalizing (stretch) blocks $\langle\alpha(\theta)|\hat{H}(\theta, r_1, r_2)|\alpha(\theta)\rangle$ to get eigenfunctions $\phi_n^\alpha(r_1, r_2)$, where $\alpha(\theta)$ is a DVR bend function, $\hat{H}(\theta, r_1, r_2)$ is the full Hamiltonian operator, and θ, r_1, r_2 are the bend and stretch coordinates. The contracted basis functions are then $\alpha(\theta)\phi_n^\alpha(r_1, r_2)$. A contraction scheme of type 2 is obtained by combining the eigenfunctions of $H(\theta_e, r_1, r_2)$, denoted $\psi(r_1, r_2)$, and eigenfunctions of $H(\theta, r_1^e, r_2^e)$, denoted $\chi(\theta)$. The contracted basis functions are $\psi(r_1, r_2)\chi(\theta)$, and r_1^e, r_2^e, and θ_e are selected specific values of r_1, r_2, and θ. Often, equilibrium values will be good choices. Regardless of the route one takes, only some of the eigenvectors of the reduced-dimension Hamiltonian matrices are retained: such methods are sometimes called diagonalization–truncation–recoupling methods (31,44).

The type 1 approach has been used extensively by Bačić, Bowman, Light, Tennyson, and their co-workers (31,32,36,38, 39, 44). Luckhaus (42) and Mladenović (40, 41) have recently used type 1 contractions in 6D calculations. Both these authors use contracted basis functions with a direct eigensolver (Householder transformations). The type 2 approach was pioneered by Carter and Handy (35) and Bramley and Handy (43) and has been used with a direct eigensolver to compute rovibrational energy levels of four-atom molecules, e.g., C_2H_2 (45), H_2O_2 (46), and NH_3 (vibration only) (47).

4. Eigensolvers

4.1. Direct methods

If the Hamiltonian matrix is not too large, its eigenvalues and eigenvectors can be determined easily using a standard implementation of Householder's algorithm (11). To use the Householder algorithm, one must store the matrix whose eigenvalues are desired (i.e., N^2 numbers), where N is the size of the matrix, and the cost of the calculation scales as N^3. If N is larger than about 10 000, it is difficult to store the Hamiltonian matrix and its diagonalization becomes very costly. The disadvantages of the Householder algorithm become debilitating if one wishes to calculate rovibrational energy levels of a triatomic molecule or vibrational energy levels of a molecule with more than three atoms. Even to calculate high-lying vibrational energy levels of a triatomic molecule, it is difficult to use the Householder algorithm if a simple product basis set is used.

4.2. Iterative methods

The unfavourable scaling of the Householder algorithm has prompted the investigation and development of iterative methods for calculating spectra (28, 48–60). An iterative method requires only the computation of matrix-vector products. The matrix is not modified or stored (61). Hamiltonian matrix-vector products can be computed without storing the Hamiltonian matrix and without even calculating its matrix elements (28,62,63).

The most popular iterative methods employed to calculate energy levels, or energy levels and wavefunctions, are variants of either the Lanczos algorithm (61, 64) or the filter diagonalization method (53,56–58). In the Lanczos method, eigenvalues of an $N \times N$ symmetric matrix H are calculated by diagonalizing an associated $M \times M$ tridiagonal matrix T_M, which is generated recursively, having dimension M after M iterations. To obtain T_M one must compute M matrix-vector products. If M is large enough, among the eigenvalues of T_M there will be eigenvalues of the original matrix H (64). There are several refined versions of the Lanczos algorithm designed to accelerate the convergence of selected eigenvalues (65–67). These methods facilitate the calculation of low-lying energy levels and allow calculation of eigenvectors without redoing matrix-vector products, but they require considerably more storage than a straightforward Lanczos method. The goal of the filter diagonalization method is to calculate energy levels and wavefunctions in a selected (not necessarily low-lying) spectral window. One builds a matrix representation of the Hamiltonian using basis vectors $\mathbf{z_n} = f(\mathbf{H}, n)\mathbf{v}$, $n = 1, 2, \cdots L$, where $\mathbf{v}$ is a starting vector and $f(\mathbf{H}, n)$ is chosen so that the filtered basis vectors have only very small overlaps with eigenvectors of $\mathbf{H}$ whose eigenvalues are outside the window in which one wishes to calculate eigenvalues (53). $\mathbf{v}$ and $\mathbf{H}$ are representations in some original basis of a starting ket, and the Hamiltonian operator is scaled so that its eigenvalues are between -1 and $+1$.

© 2004 NRC Canada

In the filtered basis, one solves a generalized eigenvalue problem to obtain energy levels (and possibly wavefunctions). If the size of the original basis is large, storing the $\mathbf{z_n}$ vectors requires much more memory than would be needed to calculate eigenvalues using the Lanczos algorithm. Wall and Neuhauser (56) pointed out that if Hamiltonian and overlap matrix elements are calculated directly, eigenvalues of the Hamiltonian may be computed without computing (and storing) the $\mathbf{z_n}$ vectors. Using this low-storage approach to filter diagonalization, one is able to calculate energy levels using as little memory as one requires using a Lanczos approach. The Cullum and Willoughby (C&W) Lanczos approach and the filter diagonalization method extract energy levels from the same Krylov space. Both may be viewed as methods for dealing with numerical error introduced as the space is generated. Formally, the space spanned by the Lanczos vectors is larger than (and includes) the space spanned by the filtered $\mathbf{z_n}$ vectors.

Both low-storage filter diagonalization methods and the C&W Lanczos method (64) yield eigenvalues. To obtain eigenvectors from a Lanczos calculation, one must either recalculate or store the Lanczos vectors. To obtain eigenvectors from a low-storage filter diagonalization method calculation, one must recalculate the matrix-vector products used to compute the Hamiltonian and overlap matrix elements. If one wishes to calculate only energy levels and not wavefunctions, the C&W Lanczos method appears to be superior to low-storage filter diagonalization methods: the C&W method requires fewer matrix-vector products and it is simpler to implement (68). In its original form (which involved storing the $\mathbf{z_n}$), filter diagonalization had the advantage that it enabled one to obtain eigenvectors (69).

5. Using iterative methods with a product basis set

An important advantage of a product basis is its inherent structure. If one uses a direct linear algebra method to compute eigenvalues, this structure is not exploited. If instead one uses an iterative method, one can exploit the structure to reduce the cost of calculating matrix-vector products.

If the basis is a product basis, then it is always possible to evaluate matrix-vector products so that their cost scales as n^{f+1}, where n is a representative number of basis functions for a single degree of freedom, and f is the number of degrees of freedom. If H is factorizable (KEOs are almost always factorizable and potentials sometimes are), then it may be written as

$$[6] \qquad H = \sum_{l=1}^{g} \prod_{k=1}^{f} \hat{h}^{(k,l)}(q_k)$$

and a matrix-vector product $\mathbf{Hu} = \mathbf{u}'$ is evaluated most efficiently by doing sums sequentially

$$[7] \qquad \sum_{l=1}^{g} \sum_{i_1} h^{(1,l)}_{i'_1,i_1} \sum_{i_2} h^{(2,l)}_{i'_2,i_2} \cdots \sum_{i_f} h^{(f,l)}_{i'_f,i_f} u_{i_1,i_2,\cdots,i_f} = u'_{i'_1,i'_2,\cdots,i'_f}$$

where $h^{(k,l)}_{i'_k,i_k}$ is an element of the $n \times n$ matrix representation of the factor $\hat{h}^{(k,l)}(q_k)$ (an operator for a single coordinate) (28, 62, 63). Note that for notational simplicity we have assumed that there are n basis functions for each degree of freedom but that this is not necessary. If the lth term has c_l nondiagonal $\mathbf{h}^{(k,l)}$ matrices, the number of multiplications required to evaluate the matrix-vector product for that term is $c_l n^{f+1}$ (28). The total number of operations required for a direct-product Lanczos calculation is $Mn^{f+1}\sum_l c_l$.

What happens if the potential (or a term in the KEO) is not factorizable? In this case, it is still possible to do matrix-vector products at a cost that scales as n^{f+1}, *if a direct product quadrature grid is used*. For example, the quadrature approximation for the integral

$$[8] \qquad V_{n'm',nm} = \int \mathrm{d}q_1\, \mathrm{d}q_2\, f_{n'}(q_1) g_{m'}(q_2) V(q_1, q_2) f_n(q_1) g_m(q_2)$$

is

$$[9] \qquad \sum_{\alpha}\sum_{\beta} \sqrt{\frac{\omega_\alpha}{w((q_1)_\alpha)}}\sqrt{\frac{\omega_\beta}{w((q_2)_\beta)}} f_{n'}((q_1)_\alpha) g_{m'}((q_2)_\beta) \times V((q_1)_\alpha, (q_2)_\beta) f_n((q_1)_\alpha) g_m((q_2)_\beta) \times \sqrt{\frac{\omega_\alpha}{w((q_1)_\alpha)}}\sqrt{\frac{\omega_\beta}{w((q_2)_\beta)}}$$

where $(q_1)_\alpha$ and $(q_2)_\beta$ are quadrature points for the q_1 and q_2 coordinates, ω_α and ω_β are the corresponding quadrature weights, and $w(q_1)$ and $w(q_2)$ are the corresponding weight functions. In terms of $\mathbf{T}$ matrices with elements

$$[10] \qquad \left({}^{[q_1]}T\right)_{n',\alpha} = f_n((q_1)_\alpha)\sqrt{\frac{\omega_\alpha}{w((q_1)_\alpha)}}$$

$$[11] \qquad \left({}^{[q_2]}T\right)_{n',\beta} = f_n((q_2)_\beta)\sqrt{\frac{\omega_\beta}{w((q_2)_\beta)}}$$

the potential integral is

$$[12] \qquad V_{n'm',nm} \approx \sum_{\alpha}\sum_{\beta} \left({}^{[q_1]}T\right)_{n',\alpha} {}^{[q_2]}T_{m',\beta} \times V((q_1)_\alpha, (q_2)_\beta) \left({}^{[q_1]}T^\dagger\right)_{\alpha,n} \left({}^{[q_2]}T^\dagger\right)_{\beta,m}$$

The matrix-vector product can now be written

$$[13] \qquad \sum_{\alpha} \left({}^{[q_1]}T\right)_{n',\alpha} \sum_{\beta} {}^{[q_2]}T_{m',\beta} V((q_1)_\alpha, (q_2)_\beta) \times \sum_{m} \left({}^{[q_2]}T^\dagger\right)_{\beta,m} \sum_{n} \left({}^{[q_1]}T^\dagger\right)_{\alpha,n} u_{nm} = u'_{n'm'}$$

and the n^{f+1} scaling is evident.

The favourable n^{f+1} scaling relation is not due to the sparsity of the Hamiltonian matrix nor to the sparsity of the $\mathbf{h}^{(k,l)}$ matrices, it is not due to the absence of mixed second-order

© 2004 NRC Canada

differential operators, and it is not due to choosing special single coordinate functions from which to build the product basis functions. (Note that it is sometimes advantageous to choose the single coordinate functions so that the $\mathbf{h}^{(k,l)}$ matrices are sparse to further accelerate the matrix-vector product (70). The n^{f+1} scaling relation is a result of using a product basis. Note that if one evaluates matrix-vector products by doing sums sequentially, one never actually calculates matrix elements of the Hamiltonian (not even "on the fly"): one uses matrix elements of the factors of the terms of the Hamiltonian to build up the Hamiltonian matrix-vector product.

For some problems it is advantageous to use a nondirect product basis. We use the term nondirect product function to mean a function that is a product of functions of a single coordinate, but for which at least one of the single coordinate functions is labelled not only by the index for its coordinate but also by the index for another coordinate, i.e., there is a shared index. The most familiar example of a nondirect product basis function is a spherical harmonic ($Y_{lm} = \Theta_l^m(\theta)\Phi_m(\phi)$); m is the shared index. Convergence of the Lanczos algorithm is poorer if the spectral range (the difference between the largest and the smallest eigenvalues) of the matrix is large. For many molecules, this problem is not really debilitating but it is exacerbated by any important singularities in the kinetic energy operator (71, 72). An important singularity is one for which the wavefunctions one wishes to calculate have significant amplitude at points in configuration space at which the kinetic energy operator is infinite. To deal with important singularities, it is useful to use nondirect product basis functions to reduce the spectral range of the Hamiltonian matrix.

Singularities occur whenever one coordinate takes a limiting value and another becomes undefined. If a singularity is important, optimal basis functions are nondirect product functions, which are eigenfunctions of part of the Hamiltonian, which includes the kinetic energy term(s) with the singularity. To evaluate the matrix-vector product efficiently for basis functions that have the form $f_n^m(q_1)g_m(q_2)$ (m is the shared index and the singularity occurs when q_1 takes a limiting value and q_2 becomes undefined), one uses equations very similar to those given previously. The nondirect product basis functions will usually be eigenfunctions either of part of the kinetic energy operator or of the sum of part of the kinetic energy operator and part of the potential, and therefore the only nontrivial matrix-vector product will be for the potential or for part of the potential. One may always attain n^{f+1} scaling by choosing the same set of q_1 quadrature points for all values of m (73). In this case, the integral

$$[14]\quad V_{n'm',nm} = \int \mathrm{d}q_1\,\mathrm{d}q_2\, f_{n'}^{m'}(q_1)g_{m'}(q_2)V(q_1,q_2)f_n^m(q_1)g_m(q_2)$$

is

$$[15]\quad \sum_\alpha\sum_\beta \sqrt{\frac{\omega_\alpha}{w((q_1)_\alpha)}}\sqrt{\frac{\omega_\beta}{w((q_2)_\beta)}} f_{n'}^{m'}((q_1)_\alpha)g_{m'}((q_2)_\beta) \times V((q_1)_\alpha,(q_2)_\beta) f_n^m((q_1)_\alpha)g_m((q_2)_\beta) \times \sqrt{\frac{\omega_\alpha}{w((q_1)_\alpha)}}\sqrt{\frac{\omega_\beta}{w((q_2)_\beta)}}$$

In terms of $\mathbf{T}$ matrices

$$[16]\quad V_{n'm',nm} \approx \sum_\alpha\sum_\beta \left({}^{[q_1]}T^{m'}\right)_{n',\alpha} {}^{[q_2]}T_{m',\beta} \times V\left((q_1)_\alpha,(q_2)_\beta\right)\left({}^{[q_1]}T^{m\dagger}\right)_{\alpha,n}\left({}^{[q_2]}T^{\dagger}\right)_{\beta,m}$$

As the notation implies, there is a different ${}^{[q_1]}T^m$ for each value of m (because there is a different set of q_1 functions for each m). The matrix-vector product can now be written

$$[17]\quad \sum_\alpha \left({}^{[q_1]}T^{m'}\right)_{n',\alpha}\sum_\beta {}^{[q_2]}T_{m',\beta}V\left((q_1)_\alpha,(q_2)_\beta\right) \times\sum_m\left({}^{[q_2]}T^{\dagger}\right)_{\beta,m}\sum_n\left({}^{[q_1]}T^{m\dagger}\right)_{\alpha,n}u_{nm} = u'_{n'm'}$$

The n^{f+1} scaling is evident. It has been exploited in many calculations (71, 74–76).

6. Exploiting symmetry with an iterative method

Molecular symmetry is useful because symmetry labels enable one to understand spectra (selection rules) and because symmetry facilitates computing spectra (77). If basis functions can be chosen so that they transform like irreducible representations, then the size of the matrices one must diagonalize to compute a spectrum can be reduced. Matrix elements between basis functions that transform like different irreducible representations are zero. Such basis functions are called symmetry-adapted basis functions. If they are ordered properly, the Hamiltonian matrix in the symmetry-adapted basis is block diagonal. If one wishes to use a direct method to compute the spectrum, it is immediately obvious that having a block diagonal matrix is a significant advantage. To diagonalize a block diagonal matrix, one requires both less memory and less CPU time. Consequently, it is always advantageous when using a direct method to exploit symmetry. Symmetry-adapted basis functions may be more complicated than simpler basis functions but the advantage of reducing the size of the matrix is extremely important.

It is natural to think that one should also exploit symmetry when using an iterative method to compute a spectrum. It is reasonable to expect that doing so should enable one to reduce the size of the vectors (decrease the memory required) and speed up the evaluation of matrix-vector products (reduce the CPU time). However, there is a problem. The cost of an iterative calculation is a product of the number of matrix-vector products required to converge the energy levels of interest and the cost of a single matrix-vector product. In the previous section it was stressed that matrix-vector products are simple and surprisingly inexpensive if one uses a product basis. If, instead of using a product basis, one uses a symmetry-adapted basis, both the simplicity and the favourable n^{f+1} scaling relation are, in general, sacrificed. This is a significant loss. As discussed by Bramley and Carrington (28), symmetry-adapted basis functions can be used efficiently if a symmetry operation affects only one coordinate. However, symmetry-adapted basis functions for a

© 2004 NRC Canada

symmetry operation that mixes or exchanges coordinates are linear combinations of the original product basis functions, and the corresponding matrix-vector product is difficult to evaluate efficiently. In this section, a symmetry-adapted Lanczos (SAL) method is described with which one can use a product basis to calculate energy levels of different symmetries separately, but from one set of matrix-vector products (78, 79).

6.1. Symmetry-adapted Lanczos method

The conventional Lanczos iteration is based on a simple three-term recurrence relation (61)

$$[18] \qquad \beta_{i+1}\mathbf{v}_{i+1} = \mathbf{H}\mathbf{v}_i - \alpha_i\mathbf{v}_i - \beta_i\mathbf{v}_{i-1}$$

with $\beta_1 = 0$.

In exact arithmetic, the Lanczos vectors ($\mathbf{v_i}$) calculated using eq. [18] are orthogonal and the Hamiltonian matrix in the basis of the Lanczos vectors is tridiagonal. The β_i and α_i are elements of the tridiagonal matrix. If one requires more than a small number of iterations, the orthogonality of the Lanczos vectors is lost due to the finite precision of computer arithmetic. However, it is still possible, using a scheme suggested by Cullum and Willoughby (64), to extract accurate eigenvalues from the tridiagonal matrix .

In the symmetry-adapted Lanczos method, the Lanczos vectors $\mathbf{v}_i^{(m)}$ and the $\alpha_i^{(m)}$ and $\beta_i^{(m)}$ coefficients are calculated for all irreducible representations m from a single set of matrix-vector products. Each set of Lanczos vectors is computed from the usual three-term recurrence relation

$$[19] \qquad \beta_{i+1}^{(m)}\mathbf{v}_{i+1}^{(m)} = \mathbf{H}\mathbf{v}_i^{(m)} - \alpha_i^{(m)}\mathbf{v}_i^{(m)} - \beta_i^{(m)}\mathbf{v}_{i-1}^{(m)}$$

but rather than applying H to symmetry-adapted Lanczos vectors to compute the first term on the right-hand-side (RHS) of this equation, we use projection operators.

Each projection operator is defined

$$[20] \qquad \hat{P}_{ii}^{(m)} = \frac{d_m}{h}\sum_R D_{ii}^{(m)}(R)\hat{R}$$

where m labels an irreducible representation, i labels a basis function (ϕ_i^m) that transforms like irreducible representation m (irreducible representations may be degenerate), $\hat{R}$ is a symmetry operation in the group, h is the order of the group, d_m is the dimension of irreducible representation m, and $D_{ii}^{(m)}(R)$ is the ith diagonal element of the matrix representation of $\hat{R}$ in the ϕ_i^m basis. To calculate energy levels, $\hat{P}_{ii}^{(m)}$ is only required for one i and we shall write $\hat{P}_{ii}^{(m)}$ as $\hat{P}^{(m)}$. If an irreducible representation is multidimensional, an index i is implied. The projection operator $\hat{P}^{(m)}$ projects the mth symmetry component from a general vector with N symmetry components without changing the amplitude and sign of the component. For example,

$$[21] \qquad \hat{P}^{(m)}\sum_{n=1}^{N}\mathbf{v}^{(n)} = \mathbf{v}^{(m)}$$

Projection operators commute with the Hamiltonian, i.e.,

$$[22] \qquad \hat{P}^{(m)}H - H\hat{P}^{(m)} = 0$$

Combining eq. [21] with eq. [22], it is clear that

$$[23] \qquad \mathbf{H}\mathbf{v}^{(m)} = \hat{P}^{(m)}\left[\mathbf{H}\sum_{n=1}^{N}\mathbf{v}^{(n)}\right]$$

Therefore, rather than computing $\mathbf{H}\mathbf{v}^{(m)}$ in eq. [19] directly, one can obtain it from eq. [23]. At each iteration, one applies $\mathbf{H}$ to the sum of the Lanczos vectors computed at the previous iteration. Note that in this fashion $\mathbf{H}\mathbf{v}_i^{(m)}$ is obtained for all m from one set of matrix-vector products.

It has been observed that in some cases, after computing $\beta_{i+1}^{(m)}\mathbf{v}_{i+1}^{(m)}$, it is necessary to purify it by applying the projection operator to it; i.e., $\beta_{i+1}^{(m)}\mathbf{v}_{i+1}^{(m)}$ is replaced by $\hat{P}^{(m)}\beta_{i+1}^{(m)}\mathbf{v}_{i+1}^{(m)}$. This purification step is not always required (78).

Using the Lanczos algorithm to calculate separately energy levels in all N irreducible representations by using symmetry-adapted starting vectors would require a factor of N more matrix-vector products. It is noted that the SAL method can be used to calculate energy levels in any number of symmetry species. One might wish to calculate energy levels of some but not all of the symmetries.

The most efficient way to implement the symmetry-adapted Lanczos algorithm entails storing Lanczos vectors for each irreducible representation. To reduce the storage requirement, one must necessarily apply projection operators more frequently. Here, I discuss two schemes for using the SAL method (75). The first requires storing six vectors and applying the projection operators twice per iteration. The second requires storing only five vectors, but one needs three applications of the projection operators per iteration.

The first scheme is shown in Table 1, where K is the number of Lanczos iterations and M is the number of irreducible representations. The starting vector $\mathbf{v}_1 = \sum_{m=1}^{M}\mathbf{v}_1^{(m)}$ is a sum of unit vectors of different symmetries. With this scheme, one needs to store (in addition to vectors required to compute the matrix-vector product) six vectors: $\mathbf{v}_{k-1}$, $\mathbf{v}_k$, $\tilde{\mathbf{v}}_k$, $\mathbf{t}_1$, $\mathbf{t}_2$, and one scratch vector to do the projection in step (7) (note that $\mathbf{v}_k$, $\mathbf{v}_{k+1}$ at steps (11) and (12) occupy the memory previously used to store $\mathbf{v}_{k-1}$, $\mathbf{v}_k$), and do two projections per iteration. Note that the vector is purified at step (7) (78). We find that this purification is necessary (if there are multidimensional irreducible representations) to avoid computing erroneous eigenvalues. At the end of step (10), $\mathbf{t_2}$ is equal to the sum of the kth Lanczos vectors for the M irreducible representations. Note that at step (6) it would be possible to compute

$$[24] \qquad \alpha_k^{(m)} = \mathbf{t}_1^t\hat{P}^{(m)}\mathbf{v}_k$$

but this projection is not necessary because $\mathbf{t}_1$ is of symmetry m.

It is possible to reduce the number of vectors that one must store by one, at the expense of increasing by one the number of applications, per iteration, of the projection operators (75). Because more applications of projection operators are required, this scheme is more expensive, but if the basis size is large, it might be necessary to reduce the number of stored vectors from six to five to calculate energy levels. In the first scheme, to calculate $(\tilde{\mathbf{v}}_k - \beta_k^{(m)}\mathbf{v}_{k-1})$ at step (5), it is necessary to have both $\tilde{\mathbf{v}}_k$ and $\mathbf{v}_{k-1}$. To reduce storage requirements one could store the

© 2004 NRC Canada

Table 1. Implementation of the SAL using 6 vectors and 2 projections.

(0)	Start with $\beta_1^{(m)} = 1$, initial vectors $\mathbf{v}_1 = \sum_{m=1}^{M} \mathbf{v}_1^{(m)}$ and $\mathbf{v}_0 = 0$,
(1)	DO k=1, K
(2)	$\tilde{\mathbf{v}}_k = \mathbf{H}\mathbf{v}_k$
(3)	$\mathbf{t}_2 = 0$
(4)	DO m=1, M
(5)	$\mathbf{t}_1 = \hat{P}^{(m)}(\tilde{\mathbf{v}}_k - \beta_k^{(m)}\mathbf{v}_{k-1})$
(6)	$\alpha_k^{(m)} = \mathbf{t}_1^t\mathbf{v}_k$
(7)	$\mathbf{t}_1 \Leftarrow \hat{P}^{(m)}(\mathbf{t}_1 - \alpha_k^{(m)}\mathbf{v}_k)$
(8)	$\beta_{k+1}^{(m)} = \|\mathbf{t}_1\|$
(9)	$\mathbf{t}_2 \Leftarrow \mathbf{t}_2 + \mathbf{t}_1/\beta_{k+1}^{(m)}$
(10)	END DO
(11)	$\mathbf{v}_k = \mathbf{v}_{k-1}$
(12)	$\mathbf{v}_{k+1} = \mathbf{t}_2$
(13)	END DO

Table 2. Implementation of the SAL using 5 vectors and 3 projections.

(0)	Start with $\beta_1^{(m)} = 1$, initial vectors $\mathbf{v}_1 = \sum_{m=1}^{M} \mathbf{v}_1^{(m)}$ and $\mathbf{w}_0 = 0$,
(1)	DO k=1, K
(2)	$\mathbf{w}_{k-1} \Leftarrow \mathbf{H}\mathbf{v}_k - \mathbf{w}_{k-1}$
(3)	$\mathbf{t}_2 = 0$
(4)	DO m=1, M
(5)	$\mathbf{t}_1 = \hat{P}^{(m)}\mathbf{w}_{k-1}$
(6)	$\alpha_k^{(m)} = \mathbf{t}_1^t\mathbf{v}_k$
(7)	$\mathbf{t}_1 \Leftarrow \hat{P}^{(m)}(\mathbf{t}_1 - \alpha_k^{(m)}\mathbf{v}_k)$
(8)	$\beta_{k+1}^{(m)} = \|\mathbf{t}_1\|$
(9)	$\mathbf{t}_2 \Leftarrow \mathbf{t}_2 + \mathbf{t}_1/\beta_{k+1}^{(m)}$
(10)	END DO
(11)	$\mathbf{t}_1 = 0$
(12)	DO m=1, M
(13)	$\mathbf{t}_1 \Leftarrow \mathbf{t}_1 + \beta_{k+1}^{(m)}\hat{P}^{(m)}\mathbf{v}_k$
(14)	END DO
(15)	$\mathbf{w}_k = \mathbf{t}_1$
(16)	$\mathbf{v}_{k+1} = \mathbf{t}_2$
(17)	END DO

combination, $(\tilde{\mathbf{v}}_k - \mathbf{w}_{k-1})$, where $\mathbf{w}_{k-1} = \sum_{m=1}^{M} \beta_k^{(m)}\mathbf{v}_{k-1}^{(m)}$, with $\mathbf{v}_{k-1}^{(m)} = \hat{P}^{(m)}\mathbf{v}_{k-1}$. Then $\mathbf{t}_1 = \hat{P}^{(m)}(\tilde{\mathbf{v}}_k - \mathbf{w}_{k-1})$ because $\hat{P}^{(m)}\mathbf{w}_{k-1} = \beta_k^{(m)}\mathbf{v}_{k-1}^{(m)} = \hat{P}^{(m)}\beta_k^{(m)}\mathbf{v}_{k-1}$. Note that if one stores only the combination $(\tilde{\mathbf{v}}_k - \mathbf{w}_{k-1})$, the vector $\mathbf{w}_{k-1}$ must be computed (at the cost of an additional projection) at the end of the kth iteration. The second scheme is shown in Table 2. Using this scheme, one needs to store five vectors: $\mathbf{w}_{k-1}, \mathbf{v}_k, \mathbf{t}_1$, $\mathbf{t}_2$, and one scratch vector to do the projections at lines (7) and (13) (note $\mathbf{w}_k$, $\mathbf{v}_{k+1}$ at steps (15) and (16) occupy the memory previously used to store $\mathbf{w}_{k-1}$, $\mathbf{v}_k$) and three projections. Note that, as in the first scheme, $\mathbf{v_k}$ is the sum of the kth Lanczos vectors for the M irreducible representations.

If one is interested only in a single symmetry species, one can use the conventional Lanczos algorithm with a starting vector that transforms like the irreducible representation of interest. However, to avoid converging energy levels of other symmetries, it is necessary to apply the corresponding projection operator $\hat{P}^{(m)}$ to the vector $\beta_{i+1}\mathbf{v}_{i+1}$ at each iteration. This is certainly better than using the method of ref. 80 to distinguish between correct-symmetry and wrong-symmetry energy levels.

The symmetry-adapted Lanczos method enables one to calculate energy levels of different symmetries from a single set of matrix-vector products. It has been used in several calculations (75,81). The SAL method has two important advantages: (*i*) using it one obtains symmetry-labelled energy levels; (*ii*) it significantly reduces the number of matrix-vector products required to achieve convergence. The number of matrix-vector products is reduced because convergence is not hampered by near degeneracies if the nearly degenerate levels occur in different symmetry blocks. The reduction is more important the higher the symmetry of the molecule.

© 2004 NRC Canada

7. The preconditioned, inexact spectral transform method

Using the C&W Lanczos approach, it is easiest to calculate low-lying energy levels. The simple C&W Lanczos method is effective and useful but it has two deficiencies: (*i*) it is necessary to evaluate many matrix-vector products to compute high-lying energy levels; (*ii*) it is not possible to calculate both energy levels and wavefunctions simultaneously without storing a large number of vectors, each with as many components as the number of basis functions required to converge the energy levels of interest. The preconditioned inexact spectral transform (PIST) method overcomes both of these disadvantages (82, 83).

One way to use the Lanczos algorithm to calculate both eigenvalues and eigenvectors without being obliged to store a large number of vectors is to use a spectral transform (84–87). Rather than using the Lanczos algorithm on $\mathbf{H}$, one uses it on $F(\mathbf{H})$, where $F(\mathbf{H})$ is chosen so that the desired eigenvalues of $\mathbf{H}$ correspond to widely separated eigenvalues of $F(\mathbf{H})$. Because widely separated eigenvalues converge quickly, this means that the desired eigenvalues of $\mathbf{H}$ are obtained after only a small number of iterations. If the number of iterations is small, the number of Lanczos vectors that must be stored to permit calculation of eigenvectors is also small. However, computing matrix-vector products with $F(\mathbf{H})$ is, in general, costly.

A very natural spectral transform function (84,87) is $F(\mathbf{H}) = (E\mathbf{I} - \mathbf{H})^{-1}$. Eigenvalues of $F(\mathbf{H})$, which correspond to eigenvalues of $\mathbf{H}$ close to the shift E, are widely spaced and converge quickly. Many authors have used $F(\mathbf{H}) = (E\mathbf{I} - \mathbf{H})^{-1}$ to accelerate the convergence of eigenvalues of $\mathbf{H}$ close to E (87). It is costly to compute $F(\mathbf{H})\ \mathbf{v}$, where $\mathbf{v}$ is a vector, accurately. One way to do so is to expand $F(\mathbf{H})$ in a Chebyshev series. Many terms are required to obtain an accurate estimate of $F(\mathbf{H})\ \mathbf{v}$. Another way to obtain $\mathbf{w} = F(\mathbf{H})\ \mathbf{v}$ is to solve the system of linear equations $(E\mathbf{I} - \mathbf{H})\mathbf{w} = \mathbf{v}$ for $\mathbf{w}$. To do so one could choose an iterative linear equation solver such as MINRES, CGS, or QMR (88). Again, many iterations (many matrix-vector products) are required to obtain an accurate $\mathbf{w}$. With a spectral transform method, which uses a linear equation solver to compute $\mathbf{w} = F(\mathbf{H})\ \mathbf{v}$, the total number of matrix-vector products required is the product of the number of matrix-vector products performed to solve the system of linear equations and the number of Lanczos iterations needed to converge the eigenvalues (assuming that at each Lanczos iteration the same number of matrix-vector products are used for solving the linear equations). If the system of linear equations is solved accurately, this product is quite large.

The PIST method uses an inexact preconditioned spectral transform. The Lanczos algorithm is applied to $(E\mathbf{I} - \mathbf{H})^{-1}$, where $\mathbf{H}$ is the matrix representation of the Hamiltonian. Rather than evaluating matrix-vector products with $(E\mathbf{I} - \mathbf{H})^{-1}$ accurately (which is costly), computing exact eigenvalues of $(E\mathbf{I} - \mathbf{H})^{-1}$, and extracting exact eigenvalues of $\mathbf{H}$ from those of $(E\mathbf{I} - \mathbf{H})^{-1}$, we evaluate matrix-vector products with $(E\mathbf{I} - \mathbf{H})^{-1}$ approximately and diagonalize $\mathbf{H}$ in a basis of the approximate Lanczos vectors of $(E\mathbf{I} - \mathbf{H})^{-1}$. We deliberately compute *approximate* Lanczos vectors knowing that we can compensate by diagonalizing $\mathbf{H}$ in a basis composed of them to obtain *exact* energy levels and wavefunctions. It is much less costly to compute approximate than accurate Lanczos vectors. This is a critical advantage of an inexact spectral transform method. The Lanczos vectors computed in this fashion are orthogonalized using an iterated modified Gram–Schmidt algorithm.

Approximate matrix-vector products with $(E\mathbf{I} - \mathbf{H})^{-1}$ are computed by solving systems of linear equations $(E\mathbf{I} - \mathbf{H})\mathbf{w} = \mathbf{v}$ using an iterative linear solver and stopping the linear solver when the residual is smaller than a predefined error. Because the systems of linear equations are solved approximately, a matrix representation of $(E\mathbf{I} - \mathbf{H})^{-1}$ in the basis of the Lanczos vectors would not be formally tridiagonal. A key advantage of using a linear solver to evaluate the $(E\mathbf{I} - \mathbf{H})^{-1}$ matrix-vector products is the fact that it allows us to use preconditioning to (greatly) speed up their computation. Instead of solving $(E\mathbf{I} - \mathbf{H})\mathbf{w} = \mathbf{v}$ directly, we solve the preconditioned system $(\mathbf{P})^{-1}(E\mathbf{I} - \mathbf{H})\mathbf{w} = (\mathbf{P})^{-1}\mathbf{v} = \mathbf{v}'$, where $\mathbf{P}$ is an approximate preconditioner. Preconditioning is extremely important because the number of $\mathbf{A}$ matrix-vector products required to compute the solution of $\mathbf{Ax} = \mathbf{b}$ depends on the distribution of the eigenvalues of $\mathbf{A}$, and the eigenvalue distribution of $(\mathbf{P})^{-1}(E\mathbf{I} - \mathbf{H})$ is more favourable than the eigenvalue distribution of $(E\mathbf{I} - \mathbf{H})$ (88).

The method is straightforward to implement. There are two parameters. The first parameter (ϵ) determines the accuracy with which the linear equations are solved. To solve the equations $(E\mathbf{I} - \mathbf{H})\mathbf{w_i} = \mathbf{v_i}$, we iterate QMR until $\| (E\mathbf{I} - \mathbf{H})\mathbf{w_i} - \mathbf{v_i} \| \leq \epsilon$ (the vector $\mathbf{v_i}$ always has a norm of unity). The second parameter is M_L, the number of vectors in the space used to calculate eigenvalues and eigenvectors. The method works well as long as ϵ is small enough. To calculate bound states we usually use $\epsilon = 10^{-2}$.

7.1. Preconditioning

It is well-known that to solve $\mathbf{Ax}$= $\mathbf{b}$ using an iterative linear solver, it is best to precondition the system of linear equations (61, 88). One simple way to do this is to multiply on the left by $\mathbf{P}^{-1}$ to obtain $\mathbf{P}^{-1}\mathbf{Ax} = \mathbf{P}^{-1}\mathbf{b} = \mathbf{c}$. If $\mathbf{P}$ is chosen so that $\mathbf{P}^{-1}\mathbf{A}$ is close to the identity, the number of matrix-vector products required to solve $\mathbf{P}^{-1}\mathbf{Ax} = \mathbf{c}$ is much smaller than the number required to solve $\mathbf{Ax} = \mathbf{b}$.

An "approximate Hamiltonian preconditioner" (AHP) of the form $\mathbf{P} = (E\mathbf{I} - \mathbf{H_0})$, where H_0 represents some approximation to the true Hamiltonian operator H, often works quite well. A good choice is $H_0 = T + V_0$, where V_0 is a separable sum of effective potentials in each degree of freedom (82).

The separable preconditioner exhibits a drawback inherent to all AHPs — namely, the number of iterations required to solve $(E\mathbf{I} - \mathbf{H})\ \mathbf{x} = \mathbf{b}$ grows quickly as E is increased. This is due to the density of states, which is (generally) greater at higher energies, and which has an adverse effect on the convergence. Therefore, if iterative methods are to be effective for problems for which many basis functions are necessary — the promise of which is a large part of their appeal — it is *vital* to devise a preconditioner that scales favorably with the density of states.

One way to do so is to use the optimized separable basis (OSB) of Poirier with an idea suggested by Wyatt (87). The OSB is obtained from an original product basis by doing block Jacobi rotations (89). The rotation angles are chosen to minimize the Frobenius norm of the off-block diagonal part of the Hamiltonian matrix. Rather than using the block-diagonal part of the matrix as the preconditioner, we incorporate into the preconditioner off-diagonal matrix elements for some of the OSB

© 2004 NRC Canada

functions whose energies are in the vicinity of E (the energy close to which we wish to compute energy levels). The resultant OSB+Wyatt (OSBW) preconditioner is a particularly effective combination, because Wyatt preconditioning is most efficient when the matrix (from which off-diagonal elements are incorporated into the preconditioner) is nearly diagonal. Using the OSBW preconditioner, we were able to compute high-lying vibrational levels of H_2O with orders of magnitude fewer matrix-vector products than are required using the CW Lanczos approach (83).

8. Using contracted basis with the Lanczos method

The efficacy of iterative methods for solving the Schrödinger equation is contingent on the cost of matrix-vector products. If one uses a product basis, matrix-vector products can always be evaluated at a cost that scales as n^{f+1}. The n^{f+1} scaling relation is attained by exploiting the special structure of the product basis and evaluating summations (over basis or quadrature indices) sequentially. Although n^{f+1} is certainly favourable, it is nevertheless clear that as f or n increases, the cost of the matrix-vector product calculation will become prohibitive. In addition, although iterative methods obviate the need to store a Hamiltonian matrix, one does need to store vectors, with as many components as there are basis functions, and eventually, as f (or n) is increased, one finds that the core memory of the computer is not large enough to do so. To mitigate both these problems, it is natural to consider using iterative methods with basis functions, which represent wavefunctions or wavepackets more compactly (so that one will require fewer basis functions than would be needed if product basis functions were used). If fewer basis functions are required, one expects the memory of the calculation to be reduced. It might appear that the cost of each matrix-vector product should also be reduced.

It is not at all obvious that contracted-basis matrix-vector products are less expensive than product-basis matrix-vector products. Recall that the n^{f+1} scaling relation (responsible for the efficiency of the product-basis matrix-vector product) is due to the simplicity of the product basis. In fact, because better basis functions are necessarily more complicated (the structure of the basis is less simple), the corresponding matrix-vector products are, in general, more costly. If one considers only the cost of a single matrix-vector product, it appears that using better basis functions may increase (and not decrease) the computer time required, but in fact using contracted basis functions will, in general, make Lanczos calculations more efficient (90–92). Why? The cost of an iterative calculation depends not only on the cost of the matrix-vector product but also on the number of matrix-vector products required to achieve convergence. Using a better basis reduces the spectral range of the Hamiltonian matrix and uniformizes the gaps between neighbouring large basis-unconverged eigenvalues and thus decreases the number of iterations required to converge the energy levels of interest.

To efficiently evaluate matrix-vector products for a contracted representation, one uses matrices (much like the quadrature **T** matrices) to transform between the contracted representation and a representation in which matrix elements of Hamiltonian terms can be computed easily and inexpensively. The number of labels on the transformation matrices and the number of values each label assumes determine the cost of the matrix-vector products.

There are two major classes of contracted basis functions (cf. sect. 3.3). Contracted functions of type 1 are excellent and might fruitfully be combined with iterative methods. Consider first the type 1 contracted matrix-vector product for a triatomic. In this section, we label with j functions of q_1 and q_2 obtained by diagonalizing a two-dimensional Hamiltonian for each DVR point $(q_3)_\gamma$ for coordinate q_3. If the two-dimensional Hamiltonian is diagonalized in a direct product q_1 q_2 basis and α and β are DVR labels for the q_1 and q_2 DVR basis functions, then the matrix of eigenvectors is the transformation matrix whose elements are $C^{\gamma}_{\alpha\beta,j}$. In a basis of functions labelled by j and γ, the triatomic Hamiltonian (written in Radau, symmetrized Radau, or Jacobi coordinates) matrix elements are

$$[25]\qquad \langle j'\gamma'|\hat{H}|j\gamma\rangle = E^{\gamma}_{j}\delta_{j'j}\delta_{\gamma\gamma'} + \sum_{\alpha\beta} C^{\gamma'}_{\alpha\beta,j'}\mu((q_1)_\alpha,(q_2)_\beta)l_{\gamma'\gamma}C^{\gamma}_{\alpha\beta,j}$$

where μ is an inverse moment of inertia function, and $l_{\gamma'\gamma}$ is a DVR matrix element of an operator proportional to $\frac{\partial^2}{\partial\theta^2} + \cot\theta\frac{\partial}{\partial\theta}$. In this representation, applying the Hamiltonian to a vector implicates only one nontrivial matrix-vector product. When sums are evaluated sequentially, the cost of the matrix-vector product

$$[26]\qquad \sum_{\alpha\beta} C^{\gamma'}_{\alpha\beta,j'}\mu((q_1)_\alpha,(q_2)_\beta)\sum_{\gamma} l_{\gamma'\gamma}\sum_{j} C^{\gamma}_{\alpha\beta,j}v_{\gamma j}$$

scales as $2(n_j n_\alpha n_\beta n_\gamma + n_\gamma^2 n_\alpha n_\beta + n_\alpha n_\beta n_\gamma$ (n_j is the number of eigenfunctions of the two-dimensional Hamiltonians that are retained). If $n_\alpha = n_\beta = n_\gamma = n$ and it were necessary to retain all n^2 eigenvectors (i.e., $n_j = n^2$) of the two-dimensional Hamiltonians, then the cost would scale as n^5 (and in general as n^{2f-1}). This should be compared to the cost of the product-basis matrix-vector product (n^{f+1}). Clearly, if at each stage of the sequential diagonalization procedure it were necessary to retain all the eigenvectors of the reduced dimensional Hamiltonians, the sequential-diagonalization and the product matrices would have the same eigenvalues (same spectral range, same gap structure), and the same number of iterations would be required to converge eigenvalues of interest for both representations, and it would be much more expensive to use the sequential-diagonalization basis. However, the utility of the sequential-diagonalization basis is derived from the truncation and if it is truncated, one reduces *both* the cost of each individual matrix-vector product and the number of iterations required. For the three-dimensional example, if n_j is reduced from n^2 to n (by retaining only n of the n^2 eigenvectors of the two-dimensional Hamiltonians), the cost of each matrix-vector product is reduced from n^5 to n^4. The cost of a product-basis matrix-vector product also scales as n^4 but because the spectral range and (or) gap structure of the sequential-diagonalization basis are much more favourable, the number of required iterations is reduced and the calculation is less costly (91). Although it is not possible to know a priori how effective the sequential-diagonalization procedure will be (how much one will be able to truncate), it seems clear

© 2004 NRC Canada

that for Lanczos calculations of energy levels the sequential-diagonalization – Lanczos method will, for many, but not all, triatomic molecules, be more efficient than the product-basis - Lanczos method (90, 91). For molecules with four or more atoms, the advantages of the sequential-diagonalization basis are even more convincing: as the number of degrees of freedom increases, it becomes more and more important to reduce the size of the product basis and to exclude poor (unimportant) functions from the basis (93).

8.1. Using simply contracted basis with the Lanczos method

Contracted basis functions of the type discussed in the previous section are certainly very efficient. If there is a good separation of timescales (for example, for a triatomic molecule, if the bend is much slower than the stretches), the coupling between blocks labelled by eigenvectors of the reduced-dimension problem is very weak. Nonetheless, the combination of iterative methods with these contracted functions has two important deficiencies: (*i*) matrix-vector products are expensive, and (*ii*) the storage cost is high. This might appear surprising because it seems natural to expect that one should need fewer contracted (than product) basis functions and that therefore a contracted-Lanczos method should be more efficient and require less memory.

The somewhat unexpected disadvantages of contracted-Lanczos methods are due to the way the matrix-vector products are evaluated. To evaluate a matrix-vector product, the vector is transformed to a simple product representation in which it is easy to apply the KEO and the potential and then back transformed to the contracted representation. This inevitably entails storing a vector in the product representation. Thus, despite the fact that the vector in the contracted basis is not large, one must store a large vector to evaluate matrix-vector products. It is the complexity of the contracted functions that makes matrix-vector products costly. Both of these disadvantages can be overcome by using "simply contracted" basis functions (91, 94).

In orthogonal polyspherical coordinates the KEO (for $J = 0$) can be written (15, 17, 25)

$$[27] \qquad H = T_{\text{ben}}(\theta, r) + T_{\text{str}}(r) + V(\theta, r)$$

with

$$[28] \qquad T_{\text{ben}}(\theta, r) = \sum_i G_b^{(i)}(r) T_b^{(i)}(\theta)$$

$$T_{\text{str}}(r) = \sum_i G_s^{(i)} \frac{\partial^2}{\partial r_i^2}$$

where θ represents all of the bend coordinates and r represents all of the stretch coordinates. The functions $G_b^{(i)}(r)$, $G_s^{(i)}$ and the operators $T_b^{(i)}(\theta)$ are known (17, 25).

The contraction schemes we present may be used with either a FBR (e.g., spherical harmonics) or DVR primitive bend basis. On the other hand, our contraction schemes rely on the use of DVR primitive stretch basis functions.

We first construct contracted bend functions from a Hamiltonian obtained by freezing all the stretch coordinates at their equilibrium values and contracted stretch functions from a Hamiltonian obtained by freezing all the bend coordinates at their equilibrium values. Products of the bend contracted functions and stretch contracted functions are our final basis functions.

The reduced-dimension Hamiltonian for the bend contraction is

$$[29] \qquad H^{(b)} = T_{\text{ben}}(\theta, r_e) + V(\theta, r_e)$$

Its wavefunctions are denoted by

$$[30] \qquad X_b(\theta) = \sum_l C_{lb} f_l(\theta)$$

and the energies by E_b. The f_l are primitive FBR or DVR bend basis functions (if there is more than one bend coordinate, l is a composite index), and the number of retained bend wavefunctions is denoted by n_b.

Similarly, the reduced-dimension Hamiltonian for the stretch contraction is

$$[31] \qquad H^{(s)} = T_{\text{str}}(r) + V(\theta_e, r)$$

with the wavefunctions denoted by

$$[32] \qquad Y_s(r) = \sum_\alpha D_{\alpha s} g_\alpha(r)$$

and the energies by E_s. The g_α are primitive DVR stretch basis functions (if there is more than one stretch coordinate, α is a composite index representing a multidimensional DVR function), and the number of retained stretch wavefunctions is denoted by n_s. θ_e and r_e represent equilibrium values of (respectively) all the bend coordinates and all the stretch coordinates. The final basis is a product of the retained stretch and bend eigenfunctions

$$[33] \qquad |bs\rangle = |X_b\rangle |Y_s\rangle$$

To facilitate calculation of its matrix elements in this basis, we write the full Hamiltonian

$$[34] \qquad H = H^{(b)} + H^{(s)} + \Delta T + \Delta V$$

where

$$[35] \qquad \Delta V(r, \theta) = V(r, \theta) - V(r_e, \theta) - V(r, \theta_e)$$

and

$$[36] \qquad \Delta T = \sum_i \Delta G_b^{(i)}(r) T_b^{(i)}(\theta)$$

with

$$[37] \qquad \Delta G^{(i)}(r) = G_b^{(i)}(r) - G_b^{(i)}(r_e)$$

Since $H^{(b)}$ and $H^{(s)}$ are diagonal in the product contracted basis and the diagonal matrix elements are known (they are the eigenvalues of $H^{(b)}$ and $H^{(s)}$), one only needs to calculate matrix elements of ΔT and ΔV in the product contracted basis. If it were possible to store the Hamiltonian matrix in the product contracted basis $|bs\rangle$, a direct linear algebra method could be used to compute the energy levels. If this is not possible, one *must* use an iterative method and evaluate matrix-vector products.

© 2004 NRC Canada

8.1.1. Matrix-vector products for ΔT

In the orthogonal vector formalism, the kinetic matrix elements are simple. Because there are no momentum cross terms coupling bend and stretch coordinates, we only have to deal with the coupling term of eq. [36].

This term is diagonal in the stretch PODVR basis (note that there are no derivatives with respect to stretch coordinates in eq. [36]). Due to the product structure of eq. [36], it is best to store the bend and stretch matrices separately. The matrix-vector product for ΔT can be performed sequentially without summing over n_b bend functions and n_s stretch functions simultaneously. Note that it not necessary to store any vectors in the primitive basis.

Specifically, the ΔT matrix-vector product can be calculated

$$[38] \qquad u'_{b's'} = \sum_{i,s} \langle s'|\Delta G_b^{(i)}|s\rangle \sum_b \langle b'|T_b^{(i)}|b\rangle u_{bs}$$

The $\Delta G_b^{(i)}$ and $T_b^{(i)}$ matrices are both small and are stored. The $\Delta G^{(i)}$ matrix elements are computed from

$$[39] \qquad \langle s'|\Delta G_b^{(i)}|s\rangle = \sum_\alpha D_{\alpha s'} \Delta G_b^{(i)}(r_\alpha) D_{\alpha s}$$

The $T_b^{(i)}$ matrix elements are computed from

$$[40] \qquad \langle b'|T_b^{(i)}|b\rangle = \sum_{l,l'} C_{l'b'} \langle f_l|T_b^{(i)}|f_{l'}\rangle C_{lb}$$

Because $\Delta G_b^{(i)}$ is diagonal in the DVR basis it is inexpensive to calculate matrix elements of it. Regardless of whether DVR or FBR primitive basis functions are used, matrix elements of $T_b^{(i)}$ are inexpensive to compute because each of the $T_b^{(i)}$ operators is factorizable and involves at most derivatives with respect to two coordinates. Assuming that $n_b > n_s$ (which almost always holds), the memory cost of the ΔT matrix-vector product is n_b^2 and the CPU cost is $n_b^2 n_s$ (if n_s were greater than n_b, then the memory and CPU costs would be n_s^2 and $n_s^2 n_b$). The memory and CPU costs of the ΔV matrix-vector product are much higher (94).

8.1.2. Matrix-vector products for ΔV

In this subsection, I present a method for calculating the ΔV matrix-vector product (94). If one uses an FBR primitive bend basis, a matrix element of ΔV in the product contracted basis is

$$[41] \qquad \begin{aligned} &\langle b's'|\Delta V(\theta, r)|bs\rangle \\ &\quad = \sum_{\substack{l'l \\ \alpha}} C_{l'b'} C_{lb} D_{\alpha s'} D_{\alpha s} \langle l'\alpha|\Delta V(\theta, r)|l\alpha\rangle \\ &\quad = \sum_{\substack{l'l \\ \alpha\beta}} C_{l'b'} C_{lb} D_{\alpha s'} D_{\alpha s} T_{l'\beta} T_{l\beta} \Delta V_{\beta\alpha} \end{aligned}$$

where

$$[42] \qquad \begin{aligned} T_{l\beta} &= \sqrt{w_\beta} f_l(\theta_\beta) \\ \Delta V_{\beta\alpha} &= \Delta V(\theta_\beta, r_\alpha) \end{aligned}$$

(θ_β, w_β) are quadrature points and weights for the angles. Note that if there is more than one bend coordinate, l and β are composite indices, and if there is more than one stretch coordinate, α is a composite index. It is sometimes advantageous to rewrite eq. [41] as

$$[43] \qquad \langle b's'|\Delta V(\theta, r)|bs\rangle = \sum_{\alpha\beta} \tilde{C}_{\beta' b'} \tilde{C}_{\beta b} D_{\alpha s'} D_{\alpha s} \Delta V_{\beta\alpha}$$

where

$$[44] \qquad \tilde{C}_{\beta b} = \sum_l C_{lb} T_{l\beta}$$

Note that the columns of $\mathbf{C}$ are the eigenvectors of $H^{(b)}$ in the FBR basis, and the columns of $\tilde{\mathbf{C}}$ are the eigenvectors of $H^{(b)}$ in the DVR basis. If the primitive bend basis is a DVR basis, a ΔV matrix element is also given by eq. [43] but with $\tilde{C}_{\beta b}$ replaced by $C_{\beta b}$.

One obvious way to evaluate the ΔV matrix-vector product is by doing sums sequentially (90–93),

$$[45] \qquad \begin{aligned} u'_{b's'} &= \sum_{bs} \langle b's'|\Delta V(\theta, r)|bs\rangle u_{bs} \\ &= \sum_\alpha D_{\alpha s'} \sum_\beta \tilde{C}_{\beta b'} \Delta V_{\beta\alpha} \sum_s D_{\alpha s} \sum_b \tilde{C}_{\beta b} u_{bs} \end{aligned}$$

This approach has two important disadvantages: (*i*) one needs to store at least one (more vectors are required to exploit symmetry using the symmetry-adapted Lanczos algorithm (78, 79)) very large vector (with as many components as there are quadrature points) and a potential vector $\Delta V_{\beta\alpha}$; (*ii*) the matrix-vector product is costly because the $\mathbf{D}$ and $\tilde{\boldsymbol{C}}$ matrices cannot be factorized. In this subsection, we discuss a method for overcoming these problems.

A potential matrix element in the product contracted basis is rewritten

$$[46] \qquad \begin{aligned} \langle b's'|\Delta V(\theta, r)|bs\rangle &= \sum_{\alpha\beta} \tilde{C}_{\beta' b'} \tilde{C}_{\beta b} D_{\alpha s'} D_{\alpha s} \Delta V_{\beta\alpha} \\ &= \sum_\alpha F_{b'b,\alpha} D_{\alpha s'} D_{\alpha s} \end{aligned}$$

where we have introduced a $\mathbf{F}$ matrix defined by

$$[47] \qquad F_{b'b,\alpha} = \sum_\beta \tilde{C}_{\beta b'} \tilde{C}_{\beta b} \Delta V_{\beta\alpha}$$

To use our method, one calculates and stores all the $F_{b'b,\alpha}$. One then does the ΔV matrix-vector product

$$[48] \qquad u'_{b's'} = \sum_{bs} \langle b's'|\Delta V|bs\rangle u_{bs}$$

This is most efficiently done in three steps:

$$[49] \qquad \begin{aligned} u^{(1)}_{b\alpha} &= \sum_s D_{\alpha s} u_{bs} \\ u^{(2)}_{b'\alpha} &= \sum_b F_{b'b\alpha} u^{(1)}_{b\alpha} \\ u'_{b's'} &= \sum_\alpha D_{\alpha s'} u^{(2)}_{b'\alpha} \end{aligned}$$

© 2004 NRC Canada

The CPU cost of the matrix-vector product in eq. [49] is $n_\alpha(n_b^2 + 2n_b n_s)$. Assuming $n_b > n_s$, the CPU cost scales as $n_\alpha n_b^2$. Each matrix-vector product is therefore very cheap. The cost is comparable to, or less than, the cost of a product-basis matrix-vector product $f n_{1d}^{f+1}$ (it is actually *much* less for many examples), where n_{1d} is the number of basis functions and quadrature points for each coordinate. Because n_b is much smaller than n_β, it is also more efficient to evaluate the matrix-vector product with eq. [49] than with eq. [45] (for which the cost of the most expensive matrix-vector product scales as $n_\alpha n_\beta n_b$). Of course, this comparison is not really fair: to estimate the total CPU cost of the calculation, one needs to also include the cost of calculating **F**. The **F** matrix is computed prior to and not during the Lanczos recursion. Calculating **F** can be costly. If one evaluates eq. [47] as it is written, the cost of computing the matrix scales as $n_\alpha n_b^2 n_\beta$. In practice, we use Level 3 BLAS for each α in eq. [47] by storing $\tilde{C}\Delta V$ first. This speeds up the calculation of **F** by about a factor of five for H_2O_2 (94).

Does the cost of calculating **F** make this method expensive? It is true that the cost of calculating **F** is formally a factor of n_β larger than the cost of a single contracted matrix-vector product (eq. [49]). However, if one wishes to calculate more than a few energy levels, the *number* of matrix-vector products required to converge the energy levels is also large, and because the cost of the matrix-vector product of eq. [49] is much less than the cost of a standard product matrix-vector product, the contracted product method is more efficient than the product method.

On a parallel computer one could *easily* reduce the total time by parallelizing the calculation of **F**. The calculation of **F** can be trivially parallelized as one can allocate the stretch DVR (α) points to different computers or processors and allow each to calculate a block of **F** for the allocated α points. The full **F** is then assembled from these blocks.

Now we estimate the memory one needs to use this method. Once **F** has been calculated, the simplest way to use eq. [49] to calculate matrix-vector products requires storing **F** and **D**. To store **F**, one must store $n_\alpha n_b^2/2$ numbers (**F** is symmetric). To store **D**, one must store $n_\beta n_s$ numbers. The memory cost is therefore dominated by the cost of storing **F** and scales as $n_\alpha n_b^2/2$. It clearly makes sense to exploit all of the memory available, but if it is not possible to store $n_\alpha n_b^2/2$ numbers, the method can nonetheless be used by storing **F** on disk and reading blocks of **F** labeled by α sequentially from the disk into memory as the ΔV matrix-vector product is computed. This is feasible as it costs only seconds to read gigabytes of data on modern desktop workstations.

The method of this section is not only quicker than a product/iterative method; it also enables one to bypass the memory bottleneck. The most costly quantities to store (**F**, **D**) are all used for one α at a time and can therefore be read one α at a time from disk. Note in addition that because **C** and $\tilde{\mathbf{C}}$ are discarded *before* matrix-vector products are evaluated, one can use an extremely large bend basis to converge the contracted bend functions without increasing the memory cost of the calculation (the CPU cost of the calculation of **F** does increase moderately). In contrast, if one uses the standard approach (eq. [45]), increasing the size of the bending basis increases both the CPU and the memory cost dramatically.

9. Conclusion

Significant progress has been made in the development of iterative methods for computing rovibrational spectra. The CPU and memory costs of a direct calculation scale as N^3 and N^2. It is very clear that no matter how much effort is put into reducing N, both N^3 and N^2 will make it impossible to use direct methods to solve many difficult and interesting problems. Iterative methods enable one to calculate a spectrum without storing a $N \times N$ Hamiltonian matrix. Instead, it is only necessary to store vectors with N components. There is no question that this makes feasible calculations with much larger basis sets. Nonetheless, for a molecule with five atoms it is not possible, if one uses a product basis set, to store even vectors. In this article I have discussed new ideas for overcoming this problem.

The cost of an iterative calculation scales as MC_{mv}, where M is the number of matrix-vector products needed to converge the energy levels of interest, and C_{mv} is the cost of a single matrix-vector product. If M is very large, then even if C_{mv} is modest the cost of an iterative calculation of a spectrum can be excessive. In this article I have reviewed new ideas for reducing M.

The simple fact that iterative methods enable one to calculate a spectrum without storing (or even calculating!) a Hamiltonian matrix immediately suggests that they should be methods of choice. So far, however, it has not been demonstrated that iterative methods enable one to solve more difficult problems. The success of iterative methods has been limited because they are almost always used with simple product basis functions. There is a good reason for this: product basis functions make it very easy to do matrix-vector products. In this article I have argued that iterative methods will reveal their true power only when they are used in conjunction with contracted basis functions. Contracted-basis matrix-vector products are necessarily more complicated but if one uses simply-contracted functions, obtained by dividing coordinates into groups, the cost of the matrix-vector products can be reduced by storing an intermediate matrix (**F**). Once **F** has been computed, the size of the primitive bend basis becomes irrelevant. With the method discussed in this article, it is not necessary to transform from the contracted basis to the primitive basis to do matrix-vector products. If the contracted basis is used as suggested in this article, the memory cost of a calculation can be reduced significantly. The CPU cost is also reduced. It is reduced both because the cost of the matrix-vector products is reduced and because the number of matrix-vector products required to converge energy levels is reduced.

The CPU cost of an iterative calculation can be reduced not only by reducing the cost of a single matrix-vector product but also by reducing their number. The PIST method discussed in this article enables one to exploit preconditioning to do so. Preconditioning has been used for many years to speed up the solution of systems of linear equations. A great deal has been learned about how to build good preconditioners. It is less obvious how to use preconditioning to accelerate the calculation of eigenvalues. PIST offers a good way of doing this.

The key to finding a good preconditioner is finding a good zeroth-order Hamiltonian. For many molecules the sum of the reduced-dimension bend Hamiltonian and the reduced-dimension stretch Hamiltonian would be a very good zeroth-order Hamiltonian. The eigenfunctions of this zeroth-order

© 2004 NRC Canada

Hamiltonian are just the contracted basis functions we have discussed using. The combination of these two ideas should be very effective.

Acknowledgements

This work has been supported by the Natural Sciences and Engineering Research Council of Canada (NSERC). Several graduate students and postdocs have made very important contributions to the work described in this article. Matthew Bramley, Bill Poirier, and Xiao-Gang Wang made especially important contributions.

References

1. G.H. Herzberg. Infrared and Raman spectra. Van Nostrand Reihnold, Toronto. 1945.
2. G.H. Herzberg. Electronic spectra of polyatomic molecules. Van Nostrand Reinhold, Toronto. 1966.
3. M.R. Aliev and J.K.G. Watson. *In* Molecular spectroscopy: Modern research. Vol. III. *Edited by* K.N. Rao. Academic Press, Orlando. 1985. pp. 1–67.
4. D. Papousek and M.R. Aliev. Molecular vibrational-rotational spectra. Elsevier, Amsterdam. 1982.
5. S. Carter and N.C. Handy. Comput. Phys. Rep. **5**, 115 (1986).
6. E.L. Sibert. Int. Rev. Phys. Chem. **9**, 1 (1990).
7. J. Tennyson. Comp. Phys. Rep. **4**, 1 (1986).
8. Z. Bačić and J.C. Light. Annu. Rev. Phys. Chem. **40**, 469 (1989).
9. T. Carrington, Jr. Encyclopedia of computational chemistry. *Edited by* Paul von Ragué Schleyer. Vol. 5. John Wiley and Sons, Bern, Switzerland. 1998.
10. A.G. Császár (*Editor*). Spectrochim. Acta Part A **58** (2002). A special issue on first principles rovibrational spectroscopy.
11. W.H. Press, B.P. Flannery, S.A. Teukolsky, and W.T. Vetterling. Numerical recipes. Cambridge University Press, Cambridge, UK. 1989.
12. B. Podolsky. Phys. Rev. **32**, 812 (1928).
13. A. Nauts and X. Chapuisat. Mol. Phys. **55**, 1287 (1985).
14. X. Chapuisat, A. Nauts, and J.-P. Brunet. Mol. Phys. **72**, 1 (1991).
15. X. Chapuisat, A. Belfhal, and A. Nauts. J. Mol. Spectrosc. **149**, 274 (1991).
16. X. Chapuisat and C. Iung. Phys. Rev. A, **45**, 6217 (1992).
17. F. Gatti, C. Iung, M. Menou, Y. Justum, A. Nauts, and X. Chapuisat. J. Chem. Phys. **108**, 8804 (1998).
18. C. Iung, F. Gatti, A. Viel, and X. Chapuisat. Phys. Chem. Chem. Phys. **1**, 3377 (1999).
19. B.T. Sutcliffe. *In* Current aspects of quantum chemistry, Studies in theoretical and physical chemistry. Vol. 21. *Edited by* R. Carbo. Elsevier, Amsterdam. 1982. pp. 99–125.
20. B.T. Sutcliffe and J. Tennyson. Int. J. Quantum Chem. **39**, 183 (1991).
21. J. Tennyson and B.T. Sutcliffe. J. Chem. Phys. **77**, 4061 (1982).
22. G. Brocks, A. Van Der Avoird, B.T. Sutcliffe, and J. Tennyson. Mol. Phys. **50**, 1025 (1983).
23. S.S. Xantheas and B.T. Sutcliffe. J. Chem. Phys. **103**, 8022 (1995).
24. N.C. Handy. Mol. Phys. **61**, 207 (1987).
25. M. Mladenović, J. Chem. Phys. **112**, 1070 (2000).
26. M. Mladenović. J. Chem. Phys. **112**, 1082 (2000).
27. T. J. Lukka, J. Chem. Phys. **102**, 3945 (1995).
28. M.J. Bramley and T. Carrington, Jr. J. Chem. Phys. **99**, 8519 (1993).
29. X.-G. Wang and T. Carrington, Jr. J. Chem. Phys. **113**, 7097 (2000).
30. R.J. Whitehead and N.C. Handy. J. Mol. Spectrosc. **55**, 356 (1975).
31. J.C. Light and T. Carrington, Jr. Adv. Chem. Phys. **114**, 263 (2000).
32. Z. Bačić and J.C. Light. Annu. Rev. Phys. Chem. **40**, 469 (1989).
33. H. Wei and T. Carrington, Jr. J. Chem. Phys. **97**, 3029 (1992).
34. J. Echave and D.C. Clary. Chem. Phys. Lett. **190**, 225 (1992).
35. S. Carter and N.C. Handy. Comput. Phys. Commun. **51**, 49 (1988).
36. J.R. Henderson and J. Tennyson. Chem. Phys. Lett. **173**, 133 (1990).
37. X.T. Wu, A.B. McCoy, and E.F. Hayes. J. Chem. Phys. **110**, 2354 (1999).
38. Y. Qiu, J.Z.H. Zhang, and Z. Bačić. J. Chem. Phys. **108**, 4804 (1998).
39. A. Bahel and Z. Bačić. J. Chem. Phys. **111**, 11164 (1999).
40. M. Mladenović. Spectrochim. Acta Part A, **58**, 809 (2002).
41. M. Mladenović. Spectrochim. Acta Part A, **58**, 795 (2002).
42. D. Luckhaus. J. Chem. Phys. **113**, 1329 (2000).
43. M.J. Bramley and N.C. Handy. J. Chem. Phys. **98**, 1378 (1993).
44. J.M. Bowman and B. Gazdy. J. Chem. Phys. **94**, 454 (1991).
45. S. Carter and N.C. Handy. Mol. Phys. **100**, 681 (2002).
46. J. Koput, S. Carter, and N. Handy. J. Chem. Phys. **115**, 8345 (2001).
47. N.C. Handy, S. Carter, and S.M. Colwell. Mol. Phys. **96**, 477 (1999).
48. R.E. Wyatt. Adv. Chem. Phys. **73**, 231 (1989).
49. H. Koeppel, W. Domcke, and L.S. Cederbaum. Adv. Chem. Phys. **57**, 59 (1984).
50. C. Iung and C. Leforestier. J. Chem. Phys. **90**, 3198 (1989).
51. J.A. Bentley, J.-P. Brunet, R.E. Wyatt, R.A. Friesner, and C. Leforestier. Chem. Phys. Lett. **161**, 393 (1989).
52. M.J. Bramley and T. Carrington, Jr. J. Chem. Phys. **101**, 8494 (1994).
53. D. Neuhauser. J. Chem. Phys. **93**, 2611 (1990).
54. R.B. Lehoucq, S.K. Gray, D.-H. Zhang, and J.C. Light. Comput. Phys. Commun. **109**, 15 (1998).
55. H.Y. Mussa and J. Tennyson. J. Chem. Phys. **109**, 10 885 (1998).
56. N.R. Wall and D. Neuhauser. J. Chem. Phys. **102**, 8011 (1995).
57. V.A. Mandelshtam and H.S. Taylor. J. Chem. Phys. **102**, 7390 (1995).
58. V.A. Mandelshtam and H.S. Taylor. J. Chem. Phys. **106**, 5085 (1997).
59. H.-G. Yu and S.C. Smith. Ber. Bunsenges. Phys. Chem. **101**, 400 (1997).
60. R. Chen and H. Guo. J. Chem. Phys. **108**, 6068 (1998).
61. G.H. Golub and C.F. Van Loan. Matrix computations. Johns Hopkins University Press, Baltimore, Md. 1989.
62. R.A. Friesner, R.E. Wyatt, C. Hempel, and B. Criner. J. Comput. Phys. **64**, 220 (1986).
63. U. Manthe and H. Koeppel. J. Chem. Phys. **93**, 345 (1990).
64. J.K. Cullum and R.A. Willoughby. Lanczos algorithms for large symmetric eigenvalue computations. Birkhäuser, Boston, Mass. 1985.
65. D.C. Sorensen. SIAM J. Math. Anal. Appl. **13**, 357 (1992).
66. R.B. Lehoucq, D.C. Sorensen, and C. Yang. ARPACK users guide: Solution of large scale eigenvalue problems by implicitly restarted Arnoldi methods. SIAM, Philadelphia, Pa. 1998.

© 2004 NRC Canada

67. J. Baglama, D. Calvetti, and L. Reichel. BIT, **36**, 400 (1996).
68. S. Huang and T. Carrington, Jr. Chem. Phys. Lett. **312**, 311 (1999).
69. P.-N. Roy and T. Carrington, Jr. J. Chem. Phys. **103**, 5600 (1995).
70. P.-N. Roy and T. Carrington, Jr. Chem. Phys. Lett. **257**, 98 (1996).
71. M.J. Bramley, J.W. Tromp, T. Carrington, Jr., and G.C. Corey. J. Chem. Phys. **100**, 6175 (1994).
72. C. Leforestier. J. Chem. Phys. **101**, 7357 (1994).
73. G.C. Corey and D.J. Lemoine. Chem. Phys. **1992**, 97, 4115.
74. C. Leforestier, L.B. Braly, K. Liu, M.J. Elrod, and R.J. Saykally. J. Chem. Phys. **106**, 8527 (1997).
75. X.-G. Wang and T. Carrington, Jr. J. Chem. Phys. **115**, 9781 (2001).
76. R. Chen, G. Ma, and H. Guo. J. Chem. Phys. **114**, 4764 (2001).
77. P.R. Bunker and Per Jensen. Molecular symmetry and spectroscopy. 2nd ed. NRC Research Press, Ottawa, Ont., Canada. 1998.
78. X.-G. Wang and T. Carrington, Jr. J. Chem. Phys. **114**, 1473 (2001).
79. R. Chen and H. Guo. J. Chem. Phys. **114**, 1467 (2001).
80. N.M. Poulin, M.J. Bramley, T. Carrington, H.G. Kjaergaard, and B.R. Henry. J. Chem. Phys. **104**, 7807 (1996).
81. X.-G. Wang and T. Carrington, Jr. J. Chem. Phys. **118**, 6946 (2003).
82. S.-W. Huang and T. Carrington, Jr. J. Chem. Phys. **112**, 8765 (2000).
83. B. Poirier and T. Carrington, Jr. J. Chem. Phys. **114**, 9254 (2001).
84. T. Ericsson and A. Ruhe. Math. Comp. **63**, 494 (1991).
85. F. Webster, P.J. Rosky, and R.A. Friesner. Comput. Phys. Commun. **63**, 494 (1991).
86. H. Kono. Chem. Phys. Lett. **214**, 137 (1993).
87. R. E. Wyatt. Phys. Rev. E, **51**, 3643 (1995).
88. J.J. Dongarra, I.S. Duff, D.C. Sorensen, and H.A. van der Vorst. Numerical linear algebra for high-performance computers. SIAM, Philadelphia, Pa. 1998.
89. B. Poirier. Numer. Linear Algebra Appl. **7**, 715 (2000).
90. R.A. Friesner, J.A. Bentley, M. Menou, and C. Leforestier. J. Chem. Phys. **99**, 324 (1993).
91. M.J. Bramley and T. Carrington, Jr. J. Chem. Phys. **101**, 8494 (1994).
92. X.T. Wu and E.F. Hayes. J. Chem. Phys. **107**, 2705 (1997).
93. A. Viel and C. Leforestier. J. Chem. Phys. **112**, 1212 (2000).
94. X.-G. Wang and T. Carrington, Jr. J. Chem. Phys. **117**, 6923 (2002).

© 2004 NRC Canada

Fermi resonance and conformation in glycolaldehyde particles[1]

Martin Jetzki, David Luckhaus, and Ruth Signorell

Abstract: The infrared spectra of gas-phase glycolaldehyde and small glycolaldehyde particles both exhibit a split carbonyl band around 1730 cm^{-1}. Ab initio calculations show that this splitting can be traced back to a Fermi resonance involving the C=O-stretching band and the first overtone of the C–C-stretching band. The analysis of this resonance leads to detailed information about the conformation of glycolaldehyde in the particles. The results can be summarized as follows. (*i*) In the particles, monomers with OCCO dihedral angles of 0° and CCOH dihedral angles around 50° are strongly preferred. (*ii*) The intramolecular hydrogen bond observed in the gas phase is partly replaced by intermolecular hydrogen bonds. (*iii*) The calculated infrared spectrum and the results from the Fermi resonance analysis are in good agreement with the formation of long chains of monomeric glycolaldehyde. This is in contrast to the solid bulk, which consists of chemically bound dimers.

Key words: Fermi resonance, conformation, glycolaldehyde particles, hydroxyacetone particles, Fourier transform infrared spectroscopy.

Résumé : Les spectres infrarouge du glycolaldéhyde en phase gazeuse et de petites particules de glycolaldéhyde présentent tous les deux une bande carbonyle dédoublée autour de 1730 cm^{-1}. Des calculs ab initio montrent que ce dédoublement provient d'une résonance de Fermi impliquant la bande d'élongation C=O et la première harmonique de la bande d'élongation C–C. L'analyse de cette résonance fournit de l'information détaillée au sujet de la conformation du glycolaldéhyde dans les particules. Les résultats peuvent être résumés de la façon suivante: (*i*) dans les particules, il existe une préférence marquée pour le OCCO avec un angle dièdre de 0° et le CCOH avec un angle dièdre d'environ 50°; (*ii*) la liaison intramoléculaire observée en phase gazeuse est en partie remplacée par des liaisons hydrogènes intermoléculaires; (*iii*) le spectre infrarouge calculé et les résultats de l'analyse de Fermi sont en bon accord avec la formation de longues chaînes de glycolaldéhyde monomère. Ces observations sont en opposition avec celles qui ont été faites à l'état solide dans lequel le glycolaldéhyde existe sous la forme de dimères chimiquement liés.

Mots clés : résonance de Fermi, conformation, particules de glycolaldéhyde, particules d'hydroxyacétone, spectroscopie infrarouge à transformée de Fourier.

[Traduit par la Rédaction]

1. Introduction

The aggregation of gas-phase molecules to oligomers, small particles, or bulk material is often accompanied by conformational changes of the molecules. They are caused by the influence of intermolecular interactions which in general are rather weak. Conformational changes are expected to be particularly pronounced in hydrogen-bonded systems when intramolecular hydrogen bonds compete with the formation of hydrogen-bonded networks.

Broad-band infrared spectroscopy is ideally suited to investigate conformational changes upon aggregation. In the spectra, such changes lead to characteristic shifts of the vibrational frequencies and to changes in the relative intensities. Corresponding characteristic group frequencies often lie in the fingerprint region. The fingerprint region, however, commonly consists of a dense manifold of vibrational transitions, which can complicate the analysis. Anharmonic resonances are particularly sensitive to conformational changes (1–3) and to aggregation processes in hydrogen-bonded systems (4–6). Compared with the characteristic group frequencies in the fingerprint region, they often appear at higher frequencies, where the infrared spectra typically are less dense. This makes the analysis simpler and more clear-cut.

With their multiple hydrogen-bonding valences, sugars are ideal model systems to study molecular aggregation processes. Depending on the experimental conditions, chemical and conformational changes are observed upon aggregation to small particles (7–9). The present work focuses on glycolaldehyde, which is the simplest monosaccharide sugar. Gas-phase glycolaldehyde also plays a role as an intermediate in the gas-phase oxidation of ethylene (10, 11). In such reactions, the formation of nonvolatile compounds, such as glycolaldehyde, can lead to gas-to-aerosol transitions, i.e., to the formation of small particles (11). Recently, interstellar gas-phase glycolaldehyde has been detected, and its formation by grain-surface reactions has

Received 12 December 2002. Published on the NRC Research Press Web site at http://canjchem.nrc.ca/ on 9 September 2004.

M. Jetzki and D. Luckhaus. Institut für Physikalische Chemie, Universität Göttingen, Tammannstr. 6, D-37077 Göttingen, Germany.
R. Signorell.[2] Institut für Physikalische Chemie, Universität Göttingen, Tammannstr. 6, D-37077 Göttingen, Germany.

[1]This article is part of a Special Issue dedicated to the memory of Professor Gerhard Herzberg.

[2]Corresponding author (e-mail: rsignor@gwdg.de).

 doi: 10.1139/V04-040 © 2004 NRC Canada

been discussed (12, 13). The understanding of these and related processes requires the knowledge of gas-phase spectra as well as of particle spectra. Very detailed information can be obtained through the analysis of infrared spectra. There exist some infrared spectra for glycolaldehyde in the vapor phase, in matrices, as a melt, and in solution (10, 11, 14–17), but no particle spectrum had been reported until now. A comparison of the available data, however, shows a contradictory assignment of some characteristic features in the spectra.

In the present study, we combine Fourier transform infrared spectroscopic investigations of small glycolaldehyde particles and gas-phase glycolaldehyde with theoretical predictions of the vibrational dynamics. The focus lies on conformational changes upon aggregation. This leads to a consistent explanation of the characteristic features in the infrared spectra, which had previously been the subject of some controversy.

2. Experiment

All infrared spectra were recorded with a Bruker Equinox 55 Fourier transform infrared spectrometer equipped with a Globar light source, a KBr beam splitter, and an HgCdTe detector. The spectral resolution was set to be 1 cm^{-1}. The spectrometer was connected to a long-path cell (White optics; optical path length ~10 m) which can be cooled down to liquid-helium temperature. This so-called collisional cooling cell and its operation are described in detail in refs. 18 and 19.

Glycolaldehyde particles were generated in the collisional cooling cell immediately before their infrared spectra were recorded. In a collisional cooling cell, particles are formed by injecting a warm sample gas into a cold bath gas where, due to the supersaturation of the sample gas, nucleation and condensation take place. In the present investigation, we have used helium as bath gas equilibrated to a temperature of 78 K using liquid nitrogen as cooling agent. To generate particles of nonvolatile substances, such as glycolaldehyde, the cell can be equipped with a heatable sample inlet (9). It consists of a heatable sample gas reservoir and a heatable stainless steel injection lance which is controlled by a magnetic valve and projects into the cold cell. In the reservoir, glycoladehyde gas (CH_2OHCHO) was formed by heating solid 2,5–dihydroxy-1,4–dioxane ($C_4H_8O_4$; Fluka research grade) to 383 K. The purity of the vapour thus obtained was obvious from its IR absorption spectrum. In particular, the vapour does not contain any dimer. The glycolaldehyde gas was then mixed with helium gas ($T = 383$ K) to increase the sample gas pressure to ~400 mbar. To form particles, short pulses of the hot sample gas (glycolaldehyde with helium) were injected into the cold bath gas (pressure: 200 mbar). From Mie scattering calculations for the particle infrared spectra (18, 20), we estimate the mean particle size to lie around 50 nm.

For the gas-phase measurements of glycolaldehyde, the same procedure was performed as described above for the particles. The only difference was the bath gas temperature, which was kept at $T = 298$ K. Under these conditions, the sample gas cools down to room temperature inside the cell. For these cell temperatures, any particle formation can be excluded.

3. Calculations

All quantum chemical calculations were performed with the Gaussian program package (21) at the B3LYP and MP2 levels of theory using different basis sets up to quadruple-ζ quality including polarization and diffuse functions (aug-cc-pVQZ). The density functional theory (DFT) calculations employed integration grids of 75 radial shells with 302 angular points each, pruned to about 7000 grid points per atom. The MP2 calculations included only valence orbitals (frozen core approximation). Equilibrium geometries, electronic energies, and harmonic vibrational wavenumbers were determined for different conformers of glycolaldehyde monomer and for several of its hydrogen-bonded oligomers. Some of the corresponding results are listed in Table 1. In the following the different conformers are labelled according to the OCCO (first letter) and CCOH (second letter) dihedral angles: Z and E indicate values around 0° and 180°, respectively; G stands for a value around 50°.

For the calculation of the Fermi resonance between the C=O-stretching vibration ($\nu_{C=O}$) and the first overtone of the C–C-stretching vibration (ν_{C-C}), we have derived two-dimensional potential energy surfaces in the corresponding reduced normal coordinates q_1 for C=O and q_2 for C–C (see eq. [1]). A major advantage of using normal coordinates lies in the fact that the coupling of the "active" coordinates (C=O and C–C stretching) to all the other vibrations of the molecule is accounted for up to quadratic terms. Moreover, anharmonic couplings occur only in the potential energy (neglecting small vibrational angular momentum terms). For each conformer of glycolaldehyde and for all monomeric units in the oligomers, we have calculated 121 single points with the Gaussian program at different levels of theory. As an example, Fig. 1 shows the corresponding point-wise potential (B3LYP/6-31+G*) for the ZZ conformer of glycolaldehyde monomer (see Fig. 2). The potential energy surfaces were then expanded in power series of the form

$$[1] \qquad V = \sum_{l,m=0}^{6} f_{lm} q_1^l q_2^m \text{ with } q_i = Q_i \sqrt{\frac{\omega_i hc}{\hbar^2}}$$

by fitting the coefficients f_{lm} to the calculated grid points (obviously $f_{10} = f_{01} = f_{11} = 0$). The index $i = 1$ refers to the C=O normal coordinate and $i = 2$ to the C–C normal coordinate, Q_i is the mass-weighted normal coordinate, ω_i is the corresponding harmonic wavenumber, c is the speed of light, and $\hbar$ is Planck's constant divided by 2π. In the reduced normal coordinates q_i and their conjugate momenta $\hat{p}_i = -i\partial/\partial q_i$, the vibrational Hamiltonian for the C=O/C–C Fermi resonance system takes the form

$$[2] \qquad \hat{H} = \hat{H}_1^{(0)} + \hat{H}_2^{(0)} + V_{\text{couple}}$$

with

$$V_{\text{couple}} = \sum_{l,m=1}^{6} f_{lm} q_1^l q_2^m$$

and

$$\hat{H}_i^{(0)} = \hat{H}(\hat{p}_{i\neq k} = 0, q_{i\neq k} = 0)$$

© 2004 NRC Canada

Table 1. Electronic energies (E), harmonic vibrational transition wavenumbers $\omega_{C=O}$ and $2\omega_{C-C}$, and anharmonic transition wavenumbers $\tilde{\nu}_{C=O}$ and $\tilde{\nu}_{2(C-C)}$ for different conformers and oligomers of glycolaldehyde (see Fig. 2).

Conformer	Method	Basis set	E/E_H	$\omega_{C=O}$ (cm^{-1})	$2\omega_{C-C}$ (cm^{-1})	$\Delta\omega$ (cm^{-1})	$\tilde{\nu}_{C=O}$ (cm^{-1})	$\tilde{\nu}_{2(C-C)}$ (cm^{-1})	$\Delta\tilde{\nu}$ (cm^{-1})
ZZ	B3LYP	6-31+G*	−229.051 654	1799	1738	61	1784	1733	51
	B3LYP	aug-cc-pVdZ	−229.082 373	1783	1742	41	1768	1740	28
	MP2	6-31+G*	−228.389 101	1755	1796	−41	1743	1792	−49
	MP2	aug-cc-pVdZ	−228.480 593	1731	1771	−40	1719	1767	−48
	MP2	aug-cc-pVtZ	−228.677 518	1753	1774	−21	1740	1770	−30
ZE	B3LYP	6-31+G*	−229.043 262	1838	1722	116	1823	1717	106
EE	B3LYP	6-31+G*	−229.046 969	1821	1989	−168	1806	1998	−192
ZE-EE	B3LYP	6-31+G*	−458.100 255	1834	1733	101	1820	1730	90
				1802	2006	−204	1790	2015	−225
ZE-ZE	B3LYP	6-31+G*	−458.097 902	1833	1734	99	1819	1728	91
				1813	1747	66	1799	1742	57
Chair	B3LYP	6-31+G*	−458.111 594	1811	1713	98	1794	1706	88
				1806	1710	96			
Half twist	B3LYP	6-31+G*	−458.111 658	1810	1701	109			
				1784	2095	−311			
Twist	B3LYP	6-31+G*	−458.108 099	1793	2100	−307			
				1787	2093	−306			
$(ZE)_3$	B3LYP	6-31+G*	−687.153 367	1832	1733	99			
				1817	1759	58			
				1809	1747	62			
$(ZE)_4$	B3LYP	6-31+G*	−916.209 381	1832	1733	99			
				1812	1756	56			
				1806	1762	44			
				1817	1748	69			
$ZZ-(ZG)_5$	B3LYP	6-31+G*	−1 374.352 241	1769	1761	8			
				1775	1728	47			
				1778	1733	45			
				1784	1739	45			
				1791	1740	51			
				1812	1708	104			

Note: $\Delta\omega = \omega_{C=O} - 2\omega_{C-C}$ and $\Delta\tilde{\nu} = \tilde{\nu}_{C=O} - \tilde{\nu}_{2(C-C)}$.

This expression neglects all vibrational-angular momentum terms and the pseudo-potential, both of which are usually small. V_{couple} is the nonseparable contribution to the potential energy V and $\hat{H}_i^{(0)}$ is the one-dimensional (1-D) separable anharmonic Hamiltonian for the vibrational motion in q_i. $\hat{H}$ is diagonalized in a product basis $|v_1 v_2\rangle = |v_1\rangle|v_2\rangle$ of the 1-D C=O-stretching function $|v_1\rangle$ and the 1-D C–C-stretching function $|v_2\rangle$. The C=O and C–C vibrations fulfill the 1:2 resonance condition almost perfectly. Since the coupling between them is much smaller than the vibrational quanta, the Fermi resonance between the C=O-stretching fundamental and the first C–C-stretching overtone can be reduced to an effective two-level Fermi resonance with the following matrix representation:

$$[3] \qquad \begin{pmatrix} \langle 10|\hat{H}|10\rangle & W \\ W & \langle 02|\hat{H}|02\rangle \end{pmatrix}$$

with the coupling matrix element

$$[4] \qquad W = \langle 10|\hat{H}|02\rangle = \langle 02|\hat{H}|10\rangle$$

Because typical anharmonicities (Table 1) are comparable to W (Table 2), the product basis has to be built from separable anharmonic wave functions. These were obtained by diagonalizing $\hat{H}_i^{(0)}$ in a basis of harmonic oscillator eigenfunctions:

$$[5] \qquad \hat{H}_i^{(0)}|v_i\rangle = E_{i,v_i}|v_i\rangle$$

The contribution of the leading harmonic basis function to the three lowest eigenfunctions exceeds 95%. Since the C=O/C–C Fermi resonance is dominated by the $q_1 q_2^2$ potential term, the coupling matrix element W can be approximated as

$$[6] \qquad W \approx \frac{1}{2} f_{12}$$

The solution of the Fermi resonance problem leads to the two eigenvalues

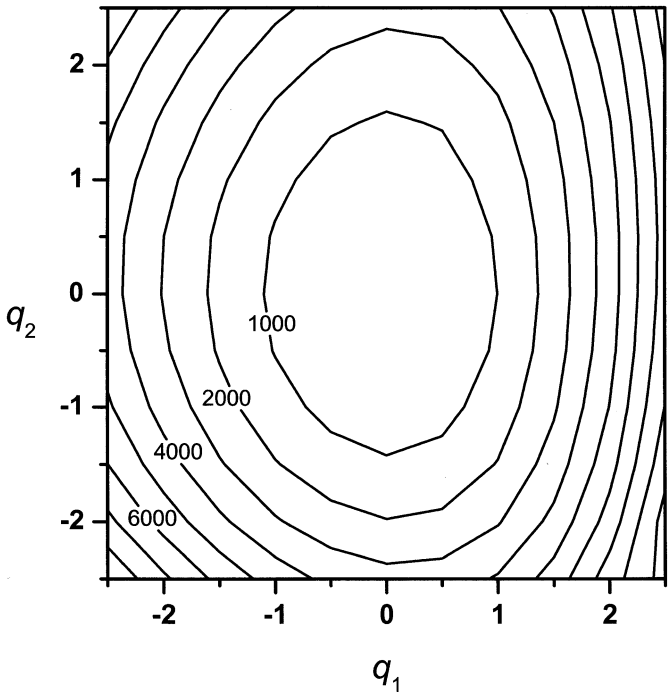
$$[7] \qquad E_A > E_B$$

and to the eigenfunctions

$$[8] \qquad \psi_A = a \cdot |10\rangle - b \cdot |02\rangle$$
$$\psi_B = b \cdot |10\rangle + a \cdot |02\rangle$$

© 2004 NRC Canada

Fig. 1. Two-dimensional potential energy surface V (eq. [1]) in the reduced normal coordinates q_1 (C=O-stretching vibration) and q_2 (C–C-stretching vibration). The contours represent equipotential lines separated by 1000 cm^{-1}.

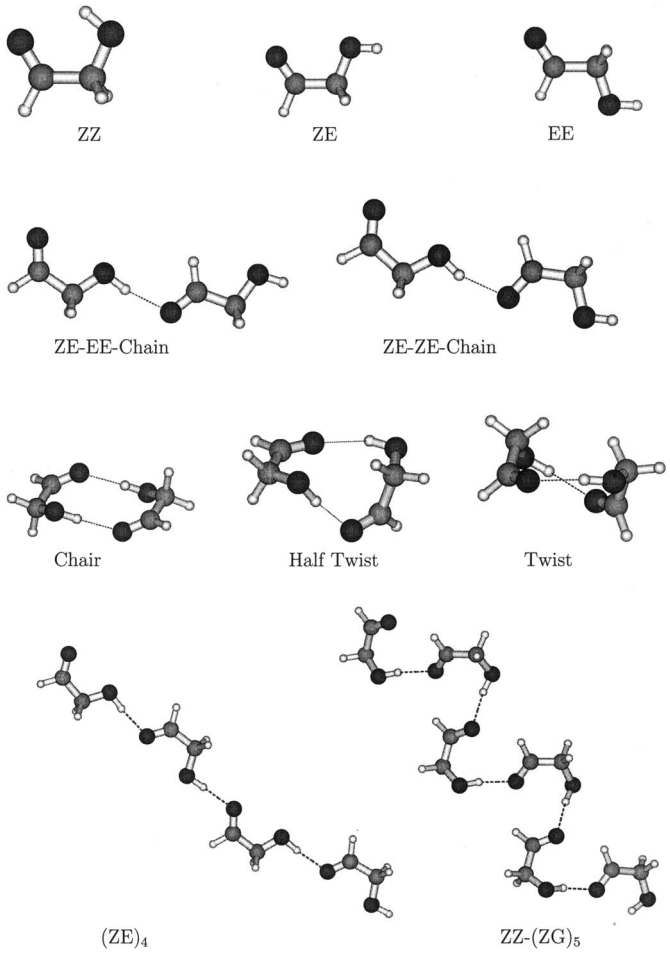


Assuming that only the C=O-stretching fundamental carries intensity, the relative band strength $\frac{I_A}{I_B}$ is given approximately by:

$$[9] \qquad I = \frac{I_A}{I_B} \approx \frac{a^2}{b^2}$$

The approximations inherent in eqs. [3]–[6] were checked against a numerically exact diagonalization of the full Hamiltonian (eq. [2]). The corresponding eigenvalues agree to within 2 cm^{-1}.

Fig. 2. Equilibrium structures for different conformers (ZZ, ZE, and EE) and small oligomers (chair, half twist, twist, ZE–EE, ZE–ZE, $(ZE)_4$, and ZZ–$(ZG)_5$) of glycolaldehyde. O, C, and H atoms are represented by dark, medium, and light grey spheres, respectively. The different conformers are labelled according to the OCCO (first letter) and CCOH (second letter) dihedral angles. Z and E indicate values around 0° and 180°, respectively. G stands for a value around 50°.



4. Results

Figure 3 shows the gas-phase infrared spectrum of glycolaldehyde (trace *a*) in comparison with the corresponding particle spectrum (trace *b*) between 600 and 3750 cm^{-1}. The comparison of the two spectra provides insight into the conformational changes that accompany the aggregation of the gas-phase monomers to hydrogen-bonded aggregates in the particles. The overall agreement between the gas-phase spectrum and the particle spectrum confirms that the chemical composition does not change upon aggregation even though the solid bulk phase consists of the chemically bound dimer 2,5-dihydroxy-1,4-dioxane (14, 16). This agrees with earlier observations on dihydroxyacetone (9): The proton-catalyzed dimerization of α-hydroxy-carbonyl compounds cannot compete with aggregation under aprotic conditions. Consequently, the main differences between the two spectra arise from the formation of hydrogen bonds in the particles and from conformational changes of the monomers upon aggregation. The most prominent difference between the two spectra appears in the OH-stretching region around 3300 cm^{-1}. Compared with the gas phase, the OH-stretching band of the particles is red shifted and distinctly broader. This observation can clearly be explained by the formation of intermolecular hydrogen bonds in the particles, which are evidently more favorable than the intramolecular one in the gas phase (probably due to cooperative effects). However, the hardly characteristic OH-stretching region of the particle spectrum cannot provide any further information about conformations. More informative with regard to conformation is the region below 2000 cm^{-1} with the following most notable features: (*i*) The band labelled with an asterisk in the gas-phase spectrum has disappeared in the particle spectrum. (*ii*) In both spectra, the C=O-stretching bands around 1750 cm^{-1} are split. The intensity ratio, however, of the higher frequency band to the lower frequency band is smaller in the particle spectrum (2:1) than in the gas-phase spectrum

© 2004 NRC Canada

(5:1). In the following, we demonstrate how these observations can be exploited to extract information about conformational changes upon particle formation.

4.1. Fermi resonance in the gas phase

In agreement with the results of an early microwave investigation (22) and a matrix study (15), our analysis of the gas-phase spectrum (trace *a* in Fig. 3) shows that the hydrogen-bonded ZZ conformer (Fig. 2) is the dominant species in the gas phase at 293 K. Harmonic ab initio calculations of the infrared spectrum of the energetically most favorable ring conformer ZZ agree best with the experimental spectrum. For illustration, Fig. 4 compares the experimental gas-phase spectrum (trace *d*) with the calculated spectrum of the ring conformer ZZ (trace *c*) and with the calculated spectra of the open conformers ZE (trace *b*) and EE (trace *a*). In contrast to all open forms of glycolaldehyde, only the intramolecularly hydrogen-bonded ZZ conformer shows the characteristic absorption band observed at 1276 cm^{-1}, which is labelled by an asterisk in Figs. 3 and 4. This band arises from the excitation of the OH-bending motion in combination with the CH_2-wagging motion of the intramolecularly hydrogen-bonded ring structure. Analogous characteristic absorption bands can be observed in the gas-phase spectra of hydroxyacetone at 1288 cm^{-1} (trace *a* in Fig. 5) and dihydroxyacetone at 1288 cm^{-1} (8,9). As demonstrated previously (8,9), this absorption band is highly characteristic for the intramolecularly hydrogen-bonded ring structures common to the most stable conformers of these molecules.

An assignment of the bands observed in the gas-phase spectrum is given in Table 3 based on the harmonic ab initio calculations. Compared with refs. 10 and 14, some transitions are reassigned here. Our assignment matches the assignment of matrix spectra by Aspiala et al. (15) within the expected wavenumber shifts. From Fig. 4 and Table 3, it is clear that the two rather weak bands at 2709 and 1706 cm^{-1} (Fig. 3*a*) cannot be explained within a harmonic analysis. In principle, three explanations could account for this: The two bands arise from a second less stable conformer or from hot band transitions or from anharmonic resonances. A second minor species would obviously have to be an open conformer, i.e., one without intramolecular hydrogen bonds. Compared with the ZZ conformer, the open conformers show blue shifted OH-stretching bands and blue shifted C=O-stretching bands. The additional C=O band at 1706 cm^{-1}, however, is red shifted and not blue shifted relative to the C=O band of the ZZ conformer, nor is there any indication in Fig. 3 of a blue shifted OH-stretching absorption or any other of the characteristic bands predicted for open forms of glycolaldehyde. The presence of a second conformer in the gas phase can therefore be excluded. The same holds for the alternative explanation of the bands at 2709 and 1706 cm^{-1} in terms of vibrationally hot transitions as there are two observations that clearly contradict it. First, hot bands should also be observable in other regions of the spectrum, which is not the case. Moreover and more importantly, the presence of both transitions in the particle spectrum (Fig. 3*b*) recorded at much lower temperature ($T = 78$ K) contradicts the assignment as hot bands. This leaves anharmonic resonances as the only plausible explanation for the bands at 2709 and 1706 cm^{-1}. This possibility had already been considered in the analysis of the matrix spectra of glycolaldehyde (15). The transition at 2709 cm^{-1} arises from the first in-plane bending overtone of the aldehyde group with its CH-stretching fundamental. Consequently, the bending fundamental would be expected above 1360 cm^{-1}. This value coincides with the CH_2-bending multiplet (1356–1456 cm^{-1}). In this range, four peaks are observed instead of only the three calculated fundamental transitions. This is consistent with a second Fermi resonance between the aldehydic in-plane and out-of-plane bending vibrations (fundamental transition calculated at 721 cm^{-1} with vanishing intensity). Similar resonances have been observed for other aldehydes (23) such as acetaldehyde (24) with typical stretch–bend coupling matrix elements around 50 cm^{-1}. This Fermi resonance is thus not particularly characteristic for glycolaldehyde nor is it particularly sensitive to conformational changes. Although the resonance is still observed in the particles, it is therefore ill suited to extract information about specific conformational changes upon aggregation. More characteristic is the Fermi resonance that causes the splitting of the C=O band. In this case, the C=O-stretching mode couples most probably to the first overtone of the C–C-stretching vibration, which appears at 859 cm^{-1} in the gas-phase spectrum. Because both the C=O and the C–C-stretching vibrations shift only slightly upon aggregation, the splitting is also observed in the particle spectrum in Fig. 3*b*. In systems where the C–C-stretching vibrations move to higher or lower frequencies compared with glycolaldehyde, e.g., in dihydroxyacetone (9) or hydroxyacetone (see Fig. 5), no splitting of the C=O band is observed.

To support this explanation, we have modeled the Fermi resonance between the C=O band and the first overtone of the C–C-stretching band for the ZZ conformer by ab initio calculations, as explained in Sect. 3. Note that the resulting evidence is quite independent from our experimental observations. The harmonic wavenumbers ($\omega_{C=O}$ and $2\omega_{C-C}$) and the anharmonic wavenumbers ($\tilde{\nu}_{C=O}$ and $\tilde{\nu}_{2(C-C)}$) for the uncoupled 1-D problems (eq. [5]) are summarized in Table 1 for different levels of theory. These data reveal anharmonicities less than 1% nearly independent of the methods used. Thus, the resonance defect is largely determined by the harmonic contribution $\Delta\omega$, which differs significantly for different levels of ab initio theory. Table 2 lists values of the coupling matrix element W (eq. [4]), the relative band strength I (eq. [9]), and the calculated transition wavenumbers $\tilde{\nu}_{A,B} = E_{A,B} - E_{1,0} - E_{2,0}$ (eqs. [5] and [7]). For the matrix element W, all levels of theory lead to a similar value of about 20 cm^{-1}. A simple two-level data analysis (see p. 216 in ref. 25) of the doublet at 1754 and 1706 cm^{-1} with an intensity ratio $I_{exptl.} = 5{:}1$ leads to an experimental value of $W_{exptl.} = 18$ cm^{-1} in perfect agreement with our theoretical value. Because the anharmonicities and the coupling matrix element both are stable with respect to the increasing level of theory, the differences in the values of I, $\tilde{\nu}_A$, and $\tilde{\nu}_B$ calculated for the ZZ form with different methods arise almost exclusively from remaining small errors in the harmonic wavenumbers $\omega_{C=O}$ and ω_{C-C} (Table 1), which are to be expected at the levels of theory employed. The intensity ratio I of the doublet (eq. [9]) reacts very sensitively to minor shifts of the vibrational wavenumbers. The B3LYP calculation consistently overestimates the C=O-stretching wavenumber, increasing the resonance defect, and thus weakening the resonance (I becomes too large). The MP2 calculation by contrast predicts the C–C-stretching vibration too high, effectively inverting the

© 2004 NRC Canada

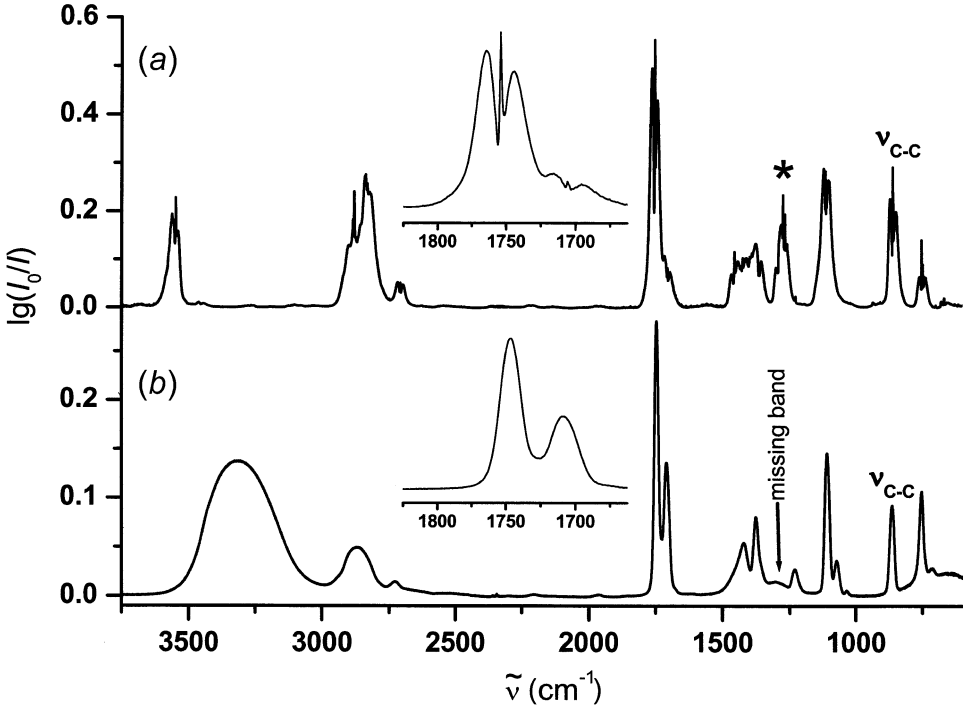
Table 2. Coupling matrix elements W (eq. [4]), coefficients a and b of the eigenfunctions (eq. [8]), relative band strengths I (eq. [9]), and calculated transition wavenumbers $\tilde{\nu}_A = E_A - E_{1,0} - E_{2,0}$ and $\tilde{\nu}_B = E_B - E_{1,0} - E_{2,0}$ from eqs. [5] and [7] for different conformers of glycolaldehyde and experimental values for gas-phase and particle spectra.

Conformer	Method	Basis set	W (cm^{-1})	$\|a\|$	$\|b\|$	$I \approx \frac{a^2}{b^2}$	$\tilde{\nu}_A$ (cm^{-1})	$\tilde{\nu}_B$ (cm^{-1})	$\Delta\tilde{\nu}_{A-B}$ (cm^{-1})[a]
ZZ	B3LYP	6-31+G*	21	0.9416	0.3368	8:1	1792	1726	66
	B3LYP	aug-cc-pVdZ	20	0.8854	0.4648	4:1	1779	1730	49
	MP2	6-31+G*	20	0.3365	0.9417	1:8	1735	1799	−64
	MP2	aug-cc-pVdZ	19	0.3359	0.9419	1:8	1712	1774	−62
	MP2	aug-cc-pVtZ	20	0.4507	0.8927	1:4	1730	1780	−50
ZE	B3LYP	6-31+G*	24	0.9783	0.2074	22:1	1828	1712	116
EE	B3LYP	6-31+G*	22	0.1132	0.9936	1:77	1803	2001	−198
ZE-EE	B3LYP	6-31+G*	23	0.9722	0.2341	18:1	1826	1724	102
			22	0.0959	0.9954	1:108	1788	2017	−229
ZE-ZE	B3LYP	6-31+G*	21	0.9760	0.2176	20:1	1824	1723	101
			21	0.9495	0.3138	9:1	1805	1736	69
Chair	B3LYP	6-31+G*	22	0.9733	0.2297	18:1	1799	1701	98
Experiment	Gas phase		18[b]			5:1	1754	1706	48
	Particles		18[b]			2:1	1747	1708	39

[a] $\Delta\tilde{\nu}_{A-B} = \tilde{\nu}_A - \tilde{\nu}_B$.

[b] From a simple data analysis (see ref. 25, p. 216).

Fig. 3. Experimental infrared spectra of glycolaldehyde. (*a*) Gas-phase spectrum recorded at $T = 293$ K. (*b*) Particle spectrum recorded at $T = 78$ K. $\tilde{\nu}$ is the transition wavenumber.



intensity ratio. Notwithstanding these small errors, all values for I consistently indicate a pronounced Fermi resonance for the ZZ conformer. The (expected) deviations in calculated harmonic wavenumbers (and consequently in absolute band positions) do not affect this conclusion. Since the fundamental band centers are known experimentally, the ab initio prediction of anharmonicities and coupling matrix elements proves — independent from the experiment — that the observed splitting in the gas-phase spectrum around 1730 cm^{-1} arises from a Fermi resonance involving the C=O-stretching vibration and the first overtone of the C–C-stretching vibration. In particular, the comparison of B3LYP and MP2 calculations with systemat-

© 2004 NRC Canada

Table 3. Vibrational assignment of the IR spectrum of glycolaldehyde vapor and particles (transition wavenumbers $\tilde{\nu}$ in cm^{-1}).

			Assignment[b]	
$\tilde{\nu}$ (vapor)	$\tilde{\nu}$ (particles)	ω (B3LYP)[a]	Present study	Refs. 10 and 14
3549	3313	3708	ν_{OH}	ν_{OH}
2881		2984	$\nu_{CH_2(as)}$	
2840	2858	2973	$\nu_{CH_2(s)}$	ν_{C-H}
2820		2922	ν_{CH}[c]	
2710	2719		$2\beta_{CH}$[c]	ν_{CH}
1754	1747	1793	$\nu_{C=O}$[d]	$\nu_{C=O}$
1706	1708		$2\nu_{C-C}$[d]	
1456		1473	$\delta_{CH_2(scissor)}$	
1425	1423	1433	$\delta_{CH_2(wag)}$, β_{OH}	$\delta_{CH_2(wag)}$
1378	1357	1394	β_{CH}	
1356				
1275		1293	β_{OH}, $\delta_{CH_2(wag)}$	ν_{C-O}
1112	1109	1128	ν_{C-O}	ν_{C-C}
	1073			β_{OH}
859	863	863	ν_{C-C}	$\beta_{O=C-C}$
752	753	763	$\beta_{O=C-C}$, β_{C-C-O}	

[a] Harmonic wavenumbers calculated with the aug-cc-pVQZ basis set.
[b] ν = stretching, β = in-plane bending, δ = deformation and out-of-plane bending.
[c] Fermi resonance $\nu_{CH}/2\beta_{CH}$.
[d] Fermi resonance $\nu_{C=O}/2\nu_{C-C}$.

ically increasing basis size clearly shows that the rather modest B3LYP/6-31+G* level of theory is sufficient to derive a realistic model of this characteristic Fermi resonance.

4.2. Conformation in the particles

The analysis of the gas-phase spectrum in the previous section enables us to obtain information on the type of conformers and aggregates in the particles. As mentioned at the beginning of Sect. 4, this is mainly based on two prominent features in the experimental spectra: (*i*) the band at 1276 cm^{-1} in the gas-phase spectrum which is missing in the particle spectrum, and (*ii*) the C=O-stretching doublet observed both in the gas-phase and in the particle spectra.

Observation (*i*) hints at an at least partial breakup of the intramolecular hydrogen bond in the ZZ conformer upon aggregation. As outlined in the previous section, this band is characteristic only for the intramolecularly hydrogen-bonded ring conformer ZZ. The fact that the transition near 1276 cm^{-1} is missing in the particle spectrum therefore indicates that the particles consist of open forms of glycolaldehyde, for example, the ZE or the EE conformer of Fig. 2. The same effect upon aggregation is also found for dihydroxyacetone (9) and hydroxyacetone (Fig. 5). Both molecules form an intramolecular ring in the gas phase that is broken up upon particle formation. With the predominance of open forms in glycolaldehyde particles thus established, we can derive more detailed information about the nature of these conformers from the C=O-stretching doublet. To this end, we first investigate the influence of the conformation on the corresponding Fermi resonance. In a second step, the influence of the aggregation, i.e., the formation of intermolecular hydrogen bonds, on the Fermi resonance is studied.

To account for the effect of conformational changes, we have modeled the Fermi resonance for different conformers via ab initio calculations as explained in Sect. 3. Here, we restrict ourselves to the conformers ZZ, ZE, and EE (Fig. 2) because all important points can be discussed with these three examples. The results from our calculations for these conformers are listed in Tables 1 and 2. For clarity, we only show the results of the B3LYP/6-31+G* calculations for the new conformers; however, in extensive calculations with basis sets up to aug-cc-pVQZ at the B3LYP and at the MP2 level of theory (not shown here), the ZE and EE conformers show the same behavior as described above for the ZZ form: Harmonic wavenumbers vary within expected errors while anharmonicities and coupling matrix elements remain stable. In particular, we note that B3LYP and MP2 calculations yield essentially the same wavenumber shifts upon hydrogen bonding (comparing ZZ vs. ZE) with only weak basis set dependence. Dispersion forces, which cannot be described by local density approximations (such as B3LYP), apparently do not play any major role in this context. The relative band strength I for the EE conformer indicates that the Fermi resonance is negligible for this form. In the ZE conformer, the resonance is stronger than in the EE conformer but weaker than in the ZZ conformer. The data in Tables 1 and 2 clearly reveal the origin of this behavior. The matrix element W has a similar magnitude for all different conformers as do the anharmonicities. Consequently, the difference between the two conformers arises from different harmonic wavenumbers $\omega_{C=O}$ and $2\omega_{C-C}$ (Table 1).

In the most stable ZZ conformer, the intramolecular hydrogen bond weakens the C=O bond, which acquires more single-bond character compared with the free C=O group. At the same time, the C–C bond stiffens as the enolic resonance structure obtains more weight in the hydrogen-bonded form. By the reverse argument, the $\nu_{C=O}/2\nu_{C-C}$ resonance defect increases significantly in the ZE conformer, and the Fermi resonance becomes less pro-

© 2004 NRC Canada

Fig. 4. Theoretical infrared spectra of the (*a*) EE conformer, (*b*) ZE conformer, and (*c*) ZZ conformer of glycolaldehyde calculated at the B3LYP/6-31+G* level. For better comparison with the experimental gas-phase spectrum in trace *d*, the calculated stick spectra are convoluted with a Gaussian band shape of 35 cm^{-1} fwhm. The absolute intensity scale refers to the calculated stick spectra. The integrated absorption intensity S may be converted to integrated absorption cross sections G via $G = S/\tilde{\nu}_0$, where $\tilde{\nu}_0$ is the band centre. $\tilde{\nu}$ is the transition wavenumber.

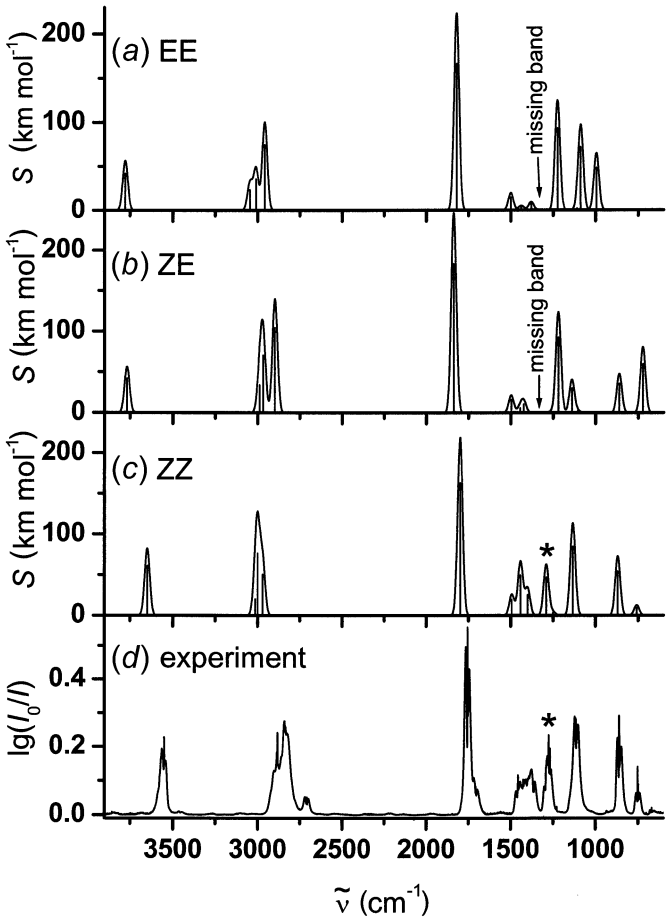
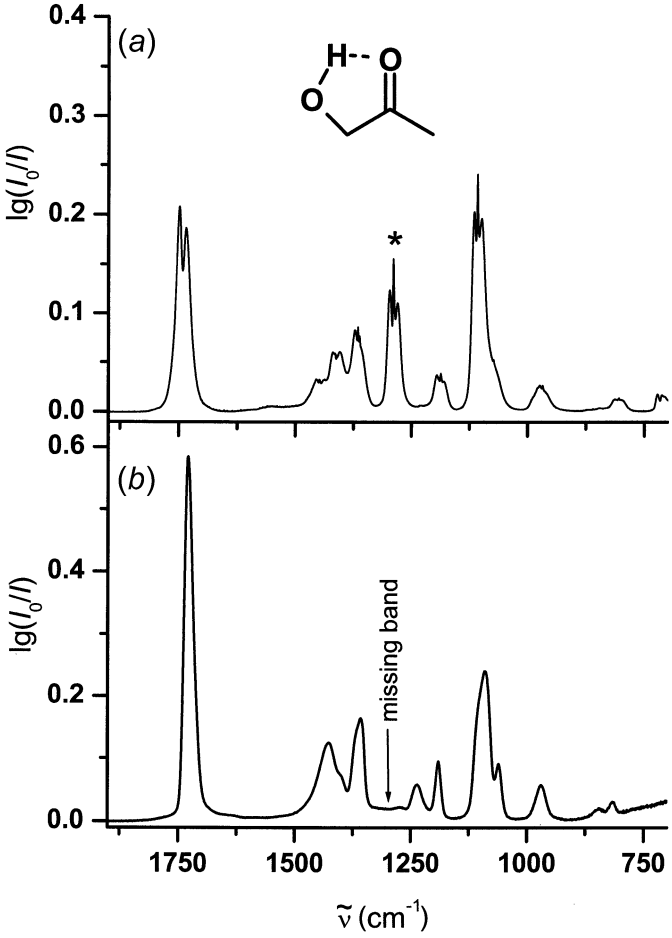


Fig. 5. Experimental infrared spectra of hydroxyacetone ($CH_2OHCOCH_3$). (*a*) Gas-phase spectrum recorded at $T = 293$ K. (*b*) Particle spectrum recorded at $T = 78$ K. The band at 1288 cm^{-1} labelled with an asterisk in the gas-phase spectrum has disappeared in the particle spectrum. $\tilde{\nu}$ is the transition wavenumber.



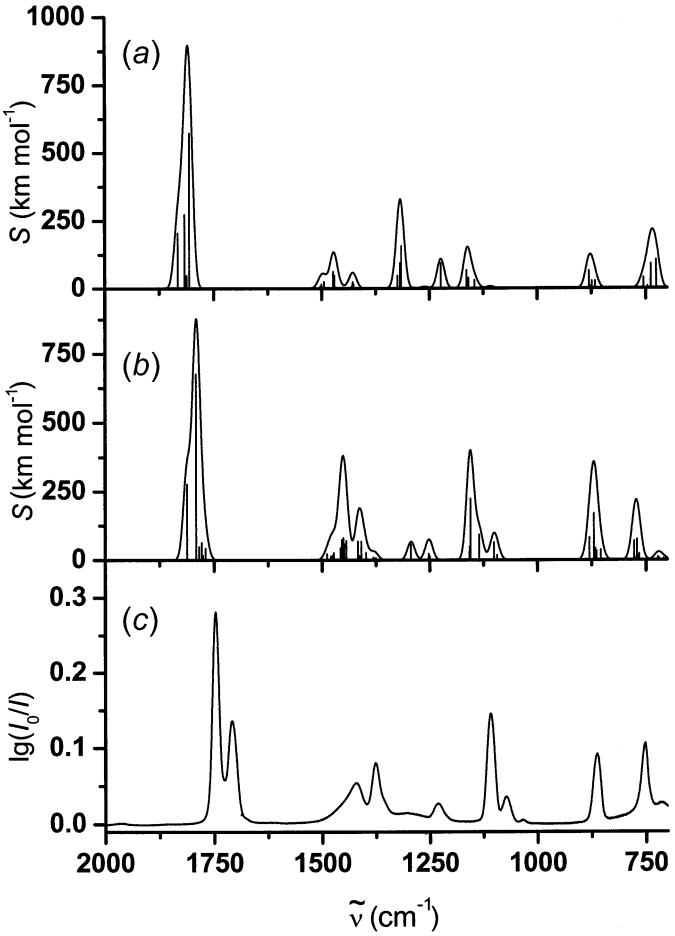
nounced. Beyond the breaking of the intramolecular hydrogen bond, the torsion of the OH group itself hardly influences the Fermi resonance, so that we cannot distinguish between different CCOH dihedral angles.

In contrast to the ZE conformer, the increased value of $\omega_{C=O}$ is only of minor influence in the EE conformer. Here, the main influence arises from the huge increase of ω_{C-C}, which depends very sensitively on the OCCO dihedral angle. For a torsional angle of 180°, this increase is so large that $2\omega_{C-C}$ is no longer in resonance with the C=O-stretching fundamental. The EE conformer can thus be excluded as a major component in glycolaldehyde particles. This is confirmed by calculations for small hydrogen-bonded dimers of glycolaldehyde. The ZE–EE dimer shows an increased C–C transition wavenumber only in its EE moiety. In the ZE unit, this value stays nearly stable (Table 1). Consequently, the Fermi resonance is negligible in the EE moiety but not in the ZE moiety, as indicated in Table 2. In the same way, the value of $2\omega_{C-C}$ explains why the Fermi resonance is important in both subunits of the ZE–ZE dimer and of the "chair" dimer (Z-arrangement of the C=O group and the C–O group). The half twist (only for one unit) and the twist conformer (for both units) show what happens when the relative arrangement of the C=O group and the C–O group lies between an E-arrangement and a Z-arrangement. Tables 1 and 2 show that this arrangement also leads to a strong increase of the C–C transition wavenumber and a negligible Fermi resonance as a consequence. Thus, the strong Fermi resonance observed in the experimental particle spectrum is only compatible with a Z-arrangement of the OCCO dihedral angle in the monomeric subunits.

As a second step, we consider the influence of intermolecular hydrogen bonds on the Fermi resonance with ZE-chains as examples. In the following, we have disregarded basis set superposition effects as our discussion focuses on spectral features rather than the absolute stability of particular oligomers. As mentioned above, due to the missing intramolecular hydrogen bond, the value of $\omega_{C=O}$ is increased in the open forms compared with the ZZ conformer of the gas phase. To explain the stronger Fermi resonance in the particle spectra, the

© 2004 NRC Canada

Fig. 6. (*a*) Theoretical infrared spectrum of the tetramer $(ZE)_4$ of glycolaldehyde calculated at the B3LYP/6-31+G* level. (*b*) The same for the hexamer ZZ–$(ZG)_5$. (*c*) Part of the experimental particle spectrum of glycolaldehyde shown in Fig. 3*b*. For better comparison with the experimental spectrum in trace c, the calculated stick spectra are convoluted with a Gaussian band shape of 20 cm^{-1} fwhm. The absolute intensity scale refers to the calculated stick spectra. $\tilde{\nu}$ is the transition wavenumber.



C=O groups obviously have to act as acceptors of intermolecular hydrogen bonds (as illustrated in Fig. 2), thus restoring $\omega_{C=O}$ roughly to its gas-phase value. This effect is found for the dimers, for the trimer $(ZE)_3$, and for the tetramer $(ZE)_4$ in Table 1. The calculations also show the corresponding slight blue shift of $2\omega_{C-C}$ upon aggregation. It is most interesting to note that the aggregation to longer chains reduces the resonance defect even beyond the gas-phase values. While the end groups mimic the behavior of the dimer, the inner monomer units appear to be subject to cooperative effects that put the Fermi resonance levels closer into resonance. The formation of hydrogen bonds apparently improves the resonance condition $\Delta\omega$ for conformers inside long chains compared to free monomers. This result qualitatively explains the observed stronger Fermi resonance in the experimental particle spectrum.

From the above arguments, long hydrogen-bonded chains of ZE conformers would appear as probable main constituents of glycolaldehyde particles. With the Z conformation of the OCCO dihedral angle, the necessary condition for the $\nu_{C=O}/2\nu_{C-C}$ Fermi resonance is fulfilled. Its increased strength compared with the gas-phase spectrum results from the above-mentioned cooperativity in longer chains. The E conformation of the CCOH dihedral angle explains the absence of the band near 1280 cm^{-1}. The agreement, however, between the calculated harmonic spectrum of the $(ZE)_4$ oligomer (Fig. 6*a*) and the experimental particle spectrum (Fig. 6*c*) is less than satisfactory. The most prominent deviations arise from the intensity distribution in the C–O-stretching region ($\sim$1150 cm^{-1}). In fact, much better qualitative agreement is obtained for the chair-dimer featuring a gauche conformation of OH relative to CC (CCOH $\sim$50°) while the OCCO dihedral angle remains at the required 180°. Although the intramolecular hydrogen bond is not completely broken in this arrangement, it is sufficiently weakened to make the characteristic 1280 cm^{-1} band disappear. In this conformation the glycolaldehyde monomers preferably arrange in "zig-zag" chains enabling the formation of a weak CH$\cdots$O=C hydrogen bond in addition to the strong OH$\cdots$O=C hydrogen bond. As an example, Fig. 2 shows the hexamer ZZ–$(ZG)_5$. The corresponding calculated harmonic absorption spectrum is depicted in Fig. 6*b*. Except for the marked overestimation of the C=O-stretching fundamental wavenumber, the agreement with the experimental particle spectrum is very good. Allowance has obviously to be made for the finite length of the short chains accessible to ab initio calculations. The main boundary effect in the calculated hexamer spectrum is a high-frequency shoulder on the C=O-stretching band due to the one "free" carbonyl group of the chain (the ZG end unit). In longer chains this effect will become negligible. However, the exact length of the hydrogen-bonded chains remains unknown nor can we distinguish between long chains and large rings. Both types of aggregates would lead to very similar spectral features.

5. Summary

The present study shows that Fermi resonances in infrared spectra can be used as a sensitive probe for conformational changes upon aggregation of molecular substances. This is demonstrated here by the example of glycolaldehyde, which shows a split carbonyl band around 1730 cm^{-1} in the gas-phase spectrum as well as in the spectrum of small (size: $\sim$50 nm) glycolaldehyde particles. The gas phase of glycolaldehyde consists of an intramolecularly hydrogen-bonded ring (ZZ conformer). With the help of ab initio calculations, we have shown that the doublet around 1730 cm^{-1} can clearly be traced back to a Fermi resonance involving the C=O-stretching vibration and the first overtone of the C–C-stretching vibration. The corresponding result is in agreement with a simple two-level analysis of the experimental data.

Upon the aggregation to particles, the intramolecular hydrogen bond of the gas-phase ZZ conformer partially breaks and intermolecular hydrogen bonds are formed. Consequently, the aggregates in the particles consist of open conformers of glycolaldehyde monomer. The ab initio calculations reveal a strong dependence of the Fermi resonance on the monomeric conformations. Here, the important factor is the transition wavenumber of the C–C-stretching vibration, whereas the coupling matrix element W and the anharmonicities hardly change at all. In particular, the value of W is apparently characteristic for the particular structural (α-hydroxy-carbonyl) feature, quite

© 2004 NRC Canada

independent of the details of the molecular environment. By contrast, the value of the C–C-stretching wavenumber sensitively determines the relative arrangement of the C=O group and the C–O group. The observed strong Fermi resonance in the particle spectra is only consistent with a Z-arrangement (cis-configuration) of these two groups. Furthermore, the formation of intermolecular hydrogen bonds has an influence on the Fermi resonance. We find that the formation of longer chains improves the resonance condition between the C=O vibration and the C–C vibration. Taken together, these results explain the strong Fermi resonance observed in the particle spectrum, at least qualitatively. The particular value of the OH torsion angle has only negligible effects on the Fermi resonance, but the intensity distribution in the C–O-stretching region suggests an out-of-plane angle of around 50°. This conformation is particularly favorable as it enables the formation of secondary hydrogen bonds between the carbonyl group and the aldehydic C–H group. These results demonstrate how characteristic anharmonic resonances can serve as sensitive probes into structural details of intermolecular arrangements.

Acknowledgements

We thank Professor M.A. Suhm for measurement time on the Bruker Equinox 55. Financial support by the Deutschen Forschungsgemeinschaft (grant Nr. SI 833/1-1, GRK 782, and SFB 357) is gratefully acknowledged.

References

1. S. Abbate, S.L. Wunder, and G. Zerbi. J. Phys. Chem. **88**, 5931 (1984).
2. G. Heimel, D. Somitsch, P. Knoll, and E. Zojer. J. Chem. Phys. **116**, 10921 (2002).
3. E.M.S. Maçôas, J. Lundell, M. Pettersson, L. Khriachtchev, R. Fausto, and M. Räsänen. J. Mol. Spectrosc. **219**, 70 (2003).
4. H. Ratajczak and A.M. Yaremko. Chem. Phys. Lett. **314**, 122 (1999).
5. G.M. Florio, E.L. Sibert III, and T.S. Zwier. Faraday Discuss. **118**, 315 (2001).
6. C. Emmeluth, M.A. Suhm, and D. Luckhaus. J. Chem. Phys. **118**, 2242 (2003).
7. R. Signorell, M.K. Kunzmann, and M.A. Suhm. Chem. Phys. Lett. **329**, 52 (2000).
8. R. Signorell and D. Luckhaus. J. Phys. Chem. A, **106**, 4855 (2002).
9. M. Jetzki and R. Signorell. J. Chem. Phys. **117**, 8063 (2002).
10. H. Niki, P.D. Maker, C.M. Savage, and L.P. Breitenbach. Chem. Phys. Lett. **80**, 499 (1981).
11. H. Niki, P.D. Maker, C.M. Savage, and L.P. Breitenbach. J. Phys. Chem. **85**, 1024 (1981).
12. J.M. Hollis, F.J. Lovas, and P.R. Jewell. Astrophys. J. **540**, L107 (2000).
13. J.M. Hollis, S.N. Vogel, L.E. Snyder, P.R. Jewell, and F.J. Lovas. Astrophys. J. **554**, L81 (2001).
14. H. Michelsen and P. Klaboe. J. Mol. Struct. **4**, 293 (1969).
15. A. Aspiala, J. Murto, and P. Stén. Chem. Phys. **106**, 399 (1986).
16. Y. Kobayashi, H. Takahara, H. Takahashi, and K. Higasi. J. Mol. Struct. **32**, 235 (1976).
17. V.A. Yaylayan, S. Harty-Majors, and A.A. Ismail. Carbohydr. Res. **309**, 31 (1998).
18. M.K. Kunzmann, R. Signorell, M. Taraschewski, and S. Bauerecker. Phys. Chem. Chem. Phys. **3**, 3742 (2001).
19. S. Bauerecker, M. Taraschewski, C. Weitkamp, and H.K. Cammenga. Rev. Sci. Instrum. **72**, 3946 (2001).
20. C.F. Bohren and D.R. Huffman. Absorption and Scattering of Light by Small Particles. Wiley-Interscience, New York. 1998.
21. M.J. Frisch, G.W. Trucks, H.B. Schlegel, G.E. Scuseria, M.A. Robb, J.R. Cheeseman, V.G. Zakrzewski, J.A. Montgomery, Jr., R.F. Stratmann, J.C. Burant, S. Dapprich, J.M. Millam, A.D. Daniels, K.N. Kudin, M.C. Strain, O. Farkas, J. Tomasi, V. Barone, M. Cossi, R. Cammi, B. Mennucci, C. Pomelli, C. Adamo, S. Clifford, J. Ochterski, G.A. Petersson, P.Y. Ayala, Q. Cui, K. Morokuma, D.K. Malick, A.D. Rabuck, K. Raghavachari, J.B. Foresman, J. Cioslowski, J.V. Ortiz, A.G. Baboul, B.B. Stefanov, G. Liu, A. Liashenko, P. Piskorz, I. Komaromi, R. Gomperts, R.L. Martin, D.J. Fox, T. Keith, M.A. Al-Laham, C.Y. Peng, A. Nanayakkara, C. Gonzalez, M. Challacombe, P.M.W. Gill, B. Johnson, W. Chen, M.W. Wong, J.L. Andres, C. Gonzalez, M. Head-Gordon, E.S. Replogle, and J.A. Pople. Gaussian 98, Revision A.7 [computer program]. Gaussian, Inc., Pittsburgh, Pa. 1998.
22. K.-M. Marstokk and H. Møllendal. J. Mol. Struct. **5**, 205 (1970).
23. M. Horák and A. Vítek. Interpretation and processing of vibrational spectra. Wiley, London. 1978.
24. T.-K. Ha, M. Quack, and J. Stohner. Mol. Phys. **100**, 1797 (2002).
25. G. Herzberg. Molecular spectra and molecular structure. II Infrared and Raman spectra of polyatomic molecules. Krieger Publishing Company, Melbourne, Fla. 1991.

© 2004 NRC Canada

The ν_1 and ν_2 vibrational bands of the OCCN radical detected through time-resolved Fourier transform IR emission spectroscopy[1]

William McNavage, William Dailey, and Hai-Lung Dai

Abstract: Through monitoring the IR emission from vibrationally excited radicals generated by exothermic photolysis reactions, the CN stretch (ν_1) and the CO stretch (ν_2) vibrational bands of the cyanooxomethyl radical (OCCN) have been observed for the first time at 2093 cm^{-1} and 1774 cm^{-1}, respectively. The OCCN radical was produced through 193 nm photolysis of methyl cyanoformate ($NCC(O)OCH_3$), carbonyl cyanide (NCC(O)CN), and pivaloyl cyanide ($NCC(O)C(CH_3)_3$). The IR emission spectra were recorded by using nanosecond time-resolved Fourier transform IR emission spectroscopy. Assignments of the spectral peaks were made based on observed time and pressure dependences of IR emission intensities, ab initio calculations, and two-dimensional cross-spectra correlation analysis.

Key words: radical, cyanooxomethyl, OCCN, time-resolved vibrational spectroscopy, FTIR, substituted carbonyl dissociation reactions, two-dimensional cross-spectra correlation analysis

Résumé : En se basant sur une détermination de l'émission IR de radicaux vibrationnellement excités, générés par des réactions de photolyse exothermique, on a pu observer pour la première fois les bandes de vibration d'élongation CN (ν_1) et de vibration d'élongation CO (ν_2) du radical cyanooxométhyle (OCCN), respectivement à 2093 cm^{-1} et 1774 cm^{-1}. On a produit le radical OCCN par une photolyse à 193 nm du cyanoformiate de méthyle, $NCC(O)OCH_3$, du cyanure de carbonyle, NCC(O)CN, et du cyanure de pivaloyle, $NCC(O)C(CH_3)_3$. Les spectres d'émission ont été enregistrés en faisant appel à la spectroscopie d'émission IR à transformation de Fourier, résolue en fonction du temps au niveau de la nanoseconde. On a effectué les attributions des bandes spectrales sur la base des dépendances en fonction du temps et de la pression des intensités d'émission IR, de calculs ab initio et d'une analyse de corrélation interspectre bidimensionnelle.

Mots clés : radical, cyanooxométhyle, OCCN, spectroscopie vibrationnelle résolue en fonction du temps, FTIR, réactions de dissociation de carbonyles substitués, analyse de corrélation interspectre bidimensionnelle.

[Traduit par la Rédaction]

Introduction

In 1971, Herzberg published one of his seminal books on spectroscopy, *The Spectra and Structure of Simple Free Radicals*. In this book, works appearing as early as 1925 were quoted. Though great advances have been made over the years, the spectroscopy of free radicals remains a challenge for research in many disciplines of science owing to the transient and unstable nature of these species. This is particularly the case for radical vibrational spectroscopy because of the generally weaker intensity of vibrational transitions. For example, understanding and characterizing the vibrational modes of the small but important cyanooxomethyl radical, OCCN, in the electronic ground state has, until this work, remained elusive despite the significant role of this radical in the atmosphere. OCCN is an important dissociation product of many substituted carbonyls (1–10) with the general structure NCC(O)X, a class of carbonyl-containing compounds that are major constituents of urban atmospheric pollution related to motor vehicles (9). None of its vibrational bands, however, have been reported previously.

Prior studies have focused on the dissociation dynamics of symmetrically or asymmetrically substituted carbonyls such as pivaloyl cyanide (X = $C(CH_3)_3$), methyl cyanoformate (X = OCH_3), and acetyl cyanide (X = CH_3) (2, 4–6, 8, 11–13). Molecules of this type fall into the Norrish type I group (14) in organic photochemistry, and their reactions involve an α-bond cleavage upon $^1(n, \pi^*)$ excitation, which can be facilitated through direct optical transition or internal conversion following the $^1(n, 3s)$ excitation to a Rydberg state (8). One of the major interests in studying the dissociation dynamics relates to bond selectivity (4–6, 8, 11, 13) — which of the two α-bond dissociation channels dominates upon electronic excitation and which is the weaker of the two bonds? For example, 193 nm photodissociation of acetyl cyanide ($CH_3C(O)CN$) shows a strong preference for primary CN elimination over CH_3 elimination even though CN elimination involves the rupture of the stronger C—C bond (8). In the case of the dissociation of acetyl chloride

Received 7 January 2004. Published on the NRC Research Press Web site at http://canjchem.nrc.ca on 26 August 2004.

W. McNavage, W. Dailey, and H.-L. Dai.[2] Department of Chemistry, The University of Pennsylvania, Philadelphia, PA 19104–6363, USA.

[1]This article is part of a Special Issue dedicated to the memory of Professor Gerhard Herzberg.

[2]Corresponding author (e-mail: dai@sas.upenn.edu).

 doi: 10.1139/V04-041 © 2004 NRC Canada

Table 1. Summary of results on OCCN vibrational modes from ab initio calculations.

			QCISD/6-31G(d) predictions	
Mode	Symmetry	Mode description	Frequency (cm^{-1})	Intensity (km/mol)
1	a′	CN stretch	2293	1333
2		CO stretch	1939	135
3		CC stretch	795	30
4		OCC bend + CCN bend	562	2
5		CCN bend + OCC bend	205	9
6	a″	Torsion	271	9

Note: The QCISD/6-31G(d) calculations were conducted by Francisco and Liu (15).

($CH_3C(O)Cl$), there is a preferential cleavage of the C—Cl bond over the C—C bond with nearly identical dissociation energy (13). For most systems, the dissociation process has been understood to be complex and not straightforward.

The only experimental study of the OCCN radical itself has been by Huber and co-workers, who used photofragment translational energy spectroscopy to probe the 193 nm dissociation of various asymmetrically substituted carbonyls that produced OCCN as a common product (4). Even though these experiments were revealing on OCCN production following UV excitation of the precursor molecules, they yielded little structural information on OCCN. In prior theoretical studies, Francisco and Liu performed QCISD level ab initio calculations on the OCCN radical and determined its structure, rotational constants, and vibrational frequencies on the basis of these calculations (15). Results from these calculations are listed in Table 1 and will be discussed later.

In this work, we will report the detection of the first two normal modes of the electronic ground state of the OCCN radical using time-resolved Fourier transform IR emission spectroscopy (TR-FTIRES). In general, vibrational spectroscopy of radicals has been challenging owing to the transient nature of radical species and because they are generally produced in small quantities (16). The TR-FTIRES approach, on the other hand, has proven to be an efficient (sensitive) and versatile technique that can detect IR-active vibrational modes with modest spectral resolution (17–20).

In our approach, UV (193 nm) photodissociation of a carbonyl-containing molecule is first used to generate the OCCN radical. A precursor is chosen for which the photodissociation reaction has a high quantum yield and is highly exothermic so that the OCCN generated has abundant internal excitation to facilitate IR emission through its IR-active modes. TR-FTIRES offers nanosecond time resolution (19) and is thus capable of detecting IR emission from short-lived transient species. Another advantage is that the entire mid-IR region can be investigated in one experiment with temporal information. The gas sample is mixed with a modest pressure of inert gas to promote collisional quenching of the vibrational excitation energy in OCCN so that in emission spectra recorded at longer times, the emission frequencies approach the values of the fundamental transitions. This technique has been successfully applied to the study of the vinyl radical (17, 20), for which the first complete experimental observation of all nine modes was made, and the cyanovinyl radical (18, 20, 21).

In the experiments reported here, the NCC(O)X precursors chosen for OCCN production were carbonyl cyanide (CC; X = CN), pivaloyl cyanide (PC; X = $C(CH_3)_3$), and methyl cyanoformate (MC; X = OCH_3). Their structures are shown in Fig. 1. All three molecules are known to be stable sources of OCCN as evidenced by photofragment translational energy spectroscopy experiments (4). MC is expected to dissociate along the following channels:

$$NCC(O)OCH_3 + h\nu \text{ (193 nm)}$$

$$[1] \quad \rightarrow OCCN + OCH_3 \quad (95 \pm 2\%, \Delta H = -104.2 \text{ kcal/mol})$$

$$[2] \quad \rightarrow OCOCH_3 + CN \quad (5 \pm 2\%, \Delta H = -115.4 \text{ kcal/mol})$$

Dissociation of PC was found to proceed along the following channels:

$$NCC(O)C(CH_3)_3 + h\nu \text{ (193 nm)}$$

$$[3] \quad \rightarrow OCCN + C(CH_3)_3 \quad (83 \pm 10\%, \Delta H = -80.3 \text{ kcal/mol})$$

$$[4] \quad \rightarrow OCC(CH_3)_3 + CN \quad (17 \pm 10\%, \Delta H = -101.1 \text{ kcal/mol})$$

Finally, CC was found to dissociate along both a radical elimination pathway and a molecular elimination pathway:

$$NCC(O)CN + h\nu \text{ (193 nm)}$$

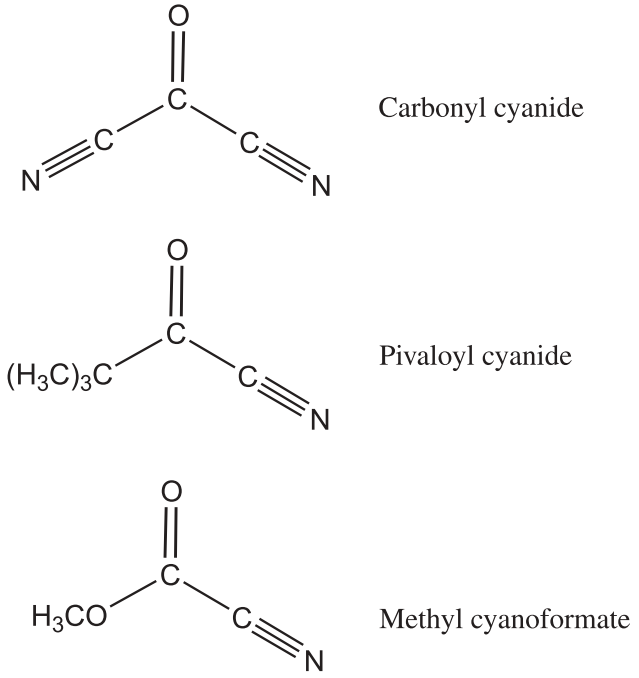
$$[5] \quad \rightarrow OCCN + CN \quad (94 \pm 2\%, \Delta H = -98.0 \text{ kcal/mol})$$

$$[6] \quad \rightarrow NCCN + CO \quad (6 \pm 2\%, \Delta H = -102.6 \text{ kcal/mol})$$

In TR-FTIRES, following photodissociation of the precursor molecule, IR emission from all the dissociation products that are vibrationally excited can be observed with time resolution. Information on the time evolution of the intensity and frequency of the emission features is used to assign vibrational modes of emitting species. Also, a newly developed spectral analysis technique, two-dimensional cross-spectra correlation (2DCSC), is used to confirm the assignment. The spectral features identified from the common OCCN product among the spectra from the three precursors are then compared with ab initio calculations to assist in the assignment of vibrational modes. Based on these observations/analyses, we present here the first experimental evi-

© 2004 NRC Canada

Fig. 1. Precursors for study: carbonyl cyanide (CC), pivaloyl cyanide (PC), and methyl cyanoformate (MC).



dence on the ν_1 CN stretch and ν_2 CO stretch vibrational bands of the OCCN radical.

Experimental

A detailed description of the experimental setup has been given elsewhere (19). Briefly, output from an ArF excimer (λ = 193 nm, 20 Hz, ≤30 mJ/pulse) laser (Lambda Physik, EMG 201 MSC) was lightly focused (fl = 1 m) into a photolysis cell mounted with CaF_2 windows. Pressures inside the cell were typically maintained between 20×10^{-3} and 120×10^{-3} torr (1 torr = 133.322 Pa) of precursor molecules and ~4 torr of Ar bath gas under constant flow conditions and were monitored with a capacitance manometer (MKS Baratron, 0–10 torr). Emission was collected perpendicular to the axis of the photolysis laser beam by a gold mirror Welsh cell arrangement and collimated and focused into the FTIR spectrometer by two KCl lenses that match the *f*/4 focusing characteristics of the spectrometer. The FTIR spectrometer (Bruker IFS-88) was equipped with an interferometer with step-scan capability and a mercury cadmium telluride detector (MCT J15D14, Judson Technologies) with a 500-ns rise time and a spectral range of 8000–720 cm^{-1}. The interferograms were recorded at 50-ns time intervals with averaging over 32–64 laser shots for a total observation window of 20 μs. The interferometric signal was amplified (10×) by a fast amplifier (SRS SR445) before reaching the transient digitizer (Tektronix TDS380) for signal processing. Subsequent Fourier transformation of each time-resolved interferogram yielded a time-resolved spectrum at every 50 ns with a spectral resolution of 12 cm^{-1}.

Carbonyl cyanide was synthesized through a published procedure (22) and purified by vacuum distillation before use. Commercially available methyl cyanoformate (Aldrich, 99%) and pivaloyl cyanide (Fluka, >97%) were used after undergoing several freeze–pump–thaw cycles. FTIR spectra taken after sample preparation showed no detectable impurities. The argon gas from the supplier (Spectra Gas, research grade, 99.9%) was used directly.

Results and analysis

Time-resolved emission spectra in the mid-IR range

As an example of the time-resolved emission spectra obtained for all three precursors, Fig. 2 shows a sampling of the time-resolved emission spectra in the range between 700 and 4000 cm^{-1} taken following the 193 nm dissociation of CC. Data was collected at 50-ns intervals for a total period of 20 μs, with $t = 0$ set at the arrival of the photolysis pulse. The time-resolved spectra should contain emission features from all species that are sufficiently vibrationally excited and have IR-active modes.

Owing to anharmonicities of vibrational modes, the emission features in general are at the lower energy side of the fundamental transition frequencies. In earlier time slices, when the emitting molecules are highly excited, the red shift is more prominent. As collisions occur over time, the IR emission detected at longer times eventually arises from the fundamental transitions as the vibrationally excited molecules cascade down the vibrational manifold.

IR emission spectra from different precursors

Common emission features associated with OCCN are expected in all emission spectra obtained using the three different precursor molecules. Since at longer time slices the IR emission features are closer to the fundamental transitions, we first compare these longer-time (9.8 μs after photolysis pulse) emission spectra from the three precursors as shown in Fig. 3. Each spectrum consists of many vibrational features although only one apparent frequency overlap is observed, slightly below 2100 cm^{-1}. Other frequency overlaps may occur among these spectra but are not immediately apparent.

The center frequencies of emission features were determined by fitting each of these features to a Gaussian line shape. Uncertainties reported were determined as a quarter of the half-width at half-maximum of each line shape. Emission spectra following MC dissociation show features (at longer times) at 1242 ± 11 and 1763 ± 26 cm^{-1} as well as a broad feature between 1829 and 2369 cm^{-1}. The PC precursor spectra show emission features at 950 ± 6 and 1090 ± 7 cm^{-1} and one other feature at 2093 ± 6 cm^{-1}. Finally, the CC precursor emission exhibits four features at 1105 ± 17, 1703 ± 22, 2096 ± 26, and 2199 ± 22 cm^{-1}. Table 2 is a summary of all the IR emission features observed in spectra obtained using these different precursors.

Time dependence of the intensity of IR emission features

In the gas cell in which the experiments were carried out, collisions among precursor molecules, bath molecules, and product molecules from the primary (photolysis) reactions occur. Further, secondary reactions of the photolysis products may be induced, and these may produce vibrationally excited by-products that also give IR emission. To determine whether the observed IR emission features result from pri-

© 2004 NRC Canada

Fig. 2. Selected time slices of the IR emission spectra spanning 1.275 to 19.775 μs following photodissociation of CC.

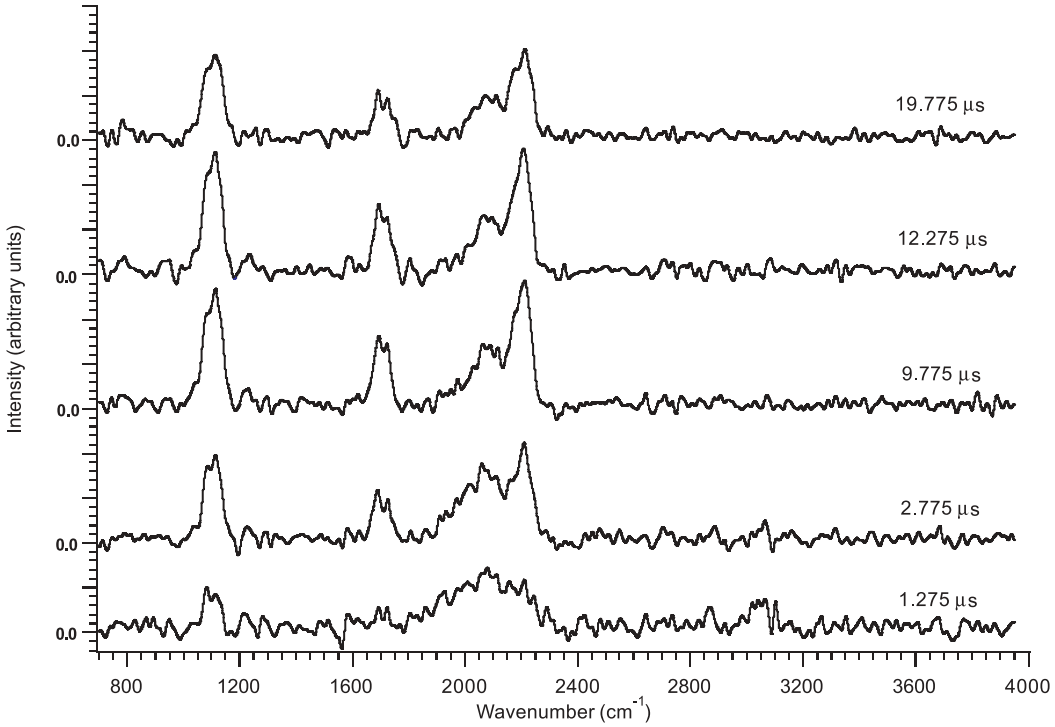
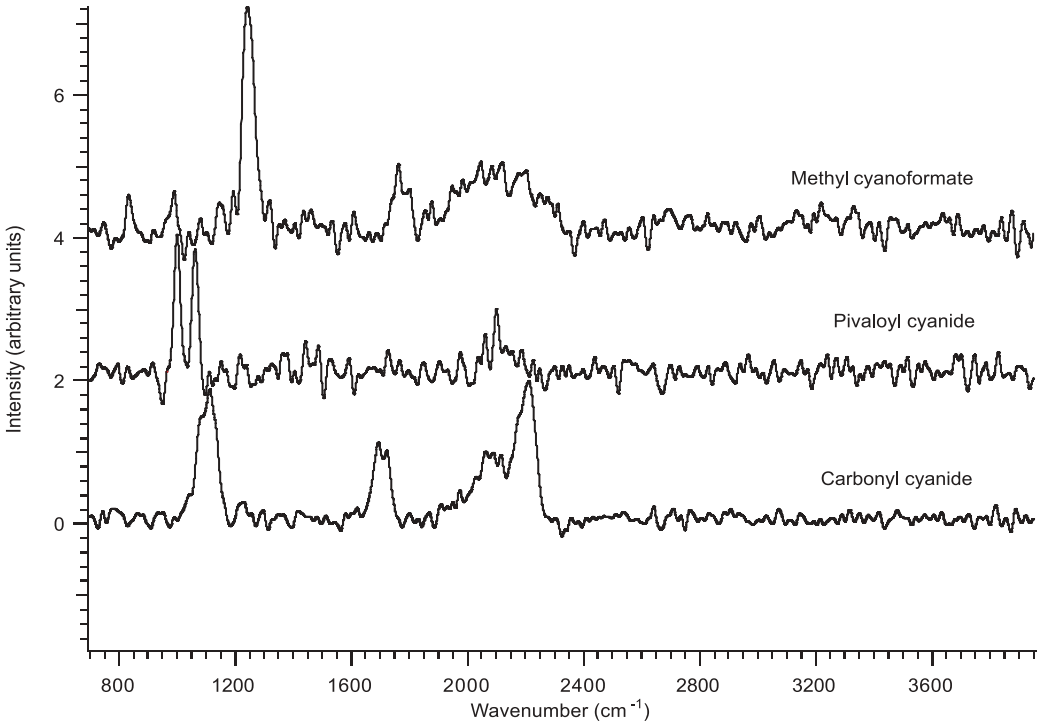


Fig. 3. IR emission spectra following photodissociation of MC, PC, and CC as OCCN precursors. The spectra were taken 9.8 μs after the photolysis pulse, at which time the emitting species are quenched to the lowest excited vibrational level.



mary photodissociation or secondary reactions, the time dependence of the emission intensity was examined for each feature. Figure 4 shows for comparison the intensity of two peaks as a function of time following the photolysis pulse in CC dissociation: one at 2093 cm^{-1} labeled as (*a*) and the other at 2199 cm^{-1} labeled as (*b*). The intensity plotted was integrated over the entire feature under the Gaussian line shape in that particular time-slice spectrum. Two clearly different time dependences are observed. These time dependences can be well fitted to a rise and a decay function (with

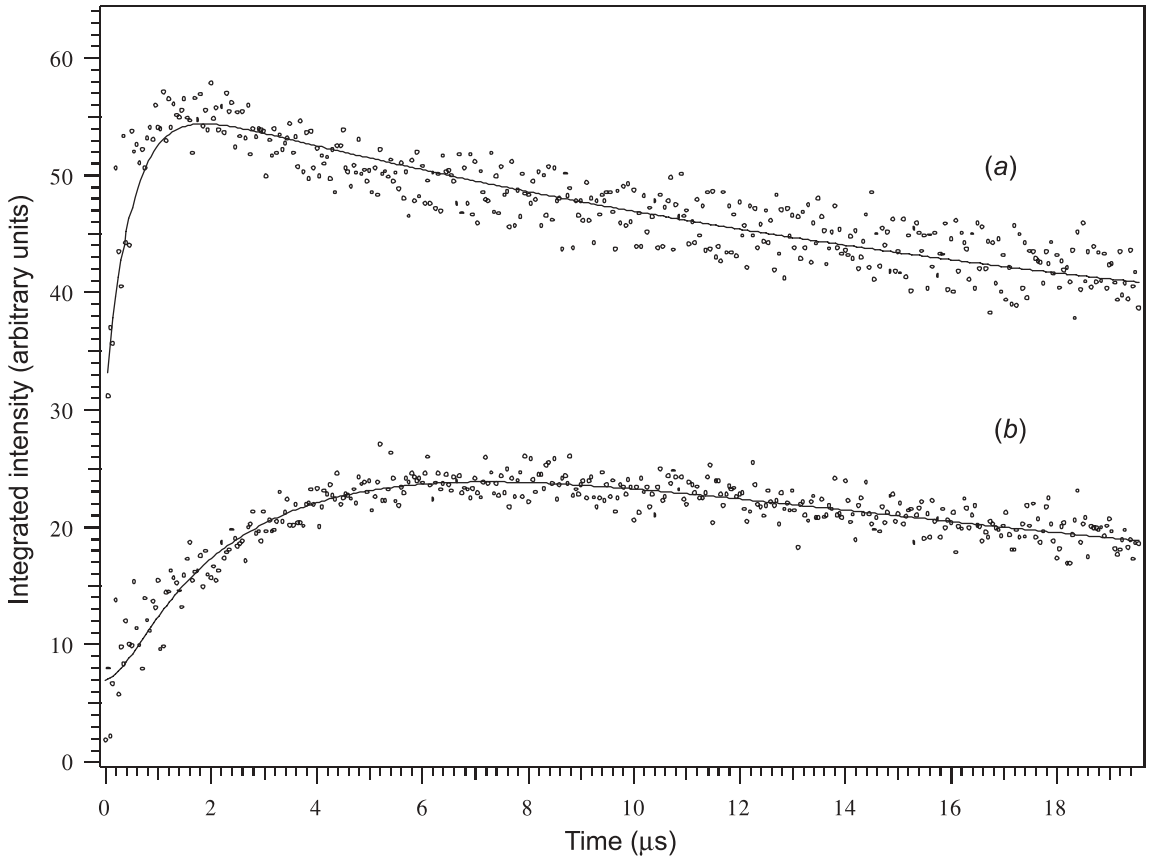
© 2004 NRC Canada

Table 2. Comparison of all observed mid-IR features from each precursor dissociation reaction.

Precursor	Frequency (cm^{-1})	Assignment	Origin[a]
CC	1105±35	$2\nu_7$ overtone	S
	1703±45	ν_2 CO stretch	S
	2093±53	OCCN CN stretch	P
	2199±44	ν_9 CN antisymmetric stretch	S
PC	950±12	Unassigned	S
	1090±13	Unassigned	S
	2093±12	OCCN CN stretch	P
MC	1242±22	ν_7 CO stretch	S
	1763±53	ν_4 COC antisymmetric stretch	S
	1829–2369	Multiple features	P and S

[a]P, primary reaction; S, secondary reaction.

Fig. 4. Time dependence of integrated intensity of emission features, using CC as precursor, at 2093 cm^{-1} (*a*) and 2199 cm^{-1} (*b*). Each point of the intensity time profile is separated by 50 ns.



rate constants k_r and k_d), with an instrument response function (k_{Det}) convoluted in, according to:

$$[7] \qquad I = A_0(\exp(-k_d t) - \exp(-k_r t))(1 - \exp(-k_{Det} t))$$

For trace (*a*), the rise can be characterized by a time constant << 500 ns, well below the rise time of the MCT detector. This feature at 2093 cm^{-1} can therefore be attributed to a product from the primary photolysis reaction. In comparison, trace (*b*) was found to have a rise time on the order of 3 μs and is more likely to result from a secondary reaction. Similar analyses of other CC dissociation features at 1105 and 1703 cm^{-1} also show rise times on the order of 3 μs, suggesting they too are from secondary reaction products.

The time dependence of the intensities of emission features in spectra from precursors PC and MC was also analyzed. In PC dissociation, the features at 950 and 1090 cm^{-1} result from secondary reactions while the feature at 2093 cm^{-1} has a time evolution consistent with a primary dissociation product. In MC dissociation, features at 1242 and 1763 cm^{-1} were observed to have very long rise times, indicating that they are from secondary reactions. The very broad feature between 1829 and 2369 cm^{-1} showed a rise time in between those assignable to primary and to second-

© 2004 NRC Canada

ary reactions. As this feature does not show a distinctly assignable time evolution and may contain emission features from several species, it cannot wholly be attributed to either a secondary or a primary reaction product. The feature at 2093 cm^{-1} once again can be assigned to a primary dissociation product.

In all precursor dissociation reactions, every emission feature except that at 2093 cm^{-1} shows a dramatic pressure dependence induced by varying precursor concentration in its rise time. This further confirms the assignment of the emission feature at 2093 cm^{-1} to the primary photodissociation reaction.

Discussion

Based on the time dependence of the intensities of the emission features and the overlap among the emission spectra from the three different precursors, the feature at 2093 cm^{-1} is assigned to the OCCN radical. Comparisons with theoretical calculations (15) suggest that this feature is the ν_1 CN stretch of OCCN. Application of the two-dimensional cross-spectra correlation analysis (see below) revealed that there is another emission feature that is common to spectra from all three precursors at 1774 cm^{-1}. This feature can be assigned to the ν_2 CO stretching mode of OCCN.

Comparison with ab initio calculations

Francisco and Liu performed ab initio calculations on the OCCN radical and its corresponding cation (15). These calculations were performed at the QCISD/6-31G(d) level. The calculations show that the radical is a bent molecule with C_s symmetry, and the predictions of its vibrational modes are shown in Table 1. Three of the six vibrational modes are stretching vibrations, two are low-frequency bending motions, and the sixth mode is a torsional motion around the C—C bond. According to the calculations, the CN stretch harmonic frequency is predicted at 2293 cm^{-1}. Comparison with the experimentally observed fundamental frequency of this mode at 2093 cm^{-1} indicates a correction factor of 0.91 to the ab initio value. This is a reasonable correction considering that the fundamental frequencies are usually somewhat smaller than the corresponding harmonic frequencies. Similar correction factors have been observed for the vibrational modes of the cyanovinyl radical that were calculated using the same method/basis set (21). Using a similar correction factor of 0.91, the frequency of the CO stretch can be scaled from the calculated 1939 cm^{-1} to 1765 cm^{-1}. The emission feature that we observed at 1774 cm^{-1} matches the scaled frequency within the uncertainty of the band.

The ab initio calculations predict the CN stretch to be the mode with the strongest emission intensity, with the CO stretch being the next strongest. After converting absorption intensities to emission intensities, the calculation indicates that emission from the CN stretch is 16 times stronger than that from the CO stretch. The weak intensity in the 1770 cm^{-1} region of the spectra in Fig. 3 is consistent with the ν_2 CO stretch being present but very weak.

Two-dimensional cross-spectra correlation analysis

The common features in the emission spectra obtained using different precursors can be quantitatively identified by two-dimensional correlation analysis of the spectra. This analysis is particularly useful for identifying weak features that are common to all the spectra. The particular algorithm we have developed for analyzing the emission spectra is an application of Noda's generalized two-dimensional correlation spectroscopy (23), which is commonly used for revealing correlation among the spectral features within the same spectra. However, our algorithm, which we denote as two-dimensional cross-spectra correlation analysis (2DCSC), is aimed at revealing the correlation between spectral features of two *different* spectra. The details of the theoretical modeling and analysis procedure as well as the detailed application to the OCCN emission spectra will be reported elsewhere.[3] A brief description of 2DCSC and the results on OCCN are presented here.

In correlation spectroscopy, a perturbation is introduced into the system to induce a dynamic response in the spectral features. The principle that spectral features associated with the same group of atoms or the same molecule should have the same response to the perturbation is the basis for generalized two-dimensional correlation analysis (23). The same idea holds true for 2DCSC. Here the collisions between the emitting molecules and the ambient molecules (in excess amount) over time serve as the perturbation, and the time-resolved emission intensity contains the dynamic information that can be used for correlation analysis.

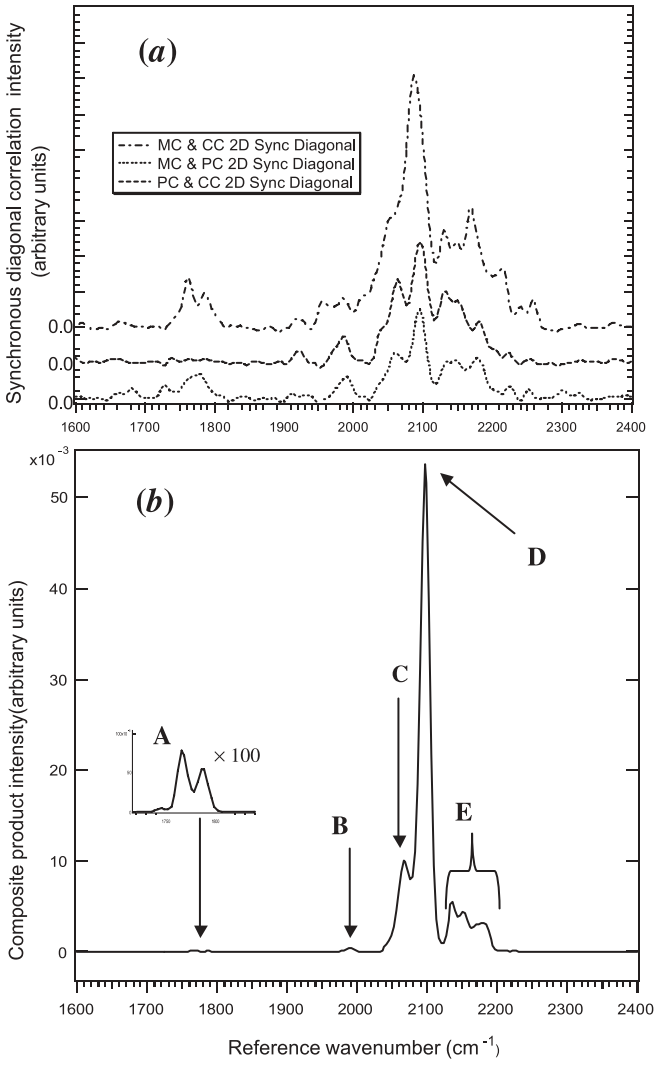
2DCSC analysis can be applied to any two sets of time-resolved spectra obtained from the OCCN precursor dissociation reactions. Following photolysis, all three precursors generate OCCN radicals with similar internal excitation energies. The excited radicals, in all three cases, experience a similar collisional perturbation as a function of time. As a result, the time dependence of the intensity of the same spectral feature from OCCN, though in different spectra, ought to be similar. Under correlation analysis, this same feature from any two spectra would show positive correlation. In each correlation analysis, the features common to OCCN should therefore be revealed due to the similar dynamic response of internally excited OCCN to collision quenching. Even in the cases where the internal excitation of the OCCN radicals generated from the two different precursors is not identical, the ones with higher energy will be quenched and will eventually reach the same energy as the ones resulting from the other precursor. Thus, the time dependence of the intensity in the time period leading to the emission at the fundamental transition frequency will be identical and suitable for correlation analysis.

In the 2DCSC procedure, first a dynamic spectrum is constructed based on the time dependence of the intensity in the frequency spectrum. The intensity as a function of time at each frequency is then Fourier analyzed. Multiplication of the Fourier-transformed functions at each pair of frequencies allows the construction of a correlation map. There are two portions of the correlation map: real and imaginary. The real portion of the map is referred to as the synchronous map and highlights the similarity in evolution of the intensity of spec-

[3] W. McNavage and H.-L. Dai. Manuscript in preparation (2004).

© 2004 NRC Canada

Fig. 5. (*a*) Extracted diagonal elements from each pair of synchronous correlation spectra. (*b*) Composite product of extracted diagonal elements shown in (*a*). Five clearly identifiable features A through E are assigned (see text).



tral features. The imaginary portion is the asynchronous map and shows how dissimilar the two features are.

The synchronous map's diagonal displays activity at the same frequency in the two spectra. If the two spectra contain the same spectral feature, i.e., the same time-dependent intensity at the same frequency, there is a positive correlation at that frequency. Three sets of 2DCSC results are obtained between MC/PC, MC/CC, and CC/PC, and the correlation spectrum along the diagonal for each pair of spectra is shown in Fig. 5*a*. A corresponding zero in the asynchronous map should confirm a positive correlation in the synchronous map. Both indications from the synchronous and asynchronous correlations identify the set of spectral features that are common to each pair of spectra. Furthermore, the product of all three synchronous correlation functions along the diagonal, shown in Fig. 5*b*, can be used to represent the overall correlation among all three spectra.

From this analysis, it is evident that the correlation activity at 2093 cm^{-1}, shown as feature D in Fig. 5*b*, is overwhelming. There are other prominent features present as well. Of these features, the one below 1800 cm^{-1}, labeled as A, falls near the predicted position of the CO stretch based on the scaled ab initio frequency. The relative intensity values of this mode and the strongest CN stretch are also in qualitative agreement with the one order of magnitude intensity ratio predicted from ab initio calculations (Table 1).

The features in Fig. 5*b* other than the two assigned to OCCN can be assigned to common dissociation products after photolysis reactions of the three precursors. For example, feature E may be due to the antisymmetric CN stretch of NCCN that is a by-product produced from the combination of two CN radicals or, in the case of precursor CC, from dissociation along its minor pathway. Energetics determined from photofragment translational energy spectroscopy (4) indicates that some of the OCCN produced in our experiments would have had enough energy to spontaneously dissociate to form CN + CO. If this were the case, the stretch of the CN radical may appear at the position of peak C, with the stretch of the CO overlapping with that of NCCN at the position of feature E. Finally, NCCN's less stable but energetically accessible isomer CNNC has a strong antisymmetric stretching mode below 2000 cm^{-1} that may account for the peak labeled B.

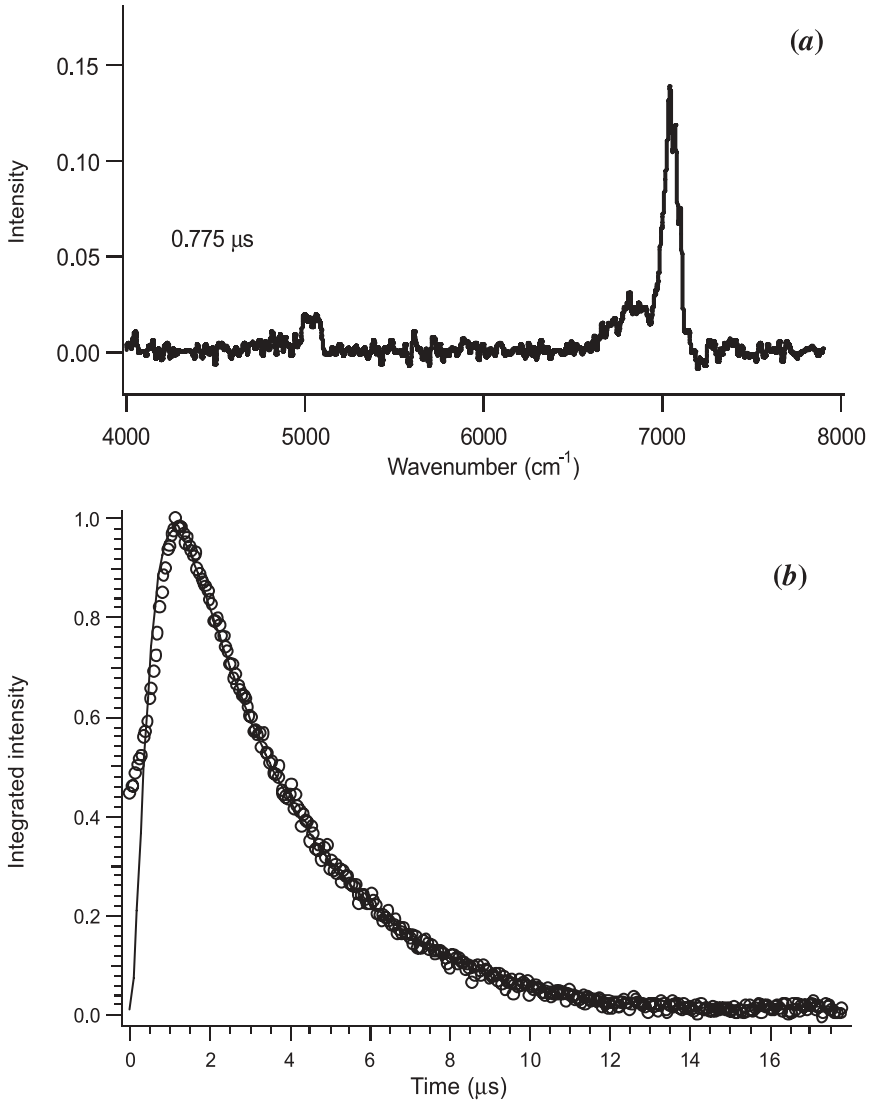
Products from secondary reactions

Table 2 summarizes all IR features directly observed in all spectra presented here. The emission features from secondary reactions in the MC and CC spectra can all be assigned. Emission at 1242 and 1763 cm^{-1} in MC experiments can be assigned to the ν_7 C=O stretch and ν_4 C-O-C antisymmetric stretch, respectively, of vibrationally excited MC (24). Emission at 1105, 1703, and 2199 cm^{-1} in the CC spectra corresponds to the $2\nu_7$ overtone, ν_2 C=O stretch, and ν_9 antisymmetric CN stretch, respectively, of vibrationally excited CC (1). On the other hand, the broad secondary emission feature observed in PC experiments remains currently unassigned.

The dissociation quantum yield following photoexcitation at 193 nm is unity for all three precursors. Vibrationally excited precursor molecules do not result from photoexcitation directly. Rather, vibrationally excited MC and CC can be related to the electronically excited CN generated directly from precursor photodissociation. Figure 6*a* shows the emission spectrum in the region from 4000 to 8000 cm^{-1} acquired 0.775 μs following the dissociation of CC. The strongest feature at 7046 cm^{-1} can be assigned to the CN $A(v' = 0) \rightarrow X(v'' = 1)$ transition (25), and the ones at 6834, 6606, and 5028 cm^{-1} correspond to the CN $A(v' = 1) \rightarrow X(v'' = 2)$, $A(v' = 2) \rightarrow X(v'' = 3)$, and $A(v' = 0) \rightarrow X(v'' = 2)$ transitions, respectively. Figure 6*b* shows the integrated intensity of the 7046 cm^{-1} feature over time. The time dependence can be fitted to a single exponential decay with a lifetime of 3.0 μs. This decay time constant appears to correlate with the rise times of the mid-IR secondary emission features in CC spectra that are assignable to emission from vibrationally excited CC. Similarly, electronically excited CN(A) is also observed in MC dissociation, and its decay also corresponds to the slow rise of the secondary features in the mid-IR emission spectrum that are assignable to vibrationally excited MC. The correlation between the loss of

© 2004 NRC Canada

Fig. 6. (*a*) The near-IR emission spectrum 0.775 μs after photodissociation of carbonyl cyanide. (*b*) Time dependence of the integrated intensity of the strongest CN emission feature in (*a*), the A(v′ = 0) → X(v′′ = 1) transition at 7046 cm^{-1}.



electronically excited CN and the formation of vibrationally excited precursor molecules may arise through the following proposed mechanism. The electronically excited CN may react with the carbonyl group of the precursor molecules, causing the elimination of a CN radical. This bimolecular reaction does not lead to the destruction of the precursor molecules but does result in vibrational excitation in the precursor molecules as product.

Summary

This work presents the first experimental report of the observation of the vibrational modes of the OCCN radical. The vibrational modes of OCCN have been detected through the IR emission from vibrationally excited OCCN produced in 193 nm photodissociation of a substituted carbonyl molecule as precursor. Three different precursors, carbonyl cyanide, pivaloyl cyanide, and methyl cyanoformate, have been used, and the IR emission spectra as a function of time following photodissociaiton have been recorded by the nanosecond time-resolved Fourier transform emission spectroscopy technique.

The CN stretch (ν_2) at 2093 cm^{-1} is the mode with the strongest transition intensity and can be readily identified in the emission spectra from all three precursors. The CO stretch (ν_1) at 1774 cm^{-1} is more than one order of magnitude weaker and not as apparent as the strongest mode in the emission spectra but can be identified after a two-dimensional cross-spectra correlation analysis of the spectra. Ab initio calculation results confirm the reasonableness of the assignment of the two modes with respect to both frequency and relative intensity.

Acknowledgements

This work is supported by Basic Energy Sciences, U.S. Department of Energy, through grant no. DEFG 02–86ER 134584. WM acknowledges the receipt of a NASA Earth System Science Fellowship (R-ESSF/03–0000–0110).

© 2004 NRC Canada

References

1. J.B. Bates and W.H. Smith. Spectrochim. Acta Part A, **26**, 455 (1970).
2. S. Deshmukh and W.P. Hess. J. Chem. Phys. **100**, 6429 (1994).
3. A. Furlan, H.A. Scheld, and R.J. Huber. Chem. Phys. Lett. **282**, 1 (1998).
4. A. Furlan, H.A. Scheld, and R.J. Huber. J. Phys. Chem. A, **104**, 1920 (2000).
5. R.J. Horwitz, J.S. Francisco, and J.A. Guest. J. Phys. Chem. A, **101**, 1231 (1997).
6. I.-R. Lee, Y.-C. Chung, W.-K. Chen, X.-P. Hong, and P.-Y. Cheng. J. Chem. Phys. **115**, 10 656 (2001).
7. Q. Li, R.T. Carter, and R.J. Huber. Chem. Phys. Lett. **323**, 105 (2000).
8. S.W. North, A.J. Marr, A. Furlan, and G.E. Hall. J. Phys. Chem. A, **101**, 9224 (1997).
9. H.A. Scheld, A. Furlan, and R.J. Huber. J. Chem. Phys. **111**, 923 (1999).
10. H.U. Suter, R.J. Huber, and T.-K. Ha. Chem. Phys. Lett. **311**, 474 (1999).
11. E. Arunan. J. Phys. Chem. A, **101**, 4838 (1997).
12. S.W. North, D.A. Blank, J.D. Gezelter, C.A. Longfellow, and Y.T. Lee. J. Chem. Phys. **102**, 4447 (1995).
13. M.D. Person, P.W. Kash, and L.J. Butler. J. Chem. Phys. **97**, 355 (1992).
14. J.G. Calvert and J.N. Pitts. Photochemistry. John Wiley & Sons, New York. 1966.
15. J.S. Francisco and R. Liu. J. Chem. Phys. **107**, 3840 (1997).
16. G.H. Herzberg. Molecular spectra and molecular structure. D. Van Nostrand Company, Princeton, N.J. 1939.
17. D.-K. Liu, L. Letendre, and H.-L. Dai. J. Chem. Phys. **115**, 1734 (2001).
18. L. Letendre, D.-K. Liu, C.D. Pibel, J.B. Halpern, and H.-L. Dai. J. Chem. Phys. **112**, 9209 (2000).
19. L. Letendre, H.-L. Dai, I.A. McLaren, and T.J. Johnson. Rev. Sci. Instrum. **70**, 18 (1999).
20. L. Letendre. Ph.D. thesis, Department of Chemistry, The University of Pennsylvania, Philadelphia, Pa. 2000.
21. L. Letendre and H.-L. Dai. J. Phys. Chem. A, **106**, 12 035 (2002).
22. W.J. Linn, O.W. Webster, and R.E. Benson. J. Am. Chem. Soc. **87**, 3651 (1965).
23. (*a*) I. Noda. Appl. Spectrosc. **44**, 550 (1990); (*b*) I. Noda. Appl. Spectrosc. **47**, 1329 (1993); (*c*) I. Noda, A.E. Dowrey, and C. Marcott. Appl. Spectrosc. **47**, 1317 (1993); (*d*) I. Noda, A.E. Dowrey, C. Marcott, G.M. Story, and Y. Ozaki. Appl. Spectrosc. **54**, 236A (2000); (*e*) I. Noda, A.E. Dowrey, G.M. Story, and C. Marcott. *In* Fourier transform spectroscopy: Twelfth international conference. *Edited by* K. Itoh and M. Tasumi. Waseda University Press, Tokyo. 1999. pp. 57–60; (*f*) H. Wang and R.A. Palmer. *In* Two-dimensional correlation spectroscopy. *Edited by* Y. Ozaki and I. Noda. American Institute of Physics, Kobe-Sanda, Japan. 1999; (*g*) S. Sasic, A. Muszynski, and Y. Ozaki. Appl. Spectrosc. **55**, 343 (2001).
24. J.R. Durig, P. Groner, A.S. Drew, G.A. Guirgis, and B.J. van der Veken. J. Raman Spectrosc. **26**, 43 (1995).
25. D. Cerney, R. Bacis, G. Guelachvili, and F. Roux. J. Mol. Spectrosc. **73**, 154 (1973).

© 2004 NRC Canada

Infrared photodissociation spectroscopy of $Si^+(CO_2)_n$ and $Si^+(CO_2)_nAr$ complexes — Evidence for unanticipated intracluster reactions[1]

J.B. Jaeger, T.D. Jaeger, N.R. Brinkmann, H.F. Schaefer, and M.A. Duncan

Abstract: $Si^+(CO_2)_n$ and $Si^+(CO_2)_nAr$ ion–molecule complexes were produced by laser vaporization in a pulsed supersonic expansion. The ions were mass-selected in a reflectron time-of-flight spectrometer and studied with infrared photodissociation spectroscopy near the asymmetric stretch vibration of CO_2. $Si^+(CO_2)_n$ clusters fragment by the loss of CO_2 whereas $Si^+(CO_2)_nAr$ complexes fragment by the loss of argon. All clusters have resonances near the CO_2 asymmetric stretch, but with shifts in frequency that are size dependent. The patterns seen in the small clusters are consistent with electrostatic bonding, while the larger systems provide evidence for an intracluster reaction forming oxide-carbonyl species. Density functional theory was employed to examine the structures of these clusters, and their calculated vibrational frequencies were compared to the measured values. Ligand assembly in $Si^+(CO_2)_n$ complexes is dominated by the presence of the occupied 3*p* valence orbital of the silicon cation.

Key words: ion–molecule complexes, infrared spectroscopy, photodissociation, density functional theory.

Résumé : Les complexes ion-molécule $Si^+(CO_2)_n$ et $Si^+(CO_2)_nAr$ ont été produits par une vaporisation au laser dans une expansion supersonique pulsée. Les ions ont été sélectionnés en fonction de leur masse dans un spectromètre à temps d'envol à réflectron et on les a étudiés par spectroscopie de photodissociation infrarouge près de la vibration d'élongation asymétrique du CO_2. Les agrégats de $Si^+(CO_2)_n$ se fragmentent par la perte de CO_2 alors que les complexes $Si^+(CO_2)_nAr$ se fragmentent par une perte d'argon. Tous les agrégats présentent des résonances près de l'élongation asymétrique du CO_2; toutefois, elles présentent des déplacements dans la fréquence qui dépendent de leur taille. Les patrons observés dans les petits agrégats sont en accord avec une liaison électrostatique alors que pour ceux des systèmes plus gros il y a des indications à l'effet qu'il pourrait y avoir une réaction intra-agrégat qui conduirait à la formation d'espèces oxyde-carbonyle. On a utilisé la théorie de la densité fonctionnelle pour étudier les structures de ces agrégats et on a comparé les valeurs calculées pour les fréquences vibrationnelles avec les valeurs mesurées. L'assemblage du ligand $Si^+(CO_2)_n$ est dominé par la présence de l'orbitale de valence 3*p* occupée du cation silicium.

Mots clés : complexes ion–molécule, spectroscopie infrarouge, photodissociation, théorie de la densité fonctionnelle.

[Traduit par la Rédaction]

Introduction

Silicon cations occur in the Earth's atmosphere following meteor ablation (1, 2), in both diffuse and dense interstellar clouds (3, 4), and in stellar atmospheres (5). Silicon ions and neutrals play a critical role in chemical-vapor deposition (CVD) of silicon and in the plasma etching of semiconductor surfaces (6). For these reasons and others, silicon ions have been explored extensively in gas-phase ion chemistry and mass spectrometry (7–12). Reaction pathways for silicon anions and cations have been investigated with a number of small molecules, and ion–molecule complexes have been studied with collision-induced dissociation experiments to explore bonding energetics. However, there is essentially no spectroscopy of small silicon ion–molecule complexes to investigate their structures. In this study, we report infrared (IR) photodissociation spectroscopy of small silicon cation complexes with carbon dioxide, e.g., $Si^+(CO_2)_n$, for $n = 1$–10. These experiments are supplemented by density functional theory (DFT) predictions of the structures and vibrations of these complexes.

The chemical reactions, rate constants, and branching ratios of ground-state silicon ions with numerous small molecules have been investigated by several mass spectrometry research groups (7–11). Armentrout and co-workers have used guided ion-beam mass spectrometry and threshold collision-induced dissociation to determine the bonding energetics of silicon cations with several small organics (8).

Received 15 December 2003. Published on the NRC Research Press Web site at http://canjchem.nrc.ca on 17 June 2004.

J.B. Jaeger, T.D. Jaeger, N.R. Brinkmann,[2] H.F. Schaefer, and M.A. Duncan.[3] Department of Chemistry, University of Georgia, Athens, Georgia 30602–2556, USA.

[1]This article is part of a Special Issue dedicated to the memory of Professor Gerhard Herzberg.
[2]Present address: University of Notre Dame, Radiation Laboratory, South Bend, IN 46556, USA.
[3]Corresponding author (e-mail: maduncan@uga.edu).

 doi: 10.1139/V04-044 © 2004 NRC Canada

Dunbar and co-workers used laser vaporization to make silicon ions in a Fourier transform ion cyclotron resonance (FT-ICR) mass spectrometer and reacted these ions with polycyclic aromatic hydrocarbons (PAHs) (11). Radiative association kinetics were employed to study dissociation energies in these complexes. In many of the previous mass spectrometry studies, silicon ions were produced from organosilicon precursors, and the production of bare Si^+ ions was relatively inefficient. The laser vaporization method employed by Dunbar and co-workers, and also used in the present work, provides a clean source of Si^+ without hydrocarbon by-products. Velegrakis and co-workers investigated the Si^+–Ar_n clusters produced by laser vaporization in a supersonic expansion (12).

Our research group has previously investigated the spectroscopy of ion–molecule complexes of the third-row elements magnesium (13–16) and aluminum (16, 17), and the structural trends in these species have been compared with those of transition-metal-cation complexes (16, 18, 19). These species have also been investigated using theory (15, 17, 20). The combined results from theory and experiment have revealed an interesting trend in the structures of multiligand complexes. While ligands tend to cluster symmetrically around transition-metal ions, clustering around Mg^+ and Al^+ is notably asymmetric. This behavior arises because the valence electron(s) in these ions resides in the 3*s* orbital, which has high polarizability (15, 17, 20). Electrostatic bonding via charge–dipole (e.g., M^+–OH_2 complexes) or charge–quadrupole (e.g., M^+–OCO complexes) interactions leads to polarization of the 3*s* electrons, which causes electron density to localize spatially opposite the first ligand. Subsequent ligands tend to bind away from this electron density and more on the same side as the first ligand, leading eventually to a metal ion located in the surface of a molecular cluster rather than at its core. Silicon cations have the same 3*s* orbital occupation found for Mg^+ and Al^+, but with an additional single electron in the 3*p* orbital. It is therefore interesting to investigate the structures of $Si^+(L)_n$ complexes via spectroscopy and theory. Although Mg^+ has a convenient atomic resonance line that provides a chromophore for electronic spectroscopy of its complexes (14), Al^+ and Si^+ do not have low-lying atomic resonances. We therefore investigate these complexes using IR spectroscopy, taking advantage of the IR photodissociation methodology.

Previous experiments in our lab have studied the IR photodissociation spectroscopy of a number of metal-cation complexes with small molecules (15–19, 21–23). Of these, carbon dioxide complexes are convenient for study because of the energetics of the charge–quadrupole electrostatic interaction, which is strong enough to allow efficient complex formation yet weak enough to allow efficient photodissociation. The convenient IR transition associated with the asymmetric stretch vibration (2349 cm^{-1}) falls within the tuning range of our infrared laser system. The IR spectroscopy of $M^+(CO_2)_n$ complexes has previously been studied for M = Fe (18), Ni (19), Co (23), V (23), Mg (15), and Al (17). These IR studies were complemented by earlier work on electronic spectroscopy of the monoligand complexes Mg^+–CO_2 (13), Ca^+–CO_2 (24), Ni^+–CO_2 (25), and Co^+–CO_2 (25). These studies, and corresponding theoretical investigations (15, 17, 20), showed that M^+–OCO binding occurs in an overall linear configuration for the monoligand complexes as a result of the charge–quadrupole interaction. Multiligand complexes bind with each ligand in a similar linear configuration with respect to the metal. The metal coordination number for the $Ni^+(CO_2)_n$ system (four) corresponded to the known value for stable inorganic complexes (19), while no clear coordination was evident for Mg^+ and Al^+ because of the asymmetric clustering (15, 17). In the present study, we find that IR photodissociation spectroscopy does allow measurement of the vibrational spectra of $Si^+(CO_2)_n$ complexes, providing information about their structures. Except for a recent study of $SiOH^+$–Ar_n clusters (26), there appears to be no other IR spectroscopy on silicon ion complexes. Additionally, these measurements reveal unanticipated evidence for intracluster reactions between Si^+ and CO_2.

Experimental

$Si^+(CO_2)_n$ and $Si^+(CO_2)_nAr$ clusters were produced by laser vaporization in a pulsed nozzle cluster source and mass-analyzed in a reflectron time-of-flight mass spectrometer, as has been described previously (13–19). The third harmonic (355 nm) of a Spectra-Physics Nd:YAG laser (Quanta Ray INDI 30) was used to vaporize a rotating and translating silicon rod (ESPI, 99.999% purity). Ionized clusters of $Si^+(CO_2)_n$ and $Si^+(CO_2)_nAr$ were produced in an expansion of pure CO_2, or a few percent of CO_2 seeded in argon, using a Series 9 valve (General Valve, Brookshire, Texas) operated at 10 Hz with a backing pressure of 40 psi. The expansion was skimmed from the source chamber into the differentially pumped mass spectrometer chamber, where the ions were pulse extracted into a reflectron time-of-flight spectrometer. Ions of interest were mass-selected by pulsed deflection plates before they entered the reflectron. In the turning region of the reflectron, selected ions were photodissociated by the infrared output of an optical parametric oscillator/amplifier (OPO/OPA). Photodissociation is enhanced on resonance with vibrations of the ligand, which may be shifted in frequency from those associated with the free molecule due to interactions with the cation. The parent and fragment ions were mass-analyzed in a second flight tube and detected using an electron multiplier tube and a digital oscilloscope (LeCroy Waverunner LT-342). Data was transferred to a PC via an IEEE-488 interface. Infrared resonance-enhanced photodissociation (IR-REPD) spectra were recorded by monitoring the fragment ion intensity as a function of the infrared wavelength.

An IR OPO/OPA laser (Laser Vision, Bellevue, Wash.) pumped by a Continuum 9010 Nd:YAG laser was used to photodissociate the clusters. This system has two 532-nm-pumped KTP crystals in the grating tuned oscillator section and four KTA crystals in the amplifier section. The idler output from the oscillator is combined with residual 1064 nm in the amplifier, and difference frequency generation here provides the tunable near-IR output from 2.2 to 4.9 μm (4500 to 2050 cm^{-1}). The OPO/OPA was tuned near the ν_3 asymmetric stretch of CO_2, where the pulse energies range from 1 to 3 mJ/pulse, with an approximate linewidth of 0.3 cm^{-1}. Typically, spectra were obtained with a 1 cm^{-1} scan step and averaged over 50 laser shots per step.

© 2004 NRC Canada

Density functional theory quantum-mechanical computations were performed on $Si^+(CO_2)_n$, where $n = 1$ and 2, using the Gaussian94 program package (27). Calculations on the $n = 3$ complex were done using Gaussian03 (28). Two gradient-corrected functionals, denoted B3LYP and BP86, were used to compute the geometries, energies, and harmonic vibrational frequencies. Energies were converged to at least 10^{-6} hartrees (1 hartree (Ha) = 27.211 eV) in the self-consistent field procedures, although the absolute accuracy may be somewhat lower owing to numerical integration procedures. The B3LYP functional is a hybrid Hartree–Fock and density functional theory (HF/DFT) method using Becke's three-parameter exchange functional (B3) (29) with the Lee, Yang, and Parr (LYP) correlation functional (30). The BP86 functional uses Becke's 1988 exchange functional (B) (31) and the 1986 correlation correction of Perdew (P86) (32).

A double-ζ basis set with polarization functions, denoted DZP, was employed. This basis was constructed from the Huzinaga–Dunning–Hay (33, 34) set of contracted double-ζ Gaussian functions. Added to this was one set of five d-type polarization functions for each Si, C, and O atom ($\alpha_d(Si) = 0.550$, $\alpha_d(C) = 0.750$, and $\alpha_d(O) = 0.850$). The final contraction scheme for this basis is Si(12s8p1d/6s4p1d) and C,O(9s5p1d/4s2p1d). Geometries were optimized for each molecular species with each functional using analytic gradient techniques. Residual Cartesian gradients were less than 1.5×10^{-5} hartree/bohr (1 bohr = 5.292×10^{-11} m). Stationary points found in optimizations were confirmed as minima by computing the harmonic vibrational frequencies using analytic second derivatives with each functional. Harmonic vibrations were scaled by calculating the asymmetric stretch of CO_2 at the same level of theory and calculating a correction factor needed to bring this mode into agreement with the known experimental value (2349 cm^{-1}). This same factor was then applied to scale the vibrations in the silicon cation complexes that are derived from the CO_2 asymmetric stretch.

Results and discussion

Figure 1 shows the mass spectrum observed for the cation complexes following laser vaporization of silicon in an expansion of pure CO_2. As indicated, a variety of cluster masses are formed. The major mass peaks correspond to ions of the form $Si^+(CO_2)_n$. A series of minor peaks is also observed at intermediate masses that correspond to either $SiO^+(CO_2)_n$ or $(CO_2)_n^+$ complexes. We are not able to assign these peaks without uncertainty, because there is a mass coincidence at 44 amu between SiO and CO_2. However, in our previous studies of other metal–CO_2 complexes under similar conditions, we did not see pure CO_2 cluster ions. Therefore, $SiO^+(CO_2)_n$ is the most likely assignment for these masses. This indicates that silicon ions are somewhat more reactive in the plasma than the main-group metals Mg and Al that we have studied previously. In similar experiments with CO_2, essentially no oxide masses were observed for those systems (15, 17). Velegrakis and co-workers observed a magic number of $n = 4$ for Si^+Ar_n complexes (12). However, there is no evidence for any magic number in the present distribution.

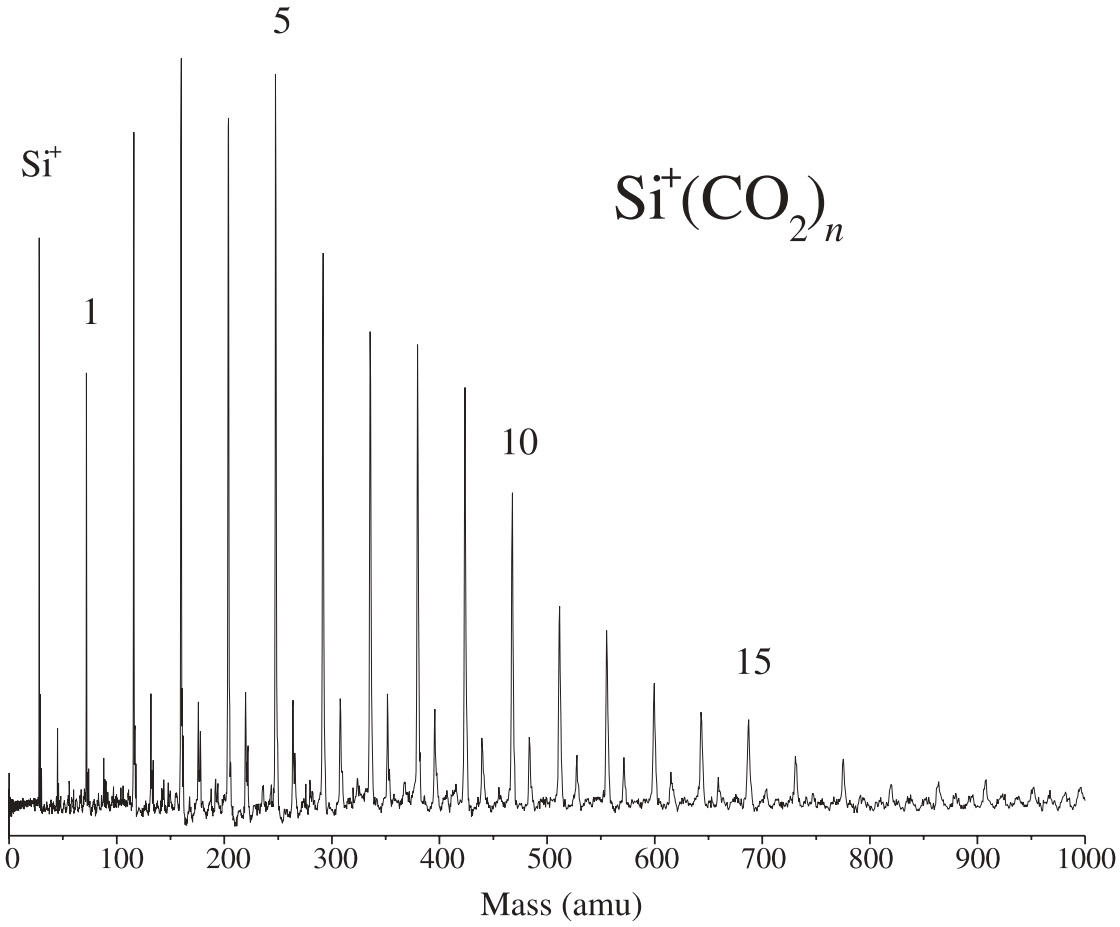
Figure 2 shows the photodissociation mass spectra of various $Si^+(CO_2)_n$ complexes that were mass-selected and excited with the IR laser in the vicinity of the CO_2 asymmetric stretch vibration near 2350 cm^{-1}. As indicated, these complexes dissociate by eliminating one or more intact CO_2 molecules. There is no evidence for the loss of CO or O masses that might occur if these clusters reacted to make oxides within these clusters. If these moieties are present, they are apparently more strongly attached to the cation than the CO_2 molecules that we see as leaving groups. It is apparent in this data that larger clusters dissociate by losing more CO_2 molecules on average than smaller ones do. This is understandable, because the average ligand binding energy to a central cation often decreases as the number of ligands increases. Additionally, it is likely in larger clusters that not all ligands are bound directly to the cation. Conditions in these supersonic expansions are cold enough so that van der Waals clusters can form, and previous studies have shown that large clusters have outer ligands bound by ligand–ligand interactions rather than ligand–metal interactions. Such outer ligands are bound more weakly to the cluster, and they dissociate more easily, explaining in a general way the more extensive fragmentation of larger complexes. The inner ligands that are attached directly to the metal are expected to be more strongly bound. Consistent with this, we find very weak photodissociation signals for the $n = 1$ and $n = 2$ complexes. Complexes for which $n > 2$ dissociate much more easily (see below). In previous studies on transition-metal ions (19, 23), we have seen a sharp final cluster size from the elimination of weakly bonded exterior ligands. The remaining ligands define the coordination sphere of the cation. However, there is no evidence in these dissociation channels for a common termination point, again indicating no strongly preferred coordination number.

As previous studies have shown, more information can be obtained through the wavelength dependence of these fragmentation processes, which reveals the vibrational frequencies of these clusters. The three vibrations of CO_2 are well known ($\nu_1 = 1333$ cm^{-1}, $\nu_2 = 667$ cm^{-1}, $\nu_3 = 2349$ cm^{-1}) (35). In the free molecule, the bend (ν_2) and asymmetric stretch (ν_3) are IR-active, while the symmetric stretch (ν_1) is not. However, regardless of what the structure is, all of these modes are IR-active in cation complexes because of the reduced symmetry. The tuning range of our IR laser system allows us to study only the asymmetric stretch or possible overtone and combination bands that would occur at higher frequencies. Figure 3 shows the wavelength dependence of the photodissociation yield for the $Si^+(CO_2)_n$ complexes for $n = 1$–4 in the vicinity of the asymmetric stretch of CO_2, whose position is indicated by the vertical dashed line. As shown, only a very weak photodissociation signal is detected for the $n = 1$ cluster. The signal is slightly more evident for $n = 2$, with a broad, noisy region of signal and a superimposed peak near the free-CO_2 resonance. Both the $n = 3$ and the $n = 4$ cluster have more clearly defined vibrational resonances that occur at or just to the blue from the free-CO_2 frequency.

The general characteristics of these spectra are understandable based on our previous studies of various metal-cation complexes with CO_2. First of all, the occurrence of a resonance-enhanced absorption near the frequency of the

© 2004 NRC Canada

Fig. 1. The mass distribution of $Si^+(CO_2)_n$ clusters produced by laser vaporization. Although there is a mass coincidence between CO_2 and SiO^+, the intermediate masses are most likely $SiO^+(CO_2)_n$ complexes.



free-CO_2 vibration, together with the observation of intact CO_2 as the elimination product, confirms that these complexes are cation–molecule complexes rather than the products of insertion chemistry. The dissociation yield is low for the smallest complexes, and it increases with additional ligands, as we have seen in essentially all other $M^+(CO_2)_n$ systems. This is likely a result of the stronger binding in the smaller complexes, which makes dissociation more difficult. In the systems we have studied previously (Mg^+, Al^+, Fe^+, and Ni^+), the cation binding energies to CO_2 were measured via collision-induced dissociation experiments. Unfortunately, such data is not available for $Si^+(CO_2)_n$ clusters. However, in the previously studied systems, the low dissociation yield in the smaller clusters came about because the binding energies were greater than the one-photon excitation energy. As we discussed, two-photon photodissociation is possible for these systems, but it is less efficient than one-photon dissociation. The latter process can occur for larger complexes that have weaker bonding, consistent with the improved dissociation yield seen here. If the most stable geometries of the small clusters are strongly bound, these structures will not dissociate efficiently, producing either no signal at all or a region of weak, broad signal from a small amount of multiphoton dissociation. However, isomeric clusters having less stable geometries may be present in minor amounts, and these species may have an advantage in dissociation because of their weaker bonding. Thus, spectra for the smallest clusters may have misleading resonances that are not characteristic of the most stable structures. We have used tagging experiments (see below) to investigate this possibility further.

Another issue discussed previously is the comparison of the CO_2 asymmetric stretch resonance in the cation complexes to this frequency in the free CO_2 molecule. In nearly all of the small complexes studied previously, the asymmetric stretch in the small complexes was shifted 10–80 cm^{-1} to the blue from the free-CO_2 frequency. This blue shift was attributed to increased repulsion on the inner wall of the vibrational potential arising from the presence of the metal ion bound in a linear M^+–OCO configuration. The magnitude of the blue shift was correlated with the binding energy of the clusters; stronger binding was associated with a greater blue shift. A similar effect was found for all cluster sizes that contained different numbers of so-called "core" ligands attached to the metal cation. This effect was also predicted with excellent accuracy by DFT for the $M^+(CO_2)_n$ (n = 1–3) complexes of Mg^+ (15) and Al^+ (17). In larger complexes that contained CO_2 ligands not attached to the cation, the same kind of blue-shifted bands occurred and there was an additional resonance with no blue shift. The latter comes from the so-called "surface" ligands, for which the asymmetric stretch vibration is found at almost exactly the free-

© 2004 NRC Canada

Fig. 2. The photodissociation mass spectra of mass-selected $Si^+(CO_2)_n$ complexes, for n = 4, 5, 8, and 9. The spectra are recorded with a difference method (dissociation laser off–on). The negative peaks indicate the depletion of the selected parent ion, and the positive peaks indicate the fragments. All complexes dissociate by the loss of one or more intact CO_2 molecules.

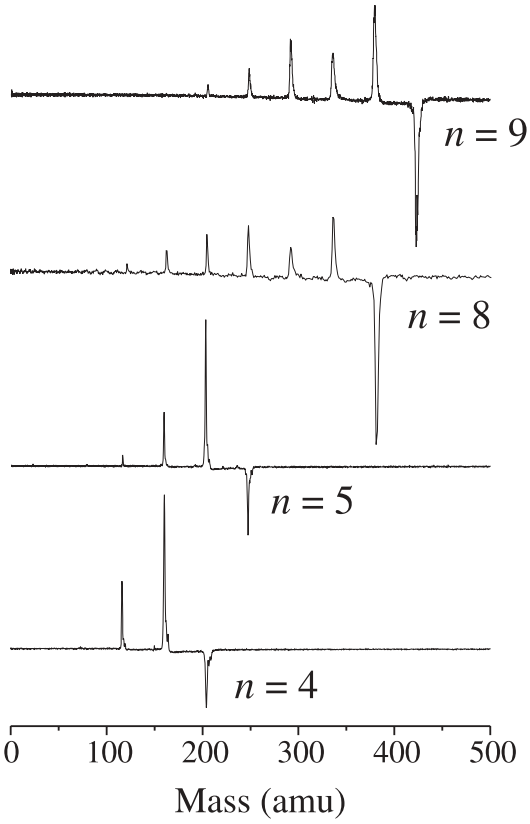
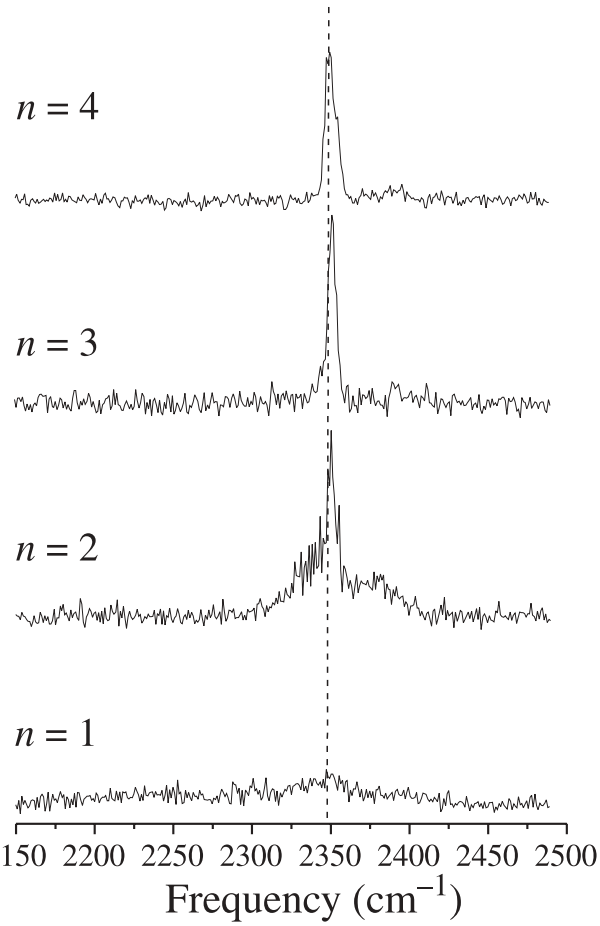


Fig. 3. The wavelength-dependent photodissociation spectra of mass-selected complexes. The vertical dashed line indicates the absorption frequency for the asymmetric stretch (ν_3) of the isolated CO_2 molecule (2349 cm^{-1}). The n = 1 complex has essentially no photodissociation; the n = 2 complex has a weak resonance and the n = 3 and n = 4 complexes have stronger signals, all occurring near the free-CO_2 band.



CO_2 frequency. A similar frequency for this vibration occurs in pure molecular clusters of CO_2 that do not contain any metal (36–41). We also noted in the previous work that any isomeric cluster that has CO_2 not bound in a linear configuration with the cation could also have a resonance near the free-CO_2 value. In the present systems, we see essentially no dissociation signal for the n = 1 complex, but the signals that we do see for the n = 2–4 complexes exhibit only a slight blue shift from the free-CO_2 frequency. These spectra are therefore quite different from those of the small $M^+(CO_2)_n$ complexes. It is not clear whether these spectra indicate clusters with very weakly bound CO_2 or clusters with some new dynamics regarding the CO_2 resonances.

To provide further insight into the structure and bonding in these small $Si^+(CO_2)_n$ complexes, we have performed DFT calculations of their structures, bonding energies, and vibrational frequencies. The results of calculations on the n = 1, n = 2, and n = 3 complexes are given in Tables 1 and 2 and Fig. 4. Stable minima are found for all three complexes, as indicated in the tables. Real frequencies are found for all vibrations except in the case of the n = 3 complex, where some of the lower frequency vibrations have small imaginary values (indicated in italics). The lowest energy structures are shown in Fig. 4. In all of these structures, the CO_2 ligands bind in a linear (or near-linear) configuration with the Si^+ ion. There is no evidence for structures with bent CO_2 molecules or side-bonded CO_2 molecules.

As indicated in Table 1 and shown in Fig. 4*a*, the n = 1 complex has its lowest energy structure with CO_2 bonded in a linear configuration with respect to the Si^+ ion and perpendicular to the p orbital. This leads to an overall ground state of $^2\Pi$ symmetry. Another electronic state of $^2\Sigma^+$ symmetry is derived from the same ground-state Si^+ ion but with the p orbital pointing at the ligand. This configuration is repulsive at all separations of metal and CO_2. We have seen similar binding trends in the excited states of Mg^+ and Ca^+ complexes that correlate to the atomic ^2P asymptote (13, 24). In several systems that we studied, including binding to rare-gas atoms, nitrogen, and CO_2, the $p\pi$ binding configuration always led to much stronger binding than the $p\sigma$ configuration, as seen here. The $p\pi$ configuration exposes the negatively charged oxygen end of the CO_2 ligand to the more positive region of the cation along the nodal plane of the p orbital, and it reduces the strong repulsion that is present between the p orbital and the negative charge on the ligand in the $p\sigma$ configuration. We have also investigated the small com-

© 2004 NRC Canada

Table 1. Total electronic energies of Si^+, CO_2, $Si^+(CO_2)$, $OSi^+(CO)$, $Si^+(CO_2)_2$, $OSi^+(CO)(CO_2)$, and $Si^+(CO_2)_3$ minima with a DZP basis set and calculated ligand dissociation energies (D_e).

	B3LYP			BP86		
System	Total electronic energy (hartree)		D_e (kcal/mol)	Total electronic energy (hartree)		D_e (kcal/mol)
Si^+	–289.07565	(–289.07565)		–289.07379	(–289.07379)	
CO_2	–188.62082	(–188.60916)		–188.63002	(–188.61878)	
$Si^+(CO_2)$	–477.73365	(–477.72128)	23.3 (22.9)	–477.74477	(–477.73291)	25.7 (25.3)
$OSi^+(CO)$	–477.70300	(–477.69359)	4.1 (2.3)	–477.71808	(–477.70874)	9.0 (7.4)
$Si^+(CO_2)_2$ ($D_{\infty h}$)	–666.36757	(–666.34334)	31.6 (31.0)	–666.38802	(–666.36475)	34.0 (33.5)
$Si^+(CO_2)_2$ (C_{2v})	–666.37658	(–666.35178)	37.2 (36.3)	–666.39887	(–666.37491)	40.8 (39.9)
$OSi^+(CO)(CO_2)$	–666.34882	(–666.32595)	19.8 (18.6)	–666.37497	(–666.35275)	25.8 (24.7)
$Si^+(CO_2)_2$ (C_{2h})	—*		—*	–666.38802	(–666.36482)	34.0 (33.6)
$Si^+(CO_2)_3$ (D_{3h})	–855.00309	(–854.96711)	40.8 (40.1)	–855.03260	(–854.99808)	43.1 (42.6)

Note: Zero-point vibrationally corrected values are listed in parentheses. The D_e values discussed in the text are for the process $Si^+(CO_2)_n \rightarrow Si^+(CO_2)_{n-1} + CO_2$ and therefore represent differences between binding energies for the n and $n - 1$ clusters. Likewise, the D_e values for the $OSi^+(CO)(CO_2)$ cluster are for removal of the CO_2 whereas those for $OSi^+(CO)$ are for loss of CO.

*The C_{2h} structure for the $n = 2$ complex was not a minimum with the B3LYP functional.

plexes that might result from insertion chemistry, e.g., $OSi^+(CO)(CO_2)_{n-1}$, and these results are also contained in Tables 1 and 2.

Surprisingly, the binding energy (D_0) of the $n = 1$ complex (22.9 kcal/mol (1 kcal = 4.184 kJ)) here is much greater than those we have calculated previously for the $Mg^+(CO_2)$ (D_0 = 15.4 kcal/mol) (15) and $Al^+(CO_2)$ (D_0 = 12.4 kcal/mol) (17) complexes. Apparently, the increased nuclear charge on the Si^+ ion increases the attractive charge–quadrupole interaction, and there is no additional screening of this nuclear charge from the extra valence electron because of the favorable $p\pi$ binding configuration. The binding energy here for the $p\pi$ configuration can be compared to that which we found for the *excited* state of $Mg^+(CO_2)$ (D_0' = 32.0 kcal/mol) (13), which has a similar $p\pi$ bonding configuration.

The $n = 2$ complex is calculated to have a bent structure. Both CO_2 ligands are oriented end-on with respect to Si^+ and perpendicular with respect to the p orbital as shown for the $n = 1$ complex. However, they are bent with respect to each other in a C_{2v} structure rather than being on opposite sides of the cation. The O-Si^+-O angle is calculated to be 82°. This bent orientation is presumably due to the same polarization effect involving the 3*s* orbital that we saw before for $Mg^+(CO_2)_n$ and $Al^+(CO_2)_n$ complexes (15, 17). The axes of the two CO_2 molecules are tilted away from each other with an angle slightly greater than the O-Si^+-O angle, as we have seen previously for $Mg^+(CO_2)_2$ and $Al^+(CO_2)_2$ complexes (15, 17). Apparently, this configuration enhances the interaction of the cation with the lone-pair electrons on the adjacent oxygen atoms. The $n = 3$ complex continues the $p\pi$ orientation for each Si^+–OCO interaction but ends up with a calculated D_{3h} structure with the three ligands distributed equally around the waist of the p orbital. The binding energy (with respect to the loss of the outer ligand) is 13.9 kcal/mol for the $n = 2$ species, which is significantly less than the binding energy for the $n = 1$ species. For the $n = 3$ species, the binding energy is only 3.6 kcal/mol, which represents another dramatic decrease.

Such a strong decrease in binding energy with the number of CO_2 ligands was not seen previously for the corresponding Mg^+ and Al^+ complexes. Table 3 shows a comparison of the binding energies versus cluster size for the small Mg^+, Al^+, and Si^+ complexes. All the complexes exhibit the pattern of decreasing binding energy with cluster size, but the $n = 1 \rightarrow n = 2$ and $n = 2 \rightarrow n = 3$ decreases are, respectively, 27% and 25% for Mg^+ and 35% and 23% for Al^+, while the corresponding values for Si^+ are 40% and 74%. The greatest drop is the $n = 2 \rightarrow n = 3$ decrease for Si^+, owing to the particularly low binding energy for the $n = 3$ complex. Consistent with this, we see a significant increase in the photodissociation yield between the $n = 2$ and $n = 3$ complexes. If the binding energy of the $n = 3$ complex is close to the calculated value (3.6 kcal/mol = 1260 cm^{-1}), it can be dissociated with a single photon at 2350 cm^{-1}, which explains the increased dissociation yield that we observe. Thus, the low dissociation energy calculated for $n = 3$ is consistent with experiment, as were the calculated dissociation energies for the Mg^+ and Al^+ complexes, suggesting that the more rapid decrease in binding energy occurs only for the Si^+ complexes. The key difference in electronic structure between Si^+ and the Mg^+ and Al^+ ions studied previously is the occupation of the 3*p* orbital. In the Mg^+ and Al^+ complexes, bent structures resulted from the highly polarizable 3*s* orbital, as discussed above. However, at least three CO_2 ligands could bind on the same side of the cation before additional ligands were forced to bind on the negative side of the distorted orbital or in the second sphere. The most noticeable decrease in binding energy occurred after $n = 3$ for these complexes. For Si^+, the 3*p* orbital provides an additional steric constraint on ligand assembly. Two CO_2 molecules can be accommodated in a bent structure, but this orbital blocks same-side binding of a third CO_2 molecule. Thus, for the $n = 3$ complex, the third ligand is forced into a site opposite the first two ligands, causing all three to interact less favorably with the 3*s* orbital.

To obtain further information about the small $Si^+(CO_2)_n$ complexes, we have also studied their photodissociation spectroscopy using the technique of "rare-gas tagging" (15–18, 42–46) with argon. In previous studies on other metal–CO_2 complexes, we have found that a complex tagged with argon has essentially the same spectrum as one with the same number of ligands without argon, except that the dissociation yield is greater and the lines in the spectrum are

© 2004 NRC Canada

Table 2. Theoretical harmonic vibrational frequencies for CO_2, $Si^+(CO_2)$, $OSi^+(CO)$, $Si^+(CO_2)_2$, $OSi^+(CO)(CO_2)$, and $Si^+(CO_2)_3$ with a DZP basis set.

	Frequency (cm^{-1})		
Vibrational mode	B3LYP	BP86	Exptl.
CO_2			
ω_1 (Σ_g)	1363 (0)	1308 (0)	1333
ω_2 (Π_u)	660 (30)	627 (21)	667
ω_3 (Σ_u)	2439 (652)	2375 (530)	2349
$Si^+(CO_2)$			
ω_1 (Σ)	2476 (984.6)	2401 (787.0)	
ω_1 (scaled)	2386		2363
ω_2	1352 (118.4)	1283 (60.5)	
ω_3	278 (145.8)	297 (113.1)	
ω_4 (Π)	619 (42.3)	582 (33.6)	
ω_5	578 (36.5)	505 (25.5)	
ω_6	77 (1.6)	79 (1.5)	
ω_7	51 (2.0)	59 (2.1)	
$OSi^+(CO)$			
ω_1 (A′)	2307 (50.7)	2193 (69.2)	
ω_1 (scaled)	2217		
ω_2	930 (43.3)	1023 (9.1)	
ω_3	323 (69.3)	362 (41.0)	
ω_4 (Π)	256 (18.4)	248 (8.9)	
ω_5	95 (17.6)	80 (18.6)	
ω_6 (A′′)	220 (7.2)	191 (4.8)	
$Si^+(CO_2)_2$ (C_{2v})			
ω_1 (A_1)	2474 (344.9)	2400 (214.4)	
ω_1 (scaled)	2384		
ω_2	1358 (36.8)	1294 (14.9)	
ω_3	629 (49.6)	592 (32.5)	
ω_4	267 (91.2)	283 (69.6)	
ω_5	108 (1.4)	119 (0.9)	
ω_6	40 (0.7)	44 (0.6)	
ω_7 (A_2)	604 (0)	550 (0)	
ω_8	51 (0)	63 (0)	
ω_9 (B_1)	605 (66)	550 (47.0)	
ω_{10}	47 (0.8)	50 (0.6)	
ω_{11} (B_2)	2452 (1888.8)	2382 (1672.6)	
ω_{11} (scaled)	2362		2350
ω_{12}	1352 (130.0)	1289 (82.4)	
ω_{13}	627 (14.7)	592 (12.1)	
ω_{14}	201 (124.4)	227 (105.7)	
ω_{15}	70 (0.5)	81 (0.3)	
$OSi^+(CO)(CO_2)$			
ω_1	2453 (1008.7)	2380 (849.7)	
ω_1 (scaled)	2363		
ω_2	2283 (110.7)	2145 (219.5)	
ω_2 (scaled)	2193		
ω_3	1338 (128.5)	1285 (105.1)	
ω_4	1081 (23.1)	1089 (12.7)	
ω_5	633 (31.2)	596 (20.4)	
ω_6	616 (32.1)	578 (24.4)	
ω_7	381 (59.0)	402 (27.3)	
ω_8	304 (48.6)	311 (84.3)	
ω_9	244 (80.8)	268 (10.4)	

© 2004 NRC Canada

Table 2 (*concluded*).

Vibrational mode	Frequency (cm^{-1}) B3LYP	BP86	Exptl.
ω_{10}	205 (44.4)	211 (67.6)	
ω_{11}	199 (22.4)	194 (10.8)	
ω_{12}	123 (6.7)	127 (4.9)	
ω_{13}	80 (9.4)	68 (7.9)	
ω_{14}	56 (1.1)	59 (1.3)	
ω_{15}	41 (2.2)	41 (2.1)	
$Si^+(CO_2)_3$ (D_{3h})			
ω_1 (A_1')	2468 (0.0)	2401 (0.0)	
ω_1 (scaled)	–2378		2371 (?)
ω_2	1366 (0.0)	1310 (0.0)	
ω_3	120.0 (0.0)	130 (0.0)	
ω_4 (A_2')	638 (0.0)	601 (2.7)	
ω_5	20 (0.0)	*29 (0.0)*	
ω_6 (A_2')	631 (3.0)	588 (75.0)	
ω_7	112 (5.9)	112 (0.03)	
ω_8	13 (0.2)	*13 (0.03)*	
ω_9 (E′)	2449 (1581.7)	2384 (1342.7)	
ω_{10}	2449 (1581.6)	2384 (1342.7)	
$\omega_{9.10}$ (scaled)	2359		2353
ω_{11}	1361 (96.8)	1305 (83.3)	
ω_{12}	1361 (96.8)	1305 (83.3)	
ω_{13}	639 (52.8)	602 (2.7)	
ω_{14}	639 (52.8)	602 (2.7)	
ω_{15}	117 (163.2)	125 (174.0)	
ω_{16}	117 (163.3)	125 (174.0)	
ω_{17}	17 (0.3)	5 (0.01)	
ω_{18}	17 (0.3)	5 (0.01)	
ω_{19}	*34 (2.1)*	49 (1.2)	
ω_{20}	*34 (2.1)*	49 (1.2)	
ω_{21} (E″)	630 (0.0)	586 (0.0)	
ω_{22}	630 (0.0)	586 (0.0)	
ω_{23}	*8 (0.0)*	*32 (0.0)*	
ω_{24}	*8 (0.0)*	*32 (0.0)*	

Note: Computed IR intensities (km/mol) are listed in parentheses. Imaginary vibrational frequencies are in italics.

sharper. Dissociation in these experiments leads to loss of argon rather than CO_2, because the former is more weakly bound. The rare gas in these experiments acts essentially as a spectator that enhances the dissociation spectroscopy. The "spectator" character of the added rare gas is only expected to be valid if there is a large difference in the binding energy for the rare gas versus the other ligand. Because the spectra of the small $Si^+(CO_2)_n$ complexes (particularly for $n = 1$ and $n = 2$) without tagging are difficult to obtain and do not have clear sharp bands, we made a mixed expansion gas containing argon and carbon dioxide to produce mixed clusters of the form $Si^+(CO_2)_nAr$. As in the systems previously studied via this approach, we found that photodissociation of $Si^+(CO_2)_nAr$ leads to elimination of argon.

The IR spectra measured in this way for the $Si^+(CO_2)_nAr$ ($n = 1$–3) complexes are shown in Fig. 5. The argon tagging does indeed improve the dissociation yield for all the small clusters. We now see sharp resonant structure for the $n = 1$ and $n = 2$ complexes, whereas without the argon these complexes were extremely difficult to dissociate and the band structure in the IR spectra was broad. For comparison to these spectra, vibrational bands calculated for the neat clusters are shown as solid vertical bars in the figure. The harmonic vibrations from the DFT/B3LYP calculations are scaled to obtain these predicted vibrational bands, as described above. The correction factor needed to bring the calculated asymmetric stretch for the free CO_2 molecule into agreement with the experimental value is –90 cm^{-1}. This factor is applied to all the bands related to the asymmetric stretch for the complexes here. Table 2 shows all the vibrational bands calculated for these complexes and the scaled asymmetric stretch frequencies are compared to the experimental values. As shown in Fig. 5, the vibrational bands computed for these small complexes are all predicted to be found at higher frequencies than the asymmetric stretch in free CO_2 (indicated with the dashed vertical line). Similar blue shifts for corresponding complex vibrations were predicted and measured in the spectra of $Mg^+(CO_2)_n$ (15) and $Al^+(CO_2)_n$ (17) complexes. In those previous experiments, DFT calculations at about the same level as here gave al-

© 2004 NRC Canada

Fig. 4. The calculated structures for the $Si^+(CO_2)_n$ complexes: (*a*) $n = 1$; (*b*) $n = 2$; (*c*) $n = 3$. The ground state of the $n = 1$ complex is $^2\Pi$, with the CO_2 molecule binding in a linear configuration perpendicular to the *p* orbital of Si^+. The $n = 2$ complex has C_{2v} symmetry, with the two CO_2 molecules binding perpendicular to the *p* orbital in a bent configuration with respect to each other. The $n = 3$ complex has D_{3h} symmetry (view shown from above the *p* orbital), with all three CO_2 molecules binding around the waist of the *p* orbital. In all cases, the CO_2 molecules are distorted slightly, with the C=O bond nearest the cation elongated.

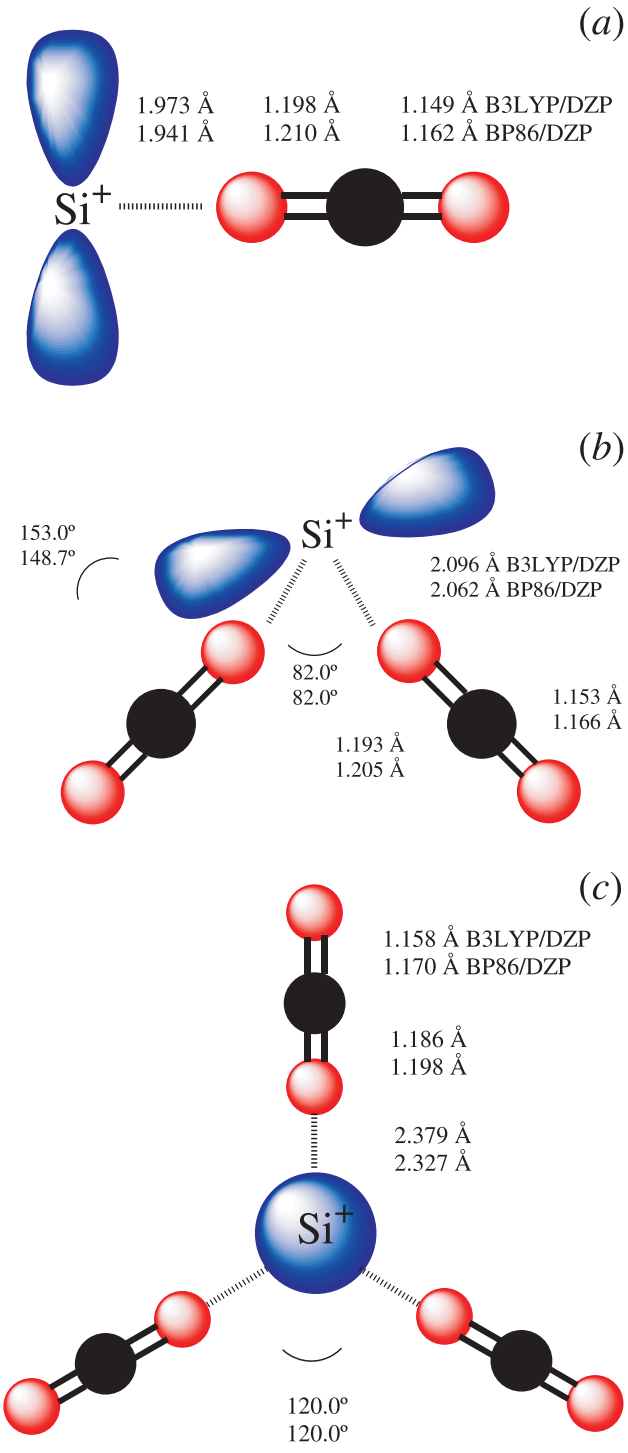
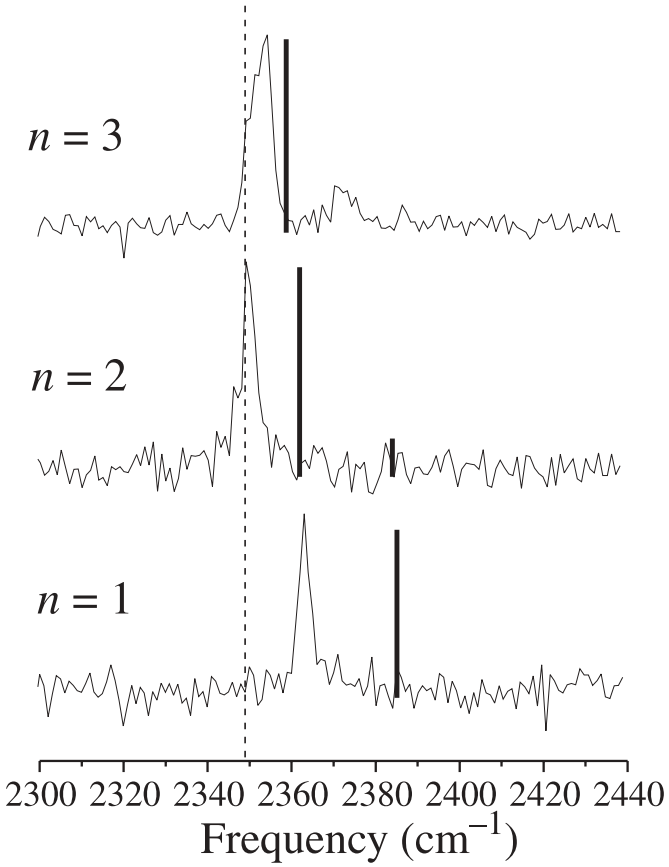


Table 3. A comparison of the calculated binding energies for the last ligand (i.e., $M^+(CO_2)_n \rightarrow M^+(CO_2)_{n-1}$) for magnesium, aluminum, and silicon complexes.

	D_e (kcal/mol)		
M^+	$n = 1$	$n = 2$	$n = 3$
Mg^+	15.8	11.6	8.7
Al^+	12.4	8.1	6.2
Si^+	23.3	13.9	3.6

Fig. 5. The IR photodissociation spectra of the $Si^+(CO_2)_n$ ($n = 1$–3) complexes when they are tagged with argon and the spectrum is detected in the argon elimination channel.The vertical dashed line indicates the free-CO_2 band, while the vertical bars indicate the (scaled) predictions of theory for the $Si^+(CO_2)_n$ complexes.



most perfect agreement (within 1–2 cm^{-1}) with the experimental vibrational bands. In the present experiments, however, there is some disparity between the predictions of DFT and the experimentally observed bands. For $n = 1$, for example, DFT predicts a strongly bound complex and a rather large blue shift of about 37 cm^{-1} from the free-CO_2 vibration. In the argon-tagged $n = 1$ complex, we measured a shift to the blue, but it is only about 14 cm^{-1}. The $n = 2$ complex is predicted to have two bands at 2362 and 2384 cm^{-1}, whereas we measured only one at 2350 cm^{-1}. The 2384 cm^{-1} band is predicted to have a much smaller intensity, and so we might miss it in our experiment, but the

© 2004 NRC Canada

one band we observe is essentially unshifted from the free-molecule vibration. The $n = 3$ complex is predicted to have D_{3h} symmetry, which leads to one doubly degenerate IR-active mode expected at 2359 cm^{-1}. In this case we observe one strong band close to this position, but another unexpected band is observed as a weak feature at about 2371 cm^{-1}. So, with respect to band positions, and even the number of bands observed, theory and experiment do not agree very well for these small complexes.

This disparity between theory and experiment is puzzling, especially in light of the excellent agreement seen before for Mg^+–CO_2 and Al^+–CO_2 complexes. It is clear that either theory has some special problem with Si^+ that it does not have with Mg^+ and Al^+ in predicting vibrations or the argon-tagged complexes here are somehow different from those studied for Mg^+ and Al^+ complexes regarding the relative inertness of the tagging. It is not clear why there should be any special problem with theory for this system. The strange pattern of calculated dissociation energies seen above, however, suggests that adding an additional ligand to these complexes has a dramatic effect in lowering the binding energies. Although argon is not expected to bind as strongly as CO_2, it may bind strongly enough to have a non-negligible effect on the spectroscopy of these complexes, thus explaining in part the mediocre agreement between theory and the tagged spectra.

The possible effect of the argon can be seen by closer inspection of the spectra and the theoretical predictions of the spectra. The $n = 1$ complex, for example, has a tagged spectrum with one band that is not shifted to the blue as much as theory predicts. However, if we consider the tagged $n = 1$ complex as actually having two ligands, we can compare it to the spectrum predicted for the $n = 2$ complex. It is perhaps no accident that the strongest band predicted for n = 2 matches the band observed for $n = 1$ almost perfectly. We can use the same logic to consider the tagged spectrum for $n = 2$, where again the blue shift is less than expected. The calculations predict a similarly small blue shift for $n = 3$. In the $n = 3$ complex, we have an extra weak band near 2371 cm^{-1}, which is close to the frequency predicted for the ν_1 vibration (2378 cm^{-1}). However, this mode is not IR-active for a cluster with D_{3h} symmetry. On the other hand, if the argon acts as a fourth ligand, we might have a square-planar arrangement around the Si^+, and then the three CO_2 ligands would be in a less symmetric configuration. This reduced symmetry would give some weak activity to the ν_1 vibration (2378 cm^{-1}) predicted to be forbidden for the $n = 3$ D_{3h} complex without tagging. In a qualitative way then, the presence of argon as a real perturbation on the system instead of as a spectator can explain the disparity between theory and experiment in these spectra. This suggests that measuring the "real" unperturbed spectra of the small complexes here may be very difficult with any tagging method. To see if this proposal holds up under closer scrutiny, we would need to calculate explicitly the spectra for complexes with and without argon.

Another clear possibility for the spectra of these small multiligand clusters (i.e., $n = 2, 3$) is the presence of minor isomers with one CO_2 molecule not attached to the cation, i.e., bound a bound externally only to CO_2. The binding energy of CO_2 in a free dimer is substantial (about 500 cm^{-1}) (47), and the induction of charge on one ligand caused by the silicon cation would enhance this kind of binding in these complexes. In our previous calculations on aluminum and magnesium complexes with CO_2, we investigated such configurations and found stable minima for them. We have not done these calculations here for silicon complexes owing to difficulties in getting the multiligand complexes to converge. However, as we have indicated above and discussed elsewhere, if such external CO_2 molecules are present, they would have resonances near the free-CO_2 value. We suspect this to be the case for the $n = 2$ complex, which has its main absorption near this value. The $n = 3$ complex has a main band shifted to the blue, but its shape is asymmetric and there is evidence for a shoulder overlapping the free-CO_2 band. The steeply decreasing binding energy seen in the calculations for the $n = 2$ and $n = 3$ complexes when the ligands are attached to the cation makes it reasonable that isomers with externally bound CO_2 might also be present at some concentration in the molecular beam.

Figure 6 shows the spectra measured for complexes in the $n = 4$–6 size range without argon tagging. For $n = 4$, the spectrum exhibits a single peak positioned mostly on the free-CO_2 resonance, but with a noticeable shoulder in the neighborhood of the core peak seen for the tagged $n = 3$ cluster. The simplest explanation for this spectrum is that this complex is basically an $n = 3$ species but with one external CO_2 ligand, giving this spectrum intensity near the free-CO_2 resonance. Interesting new features arise in the spectra for $n = 5$ and $n = 6$. We have similar strong resonances near the free-CO_2 position, just as in the $n = 4$ spectrum, but there is a noticeable new peak further to the blue (near 2370 cm^{-1}) for both of these clusters. This peak occurs at about the same position as the weak peak in the spectrum of the argon-tagged $n = 3$ complex, but it appears to be due to a new kind of chromophore. It has significant intensity beginning at $n = 5$ and growing in at $n = 6$. In the spectra of the larger clusters ($n = 7$–10), shown in Fig. 7, this peak continues to grow, eventually becoming the most intense in the spectrum. In addition to this blue-shifted peak, there is a much weaker peak near 2290 cm^{-1}. This peak is weak, but reproducible, in both the $n = 5$ and $n = 6$ spectra, but it is not present in the spectra of the larger clusters where the 2370 cm^{-1} band is more evident.

An interpretation of these new bands is possible by comparison to our previous studies of other metal ion–CO_2 clusters. In most of the systems we have studied, $M^+(CO_2)_n$ clusters have only resonances associated with the core ligands and those on the surface of the cluster. The core ligand bands occur about 10–30 cm^{-1} to the blue of the free-CO_2 band, with the biggest shift occurring for the smallest clusters and smaller shifts seen as cluster size increases. The surface bands appear near the free-CO_2 band, and this splits slightly into a doublet in the spectra of the larger clusters. In the present clusters, only the $n = 1$ complex has a significant blue shift associated with core ligands. The new blue-shifted band and the weak red-shifted band appear suddenly and only for larger clusters. This suggests that these features are not associated with any gradual solvation process in the clusters. While we have seen only progressive solvation in most of our previous studies on metal ion–CO_2 complexes(15–18), there have been two examples (Ni^+ and V^+)

© 2004 NRC Canada

Fig. 6. The photodissociation spectra of the $Si^+(CO_2)_n$ (n = 4–6) complexes detected in the CO_2 elimination channel. New bands are observed to the blue and to the red.

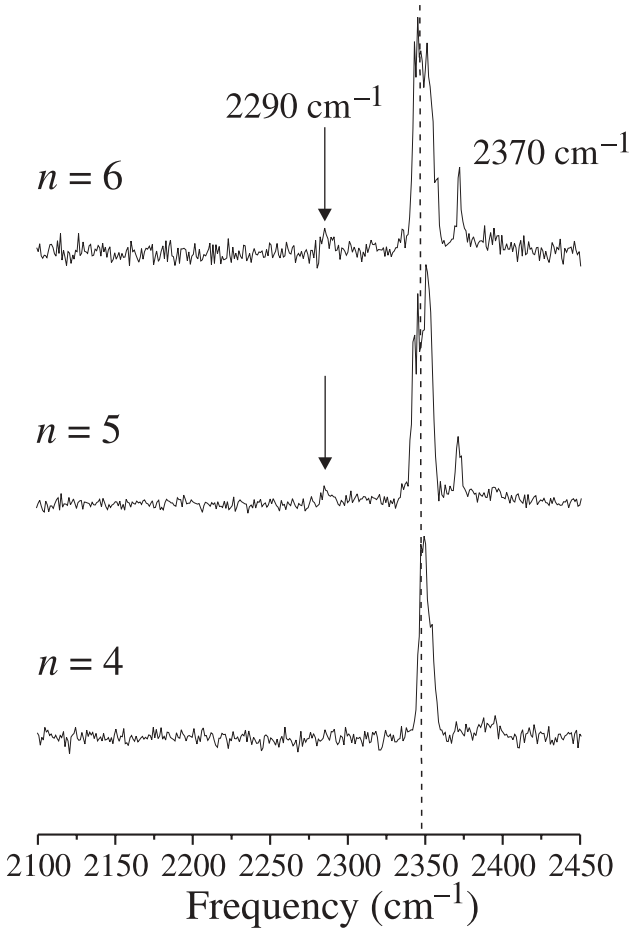
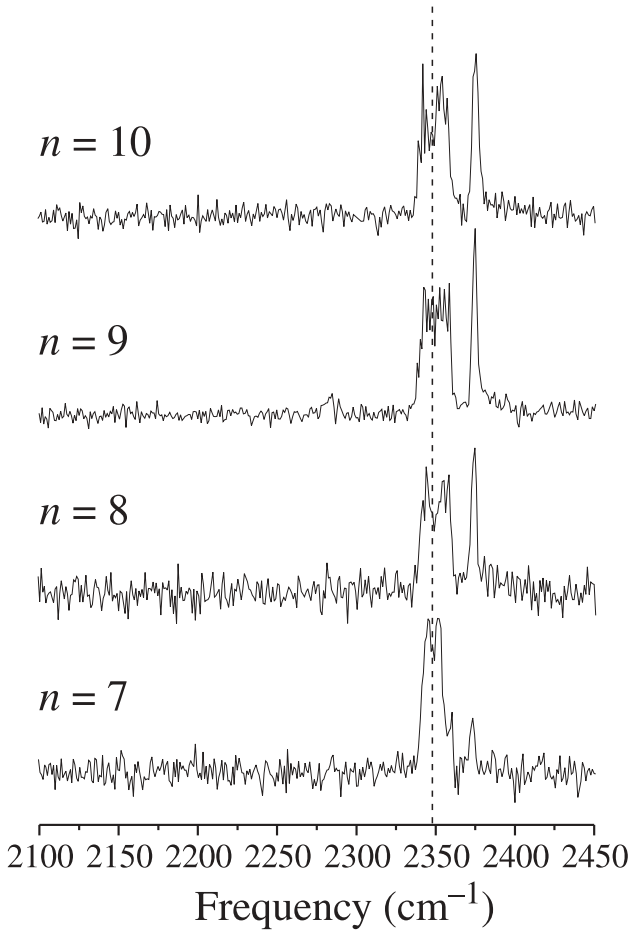


Fig. 7. The photodissociation spectra of the $Si^+(CO_2)_n$ (n = 7–10) complexes, showing the strong blue-shifted band growing in intensity.



(23 and unpublished results) in which there was a sudden appearance of similar blue-shifted bands. In both cases, we have interpreted these bands to arise from an intracluster reaction, in which the metal ion reacts with one CO_2 to form an oxide-carbonyl species, i.e., $OM^+(CO)(CO_2)_{n-1}$. Such a reaction would not be detected based on mass spectrometry alone. A similar reaction makes sense here and provides a convenient explanation for the new IR bands seen.

To further investigate such an intracluster reaction, we have done DFT calculations on the $OSi^+(CO)$ and $OSi^+(CO)(CO_2)$ ions to investigate their properties. As shown in Table 1, the covalent bonding interactions of the oxide and the carbonyl are not favorable compared to the cation–CO_2 bonding, and the oxide-carbonyl species is much less stable for the n = 1 complex. However, the diatomic oxide has partial ionic character (e.g., Si^{2+}, O^-) as well as a significant dipole moment. In the larger clusters, binding of other CO_2 molecules to such a core ion would perhaps be stronger than binding to a singly charged silicon cation, especially considering the problems noted above for clustering about Si^+. CO_2 molecules bound strongly to a (Si^{2+}, O^-) core ion would get a stronger blue shift in their spectrum than those bound more weakly to Si^+. This can explain the 2370 cm^{-1} peak observed in the spectra of the larger clusters. Consistent with this, our calculations for the $OSi^+(CO)(CO_2)$ insertion complex find an asymmetric stretch for the CO_2 at 2363 cm^{-1}. Additionally, the DFT calculations find a much greater oscillator strength for this CO_2 mode in the oxide-carbonyl complex than that in the Si^+ complexes, consistent with the increasing prominence of the 2370 cm^{-1} band in larger clusters. The 2290 cm^{-1} band, which is red-shifted from the free-CO_2 band, can be assigned to the carbonyl stretch in such an oxide-carbonyl core ion. A similar peak has been seen in matrix isolation spectroscopy of neutral OSi(CO) complexes, and DFT calculations on the neutral predicted the carbonyl stretch band near 2260 cm^{-1} (48). Likewise, our DFT calculations here predict a carbonyl stretch (scaled) near 2217 cm^{-1} in the monomer complex and 2193 cm^{-1} in the dimer, which might easily shift to higher frequencies in the larger clusters. The IR intensity of this carbonyl band is extremely weak here, and this band is only seen for the n = 5 and n = 6 clusters. In our previous studies on the Ni^+ and V^+ complexes, only the blue-shifted band was observed and there was no evidence for the carbonyl band (23 and unpublished results). Apparently, in all of these various clusters with oxide-carbonyl moieties believed to be present, the carbonyl stretch does not have a strong oscillator strength. Consistent with these observations, our calculations find a

© 2004 NRC Canada

particularly low value for the IR intensity of the carbonyl stretch compared to the CO_2 asymmetric stretch. Overall then, the suggested intracluster reaction producing an oxide-carbonyl species is consistent with the vibrational spectrum observed.

The formation of $SiO^+(CO_2)_n$ clusters was noted above in the mass distribution produced from the cluster source. However, the formation of the intracluster oxide-carbonyl species here is apparently not driven by the plasma chemistry, because it is not found in the small clusters. The occurrence of a reaction product only in larger clusters is possible via a solvation-induced reaction mechanism. The new covalent Si^+—O and Si^+—CO bonds may be present at all cluster sizes, but our calculations for the $n = 1$ and $n = 2$ complexes indicate that these are not as favorable as the Si^+–OCO electrostatic interactions. However, if the reaction product (SiO^+) can be solvated more easily than the reactant species (Si^+), then the energetics of solvation will eventually stabilize the oxide-carbonyl complexes more beyond some critical cluster size. In this case, the calculated binding energy of the first CO_2 molecule to Si^+ is significant, but there is a dramatic decrease in the binding energy of subsequent molecules to this atomic ion, as discussed above. SiO^+, however, would have more ionic character and a dipole moment, as noted above, facilitating its solvation. If there is indeed some transfer of charge from silicon to oxygen, then the steric hindrance for ligand binding caused by the 3*p* orbital of Si^+ will be reduced for SiO^+. Therefore, the lowest-energy structures for the small clusters could be the simple electrostatic complexes with Si^+, as found in our DFT calculations. The larger clusters, whose structures are less accessible with theory, may be more stable in the oxide-carbonyl geometries because of the more efficient solvation of these species. This picture makes sense for these silicon-ion clusters in the same way that it does for the transition-metal-cation systems of nickel and vanadium.

Conclusions

Weakly bound $Si^+(CO_2)_n$ complexes have been studied with IR photodissociation spectroscopy near the asymmetric stretch vibration in CO_2. The smallest complexes studied ($n = 1, 2$) do not dissociate efficiently, but as the size of the complex increases, the dissociation proceeds by the loss of intact CO_2 molecules. Mixed clusters of the form $Si^+(CO_2)_nAr$ dissociate by the loss of argon. Both the pure CO_2 and argon-tagged complexes have vibrational resonances near the frequency of the asymmetric stretch vibration in CO_2, indicating that there are weakly bound ligands present. Density functional theory was employed to investigate the structures of these complexes and their vibrational spectra. The dissociation energy for the $n = 1$ complex is quite high, but the binding energy for subsequent ligands drops steeply. This decline is interpreted to arise because of the difficulty in assembling multiple ligands around the 3*p* orbital. The agreement between theory and experiment on vibrational resonances is much less satisfactory than it was for the previously studied $Mg^+(CO_2)_n$ and $Al^+(CO_2)_n$ complexes. This is likely because the argon used to tag these clusters is not legitimate as an inert spectator atom, as it was in the earlier systems. The acute sensitivity of the binding energy in these complexes amplifies the effect of each added atom, and therefore argon induces significant perturbations on the spectra.

In complexes with five or more CO_2 ligands, new vibrational bands are measured that are assigned to an intracluster reaction producing an oxide-carbonyl species. This reaction is apparently induced because of the differential solvation interactions of the bare silicon cation versus the diatomic SiO^+ species. The latter is more effectively solvated because of its partial ionic character and its dipole moment. The differential binding is also presumably enhanced because of the severely ineffective binding of the bare silicon cation to additional ligands, as discussed above.

If the weak electrostatic binding seen here is indeed associated with the presence of an occupied valence *p* orbital, then this would imply very weak electrostatic interactions for similar cations or those with greater occupation in similar *p* orbitals. For example, we could predict weak binding for ligands to ions such as P^+ or S^+ in the third row. Ion–molecule complexes have not been studied extensively for these cations, but it would be interesting to examine these systems to follow the trend suggested. Larger ions, such as those in the fourth row, would necessarily have *d* orbitals populated before the *p* orbitals, and so such simple predictions are not likely to apply to their binding.

Acknowledgements

We gratefully acknowledge support for this work from National Science Foundation (Grant Nos. CHE-0244143 (Duncan) and CHE-0136186 (Schaefer)). Some of the calculations reported herein were performed at the Notre Dame Radiation Laboratory, which is supported by the United States Department of Energy, Office of Basic Energy Sciences.

References

1. P.A. Zbinden, M.A. Hidalgo, P. Eberhardt, and J. Geiss. Planet. Space Sci. **23**, 1621 (1975).
2. S.K. Atreya, J.B. Pollack, and M.S. Matthews (*Editors*). Origin and evolution of planetary and satellite atmospheres. University of Arizona Press, Tucson. 1989.
3. J.L. Turner and A. Dalgarno. Astrophys. J. **213**, 386 (1977).
4. J. Millar. Astrophys. Space Sci. **72**, 509 (1980).
5. R.E.S. Clegg, L.J. van Ijzendoorn, and L.J. Allamandola. Mon. Not. Astr. Soc. **203**, 125 (1983).
6. (*a*) M.J. Powell, B.C. Easton, and O.F. Hill. Appl. Phys. Lett. **38**, 794 (1981); (*b*) L.G. J. Meiners. Vac. Sci. Technol. **21**, 655 (1982).
7. (*a*) D.K. Bohme. Advances in gas phase ion chemistry. Vol. 1. JAI Press, Greenwich, Conn. 1992. p. 225; (*b*) D.K. Bohme, S. Wlodek, and H. Wincel. J. Am. Chem. Soc. **113**, 6396 (1991); (*c*) R. Srinivas, J. Hrusak, D. Sülzle, D.K. Bohme, and H. Schwarz. J. Am. Chem. Soc. **114**, 2802 (1992).
8. (*a*) B.H. Boo, J.L. Elkind, and P.B. Armentrout. J. Am. Chem. Soc. **112**, 2083 (1990); (*b*) B.H. Boo and P.B. Armentrout. J. Am. Chem. Soc. **113**, 6401 (1991); (*c*) B.H. Boo and P.B. Armentrout. J. Am. Chem. Soc. **109**, 3549 (1987); (*d*) B.L. Kickel, E.R. Fisher, and P.B. Armentrout. J. Phys. Chem. **96**, 2603 (1992).
9. (*a*) J. Glosik, P. Zakouril, V. Skalsky, and W. Lindinger. Int. J. Mass. Spectrom. Ion Processes **149/150**, 499 (1995); (*b*) J.

© 2004 NRC Canada

Glosik, P. Zakouril, and W. Lindinger. J. Chem. Phys. **103**, 6490 (1995); (*c*) J. Glosik, P. Zakouril, and W. Lindinger. Int. J. Mass. Spectrom. Ion Processes **145**, 155 (1995).
10. K.P. Lim and F.W. Lampe. J. Chem. Phys. **96**, 2819 (1992).
11. (*a*) R.C. Dunbar, S.J. Klippenstein, J. Hrusak, D. Stockigt, and H. Schwarz. J. Am. Chem. Soc. **118**, 5277 (1996); (*b*) B.P. Pozniak and R.C. Dunbar. J. Am. Chem. Soc. **119**, 10 439 (1997); (*c*) R.C. Dunbar, G.T. Uechi, and B. Asamoto. J. Am. Chem. Soc. **116**, 2466 (1994).
12. C. Luder, E. Georgiou, and M. Velegrakis. Int. J. Mass. Spectrom. Ion Processes **153**, 129 (1996).
13. C.S. Yeh, K.F. Willey, D.L. Robbins, J.S. Pilgrim, and M.A. Duncan. J. Chem. Phys. **98**, 1867 (1993).
14. (*a*) C.S. Yeh, J.S. Pilgrim, D.L. Robbins, K.F. Willey, and M.A. Duncan. Int. Rev. Phys. Chem. **13**, 231 (1994); (*b*) M.A. Duncan. Annu. Rev. Phys. Chem. **48**, 63 (1997).
15. G. Gregoire, N.R. Brinkmann, D. van Heijnsbergen, H.F. Schaefer, and M.A. Duncan. J. Phys. Chem. A, **107**, 218 (2003).
16. M.A. Duncan. Int. Rev. Phys. Chem. **22**, 407 (2003).
17. R.S. Walters, T.D. Jaeger, N. Brinkmann, H.F. Schaefer, and M.A. Duncan. J. Phys. Chem. A, **107**, 7396 (2003).
18. (*a*) G. Gregoire, J. Velasquez, and M.A. Duncan. Chem. Phys. Lett. **349**, 451 (2001); (*b*) G. Gregoire and M.A. Duncan. J. Chem. Phys. **117**, 2120 (2002).
19. N.R. Walker, G.A. Grieves, R.S. Walters, and M.A. Duncan. Chem. Phys. Lett. **380**, 230 (2003).
20. (*a*) M. Sodupe, C.W. Bauschlicher, Jr., and H. Partridge. Chem. Phys. Lett. **192**, 185 (1992); (*b*) M. Sodupe and C.W. Bauschlicher, Jr. Chem. Phys. Lett. **181**, 321 (1991); (*c*) M. Sodupe, V. Branchadell, M. Rosi, and C.W. Bauschlicher, Jr. J. Phys. Chem. A, **101**, 7854 (1997); (*d*) C.W. Bauschlicher, Jr. and H. Partridge. J. Phys. Chem. **95**, 9694 (1991); (*e*) C.W. Bauschlicher, Jr., M. Sodupe, and H. Partridge. J. Chem. Phys. **96**, 4453 (1992); (*f*) H. Partridge, C.W. Bauschlicher, Jr., and L. Visscher. Chem. Phys. Lett. **246**, 33 (1995).
21. R.S. Walters, T.D. Jaeger, N.R. Brinkmann, H.F. Schaefer, and M.A. Duncan. J. Phys. Chem. A, **107**, 7396 (2003).
22. R.S. Walters, N.R. Walker, D. Pillai, and M.A. Duncan. J. Chem. Phys. **119**, 10471 (2003).
23. N.R. Walker, R.S. Walters, and M.A. Duncan, J. Chem. Phys. **120**, 10 037 (2004).
24. C.T. Scurlock, S.H. Pullins, and M.A. Duncan. J. Chem. Phys. **105**, 3579 (1996).
25. (*a*) R.L. Asher, D. Bellert, T. Buthelezi, G. Weerasekera, and P.J. Brucat. Chem. Phys. Lett. **228**, 390 (1994); (*b*) R.L. Asher, D. Bellert, T. Buthelezi, and P.J. Brucat. Chem. Phys. Lett. **227**, 623 (1994); (*c*) D. Bellert, T. Buthelezi, and P.J. Brucat. Chem. Phys. Lett. **290**, 316 (1998).
26. R.V. Olkhov, S.A. Nizkorodov, and O. Dopfer. Chem. Phys. **239**, 393 (1998).
27. M.J. Frisch, G.W. Trucks, H.B. Schlegel, P.M.W. Gill, B.G. Johnson, M.A. Robb, J.R. Cheeseman, T. Keith, G.A. Petersson, J.A. Montgomery, K. Raghavachari, M.A. Al-Laham, V.G. Zakrzewski, J.V. Ortiz, J.B. Foresman, J. Cioslowski, B.B. Stefanov, A. Nanayakkhara, M. Challacombe, C.Y. Peng, W. Chen, M.W. Wong, J.L. Andres, E.S. Replogle, R. Gomperts, R. L. Martin, D.J. Fox, J.S. Binkley, D.J. Defrees, J. Baker, J.P. Stewart, M. Head-Gordon, C. Gonzalez, and J.A. Pople. Gaussian94. Revision C.3 [computer program]. Gaussian, Inc., Pittsburgh, Pa. 1995.
28. M.J. Frisch, G.W. Trucks, H.B. Schlegel, G.E. Scuseria, M.A. Robb, J.R. Cheeseman, J.A. Montgomery, T. Vreven, K.N. Kudin, J.C. Burant, J.M. Millam, S.S. Iyengar, J. Tomasi, V. Barone, B. Mennucci, M. Cossi, G. Scalmani, N. Rega, G.A. Petersson, H. Nakatsuji, M. Hada, M. Ehara, K. Toyota, R. Fukuda, J. Hasegawa, M. Ishida, T. Nakajima, Y. Honda, O. Kitao, H. Nakai, M. Klene, X. Li, J.E. Knox, H.P. Hratchian, J.B. Cross, C. Adamo, J. Jaramillo, R. Gomperts, R.E. Stratmann, O. Yazyev, A.J. Austin, R. Cammi, C. Pomelli, J.W. Ochterski, P.Y. Ayala, K. Morokuma, G.A. Voth, P. Salvador, J.J. Dannenberg, V.G. Zakrzewski, S. Dapprich, A.D. Daniels, M.C. Strain, O. Farkas, D.K. Malick, A.D. Rabuck, K. Raghavachari, J.B. Foresman, J.V. Ortiz, Q. Cui, A.G. Baboul, S. Clifford, J. Cioslowski, B.B. Stefanov, G. Liu, A. Liashenko, P. Piskorz, I. Komaromi, R.L. Martin, D.J. Fox, T. Keith, M.A. Al-Laham, C.Y. Peng, A. Nanayakkara, M. Challacombe, P.M.W. Gill, B. Johnson, W. Chen, M.W. Wong, C. Gonzalez, and J.A. Pople. Gaussian03. Revision B.02 [computer program]. Gaussian, Inc., Pittsburgh, Pa. 2003.
29. A.D. Becke. J. Chem. Phys. **98**, 5648 (1993).
30. C. Lee, W. Yang, and R.G. Parr. Phys. Rev. B, **37**, 785 (1988).
31. A.D. Becke. Phys. Rev. A, **98**, 3098 (1988).
32. J.P. Perdew. Phys. Rev. B, **33**, 7046 (1986).
33. S. Huzinaga. J. Chem. Phys. **42**, 1293 (1965).
34. (*a*) T.H. Dunning. J. Chem. Phys. **53**, 2823 (1970); (*b*) T.H. Dunning and P.J. Hay. *In* Modern theoretical chemistry. Vol. 3. *Edited by* H.F. Schaefer. Plenum, New York. 1977.
35. T. Shimanouchi. Molecular vibrational frequencies. Chemistry WebBook, NIST Standard Reference Database 69. 2001. http://webbook.nist.gov.
36. (*a*) G.T. Fraser, A.S. Pine, W.J. Lafferty, and R.E. Miller. J. Chem. Phys. **87**, 1502 (1987); (*b*) T.E. Gough, R.E. Miller, and G. Scoles. J. Phys. Chem. **85**, 4041 (1981); (*c*) K.W. Jucks, Z.S. Huang, D. Dayton, R.E. Miller, and W.J. Lafferty. J. Chem. Phys. **86,** 4341 (1987); (*d*) K.W. Jucks, Z.S. Huang, R.E. Miller, G.T. Fraser, A.S. Pine, and W.J. Lafferty. J. Chem. Phys. **88**, 2185 (1988).
37. J.S. Muenter. J. Chem. Phys. **94**, 2781 (1991).
38. M.A. Walsh, T.H. England, T.R. Dyke, and B.J. Howard. Chem. Phys. Lett. **120,** 313 (1985).
39. M.J. Weida, J.M. Spherhac, and D. Nesbitt. J. Chem. Phys. **103**, 7685 (1995).
40. R. Disselkamp and G.E. Ewing. J. Chem. Phys. **99,** 2439 (1993).
41. A. Bonnamy, R. Georges, A. Benidar, J. Boissoles, A. Canosa, and B.R. Rowe. J. Chem. Phys. **118**, 3612 (2003).
42. (*a*) M. Okumura, L.I. Yeh, and Y.T. Lee. J. Chem. Phys. **83**, 3705 (1985); (*b*) M. Okumura, L.I. Yeh, and Y.T. Lee. J. Chem. Phys. **88**, 79 (1988).
43. (*a*) M. Meuwly, S.A. Nizkorodov, J.P. Maier, and E.J. Bieske. J. Chem. Phys. **104**, 3876 (1996); (*b*) O. Dopfer, D. Roth and J.P. Maier. J. Phys. Chem. A**, 104**, 11 702 (2000); (*c*) E.J. Bieske and O. Dopfer. Chem. Rev. **100**, 3963 (2000).
44. P. Ayotte, G.H. Weddle, J. Kim, and M.A. Johnson. J. Am. Chem. Soc. **120**, 1236 (1998).
45. T. Pino, N. Boudin, and P. Brechignac. J. Chem. Phys. **111**, 7337 (1999).
46. R.G. Satink, H. Piest, G. von Helden, and G. Meijer. J. Chem. Phys. **111**, 10 750 (1999).
47. R. Bukowski, J. Sadlej, B. Jeziorski, P. Jankowski, K. Szalewicz, S.A. Kucharski, H.A. Williams, and B.M. Rice. J. Chem. Phys. **110**, 3785 (1999).
48. L. Miao, L. Shao, W. Wang, K. Fang, and M. Zhou. J. Chem. Phys. **116**, 5643 (2002).

© 2004 NRC Canada

The antisymmetric stretching fundamental band of free MgD_2[1]

Alireza Shayesteh, Dominique R.T. Appadoo, Iouli Gordon, and Peter F. Bernath

Abstract: The gaseous MgD_2 molecule has been synthesized for the first time in an electrical discharge inside a high-temperature furnace. The high-resolution infrared emission spectrum of MgD_2 was recorded with a Fourier transform spectrometer, and the antisymmetric stretching mode (ν_3) was detected near 1176.5 cm^{-1}. The ν_3 band was rotationally analyzed, and the r_0 Mg—D bond distance was determined to be 1.700 874(8) Å.

Key words: gaseous MgD_2, vibration–rotation emission spectrum, Mg-D bond distance.

Résumé : Faisant appel à une décharge électrique dans une fournaise à haute température, on a synthétisé pour la première fois une molécule de MgD_2 gazeuse. On en a enregistré le spectre d'émission infrarouge à haute résolution à l'aide d'un spectrophotomètre à transformée de Fourier et on a détecté le mode d'élongation antisymétrique (ν_3) près de 1176,5 cm^{-1}. On a analysé la bande ν_3 d'un point de vue rotationnel et on a déterminé que la longueur r_0 de la liaison Mg—D est égale à 1,700 874(8) Å.

Mots clés : MgD_2 gazeux, spectre d'émission vibration-rotation, longueur de la liaison Mg-D.

[Traduit par la Rédaction]

Introduction

We recently published a paper on the discovery of MgH_2 in the gas phase and the analysis of its vibration–rotation emission spectrum (1). The MgH_2 molecule is a favorite target for ab initio methods (2–6) because it is a closed-shell system with only a few electrons. The previous studies on the reaction of the magnesium atom with molecular hydrogen and the properties of solid MgH_2 were discussed in our earlier paper (1). Although the ground-state reaction

$$Mg\ (^1S)\ (g) + H_2\ (g) \rightarrow MgH_2\ (g)$$

was predicted to be slightly endoergic (2, 3), we were able to produce gaseous MgH_2 in our furnace-discharge emission source.

The previous experimental work on MgD_2 is limited to matrix isolation experiments. McCaffrey et al. (7) recorded the infrared spectra of MgH_2, MgHD, and MgD_2 in krypton and xenon matrices at 12 K. They found the antisymmetric stretching frequency (ν_3) of MgD_2 at 1153 and 1144 cm^{-1} in krypton and xenon matrices, respectively, while the bending modes (ν_2) were observed at 309 and 300 cm^{-1}. Tague and Andrews (8) recorded the infrared spectra of MgH_2 and MgD_2 in an argon matrix at 10 K, and they detected the antisymmetric stretching mode of MgD_2 at 1163.2 cm^{-1}.

We have produced gaseous MgD_2 in a discharge source, and the analysis of its vibration–rotation emission spectrum is reported in this paper.

Experiment and results

The high-resolution vibration–rotation spectrum of MgD_2 was recorded with a Bruker IFS 120 HR Fourier transform spectrometer. An emission source that combines a high-temperature furnace with an electrical discharge was used to generate gaseous MgD_2. Except for some minor changes, the same experimental setup was used as described in the earlier paper on MgH_2 (1). About 50 g of magnesium (cut from a rod) was placed in the central part of an alumina tube and was heated to 600 °C to produce approximately 1 torr of magnesium vapor (1 torr = 133.322 Pa). Although we used a mixture of argon and hydrogen in our MgH_2 experiment (1), it was found later that pure hydrogen yields a stronger signal. About 1 torr of pure deuterium flowed slowly through the cell. The tube was sealed with BaF_2 windows, and a BaF_2 lens was used to focus the emission from the tube onto the entrance aperture of the spectrometer. A KBr beamsplitter was used, and the spectrum was recorded with a liquid-nitrogen-cooled HgCdTe (MCT) detector at an instrumental resolution of 0.01 cm^{-1}. The detector response, the BaF_2 lens, and a 1700 cm^{-1} longwave pass filter limited the spectral region to 800–1700 cm^{-1}. In order to improve the

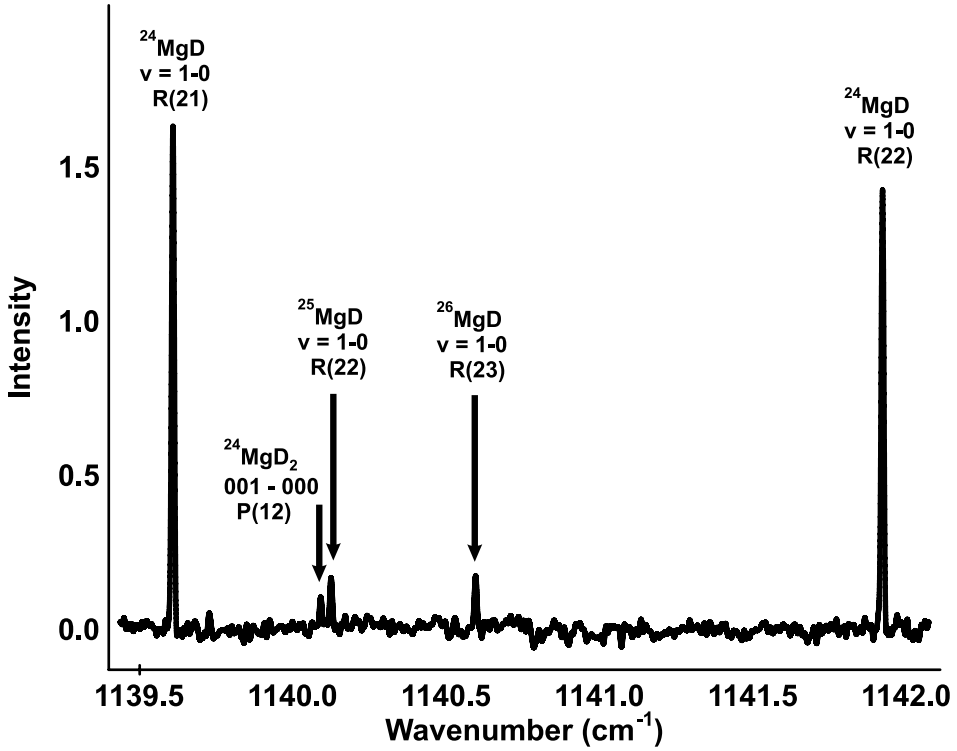
Received 17 November 2003. Published on the NRC Research Press Web site at http://canjchem.nrc.ca on 26 August 2004.

A. Shayesteh, D.R.T. Appadoo, and P.F. Bernath.[2] Department of Chemistry, University of Waterloo, Waterloo, ON N2L 3G1, Canada.
I. Gordon. Department of Physics, University of Waterloo, Waterloo, ON N2L 3G1, Canada.

[1]This article is part of a Special Issue dedicated to the memory of Professor Gerhard Herzberg.
[2]Corresponding author (e-mail: bernath@uwaterloo.ca).

 doi: 10.1139/V04-043 © 2004 NRC Canada

Fig. 1. An expanded view of the spectrum showing the relative intensities of MgD_2 lines, compared to the lines from MgD.



signal-to-noise ratio, about 1200 scans were co-added during 18 h of integration.

The spectrum contained blackbody emission from the hot tube, plus atomic and molecular emission lines, and absorption lines from atmospheric water vapor. The strongest emission lines in the spectrum are from the ^{24}MgD $v = 1 \rightarrow 0$ band and from atomic lines. Four hot bands of ^{24}MgD ($v = 2 \rightarrow 1$ to $v = 5 \rightarrow 4$) were also found and rotationally analyzed (9). The natural abundances of the magnesium isotopes ^{24}Mg,^{25}Mg, and ^{26}Mg are 79:10:11, and for the minor isotopomers, ^{25}MgD and ^{26}MgD, only the $v = 1 \rightarrow 0$ to $v = 4 \rightarrow 3$ bands were detected. In addition to these bands, a series of very weak lines, which was assigned to the ν_3 antisymmetric stretching fundamental band of $^{24}MgD_2$, was observed to higher wavenumbers. An expanded view of the spectrum showing the relative intensities of the MgD and MgD_2 lines is given in Fig. 1. The signal-to-noise ratio for the MgD_2 lines was much smaller than that for the MgH_2 lines (1) for several reasons:

- The intrinsic band strength for ν_3 of MgD_2 was calculated by Tague and Andrews (8) to be about 2 times smaller than that of MgH_2.
- The Einstein A coefficient for spontaneous emission is proportional to $\tilde{\nu}^3$. The band origin of MgH_2 is at 1588.7 cm^{-1}, while the band origin of MgD_2 is at 1176.5 cm^{-1}. This difference makes the Einstein A coefficient of MgD_2 about 2.5 times smaller than that of MgH_2.
- For technical reasons, the quality of spectra generally decreases at lower wavenumbers. In this case, for example, the 1700 cm^{-1} longwave pass filter that was used for MgD_2 is made of germanium, and it has a transmittance of ~50% in the 1200 cm^{-1} spectral region. The 2200 cm^{-1} longwave pass filter used for MgH_2 is made of CaF_2, and it has a transmittance of ~90% in the 1600 cm^{-1} spectral region.

Analysis and discussion

The line positions were determined using the program WSpectra written by M. Carleer (Université Libre de Bruxelles). The spectrum was calibrated using several atomic lines common to both the MgH_2 and MgD_2 spectra, while the MgH_2 spectrum was calibrated using impurity CO lines. The absolute accuracy of calibrated MgD_2 lines is better than 0.002 cm^{-1}. The assignment of the bands was facilitated by the use of a color Loomis–Wood program.

The antisymmetric stretching vibrational mode of MgD_2 (linear) has σ_u symmetry, and the observed vibration–rotation band ($001 \rightarrow 000$) is a Σ_u^+–Σ_g^+ transition having only P and R branches. A list of line positions and assignments is presented in Table 1. For the MgD_2 molecule with $D_{\infty h}$ symmetry, the adjacent rotational lines have a 2:1 intensity ratio ($(I + 1)/I$) due to the ortho–para nuclear spin statistical weights associated with the $I = 1$ deuterium nuclei. In this particular band (Σ_u^+–Σ_g^+), the lines with even J'' should be twice as intense as odd-J'' lines, because deuterium nuclei are bosons. The signal-to-noise ratio for MgD_2 lines was small and the 2:1 intensity ratio was not clearly observed, but the even-J'' lines were stronger than the odd-J'' lines. A few lines near the band origin were missing (i.e., too weak to be observed), and this made the absolute rotational numbering difficult. The absolute rotational assignment was made based on three criteria:

© 2004 NRC Canada

Table 1. The line positions of the 001 → 000, Σ_u^+–Σ_g^+, band of $^{24}MgD_2$.

Assignment	Line position (cm^{-1})	Assignment	Line position (cm^{-1})
P(34)	1064.7581(–16)	R(4)	1190.5640(3)
P(32)	1072.0120(6)	R(6)	1195.9973(24)
P(31)	1075.6099(3)	R(7)	1198.6693(9)
P(30)	1079.1882(–7)	R(8)	1201.3190(57)
P(28)	1086.2911(10)	R(10)	1206.5151(–19)
P(27)	1089.8115(1)	R(11)	1209.0786(34)
P(26)	1093.3130(3)	R(12)	1211.6035(–7)
P(25)	1096.7928(–11)	R(14)	1216.5708(–25)
P(24)	1100.2550(4)	R(15)	1219.0145(15)
P(22)	1107.1143(7)	R(16)	1221.4244(17)
P(20)	1113.8870(–5)	R(18)	1226.1510(4)
P(18)	1120.5743(–1)	R(20)	1230.7547(–8)
P(16)	1127.1724(3)	R(23)	1237.4242(–48)
P(15)	1130.4315(–54)	R(24)	1239.5880(–22)
P(14)	1133.6775(–11)	R(25)	1241.7188(–7)
P(13)	1136.8975(5)	R(29)	1249.9150(11)
P(12)	1140.0935(17)	R(30)	1251.8824(16)
P(10)	1146.4112(14)	R(32)	1255.7142(–12)
P(9)	1149.5300(–24)		
P(8)	1152.6289(–16)		
P(7)	1155.7024(–15)		
P(6)	1158.7515(–6)		
P(5)	1161.7764(12)		

Note: The numbers in parentheses (in units of 10^{-4} cm^{-1}) are the observed minus calculated line positions computed with the constants of Table 2.

- The rotational lines with even J'' should be stronger than odd-J'' lines.
- The r_0 value of MgD_2, which is determined from B_0, should be close to the r_0 value of MgH_2.
- The band origin should be relatively close to the matrix isolation values (7, 8) when small matrix shifts are taken into account.

Three different rotational numberings were attempted, and only one rotational assignment (Table 1) satisfies all of the conditions listed above.

The rotational lines were fitted to the customary energy level expression:

$$[1] \qquad E(v_1, v_2, v_3, J) = G(v_1, v_2, v_3) + BJ(J+1) - DJ^2(J+1)^2$$

using our least-squares fitting program, and the constants of Table 2 were determined. We determined the Mg—D bond distance (r_0) for $v = 0$ to be 1.700 874(8) Å (1 Å = 0.1 nm), using the atomic mass of 2.014 101 779 amu (10) for deuterium.

In our earlier paper on MgH_2 (1), we found the r_0 Mg—H bond distance to be 1.703 327(3) Å. The average Mg—D bond distance is expected to be slightly smaller than the Mg—H bond distance at the zero-point level because the potential energy surface is anharmonic. The vibrational frequencies of MgD_2 are smaller than those of MgH_2, so the MgD_2 zero-point level lies deeper in the anharmonic potential surface.

The ν_3 band origins of MgH_2 and MgD_2 observed or calculated in different studies are compared in Table 3. The argon matrix shift (8) for MgH_2 is –16.8 cm^{-1}, which is –1.06% in relation to the gas-phase band origin. Similarly, the shift for MgD_2 is –13.3 cm^{-1} or –1.13% in relation to the observed ν_3 band origin. The relative shifts for the MgH_2 and MgD_2 band origins in krypton and xenon matrices (7) are also very similar. This consistency in the relative matrix shifts for MgH_2 and MgD_2 supports our absolute rotational assignment.

Table 2. Spectroscopic constants (in cm^{-1}) of $^{24}MgD_2$.

v_1 v_2 v_3	G_v	B_v	10^6 D_v
000	0.0	1.446 575(14)	9.5872(92)
001	1176.502 82(51)	1.433 237(14)	9.5221(94)

Note: All uncertainties are 1σ.

Summary

The gaseous MgD_2 molecule was produced for the first time and was identified via its infrared emission spectrum. The antisymmetric stretching fundamental band 001 → 000 was observed and rotationally analyzed to yield spectroscopic constants. MgD_2 has a linear structure with an r_0 Mg—D bond distance of 1.700 874(8) Å.

Acknowledgement

This work was supported by the Natural Sciences and Engineering Research Council (NSERC) of Canada.

© 2004 NRC Canada

Table 3. A comparison of the antisymmetric stretching frequencies (in cm^{-1}) of MgH_2 and MgD_2 observed in the gas phase and in matrices.

Molecule	Gas phase	Ar matrix	Kr matrix	Xe matrix	Ab initio
MgH_2	1588.6716(2)[a]	1571.9[b]	1558[c]	1544[c]	1628.2[d] 1641.3[b]
MgD_2	1176.5028(5)[e]	1163.2[b]	1153[c]	1144[c]	1205.1[b]

[a]Reference 1.
[b]Reference 8.
[c]Reference 7.
[d]Reference 6.
[e]This work.

References

1. A. Shayesteh, D.R.T. Appadoo, I. Gordon, and P.F. Bernath. J. Chem. Phys. **119**, 7785 (2003).
2. J.A. Pople, B.T. Luke, M.J. Frisch, and J.S. Binkley. J. Phys. Chem. **89**, 2198 (1985).
3. R. Ahlrichs, F. Keil, H. Lischka, W. Kutzelnigg, and V. Staemmler. J. Chem. Phys. **63**, 455 (1975).
4. L. von Szentpály. J. Phys. Chem. A, **106**, 11 945 (2002).
5. P. Chaquin, A. Sevin, and H. Yu. J. Phys. Chem. **89**, 2813 (1985).
6. G.S. Tschumper and H.F. Schaefer. J. Chem. Phys. **108**, 7511 (1998).
7. J.G. McCaffrey, J.M. Parnis, G.A. Ozin, and W.H. Breckenridge. J. Phys. Chem. **89**, 4945 (1985).
8. T.J. Tague, Jr., and L. Andrews. J. Phys. Chem. **98**, 8611 (1994).
9. A. Shayesteh, D.R.T. Appadoo, I. Gordon, and P.F. Bernath. J. Chem. Phys. **120**, 10 002 (2004).
10. I. Mills, T. Cvitaš, K. Homann, N. Kallay, and K. Kuchitsu. Quantities, units and symbols in physical chemistry, 2nd ed. Blackwell Scientific Publications, Oxford. 1993.

© 2004 NRC Canada

Vibrational spectra and electron–vibration interactions of the naphthalene radical anion — Experimental and theoretical study[1]

Hajime Torii, Yuko Ueno, Akira Sakamoto, and Mitsuo Tasumi

Abstract: Vibrational analysis is carried out for the radical anions of naphthalene-h_8 and -d_8. Their infrared (IR) spectra are observed in tetrahydrofuran by using a cell designed for IR measurements of unstable species. The vibrational force field and the IR intensities are calculated by the ab initio molecular orbital and density functional methods at various theoretical levels. As found in the cases of the radical cations of many polycyclic aromatic hydrocarbons (PAHs), a few strong IR bands with intensities of the order of 10^2 km mol^{-1} are observed in the 1700–900 cm^{-1} region. These observed spectral features are well reproduced by the calculations at the CASSCF (complete active space self-consistent field) and B3LYP (Becke's three-parameter hybrid method using the Lee–Yang–Parr correlation functional) levels. The calculation at the B3LYP level gives a better fit between the observed and calculated absolute IR intensities. Normal modes and the origin of the strong IR intensities characteristic of the radical anions are discussed in terms of molecular symmetry coordinates and the dipole derivatives based on these coordinates. It is found that the IR intensities of the b_{2u} modes below 2000 cm^{-1} are dominated by the contribution from one molecular symmetry coordinate, in which the C—C bonds in one ring stretch while those in the other ring shrink. The mechanism that gives rise to the strong IR intensity for this vibration is discussed by examining the changes in the electronic structure induced by this vibration.

Key words: vibrational spectra, electron–vibration interaction, naphthalene, radical anion.

Résumé : On a effectué des analyses vibrationnelles sur des anions radicaux du naphtalène-h_8 et naphtalène-d_8. On a observé leurs spectres infrarouge (IR) dans le tétrahydrofurane à l'aide d'une cellule construite pour des mesures IR d'espèces instables. On a calculé le champ de force vibrationnelle et les intensités IR par la méthode ab initio des orbitales moléculaires et par la méthode de la densité fonctionnelle, à divers niveaux théoriques. Tel qu'il a été observé dans les cas des cations radicaux de plusieurs hydrocarbures aromatiques polycycliques (PAH), on a observé quelques bandes IR fortes dans la région de 1700–900 cm^{-1}, avec des intensités de l'ordre de 10^2 km mol^{-1}. Ces caractéristiques spectrales observées sont très bien reproduites par les calculs aux niveaux CASSCF (champ autocohérent de l'espace actif complet) et B3LYP (méthode hybride de Becke à trois paramètres utilisant la corrélation fonctionnelle de Lee–Yang–Parr). Les calculs au niveau B3LYP conduisent à une meilleure corrélation entre les intensités IR absolues observées et calculées. Les modes normaux et l'origine des fortes intensités IR caractéristiques des anions radicaux sont discutés en fonction des coordonnées de symétrie moléculaire et des dérivées des moments dipolaires basées sur ces coordonnées. On a trouvé que les intensités IR des modes b_{2u} en-dessous de 2000 cm^{-1} sont dominées par la contribution d'une coordonnée de symétrie moléculaire dans laquelle les liaisons C—C d'un cycle s'allongent alors que celles de l'autre deviennent plus courtes. Pour discuter du mécanisme qui donne lieu à la forte intensité IR de cette vibration, on examine les changements dans la structure électronique induite par cette vibration.

Mots clés : spectre vibrationnel, interaction électron–vibration, naphtalène, anion radical.

Introduction

The radical cations of polycyclic aromatic hydrocarbons (PAHs) are known to exhibit distinctive features in their infrared (IR) spectra (1–16); the IR intensities of some bands of these species in the fingerprint region (1700–900 cm^{-1}), which arise from the C-C stretching and C-H in-plane bending modes, are stronger by one or two orders of magnitude than those of the corresponding neutral species. In our previous study (17), the mechanism that gives rise to the IR intensities of these bands has been examined theoretically. It has been shown that these IR intensities are induced by charge fluxes generated by specific vibrational modes that are determined by the electronic structure of the molecule.

Received 31 October 2003. Published on the NRC Research Press Web site at http://canjchem.nrc.ca on 28 August 2004.

H. Torii. Department of Chemistry, School of Education, Shizuoka University, 836 Ohya, Shizuoka 422-8529, Japan.
Y. Ueno. NTT Lifestyle and Environmental Technology Laboratories, Atsugi, Kanagawa 243–0198, Japan.
A. Sakamoto and M. Tasumi.[2] Department of Chemistry, Faculty of Science, Saitama University, Saitama 338-8570, Japan.

[1]This article is part of a Special Issue dedicated to the memory of Professor Gerhard Herzberg.
[2]Corresponding author (e-mail: tasumi@chem.saitama-u.ac.jp).

 doi: 10.1139/V04-050 © 2004 NRC Canada

Strong electron–vibration interaction is responsible for the generation of the charge fluxes. This situation is closely related to that encountered in previous studies (18–26) on charged polyenes and related molecules, in which some bands in the fingerprint region have strong IR intensities. In those cases, the strong IR intensities are induced by charge fluxes generated by the vibrations along the bond-alternation coordinate.

In the subsequent studies by one of the present authors (HT) (27–29), the nature of the electron–vibration interaction that is responsible for the generation of charge fluxes (or dipole derivatives) in charged conjugated π-electron systems has been analyzed theoretically by using a model Hamiltonian. It has been shown that the dipole derivatives for the C-C stretches of these species are mainly generated by a mixing of a few one-electron excited electronic configurations. The changes in the electronic structure occurring upon the mixing of those configurations, as well as the signs and the magnitudes of the dipole derivatives generated by the mixing, support the concept of long-range and short-range charge fluxes introduced in ref. 17. The small IR intensities of the C-C stretches of neutral species are explained by the cancellation of the contributions of various one-electron excited configurations, which results from the pairing theorem (30) that holds for the molecular orbitals of the model Hamiltonian for alternant hydrocarbons.

Although only the cationic and neutral species have been treated in the model Hamiltonian approach described above, it is expected that the concept obtained there also holds for the anionic species because of the pairing theorem. To examine the extent of such generality, it is interesting to analyze the IR spectra of anionic species and compare the results with those obtained for the cationic species. One problem that arises at this point is that there are only a small number of anionic conjugated π-electron systems for which reliable IR spectra have been measured. This is partly because radical anions are very sensitive to molecular oxygen and water, and partly because many radical anions are intrinsically unstable toward electron detachment in the isolated state. For example, IR spectra have been measured for the cationic species (in the matrix-isolated condition) of many PAHs (2–11), including linear polyacenes ranging from naphthalene to pentacene, and other PAHs such as perylene and coronene, but to the best of our knowledge, the IR spectra of only a few anionic counterparts have been measured (6, 31, 32).

In the present study, the IR spectra of the radical anions of naphthalene-h_8 and -d_8 in tetrahydrofuran (THF) are measured by using a cell designed for measuring the IR spectra of unstable species in solution. The absolute IR intensity of each observed band is determined. The observed IR spectra are compared with those obtained from ab initio molecular orbital (MO) and density functional (DFT) calculations carried out at various theoretical levels for an isolated species of the radical anions. The radical anions in solution are of course not isolated, but vibrational spectra are not affected greatly by solvent molecules unless strong intermolecular interactions such as hydrogen bonding exist. It is, therefore, reasonable to expect that the results of calculation for a single molecule would be useful for analysing the spectra observed in solution. It is shown that the main features of the observed IR spectra are best reproduced by the DFT calculation at the B3LYP (Becke's three-parameter hybrid method (33) using the Lee–Yang–Parr correlation functional (34)) level. By using the vibrational force field and the dipole derivatives calculated at this theoretical level, a detailed analysis of the observed spectra is carried out. As in the case of the cationic counterpart (17), IR intensities are particularly large for some specific modes determined by the electronic structure. The mechanism that gives rise to large dipole derivatives for such vibrations is discussed.

Experimental procedure

As described in the *Introduction*, measurements of reliable IR spectra of radical anions in solution need a special technique for keeping the anions intact during the measurement. In the present study, we used CaF_2 cavity cells (Spectra Tech and Pier Optics) and a vacuum-tight holder (Spectra Tech) modified for this purpose. By using the modified vacuum-tight holder, we can connect the CaF_2 cavity cell for IR measurements through a glass joint and a Teflon O-ring to a completely sealed glass apparatus for preparation of radical anions in solution. The optical pathlength was set at 0.3 mm for measurements in the 3200–1200 cm^{-1} region and at 0.1 mm for the 1200–900 cm^{-1} region.

Tetrahydrofuran (THF) was used as a solvent for IR measurements: THF-d_8 in the 3200–2400 and 1700–1200 cm^{-1} regions, and THF-h_8 in the 2400–2000 and 1200–900 cm^{-1} regions. THF-h_8 and THF-d_8 were degassed and dehydrated by distillation in vacuum several times and were stored in vacuum in contact with a sodium mirror. Reduction of naphthalene-h_8 and -d_8 was performed by bringing their degassed and anhydrous THF solution into contact with a sodium mirror in a completely sealed glass apparatus. The concentrations of the sample solutions were determined by measuring electronic absorption spectra and using the absorption coefficients reported in previous studies (35–37) as a reference. The concentrations were 2.9×10^{-2} mol dm^{-3} for the naphthalene-h_8 radical anion in THF-d_8 (used for the measurements in the 3200–1200 cm^{-1} region), 1.3×10^{-1} mol dm^{-3} for the naphthalene-h_8 radical anion in THF-h_8 (1200–900 cm^{-1}), 2.5×10^{-2} mol dm^{-3} for the naphthalene-d_8 radical anion in THF-h_8 (2400–2000 cm^{-1}), and 2.4×10^{-2} mol dm^{-3} for the naphthalene-d_8 radical anion in THF-d_8 (1700–1200 cm^{-1}).

IR spectra were observed at room temperature on a JEOL JIR-5500 Fourier-transform IR spectrophotometer equipped with a mercury–cadmium–telluride (MCT) detector (3200–1200 cm^{-1}) or a triglycine sulfate (TGS) detector (1200–900 cm^{-1}). Spectral resolution was 4 cm^{-1}. Solvent bands were subtracted from the spectra measured in solution. Electronic absorption spectra were measured on a Hitachi U-3500 spectrophotometer.

Computational procedure

Ab initio MO calculations of the structure, vibrational force field, and dipole derivatives of the naphthalene radical anion were carried out at the unrestricted Hartree–Fock (UHF), restricted open-shell Hartree–Fock (ROHF), unrestricted second-order Møller–Plesset perturbation (UMP2), and complete active space self-consistent field (CASSCF) levels in combination with the 6-31G* basis set. In the

© 2004 NRC Canada

Table 1. In-plane local coordinates of the naphthalene radical anion.

Type	Coordinate	Definition
C-C stretching	R_1	$\Delta r(C_9\text{-}C_1)$
	R_2	$\Delta r(C_1\text{-}C_2)$
	R_3	$\Delta r(C_2\text{-}C_3)$
	R_4	$\Delta r(C_3\text{-}C_4)$
	R_5	$\Delta r(C_4\text{-}C_{10})$
	R_6	$\Delta r(C_{10}\text{-}C_5)$
	R_7	$\Delta r(C_5\text{-}C_6)$
	R_8	$\Delta r(C_6\text{-}C_7)$
	R_9	$\Delta r(C_7\text{-}C_8)$
	R_{10}	$\Delta r(C_8\text{-}C_9)$
	R_{11}	$\Delta r(C_9\text{-}C_{10})$
C-H stretching	R_{12}	$\Delta r(C_1\text{-}H_1)$
	R_{13}	$\Delta r(C_2\text{-}H_2)$
	R_{14}	$\Delta r(C_3\text{-}H_3)$
	R_{15}	$\Delta r(C_4\text{-}H_4)$
	R_{16}	$\Delta r(C_5\text{-}H_5)$
	R_{17}	$\Delta r(C_6\text{-}H_6)$
	R_{18}	$\Delta r(C_7\text{-}H_7)$
	R_{19}	$\Delta r(C_8\text{-}H_8)$
C-C-C bend	R_{20}	$\Delta\theta(C_{10}\text{-}C_9\text{-}C_1)$
	R_{21}	$\Delta\theta(C_9\text{-}C_1\text{-}C_2)$
	R_{22}	$\Delta\theta(C_1\text{-}C_2\text{-}C_3)$
	R_{23}	$\Delta\theta(C_2\text{-}C_3\text{-}C_4)$
	R_{24}	$\Delta\theta(C_3\text{-}C_4\text{-}C_{10})$
	R_{25}	$\Delta\theta(C_4\text{-}C_{10}\text{-}C_9)$
	R_{26}	$\Delta\theta(C_9\text{-}C_{10}\text{-}C_5)$
	R_{27}	$\Delta\theta(C_{10}\text{-}C_5\text{-}C_6)$
	R_{28}	$\Delta\theta(C_5\text{-}C_6\text{-}C_7)$
	R_{29}	$\Delta\theta(C_6\text{-}C_7\text{-}C_8)$
	R_{30}	$\Delta\theta(C_7\text{-}C_8\text{-}C_9)$
	R_{31}	$\Delta\theta(C_8\text{-}C_9\text{-}C_{10})$
C-H bend	R_{32}	$[\Delta\theta(C_9\text{-}C_1\text{-}H_1) - \Delta\theta(C_2\text{-}C_1\text{-}H_1)]/\sqrt{2}$
	R_{33}	$[\Delta\theta(C_1\text{-}C_2\text{-}H_2) - \Delta\theta(C_3\text{-}C_2\text{-}H_2)]/\sqrt{2}$
	R_{34}	$[\Delta\theta(C_4\text{-}C_3\text{-}H_3) - \Delta\theta(C_2\text{-}C_3\text{-}H_3)]/\sqrt{2}$
	R_{35}	$[\Delta\theta(C_{10}\text{-}C_4\text{-}H_4) - \Delta\theta(C_3\text{-}C_4\text{-}H_4)]/\sqrt{2}$
	R_{36}	$[\Delta\theta(C_9\text{-}C_1\text{-}H_1) - \Delta\theta(C_2\text{-}C_1\text{-}H_1)]/\sqrt{2}$
	R_{37}	$[\Delta\theta(C_5\text{-}C_6\text{-}H_6) - \Delta\theta(C_7\text{-}C_6\text{-}H_6)]/\sqrt{2}$
	R_{38}	$[\Delta\theta(C_8\text{-}C_7\text{-}H_7) - \Delta\theta(C_6\text{-}C_7\text{-}H_7)]/\sqrt{2}$
	R_{39}	$[\Delta\theta(C_9\text{-}C_8\text{-}H_8) - \Delta\theta(C_7\text{-}C_8\text{-}H_8)]/\sqrt{2}$

CASSCF calculations, 11 electrons were included in the active space consisting of 10 valence π orbitals. DFT calculations at the B3LYP level were also performed in combination with the 6-311G* basis set. To support the discussion on the mechanism that gives rise to strong IR intensities of some normal modes, structural parameters were calculated also for the two Jahn–Teller distorted structures of the benzene radical anion as well as neutral benzene and naphthalene at the CASSCF and B3LYP levels. We used the HONDO 8 program (38) for the calculations at the CASSCF level and the Gaussian 92 and 94 programs (39, 40) for the calculations at the other levels. All these calculations were carried out on IBM SP2 computers at the Computer Center of the Institute for Molecular Science, Okazaki, Japan.

For the vibrational analysis of the naphthalene radical anion, two sets of intramolecular coordinates were needed: local coordinates and molecular symmetry coordinates. The in-plane local coordinates R_1–R_{39} were defined as shown in Table 1, with the numbering of atoms shown in Fig. 1. By using these coordinates, the molecular symmetry coordinates for the IR-active b_{2u} and b_{1u} symmetry species of the D_{2h} point group (S_{18}–S_{33}) were defined as given in Table 2. The latter set of coordinates was used to represent the vibrational force field and the dipole derivatives in the vibrational analysis. Two points are noteworthy in relation to the definition of coordinates. (*i*) No hydrogen atoms are involved in the definition of the C-C-C bending local coordinates (R_{20}–R_{31}) to define the corresponding molecular symmetry coordinates

© 2004 NRC Canada

Table 2. Molecular symmetry coordinates belonging to the IR-active b_{2u} and b_{1u} symmetry species of the naphthalene radical anion.

Symmetry	Type	Coordinate	Definition
b_{2u}	C-C stretching	S_{18}	$(R_1 + R_2 + R_4 + R_5 - R_6 - R_7 - R_9 - R_{10})/2\sqrt{2}$
		S_{19}	$(R_1 - R_2 - R_4 + R_5 - R_6 + R_7 + R_9 - R_{10})/2\sqrt{2}$
		S_{20}	$(R_3 - R_8)/\sqrt{2}$
	C-H stretching	S_{21}	$(R_{12} + R_{13} + R_{14} + R_{15} - R_{16} - R_{17} - R_{18} - R_{19})/2\sqrt{2}$
		S_{22}	$(R_{12} - R_{13} - R_{14} + R_{15} - R_{16} + R_{17} + R_{18} - R_{19})/2\sqrt{2}$
	C-C-C bend	S_{23}	$(R_{20} - 2R_{21} + R_{22} + R_{23} - 2R_{24} + R_{25} - R_{26} + 2R_{27} - R_{28} - R_{29} + 2R_{30} - R_{31})/2\sqrt{3}$
	C-H bend	S_{24}	$(R_{32} - R_{33} - R_{34} + R_{35} - R_{36} + R_{37} + R_{38} - R_{39})/2\sqrt{2}$
		S_{25}	$(R_{32} + R_{33} + R_{34} + R_{35} - R_{36} - R_{37} - R_{38} - R_{39})/2\sqrt{2}$
b_{1u}	C-C stretching	S_{26}	$(R_1 + R_2 - R_4 - R_5 - R_6 - R_7 + R_9 + R_{10})/2\sqrt{2}$
		S_{27}	$(R_1 - R_2 + R_4 - R_5 - R_6 + R_7 - R_9 + R_{10})/2\sqrt{2}$
	C-H stretching	S_{28}	$(R_{12} + R_{13} - R_{14} - R_{15} - R_{16} - R_{17} + R_{18} + R_{19})/2\sqrt{2}$
		S_{29}	$(R_{12} - R_{13} + R_{14} - R_{15} - R_{16} + R_{17} - R_{18} + R_{19})/2\sqrt{2}$
	C-C-C bend	S_{30}	$(R_{20} - R_{21} + R_{22} - R_{23} + R_{24} - R_{25} - R_{26} + R_{27} - R_{28} + R_{29} - R_{30} + R_{31})/2\sqrt{3}$
		S_{31}	$(R_{20} - R_{22} + R_{23} - R_{25} - R_{26} + R_{28} - R_{29} + R_{31})/2\sqrt{2}$
	C-H bend	S_{32}	$(R_{32} + R_{33} - R_{34} - R_{35} - R_{36} - R_{37} + R_{38} + R_{39})/2\sqrt{2}$
		S_{33}	$(R_{32} - R_{33} + R_{34} - R_{35} - R_{36} + R_{37} - R_{38} + R_{39})/2\sqrt{2}$

Fig. 1. Numbering of atoms and the Cartesian coordinate system for the naphthalene radical anion.

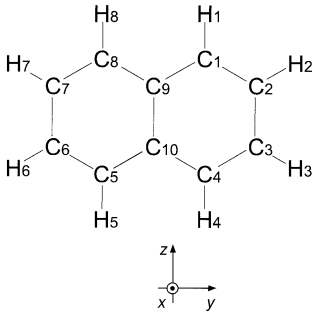
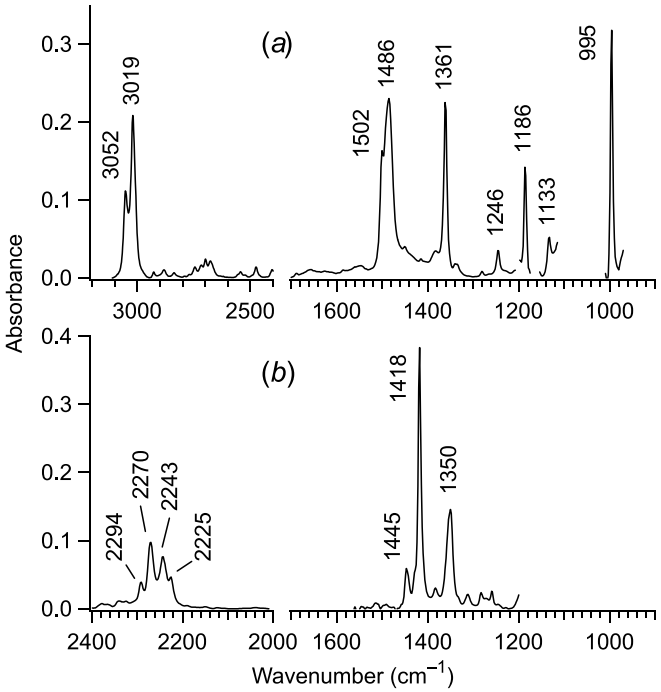


Fig. 2. Observed IR spectra of the (*a*) naphthalene-h_8 and (*b*) naphthalene-d_8 radical anions in THF.



in a systematic way. (*ii*) The redundancies intrinsic to the ring systems (called the ring redundancies) (41) are removed in the definition of the molecular symmetry coordinates as shown in Table 2, so that the vibrational pattern represented by each coordinate is easily understandable.

All the calculations related to the vibrational analysis were carried out on a Hitachi M5800/320 computer at the Computer Center of the University of Tokyo.

Results and discussion

(A) Observed spectra

The observed IR spectrum of the naphthalene-h_8 radical anion in THF is shown in Fig. 2*a*. The vibrational wavenumbers and the absolute IR intensities of the observed bands are shown on the right side of Table 3.

In Fig. 2*a*, a few strong IR bands are seen in the 1700–900 cm^{-1} region. The absolute IR intensities of the strongest bands are on the order of 10^2 km mol^{-1}, which are one to two orders of magnitude larger than those of the corresponding bands of the neutral species. This situation is similar to the cases of the PAH radical cations. It is, therefore, expected that the strong IR intensities of these bands arise from the same mechanism as those of the PAH radical cations (17). The discussion on this point is described in section D. In contrast to the cases of the PAH radical cations, however, the IR intensities of the C-H stretching bands of the naphthalene radical anion are very strong. This result suggests that the atomic charges on the hydrogen atoms are significantly different between the cationic and anionic species. The Mulliken atomic charges of the hydrogen atoms obtained by the calculations at the B3LYP/6-311G* level are indeed different between the two species (~0.27 *e* in the cationic species and ~0.11 *e* in the anionic species).

Because of the existence of strong solvent bands, all the IR bands in the 1300–900 cm^{-1} region may not be observed

© 2004 NRC Canada

Table 3. Calculated and observed vibrational wavenumbers (cm^{-1}) and IR intensities (km mol^{-1}) of the IR-active modes of the naphthalene-h_8 radical anion.

		UHF/6-31G*		ROHF/6-31G*		UMP2/6-31G*		CASSCF/6-31G*		B3LYP/6-311G*		Observed[f]	
Symmetry	Mode	Wave-number[a] (cm^{-1})	Intensity (km mol^{-1})	Wave-number[b] (cm^{-1})	Intensity (km mol^{-1})	Wave-number[c] (cm^{-1})	Intensity (km mol^{-1})	Wave-number[d] (cm^{-1})	Intensity (km mol^{-1})	Wave-number[e] (cm^{-1})	Intensity (km mol^{-1})	Wave-number (cm^{-1})	Intensity (km mol^{-1})
b_{2u}	ν_{18}	3013	243	3014	238	3087	192	3075	327	3068	258	3052	74
	ν_{19}	2982	114	2982	146	3056	97	3038	80	3036	76		
	ν_{20}	1491	304	1483	414	1514	313	1520	299	1504	131	1486	198
	ν_{21}	1308	141	1302	19	1470	73	1352	96	1374	44	1361	68
	ν_{22}	1150	507	1121	160	1211	173	1199	281	1189	134	1186	(23)
	ν_{23}	1118	9	1115	444	1152	59	1138	9	1135	6	1133	10
	ν_{24}	966	290	970	461	1016	136	988	96	1002	105	995	98
	ν_{25}	580	58	572	117	577	53	593	36	599	11		
b_{1u}	ν_{26}	3002	283	3003	328	3104	25 727	3059	353	3055	349	3019	177
	ν_{27}	2973	29	2975	1	3071	19	3036	3	3030	0		
	ν_{28}	1499	0	1508	10	2067	143 962	1526	7	1505	12	1502	13
	ν_{29}	1376	41	1382	2	1533	105	1404	4	1371	2		
	ν_{30}	1225	142	1239	9	1336	921	1257	19	1242	10	1246	11
	ν_{31}	1077	42	1084	20	1101	587	1092	14	1085	21		
	ν_{32}	717	141	770	4	1063	4 798	781	1	783	6		
	ν_{33}	327	110	356	6	439	487	358	9	359	5		
b_{3u}	ν_{38}	771	3	786	15	667	80	715	4	702	12		
	ν_{39}	715	174	723	164	573	60	677	147	679	147		
	ν_{40}	464	4	469	4	413	0	462	4	459	11		
	ν_{41}	177	3	181	4	164	5	174	4	173	4		

[a]Scaled by 0.9064.
[b]Scaled by 0.9064.
[c]Scaled by 0.9671.
[d]Scaled by 0.9258.
[e]Scaled by 0.9805.
[f]In THF.

© 2004 NRC Canada

even after the subtraction of the solvent bands. For the same reason, two solvents were used in the present study: THF-d_8 for the measurement in the 3200–1200 cm^{-1} region and THF-h_8 in the 1200–900 cm^{-1} region. The 1246 cm^{-1} band is observed both in THF-h_8 and in THF-d_8. The absolute IR intensities of this band measured in the two solvents are in good agreement with each other. As shown in section B, it is expected from the calculation at the B3LYP level that there is an IR band at ~1085 cm^{-1} for the naphthalene-h_8 radical anion. We could not find an appropriate solvent to observe this band. The absolute IR intensity of the 1186 cm^{-1} band may not be accurate because of the overlap of a solvent band. The weak IR bands observed in the whole wavenumber region may be due to the solvent or to overtones and combinations.

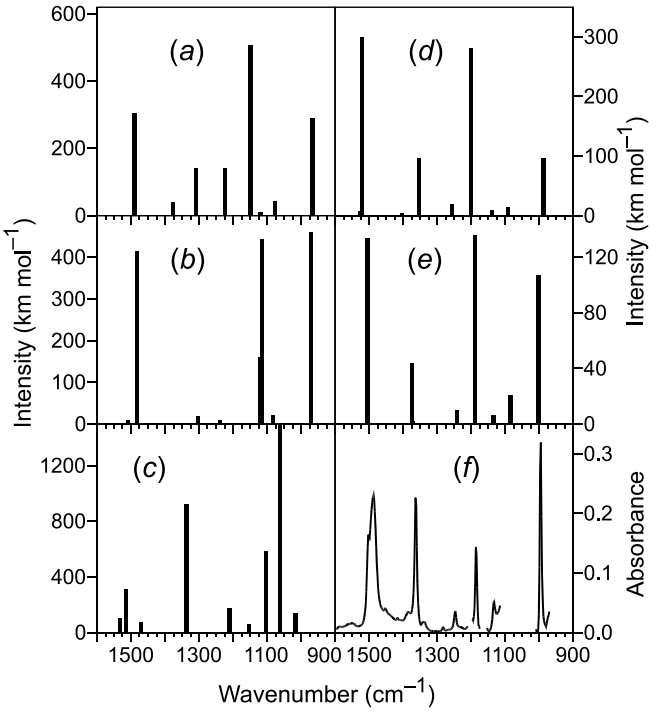
The IR spectrum of the naphthalene-h_8 radical anion was reported in 1965 by Kachkurova (31). In that study, many bands of the neutral species were observed, and the solvent (THF) bands were not subtracted. The observation of many bands of the neutral species in ref. 31 indicates that a great amount of the neutral species remained in the sample, probably because of incomplete sealing of the measurement system used in ref. 31. In the present study, the solvent bands could be subtracted to a satisfactory degree thanks to the high performance of the FT-IR spectrophotometer used. For these reasons, the IR bands at 1502, 1246, and 1133 cm^{-1} observed in the present study were not detected in ref. 31. The absolute intensities of the IR bands of the radical anion (determined for the first time in the present study) are one to two orders of magnitude larger than those of the corresponding bands of the neutral. The IR spectrum of the naphthalene-h_8 radical anion was also observed in 1973 by Dodson and Graham (42). In their spectrum, the IR bands at 1502, 1361, 1246, and 1133 cm^{-1} were not observed. As a consequence, other weak bands arising (probably) from overtones and combinations or from some impurities were erroneously assigned to fundamental modes of the radical anion.

The observed IR spectrum of the naphthalene-d_8 radical anion in THF is shown in Fig. 2*b*. The absolute IR intensities of the observed bands are shown on the right side of Table 4. In this case also, a few strong IR bands are observed in the 1700–1200 cm^{-1} region, and the absolute IR intensities of the strongest bands are on the order of 10^2 km mol^{-1}. The spectral pattern in the 1700–1200 cm^{-1} region observed for the d_8 species is substantially different from that observed for the h_8 species, because the C-C stretches are mixed with the C-H bends more strongly in the h_8 species than with the C-D bends in the d_8 species. The spectral pattern in the C-D stretching (2400–2000 cm^{-1}) region is different from that in the C-H stretching (3200–2800 cm^{-1}) region of the h_8 species, probably because of the difference in the coupling with overtones and combinations.

(B) Calculated spectra

The vibrational wavenumbers and the IR intensities of the naphthalene-h_8 radical anion calculated at various theoretical levels are shown in Table 3. The calculated wavenumbers are uniformly scaled by using a single scale factor at each theoretical level. The scale factors (given in the footnote of Table 3) are determined from the comparison between the observed (43) and calculated wavenumbers of the in-plane

Fig. 3. IR spectra of the naphthalene-h_8 radical anion in the 1600–900 cm^{-1} region calculated at the (*a*) UHF/6-31G*, (*b*) ROHF/6-31G*, (*c*) UMP2/6-31G*, (*d*) CASSCF/6-31G*, and (*e*) B3LYP/6-311G* levels, in comparison with (*f*) the spectrum observed in THF.



modes in the region below 2000 cm^{-1} (except those involving the Kekulé vibration) of four isotopic species of neutral benzene (C_6H_6, C_6D_6, $^{13}C_6H_6$, and $^{13}C_6D_6$). The observed and calculated IR spectra in the 1600–900 cm^{-1} region are shown in Fig. 3 for ease of comparison.

It is evident from Table 3 and Fig. 3 that the observed IR spectrum is reproduced reasonably well only by the calculations at the CASSCF and B3LYP levels (shown in Fig. 3*d* and 3*e*, respectively). Comparison between the observed and calculated absolute IR intensities suggests that the calculation at the B3LYP level gives a better result. It is, therefore, concluded that the vibrational force field and the dipole derivatives calculated at the B3LYP level are sufficiently reliable. These quantities are used in the subsequent vibrational analysis described in sections C and D.

The IR spectra calculated at the three other theoretical levels are substantially different from the observed spectrum. At the ROHF level, the relative IR intensities of the bands in the 1400–1200 cm^{-1} region are too small as shown in Fig. 3*b*, and the vibrational wavenumbers of the ν_{21} and ν_{22} modes are too low as shown in Table 3. At the UHF level also, the vibrational wavenumber of ν_{21} is too low. These discrepancies are considered to arise from the neglect of electron correlation in the calculations at the ROHF and UHF levels. At the ROHF level, the contribution of molecular symmetry coordinate S_{19}, which corresponds to the vibration along the bond-alternation coordinate and is similar to the Kekulé vibration, to ν_{21} and ν_{22} is 50% and 38%, respectively, in terms of potential energy distribution (PED). The corresponding values in the UHF calculation are 58% and

© 2004 NRC Canada

Table 4. Calculated and observed vibrational wavenumbers (cm^{-1}) and IR intensities (km mol^{-1}) of the IR-active modes of the naphthalene-d_8 radical anion.

		UHF/6-31G*		ROHF/6-31G*		UMP2/6-31G*		CASSCF/6-31G*		B3LYP/6-311G*		Observed[f]	
Symmetry	Mode	Wave-number[a] (cm^{-1})	Intensity (km mol^{-1})	Wave-number[b] (cm^{-1})	Intensity (km mol^{-1})	Wave-number[c] (cm^{-1})	Intensity (km mol^{-1})	Wave-number[d] (cm^{-1})	Intensity (km mol^{-1})	Wave-number[e] (cm^{-1})	Intensity (km mol^{-1})	Wave-number (cm^{-1})	Intensity (km mol^{-1})
b_{2u}	ν_{18}	2234	98	2235	103	2289	79	2278	142	2273	102	2270	71
	ν_{19}	2195	120	2193	160	2249	123	2236	98	2235	68	2225	22
	ν_{20}	1397	376	1385	511	1465	1	1427	380	1428	145	1418	142
	ν_{21}	1267	322	1245	186	1440	458	1321	146	1358	71	1350	92
	ν_{22}	1001	466	991	703	1065	224	1042	198	1050	164		
	ν_{23}	834	21	835	16	841	7	845	9	832	13		
	ν_{24}	811	13	813	14	824	16	826	7	816	7		
	ν_{25}	554	54	546	109	553	49	567	33	574	10		
b_{1u}	ν_{26}	2219	164	2220	149	2387	74 671	2259	170	2256	159	2243	33
	ν_{27}	2187	34	2189	0	2270	522	2235	1	2229	0		
	ν_{28}	1429	35	1437	29	1921	88 332	1453	27	1447	31	1445	16
	ν_{29}	1209	85	1229	0	1475	1 013	1239	2	1227	0		
	ν_{30}	1037	6	1039	0	1087	2 956	1056	1	1033	0		
	ν_{31}	848	136	868	8	1017	497	878	10	868	7		
	ν_{32}	665	84	703	8	795	709	716	3	714	11		
	ν_{33}	300	90	325	6	397	396	327	8	327	4		
b_{3u}	ν_{38}	651	39	667	45	524	59	604	38	606	36		
	ν_{39}	573	62	576	57	454	16	538	43	533	42		
	ν_{40}	385	15	390	15	369	12	384	17	380	24		
	ν_{41}	163	4	166	4	152	5	160	4	159	5		

[a]Scaled by 0.9064.
[b]Scaled by 0.9064.
[c]Scaled by 0.9671.
[d]Scaled by 0.9258.
[e]Scaled by 0.9805.
[f]In THF.

© 2004 NRC Canada

32%. As in the case of neutral benzene (44–46), the calculated diagonal force constant for S_{19} is considered to be too low at the HF level. Another source of the discrepancies in the calculation at the UHF level may be the spin contamination of the electronic wave function. The $\langle s^2 \rangle$ value obtained from the present UHF calculation is 0.8589, which is noticeably larger than the ideal value of 0.75. At the UMP2 level, the discrepancies between the observed and calculated results are more serious. As shown in Table 3, the calculated IR intensities of many b_{1u} modes are extraordinarily large, and the calculated wavenumber of ν_{28} appears to be strange. These discrepancies are considered to arise (at least partly) from the spin contamination of the electronic wave function, since the calculated $\langle s^2 \rangle$ value is as large as 0.8600. In contrast, in the calculation at the B3LYP level, the calculated $\langle s^2 \rangle$ value is 0.7603, which is close to the ideal value of 0.75, and the effect of electron correlation is also taken into account. The good agreement between the observed and calculated spectra obtained at the B3LYP level is therefore reasonable.[3]

The vibrational wavenumbers and the IR intensities of the naphthalene-d_8 radical anion calculated at the five theoretical levels are shown in Table 4. The calculated and observed IR spectra in the 1600–900 cm^{-1} region are compared in Fig. 4. In this case also, good agreement with the observed spectral pattern is obtained by the calculations at the CASSCF and B3LYP levels, and the latter calculation yields a better result with regard to the absolute IR intensities. At the UHF and ROHF levels, the discrepancies between the observed and calculated wavenumbers of ν_{21} are more noticeable for the d_8 species than for the h_8 species. This result is reasonable by considering that the PEDs of S_{19} in ν_{21} calculated at these two levels are 92% and 96%, respectively, for the d_8 species, which are significantly larger than the values calculated for the h_8 species (58% and 50%, respectively).

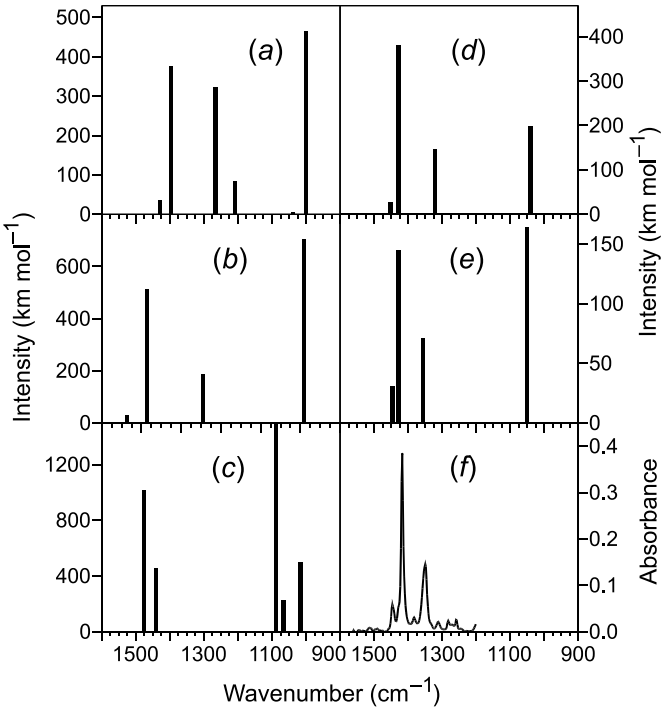
(C) Characterization of normal modes

The normal modes of the naphthalene-h_8 and -d_8 radical anions are discussed here in terms of the molecular symmetry coordinates (S_j) defined in Table 2. In the same way as in the vibrational analysis in refs. 24 and 26, the origin of the IR intensity of each normal mode (Q_m) is examined by calculating $\partial \boldsymbol{\mu}/\partial S_j \times \partial S_j/\partial Q_m$. The direction of the dipole derivative vector is determined by the symmetry species to which S_j and Q_m belong. As shown in Fig. 1, it is in the x direction for the b_{3u} (out-of-plane, IR-active) modes, y for the b_{2u} (in-plane, IR-active) modes, and z for the b_{1u} (in-plane, IR-active) modes.

The results obtained for the b_{1u} and b_{2u} modes of the naphthalene-h_8 radical anion are shown in Table 5. It is evident from the calculated PEDs that the C-C stretches and the C-H bends are strongly mixed with each other in the normal modes in the 1600–900 cm^{-1} region (ν_{20}–ν_{24} and ν_{27}–ν_{30}). Because of the large contributions of the off-diagonal force constants to the vibrational potential energy, the sum of the PEDs exceeds 100% to a great extent for some normal modes (e.g., the ν_{21} mode).

The strong IR bands observed at 1486 and 995 cm^{-1} correspond to the ν_{20} and ν_{24} modes, respectively. In terms of PED, the former mainly derives from S_{25} (C-H bend) and S_{20} (C-C stretch), and the latter from S_{18} and S_{20} (C-C stretches). The calculated IR intensity of ν_{22} is also strong. This mode arises from S_{18} (C-C stretch) as well as S_{24} and S_{25} (C-H bends). From these results, it may seem as if the IR intensities of these three modes originate from both the C-C stretches and the C-H bends. However, as shown by the values of $\partial \mu_y/\partial S_j \times \partial S_j/\partial Q_m$ in Table 5, they are determined primarily by the contributions from S_{18}. The value of $\partial \mu_y/\partial S_{18} \times \partial S_{18}/\partial Q_m$ exceeds 1.0 D $Å^{-1}$ $amu^{-1/2}$ only in the ν_{20}, ν_{22}, and ν_{24} modes, and the other normal modes below 2000 cm^{-1} have medium to weak IR intensities. The dominance of the contribution of S_{18} to the IR intensities arises from the magnitude of $\partial \mu_y/\partial S_{18}$, the absolute value of which exceeds 7.0 D $Å^{-1}$ in both the CASSCF/6-31G* and B3LYP/6-311G* calculations and is significantly larger than the absolute value of any other $\partial \boldsymbol{\mu}/\partial S_j$ listed in Table 6.

Fig. 4. IR spectra of the naphthalene-d_8 radical anion in the 1600–900 cm^{-1} region calculated at the (*a*) UHF/6-31G*, (*b*) ROHF/6-31G*, (*c*) UMP2/6-31G*, (*d*) CASSCF/6-31G*, and (*e*) B3LYP/6-311G* levels, in comparison with (*f*) the spectrum observed in THF.



For the coordinates belonging to the b_{1u} symmetry species, the magnitude of $\partial \mu_z/\partial S_{26}$ is the largest (3.355 D $Å^{-1}$). However, because this value is not particularly larger than those for the other b_{1u} coordinates, the contributions from the vibrations along many coordinates should be taken into account to understand the IR intensities of the b_{1u} modes.

The values of $\partial \boldsymbol{\mu}/\partial S_j \times \partial S_j/\partial Q_m$ and the PEDs calculated for the b_{1u} and b_{2u} modes of the naphthalene-d_8 radical anion are shown in Table 7. Since the C-D bends are intrinsically lower in wavenumber than the C-H bends, the vibrations along the C-D bends (S_{24}, S_{25}, S_{32}, and S_{33}) contribute

[3] The $\langle s^2 \rangle$ value calculated at the ROHF and CASSCF levels is 0.75 by definition.

© 2004 NRC Canada

Table 5. Values of $\partial\boldsymbol{\mu}/\partial S_j \times \partial S_j/\partial Q_m$ and the potential energy distributions for the b_{1u} and b_{2u} modes of the naphthalene-h_8 radical anion.

Symmetry	Mode	Wavenumber (cm^{-1})	IR intensity (km mol^{-1})	$\partial\boldsymbol{\mu}/\partial S_j \times \partial S_j/\partial Q_m$ (D $Å^{-1}$ $amu^{-1/2}$)[a]				PED			
b_{2u}	ν_{18}	3068	258	–0.40(S_{18})	2.36(S_{21})	0.51(S_{22})		91(S_{21})	9(S_{22})		
	ν_{19}	3036	76	0.28(S_{18})	–0.73(S_{21})	1.66(S_{22})	0.12(S_{23})	92(S_{22})	9(S_{21})		
	ν_{20}	1504	131	1.37(S_{18})	0.32(S_{19})	–0.37(S_{20})	0.16(S_{23})	49(S_{25})	38(S_{20})	15(S_{18})	8(S_{19})
				0.34(S_{25})							
	ν_{21}	1374	44	–0.13(S_{18})	0.91(S_{19})	0.31(S_{20})	–0.16(S_{23})	76(S_{19})	31(S_{20})	26(S_{24})	
	ν_{22}	1189	134	1.71(S_{18})	0.30(S_{19})	–0.18(S_{25})		38(S_{18})	23(S_{24})	23(S_{25})	11(S_{19})
	ν_{23}	1135	6	0.71(S_{18})	–0.11(S_{19})	–0.18(S_{20})	–0.16(S_{25})	51(S_{24})	18(S_{25})	15(S_{20})	7(S_{18})
	ν_{24}	1002	105	1.50(S_{18})	–0.25(S_{19})	0.18(S_{20})	0.10(S_{25})	41(S_{18})	21(S_{20})	11(S_{19})	10(S_{25})
	ν_{25}	599	11	0.40(S_{23})				99(S_{23})			
b_{1u}	ν_{26}	3055	349	–0.22(S_{26})	2.75(S_{28})	0.25(S_{29})		92(S_{28})	9(S_{29})		
	ν_{27}	3030	0	–0.84(S_{28})	0.82(S_{29})	0.13(S_{30})		93(S_{29})	9(S_{28})		
	ν_{28}	1505	12	0.51(S_{26})	0.64(S_{27})	–0.24(S_{31})	–0.47(S_{33})	56(S_{27})	42(S_{33})	12(S_{26})	8(S_{31})
	ν_{29}	1371	2	–0.42(S_{26})	0.24(S_{27})	0.16(S_{30})	0.20(S_{32})	79(S_{32})	10(S_{26})	9(S_{27})	5(S_{30})
	ν_{30}	1242	10	–0.40(S_{26})	0.37(S_{27})	0.33(S_{30})	0.25(S_{33})	28(S_{27})	27(S_{30})	19(S_{32})	18(S_{33})
								10(S_{26})			
	ν_{31}	1085	21	0.56(S_{26})	0.16(S_{27})	–0.31(S_{30})	0.31(S_{33})	34(S_{33})	29(S_{30})	27(S_{26})	7(S_{27})
	ν_{32}	783	6	0.38(S_{26})	0.28(S_{30})	–0.30(S_{31})	0.10(S_{33})	49(S_{31})	46(S_{30})	24(S_{26})	7(S_{33})
	ν_{33}	359	5	0.16(S_{26})	0.15(S_{31})			55(S_{31})	20(S_{26})		

Note: Calculated at the B3LYP/6-311G* level.
[a] $\partial\mu_y/\partial S_j \times \partial S_j/\partial Q_m$ for the b_{2u} modes and $\partial\mu_z/\partial S_j \times \partial S_j/\partial Q_m$ for the b_{1u} modes are given.

Table 6. Dipole derivatives ($\partial\boldsymbol{\mu}/\partial S_j$ in D $Å^{-1}$) for the in-plane molecular symmetry coordinates of the naphthalene-h_8 and -d_8 radical anions.

		h_8 species		d_8 species	
Symmetry	Coordinates	CASSCF/6-31G*	B3LYP/6-311G*	CASSCF/6-31G*	B3LYP/6-311G*
b_{2u}	S_{18}	–8.827	–7.317	–8.803	–7.293
	S_{19}	–4.331	–2.172	–4.295	–2.135
	S_{20}	–0.635	–1.349	–0.664	–1.377
	S_{21}	–2.573	–2.383	–2.532	–2.342
	S_{22}	1.711	1.676	1.671	1.635
	S_{23}	–1.720	–0.903	–1.724	–0.906
	S_{24}	0.081	0.081	0.099	0.099
	S_{25}	0.335	0.305	0.389	0.359
b_{1u}	S_{26}	–3.067	–3.355	–3.150	–3.439
	S_{27}	2.178	1.859	2.191	1.872
	S_{28}	–2.751	–2.775	–2.681	–2.704
	S_{29}	–0.783	–0.828	–0.760	–0.805
	S_{30}	1.089	0.887	1.126	0.924
	S_{31}	1.725	0.940	1.780	0.995
	S_{32}	–0.187	–0.152	–0.218	–0.184
	S_{33}	0.423	0.451	0.453	0.482

Note: $\partial\mu_y/\partial S_j$ for b_{2u} and $\partial\mu_z/\partial S_j$ for b_{1u} are given.

mainly to the modes below 1100 cm^{-1} rather than to the modes in the 1600–1100 cm^{-1} region. The C-C stretches are therefore mixed to a minor extent with the C-D bends in the d_8 species.

The strong IR band observed at 1418 cm^{-1} corresponds to ν_{20}. The calculated IR intensity of ν_{22} is also strong, although the IR spectrum could not be measured in the wavenumber region where the IR band corresponding to this mode is expected to be observed. The value of $\partial\mu_y/\partial S_{18} \times \partial S_{18}/\partial Q_m$ exceeds 1.0 D $Å^{-1}$ $amu^{-1/2}$ only for these two modes. The IR intensities of the b_{2u} modes below 2000 cm^{-1} are dominated by the contribution from S_{18}. By contrast, the contributions from the vibrations along many coordinates are important to analyze the IR intensities of the b_{1u} modes. The situation found for the d_8 species is thus similar to that for the h_8 species.

© 2004 NRC Canada

Table 7. Values of $\partial\boldsymbol{\mu}/\partial S_j \times \partial S_j/\partial Q_m$ and the potential energy distributions for the b_{1u} and b_{2u} modes of the naphthalene-d_8 radical anion.

Symmetry	Mode	Wavenumber (cm^{-1})	IR intensity (km mol^{-1})	$\partial\boldsymbol{\mu}/\partial S_j \times \partial S_j/\partial Q_m$ (D $Å^{-1}$ $amu^{-1/2}$)[a]				PED			
b_{2u}	ν_{18}	2273	102	$-0.55(S_{18})$	$-0.13(S_{20})$	$1.67(S_{21})$	$0.42(S_{22})$	$86(S_{21})$	$11(S_{22})$		
	ν_{19}	2235	68	$0.50(S_{18})$	$-0.60(S_{21})$	$1.17(S_{22})$	$0.18(S_{23})$	$88(S_{22})$	$12(S_{21})$		
	ν_{20}	1428	145	$1.71(S_{18})$	$0.29(S_{19})$	$-0.42(S_{20})$	$0.15(S_{23})$	$53(S_{20})$	$27(S_{18})$	$21(S_{25})$	$7(S_{19})$
				$0.25(S_{25})$							
	ν_{21}	1358	71	$0.10(S_{18})$	$0.97(S_{19})$	$0.29(S_{20})$	$-0.15(S_{23})$	$90(S_{19})$	$28(S_{20})$	$10(S_{24})$	
	ν_{22}	1050	164	$2.02(S_{18})$	$0.10(S_{20})$	$0.12(S_{21})$	$-0.14(S_{25})$	$68(S_{18})$	$13(S_{25})$	$5(S_{20})$	
	ν_{23}	832	13	$0.19(S_{18})$	$0.14(S_{20})$	$0.24(S_{25})$		$55(S_{25})$	$17(S_{20})$	$13(S_{24})$	
	ν_{24}	816	7	$0.38(S_{18})$	$-0.15(S_{19})$			$71(S_{24})$	$7(S_{25})$	$6(S_{19})$	
	ν_{25}	574	10	$0.10(S_{18})$	$0.38(S_{23})$			$96(S_{23})$	$6(S_{25})$		
b_{1u}	ν_{26}	2256	159	$-0.37(S_{26})$	$1.95(S_{28})$	$0.19(S_{29})$		$89(S_{28})$	$9(S_{29})$		
	ν_{27}	2229	0	$-0.64(S_{28})$	$0.58(S_{29})$	$0.21(S_{30})$	$-0.14(S_{31})$	$91(S_{29})$	$10(S_{28})$		
	ν_{28}	1447	31	$0.42(S_{26})$	$0.75(S_{27})$	$0.12(S_{28})$	$0.11(S_{30})$	$82(S_{27})$	$17(S_{33})$	$8(S_{26})$	$8(S_{31})$
				$-0.24(S_{31})$	$-0.31(S_{33})$						
	ν_{29}	1227	0	$0.84(S_{26})$	$-0.22(S_{27})$	$0.10(S_{28})$	$-0.37(S_{30})$	$46(S_{26})$	$31(S_{30})$	$13(S_{32})$	$10(S_{27})$
				$-0.16(S_{33})$				$7(S_{33})$			
	ν_{30}	1033	0	$0.23(S_{30})$	$-0.18(S_{32})$			$81(S_{32})$	$17(S_{30})$		
	ν_{31}	868	7	$0.16(S_{27})$	$-0.25(S_{30})$	$0.15(S_{31})$	$0.30(S_{33})$	$43(S_{33})$	$29(S_{30})$	$10(S_{27})$	$9(S_{31})$
	ν_{32}	714	11	$0.37(S_{26})$	$0.20(S_{30})$	$-0.27(S_{31})$	$0.22(S_{33})$	$41(S_{31})$	$34(S_{33})$	$26(S_{26})$	$26(S_{30})$
	ν_{33}	327	4	$0.15(S_{26})$	$0.14(S_{31})$			$52(S_{31})$	$20(S_{26})$		

Note: Calculated at the B3LYP/6-311G* level.
[a] $\partial\mu_y/\partial S_j \times \partial S_j/\partial Q_m$ for the b_{2u} modes and $\partial\mu_z/\partial S_j \times \partial S_j/\partial Q_m$ for the b_{1u} modes are given.

It is clear from these results that the significant enhancement of the IR intensities in the 1600–900 cm^{-1} region observed for the naphthalene radical anion as compared with the neutral species is primarily due to the large dipole derivative induced by the vibration along S_{18}, as found in ref. 17 for the cationic species.

(D) Mechanism that gives rise to strong IR intensities

To discuss the mechanism that gives rise to such a large dipole derivative, we first examine the relation between the molecular structural parameters and the electronic wave function of the radical anions of benzene and naphthalene, paying attention to the form of the singly occupied molecular orbital (SOMO).

The calculated structural parameters of these anions and their neutral species are shown in Table 8. The numbering of atoms and the Cartesian coordinate system defined for naphthalene (Fig. 1) are also used for benzene. The structural parameters calculated at the CASSCF and B3LYP levels are in good agreement with each other.

Because of the Jahn–Teller effect, two structures (A and B) with D_{2h} symmetry are considered for the benzene radical anion. In structure A, the C_1—C_2 and C_2—C_3 bonds are longer and shorter, respectively, than those of the neutral species. By contrast, the C_2—C_3 bond of structure B is longer than that of the neutral, while the C_1—C_2 bond length remains almost the same. These structural changes are reasonably explained by the SOMOs of the anionic species, which are shown in Fig. 5*a*. In structure A, the SOMO is antibonding and bonding, respectively, for the C_1—C_2 and C_2—C_3 bonds. Therefore, when neutral benzene is reduced to this form of the anion, the C_1—C_2 bond becomes longer and the C_2—C_3 bond shorter. In structure B, the SOMO is antibonding for the C_2—C_3 bond and nonbonding for the C_1—C_2 bond. Therefore, the C_2—C_3 bond becomes longer and the C_1—C_2 bond length remains almost the same when benzene is reduced to this form of the anion.

The SOMO of the naphthalene radical anion is shown on the upper left part of Fig. 5*b*. It is antibonding and bonding, respectively, for the C_1—C_2 and C_2—C_3 bonds, and nonbonding for both the C_9—C_1 and C_9—C_{10} bonds. By the same reasoning as employed for the benzene radical anion, it is expected that the C_1—C_2 and C_2—C_3 bonds become longer and shorter, respectively, when naphthalene is reduced to the radical anion, while the C_9—C_1 and C_9—C_{10} bond lengths remain almost the same. As shown in Table 8, the changes in the C_9—C_1, C_1—C_2, and C_2—C_3 bond lengths match this expectation. By contrast, the C_9—C_{10} bond of the radical anion is calculated to be longer than that of the neutral. At present, we have no reasonable explanation for this change of bond length.

It is clear from Fig. 5*b* that the electronic structure of each ring in the naphthalene radical anion is similar to that of structure A of the benzene radical anion. The coefficients of the SOMO on the C_9 and C_{10} atoms are zero because the contributions from the two rings cancel each other. In the subsequent analysis of the origin of IR intensities, structure A of the benzene radical anion is regarded as the building block for the naphthalene radical anion.

The vibrational pattern of S_{18} is schematically shown on the upper right part of Fig. 5*b*. It is noticed that one of the rings vibrates in the direction of the structural change from neutral benzene to its radical anion (structure A), and the other ring vibrates in the opposite phase. As a result, the former becomes more anionic and the latter less anionic by this

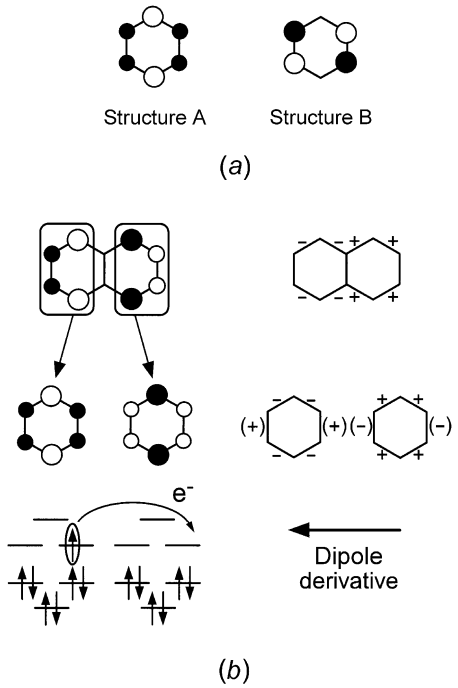
© 2004 NRC Canada

Table 8. Structural parameters of benzene, naphthalene, and their radical anions.

Theoretical level	$r(C_9\text{-}C_{10})$ (Å)	$r(C_9\text{-}C_1)$ (Å)	$r(C_1\text{-}C_2)$ (Å)	$r(C_2\text{-}C_3)$ (Å)	$\theta(C_{10}\text{-}C_9\text{-}C_1)$ (°)	$\theta(C_9\text{-}C_1\text{-}C_2)$ (°)	$\theta(C_1\text{-}C_2\text{-}C_3)$ (°)
Benzene neutral							
CASSCF/6-31G*			1.3963	1.3963		120.00	120.00
B3LYP/6-311G*			1.3940	1.3940		120.00	120.00
Benzene radical anion (structure A)							
CASSCF/6-31G*			1.4357	1.3756		116.78	121.61
B3LYP/6-311G*			1.4384	1.3757		117.00	121.50
Benzene radical anion (structure B)							
CASSCF/6-31G*			1.3951	1.4568		123.04	118.48
B3LYP/6-311G*			1.3956	1.4614		122.96	118.52
Naphthalene neutral							
CASSCF/6-31G*	1.4174	1.4276	1.3731	1.4211	119.01	120.79	120.19
B3LYP/6-311G*	1.4315	1.4195	1.3736	1.4148	118.82	120.89	120.29
Naphthalene radical anion							
CASSCF/6-31G*	1.4527	1.4163	1.4098	1.3859	118.47	121.37	120.17
B3LYP/6-311G*	1.4523	1.4201	1.4084	1.3880	118.33	121.59	120.08

Note: Numbering of atoms is shown in Fig. 1.

Fig. 5. (*a*) Singly occupied molecular orbitals (SOMOs) of the benzene radical anion (structures A and B). (*b*) Decomposition of the SOMO and the vibrational pattern of S_{18} of the naphthalene radical anion into those of two benzene rings and scheme of the charge flux induced by the vibration along S_{18}.



vibration. In other words, as shown on the lower left part of Fig. 5*b*, a partial negative charge is transferred from the latter ring to the former by this vibration. Of course, the charge goes back and forth as the vibration proceeds. This mechanism of generating large dipole derivatives, called "long-range charge flux" in our previous study (17), is considered to be important also for other PAH radical ions. The result that the total IR intensities calculated for the radical cations of polyacenes are approximately proportional to the square of the number of rings (17) supports this mechanism.

To see more closely the change in the electronic structure induced by the vibration along S_{18}, the form of the SOMO (more specifically, the singly occupied natural orbital derived from the CASSCF calculation) is examined for the naphthalene radical anion displaced along S_{18}. Since the 6-31G* basis set used in the calculation is of split-valence type, there are two contracted basis functions for valence π orbitals on each carbon atom. As shown in Table 2, the C_9—C_1, C_1—C_2, C_3—C_4, and C_4—C_{10} bonds stretch while the C_{10}—C_5, C_5—C_6, C_7—C_8, and C_8—C_9 bonds shrink by the displacement in the positive direction along S_{18}. Because these eight C—C bonds are involved in S_{18}, the displacement of 1 Å along S_{18} means that each bond stretches or shrinks by $1/\sqrt{8}$ Å.

The result is shown in Table 9. The coefficients of the singly occupied natural orbital on the C_1 and C_2 atoms (and the other two equivalent atoms on the same ring) increase by the displacement in the positive direction along S_{18}, while those on the C_5 and C_6 atoms decrease. This result indicates that the electron–vibration interaction involving the vibration along S_{18} is strong, and the motion of the unpaired electron between the two rings is induced by this vibration.

The change in the electronic structure induced by the vibration along S_{18} may be examined also by using the model Hamiltonian approach developed in refs. 27 and 28. In this approach, dipole derivatives of individual C-C stretches ($\partial\mu_k/\partial R_l$) are represented in atomic units as

$$[1] \qquad \frac{\partial \mu_k}{\partial R_l} = -0.07 \sum_s f_{k,s} P_{ij,s}$$

where

$$[2] \qquad f_{k,s} = \frac{\partial}{\partial E_k} \langle \nu_s \mid g(\boldsymbol{E}) \rangle$$

© 2004 NRC Canada

Table 9. Coefficients of the singly occupied natural orbital of the naphthalene radical anion displaced along S_{18}.

		Inner valence shell				Outer valence shell			
Displacement (Å)	Occupation number	C_1	C_2	C_5	C_6	C_1	C_2	C_5	C_6
0.00	1.00271	0.25893	0.15239	0.25893	0.15239	0.32184	0.19401	0.32184	0.19401
0.05	1.00278	0.27715	0.15699	0.23982	0.14672	0.34335	0.19979	0.29829	0.18664
0.10	1.00298	0.29365	0.16033	0.22081	0.14038	0.36178	0.20362	0.27409	0.17827
0.15	1.00325	0.30800	0.16240	0.20276	0.13379	0.37671	0.20549	0.25048	0.16955

Note: Calculated at the CASSCF/6-31G* level. Numbering of atoms is shown in Fig. 1. Only the absolute values are shown. Phase of the orbital is shown in Fig. 5*b*.

is the electric-field-induced mixing of one-electron excited electronic configurations $|\nu_s\rangle$ (numbered by s) into the ground electronic state $|g(\boldsymbol{E})\rangle$, and

$$[3] \qquad P_{ij,s} = \langle g_0 \mid \sum_{\sigma} (a_{i\sigma}^{\dagger} a_{j\sigma} + a_{j\sigma}^{\dagger} a_{i\sigma}) \mid \nu_s \rangle$$

is an element of the one-particle transition density matrix (47) between $|g_0\rangle$ ($\equiv |g(\boldsymbol{E} = 0)\rangle$) and $|\nu_s\rangle$. In the last equation, $a_{i\sigma}^{\dagger}$ is the creation operator of a π electron of spin σ at the ith carbon atom, and $a_{i\sigma}$ is the corresponding annihilation operator. It is assumed that the lth C—C bond connects the ith and jth carbon atoms.

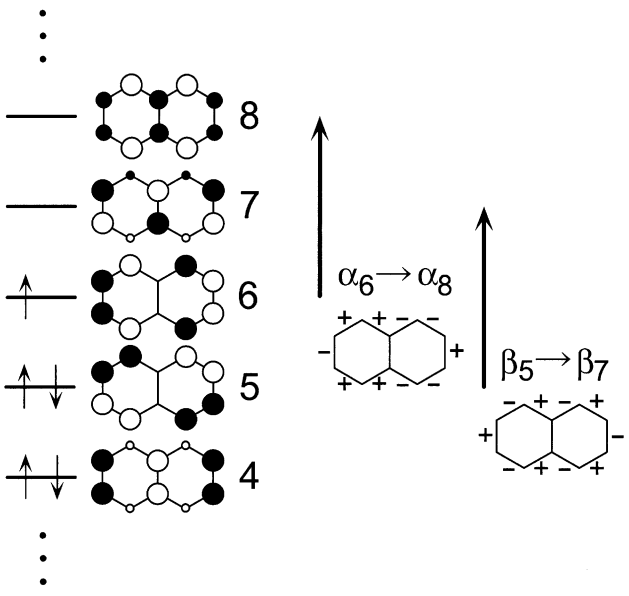
The configurations ($|\nu_s\rangle$) that are important for generating the IR intensity of the b_{2u} modes are shown in Fig. 6. By the mixing of the $\alpha_6 \rightarrow \alpha_8$ configuration (where the α electron on the 6th orbital is excited to the 8th orbital), the dipole derivatives of individual C-C stretches ($\partial\mu_y/\partial R_l$) are generated with the signs as shown just below the "$\alpha_6 \rightarrow \alpha_8$" label in Fig. 6. From the comparison with the definition of S_{18} shown in Table 2, it is seen that the large dipole derivative in the $-y$ direction is induced for S_{18} by this mixing. It is also seen that the dipole derivative in the $-y$ direction is induced for S_{19} by the mixing of the $\beta_5 \rightarrow \beta_7$ configuration. As discussed in the *Introduction*, the contributions of many one-electron excited configurations cancel each other in the neutral species. Because of the existence of an electron on the 6th orbital in the naphthalene radical anion, we have the contribution of the $\alpha_6 \rightarrow \alpha_8$ configuration. For the same reason, the contribution of the $\beta_5 \rightarrow \beta_7$ configuration is not canceled by that of the $\alpha_4 \rightarrow \alpha_6$ configuration. The IR intensity enhancement observed for the naphthalene radical anion (as well as for the cationic species (27–29)) as compared with the neutral species is thus reasonably explained by the difference in their electronic structures.

From the forms of the 6th and 8th orbitals shown in Fig. 6, it is also clear that the electronic populations on the C_1 through C_4 atoms decrease, while those on the C_5 through C_8 atoms increase by the mixing of the $\alpha_6 \rightarrow \alpha_8$ configuration. This result is fully consistent with that obtained from the CASSCF calculation show in Table 9.

Concluding remarks

The purposes of the present study were to observe the IR spectra of the naphthalene-h_8 and -d_8 radical anions and to elucidate the mechanism that gives rise to the spectral features characteristic of these species. It has been shown from the comparison of the observed spectra with those calculated at the B3LYP level that the strong IR bands observed in the 1600–900 cm^{-1} region with intensities of the order of 10^2 km mol^{-1} originate from the normal modes of b_{2u} symmetry. The IR intensities of these bands are primarily determined by the contribution from the one molecular symmetry coordinate, which is denoted as S_{18} in the present study, because the dipole derivative calculated for this coordinate is substantially larger than those for the other coordinates. From detailed examination of the change in the electronic structure induced by the vibration along this coordinate, it is shown that this vibration generates a large charge flux between the two rings of the naphthalene radical anion. Strong electron–vibration interaction is responsible for this mechanism.

Fig. 6. The forms of orbitals 4–8, the occupation of α and β electrons in these orbitals, the electronic excitations involved in the configurations that are important for generating the IR intensity of the b_{2u} modes, and the signs of the dipole derivatives generated by the mixing of these configurations calculated for the naphthalene radical anion.



Conjugated π-electron systems in general are known to have interesting electronic and vibrational properties. It is expected that electron–vibration interactions are important to understand the molecular aspects of the functions of some conjugated π-electron systems related to those properties, such as electric conductivity and nonlinear optical susceptibilities.

References

1. L.J. Allamandola, A.G.G.M. Tielens, and J.R. Barker. Astrophys. J. **290**, L25 (1985).

© 2004 NRC Canada

2. J. Szczepanski, D. Roser, W. Personette, M. Eyring, R. Pellow, and M. Vala. J. Phys. Chem. **96**, 7876 (1992).
3. J. Szczepanski, M. Vala, D. Talbi, O. Parisel, and Y. Ellinger. J. Chem. Phys. **98**, 4494 (1993).
4. J. Szczepanski, C. Chapo, and M. Vala. Chem. Phys. Lett. **205**, 434 (1993).
5. M. Vala, J. Szczepanski, F. Pauzat, O. Parisel, D. Talbi, and Y. Ellinger. J. Phys. Chem. **98**, 9187 (1994).
6. J. Szczepanski, C. Wehlburg, and M. Vala. Chem. Phys. Lett. **232**, 221 (1995).
7. J. Szczepanski, J. Drawdy, C. Wehlburg, and M. Vala. Chem. Phys. Lett. **245**, 539 (1995).
8. D.M. Hudgins, S.A. Sandford, and L.J. Allamandola. J. Phys. Chem. **98**, 4243 (1994).
9. D.M. Hudgins and L.J. Allamandola. J. Phys. Chem. **99**, 3033 (1995).
10. D.M. Hudgins and L.J. Allamandola. J. Phys. Chem. **99**, 8978 (1995).
11. D.M. Hudgins and L.J. Allamandola. J. Phys. Chem. A, **101**, 3472 (1997).
12. F. Pauzat, D. Talbi, M.D. Miller, D.J. DeFrees, and Y. Ellinger. J. Phys. Chem. **96**, 7882 (1992).
13. Y.-P. Ho, Y.-C. Yang, S.J. Klippenstein, and R.C. Dunbar. J. Phys. Chem. **99**, 12115 (1995).
14. S.R. Langhoff. J. Phys. Chem. **100**, 2819 (1996).
15. J. Szczepanski and M. Vala. Nature (London), **363**, 699 (1993).
16. D.J. Cook, S. Schlemmer, N. Balucani, D.R. Wagner, B. Steiner, and R.J. Saykally. Nature (London), **380**, 227 (1996).
17. H. Torii, Y. Ueno, A. Sakamoto, and M. Tasumi. J. Phys. Chem. A, **103**, 5557 (1999).
18. C.R. Fincher, Jr., M. Ozaki, A.J. Heeger, and A.G. MacDiarmid. Phys. Rev. B, **19**, 4140 (1979).
19. I. Harada, Y. Furukawa, M. Tasumi, H. Shirakawa, and S. Ikeda. J. Chem. Phys. **73**, 4746 (1980).
20. P. Piaggio, D. Dellepiane, L. Piseri, R. Tubino, and C. Taliani. Solid State Commun. **50**, 947 (1984).
21. M. Gussoni, C. Castiglioni, and G. Zerbi. *In* Spectroscopy of advanced materials. Advances in spectroscopy. Vol. 19. *Edited by* R.J.H. Clark and R.E. Hester. Wiley, New York. 1991. p. 251.
22. S. Masuda, H. Torii, and M. Tasumi. J. Phys. Chem. **100**, 15335 (1996).
23. H. Torii and M. Tasumi. J. Phys. Chem. B, **101**, 466 (1997).
24. K. Furuya, Y. Inagaki, H. Torii, Y. Furukawa, and M. Tasumi. J. Phys. Chem. A, **102**, 8413 (1998).
25. H. Torii, K. Furuya, and M. Tasumi. J. Phys. Chem. A, **102**, 8422 (1998).
26. K. Furuya, H. Torii, Y. Furukawa, and M. Tasumi. J. Phys. Chem. A, **104**, 11203 (2000).
27. H. Torii. Chem. Phys. Lett. **306**, 381 (1999).
28. H. Torii. J. Phys. Chem. A, **104**, 413 (2000).
29. H. Torii. Vib. Spectrosc. **24**, 3 (2000).
30. C.A. Coulson and H.C. Longuet-Higgins. Proc. R. Soc. London Ser. A, **192**, 16 (1947).
31. I.Ya. Kachkurova. Dokl. Akad. Nauk S.S.S.R. **163**, 1198 (1965).
32. I.Ya. Kachkurova. Teor. Eksp. Khim. **3**, 498 (1967).
33. A.D. Becke. J. Chem. Phys. **98**, 5648 (1993).
34. C. Lee, W. Yang, and R.G. Parr. Phys. Rev. B, **37**, 785 (1988).
35. D.E. Paul, D. Lipkin, and S.I. Weissman. J. Am. Chem. Soc. **78**, 116 (1956).
36. P. Balk, G.J. Hoijtink, and J.W.H. Schreuers. Recl. Trav. Chim. **76**, 813 (1957).
37. K.K. Brandes and R.J. Gerdes. J. Phys. Chem. **71**, 508 (1967).
38. M. Dupuis, F. Johnston, and A. Marquez. HONDO 8 [computer program]. IBM Corporation, Kingston, N.Y. 1994.
39. M.J. Frisch, G.W. Trucks, M. Head-Gordon, P.M.W. Gill, M.W. Wong, J.B. Foresman, B.G. Johnson, H.B. Schlegel, M.A. Robb, E.S. Replogle, R. Gomperts, J.L. Andres, K. Raghavachari, J.S. Binkley, C. Gonzalez, R.L. Martin, D.J. Fox, D.J. Defrees, J. Baker, J.J.P. Stewart, and J.A. Pople. Gaussian 92 [computer program]. Gaussian Inc., Pittsburgh, Pa. 1992.
40. M.J. Frisch, G.W. Trucks, H.B. Schlegel, P.M.W. Gill, B.G. Johnson, M.A. Robb, J.R. Cheeseman, T. Keith, G.A. Petersson, J.A. Montgomery, K. Raghavachari, M.A. Al-Laham, V.G. Zakrzewski, J.V. Ortiz, J.B. Foresman, J. Cioslowski, B.B. Stefanov, A. Nanayakkara, M. Challacombe, C.Y. Peng, P.Y. Ayala, W. Chen, M.W. Wong, J.L. Andres, E.S. Replogle, R. Gomperts, R.L. Martin, D.J. Fox, J.S. Binkley, D.J. Defrees, J. Baker, J.J.P. Stewart, M. Head-Gordon, C. Gonzalez, and J.A. Pople. Gaussian 94 [computer program]. Gaussian Inc., Pittsburgh, Pa. 1995.
41. H. Torii and M. Tasumi. J. Mol. Struct. **352/353**, 465 (1995).
42. C.L. Dodson and J.F. Graham. J. Phys. Chem. **77**, 2903 (1973).
43. L. Goodman, A.G. Ozkabak, and S.N. Thakur. J. Phys. Chem. **95**, 9044 (1991).
44. A.G. Ozkabak, L. Goodman, and K.B. Wiberg. J. Chem. Phys. **92**, 4115 (1990).
45. H. Torii and M. Tasumi. J. Mol. Struct. THEOCHEM, **334**, 15 (1995).
46. H. Torii and M. Tasumi. J. Mol. Struct. **376**, 317 (1996).
47. I. Shavitt. *In* Methods of electronic structure theory. Vol. 3. *Edited by* H.F. Schaefer III. Plenum, New York. 1977. p 189.

© 2004 NRC Canada

Conformational stability, infrared and Raman spectra, and vibrational assignment of ethyl bromogermane[1]

James R. Durig, Chunhua Pan, Witold Witkowski, and Gamil A. Guirgis

Abstract: The infrared spectra (3200–30 cm^{-1}) of ethyl bromogermane, $CH_3CH_2GeH_2Br$, in the gaseous phase and of amorphous and annealed solid samples as well as the Raman spectrum (3200–100 cm^{-1}) of the liquid have been recorded. Variable-temperature (–105 to –150 °C) studies of the infrared spectra of a sample dissolved in liquid krypton have been carried out. From these data, the enthalpy difference between the gauche and trans conformers has been determined to be 158 ± 16 cm^{-1} (1.89 ± 0.20 kJ/mol), with the gauche conformer being the more stable form. This result is consistent with the prediction from ab initio calculations at both the Hartree–Fock level and with full electron correlation by the perturbation method to second order. It is estimated that at ambient temperature 81 ± 2% of the sample is in the gauche form. A relatively complete vibrational assignment is proposed for both the gauche and trans conformers based on infrared band contours, relative intensities, depolarization values, and group frequencies which is supported by normal coordinate calculations utilizing the force constants from the ab initio MP2/6-31G(d) calculations. The optimized geometries and conformational stabilities have also been obtained from ab initio calculations utilizing several different basis sets with full electron correlation by the perturbation method up to MP2/6-311+G(2d,2p). Additionally, the potential functions governing the conformation interchange have been estimated from ab initio MP2/6-31G(d) and density functional theory calculations by the B3LYP method, with barriers to conformational interchange of 560, 924, and 852 cm^{-1} from MP2/6-31G(d) and 418, 771, and 606 cm^{-1} from B3LYP/6-31G(d) calculations for the trans to gauche, gauche to gauche, and gauche to trans conformers, respectively. The results are discussed and compared to some corresponding quantities for several related molecules.

Key words: conformational stability, Raman spectra, infrared spectra; ab initio calculations, ethyl bromogermane.

Résumé : On a déterminé les spectres infrarouge (3200 à 30 cm^{-1}) de l'éthylbromogermane, $CH_3CH_2GeH_2Br$, en phase gazeuse et ceux d'échantillons solides amorphes et recuits ainsi que les spectres Raman (3200 à 100 cm^{-1}) en phase liquide. On a effectué des études à température variable (–105 à –150 °C) des spectres infrarouge des échantillons dissous dans le krypton liquide. Sur la base de ces données, on a déterminé que la différence d'enthalpie entre les conformères gauche et trans est de 158 ± 16 cm^{-1} (1,89 ± 0,20 kJ/mol) et que le conformère gauche est le plus stable, ce qui est en accord avec la prédiction faite sur la base de calculs ab initio, tant au niveau de Hartree–Fock qu'avec la corrélation électronique complète faisant appel à la méthode de perturbation du deuxième ordre. À la température ambiante, il a été évalué que 81 ± 2 % de l'échantillon est sous la forme gauche. Sur la base des contours des bandes infrarouges, des intensités relatives, des valeurs de dépolarisation et des fréquences de groupe qui est supportée par des calculs de coordonnées normales à l'aide de constantes de force obtenues par des calculs ab initio MP2/6-31G(d), on propose une attribution vibrationnelle relativement complète pour les conformères tant gauche que trans. On a aussi obtenu les géométries optimisées et les stabilités conformationnelles à partir de calculs ab initio utilisant plusieurs ensembles de base différents, avec une corrélation électronique complète à l'aide de la méthode de perturbation jusqu'au niveau MP2/6-311+G(2d,2p). En se basant sur des calculs ab initio MP2/6-31G(d) et des calculs selon la théorie de la densité fonctionnelle (TDF) à l'aide de la méthode B3LYP, on a aussi évalué les fonctions de potentiel gouvernant l'échange de conformation. Les barrières à l'échange conformationnel sont respectivement de 560, 924 et 852 cm^{-1} par la méthode MP2/6-31G(d) et de 418, 771 et 606 cm^{-1} par la méthode B3LYP/6-31G(d) pour les échanges de conformère trans à gauche, de gauche à gauche et de gauche à trans. On discute des résultats et on les compare à des valeurs correspondantes obtenues pour plusieurs autres molécules.

Received 10 December 2003. Published on the NRC Research Press Web site at http://canjchem.nrc.ca on 3 September 2004.

Dedicated to the memory of Gerhard Herzberg, a pillar in the field of spectroscopy in the twentieth century.

J.R. Durig[2] and C. Pan.[3] Department of Chemistry, University of Missouri-Kansas City, Kansas City, MO 64110–2499, USA.
W. Witkowski and G.A. Guirgis. Department of Chemistry and Biochemistry, College of Charleston, Charleston, SC 29403, USA.

[1]This article is part of a Special Issue dedicated to the memory of Professor Gerhard Herzberg.
[2]Corresponding author (email: durigj@umkc.edu).
[3]Taken in part from the dissertation of C. Pan, which will be submitted to the Department of Chemistry at the University of Missouri-Kansas City in partial fulfillment of the Ph.D degree.

 doi: 10.1139/V04-048 © 2004 NRC Canada

Mots clés : stabilité conformationnelle, spectres Raman, spectres infrarouge, calculs ab initio, éthylbromogermane.

[Traduit par la Rédaction]

Introduction

To investigate the conformational stability of a series of YCH_2CH_2X, YCH_2SiH_2X, and YCH_2GeH_2X molecules, where Y is a halogen or methyl group and X is F, Cl, Br, or CH_3, we have carried out a number of vibrational spectroscopic and theoretical studies on the 1,2-disubstituted ethane and 1,2-disubstituted methylsilane molecules. For YCH_2CH_2X, when Y is a methyl group and X is F (1), Cl (2), or Br (2), the enthalpy differences between the trans and gauche conformers, obtained from rare-gas solutions, are 104 ± 6, 52 ± 3, and 72 ± 7 cm^{-1} (1 cm^{-1} = 11.963 J/mol), respectively, with the gauche conformer being the more stable form. However, for molecules in which Y and X are both either halogens (except when they are both F atoms (3)) or methyl groups, such as 1,2-dichloroethane (4), 1,2-fluorochloroethane (4), 1,2-fluorobromoethane (5), and *n*-butane (6), the trans conformers were determined to be the more stable forms. Enthalpy differences of 318 ± 25, 17 ± 8, 109 ± 9, and 221 ± 21 cm^{-1} between the trans and gauche conformers were determined in krypton solutions for 1,2-dichloroethane, 1,2-fluorochloroethane, 1,2-fluorobromoethane, and *n*-butane, respectively. However, the 1,2-difluoroethane molecule has the gauche conformer as the more stable rotamer (3) with an enthalpy difference of 283 ± 47 cm^{-1}.

Similar studies of conformational stabilities have been carried out for the corresponding silicon-containing compounds, YCH_2SiH_2X. When Y is a methyl group and X is F (7), Cl (8), or Br (9), the most stable conformer is also the gauche form, with enthalpy differences between the trans and gauche conformers of 54 ± 16, 78 ± 11, and 140 ± 22 cm^{-1}, respectively, again determined in rare-gas solutions. For molecules in which both Y and X are halogens, such as chloromethyl silyl chloride (10), $ClCH_2SiH_2Cl$, and chloromethyl silyl bromide (11), $ClCH_2SiH_2Br$, the trans conformer is found to be more stable by 177 ± 35 and 216 ± 22 cm^{-1}, respectively. However, when both Y and X are methyl groups, there is a large difference in conformational stability between YCH_2CH_2X and YCH_2SiH_2X since *n*-butane ($CH_3CH_2CH_2CH_3$) has the trans conformer as the more stable rotamer with a large enthalpy difference of 221 ± 21 cm^{-1} (6) whereas the trans and gauche forms of ethyl methylsilane ($CH_3CH_2SiH_2CH_3$) were initially reported (12) to have nearly the same energy. In our recent temperature-dependent infrared study of ethyl methylsilane in krypton solution (13), we found the trans conformer to be only 20 ± 5 cm^{-1} more stable than the gauche form.

As a continuation of these conformational stability studies, we have now turned our attention to the corresponding germanium compounds for comparison with the carbon and (or) silicon analogues. There is very little conformational data available for these compounds, although ethyl methylgermane, $CH_3CH_2GeH_2CH_3$, has been predicted to have the gauche form as the more stable rotamer (14). Also, we have recently carried out conformational stability studies of ethyl chlorogermane, $CH_3CH_2GeH_2Cl$, from temperature-dependent Fourier transform infrared (FT-IR) spectra of krypton solutions and determined an enthalpy difference of 143 ± 30 cm^{-1} with the gauche conformer the more stable form (15). Because ethyl bromogermane, $CH_3CH_2GeH_2Br$, is an interesting molecule in this series of studies, we have initiated investigations of the temperature dependence of its vibrational spectra. Additionally, we carried out ab initio calculations utilizing the 6-31G(d) basis set at the restricted Hartree–Fock (RHF) and (or) with full electron correlation by the perturbation method (16) to second order (MP2) as well as density functional theory (DFT) calculations by the B3LYP method to determine the optimized structural parameters, harmonic force constants, vibrational wavenumbers, infrared intensities, Raman activities, and conformational stabilities. We also calculated the structural parameters and conformational stabilities utilizing the larger 6-311+G(d,p) and 6-311+G(2d,2p) basis sets at the MP2 level. The results of these vibrational spectroscopic and theoretical studies are reported herein.

Experimental

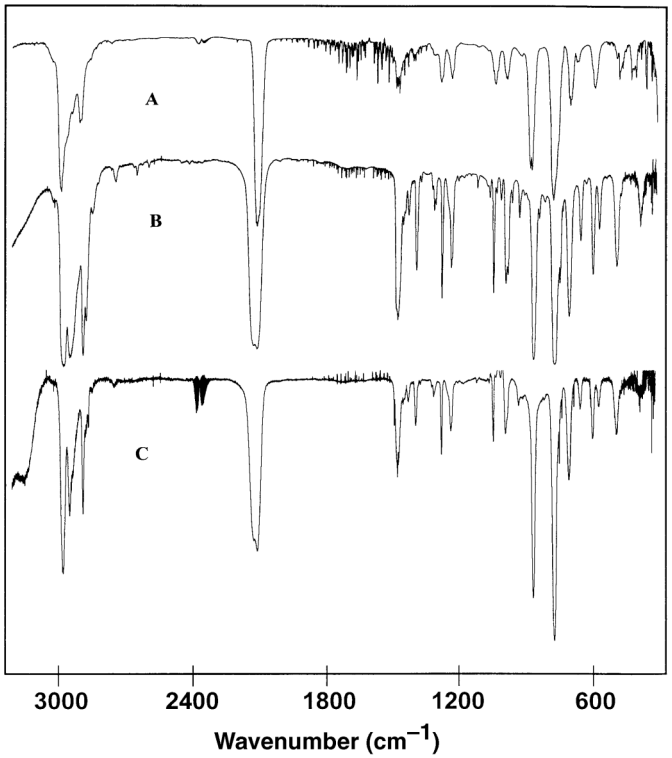
The sample of ethyl bromogermane was prepared by a two-step reaction. In the first step, ethyl trichlorogermane (Aldrich Chemical Co., Milwaukee, WI) was reacted with lithium aluminum hydride in dry *n*-butyl ether at room temperature. In the second step, the purified sample of ethyl germane was brominated with equivalent amounts of boron tribromide at 0 °C for 20 h. The ethyl bromogermane was first purified by trap-to-trap distillation. Further purification was performed with a low-temperature, low-pressure fractionating column. The purity was checked by recording the mass spectrum and the mid-infrared spectrum of the gas. The sample was stored under vacuum at low temperature.

The mid-infrared spectra of gaseous, amorphous, and annealed solid ethyl bromogermane were recorded with a Perkin-Elmer model 2000 Fourier transform spectrometer equipped with a Ge/CsI beamsplitter and DTGS detector. Atmospheric water vapor was removed from the spectrometer housing by purging with dry nitrogen. The spectrum of the gas was obtained with the sample contained in a 10-cm cell fitted with CsI windows. The spectra of the solids were obtained by depositing the sample onto a CsI substrate held at the temperature of boiling liquid nitrogen, housed in a vacuum cell fitted with CsI windows. The sample was condensed as an amorphous or glassy solid and repeatedly annealed until no further changes were observed in the spectrum (Fig. 1).

The mid-IR spectra of ethyl bromogermane dissolved in liquid krypton (Fig. 2) as a function of temperature were recorded on a Bruker model IFS 66 Fourier transform spectrometer equipped with a globar source, a Ge/KBr beamsplitter, and a DTGS detector. In all cases, 100 interferograms were collected at 1.0 cm^{-1} resolution, averaged, and trans-

© 2004 NRC Canada

Fig. 1. Mid-infrared spectra of ethyl bromogermane: (A) gas; (B) amorphous; (C) solid.

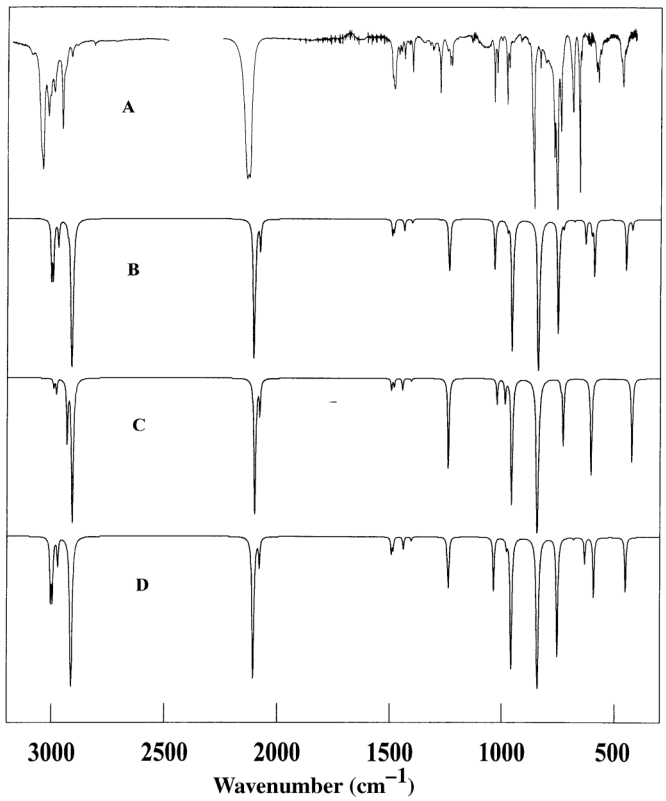


formed with a boxcar truncation function. A specially designed cryostat cell was used to obtain the spectral data. It consists of a copper cell with a path length of 4 cm, with wedged silicon windows sealed to the cell with indium gaskets. This cell was cooled with boiling liquid nitrogen, and the temperature was monitored with a Pt thermoresistor. The complete cell was connected to a pressure manifold, allowing the filling and evacuation of the cell. After the cell had cooled to the desired temperature, a small amount of the compound was condensed into the cell. Next, the pressure manifold and the cell were pressurized with the noble gas, which immediately began condensing in the cell, allowing the compound to dissolve.

The Raman spectrum of liquid ethyl bromogermane from 3200 to 100 cm^{-1} (Fig. 3) was recorded on a Spex model 1403 spectrophotometer equipped with a Spectra-Physics model 164 argon-ion laser operating on the 514.5-nm line. Laser power at the sample ranged from 0.4 to 1 W depending on the physical state of the sample, and a bandpass of 3 cm^{-1} was utilized. The spectrum of the liquid was obtained from the sample sealed in a glass capillary with a spherical bulb on the end (17). The reported frequencies are expected to be accurate to ±2 cm^{-1}.

The far-infrared spectra of gaseous and amorphous and annealed solid samples (Fig. 4) were recorded on the Perkin-Elmer 2000 spectrometer described above. A grid beamsplitter and a cryostat cell with polyethylene windows were used to record the spectrum of the solid sample, which was deposited on a silicon substrate at 77 K and subjected to multiple annealings to obtain a good polycrystalline solid. For the spectrum of the gas, the sample was contained in a 10-cm cell equipped with polyethylene windows. The spec-

Fig. 2. (A) Mid-infrared spectrum of ethyl bromogermane in krypton solution at –125 °C (the bands marked with an asterisk arise from impurities); (B) simulated infrared spectrum of the gauche and trans conformer mixture with ΔH = 158 cm^{-1}; (C) calculated infrared spectrum for the pure gauche conformer; and (D) calculated infrared spectrum for the pure trans conformer.



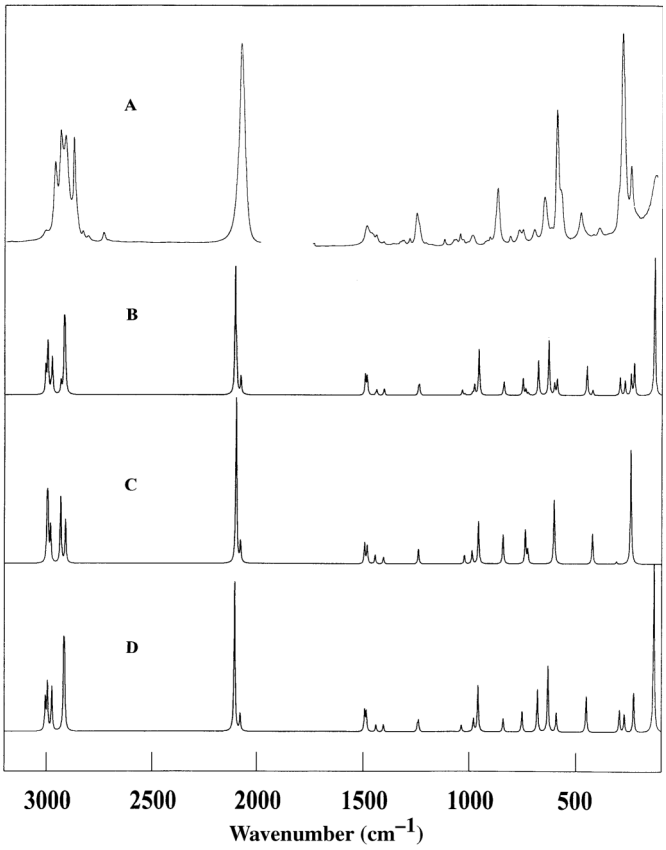
tra were recorded at a spectral resolution of 1.0 cm^{-1}. Typically, 256 scans were used for both the sample and reference data to give a satisfactory signal-to-noise ratio. The interferograms were averaged and then transformed with a boxcar truncation function. All observed infrared and Raman bands assigned as fundamentals are listed in Table 1.

Quantum-chemical calculations

LCAO-MO-SCF calculations were performed by using the Gaussian 98 program (18) with the Gaussian-type basis functions. The energy minima with respect to the nuclear coordinates were obtained by the simultaneous relaxation of all the geometric parameters using the gradient method of Pulay (19). DFT calculations utilizing the B3LYP method were also carried out up to the 6-311+G(2d,2p) basis set. The results of these ab initio calculations are listed in Table 2. All calculations except MP2 (full) and DFT calculations with the 6-31+G(d) basis set, both of which gave the trans conformer as the more stable form, predicted the gauche conformer to be more stable. From either MP2 (full) or DFT calculations with large basis sets such as 6-311G(d) or even larger ones, the conformational energy differences vary little, from 112 to 182 cm^{-1} and from 40 to 56 cm^{-1}, respectively, with the basis sets from 6-311G(d) up to 6-311+G(2d,2p). In addition, structural parameters were ob-

© 2004 NRC Canada

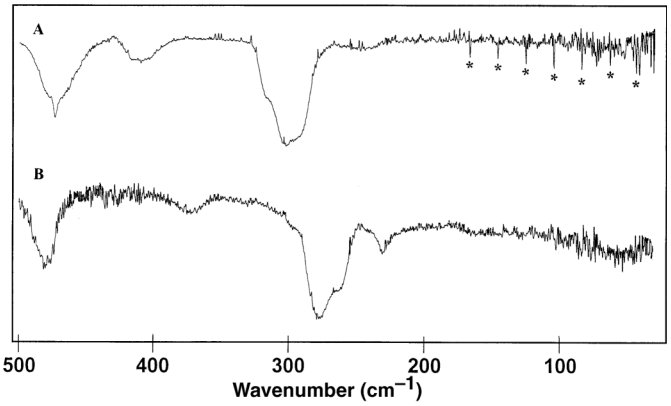
Fig. 3. (A) Raman spectrum of liquid ethyl bromogermane; (B) simulated Raman spectrum of the gauche and trans conformer mixture with ΔH = 158 cm^{-1}; (C) calculated Raman spectrum for the pure gauche conformer; and (D) calculated Raman spectrum for the pure trans conformer.



tained from restricted Hartree–Fock (RHF) calculations with the 6-31G(d) basis set as well as with full electron correlation with Møller–Plesset perturbation at the second order (MP2) with the 6-31G(d), 6-311+G(d,p), and 6-311+G(2d,2p) basis sets. The results of these calculations are listed in Table 3.

For the normal coordinate analysis, the force field in Cartesian coordinates was obtained with the Gaussian 98 program (18) from the MP2/6-31G(d) calculations. The complete set of internal coordinates is shown in Fig. 5, which was used to form the symmetry coordinates listed in Table 4. The **B**-matrix elements were used to convert the ab initio force field in Cartesian coordinates to the force field in the desired internal coordinates (20). The resulting force fields for the *t*rans and gauche conformers are available from the authors. These force fields were used in a mass-weighted Cartesian coordinate calculation to reproduce the ab initio vibrational frequencies and to determine the potential energy distributions (P.E.D.), which are given in Table 1. The diagonal and off-diagonal elements of the force field in internal coordinates were then assigned scaling factors of 0.88 for the CH stretches and 0.9 for the CH bends and heavy-atom stretches; the other coordinates were not scaled. The geometric average was used for the off-diagonal elements. The calculation was repeated to obtain the fixed-scale force field and scaled vibrational frequencies.

Fig. 4. Far-infrared spectra (30 to 500 cm^{-1}) of ethyl bromogermane: (A) gas; (B) annealed solid. Bands marked with an asterisk are due to HCl impurity.



The theoretical Raman (Fig. 3) and infrared spectra (Fig. 2) have been calculated using the scaled wavenumbers, Raman scattering activities, and infrared intensities determined from the MP2/6-31G(d) ab initio calculations. The Raman scattering cross sections, $\partial\sigma_j/\partial\Omega$, which are proportional to the Raman intensities, can be calculated from the scattering activities and the predicted wavenumber for each normal mode (21–24). To obtain the polarized Raman scattering cross sections, the polarizabilities are incorporated into S_j by $S_j[(1 - \rho_j)/(1 + \rho_j)]$, where ρ_j is the depolarization ratio of the *j*th normal mode. The Raman scattering cross sections and calculated frequencies were used, together with a Lorentzian function, to obtain the calculated spectrum. The predicted Raman spectra of the gauche and trans conformers are shown in Figs. 3C and 3D, respectively. Figure 3B is a simulated spectrum of the mixture of the two conformers for the determined ΔH of 158 cm^{-1} (see *Conformational stability* section) with the gauche conformer the more stable rotamer. This spectrum should be compared to the experimental Raman spectrum (Fig. 3A) of the liquid. The calculated spectrum has some differences from the experimental spectrum, especially in the relative intensities of the bands in the low-frequency region. Nevertheless, it provides support for the assignment of the observed bands to the indicated fundamentals to the correct conformers.

Infrared intensities were calculated based on the dipole moment derivatives with respect to the Cartesian coordinates. The derivatives were taken from the ab initio calculations (MP2/6-31G(d)) transformed to normal coordinates by

$$[1] \qquad \left(\frac{\partial \mu_u}{\partial Q_i}\right) = \sum_j \left(\frac{\partial \mu_u}{\partial X_j}\right) L_{ij}$$

where Q_i is the *i*th normal coordinate, X_j is the *j*th Cartesian displacement coordinate, and the L_{ij} are the elements of the transformation matrix between the Cartesian displacement coordinates and normal coordinates.

The predicted infrared spectra of the gauche and trans conformers are shown in Figs. 2C and 2D, respectively, and Fig. 2B is the simulated spectrum of the mixture of the two conformers. The calculated spectrum is in good agreement with the experimental spectrum of the sample dissolved in

© 2004 NRC Canada

Table 1. Calculated and observed infrared and Raman wavenumbers for ethyl bromogermane.

		gauche								
		Calcd. (cm^{-1})				Obs. (cm^{-1})				
						Infrared				
Vib. no.	Approximate description	Ab initio[a]	Fixed scaled[b]	IR int.[c]	Raman act.[d]	Gas	Krypton solution[e]	Solid	Raman	P.E.D.[f]
ν_1	CH_3 antisymmetric stretch	3203	3004	14.0	32.9	2980	2974	—	2977	59 S_1, 37 S_2
ν_2	CH_3 antisymmetric stretch	3192	2994	20.4	58.7	2970	2965	2958	2962	61 S_2, 31 S_1
ν_3	CH_2 antisymmetric stretch	3169	2973	1.2	88.4	2944	2939	2930	2935	87 S_3
ν_4	CH_2 symmetric stretch	3110	2917	8.1	79.9	2925	2913	2915	2914	94 S_4
ν_5	CH_3 symmetric stretch	3106	2913	17.7	122.4	2887	2881	2871	2876	98 S_5
ν_6	GeH_2 antisymmetric stretch	2107	2106	110.2	117.3	2097	2096	2107	2105	80 S_6, 20 S_7
ν_7	GeH_2 symmetric stretch	2080	2079	91.4	158.6	2087	2085	2089	2081	80 S_7, 20 S_6
ν_8	CH_3 antisymmetric deformation	1573	1492	8.2	17.4	1470	1465	1460	1457	75 S_8, 16 S_9
ν_9	CH_3 antisymmetric deformation	1564	1484	4.6	13.4	1463	1461	1456	1439	77 S_9, 16 S_8
ν_{10}	CH_2 deformation	1516	1439	3.4	12.3	1421	1417	1411	1413	95 S_{10}
ν_{11}	CH_3 symmetric deformation	1480	1404	3.3	4.2	1383	1384	1378	1382	96 S_{11}
ν_{12}	CH_2 wag	1310	1243	1.1	4.1	1270	1264	1261	1260	36 S_{12}, 26 S_{13}, 15 S_{15}, 10 S_{16}
ν_{13}	CH_2 twist	1304	1238	4.8	3.2	1221	1215	1219	1216	27 S_{13}, 32 S_{12}, 17 S_{15}
ν_{14}	CC stretch	1090	1038	14.6	5.6	1029	1030	1028	1028	55 S_{14}, 33 S_{16}
ν_{15}	CH_3 rock	1030	981	20.7	2.8	977	976	974	972	39 S_{15}, 41 S_{13}
ν_{16}	CH_3 rock	1009	956	2.7	4.9	968	967	965	969	33 S_{16}, 34 S_{14}, 26 S_{12}
ν_{17}	GeH_2 deformation	885	885	73.8	17.1	864	862	848	856	100 S_{17}
ν_{18}	GeH_2 wag	793	778	146.5	5.3	773	773	754	766	53 S_{18}, 30 S_{19}, 12 S_{15}
ν_{19}	CH_2 rock	716	700	33.3	6.1	690	691	690	687	29 S_{19}, 40 S_{18}, 15 S_{20}
ν_{20}	GeH_2 twist	663	652	1.3	8.3	654	655	641	640	56 S_{20}, 16 S_{19}, 12 S_{21}
ν_{21}	CGe stretch	623	599	10.7	13.9	580	581	585	580	62 S_{21}, 18 S_{20}
ν_{22}	GeH_2 rock	475	471	18.8	4.1	472	475	478	473	75 S_{22}, 10 S_{21}
ν_{23}	GeBr stretch	310	297	21.8	5.1	303	—	277	279	69 S_{23}, 19 S_{24}
ν_{24}	CH_3 torsion	278	267	6.2	1.8	—	262*	262	—	42 S_{24}, 31 S_{23}, 16 S_{25}
ν_{25}	CCGe bend	233	231	0.4	1.2	230	—	230	230	52 S_{25}, 26 S_{24}
ν_{26}	CGeBr bend	136	136	0.8	2.0	—	—	140	130	73 S_{26}, 12 S_{25}
ν_{27}	Antisymmetric torsion	75	75	0.3	0.8	—	—	—	—	84 S_{27}

[a]Calculated with the MP2/6-31G* basis set.
[b]Scaled ab initio calculations with factors of 0.88 for CH stretches, 0.9 for CH bends and heavy-atom stretches, and 1.0 for all other modes using the MP2/6-31G* basis set.
[c]Calculated infrared intensities in km/mol.
[d]Calculated Raman activities in $Å^4$/amu.
[e]Values marked with an asterisk are from the spectrum of an amorphous sample.
[f]Values less than 10% are omitted.

krypton (Fig. 2A) with the major differences being in the intensity of the bands located at 976, 743, and 691 cm^{-1}.

Results

Vibrational assignment

The nearly complete vibrational assignment for the gauche conformer and partial assignment for the trans conformer of ethyl bromogermane are listed in Table 1. These assignments are based on the frequencies obtained from the ab initio calculations along with relative intensities and Raman activities. The previous assignment for ethyl chlorogermane (15) was also used in this study since most of the predicted wavenumbers for the fundamentals of ethyl bromogermane and ethyl chlorogermane are nearly the same, particularly for the CH_3 and CH_2 group frequencies. Therefore, only the assignment of the bands that have significantly different frequencies from the corresponding ones of the chloride will be discussed.

In the "fingerprint" region (Fig. 6), six predicted wavenumbers for the gauche conformer (1038, 981, 956, 885, 778, and 700 cm^{-1}) differ significantly from the correspond-

© 2004 NRC Canada

Table 1 (*concluded*).

		trans							
		Calcd. (cm^{-1})				Obs. (cm^{-1})			
						Infrared			
Vib. no.	Approximate description	Ab initio[a]	Fixed scaled[b]	IR int.[c]	Raman act.[d]	Gas	Krypton solution[e]	Raman	P.E.D.[f]
ν_1	CH_3 antisymmetric stretch	3194	2996	17.4	7.1				48 S_1, 52 S_3
ν_2	CH_3 antisymmetric stretch	3190	2992	19.1	102.6				99 S_2
ν_3	CH_2 antisymmetric stretch	3177	2980	2.5	88.4				48 S_3, 52 S_1
ν_4	CH_2 symmetric stretch	3126	2932	4.1	65.4				99 S_4
ν_5	CH_3 symmetric stretch	3101	2909	20.8	118.2				100 S_5
ν_6	GeH_2 antisymmetric stretch	2100	2100	102.0	71.5				100 S_6
ν_7	GeH_2 symmetric stretch	2079	2079	80.5	174.5				100 S_7
ν_8	CH_3 antisymmetric deformation	1575	1494	10.1	21.3				91 S_8
ν_9	CH_3 antisymmetric deformation	1563	1482	3.2	13.3				94 S_9
ν_{10}	CH_2 deformation	1523	1445	2.3	11.4				96 S_{10}
ν_{11}	CH_3 symmetric deformation	1482	1406	3.1	5.6				97 S_{11}
ν_{12}	CH_2 wag	1308	1241	1.2	4.4		1233		69 S_{12}, 20 S_{16}
ν_{13}	CH_2 twist	1307	1241	0.9	4.0		1223	1227	54 S_{13}, 32 S_{15}
ν_{14}	CC stretch	1078	1025	36.1	2.9		1017	1015	58 S_{14}, 33 S_{16}
ν_{15}	CH_3 rock	1040	991	7.9	3.6		997	996	39 S_{15}, 41 S_{13}
ν_{16}	CH_3 rock	1010	958	7.6	5.1		948		33 S_{16}, 36 S_{14}, 26 S_{12}
ν_{17}	GeH_2 deformation	889	888	65.9	15.6		865		100 S_{17}
ν_{18}	GeH_2 wag	767	765	153.7	8.8	763	762	757	94 S_{18}
ν_{19}	CH_2 rock	778	749	21.3	4.3	743	743	740	56 S_{19}, 20 S_{15}, 18 S_{20}
ν_{20}	GeH_2 twist	636	631	3.9	7.8	591	588		75 S_{20}, 11 S_{22}, 11 S_{19}
ν_{21}	CGe stretch	637	607	24.7	12.6	591	588		81 S_{21}
ν_{22}	GeH_2 rock	444	442	12.1	1.1	408	403		73 S_{22}, 12 S_{24}
ν_{23}	GeBr stretch	326	314	30.8	3.9	315		300	65 S_{23}, 23 S_{25}
ν_{24}	CH_3 torsion	250	237	0.5	0.1				83 S_{24}
ν_{25}	CCGe bend	247	243	4.9	6.6			243	44 S_{25}, 21 S_{26}, 36 S_{23}
ν_{26}	CGeBr bend	94	94	0.4	2.1				78 S_{26}, 20 S_{25}
ν_{27}	Antisymmetric torsion	69	69	0.4	0.02				93 S_{27}

ing predicted ones for the trans conformer (1025, 991, 958, 888, 765, and 749 cm^{-1}), such that these differences should be easily identified in the experimental spectra. The 1050–1000 cm^{-1} portion of the spectrum of the sample in liquid krypton solution (Fig. 7) clearly shows that the band at 1030 cm^{-1} arises from the gauche conformer and that the 1017 cm^{-1} band arises from the trans form. In the region from 800 to 700 cm^{-1}, only three bands located at 773, 762, and 743 cm^{-1} were observed, matching the predicted ones at 778(g), 765(t), and 749(t) cm^{-1}, where g and t in the parentheses indicate the gauche and the trans conformer, respectively. The band at 691 cm^{-1} can undoubtedly be assigned to the predicted band at 700 cm^{-1} from the gauche conformer since this band is so isolated from other bands in the spectrum. For the region from 1000 to 800 cm^{-1}, since the predicted wavenumbers for both conformers are very close and since about 90% of the sample is in the gauche form in the liquid krypton solution (at about –125 °C), the bands observed at 976, 967, and 862 cm^{-1} are only assigned to the predicted frequencies at 981, 956, and 885 cm^{-1} arising from the gauche conformer. The bands below 650 cm^{-1} in the infrared spectrum of the krypton solution are difficult to assign because of the poor signal-to-noise ratio and some decomposition of the sample. However, the infrared spectrum of the amorphous solid and the Raman spectrum of the liquid (Fig. 8) give very clear indication that the bands in the spectrum of the amorphous solid at 641 and 585 cm^{-1} must arise from the gauche conformer and the band of 617 cm^{-1} from the trans form. Also, the bands at 479 and 461 cm^{-1} can confidently be assigned to the GeH_2 rocking (ν_{22}) fundamental from the gauche and trans conformers, respectively.

The assignments for all of the fundamentals in the low-frequency region (below 400 cm^{-1}) cannot be made since the bands for some of these modes have too low intensities to be

© 2004 NRC Canada

Table 2. Calculated energies and energy differences for several conformations of ethyl bromogermane by ab initio and hybrid DFT methods.

	Energy (E_h)	Energy differences (cm^{-1})				
Method/basis	Gss	Tss[a]	Css[a]	Sss[a]	Tes[b]	Ges[b]
RHF/6-31G(d)	–4723.002950	169				
MP2(full)/6-31G(d)	–4723.528706	292	924	852	1191	1204
MP2(full)/6-31+G(d)	–4723.568673	–33				
MP2(full)/6-311G(d,p)	–4728.935298	112				
MP2(full)/6-311+G(d,p)	–4728.938352	158				
MP2(full)/6-311G(2d,2p)	–4728.997578	159				
MP2(full)/6-311+G(2d,2p)	–4728.999907	182				
B3LYP/6-31G(d)	–4727.170111	188	771	606	1092	1086
B3LYP/6-31+G(d)	–4727.207484	–120				
B3LYP/6-311G(d)	–4731.646756	41				
B3LYP/6-311+G(d)	–4731.647818	40				
B3LYP/6-311G(d,p)	–4731.656822	48				
B3LYP/6-311+G(d,p)	–4731.657884	49				
B3LYP/6-311G(2d,2p)	–4731.655236	56				
B3LYP/6-311+G(2d,2p)	–4731.656183	56				

Note: Conformations are designated as follows. Capital letter refers to main skeletal torsional angle, CCGeBr: T, trans; G, gauche; C, cis; S, skew. The lower case letters refer to methyl torsional angles, staggered or eclipsed.

[a]Energies of conformations relative to Gss.

[b]Tes energy is relative to Tss and Ges energy is relative to Gss to obtain barriers to methyl rotation for the trans and gauche conformers, respectively.

observed. However, the GeBr stretch (ν_{23}), CH_3 torsion (ν_{24}), and CCGe bend (ν_{25}) can confidently be assigned for both conformers from the infrared spectrum of the gaseous sample or the Raman spectrum of the liquid. The large shift to lower frequency of the GeBr stretch in the condensed phases is similar to what is observed for two similar chlorides (15, 25). The CGeBr bend for the gauche conformer is observed at about 130 cm^{-1} in the Raman spectrum of the liquid, but the corresponding band for the trans conformer was not observed nor were those for the asymmetric torsion for either conformer. However, it is expected that the predicted values for these three modes should be relatively close to the frequencies for these modes.

Conformational stability

Although only a few bands disappeared from the infrared spectrum of the amorphous solid of ethyl bromogermane with annealings (Fig. 9), there was still evidence for the presence of a second conformer in the fluid phases. For example, the bands at 733, 617, and 462 cm^{-1} in the spectrum of the amorphous solid (Fig. 9A), which are assigned to the trans conformer, disappeared in the spectrum of the annealed solid (Fig. 9B). The observed band at 965 cm^{-1} in the spectrum of the amorphous solid (Fig. 9A) is predicted at 958 cm^{-1} for both the trans and gauche conformers, whereas the predicted infrared intensity of this mode is 6.6 km/mol for the trans form, compared with a much smaller value of 2.5 km/mol for the gauche form. Therefore, its intensity decreases significantly in the spectrum of the annealed solid.

From ab initio predicted wavenumbers, several conformer pairs at 1036(g)/1024(t), 752(g)/728(t), 680(g)/739(t), 631(g)/604(t), 592(g)/606(t), and 452(g)/425(t) cm^{-1} can be easily identified. However, many of these bands in the infrared spectrum of the krypton solution are overlapped and some are too weak to obtain accurate intensity measurements so they cannot be used for the conformational stability determinations. The exceptions are the fundamentals at 1030, 1017, 773, 743, and 691 cm^{-1}, which are sufficiently separated from other bands in the spectrum of the krypton solution and also have reasonable intensities that can be confidently used for the determination of the enthalpy difference between the two conformers.

Variable-temperature studies of the krypton solution were carried out to determine the enthalpy difference between the conformers of ethyl bromogermane. Infrared spectral data were collected at 10 different temperatures in the range from –105 to –150 °C. The peak areas of the 1030 cm^{-1} band arising from the gauche rotamer and the 1017 cm^{-1} band arising from the trans form (Fig. 7) were used for the intensity determinations, and the data for this conformer pair (Table 5) were fit to the equation $-\ln K = (\Delta H/RT) - (\Delta S/R)$, where K is the intensity ratio (I_g/I_t) times a constant, ΔS is the entropy change, and it is assumed that ΔH is not a function of temperature over the relatively small temperature range. The slope of the line obtained from a least-squares fit yielded a ΔH value for this conformer pair of 129 ± 8 cm^{-1} with the gauche conformer the more stable form. Additionally, it is very obvious from the spectra in Fig. 7 that as the temperature decreases, the intensity of the 1030 cm^{-1} band assigned to the gauche conformer increases relative to that of the band at 1017 cm^{-1} assigned to the trans form, showing conclusively that the gauche conformer is the more stable rotamer. Similar studies were also carried out for the two other conformer pairs at 773(g)/743(t) and 691(g)/743(t) cm^{-1}, which yielded ΔH values of 224 ± 10 and 118 ± 10 cm^{-1}, respectively, with again the gauche conformer the more stable form. The statistical average of the three ΔH values is 158 ± 11 cm^{-1} (1.89 ± 0.14 kJ/mol).

The above uncertainty value is the statistical uncertainty and does not take into account any underlying overtone or

© 2004 NRC Canada

Table 3. Structural parameters for ethyl bromogermane.

	RHF/6-31G(d)		MP2/6-31G(d)		MP2/6-311+G(d,p)		MP2/6-311+G(2d,2p)	
Parameter	gauche	trans	gauche	trans	gauche	trans	gauche	trans
Bond lengths (Å)								
$r(C_1—C_2)$	1.533	1.534	1.529	1.530	1.531	1.534	1.527	1.529
$r(C_2—Ge)$	1.942	1.941	1.931	1.930	1.943	1.943	1.941	1.941
r(Ge—Br)	2.325	2.323	2.324	2.320	2.326	2.323	2.334	2.331
$r(Ge—H_5)$	1.536	1.539	1.547	1.551	1.518	1.519	1.523	1.524
$r(Ge—H_6)$	1.540	1.539	1.553	1.551	1.519	1.519	1.524	1.524
$r(C_2—H_7)$	1.085	1.085	1.094	1.094	1.094	1.094	1.087	1.087
$r(C_2—H_8)$	1.087	1.085	1.096	1.094	1.096	1.094	1.089	1.087
$r(C_1—H_9)$	1.085	1.085	1.093	1.094	1.094	1.094	1.086	1.086
$r(C_1—H_{10})$	1.084	1.086	1.093	1.094	1.093	1.094	1.086	1.087
$r(C_1—H_{11})$	1.086	1.086	1.094	1.094	1.094	1.094	1.087	1.087
Bond angles (°)								
$\angle GeC_2C_1$	112.8	111.7	110.7	109.7	113.2	111.9	113.0	111.9
$\angle BrGeC_2$	108.3	109.0	107.2	109.7	107.5	108.6	107.1	108.3
$\angle H_5GeC_2$	113.5	112.5	115.1	112.1	113.4	112.3	113.8	112.4
$\angle H_6GeC_2$	112.3	112.5	111.7	112.1	112.3	112.3	112.5	112.4
$\angle H_7C_2C_1$	111.0	110.8	111.5	111.4	110.8	111.0	110.9	111.0
$\angle H_8C_2C_1$	110.6	110.8	111.2	111.4	110.8	111.0	110.9	111.0
$\angle H_9C_1C_2$	111.1	111.1	111.5	111.4	110.9	111.0	111.1	111.1
$\angle H_{10}C_1C_2$	111.0	111.4	110.6	111.2	111.0	111.4	111.0	111.5
$\angle H_{11}C_1C_2$	111.2	111.4	110.9	111.2	111.2	111.4	111.3	111.5
τC_1C_2GeBr	64.4	180.0	61.3	180.0	61.5	180.0	61.5	180.0
τH_5GeC_2Br	117.5	117.4	118.0	117.8	117.0	117.3	116.8	117.1
τH_6GeC_2Br	–116.2	–117.4	–115.0	–117.8	–115.7	–117.3	–115.7	–117.1
$\tau H_7C_2C_1Ge$	121.1	120.7	120.4	120.1	121.0	120.5	120.9	120.6
$\tau H_8C_2C_1Ge$	–120.5	–120.7	–120.0	–120.1	–120.2	–120.5	–120.5	–120.6
$\tau H_9C_1C_2Ge$	179.2	180.0	178.8	180.0	179.9	180.0	180.1	180.0
$\tau H_{10}C_1C_2H_9$	120.2	120.0	120.5	120.2	119.9	119.8	120.0	119.8
$\tau H_{11}C_1C_2H_9$	–120.1	–120.0	–120.4	–120.2	–120.0	–119.8	–120.0	–119.8
Rotational constants (MHz)								
A	4205	8686	4144	9016	4110	8580	4096	8476
B	1506	1131	1559	1133	1535	1133	1536	1133
C	1179	1026	1206	1033	1186	1026	1186	1025
Dipole moments (debye)								
$\lvert\mu_a\rvert$	2.697	2.814	2.683	2.800	2.890	2.995	2.822	2.952
$\lvert\mu_b\rvert$	0.299	0.101	0.244	0.165	0.486	0.069	0.402	0.035
$\lvert\mu_c\rvert$	0.247	0.000	0.278	0.000	0.184	0.000	0.188	0.000
$\lvert\mu_t\rvert$	2.725	2.816	2.708	2.805	2.937	2.996	2.856	2.952
–(*E*+4723)	0.002950	0.002178	0.528705	0.527375	5.938352	5.937634	5.999907	5.999079
ΔE (cm^{-1})		169		292		158		182

combination bands. Therefore, a more realistic uncertainty is 10%, which gives a value of 158 ± 16 cm^{-1} (1.89 ± 0.20 kJ/mol) for the enthalpy difference, with the gauche rotamer the more stable form. Thus, at ambient temperature, it is estimated that 81 ± 2% of the sample is in the gauche form.

Discussion

The experimentally determined enthalpy difference between the gauche and trans conformers of ethyl bromogermane is in excellent agreement with the predicted values obtained from the ab initio calculations with full electron correlation at the MP2 level, even with the relatively small 6-31G(d) basis set. In fact, there is only a small change in the predicted energy difference between the conformers in going from the 6-31G(d) basis set to the 6-311+G(2d,2p) basis set (82 vs. 187 functions). Although the experimental ΔH value seems low compared to the relative intensity of the fundamentals for the trans conformer, the ab initio predicted value indicates that the actual value should be within the experimentally indicated error limits.

The asymmetric torsional potential has been predicted from the ab initio calculations. Beginning at the minimum

© 2004 NRC Canada

Fig. 5. Internal coordinates for ethyl bromogermane.

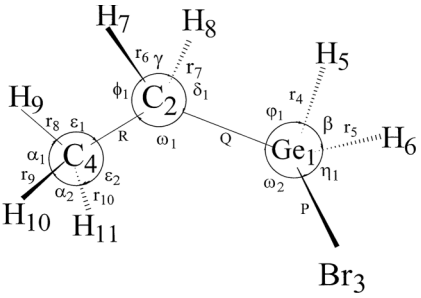
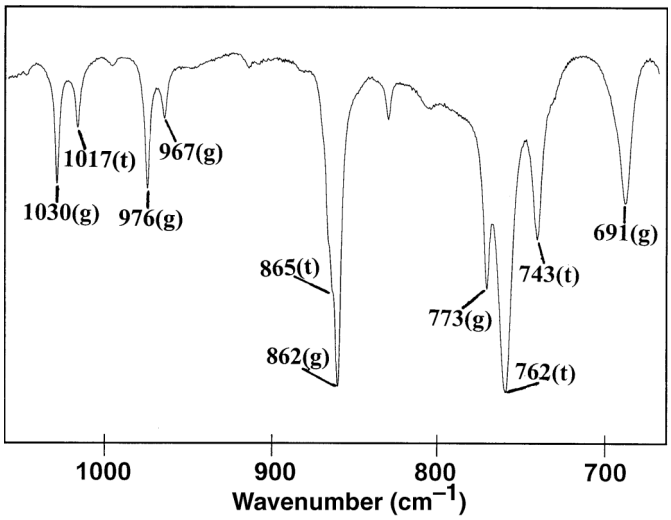


Fig. 6. Mid-infrared spectrum in the region of 1060–670 cm^{-1} of ethyl bromogermane in krypton solution at –125 °C.



for the trans conformer at zero, a potential function was initially determined by first calculating the energy every 30° with optimization of the structural parameters at each point from the MP2/6-31G(d) calculations. Both the minima and the maxima were determined with optimization, and the resulting potential function is shown as a dashed line in Fig. 10. With this basis set, the energy difference is 188 cm^{-1} between the more stable gauche conformer and the trans form. The torsional potential is represented as a Fourier cosine series in the internal angle (ϕ):

$$[2] \qquad V(\phi) = \sum_{i=1}^{6} (V_i/2)(1 - \cos i\phi)$$

The values for the potential terms V_1~V_4 and V_6 are presented in Table 6; the V_5 term is negligible. For this potential, the dihedral angle, CCGeBr, is 61.3°, and the gauche-to-gauche barrier of 924 cm^{-1} is much larger than the trans-to-gauche barrier of 560 cm^{-1} (Fig. 10). The potential function was also obtained from DFT calculations by the B3LYP method with the same basis set. Because the energy difference between the two conformers is much larger (292 cm^{-1}) in this case, the V_1 term is very small (–11 cm^{-1}) and the V_3 term is also much smaller (595 cm^{-1}) than the value obtained for the first potential. Also, the gauche-to-gauche barrier is predicted to be 771 cm^{-1} with a similarly smaller trans-to-gauche barrier of 418 cm^{-1}. This potential is also shown in Fig. 10 (solid line), and it is expected to be closer to the actual one since the predicted energy difference from the B3LYP calculations is closer to the experimentally determined ΔH value than that from the MP2 calculations.

Table 4. Symmetry coordinates for ethyl bromogermane.

Description	Symmetry coordinate
CH_3 antisymmetric stretch	$S_1 = r_9 - r_{10}$
CH_3 antisymmetric stretch	$S_2 = 2r_8 - r_9 - r_{10}$
CH_2 antisymmetric stretch	$S_3 = r_6 - r_7$
CH_2 symmetric stretch	$S_4 = r_6 + r_7$
CH_3 symmetric stretch	$S_5 = r_8 + r_9 + r_{10}$
GeH_2 antisymmetric stretch	$S_6 = r_4 - r_5$
GeH_2 symmetric stretch	$S_7 = r_4 + r_5$
CH_3 antisymmetric deformation	$S_8 = \alpha_1 - \alpha_3$
CH_3 antisymmetric deformation	$S_9 = 2\alpha_2 - \alpha_1 - \alpha_3$
CH_2 deformation	$S_{10} = 4\gamma - \phi_1 - \phi_2 - \delta_2 - \delta_1$
CH_3 symmetric deformation	$S_{11} = \alpha_1 + \alpha_2 + \alpha_3 - \varepsilon_1 - \varepsilon_2 - \varepsilon_3$
CH_2 wag	$S_{12} = \phi_1 + \phi_2 - \delta_1 - \delta_2$
CH_2 twist	$S_{13} = \phi_1 - \phi_2 - \delta_2 + \delta_1$
CC stretch	$S_{14} = R$
CH_3 rock	$S_{15} = \varepsilon_3 - \varepsilon_2$
CH_3 rock	$S_16 = 2\,\varepsilon_1 - \varepsilon_2 - \varepsilon_3$
GeH_2 deformation	$S_{17} = 4\beta - \varphi_1 - \varphi_2 - \eta_2 - \eta_1$
GeH_2 wag	$S_{18} = \varphi_1 + \varphi_2 - \eta_2 - \eta_1$
CH_2 rock	$S_{19} = \phi_1 - \phi_2 + \delta_2 - \delta_1$
GeH_2 twist	$S_{20} = \varphi_1 - \varphi_2 - \eta_2 + \eta_1$
CGe stretch	$S_{21} = Q$
GeH_2 rock	$S_{22} = \varphi_1 - \varphi_2 + \eta_2 - \eta_1$
GeBr stretch	$S_{23} = P$
CH_3 torsion	$S_{24} = \tau_1$
CCGe bend	$S_{25} = \omega_1$
CGeBr bend	$S_{26} = \omega_2$
Antisymmetric torsion	$S_{27} = \tau_2$

Note: Symmetry coordinates are not normalized. The symmetry coordinates S_1, S_3, S_6, S_8, S_{13}, S_{15}, S_{19}, S_{20}, S_{22}, S_{24}, and S_{27} are A′′ modes for the trans conformer.

The barrier to methyl rotation has been predicted from MP2(full)/6-31G(d) and B3LYP/6-31G(d) calculations for both conformers, and the values from the MP2 calculations are about 100 cm^{-1} higher than those from the B3LYP results. Also, there is only a minor difference between the barriers for the two conformers, with the one of 1204 cm^{-1} for the gauche rotamer from the MP2 calculations being 13 cm^{-1} higher than that for the trans form from the same calculations whereas the B3LYP predictions indicate that the barrier for the gauche conformer is 6 cm^{-1} lower than that for the trans form (Table 2). The torsional mode was observed at 262 cm^{-1} in the infrared spectrum of the solid for the gauche form, but the P.E.D. indicates that this mode is only 42% torsion with contributions of 31% from the Ge–Br stretch and 16% from the CCGe bend. Thus, the barrier of 1412 cm^{-1} predicted from this frequency is considerably higher than the predicted value from the MP2 calculation, which is probably closer to the actual value.

The mixing of the symmetry coordinates for the gauche conformer is not as extensive as one might expect for a molecule with no symmetry. The heavy mass of the germanium

© 2004 NRC Canada

Fig. 7. Temperature-dependent infrared spectra in the region of 1050–1000 cm^{-1} of ethyl bromogermane dissolved in liquid krypton.

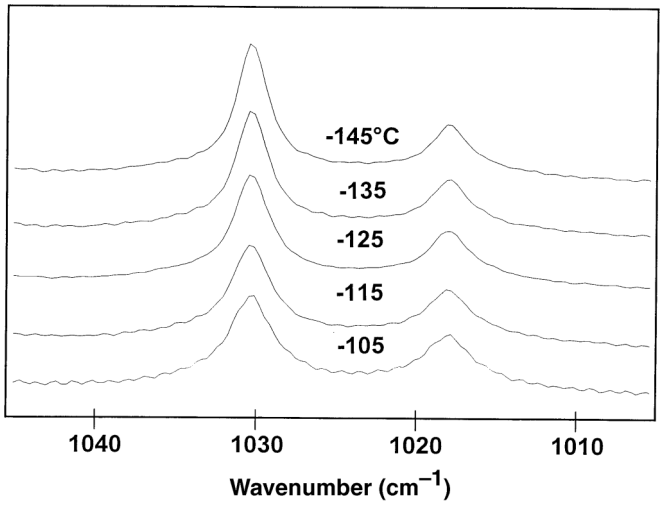
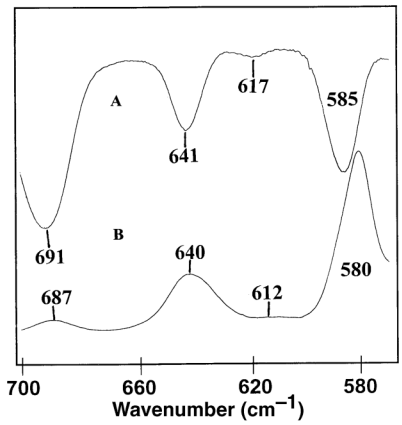


Fig. 8. Comparison of spectra of ethyl bromogermane in the region of 700-570 cm^{-1}: (A) infrared spectrum of amorphous sample; (B) Raman spectrum of liquid.



atom reduces significantly the mixing of the Ge–H bends with the C–H bends of the ethyl moiety except for the CH_2 rock and GeH_2 wag, which are heavily mixed. The mixing is even slightly less for the trans conformer, with more mixing of the CH_2 and CH_3 bending modes, which is probably due to the symmetry plane.

There is little difference in the ab initio predicted structural parameters for the two conformers. The only significant bond distance difference is that for the Ge—Br bond, which is predicted to be ~0.003 Å shorter for the trans conformer compared to the corresponding distance in the gauche form. The significant angle differences for the heavy atoms are those for the BrGeC angle, which is predicted to be 1.1° larger for the trans conformer, and the CCGe angle, which is predicted to be 1.3° smaller for the trans conformer compared to the corresponding angles for the gauche rotamer. These changes then result in the H_5GeC_2 angle being predicted to be 1.1° larger in the gauche conformer than the corresponding angle for the trans form. These angle differences then cause several of the force constants to have

Fig. 9. Mid-infrared spectra of ethyl bromogermane in the region of 1200–400 cm^{-1}: (A) amorphous solid; (B) annealed solid.

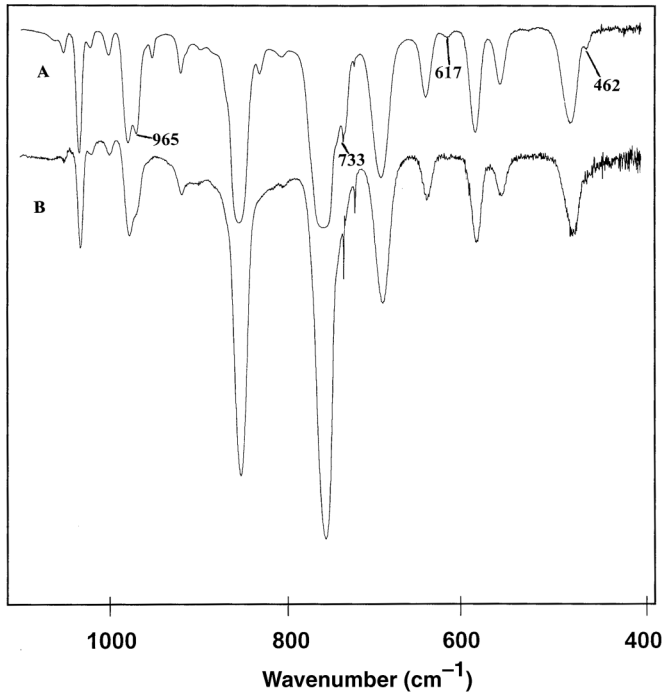
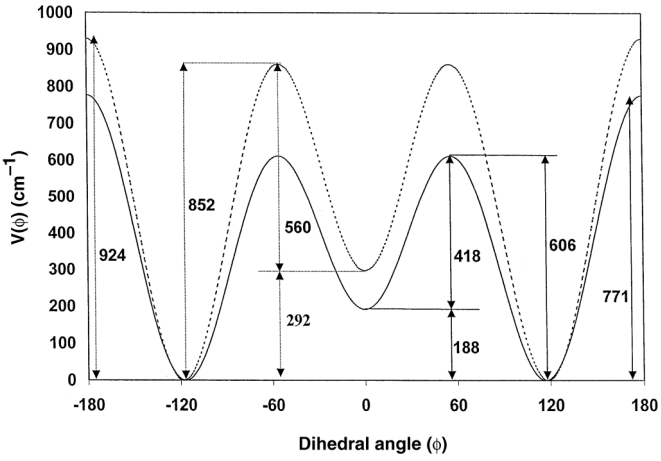


Fig. 10. Potential function governing conformational interchange of ethyl bromogermane determined from the MP2/6-31G(d) (dashed line) and B3LYP/6-31G(d) (solid line).calculations.



significantly different values. For example, the force constants for the deformations of the CGeBr, CCGe, $CGeH_6$, CCH_8, $BrGeH_5$, and $BrGeH_6$ angles are larger by 26.2, 19.0, 1.8, 2.4, 2.2, and 6.1%, respectively, for the gauche conformer compared to those for the trans rotamer, whereas the force constants for the deformations of the $CGeH_5$ and HGeH angles are larger by 3.5 and 2.2%, respectively, for the trans conformer. These differences produce some notable differences in the predicted frequencies for the normal modes associated with the motions involving the corresponding atom displacements.

Using two scaling factors of 0.88 for the CH stretches and 0.90 for the CH bends and heavy-atom stretches, the wavenumbers for the fundamentals predicted from the MP2/6-

© 2004 NRC Canada

Table 5. Temperature and infrared intensity ratios from the conformational study of ethyl bromogermane in krypton solution and resulting values for the enthalpy difference between the gauche and trans conformers.

T (°C)	1000/T (K^{-1})	$I_{773(g)}/I_{743(t)}$	$I_{691(g)}/I_{743(t)}$	$I_{1030(g)}/I_{1017(t)}$
–105	5.95	0.4768	1.6982	—
–110	6.15	—	—	1.8180
–115	6.32	0.5262	1.7465	1.9696
–120	6.53	0.5842	1.7982	2.0420
–125	6.75	0.6266	1.7879	2.1366
–130	6.98	0.7011	1.9364	2.1970
–135	7.24	0.7458	2.0660	2.2514
–140	7.51	0.8220	2.2270	2.4181
–145	7.80	0.8666	2.2890	2.4848
–150	8.13	0.9382	2.3293	2.7628
ΔH^a (cm^{-1})	—	224±10	118±10	129±8

[a]The average value of ΔH is 158 ± 11 cm^{-1} (1.89 ± 0.14 kJ/mol) with the gauche conformer the more stable form.

Table 6. Potential coefficients (cm^{-1}) and barriers (cm^{-1}) for the conformational interchange of ethyl bromogermane.

Parameter	B3LYP/6-31G(d)	MP2/6-31G(d)
V_1	–11	–145
V_2	–224	–237
V_3	595	777
V_4	–15	–14
V_6	—	7
trans-to-gauche barrier	418	560
gauche-to-gauche barrier	771	924
gauche-to-trans barrier	606	852
Energy difference	188	292
gauche dihedral angle $\tau(C_1C_2Ge_3Br_4)$	62.7°	61.3°

31G(d) calculations are in good agreement with the observed values. The average error in the frequency predictions for the normal modes is 13.3 cm^{-1} for the gauche conformer, which represents an average 1.0% error. Thus, these two scaling factors are sufficient to predict the wavenumbers for the observed fundamentals for this type of organogermane molecule, and these predictions then can be used for making vibrational assignments and identifying the correct modes for two different conformers.

The structural parameters obtained from the MP2/6-311+G(d,p) calculations predict the r_0 values for hydrocarbons with a bromine atom very well (26), as do those for many silanes (27–30). Therefore, it is expected that the predicted bond distances from the MP2/6-311+G(d,p) calculations for ethyl bromogermane should be within 0.005 Å of the actual values, except for the Ge–Br distance, which is expected to be predicted too long, as well as possibly the Ge–H distance. For example, the ab initio MP2/6-311+G(d,p) predictions for Si–H distances are too long by 0.007 Å compared to values obtained for this distance from isolated Si–H stretching frequencies (31). Similarly, the predicted angles are expected to be within one-half of a degree of the actual angles, with the exception of the gauche dihedral angle.

To evaluate how well the ab initio MP2/6-311+G(d,p) calculations predict the Ge–H and Ge–Br distances, we carried out structural calculations for some organogermanes for which these parameters are known. For example, the Ge–H distance of germane, GeH_4, was calculated, and the predicted value of 1.517 Å is smaller by 0.008 Å than the experimentally determined value (32) of 1.5251 ± 0.0005 Å (Table 7). As a check, similar calculations were also carried out for methyl germane, CH_3GeH_3 (15). This molecule is a symmetric top, and the initial structural parameters obtained from a microwave study (33) have larger error limits than indicated based on the distances obtained (34) from the frequencies of the "isolated" C–H and Ge–H stretching vibrations. In the latter study (34), the authors pointed out the problem with the parameters previously proposed for methyl germane, particularly the r_s parameter of 1.083 Å for the C–H distance, which was the preferred value (33). The ab initio predictions (15) from the MP2/6-311+G(d,p) calculations agreed reasonably well with the new proposed parameters (34). The predicted Ge–H distance is too short by 0.006 Å and the two angles are too small by 0.3°, but the predicted Ge–C distance of 1.949 Å is the same as the experimental value (34) of 1.949(1) Å. However, a similar prediction for this parameter (Ge–C distance) for ethyl germane (15) gave a value of 1.955 Å compared to an experimental value of 1.959(5) Å, which may indicate that the predicted value is a little short.

Therefore, we have carried out a determination of the adjusted r_0 parameters for methyl bromogermane, CH_3GeH_2Br, using a new program that we developed in this laboratory (35) by combining the previously reported microwave data

© 2004 NRC Canada

Table 7. Structural r_0 parameters of some organogermanes.

	GeH_4		GeH_3Br			CH_3GeH_2Br			$CH_3CH_2GeH_2Br$[f]	
Parameter	Theory[a]	Exptl.[b]	Theory[a]	Exptl.[c]	This study[d]	Theory[a]	Exptl.[e]	This study[d]	gauche	trans
Bond lengths (Å)										
r(Ge—H_a)						1.517	1.519(9)	1.520(3)	1.521	1.522
r(Ge—H_s)	1.517	1.5251(5)	1.513	1.527(1)	1.519(3)				1.522	1.522
r(C—H)									1.094	1.094
r(C—H_a)						1.093	1.097(30)	1.093(2)	1.093	1.094
r(C—H_s)						1.091	1.100(12)	1.091(2)	1.094	1.094
r(Ge—C)						1.935	1.933(2)	1.933(3)	1.943	1.943
r(C—C)									1.531	1.534
r(Ge—Br)			2.314	2.297(1)	2.299(3)	2.323	2.308(2)	2.307(3)	2.311	2.308
Bond angles (°)										
∠HGeH	109.5	109.5				110.9	111.9(2)	110.8(5)	111.2	110.5
∠H_aGeC						112.9	112.6(3)	113.0(5)	113.4	112.3
∠H_sGeC									112.3	112.3
∠H_sCGe						109.9	110.3(47)	110.0(5)	107.6	107.8
∠HCGe						110.0	111.9(17)	110.1(5)	107.0	107.8
∠HCH						108.9	107.3	108.8(5)	107.0	107.1
∠H_sCC									110.8	111.0
∠H_aCC									110.9	111.4
∠H_aCH_s						109.0	108.0	108.9(5)	107.9	107.6
∠HGeBr									105.6	106.4
∠HGeBr			107.0	106.2(1)	106.8(2)	106.0	106.3	106.0(5)	106.2	106.4
∠CGeBr						107.7	107.3(1)	107.4(5)	107.5	108.6
∠CCGe									113.2	111.9

[a]This study from MP2/6-311+G(d,p) calculations; values in parentheses for experimental parameters are the statistical uncertainties.
[b]Reference 32.
[c]Reference 38.
[d]Obtained from adjusted ab initio predictions using the previously reported microwave rotational constants.
[e]Reference 37.
[f]From MP2/6-311+G(d,p) with adjusted GeH and GeBr distances.

of the values of the rotational constants for several isotopomers (36) and the ab initio predicted parameters. This A&M program fits the rotational constants, with the structural parameters remaining close to the ab initio values. To reduce the number of independent variables, the structural parameters are separated into sets according to their type. Each set uses only one independent parameter in the optimization, and all structural parameters in one set are adjusted by the same adjustment factor. The differences between similar parameters in one set are adjusted by the same adjustment factor. The differences between similar parameters from the ab initio calculations are retained in the final results. Bond lengths in the same set keep their relative ratio in distances, and bond angles and torsional angles in the same set keep their differences in degrees. This assumption is based on the fact that errors from ab initio calculations are systematic.

Among the structural parameters for methyl bromogermane, the major questionable ones are the C–H distances of 1.100 ± 0.012 Å (C–H_s) and 1.097 ± 0.030 Å (C–H_a), which have extremely large uncertainties, and possibly the Ge–C distance of 1.933(2) Å, which seems a little short compared to this distance in methyl germane and ethyl germane (15). We have utilized the rotational constants (36) for the six isotopomers, which include ^{70}Ge, ^{72}Ge, and ^{74}Ge, ^{12}C, and ^{79}Br and ^{81}Br, along with the predicted parameters from the ab initio MP2/6-311+G(d,p) calculation. The fit of 21 of these rotational constants by the adjustment of the ab initio parameters is shown in Table 8, with all of the *B* and *C* rotational constants fit to less than one-tenth of a megahertz. There was a very large uncertainty for the *A* rotational constants (average uncertainty of 3.8 MHz) since only a-type transitions were assigned and their observed frequencies are not very dependent on the *A* rotational constant. Nevertheless, the differences between the experimental and predicted values are well within the expected uncertainties of these constants. The adjusted r_0 parameters, which are listed in Table 7, have C–H distances with normal values of 1.091 (in-plane) and 1.093 Å (out-of-plane) and a Ge–H distance of 1.520 Å. The Ge–Br distance is only slightly smaller than the previously reported value (36). We believe the C–H and Ge–H distances should not be in error by more than 0.002 and 0.003 Å, respectively, and the heavy-atom distances by 0.003 Å, with estimated error limits on the angles of 0.5°.

We have evaluated the ab initio predicted value for the Ge–Br distance using the germyl bromide molecule, for which the distances have been reported (37). From this calculation, the Ge–Br distance is predicted too long by 0.015 Å, and the Ge–H distance too short by 0.008 Å. All of these data indicated that the ab initio MP2/6-311+G(d,p) predictions for the Ge–H bond distances should be slightly too

© 2004 NRC Canada

Table 8. Comparison of rotational constants (MHz) obtained from ab initio structural parameters and fit to the microwave-determined rotational constants of bromogermane and methyl bromogermane.

	Bromogermane				Methyl bromogermane			
Rotational constant	Isotopomer	Obs.	Calcd.	Δ	Isotopomer	Obs.	Calcd.	Δ
A					$^{12}CH_3{}^{74}GeH_2{}^{79}Br$	10 551.95	10 553.28	–1.33
B	$^{70}GeH_3{}^{79}Br$	2438.48	2438.52	–0.04		1 895.13	1 895.13	0.00
C						1 655.21	1 655.21	0.00
A					$^{12}CH_3{}^{72}GeH_2{}^{79}Br$	10 609.28	1 0613.45	–4.17
B	$^{70}GeH_3{}^{81}Br$	2410.11	2410.12	–0.01		1 908.42	1 908.42	0.00
C						1 666.83	1 666.83	0.00
A					$^{12}CH_3{}^{70}GeH_2{}^{79}Br$	10 675.26	10 676.78	–1.52
B	$^{72}GeH_3{}^{79}Br$	2406.35	2406.34	0.01		1 922.13	1 922.18	–0.05
C						1 678.89	1 678.89	0.00
A					$^{12}CH_3{}^{74}GeH_2{}^{81}Br$	10 549.93	10 548.29	1.64
B	$^{72}GeH_3{}^{81}Br$	2377.95	2377.91	0.04		1 871.78	1 871.74	0.04
C						1 637.22	1 637.22	0.00
A					$^{12}CH_3{}^{72}GeH_2{}^{81}Br$	10 610.57	10 608.41	2.16
B	$^{74}GeH_3{}^{79}Br$	2375.82	2375.74	0.08		1 885.15	1 885.13	0.02
C						1 648.91	1 648.92	–0.01
A					$^{12}CH_3{}^{70}GeH_2{}^{81}Br$	10 674.95	10 671.70	3.25
B	$^{74}GeH_3{}^{81}Br$	2347.40	2347.29	0.11		1 899.00	1 898.99	0.01
C						1 661.04	1 661.05	–0.01

short (0.005 Å) for this bond whereas the Ge–Br distances will be significantly longer (0.015 Å) than the actual distance.

We have predicted the r_0 structural parameters for ethyl bromogermane by decreasing the Ge–Br distance by 0.015 Å from the predicted value from the MP2/6-311+G(d,p) calculations. The Ge–H distances are increased by 0.004 Å whereas the remaining parameters are the same as the predicted values. Therefore, a microwave study of ethyl bromogermane would be of interest to determine the Ge–Br bond distance as well as the other structural parameters to evaluate the quality of the MP2/6-311+G(d,p) ab initio predictions for this organobromogermane molecule. Since at ambient temperature 19 ± 2% of the sample is predicted to be the trans conformer, it should be possible to assign the microwave spectra for both conformers.

Acknowledgement

J.R. Durig acknowledges the University of Missouri-Kansas City for a Faculty Fellowship award for partial financial support of this research.

References

1. G.A. Guirgis, X. Zhu, and J.R. Durig. Struct. Chem. **10**, 445 (1999).
2. J.R. Durig, X. Zhu, and S. Shen. J. Mol. Struct. **570**, 1 (2001). J.R. Durig, J. Liu, T.S. Little, and V.F. Kalasinsky. J. Phys. Chem. **96**, 8224 (1992).
3. W.A. Herrebout and B.J. van der Veken. J. Phys. Chem. **100**, 9671 (1996).
4. J.R. Durig, R.R. Hester, and J.B. Robb II. J. Mol. Struct. **500**, 293 (2000).
5. W.A. Herrebout, B.J. van der Veken, A. Wang, and J.R. Durig. J. Phys. Chem. **99**, 578 (1995).
6. J.R. Durig, Y.E. Nashed, J. Tao, and G.A. Guirgis, J. Mol. Struct. **560**, 39 (2001).
7. T.A. Mohamed, G.A. Guirgis, Y.E. Nashed, and J.R. Durig. Struct. Chem. **10**, 333 (1999).
8. D.L. Powell, P. Klaeboe, A. Grudis, C.J. Nielsen, G.A. Guirgis, J.R. Durig, and V. Aleksa. J. Mol. Struct. **482/483**, 391 (1999).
9. G.A. Guirgis, C. Pan, S. Shen, and J.R. Durig. Struct. Chem. **12**, 445 (2001).
10. G.A. Guirgis, C. Pan, and J.R. Durig. J. Raman Spectrosc. **33**, 677 (2002).
11. H. Matsuura, K. Ohno, T. Sato, and H. Murata. J. Mol. Struct. **52**, 13 (1979).
12. J.R. Durig, C. Pan, and G.A. Guirgis. Spectrochim. Acta Part A, **59,** 979 (2003).
13. R.J. Ouellette. J. Am. Chem. Soc. **94**, 7674 (1972).
14. J.R. Durig, C. Pan, and G.A. Guirgis. J. Mol. Struct. **607**, 117 (2002).
15. C. Møller and M.S. Plesset. Phys. Rev. **46**, 618 (1934).
16. K. Furic and J.R. Durig. Appl. Spectrosc. **42**, 175 (1988).
17. M.J. Frisch, G.W. Trucks, H.B. Schlegel, G.E. Scuseria, M.A. Robb, J. Cheeseman, V. Zakrzewski, J. Montgomery Jr., R. Stratmann, J.C. Burant, S. Dapprich, J.M. Millam, A.D. Daniels, K.N. Kudin, M.C. Strain, O. Farkas, J. Tomasi, V. Barone, M. Cossi, R. Cammi, B. Mennucci, C. Pomelli, C. Adamo, S. Clifford, J. Ochterski, G.A. Petersson, P.Y. Ayala, Q. Cui, K. Morokuma, D.K. Malick, A.D. Rabuck, K. Raghavachari, J.B. Foresman, J. Cioslowski, J.V. Ortiz, B.B. Stefanov, G. Liu, A. Liashenko, P. Piskorz, I. Komaromi, R. Gomperts, R.L. Martin, D.J. Fox, T. Keith, M.A. Al-Laham, C.Y. Peng, A. Nanayakkara, M.W. Wong, J.L. Andres, C. Gonzalez, M. Challacombe, P.M.W. Gill, B. Johnson, W. Chen, M. Head-Gordon, E.S. Replogle, and J.A. Pople. Gaussian 98 (Re-

© 2004 NRC Canada

vision A.6) [computer program], Gaussian Inc., Pittsburgh, Pa. 1998.
18. P. Pulay. Mol. Phys. **17,** 197 (1969).
19. G.A. Guirgis, X. Zhu, Z. Yu, and J.R. Durig. J. Phys. Chem. A, **104**, 4383 (2000).
20. M.J. Frisch, Y. Yamaguchi, J.F. Gaw, H.F. Schaefer III, and J.S. Binkley. J. Chem. Phys. **84**, 531 (1986).
21. R. D. Amos. Chem. Phys. Lett. **124**, 376 (1986).
22. P.L. Polavarapu. J. Phys. Chem. **94**, 8106 (1990).
23. G.W. Chantry. *In* The Raman Effect. Vol. 1. *Edited by* A. Anderson. Marcel Dekker, New York. 1971. Chap. 2.
24. G.K. Barker, J.E. Drake, R.T. Hemmings, and B. Rapp. Spectrochim. Acta Part A, **28**, 1113 (1972).
25. J.R. Durig, X. Zhu, and S. Shen. J. Mol. Struct. **570**, 1 (2001).
26. G.A. Guirgis, Y.E. Nashed, J.B. Robb II, and J.R. Durig. J. Mol. Struct. **446**, 15 (1986).
27. T.A. Mohamed, G.A. Guirgis, Y.E. Nashed, and J.R. Durig. Struct. Chem. **9**, 255 (1998).
28. T.A. Mohamed, G.A. Guirgis, Y.E. Nashed, and J.R. Durig. Struct. Chem. **10**, 333 (1999).
29. J.R. Durig, Y.E. Nashed, M.A. Qtaitat, and G.A. Guirgis. J. Mol. Struct. **525**, 191 (2000).
30. J.L. Duncan, J.L. Harvie, D.C. McKean, and S. Cradock. J. Mol. Struct. **145**, 225 (1986).
31. H.W. Kattenberg, W. Gabes, and A. Oskam, J. Mol. Spectrosc. **44**, 425 (1972).
32. V.W. Laurie. J. Chem. Phys. **30**, 1210 (1959).
33. D.C. McKean, M.W. Mackenzie, and A.R. Morrisson. J. Mol. Struct. **116**, 331 (1984).
34. B.J. van der Veken, W.A. Herrebout, D.T. Durig, W. Zhao, and J.R. Durig. J. Phys. Chem. A, **103**, 1976 (1999).
35. J.R. Durig, J.F. Sullivan, A.B. Mohamad, S. Cradock, and Y.S. Li. J. Chem. Phys. **84**, 5796 (1986).
36. J.R. Durig, A.B. Mohamad, P.L. Trowell, and Y.S. Li. J. Chem. Phys. **75**, 2147 (1981).

© 2004 NRC Canada

Temporal evolution of an ultrathin, noncrystalline ice deposit at crystallization near 160 K studied by FT-IR reflection–absorption spectroscopy[1]

S. Mitlin and K.T. Leung

Abstract: The temporal evolution of the OH stretching modes of a noncrystalline ice deposit upon annealing followed by crystallization near 160 K has been investigated by FT-IR reflection–absorption spectroscopy. Using the earlier theoretical results from Whalley (E. Whalley. Can. J. Chem. **55**, 3429 (1977)) and from Buch and Devlin (V. Buch and J.P. Devlin. J. Chem. Phys. **110**, 3437 (1999)), the most prominent changes in these modes have been characterized for the first time. A dynamical picture of the structural transformation during crystallization has been developed, and it supports the observation that crystallization proceeds directly from a noncrystalline to a crystalline state without any long-lived intermediate state structurally different from its noncrystalline predecessor.

Key words: crystallization, noncrystalline ice, FT-IR reflection–absorption spectroscopy, temporary evolution.

Résumé : Faisant appel à la spectroscopie de réflexion–absorption infrarouge à transformée de Fourier, on a étudié l'évolution en fonction du temps des modes d'élongation OH d'un dépôt de glace non cristalline soumise à un réchauffement puis à une cristallisation près de 160 K. Utilisant des résultats théoriques antérieurs de Whalley (E. Whalley. Can. J. Chem. **55**, 3429 (1977)) et d'autres de Buch et Devlin (V. Buch et J.P. Devlin. J. Chem. Phys. **110**, 3437 (1999)), on a pu caractériser les changements les plus importants dans ces modes pour la première fois. On a développé une image dynamique de la transformation de structure au cours de la cristallisation et elle est en accord avec l'observation que la cristallisation procède directement d'un état non cristallin à un état cristallin sans l'intermédiaire d'un état de longue durée qui serait différent d'un point de vue structural de son prédécesseur non cristallin.

Mots clés : cristallisation, glace non cristalline, spectroscopie de réflexion–absorption infrarouge à transformée de Fourier, évolution en fonction du temps.

[Traduit par la Rédaction]

Introduction

At cryogenic temperature, water medium exhibits both crystalline form, such as cubic Ic and hexagonal Ih arrangements, and noncrystalline (nc) form. For the nc-ice form, a number of distinct polyamorphs can be generally classified according to their density: the high-density amorph (HDA) with density $\rho > 1.1$ g cm^{-3} and the low-density amorph (LDA) with $\rho \sim 0.94$ g cm^{-3} (1–4). Physico-chemical properties of these two types of polyamorphs are known to be quite different, which suggests qualitative differences in the packing arrangements in their intrinsic local structures and in the arrangements of the network of hydrogen bonds (5). Using elastic neutron diffraction, Finney et al. (5) found structural similarities between the LDA and hexagonal ice and between HDA and liquid water. Furthermore, the observable bulk and surface properties of a particular nc-ice sample appear to depend critically on the preparation method and the post-growth history, as expected for the metastable states that are structurally unrelaxed. In particular, the inelastic neutron scattering measurements by Kolesnikov et al. (6) confirmed the dependence of the local structure of the LDA ice on the preparation method. Computer simulations (7–10) revealed that the LDA could exhibit a fractal structure with a large variation in the local density. However, the characteristic size of the intrinsic "building block" (or molecular cluster) of the fractal structure remains unknown.

The morphology of the nc-ice medium has also been found to depend on the preparation technique. In particular, by varying the direction of the incident (water) molecular beam, Stevenson at al. (11) observed a systematic change in the morphology of the vapour-deposited LDA ice films, which could accommodate nitrogen as much as 2700 m^2 g^{-1} at 22 K and 640 m^2 g^{-1} at 77 K, if prepared at glancing incidence. Large uptakes of argon and methane by the LDA ice films have also been reported recently by Dohlanek et al. (12), which similarly suggests the presence of a fractal, grassy-like structure for the low-temperature vapour-deposit, in agreement with the earlier studies of Mayer and Pletzer (13) and Laufer et al. (14) that support a morphologically porous medium for the LDA. As expected for fractal behaviour, the LDA appears to exhibit recurrent features on different length scales, from ~10 Å for a typical cluster size in the

Received 8 February 2004. Published on the NRC Research Press Web site at http://canjchem.nrc.ca on 31 August 2004.

S. Mitlin and K.T. Leung.[2] Department of Chemistry, University of Waterloo, Waterloo, ON N2L 3G1, Canada.

[1]This article is part of a Special Issue dedicated to the memory of Professor Gerhard Herzberg.

[2]Corresponding author (e-mail: tong@uwaterloo.ca).

 doi: 10.1139/V04-076 © 2004 NRC Canada

hydrogen-bonding network (8) to larger though yet-to-be-determined nanopores (13, 15), and to much larger mesoscopic features (14).

Crystallization of a LDA medium has been found to occur abruptly at a rapid rate over a narrow temperature range above 150 K (16). At a lower temperature, crystallization is too slow to be observed at a laboratory timescale, in spite of the metastable nature of nc ice with respect to its crystalline polymorphs. However, internal motions in these nc-ice structures have clearly been discernible below 130 K. In particular, on annealing thick LDA ice films vapour-deposited at 77 K, Hallbruker et al. (17) observed a rapid reduction in the surface area from several hundreds to 40 $m^2\ g^{-1}$ at 113 K, which was interpreted as the result of the collapse of micropores accompanied by significant exothermic effects. By hyperquenching the micrometer-sized water droplets at 140 K, Kohl et al. (16) were able to obtain LDA samples that exhibit no exothermic effects upon a small anneal, which leads us to suggest that just above the expected glass-to-liquid transition temperature, the hyperquenched nc-ice samples become substantially more homogeneous though remain primarily noncrystalline. By measuring the time dependence of the OH dangling-bond signal of vapour-deposited nc-ice films by FT-IR reflection–absorption spectroscopy (FT-IR–RAS), Zondlo et al. (18) showed that the collapse of the micropores occurs rapidly on a timescale of 10^3–10^4 s at a temperature as low as 105 K, indicative of plausible structural relaxation. By measuring the isotope intermixing, Smith and Kay (19) and Smith et al. (20) found the self-diffusion coefficient ($1 \times 10^{-16} - 1 \times 10^{-13}\ cm^2\ s^{-1}$) in the temperature range of 146–155 K for nc-ice films to be substantially larger than that of crystalline films. Furthermore, they also determined the apparent Arrhenius activation energy for diffusion in a crystalline film to be 14 kcal mol^{-1} and that in an amorphous film to be as high as 41 kcal mol^{-1}. These observations led them to favour the existence of supercooled liquid domains in the temperature range of 145–155 K, which lies between the onset of plausible glass-to-liquid transition in the LDA (135 K) (17) and the onset of crystallization (160 K). Thermal desorption studies by Dohnalek et al. (21, 22) revealed the difference in the desorption spectra of N_2 from the surfaces of nc- and crystalline-ice films and the dependence of the desorption spectra on the annealing history of the pore-less nc-ice films, both of which have been used to follow the crystallization kinetics. The crystallization of thin (15–150 bilayers) nc-ice films deposited on Pt (111) and on smooth crystalline ice films was found to be consistent with bulk nucleation and three-dimensional growth of the crystalline phase, except for very thin amorphous deposits on the crystalline-ice film that was found to crystallize by a two-dimensional substrate-induced growth mechanism. These studies appear to be in accord with the direct transformation of solid amorph to ice crystallites without the formation of an intermediate liquid-like amorphous state (22). In an earlier calorimetric work, MacFarlane and Angell (23) argued that the glass-to-liquid transition in nc ice should be above the crystallization onset at 160 K, because given the very large nucleation rate for water, the driving force towards crystallization (being proportional to the difference between the homogeneous nucleation temperature and the glass-to-liquid transition temperature) should be sufficiently large. In more recent studies, Velikov et al. (24) further argued that the glass-to-liquid transition should be above the onset of crystallization and have estimated the former transition temperature to be 165 K.

To date, there has been no direct spectral evidence for the presence of the glass-to-liquid transition before the onset of crystallization, although it is possible that no spectral difference in the OH stretching modes exist between the glass amorphous and liquid-like amorphous states. The present work examines the spectral evolution of the relevant OH stretching modes before and during crystallization of an nc-ice film by using FT-IR–RAS, with the goal to not only assign these spectral features with the vibrational modes in nc and polycrystalline (pc) ice films, but also correlate the spectral changes to the structural evolution.

Experimental details

The details of the experimental setup and procedures have been described elsewhere (25). Briefly, the FT-IR–RAS experiments were conducted in an ultrahigh vacuum (UHV) chamber evacuated to a base pressure better than 3×10^{-9} torr (1 torr = 133.322 4 Pa). Ice films were grown by water vapour deposition on an optically flat polycrystalline copper disk mounted on a four-motion manipulator. The copper substrate could be cooled to 120 K or annealed to a preset temperature (up to 400 K) by a resistance heater attached to the backside of the substrate. The substrate temperature was monitored by two K-type thermocouples separately fastened to the front surface of the copper disk, with the accuracy of the temperature measurement of ±1 K. Deposition of the ice films was performed by backfilling of the UHV chamber with vapours of H_2O (Millipore) or of D_2O (Isotech) with a small fraction of HDO by a variable leak valve. The liquid water samples were thoroughly degassed by several freeze–pump–thaw cycles prior to use. The deposition pressure was measured by an uncalibrated ionization gauge and held at 1×10^{-6} torr (1 torr = 133.322 4 Pa) unless stated otherwise.

The IR beam from a FT-IR spectrometer (Bruker Equinox 55) was directed to the target surface at ~83° from the surface normal by two external mirrors. The specularly reflected light was collected by another external focusing mirror positioned on the opposite side of chamber, and focused onto a mercury–cadmium–telluride detector. The entire optical path was purged with dry N_2 gas. Spectral data are represented in units of absorbance defined as $A = -\log(R/R_0)$, where R/R_0 is the ratio of reflectances with and without the ice film. In an attempt to elucidate the nature of the observed spectral changes with increasing film thickness, the Fresnel method applied to a triple-layer (vacuum–ice–metal) stratified medium (18, 26, 27) was used to simulate the FT-IR–RA spectra using optical constants for pc and nc ice available in the literature (28, 29). Details of our computational procedure have been given in our earlier work (25).

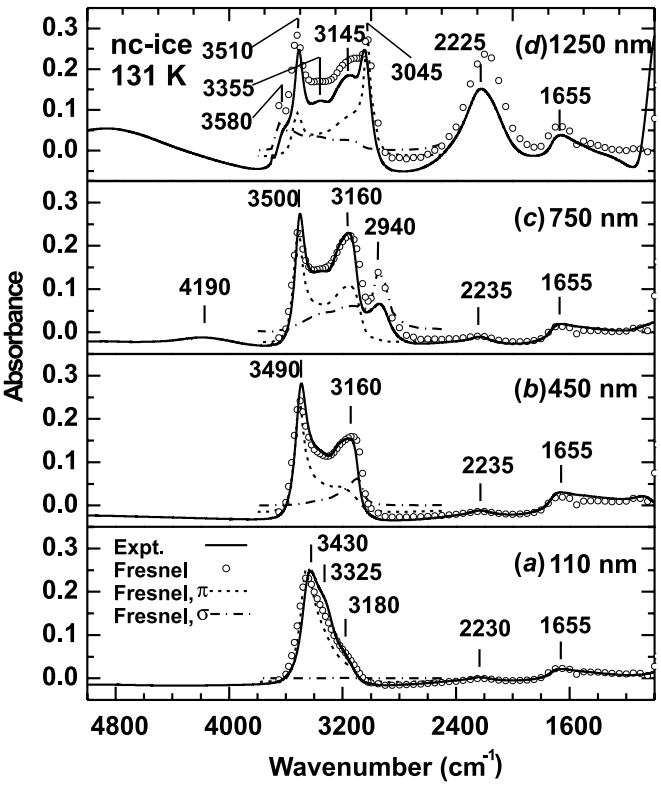
Results and discussion

The growth of pc- and nc-ice films by vapour deposition has been studied by FT-IR–RAS over a range of film thick-

© 2004 NRC Canada

ness from 10 to 1500 nm. In accord with earlier results (18, 25, 30), there are two established optical effects associated with the reflection–absorption of IR light in a stratified ice medium: (*i*) blue shift and profile deformation of the OH stretch (the strongest RA band in the ice spectrum) with respect to that obtained in the transmission mode, and (*ii*) optical interference in the smooth films. There is generally good agreement between the experimental spectra and the simulated Fresnel spectra of ice films for a wide range of thickness from 50 to 1500 nm. However, there are other possible spectral effects associated with the particle size and shape of the ice medium and with scattering from a rough film–vacuum interface, which are more difficult to characterize. These effects could become dominant in the present cases of interest, i.e., the early stage of deposition and during annealing and crystallization. The spectral effects associated with the size and shape of the constituent particles in the absorbing medium were investigated theoretically for finite-sized ionic crystals by Englman and Ruppin (31) and experimentally demonstrated for KCl films and crystals by Martin (32). Later, Buch and Devlin (33) provided a spectral simulation of the crystalline ice in the forms of a sphere and a slab, and illustrated that the OH stretching band strongly depends on not only the polarization of the light but also the shape of the absorbing medium. Following the theoretical treatment of Buch and Devlin (33) and the earlier spectral assignment of the OH stretch features by Whalley (34), we provide a detailed interpretation of the experimentally observed RA features of the OH band at the early stage of pc-ice formation and during crystallization of an ultrathin nc-ice deposit.

Fig. 1. Comparison of experimental FT-IR–RA spectra of noncrystalline (nc) ice films obtained by vapour deposition at 131 K for (*a*) 3.5 min, (*b*) 20.5 min, (*c*) 33.5 min at 1×10^{-6} torr, and (*d*) 11 min at 5×10^{-6} torr (1 torr = 133.322 4 Pa) with the corresponding Fresnel spectra for non-polarized light and their σ- and π-polarized components (arbitrarily normalized) involving 110, 450, 750, and 1200 nm thick films, respectively.



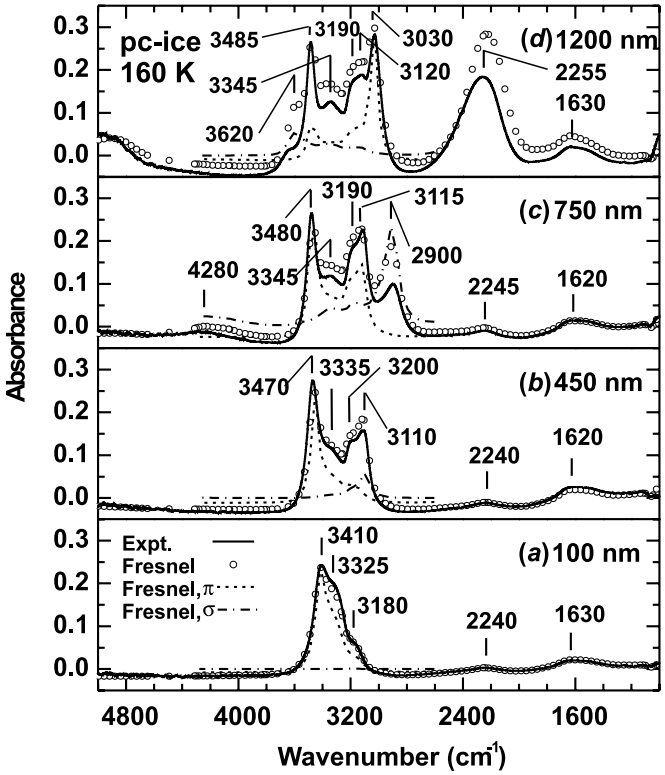
FT-IR–RA spectral features of the noncrystalline and polycrystalline ice in the Fresnel regime (for over 50 nm thick films)

Figure 1 shows typical spectra of nc-ice films obtained by water vapour deposition at 1×10^{-6} torr (1 torr = 133.322 4 Pa) with the copper substrate held at 131 K as a function of film thickness. The features near 1655 and 2230 cm^{-1} (Fig. 1*a*) can be assigned as the OH bending band (ν_2) with contribution from the first overtone ($2\nu_R$) of the hindered rotational lattice mode (ν_R), and as the combination band ($\nu_2 + \nu_R$) of the OH bending and hindered rotation modes, respectively, (35, 36, 37). These features remain essentially in the same peak positions with increasing film thickness. Furthermore, three relatively "stationary" (ν_1, ν_3) OH stretch features at 3490–3510 cm^{-1} (band maximum), 3355 cm^{-1}, and 3160–3145 cm^{-1} can be resolved for film thickness greater than 450 nm (Figs. 1*b*–1*d*). For film thickness below 250 nm, the shape of the (ν_1, ν_3) OH stretching band is predominantly determined by reflection–absorption of the π-polarized component of the incident light (Fig. 1*a*), with negligible contribution from the σ-polarized component. For film thickness greater than 250 nm, the σ-polarized component is generally found to strengthen with the emergence of an interference feature traveling from 3160 cm^{-1} at 450 nm (Fig. 1*b*) to 2940 cm^{-1} at 750 nm (Fig. 1*c*) and to 2225 cm^{-1} at 1250 nm (Fig. 1*d*). Another σ-polarized interference feature near 4190 cm^{-1} for film thickness of 750 nm (Fig. 1*c*) is also seen to travel to 3580 cm^{-1} for the 1250 nm thick film (Fig. 1*d*). It is evident that the π-polarized component also contributes prominently to the three aforementioned stationary OH stretch features over the film thickness range covered in Fig. 1. The movement of the main π-polarized feature (near 3430 cm^{-1} for the 110 nm thick film in Fig. 1*a*) to a higher frequency with increasing film thickness gives rise to the observed blue shift of the band maximum. This shift is therefore related to the physics of reflection–absorption of IR light and not to any possible structural change in the nc-ice network as a result of an increase in the film thickness. For thicker films, the π-polarized interference feature observed at 3160 cm^{-1} for the 750 nm thick film (Fig. 1*c*) is also found to travel to a lower frequency with increasing film thickness, e.g., 3045 cm^{-1} for the 1250 nm thick film (Fig. 1*d*).

Figure 2 demonstrates typical spectral evolution of pc-ice films obtained by water vapour deposition at 1×10^{-6} torr (1 torr = 133.322 4 Pa) with the substrate held at 160 K as a function of film thickness. Evidently, three major absorption features related to the vibrational modes of the water molecules in the pc-ice film are also observed: the OH stretching band (ν_1, ν_3) at 3410 cm^{-1}, the first overtone ($2\nu_R$) of the hindered rotational lattice mode ($\nu_R \approx 850$ cm^{-1} (35, 36)) at 1630 cm^{-1} with higher-frequency contribution from the OH bending band (ν_2), and the ($\nu_2 + \nu_R$) combination band and (or) the $3\nu_R$ second overtone at 2240 cm^{-1} (Fig. 2*a*) (36, 37). There is also generally good accord between the experimen-

© 2004 NRC Canada

Fig. 2. Comparison of experimental FT-IR–RA spectra of polycrystalline (pc) ice films obtained by vapour deposition at 160 K and 1 × 10^{-6} torr (1 torr = 133.322 4 Pa) for (*a*) 3.5 min, (*b*) 20 min, (*c*) 33.5 min, and (*d*) 52.5 min with the corresponding Fresnel spectra for non-polarized light and their σ- and π-polarized components (arbitrarily normalized) involving 100, 450, 750, and 1200 nm thick films, respectively.



tal spectrum and the corresponding Fresnel spectrum of a pc-ice film for all the film thicknesses depicted in Fig. 2. As with nc-ice films, the residual, non-vibration-related spectral features of the thicker (>100 nm) pc-ice films can be attributed to the σ- and π-polarized IR interference patterns, which are well approximated by the σ- and π-components of the corresponding Fresnel spectra. In particular, the low-frequency shoulder of the σ-polarized profile is seen to travel from 3110 cm^{-1} for the 450 nm thick film (Fig. 2*b*) to 2900 cm^{-1} for the 750 nm thick film (Fig. 2*c*), which evidently contributes to the corresponding features at 3110 and 2900 cm^{-1} in the respective experimental spectra. Further increase in the film thickness to 1200 nm causes the σ-polarized feature to move towards the lower frequency, giving rise to the strong enhancement of the spectral intensity at 2255 cm^{-1} (Fig. 2*d*). Furthermore, a second σ-polarized feature near 4280 cm^{-1} appearing in the spectrum for the 750 nm thick film (Fig. 2*c*) is also found to migrate to 3620 cm^{-1} for the 1200 nm thick film (Fig. 2*d*). Similar interference peak movement is also evident for the π-polarized feature at 3115 cm^{-1} for the 750 nm thick film (Fig. 2*c*), which travels to 3030 cm^{-1} as the film thickness is increased to 1200 nm (Fig. 2*d*). The evolution of the underlying σ- and π-polarized Fresnel contributions to the overall spectrum of pc ice with increasing film thickness (Fig. 2) is therefore similar to that found for the nc ice (Fig. 1). The observed movements of the destructive interference peaks generally reflect the quality of film uniformity obtainable for pc ice by vapour deposition.

Spectral characterization of the OH (OD) stretch manifold of an ultrathin (<50 nm) polycrystalline ice deposit

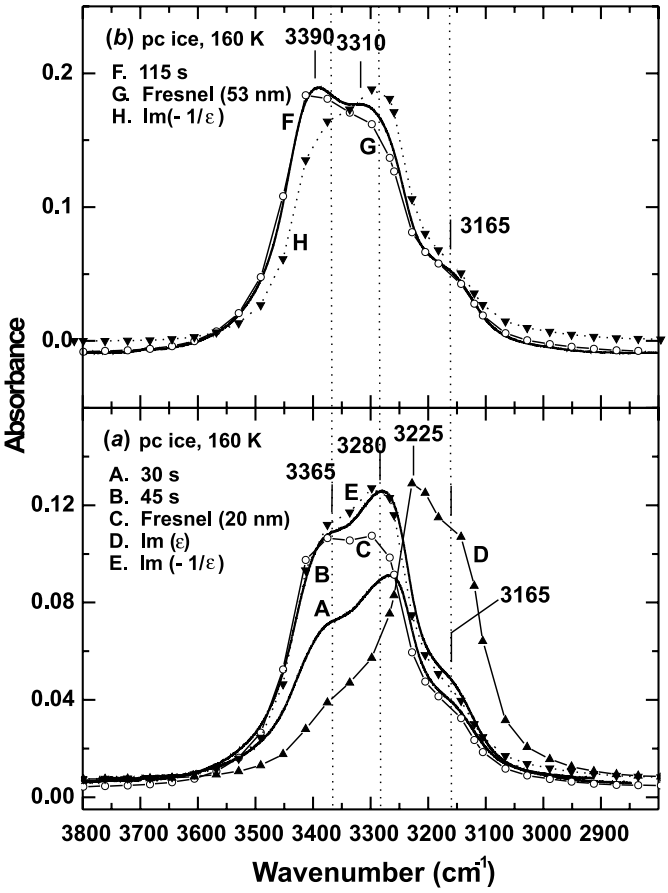
By using proton-ordered and disordered Ic and Ih ice models, Buch and Devlin (33) made use of four oscillating dipoles tetrahedrally arranged around a central O atom as the basis to calculate the OH stretching band. They attributed the central peak of the OH stretching band at 3220 cm^{-1} to the zero wave-vector modes of two transversal (TO) branches and a longitudinal (LO) branch (which corresponds to two dipoles moving "in" with the other two diploes moving "out" in a way that correlates with the asymmetric stretching character of the ν_3 molecular mode of an isolated water molecule). The asymmetric ν_3 character of the OH central peak is in agreement with the spectral assignment made by Whalley (34). The shoulder located at the lower-frequency side of the central peak appears to originate from the transversal modes strongly perturbed by intramolecular interactions and was therefore attributed to the in-phase ν_1 TO branch by Buch and Devlin (33), again in accord with Whalley's earlier assignment (34). The state with the lowest OH stretch frequency corresponds to the globally in-phase ν_1 vibration, which dominates in the Raman spectra obtained with parallel polarization (38). In the higher-frequency region of the OH stretching band, an intermediate branch (i.e., one that exhibits no systematic variation in the angle between the dipole moment of the lattice and the wave-vector) and nonzero wave-vector modes of the aforementioned longitudinal branch were found (33). Originated from the higher-frequency out-of-phase ν_1 vibration of the four dipoles surrounding the O atom, the intermediate branch was characterized by a small dipole moment near the center of the Brillouin zone, in marked contrast to the longitudinal modes (with origin from the ν_3 molecular vibration), which carry a significant dipole moment over the entire Brillouin zone (33).

Buch and Devlin (33) further demonstrated that the OH stretch absorption band can be strongly affected by the shape of the ice medium and by the polarization of the electric field. In particular, in the case of an ice slab, the modes of the higher-frequency intermediate and longitudinal branches are stimulated with surface-perpendicular polarization, while the lower-frequency transversal modes of the ν_1 branch are preferentially excited with surface-parallel polarization. The dependence of the absorption spectra on the shape is caused by the long-range dipole–dipole interaction, which was found to include a shape-dependent component associated with the surface polarization charge (39). The oscillating surface charge creates an electric field inside the sample that changes the energy gap between the ground and excited vibrational levels (39), and consequently the corresponding vibrational frequencies become shape-dependent. However, the shape-dependent effect predicted by the model was found to be considerably stronger than that observed experimentally (33). This discrepancy was attributed to a limitation on the spatial extent of the vibrational excited states imposed by the imperfections in the pc-ice medium.

© 2004 NRC Canada

The Buch–Devlin simulation of IR absorption by an ice slab for the surface-perpendicular polarization (33) could be directly compared with the experimental RA spectra of ultrathin ice films on a metal surface at grazing-angle illumination with π-polarized or nonpolarized light. Upon reflection on a highly conductive metal, the σ-polarized component of the incident electric field is almost completely eliminated near its surface and only the π-polarized component of the electric field remains, which provides the physical justification for comparing the experimental RA spectra with the simulated spectrum for excitation of an ice slab by just the (surface-perpendicular) π polarization. In particular, the Buch–Devlin model (33) predicts that the absorption spectra of the ice slab for the surface-perpendicular polarization are primarily originated from excitation of the intermediate and ν_3 LO branches, of which the former is of a higher frequency. Figure 3 compares our experimental RA spectra of the OH stretching band obtained for ultrathin pc-ice deposits (with an estimated thickness below 50 nm) with the corresponding Fresnel spectra and with the Berreman and transmission profiles (40) (arbitrarily normalized to the band maxima of the respective experimental spectra). The Berreman profile corresponds to the energy loss function defined as $\mathrm{Im}(-\varepsilon^{-1}) = \varepsilon''/(\varepsilon'^2 + \varepsilon''^2)$, where the dielectric function $\varepsilon = \varepsilon' - i\varepsilon''$ (with its real ε' and imaginary ε'' parts), while the transmission profile is given by $\mathrm{Im}(\varepsilon)$ (i.e., ε''). The Fresnel spectra and both of these profiles are generated based on the spectral data reported by Toon et al. (28). Evidently, the spectra for pc-ice deposited at 160 K and 1×10^{-6} torr (1 torr = 133.322 4 Pa) for 30 and 45 s (curves A and B, Fig. 3*a*) are in good accord in shape with the Buch–Devlin spectrum for the ice slab (see Fig. 3*c* in ref. 33), supporting the assignment of the higher-frequency shoulder at 3365 cm^{-1} to the intermediate branch and of the 3280-cm^{-1} feature to the ν_3 LO band. The band maximum for the 3280 cm^{-1} peak is also found to be in good agreement with that of the ν_3 LO band (3299 cm^{-1}) predicted by Whalley (34). Furthermore, the 45 s spectrum (curve B, Fig. 3*a*) closely follows the energy loss function as represented by the Berreman profile (curve E, Fig. 3*a*), which again indicates that the blue shift of the central OH stretch peak with respect to the transmission profile (curve D, Fig. 3*a*) is due to stimulation of the longitudinal modes of the ν_3 branch. The apparent enhancement of the higher-frequency part of the OH stretch with the corresponding weakening of the lower-frequency part could be associated with the blue shift of the most intense ν_3 branch alone and not to the actual changes in their own respective intensities. As expected for thicker deposits, the 115 s RA spectrum shown in Fig. 3*b* (curve F) evidently begins to deviate from the Berreman profile (curve H, Fig. 3*b*) and converge to the Fresnel spectrum (curve G, Fig. 3*b*), indicating the onset of the formation of a stratified ice film with smooth interfaces. The continual blue shift of the OH stretch and the apparent changes in the relative intensities of the band components (band shape deformation) with increasing thickness are likely caused by optical effects in the film on a metal substrate (41). Accordingly, at the initial stage of pc-ice film formation the ice deposit exists in the form of crystallites, which causes the experimental spectra to deviate from the Fresnel model. This is illustrated by the differences between the 30 and 45 s spectra (both with a common shape, curves A and B in Fig. 3*a*) and the corresponding Fresnel spectrum. In this case, the frequency position of a band associated with the ν_3 LO modes becomes dependent upon the particle shapes of the crystallites (31, 32, 38, 39).

Fig. 3. Comparison of the OH stretching band of the experimental FT-IR–RA spectra of early-stage polycrystalline (pc) ice deposits obtained by vapour deposition at 160 K and 1×10^{-6} torr (1 torr = 133.322 4 Pa) for 30 s (A), 45 s (B), and 115 s (F) with the Fresnel spectra of 20 nm (C) and 53 nm (G) thick pc-ice films and the Berreman (E, H) and transmission profiles (D), all arbitrarily normalized.



Temporal evolution of the OH (OD) stretch manifold during crystallization of an ultrathin, noncrystalline ice deposit

Because nc ice is considered metastable with respect to the crystalline ice form, annealing of an nc-ice deposit could promote crystallization to occur at a detectable rate above an appropriate temperature. Indeed, rapid changes in the OH stretch region are found at 153–163 K in the present work, in good accord with the earlier observations made by using different techniques (16, 17, 23). In particular, Fig. 4 shows the temporal evolution of the OH stretching band at 155 K for 30 min and at 163 K for 6 min for an nc-ice film deposited at 124 K and 1×10^{-6} torr (1 torr = 133.322 4 Pa) for 240 s. In Fig. 5, we compare selected experimental profiles in Fig. 4 with the appropriate calculated spectra. While no significant temporal spectral changes are found at 155 K

© 2004 NRC Canada

Fig. 4. Evolution of the OH stretching band of the experimental FT-IR–RA spectra for an early-stage, noncrystalline ice deposit obtained by vapour deposition at 124 K and 1×10^{-6} torr (1 torr = 133.322 4 Pa) for 240 s (A), followed by annealing to 155 K for 30 min (B), and to 163 K for 60 s (C), 90 s (D), 120 s (E), 150 s (F), 180 s (G), 210 s (H), 240 s (I), 270 s (J), and 300 s (K).

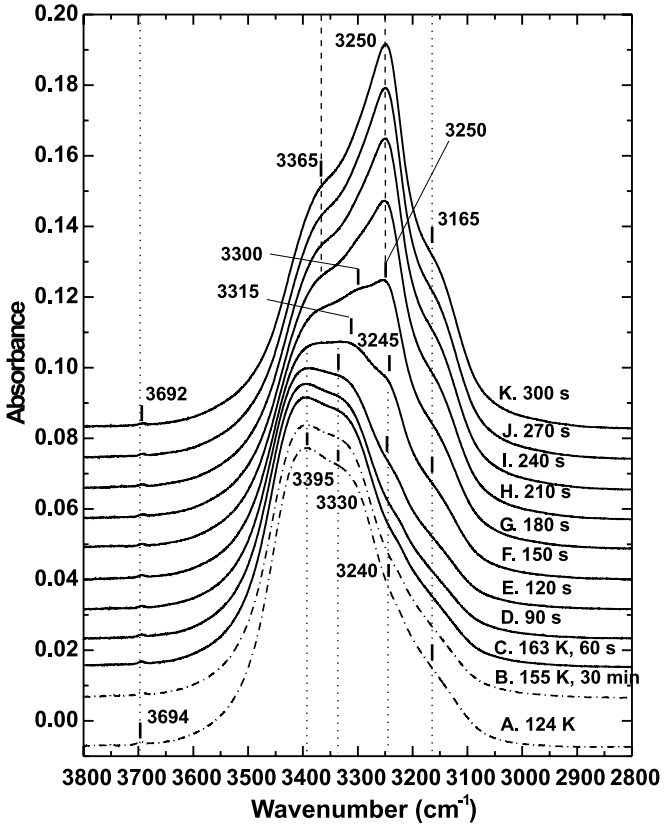
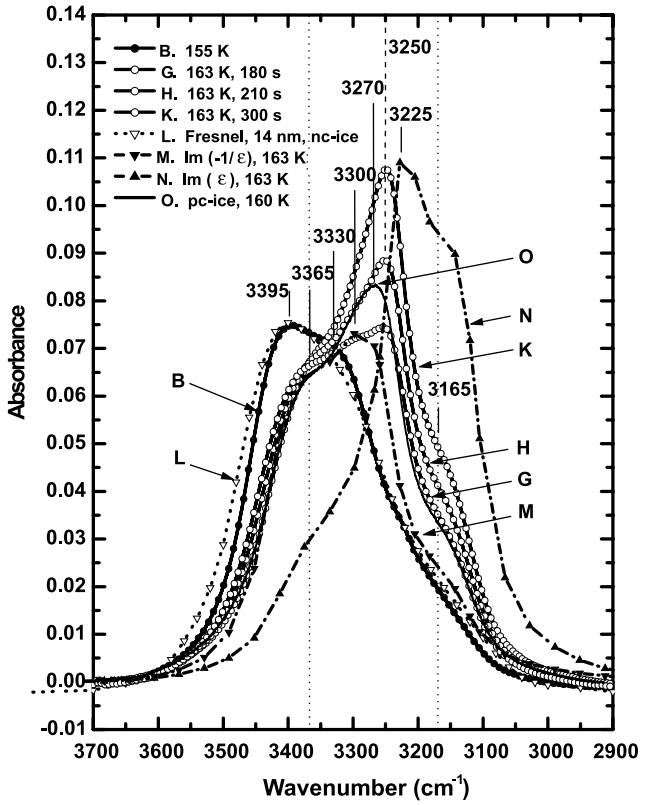


Fig. 5. Comparison of the OH stretching band of the experimental FT-IR–RA spectra of an early-stage, noncrystalline (nc) ice deposit obtained by vapour deposition at 124 K and 1×10^{-6} torr (1 torr = 133.322 4 Pa) for 240 s followed by annealing to 155 K for 30 min (B) and to 163 K for 180 s (G), 210 s (H), and 300 s (K) with that of a polycrystalline (pc) ice deposit obtained by vapour deposition at 160 K and 1×10^{-6} torr (1 torr = 133.322 4 Pa) for 30 s (O), and with the Fresnel spectrum of a 14 nm thick nc-ice film (L) and the Berreman (M) and transmission profiles for the pc ice (N), all arbitrarily normalized.



(curve B, Fig. 4) relative to the as-deposited nc-ice spectrum at 124 K (curve A, Fig. 4), rapid dramatic changes in the shape of the OH stretching band are observed at 163 K (curves C–K, Fig. 4). By analogy with the assignment for pc ice, the weak peak at 3694 cm^{-1} can be attributed to the OH dangling bonds, while the features at 3395, 3330, and 3165 cm^{-1} likely correspond to the out-of-phase ν_1 intermediate modes, the ν_3 LO branch, and the in-phase ν_1 branch, respectively. As shown in Fig. 5, the OH stretch profiles for the nc-ice film as-deposited at 124 K and upon annealing to 155 K (curve B, Fig. 5) are well approximated by the Fresnel spectrum for a 14 nm thick nc-ice film (curve L, Fig. 5), indicating the preservation of the smooth stratified film even upon annealing at 155 K for 30 min. On the other hand, discernible spectral changes near 3245 cm^{-1} are found upon annealing at 163 K for just 2 min (curves C–E, Fig. 4). This feature develops into a strong, well-defined peak at 3250 cm^{-1} upon further annealing at the same temperature for 3 more min (curves F–K, Fig. 4). In contrast, the dangling-bond feature at 3694 cm^{-1} remains essentially unchanged except for the minor red shift during this anneal.

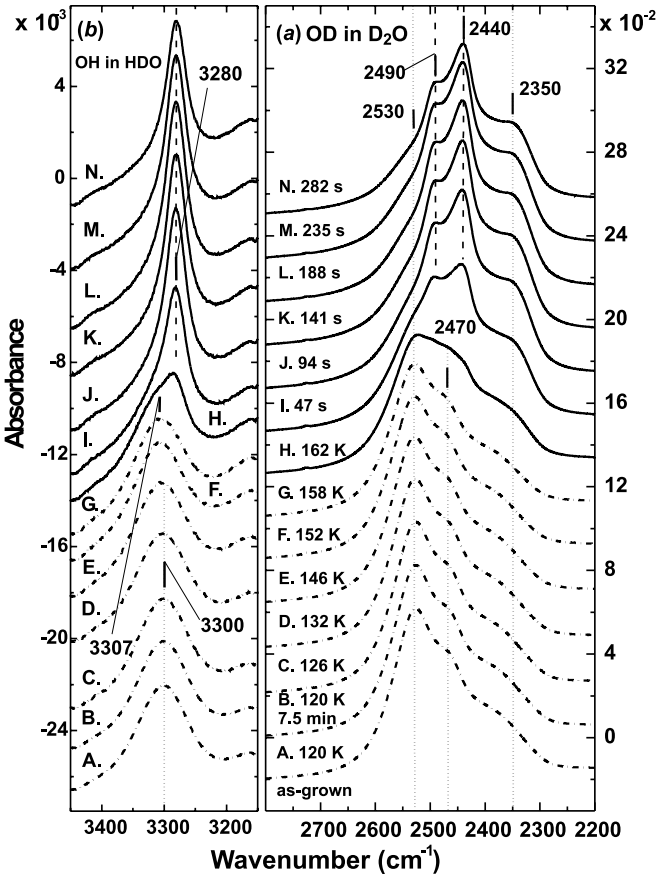
Figure 5 also compares selected spectra obtained during the 163 K anneal with the RA spectrum of the 30 s pc-ice film deposited at 160 K discussed earlier in Fig. 3, and with the Berreman and transmission profiles for pc-ice films. Evidently, the major differences between the OH stretch profiles of the annealed nc-ice film (curves G, H, and K, Fig. 5) and that of the as-grown 30 s pc-ice film (curve O, Fig. 5) are the location and relative intensity of the ν_3 LO manifold (at 3250 vs. 3270 cm^{-1}). According to the theoretical study by Wojcik et al. (42), the emergence of a prominent ν_3 LO band during annealing in the present work can be used as evidence of a rapid increase in the density of excited vibrational states in this narrow frequency region, which in turn indicates the onset of a crystallization process. The intensity increase of the overall OH stretching band during the anneal (curves G, H, and K, Fig. 5) is also consistent with the general chemical principle that crystallization leads to strengthening of the hydrogen bonds in the ice medium (43). Furthermore, the peak maximum of the observed ν_3 band (3250 cm^{-1}) is found to be in between those of the Berreman profile (3300 cm^{-1}, curve M, Fig. 5) and the transmission profile (3225 cm^{-1}, curve N, Fig. 5). (It should be noted that the Berreman profile and the transmission profile are arbitrarily normalized to the experimental spectra shown as curve G and curve K, respectively.) The intermediate peak

© 2004 NRC Canada

location is due to the presence of surface modes in the crystallites, as discussed by Englman and Ruppin (31) and Martin (32). Moreover, the formation and growth of the crystallites introduce tension into the film and could lead to cracking in a sufficiently thin film.

Figure 6 shows the temporal evolution of the OH and OD stretching modes of deuterated nc ice as deposited at 120 K and 1.5×10^{-6} torr (1 torr = 133.322 4 Pa) for 9 min and during annealing to 162 K. Evidently, no discernible change is observed in the OD stretching mode upon annealing from 120 to 162 K (curves A–H, Fig. 6*a*). Furthermore, the temporal evolution in the OD stretch features at 162 K for nearly 5 min (curves H–N, Fig. 6*a*) is found to be remarkably similar to that of the OH stretch observed earlier in the undeuterated nc-ice sample (Figs. 4 and 5), which again indicates the onset of rapid crystallization at this temperature. (Figure 6*a* also shows only minor changes in the dangling-bond signal of the OD surface groups at 2727 cm^{-1} during crystallization). Moreover, the uncoupled OH stretching mode of HOD in the deuterated ice sample exhibits a red shift from 3300 cm^{-1} at 120 K (curve A, Fig. 6*b*) to 3280 cm^{-1} at 162 K (curve N, Fig. 6*b*) with concomitant narrowing of the peak, which is also consistent with the crystallization process. The changes in this vibrational mode are in excellent agreement with the transmission spectra for thick amorphous and polycrystalline ice samples obtained by Bergren et al. (44). Between 120 K (curve A, Fig. 6*b*) and the crystallization onset at 162 K (curve H, Fig. 6*b*), there is a small but discernible blue shift of 7 cm^{-1} accompanied with peak broadening in this structure-sensitive mode, which could be argued as spectral evidence for further disordering of this nc-ice deposit immediately before crystallization. This spectral change might also be associated with an endothermic peak in the calorimetric upscan of an nc-ice medium often appearing just before the crystallization onset, which has been attributed to a glass-to-liquid transition in the earlier studies (16, 17) because frequency shifts for the structure-sensitive modes (including, e.g., the aforementioned modes) are expected in the case of a supercooled liquid state. In particular, Jenniskens et al. (45) used this approach to interpret their FT-IR–RAS data for the transition of nc ice to pc ice. Smith and Kay (19) and Smith et al. (20) also attributed the significant enhancement in the self-diffusivity of nc ice over this temperature range to a glass-to-liquid transition. However, the observed blue shift for this nc-ice feature is also in remarkably good agreement with the blue shift of the corresponding feature for pc-ice solids upon annealing (from 3275.2 cm^{-1} at 120 K to 3280.5 cm^{-1} at 150 K) observed by Sivakumar et al. (46) using Raman spectroscopy. Indeed, we also observed a corresponding red shift in the OH stretch feature in the crystallized ice (curve N, Fig. 6*b*) upon recooling from 162 to 120 K (not shown). The blue shift in the isolated OH stretch observed for nc ice upon annealing in the present work is therefore most likely just the natural consequence of thermal expansion of the ice medium. We favour the latter, simpler explanation over the former explanation invoking the glass-to-liquid transition because such an equilibrium thermodynamic effect is expected to occur regardless of the existence of the glass-to-liquid transition. Together with the early spectroscopic studies on ice crystallization by Hardin and Harvey (36) and

Fig. 6. Evolution of (*a*) the OD stretching band (for D_2O) and (*b*) the OH stretching band (for HDO) of the experimental FT-IR–RA spectra for an early-stage noncrystalline ice deposit obtained by vapour deposition at 120 K and 1.5×10^{-6} torr (1 torr = 133.322 4 Pa) for 9 min (A), followed by annealing to 120 K for 7.5 min (B) and to 132 K (C), 146 K (E), 152 K (F), 158 K (G), and 162 K (H) for 47 s (I), 94 s (J), 141 s (K), 188 s (L), 235 s (M), and 282 s (N).



Hagen et al. (47), the present data therefore provides no conclusive spectroscopic evidence for the existence of a distinct glass-to-liquid transition in nc ice in the 120–163 K range. Although any difference in the rates of relaxation processes is expected to manifest in the shape and width of the OH stretch band, we cannot rule out the possibility that the local structures of the water glass and supercooled liquid states happen to be almost identical, in which case the intermolecular interactions in both media are so close to each other that no spectral differences in the OH (OD) stretching region could be resolved. In a separate experiment, we also obtained FT-IR–RA spectra for an organic guest species, acetone or acetaldehyde, codeposited with water to form a noncrystalline guest–ice matrix at 130 K (48). The temporal evolution of the spectral features of the embedded guest species upon annealing followed by crystallization of the ice at 165 K shows only steady escape of the guest species from the matrix. While spectral differences between the adsorption (absorption) states of the guest species in the nc- and pc-ice samples were clearly resolved, no signature of the intermediate states in the guest-supercooled liquid water matrix in the 130–165 K temperature region could be observed

© 2004 NRC Canada

(48). Similar spectral observations of a steady escape and the absence of any frequency shift for dimethyl ether in a dimethyl ether – water matrix at 130–160 K have also been reported recently by Schriver-Mazzuoli et al. (49), although the spectral changes for dimethyl ether have been found at 120–130 K and attributed to clathrate–hydrate formation (49). These results further support our above observation of direct transition from nc ice to pc ice (i.e., without an intermediate glass-to-liquid transition). Furthermore, the results on crystallization kinetics of thin compact nc ice films by Dohnalek et al. (22) are also consistent with the direct solid-to-solid phase transformation.

It should be noted that for thicker ice deposits, for example those above 100 nm thick shown in Figs. 1 and 2, the temporal evolution of the main peak in the OH or OD stretch manifold upon annealing followed by crystallization is found to be less pronounced, likely due to the optical effects of the film–metal medium as discussed earlier by La Spisa et al. (50).

Concerning the state of surfaces at nc-ice and pc-ice films investigated in the present and early studies (25), it should be noted that the amount of OH dangling bonds as estimated by the intensity of the corresponding spectral feature at 3694 cm^{-1} (Fig. 4) on the as-grown thin (and compact) nc-ice films is similar to that on the pc-ice films prepared by crystallization of nc-ice films or by direct deposition. However, our FT-IR–RAS data on acetone adsorption (48, 51) appear to indicate a dynamical difference in the surface states of the adsorbate on nc- and pc-ice films. This difference is clearly related not only to the "snap-shot" structure of the surface but also to the stability and dynamics of the surface and near-surface regions of nc- and pc-ice films as discussed by Buch et al. (52).

Concluding remarks

The temporal evolution of the OH (and OD) stretch manifold(s) in the (deuterated) nc-ice deposits upon annealing followed by crystallization has been investigated by using FT-IR–RAS at grazing-angle incidence. We provide a microscopic interpretation of the spectral data using the theoretical results of Buch and Devlin (33) and Whalley's assignment (34). For the ultrathin nc-ice deposits, crystallization near 160 K has been demonstrated for the first time to be marked spectroscopically by an abrupt enhancement along with a concomitant red shift in the longitudinal branch of the ν_3 OH (OD) stretching mode at 3250 (2440) cm^{-1}. These observations are consistent with strengthening of the hydrogen bonds in the molecular water network and with increased ordering of an ice medium during crystallization. Furthermore, the spectral dynamics of the OH and OD stretch manifolds and of the isolated OH stretching mode in a deuterated ice matrix near 160 K observed in the present work indicate that rapid crystallization proceeds directly from a noncrystalline to a crystalline state, i.e., without any long-lived intermediate state that involves a hydrogen-bonded network structurally different from that of nc ice at a lower temperature (120 K). While the present interpretation of the OH spectral dynamics does not favour the existence of a glass-to-liquid transition during crystallization, we cannot rule out the existence of a supercooled-liquid state that happens to have a nearly identical local structure to glass. Further studies possibly involving non-spectroscopic data would be of great interest to resolve this intricate fundamental issue about ice.

Acknowledgement

This work was supported by the Natural Sciences and Engineering Research Council of Canada (NSERC).

References

1. P.V. Hobbs. Ice physics. Clarendon Press, Oxford. 1974.
2. O. Mishima and H.E. Stanley. Nature (London), **396**, 329 (1998).
3. O. Mishima. J. Chem. Phys. **100**, 5910 (1994).
4. J.L. Finney, D.T. Bowron, A.K. Soper, T. Loerting, E. Mayer, and A. Hallbrucker. Phys. Rev. Lett. **89**, 205 503 (2002).
5. J.L. Finney, A. Hallbrucker, I. Kohl, A.K. Soper, and D.T. Bowron. Phys. Rev. Lett. **88**, 225 503 (2002).
6. A.I. Kolesnikov, J. Li, S.F. Parker, R.S. Eccleston, and C.-K. Loong. Phys. Rev. B, **59**, 3569 (1999).
7. V.P. Shpakov, P.M. Rodger, J.S. Tse, D.D. Klug, and V.R. Belosludov. Phys. Rev. Lett. **88**, 155 502 (2002).
8. V.P. Voloshin, E.A. Zhelegovskaya, G.G. Malenkov, and Yu.I. Naberukhin. J. Struct. Chem. **42**, 794 (2001).
9. H. Tanaka. J. Chem. Phys. **105**, 5099 (1996).
10. J.P. Devlin and V. Buch. J. Phys. Chem. **99**, 16 534 (1995).
11. K.P. Stevenson, G.A. Kimmel, Z. Dohlanek, R.S. Smith, and B.D. Kay. Science, **28**, 1505 (1999).
12. Z. Dohlanek, G.A. Kimmel, P. Ayotte, R.S. Smith, and B.D. Kay. J. Chem. Phys. **118**, 364 (2003).
13. E. Mayer and R. Pletzer. Nature (London), **319**, 298 (1986).
14. D. Laufer, E. Kochavi, and A. Bar-Nun. Phys. Rev. B, **36**, 9219 (1987).
15. M.S. Westley, G.A. Baratta, and R.A. Baragiola. J. Chem. Phys. **108**, 3321 (1998).
16. I. Kohl, E. Mayer, and A. Hallbrucker. Phys. Chem. Chem. Phys. **2**, 1579 (2000).
17. A. Hallbrucker, E. Mayer, and G.P. Johari. J. Phys. Chem. **93**, 4986 (1989).
18. M.A. Zondlo, T.B. Onasch, M.S. Warshawsky, M.A. Tolbert, G. Mallick, P. Arentz, and M.S. Robinson. J. Phys. Chem. B, **101**, 10 887 (1997).
19. R.S. Smith and B.D. Kay. Nature (London), **398**, 788 (1999).
20. R.S. Smith, Z. Dohnalek, G.A. Kimmel, K.P. Stevenson, and B.D. Kay. ACS Symposium Series 820. American Chemical Society, Washington, D.C. 2002. p. 198.
21. Z. Dohnalek, R.L. Ciolli, G.A. Kimmel, K.P. Stevenson, R.S. Smith, and B.D. Kay. J. Chem. Phys. **110**, 5489 (1999).
22. Z. Dohnalek, G.A. Kimmel, R.L. Ciolli, K.P. Stevenson, R.S. Smith, and B.D. Kay. J. Chem. Phys. **112**, 5932 (2000).
23. D.R. MacFarlane and C.A. Angell. J. Phys. Chem. **88**, 759 (1984).
24. V. Velikov, S. Borick, and C.A. Angell. Science, **294**, 2335 (2001).
25. S. Mitlin and K.T. Leung. J. Phys. Chem. B, **106**, 6234 (2002).
26. R.G. Greenler. J. Chem. Phys. **44**, 310 (1966).
27. J.D.E. McIntyre and D.E. Aspnes. Surf. Sci. **24**, 417 (1971).
28. O.B. Toon, M.A. Tolbert, B.G. Koehler, and A.M. Middelebrook. J. Geophys. Res. **99**(D12), 631 (1994).
29. A. Leger, S. Gauthier, D. Deforneau, and D. Rouan. Astron. Astrophys. **117**, 164 (1983).
30. B. Mate, A. Medialdea, M.A. Moreno, R. Escribano, and V.J. Herrero. J. Phys. Chem. B, **107**, 11 098 (2003).

© 2004 NRC Canada

31. R. Englman and R. Ruppin. J. Phys. C. (Proc. Phys. Soc.) **1**, 614 (1968).
32. T.P. Martin. Phys. Rev. **177**, 1349 (1969).
33. V. Buch and J.P. Devlin. J. Chem. Phys. **110**, 3437 (1999).
34. E. Whalley. Can. J. Chem. **55**, 3429 (1977).
35. C. Haas, D.F. Hornig. J. Chem. Phys. **32**, 1763 (1960).
36. A.H. Hardin and K.B. Harvey. Spectrochim. Acta, **29A**, 1139 (1973).
37. J.E. Bertie and E. Whalley. J. Chem. Phys. **40**, 1637 (1964).
38. J.P. Devlin. J. Chem. Phys. **90**, 1322 (1989).
39. D. Fox and R. Hexter. J. Chem. Phys. **41**, 1125 (1964).
40. D.W. Berreman. Phys. Rev. **130**, 2193 (1963).
41. R.G. Tobin. Phys. Rev. **45**, 12 100 (1992).
42. M.J. Wojcik, V. Buch, and J.P. Devlin. J. Chem. Phys. **99**, 2332 (1993).
43. A.V. Iogansen. Spectrochim. Acta, **A55**, 1585 (1999).
44. M.S. Bergren, D. Schuh, M.G. Sceats, and S.A. Rice. J. Chem. Phys. **69**, 3477 (1978).
45. P. Jenniskens, S.F. Banham, D.F. Blake, and M.R.S. McCoustra. J. Chem. Phys. **107**, 1232 (1997).
46. T.C. Sivakumar, S.A. Rice, and M.G. Sceats. J. Chem. Phys. **69**, 3468 (1978).
47. W. Hagen, A.G.G.M. Tielens, and J.M. Greenberg. Chem. Phys. **56**, 367 (1981).
48. S. Mitlin, and K.T. Leung. (2004) to be published.
49. L. Schriver-Mazzuoli, J.M. Coanga, A. Schriver, and P. Ehrenfreund. Vib. Spec. **30**, 245 (2002).
50. S. La Spisa, M. Waldheim, J. Lintemoot, T. Thomas, J. Naff, and M. Robinson. J. Geophys. Res. **106**(E12), 33 351 (2001).
51. S. Mitlin and T. Leung. Surf. Sci. **505**, L227 (2002).
52. V. Buch, L. Delzeit, C. Blackledge, and J.P. Devlin. J. Phys. Chem. **100**, 3732 (1996).

© 2004 NRC Canada

Chemical adsorption of salicylate on silver — A systematic approach to the interpretation of surface-enhanced vibrational spectra[1]

P.J.G. Goulet and R.F. Aroca

Abstract: In this work, surface-enhanced vibrational spectroscopy and normal vibrational spectroscopy as well as density functional theory (DFT) computational methods have been employed to investigate the nature of the chemical adsorption and orientation of the surface species generated from salicylic acid at silver surfaces. The structure of salicylic acid and its IR and Raman spectra are determined at the B3LYP/6-311+G(d,p) level of theory. These results are used in the assignment of the vibrational spectra. Surface-enhanced Raman scattering (SERS) spectra obtained from silver island films thinly coated with salicylic acid confirm chemical adsorption on the Ag nanostructures. To probe the nature of this surface complex, the optimized geometries and IR and Raman spectra of two model salicylate–silver complexes (Ag1 and Ag2) were calculated at the B3LYP/Lanl2DZ level of theory. It was found that good agreement exists between experimentally observed SERS spectra and the simulated SERS spectra of a complex with the salicylate monoanion bound to a Ag^+ ion through its carboxylate group (Ag1). The carboxylate silver salt of salicylic acid (essentially the Ag1 complex) was also prepared, and its IR and Raman spectra were recorded for comparison with the surface-enhanced vibrational spectra. These results, along with the application of surface selection rules, suggest that salicylic acid is deprotonated at silver surfaces, interacting through its carboxylate group alone, and is preferentially in a tilted head-on orientation.

Key words: chemisorption, salicylic acid, silver, density functional theory, surface-enhanced Raman scattering, reflection–absorption IR spectroscopy, surface-enhanced IR absorption.

Résumé : Dans ce travail, on a utilisé la spectroscopie vibrationnelle exaltée de surface, la spectroscopie vibrationnelle normale ainsi que des méthodes de calculs de la théorie de la densité fonctionnelle (TDF) pour étudier la nature de l'adsorption chimique et l'orientation des espèces en surface générées à partir de l'acide salicylique sur des surfaces d'argent. La structure de l'acide salicylique et ses spectres infrarouge et Raman ont été déterminés au niveau B3LYP/6-311+G(d,p) de la théorie. On a utilisé ces résultats dans l'attribution des spectres vibrationnels. Les spectres de diffusion Raman exaltée de surface (« SERS ») obtenus pour des films d'îles d'argent légèrement recouverts d'acide salicylique confirment l'adsorption chimique sur la nanostructure d'argent. Afin de pouvoir étudier la nature de ce complexe en surface, on a calculé les géométries optimisées et les spectres infrarouge et Raman de deux modèles de complexes de salicylate d'argent (Ag1 et Ag2) au niveau B3LYP/Lan12DZ de la théorie. On a trouvé qu'il existe un bon accord entre les spectres SERS observés expérimentalement et les spectres SERS simulés d'un complexe dans lequel le monoanion salicylate est lié à un ion Ag^+ par le biais de son groupe carboxylate (Ag1). On a aussi préparé le sel d'argent du carboxylate de l'acide salicylique (essentiellement un complexe Ag1) et, pour fins de comparaison avec le spectre vibrationnel exalté de surface, on en a aussi enregistré ses spectres infrarouge et Raman. Ces résultats, en relation avec l'application des règles de sélection de surface, suggèrent que l'acide salicylique est déprotoné au niveau des surfaces d'argent, qu'il interagit uniquement par le biais de son groupe carboxylate et qu'il est préférentiellement dans une orientation face à face décalée.

Mots clés : chimisorption, acide salicylique, argent, théorie de la densité fonctionnelle, diffusion Raman exaltée de surface, spectroscopie infrarouge de réflexion–absorption, absorption infrarouge exaltée de surface.

[Traduit par la Rédaction]

Introduction

In the late 1970s, the phenomenon of surface-enhanced Raman scattering (SERS) was discovered (1–3). Since then, research into and employing surface-enhanced spectroscopies has exploded with activity (4–6). SERS is primarily due to the enhancement of Raman scattering cross sections of analytes as a result of their interaction with the strong

Received 28 November 2003. Published on the NRC Research Press Web site at http://canjchem.nrc.ca on 3 September 2004.

P.J.G. Goulet and R.F. Aroca.[2] Materials and Surface Science Group, Department of Chemistry and Biochemistry, University of Windsor, Windsor ON N9B 3P4, Canada.

[1]This article is part of a Special Issue dedicated to the memory of Professor Gerhard Herzberg.
[2]Corresponding author (e-mail: g57@uwindsor.ca).

 doi: 10.1139/V04-075 © 2004 NRC Canada

electromagnetic fields at or near the surface of appropriate enhancing metal nanostructures. The total enhancement of Raman intensities observed in SERS may span several orders of magnitude, up to ~10^{14}, and will depend critically on the architecture of the enhancing nanoparticles or surfaces used (7–9). Typically, SERS measurements are carried out on island films, electrochemically roughened electrodes, and colloidal metal particles of coinage metals such as Ag, Au, and Cu. These nanostructures support dipole particle plasmon resonance (DPPR) in the visible and thus are readily accessible to several excitation laser lines commonly used in Raman measurements (10).

Surface-enhanced Raman scattering and surface-enhanced IR absorption (SEIRA) occur near the surface of metal nanostructures that polarize the electric field of incident light, and, consequently, it is necessary to account for the orientation of adsorbates in the interpretation of experimental spectra. This is similar to the situation that exists for IR and Raman spectra of molecules adsorbed on reflecting flat metal surfaces. Greenler (11) demonstrated that the light at these surfaces is highly polarized, and at appropriate angles of incidence the p-polarized (parallel to the plane of incidence) component of the electromagnetic wave is three orders of magnitude larger than the s-component. Since the component perpendicular to the surface (P) dominates, we expect to see only those vibrational modes whose polarizability derivatives (Raman) or dipole moment derivatives (IR) align well with the field. This leads to the concept of surface selection rules (12), where the vibrational intensities predicted depend upon the contribution of the normal and tangential components of the local electric field near the surface. To the knowledge of the light polarization at the surface, one must also add the very important distinction between physically adsorbed and chemically adsorbed molecules for the interpretation of surface and surface-enhanced vibrational spectroscopy (SEVS). Physisorbed molecules show weak interactions with surfaces and, because of this, are often oriented randomly, loosely maintaining their native symmetry. This, in effect, makes the interpretation of the SEVS spectra of randomly oriented physisorbed molecules relatively simple, as the molecular selection rules do not change, and a comparison can be made directly to reference Raman scattering and IR absorption spectra. In the cases of chemical adsorption or physical adsorption with preferential orientation, however, a new complexity is introduced that can make the interpretation of SEVS spectra very challenging.

Chemisorption is a strong interaction of an analyte with a surface at energies comparable to those of chemical bonds. This results in the formation of surface complexes and therefore leads to striking changes in Raman and IR spectra. In addition to the changes in symmetry and structure that result from strong chemisorption, we will also have the additional factor of a preferred molecular orientation at the surface. A preferred orientation, whether involving chemisorption or physisorption, introduces the necessity for the above-mentioned surface selection rules, as the electric field (polarized perpendicular to the surface) will not interact strongly with those modes that are tangential to the electromagnetic field-enhancing surface. The phenomenon of chemisorption can thus be a very complicating factor for the assignment of SERS and SEIRA spectra, and so presents a perfect opportunity for the strengths of theoretical computational methods to be employed. Notably, if the electronic absorption of the surface complex happens to be in resonance with the exciting laser line, the observed spectrum will be that of resonance Raman scattering, a case that is not considered here for this salicylate complex.

Theoretical methods, such as those available in Gaussian 98 (13), have been recently employed in the study of the chemical adsorption of two different molecules on Ag (14, 15). In these studies the authors calculated the optimized geometries and Raman spectra of analyte–Ag complexes using density functional theory (DFT) methods and compared them to experimental SERS spectra. In both reports, fairly good agreement was found for simulated (computed) and experimental SERS spectra, and as theoretical modeling of chemical systems continues to improve and become more computationally affordable, it is expected that this will become a very useful and common method for predicting and assigning SERS spectra. In this work, strategies similar to those mentioned above have been employed in the study of a molecular system that has not before been submitted to a full theoretical treatment (16) and for which the chemisorption on Ag does not appear to be fully understood. This system is that of salicylic acid (2-hydroxybenzoic acid) and its deprotonated monoanion and dianion forms.

Salicylic acid is a molecule that is of interest to science for several reasons, and perhaps the most important of these is its application in commercial drugs, including its use in the synthesis of drugs such as aspirin (acetylsalicylic acid) (17). However, another significant point of interest about this system is that the salicylate ion is a very important metal-binding agent in nature (18). Several vibrational studies of salicylic acid and its ions have been reported in the literature (16) including a few that have employed SERS (17, 19–21). These reports show inconsistencies with regard to the question of the adsorption of the molecule on Ag. In one report, it is claimed that salicylic acid interacts with the colloidal Ag surface through both its carboxylate and phenolate groups (17), while in other reports adsorption is concluded to occur only through the carboxylate group (19, 20), or in a "tilted side-on orientation", where the C=O stretch was incorrectly assigned (21). Additionally, one recently reported SERS spectrum shows large discrepancies with previous work (19). Much of the confusion that seems to exist in the literature is likely due to the difficulty of accurately assigning peaks in the SERS spectra of this chemisorbed molecule. This is due to the reasons that have been mentioned earlier, but also to the fact that salicylic acid has a very crowded Raman spectrum with many closely spaced bands and shows strong photodegradation at relatively low laser powers. Thus, in an attempt to simplify the assignment of bands in the SERS spectra of this molecule, and to shed light on the question of how it chemically adsorbs to Ag, we have employed DFT techniques to compute optimized geometries and vibrational spectra for salicylic acid and two silver–salicylate complexes.

DFT methods have recently become very widely used and popular owing to their accuracy and low computational cost. These methods minimize an energy functional rather than handling a wave function for each of the electrons in an

© 2004 NRC Canada

N-electron system, and because of this simplification they are of much lower computational cost than other correlational techniques. In this study, Becke's three-parameter functional (22) including the correlational functional of Lee et al. (23) (B3LYP) has been employed for all reported results. This functional has been shown to perform very well in the calculation of vibrational spectra. However, the accuracy of the results for the two different Ag complexes may be expected to be lacking because of the limited size of the Lanl2DZ (24, 25) basis set that was used. Lanl2DZ was employed, despite its small size, as it is one of the only basis sets available for silver that is also available for second-row elements (15).

Extracting from the spectra the molecular orientation of the surface species on Ag nanostructures and smooth Ag surfaces was an important goal of this work and was done with the hope of gaining a more complete understanding of the molecule–surface interaction. The molecular orientation at the surface was determined by detailed examination of spectra obtained from SERS, SEIRA (26), and reflection–absorption IR spectroscopy (RAIRS) (27) measurements. In RAIRS, the standing electric field at the reflecting metal surface is polarized parallel to the surface normal, and thereby, only those modes that have dipole moment changes perpendicular to the surface will demonstrate appreciable relative intensity in the absorption spectrum. SEIRA experiments, on the other hand, are performed on roughened surfaces having nanoscale features randomly oriented, and so determination of molecular orientation can sometimes be challenging. SEIRA enhancement factors (EF) are modest compared to those of SERS (EF of SEIRA are commonly less than 10^2), and SEIRA spectra may have contributions from molecules more distant from the surface, and thus reflect the effect of random orientation above the first layer for films lacking epitaxy. Conversely, SERS shows a very strong first-layer effect (28). This means that the SERS spectra of oriented chemisorbed species will generally be dominated by those molecules in the first layer on the surface and therefore will reflect their orientation. Notably, however, in the case of a SERS experiment where molecules are adsorbed in the interstitial volumes between multiple particles, where electromagnetic enhancements are known to be highest, spectra may seem to indicate a random orientation.

In summary, in this work, the structures and vibrational spectra of salicylic acid and two silver–salicylate complexes are calculated using DFT methods. By employing an analysis of the calculated polarizability derivative tensor and dipole moment derivatives for each normal mode, with respect to light polarization and a given fixed molecular orientation, we utilize a systematic approach for the interpretation of experimental Raman, SERS, IR, RAIRS, and SEIRA spectra. In addition, the experimental IR and Raman spectra of prepared silver salicylate are presented for comparison with the surface-enhanced vibrational spectra. Insight is provided into the chemical adsorption and the specificity of the interaction of molecular groups on Ag nanostructures. The selection of the vibrational techniques of Raman, IR, SERS, RAIRS, and SEIRA for this work is in recognition of the fact that they represent a complete set of complementary data required for a meaningful interpretation of a molecular system and its interaction with a particular metal surface.

Experimental

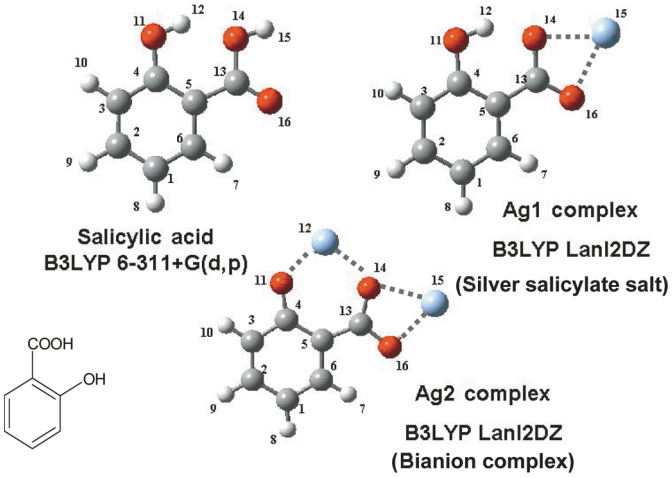
Analytical-grade salicylic acid, sodium salicylate, and silver nitrate were obtained from Sigma Aldrich and used without further purification. The complex of silver salicylate was prepared according to the methods described by Alvarez-Ros et al. (17). Raman and attenuated total reflection (ATR) IR spectra of the pure salicylic acid solid were obtained directly from the powder. Raman measurements on silver salicylate were also obtained directly from powder, while IR spectra were recorded from the powder dispersed in KBr pellets. To prepare SERS and SEIRA samples, vacuum evaporated 10 nm (mass thickness) Ag island films were dipped into 10^{-3} and 10^{-4} mol/L solutions of salicylic acid in spectrophotometric-grade acetone. These Ag island films were previously prepared by vacuum evaporation at a pressure of about 10^{-7} torr (1 torr = 133.322 Pa) and a temperature of +200 °C (maintained for 1 h after evaporation), where mass thickness was monitored with a quartz crystal balance. The slides were allowed to remain several minutes in the salicylic acid solution before removal and drying. All Raman spectra were collected with a Renishaw research Ramanscope 2000 or a Renishaw inVia Raman microscope, both equipped with Peltier-cooled CCD detectors (–70 °C) and Leica microscopes. The spectrographs use 1800 g/mm gratings with additional bandpass filter optics. Excitation lines of 488, 514, and 633 nm were used, and did not reveal any significant differences. All IR absorption measurements were recorded with a Bruker Equinox 55 FT-IR spectrometer, employing a nitrogen-cooled MCT detector. Each spectrum was measured with 1024 scans and 4 cm^{-1} resolution. ATR measurements of salicylic acid powder were obtained using an ATR accessory from Pike Technologies. SEIRA measurements on a Ge substrate were collected in transmission mode using the IRscope II microscope from Bruker. Finally, RAIRS spectra were collected from a thin salicylic acid film on a 100 nm mass thickness Ag mirror with the Harrick Auto Seagull variable-angle reflectance accessory. Reported RAIRS measurements were made with p-polarized light at an angle of incidence of 80° to the surface normal.

Computational methods

All reported calculations were performed using the Gaussian 98 (revision A.3) suite of programs (13) and employed Becke's three-parameter functional including the correlational functional of Lee et al. (23) (B3LYP). To calculate an optimized structure and vibrational spectra for salicylic acid, the 6-311+G(d,p) basis set was employed using tight convergence criteria. This basis set was deemed to be a reasonable compromise between accuracy and computational expense for this molecule. The optimized structures and vibrational spectra of the two Ag–salicylic acid complexes were computed using the Lanl2DZ basis set (24, 25), also employing tight convergence criteria. GaussView for Windows was used to view all computed results, and an in-house program (VibWidth) was used to artificially apply a 5 cm^{-1} bandwidth to all peaks in the presented calculated Raman and IR spectra. Raman frequencies were not scaled, as scaling factors are not available for the basis sets used in this study. It is expected, however, that an appropriate scaling

© 2004 NRC Canada

Fig. 1. Optimized structures of salicylic acid and the Ag1 (molecular plane is *xy*) and Ag2 complexes. Also shown is the molecular structure of salicylic acid.



factor for the 6-311+G(d,p) basis set would be close to unity for the B3LYP functional. As a general rule, neglecting scaling results in an overestimation of harmonic frequencies (29), and so this must be considered when reviewing the results for the two calculated silver complexes. In calculations of the Ag1 complex, the molecule was fixed in the *x–y* plane to simplify the application of surface selection rules in the spectral interpretation.

Results and discussion

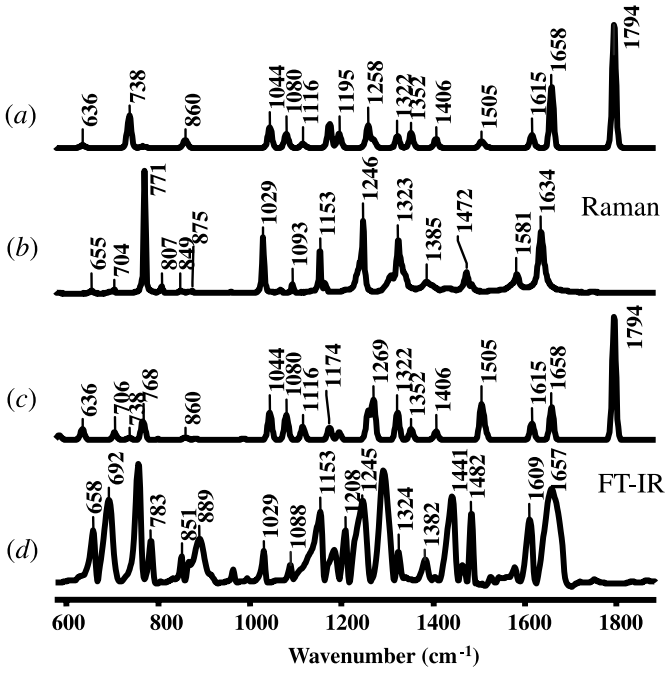
The optimized geometries of salicylic acid, a salicylate monoanion – Ag^+ complex (Ag1), and a salicylate dianion – $2Ag^+$ complex (Ag2) are shown in Fig. 1. Salicylic acid was calculated at the B3LYP/6-311+G(d,p) level of theory, while the two silver complexes were calculated at the B3LYP/Lanl2DZ level of theory. All three of these structures belong to the C_s symmetry point group and have 42 vibrational degrees of freedom, or normal vibrational modes. A summary of pertinent structural parameters for the three optimized geometries is presented in Table 1, where all bond and angle numbering refers to those numbers assigned in Fig. 1. Upon close examination of these results, it can be seen that the substitution of Ag atoms for H atoms causes drastic changes in the structural parameters of these molecules. These changes are largely concentrated on the carboxyl and hydroxyl groups of these structures and have very little impact on the aromatic ring parameters, especially at parts distant from the affected groups of the molecule.

The experimental Raman and FT-IR (ATR) spectra of bulk salicylic acid powder are directly compared in Fig. 2 with those calculated at the B3LYP/6-311+G(d,p) level of theory. To supplement these spectra, Table 2 shows the calculated and observed IR and Raman frequencies, calculated symmetries, IR intensities, Raman activities, and assignments for the fundamental vibrational modes of salicylic acid. It can be seen from these results that acceptable agreement exists between the calculated and experimentally observed Raman spectra at this level of theory. As well, it should be noted that these spectra also agree very well with results previ-

Table 1. Selected geometrical parameters for salicylic acid and the Ag1 and Ag2 complexes.

Bond lengths (Å)			
Bond	Salicylic acid	Ag1 complex	Ag2 complex
1–2	1.400	1.416	1.422
2–3	1.380	1.400	1.380
3–4	1.400	1.410	1.440
4–5	1.410	1.420	1.450
5–6	1.400	1.410	1.430
6–1	1.380	1.400	1.390
6–7	1.080	1.080	1.080
1–8	1.080	1.080	1.080
2–9	1.080	1.080	1.080
3–10	1.080	1.080	1.080
4–11	1.350	1.370	1.330
11–12	0.970	1.000	2.150
5–13	1.470	1.470	1.470
13–14	1.370	1.330	1.330
14–15	0.960	2.310	2.400
13–16	1.200	1.290	1.310
Interatomic angles (°)			
Angle	Salicylic acid	Ag1 complex	Ag2 complex
3-4-11	115.999	118.121	115.450
4-11-12	109.700	108.550	126.490
5-13-14	113.370	118.540	125.590
13-14-15	107.400	91.050	89.580
14-13-16	120.300	119.550	115.630

Fig. 2. Comparison of salicylic acid vibrational spectra. (*a*) B3LYP/6-311+G(d,p) calculated Raman spectrum, (*b*) experimental Raman spectrum (obtained from powder at 633 nm excitation), (*c*) B3LYP/6-311+G(d,p) calculated IR absorption spectrum, (*d*) experimental attenuated total reflection (ATR) IR absorption spectrum (powder).



© 2004 NRC Canada

Table 2. Calculated and observed IR and Raman frequencies with corresponding symmetries, IR intensities (in km/mol), Raman activities (in Å^4/amu), and assignments for the fundamental vibrational modes of salicylic acid.

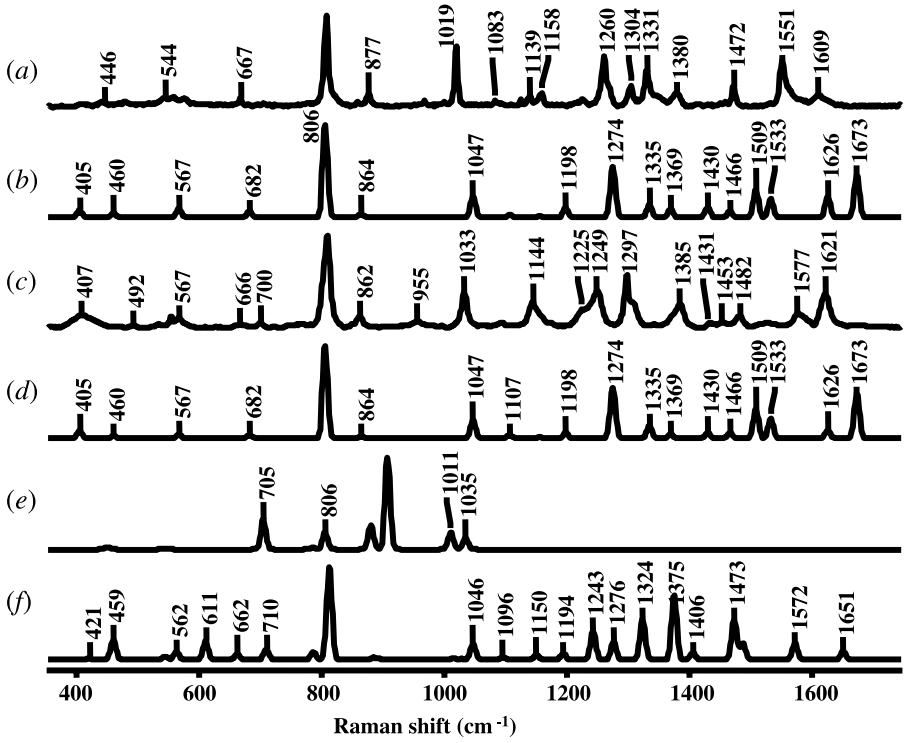
B3LYP/6-311+G(d,p)						
		Calculated		Experimental		
Frequency (cm^{-1})	Symmetry	IR intensity (km/mol)	Raman activity (Å^4/amu)	IR (cm^{-1})	Raman (cm^{-1})	Assignment
54	A″	1	0			Out-of-plane COO bend
132	A″	0	2		122	Out-of-plane butterfly
243	A′	3	1		178	Out-of-plane butterfly
254	A′	1	1		257	Rocking of carboxyl group
378	A′	2	3		284	Ring stretch
411	A′	8	2			Rocking of carboxyl and hydroxyl groups
425	A″	31	1	433	433	Out-of-plane C-H and O-H bends
491	A″	124	3	466	451	Out-of-plane C-H and O-H bends
540	A″	47	0			Out-of-plane C-H and O-H bends
548	A′	7	3	533	533	Rocking of carboxyl and hydroxyl groups
565	A′	11	8	567	565	Ring stretch
585	A″	16	0			Out-of-plane O-H bends
636	A′	39	2	658	655	Ring stretch, COO bend
706	A″	27	0	692	704	Out-of-plane C-H bend
738	A′	6	26	759	771	Ring stretch, COO scissor
768	A″	72	1	783		Out-of-plane C-H bend
800	A″	1	0	806	807	Out-of-plane C-H bend
860	A′	9	6	851	849	Ring stretch
882	A″	2	0	889	875	Out-of-plane C-H bend
986	A″	2	0	963	961	Out-of-plane C-H bend
1002	A″	0	0	995	995	Out-of-plane C-H bend
1044	A′	103	16	1029	1029	Ring stretch, C-O stretch
1080	A′	94	11	1088	1093	C-H bend, C-O stretch
1116	A′	51	3	1153	1153	C-H bend, O-H bend
1174	A′	46	19	1169	1165	C-H bend, O-H bend
1195	A′	27	11	1208	1208	C-H bend, O-H bend
1258	A′	110	18	1245	1246	C-H bend, O-H bend
1269	A′	150	6	1290		C-H bend, O-H bend
1322	A′	102	9	1306	1307	C-O-H bend
1352	A′	42	12	1324	1323	C-H bend, O-H bend, ring stretch
1406	A′	31	7	1382	1385	C-H bend, O-H bend
1505	A′	131	5	1442	1432	Ring stretch, O-H bend
1513	A′	33	1	1482	1472	Ring stretch, O-H bend
1615	A′	62	10	1580	1581	Ring stretch, O-H bend
1658	A′	124	49	1609	1634	Ring stretch, O-H bend
1794	A′	471	99	1657		C=O stretch, O-H bend, ring stretch
3172	A′	5	71		3019	C-H stretch
3189	A′	6	88	3062	3059	C-H stretch
3198	A′	4	82		3078	C-H stretch
3205	A′	7	200		3090	C-H stretch
3691	A′	288	100	3235	3239	O-H stretch
3769	A′	88	128		3239	O-H stretch

ously reported in the literature (17, 19, 20). However, there are some differences between the two, and they can be explained as being a result of condensed-phase effects. The calculated spectrum reported is for a noninteracting gas-phase system, whereas the experimental results presented are for a solid powder. This difference is known to account for very significant changes in relative vibrational intensities and can produce spectra that appear to be quite dissimilar (15). This is certainly not surprising, as salicylic acid is known to form both inter- and intramolecular hydrogen bonds in condensed phases. Indeed, this effect is even more pronounced in the IR absorption spectra where strong hydrogen bonding in the condensed phase clearly leads to differences between the calculated IR and FT-IR ATR spectra of salicylic acid.

The most striking example of this condensed-phase effect is the C=O stretch, which is calculated at 1794 cm^{-1} as an intense band but is not observed in the experimental Raman spectrum (Fig. 2). The disappearance of this band is likely the result of C=O participation in intermolecular interactions

© 2004 NRC Canada

Fig. 3. Comparison of (*a*) the Raman spectrum of silver salicylate salt (obtained from powder at 633 nm excitation), (*b*) the B3LYP/Lanl2DZ calculated Ag1 Raman spectrum (random orientation), (*c*) the experimental SERS spectrum, (*d*) the B3LYP/Lanl2DZ calculated Raman spectrum for the Ag1 complex with head-on orientation (only *xx* and *xy* polarizability derivative components used to calculate Raman activity), (*e*) the B3LYP/Lanl2DZ calculated Raman spectrum for the Ag1 complex with face-on orientation (only *xz* and *yz* polarizability derivative components used to calculate Raman activity), and (*f*) the B3LYP/Lanl2DZ calculated Ag2 Raman spectrum (random orientation).



in the condensed phase. It is, however, observed in the experimental IR spectrum as a broad peak showing a maximum at 1657 cm^{-1}. This is in agreement with the vibrational spectra recorded for salicylic acid in aqueous solution, where the C=O stretching was observed in both the Raman and IR at 1660 cm^{-1} (16). Dissolving the salicylic acid in organic solvents shows that this IR band wanders to higher wavenumbers, indicating less association via C=O interactions. A pair of bands at 1580 and 1609 cm^{-1} in the IR spectrum are assigned to C=C stretching vibrations of the aromatic ring. In the Raman spectrum, similar bands are seen at 1581 and 1634 cm^{-1}, as confirmed by the literature (17). The computed spectra clearly show that there are only two ring stretching vibrations in this region, the 1581 and 1609 cm^{-1} bands observed in the IR spectrum. The 1634 cm^{-1} band in the Raman spectrum cannot be assigned to the C=O stretching, since this vibration is clearly observed at 1657 cm^{-1} in the IR spectrum. Therefore, we must conclude that the 1634 cm^{-1} vibration observed in the Raman spectrum is a result of dimers or higher order aggregates formed in the condensed phase.

A direct comparison of several key Raman spectra for this system is presented in Fig. 3 for the region below 1700 cm^{-1}. The spectra are supported by Table 3, which contains the calculated frequencies, symmetries, Raman activities, IR intensities, and assignments for the fundamental vibrational modes of the Ag1 complex, along with the corresponding experimental frequencies for the silver salicylate salt, SERS, and SEIRA samples. The Raman spectrum of the prepared silver salicylate monoanion salt and the SERS spectrum obtained from 10 nm Ag island films coated with thin films of salicylic acid agree well with those previously reported in the literature (17, 19, 20). However, they show some differences with one another, because of the effect of hydrogen bonding that occurs for the salt sample, as well the fact that the spectrum of the salt represents a random spatial distribution, whereas the SERS spectrum is primarily derived from an oriented first layer. Results obtained using different excitation laser energies for these samples did not reveal meaningful changes in the obtained spectra.

When the obtained SERS results are compared with the Raman spectrum of the powder salicylic acid, it becomes immediately clear that the molecule has been altered due to association with the silver nanostructured surface. It is evident that salicylic acid is in fact chemisorbed on the Ag islands, forming a surface complex. This surface complex adopts a preferred orientation at the surface, and it is these two effects that are responsible for the changes in the observed spectral properties. However, it is not immediately clear from these results what the structure of the surface complex is, or what its orientation on the surface is, but there are many valuable pieces of information contained in the spectra.

The first of these pieces of information is the presence of very strong Ag-O bands in the low wavenumber region of the SERS spectrum. These bands appear to be strengthened

© 2004 NRC Canada

Table 3. Calculated frequencies, symmetries, Raman activities (in Å^4/amu), IR intensities (in km/mol), and assignments for the fundamental vibrational modes of the Ag1 complex.

B3LYP/Lanl2DZ								
		Calculated		Experimental				
Frequency (cm^{-1})	Symmetry	Raman activity (Å^4/amu)	IR intensity (km/mol)	Ag salt Raman (cm^{-1})	Ag salt IR (cm^{-1})	SERS (cm^{-1})	SEIRA (cm^{-1})	Assignment
68	A″	2	10					Ring wagging
87	A′	0	3					Ring rocking
109	A″	1	1					COO twisting
178	A″	2	2					Ring twisting
186	A′	12	11	204		Broad		COO-Ag symmetric stretch
262	A″	2	1	276				COO-ring butterfly
289	A′	0	3			Broad		COO-Ag antisymm. stretch
405	A′	8	25			407		C-OH rocking
450	A″	0	0					Ring twisting
460	A′	5	13			492		Ring stretch, Ag-O stretch
538	A′	1	5					C-C-O deformation
545	A″	0	11					Ring twisting
567	A′	10	6	575		567		Ring stretch
682	A′	7	29	669	670	700		Ring stretch, COO scissor
705	A″	0	13		708			C-H bend
785	A″	0	30		780			C-H bend, O-H bend
806	A′	99	9	809	809	809		Ring stretch, COO scissor
806	A′	0	84				757	Out-of-plane C-H bend
864	A′	4	7	859	860	862	852	Ring stretch
879	A″	0	152	877	881		888	O-H bend
908	A″	1	0					C-H bend, O-H bend
1011	A″	0	3					Out-of-plane C-H bend
1035	A″	0	0					Out-of-plane C-H bend
1047	A′	23	23	1019	1021	1033	1033	C-H bending, ring stretch
1107	A′	3	4	1083	1086	1093	1089	C-H bend, COO stretch
1156	A′	2	33	1139	1141	1144	1159	C-H bend, COO stretch
1198	A′	11	14	1224		1225		C-H bend
1269	A′	1	54		1213		1210	C-H bend, O-H bend
1274	A′	54	72	1260	1261	1249	1248	C-O stretch + C-H bend
1335	A′	14	275	1304	1302	1297	1307	COO stretch + O-H bending
1369	A′	10	126	1380	1382	1385	1382	Ring stretch
1430	A′	11	106			1431		Ring stretch, O-H bend, COO stretch
1466	A′	7	197		1454	1453	1447	Ring stretch, O-H bend, COO stretch
1509	A′	30	174	1472	1481	1482	1458	Ring stretch, C-H bend
1533	A′	20	26			1524	1484	Ring stretch, O-H bend, COO stretch
1626	A′	23	82	1551	1555	1577	1612	Ring stretch, O-H bend
1673	A′	46	114	1609	1588	1621	1655	Ring stretch, O-H bend
3162	A′	207	434		broad	2927	broad	O-H stretch
3198	A′	49	3					C-H stretch
3217	A′	95	13			3022		C-H stretch
3236	A′	27	12					C-H stretch
3243	A′	228	20	3058	3062	3064		C-H stretch

Note: Also shown are the corresponding experimental Raman and IR frequencies for the Ag salt, SERS, and SEIRA samples.

relative to the usual Ag-O peaks that are nearly always found in the spectra of Ag island films (resulting from an ever-present silver oxide layer). The presence of these Ag-O stretching bands provides very strong evidence for the formation of a surface complex (chemisorption). Further strength is provided to this hypothesis by several key spectral changes in the SERS relative to the Raman spectra of salicylic acid. Among these changes are shifts in vibrations resulting from both the carboxyl and hydroxyl groups of the molecule. For example, a clear upshift of the ring stretching + COO scissoring from 771 to 809 cm^{-1} takes place (attributed to deprotonation producing the monoanion (16)), while downshifts in several bands with considerable phenolic O-H contribution, in particular, those found at 451 and 3239 cm^{-1} in the Raman (seen at 407 and 2927 cm^{-1} in the SERS) are observed upon adsorption of the molecule on Ag. Shifts in

© 2004 NRC Canada

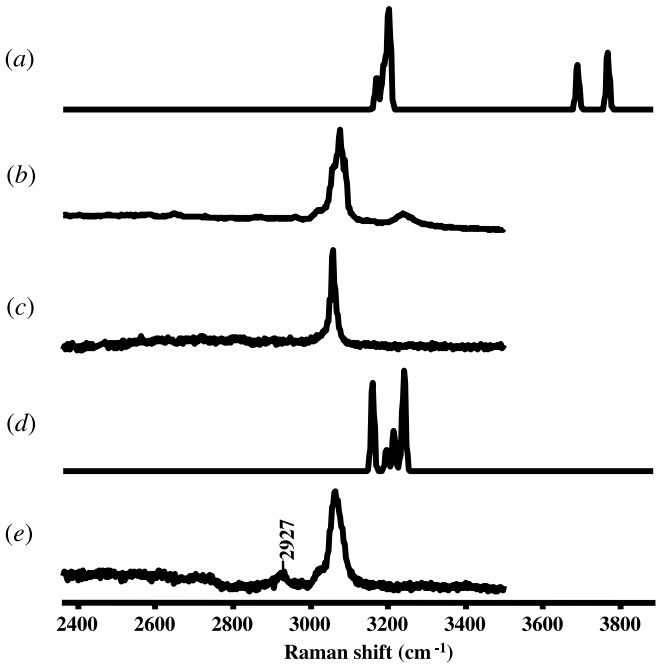
bands associated with the carboxylate group suggest that adsorption is occurring through it, while the presence of several downshifted O-H related modes indicates that the molecule is not reacting with the metal through its hydroxyl group, but rather is experiencing drastic changes in the strength of its hydrogen bonds as a result of the adsorption. This is made particularly clear by the unmistakable presence of the O-H stretching band (2927 cm^{-1}) that has shifted below the C-H stretches in the SERS spectrum, as shown in Fig. 4 (and predicted by theoretical results). Moreover, several other bands involving contributions from the O-H group are clear in the SERS spectrum (Table 3). These bands provide direct evidence that salicylic acid is not chemically adsorbed through its hydroxyl group. However, from experimental results alone, where peak assignments are unreliable, this problem remains difficult to solve, as evidenced by unclear and conflicting reports on this matter in the literature. Therefore, attempts have been made to clarify this problem through the use of DFT computational methods.

As mentioned earlier, the structure and vibrational (IR and Raman) spectra of two different Ag–salicylate complexes (Ag1 and Ag2) were calculated at the B3LYP/Lanl2DZ level of theory to determine if one would agree strongly with experimentally observed SERS spectra, and therefore clarify how the chemisorption of this molecule occurs on Ag. (Notably, an interaction of the metal with the π system of the ring was ruled out as a possibility based on early experimental results.) The Raman results derived from these calculations are shown in Fig. 3, where the calculated spectra of these two complexes (Ag1 and Ag2) are compared to the experimentally observed silver salicylate salt and SERS spectra. Tables 3 and 4, which show the calculated frequencies, symmetries, Raman activities, IR intensities, and assignments for the fundamental vibrational modes of Ag1 and Ag2, respectively, support these spectra.

It can be seen in Fig. 3 that both model complexes seem to approximate the SERS spectrum of the surface species to some extent. However, there are once again some very clear signs that will allow us to eliminate one of these possibilities. The calculated Raman spectrum of the Ag2 complex, as expected, does not account for the presence of O-H vibrational bands in the experimental SERS spectrum as that of the Ag1 complex does. The O-H stretching (2927 cm^{-1}), in particular, in the SERS spectrum confirms that the phenolate has not been formed. As shown in Fig. 4, this band demonstrates nearly identical band shape and relative intensity to the O-H stretching band in the experimental Raman spectrum of salicylic acid. As well, it cannot be reasonably assigned to a combination band, as there are no two fundamentals in the SERS spectrum whose frequencies can be summed to arrive close to 2927 cm^{-1}. Thus, given this quite clear assignment, we can conclude with a great deal of certainty that the Ag2 complex does not approximate the chemical adsorption of the salicylate surface complex on Ag.

The calculated Raman spectrum of the Ag1 complex, on the other hand, shows good agreement with the experimental SERS spectrum, especially considering the previously discussed complications created by condensed-phase and field polarization effects. Not only does the Ag1 complex calculation account for the presence of the O-H bands in the SERS spectrum, but it also predicts successfully the shifting of

Fig. 4. Comparison of Raman spectra above 2400 cm^{-1} for (*a*) B3LYP/6-311+G(d,p) calculated salicylic acid, (*b*) salicylic acid powder (experimental), (*c*) silver salicylate salt (experimental), (*d*) B3LYP/Lanl2DZ calculated Ag1 complex, and (*e*) SERS (experimental).



these bands. As shown in Table 3, the Ag1 complex has its O-H stretching mode shifted below the C-H stretches as was also observed in the experimental SERS spectra. In light of this theoretical result, there can be little doubt about the assignment of the O-H stretch in the experimental SERS spectrum. Moreover, the calculated spectrum of the Ag1 complex shows generally good agreement with the entire experimental SERS spectrum in terms of band frequencies and relative intensities. Thus, based on the results presented here, and the results found in the literature, it can be concluded that the chemical adsorption of this analyte on Ag occurs only through its carboxylate group. In fact, the calculated Raman spectrum of the Ag1 complex approximates the experimental SERS spectrum far better than it does the silver salicylate salt Raman spectrum. This may seem unexpected, but it simply demonstrates, once again, the importance of intermolecular interactions in this system. The prepared salt complex experiences strong hydrogen bonding, while the salicylate ions at the surface of the Ag nanoparticles are much more isolated from one another. In fact, for example, the Raman spectrum of the silver salicylate salt does not have an apparent O-H stretching band, as the Ag1 and SERS spectra do.

Having a clear notion about the chemical adsorption of salicylate on silver, the next logical problem becomes that of the molecular orientation at the surface. In a previous study (15), SERS surface selection rules were applied to a different adsorbate by orienting the calculated surface complex and then plotting a simulated SERS spectrum by only including those modes of symmetry with polarizability derivative tensor components parallel to the electromagnetic field at the surface. In this way, the surface selection rules were accounted for by the theoretical methods, and good agree-

© 2004 NRC Canada

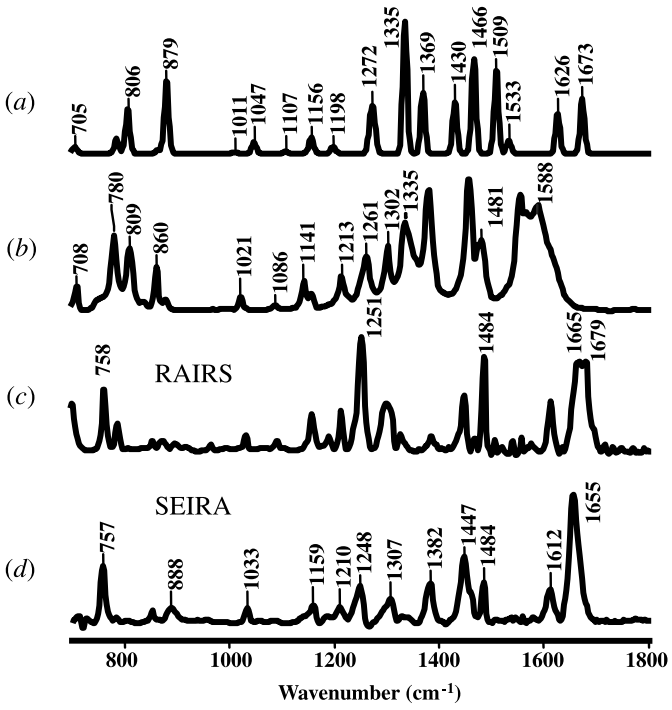
Table 4. Calculated frequencies, symmetries, Raman activities (in Å^4/amu), IR intensities (in km/mol), and assignments for the fundamental vibrational modes of the Ag2 complex.

Frequency (cm^{-1})	Symmetry	Raman activity (Å^4/amu)	IR intensity (km/mol)	Assignment
32	A″	1	6	C-C torsion
66	A′	1	1	Ring rocking
66	A′	1	11	Ring wagging
94	A″	1	2	COO twisting
126	A′	6	19	Ag-O stretch
139	A″	6	2	Out-of-plane C-C torsion
173	A′	23	5	Ring rocking
232	A′	40	22	Ag-O stretching (both Ag atoms)
252	A″	24	2	Ring wagging
332	A′	11	6	Ring rocking
421	A′	3	9	Ag-O stretch
452	A″	1	0	C-H bend
460	A′	33	4	Ag-O stretching, ring stretch
545	A″	6	11	C-H bend
563	A′	13	29	Ring stretch
611	A′	31	3	Ring stretch
662	A′	10	25	Ring stretch, COO scissoring
710	A″	17	21	C-H bend
786	A″	13	58	C-H bend
802	A″	1	26	C-H bend
813	A′	152	2	COO scissor, ring stretch
884	A′	4	19	Ring stretch, COO stretch, C-O stretch
894	A″	2	5	C-H bend
1015	A″	3	3	C-H bend
1029	A″	2	0	C-H bend
1047	A′	26	26	Ring stretch
1096	A′	5	15	Ring stretch, COO stretch
1150	A′	8	76	C-H bend,
1194	A′	11	25	C-H bend
1243	A′	48	173	C-H bend, COO stretch, C-O stretch
1276	A′	31	89	C-H bend
1324	A′	67	202	C-H bend, COO stretch
1375	A′	106	264	COO stretch, ring stretch
1406	A′	12	176	COO stretch, ring stretch
1473	A′	66	203	Ring stretch, C-O stretch, C-H bend
1487	A′	27	223	Ring stretch, C-H bend
1572	A′	28	93	Ring stretch, C-H bend
1651	A′	15	117	Ring stretch, C-H bend
3183	A′	87	15	C-H stretch
3210	A′	123	21	C-H stretch
3228	A′	110	27	C-H stretch
3243	A′	89	21	C-H stretch

ment between the calculated and experimental results was obtained. To produce simulated spectra that account for surface selection rules, we must calculate Raman activities of each mode using only the polarizability derivative tensor components that align with the electromagnetic field at the surface. In this study, the Ag1 salicylate–silver complex, having C_s symmetry, shows modes of only two symmetries (A′ and A″). (The Ag2 complex was not considered in determining the molecular orientation of the surface species, as its calculated spectrum showed poor agreement with the experimental SERS results.) Thus, knowing that salicylic acid is adsorbed through its carboxylate group, we arrive at two test cases for orientation: the molecule standing (head-on) or lying flat on the surface (face-on). In calculations of the Ag1 complex, the molecule was fixed in the *x–y* plane. Consequently, for the case of the molecule lying flat on the surface, the *x–y* plane of the molecular system is parallel to the tangential components of the field, and we can simply calculate the Raman activity of each mode using only the *xz* and *yz* components of the polarizability derivative tensor. This effectively means that we are plotting only the A″, or out-of-plane, modes for the molecule. If, however, the molecule is standing head-on to the surface, then the perpendicular component of the polarized surface field will be parallel to

© 2004 NRC Canada

Fig. 5. Comparison of (*a*) B3LYP/Lanl2DZ calculated IR spectrum for the Ag1 complex, (*b*) IR absorption spectrum of silver salicylate salt (KBr pellet), (*c*) reflection–absorption IR spectrum (RAIRS), and (*d*) surface-enhanced IR absorption spectrum.



the plane of the molecular system, and the Raman activity of each mode can be calculated using only the *xx* and *xy* components of the polarizability derivative tensor (assuming the molecule is standing with its *x*-axis parallel to the surface normal). In this way, we are accounting for all in-plane vibrations that have polarizability derivative components parallel to the surface electromagnetic field. Polarizability derivative tensor components are readily obtained from quantum chemical calculations performed with software packages such as Gaussian 98 (13), and Raman activities can be calculated from the invariants of the derived polarizability tensor (30).

The two cases mentioned above have been tested in this work, and the results are shown in Fig. 3. Upon close examination, it can be seen that the spectrum representing head-on orientation, as expected, is clearly in closer agreement with the experimental SERS spectrum than the spectrum representing face-on orientation. This is unambiguous evidence suggesting that the molecule is not lying flat on the surface. However, it appears that experimental SERS results are likely best approximated by the Ag1 spectrum (average of spatial directions), and from this we can conclude that the molecule is slightly tilted at the surface.

In attempts at obtaining corroborating evidence about the orientation of salicylate chemically adsorbed at silver surfaces, RAIRS and SEIRA measurements were made and used in conjunction with theoretical results for the Ag1 complex. These results are summarized in Fig. 5, which also includes the IR absorption spectrum of silver salicylate dispersed in a KBr pellet. It can be seen that the RAIRS and SEIRA results show agreement with one another and with results for salicylic acid powder (spectrum in Fig. 1), while the silver salt spectrum is quite dissimilar. This can be explained as being the result of strong intermolecular attractions that salicylic acid and the salt complex both exhibit, as confirmed by the observation of several broad IR bands (more than average full width at half-maximum) in the spectra. Due to very modest enhancements in the IR (SEIRA and RAIRS), and thus a weak first-layer effect, even moderate surface concentrations bring about the spectrum of the bulk material. This is in contrast with what is observed in SERS measurements, where first-layer effects are dominant.

However, let us follow the relative intensities of two bands: the strong in-plane vibration at 1655 cm^{-1}, characteristic of the carboxylate moiety, and the out-of-plane C-H bending vibration observed at 757 cm^{-1} in the SEIRA spectrum. Assuming a predominant perpendicular polarization at the silver nanostructures, the intensity ratio for the two bands (I_{1655}/I_{757}), may be used as an indicator for the molecular orientation of the adsorbate at or near the surface. The reference ratio, for a random distribution, is in this case the spectrum of the salicylic acid powder. The ratio will show a maximum for a head-on orientation, and a minimum for flat or face-on (molecular plane parallel to the surface) orientation. The latter is a direct application of the surface selection rules. It can be seen that the ratio increases in the SEIRA spectra, confirming a preferential orientation in favor of the head-on model for the adsorbate. Since the relative intensity of the 757 cm^{-1} mode is diminished, but still clearly observed, it must be concluded that, on average, the molecule demonstrates a predominant tilted head-on orientation at the surface.

Conclusions

In this report, DFT methods were employed to investigate the nature of the chemical adsorption of salicylic acid on silver surfaces. The structure of salicylic acid, along with its IR and Raman spectra, was determined at the B3LYP/6-311+G(d,p) level of theory. These results were then used in the assignment of vibrational spectra and generally showed good agreement with those obtained experimentally, accounting, of course, for condensed-phase effects. SERS spectra obtained from silver island films thinly coated with salicylic acid showed good agreement with results previously reported in the literature for colloidal solutions. To determine the structure and orientation of the surface complex of salicylate formed at Ag surfaces, the optimized geometries and Raman spectra of two model salicylate–silver complexes (Ag1, Ag2) were calculated at the B3LYP/Lanl2DZ level of theory. Experimental vibrational spectra were obtained for a silver salicylate salt for comparison with SERS results. It was found that experimentally observed SERS spectra and simulated SERS spectra of a salicylate complex chemisorbed through its carboxylate group (Ag1) show good agreement with one another. It is concluded that salicylate chemically adsorbs only through its carboxylate group. Conclusive evidence for a tilted head-on orientation of the salicylic acid complex on the surface was obtained from calculations of simulated SERS spectra that account for po-

© 2004 NRC Canada

larization, as well as from comparisons of reference powder results with SEIRA and RAIRS spectra.

Acknowledgements

Thanks to J.W. Gauld, M.D. Halls, and current MSSG members for their kind assistance and enlightening discussion. Financial assistance from the Natural Sciences and Engineering Research Council of Canada (NSERC) is gratefully acknowledged.

References

1. M. Fleischmann, P.J. Hendra, and A.J. McQuillan. Chem. Phys. Lett. **26**, 163 (1974).
2. D.L. Jeanmaire and R.P. Van Duyne. J. Electroanal. Chem. **84**, 1 (1977).
3. M.G. Albrecht and J.A. Creighton. J. Am. Chem. Soc. **99**, 5215 (1977).
4. M. Kerker. Selected papers on surface-enhanced Raman scattering. SPIE Milestone Series. *Edited by* B.J. Thompson. SPIE, Bellingham, Wash. 1990.
5. K. Kneipp, H. Kneipp, I. Itzkan, R.R. Dasari, and M.S. Feld. Chem. Rev. **990**, 2957 (1999).
6. M. Moskovits. Rev. Mod. Phys. **57**, 783 (1985).
7. B. Pettinger, G. Picardi, and G. Ertl. Electrochemistry, **68**, 942 (2000).
8. G.C. Schatz and R.P. Van Duyne. *In* Handbook of vibrational spectroscopy. *Edited by* J.M. Chalmers and P.R. Griffiths. John Wiley and Sons, Chichester, UK. 2002. p. 759.
9. P.J.G. Goulet, N.P.W. Pieczonka, and R.F. Aroca. Anal. Chem. **75**, 1918 (2003).
10. R. Aroca and G.J. Kovacs. *In* Vibrational spectra and structure. *Edited by* J.R. Durig. Elsevier Science Publishing Company, Amsterdam. 1991. p. 55.
11. R.G. Greenler. J. Chem. Phys. **44**, 310 (1966).
12. M. Moskovits. J. Chem. Phys. **77**, 4408 (1982).
13. M.J. Frisch, G.W. Trucks, H.B. Schlegel, G.E. Scuseria, M.A. Robb, J.R. Cheeseman, V.G. Zakrzewski, J.A. Montgomery, R.E. Stratmann, J.C. Burant, S. Dapprich, J.M. Millam, A.D. Daniels, K.N. Kudin, M.C. Strain, O. Farkas, J. Tomasi, V. Barone, M. Cossi, R. Cammi, B. Mennucci, C. Pomelli, C. Adamo, S. Clifford, J. Ochterski, G.A. Petersson, P.Y. Ayala, Q. Cui, K. Morokuma, D.K. Malick, A.D. Rabuck, K. Raghavachari, J.B. Foresman, J. Cioslowski, J.V. Ortiz, B.B. Stefanov, G. Liu, A. Liashenko, P. Piskorz, I. Komaromi, R. Gomperts, R.L. Martin, D.J. Fox, T. Keith, M.A. Al-Laham, C.Y. Peng, A. Nanayakkara, C. Gonzalez, M. Challacombe, P.M.W. Gill, B. Johnson, W. Chen, M.W. Wong, J.L. Andres, C. Gonzalez, M. Head-Gordon, E.S. Replogle, and J.A. Pople. Gaussian 98. Revision A.3 [computer program]. Gaussian Inc., Pittsburgh, Pa. 1998.
14. G. Cardini and M. Muniz-Miranda. J. Phys. Chem. B, **106**, 6875 (2002).
15. R.F. Aroca, R.E. Clavijo, M.D. Halls, and H.B. Schlegel. J. Phys. Chem. A, **104**, 9500 (2000).
16. B. Humbert, M. Alnot, and F. Quiles. Spectrochim. Acta Part A, **54**, 465 (1998).
17. M.C. Alvarez-Ros, S. Sanchez-Cortes, and J.V. Garcia-Ramos. Spectrochim. Acta Part A, **56A**, 2471 (2000).
18. R. Francois. Rev. Aquat. Sci. **3**, 41 (1990).
19. Y. Wang, Y.-S. Li, Z. Zhang, and D. An. Spectrochim. Acta Part A, **59A**, 589 (2003).
20. S. Sanchez-Cortes and J. V. Garcia-Ramos. J. Colloid Interface Sci. **231**, 98 (2000).
21. D. Philip, A. John, C.Y. Panicker, and H.T. Varghese. Spectrochim. Acta Part A, **57**, 1561 (2001).
22. A.D. Becke. J. Chem. Phys. **98**, 5648 (1993).
23. C. Lee, W. Yang, and R.G. Parr. Phys. Rev. B, **37**, 785 (1988).
24. P.J. Hay and W.R. Wadt. J. Phys. Chem. **82**, 299 (1985).
25. T.H. Dunning and P.J. Hay. Methods of electronic structure theory. Plenum Press, New York. 1977.
26. M. Osawa. Bull. Chem. Soc. Jpn. **70**, 2861 (1997).
27. F.M. Hoffmann. Surf. Sci. Rep. **3**, 107 (1983).
28. A. Otto. Phys. Stat. Sol. (a), **188**, 1455 (2001).
29. A.P. Scott and L. Radom. J. Phys. Chem. **100**, 16 502 (1996).
30. D.A. Long. The Raman effect. John Wiley and Sons, Chichester, UK. 2002. p. 121.

© 2004 NRC Canada

The Br—O bond in halogen oxides — Empirical force constants and electronic characteristics[1]

Rafael Escribano, Ismael K. Ortega, Rafael G. Mosteo, and Pedro C. Gómez

Abstract: A number of bromine oxides and mixed chlorine–bromine oxides for which spectroscopic information is available have been chosen to investigate the nature and characteristics of the Br—O bond. The study consists of the empirical determination of stretching force constants for these bonds from observed vibrational spectroscopic data and the analysis of the topological characteristics of the bonds via ab initio calculations. The latter have been performed at the MP2 level with a 6-311+G(2df) basis set, to provide a uniform and systematic framework for comparing these species. Three types of Br—O bonds have been found, with different characteristics of strength and electron density. The results are compared with those recently found for the Cl—O bond in chlorine oxides.

Key words: bromine oxides, bond electronic structure.

Résumé : On a choisi un certain nombre d'oxydes de brome et de chlore, ainsi que d'oxydes mixtes de brome et de chlore au sujet desquels on disposait d'information spectroscopique dans le but d'étudier la nature des liaisons chimiques Br—O. L'étude a consisté à déterminer la constante de force d'élongation (« stretching ») à partir des données de spectroscopie vibrationnelle ainsi qu'à étudier les caractéristiques topologiques de la densité de ces liens qui ont été obtenues à partir de calculs ab initio. Pour ces calculs, on a choisi la méthodologie MP2/6-311+G(2df) qui comporte un niveau uniforme de la théorie pour toutes les espèces étudiées. On a trouvé trois classes de liens Br—O qui présentent des différences en ce qui concerne la force du lien ainsi que la densité électronique et on a fait une comparaison avec des résultats publiés antérieurement pour le lien Cl—O.

Mots clés : oxydes de brome, structure électronique de liaison.

[Traduit par la Rédaction]

Introduction

In a recent investigation (1), the electronic structure of the Cl—O bond was studied, taking as subject of research a number of chlorine oxides for which vibrational spectroscopic data were available. It was found that Cl and O can form three types of markedly different bonds, which were characterized by their force constants, obtained from the analysis of the experimental data, and by their electronic density distribution, studied by ab initio methods based on the atoms in molecules (AIM) analysis (2). A similar investigation is presented here for the Br—O bond in bromine oxides and mixed bromine–chlorine oxides.

The halogen oxides, especially those with Cl and Br, have received considerable attention in recent years, since they are involved in atmospheric processes and play a leading role in ozone depletion reactions (3–9). Much more is known of chlorine oxides (1, and refs. cited therein), but there are also a number of papers on the compounds formed by oxygen and bromine with different stoichiometries, as well as on chlorine–bromine oxides. We restrict the scope of this investigation to molecules whose vibrational or rovibrational spectrum has been reported in the literature and leave aside other species of undoubted interest for which only theoretical predictions are available, and which have never been detected experimentally. The list of molecules under study is given in Table 1.

Most of the published spectroscopic information concerns the simplest and more stable species, namely, BrO, OBrO, and BrOBr, which have mainly been observed in matrices, but, when available, gas-phase values for the vibrational frequencies were selected as data for force field refinements. BrO has been extensively studied, both in the gas phase and in matrices (see ref. 10 and refs. cited therein; see also ref. 11 for works prior to 1996). The most recent data on the geometry of OBrO comes from the microwave experiment

Received 17 March 2003. Published on the NRC Research Press Web site at http://canjchem.nrc.ca on 01 September 2004.

R. Escribano.[2] Instituto de Estructura de la Materia, Consejo Superior de Investigaciones Científicas, Serrano 123, 28806 Madrid, Spain.
I.K. Ortega. Instituto de Estructura de la Materia, Consejo Superior de Investigaciones Científicas, Madrid, and Departamento de Química Física y Analítica, Universidad de Jaén, Spain.
R.G. Mosteo. Escuela Universitaria Politécnica, Universidad de Zaragoza, Ciudad Escolar s/n, 44071 Teruel, Spain.
P.C. Gómez. Departamento de Química Física I, Facultad de Química, Universidad Complutense, 28040 Madrid, Spain.

[1]This article is part of a Special Issue dedicated to the memory of Professor Gerhard Herzberg.
[2]Corresponding author (e-mail: rescribano@iem.cfmac.csic.es).

 doi: 10.1139/V04-016 © 2004 NRC Canada

Table 1. Data for the bromine oxides and mixed chlorine–bromine oxides studied in this work and results of the force constant refinements carried out for individual molecules and their isotopomers.

		Length (Å)			Frequency (cm^{-1})		Force constants (10^2 N m^{-1})[c]			
Molecule	Bond	Exptl.[a]	Optim.[b]	Mode	Exptl.[a]	Calcd.[b]	Type	Exptl.[a]	Optim.[b]	Bond type
BrO	Br—O	1.717	1.707	str.	723.41	723.4	$f_{str.}$	4.127	4.1005(—)	I
OBrO	Br—O	1.644	1.637	sym. str.	800.4	798.4	$f_{str.}$	5.4696	5.8254(73)	I
				antisym. str.	848.5	847.3	$f_{str.\text{-}str.}$	–0.008	0.0251(73)	
				bend	317.5	317.2	f_{bend}	1.026	1.0325(20)	
BrOO	Br—O		2.318							III
	O—O		1.164	str.	1485.1	1486.0	$f_{str.}$		10.0948(178)	
BrOBr	Br—O	1.838	1.846	sym. str.	532.9	530.0	$f_{str.}$	2.874	2.5659(276)	II
				bend	197	197.0	f_{bend}	1.023	1.3698(360)	
				antisym. str.	629.0	626.6	$f_{str.\text{-}str.}$	0.0334	0.2258(276)	
BrBrO	Br—Br		2.426	str.	236	237.1	$f_{str.}$		1.2102(69)	
	Br—O		1.637	str.	804.8	804.7	$f_{str.}$		5.0395(206)	I
BrO_3	Br—O		1.607	antisym. str.	828	828.0	$f_{str.}$		5.2493(—)	I
	Br—O(2)			sym. str.	800	800.0	$f_{str.\text{-}str.}$		0.2736(—)	
				bend	350	350.0	f_{bend}		1.4380(—)	
$BrOBrO_3$	Br—O		1.840	str.	582	555.1	$f_{str.}$		1.5882(715)	II
	O—Br		1.836	str.	594	620.1	$f_{str.}$		2.5915(528)	II
	Br—O		1.576	sym. str.	856	851.8	$f_{str.}$		5.5920(579)	I
	Br—O(2)		1.580	antisym. str.	842	845.4				
				bend	453	452.9	f_{bend}		1.3355(265)	
ClOBr	Cl—O		1.705	str.	676	676.0	$f_{str.}$		2.9536(—)	II
	O—Br		1.846	str.	559	559.0	$f_{str.}$		2.5574(—)	II
ClBrO	Cl—Br		2.253							
	Br—O		1.633	str.	818.9	819.0	$f_{str.}$		5.2254(21)	I
BrClO	Br—Cl		2.317							
	Cl—O		1.500	str.	940.9	941.0	$f_{str.}$		5.6262(7)	I
BrOClO	Br—O		1.845							II
	O—Cl		1.775							II
	Cl—O		1.488	str.	991.1	991.4	$f_{str.}$		6.2000(35)	I
ClOBrO	Cl—O		1.706							II
	O—Br		1.905							II
	Br—O		1.629	str.	834.4	834.4	$f_{str.}$		5.4037(1)	I
$BrClO_2$	Br—Cl		2.448							
	Cl—O		1.442	sym. str.	1019.2	1019.2	$f_{str.}$		7.7990(—)	I
				antisym. str.	1193.5	1193.5	$f_{str.\text{-}str.}$		–0.3025(—)	

[a]Data experimentally determined. See text for references.
[b]Calculated results from this work; optim., optimized. Uncertainties for the force constants are given in parentheses in units of the last digit.
[c]10^2 N m^{-1} = 1 mdyn $Å^{-1}$.

of Müller et al. (12), who also determined the empirical force field of this species, whereas the vibrational frequencies have been measured in works on FT-IR (13), visible (14), and matrix (15) spectroscopy, including data on several isotopic derivatives. Müller and Cohen (16) also determined the geometry and force field of BrOBr, for which frequencies were recorded in the gas phase (13) and in matrices (17–19) or were estimated for isotopic derivatives by correcting matrix values or from rotational spectra measurements (16). We have not found in the literature any empirical determination of the geometry for the rest of the oxides studied here, with the exception of some X-ray measurements for $BrOBrO_3$ that will be discussed below, as this molecule deserves special attention. Some vibrational frequencies have been reported for the remaining molecules, although a complete spectrum has not been recorded for any of them. The appropriate references are indicated, together with other data, in the *Results* section.

High-quality ab initio calculations have been previously published for specific bromine or mixed oxides (20–28), at different degrees of theory. On the other hand, the aim of this contribution, from the computational point of view, is to present a uniform and systematic description of these species, calculated at a reasonably high level. This has been chosen as an MP2/6-311+G(2df) combination of method and basis set. We used the refined geometrical structure given in the literature as input for our force field or ab initio calculations, when experimentally derived information on the geometry of the molecules was not available.

We present in the next section a brief description of the

© 2004 NRC Canada

tools and methods used in this work. In the following one, we describe the results, with special emphasis on specific molecules, and we present the main conclusions in the final section of the paper.

Methodology

We have followed the same procedure as in ref. 1, where a detailed description was given of the methods used in this work. In brief, the force field refinement was done in two steps. In the first, the observed frequencies for each individual molecule and its isotopomers were taken as data for a standard fitting to determine the stretching force constants of the bonds involved in the corresponding vibrational mode. In a few cases, a bending force constant or a stretch–stretch interaction constant was also refined. We followed the usual Wilson's GF method (29) using computer programs written by us (30). The results are commented on below. In the second step, we used the so-called group force constants or characteristic force constants method (31), which enables the refinement of a set of force constant parameters common to a series of molecules that contain a common group of atoms. The molecules may have the same number or different numbers of atoms and various symmetries. The refinement yields, in this case, the average values of the force constants for the common bonds in the series of molecules. The observed frequencies are not necessarily reproduced perfectly, but the refined force constants provide a good representation for the forces between the atoms present in the common groups. In our case, we have fitted seven different force constants, corresponding to three markedly different types of Br—O and Cl—O bonds.

For the topological analysis, we have used Bader's AIM analysis (2) as implemented in the Gaussian 98 (G98) set of programs (32). First, we carried out a structure optimization for each molecule at the MP2 level of theory with a 6-311+G(2df) basis, which proved to be a good compromise between use of computational resources and quality of results. Some tests at the CCSD(T) level of theory failed to converge for some of the more difficult radicals, like BrO_3 or BrOO. In the case of the ground-state doublet radicals like OBrO or BrOO, UMP2 rather than MP2 calculations were carried out in this work. These UMP2 calculations often suffer from spin contamination, i.e., mixing of higher spin states (in the present case, quadruplets, sextuplets, etc.), which can be partially removed by means of appropriate projection operators. The amount of spin contamination is normally evaluated by means of the expectation value of the total spin angular momentum, $\langle \mathbf{S}^2 \rangle$, corresponding to the appropriate wave function. For the radicals studied here with only one unpaired electron, $\langle \mathbf{S}^2 \rangle$ should be 3/4, but initial values obtained for the UHF wave function were 0.790 for OBrO and 0.770 for BrOO. This implies a moderate spin contamination that is further diminished after annihilation of the contribution of the next higher state, yielding $\langle \mathbf{S}^2 \rangle$ values of 0.762 and 0.757 for OBrO and BrOO, respectively. The relative agreement with the predicted value is thus within 2%, and therefore the effect of spin contamination on relative energies, equilibrium geometries, and electron density is not likely to be relevant. As for its effect on the calculated harmonic frequencies, the spin contamination for these molecules has already been studied in a previous paper (33) and found to be small as well.

For the optimized geometry of each molecule, we studied several topological properties of the total electron density ρ, which characterize the bonds in the molecule. These properties are the bond critical point of the electron density and its distance to the bonded atoms (r_{bcp}), the density (ρ_{bcp}) and the Laplacian of the density ($\nabla^2\rho_{bcp}$) at the critical point, and the ellipticity of the critical point (ε). In most cases, the critical points are saddle points at which two curvatures of the electron density (λ_1, λ_2) are negative and one is positive. When two atoms are bonded, the electron density reaches a minimum along the bond line precisely at r_{bcp}, whereas this point is a maximum in the perpendicular plane. If we choose λ_2 to be the smallest (absolute value) eigenvalue, the ellipticity of the bond is defined as $\varepsilon = (\lambda_1/\lambda_2) - 1$. It provides an indication about the extent to which the density is accumulated in a plane containing the bond line. Thus, if a particular bond has cylindrical symmetry, it would display equal λ_1 and λ_2 values and the ellipticity would be zero; on the other hand, if some density is accumulated in a perpendicular plane to the bond line, ε would have a nonzero value and would inform about the extent of such concentration. As the λ_2 value diminishes, the bond is thought to become less stable, leading to the point of instability and rupture when it approaches zero. The Laplacian of the density, $\nabla^2\rho(r)$, tells us how the charge is distributed, so that in the regions where $\nabla^2\rho < 0$ the charge is locally concentrated, whereas in the regions where $\nabla^2\rho > 0$ charge depletion is found.

For reference purposes only, we may quote some typical values of the electron density at the bond critical point ρ_{bcp} taken from ref. 34 for the C—C bond: 0.24 au for ethane, 0.36 au for the double bond in ethylene, and 0.45 au for the triple bond in ethyne. In the molecules we study here, values range from 0.06 to 0.28 au.

We have estimated the average values of these magnitudes for the different types of bonds and evaluated their usefulness for describing the bonds. We have also calculated the covalent bond orders for the Br—O and Cl—O bonds under study, based on partitioning of the number of electrons within the topological theory of AIM implemented in the G98 package, as discussed in refs. 35–37. This method does not imply any empirical fitting to specific types of bonds.

Results

We present in Table 1 a summary of the data collected for the set of molecules under study. Where available, we indicate experimental bond lengths and observed vibrational frequencies. We also include previously calculated empirical force constants, which come from ref. 12 for BrO and OBrO and from ref. 16 for BrOBr. Together with these data, we display the results obtained in the present work, both for optimized geometry from our ab initio calculations and for refined wavenumbers and force constants from the individual refinements of each molecule and its isotopomers. These individual refinements are carried out in a standard way (38). When the frequency of a specific normal mode has not been observed, the corresponding force constant is not refined and

© 2004 NRC Canada

Table 2. Best-estimate values of the force constant parameters refined in a joint fit of the complete set of halogen oxides studied in this work.

Bond	Type	Molecules[a]	Best estimate (10^2 N m^{-1})[b]
$Cl_xBr_yO_z$			
Br—O	I	*OBrO*, Br*BrO*, *BrO*$_3$, BrO*BrO*$_3$, Cl*BrO*, ClO*BrO*	5.259(34)
	I	*BrO*	4.100(86)
	II	*BrOBr*, Br*OBr*O$_3$, Cl*OBr*	2.536(37)
	II	*BrO*BrO$_3$	1.676(138)
Cl—O	I	Br*ClO*$_2$	7.799(172)
	I	Br*ClO*, BrO*ClO*	5.811(81)
	II	*ClO*Br	2.960((99)
Cl_xO_y			
Cl—O[c]	I	Cl*ClO*$_2$, *ClO*$_2$O$_2$, ClO*ClO*$_2$	8.203(91)
	I	Cl*ClO*, ClO*ClO*	6.121(78)
	II	*ClOCl*, *ClO*ClO, *ClO*ClO$_2$	2.720(53)

[a] The relevant bonds within each molecule are indicated in italic type.
[b] Uncertainties are given in parentheses in units of the last digit.
[c] From ref. 1.

a blank is left in the appropriate entry of the table (see, e.g., BrOO and ClBrO). The complete set of data included vibrational frequencies from the following isotopic species: bromine-79 and bromine-81 isotopomers for $Br^{16}O$ (39); 16–79–16, 16–81–16, 18–79–18, and 18–81–18 for OBrO (14, 15); 79–79–16, 79–79–18, 81–81–16, and 81–81–18 for BrBrO (17, 40); 79–16–79, 79–18–79, 79–16–81, and 79–18–81 for BrOBr (13, 16, 18, 19); 16–16, 16–18, and 18–18 for ^{79}BrOO (15); 79–16, 81–16, 79–18, and 81–18 for ^{35}ClBrO (41); 35–16, 35–18, and 37–16 for ^{79}BrClO (41); chlorine-35 and chlorine-37 isotopes for $^{79}Br^{16}OCl^{16}O$ (42); bromine-79 and bromine-81 isotopes for $^{35}Cl^{16}OBr^{16}O$ (42); and the more abundant isotopic species only for BrO_3 (11), $BrOBrO_3$ (43), ClOBr (27), and $BrClO_2$ (42). Only frequencies for the parent molecules are reported in Table 1, values for the minor isotopomers being reproduced with a similar quality in the force field analysis. The last column of Table 1 indicates our labelling of the type of bond formed between the oxygen atom and the halogen, Br or Cl, according to the value of the refined force constant of the corresponding bond stretching.

Based upon these results, we performed a joint fit using the stretching frequencies of all halogen oxides as input to refine a reduced set of stretching force constants. The best estimates of the refined force constants are given in Table 2, with an indication of the molecule in which the appropriate bond is found. For the Cl—O bond, the corresponding refined values reported in the chlorine oxides paper (1) are also listed for comparison.

Table 3 collects the results of the topological analysis performed on these molecules, and Table 4 presents the average values of the electronic density characteristics for the types of bonds found, to facilitate the forthcoming discussion.

From the analysis of the preceding data, we have found three different types of Br—O bonds, similar to the findings for the Cl—O bond. The stronger type of bond, termed type I, occurs in molecules in which the bromine atom is linked to two or more oxygen atoms that are located at the end of the molecule, and it is thus denominated "central". Type II corresponds to weaker bonds, found in molecules with bromine atoms at end positions, called "external". A type III bond is formed when a very weak link occurs between a bromine atom and an otherwise stable molecule, as in BrOO, and we term it simply "weak". The same characteristics apply for the Cl—O bonds present in the mixed oxides studied here, as well as in the Cl_xO_y species studied previously (1).

The frequencies where the Br—O bond stretching modes appear in the spectrum give a straightforward indication of the type of bond, with values around 800 cm^{-1} for the central type and 500 cm^{-1} for the external type. Accordingly, the corresponding force constants have typical values for a strong or for a moderate single bond of 5×10^2 or 2.5×10^2 N m^{-1}, respectively. The strength of the binding is also reflected in the bond length, which varies between values of 1.6 and 1.9 Å (1 Å = 0.1 nm) for central and external bonds, respectively, whereas it is much longer (2.3 Å) for the weak bond in BrOO. Similarly, the covalent bond order has decreasing values in the series, indicating a fairly strong single bond (bond order of 1.7) in the first case, a standard single bond (bond order of 1.1) in the second, and a very weak binding (bond order of 0.6) in the third. There are some special cases that will be discussed in more detail below.

The analysis of the topological characteristics of these bonds presents some interesting results, which are more manifest when one looks at the average values of the electron distribution properties. Table 4 lists the mean values of the electron density at the bond critical point, the Laplacian of the density distribution, and the ellipticity of the bond. These values are calculated for each type of bond from the results given in Table 3 for the corresponding specific bond in the molecules listed in the footnotes to Table 4. We have also included the standard deviation about each mean value. Thus, when comparing the ellipticity mean values of the Br—O bonds, we can see that they increase as the bond gets weaker, indicating a less cylindrical symmetry of the bond, but the uncertainties are very large, overlapping consecutive mean values. The use of this quantity as an indicator of the bond type seems therefore inadvisable. A similar result is found for the Laplacian of the density. Increasing positive values are found as the bonds get weaker, indicating increas-

© 2004 NRC Canada

Table 3. Properties of the bonds in the halogen oxides studied in this work, obtained with the MP2/6-311+G(2df) method and basis set, for the converged equilibrium geometries.

Molecule	Bond A—B	d_{bcp}[a] (Å)	ε_{bcp}[b]	$\nabla^2\rho_{bcp}$[c] (au)	ρ_{bcp}[d] (au)	Bond order[e]	Bond type
BrO	Br—O	0.881	0.024	0.076	0.205	1.6	I
OBrO	O—Br	0.793	0.051	0.116	0.240	1.8	I
BrOO	Br—O	1.080	0.082	0.140	0.056	0.6	III
	O—O	0.572	0.003	–0.462	0.579	2.2	
BrOBr	Br—O	0.938	0.047	0.111	0.149	1.1	II
BrBrO	Br—Br	1.201	0.124	0.075	0.080	1.2	
	Br—O	0.846	0.039	0.126	0.237	1.7	I
BrO_3	Br—O	0.820	0.058	0.055	0.260	1.6	I
	Br—O(2)	0.828	0.073	0.128	0.256	1.7	I
$BrOBrO_3$	Br—O	0.940	0.006	0.123	0.149	1.1	II
	O—Br	0.926	0.092	0.087	0.166	0.9	II
	Br—O	0.810	0.042	0.067	0.280	1.6	I
	Br—O(2)	0.812	0.057	0.073	0.278	1.7	I
ClOBr	Cl—O	0.875	0.049	0.029	0.187	1.2	II
	O—Br	0.907	0.055	0.110	0.149	1.1	II
ClBrO	Cl—Br	1.112	0.129	0.083	0.099	1.2	
	Br—O	0.844	0.035	0.124	0.240	1.8	I
BrClO	Br—Cl	1.147	0.118	0.081	0.089	1.3	
	Cl—O	0.801	0.053	–0.436	0.300	1.7	I
BrOClO	Br—O	0.934	0.024	0.106	0.150	1.1	II
	O—Cl	0.888	0.105	0.191	0.164	1.1	II
	Cl—O	0.799	0.044	–0.494	0.310	1.9	I
ClOBrO	Cl—O	0.870	0.022	0.036	0.187	1.2	II
	O—Br	0.960	0.085	0.171	0.134	1.0	II
	Br—O	0.843	0.035	0.132	0.242	1.8	I
$BrClO_2$	Br—Cl	1.207	0.028	0.088	0.073	1.1	
	Cl—O	0.809	0.114	–0.748	0.351	1.8	I

[a] *d*, distance from bond critical point (bcp) to atom A.
[b] Ellipticity at bcp.
[c] Laplacian of the electron density at bcp.
[d] Charge density at bcp.
[e] Bond order based on partitioning of the number of electrons; see text.

ing withdrawal from the maximum of charge concentration, where $\nabla^2\rho$ should be negative for a strong bond. However, again the standard deviations about the mean values are larger than the differences between the mean values characteristic of each type of bonds. On the other hand, the electron density at the bond critical point offers a good indication of the bond type. The mean value of ρ decreases substantially from central to external to weak bonds, and the standard deviations about the mean values are relatively small.

In view of these results, the chemical nature of these bonds can be envisaged in the following way. A central type Br—O bond, as found in the BrO_3 molecule, is formed by both the oxygen atom and the bromine atom contributing two electrons each, giving rise to a kind of π-type bonding, comparatively shorter and with higher density in the plane perpendicular to the bond. The typical value of the covalent bond order, 1.6 to 1.8, is consistent with this description. On the other hand, in an external bond, as in BrOBr, the oxygen and bromine atoms contribute one electron each, resulting in a σ-type bond, longer, more cylindrical, and with lower density. The O atom in this case would accommodate its electrons in sp^3 hybrid orbitals, with two pairs of nonbonding electrons. Correspondingly, a covalent bond order close to 1 is calculated for this type of bond. Finally, the weak type of bond is mainly of electrostatic nature; the covalent bond order of ~0.6 reflects that there is still some electron sharing between bromine and oxygen atoms.

It is interesting to see that these topological properties have very similar values for Cl—O bonds, both in pure chlorine oxides and in the mixed species studied here. The substitution of a Cl atom by a Br atom does not alter in any appreciable amount the charge density or the Laplacian of the density of any other Cl—O bonds contained in the molecule. For example, ρ and $\nabla^2\rho$ for the external Cl—O bond in ClO*ClO* and BrO*ClO* are calculated as 0.312 and –0.426 au (ClOClO; ref. 1) and 0.310 and –0.494 au (BrOClO). The computed values for Cl_xO_y species of ref. 1 were obtained with the same basis set as in this work, namely, 6-311+G(2df), although in ref. 1 a density functional method (B3LYP) was used. Thus, it seems that the basis set is more a determinant than the method of calculation in the evaluation of these electronic properties.

It is also illustrative to make a comparison of the charac-

© 2004 NRC Canada

Table 4. Average values of ellipticity ε, Laplacian of the density $\nabla^2\rho$, and electron density ρ at bond critical point, calculated from Table 3 of this work and Table 4 of ref. 1.

Bond	Type	ε	$\nabla^2\rho$ (au)	ρ (au)
$Cl_xBr_yO_z$				
Br—O	I[a]	0.045(16)	0.103(31)	0.245(22)
	II[b]	0.052(34)	0.118(27)	0.150(10)
	III[c]	0.082	0.140	0.056
Cl—O	I[d]	0.070(38)	–0.559(17)	0.320(27)
	II[e]	0.059(42)	0.085(92)	0.179(13)
Cl_xO_y				
Cl—O	I[f]	0.068(38)	–0.709(216)	0.348(29)
	II[g]	0.068(19)	0.068(48)	0.186(8)
	III[h]	0.093(22)	0.199(19)	0.100(40)

Note: Standard deviations are given in parentheses in units of the last digit.
[a]In molecules BrO, OBrO, BrBrO, BrO_3, $BrOBrO_3$, ClBrO, and ClOBrO.
[b]BrOBr, $BrOBrO_3$, ClOBr, BrOClO, and ClOBrO.
[c]BrOO.
[d]BrClO, BrOClO, and $BrClO_2$.
[e]ClOBr, BrOClO, and ClOBrO.
[f]OClO, ClClO, ClOClO, $ClClO_2$, ClO_3, ClO_4, and $ClOClO_2$; from ref. 1.
[g]ClOCl, ClOOCl, and ClOClO; from ref. 1.
[h]ClOO and $ClOClO_2$; from ref. 1.

Table 5. Summary of typical values of characteristics of the Cl—O and Br—O bonds in halogen oxides.

	Cl—O bonds	Br—O bonds
Type I: central		
Bond length (Å)	1.45–1.50	1.60–1.65
Stretching frequency (cm^{-1})	950–1150	800
Force constant (10^2 N m^{-1})	6–8	5–6
Covalent bond order	1.8–2.0	1.6–1.8
Electron density at bcp (au)	0.33	0.25
Laplacian of density at bcp (au)	–0.60	0.1
Type II: external		
Bond length (Å)	1.70–1.75	1.85–1.90
Stretching frequency (cm^{-1})	500–700	500–600
Force constant (10^2 N m^{-1})	2.5–3.0	1.5–2.5
Covalent bond order	1.3	1.1
Electron density at bcp (au)	0.18	0.15
Laplacian of density at bcp (au)	0.09	0.12
Type III: weak		
Bond length (Å)	2	2.3
Stretching frequency (cm^{-1})	200	—
Force constant (10^2 N m^{-1})	0.5	—
Covalent bond order	0.5	0.6
Electron density at bcp (au)	0.1	0.06
Laplacian of density at bcp (au)	0.2	0.14

Note: bcp, bond critical point.

teristics of Br—O bonds with those of Cl—O bonds. Table 5 lists both typical values for the properties already discussed for Br—O bonds and the corresponding ones for Cl—O bonds, taken from the results of the present work and of ref. 1. For Cl—O, the same three types of bonds are found, as discussed in ref. 1 and reflected in the table, with characteristics that show the same trends as for Br—O. When comparing Cl—O and Br—O bonds, the higher force constants and larger bond orders of the former with respect to the latter indicate that Cl—O bonds are on average 10% stronger than Br—O bonds of a similar type. The different masses and sizes of the chlorine and bromine atoms account also for the corresponding shorter bond lengths and higher stretching frequencies. The electron densities at bond critical points are also systematically larger for Cl—O bonds, by a factor of 1.1 or 1.2. On the other hand, the Laplacian of the density, which we discarded as a poor indicator for Br—O bonds, was found to change drastically from one type of Cl—O bond to the next. Thus, for central Cl—O bonds, the Laplacian is large and negative, indicating a clear maximum of density distribution at the critical point. This value is close to 0 for the external type of Cl—O bonds and becomes large and positive for the weaker bonds. The absence of negative values for the Laplacian of the density of all Br—O bonds shows the relative weakness of these bonds.

Some special cases

The first molecule under study, bromine oxide (BrO), has special characteristics, as was true for ClO in the Cl_xO_y series (1). All the indicators that we have derived to ascribe the bond to a certain type have values that are between those of a central and those of an external bond, although closer to the former. Thus, this specific Br—O bond shares the properties of both types: the oxygen atom is located at one end of the molecule, which would make this bond of the central type, but the Br atom is also at an end, which would make the bond external. It seems that the existence of an external O atom is the more relevant to impress character to the bond. A rather similar situation is found for the BrBrO molecule, where the Br—O bond shows characteristics intermediate between those of central and external bonds, but again closer to those corresponding to the definition of a central bond adopted in this work.

We thought it interesting to present here a more detailed study of $BrOBrO_3$. The only reference to the geometry of this molecule that we have found comes from X-ray data (43), providing a tentative structure where both bonds of the Br–O–Br bridge have the same length (1.862 Å), and those of the BrO_3 end group are also identical but shorter (1.605 Å). A value of 110° is reported for the angle of the Br–O–Br bridge, but nothing is stated about the other angles of the molecule. The same authors (43) report a Raman spectrum at 77 K, from which the bands in the 500–600 cm^{-1} region are assigned to vibrations of the Br–O–Br bridge. With this information, we carried out ab initio refinements of the geometry, starting at different initial structures and working at a lower level of theory, until we found good convergence for the highest level of calculations performed in this work. The corresponding geometry is represented in Fig. 1, where the electronic density is depicted by contour regions of different shading, and bond critical points are marked by open triangles. Bond lengths for this structure are indicated in Table 1, with values of 115.5° for the angle of the bridge, 97.6° for the in-plane adjacent BrOBr angle, and 115.9° (twice) and 114.1° for the three OBrO angles of the BrO_3 end group, whose symmetry is therefore not exactly threefold. With the optimized structure and by comparison

© 2004 NRC Canada

Fig. 1. Electron density contour map of the $BrOBrO_3$ molecule for the bonds in the plane of the figure. Triangles indicate bond critical points (saddle points of the electron density). Dotted lines represent bonds above or below the plane.

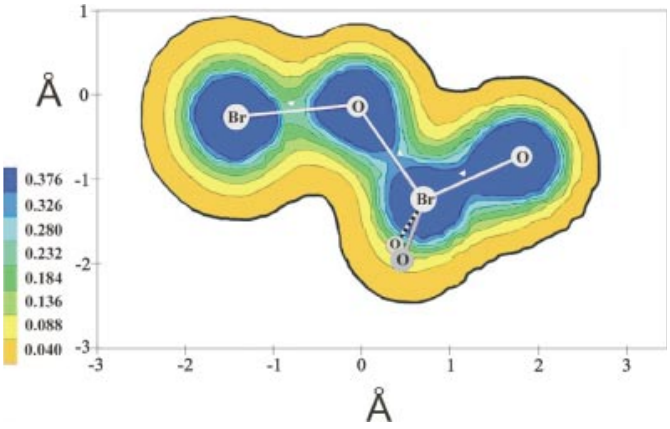
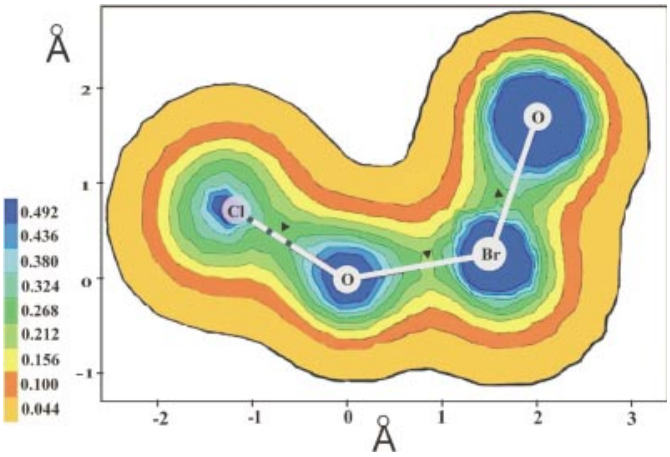


Fig. 2. Electron density contour map for the ClOBrO molecule. Triangles indicate bond critical points. The dotted part of a line represents the corresponding part of the bond below the plane of the figure.



with other bromine oxides, we performed various normal mode analyses until we reached an acceptable interpretation of the vibrational spectrum reported in ref. 43. The corresponding force constants and calculated wavenumbers are also given in Table 1. It is interesting to see that where the first two bonds are of type II, clearly weaker than those of the BrO_3 end group (type I), they are also significantly different from each other, as illustrated by their stretching force constants and as shown by the lower electron density at the bond critical point of the first Br—O bond with respect to that of the adjacent O—Br. It seems that the first Br—O bond is weakened by having part of its electron density transferred to the second. Surprisingly, the covalent bond order values of these two bonds are reversed from the expected trend, the first weaker bond having a larger bond order than the stronger second O—Br bond, although the values are not widely different. We cannot find an explanation for these abnormal bond order values. The BrO_3 end group behaves in accordance with other central Br—O bonds in the series, as far as all indicators are concerned.

Figure 2 depicts the ClOBrO molecule, with the OBrO group in the plane of the figure and the Cl atom below the plane. Here again we have two markedly different Br—O bonds. Although the Br atom is in a central position, only the last Br—O bond is of the central type I, whereas the presence of the Cl atom at the other end draws electron density from the central O—Br bond to the external Cl—O bond, both of which thus have type II or external characteristics. The different distribution of electron density for the two Br—O bonds is clearly shown in the figure.

Conclusions

This work characterizes three different types of Br—O bonds in bromine oxides, which roughly correspond to bonds where the Br atom occupies a central or apex position in the first and stronger case, occupies an external position in the second, or is loosely linked to a stable structure in the third and weaker type. These three bond types exhibit quite different values for bond lengths, stretching frequencies, force constants, and electron densities at the bond critical point. These types of bonds parallel those previously described for Cl—O in chlorine oxides, the Br—O bonds being on average 10%–15% weaker than the corresponding Cl—O bonds of the same type. The scant spectroscopic information available for the bromine oxides would make further experimental work on these species highly recommendable.

Acknowledgements

We acknowledge financial support from the Spanish Ministry of Science and Technology, Projects REN 2000-1557 and BQU2002-04005-C02-02, and the use of computing facilities at Centro de Supercomputación de Galicia (CESGA). This work has been carried out within the frame of a Unidad Asociada between the Consejo Superior de Investigaciones Científicas (CSIC) and the University of Jaén (Spain). We are grateful to V.J. Herrero for suggestions on the manuscript.

References

1. R. Escribano, R.G. Mosteo, and P.C. Gómez. Can. J. Phys. **79**, 597 (2001).
2. R.F.W. Bader. Atoms in molecules: A quantum theory. Clarendon Press, Oxford. 1990.
3. L.T. Molina and M.J. Molina. J. Geophys. Res. **91**, 14 501 (1986).
4. S. Solomon, R.R. Garcia, F.S. Rowland, and D.J. Wuebbles. Nature (London), **321**, 755 (1986).
5. M.B. McElroy, R.J. Salawitch, S.C. Wofsy, and J.A. Logan. Nature (London), **321**, 759 (1986).
6. K.A. McKinney, J.M. Pierson, and D.W. Toohey. Geophys. Res. Lett. **24**, 853 (1997).
7. J.G. Anderson, D.W. Toohey, and W.H. Brune. Science (Washington, D.C.), **251**, 39 (1991).
8. W.B. DeMore, S.P. Sander, D.M. Golden, R.F. Hampson, M.J. Kurylo, C.J. Howard, A.R. Ravishankara, C.E. Kolb, and M.J. Molina. JPL Publication 97-4. Jet Propulsion Laboratory, Pasadena, Calif. 1997.

© 2004 NRC Canada

9. B.J. Finlayson-Pitts and J.N. Pitts, Jr. Chemistry of the upper and lower atmosphere. Academic Press, San Diego. 2000, and refs. cited therein.
10. B.J. Drouin, C.E. Miller, H.S.P. Müller, and E.A. Cohen. J. Mol. Spectrosc. **205**, 128 (2001).
11. M.W. Chase, Jr. J. Phys. Chem. Ref. Data, **25**, 1069 (1996).
12. H.S.P. Müller, C.E. Miller, and E.A. Cohen. J. Chem. Phys. **107**, 8292 (1997).
13. L.T. Chu and Z. Li. Chem. Phys. Lett. **330**, 68 (2000).
14. C.E. Miller, S.L. Nickolaisen, J.S. Francisco, and S.P. Sander. J. Chem. Phys. **107**, 2300 (1997).
15. J. Kölm, A. Engdahl, O. Schrems, and B. Nelander. Chem. Phys. **214**, 313 (1997).
16. H.S.P. Müller and E.A. Cohen. J. Chem. Phys. **106**, 8344 (1997).
17. Y.-C. Lee and Y.-P. Lee. J. Phys. Chem. A, **104**, 6951 (2000).
18. S.D. Allen, M. Poliakoff, and J.J. Turner. J. Mol. Struct. **157**, 1 (1987).
19. C. Campbell, J.P.M. Jones, and J.J. Turner. J. Chem. Soc. Chem. Commun. 888 (1968).
20. T.J. Lee, C.E. Dateo, and J.E. Rice. Mol. Phys. **96**, 633 (1999).
21. P.C. Gómez and L.F. Pacios. J. Phys. Chem. A, **103**, 739 (1999).
22. L.F. Pacios and P.C. Gómez. THEOCHEM, **467**, 223 (1999).
23. M. Alcami, O. Mo, M. Yánez, and I.L. Cooper. J. Chem. Phys. **112**, 6131 (2000).
24. Y. Xie, H.F. Schaefer III, Y. Wang, X.-Y. Fu, and R.-Z. Liu. Mol. Phys. **98**, 879 (2000).
25. S. Guha and J.S. Francisco. J. Phys. Chem. A, **102**, 6702 (1998).
26. S. Guha and J.S. Francisco. J. Phys. Chem. A, **101**, 5347 (1997).
27. P. Chaquin, M. Bahou, A. Schriver, and L. Schriver. Chem. Phys. Lett. **256**, 609 (1996).
28. T. Lee. J. Phys. Chem. **99**, 15 074 (1995).
29. E.B. Wilson, J.C. Decius, and P.C. Cross. Molecular vibrations, McGraw-Hill New York. 1955.
30. R. Escribano, S. Martin, V. Botella, and A.B. Altabef. J. Mol. Struct. **517**, 227 (2000).
31. R.G. Mosteo, M.I. Suero, V. Botella, and R. Escribano. J. Mol. Struct. **443**, 57 (1998).
32. M.J. Frisch, G.W. Trucks, H.B. Schlegel, G.E. Scuseria, M.A. Robb, J.R. Cheeseman, V.G. Zakrzewski, J.A. Montgomery, Jr., R.E. Stratmann, J.C. Burant, S. Dapprich, J.M. Millam, A.D. Daniels, K.N. Kudin, M.C. Strain, O. Farkas, J. Tomasi, V. Barone, M. Cossi, R. Cammi, B. Mennucci, C. Pomelli, C. Adamo, S. Clifford, J. Ochterski, G.A. Petersson, P.Y. Ayala, Q. Cui, K. Morokuma, D.K. Malick, A.D. Rabuck, K. Raghavachari, J.B. Foresman, J. Cioslowski, J.V. Ortiz, A.G. Baboul, B.B. Stefanov, G. Liu, A. Liashenko, P. Piskorz, I. Komaromi, R. Gomperts, R.L. Martin, D.J. Fox, T. Keith, M.A. Al-Laham, C.Y. Peng, A. Nanayakkara, C. Gonzalez, M. Challacombe, P.M.W. Gill, B. Johnson, W. Chen, M.W. Wong, J.L. Andres, C. Gonzalez, M. Head-Gordon, E.S. Replogle, and J.A. Pople. Gaussian 98 (G98W) [computer program]. Gaussian, Inc., Pittsburgh, Pa. 1998.
33. L.F. Pacios and P.C. Gómez. J. Phys. Chem. A, **101**, 1767 (1997).
34. P. Popelier. Atoms in molecules: An introduction. Prentice Hall, London. 2000.
35. J. Cioslowski and S.T. Mixon. J. Am. Chem. Soc. **113**, 4142 (1991).
36. J. Cioslowski and B.B. Stefanov. Mol. Phys. **84**, 707 (1995).
37. B.B. Stefanov and J. Cioslowski. J. Comput. Chem. **16**, 1394 (1995), and refs. cited therein.
38. L. Hedberg and I. M. Mills. J. Mol. Spectrosc. **160**, 117 (1993).
39. F. Tamassia, S.M. Kermode, and J.M. Brown. J. Mol. Spectrosc. **205**, 92 (2001).
40. D.E. Tevault, N. Walker, R.R. Smardzewski, and W.B. Fox. J. Phys. Chem. **82**, 2733 (1978).
41. L. Schriver-Mazzuoli, O. Abdelaoui, C. Lugez, and L. Schriver. Chem. Phys. Lett. **214**, 519 (1993).
42. K. Johnsson, A. Engdahl, J. Kölm, J. Nieminen, and B. Nelander. J. Phys. Chem. **99**, 3902 (1995).
43. T.R. Gilson, W. Levason, J.S. Ogden, M.D. Spicer, and N.A. Young. J. Am. Chem. Soc. **114**, 5469 (1992).

© 2004 NRC Canada

Torsional isomers in methylated aminoethanols — A jet–FT-IR study[1]

Yaqian Liu, Corey A. Rice, and Martin A. Suhm

Abstract: Jet–FT-IR spectra of aminoethanol (AE), *N*-methylaminoethanol (MAE), and *N*,*N*-dimethylaminoethanol (DMAE) are presented and compared to gas-phase and matrix isolation IR, microwave, and quantum chemical data. The intramolecular O-H··N hydrogen bond gives rise to characteristically shifted O-H stretching bands and torsional difference bands in the monomer spectra. It stabilizes one out of 14 diastereomeric monomer conformations of AE and DMAE and two out of 27 diastereomeric MAE conformations. The latter two correspond to torsional or *N*-inversional isomers, the interconversion of which is hindered by the intramolecular hydrogen bond. Their energy difference is found to be <1.2 kJ/mol. The intermolecular aggregation patterns of the three aminoethanols are quite distinct and non-monotonic, as suggested by their O-H stretching fingerprints.

Key words: aminoethanol, IR spectroscopy, conformation, hydrogen bond, supersonic jet.

Résumé : On a déterminé les spectres FT-IR à jet de l'aminoéthanol (AE), du *N*-méthylaminoéthanol (MAE) et du *N*,*N*-diméthylaminoéthanol (DMAE) et on les compare aux données relatives aux spectres IR en phase gazeuse et isolement matriciel, aux spectres de microondes ainsi qu'aux données obtenues par calculs quantiques. Dans les spectres des monomères, la liaison hydrogène O-H··N donne lieu à des bandes d'élongation O-H qui sont déplacées d'une façon caractéristique et des bandes de différence de torsion. Elle stabilise une seule des quatorze conformations monomères diastéréomères du AE et du DMAE et deux des vingt-sept conformations diastéréomères du MAE. Ces deux dernières correspondent aux isomères de torsion ou d'inversion autour de l'azote, l'interconversion qui subit un empêchement en raison de la liaison intramoléculaire. On a trouvé que leur différence d'énergie est de <1,2 kJ/mol. Les patrons d'agrégation intermoléculaire des trois aminoéthanols sont très différents et ne sont pas monotoniques, tel que suggéré par leurs profils caractéristiques dans la région des bandes d'élongation O-H.

Mots clés : aminoéthanol, spectroscopie IR, conformation, liaison hydrogène, jet supersonique.

[Traduit par la Rédaction]

Introduction

Hydroxy and amino groups rank among the most important hydrogen-bond building blocks in nature. If they are separated by a backbone of two sp^3 carbon atoms, an interesting interplay between intra- and intermolecular hydrogen bonding is possible. The resulting simplest prototype, 2-aminoethanol (AE) — an 11-atomic molecule with a single reference (1) in Herzberg's compilation of *Molecular Spectra and Molecular Structure* (2) — has three torsional degrees of freedom, which allow for rich conformational isomerism. This conformational isomerism in AE has been the subject of a number of experimental and theoretical investigations (3, 4). Despite the large number of conformers, microwave (MW) and millimeter-wave studies (5–7) have shown the most stable enantiomeric pair (g′Gg′ and gG′g) to be the dominant species in the gas phase. Here, the notation employed by Radom et al. (8) is applied: G denotes a gauche (≈60°) N-C-C-O torsional angle, whereas g′ refers to an opposite gauche (≈−60°) conformation of the C-C-O-H and C-C-NLp (Lp stands for the N-atom lone pair) dihedral angles. The stability of this pair of conformers is attributed to the formation of an intramolecular hydrogen bond of O-H··N type (see Fig. 1). This finding is also supported by the gas-phase IR spectrum of AE, which shows a dominant absorption centred at 3570 cm^{-1} (9). The same was found for *N*,*N*-dimethylaminoethanol (DMAE, see Fig. 1), which features a somewhat stronger hydrogen bond because of the electron-donating properties of the methyl groups (10). Obviously, all other conformers are energetically less favourable, although some of them can be trapped by rapid cooling in a rare gas matrix (9). Vibrational spectroscopy provides an appropriate tool for the investigation of such conformational isomerism, as the exact frequency of the strong O-H stretching transition depends sensitively on the hydrogen-bond environment. To characterize the low-temperature conformations of isolated AE and DMAE, we have undertaken a ragout-jet–FT-IR (11, 12) investigation. The ragout-jet–FT-IR technique, while originally designed for the study of hydrogen-bonded clusters, can also be used to investigate hydrogen-bonded monomer conformations of moderately volatile compounds. With this technique, we went on to in-

Received 29 October 2003. Published on the NRC Research Press Web site at http://canjchem.nrc.ca on 7 September 2004.

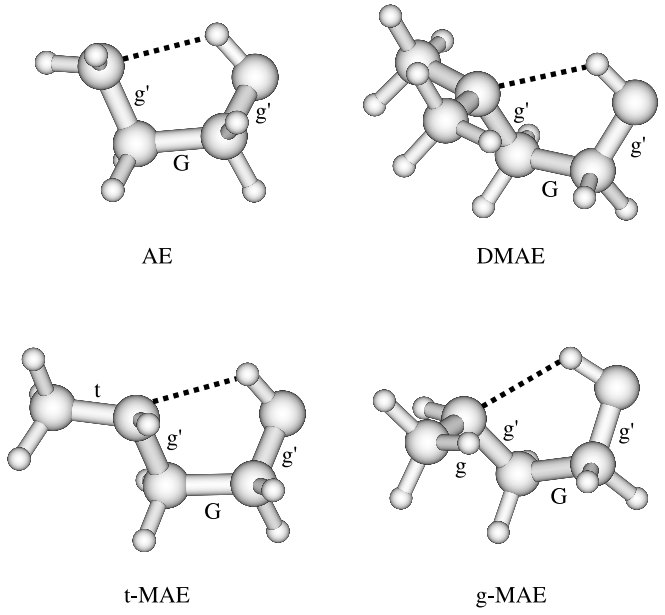
Y. Liu, C.A. Rice, and M.A. Suhm.[2] Institut für Physikalische Chemie, Universität Göttingen, Tammannstr. 6, D-37077 Göttingen, Germany.

[1]This article is part of a Special Issue dedicated to the memory of Professor Gerhard Herzberg.

[2]Corresponding author (e-mail: msuhm@gwdg.de).

 doi: 10.1139/V04-046 © 2004 NRC Canada

Fig. 1. MP2/6-311++G(2d,2p) g′Gg′ structures of aminoethanols. For MAE, an additional prefix is needed to describe the chirality at the N-atom: *t*- and *g*- refer to trans and gauche positions of the methyl group with respect to the CH_2OH group. The gauche conformation is predicted to be 0.5 kJ/mol above the trans conformation at this level, including zero-point energy contributions.



vestigate the effect of replacing only one amino hydrogen by a methyl group in *N*-methylaminoethanol (MAE, see Fig. 1) (13). This single methyl group introduces a labile chiral centre at the nitrogen, which gives rise to additional diastereoisomerism. At room temperature, two MAE diastereomers, as depicted in Fig. 1, were observed by MW spectroscopy (14). A ground-state energy difference of 1.9 kJ/mol was determined from relative intensity measurements. The question is then: will these two MAE diastereomers relax to a single one in a free jet expansion, as in the case of AE and DMAE, or will they persist even at low temperatures?

Methods

The IR spectra in the O-H stretching region of the three aminoethanols were recorded with our ragout-jet–FT-IR cluster spectrometer. The setup and operating principles of the spectrometer are given in detail elsewhere (11). Briefly, a commercial Bruker IFS 66v/S rapid-scan FT-IR spectrometer probes a pulsed supersonic expansion into a 15-m^3 vacuum chamber. The expansion is generated by a 12 cm long and 0.5 mm wide pulsed slit nozzle (modified General Valve Series 97). The size of the vacuum chamber allows for the use of long and intense gas pulses, during which entire FT-IR spectra are recorded. At 2 cm^{-1} spectral resolution, a typical gas pulse extends over 140 ms. After a pulse, the buffer volume is pumped for about 30 s at 2000 m^3/h, to prevent the buildup of excessive background gas pressure. Therefore, the actual scan time is quite short, but the idle time is more than two orders of magnitude higher. The low duty cycle is at the heart of the success of this technique (11). A 65-L sample reservoir keeps the stagnation pressure within 10% during a gas pulse.

The three aminoethanols (AE (>99%), Aldrich; MAE (99.8%), Acros; DMAE (>99.5%), Aldrich) were dried over molecular sieves and injected into a saturator. Helium (>99.996%, Messer) was passed through the saturator before entering the sample reservoir. The temperature of the saturator was varied to optimize the monomer absorptions. The optimal temperatures were 20 °C for AE and MAE, and 0 °C for DMAE. The estimated concentration in the gas mixture is 0.005%. An InSb detector with appropriate optical components was used. Representative room temperature, gas-phase and ragout-jet–FT-IR spectra of the three compounds are collected in Fig. 2.

The conformational isomerism of the aminoethanols was also investigated by quantum chemical calculations at double-harmonic level using the Gaussian 98 (15) electronic structure package.

Results and discussion

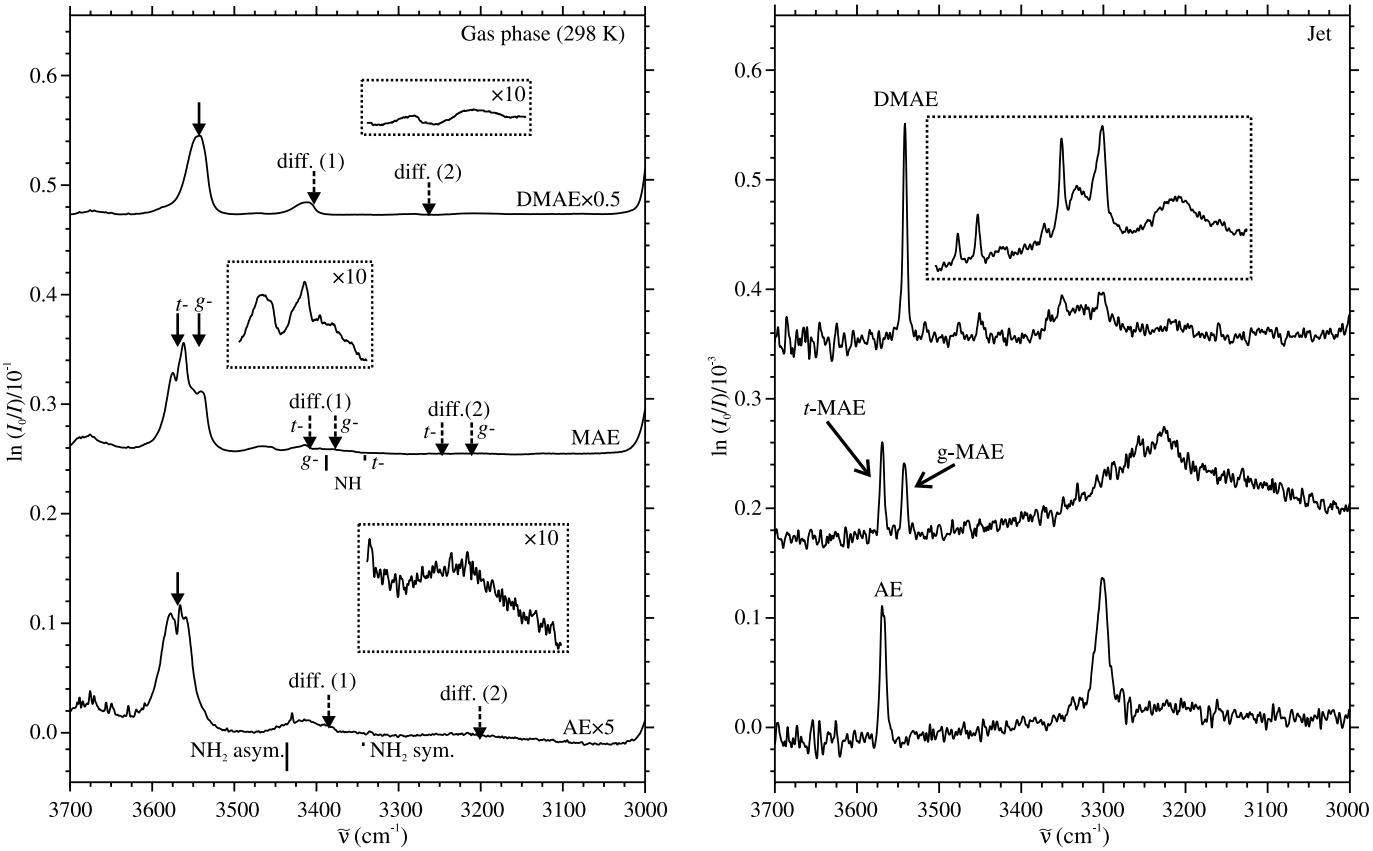
Geometry optimizations for all 14 spectroscopically distinguishable conformers were not repeated for AE, because of the large number of existing data (3, 4, 8). Geometry optimization followed by harmonic frequency calculation was restricted to the most stable g′Gg′ conformer and the open-chain gTt conformer, at HF, B3LYP, and MP2 levels of theory, with the 6-31+G* basis set. The relative energies are in line with previous data (3, 4).

For DMAE, all 14 energetically distinct conformers were optimized. The relative energies, harmonic O-H stretching wavenumbers, and band strengths are given in Table 1. The HF values are in reasonable agreement with a previous study by Ohno et al. (16). Calculations at all levels predict the g′Gg′ conformer as the most stable conformer. All other conformers are at least 8–14 kJ/mol higher in energy. The energy difference between the g′Gg′ conformer and the open-chain gTt conformer may be used as a rough approximation to the intramolecular H-bond stabilization energy. For the 6-31+G* basis set, it amounts to 8.8, 12.8, and 15.7 kJ/mol at the HF, B3LYP, and MP2 levels, respectively, for DMAE. These values are slightly larger than those for AE (8.0 kJ/mol at the HF level, 12.3 kJ/mol at the B3LYP level, and 13.8 kJ/mol at the MP2 level), consistent with a relatively stronger intramolecular hydrogen bond. This is confirmed by the O-H stretching wavenumber red shift in the g′Gg′ conformer compared to that of the gTt conformer. The values are 123/104 cm^{-1} (DMAE/AE) at the MP2/6-31+G* level. The intramolecular hydrogen bond is also reflected by an increased IR band strength for the g′Gg′ conformer (see Table 1). For the remaining conformers, different relative orders of stability are predicted at different levels. The same phenomenon was previously observed (3, 16).

The 27 conformers of MAE were also optimized at the HF, B3LYP, and MP2 levels with the 6-31+G* basis set. The obtained results are given in Table 2. The HF values are consistent with the study by Ohno et al. (17). As in the case of AE and DMAE, the g′Gg′ conformations are predicted to be the most stable isomers. The introduction of an additional chiral centre at the N atom by single methyl substitution gives rise to two distinct g′Gg′conformers, namely, *t*-g′Gg′ where the methyl group is located trans (~180°) with respect to the CH_2OH group, and *g*-g′Gg′ where the methyl group is

© 2004 NRC Canada

Fig. 2. Gas-phase spectra (left, including some enlarged sections) and ragout-jet–FT-IR spectra (right) in the O-H stretching region of aminoethanols. The gas-phase spectra correspond to a scan time of 19.2 s, while the jet spectra correspond to scan times of 37, 48, and 29 s for AE, MAE, and DMAE, respectively. Experimental conditions are p = 1.0 bar (1 bar = 100 kPa), T = 20 °C for AE; p = 0.8 bar, T = 20 °C for MAE; and p = 1.0 bar, T = 0 °C for DMAE. Dashed arrows mark harmonic MP2/6-311++G(2d,2p) predictions of O-H stretching/O-C-C-N torsion difference bands originating from the first and second excited O-C-C-N torsional states, shifted from the experimental O-H stretching bands (solid arrow). Predicted N-H stretching modes are shown as vertical bars below the corresponding spectrum, shifted in the same manner. The lengths of the bars correspond to relative intensities, but are amplified 10-fold.



gauche (~60°) with respect to the CH_2OH group (see Fig. 1). In this notation, we conserve the underlying AE nomenclature for comparison purposes. At the HF level, the gauche conformer is 2.6 kJ/mol higher in energy than the trans conformer. The energy difference reduces to 1.6 kJ/mol at the B3LYP level, and further to 0.9 kJ/mol at the MP2 level. Relative to the corresponding gTt conformer, the intramolecular O-H··N bond stabilizes *t*-MAE by 7.9, 11.6, and 14.1 kJ/mol and *g*-MAE by 8.6, 12.9, 15.3 kJ/mol at HF, B3LYP, and MP2 levels, respectively. The predicted O-H stretching wavenumber red shifts are 99/122 cm^{-1} for *t*-/*g*-MAE at the MP2/6-31+G* level.

MP2 geometry optimizations and harmonic frequency calculations were extended to larger basis sets, namely, 6-311++G** and 6-311++G(2d,2p), for the most stable g′Gg′ conformers of the three aminoethanols. The predicted equilibrium rotational constants are in good agreement (1 ± 1%) with MW data (5, 10, 14). Calculated O-H stretching harmonic wavenumbers together with IR intensities are given in Table 3. One might expect that the O-H stretching frequencies of the two MAE conformations should fall in between those of AE and DMAE, because of the intermediate inductive methyl influence. In fact, *t*-MAE is predicted by the MP2/6-311++G(2d,2p) calculations to absorb very close to AE, whereas the *g*-MAE absorption falls rather close to the DMAE absorption (see Table 3). It appears that the O-H stretching frequencies correlate with the N-substituent at the gauche position relative to the CH_2OH group. The N-H stretching intensities are predicted to be at least an order of magnitude weaker than the O-H stretching fundamentals. With these quantum chemical predictions, it is rather straightforward to interpret the recorded ragout-jet–FT-IR spectra of the three aminoethanols, which are shown in Fig. 2.

For AE, a single narrow monomer absorption centred at 3569 cm^{-1} is observed, corresponding to the broad absorption band centred at 3570 cm^{-1} in the room-temperature, gas-phase spectrum. This is assigned to the O-H stretching mode of the g′Gg′conformer. Its average number density in the jet is estimated to be 10^{13} cm^{-3}, using the predicted band strength at the MP2/6–311++G(2d,2p) level. The obtained O-H stretching frequency is in agreement with a previously reported gas-phase value of 3570 cm^{-1} (3, 18), an Ar matrix isolation value of 3555 cm^{-1} (9), and a value of 3526 cm^{-1} in C_2Cl_4 solution (19). In the gas-phase spectrum, a weak broad absorption feature is observed to higher frequencies, near 3680 cm^{-1}. The occurrence of this peak was attributed to the O-H stretching absorption of other conformers such as gGt, tGt, and gGg (3). No significant monomer absorption is

© 2004 NRC Canada

Table 1. Calculated relative energies including harmonic zero-point energy contributions ($E_{0,\,rel} = E_0 - E_0$(g′Gg′), in kJ/mol), harmonic O-H stretching wavenumbers (ω, in cm^{-1}), and IR band strengths (in parentheses, km/mol) of the 14 DMAE conformations.

	HF/6-31+G*		B3LYP/6-31+G*		MP2/6-31+G*	
Conformer	$E_{0,\,rel}$	ω	$E_{0,\,rel}$	ω	$E_{0,\,rel}$	ω
g′Gg′	0.0	4071 (71)	0.0	3651 (67)	0.0	3638 (89)
gGt	12.0	4117 (59)	12.7	3762 (25)	14.4	3753 (36)
gGg	13.3	4110 (45)	12.9	3747 (18)	14.4	3752 (29)
gTt	8.8	4121 (60)	12.8	3767 (27)	15.7	3761 (38)
gTg	10.2	4109 (44)	13.0	3746 (18)	16.6	3749 (27)
g′Tg	10.3	4111 (44)	12.8	3747 (17)	16.7	3751 (27)
tGt	15.7	4115 (55)	17.5	3758 (22)	20.2	3749 (32)
g′Gt	16.1	4122 (56)	17.1	3766 (17)	20.8	3672 (36)
tGg	17.7	4107 (43)	18.8	3745 (17)	22.4	3749 (27)
tGg′	19.1	4137 (40)	19.4	3768 (19)	22.4	3783 (28)
tTt	14.6	4118 (57)	18.6	3761 (23)	23.1	3757 (35)
tTg	16.2	4105 (43)	18.7	3740 (16)	24.0	3744 (26)
gGg′	Relaxes to g′Gg′					
g′Gg	Relaxes to g′Gg′					

Table 2. Calculated relative energies ($E_{0,\,rel}$, in kJ/mol), harmonic O-H stretching wavenumbers (ω, in cm^{-1}), and IR band strengths (in parentheses, km/mol) of the 27 diastereomeric MAE conformations.

	HF/6-31+G*		B3LYP/6-31+G*		MP2/6-31+G*	
Conformer	$E_{0,\,rel}$	ω	$E_{0,\,rel}$	ω	$E_{0,\,rel}$	ω
t-g′Gg′	0.0	4073 (76)	0.0	3661 (64)	0.0	3663 (81)
g-g′Gg′	2.6	4067 (74)	1.6	3644 (67)	0.9	3641 (82)
t-gGt	2.8	4123 (63)	4.7	3772 (31)	4.8	3764 (41)
t-gGg	5.5	4108 (46)	6.0	3745 (19)	7.3	3749 (29)
t-gGg′	6.3	4121 (56)	7.8	3759 (25)	8.3	3756 (36)
t-g′Tg	9.7	4110 (44)	10.7	3746 (17)	11.2	3752 (26)
g-tGg	12.1	4106 (48)	12.2	3742 (19)	13.2	3747 (30)
t-gTt	7.9	4120 (59)	11.6	3768 (26)	14.1	3762 (37)
t-gTg	9.1	4111 (47)	11.7	3750 (19)	14.9	3755 (29)
g-tGg′	14.5	4124 (42)	15.0	3757 (15)	15.1	3763 (25)
g-tGt	9.6	4121 (61)	11.9	3770 (29)	15.3	3762 (39)
g′-gGt	14.4	4118 (56)	14.6	3762 (24)	15.7	3756 (34)
g′-gTt	11.2	4121 (58)	14.5	3768 (26)	16.2	3763 (37)
g-tTg	16.9	4109 (45)	16.2	3746 (18)	17.2	3744 (26)
g′-gTg	12.9	4110 (45)	15.0	3746 (17)	17.3	3751 (27)
g-g′Tg	13.1	4111 (42)	14.9	3745 (17)	17.4	3752 (25)
g-tGt	17.1	4115 (55)	17.6	3757 (22)	19.0	3752 (33)
g-tTt	15.0	4118 (57)	17.2	3761 (22)	20.2	3758 (35)
g-tTg	16.1	4104 (44)	17.1	3740 (17)	20.4	3750 (28)
g-tGg	18.9	4108 (43)	18.6	3747 (18)	20.7	3752 (28)
g′-gGg	16.5	4102 (42)	17.7	3745 (16)	21.1	3750 (26)
t-g′Gt	17.2	4118 (55)	18.2	3762 (23)	21.4	3759 (34)
g-g′Gt	19.5	4123 (55)	19.9	3769 (25)	22.2	3768 (37)
g-tGg′	20.9	4142 (43)	19.9	3773 (23)	23.4	3792 (33)
g′-gGg′	Relaxes to *t*-g′Gg′					
t-g′Gg	Relaxes to *t*-g′Gg′					
g-g′Gg	Relaxes to *g*-g′Gg′					

located in the jet spectrum in that region, consistent with a relative energy of 6.6 kJ/mol (4) for the second most stable gGt conformer, even if we assume that the conformational equilibrium is frozen at room temperature. It would require a significantly better signal-to-noise ratio in this difficult spectral region to see such high-lying conformers. Towards lower frequencies, an additional weak, broad feature centred around 3410 cm^{-1} with a sharp peak at 3430 cm^{-1} appears in the room-temperature, gas-phase spectrum. The sharp peak was previously assigned to the asymmetric NH_2 stretch of the g′Gg′conformer (9). This assignment is consistent with the MP2/6-311++G(2d,2p) prediction, as denoted by the ver-

© 2004 NRC Canada

Table 3. Calculated harmonic O-H stretching wavenumbers (in cm^{-1}) and IR band strengths (in parentheses, km/mol) of the most stable conformers (g′Gg′) of aminoethanols.

		MAE					
O-H stretching frequency	AE	*t*-Conformer	*g*-Conformer	ΔE_e	ΔE_0	$\Delta G^\circ_{298.15}$	DMAE
HF/6-31+G*	4068 (80)	4073 (76)	4067 (74)	2.3	2.6	2.5	4071 (71)
B3LYP/6-31+G*	3654 (64)	3661 (64)	3644 (67)	1.5	1.6	1.4	3651 (67)
MP2/6-31+G*	3661 (77)	3663 (81)	3641 (82)	0.7	0.9	0.7	3638 (89)
MP2/6-31++G**	3798 (74)	3796 (78)	3776 (82)	0.5	0.6	0.4	3770 (89)
MP2/6-311++G(2d,2p)	3779 (70)	3777 (73)	3752 (79)	0.1	0.5	0.3	3745 (87)
Exptl. (anharmonic)	3569	3569	3543		1.9[a]		3542

Note: The equilibrium energy differences ($\Delta E_e = E_{e,g\text{-conformer}} - E_{e,t\text{-conformer}}$, in kJ/mol), the zero-point corrected values (ΔE_0), and the Gibbs free-energy differences ($\Delta G^\circ_{298.15}$, in kJ/mol) between the two MAE conformers are also given.

[a]From ref. 13.

tical bar labelled as NH_2 asym. (Fig. 2). Position and height of this bar are determined by the calculated relative wavenumber and intensity with respect to the experimental O-H stretching fundamental (solid arrow, Fig. 2). For better visibility, a factor of 10 is applied to calculated NH stretching intensities. The symmetric NH_2 stretching intensity is predicted to be an order of magnitude weaker than the asymmetric NH_2 stretch, and it might correspond to the very weak feature at 3335 cm^{-1}. Neither of the NH_2 bands is observed in the jet spectrum because of their low intensities. This is consistent with a detection limit of 10^{13} cm^{-3} based on the predicted band strength for the asymmetric NH_2 stretching mode (9 km/mol at the MP2/6-311++G(2d,2p) level) at our noise level. The broad band near 3410 cm^{-1} was previously not assigned (9). It disappears in the jet spectrum, which points to a hot-band origin. Among the low-frequency modes of AE (τ_{OCCN} = 184 cm^{-1}, τ_{NH_2} = 263 cm^{-1}, δ_{CCN} = 328 cm^{-1} at MP2/6-311++G(2d,2p) level), the O-C-C-N torsional motion can give rise to a difference band $\nu_{OH} - \tau_{OCCN}$ in this region, in particular as it modulates the H-bond distance. Its harmonic prediction relative to the experimental ν_{OH} band centre is shown by a dashed arrow (diff. (1), see Fig. 2) and agrees reasonably well with the broad feature. The $\nu_{OH} - 2\tau_{OCCN}$ difference band is also predicted (diff. (2)) close to a weak and broad absorption in the spectrum (magnified 10-fold in the insert).

The jet spectrum of DMAE is rather similar to that of AE (Fig. 2). A single monomer absorption band at 3542 cm^{-1} is observed and assigned to the O-H stretch of the g′Gg′ conformer. It corresponds to the broad absorption band centred at 3543 cm^{-1} in the room-temperature, gas-phase spectrum. It is in line with the values obtained in dilute C_2Cl_4 solutions (3506 cm^{-1} in ref. 19 and 3510 cm^{-1} in ref. 20) and the Ar matrix isolation value (3498 cm^{-1}, ref. 16). It is red shifted by 27 cm^{-1} relative to AE, because of a slightly stronger intramolecular H-bond. Similar to AE, the ν_{OH} jet band centre is labelled by a solid arrow in the gas-phase spectrum. Predicted band centres of $\nu_{OH} - \tau_{OCCN}$ and $\nu_{OH} - 2\tau_{OCCN}$ with τ_{OCCN} = 140 cm^{-1} at the MP2/6-311++G(2d,2p) level are also shown by dashed arrows. The $\nu_{OH} - \tau_{OCCN}$ prediction (diff. (1)) agrees rather well with the absorption band around 3410 cm^{-1}, 132 cm^{-1} to the red relative to the O-H stretching fundamental. There is also an absorption near $\nu_{OH} + \tau_{OCCN}$, but it falls in a range where water absorptions and excited conformers make an analysis difficult.

Two O-H absorption bands are observed in the MAE jet expansion. One almost coincides with the AE absorption and is assigned to the *t*-g′Gg′ conformer. The other one is at nearly the same position as in DMAE. It is assigned to the gauche conformer (see Table 3 and Fig. 2). For comparison, the O-H stretching wavenumbers are 3515 cm^{-1} in C_2Cl_4 (only one value was reported) (19) and 3485, 3516, and 3555 cm^{-1} in an Ar matrix (not definitely assigned, ref. 17). The presence of more than one conformation is also apparent in the room-temperature, gas-phase spectrum (Fig. 2). As in the spectra of AE and DMAE, $\nu_{OH} - \tau_{OCCN}$ and $\nu_{OH} - 2\tau_{OCCN}$ predictions relative to the experimental ν_{OH} bands are shown using dashed arrows (τ_{OCCN} = 161/166 cm^{-1} for *t*-/*g*-MAE at the MP2/6-311++G(2d,2p) level). This leaves a peak around 3470 cm^{-1} unexplained. It corresponds nicely to other torsional difference bands involving the N-CH_3 group, predicted at 3465 (*t*-) and 3466 cm^{-1} (*g*-). The predicted NH stretching fundamentals are again shown as vertical bars with appropriate relative intensities (Fig. 2).

It is instructive to discuss the *t*- and *g*-MAE O-H stretching intensities in the jet spectrum. On the basis of the MP2/6-311++G(2d,2p) energy difference (ΔE_e = 0.09 kJ/mol in favour of *t*-MAE, see Table 3) and band strength ratio (nearly 1:1), the experimental intensity ratio of 1:0.84 would be consistent with thermal equilibrium frozen at ~40 K. This is somewhat low, considering the various conceivable isomerization paths, which all involve substantial heavy-atom motion. Likely, the lowest paths do not involve *N*-inversions, but rather g–g′, G′–G torsions. However, this requires closer investigation. Inclusion of zero-point energy raises the energy difference to 0.5 kJ/mol and brings the effective isomerization temperature to ~240 K, a more plausible value for a jet expansion under kinetic control. Actually, the more appropriate quantity in the IR experiment would be ΔG°_T, which is 0.3 kJ/mol at 298.15 K at the MP2/6-311++G(2d,2p) level, i.e., quite similar to the energy difference. Interestingly, there is an experimental value for the energy difference between the conformers based on MW spectroscopy (14), which is substantially higher (1.9 ± 0.4 kJ/mol). This value appears to be inconsistent with our observed jet band intensities, even if equilibrium is frozen already at room temperature. Even if we allow for a 10% error in the calculated *t*-/*g*-band strength ratio and another 10% difference in the partition functions of the two isomers, we get an upper limit for ΔE of about 1.2 kJ/mol. This is

© 2004 NRC Canada

also consistent with our large basis set MP2 calculations, but higher level electronic structure calculations including an analysis of interconversion pathways would be desirable to confirm this finding. On the experimental side, further MW investigations on this delicate conformational equilibrium would be valuable. One might also consider a higher resolution IR study.

In the jet spectra of the aminoethanols (Fig. 2), bands due to aggregates appear to lower frequencies. A single absorption band around 3300 cm^{-1} is observed for AE, possibly corresponding to the IR-active O-H stretch of the most stable cyclic dimer with two intermolecular O-H··N bonds (4). Quite in contrast, a very broad absorption band is observed for MAE, with a peak position near 3225 cm^{-1}. This is in line with a broad band around 3220 cm^{-1} observed in the Ar matrix, assigned to the intermolecular O-H stretching band. The increased width of the cluster band relative to that of AE may be due to a larger number of isomers or to a preference for larger clusters. Rather than restoring the simplicity of AE, the cluster absorptions of DMAE are more complex. They involve several groups of sharp and broad bands over a wide frequency range. This is illustrated by a spectrum at higher concentration, shown as an insert in Fig. 2. The broad bands at lower frequencies might be due to intermolecular O-H stretching modes, while intramolecularly hydrogen-bonded O-H stretches could give rise to the sharp bands. Intramolecular O-H··N bonds should be more persistent in DMAE because of the enhanced strength. Also, N-H vibrations may come into play for intermolecular hydrogen bonds (4). A more detailed discussion of these variations in clustering tendency will be given elsewhere.

We finally note that our accurate ragout-jet–FT-IR aminoethanol monomer band centres can be useful for the interpretation of IR hole burning spectra of clusters involving an aromatic chromophore and an aminoethanol. In those experiments, the corresponding aminoethanol O-H stretch can only be observed in the complex (21, 22). Estimates of the shifts so far had to rely on relatively broad room-temperature, gas-phase band profiles or matrix isolation values.

Conclusions

The intramolecular O-H··N hydrogen bond in symmetrically substituted aminoethanols stabilizes a single pair of enantiomeric conformations (g′Gg′ and gG′g) over all other 25 conceivable structures, so that no significant isomerism is observed in supersonic jet expansions. By breaking the symmetry at the amino group via single methyl substitution, the O-H stretching band splits into two. The two components almost coincide with the band centres of the doubly and the non-methylated aminoethanol. It is shown that these two bands are due to conformations that differ in their relative chirality at the N atom and that their energy difference is probably less than 1.2 kJ/mol, somewhat in contrast to previous MW evidence. In the future, it will be interesting to carry out jet isomerization experiments between *t*- and *g*-MAE, including also Ar coating (23). It will be challenging to analyse in detail the clustering behaviour of these compounds, which clearly shows a non-monotonic trend with increasing *N*-methylation. *N*-Methylaminoethanol may be viewed as an extremely simplified cartoon of the torsional isomerization and intra- versus intermolecular hydrogen-bond competition, which is so vital in protein folding. Even in this simple example, there remains a lot to be explored.

Acknowledgements

We are indebted to N. Borho and C. Emmeluth for substantial help and discussions. We thank A. Zehnacker, F. Lahmani, and R. Fausto for discussions and correspondence. This work was supported by the Deutsche Forschungsgemeinschaft (DFG) via Graduiertenkolleg (GRK) 782 and via Sonderforschungsbereich (SFB) 357 as well as by the Fonds der Chemischen Industrie. C.A.R. acknowledges a student visitor scholarship from the GRK 782. This contribution is dedicated to the memory of G. Herzberg, whose seminal book on polyatomic molecules (2) got M.A.S. interested in molecular spectroscopy at the age of 17, when he received a copy as a gift from a former student colleague of Herzberg. Y.L. received a copy of the same book as a Rao prize at the Molecular Spectroscopy Symposium in 2001, and it will continue to educate molecular spectroscopists for generations to come.

References

1. H.W. Thompson. J. Am. Chem. Soc. **61**, 1396 (1939).
2. G. Herzberg. Molecular spectra and molecular structure II. Infrared and Raman spectra of polyatomic molecules. Van Nostrand, Princeton, N.J. 1945.
3. C.F.P. Silva, M.L.T.S. Duarte, and R. Fausto. J. Mol. Struct. **482–483**, 591 (1999), and refs. therein.
4. I. Vorobyov, M.C. Yappert, and D.B. Dupré. J. Phys. Chem. A, **106**, 668 (2002).
5. R.E. Penn and R.F. Curl, Jr. J. Chem. Phys. **55**, 651 (1971).
6. M.J. Tubergen, C.R. Torok, and R.J. Lavrich. J. Chem. Phys. **119**, 8397 (2003).
7. S.L.Widicus, B.J. Drouin, K.A. Dyl, and G.A. Blake. J. Mol. Spectrosc. **217**, 278 (2003).
8. L. Radom, W.A. Lathan, W.J. Hehre, and J.A. Pople. J. Am. Chem. Soc. **95**, 693 (1973).
9. M. Räsänen, A. Aspiala, L. Homanen, and J. Murto. J. Mol. Struct. **96**, 81 (1982).
10. R.E. Penn and J.A. Birkenmeier. J. Mol. Spectrosc. **62**, 416 (1976).
11. T. Häber, U. Schmitt, and M.A. Suhm. Phys. Chem. Chem. Phys. **1**, 5573 (1999).
12. T. Häber, U. Schmitt, C. Emmeluth, and M.A. Suhm. Faraday Discuss. **118**, 331 (2001).
13. M. Kuhn, W. Lüttke, and R. Mecke. Z. Anal. Chem. **170**, 106 (1959).
14. R.E. Penn and L.W. Buxton. J. Mol. Spectrosc. **56**, 229 (1975).
15. M.J. Frisch, G.W. Trucks, H.B. Schlegel, P.M.W. Gill, B.G. Johnson, M.A. Robb, J.R. Cheeseman, T. Keith, G.A. Petersson, J.A. Montgomery, K. Raghavachari, M.A. Al-Laham, V.G. Zakrzewski, J.V. Ortiz, J.B. Foresman, J. Cioslowski, B.B. Stefanov, A. Nanayakkara, M. Challacombe, C.Y. Peng, P.Y. Ayala, W. Chen, M.W. Wong, J.L. Andres, E.S. Replogle, R. Gomperts, R.L. Martin, D.J. Fox, J.S. Binkley, D.J. Defrees, J. Baker, J.P. Stewart, M. Head-Gordon, C. Gonzalez, and J.A. Pople. Gaussian 94. Revision A.1 [computer program]. Gaussian, Inc., Pittsburgh, Pa. 1998.
16. K. Ohno, H. Matsumoto, H. Yoshida, H. Matsuura, T. Iwaki, and T. Suda. J. Phys. Chem. A, **102**, 8056 (1998).

© 2004 NRC Canada

17. K. Ohno, Y. Inoue, H. Yoshida, and H. Matsuura. J. Phys. Chem. A, **103**, 4283 (1999).
18. EPA Vapour Phase Library (CAS Number 141-43-5). Galactic Industries Corp., Salem, N.H. 1994.
19. P.J. Krueger and H.D. Mettee. Can. J. Chem. **43**, 2970 (1965).
20. S.T. Mulla and C.I. Jose. J. Chem. Soc. Faraday Trans. 1, **82**, 691 (1986).
21. K. Le Barbu, F. Lahmani, and A. Zehnacker-Rentien. J. Phys. Chem. A, **106**, 6271 (2002).
22. N.A. Macleod and J.P. Simons. Phys. Chem. Chem. Phys. **5**, 1123 (2003).
23. N. Borho and M.A. Suhm. Phys. Chem. Chem. Phys. **4**, 2721 (2002).

© 2004 NRC Canada

An intercomparison of measured pressure-broadening and pressure-shifting parameters of water vapor[1]

Robert R. Gamache and Jean-Michel Hartmann

Abstract: The present work is an intercomparison of experimental results on the pressure broadening and pressure shifting of water vapor absorption lines. The work focuses on application to the Earth's atmosphere; hence measurements of nitrogen, oxygen, air, and H_2O as the buffer, or perturbing gas, were considered. The literature was searched and over 100 papers found. The data, measured half-widths, their temperature dependence, and the line shifts, were taken and databases created for each perturbing gas. The databases were reordered, grouping data for rovibrational transitions, and intercomparisons of the measurements made. Trends in the data, relationships between the data sets, and dependences on temperature and quantum numbers were investigated. The data were averaged and an estimated uncertainty determined. The averaged data sets are evaluated with respect to the need of the spectroscopic and remote sensing communities. Based on these studies, recommendations for new measurements are made.

Key words: water vapor, half-widths, line shifts, temperature dependence of half-width.

Résumé : Dans le présent travail, on présente une intercomparaison de résultats expérimentaux relatifs à l'élargissement et au déplacement des raies d'absorption dus à la pression. Le travail est principalement orienté vers l'application à la chimie de l'atmosphère de la terre et, en conséquence, des mesures d'azote, d'oxygène, d'air et d'eau comme tampon ou comme gaz provoquant une perturbation. On a fait un relevé de la littérature dans laquelle on a trouvé plus de cent études. Les données relevées pour les demi-largeurs mesurées, leur dépendance sur la température et les déplacements des raies ont été insérées dans des bases de données créées pour chacun des gaz provoquant une perturbation. Ces bases de données ont été réorganisées en regroupant les données pour les transitions rovibrationnelles et on a effectué une intercomparaison des mesures. On a étudié les tendances observées dans les données, les relations entre les ensembles de données et leur dépendance sur la température et les nombres quantiques. On a établi les moyennes des données et on a évalué les incertitudes. On a évalué les ensembles de données pour lesquels les moyennes avaient été établies par rapport à la nécessité des communautés spectroscopiques et de détection à distance. Sur la base de ces études, on fait des recommandations relativement aux nouvelles mesures qui devraient être faites.

Mots clés : vapeur d'eau, demi-largeur, déplacement de raies, dépendance de la demi-largeur sur la température.

[Traduit par la Rédaction]

Introduction

Some 10 years ago the current authors, with L. Rosenmann, published a critical survey (1) of measured half-widths of water vapor perturbed by H_2O, N_2, O_2, air, CO_2, and Ar. There were four goals identified in that work: (1) to use the available data to draw conclusions concerning the influence of vibration, relations between half-widths and their temperature dependence, ratios between broadening by different collision partners, etc.; (2) to extract different broadening values for selected transitions in which one may be very confident by comparing measurements from different authors. Such accurate etalon lines should be of great use to experimentalists as tests of their measurement procedures, for remote sensing, and comparisons with theoretical models.; (3) to propose measurements that are crucially missing to complete the selected set in regard to the requirements of applications and testing of theoretical models; and (4) to make a first test of theoretical results. A literature search at the time revealed a large number of papers concerning measured half-widths of water vapor (2–84). These data gave 1091, 194, 941, and 942 half-widths for N_2-, O_2-, air-, and self-broadening and roughly 500 temperature dependence measurements. Unfortunately, the disagreement among the data was much larger than the experimental uncertainty, making it difficult to address the goals of the work. Goal 1 was addressed as well as could be done at the time with the available data; goal 2 yielded a very small number of transitions for which the confidence in the half-width was high;

Received 31 October 2003. Published on the NRC Research Press Web site at http://canjchem.nrc.ca on 8 September 2004.

R.R. Gamache.[2] Department of Environmental, Earth, and Atmospheric Sciences, University of Massachusetts Lowell, 265 Riverside Street, Lowell, MA 01854, USA.
J.-M. Hartmann. Laboratoire de Photophysique Moléculaire, CNRS (UPR3361) et Université Paris-sud (bât. 350), 91405 Orsay CEDEX, France.

[1]This article is part of a Special Issue dedicated to the memory of Professor Gerhard Herzberg.
[2]Corresponding author (e-mail: robert_gamache@uml.edu).

 doi: 10.1139/V04-069 © 2004 NRC Canada

we were able to address goal 3 based on the measurements at the time, whereas goal 4 was not possible.

Over the past 10 years there have been a number of measurements of pressure-broadened half-widths and pressure-induced line shifts of water vapor transitions (85–112)[3]. The data sets have grown to 7683, 598, 14 067, and 10 596 measurements of N_2-, O_2-, air-, and self-broadened half-widths and 7097, 461, 8754, and 1543 measurements of N_2-, O_2-, air-, and self-induced line shifts. Using these databases of half-widths and line shifts, the goals of the previous survey are readdressed and the current state-of-the-art of measuring line broadening and shifting is considered.

In the terrestrial atmosphere, water is the principal absorber of longwave radiation, responsible for some 80% of "greenhouse" warming of the Earth's surface (113), and is present in significant amounts in most media. Many water vapor transitions are used or must be accounted for in remote sensing applications. These applications require the calculation of spectra resulting from the interaction of molecular gases with radiation. The data needed for the computation of the spectra consist mainly of the line parameters for each line in the spectrum: the vacuum line position, the line intensity of the molecule–radiation interaction, the lower state energy, the pressure-broadened half-width, and the pressure-induced line shift. For most applications the temperature dependence of these parameters must also be known. The parameters are found in spectral databases such as HITRAN (114), GEISA (115), or the JPL catalogue (116). Some of these catalogues contain collisional-broadening information based on the Voigt or Van Vleck – Weisskopf profile model. Often it is necessary to account for deviations from this model, such as line mixing as in H_2O Raman Q-branch spectra (117–119), finite duration of collision effects in the far wings of the lines (120) of H_2O atmospheric continua (121–123) and high-pressure spectra (124), collisional narrowing effects (2–3), and effects from velocity-changing collisions (125–129).

Currently, the largest source of uncertainty in determining molecular profiles is the pressure-broadening coefficient (130). The effect of errors in the half-width on retrieved profiles has been systematically investigated (131, 132)[4] with the conclusion that inaccurate collision-broadened half-width values and the temperature dependence of the half-width lead to significant errors in retrieved profiles. Traub and Chance[4], using a balloon-borne far-IR FTS during the Balloon Intercomparison Campaign (BIC-2), showed that the estimated uncertainty of 10% rms in the broadening coefficient was by far the dominant error source in H_2O and O_3 profiles at nearly all altitudes. Smith and Gordley (131) and Chu et al. (132) have shown that the magnitude of the error is dependent on altitude and differs with the molecular species in question and depends on the particular transitions under consideration. Chu et al. (132) have also shown that the uncertainty in the temperature dependence of the half-width leads to errors in the retrieved mixing ratios.

The half-widths are also the dominant source of uncertainty in calculation of radiance. Kivel et al. (133) have demonstrated that a 30% increase in the air-broadened half-width of CO_2 leads to a 5% increase in the predicted radiant energy at ~710 cm^{-1}. Smith and Gordley (131) have commented that this change in calculated radiance would correspond to an increase in retrieved temperature on the order of 3 K. In regard to the radiative effects of trace gases, a WMO report on atmospheric ozone (134) cites the lack of data for the half-width and its temperature dependence as a major source of uncertainty in the line-by-line calculations.

The spectroscopic community (130, 135, 136)[5] has determined that for accurate retrievals the half-width and its temperature dependence should be known with an uncertainty of *3%* for strong lines and *10%* for weak lines. The effect of the line shift on reducing data from remote sensing measurements is now known to be significant (137, 138)[6].

This work presents an intercomparison of the measured half-widths and line shifts of water vapor important for terrestrial applications. The goals set forth in the previous survey (1) can be better addressed by the addition of the newer data, and the line shift may now be considered. A survey of the experimental results is presented in the next section and is followed by the analysis of the data including the dependence of the collision-induced parameters on vibration, rotation, temperature, and broadening partner. Intercomparisons of the data are also discussed in the latter section. In the final section, conclusions and recommendations are made.

The experimental results

This work considers the collision-broadened half-widths and pressure-induced line shifts of water vapor for terrestrial applications. A search of the literature was made for half-widths and line shifts of H_2O perturbed by N_2, O_2, air, and H_2O. The result was 112 papers spanning seven decades. Twenty-four have been published since the work of ref. 1. They have increased the half-width data sets by factors of 6.5, 2.0, 7.3, and 10.4 for N_2-, O_2-, air-, and self-broadening. Most of the line shift data are from studies more recent than the study of ref. 1. These data have been organized into databases for each perturbing gas with the half-widths corrected, when necessary, to 296 K by the usual power law model. Table 1 presents a summary of the data. Presented are the number of measurements of the half-width and line shift for a particular broadening gas as a function of vibrational band. The ranges of the data are presented in Table 2; however, to understand this better, some of the newer data must be discussed.

Several of the more recent studies have produced large data sets. Reference 88 reported 5423 N_2-broadened half-widths of water vapor, ref. 89 reported 4168 air-broadened half-widths, and refs. 106 and 107 reported over 6000 half-widths and line shifts for air as the perturbing gas and over 8000 self-broadened half-widths. The analysis of the spectra was automated to produce such large data sets. The codes

[3] V. Zeninari. Private communication, University of Reims. 2003.
[4] W. Traub and K. Chance. BIC-2 Campaign. Private communication. 1985.
[5] M.A.H. Smith. Private communication. Third Langley Spectroscopic Parameters Workshop, NASA Langley Research Center, Hampton, Va. 1992.
[6] J. Margolis. Private communication. Jet Propulsion Laboratory. 1997.

© 2004 NRC Canada

Table 1. The number of half-width (γ) and line shift (δ) data as a function of vibrational band.

	N_2		O_2		Air		Self	
Band	γ	δ	γ	δ	γ	δ	γ	δ
000←000	258	168	74	1	341	163	158	110
010←000	1358	1186	373	342	1971	1384	1518	1198
020←000					62	18	47	
100←000	6	6			132	118	142	
001←000	98	98			245	239	164	
011←000					5		5	
200←000	8		6				6	
101←000	27	4	22	4	11		24	
002←000							2	
130←000	1				9			
031←000	1				29			
210←000	7				78	3	4	
111←000	67				352	32	30	
012←000	19				231	38	36	
041←000					311	166	170	
220←000	1	1			262	134	126	
121←000	76	1			768	410	321	
022←000	1				164	81	96	
300←000	55	26			608	320	276	
201←000	114	13			996	529	378	
102←000	17	21			508	252	260	
003←000	56				655	367	314	
131←000					170	49	84	
310←000					133	35	57	
211←000					458	169	162	
112←000					183	56	99	
013←000					224	94	111	
141←000	32	38			30	21	42	
042←000	15	15			15	8	22	
320←000	85	103	1	1	93	65	103	
221←000	307	273	29	28	417	243	320	
301←000	470	381	78	77	646	366	443	
202←000	247	238	9	8	338	207	270	
122←000	79	86			77	59	87	
023←000	76	90			98	66	86	
400←000	216	225			314	190	235	
103←000	313	294	3		413	248	296	
004←000	99	116			71	66	124	
151←000	4	9			1	1	14	
330←000	21	22			15	13	25	
231←000	158	168			127	124	169	
212←000	77	94			59	58	102	
311←000	301	282			236	235	270	
410←000	153	159			134	131	152	
113←000	170	179			143	142	176	
321←000	165	162			135	132	160	
222←000	48	55			23	21	56	
302←000	144	147			113	112	149	
401←000	242	243			207	206	241	
420←000	102	104			76	75	103	
123←000	76	80			59	58	83	
500←000	161	169			144	144	171	
203←000	223	205			142	142	211	
104←000	47	63			16	16	74	
331←000	113	116			78	75	123	
213←000	70	76			47	43	81	

© 2004 NRC Canada

Table 1 (*continued*).

	N_2		O_2		Air		Self	
Band	γ	δ	γ	δ	γ	δ	γ	δ
312←000	1	1			1	1	1	
411←000	118	125			91	90	124	
303←000	56	56			24	24	63	
402←000	15	16			3	3	21	
421←000	20	20			10	9	23	
501←000	139	139			118	117	140	
313←000					3	3	2	
060←000					3			
070←000					3			
032←000					3			
051←000					3			
061←000	2	2			2	2	2	
080←000					3	3	3	
140←000					4			
240←000	11	16			11	7	18	
160←000	2	3			2	2	2	
071←000	5	4			5	5	4	
170←000	4	5			3	3	4	
033←000	78	88			62	61	97	
132←000	10	15			5	5	15	
241←000	34	43			17	17	42	
142←000	73	76			52	52	76	
340←000	32	39			17	17	43	
043←000	15	16			8	8	16	
510←000	59	62			49	48	62	
430←000	7	7			5	5	7	
053←000	16	18			8	8	18	
133←000	26	30			8	8	32	
034←000	9	9			3	3	10	
600←000	79	81			60	60	90	
341←000	55	58			31	31	62	
063←000	6	6			4	4	5	
322←000	23	24			9	9	26	
511←000	42	44			21	20	47	
610←000	8	8					11	
431←000	13	14			3	3	16	
115←000	5	6			1	1	8	
620←000	4	5					5	
601←000	80	85			19	19	89	
521←000	5	5					9	
800←000	15	16					16	
701←000	16	22					25	
700←000	61	65			8	8	81	
223←000	15	19			3	3	22	
230←000					17			
611←000		2					11	
010←010	2	1			1	1	2	2
020←010	96	82	3		119	111	205	203
100←010	15	16			13	16	31	30
001←010	27	28			27	28		
011←010							8	
131←010					8	8	10	
310←010					3	2	2	
211←010					6	5	9	
311←010		1					2	

© 2004 NRC Canada

Table 1 (*concluded*).

	N_2		O_2		Air		Self	
Band	γ	δ	γ	δ	γ	δ	γ	δ
410←010		1						
113←010		2					1	
121←001					3			
131←001					3			
211←001					9			
Number of data	7683	7097	598	461	14 067	8754	10 596	1543

Table 2. Minimum and maximum values of measured half-width (γ) and line shift (δ) in units of 10^{-3} cm^{-1} atm^{-1} (1 std atm = 101.325 kPa) as a function of perturbing species.

	N_2		O_2		Air		Self	
	γ	δ	γ	δ	γ	δ	γ	δ
Min. value	4.7	–30.4	6.0	–37.7	4.3	–83.2	108	–63.0
Max. value	182	24.8	91.5	48.8	190	41.2	805	65.2

that were implemented do not ensure that every spectral line is correct. The assignments for the lines, many of which were very weak transitions, came from ab initio predictions. This fact coupled with transcription errors has led to a small number of transitions with incorrect rotational quantum numbers or a number of transitions with identical rovibrational quantum numbers in the data of ref. 89. One of the current authors (RRG) has corresponded with the authors about these problems.

The data from refs. 88, 106, and 107 have problems that arise from the automated reduction algorithms. For example, in ref. 88, N_2-broadened half-widths as large as 1.65 cm^{-1} atm^{-1} and as small as 0.00099 cm^{-1} atm^{-1} (1 std atm = 101.325 kPa) are reported, values that are much too large and small, respectively. The current authors have been collaborating with the authors of these works. It appears that the spurious values arise for very weak transitions or noise in the spectrum. In the intercomparisons for transitions with reasonable strength (a qualitative guide might be transitions with more than ~5% absorption in the spectra), their data agree well with the data from other groups. We have provided to them an algorithm to identify line shape data that are potentially in error. While they are currently reanalyzing their data, the data used in this intercomparison are from the published work.

Given these facts, when we discuss the range of the data we have not included the data from refs. 88, 106, and 107. However, we have included their data in the intercomparisons since the data that appears to be in question is generally for very weak transitions, which have not been measured by other groups. Hence, there are no intercomparisons of the questionable data. The ranges of the data for the different perturbing molecules are presented in Table 2. These data indicate that the half-widths change by a factor of 39, 15, 44, and 8 from low- to high-J lines for N_2-, O_2-, air-, and self-broadening, respectively. The maximum values of J (K_a) for the data are 20 (11), 16 (10), 19 (11), and 20 (11) for N_2-, O_2-, air-, and self-broadening, respectively. A complete list of J_{max}, J_{min}, $K_{a,max}$, and $K_{a,min}$ for each vibrational band studied can be obtained at faculty.uml.edu/RobertGamache.

There have been a number of investigations into the dependence of the half-width on vibration. Mandin et al. (10, 27), in studies in the 8500–9300 and 9500 – 11 500 cm^{-1} regions, took ratios of their measured half-widths to those of the HITRAN database (114). From this study, Mandin et al. concluded that there was a small (±3%) vibrational dependence of the half-width. Grossman and Browell (5) reported a 5% difference between transitions in the $3\nu_1 + \nu_3$ and $2\nu_1 + 2\nu_2 + \nu_3$ bands, with the $3\nu_1 + \nu_3$ lines having the larger broadening values. This study compared average broadening values, not J-dependent half-widths. In a 1996 study by Brown and Plymate (139) on H_2O broadened by hydrogen, the ratios of half-widths for the same set of rotational quantum numbers were formed for the rotation and ν_1 bands divided by the ν_2 band (51 and 63 pairs of transitions, respectively). The ratios of the rotation to the ν_2 band range from 0.92 to 1.1 and those of the ν_1 to ν_2 band range from 0.98 to 1.19 for the transitions studied. For rotational/ν_2 transitions, the rms ratio is 1.016 (±2.6%), and it is 1.08 (±4%) for ν_1/ν_2 transitions. Brown and Plymate concluded that these differences are too large to be caused by experimental error and that there is a vibrational dependence in the half-width.

Zou and Varanasi (85), in a 2002 study, investigated the vibrational dependence of self- and air-broadening of water vapor in the 950–2100 and 3000–4050 cm^{-1} regions. They considered ratios of the half-widths for the same rotational transition for the $2\nu_2$ and the ν_2 bands, the ν_1 and the ν_2 bands, and the $2\nu_2$ and the ν_1 bands for both self- and air-broadening. From the analysis of the self-broadening data, they concluded that the half-widths in the $2\nu_2$ band are smaller than their counterparts in the ν_2 band by about 10%. The differences in the ratios for the ν_1 and the ν_2 bands and for the $2\nu_2$ and the ν_1 bands contained too much scatter to state conclusively if there was a definite vibrational dependence. Their analysis of the air-broadening data indicated that the half-widths in the ν_1 band are larger than the correspond-

© 2004 NRC Canada

ing half-widths in the ν_2 band by about 5%. This is in rough agreement with the work of Brown and Plymate (139). There were too few ratios for the $2\nu_2$ and the ν_2 bands and the $2\nu_2$ and the ν_1 bands to draw any solid conclusions about the vibrational dependence of the half-widths.

The vibrational dependence of the half-widths of water vapor was addressed in a survey paper (1) and several workshops (130, 135)[5]. It was estimated that, in general, the effect of the vibrational states of the transition was smaller than experimental uncertainties and could change the half-width by ~3%–5%.

A recent theoretical work (140) on the vibrational dependence of the half-widths of water vapor lines found that the half-widths of certain transitions (doublet transitions where $K_c = J$ or $J - 1$) exhibit a strong vibrational dependence. The difference in the half-widths can be up to a factor of 6 for high-J transitions for bands involving 4 quanta of stretch modes. Using the database of measured half-widths, the authors were able to confirm their prediction with experimental data. They were also able to determine the mechanism leading to the vibrational dependence of these half-widths. Given this fact, the intercomparisons made here will not consider identical rotational transitions of different vibrational bands; i.e., the vibrational dependence will be neglected. This greatly reduces the number of transitions that can be compared, but it is necessary. Hence, intercomparisons between measurements made by different groups will be made for transitions with the same quantum numbers: $v_1'v_2'v_3'J'K_a'K_c' \leftarrow v_1''v_2''v_3''J''K_a''K_c''$.

The temperature dependence of the half-width in the databases assumes the usual power law model

$$[1] \qquad \gamma(T) = \gamma(T_0)\left[\frac{T_0}{T}\right]^n$$

where n is the temperature exponent. Measurements (141)[7] and predictions from theory (140) show that for N_2-broadening of water vapor, the temperature exponents range from about 0.8 to –0.3. This is a recent finding. The databases that were created here allow for negative temperature exponents.

Each record of each database contains the wavenumber of the transition, the upper and lower state vibrational quantum numbers ($v_1'v_2'v_3'$ $v_1''v_2''v_3''$), the upper and lower rotational quantum numbers ($J'K_a'K_c'$ $J''K_a''K_c''$), the half-width in units of 10^{-3} cm^{-1} atm^{-1} (1 std atm = 101.325 kPa), the uncertainty in the half-width (same units), the temperature dependence of the half-width and its uncertainty, the line shift in units of 10^{-3} cm^{-1} atm^{-1} (1 std atm = 101.325 kPa), the uncertainty in the line shift (same units), the temperature dependence of the line shift and its uncertainty, an isotopologue code (HITRAN values), and a reference number. While fields in the database have been reserved for the temperature dependence of the line shift, these fields are currently not used. The reference number in the databases refers to a bibliography file that one can download with the database files. These files are available at faculty.uml.edu/Robert_Gamache.

An intercomparison of the collision-induced parameters

Using the database files, codes were written to sort the data into groups for particular rovibrational transitions. All transitions for which only a single measurement was made are eliminated and the resulting data are plotted and intercomparisons made. This procedure results in groups of 2, 3, 4, …, 8 points depending on the number of measurements made for a particular rovibrational transition. For a number of rovibrational transitions, different isotopologues were measured. Intercomparisons were not made between different isotopologues. This procedure yields 499, 19, 3514, and 440 rovibrational transitions for which intercomparisons could be made for N_2-, O_2-, air-, and self-broadening, respectively.

The data for each rovibrational transition are taken and average values of the parameters and their uncertainty produced. Because the uncertainties reported in the literature are not consistent, i.e., some report 1σ of the fit to the data as the uncertainty, others report 2σ or 3σ, others give an overall percentage error for the uncertainty, and in some instances the uncertainty is not reported, it is not possible to use an elaborate scheme to construct the uncertainty. Here, the average value of the half-width was determined as the simple arithmetic average. When five or more points were compared, the uncertainty assigned was twice the standard deviation; otherwise, the uncertainty assigned was the maximum difference between the average and the individual half-width values for the transition or the maximum uncertainty of the measured points, whichever was the greater value. For intercomparisons of two points, the separation of the two data points was considered and compared with the reported uncertainty of the data. This approach yielded a conservative estimate of the accuracy of the data. A similar scheme was used for the line shifts; however, there were far fewer intercomparisons.

Table 3 lists the number of intercomparisons of half-widths made as a function of the number of points in the group, the number of the intercomparisons for which the estimated uncertainty is less than or equal to 3%, 5%, and 10%, the number with estimated uncertainty greater than 10%, and the maximum estimated uncertainty. Table 4 lists the number of comparisons of line shifts made as a function of the number of points in the group, the number of the intercomparisons for which the estimated uncertainty is less than or equal to 5%, 10%, and 20%, and the number with estimated uncertainty greater than 20%. Note that for the line shift there are intercomparisons only for N_2- and air-broadening of water vapor.

Before commenting on the statistics, it should be noted that most of the intercomparisons are for pairs of points, from 80% for air-broadening to 93% for self-broadening. Certainly, at the same level of agreement, more confidence is gained as the number of points compared increases. Unfortunately, the number of intercomparisons with n greater than 3 is small: 6%, 10%, 2%, and 0.9% for N_2-, O_2-, air-, and self-broadening, respectively.

[7] A. Valintin. Private communication. Université de Pierre et Marie Curie, Paris. 2002.

© 2004 NRC Canada

Table 3. Half-width intercomparisons: number of data in 2, 3, 4, …, 8 point intercomparisons, number of intercomparisons with estimated uncertainties (U) in the given ranges, and maximum estimated uncertainties for the H_2O–N_2, H_2O–O_2, H_2O–air, and H_2O–self systems.

		Number of data in the intercomparison						
System	Uncertainty	2	3	4	5	6	7	8
H_2O–N_2	N^a	420	48	30			1	
	$U \leq 3\%$	46						
	$3\% < U \leq 5\%$	67	6	1				
	$5\% < U \leq 10\%$	216	30	25				
	$10\% < U$	91	12	4			1	
	$U_{max} = 140\%$							
H_2O–O_2	N^a	16	1	1		1		
	$U \leq 3\%$							
	$3\% < U \leq 5\%$	1						
	$5\% < U \leq 10\%$	4	1	1		1		
	$10\% < U$	11						
	$U_{max} = 51.8\%$							
H_2O–air	N^a	2818	615	63	11	4	2	1
	$U \leq 3\%$	65	48					
	$3\% < U \leq 5\%$	297	83	8	1	1		
	$5\% < U \leq 10\%$	967	382	37	5	1	1	
	$10\% < U$	1489	102	18	5	2	1	1
	$U_{max} = 137\%$							
H_2O–self	N^a	409	27	3	1			
	$U \leq 3\%$	2						
	$3\% < U \leq 5\%$	3						
	$5\% < U \leq 10\%$	156	8					
	$10\% < U$	248	19	3	1			
	$U_{max} = 186\%$							

[a]Number of intercomparisons.

Table 4. Line shift intercomparisons: number of data in 2- and 3-point intercomparisons and number of intercomparisons with estimated uncertainties (U) in the given ranges for the H_2O–N_2 and H_2O–air systems.

		Number of data in the intercomparison	
System	Uncertainty	2	3
H_2O–N_2	N^a	145	
	$U \leq 5\%$	21	
	$5\% < U \leq 10\%$	35	
	$10\% < U \leq 20\%$	36	
	$20\% < U$	53	
H_2O–air	N^a	675	5
	$U \leq 5\%$	21	0
	$5\% < U \leq 10\%$	45	0
	$10\% < U \leq 20\%$	201	3
	$20\% < U$	408	2

[a]Number of intercomparisons.

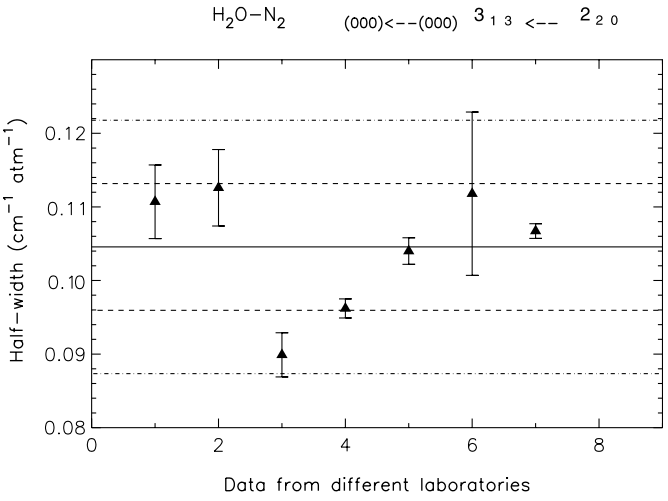
For N_2-broadening, there are no three-point or greater intercomparisons with an estimated uncertainty less than or equal to 3%, and among the pair intercomparisons, only 11% meet this criterion. A look at Table 3 shows that most of the estimated uncertainties are in the range greater than 5% to less than or equal to 10%, with a fair number greater than 10%. One rovibrational transition, the $3_{12} \leftarrow 2_{20}$ transition of the rotational band or 183 GHz line, was studied by seven groups, and here the estimated uncertainty is greater than 10%. These data are shown in Fig. 1. This plot is typical of the intercomparisons. Often the data are separated by more than the uncertainty assigned to the data. This fact certainly leads to questions about the uncertainties reported in the literature. For the line shifts, there are only intercomparisons of pairs of points. Often in the plots, the error bars do not overlap (see Fig. 2). Table 4 shows the distribution of the estimated uncertainties. Some 14% of the intercomparisons have agreement to better than 5%.

For O_2-broadening of water vapor, there are only 19 intercomparisons, mostly pairs of data. The estimated uncertainties are mostly greater than 10%. Figure 3 shows the only six-point intercomparison for this database. The estimated uncertainty for this line is 6.2%. There are no shift measurements for intercomparison.

The largest data set is for air-broadening of H_2O, which allows 3514 intercomparisons to be made. Unfortunately, only 81 of the intercomparisons have more than three data points. Of these intercomparisons, none meet the 3% uncertainty criterion of the spectroscopic community. Most of the error estimates are in the 5%–10% range or above 10%. There are two transitions for which seven measurements have been made and one transition for which eight measurements have been made (183 GHz transition). These transi-

© 2004 NRC Canada

Fig. 1. Measured half-widths (cm^{-1} atm^{-1}, 1 std atm = 101.325 kPa) for nitrogen-broadening of the 183 GHz line of water vapor with reported uncertainties. The solid line is the average half-width, and the dashed lines are 1 and 2 standard deviations.



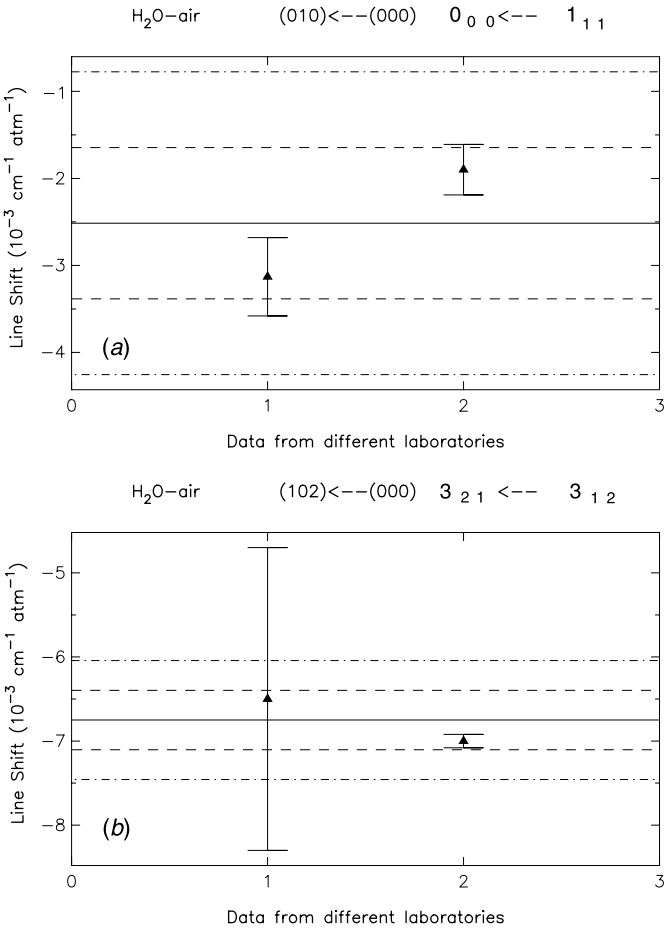
tions have 26%, 8%, and 18% estimated uncertainty, respectively. Figures 4*a* and 4*b* show the two transitions for which there are seven measurements for intercomparison. The first of these (Fig. 4*a*) is typical of many of the air-broadening plots with the error bars of the data points not overlapping. While the error bars do overlap in Fig. 4*b*, the overall 2σ uncertainty is almost 3 times that needed for remote sensing. The intercomparisons for the line shifts only occur as pairs of measurements. As shown in Table 4, these data are heavily skewed toward the 10%–20% and >20% uncertainty ranges. There are 21 intercomparisons with an estimated uncertainty of less than 5%.

The data set for self-broadening of H_2O is also large, some 10 596 measurements. From this data set, it is possible to make 440 intercomparisons of half-widths. There are no intercomparisons of the line shifts. Only four intercomparisons are possible for more than three data points: three four-point intercomparisons and one five-point intercomparison. The estimated uncertainty for these intercomparisons is greater than 10%. The five-point intercomparison for the $3_{1\,3} \leftarrow 2_{2\,0}$ transition of the rotational band is shown in Fig. 5, demonstrating the spread in the measurements. The intercomparison of pairs of points contstitutes 92% of the self-broadening intercomparisons, of which 61% have estimated uncertainties greater than 10%.

Data trends

For the purpose of developing a database of spectral parameters or in running radiative transfer codes, trends in the half-width data have been exploited. One method was to compile an average half-width as a function of the rotational quantum number J'' (or a combination such as $(J' + J'')/2$) and use these values when measurement or calculation was not available for a transition. In Fig. 6, the measured air-broadened half-widths for the ν_2 band are plotted vs. $(J' + J'')/2$. For many of the columns of points the half-width changes by a factor of 6, and hence an algorithm based on averages as a function of J is prone to large error.

Fig. 2. (*a*) Measured line shifts (cm^{-1} atm^{-1}, 1 std atm = 101.325 kPa) for air-broadening of the $0_{0\,0} \leftarrow 1_{1\,1}$ transition in the ν_2 band of water vapor with reported uncertainties. The solid line is the average line shift, and the dashed lines are 1 and 2 standard deviations. (*b*) Measured line shifts (cm^{-1} atm^{-1}, 1 std atm = 101.325 kPa) for air-broadening of the $3_{2\,1} \leftarrow 3_{1\,2}$ transition in the $\nu_1 + 2\nu_3$ band of water vapor with reported uncertainties. The solid line is the average line shift, and the dashed lines are 1 and 2 standard deviations. Note that the data of ref. 106 are included.



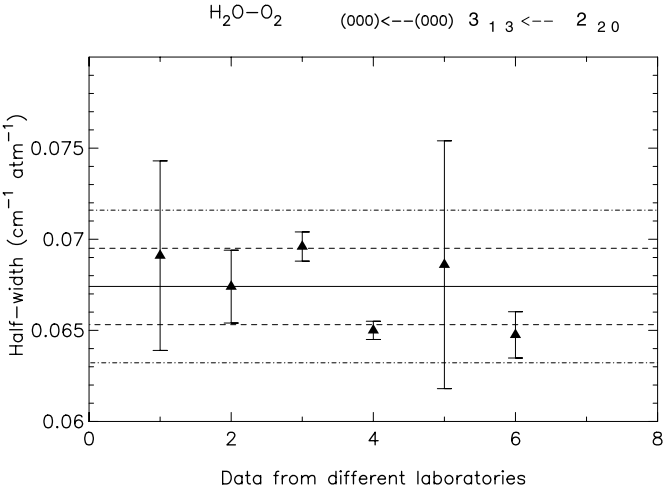
Polynomial expressions have been used to fit half-width data for a particular band (142–145). These are typically of the form

$$[2] \qquad \gamma = a + bJ'' + cJ''^2 + dK_a''$$

where a, b, c, and d are fitting constants. In ref. 145, J'' was replaced by $(J'' + J')/2$, and K_a'' was replaced by $(K_a'' + K_a')/2$. The application of eq. [2] to asymmetric rotors has been mostly to heavy species such as ozone. References 142 and 143 consider pressure-broadened half-widths of ozone where the values change by about a factor of 2 from the maximum to the minimum. While there is no physics in the polynomial fit, it sometimes gives a reasonable representation of the half-widths. In refs. 144 and 145, the application is to CO_2- and H_2-broadening of water vapor, a light asym-

© 2004 NRC Canada

Fig. 3. Measured half-widths (cm^{-1} atm^{-1}, 1 std atm = 101.325 kPa) for oxygen-broadening of the $3_{1\,3} \leftarrow 2_{2\,0}$ transition in the rotation band of water vapor with reported uncertainties. The solid line is the average half-width, and the dashed lines are 1 and 2 standard deviations.

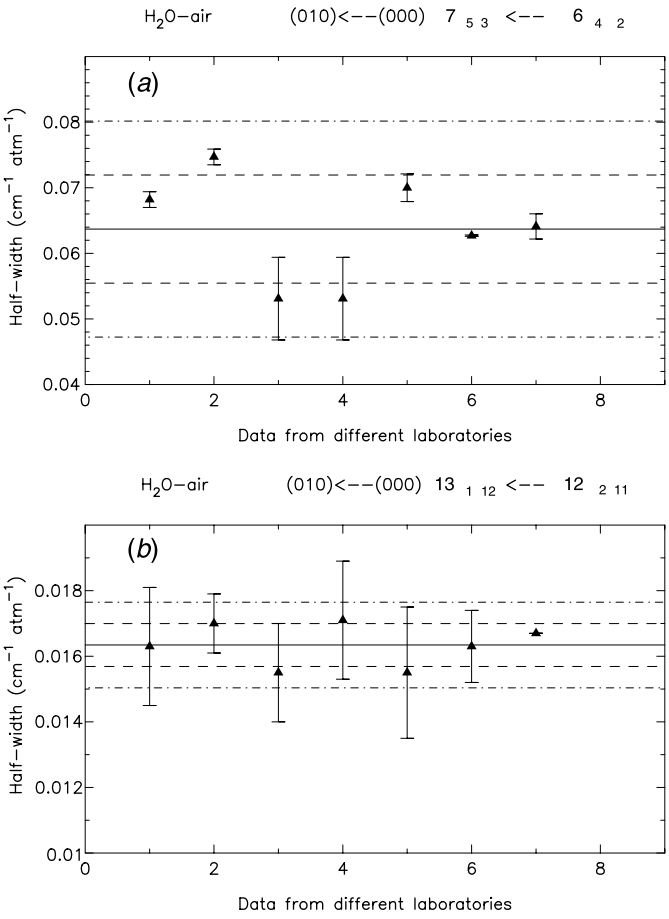


metric rotor. Here, the half-widths change by factors of 15 and 3, respectively. In both of these studies, the authors found that the polynomial expression gave only slightly better results than averaging as a function of $(J'' + J')/2$. This is due to both the range of the half-widths being large and to the energy structure of H_2O (energy gap) and the effect on the half-width. The minimum to maximum half-widths observed in the databases studied here change by factors of 39, 15, 44, and 7 for N_2-, O_2-, air-, and self-broadening, respectively. Hence, it is not expected that polynomial fits of the type in eq. [2] will give reasonable results.

More recently, Wagner et al. (146) used the polynomial fit applied to particular K_a sub-bands of ozone, which are similar to the spectrum of a diatomic molecule. Note, this requires a separate set of coefficients for each sub-band considered. Wagner et al. (146) found that a third-order polynomial gave reasonable results. For water vapor this approach may be possible. To test this, the P and R B-type transitions of the ν_2 band for particular values of K_a'' were extracted from the air-broadening database and plotted vs. J'' and are given in Fig. 7 for $K_a'' = 2$ and 5. Although there is spread due to measurements from different groups in Fig. 7*a* ($K_a'' = 2$), there are clear trends that could be fit with a polynomial. However, a similar plot (Fig. 7*b*) for $K_a'' = 5$ does not demonstrate any clear trend that could be represented by a polynomial. The plots for many other K_a'' values were similar to Fig. 7*b*, from which it can be concluded that this type of polynomial fit should not be applied to water vapor.

Brown and Plymate (139) made plots for a subset of transitions chosen such that $K_a + K_c - J = 0$ for both the upper and the lower state or $K_a + K_c - J = 1$ for both the upper and the lower state and plotted these values vs. $J_m + 0.1(J_m - K_{am})$, where J_m and K_{am} are the larger of the values of J and K_a of the rotational transition quantum numbers. Figures 8*a* and 8*b* are plots for $K_{am} = 2$ and 5. The trends are more evident than those of previous plots; however, at $K_{am} = 5$, it is not clear that a polynomial fit will give a good representation of the data.

Fig. 4. (*a*) Measured half-widths (cm^{-1} atm^{-1}, 1 std atm = 101.325 kPa) for air-broadening of the $7_{5\,3} \leftarrow 6_{4\,2}$ transition in the ν_2 band of water vapor with reported uncertainties. The solid line is the average half-width, and the dashed lines are 1 and 2 standard deviations. (*b*) Measured half-widths (cm^{-1} atm^{-1}, 1 std atm = 101.325 kPa) for air-broadening of the $13_{1\,12} \leftarrow 12_{2\,11}$ transition in the ν_2 band of water vapor with reported uncertainties. The solid line is the average half-width, and the dashed lines are 1 and 2 standard deviations.



One additional method used to estimate the half-width for a particular transition broadened by a gas for which there is no data is by scaling the half-width for a different broadening gas by an average ratio of the half-widths obtained from other transitions (5, 145). To test the soundness of this approach, the databases for N_2-, O_2-, air-, and self-broadening were taken and for each gas the average half-width for each rovibrational transition was determined. Next, the ratios of self-, O_2-, and air-broadening to N_2-broadening were taken for each rovibrational transition for which data was available. The three sets of ratios have similar structure. In Fig. 9, the ratios are plotted vs. J'' of the transition for air-broadening divided by N_2-broadening. The solid line is the average ratio. It is clear that an algorithm to estimate half-widths for one perturbing gas from the data of another per-

© 2004 NRC Canada

Fig. 5. Measured half-widths (cm^{-1} atm^{-1}, 1 std atm = 101.325 kPa) for self-broadening of the $3_{13} \leftarrow 2_{20}$ transition in the rotation band of water vapor with reported uncertainties. The solid line is the average half-width, and the dashed lines are 1 and 2 standard deviations.

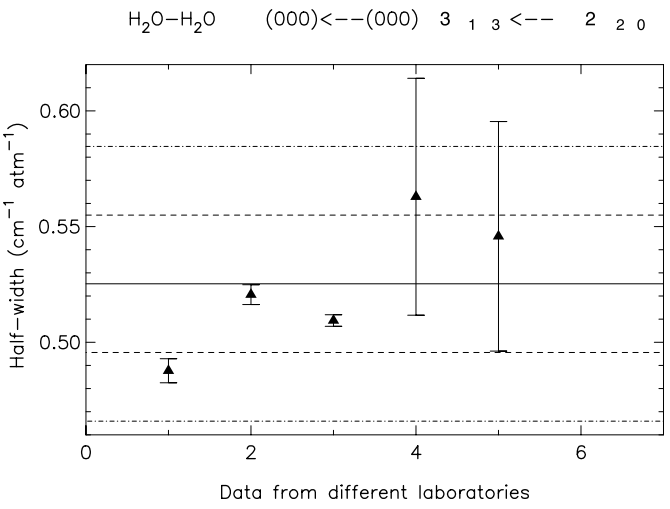
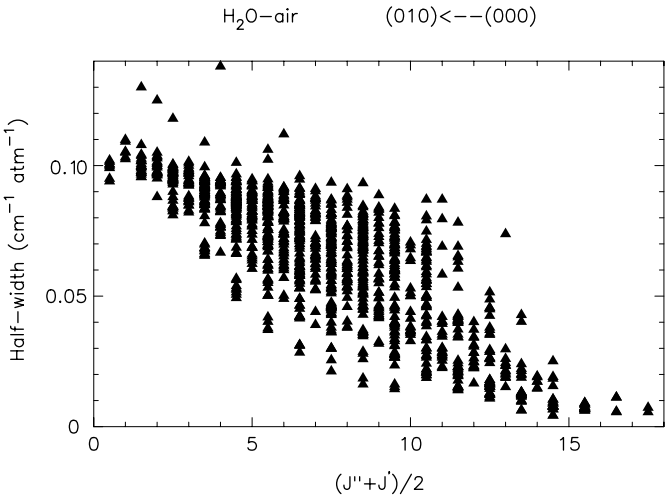


Fig. 6. Measured air-broadened half-widths (cm^{-1} atm^{-1}, 1 std atm = 101.325 kPa) in the ν_2 band vs. $(J'' + J')/2$.



turbing gas from the average ratio will result in data with very large uncertainties.

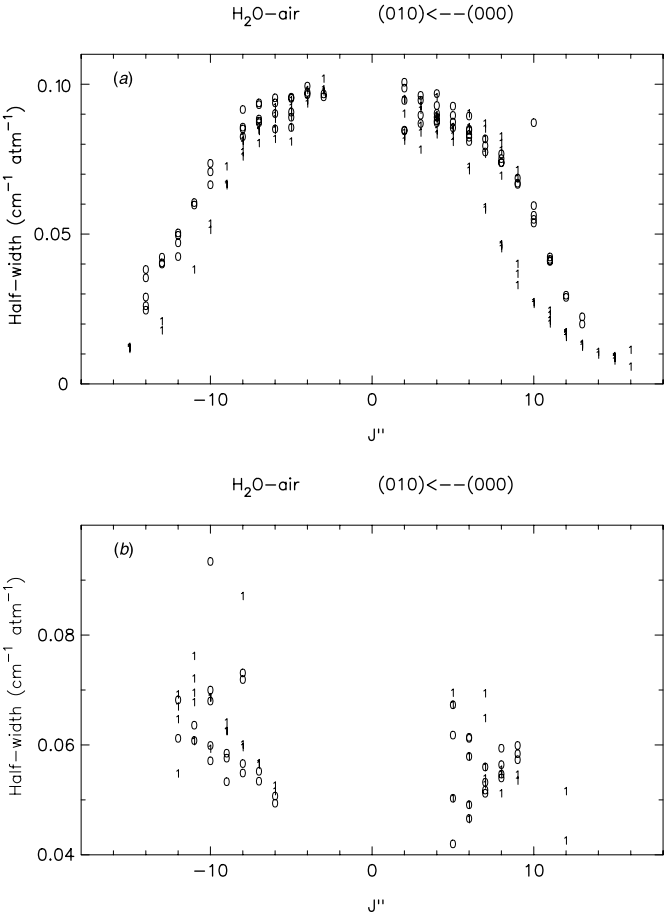
The line shift is a quantity that is dependent on the vibrational states of the transition. As discussed by Gamache and Hartmann (140), the dominant term in the potential is the vibrational dependence of the polarizability, part of the vibrational dephasing term. The expression is given by

$$[3] \quad \alpha = \alpha_0 + 0.29n_{\nu_1} + 0.07n_{\nu_2} + 0.28n_{\nu_3}$$

$$\alpha \approx \alpha_0 + 0.29(n_{\nu_1} + 0.25n_{\nu_2} + n_{\nu_3})$$

where n_{ν_1}, n_{ν_2}, and n_{ν_3} are the number of ν_1, ν_2, and ν_3 quanta exchanged in the transition. The database of measurements for air-broadening was reordered and grouped on rotational quantum numbers. The line shift data were plotted vs. the

Fig. 7. (*a*) Air-broadened half-widths (cm^{-1} atm^{-1}, 1 std atm = 101.325 kPa) of P and R B-type transitions of the ν_2 band for $K_a'' = 2$ vs. J''. Symbols (0 or 1) correspond to values of $K_a'' + K_c'' - J''$. (*b*) Air-broadened half-widths (cm^{-1} atm^{-1}, 1 std atm = 101.325 kPa) of P and R B-type transitions of the ν_2 band for $K_a'' = 5$ vs. J''. Symbols (0 or 1) correspond to values of $K_a'' + K_c'' - J''$.

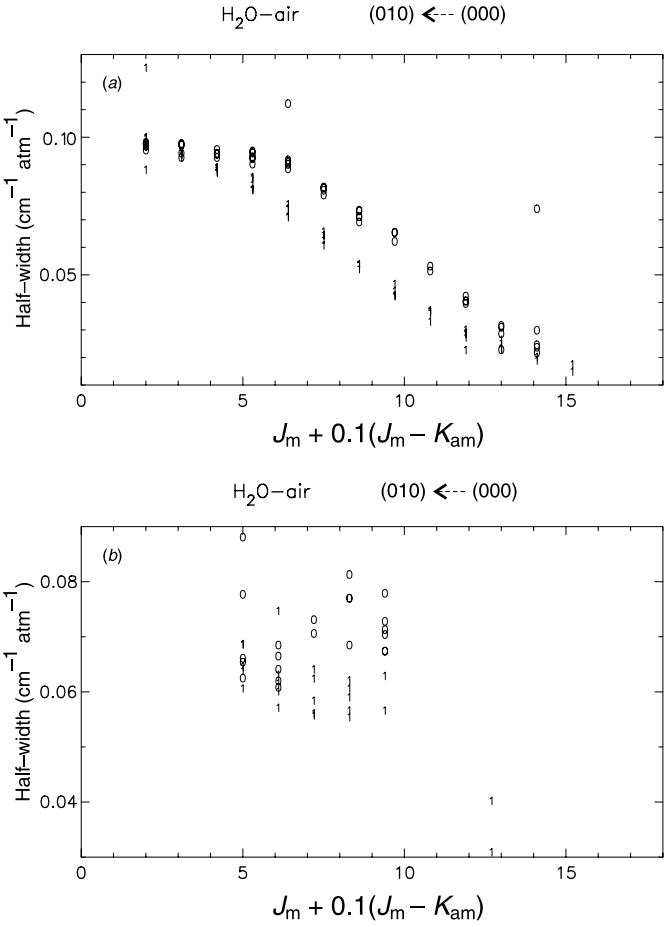


number of vibrational quanta defined as $(n_{\nu_1} + 0.25n_{\nu_2} + n_{\nu_3})$. Figure 10 is a plot of the line shift for the $4_{14} \leftarrow 3_{03}$ rotational transition vs. the number of vibrational quanta; the straight line is a fit of the data, showing the linear dependence of the line shift on the number of vibrational quanta exchanged in the transition. The problem is more complicated in that there is also a dependence on the other terms in the potential, leading to different slopes and intercepts for each rotational transition. This fact limits the use of eq. [3] for making predictions of the line shift.

Gamache and Hartmann (140) reported a strong vibrational dependence of the half-width for certain types of transitions. Readers are referred to that paper for full details. The basic notion is that rotational states of water vapor that have large energy gaps to other collisionally connected states demonstrate large vibrational dependence of the half-width. Those states with a small energy gap to other states appear independent of the vibrational states. The states showing the large energy gaps are for high J and $K_c = J$ or $J - 1$, e.g., $15_{0\,15}$. Figures 11*a* and 11*b* show the half-width vs. the num-

© 2004 NRC Canada

Fig. 8. (*a*) Air-broadened half-widths (cm^{-1} atm^{-1}, 1 std atm = 101.325 kPa) of transitions with $K_a + K_c - J = 0$ or $K_a + K_c - J = 1$ for both the upper and lower states vs. $J_m + 0.1(J_m - K_{am})$, where J_m and K_{am} are the larger of the values of J and K_a of the rotational transition quantum numbers and $K_{am} = 2$. Symbols (0 or 1) correspond to values of $K_a'' + K_c'' - J''$. (*b*) Air-broadened half-widths (cm^{-1} atm^{-1}, 1 std atm = 101.325 kPa) of transitions with $K_a + K_c - J = 0$ or $K_a + K_c - J = 1$ for both the upper and lower states vs. $J_m + 0.1(J_m - K_{am})$, where J_m and K_{am} are the larger of the values of J and K_a of the rotational transition quantum numbers and $K_{am} = 5$. Symbols (0 or 1) correspond to values of $K_a'' + K_c'' - J''$.



ber of vibrational quanta for the $3_{1\,3} \leftarrow 2_{1\,2}$ and the $9_{1\,9} \leftarrow 8_{1\,8}$ rotational transition, respectively. For the first of these transitions, the energy gaps to other states are small and the half-width is only weakly dependent on the vibrational states involved in the transition (Fig. 11*a*). For the second transition, the energy gap is becoming large and the figure shows the half-width increasing by almost a factor of 3 in agreement with the theoretical calculations of ref. 140. As the rotational quantum numbers increase, the energy gaps increase as well, and by $\sim J'' \sim 16$, the half-widths are dominated by the vibrational dephasing terms.

It is still too early to discuss trends in the temperature dependence of the half-width. Measurements are available for 76, 12, 341, and 213 transitions for N_2-, O_2-, air-, and self-broadening of H_2O. While a number of plots were made, the data are too sparse to identify trends at this time.

Fig. 9. Ratio of air-broadened half-widths to nitrogen-broadened half-widths for identical rovibrational transitions vs. J'' of the transition. The solid line is the average ratio.

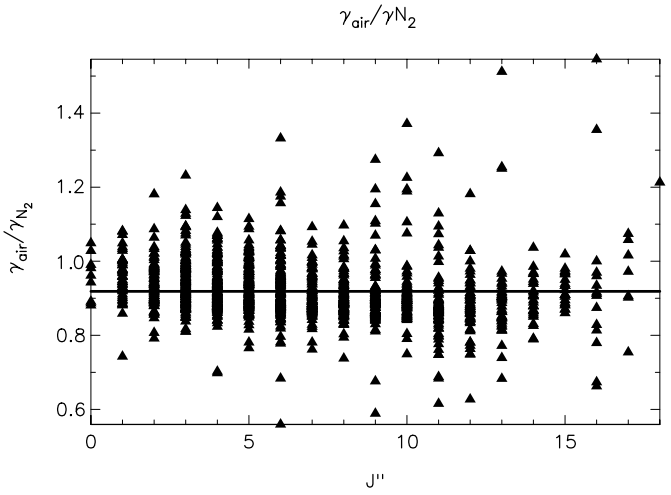
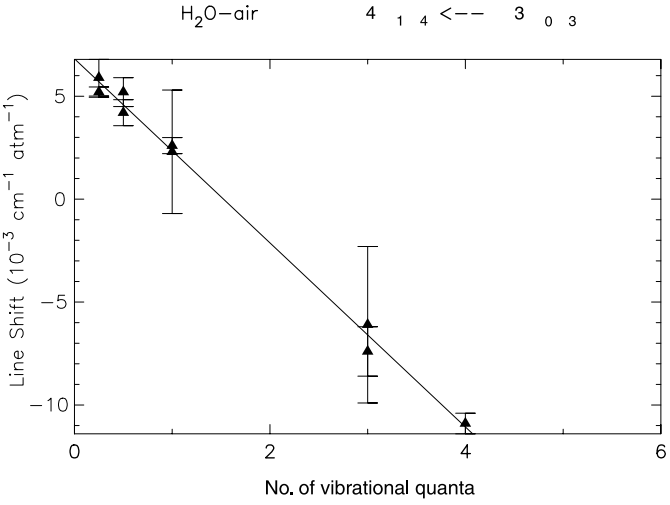


Fig. 10. Measured line shifts (10^{-3} cm^{-1} atm^{-1}, 1 std atm = 101.325 kPa) with reported uncertainties for air-broadening of the $4_{1\,4} \leftarrow 3_{0\,3}$ transition vs. the number of vibrational quanta ($n_{\nu_1} + 0.25n_{\nu_2} + n_{\nu_3}$), where n_{ν_1}, n_{ν_2}, and n_{ν_3} are the number of ν_1, ν_2, and ν_3 quanta exchanged in the transition. The solid line is a least-squares fit of the data to eq. [3].

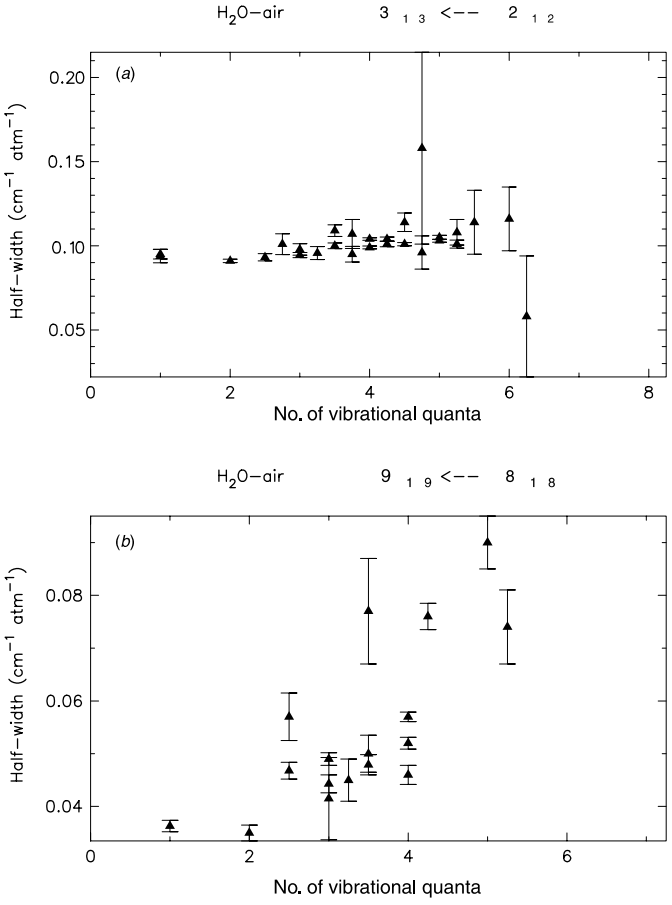


Conclusions and recommendations

We may now consider the four goals stated at the start of this paper. Since the previous study, the data sets for pressure-broadened half-widths have increased by factors of 7, 3, 14, and 10 for N_2-, O_2-, air-, and self-broadening, respectively. The line shift data, which was almost nonexistent in 1994, has grown considerably so that trends are now evident in the data. The influence of vibration, rotational quantum states, and relationships between broadening by different collision partners can be addressed. While there are many more measurements than in 1994, more work needs to be done on the relations between half-widths and their temperature dependence. Overall, there have been big improvements

© 2004 NRC Canada

Fig. 11. (*a*) Measured half-widths (cm^{-1} atm^{-1}, 1 std atm = 101.325 kPa) with reported uncertainties for air-broadening of the $3_{1\,3} \leftarrow 2_{1\,2}$ transition vs. the number of vibrational quanta ($n_{\nu_1} + 0.25n_{\nu_2} + n_{\nu_3}$), where n_{ν_1}, n_{ν_2}, and n_{ν_3} are the number of ν_1, ν_2, and ν_3 quanta exchanged in the transition. Note that the data of refs. 88, 106, and 107 are included. (*b*) Measured half-widths (cm^{-1} atm^{-1}, 1 std atm = 101.325 kPa) with reported uncertainties for air-broadening of the $9_{1\,9} \leftarrow 8_{1\,8}$ transition vs. the number of vibrational quanta ($n_{\nu_1} + 0.25n_{\nu_2} + n_{\nu_3}$), where n_{ν_1}, n_{ν_2}, and n_{ν_3} are the number of ν_1, ν_2, and ν_3 quanta exchanged in the transition. Note that the data of refs. 88, 106, and 107 are included.



in the state of the knowledge since the last study of this kind.

Goal 2, which was to extract different broadening values for selected transitions in which one may be very confident by comparing measurements from different authors, is still far from being realized. A review of Tables 3 and 4 indicated that far too few of the intercomparisons meet the uncertainty criterion set forth by the spectroscopic and remote sensing communities. Of the nearly 4500 intercomparisons made, only 3.6% meet this criterion and these are mostly intercomparisons of pairs. Files of the averaged half-widths and line shifts with the associated estimated uncertainty have been produced and are available with the database files.

The third goal was to propose measurements that are needed to augment the databases. The results of the intercomparisons have identified certain weaknesses in the databases. In particular, the data set on water vapor in collision with oxygen is much smaller than any of the other databases and none of the intercomparisons meet the 3% uncertainty criterion. One advantage of the H_2O–O_2 system is that it can be studied directly via theoretical calculations, unlike the H_2O–air system, allowing comparisons with measurement to be made.

In a study of isotopologues of water vapor (147), it was observed that a relatively small change in the atom–atom parameters of D based on new H_2 and D_2 parameters (148) using conventional combination rules (149) resulted in noticeable changes in the calculated half-widths of HDO and D_2O. These results gave much better agreement with experimental values. There are a number of different methods that have been proposed to determine heteronuclear potential parameters from homonuclear parameters (150 and refs. therein, 151, 152). Thus, the resulting parameters have an uncertainty that depends on the method chosen to go from the homonuclear to the heteronuclear parameters. Differences are on the order of 15% and 5% for the σ and ε parameters. The results in ref. 147 show that such changes in the atom–atom parameters are significant. To refine the intermolecular potential, accurate measurements of O_2-broadening of water vapor are needed. This can best be accomplished with mid- to high-*J* rotational lines of the rotation or ν_2 band.

For the other perturbing gases of this study, additional measurements need to be made. However, the emphasis should be on the accuracy of the measurement rather than the number of transitions measured. Given the results of ref. 140, measurements of the doublet transitions ($K_c = J$ or $J + 1$) would be interesting. Also, half-width and line shift measurements of mid- to high-*J* rotational lines for a number of vibrational bands would be useful for the adjustment of the intermolecular potential.

Measurements of the temperature dependence of the half-width and the line shift need to be made. Currently, there are far too few measurements of the temperature dependence of the half-width to identify trends. There is also some evidence that the temperature dependence model (eq. [1]) may not be valid over large temperature ranges (153) or for certain transitions (141).

Goal 4, a first test of theoretical results, cannot be fully accomplished until goal 3 is better addressed.

While the number of half-width and line shift measurements of water vapor broadened by nitrogen, oxygen, air, and water vapor has increased substantially since the survey paper of 1994, there is still a need for more measurements of high accuracy. The results of the intercomparisons show that the current databases of measured parameters do not demonstrate good agreement with each other, certainly not of the quality needed to meet the needs of remote sensing. Trends in line shift parameters are now becoming evident, but more measurements are needed. The study of the temperature dependence of the half-width needs more measurements to identify trends, and the study of temperature dependence of the line shift is still in its infancy. There is much to be learned for both properties.

From the point of view of the theory, measurements are needed for nitrogen-, oxygen-, and self-broadening. In particular, measurements for high-*J* lines of bands such as the rotation band and ν_2 and the doublet transitions for high vi-

© 2004 NRC Canada

brational bands would be useful for adjusting the interaction potential. Temperature dependence of the half-width and line shift for these transitions would also be useful, given the results of refs. 140 and 141.

Acknowledgement

One of the authors (RRG) is pleased to acknowledge support of this research by the National Science Foundation through grant No. ATM-0242537. Any opinions, findings, and conclusions or recommendations expressed in this material are those of the author(s) and do not necessarily reflect the views of the National Science Foundation.

References

1. R.R. Gamache, J.-M. Hartmann, and L. Rosenmann. J. Quant. Spectrosc. Radiat. Transfer, **52**, 481 (1994).
2. R.S. Eng, A.R. Calawa, T.C. Harman, P.L. Kelley, and A. Javan. Appl. Phys. Lett. **21**, 303 (1972).
3. B.E. Grossmann and E.V. Browell. J. Quant. Spectrosc. Radiat. Transfer, **45**, 339 (1991).
4. B.E. Grossmann and E.V. Browell. J. Mol. Spectrosc. **136**, 264 (1989).
5. B.E. Grossmann and E.V. Browell. J. Mol. Spectrosc. **138**, 562 (1989).
6. S.D. Gasster, C.H. Townes, D. Goorvitch, and F.P.J. Valero. J. Opt. Soc. Am. B, **5**, 593 (1988).
7. J.-Y. Mandin, J.P. Chevillard, J.-M. Flaud, and C. Camy-Peyret. J. Mol. Spectrosc. **138**, 430 (1989).
8. T.D. Wilkerson, G. Schwemmer, B. Gentry, and L.P. Giver. J. Quant. Spectrosc. Radiat. Transfer, **22**, 315 (1979).
9. L.P. Giver, B. Gentry, G. Schwemmer, and T.D. Wilkerson. J. Quant. Spectrosc. Radiat. Transfer, **27**, 423 (1982).
10. J.-Y. Mandin, J.P., Chevillard, C. Camy-Peyret, and J.-M. Flaud. J. Mol. Spectrosc. **138**, 272 (1989).
11. J.-Y. Mandin, J.-M. Flaud, and C. Camy-Peyret. J. Quant. Spectrosc. Radiat. Transfer, **23**, 35 (1980).
12. J.-Y. Mandin, J.-M. Flaud, and C. Camy-Peyret. J. Quant. Spectrosc. Radiat. Transfer, **26**, 483 (1981).
13. C. Cahen, B.E. Grossmann, J.L. Lesne, J. Benard, and G. Leboudec. Appl. Opt. **25**, 4268 (1986).
14. V.M. Devi, D.C. Benner, C.P. Rinsland, M.A.H. Smith, and B.D. Sidney. J. Mol. Spectrosc. **117**, 403 (1986).
15. T.M. Goyette and F.C. De Lucia. J. Mol. Spectrosc. **143**, 346 (1990).
16. C.P. Rinsland, A. Goldman, M.A.H. Smith, and V.M. Devi. Appl. Opt. **30**, 1427 (1991).
17. F.M. Nicolaisen. 2nd International Workshop on Atmospheric Spectroscopy Applications (ASA), Moscow, 6–8 June 1990. Paper 5.8. University of Reims, Reims, France. 1990.
18. P. Cardinet, F. Sverin, A. Valentin. M.L. Claude, and A. Henri. C.R. Acad. Sci. Paris, **284**, 37 (1977).
19. V.M. Devi, B. Fridovich, G.D. Jones, and D.G.S. Snyder. J. Mol. Spectrosc. **111**, 114 (1985).
20. R.S. Eng, P.L. Kelley, A. Mooradian, A.R. Calawa, and T.C. Harman. Chem. Phys. Lett. **19**, 524 (1973).
21. R.A. Toth. J. Quant. Spectrosc. Radiat. Transfer, **13**, 1127 (1973).
22. S. Salimian and R.K. Hanson. J. Quant. Spectrosc. Radiat. Transfer, **30**, 1 (1983).
23. R.E. Eng and A.W. Mantz. J. Mol. Spectrosc. **74**, 388 (1979).
24. Y.S. Chang and J.H. Shaw. J. Quant. Spectrosc. Radiat. Transfer, **18**, 491 (1977).
25. Y. Ben Aryeh. J. Quant. Spectrosc. Radiat. Transfer, **7**, 211 (1967).
26. J.R. Izatt, H. Sakai, and W.S. Benedict. J. Opt. Soc. Am. **59**, 19 (1969).
27. J.-Y. Mandin, J.P. Chevillard, J.-M. Flaud, and C. Camy-Peyret. J. Mol. Spectrosc. **132**, 352 (1988).
28. M.M. Johnson and A.H. LaGrone. Radio Sci. **8**, 407 (1973).
29. V. Dana, J.-Y. Mandin, C. Camy-Peyret, J.-M. Flaud, J.P. Chevillard, R.L. Hawkins, and J.L. Delfau. Appl. Opt. **31**, 1928 (1992).
30. V. Dana, J.-Y. Mandin, C. Camy-Peyret, J.-M. Flaud, and L.S. Rothman. Appl. Opt. **31**, 1179 (1992).
31. J.-Y. Mandin, V. Dana, C. Camy-Peyret, and J.-M. Flaud. J. Mol. Spectrosc. **152**, 179 (1992).
32. M.A. Guerra, M. Ketabi, A. Sanchez, M.S. Feld, and A. Javan. J. Chem. Phys. **63**, 1317 (1975).
33. F.A. Blum, K.W. Nill, P.L. Kelley, A.R. Calawa, and T.C. Harman. Science (Washington, D.C.), **177**, 694 (1972).
34. A. Bauer, M. Godon, and B. Duterage. J. Quant. Spectrosc. Radiat. Transfer, **33**, 167 (1985).
35. D. Mrowinski. Z. Angew. Phys. **29**, 323 (1970).
36. C.O. Hemmi and A.W. Straiton. Radio Sci. **4**, 9 (1969).
37. M. Godon and A. Bauer. Chem. Phys. Lett. **147**, 189 (1988).
38. J.A. Mucha. Appl. Spectrosc. **36**, 141 (1982).
39. R.S. Eng, P.L. Kelley, A.R. Calawa, T.C. Harman, and K.W. Nill. Mol. Phys. **28**, 653 (1974).
40. T.M. Goyette, F.C. DeLucia, J.M. Dutta, and C.R. Jones. J. Quant. Spectrosc. Radiat. Transfer, **49**, 485 (1993).
41. J.M. Dutta, C.R. Jones, T.M. Goyette, and F.C. DeLucia. Icarus, **102**, 232 (1993).
42. J.-Y. Mandin, C. Camy-Peyret, J.-M. Flaud, and G. Guelachvili. Can. J. Phys. **60**, 94 (1982).
43. L. Frenkel and D. Woods. Proc. IEEE, **54**, 498 (1966).
44. G.E. Becker and S.H. Autler. Phys. Rev. **70**, 300 (1946).
45. J.E Pearson, D.T. Llewellyn-Jones, and R.J. Knight. Infrared Phys. **9**, 53 (1969).
46. V.N. Markov. J. Mol. Spectrosc. **164**, 233 (1994).
47. F.M. Nicolaisen and L. Nielsen. Mol. Phys. **62**, 1111 (1987).
48. V.Y. Ryadov and N.I. Furashov. Opt. Spectrosc. (Transl. of Opt. Spektrosk.) **24**, 93 (1968).
49. J.-M. Hartmann, J. Taine, J. Bonamy, B. Labani, and D. Robert. J. Chem. Phys. **86**, 144 (1987).
50. A. Bauer, M. Godon, M. Kheddar, J.-M. Hartmann, J. Bonamy, and D. Robert. J. Quant. Spectrosc. Radiat. Transfer, **37**, 531 (1987).
51. H.J. Liebe and T.A. Dillon. J. Chem. Phys. **50**, 727 (1969).
52. H.J. Liebe, M.C. Thompson, and T.A. Dillon. J. Quant. Spectrosc. Radiat. Transfer, **9**, 31 (1969).
53. J.R. Rusk. J. Chem. Phys. **42**, 493 (1965).
54. A. Bauer, M. Godon, M. Kheddar, and J.-M. Hartmann. J. Quant. Spectrosc. Radiat. Transfer, **41**, 49 (1989).
55. P. Varanasi. J. Quant. Spectrosc. Radiat. Transfer, **11**, 223 (1971).
56. V.M. Devi, D.C. Benner, M.A.H. Smith, and C.P. Rinsland. J. Mol. Spectrosc. **155**, 333 (1992).
57. M.P. Arroyo and R.K. Hanson. 30th Aerospace Sciences Meeting and Exhibit, Reno, Nevada, 6–9 Jan. 1992. Paper No. 92-0510. American Institute of Aeronautics and Astronautics, Reston, Va. 1992.
58. T. Kasuga, H. Kuze, and T. Shimizu. J. Chem. Phys. **69**, 5195 (1978).

© 2004 NRC Canada

59. B.G. Aggev, Yu.N. Ponomarev, B.A. Tikhomirov, and I.S. Tyryshkin. 2nd International Workshop on Atmospheric Spectroscopy Applications (ASA), Moscow, 6–8 June 1990. Paper 5.9. University of Reims, Reims, France. 1990.
60. T. Giesen, R. Schieder, G. Winnewisser, and K.M.T. Yamada. J. Mol. Spectrosc. **153**, 406 (1992).
61. C.K.N. Patel. Phys. Rev. Lett. **28**, 649 (1972).
62. R. Emery. Infrared Phys. **12**, 65 (1972).
63. V.Y. Ryadov and N.I. Furashov. Opt. Spectrosc. (USA), **35**, 255 (1973).
64. R.B. Sanderson and N. Ginsburg. J. Quant. Spectrosc. Radiat. Transfer, **3**, 435 (1963).
65. A.F. Aushev, N.F. Borisova, E.S. Bykova, V.M. Osipov, and V.V. Tsukanov. Opt. Spectrosc. **68**, 700 (1990).
66. T.D. Adiks, A.A. Vinogradova, and I.P. Malkov. J. Appl. Spectrosc. **45**, 778 (1986).
67. V.Y. Ryadov and N.I. Furashov. Izv. VUZ. Radiofis. **9**, 1073 (1966).
68. V.G. Avetisov, A.I. Nadezhdinskii, A.N. Khusnutdinov, P.M. Omarova, and M.V. Zyrianov. J. Mol. Spectrosc. **160**, 326 (1993).
69. S. Adler-Golden, J. Lee, and N. Goldstein. J. Quant. Spectrosc. Radiat. Transfer, **48**, 527 (1992).
70. A.P. Godlevskii and V.A. Kapitanov. J. Appl. Spectrosc. **28**, 142 (1978).
71. V.Y. Ryadov and N.I. Furashov. Radiophys. Quantum Electron. **18**, 256 (1975).
72. P. Varanasi, and C.R. Prasad. J. Quant. Spectrosc. Radiat. Transfer, **10**, 65 (1970).
73. J.J. Remedios. Ph.D thesis, University of Oxford, Oxford, UK. 1990.
74. N. Goldstein, S. Adler-Golden, J. Lee, and F. Bien. Appl. Opt. **31**, 3409 (1992).
75. C.H. Townes and F.R. Merritt. Phys. Rev. **70**, 558 (1946).
76. A. Adel. Phys. Rev. **71**, 806 (1947).
77. K.M.T. Yamada, M. Harter, and T. Giesen. J. Mol. Spectrosc. **157**, 84 (1993).
78. Z. Chu, T.D. Wilkerson, and U.N. Singh. Appl. Opt. **32**, 992 (1993).
79. J.T. Bradley. Ph.D thesis, University of New York, New York. 1970.
80. S. Langlois, T.P. Birbeck, and R.K. Hanson. J. Mol. Spectrosc. **163**, 27 (1994).
81. M.P. Arroyo and R.K. Hanson. Appl. Opt. **32**, 6104 (1993).
82. S. Langlois, T.P. Birbeck, and R.K. Hanson. J. Mol. Spectrosc. **167**, 272 (1994).
83. L.A. Rahn and D.A. Greenhalgh. J. Mol. Spectrosc. **119**, 11 (1986).
84. D.A. Greenhalgh and L.A. Rahn. J. Raman Spectrosc. **21**, 847 (1990).
85. Q. Zou and P. Varanasi. J. Quant. Spectrosc. Radiat. Transfer, **82**, 45 (2003).
86. R.A. Toth. J. Mol. Spectrosc. **201**, 218 (2000).
87. D.W. Steyert, W.F. Wang, J.M. Sirota, N.M. Donahue, and D.C. Reuter. J. Quant. Spectrosc. Radiat. Transfer, **72**, 775 (2002).
88. P.-F. Coheur, S. Fally, M. Carleer, C. Clerbaux, R. Colin, A. Jenouvrier, M.-F. Mérienne, C. Hermans, and A. Vandaele. J. Quant. Spectrosc. Radiat. Transfer, **74**, 493 (2002).
89. R. Schermaul, R.C.M. Learner, D.A. Newnham, R.G. Williams, J. Ballard, N.F. Zobov, D. Belmiloud, and J. Tennyson. J. Mol. Spectrosc. **208**, 32, (2001).
90. P.L. Ponsardin and E.V. Browell. J. Mol. Spectrosc. **185**, 58 (1997).
91. K. Singh and J.J. O'Brien. J. Mol. Spectrosc. **167**, 99 (1994).
92. B.L. Upschulte and M.G. Allen. J. Quant. Spectrosc. Radiat. Transfer, **59**, 653 (1998).
93. M. Lepere, A. Henry, A. Valentin, and C. Camy-Peyret. J. Mol. Spectrosc. **208**, 25 (2001).
94. V. Nagali, S.L. Chou, D.S. Baer, and R.K. Hanson. J. Quant. Spectrosc. Radiat. Transfer, **57**, 795 (1997).
95. K.V. Chance, K. Park, and K.M. Evenson. J. Quant. Spectrosc. Radiat. Transfer, **59**, 687 (1998).
96. A. Lucchesini, S. Gozzini, and C. Gabbanini. Eur. Phys. J. **D8**, 223 (2000).
97. C. Claveau, A. Henry, D. Hurtmans, and A. Valentin. J. Quant. Spectrosc. Radiat. Transfer, **68**, 273 (2001).
98. C. Claveau, A. Henry, M. Lepere, A. Valentin, and D. Hurtmans. J. Mol. Spectrosc. **212**, 171 (2002).
99. S.J. Davis, W.J. Kessler, and M. Bachmann. Proc. SPIE, **3612**, 157 (1999).
100. J. Gao, H. Chen, J. Zhou, Z. Ma, and Z. Gong. Chin. J. Quantum Electron. **15**, 186 (1998).
101. J.-Y. Mandin,V. Dana, M. Badaoui, A. Barbe, A. Hamdouni, and J.-J. Plateaux. J. Mol. Spectrosc. **164**, 328 (1994)
102. L.R. Brown, R.A. Toth, and M. Dulick. J. Mol. Spectrosc **212**, 57 (2002).
103. R.A. Toth and L.R. Brown. J. Mol. Spectrosc. **218**, 135 (2003).
104. R.C.M. Learner, R. Schermaul, J. Tennyson, N.F. Zobov, J. Ballard, D. Newnham, and M.G. Wickett. Measurememt of H_2O absorption cross-sections for exploitation of GOME data. Final report, ESTEC contract No. 13312/99/NL/SF. European Space Agency, 1999.
105. R.A. Toth, L.R. Brown, and C. Plymate. J. Quant. Spectrosc. Radiat. Transfer, **59**, 529 (1998).
106. M.-F. Merienne, A. Jenouvrier, C. Hermans, A.C. Vandaele, M. Carleer, C. Clerbaux, P.-F. Coleur, R. Colin, S. Fally, and M. Bach. J. Quant. Spectrosc. Radiat. Transfer, **82**, 99 (2003).
107. S. Fally, P.-F. Coleur, M. Carlee, C. Clerbaux, R. Colin, A. Jenouvrier, M.-F. Merienne, C. Hermans, and A.C. Vandaele. J. Quant. Spectrosc. Radiat. Transfer, **82**, 119 (2003).
108. A. Lucchesinia, S. Gozzini, and C. Gabbanini. Eur. Phys. J. **D 8**, 223 (2000).
109. M. Lepere, A. Henry, A. Valentin, and C. Camy-Peyret. J. Mol. Spectrosc. **208**, 25 (2001).
110. L. Moretti, A. Sasso, L. Gianfrani, and R. Ciurylo. J. Mol. Spectrosc. **205**, 20 (2001).
111. M.Yu. Tretyakov, V.V. Parshin, M.A. Koshelev, V.N. Shanin, S.E. Myasnikova, and A.F. Krupnov. J. Mol. Spectrosc. **218**, 239 (2003).
112. A. Valentin, C. Rachet, A.D. Bykov, N.N. Lavrentieva, V.N. Saveliev, and L.N. Sinitsa. J. Quant. Spectrosc. Radiat. Transfer, **59**, 165 (1998); A. Valentin, C. Claveau, A.D. Bykov, N.N. Lavrentieva, V.N. Saveliev, and L.N. Sinitsa. J. Mol. Spectrosc. **198**, 218 (1999).
113. D.L. Hartmann. Global physical climatology. Academic Press, Boston, Mass. 1994.
114. L.S. Rothman, C. Clerbaux, V. Dana, V.M. Devi, A. Fayt, J.-M. Flaud, R.R. Gamache, A. Goldman, D. Jacquemart, K.W. Jucks, W.J. Lafferty, J.-Y. Mandin, S.T. Massie, V. Nemtchinov, D.A. Newnham, A. Perrin, C.P. Rinsland, J. Schroeder, K.M. Smith, M.A.H. Smith, K. Tang, R.A. Toth, J. Vander Auwera, P. Varanasi, and K. Yoshino. J. Quant. Spectrosc. Radiat. Transfer, **82**, 5 (2003).
115. N. Jacquinet-Husson, E. Arié, J. Ballard, A. Barbe, G. Bjoraker, B. Bonnet, L.R. Brown, C. Camy-Peyret, J.P. Champion, A. Chédin, A. Chursin, C. Clerbaux, G. Duxbury, J.-M. Flaud, N. Fourrié, A. Fayt, G. Graner, R.R. Gamache,

© 2004 NRC Canada

A. Goldman, Vl. Golovko, G. Guelachvili, J.-M. Hartmann, J.C. Hilico, J. Hillman, G. Lefèvre, E. Lellouch, S.N. Mikhailenko, O.V. Naumenko, V. Nemtchinov, D.A. Newnham, A. Nikitin, J. Orphal, A. Perrin, D.C. Reuter, C.P. Rinsland, L. Rosenmann, L.S. Rothman, N.A. Scott, J. Selby, L.N. Sinitsa, J.M. Sirota, A.M. Smith, K.M. Smith, Vl.G. Tyuterev, R.H. Tipping, S. Urban, P. Varanasi, and M. Weber. J. Quant. Spectrosc. Radiat. Transfer, **62**, 205 (1999).
116. H.M. Pickett, R.L. Poynter, E.A. Cohen, M.L. Delitsky, J.C. Pearson, and H.S.P. Muller. Submillimeter millimeter and microwave spectral line catalog. 1996 ed. Caltech, Pasadena Calif. JPL Publication 80-23. Rev. 4.
117. D.A. Greenhalgh, R.J. Hall, F.M. Porter, and W.A. Engmand. J. Raman Spectrosc. **15**, 71 (1984)
118. F.M. Porter and D.R. Williams. Appl. Phys. **B54**, 103 (1992).
119. F. Grisch and M. Péalat. J. Raman Spectrosc. **25**, 145 (1994).
120. R.W. Davies, R.H. Tipping, and S.A. Clough. Phys. Rev. A, **26**, 3378 (1982).
121. Q. Ma and R.H. Tipping. J. Chem. Phys. **95**, 6290 (1991).
122. Q. Ma and R.H. Tipping. J. Chem. Phys. **96**, 818 (1992).
123. Q. Ma and R.H. Tipping. J. Chem. Phys. **96**, 8655 (1992).
124. J.-M. Hartmann, M.Y. Perrin, Q. Ma, and R.H. Tipping. J. Quant. Spectrosc. Radiat. Transfer, **49**, 675 (1993).
125. J.-F. D'Eu, B. Lemoine, and F. Rohart. J. Mol. Spectrosc. **212**, 96 (2002).
126. C. Claveau, A. Henry, M. Lepere, A. Valentin, and D. Hurtmans. J. Mol. Spectrosc. **212**, 171 (2002).
127. R. Ciurylo and J. Szudy. J. Quant. Spectrosc. Radiat. Transfer, **57**, 411 (1997).
128. R. Ciurylo, R. Jaworski, J. Jurkowski, A.S. Pine, and J. Szudy. Phys. Rev. A, **63**, 1 (2001).
129. A.S. Pine. J. Quant. Spectrosc. Radiat. Transfer, **62**, 397 (1999).
130. A. Barbe (*Editor*). Workshop proceedings, Atmospheric Spectroscopy Applications Workshop, ASA REIMS 96, Université de Reims Champagne Ardenne, 4–6 Sept. 1996. University of Reims, Reims, France. 1996.
131. M.A.H. Smith and L.L. Gordley. J. Quant. Spectrosc. Radiat. Transfer, **29**, 413 (1983).
132. W.P. Chu, E.W. Chiou, J.C. Larsen, L.W. Thomason, D. Rind, J.J. Buglia, S. Oltmans, M.P. McCormick, and L.M. McMaster. J. Geophys. Res. **98**, 4857 (1993).
133. B. Kivel, H.E. Fleming, and W.G. Planet. J. Quant. Spectrosc. Radiat. Transfer, **17**, 181 (1977).
134. Global Ozone Research and Monitoring Project. Atmospheric ozone 1985. Report No. 16. Vol. III. World Meteorological Organization, Geneva. 1985. p. 845.
135. M.A.H. Smith (*Editor*). NASA Conference Publication 2396. NASA, Scientific and Technical Information Branch, Washington, D.C. 1985.
136. C.A. Reber. NASA Goddard Space Flight Center Publication 430-1003-001. 1985.
137. J. Bosenberg. Appl. Opt. **24**, 3531 (1985).
138. H.C. Pumphrey and S. Buehler. J. Quant. Spectrosc. Radiat. Transfer, **64**, 421 (2000).
139. L.R. Brown and C. Plymate. J. Quant. Spectrosc. Radiat. Transfer, **56**, 263 (1996).
140. R.R. Gamache and J.-M. Hartmann. J. Quant. Spectrosc. Radiat. Transfer, **83**, 119 (2004).
141. G. Wagner, M. Birk, R.R. Gamache, and J.-M. Hartmann. J. Quant. Spectrosc. Radiat. Transfer. In press.
142. M.A.H Smith, C.P. Rinsland, V.M. Devi, D.C. Benner, and K.B. Thakur. J. Opt. Soc. Am. B, **5**, 585 (1988).
143. J.-M. Flaud, C. Camy-Peyret, C.P. Rinsland, M.A.H. Smith, and V.M. Devi. Atlas of ozone spectral line parameters from microwave to medium infrared. Academic Press, Boston, Mass. 1990.
144. R.R. Gamache, S.P Neshyba, J.J. Plateaux, A. Barbe, L Régalia, and J.B. Pollack. J. Mol. Spectrosc. **170**, 131 (1995).
145. R.R. Gamache, R. Lynch, and L.R. Brown. J. Quant. Spectros. Radiat. Transfer, **56**, 471 (1996).
146. G. Wagner, M. Birk, F. Schreier, and J.-M. Flaud. J. Geophys. Res. **107**, 4626 (2002).
147. R.R. Gamache and J. Fischer. J. Quant. Spectrosc. Radiat. Transfer, **78**, 305 (2003).
148. W.F. Wang. J. Quant. Spectrosc. Radiat. Transfer, **76**, 23 (2003).
149. J.O. Hirschfelder, C.F. Curtiss, and R.B. Bird. Molecular theory of gases and liquids. Wiley, New York. 1964.
150. M. Diaz Pena, C. Pando, and J.A.R. Renuncio. J. Chem. Phys. **76**, 325 (1982).
151. M. Diaz Pena, C. Pando, and J.A.R. Renuncio. J. Chem. Phys. **76**, 333 (1982).
152. R.J. Good and C.J. Hope. J. Chem. Phys. **55**, 111 (1971).
153. D. Priem, J.-M. Colmont, F. Rohart, G. Wlodarczak, and R.R. Gamache. J. Mol. Spectrosc. **204**, 204 (2000).

© 2004 NRC Canada

The Canadian Light Source — History and scientific prospects[1,2]

G.M. Bancroft

Abstract: The Canadian Light Source (CLS) in Saskatoon has been under construction for the last 4 years, and will be producing a number of very intense beams of far-IR, IR, soft and hard X-rays in 2004 for use by several hundred Canadian scientists in chemistry, surface and material science, and a host of other scientific disciplines. The CLS will dramatically enhance the Canadian spectroscopic tradition that Gerhard Herzberg help create. I begin this article (from my 2002 CIC Montreal Medal lecture) with an overview of the history of SR in Canada, beginning in 1972 with the first Canadian synchrotron workshop organized at the University of Western Ontario by Bill McGowan, and attended by Dr. Herzberg. The CLS facility is then described, along with the properties of the first and second set of beamlines to be built at the CLS. These SR beams, in the IR and X-ray regions from the third generation CSL ring, will be competitive in brightness and intensity with the best beamlines in the world for most applications. Finally, some of the present Canadian SR research at foreign SR sources is described across the entire SR spectrum. All known spectroscopic and diffraction experiments are dramatically enhanced with SR; and SR opens up new areas of spectroscopy, microscopy, and spectromicroscopy that cannot be studied with any other source of radiation.

Key words: synchrotron light, X-rays, infrared, spectroscopy.

Résumé : La construction du Centre canadien de rayonnement synchrotron (CCRS) de Saskatoon a débuté il y a quatre ans et, à partir de 2004, celui-ci sera en mesure de produire des faisceaux très intenses de rayonnements IR et IR lointain, de rayons X de basses et de hautes énergies qu'utiliseront plusieurs centaines de scientifiques canadiens oeuvrant dans le domaine de la chimie des matériaux et des surfaces ainsi que dans plusieurs autres disciplines. Le CCRS augmentera d'une façon dramatique la tradition spectroscopique canadienne que Gerhard Herzberg a su créer. Je débute cet article (tiré de la conférence que j'ai présentée lors de la remise de la Médaille de Montréal de l'Institut de chimie du Canada qui m'a été faite en 2002) en passant en revue l'histoire du rayonnement synchrotron (RS) au Canada, en commençant en 1972, avec la première table ronde canadienne sur le synchrotron qui a été organisée à l'Université de Western Ontario par Bill McGowan et à laquelle a participé le Dr. Herzberg. Je passe ensuite à une description du CCRS et des propriétés des deux premiers ensembles de lignes de faisceaux à être construites au centre. Pour la plupart des applications, la brillance et l'intensité des faisceaux de RS des régions de l'IR et des rayons X obtenus à partir de l'anneau de troisième génération du CCRS pourront supporter la compétition de celles des meilleurs faisceaux du monde. Enfin, je décris les travaux de recherches actuels de RS effectués par des canadiens, sur l'ensemble des domaines du RS, sur des sources étrangères de RS. Toutes les expériences connues de spectroscopie et de diffraction sont améliorées par le RS et le RS ouvre de nouveaux horizons de la spectroscopie, de la microscopie et de la spectromicroscopie qui ne peuvent pas être étudiés par toute autre source de rayonnement.

Mots clés : rayonnement synchrotron, rayons X, infrarouge, spectroscopie.

[Traduit par la Rédaction]

Introduction

The Canadian Light Source (CLS), the Canadian national synchrotron facility, has been under construction on the University of Saskatchewan campus in Saskatoon since 1999. The construction has proceeded very smoothly, and in early February 2004 when the final corrections were done on this article, over 25 mA of a well-characterized electron beam have been stored in the storage ring (with a lifetime of an hour), and synchrotron radiation has been observed. The facility is on-budget and a few beamlines are due to start working in mid-2004 — only a few months behind schedule.

This is probably the largest scientific facility in Canada to be constructed in the last 30 years, both because of its size and $173M capital budget; and it should have a dramatic impact on Canadian science (both academic and industrial) in the next 30 years. Beginning in early 2004, a number of very intense and bright monochromatic beams of IR, soft and hard X-ray radiation will be available for several hundred Canadian researchers in chemistry, physics, geology, materi-

Received 29 October 2003. Published on the NRC Research Press Web site at http://canjchem.nrc.ca on 20 May 2004.

G.M. Bancroft. Chemistry Department, University of Western Ontario, London,ON N6A 5B7, Canada and Canadian Light Source, University of Saskatchewan, Saskatoon, SK S7N 0X4, Canada. (e-mail: gmbancro@uwo.ca).

[1]This article is part of a Special Issue dedicated to the memory of Professor Gerhard Herzberg.
[2]Presented as the Montreal Medal Lecture at the June 2002 Vancouver CSC meeting.

 doi: 10.1139/V04-027 © 2004 NRC Canada

als science, surface science, soils science, and many areas of engineering and biochemistry. Medical imaging and radiation therapy will probably be added to that list in the near future. The CLS will also be very important to industries in a wide variety of sectors spanning the pharmaceutical, biotechnology, mining, environmental, materials and coatings, petrochemical, and micromachining.

In October 1972, Gerhard Herzberg and several of his close NRC spectroscopic colleagues (along with the Director of the Madison, Wisconsin Tantalus SR facility, Ed Rowe) attended the first Canadian workshop organized by Bill McGowan on the uses of synchrotron radiation (SR) at the University of Western Ontario. At that early time, the most important uses of SR appeared to be in the far-UV, soft and hard X-ray regions. Mostly because Dr. Herzberg's outstanding spectroscopic research used much lower photon energies in the microwave and IR, he never became involved directly in the Canadian synchrotron effort. He would now probably be somewhat surprised, and I think delighted, to notice the rapid development of the synchrotron beams at the CLS and the heavy involvement of some of his NRC spectroscopic colleagues in the development of strong research efforts at the CLS in the far- and mid-IR regions as well as in the "traditional" higher energy areas. Indeed, the CLS will certainly greatly enhance the great Canadian spectroscopic tradition that Dr. Herzberg helped create.

Most of the material in this current article was presented as the Montreal Medal Lecture at the June 2002 Vancouver CSC. The above mentioned 1972 workshop was the beginning of my 30 year odyssey to develop Canadian SR capabilities in the US and then in Canada. Because the Montreal Medal "is presented as a mark of distinction for significant leadership in, or for an outstanding contribution to, the profession of chemistry or chemical engineering in Canada", in the first part of this article, I will devote a significant part of this article to the long and somewhat tortuous historical development of SR in Canada. Second, I will describe the CLS facility and the progress towards operation, along with comments on the CLS vision and opportunities. Third, I will describe the seven so-called Phase 1 beamlines, and also comment on the seven Phase 2 beamlines that are hopefully funded by the Canada Foundation for Innovation (CFI) in February 2004. Finally, to give readers a flavour of the kind of research that will be carried out on the Phase 1 beamlines, I will describe some of the Canadian research currently being performed at foreign synchrotrons in the IR, soft, and hard X-ray regions.

History of SR in Canada

The construction of the CLS has involved intense effort by many, many dedicated Canadian scientists over the last 30 years, and I have perused many of my old documents to try to give credit to the major players in this effort. Certainly, Bill McGowan was the initiator of the Canadian SR effort beginning with the above workshop that Herzberg attended in 1972. As the first Director of the Centre for Chemical Physics (CCP) at the University of Western Ontario, Dr. McGowan pushed extremely hard for a Canadian synchrotron in the period 1972–1977. For example, he applied in July 1973 to NRC for a feasibility study for a Canadian SR source. As there were NO known Canadian users at the time (very limited SR work at Stanford, Tantalus, Cornell, and several European sites had only begun about 1969), that request (and many later requests, see below) was rejected. In January 1975, Dr. McGowan hosted a CCP SR workshop to consider a design from Roger Servranckx of the University of Saskatchewan for a Canadian low-energy synchrotron, and Dr. McGowan suggested a possible site for the synchrotron at the University of Western Ontario to the UWO senior administration. This 1975 meeting initiated a long collegial interaction of UWO scientists with the high-energy electron accelerator group from the University of Saskatchewan (the Saskatchewan Accelerator Laboratory (SAL)) which began with the hiring of Leon Katz in the Physics Department in 1947, the construction of a 300 MeV linac in 1962, the construction of a 300 MeV beam stretcher in 1985 directed by Henry Kaplan, and the push for the Canadian Light Source spearheaded by Dennis Skopik in 1995. This group developed state-of-the-art expertise in design and construction of electron accelerators (critical to the construction of the CLS), and operated a very successful high-energy nuclear physics program until the late 1990s.

Dr. McGowan then submitted in September 1975 a very large proposal, entitled "A National Laboratory for SR Studies" to Paul Redhead, the Director of the Physics Division at NRC. Paul Redhead chaired an ad-hoc NRC committee on SR, and that committee met in June, August, and October 1976. The chemists on that committee were Camille Sandorfy, Chris Brion, and myself. Several Canadian scientists began using SR in this period. For example, Daryl Crozier from Simon Fraser began high-energy EXAFS studies at the Stanford Synchrotron Radiation facility (SSRL) in the fall of 1974, and I began SR studies at Tantalus in March 1975 as a result of the contact with Ed Rowe that resulted from the 1972 meeting. Meanwhile, Bill McGowan organized the first very large international SR workshop at Laval University in June 1976. There were 55 attendees at this workshop, with just 11 Canadian scientists. A 624 page report on the many uses of SR was submitted to Paul Redhead's ad-hoc committee. There was still very little Canadian involvement at this time, but it was obvious even then to nearly all the committee members that SR research was going to be very important for Canadian science, and Canada should be a major player in SR research along with all the other G7 countries that already had SR facilities (1, 2). However, because there were still very few Canadian users, and Canada does not take any "risks", this proposal was turned down.

With a cordial invitation from Ed Rowe, excellent scientific support from Ed Rowe and Charlie Pruett from Tantalus, great administrative and financial support from Dean John Bancroft, President George Connell, and the UWO Second Century Fund, I spearheaded (co-applicants were Bill McGowan and Bill Ware, both from UWO) an application to NRC in October1977 for the Canadian Synchrotron Radiation Facility (CSRF) to construct a Canadian soft X-ray beamline and three endstations at the existing Tantalus and newly designed Aladdin SR sources outside Madison, Wisconsin. In July 1978, the newly-created NSERC awarded $320 000 capital for the beamline and two end-stations (photoelectron spectroscopy and X-ray microscopy of cells). NRC

© 2004 NRC Canada

was to own, staff, and manage the facility (and NRC appointed Norman Sherman as the NRC manager for close to two decades), I was appointed the Scientific Director for CSRF (and I continued until 1999), and NRC allotted $5000 annually to own, operate, and maintain the equipment!! This inappropriate small amount created enormous problems for me and for the development of CSRF. Fortunately, UWO (with John Bancroft, George Connell, and Howard Baldwin being enormously helpful) scraped together enough funding, mainly to hire Kim Tan in January 1980 for most of 5 years as the CSRF Operations Manager in Madison. Kim Tan worked closely with Baker Manufacturing outside Madison (with excellent cooperation and collaboration with the monochromator designers Charlie Pruett, Fred Brown, and Niel Lien) in assembling the soft X-ray "Grasshopper" monochromator, and in 1 year the monochromator was successfully tested on Tantalus, the first publication appeared in 1982 (3), and the beamline plus XPS was working routinely by January 1983 (4). The first significant NSERC infrastructure funding ($32 000) was obtained in April 1984, along with an increasing amount of $16 000 from NRC.

CSRF expanded in 1990, with the construction of a higher energy soft X-ray beamline (the double crystal monochromator (DCM) beamline) in the late 1980s, funded by the Ontario Centre for Materials Research (OCMR), and designed and constructed mainly by Bing Xing Yang and T.K. Sham (5, 6). Funding for a third beamline (the spherical grating beamline (SGM)) was obtained from NSERC in 1995; and this beamline,constructed by Brian Yates, began working in 1998 (7). It is important to emphasize that all three beamlines have been working routinely at CSRF. The SGM beamline is being shipped to the Canadian Light Source as I write. As well as Sherman, Sham, Tan, and myself, Ron Cavell and Adam Hitchcock were very helpful over many years on the CSRF management committee, and in providing scientific expertise and equipment at CSRF. Over 400 publications have been generated by many Canadian scientists, and CSRF (T.K. Sham has been the Scientific Director since 1999) has had one of the highest NSERC MFA grants in Canada (e.g., $300 000 in the last few years).

The next big push for a Canadian synchrotron began in 1990. Many countries were designing and building third-generation SR sources with much smaller and brighter beams of radiation that could be used very effectively for protein crystallography, a field that has grown exponentially in the last 10 years. Bruce Bigham from AECL initiated the Canadian Institute for Synchrotron Radiation (CISR), which became very important in coordinating the Canadian SR effort. The first Directors of CISR included myself as President, along with Bruce Bigham, and Daryl Crozier. Cavell, Hitchcock, Sham, and Skopik became prominent. Initially, there was interest from AECL and TRIUMF to design and build the ring, but the Saskatchewan Accelerator Laboratory (with Dennis Skopik as Director, and Les Dalin and Roger Servrankx as the main designers), became prominent in pushing the design of the Canadian SR facility. In October 1991, a proposal from CISR was presented to NSERC for study funds to finalize a Canadian design, and this was turned down. In the early- and mid-1990s, CISR supported several Canadian initiatives at US synchrotrons; Mark Sutton and Daryl Crozier at the APS; Adam Hitchcock at the ALS; and Alice Vrielink and Eastern Canadian protein crystallographers at Brookhaven. NSERC and the President of NSERC, Peter Morand, became very supportive of a Canadian synchrotron, and an NSERC Committee on Materials Research Facilities (Chaired by John Strom-Olsen of McGill) recommended a Canadian SR source in 1994, but of course there was no NSERC money for such a proposal of about $100M. In 1994 to 1995, NSERC sponsored three workshops to better define the machine design and the possible beamlines; and in August 1995, NSERC set up a committee chaired by Alex McAuley of the University of Victoria to assist CISR to select between two bids for the Canadian SR source — the Western Canadian bid from the University of Saskatchewan (headed by Dennis Skopik) and the Eastern Canadian bid (headed by me) from the University of Western Ontario. Both of these bids took over 6 months to put together, and were over 500 pages long each. Dennis Skopik and his University of Saskatchewan (U. Sask.) colleagues (including the President George Ivany, and the Vice-President Dennis Johnson) did a magnificent job on behalf of all Canadian scientists in raising both financial and political support for their bid (a VERY difficult thing to do for such a huge facility at any University!!); and in June 1996, the NSERC committee recommended that a Canadian SR facility should be built, and that it should be built at the University of Saskatchewan. A joint U. Sask./UWO proposal was finalized and submitted to NSERC in September 1996.

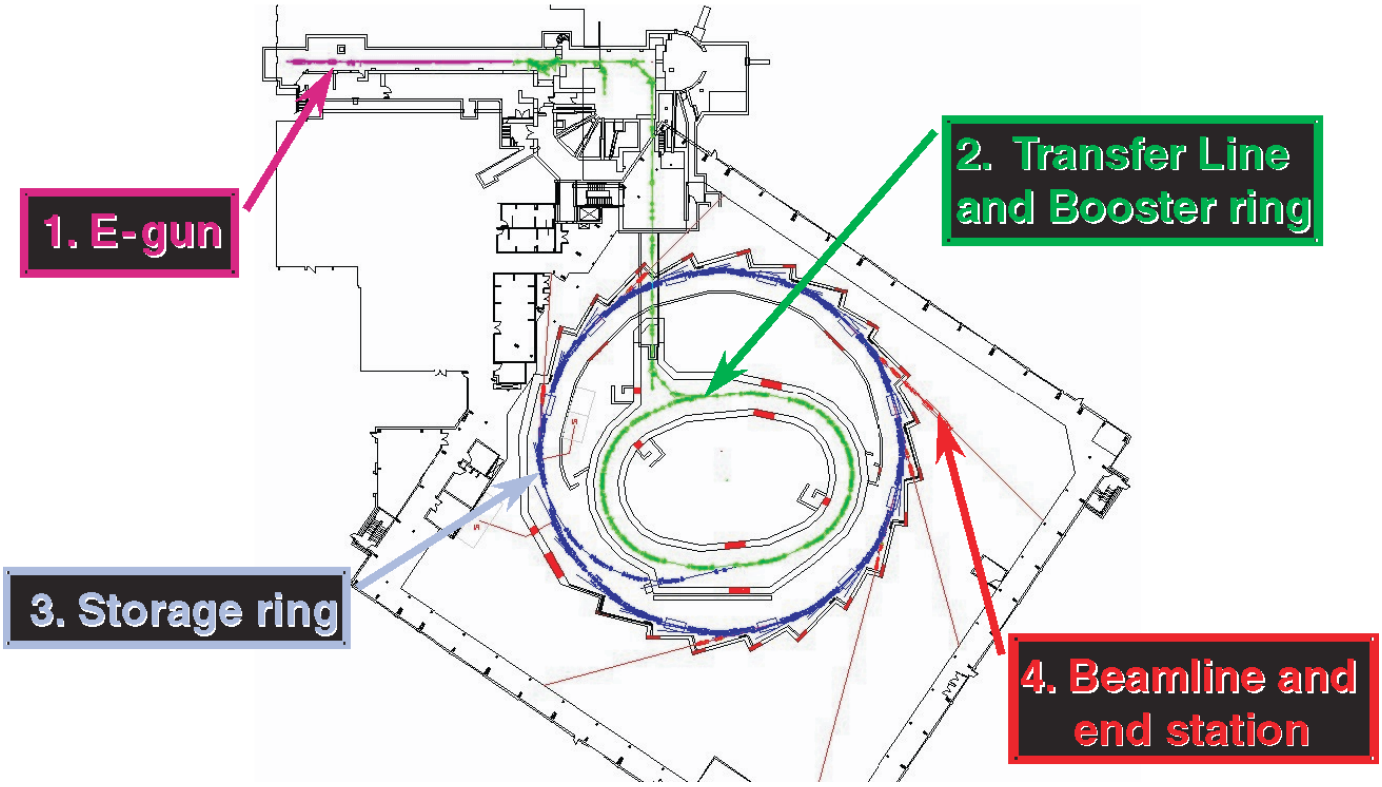
But where was the funding coming from? Even in early 1996, the NSERC President Peter Morand wrote to us stating that he could not see this facility funded in the next 5 years! How quickly things can turn around, as the federal government began to run surpluses in 1997; and in June 1997, the federal government announced the creation of the Canada Foundation for Innovation with $800M to fund large University and hospital projects, including national projects such as the Canadian Light Source. Some pundits claim that the CFI was set up in large part to provide a mechanism for funding the CLS. In May 1998, Dennis Skopik and the University of Saskatchewan submitted the CLS proposal to the CFI for $71.3M (40% of the total of $178M) after raising many tens of $Ms from the University, City of Saskatoon, Sask Power, NRC, the province, and Western Economic Diversification to cover a large fraction of the remaining about $100M — a Herculean effort by the Saskatoon team over 3 years. And indeed, on 31 March 1999, the CFI announced that they would fund $56.4M towards a $141M project. The University of Saskatchewan team had raised $65.6M of the remaining $84.5M, as well as having promises of operating funding of $8.6M a year. See my CISR President's report at www.cisr.ca/reports/pres_rep_199906.html for a more complete account. As the 31 March 1999 press announcement from Saskatoon said: "The CLS represents an unprecedented level of collaboration among governments, Universities, and Industry in Canada". In addition to the U. Sask., 18 Canadian universities endorsed the CLS project on behalf of the over 300 users of SR in Canada.

The CLS Facility and Progress

The Canadian Light Source Inc. is a separate, nonprofit company wholly owned by the University of Saskatchewan.

© 2004 NRC Canada

Fig. 1. Floor plan of the Canadian Light Source showing the main components of the facility.



Partly because of timely strategic planning by the University of Saskatchewan in 1998 and 1999, and the hiring of UMA as project manager, CLS progress in the last 4 years has been quite remarkable. First, the immense new building (3) (84 m by 83 m and 20 m high at the center) was completed on schedule in early 2001. Second, all of the new $141M to complete the initial project (including seven beamlines) was identified from 14 different partners, and the project is on budget, and is only a few months behind schedule. Third, over 60 talented employees have been hired to complement the fine core of 25 employees remaining from the Saskatchewan Accelerator Laboratory (SAL). Fourth, a large number of academics from across Canada have coordinated with the CLS to design and build the initial seven beamlines to be operating in 2004. Fifth, a significant amount of industrial business has already been identified (mainly with mining companies), and an impressive marketing and communication effort is well advanced at the CLS and the University of Saskatchewan. Indeed, the CLS vision statement includes a significant industrial mandate: "To advance Canadian scientific and industrial capabilities by operating the CLS facility as the national research and development center of excellence".

The CLS facility has four major components, as shown in Figs. 1 and 2: (1) a 250 MeV linac; (2) a full-energy (2.9 GeV electron energy) booster synchrotron; (3) the storage ring; and (4) a number of beamlines optimized for use in the IR or X-ray regions. Electrons are emitted from a hot metal filament (top left) and accelerated in a high vacuum to 250 MeV by the refurbished original SAL linac (magenta). The 250 MeV electrons are then transferred to the booster ring (green), where the electron energy is increased to 2900 MeV (2.9 GeV). These very high-energy electrons are then transferred to the storage ring (blue) where the electrons circulate for several hours. The 2.9 GeV storage ring (170 m in circumference, and designed by Les Dallin and SAL staff), has a very compact design, and 12-fold symmetry with 24 bending magnets in 12 cells (Fig. 3) to bend the electrons around the whole storage ring. Figure 2 (bottom) illustrates some of the thick concrete shielding that encases the storage ring (represented by black double lines in Fig. 1). The synchrotron light (SL) beams emerge through a rectangular hole in the short side of the concrete saw-tooth (see the lower right part of Fig. 2 for one of these).

One of the 12 equivalent cells of the CLS is illustrated in Fig. 3. Each cell has two large bending magnets, along with six quadrupole and three sextupole magnets for focusing the electron beam, and correcting the orbit of the electron beam, respectively. Twelve straight sections (each 5.2 m long) separate each cell. Three of these will be used for injection and supply of radio frequency (RF) power to the electron beam, and the other 9 straight sections can be used for linear arrays of dipole magnets (so-called insertion devices) — either undulators or wigglers that alternately bend the electrons back and forth many times (8, 9).

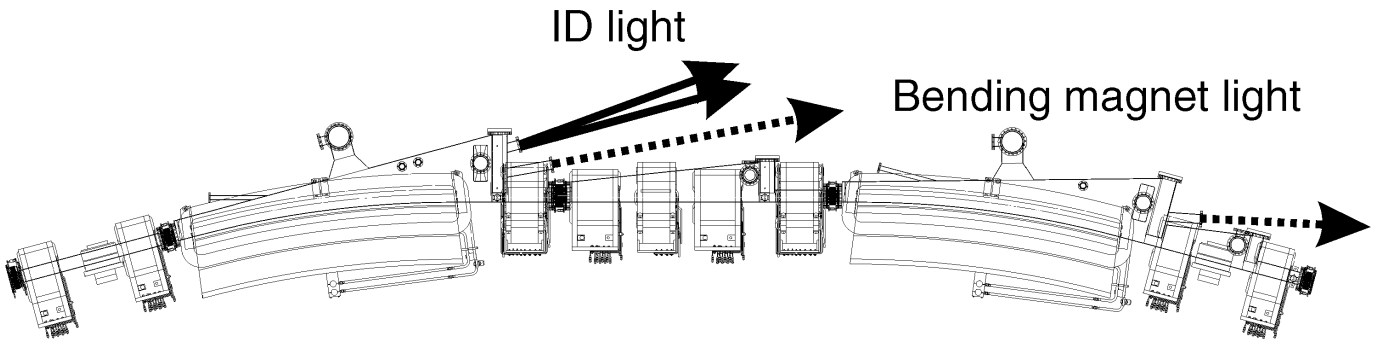
Bending of these high-energy electrons — either by the bending magnets or the insertion devices — results in emission of up to 35 beams of synchrotron light (see the four beams, one from each of two insertion devices in a single straight section and one from each bending magnet, from the one cell in Fig. 3). These beams have several remarkable properties (8, 9) (Fig. 4). First, all of the bending magnet

© 2004 NRC Canada

Fig. 2. The CLS experimental hall (84 m × 83 m), taken in early 2002. Note the sawtooth concrete shielding that encases the storage ring. The SL beam emerges from the rectangular hole in the concrete shielding on the lower right. Note also the ceiling crane on the top.



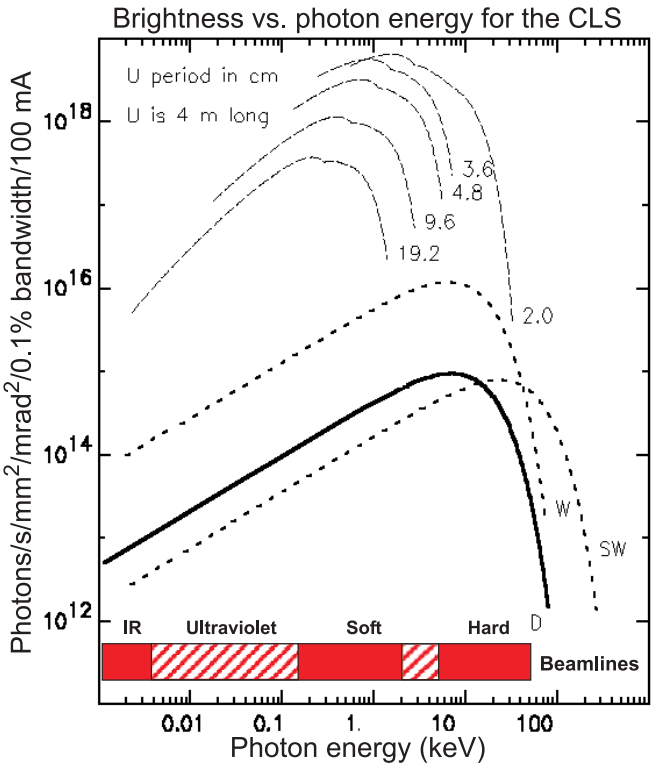
Fig. 3. One storage ring cell of the CLS. The long two magnets are the dipoles, and the short nine magnets are the quadrupoles and hextapoles. Bold solid lines show the SR from the insertion device (from the straight section off scale on the left), dotted lines show SR from the two bending magnets.



beams and some of the insertion device beams of synchrotron light (SL) contain the whole upper two-thirds of the electromagnetic spectrum — the far-IR, IR, visible, UV, to the soft and hard X-ray region. Notice the much higher brightness curves for the undulator (U) and wiggler (W) beams compared to the bending magnet beam in thick black. Also notice that the superconducting wiggler (SW) extends the SR "spectrum" to much higher X-ray energies — even above 50 keV. Second, the intensity of all of these beams is orders of magnitude greater than laboratory sources. Third, the beam sizes are very small, much less than 1 mm^2. For example the bending magnet "point" source, on this third generation ring will be about 0.3 mm (horizontal) × 0.1 mm (vertical); and the beam size increases very slowly with distance — the beam has a small divergence of about 200 μrad (horizontal) × 20 μrad (vertical). This gives a vertical beam size 10 m from the ring of only 0.2 mm, with a horizontal beam size substantially larger depending on the how much beam is accepted horizontally. The very high intensities, combined with the very small size results in a beam bright-

© 2004 NRC Canada

Fig. 4. Plot of the SR brightness vs. photon energy from different magnets on the CLS storage ring (from the bottom curves up): solid line at the bottom (D) from a bending magnet; W, from a wiggler; SW, from a superconducting wiggler as in the XAFS beamline; top five curves (U), for different undulators.



ness or brilliance that can be millions of times greater than any laboratory source of X-rays. Beamlines are constructed to optimize the performance in specific energy regions (for example, the CLS will have IR beamlines, soft X-ray beamlines, and hard X-ray beamlines) with monochromators to vary the energy within that region, and mirrors to focus the slightly diverging beam to the sample, so that the same sub-mm^2 beam size is obtained at the sample to be analyzed. The next section will describe these beamlines in more detail.

It is important to emphasize that the CLS is a so-called "third" generation ring with the above very small beam sizes. There are seven other third generation rings working in the world at present, with two in the US. The CLS should be competitive for most experiments with the best in the world, and will have comparable performance with the other two in North America.

What is the progress on the electron accelerators at the end of October 2003? The 1962 linac from the Saskatchewan Accelerator Laboratory was refurbished almost completely in 2002, and is now generating 250 MeV beams ready to be transferred to the booster ring. Danfysik delivered the booster ring in late 2001, and it exceeded specifications in the fall of 2002. The major storage ring components are now completely assembled, and at the time of writing (October 2003) a few milliamps of electrons have been stored for milliseconds (over 5000 turns) in the storage ring. It is expected that tens of milliamps of beam will be stored in the outer ring by the end of this year. (indeed, 25 mA have been stored as of early February 2004). All of the seven initial beamlines were designed by early 2002, and nearly all beamline components have now been ordered. It is expected that most of the seven beamlines will be working by mid-2004.

The beamlines

The seven beamlines in Table 1 have been approved for construction by several CLS committees after scientific recommendation by the CLS International Facility Advisory Committee (FAC) based on the scientific excellence of the proposals. In addition to these seven, a facility diagnostic beamline (Table 1, top) will be built to monitor the performance of the storage ring. All of these proposals are cooperative efforts between the CLS and Canadian scientific groups. For example, over 150 scientists (mostly academics) from all across Canada are involved in the initial seven beamlines. These academics provide the performance requirements of the beamlines to the CLS (included in the beamline proposal that they write, with assistance from CLS scientists as required) and liaise with CLS beamline scientists who coordinate the design, construction, and operation of the beamlines.

The initial seven beamlines (two IR lines, three soft X-ray lines (the variable line spacing plane grating monochromator beamline (VLS PGM), the spherical grating monochromator beamline (SGM), and the spectromicroscopy beamline (SM)), and the two hard X-ray lines (protein crystallography at the first beamline of the Canadian Macromolecular Crystallography Facility (CMCF), and the micro-XAFS beamline) utilize the full useful spectral range offered by the CLS (see the energy range for each beamline on the right-hand side of Table 1). The far-IR beamline will enable IR measurements from 1.2×10^{-3} eV (10 cm^{-1}) to 0.5 eV (4000 cm^{-1}), the soft X-ray lines will yield energies between 5 eV and 2000 eV, and the hard X-ray lines give photon energies between 4 keV and 30 keV. The academic project leaders are listed first below the name of the beamline, and the CLS beamline scientists are given next in brackets.

Applications to the May 2003 CFI competition were made for the seven "Phase 2" beamlines listed in Table 2, plus an XPS end station for the Phase 1 SGM beamline. These eight applications came from three universities — the University of Saskatchewan, the University of Western Ontario, and the University of British Columbia, and the project leaders are listed in Table 2. These beamlines concentrate on the hard X-ray part of the spectrum with diffraction, microprobe, and medical imaging being prominent. In addition, two soft X-ray beamlines were applied for. The soft X-ray DCM is a replacement for the CSRF DCM mentioned above. The CFI will announce the results of the competition in March 2004.

The most important device for all beamlines is the monochromator that converts the polychromatic SL beam (Fig. 4) into a variable energy monochromatic beam: a double crystal for the hard X-ray region, a grating for the soft X-ray region, and a laboratory interferometer for the IR region. For the hard X-ray micro-XAFS line (Fig. 5*a*) after some filtering and focusing, the SL beam impinges on the first crystal of an identical, and parallel, crystal pair (labeled DCM). The first crystal diffracts the incident polychromatic beam onto

© 2004 NRC Canada

Table 1. Phase I beamlines under construction.

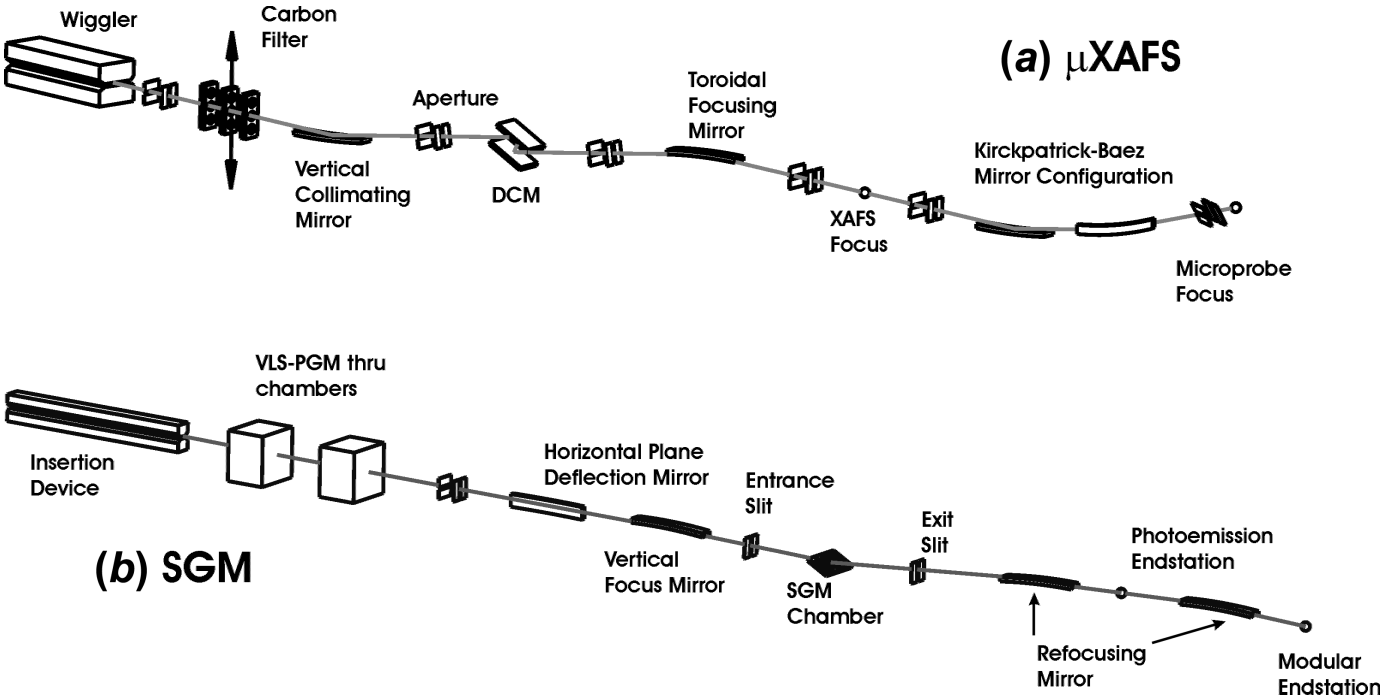
Facility diagnostic Jack Bergstrom bending magnet (BM) white	
(1) Far-IR spectroscopy, high resolution, high pressure	
Bob McKellar, Tom Ellis (Tim May)	BM 0.001–0.13 eV
(2) Mid-IR biological spectromicroscopy, imaging, industry	
Mike Jackson, Farid Bensebaa (Tim May)	BM 0.008–0.8 eV
(3) Plane grating monochromator (PGM)	
T.K. Sham (Yongfeng Hu)	Undulator (Und) 5–250 eV
(4) High resolution SGM, photoemission, XAFS, UHV	
T.K. Sham (Ian Coulthard)	Und 0.22–1.9 keV
(5) Soft X-ray spectromicroscopy, STXM, NEXAFS	
Adam Hitchcock (Kon Kaznatcheev)	EPU 0.2–2.0 keV
(6) Macromolecular protein crystallography	
Louis Delbaere (Pawel Grochulski)	SG-U 6.5–18 keV
(7) Hard X-ray absorption spectroscopy, XAFS/microprobe, industry	
De Tong Jiang	(Wiggler) 5–540 keV

Note: CLSI beamlines team leader, Emil Hallin.

Table 2. Phase II beamlines.

(1) SXRBM: soft X-ray DCM; T.K. Sham	BM 1.7–5.5 keV
(2) CCAXRDS: general purpose diffraction; D.T. Jiang	W 4–40 keV
(3) REIXS: soft X-ray spectroscopy; G. Sawatzky	EPU 80–2000 eV
(4) BMIT; biomedical imaging and therapy; D. Chapman	Und 15–85 keV
(5) CMCF No. 2: 2nd PX; N. Strynadka	BM 5–20 keV
(6) VESPERS (microdiffraction, XRF); N.S. McIntyre	BM pink light 5–50 eV
(7) CSNF (MEMS, etc.); D. Klymyshyn	BM 1–10 keV

Fig. 5. Cartoon layout for: (*a*) hard X-ray micro-XAFS beamline, and (*b*) soft X-ray SGM beamline. Note that the microprobe focus and XAFS focus in (*a*) are in the same place and are shown separately only for clarity. In the SGM case (*b*), the two foci are at different physical locations for two different end stations. (1 atm = 101.325 kPa; 1 bar = 100 kPa).



the second crystal where a second diffraction occurs. If the two crystals are held so they are parallel and have the correct relative position, then a "monochromatic" beam will emerge from the second crystal. The energy of that beam is determined by the angle of incidence on the first crystal. If the motion of the two crystals (rotation and translation as

© 2004 NRC Canada

appropriate) is coordinated, the outgoing beam will be parallel to the incoming beam with a fixed offset. The wavelength (λ) of the diffracted X-rays is given by Bragg's law (for first order, set $n = 1$):

$$[1] \qquad n\lambda = 2d \sin \theta$$

where $2d$ is the spacing of the lattice planes in the crystal, θ is the angle of incidence onto the two crystals, and n is the order of the refraction.

For soft X-ray energies lower than about 1.5 keV (e.g., the VLS PGM and the SGM), larger d spacings are essential for the larger wavelengths; in this case, the array of scattering centers is conveniently achieved by ruling a grating according to some well-defined equation. Such "grating monochromators" provide the same function as the parallel crystals used for hard X-rays but are normally used in a single grating configuration. Additional optics are used to keep the monochromatic beam in the right spot; commonly a grating monochromator consists of a grating and at least one more X-ray optical device together with a means to provide coordinated motion of some of the devices (Fig. 5*b*). The polychromatic beam strikes a reflecting surface with a periodic array of lines (the SGM in Fig. 5*b*), usually at a glancing angle. Diffraction of different wavelengths (λ) is given by the well-known equation (set $n = 1$ for first order):

$$[2] \qquad n\lambda = 2d(\sin \alpha + \sin \beta)$$

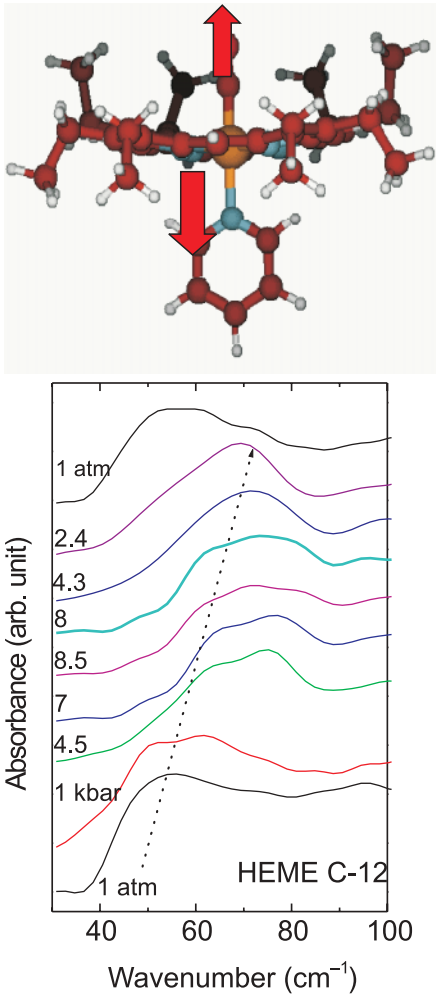
where d is the distance between two adjacent grating lines, n is the order of the diffraction, and α and β are the incidence and diffraction angles measured perpendicular to the grating surface.

In typical implementations at the CLS, mirrors of various surface figures are used to collimate and focus the photon beam both before and after the monochromator (see the mirrors labeled in Figs. 5*a* and 5*b*). Performance of the beamlines at CLS will be competitive with the best in the world. For example, the SGM beamline will yield a beam size of 0.05 mm (vertical) × 0.1 mm (horizontal), a photon flux of 10^{12} photons/s into that area, and give an energy resolution of 10 000 (e.g., a line width of 0.1 eV at 1000 eV). The SGM is presently working well at CSRF, giving about the same excellent resolution, but with a larger beam size, and only 10^8 photons/s (7). The micro-XAFS and SM will also give a great combination of small beam sizes (down to 50 nm for SM and 2 μ for XAFS) along with very high intensity with special optics. The design of the micro-XAFS line was optimized for spectroscopy; that of the SM line was chosen to preserve brilliance and maximize flexibility in delivering highly customized beams into each of two different endstations (PEEM and STXM). In the IR and far-IR, the small parallel SL beam can deliver far more IR photons through a small aperture in a commercial spectrometer than can a thermal source like a globar normally used in IR spectrometers. This results in better spectral resolution, and much better spatial resolution (3–5 μ resolution compared to the 30 μ available with a laboratory source).

Canadian science

In this section, I will illustrate the power of SR for research in all regions of the SR spectrum, beginning with recent Canadian research at foreign synchrotrons in the far-IR, working up in energy with Canadian examples from the IR, soft X-ray, and finally hard X-ray regions.

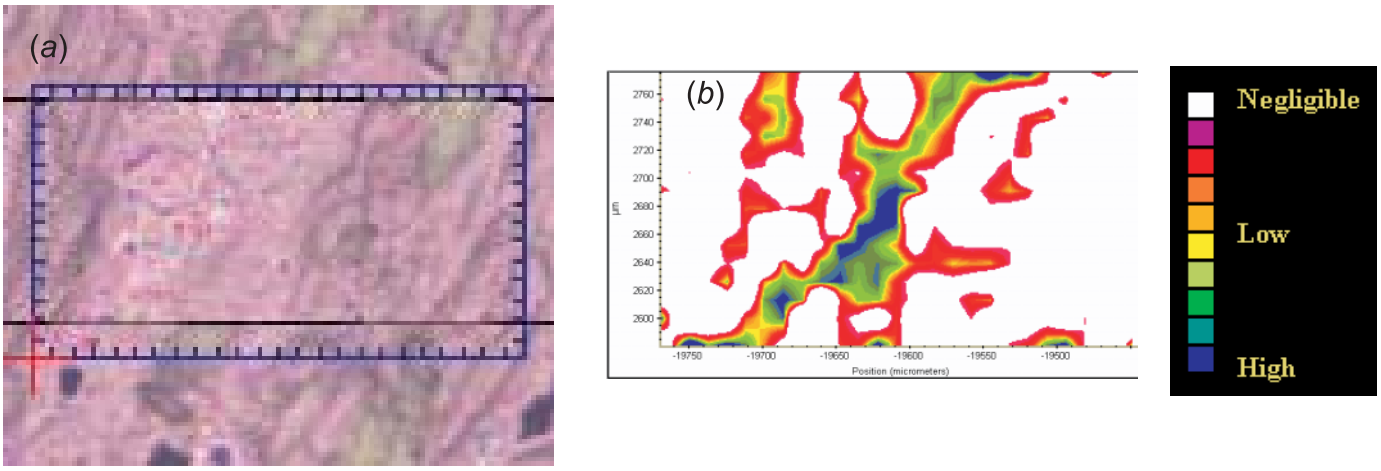
Fig. 6. Far-IR spectra of the model heme compound COFe(OEP)Py (carboxy-octaethyl-ironporphyrinpyridine) (10). The model structure is shown at the top.



The very small, intense, synchrotron beam is absolutely essential for high-pressure experiments from the far-IR (10) to the hard X-ray (11) in which the gaskets in diamond–anvil cells yield experimental apertures of a few hundred μm for absorption experiments. NRC scientists from the Institute for Microstructural Sciences have been especially active in this area. These researchers have been able to obtain the far-IR spectra of model heme compounds (COFe(OEP)Py) (Fig. 6) as a function of pressure. The peak at about 53 cm^{-1} (top spectrum at 1 atm, 1 std. atm = 101.325 kPa) shifts markedly to about 70 cm^{-1} within 0.24 GPa and then more slowly up to 0.85 GPa. The pressure dependency of the peak was completely reversible as the pressure was decreased to 1 atm (1 std. atm = 101.325 kPa) (bottom spectrum). Other higher frequency peaks had a complex structure, including several peaks within a broad absorption feature. Density functional calculations showed that the low-frequency peak was due to the fundamental excitation of the "doming" vibrational mode in which the iron atom moves out of the

© 2004 NRC Canada

Fig. 7. FT-IR imaging of collagen in damaged hamster heart tissue. Newly formed scar tissue is detected as collagen in areas of necrosis (12).



porphyrin plane while the periphyry of the ring moves in the opposite direction (Fig. 6, top). The calculations indicated that this peak should have a large pressure dependence as observed. This "doming" mode is thought to determine the reactivity of oxygen with this type of molecule in biological systems (10). The pressure dependence and the calculations were essential for the first definitive assignment of these very low-frequency vibrations.

The mid-IR of the SR spectrum has been used in the last 10 years in many different scientific areas (see for example the web sites: http://nslsweb.nsls.bnl.gov/infrared and http://infrared.als.lbl.gov/).

Biomedical uses of IR from SR have been the focus of the group at the University of Manitoba. In one study (12), the IR spectroscopy and microscopy of damaged hamster heart tissue was investigated. The high brightness of the IR from SR enabled rapid aquisition of data from a 10 μm × 10 μm area of an 8 μm thick tissue section. The IR spectra in such a small volume yield information on the major chemical components including collogen, lipid, DNA, and noncollagen tissue proteins. The IR absorption spectrum of collagen, which is a major indication of cardiac dysfunction after cardiomyopathy, is well known. Using the intensities of the major IR bands of collagen and the computer-controlled mapping stage, the distribution of collagen can readily be obtained in the damaged hearts (Fig. 7*b*) across an area of about 200 μm vertical × 300 μm horizontal and at about 10 μm resolution. The highest collagen content, and greatest tissue damage is shown in the blue–green region.

Most of the studies in the soft X-ray region look at the excitation of core level electrons, using photoabsorption, photoelectron, Auger, and resonance Auger techniques. The narrow core level edges that can be studied in the soft X-ray region are: the 1*s* (so-called K edges) of the light elements from Li to Ar, the 2*p* (so-called L edges) of the elements from Na to Zn, and the 3*d* (so-called M edges) of many of the heavier elements. The new PGM and SGM Phase 1 beamlines will be ideal sources from 5 eV to 1900 eV to cover all the core levels as well as valence bands at low energy.

In our high-resolution SR gas phase studies in the early 1990s, we were able to resolve ligand field and vibrational effects on core level X-ray photoelectron spectra (XPS) of molecules (13). In recent studies at about 50 meV total resolution (Fig. 8*a*) we have been able to resolve both the ligand field and vibrational splitting on the Br 3*d* level that splits the $3d_{3/2}$ and $3d_{5/2}$ levels into a doublet and triplet, respectively (14). The vibrational profile on the left hand side of each of the five peaks is also evident. Using a commercial XPS source with the best resolution of 0.35 eV, none of these splittings could be observed. The observation of this splitting was essential to interpret the very complex Br 3*d* photoabsorption spectrum in Fig. 8*b*, which show transitions from the five ligand field split states to the Br 5*s*, 6*s*, and *np* (n = 5–9) Rydberg orbitals (15). The ligand field splitting was also necessary to interpret the very complex $3d^{-1}$ ▶ $4p_{\pi}^{-2}$ normal Auger spectrum (Fig. 9*a*), which had been recorded a decade earlier with an electron source at similar resolution (16). The splitting of the three Auger final states, $^1\Sigma^+$, $^1\Delta$, and $^3\Sigma^-$, by the five ligand split 3*d* states is shown at the bottom Fig. 9. The intense vibrational structure on each state is shown beneath the experimental results at the top the figure. Having interpreted the XPS, absorption, and Auger spectrum, the real challenge is to record and interpret the resonant Auger spectra, where the Br 3*d* electron is resonantly excited to the Rydberg orbitals found in Fig. 8*b* — i.e., the 5*s*, 6*s*, or *np* Rydberg orbitals, and the Br atom decays via the Auger process with the Rydberg electron as a "spectator". An example of these spectra is given in Fig. 9*b*, where we show the resonant Auger spectrum of a $3d_{5/2}^{-1}5p_{\pi}$ resonance taken at a photon energy of 74.53 eV (17). The interpretation of these spectra depend on the accurate interpretation of the photoelectron, absorption, and Auger spectra. In these spectra, the inherent line width of about 90 meV does not contribute to the observed line width, and total line widths of 30 meV are observed in this very complex spectrum. The splitting of the normal Auger states (about 1.2 eV) is preserved in this spectrum (see top of horizontal bars), and a kind of angular "shake-up" occurs to give an overlapping $3d^{-1}4d_{\pi}$ resonance Auger spectrum. In contrast to the normal Auger spectra, no spin-orbit splitting, ligand field splitting, or vibrational splitting is observed in this spectrum. The higher energy resonant Auger (e.g., 7*p*, 8*p*, etc.) are enormously complex; but recent analysis shows that

© 2004 NRC Canada

Fig. 8. (*a*) High-resolution photoelectron spectrum of the Br 3*d* level in HBr taken at 50 meV total resolution (14). (*b*) High-resolution Br 3*d* photoabsorption spectrum of HBr taken at different angles (15).

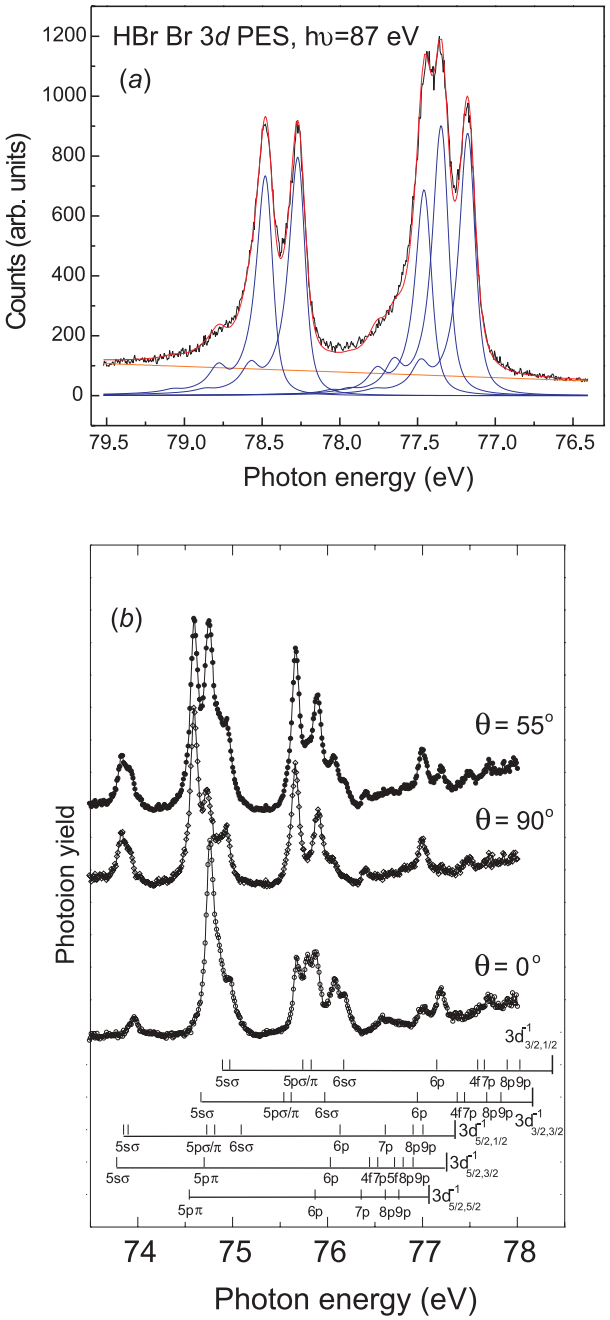
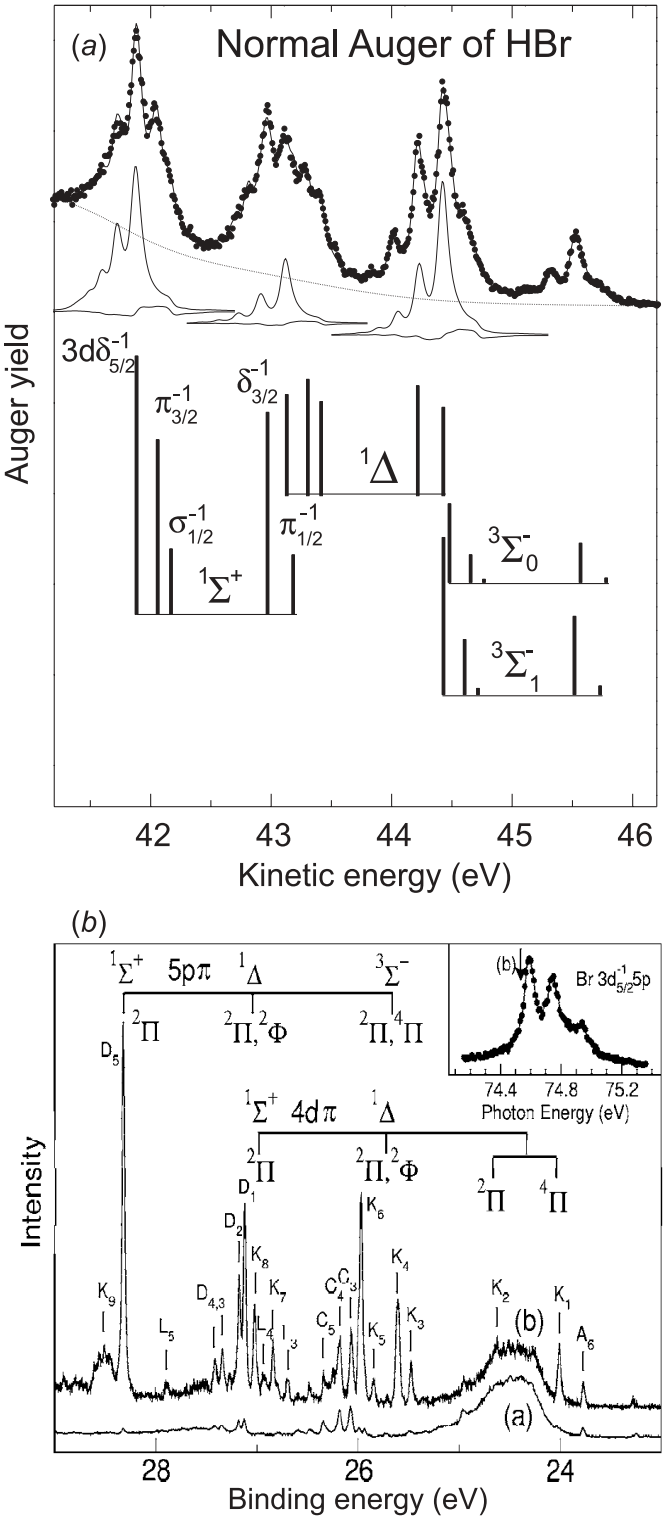


Fig. 9. (*a*) The normal Auger MVV spectrum showing the vibrational envelopes (top) and the ligand field states (bottom) required to fit the spectrum (bold solid line through the spectrum) (16). (*b*) The resonance Auger spectrum after the resonance excitation of a $3d_{5/2}$ electron to the $5p_{\pi}$ Rydberg orbital (17).

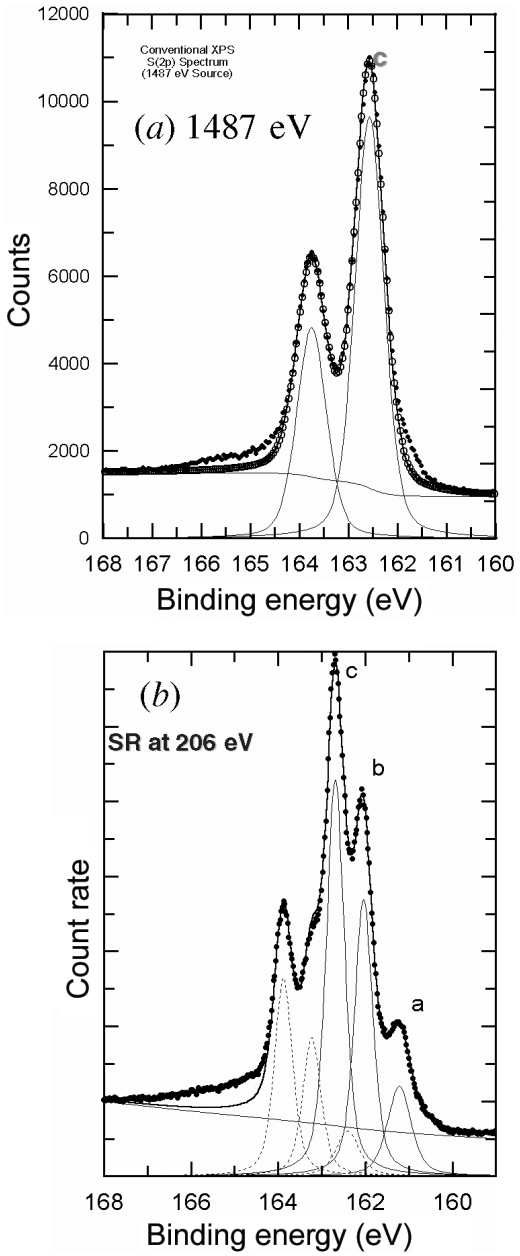


they can be interpreted using very extensive shake-up phenomena (17).

SR also greatly enhances XPS spectra of solids (Fig. 10). A S 2*p* XPS spectrum of pyrite FeS_2 taken with a conventional XPS source is shown in Fig. 10*a*. The normal S 2*p* spin-orbit doublet is immediately obvious, with hints of shoulders on the left and right hand sides of the two peaks. When this spectrum is taken with SR at 206 eV (Fig. 10*b*), the spectrum is dramatically changed due to the great surface enhancement at about 50 eV above threshold. The hint of a shoulder at about 162 eV in Fig. 10*a* turns into two intense peaks b and a in Fig. 10*b* due to a surface disulphide (b) and a surface monosulphide (a) (18). Also the peak

© 2004 NRC Canada

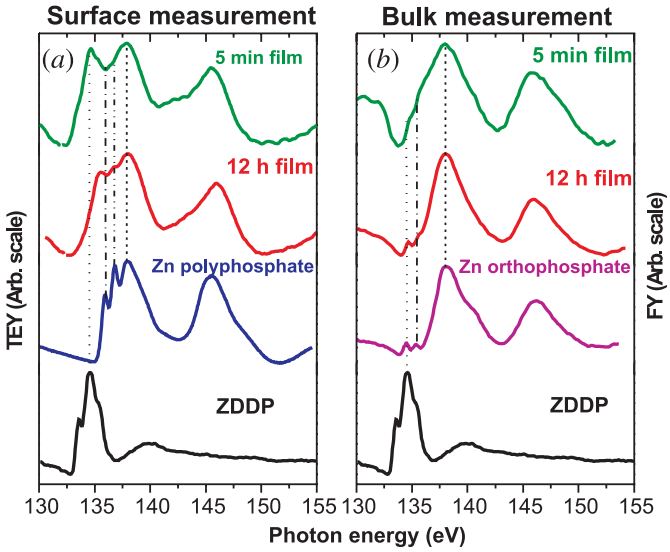
Fig. 10. The S 2*p* XPS spectra of FeS_2 taken: (*a*) with a conventional monochromatic laboratory Al K_α XPS source at 1487 eV; and (*b*) with a high-resolution SR source at 206 eV (18, 19).



widths in Fig. 10*b* are appreciably narrower than in Fig. 10*a*. The surface sensitivity of about two monolayers in Fig. 10*b* make it possible to study the oxidation and reactions of mineral surfaces in great detail (e.g., 18, 19).

X-ray absorption spectra (XAS) in both the soft and hard X-ray regions are extremely useful for obtaining chemical information on the widest variety of samples — gases, liquids, and amorphous and crystalline solids. These spectra (both the near-edge XANES and extended fine structure (EXAFS) can be obtained usually in five modes: absorption, total electron yield (TEY), fluorescence yield (FY), Auger or resonance Auger yield (AY), or optical luminescence yield (PY). Often, more than one of these modes can be obtained simultaneously on the same sample. The AY, TEY,

Fig. 11. The P L-edge XANES spectra of model compounds (bottom two spectra) and tribofilms from ZDDP (top two spectra) taken simultaneously in TEY mode (*a*, left) and FY mode (*b*, right) (20–22).



and FY modes give spectra that are very similar to the straight absorption spectra (the same peaks, but different intensities), but the sampling depths are very different. The AY technique monitors high energy Auger electrons with sampling depths of about 50 Å, so this technique is always fairly surface-sensitive. The TEY technique, often obtained by monitoring the sample current, monitors very low-energy electrons (less than 2 eV), and the sampling depth can be over 1000 Å. For example, the TEY sampling depth in Si for 100 eV photons and electrons at the Si L edge has been shown to be only about 50 Å, while the sampling depth for the Si K edge at 1800 eV is 700 Å (20).

Some of the power of the XANES technique for studying surfaces and materials is illustrated in Fig. 11 (21–23). The phosphate results described below should also be useful for studying environmental phosphate samples. All engine oil contains additives, so-called antiwear agents, anti-oxidants, detergents, and dispersants. The usual antiwear agent is zinc dialkyldithiophosphate (so-called ZDDPs), and this compound decomposes on hot metal surfaces in engines to give very thin "antiwear" films. The chemistry of antiwear films have been studied for many years using conventional surface techniques such as XPS; and XPS showed that the major component of the film was phosphate from decomposition of the ZDDP. The P L-edge and K-edge XANES using TEY and FY detection combined are ideally suited to give details of the chemistry and microchemistry of these films because the analysis depths of these techniques (about 50 Å for TEY and 700 Å for FY at the L-edge) match the thicknesses of these inhomogeneous films (about 1000 Å on average).

Figure 11 gives the P L-edge spectra on about 5 mm^2 samples of ZDDP, two Zn phosphate standards (Zn orthophosphate ($Zn_3(PO_4)_2$) and a Zn polyphosphate with bridging oxygens (formally $Zn(PO_3)_2$)), and two antiwear films produced by rubbing a steel cylindrical pin against a flat piece of steel in hot oil containing ZDDP. This rubbing

© 2004 NRC Canada

Fig. 12. Top right: the Si K-edge XANES spectra of clean Si (top), porous Si (middle) in PY mode, and porous Si in TEY mode Si (bottom). The X-ray excited optical luminescence (XEOL) spectra from the porous Si sample are shown in the central figure (24, 25).

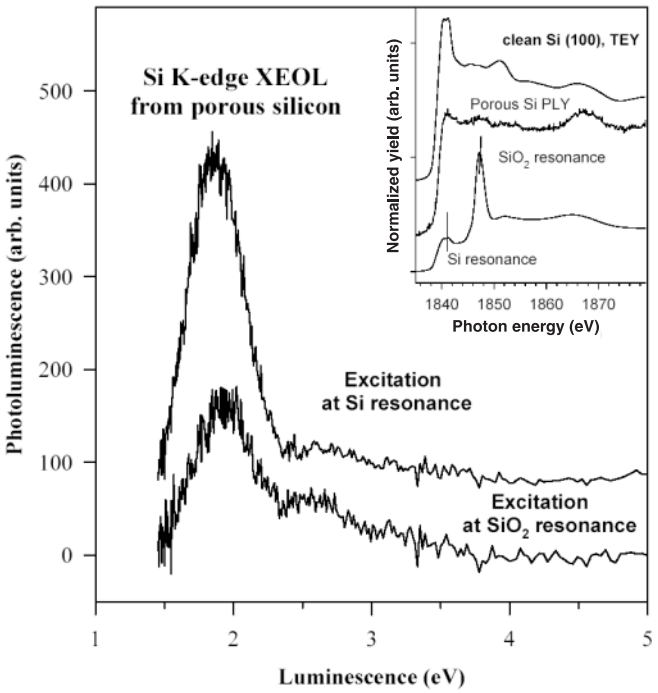
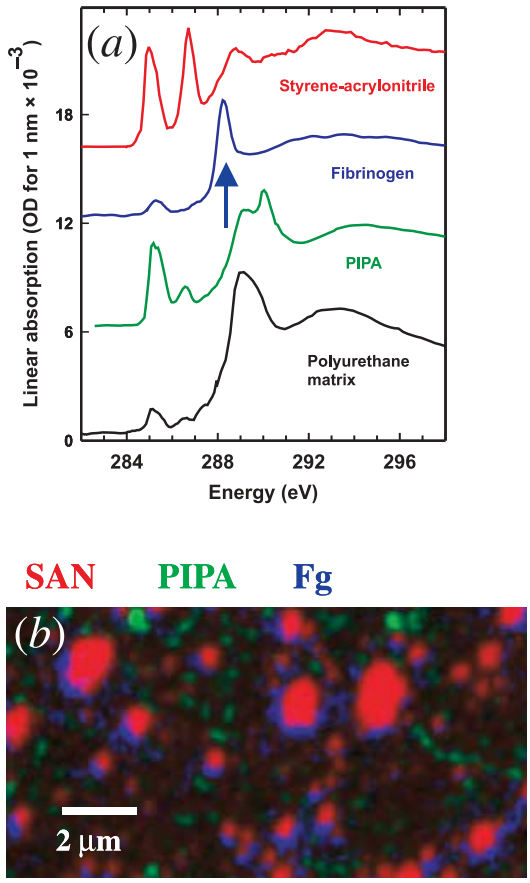


Fig. 13. (*a*) The C 1*s* XANES spectra of two polymer components (SAN (top) and PIPA) and the protein fibrinogen (Fg), along with the polyurethane matrix. The microscopic image from the STXM technique is shown below with colour coding for the four components (27, 29, 30). (Chemical map derived from pixel-by-pixel fit of reference spectra to image sequence).



occurs in a commercial Plint machine to simulate conditions in an engine. TEY spectra (Fig. T11*a*) and FY spectra (Fig. 11*b*) were obtained simultaneously from the two films and ZDDP, with separate TEY and FY spectra taken of the Zn orthophosphate and Zn polyphosphate, respectively, as standards (bottom two spectra in both Figs. 11*a* and 11*b*). Note that the ZDDP gives a triplet peak structure centered around about 135 eV in both TEY and FY modes. The two phosphate model compounds both give a major, rather broad peak in TEY and FY at about 138 eV, with a narrow doublet at lower energy. Somewhat surprisingly, the intensity of this doublet is VERY different for the two phosphates — orthophosphate gives a very small doublet at about 135 eV, while the polyphosphate gives an intense doublet at about 137 eV. Indeed, the intensity of this doublet increases more or less linearly with an increase in chain length of the phosphate. TEY analysis of the film after 5 min of rubbing (top left) shows the presence of undecomposed ZDDP and phosphate; whereas FY analysis of the same film (top right) shows only phosphate, showing that the ZDDP is only present at the surface of the film. The spectra of the 12 h film are more interesting. The TEY analysis gives a spectrum which is very similar to the spectrum of the model Zn polyphosphate spectrum with the intense doublet at about 137 eV in both cases. In contrast, the FY spectrum of the 12 h film is very similar to the spectrum of the Zn orthophosphate with a very weak doublet at about 135 eV. Obviously, the surface of the 12 h film (the first 50 Å) contains mostly polyphosphate, with the bulk of the 1000 Å film being mostly orthophosphate. From this and other information, a mechanism of formation has been suggested (21–23).

The PY technique has been pioneered by T.K. Sham, and is very useful for investigating the source of luminescence in light-emitting compounds such as porous Si or metal-containing polymers, which may be very useful in the future for optoelectronics applications (24, 25). In the initial study, the photoluminescence intensity was studied on a slightly oxidized porous Si. The Si K-edge XANES in the TEY mode of this sample is seen in the upper right insert in Fig. 12. The relatively weak absorption at about 1840 eV generates a very intense luminescent signal at 690 nm; whereas, the strong SiO_2 signal about 1848 eV generates a very weak luminescent signal. The source of the luminescence must be the porous Si itself rather than the oxide; and this result is consistent with the so-called quantum confinement model in the porous Si. The energy of this luminescence peak position varies with the conditions of electrochemical preparation and the history of the sample (24).

Considering sample size, most measurements have been done on a few mm^2 of sample. However, recently, photoelectron emission microscopy (PEEM) (26) and scanning transmission X-ray microscopy (STXM) (27), with resolutions of

© 2004 NRC Canada

Fig. 14. The crystal structure of $Nb_5Pd_4As_4$ from a 5 X × 5 X × 5μm crystal. (Nb atoms in green, Pd atoms in blue, and As atoms in red). (*I*4/*m*, *a* = 10.4457(17), *c* = 3.7868(6), *Z* = 2, synchrotron λ = 0.6880 Å, μ = 309.6 cm^{-1}, R_1 = 0.0262, wR_2 = 0.0694).

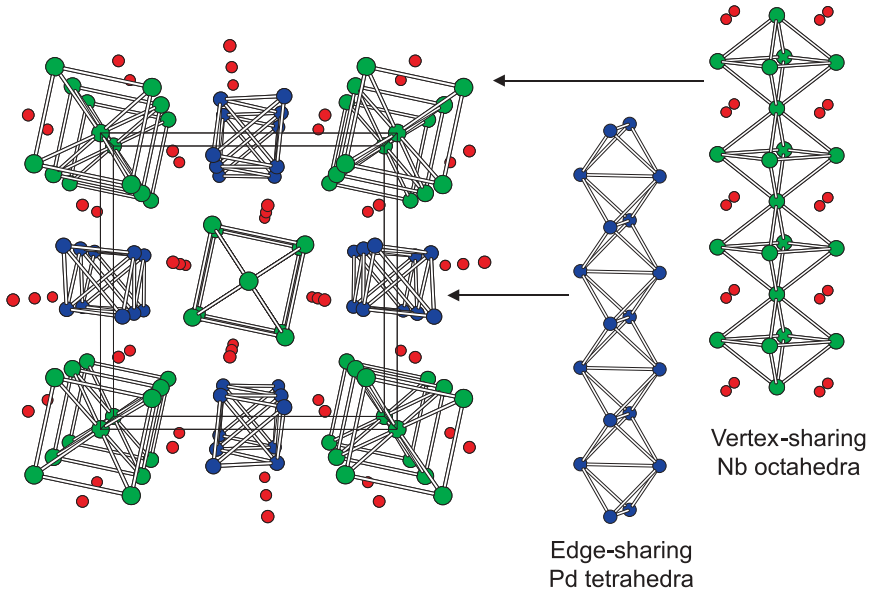


Fig. 15. The As K-edge XANES spectra of three model compounds and a tailings sample (32). The tailings sample contains mostly As(V), but the broadening at low energy (circled) shows a significant amount of a lower oxidation state.

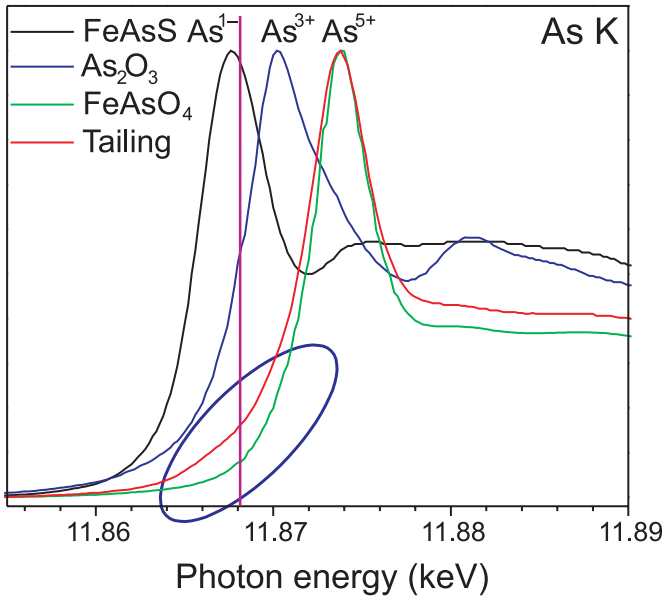
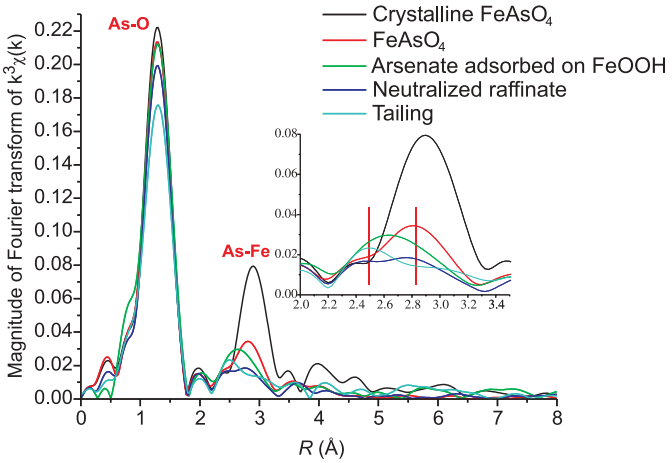


Fig. 16. The As K-edge EXAFS three model samples and two samples from a tailings pond (32). Notice the blowup of the *R* = 2.0–3.4 region in the right top figure.



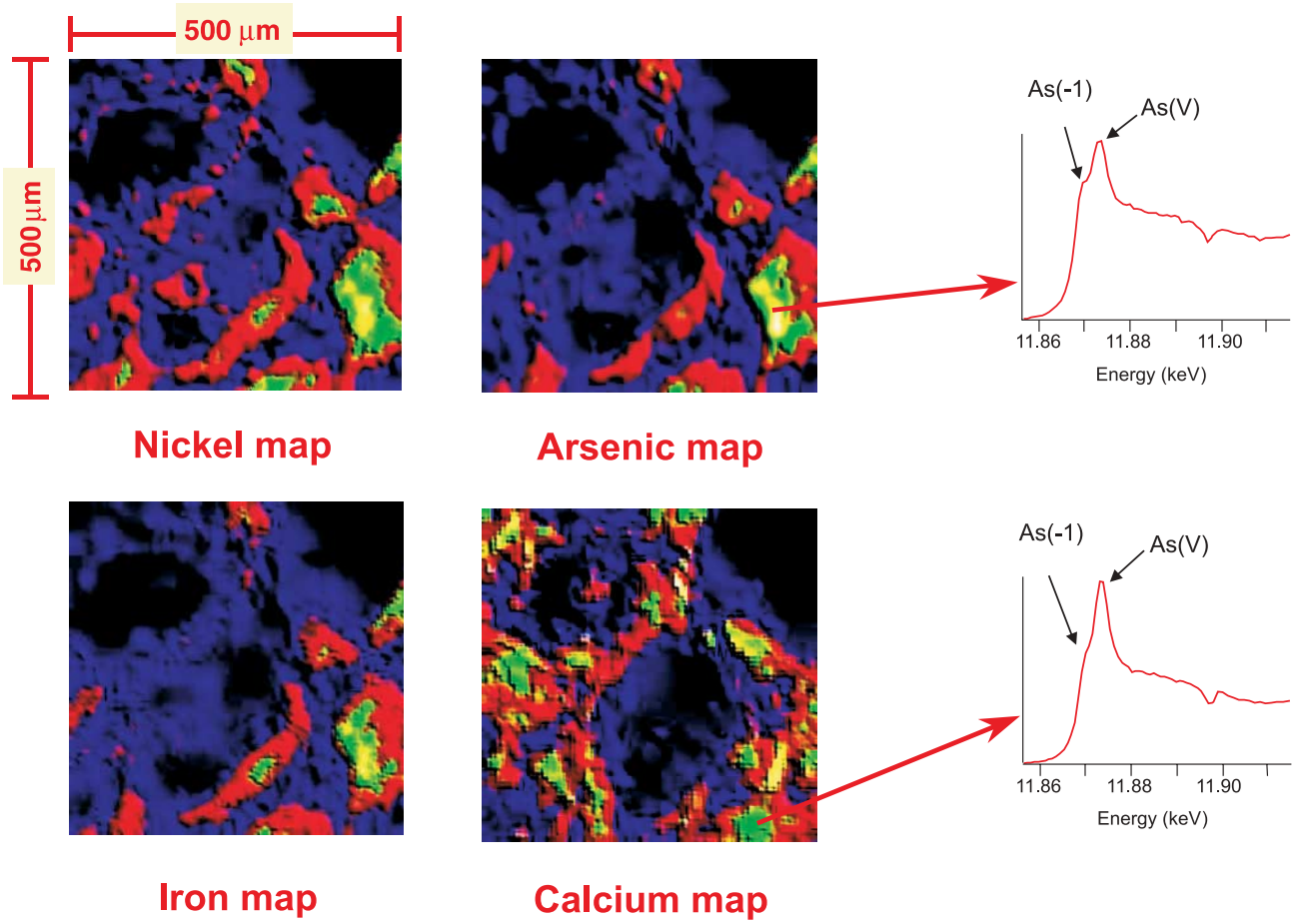
less than 1000 Å, have obtained very novel results on spatially inhomogeneous samples, and both of these techniques will be optimized on a Phase I beamline at the CLS. In PEEM, X-ray absorption spectroscopy and electron microscopy (as in scanning electron microscopy (SEM)) are combined. As for TEY measurements, electron yield from the sample is monitored. XANES can be obtained on very small areas (much less than 1 μm^2); and when the X-ray energy is tuned to a given absorption edge, a microscopic image is obtained for a given chemical species that is absorbing the X-rays.

Using PEEM, it is possible to examine the above antiwear films in much more detail. Very recent results (28), show that the chemistry of these films can be obtained at the 0.5 μm level. The images all show a very patchy film with pads of varying sizes from ~1 μm to ~10 μm. Spectra show that the polyphosphate chain length was smaller on the small pads than on the large pads.

STXM is another powerful spectromicroscopy technique that requires the high brightness of SR. The SR beam is focused with a zone plate to about 20 nm, and the sample is scanned across the stationary SR beam very precisely. On a polymer sample such as seen in Fig. 13, the different polymer components have very different C 1*s* XANES. By sitting on characteristic peaks for each polymer, an image is built up of each component in the polymer, and the amount of each component in a polymer or polymer spheres (29) can be quantified. This technique is now being used as a tool to

© 2004 NRC Canada

Fig. 17. Elemental microscopy of a tailings sample (33) (left), with the As K-edge XANES spectra from 5 μ spots as indicated on the right.



study the biointeractions of proteins on polymers that might be used as medical implants (30). In Fig. 13, the interaction of a protein fibrinogen (Fb) with the polymer shows: the protein Fb in monolayer amounts (blue) can be detected associated with the styrene acrylonitrile (SAN, red), and Fb is not associated with the PIPA (green) or matrix (black).

The hard X-ray uses of SR are even more numerous than the soft X-ray uses, but I only have time to mention the two major areas of hard X-ray research — diffraction and EXAFS. First, the very small intense SR beams are essential for obtaining atomic resolution on very small crystals of proteins and other large molecules. Indeed all 52 protein crystallography groups in Canada go to foreign synchrotrons to obtain their final data. It is anticipated that smaller molecule diffraction will have a separate phase II beamline. In Fig. 14, the structure of an incredibly small crystal from a powder (5 μm × 5 μm × 5 μm) of $Nb_5Pd_4As_4$ is shown (31). The data was obtained at the second generation Daresbury SR source.

EXAFS is the technique of choice to obtain chemical information on noncrystalline samples. The CLS has initiated a strong research initiative with Canadian mining companies to characterize the chemistry of As (and other heavy metal toxins) in amorphous mine wastes. The toxicity of the As depends on its chemistry (for example, As(III) is generally much more toxic than As(V)), and the mobility of the As species in the tailings pond is dependent on the As chemistry (for example, $FeAsO_4$ is more stable than adsorbed As on FeOOH). The As K-edge XANES in Fig. 15 shows that the As oxidation state can be readily distinguished, and the amount of each As oxidation state in tailings samples can be obtained using these model spectra (32). The As K-edge EXAFS in Fig. 16 shows that the nature of the AsO_4^{3-} can be obtained from the EXAFS. For example, the peak at 2.5–2.8 Å due to As–Fe scattering is very sensitive to the nature of the AsO_4^{3-}. The two mine waste samples (dark blue and light blue) have very different spectra than either crystalline or amorphous $FeAsO_4$ (black and green, respectively). In particular the intensities of the black and red spectra are much larger than for the two tailings samples. The tailings spectra are much more similar to that of adsorbed AsO_4^{3-} on FeOOH, and detailed modeling of these spectra has indicated that the predominant species is arsenate bonded to the FeOOH in a bidentate mode.

In the hard X-ray region it is possible to focus the beam down to 1 μm or so, and then microscopy and spectromicroscopy is possible as in the soft X-ray region. Figure 17 shows the element distribution in a tailings sample at about 5 μm spot size (33). It is obvious that the high concentrations of As are associated with high concentrations of Fe and Ni (the yellow green regions) and not associated with

© 2004 NRC Canada

Ca. EXAFS can be obtained from those small yellow regions, and they show that the As is a combination of the two oxidation states (As(-I) and As(V)).

Acknowledgements

This project has required the great effort of at least 200 people in the last 10 years, and I am extremely grateful to all of them. I am hopefully representing many of them in this article. In my 1999 CISR President's report (www.cisr.ca/reports/pres_rep_199906.html) I have acknowledged the many people who were critical in getting the project off the ground. The CLS staff have done a great job in the last 5 years to bring the initial project very close to completion (see the CLS web site: www.lightsource.ca).

I am very grateful to my colleagues (see the text) for providing me with an example of their exciting recent results. Kim Tan deserves a special thank you, for his critical role in making the CSRF in Madison such a successful and productive facility in the last 20+ years. Many thanks to all of my 16 post-graduate students and 18 post-docs who traveled from London, Ontario to CSRF outside Madison, Wisconsin for the last 20 years to obtain their results. They all were productive in a very high-pressure environment. Thanks to all of them, and also to the CSRF staff and my senior colleagues. A number of my former students and post-docs are now working at the CLS in Saskatoon. I am particularly grateful in the last few years to Masoud Kasrai and Wayne Nesbitt for helping supervise joint students and post-docs. It is still exciting to be producing state-of-the-art research, and this would not have been possible without their fine cooperation.

References

1. G.M. Bancroft and P.W.M. Jacobs. Sci. Forum. December, 21 (1975).
2. J. Wm. McGowan. Phys. Can. **31**, 67 (1975).
3. K.H. Tan, G.M. Bancroft, L.L. Coatsworth, and B.W. Yates. Can. J. Phys. **60**, 131 (1982).
4. G.M. Bancroft, B.W. Yates, K.H. Tan, and L.L. Coatsworth. J. Chem Soc. Chem. Commun. 1613 (1984).
5. B.X. Yang, F. H. Middleton, B.G. Olsson, G.M. Bancroft, J.M. Chen, T.K. Sham, K.H. Tan, and D. Wallace. Nucl. Instrum. Methods, **316**, 422 (1992).
6. G.M. Bancroft. Chem. Can. **44**, 15 (1992).
7. B.W. Yates, Y.F. Hu, K.H. Tan, G. Retzlaff, R.G. Cavell, T.K. Sham, and G.M Bancroft. J. Synchrotron Radiation, **7**, 296 (2000).
8. G. Margaritondo. Introduction to synchrotron radiation. Oxford University Press, New York. 1988. pp. 1–280.
9. T.K. Sham. Synchrotron radiation: Earth, environmental and material sciences applications. Mineralogical Association of Canada. *Edited by* G.S. Henderson and D.R. Baker. Can. Mineral. Special Publication, **30**, 1 (2002).
10. D. Klug, M.Z. Zgierski, J.S. Tse, Z. Liu, J.R. Kincaid, K. Czarnecki, and R.J Hemley. Proc. Nat. Acad. Sci. U.S.A. **99**, 12 526 (2002).
11. J.S. Loveday, R.J. Nelmes, D.D. Klug, J.S. Tse, and S. Desgreniers. Can. J. Phys. **81**, 539 (2003), and refs. therein.
12. K.M. Gough, D. Zielinski, R. Wiens, M. Rak, and I.M.C. Dixon. Anal. Biochem. **316**, 232 (2003).
13. G.M. Bancroft and Y.F. Hu. *In* Inorganic electronic structure and spectroscopy. *Edited by* A.B.P. Lever and E.I. Solomon. Wiley and Sons, New York. 1999. Chap. 8. p. 443.
14. Y.F. Hu, Z.F. Liu, R. Puttner, G.M. Bancroft, and S. Aksela. J. Phys. B, **32**, 4091 (1999).
15. R. Puttner, Y.F. Hu, E. Nommiste, G.M. Bancroft, and S. Aksela. Phys. Rev. A, **65**, 32 513 (2002).
16. R. Puttner, Y.F. Hu, G.M. Bancroft, H. Aksela, E. Nommiste, J. Karvonen, A. Kivimaki, and S. Aksela. Phys. Rev. A, **59**, 4438 (1999).
17. R. Puttner, Y.F. Hu, G.M. Bancroft, A. Kivimaki, M. Jurvansuu, H. Aksela, and S. Aksela. Phys. Rev. A, **68**, 32 705 (2003), and in preparation.
18. A.G. Schaufuss, H.W. Nesbitt, I. Kartio, K. Laajalehto, G.M. Bancroft, and R. Szargan. Surf. Sci. Lett. 411, 321 (1998).
19. H.W. Nesbitt, A. Schaufuss, M. Scaini, H. Hochst, G.M. Bancroft, and R. Szargan. Geochim. Cosmochim. Acta, **67**, 845 (2003).
20. M. Kasrai, R.W. Brunner, G.M. Bancroft, J.A. Bardwell, W.N. Lennard, and K.H. Tan. Appl. Surf. Sci. **99**, 303 (1996).
21. Z.Yin, M. Kasrai, G.M. Bancroft, K. Fyfe, and K.H. Tan. Wear, **202**, 172 (1997).
22. Z. Yin, M. Kasrai, M. Fuller, G.M. Bancroft, K. Fyfe, K.H. Tan. Wear, **202**, 192 (1997).
23. M. Suominen Fuller, L. Rodriquez-Fernandez, G.R. Massoumi, W.L. Lennard, and G.M. Bancroft. Tribol. Lett. **8**, 187 (2000).
24. D.T. Jiang, I. Coulthard, T.K. Sham, J.W. Lorimer, S.P. Frigo, X.H. Feng, and R.A. Rosenberg. J. Appl. Phys. **74**, 6335 (1993); I. Coulthard. Ph.D. thesis, University of Western Ontario, London, Ontario, Canada, 1998.
25. P.G. Kim, M.C. Brandys, Y.F. Hu, R.J. Puddephatt, and T.K. Sham. J. Lumin. **105**, 21 (2003).
26. G. DeStasio, B. Gilbert, B.H. Fraser, K.H. Nealson, P.G. Conrad, V. Levi, M. Labrenz, and J.L. Banfield. J. Electron Spectrosc. Relat. Phenom. **114–116**, 997 (2001).
27. T. Warwick, H. Ade, A.P. Hitchcock, H. Padmore, B. Tonner, and E. Rightor. J. Electron Spectrosc. Relat. Phenom. **84**, 85 (1997).
28. M.A. Nicholls, P.R. Norton, G.M. Bancroft, M. Kasrai, T. Do, G. DeStasio, and B. Fraser. Tribol. Lett. Accepted for publication.
29. I. Koprinarov, A.P. Hitchcock, W.H. Li, Y.M. Heng, and H.D.H. Stover. Macromolecules, **34**, 4424 (2001).
30. A.P. Hitchcock, C. Morin, Y.M. Heng, R.M. Cornelius, and J.L. Brash. J. Biomater. Sci. Polymer Ed. **13**, 919 (2002).
31. M. Wang, A. Mar, and E.J. MacLean. J. Solid State Chem. **172**, 232 (2003).
32. J.N. Cutler, N. Chen, D.T. Jiang, G.P. Demopoulos, Y. Jia, and J.W Rowson. J. Phys. IV, **107**, 337 (2003).
33. B.T. Moldovan, D.T. Jiang, and M.J. Hendry. Environ. Sci. Technol. **37**, 873 (2003), and to be published.

© 2004 NRC Canada

Intrachannel vibronic coupling in molecular photoionization[1]

G.J. Rathbone, E.D. Poliakoff, John D. Bozek, and R.R. Lucchese

Abstract: We discuss the excitation of forbidden vibrational transitions accompanying photoionization of linear triatomic molecules. Excitation of a single quantum of the antisymmetric stretching vibration is observed for molecules with inversion symmetry, as is the bending mode. Photoelectron spectra of the $N_2O^+(A^2\Pi)$, $CO_2^+(C^2\Sigma_g^+)$, and $CS_2^+(B^2\Sigma_u^+)$ states obtained over a range of ionization energies exhibit contrasting behavior for the relative intensities of the forbidden vibrations. These energy-dependent vibrational branching ratios are shown to result from an intrachannel vibronic coupling mechanism. Moreover, this intrachannel coupling can be further divided into two cases, one in which the photoionization cross section is sensitive to geometry changes, and a second case in which it is not. These different cases can be distinguished by comparing the experimental and theoretical results for all three molecules.

Key words: photoelectron spectroscopy, vibronic coupling, photoionization.

PACS Nos.: 33.60.Cv, 33.20.Ni, 33.20.Wr, 33.80.Eh

Résumé : On discute de l'excitation des transitions vibrationnelles défendues qui accompagnent la photoionisation de molécules triatomiques linéaires. Pour les molécules avec inversion de symétrie, on observe l'excitation d'un seul quantum de vibration d'élongation antisymétrique, tel qu'observé dans le mode de déformation angulaire. Les spectres photoélectroniques des états indiqués du $N_2O^+(A^2\Pi)$, du CO_2^+ $(C^2\Sigma_g^+)$ et du $CS_2^+(B^2\Sigma_u^+)$, obtenus sur une large plage d'énergies d'ionisation, présentent des comportements différents pour les intensités relatives des vibrations défendues. On montre que ces rapports de branchements vibrationnels qui dépendent de l'énergie résultent d'un mécanisme de couplage vibronique entre canaux. De plus, ce couplage entre canaux peut se diviser dans deux cas, dont l'un dans lequel la section droite de photoionisation est sensible aux changements de géométrie alors que dans l'autre il ne l'est pas. On peut faire la distinction entre ces différents cas en comparant les résultats expérimentaux et théoriques pour les trois molécules.

Mots clés : spectroscopie photoélectronique, couplage vibronique, photoionisation.

[Traduit par la Rédaction]

Introduction

Among Herzberg's many accomplishments are his explanations of forbidden transitions, and a prominent example is the phenomenon of Herzberg–Teller coupling, which bears his name. In this paper, we discuss recent results that focus on a closely related topic — the excitation of forbidden vibrations in molecular photoionization. A photoionization process is an electronic transition where the final state electronic wave function includes a continuum photoelectron. As for all electronic transitions, the excitation of a single quantum in a non-totally symmetric vibrational mode is forbidden within the Franck–Condon approximation. While they are forbidden, such vibrations have been observed frequently in photoelectron spectra (1–5), where their occurrence has traditionally been attributed to interchannel vibronic coupling (6–8), and are examples of one type of Herzberg–Teller coupling (7, 9–11). To interpret photoelectron spectra that exhibit such features correctly, it is necessary to understand the mechanism by which such transitions occur. For selected linear triatomic targets, we have performed high-resolution photoelectron spectroscopy and Schwinger variational calculations (12–14) to elucidate the underlying physics of these forbidden transitions. In previous studies, the explanation for these transitions had not been well-established because the photoelectron spectra were limited to fixed photoionization energies. By studying the relative intensities of these transitions as a function of incident photon energy — and combining such experimental data with physically realistic theoretical treatments of the continuum

Received 7 November 2003. Published on the NRC Research Press Web site at http://canjchem.nrc.ca on 3 September 2004.

G.J. Rathbone and E.D. Poliakoff.[2] Department of Chemistry, Louisiana State University, Baton Rouge, LA 70803, USA.
J.D. Bozek. Advanced Light Source, Lawrence Berkeley National Laboratory, University of California, Berkeley, CA 94720, USA.
R.R. Lucchese. Department of Chemistry, Texas A&M University, College Station, TX 77843, USA.

[1]This article is part of a Special Issue dedicated to the memory of Professor Gerhard Herzberg.
[2]Corresponding author (e-mail: epoliak@lsu.edu).

 doi: 10.1139/V04-079 © 2004 NRC Canada

photoelectron — it is possible to discern new and unanticipated phenomena for polyatomic photoionization. In particular, we will demonstrate the importance of *intrachannel* vibronic coupling, or photoelectron-mediated coupling, in polyatomic photoionization processes. For our purposes, we define a channel to be the ion–electron complex at a fixed molecular geometry. Thus, interchannel coupling involves more than a single ion core electronic state, while intrachannel coupling necessarily does not.

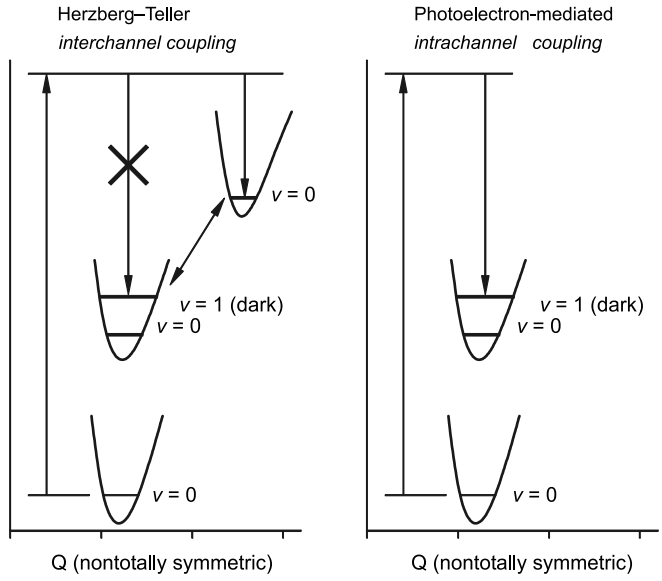
We present photoelectron spectra of the $CO_2^+(C^2\Sigma_g^+)$, $CS_2^+(B^2\Sigma_u^+)$, and $N_2O^+(A^2\Sigma^+)$ states. In all cases, the spectra are vibrationally resolved and are acquired as a function of photon energy, which is equivalent to tuning the photoelectron energy. By examining the results for these three similar systems, it is possible to categorize the mechanisms responsible for the forbidden transitions; moreover, these results give us additional insights into non-Franck–Condon effects, which arise for polyatomic systems generally (15–17), and the mode-specificity that is frequently characteristic of such data (16–19).

The strategy of the current study is straightforward. Studies that tune the photoelectron energy can clarify the mechanism of forbidden vibrational transitions because they assess whether the continuum electron has a role in such phenomena. To demonstrate this, it is instructive to consider the normal description of why such forbidden photoelectron features are observed — namely, interchannel coupling, which is represented schematically in the left frame of Fig. 1. Assume that the initial state is a Σ electronic state of the neutral molecule (e.g., $CO_2(X^1\Sigma_g^+)$) and that an ionic state is created with Σ electronic symmetry and a single quantum of bending excitation (e.g., $CO_2^+(C^2\Sigma_g^+)$, $v^+ = (010)$). Traditionally, such observations have been rationalized by assuming that there is a violation of the Born–Oppenheimer approximation and that there is mixing between electronic channels. In other words, the transition is occurring because the Born–Oppenheimer breakdown leads to intensity borrowing between electronic channels, i.e., *interchannel* coupling. Note that the argument listed above does not involve the photoelectron, only the residual ion core.

We have tested this argument that the excitation of the forbidden vibronic level occurs via intensity borrowing because there is a simple experiment one can perform (7). Namely, the ionization properties of the forbidden transition (cross section, asymmetry parameter) should mimic the results for the electronic channel that is donating the oscillator strength. For the CO_2 example, the $CO_2^+(C^2\Sigma_g^+, v^+ = (010))$ level has a total vibronic symmetry of Π_u, i.e., the direct product of Σ_g (electronic) $\otimes$ Π_u (vibrational). So, the only state of the same total symmetry that might donate oscillator strength in this CO_2 example is the $CO_2^+(A^2\Pi_u)$ state. In fact, our previous work has demonstrated that the oscillator strength for the forbidden transition does not have the same energy dependence as the allowed level from which it is borrowing its oscillator strength. In two previous investigations (20, 21), we have shown that this prediction is not followed even qualitatively in the case of some forbidden photoelectron features.

There is an alternative explanation for the existence of these forbidden vibrations involving intrachannel coupling,

Fig. 1. Cartoon comparison of interchannel coupling, as compared with the intrachannel mechanism described in the text.



and it appears that it might be common for the observation of these forbidden transitions in molecular photoelectron spectra. In a previous communication (22), we showed that an intrachannel mechanism — resonantly amplified vibronic symmetry breaking — was responsible for excitation of the symmetry-forbidden bending vibration, $v^+ = (010)$, in $4\sigma_g^{-1}$ photoionization of CO_2. In this intrachannel formulation, it is the photoelectron that is responsible for the symmetry breaking, not the ionic core, as sketched schematically in Fig. 1. In this paper, we describe how the continuum electron induces the symmetry breaking alluded to in the right frame in Fig. 1. Most importantly, we show that these intrachannel phenomena can exhibit two qualitatively distinct phenomena and that these differing mechanisms have significant implications for vacuum UV (VUV) spectroscopy, in general.

Experimental

The experiments were carried out at beam line 10.0.1 at the Advanced Light Source (ALS), and details of the beam line and the high-resolution photoelectron spectrometer are described elsewhere (23). The VUV radiation was generated by an undulator insertion device, and the beam line was equipped with a spherical grating monochromator. The measurements reported here used the 380 line/mm grating for $20 \leq h\nu \leq 50$ eV and 925 line/mm grating for $50 \leq h\nu \leq 110$ eV. The excitation bandwidth in these studies was maintained at 10 meV, which was essential for obtaining vibrationally resolved electron spectra over a wide range of photon energies. The sample pressure in the interaction region (gas cell) was $\sim 5 \times 10^{-3}$ torr, dropping rapidly to 5×10^{-6} torr (1 torr = 133.322 Pa) in the bulk of the spectrometer. Spectra were acquired at several different pressures to ensure that data were not influenced by secondary scattering processes (3). The photoelectron spectrometer was a hemispherical electron energy analyzer (Scienta model SES-200), and the pass energy for these measurements was 2 eV. Slit widths between 0.4 and 0.6 mm were used and were selected

© 2004 NRC Canada

to achieve both good electron energy resolution and adequate counting rates. At 25 eV, for example, the electron analyzer resolution was adjusted to be 7 meV and the overall photoelectron energy resolution was ~12 meV, which was consistent with the values for the photon and photoelectron energy bandwidths. All data were obtained at the magic angle of 54.7°, so the observed intensities are proportional to partial cross sections.

Background: photoelectron-mediated vibronic symmetry breaking

The calculations for all of the systems studied use methods that have been reported previously (22, 24). Before discussing the details of the procedure, this section provides a qualitative overview of the approach to delineate the differences between the photoelectron-mediated intrachannel mechanisms that are relevant in the current study and the interchannel picture, which has been invoked in the past.

The partial cross section for creation of the final vibrational level (f) of the ionic state depends on the magnitudes of the dipole amplitudes $f^{(f\leftarrow i)}(\hat{k},\hat{n})$, where $\hat{k}$ is the direction of emission of the photoelectron and $\hat{n}$ is the polarization vector of the incident radiation. For simplicity, consider the case of a nondegenerate vibrational mode, although a degenerate degree of freedom (such as triatomic bending) can be shown to be equivalent to the description given here. In general, the dipole amplitude can be expressed in the following form, assuming that the wave function is separable into electronic and vibrational components.

$$[1]\qquad f^{(f\leftarrow i)}(\hat{k},\hat{n}) = \left\langle \chi^{(i)}_{v_i}(q)\middle| f(\hat{k},\hat{n},q)\middle|\chi^{(f)}_{v_f}(q)\right\rangle_q$$

Here, $f(\hat{k},\hat{n},q)$ is an electronic dipole amplitude, which depends parametrically on q (the normal coordinate of interest), and no restriction is placed on its symmetry classification. If one does *not* invoke the Franck–Condon approximation, then there is a possibility of single quantum excitations of nonsymmetric modes. This can be seen by expanding the electronic dipole amplitude $f(\hat{k},\hat{n},q)$, as a Taylor series about the vibrational coordinate q to first order, and the result is

$$[2]\qquad f(\hat{k},\hat{n},q) = F_0(\hat{k},\hat{n}) + F_1(\hat{k},\hat{n})q + \ldots$$

where

$$F_0(\hat{k},\hat{n}) = f(\hat{k},\hat{n})_{q=0}$$

$$F_1(\hat{k},\hat{n}) = \left[\frac{\partial f(\hat{k},\hat{n},q)}{\partial q}\right]_{q=0}$$

Substituting eq. [2] into eq. [1] leads to

$$[3]\qquad f^{(f\leftarrow i)}(\hat{k},\hat{n}) = F_0(\hat{k},\hat{n})\left\langle \chi^{(i)}_{v_i}(q)\middle|\chi^{(f)}_{v_f}(q)\right\rangle_q + F_1(\hat{k},\hat{n})\left\langle \chi^{(i)}_{v_i}(q)\middle|q\middle|\chi^{(f)}_{v_f}(q)\right\rangle_q + \ldots$$

The first term leads to the usual Franck–Condon selection rules: allowed transitions have $v_i + v_f = 2n$ (assuming no change in equilibrium structure upon ionization). The second term will lead to transitions where $v_i + v_f = 2n + 1$. However, it contributes to the dipole amplitude only if $F_1(\hat{k},\hat{n})$ is nonzero — in other words, single-quantum excitation occurs in a non-totally symmetric normal mode only if the electronic dipole amplitudes vary with changes in that normal coordinate.

We now apply the above discussion to the specific example of the CS_2 case studied here. Consider a system which has g–u symmetry at the equilibrium geometry and where the vibrational coordinate under consideration (q) is an antisymmetric stretching mode that breaks the g–u symmetry. Then assume that the initial electronic state $\Phi^{(i)}_g(q)$ has g symmetry at the equilibrium, $q = 0$, as indicated by the subscript, and that the final ion state $\Phi^{(f)}_u(q)$ has u symmetry. Now consider the photoionization amplitude for ionization to a continuum of u symmetry $\psi_u(\hat{k},q)$.

$$[4]\qquad f(\hat{k},\hat{n},q) = \left\langle \Phi^{(i)}_g(q)\middle|\hat{n}\cdot\vec{\mu}\middle|\Phi^{(f)}_u(q)\,\psi_u(\hat{k},q)\right\rangle$$

Note that the final electronic state has an overall symmetry of g, i.e., u(ion) ⊗ u(photoelectron) = g(total electronic), so that in this case the photoelectron channel under consideration is forbidden in a symmetric geometry ($q = 0$), i.e.,

$$[5]\qquad \begin{aligned} f(\hat{k},\hat{n},q=0) &= F_0(\hat{k},\hat{n}) \\ &= \left\langle \Phi^{(i)}_g(q=0)\middle|\hat{n}\cdot\vec{\mu}\middle|\Phi^{(f)}_u(q=0)\,\psi_u(\hat{k},q=0)\right\rangle \\ &= 0 \end{aligned}$$

where $\vec{\mu}$ is the dipole operator that has u symmetry. Now all three electronic wave functions will acquire components of the opposite symmetry as the molecule stretches. These changes in the wave functions can be expanded to first order in q to give

$$[6]\qquad \Phi^{(i)}_g(q) = \Phi^{(i)}_g(q=0) + q\bar{\Phi}^{(i)}_u \qquad \text{(initial electronic state)}$$

$$[7]\qquad \Phi^{(f)}_u(q) = \Phi^{(f)}_u(q=0) + q\bar{\Phi}^{(f)}_g \qquad \text{(final ion state)}$$

$$[8]\qquad \psi_u(\hat{k},q) = \psi_u(\hat{k},q=0) + q\bar{\psi}_g(\hat{k}) \qquad \text{(photoelectron)}$$

The first derivative of f is then given by

$$[9]\qquad \begin{aligned} F_1(\hat{k},\hat{n}) = &\left\langle \Phi^{(i)}_g(q=0)\middle|\hat{n}\cdot\vec{\mu}\middle|\Phi^{(f)}_u(q=0)\bar{\psi}_g(\hat{k})\right\rangle \\ &+ \left\langle \Phi^{(i)}_g(q=0)\middle|\hat{n}\cdot\vec{\mu}\middle|\Phi^{(f)}_g\psi_u(\hat{k},q=0)\right\rangle \\ &+ \left\langle \bar{\Phi}^{(i)}_u\middle|\hat{n}\cdot\vec{\mu}\middle|\Phi^{(f)}_u(q=0)\psi_u(\hat{k},q=0)\right\rangle \end{aligned}$$

Thus, the symmetry-breaking coordinate q can induce transitions to a continuum symmetry, which is not allowed at the equilibrium. Also, we see that the symmetry breaking of all three wave functions involved in the transition matrix element can contribute to the value of F_1. If the initial state has vibrational quantum number $v = 0$, then these first-order terms will allow excitation of the $v = 1$ level of the antisymmetric stretching mode of the ion state. Note that if there are resonance features in the "forbidden" continuum,

© 2004 NRC Canada

then the final state vibrational populations that depend on coupling to that continuum will also exhibit resonance features.

To put this result into context, we note that Franck–Condon breakdown in diatomics will occur as a result of the sensitivity of the trapping of the continuum electron to changes in bond length (25, 26). It is well known that this sensitivity results in a relative enhancement of the cross section for weaker vibrational levels in diatomics (25). This leads to an extension for polyatomic systems based on the above discussion, which is general and potentially useful. Specifically, the same effect that amplifies weak transitions in diatomics can be responsible for nonvanishing cross sections in forbidden vibrational transitions for polyatomics.

It is useful to consider the implications of this mechanism of symmetry breaking with the more traditional explanation used in photoionization studies, namely, the interchannel type of Herzberg–Teller coupling. First, this formulation described above does not assume any violation of the Born–Oppenheimer approximation, with a concomitant mixing of different electronic channels. In fact, the treatment described above — as described in detail in the following section — is explicitly adiabatic, and therefore *not* an interchannel coupling phenomenon. It is inherently intrachannel in nature, and this actually can serve as a powerful tool, as discussed in the following sections. Moreover, it is a qualitatively distinct effect, in that the interchannel explanation typically applied to photoionization transitions involves only the vibronic mixing in the ion core (10) and does not consider any influence of the continuum electron, while the intrachannel mechanism described above (22, 24) arises solely because of the behavior of the photoelectron. If both interchannel and intrachannel mechanisms are active, a vibrational close-coupling treatment would be needed. In such a treatment, the interchannel coupling would modify the vibronic states and thus would also influence the intrachannel mechanism. Thus, the schematic representation of the competing explanations introduced in Fig. 1 takes on a more explicit meaning. In the case of interchannel coupling, effects involving the ion core induce the forbidden transition. By way of contrast, the intrachannel mechanism has the photoelectron mediating the vibrational coupling; that is why the second frame in Fig. 1 does *not* include any additional potential surfaces. It is the photoelectron that is responsible for the effect. There is an important corollary to this distinction, namely, one can uncover new aspects of continuum electron dynamics as well as VUV molecular spectroscopy by studying such effects.

Theory and computational methods

For vibrationally specific photoionization transitions, we used the adiabatic approximation so that the cross section leading to a specific vibrational state was obtained as an integral over the coordinates of the nuclear motion of the product of the initial and ion-state vibrational wave functions and the dipole matrix element for photoionization obtained within the fixed-nuclei approximation over the range of geometries need to converge the vibrational integral. In calculations on the triatomic systems considered here, we have approximated the vibrational wave functions by harmonic oscillator wave functions.

The fixed nuclei photoionization matrix elements were obtained using the single-channel Schwinger method. For linear geometries, we used either Hartree–Fock wave functions for the initial and ion-target states or configuration interaction wave functions. The scattering equations were then solved using numerical techniques based on single-center expansions of the electronic wave function (12–14). For nonlinear geometries, the bound states were represented by Hartree–Fock wave functions, and the resulting scattering equations were solved using methods we developed for studying electron scattering from nonlinear molecules (27–29).

In addition to the Schwinger variational calculations, we also analyzed the various shape resonances using the adiabatic static model-exchange (ASME) potential, which is a simple local model potential for the electron–molecule interaction. This approach has been previously used to visualize resonant states in electron–molecule scattering (30) and molecular photoionization (27) and has been discussed in detail previously (30, 31).With the ASME potential, the scattering calculations are performed at complex energy allowing for the resonances in the scattering system to be directly determined by locating the poles of the *S* matrix at complex energy. The wave functions at resonance energies can then be analyzed. The position and width of the resonances in the ASME model are usually within a few eV of those found in the Schwinger variational calculation, and thus we can use the resonance wave functions found with the model potential to interpret the resonances found in the full calculation.

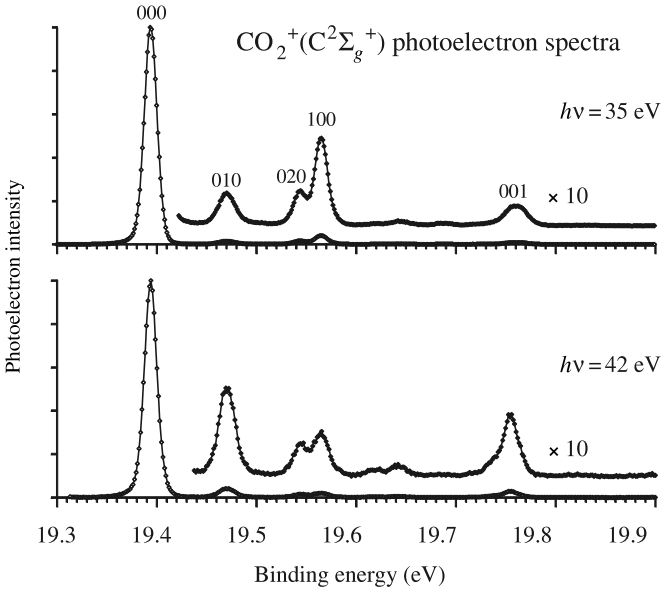
Results

The photoelectron spectra for all three molecules studied have been reported previously (1–5, 8,11, 18, 32–36), and the current results agree well with previous investigations. Representative results are shown for the $CO_2^+(C^2\Sigma_g^+)$ state in Fig. 2, and the vibrational structure is very clear. In particular, the v^+ = (010) and (001) levels (i.e., the symmetry forbidden vibrational excitations) are clearly evident. As mentioned earlier, such transitions were observed previously (2–4, 6–8), although the energy dependence for their relative partial cross sections has not been investigated until the work reported here and a few other studies (7, 21, 22, 24, 37). In Fig. 2, data are shown for two different photon energies, and it is apparent that the relative intensities are varying substantially between these two spectra. This is true for both the allowed vibrational transitions as well as for the forbidden ones.

The ratios of intensities for alternative vibrational levels provide branching ratios, and we acquire such data over a dense energy mesh, as shown in Figs. 3–5. Figure 3 shows results for N_2O, and data are presented for the two stretching motions. In N_2O, both stretching vibrations are allowed because there is no inversion symmetry. Note that the branching ratio for the antisymmetric stretch is relatively constant with photon energy, while the branching ratio curve for the symmetric stretch is varying significantly as a function of photon energy for approximately 6 to 7 eV above threshold.

© 2004 NRC Canada

Fig. 2. Photoelectron spectra of the $CO_2^+(C^2\Sigma_g^+)$ state at two selected photon energies. Note the forbidden vibrational excitations (v^+ = (010) and (001)) and the changes in relative intensities for all of the vibrational levels.



Data from two previous investigations are also shown, and the agreement between these data sets is good.

Figure 4 shows theoretical and experimental branching ratio curves for the $CO_2^+(C^2\Sigma_g^+)$ state (21). These data are only for the single quantum excitations; the results for all the other observed vibrational transitions are reported elsewhere (21). Both the antisymmetric stretch and the bending vibration exhibit significant maxima in the region of the $4\sigma_g \rightarrow k\sigma_u$ shape resonance (21, 22, 38–45) at $h\nu \approx 45$ eV. In contrast, the symmetric stretch branching ratio exhibits a pronounced minimum in the same energy range. Comparing the various branching ratio curves, we see that the branching ratios for the forbidden vibrations actually exceed the value for the allowed symmetric stretch vibration at selected energies. This underscores the point that the partial cross section for these forbidden transitions can become significant under certain conditions.

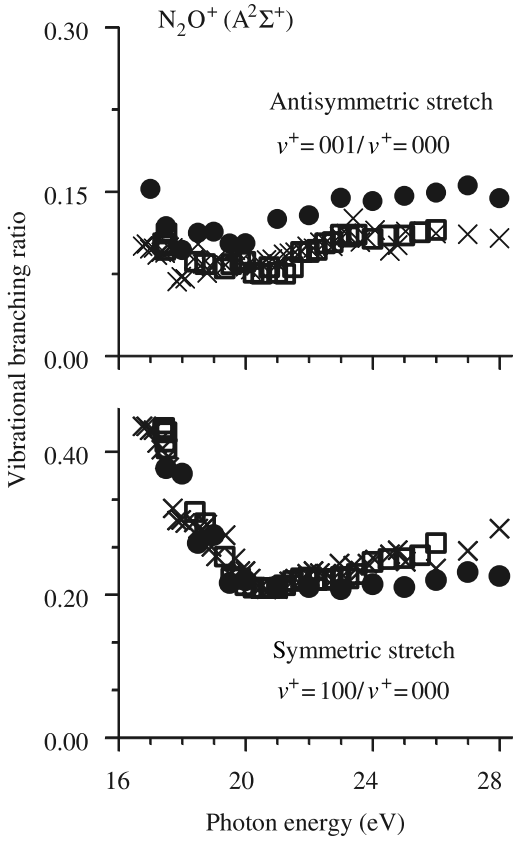
The vibrational branching ratio curves for the $CS_2^+(B^2\Sigma_u^+)$ stretching vibrations are shown in Fig. 5. The data are very striking in their mode-specificity, although the trends are the opposite of what was observed for N_2O. For $CS_2^+(B^2\Sigma_u^+)$, the antisymmetric stretch branching ratio curve exhibits a pronounced maximum, while the symmetric stretch is comparatively constant.

Discussion

Non-Franck–Condon mode-specificity for allowed transitions ($N_2O^+(A_2\Sigma^+)$)

In the following sections, we will show that both the occurrence and the energy dependence of the forbidden vibrational transitions in CO_2 and CS_2 are due to effects of shape resonances. Thus, it is useful to consider more generally how shape resonances induce deviations from Franck–Condon behavior in polyatomic systems. We present results

Fig. 3. Vibrational branching ratios obtained as a function of energy for the stretching modes of N_2O from this study compared with earlier data. Current study (solid circles), ref. 18 (hollow squares), ref. 16 (×).



on non-Franck–Condon effects for N_2O to illustrate the main effects, as they are common to both the molecules with and without inversion symmetry. The basic picture describes the photoionization shape resonance as an above-threshold quasibound state, which results from angular momentum barriers that trap the continuum photoelectron at specific energies. The energy at which trapping occurs is strongly dependent on the shape of the potential experienced by the photoelectron, which in turn depends strongly on the molecular geometry. As a result of the sensitivity of the resonance excitation to changes in geometry, the energy-dependence of the dipole transition amplitudes depends strongly on molecular geometry, implying that deviations from Franck–Condon behavior will occur. While this picture is clearly established for diatomic molecules with a well-characterized connection between bond length and resonance changes (25, 46), polyatomic systems present nuances that have no analog in diatomic systems. In particular, the details of the photoelectron localization for polyatomic systems — as well as the effects it has on alternative molecular motions — are not well understood.

Figure 3 shows the vibrational branching ratios for the $N_2O^+(A^2\Sigma^+)$ state. It is striking that the symmetric stretch ratio is varying significantly near threshold, while the antisymmetric stretch is rather constant. There is a well-characterized shape resonance near threshold (16, 18, 19), and it is responsible for the observed behavior. It is interest-

© 2004 NRC Canada

Fig. 4. Vibrational branching ratios obtained as a function of energy for the three vibrational modes of CO_2. The symbols are experimental data, and they correspond to the left-hand y axes. The solid lines are theoretical predictions and correspond to the right-hand y axes.

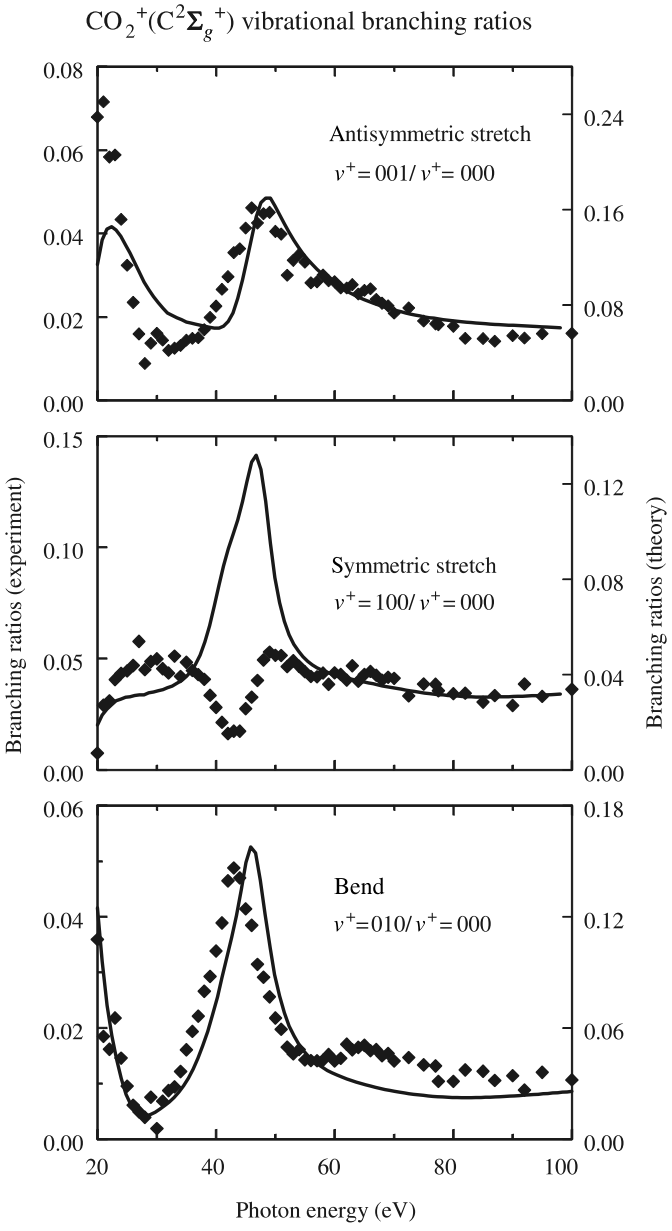
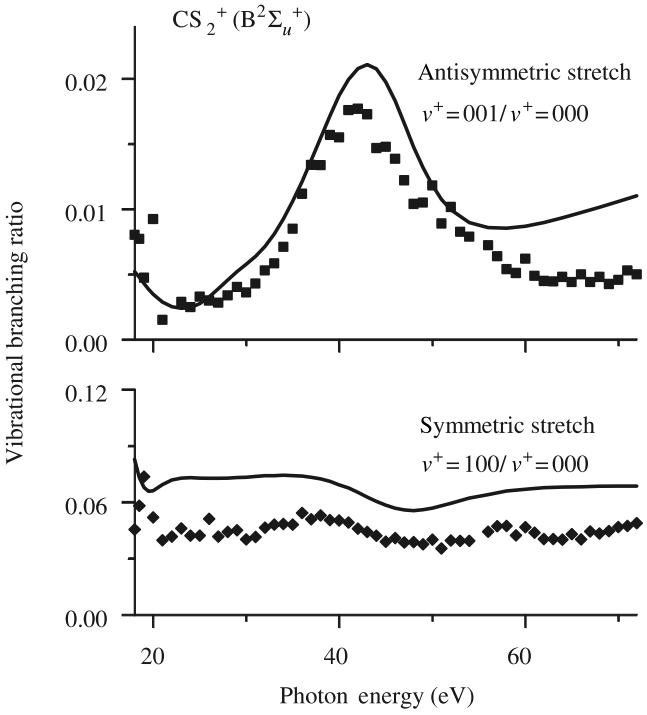


Fig. 5. Vibrational branching ratios obtained as a function of energy for the stretching modes of CS_2. The symbols are experimental data and the solid lines are theoretical predictions.



ing to note that the shape resonance is very sensitive to changes in the breathing mode of the ion, but rather insensitive to the antisymmetric stretching vibration. In previous theoretical studies (19), it was suggested that this mode specificity could be rationalized by noting that the shape resonant dynamics were sensitive to the overall size of the molecule, as the end-to-end length of the molecule does not change much for the antisymmetric stretching motion. The contour map for this shape resonant wave function has been calculated for the first time using methods mentioned above (27, 30, 31), and the result is shown in the top panel of Fig. 6. The resonant state clearly has the nature of an antibonding σ orbital constructed from *sp* hybrid orbitals on the outer N and O atoms and an *s* orbital on the central N atom. The nodal structure is characteristic of an $l = 4$ angular momentum shape resonance when analyzed in terms of confocal elliptic coordinates (47). It is clear that the electron is not associated with a specific bond of the molecule, but it is not straightforward to correlate the earlier arguments regarding mode specificity with the picture of the resonant wave function shown in Fig. 6. This remains a topic of continuing investigation.

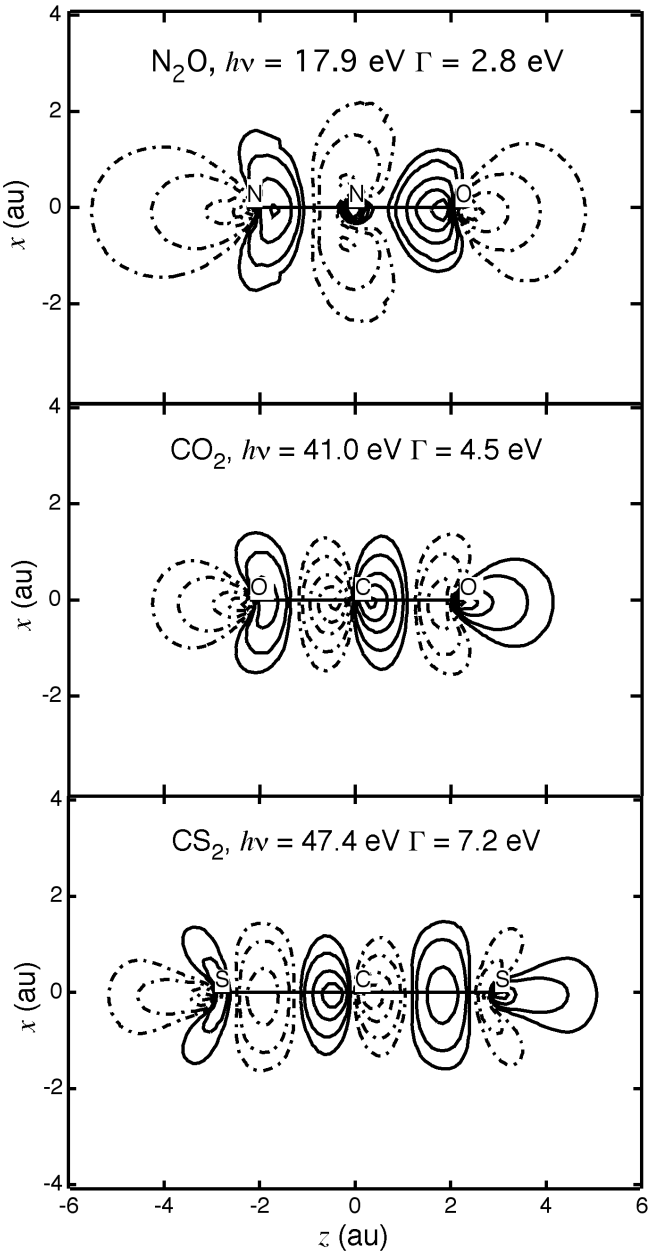
These N_2O results have bearing on the observation of forbidden transitions, because they show that it is possible, and even likely, that shape resonance behavior might change as the geometry is altered along a normal coordinate, a prerequisite for the photoelectron-mediated vibronic symmetry breaking mechanism described in the earlier discussion on photoelectron-mediated vibronic symmetry breaking. While the N_2O results do not show much sensitivity to the antisymmetric stretch, it is certainly possible that other cases might exhibit sensitivity to non-totally symmetric vibrations. The results shown for CO_2 and CS_2 reinforce this point, and they also demonstrate that there can be considerable diversity in terms of how mode-specific behavior is manifested.

Photoelectron-mediated intrachannel vibronic coupling ($CO_2^+(C^2\Sigma_g^+)$)

The CO_2 results are shown in Fig. 4, and they are strikingly different from those for N_2O. There is an intensively studied shape resonance at ca. 40 eV (21, 22, 38–45), and we have shown previously (22) that this resonance is responsible for the amplification of the bending branching ratio also shown in Fig. 4. Note that the profiles for the experi-

© 2004 NRC Canada

Fig. 6. The real part of the resonant wave function in the $k\sigma$ continua of N_2O, CO_2, and CS_2 computed using the ASME model potential. The solid contours are for positive values of the wave function and the dashed contours are for negative values of the wave function.



mental and theoretical curves match closely for the (010) and (001) levels; the theoretical treatment uses the Chase adiabatic approximation (48) that does *not* include effects of interchannel Herzberg–Teller coupling or the intensity borrowing mechanism alluded to in Fig. 1. This is additional evidence that the sensitivity of the shape resonance to selective changes in molecular geometry is the mechanism by which these forbidden vibrational levels are being excited. Because the electron trapping is sensitive to the geometry changes, it is the electron scattering dynamics that result in the forbidden excitation. This is why we refer to this mechanism as a *photoelectron-mediated vibronic coupling*.

To clarify the details of the transitions — and to lay the groundwork for a comparison with CS_2 — it is useful to consider the electronic and vibrational symmetry considerations. The target state is Σ_g (both electronic and vibrational). The electronic symmetry of the ion state is Σ_g, while the electronic symmetry of the continuum shape resonance is $k\sigma_u$. Thus, the electronic symmetry of the final electronic state (ion plus electron) is also Σ_u. The implication is that the electronic transition is allowed, even for the symmetric equilibrium geometry. We will show how this contrasts with the CS_2 case in the following section. Of course, the vibrational symmetry for the antisymmetric stretch is Σ_u, so the overall vibronic symmetry of the final state is Σ_g. Note that this resonant channel in CO_2 is allowed even in the absence of symmetry-breaking vibrations.

A comparison between the CO_2 and N_2O results is revealing. The main difference is that all three single quantum excitations are clearly sensitive to the shape resonance for CO_2, while the antisymmetric stretch was relatively insensitive to the shape resonance occurring in N_2O. The dip in the branching ratio curve for the symmetric stretch is not well-reproduced by theory. In fact, it is likely that this discrepancy results from a Fermi resonance between the $v^+ = (020)$ and (100) vibrational levels that is not accounted for by the theoretical formulation. The evidence for the influence of a Fermi resonance is described in detail elsewhere (21). The key point for the CO_2 results is that all vibrational levels are affected by the resonance. The fact that the CO_2 and N_2O branching ratio data are qualitatively different drives home the point that the photoelectron scattering dynamics can vary considerably from molecule to molecule; moreover, the comparison also shows that experiments that interrogate the vibrational motion provide a useful means of investigating the photoelectron escape in the anisotropic molecular field. While the results for CO_2 are different from those of N_2O, they are analogous in one important respect. Namely — for both molecules — the variation of the branching ratio with energy is a direct result of the resonance profile with changes in geometry. This is an extension of the effect observed for diatomics (26) described earlier, and we will see that this behavior is qualitatively distinct from what is observed for CS_2.

The contour map for the CO_2^+ $k\sigma_u$ shape resonant photoelectron is shown in the middle panel of Fig. 6. This resonance is also a typical σ^* type resonance composed of *sp* hybrid orbitals on the terminal O atoms and a *p* orbital on the central C atom. The characteristic angular momentum of this state is $l = 5$, which leads to the fairly narrow resonance found in the full calculations. While clearly different from the one shown for N_2O in the top panel, it is not obvious why the response of the resonance to the antisymmetric stretch is qualitatively different from that of N_2O.

A photoelectron-mediated, vibrationally driven resonance ($CS_2^+(B^2\Sigma_u^+)$)

The $CS_2^+(B^2\Sigma_u^+)$ stretching vibration branching ratio curves are shown in Fig. 5. These data appear similar to both the N_2O and the CO_2 results in some respects, i.e., there is an excursion in a branching ratio curve driven by a reso-

© 2004 NRC Canada

nance, and the results are strongly mode-specific. While these characteristics of the CS_2 data are similar to those of the N_2O and CO_2 data, there are fundamental differences, as we will show. In Fig. 6, we also show the resonant state that is responsible for non-Franck–Condon effects seen in the vibrational branching ratios. This state can be described as a linear combination of $d\sigma$ orbitals on the S atoms and a *p* orbital on the central C atom. An analysis of the nodal surfaces of this state suggests that it is trapped behind an $l = 7$ angular momentum barrier, leading to its relatively high energy of $h\nu = 47.4$ eV, which corresponds to a photoelectron energy of 32.8 eV.

The first empirical difference between the CS_2 and N_2O data is that the mode-sensitivity is the opposite in these two cases. For N_2O, the antisymmetric stretch did not influence the shape resonance and the symmetric stretch did; the situation is reversed for CS_2. This result is of central importance, and the explanation for this difference is particularly revealing because it illustrates how the CS_2 results arise from an alternative type of resonant behavior. The peak in the CS_2 results is due to a resonance in the $k\sigma_u$ continuum channel (37), and it appears that this assignment is correct, given the agreement between theory and experiment (cf. Fig. 5). It is significant that the resonant electronic channel responsible for the observed results has σ_u symmetry. To see why, consider the symmetries for the electronic wave functions. The lower state is Σ_g, and the upper electronic state (ion plus electron) is also Σ_g; the ion has Σ_u symmetry, as does the resonant photoelectron, so $\Sigma_u \otimes \Sigma_u = \Sigma_g$. At the equilibrium geometry, this *gerade–gerade* transition is rigorously forbidden. However, the resonance is "activated" when the molecule undergoes the zero-point antisymmetric stretching motion; i.e., the instantaneously broken symmetry allows the molecule to be excited to this resonance, *provided that the overall vibronic symmetry selection rules are obeyed*. In this instance, the implication is that the total vibronic symmetry must be *ungerade*, which can be accomplished by exciting an odd number of quanta in the antisymmetric stretching vibration (or alternatively the bending mode, as well).

There is an important facet that is not apparent from the figures. For N_2O and CO_2, the non-Franck–Condon effects occur because the resonant trapping of the electron depends strongly on the molecular geometry; i.e., the profile for the cross section calculated as a function of energy depends on the molecular geometry. In fact, for the calculations used to generate the theoretical N_2O (49) and CO_2 (21) branching ratio curves, the resonance shifted and broadened as the geometry was altered, as was originally described for diatomics by Wallace and co-workers (25). However, the calculations show that the resonance profile does *not* change for CS_2; i.e., the profile of the resonance is insensitive to changes in the geometry. The resonant contribution to the cross-section curve is turning on and off as the distortion from equilibrium geometry occurs during a non-totally symmetric vibrational motion. The magnitude of the $k\sigma_u$ resonant cross section (at all energies) is zero at the equilibrium geometry and increases in the region of the symmetry-forbidden resonance as the molecule is distorted from its equilibrium geometry.

There is a very close connection between this CS_2 result and the traditional Herzberg–Teller effect in bound–bound electronic transitions. To illustrate the similarities and highlight the differences, consider the famous case of the $\tilde{A}^1B_{2u} - \tilde{X}^1A_{1g}$ band system of benzene (50). Like the CS_2 case, this electronic transition is forbidden at the equilibrium geometry. This electronic transition only occurs when $\Delta\nu_6 = 1$; ν_6 has e_{2g} symmetry, and the direct product corresponding to the total vibronic symmetry of the excited state is $B_{2u} \otimes E_{2g} \supset E_{1u}$, which is connected to the A_{1g} ground state of benzene via dipole transitions. The similarities with the CS_2 case are clear. For CS_2, the shape resonant $k\sigma_u$ final state is inaccessible at the equilibrium geometry and is excited only when a non-totally symmetric vibration is also accessed. On the other hand, the explanation for the benzene example is that there is a breakdown of the Born–Oppenheimer approximation and that this induces mixing between the target vibrational state and other nearby vibronic levels of the same total symmetry. The CS_2 case is fundamentally different in that the effect occurs without any violation of the Born–Oppenheimer approximation. There is no intensity-borrowing that is invoked to explain the results. Indeed, the theoretical treatment that reproduces the experimental result faithfully is performed explicitly within an adiabatic framework.

Implications for other ionization processes

It is likely that these effects will be manifested in many ways, some of which are not immediately apparent. First, analogous effects can arise for linear systems that do not have Σ electronic symmetry. For linear molecules, this suggests that some observations of bending vibrational excitation attributed to Renner–Teller coupling might be due — wholly or in part — to intrachannel analogs of the effects described above for CO_2 and CS_2. It also implies that analogous effects might occur for nonlinear systems, where excited vibrations have been attributed to Jahn–Teller coupling (51, 52). Second, these effects can occur near threshold, not just at 20 eV above threshold. Third, the intrachannel effects described in these systems do not imply that the interchannel, Herzberg–Teller mechanism is not responsible for some of the previous observations of forbidden vibrational excitation in photoelectron spectroscopy. In this same vein, the two mechanisms are not mutually exclusive and can, in fact, be occurring simultaneously in a single vibronic channel; i.e., some enhancement of a forbidden vibration might be the result of intensity borrowing via interchannel coupling that involves only the ionic core, and additional enhancement results from effects of the continuum electron. Finally, it is clear that in cases where the intrachannel mechanism is operative, it is possible to learn how the photoelectron dynamics respond to changes in molecular geometry, even for those modes that are nominally forbidden. Thus, this effect opens up the possibility of studying even more complex molecular systems, which naturally have a larger number of vibrational degrees of freedom.

Acknowledgements

EDP acknowledges that this work was supported by the Chemical Sciences, Geosciences and Biosciences Division, Office of Basic Energy Sciences, Office of Science, US Department of Energy. This work was also supported in part by

© 2004 NRC Canada

the Robert A. Welch Foundation (Houston, Texas) under grant No. A-1020. We also acknowledge the support of the Texas A&M University Supercomputing Facility. Finally, we wish to thank the reviewers of this paper, who helped to clarify several important points.

References

1. A.W. Potts and G.H. Fattahallah. J. Phys. B, **13**, 2545 (1980).
2. I. Reineck, C. Nohre, R. Maripuu, P. Lodin, S.H. Al-Shamma, H. Veenhuizen, L. Karlsson, and K. Siegbahn. Chem. Phys. **78**, 311 (1983).
3. B. Wannberg, H. Veenhuizen, L. Mattsson, K.E. Norell, L. Karlsson, and K. Siegbahn. J. Phys. B: At. Mol. Opt. Phys. **17**, L259 (1984).
4. L.S. Wang, J.E. Reutt, Y.T. Lee, and D.A. Shirley. J. Electron Spectrosc. Relat. Phenom. **47**, 167 (1988).
5. J.B. Liu, W.W. Chen, M. Hochlaf, X.M. Qian, C. Chang, and C.Y. Ng. J. Chem. Phys. **118**, 149 (2003).
6. P. Roy, I. Nenner, M.Y. Adam, J. Delwiche, M.J.H. Franskin, P. Lablanquie, and D. Roy. Chem. Phys. Lett. **109**, 607 (1984).
7. P. Roy, R.J. Bartlett, W.J. Trela, T.A. Ferrett, A.C. Parr, S.H. Southworth, J.E. Hardis, V. Schmidt, and J.L. Dehmer. J. Chem. Phys. **94**, 949 (1991).
8. P. Baltzer, B. Wannberg, M. Lundqvist, L. Karlsson, D.M.P. Holland, M.A. MacDonald, M.A. Hayes, P. Tomasello, and W. von Niessen. Chem. Phys. **202**, 185 (1996).
9. W. Domcke and L.S. Cederbaum. Chem. Phys. **25**, 189 (1977).
10. W. Domcke. Phys. Scr. **19**, 11 (1979).
11. W. Domcke, L.S. Cederbaum, J. Schirmer, W. von Niessen, C.E. Brion, and K.H. Tan. Chem. Phys. **40**, 171 (1979).
12. R.R. Lucchese, K. Takatsuka, and V. McKoy. Phys. Rep. **131**, 147 (1986).
13. R.E. Stratmann and R.R. Lucchese. J. Chem. Phys. **102**, 8493 (1995).
14. R.E. Stratmann, R.W. Zurales, and R.R. Lucchese. J. Chem. Phys. **104**, 8989 (1996).
15. S. Kakar, E.D. Poliakoff, and R.A. Rosenberg. J. Chem. Phys. **96**, 23 (1992).
16. L.A. Kelly, L.M. Duffy, B. Space, E.D. Poliakoff, P. Roy, S.H. Southworth, and M.G. White. J. Chem. Phys. **90**, 1544 (1989).
17. S. Kakar, H.-C. Choi, and E.D. Poliakoff. J. Chem. Phys. **97**, 4690 (1992).
18. T.A. Ferrett, A.C. Parr, S.H. Southworth, J.E. Hardis, and J.L. Dehmer. J. Chem. Phys. **90**, 1551 (1989).
19. M. Braunstein and V. McKoy. J. Chem. Phys. **90**, 1535 (1989).
20. J.S. Miller and E.D. Poliakoff. J. Chem. Phys. **113**, 899 (2000).
21. G.J. Rathbone, E.D. Poliakoff, J.D. Bozek, R.R. Lucchese, and P. Lin. J. Chem. Phys. **120**, 612 (2004).
22. G.J. Rathbone, E.D. Poliakoff, J.D. Bozek, and R.R. Lucchese. J. Chem. Phys. **114**, 8240 (2001).
23. G. Ohrwall, J. Bozek, and P. Baltzer. J. Electron Spectrosc. Relat. Phenom. **104**, 209 (1999).
24. J.S. Miller, E.D. Poliakoff, T.F. Miller, A.P.P. Natalense, and R.R. Lucchese. J. Chem. Phys. **114**, 4496 (2001).
25. J.L. Dehmer, D. Dill, and S. Wallace. Phys. Rev. Lett. **43**, 1005 (1979).
26. J.B. West, A.C. Parr, B.E. Cole, D.L. Ederer, R. Stockbauer, and J.L. Dehmer. J. Phys. B, **13**, L105 (1980).
27. A.P.P. Natalense and R.R. Lucchese. J. Chem. Phys. **111**, 5344 (1999).
28. F.A. Gianturco, R.R. Lucchese, N. Sanna, and A. Talamo. *In* Electron collisions with molecules, clusters, and surfaces. *Edited by* H. Ehrhardt and L.A. Morgan. Plenum Press, New York. 1994. pp. 71–86.
29. F.A. Gianturco, R.R. Lucchese, and N. Sanna. J. Chem. Phys. **100**, 6464 (1994).
30. R.R. Lucchese and F.A. Gianturco. Int. Rev. Phys. Chem. **15**, 429 (1996).
31. F.A. Gianturco and R.R. Lucchese. J. Chem. Phys. **111**, 6769 (1999).
32. P. Baltzer, F.T. Chau, J.H.D. Eland, L. Karlsson, M. Lundqvist, J. Rostas, K.Y. Tam, H. Veenhuizen, and B. Wannberg. J. Chem. Phys. **104**, 8922 (1996).
33. D.M.P. Holland, J.B. West, and M.A. Hayes. Chem. Phys. **148**, 241 (1990).
34. L.S. Wang, C.F. Ding, X.B. Wang, J.B. Nicholas, and B. Nicholas. Phys. Rev. Lett. **81**, 2667 (1998).
35. A.W. Potts and T.A. Williams. J. Electron Spectrosc. Relat. Phenom. **3**, 3 (1974).
36. D.M.P. Holland, M.A. MacDonald, and M.A. Hayes. Chem. Phys. **142** (1990).
37. G.J. Rathbone, E.D. Poliakoff, J.D. Bozek, and R.R. Lucchese. Phys. Rev. Lett. **92**, 143002: 1–4 (2004).
38. T.A. Carlson, M.O. Krause, F.A. Grimm, J.D. Allen, Jr., D. Mehaffy, P.R. Keller, and J.W. Taylor. Phys. Rev. A, **23**, 3316 (1981).
39. M.R.F. Siggel, J.B. West, M.A. Hayes, A.C. Parr, J.L. Dehmer, and I. Iga. J. Chem. Phys. **99**, 1556 (1993).
40. J.R. Swanson, D. Dill, and J.L. Dehmer. J. Phys. B, **13**, L231 (1980).
41. P.M. Dittman, D. Dill, and J.L. Dehmer. Chem. Phys. **78**, 405 (1983).
42. R.R. Lucchese and V. McKoy. Phys. Rev. A, **26**, 1992 (1982).
43. R.R. Lucchese and V. McKoy. Phys. Rev. A, **26**, 1406 (1982).
44. L.A. Collins and B.I. Schneider. Phys. Rev. A, **29**, 1695 (1984).
45. C.-H. Yu, R.M. Pitzer, and C.W. McCurdy. J. Phys. Chem. **92**, 3116 (1988).
46. J. Stohr. NEXAFS spectroscopy. Springer-Verlag, Berlin. 1992.
47. R.W. Zurales. Ph.D. thesis, Texas A&M University, College Station, Texas, 1997.
48. D.M. Chase. Phys. Rev. A, **104**, 838 (1956).
49. M. Braunstein, V. McKoy, and M.E. Smith. J. Chem. Phys. **90**, 3931 (1989).
50. G. Herzberg. Electronic spectra and electronic structure of polyatomic molecules. Krieger Publishing, Malabar, Fla. 1991.
51. E. Haller, H. Koppel, L.S. Cederbaum, W. von Niessen, and G. Bieri. J. Chem. Phys. **78**, 1359 (1983).
52. D.M.P. Holland, M.A. MacDonald, M.A. Hayes, L. Karlsson, and B. Wannberg. Chem. Phys. **226**, 351 (1998).

© 2004 NRC Canada

Quantitative oscillator strengths for ionic fragmentation of C 1*s* and O 1*s* excited CO[1]

A.C.O. Guerra, J.B. Maciel, C.C. Turci, R.C. Bilodeau, and A.P. Hitchcock

Abstract: Ionic photofragmentation of carbon monoxide following carbon 1*s* and oxygen 1*s* excitation has been measured quantitatively with tuned synchrotron light and time-of-flight mass spectrometry using a Wiley–McLaren apparatus modified with an additional ion lens for improved quantitative performance. The sensitivity of the apparatus to kinetic energy and angular distribution effects has been characterized for selected lens settings through ion trajectory simulations and experimental measurements. Three distinct modes of the added lens have been identified (focus, defocus, and maximum). The focus mode has the least sensitivity to details of the angular and ion kinetic energy distribution and, therefore, is the best mode for measuring quantitative partial ion and ion-pair yields. The defocus mode has the most sensitivity to angular and kinetic energy distributions and, therefore, is the mode that provides the most information about the kinematics of photofragmentation. Branching ratios for ion and ion-pair production in all positive ion fragmentation channels were recorded from 280 to 330 eV (C 1*s*) and from 520 to 570 eV (O 1*s*) in the "focus" mode. Quantitative oscillator strengths were derived by combining these branching ratios with absolute total ion yield spectra. The results are compared to literature values.

Key words: CO, time-of-flight mass spectrometry, inner-shell excitation, quantitative oscillator strengths, cross sections.

Résumé : On a mesuré quantitativement le photofragmentation ionique du monoxyde de carbone qui suit les excitations 1*s* du carbone et 1*s* de l'oxygène à l'aide d'un rayonnement synchrotron et un spectromètre de masse à temps d'envol utilisant un appareil Wiley–McLaren modifié par l'addition d'une lentille ionique afin d'en améliorer la performance quantitative. Utilisant des simulations de trajectoires ioniques et des mesures expérimentales, on a caractérisé la sensibilité de l'appareil à l'énergie cinétique et aux effets de distribution angulaire pour divers ajustements choisis des lentilles. On a identifié trois modes distincts de lentilles ajoutées (focalisation, défocalisation et maximum). Le mode de focalisation est le moins sensible aux détails de la distribution de l'énergie angulaire et cinétique des ions et est donc le meilleur mode pour la mesure quantitative des rendements ioniques partiels et de paires d'ions. Le mode de défocalisation est le plus sensible aux distributions de l'énergie angulaire et cinétique et est donc le mode qui fournit le plus d'information concernant la cinématique de la photofragmentation. Les rapports de bifurcation dans la production de l'ion et de la paire d'ions dans les voies de fragmentation de tous les ions positifs ont été enregistrés de 280 à 330 eV (C 1*s*) et de 520 à 570 eV (O 1*s*) dans le mode de « focalisation ». On a dérivé les forces quantitatives de l'oscillateur en combinant ces rapports de bifurcation au spectre de rendement ionique total absolu. On compare les résultats aux valeurs rapportées dans la littérature.

Mots clés : CO, spectrométrie de masse en temps de vol, excitation de la couche interne, forces quantitatives de l'oscillateur, sections droites.

[Traduit par la Rédaction]

Introduction

Inner-shell excitation and associated decay spectroscopies are site-specific probes of electronic and geometrical structure and photoionization dynamics. Auger decay of inner-shell excited and ionized states is an efficient source of multiply charged ions. The fragmentation of these species, studied by photoelectron – photoion – photoion coincidence (PEPIPICO) and photoion–photoion coincidence (PIPICO) spectroscopy (also called charge separation mass spectrometry), gives insight into bonding and electronic structure. In triatomic and larger polyatomic molecules, the dependence

Received 5 December 2003. Published on the NRC Research Press Web site at http://canjchem.nrc.ca on 14 September 2004.

A.C.O. Guerra. BIMR, Department of Chemistry, McMaster University, Hamilton, ON L8S 4M1, Canada and Instituto de Química, Universidade Federal do Rio de Janeiro, Rio de Janeiro, RJ 21949-900, Brazil.
J.B. Maciel and C.C. Turci. Instituto de Química, Universidade Federal do Rio de Janeiro, Rio de Janeiro, RJ 21949–900, Brazil.
R.C. Bilodeau.[2] Department of Physics, Western Michigan University, Kalamazoo, MI 49008, USA.
A.P. Hitchcock.[3] BIMR, Department of Chemistry, McMaster University, Hamilton, ON L8S 4M1, Canada.

[1]This article is part of a Special Issue dedicated to the memory of Professor Gerhard Herzberg.
[2]Present address: Lawrence Berkeley National Laboratory (ALS Division), 1 Cyclotron Road, Berkeley, CA 94720, USA.
[3]Corresponding author (e-mail: aph@mcmaster.ca).

 doi: 10.1139/V04-055 © 2004 NRC Canada

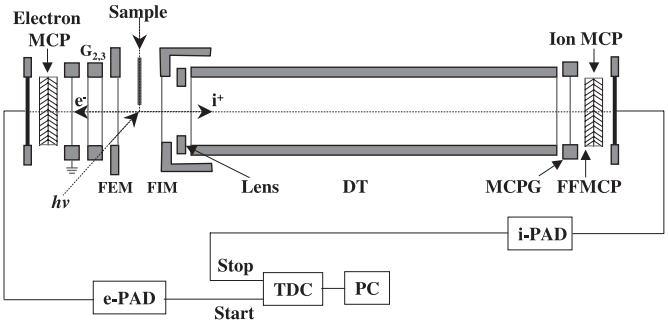
of the fragmentation process on the X-ray energy can reveal cases of site- and (or) state-selective fragmentation. The identification of potential candidates for selective X-ray photochemistry is an ongoing goal of our research program. To identify selectivity in fragmentation processes, quantitative yields are required, and thus it is important to understand the relationship between measured signals and the true partial photoionization cross sections (1). Some previous claims of selectivity in core level ionic fragmentation have been found to be, at least in part, an artefact of strong selectivity of the instrumentation to kinetic energy release distribution (KER or KERD) or angular distributions, combined with simultaneous changes of these factors among different core excited or ionized states (2).

To improve its quantitative performance, we have recently modified our Wiley–McLaren (3) time-of-flight (TOF) mass spectrometer to incorporate an ion-focussing lens (4). Here, we have used SIMION^{TM} trajectory simulations (5) and experimental measurements of CO to investigate the sensitivity of the modified apparatus to kinetic energy and ion angle distributions. We have found the additional ion lens has produced an instrument with three distinct modes — maximum signal rate (maximum mode), minimum selectivity to angle and kinetic energy distributions (focus mode), and maximum selectivity to ion angle and kinetic energy distributions (defocus mode). The focus mode of our apparatus is shown to provide the most representative partial ion and ion-pair yields — i.e., those with the least distortions associated with varying kinetic energy or angular distributions, as judged by absence of structure in the ion and ion-pair yields for high kinetic energy ions. Photoelectron–photoion coincidence (PEPICO) and PIPICO measurements of the ionic fragmentation following C 1*s* and O 1*s* excitation and ionization of CO are used to demonstrate these modes. The CO molecule was chosen because its electronic spectroscopy and core level photofragmentation have been studied extensively, and because there have been several previous studies of the core level photofragmentation yields claiming quantitative results (6, 7). Photoionization mass spectroscopy (6–15), photoelectron spectroscopy (16, 17), electron–ion coincidence spectroscopy (18, 19), and electron energy loss spectroscopy (20–24) measurements on CO were performed. The results are compared to an early time-of-flight photoionization mass spectrometry study, in which a very short extraction pulse was used to improve quantitative collection (6), and to (e,e + ion) coincidence measurements (7) simulating photoionization, which are generally accepted to produce branching ratios free from kinetic energy distortion. We discuss our results relative to a wider range of partial ion yield results on CO (6, 7–11, 25).

Experimental

The experiments were performed using two different beamlines at the Synchrotron Radiation Center (SRC), University of Wisconsin at Madison. One was a modest resolution grasshopper monochromator (Mark II) equipped with a 1200 lines/mm grating. The other was the high-resolution spherical grating monochromator (SGM) of the Canadian Synchrotron Radiation Facility (CSRF). The X-ray beam

Fig. 1. Schematic diagram of the experimental TOF apparatus. Drift tube (DT), first electron mesh (FEM), first ion mesh (FIM), multichannel plate grid (MCPG, prevents ion feedback), microchannel plate (MCP), front electrode of the MCP (FFMCP), electron pre-amplifier, amplifier, discriminator (e-PAD), ion pre-amplifier, amplifier, discriminator (i-PAD), time-to-digital converter (TDC), personal computer (PC).



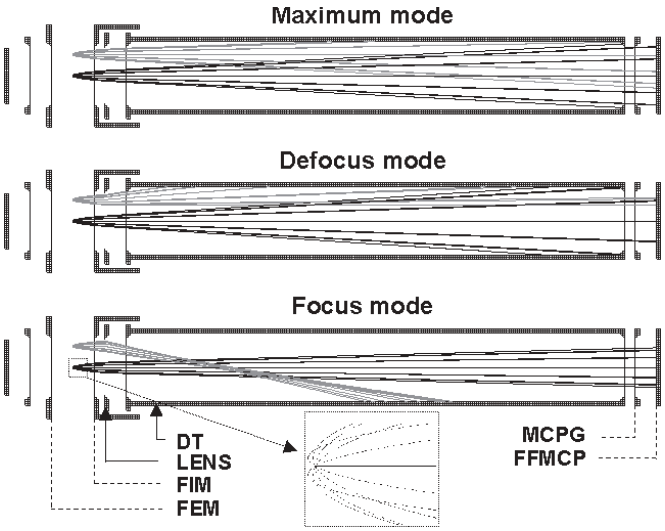
cross section in the ionization region was 2 × 1 mm in each case. For C 1*s* measurements, a 100 nm thin film of Ti was placed in the beam path to reduce second-order radiation by 70%. The sample was introduced into the experimental chamber as an effusive jet through a high-aspect-ratio stainless steel needle oriented perpendicular to both the time-of-flight (TOF) axis and the monochromatized photon beam. There was very little variation in gas density over the volume of the X-ray beam in the interaction region, as evidenced by negligible variation in signal strengths or spectral shapes as the position of the tip of the needle was varied over large ranges. Thus, signal is generated all along the X-ray beam path as it traverses the interaction region defined by the 25 mm mesh-covered openings into the electron detector and ion TOF drift tube. The sample pressure was maintained at ~6×10^{-6} torr (1 torr = 133.322 Pa) during data acquisition. The base pressure was ~2×10^{-8} torr so that residual gas signals contributed negligibly.

The TOF apparatus, prior to modification for addition of the ion lens, along with the PEPICO, PIPICO, and PEPIPICO modes, has been described earlier (1). Figure 1 shows a schematic diagram of the modified TOF apparatus, along with the electronic setup. It consists of a Wiley–McLaren type space charge focusing instrument (3) in which an electric field of up to 1050 V/cm (2000 V over 19 mm) was used to extract the parent and fragment ions. An additional lens (4) was installed between the drift tube (DT) and the ion extraction grid (FIM). The lens was designed to focus the fragment ions on a microchannel plate (MCP) detector.

Electrons and ions produced from photoionization were detected by two microchannel plate detectors (MCP), positioned directly opposite in relation to the TOF axis. Signals from the two MCP detectors were amplified and fed into LeCroy 688AL amplifier/discriminators. Coincidence detection was performed using an Ortec picosecond time analyzer (pTA) operated in a list mode, in which the arrival times of start (electron) and one or more stop (ion) signals were stored in a local memory and periodically downloaded to a microcomputer for further processing to generate the PEPICO, PIPICO, and other visualizations.

© 2004 NRC Canada

Fig. 2. C^+ ion trajectories computed by SIMION^{TM}, showing the existence of three modes of lens operation. Ions (20 eV) were started from the centre of the ionization region with initial ejection angles covering the full 360° (see insert figure at the bottom). One set of trajectories was started on the TOF axis and a second was started close to the edge of the entrance aperture into the drift tube. Potentials for the simulation: DT (–3800 V), FEM (+1000 V), FIM (–1000 V), MCPG (–3900 V), FFMCP (–3800 V), lens (–800 V for focus mode, –2200 V for maximum ion signal mode, and –3000 V for defocus mode).



Results and discussion

Characterization of the lens

Figure 2 shows the SIMION^{TM} simulations using potentials identified empirically for the instrument. The simulations are for the three different lens modes and an extraction field of 1050 V/cm (2000 V over 19 mm). The geometric parameters used in the simulation are listed in Table 1. For this geometry, the simulation flight times agree quite well with the measured times, indicating that the SIMION^{TM} model closely approximates the actual apparatus. The existence of the three modes was deduced from the SIMION^{TM} simulations, although the optimum lens voltages (summarized in Table 2) were found experimentally by determining optimal performance of each type — maximum ion signal for maximum mode; minimum kinetic energy discrimination, as evidenced by absence of the dip in the PIPICO signals, for "focus" mode; and maximum kinetic energy discrimination, as evidenced by the deepest dip in the PIPICO signals, for "defocus" mode. The PEPICO and PIPICO signals at 305 eV, for a 1050 V/cm extraction field and these three lens conditions, are compared in Fig. 3. The trajectories displayed in Fig. 2 are those of a positive ion with 20 eV kinetic energy, emitted at two points along the photon trajectory, one at the centre of the ionization region, the other 10 mm from the centre of the DT. The DT inner diameter is 25 mm, and thus the 10 mm off-centre starting point is still 2.5 mm away from the edge of the opening in the DT. Since the SIMION^{TM} geometry is a close approximation to the actual geometry, any edge effects not included in the simulation are expected to be minimal. From each of these points, a set of ion trajectories are plotted using take-off angles covering the full 360° (see insert to Fig. 2).

Table 1. Geometric parameters used in the SIMION^{TM} simulations.

Geometric feature	Dimension in simulation (mm)
FEM–FIM gap	19.0
FIM lens and DT thickness	1.0
FIM (grid) – lens (front surface)	5.0
Lens (front surface) to DT (grid)	10.0
DT grid-to-grid	232.0

In the *focus* mode (V_{lens} = –800 V for V_{DT} = –3800 V), a convergent potential is used in which the ions emitted at any angle from a single spot are transported to the detector without loss, for all kinetic energies up to 20 eV. Of the three modes, this one provides the least kinetic energy or angular discrimination, and thus it should be the best for measuring representative partial ion yields, which can form the basis for quantitative partial ion yields. In the *defocus* mode (V_{lens} = –3000 V for V_{DT} = –3800 V), a divergent potential is used in which the ions emitted along the TOF axis from a wide range of lateral positions along the X-ray beam are transported to the detector. Ions starting with large off-axis angles tend to hit the walls. This mode provides the most information about on-axis kinetic energy distributions since the system has a narrow acceptance angle (approximately ±30°). In the *maximum* mode, ions emitted all along the photon path are focused to the detector. The simulation shows that, for many positions along the photon path, an approximately ±60° acceptance angle is achieved at an extraction field of 1050 V/cm. Note that although, relative to the defocus mode, poorer kinetic energy distribution information results from the larger acceptance angle, the angle is better defined (all positions on the X-ray beam axis have the same angular distribution sampled), resulting in significantly larger signals (about 3 to 4 times more than in the focus or defocus modes).

PEPICO and PIPICO signals from CO in the three lens modes

Figure 3 shows the PEPICO and PIPICO signals for CO ionized at 305 eV, the peak of the excitation to the quasi-bound (C $1s^{-1}$, σ*) state, also called the σ* shape resonance. The extraction field was 1050 V/cm and the lens voltages for the three modes are those for which the SIMION^{TM} calculations were performed. The first stop signal (from single and the faster ion produced in dissociative double ionization) and the second stop signal (from the slower ion of dissociative double ionization) have been summed in each case. The peak shapes of high kinetic energy species (C^{++}, O^{++}, C^+, O^+), and especially the PIPICO signals that correspond mostly to highly energetic ions, show significant changes between the focus and defocus modes. For example, $I(C^+)/I(O^+) > 1$ for the focus mode but $I(C^+)/I(O^+) < 1$ for the defocus mode (I(x) = intensity of ion x). These changes are consistent with loss of fast C^+ ions, and thus much higher KER sensitivity in the defocus mode but very little KER or angular selectivity in the focus mode. The maximum mode gives a significantly higher signal in both PEPICO and

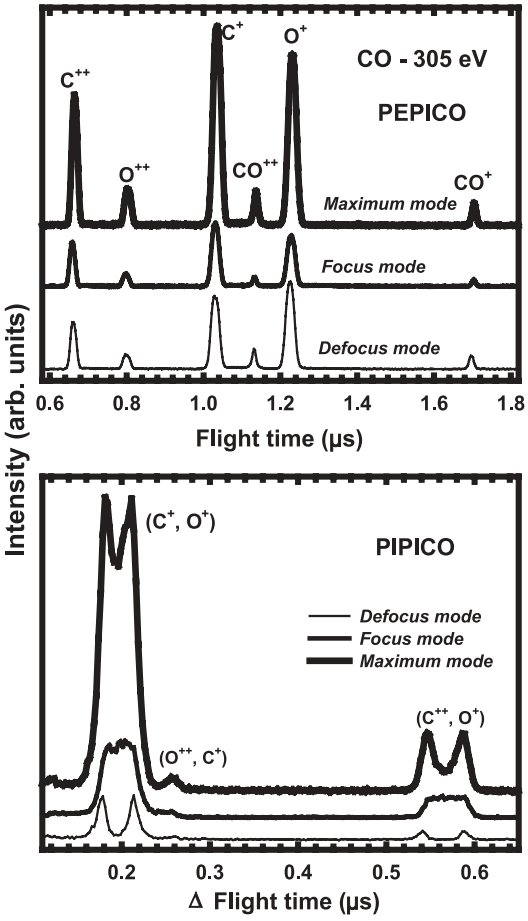
© 2004 NRC Canada

Table 2. Voltages and lens ratios for the three modes at the various extraction fields explored.

			Lens voltages (–V)			Lens ratios	
FEM (+V)	FIM (–V)	DT (–V)	Focus	Maximum	Defocus	V_d[a]/V_f[b]	V_d/V_m[c]
120	120	600	80	200	300	3.75	1.50
200	200	950	150	400	550	3.67	1.38
300	300	1400	300	700	1000	3.33	1.43
500	500	2700	500	1150	1650	3.30	1.43
1000	1000	3800	800	2200	3000	3.75	1.36

[a] V_d is the applied lens voltage used for defocus mode.
[b] V_f is the applied lens voltage used for focus mode.
[c] V_m is the applied lens voltage used for maximum mode.

Fig. 3. PEPICO (upper) and PIPICO (lower) spectra for C 1*s* ionized CO at 305 eV, measured with the lens set for focus, defocus, and maximum modes, as indicated in the legend. For clarity, the ordinates of the curves have been shifted with respect to each other. The intensities are in correct proportions.



PIPICO and has a KER discrimination somewhere in between the focus and defocus modes. Since the kinetic energy release distribution (KERD) is spread over more time at weak extraction fields and is thus easier to sample, it is often favorable to use the low extraction field to explore kinetic energy distributions and polarization-dependent ion yields. We stress the extremely flat-topped character of the (C^+, O^+) PIPICO signals in the focus mode. This is an unambiguous indication of the absence of angular discrimination and strongly supports our claim that this mode provides relative ion yields that are proportional to the quantitative ion yields.

Experimental conditions with these three limiting behaviors could be found for a wide range of different extraction fields, indicating they are a fundamental aspect of the ion optics. Table 2 lists the voltages and lens ratios for the three modes at the various extraction fields explored. We chose to use an extraction field of 1050 V/cm to maximize the yield. Even below 200 V/cm extraction field, it is possible to see the characteristic changes in the TOF or PIPICO shapes seen in Fig. 3 as a function of lens voltages, indicating there are distinct modes, even under weak extraction field conditions. Within experimental error, the lens ratios V_d/V_f and V_d/V_m are independent of extraction fields (V_d, V_f, and V_m are the optimal lens voltages in defocus, focus, and maximum modes, respectively). This observation suggests to us that our experimental procedure used to define the optimal lens voltages is valid and that the conditions we are identifying in this manner are general properties of the lens, and not specific to a narrow range of extraction fields.

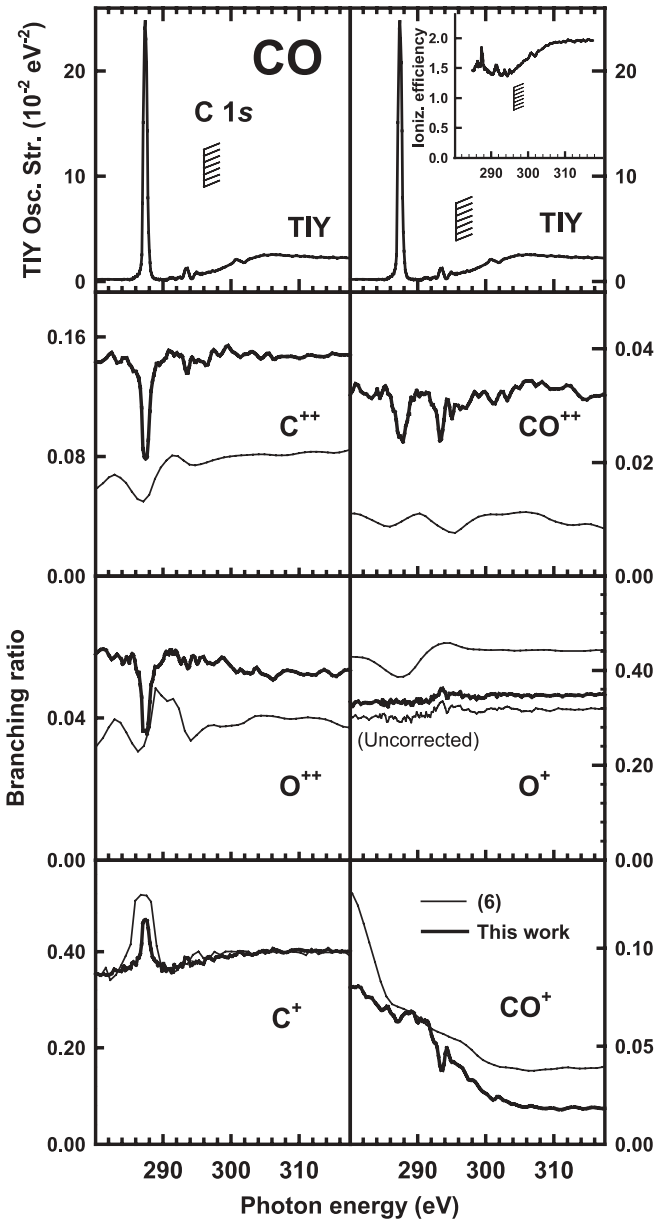
At 305 eV photon energy, the CO^+ yield is very small since this species only arises from the weak underlying valence shell ionization or from the even weaker fluorescence decay of the C 1*s* core hole. In fact, there is also a small contribution from CO^+ produced by low-energy UV stray light. Since virtually all of the 1*s* ion states decay by Auger, a final charge state of at least 2+ must exist. Although there is a small yield of CO^{++}, most of the CO^{++} states undergo symmetric dissociative double ionization producing C^+ and O^+, as explained by the "Coulomb explosion" model (26). The C^+ and O^+ signals from core ionization are very similar and dominate the spectra. These signals arise mainly from (C^+, O^+) ion-pair production (6). The yields of C^{++} and O^{++} are likely associated with asymmetric dissociation, although some also arise from the weak triple ionization processes producing (C^{++}, O^+) or (O^{++}, C^+) ion pairs detected in the PIPICO and PEPICO measurements.

Photoion branching ratios

The branching ratio (BR) is the ratio of the yield of a specific ion to the total ion yield. Figure 4 shows the C 1*s* photoion branching ratios between 280 and 320 eV measured in the focus mode, as compared to literature values (6). The branching ratio data shown in Fig. 4 are the average from two sets of measurements. The curves for each ion were derived from the peak areas in the PEPICO spectra measured at a series of energies, with high extraction fields and the focus mode of the lens. After subtraction of the background of accidental coincidences, the first stop and second stop signals were summed to generate the branching

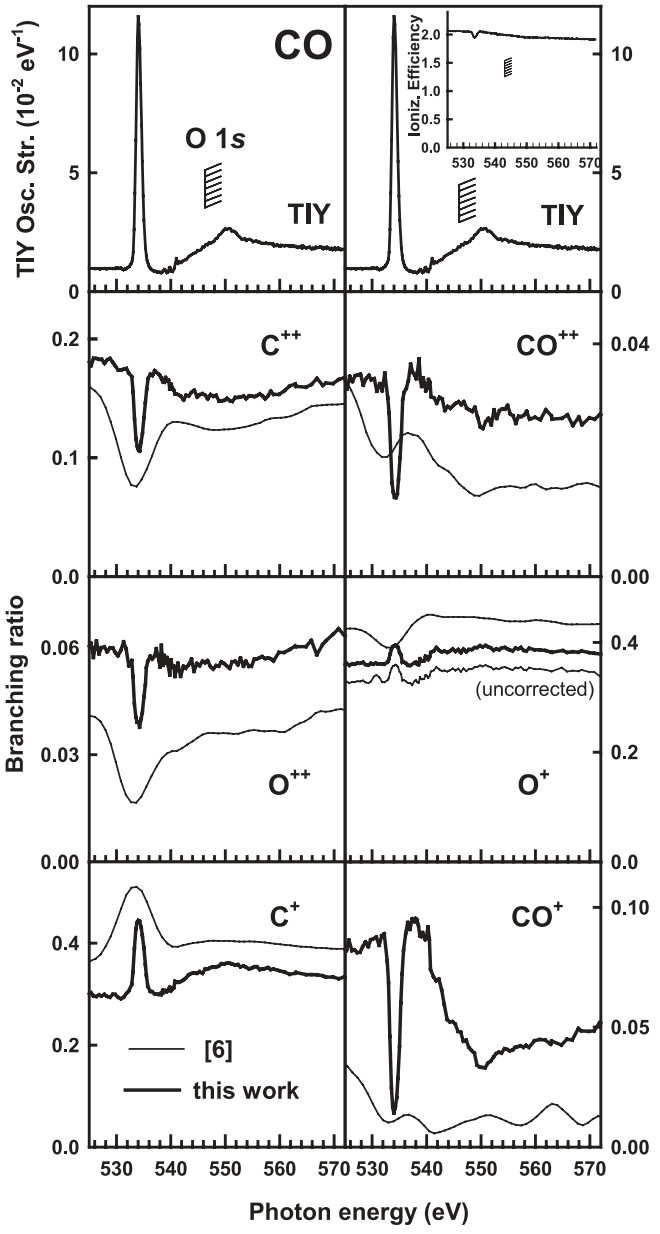
© 2004 NRC Canada

Fig. 4. Branching ratios for positive ion production from CO in the C 1*s* region derived from PEPICO mass spectra recorded with a Mark II grasshopper monochromator, as compared to literature values (6), which were digitized. The top of each column displays the total ion yield (TIY) spectra measured simultaneously and placed on an absolute scale, taking into account the estimated ionization efficiency of 2 in the C 1*s* continuum. The inset figure in the upper right panel is the estimated ionization efficiency. The O^+ curve marked uncorrected is prior to addition of 20% of the C^+ signal (followed by renormalization of all branching ratios to sum to unity). This correction compensates the fraction of the O^+ signal lost because of masking by first arrival of a C^+ signal. (A similar correction was applied in ref. 6.)



ratio. However, because the efficiency of ion detection is low (estimated to be 20%), this procedure does not account for the large loss of the O^+ signal from the "masking" of that species by the C^+ species for the (C^+, O^+) ion-pair process, which dominates the decay of C 1*s* ionized states. To compensate for the loss of the O^+ signal, 20% of the signal from

Fig. 5. Branching ratios for positive ion production from CO in the O 1*s* region derived from PEPICO mass spectra recorded with the spherical grating monochromator, as compared to literature values (6). The top of each column displays the total ion yield (TIY) spectrum, with the oscillator strength scale set from published oscillator strength data (24, 27), taking into account the estimated ionization efficiency of 2 in this energy region. The O^+ curve marked uncorrected is prior to the addition of 20% of the C^+ signal (see caption to Fig. 4 for further details).



the C^+ yield was added to the O^+ yield and the branching ratios recomputed. Figure 4 plots both the uncorrected and corrected O^+ branching yield spectra. Figure 5 shows the measured O 1*s* photoion branching ratios, derived from a sequence of PEPICO spectra measured in the 525–570 eV range with high extraction fields and the focus mode of the lens. As with the C 1*s* region, the O^+ signal was augmented by 20% of the C^+ signal to compensate for loss of the O^+ from the dominant (C^+, O^+) ion-pair process.

© 2004 NRC Canada

Table 3. Branching ratios following soft X-ray photoionization of CO.

	(Valence)$^{-1}$			C 1$s \rightarrow 2\pi^*$[a]		
Ion	280 eV (This work)	280 eV (Reference 6)	280 eV (Reference 7)	287.4 eV (This work)	287.4 eV (Reference 6)	287.4 eV (Reference 7)
C^{++}	0.143(8)[b]	0.05	0.02	0.080(7)	0.03	0.05
O^{++}	0.057(2)	0.03	0.01	0.042(2)	0.01	0.02
C^+	0.35(2)	0.35	0.22	0.46(2)	0.52	0.51
CO^{++}	0.033(5)	0.01	0.02	0.025(5)	0.01	0.02
O^+	0.33(2)	0.46	0.26	0.33(2)	0.39	0.24
CO^+	0.080(7)	0.11	0.46	0.063(7)	0.05	0.17
O^++C^+	0.68(3)	0.81	0.48	0.79(3)	0.91	0.75
C^+/O^+	1.06	0.76	0.85	1.39	1.33	2.1

[a]Branching ratio at peak energy.
[b]The cited uncertainties are based on local statistical fluctuations in the data and do not reflect uncertainties associated with systematic errors.

The general shapes of the branching ratios are similar to those reported earlier, but there are differences in the quantitative yields. In particular, relative to ref. 6, in this work the yield of all doubly charged ion species is larger by 50%–100%, while that of the C^+ and O^+ singly charged species is about 20% smaller. This suggests that the earlier measurements underestimated the lower kinetic energy ion species. Note that the structure in the π^* region is much broader in the literature branching ratios (6) simply because of the poorer energy resolution of the earlier measurements (2.5 eV (6) vs. 0.6 eV fwhm (full width at half-maximum) in C 1*s*; 5 eV (6) vs. 1.5 eV fwhm in O 1*s*).

Figures 4 and 5 each include the total ion yield spectrum at the top of each column to help in the location of the states. This signal was measured simultaneously with the photoionization yields. For the O 1*s* spectrum, a small signal from impurity O_2 was subtracted (the O_2 π^* signal at 530.8 eV was about 3% of the CO π^* signal). Both C 1*s* and O 1*s* signals are set on an absolute oscillator strength scale by matching to earlier absorption oscillator strengths (6, 7, 24, 27), with a correction for the ionization efficiency, which is taken to be two above the C 1*s* ionization potential (6).

The inner-shell spectroscopy of CO has been described previously (6, 24) and is not controversial. Briefly, for the C 1*s* spectrum, the first strong peak at 287.4 eV is due to the C 1$s \rightarrow 2\pi^*$ transition. The weak structures at 292.4 and 293.4 eV correspond to C 1$s \rightarrow 3s$ and C 1$s \rightarrow 3p$ Rydberg excitations, respectively. The 294.8 eV feature is assigned as the overlap of 4*s* and 3*d* Rydberg transitions. The C 1*s* ionization potential (IP) is 296.1 eV (10). The feature in the near continuum at 300.7 eV is assigned to double excitation, while the broad structure at 305 eV is the σ^* shape resonance. The O 1*s* spectral features are assigned similarly: 534.1 eV (O 1$s \rightarrow 2\pi^*$), 539.1 eV (O 1$s \rightarrow 3s$), 540.4 eV (O 1$s \rightarrow 3p$), 541.7 eV (O 1$s \rightarrow 4s$, 3*d*), 542.4 eV (IP) (10), and 550.6 eV (shape resonance).

The C 1*s* branching ratio spectra can generally be divided into five regions: that below the onset of C 1*s* excitation (<287 eV), the C 1*s* discrete region (287–296 eV), the region just above the C 1*s* ionization threshold (296–300 eV), the near continuum (300–320 eV), and the continuum above the shake-off threshold (>320 eV). In contrast to the essentially constant ion branching ratios in the core ionization continua, at the π^* resonance there are large increases in the C^+ yield and significant decreases in the C^{++} and O^{++} yields. Similar observations can be made about the O 1*s* branching ratios, although the pre-O1*s*-edge signal is characteristic of C 1*s* ionization, rather than valence ionization, as in the pre-C 1*s*-edge signal, and thus the change from below to above the O 1*s* IP is smaller.

The C 1*s* branching ratios are also compared to results from a dipole regime electron–ion (e,e + ion) experiment (7) (Table 3). We found considerable disagreement, which was unexpected, since such measurements are generally considered quantitative. The CO (e,e + ion) study was one of the very first performed with that apparatus. It would be interesting to see the results of a modern (e,e + ion) measurement of CO.

Table 3 presents branching ratios at selected energies derived from the quantitative focus mode, in comparison to literature values (6, 7). The $I(C^+)/I(O^+)$ ratio for the C 1s π^* state is 1.39, very similar to the 1.33 value from ref. 6, but 34% lower than that from ref. 7. The $I(C^+)/I(O^+)$ ratio for the O 1s π^* state is 1.12, as compared to 1.30 from ref. 6. As noted in ref. 6, these similar ratios in the C 1*s* and O 1*s* regions indicate that the site of the core hole in CO has relatively little influence on the final ion distribution for this molecule. The largest factor determining variation in the fragmentation pattern is discrete vs. continuum excitation, associated with essentially complete double ionization above the C 1*s* IP, but only partial double ionization below the IP.

Partial ion and ion-pair yields for CO

C 1s partial ion yields

Figure 6 presents the quantitative partial ion yield (PIY) spectra of C 1*s* excited – ionized CO from 280 to 320 eV, derived by taking the product of the branching ratio and the absolute total ion yield signal. The partial ion yield spectra of C^{++}, O^{++}, and CO^{++} have enhanced continuum signals relative to the total ion yield (TIY). As found earlier (6), the C^{++} and O^{++} signals show a further rise at ~320 eV (not shown) corresponding to the onset of shake-off (simultaneous core and valence ionization) (6). The CO^+ signal has negligible signal in the C 1*s* continuum since the only channel that can give rise to CO^+ is fluorescence decay of the core hole, which has an extremely low probability. Note there is a very weak residual CO^+ signal, amounting to less than 2% of the total signal, which is most likely from low-

© 2004 NRC Canada

Fig. 6. Quantitative partial ion yield (PIY) oscillator strength spectra of all positive ions produced from CO in the 280–320 eV region recorded in the focus mode.

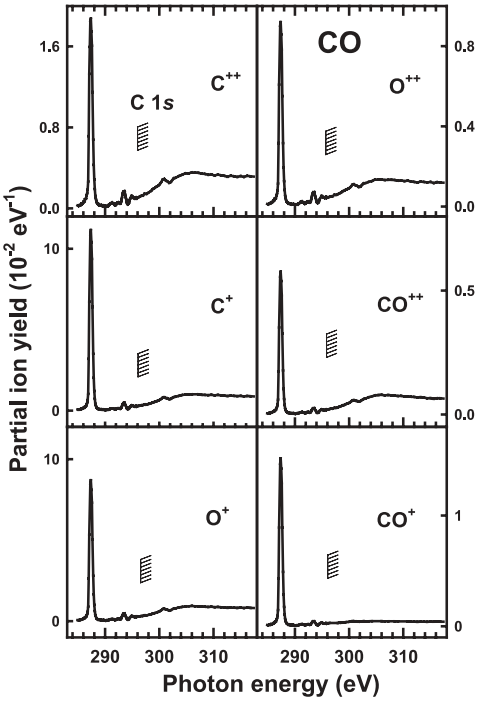
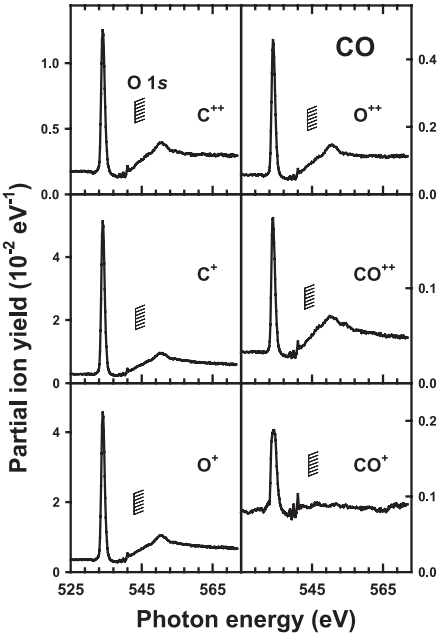


Fig. 7. Quantitative partial ion yield (PIY) oscillator strength spectra of all positive ions produced from CO in the 525–570 eV region recorded in the focus mode.



energy UV stray light. The relative strength of the C $1s \rightarrow 2\pi^*$ peak varies for the different ion products, indicating changes in the branching ratio for ionic fragmentation as discussed in the previous section and listed in Table 3.

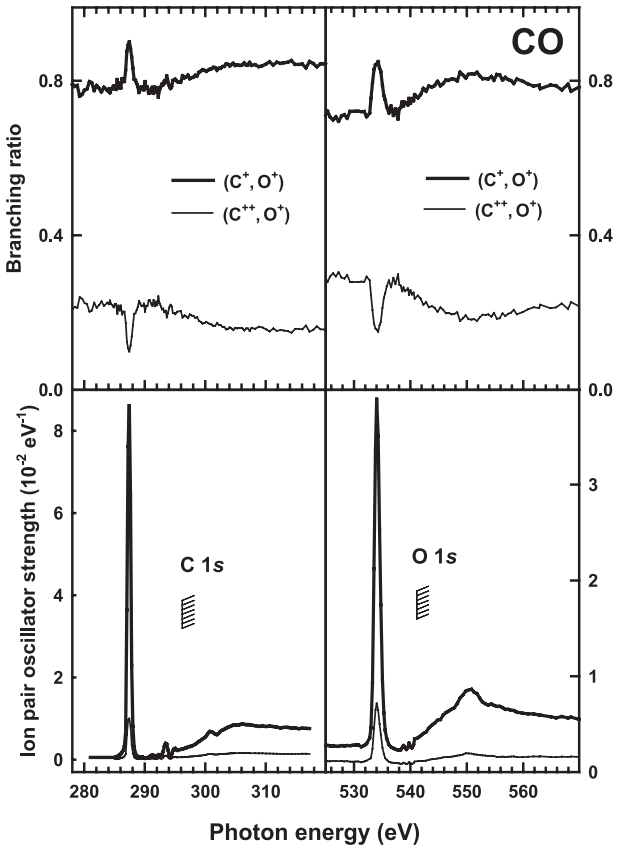
O 1s partial ion yields

Figure 7 presents the quantitative PIY spectra of O 1*s* excited – ionized CO from 525 to 570 eV, derived by taking the product of the branching ratio and the absolute TIY signal. As with the C 1*s* partial ion yields, the yields of the doubly charged products are increased in the O 1*s* continuum, although the effect is less dramatic since the underlying signal arises mostly from C 1*s* ionization, where already the double ionization dominates. The CO^+ parent ion signal shows a constant contribution from underlying valence ionization, with additional yield at the O $1s \rightarrow \pi^*$ transition and relatively more at the O $1s \rightarrow$ Rydberg transitions, but no signal in the O 1*s* continuum.

C 1s and O 1s ion-pair yields

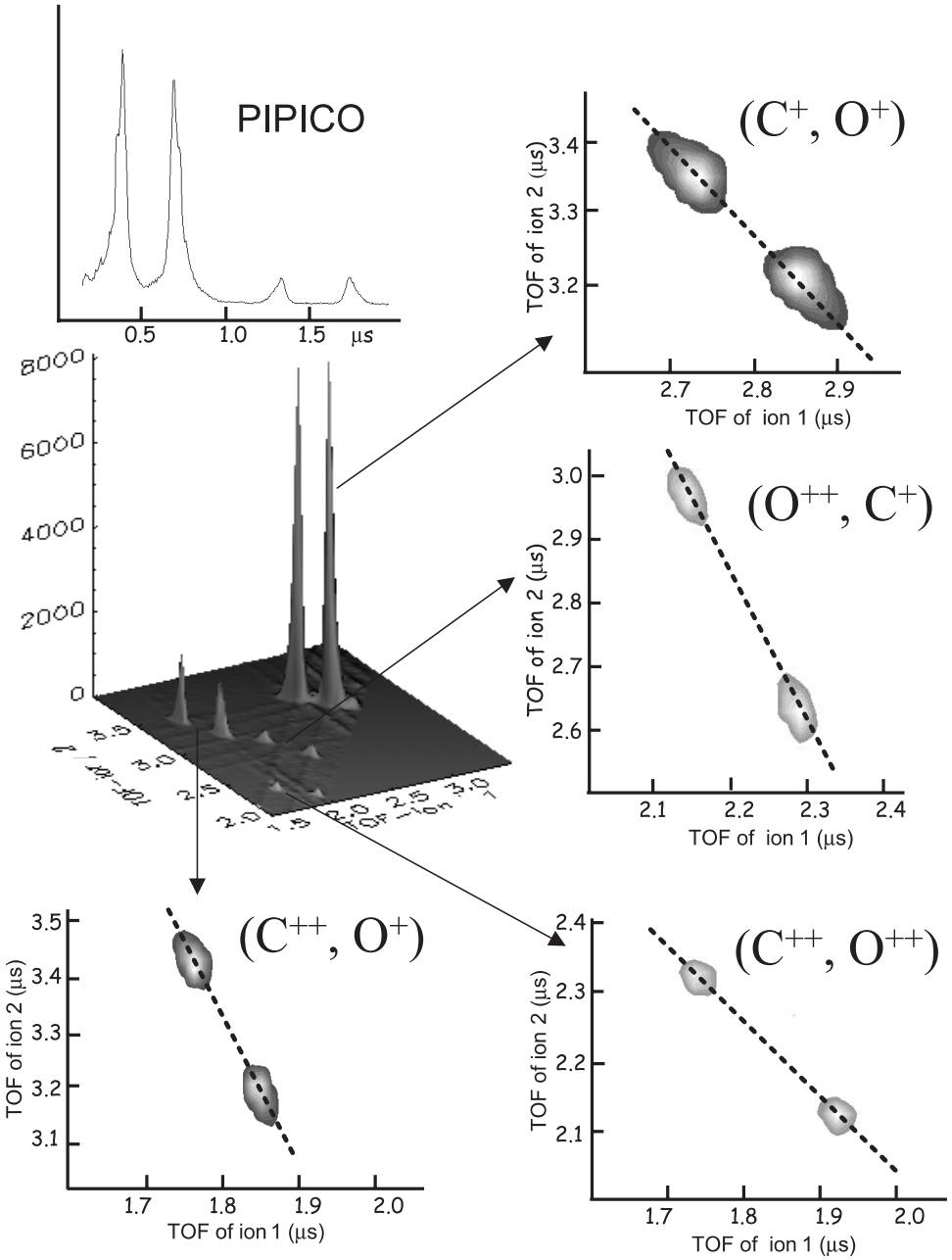
Figure 8 plots the branching ratios and the PIY spectra for the (C^+, O^+) and (C^{++}, O^+) ion pairs in the C 1*s* and O 1*s* regions derived from PIPICO data. The (C^+, O^+) ion-pair signal dominates the C 1*s* and O 1*s* continua. From the sum of the C^+ and O^+ branching ratios, we estimate that the ion-pair signal is 80% of the total ion signal. Since the TIY counts each ion separately, the derived total ion-pair yield (80% of the continuum TIY) was further divided by two to derive the oscillator strength for only ion-pair production. Thus, the absolute oscillator strength for producing the individual ion pairs was obtained by multiplying the ion-pair branching ratio times the TIY signal scaled by 0.40. (C^+, O^+) pair production is the strongest pair process in both core ionization

Fig. 8. Branching ratios (upper) and oscillator strength spectra (lower) for production of (C^+, O^+) and (C^{++}, O^+) ion pairs from CO in the C 1*s* and O 1*s* regions, derived from PIPICO spectra recorded with a high extraction field (1050 V/cm) and in the focus mode.



© 2004 NRC Canada

Fig. 9. PEPIPICO signals recorded in defocus mode at 305 eV with a weak extraction field (125 V/cm). The upper left curve is the PIPICO signal from the same data set.



continua. The dissociative triple ionization channel that produces the (C^{++}, O^{+}) pair constitutes ~10% of the total ion-pair signal, while the (O^{++}, C^{+}) signal, which is almost invisible in PIPICO but readily visible in PEPIPICO, is only a few percent of the ion-pair signal.

PEPIPICO

The PEPIPICO spectrum measured at 305 eV (C $1s \rightarrow \sigma^*$ resonance maximum) under weak extraction field conditions and with the lens operated in defocus mode, using the voltages displayed in the first row of Table 2, is presented in Fig. 9 in comparison to the PIPICO spectrum recorded at the same time. The defocus mode with a weak extraction field is the best condition for examining kinematics of ionic fragmentation since these conditions provide the largest sensitivity to kinetic energy and angular distributions. Figure 9 illustrates clearly the advantage of PEPIPICO relative to PIPICO. A total of four distinct ion-pair signals are clearly observed by PEPIPICO, whereas only two distinct signals are detected in the PIPICO signal recorded simultaneously. The (O^{++}, C^{+}) signal is clearly observed in PEPIPICO, whereas it is masked by the much stronger (C^{+}, O^{+}) signal in PIPICO. The very weak (C^{++}, O^{++}) signal from quadruple ionization is also clearly detected. Figure 9 also illustrates the power of the defocus mode to reveal details of the kinetic energy release distributions. The differences in the slope of the major axis of the coincidence signal are trivially related to the changes in the charge state of the ions in-

© 2004 NRC Canada

volved (1), since the events are pair dissociations in which all particles are detected. The separation of the two peaks along the major axis is related to the average kinetic energy release, which is significantly larger for 2+/1+ than for 1+/1+ and larger again for 2+/2+ charge separation. Detailed analysis of the full line shape (1) provides quantitative kinematic information, which can be compared to computed potential energy surfaces of CO^{++} (6).

Summary

Three different operation modes of a newly installed ion lens were found, corresponding to conditions predicted from SIMION™ simulations. The focus mode was found to produce yields that have minimal kinetic energy or angular discrimination and thus are likely to correspond to the true quantitative yields. The photoion branching ratios for C 1*s* and O 1*s* excited and ionized CO were measured in the focus mode and converted to absolute partial ion yield oscillator strengths. When compared with an early literature result (6), claimed to be quantitative, we find significant differences in the individual ion yields. While we believe the present system operated in the focus mode provides more quantitative ion yields than the method used in the earlier study, beamline-specific factors such as interference from stray light or residual second-order radiation may still have distorted the results presented in this work. Comparison to other independent photoionization or (e,e + ion) coincidence measurements with mass spectrometers optimized for quantitative results is required to properly establish the accuracy of these results. We encourage other researchers to provide such results. In the meanwhile, we will continue to use our apparatus in the focus mode to study the photon energy dependence of molecular photofragmentation in our ongoing search for X-ray selective photochemistry.

Acknowledgements

This research is supported financially by the Natural Sciences and Engineering Research Council of Canada (NSERC), the Canada Research Chair program, and Fundação Universitária José Bonifácio (FUJB) (Brazil). Joselito Maciel acknowledges support of a Fundação de Amparo à Pesquisa do Estado do Rio de Janeiro (FAPERJ) postdoctoral fellowship, Antonio Guerra gratefully acknowledges a Comissão de Aperfeiçoamento de Pessoal de Nível Superior (CAPES) graduate fellowship, and Rene Bilodeau acknowledges an NSERC postdoctoral fellowship. The Synchrotron Radiation Center is funded by the National Science Foundation (award No. DMR-0084402) and operated by the Graduate School of the University of Wisconsin-Madison. We thank Yong-Feng Hu, Astrid Jurgensen, and Kim Tan of the SRC-based Canadian Synchrotron Radiation Facility for assistance with operation of the TOF on the SGM.

References

1. A.P. Hitchcock and J.J. Neville. *In* Chemical applications of synchrotron radiation. *Edited by* T.K. Sham. World Scientific, Singapore. 2001.
2. W. Eberhardt, T.K. Sham, R. Carr, S. Krummacher, M. Strongin, S.L. Weng, and D. Wesner. Phys. Rev. Lett. **50**, 1038 (1983); W. Eberhardt and T.K. Sham. Proc. SPIE, **447**, 143 (1984).
3. W.C. Wiley and H. McLaren. Rev. Sci. Instrum. **26**, 1150 (1955).
4. J.B. Maciel, E. Morikawa, and G.G.B. de Souza. Presented at the 10th US National Conference on Synchrotron Radiation Instrumentation, Ithaca, NY, 1997; A.C.F. Santos, C.A. Lucas, and G.G.B. de Souza. Chem. Phys. **282**, 315 (2002).
5. D.A. Dahl. SIMION 3D. Version 6.0 [computer program]. Ion Source Software, PO Box 2726, Idaho Falls, ID 83403.
6. A.P. Hitchcock, P. Lablanquie, P. Morin, M. Simon, E. Lizon, A. Lugrin, P. Thiry, and I. Nenner. Phys. Rev. A, **37**, 2448 (1988).
7. R.B. Kay, P.E. Van der Leeuw, and M.J. Van der Wiel. J. Phys. B, **10**, 2521 (1977).
8. W.C. Stolte, D.L. Hansen, M.N. Piancastelli, I. Dominguez Lopez, A. Rizvi, O. Hemmers, H. Wang, A.S. Schlachter, M.S. Lubell, and D.W. Lindle. Phys. Rev. Lett. **86**, 4504 (2001).
9. N. Saito, F. Heiser, O. Hemmers, A. Hempelmann, K. Wieliczek, J. Viefhaus, and U. Becker. Phys. Rev. A, **51**, R4313 (1995).
10. M. Benndorf, W.B. Westerveld, J. van Eck, J. van der Weg, and H.G.M. Heideman. J. Phys. B, **32**, 2503 (1999).
11. P. Erman, A. Karawajczyk, E. Rachlew-Källne, and C. Strömholm. J. Phys. B, **28**, 2069 (1995).
12. P. Erman, A. Karawajczyk, U. Köble, E. Rachlew-Källne, and K. Yoshiki Franzén. Phys. Rev. A, **53**, 1407 (1996).
13. N. Saito, F. Heiser, O. Hemmers, K. Wieliczek, J. Viefhaus, and U. Becker. Phys. Rev. A, **54**, 2004 (1996).
14. N. Saito, A. Hempelmann, F. Heiser, O. Hemmers, K. Wieliczek, J. Viefhaus, and U. Becker. Phys. Rev. A, **61**, 022709 (2000).
15. F. Heiser, O. Geßner, J. Viefhaus, K. Wieliczek, R. Hentgens, and U. Becker. Phys. Rev. Lett. **79**, 2435 (1997).
16. O. Gessner, F. Heiser, N.A. Cherpkov, B. Zimmermann, and U. Becker. J. Electron. Spectrosc. **101–103**, 113 (1999).
17. P.A. Hatherly, J. Adachi, E. Shigemasa, and A. Yagishita. J. Phys. B, **28**, 2643 (1995).
18. A. Hamnett, W. Stoll, and C.E. Brion. J. Electron. Spectrosc. **8**, 367 (1976).
19. W.B. Westerveld, J. van der Weg, J. van Eck, H.G.M. Heideman, and J.B. West. Chem. Phys. Lett. **252**, 107 (1996).
20. M.J. Van Der Wiel, Th.M. El-Sherbini, and C.E. Brion. Chem. Phys. Lett. **7**, 161 (1970).
21. G.R. Wight, C.E. Brion, and M.J. Van Der Wiel. J. Electron. Spectrosc. **1**, 457 (1972/1973).
22. R.B. Kay, P.E. Van der Leeuw, and M.J. Van der Wiel. J. Phys. B, **10**, 2513 (1977).
23. M. Tronc, G.C. King, and F.H. Read. J. Phys. B, **12**, 137 (1979).
24. A.P. Hitchcock and C.E. Brion. J. Electron. Spectrosc. **18**, 1 (1980).
25. I. Nenner. *In* Proc. XV Int. Conf. Photon, Electron and Atomic Collisions (ICPEAC), Brighton, UK, 1987. Plenum Press, New York. 1988. p. 15.
26. T.A. Carlson and R.M. White. J. Chem. Phys. **44**, 4510 (1966).
27. A.P. Hitchcock. Data base of absolute photoabsorption cross sections for gaseous species [online]. Available from http://unicorn.mcmaster.ca/corex.html. (2003).

© 2004 NRC Canada

Threshold photoelectron spectroscopy of benzene up to 26.5 eV[1]

Andrew J. Yencha, Richard I. Hall, Lorenzo Avaldi, Grant Dawber, Andrew G. McConkey, Michael A. MacDonald, and George C. King

Abstract: The threshold photoelectron spectrum of benzene has been recorded up to 26.5 eV photon energy under high-resolution conditions using synchrotron radiation and employing the penetrating-field threshold electron collection method. By means of a direct comparative study with a recent HeI photoelectron spectrum of benzene of equally high resolution, numerous autoionization effects are observed in the formation of the ionic band systems of benzene in the outer valence ionization region in the threshold photoelectron spectrum. The Rydberg states responsible for these effects are identified. Autoionization does not appear to play a role in the formation of the two lowest-energy, inner-valence bands of $C_6H_6^+$.

Key words: threshold photoelectron spectroscopy, photoelectron spectroscopy, benzene, ionization, autoionization, Rydberg states.

Résumé : On a enregistré le spectre de seuil photoélectronique du benzène jusqu'à une énergie photonique de 26,5 eV, dans des conditions de haute résolution, utilisant un rayonnement synchrotron et la méthode du champ pénétrant pour la collection des électrons de seuil. Faisant appel à une étude comparative directe avec un spectre photoélectronique HeI récent du benzène d'une résolution aussi haute, on a pu observer divers effets d'autoionisation dans la formation des systèmes de bandes ioniques du benzène dans la région d'ionisation de valence externe du spectre de seuil photoélectronique. On a identifié les états de Rydberg responsables de ces effets. L'autoionisation ne semble pas jouer un rôle dans la formation des deux bandes de valence interne de plus faible énergie du $C_6H_6^+$.

Mots clés : spectroscopie de seuil photoélectronique, spectroscopie photoélectronique, benzène, ionisation, autoionisation, états de Rydberg.

[Traduit par la Rédaction]

Introduction

The electronic structure of benzene has been of great interest to both experimentalists and theoreticians for more than seven decades due to its being the simplest example of a large class of polyatomic aromatic molecules. In fact, there are 24 separate entries in the subject index on this molecule in the 1966 seminal book on the electronic spectra and electronic structure of polyatomic molecules by Gerhard Herzberg (1). On the other hand, only a single entry is given in the book for the cation of benzene. Thus, most of our knowledge about the electronic structure of the benzene cation has occurred since and largely because of the advent of photoelectron spectroscopy (PES) in the 1960s. The first report of the PE spectrum of benzene was given by Akopian et al. (2) in 1961 using a variable-wavelength light source, but it has been reported on numerous times since. In the early days of PES, there was considerable controversy over the assignment of the low-lying ionization bands of benzene, primarily over the ordering of the three lowest-energy bands (3). The controversy stems from the assignment given by El-Sayed et al. (4) that the second ionization potential (IP) at 11.489 eV was due to the $1a_{2u}$ (π) orbital. This controversy has now long been settled with the ordering of the first three IPs of benzene being generally accepted to be $1e_{2g}$ (π) (ground state), $3e_{2g}$ (σ), $1a_{2u}$ (π). The most recent and, to date, the most extensive study of benzene by PES was that by Baltzer et al. (5) in 1997 using both synchrotron and HeI radiation. In spite of all the activity over the years on the PES of benzene, it is surprising that no report on the threshold photoelectron spectroscopy (TPES) of benzene has yet appeared to our knowledge. Since TPES provides a different

Received 27 November 2003. Published on the NRC Research Press Web site at http://canjchem.nrc.ca on 7 September 2004.

A.J. Yencha.[2] Department of Chemistry, State University of New York at Albany, Albany, NY 12222, USA.
R.I. Hall. Laboratoire de Dynamique Moléculaire et Atomique, Université Pierre et Marie Curie, 75252 Paris CEDEX 05, France.
L. Avaldi. CNR-IMIP, Area della Ricerca di Roma, CP10-00016 Monterotondo, Italy.
G. Dawber, A.G. McConkey, and G.C. King. Department of Physics, Schuster Laboratory, Manchester University, Manchester M13 9PL, UK.
M.A. MacDonald. CLRC, Daresbury Laboratory, Daresbury, Warrington WA4 4AD, UK.

[1]This article is part of a Special Issue dedicated to the memory of Professor Gerhard Herzberg.
[2]Corresponding author (e-mail: yencha@albany.edu).

 doi: 10.1139/V04-057 © 2004 NRC Canada

perspective of photoionization, it is of interest to see what we can learn about the formation of the cationic states of benzene by recording and analyzing the TPE spectrum of benzene at a resolution comparable to that of the highest resolution PE spectrum of benzene yet obtained. The object of this report is then to compare and contrast the TPE spectrum of benzene with the HeI PE spectrum of benzene. As such, we will not dwell on the details of the vibrational and electronic-state analysis of the HeI PE spectrum (5) but generally accept it.

Experimental

The TPE spectrum of benzene reported here was obtained on beamline 3.2 of the Synchrotron Radiation Source (SRS) of the Daresbury Laboratory. Details of the experimental procedure for taking TPE spectra have been given previously (6, 7), so only a brief description will be given here. Synchrotron radiation emanating from the electron storage ring of the SRS was dispersed using the 5 m McPherson monochromator of the station prior to entering the experimental apparatus. Near-zero-kinetic-energy electrons (<20 meV, although ~95% were within 3 meV of zero) were detected as a function of the scanning photon energy using a penetrating-field energy analyzer (8, 9) tuned to accept primarily threshold electrons using the argon ion doublet lines, $^2P_{3/2}$ and $^2P_{1/2}$. An effusive beam of benzene gas entered the ionization region of the apparatus through a platinum/iridium needle of 0.8 mm bore mutually perpendicular to the photon beam (1 mm diameter) and the entrance aperture (5 mm) of the analyzer and positioned ~3 mm above the photon beam. The temperature of the main chamber of the apparatus was maintained at ~100 °C to minimize local patch fields because of contact potential variations.

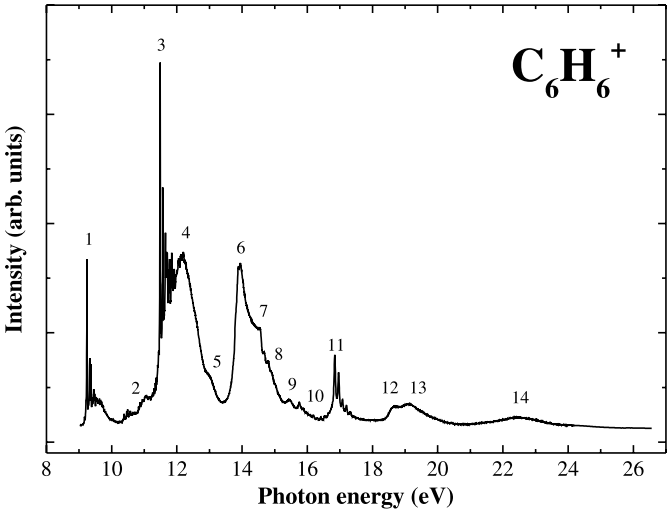
The TPE spectrum of benzene presented here was obtained by joining together spectra recorded in four energy regions: 9.0–14.0, 13.9–19.0, 18.9–24.1, and 24.0–26.5 eV, respectively. The first three of these regions were recorded in 5 meV steps, while the last region was recorded in 20 meV steps. These spectra were independently corrected for the variation in the photon flux as a function of energy and the decay of the synchrotron current with time. Normalization of the individual spectra in the overlapping regions resulted in the complete TPE spectrum of benzene over the photon energy range 9.0–26.5 eV. This spectrum was energy calibrated by measuring the TPE spectra of Xe in the presence of benzene over the $5p^{-1}$ (13.436 eV) and $5s^{-1}$ (23.397 eV) ionization peaks. These spectra also enabled a determination of the resolution of the benzene spectrum that was found to range smoothly from ~6 meV at 9 eV photon energy to ~19 meV at 26.5 eV photon energy. The pressure of benzene in the apparatus was of the order of 2×10^{-5} to 3×10^{-5} mbar (1 bar = 100 kPa). Benzene was supplied by the Aldrich Chemical Co. (Milwaukee, Wis.) and used directly.

Results and discussion

General considerations

Benzene is a planar molecule of D_{6h} symmetry containing 30 valence electrons whose orbital configuration is generally accepted to be (10):

Fig. 1. The full TPE spectrum of benzene up to 26.5 eV photon energy. The band features shown are identified in Table 1 as discussed in the text.



$$(2a_{1g})^2(2e_{1u})^4(2e_{2g})^4(3a_{1g})^2(2b_{1u})^2(1b_{2u})^2(3e_{1u})^4$$
$$(1a_{2u})^2(3e_{2g})^4(1e_{1g})^4$$

where $1a_{2u}$ and $1e_{1g}$ are pure π orbitals — all others being σ orbitals. On the basis of the independent-particle approximation for ionization, removal of an electron from each of these orbitals is expected to produce 10 single-hole states. However, it has been shown theoretically that electron correlation effects are important in the photoionization of benzene, even in the removal of outer valence electrons (11). In fact, an additional outer valence satellite state was predicted (11) and a band later confirmed in the Penning ionization electron spectrum of benzene (12), even though this band had eluded detection in any HeI or HeII PE spectrum of benzene. In addition, one might anticipate because of the high symmetry of the benzene molecule that the Jahn–Teller effect (1) would be important in describing the vibronic bands of $C_6H_6^+$ of *E*-symmetry in the PE spectrum of benzene. This would manifest itself in the observation of Jahn–Teller active modes of vibration of e_{2g} symmetry in the vibronic structure of states of *E*-symmetry as well as the possibility of splitting of the electronic state into two components (13). Hence, the details of the ionization of benzene are expected to be far more complicated than would at first appear. These aspects have been thoroughly considered and discussed in the most recent PE study of benzene (5) and will not be considered further here.

The TPE spectrum of benzene

The full TPE spectrum of benzene over the photon energy range 9.0–26.5 eV is shown in Fig. 1. Many individual features can be identified in this figure and are labeled 1–14. The identities of these features are given in Table 1 based on the discussion in the text. How this spectrum compares with the conventional HeI PE spectrum of benzene (5) can be seen in Fig. 2. The high-resolution HeI PE spectrum shown here displays the seven well-known band systems of $C_6H_6^+$ lying below 18 eV binding energy. The labeling of these sys-

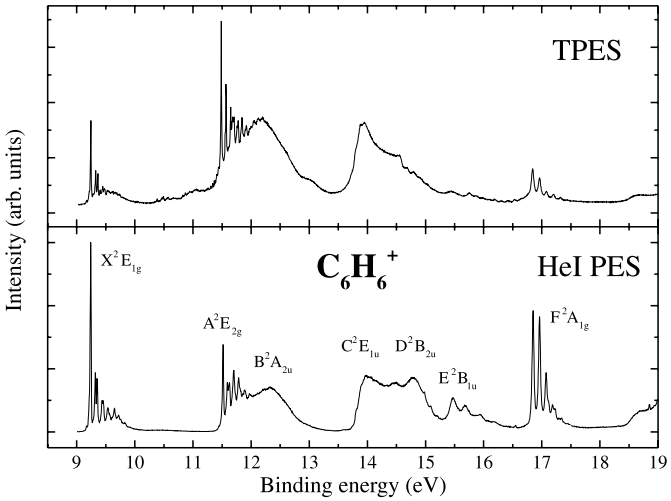
© 2004 NRC Canada

Table 1. Identification of the band features in the TPE spectrum of benzene shown in Fig. 1 resulting in the populating of different states of $C_6H_6^+$ by the autoionization of Rydberg states formed through various Rydberg transitions.

Feature number	$C_6H_6^+$ state	Rydberg transition
1	X^2E_{1g}	$(3e_{2g} \rightarrow 3pe_{1u})$
2	X^2E_{1g}	$3e_{2g} \rightarrow npe_{1u}$, n = 4–6
3	A^2E_{2g}	$(3e_{1u} \rightarrow 3da_{1g})$
4	A^2E_{2g}/B^2A_{2u}	$(3e_{1u} \rightarrow 3de_{2g})$
5	B^2A_{2u}	$1b_{2u} \rightarrow 3de_{2g}$
6	C^2E_{1u}	$2b_{1u} \rightarrow 3de_{2g}$
7	C^2E_{1u}	$2b_{1u} \rightarrow 4de_{2g}$
8	D^2B_{2u}	$3a_{1g} \rightarrow 3pe_{1u}$
9	E^2B_{1u}	$(3a_{1g} \rightarrow 3pa_{2u})$
10	E^2B_{1u}	$3a_{1g} \rightarrow npe_{1u}$, n = 4–6
11	F^2A_{1g}	$(2e_{2g} \rightarrow 3pe_{1u})$
12	G^2E_{2g}	
13	G^2E_{2g}	
14	H^2E_{1u}	

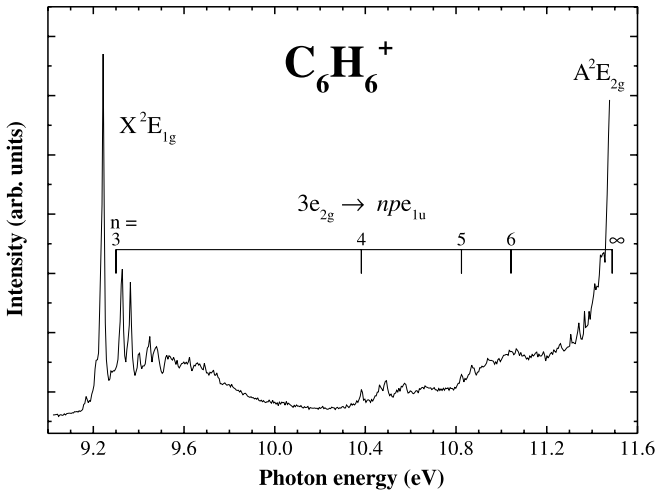
Note: Transitions in parentheses are postulated (see text).

Fig. 2. Comparison between the TPE spectrum (upper panel) and the HeI PE spectrum (lower panel) of benzene (5), reproduced with permission, below a binding energy of 19 eV.



tems follows the orbital ordering used in ref. 5. Upon inspection of these two spectra (TPE vs. HeI PE), one is immediately struck by the dramatic changes in relative intensities in features within one spectrum as compared with the other. For example, the X^2E_{1g} and F^2A_{1g} bands in the PE spectrum are the dominant two systems (most intense peak heights), while the corresponding features in the TPE spectrum appear much suppressed compared with the central part of the spectrum. Upon closer inspection, one finds considerable "filling-in" in the Franck–Condon (FC) gap regions in the TPE spectrum, especially noticeable between the X^2E_{1g} and A^2E_{2g} bands and between the B^2A_{2u} and C^2E_{1u} bands. In addition, in the binding energy region encompassing the C^2E_{1u}, D^2B_{2u}, and E^2B_{1u} bands in the PE spectrum, the TPE

Fig. 3. A portion of the TPE spectrum of benzene covering the X^2E_{1g} band of $C_6H_6^+$ showing an identified Rydberg series contributing to the formation of this band (see text). The energy resolution in this part of the TPE spectrum is 6–8 meV.



spectrum is dramatically different. We shall now examine the various regions of the TPE spectrum in detail.

TPE spectrum in the 9.0–11.5 eV photon energy region

This expanded region of the TPE spectrum is presented in Fig. 3. It shows considerable filling-in between the X^2E_{1g} and A^2E_{2g} band systems as noted previously with some sharp features evident between about 10.4 and 11.4 eV. In addition, the breadth of the X^2E_{1g} band system appears larger than in the PE spectrum (see Fig. 2) with a long high-energy tail merging with sharp features beginning at about 10.4 eV. We attribute all these differences between the TPE and PE spectra to the autoionization of Rydberg states of benzene converging on the A^2E_{2g} cationic state as identified in Fig. 3 as the series $(3e_{2g} \rightarrow npe_{1u}$, for n = 3–6). This Rydberg series has been identified previously in the absorption spectrum (4, 14) and in the electron impact energy loss spectrum (15) as interpreted by Jonsson and Lindholm (16). Autoionizing structure in this energy range has also been observed in the ion yield spectrum of benzene (17). The position of the n = 3 member of this series was set at 9.3 eV in Fig. 3 as given by Jonsson and Lindholm (16), while the other members shown are experimental positions from this work. The sharp peaks between 11.3 and 11.4 eV are possibly due to hot-band structure associated with the A^2E_{2g} band of $C_6H_6^+$ due to the elevated temperature (100 °C) of the benzene used in obtaining the TPE spectrum. Similar hot-band effects are to be found in other band systems in the TPE spectrum but will not be dwelled upon.

TPE spectrum in the 11.4–13.4 eV photon energy region

The TPE spectrum in this expanded photon energy region is shown in Fig. 4. This binding energy region encompasses the overlapping A^2E_{2g} and B^2A_{2u} band systems of $C_6H_6^+$. There are a number of features in the TPE spectrum that differ from the PE spectrum (see Fig. 2): (*i*) the sharp vibrational structure of the A^2E_{2g} band differs qualitatively, i.e., the relative intensities of peaks are different; (*ii*) the peak

© 2004 NRC Canada

Fig. 4. A portion of the TPE spectrum of benzene covering the A^2E_{2g} and B^2A_{2u} bands of $C_6H_6^+$ showing the influence of three Rydberg transitions contributing to the formation of these bands (see text). The energy resolution in this part of the TPE spectrum is 8–10 meV.

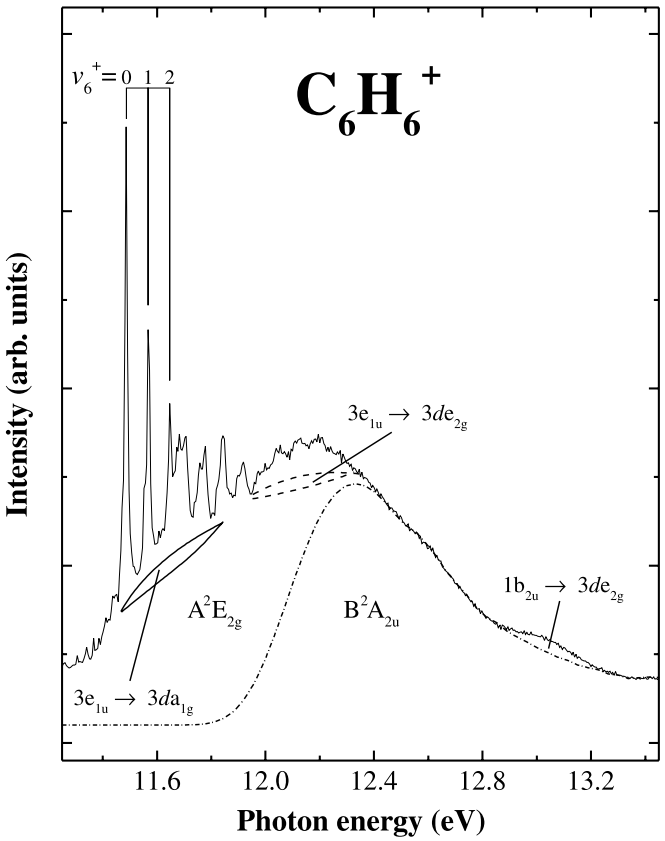
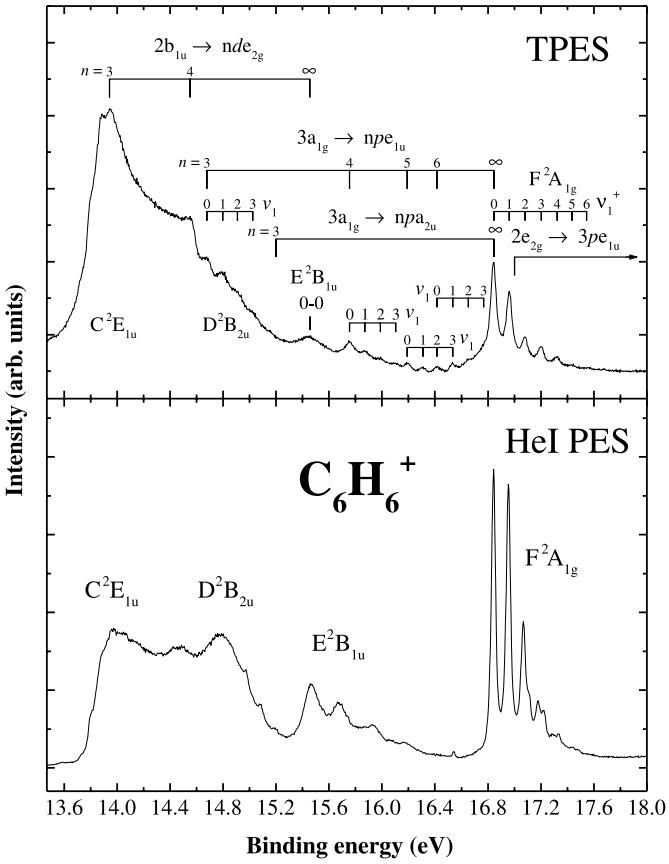


Fig. 5. Comparison between the TPE spectrum (upper panel) and the HeI PE spectrum (lower panel) of benzene (5), reproduced with permission, covering the C^2E_{1u}, D^2B_{2u}, E^2B_{1u}, and F^2A_{1g} bands of $C_6H_6^+$ in the 13.5–18.0 eV binding energy region. In the TPE spectrum numerous Rydberg transitions are identified as contributing to the formation of these bands (see text). The energy resolution in this part of the TPE spectrum is 10–13 meV.



maximum in the broad-band region following the sharp structure of the A^2E_{2g} band representing the vertical energy position of the B^2A_{2u} band in the PE spectrum at 12.3 eV (5) is not at all evident in the TPE spectrum; (*iii*) there appears to be a broad band on the high-energy tail of the B^2A_{2u} band in the TPE spectrum not seen in the PE spectrum (see Fig. 2). We attribute all of these effects in the TPE spectrum to autoionization of Rydberg states lying in this energy region. To interpret these observations, we have schematically drawn in Fig. 4 (dot–dashed curve) the expected vibronic band shape of the B^2A_{2u} system based on the calculated ionization profile (Fig. 4*a* in ref. 18) and positioned the band maximum at the measured vertical ionization potential of 12.3 eV (5). Based on the interpretation by Jonsson and Lindholm (16) of the electron impact energy loss spectrum of benzene by Lassettre et al. (15), we identify the Rydberg states in Fig. 4 as follows. Autoionization of the Rydberg state $3da_{1g}$ ($\leftarrow 3e_{1u}$) predicted to lie at 11.6 eV (16) would account for the vibrational intensity variations in the A^2E_{2g} band as noted above in point (*i*). The location of this state is schematically shown as the solid curves in Fig. 4. The rising of the broad vibrational band features following the sharp vibrational peaks of the A^2E_{2g} band is ascribed to the $3de_{2g}$ ($\leftarrow 3e_{1u}$) Rydberg state predicted to lie at 12.2 eV (16) and would account for point (*ii*) above. The location of this state is schematically shown as the dashed curves in Fig. 4.

The broad-band feature noted in point (*iii*) above is assigned to the $3de_{2g}$ ($\leftarrow 1b_{2u}$) Rydberg state identified to lie at 13.1 eV (16). A broad feature at ~13.0 eV in the absorption spectrum of benzene was assigned to the $5sa_{1g}$ ($\leftarrow 3e_{1u}$) Rydberg state. We favor the former assignment simply because of the lower principal quantum number of the Rydberg state.

TPE spectrum in the 13.6–18.0 eV photon energy region

The TPE spectrum in this photon energy region is shown in the upper panel of Fig. 5. It covers the binding energy range encompassing the C^2E_{1u}, D^2B_{2u}, E^2B_{1u}, and F^2A_{1g} PE bands of $C_6H_6^+$ as identified in the lower panel of Fig. 5. This portion of the TPE spectrum is by far the most different from the PE spectrum. Only the F^2A_{1g} band is fully recognizable by comparison with the PE spectrum, but even in this case, there are some differences to be noted (see the following). The shapes of the C^2E_{1u} and D^2B_{2u} vibronic bands in the TPE spectrum are dramatically altered in comparison with the PE spectrum. The three broad-peak maxima of the overlapping C^2E_{1u} and D^2B_{2u} bands of the PE spectrum *do not* have *any* correspondence in the TPE spectrum, although

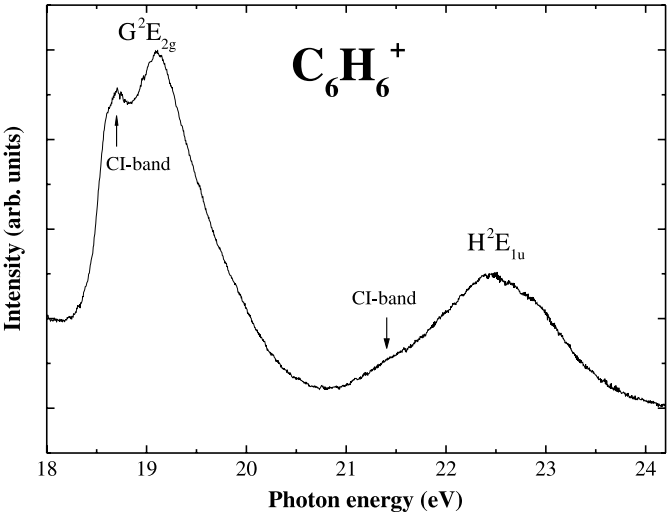
© 2004 NRC Canada

the weak vibrational structure on the low-energy side of the C^2E_{1u} band does appear in both spectra. The dominant features in the C^2E_{1u}/D^2B_{2u} bands region in the TPE spectrum of benzene are ascribed to the autoionization of three overlapping Rydberg states as shown in the upper panel of Fig. 5. This is based on the interpretation given by Jonsson and Lindholm (16) of the electron impact energy loss spectrum of benzene of Lassettre et al. (15). The first two Rydberg states, ($3de_{2g}$ and $4de_{2g}$) converging on the E^2B_{1u} ionic state, primarily populate the C^2E_{1u} state of $C_6H_6^+$, while the third Rydberg state ($3pe_{1u}$), converging on the F^2A_{1g} ionic state, primarily populates the D^2B_{2u} state of $C_6H_6^+$ based on the energy location of the Rydberg states in relationship to the ionic states of benzene (see lower panel of Fig. 2). The electronic band structure due to the latter exhibits four vibrational peaks of the dominant ν_1 mode familiar in the F^2A_{1g} ionic band of benzene as shown in the upper panel of Fig. 5. In addition, three other members of the $3a_{1g} \rightarrow npe_{1u}$ Rydberg series, for n = 4–6, display the same four vibrational bands of the ν_1 mode. The only feature in the TPE spectrum of benzene that can be assigned to the E^2B_{1u} ionic band is the 0–0 vibration at 15.46 eV as identified in the upper panel of Fig. 5. We postulate that this feature is, in fact, produced by autoionization of a Rydberg state lying in this energy region based on the extensive Rydberg-state activity in this photon energy range. The likely Rydberg state would be the $3pa_{2u}$ ($\leftarrow 3a_{1g}$) state converging on the F^2A_{1g} ionic state of benzene identified to lie at 15.2 eV (16) in the electron impact energy loss spectrum of Lassettre et al. (15). Finally, the F^2A_{1g} band in the TPE spectrum, although generally similar to the same band in the PE spectrum (see Fig. 5), does show broader vibrational peaks, a different vibrational distribution, and a longer progression in ν_1. These suggest that autoionization plays some role in the formation of the F^2A_{1g} band in the TPE spectrum. A likely Rydberg-state candidate would be the $3pe_{1u}$ ($\leftarrow 2e_{2g}$) state converging on the G^2E_{2g} ionic state of benzene (see Fig. 1 and the following) predicted to lie at 17.0 eV (16). No evidence is found in the TPE spectrum of benzene shown in Fig. 5 for the shake-up band ($(1e_{1g})^{-2}(1e_{2u})^1$, $^2A_{2u}$) found to appear at 16.2 eV in the Penning ionization electron spectrum of benzene (12) and confirmed theoretically (18) as well as being detected, most likely, in the $\Theta = 0°$ photoelectron spectrum of benzene using synchrotron radiation of energy 38 eV (5).

TPE spectrum in the 18.0–24.2 eV photon energy region

In this photon energy region, ionization of benzene is mainly attributed to the inner-valence orbitals $2e_{2g}$ and $2e_{1u}$ giving rise to the main lines and several satellites (19). The TPE spectrum given in Fig. 6 clearly shows two broad bands with peak maxima at 19.09 and 22.45 eV associated with ionization from these orbitals with subsidiary bands at 18.71 and ~21.4 eV identified as configuration interaction (CI) bands in the HeII PE spectrum of benzene (20). In general, the overall appearance of the TPE spectrum in this photon energy region is quite similar to that of the HeII PE spectrum of benzene (20) except for the CI feature at ~21.4 eV, which appears somewhat weaker in the TPE spectrum. Thus, autoionization does not appear to play a significant role in the formation of these bands in the TPE spectrum.

Fig. 6. A portion of the TPE spectrum of benzene covering the G^2E_{2g} and H^2E_{1u} bands of $C_6H_6^+$ with associated configuration interaction (CI) bands. The energy resolution in this part of the TPE spectrum is 13–17 meV.



Summary

The complete TPE spectrum of benzene up to 26.5 eV photon energy is presented for the first time at a resolution ranging smoothly from ~6 meV at 9 eV photon energy to ~19 meV at 26.5 eV photon energy. Analysis of the TPE spectrum by comparison with the HeI PE spectrum reveals dramatic differences in the appearance of the observed bands of $C_6H_6^+$ in the outer valence ionization region (9–18 eV). These differences are attributed in the TPE spectrum to the autoionization of Rydberg states found across the entire photon energy region. These Rydberg states appear to be major contributors to the TPE spectrum. In the inner-valence ionization region studied (18–26.5 eV), the TPE spectrum is similar in appearance to the HeII PE spectrum of benzene (20), suggesting that autoionization is not an important factor in the formation of the band systems of $C_6H_6^+$ in this binding energy region. This study demonstrates how TPE spectroscopy affords a different perspective of the photoionization of molecules as compared with conventional PE spectroscopy.

Acknowledgements

The authors thank the CLRC Daresbury Laboratory for providing beam time and facilities for carrying out this study. The authors are most grateful to Professor Leif Karlsson for providing the high-resolution photoelectron spectrum of benzene in digital form used in this paper. Financial support for this research from the Engineering and Physical Sciences Research Council (UK) (EPSRC) is acknowledged.

© 2004 NRC Canada

References

1. G. Herzberg. Molecular spectra and molecular structure III. Electronic spectra and electronic structure of polyatomic molecules. D. Van Nostrand Co., Inc., Princeton, N.J. 1966.
2. M.E. Akopian, F.I. Vilesov, and A.N. Terenin. Sov. Phys. Doklady (Engl. Transl.), **6**, 490 (1961).
3. A.D. Baker, C.R. Brundle, and D.W. Turner. J. Mass Spectrom. Ion Phys. **1**, 443 (1968).
4. M.F.A. El-Sayed, M. Kasha, and Y. Tanaka. J. Chem. Phys. **34**, 334 (1961).
5. P. Baltzer, L. Karlsson, B. Wannberg, G. Öhrwall, D.M.P. Holland, M.A. MacDonald, M.A. Hayes, and W. von Niessen. Chem. Phys. **224**, 95 (1997).
6. A.J. Yencha, A. Hopkirk, A. Hiraya, G. Dujardin, A. Kvaran, L. Heller, M.J. Besnard-Ramage, R.J. Donovan, J.G. Goode, R.R.J. Maier, G.C. King, and S. Spyrou. J. Electron Spectrosc. Relat. Phenom. **70**, 29 (1994).
7. L. Avaldi, G. Dawer, R.I. Hall, G.C. King, A.G. McConkey, M.A. MacDonald, and G. Stefani. J. Electron Spectrosc. Relat. Phenom. **71**, 93 (1995).
8. S. Cvejanovic and F.H. Read. J. Phys. B, **7**, 1180 (1974).
9. G.C. King, M. Zubek, P.M. Rutter, and F.H. Read. J. Phys. E, **20**, 440 (1987).
10. H.-G. Weikert and L.S. Cederbaum. Chem. Phys. Lett. **237**, 1 (1995).
11. L.S. Cederbaum, W. Domcke, J. Schirmer, W. von Niessen, G.H.F. Diercksen, and W.P. Kraemer. J. Chem. Phys. **69**, 1591 (1978).
12. S. Masuda, M. Aoyama, K. Ohno, and Y. Harada. Phys. Rev. Lett. **65**, 3257 (1990).
13. J.H.D. Eland. Photoelectron spectroscopy. Butterworths, London. 1974. p. 130.
14. E.E. Koch and A. Otto. Chem. Phys. Lett. **12**, 476 (1972).
15. E.N. Lassettre, A. Skerbele, M.A. Dillon, and K.J. Ross. J. Chem. Phys. **48**, 5066 (1968).
16. B-Ö. Jonsson and E. Lindholm. Ark. Fys. **39**, 65 (1969).
17. J. Momigny, C. Goffart, and L. D'Or. J. Mass Spectrom. Ion Phys. **1**, 53 (1968).
18. H. Köppel, L.S. Cederbaum, and W. Domcke. J. Chem. Phys. **89**, 2023 (1988).
19. M.S. Deleuze, A.B. Trofimov, and L.S. Cederbaum. J. Chem. Phys. **115**, 5859 (2001).
20. G. Bieri and L. Åsbrink. J. Electron Spectrosc. Relat. Phenom. **20,** 149 (1980).

© 2004 NRC Canada

Zero electron kinetic energy photoelectron and threshold photoionization spectroscopy of M-X$(CH_3)_3$ (M = Ga, In; X = P, As)[1]

Shenggang Li, Gretchen K. Rothschopf, Bradford R. Sohnlein, Jason F. Fuller, and Dong-Sheng Yang

Abstract: This paper presents pulsed-field ionization, zero electron kinetic energy (ZEKE) photoelectron and threshold photoionization spectra of M-X$(CH_3)_3$ (M = Ga, In; X = P, As). The ZEKE spectra exhibit well-resolved vibrational structures. A comparison with B3LYP calculations shows that the spectrum of In-P$(CH_3)_3$ arises from the $^1A_1 \leftarrow {}^2E$ transition and the spectra of Ga-P$(CH_3)_3$ and Ga-As$(CH_3)_3$ arise from transitions of a Jahn–Teller distorted doublet state to the $^1A_1$ state. The intensities of the $^1A_1$–^2E transition in the indium species are described with the Franck–Condon approximation, while the transitions in the gallium complexes are more complicated due to the dynamic Jahn–Teller effect. The adiabatic ionization potentials of Ga-P$(CH_3)_3$, In-P$(CH_3)_3$, and Ga-As$(CH_3)_3$ are 39 635, 38 930, and 40 322 cm^{-1}, respectively, and the ionization threshold of In-As$(CH_3)_3$ is ~39 550 cm^{-1}. The metal–ligand stretching frequencies are 143, 116, and 125 cm^{-1} for Ga^+-P, In^+-P, and Ga^+-As, respectively, and 96 cm^{-1} for In-P. The intermolecular bending frequencies are 71, 65, and 42 cm^{-1} for Ga^+-P-C, In^+-P-C, and Ga^+-As-C, respectively, and 47 cm^{-1} for In-P-C. In addition, ligand-based vibrational frequencies are determined for the CH_3 wag, PC_3 and AsC_3 umbrella, and P-C stretching vibrations.

Key words: ZEKE photoelectron, photoionization, DFT, gallium–phosphine, gallium–arsine, indium–phosphine, indium–arsine.

Résumé : Dans ce travail, on décrit les spectres photoélectroniques d'énergie cinétique électronique nulle (« ZEKE »), à ionisation par champ pulsé, ainsi que les spectres de seuil de photoionisation des composés M-X$(CH_3)_3$ (M = Ga, In; X = P, As). Les spectres ZEKE présentent des structures vibrationnelles bien définies. Une comparaison avec les calculs B3YLP permet de montrer que le spectre de In-P$(CH_3)_3$ découle de la transition $^1A_1 \leftarrow {}^2E$ alors que les spectres de Ga-P$(CH_3)_3$ et Ga-As$(CH_3)_3$ découlent de transitions d'un état doublet déformé de Jahn–Teller vers un état $^1A_1$. Les intensités de la transition $^1A_1$–^2E dans l'espèce contenant de l'indium peuvent être décrites par l'approximation de Franck–Condon alors que les transitions dans les complexes du gallium sont plus compliquées en raison de l'effet Jahn–Teller dynamique. Les potentiels d'ionisation adiabatique des complexes Ga-P$(CH_3)_3$, In-P$(CH_3)_3$ et Ga-As$(CH_3)_3$ sont respectivement 39 635, 38 930 et 40 322 cm^{-1}; le seuil d'ionisation du complexe In-As$(CH_3)_3$ est ~39 550 cm^{-1}. Les fréquences d'élongation métal–ligand sont de 143, 116 et 125 cm^{-1} pour Ga^+-P, In^+-P et Ga^+-As et 96 cm^{-1} pour In-P. Les fréquences de déformation angulaire intermoléculaires sont de 71, 65 et 42 cm^{-1} pour Ga^+-P-C, In^+-P-C et Ga^+-As-C et 47 cm^{-1} pour In-P-C. De plus, on a déterminé les fréquences vibrationnelles basées sur le ligand pour le balancement du CH_3, pour les parapluies PC_3 et AsC_3 et pour les vibrations d'élongation P-C.

Mots clés : photoélectron d'énergie cinétique électronique nulle, photoionisation, « DFT », gallium–phosphine, gallium–arsine, indium–phosphine, indium–arsine.

Introduction

The importance of group 13–15 compounds has stimulated great interest in characterizing compounds formed by reactions of the group 13 metal atoms with the group 15-containing molecules. A majority of these studies have focused on the metal complexes of nitrogen-bearing molecules. Experimental investigations have included matrix isolation IR spectra of reaction products of M (M = Al, Ga, In) with NH_3 (1–3) and N_2 (4, 5), photoionization efficiencies of M-NH_3 (6, 7) and Al-$(N_2)_x$ (x = 1–14) (8), resonant two-photon photoionization of Al-ND_3 (9) and In-N_2 (10), pulsed-field ionization, zero electron kinetic energy photoelectron (ZEKE) of M-$NH_{3-n}(CH_3)_n$ (n = 0–3) (11–17), laser fluorescence of Al-N_2 (18, 19) and Ga-N_2 (20), laser-induced plasma of Al^+-N_2 (21), electrostatic multipole field of Al-NH_3 (22), and electron paramagnetic resonance of Al-$(NH_3)_{2,4}$ (23). Computationally, ab initio and density functional theory (DFT) calculations were performed on Al-NH_3 (24–27), Al^+-NH_3 (28–31), and Al-N_2 (32). However, there have been relatively few studies on group 13 metal complexes with phosphorus- and arsenic-containing molecules.

Received 17 November 2003. Published on the NRC Research Press Web site at http://canjchem.nrc.ca on 14 September 2004.

S. Li, G.K. Rothschopf, B.R. Sohnlein, J.F. Fuller, and D.-S. Yang.[2] Department of Chemistry, University of Kentucky, Lexington, KY 40506-0055, USA.

[1]This article is part of a Special Issue dedicated to the memory of Professor Gerhard Herzberg.

[2]Corresponding author (e-mail: dyang0@uky.edu).

 doi: 10.1139/V04-053 © 2004 NRC Canada

These have involved matrix isolation IR absorption of MPH_3, $HMPH_2$, and H_2MPH (33), photoionization and ZEKE photoelectron of M-XH_3 (34) and Al-$X(CH_3)_3$ (X = P, As) (35), and ab initio calculations of Al-PH_3 (25, 36).

Previously, we reported ZEKE studies of the group 13 metal complexes with ammonia and methylamine ligands (11–17) and aluminum complexes with phosphine and arsine ligands (35). From the vibrationally resolved ZEKE spectra, we were able to determine adiabatic ionization potentials (AIPs), metal–ligand and ligand-based vibrational frequencies, low-lying electronic states, and molecular conformations of these complexes. In this paper, we present the first photoionization and ZEKE photoelectron study of the Ga- and In-$X(CH_3)_3$ (X = P, As) complexes. The vibrationally resolved ZEKE spectra reveal a strong Jahn–Teller distortion in Ga-$P(CH_3)_3$ and Ga-$As(CH_3)_3$, but no significant effect in In-$P(CH_3)_3$. The ZEKE spectra of the gallium and indium complexes will be discussed in combination with DFT calculations and compared with other group 13–15 complexes.

Experimental and computational details

The ZEKE apparatus has been described in a previous publication (12). Briefly, it consists of a Smalley-type laser ablation molecular beam source (37) and a Wiley–McLaren type of time-of-flight mass spectrometer (38). The molecular beam source is housed in a cubic chamber that is pumped by a 2200 L s^{-1} oil-diffusion pump (BOC Edwards). The spectrometer is placed in a six-way cross chamber evacuated by two 400 L s^{-1} turbomolecular pumps (Seiko Seiki) and is isolated from the Earth's magnetic field by a cylindrical, double-walled μ-metal shield. The spectrometer is used to detect both ions and electrons.

Metal complexes were produced by reactions of metal atoms with trimethylphosphine (99%, Aldrich) or trimethylarsine (99%, Strem). The metal atoms were produced by pulsed-laser vaporization of a pure metal rod (Al, 99.999%, Aldrich) or an alloy target (GaSb, 99.99%, Aldrich). The target was rotated and translated by a motor-driven mechanism and vaporized with the second-harmonic output of a Nd:YAG laser (2 mJ, 532 nm, Quanta-Ray GCR-3). $P(CH_3)_3$ or $As(CH_3)_3$ vapor at 0 and 25 °C, respectively, was mixed with helium (UHP, Scott-Gross) or argon (UHP, Scott-Gross) at a stagnation pressure range of 40~60 psi and delivered to the vaporization region by a piezoelectric pulsed valve (39). The mixture pulses were synchronized with the vaporization laser pulses to optimize the metal–ligand reactions.

Masses of the products formed in the molecular beams were determined by photoionization time-of-flight (TOF) mass spectrometry. Approximate ionization potentials of Ga-$P(CH_3)_3$, In-$P(CH_3)_3$, Ga-$As(CH_3)_3$, and In-$As(CH_3)_3$ were located by threshold photoionization measurements in the TOF mass operation mode. Prior to ZEKE experiments, intensities of ionized metal complexes were maximized by optimizing the timing and power of the ablation and ionization lasers, the temperature and concentration of the reactants, and the backing pressure of the carrier gas. The ZEKE measurements were carried out by photoexcitation of the molecules to high-lying Rydberg states, followed by pulsed-electric-field ionization. The second-harmonic output of a dye laser (Lumonics HD-500), pumped by a XeCl excimer laser (Lumonics PM-884), was used as photoionization and photoexcitation sources. A delay pulse generator (Stanford SR 445) was used to provide electric pulses (1.2 V cm^{-1}, 100 ns) for field ionization. The ZEKE electron signal was capacitively decoupled from a dual microchannel plate anode (Galileo), amplified by a preamplifier (Stanford SR445), averaged by a gated integrator (Stanford SR250), and collected and stored in a computer. A small dc field (0.08 V cm^{-1}) was applied to help remove prompt electrons from direct photoionization. A field dependence study was not performed due to the limited size of the ZEKE signal. Laser wavelengths were calibrated against vanadium or titanium atomic transitions in the frequency range of each individual spectrum. Attempts to record ZEKE spectra for In-$As(CH_3)_3$ were not successful. This may indicate that the lifetime of the ZEKE Rydberg states in this molecule is shorter than the microsecond timescale used in our measurements.

To aid in the ZEKE spectral interpretation, geometries, harmonic vibrational frequencies, and dissociation energies of the neutral and ionized complexes were calculated using the hybrid DFT B3LYP method implemented in the Gaussian 98 program package (40). The 6-311+G(d,p) basis was used for all atoms except for indium, for which the Los Alamos ECP plus DZ basis (Lanl2DZ) was employed. Multidimensional Franck–Condon (FC) factors were computed using the equilibrium geometries and normal modes of the neutral and ionized molecules. In these calculations, the Duschinsky effect (41) was considered to account for normal mode differences in the neutral and ionic species. Details of the FC calculations were previously described (42, 43). Spectral broadening was simulated by giving each line a Lorenztian line shape with the linewidths of experimental ZEKE spectra. Boltzmann factors were used to simulate spectra at finite temperatures.

Results and discussion

Computation

Table 1 lists the electronic energies and major equilibrium bond lengths and angles of low-lying electronic states of M^+/M-$X(CH_3)_3$ (M = Ga, In; X = P, As) from the B3LYP calculations. Bond lengths and angles involving hydrogen atoms are not included as they are insensitive to metal coordination. The ground state of M-$X(CH_3)_3$ is predicted to be $^2A''$ in the C_s point group. This doublet state is formed by the interaction of a $p\pi$ orbital of the metal atom with the lone-pair orbital of the ligand. The metal $p\pi$ electron is oriented to be perpendicular to the M-X internuclear axis to minimize the electron repulsion with the electron lone pair of the ligand. In this configuration, the ligand donates the electron lone pair to the empty metal $p\sigma$ orbital, and the metal $p\pi$ orbital interacts with one or more ligand orbitals of appropriate symmetry. Since the metal $p\pi$ orbital lies much higher in energy than filled ligand orbitals, the highest occupied molecular orbital (HOMO) formed by the interaction largely consists of the metal character, as shown in Fig. 1. The mixing of the ligand orbital with the metal $p\pi$ orbital will depend on the relative energies of the interacting orbitals. Because there are two possible perpendicular orientations of the $p\pi$ orbital, the HOMO is expected to be doubly

© 2004 NRC Canada

Table 1. Electronic energies (E_e), molecular geometries, and vibrational frequencies from the B3LYP/6–311+G(d,p) calculations.

Energy (a.u.)	Bond lengths (Å)	Bond angles (°)	Frequencies (cm^{-1})
Ga-P$(CH_3)_3$			
$^2A''$ –2386.005038	Ga—P = 2.747	∠Ga-P-C = 105.9, 121.5	a′: 3120, 3107, 3102, 3030, 3021, 1482, 1469, 1465, 1345, 1321, 977, 967, 845, 705, 633, 299, 248, 204, 112, 68
	P—C = 1.852, 1.856	∠C-P-C = 101.7, 101.2	a″: 3119, 3118, 3101, 3019, 1461, 1459, 1452, 1319, 954, 836, 805, 693, 235, 186, 149, 71
$^1A_1$ –2385.825538	Ga—P = 2.771	∠Ga-P-C = 113.5	a_1: 3120, 3037, 1476, 1363, 987, 640, 303, 132
	P—C = 1.839	∠C-P-C = 105.1	a_2: 3126, 1450, 814, 158
			e: 3127, 3119, 3038, 1467, 1456, 1338, 978, 854, 725, 238, 189, 76
In-P$(CH_3)_3$			
$^2A''$ –463.024499	In—P = 3.024	∠In-P-C = 107.2, 121.3	a′: 3118, 3104, 3101, 3027, 3019, 1481, 1467, 1464, 1345, 1321, 976, 966, 847, 704, 635, 287, 242, 194, 82, 56
	P—C = 1.854, 1.855	∠C-P-C = 101.3, 101.1	a″: 3117, 3115, 3099, 3018, 1462, 1458, 1452, 1321, 956, 839, 804, 698, 238, 186, 158, 51
^2E –463.024200	In—P = 3.050	∠In-P-C = 116.7	3117, 3116, 3110, 3103, 3101, 3076, 3023, 3019, 3007, 1481, 1470, 1463, 1460, 1453, 1347, 1323, 1321, 1293, 977, 966, 918, 847, 804, 704, 699, 636, 315, 293, 243, 237, 192, 159, 142, 80, 60, 1019i
	P—C = 1.855	∠C-P-C = 101.4	
$^1A_1$ –462.852548	In—P = 3.003	∠In-P-C = 114.3	a_1: 3117, 3036, 1477, 1362, 984, 641, 293, 106
	P—C = 1.842	∠C-P-C 104.3	a_2: 3125, 1451, 814, 160
			e: 3125, 3118, 3038, 1468, 1458, 1337, 978, 853, 721, 240, 190, 71
Ga-As$(CH_3)_3$			
$^2A''$ –4280.499934	Ga—As = 2.876	∠Ga-As-C = 106.7, 123.8	a′: 3132, 3125, 3123, 3040, 3035, 1481, 1468, 1465, 1305, 1282, 913, 911, 807, 575, 545, 233, 207, 162, 95, 49
	As—C = 1.979, 1.984	∠C-As-C = 99.4, 98.8	a″: 3132, 3131, 3122, 3034, 1462, 1461, 1453, 1279, 900, 795, 778, 561, 198, 153, 126, 51
$^1A_1$ –4280.317609	Ga—As = 2.877	∠Ga-As-C = 115.3	a_1: 3140, 3049, 1476, 1325, 927, 558, 223, 120
	As—C = 1.965	∠C-As-C = 103.0	a_2: 3145, 1451, 797, 133
			e: 3145, 3140, 3050, 1466, 1458, 1302, 932, 824, 591, 196, 155, 63
In-As$(CH_3)_3$			
$^2A''$ –2357.520471	In—As = 3.153	∠In-As-C = 109.0, 123.3	a′: 3131, 3124, 3121, 3038, 3034, 1481, 1467, 1464, 1304, 1281, 912, 910, 806, 575, 549, 231, 207, 163, 66, 43
	As—C = 1.981, 1.983	∠C-As-C = 98.9, 98.6	a″: 3130, 3129, 3120, 3033, 1462, 1460, 1453, 1281, 900, 798, 775, 565, 201, 159, 140, 44
$^1A_1$ –2357.345511	In—As = 3.097	∠In-As-C = 116.0	a_1: 3139, 3047, 1477, 1324, 926, 559, 224, 93
	As—C = 1.967	∠C-As-C = 102.2	a_2: 3142, 1453, 795, 138
			e: 3143, 3139, 3049, 1468, 1459, 1300, 930, 822, 589, 200, 161, 61

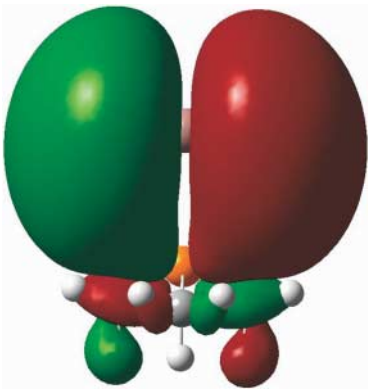
Note: The basis for the indium atom is Lanl2DZ.

degenerate under C_{3v} symmetry. However, a partially filled degenerate orbital is liable to the Jahn–Teller distortion, leading to a lower molecular symmetry by the removal of the orbital degeneracy. This is exactly what is predicted by the B3LYP calculations. The extent of the distortion is evident from the two sets of nonequivalent M-X-C angles, which differ by as much as 17°. Interestingly, the distortion for the ligand framework is very small, as the C-X-C angles are different by less than 1°. Furthermore, the M-X-C angle differences are slightly larger in the Ga complexes than in the corresponding In analogues, while the distortions in both the Ga and In species are smaller than those in the Al complexes (35).

The prediction seems to be reasonable, so far as it goes. However, it does not explain the ZEKE spectrum of In-P$(CH_3)_3$ (see the section titled In-P$(CH_3)_3$ in *ZEKE spectra*). As a further effort, we have also carried out the B3LYP calculations for this species by enforcing the C_{3v} point group. In this symmetry, the ground state is predicted to be ^2E. Compared to the $^2A''$ state in C_s symmetry, the doubly

© 2004 NRC Canada

Fig. 1. The HOMO of the $^2A''$ state of In-P$(CH_3)_3$ showing a predominant In $p\pi$ character with some ligand contributions.



degenerate state is ~70 cm^{-1} higher in energy, the In—P bond length is ~0.03 Å longer, and the In-P-C angle is ~2° larger than the average of the In-P-C angles. The ^2E state also shows an imaginary frequency, indicating that this state may not be a minimum at the potential energy surface. The imaginary frequency was calculated to be 1019i cm^{-1} with the default convergence defined in Gaussian 98 (40). With a tighter convergence criterion (e.g., cutoff values of 1.5×10^{-5} au for forces and 6×10^{-5} au for step sizes) and a finer grid (e.g., 99 radial shells, each with 590 angular points), the frequency was reduced to 193i cm^{-1}. However, it will be clear from the section on *ZEKE spectra* that spectral simulations from the C_{3v} structure yield far better agreement with the experimental spectra than the simulation from the C_s structure.

Ionization of the M-X$(CH_3)_3$ complexes leads to an $^1A_1$ ground electronic state in C_{3v} symmetry. The ionized species possesses a higher symmetry because the orbital degeneracy is lost by the removal of the metal *p*-based electron. The three M^+-X-C angles in the ion are the same size, with a value equivalent to the average of the corresponding M-X-C angles of the neutral molecule. The Ga-P/As bond lengths increase by 0.024 and 0.001 Å, while the In-P/As bond lengths shrink by 0.021 and 0.056 Å, respectively. It seems to be surprising that ionization leads to elongation of the Ga-P/As bonds, as their bond energies increase by as much as four times from the neutral $^2A''$ state to the ion $^1A_1$ state. Moreover, the metal–ligand distances of the Ga/In-N$(CH_3)_3$ complexes decrease by 0.17/0.25 Å upon ionization (15, 17). However, it has been known in inorganic chemistry that phosphine as well as arsine ligands can function not only as σ donors, but also as π acceptors because of the availability of relatively low energy empty orbitals. On the other hand, the amine ligand can only act as a σ donor since it has no low energy empty orbitals available for such a π interaction (44, 45). Thus, the metal atom may donate its pπ electron to an appropriate empty π orbital of the phosphine or arsine in the neutral complex. Such back-donation is lost upon the removal of the metal $p\pi$ electron. This means that the short-range interaction due to the π-orbital overlap between the metal and ligand is reduced in the ion, resulting in a possible increase of the metal–ligand bond length. On the other hand, ionization results in an additional long-range, charge–dipole interaction, strengthening the metal–ligand bonding. Of course, the degree of the variation in the bond length depends on the strength of the orbital overlap interaction. The predicted changes in the bond distances indicate that the π-back-donation to the phosphine ligand is slightly stronger than that to the arsine ligand. Previously, DFT calculations predicted an increase of the Al-P/As distances from the neutral to the ionized Al-P(CH_3) and -As(CH_3) complexes (35).

Table 1 also lists the harmonic vibrational frequencies of the Ga and In complexes, which will be compared with the ZEKE measurements.

Photoionization spectra

Figure 2 presents the photoionization efficiency (PIE) spectra of M-X$(CH_3)_3$ (M = Ga, In; X = P, As) seeded in helium and the PIE spectrum of In-P$(CH_3)_3$ in argon. Photoionization wavelengths in these spectra are corrected by +110 cm^{-1}, an energy shift induced by a dc field of 315 V cm^{-1} applied in the ionization region of the TOF spectrometer. The energy correction is given by $\Delta E = 6.1 F_{dc}^{1/2}$, where ΔE is in units of cm^{-1} and F_{dc} is the dc extraction field in units of V cm^{-1} (46). There is an onset of the ion signal in each of the PIE spectra, which corresponds to the ionization threshold of the complex. To estimate the threshold, a line through the onset is drawn to intersect with the baseline. Using this method, the ionization thresholds from the spectra with the helium carrier are estimated to be 39 650 (100), 40 300 (100), 38 850 (150), and 39 550 (100) cm^{-1} for Ga-P$(CH_3)_3$, Ga-As$(CH_3)_3$, In-P$(CH_3)_3$, and In-As$(CH_3)_3$, respectively.

Although the thresholds obtained from the PIE measurements are only approximate, they are very useful for the search of the ZEKE signal. Moreover, the accuracy of the PIE measurements may be significantly improved by using a heavier carrier gas. This is because heavier carriers are often more efficient in cooling the internal degrees of freedom of molecular systems, reducing the number of hot transitions from the neutral molecule. To show the carrier effect, Fig. 2*c* compares the PIE spectra of In-P$(CH_3)_3$ in helium and argon. Clearly, the ionization onset with argon is much sharper than the onset with helium, and the threshold is more accurately measured to be 38 930 (20) cm^{-1}. The carrier effect has also been observed in other complexes (17, 47, 48).

Above the ionization threshold, there appear to be some spectral features superimposed on the rising ion signal (Figs. 2*a* and 2*b*). In the PIE spectrum of In-P$(CH_3)_3$ seeded in argon, some step-like structures exist, which may be associated with transitions to higher vibrational levels of the ion state. However, definitive assignments of these structures are difficult because autoionization often obscures the observation of true threshold ion signals.

ZEKE spectra

In-P$(CH_3)_3$

Figures 3*a* and 3*b* present the ZEKE spectra of In-P$(CH_3)_3$ seeded in helium and argon carriers. The linewidth (the full width at half-maximum) of the spectrum with helium is ~8 cm^{-1}, and it is reduced to ~5 cm^{-1} with argon. Two observations can be made from the spectra. First, the spectrum in helium shows more transitions compared with that in argon. By comparing the two spectra, hot transitions

© 2004 NRC Canada

Fig. 2. PIE spectra of: (*a*) Ga-P(CH_3)$_3$, (*b*) Ga-As(CH_3)$_3$, (*c*) In-P(CH_3)$_3$, and (*d*) In-As(CH_3)$_3$ with the helium carrier gas. The spectrum of In-P(CH_3)$_3$ with an argon carrier gas is also shown in (*c*).

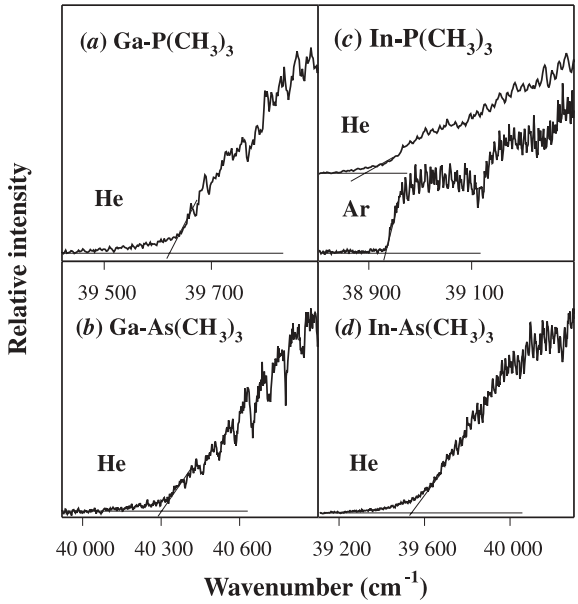
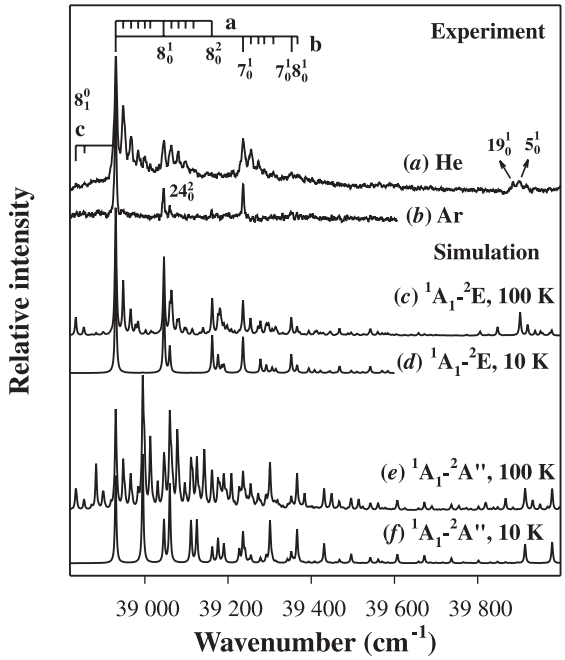


Fig. 3. ZEKE spectra and simulations of In-P(CH_3)$_3$: (*a*, *b*) The experimental spectra with helium and argon carrier gases, (*c*, *d*) the simulations from the $^1A_1 \leftarrow {}^2E$ transition at 100 and 10 K, and (*e*, *f*) the simulations from the $^1A_1 \leftarrow {}^2A''$ transition at 100 and 10 K.



can be quickly identified. Second, the spectra exhibit relatively short progressions, indicating that the change in the molecular structure is small upon ionization.

Figures 3*c* and 3*d* show the simulations from the $^1A_1 \leftarrow {}^2E$ transition, and Figs. 3*e* and 3*f* display the simulations from the $^1A_1 \leftarrow {}^2A''$ transition. In these simulations, the theoretical energy of the 0–0 transition is referenced to the experimental value for simplicity. Simulations for both transitions were carried out at various temperatures to estimate the vibrational temperatures of the complex in the argon and helium beams. In general, vibrational temperatures are dependent on frequencies of normal modes, since different modes are expected to cool with different efficiencies. In supersonic beams, however, transitions from vibrationally excited levels of the neutral molecule are limited to the smallest frequency mode(s). Thus, simulations at finite temperatures often reproduce hot transitions in ZEKE spectra (12–17, 35, 47, 48). It is clear that the $^1A_1 \leftarrow {}^2E$ simulations at 10 and 100 K match well to the experimental spectra with the argon and helium carriers, respectively. In contrast, the $^1A_1 \leftarrow {}^2A''$ simulations have little similarity with the experimental spectra. The comparison between the simulated and measured spectra suggests that the neutral complex is in the ^2E ground state, rather than the Jahn–Teller distorted $^2A''$ state. This is contrary to the B3LYP calculations, which predict that the ^2E state is ~70 cm^{-1} higher in energy than the $^2A''$ state. One should keep in mind, however, that the relativistic effect is not included in the B3LYP method. Such an effect is expected to yield a sizeable spin–orbit splitting for an indium-containing molecule. For the atomic indium, the splitting between the two *J* levels of the ground ^2P state is 2212 cm^{-1} (49). The splitting is expected to be reduced by complex formation because of the recoupling of the angular momentum in a molecular framework. The reduction is estimated to be a factor of one-third in a strong-field approximation (50), resulting in a splitting of about 1500 cm^{-1} in an In complex. Thus, if the spin–orbit effect were included in the B3LYP calculations, the lower spin component ($^2E_{1/2}$) would be below the $^2A''$ state.

The spectral assignment is trivial with the excellent agreement between the $^1A_1 \leftarrow {}^2E$ simulations and experimental spectra and is listed in Table 2 and labeled in Fig. 3 as well. The ν_8 mode is identified as the In-P stretching (a_1), with a ν_8^+ frequency of 116 cm^{-1} in the cation and a ν_8'' frequency of 96 cm^{-1} in the neutral molecule. The ν_{24} mode is the In-P-C bending vibration that has an ion frequency (ν_{24}^+) of 65 cm^{-1} and a neutral frequency (ν_{24}'') of 47 cm^{-1}. In addition to the metal–ligand stretching and bending vibrations, two CH_3 wag vibrations (ν_5^+/ν_{19}^+) and a PC_3 umbrella vibration (ν_7^+) in the ionized complex are also identified from these spectra. The CH_3 wag frequencies are measured to be 972 cm^{-1} for ν_5^+ and 956 cm^{-1} for ν_{19}^+. The PC_3 umbrella frequency is determined to be 306 cm^{-1}. No hot transitions were observed from the excited levels of these relatively high frequency modes.

Ga-P(CH_3)$_3$

The ZEKE spectra of Ga-P(CH_3)$_3$ are presented in Fig. 4. The top trace was recorded with argon and the bottom one was obtained with helium. As in the case of the indium complex, argon shows more efficient cooling than helium. Furthermore, the spectrum of Ga-P(CH_3)$_3$ in argon exhibits many more transitions than the spectrum of In-P(CH_3)$_3$ (Figs. 3*b* and 4*a*). At this point, we may also compare Ga-P(CH_3)$_3$ with previously studied Al-P(CH_3)$_3$ (35). The ZEKE spectrum of Al-P(CH_3)$_3$ is dominated by the Al^+-P-C degenerate bending progression and its combination with the

© 2004 NRC Canada

Table 2. ZEKE peak positions (cm^{-1}) and assignments.

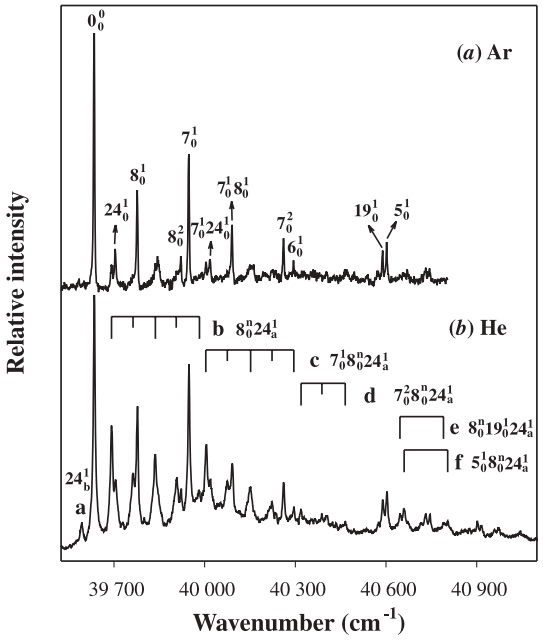
Ga-P$(CH_3)_3$[a]		In-P$(CH_3)_3$		Ga-As$(CH_3)_3$	
Peak position (cm^{-1})	Assignment	Peak position (cm^{-1})	Assignment	Peak position (cm^{-1})	Assignment
39 594	24^1_b	38 834	8^1_1	40 322	0^0_0
39 635	0^0_0	38 855	$8^0_1 24^1_1$	40 364	24^1_0
39 692	24^1_a	38 930	0^0_0	40 447	8^1_0
39 706	24^1_0	38 948	24^1_1	40 490	$8^1_0 24^1_0$
39 763	24^2_a	38 967	24^2_2	40 550	7^1_0
39 778	8^1_0	38 984	24^3_3	40 576	8^2_0
39 837	$8^1_0 24^1_a$	39 000	24^4_4	40 594	$7^1_0 24^1_0$
39 844	$8^1_0 24^1_0$	39 013	24^5_5	40 617	$8^2_0 24^1_0$
39 906	$8^1_0 24^2_a$	39 046	8^1_0	40 674	$7^1_0 8^1_0$
39 923	8^2_0	39 060	24^2_0	40 699	8^3_0
39 948	7^1_0	39 064	$8^1_0 24^1_1$	40 719	$7^1_0 8^1_0 24^1_0$
39 983	$8^2_0 24^1_a$	39 081	$8^1_0 24^2_2$	40 780	7^2_0
40 004	$7^1_0 24^1_a$	39 098	$8^1_0 24^3_3$		
40 019	$7^1_0 24^1_0$	39 117	$8^1_0 24^4_4$		
40 075	$7^1_0 24^2_a$	39 161	8^2_0		
40 091	$7^1_0 8^1_0$	39 236	7^1_0		
40 152	$7^1_0 8^1_0 24^1_a$	39 255	$7^1_0 24^1_1$		
40 162	$7^1_0 8^1_0 24^1_0$	39 273	$7^1_0 24^2_2$		
40 223	$7^1_0 8^1_0 24^2_a$	39 287	$7^1_0 24^3_3$		
40 261	7^2_0	39 309	$7^1_0 24^4_4$		
40 295	6^1_0	39 353	$7^1_0 8^1_0$		
40 319	$7^2_0 24^1_a$	39 367	$7^1_0 8^1_0 24^1_1$		
40 388	$7^2_0 24^2_a$	39 886	19^1_0		
40 404	$7^2_0 8^1_0$	39 902	5^1_0		
40 465	$7^2_0 8^1_0 24^1_a$				
40 575	7^3_0				
40 589	19^1_0				
40 603	5^1_0				
40 646	$19^1_0 24^1_a$				
40 660	$5^1_0 24^1_a$				
40 670	$5^1_0 24^1_0$				
40 716	$7^3_0 8^1_0$				
40 732	$8^1_0 19^1_0$				
40 746	$5^1_0 8^1_0$				
40 804	$5^1_0 8^1_0 24^1_a$				
40 902	$7^1_0 19^1_0$				
40 916	$5^1_0 7^1_0$				
40 959	$7^1_0 19^1_0 24^1_a$				
40 973	$5^1_0 7^1_0 24^1_a$				
41 045	$7^1_0 8^1_0 19^1_0$				

[a] 24_a (14 cm^{-1}) and 24_b (112 cm^{-1}) are two sublevels of 24_1, split by the linear Jahn–Teller effect.

PC_3 umbrella vibration. The spectrum has been identified from the $^1A_1 \leftarrow {}^2A''$ transition. In contrast, the In-P$(CH_3)_3$ spectrum exhibits a predominant In^+-P stretching progression combined with the PC_3 vibration and is described by the $^1A_1 \leftarrow {}^2E$ transition. This indicates that the Jahn–Teller distortion is reduced from Al to In. This is not surprising because the spin–orbit coupling increases with increasing atomic number and competes with the Jahn–Teller effect in lifting orbital degeneracies. With this in mind, we expect the degrees of the Jahn–Teller distortion and spin–orbit splitting in Ga-P$(CH_3)_3$ to be between those in Al- and In-P$(CH_3)_3$. Indeed, the ZEKE spectrum of Ga-P$(CH_3)_3$ shows significant activities from both the Ga^+-P stretching and Ga^+-P-C bending vibrations. Due to the dynamic Jahn–Teller effect, the observed intensities in the spectrum of Ga-P$(CH_3)_3$ cannot be satisfactorily described with the FC approximation.

© 2004 NRC Canada

Fig. 4. ZEKE spectra of Ga-P$(CH_3)_3$ with (*a*) argon and (*b*) helium carrier gases.



However, cold transitions from the vibrationless level of the neutral state to excited vibrational levels of the ionic $^1A_1$ state can be easily identified by comparing them to the theoretical predictions and to the vibrations in the In-P$(CH_3)_3$ complex.

The spectrum recorded with the argon beam displays short progressions with 71, 143, and 313 cm^{-1} intervals as well as their combinations. In addition, the spectrum exhibits three peaks located at 660, 954, and 968 cm^{-1} to the blue of the band origin (39 635 cm^{-1}). The 71 and 143 cm^{-1} intervals are in good agreement with the predicted Ga^+-P-C bending (ν_{24}^+, e) and Ga^+-P stretching (ν_8^+, a_1) fundamentals of 76 and 132 cm^{-1}. Thus, these two progressions are assigned to the 8_0^n and 24_0^n transitions. Because the ν_{24}^+ frequency is about one-half of the ν_8^+ frequency, the 8_0^n progression may also contain the contribution from the 24_0^n transitions. The observation of the 24_0^n transitions is the result of the vibronic coupling.

From the spectrum of In-P$(CH_3)_3$, we identified two CH_3 wags (972/956 cm^{-1}) and a PC_3 umbrella (306 cm^{-1}) vibration. Since these are ligand-based vibrations, their frequencies are expected to be similar in both In-P$(CH_3)_3$ and Ga-P$(CH_3)_3$. By comparison, the 968 and 954 cm^{-1} peaks in the spectrum of Ga-$(CH_3)_3$ are assigned to the two CH_3 wag modes, and the 313 cm^{-1} interval to the PC_3 umbrella motion. The weak peak at 660 cm^{-1} to the blue of the band origin is also expected to be from a ligand-based vibration. On the basis of the B3LYP prediction, this peak can only be assigned to the P-C stretching (ν_6^+, a_1) in the ion, which has a theoretical frequency of 640 cm^{-1}. There are a few unlabeled peaks in Fig. 4*a*, which are identified as hot transitions by comparing with the spectrum in helium. The analysis of these hot transitions is discussed in the following.

The helium spectrum of Ga-P$(CH_3)_3$ (Fig. 4*b*) shows increased intensities for the hot transitions observed in argon and additional peaks that are not observed in the argon spectrum. To the red of the band origin, a hot transition (labeled a) appears at 41 cm^{-1}. To the blue of the band origin, hot transitions (labeled b–f) lie 57 cm^{-1} above each of the 8_0^n, $7_0^1 8_0^n$, $7_0^2 8_0^n$, $8_0^n 19_0^1$, and $5_0^1 8_0^n$ peaks. Assigning these hot transitions requires at least two neutral frequencies to be involved. Two possible assignments are presented below. In the first scenario, the peak at 41 cm^{-1} below the 0–0 transition is attributed to $8_1^1 24_1^0$ and the peaks at 57 cm^{-1} above various ion vibrations are assigned to the transitions from the first excited level of ν_{24}'' (e.g., $8_0^1 24_1^0$ for the first peak). This assignment yields a ν_{24}'' frequency of 86 cm^{-1} and a ν_8'' frequency of 98 cm^{-1}, which are in fair agreement with the calculated values of 68 and 112 cm^{-1}, respectively. Although the frequency comparison between the theory and experiment is not unacceptable, this assignment has difficulty explaining why the transitions from the first excited level of ν_{24}'' remain in the cooler argon spectrum. In the case of In-P$(CH_3)_3$, ν_{24}'' has a frequency of 47 cm^{-1} and ν_8'' has a frequency of 96 cm^{-1}, and the transitions associated with these two modes disappear by changing the carrier from helium to argon. If the ν_{24}'' mode of Ga-P$(CH_3)_3$ has a frequency of 86 cm^{-1}, then the transitions associated with 24_1 should also disappear from the argon spectrum. However, this is not the case although the transition intensities are reduced. Therefore, we propose another assignment for these hot transitions. The second scenario assumes that the 24_1 level is split into two sublevels by the linear Jahn–Teller effect (51). The relative energies of these two levels with respect to the vibrationless level are assumed to be $\omega_e \pm 2D\omega_e$, where ω_e is the harmonic frequency of ν_{24}'' and D is a small, linear Jahn–Teller coefficient. With this assumption, the peak at 41 cm^{-1} to the red of the band origin can be assigned to the higher energy sublevel of 24_1, which is labeled as 24_b in Fig. 4*b* and Table 2. The peaks at 57 cm^{-1} above various cold transitions are attributed to the transitions associated with the lower energy sublevel of 24_1, which is labeled as 24_a. On the basis of this assignment, the 24_a and 24_b sublevels are located at 14 and 112 cm^{-1} above the vibrationless level of the neutral ground state. This gives a 24_1 frequency of 63 cm^{-1} prior to Jahn–Teller splitting and a linear Jahn–Teller coefficient of 0.39. Now the ν_{24}'' frequency of 63 cm^{-1} is in excellent agreement with the calculated value of 68 cm^{-1}. Although the D value is relatively large, it is not unusual. A linear Jahn–Teller coefficient as large as 0.45 has been reported for the ^2E state of OCF_3 (52). Furthermore, the very small frequency of 24_a much better explains the observation of the weak peaks in the argon spectrum.

Ga-As$(CH_3)_3$

The ZEKE spectrum of Ga-As$(CH_3)_3$ with helium is shown in Fig. 5. Attempts to record a ZEKE spectrum in argon were not successful due to the limited size of the signal. In coordination with the B3LYP calculations, we identified short 7_0^n and 8_0^n progressions and their combinations as well as a 24_1^0 transition and its combinations with ν_7^+ and ν_8^+. The vibrational frequencies of the ν_7^+, ν_8^+, and ν_{24}^+ modes are determined to be 228, 125, and 42 cm^{-1}, respectively. The measured ν_7^+ and ν_8^+ frequencies match well to the cal-

© 2004 NRC Canada

Fig. 5. The ZEKE spectrum of Ga-As$(CH_3)_3$ with a helium carrier gas.

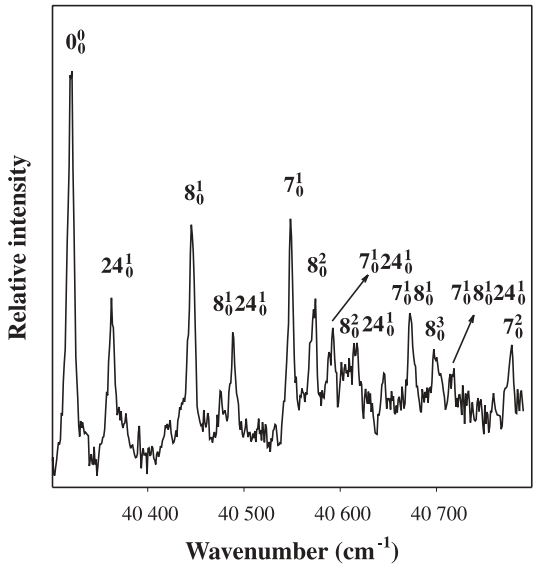


Table 3. Vibrational frequencies (cm^{-1}) from the ZEKE measurements and B3LYP calculations.

	Ga-P$(CH_3)_3$	In-P$(CH_3)_3$	Ga-As$(CH_3)_3$
$^1A_1$			
CH_3 (ν_5^+, a_1)	968 (987)	972 (984)	
X-C (ν_6^+, a_1)	660 (640)		
XC_3 (ν_7^+, a_1)	313 (303)	306 (293)	228 (223)
M-X (ν_8^+, a_1)	143 (132)	116 (106)	125 (120)
CH_3 (ν_{19}^+, e)	954 (978)	956 (978)	
M-X-C (ν_{24}^+, e)	71 (76)	65 (71)	42 (63)
^2E			
M-X (ν_8'', a_1)		96 (80)	
M-X-C (ν_{24}'', e)		47 (60)	

Note: Values in parentheses are from the B3LYP calculations.

Table 4. Adiabatic ionization potentials (AIP) and dissociation energies (D_0/D_0^+) of M-X$(CH_3)_3$ (M = Al, Ga, In; X = N, P, As).

	AIP[a] (cm^{-1})	D_0 (kcal/mol)[b]	D_0^+ (kcal/mol)	Reference
Al	48 278			53
Al-N$(CH_3)_3$	37 373 (37 682)	9.9	40.3	16
Al-P$(CH_3)_3$	39 981 (39 710)	10.4	35.5	35
Al-As$(CH_3)_3$	40 451 (40 284)	7.8	31.3	35
Ga	48 378			53
Ga-N$(CH_3)_3$	38 081 (38 630)	8.5	37.1	17
Ga-P$(CH_3)_3$	39 635 (39 558)	9.7	35.7	This work
Ga-As$(CH_3)_3$	40 322 (40 218)	7.6	31.7	This work
In	46 670			53
In-N$(CH_3)_3$	38 236 (37 008)	6.9	32.9	15
In-P$(CH_3)_3$	38 930 (37 914)	7.2	31.2	This work
In-As$(CH_3)_3$	39 550[c] (38 602)	5.6	27.7	This work

Note: AIPs are obtained from the ZEKE spectra and B3LYP calculations (in parentheses). D_0/D_0^+ are from the B3LYP calculations.

[a]The uncertainty of the AIP values is ±8 cm^{-1}.

[b]1 kcal/mol = 349.8 cm^{-1}.

[c]This value was obtained from the PIE spectrum and has an uncertainty of ±100 cm^{-1}.

culated values of 223 and 120 cm^{-1}, while the agreement for ν_{24}^+ is not as good.

Table 3 summarizes the vibrational frequencies from the ZEKE measurements and the B3LYP calculations. It can be seen that the agreement between the experiment and theory is excellent for most vibrational modes, but the predicted values are in larger error for some of the very low frequency modes.

Adiabatic ionization potentials and bond dissociation energies

Table 4 lists the AIPs and dissociation energies of the gallium and indium complexes reported in this work and those of other similar molecular systems for comparison. The AIPs were obtained from the ZEKE measurements and B3LYP calculations, and the dissociation energies were calculated with the B3LYP methods. The theoretical AIPs are a few hundreds of wavenumbers from the experimental values for the aluminum and gallium complexes and are about a thousand wavenumbers smaller for the indium systems. The larger errors for the heavy metal systems likely arise from the use of the pseudopotential Lanl2DZ basis set. Although the accuracy of the calculated dissociation energies cannot be evaluated directly, the differences between the ion and neutral dissociation energies can be compared with the experimental AIP shifts from the bare metal atoms to the complexes [AIP(M) – AIP(ML) = $D_0^+(M^+L) - D_0(ML)$, where M = Al, Ga, In; L = X$(CH_3)_3$; X = N, P, As]. Differences

© 2004 NRC Canada

between the experimental Δ(AIP) and the theoretical Δ(D_0^+ – D_0) are about 1 kcal mol^{-1} for the aluminum and gallium complexes and around 2 kcal mol^{-1} for the indium species.

A number of trends in the AIPs and bond energies can be drawn from Table 4. First, the AIPs of the metal atoms are reduced upon ligand coordination, and the reduction is substantially larger for Al/Ga-N(CH_3)$_3$ than for other systems. The AIP reduction correlates with the increase of the bond energy from the neutral to the ionized complex. This binding enhancement is the result of the removal of an antibonding electron in the neutral and the addition of a charge–dipole interaction. Second, the bond dissociation energies of the neutral complexes follow the order P(CH_3)$_3$ > N(CH_3)$_3$ > As(CH_3)$_3$ for a given metal and Al > Ga > In for a given ligand. Interestingly, the ion bond energies do not follow the same trends as those of the neutral complexes. For a given metal ion, the bond energies are in the order N(CH_3)$_3$ > P(CH_3)$_3$ > As(CH_3)$_3$. For the nitrogen ligand, the order is Al^+ > Ga^+ > In^+; for the phosphine and arsine ligands, it is Al^+ ~ Ga^+ > In^+. To explain these bonding trends, both short- and long-range forces must be considered to include orbital, σ/π dative, charge–dipole, dipole – induced-dipole, and polarization interactions. A quantitative analysis of each interaction is in progress and will be reported in the future.

Conclusions

The analysis of the vibrationally resolved ZEKE spectra shows that the spectrum of In-P(CH_3) arises from the $^1A_1$–^2E transition and the spectra of Ga-P(CH_3)$_3$ and Ga-As(CH_3)$_3$ are due to the transitions from the Jahn–Teller distorted doublet state to the $^1A_1$ state. The spectrum of the indium complex can be treated with the FC approximation, while the spectra of the gallium systems cannot be so described because of significant vibronic couplings. The adiabatic ionization energies of the metal complexes are substantially lower than those of the bare metal atoms, and the metal–arsine complexes have slightly higher ionization energies than the corresponding phosphine systems. The metal–phosphine binding is significantly stronger than the metal–arsine binding, in both the neutral and ionized complexes. In comparison with the ZEKE measurements, the B3LYP calculations yield excellent frequencies for most vibrational modes, but the agreement is less desirable for some of the low frequency modes. The calculated ionization energies are in better agreement for the gallium systems than for the indium species.

Acknowledgements

This work was supported by the National Science Foundation (CHE-0111227) and the donors of the Petroleum Research Fund of the American Chemical Society.

References

1. H. Himmel, A.J. Downs, and T.M. Greene. J. Am. Chem. Soc. **122**, 9793 (2000).
2. H. Himmel, A.J. Downs, J.C. Green, and T.M. Greene. J. Chem. Soc. Dalton Trans. **5**, 535 (2001).
3. D.V. Lanzisera and L. Andrews. J. Phys. Chem. A, **101**, 5082 (1997).
4. L. Andrews, M. Zhou, G.V. Chertihin, W.D. Bare, and Y. Hannachi. J. Phys. Chem. A, **104**, 1656 (2000).
5. M. Zhou and L. Andrews. J. Phys. Chem. A, **101**, 1648 (2000).
6. T.M. Di Palma, A. Latini, M. Satta, M. Varvesi, and A. Giardini. Chem. Phys. Lett. **284**, 184 (1998).
7. T.M. Di Palma, A. Latini, M. Satta, and A. Giardini. Eur. Phys. J. D, **4**, 225 (1998).
8. L.R. Brock and M.A. Duncan. J. Phys. Chem. **99**, 16 571 (1995).
9. J. Jakubek and B. Simard. J. Chem. Phys. **112**, 1733 (2000).
10. L.R. Brock and M.A. Duncan. J. Chem. Phys. **102**, 9498 (1995).
11. D.-S. Yang and J. Miyawaki. Chem. Phys. Lett. **313**, 514 (1999).
12. G.K. Rothschopf, J.S. Perkins, S. Li, and D.-S. Yang. J. Phys. Chem. A, **104**, 8178 (2000).
13. D.-S. Yang. Coord. Chem. Rev. **214**, 187 (2001).
14. S. Li, G.K. Rothschopf, D. Pillai, B.R. Sohnlein, B.M. Wilson, and D.-S. Yang. J. Chem. Phys. **115**, 7968 (2001).
15. G.K. Rothschopf, S. Li, J.S. Perkins, and D.-S. Yang. J. Chem. Phys. **115**, 4565 (2001).
16. S. Li, G.K. Rothschopf, J.F. Fuller, and D.-S. Yang. J. Chem. Phys. **118**, 8636 (2003).
17. S. Li, J.F. Fuller, G.K. Rothschopf, B.R. Sohnlein, and D.-S. Yang. J. Chem. Phys. **119**, 8882 (2003).
18. X. Yang, I. Gerasimov, and P.J. Dagdigian. Chem. Phys. Lett. **239**, 207 (1998).
19. X. Tan and P.J. Dagdigian. J. Phys. Chem. A, **105**, 11 009 (2001).
20. G.M. Greetham, M.J. Hanton, and A.M. Ellis. Phys. Chem. Chem. Phys. **1**, 2709 (1999).
21. K.X. He, T.D. Hammond, C.B. Winstead, J.L. Gole, and D.A. Dixon. J. Chem. Phys. **95**, 7183 (1991).
22. K. Imura, T. Kawashima, H. Ohoyama, and T. Kasai. J. Am. Chem. Soc. **123**, 6367 (2001).
23. J.A. Howard, H.A. Joly, P.P. Edwards, R.J. Singer, and D.E. Logan. J. Am. Chem. Soc. **114**, 474 (1992).
24. R.D. Davy and K.L. Jaffrey. J. Phys. Chem. **98**, 8930 (1994).
25. S. Sakai. J. Phys. Chem. **96**, 8369 (1992).
26. B.S. Jursic. Chem. Phys. Lett. **237**, 51 (1998).
27. T. Fängström, S. Lunell, P.H. Kasai, and L.A. Eriksson, J. Phys. Chem. A, **102**, 1005 (1998).
28. D. Stökigt. Chem. Phys. Lett. **250**, 387 (1996).
29. M. Sodupe and C.W. Bauschlicher, Jr. Chem. Phys. Lett. **181**, 321 (1991).
30. M. Alcamí, O. Mó, and M.J. Yáñez. Mol. Struct: THEOCHEM, **234**, 357 (1991).
31. S.F. Smith, J. Chandrasekhar, and W.L. Jorgensen. J. Phys. Chem. **87**, 1898 (1983).
32. G. Chaban and M.S. Gordon. J. Chem. Phys. **107**, 2160 (1997).
33. H.-J. Himmel, A.J. Downs, and T.M. Greene. Inorg. Chem. **40**, 396 (2001).
34. S. Li, G.K. Rothschopf, B.R. Sohnlein, and D.-S. Yang. J. Phys. Chem. A, **106**, 6941 (2002).
35. S. Li, G.K. Rothschopf, and D.-S. Yang. J. Chem. Phys. **116**, 6589 (2002).
36. R.D. Davy and H.F. Schaefer. J. Phys. Chem. A, **101**, 3135 (1997).
37. T.G. Dietz, M.D. Duncan, D.E. Powers, and R.E. Smalley. J. Chem. Phys. **74**, 6511 (1981).
38. W.C. Wiley and I.H. McLaren. Rev. Sci. Instrum. **26**, 1150 (1955).
39. D. Proch and T. Trickl. Rev. Sci. Instrum. **60**, 713 (1989).

© 2004 NRC Canada

40. Gaussian 98. Revision A.11 [computer program]. Gaussian Inc., Pittsburgh, Pa. 1998.
41. F. Duschinsky. Acta Physicochim. URSS, **7**, 551 (1937).
42. D.-S. Yang, M.Z. Zgierski, D.M. Rayner, P.A. Hackett, A. Martinez, D.R. Salahub, P.N. Roy, and T. Carrington, Jr. J. Chem. Phys. **103**, 5335 (1995).
43. A. Berces, M.Z. Zgierski, and D.-S. Yang. *In* Computational molecular spectroscopy. *Edited by* P. Jensen and P. Bunker. Wiley, New York. 2000. p. 110.
44. F.A. Cotton, G. Wilkinson, C.A. Murillo, and M. Bochmann. *In* Advanced inorganic chemistry. 6th ed. Wiley, New York. 1999.
45. M.S. Davis, R.K. Pierens, and M.J. Aroney. J. Organomet. Chem. **458**, 141 (1993); G. Pacchioni and P.S. Bagus. Inorg. Chem. **31**, 4391 (1992); D.S. Marynick. J. Am. Chem. Soc. **106**, 4064 (1984).
46. M.A. Duncan, T.G. Dietz, and R.E. Smalley. J. Chem. Phys. **75**, 2118 (1981).
47. J.F. Fuller, S. Li, B.R. Sohnlein, G.K. Gretchen, and D.-S. Yang. Chem. Phys. Lett. **366**, 141 (2002).
48. S. Li, B.R. Sohnlein, G.K. Gretchen, J.F. Fuller, and D.-S. Yang. J. Chem. Phys. **119**, 5406 (2003).
49. C.E. Moore. *In* Atomic energy levels. Vol. 3. Natl. Stand. Ref. Data, Ser. No. 35. Natl. Bur. Stand., Washington, D.C. 1971.
50. H. Lefebvre-Brion and R.W. Field. Perturbations in the spectra of diatomic molecules. Academic Press, Orlando, Fla. 1986.
51. T.A. Barckholtz and T.A. Miller. Int. Rev. Phys. Chem. **17**, 435 (1998).
52. T.A. Barckholtz, M.-C. Yang, and T.A. Miller. Mol. Phys. **97**, 239 (1999).
53. D.R. Lide and H.P.R. Frederikse. *In* CRC handbook of chemistry and physics. 78th ed. CRC Press, New York. 1997. pp. 10–214.

© 2004 NRC Canada

A vacuum ultraviolet laser single-photon zero kinetic energy photoelectron spectroscopic study of the $\tilde{X}^2E_{3/2}$ ground electronic state of CH_3Br^+ [1]

Y.J. Shi, S. Wang, Z.J. Jakubek, and B. Simard

Abstract: The vacuum ultraviolet laser single-photon zero kinetic energy (ZEKE) photoelectron spectrum of the $\tilde{X}^2E_{3/2}$ ground electronic state of the methyl bromide cation is reported. The spectrum is dominated by the origin band 0_0^0 of the transition $\tilde{X}^2E_{3/2} \leftarrow \tilde{X}^1A_1$. In addition, the 2_0^1 band and the 3_1^1 hot band are observed. All observed bands show similar rotational contours. Simulation of the rotational contour of the origin band yields the first ionization energy of methyl bromide (85 031.2 ± 1.0 cm^{-1}) and the rotational constants of the cation in its ground electronic state.

Key words: methyl bromide, vacuum ultraviolet laser, single-photon excitation, zero kinetic energy photoelectron spectroscopy.

Résumé : Faisant appel à un laser ultraviolet du vide, on a déterminé le spectre photoélectronique d'énergie cinétique électronique nulle (« ZEKE »), à excitation photonique unique, de l'état électronique fondamental $\tilde{X}^2E_{3/2}$ du cation bromure de méthyle. Le spectre est dominé par la bande d'origine, 0_0^0, de la transition $\tilde{X}^2E_{3/2} \leftarrow \tilde{X}^1A_1$. On a de plus observé la bande 2_0^1 et la bande chaude 3_1^1. Toutes les bandes observées présentent des contours rotationnels semblables. La simulation du contour rotationnel de la bande d'origine permet d'obtenir l'énergie de première ionisation du bromure de méthyle (85 031,2 ± 1,0 cm^{-1}) et les constantes de rotation du cation dans son état électronique fondamental.

Mots clés : bromure de méthyle, laser ultraviolet du vide, excitation photonique unique, spectroscopie photoélectronique d'énergie cinétique électronique nulle.

[Traduit par la Rédaction]

Introduction

Methyl bromide has recently received considerable interest from atmospheric and environmental scientists owing to its role as the most abundant atmospheric source of bromine in the gas phase (1–4), which is found to be extremely efficient, nearly 40 times more than chlorine, in removing ozone in the stratosphere (5, 6). Atmospheric CH_3Br comes essentially from natural and anthropogenic sources (2). The major process of the destruction of CH_3Br in the atmosphere involves its reaction with the hydroxyl radical. Investigation of the role that methyl bromide plays in atmospheric chemistry has stimulated many laboratory studies of the physicochemical and spectroscopic properties of methyl bromide in the last several decades.

The molecular structure and the thermodynamic and spectroscopic properties of neutral CH_3Br have been extensively investigated in the past (7–11). However, less is known about the methyl bromide cation. The lowest ionization energy (IE = 85 020 cm^{-1}) of CH_3Br was first obtained by Price from an analysis of the Rydberg series observed in the vacuum ultraviolet (VUV) absorption spectrum (12). Two other VUV absorption studies of the same molecule in the mid-1970s yielded the lowest IE of 85 020 cm^{-1} (13) and 85 012 cm^{-1} (14). The photoelectron spectra in the outer valence region of methyl bromide have been reported by several research groups (15–20). In these studies, the ionization energies of the ground electronic state and several excited electronic states of CH_3Br^+ were obtained. The vibrational frequencies of the totally symmetric ν_2 and ν_3 modes, as well as the degenerate ν_4 and ν_6 modes in the cationic ground electronic states, were also determined. However, these studies suffered from the major deficiency of conventional photoelectron spectroscopy, namely its poor resolution, typically no better than 10 meV. This problem was overcome with the development of zero kinetic energy (ZEKE) photoelectron spectroscopy in the 1980s (21, 22). ZEKE spectroscopy offers a significantly higher spectral resolution and has become a method of choice for high-resolution spectroscopy of molecular ions. Song et al. (23) reported the pulsed-field ionization photoelectron (PFI–PE) spectra of CH_3Br^+ using a VUV synchrotron radiation. They obtained the lowest IE value of 10.5427 ± 0.0010 eV (85 032.6 ± 8.0 cm^{-1}), with a resolution of 1 meV. Very recently, Urban and Bondybey (24) reported the threshold photoelectron spectra (ZEKE) of CH_3Br^+ using one-color,

Received 31 October 2003. Published on the NRC Research Press Web site at http://canjchem.nrc.ca on 10 September 2004.

Y.J. Shi,[2,3] S. Wang, Z.J. Jakubek, and B. Simard. Steacie Institute for Molecular Sciences, National Research Council of Canada, Ottawa, ON K1A 0R6, Canada.

[1]This article is part of a Special Issue dedicated to the memory of Professor Gerhard Herzberg.

[2]Present address: Department of Chemistry, University of Calgary, 2500 University Drive NW, Calgary, AB T2N 1N4, Canada.

[3]Corresponding author (e-mail: shiy@ucalgary.ca).

 doi: 10.1139/V04-051 © 2004 NRC Canada

two- and three-photon excitations. The lowest IE was determined to be 85 024.6 ± 4.0 cm^{-1}; the frequencies of the six vibrational modes of the ground electronic state of CH_3Br^+ were also obtained. However, none of the observed features in the previous studies showed resolved rotational structures or rotational contours.

In this work, the high-resolution ZEKE photoelectron spectrum of CH_3Br^+ was recorded using single-photon VUV excitation, in which the coherent VUV laser radiation was generated by a two-photon resonance-enhanced four-wave mixing process in Hg vapor. By carefully optimizing the ZEKE detection scheme, we obtained a spectral resolution in the range 1.0–1.2 cm^{-1}, which was mainly determined by the line widths of the lasers used. The resolution was insufficient to fully resolve the rotational structures of the bands, but it allowed for the observation of the rotational contours of the origin band and some excited vibrational bands of the ground electronic state of CH_3Br^+. Simulation of the rotational contours of the origin band resulted in the determination of the adiabatic ionization energy and the rotational constants for the ground electronic state of CH_3Br^+.

Experimental

The ZEKE photoelectron spectrum of the CH_3Br^+ ion was obtained using a home-built, versatile high-resolution ZEKE/MATI (mass analyzed threshold ionization) spectrometer. Details of the apparatus have been described elsewhere (25). Only the new features relevant to the present work are discussed here. Two Nd:YAG pumped dye lasers were used to generate tunable, coherent, and monochromatic VUV light by two-photon resonance-enhanced four-wave mixing in Hg vapor (26, 27). The red beam of the first dye laser (ν_1) was frequency doubled in a KDP crystal to be two-photon resonant with the Hg $6s7s$ ($^1S_0$) $\leftarrow$ $6s^2$ ($^1S_0$) transition at 63 928.243 cm^{-1} (28). The second dye laser (ν_2) was scanned between 20 960 and 22 420 cm^{-1} to produce VUV light tunable between 84 890 and 86 350 cm^{-1}. The wavenumber of this visible beam (ν_2) was calibrated using a Fizeau wavelength meter (New Focus, 7711) with a factory-specified precision of 0.4 cm^{-1}. The maximum error in the ionization potential, including the maximum calibration error of 0.4 cm^{-1}, was estimated to be 1.0 cm^{-1}. Both visible beams (ν_1 and ν_2) have a line width of 0.15 cm^{-1}. Hg vapor was produced in a heated Pyrex cell equipped with a water-cooling jacket on each end to prevent condensation of Hg vapor on both the quartz entrance window and the LiF (lithium fluoride) exit window. Krypton gas (≤5 torr; 1 torr = 133.322 Pa) was added to the Hg vapor to satisfy the phase-matching condition. The Hg cell was mounted on the front end of the vacuum chamber housing a linear time-of-flight (TOF) mass spectrometer.

The VUV light was directed into the ionization chamber to cross a skimmed molecular beam of the CH_3Br–He mixture located between the E_2 and E_3 grids of the TOF mass spectrometer. It should be noted that the ion optics of the TOF mass spectrometer is composed of four parallel copper mesh grids, labeled from bottom to top as E_1, E_2, E_3, and E_4. The CH_3Br–He mixture was prepared by diluting 300 torr of CH_3Br in ultrahigh purity helium to a total pressure of 4 atm (1 atm = 101.325 kPa). The sample was subsequently introduced into the vacuum chamber in a supersonic jet expansion through a nozzle of a pulsed piezoelectric valve. The arrival of the VUV light was synchronized to the valve opening using a digital delay generator (Stanford Research Systems, DG 535).

In the ZEKE experiment, the methyl bromide molecule was excited in a VUV single-photon process to high-n* Rydberg states converging to an eigenstate of the methyl bromide cation. After a 30-ns delay with respect to the firing of the excitation laser, the first pulsed electric field (discrimination) of 333 mV/cm (duration = 600 ns) was created between the E_2 and E_3 electrodes by applying a negative voltage to the E_3 grid. The second pulsed field (ionization) of 667 mV/cm was created between the E_2 and E_3 electrodes by applying a negative voltage on the E_2 grid 830 ns after the laser excitation. The third pulsed electric field (acceleration) between E_3 and E_4 with an amplitude of 28 V/cm and a duration of 20 ns was generated by applying a short positive voltage pulse to the E_4 grid 51 ns after the start of the ionization pulse. The E_1 grid was grounded in the ZEKE experiment. The electrons, generated either by direct photoionization or by pulsed-field ionization, were extracted into a 40-cm-long field-free flight tube of the TOF mass spectrometer and detected by a Z-stack microchannel plate (MCP) detector. The previously described ZEKE detection scheme resulted in the spectral resolution of 1.0–1.2 cm^{-1}.

We also tried to detect the zero kinetic energy ions using MATI techniques. In our MATI experiment, both E_1 and E_4 grids were grounded. Constant positive voltages of 1548 V and 1550 V were applied to both E_2 and E_3 grids, respectively. The resulting 667 mV/cm constant field was used to separate the prompt ions created by direct photoionization from the highly excited neutral molecules remaining at the center. A pulsed field of 217 V/cm between E_2 and E_3 electrodes was triggered 3.53 μs after the laser excitation by applying a high positive voltage to the E_2 grids. This delayed pulsed field produced the MATI ions and also served to extract and accelerate the MATI and prompt ions. The two groups of ions arrived at the detector at different times. By gating at the signals on the MATI ion group, the MATI spectrum was obtained.

Results

The most prominent features in the TOF mass spectrum of the CH_3Br–He mixture recorded following one-photon excitation–ionization at 86 310 cm^{-1} are the methyl bromide parent-ion peaks corresponding to the two isotopomers, $CH_3{}^{79}Br^+$ and $CH_3{}^{81}Br^+$. The methyl fragment ion peak is just discernable above the noise, which is not surprising since soft ionization can be easily achieved with single-photon VUV ionization. It should be noted that a very high mass resolution ($m/\Delta m \approx 450$) was obtained, bearing in mind that the VUV light is not focused and the flight tube of the TOF mass spectrometer is only 40 cm long. The reason behind this is that a delayed pulsed extraction field rather than a constant field was used. For ion detection, a constant high voltage of 1550 V was applied to both E_2 and E_3 grids. A pulsed field of 217 V/cm between the E_2 and E_3 grids was triggered 3.53 μs after the excitation laser by applying a high positive voltage to the E_2 grid. The photoionization effi-

© 2004 NRC Canada

Fig. 1. Photoionization efficiency curves of $CH_3{}^{79}Br$ (solid line) and $CH_3{}^{81}Br$ (dotted line).

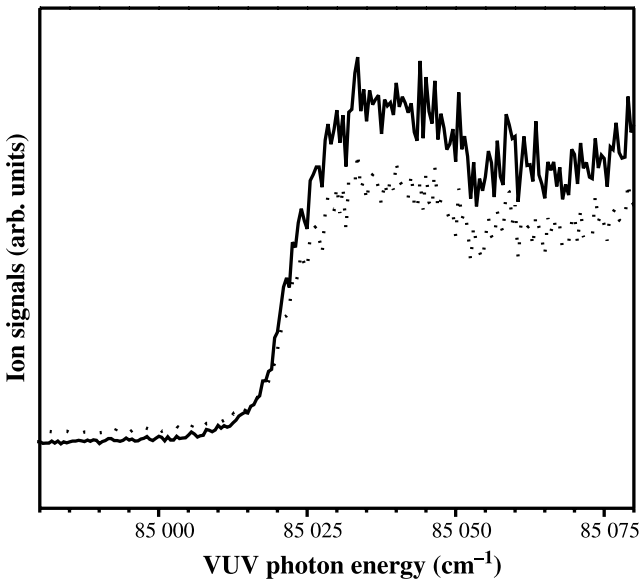
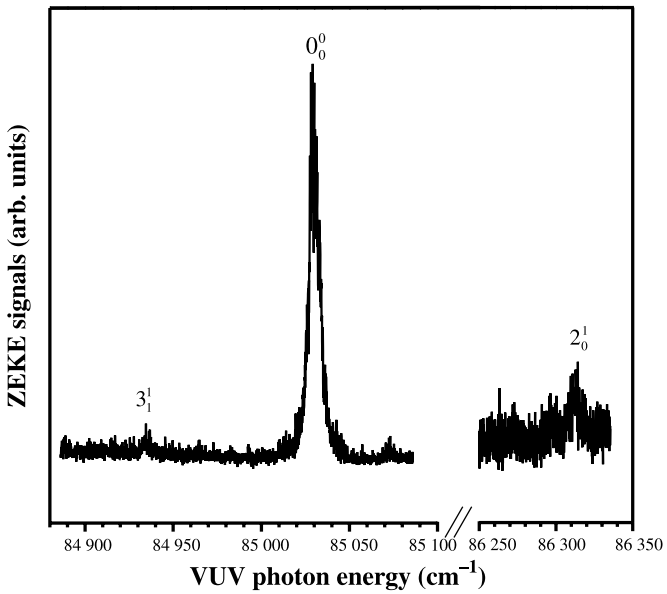


Fig. 2. The ZEKE photoelectron spectrum of CH_3Br^+ in its $\tilde{X}^2E_{3/2}$ ground electronic state.



ciency curves of the two isotopomers of methyl bromide show a mid-rise at ~85 022 cm^{-1}, as is seen in Fig. 1.

An overview scan of the transitions to the lowest vibrational levels of the $\tilde{X}^2E_{3/2}$ electronic ground state of the methyl bromide cation recorded using the ZEKE scheme described previously is shown in Fig. 2. No feature has been observed in the gap between the disconnected lines. The intensities of the features in the two separate parts of the spectrum are not directly comparable. We did not attempt to normalize the spectrum since the ZEKE signal intensity is not expected to be proportional to the laser intensity (29). The dominating feature in the ZEKE spectrum is assigned as the origin band (0_0^0) of the $\tilde{X}^2E_{3/2} \leftarrow \tilde{X}^1A_1$ transition. The weak peak at the higher energy side of the origin band remains unassigned. Vibrational features observed in the spectrum are labeled by both the upper and the lower vibrational level using the symbol i_m^n, where i indicates a vibrational mode, as in ν_i, n is the number of quanta of the ν_i mode excited in the upper electronic state, and m is the number of quanta of the ν_i mode in the lower electronic state. Excitation of one quantum of the symmetric CH_3 bending vibration, ν_2 (a_1 symmetry), is observed at 1281 cm^{-1} above the 0_0^0 band. The peak observed 94 cm^{-1} below the origin is assigned as the 3_1^1 hot band, based on the ν_3 vibrational frequency in the $\tilde{X}^2E_{3/2}$ cationic ground state determined in the multiphoton ZEKE photoelectron spectroscopic study (24). The origin band and the 2_0^1 band were previously observed in the low-resolution HeI photoelectron spectrum (19) and the one-color multiphoton ZEKE spectrum (24). However, the better resolution (1.0–1.2 cm^{-1}) of our ZEKE detection scheme allows for the observation of the rotational contours of the three vibrational bands but is insufficient to fully resolve the rotational structures of these bands. It is found that the origin band and the other two vibrational bands in Fig. 2 show similar rotational contours. Figure 3*a* shows the rotational contour of the origin band.

The one-photon VUV spectrum was also recorded using the MATI detection scheme described in the *Experimental* section. Weak MATI ions were observed at a shorter flight time as compared with the prompt ions. The MATI spectrum of the origin band appeared as a broad feature with unresolved rotational structures because of poorer resolution of the MATI scheme as compared with the ZEKE detection scheme, but it confirmed the attribution of the ZEKE signal to the CH_3Br.

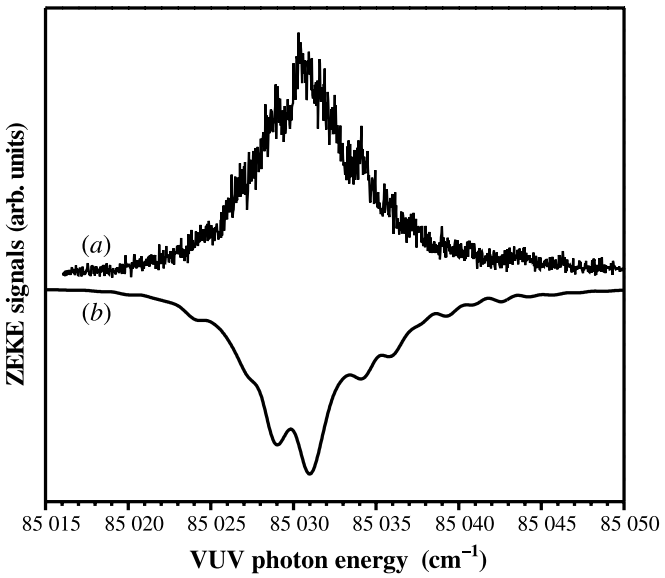
Discussion

The ground electronic state of methyl bromide has C_{3v} symmetry and a $1a_1{}^2 2a_1{}^2 1e^4 3a_1{}^2 2e^4$ electronic configuration yielding the total symmetry of A_1. The highest occupied molecular orbital (2e) has the predominant character of the halogen lone pairs. The lowest (ground) electronic state of the cation is ^2E formed by the removal of a nonbonding 2e electron. The degenerate ^2E electronic state is subject to vibronic coupling of the Jahn–Teller type and spin–orbit coupling. For methyl bromide, the latter is found to be significant in the outermost, lone-pair orbital. Therefore, the ^2E ground state is split into two spin–orbit components ($^2E_{3/2}$ and $^2E_{1/2}$), with the $^2E_{3/2}$ component lying lower in energy. The strongest feature observed in Fig. 2 is attributed to the origin band of the lower spin–orbit component of the degenerate ^2E ground ionic state $\tilde{X}^2E_{3/2}$, based on the comparison with previous photoelectron (19) and ZEKE (23, 24) spectroscopic studies. The fact that this band dominates the ZEKE photoelectron spectrum indicates that the geometry of the $\tilde{X}^2E_{3/2}$ ground ionic state is nearly the same as that of neutral CH_3Br in its ground electronic state. This is consistent with the electron being ejected from the nonbonding halogen lone-pair orbit upon ionization.

Neutral CH_3Br in its $\tilde{X}^1A_1$ vibronic ground state is a prolate ($A'' = 5.08$ cm^{-1}, $B'' = C'' = 0.31916$ cm^{-1} (8)) symmetric top molecule possessing C_{3v} symmetry. As was discussed earlier, the dominating appearance of the origin band in the obtained ZEKE spectrum suggests that the CH_3Br cat-

© 2004 NRC Canada

Fig. 3. The ZEKE photoelectron spectrum of the origin band of the ground electronic state of the CH_3Br^+ cation, showing the rotational contour from (*a*) experiment and (*b*) simulation (inverted). The energy scale has been corrected for the shifts owing to electric fields. The *A*, *B*, and *C* constants of the neutral ground state used in the simulation are from ref. 8.



ion is also of C_{3v} symmetry in its $\tilde{X}^2E_{3/2}$ state. The highest occupied molecular orbital of CH_3Br in its $\tilde{X}^1A_1$ ground state is a doubly occupied 2e orbital, which is predominantly nonbonding localized on the Br atom with some C—H bonding character (20). The 2e orbital is, therefore, essentially composed of the Br 4*p* atomic orbitals with minor contributions from the carbon 2*p* and the hydrogen 1*s* orbitals (17). For atomic-like, one-photon transition, $\Delta l = \pm 1$. Therefore, the Rydberg states excited by one photon from the 2e orbital are most probably predominantly of *ns* ($l = 0$) and *nd* ($l = 2$) characters, with some weak *np* ($l = 1$) characters. However, the absorption spectroscopic studies (9, 12) showed that the high Rydberg states converging to the first ionization potential of CH_3Br are predominantly of *s* with some *p* character.

It can be easily shown that only perpendicular transitions are allowed to *s* Rydberg states. For the *p* and *d* Rydberg states, both perpendicular and parallel transitions are possible, but their contributions to the ZEKE states of the ground electronic state of CH_3Br^+ are small compared with the *s* Rydberg states. The general rotational selection rules for a perpendicular band are:

$$[1] \qquad \Delta J' = J' - J'' = 0, \pm 1; \qquad \Delta K = K' - K'' = \pm 1$$

where *J* and *K* are the total angular momentum and its projection on the symmetry axis quantum numbers, respectively. The "′" ("″") superscript indicates the upper (lower) state. In a ZEKE state ($n \geq 100$), the Rydberg electron is asymptotically decoupled from the ion core, and we can write

$$[2] \qquad \mathbf{J}' = \mathbf{J}^+ + \mathbf{l} + \mathbf{s}$$

where vector $\mathbf{J}^+$ is the total angular momentum of the cation core, while vectors **l** and **s** are the orbital and the spin angular momenta of the Rydberg electron, respectively. Taking the experimental evidence into account and using eq. [2], the rotational selection rules can be expressed in terms of $\Delta J^+ = J^+ - J''$ as follows:

$$[3] \qquad \Delta J^+ = J^+ - J'' = -3/2, -1/2, +1/2, +3/2 \text{ for } l = 0$$

$$[4] \qquad \Delta J^+ = J^+ - J'' = -5/2, -3/2, -1/2, +1/2, +3/2, +5/2 \text{ for } l = 1$$

The spin–orbit splitting of the ^2E state of CH_3Br^+ is as large as 2541 cm^{-1} (315 meV) (12), and the Hund case (*c*) coupling scheme applies. In this case, the projection of the total angular momentum quantum number *J* along the principal symmetry axis of a symmetric rotor is equal to (30)

$$[5] \qquad P = \sum_i l_i + K + \Sigma$$

where l_i is the projection of the vibrational angular momentum on the principal symmetry axis for degenerate vibration ν_i, while Σ and *K* are the projections of the spin and the angular momentum without spin on the principal symmetry axis, respectively. For the origin band of the $\tilde{X}^2E_{3/2} \leftarrow \tilde{X}^1A_1$ transition in CH_3Br, $\sum_i l_i = 0$ and $\Sigma = 1/2$. Therefore, we can write

$$[6] \qquad P^+ = K^+ + 1/2$$

for the $\tilde{X}^2E_{3/2}$ state of CH_3Br^+. Now, the rotational selection rules in eq. [1] can be expressed in terms of $\Delta K^+ = P^+ - K''$ as

$$[7] \qquad \Delta K^+ = +3/2, -1/2$$

As described previously, the origin band and two vibrational bands of the $\tilde{X}^2E_{3/2} \leftarrow \tilde{X}^1A_1$ transition show similar rotational contours. As the rotational structure of the origin band is unresolved in our spectra, to determine the ionization energy and estimate the rotational constants of the CH_3Br^+ ion, we have simulated the profile of the origin band and compared it with the observed spectrum. The rotational Hamiltonian of a symmetric rotor can be written as

$$[8] \qquad \mathbf{H} = B[\mathbf{R_x}^2 + \mathbf{R_y}^2] + A\mathbf{R_z}^2$$

where *A* and *B* are rotational constants, and **R** ($\mathbf{R_x}$, $\mathbf{R_y}$, $\mathbf{R_z}$) is the operator of molecular rotation. The **R** operator can be written in terms of molecular angular momenta as

$$[9] \qquad \mathbf{R} = \mathbf{J} - \mathbf{L} - \mathbf{S}$$

where **J**, **L**, and **S** are the total, orbital, and spin angular momenta of a molecule, respectively. Substituting eq. [9] into eq. [8] and evaluating diagonal matrix elements of a symmetric rotor, we obtain

$$[10] \qquad T = B[J(J+1) - P^2] + A(P - \Omega)^2 + B[L(L+1) + S(S+1) + 2(\Omega - \Sigma)\Sigma - \Omega^2]$$

where *J* and *P* are the total angular momentum and its projection on the principal symmetry axis quantum numbers, *S* and Σ are the spin and its projection on the principal symmetry axis quantum numbers, *L* is the expectation value of the orbital angular momentum, and Ω is the expectation value of

© 2004 NRC Canada

the projection of the electronic angular momentum (orbital and spin) on the principal axis. The last term in eq. [10] reduces to zero for the ground state of the neutral CH_3Br molecule $\tilde{X}^1A_1$, and the diagonal matrix elements can be written as

$$[11] \quad T'' = B''[J''(J'' + 1) - K''^2] + AK''^2$$

where we substitute $P'' = K''$. For the ground state of the CH_3Br^+ ion ($\tilde{X}^2E_{3/2}$), the last term of eq. [10] cannot be evaluated explicitly because L and Ω are not good quantum numbers. By substituting $L = 1$, $S = 1/2$, $\Sigma = 1/2$, and $\Omega = 3/2$, we estimate that this term is expected to be small, approximately equal to $3/2B$, constant for a given vibronic state. Consequently, we constrain this term in the simulation at the value of $3/2B$. Thus, we write the diagonal matrix elements of the Hamiltonian of the $\tilde{X}^2E_{3/2}$ state as

$$[12] \quad T^+ = B^+[J^+(J^+ + 1) - (P^+)^2] + A^+(P^+ - \Omega)^2 + 3/2B$$

The rotational constants of the ground state of the neutral molecule have been constrained at the values $A'' = 5.08$ cm^{-1} and $B'' = 0.31916$ cm^{-1} taken from ref. 8. The ionization energy (IE), the rotational constants of the CH_3Br^+ ion ground state (A^+ and B^+), and the expectation value of the electronic angular momentum projection (Ω^+) were varied to reproduce the observed spectrum. Only excitations to s ($l = 0$, weight 1.0) and p ($l = 1$, weight 0.2) Rydberg states from $K'' = 0$ and $K'' = 1$ levels were included in the simulation. Rotational lines satisfying the $\Delta J^+ = J^+ - J'' = -1.5, \ldots, +1.5$ (for s Rydberg states) and $\Delta J^+ = -2.5, \ldots, +2.5$ (for p Rydberg states) selection rules were included, with the extreme branches of one-half the intensity of the main branches. The width of the rotational lines was set equal to 1.0 cm^{-1}. The rotational temperature of the ground state of the neutral molecule was optimized at $T = 6.0(5)$ K. The ionization energy (IE), the rotational constants of the ground state of the CH_3Br^+ ion (A^+ and B^+), and the expectation value of the electronic angular momentum projection (Ω), were fitted to be equal to 85 031.2(1.0) cm^{-1}, 4.75(5) cm^{-1}, 0.32(1) cm^{-1}, and 1.48(2), respectively. The simulated spectrum is shown in Fig. 3*b* (lower trace).

The adiabatic ionization energy of CH_3Br of 85 031.2 ± 1.0 cm^{-1} obtained in this work is in very good agreement with the values recently obtained from the ZEKE spectroscopic studies using VUV synchrotron radiation (85 032.6 ± 8.0 cm^{-1}) (23). It also agrees very well with the value of 85 035 ± 50 cm^{-1} obtained by Karlsson et al. (19) in their HeI photoelectron spectroscopic study.

The A^+ rotational constant value of 4.75 cm^{-1} is 0.33 cm^{-1} smaller than that of the neutral ground state ($A = 5.08$ cm^{-1}), which indicates that the three H atoms move away from the *a* rotational axis upon ionization. This is consistent with the lowering from 1305 cm^{-1} in $\tilde{X}^1A_1$ to 1281 cm^{-1} in $\tilde{X}^2E_{3/2}$ in the wavenumber of the vibrational mode (ν_2, CH_3 symmetric bend) (8). This wavenumber lowering in ν_2 upon excitation should also translate into an increase in the rotational constant B^+; however, it is found from the simulation of the rotational profile of the origin band that B^+ (0.32 cm^{-1}) does not change from its neutral ground state value ($B'' = 0.31916$ cm^{-1}). The 3_1^1 band is observed 94 cm^{-1} below the origin band (see Fig. 2), indicating that the wavenumber of the ν_3 vibrational mode (the C-Br stretch) in the cationic ground state is lowered by 94 cm^{-1} compared with that in the neutral ground state. This suggests that the C—Br bond is elongated upon ionization, which in turn should cause a decrease in the B^+ rotational constant. Consequently, we attribute the little change in the B value upon excitation to a canceling of the opposing effect caused by the decrease in ν_2 and ν_3.

Conclusions

The VUV single-photon ZEKE photoelectron spectrum of CH_3Br^+ in its $\tilde{X}^2E_{3/2}$ ground electronic state has been recorded. The dominating feature in the spectrum is the origin band 0_0^0 of the transition $\tilde{X}^2E_{3/2} \leftarrow \tilde{X}^1A_1$. The excitation of the totally symmetric vibrational mode (ν_2) is observed. The 3_1^1 hot band is also present. The rotational contours of three vibrational bands have been observed. Simulation of the rotational contour of the origin band has yielded the improved value of the first adiabatic ionization energy (85 031.2 ± 1.0 cm^{-1}) and the rotational constants of CH_3Br^+ in its $\tilde{X}^2E_{3/2}$ ground state.

References

1. M.J. Molina, L.T. Molina, and C.E. Kolb. Annu. Rev. Phys. Chem. **47**, 327 (1996).
2. H.B. Singh and M. Kanakidou. Geophys. Res. Lett. **20**, 133 (1993).
3. C.E. Reeves and S.A. Penkett. Geophys. Res. Lett. **20**, 1563 (1993).
4. J.H. Butler. Geophys. Res. Lett. **21**, 185 (1994).
5. A. Mellouki, R.K. Talukdar, A.M. Schmolter, T. Gierczak, M.J. Mills, S. Solomon, and A.R. Ravishankara. Geophys. Res. Lett. **19**, 2059 (1992).
6. M.B. McElroy, R.J. Salawitch, S.C. Wofsy, and J.A. Logan. Nature (London), **321**, 759 (1986).
7. S.A. Kudchadker and A.P. Kudchadker. J. Phys. Chem. Ref. Data, **4**, 457 (1975).
8. G. Herzberg. Molecular spectra and molecular structure III. Electronic spectra and electronic structure of polyatomic molecules. Van Nostrand Reinhold, New York. 1945.
9. T.N. Olney, G. Cooper, W.F. Chan, G.R. Burton, C.E. Brion, and K.H. Tan. Chem. Phys. **218**, 127 (1997).
10. S.J. Paddison and E. Tschuikow-Roux. J. Phys. Chem. A, **102**, 6191 (1998).
11. R. Venkatraman, J.S. Kwiatkowski, G. Bakalarski, and J. Leszczynski. Mol. Phys. **98**, 371 (2000).
12. W.C. Price. J. Chem. Phys. **4**, 539 (1936).
13. P. Hochmann, P.H. Templet, H.-T. Wang, and S.P. McGlynn. J. Chem. Phys. **62**, 2588 (1975).
14. G.C. Causley and B.R. Russell. J. Chem. Phys. **62,** 848 (1975).
15. D.W. Turner, C. Baker, A.D. Baker, and C.R. Brundle. Molecular photoelectron spectroscopy. Wiley-Interscience, London. 1970.
16. A.W. Potts, H.J. Lempka, D.G. Streets, and W.C. Price. Phil. Trans. Roy. Soc. Lond. A. **268**, 59 (1970).
17. J.L. Ragle, I.A. Stenhouse, D.C. Frost, and C.A. McDowell. J. Chem. Phys. **53**, 178 (1970).
18. R.N. Dixon, J.N. Murrell, and B. Narayan. Mol. Phys. **20**, 611 (1971).
19. L. Karlsson, R. Jadrny, L. Mattsson, F.T. Chau, and K. Siegbahn. Phys. Scripta, **16**, 225 (1977).

© 2004 NRC Canada

20. C.E. Brion, W.B. Stewart, D.S.C. Yee, and P. Cowley. J. Electron Spectrosc. Relat. Phenom. **23**, 399 (1981).
21. K. Müller-Dethlefs, M. Sander, and E.W. Schlag. Chem. Phys. Lett. **112**, 291 (1984).
22. K. Müller-Dethlefs, E.W. Schlag. E.R. Grand, K. Wang, and V.B. McKoy. *In* Advances in chemical physcis. *Edited by* I. Prigogine and S.A. Rice. Wiley, New York. 1995.
23. Y. Song, X.-M. Qian, K.-C. Lau, C. Y. Ng, J. Liu, and W. Chen. J. Chem. Phys. **115**, 4095 (2001).
24. B. Urban and V. Bondybey. J. Chem. Phys. **116**, 4938 (2002).
25. S. Wang, Y.J. Shi, Z.J. Jakubek, M. Barnett, B. Simard, K. Müller-Dethlefs, C.P. Liu, and Y.P. Lee. J. Chem. Phys. **117**, 6546 (2002).
26. R. Hilbig and R. Wallenstein. IEEE J. Quantum Electron. QE-**19**, 1759 (1983).
27. P.R. Herman, P.E. LaRocque, R.H. Lipson, W. Jamroz, and B.P. Stoicheff. Can. J. Phys. **63**, 1581 (1985).
28. C.E. Moore. Atomic energy levels. Natl. Bur. Stand. (U.S.) Circ. No. 467. U S GPO, Washington, D.C. 1971.
29. F. Merkt. Annu. Rev. Phys. Chem. **48**, 675 (1997).
30. C.J.H. Schutte, J.E. Bertie, P.R. Bunker, J.T. Hougen, I.M. Mills, J.K.G. Watson, and B.P. Winnewisser. Pure Appl. Chem. **69**, 1633 (1997).

© 2004 NRC Canada

Temperature- and pressure-dependent luminescence spectroscopy on the *trans*-$[ReO_2(pyridine)_4]^+$ complex — Analysis of vibronic structure, luminescence energies, and bonding characteristics[1]

John K. Grey, Ian S. Butler, and Christian Reber

Abstract: Resolved vibronic structure in electronic spectra provides a detailed view into how molecular structure changes after absorption or emission of a photon. We report temperature- and pressure-dependent luminescence spectra of *trans*-$[ReO_2(pyridine)_4]I$. Low-temperature spectra reveal long vibronic progressions in the totally symmetric O=Re=O (907 cm^{-1}) and Re-pyridine (211 cm^{-1}) stretching modes, indicating large structural displacements along these normal coordinates. The luminescence band maximum is at ca. 15 500 cm^{-1}. Room-temperature spectra are somewhat less-resolved; however, intervals closely matching the O=Re=O frequency (~870 cm^{-1}) persist at higher temperatures. The variable pressure spectra exhibit distinct changes in the vibronic patterns, and luminescence energies decrease by 16 ± 2 cm^{-1}/kbar (1 bar = 100 kPa). Low-temperature spectra are modeled using two-dimensional potential energy surfaces to represent the initial and final electronic states, from which the quantitative normal coordinate offsets can be determined. We then adapt this model to the room-temperature, pressure-dependent data where it is possible to determine how the offsets and other important spectroscopic parameters vary with the pressure-induced changes of the molecular structure.

Key words: trans-$[ReO_2(pyridine)_4]I$, low-temperature luminescence spectroscopy, high-pressure luminescence spectroscopy, vibronic structure, emitting state distortions.

Résumé : La structure vibronique résolue des spectres électroniques nous permet d'obtenir de l'information détaillée concernant les changements de la structure moléculaire suite à l'absorption ou l'émission d'un photon. Nous présentons et analysons les spectres de luminescence du *trans*-$[ReO_2(pyridine)_4]I$ en fonction de la température et de la pression. Les progressions vibroniques observées impliquent les modes de vibration totalement symétriques O=Re=O et Re-pyridine avec des fréquences Raman de 907 cm^{-1} et de 211 cm^{-1} et indiquent d'importants déplacements le long de ces coordonnées normales. Le maximum de la bande de luminescence est à approximativement 15 500 cm^{-1}. Les spectres de luminescence à la température ambiante montrent une résolution inférieure, mais suffisante pour distinguer des intervalles de 870 cm^{-1} se rapprochant de la fréquence de vibration O=Re=O. Les spectres à pression variable montrent des changements dans la structure vibronique ainsi qu'une décroissance des énergies de luminescence de 16 ± 2 cm^{-1}/kbar (1 bar = 100 kPa). Les spectres expérimentaux à basse température sont comparés à des spectres calculés selon un modèle impliquant des surfaces d'énergie potentielle bidimensionnelles. Ces surfaces représentent les états électroniques initial et final et permettent de déterminer quantitativement les écarts le long des coordonnées normales. Ce modèle est ensuite adapté aux données à température ambiante et à pression variable, de façon à déterminer la nature des déplacements et des variations des paramètres spectroscopiques amenés par les changements dans la structure moléculaire induits par la pression.

Mots clés : *trans*-$[ReO_2(pyridine)_4]I$, spectroscopie de luminescence à basse temperature et à haute pression, structure vibronique, distorsions structurales à l'état excité.

Received 31 October 2003. Published on the NRC Research Press Web site at http://canjchem.nrc.ca on 14 September 2004.

J.K. Grey. Department of Chemistry, McGill University, Montreal, QC H3A 2K6, Canada and Département de Chimie, Université de Montréal, Montréal, QC H3C 3J7, Canada.
I.S. Butler. Department of Chemistry, McGill University, Montreal, QC H3A 2K6, Canada.
C. Reber.[2] Département de Chimie, Université de Montréal, Montréal, QC H3C 3J7, Canada.

[1]This article is part of a Special Issue dedicated to the memory of Professor Gerhard Herzberg.
[2]Corresponding author (e-mail: reber@chimie.umontreal.ca).

 doi: 10.1139/V04-031 © 2004 NRC Canada

Introduction

Transition metal complexes with metal–oxygen multiple bonds have received much attention for uses in oxygen atom transfer catalysis and as photochemical sensitizers (1–4). The electronic structures of many second- and third-row metal–oxo complexes have been well studied both spectroscopically and theoretically since the seminal work of Winkler and Gray (5, 6). We present and analyze temperature- and pressure-dependent luminescence spectra of the *trans*-[ReO_2(pyridine)$_4$]I compound that show well-resolved vibronic structure, even at room temperature, and provide an in-depth view into how the molecular geometry changes in the emitting state. Perhaps the most relevant application of *trans*-dioxo complexes to the results presented in the following is their use as luminescent probes to determine the influence of host–guest interactions in layered materials (7), where a *trans*-[ReO_2(pyridine)$_4$]$^+$ complex was intercalated into hectorite lattices and changes in the resolved vibronic structure and luminescence energies determined from low-temperature luminescence spectra were used to understand the nature of interaction between the host lattice and the guest luminophore. These host–guest interactions represent what has become known as a "chemical pressure" and here we use a *trans*-dioxo rhenium(V) complex to study the effect of external pressure on the resolved luminescence spectrum. Pressure-dependent emitting state normal coordinate offsets, luminescence band maxima energies, and energies of the electronic origin transition are determined quantitatively based on a model developed from the low-temperature luminescence spectrum.

The six-coordinate [Xe $5d^2$] *trans*-dioxo class of complexes usually are described in idealized D_{4h} point group symmetry and show well-resolved vibronic structure in their low-temperature electronic spectra (6). Long progressions in high frequency (900–1000 cm^{-1}) metal–oxo stretching modes are often observed, indicating a large structural change along metal–oxo coordinates in the emitting state, and the offset of the ground and emitting state potential energy minima can be determined from the intensity distribution of the resolved vibronic progressions. The high vibrational frequencies of the metal–oxo modes are due to the strength of the formal M=O double bonds. This feature makes such complexes amenable to room-temperature spectroscopic studies because of the low thermal population of higher vibrational levels allowing vibronic structure to persist even at relatively high temperatures. By applying high external pressures to single crystals of these systems, it is possible to determine the change in the metal–oxo normal coordinate offset as a function of pressure through the changes in vibronic patterns. We have previously used the resolved structure in a O=Re=O totally symmetric stretching mode to study the influence of pressure on coupling interactions between the ground- and excited-electronic-state potential energy surfaces in a series of *trans*-[ReO_2(*N*,*N*,*N*′,*N*′-ethylenediamine)$_2$]$^+$ complexes (8, 9). The ethylenediamine ligands effectively "clamp" to the metal center, thus resisting changes in molecular geometry because of changes in intermolecular packing forces with increasing pressure, whereas the pyridine ligands of the title compound are expected to be more susceptible to pressure-induced changes in molecular geometry. Furthermore, the luminescence properties of the title complex show a strong dependence on the environment whereby the luminescence energy and intensity distribution of vibronic progressions change noticeably upon changing counter-ions.

The ground- and excited-state electronic structures of d^2 *trans*-dioxo complexes are well-known and have been parameterized in terms of ligand-field strength and interelectronic repulsion (10). For these and other six-coordinate tetragonal complexes, the five *d*-orbitals are split in the following fashion in increasing energy: $d_{xy}(b_{2g})$, d_{xz}, $d_{yz}(e_g)$, $d_{x^2-y^2}(b_{1g})$, $d_{z^2}(a_{1g})$. The ground electronic state in the title complex is both spin and orbitally nondegenerate ($^1A_{1g}$) in D_{4h} symmetry because of the pairing of the two *d* electrons in the d_{xy} orbital (HOMO). The energy of this state depends on the two-electron parameter (K_{xy}), which is defined as $3B + C$, where *B* and *C* are the Racah parameters describing interelectronic repulsion. Promotion of one electron to the e_g orbitals (LUMO) leads to both ^1E_g and ^3E_g excited states separated by $2K_{xy}$ with the triplet state at lower energy. Due to strong spin–orbit coupling effects intrinsic to third-row transition metal atoms, the ^3E_g state is split into several components and luminescence occurs from the lowest energy spin–orbit components. The energy of the LUMO depends on the difference in π overlap between the oxo and ancillary ligands to the metal *d* orbitals, which is defined by the ligand-field parameter Δ_π. In *trans*-dioxo complexes with anisotropic π-donating ligands, such as the pyridine ligands in the title compound, Δ_π is represented as $2e_\pi(O) + 2e_\pi(ligand) - 4e_\pi(ligand)$, where e_π is the angular-overlap parameter describing π overlap between the metal e_g and b_{2g} orbitals with ligand orbitals of π-symmetry that accounts for contributions both parallel and perpendicular to the ML_4 equatorial plane (10). The pyridine ligands are oriented perpendicular to the equatorial plane where the lone unhybridized *p*-orbital on the nitrogen atom has the maximum π interaction with the metal center, causing $e_\pi \approx 0$ and Δ_π then becomes $2e_\pi(O) - 4e_{\pi\perp}(ligand)$ (10). Because the energy difference between the ground and emitting states depends on both ligand-field effects arising from metal–ligand bond lengths and interelectronic repulsion parameters, one of the goals of this work is to rationalize the pressure-dependent change in luminescence energies in terms of K_{xy} and Δ_π and compare to previous studies of *trans*-dioxo complexes.

We calculate the well-resolved 5 K luminescence spectrum of the title complex using harmonic potential energy surfaces with the ground and emitting states displaced along the O=Re=O and Re-N(pyridine) symmetric stretching modes. The two-dimensional model can then be adapted to calculate room-temperature pressure-dependent luminescence spectra using potential energy surfaces displaced along a single effective coordinate with predominant O=Re=O stretching character. The pressure-induced changes of the most important parameters are compared to those reported for complexes with less π-bonding characteristics (8, 9, 11). The title complex demonstrates the quantitative transferability of parameters obtained from low-temperature spectra to less resolved room temperature spectra.

Experimental

Synthesis and spectroscopy

trans-[ReO_2(py)$_4$]I was synthesized following literature

© 2004 NRC Canada

methods (12) and all starting materials were used as received. Luminescence and Raman spectra were recorded as a function of temperature and pressure on a microscope spectrometer described previously (8, 9). Crystalline samples were placed in a liquid helium cryostat (Janis ST 500) and temperature was controlled between 300 and 5 K. Variable pressure experiments were carried out by placing samples in a gasketed diamond-anvil cell (DAC). All spectra were unpolarized and corrected for spectrometer response. Absorption measurements were performed on a Varian CARY 5E spectrometer. For the absorption spectra, the *trans*-$[ReO_2(py)_4]I$ compound was dissolved in water and the solution was allowed to evaporate slowly on quartz plates, which produced a thin layer of microcrystals on the surface.

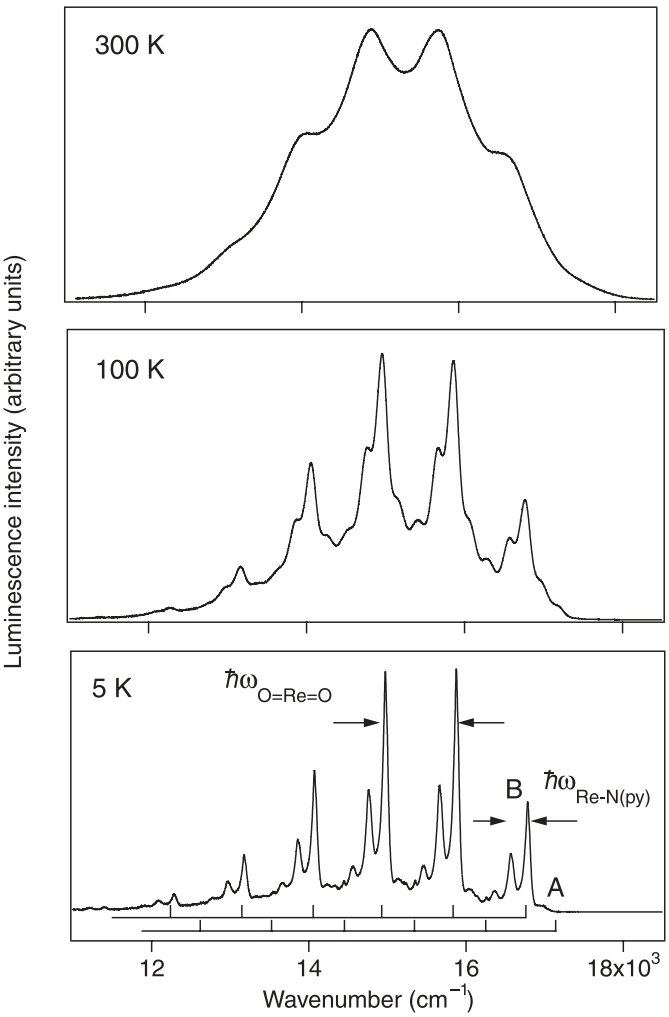
Spectroscopic results

Variable temperature luminescence spectroscopy

Figure 1 shows the luminescence spectra of *trans*-$[ReO_2(py)_4]I$ at 5 K (bottom panel), 100 K (middle panel), and 300 K (top panel). All spectra measured over the indicated temperature range show resolved vibronic structure in the high-frequency O=Re=O totally symmetric stretching mode, with an average progression interval of 905 cm^{-1}. This mode is observed in the 300 K Raman spectrum at 907 cm^{-1}. At temperatures lower than 150 K, progressions in the lower frequency (211 cm^{-1}) Re-N(pyridine) totally symmetric stretching mode are visible on the lower energy side of the main (O=Re=O) progression. In the 5 K spectrum shown in Fig. 1, up to seven quanta of the O=Re=O mode can be observed, indicating a large change in emitting-state rhenium–oxo bond length compared to the ground-state equilibrium configuration. At 300 K the vibronic structure in the luminescence spectrum becomes less resolved and the observed high frequency progression interval decreases to an average 870 cm^{-1}.

The highest energy discernible maximum of the 5 K spectrum appears at approximately 17 200 cm^{-1} and overlaps with the lowest energy absorption onset, shown in Fig. 2. The luminescence spectrum consists of two bands, the first (labeled **A** in Fig. 1) originates from the highest energy peak and the more intense band (labeled **B** in Fig. 1) begins at 314 cm^{-1} lower in energy. The beginning of each cluster of lower frequency Re-N(py) progressions is indicated by tick marks for both bands **A** and **B** for the 5 K spectrum in Fig. 1 and the clusters of vibronic transitions are exact replicas, i.e., they have the same relative intensity distributions across the entire luminescence spectrum. All energy positions of individual vibronic peaks and frequency intervals are listed in Table 1 for the dominant vibronic band (**B**). It is also interesting to note the decrease in the O=Re=O frequency toward the lower energy side of the spectrum by approximately 4 cm^{-1} for each subsequent quantum of the O=Re=O mode, which becomes 21 cm^{-1} lower at the highest quantum of this mode. Comparison with the 5 K luminescence spectrum of the tetraphenylborate $(BPh_4)^-$ salt of this complex reveals a similar trend where this interval decreased by 10 cm^{-1} between the second and third quanta followed by an anomalous large increase between the third and fourth quanta by 30 cm^{-1} (6). This apparent anharmonicity was also observed

Fig. 1. Luminescence spectra of single crystals of *trans*-$[ReO_2(pyridine)_4]I$ at three temperatures: 300 K (top panel), 100 K (middle panel), and 5 K (bottom panel). Frequency intervals of the two resolved progressions are indicated by arrows. The tick marks below the 5 K spectrum mark the main progressions for the two band systems, labeled **A** and **B**, that comprise the total spectrum.



in theoretical calculations on the *trans*-$[ReO_2(ethylenediamine)_2]^+$ complex where it was revealed that the ground electronic state potential energy surface was anharmonic along the O=Re=O coordinate (13).

Figure 2 shows the effect of temperature on the intensity distribution between the two bands (**A** and **B**). As temperature increases, the intensity of band system **A** increases, whereas band system **B** shows a slight decrease. The higher energy bands (**A**) of the BPh_4^- salt also demonstrate similar temperature-dependent characteristics as those observed in Fig. 2 and were assigned as transitions from a second luminescent state slightly higher in energy (6). This assignment was consistent with temperature-dependent luminescence lifetimes where the higher energy state becomes thermally populated at higher temperatures and leads to a decrease in the lifetime from 68 μs (5–70 K) to 32 μs at room temperature (6). The temperature-dependent features in Fig. 2 are in agreement with this assignment, further supported by the

© 2004 NRC Canada

Fig. 2. Temperature-dependent luminescence spectra of *trans*-[ReO_2(pyridine)$_4$]I. Upward arrows show the increase of intensity for band system **A** and downward arrows show the decrease of intensity for band system **B** with increasing temperature. The 300 K absorption spectrum from microcrystals of the title compound is indicated as a hatched line on the right-hand side.

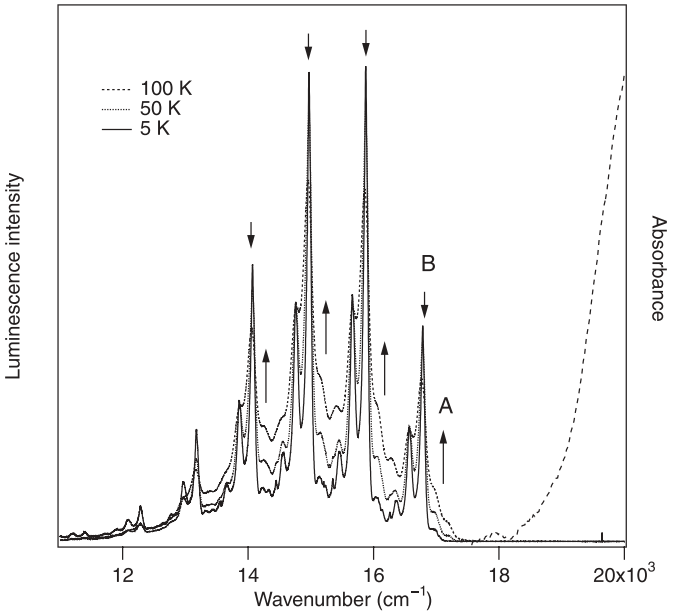
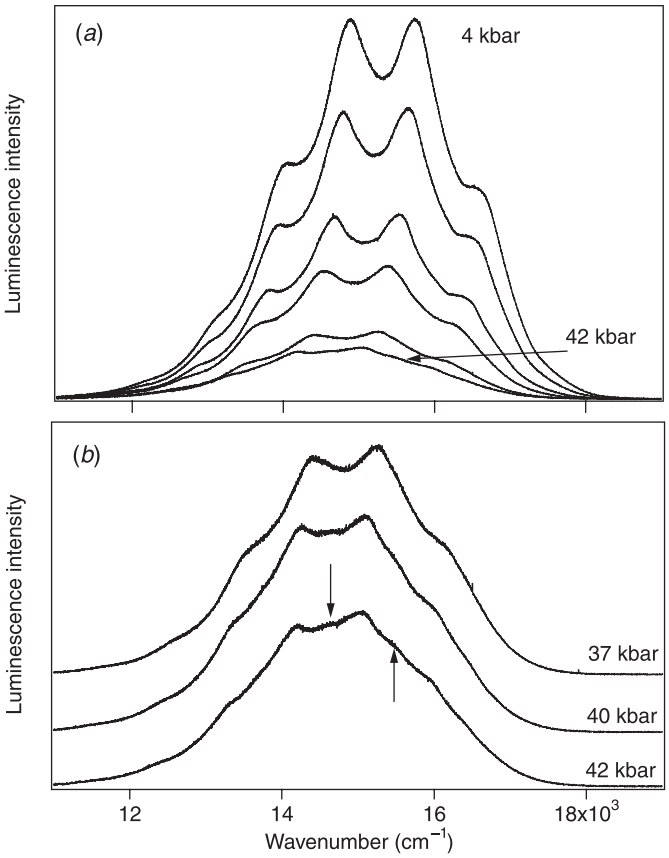


Table 1. Vibronic energy spacings in the 5 K luminescence spectrum of *trans*-[ReO_2(py)$_4$]I.

	Energy intervals (cm^{-1})	
Peak energy (cm^{-1})[a]	Re-N[b]	O=Re=O[c]
16 784		
16 573	211	
16 364	209	
15 877		907
15 666	211	
15 460	206	
14 972		905
14 764	208	
14 561	203	
14 073		899
13 866	207	
13 668	198	
13 178		895
12 974	204	
12 783	191	
12 286		892
12 091	195	
11 911	180	
11 400		886
11 211	189	
11 028	183	

[a]±3 cm^{-1}.
[b]Raman: 211 cm^{-1} (300 K).
[c]Raman: 905 cm^{-1} (300 K).

Fig. 3. (*a*) Selected pressure-dependent single-crystal luminescence spectra of *trans*-[ReO_2(pyridine)$_4$]I recorded at room temperature (ca. 300 K). Individual pressures are in descending order: 4 kbar (top trace), 13 kbar, 21 kbar, 29 kbar, 37 kbar, and 42 kbar (bottom trace) (1 bar = 100 kPa). (*b*) High-pressure luminescence spectra with additional features indicated by arrows.



different bandwidths for transitions labeled as **A** and **B**, indicating transitions originating from different components of the ^3E_g excited state.

Variable pressure luminescence spectroscopy

Figure 3 shows the effect of pressure on the luminescence spectrum of the title complex. The dominant progression interval in the room-temperature spectra is 870 cm^{-1}, almost 40 cm^{-1} less than the observed O=Re=O vibrational frequency in the Raman spectrum. As pressure increases, the luminescence intensities show steady decreases, an effect that is often observed and most likely due to efficient energy transfer to deep traps at high pressure. In addition, the intensity distribution within the resolved progression change with increasing pressure, which can be observed by comparing the second and third members of the 4 kbar spectrum in Fig. 3*a* and the 42 kbar spectrum in Fig. 3*b*. The energy of the luminescence band maximum (E_{max}) shows a visible decrease with increasing pressure that can be seen qualitatively by following a particular vibronic peak. Luminescence spectra at the highest working pressures (37–42 kbar) also reveal additional features not observed in the lower pressure spectra and indicated in Fig. 3*b* by arrows. Pressure-dependent

© 2004 NRC Canada

Raman spectra of the title compound show smooth shifts of the O=Re=O stretching mode to higher frequencies by 0.53 cm^{-1}/kbar. This value is similar to the pressure-induced shifts determined for various *trans*-dioxo rhenium(V) complexes with substituted imidazole ligands, which range from 0.55 to 0.69 cm^{-1}/kbar, and larger than those found in complexes with ethylenediamine ligands (0.37–0.42 cm^{-1}/kbar) (11).

Discussion

The title complex has exact D_{4h} point group symmetry for the *trans*-ReO_2N_4 fragment and we use the labels from this symmetry group to describe the electronic states and relevant vibrational modes. The removal of electron density in the x,y plane to the π* LUMO orbital results in large changes in metal–ligand bond lengths along the Re-N(py) and O=Re=O coordinates, therefore these modes are expected to have the largest displacements between ground- and emitting-state potential minima. Only one emitting state is considered in the model for both temperature- and pressure-dependent luminescence spectra where the most intense luminescence band (**B**) is analyzed.

Analysis of the temperature-dependent vibronic structure

The detailed spectroscopic features shown in Figs. 1 and 2 provide a means to analyze the rich vibronic structure and characterize the ground- and emitting-state potential energy surfaces. We use two-dimensional harmonic potential surfaces with the ground and emitting states displaced along the totally symmetric O=Re=O and Re-N(pyridine) stretching modes. The luminescence spectrum is calculated using the time-dependent theory of luminescence spectroscopy, an approach that has been described in detail before (14–16). Briefly, a wave packet is created on the final potential energy surface (ground state) upon emission of a photon from a molecule in the emitting state at $t = 0$. The shape of the luminescence spectrum is given by eq. [1]

$$[1] \qquad I_{\mathrm{lum}}(\omega) = C\omega^3 \int_{-\infty}^{+\infty} e^{i\omega t} \left\langle \phi \middle| \phi(t) \right\rangle \mathrm{d}t$$

where $I_{\mathrm{lum}}(\omega)$ is the luminescence intensity at the frequency ω, C is a constant scaling factor, and $\langle\phi|\phi(t)\rangle$ is the autocorrelation function. Its absolute value can be visualized as the overlap of the initial wavepacket ($\phi = \phi(t = 0)$) with the time-dependent wavepacket ($\phi(t)$). The autocorrelation is calculated from a closed-form analytical equation obtained by making several assumptions: (*i*) the vibrational frequencies (ω) in the ground and excited states are identical and both states are represented by harmonic potential energy surfaces, (*ii*) there is no mixing of normal coordinates, and (*iii*) the transition dipole moment is constant. The autocorrelation for the *k*th mode is then given by eq. [2]

$$[2] \qquad \left\langle \phi_k \middle| \phi_k(t) \right\rangle = \exp\left[-\frac{\Delta_k^2}{2}(1 - \exp(-i\omega_k t)) - \frac{i\omega_k t}{2} \right]$$

for harmonic ground- and emitting-state potential energy surfaces with minima displaced by Δ_k in dimensionless units.[3] For multiple displaced modes, the total autocorrelation is the product of autocorrelations for each individual mode

$$[3] \qquad \left\langle \phi \middle| \phi(t) \right\rangle = \prod_k \left\langle \phi_k \middle| \phi_k(t) \right\rangle \exp\left(\frac{-iE_{00}t}{\hbar} - \Gamma^2 t^2 \right)$$

where E_{00} is the energy of the electronic origin, and Γ is a Gaussian damping factor that determines the width of individual vibronic transitions, both in cm^{-1} units. After calculating the total overlap, the result is Fourier transformed (eq. [1]) to give the spectrum. The uncoupled coordinates for the ground state are a good assumption because clusters of vibronic transitions observed across the entire luminescence band are "replicas" of each other. This feature arises from Lissajous motion of the wave packet along the two displaced normal coordinates, as was superbly illustrated by Herzberg for two orthogonal harmonic oscillators with different force constants, k_x and k_y, leading to a complicated pattern resulting from the superposition of the individual motions (17, 18). The appearance of replicas in the vibronic structure of electronic spectra is due to these uncoupled individual motions, justifying the use of harmonic potential energy surfaces and eq. [3] to describe the wave packet motion on the final (ground) state potential energy surface. Two other salts of the *trans*-$[ReO_2(py)_4]^+$ complex also show such replicas (6), however, the I^- salt studied here shows the best resolution of vibronic structure where there are two distinct progression-forming modes and details of the vibronic patterns can be carefully scrutinized.

Figure 4*a* compares the experimental luminescence spectrum at 5 K to the spectrum calculated with eq. [1]. The energy (E_{00}) of the origin transition for the calculation was set to the first resolved peak in progression **B** at 16 786 cm^{-1}. All parameters used in this calculation are shown in Table 2. Literature values for the emitting-state bond length changes for individual Re=O and Re-N(py) bonds were found to be 0.07 and 0.03 Å, respectively, for the BPh_4^- salt (6). The offset along the Re-N coordinate is negative due to the removal of electron density from the x,y plane, thus decreasing these bonds and resulting in a negative emitting state offset along this coordinate (19). In the model used here, only the absolute values can be determined since harmonic potential energy surfaces are used. From the calculated 5 K luminescence spectra, we determine values of 0.074 and 0.022 Å for the Re=O and Re-N(pyridine) bond length

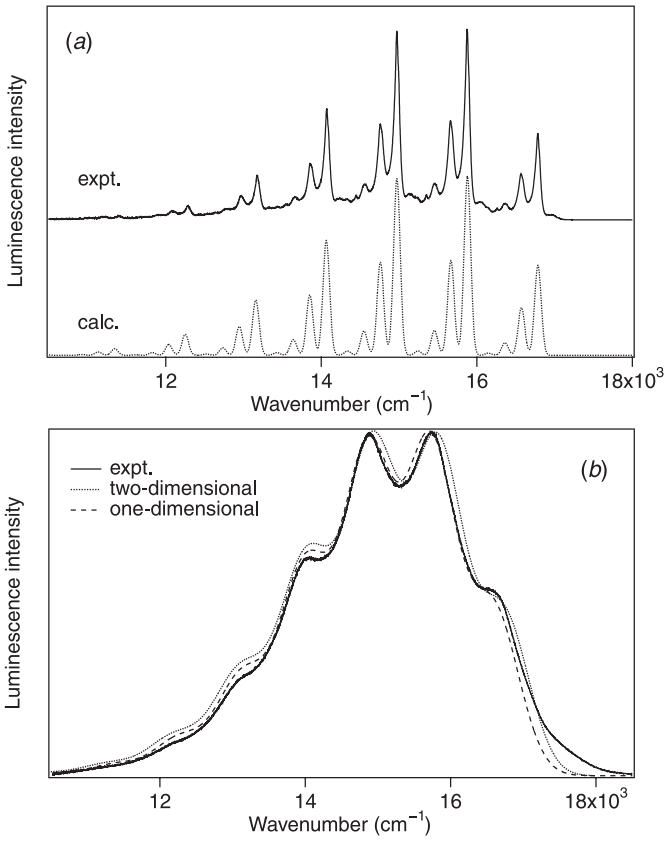
[3] The conversion of the emitting-state offset for a particular mode from dimensionless units to Å is given by

$$\Delta Q_k = \sqrt{\frac{N_A \hbar}{4\pi^2 c \hbar \omega_k M}}\, 10^8 \Delta_k$$

where N_A is Avogadro's number, $\hbar$ is Planck's constant in erg s (1 erg = 0.1 μJ), c is the speed of light in cm s^{-1}, $\hbar\omega_k$ is the frequency of the vibration in cm^{-1}, and M is the mass of the mode in g mol^{-1}.

© 2004 NRC Canada

Fig. 4. (*a*) Experimental (solid trace, 5 K) and calculated (dotted trace) luminescence spectra using two-dimensional harmonic potential energy surfaces and parameters from Table 2. (*b*) Comparison of the 300 K luminescence spectrum with the broadened two-dimensional calculated spectrum (dotted trace) and best-fit one-dimensional effective mode model (dashed trace).



changes based on the normal coordinate offsets in Table 2,[4] values similar to those calculated for the BPh_4^- salt indicating that different counter-ions do not lead to large changes in emitting-state distortions along the same normal coordinates. For other *trans*-$[ReO_2]^+$ complexes with aromatic nitrogen-donor ligands, such as substituted imidazoles, the emitting-state distortions along the Re=O bond lengths are in a similar range to those given above, between 0.07 and 0.09 Å, whereas some Re-N(ligand) distortions are much larger (19, 20).

Previous luminescence measurements and analyses of near-IR emitting *trans*-$[ReO_2]^+$ complexes revealed coupling between normal coordinates in the ground electronic state based on the nonreplica clusters of vibronic bands (20, 21). The coupling is induced by avoided crossings between the ground and excited states of the same symmetry (13). This effect is also mediated by the magnitude of the normal coordinate offset for each displaced vibrational mode. In lower energy emitting systems with large emitting state normal coordinate displacements, the coupling effect is much stronger and leads to noticeably anharmonic luminescence bandshapes. However, the title complex luminesces at higher energy and the emitting-state distortion along the Re-N(py) stretching mode is much less than in other *trans*-dioxo rhenium(V) complexes, thus making the coupling effect comparatively smaller since the avoided crossings between same-symmetry states occur farther away from the Franck–Condon region of the luminescence transition. These trends explain why there is no spectroscopic manifestation of coupling interactions between the ground and excited states in the title complex, which further justifies the use of harmonic potential energy surfaces with uncoupled coordinates to describe the ground electronic state.

Table 2. Parameter values used to calculate the spectra in Fig. 4.

Parameter	5 K	300 K
E_{00}	16 786	16 570
$\hbar\omega_{O=Re=O}$ (cm^{-1})	907	870
$\hbar\omega_{Re-N}$ (cm^{-1})	212	
$\Delta Q_{O=Re=O}$ (Å)	0.105	0.106
ΔQ_{Re-N} (Å)	0.045	
Γ (cm^{-1})	30	250

Luminescence spectra of *trans*-dioxo complexes of rhenium (V) with substituted ethylenediamine ligands measured at room temperature display partially resolved vibronic structure in the O=Re=O totally symmetric stretching mode (9). Analyses of these bandshapes were achieved with one-dimensional potential surfaces because of the lack of resolution in the lower frequency Re–ligand modes at higher temperatures. Figure 4*b* shows the 300 K spectrum with a calculated spectrum using the same parameter values in Table 2 for the 5 K spectrum (Fig. 4*a*, bottom trace), but with the damping factor (Γ) increased to 250 cm^{-1}. The agreement is very good between the experimental spectrum at 300 K and the broadened two-dimensional calculated spectrum; however, for the pressure-dependent spectra measured at 300 K, the lack of resolved structure in the Re-N(py) lower frequency mode forbids the use of a two-dimensional model to determine changes in emitting-state offsets.

The room-temperature spectra can also be calculated with a model based on effective one-dimensional potential energy surfaces, which is necessary to extract the normal coordinate offsets as a function of pressure. To fit the 300 K spectrum with the one-dimensional model, a lower vibrational frequency of 870 cm^{-1}, a value close to the O=Re=O frequency of 907 cm^{-1}, but not observed in the ground-state Raman spectrum of the title compound is used. Figure 4*b* shows the best-fit two-dimensional calculated spectrum (5 K) broadened to achieve the same resolution as the spectrum measured at 300 K compared to the best-fit calculated spectrum obtained from the one-dimensional effective coordinate model. The agreement between calculated spectra from these two models is very good and the values for the $\Delta Q_{O=Re=O}$ parameter do not vary significantly, indicating that the O=Re=O mode is the dominant contribution to the effective

[4] The conversion of the emitting-state distortion (ΔQ (Å)) to individual bond-length distortions is: for O=Re=O, $1/\sqrt{2}\,\Delta Q_{O=Re=O} = \Delta r_{Re=O}$, and for Re-N(pyridine), $1/2\,\Delta Q_{Re-N} = \Delta r_{Re-N}$, assuming that these coordinates are the sole contributors to the normal modes.

© 2004 NRC Canada

Table 3. Parameter values used to calculate the pressure-dependent luminescence spectra in Fig. 5.

P (kbar)	E_{00} (cm^{-1})	$\hbar\omega_{O=Re=O}$ (cm^{-1})	$\Delta Q_{O=Re=O}$ (Å)	Γ (cm^{-1})	E_{max} (cm^{-1})
4	16 570	865	0.1063	245	15 299
13	16 505	865	0.1062	245	15 243
21	16 380	870	0.1061	245	15 121
29	16 245	870	0.1053	250	15 008
37	16 145	870	0.1050	260	14 911
40	15 955	870	0.1049	260	14 736
42	15 885	870	0.1035	275	14 706

Note: 1 bar = 100 kPa.

coordinate, and confirming that the offsets ΔQ obtained from the one-dimensional model can be reliably interpreted as Re=O bond length changes. We use the effective coordinate model to determine pressure-induced changes in 300 K luminescence spectra.

Effect of pressure on the luminescence spectrum at room temperature

The majority of previous pressure-dependent spectroscopic studies involving transition metal complexes have focused largely on octahedral systems where the pressure-induced decrease in metal–ligand bond lengths leads to increases in $10Dq$ (22–25). Because changes in both π (t_{2g}) and σ (e_g) bonding contribute to this ligand-field parameter and spectra are usually devoid of resolved vibronic structure, analyses are usually restricted to qualitative energy level diagrams whereby states (orbitals) shift in energy relative to one another. In the idealized D_{4h} point group symmetry of the title complex, the t_{2g} level splits into the b_{2g} (HOMO) and e_g (LUMO) levels and we only consider this orbital energy difference that depends on Δ_π. The energy difference between the $^1A_{1g}$ ground state and the ^3E_g emitting state is then $\Delta_\pi - 3K_{xy}$. As an external pressure is applied to the title compound, the energy of the luminescence transition will change according to the variation of both parameters. It has been found in pressure-dependent spectroscopic studies involving doped transition metal ions (i.e., Cr^{3+} in ruby) and molecular coordination compounds that the Racah parameters decrease with increasing pressure resulting in an increase of covalency (22–26). In the title compound, this expected decrease of K_{xy} leads to a blue shift of the spectrum if the value of Δ_π does not change appreciably. However, the experimental pressure-dependent spectra shown in Fig. 3 reveal a substantial red shift with increasing pressure, which implies a strong decrease of Δ_π with pressure. The dominance of this parameter is apparent in its definition where the π contribution from the pyridine ligand ($e_{\pi\perp}$) has a large influence on Δ_π. Because it is easier to compress metal–ligand single bonds (Re-N) than double bonds (Re=O), an increasing pressure corresponds to a large increase of $e_{\pi\perp}$ but only a small increase of e_π(O), leading to a large decrease of Δ_π if no changes in the orientation of the pyridine ligands occur. This significant decrease of Δ_π as a function of pressure is a manifestation of strong π bonding between the metal center and ancillary ligands. This is confirmed by a comparison with systems having similar luminescence energies as the title compound, but smaller π interactions from the ancillary ligands, such as *trans*-[ReO_2(*N*,*N*,*N*′,*N*′-tetramethylethylenediamine)$_2$]Cl (9). In this compound, the luminescence band maximum shows a much smaller pressure-dependent red shift that indicates a smaller variation of Δ_π in complexes with ancillary ligands that do not form strong metal–ligand π bonds.

In the pressure-dependent luminescence spectra reported in Fig. 3, the partially resolved vibronic structure provides an opportunity to study the effect of pressure on the Re=O bond length differences from the changes in vibronic patterns and energies of the luminescence origin and band maximum. These important spectroscopic parameters are extracted by fitting a calculated spectrum to the experimental spectrum at each measured pressure using the effective coordinate one-dimensional harmonic potential energy surface model described in the previous section. The energy of the electronic origin transition at each pressure was assumed to be the first resolved shoulder observed in the luminescence bands. This assumption is necessary due to thermal broadening of the vibronic bands and, at ambient pressure, leads to an energy that is lower than the 5 K value by approximately 200 cm^{-1}. Figure 5 shows the comparison between calculated and experimental spectra at selected pressures. The agreement between the calculated spectra and the pressure-dependent luminescence bands is excellent and the parameters used to calculate the spectra are summarized in Table 3. At the highest pressures, starting from 37 kbar (Fig. 3*b*) there is additional intensity to the blue side of the first vibronic transition. This feature closely corresponds to the position of the less-intense band system (**A**) observed in the temperature-dependent luminescence spectra. This band could gain intensity if the two emitting states have different pressure dependence, thus leading to an increased population of **A** at the expense of **B**. Another possibility for the appearance of this feature arises from a pressure-induced increase of inhomogeneity throughout the lattice, creating a luminophore slightly different in structure than that found in ambient pressure spectra. Because the pyridine ligands are oriented perpendicular to the ML_4 plane, a pressure-induced change in crystal-packing forces could favor a structure where the pyridine ligand twists around the Re—N single bond axes. This change in orientation of the pyridine ligand would then alter its contribution to Δ_π and the magnitude of red shift would be expected to decrease at higher pressures. We cannot rule out any of these possibilities in rationalizing the pressure-dependent luminescence properties of the title compound based on the spectra in Fig. 3.

© 2004 NRC Canada

Fig. 5. Selected pressure-dependent luminescence spectra with the calculated spectra shown as dotted traces calculated using parameter values from Table 3. The slanted lines shown in the top and bottom panels are included as a guide for the eye to illustrate the change in intensity distribution for the resolved vibronic progression.

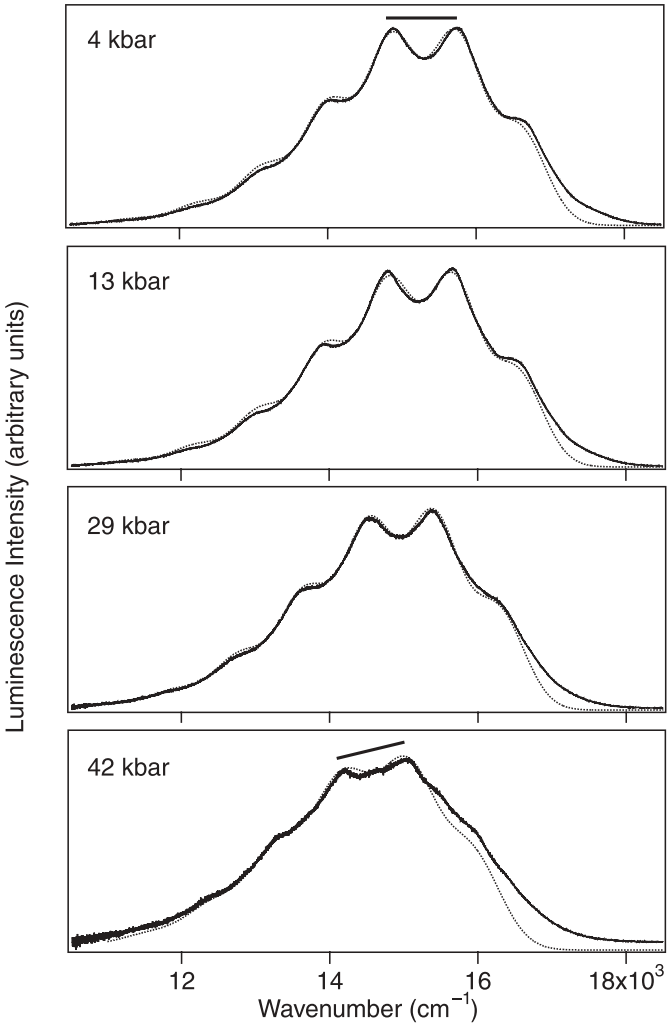
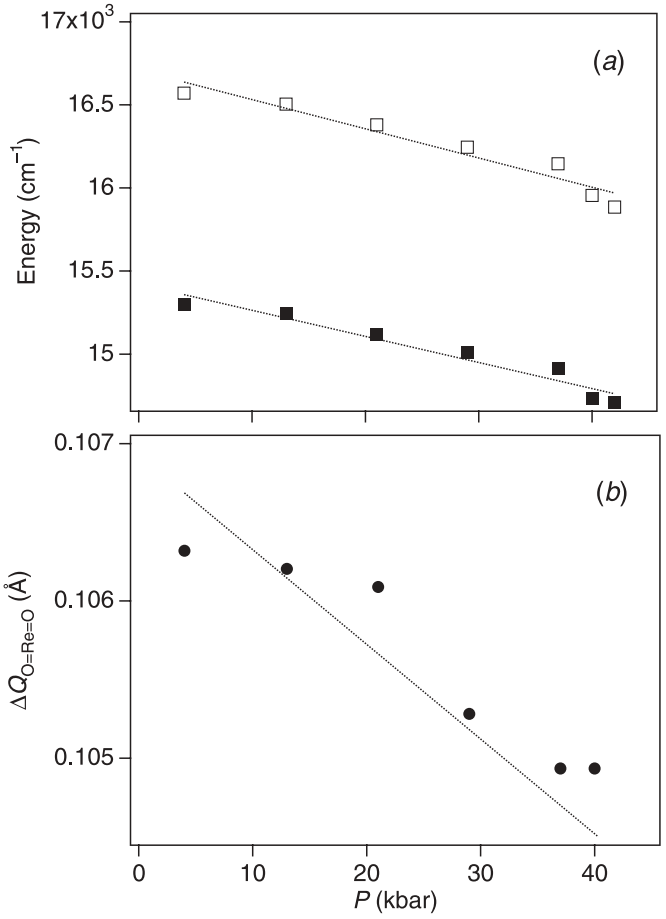


Fig. 6. (*a*) Pressure dependence of the origin transition (E_{00}) (open squares) and the energy of the luminescence band maximum (E_{max}) (solid squares). (*b*) Pressure dependence of the normal coordinate offset ($\Delta Q_{O=Re=O}$) from the one-dimensional model.



In typical pressure-dependent studies, the energy of the band maximum is the only spectroscopic parameter reported quantitatively. Because most pressure-dependent electronic spectra of transition metal complexes are devoid of any resolved vibronic structure, the unresolved bands (absorption or luminescence) are fitted with Gaussian functions from which the energy of the band maxima can be determined and qualitative energy level diagrams can be used to rationalize pressure-induced shifts in energy. In contrast, our spectra with resolved vibronic structure allow us to determine not only the shift of the band maximum, but also the pressure-induced shift of the normal coordinate offset ($\Delta Q_{O=Re=O}$) and the energy of the electronic origin (E_{00}) quantities obtained from the fit of calculated spectra to the experimental results. The quantitative calculated spectra in Fig. 5 can be phenomenologically broadened (by increasing Γ) to give an unresolved band whose overall maximum (E_{max}) is easily determined. This procedure is necessary due to the fact that individual vibronic maxima are not suitable to describe how the overall band maximum changes with pressure. Figure 6 shows the effect of pressure on the parameters used in the calculation of the room-temperature, pressure-dependent luminescence spectra.

Figure 6*a* demonstrates that E_{00} and E_{max} have very similar pressure-dependent behavior, which justifies the choice of harmonic potential energy surfaces to describe the ground electronic state and our rationalization in the changes in luminescence energies in terms of purely electronic parameters, Δ_π and K_{xy}. This is in contrast to the trends observed in the substituted ethylenediamine complexes, where E_{00} and E_{max} have a markedly different response to increasing pressure because of avoided crossings between the ground state and excited states of the same symmetry (9).

Figure 6*b* illustrates the effect of pressure on the normal coordinate offset ($\Delta Q_{O=Re=O}$) determined from the one-dimensional calculated spectra. All normal coordinate offsets decrease as a function of pressure because of the reduced sample volume; however, the extent to which they vary depends on the influence of intermolecular packing forces on the intramolecular properties, such as metal–ligand bond lengths and angles. The pressure-induced decrease of

© 2004 NRC Canada

$\Delta Q_{O=Re=O}$ was found to be -6×10^{-5} Å/kbar, much smaller than determined for substituted ethylenediamine complexes of rhenium(V), where this decrease is on the order of -1×10^{-4} Å/kbar (9). This previous study showed that as luminescence energies increase, bandshapes become more harmonic and the decrease of $\Delta Q_{O=Re=O}$ became smaller, and the title complex confirms this trend.

In contrast, the pressure-induced red shift of the luminescence band maximum is much larger (16 ± 2 cm^{-1}/kbar) than determined for *trans*-dioxo rhenium(V) complexes with substituted ethylenediamine ligands, with red shifts of less than 10 cm^{-1}/kbar (9). We attribute this large red shift to the ancillary pyridine ligands that form strong π bonds with the metal center, illustrating that both interactions between electronic states (9) and the detailed nature of the metal–ligand bonds can be probed via the observed pressure effects on the luminescence spectra of *trans*-dioxo complexes.

Conclusion

The *trans*-[ReO_2(pyridine)$_4$]I luminophore is an excellent system to study the effect of an external perturbation on the resolved vibronic luminescence spectrum at room temperature because of the sensitivity of its luminescence properties to the crystalline environment. We find that the luminescence energies of complexes with monodentate ligands that have strong π-bonding interactions with the metal center, such as pyridine, are more susceptible to changes in the crystalline environment whereas *trans*-[ReO_2]$^+$ complexes with chelating and weakly π interacting ligands tend to show smaller variations. The analysis of less-resolved room-temperature spectra with one-dimensional potential energy surfaces reveals the effects of pressure on the spectroscopic parameters defining the ground and emitting states. These subtle aspects of metal–ligand bonding can be quantitatively derived from the temperature- and pressure-dependent luminescence spectra of related *trans*-dioxo complexes.

Acknowledgements

Financial support through research grants and a postgraduate scholarship (JKG) from the Natural Sciences and Engineering Research Council of Canada (NSERC) is gratefully acknowledged.

References

1. C.-M. Che, V.W.-W. Yam, K.-C. Cho, and H.B. Gray. Chem. Comm. 948 (1987).
2. H.H. Thorp, C.V. Kumer, N.J. Turro, and H.B. Gray. J. Am. Chem. Soc. **111**, 4364 (1989).
3. H.H. Thorp, J. Van Houten, and H.B. Gray. Inorg. Chem. **28**, 889 (1989).
4. C.-M. Che, W.-K. Cheng and V.W.-W. Yam. J. Chem. Soc. Dalton Trans. 3095 (1990).
5. J.R. Winkler and H.B. Gray. J. Am. Chem. Soc. **105**, 1373 (1983).
6. J.R. Winkler and H.B. Gray. Inorg. Chem. **24**, 346 (1985).
7. M.D. Newsham, E.P. Giannelis, T.J. Pinnavaia, and D.G. Nocera. J. Am. Chem. Soc. **110**, 3885 (1988).
8. J.K. Grey, M. Triest, I.S. Butler, and C. Reber. J. Phys. Chem. A, **105**, 6269 (2001).
9. J.K. Grey, I.S. Butler, and C. Reber. J. Am. Chem. Soc. **124**, 11 699 (2002).
10. V.M. Miskowski, H.B. Gray, and M.D. Hopkins. *In* Adv. in Trans. Met. Coord. Chem. Vol. 1. *Edited by* C.-M. Che and V.W.-W. Yam. JAI Press, Greenwich, Conn. 1996. p. 159.
11. J.K. Grey, M. Marguerit, I.S. Butler, and C. Reber. Chem. Phys. Lett. **366**, 361 (2002).
12. J.H. Beard, J. Casey, and R.K. Murmann. Inorg. Chem. **4**, 797 (1965).
13. J. Landry-Hum, V. Tessier, M. Ernzerhof, and C. Reber. Coord. Chem. Rev. **233–234**, 63 (2002).
14. E.J. Heller. J. Chem. Phys. **62**, 1544 (1975).
15. E.J. Heller. Acc. Chem. Res. **14**, 368 (1981).
16. J.I. Zink and K.-S. Kim Shin. *In* Adv. Photochem. Vol. 16. *Edited by* D.H. Volman, G.S. Hammond and D.C. Neckers. John Wiley, New York. 1991. p. 119.
17. G. Herzberg. Molecular structure and molecular spectra. Vol. II. Infrared and Raman spectra of polyatomic molecules. Van Nostrand, New York. 1945. p. 63.
18. M. Triest, S. Masson, J.K. Grey, and C. Reber. Phys. Chem. Comm. Article 12, 64 (2000) [online]. Available from http://www.rsc.org/CFmuscat/intermediate_abstract.cfm?FURL=/ej/qu/2000/b008386k/index.htm&TYP=EON [cited 26 January 2004].
19. C. Savoie and C. Reber. Coord. Chem. Rev. **171**, 387 (1998).
20. C. Savoie and C. Reber. J. Am. Chem. Soc. **122**, 844 (2000).
21. C. Savoie, C. Reber, S. Bélanger, and A.L. Beauchamp. Inorg. Chem. **34**, 3851 (1995).
22. R.W. Parsons and H.G. Drickamer. J. Chem. Phys. **29**, 930 (1958).
23. D.R. Stephens and H.G. Drickamer. J. Chem. Phys. **34**, 937 (1961).
24. D.R. Stephens and H.G. Drickamer. J. Chem. Phys. **35**, 429 (1961).
25. A.S. Balchan and H.G. Drickamer. J. Chem. Phys. **35**, 356 (1961).
26. K.L. Bray. Top. Curr. Chem. **213**, 1 (2001).

© 2004 NRC Canada

The dependence of thymine and thymidine Raman spectra on solvent[1]

L. Beyere, P. Arboleda, V. Monga, and G.R. Loppnow

Abstract: Recent work has focused on developing Raman spectroscopy as a noninvasive probe of DNA interactions with solvents, intercalants, proteins, and other ligands. Here, we report the Raman spectra of thymine in eight solvents and thymidine in nine solvents obtained with visible excitation. Raman spectra under acidic, neutral, and basic conditions were also obtained of both thymine and thymidine. Changes in both the frequencies and intensities of several of the vibrational bands in the 800–1800 cm^{-1} region are observed. No evidence of deprotonation in the different solvents is observed for either thymine or thymidine. Correlations of the observed frequency shifts of specific vibrational modes with characteristic properties of the solvent for both thymine and thymidine show a significant correlation with acceptor and donor numbers, measures of the hydrogen-bonding ability of the solvent, in both thymine and thymidine. These results are interpreted in terms of hydrogen-bonding interactions between the N-H protons of the thymine base and lone pairs of electrons on the solvent molecules and between the solvent hydrogens and lone pairs on C=O sites. The solvent-dependent intensity in vibrational bands of thymine between 1500 and 1800 cm^{-1} indicates a strong interaction between thymine and solvent at the C=O and N-H sites that leads to separation of the C=O stretches from the C=C stretch. The intensity variations with solvent were much smaller for thymidine than for thymine, perhaps as a result of replacing the N_1 proton by the sugar. These results suggest that Raman spectroscopy is uniquely sensitive to specific interactions of thymine and thymidine with their environment.

Key words: Raman spectroscopy, thymine, thymidine, solvent effects, hydrogen bonding.

Résumé : Un récent travail a été orienté vers le développement de la spectroscopie Raman comme sonde non invasive des interactions de l'ADN avec des solvants, des intercalants, des protéines et d'autres ligands. Dans ce travail, on a mesuré les spectres Raman de la thymine dans huit solvants et de la thymidine dans neuf solvants, obtenus à l'aide d'une excitation visible. On a aussi déterminé les spectres Raman de la thymine et de la thymidine dans des milieux acide, neutre et basique. On a observé des changements tant dans les fréquences que dans les intensités de plusieurs bandes vibrationnelles dans la région de 800 à 1800 cm^{-1}. On n'a observé aucun donnée pouvant laisser croire qu'il se produit une déprotonation de la thymine ou de la thymidine dans les différents solvants. Des corrélations entre les propriétés caractéristiques des solvants et les déplacements de fréquence observés pour des modes vibrationnels spécifiques tant de la thymine que de la thymidine présentent une corrélation significative avec les nombres de donneur et d'accepteur, des mesures du pouvoir d'un solvant à former des liaisons hydrogènes tant avec la thymine qu'avec la thymidine. On interprète ces résultats en fonction d'interactions de liaisons hydrogènes entre les protons N-H de la base, la thymine, et les paires d'électrons libres des molécules de solvant et entre les hydrogènes du solvant et les paires libres des sites C=O. L'intensité qui varie en fonction du solvant des bandes vibrationnelles de la thymine entre 1500 et 1800 cm^{-1} est un reflet d'une interaction forte entre la thymine et le solvant au niveau des sites C=O et N-H qui conduit à une séparation des bandes d'élongation C=O par rapport à la bande d'élongation C=C. Les variations d'intensité en fonction du solvant sont beaucoup plus faibles dans le cas de la thymidine que dans celui de la thymine et ceci est peut-être le résultat du remplacement du proton en N_1 par un sucre. Ces résultats suggèrent que la spectroscopie Raman comporte une sensibilité unique aux interactions spécifiques de la thymine et de la thymidine dans leur environnement.

Mots clés : spectroscopie Raman, thymine, thymidine, effets de solvant, liaison hydrogène.

[Traduit par la Rédaction]

Received 2 November 2003. Published on the NRC Research Press Web site at http://canjchem.nrc.ca on 10 September 2004.

L. Beyere, P. Arboleda, V. Monga, and G.R. Loppnow.[2] Department of Chemistry, University of Alberta, Edmonton, AB T6G 2G2, Canada.

[1]This article is part of a Special Issue dedicated to the memory of Professor Gerhard Herzberg.
[2]Corresponding author (e-mail: glen.loppnow@ualberta.ca).

 doi: 10.1139/V04-052 © 2004 NRC Canada

Introduction

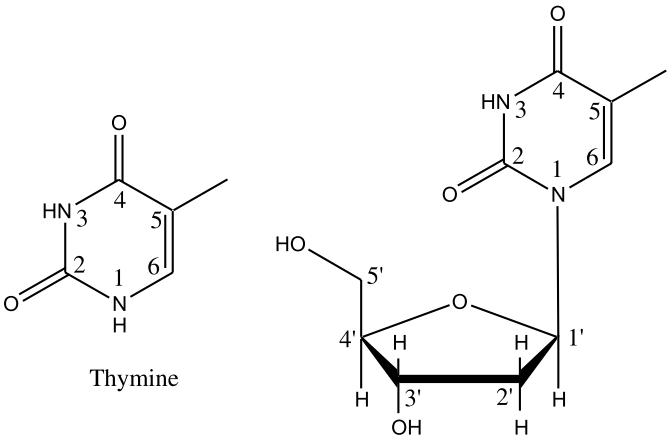
Thymidine (1-[2′-deoxy-β-ribofuranosyl]-5-methyluracil) is one of the four nucleoside constituents of DNA and consists of 2′-deoxyribose attached to the pyrimidine base thymine (2,4-dioxo-5-methylpyrimidine) (Scheme 1). The pyrimidine nucleosides are more photochemically active than their purine counterparts, with thymidine and its derivatives being the most photochemically active (1). Of the pyrimidine bases, thymine is particularly prone to damage by UV light, forming a variety of photoproducts such as cyclobutane photodimers, 6–4 photoproducts, spore photoproducts, and photohydrates (2, 3). Many aspects of the photophysical, photochemical, and photobiological properties of DNA and related compounds have been intensively studied (4–8), resulting in a large body of information on the various structural features of the photoproducts (9). However, most methods for detecting and quantifying DNA photodamage and repair, such as chromatography, gel electrophoresis, and immunological approaches (8, 10–12), are invasive and destructive. The ultimate aim of this work is to probe DNA structure and interactions using Raman spectroscopy, a noninvasive method.

Vibrational spectroscopy is a powerful probe of structure and interactions. For example, infrared (IR) absorption spectroscopy has been used to assign the IR-allowed vibrational modes of uracil and thymine (13–16). Raman vibrational spectroscopy, the inelastic scattering of light (17, 18), has been applied to DNA by a number of groups, in an effort to understand its structure and dynamics (16, 19–28). Raman spectroscopic studies of thymidine-containing molecules have also been performed, leading to the preliminary assignment of thymidine vibrational Raman bands (29–32). Advantage has been taken of the more selective and sensitive method of UV-resonance Raman spectroscopy to probe nucleic acids, their constituents, and related molecules (21, 24, 25). However, these studies have focused on the structure of nucleic acids, and few studies have explored the applicability of using Raman spectroscopy to probe nucleic acid interactions with different chemical environments and other molecules. The solvent dependence of the UV Raman spectrum of only adenine among the nucleobases has been reported (26). Recently, Raman spectroscopy with excitation at 532 nm has shown that thymines are particularly sensitive to the binding of HU protein to the minor groove of DNA (27).

Since thymine and thymidine both have proton-accepting and -donating sites, spectral changes are expected to result from their interaction with proton-acceptor and acceptor–donor solvents (33). Raman spectroscopy has been used recently to explore the dependence of the Raman spectra of ethyl 4-(dimethylamino)benzoate (DMABEE) (34) and of sunscreens (35) on solvent.

In this paper, we explore the Raman frequency shifts of thymine and thymidine as a function of solvent environment. Guided by an experimental assignment of the normal modes in thymine (28) and by solvent parameter scales, we attempt to elucidate the specific interaction sites of solvent molecules with thymine and thymidine in the condensed phase. Several of the observed thymine modes exhibit frequency shifts as a function of solvent parameters. Interestingly, the magnitude of the shifts in a particular solvent is different for different modes, suggesting that Raman spectroscopy is a structurally specific probe of solvent–thymine interactions. In addition, intensity changes in thymine C=O stretch-containing modes indicate particularly strong interactions with solvent. These results provide an important foundation for analyzing the spectra of nucleic acids in different chemical environments, which will eventually lead to developing Raman spectroscopy as a better probe of DNA interactions with other nucleic acids, proteins, and smaller molecules such as drugs and intercalants.

Scheme 1.



Experimental

Thymine and thymidine (99%) were obtained from the Sigma Chemical Company (St. Louis, Missouri) and used as received. Acetic acid (glacial), benzyl alcohol, *N*,*N*-dimethylformamide, ethanol, ethylene glycol, formamide, formic acid (88%), pyridine, trifluoroacetic acid, and water (deionized, 18 MΩ) were reagent grade or better from freshly opened bottles and were used without further purification. The important solvent parameters are collected in Table 1.

Room-temperature Raman spectra were obtained of freshly prepared solutions of thymine and thymidine in various solvents. Due to the differences in solubility of thymine and thymidine in the various solvents used, the concentration varied from a high range of 0.5–4 mol L^{-1} for the acidic solvents to a low range of 1–20 mmol L^{-1} in the other solvents (the highest concentration was 4 mol L^{-1} for thymidine in formic acid and the lowest concentration was ~1 mmol L^{-1} for thymine in pyridine), as determined from the UV–vis absorption measurements of the saturated solutions using ε = 10 200 L mol^{-1} cm^{-1} at 260 nm. Raman spectra were excited by 250 mW of 457.9 nm light from an Ar^+ ion laser (Coherent, Santa Clara, California) spherically focused on a 5 mm diameter (o.d.) spinning NMR tube in a 135° backscattering geometry (34, 36, 37) containing approximately 300 μL of the solution. Multichannel detection of the resulting Raman scattering was accomplished with a liquid-nitrogen-cooled, charged-coupled device (CCD) detector (Princeton Instruments, Trenton, New Jersey) coupled to the first half of a double monochromator (Spex, Metuchen, New Jersey).

© 2004 NRC Canada

Table 1. Solvent parameters used in this study.

Solvent	n	ε	AN	DN	$\pi^*/\pi^*\Pi$	Y	Π	B	K	Θ	ε_p	M'	M	L	KL
Acetic acid	1.3716	6.15[20]	52.9	12.7[a]	0.664/0.64	0.649	0.227	0.163	0.387	0.263	5.27	0.369	0.405	0.185	0.0717
Benzyl alcohol	1.5396	13.1	34.5	15.8	0.984/—	0.801	0.314	0.0764	0.429	0.826	11.73	0.345	0.488	0.314	0.153
N,*N*-DMF	1.4305	36.5[a]	16.0	26.6	0.882[b]/0.88	0.922	0.259	0.0274	0.480	0.444	35.5	0.461	0.663	0.205	0.0986
Ethanol	1.3611	24.3	37.9	20	0.54/—	0.886	0.221	0.0411	0.460	0.573	23.45	0.499	0.665	0.221	0.147
Ethylene glycol	1.4318	37.7[25]	—	—	0.932/0.92	0.924	0.259	0.0265	0.480	0.446	36.7	0.461	0.665	0.206	0.0989
Formamide	1.4472	109[20]	39.8	24.0	1.118/0.97	0.973	0.267	9.2×10^{-5}	0.500	0.716	10 900	0.477	0.732	0.211	0.105
Formic acid	1.3714	58.5[16]	—	—	—	0.950	0.227	0.0171	0.487	0.481	57.6	0.515	0.723	0.185	0.0901
Pyridine	1.5095	12.3[25]	14.2	33.1	0.867/0.87	0.790	0.299	0.0811	0.442	0.342	11.0	0.358	0.492	0.230	0.102
Trifluoroacetic acid	1.6506[a]	8.6[a]	105.3	7.1[a]	0.50[c]	0.717	0.365	0.116	0.418	0.302	6.88	0.251	0.352	0.267	0.112
Water	1.333	80.37[20]	54.8	18.0	1.090/1.09	0.964	0.206	0.0124	0.491	0.504	79.6	0.550	0.758	0.171	0.0837

Note: n (refractive index) and ε (dielectric constant; superscripts represent temperature in °C) data from ref. 48. AN (acceptor number) data from ref. 49. DN (donor number) data from ref. 40. $\pi^*/\pi^*\Pi$ (Kamlet–Taft dipolarity numbers) data from ref. 50. $Y = (\varepsilon - 1)/(\varepsilon + 2)$ and $\Pi = (n^2 - 1)/(n^2 + 2)$ from ref. 51. $B(\varepsilon) = 1/\varepsilon$, $K(\varepsilon) = (\varepsilon - 1)/(2\varepsilon + 1)$, $\Theta(\varepsilon) = [(3\varepsilon \ln \varepsilon)/(\varepsilon \ln \varepsilon - \varepsilon + 1)] - (6/\ln \varepsilon) - 2$, $\varepsilon_p = \varepsilon - n^2 + 1$, $M'(\varepsilon, n^2) = 1/n^2 - 1/\varepsilon$, $M(\varepsilon, n^2) = [(\varepsilon - 1)/(\varepsilon + 2)] - [(n^2 - 1)/(n^2 + 2)]$, and $L(n^2) = (n^2 - 1)/(2n^2 + 1)$ from ref. 52.

[a]From ref. 51.

[b]Used value for *N*,*N*-dimethylacetamide.

[c]From ref. 53.

Spectral slit widths were 5–7 cm^{-1} and typical spectral acquisition times were 1 h. UV–vis absorption spectra of the samples were measured using a diode array spectrophotometer (Hewlett-Packard, Sunnyvale, California) before and after irradiation. In addition, NMR spectra of thymine and thymidine in the perdeuterated forms of the solvents used here showed no perturbations from the NMR spectra of thymine and thymidine in D_2O. A solvent spectrum was subtracted from the spectrum of each solution, and the resulting spectrum was frequency calibrated by measuring the Raman scattering of solvents with known frequencies (acetone, benzene, carbon tetrachloride, and chloroform). The reported frequencies are accurate to ±1.5 cm^{-1}. The baselines were leveled by subtraction of multiple joined line segments. Raman spectra of freshly prepared saturated solutions of thymine in acid (0.31 mol L^{-1}, H_2O, pH ~ 3) and base (0.60 mol L^{-1}, H_2O, pH ~ 11) were also obtained under similar conditions.

Results

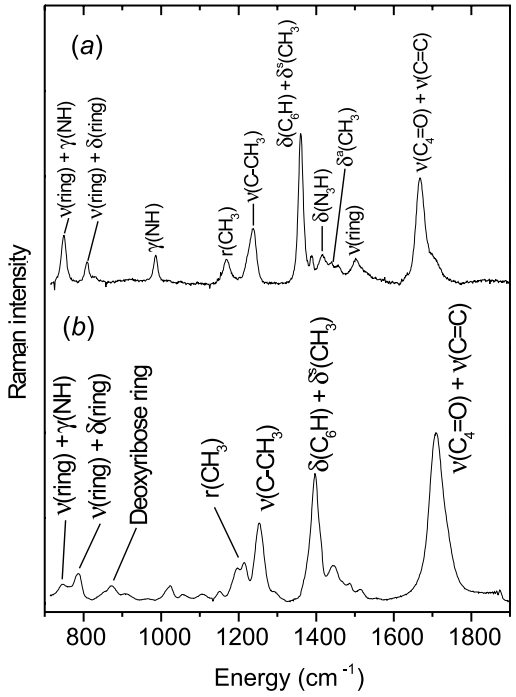
Figure 1 shows the Raman spectrum and vibrational assignments of thymine and thymidine in water for the 700–1800 cm^{-1} region. The Raman spectra of thymine and thymidine obtained in this work agree with previously reported Raman spectra (29–32). No significant bands due to thymine or thymidine are observed at frequencies above 1800 cm^{-1}. Very weak bands are observed below 700 cm^{-1}, too weak to determine accurate frequencies. Therefore, only the vibrational bands within the 700–1800 cm^{-1} region were considered. The vibrational assignments of thymine were determined earlier from an extensive isotopic labeling study (28). For thymidine, modes assigned to the 2′-deoxyribose sugar ring only and vibrations due to coupling of the base and sugar ring are based on Raman studies of thymidine (29–32), while the assignment of the 740, 787, 1180, 1235, 1372, and 1660 cm^{-1} modes to the thymine base are from an extensive isotopic labeling study of Zhang et al. (28).

For thymine, the 700–800 cm^{-1} region is dominated by bands assigned to ring-breathing modes of the thymine base, while more localized vibrations are observed from 800 to 1800 cm^{-1} (30). Several bands are observed in this latter region of the spectrum, arising mainly from ring stretches, as well as stretches, bends, wags, and rocks of the exocyclic groups (28). Because the vibrations in this region of the spectrum arise from all of the groups of the molecule, particularly the NH and CO groups that are expected to interact strongly with solvent, this "fingerprint" region should allow a determination of the interaction sites with solvent.

For thymidine, modes in the 800–1200 cm^{-1} region are thought to be localized on the 2′-deoxyribose sugar ring, while in the 1200–1600 cm^{-1} region we expect modes resulting from the coupling of the vibrational coordinates of the thymine base and the sugar ring (29–32). It is evident from the spectra in Fig. 1 that the Raman modes due to the sugar ring are very weak, the most intense peaks being those due to coupled vibrations of the base and sugar, and those due to the base only, with the mode assigned to the C=C and C=O double bond stretches of the base being the most intense. In fact, many of the same vibrations are observed in the Raman spectra of both thymine and thymidine, although they are

© 2004 NRC Canada

Fig. 1. Raman spectra of (*a*) thymine and (*b*) thymidine in water excited at 457.9 nm. The spectra are the sum of 3–9 scans, and a Raman spectrum of water has been subtracted. The vibrational assignments for thymine (28) and thymidine (28–32) are shown above the bands: ν stretch; δ in-plane bend; γ out-of-plane bend (wag); r rock. The superscripts "a" and "s" stand for asymmetric and symmetric, respectively.



shifted slightly to higher frequency in thymidine. This result suggests that the most intense modes arise from vibrations of the base with slight perturbations to the frequency by the sugar attached to N_1 instead of a proton. Thus, the intense modes at 1235, 1415, and 1690 cm^{-1} are assigned to the methyl stretch, $C_6H + CH_3$ deformation, and $C_4=O + C=C$ stretch of the thymine base, respectively.

To determine the sensitivity of Raman spectroscopy to specific solvent–solute interactions, and to identify the molecular sites of interaction with thymine, the Raman spectra of thymine dissolved in eight solvents and thymidine dissolved in nine solvents with a wide range of properties were obtained. Since thymine and thymidine each have multiple proton-accepting and proton-donating sites, their vibrations are expected to be sensitive to solvent interaction. The Raman spectra of the thymine and thymidine solutions are presented in Figs. 2 and 3. Table 1 lists the major fundamental and derived parameters of the solvents used. Good-quality spectra were obtained in all cases. In some solvents, Raman scattering from the solvent interfered with the precise determination of the data in some regions of the spectrum. These regions have been blanked out in Figs. 2 and 3. Examination of Figs. 2 and 3 shows that the general pattern of the Raman spectrum is the same in all of the different solvents. To ensure that no reaction was occurring between thymine and the solvent, UV-absorption and NMR spectra were taken of the thymine and thymidine solutions before and after irradiation in the Raman excitation laser beam. The absorption spectra of thymine and thymidine were similar, with

Fig. 2. Raman spectra of thymine in (*a*) glacial acetic acid, (*b*) *N*,*N*-dimethylformamide, (*c*) ethylene glycol, (*d*) formamide, (*e*) formic acid, (*f*) pyridine, (*g*) trifluoroacetic acid, and (*h*) water. Solvent spectra have been subtracted from each spectrum. The portions of each spectrum where no data are reported have been blanked out owing to strong solvent interference in those regions.

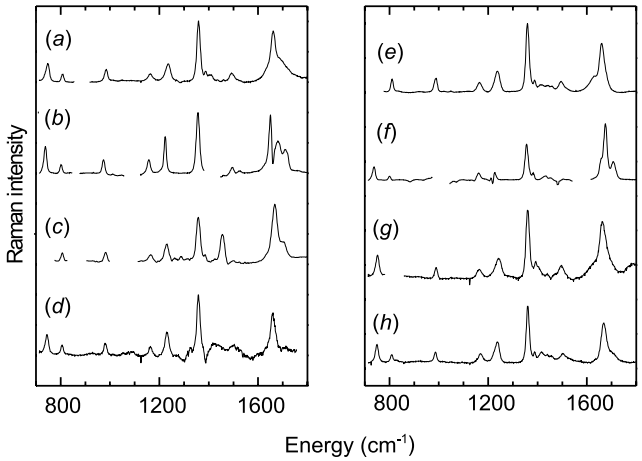
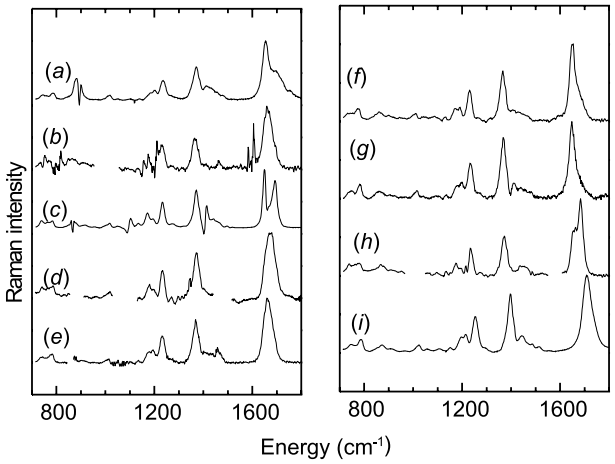


Fig. 3. Raman spectra of thymidine in (*a*) glacial acetic acid, (*b*) benzyl alcohol, (*c*) *N*,*N*-dimethylformamide, (*d*) ethanol, (*e*) ethylene glycol, (*f*) formamide, (*g*) formic acid, (*h*) pyridine, and (*i*) water. Solvent spectra have been subtracted from each spectrum. The portions of each spectrum where no data are reported have been blanked out owing to strong solvent interference in those regions.



only slight absorption maxima shifts, in all of the solvents studied. Except for slight changes in coupling constants, expected from the different hydrogen-bonding properties of the solvents, no changes were seen in any ^1H NMR spectrum of fresh solutions or of solutions left sitting for 3–5 days. All of these observations suggest that there is no reaction between thymine or thymidine and any of the solvents used.

Although no major changes in the absorption or Raman spectra of thymine were observed in any solvent, there are obvious frequency shifts and relative intensity changes in the Raman spectra as a function of the solvent environment. The frequencies of the bands at ca. 740, 980, 1230, 1360, 1390,

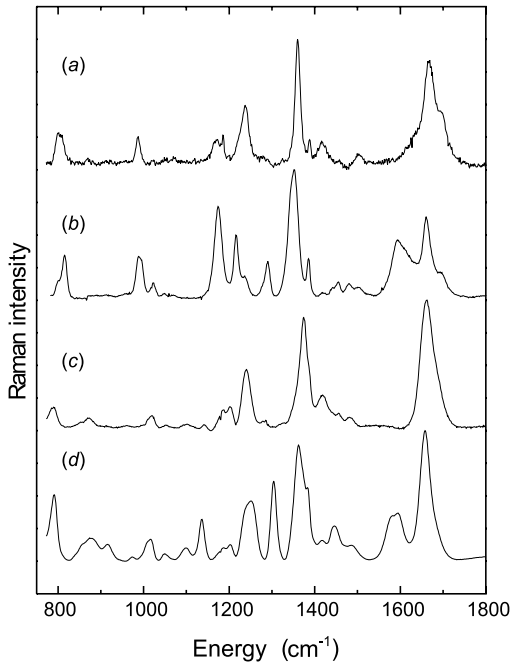
© 2004 NRC Canada

and 1500 cm^{-1} all vary with the solvent (Fig. 2). In addition to these frequency shifts, striking changes in relative intensity also appear as a function of solvent. The most dramatic of these intensity changes occur in the 1600–1800 cm^{-1} region. In some solvents, such as acetic acid, water, trifluoroacetic acid, and formamide, a single peak is observed at ca. 1680 cm^{-1}. However, in other solvents, one or more additional peaks are seen in this region. For example, the band at 1680 cm^{-1} exhibits a high-frequency shoulder in ethylene glycol and pyridine, a low-frequency shoulder in formic acid and pyridine, and two or more peaks at higher frequency in *N*,*N*-DMF. The presence of a solvent peak at 1660 cm^{-1} in *N*,*N*-DMF (Fig. 2*c*) raises a doubt as to the assignment of these two new peaks to thymine in this solvent. However, in the subtraction, the three most intense solvent peaks at 865, 1406, and 1439 cm^{-1} were well subtracted and any contribution from the less intense 1660 cm^{-1} peak should have been completely removed. Hence, we assign the three peaks to actual thymine peaks, not to solvent subtraction artifacts. In addition to these dramatic changes, smaller changes in relative intensity also occur between the 1680 and 1360 cm^{-1} peaks in many of the solvents, in the 1230 cm^{-1} peak in *N*,*N*-DMF, and in the 1460 cm^{-1} peak in ethylene glycol.

For thymidine, similar spectral features are also observed in all the solvents (Fig. 3). Although there are no obvious major changes in the Raman spectra, some frequency shifts and slight intensity changes are observed. The frequencies of the bands at ca. 740, 787, 1140, 1180, 1450, and 1690 cm^{-1} all shift significantly with the solvent, while slight shifts occur for the modes at 867, 1100, and 1200 cm^{-1}. Some slight intensity changes are also evident, especially in the 1600–1800 cm^{-1} region. Two peaks appear in *N*,*N*-DMF, while a single peak appears around 1660 cm^{-1} in all the other solvents. As was observed for thymine, the presence of a solvent peak at 1660 cm^{-1} in *N*,*N*-DMF (Fig. 3*c*) raises a doubt as to the assignment of the two peaks in this region to thymidine. However, in the subtraction, the three most intense solvent peaks at 865, 1406, and 1439 cm^{-1} were well subtracted, and any contribution from the less intense 1660 cm^{-1} peak should have been completely removed. Hence, we assign the two peaks to thymidine, and not to solvent subtraction artifacts. In pyridine, a low-frequency shoulder is seen, while for acetic acid a high-frequency shoulder is observed. However, there is very little change in the relative intensities of the 1660 cm^{-1} peak to the 1240 and (or) the 1450 cm^{-1} peak.

Since the most logical interaction of solvent with thymine or thymidine would be a hydrogen-bonding interaction, because of the extensive number of sites on thymine where hydrogen bonding can occur, Raman spectra were also obtained of thymine and thymidine at low and high pH. These spectra in the 800–1800 cm^{-1} region are presented in Fig. 4. The Raman spectra of thymine at neutral and acidic pH (pH ~ 3) were essentially identical, so only the spectrum at neutral pH is shown. This was similarly true for thymidine. However, significant differences between the Raman spectra at neutral and basic pH are observed for both thymine and thymidine. In the pH range 2–11, thymine is neutral in the acidic region and negatively charged in the alkaline region (38). Therefore, at the pH used in this study (pH ~ 11), thymine exists mostly as the monovalent anion, since the N_3 pK_a of thymine is 10.0 (38). The Raman spectrum at pH ~ 11 therefore represents a weighted mixture of the spectra for the monovalent anion and neutral. The largest differences between the neutral and basic thymine Raman spectra are the presence of two strong new bands at 1290 and 1593 cm^{-1} and an increase in intensity of the band at 1160 cm^{-1} in the high-pH spectrum. Thus, the presence of the two new bands can be used as a diagnostic for the deprotonation of thymine in the solvents used in this study. Since none of the spectra in Fig. 2 show bands at either 1290 or 1593 cm^{-1}, no deprotonation of thymine occurs in any of the solvents tested.

Fig. 4. Raman spectra of thymine in (*a*) neutral and (*b*) basic aqueous solution, and thymidine in (*c*) neutral and (*d*) basic aqueous solution. The Raman spectra of thymine and thymidine in acidic solution were indistinguishable from those in neutral solution. A solvent spectrum has been subtracted from each spectrum.



A comparison of the neutral and base spectra of thymidine (Figs. 4*c* and 4*d*) to those of thymine shows great similarities. This is expected, since thymine is the main contributor to the Raman spectrum of thymidine. For thymidine, three new strong bands are seen at 1136, 1303, and 1594 cm^{-1} in the basic spectrum, which are not present in the neutral spectrum. A number of bands also experience relative intensity changes such as the bands at 1100 and 1450 cm^{-1}. Because thymidine can be deprotonated–protonated at the N_3-H site, which has a pK_a of 9.93 (38, 39), thymidine exists mostly as the monovalent anion at the pH ~ 11 used for this study. Thus, the presence of these three new bands in the basic pH spectrum can be used as a diagnostic for the deprotonation of the thymidine in the other solvents used for this study. Since the 1136, 1303, and 1594 cm^{-1} bands are not observed in any of the spectra in Fig. 3, we conclude that no deprotonation of thymidine occurred in any of the solvents used for the study.

© 2004 NRC Canada

Discussion

Frequency changes with solvent

To understand the significant changes in the Raman spectra of thymine and thymidine observed in Figs. 2 and 3 as a function of environment, correlations were obtained between the observed Raman frequencies and the solvent properties (Table 1) expected to be important in solvent–solute interactions, such as polarity, polarizability, and hydrogen bonding. Tables of all the resulting correlation coefficients are given in the supplementary information.[3] From these results, it is clear that only two solvent properties are well-correlated with the observed frequency shift in thymine, acceptor number (AN) and donor number (DN), generally thought to be measures of hydrogen-bonding ability of the solvent with solute. No correlations greater than 0.75 were obtained between any of the "nonspecific" solvent properties, such as polarity (ε, *K*) and polarizability (*n*, *L*), or mixed terms (ε_p, *KL*), and the vibrational frequency of any thymine mode, except between the 1500 cm^{-1} mode and ε, a measure of solvent polarity. The acceptor numbers are derived from ^{31}P NMR chemical shifts of triethylphosphine oxide (Et_3PO) (40):

$$[1] \qquad AN = 100\delta_{corr}/\delta_{corr}(Et_3PO{\cdot}SbCl_5) = (2.348)\delta_{corr}$$

where δ_{corr} ($Et_3PO{\cdot}SbCl_5$) = 42.59 ppm and acceptor numbers range from 0 (hexane) to 100 ($SbCl_5$). Donor numbers are obtained directly from calorimetric measurements with $SbCl_5$ and are defined as the molar enthalpy value for the reaction of the donor (D) with $SbCl_5$ as a reference acceptor in 10^{-3} mol L^{-1} solution of dichloroethane (40):

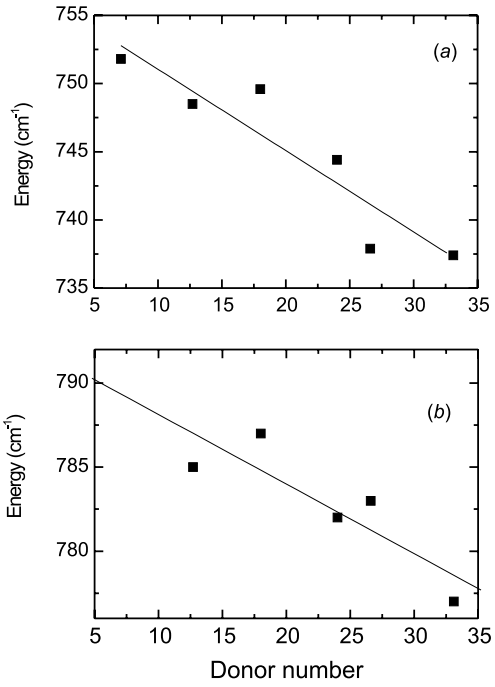
$$[2] \qquad D + SbCl_5 = D{\cdot}SbCl_5 \ (-\Delta H_{D\cdot SbCl_5} \equiv DN)$$

Donor numbers can also be inferred indirectly from ^{23}Na NMR chemical shifts of $NaClO_4$ (40).

Correlation coefficients of 0.83 or greater are observed for the 740, 980, 1230, 1360, and 1390 cm^{-1} modes with both solvent donor and acceptor numbers for thymine. This clear correlation with acceptor and donor numbers indicates the interaction between thymine and solvent is a *specific* interaction, nominally involving hydrogen bonding. The correlation between the 740 cm^{-1} mode frequency for thymine and donor number is shown in Fig. 5*a*. Figure 5*b* shows the correlation between the 740 cm^{-1} mode frequency of thymidine and donor number.

The nature of the vibrations affected by the hydrogen-bonding properties of the solvent can be used to determine the sites of interaction between thymine and solvent. The modes at 740, 980, and 1390 cm^{-1} all contain contributions from NH bending vibrations, either in-plane or out-of-plane (Fig. 1). The sensitivity of these NH vibrations to the hydrogen-bonding ability of the solvent is expected and indicates solvent donation of a pair of electrons involved in a hydrogen bond at the hydrogens on the N_1 and (or) N_3 nitrogens. The mode at 1230 cm^{-1} is the isolated C_5-$C_\alpha H_3$ stretch and correlates very well with solvent hydrogen-bonding strength. It is difficult to imagine why this should be so. This result may indicate that this C-C stretching internal coordinate is also mixed with N-H internal coordinates. Significant hydrogen-bonding correlation is also observed for the 1360 cm^{-1} mode, which has been assigned to $\delta(C_6H) + \delta(C_\alpha H_3)$. This could be due to the influence of the π electrons from the $C_5{=}C_6$ bond, although the $C_5{=}C_6$ stretch itself does not appear to be sensitive to solvent hydrogen bonding.

Fig. 5. Correlations of the Raman frequency with donor number, a measure of hydrogen bonding ability of the solvent, for (*a*) thymine (r = –0.93) and (*b*) thymidine (r = –0.86). The correlations presented here have some of the largest correlation coefficients of all of the solvent parameters tested.



As observed in Fig. 3, there are some significant frequency shifts in the Raman spectra of thymidine with solvent. As with thymine, correlations (supplementary information)[3] were obtained between the observed Raman frequencies and solvent properties to understand the molecular origin of these shifts. Again, only a few solvent properties correlate well with the observed frequency shifts. The modes at 740, 787, 1450, and 1690 cm^{-1} all correlate very well with the acceptor and (or) donor numbers. These modes are due to vibrations of the thymine base only or to coupling of the base and sugar ring. However, none of the sugar ring modes correlates well with the solvent property of hydrogen bonding, although the 1180 cm^{-1} mode correlates well with acceptor number (r = –0.87). This results suggests that the proton-accepting and (or) -donating sites of the molecule localized on the thymine base are more solvent-sensitive than those on the sugar ring. There is also significant correlation between several thymidine modes and nonspecific solvent properties such as the 787, 1100, 1200, and 1690 cm^{-1} modes with polarizability (*n*, *L*, Π), 1180 and 1450 cm^{-1}

[3] Supplementary data may be purchased from the Directory of Unpublished Data, Document Delivery, CISTI, National Research Council Canada, Ottawa, ON K1A 0S2, Canada (http://www/nrc.ca/cisti/irm/unpub_e.shtml for information on ordering electronically).

© 2004 NRC Canada

modes with dipolarity (π^*/π^*II), and 1140 cm^{-1} mode with polarity (Θ).

Therefore, unlike in thymine where good correlation is only observed between certain modes and the specific solvent property of hydrogen bonding, good correlation of the observed frequency shifts with a few nonspecific solvent properties, such as polarity and polarizability, exists for thymidine. Here, we are only considering the dynamic, or AC, component of the polarizability in the high-frequency optical range. We attribute this correlation difference with nonspecific solvent properties between thymine and thymidine as being due to the larger size of the thymidine molecule compared with the smaller thymine molecule. The somewhat surprising fact that the modes most sensitive to polarizability are those localized on the thymine moiety may be more related to the absence of intense sugar modes in the Raman spectra excited here in the visible than to any inherent insensitivity of the sugar modes to solvent. Resonance Raman spectra at wavelengths below 200 nm or near-IR excited Raman spectra may be more sensitive to the sugar modes and reveal the solvent dependence, if any, of these modes.

While it is difficult to explain all these varied correlations of several modes with numerous and diverse solvent properties, it is clear that the modes that correlate very well with acceptor and donor numbers, i.e., the 740, 787, 1180, 1450, and 1690 cm^{-1} modes, are due mainly to the N_3-H and C=O sites or contain contributions from these sites. These results are similar to those obtained for thymine, where all the modes with N-H contributions showed good correlation with acceptor and donor numbers. This clear correlation suggests that the major interaction between thymidine and solvent is a specific interaction involving hydrogen bonding.

Intensity changes with solvent

Similar arguments can be used to understand the relative intensity changes in the 1600–1800 cm^{-1} region. The two CO stretches $\nu(C_2{=}O)$ and $\nu(C_4{=}O)$ as well as the $\nu(C_5{=}C_6)$ bands are all expected in this region. The most intense peak in this region around 1680 cm^{-1} in all the spectra in Figs. 2 and 3 has been assigned to $\nu(C_4{=}O)$ coupled with $\nu(C_5{=}C_6)$ from an extensive isotopic labeling experiment (28). Spiro and co-workers (21, 41) reported from UV-resonance Raman experiments on thymine and its derivatives that, at longer excitation wavelengths (240–266 nm), a single broad band appears around 1665 cm^{-1}. However, with shorter wavelength excitation (218, 200 nm), a narrower band is observed at 1648 cm^{-1}, with a shoulder at 1700 cm^{-1}. They interpreted the results to show that the $\nu(C_5{=}C_6)$ and $\nu(C_4{=}O)$ were coupled or degenerate in water solutions to give a single peak at 1665 cm^{-1} and the $\nu(C_2{=}O)$ vibration gave the band at 1700 cm^{-1}. This is an indication that the $\nu(C_4{=}O)$ is part of the composite band at 1665 cm^{-1}, in agreement with our assignment of the mode around 1680 cm^{-1} in our spectra to accidentally degenerate $\nu(C_4{=}O)$ and $\nu(C_5{=}C_6)$ (33). While these assignments may imply that the peaks are due to localized internal coordinates, in reality, they should be regarded as due to normal modes with different contributions from each internal coordinate, with, say, the $\nu(C_5{=}C_6)$ contribution being dominant for the 1680 cm^{-1} peak. Also, the lack of correlation between the mode at 1680 cm^{-1} and any property of the solvent supports a previous assignment of this mode in the Raman spectrum primarily to the C=C vibration, which should be relatively insensitive to solvent polarity, polarizability, and (or) hydrogen bonding. This result suggests that the C=O contribution to this band's intensity is minimal, as the C=O stretch is expected to be solvent sensitive. This assignment is confirmed by spectral intensity changes in this region.

There are three possible explanations for the spectral intensity changes observed in the 1600–1800 cm^{-1} region: symmetry breaking of the vibrational bands due to strong solvent–solute interactions, interaction at the C=O sites only, and (or) interaction with both the N-H and C=O sites. Johnson and Myers (42, 43) observed in resonance Raman experiments for the photodissociation of I_3^- that, in addition to the allowed symmetric stretch band seen in all the solvents, the symmetry-forbidden asymmetric stretch was also observed in ethanol, the most polar solvent used. This was attributed to solvent-induced symmetry breaking of the "chromophore", effectively lowering its symmetry and giving some allowed character to the nominally forbidden bands. However, in our results, a doublet appears in the less or non-polar solvents such as *N*,*N*-DMF and pyridine, while a single peak is seen in the more polar, hydrogen-bonding solvents of water, formamide, and trifluoroacetic acid. Therefore, the intensity changes observed in our spectra cannot be due to solvent-induced symmetry breaking, as they are inconsistent with increased symmetry breaking as the solvent polarity increases.

The second possible cause for these intensity changes is interaction of the solvent with the C=O sites alone of thymine. UV-resonance Raman (UVRR) experiments on nucleobase derivatives in several solvents (33) have shown that, for uracil, the $\nu(C_5{=}C_6)$ appears at 1620–1630 cm^{-1} in all the solvents, with little or no frequency shift with solvent. The $\nu(C_4{=}O)$ band at 1673 cm^{-1} in water was seen to shift to higher frequency, however, as the polarity of the solvents decreased, an indication of a stronger C=O bond and a weaker hydrogen bonding of the solvent at the C=O sites. For thymine, only one band is observed at 1600–1800 cm^{-1} in the polar solvents water and methanol, around 1665 cm^{-1} in the UVRR spectrum, assigned to overlap of the $\nu(C_4{=}O)$ and $\nu(C_5{=}C_6)$. Because the $\nu(C_5{=}C_6)$ is shifted to higher frequency in thymine compared with uracil (22), due to the electron-donating effect of the C_5-$C_\alpha H_3$ group, it overlaps with the $\nu(C_4{=}O)$ in the polar solvents, giving rise to a single peak. The $\nu(C_2{=}O)$ has a weak Raman signal, which only has intensity at excitation wavelengths of 218 nm and below. However, in non-hydrogen-bonded solvents such as 1,4-dioxane and chloroform, doublets are seen with the $\nu(C_5{=}C_6)$ well-separated from the $\nu(C_4{=}O)$. Because of weaker or no hydrogen bonding at the C=O sites in these low-polarity or non-polar solvents, the $\nu(C_4{=}O)$ vibration shows up well-separated and at higher frequency than the unshifted $\nu(C_5{=}C_6)$. Although these results were obtained in UVRR experiments, we observe similar spectral features in the 1600–1800 cm^{-1} region in our Raman data. Therefore, the single peak observed in the polar solvents of water, trifluoroacetic acid, formamide, and formic acid in the 1600–1800 cm^{-1} region (Fig. 2) is due to interaction of the solvent with the C=O sites, lowering the $\nu(C_4{=}O)$ and making it

© 2004 NRC Canada

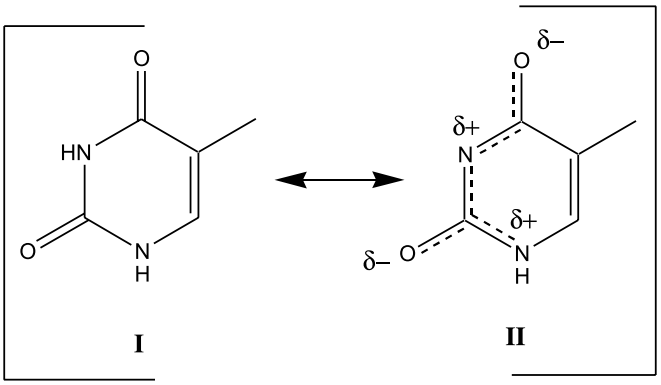
overlap with the $\nu(C_5{=}C_6)$. The doublets in pyridine and *N*,*N*-DMF, which have low H-bonding capability as shown by their lower acceptor numbers (Table 1), result from separation of the $\nu(C_5{=}C_6)$ from the $\nu(C_4{=}O)$, which appears at a higher frequency owing to less or no interaction in these solvents. However, interaction solely at the $C_4{=}O$ bond does not explain the frequency shifts and sensitivity of the N-H modes with the solvent. From the comparison of the spectra in Fig. 2 to the base spectrum of thymine in Fig. 4*b*, we conclude that thymine is not deprotonated in any of the solvents. Depending on the polarity of the solvent and the extent of the interaction mainly at the N_3-H site, the electronic structure of thymine may resemble a zwitterionic or neutral thymine in solution (Fig. 6). Increased interaction at the C=O sites would be expected to stabilize the zwitterionic structure in Fig. 6. Since the N-H bends are not directly affected, it is unclear how this interaction could explain the sensitivity of the N-H deformations and wags to the solvent. The dramatic intensity changes cannot therefore be completely explained only by H-bonding with solvent at the C=O sites.

The only other possible explanation for the intensity changes observed is a strong interaction of solvent with the C=O and N-H sites of thymine. This explanation can best be understood by considering the resonance structures of thymine. In polar solvents, the zwitterionic structure (Fig. 6) is expected to dominate, lowering the $\nu(C_4{=}O)$ band and making it overlap with the $\nu(C_5{=}C_6)$. This gives rise to a single peak in these solvents. However, in the less or non-polar solvents, because of little or no electron-pair donation to the N_3-H site, the neutral resonance structure of thymine (Fig. 6) dominates, giving rise to a higher frequency $\nu(C_4{=}O)$ band, which is well-separated from the $\nu(C_5{=}C_6)$, and a doublet is observed in these solvents. Again, this interaction only accounts for the intensity changes in the 1600–1800 cm^{-1} region and does not explain the changes in the N-H modes as a function of solvent observed in our results. As suggested by Zhang et al. (28), the peaks in the 1600–1800 cm^{-1} region may not be due to localized internal coordinates or overlapping bands but may be due to mixed and (or) coupled vibrational modes. It is, therefore, also possible that the spectral changes observed are due to solvent "turning on" intensity in weak and (or) forbidden modes, such as the $\nu(C_2{=}O)$. However, since this band has a weak Raman signal and is only strongly enhanced at shorter excitation wavelengths, the contribution of this effect is minimal.

We, therefore, conclude that the intensity changes observed in thymine are not due to solvent-induced symmetry breaking but are rather a result of the interaction of solvent with thymine at both the C=O and N-H sites. This leads to a weakening of the $\nu(C_4{=}O)$ frequency in the polar solvents, resulting in an overlap with the $\nu(C_5{=}C_6)$ and giving rise to a single peak. However, the interaction of solvent with thymine at these sites also results in the frequency shifts and good correlation of the N-H modes with solvent as shown by the sensitivity of the N-H modes to acceptor and donor numbers.

Some intensity changes in the Raman spectra of thymidine as a function of solvent are observed mainly in the 1600–1800 cm^{-1} region. As in the case of thymine, a peak appears around 1660 cm^{-1} in all the spectra in Fig. 3, assigned to the $\nu(C_4{=}O)$ coupled with the $\nu(C_5{=}C_6)$ (21, 25, 29). Again, we note that these assignments do not refer to localized internal coordinates but to normal modes with different contributions from each internal coordinate. Hence, the contribution of the $\nu(C_5{=}C_6)$ internal coordinate is dominant for the 1660 cm^{-1} mode, with the $\nu(C_4{=}O)$ contribution to the intensity of this band being minimal as shown by the lack of correlation of this band with any solvent property, and the $\nu(C_2{=}O)$ contribution being negligible, since it has a weak Raman signal, which only has intensity at excitation wavelengths of 218 nm and below. While a single peak is observed in the more polar and (or) hydrogen-bonding solvents such as water, formamide, formic acid, and the alcoholic solvents, a doublet appears in the less or non-polar solvents pyridine and *N*,*N*-DMF. However, it is not clear why a doublet appears in acetic acid, a very polar solvent. Acetic acid is known to associate in solution, forming dimers and to a smaller extent higher polymers (44–47). The dimerization is due to the formation of hydrogen bonds between two or more monomers of acetic acid. In fact, IR spectra have been reported (46, 47) for acetic acid solutions in carbon tetrachloride where absorption bands for monomers and dimers were observed. Hence, dimer formation by acetic acid may make it interact to a lesser extent with thymidine, as is the case for the non-polar solvents, resulting in the doublet and (or) higher shoulder peak. As in the case of thymine, based on UVRR experiments on nucleobase derivatives in several solvents (33), these intensity changes are due partly to the interaction of solvent with thymidine at the C=O sites. This interaction weakens the C=O bond strength, leading to a lowering of the $\nu(C_4{=}O)$ frequency in the polar solvents that causes it to overlap with the $\nu(C_5{=}C_6)$, giving rise to a single peak. In the less polar solvents, due to less or no interaction of solvent with thymidine, the $\nu(C_4{=}O)$ appears at a higher frequency, well-separated from the $\nu(C_5{=}C_6)$, and gives rise to a doublet in these solvents. However, interaction of solvent solely at the $(C_4{=}O)$ site cannot explain the dramatic intensity changes observed, nor does it account for the sensitivity of the N_3-H modes to solvent. A comparison of the spectra in Fig. 3 to the base spectrum in Fig. 4*d* shows that thymidine is not deprotonated in any of the solvents. Again, as in thymine, depending on the polarity of the solvent, there is electron pair donation to the proton at the N_3 site, leading to a change in the balance of resonance structures between a zwitterionic and a neutral thymine spe-

Fig. 6. Neutral and zwitterionic resonance structures of thymine.



© 2004 NRC Canada

cies in solution (Fig. 6). Increased interaction at the C=O sites would be expected to stabilize the zwitterionic structure, weakening the (C_4=O) bond strength, making the $\nu(C_4=O)$ appear at a lower frequency and thus overlapping with the $\nu(C_5=C_6)$ in the polar solvents. These observed intensity changes can only be explained by interaction of solvent with thymidine at both the C=O and N_3-H sites. Since the zwitterionic species is a better representation of thymine in the more polar solvents, the $\nu(C_4=O)$ stretch, with its weaker (C_4=O) bond, appears at a lower frequency and overlaps with the $\nu(C_5=C_6)$ stretch. Hence, a single peak is observed in these solvents. However, in the less polar solvents, owing to less or no interaction of solvent with thymidine, the neutral species predominates. Therefore, the $\nu(C_4=O)$ stretch, with its stronger bond, appears at higher frequency, well-separated from the $\nu(C_5=C_6)$ stretch. We, therefore, conclude that the interaction of thymidine with solvent results in frequency shifts and slight intensity changes. The major interaction is at the proton-accepting and -donating sites of the thymine base, i.e., at both the N_3-H and C=O sites, with little or no apparent interaction with the proton-accepting and -donating sites of the sugar ring.

Conclusion

In this paper, the Raman spectra of thymine in eight solvents and thymidine in nine solvents were obtained with visible excitation. Spectra of both thymine and thymidine under acidic, neutral, and basic conditions were also obtained. Correlations of the observed frequency shifts of specific vibrational modes with characteristic properties of the solvent for both thymine and thymidine show that a significant hydrogen-bonding interaction occurs between the N-H protons of the thymine base and lone pairs of electrons on the solvent molecules and between the solvent hydrogens and lone pairs on C=O sites. The solvent-dependent intensity of vibrational bands of thymine between 1500 and 1800 cm^{-1} indicates a strong interaction between thymine and solvent at the C=O and N-H sites that leads to separation of the C=O stretches from the C=C stretch. The intensity variations with solvent were much smaller for thymidine than for thymine, perhaps as a result of replacing the N_1 proton by the sugar. These results suggest that Raman spectroscopy is uniquely sensitive to specific interactions of thymine and thymidine with their environment and that it may be a useful technique in probing DNA binding of intercalants, proteins, and other substances.

Acknowledgements

The authors thank the Natural Sciences and Engineering Research Council of Canada (NSERC) Discovery Grants-in-Aid of Research for funding. In addition, VM thanks the Reactive Intermediates Student Exchange (RISE) program for providing a summer research opportunity.

References

1. M.H. Patrick and R.O. Rahn. *In* Photochemistry and photobiology of nucleic acids. Vol. 2. *Edited by* S.Y. Wang. Academic Press, New York. 1976. pp. 35–95.
2. G.J. Fisher and H.E. Johns. *In* Photochemistry and photobiology of nucleic acids. Vol. 1. *Edited by* S.Y. Wang. Academic Press, New York. 1976. pp. 169–224.
3. G.J. Fisher and H.E. Johns. *In* Photochemistry and photobiology of nucleic acids. Vol. 1. *Edited by* S.Y. Wang. Academic Press, New York. 1976. pp. 225–294.
4. H. Görner. J. Photochem. Photobiol. B, **26**, 117 (1994).
5. K. Morikawa, O. Matsumoto, M. Tsujimoto, K. Katayangi, M. Ariyoshi, T. Doi, M. Ikehara, T. Inaoka, and E. Ohtsuka. Science (Washington, D.C.), **256**, 523 (1992).
6. M. Ishida, Y. Kanamori, N. Hori, T. Inaoka, and E. Ohtsuka. Biochemistry, **29**, 3817 (1990).
7. M.L. Kripke. *In* Dermatology in general medicine. *Edited by* T.B. Fitzpatrick, A.Z. Eisen, K. Wolff, I.M. Freedberg, and K.F. Austen. McGraw-Hill, New York. 1993. pp. 797–804.
8. D.L. Mitchell and D. Karentz. *In* Environmental UV photobiology. *Edited by* A.R. Young, L.O. Björn, J. Moan, and W. Nultsch. Plenum Press, New York. 1993. pp. 345–377.
9. J. Cadet, C. Anselmino, T. Douki, and L. Voituriez. J. Photochem. Photobiol. B, **15**, 277 (1992).
10. P.G. Sealey and E.M. Southern. *In* Gel electrophoresis of nucleic acids: A practical approach. *Edited by* D. Rickwood and B.D. Hames. IRL Press, Oxford. 1990. pp. 51–100.
11. W.L. Fangman. Nucleic Acids Res. **5**, 653 (1978).
12. T.M. Jovin. *In* Methods in enzymology. Vol. 21. *Edited by* L. Grossman and K. Moldave. Academic Press Inc., London. 1971. pp. 179–187.
13. L. Andrzej, L. Adamowica, M. Nowak, and L. Lapinski. Spectrochim. Acta Part A, **48A**, 1385 (1992).
14. P. Colarusso, K. Zhang, B. Guo, and P.F. Bernath. Chem. Phys. Lett. **269**, 39 (1997).
15. A.Y. Ivanov, A.M. Plokhotnichenko, E.D. Radchenko, G.G. Sheina, and Y.P. Blagoi. J. Mol. Struct. **372**, 91 (1995).
16. M. Tsuboi. *In* Basic principles in nucleic acid chemistry. Vol. 1. *Edited by* P.O.P. Ts'o. Academic Press, New York. 1974. pp. 399–452.
17. K. Nakamoto and J.R. Ferraro. *In* Introductory Raman spectroscopy. Academic Press Inc., San Diego. 1994. pp. 1–94.
18. J.L. McHale. *In* Molecular spectroscopy. Prentice Hall, Upper Saddle River, N.J. 1999. pp. 364–409.
19. M. Tsuboi, S. Takahushi, and I. Harada. *In* Physico-chemical properties of nucleic acids. Vol. 2. *Edited by* J. Duchesne. Academic Press, New York. 1973. pp. 91–145.
20. K.A. Hartman, R.C. Lord, and G.J. Thomas, Jr. *In* Physicochemical properties of nucleic acids. Vol. 2. *Edited by* J. Duchesne. Academic Press, New York. 1973. pp. 1–89.
21. S.P.A. Fodor, R.P. Rava, T.R. Hays, and T.G. Spiro. J. Am. Chem. Soc. **107**, 1520 (1985).
22. M. Tsuboi, Y. Nishimura, A.Y. Hirakawa, and W.L. Peticolas. *In* Biological applications of Raman spectroscopy. Vol. 2. *Edited by* T.G. Spiro. Wiley-Interscience, New York. 1987. pp.109–179.
23. W.L. Peticolas, W.L. Kubasek, G.A. Thomas, and M. Tsuboi. *In* Biological applications of Raman spectroscopy. Vol. 1. *Edited by* T.G. Spiro. Wiley-Interscience, New York. 1987. pp. 81–133.
24. P.R. Carey. *In* Biochemical applications of Raman and resonance Raman spectroscopies. Academic Press, New York. 1982. pp. 184–207.
25. S.P.A. Fodor and T.G. Spiro. J. Am. Chem. Soc. **108**, 3198 (1986).
26. N. Fujimoto, A. Toyama, and H. Takeuchi. J. Mol. Struct. **447**, 61 (1998).
27. D. Serban, J.M. Benevides, and G.J. Thomas, Jr. Biochemistry, **42**, 7390 (2003).

© 2004 NRC Canada

28. S.L. Zhang, K.H. Michaelian, and G.R. Loppnow. J. Phys. Chem. **102**, 461 (1998).
29. M. Tsuboi, M. Komatsu, J. Hoshi, E. Kawashima, T. Sekine, Y. Ishido, M.P. Russell, J.M. Benevides, and G.J. Thomas, Jr. J. Am. Chem. Soc. **119**, 2025 (1997).
30. A.F. Bell, L. Hecht, and L.D. Barron. J. Chem. Soc. Faraday Trans. **93**, 553 (1997).
31. R. Escobar, P. Carmona, and M. Molina. The Analyst, **121**, 105 (1996).
32. K. Ushizawa, T. Ueda, and M. Tsuboi. J. Mol. Struct. **412**, 169 (1997).
33. A. Toyama, H. Takeuchi, and I. Harada. J. Mol. Struct. **242**, 87 (1991).
34. M.M. Mitambo and G.R. Loppnow. Chem. Phys. Lett. **261**, 691 (1996).
35. L. Beyere, S. Yarasi, and G.R. Loppnow. J. Raman Spectrosc. **34**, 743 (2003).
36. M.A. Webb, E. Fraga, and G.R. Loppnow. J. Phys. Chem. **100**, 3278 (1996).
37. E. Fraga and G.R. Loppnow. J. Phys. Chem. B, **102**, 7659 (1998).
38. P.O.P. Ts'o. *In* Basic principles in nucleic acid chemistry. Vol. 1. *Edited by* P. O. P. Ts'o. Academic Press, New York. 1974. pp. 453–584.
39. W. Saenger. *In* Principles of nucleic acid structure. Springer Verlag, New York. 1984. pp. 105–115.
40. V. Gutmann. *In* The donor–acceptor approach to molecular interactions. Plenum, New York. 1978. pp. 17–33.
41. C.A. Grygon and T.G. Spiro. Biopolymers, **29**, 707 (1990).
42. A.E. Johnson and A.B. Myers. J. Phys. Chem. **100**, 7778 (1996).
43. A.E. Johnson and A. B. Myers. J. Chem. Phys. **102**, 3519 (1995).
44. I.M. Shiah and H.C. Tseng. Fluid Phase Equilib. **124**, 1 (1996).
45. I.M. Shiah and H.C. Tseng. Fluid Phase Equilib. **19**, 1074 (1954).
46. I. Malijevskha and M. Polasek. Collect. Czech. Chem. Commun. **60**, 1094 (1995).
47. J.T. Bolmer and H.F. Shurvell. J. Phys. Chem. **77**, 256 (1973).
48. R.C. Weast (*Editors*). CRC handbook of chemistry and physics. 53rd ed. CRC Press, Cleveland. 1972. pp. C75-E47.
49. F.L. Riddle, Jr. and F.M. Fowkes. J. Am. Chem. Soc. **112**, 3259 (1990).
50. M.J. Kamlet, J.-L.M. Abboud, and R.W. Taft. J. Am. Chem. Soc. **99**, 6027 (1977).
51. O.W. Kolling. J. Phys. Chem. **100**, 16 087 (1996).
52. W.R. Fawcett and A.A. Kloss. J. Phys. Chem. **100**, 2019 (1996).
53. M.J. Kamlet, J.-L.M. Abboud, M.H. Abraham, and R.W. Taft. J. Org. Chem. **48**, 2877 (1983).

© 2004 NRC Canada

A computational study of a cyano-bridged dinuclear ruthenium complex containing the non-innocent methylpyrazinium ligand[1]

A.B.P. Lever

Abstract: The properties of a series of complexes *trans*-[LRu(NH_3)$_4$-NC-Ru(NH_3)$_4$(methylpyrazinium)]$^{n+}$ where L is an anion (Cl^-, F^-, CN^-, OH^-) or neutral ligand (CO, H_2O, pyridine, CH_3NO_2) were analyzed using density functional theory. The objective was to probe the change in electronic coupling between the two ruthenium atoms and between ruthenium and the non-innocent methylpyrazinium ligand as L is varied. Molecular orbital coefficients and optical spectra were derived. The electronic interactions involved are seen to be quite sensitive to the charge on the ruthenium to which the ligand L is attached as L is varied. Exchange (*K*) and Coulomb (*J*) energies are also calculated, using the INDO/S model, for the various metal-to-ligand charge-transfer transitions. *K* correlates well with the energy and intensity of the transitions and specifically with the variation in delocalization induced by variation of L.

Key words: DFT, ruthenium, non-innocent ligand, methylpyrazinium, ZINDO.

Résumé : Faisant appel à la théorie de la densité fonctionnelle, on a analysé les propriétés d'une série de complexes *trans*-[LRu(NH_3)$_4$-NC-Ru(NH_3)$_4$(méthylpyrazinium)]$^{n+}$ dans lesquels L est un anion (Cl^-, F^-, CN^-, OH^-) ou un ligand neutre (CO, H_2O, pyridine, CH_3NO_2). L'objectif était d'étudier le changement dans le couplage électronique entre les deux atomes de ruthénium ainsi qu'entre le ruthénium et le ligand méthylpyrazinium qui n'est pas innocent en fonction d'une variation de L. On en a dérivé les coefficients d'orbitales moléculaires et les spectres optiques. On a observé que lors des variations de L, les interactions électroniques impliquées sont très influencées par la charge portée par le ruthénium sur lequel le ligand L est attaché. Faisant appel au modèle INDO/S, on a aussi calculé les énergies d'échange (*K*) et de Coulomb (*J*) pour diverses transitions de transfert de charge du métal au ligand. Il existe une bonne corrélation entre les valeurs de *K* et l'énergie et l'intensité des transitions et, plus spécifiquement, avec la variation dans la délocalisation induite par une variation de L.

Mots clés : théorie de la densité fonctionnelle, ruthénium, ligand non innocent, méthylpyrazinium, ZINDO.

[Traduit par la Rédaction]

Introduction

We have been interested in developing methods to describe the electronic coupling in ruthenium complexes of π-accepting ligands, especially so-called non-innocent ligands (1–14). For the most part, these studies have involved mononuclear ruthenium species except for a couple of recent studies (5, 12). We are now concerned with exploring how information might be electronically transmitted along a chain by modifying the terminus L of the species *trans*-[LRu^{II}(NH_3)$_4$-NC-Ru^{II}(NH_3)$_4$(Mpz+)]$^{n+}$ (**I**) (Mpz+ = methylpyrazinium; L = Cl^-, OH^-, CN^-, F^-, CH_3CN, CO, pyridine, CH_3NO_2, H_2O; *n* = 4 or 3 depending on whether L is neutral or mononegative). Both density functional theory (DFT) (15–17) and the semiempirical INDO/S in its Zerner manifestation (ZINDO) (18–22) have been employed in our studies.

The bonding between ruthenium(II) and the methylpyrazinium ligand has long been a subject of interest (14, 23–29). Two relevant crystal structures have been reported. In the species [Ru^{II}(NH_3)$_5$(Mpz+)]I_3, the Ru—N(Mpz) bond distance is reported (14) to be as short as 195 pm, supposedly as a consequence of strong π-back-donation. On the other hand, in the species *trans*-RuCl(pdma)(phen)(Mpz+)]$^{2+}$ (pdma = 1,2-phenylenebis(dimethylarsine), phen = 1,10-phenanthroline) the distance is 202 pm (30).

The title dinuclear complexes are, as yet, experimentally unknown. Yet, the predictive capabilities of both the INDO/S and DFT methods have been shown (1–13, 31–39, 39–47) to be sufficiently precise that the overall properties of these species can be deduced without proceeding to the laboratory. Previously, we demonstrated that a good to excellent agreement can be achieved between the experimental optical spectra of ruthenium(II) complexes and those predicted by time-dependent density functional response theory (TD-DFRT) or INDO/S. Certainly, the future of chemistry will involve computation followed by the laboratory synthesis only of specifically desired species. The geometries of the complexes were all optimized using DFT.

Received 13 January 2004. Published on the NRC Research Press Web site at http://canjchem.nrc.ca on 10 September 2004.

A.B.P. Lever. Department of Chemistry, York University, 4700 Keele Street, Toronto, ON M3J 1P3, Canada. (e-mail: blever@yorku.ca).

[1]This article is part of a Special Issue dedicated to the memory of Professor Gerhard Herzberg.

 doi: 10.1139/V04-068 © 2004 NRC Canada

The discussion that follows deals specifically with these complexes in the gas phase, i.e., there is no solvent, and further, the counter anions are not considered. In the solid state, the counter anions will most likely occupy positions hydrogen bonding to the NH_3 hydrogen atoms, and this will influence the electronic characteristics through modification of the charge on the ruthenium atoms. The study probes how modification of the electron density at one end of the molecule is recognized by a corresponding change at the other end. The application might be to molecular wires where an electrochemical perturbation at one end is recognized by a response at the other end.

Computational details

The DFT calculations employed in this article were carried out with the Gaussian 98 program (48). Becke's three-parameter hybrid functional (49) with the LYP correlation functional (50) (B3LYP) and an effective core potential basis set LanL2DZ (51–54) were used. The self-consistent field (SCF) convergence criterion was a change of less than 10^{-8} hartree (1 hartree = 27.211 eV) in the total energy. Harmonic frequency calculations were performed to establish the nature of the critical points (minimum or transition state). The energies and intensities of the lowest 40 singlet–singlet electronic transitions were calculated with TD-DFRT (15–17, 55–61). The profiles of the absorption spectra of the complexes were calculated using the SWizard program (62). The half-bandwidths of all electronic transitions ($\Delta_{1/2}$) were assumed to be 3000 cm^{-1} (a typical half-bandwidth value for the complexes under consideration). The atomic orbital compositions of the molecular orbitals (MOs) were calculated using Mulliken population analysis (MPA) and the AOMix program (63).

Coulomb J and exchange K values were derived for the specific electronic excitations responsible for the optical spectra using the SIG-JK program (64) and DFT-optimized structures. This program computes these values for the electron excitations involved in the transitions, prior to configurational interaction. However, the computational basis for this calculation is the Hartree–Fock semiempirical INDO/S model as implemented by Zerner and co-workers (ZINDO/S) (18–22). We have demonstrated, in a comparative study, that for species of the type discussed here, both methods give very similar results (9). Recently, it has been concluded that the Kohn–Sham MOs generated by the DFT model are equivalent in meaning to the Hartree–Fock MOs, generated, for example, by ZINDO/S (65–69). To confirm that the ZINDO/S calculations do give essentially the same interpretation as the DFT for the specific complexes under study, we report in the following a comparison of MOs generated by each model (Fig. 1).

Results and discussion

Optimized geometries

Geometries were optimized using DFT as described in *Computational details*. Table 1 displays some of the relevant data for key bond distances.

The average Ru—N(NH_3) bond distances are effectively independent of ligand L, but the distances around the local ruthenium atom (Ru_L) are marginally but systematically longer than those around the remote Ru atom (Ru_R). These distances lie within, but at the longer end of, the range observed previously for Ru(II)—N(NH_3) distances (70–80). Both the Ru—N(MPz+) and Ru—CN distances are clearly and significantly dependent on L, with both decreasing with the electron richness of the metal as the ligand donicity increases. Anionic ligands yield much shorter distances than strongly π-acidic ligands such as CO and CH_3NO_2. The predicted Ru—N(Mpz+) distances are longer than those seen in the two crystal structures. A parallel DFT study of the mononuclear $[LRu(NH_3)_4(Mpz+)]^{n+}$ species[2] reveals that the Ru—N(Mpz+) distance is very sensitive to the net electron density on the Ru atom, becoming substantially shorter with increasing electron richness on Ru. Gas-phase calculated Ru—N(Mpz+) distances are likely to be longer than the solid-state observed distances because of the effect of the counter anions in donating charge to the metal centre through hydrogen bonding in the latter case.

The ammine ligands on each metal atom lie in an almost eclipsed configuration. A cross check of the total binding energy for L = OH^- as an example (using ZINDO/S and Hyperchem) showed that the optimized DFT structure deviating slightly from an eclipsed configuration was indeed more stable than either the totally eclipsed or totally staggered configurations. This is likely true for all the species.

Electronic coupling

We are concerned with how information input at the remote ruthenium (Ru_R) by variation of L influences the Ru_R–Ru_L electronic coupling and how the perturbation is "felt" by the local ruthenium (Ru_L) bound to the methylpyrazinium ligand. The methylpyrazinium ligand is a strong π-acceptor ligand with non-innocent character (81). We can expect that the "back donation" to that ligand will be sensitive to the donicity or electron richness of the local ruthenium atom. There are a number of computational methods to probe this. We can evaluate the $d\pi$ metal contribution to the LUMO from the local or remote Ru centre and mixing of filled $d\pi$ orbitals of Mpz with Ru $d\pi$, and also evaluate the coupling between the remote and local ruthenium atoms as a function of symmetry, $d\sigma$, $d\pi$, or $d\delta$. Further, the metal-to-ligand charge-transfer (MLCT) energies can be calculated and the exchange-energy contributions to these excitations evaluated.

The data in Table 2 can be summarized from the viewpoint of symmetry as follows. The $d\delta$-symmetry orbitals (with respect to the metal–metal axis) are more than 90% localized on one metal (see Fig. 1). Orbitals that have $d\pi$ symmetry with respect to the MPz+ plane invariably also have π-MPz+ or π*-Mpz+ character; usually both Ru atoms are involved to a greater or lesser degree. The two Ru localized orbitals having $d\sigma$ symmetry with respect to the MPz+ plane (see Fig. 1) are coupled via an in-MPz+-plane π orbital on the cyanide bridge. They contain little or no MPz+ character. With these aforementioned attributes, it is fairly easy to identify the symmetries of the metal-localized

[2] A.B.P. Lever. Paper in preparation.

© 2004 NRC Canada

Fig. 1. Frontier molecular orbitals of $[Cl\text{-}Ru(NH_3)_4\text{-}NC\text{-}Ru(NH_3)_4(Mpz+)]^{3+}$. Left: DFT Kohn–Sham orbitals of the LUMO (top) (91), HOMO, HOMO-1, and HOMO-2 (88). Right: ZINDO/S orbitals of the LUMO (top) (66), HOMO, HOMO-1, and HOMO-2 (63). Numbers in parentheses refer to MO numbering.

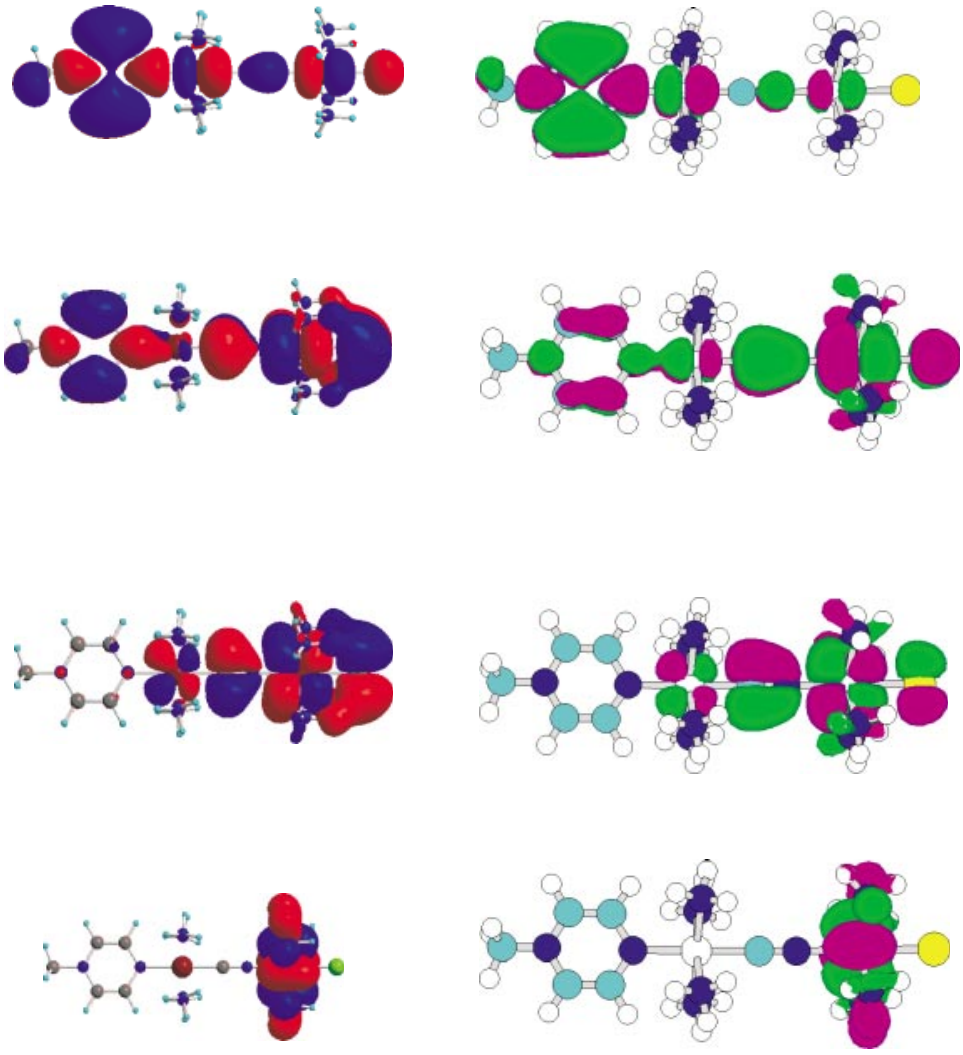


Table 1. Selected distances (in pm) in optimized geometries of $[LRu(NH_3)_4\text{-}NC\text{-}Ru(NH_3)_4(Mpz+)]^{n+}$.

L	*d* [Ru—Mpz+]	*d* [Ru—CN-]	Avg. Ru_R—$N(NH_3)$	Avg. Ru_L—$N(NH_3)$
F	209	203	217	219
Cl	210	203.5	218	220
CN	210	204	219	219.5
OH	210	203	218	219
Py	212	207	219	220
H_2O	212	207	219	220
CH_3CN	212	207	219	220
CH_3NO_2	213	207	219	220
CO	215	206	219	220

orbitals listed in Table 2. In certain cases (especially L = H_2O), the lack of axial symmetry causes a small degree of mixing between the $d\sigma$ and $d\pi$ orbitals, generating two MOs that are canted with respect to the MPz+ plane. This has an effect on the electronic spectrum as discussed in the following.

Local–remote ruthenium coupling

While both ruthenium atoms contain a tetraammine ligand set, the presence of the strongly Lewis acidic methylpyrazinium ligand at the local end and an anion at the remote end causes a rather substantial difference in mean energies and reduces the interaction between the two ruthenium cen-

© 2004 NRC Canada

Table 2. Contributions (%) of local (Ru_L) and remote (Ru_R) ruthenium atoms and methylpyrazinium to $[LRu(NH_3)_4\text{-}NC\text{-}Ru(NH_3)_4(Mpz+)]^{n+}$ molecular orbitals (DFT).

No. MO	*E* (eV)	Ru_R (%)	Ru_L (%)	Mpz+ (%)
L = CH_3NO_2				
105	–12.82	0	0.1	98.8
104			–12.87	5.5
103 L	–14.23	1.1	11.1	86.1
102 H	–15.71	76.8	4	2.5
101	–15.74	82.7	5.3	1.1
100	–15.82	95.9	0	0
99	–16.89	0	96.1	0.1
98	–17.02	5.5	74.4	12.5
97	–17.07	6.2	83.5	1.1
L = pyridine				
109	–12.61	0	0.1	98.6
108 L	–14.03	2.5	11.5	84.3
107 H	–15.12	79.5	1.2	4.3
106	–15.28	87.5	3.6	0.1
105	–15.34	96.1	0	0
104	–16.68	0	0	0
103	–16.72	0	96.1	0.1
102	–16.79	2.1	74.4	13.4
101	–16.85	4.1	85.2	1.2
L = H_2O				
93	–12.87	0	0.1	98.7
92	–14.28	1.6	11.1	85.8
91	–15.63	82.4	4.2	2.2
90	–15.81	83.4	5.0	2.0
89	–15.82	96.3	0	0
88	–16.96	0	96.1	0.1
87	–17.09	5.9	74.7	12.3
86	–17.15	6.3	83.8	1.2
93	–12.87	0	0.1	98.7
L = CO				
95	–13.26	0	0.1	98.8
94 L	–14.65	0.1	9.3	89.1
93 H	–16.79	96.0	0	0
92	–17.09	51.7	31.1	1.3
91	–17.1	49.5	30.5	5.0
90	–17.25	0	96.1	0.1
89	–17.49	34.0	49.0	6.8
88	–17.52	31.0	57.3	0.7
L = CN^-				
95	–10.32	0	0.1	98.3
94 L	–11.86	11.2	12.3	72.5
93 H	–12.61	64.1	0.3	15.5
92	–12.71	74.8	2.3	0.1
91	–13.02	96.1	0	0
90	–14.47	8.8	0	0
89	–14.62	0.1	57.8	12.0
88	–14.66	0.3	61.5	0.9
87	–14.68	0	96.0	0.1
86	–14.91	13.5	16.2	2.6
85	–14.94	14.1	23.5	0.3
L = F^-				
93	–105	0	0.2	98.2
92 L	–11.61	12.9	13.2	70.1
91 H	–12.48	63.9	0.6	18.5
90	–12.58	76.6	4.0	0.2
89	–13.15	95.6	0	0
88	–14.51	0	96.1	0.1
87	–14.52	3.1	72.1	14.1
86	–14.6	3.2	82.5	1.2
85	–15.55	6.6	1.5	90.3
L = Cl^-				
92	–10.23	0	0.1	98.3
91 L	–11.78	11.3	12.9	71.7
90 H	–12.61	59.6	0.5	16.5
89	–12.7	69.8	3.3	0.3
88	–13.12	95.7	0	0
87	–14.19	12.4	5.8	1.7
86	–14.2	13.4	6.2	0.3
85	–14.65	0	95.9	0.1
84	–14.71	8.1	68	12.7
83	–14.78	8.2	78.5	1.2
82	–14.8	15.4	0.8	0.1
L = OH^-				
93	–9.76	0	0.2	97.9
92 L	–11.37	15.0	11.9	66.8
91 H	–12.12	51.5	0.4	22.4
90	–12.63	78	4.6	0.1
89	–13.11	95.7	0	0
88	–14.21	1.9	51.9	10.5
87	–14.32	0	96.1	0.1
86	–14.39	2.9	76.4	1.2
85	–14.61	21.8	22.8	3.3

Note: L = LUMO, H = HOMO.

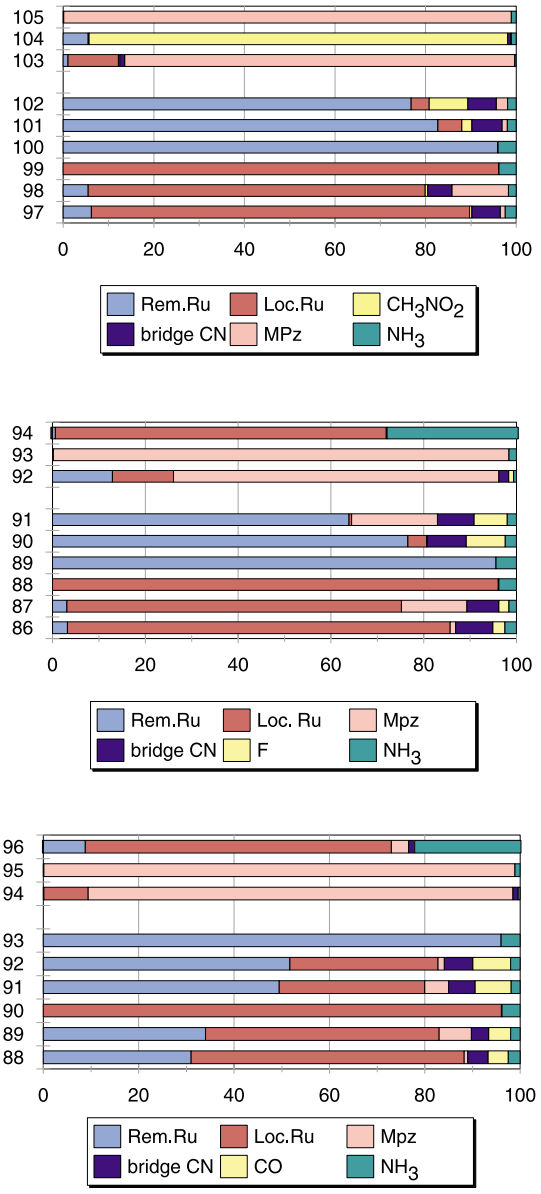
tres. The mean energies of the *d* shells on the remote and local ruthenium centres can be compared by considering the average energies of the easily recognizable "t_{2g}" sets in Table 2. Thus, the *d* orbitals of Ru_R are the frontier filled orbitals and lie $\Delta eV > 1.6$ eV above the mean energy of the *d* orbitals of Ru_L. The difference is significantly smaller when neutral ligands are bound to Ru_R. In the case of L = CO, the difference decreases to 0.43 eV. The value of ΔeV shows a definite linear trend with the value of the ligand electrochemical parameter for ligand L ($E_L(L)$) (82).

Thus, as a consequence, for anionic L the MOs are essentially localized on each ruthenium atom with little interaction between the two ruthenium atoms. With neutral ligands, as ΔeV decreases, mixing between the ruthenium centres (via σ and π pathways) increases but remains small for all species except L = CO, where mixing involving remote and local ruthenium $d\pi$ and $d\sigma$ orbitals is extensive.

The HOMO in all cases (except L = CO) is localized on Ru_R, and for L = anion, it has a substantial contribution from π^*-Mpz+. This arises because the HOMO–LUMO gap is significantly smaller for the anionic ligands than for the neutral ligands and the frontier $d\pi$ orbital on Ru_R lies close in energy to the LUMO on Mpz+. With L = neutral, the HOMO is still $d\pi$ and localized on Ru_R but has very little contribution from π^*-Mpz+. For L = CO, it is the HOMO-2 that is $d\pi$ with 5% contribution from π^*-Mpz+. This is larger than the contributions observed with the other neutral L but much smaller than with anionic L.

© 2004 NRC Canada

Fig. 2. Molecular orbital coefficients expressed in a bar graph for: L = CH_3NO_2 (upper), L = F (middle), and L = CO (lower). The HOMO–LUMO gap is noted as a white intermission, and all orbitals below this gap are filled (DFT).



For all species, except L = CH_3NO_2, which has an intervening π* orbital on CH_3NO_2, the LUMO and LUMO + 1 are π* orbitals localized on Mpz+. The LUMO has the correct symmetry to interact with metal *d*π, while the LUMO + 1 does not and is essentially entirely localized on Mpz+. For the neutral L species, it is not surprising that only the local Ru_L *d*π orbital will back-donate to this π*-LUMO on Mpz+; there is very little contribution from Ru_R *d*π. However, because of the smaller HOMO–LUMO gap, there is a greater contribution of the remote Ru_R *d*π back-bonding to π*-LUMO for the anionic ligands. Indeed, back-bonding from the remote ruthenium is comparable to, or even greater than, that from the local ruthenium. The magnitude of the Ru_L π-back-bonding at 10%–15% is significantly greater than observed in ruthenium(II) bipyridine complexes (ca. 5%) (3).

Table 3. Predicted electronic transition energies (*E*), intensities (*f*), and assignments.

E (10^3 cm^{-1}) (*f*)	Assignment
L = CH_3NO_2	
10.4 (0.16)	102 → 103 (58%), 101 → 103 (25%)
19.9 (0.30)	102 → 104 (68%), 98 → 103 (6%)
21.8 (0.20)	98 → 103 (64%), 102 → 104 (5%)
L = pyridine	
8.2 (0.18)	107 → 108 (67%)
21.6 (0.37)	102 → 108 (69%)
24.5 (01)	100 → 108 (99%)
L = H_2O	
7.7 (007)	91 → 92 (65%), 90 → 92 (29%)
10.5 (0.13)	90 → 92 (59%), 91 → 92 (21%)
21.8 (0.33)	87 → 92 (70%)
L = CO	
17.8 (0.13)	91 → 94 (71%), 92 → 94 (12%), 89 → 94 (10%)
21.3 (0.26)	89 → 94 (73%)
L = CN^-	
8.7 (0.34)	93 H → 94 L (33%)
21.2 (0.08)	89 → 94 (64%), 86 → 94 (21%)
22.7 (0.20)	86 → 94 (70%), 89 → 94 (10%)
L = F^-	
10.2 (0.38)	91 → 92 (35%)
22.8 (0.23)	87 → 92 (71%)
L = Cl^-	
9.5 (0.37)	90 H → 91 L (36%)
17.4 (0.009)	87 → 91 L (81%)
22.8 (0.26)	84 → 91 L (71%)
L = OH^-	
9.8 (0.42)	91 H → 92 L (29%)
21.8 (0.09)	88 → 92 L(75%)
24.0 (0.12)	85 → 92 L(81%)

Note: Assignments are based on MO numbering in Table 2. L = LUMO, H = HOMO.

The HOMO (HOMO-2 for L = CO) and LUMO can be described as a pair of in- and out-of-phase coupled (Ru_R) *d*π ± *d*π (Ru_L) orbitals, the bonding combination, of course, being the HOMO.

There is a further pair of deeper-lying in- and out-of-phase coupled Ru_R(*d*π) – Ru_L(*d*π) MOs with nonzero contributions from a π-symmetry Mpz+ orbital but which have a much larger contribution from the local Ru_L *d*π orbital. For clarity, we identify the HOMO orbital as ***dπ***-*d*π-Mpz and the deeper orbitals as *d*π-***dπ***-Mpz (1, 2), where the bolded orbital is the dominant orbital in the order Ru_R-Ru_L-Mpz+. We also note that a frontier π orbital on L, especially L = CN^-, Cl^-, or OH^-, is coupled with these *d*π-*d*π-Mpz+ orbitals. As we describe in the following section, transitions from these three orbitals to the LUMO provide the principal features of the visible-region electronic spectra.

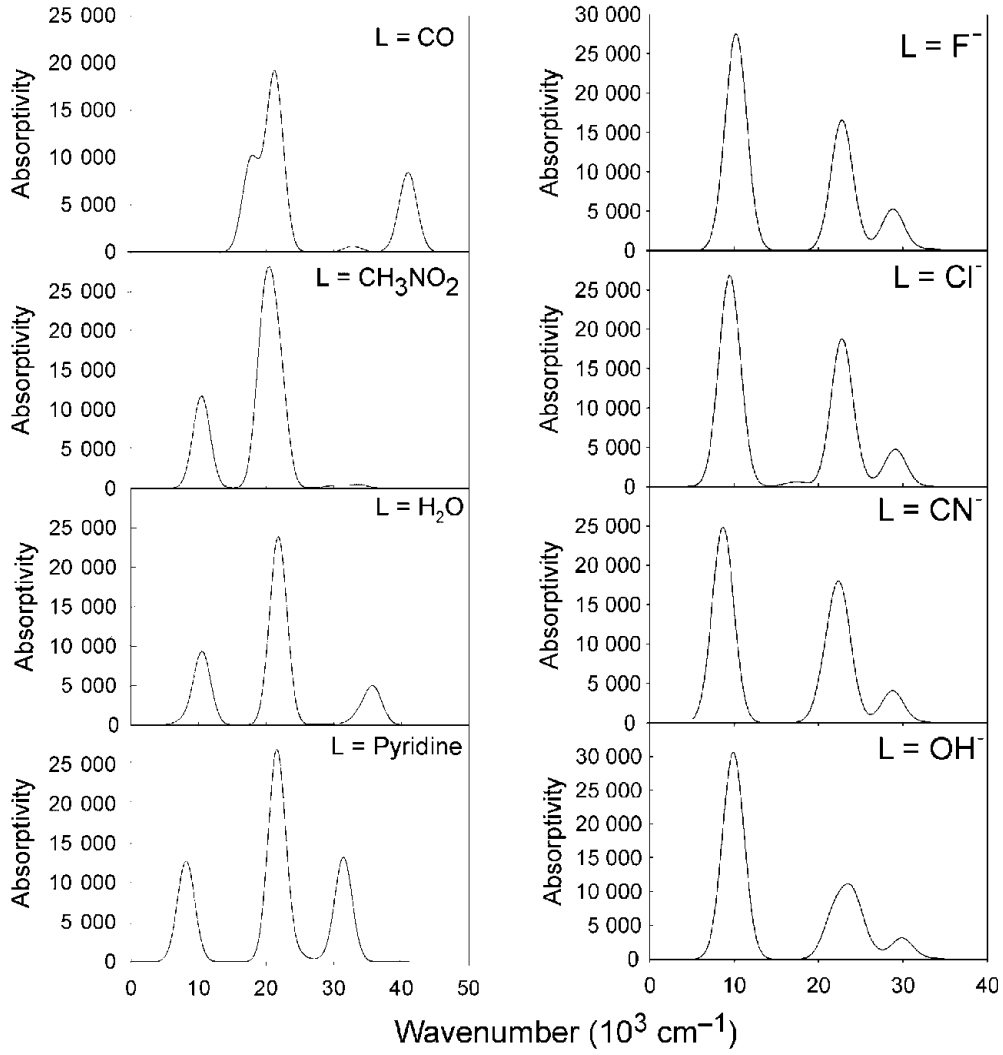
Examples of MO data are displayed in Fig. 2 as bar graphs, which provide a convenient visual display of the extent of mixing between the various components.

Gas-phase optical spectra

The predicted gas-phase optical spectra are presented in Table 3 and illustrated in Fig. 3. They all involve essentially

© 2004 NRC Canada

Fig. 3. TD-DFRT predicted optical spectra for the neutral L species as identified (left) and the anionic L species as identified (right).



the same assignments, but with quite markedly different predicted intensities. There are two principal features common to all the species. These are the first pair of bands shown in Fig. 3, where it is evident that they are not fully resolved for L = CO. For L = neutral (Fig. 3, left-hand panel), the first band is weaker than the second. The same pair is identified for L = anion (Fig. 3, right-hand panel), but now the first transition is the more intense.

The lowest-energy, nonzero-intensity transition is the ***dπ***-*d*π-Mpz → LUMO (usually HOMO → LUMO) excitation lying in the range 7700 – 10 500 cm^{-1} for all except L = CO, where it lies at 17 800 cm^{-1}. This has a significant intensity for anionic L but less so for the neutral L. This can be understood readily from Table 2 as follows. For the neutral ligands, the LUMO is almost totally localized on π*-Mpz+ with only a very small contribution from *d*π Ru_R, while the donor orbital is mostly *d*π Ru_R with very little contribution from π*-Mpz+; thus, the overlap between the ground and the excited state is small and hence the intensity is small (83, 84). For anionic L, on the other hand, the LUMO has substantial *d*π Ru_R character and the donor orbital has substantial π*-MPz+ character; hence, overlap is greater and this is reflected in the greater intensity (83).

The second common feature, which is usually a composite of two closely lying excitations, lies in the range 19 900 – 24 000 cm^{-1}, appearing near 21 500 – 21 800 cm^{-1} for all the L = neutral and at 22 700 – 24 000 cm^{-1} for the L = anion species. This second feature arises through excitations from the deeper-lying pair of *d*π-coupled orbitals, localized primarily on the local Ru_L, again to the LUMO. This feature is moderately intense for all L because these donor orbitals always have substantial π-MPz+ character and we are generally observing the overlap of two transitions, the higher-energy component of which is the more intense. These transitions are all most simply described as MLCT transitions to the LUMO of the Mpz+ ligand. However, both metal ions are usually involved, to a greater or lesser extent. To ascertain the dominant contribution, i.e., local or remote Ru to Mpz+ MLCT, one needs to compare the details of the assignment in Table 3 with the MO composition in Table 2.

In the examples where *d*σ–*d*π mixing occurs yielding canted orbitals, transitions from each of these to the LUMO is predicted, yielding thereby an extra transition, though one is generally much weaker than the other (e.g., L = H_2O).

Some species have additional moderately intense transitions associated with the group L. For example, with L = Py,

© 2004 NRC Canada

Table 4. Comparison of DFT and ZINDO/S electronic coupling for L = fluoride and L = CO species.

	DFT					ZINDO/S					
No. MO	Ru_R	Ru_L	Mpz+	-CN-	L	Ru_R	Ru_L	Mpz+	-CN-	L	No. MO
L = F^-											
93	0	0.2	98.2	0	0	0	0.1	99.5	0	0	67
92 L	12.9	13.2	70.1	2.1	0	4.0	9.5	84.2	1.7	0.1	66 L
91 H	63.9	0.6	18.5	7.9	7.1	75.5	1.9	7.5	10.7	1.9	65 H
90	76.6	4.0	0.2	8.4	8.4	81.0	4.0	0.1	10.5	2	64
89	95.6	0	0	0	0	96.4	0	0	0	0	63
88	0	96.1	0.1	0	0	0	96.5	0	0	0	60
87	3.1	72.1	14.1	6.9	2.2	6.1	68.3	13.3	10.2	0.5	62
86	3.2	82.5	1.2	8.0	2.6	5.7	78.7	1.0	12.2	0.5	61
L = CO											
95	0	0.1	98.8	0	0	0	0.1	99.6	0	0	68
94 L	0.1	9.3	89.1	1.1	0	0	3.3	95.8	0.6	0	67 L
93 H	96.0	0	0	0	0	95.7	0.4	0	0.1	0.1	65
92	51.7	31.1	1.3	6.0	7.9	38.8	36.7	3.6	9.5	9.8	66 H
91	49.5	30.5	5.0	5.6	7.5	44.7	32.5	0.3	9.4	11.6	64
90	0	96.1	0.1	0	0	0.1	96.6	0	0	0	63
89	34.0	49.0	6.8	3.6	4.6	37.8	42.3	3.9	4.1	9.8	62
88	31.0	57.3	0.7	4.3	4.2	31.5	52.1	0.5	5.7	8.2	61

Note: MOs are ordered sequentially with respect to the DFT calculation. The ZINDO/S MOs are ordered to match the corresponding DFT orbitals. L = LUMO, H = HOMO.

the band at 24 500 cm^{-1} (100 → 108) is mostly an interligand Py → Mpz+ ligand-to-ligand charge transfer (LLCT), while the most intense transition in the visible region for L = CH_3NO_2, at 19 900 cm^{-1}, is mostly $Ru_R \rightarrow \pi^*$ CH_3NO_2 MLCT. For L = anion, there is an additional band near 30 000 cm^{-1}, which is a composite transition involving excitations both to the LUMO and to higher virtual orbitals. These are not germane to this study and are not discussed further.

The question of overlap is addressed again immediately below in terms of the exchange contributions involved in these transitions.

Exchange (*K*) and Coulombic (*J*) integral contributions

It has been previously demonstrated (3, 7, 10, 26, 70, 85, 86) that evaluation of the *J* and *K* integrals, especially *K*, involved in the electronic excitations, can provide additional insight into the delocalization extant in the complex. As noted in the previous section, this calculation utilizes the ZINDO/S calculated data; it is, therefore, relevant to ensure that the INDO/S calculation essentially reproduces the DFT calculations. Table 4 describes the ZINDO/S computed electronic coupling for one neutral and one anionic ligand species for comparison with the DFT data. The MO numbering system differs for the two models and, since some MOs have very similar energies, the ordering of the MOs is not exactly the same in the two calculations. Nevertheless, one can readily identify corresponding orbitals between the two models by their σ, δ, or π symmetry and their composition. Figure 1 illustrates that the ZINDO/S MOs are closely similar to the DFT Kohn–Sham orbitals.

Table 5 collects the *J* and *K* values derived for the dominant electronic excitations listed in Table 3. The value of *K* is inversely and exponentially proportional (84, 86–88) to the distance travelled by the electron in the excitation. Thus, if the electron formally leaves an orbital 100% localized on the metal to arrive at one 100% localized on the ligand, then the formal distance travelled might be supposed to approximate to the distance between the metal centre and ligand centre. However, if the initial orbital involves delocalization over metal and ligand and the terminating ligand orbital is also delocalized over the same metal and ligand orbitals,

Table 5. Coulomb and exchange integral values.

Ligand (L)	Transition	*J* (10^3 cm^{-1})	*K* (10^3 cm^{-1})
CH_3NO_2	102 H → 103 L	15.4	0.43
	102 H → 104	31.3	2.93
	98 → 103 L	28.1	2.81
Pyridine	107 H → 108 L	14.35	0.35
	102 → 108 L	25.8	2.63
	100 → 108 L	13.7	0.49
H_2O	91 H → 92 L	15.9	0.3
	90 → 92 L	15.9	0.3
	87 → 92 L	27.7	2.7
CO	91 → 94 L	20.3	1.18
	89 → 94 L	21.0	1.26
CN^-	93 H → 94 L	16.0	2.28
	89 → 94 L	16.9	1.45
	86 → 94 L	26.5	3.59
F^-	91 H → 92 L	19.7	4.18
	87 → 92 L	30.6	5.0
Cl^-	90 H → 91 L	18.3	2.8
	87 → 91 L	14.9	0.8
	84 → 91 L	28.7	4.4
OH^-	91 H → 92 L	20.6	5.5
	88 → 92 L	28.2	4.4
	85 → 92 L	17.0	1.0

Note: Assignment of transitions is based on MO numbering in Table 2 (see Table 3). L = LUMO, H = HOMO.

© 2004 NRC Canada

then we may suppose that the time-average distance the electron jumps will be much smaller than in the localized case. This description has been shown to be accurate experimentally via measurement of the Stark effect in related species (89).

Transitions between similarly delocalized MOs are indicated by a much larger value of K than in the case of the localized excitation. Thus, the lowest energy transition displays higher values for K (2280–5500 cm^{-1}) for L = anions, where both the donor and acceptor orbitals contain substantial contributions from the same ligand π^* and same metal $d\pi$ orbital and smaller values for L = neutral ligands (300–1180 cm^{-1}), where such delocalization is smaller. For the second major transition, where delocalization is greater for both neutral and anionic L, we observe the range 1260–2810 cm^{-1} for neutral L and 3590–5000 cm^{-1} for anionic L. As expected, there is a general trend whereby the higher values of K are associated with the more intense transitions. Moreover, the grouping of the second pair of transitions appearing at slightly higher energy for L = anion than for L = neutral is due to the higher value of K, whose magnitude contributes directly to the transition energy (83, 86). The variation in J generally follows the same patterns, becoming larger along with K when delocalization causes significant overlap between ground and excited state, but there are a few exceptions. For some useful comparative J and K values, see Table 4 of ref. 7.

Comparison with experimental data

For further confirmation that the methodologies discussed in this report are valid, we calculate optical data for a cyano-bridged dinuclear ruthenium(II) species (**II**) reported by Bignozzi et al. (90, 91) and Endicott et al. (92). Species **II** ($[(NH_3)_5Ru^{II}\text{-}NC\text{-}Ru^{II}(CN)(bpy)_2]^{4+}$) contains a ruthenium bound by two 2,2′-bipyridine (bpy) groups and a cyanide residue linked, in a cis conformation, via a bridging cyanide to a $[Ru(NH_3)_5]^{2+}$ fragment.

This is actually quite an interesting system. The two bpy groups are inequivalent since one is trans to a negatively charged cyano group and the other to the positively charged $[Ru(NH_3)_5\text{-}NC]^+$ residue. The π^* LUMO is localized essentially entirely (94%, INDO/S; 94% DFT) on the former, while the π^* LUMO + 1, lying ca. 0.35 eV above the LUMO (INDO/S), is almost entirely localized (95%, INDO/S; 93% DFT) on the latter.

For convenience, we define a molecular plane on the pentaamminoruthenium centre (designated as Ru_t) to contain the terminal cyano group on the bpy-bound ruthenium centre (designated Ru_c) and three NH_3 groups including the terminal one. The $d(t_{2g})$ orbitals on Ru_t can be identified as σ, π, or δ with respect to this plane, in a similar fashion to the arguments above. The HOMO is predominantly $d\sigma(Ru_c)$, the HOMO-1 is $d\delta(Ru_c)$, and the HOMO-2 is $d\pi((56\%)Ru_c\text{–}(25\%)Ru_t)$ (DFT). Thus, the HOMO-2 is quite extensively mixed and phased so that the two Ru $d\pi$ orbitals are in a bonding phase with one another but separated by an antibonding interaction with the bridging cyano group.

The visible absorption spectrum of this species (shown in Fig. 1 of ref. 90) exhibits an intense MLCT band centred at 21 600 cm^{-1} (ε = 6400 L mol^{-1} cm^{-1}) (in DMF) with well-defined shoulders at 19 300 and 16 000 cm^{-1}. The intense band is calculated to be a composite of two transitions, HOMO-2 $\rightarrow$ LUMO (50%) and HOMO $\rightarrow$ LUMO + 1 (30%), and so is mostly from the heavily mixed $d\pi$ orbital on both Ru centres to the π^* localized on the bpy trans to the terminal pentaammino group. Its calculated energy and intensity (22 600 cm^{-1}, f = 0.14 (ε = 7500 L mol^{-1} cm^{-1}),[3] INDO/S) are in excellent agreement with the experimental data. The calculation predicts several weaker and lower-energy transitions to explain the experimental shoulder, the two more intense of these being 20 900 cm^{-1} (f = 0.03) HOMO $\rightarrow$ LUMO (77%) and 22 200 cm^{-1} (f = 0.009) HOMO – 1 $\rightarrow$ LUMO + 1 (66%) (INDO/S). These are both MLCT transitions involving predominantly the central bpy-bound ruthenium atom in contrast to an earlier assignment (91) that assigned them as MLCT involving the terminal Ru. Overall, the agreement between theory and experiment is excellent, in terms of energy, intensity, and the number of observed bands. This short analysis provides additional support for the validity of the analyses of the experimentally unknown species discussed herein.

Summary

This analysis has demonstrated the significant but often subtle effects of changing the terminal ligand on the electronic structure of these molecules. The changes can readily be mapped via the application of density functional theory and lead to a firmer understanding of the factors that determine electronic interactions between the metal centres. The variations in the predicted optical spectra follow from careful analysis of the MO coefficients. Exchange integral values are seen to correlate well with the degree of delocalization and with both the energy and intensity of the electronic transitions. The extent of π-back-donation to the non-innocent methylpyrazinium ligand can evidently be tuned over quite a wide range, involving either or both metal centres, leading to exquisite control not only of electronic structure but also of geometry from the viewpoint of bond distances.

Acknowledgements

I am indebted to the Natural Sciences and Engineering Research Council of Canada (NSERC) for financial support, to the Canada Council for the Arts, for a Killam Fellowship (2000–2002), and especially to Dr. Serge I. Gorelsky for many years of expert computational and theoretical chemical assistance. This paper also benefited greatly from the availability of the programs AOMix, SIG-JK, and SWizard written by Dr. Gorelsky and available as noted in the appropriate references cited herein.

References

1. C.J. Da Cunha, S.S. Fielder, D.V. Stynes, H. Masui, P.R. Auburn, and A.B.P. Lever. Inorg. Chim. Acta, **242**, 293 (1996).
2. R.A. Metcalfe and A.B.P. Lever. Inorg. Chem. **36**, 4762 (1997).

[3] Scaled by 2. ZINDO/S routinely overestimates intensities; therefore, the calculated intensity is decreased by a factor of two.

© 2004 NRC Canada

3. S.I. Gorelsky, E.S. Dodsworth, A.B.P. Lever, and A.A. Vlcek. Coord. Chem. Rev. **174**, 469 (1998).
4. A.B.P. Lever and E.S. Dodsworth. *In* Inorganic electronic structure and spectroscopy. Vol. 2. *Edited by* E.I. Solomon and A.B.P. Lever. John Wiley & Sons, New York. 1999. p. 227.
5. R.A. Metcalfe, L.C.G. Vasconcellos, H. Mirza, D.W. Franco, and A.B.P. Lever. J. Chem. Soc. Dalton Trans. 2653 (1999).
6. H. Masui, A.L. Freda, M.C. Zerner, and A.B.P. Lever. Inorg. Chem. **39**, 141 (2000).
7. A.B.P. Lever and S.I. Gorelsky. Coord. Chem. Rev. **208**, 153 (2000).
8. Md.K. Nazeeruddin, S.M. Zakeeruddin, R. Humphry-Baker, S.I. Gorelsky, A.B.P. Lever, and M. Grätzel. Coord. Chem. Rev. **208**, 213 (2000).
9. S.I. Gorelsky and A.B.P. Lever. J. Organomet. Chem. **635** (2001).
10. S.I. Gorelsky, A.B.P. Lever, and M. Ebadi. Coord. Chem. Rev. **230**, 97 (2002).
11. S.I. Gorelsky and A.B.P. Lever. Can. J. Appl. Spectrosc. **48**, 93 (2003).
12. A.P. Meacham, K.L. Druce, Z.R. Bell, M.D. Ward, J.B. Keister, and A.B.P. Lever. Inorg. Chem. **42**, 7887 (2003).
13. E.S. Dodsworth, E. Del Medico, and A.B.P. Lever. Inorg. Chem. **43**, 2654 (2004).
14. A.B.P. Lever and S.I. Gorelsky. Struct. Bond. In press.
15. J. Li, L. Noodleman, and D.A. Case. *In* Inorganic electronic structure and spectroscopy. Vol. 1. John Wiley & Sons, New York. 1999. p. 661.
16. M.E. Casida. *In* Recent advances in density functional methods. Vol. 1. *Edited by* D.P. Chong. World Scientific, Singapore. 1995. Chap. 5.
17. M.E. Casida. *In* Recent developments and applications of modern density functional theory. *Edited by* J.M. Seminario. Elsevier Science, Amsterdam. 1996. p. 391.
18. J. Ridley and M.C. Zerner. Theor. Chim. Acta, **32**, 111 (1973).
19. J. Ridley and M.C. Zerner. Theor. Chim. Acta, **42**, 223 (1976).
20. M.C. Zerner. Reviews in computational chemistry. Vol. 2. VCH Publishers, New York. 1991. p. 313.
21. M.C. Zerner. *In* Metal–ligand interactions. *Edited by* N. Russo and D.R.E. Salahub. Kluwer Academic Publishers, Amsterdam. 1996. p. 493.
22. C. Martin and M.C. Zerner. *In* Inorganic electronic structure and spectroscopy. Vol. 1. *Edited by* E.I. Solomon and A.B.P. Lever. John Wiley & Sons, New York. 1999. p. 555.
23. J.F. Wishart, H. Taube, K.J. Breslauer, and S.S. Isied. Inorg. Chem. **23**, 2997 (1984).
24. R.E. Shepherd, A. Proctor, W.W. Henderson, and T.K. Myser. Inorg. Chem. **26**, 2440 (1987).
25. C. Creutz and M.H. Chou. Inorg. Chem. **26**, 2995 (1987).
26. Y.G.K. Shin, B.S. Brunschwig, C. Creutz, M.D. Newton, and N. Sutin. J. Phys. Chem. **100**, 1104 (1996).
27. F. Hilgers, W. Bruns, J. Fiedler, and W. Kaim. J. Organomet. Chem. **511**, 273 (1996).
28. D.A. Estrin, O.Y. Hamra, L. Paglieri, L.D. Slep, and J.A. Olabe. Inorg. Chem. **35**, 6832 (1996).
29. E. Waldhor, W. Kaim, J.A. Olabe, L.D. Slep, and J. Fiedler. Inorg. Chem. **36**, 2969 (1997).
30. B.J. Coe, C.I. Mcdonald, S.M. Couchman, J.C. Jeffery, L.H. Rees, S.J. Coles, T. Gelbrich, and M.B. Hursthouse. Polyhedron, **19**, 1193 (2000).
31. M.P. Aarnts, D.J. Stufkens, M.P. Wilms, E.J. Baerends, A. Vlcek, Jr., I.P. Clark, M.W. George, and J.J. Turner. Chem.—Eur. J. **2**, 1556 (1996).
32. J.-F. Guillemoles, V. Barone, L. Joubert, and C. Adamo. J. Phys. Chem. A, **106**, 11354 (2002).
33. J.E. Monat, J.H. Rodriguez, and J.K. McCusker. J. Phys. Chem. A, **106**, 7399 (2002).
34. C.E Powell, M.P. Cifuentes, J.P. Morrall, R. Stranger, M.G. Humphrey, M. Samoc, B. Luther-Davies, and G.A Heath. J. Am. Chem. Soc. **125**, 602 (2003).
35. M. Turki, C. Daniel, S. Zalis, A. Vlcek, Jr., J. van Slageren, and D.J. Stufkens. J. Am. Chem. Soc. **123**, 11 431 (2001).
36. J.A. Weinstein, J. van Slageren, D.J. Stufkens, S. Zalis, and M.W. George. J. Chem. Soc. Dalton Trans. 2587 (2001).
37. K.C. Zheng, Y. Shen, J.P. Wang, X.W. Liu, and F.C. Yun. Inorg. Chim. Acta, **335**, 100 (2002).
38. K. Zheng, J. Wang, W. Peng, X. Liu, and F. Yun. J. Phys. Chem. A, **105**, 10 899 (2001).
39. K.C. Zheng, J.P. Wang, W.L. Peng, X.W. Liu, and F.C. Yun. THEOCHEM, **582**, 1 (2002).
40. K.C. Zheng, J.P. Wang, W.L. Peng, Y. Shen, and F.C. Yun. Inorg. Chim. Acta, **328**, 247 (2002).
41. O.V. Sizova, V.I. Baranovskii, N.V. Ivanova, and A.I. Panin. Russ. J. Coord. Chem. **24**, 219 (1998).
42. O.V. Sizova, V.I. Baranovskii, and A.I. Panin. Russ. J. Coord. Chem. **24**, 601 (1998).
43. A.Y. Ershov, A.D. Shashko, O.V. Sizova, and N.V. Ivanova. Russ. J. Gen. Chem. **72**, 1327 (2002).
44. O.V. Sizova, N.V. Ivanova, and A.Y. Ershov. Russ. J. Coord. Chem. **29**, 494 (2003).
45. O.V. Sizova, N.V. Ivanova, and A.B. Nikol'skii. Russ. J. Gen. Chem. **67**, 23 (1997).
46. V.I. Baranovski and O.V. Sizova. Chem. Phys. Lett. **315**, 130 (1999).
47. N.V. Ivanova, V.V. Sizova, A.B. Nikolskii, and A.I. Panin. J. Struct. Chem. **40**, 620 (2000).
48. M.J. Frisch, G.W. Trucks, H.B. Schlegel, G.E. Scuseria, M.A. Robb, J.R. Cheeseman, V.G. Zakrzewski, J.A. Montgomery, Jr., R.E. Stratmann, J.C. Burant, S. Dapprich, J.M. Millam, A.D. Daniels, K.N. Kudin, M.C. Strain, O. Farkas, J. Tomasi, V. Barone, M. Cossi, R. Cammi, B. Mennucci, C. Pomelli, C. Adamo, S. Clifford, J. Ochterski, G.A. Petersson, P.Y. Ayala, Q. Cui, K. Morokuma, D.K. Malick, A.D. Rabuck, K. Raghavachari, J.B. Foresman, J. Cioslowski, J.V. Ortiz, B.B. Stefanov, G. Liu, A. Liashenko, P. Piskorz, I. Komaromi, R. Gomperts, R.L. Martin, D.J. Fox, T. Keith, M.A. Al-Laham, C.Y. Peng, A. Nanayakkara, C. Gonzalez, M. Challacombe, P.M.W. Gill, B. Johnson, W. Chen, M.W. Wong, J.L. Andres, C. Gonzalez, M. Head-Gordon, E.S. Replogle, and J.A. Pople. Gaussian 98. Revision A11 [computer program]. Gaussian Inc., Pittsburgh, Pa. 1998.
49. A.D. Becke. J. Chem. Phys. **98**, 5648 (1993).
50. C. Lee, W. Yang, and R.G. Parr. Phys. Rev. B, **37**, 785 (1988).
51. T.H. Dunning, Jr. and P.J. Hay. *In* Modern theoretical chemistry. Vol. 3. *Edited by* H.F. Schaefer. Plenum, New York. 1976. p. 1.
52. P.J. Hay and W.R. Wadt. J. Chem. Phys. **82**, 270 (1985).
53. P.J. Hay and W.R. Wadt. J. Chem. Phys. **82**, 284 (1985).
54. P.J. Hay and W.R. Wadt. J. Chem.Phys. **82**, 299 (1985).
55. R. Bauernschmitt and R. Ahlrichs. Chem. Phys. Lett. **256**, 454 (1996).
56. M.E. Casida, C. Jamorski, K.C. Casida, and D.R. Salahub. J. Chem. Phys. **108**, 4439 (1998).
57. R.E. Stratmann, G.E. Scuseria, and M.J. Frisch. J. Chem. Phys. **109**, 8218 (1998).
58. R. Bauerschmitt, R. Ahlrichs, F.H. Hennrich, and M.M. Kappes. J. Am. Chem. Soc. **120**, 5052 (1998).
59. J. Juan, M.E. Casida, and D.R. Salahub. J. Mol. Struct: THEOCHEM, **527**, 229 (2000).

© 2004 NRC Canada

60. F. Della Sala and A. Gorling. Int. J. Quantum Chem. **91**, 131 (2003).
61. P. Bour. Chem. Phys. Lett. **345**, 331 (2001).
62. S.I. Gorelsky. SWizard [computer program]. Available at http://www.sg-chem.net/swizard/.
63. S.I. Gorelsky. AOMix [computer program]. Available at http://www.sg-chem.net/aomix/.
64. S.I. Gorelsky. SIG-JK [computer program]. Available at http://www.sg-chem.net/sig-jk/.
65. F.M. Bickelhaupt and E.J. Baerends. *In* Reviews in computational chemistry. Vol. 15. *Edited by* K.B. Lipkowitz and D.R.E. Boyd. Wiley, New York. 2000. pp. 1–86.
66. P. Bour. J. Comput. Chem. **21**, 8 (2000).
67. J. Zevallos and A. Toro-labbe. J. Chilean Chem. Soc. **48**, 39 (2003).
68. T. Hupp, B. Engels, and A. Gorling. J. Chem. Phys. **119**, 11591 (2003).
69. S. Hamel, P. Duffy, M.E. Casida, and D.R. Salahub. J. Electron Spectrosc. Relat. Phenom. **123**, 345 (2002).
70. Y.K. Shin, D.J. Szalda, B.S. Brunschwig, C. Creutz, and N. Sutin. Inorg. Chem. **36**, 3190 (1997).
71. H.A.d.S. Silva, B.R. McGarvey, R.H.d.A. Santos, M. Bertotti, V. Mori, and D.W. Franco. Can. J. Chem. **79**, 679 (2001).
72. Q.-F. Zhang, H. Zheng, W.-Y. Wong, W.-T. Wong, and W.-H. Leung. Inorg. Chem. **39**, 5255 (2000).
73. A.N. Sobolev and B.N. Figgis. Aust. J. Chem. **50**, 825 (1997).
74. T. Sugaya, A. Tomita, H. Sago, and M. Sano. Inorg. Chem. **35**, 2692 (1996).
75. J.F. Wishart, X.H. Zhang, S.S. Isied, J.A. Potenza, and H.J. Schugar. Inorg. Chem. **31**, 3179 (1992).
76. K. Kroghjespersen, X.H. Zhang, Y.B. Ding, J.D. Westbrook, J.A. Potenza, and H.J. Schugar. J. Am. Chem. Soc. **114**, 4345 (1992).
77. M. Henn, E. Alessio, G. Mestroni, M. Calligaris, and W.M. Attia. Inorg. Chim. Acta, **187**, 39 (1991).
78. P.S. Moritz, A.A. Diamantis, F.R. Keene, M.R. Snow, and E.R.T. Tiekink. Aust. J. Chem. **41**, 1353 (1988).
79. R.C. Elder and M. Trkula. Inorg. Chem. **16**, 1048 (1977).
80. F. Bottomley. J. Chem. Soc. Dalton Trans. 1600 (1974).
81. J.F. Wishart, A. Bino, and H. Taube. Inorg. Chem. **25**, 3318 (1986).
82. A.B.P. Lever. Inorg. Chem. **29**, 1271 (1990).
83. A.B.P. Lever. Inorganic electronic spectroscopy. Elsevier Science, Amsterdam. 1984.
84. A.B.P. Lever and E.I. Solomon. *In* Inorganic electronic structure and spectroscopy. Vol. 1. *Edited by* E.I. Solomon and A.B.P. Lever. John Wiley & Sons, New York. 1999. p. 1.
85. C. Creutz, M.D. Newton, and N. Sutin. J. Photochem. Photobiol. A. **82**, 47 (1994).
86. S.I. Gorelsky and A.B.P. Lever. Can. J. Appl. Spectrosc. **48**, 93 (2003).
87. R.G. Parr. Quantum theory of molecular electronic structure. W.A. Benjamin, New York. 1963.
88. A. Szabo and N.S. Ostlund. Modern quantum chemistry. Macmillan, New York. 1982.
89. G.U. Bublitz, W.M. Laidlaw, R.G. Denning, and S.G. Boxer. J. Am. Chem. Soc. **120**, 6068 (1998).
90. C.A. Bignozzi, S. Roffia, and F. Scandola. J. Am. Chem. Soc. **107**, 1644 (1985).
91. C.A. Bignozzi, C. Paradisi, S. Roffia, and F. Scandola. Inorg. Chem. **27**, 408 (1988).
92. M.A. Watzky, A.V. Macatangay, R.A. Vancamp, S.E. Mazzetto, X.Q. Song, J.F. Endicott, and T. Buranda. J. Phys. Chem. A, **101**, 8441 (1997).

© 2004 NRC Canada

Taxol interaction with DNA and RNA — Stability and structural features[1]

A. Ahmed Ouameur, H. Malonga, J.F. Neault, S. Diamantoglou, and H.A. Tajmir-Riahi

Abstract: Taxol (paclitaxel) is an anticancer drug that interacts with microtubule proteins in a manner that catalyzes their formation from tubulin and stabilizes the resulting structures. However, in the human lung tumor cell, the concentration of paclitaxel is highest in the nucleus. Therefore, it was of interest to examine the interaction of taxol with DNA and RNA in aqueous solution at physiological pH. Capillary electrophoresis and Fourier transform infrared (FTIR) difference spectroscopic methods were used to characterize the nature of drug–DNA and drug–RNA interactions and to determine the taxol binding site, the binding constant, the sequence selectivity, the helix stability, and the biopolymer secondary structure in the taxol–polynucleotide complexes in vitro. The FTIR spectroscopic studies were conducted with taxol/polynucleotide (phosphate) ratios of 1/80, 1/40, 1/20, 1/10, 1/4, and 1/2 with a final DNA(P) or RNA(P) concentration of 12.5 mmol/L, and capillary electrophoresis was performed after incubation of taxol with polynucleotides at ratios of 1/200 to 1/12 with a final polynucleotide concentration of 1.25 mmol/L. Taxol was shown to bind to DNA and RNA at G–C, A–T, or A–U bases and the backbone PO_2 group. Two types of binding were observed for taxol–DNA with $K_1 = 1.3 \times 10^4$ L mol^{-1} and $K_2 = 3.5 \times 10^3$ L mol^{-1}, whereas taxol–RNA complexes showed one type of binding with $K = 1.3 \times 10^4$ L mol^{-1}. The taxol–polynucleotide complexation is associated with a partial helix stabilization and no major alterations of B-DNA or A-RNA structure.

Key words: DNA, RNA, taxol, binding site, binding constant, conformation, helix stability, electrophoresis, FTIR spectroscopy.

Résumé : Le taxol est un médicament anticancéreux qui interagit avec les protéines microtubulaires d'une façon qui catalyse leur formation à partir de la tubuline et qui stabilise les structures qui en résultent. Toutefois, il a été démontré que les concentrations de taxol dans la cellule d'une tumeur d'un poumon humain sont plus élevées dans le noyau. Il y avait donc un intérêt à examiner l'interaction entre le taxol et l'ADN et l'ARN en solution aqueuse, au pH physiologique. On a utilisé l'électrophorèse capillaire et des méthodes de spectroscopie infrarouge à transformée de Fourier (FTIR) pour caractériser la nature des interactions médicament–ADN et médicament–ARN et pour déterminer le site de fixation du taxol, la constante d'association, la sélectivité séquentielle, la stabilité de l'hélice et la structure secondaire du biopolymère dans les complexes taxol–acides nucléiques. On a effectué ces études avec des rapports (r) de taxol/polynucléotides (phosphate) de 1/80, 1/40, 1/20, 1/10, 1/4 et 1/2, avec une concentration finale d'ADN(P) ou d'ARN(P) de 12,5 mmol/L pour l'infrarouge et de 1/200 à 1/12, avec une concentration finale de polynucléotides de 1,25 mmol/L pour l'électrophorèse capillaire. L'analyse structurale a montré que le taxol se fixe avec l'ADN et l'ARN au niveau des bases G–C, A–T ou A–U et aux groupements phosphates (PO_2). Deux types de liaison ont été observés pour les complexes taxol–ADN, avec $K_1 = 1{,}3 \times 10^4$ L mol^{-1} et $K_2 = 3{,}5 \times 10^3$ L mol^{-1}, alors que les complexes taxol–ARN ne comportent qu'un seul type de liaison, avec $K = 1{,}3 \times 10^4$ L mol^{-1}. Les interactions taxol–polynucléotides stabilisent partiellement la structure secondaire des acides nucléiques, qui restent dans leur conformation naturelle (conformation B pour l'ADN et A pour l'ARN).

Mots clés : ADN ARN, taxol, site de fixation, constante d'association, conformation, stabilité de l'hélice, électrophorèse, spectroscopie infrarouge à transformée de Fourier.

Introduction

Taxol (paclitaxel) is an anticancer drug with the structure shown in Scheme 1. It interacts with microtubule proteins in a manner that catalyzes the formation of microtubules from tubulin and stabilizes the resulting structures (1). Its antitumor activity is based on increasing the stability of microtubules and preventing mitosis (2–4). In the cell, this

Received 13 February 2004. Published on the NRC Research Press Web site at http://canjchem.nrc.ca on 10 September 2004.

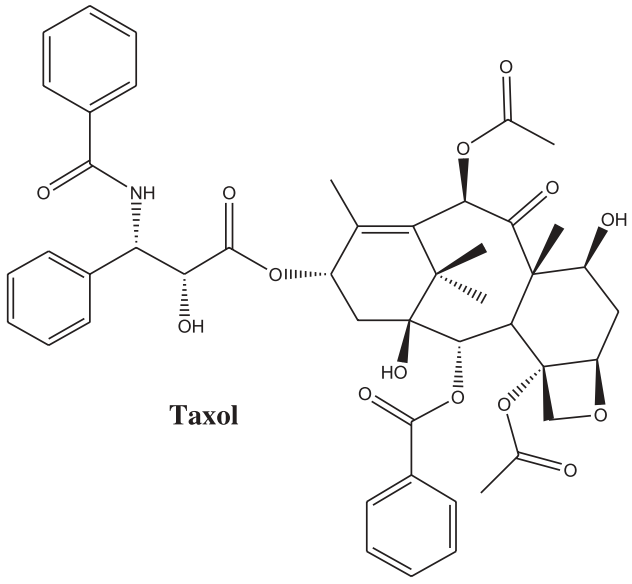
A. Ahmed Ouameur, H. Malonga, J.F. Neault, S. Diamantoglou, and H.A. Tajmir-Riahi.[2] Department of Chemistry–Biology, University of Québec at Trois-Rivières, C.P. 500, Trois-Rivières, QC G9A 5H7, Canada.

[1]This article is part of a Special Issue dedicated to the memory of Professor Gerhard Herzberg.

[2]Corresponding author (e-mail: tajmirri@uqtr.ca).

 doi: 10.1139/V04-061 © 2004 NRC Canada

Scheme 1.



Taxol

phenomenon leads to an altered morphology, with microtubules forming stable bundles and the cell being unable to assemble a normal mitotic spindle (5). In cells treated with taxol, the transition between interphase and mitosis is normally arrested and the cells die. The elucidation of this unique mechanism of action during the late 1970s and 1980s promoted the development of taxol as an anticancer drug. Taxol has shown unusual efficacy as a clinical agent for the treatment of breast, ovarian, skin, lung, head, and neck cancers (6). In 1993, taxol was approved by the U.S. Food and Drug Administration for use in the treatment of breast and ovarian cancers.

In recent years, to further elucidate the mechanism of action of taxol's antitumor activity, the structures of several taxol–protein and taxol–lipid complexes have been investigated (7, 8). On the other hand, it has been demonstrated that the presence of nucleotide strongly affects the taxol–tubulin complexation (9). It has also been demonstrated in the human lung tumor cell that paclitaxel is concentrated (twofold) in the nucleus (10). Recently, it was reported that paclitaxel exhibits major interaction with poly(dA–dT), inducing partial helical stability of the oligonucleotides, but not with poly(dG–dC) (11).[3] This prompted us to examine the interaction of taxol with DNA and RNA in vitro.

We report the results of capillary electrophoresis and FTIR difference spectroscopic studies on the interaction of taxol with calf-thymus DNA and yeast RNA in aqueous solution at physiological pH. Taxol/polynucleotide molar ratios of 1/80 to 1/2, with a final polynucleotide (phosphate) concentration of 12.5 mmol/L, and of 1/200 to 1/12, with a final polynucleotide (phosphate) concentration of 1.25 mmol/L, were employed for the FTIR spectroscopic studies and for capillary electrophoresis, respectively. Structural analyses regarding the drug binding site, the binding constant, sequence preference, helix stability, and nucleic acid conformation are reported here. The structural evidence presented provides major information on taxol–polynucleotide complexation and helps to elucidate the nature of this biologically important complex formation in vitro and in vivo.

Materials and methods

Materials

Highly polymerized type I calf-thymus DNA sodium salt (7% Na content) and Baker's yeast RNA sodium salt were purchased from Sigma Chemical Co. and used without further purification. To check the protein content of DNA and RNA solutions, the absorbance bands at 260 and 280 nm were used. The A_{260} / A_{280} ratio was 1.80 for DNA and 2.1 for RNA, showing that the DNA and RNA samples were sufficiently free from protein (12). Taxol was obtained from Biolyse Pharmacopée (Port-Daniel, QC) and recrystallized from methanol. Other chemicals were of reagent grade and were used without further purification.

Preparation of stock solutions

Sodium-DNA or sodium-RNA was dissolved to 1% *w*/*v* (25 mmol polynucleotide (phosphate)/L) in an aqueous solution containing 0.1 mol NaCl/L and 1 mmol sodium cacodylate/L (pH 7.30) at 5 °C for 24 h with occasional stirring to ensure the formation of a homogeneous solution. The appropriate amount of taxol (0.3–25 mmol/L) was dissolved in a 20/80 methanol–water mixture. (Taxol is not soluble in H_2O or D_2O but is soluble in this methanol–water mixture.) The drug solution was then added dropwise to the DNA or the RNA solution to attain desired taxol/DNA(P) and taxol/RNA(P) molar ratios of 1/80, 1/40, 1/20, 1/10, 1/4, and 1/2 at a final DNA or RNA concentration of 0.5% *w*/*v* (12.5 mmol polynucleotide (phosphate)/L) for infrared measurements. For capillary electrophoresis, the taxol/polynucleotide ratios were 1/200 to 1/12 with a final DNA or RNA concentration of 1.25 mmol polynucleotide (phosphate)/L. The pH of the solutions was adjusted to 6.5–7.5, using NaOH solution.

FTIR spectra

Infrared spectra were recorded on a Bomem DA3–0.02 FTIR spectrometer equipped with a liquid-nitrogen-cooled HgCdTe (MCT) detector and a KBr beam splitter. The spectra of the taxol/polynucleotide solutions were acquired using a cell assembled with AgBr windows. Spectra were collected after 2 h incubation of taxol with the polynucleotide solution and were measured in triplicate (three individual samples of the same polynucleotide and taxol concentrations). For each spectrum, 100–500 scans were collected at a resolution of 2 to 4 cm^{-1}. The water subtraction was carried out using an NaCl (0.1 mol/L) solution at pH 6.5–7.5 as a reference (13). A good water subtraction was considered to be achieved when there was a flat baseline around 2200 cm^{-1}, where the water combination mode is located. This method yields a rough estimate of the subtraction scaling factor, but it removes the spectral features of water in a satisfactory way (13). Owing to the insolubility of taxol in aqueous solution, we did not perform the same experiments in D_2O solution. The difference spectra [(polynucleotide solution + taxol solution) – (polynucleotide solution)] were obtained using a

[3] Abbreviations: dA, deoxyadenylic acid; dC, deoxycytidylic acid; dG, deoxyguanylic acid; dT, thymidylic acid.

© 2004 NRC Canada

sharp DNA band at 968 cm^{-1} and an RNA band at 861 cm^{-1} as internal references. These bands, which are due to sugar C–C and C–O stretching vibrations, exhibit no spectral changes (shifting or intensity variations) upon taxol–polynucleotide complexation, and they were cancelled out upon spectral subtraction (Fig. 1). The intensity ratios of bands due to several DNA or RNA in-plane vibrations related to A–T, A–U, and G–C base pairs[4] and the PO_2 stretching vibrations were measured with respect to the reference band at 968 (DNA) or 861 cm^{-1} (RNA) as a function of taxol concentration with an error of ±3%.

Capillary electrophoresis

A P/ACE System MDQ (Beckman) with a photodiode array detector was used to study taxol–polynucleotide complexation. An uncoated fused-silica capillary of 75 µm i.d. and 50 cm effective length was used. The capillary was initially conditioned by washing with an NaOH (1 mol/L) solution for 30 min, followed by a 15-min wash with a more dilute (0.1 mol/L) NaOH solution. It was then extensively rinsed with deionized water and running buffer before use. Samples were injected using a voltage injection at 10 kV for 5 s. Electrophoresis was carried out at a voltage of 25 kV for 10 min using normal polarity. All runs were carried out at 25 °C. A stock solution of taxol (2 mmol/L) was prepared in 20% methanol. The capillary inlet and outlet vials were replenished after every five runs. The taxol binding experiments were performed on a sample buffer containing 15 mmol Tris-HCl/L, pH 7.2 (with 4 mmol NaCl/L and 20% methanol) using constant concentrations of DNA or RNA and various concentrations of taxol. The taxol solution (20% methanol) was added to the DNA or RNA solution to attain desired drug/polynucleotide (phosphate) molar ratios of 1/200 to 1/12. Each sample was allowed to equilibrate for 30 min and subjected to two separate runs. The electropherograms were monitored at 260 nm for taxol–DNA and taxol–RNA complexes and were collected and analyzed with the Beckman P/ACE Windows controller software.

Data analysis

The binding constants for taxol–DNA and taxol–RNA adducts can be determined by capillary electrophoresis, using Scatchard analysis (14, 15). The extent of saturation (R_f) of the polynucleotide was determined from the change of the peak heights of the polynucleotide in the presence of various concentrations of taxol by the following equation:

$$[1] \qquad R_f = \frac{h - h_0}{h_s - h_0}$$

where h is the peak height of DNA or RNA measured for any added taxol concentration, while h_0 and h_s correspond to the peak heights of free and drug-saturated DNA or RNA, respectively.

The binding constant K_b, given by

$$[2] \qquad K_b = \frac{[\text{taxol–polynucleotide adduct}]}{[\text{polynucleotide}][\text{taxol}]}$$

was determined by fitting the experimental values of R_f and taxol concentration to the equation

$$[3] \qquad R_f = \frac{K_b[\text{taxol}]}{1 + K_b[\text{taxol}]}$$

Rearrangement of this equation gives a convenient form for Scatchard analysis:

$$[4] \qquad \frac{R_f}{[\text{taxol}]} = K_b - K_b R_f$$

Results and discussion

Taxol–DNA complexes

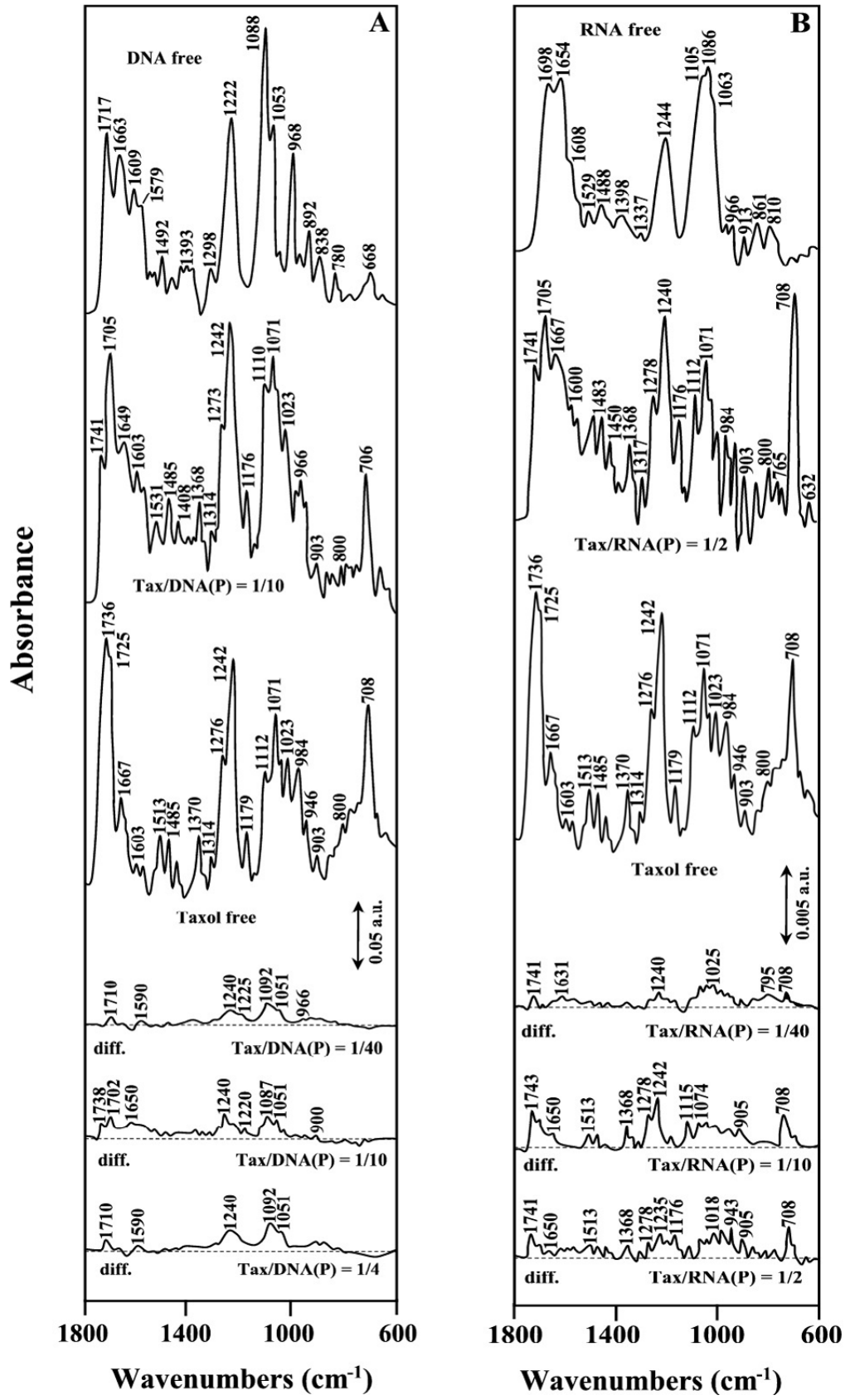
At a low taxol concentration (taxol/DNA ratio r = 1/80), no major drug–DNA interaction occurred, as indicated by the minor decrease in the intensity of several DNA bands related to the G–C, A–T, and backbone phosphate vibrational modes in the presence of taxol, such as the bands at 1717 (G), 1663 (T), 1609 (A), 1529 (C), 1492 (C), and 1222 cm^{-1} (asymmetric PO_2 stretching vibration) (16–25) (Fig. 2A). As drug content increased (r = 1/40 to 1/20), major increases in the intensities of the bands at 1717 (G) and 1222 cm^{-1} (phosphate) were observed (Fig. 2A). These results are supported by the difference spectra presented in Fig. 1A. The positive features at 1710 and 1225 cm^{-1} in the difference spectra of the taxol–DNA complexes (Fig. 1A, r = 1/40) have been attributed to drug interaction with the guanine-N7 reactive site and backbone PO_2 group. At r = 1/10, the interaction continues with the guanine bases and the PO_2 group, as well as with the thymine-O2 atom. Evidence for this comes from the further increase in the intensities of the bands at 1717 (G), 1663 (T), and 1222 cm^{-1} (phosphate) (Fig. 2A). These intensity changes were associated with positive features at 1702, 1650, and 1220 cm^{-1} in the difference spectra of the taxol–DNA complexes (Fig. 1A, r = 1/10). These spectral changes are due to taxol interaction with the guanine-N7 and thymine-O2 reactive sites and PO_2 groups, respectively. The other positive features centered at 1738, 1248, 1240, 1087, and 1092 cm^{-1} in the difference spectra of the drug–DNA complexes arise from the vibrational modes of taxol (26) and are not due to DNA vibrations (Fig. 1A). In the spectra of taxol–DNA complexes (Fig. 1A, r = 1/10), several other bands at 1741, 1707, 1603, 1485, 1368, 1273, 1242, 1176, 1110, 1071, 1023, and 706 cm^{-1} are also related to the taxol vibrational frequencies (26). The band at 1492 cm^{-1} (mainly cytosine) showed no spectral changes upon drug interaction, which is indicative of no participation of cytosine bases in taxol–DNA complexation (Fig. 2A).

At high taxol concentration (r > 1/10), a partial stabilization of the DNA helix occurs, which is associated with minor decreases in the intensities of the bands at 1717 and 1222 cm^{-1} and a minor increase in the intensity of the band at 1663 cm^{-1} (Fig. 2A). Similar infrared spectral changes were observed for DNA vibrations in cases in which metal–cation interaction induced helical stability (27–29). Recent calorimetric titration of several synthetic DNAs by

[4] Abbreviations: A, adenine; C, cytosine; G, guanine; T, thymine; U, uracil.

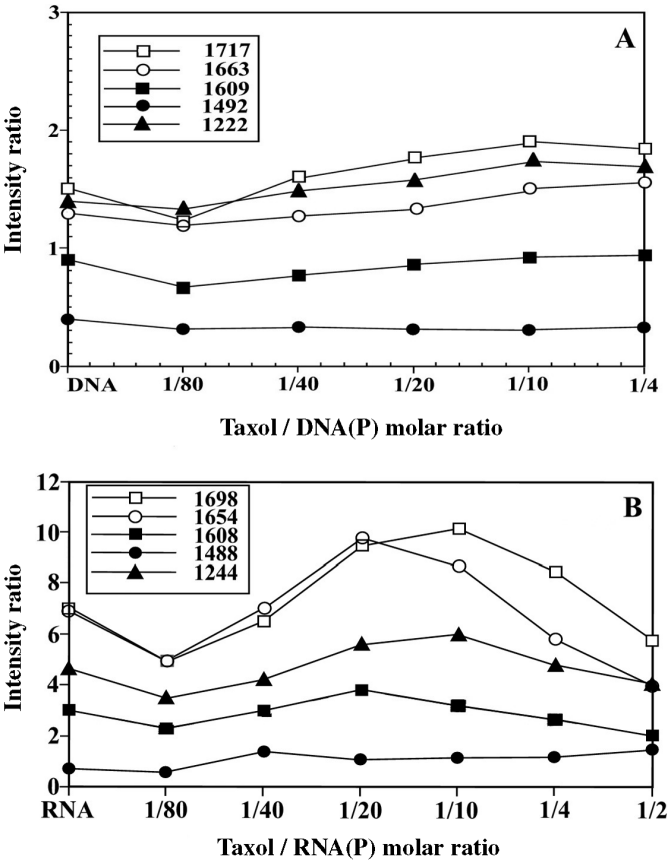
© 2004 NRC Canada

Fig. 1. FTIR spectra in the region of 1800–600 cm^{-1} for free calf-thymus DNA (A) and yeast RNA (B), free taxol, and taxol–polynucleotide adducts in aqueous solution at pH 6.5–7.5 (top three spectra) and difference spectra for taxol–polynucleotide adducts obtained at various taxol/polynucleotide (phosphate) molar ratios (bottom three spectra).



© 2004 NRC Canada

Fig. 2. Intensity ratio variations for several DNA and RNA in-plane vibrations as a function of taxol concentration. (A) Intensity ratios for the DNA bands at 1717 (G, T), 1663 (T), 1609 (A), 1492 (C, G), and 1222 cm^{-1} (PO_2 stretch), referenced to the DNA band at 968 cm^{-1}; (B) intensity ratios for the RNA bands at 1698 (G, U), 1654 (U), 1608 (A), 1488 (C, G), and 1244 cm^{-1} (PO_2 stretch), referenced to the RNA band at 861 cm^{-1}.



pacilitaxel also showed major increases in helical stability for poly(dA–dT) oligonucleotides (11).

Taxol–RNA complexes

No major taxol–RNA interaction occurred at low drug concentration (r = 1/80), as indicated by the minor decrease in intensity of bands due to RNA in-plane vibrations at 1698 (mainly G), 1654 (mainly U), 1608 (A), 1488 (mainly C), and 1244 cm^{-1} (asymmetric PO_2 stretch) (17–25) in the presence of taxol (Fig. 2B). As drug concentration increased (r = 1/40 and 1/20), major increases in the intensities of the bands at 1698, 1654, 1608, and 1244 cm^{-1} were observed (Fig. 2B). These intensity changes arise from major drug interaction with the guanine, uracil, and, to a lesser extent, adenine bases, as well as the backbone phosphate groups. However, the cytosine band at 1488 cm^{-1} exhibited no major spectral changes, which is indicative of no drug–cytosine interaction (Fig. 2B). Several positive features centered at 1741, 1743, 1631, 1513, 1368, 1278, 1235–1242, 1175, 1115, 1074, 1025, 1018, 905, and 708 cm^{-1} in the difference spectra of the taxol–RNA complexes arise from taxol vibrational frequencies (26) and are not due to the RNA vibrations (Fig. 1B).

Effects of complexation on taxol vibrational modes

Additional evidence regarding taxol–DNA and taxol–RNA complexation comes from the major shifts of the taxol vibrational bands. A strong band at 1736 cm^{-1} related to the drug's exocyclic carbonyl C=O stretching vibration (26) is shifted to 1741 cm^{-1} in the spectra of taxol–polynucleotide complexes (Figs. 1A and 1B; r = 1/10 and 1/2, respectively). Similarly, a shoulder band at 1725 cm^{-1} due to taxol ring carbonyl vibrations (26) is shifted to 1705 cm^{-1} upon DNA and RNA complexation. A band with medium intensity at 1667 cm^{-1}, related to the free taxol OH bending and C–N stretching vibrations (26), is also shifted toward lower frequency in the spectra of drug–DNA and drug–RNA complexes (Figs. 1A and 1B). The observed spectral changes are indicative of taxol–polynucleotide complexation through taxol's polar groups and alterations of its H-bonding network. The rearrangement of the drug's H-bonding network to a drug – nucleic acid H-bonding system may stabilize taxol–DNA and taxol–RNA adduct formation.

DNA and RNA conformations

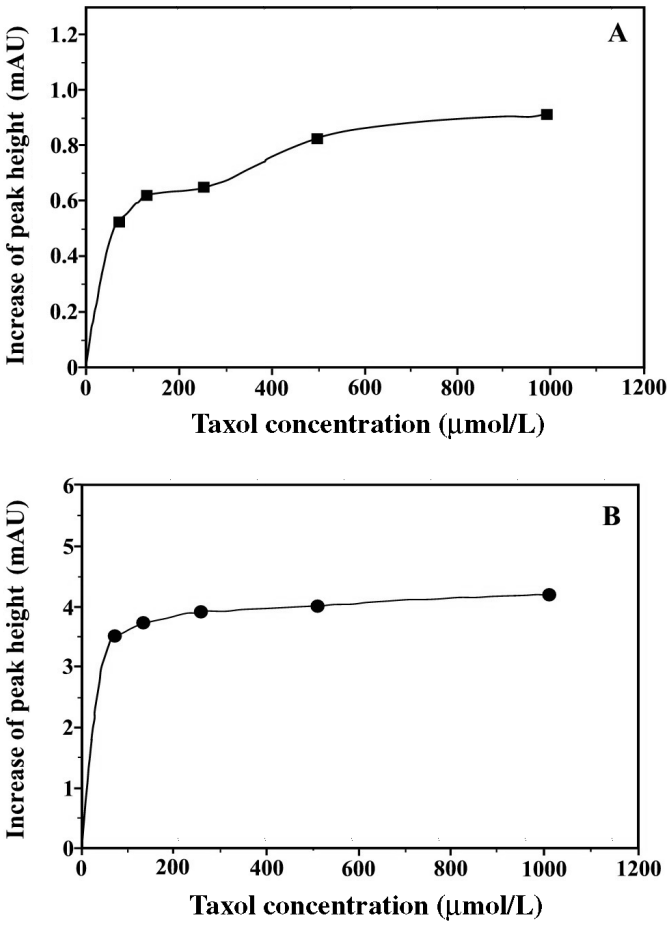
The infrared spectra also provided evidence that taxol–polynucleotide interaction leads to no major biopolymer conformational changes, with DNA maintaining the B-family structure and RNA maintaing the A-conformation. No major shifts of the B-DNA marker bands (22, 25, 29) at 1717 (G), 1222 (PO_2), and 836 cm^{-1} (phosphodiester) occurred in our experiments (Fig. 1A). Similarly, the marker bands for A-form RNA were observed at 1698 (G), 1244 (PO_2), and 861 and 810 cm^{-1} (phosphodiester modes) (Fig. 1B). When the B to A transition occurs, the DNA marker bands are shifted to 1710–1700, 1225–1240, and 825–800 cm^{-1}, respectively, and a new band appears at about 870–860 cm^{-1} (22, 25, 29). In the B to Z conformational transition, the sugar–phosphate band at 836 cm^{-1} appears at 800–780 cm^{-1}, and the guanine band is displaced to 1690 cm^{-1}, while the phosphate band shifts to 1216 cm^{-1} (22, 25, 29). Since no such spectral changes occurred in our experiment, DNA remained in the B-conformation upon interaction with taxol. Similarly, the RNA remained in the A-conformation in the taxol–RNA complexes, since there was no major shifting of the A-form RNA marker bands at 810 (phosphodiester mode), 1244 (PO_2 stretch), and 1698 cm^{-1} (mainly guanine carbonyl stretch) (22, 25, 29) upon drug complexation (Fig. 1B).

Stability of taxol–DNA and taxol–RNA adducts

The binding of the taxol–DNA and taxol–RNA complexes was also studied by capillary electrophoresis. Mixtures containing various concentrations of taxol and either DNA or RNA with molar ratios of 1/200 to 1/12 were prepared and subjected to electrophoresis, using an uncoated silica capillary of 75 μm i.d. (50 cm effective length) at 25 kV. The electropherogram was monitored at 260 nm for DNA and RNA in the run buffer (15 mmol Tris-HCl/L, pH 7.2, 4 mmol NaCl/L) at 25 °C. The peak heights of taxol–DNA and taxol–RNA adducts gradually increased as the taxol concentration increased and nearly reached a plateau at a

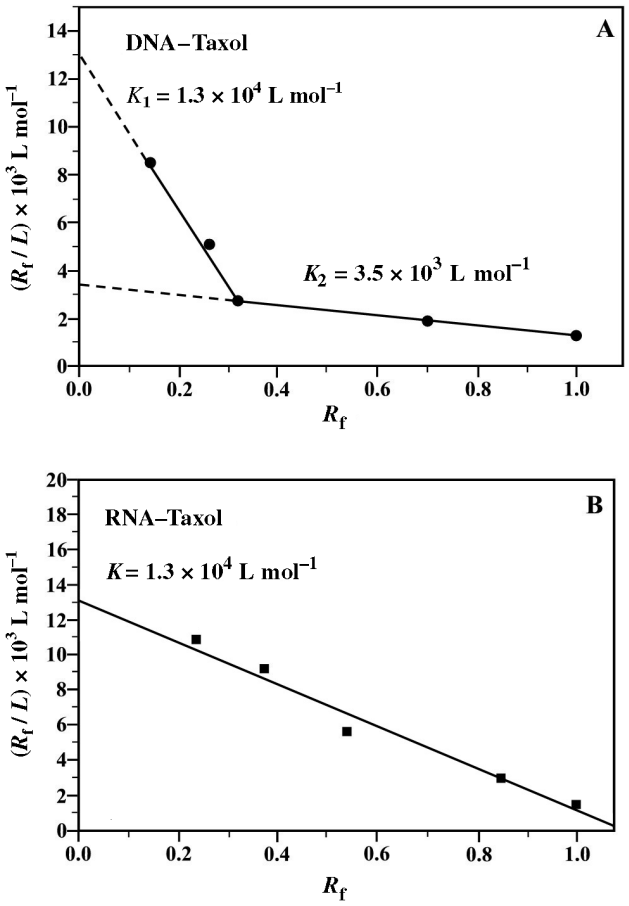
© 2004 NRC Canada

Fig. 3. Plots of increase of peak heights (in milliabsorbance units (mAU)) of taxol–polynucleotide complexes from capillary electrophoresis following incubation of a constant concentration of DNA (A) or RNA (B) (1.25 mmol phosphate/L) with various concentrations of taxol. Incubations were carried out in the run buffer (15 mmol Tris-HCl/L, pH 7.2, 4 mmol NaCl/L) at 25 °C for 30 min prior to capillary electrophoresis. The increase in peak height of the taxol–DNA and taxol–RNA complexes at 260 nm was determined by subtracting the peak height of the free DNA or RNA from that of each taxol–polynucleotide adduct.



taxol concentration of 1 mmol/L (Fig. 3). Based on these results, binding constants of the drug–DNA complexes were determined by Scatchard analysis as described in *Materials and methods*. As shown by the saturation curves in Fig. 3, the slope for the taxol–DNA complexes is biphasic (Fig. 3A), suggesting the presence of low-affinity and high-affinity binding sites for the drug–DNA complexes, whereas the slope for the taxol–RNA complexes is monophasic with one binding site (Fig. 3B). Scatchard analysis of the data for the taxol–DNA adducts showed high- and low-affinity sites with binding constants of $K_1 = 1.3 \times 10^4$ L mol^{-1} and $K_2 = 3.5 \times 10^3$ L mol^{-1}, respectively (Fig. 4A). Similar Scatchard analysis for the taxol–RNA complexes showed one binding site with $K = 1.3 \times 10^4$ L mol^{-1} (Fig. 4B). These results suggest that taxol binds at two distinct binding sites on DNA and at one binding site on RNA. Furthermore, it may be

Fig. 4. Scatchard plots for taxol–DNA (A) and taxol–RNA complexes (B). L = [taxol].



speculated that the stronger interaction is due to binding to G–C bases, while the weaker is due to binding to A–T bases.

Concluding remarks

Our capillary electrophoresis and spectroscopic results on DNA and RNA complexes with taxol showed that (*a*) taxol binds to the major and minor grooves of DNA with apparent binding constants of $K_1 = 1.3 \times 10^4$ L mol^{-1} and $K_2 = 3.5 \times 10^3$ L mol^{-1}; (*b*) taxol binds to RNA via G–C and A–U bases with $K = 1.3 \times 10^4$ L mol^{-1}; and (*c*) taxol–polynucleotide complexation results in a partial helix stabilization with no alterations of the B-DNA or A-RNA structure.

Acknowledgements

The financial support of the Natural Sciences and Engineering Research Council of Canada (NSERC) and FCAR (Québec) for this work is highly acknowledged.

References

1. E. Nogales, S.G. Wolf, I.A. Khan, R.F. Luduena, and K.H. Downing. Nature (London), **375**, 424 (1995).
2. P.B. Schiff and S.B. Horwitz. Nature (London), **277**, 665 (1979).
3. E. Mandelkow and E.-M. Mandelkow. Curr. Opin. Struct. Biol. **4**, 171 (1994).

© 2004 NRC Canada

4. J.J. Manfredi and S.B. Horwitz. Pharmacol. Ther. **25**, 83 (1984).
5. P.B. Schiff and S.B. Horwitz. Proc. Natl. Acad. Sci. U.S.A. **77**,1561 (1980).
6. R. Pazdur, A.P. Kudelka, J.K. Kavanagh, P.R. Cohen, and M.N. Raber. Cancer Treat. Rev. **19**, 351 (1988).
7. D. Song, L.F. Hsu, and J.L.-S. Au. J. Pharm. Sci. **85**, 29 (1996).
8. S.V. Balasubramanian and R.M. Straubinger. Biochemistry, **33**, 8941 (1994).
9. E. Hamel, A.A. del Campo, M.C. Lowe, and C.M. Lin. J. Biol. Chem. **256**, 11 887 (1981).
10. M.G. Solis Recendez, F. Bichat, F. Grossin, H. Barbault, D. Khayat, and G. Bastin. Paper presented at the 6th International Congress on Anti-Cancer Treatment, Paris, 6–9 February 1996. p. 105. [Abstr.]
11. G. Bischoff, U. Gromann, S. Lindau, E. Birch-Hirschfeld, R. Bischoff, C. Bohley, W.V. Meister, and S. Hoffmann. *In* Proceedings of the 11th Conversation in Biomolecular Stereodynamics, Albany, N.Y., 15–19 June 1999. Adenine Press, Schenectady, N.Y. 2000. p. 349.
12. J. Marmur. J. Mol. Biol. **3**, 208 (1961).
13. S. Alex and P. Dupuis. Inorg. Chim. Acta, **157**, 271 (1989).
14. I.M. Klotz and D.L. Hunston. Biochemistry, **16**, 3065 (1971).
15. I.M. Klotz. Science (Washington, D.C.), **217**, 1247 (1982).
16. J.-F. Neault and H.A. Tajmir-Riahi. Biophys. J. **76**, 1776 (1999).
17. D.E. DiRico Jr., P.B. Keller, and K.A. Hartman. Nucleic Acids Res. **13**, 251 (1985).
18. P.B. Keller and K.A. Hartman. Spectrochim. Acta Part A, **42**, 299 (1986).
19. M. Langlais, H.A. Tajmir-Riahi, and R. Savoie. Biopolymers, **30**, 743 (1990).
20. D.M. Loprete and K.A. Hartman. Biochemistry, **32**, 4077 (1993).
21. T.G. Spiro (*Editor*). Biological applications of Raman apectroscopy, John Wiley & Sons, New York. 1987. pp. 83–133.
22. E.B. Starikov, M.A. Semenov, V.Y. Maleev, and I.A. Gasan. Biopolymers, **31**, 255 (1991).
23. E. Taillandier and J. Liquier. Methods Enzymol. **211**, 307 (1992).
24. B. Prescot, W. Steinmetz, and G.J. Thomas, Jr. Biopolymers, **23**, 235 (1984).
25. M. Tsuboi. Appl. Spectrosc. Rev. **3**, 45 (1969).
26. M. Purcell, J.F. Neault, and H.A. Tajmir-Riahi. Biochim. Biophys. Acta, **1478**, 61 (2000).
27. H. Arakawa, R. Ahmad, M. Naoui, and H.A. Tajmir-Riahi. J. Biol. Chem. **275**, 10 150 (2000).
28. H.A. Tajmir-Riahi, J.-F. Neault, and M. Naoui. FEBS Lett. **370**, 105 (1995).
29. H.A. Tajmir-Riahi, R. Ahmad, M. Naoui, and S. Diamantoglou. Biopolymers, **35**, 493 (1995).

© 2004 NRC Canada

This special issue is dedicated to the memory of

Professor Gerhard Herzberg

to honour his outstanding contributions to spectroscopy.

Associate Editors: Rob Lipson and Benoit Simard

Ce numéro spécial est dédié à la mémoire du

Professeur Gerhard Herzberg

en reconnaissance de ses inestimables contributions au domaine de la spectroscopie.

Directeurs scientifiques associés : Rob Lipson et Benoit Simard

© 2004 NRC Canada

TRIBUTE / HOMMAGE

This issue of the *Canadian Journal of Chemistry* is dedicated to the memory of one of Canada's greatest scientists: Gerhard Herzberg. There have been many special journal issues honoring Herzberg, or "GH" as all his scientific colleagues called him. Nevertheless, the timing of this particular one is significant. GH was born 100 years ago this year, in Hamburg, Germany, on 25 December 1904. He passed away five years ago on 3 March 1999 at the age of 94, and in the time since his passing we have entered the 21st century. It therefore seems appropriate to take a "scientific snapshot" of what is happening in the field of high-resolution molecular spectroscopy. By doing so, we are able not only to acknowledge the tremendous advances that have been made but also to illustrate the debt the community owes to Herzberg and his profound contributions to the field.

The first anecdote in Boris Stoicheff's wonderful biography *Gerhard Herzberg: An Illustrious Life in Science* refers to a humorous statement Herzberg made when reminded that he shared a very famous birthday, coming as it did on Christmas Day: "Yes, with Sir Isaac Newton". Of course, his connection to Newton runs deeper than that of a mere chronological coincidence. In 1666, Newton was the first to observe a spectrum obtained from a prism, and for many laypeople that achievement is their main knowledge of spectroscopy, even if the word spectroscopy itself is not part of their vocabulary. It can be said that Herzberg's accomplishments link not only scientifically back through history to Newton but, even five years after his passing, continue to be relevant today. The reason for this is that GH's career spanned both the birth of quantum mechanics and the development of the laser. His work, insight, and influence, therefore, set the agenda for generations of spectroscopists.

Although GH was a scientific icon even during his lifetime, those who were privileged to work with him knew him to be a true gentleman, always accessible, deeply inquisitive, and caring. In the voluminous amount of correspondences with authors and referees from all around the globe that was exchanged during the past year in putting this issue together, numerous references were made to Herzberg's style and wisdom. It is clear that GH continues to be a tremendously positive influence.

Many people consider Herzberg to be a physicist; perhaps even GH did. Furthermore, his association with the astronomy community has also been nothing short of profound. Yet, it is probably fairest to say that the field of molecular spectroscopy rests very happily at the interface of physics, astronomy, and chemistry. For one thing, GH did win the Nobel Prize in Chemistry, and today many chemists from around the world are carrying out some of the most innovative and creative spectroscopy. For this reason, we are grateful to the Editorial Board of the *Canadian Journal of Chemistry* for recognizing GH's extraordinary contributions to the chemistry community in Canada and beyond, and for allowing these papers to be published in this venue. We are particularly grateful for the help provided by Judy Murdoch in the Editorial Office.

The quality of the papers in this issue is extremely high. Knowing that Herzberg's standards were the highest possible, we believe he would approve of the progress the spectroscopy community continues to make in building upon his legacy.

Rob Lipson and Benoit Simard

Le présent numéro de la *Revue canadienne de chimie* est dédié à la mémoire d'un des plus éminents scientifiques du Canada : Gerhard Herzberg. Certes, ce n'est pas la première fois qu'une revue honore Herzberg, ou « GH » comme l'appelaient affectueusement ses collègues. Cette année marque toutefois ce qui aurait été le 100e anniversaire de naissance de GH, qui est né à Hambourg, en Allemagne, le 25 décembre 1904, et marque également le 5e anniversaire de sa mort, à 94 ans, le 3 mars 1999. Nous avons donc cru probant, à la lumière des précédentes et en ce début de siècle, de « faire le portrait » du domaine de la spectroscopie moléculaire à haute résolution, dans son incarnation contemporaine. Par ce geste, nous levons le voile sur les avancées déterminantes dans ce secteur tout en rendant hommage aux inestimables contributions d'Herzberg à notre collectivité.

La première anecdote relatée par Boris Stoicheff dans sa fascinante biographie de GH intitulée *Gerhard Herzberg: An Illustrious Life in Science* atteste de l'humour fin d'Herzberg, qui, lorsqu'on lui rappelait qu'il partageait son anniversaire (le 25 décembre) avec un personnage d'exception, rétorquait volontiers : « Effectivement, avec Sir Isaac Newton! » La date de son anniversaire n'était toutefois pas le seul point en commun que GH avait avec Newton. Ainsi, en 1666, Newton a fait la première observation du spectre produit par un prisme. Pour plusieurs, cet événement constitue leur seul niveau d'intimité avec la spectroscopie, même s'ils ne connaissent peut-être même pas ce mot. Autant la science passée a influé sur les réalisations d'Herzberg, autant ses réalisations ont influé sur l'avenir de la science. En effet, pendant sa carrière, GH aura vu éclore la mécanique quantique et le laser. Ses travaux, ses réflexions et son influence sur ces découvertes marquantes aiguillent encore aujourd'hui le travail des spectroscopistes.

Bien que GH ait connu la gloire pendant sa carrière, ceux et celles qui ont eu la chance de le côtoyer admiraient son caractère charmant, affable, curieux et sensible. À maintes reprises, dans la vaste correspondance échangée pendant l'année de préparation du présent numéro honorifique, auteurs et arbitres du monde entier ont loué la finesse et la sagesse d'Herzberg. Même sur le plan humain, GH continue d'inspirer.

Plusieurs affirment qu'Herzberg était un physicien, ce à quoi GH ne s'objecterait probablement pas, et une étroite association avec la collectivité de l'astronomie ne saurait lui être contestée. Nous ne croyons pas nous tromper, cependant, en affirmant que la spectroscopie moléculaire se situe véritablement à l'intersection de trois disciplines : la physique, l'astronomie et la chimie. Après tout, GH a été lauréat de prix Nobel de chimie et nombreux chimistes du monde entier sont au premier rang des chercheurs et des innovateurs dans le domaine de la spectroscopie. Nous désirons remercier le Comité de rédaction de la *Revue canadienne de chimie* de reconnaître les exceptionnelles contributions de GH à la collectivité des chimistes du Canada et du monde entier en nous permettant de publier les articles qui suivent sous la bannière de la *Revue*. Nous sommes particulièrement reconnaissants de l'aide que nous a portée Judy Murdoch, du Comité de rédaction.

Les articles qui suivent ont de l'étoffe. Sachant qu'Herzberg jurait par la rigueur, nous croyons qu'il conviendrait, avec nous, que les progrès faits par ses successeurs demeurent nettement dans son sillage.

Rob Lipson et Benoit Simard

© 2004 NRC Canada

GERHARD HERZBERG PC CC[1]

25 December 1904 — 3 March 1999

Elected FRS 1951

BY BORIS P. STOICHEFF OC FRS

Department of Physics, University of Toronto, Toronto, Ontario, Canada M5S 1A7

Gerhard Herzberg, Nobel Laureate in Chemistry, had broad interests and achieved supreme accomplishments in physics, chemistry and astrophysics. The high points in his research were many. In physics they were the work on atomic hydrogen and helium, and evaluations of energy levels and constants of molecular hydrogen and its isotopes. His determinations of many molecular structures and discoveries of spectra of the free radicals CH_2 and CH_3, and of the Rydberg molecule H_3, were each outstanding contributions in chemistry. In astrophysics, his reproduction in the laboratory of the spectrum of CH^+, proving its presence in the interstellar medium, and of spectra of C_3 and H_2O^+ and their presence in comets, his observation of the quadrupole spectrum of H_2 and his discovery of hydrogen in the atmospheres of the planets opened up new applications of spectroscopy for our knowledge of the universe. His classic volumes on molecular spectra and molecular structures remain as encyclopaedias of molecular knowledge for all time. And his famous laboratory, the 'Temple of spectroscopy', served as a home for hundreds of scientists around the world, and helped to bring Canadian science to international prominence.

FAMILY AND EDUCATION, 1904–24

Gerhard Herzberg was born on 25 December 1904 in Osdorf, Pinneberg, a northwestern suburb of Hamburg, Germany. He was the younger son of Albin and Ella Herzberg, his brother Walter having been born in January of the same year. Gerhard was christened Gerhard Heinrich Friedrich Otto Julius on 9 July 1905, in the Lutheran St Gertrudkirche. This was a middle-class family; Albin Herzberg worked as the assistant manager of a small company that manufactured electrical products. The Herzberg genealogy has been traced back to 1573 through records of two Lutheran churches in the town of Langensalza (now Bad Langensalza) where 11 generations of Herzberg families had lived for almost 400 years. Albin was born

[1]Reprinted from Biogr. Mems Fell. R. Soc. Lond. **49**: 179–195 (2003)

© 2003 The Royal Society

there on 12 April 1872, in a family of five sisters and two brothers. His father, Franz Otto, and mother, Anna Sophia Christina (*née* Kürsten), were both born in Langensalza, where Franz Otto spent his life as a merchant. Albin was not a healthy youth: he suffered from dropsy, and became a vegetarian for the good of his health. He and Ella Biber were married in November 1902, Ella at 17 years of age and Albin 13 years her senior. Ella was born in Hamburg to Henrietta Maria and Rudolf Albert Biber, a master glazier.

Albin Herzberg was anxious that his two sons should have the best education possible and more advanced than was the custom in the Herzberg or Biber families. With Ella's interest in music, a piano was purchased and Walter began his serious study of the piano in what was to become his profession, while Gerhard took up the violin.

Just before Gerhard's graduation from the Vorschule, his father died in February 1915 at 43 years of age, leaving a young widow and the boys aged 10 and 11. On the advice of his teachers, Gerhard enrolled in the Realgymnasium of the Johanneum, and thanks to his excellent Vorschule record, he won a scholarship for his nine years at the Johanneum. He immersed himself in science studies and developed a particular love for astronomy. This led to his building a telescope and to his lasting fascination with the heavens. Along with his favourite subjects of mathematics, physics and chemistry, he studied Latin, French, Spanish and English, as well as the works of Goethe, Schiller, Kant and others. Gerhard formed a close friendship with Hans-Werner Döring and Alfred Schulz during the gymnasium years, and the three maintained lifelong relationships, while continuing their studies and professions in different cities.

What especially caught Gerhard's attention in science was a stimulating course in modern atomic physics during special classes, held at 7 o'clock each morning. Lectures on Bohr's model of the atom with spectacular demonstrations of the emission and absorption of light, and the spectra of different gases, entranced the young Gerhard. He was intrigued to learn that light was produced when electrons in atoms jumped from higher orbits to lower ones. These results remained embedded in his mind.

At Easter in 1924, Gerhard graduated with the 'Abitur', the prerequisite for entry into university, and, being one of the best students in his graduating class, he began to think about university. Astronomy was at the top of his list, but he became discouraged when the Director of the Hamburg Observatory thought it unwise unless he had private means of support. Gerhard then considered the more practical possibility of enrolling in a new programme of engineering physics recently introduced in several universities, and chose the Technische Hochschule in Darmstadt (now the Darmstadt University of Technology). By good fortune he was awarded a scholarship by the Stinnes Company, a huge corporation, which had worldwide holdings in mines, shipbuilding, paper mills and foundries.

Early career, 1924–35

Darmstadt, Göttingen and Bristol, 1924–30

All of Herzberg's undergraduate and graduate studies took place in Darmstadt. Although his original idea was to devote himself to engineering physics, he changed his mind and concentrated on basic research in physics. He came under the influence of Professor Hans Rau, whom Herzberg cherished as an exceptional mentor. Along with his heavy duties as Director of the Physics Institute and then as Rector, Rau supervised the research of several students, yet he did not add his name to their publications. As an undergraduate, Herzberg followed the current

literature, and saw in a new issue of *Annalen der Physik* Schrödinger's first paper 'Quantization as an eigenvalue problem'. This aroused his interest because he had just taken a course in partial differential equations and had learned about eigenvalues and eigenfunctions. He gave a talk about the paper in the Physics Colloquium; subsequently, Rau sent him to Freiburg, where Schrödinger was lecturing, and he had the thrilling experience of meeting Schrödinger. In 1927, Herzberg was granted the Dipl.Ing., and received the Müller–Alewyn–Plakette Medal as the best student. His first research resulted in one of the most complete spectra of the Balmer series of hydrogen to the ionization limit. This work was part of his first three papers, including a brief note on spectra of H_2, a subject to which he returned on many occasions in the next 50 years. He also mentioned the possibility of H_3, a radical he was to observe in 1979. In 1928 he was awarded the Dr.Ing., his thesis being on the afterglow of nitrogen and the spectra of N_2 and the ion N_2^+. This intriguing investigation decided him to pursue molecular spectroscopy as his life's work.

He then spent a very profitable postdoctoral year in Göttingen working on theoretical problems in the group of Max Born (FRS 1939), and on an experimental study of the far ultraviolet absorption spectra of methyl halides in the institute of James Franck (ForMemRS 1964). In Göttingen he met many of the giants of mathematics and science, including the younger members E.P. Wigner (ForMemRS 1970), F. Hund, W.H. Heitler (FRS 1948), L.W. Nordheim, V.F. Weisskopf, M. Goeppert, M.L.H. Delbrück (ForMemRS 1967), among others, all destined to become founders of twentieth-century science. While in Göttingen, Herzberg met Luise Oettinger, a physics student in Franck's group, and they married in December 1929. It was also in Göttingen that his acclaimed series of texts on atomic and molecular spectra and structures had their origin: students had asked him to give introductory lectures on atomic and molecular spectra because they had difficulty following discussions in the colloquia. G. Scheibe, a visiting professor from Erlangen, then suggested that he publish the lectures in a book. What began as an introductory volume of about 160 pages eventually blossomed into six volumes of more than 3200 pages, written over four decades.

Herzberg's research made use of several theoretical concepts. He showed that according to the correlation rules just enunciated by Wigner and E. Witmer, the dissociation energy of O_2 was wrong because the excited state could not arise from normal atoms. An important work with Heitler has all but been forgotten over the years. On examining the N_2 rotational Raman spectrum observed by F. Rasetti, they recognized that the even-numbered lines being stronger than the odd-numbered lines meant that nitrogen nuclei obeyed Bose rather than Fermi statistics, contrary to the theory of that time. Although this result was the first indication that electrons are not present in nuclei, Heitler and Herzberg explained the discrepancy by suggesting that electrons in the nucleus lose their spin and thus their influence on statistics of nuclei. This result was clarified three years later with the discovery of the neutron by J. (later Sir James) Chadwick FRS. Herzberg also became interested in Hund's theory of molecular orbitals and produced a paper on bonding and antibonding electrons. This caught the attention of J.E. (later Sir John) Lennard-Jones (FRS 1933) of the University of Bristol, who was visiting Göttingen, and he offered Herzberg a research fellowship in Bristol.

In Bristol, a grating spectrograph was built with the assistance of H.W.B. Skinner (FRS 1942), and spectra of P_2, CP, N_2, C_2H_2 and CH_2O were investigated, some with the help of Luise. Herzberg found a striking case of predissociation in the spectrum of P_2: he observed a breaking-off of rotational structure in two successive vibrational levels and was able to determine the dissociation energy of P_2. Beginning with this study, he became well versed in the concept of

predissociation and wrote a review on this topic. He attended his first of many Faraday Society conferences, visited universities in London and became acquainted with many English scientists. At that time, he completed the procedure of *Habilitation* and was given a position as *Privatdozent* in Darmstadt, to build a spectroscopy laboratory, after his year in Bristol.

Privatdozent in Darmstadt, 1930–35

Back in Darmstadt in 1930, Herzberg built two grating spectrographs, one of 3 m length for the visible and infrared regions, for which he obtained an excellent grating from R.W. Wood ForMemRS, and a 2 m vacuum instrument for the far ultraviolet. He was an invited speaker at many conferences, one being the prestigious 'Week of Physics' on spectra of polyatomic molecules, organized by Peter Debye (ForMemRS 1933) in Leipzig. The other speakers were R. Mecke, F. Rasetti, G. Placzek, H. Sponer, V. Henri and R. de L. Kronig. There he met Werner Heisenberg (ForMemRS 1955), Michael Polanyi (FRS 1944) and Edward Teller for the first time. With Hund present, Herzberg decided to present his ideas on bonding and antibonding electrons. Discussions with Teller led to a two-year collaboration on the vibrational structure of electronic transitions in polyatomic molecules. The main result was that in allowed electronic transitions, totally symmetric vibrations are predominantly excited, whereas transitions with changes in non-totally symmetric vibrations are weak. In 1931, Herzberg became an assistant to Rau, with responsibilities to supervise students. He launched an ambitious research programme with students, postdoctoral fellows from the USA, China and Sweden, a senior assistant from Germany, and Luise.

By photographing the solar spectrum to 12 900 Å, the forbidden $^1\Delta_g$–$^3\Sigma_g$ (magnetic dipole) bands of O_2 were found. New ultraviolet spectra of O_2 were observed at low resolution, consisting of a progression of single Q branches ($^3\Sigma_u^+$–$^3\Sigma_g^-$ transitions, $\Delta K = 0$), now known as the 'Herzberg bands'. Other diatomic molecules investigated were PN, CP, HCl and BeO (which Luise had started in Bristol, completed at high resolution in Darmstadt, and submitted for her PhD thesis to the University of Frankfurt in 1933). Spectra of the polyatomic molecules CO_2, H_2O, HCN, C_2H_2 and CH_3CCH were obtained in the photographic infrared, and of C_2H_2, H_2CO and B_2H_6 in the ultraviolet. Fluorescence spectra of H_2CO confirmed the selection rules proposed by Herzberg and Teller.

Herzberg's laboratory quickly became known internationally and attracted many visitors, including R.S. Mulliken (ForMemRS 1967) and F.A. Jenkins from the USA. With the discovery of deuterium by H.C. Urey (ForMemRS 1947) in 1932, Herzberg recognized its importance for studies of molecular structure. When John W.T. Spinks, from the University of Saskatchewan in Saskatoon, Canada, spent a year with Herzberg, they succeeded in concentrating a spoonful of heavy water by electrolysis, sufficient to make samples of deuterated HCl, HCN, H_2O, C_2H_2 and CH_3CCH, and obtained their spectra.

With the Nazis in power in 1933, life became difficult for the Herzbergs because Luise was of Jewish descent. A year later, Herzberg was informed that his appointment would not be renewed, and he realized he would have to leave Germany. He sought the assistance of the emergency committees in London and Zurich, and found that positions in all six continents were scarce because of the Depression, and those that had been available were filled by refugees. Finally, through the efforts of Spinks, back in Canada, he was offered a guest professorship for two years at the University of Saskatchewan, funded by the Carnegie Corporation. He accepted and arrived there in September 1935. Just before leaving Germany, Herzberg submitted the manuscript of *Atomspektren und Atomstruktur* for publication.

Research professor, University of Saskatchewan, 1935–45

The University of Saskatchewan was one of the most unlikely universities to which someone of Herzberg's stature might have gone. It had a faculty of about 100, 5 in physics, a student enrolment of 2000, and was situated in a city with a population of about 45 000, in the middle of the Canadian prairies, hundreds of miles away from any major city. The university lacked equipment for spectroscopic research, and funds for apparatus or additional staff were almost non-existent.

Within two weeks of his arrival, Herzberg was teaching two courses, one in elementary mechanics to undergraduates and the other in atomic and molecular spectroscopy to students in the Master's degree programme, the highest degree given at the university. To his pleasant surprise, he found the standards at the university to be remarkably high, with top-quality, hard-working students. Among the students in his first graduate class were William G. Schneider (FRS 1962), who was destined to serve as President of the National Research Council in Ottawa from 1967 to 1980, and Henry Taube (ForMemRS 1988), who joined Stanford University and received the 1983 Nobel Prize in Chemistry for his work on electron transfer reactions. Within three months, the Head of the Physics Department and the President could hardly believe their good fortune in having acquired Herzberg. He was given a permanent faculty appointment as Research Professor, and he and Luise decided to make Canada their home and to start a family. Paul Albin was born in 1936 and Agnes Margaret two years later.

An early task was to read the galley proofs of *Atomspektren und Atomstruktur*, which was published in 1936. An English version, *Atomic spectra and atomic structure*, was translated with the help of Spinks, and appeared in 1937. Herzberg then completed *Spectra of diatomic molecules*, the first of three volumes in the series *Molecular spectra and molecular structure*, published in German and in English in 1939, before World War II erupted.

An important result for molecular structure was Herzberg's discovery in 1937 that the length of the C–C single bond was dependent on the number of adjacent atoms. When spectra of methylacetylene (CH_3CCH and CH_3CCD) taken in Darmstadt were analysed, the C–C bond length was found to be 1.460 Å, considerably shorter than the 1.543 Å accepted for ethane, much to the surprise of Linus Pauling (ForMemRS 1948), who accepted this result only after his colleague R.M. Badger confirmed it by electron diffraction. In C_2H_6 the C–C bond is surrounded by three single bonds on each side, and in methylacetylene by three single bonds on one side and a triple bond on the other. Herzberg was to continue such studies for the remaining C–C and C=C bonds.

He was regularly invited to attend conferences in Canada and the USA. A small meeting on interstellar molecules, organized by Otto Struve (FRS 1954), Director of the Yerkes Observatory, in 1941 was attended by Mulliken, Teller and H. Beutler, from the Chicago campus, and P. Swings, Herzberg, and staff of the Observatory. The purpose was to discuss a series of lines near 4000 Å, observed in absorption spectra of distant stars by T. Dunham and W.S. Adams (ForMemRS 1950) at Mount Wilson Observatory. One of the lines had been identified as being due to CH; however, four other lines posed a problem. Swings thought they might belong to an ionized molecule like C_2^+, CH^+, CN^+, NH^+ or NO^+, and Mulliken suggested the free radical CH_2. Herzberg and Teller favoured CH^+: they surmised it would have an electronic band near 4000 Å because of the similarity of CH^+ to iso-electronic BH, whose spectrum was in this wavelength region.

Herzberg attempted to reproduce these unidentified lines in the laboratory. He had been

awarded $1500 by the American Philosophical Society to build a 6 m grating spectrograph, which was now ready. He also had a good student, Alex E. Douglas (FRS 1970), who was later instrumental in assisting Herzberg in establishing the Spectroscopy Laboratory in Ottawa. A discharge in helium with a trace of benzene produced a molecular spectrum in the 4000 Å region. Closer examination showed that three R(0) lines, the only lines expected to occur at the extremely cold temperatures of space, were exactly at the positions of the unidentified interstellar lines. Further experiments convinced Herzberg and Douglas that the spectrum was due to the ion CH^+. This was the first molecular ion to be identified in the interstellar medium. (Later, Douglas found that the fourth line was also an R(0) line of a CH^+ band.)

Herzberg's work on the free radical CH_2 began on receiving a letter and spectrum from Swings: 'We observed in a comet a group of features around 4050 Å, and we can't understand what they are'. Herzberg, who was then writing *Infrared and Raman spectra of polyatomic molecules*, thought the spectrum looked like a perpendicular band of a nearly symmetrical top molecule, and had the idea that it might be due to CH_2. He reproduced the spectrum with an interrupted discharge in CH_4 and assumed that it was due to CH_2, but did not rule out CH_3 or CH_4. This result on the comet bands and the identification of CH^+ in interstellar space quickly established Herzberg's reputation among astronomers. Even so, about seven years later, his identification of the 4050 Å group with CH_2 was shown to be wrong; this induced him to search for the spectrum of CH_2 until he discovered it two decades later. He and Douglas later showed the 4050 Å group to be due to C_3.

In 1942, Herzberg presented his idea of *l*-type doubling. He showed that infrared spectra of C_2H_2, CO_2, and HCN exhibited a splitting of Π vibrational levels into two components, the double degeneracy being removed by the interaction of rotation and vibration. His simple theoretical treatment caused some controversy, but was later accepted to be correct. During his 10 years in Saskatchewan, Herzberg supervised the research of 10 students who received their Master's degrees with studies of B_2, C_2, S_2, CH, CN, CO, NO, BCl, B_2H_6 and active nitrogen. After the war he learned that two of his students, J.G. Fox and R.B. Sutton, had worked on the atomic bomb project at Los Alamos, New Mexico.

Although technically 'an enemy alien', Herzberg was invited to investigate spectra of explosives. He signed an Oath of Secrecy and attended classified meetings on explosives in the USA with G.B. Kistiakowski, H. Eyring, G. Gamow and B. Crawford Jr, among others. As Herzberg was to say later, the explosives work was challenging and interesting scientifically, but it did not help to end the war.

On completing *Infrared and Raman spectra of polyatomic molecules*, Herzberg began taking singing lessons for relaxation. His resonant bass-baritone voice was suited to lieder by Schubert and Brahms and some arias by Mozart and Verdi, which he especially enjoyed.

Professor of Spectroscopy, Yerkes Observatory, 1945–48

Just before the end of World War II, Herzberg was surprised to receive a letter from Otto Struve inquiring whether he would be interested in joining the Yerkes Observatory of The University of Chicago to set up a spectroscopy laboratory. This was an opportunity to work with the major astronomers in the world and to concentrate on molecules of astrophysical interest. He accepted a position as an associate professor, then as Professor of Spectroscopy, arrived in Williams Bay in September 1945, and spent three productive years there. His col-

leagues at Yerkes were Otto Struve, G.P. Kuiper, W.A. Hiltner, W.W. Morgan and Subrahmanyan Chandrasekhar FRS, all distinguished astronomers. He also had the opportunity to continue his association with Mulliken, Beutler, Teller and Franck at the Chicago campus. Herzberg valued highly his close and lasting friendship with Chandra (Chandrasekhar).

To emulate planetary atmospheres, Herzberg built a cell 22 m long, running under the ceiling, through almost the whole length of the observatory basement. This iron pipe was fitted with concave mirrors, which could be aligned for multiple traversals of the cell to provide an extremely long absorbing path. This made possible the study of absorption spectra of diatomic and polyatomic molecules of astrophysical interest, and others for determination of their structures. Spectra of O_2, CO, NO, CO_2, N_2O, C_2H_2, CH_4, CHF_3, CH_3I and CH_3CF_3 were investigated with the assistance of Luise, Harold J. Bernstein from the National Research Council in Ottawa, S.P. Sinha from Patna University in India, and two graduate students, R. Narahari Rao and John G. Phillips.

The observation of the quadrupole spectrum of hydrogen turned out to be Herzberg's major achievement at Yerkes Observatory. He had predicted 10 years earlier that large amounts of H_2 in planetary atmospheres would make up for the weak quadrupole spectrum and was determined to find this spectrum of hydrogen in laboratory experiments. For the 3–0 band in the 8000–8600 Å region he used a path length of 5370 m and a gas pressure of nine atmospheres, and observed four lines in their predicted positions. Another four lines of the 2–0 band were found in the region 11 300–12 400 Å. As expected, all eight lines were extremely sharp. Twelve years later, the H_2 quadrupole spectrum was observed in the atmospheres of Jupiter and Uranus. Later still, its emission spectrum was observed in the Orion nebula and in planetary ionospheres, and superluminous galaxies.

In spite of the many research activities and a light teaching load, Herzberg missed the daily contact with humanists, chemists, and physicists that he had enjoyed in Saskatoon. He and Luise realized they were homesick for Canada, and let friends know they were eager to return. John Spinks mentioned their hopes to C.J. Mackenzie FRS, President of the National Research Council of Canada (NRC) in Ottawa, and E.W.R. (Ned) Steacie (FRS 1948), Director of the Division of Chemistry, and they quickly set into motion the means for enticing Herzberg to join the NRC. He was invited to establish a major spectroscopy laboratory for basic research, with an appointment to the new and highest non-administrative position of Principal Research Officer. This was an opportunity not to be missed, and one in which he would realize his full potential. He accepted in July 1947 for arrival a year later, when he felt he would have adequately discharged his obligations to Yerkes Observatory.

A HALF-CENTURY AT THE NATIONAL RESEARCH COUNCIL, OTTAWA, 1948–94

The NRC had its beginnings in 1916 as an Advisory Council appointed by the Government to promote and undertake scientific and industrial research for national development. It enjoyed arm's-length treatment from the Government and became a major scientific resource for the Armed Services during World War II, winning strong support for increased research activity in peacetime. Under these favourable conditions, Herzberg was given complete freedom in research, and substantial space and funds for staff and equipment. The availability of devices and techniques developed during the war, such as radar, sensitive detectors for infrared radiation, and photomultipliers for the visible and ultraviolet regions, made this an ideal time at

which to develop a spectroscopy laboratory. Herzberg rose to the challenge and established a major laboratory that quickly won acclaim for its many accomplishments in atomic and molecular spectroscopy.

A month after his arrival in Ottawa, Herzberg was informed that R.W. Boyle, Director of the Division of Physics, would retire in October, and was urged to take the position. Because his main interest in joining the NRC was research and not administration, he finally accepted when L.E. Howlett agreed to be the Assistant Director, to lead the applied research groups and to take care of the day-to-day administration of the Division of Physics. Herzberg served as Director from 1949 to 1955, when the Division of Physics was split into the Division of Pure Physics and the Division of Applied Physics. Howlett took over the latter and Herzberg directed the former until his retirement from administrative duties at age 65 in 1969. As Herzberg often noted to visitors, 'I am the Director but I don't direct': he provided the physics groups with the best facilities possible for scientists to work on problems of their own choosing, and encouraged them to include postdoctoral fellows in their programmes and to invite leading scientists from around the world to visit, give lectures and collaborate in research. He also initiated research in several new areas, including low-temperature and solid state physics under the leadership of the dynamic D.K.C. MacDonald (FRS 1960), theoretical physics under Ta-You Wu, and laser and plasma physics headed by S.A. Ramsden.

The enlightened leadership provided by Herzberg in physics, and by Steacie as Director of the Division of Chemistry (and then as President of the NRC from 1952 to 1962), was instrumental in bringing world recognition of the NRC. While continuing an active research programme and attending scientific conferences usually as a keynote speaker, Herzberg served on many international committees looking after problems in notation, standards and related matters in spectroscopy, and kept in constant touch with colleagues all over the world. In the midst of these many activities, Herzberg always found time to make the way a little easier for fellow scientists, young and old, by writing letters of encouragement, making recommendations about jobs and advancements, and nominating deserving candidates for awards. Such unselfish interest in other people's careers was unique.

As Canadian politicians jumped on the 'world bandwagon' of the 1960s, for development of coherent national science policies to help in solving social and economic problems, and criticized the NRC and its presidents past and present, the usually mild-mannered Herzberg ventured out of his laboratory to speak in the defence of science. He argued vigorously for the freedom of choice for scientists and against the encroaching bureaucratic control of science and technology. His pleas for freedom were not confined to scientists and the NRC, but embraced human rights, and he persistently appealed on behalf of unjustly detained dissidents worldwide, even participating in demonstrations in front of the Soviet Embassy in Ottawa on several occasions.

Herzberg received numerous awards, the most prestigious being the Faraday and Royal Medals, and in 1971 the Nobel Prize in Chemistry. The death of Luise five months before the announcement of the Nobel Prize was a severe blow. She had admirably managed a busy household, yet had the energy to work and publish papers with Gerhard, and provide figures and tables of molecular data for his texts. Since the 1950s she had performed independent research on solar spectra and photochemical processes in the upper atmosphere at the Dominion Observatory and then the Radio Physics Laboratory. With her death, Canada lost one of its few accomplished women physicists.

Among the many honours that Herzberg received from his adopted country, he was especially

pleased to receive his first honorary degree from the University of Saskatchewan, to be appointed a Companion of the Order of Canada (CC) in 1968 and a Member of the Queen's Privy Council for Canada in 1992, in recognition of his outstanding contributions to Canada. As a Privy Councillor, his title was The Honourable Gerhard Herzberg PC.

At a conference on 'Free radical spectroscopy', held in honour of Herzberg's 65th birthday, the NRC's President W.G. Schneider announced that Herzberg would be appointed Distinguished Research Scientist and would continue his research at the NRC. This occasion was the first in a series of birthday conference celebrations, held every five years in Canada, the one in 1994 being the last that Herzberg was able to attend. On his 70th birthday in 1974, the creation of the Herzberg Institute of Astrophysics (HIA) was announced by Schneider. In March 1972, Herzberg married Monika Tenthoff, the niece of his gymnasium friend Alfred Schulz.

Herzberg continued with his research activities, completed *Electronic spectra of polyatomic molecules*, the last of his trilogy on *Molecular spectra and molecular structure*, and published *The spectra and structures of simple free radicals*, based on his George Fisher Baker Lectures at Cornell University. Extensive tables of data on electronic states and constants of over 900 diatomic molecules and ions were published in 1979 with K.P. Huber in *Constants of diatomic molecules*. After a few mild heart attacks in the 1970s, Herzberg began to reduce his travels but maintained an active research agenda. He also found the energy to publish revised editions of all three volumes of *Molecular spectra and molecular structures* in 1989–91. As he approached his 90th birthday, his health and failing eyesight prevented him from maintaining an active eight-hour workday, and he proposed to retire. A ceremonial retirement tribute took place at the NRC on 13 December 1994, his official retirement date being 31 December.

The Spectroscopy Laboratory

Herzberg was fortunate in being able to recruit Alex Douglas as his principal assistant in the development of the Spectroscopy Laboratory. Thus began the fruitful collaboration, lasting for 33 years, which Herzberg often emphasized: 'Douglas made a towering contribution to the laboratory'. They planned to achieve the highest resolution possible, with access from the longest to the shortest wavelengths for the study of atomic and molecular spectra. Four grating instruments were designed and built to cover the visible, infrared and far ultraviolet regions: a 7 m spectrograph for 2000–12 000 Å; an infrared spectrometer beyond 12 000 Å, equipped with sensitive detectors; and 3 m and later 10 m instruments for the vacuum ultraviolet below 2000 Å.

Others in the founding staff included Donald A. Ramsay (FRS 1978), who initially helped Herzberg in developing the flash-photolysis technique, Hin Lew, whose interests were in atomic and molecular beams, and Cecil C. Costain, who established the microwave laboratory. In time, each had the assistance of an expert technician and two postdoctoral fellows, and given the means for inviting visiting scientists, and encouragement to attend conferences to report on research. Also, on average about six postdoctoral fellows (PDFs) participated each year. By 1975, over 130 PDFs from the best laboratories around the world had spent up to two years in the Spectroscopy Laboratory, and more than 100 visiting scientists had worked there for periods of four months or more. Over the years a small number of PDFs were offered permanent appointments: I was the first of the lucky ones, followed by John W.C. Johns, Takeshi Oka (FRS 1984), Klaus P. Huber and A. Robert W. McKellar, mainly involved in experimen-

tal work, and theorists Jon T. Hougen, Philip R. Bunker and James K.G. Watson (FRS 1987), among others.

Scientific life in the Spectroscopy Laboratory was intense, with excellent equipment and facilities at hand, and much exciting research was done. Herzberg gave guidance to the group by his own inimitable example of working long hours, six days a week. Neither he nor Douglas directed our research, and each PDF was free to collaborate with a staff member or to work independently. There were weekly group meetings, seminars and colloquia by distinguished visitors, and daily afternoon tea, with all members taking part in discussions on science, and sometimes on hockey or cricket. In the lively environment created by Herzberg and Douglas it is easy to understand that, in the words of the Nobel citation, 'A noted English chemist has said that the only institutions which have previously played such a role were the Cavendish Laboratory in Cambridge and Bohr's institute in Copenhagen'.

Scientific research

Within a few years the Spectroscopy Laboratory was in full swing, with numerous investigations on a variety of topics. The spin and magnetic moments of nuclei were measured, and the interaction between nuclear and electronic motions was studied; spectra of many diatomic and polyatomic molecules, ions and free radicals were obtained, many for the first time; and a variety of forbidden transitions were investigated. These studies were important for elucidating ground and excited states and structures and for developing and confirming atomic and molecular theory, and were often significant for astrophysics.

Herzberg's own interests and experiments in molecular spectroscopy continued on a broad front, and he also became involved with some problems in atomic spectroscopy and structures. The first experiment carried out in the new laboratory was the determination of the spin and statistics of the ^{3}He nucleus. Herzberg and Douglas established the value $\frac{1}{2}$ for the spin and Fermi statistics from the 3:1 intensity alternation of odd to even rotational lines in the spectrum of $^3He_2$, in agreement with theory. Herzberg began a lengthy programme of accurate measurements of absolute wavelengths for spectra of D, He and He^+ in the vacuum ultraviolet to test theoretical predictions for Lamb shifts. For the 1S level of deuterium he obtained the value 0.264 cm^{-1}, in agreement with the theoretical value 0.2726 cm^{-1}. Experimental values for the ground states of ^{3}He and ^{4}He were also in general agreement with theory (to ± 0.05 cm^{-1}). Measurements were also made for excited states of He, He^+ and Li^+. Because some of these determinations were dependent on theoretical values of specific energy levels and ionization potentials, which turned out to be less reliable than assumed, Herzberg became involved with Chandra, in lengthy computations of He, Li^+ and O^{6+}, using variational methods.

From his earliest work with hydrogen, Herzberg realized that experimental data on H_2 and its isotopes would be of fundamental importance for astrophysics and for testing quantum theory. He began a concerted study of hydrogen spectra and reported the results in over 40 publications. Because HD has a dipole moment, although small, he had suggested in 1938 that its spectrum could be used to detect deuterium in planetary and stellar atmospheres. In 1950 he observed the 3–0 and 4–0 bands, and later the 1–0 band in the infrared. Two decades later, HD was detected in a spectrum of Jupiter.

In 1949 Kuiper found broad features in spectra of Uranus and Neptune, and asked Herzberg whether he had any idea of their origin. A feature at 8270 Å agreed closely with a line of the 3–0 spectrum of H_2 but was clearly not a quadrupole line because these are extremely sharp. He surmised that it could be caused by pressure-induced absorption (an effect discovered at

the University of Toronto a year earlier), and began experiments with H_2 at high gas pressure in a long absorbing path cooled to liquid nitrogen temperature. He observed a broad 3–0 band, in agreement with the spectra of Uranus and Neptune, and established for the first time the presence of hydrogen in extraterrestrial atmospheres.

The improved techniques in high-resolution spectroscopy at the NRC provided precise values of energy levels of the ground and excited states of hydrogen and its isotopes. To test quantum theory, comparisons of experimental and *ab initio* values were made of rotational and vibrational energy levels, dissociation energies and ionization potentials. From spectra with the 10 m ultraviolet spectrograph, Herzberg and colleagues obtained precise values for the dissociation energy and ionization potential, in good agreement with theoretical values. He continued the investigations of electronic spectra of hydrogen and its isotopes into the 1990s and obtained improved ionization potentials, as well as detailed data of high orbital angular momentum states for H_2 and D_2. Many of these investigations were performed with the assistance of PDFs and visiting scientists.

Along with the above studies, Herzberg concentrated his efforts on obtaining the spectra of short-lived free radicals, particularly methylene (CH_2) and methyl (CH_3). Although these building blocks of organic molecules had long been postulated as intermediates in chemical reactions, Herzberg argued that he wanted to observe their spectra before he could feel entirely convinced of their presence in chemical reactions, flames, explosions or discharges. His pursuit of this question after his first involvement with CH_2, 17 years earlier, culminated in what undoubtedly became one of his most notable and satisfying achievements.

With the help of his superb technician Jack Shoosmith, Herzberg explored several different experimental approaches, chose the technique of flash photolysis and succeeded in obtaining spectra of CH_3 from the parent molecules $Hg(CH_3)_2$, and $(CH_3)_2CO$ in 1956. Proof that these were spectra of CH_3 was established by using partly deuterated samples, which produced four slightly shifted bands arising from the isotopic species CH_3, CH_2D, CHD_2 and CD_3. Two years later, a spectrum of CH_2 was found in the extreme ultraviolet region at 1415 Å by using the parent molecule CH_2N_2. Further experiments with deuterated compounds showed three slightly shifted bands (due to CH_2, CHD and CD_2), proving that the radical had two H atoms. The spectrum with $^{13}CH_2N_2$ established the presence of a single carbon atom. Analyses of the spectra led to a nonlinear symmetrical structure with C–H distances of 1.071 Å and an H–C–H angle of 140°. The discovery of the spectra of CH_2 and CH_3 was undoubtedly the criterion leading to the award of the Nobel Prize in Chemistry in 1971, with the citation 'for contributions to the knowledge of electronic structure and geometry of molecules, particularly free radicals'. Four decades later, CH_2 was detected in the interstellar medium, and CH_3 in the atmospheres of Saturn and Neptune and the interstellar medium.

Spectra of over 30 free radicals were discovered and studied by Herzberg, Ramsay and other members of the laboratory during the 1950s and 1960s. Their use of flash photolysis coupled with the superb spectrographs built at the NRC changed in a dramatic manner the field of free radicals from unobservable chemical intermediates to well-known molecules, and provided new molecules for study. Investigations with a variety of sources, resulted in the excitation of spectra of many molecular ions, C_2^+, CO_2^+, N_2O^+, $C_4H_2^+$ and H_2S^+, and in the discovery of the first discrete spectrum of a gaseous negative molecular ion, C_2^-.

With its studies of spectra of free radicals and molecular ions, and Herzberg's interests in molecular astrophysics, the Spectroscopy Laboratory was an integral part of the HIA. The

study of molecular ions provided an important confirmation of early ideas that comets consisted mainly of ices, including water (H_2O). Because the water molecule does not exhibit an emission spectrum, various groups had attempted in vain to obtain the laboratory spectrum of H_2O^+ to compare with spectra of comets. At Herzberg's suggestion, Hin Lew succeeded in obtaining a rich and complex emission spectrum in the visible region, just as astronomers were awaiting the reappearance of Comet Kohoutek. When spectra of the tail of the comet were sent to Herzberg by colleagues in Italy and Israel, he and Lew immediately identified parts of the spectrum to be identical with the laboratory spectrum of H_2O^+, thus proving that Comet Kohoutek was partly composed of ice.

Herzberg believed that because of the great stability of H_3^+ and the simple reaction forming it from collisions of H_2 and H_2^+, H_3^+ must be present in interstellar space, where hydrogen is by far the most abundant element. Meanwhile, others predicted that it was the starting point for the creation of most of the molecules found in interstellar space. A friendly competition in the search for this elusive species developed at the HIA, with Takeshi Oka looking for an absorption spectrum and Herzberg an emission spectrum, expected to occur near 2522 cm^{-1}.

Herzberg also kept up a search in the visible region and found a spectrum at 5600 Å with broad lines for hydrogen and sharper lines for deuterium. He concentrated on the deuterium spectrum but deduced that it was due to neither D_2 nor D_3^+ but to D_3, a molecule stable in its excited states. The structure was an equilateral triangle, as predicted for D_3^+ (H_3^+), but with the third electron in an orbit far from the protons, and he called it a 'Rydberg molecule'. He also examined spectra of the diatomic Rydberg molecules HeH^+, $HeNe^+$, $HeAr^+$, KrH, KrD, XeH, XeD, ArH and ArD, keeping in mind the possibility that they could be detected in space and might be the cause of the diffuse interstellar bands.

Meanwhile, Oka searched for the absorption spectrum of H_3^+, using laser techniques, and after four years of concentrated effort he succeeded in detecting its infrared spectrum in 1980. This was a fundamental discovery for interstellar spectroscopy and chemistry. Another important achievement of the HIA was the detection of spectra of the long-carbon-chain molecules HC_5N, HC_7N and HC_9N in the interstellar medium. This work was initiated by Harry (later Sir Harold) Kroto (FRS 1990), a former PDF at NRC and a Nobel laureate in chemistry (1996), and was carried out by him together with Oka and colleagues with the HIA radio telescope.

THE LAST YEARS, 1995–99

As expected, Herzberg continued to work in his office daily, mainly carrying on his voluminous correspondence and reading technical papers. He persisted in his search for the rare molecular species or chemical processes that could give rise to the ubiquitous diffuse interstellar bands: 'It is one of my aims to solve that problem before I quit'. But this was not to be. A fall down a short flight of stairs at home prevented him from spending more than a few hours each day at the office. After a severe heart attack in 1996, his health noticeably failed. He ceased working in his office and was often in hospital for tests lasting a day or more. With the progressing effects of Parkinson's disease, increasing medication and loss of appetite, he weakened rapidly and was confined to his home, where Monika cared for him faithfully in the last three years of his life. He died at home on 3 March 1999.

At a Memorial Tribute held on 11 May 1999 in the Auditorium of the National Research

Council, President Arthur Carty announced the creation of the Herzberg Memorial Prize and Fellowship, open to applicants in Canada and around the world to work at the NRC for up to a year. In November 2000 the Federal Government also launched the country's premier research award, the annual Gerhard Herzberg, Canada Gold Medal for Science and Engineering with a $1 million research award over five years. Such awards to applaud and encourage outstanding research would have pleased Herzberg immensely. His office, Room 2057 in the NRC Laboratories at 100 Sussex Drive, was renovated and named The Gerhard Herzberg Reading Room, as a lasting tribute to this gentle and peaceful man, one of Canada's most renowned scientists.

Honours and awards

Fellowships, medals and special lectures

1927	Mueller–Alewyn–Plakette Medal, Darmstadt
1939	Fellow, Royal Society of Canada
1950	Médaille de l'Université de Liège
1951	Fellow, The Royal Society of London
1953	Henry Marshall Tory Medal, Royal Society of Canada
1954	Honorary Fellow, Indian Academy of Sciences
	Joy Kissen Mookerjee Gold Medal, Indian Assoc. for the Cultivation of Science
1957	Gold Medal for Achievement in Physics, Canadian Association of Physicists
	Honorary Fellow, National Academy of Sciences, India
1959	Medal of the Society for Applied Spectroscopy
1959–60	Chair Francqui, Université de Liège
1960	Médaille de l'Université de Liège
	Médaille de l'Université de Bruxelles
	Corresponding Member, Société Royale des Sciences de Liège
	Bakerian Lecture, The Royal Society of London
1962	Spectroscopy Award, Spectroscopy Society of Pittsburgh
1963	Twelfth Spiers Memorial Lecture, Faraday Society
1964	Frederic Ives Medal, Optical Society of America
	Honorary Member, Hungarian Academy of Sciences
	Academician, Pontifical Academy of Sciences
1965	Foreign Honorary Member, American Academy of Arts and Sciences
1966–67	President, The Royal Society of Canada
1968	Honorary Fellow, Optical Society of America
	Honorary Fellow, Chemical Society of London (now Royal Society of Chemistry)
	Foreign Associate, National Academy of Sciences, Washington
	Companion of the Order of Canada
	George Fisher Baker Non-Resident Lecturer in Chemistry, Cornell University
1969	Willard Gibbs Medal, American Chemical Society
	Gold Medal, Professional Institute of the Public Service of Canada
	Honorary Member, Society for Applied Spectroscopy
1970	Faraday Medal, Chemical Society of London
	Honorary Member, Royal Irish Academy

1970	Honorary Fellow, Chemical Institute of Canada
	Honorary Member, Spectroscopy Society of Canada
1971	Royal Medal, The Royal Society of London
	Linus Pauling Medal, American Chemical Society
	Nobel Prize in Chemistry, Swedish Royal Academy of Sciences
1972	Foreign Member, American Philosophical Society
	Chemical Institute of Canada Medal
1973–80	Chancellor, Carleton University
1973	Member, International Academy of Quantum Molecular Science
	Honorary Fellow, Indian Chemical Society
1974	Madison Marshall Award, American Chemical Society (North Alabama Section)
	Foreign Fellow, Indian National Science Academy
	Honorary Member, La Asociacion de Quimicos Farmaceuticos de Colombia
	Foreign Associate, Royal Academy of Belgium
1976	ACS Centennial Foreign Fellow, American Chemical Society
	Honorary Member, Japan Academy
1978	Honorary Member, Chemical Society of Japan
	Honorary Member, Real Sociedad Espanola de Fisica y Quimica
1980	Member, European Academy of Arts, Sciences and Humanities
1981	Foreign Member (Physics), Royal Swedish Academy of Sciences
1985	Earle K. Plyler Prize, American Physical Society
1986	Korrespondierendes Mitglied Bayerische Akademie der Wissenschaften
1987	Jan Marcus Marci Memorial Medal, Czechoslovak Spectroscopy Society
	Minor planet 3316–1984 CN1 officially named ‘Herzberg’
1990	Ohio Engineering Hall of Fame, Dayton
1992	Member of the Queen’s Privy Council for Canada

Honorary degrees

1953	LLD, University of Saskatchewan
1954	DSc, McMaster University, Hamilton
1956	DSc, National University of Ireland, Dublin
1958	LLD, University of Toronto
1960	LLD, Dalhousie University
	DSc, Oxford University
1961	LLD, University of Alberta
1964	DSc, University of British Columbia
1965	DSc, Queen’s University, Kingston
1966	DSc, University of New Brunswick
	Fil.Hed.-Dr., University of Stockholm
1967	DSc, University of Chicago
	DSc, Carleton University, Ottawa
1968	Dr.rer.nat., University of Göttingen
	DSc, Memorial University, Newfoundland
1969	DSc, York University, Toronto
1970	DSc, University of Windsor
1971	DSc, Royal Military College of Canada

1972	DSc, Drexel University, Philadelphia
	LLD, St. Francis Xavier University
	DSc, University of Montreal
	LLD, Simon Fraser University
	DSc, Université de Sherbrooke
	DSc, Cambridge University
	DSc, McGill University, Montreal
1973	DSc, University of Manitoba
1974	Dr.rer.nat., University of Hamburg
1975	DSc, University of Bristol
	DSc, Andhra University
1976	DSc, Osmania University
	DSc, University of Delhi
	DPhil, Weizmann Institute of Science
	DSc, University of Western Ontario
1979	DSc, Laval University
1983	Dr.phil.nat., University of Frankfurt
1984	PhD, University of Toledo
1991	DSc, St. Mary's University

Acknowledgements

In this memoir I have drawn on my knowledge of Gerhard Herzberg, whom I had known for almost five decades as a mentor and friend, and whose life and achievements I have described in more detail in *Gerhard Herzberg: an illustrious life in science*, published by the NRC Press in 2002. I am particularly appreciative of the assistance of Mrs Monika Herzberg, and Paul and Agnes Herzberg, as well as colleagues of the Spectroscopy Laboratory, who provided much material and advice in preparation of the biography.

The frontispiece photograph was taken in 1967, and is reproduced by courtesy of the Public Relations Office of the National Research Council of Canada.

Bibliography

A full bibliography appears on the accompanying microfiche, a photocopy of which is available from The Royal Society's Library at cost.

AWARD LECTURE / CONFÉRENCE D'HONNEUR

The 2003 CSC Pure or Applied Inorganic Chemistry Award Lecture
Adventures in stable radical chemistry

Robin G. Hicks

Abstract: Stable radicals are of intense fundamental interest because they challenge conventional bonding paradigms, and they find a wide range of uses ranging from organic and polymer synthesis to biological and medicinal applications to materials science. Yet the directed synthesis and study of stable radicals for either fundamental or applied purposes are rarely pursued strategies. This Award Lecture describes my research group's efforts in exploratory and targeted research focusing on stable radical design.

Key words: stable radicals, verdazyls, molecular magnetism.

Résumé : Les radicaux stables présentent un intérêt fondamental intense en raison de leur défi aux paradigmes conventionnels des liaisons et on leur connaît beaucoup d'applications en sciences biologiques, médicinales et celles des matériaux en plus de les utiliser en synthèse organique et celle des polymères. Toutefois, il y a rarement de travaux orientés directement à la synthèse et à l'étude de radicaux stables pour des fins fondamentales ou appliquées. Dans cette présentation, on décrit les recherches exploratoires et orientées effectués dans mon groupe pour le développement de radicaux stables.

Mots clés : radicaux stables, verdazyles, magnétisme moléculaire.

[Traduit par la Rédaction]

Introduction

One of the fundamental tenets of molecular structure and bonding is that closed-shell electronic configurations are stable. The corollary to this principle is that species with unpaired electrons — *radicals* — are transient or reactive intermediates. However, there are examples of open-shell compounds that do not exhibit the high reactivity normally associated with radicals (dimerization, autoxidation, H· or R· abstraction, etc.). These relatively inert species, generally referred to as *stable radicals*,[1] stand out as molecules of exceptional structure and properties.

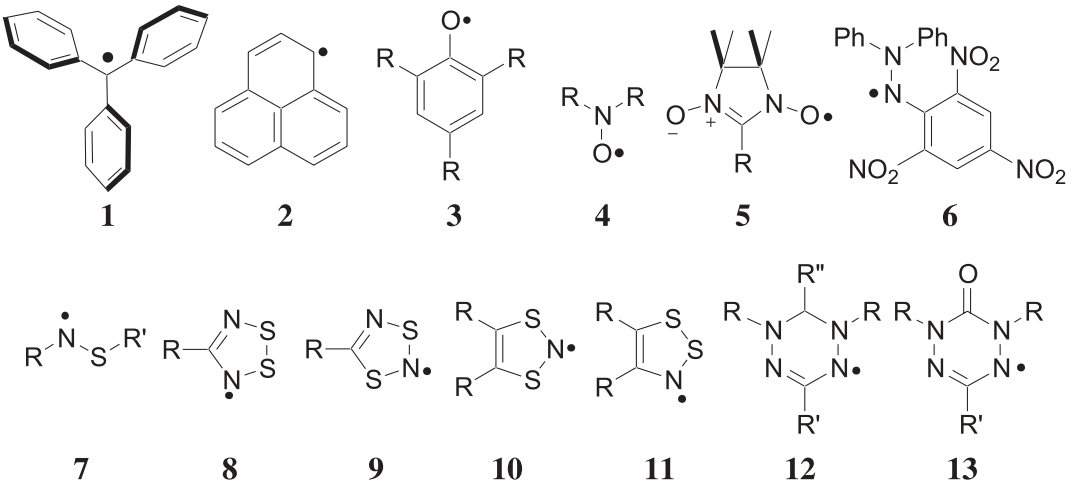
Gomberg's discovery of the triphenylmethyl radical **1** (2) marked the dawn of stable radical chemistry. Triarylmethyl derivatives remain the best known class of stable radicals based on hydrocarbons — although only heavily substituted derivatives are isolable (3). Other stable organic radicals include phenalenyl radicals **2** (4) and substituted phenoxyl radicals **3** (5), though like the triarylmethyls these also require bulky substituents for stability. Most of the general families of stable radicals are based on catenated *inorganic elements*

Received 19 January 2004. Published on the NRC Research Press Web site at http://canjchem.nrc.ca on 15 September 2004.

R.G. Hicks. Department of Chemistry, University of Victoria, PO Box 3065, STN CSC. Victoria, BC V8W 3V6, Canada. (e-mail: rhicks@uvic.ca).

[1]The terms stable and persistent have long been used loosely with respect to radicals, and indeed both are subjective terms. In general, persistence is a kinetic phenomenon related to lifetime whereas stability implies thermodynamic stability under a certain set of conditions. From a practical perspective, "stable" radicals are arbitrarily defined here as those that persist for many days in solution and can be isolated and (or) stored as radicals without appreciable decomposition. For a more detailed account of the use of these terms, see ref. 1.

 doi: 10.1139/V04-064 © 2004 NRC Canada



such as nitrogen, oxygen, and sulfur. This is exemplified by small molecules such as NO, NO_2, and O_2. By far the most familiar stable organomain group[2] radicals are the nitroxides **4** and the closely related nitronyl nitroxides **5** (6). The *N*,*N*-diphenyl-*N′*-picrylhydrazyl (DPPH) radical **6** is well known, although hydrazyls as a class are not very long-lived (7). Other established stable radicals include a multitude of sulfur–nitrogen-based species **7–11** (8) and verdazyls **12** and **13** (9). In addition to these, new individual examples continue to be discovered (10), many of which appear to warrant publication largely on the basis that they are stable radicals (11). This lends support to the notion that, despite their existence for over a century, to this day the chemical community views stable radicals as highly unusual and intriguing species.

But stable radicals offer much more than pure novelty. From a fundamental perspective, they challenge conventional thinking about molecular electronic structure. Gomberg's triphenylmethyl was the first example of a molecule with trivalent carbon, a bonding arrangement thought at the time to be nonexistent. Recent examples of molecules possessing features such as "one-electron bonds" (12) or so-called "singlet diradicals" (13) offer further evidence that we can and should continue to look to open-shell molecules in order to improve our understanding of structure and bonding. Stable radicals are also central to a diverse array of applications:

1. The incorporation of stable radicals into chemical and particularly biological systems facilitates structural, mechanistic, and dynamic investigations using electron paramagnetic resonance (EPR) spectroscopic methods. Of particular importance are techniques such as spin labeling (14), spin trapping (15), and EPR imaging (16).
2. There is tremendous interest in the electronic and magnetic properties of stable radical-based materials as part of the general pursuit of new generations of functional molecular-based materials (17). These efforts stem from the simple fact that many interesting and technologically relevant charge transport and magnetic properties require unpaired electrons.
3. The chemical biology of stable radicals is well established. Small-molecule radicals such as dioxygen, superoxide, and nitric oxide, as well as tyrosyl radicals (18), are known to play crucial roles arising from their reactions with reactive free radicals and metals.
4. Most "stable" radicals in fact do possess some chemical reactivity, but of a much more controlled nature than is normally associated with radicals. A variety of synthetically useful reactions have been developed based on the "persistent radical effect" (PRE) (19), i.e., the selective cross-coupling reactions of stable and reactive radicals. A particularly exciting synthetic application of the PRE is the development of "living" free-radical polymerization processes (20). In addition to PRE-based chemistry, stable radicals exhibit a rich redox chemistry that has led to their development as practical oxidizing agents (21) and as *anti*oxidants too (22).

Personal motivations

My own fascination with stable radicals began during my graduate school days at the University of Guelph. My doctoral research, carried out under the supervision of Rich Oakley, focused on the solid-state packing and charge transport properties of heterocyclic sulfur–nitrogen and selenium–nitrogen radicals (23). I maintained a fleeting interest in radical ions (24) (through electrochemistry) and neutral radicals (25) while acquiring expertise in synthetic organic chemistry and electrochemistry during my postdoctoral stint with Fred Wudl at the University of California-Santa Barbara. As I developed ideas for what would become my own research program, I was certainly mindful of the general (unwritten) rule that assistant professors avoid repeating previous doctoral or postdoctoral research (26). But this gen-

[2] Most of the common stable radicals (in addition to a great many other compounds based on *p*-block elements) combine carbon with other elements and, as such, are not readily categorized as either "organic" or "inorganic" molecules. In fact, one of our early synthetic publications on verdazyl radicals was rejected by an inorganic journal without review on the grounds that the molecules were not inorganic enough! Although "heteroatom chemistry" has been employed to describe compounds of this sort, I think that the term "organomain group" better captures the dichotomous nature of these molecules, as do the corresponding ingrained terms "organometallic" or "organotransition metal" for compounds containing metallic and organic fragments.

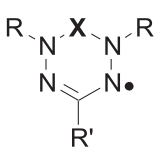
© 2004 NRC Canada

eral field seemed to me to be wide open with possibilities. Fundamentally, almost all new examples of stable radicals appear to be serendipitous discoveries. In the many applied forums described above, the stable radicals that are employed are usually the most readily available ones, typically nitroxide derivatives **4** or **5**. In many of these areas, there is still much room for improvement in the efficacy of the radicals that are used. It seemed to me that the collective shortcomings in these and other areas originated from the fact that few researchers were *actively* pursuing the *design* of stable radicals with a view to understanding, or "tuning", their properties (e.g., spin distributions, redox properties, and reactivity, to name a few). There appeared to be many areas ripe for discovery that would allow me to build on my expertise and take stable radical chemistry into new directions, with the long-term goal of a rational stable radical science, including a deeper understanding of why stable radicals are stable and the development of structure–property relationships in selected targeted areas.

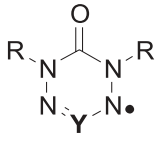
Expanding the verdazyl family

Many stable radicals rely on the steric bulk of substituents for their stability. This strategy of stabilizing reactive fragments has long been practiced by inorganic chemists, but it turns out to be the wrong strategy for radical stabilization if one is interested in ultimately *doing* anything with the resulting radicals: Virtually all of the "applications" described above require that the radical (in addition to being stable) must be able to interact — chemically, magnetically, etc. — with other substrates. Too much steric protection can inhibit or prohibit these interactions. So the challenge from a molecular design perspective was to find new templates for radical stability while relying as little as possible on steric stabilization.

Rather than try to create new radicals from scratch, I opted to start with an established architecture that was amenable to modification. In this respect, verdazyl radicals **12** and **13** represented appealing systems. Although they were discovered over 40 years ago (27) and are generally quite stable, almost the entire body of work on these radicals focused on synthesis and spectroscopic analyses. I viewed verdazyls as templates that could be converted (on paper) to



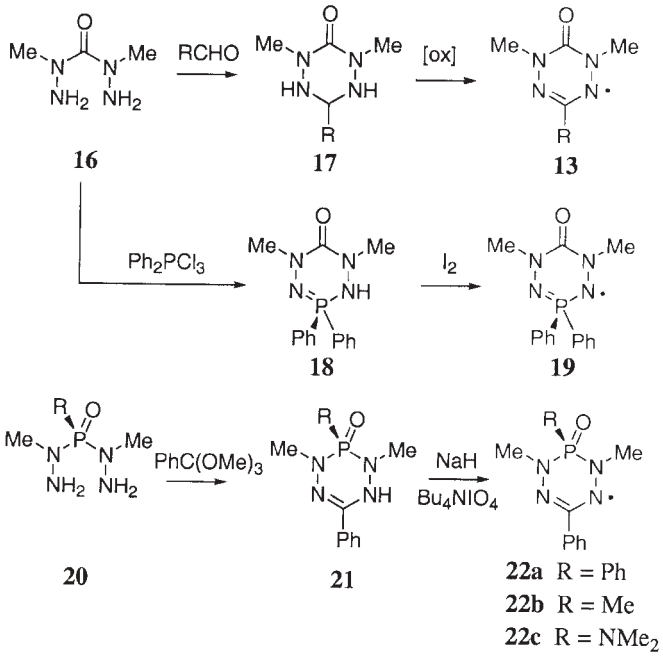
14



15

new radicals by skeletal atom substitution. Given that the stability of verdazyls is due in large part to the nitrogen-rich ring, it seemed prudent to start out with the relatively modest goal of making new radicals in which the ring carbon atoms were replaced by other elements, hence their general moniker "heteroverdazyls", generically depicted as **14** and **15**. I hoped that this would give us a fighting chance of obtaining something stable, and also provide a handy reference point (the "parent" verdazyl) for comparisons of electronic

Scheme 1.



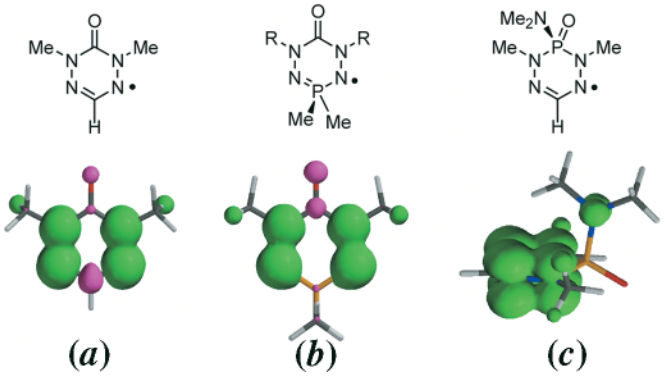
structure. Phosphorus stood out as an ideal element to start with, as the introduction of another spin-active nucleus (^{31}P: I = 1/2, 100% abundance) would give us a direct handle on the electronic structure of the radicals through EPR spectroscopy. There were, in fact, already a few reports on these sorts of "phosphaverdazyls", but the characterization was far from complete (28).

The synthesis of the phosphaverdazyls built on established routes to the parent verdazyl ring **13** (Scheme 1). The latter are made by condensations of dimethyl carbohydrazide **16** with aldehydes to give tetrazanes **17**, followed by oxidation to give radicals **13** (9*b*, 29). We found that **16** could be condensed with Ph_2PCl_3 to give the 3-phosphatetrazine **18** and then oxidized with iodine to give the 3-phosphaverdazyl **19**. Phosphorus could also be introduced into the 6-position of the verdazyl via analogous chemistry. Derivatives of **20**, the phosphorus analogues of bis-hydrazide **16**, were originally synthesized by Majoral et al. (30). Reactions of **20** with aldehydes were problematic, so we turned to orthoesters $RC(OMe)_3$, which gave the desired 6-phosphatetrazines **21.** Subsequent oxidations with periodate gave the 6-phosphaverdazyl radicals **22a**-**c** (31).

The stability of the phosphaverdazyl radicals was unfortunately not quite as high as that of their carbon counterparts. They survive for several days in solution or in the solid state and are essentially insensitive to oxygen or water, but they slowly decompose to give mixtures of products (mainly the corresponding precursor phosphatetrazines). This has made it a challenge to obtain X-ray crystallographic data for these radicals. However, we were able to gain insights into their molecular and electronic structures through a combination of EPR spectroscopy and density functional theory (DFT) calculations. The calculated spin densities of three radicals that are simpler models of verdazyls and phosphaverdazyl radicals are shown in Fig. 1. All three share the common feature of having the majority of their spin on the four heterocyclic

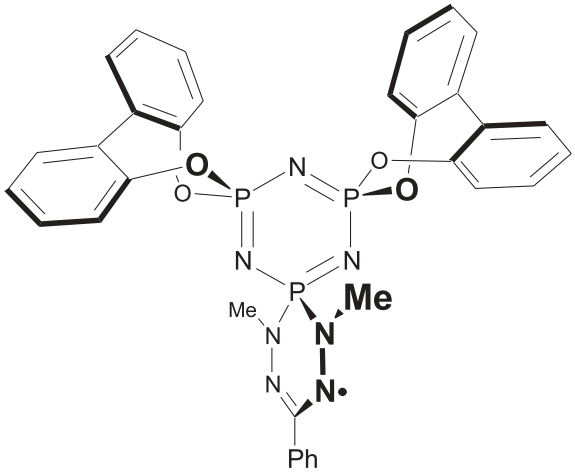
© 2004 NRC Canada

Fig. 1. Molecular structure and calculated spin densities of model compounds for (*a*) a 6-oxoverdazyl radical, (*b*) a 3-phosphaverdazyl radical, and (*c*) the dimethylamino-substituted 6-phosphaverdazyl radical. Positive spin density is green and negative spin density is pink.



nitrogen atoms. In this regard, the electronic structures of the phosphaverdazyls are qualitatively similar to that of the parent radical. However, closer inspection reveals subtle but important differences between the phosphorus-based radicals and the parent verdazyl. We were quite surprised, for example, to find that in the 3-phosphaverdazyls **19** there is essentially *no* spin on the phosphorus atom (Fig. 1*b*), whereas the carbon analogue **13** is known to have appreciable *negative* spin density on the corresponding carbon atom (Fig. 1*a*). These differences can be understood through a combination of spin polarization effects coupled with the specific nature of each radical's singly occupied molecular orbital (SOMO) (31*b*). The 6-phosphaverdazyls, exemplified by **22a–c**, turn out to be more complex, as the ring conformation (planar vs. bent) and the spin density at phosphorus turn out to be exquisitely sensitive to the substituents on the phosphorus. In one example, **22c**, the orientation of the dimethylamino group in its minimum-energy conformation permits through-space overlap between the exocyclic nitrogen and the π-SOMO of the verdazyl moiety (Fig. 1*c*). Calculations and EPR spectra corroborated one another and established *spiroconjugation* as a new form of spin delocalization in radicals that is distinct from the common π-conjugated delocalization in π radicals.

Intrigued by the novel spiroconjugation spin propagation mechanism in **22c**, we designed a phosphaverdazyl radical (**23**) in which this phenomenon might be enhanced. The phosphorus atom in this structure is in a spiro*cyclic* environment, simultaneously part of both the phosphaverdazyl ring and a phosphazene heterocycle. The synthesis of this compound conveniently built on our established "bis-hydrazide" route for 6-phosphaverdazyls **22** and the known substitution chemistry patterns of the dichlorocyclotriphosphazene starting material. Analyses of the EPR spectrum of the radical, which required additional experiments based on the ENDOR double-resonance technique, indeed indicated that spin density was being transferred from the verdazyl ring onto the phosphazene ring, presumably by a spiroconjugation-type mechanism (32). This is an intriguing result because it is an extremely rare example of spin injection into a PN backbone. Phosphazene rings and polymers are among the most well-known and robust inorganic systems, but they are poor electronic conductors despite the presence of a formally π-conjugated framework. The behavior of ompound **23** suggests that phosphazenes may be able to transmit *spin* — and spin *communication* — in verdazyl/phosphazene materials. Work is underway to explore these possibilities in model systems related to **23** but in which multiple verdazyl radicals are linked to the central phosphazene ring in a spirocyclic manner.



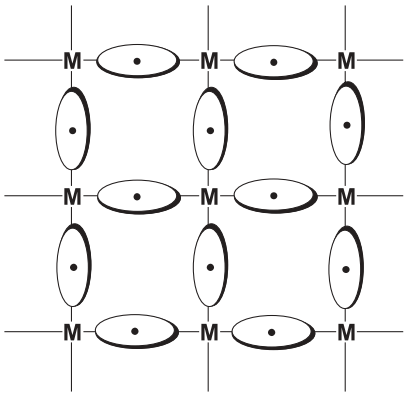
23

Verdazyl coordination chemistry

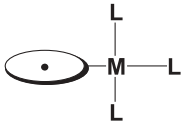
One intensively pursued facet of stable radical chemistry concerns their magnetic properties. One of the holy grails of the field of "molecular magnetism" is the realization of bulk magnetic materials based in whole or in part on nonmetal building blocks. A promising strategy in pursuit of this goals involves combining paramagnetic metal ions and stable radicals. The ideal architecture, depicted schematically in **24**, is a coordination network in which the bridging ligands are radicals. The presence of spin on the ligands as well as the metals is an improvement in design over conventional coordination networks containing conventional (diamagnetic) ligands. Paralleling the effort to make high critical temperature (high-T_C) magnets has been the development of the fundamental coordination chemistry of stable radicals. Discrete complexes of the type depicted in **25** can yield insights into how metal- and radical-based spins interact and can, in principle, guide the way towards magnetically functional network solids.

Not surprisingly, metal–radical complex chemistry has been dominated by nitroxides (33). Although these radicals have the requisite stability, they are weak Lewis bases and consequently require Lewis acidic metal ions for effective binding. More problematic is the fact that the structure of the nitroxide–metal interaction is quite flexible: Nitroxides bind to metals through the oxygen atom and the N-O-M bond angle takes on a range of values from linear to strongly bent. This variation in structure is difficult to control and renders the magnetic interactions between radical and metal — which depend crucially on structure — unpredictable. This makes it difficult to carry out meaningful structure–

© 2004 NRC Canada



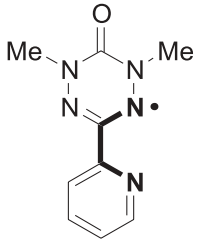
24



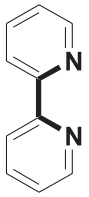
25

property correlations or to *design* structures like **24** that have the "best" magnetic properties.

When I arrived at the University of Victoria in 1996, there was not a single report in the literature of a transition-metal complex of a verdazyl radical. We decided to attempt to control the mode of coordination by preparing chelating verdazyls by using substituents with donor atoms. The prototype ligand for this approach is the 3-(2-pyridyl) derivative **26**: It possesses a diimine-type environment closely structurally related to the ubiquitous 2,2'-bipyridine **27**. The use of this simple chelating ligand would facilitate the preparation of discrete complexes; our strategy was to develop the fundamental coordination chemistry of verdazyls and then use information gleaned from these first-generation studies to eventually push toward extended networks (i.e., **24**).

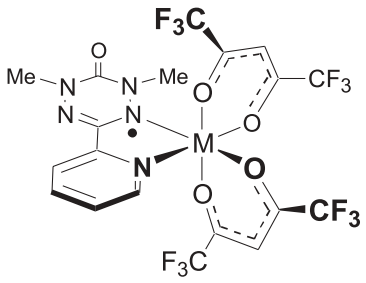


26



27

Our first breakthrough came with complexes based on manganese and nickel with hexafloruo-β-diketonate ancillary ligands (34). Although X-ray structures proved elusive, all of our data were consistent with the expected structure **28**, consisting of pseudo-octahedral metal ions and radical ligand **26** in a chelating binding mode. Importantly, UV–visible spectra confirmed that the radicals remained genuine radicals when coordinated; no electron transfer chemistry with the metals had occurred. Magnetic susceptibility data indicated that the metal–verdazyl magnetic exchange interactions are metal dependent. The manganese complex exhibited moderate antiferromagnetic coupling between the $S = 5/2$ Mn(II) center and the $S = 1/2$ radical, with an exchange interaction energy (J) of –45 cm^{-1}, which is a typical value for a metal–radical complex. In sharp contrast, the exchange interaction between the $S = 1$ Ni(II) ion and the $S = 1/2$ radical was very strongly ferromagnetic, with a value of at least +200 cm^{-1}. This was one of the largest ferromagnetic metal–radical interactions ever observed. The large magnitude of J (a measure of the strength of the interaction) can be rationalized based on the large amount of spin density at the verdazyl N atom directly bound to the metal, while the sign of J (which indicates whether the interaction is ferromagnetic or antiferromagnetic) is determined by straightforward orbital symmetry considerations (34). These were the first examples of verdazyl complexes showing metal–radical exchange interactions (some verdazyl complexes of diamagnetic Cu(I) were reported in 1997 (35)), and the nickel–verdazyl exchange, in particular, represented a major development: Strong ferromagnetic metal–radical interactions are precisely the kind needed in order to realize high-T_C magnetic ordering in structures like **24**.



28 (M = Mn, Ni)

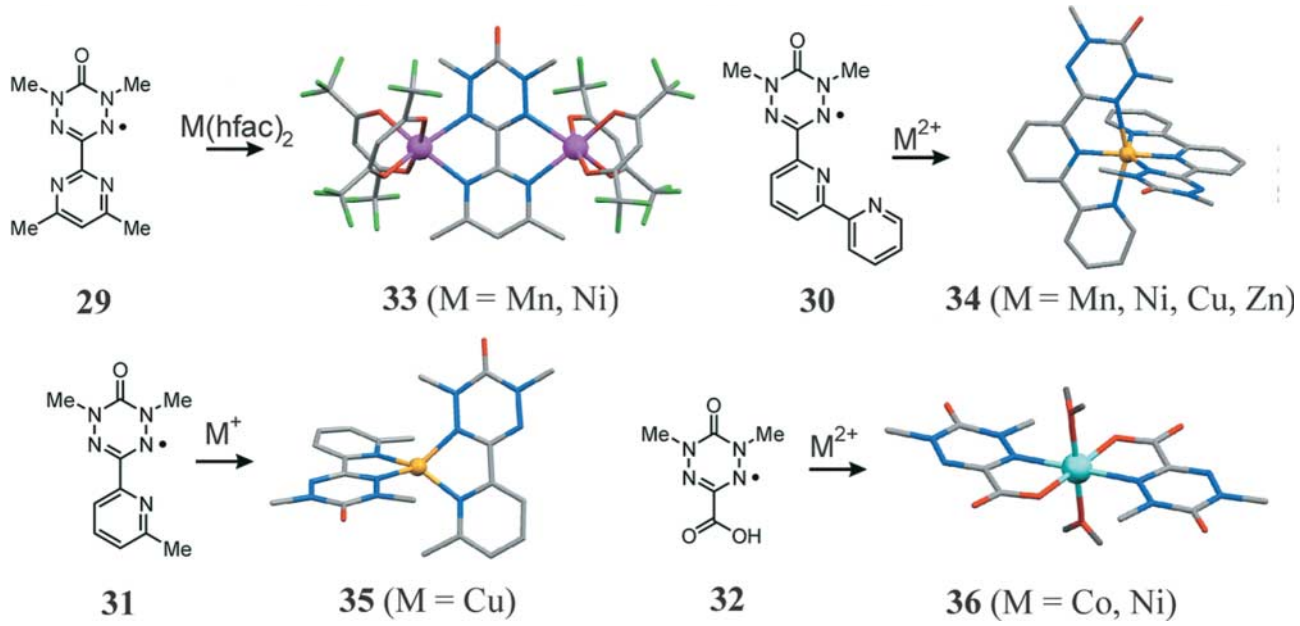
We have since prepared several chelating verdazyl-based ligands that present different binding topologies to metal ions (Fig. 2) (36). The chelate effect makes the verdazyls better ligands and also constrains the geometry of the metal–radical binding, which leads to consistent (metal-dependent) magnetic exchange interactions. Thus, *all* of the Ni(II) verdazyl complexes we have prepared to date exhibit strong ferromagnetic coupling, whereas the Mn(II) complexes are moderately antiferromagnetic. To be sure, there are other factors (e.g., ancillary ligands, metal–verdazyl bond lengths, inter-radical exchange in bis-ligand complexes) that influence the magnetic properties, but to a first approximation the magnetic interactions between verdazyls and metals are predictable. Examples of verdazyls with at least two binding sites are now in hand (e.g., **29** and **32** in Fig. 2), and we have begun to explore their coordination chemistry (36*b*, 36*d*). These ligands are also building blocks for extended structures akin to **24**, which, based on the magnetochemistry of the discrete complexes, are excellent candidates for high-T_C magnets. Future work in our group will also involve verdazyl coordination chemistry of these radicals with a wider range of metals.

Supramolecular chemistry of radicals

The verdazyl radical ligands described above can usually be made, handled, and purified using "normal" procedures. However, our early efforts to purify the pyridine derivative **26** were frustrated by this radical's gradual decomposition in solution or in the solid state. However, we found that by switching from ferricyanide to *p*-benzoquinone as the oxidizing agent in the synthesis of the radical, **26** cocrystallized in a 1:1 stoichiometry with hydroquinone, the by-product of the reaction. These crystals can be stored indefinitely without decomposition of the radical. The hydroquinone can be

© 2004 NRC Canada

Fig. 2. Verdazyl ligands **29**–**32** and X-ray structures of corresponding metal complexes **33**–**36**.



readily separated from the radical by chromatography, thereby affording solutions of pure radical that can then be used for subsequent chemistry. This fortuitous development certainly facilitated the verdazyl coordination chemistry described above. In addition, the structure and magnetic properties of the radical:hydroquinone material turn out to have significant implications for the magnetochemistry of molecular systems.

The crystal structure contains π stacks of **26** assembled in a head-over-tail manner, with each verdazyl ring sandwiched between two pyridines and vice versa (Fig. 3*a*) (37). The mean interplanar separation between molecules within the stacks is close to the normal van der Waals distance for π stacks of ~3.4 Å (1 Å = 0.1 nm). Rows of these stacks fill the *ac* plane and are separated from one another by layers of hydroquinone. There is an extensive two-dimensional hydrogen-bond network involving the hydroxyl groups and the pyridine nitrogen atoms (Fig. 3*b*) perpendicular to the π stacking axis.

Analysis of the variable-temperature magnetic susceptibility data indicated fairly strong antiferromagnetic interactions, and the data could be fit to a model in which one-dimensional chains of spins couple antiferromagnetically to one another. The exchange interaction obtained from the best fit to the data is $J = -56$ cm^{-1}. This is by no means a record, but it is fairly strong for an intermolecular radical interaction. In general, the observation of strong exchange in molecular solids is always ascribed to close intermolecular contacts (within van der Waals distances) between radicals, *in particular between atoms that bear a significant portion of the radical's spin density*. EPR and computational work had established that the spin density in **26** is essentially confined to the four nitrogen atoms of the verdazyl ring. But there are no intermolecular N–N contacts under 4 Å in this structure! The antiparallel nature of the π stacks prevents the verdazyl π systems from overlapping directly with one another, and there are no interstack N–N contacts to speak of. As such, this system is unique in that its magnetic properties run counter to current paradigms about the requirements for strong intermolecular exchange.

To rationalize these observations, we proposed a mechanism of exchange within the π stacks that invokes the pyridine substituents. The pyridine moiety possesses an empty orbital with the same symmetry properties as the radical SOMO. Interactions between two SOMOs via direct (albeit weak) orbital overlap mediated by the pyridine π* orbital could permit through-space (or *supramolecular) superexchange* (Fig. 4*a*). Conceptually, this mechanism is closely related to the superexchange mechanism for metal–metal antiferromagnetic coupling in transition-metal oxides (Fig. 4*b*). However, two key differences in our system are that the orbitals involved are molecular, not atomic, and the interactions are through-space because the molecules are not covalently attached.

One of the biggest challenges in the development of purely organic magnetic materials is that the relationships between molecular packing in the solid state and intermolecular exchange are not well understood (38). The magnetic properties of verdazyl **26**, and our proposed mechanism to explain them, offer a partial explanation as to why structure–magnetism correlations have been so tricky to delineate: Although it is undoubtedly true that close approach between radicals can lead to strong magnetic interactions, through-space magnetic exchange does not *require* spin centers to be as close together as once thought. Although the magnetism of molecular crystals or the radicals themselves was not initially a focus of my research program, the results described here have motivated us to study intermolecular exchange in verdazyls more actively. Structural and magnetic characterization of other radicals is underway, as are efforts to build model systems designed to probe more deeply the intimate mechanism of supramolecular superexchange.

Summary

The work described herein began with what seemed to be

© 2004 NRC Canada

Fig. 3. Crystal structure of **26**:hydroquinone. (*a*) View of *ac* plane depicting verdazyl π stacks (hydroquinones not shown). (*b*) View of *bc* plane. Hydrogen bonds are indicated by red lines.

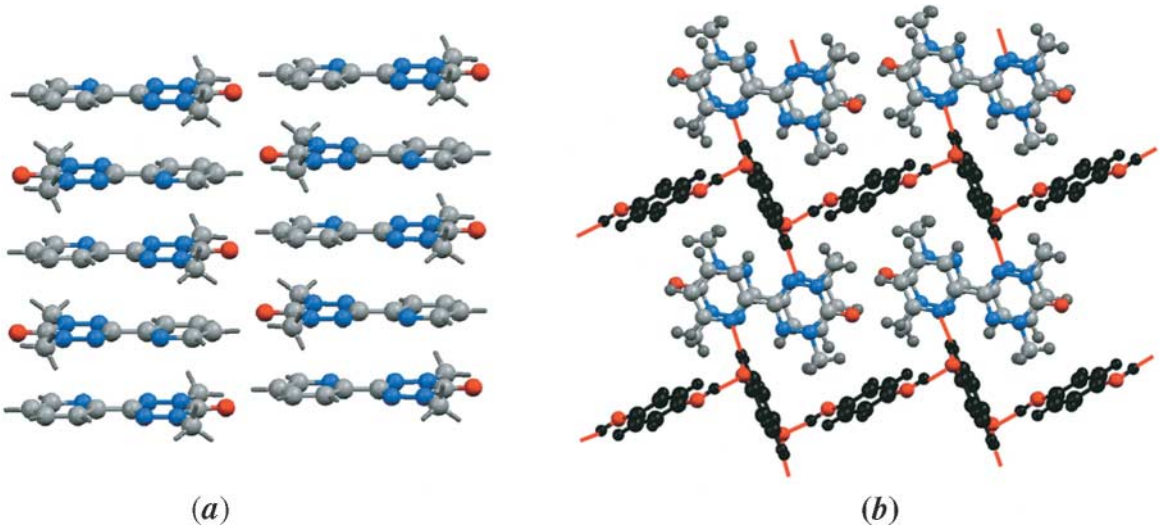
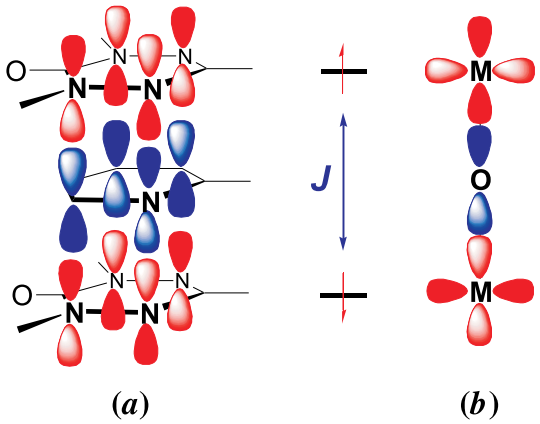


Fig. 4. (*a*) Proposed pyridine π* orbital-mediated superexchange between stacked radicals and (*b*) superexchange in metal oxides.



straightforward ideas for modifying or building on a well-established stable radical system in a number of different ways. The long-term goals of these pursuits were, and continue to be, to bring rational design and the development of structure–property relationships – themes that lie at the very heart of inorganic chemistry – to stable radical chemistry. There are a number of challenges specific to carrying out research on stable radicals (the inability to obtain conventional NMR spectra of open-shell molecules being just one practical obstacle!), and we have certainly encountered our share of these problems along the way. However, overall our progress over the past several years has shown that verdazyl radical chemistry and magnetochemistry are proving to be rich and fruitful areas of study. Our recent successes have emboldened us to pursue new radical architectures that depart more dramatically from the verdazyl template. As progress in basic science is made, we anticipate making significant inroads in selected applications of stable radical science.

Acknowledgements

I thank the CSC Division of Inorganic Chemistry for sponsoring the Award for Pure or Applied Inorganic Chemistry and, in particular, for creating an award that recognizes early career achievement. The work described herein was supported initially by generous startup funds from the University of Victoria and has been sustained through grants from the Natural Sciences and Engineering Research Council of Canada (NSERC), the Petroleum Research Fund, and the Department of National Defense.

This article summarizes "my" research efforts at the University of Victoria over the past several years. Of course, the achievements described herein would not have been possible without the efforts of, and assistance from, many people. The Chemistry Department at the University of Victoria has provided me with a tremendously supportive and stimulating environment, and I offer the faculty and staff there my sincere gratitude; in particular, I thank my colleagues Tom Fyles, Cornelia Bohne, Terry Gough, Peter Wan, and Penny Codding for their guidance and enthusiasm. I have also benefited enormously from a number of fruitful collaborations. First and foremost among these is Laurie Thompson (Memorial University), who for the past six years has provided me with a wealth of magnetic data and has been a willing and patient tutor to a group that had essentially no experience in magnetochemistry at the outset. I also thank my other collaborators for their expertise in X-ray crystallography (Tosha Barclay, North Harris College; John F. Richardson, Louisville), computational chemistry (Lars Ohrstrom, Chalmers Institute of Technlogy, Sweden), and ENDOR spectroscopy (Andrew Ichimura, San Francisco State).

Lastly, and most importantly, I tip my hat to the past and present members of my research group. Although space did not permit a full discussion in this article of all aspects of my program, the contributions of all of my co-workers are deeply appreciated. This includes postdocs (Richard Hooper, Mhamed Chahma, Rajsapan Jain, Khayrul Kabir, and Peter Otieno), graduate students (Greg Patenaude, Martin Lemaire, Matt Nodwell, Bryan Koivisto, Dan Myles, Steve McKinnon, Joe Gilroy, and Sharon Caldwell), and a group of undergraduate researchers too long to list here but whose contributions were, are, and will continue to be crucial.

© 2004 NRC Canada

References

1. (*a*) D. Griller and K.U. Ingold. Acc. Chem. Res. **9**, 13 (1976); (*b*) M.B. Smith and J. March. March's advanced organic chemistry. 5th ed. John Wiley & Sons, New York. 2001. pp. 238–247; (*c*) A.R. Forrester, J.M. Hay, and R. H. Thomson. Organic chemistry of stable free radicals. Academic Press, London. 1968.
2. M. Gomberg. J. Am. Chem. Soc. **22**, 757 (1901).
3. (*a*) M. Ballester. Acc. Chem. Res. **18**, 380 (1985); (*b*) A. Rajca. Chem. Eur. J. **8**, 4834 (2002).
4. (*a*) K. Goto, T. Kubo, K. Yamamoto, K. Nakasuji, K. Sato, D. Shiomi, T. Takui, M. Kubota, T. Kobayashi, K. Yakusi, and J. Ouyang. J. Am. Chem. Soc. **121**, 1619 (1999); (*b*) R.C. Haddon, F. Wudl, M.L. Kaplan, J.H. Marshall, and F.B. Bramwell. J. Chem. Soc. Chem. Commun. 429 (1978); (*c*) S.J. Zheng, J. Lan, S.I. Khan, and Y. Rubin. J. Am. Chem. Soc. **125**, 5786 (2003).
5. E.R. Altwicker. Chem. Rev. **67**, 475 (1967).
6. (*a*) E.G. Rozanstev and V.D. Sholle. Synthesis, 190 (1971); (*b*) E.G. Rozanstev and V.D. Sholle. Synthesis, 401 (1971); (*c*) E.F. Ullman, J.H. Osiecki, D.G.B. Boocock, and R. Darcy. J. Am. Chem. Soc. **94**, 7049 (1972).
7. A.R. Forrester, J.M. Hay, and R. H. Thomson. Organic chemistry of stable free radicals. Academic Press, London. 1968. Chap. 4.
8. (*a*) K.F. Preston and L.H. Sutcliffe. Magn. Reson. Chem. **28**, 189 (1990); (*b*) R.T. Oakley. Can. J. Chem. **71**, 1775 (1993).
9. (*a*) F.A. Neugebauer. Angew. Chem. Int. Ed. Engl. **12**, 455 (1973); (*b*) F.A. Neugebauer, H. Fischer, and R. Siegel. Chem. Ber. **121**, 815 (1988).
10. P.P. Power. Chem. Rev. **103**, 789 (2003).
11. Selected examples: (*a*) N. Jux, K. Holczer, and Y. Rubin. Angew. Chem. Int. Ed. Engl. **35**, 1986 (1996); (*b*) B.T. King, B.C. Noll, A.J. McKinley, and J. Michl. J. Am. Chem. Soc. **118**, 10 902 (1996); (*c*) M.M. Olmstead, L. Pu, R.S. Simmons, and P.P. Power. Chem. Commun. 1595 (1997); (*d*) H. Tomioka, E. Iwamoto, H. Itakura, and K. Hirai. Nature (London), **412**, 626 (2001); (*e*) N. Wiberg, T. Blank, W. Kaim, B. Schwederski, and G. Linti. Eur. J. Inorg. Chem. 1475 (2000); (*f*) Y. Miura and T. Tomimura. Chem. Commun. 627 (2001); (*g*) S. Loss, A. Magistrato, L. Cataldo, S. Hoffmann, M. Geoffroy, U. Rothlisberger, and H. Grutzmacher. Angew. Chem. Int. Ed. **40**, 723 (2001); (*h*) A. Armstrong, T. Chivers, M. Parvez, and R.T. Boeré. Angew. Chem. Int. Ed. **43**, 502 (2004).
12. (*a*) Y. Canac, D. Bourissou, A. Baceiredo, H. Gornitzka, W.W. Schoeller, and G. Bertrand. Science (Washington, D.C.), **279**, 2080 (1998); (*b*) J.D. Hoefelmeyer and F.P. Gabbai. J. Am. Chem. Soc. **122**, 9054 (2000); (*c*) L. Cataldo, S. Choua, T. Berclaz, M. Geoffroy, N. Mezailles, L. Ricard, F. Mathey, and P.F. Le Floch. J. Am. Chem. Soc. **123**, 6654 (2001).
13. (*a*) E. Niecke, A. Fuchs, F. Baumeister, M. Nieger, and W.W. Shcoeller. Angew. Chem. Int. Ed. **34**, 555 (1995); (*b*) D. Scheschkewitz, H. Amii, H. Gornitzka, W.W. Schoeller, D. Bourissou, and G. Bertrand. Science (Washington, D.C.), **295**, 1880 (2002); (*c*) H. Sugiyama, S. Ito, and M. Yoshifuji. Angew. Chem. Int. Ed. **42**, 3802 (2003).
14. (*a*) J.F.W. Keana. Chem. Rev. **78**, 37 (1978); (*b*) L.J. Berliner. Spin labelling: Theory and applications. Academic Press, New York. 1979; (*c*) P.P. Borbat, A.J. Costa-Filho, K.A. Earle, J.K. Moscicki, and J.H. Freed, Science **291**, 266 (2001).
15. (*a*) M.J. Perkins. Adv. Phys. Org. Chem. **17**, 1 (1980); (*b*) D. Rehorek. Chem. Soc. Rev. **20**, 341 (1991); (*c*) A.J.L. Beckwith, V.W. Bowry, and K.U. Ingold. J. Am. Chem. Soc. **114**, 4983 (1992); (*d*) V.W. Bowry and K.U. Ingold. J. Am. Chem. Soc. **114**, 4992 (1992).
16. (*a*) L.J. Berliner and H. Fujii. Science (Washington, D.C.), **227**, 517 (1985); (*b*) J.L. Zweier and P. Kuppusamy. Proc. Natl. Acad. Sci. U.S.A. **85**, 5703 (1988); (*c*) A.T. Yordanov, K. Yamada, M.C. Krishna, J.B. Mitchell, E. Woller, M. Cloninger, and M.W. Brechbiel. Angew. Chem. Int. Ed. **40**, 2690 (2001); (*d*) T.J. Reddy, T. Iwama, H.J. Halpern, and V.H. Rawal. J. Org. Chem. **67**, 4635 (2002).
17. (*a*) A. Rajca. Chem. Rev. **94**, 871 (1994); (*b*) J.S. Miller and A.J. Epstein. Angew. Chem. Int. Ed. **33**, 385 (1994); (*c*) P.M. Lahti (*Editor*). Magnetic properties of organic materials. Marcel Dekker, New York. 1999; (*d*) X. Chi, M.E. Itkis, B.O. Patrick, T.M. Barclay, R.W. Reed, R.T. Oakley, A.W. Cordes, and R.C. Haddon. J. Am. Chem. Soc. **121**, 10 395 (1999); (*e*) T.M. Barclay, A.W. Cordes, R.C. Haddon, M.E. Itkis, R.T. Oakley, R.W. Reed, and H. Zhang. J. Am. Chem. Soc. **121**, 969 (1999); (*f*) M.E. Itkis, X. Chi, A.W. Cordes, and R.C. Haddon. Science (Washington, D.C.), **296**, 1443 (2002).
18. (*a*) J. Stubbe and W.A. van der Donk. Chem. Rev. **98**, 705 (1998); (*b*) J. Stubbe. Chem. Commun. (Cambridge), 2511 (2003).
19. (*a*) A. Studer. Chem. Eur. J. **7**, 1159 (2001); (*b*) H. Fischer. Chem. Rev. **101**, 3581 (2001).
20. M.K. Georges, R.P.N. Veregin, P.M. Kazmeier, and G.K. Hamer. Macromolecules, **26**, 2987 (1993); (*b*) C.J. Hawker, A.W. Bosman, and E. Harth. Chem. Rev. **101**, 3661 (2001).
21. (*a*) H. Zimmer, D.C. Lankin, and S.W. Horgan. Chem. Rev. **71**, 229 (1971); (*b*) A.E.J. deNooy, A.C. Besemer, and H.v. Bekkum. Synthesis, 1153 (1996); (*c*) R.A. Sheldon. Acc. Chem. Res. **35**, 774 (2002).
22. (*a*) J.B. Mitchell, A. Samuni, M.C. Krishna, W.G, Degraff, M.S. Ahn, U. Samuni, and A. Russo. Biochemistry, **29**, 2802 (1990); (*b*) D. Metodiewa, J. Skolimowski, A. Kochman, K. Gwozdzinski, and J. Glebska. Anticancer Res. **18**, 369 (1998); (*c*) P. Bar-On, M. Mohsen, R.L. Zhang, E. Feigin, M. Chevion, and A. Samuni. J. Am. Chem. Soc. **121**, 8070 (1999); (*d*) A.M. Samuni and Y. Barenholz. Free Radicals Biol. Med. **34**, 177 (2003).
23. Selected publications: (*a*) A.W. Cordes, R.C. Haddon, R.G. Hicks, R.T. Oakley, T.T.M. Palstra, L.F. Schneemeyer, and J.V. Waszczak. J. Am. Chem. Soc. **114**, 5000 (1992); (*b*) A.W. Cordes, R.C. Haddon, R.G. Hicks, R.T. Oakley, and T.T.M. Palstra. Inorg. Chem. **31**, 1802 (1992); (*c*) A.W. Cordes, S.H. Glarum, R.C. Haddon, R. Hallford, R.G. Hicks, D.K. Kennepohl, R.T. Oakley, T.T.M. Palstra, and S.R. Scott. J. Chem. Soc. Chem. Commun. 1265 (1992); (*d*) A.W. Cordes, C.D. Bryan, W.M. Davis, R.H. DeLaat, S.H. Glarum, J.D. Goddard, R.C. Haddon, R. Hallford, R.G. Hicks, D.K. Kennepohl, R.T. Oakley, S.R. Scott, and N.P.C. Westwood. J. Am. Chem. Soc. **115**, 7232 (1993); (*e*) C.D. Bryan, A.W. Cordes, R.C. Haddon, R.G. Hicks, D.K. Kennepohl, C.D. MacKinnon, R.T. Oakley, T.T.M. Palstra, A.S. Perel, S.R. Scott, L.F. Schneemeyer, and J.V. Waszczak. J. Am. Chem. Soc. **116**, 1205 (1994); (*f*) C.D. Bryan, A.W. Cordes, R.C. Haddon, R.G. Hicks, R.T. Oakley, T.T.M. Palstra, A.S. Perel, and S.R. Scott. Chem. Mater. **6**, 508 (1994); (*g*) C.D. Bryan, A.W. Cordes, R.C. Haddon, R.G. Hicks, R.T. Oakley, T.T.M. Palstra, and A.S. Perel. J. Chem. Soc. Chem. Commun. 1447 (1994); (*h*) C.D. Bryan, A.W. Cordes, J.D. Goddard, R.C. Haddon, R.G. Hicks, C.D. MacKinnon, R.C. Mawhinney, R.T. Oakley, T.T.M. Palstra, and A.S. Perel. J. Am. Chem. Soc. **118**, 330 (1996).

© 2004 NRC Canada

24. (*a*) M. Keshavarz-K., R. Gonzalez, R.G. Hicks, G. Srdanov, V.I. Srdanov, T.G. Collins, J.C. Hummelen, C. Bellavia-Lund, F. Wudl, and K. Holczer. Nature (London), **383**, 147 (1996); (*b*) C. Bellavia-Lund, R. Gonzalez, J.C. Hummelen, R.G. Hicks, A. Sastre, and F. Wudl. J. Am. Chem. Soc. **119**, 2946 (1997).
25. K. Hutchison, G. Srdanov, R.G. Hicks, H. Yu, F. Wudl, T. Strassner, M. Nendel, and K.N. Houk. J. Am. Chem. Soc. **120**, 2989 (1998).
26. M.D. Fryzuk. Can. J. Chem. **70**, 2839 (1992).
27. R. Kuhn and H. Trischmann. Angew. Chem. Int. Ed. **2**, 155 (1963).
28. (*a*) P.P. Kornuta, V.N. Bobkov, O.M. Polumbrik, and L.N. Markovskii. Zh. Obshch. Khim. **51**, 2449 (1982); (*b*) F.A. Neugebauer and H. Fischer. Z. Naturforsch. **35B**, 250 (1980).
29. P.A. Chase, C.L. Barr, R.G. Hicks, M.T. Lemaire, and C.L. Stevens. J. Org. Chem. **64**, 8893 (1999).
30. J.P. Majoral, R. Kraemer, J. Navech, and F. Mathis. Tetrahedron, **32**, 2633 (1976).
31. (*a*) R.G. Hicks and R. Hooper. Inorg. Chem. **38**, 284 (1999); (*b*) R.G. Hicks, L.Öhrström, and G.W. Patenaude. Inorg. Chem. **40**, 1865 (2001).
32. T.M. Barclay, R.G. Hicks, A.S. Ichimura, and G.W. Patenaude. Can. J. Chem. **80**, 1501 (2002).
33. (*a*) A. Caneschi, D. Gatteschi, and R. Sessoli. Acc. Chem. Res. **22**, 392 (1989); (*b*) A. Caneshi, D. Gatteschi, and P. Rey. Prog. Inorg. Chem. **39**, 331 (1991).
34. R.G. Hicks, M.T. Lemaire, L.K. Thompson, and T.M. Barclay. J. Am. Chem. Soc. **122**, 8077 (2000).
35. D.J.R. Brook, V. Lynch, B. Conklin, and M.A. Fox. J. Am. Chem. Soc. **119**, 5155 (1997).
36. (*a*) T.M. Barclay, R.G. Hicks, M.T. Lemaire, and L.K. Thompson. Chem. Commun. (Cambridge), 2141 (2000); (*b*) T.M. Barclay, R.G. Hicks, M.T. Lemaire, and L.K. Thompson. Inorg. Chem. **40**, 5581 (2001); (*c*) T.M. Barclay, R.G. Hicks, M.T. Lemaire, and L.K. Thompson. Inorg. Chem. **40**, 6521 (2001); (*d*) T.M. Barclay, R.G. Hicks, M.T. Lemaire, L.K. Thompson, and Z. Xu. Chem. Commun. (Cambridge), 1688 (2002); (*e*) T.M. Barclay, R.G. Hicks, M.T. Lemaire, and L.K. Thompson. Inorg. Chem. **42**, 2261 (2003).
37. R.G. Hicks, M.T. Lemaire, L. Öhrström, J.F. Richardson, L.K. Thompson, and Z. Xu. J. Am. Chem. Soc. **123**, 7154 (2001).
38. (*a*) M. Deumal, J. Cirujeda, J. Veciana, and J.J. Novoa, Adv. Mater. **10**, 1461 (1998); (*b*) M. Deumal, J. Cirujeda, J. Veciana, and J.J. Novoa, Chem. Eur. J. **5**, 1631 (1999).

© 2004 NRC Canada

Revisiting lipid – general anesthetic interactions (I): Thinned domain formation in supported planar bilayers induced by halothane and ethanol

Zoya V. Leonenko and David T. Cramb

Abstract: A long-standing question in anesthesia is that of the molecular mechanism. Do anesthetics target proteins or change membrane properties or both? We used temperature-dependent magnetic A/C mode atomic force microscopy (AFM) to study interaction of the volatile anesthetics halothane and ethanol with model membranes made from supported planar bilayers (SPBs) of 1,2-dioleoyl-*sn*-3-glycero-3-phosphocholine (DOPC), dioleoyltrimethylammonium propane (DOTAP), or 1,2-dipalmitoyl-*sn*-3-glycero-3-phosphocholine (DPPC). We found that the incorporation of halothane or ethanol induces structural changes in the bilayer. These compounds cause thickness reduction in L_α bilayers (either globally or in domains) and the formation of domains with reduced thickness in L_β phase bilayers. We propose that an anesthetic-induced increased area per lipid drives local chain disorder, thus promoting local phase change. The characteristics of SPBs with halothane or ethanol incorporated were compared with characteristics of the L_α and L_β phases of anesthetic-free SPBs.

Key words: atomic force microscopy, anesthesia, lipid bilayer domains, phase transition

Résumé : Le mécanisme moléculaire de l'anesthésie n'a toujours pas été résolu. On se demande encore est-ce que les produits anesthésiques s'attaquent aux protéines ou s'ils changent les propriétés des membranes ou agissent-ils sur les deux fronts. On a fait appel à la microscopie de forces atomiques (MFA) en mode A/C magnétique et dépendante de la température pour étudier l'interaction d'anesthésiques volatiles, tels l'halothane et l'éthanol, avec des membranes modèles faites à partir de bicouches planaires supportées (BPS) de 1,2-dioléoyl-*sn*-3-glycéro-3-phosphocholine (DOPC), de dioléoyltriméthylammonium propane (DOTAP) ou de 1,2-dipalmitoyl-*sn*-3-glycéro-3-phosphocholine (DPPC). On a observé que l'incorporation d'halothane ou d'éthanol induit des changements structuraux dans la bicouche. Ces composés provoquent une réduction de l'épaisseur des bicouches L_α (globalement ou dans les domaines) accompagnée de la formation de domaines comportant des épaisseurs réduites dans les bicouches de la phase L_β. On suggère qu'une surface par lipide accrue, induite par l'anesthésique, provoque un désordre de chaîne local qui induit un changement de phase local. On a comparé les caractéristiques des BPS dans lesquelles on a incorporé de l'halothane ou de l'éthanol avec les caractéristiques des phases L_α et L_β de BPS ne contenant pas d'anesthésique.

Mots clés : microscopie de forces atomiques, anesthésie, domaines de bicouches lipidiques, transition de phase.

[Traduit par la Rédaction]

Introduction

The phenomenon of domain formation in model membranes is of great interest, as membrane structural changes define changes in membrane functional properties. This may also be true for anesthesia. Indeed, there have been paradigm shifts in the molecular theory of anesthetic action over the past century. The correlation found by Meyer and Overton (1, 2) between anesthetic potency and lipid solubility suggested that alteration of the lipid membrane structure was key to anesthetic efficiency. As membrane protein studies became possible at the molecular level, attention shifted to the direct action of anesthetics on ligand-gated ion channels (3, 4). More recently, it has been suggested that volatile anesthetics indirectly affect membrane protein by altering the lateral pressure within bilayers (5). Also, a multiple-sites-of-action hypothesis has been forwarded in which general anesthetics may bind to many protein and lipid sites with relatively low affinity (1–10 mmol/L) (6). Despite considerable study, the exact molecular effect of volatile anesthetics on membranes is only beginning to emerge. It has been demonstrated that volatile anesthetics can induce a change in lipid packing in membranes (7–9). For example, several experimental and theoretical studies were devoted to investigation of changes in membrane properties due to the incorporation of alcohols. For example, Holte and Gawrish (10) found that ethanol partitions near the lipid–water interface close to the lipid glycerol backbone and upper segments of lipid hydrocarbon chains and increases the degree of motional disorder in lipid chains. The implication is that a contributing factor in the physiological effect of ethanol results from the mole-

Received 8 October 2003. Published on the NRC Research Press Web site at http://canjchem.nrc.ca on 27 May 2004.

Z.V. Leonenko and D.T. Cramb.[1] Department of Chemistry, University of Calgary, 2500 University Drive NW, Calgary, AB T2N 1N4, Canada.

[1]Corresponding author (e-mail: dcramb@ucalgary.ca).

 doi: 10.1139/V04-023 © 2004 NRC Canada

cules dissolving in specific lipid hydrophobic sites, which significantly modifies membrane structure and may lead to bilayer thinning. Thinned bilayers could contain both interdigitated lipids (interpenetration of hydrocarbon chains of the upper leaflet to the lower leaflet of the bilayer, resulting in disappearance of the bilayer midplane) and lipids with vastly increased tilt angles. It has been reported that bilayer thinning occurs when the local concentration of the species in the bilayer is higher than a threshold value (11). Bilayer thickness changes may have a strong effect on the function of membrane-associated proteins because of a mismatch of the protein–lipid hydrophobic interaction region. Changes in lipid packing in the presence of ethanol have been examined by X-ray diffraction, and they have been suggested in fluorescence spectroscopic studies (12, 13). Interdigitated domains caused by ethanol were proposed by Mou et al. (14) to explain the thinned dipalmitoylphosphatidylcholine (DPPC) bilayer they observed using atomic force microscopy (AFM). Recently, AFM studies by McClain and Breen (15) suggest that 2-propanol-induced DPPC bilayer thinning is strictly due to interdigitation.

Halothane is a clinical anesthetic that has received increasing attention as a model molecule for fundamental studies on anesthetic action. Molecular dynamics simulations (16) of halothane in a DPPC bilayer revealed that halothane self-associates and also is distributed nonuniformly across the membrane interior. This resulted in significant modifications of the lipid bilayer, including thinning. A decrease in lipid wobble and an increase in tail defects of the lipid system were also observed.

A temperature-dependent AFM study may provide valuable information about the effect of anesthetics on the thinned-bilayer formation by monitoring the effect of anesthetics on the chain-melting phase transition. Very recently, three temperature-dependent AFM studies involving bilayers have been reported (17–19). In these papers, increases in temperature were used to induce L_β–L_α phase changes in the supported planar bilayers (SPBs). In our studies of DNA – cationic bilayer interactions as a function of temperature, we have shown that topology can be accurately measured using magnetic A/C (MAC) mode AFM to temperatures as high as 70 °C in a liquid sample cell (19). Temperature-dependent AFM allows a novel examination of halothane-induced changes in lipid bilayer properties and permits powerful re-examination of some previous results (14) for anesthetic – DPPC bilayer interactions, because the characteristics of both the gel- and the liquid-phase SPB can be measured on the same sample in the presence and absence of anesthetic.

In the present work, we have concentrated our efforts on studying the incorporation of ethanol and halothane into SPBs. We employed MAC mode AFM to study anesthetic-induced changes in supported phospholipid bilayers of dioleoylphosphatidylcholine (DOPC), DPPC, or dioleoyltrimethylammonium propane (DOTAP). The goal of this study was to extend the knowledge that exists in the literature for ethanol and to examine the incorporation of halothane into a bilayer. We were also able to measure the bilayer properties as a function of temperature and to induce the L_β–L_α phase transition in DPPC, and we used a temperature increase to irreversibly drive ethanol out of the SPBs. In the following companion paper (20), the results of our AFM studies for halothane are compared with those obtained using spectroscopic techniques.

Materials and methods

Dioleoylphosphatidylcholine (DOPC, lyophilized or in chloroform solution), dioleoyltrimethylammonium propane (DOTAP, chloroform solution), and dipalmitoylphosphatidylcholine (DPPC) were obtained from Avanti Polar Lipids Inc. (Alabaster, Ala.) and were used without further purification. Tris–EDTA (TE) buffer, pH 7.6, and distilled, ultrapure water were used in the generation of all vesicles. Freshly cleaved ASTMV-2 quality, scratch-free ruby mica (Asheville-Schoonmaker Mica Co., Newport News, Va.) was used throughout this study as a substrate. In some cases, mica was modified by addition of a dilute solution of 3-aminopropyltriethoxysilane (APTES) using standard procedures (21).

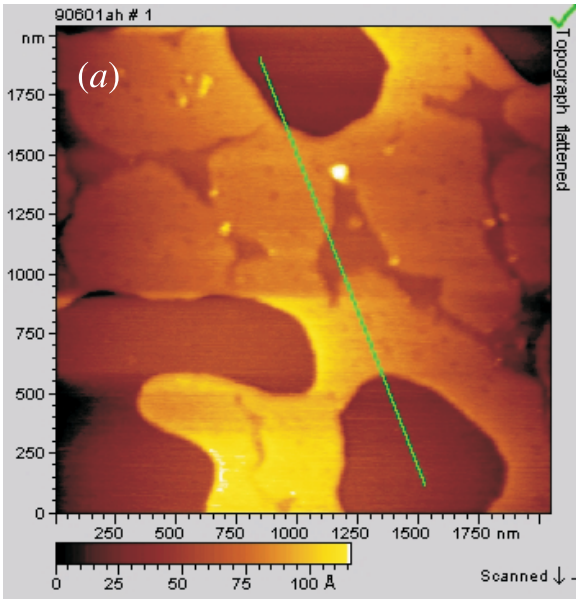
All vesicles were prepared using the "dry" method as previously reported (22). An appropriate aliquot of phospholipid chloroform solution was measured into a small vessel, and the chloroform was removed using a stream of dry nitrogen. The dry phospholipid was then resuspended in buffer to its final concentration and stirred for 30 min. The solution was sonicated (Branson 1200; Branson Ultrasonics, Danbury, Conn.) at room temperature for 10-min periods. Between each 10-min period, there was a 15-min "rest" interval where the solution was placed in an ice bath and then stirred at room temperature. For this method, the solutions were cycled an average of 10 times or until they were observed to clear.

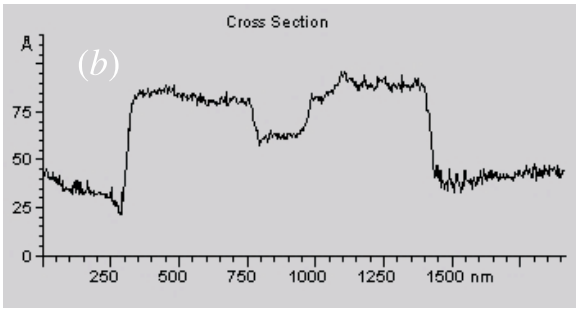
Supported planar bilayers were prepared for AFM imaging by the method of vesicle fusion (22, 23). Aliquots of liposome solution were deposited on modified or unmodified freshly cleaved mica. After a controlled period of time, the mica was gently rinsed with ultrapure water, and the surface was imaged under water in the liquid cell, at room temperature and at various higher temperatures.

Addition of ethanol and halothane was performed in two ways: (*i*) by addition of pure anesthetic into the vesicle solution with an incubation time of 1.5 h and (*ii*) by addition of an ethanol/water mixture (50% by volume) or pure liquid halothane into the AFM liquid cell with the established supported bilayer and incubation for the same period of time. A time of 1.5 h was shown by fluorescence experiments to be optimal for halothane distribution between buffer and membrane (20).

We employed MAC mode AFM, where a magnetically coated probe oscillates near its resonant frequency driven by an alternating magnetic field. This technique has proven to be advantageous for measuring supported planar bilayers in liquid media (22, 24, 25). All images were taken using a Pico SPM microscope with AFMS-165 scanner (Molecular Imaging Inc., Phoenix, Ariz.). Magnetically coated type I Maclevers® (Molecular Imaging Inc.) were used for MAC mode imaging. Their specifications include a length of 85 μm, a force constant of 0.06–0.1 N/m, a resonant frequency of 20–40 kHz in water, and a tip radius of curvature quoted as less than 10 nm. The standard MAC mode fluid cell (Molecular Imaging Inc.) was used throughout. The scanning speed was 1–2 lines per second. The height scale

© 2004 NRC Canada





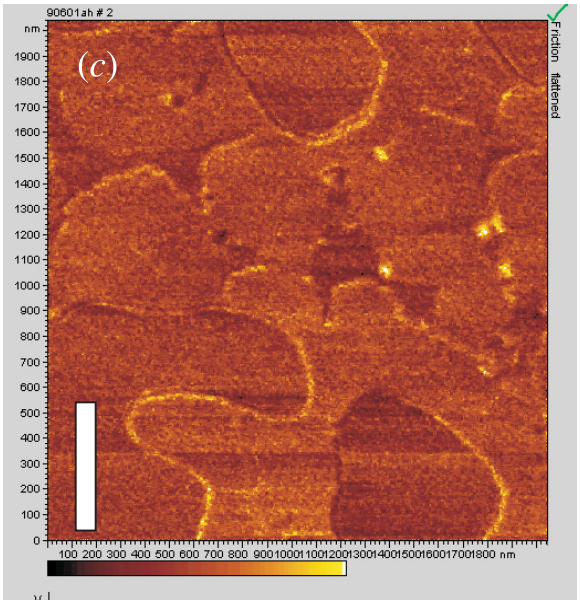


Fig. 1. Topography image (*a*), cross section (*b*), and phase image (*c*) of a supported dipalmitoylphosphatidylcholine (DPPC) bilayer in the presence of ethamol obtained by AFM. An EtOH–water mixture (50:50 by volume) was added to a supported DPPC bilayer, incubated for 1.5 h, and then rinsed with pure water prior to the AFM measurements. The scale bar in panel (*c*) is 500 nm long.

was calibrated using colloidal gold spheres of 5 nm and 14 nm in diameter (26). For elevated-temperature experiments, the AFM Temperature Controller and Hot Mac Mode Stage from Molecular Imaging Inc. were used. Heating and cooling were performed at ΔT = 1 °C/min, with the possibility to hold at any given temperature. The mean value(s) of the bilayer thickness was calculated using between 50 and 70 measurements over several scanned regions, where appropriate. The standard deviation is quoted at the 99% confidence level.

Results and discussion

DPPC

The changes in a L_β DPPC bilayer structure as a function of incorporation of halothane and ethanol were examined and compared with the effect of temperature. The reason for using ethanol was to compare our data, obtained by MAC mode AFM, with the results of previous studies (14, 15). There are several studies in the literature that have examined incorporation of ethanol and other alcohols into phospholipid bilayers using various methods, including fluorescence (27) and AFM (14, 15). It has been suggested that a high concentration of ethanol in a lipid-containing aqueous solution can induce transformation of a lipid bilayer from (L_β) gel phase to the fully interdigitated ($L_{\beta I}$) phase of monounsaturated phosphatidylcholine (PC) lipids, which alters the L_β–L_α melting transition temperature of the phospholipid bilayer (28). In our study, ethanol was added to a supported DPPC bilayer on mica. After 1.5 h, the cell was then rinsed and imaged in water. In the absence of ethanol, we measured the thickness of a pure supported DPPC bilayer on mica as 5.5 nm, from natural defects, which is in good agreement with the value of 5.7 nm reported earlier (14). We observed the formation of thin domains in the presence of ethanol (Fig. 1). The thickness of the higher domains was 5.6 nm, and that of the lower domains was 3.6 nm (Table 1). The difference in thickness of the two domains was 2.0 nm, compared with 1.9 nm previously reported (14). The ethanol/SPB system remained stable at room temperature for up to 2 days. Changing the relative concentration of ethanol only changed the extent of thin domains, but not their thickness. The stability of the thin domains suggests that ethanol remains preferentially in the bilayer at room temperature. When the bilayer was heated to 50 °C (i.e., above the melting transition point, T_m = 41 °C) while imaging was performed and then slowly cooled back to room temperature, the lower domains disappeared and the original bilayer thickness was restored. This reversibility of the ethanol effect is in agreement with data of Mou et al. (14), although the latter authors were not able to simultaneously image and scan temperature. These findings suggest that ethanol repartitions into water when DPPC is at elevated temperature and that this repartitioning depends on the phase of the bilayer. Recently, we investigated the temperature dependence of a pure DPPC SPB (data not shown). As the tempera-

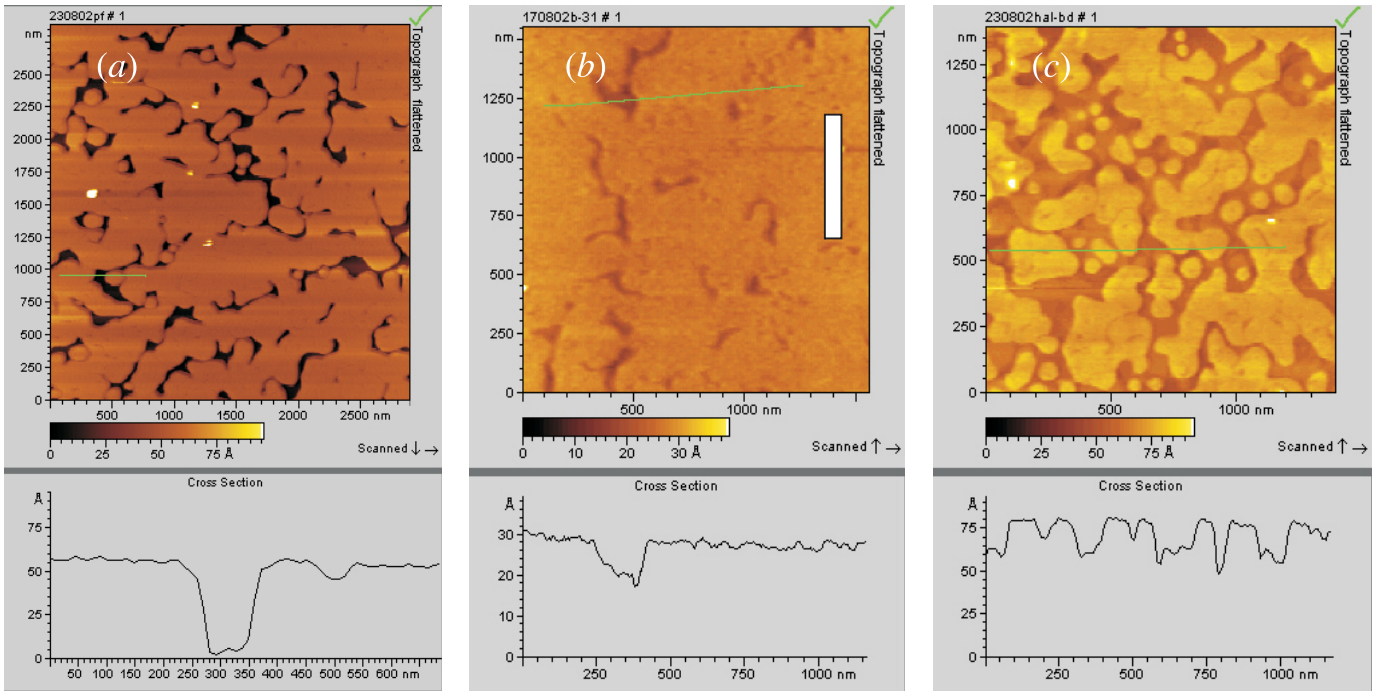
© 2004 NRC Canada

Table 1. Dependence of thickness (nm) of supported planar bilayers (SPBs) on the incorporation of halothane and ethanol.

SPB[a]	Thickness of pure lipid bilayer	Thickness after addition of ethanol		Thickness after addition of halothane	
		$C_{EtOH\ in\ water}$ = 75 mmol/L	$C_{EtOH\ in\ water}$ = 1.4 mol/L	MR = 3.6:1	MR = 7.3:1
DOTAP	3.7 ± 0.2		3.6 ± 0.2		3.5 ± 0.2
					2.9 ± 0.2
DOPC	5.4 ± 0.1	5.3 ± 0.3	3.5 ± 0.2	5.0 ± 0.5	3.6 ± 0.2
		3.5 ± 0.2		3.6 ± 0.3	
DPPC	5.5 ± 0.1		5.6 ± 0.2	5.5 ± 0.1	5.5 ± 0.1
			3.6 ± 0.3		3.5 ± 0.1

Note: MR is the ratio of the number of moles of halothane in the membrane to the number of moles of lipids.
[a]DOTAP, dioleoyltrimethylammonium propane; DOPC, dioleoylphosphatidylcholine; DPPC, dipalmitoylphosphatidylcholine.

Fig. 2. Topography images and cross sections showing the effects of incorporation of halothane into a DPPC bilayer. (*a*) Pure DPPC bilayer; (*b*) DPPC with halothane, at an estimated molar ratio of halothane in the membrane to lipid of 3.4:1; (*c*) DPPC with halothane, molar ratio = 14.6:1. In these experiments, halothane was added into the vesicle solution prior to SPB formation.

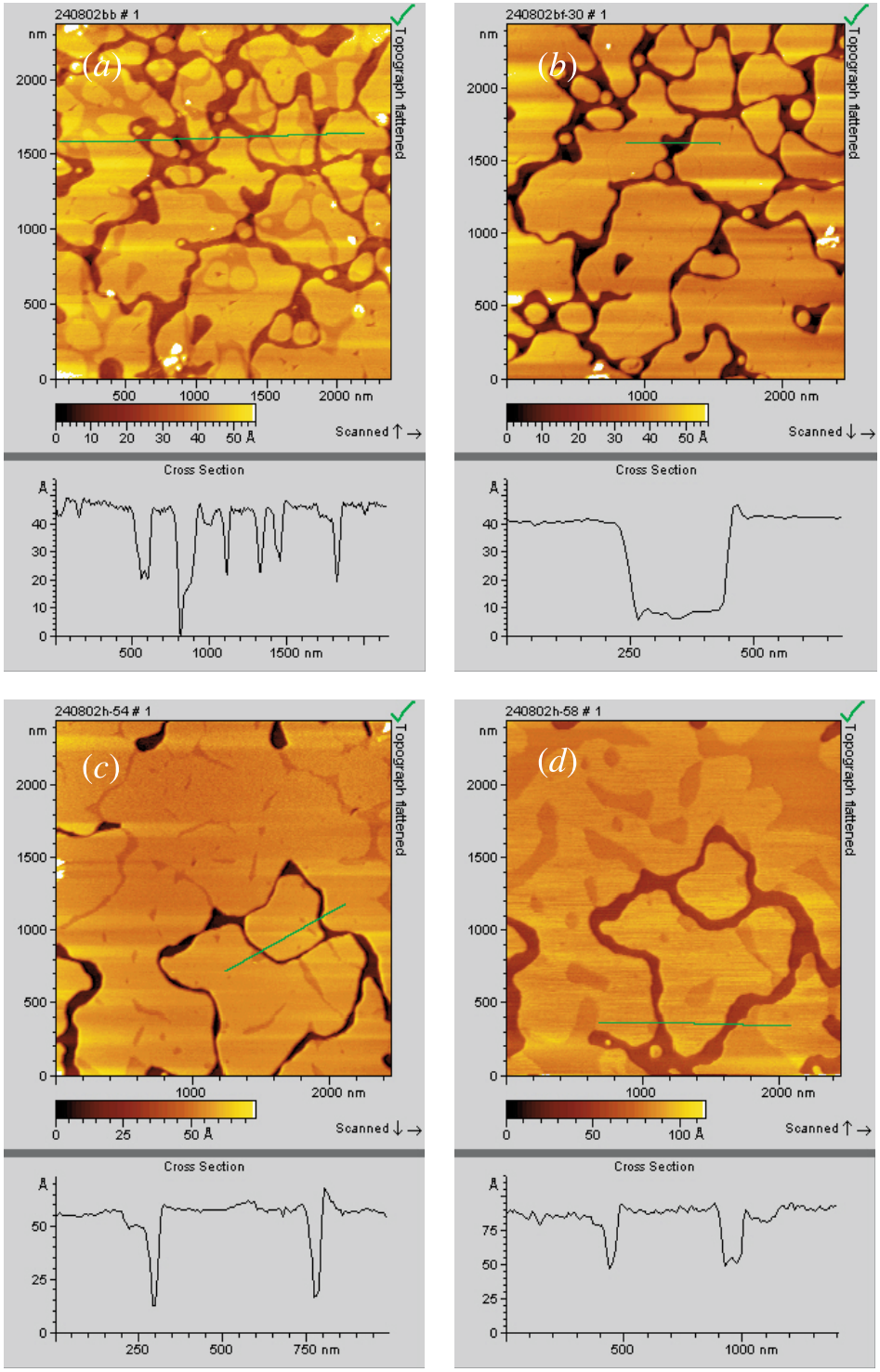


ture approached the L_β–L_α phase transition, thinned domains appeared. The heights of the domains were exactly the same as those induced by ethanol, described above. When holding at a temperature of 50 °C, the lower domains coalesced and grew in extent. There is every reason to believe that these thinner domains represent a DPPC SPB in its L_α state. The value of 3.6 nm for L_α DPPC thickness is in the range previously determined using X-ray scattering ($X_{head\text{-}to\text{-}head}$ = 3.6–4.0 nm) (29). A similar range was also calculated by Feller et al. (30) by molecular dynamics simulation. Interestingly, the simulation illustrated that the DPPC lipid chains in the L_α phase displayed both some interdigitation and significant tilting. However, there was no indication of the completely interdigitated $L_{\beta I}$ phase, where methyl end groups would be exposed to water.

We have also examined the incorporation of halothane into a DPPC bilayer to compare the effects of ethanol and halothane. The halothane was added into the vesicle solution or into the liquid cell with a preformed supported bilayer. In Fig. 2 we illustrate the effects of incorporating halothane into vesicles prior to SPB formation. In the presence of halothane, we observed similar domain formation in a DPPC bilayer to that induced by ethanol. The thickness of the higher and lower domains was measured as 5.5 and 3.5 nm, respectively, giving the same difference of 2.0 nm as we observed in the case of ethanol (Table 1). The surface coverage of the thin domains was 2–3% at lower halothane concentrations (Fig. 2*b*) and comparable to that naturally formed in pure DPPC SPBs (1–2%). At higher halothane content, we observed a considerable amount of lower domain surface coverage (25–50%, Fig. 2*c*). We were able to image the surface during slow heating of the bilayer above the melting transition point (T_m = 41 °C). Heating the system to 42 °C did not induce considerable changes in the domain structure. After 1 h of scanning at 42 °C, lower domains in the bilayer were still present. A further increase in temperature to 50 °C

© 2004 NRC Canada

Fig. 3. Topography images and cross sections of supported DPPC bilayer with halothane recorded as a function of temperature and time. Halothane was added into the liquid cell containing a supported DPPC bilayer covered with 1 mL of water; no rinsing was performed for this sample. Halothane remained in the water and the sample was scanned during heating. (*a*) Room temperature; (*b*) 30-min scanning at room temperature; (*c*) heated to 50 °C; (*d*) heated to 58 °C; (*e*) heated to 62 °C; (*f*) cooled to 55 °C; (*g*) cooled to 50 °C; (*h*) cooled to room temperature. The estimated molar ratio of halothane in the membrane to lipid was 3.4:1.

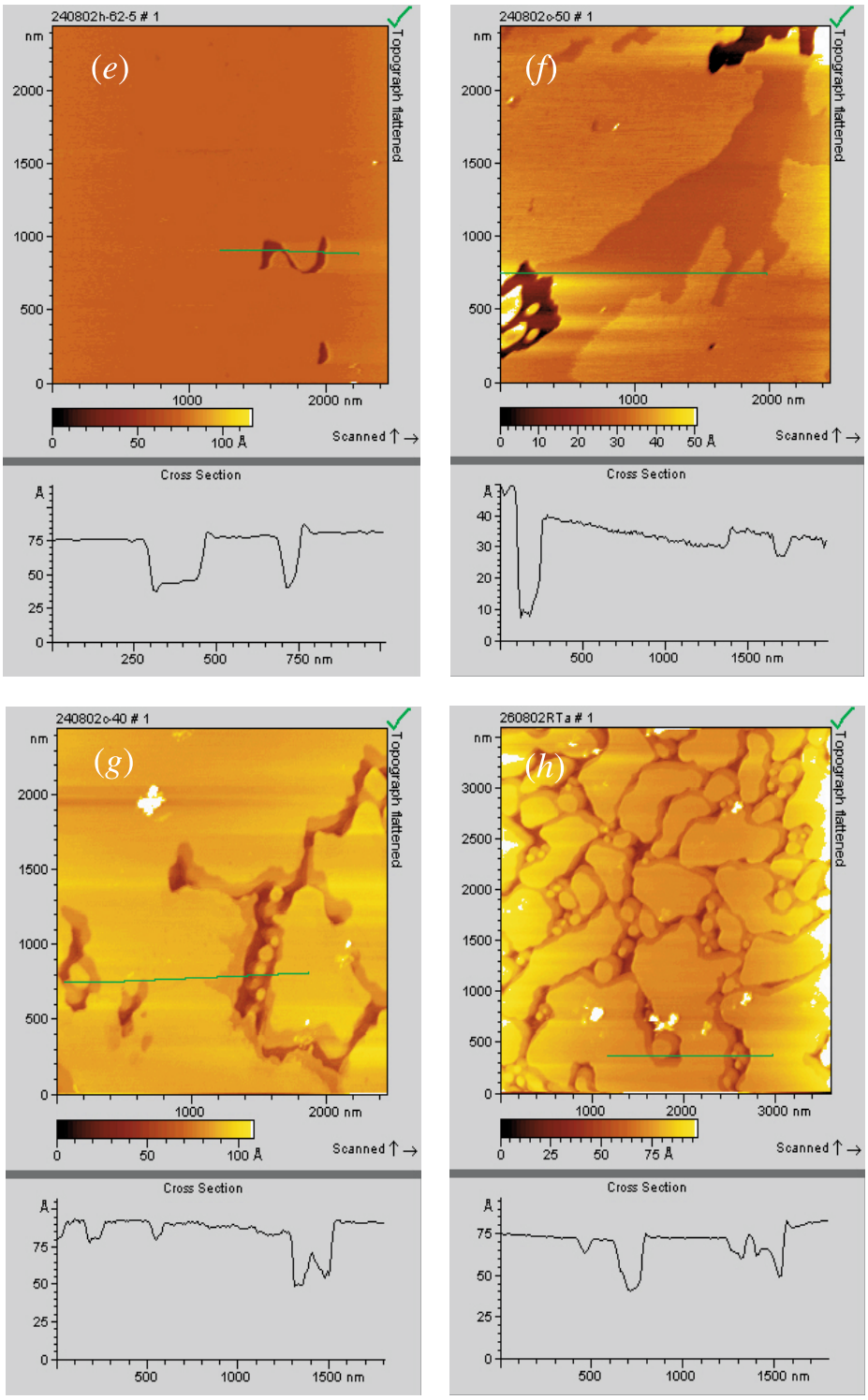


demonstrated that the remaining thicker domains melted at a higher temperature than the pure DPPC free-standing bilayer and the phase transition was broad. This is consistent with the melting of a pure DPPC SPB (data not shown).

In the alternate preparation, halothane was added into the liquid cell containing the supported DPPC bilayer covered with 1 mL of water. After the addition of halothane, no rinsing was performed. In Fig. 3, we follow the SPB containing

© 2004 NRC Canada

Fig. 3 (*concluded*).



halothane as a function of temperature and time. In this case we observed a very interesting transition of the bilayer containing halothane at room temperature during the first 30 min of scanning. Domains (thickness of higher domains was 4.5 ± 0.2 nm) initially present (Fig. 3*a)* disappeared and the bilayer became generally thin (3.3 ± 0.3 nm, Fig. 3*b*). Because the bilayer was supported on mica, we consider that halothane first causes structural changes in the upper leaflet, and scanning at room temperature might induce equilibration of halothane between the two leaflets. After this thinner bilayer is formed, the system is stable during scanning at room temperature and becomes thinner yet at a temperature higher than that of the L_β–L_α transition for a pure DPPC bilayer. Further thinning was observed to start at 50 °C and was complete at 62 °C (Figs. 3*c*–*e*). After the system was cooled back to room temperature (Figs. 3*f*–*h*), bilayer thick-

© 2004 NRC Canada

ness was 3.9 ± 0.2 nm, which is lower than that of pure L_β DPPC bilayer. The initial thickness of pure DPPC without halothane was restored during a similar cooling process (data not shown). The molar ratio of the amount of halothane in the membrane to that of lipid was estimated as $n_{Hal}/n_L = 3.4$ at room temperature and has been shown to increase by a factor of 4 above the chain-melting transition temperature (31). The amount of halothane in the bilayer was estimated using the partition coefficient of halothane in DPPC provided by Simon et al. (31). This increase in halothane partitioning during heating is probably responsible for a saturation of the bilayer with halothane and stabilization of thinned domains when the system was cooled back to room temperature.

The persistence of thinner domains and the complete thinning of the bilayer show that interaction of halothane with the lipids is very strong and increases at elevated temperature. These results are consistent with those reported in the companion paper (20) as well as with those obtained by Simon et al. (31) and by Hill (32).

When compared with ethanol, halothane shows different behavior during heating. Whereas ethanol leaves the bilayer, thus restoring its initial thickness, halothane partitioning increases with temperature, leading to more extensive domain formation. The reason for this difference in behavior likely originates from the higher hydrophobicity of halothane and its lower solubility in water (17 mmol/L) (20) compared with that of ethanol. Ethanol can escape during heating when the mobility of phospholipids and ethanol is high, whereas for solubility reasons halothane remains in the bilayer.

The transitions observed upon heating the bilayer with and without halothane were compared. For a pure DPPC bilayer, we observed a broad main transition between 42 °C and 52 °C and further change between 52 °C and 60 °C; upon cooling back to room temperature, a transition between 35 °C and 36 °C occurred. When the bilayer with halothane incorporated was heated, the lower temperature transition was not observed, and only one transition at 52–60 °C occurred. The presence of halothane likely changes structural properties of the bilayer in such a way that the other transitions observed for a pure bilayer are not possible. The transition below T_m likely involves reorganization of water molecules at the interface. In the presence of halothane, water molecules are exchanged for halothane molecules, which eliminates the low-temperature transition.

The inhomogeneous domain formation observed with both ethanol and halothane incorporation is presumably due to a cooperative mechanism of anesthetic penetration and partitioning into the bilayer. This mechanism may include localized dehydration of headgroups by disruption of the coordinated hydration shell. The existence of such a hydration shell has been suggested by molecular dynamics simulations (33). Additionally, the initial rupture of the hydration shell may promote inhomogeneous anesthetic incorporation into the bilayer at the exposed location. After water shell rupture, further incorporation of anesthetic into the bilayer increases the headgroup area and motional disorder in lipid chains and leads to formation of the thinned state. The possible role of water in the mechanism of anesthesia was emphasized in previous studies (33, 34). Ueda and co-workers (34, 35) have obtained evidence, through proton NMR measurements and FTIR spectroscopy, for the release of bound interfacial water by inhalation anesthetics in a water-in-oil emulsion. This suggested that some anesthetics compete with water for binding sites. Both ethanol and halothane are able to form hydrogen bonds. Halothane contains a so-called acidic hydrogen, which is considered to be involved in a "hydrogen bond breaking effect". It has been shown that anesthetics with "acidic hydrogen" and therefore with high "hydrogen bond breaking" ability have higher anesthetic potency than halogenated molecules containing no acidic hydrogen (36). An NMR study (10) has shown that ethanol incorporates into the lipid–water interface near the lipid glycerol backbone and upper segments of lipid hydrocarbon chains and increases the degree of motional disorder in the lipid chains, which promotes formation of a thinned bilayer.

Molecular dynamics simulations (16) indicate that halothane induces lateral expansion and contraction of the L_α DPPC bilayer. Koubi et al. (16) reported a thickness reduction of 8 Å (from 42 to 34 Å; 1 Å = 0.1 nm) and an increase in area per lipid of 16% (from 63.6 to 72.0 $Å^2$). We observed a thickness reduction from 5.5 to 3.5 nm (2.0 nm) in the L_β DPPC bilayer due to incorporation of halothane. We also have observed a thinning of a pure DPPC bilayer to 3.6 nm upon heating above 42 °C. Thus, incorporation of halothane produces a similar thinning effect as heating the bilayer above the chain melting transition temperature. The difference in an L_α DPPC SPB with and without halothane is small (0.1 nm) compared with that predicted (0.8 nm (16)). This might reflect the differences between supported planar bilayers and free-standing bilayers.

The fact that very similar DPPC bilayer changes are observed for both ethanol and halothane incorporation suggests a common mechanism. Moreover, because the formation of thin bilayer domains surrounded by thick domains is analogous to what we observe for a DPPC SPB near the L_β–L_α phase transition temperature, it is likely that ethanol and halothane induce something similar to a local phase change in the SPB. The mechanism may include initially smaller L_α-like domains coalescing into larger thin domains. The stability of these domains for periods of days would be due to a cage effect by the surrounding thicker and less mobile L_β regions. Fluorescence results from our companion paper (20) also suggest that increased disorder of the lipid packing and penetration of water near the headgroup region of DPPC small unilamellar vesicles is induced by the incorporation of halothane.

DOPC

To gain insight into how the lipid phase might affect the interaction of ethanol and halothane with SPBs, we used DOPC. DOPC exists in a fluid phase (L_α) at room temperature and serves as a fluid-phase analog of the DPPC bilayer. A pure DOPC SPB (Fig. 4*a*) has a thickness of 5.4 nm, as we reported earlier (22). In the presence of ethanol (Fig. 4*b*) or halothane (Fig. 4*c*) at a molar ratio of 7.2:1, the DOPC SPB transforms to a uniform thickness of 3.5 and 3.6 nm, respectively (Table 1). We assume that the higher lipid disorder of a DOPC bilayer results in much less cooperativity in

© 2004 NRC Canada

Fig. 4. Topography images and cross sections showing the effects of incorporation of ethanol or halothane into a dioleoylphosphatidylcholine (DOPC) bilayer. (*a*) Pure DOPC bilayer; (*b*) DOPC bilayer with ethanol, $C_{\mathrm{EtOH\ in\ water}}$ = 1.4 mol/L; (*c*) DOPC bilayer with halothane, at an estimated molar ratio of halothane in the membrane to lipid of 7.5:1. Ethanol and halothane were added into the vesicle solution prior to SPB formation. The scale bars in all panels are 500 nm long. The arrows in all cross sections represent 4.0 nm in height.

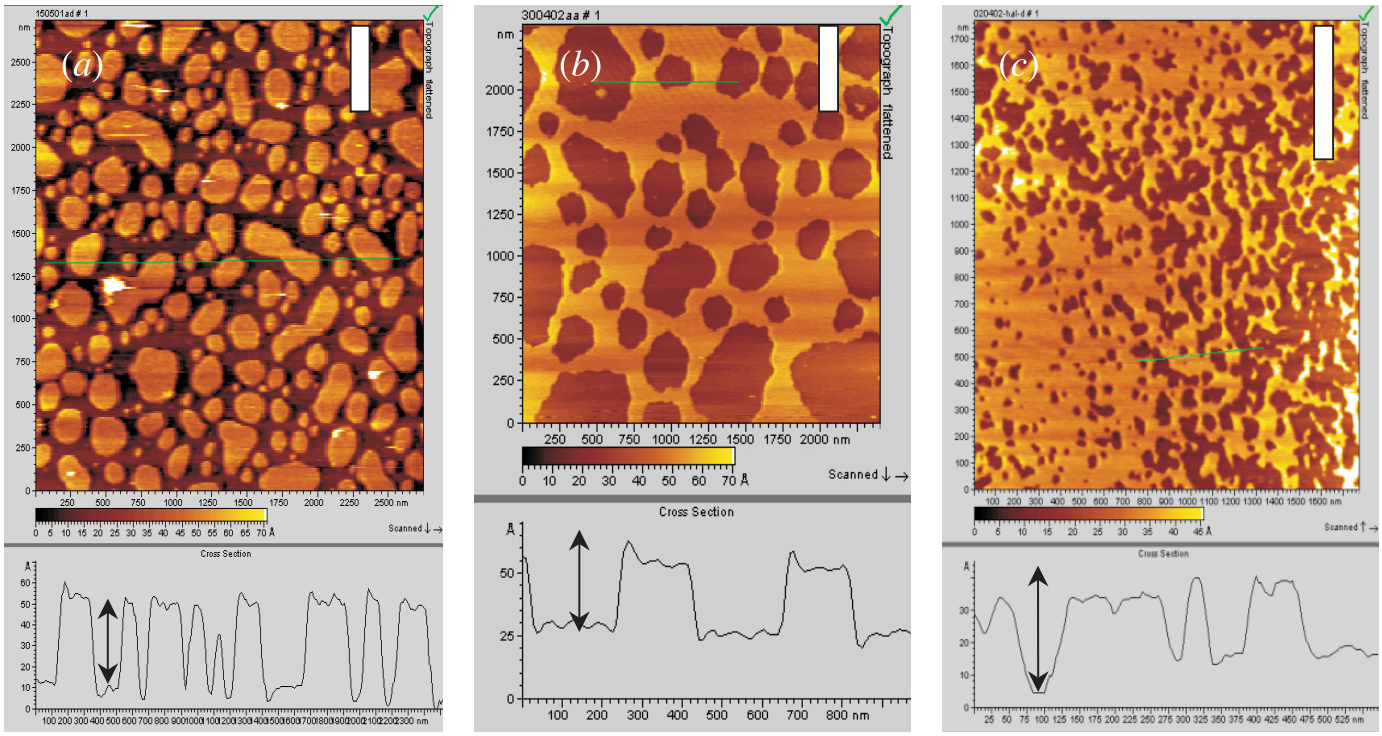
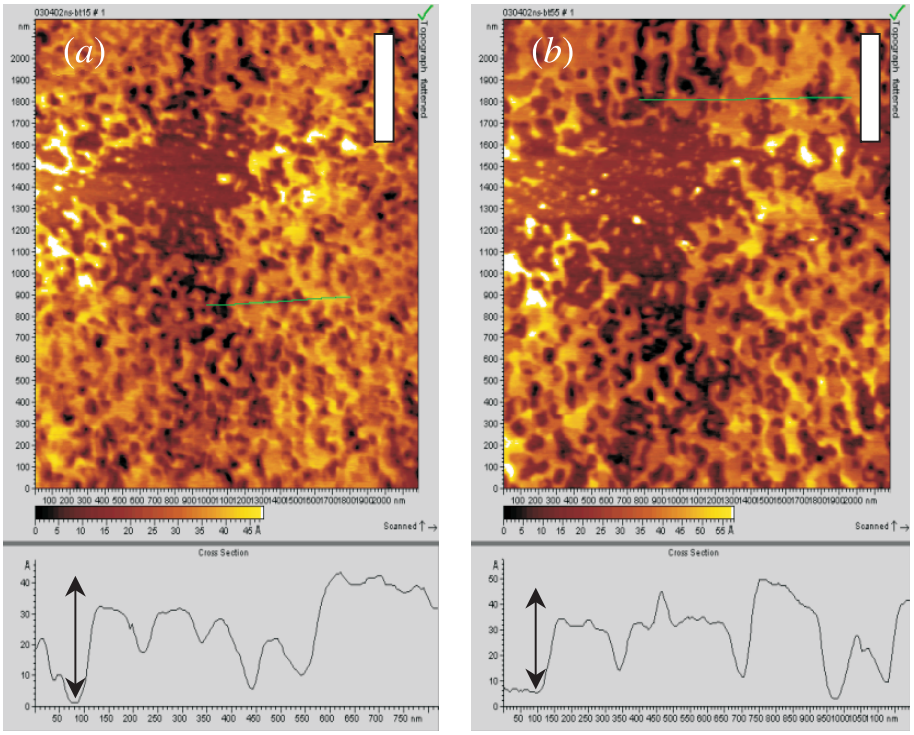
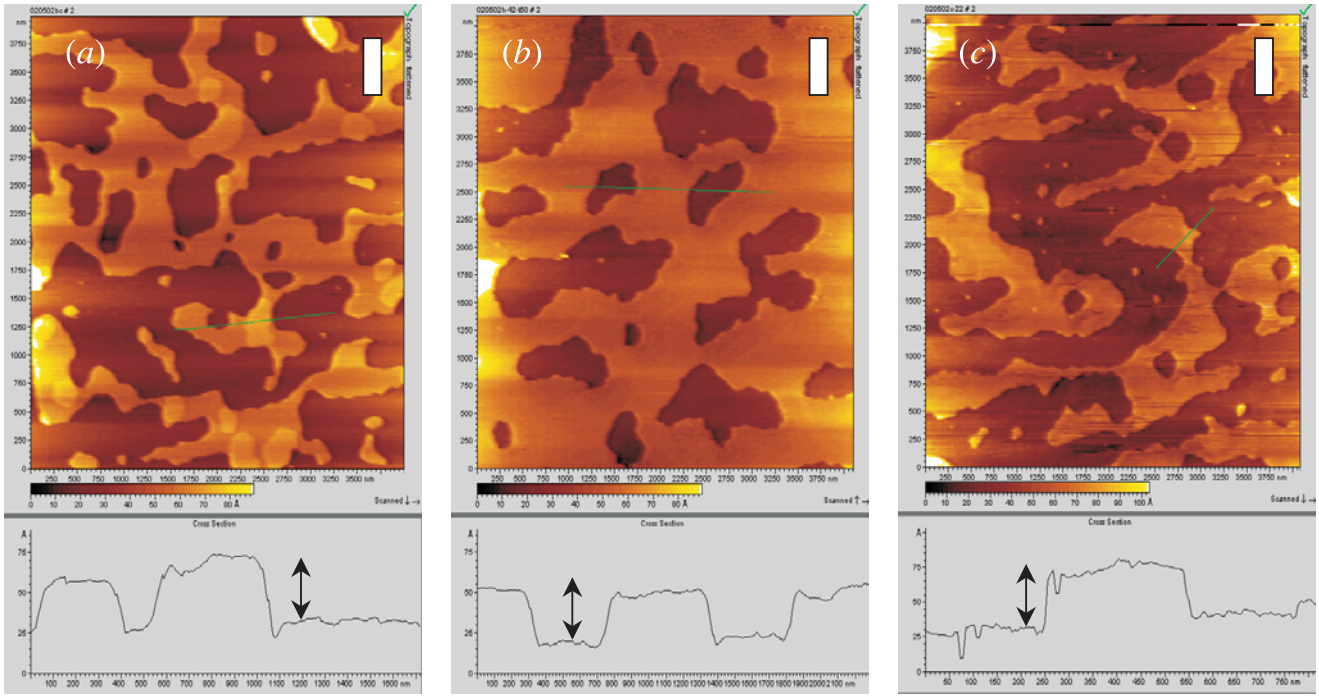


Fig. 5. Topography images and cross sections of DOPC bilayer with halothane, at an estimated molar ratio of halothane in the membrane to lipid of 3.7:1. (*a*) Initial scan; (*b*) after 40 min of scanning. Halothane was added into the vesicle solution prior to SPB formation. The scale bars in all panels are 500 nm long. The arrows in all cross sections represent 4.0 nm in height.



© 2004 NRC Canada

Fig. 6. Topography images and cross sections obtained during heating and cooling of DOPC bilayer with ethanol incorporated. (*a*) At room temperature; (*b*) at 42 °C; (*c*) after cooling back to room temperature. Ethanol ($C_{EtOH\ in\ water}$ = 75 mmol/L) was added into the vesicle solution prior to SPB formation. The scale bars in all panels are 500 nm long. The arrows in all cross sections represent 4.0 nm in height.



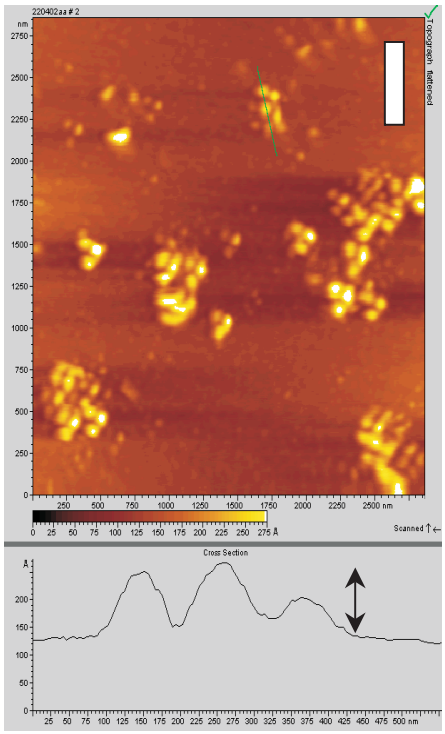
the incorporation of anesthetic at these higher molar ratios, and thus no domains are formed.

Interestingly, at a lower concentration of halothane (molar ratio = 3.6:1), domain formation was observed (Fig. 5*a*). These domains were 5.0 and 3.6 nm thick (Table 1), and the domain shape and size changed during 40 min of scanning (Fig. 5*b*). The fact that DOPC domains were not well resolved and more dynamic compared to DPPC bilayer may be explained by higher mobility of anesthetic in DOPC bilayer than in DPPC L_β bilayer. Thinned DOPC domains were observed in the presence of ethanol as well (Fig. 6*a*).

Although the ethanol-induced domains were more stable at room temperature than those induced by halothane, they started to disappear at 35 °C as the sample was heated and simultaneously imaged. We found that heating the DOPC bilayer with ethanol incorporated and then cooling it back to room temperature revealed changes in SPB surface coverage (Figs. 6*a*–*c*) and bilayer thickness. Initially, we observed a bilayer with domains of 5.5 and 3.5 nm. Upon heating and slow cooling, the bilayer was restored to 5.3 nm. This implies that the release of ethanol from DPPC is largely due to elevated temperature rather than the lipid phase, since the ethanol–DOPC system is stable at room temperature but releases ethanol at elevated temperature.

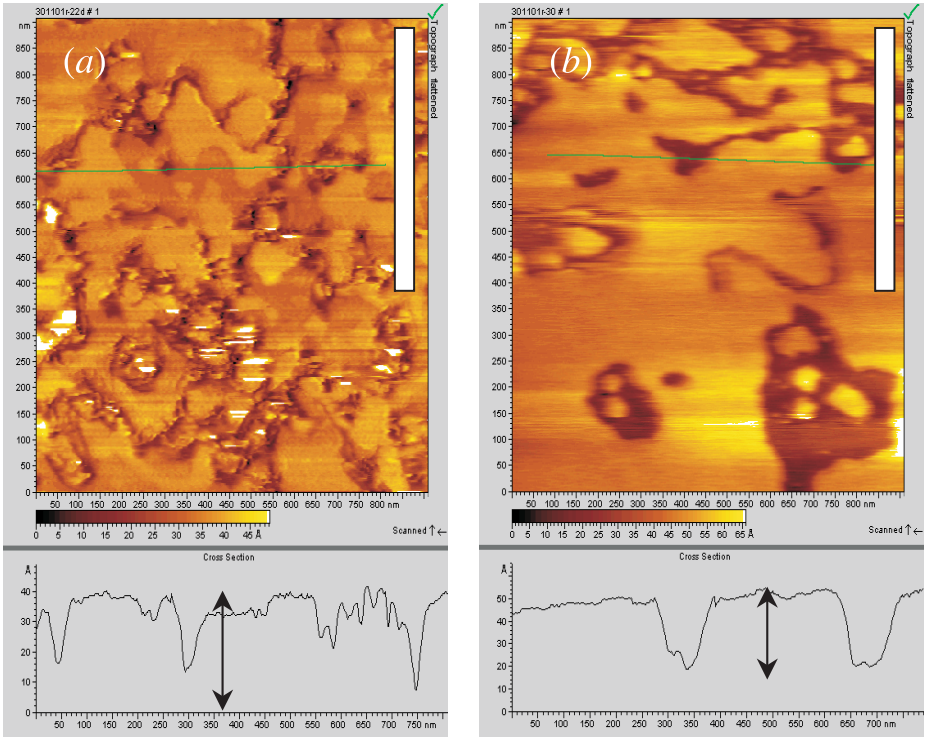
For an SPB with anesthetic incorporated, changes in surface coverage as a function of temperature can be used to provide insight into the amount of lateral expansion the SPB undergoes during incorporation. For the ethanol-containing bilayer, surface coverage increased by 42.3% (compared to the surface coverage at room temperature) upon heating to 43 °C (observed after 50 min of scanning at 43 °C). After

Fig. 7. Topography image and cross section of DOPC aggregates deposited on mica. Vesicles were prepared in an aqueous solution of ethanol (3 mol/L). The scale bar is 500 nm long. The arrow in the cross section represents 12.5 nm in height.



© 2004 NRC Canada

Fig. 8. Topography images and cross sections of a dioleoyltrimethylammonium propane (DOTAP) bilayer with halothane, at an estimated molar ratio of halothane in the membrane to lipid of 7.3:1. (*a*) At room temperature; (*b*) at 30 °C, 30-min scanning. An aqueous solution of halothane (41 mmol/L) was added into the vesicle solution prior to SPB formation. The scale bars in all panels are 500 nm long. The arrows in all cross sections represent 4.0 nm in height.



the bilayer was slowly cooled back to room temperature, the surface coverage was decreased by 6.2% compared to the initial value before heating. The increase in surface area at 43 °C (with a concomitant decrease in thickness to 3.6 nm) indicates an increase in lipid disorder. Restoring of the bilayer full thickness and a decrease of surface area indicate ethanol escape and formation of the L_α DOPC bilayer. For our conditions, we estimate that incorporation of ethanol produces a 10% increase in DOPC area per lipid compared to that of a pure DOPC bilayer at room temperature. This estimation has been made on the basis of surface changes we observed and known DOPC area per lipid in pure DOPC bilayer without ethanol (A_{DOPC} = 64 Å^2) (37). The increase in DOPC area per lipid can be compared to that of an L_α DPPC bilayer (16%) in the presence of halothane at high concentrations (16) and to that of DPPC in the presence of 2-propanol (15) (57.8% — from 52 Å^2 to 90 Å^2). The smaller increase in the case of DOPC can be explained by taking into account the liquid phase of DOPC bilayer, which is more disordered compared to gel-phase DPPC bilayer, and also to differences in the volume of incorporated molecules.

At a higher concentration of ethanol (3 mol/L) in the vesicle incubation solution, we observed formation of small disk-shaped aggregates and clusters of these aggregates upon exposure of the solution to a mica surface (Fig. 7). No bilayers were observed for this preparation. The height of the circular aggregates was in the range 10–15 nm. We assume that these aggregates could be flattened vesicles, which were stabilized by the partitioning of more ethanol molecules in the upper leaflet. This seems to make vesicles more susceptible to a pre-fusion type of aggregation but resistant to rupture upon adsorption to the mica surface. Mou et al. (14) mentioned previously the existence of such small globular structures in the presence of high concentrations of ethanol.

DOTAP

To help elucidate the influence of the headgroup on the anesthetic-induced changes in SPB structure, we performed analogous experiments using DOTAP. DOTAP is L_α at room temperature, and its headgroup carries a positive charge at neutral pH. A pure DOTAP supported bilayer was described in our earlier publication (18). Halothane was incorporated into the DOTAP bilayer via incubation in the vesicle solution at a 7.3:1 molar ratio of halothane to lipid. An AFM image of the resulting SPB is presented in Fig. 8. Although a DOTAP SPB is already very thin, we again observed formation of thinner domains. The thickness of the higher domain was 3.5 nm and that of the lower domain was 2.9 nm (Table 1). The difference in thickness of the two domains was 0.5–0.6 nm. This difference is close to that calculated (0.4 nm) by Koubi et al. (16) for halothane in L_α DPPC using molecular dynamics. We assume that high lateral mobility of lipid in a DOTAP bilayer, which exists in L_α phase at room temperature, explains the higher mobility of the domains that we observed (Fig. 8).

Conclusions

We have demonstrated by AFM that the thinned domains in DOPC, DPPC, and DOTAP supported planar bilayers in-

© 2004 NRC Canada

duced by halothane and ethanol are similar, regardless of whether the headgroup is the zwitterionic PC or the cationic TAP. This is consistent with the molecular dynamics simulations of Koubi et al. (16) for halothane in the L_α phase of DPPC, where halothane was observed to partition preferentially on the lipid side of the headgroup region. A room temperature DPPC bilayer showed stable domains when either ethanol or halothane was present in the bilayer. Upon heating above the phase transition temperature, ethanol was released whereas halothane was retained. This indicates that the effects we observe are solely due to anesthetic within the bilayer and not an effect of anesthetic content in aqueous solution. In a fluid-phase DOPC bilayer, inhomogeneous, dynamic domains were formed at a ratio of incorporated anesthetic to lipid of less than 7:1. DOPC SPBs completely thinned when this ratio was 7.3:1. The fact that domain formation was almost universally observed implies that anesthetic-induced bilayer thinning is a cooperative process. For gel-phase bilayers, it seems that volatile anesthetics induce a localized phase transformation to L_α, whereas for lipids already in L_α, even thinner domains are generated. Heating of the DPPC bilayer with halothane showed that halothane affects the transition in the bilayer. For the anesthetics studied here, the mechanism likely involves partitioning of the anesthetic preferentially near the headgroups. This is in agreement with the findings of the following companion paper and with previous theoretical and experimental studies. The fact that thinning seems to be universal means that this effect cannot be ignored when considering the physiological mechanism of anesthesia, since membrane thinning may affect the function of some membrane-associated proteins.

Acknowledgements

We thank Professor Y. Tarahovsky for helpful discussions and Molecular Imaging Inc. for continuous support. This research is supported by the Natural Sciences and Engineering Research Council of Canada.

References

1. H.H. Meyer. Arch. Exp. Pathol. Pharmakol. **46**, 338 (1901).
2. C.E. Overton. Studies of narcosis. Chapman and Hall, London. 1990.
3. J.W. Tanner, J.S. Johansson, P.A. Liebman, and R.G. Eckenhoff. Biochemistry, **40**, 5075 (2001).
4. J.E. Sirois, Q. Lei, E.M. Talley, C. Lynch, and D.A. Bayliss. J. Neurosci. **20**, 6347 (2000).
5. R.S. Cantor. Biophys. J. **80**, 2284 (1994).
6. G.E. Morgan, Jr., and M.S. Mikhail. *In* Clinical anesthesiology. Appleton and Lange, Stamford, Conn. 1996. pp. 109–120.
7. E.S. Rowe. Biochemistry **26**, 46 (1987).
8. S.A. Simon and T.J. McIntosh. Biochim. Biophys. Acta, **773**, 169 (1984).
9. P. Nambi, E.S. Rowe, and T.J. McIntosh. Biochemistry, **27**, 9175 (1988).
10. L.L. Holte and K. Gawrish. Biochemistry, **36**, 4669 (1997).
11. E.S. Rowe and J.M. Champion. Biophys. J. **67**, 1888 (1994).
12. H. Komatsu, P.T. Guy, and E.S. Rowe. Chem. Phys. Lipids, **65**, 11 (1993).
13. L.T. Boni, S.R. Minchey, W.R. Perkins, P.L. Ahl, J.L. Slater, M.W. Tate, S.M. Gruner, and A.S. Janoff. Biochim. Biophys. Acta, **1146**, 247 (1993).
14. J. Mou, J. Yang, C. Huang, and Z. Shao. Biochemistry. **33**, 9981 (1994).
15. R.L. McClain and J.J. Breen. Langmuir, **17**, 5121 (2001).
16. L. Koubi, M. Tarek, M. Klein, and D. Scharf. Biophys. J. **78**, 800 (2000).
17. M.C. Giocondi, V. Vie, E. Lesniewska, P.E. Milhiet, M. Zinke-Allmang, and C. Le Grimellec. Langmuir, **17**, 1653 (2001).
18. Z. Leonenko, D. Merkle, S.P. Lees-Miller, and D.T. Cramb. Langmuir, **18**, 4873 (2002).
19. Z. Leonenko and D. Cramb. D. Nanoletters, **2**, 305 (2002).
20. A. Carnini, H.A. Phillips, L.G. Shamrakov, and D.T. Cramb. Can J. Chem. **82** (2004). This issue.
21. S.M. Lindsay, Y.L. Lyubchenko, A.A. Gall, L.S. Shlyakhtenko, and R.E. Harrington. Proc. SPIE (Scanning Probe Microscopies), **1639**, 84 (1992).
22. Z.V. Leonenko; A. Carnini, and D.T. Cramb. Biochim. Biophys. Acta, **1509**, 131 (2000).
23. A.A. Brian and H.A. McConnell. Proc. Natl. Acad. Sci. U.S.A. **81**, 6159 (1984).
24. W. Han, S.M. Lindsay, and T. Jing. Appl. Phys. Lett. **69**, 1 (1996)
25. W. Han and S.M. Lindsay. Appl. Phys. Lett. **72**, 1656 (1998).
26. J. Vesenka, S. Manne, T. Giberson, E. Marsh, and E. Henderson. Biophys J. **65**, 992 (1993).
27. Q.-T. Li and W.K. Kam. J. Biochem. Biophys. Methods, **35**, 11 (1997).
28. T.J. McIntosh, H. Lin, S. Li, and C. Huang. Biochim. Biophys. Acta, **1510**, 219 (2001).
29. J.F. Nagle, R. Zhang, S. Tristram-Nagle, W. Sun, H.I. Petrache, and R.M. Suter. Biophys. J. **70**, 1419 (1996).
30. S.E. Feller, R.M. Venable, and R.W. Pastor. Langmuir, **13**, 6555 (1997).
31. S.A. Simon, T.J. McIntosh, P.B. Bennet, and B.B. Shrivastav. Mol. Pharmacol. **16**, 163 (1979).
32. M.W. Hill. Biochim. Biophys. Acta, **356**, 117 (1974).
33. L. Perera, U. Essman, and M.L. Berkowirz. Langmuir, **12**, 2625 (1996).
34. T. Yoshida, H. Okabayashi, K. Takahashi, and I. Ueda. Biochim. Biophys. Acta, **772**, 102 (1984).
35. Y.S. Tsai, S.M. Ma, H. Kamaya, and I. Ueda. Mol. Pharmacol. **31**, 623 (1987).
36. G. Trudeau, K.C. Cole, R. Massuda, and C. Sandorfy. Can. J. Chem. **56**, 1681 (1978).
37. N. Cuvillier, F. Millet, V. Petkova, M. Nedyalkov, and J.-J. Benattar. Langmuir, **16**, 5029 (2000).

© 2004 NRC Canada

Revisiting lipid – general anesthetic interactions (II): Halothane location and changes in lipid bilayer microenvironment monitored by fluorescence

Anna Carnini, Heather A. Phillips, Leanne G. Shamrakov, and David T. Cramb

Abstract: A universal mechanism for the action of general anesthetics (GA) is not yet available. In this study, we investigated the interaction between halothane and 1,2-dipalmitoyl-*sn*-3-glycero-3-phosphocholine (DPPC) and 1,2-dioleoyl-*sn*-3-glycero-3-phosphocholine (DOPC) bilayers labeled with Laurdan, Prodan, and NBD-C_6-PC as the reporter probes using steady-state fluorescence spectroscopy. We have evidence that halothane is located on the acyl chain side, near the headgroup region of the bilayer. Additionally, we find that halothane may be inhomogeneously distributed within DOPC and DPPC bilayers. We also show data that indicate halothane increases the free volume available to fluorescent probes. Differential scanning calorimetry and UV scanning calorimetry experiments were implemented to further observe the effects of halothane addition to the DPPC lipid bilayer. A significant shift of the phase-transition temperature of the DPPC system was observed. Our findings suggest that general anesthetic – lipid bilayer interactions may play a significant role in the overall mechanism of anesthetic action, and these effects should not be ignored when interactions between membrane proteins and anesthetics are considered.

Key words: liposomes, anesthesia, fluorescence, phase transition, phospholipid bilayers.

Résumé : On ne connaît pas encore de mécanisme universel d'action pour l'action des anesthésiques généraux (AG). Dans cette étude, faisant appel à la spectroscopie de fluorescence en état stationnaire, on a étudié l'interaction de l'halothane et de bicouches de 1,2-dipalmitoyl-*sn*-3-glycéro-3-phosphocholine (DPPC) et de 1,2-dioléoyl-*sn*-3-glycéro-3-phosphocholine (DOPC) marquées avec du Laurdan, du Prodan et du NBD-C_6-PC comme sondes. On a obtenu des résultats qui suggèrent que l'halothane se situe sur la chaîne acyle latérale, près de la région du groupe de tête de la bicouche. De plus, on a trouvé que l'halothane n'est peut être pas distribué de façon homogène dans les bicouches de DOPC ou de DPPC. On présente aussi des données qui suggèrent que l'halothane augmente le volume libre pour les sondes fluorescentes. Des expériences d'analyse calorimétrique différentielle et de calorimétrie à balayage UV ont été réalisées pour mieux observer les effets de l'addition de l'halothane à la bicouche de lipide DPPC. On a observé un déplacement notable de la température de transition du système DPPC. Nos observations suggèrent que les interactions entre une bicouche de lipide et un anesthésique général peuvent jouer un rôle significatif dans le mécanisme global de l'action anesthésique et que ces effets ne devraient pas être ignorés lorsqu'on considère les interactions entre la protéine de la membrane et les anesthésiques.

Mots clés : liposomes, anesthésie, fluorescence, transition de phase, bicouches de phospholipides.

[Traduit par la Rédaction]

Introduction

There is a lack of a detailed universal mechanism for general anesthetics (GA). Historically, a strong correlation between oil solubility of general anesthetics and their anesthetic potency was noted at the beginning of the twentieth century (Overton–Meyer correlation) (1, 2). As a result, it was speculated that anesthetics exerted their action by affecting unidentified fatty components of cells. Only later, with a greater understanding of membrane structure and composition, was it hypothesized that general anesthetics targeted the lipid matrix of cell membranes (3). In recent years, a protein-mediated mechanism of general anesthesia has been favored over the lipid-mediated mechanism. Extensive work has been carried out to establish the interaction of general anesthetics with water-soluble proteins as well as with integral membrane proteins (4, 5). A specific class of proteins, ligand-gated ion channels, was found to be an important target of volatile anesthetics (5). Existing models for the mechanism of action of GA include a GA–lipid mediated mechanism, a GA – ion-channel mediated mechanism, and lipid lateral pressure (6). Consistent with a variety of putative mechanisms, volatile anesthetics have a wide range of structures. Small anesthetics such as xenon, organic solvents, steroids, arabinosides, and pyrimidines can induce general anesthesia if present at high enough concentration. It may thus be naive to think that there is a single mechanism

Received 8 October 2003. Published on the NRC Research Press Web site at http://canjchem.nrc.ca on 27 May 2004.

A. Carnini, H.A. Phillips, L.G. Shamrakov, and D.T. Cramb.[1] Department of Chemistry, University of Calgary, 2500 University Drive NW, Calgary, AB T2N 1N4, Canada.

[1]Correponding author (e-mail: dcramb@ucalgary.ca).

 doi: 10.1139/V04-024 © 2004 NRC Canada

for all general anesthetics, and many factors may be operating synchronously. That is, even if general anesthetics directly affect ion channels, they may also alter membrane characteristics. We therefore need a simple, understandable model to help separate the variables.

Halothane has been prevalent in studies of the effects of volatile anesthetics on model membranes, and several techniques have been applied to the study of its anesthetic mechanism. These include X-ray diffraction, NMR, fluorescence, differential scanning calorimetry (DSC) (7), atomic force microscopy (AFM) (8), and, more recently, molecular dynamics (9–12). Previous work using X-ray diffraction showed that bilayers manifested an increased disorder upon halothane incorporation while maintaining constant membrane thickness (13). Our AFM work (8) suggests that there is change in local structure in the bilayer upon halothane incorporation, resulting from an inhomogeneous distribution of anesthetic in the bilayer. However, AFM cannot provide information about the depth distribution of halothane molecules in the bilayer.

The amphiphilic nature of anesthetics, including halothane, suggests that these molecules would reside mainly at the hydrophobic–hydrophilic interface in model systems such as phospholipid vesicles or micelles. NMR (^{19}F, ^{1}H) and nuclear Overhauser effect (NOE) studies of halothane in sodium dodecyl sulfate (SDS) micelles revealed that halothane molecules reside mostly at the water–micelle interface region (14). At low halothane:SDS ratios, the anesthetic interacted mainly with protons closer to the water–micelle interface; at higher halothane:SDS ratios, the anesthetic interacted with protons that are farther away from the hydrophilic interface. Halothane did not interact with the core of the micelle, even at high concentration (15). Kaneshina et al. (16) and Yoshida et al. (17) demonstrated by ^{19}F and ^{1}H NMR that volatile anesthetics remain at the surface of SDS micelles without losing contact with water. Additionally, NMR studies of halothane, enflurane, and isoflurane distribution in palmitoyloleoylphosphatidylcholine (POPC) bilayers suggested that these anesthetics locate primarily in the interfacial region of the bilayer (18). Other work by Tang and Xu (19) has shown that anesthetics 1-chloro-1,2,2-trifluorocyclobutane and isoflurane locate preferentially in the headgroup region, whereas nonanesthetics locate deeper in the bilayer.

Molecular dynamics simulations (10) of halothane in a DPPC bilayer revealed that halothane self-associates and is also distributed nonuniformly across the membrane interior. This resulted in significant modifications of the lipid bilayer. Because of its nonzero electric dipole moment, this anesthetic was found to reside in a region of the bilayer most accessible to water (i.e., preferentially in the upper portion of the acyl chain). A decrease in lipid wobble and an increase in tail defects of the lipid system were also observed.

To further our understanding of the localization of general anesthetics in a membrane system, we have used fluorescence spectroscopy, temperature-scanned UV–vis spectrophotometry, and DSC on small unilamellar vesicles (SUVs) as a method to examine the location of halothane in model membranes and examine localized lipid order/organization changes. In the present work, we studied the interaction between halothane and 1,2-dipalmitoyl-*sn*-glycero-3-phosphocholine (DPPC) and 1,2-dioleoyl-*sn*-3-glycero-3-phosphocholine (DOPC) bilayers labeled with Laurdan, Prodan, and NBD-C_6-PC as the reporter probes. Laurdan (20–22) has been previously used to detect lipid phase changes from gel (L_β) to liquid crystalline (L_α). We have chosen to study single lipid systems to understand the fundamental nature of halothane distribution and to directly compare our results with those of others and of our AFM study in the companion paper (8).

Materials

DPPC and DOPC were purchased from Avanti Polar Lipids (Alabaster, Ala.) and were used with no further purification. 2-Bromo-2-chloro-1,1,1-trifluoroethane (halothane) 99% (0.01% thymol) was obtained from Sigma (St. Louis, Mo.). 2-Dimethylaminonaphthalene (Prodan), 6-dodecanoyl-2-dimethylaminonaphthalene (Laurdan), and 2-(6-(7-nitrobenz-2-oxa-1,3-diazol-4-yl)amino)hexanoyl-1-hexadecanoyl-*sn*-glycero-3-phosphocholine (NBD-C_6-PC) were obtained from Molecular Probes (Eugene, Ore.). All lipids, anesthetics, and fluorescent labels were used without further purification. Ultrapure water was used in the preparation of buffer and aqueous solutions using a Mega Pure System ACS by Corning.

Saturated aqueous solutions of halothane were made at room temperature using ultrapure water. The halothane concentration of this saturated solution was 17.5 mmol/L (23). All stock solutions were prepared at room temperature.

Methodology

Preparation of small unilamellar vesicles and large unilamellar vesicles

Solutions of DPPC and DOPC unilamellar vesicles were prepared using a chloroform stock solution (2.5 mg/mL). An appropriate aliquot of the chloroform stock was transferred to a 10-mL volumetric flask to give a final lipid concentration of 0.1 mmol/L (0.25 mg/mL). Chloroform was driven off using nitrogen gas until a lipid film was visible in the flask. The resulting lipid film was resuspended in phosphate buffer (0.01 mol/L, pH 7.0). Unilamellar vesicles were formed by sonication in a sonicator bath from Laboratory Supplies Co. (Hicksvile, N.Y.) followed by extrusion with a miniextruder from Avanti Polar Lipids. DOPC vesicles were extruded after a 10-min sonication–stirring cycle for a total sonication time of 30 min. The DOPC and DPPC unilamellar vesicles were determined to be 100 and 43 nm in diameter, respectively, using a Dyne Pro (Protein Solutions, Piscataway, N.J.) light scattering particle sizer.

Vesicle labeling

DPPC and DOPC vesicles were labeled with fluorescent probes following the procedure outlined by Gratton and coworkers (21). Stocks of fluorescent probes (Laurdan, Prodan, and NBD-C_6-PC) were prepared in chloroform, and appropriate aliquots were added to the lipid fraction in chloroform to obtain a probe:lipid ratio of 1:100 (lipid and dye concentrations of 10^{-4} and 10^{-6} mol/L, respectively). The lipid/dye mixtures were dried under nitrogen gas and then resuspended in buffer.

© 2004 NRC Canada

Table 1. Results of fitting Laurdan fluorescence spectra to a sum of two Gaussian functions.

	Red peak			Blue peak		
Sample	Band centre (cm^{-1})	Bandwidth (cm^{-1})	Intensity (a.u.)	Band centre (cm^{-1})	Bandwidth (cm^{-1})	Intensity (a.u.)
DPPC (SUVs)	21 415	3128	9	22 740	7 103	3
DPPC (SUVs/halothane)	21 720	3500	4	24 219	11 778	2
DPPC (MLVs)	21 562	3275	82	22 993	2 296	167
DPPC (MLVs/halothane)	21 789	7647	7	22 284	3 762	75
DOPC (SUVs)	20 651	2954	253	23 432	1 803	73
DOPC (SUVs/halothane)	20 842	3201	35	23 540	2 490	18
DOPC (MLVs)	20 599	2929	639	23 495	1 851	196
DOPC (MLVs/halothane)	20 831	3176	202	23 650	2 048	103

Note: a.u., arbitrary units.

Loading of halothane into vesicle solution

Halothane was used in its pure liquid form or as a saturated aqueous solution (17.5 mmol/L). The anesthetics were either delivered to the fluorescence cuvette using an Eppendorf pipette or a gas-tight syringe as required. To avoid loss of anesthetic, the cuvette was immediately stoppered, sealed with Parafilm, and neither shaken nor stirred. Solutions were not shaken prior to collecting fluorescence spectra.

Preparation of aqueous micelle solutions

For fluorescence quenching experiments, stock solutions of SDS micelles (80 mmol/L) were prepared. Micelles were labeled with Laurdan using the dry preparation method to give a 1:1 Laurdan:micelles molar ratio. Solutions were allowed to stir for 1.5 h prior to use. Aliquots of pure anesthetics were added to 3-mL aliquots of stock SDS solution to obtain anesthetics concentration in the range of 0.1-20 mmol/L. Solutions were allowed to equilibrate with anesthetics for 2 h prior to recording of their fluorescence spectra.

Collection of emission and excitation spectra

All steady-state fluorescence spectra were collected using a Varian Eclipse fluorimeter (Varian, Palo Alto, Calif.) equipped with a Peltier cryobath. Emission and excitation spectra were collected approximately every 10 min after the addition of halothane. Spectra were collected until no further change in the fluorescence emission intensity occurred. Laurdan and Prodan were excited at 360 nm, and NBD-C_6-PC was excited at 460 nm.

Calorimetry

UV temperature-scanning experiments (22) were carried out using a Varian UV–vis spectrophotometer equipped with a Peltier temperature control unit. Unlabeled DPPC liposome samples were allowed to equilibrate at 25 °C for 10 min prior to beginning the heating/cooling cycle. Heating/cooling cycles were carried out from 25 °C to 45 °C and from 45 °C to 20 °C. Samples were let rest for 10 min at 45 °C prior to starting the cooling cycle. The temperature was scanned at 0.5 °C/min. DPPC liposome samples were prepared in the same manner as for the fluorescence experiments following the procedure outlined above.

Thermograms were collected using a MicroCal (Northampton, Mass.) calorimeter. The data was analyzed using Microcal Origin. The temperature was scanned from 20 °C to 45 °C and back at a rate of 0.5 °C/min. Samples were allowed to equilibrate for 10 min prior to scanning the temperature. The DPPC lipid concentration used was 1 mmol/L (2.5 mg/mL). Vesicles were prepared by sonication and by extrusion through a 50-nm polycarbonate membrane using a miniextruder from Avanti Polar Lipids.

Results

The interaction of the volatile anesthetic halothane with DPPC and DOPC single unilamellar and multilamellar vesicles was investigated by following changes in fluorescent emission of the probes Laurdan, Prodan, and NBD-C_6–PC over time. Studies of anesthetics incorporation were carried out at temperatures below and above the phase transition temperature (T_m) of DPPC (41 °C). This allowed for the investigation of the interaction of the drugs with the bilayer in both its gel and its liquid-crystalline phase. DOPC single unilamellar vesicles were used to study lipid bilayer – volatile anesthetic interactions in a room temperature liquid-crystalline-phase lipid environment. To quantify the degree to which the emission spectra of Laurdan in DPPC and DOPC in SUVs and multilamellar vesicles (MLVs) were altered in the presence of halothane, they were modeled using a sum of two Gaussian functions. The results of these fits are presented collectively in Table 1.

Incorporation of halothane in DPPC MLVs below the L_β–L_α transition temperature

Pure halothane was pipetted into a quartz cuvette containing the vesicle solution and allowed to mix without stirring to give a final concentration of 17.5 mmol/L This is the saturation concentration of halothane in a pure aqueous solution. Stirring or shaking was avoided to minimize volatilization of the anesthetic. Emission and excitation spectra were collected approximately every 10 min after the addition of halothane. Spectra were collected until no further change in the fluorescence intensity occurred. Figure 1*a* shows the intensity changes observed during incorporation of halothane in DPPC MLVs at 20 °C. As halothane was loaded into the vesicles, there was a decrease in Laurdan emission until an equilibrium state was reached 2 h after injecting the drug. This amount of time was required for purely diffusive mixing. Shaking and stirring of the sample was avoided so as to minimize volatilization of halothane. Figure 1*a* also shows

© 2004 NRC Canada

Fig. 1. (*a*) Incorporation of halothane in DPPC MLVs labeled with Laurdan at room temperature (gel phase). Equilibrium is reached after 2 h from drug injection, as indicated by no further change in Laurdan emission intensity. (*b*) Two-Gaussian deconvolution of the Laurdan spectrum without halothane. (*c*) Two-Gaussian deconvolution of the Laurdan spectrum with halothane. The dye:lipid ratio was 1:100.

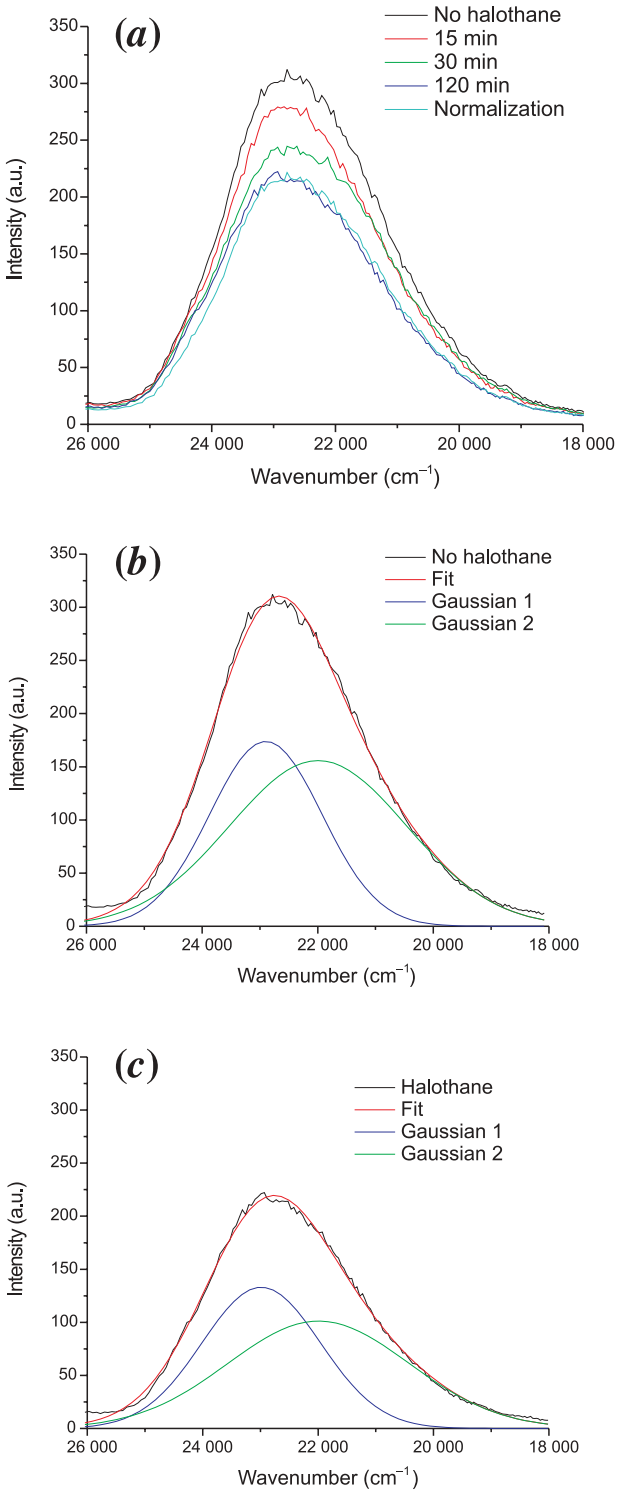
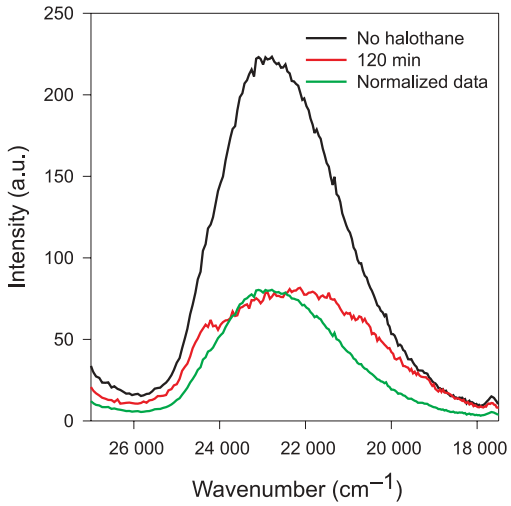


Fig. 2. Incorporation of halothane in DPPC MLVs above the phase transition temperature followed by Laurdan fluorescence. No shift in the λ_{max} of emission occurs. Slight broadening of the Laurdan emission peak occurs upon the incorporation of halothane. The dye:lipid ratio was 1:100.



an emission spectrum of Laurdan with no drug present that has been normalized to the trace collected after 2 h from injection time. No significant shift in the emission wavelength of the probe is observed between these two traces, suggesting no change in the probe environment upon incorporation of halothane. Figures 1*b* and 1*c* depict deconvolutions of the spectra in Fig. 1*a* using the sum of two Gaussian functions. The use of two Gaussian functions suggests that Laurdan finds itself in two environments of differing polarity. The lineshape parameters determined for these deconvolutions are given in Table 1.

The gel to liquid-crystalline phase (L_β–L_α) transition in DPPC MLVs can be monitored using Laurdan (20–22). The vesicle solution was heated in stages above the phase transition temperature of DPPC (T_m = 41 °C). As the bilayer becomes more fluid, the fluorescence λ_{max} shifts to the red, indicating that the probe environment becomes more polar owing to more water molecules percolating into the upper region of the bilayer. Since we observe only a slight red-shifting with added anesthetic, the anesthetic-related loss of fluorescence intensity may be due to direct quenching. This will be addressed further in the Discussion section

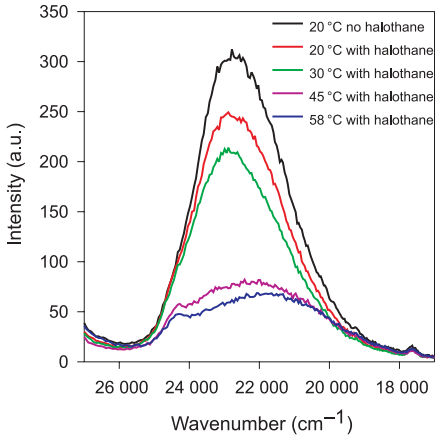
At a "clinical" (i.e., very low) concentration of 280 µmol/L, halothane shows no significant effect on the Laurdan emission. This indicates that at these concentrations Laurdan may not report on any localized changes in bilayer properties.

Incorporation of halothane at elevated temperatures in nonextruded DPPC vesicles

Halothane was incubated with DPPC liposomes at 42 °C. Although this temperature is above the chain melting temperature, it is clear from Fig. 2 that the vesicle system has not completely transformed to L_α. We therefore consider that there was a mixture of L_β and L_α in the liposomes. Again, we found that Laurdan fluorescence decreased as halothane was incorporated in the vesicles and that 2 h was

© 2004 NRC Canada

Fig. 3. Study of the effect of temperature on halothane incorporated in DPPC MLVs labeled with Laurdan. The drug was not fully expelled from the vesicles despite heating the sample up to 58 °C. The concentrations of halothane and lipid were 17.5 and 0.1 mmol/L, respectively. The dye:lipid ratio was 1:100.



required for this preparation to reach equilibrium. Incorporation of halothane caused a broadening of the main Laurdan fluorescence peak; no shift of the λ_{max} was observed (Fig. 2). The spectra were fitted using a sum of two Gaussian functions. The fit produced one major peak at 435 nm (22 993 cm^{-1}) and a second smaller peak at 464 nm (21 562 cm^{-1}). The peak at 435 nm was quenched 55% by halothane. The redder contribution to the spectrum at 464 nm was quenched by 92%.

After equilibrium was reached, the sample was cooled to 20 °C and then reheated. During reheating, spectra were collected at different temperatures (Fig. 3) to study the effect of temperature cycling on halothane partitioning in the vesicles. Halothane was not entirely expelled from the bilayer even when the vesicle solution was heated above the boiling point of halothane (50.2 °C) for up to 30 min.

Incorporation of halothane in DPPC SUVs above the phase transition temperature

For incorporation of halothane in DPPC (L_α) SUVs, just less than 2 h was required to reach an equilibrium point as indicated by no further change in Laurdan fluorescence intensity. The λ_{max} of emission was at 468 nm. This value is much redder than in the case of nonextruded DPPC vesicles (λ_{max} = 439 nm), and thus we can assume that our sample was in the L_α phase. Fitting to the data revealed again that two peaks contributed to the overall Laurdan spectrum: one major peak at 456 nm (21 930 cm^{-1}) and a smaller redder peak at 477 nm (20 964 cm^{-1}). Upon halothane incorporation, the predominant peak at 456 nm was quenched considerably (65%), whereas the second, red peak was only quenched by 11%, and a 6-nm blue shift occurred (Fig. 4); no broadening of the spectrum was observed.

Direct quenching of probes by halothane SDS micelles

Since the SUV and MLV work indicates that direct quenching of the fluorescent probe may take place, we were motivated to investigate the direct interactions of fluorescent probes with volatile anesthetics. An easy method to ensure

Fig. 4. Incorporation of halothane in DPPC SUVs above the phase transition temperature followed by changes in Laurdan intensity of emission. Equilibrium was reached after 100 min from drug injection. The concentrations of halothane and lipid were 10 and 0.1 mmol/L, respectively. The dye:lipid ratio was 1:100.

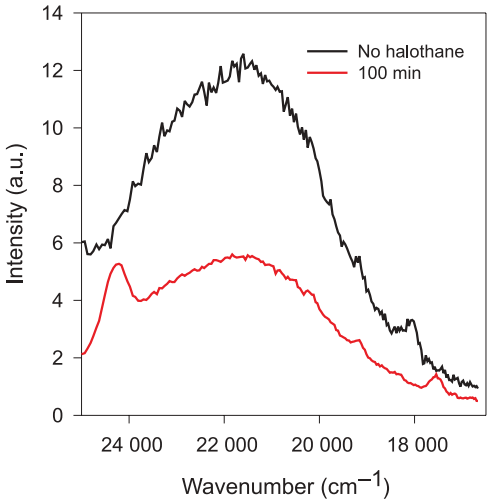
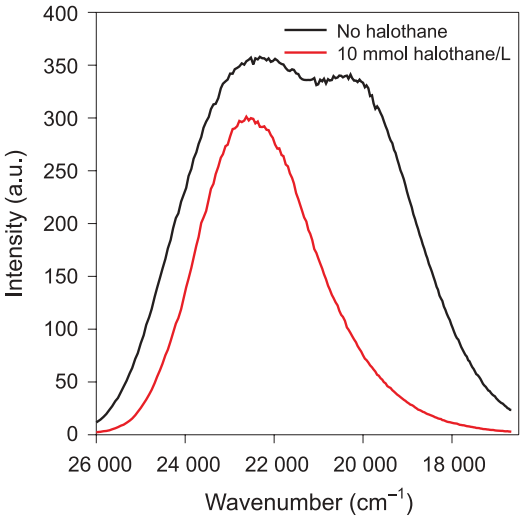


Fig. 5. Incorporation of halothane in SDS micelles labeled with Laurdan. The red shoulder is quenched preferentially by the drug at all halothane concentrations. The dye per micelle ratio was 1:1. The halothane concentration was 10 mmol/L.

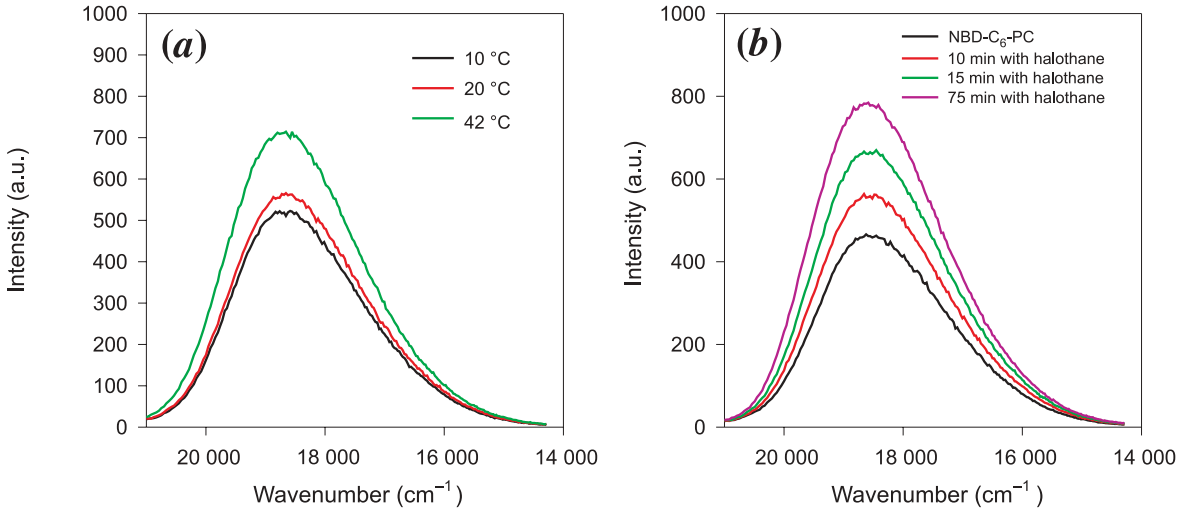


that probe and anesthetic are in close proximity is to solubilize them both using micelles. The relative concentrations can then be arranged such that each micelle contains one probe and one anesthetic molecule on average, given Poisson occupation statistics.

Halothane was incorporated in Laurdan-labeled SDS micelles. The range of concentrations of halothane used was between 0.1 and 10 mmol/L. Laurdan in SDS shows its fluorescence λ_{max} at 450 nm with a red shoulder at 510 nm (Fig. 5). This is suggestive of a bimodal distribution of Laurdan within the micelle environment. The blue peak would likely represent a dimerized probe, and the red peak probe near the micelle–water interface. Inspection of the

© 2004 NRC Canada

Fig. 6. (*a*) Effect of heat on the emission spectrum of NBD-C_6-PC in DPPC MLVs (no halothane). Temperature increase leads to an increase of NBD-C_6-PC emission intensity. (*b*) Effect of halothane incorporation in DPPC MLVs vesicles on NBD-C_6-PC fluorescence intensity of emission at room temperature. As halothane partitions in the vesicles, NBD-C_6-PC emission intensity increases. Halothane and lipid concentrations were 17.5 and 0.1 mmol/L, respectively. The dye:lipid ratio was 1:100.



spectra versus halothane concentration added showed that the intensity across the entire spectrum is reduced, but the red peak is quenched to a greater degree. This confirms that direct quenching of Laurdan by halothane is possible.

Do anesthetic–bilayer interactions induce local phase changes?

It is known that the incorporation of molecules in a lipid bilayer can induce structural changes in membranes that may reflect changes in lipid phase (25, 26). Laurdan is, in principle, sensitive to L_β–L_α phase transitions, as has been shown for DPPC; however, because the anesthetic may quench the fluorescent probe located exactly in those microdomains with nearby anesthetic, its ability to report on the local phase of the bilayer may be compromised. Thus, it was not possible to use the generalized polarization fluorescence technique (21) in the present work. Alternatively, NBD-C_6-PC is a highly effective fluorescent probe for monitoring changes in membrane lipid packing. An increase in lipid disorganization and interlipid free space is accompanied by an increase in the fluorescence emission intensity, possibly due to a reduction in self-quenching (27) as the vesicle expands. To confirm this, a solution of DPPC vesicles labeled with NBD-C_6-PC was heated from 20 to 45 °C above the DPPC phase transition temperature (Fig. 6*a*) at three different probe concentrations (0.5, 1, and 2 mol% in DPPC). As the vesicles underwent a chain-melting transition, the fluorescence emission of the NBD-C_6-PC probe increased, without any substantial excitation or emission spectral shifts. This same trend was observed upon the incorporation of halothane in the NBD-C_6-PC-labeled vesicles at room temperature (Fig. 6*b*). This suggests that halothane incorporation increases the DPPC lipid bilayer disorder and the free volumes within the bilayer.

Calorimetry

A calorimetric analysis was undertaken to assess the halothane-induced changes in melting temperature of DPPC. Temperature-scanning UV spectrophotometry was used to follow phase transition events of unlabeled DPPC MLV suspensions in the absence and presence of halothane. The change in absorbance with temperature was followed at 250 nm, which has been shown to be sensitive to changes in lipid packing. Heating was carried out from 25 °C to 45 °C followed by a cooling cycle from 45 °C to 25 °C. The heating cycles showed a broad drop in absorbance between 34 °C and 36 °C followed by a second sharp decrease in absorbance between 41 °C and 44 °C (Fig. 7*a*). Cooling cycles showed this process to be reversible (cooling scan not shown). To better visualize the changes in absorbance associated with the phase transition of DPPC vesicles, the first derivative with respect to temperature was taken and plotted against the temperature (Fig. 7*b*). The first derivative for the heating cycle showed a major peak at 42.0 °C, corresponding to the main phase transition of the DPPC system from gel to liquid-crystalline phase (L_β to L_α). The second peak at 35 °C is due to the pretransition of DPPC MLVs (gel to gel ripple phase).

Samples incubated with halothane were subjected to the same heating/cooling cycle as described above. The incorporation of halothane in the liposome solution caused the shape of the absorbance curve to change. The broad drop in absorbance at 35.0 °C was no longer detectable, and the sharper loss of absorbance, observed between 41°C and 44 °C in the absence of halothane, occurred at the lower temperature range of 33–35.5 °C. Again, to better visualize the changes in absorbance associated with the phase transition of DPPC vesicles, the first derivative was taken and plotted against the temperature (Fig. 7*b*). The first derivative shows only one sharp peak at 34 °C. This suggests that incorporation of halothane in the DPPC solution caused a significant lowering of the phase transition temperature from 42.0 °C to 34.0 °C. Samples that were subjected to the heating/cooling cycle twice produced the same results as the samples exposed to only one heating/cooling cycle.

To verify the temperature-scanning spectrophotometric results, the same sample conditions were examined using differential scanning microcalorimetry. The resulting ther-

© 2004 NRC Canada

Fig. 7. (*a*) UV scanning thermogram for an MLVs DPPC solution containing no halothane (black line) and for a solution containing halothane (red). (*b*) First derivatives of the thermograms in (*a*). The phase transition temperature in the absence of halothane was 42 °C, and it decreased to 34 °C in the presence of the drug. Halothane and lipid concentrations were 17.5 and 0.1 mmol/L, respectively. The vesicles were unlabeled.

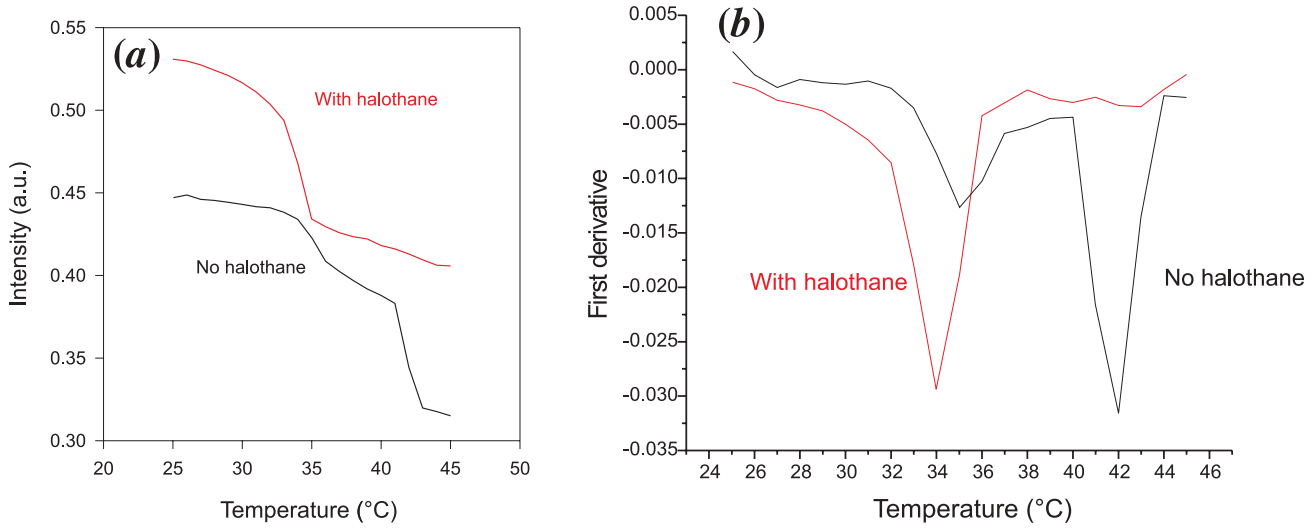
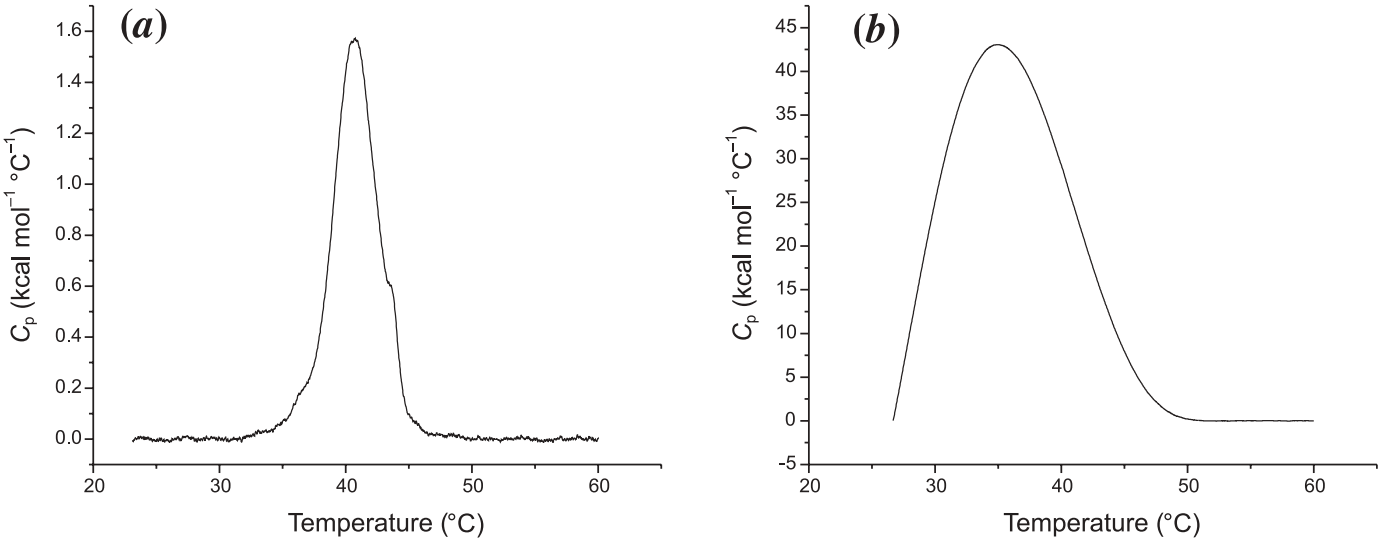


Fig. 8. (*a*) Thermogram for a solution of extruded DPPC vesicles, showing the main phase transition T_m at 41 °C. (*b*) Thermogram for a solution of extruded DPPC vesicles loaded with halothane (17.5 mmol/L), showing a shift in the T_m to 35 °C. Halothane and lipid concentrations were 17.5 and 1 mmol/L, respectively.



mogram for a sample of pure lipid SUVs, presented in Fig. 8*a*, shows a broad peak typical of SUVs and of large unilamellar vesicles (LUVs), with the main phase transition, T_m, occurring at 40.7 ± 1 °C. Two shoulders are visible in the thermogram at 36.6 ± 1 °C and at 43.5 ± 1 °C, and deconvolution of the thermogram confirmed the existence of these two smaller peaks hidden beneath the main peak. The first one is possibly due to the ripple phase transition, and the second to the presence of multilamellar vesicles.

The thermogram for a sample containing halothane at a concentration of 17.5 mmol/L shows a much broader peak than for the sample containing no halothane (Fig. 8*b*). The center of this broad peak is around 34 °C, consistent with the above shift. The considerable broadening may have resulted from aggregation and possibly fusion of the DPPC SUVs during heat cycling; however, the solution did not appear to become more translucent. The broadening could suggest that halothane is reducing the cooperativity between the lipids during phase transition. Interestingly, this does not occur in the absence of halothane.

Incorporation of halothane in extruded DOPC unilamellar vesicles

Because most bilayers found in mammalian cells exist in the liquid-crystalline phase (L_α) at physiological temperature, it is important to examine the effect of volatile anesthetics on a system appropriate to this. DOPC liposomes represent such a system. A sample of DOPC vesicles labeled with Laurdan (Fig. 9*a*) shows a 490 nm emission peak characteristic of a liquid-crystalline-phase bilayer. A significant

© 2004 NRC Canada

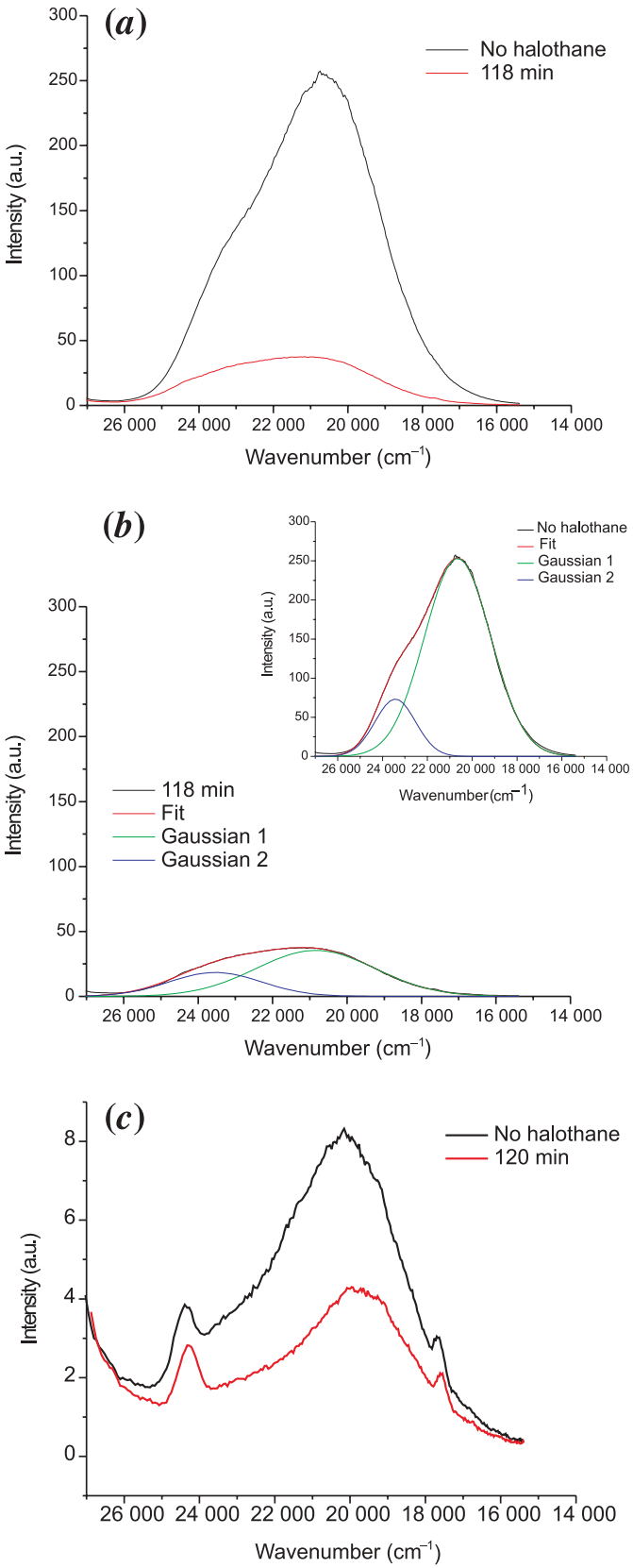


Fig. 9. (*a*) Incorporation of halothane in DOPC SUVs followed by Laurdan fluorescence. Equilibrium was reached after 2 h from adding halothane. (*b*) Deconvolution of the data by fitting Gaussian functions, showing that the red shoulder of the Laurdan spectrum is preferentially quenched by halothane. The insert shows the Gaussian fits obtained for a sample containing no halothane. The concentrations of halothane and lipid were 17.5 and 0.1 mmol/L, respectively. The dye:lipid ratio was 1:100. (*c*) Incorporation of halothane into DOPC SUVs followed by Prodan fluorescence. Equilibrium was again reached after 2 h from adding halothane.

shoulder is visible to the blue of this peak at ~440 nm. This blue peak is indicative of a more nonpolar probe environment and (or) of probe aggregation. This peak was found to be dependent on the dye concentration (data not shown). The incorporation of halothane in DOPC unilamellar vesicles was followed over time. Two hours was required to reach an equilibrium point for halothane incorporation (Fig. 9*a*), after which no further change in fluorescence intensity was observed. The spectra were fitted using a sum of two Gaussian functions (Fig. 9*b*). Both peaks were quenched by halothane, 86% of the red peak (484 nm, 20 651 cm^{-1}) and 75% of the blue peak (426 nm, 23 432 cm^{-1}). It is also notable that the quenched spectrum is slightly broader near the band center (Fig. 9*a*), and when this spectrum was normalized to the initial intensity, it appeared to have broadened significantly. However, as in the case of DPPC, total loss of fluorescence was never achieved.

Extruded DOPC unilamellar vesicles were also labeled with Prodan, which reports on conditions near the headgroup–water interface. In Fig. 9*c*, the same 490 nm peak, indicative of a L_α bilayer, is observed. However, in contrast to the spectrum of Laurdan, no significant peak is found at 440 nm. Upon incorporation of halothane into the vesicles, the spectrum loses intensity, although not as significantly as in the case of Laurdan, and there seems to be a slight (5 nm) red shift of the spectrum.

Incorporation of halothane in DOPC MLVs

The interaction of halothane with Laurdan-labeled DOPC was studied to investigate the drug partitioning in a multicompartment system. As in the case of extruded DOPC vesicles, nonextruded DOPC samples showed a 490 nm emission peak characteristic of a liquid-crystalline-phase bilayer and a significant blue shoulder at ~440 nm. The red peak of Laurdan was quenched by 68% of its original intensity, whereas the 440 nm peak was quenched by 47% (data not shown).

Discussion

Location of volatile anesthetics in bilayers

In this paper, Prodan and Laurdan were used to help elucidate halothane location in the DPPC and DOPC bilayers. Prodan monitors the headgroup region; Laurdan monitors the region immediately below the headgroup. We found that the fluorescence of both Prodan and Laurdan was quenched by halothane for DPPC (L_α and L_β) and for DOPC (L_α) liposomes. The reduction in Laurdan and Prodan fluorescence

© 2004 NRC Canada

intensity is likely due to direct quenching by halothane via the Br heavy-atom effect. This hypothesis is corroborated by our SDS micelle studies, where similar quenching was observed when the micelles were occupied by a single probe molecule and a single halothane molecule. Additionally, some change in fluorescence yield would be expected in DPPC from the induction of lipid melting by halothane. It has been demonstrated that the strongest effect of DPPC melting on Laurdan is a spectral shifting to the red, rather than general loss of intensity (21). The degree of quenching observed upon halothane incorporation both into DPPC and into DOPC cannot be explained solely by alteration in the bilayer structure. Taken together, these results suggest that a fraction of halothane is near the headgroup region.

Since Prodan and Laurdan report on different regions near the bilayer–water interface, a heterogeneous distribution of anesthetic in the bilayer should result in differential quenching of these probes. This is indeed observed for DOPC vesicles. Laurdan experiences a greater loss in fluorescence intensity as anesthetic partitions into the liposomes than does Prodan. Moreover, the reddest feature (490 nm) of Laurdan fluorescence in DOPC is quenched to a greater extent than the blue feature (440 nm). The differential quenching of Laurdan over Prodan by halothane is very suggestive that a significant fraction of these anesthetics take up positions just below the headgroups of DOPC.

For both Prodan and Laurdan, there is minimal spectral shifting as a function of anesthetic incorporation. This is somewhat counterintuitive, since both these probes should report localized induction of more L_α-like domains. However, since changes in the L_α domains are observed using AFM (8), it is possible that the anesthetics quench exactly those probes that are proximal to the bilayer region undergoing change.

It is informative to compare the behaviour of the system above and below T_m for DPPC. The fluorescence spectrum of Laurdan is already broad for L_α DPPC (SUVs at 42 °C), and incorporation of halothane only serves to quench the fluorescence, but not to broaden it further. Furthermore, the quenching of Laurdan is greater when DPPC is at elevated temperatures. This is consistent with the study of Simon et al. (28), in which the partition coefficient of halothane in L_α DPPC was observed to increase by a factor of 4 compared with that in L_β. The slight shift (5–10 nm) of the unquenched probe is in a sensible direction for L_α DPPC and DOPC (i.e., to the red). The fact that there is incomplete quenching, even at levels at which the liposomes appear to be saturated with halothane, indicates that the anesthetic is distributed within the bilayer at several locations.

The present study, nevertheless, indicates that a significant fraction of the membrane-bound halothane is located near the headgroup region of DPPC and DOPC bilayers. This appears to be independent of whether the system examined is unilamellar or multilamellar. Moreover, preferential quenching of Laurdan located near the surface of SDS micelles suggests that halothane also partitions near the water–surfactant interface in micelles. These findings are consistent with the NMR work of Yoshino et al. (14). NMR spectroscopy has also been used to examine the location of halothane in lipid bilayers (29). The apparent disagreement on halothane location (water side of headgroups versus lipid side of headgroups) was reconciled by molecular dynamics simulation (10), which concluded that the distribution of halothane in a DPPC bilayer is concentration dependent and nonuniform. In the present study, experiments were performed in the high concentration regime, i.e., greater than 50 mol%. In this regime, halothane has consistently been suggested to partition largely just under the headgroups on the acyl chain side, in agreement with our results. Additionally, NMR studies (18, 19) have revealed that other volatile anesthetics locate in this region of the bilayer, whereas nonanesthetics partition deeper into the hydrophobic region.

We found that the red peak of Laurdan is quenched to a greater degree in DOPC than in L_α DPPC SUVs (86% vs. 65%, respectively). This peak is due to probe molecules that are more exposed to water, and the difference in quenching may simply reflect the relative partition coefficients of halothane in these two systems, given that L_α DPPC is at elevated temperature (50 °C). Future studies will help reveal any correlation between halothane location and unsaturation in the lipid tails. The challenge of future studies will be to find a fluorescent probe that reliably reports on the inner core of the bilayer.

We recognize that DOPC SUV aggregation and fusion may take place in the presence of higher concentration anesthetic. Our companion paper (8) indicates that this has happened for DOPC SUVs in ethanol solution (3 mol ethanol/L). Thus, aggregation/fusion is also possible for DOPC SUVs in a solution containing 17 mmol halothane/L. However, we do not believe that this significantly influences our fluorescence data. Fusion to form LUVs should not affect the local environment of Laurdan. Moreover, the minor differences observed in the fluorescence behaviour of Laurdan-labeled MLVs compared with SUVs suggest that the quenching of fluorescence does not result from MLV formation via fusion.

Anesthetic-induced phase changes

In the companion paper to this (8), we observed by AFM that incorporation of anesthetics into supported planar bilayers induced domain formation. These domains were thinner and may have been more disordered than the original bilayer. This is suggestive that volatile anesthetics induce local chain-melting phase changes (L_β–L_α) in DPPC and transformation to an increasingly disordered liquid-crystalline phase in DOPC. In the present study, we further investigated this possibility using fluorescence and temperature-scanned UV–vis spectroscopies and DSC.

We acknowledge that the concentrations of anesthetic used in this study are high compared with those in clinical applications. However, this does not obviate the impact of the current results. As shown in our companion paper (8), halothane loads heterogeneously into bilayers, and therefore it is possible that there are regions of high local concentration within physiological bilayers even at much lower aqueous concentrations. Our examination of simple, single lipid bilayers is the first step toward examining bilayers of increasing complexity.

Traditionally, the definition of the lipid chain-melting phase transition is that the individual phospholipid molecules become more mobile or that their lateral diffusion co-

© 2004 NRC Canada

efficients increase significantly. Commensurate with this would be an increase in transverse displacement within the bilayer. The main driving force for melting is that lipid tails acquire gauche defects, which push individual lipid molecules apart. The net effect is often an increase in headgroup spacing. At first glance, it is not unreasonable to expect the same result from the incorporation of anesthetic molecules into a bilayer. Therefore, for halothane/DPPC, one would expect that a significant accumulation of anesthetic just below the headgroup would push the lipid molecules apart. This would lead to more space available for the tails, and again an increase in gauche defects and (or) greater lipid tilting may occur. Indeed, this has been observed in molecular dynamics simulations (10) and inferred from NMR studies (29). In our companion paper (8), we suggest that this increase in interlipid spacing leads to a localized thinning of the bilayer. In the following discussion, we will explore the evidence from the present study for halothane induction of increased interlipid spacing.

By examining the dependence of the fluorescence of NBD-C_6-PC (1 mol%) on the temperature of DPPC SUVs, we have demonstrated that fluorescence yield increases as the bilayer undergoes chain melting (Fig. 6*a*). Probe concentration dependences suggest that this is primarily due to dequenching (i.e., a reduction in self-association) since no change in the 325 nm vs. 470 nm peaks in the excitation spectra was observed. This is in slight contrast to the observations of Alakoskela and Kinnunen (30), who observed changes in $I_{325\ nm}/I_{470\ nm}$ for NBD-C_{12}-PC at 3 mol% in a DPPC liposome as a function of temperature. However, our results agree with the findings of Krull and co-workers (27, 31), who performed extensive studies on NBD self-quenching in monolayers and vesicles for a wide range of concentrations.

Similar to the increase in fluorescence observed when heating DPPC, an increase in fluorescence yield was observed as halothane was added to room temperature DPPC SUVs. Again, we infer that since the excitation intensity ratio, $I_{325\ nm}/I_{470\ nm}$, was constant over the fluorescence increase, the increase results from a dequenching due to changes in membrane lipid packing, i.e., an increase in the space available to the probe molecules. It would also appear that NBD-C_6-PC may be relatively insensitive to changes in local polarity induced by the incorporation of volatile anesthetics into bilayers because no spectral shifting was observed.

Changes in the lipid packing/order in bilayers at the nanometer length scale should be accompanied by changes in the phase transition temperature (T_m) for the system (32). A straightforward way to measure T_m for low-concentration SUVs is by measuring absorbance changes at 250 nm (33). For halothane in DPPC, we observed a lowering of T_m from 42 °C to 34 °C. DSC studies on unlabeled nonextruded DPPC samples (1 mmol lipid/L) supported this finding. In the DSC experiment, the T_m was shifted from 42 °C to 34 °C (Fig. 8).

Lipids that constitute a DPPC bilayer in the gel phase are tightly packed together in an orderly fashion. The partitioning of a solute in a bilayer will change the thermotropic behaviour of the liposomes. We and others (10) suggest that the incorporation of halothane in the bilayer leads to the disruption of the ordered gel-phase packing. As the disorder in the packing increases, so does the entropy of the system, and consequently the phase transition occurs at a lower temperature.

The presence of multiple peaks constituting the main peak in the DSC plot indicates that the DPPC vesicle suspension was perhaps a heterogeneous system. Vesicles of different sizes may have been present in solution. The feature at the highest temperature may be due to larger multilamellar vesicles.

Addition of halothane caused the T_m to shift to a lower temperature. This is consistent with the idea that small molecules like ethanol and 1-butanol (32) or halothane (29) inserting a lipid bilayer will decrease the lipid bilayer ordered packing and thus reduce the temperature at which the phase transition occurs. It is notable that the value obtained for the T_m of halothane/DPPC by DSC (34 ± 1 °C) agrees with the value obtained by temperature-scanning UV spectrophotometry (34 ± 1 °C). Janes et al. (34) have shown that the change in transition temperature has a linear dependence on the mole fraction of hexanol in a dimyristoylphosphatidylcholine (DMPC) bilayer. The authors argue that the incorporation of anesthetics into a bilayer is the equivalent of local thermal heating and cooling, which disrupts the domain structure.

We investigated the effect of subjecting a sample to more than one heating/cooling cycle. Interestingly, there was no indication of halothane being expelled from the vesicles despite the fact that samples were heated above the halothane boiling point (data not shown). This result is consistent with our findings from fluorescence and AFM data.

Since phase transitions in DPPC can be detected using Laurdan (21), halothane-induced packing changes localized within SUVs and MLVs should also be detectable. Using Laurdan, T_m is reported by a red shift in the fluorescence maximum owing to an increase in H_2O penetration into the bilayer and concomitant increase in polarity. Recall in Fig. 1 we observed quenching of Laurdan. In Fig. 1, the Laurdan fluorescence spectrum in DPPC is typical of the L_β phase, with a maximum at 450 nm. Although quenching is observed, no significant spectral broadening can be seen, suggesting that the domains that may undergo complete melting are exactly those where Laurdan is quenched. This is consistent with observations by Merlo and Yager on the effect of isoflurane on Laurdan fluorescence in DPPC (20).

Near the transition temperature of DPPC, an interesting effect is observed (Fig. 4). As halothane partitions into the liposomes, the intensity of the fluorescence spectrum decreases and the spectrum broadens. Thus, there seems to be a small but general increase in the polarity of unquenched Laurdan, consistent with a further departure of the liposome from pure gel phase.

The changes in lipid order suggested by our work are in harmony with the NMR-based results of North and Cafiso (35) and Baber et al. (18), where a decrease in chain order parameter was observed in the presence of volatile anesthetic. The interpretation of our fluorescence and calorimetric data agrees with the molecular dynamics study of Koubi et al. (10), where increased DPPC lipid chain disorder was also observed in the presence of high-concentration (50 mol%) halothane. Moreover, other microcalorimetry

© 2004 NRC Canada

studies have shown that volatile anesthetics lower the lipid chain-melting temperature (7).

Conclusions

In the present work, we studied the interaction between halothane and DPPC and DOPC bilayers labeled with Laurdan, Prodan, and NBD-C_6-PC as the reporter probes. Our results indicate that halothane is located on the acyl chain side, near the headgroup region of the bilayer. Additionally, we find that halothane may be inhomogeneously distributed within DOPC and DPPC bilayers, and this is consistent with what others have observed (10, 12). We also show data that indicate halothane increases the free volume available to fluorescent probes. An increase in lipid disorder is also indicated by DSC and UV scanning calorimetry experiments. The halothane-induced increase in lipid bilayer disorder is reflected in a shift of the phase transition temperature (T_m) to lower temperatures. Our findings suggest that even if anesthesia results from a protein-mediated mechanism, general anesthetic – lipid bilayer interactions cannot be ignored and may play a significant role in the overall mechanism of anesthetic action. For example, the anesthetics may bind to a hydrophobic region of ion channels via the cell membrane. Additionally, if the proteins affected in anesthesia are located in lipid rafts, the changes in lipid packing induced by anesthetics may be an important mechanistic factor.

Acknowledgements

The authors thank Natural Science and Engineering Research Council of Canada and the Alberta Cancer Board for financial support. We also thank Professors Hans Vogel and Ray Turner for the use of their equipment.

References

1. H. Meyer. Arch. Exp. Pathol. Pharmakol. **46**, 338 (1901).
2. C. Overton. Studies über die Narkose. Fisher, Jena. 1901.
3. K. Miller. Int. Rev. Neurobiol. **27**, 1 (1985).
4. R. Eckenhoff and J. Johnasson. Pharmacol. Rev. **49**, 343 (1997).
5. N. Franks and W. Lieb. Nature (London), **367**, 607 (1994).
6. R. Eckenhoff. Mol. Interventions, **1**, 258 (2001).
7. S. Forman, D. Raines, and K. Miller. *In* Anesthesia: biological foundations. *Edited by* T.L. Yaksh, C. Lynch, W.M. Zapol, M. Maze, J.F. Biebuck, and L.J. Saidman. Lippincott-Raven, Philadelphia. 1998.
8. Z. Leonenko and D. Cramb. Can. J. Chem. **82** (2004). This issue.
9. L. Koubi, M. Tarek, S. Bandyopadhyay, M. Klein, and D. Scharf. Biophys. J. **81**, 3339 (2001).
10. L. Koubi, M. Tarek, M. Klein, and D. Scharf. Biophys. J. **78**, 800 (2000).
11. K. Tu, M. Tarek, M. Klein, and D. Scharf. Biophys. J. **75**, 2123 (1998).
12. P. Tang and Y. Xu. Proc. Natl. Acad. Sci. U.S.A. **99**, 16 035 (2002).
13. N. Franks and W. Lieb. Nature (London) **274**, 339 (1978).
14. A. Yoshino, T. Yoshida, H. Okabayashi, H. Kamaya, and I. Ueda. J. Colloid Interface Sci. **198**, 319 (1998).
15. T. Yoshida, K. Takahashi, H. Kamaya, and I. Ueda. J. Colloid Interface Sci. **124**, 177 (1998).
16. S. Kaneshina, H. Lin, and I. Ueda. Biochim. Biophys. Acta, **647**, 223 (1981).
17. T. Yoshida, K. Takahashi, and I. Ueda. Biochim. Biophys. Acta, **985**, 331 (1989).
18. J. Baber, J. Ellena, and D. Cafiso. Biochemistry, **34**, 6533 (1995).
19. P. Tang and Y. Xu. Biophys. J. **72**, 1676 (1997).
20. S. Merlo and P. Yager. Anal. Chem. **62**, 2728 (1990).
21. L. Bagatolli, T. Parasassi, G. Fidelio, and E. Gratton. Photochem. Photobiol. 70, 557 (1999).
22. T. Parasassi, F. Conti, and E. Gratton. Cell. Mol. Biol. **32**, 103 (1986).
23. A. Jenkins, N. Franks, and W. Lieb. Anesthesiology, **90**, 484 (1999).
24. E. Lissi, M. Bianconi, A. do Amaral, E. de Paula, L. Blanch, and S. Schreier. Biochim. Biophys. Acta, **46**, 1021 (1990).
25. E. Rowe. Biochemistry, **26**, 46 (1987).
26. S. Simon and T. McIntosh. Biochim. Biophys. Acta, **773**, 169 (1984).
27. R. Brown, J. Brennan, and U. Krull. J. Chem. Phys. **100**, 6019 (1994).
28. S. Simon, T. McIntosh, P. Bennet, and B. Shrivastav. Mol. Pharmacol. **16**, 163 (1979).
29. S. Gaillard, J. Renou, M. Bonnet, X. Vignon, and E. Dufoure. Eur. Biophys. J. **19**, 265 (1991).
30. J. Alakoskela and P. Kinnunen. J. Phys. Chem. B, **105**, 11 294 (2001).
31. J. Shrive, S. Kanagalingam, and U. Krull. Langmuir, 12, 4921 (1996).
32. E. Rowe and F. Zhang. Biochemistry, **31**, 2005 (1992).
33. P. Royall. Thesis. Liposomes: partitioning and model drug systems. University of Kent, Canterbury, U.K. 1999.
34. N. Janes, J.Hsu, E. Rubin, and T. Taraschi. Biochemistry, **31**, 9467 (1992).
35. C. North and D. Cafiso. Biophys. J. **72**, 1754 (1997).

© 2004 NRC Canada

Electrochemical behaviour of 1-{[(3-halophenyl)-imino]methyl}-2-naphthol Schiff bases on graphite electrodes

Kamran Polat, Mustafa Uçar, M. Levent Aksu, and Hüseyin Ünver

Abstract: An electrochemical study of the reduction of 1-{[(3-halophenyl)imino]methyl}-2-naphthol compounds on graphite electrodes was carried out. All the compounds were dissolved in a 1:4 (volume fraction) mixture of tetrahydrofuran (THF) and methanol. $NaClO_4$ (0.1 mol L^{-1}) was used as the supporting electrolyte. Cyclic voltammetry, chronoamperometry, constant-potential coulometry (bulk electrolysis), and constant-potential preparative electrolysis were employed. The cyclic voltammetric data revealed that the reduction on graphite was irreversible and followed an EC mechanism. The diffusion coefficients and the number of electrons transferred were determined using the chronoamperometric Cottrell slope and the ultramicro electrode steady-state current. The number of electrons was also determined by bulk electrolysis. The products of the electroreduction were synthesized in milligram quantities by the use of constant-potential preparative electrolysis. These products were purified and characterized by spectroscopic methods. Based on these findings, a mechanism for the electroreduction process is proposed.

Key words: electrochemical reduction, hydroxynaphthylideneaniline Schiff bases, cyclic voltammetry, ultramicro electrode.

Résumé : On a effectué une étude électrochimique de la réduction de 1-{[3-halophényl)imino]méthyl}-2-naphtols sur des électrodes de graphite. On a dissous tous les composés dans des mélanges 1:4 (v/v) de tétrahydrofurane (THF) et de méthanol. Du $NaClO_4$ 0,1 mol L^{-1} a été utilisé comme électrolyte de support et on a fait appel aux techniques des voltampérométrie cyclique, de chronoampérométrie, de coulométrie à potentiel constant (électrolyse globale) et d'électrolyse préparative à potentiel constant. Les données de voltampérométrie cyclique révèlent que la réduction sur le graphite est irréversible et qu'elle suit un mécanisme EC. On a déterminé les coefficients de diffusion et le nombre d'électrons transférés à l'aide de la pente chronoampérométrique de Cottrell et du courant d'état stationnaire d'une ultramicro électrode. On a aussi déterminé le nombre d'électrons par le biais de l'électrolyse globale. On a synthétisé les produits d'électroréduction en quantités de l'ordre du milligramme en faisant appel à des électrolyses préparatives à potentiel constant. Ces produits ont été purifiés et caractérisés par des méthodes spectroscopiques. Sur la base de ces observations, on propose un mécanisme pour le processus d'électroréduction.

Mots clés : réduction électrochimique, bases de Schiff de l'hydroxynaphtylidèneaniline, voltampérométrie cyclique, ultramicro électrode.

[Traduit par la Rédaction]

Introduction

Schiff bases are used extensively as ligands in coordination chemistry (1, 2). Some Schiff bases have thermochromic and photochromic properties in the solid state (3, 4). They are also used as model systems in studies of biological macromolecules and catalytic reactions (5, 6).

Received 14 April 2003. Published on the NRC Research Press Web site at http://canjchem@nrc.ca on 19 May 2004.

K. Polat[1] and M. Uçar. Ankara University, Faculty of Science, Department of Chemistry, 06100 Tandoğan, Ankara, Turkey.
M.L. Aksu. Gazi University, Gazi Education Faculty, Department of Chemical Education, 06500 Teknikokullar, Ankara, Turkey.
H. Ünver. Ankara University, Faculty of Science, Department of Physics, 06100 Tandoğan, Ankara, Turkey.

[1]Corresponding author (e-mail: kpolat@science.ankara.edu.tr).

Aromatic Schiff bases containing a hydroxy group in the *ortho* position may have two tautomeric forms, namely phenol-imine and keto-amine structures (7). The existence of the tautomers has been documented with X-ray crystallography and UV spectroscopy (8–10). Dudek and Holm (10) observed these tautomers in hydroxynaphthylideneaniline-type compounds. UV and ^{1}H NMR studies carried out on Schiff bases derived from 2-hydroxy-1-naphthaldehyde and some aliphatic and aromatic amines revealed that the keto-amine structure is predominant in polar solvents, and the phenol-imine form is predominant in apolar solvents (11, 12).

The electrochemistry of Schiff bases in aqueous media has been studied in detail (13–16). It was observed that the reduction takes place with a transfer of two electrons and two protons, thereby converting >C=N– to –HCNH–. Two reduction waves are reported to accompany this reduction. The first reduction wave shows a strong dependence on the pH of the media, whereas the second wave was more or less independent of pH (14–16). The reaction is further complicated by the hydrolysis of the azomethine group, which

 doi: 10.1139/V04-021 © 2004 NRC Canada

yields the constituent amine and carbonyl compound (14, 15). This complication is avoided by carrying out the reaction in nonaqueous media. However, studies using aprotic media, such as dimethylformamide and acetonitrile, are few in number and lack detail (17–21).

Scott and Jura (17) proposed the electroreduction process illustrated in Scheme 1, based on their study of the electrochemistry of Schiff bases in DMF. Kononenko et al. (18), on the other hand, concluded that the first reduction wave is an irreversible, two-electron process. Andrieux and Saevant (19) studied the reduction of several imines in DMF and acetonitrile and concluded that, depending on the solvent employed, there is either an irreversible two-electron reduction leading to a saturated amine or, again, an irreversible process, consisting of one-electron steps, which results in dimerization. The first reduction step is assumed to involve an immonium cation derived from the attachment of a proton to the nitrogen atom of the >C=N– group. Dimerization has been considered to be the only cause of irreversibility when explaining the behaviour of benzaldehyde anil in linear-sweep voltammetry (19). The radical formed by protonation of the anion radical produced initially is able to dimerize or to be reduced at the electrode more easily than the imine itself. This second trend is stronger than the first one. However, dimerization was observed, at least partially, in a less acidic medium in DMF (19). Fry and Reed (20) also indicated that the reduction of several imines takes place through an irreversible two-electron transfer.

N-(Benzylidene)-2-aminopyrimidine has been found to be reduced by two electrons at pH 9.8–13.0, ending in *N*-(benzyl)-2-aminopyrimidine. The protonation precedes the electronation in the reduction process, and from voltammetric findings, the whole process is found to be diffusion-controlled and irreversible, and no dimeric product is formed (21).

In our previous work, 1-{[(3-halophenyl)imino]methyl}-2-naphthol Schiff bases were synthesized, and their structures and keto–enol tautomerism in protic and aprotic media were elucidated by the use of spectroscopic methods (22). The present study is concerned with the examination of the electrochemical behaviour of the synthesized Schiff bases using cyclic voltammetric, chronoamperometric, and coulometric methods. The studies in the literature lack detail. In addition, the electroreduction products are studied by spectroscopic methods, to determine the detailed electrochemical mechanism.

Scheme 1.

$$ArCH{=}NAr' + e \rightleftharpoons Ar\dot{C}H\text{-}\bar{N}Ar' \text{ (first wave)}$$

$$Ar\dot{C}H\text{-}\bar{N}Ar' + e \longrightarrow Ar\bar{C}H\text{-}\bar{N}Ar' \text{ (second wave)}$$

$$Ar\bar{C}H\text{-}\bar{N}Ar' + 2BH \longrightarrow ArCH_2NHAr' + 2\bar{B} \text{ (chemical reaction)}$$

Experimental

Apparatus

Melting points (uncorrected) were determined on a Gallenkamp melting point apparatus. Infrared spectra (KBr discs) were recorded with a Mattson 1000 FTIR spectrophotometer. UV–vis spectra were measured with a Perkin-Elmer Lambda 2 Series recording spectrophotometer. Mass spectra were obtained using an Agilent GC–MSD and Micromass Platform 2 mass spectrometer operated at 70 eV ionizing potential. ^{1}H and ^{13}C NMR spectra were recorded on a Bruker DPX 400-MHz FT-NMR spectrometer, operating at a proton frequency of 400.5 MHz and a carbon frequency of 100.7 MHz, using $CDCl_3$ as the solvent and tetramethylsilane (TMS) as the internal standard.

Bulk electrolysis (BE), chronoamperometry (CA), and cyclic voltammetry on ultramicro electrodes were carried out on a BAS100B Electrochemical Analyser equipped with a BAS100B Cell Stand and with a BAS100W.EXE data processing program. Cyclic voltammograms on graphite electrodes were recorded on an EG&G Princeton Applied Research Model 362 Scanning Potantiostat with scan rates between 5 and 500 mV s^{-1}. The *iR* drop was compensated. Constant-potential preparative electrolyses (CPE) were obtained on a PGZ 301 Dynamic-EIS Voltammetry (Radiometer Analytical Co.) system equipped with VoltaLab 4.0+ PC Software.

All experiments except the CPE experiments were carried out in an undivided conventional three-electrode cell with a working electrode and a platinum-wire auxiliary electrode. An Ag–$AgNO_3$ (0.01 mol L^{-1}) – CH_3CN electrode, connected to the solution by a Luggin capillary, was employed as the reference electrode. No correction for the junction potential was made. The working electrode for the electrochemical experiments (except for cyclic voltammetry on the ultramicro electrode and CPE) was a 3 mm diameter (0.071 cm^2) graphite disc (spectroscopic grade). Cyclic voltammograms on an ultramicro electrode were recorded with a 10 μm diameter platinum disc (Cypress Systems) and the CPE was performed with a 7 mm diameter (0.3848 cm^2) graphite electrode. The working electrodes were polished with 0.05 μm and 1 μm Al_2O_3 (Buehler). All measurements were run under a blanket of nitrogen. To remove the dissolved oxygen, the solutions were purged at room temperature with nitrogen saturated with the solvent for ca. 15 min prior to each experiment.

The number of electrons was calculated from the amount of charge passed and the equivalent amount of the reduced BE product. Electrolysis was continued until the current dropped to about 1% of its initial value.

To ascertain the feasibility of an electrochemical synthesis of Schiff bases, different solvents and supporting electrolytes were tested, such as DMSO–Bu_4NF_4, $NaClO_4$; DMF–Et_4NBr, $NaClO_4$; CH_3CN–Bu_4NF_4 or $NaClO_4$. Solutions containing 20% (volume fraction) methanol in THF and Bu_4NBF_4 or Et_4NBr were also examined, but none gave a reduction peak in the potential range studied. For this reason, the solvent and supporting electrolyte (SSE) were chosen as a solution of THF containing 20% (volume fraction) methanol and 0.1 mol L^{-1} $NaClO_4$, which gave the best results in the appropriate potential range.

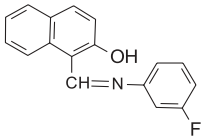
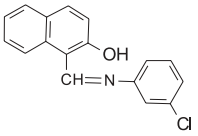
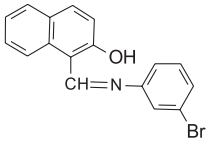
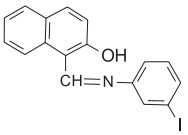
The structures of the compounds obtained by electrochemical reduction were elucidated by IR, UV–vis, ^{13}C NMR, ^{1}H NMR, and GC–MS techniques.

Reagents

Methanol and tetrahydrofuran (THF) were purchased from

© 2004 NRC Canada

Table 1. Chemical structure and melting points of the Schiff bases investigated.

Compound	Name	Structure	Melting point (°C)
I	1-{[(3-Fluorophenyl)imino]methyl}-2-naphthol		113
II	1-{[(3-Chlorophenyl)imino]methyl}-2-naphthol		115
III	1-{[(3-Bromophenyl)imino]methyl}-2-naphthol		140
IV	1-{[(3-Iodophenyl)imino]methyl}-2-naphthol		163

Note: All the structures given here are based on the assumption that the compounds are in the phenol-imine form.

Merck and purified as described in the literature (23). Sodium perchlorate ($NaClO_4$) was from Aldrich and was used without further purification. 1-{[(3-Halophenyl)imino]methyl}-2-naphthols were prepared according to the method described elsewhere (22). These compounds are listed in Table 1. The melting points relate to a reversible, true melting process. No decomposition was noticed.

Results and discussion

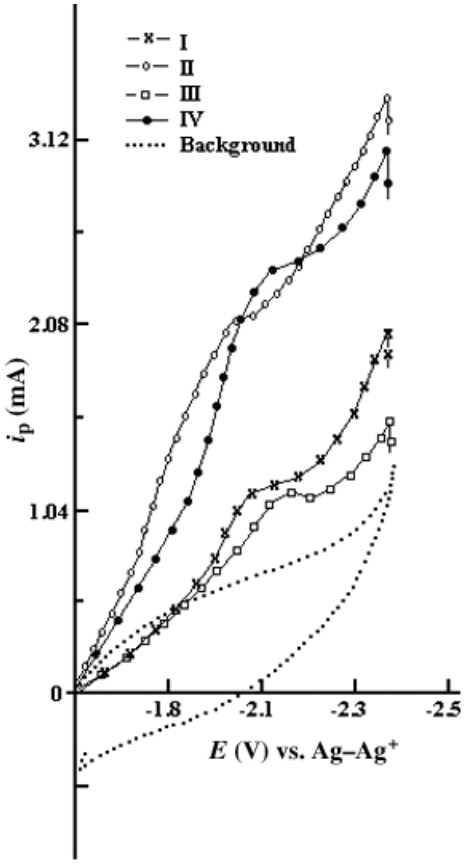
Characterization of the electrode reaction

The cyclic voltammograms of the compounds **I–IV** are shown in Fig. 1. The plotted curves represent the initial scans with a freshly cleaned graphite electrode. As evident on the voltammograms, there is only one reduction peak observed in the –2.0 to – 2.2 V potential range. Also, the anodic half cycle does not have any peak, indicating that the electroreduction is irreversible.

The electrochemical data extracted from the cyclic voltammograms are summarized in Table 2. The reduction potentials shift towards more negative values as the scan rate is increased. Because of this shift, there were no reduction peaks recorded, even at moderate scan rates such as 200 and 500 mV s^{-1}. Even for compound **IV**, with the most positive reduction potential, there was no peak observed at scan rates above 50 mV s^{-1}.

The peak current (i_p) and the current function ($i_p/v^{1/2}C$, where C is the bulk concentration) values were plotted against the scan rate in order to apply the Nicholson–Shain criteria, to elucidate the reaction mechanism (24). The plots obtained are given in Figs. 2 and 3. The plots in Fig. 2 are clearly straight lines, while in Fig. 3 the corresponding plots are concave curves whose slopes decrease towards higher scan rates. Figure 4 is a plot of current against concentration. Both Fig. 2 and Fig. 4 gave linear plots for all the com-

Fig. 1. Cyclic voltammograms of compounds **I–IV** (3 mmol L^{-1}) for solutions containing 20% (volume fraction) methanol in THF (0.1 mol L^{-1} $NaClO_4$) at a scan rate of 50 mV s^{-1} on a 3 mm diameter graphite electrode.



© 2004 NRC Canada

Table 2. Cyclic voltammetric data for the reduction of compounds **I–IV**.

v (mV s^{-1})	i_p (mA)	$-E_p$ (mV)	$E_{p/2}$ (mV)	$E_{1/2}$ (mV)	$E_p - E_{p/2}$ (mV)	$(i_p/v^{1/2})C$ (mA (mV/s)$^{-1/2}$ mmol L^{-1})
Compound I						
10	0.42	2025	1980	2003	45	0.043
20	0.55	2040	1970	2005	70	0.040
50	1.14	2100	2015	2058	85	0.034
100	1.64	2150	2060	2105	90	0.038
200	2.73	2200	2090	2145	110	0.037
Compound II						
5	0.35	2000	1960	1980	40	0.052
10	0.70	2020	1950	1985	70	0.073
20	0.96	2050	1970	2105	80	0.071
50	1.98	2150	2060	2080	90	0.093
100	2.57	2210	2090	2150	120	0.085
Compound III						
5	0.65	1940	1900	1920	40	0.0969
10	0.73	1985	1920	1953	65	0.0767
20	1.09	2050	1970	2010	70	0.0814
50	1.12	2180	2090	2135	90	0.0527
100	1.83	2240	2140	2190	100	0.0610
Compound IV						
2	0.65	1930	1890	1910	40	0.091
5	0.99	1965	1915	1940	50	0.089
10	1.50	1990	1930	1960	60	0.094
20	2.23	2025	1960	1993	65	0.097
50	2.39	2050	1970	1970	80	0.084

Note: Compounds **I–IV** in solutions containing 20% (volume fraction) methanol in THF (0.1 mol L^{-1} $NaClO_4$) at a scan rate of 50 mV s^{-1} on a graphite electrode (C: compounds **I–III**, 3 mmol L^{-1}; compound **IV**, 5 mmol L^{-1}).

Fig. 2. Current changes for compounds **I–IV** (3 mmol L^{-1}) with scan rate for solutions containing 20% (volume fraction) methanol in THF (0.1 mol L^{-1} $NaClO_4$) at a scan rate of 5–500 mV s^{-1} on a 3 mm diameter graphite electrode.

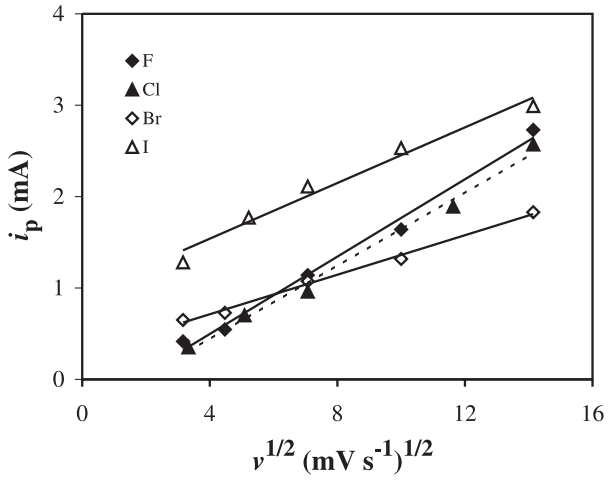
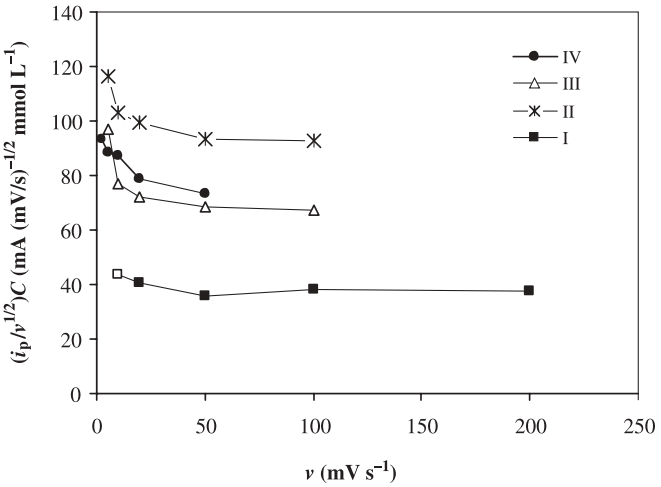


Fig. 3. Current function for compounds **I–IV** (3 mmol L^{-1}) plotted against the scan rate for solutions containing 20% (volume fraction) methanol in THF (0.1 mol L^{-1} $NaClO_4$) on a 3 mm diameter graphite electrode.



pounds investigated. The Nicholson–Shain criteria state that the linear change of the current with scan rate is an indication that the reaction is diffusion-controlled (24).

The fact that the current function decreases exponentially towards the higher scan rates is an indication that the electron transfer is followed by a chemical reaction. In the absence of chemical complications, this graph would be expected to be a nearly horizontal line. $E_{p,c} - E_{p,c/2}$ values were found to be 45–120 mV, in good agreement with those given in the literature for EC systems (24, 25). All these points suggest that the overall reaction is irreversible and follows an EC mechanism (25).

As shown in Fig. 1 and Table 2, the order of reduction of the compounds is **IV** > **I** > **II** > **III**, which reflects the de-

© 2004 NRC Canada

Scheme 2. The electrochemical reduction reaction mechanism.

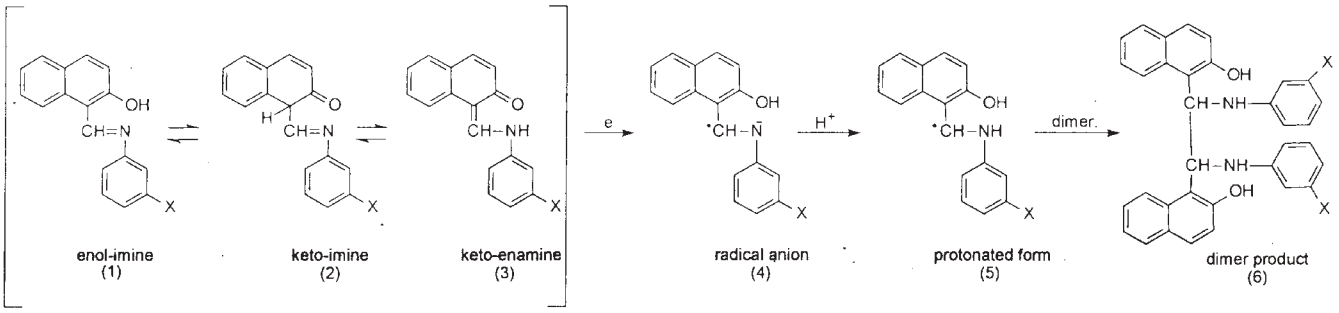
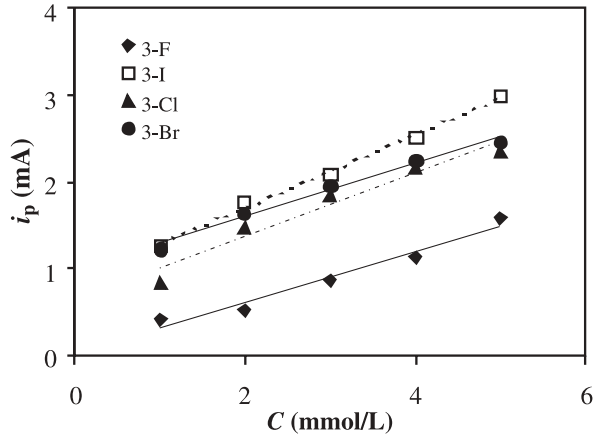


Fig. 4. The change, with concentration, of the current for compounds **I–IV** in solutions containing 20% (volume fraction) methanol in THF (0.1 mol L^{-1} $NaClO_4$) at a scan rate of 50 mV s^{-1} on a 3 mm diameter graphite electrode.



crease in the basicity of the iminic nitrogen, according to Scheme 2, as keto-imine (**2**) → keto-enamine (**3**) → radical anion (**4**) → protonated form (**5**). Such a sequence would be related to shifts in the reduction potentials caused by changes in the halogen-substituted Ar groups attached to the iminic nitrogen. The electron-withdrawing group on the aniline ring facilitates the reduction of the compound. However, it decreases the electron density at the N atom and makes proton transfer from the solvent more difficult. In Schiff bases, the phenyl ring is twisted, and the substituents are not fully conjugated with the rest of the molecule. Therefore, the tautomeric ratio does not depend, in general, on the electron action (donor or acceptor) of the substituents. Thus, the tautomeric process is localized on the naphthylmethylidene moiety. These results are in good agreement with the literature for similar compounds, except for compound **IV** (16).

Determination of the number of electrons transferred and the diffusion coefficients

First, we used both cyclic voltammetry at an ultramicro electrode (26–28) and chronoamperometry at the electrode to determine the number of electrons transferred (n) and the diffusion coefficent (D) simultaneously, for compounds **I–IV**. Equations [1] and [2] give the slope (S_{cott}) of the chronoamperometric i vs. $t^{-1/2}$ plot and the limiting steady-state current (i_{ss}) at an ultramicro electrode, respectively.

$$[1] \qquad S_{cott} = \frac{nFACD^{1/2}}{\pi^{1/2}}$$

$$[2] \qquad i_{ss} = 4nFCDr$$

When the last two equations are combined the number of electrons transferred (n) is given by the expression

$$[3] \qquad n = \frac{4\pi r S_{cott}^2}{A^2 F C i_{ss}}$$

Here, r is the radius of the ultramicro electrode, A is the area of the microelectrode, and all other symbols have their usual meaning (27). In the chronoamperometric experiments, the potential was stepped up from a value where there was no Faradaic current (about –100 mV) to a potential of –2300 mV, which is about 100 mV more cathodic than the first reduction peak for all the compounds investigated. The electrochemically active area of the 3 mm graphite electrode was determined from the slope of the chronoamperometric i vs. $t^{-1/2}$ plot, which was obtained with 5 mmol L^{-1} solutions of ferrocene in 0.1 mol L^{-1} $NaClO_4$–THF (containing 20% methanol) and was found to be 0.80 ± 0.015 cm^2. The value of D for ferrocene used in calculating this area was 4.8(± 0.1) × 10^{-6} cm^2 s^{-1} (29) and was obtained from the limiting current of the voltammograms by assuming the true geometric area of a 10 μm diameter Pt ultramicrodisc electrode as the electroactive area and by employing eq. [2]. The value of n of the ferrocene–ferrocenium couple was taken to be 1. The experimental values of n and D for all compounds are shown in Table 3.

Bulk electrolysis was performed at each peak potential (Fig. 1) for the compounds **I–IV**. The results obtained are shown in Table 3.

Controlled-potential preparative electrolyses and mechanism of the electrode reaction

Controlled-potential preparative electrolysis was carried out in a divided cell. The catholyte was 40 mL of solution containing 28 mmol of compounds **I–IV**. A Pt foil electrode was used as the anode. The anolyte was 20 mL of an SSE solution. The results are illustrated in Table 4.

The reduction products of CPE gave no absorption bands (λ_{max}) above 372 nm, indicating the disappearance of the azomethine group (>CH=N–). After the electrolysis process, the mixture was evaporated to dryness in a rotary evaporator. The solid residue was triturated with diethyl ether several times, and the ether-soluble portion was crystallized from this solvent after drying over K_2CO_3 powder (mp compound

© 2004 NRC Canada

Table 3. Diffusion coefficient, quantity of charge passed, and the number of electrons transferred for compounds **I**–**IV** at 25 °C.

Compound	Q^a/C (F mol^{-1})	$D^b/10^{-5}$ (±0.02) (cm^2 s^{-1})	Electron transferred (n) (±0.03) (equiv. mol^{-1})	
			n[c]	n^d
I	0.89	1.90	0.92	0.92
II	0.78	2.35	0.80	1.12
III	0.82	2.82	0.85	1.04
IV	0.85	3.31	0.88	0.94

Note: The concentration of the compound was 3 mmol L^{-1}.
[a]Calculated from bulk electrolysis.
[b]Calculated from the Cottrell slope (eq. [1]).
[c]Calculated from bulk electrolysis.
[d]Calculated from eq. [3].

Table 4. Controlled-potential preparative electrolysis results for the compounds **I**–**IV**.

Compound	Electrolysis products (10^{-3} mol)	t (min)	Potential (mV)	Q/C (F mol^{-1})	Product yield (%)	Current efficiency (%)
I	9.5	51.7	–2200	1785	33.9	66.1
II	9.2	50.0	–2250	1814	32.9	67.2
III	11	51.1	–2300	1640	39.3	60.7
IV	10	57.7	–2150	1736	35.7	64.3

I, 130–133 °C; compound **II**, 74–76 °C; compound **III**, 60–63 °C; and compound **IV**, 66–68 °C).

As a typical example, the following assignments have been made from the IR spectrum of compound **I** after the electrolysis process: peaks (cm^{-1}) at 3474 (OH), 3437 (NH), 3072–3046 (CH arom.), 2920–2859 (CH aliphatic), 1578 (C=C arom.), 1437 (C-N), 1334–1089 (C-O). The IR spectra in the case of compounds **II**–**IV** are similar except for the expected differences in the fingerprint region.

In addition, the broad band in the 3100–3000 cm^{-1} region, characteristic of intramolecular hydrogen bonding, and the bands between 1700 and 1600 cm^{-1}, due to C=N and C=O stretching (22), were found to disappear after CPE.

Principal mass spectral peaks observed after CPE were as follows:

Compound I

MS (EI+, 6.124 × 10^4) *m*/*z* (%): 531.5 ([M – 1(H)$^+$], 9.2), 533.5 ([M + 1]$^+$, 6.7), 437 ([M – 1(H)$^+$ – C_6H_5F], 4.76), 266 ([M – 1(H)$^+$ – $C_{17}H_{13}NOF^+$], 100), 264 ([$C_{17}H_{13}NOF$ – 2H]$^+$, 41.1), 95 ([C_6H_4F]$^+$, 88.9).

Compound II

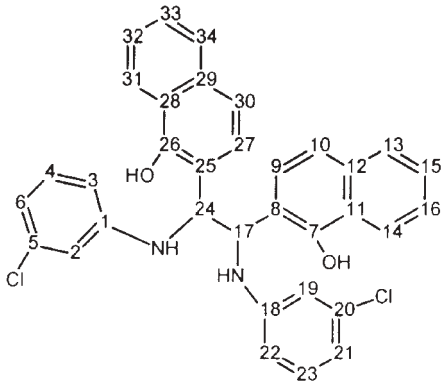
MS (EI+, 5.73 × 10^4) *m*/*z* (%): 565.55 ([M]$^{+\bullet}$, 2.4), 281 ([$C_{17}H_{12}NOCl$]$^{+\bullet}$, 60), 110.85 ([C_6H_4Cl]$^+$, 100).

FAB+ (ZabSpec) *m*/*z* (%): 580.49 ([M – 1]$^{+\bullet}$, 10.7), 579.4 ([M – 2]$^{+\bullet}$, 19.0), 341.1 ([M – C_6H_4Cl – H]$^+$, 100), 342.13 ([M – C_6H_4Cl]$^+$, 19.67).

Compound III

MS (EI+, 5.57 × 10^3) *m*/*z* (%): 652 ([M + 4]$^{+\bullet}$, 1.2), 655.50 ([M + 2]$^{+\bullet}$, 0.8), 326.01 ([M + 2]$^{+\bullet}$ – [$C_{17}H_{13}NOBr^+$], 55), 324.01 ([$C_{17}H_{13}NOBr$ – 2H]$^+$, 100), 170.52 ([C_6H_5NBr]$^+$, 3.17), 154.61 ([C_6H_4Br]$^+$, 2.93).

Scheme 3. The molecular structure for 2,2′-{1,2-bis[(3-chlorophenyl)amino]ethane-1,2-diyl}di(1-naphthol).



Compound IV

MS (EI+, 1.18 × 10^4) *m*/*z* (%): 748.35 ([M]$^{+\bullet}$, 0.62), 218.83 ([C_6H_5NHI]$^+$, 100), 126.53 ([I]$^+$, 50.81), 372.06 ([M$^{+\bullet}$ – $C_{17}H_{13}NOI$ – 1]$^+$, 30.04), 373.66 ([M$^{+\bullet}$ – $C_{17}H_{13}NOI$]$^+$, 15.73).

The molecular-ion peaks corresponding to the dimerized product (depicted in Scheme 3 for compound **II**) are observed in the MS spectra of all compounds. Also, the base peaks indicate that the fragmentation in compounds **I** and **III** was symmetrical.

Further evidence for the identity of the reduction products of compounds **I**–**IV** was provided by ^{13}C NMR and ^{1}H NMR data. As an example, ^{13}C NMR data obtained for compound **II** after CPE are given below.

^{13}C NMR (proton decoupled, ppm) δ: 148.16 (C1, C18), 109.48 (C2, C19), 115.69 (C3, C22), 129.82 (C4, C23), 133.49 (C5, C20), 119.43 (C6, C21), 156.95 (C7, C26), 120.86 (C8, C25), 127.98 (C9, C27), 121.77 (C10, C30),

© 2004 NRC Canada

135.77 (C11, C28), 137.10 (C12, C29), 126.86 (C13, C34), 116.65 (C14, C31), 128.60 (C15, C33), 124.17 (C16, C32), 56.82 (C17, C24).

DEPT (45, 90, 135) (ppm) δ: 109.48 (C2, C19), 115.69 (C3, C22), 129.82 (C4, C23), 119.43 (C6, C21), 127.98 (C9, C27), 121.77 (C10, C30), 126.86 (C13, C34), 116.65 (C14, C31), 128.60 (C15, C33), 124.17 (C16, C32), 56.82 (C17, C24).

The ^{13}C NMR DEPT results show that there are 11 methine protons ((DEPT-90 and DEPT-45) and no methylene protons (DEPT-135) and no methyl protons (DEPT-45 and DEPT-135)) in the structure. Moreover, the observation of 17 signals in the proton-decoupled spectrum shows that the structure is a symmetrical dimer.

The ^{1}H NMR data for compound **II** after electrolysis are as follows:

^{1}H NMR δ (ppm): 12.4 (s, Ar-O*H* proton), 8.5–6.5 (m, arom. protons), 3.0–4.0 (m, aliph. –C*H* protons), 2.2 (hump, -N*H* proton).

The fact of the disappearance of the characteristic peaks located at δ 9.2 (C=N-H) and δ 15.2 (OH–NH) in the original ^{1}H NMR spectra (22) of the compounds is another verification of the dimer formation.

The fact that the CPE product of compounds **I**–**IV** appears to take one electron per molecule to yield the final product suggests the formation of a protonated radical intermediate, followed by dimerization to yield the final product (Scheme 2, structure **6**). Indeed, the spectroscopic evidence on CPE of compounds **I**–**IV** supports the formation of these kinds of products.

Conclusions

The conclusions drawn from the electrochemical and spectroscopic data are the following:

The cyclic voltammetric investigation of the compounds on graphite electrodes indicates an irreversible reduction peak with a diffusion-controlled EC mechanism for all of the compounds investigated.

Cyclic voltammetry on ultramicro disc electrodes and the chronoamperometric and coulometric studies indicate $n = 1$ for each compound investigated.

The CPE data shows that the dimerized products are very stable. They were isolated and characterized spectroscopically.

It has been demonstrated that the dimeric product of electrolyses can be synthesized on a laboratory scale by the electrochemical reduction in a solution of THF containing 20% methanol, using sodium perchlorate as the supporting electrolyte. The stereochemical investigation of this dimeric product may be interesting and could be a subject of another study.

Acknowledgement

The authors are grateful to Ankara University Research Fund for financial support (Project CHE 20010705039).

References

1. H. Ünver, D.M. Zengin, and T.N. Durlu. Anal. Sci. **17**, 1021 (2001).
2. H. Ünver, D.M. Zengin, and K. Güven. J. Chem. Crystallogr. **30**, 359 (2000).
3. M.D. Cohen, G.M. Schmidt, and S.J. Flavian. J. Chem. Soc. B, 2041 (1964).
4. M.E. Kletskii, A.A. Millov, A.V. Metelitsa, and M.I. Knyazhansky. J. Photochem. Photobiol. A, **110**, 267 (1997).
5. D. Chen and A.E. Martel. Inorg. Chem. **26**, 1026 (1987).
6. D.E. Hamilton, R.S. Drago, and A. Zonbeck. J. Am. Chem. Soc. **109**, 374 (1987).
7. R. Herzfeld and P. Nagy. Curr. Org. Chem. **5**, 373 (2001).
8. M. Gavranić, B. Kaitner, and E. Mestrović. J. Chem. Crystallogr. **26**, 23 (1996).
9. B. Kaitner and G. Pavlonic. Acta Crystallogr. C, **52**, 2573 (1996).
10. G. Dudek and R.H. Holm. J. Am. Chem. Soc. **86**, 4283 (1964).
11. S.R. Salman, S.H. Shawkat, and G.M. Al-Obaidi. Can. J. Spectrosc. **35**, 27 (1990).
12. S.R. Salman, R.D. Farrant, and J.C. Lindan. Spectrosc. Lett. **24**, 1071 (1991).
13. J. Casaszar, J. Morray, and O. Herczeg. Acta Phys. Chem. **31**, 717 (1985).
14. H. Lund. Acta. Chem. Scand. **13**, 249 (1959).
15. E. Paspaleev and A. Pavlova. C. R. Acad. Bulg. Sci. **18**, 533 (1965).
16. V.N. Dmitrieva, L.V. Kononenko, and V.D. Bezuglyi. Teor. Eksp. Khim. **1**, 456 (1965).
17. J.M.V. Scott and W.H. Jura. Can. J. Chem. **45**, 2375 (1967).
18. L.V. Kononenko, V.D. Bezuglyi, and V.N. Dmitrieva. Zh. Obshch. Khim. **38**, 2153 (1968).
19. C.P. Andrieux and J.M. Saveant. Electroanal. Chem. **33**, 453 (1971).
20. A.J. Fry and R.G. Reed. J. Am. Chem. Soc. **91**, 6448 (1969).
21. T.V.D Prasad Rao, G. Veerabhadram, and K.S. Sastry. J. Indian Chem. Soc. **77**, 410 (2000).
22. H. Ünver, K. Polat, M. Uçar, and D.M. Zengin. Spectrosc. Lett. **36**, 287 (2003).
23. D.D. Perrin and W.L.F. Armarego. Purification of laboratory chemicals. 3rd ed. Pergamon Press Ltd., Oxford. 1988.
24. R.S Nicholson and I. Shain. Anal. Chem. **36**, 706 (1964).
25. C.R. Brown and R.F. Large. *In* Techniques of chemistry. Vol. 1. Part II A: Electrochemical methods. *Edited by* A. Weissberger. Wiley-Interscience, New York. 1971.
26. A.S. Baranski, W.R. Fawcett, and C.M. Gilbert. Anal. Chem. **57**, 166 (1985).
27. M. Fleischmann, S. Pons, D.R. Rolison, and P. Schmidt. Ultramicroelectrodes. Datatech Science, Morganton, N.C. 1987.
28. G. Denualt, M. Fleischmann, and D. Pletcher. J. Electroanal. Chem. **280**, 243 (1990).
29. B. Workie, C.E. Dubé, L. Aksu, S.P. Kounaves, A. Robbat, and G. Davies. J. Chem. Soc. Dalton Trans. 1739 (1997).

© 2004 NRC Canada

Is acyl migration to the aglycon avoidable in 2-acyl assisted glycosylation reactions?[1]

Attila Bérces, Dennis M. Whitfield, Tomoo Nukada, Iwona do Santos Z., Agnes Obuchowska, and Jiri J. Krepinsky

Abstract: This report unequivocally separates orthoester formation from acyl transfer for the first time and indicates possible routes to eliminate 2-*O*-acyl transfer during glycosylation reactions. Experimental evidence is shown that acyl transfer from 2-*O*-acyl-3,4,6-tri-*O*-benzyl-D-galactopyranose-derived glycosyl donors decreases in the order formyl > acetyl > pivaloyl. The 2-*O*-benzoyl derivatives are more variable, in some cases transferring easily, and in others not at all. Density functional theory (DFT) calculations of the structure and energetics of dioxolenium ion and related intermediates suggest that a proton transfer pathway from the nucleophile to O-2 provides an explanation for the observed trends. These DFT calculations of the proton transfer pathway support a mechanism in which a relay molecule is involved. Further DFT calculations used a constraint based on linear combinations of six bond lengths to establish the sequence of bond breaking and bond forming. The calculated anomeric carbon to former carbonyl oxygen bond that breaks during acyl transfer is the longest in the formyl case and shortest in those that exhibit little or no acyl transfer. Rotation about the aromatic to carbonyl Ph—C(=O) bond is different from the alkyl series. Analysis of this proposed TS led to the postulate that 2,6-substitution may hinder rotation even more. Thus, the 2,6-dimethylbenzoyl analogue was synthesized and it does not transfer directly or by rearrangement of its readily formed orthoester. DFT calculations suggested that 2,6-dimethoxybenzoyl should also not transfer easily. Experimentally, this proved to be the case and this new 2-*O*-acyl protecting group cleaves at 50 °C with a 1 mol/L solution of LiOH in methanol. Thus, a calculated transition state has led to a prototype of a protecting group that solves a major problem in oligosaccharide synthesis.

Key words: glycosylation, carbohydrates, quantum chemistry, reaction mechanism, neighboring-group effects.

Résumé : Dans ce travail, on sépare sans équivoque et pour la première fois la formation d'orthoester des transferts d'acyles et on suggère des voies possibles pour éliminer le transfert de 2-*O*-acyle lors des réactions de glycosylation. On présente des données expérimentales montrant que le transfert d'acyle de donneurs glycosyles dérivés du 2-*O*-acyl-3,4,6-tri-*O*-benzyl-D-galactopyranose diminue dans l'ordre formyle > acétyle > pivaloyle. Les dérivés 2-*O*-benzoyles sont plus variables; dans certains cas, le transfert se fait facilement alors que dans d'autres il ne se fait pas du tout. Des calculs basés sur la théorie de la densité fonctionnelle (THF) de la structure et des énergies de l'ion dioxolénium et d'intermédiaires apparentés suggèrent qu'un transfert de proton du nucléophile vers O-2 s'avère la meilleure explication pour les tendances observées. Ces calculs de THF de la voie de transfert de proton appuient un mécanisme dans lequel une molécule relais serait impliquée. Des calculs supplémentaires de THF ont été réalisés en appliquant une contrainte basée sur des combinaisons linéaires de six longueurs de liaisons pour déterminer la séquence de bris et de formation de la liaison. La longueur calculée pour la liaison entre le carbone anomérique et l'oxygène du carbonyle antérieur qui se brise au cours du transfert d'acyle est la plus longue dans le cas du formyle et elle est la plus courte dans les cas de ceux qui ne donnent que peu ou pas de transfert d'acyle. La rotation autour de la liaison aromatique vers le carbonyle de Ph—C(=O) est différente de celle observée dans la série alkyle. L'analyse de cet état de transition proposé conduit au postulat que la substitution en 2 et 6 peut empêcher la rotation encore plus. On a donc réalisé la synthèse de l'analogue 2,6-diméthoxybenzoyle et on a observé qu'il n'y a pas de transfert direct ou par le biais d'un réarrangement de la part de cet orthoester facilement formé. Des calculs de TDF suggèrent que le 2,6-diméthoxybenzoyle ne devrait pas donner lieu à des transferts. D'un point de vue expérimental, cette prédiction s'est avérée juste et ce nouveau groupe protecteur 2-*O*-acyle peut être clivé à 50 °C, avec du 1 mol/L LiOH dans du méthanol. Ainsi, un état

Received 5 December 2003. Published on the NRC Research Press Web site at http://canjchem.nrc.ca on 17 September 2004.

A. Bérces.[2] Steacie Institute for Molecular Sciences, National Research Council Canada, 100 Sussex Drive, Ottawa, ON K1A 0R6, Canada.
D.M. Whitfield.[3] Institute for Biological Sciences, National Research Council Canada, 100 Sussex Drive, Ottawa, ON K1A 0R6, Canada.
T. Nukada. The Institute for Physical and Chemical Research (RIKEN), Wako-shi, 351-01 Saitama, Japan.
I. do Santos Z., A. Obuchowska, and J.J. Krepinsky. Department of Medical Genetics & Microbiology and Protein Engineering Network of Centers of Excellence (PENCE), University of Toronto, Toronto, ON M5S 1A8, Canada.

[1]NRC paper No. 42487.
[2]Present address: Astra Zeneca R&D Mölndal, SE-431 83 Mölndal, Sweden.
[3]Corresponding author (e-mail: dennis.whitfield@nrc-cnrc.gc.ca).

 doi: 10.1139/V04-059 © 2004 NRC Canada

de transition calculé a conduit à un prototype de groupe protecteur qui résout un problème majeur dans la synthèse d'oligosaccharides.

Mots clés : glycosylation, carbohydrates, chimie quantique, mécanisme réactionnel, effets de groupes voisins.

[Traduit par la Rédaction]

Introduction

Many biologically active molecules contain sugar molecules with acetal or ketal linkages. The study of the diastereomeric complexities of joining two sugar molecules together to form such linkages is an active area of research. Most linkages are formed by glycosylation reactions between an activated electrophilic glycosyl donor and a weakly nucleophilic alcoholic acceptor. This necessity to use highly reactive donors makes these reactions prone to side reactions. Minimizing side reactions and achieving stereochemical control are the two main objectives of research into glycosylation reaction mechanisms (1).

The commonest approach to stereochemical control of glycosylation reactions is to use neighboring group participation, typically of an ester at C-2 of a hexopyranosyl donor. After activation by a promoter in the absence of nucleophiles such species form dioxolenium ions by nucleophilic attack of the ester carbonyl oxygen (O-7) on C-1 (2). It has been shown theoretically that such cations have a LUMO predominantly situated on the former carbonyl carbon (C-7) and therefore C-7 should be the site of nucleophilic attack. In the presence of nucleophiles, calculations suggest that stable intermediates that have long C-7—O_{nuc} bonds are formed (3). After shortening of this bond, hydroxylic proton transfer and pyranose ring conformational change stable orthoesters can be formed. A common side reaction long associated with orthoester formation is acyl transfer. This unwanted side reaction is the transfer of the O-2 acyl protecting group (4) to the nucleophilic acceptor to form a new ester linkage and a free OH group at O-2 of the sugar (5). This side reaction is the focus of this study.

Acyl transfer from the glycosyl donor to the sugar acceptor has been noted numerous times over many years (6). This side reaction has been observed with many different glycosyl donors (7) under many different glycosylation reaction conditions. Besides the acylated acceptor alcohols, glycosides often of both anomers with a 2-OH group, for example **5**, are frequently formed as well (8). For "conventional" solution-phase chemistry this side reaction is only a problem of yield and adds extra complexity to the reaction mixture to be purified. For solidphase methodologies, where the acceptor is bound to the polymeric support, it is particularly troublesome (9). If the acyl group is used as the cleavable group then two or more hydroxyl species instead of one will be available for the subsequent glycosylation. If the acyl group is not the cleavable protecting group then the acyl transfer itself essentially caps the polymer bound acceptor and it is the formation of polymer bound donor derived glycosides with free OH groups that can undergo further glycosylation, which is the problem.

Such a reaction was observed between the linker-polymer combination MPEG-DOXOH (**1**) and the donor ethyl 2,6-di-*O*-benzoyl-3,4-*O*-isopropylidene-1-thio-β-D-galactopyranoside (**2**) under a wide variety of reaction conditions. Donor **2** was designed to allow for subsequent branching at O-3 and O-4. Among the reaction products were: **3** the result of benzoyl transfer to the nucleophile, **4** the expected product, **5** a 2-OH glycoside, and **6** β(1 → 2)-linked oligomers that accounted for up to half the polymer bound products (see Scheme 1 (10)). Previously (1 → 2)-linked disaccharides have been isolated as side products in glycosylation reactions that also exhibited acyl transfer (11). Also, some groups have independently developed protocols to preparatively prepare (1 → 2)-linked disaccharides based on this reaction type (12). Since preparative polymer-supported chemistry requires very high yields with no side products, we adopted a program to develop strategies towards the elimination of the acyl transfer side reaction.

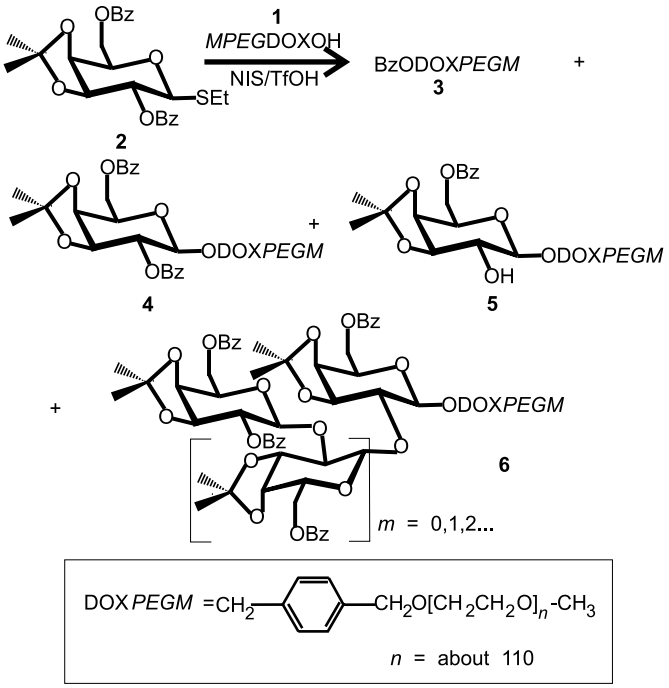
It has long been known that increasing the steric bulk about the acyl substituent minimizes acyl transfer. For example, the suppression of acyl transfer during the preparation of multigram quantitities of glucosylated sapogenins was achieved by switching from peracetyl- to perbenzoyl-substituted donors (13). Another group has shown the utility of isobutyryl to minimize acyl transfer with glucuronyl donors (14). Several groups have used pivaloyl esters to suppress acyl transfer (15). Most of these reports discuss the use of pivaloyl in terms of suppressing orthoester formation and do not discuss acyl transfer (16). Similarly, the mesitoyl (2,4,6-trimethylbenzoyl) group has also been used to suppress orthoester formation (17). Orthoesters can be rearranged to glycosides by acid catalysis (18) but acyl transfer is frequently observed in this reaction (19). As we will show below, the propensity to form orthoesters and the propensity to give acyl transfer are not directly related (20).

Results and discussion

Few studies have attempted to systematically study the effect of the acyl group on acyl transfer. We had previously studied a series of 2,3,4,6-tetra-*O*-acyl-substituted galactopyranosyl trichloroacetimidate donors (**7ab** and **8**), and shown that the order of acyl transfer was benzoyl (**12b**) << isobutyryl (**12c**) ≈ acetyl (**12a**) (8). This study also showed that trifluoromethanesulfonic anhydride as promoter with the peracetate **7a** (21) led to 1,2 linked-oligomers, whereas using silver or copper(II) triflate as promoter eliminated the 1,2-oligomers but not acetate transfer (see Scheme 2). We now show that the powerful promoter triethylsilyltriflate also leads to acetate transfer in a ratio of 40:60 (glycoside **11a** to acetate transfer **12a**) for the α-trichloroacetimidate **7a** and 33:67 for the β-trichloroacetimidate **9a**. Changing to the perbenzoyl trichloroacetimidate **9b** improves the ratio to 93:7 (see *Experimental*). This matches the previously reported result with the perbenzoyl 1-thio-galactoside donor

© 2004 NRC Canada

Scheme 1. Acyl transfer side reaction during a polymer-supported glycosylation reaction. Even after extensive optimization desired glycoside **4** could only be formed in <40% yield (10).



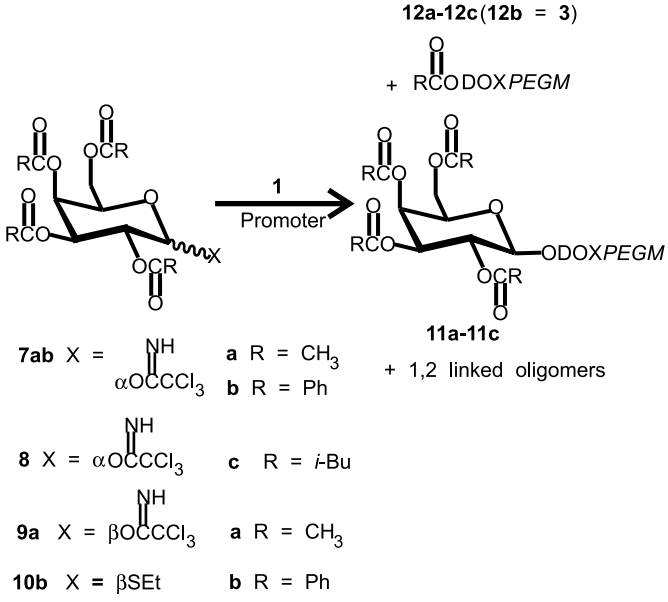
10b, where a ratio of 93:7 (**11b**:**12b**) was also found (10). We interpret these results to indicate that one or more intermediates are formed in such glycosylation reactions that eventually lead to acyl transfer or glycosylation (cf. **D** and **E** in Scheme 3).

Returning to 3,4-*O*-isopropylidene galactose derivatives, we showed that even pivaloyl esters transfer to form MPEG-DOXOPiv although 1,2-oligomer formation was suppressed.

Following a literature precedent (22), increasing the steric bulk about the alcohol acceptor by forming the α-methyl benzyl derivative MPEG-MDOXOH was undertaken for the preparation of synthetically useful amounts of MPEG-MDOXyl glycosides. Two other factors, namely operating at the highest possible concentration of TfOH and the highest possible temperature that did not lead to decomposition reactions, were also necessary to suppress acyl transfer. These last two observations can be interpreted to indicate that acyl transfer gives the apparent kinetic product and glycosylation the apparent thermodynamic product (10). The importance of the acid concentration also suggests that proton transfer is integral to the mechanism as previously proposed (11*a*).

Given the high propensity to undergo acyl transfer of the 3,4-isopropylidene galactose derivatives, we undertook to study the mechanism of acyl transfer with the 2,6-di-*O*-acetyl-3,4-*O*-isopropylidene-D-galactopyranosyl cations. The structures and energetics of the following intermediates were calculated using density functional theory (DFT) with a continuum solvent correction (see Scheme 3). The "parent" cat-

Scheme 2. Effect of acyl groups on acyl transfer with galactose donors (8, 10).



ion **B** is derived by ionization of donor **A**. Monocyclic **B** after ring inversion can cyclize to the bicyclic dioxolenium ion **C** associated with neighboring group participation with a calculated barrier of 34 kJ mol^{-1} (23). This ion has a vacant *p*-like orbital centered on the former carbonyl carbon (C-7) (3). This reacts with methanol to form an ion–dipole complex **D** with a C-7—O-8 (O-8 from MeOH) bond length of 2.81 Å. After considerable search, a pathway involving proton transfer to O-2 from **D** spontaneously led to acyl transfer and the 2-OH ion **E**.[4] Ion **E** is presumably the precursor to 2-OH glycosides and 1,2-oligomer formation but its reactivity has not been studied further.

To further study the acyl transfer pathway, we decided to study the effect of acyl substituents. For this purpose, a series of 2-*O*-acyl 3,4,6-tri-*O*-benzyl-D-galactopyranosyl donors (**13a**–**13e**), where the acyl groups are formyl, acetyl, benzoyl, pivaloyl, and levulinoyl, were prepared and reacted with **1** (see *Supplementary material*[5] and *Experimental*. The ease of acyl transfer during the preparation of glycosides **14a**–**14e** followed the order formyl > acetyl > levulinoyl >> benzoyl = pivaloyl in the amounts 56%, 5%, 2%, and 0% (cf. **15a**-**15e**, see Scheme 4). This compares to the 3,4-isopropylidene donors where benzoyl transfers more than pivaloyl with the same acceptor suggesting that the more reactive 3,4,6-tri-*O*-benzyl donors suppress acyl transfer (24).

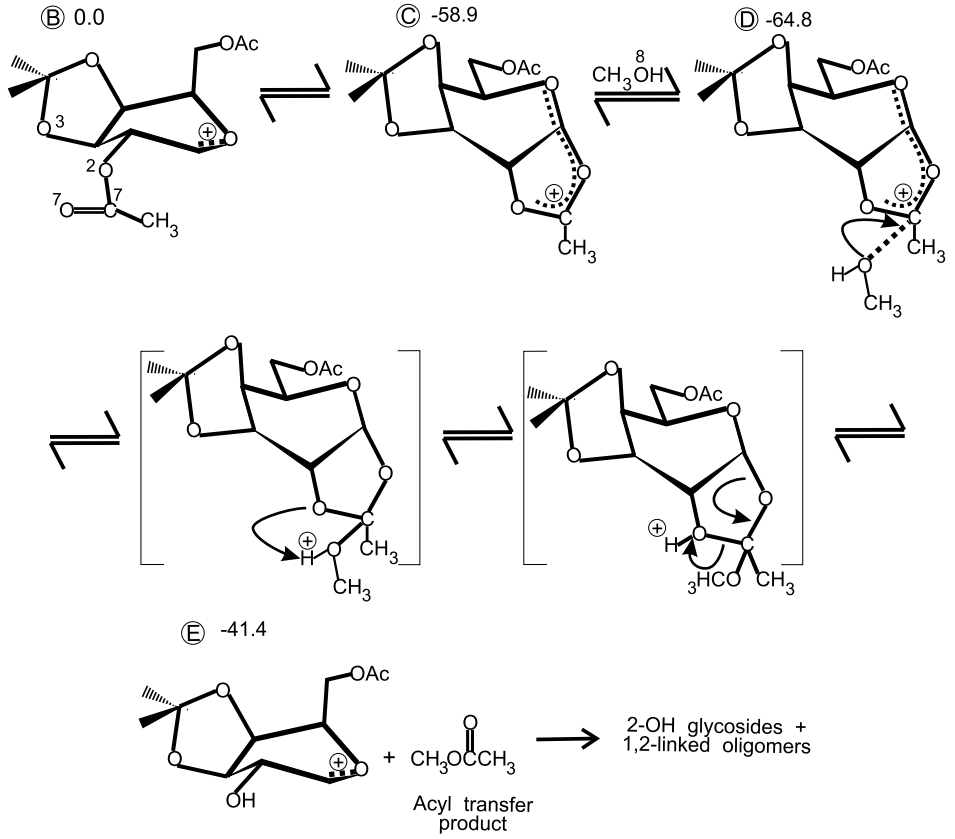
To study the acyl group effect theoretically we calculated the intermediates **B**, **C**, **D**, and **E′** for the series 2-*O*-acyl 3,4-*O*-isopropylidene-6-*O*-acetyl-D-galactopyranosyl cation plus MeOH where the acyl is formyl, acetyl, benzoyl, and pivaloyl (see Table 1). Note as shown below, **E′** in this series is an ion–dipole complex of the ion **E** and the appropriate acyl methyl ester. The pyranose ring in all **C** and **D**s is in the

[4] In the original report of ref. 3 other ion–dipole complexes resulting from the methanol approach to the anomeric center of **C**, to the β-face of **B**, and the α-face of **B**, respectively, as well as a plausible intermediate with a tetrahedral carbon were considered.

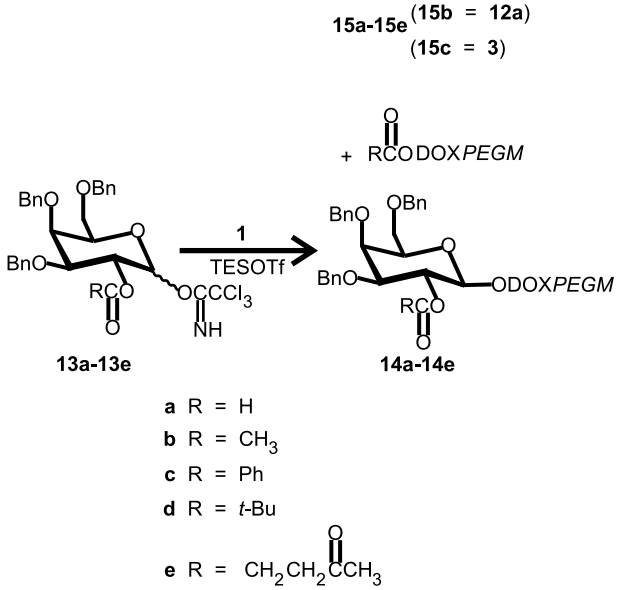
[5] Supplementary data may be purchased from the Depository of Unpublished Data, Document Delivery, CISTI, National Research Council Canada, Ottawa, ON K1A 0S2, Canada (http://www.nrc-cnrc.gc.ca/cisti/irm/unpub_e.shtml for information on ordering electronically).

© 2004 NRC Canada

Scheme 3. Previously proposed mechanism for acyl transfer via proton transfer to O-2. Intermediates **B**–**E** derived by the ionization of donor **A** (10).



Scheme 4. 2-*O*-Acyl-substituted galactose donors used to assess the substituent effect on acyl transfer.



$B_{2,5}$ conformation and in all **B**s is in an ^2S_O conformation. Figure 1 shows partial ball and stick representations of the structures of the **D** complexes. It is readily apparent that the C-1—O-7 bond length is the longest for the formyl derivative among the series formyl (1.810 Å), acetyl (1.640 Å), and pivaloyl (1.618 Å). These trends fit the observation of acyl transfer diminishing in the series formyl > acetyl > pivaloyl (see Figs. 1*a*–1*c*). The benzoyl **D** has the shortest calculated C-1—O7 bond length (1.607 Å) but is quite close to pivaloyl (cf. Figs. 1*d* and 1*c*). These results suggest some π-resonance contribution, which is not unexpected given the similarity to a substituted benzyl cation. Similarly, the benzoyl complex **D** is the most stable relative to isolated **B** and MeOH as shown in Table 1.

From our previous calculations we know that proton transfer triggers the acyl transfer and for this reason, the proton transfer is probably the rate-determining step (10). We first studied the direct transfer of the H-(O-8) to O-2 using constrained linear transit calculations explained in *Computational details*. We found that the direct proton transfer involves a 170 kJ mol^{-1} barrier, which is clearly too high and this mechanism is therefore unrealistic. For a proton transfer to take place with a reasonably low energy barrier, the donor, the acceptor, and the proton should ideally be situated on a straight line. In contrast, the angle between the H—O-8 bond and the H—O-2 hydrogen bond is 78° in the formyl case. Consequently, the proton transfer does not take place directly but likely involves a relay molecule. We note that these reactions normally take place in aprotic solvent but a small amount of water or other proton relay molecules cannot be ruled out. The counteranions or leaving-group derived entities as well as added bases and molecular sieves etc. are all possible relay molecules. To keep the model as simple as possible we considered a second methanol to be involved as

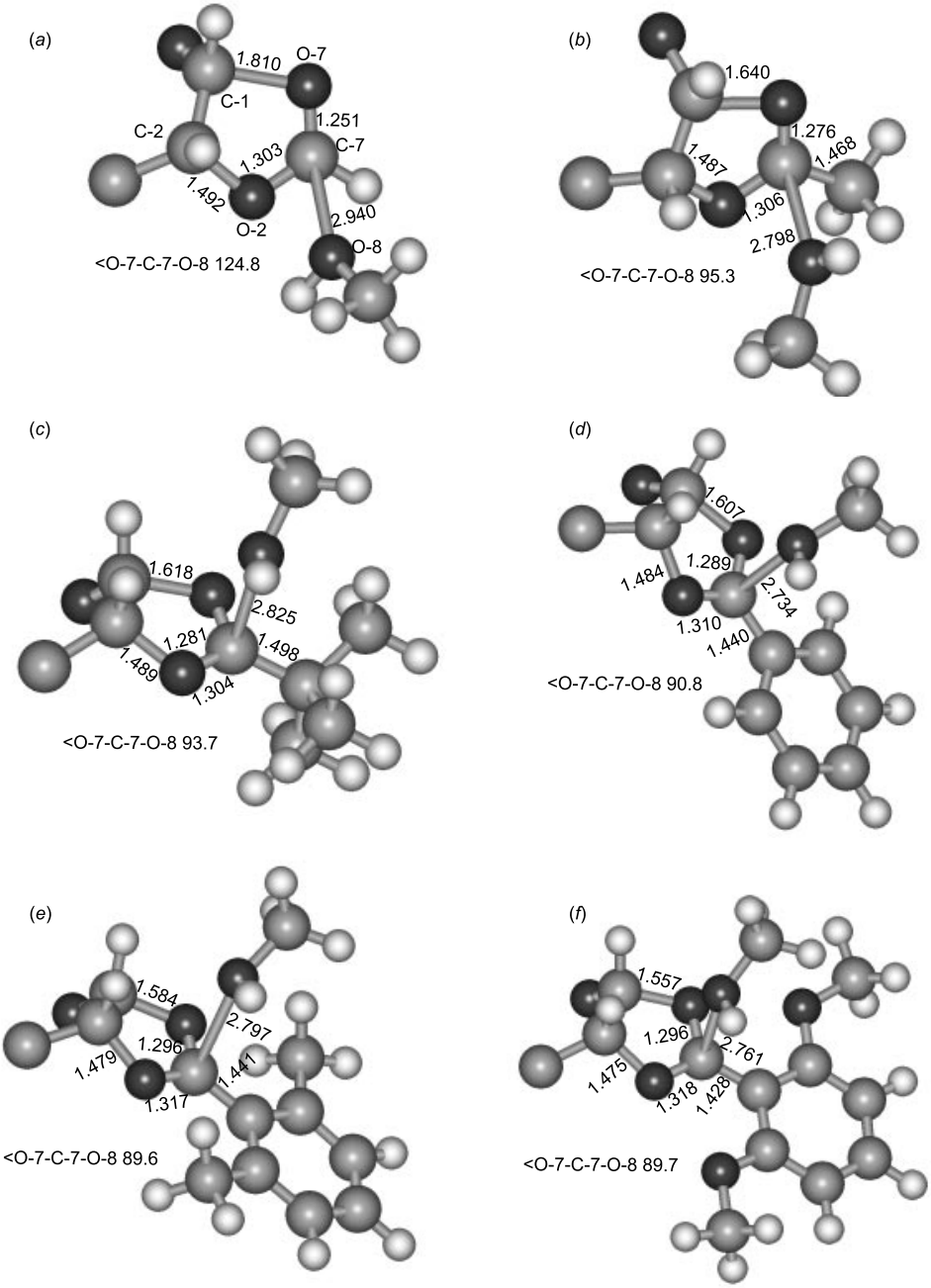
© 2004 NRC Canada

Table 1. Relative energies in kJ mol^{-1} for cations **B**–**E′** derived from 2,6-di-*O*-acyl-3,4-*O*-isopropylidene-D-galactopyranosyl donors.

	Formyl	Acetyl	Pivaloyl	Benzoyl	2,6-Dimethylbenzoyl	2,6-Dimethoxybenzoyl
B	0.0[a]	0.0	0.0	0.0	0.0	0.0
C	–34.9	–51.6	–48.7	–56.0	–65.9	–82.6
D	–35.9	–57.7	–56.1	–62.6	–70.0	–85.2
E′	–44.6	–46.2	–16.6	–30.8	–46.9	–57.6
ME (*c*)	0.0[b]	0.0	0.0	0.0	0.0	0.0
ME (*t*)	–10.7	–18.3	–44.8	–33.5	–15.7	–12.8

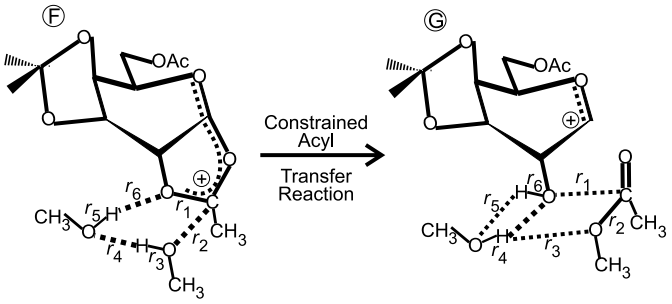
[a]Energy including solvated methanol for **B** and **C** at the same level of theory.
[b]Energy for the solvated cis (*c*) ester set to 0.0 for comparison to the trans ester (*t*) reaction (25).

Fig. 1. Partial ball and stick representations of ion–dipole complexes **D** for: (*a*) formyl, (*b*) acetyl, (*c*) pivaloyl, (*d*) benzoyl, (*e*) 2,6-dimethylbenzoyl, and (*f*) 2,6-dimethoxybenzoyl.



© 2004 NRC Canada

Scheme 5. The constraint based on r_1r_6 used for the mechanism calculation (see eq. [2]).



a relay molecule in the proton transfer. Similar relay molecules have been used in theoretical studies of the mutarotation reaction (25).

To understand the mechanism of acyl transfer we carried out calculations mapping the reaction path leading from **F** to **G** as shown in Scheme 5. General methods of reaction path following usually consider elementary reaction steps. The application of these methods becomes intractable for multistep reactions such as acyl transfer. Consequently, we customized our approach to this reaction to gain insight into the mechanism. We carried out linear transit calculations using a constraint that ensures that the reactant and the product states correspond to **F** and **G**.

This reaction involves the formation and breaking of seven bonds as well as hybridization changes such as C-1 going from sp^2 in **F** to sp^3 in neutral products. Two hydrogen bonds become covalent bonds and two covalent bonds involving hydrogen break to become hydrogen bonds. In addition, the formation of the O-8—C-7 bond and the breaking of O-2—C-7 and O-7—C-1 are key features in the mechanism. Since the O-7—C-1 bond breaking is the consequence of the rest of the rearrangements, we do not have to consider this bond as part of our linear transit constraints. To consider the breaking and formation of six separate bonds individually requires assessing the $6 \times 5 \times 4 \times 3 \times 2 = 720$ possible sequences of events. For this reason, we have to define a constraint that brings the reactants to product state without predefining the sequence of events. We shall explain how this can be carried out on a simpler example and extend the results to acyl transfer. Lets consider the transfer of H—(O-R) to O-2. There are two bonds involved in this transfer: the forming H—O-2 bond and the breaking H—(O-R) bond. A simple constraint

$$[1] \qquad Q = \mathrm{R[H—(O\text{-}R)]} - \mathrm{R[H—(O\text{-}2)]}$$

where R[H—(O-R)] and R[H—(O-2)] are the H—(O-R) and H—(O-2) bond lengths, respectively, can be used to study this mechanism. At the reactant state, the value of Q is negative while it is positive in the product state. To study this reaction by quantum mechanical methods, we can carry out constrained geometry optimization at varying values of Q representing the progress of the reaction. This procedure is called linear transit. The application of Q as a constraint has some distinct advantages compared to using either the forming or the breaking bond distance as constraint alone. Most importantly, this constraint does not specify the sequence of events, whether the bond breaking or the formation takes place first or if the two steps are synchronized. In addition, it is straightforward to extend this constraint to the case described in Scheme 5. For the exploration of the reaction path from **F** to **G** we used the following definition of the constraint:

$$[2] \qquad Q = r_1 - r_2 + r_3 - r_4 + r_5 - r_6$$

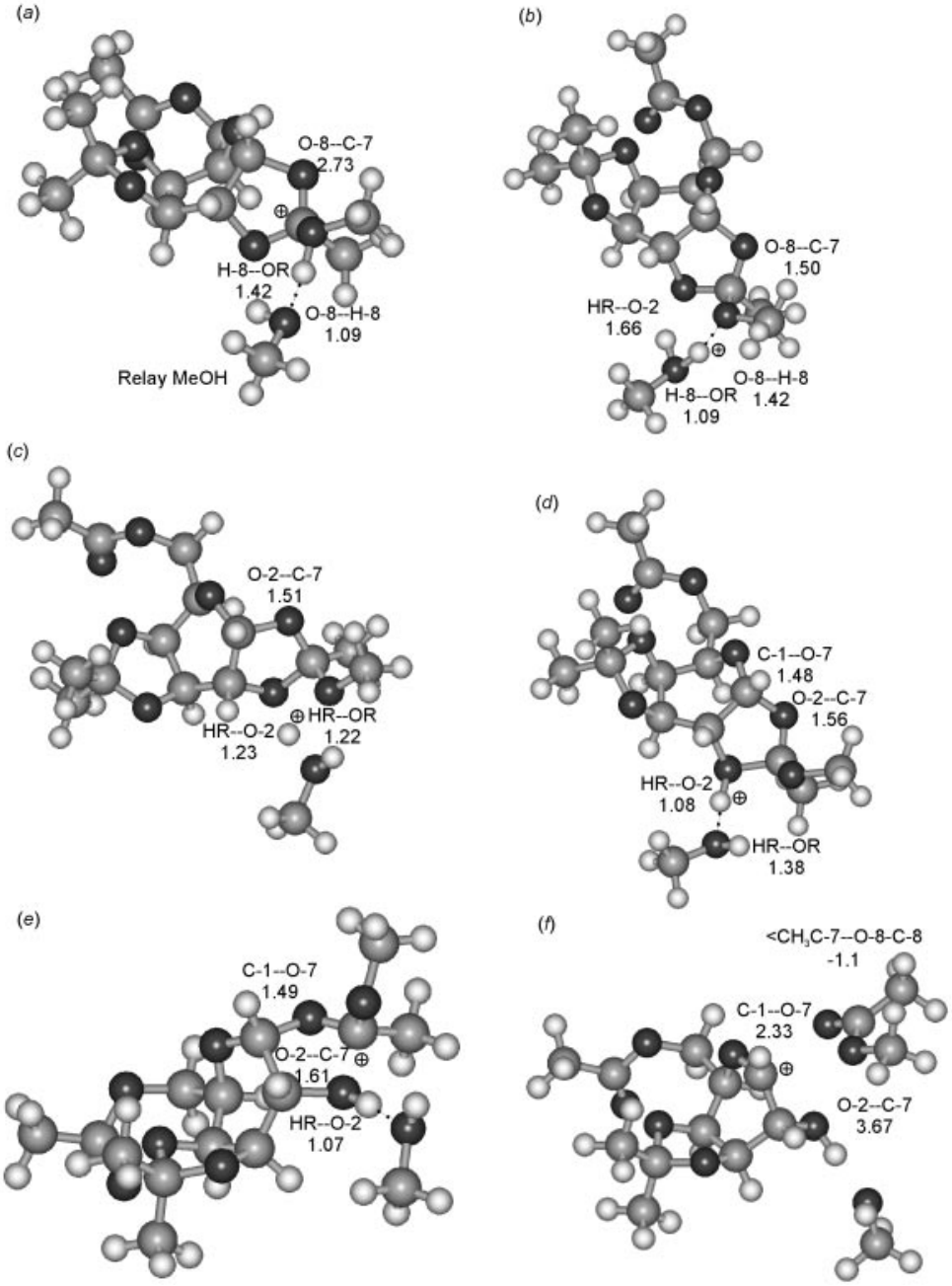
where r_1 through r_6 are defined in Scheme 5. In our calculations, we varied Q stepwise from a negative value to a positive one in 50–60 steps. At each value of the constraint the geometry was optimized subject to the constraint. Consequently, going from one value to the next of Q in the reaction path, the bond that changes its length is always whichever bond involves the least increase in the energy. These calculations enable one to find out the sequence of events without any assumption. However, this constraint has its own limitations. If the mechanism is stepwise, after the first proton transfer the broken bond involving the transferred hydrogen becomes the softest coordinate. Consequently, the lowest energy path involving the increase of Q is the increase of the distance of the broken bond, which may be irrelevant to the mechanism. For this reason, in a clearly stepwise reaction, once the first step is explored Q may be modified to the exploration of the next step to exclude the coordinates irrelevant for the rest of the reaction.

In addition, in the definition of Q we assumed that all conformational changes are the consequence of the formation and breaking of the bonds. As we found in the calculations, the products often involve different conformations from the reactants. To explore the importance of conformational change in the mechanism in a quantitative manner is a subject for future research. Even with its limitations, these calculations gave some significant insight into the reaction mechanism. It is remarkable that out of the 720 theoretically possible reaction mechanisms, all studied reactions follow essentially the same steps with four different protecting groups (see Fig. 2*a*–2*f* for the acetyl example). The potential energy surface involves an initial barrier followed by a high energy intermediate in a plateau region (see Fig. 3). The plateau is followed by a second barrier, which is higher than the first barrier except for the pivaloyl case.

The mechanism starts with the shortening of the O-8—C-7 bond length, which markedly increases the acidity of the nucleophilic hydroxlic proton. This charge movement presumably triggers transfer of this hydroxylic proton from O-8 to the relay molecule (see Fig. 2*b*) followed immediately by the transfer of the proton from the relay molecule to O-2. The first barrier (TS1) on all calculated potential surfaces corresponds to the second proton transfer step to O-2 (see Fig. 4). The first proton transfer causes the formation of a shoulder on the potential surface but no barrier can be associated with it. The intermediate is not clearly defined due to the shallow nature of the plateau region. The second barrier (TS2) involves the breaking of the O-2—C-7 bond and charge transfer to C-7 associated with the change of sp^3 to sp^2 hybridization of C-7. Subsequently the C-1—O-7 bond breaks to give **G**. This mechanism resembles the intuitive proposal of Bochkov et al. (26) except that their model has

© 2004 NRC Canada

Fig. 2. Ball and stick representations of the constrained acyl transfer reaction for the acetyl case. (*a*) Initial structure showing relay methanol (OR and OHR). (*b*) Proton transfer to the relay methanol. (*c*) Proton transferring from the relay methanol to O-2 (1st TS). (*d*) Proton transferred to O-2. (*e*) Breaking of bond O-2—C-7 (2nd TS). (*f*) Final structure with bond C-1—O-7 broken also.

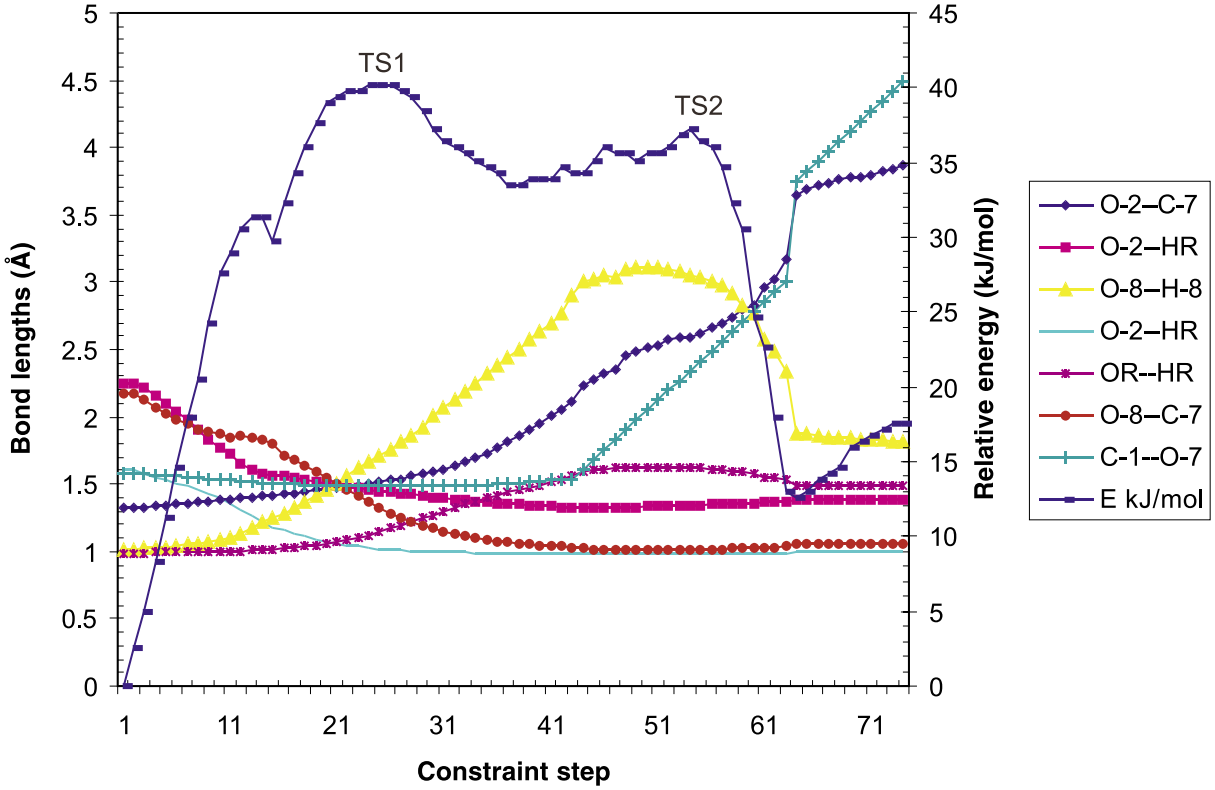


an equivalent to **E′** with a covalent O-7—C-1 bond and no proton relay.

The first barrier is between 30 and 78 kJ mol^{-1}, the formyl being the lowest and the benzoyl the highest. The second barrier is between 40 and 92 kJ mol^{-1}, the pivaloyl being the lowest and the benzoyl the highest. The second barrier appears as a sharp peak in all potential surfaces except the pivaloyl (see Fig. 3). We found that the lack of the large peak at the second barrier in the case of the pivaloyl is due to a qualitatively different pathway. The difference is best understood by considering the difference in the conformation of the final ester product. Methyl pivalate is found in the preferred trans conformation, while all other esters were found in the undesirable cis conformation at the end of the reaction path (see Figs. 2*f* and 5). The steric repulsion of the bulky pivaloyl group prevented the rotation of the methyl group towards the cis orientation. For all other systems, the rotation of the methyl group is easier towards the cis position at the beginning of the reaction. Consequently, we consider the large second barrier an artifact of the conformational orientation. This clearly points to the need to improve the reaction path following method by enabling the

© 2004 NRC Canada

Fig. 3. Bond lengths (r_1–r_6) used for the constrained acyl transfer reaction plus C-1—O-7 and the relative energy vs. the constraint step. The acyl group is pivaloyl.



involvement of conformational as well as bond distance coordinates in the constraints. Such a development is for future studies.

Taking all these finding into consideration, the rate-determining barrier is the first barrier on the calculated reaction surface associated with proton transfer to O-2. The height of this barrier is 30, 40, 40, and 78 kJ mol^{-1} for formyl, acetyl, pivaloyl, and benzoyl, respectively. Some contribution from the undesirable conformation can be attributed to the first barrier in all cases except the pivaloyl. The largest difference between the cis and trans product was found in the case of benzoyl ester, which is 33.5 kJ mol^{-1}, while it is 10.7 and 18.3 in the case of formyl and acetyl (see Table 1). Considering the relative magnitudes of these undesirable contributions, our calculated barriers are consistent with the experimentally found order of propensity to acyl transfer.

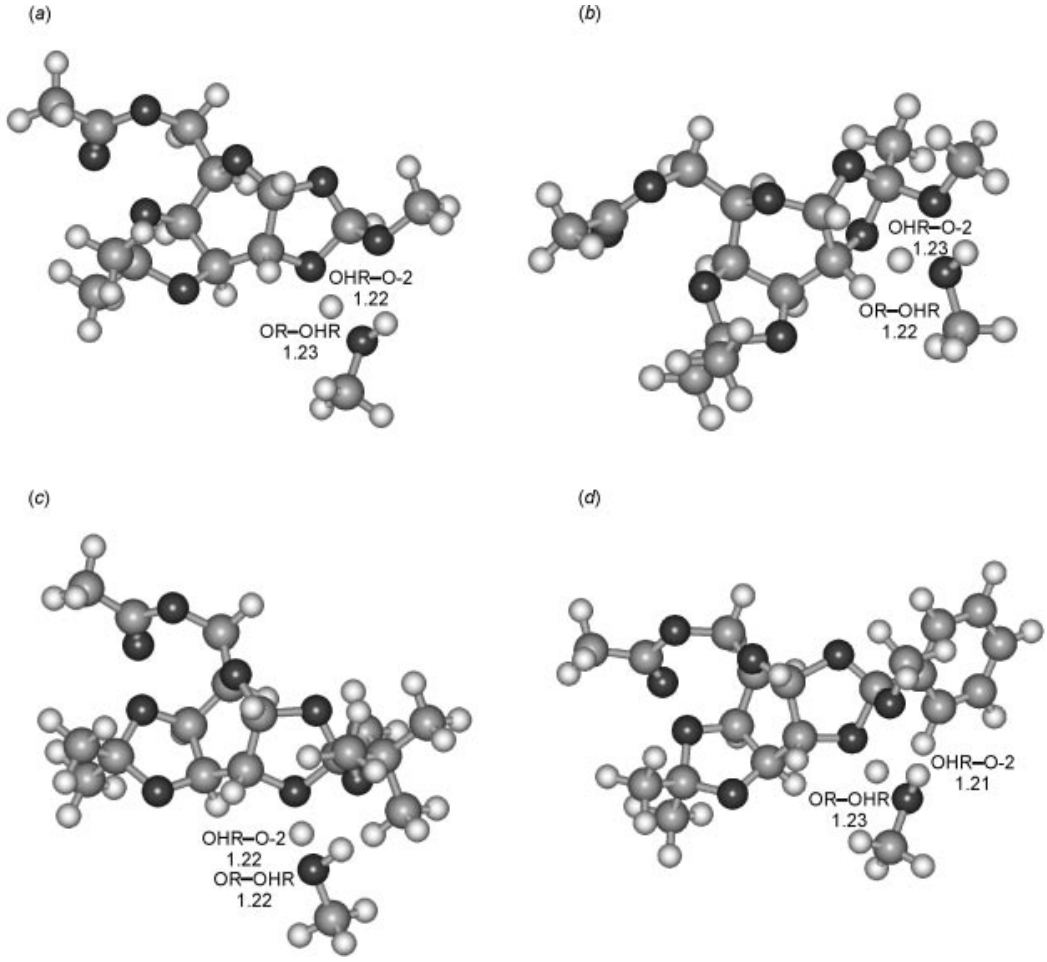
From these four trajectories we can draw some important conclusions. The conformational reorganization is driven by the change in the hybridization of C-7, which goes from sp^3 to sp^2, and consequently from tetrahedral to a planar conformation. In addition to the conformational change leading to either cis or trans in the final ester product, the protecting groups also play a role in determining the conformation around the C-7—O-7 bond, which is crucial in the reaction mechanism (see Fig. 5). In this regard, the benzoyl stands out as different from the rest and especially different from pivaloyl. The flat benzoyl group can accommodate a conformation helping the C-7—O-2 bond breaking by simply rotating around the C-7—phenyl bond.

The above analysis suggested to us that in the benzoyl case 2,6-disubstitution may inhibit this rotation and hence acyl transfer. The DFT-calculated intermediates **B**–**E′** are shown in Table 1 and Fig. 1*e*. Like the parent benzoyl, the 2,6-dimethylbenzoyl **D** is predicted to be stable with a short C-1—O-7 bond length. Thus, we synthesized the 2,6-dimethylbenzoic acid analogue in the 3,4-isopropylidene series and tested its reactivity (see *Experimental* and Scheme 6). This derivative **17** synthesized from known diol **16** (27) exhibited no acyl transfer giving an almost quantitative yield of glycoside **18**. The structure of **18** was confirmed by cleaving from the polymer to give **19** (28). Furthermore, if less triflic acid was added (0.7 equiv. vs. 1.4 equiv.) then a mixture of orthoester **20** and **18** was obtained. The orthoester **20** in the mixture could be smoothly isomerized to **18** with more triflic acid without acyl transfer. To the best of our knowledge this is the first experimental result that uncouples orthoester formation and acyl transfer.

Orthoesters (29) have been previously suggested to be intermediates to glycosides and acyl transfers (30). The acid-catalyzed isomerization of **20** to **18** without acyl transfer strongly supports a mechanism for acyl transfer that does not involve neutral orthoesters. Note that our **D** ion–dipole complexes have long C-7—O-8 bond lengths (see Figs. 1*a*–1*f*), and must undergo three major changes to become neutral orthoesters: the O-8—C-7 bond must shorten, the pyranose ring conformation must change, and the alcoholic proton must be transferred. DFT calculations (not shown) of this process suggest that proton transfer is the last of these three steps. This uncoupling of orthoester formation and acyl

© 2004 NRC Canada

Fig. 4. Ball and stick representations of putative TS1: (*a*) formyl, (*b*) acetyl, (*c*) pivaloyl, (*d*) benzoyl.



transfer is in agreement with the ease of formation of pivaloyl orthoester (31) but their reluctance to undergo acyl transfer. What the mechanism is for proceeding from **D** to glycosides is not known (32). This is a subject of current research for us (33).

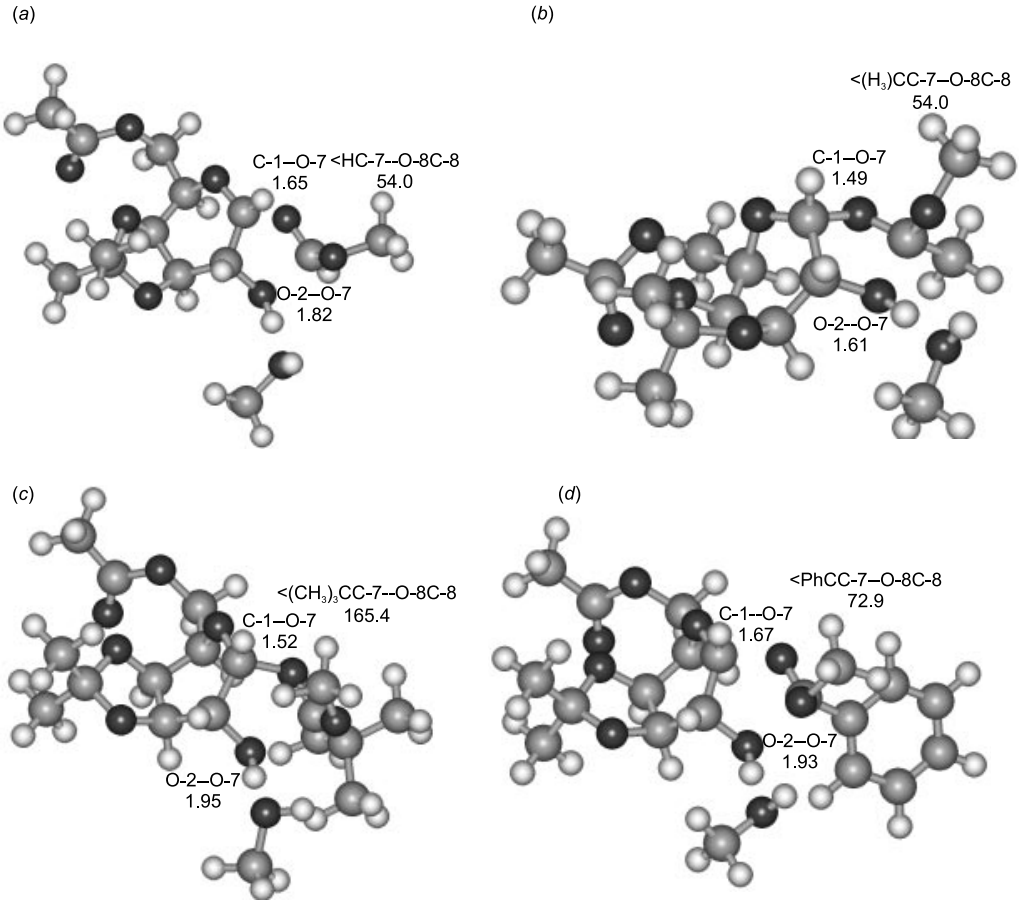
Our previous results had shown that even benzoate is difficult to cleave from polymer-supported Gal C-2 (10) and it is well-known that 2,6-dimethylbenzoyl esters are difficult to hydrolyse (34). Therefore, it was not surprising that under a variety of vigorous conditions (for example $LiAlH_4$ at reflux in THF, 1 mol/L KOHaq at 50 °C, etc.), we could not cleave the 2,6-dimethylbenzoate group from **18** without decomposition or recovery of intact **18**. Eventually we discovered that 1 mol/L LiOH in methanol at 70 °C for 48–60 h did cleave this group (see Scheme 7). This led us back to the results in Figs. 1*e* and 1*d* where the C-1—O-7 bond length (1.584 Å) in complex **D** of the 2,6-dimethylbenzoate is shorter than in **D** of the benzoate (1.607 Å). This suggested to us that the difference in this bond length may be at least in part a π-electronic effect. Therefore, we calculated the parameters for the more electron-donating 2,6-dimethoxybenzoate analogue, and the C-1—O-7 bond length (1.557 Å) is even shorter (see Fig. 1*f*). Subsequently, we synthesized this analogue **21** from **16** and reacted it with **1** (see Scheme 7). The reaction proceeded smoothly to give glycoside **22** contaminated with only a small amount of acyl transfer product **23** (**22**:**23**, 92%:8%). We had also envisaged that the 2,6-dimethoxy analogue would cleave easier than the 2,6-dimethyl one due to the possibility of chelation to the methoxy oxygens. The 2,6-dimethoxybenzoyl group is smoothly cleaved with 1 mol/L LiOH in methanol at 50 °C for 16 h to diol **24**. To improve the ease of removal, we are examining 2,6-dimethoxy-4-X-benzoyl esters, where X is an electron-withdrawing group. Thus, we have progressed from a calculated TS to a prototype of a protecting group that minimizes acyl transfer. Since the 3,4-isopropylidene galactose donors are the most prone to acyl transfer among those that we have studied, this new protecting group should be a general solution to acyl transfer.

Conclusions

Computational evidence is presented that ion–dipole complexes like **D** are formed under glycosylation reaction conditions. A pathway from **D** that most likely involves a proton relay from the nucleophile's proton to O-2 of the electrophilic sugar with accompanying formation of the O-8—O-7 bond, O-2—C-7 bond rupture, and finally O-7—C-1 bond breaking leads to an ion–dipole complex of a 2-OH glycosyl cation and the ester by-product **E′**. This order of bond forming and bond breaking was determined by computations using a complex constraint (see Scheme 5). In the model, the

© 2004 NRC Canada

Fig. 5. Ball and stick representations of putative TS2: (*a*) formyl, (*b*) acetyl, (*c*) pivaloyl, (*d*) benzoyl.



ester is formed in the unfavorable cis conformation except the pivaloyl, which perhaps explains the strong sensitivity to steric bulk of the acyl transfer side reaction. The O-7—C-1 bond in the **D** complexes is the longest in the formyl case and the shortest in the pivaloyl case along the series formyl, acetyl, pivaloyl. It is even shorter in the benzoyl case even though benzoyl still transfers in some cases suggesting an electronic component besides a steric component to this side reaction. The steric effect led us to use the 2,6-dimethyl- and 2,6-dimethoxybenzoyl groups as neighboring groups, which eliminate or greatly minimize acyl transfer especially compared to benzoate where >50% of the reaction products were 1,2-linked oligomers under the same reaction conditions. The 2,6-dimethoxybenzoyl is easier to remove and its use is under investigation in other oligosaccharide syntheses. Orthoester formation with the 2,6-dimethylbenzoyl protecting group is facile but its rearrangement to glycoside is not accompanied by acyl transfer. Although these two side reactions are probably related, this result clearly shows that the two reactions are distinct. This separation of reaction mechanisms strongly suggests that acyl transfer can be eliminated by the judicious choice of protecting groups and reaction conditions like the ones described here.

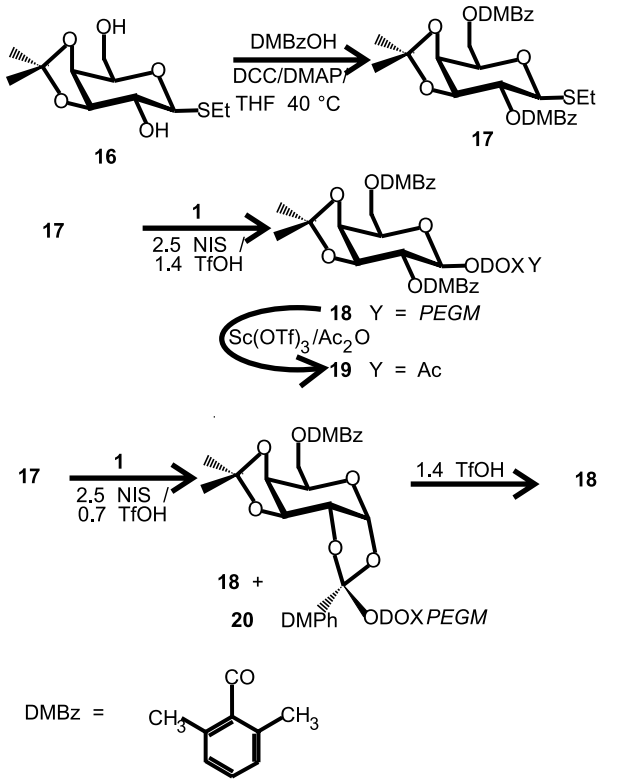
Methods

All starting materials were dried overnight in vacuo at 10^{-3} mmHg (1 mmHg = 133.322 4 Pa). All reactions were done under argon. The progress of the reactions was monitored by thin layer chromatography (TLC) on silica gel. The TLC results were visualized under UV light (254 nm) and by spraying with 50% sulphuric acid in methanol and heating at 200 °C. The ^{1}H and ^{13}C NMR spectra were recorded in deuteriochloroform solution at 500.1 MHz and 125.8 MHz, respectively, with Varian Unity Plus spectrometers. For polymer-bound samples, the *MPEG* methylenes were saturated and quantitation was made by comparing integrals to the terminal methyl of the MPEG. Assignments were made by comparison to the spectra of building blocks and cleaved compounds. ^{1}H NMR spectra in $CDCl_3$ were referenced to residual $CHCl_3$ at 7.26 ppm, and ^{13}C NMR spectra to the central peak of $CDCl_3$ at 77.0 ppm. Assignments were made by standard ^{1}H^{-1}H-COSY and ^{13}C-^{1}H-COSY experiments. The mass spectral analysis was done on a forward mass spectrometer. Fast atom bombardment (FAB) MS was performed using xenon atom at 6 kV as the source. Thioglycerol or a mixture of glycerol and thioglycerol was used as FAB matrix. Typically, 10–15 full-range, low-resolution MS scans were averaged to yield a low-resolution mass spectrum. For high-resolution MS, the electric sector was scanned over the range of interest. Typically, polyethylene glycol or polypropylene glycol was used as an internal mass standard and between 75 and 150 scans were averaged. Some MS were done by ion spray with a PerkinElmer/Sciex API triple quadrupole mass spectrometer.

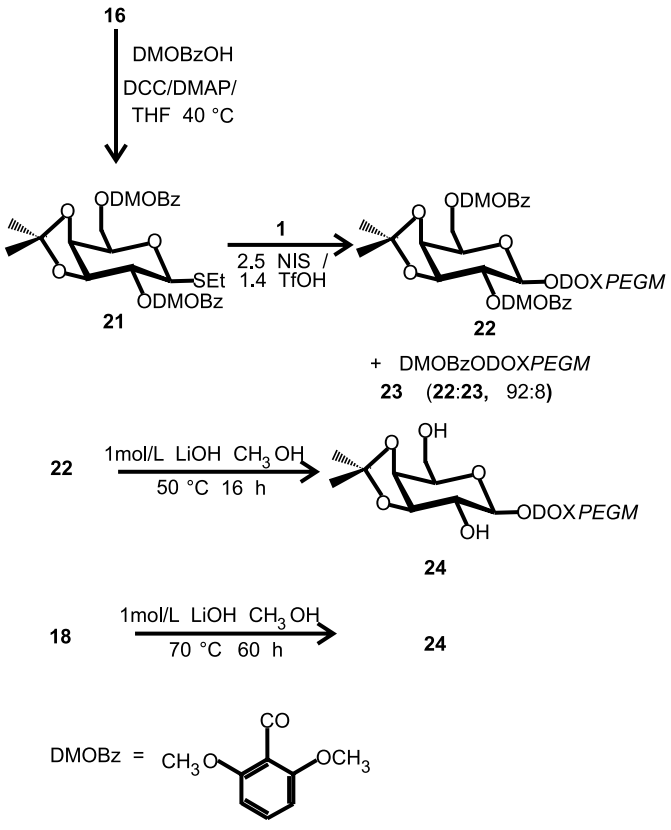
The ^{1}H NMR spectrum of the acylated MPEGDOXOH

© 2004 NRC Canada

Scheme 6. 2,6-Dimethylbenzoyl as a protecting group to eliminate acyl transfer and to separate acyl transfer from orthoester formation.



Scheme 7. 2,6-Dimethoxybenzoyl as a protecting group for minimizing acyl transfer.



were obtained by acylating the polymer i.e., either formyl, acetyl, or benzoyl. The ^{1}H NMR spectrum of MPEGDOX-*O*-formyl shows that the CHO-O-CH_2-C_6H_4-CH_2-$(OCH_2CH_2)_nOCH_3$ peak is shifted to 5.19 ppm from 4.68 ppm in MPEGDOXOH. This same peak appears at 5.09, 5.05, 5.10, 5.35, and 5.34 ppm in the acetylated (**12a**), pivaloylated (**15d**), levulinoylated (**15e**), benzoylated (**3**), and 2,6-dimethoxybenzoylated (**23**), MPEGDOXOH, respectively.

Computational details

The Amsterdam density functional (ADF) calculations use the methods described in ref. 3 and include a continuum dielectric solvent term. The basis set used was a double ζ basis set with a single polarization function. The conformational description based on the IUPAC nomenclature is described in detail in ref. 35. A fully working version of the program is available at http://www.sao.nrc.ca/ibs/6ring.html.

To enable the exploration of the reaction pathways we incorporated some changes in the ADF program. ADF enables the user to follow the reaction pathway by slowly varying a constrained coordinate from the value representative of the reactant state to the product state with geometry optimization subject to this constraint at given values of the constraint. This procedure is called a linear transit calculation. The original implementation of linear transit allows only individual internal coordinates such as bond length, bending angles, and torsion angles to be defined as a constraint. However, it is not possible to define linear combinations of individual internal coordinates, which is desirable for complicated reaction profiles such as acyl transfer. To facilitate the exploration we extended the definition of constraint by implementing a general constraint of the following form:

$$Q = l_1{*}q_1 + l_2{*}q_2 \ \ldots \ + l_nq_n$$

where q can be any bond length, bending angle, or torsion angle.

The coordinates are kept constant in the geometry optimization by simply projecting out the contribution of the Cartesian forces to the force on the constrained coordinate followed by a Cartesian geometry optimization step. After the Cartesian optimization step, the constraints are exactly imposed by an iterative correction of the coordinates (36).

MPEGDOXOH (**1**) was synthesized according to ref. 37. The synthesis of donors **13a**–**13e** is described in the *Supplementary material*.[5]

MPEGDOXyl 2,3,4,6-tetra-*O*-acetyl-β-D-galactopyranoside 11a (38)

Experiment I (using α-imidate)

A solution of TESOTf in CH_2Cl_2 (2.0 µL, 8.8 µmol) was added to a solution of 2,3,4,6-tetra-*O*-acetyl-α-D-galactopyranosyl trichloroacetimidate (39) (**8a**) (27 mg, 55 µmol) and **1** (57 mg, 27 µmol) in dry CH_2Cl_2 (2 mL) at room temperature. After 1 h of stirring, TLC (hexanes : ethyl acetate, 2:1, 2% diisopropylethylamine (DIPEA)) indicated complete disappearance of the starting imidate. The reaction was stopped 3 h after the addition of TESOTf by addition of

© 2004 NRC Canada

$NaHCO_3$ (and stirring for ~10 min), filtered, and the volume was reduced to ~0.5 mL. Dry *tert*-butylmethylether (TBME) (30 mL) was then added and the polymer was precipitated at 4 °C overnight. The polymer (64 mg) was then isolated by filtration. The ^{1}H NMR spectrum indicates that 40% yield of the β-glycosylated product **11a** and 63% yield of acyl transfer product **12a** were obtained. ^{1}H NMR (ppm) δ: 5.39 (dd, 1H, $J_{3,4}$ = 3.4 Hz, $J_{4,5}$ = 1.0 Hz, H-4), 5.27 (dd, 1H, $J_{1,2}$ = 8.1 Hz, $J_{2,3}$ = 10.5 Hz, H-2), 4.98 (dd, 1H, H-3), 4.51 (d, 1H, H-1), 4.21 (dd, 1H, $J_{5,6}$ = 6.4 Hz, $J_{6,6'}$ = 11.3 Hz, H-6), 4.16 (dd, 1H, $J_{5,6'}$ = 6.8 Hz, H-6′), 3.89 (m, 1H, H-5), 2.16 (s, 3H, CH_3CO), 2.07 (s, 3H, CH_3COO), 2.02 (s, 3H, CH_3CO), 1.98 (s, 3H, CH_3CO).

Experiment II (using β-imidate)

TESOTf (3.9 μL, 17 μmol) was added to a solution of 2,3,4,6-tetra-*O*-acetyl-β-D-galactopyranosyl trichloroacetimidate **9a** (43 mg, 87 μmol) and **1** (92 mg, 43 μmol) and were reacted as above to yield 33% of the β-glycosylated product **11a** and 67% of acyl transfer product **12a**.

MPEGDOXyl 2,3,4,6-tetra-*O*-benzoyl-β-D-galactopyranoside (11b)

2,3,4,6-Tetra-*O*-benzoyl-β-D-galactopyranosyl trichloroacetimidate (39) (**10b**) (40 mg, 54 μmol) and **1** (57 mg, 27 μmol) were reacted as for **11a** to yield 93% of the β-glycosylated product **11b** and 7% of acyl transfer product **3**. ^{1}H NMR (ppm) δ: 8.10 (d, 2H, J = 7.5 Hz, Bz_o), 8.05 (d, 2H, J = 7.5 Hz, Bz_o), 7.92 (d, 2H, J = 7.7 Hz, Bz_p), 7.78 (d, 2H, J = 7.7 Hz, Bz_p), 5.98 (d, 1H, $J_{3,4}$ = 3.0 Hz, H-4), 5.86 (dd, 1H, $J_{1,2}$ = 8.1 Hz, $J_{2,3}$ = 10.1 Hz, H-2), 5.54 (dd, 1H, H-3), 4.29 (m, 1H, H-5).

MPEGDOXyl 3,4,6-tri-*O*-benzyl-2-*O*-formyl-β-D-galactopyranoside (14a)

TESOTf (12 μL, 53 μmol) was added to a solution of compound **13a** (0.169 g, 0.271 μmol) and **1** (0.275 g, 0.130 μmol) in dry CH_2Cl_2 (3 mL). After 3 h of stirring at room temperature, TLC (hexanes : ethyl acetate, 3:1) indicated absence of the imidate. The reaction was stopped by the addition of 2 drops of DIPEA and the volume was reduced to ~0.5 mL. Dry TBME (50 mL) was added and the polymer was allowed to precipitate at 4 °C overnight. The polymer (0.278 g) was then isolated by filtration. The ^{1}H NMR spectrum indicated that ~25% yield of the β-glycosylated product **14a**, ~4% yield of the orthoester, and 56% yield of acyl transfer product **15a** were obtained. **14a**: ^{1}H NMR (ppm) δ: 8.14 (s, 1H, HCOO), 5.10 (dd, 1H, $J_{1,2}$ = 8.3 Hz, $J_{2,3}$ = 9.0 Hz, H-2), 3.96 (d, 1H, $J_{3,4}$ = 2.4 Hz, H-4).

MPEGDOXyl 2-*O*-acetyl-3,4,6-tri-*O*-benzyl-β-D-galactopyranoside (14b)

Compound **13b** (27 mg, 42 μmol) was treated as for **14a**. The ^{1}H NMR spectrum indicated that 64% yield of the β-glycosylated product **14b**, 13% yield of the orthoester, and 5% yield of acyl transfer product **15b** were obtained. **14b**: ^{1}H NMR (ppm) δ: 7.36–7.22 (m, aromatic), 5.43 (dd, 1H, $J_{1,2}$ = 7.9 Hz, $J_{2,3}$ = 10.0 Hz, H-2), 4.37 (d, 1H, H-1), 3.94 (m, 1H, H-4), 1.99 (s, 3H, CH_3CO).

MPEGDOXyl 2-*O*-benzoyl-3,4,6-tri-*O*-benzyl-β-D-galactopyranoside (14c)

Compound **13c** (47 mg, 67 μmol) was treated as for **14a**. The ^{1}H NMR spectrum indicated that 66% yield of the β-glycosylated product **14c**, 11% yield of the orthoester, and no detectable acyl transfer product were obtained. **14c**: ^{1}H NMR (ppm) δ: 7.98–7.96 (m, 2H, Bz_o), 7.59 (m, 1H, Bz_o), 7.47–7.43 (m, 2H, Bz_p), 5.71 (dd, 1H, $J_{2,1}$ = 8.0 Hz, $J_{2,3}$ = 9.8 Hz, H-2), 4.00 (m, 1H, H-4). Orthoester: 5.25 (d, 1H, H-1).

MPEGDOXyl 3,4,6-tri-*O*-benzyl-2-*O*-pivaloyl-β-D-galactopyranoside (14d)

Compound **13d** (17 mg, 25 μmol) was treated as for **14a**. The ^{1}H NMR spectrum indicated that 47% yield of the β-glycosylated product **14d**, 14% yield of the orthoester, and no detectable acyl transfer product were obtained. **14d**: ^{1}H NMR (ppm) δ: 5.49 (dd, 1H, $J_{2,1}$ = 7.9 Hz, $J_{2,3}$ = 10.0 Hz, H-2), 4.42 (d, 1H, H-1), 3.94 (m, 1H, H-4).

MPEGDOXyl 3,4,6-tri-*O*-benzyl-2-*O*-levulinoyl-β-D-galactopyranoside (14e)

Compound **13e** (23 mg, 33 μmol) was treated as for **14a**. The ^{1}H NMR spectrum indicated that 49% yield of the β-glycosylated product **14e**, 7% yield of the orthoester, and 2% yield of acyl transfer product **15e** were obtained. **14e**: ^{1}H NMR (ppm) δ: 5.42 (dd, 1H, $J_{2,1}$ = 7.9 Hz, $J_{2,3}$ = 10.0 Hz, H-2), 3.93 (m, 1H, H-4), 2.71–2.66 (m, 2H, CH_2 Lev), 2.53–2.49 (m, 2H, CH_2 Lev).

Ethyl 2,6-di-*O*-(2,6-dimethylbenzoyl)-3,4-*O*-isopropylidene-1-thio-β-D-galactopyranoside (17)

2,6-Diol (27, 40) (**16**) (1.5 g, 5.71 mmol) was dissolved in THF (30 mL) and 2,6-dimethylbenzoic acid (3.43 g, 4 equiv.), dicyclohexylcarbodiimide (5.3 g, 4.5 equiv.), and DMAP (50 mg) were added. After stirring at room temperature (RT) for 1 day, the mixture was heated to 40 °C and the temperature maintained for 1 week. Each day, further aliquots of DCC (0.5 equiv.) and DMAP (50 mg) were added until the starting material disappeared. After filtration and concentration, the residue was purified by MPLC eluting with hexanes : ethyl acetate : dichloromethane (8:1:1) to yield slightly impure material, which was recrystallized from ethanol:water about 1:1 to form colorless needles of **17** (750 mg, 25%); mp 159 to 160 °C. $[\alpha]_D$ = 35.5 (*c* 0.84, $CHCl_3$). ^{1}H NMR (ppm) δ: 7.22 (m, 2H, Bz), 7.06 (m, 4H, Bz), 5.37 (brt, 1H, H-2), 4.65 (m, 2H, H-6ab), 4.45 (d, 1H, $J_{1,2}$ = 10.3 Hz, H-1), 4.31 (m, 2H, H-3, H-4), 4.17 (t, 1H, $J_{4,5+5,6}$ = 12.2 Hz, H-5), 2.78 (m, 2H, CH_3CH_2S), 2.43, 2.37 (2s, 12H, $ArCH_3$), 1.66, 1.39 (2s, 6H, $O_2C(CH_3)_2$), 1.28 (t, 3H, J = 7.3 Hz, CH_3CH_2S). ^{13}C NMR (ppm) δ: 169.6, 168.6 (2*C*OAr), 135.3, 135.1 ($2Bz_{ip}$), 133.4 ($2Bz_o$), 129.5, 129.4 ($2Bz_p$), 127.5, 127.5 ($2Bz_m$), 110.8 ($O_2C(CH_3)_2$), 82.2 (C-1),

© 2004 NRC Canada

77.2 (C-3), 74.3 (C-5), 73.8 (C-4), 71.6 (C-2), 64.1 (C-6), 27.1, 26.0 ($2O_2C(CH_3)_2$), 23.7 (CH_3CH_2S), 19.9, 19.8 ($2ArCH_3$), 14.9 (CH_3CH_2S). FAB-MS calcd. for $C_{29}H_{36}O_7S$: 528.2181; found *m/z*: 529.1 (m + H^+), 467.1 (M – Set^+) 133 (DiMeBz$^+$). HR-MS calcd. for $C_{29}H_{36}O_7SNa$: 551.2079; found: 551.2065.

MPEGDOXyl 2,6-di-*O*-(2,6-dimethylbenzoyl)-3,4-*O*-isopropylidene-β-D-galactopyranoside (18)

Method 1

Donor **17** (77 mg, 0.15 mmol), **1** (512 mg, 0.1 mmol), and activated 4 Å molecular sieves (about 300 mg) were dried together overnight at high vacuum. Dichloromethane (3 mL) was added and the mixture cooled in an ice–salt bath. After stirring for 0.5 h, NIS (112 mg, 0.5 mmol) was added followed by TfOH (12 μL, 0.14 mmol). After stirring for 30 min, the reaction was quenched with DIPEA (50 μL) and the polymer precipitated with TBME (40 mL). The solid was recovered by filtration and after rinsing with TBME was reprecipitated from absolute ethanol (25 mL). The resulting solid was collected by filtration and after washing with cold ethanol and diethyl ether was taken up in CH_2Cl_2, filtered, and evaporated to yield **18** (490 mg, 88%). Partial ^{1}H NMR (ppm) δ: 7.31 (m, 4H, Ar*H*-DOX), 7.24 (t, 1H, *J* = 7.8 Hz, Bz_p), 7.20 (t, 1H, *J* = 7.8 Hz, Bz_p), 7.08 (d, 2H, *J* = 7.8 Hz, Bz_m), 7.03 (d, 2H, *J* = 7.8 Hz, Bz_m), 5.37 (brt, 1H, H-2), 4.95 (d, 1H, *J* = 11.7 Hz, C*H*HC$_6$H$_4$-DOX), 4.70 (m, 1H, H-6a), 4.65 (m, 1H, H-6b), 4.58 (d, 1H, *J* = 11.7 Hz, CH*H*C$_6$H$_4$-DOX), 4.56 (s, 2H, CH_2C$_6$H$_4$-DOX), 4.54 (d, 1H, $J_{1,2}$ = 7.8 Hz, H-1), 4.29 (m, 2H, H-3, H-4), 4.17 (t, 1H, $J_{4,5+5,6}$ = 9.8 Hz, H-5), 2.39, 2.29 (2s, 12H, ArCH_3), 1.68, 1.40 (2s, 6H, $O_2C(CH_3)_2$).

Method 2

Orthoester **20** was treated as for **18** above except no NIS, extra donor, or **1** were added.

6-*O*-(2,6-Dimethylbenzoyl)-3,4-*O*-isopropylidene-β-D-galactopyranosyl-1,2-*O*-MPEGDOXyl-*ortho*-(2,6-dimethylbenzoate) (20)

Orthoester **20** was prepared as for **18** except 0.7 equiv. of TfOH was used. Partial ^{1}H NMR (ppm) δ: 5.80 (d, 1H, $J_{1,2}$ = 4.9 Hz, H-1), 4.38 (m, 1H, H-2), 1.68, 1.40 (2s, 6H, $O_2C(CH_3)_2$).

[4-*O*-Acetoxymethyl]benzyl 2,6-di-*O*-(2,6-dimethylbenzoyl)-3,4-*O*-isopropylidene(-β-D-galactopyranoside (19)

Compound **18** (480 mg, 0.087 mmol) was dissolved in CH_2Cl_2 (2.0 mL) and Ac_2O (2.0 mL) under an atmosphere of argon at RT. To this solution was added $Sc(OTf)_3$ (25 mg, 0.02 mmol) and the stirring continued for 4 h. After cooling with an ice bath, the polymer was precipitated with TBME (60 mL) and collected by filtration. The filtrate was evaporated. The solid was reprecipitated from ethanol (40 mL) and collected by filtration. The filtrate was combined with the residue from TBME and evaporated. The residue was purified by preparative TLC eluting with hexanes : ethyl acetate (80:20) to yield a viscous oil **19** (12 mg, 22% assuming 100% yields for all polymer steps including linker attachment). $[\alpha]_D$ –75.0 (*c*, 0.06, $CHCl_3$). ^{1}H NMR (ppm) δ: 7.27 (q_{AB}, 4H, *J* = 8.1 Hz, Ar*H*-DOX), 7.22 (t, 1H, *J* = 7.3 Hz, *J* = 8.0 Hz, Bz_p), 7.18 (t, 1H, *J* = 7.3, *J* = 8.0 Hz, Bz_p), 7.06 (d, 2H, *J* = 8.0 Hz, Bz_m), 7.01 (d, 2H, *J* = 7.3 Hz, Bz_m), 5.39 (brt, 1H, H-2), 5.08 (s, 2H, CH_2C$_6$H$_4$-DOX), 4.94 (d, 1H, *J* = 11.7 Hz, C*H*HC$_6$H$_4$-DOX), 4.67 (m, 2H, H-6ab), 4.57 (d, 1H, *J* = 11.7 Hz, CH*H*C$_6$H$_4$-DOX), 4.52 (d, 1H, $J_{1,2}$ = 8.8 Hz, H-1), 4.28 (m, 2H, H-3, H-4), 4.15 (t, 1H, $J_{4,5+5,6}$ = 10.2 Hz, H-5), 2.36, 2.26 (2s, 12H, ArCH_3), 2.11 (s, 3H, COCH_3), 1.66, 1.38 (2s, 6H, $O_2C(CH_3)_2$). ^{13}C NMR (ppm) δ: 170.8 (*C*OCH$_3$), 169.6, 168.4 (2*C*OAr), 136.7, 135.5 ($2CH_2$-*C*Ar-DOX), 135.0, 135.1 ($2Bz_{ip}$), 133.6, 133.3 ($2Bz_o$), 129.6, 129.3 ($2Bz_p$), 128.2, 128.1 (*C*HAr-DOX), 127.6, 127.4 ($2Bz_m$), 110.9 ($O_2C(CH_3)_2$), 99.0 (C-1), 77.2 (C-3), 73.8 (C-4), 73.0 (C-2), 71.1 (C-5), 70.1 (CH_2C$_6$H$_4$), 66.0 (CH_2C$_6$H$_4$-DOX), 64.1 (C-6), 27.7, 26.6, ($2O_2C(CH_3)_2$), 21.0 (CO*C*H$_3$), 19.8, 19.6 ($2ArCH_3$). FAB-MS: +ve 669 (M + Na^+), 467 (M – DOX^+), 133 (DiMeBz$^+$). HR-MS calcd. for $C_{37}H_{42}O_{10}Na$: 669.2676; found: 669.2715.

Ethyl 2,6-di-*O*-(2,6-dimethoxylbenzoyl)-3,4-*O*-isopropylidene-1-thio-β-D-galactopyranoside (21)

Diester **21** was made from diol **16** as for **17** (750 mg, 25%). $[\alpha]_D$ = 18.2 (*c* 0.2, $CHCl_3$). ^{1}H NMR (ppm) δ: 7.27 (m, 2H, Bz), 6.53 (m, 4H, Bz), 5.34 (brt, 1H, *J* = 6 Hz, H-2), 4.73 (d, 1H, $J_{1,2}$ = 7.0 Hz, H-1), 4.57 (m, 2H, H-6ab), 4.41 (brt, 1H, *J* = 5.7 Hz, H-3), 4.31 (brd, 1H, $J_{3,4}$ = 4.5 Hz, H-4), 4.14 (t, 1H, $J_{4,5+5,6}$ = 12.2 Hz, H-5), 3.80, 3.76 (2s, 12H, ArOCH_3), 2.76 (m, 2H, CH_3CH_2S), 1.61, 1.39 (2s, 6H, $O_2C(CH_3)_2$), 1.27 (t, 3H, *J* = 7.3 Hz, CH_3CH_2S). ^{13}C NMR (ppm) δ:, 166.2, 164.7 (2*C*OAr), 157.6, 157.2 ($2Bz_o$), 131.3, 131.0 ($2Bz_p$), 112.8, 112.2 ($2Bz_{ip}$), 110.5 ($O_2C(CH_3)_2$), 103.9, 103.8 ($2Bz_m$), 82.6 (C-1), 75.6 (C-3), 73.2 (C-5), 72.8 (C-4), 72.3 (C-2), 64.0 (C-6), 56.0, 55.9 ($2ArOCH_3$), 27.8, 26.6 ($2O_2C(CH_3)_2$), 23.7 (CH_3CH_2S), 14.8 (CH_3CH_2S). FAB- MS calcd. for $C_{29}H_{36}O_{11}S$: 592; found *m/z*: 615.2 (M + Na^+), 531.2 (M – SEt^+), 165 (DiMeOBz$^+$). HR-MS calcd. for $C_{29}H_{36}O_{11}S$: 592.2115; found: 592.2128.

MPEGDOXyl 2,6-di-*O*-(2,6-dimethoxylbenzoyl-3,4-*O*-isopropylidene-β-D-galactopyranoside (22)

Donor **21** was reacted with **1** as for **18** to yield **22** and **23**. **22**: partial ^{1}H NMR (ppm) δ: 7.32 (m, 2H, Bz), 7.30 (d, 2H, *J* = 8.1 Hz, Ar*H*-DOX), 7.22 (d, 2H, *J* = 8.1 Hz, Ar*H*-DOX), 6.54 (m, 4H, Bz), 5.27 (brt, 1H, *J* = 6.1 Hz, H-2), 4.93 (d, 1H, *J* = 12.0 Hz, C*H*H-DOX), 4.38 (brt, 1H, H-3), 4.30 (dd, 1H, $J_{3,4}$ = 5.8 Hz, $J_{4,5}$ = 1.9 Hz, H-4), 4.11 (brt, 1H, *J* = 4.4 Hz, H-5), 1.60, 1.36 (2s, 6H, $O_2C(CH_3)_2$).

MPEGDOXyl 3,4-*O*-isopropylidene-β-D-galactopyranoside (24)

Diester **22** (98 mg, 0.017 mmol) was dissolved in 1 mol/L LiOH in methanol (2 mL) and heated at 50 °C for 16 h un-

© 2004 NRC Canada

der an atmosphere of argon. The heat was removed and the mixture cooled in an ice bath. The polymer was recovered by precipitation with TBME and filtration followed by dissolution in warm absolute ethanol, filtration while warm, and cooling. The resulting solid was collected by filtration and after rinsing with ethanol and diethyl ether was dissolved in CH_2Cl_2, filtered, and evaporated to yield **24** (90 mg, 97%). Partial ^{1}H NMR (ppm) δ: 7.32 (s, 4H, Ar*H*-DOX), 4.89 (d, 1H, J = 11.6 Hz, C*H*H-DOX), 4.25 (brt, 1H, H-3), 4.14 (dd, 1H, $J_{3,4}$ = 5.6 Hz, $J_{4,5}$ = 1.9 Hz, H-4), 4.06 (brt, 1H, J = 5.9 Hz, H-5), 3.97 (m, 1H, H-6a), 1.52, 1.34 (2s, 6H, $O_2C(CH_3)_2$).

Acknowledgements

The authors gratefully acknowledge the use of the VPP770 Fujitsu parallel computer situated in the RIKEN Computer Center. This work was partly supported by the PENCE program Canada.

References

1. N.K. Kochetkov. *In* Studies in natural products chemistry. Vol. 14. *Edited by.* A. Rahman. Elsevier, Amsterdam. 1994. pp. 201–266.
2. (*a*) H. Paulsen and E. Schüttpelz. Chem. Ber. **112**, 3214 (1979); (*b*) D. Crich, Z. Dai, and S. Gastaldi. J. Org. Chem. **64**, 5224 (1999).
3. T. Nukada, A. Bérces, M.Z. Zgierski, and D.M. Whitfield. J. Am. Chem. Soc. **120**, 13 291 (1998).
4. D.M. Whitfield and S.P. Douglas. Glycoconjugate J. **13**, 5 (1996).
5. R.U. Lemieux. Chem. Can. **16**, 14 (1964).
6. (*a*) G.H. Veeneman. *In* Carbohydrate chemistry. *Edited by* G.-J. Boons. Blackie Academic and Professional, London. 1998. pp. 98–174; (*b*) J.-C. Jacquinet and P. Sinaÿ. J. Chem. Soc. Perkin Trans. 1, 314 (1979).
7. (*a*) F.J. Urban, B.S. Moore, and R. Breitenbach. Tetrahedron Lett. **31**, 4421 (1990); (*b*) A.Ya. Khorlin, V.A. Nesmeyanov, and S.E. Zurabyan. Carbohydr. Res. **43**, 69 (1975); (*c*) V. Křen, A. Fišerová, C. Augé, P. Sedmera, V. Havlíček, and P. Šíma. Bioorg. Med. Chem. Lett. **4**, 869 (1996); (*d*) T. Ziegler, P. Kovac, and C.P.J. Glaudemans. J. Carbohydr. Chem. **9**, 135 (1990); (*e*) N.E. Nifant'ev, E.A. Khatuntseva, A.S. Shahkov, and K. Bock. Carbohydr. Lett. **1**, 399 (1990); (*f*) U. Nilsson, A.K. Ray, and G. Magnusson. Carbohydr. Res. **252**, 117 (1994); (*g*) V. Pozsgay, J.-R. Brisson, and H.J. Jennings. Can. J. Chem. **65**, 2764 (1987); (*h*) N.I. Uvarova, G.I. Oshitok, and G.B. Elyakov. Carbohydr. Res. **27**, 79 (1973).
8. D.M. Whitfield, S.P. Douglas, and J.J. Krepinsky. 17th International Carbohydrate Symposium, Ottawa, Ont. 1994.
9. (*a*) J.J. Krepinsky and S.P. Douglas. *In* Solid support oligosaccharide synthesis and combinatorial libraries. *Edited by* P.H. Seeberger. Wiley-Interscience, New York. 2001. pp. 175–199; (*b*) J.J. Krepinsky and S.P. Douglas. *In* Carbohydrates in chemistry and biology. Vol. 1. *Edited by* B. Ernst, G.W. Hart, and P. Sinaÿ. Wiley-VCH, Weinheim. 2000. pp. 239–265.
10. T. Nukada, A. Bérces, and D.M. Whitfield. J. Org. Chem. **64**, 9030 (1999).
11. (*a*) D.M. Whitfield, S.P. Douglas, T.H. Tang, I.G. Csizmadia, H.Y.S. Pang, F.L. Moolten, and J.J. Krepinsky. Can. J. Chem. **72**, 2225 (1994); (*b*) N.M. Spijker, J.E.M. Basten, and C.A.A. van Boeckel. Recl. Trav. Chim. Pays–Bas, **112**, 611 (1993); (*c*) A.F. Bochkov, V.I. Betaneli, N.K. Kochetkov, and N.K. Izvestiya. Akad. Nauk SSSR Ser. Khim. **6**, 1299 (1974) [In English] ; [In Russian, p. 1379]; (*d*) J. Madaj, A. Trynda, M. Jankowska, and A. Wiśniewski. Carbohydr. Res. **337**, 1495 (2002).
12. (*a*) M.Z. Liu, H.N. Fan, Z.W. Guo, and Y.Z. Hui. Carbohydr. Res. **290**, 233 (1996); (*b*) R.T. Lee and Y.C. Lee. Carbohydr. Res. **271**, 131 (1995).
13. S. Deng, B. Yu, J. Xie, and Y. Hui. J. Org. Chem. **64**, 7265 (1999).
14. (*a*) R.T. Brown, N.E. Carter, S.P. Mayalarp, and F. Scheinmann. Tetrahedron, **56**, 7591 (2000); (*b*) J.R. Ferguson, J.R. Harding, D.A. Killick, K.W. Lumbard, F. Scheinmann, and A.V. Stachulski. J. Chem. Soc. Perkin Trans. 1, 3037 (2001).
15. (*a*) H. Kunz and A. Harreus. Liebigs Ann. Chem. 41 (1982); (*b*) S. Sato, T. Nunomura, Y. Ito, and T. Ogawa. Tetrahedron Lett. **29**, 4097 (1988); (*c*) S. Sato, Y. Ito, and T. Ogawa. Tetrahedron Lett. **29**, 5267 (1988); (*d*) S. Nunomura and T. Ogawa. Tetrahedron Lett. **29**, 5681 (1988); (*e*) M.J. Thompson, E.J. Hutchinson, T.H. Stratford, W.B. Bowler, and G.M. Blackburn. Tetrahedron Lett. **45**, 1207 (2004).
16. P. Zimmermann, R. Bommer, T. Bar, and R.R. Schmidt. J. Carbohydr. Chem. **7**, 435 (1988).
17. (*a*) S. Nunomura, M. Mori, Y. Ito, and T. Ogawa. Tetrahedron Lett. **30**, 5619 (1989); (*b*) S. Nunomura, M. Mori, Y. Ito, and T. Ogawa. Tetrahedron Lett. **30**, 6713 (1989).
18. P.J. Garegg and I. Kvarnstorm. Acta Chem. Scand. Ser. B, **B30**, 655 (1976).
19. (*a*) N.I. Uvarova, G.I. Oshitok, and G.B. Elyakov. Carbohydr. Res. **27**, 79 (1973); (*b*) T.K. Lindhorst. J. Carbohydr. Chem. **16**, 237 (1997); (*c*) A.F. Bochkov, V.I. Betaneli, and N.K. Kochetkov. Bioorgan. Khim. **3**, 39 (1977). [In English].
20. (*a*) J. Banoub and D.R. Bundle. Can. J. Chem. **57**, 2091 (1979); (*b*) V. Magnus, D. Vikić-Topić, S. Iskrić, and S. Kveder. Carbohydr. Res. **114**, 209 (1983); (*c*) Z. Yang, W. Lin, and B. Yu. Carbohydr. Res. **329**, 879 (2000).
21. P.H. Amvam-Zollo and P. Sinaÿ. Carbohydr. Res. **150**, 199 (1986).
22. P.J. Garegg and I. Kvarnström. Acta Chem. Scand. Ser. B, **B31**, 509 (1977).
23. A. Bérces, T. Nukada, and D.M. Whitfield. J. Am. Chem. Soc. **123**, 5460 (2001).
24. (*a*) H. Paulsen. Angew. Chem. Int. Ed. Engl. **21**, 155 (1982); (*b*) T. Ishikawa and H.G. Fletcher. J. Org. Chem. **34**, 563 (1969).
25. (*a*) S. Morpurgo, M. Bossa, and G.O. Porpurgo. Phys. Chem. Chem. Phys. **3**, 4898 (2001); (*b*) S. Morpurgo, M. Brahimi, M. Bossa, and G.O. Morpurgo. Phys. Chem. Chem. Phys. **2**, 2707 (2000).
26. A.F. Bochkov, V.I. Betaneli, and N.K. Kochetkov. Bioorgan. Khim. **2**, 671 (1976). [In English].
27. E. Eichler, F. Yan, J. Sealy, and D.M. Whitfield. Tetrahedron, **57**, 6679 (2001).
28. S. Mehta and D.M. Whitfield. Tetrahedron Lett. **39**, 5907 (1998).
29. D. Crich, Z. Dai, and S. Gastaldi. J. Org. Chem. **64**, 5224 (1999).
30. (*a*) J.E. Wallace and L.R. Schroeder. J. Chem. Soc. Perkin Trans. 2, 795 (1977); (*b*) L.G. Green and S.V. Ley. *In* Carbohydrates in chemistry and biology. Vol. 1. *Edited by* B. Ernst, G.W. Hart, and P. Sinaÿ. Wiley-VCH, Weinheim. 2000. pp. 427–448.
31. R.U. Lemieux and A.R. Morgan. Can. J. Chem. **43**, 2199 (1965).
32. (*a*) H.S. Isbell and H.L. Frush. J. Res. Natl. Bur. Stand. **43**,

© 2004 NRC Canada

161 (1949); (*b*) Y. Zeng, J. Ning, and F. Kong. Tetrahedron Lett. **43**, 3729 (2002).
33. T. Nukada, A. Bérces, and D.M. Whitfield. Carbohydr. Res. **337**, 765 (2002).
34. J. March. Advanced organic chemistry. 2nd ed. McGraw Hill, London. 1977. p. 248.
35. T. Nukada, A. Bérces, and D.M. Whitfield. Tetrahedron, **57**, 477 (2001).
36. P. Pulay, G. Fogarasi, F. Pang, and J.E. Boggs. J. Am. Chem. Soc. **101**, 2550 (1979).
37. J.J. Krepinsky, S.P. Douglas, and D.M. Whitfield. Methods Enzymol. **242**, 281 (1994).
38. G. Hodosi and J.J. Krepinsky. Synlett, 159 (1996).
39. R.R. Schmidt and M. Stumpp. Liebigs Ann. Chem. 1249 (1983).
40. Y. Buskas and P. Konradsson. J. Carbohydr. Chem. **19**, 25 (2000).

© 2004 NRC Canada

Studies on the two-photon absorption properties of trigonal dehydrobenzo[18]annulenes

Xin Zhou, Ai-Min Ren, Ji-Kang Feng, and Xiao-Juan Liu

Abstract: The one-photon and two-photon absorption properties of donor–acceptor substituted dehydrobenzo[18]annulenes were determined by using density functional theory and ZINDO methods. The macrocycle containing C_{2v} symmetry exhibited the largest TPA cross-section value of 3376×10^{-50} cm^4 s/photon. The calculated results indicate that the TPA response in the whole molecule comes from the contribution of that in the every side in the trigon. It is notable that the magnitudes of the transition dipole moment from the virtual intermediate state to the TPA final state and the dipole moment difference between the ground state and the virtual intermediate state play important roles in increasing the TPA cross-section value. This series of molecules can circumvent the trade-off between efficiency and transparency, and they provide a promising direction for the further development of novel two-dimensional molecules with such properties.

Key words: two-photon absorption, ZINDO, sum-over-states, dehydrobenzo[18] annulenes, transparency.

Résumé : Faisant appel à la théorie de la densité fonctionnelle ainsi qu'à des méthodes ZINDO, on a déterminé les propriétés d'absorption monophotonique et biphotonique de déhydrobenzo[18]annulènes substitués, des donneurs–accepteurs. Le macrocycle comportant une symétrie C_{2v} exhibe la valeur la plus élevée de section droite de « TPA », 3376×10^{-50} cm^4 s/photon. Les résultats calculés indiquent que la réponse de TPA dans une molécule complète provient de la contribution de ce qu'on retrouve dans l'aire trigonale. Il est à noter que les amplitudes de la transition du moment dipolaire de l'état intermédiaire virtuel à l'état final de TPA ainsi que la différence de moment dipolaire entre l'état fondamental et l'état intermédiaire virtuel jouent des rôles importants dans l'augmentation de la valeur de la section droite de la TPA. Les molécules de cette série permettent de contourner le compromis entre l'efficacité et la transparence et elles s'avèrent être une direction de choix pour le développement ultérieur de nouvelles molécules bidimensionnelles ayant de telles propriétés.

Mots clés : absorption biphotonique, ZINDO, somme sur l'ensemble des états, déhydrobenzo[18]annulènes, transparence.

[Traduit par la Rédaction]

Introduction

Organic molecular two-photon absorption (TPA) has attracted increasing attention because of a variety of applications in many areas such as three-dimensional microfabrication (1–3), ultra-high-density optical data storage (4), biological imaging (5), the controlled release of biologically relevant species (6), immunoassays (7), and photodynamic cancer therapy (8). For these applications, the magnitude of the TPA cross section is crucially important. To prepare organic material with large TPA cross sections, researchers are examining various design strategies. Numerous compounds including donor–bridge–acceptor (D–π–A) dipoles (9, 10), donor–bridge–donor (D–π–D) quadrupoles (11–13), octupoles (14–16), multibranched compounds (17–19), and dendrimers (20, 21) have been synthesized and their structure–property relationships established. The studied results indicate that increasing donor and acceptor strength, extending the conjugated length and the molecular dimensionality, and changing the character of the conjugated bridge are in favor of enhancing the magnitude of the molecular TPA cross section. Recently, many groups paid attention to the nonlinear optical (NLO) properties of the octupolar molecules. Compared with the typical NLO chromophores, which are one-dimensional, conjugated π-systems with donor (D) and acceptor (A) moieties as terminal substituents, the transparency as well as efficiency of adequately tailored octupolar molecules are expected in different instances to significantly improve. The octupolar systems without permanent dipole moments would be less prone to reorientational relaxation, which is the detrimental factor for the dipolar molecules favoring undesired antiparallel pairing.

Here, we will study a series of novel two-dimensional molecules — dehydrobenzo [18]annulenes, which have been shown to be useful precursors for a variety of carbon-rich polymeric systems such as ladder polymers (22), molecular tubes (23), and novel allotropes of carbon (24, 25). Haley

Received 12 November 2003. Published on the NRC Research Press Web site at http://canjchem.nrc.ca on 17 September 2004.

X. Zhou, A.-M. Ren, J.-K. Feng,[1,2] and X.-J. Liu. State Key Laboratory of Theoretical and Computational Chemistry, Institute of Theoretical Chemistry, Jilin University, 125 Jie Fang Road, Changchun 130023, China.

[1]Corresponding author (e-mail: jikangf@yahoo.com).
[2]Second affiliation: College of Chemistry, Jilin University, 125 Jie Fang Road, Changchun 130023, China.

 doi: 10.1139/V04-086 © 2004 NRC Canada

and co-workers (26, 27) developed a straightforward synthetic scheme to easily tune the substitution pattern of the dehydrobenzo[18]annulene chromophore for maximum NLO behavior. In addition, the macrocycle is locked into a planar conformation, which increases the overall π conjugation, and thus should result in better NLO efficiency. In this paper, we theoretically investigated the one-photon absorption (OPA) and TPA properties of dehydrobenzo[18]annulenes, and analyzed the micromechanism of the increase in the molecular TPA cross-section value.

Theoretical methodology

The TPA process corresponds to simultaneous absorption of two photons. The TPA efficiency of an organic molecule, at optical frequency $\omega/2\pi$, can be characterized by the TPA cross-section $\delta(\omega)$. It can be directly related to the imaginary part of the second hyperpolarizability $\gamma(-\omega; \omega, \omega, -\omega)$ by (11):

$$[1] \qquad \delta(\omega) = \frac{8\pi^2\hbar\omega^2}{n^2c^2} L^4 Im\, \gamma(-\omega;\omega,\omega,-\omega)$$

where $\hbar$ is Planck's constant divided by 2π, n is the refractive index of medium, c is the speed of light, and L is a local field factor (equal to 1 for vacuum).

The sum-over-states (SOS) expression to evaluate the components of the second hyperpolarizability γ_{ijkl} can be induced out using perturbation theory and density matrix method. By considering a power expansion of the energy with respect to the applied field, the γ_{ijkl} Cartesian components are given by (28, 29):

$$[2] \qquad \gamma_{ijkl}(-\omega_\sigma;\omega_1,\omega_2,\omega_3) = \frac{4\pi^3}{3h^3} P(i,j,k,l;-\omega_\sigma;\omega_1,\omega_2,\omega_3)$$
$$\left[\sum_{m\neq o}\sum_{n\neq o}\sum_{p\neq o} \frac{\langle o|\mu_i|m\rangle\langle m|\bar{\mu}_j|n\rangle\langle n|\bar{\mu}_k|p\rangle\langle p|\mu_l|o\rangle}{(\omega_{mo}-\omega_\sigma-i\Gamma_{mo})(\omega_{no}-\omega_2-\omega_3-i\Gamma_{no})(\omega_{po}-\omega_3-i\Gamma_{po})} \right.$$
$$\left. - \sum_{m\neq o}\sum_{n\neq o} \frac{\langle o|\mu_i|m\rangle\langle m|\mu_j|o\rangle\langle o|\mu_k|n\rangle\langle n|\mu_l|o\rangle}{(\omega_{mo}-\omega_\sigma-i\Gamma_{mo})(\omega_{no}-\omega_3-i\Gamma_{no})(\omega_{no}+\omega_2-i\Gamma_{no})} \right]$$

where P(i,j,k,l; $-\omega_\sigma$ ω_1, ω_2, ω_3) is a permutation operator defined in such a way that for any permutation of (i,j,k,l), an equivalent permutation of ($-\omega_\sigma$; ω_1, ω_2, ω_3) is made simultaneously; $\omega_\sigma = \omega_1 + \omega_2 + \omega_3$ is the polarization response frequency; ω_1, ω_2, ω_3 indicate the frequencies of the perturbing radiation fields (considering the degenerate TPA, $\omega_1 = \omega_2 = \omega$ and $\omega_3 = -\omega$); i, j, k, and l correspond to the molecular axes x, y, and z; m, n, and p denote excited states, and o, the ground state; μ_j is the j(= x, y, z)th component of the dipole operator; ($\langle m|\vec{\mu}_j|n\rangle = \langle m|\mu_j|n\rangle - \langle o|\mu_j|o\rangle$); $(h/2\pi)\omega_{mo}$ is the transition energy between the m and o states and Γ_{mo} is the damping factor of excited state m. Considering the higher the excited state is and the shorter its lifetime is, the Γ_{mo} is expressed as follows (29):

$$[3] \qquad \Gamma_{mo} = 0.08 \times \frac{\omega_{mo}}{\omega_{1o}}$$

To compare the calculated $\delta(\omega)$ value with the experimental value measured in solution, the orientationally averaged (isotropic) value of γ is evaluated, which is defined as

$$[4] \qquad \langle\gamma\rangle = \frac{1}{15}\sum_{i,j}(\gamma_{iijj} + \gamma_{ijij} + \gamma_{ijji}) \qquad i,j = x,y,z$$

Whereafter, $\langle\gamma\rangle$ is taken into eq. [1], and then the TPA cross section $\delta(\omega)$ is obtained.

Generally, the position and relative strength of the two-photon resonance are predicted using the following simplified form of the SOS expression (30):

$$[5] \qquad \delta \propto \frac{M_{0k}^2 (M_{kn}^2 + \Delta\mu_k^2)}{(E_{0k} - E_{0n}/2)^2\Gamma}$$

where M_{ij} is the transition dipole moment from the state i to j; E_{ij} is the corresponding excitation energy, the subscripts 0, k, and n refer to the ground state S_0, the intermediate state S_k, and the TPA final state S_n, respectively; $\Delta\mu_k$ is the dipole moment difference between S_0 and S_k, which is neglected in molecules having central symmetry. So for molecules with a center of inversion symmetry, eq. [5] becomes the following formula (11):

$$[6] \qquad \delta \propto \frac{M_{0k}^2 M_{kn}^2}{(E_{0k} - E_{0n}/2)^2\Gamma}$$

In principle, any kind of self-consistent field molecular orbital procedure combined with configuration interaction can be used to calculate the physical values in the above expression. In the present paper, the B3LYP/6-31g method was firstly used to calculate molecular equilibrium geometry. Then, the property of the electronic excited state was obtained by 196 single-electron excitation and 54 double-electron excitation configuration interactions using the ZINDO program. Furthermore, UV–vis (ground-state, one-photon absorption) spectra, which were needed to predict TPA, were provided. Then according to eqs. [1]–[4], the second hyperpolarizability (γ) and TPA cross section $\delta(\omega)$ were calculated.

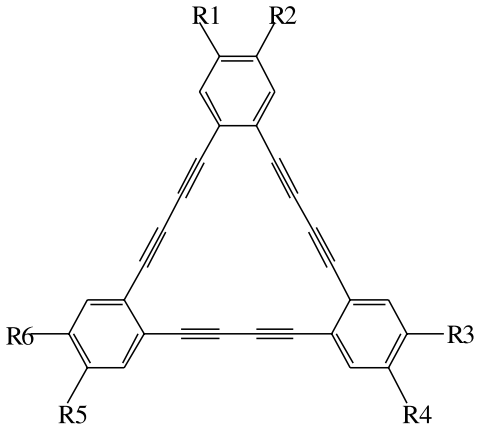
Results and discussions

Geometry optimization and electronic structure

The molecular structures were chosen according to Fig. 1

© 2004 NRC Canada

Fig. 1. Molecular structures designed for the compounds studied.



	R1	R2	R3	R4	R5	R6
D1	H	H	H	H	H	H
D2	NO_2	$N(Me)_2$	H	H	H	H
D3	NO_2	H	H	H	H	$N(Me)_2$
D4	NO_2	H	H	$N(Me)_2$	H	H
D5	NO_2	$N(Me)_2$	H	NO_2	$N(Me)_2$	H
D6	NO_2	H	OMe	OMe	H	NO_2
D7	NO_2	H	$N(Me)_2$	$N(Me)_2$	H	NO_2

with systematic donor–acceptor substitutions — in terms of donor dimethylamino ($N(Me)_2$) and oxymethyl (OMe), and acceptor nitro (NO_2) groups — on a hydrocarbon backbone. The basic building block is dehydrobenzo[18]annulene denoted by D1, which is nonsubstituted with R_i = H and possesses D_{3h} point group symmetry. When R1 and R2 are replaced by NO_2 and $N(Me)_2$, respectively, the D2 is formed, whose symmetry is reduced into C_s.

In the same way, because of the unsymmetric substituent of one pair of the donor–acceptor, the molecules D3 and D4 have C_s point group symmetry. The intention of designing D2, D3, and D4 was to study the effect of the different positions of donor or acceptor on the OPA and TPA properties. As far as the D5 compound is concerned, unsymmetric substitutions of two pairs of the donor–acceptor allow the molecule to retain C_s symmetry. To investigate the contribution of the increase of the donor strength to the OPA and TPA properties, we designed the chromophores D6 and D7, whose point group symmetry becomes C_{2v} owing to symmetric positions of two $N(Me)_2$ or OMe and two NO_2 groups. We select some bond lengths and bond angles of molecule D4 and the experimental results are given in parentheses (shown in Fig. 2). In the theoretical calculations, butyl groups in the experiment were replaced by methyl groups. The optimized geometries show that the macrocycle in all molecules are locked into a planar conformation, which is in accordance with the experimental result and are in favor of the intramolecular charge transfer.

One-photon absorption

Table 1 collects the calculated and experimental (given in parentheses) wavelengths ($\lambda^{(1)}$), oscillator strengths (f), and the nature of the transition for the maximum OPA of every compound. From Table 1, one can see that the results we calculated are in good agreement with the experimental values. The substitution of one pair of donor–acceptor in D2 makes $\lambda_{max}^{(1)}$ red-shifted by 2.4 nm on the basis of that of D1 (354.4 nm). The enhanced effects of the donor–acceptor groups in D3 and D4 result in a longer OPA maximal wavelength than that for D2 by 10–12 nm. The reason that $\lambda_{max}^{(1)}$ of D4 is longer than that of D3 is the more efficient conjugated pathway. The $\lambda_{max}^{(1)}$ value increases with the change of the substituent in the order $N(Me)_2$ (in D7) > OMe (in D6). The reason for this result is that $N(Me)_2$ group has a stronger electron-donating ability than the OMe group. As shown in Fig. 1, there are two pairs of the same donor–acceptor substitutions in both D5 and D7. However, the $\lambda_{max}^{(1)}$ displayed in Table 1 is red-shifted by 25 nm from D5 to D7, which is possibly owing to the fact that molecule D7 has a higher point group symmetry (C_{2v}) than D5 (C_s), and then is in favor of the symmetric electron transfer.

Two-photon absorption

Table 2 summarizes the position of the maximal TPA ($\lambda_{max}^{(2)}$) and the nature of the transition. According to eqs. [1]–[4], we compiled a program to calculate the third-order optical susceptibility $\langle\gamma\rangle$ abbreviated as γ, and the TPA cross section $\delta(\omega)$. Using the program, we calculated the real and imaginary part of γ as well as the δ_{max} value, which are also listed in Table 2. To examine the accuracy of the calculation method, we chose stilbene (molecule A in Tables 1 and 2) and 4,4-bis(dimethyl-amino)stilbene (molecule B in Tables 1 and 2) as comparison samples and the corresponding experimental values are given in parentheses. We can see from Tables 1 and 2 that the results we calculated are in good agreement with the experimental values.

The absorption of light by matter is a consequence of the interaction of an electromagnetic field with optically induced electric dipoles in a molecule. For the molecule that has central symmetry, a change in the parity between the initial and final states (wave functions) is required for every photon involved in the transition for electric dipole transitions. Thus, the selection rule for TPA is different from that of OPA. One change of parity is required for a one-photon transition, while two-photon transitions must have initial and final states with the same parity. In this work, all of the studied compounds have no center of inversion symmetry, so every state is of mixed parity and transition between all electronic states involving any numbers of photons are allowed. We studied the TPA spectra for all compounds by considering the 25 lowest excited states one point by one point, and at the same time obtained the maximum TPA cross section δ_{max} and the position of TPA maximum $\lambda_{max}^{(2)}$. We take the molecule D1 as an example to depict its TPA spectrum (shown in Fig. 3).

It is well-known that the simplified form of the SOS expression – three-state approximation can be used to predict the position and relative strength of the two-photon resonance (11). In this paper, there is no central symmetry in the investigated compounds, and hence eq. [5] should be applicable to this series of molecules. According to the results in Tables 2 and 3, the relationship between the maximum TPA cross section (δ_{max}) of every compound and $M_{0k}^2(M_{kn}^2 + \Delta\mu_k^2)/(E_{0k} - E_{0n}/2)^2\Gamma$ is depicted in Fig. 4. As can be seen,

© 2004 NRC Canada

Fig. 2. Optimized and experimental (given in parentheses) geometric parameters of molecule D4 (distance in Å, angles in °).

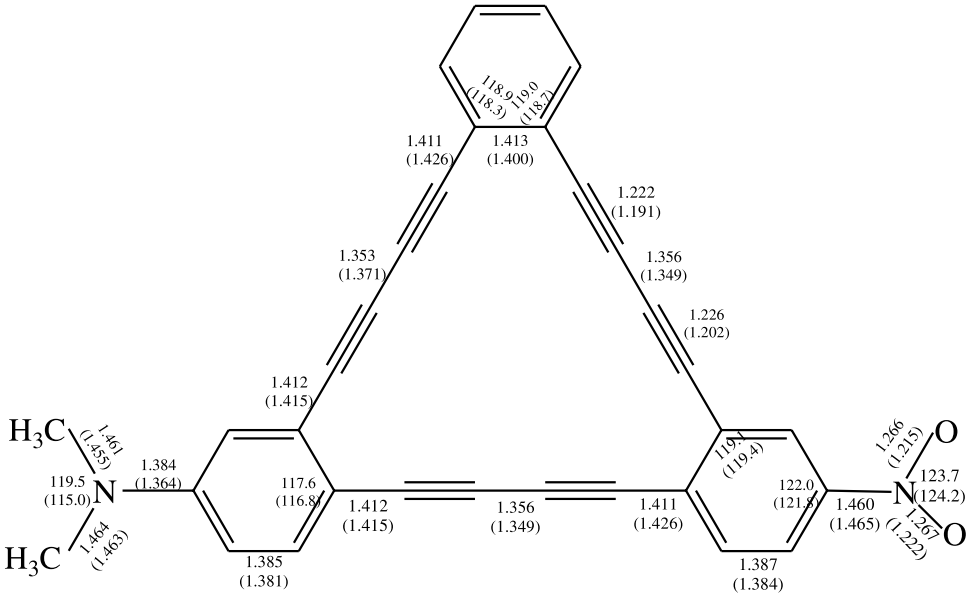


Table 1. Maximum one-photon absorption and nature of the transition for each compound.

Compound	$\lambda_{max}^{(1)}$ (nm)	f	Transition nature	Configurations	Weight (%)
D1	354.4(331) (26)	0.57704	$S_0 \rightarrow S_6$	(HOMO,0) → (LUMO,0)	23
				(HOMO – 1,0) → (LUMO + 1,0)	23
				(HOMO – 2,0) → (LUMO + 8,0)	10
D2	356.8(357) (26)	1.00401	$S_0 \rightarrow S_7$	(HOMO – 1,0) → (LUMO,0)	21
				(HOMO,0) → (LUMO + 1,0)	17
				(HOMO,0) → (LUMO + 2,0)	14
D3	367.5(362) (26)	0.90227	$S_0 \rightarrow S_7$	(HOMO – 1,0) → (LUMO,0)	27
				(HOMO,0) → (LUMO + 1,0)	25
D4	368.3(367) (26)	0.74696	$S_0 \rightarrow S_6$	(HOMO – 1,0) → (LUMO + 1,0)	31
				(HOMO,0) → (LUMO,0)	19
D5	359.6(360) (26)	1.12846	$S_0 \rightarrow S_7$	(HOMO,0) → (LUMO + 3,0)	24
				(HOMO – 1,0) → (LUMO,0)	23
				(HOMO,0) → (LUMO + 2,0)	22
D6	381.3(370) (26)	1.05739	$S_0 \rightarrow S_7$	(HOMO,0) → (LUMO + 1,0)	52
D7	385.0	1.17539	$S_0 \rightarrow S_7$	(HOMO,0) → (LUMO + 1,0)	51
A	261.7(267) (31)	1.08101	$S_0 \rightarrow S_1$	(HOMO,0) → (LUMO,0)	88
B	325.2(322) (31)	1.38312	$S_0 \rightarrow S_1$	(HOMO,0) → (LUMO,0)	93

Note: The experimental values in the literature (26) are given in parentheses. For the theoretical results, butyl groups in the experiment were replaced by methyl groups.

Table 2. Two-photon absorption properties of molecules.

Compound	$\lambda_{max}^{(2)}$ (nm)	Transition	$\gamma \times 10^{-34}$ (esu)	δ_{max} (10^{-50} cm^4 s/photon)
D1	550.8	$S_0 \rightarrow S_{13}$	–6.13+4.39i	298.9
D2	541.8	$S_0 \rightarrow S_{19}$	–16.4+8.98i	632.1
D3	600.0	$S_0 \rightarrow S_{14}$	–8.57+17.1i	979.4
D4	605.6	$S_0 \rightarrow S_{14}$	–10.2+23.6i	1325
D5	581.6	$S_0 \rightarrow S_{18}$	–23.9+26.6i	1623
D6	601.6	$S_0 \rightarrow S_{14}$	–15.6+33.9i	1934
D7	604.0	$S_0 \rightarrow S_{15}$	–20.1+59.6i	3376
A	432(425) (31)	$S_0 \rightarrow S_3$	0.44+5.33i	93.81(54) (31)
B	517.4(529) (31)	$S_0 \rightarrow S_3$	–0.51+34.9i	429.71(411) (31)

© 2004 NRC Canada

Table 3. Electronic transitions and transition dipole moments of compounds for maximum TPA.

Molecule	M_{0k}^2 (D)	M_{kn}^2 (D)	$\Delta\mu_k^2$ (D)	E_{0k} (eV)	$E_{0n}/2$ (eV)	Γ (eV)	$M_{0k}^2\ (M_{kn}^2 + \Delta\mu_k^2)/(E_{0k} - E_{0n}/2)^2\Gamma$
D1	43.41	12.38	0.120	3.49	2.25	0.09	3 921.15
D2	76.04	6.712	10.24	3.47	2.29	0.10	9 256.52
D3	70.39	19.98	12.32	3.37	2.07	0.10	14 948.0
D4	58.37	27.98	23.62	3.37	2.05	0.09	19 206.5
D5	86.12	45.43	23.04	3.45	2.13	0.09	33 842.0
D6	85.56	86.68	70.06	3.25	2.06	0.09	105 223
D7	96.04	115.56	107.95	3.22	2.05	0.09	174 234

Fig. 3. TPA spectrum of the molecule D1.

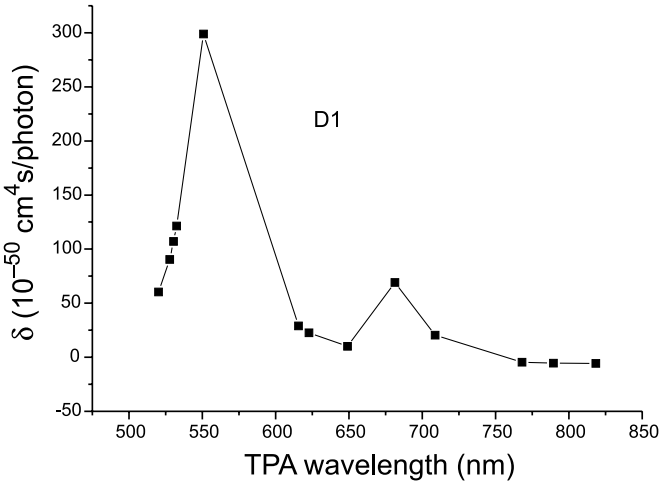
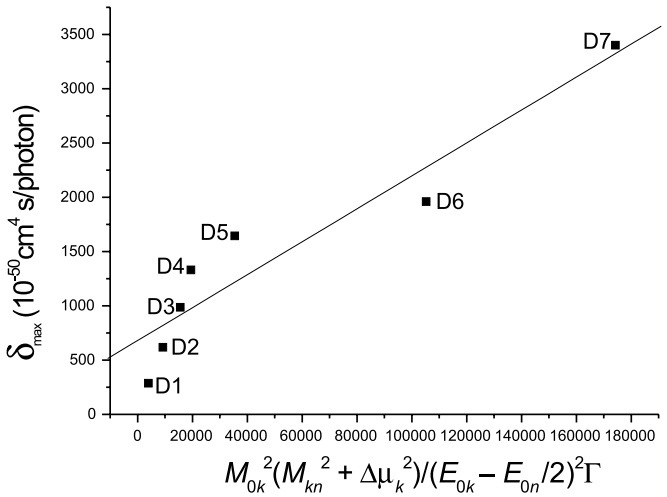


Fig. 4. Plot of δ_{max} vs. $M_{0k}^2(M_{kn}^2+\Delta\mu_k^2)/(E_{0k} - E_{0n}/2)^2\Gamma$.



the calculated points are distributed on average on the two sides of the line, which indicated the basal applicability of three-state approximation in this class of molecules. It is notable that the increasing magnitude of M_{kn}^2 and $\Delta\mu_k^2$ plays the most significant role in the enhanced TPA cross-section value from D1–D7.

To examine further the reliability of the applied method to calculate the nonlinear optical properties, we choose 4-amino-4 -nitro-diphenylacetylene as the comparison sample. We calculated its transition dipole moment M_{ge} and state dipole moment difference $\Delta\mu$. The calculated M_{ge} is equal to 8.49, which is close to the calculated result 8.62 and the experimental value 6.16 in the literature (32). The $\Delta\mu$ value is 13.62, which is larger than the experimental value 9.5 but almost equal to the calculated result 13.54 in the literature (32). From Table 3, the TPA maximum wavelength for all molecules is in the range from 540 to 610 nm, in which there is no linear absorption and so a TPA process may occur. Except for D2 with the higher-lying TPA final state, the $\lambda_{max}^{(2)}$ of the donor–acceptor substituted compounds is redshifted in comparison to that for the nonsubstituted molecule D1. As far as one pair of donor–acceptor substituted molecules are concerned, with the enhancement in the efficiency of conjugation, the $\lambda_{max}^{(2)}$ value increases in the order of D4 (605.6 nm) > D3 (600 nm) > D2 (541.8 nm). In terms of chromphores with two-pairs of donor- acceptor, because of the more symmetric substituents (C_{2v}) in D6 and D7 than that in D5 (C_s), the $\lambda_{max}^{(2)}$ is bathochromic more than 20 nm. From D6 to D7, there is a slight shift (2.4 nm) of the peak position of the TPA to a longer wavelength upon increasing the donor strength.

In general, an octupolar system should exhibit the character of the basic trigonal C_3 group included in all-trigonal groups such as C_{3h}, D_3, and D_{3h}. In this paper, only the molecule D1 possesses D_{3h} point group symmetry, but the other molecules have reduced symmetry (C_{2v} or C_s) because of substitutions of donor and acceptor and become the distorted octupolar compounds. The TPA response in octupolar compounds is highly sensitive to the actual interactions among the individual molecular branches. Then, in these distorted octupolar systems, what does result in the increase of maximum TPA cross-section δ_{max}?

As shown in Table 2, the octupolar system D1 presents the smallest TPA cross section — 298.9×10^{-50} cm^4 s/photon — since there is no outside force driving the electron transfer. As both functional groups on D2 are positioned on a single benzene ring ortho to each other, most of the electron transfer is localized in the six-membered ring. The increased quantities of electron transfer make the δ_{max} value of D2 (632.1×10^{-50} cm^4 s/photon) larger than that of D1. In the case of D3, because the effect of the donor–acceptor groups through the delocalization pathway is better than that in D2, the maximum TPA cross section is added to 979.4×10^{-50} cm^4 s/photon. The donor–acceptor substitution locates a conjugated pathway in D4 compared with the cross- conjugated pathway in D3, which makes for the electron transfer in the molecular plane. As a result, D4 exhibits a larger TPA cross-section value of 1325×10^{-50} cm^4 s/photon. To probe into the origin of the TPA response in molecule D4, we calculated the TPA cross section of the linear donor–acceptor chromophore 4-nitro-4 -dimethylaimno-diphenyldiacetylene, denoted by P. The computed δ_{max} for molecule P is up to

© 2004 NRC Canada

1338×10^{-50} cm^4 s/photon, which is almost equal to the δ_{max} for D4. The above result suggests that the TPA response in molecule D4 mostly comes from that in the side connected by donor and acceptor in the trigonal molecule. The magnitude of the TPA cross section of the molecule D5 is 1623×10^{-50} cm^4 s/photon, which is the sum of that of D2 and D3. The obtained TPA cross section increases from 1934×10^{-50} cm^4 s/photon of D6 to 3376×10^{-50} cm^4 s/photon of D7 as the electron-donating ability of substituents enhances. Examining the data in Table 3, one can find that the δ_{max} for molecule D7 (3376×10^{-50} cm^4 s/photon) is more than twice as that for D4 (1325×10^{-50} cm^4 s/photon). The result illuminates that the symmetric substitutions of donors and acceptors in molecule D7 are propitious to the electron transfer and cooperative enhancement in TPA response of the individual side.

Theoretical calculations and experimental observations indicate that the enhanced nonlinear optical properties of organic molecules quite often are hampered by an optical transparency problem. It causes the bathochromic shift of the π-π^* absorption band, and thus the requirement of high transparency to visible light will not be met. The calculation shows that the maximum TPA cross section of D7 is enhanced by one order of magnitude on the basis of that of D1, while the $\lambda^{(1)}_{max}$ has red-shifted by 30 nm. Gompper et al. (33) pointed out that the maximum wavelength ($\lambda^{(1)}_{max}$) of the electronic spectra of the chromophore molecules of the nonlinear optical materials ought to be shorter than 415 nm so that the transparency can be guaranteed. From the calculated electronic spectra listed in Table 1, it can be seen that $\lambda^{(1)}_{max}$ of all molecules is lower than 385 nm (i.e., the third-order susceptibility and the TPA cross section increase without lowering the transparency).

Conclusion

The linear and nonlinear optical properties for various dehydrobenzo[18]annulenes were systematically investigated. Overall, the effects of increasing donor strength and the efficiency of the conjugation on the OPA and TPA properties were studied in detail. The results indicate that macrocycle D7 with the stronger donors ($N(Me)_2$) and higher point group symmetry (C_{2v}) exhibits the largest TPA cross-section value. For this series of chromphores, the three-state approximation is still applicable to predict the changing trend of the TPA cross section. It is notable that the calculated TPA cross-section value for the molecule D7 is 15-fold larger than that of the famous TPA material — 4,4 -bis(di-*n*-butylamino)-*E*-stilbene (11). In general, dehydrobenzo[18]annulenes with the high transparency and the larger TPA response are worth being investigated further.

Acknowledgements

This work is supported by the National Nature Science Foundation of China (20273023), the University Doctoral Subjet Foundation of China and the Key Laboratory for Supramolecular Structure and Material of Jilin University.

References

1. S. Maruo, O. Nakamura, and S. Kawata. Opt. Lett. **22**, 132 (1997).
2. S. Kawata, H.-B. Sun, T. Tanaka, and K. Takada. Nature (London), **412**, 697 (2001).
3. S. Maruo and K. Ikuta. Proc. Soc. Photo-Opt. Instrum. Eng. **3937**, 106 (2000).
4. H.E. Pudavar, M.P. Joshi, P.N. Prasad, and B.A. Reinhardt. Appl. Phys. Lett. **74**, 1338 (1999).
5. W. Denk. Proc. Natl. Acad. Sci. U.S.A. **91**, 6629 (1994).
6. R.M. Williams, D.W. Piston, and W.W. Webb. Feb. Am. Soc. Exp. Bio. J. **8**, 804 (1994).
7. G.A. Baker, S. Pandey, and F.V. Bright. Anal. Chem. **72**, 5748 (2000).
8. J.D. Bhawalker, N.D. Kumar, C.F. Zhao, P.N. Prasad, and J. Clin. Laser Med. Surg. **15**, 201 (1997).
9. K.S. Belfield, K.J. Schafer, W. Mourad, and B.A. Reinhardt. J. Org. Chem. **65**, 4475 (2000).
10. A. Abbotto, L. Beverina, R. Bozio, A. Facchetti, C. Ferrante, G.A. Pagani, D. Pedron, and R. Signorini. Org. Lett. **4**, 1495 (2002).
11. M. Albota, D. Beljonne, J.L. Brédas, J.E. Ehrlich, J. Fu, A.A. Heikal, E. Hess, T. Kogej, M.D. Levin, S.R. Marder, D. McCord-Maughon, W. Perry, H. Röeckel, M. Rumi, G. Subramaniam, W.W. Webb, X. Wu, and C. Xu. Science (Washington, D.C.), **281**, 1653 (1998).
12. M. Rumi, J.E. Ehrlich, A.A. Heikal, J.W. Perry, S. Barlow, Z. Hu, D. McCord-Maughon, T.C. Parker, H. Röckel, S. Thayumanavan, S.R. Marder, D. Beljonne, and J.-L. Brédas J. Am. Chem. Soc. **122**, 9500 (2000).
13. S.J.K. Pond, M. Rumi, M.D. Levin, T.C. Parker, D. Beljonne, M.W. Day, J.-L. Brédas, S.R. Marder, and J.W. Perry. J. Phys. Chem. A, **106**, 11 470 (2002).
14. B.R. Cho, K.H. Son, S.H. Lee, Y.-S. Song, Y.-K. Lee, S.-J. Jeon, J.H. Choi, H. Lee,and M. Cho. J. Am. Chem. Soc. **123**, 10 039 (2001).
15. B.R. Cho, M.J. Piao, K.H. Son, S.H. Lee, S.J. Jeon, J.-H. Choi, H. Lee, and M. Cho. Chem. Eur. J. **8**, 3907 (2002).
16. L. Porrès, O. Mongin, C. Katan, M. Charlot, T. Pons, J. Mertz, and M. Blanchard-Desce. Org. Lett. **6**, 47 (2004).
17. D.W. Brousmiche, J.M. Serin, J.M.J. Fréchet, G.S. He, T.-C. Lin, S.J. Chung, and P.N. Prasad. J. Am. Chem. Soc. **125**, 1448 (2003).
18. A. Abbotto, L. Beverina, R. Bozio, A. Facchetti, C. Ferrante, G.A. Pagani, D. Pedron, and R. Signorini. Chem. Commun. 2144 (2003).
19. H.J. Lee, J. Sohn, J. Hwang, and S.Y. Park. Chem. Mater. **16**, 456 (2004).
20. A. Adronov, J.M. Fréchet, G.S. He, K.-S. Kim, S.-J. Chung, J. Swiatkiewicz, and P.N. Prasad. Chem. Mater. **12**, 2838 (2000).
21. M. Drobizhev, A. Karotki, Y. Dzenis, A. Rebane, Z. Suo, and C.W. Spangler. J. Phys. Chem. B, **107**, 7540 (2003).
22. Q. Zhou, P.J. Carroll, and T.M. Swager. J. Org. Chem. **59**, 1294 (1994).
23. K.P. Baldwin, A.J. Matzger, D.A. Scheiman, C.A. Tessier, K.P.C. Vollhardt, and W.J. Youngs. Syn. Lett. 1215 (1995).
24. Y. Tobe, N. Nakagawa, K. Naemura, T. Wakabayashi, T. Shida, and Y. Achiba. J. Am. Chem. Soc. **120**, 4544 (1998).
25. Y. Rubin, T.C. Parker, S.J. Pastor, S. Jalisatgi, C. Boulle, and C.L. Wildins. Angew. Chem. Int. Ed. **37**, 1226 (1998).
26. J.J. Pak, T.J.R. Weakley, and M.M. Haley. J. Am. Chem. Soc. **121**, 8182 (1999).

© 2004 NRC Canada

27. A. Sarkar, J.J. Pak, G.W. Rayfield, and M.M. Haley. J. Mater. Chem. **11**, 2943 (2001).
28. B.J. Orr and J.F. Ward. Mol. Phys. **20**, 513 (1971).
29. D. Beljonne, J. Cornil, Z. Shuai, J.L. Bredas, F. Rohlfing, D.D.C. Bradlley, W.E. Torruellas, V. Ricci, and G.I. Stegeman. Phys. Rev. B, **55**, 1505 (1997).
30. A.F. Garito, J.R. Heflin, K.Y. Wong, and Zamani-Khamiri, O. *In* Organic materials for nonlinear optics. *Edited by* R.A. Hann and D. Bloor. Royal Society of Chemistry, London. 1989. p. 16.
31. Y. Morel, A. Irimia, P. Najechalski, Y. Kervella, O. Stephan, P.L. Baldeck, and C. Andraud. J. Chem. Phys. **114**, 5391 (2001).
32. C. Dehu, F. Meyers, and J.L. Brédas. J. Am. Soc. Chem. **115**, 6198 (1993).
33. R. Gompper, H.J. Mair, and K. Polborn. Synthesis, **6**, 696 (1997).

© 2004 NRC Canada

A one-pot synthesis and X-ray crystallographic and computational analyses of methyl-2,4-dimethoxysalicylate — a potential anti-tumour agent

Hossein A. Dabbagh, Nader Noroozi-Pesyan, Brian O. Patrick, and Brian R. James

Abstract: The thermal decarboxylation of 2-methoxycarbonyl-5-(4′-nitrophen-oxy)tetrazole (**1a**) with the electron-rich, aromatic compounds (anisole, *N*,*N*-dimethylaniline, 1,4-dimethoxybenzene, and 1,3,5-trimethoxybenzene), neat or in polar solvents (DMSO, DMF, and CH_3CN), is investigated. The solid phase thermal decomposition of a mixture of **1a**, 1,3,5-trimethoxybenzene, and a Lewis acid ($AlCl_3$) produces methyl-2,4-dimethoxysalicylate (**8**) in good yield, instead of the expected 2,4,6-trimethoxybenzoic acid. The X-ray structure of **8** shows intramolecular hydrogen bonds between the carbonyl oxygen and hydrogens of Me and OH groups. A measured pK_a value of 6.8 compares well with a value of 6.4 estimated using the [C=O···H···O] hydrogen bond distances.

Key words: anti–tumor, novel synthesis, X-ray structure, hydrogen bonds, computational analysis.

Résumé : On a étudié la décarboxylation thermique du 2-méthoxycarbonyl-5-(4′-nitrophényl)tétrazole (**1a**) en présence de composés aromatiques riches en électrons (anisole, *N*,*N*-diméthylaniline, 1,4-diméthoxybenzène et 1,3,5-triméthoxybenzène) à l'état pur ou dans des solvants polaires (DMSO, DMF et CH_3CN). La décomposition thermique en phase solide d'un mélange de **1a**, de 1,3,5-triméthoxybenzène et d'un acide de Lewis ($AlCl_3$) conduit à la formation du 2,4-diméthoxysalicylate de méthyle (**8**) avec un bon rendement au lieu de l'acide 2,4,6-triméthoxybenzoïque attendu. La structure du composé **8** telle que déterminée par diffraction des rayons X montre la présence de liaisons hydrogènes intramoléculaires entre l'oxygène du carbonyle et les atomes d'hydrogène des groupes méthyle et hydroxyle. La valeur mesurée de 6,8 pour le pK_a se compare bien avec la valeur de 6,4 évaluée sur la base des longueurs des liaisons hydrogènes [C=O···H···O].

Mots clés : antitumoral, synthèse nouvelle, structure par diffraction des rayons X, liaisons hydrogènes, analyse conformationnelle.

[Traduit par la Rédaction]

Introduction

Trimethoxybenzoic acid derivatives are important because of their pharmaceutical and biological activities (1), and industrial applications (2). A recent patent reported that a wide range of benzoic acid derivatives have good anti-tumour properties, their activity being related to novel synergistic compositions that selectively control tumour tissue (3); the mixtures contain at least two of the following benzoic acid derivatives: 2-OH, 2-O_2CMe, 2,4-$(OMe)_2$, 2,4,6-$(OMe)_3$, 2-OH-4-NH_2. Other derivatives of dimethoxybenzoic acid have also received considerable attention (4).

Numerous methods have been reported for the synthesis of hydroxybenzoic acids and their methoxy derivatives (e.g., 2,3-$(OH)_2$ (5), 2,4-$(OH)_2$ (6), 2,5-$(OH)_2$ (7), 2,6-$(OH)_2$ (8), 3,4-$(OH)_2$ (9), 2,3,4-$(OH)_3$ (10), 2,3,5-$(OH)_3$ (11), 2,3,6-$(OH)_3$ (12), 2,4,5-$(OH)_3$ (13), and 2,4,6-$(OH)_3$ (14)). 2,4,6-Trimethoxybenzoic acid has been synthesized by methylation of 2,4,6-trihydroxyphenyl allyl ether using Me_2SO_4, followed by oxidation using $KMnO_4$ (15), or from phloroglucinol (16) or β-resorcinol (17). The best known derivative of benzoic acid is the most often recommended drug aspirin (acetylsalicylic acid), which is an analgesic, effective in relieving headaches, and has anti-inflammatory and other beneficial properties (18).

One of our groups recently reported the equilibria, kinetics, and mechanism for the isomerization of 2-methoxycarbonyl-5-(*p*-X-phenoxy)tetrazoles (X = H, Me, NHCOMe, Cl, Br, and NO_2; **1** → **2** (Scheme 1, pathways *a* and *b*)) (19, 20), and also their thermal decarboxylation to form in high yield 5-(aryloxy)tetrazoles (**3**, **4** (Scheme 1, pathways *c* and

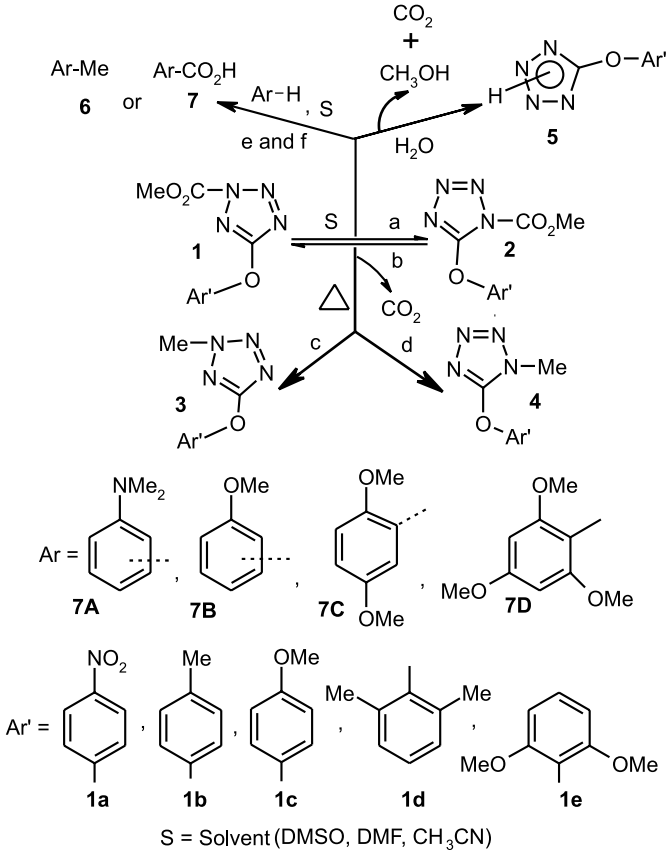
Received 24 January 2004. Published on the NRC Research Press Web site at http://canjchem.nrc.ca on 17 September 2004.

H.A. Dabbagh[1] and N. Noroozi-Pesyan. Department of Chemistry, Isfahan University of Technology, P.O. Box 84155, Isfahan, Iran.
B.O. Patrick and B.R. James. Department of Chemistry, The University of British Columbia, Vancouver, BC V6T 1Z1, Canada.

[1]Corresponding author (e-mail: dabbagh@cc.iut.ac.ir).

 doi: 10.1139/V04-113 © 2004 NRC Canada

Scheme 1. Summary of chemistry for the tetrazoles **1** and **2**.



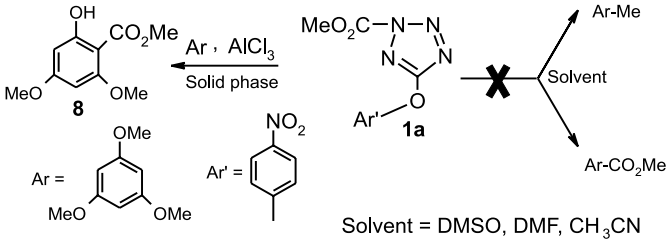
d)) (21), when CO_2 is released at temperatures below the melting points of the precursor methoxycarbonyl derivatives.

In the work reported here, we attempted to utilize **1** as a potential carboxylation and (or) alkylation agent (Scheme 1, pathways *e* and *f*) for electron-rich aromatic compounds such as *N*,*N*-dimethylaniline, anisole, 1,4-dimethoxybenzene, and 1,3,5-trimethoxybenzene (Schemes 1 and 2), the plan being to trap any released (free) alkyl or acyl groups during the reaction. However, we unexpectedly synthesized methyl-2,4-dimethoxysalicylate by a method that might aid in the synthesis of new compounds or compounds previously difficult to prepare. The new findings also shed more light on the mechanism of isomerization, decarboxylation, alkylation, and (or) acylation of 2-alkloxycarbonyl-5-aryloxytetrazoles.

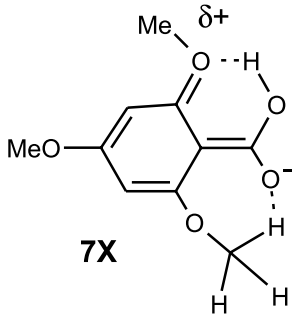
Results and discussion

The thermal decomposition of **1a**–**1e** in polar aprotic solvents (DMSO, DMF, and MeCN) gives **3a**–**3e** and **4a**–**4e** in high yield (21). In the present study, the reaction of **1a**–**1e** in the presence of the electron-rich aromatic compounds mentioned above was investigated both in polar aprotic solvents and solvent-free conditions. There was no trace of the carboxylation or alkylation of the electron-rich aromatic ring (Scheme 2). With 1,3,5-trimethoxybenzene (the most electron-rich aromatic ring) under solvent-free conditions, a low yield product was obtained (<2%), while in the presence of a Lewis acid ($AlCl_3$), the yield was increased to 30%. There were no akylation (**6A**–**6C**) or carboxylation (**7A**–**7C**) products (see Scheme 1) detected from reactions with the

Scheme 2. Formation of **8**.



other electron-rich reagents. We initially thought that the 30% product was 2,4,6-trimethoxybenzoic acid (**7D**) (Scheme 1). This was based on ^{1}H NMR (90 MHz) in DMSO-d_6: δ 3.63 (br s, 3H), 3.66 (s, 6H), and 6.0 (br s, 2H), and MS data that showed a parent M^+ peak at 212. However, the melting point (96–98 °C) did not match the value of 158 °C (decomp.) given for **7D** in the *Lancaster Chemicals* catalogue. Further examination by ^{1}H NMR (300 MHz) in $CDCl_3$ revealed a well-resolved spectrum (δ 3.73 (s, 3H), 3.74 (s, 3H), 3.83 (s, 3H), 5.89 (d, 1H, J = 8 Hz), 6.02 (d, 1H, J = 8.3 Hz), 11.91 (s, 1H)), while the corresponding ^{13}C NMR spectrum showed 10 signals (see Experimental). The NMR data show the presence of three inequivalent OMe groups and two inequivalent aromatic protons. We considered as a possibility the H-bonded structure **7X**, but an X-ray structure revealed that the product was, in fact, methyl-2,4-dimethoxysalicylate (**8**, Fig. 1; see Table 1 for crystal and structure refinement data), which accounts for the NMR data; formally, this has been formed from the "expected **7D**" by the interchange of a Me group (of a 2- or 6-OMe) with the carboxylic acid proton. The co-products isolated with **8** are 1- and 2-Me-5-aroyltetrazole (**4a** and **3a**, respectively) and the tetrazole **5**.



Of note, the structure of 2,4,6-trimethoxybenzoic acid (**7D**) has not been determined, although the structure of an inclusion compound of this acid with 2′,6′-dimethoxyflavone (in which the carboxylic acid proton is H-bonded to the flavone carbonyl) reveals a nonplanar benzoic acid component, the carboxylic acid moiety being ~66° out of the plane of the rest of the acid molecule (4*c*).

The carbon–oxygen framework of the molecular structure of **8** is essentially planar; bond lengths and angles are summarized in Table 2, while a structural diagram is shown also in Scheme 3. Planarity is maintained by a strong intramolecular H-bonding interaction between the carbonyl oxygen and phenolic H atom (H(1)···O(1) = 1.68(4) Å; O(5)-H(1) = 1.00(4) Å), and a much weaker intramolecular H-bond of distance 2.535 Å between Me hydrogens (H(8)) and the

© 2004 NRC Canada

Fig. 1. Molecular structure for **8** with 50% probability ellipsoids.

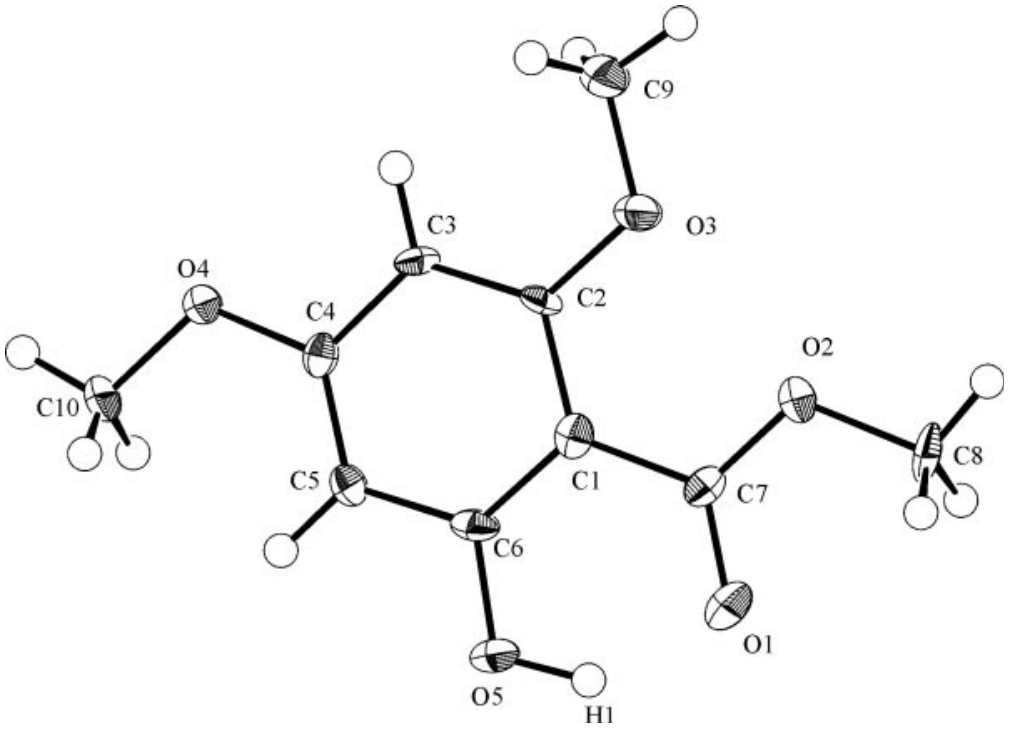


Table 1. Crystal data and structure refinement for **8.**

Empirical formula	$C_{10}H_{12}O_5$
Formula weight	212.20
Temperature (K)	173(1)
Crystal system	Monoclinic
Space group	$P2_1/c$
Unit cell dimensions	
a (Å)	7.634(1)
b (Å)	8.931(2)
c (Å)	14.274(3)
β (°)	91.82(1)
Volume (Å^3)	972.7(3)
Z	4
Density (calculated) (Mg m^{-3})	1.449
Absorption coefficient (mm^{-1})	0.117
F(000)	448.00
Crystal size (mm^3)	0.13 × 0.10 × 0.04
θ range for data collection (°)	2.67–23.65
Index ranges	$-8 \le h \le 8$, $-9 \le k \le 9$, $-15 \le l \le 15$
Reflections collected	6441
Independent/observed reflections	1390 (R(int) = 0.102)/671 ($I > 3\sigma(I)$)
$2\theta_{max}$ (°)	46.5
Data/parameters	1390/140
Goodness-of-fit on F^2	0.99
Weight parameters[a]	p = 0.0310
Final R indices ($I > 3\sigma(I)$)	$R1$ = 0.039, wR_2 = 0.074
R indices (all data)	$R1$ = 0.086, wR_2 = 0.106
Largest diff. peak[b] and hole (e Å^{-3})	0.64 and –0.45

[a] $w = [\sigma^2{}_c(F_o^2) + p^2F_o^2/4]^{-1}$.
[b] At ~1.1 Å from O(1).

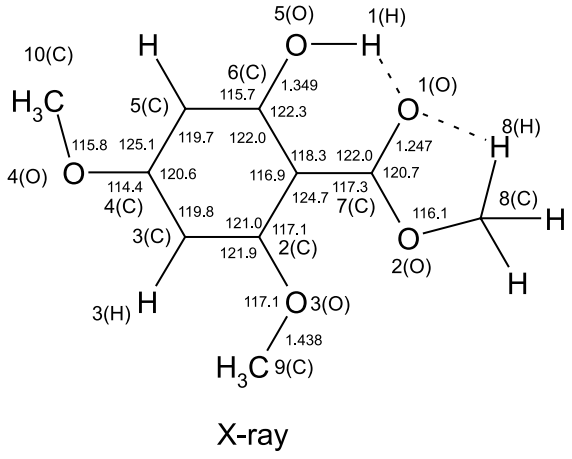
© 2004 NRC Canada

Table 2. Bond lengths (Å) and angles (°) of **8** (esds in parentheses).

Atoms[a]	Bond lengths (Å)	Atoms	Bond angles (°)
O(1)—C(7)	1.247(4)	C(7)-O(2)-C(8)	116.1(3)
O(2)—C(7)	1.325(4)	C(2)-O(3)-C(9)	117.1(3)
O(2)—C(8)	1.465(4)	C(4)-O(4)-C(10)	115.8(2)
O(3)—C(2)	1.363(4)	C(2)-C(1)-C(6)	116.9(3)
O(3)—C(9)	1.438(4)	C(2)-C(1)-C(7)	124.7(3)
O(4)—C(4)	1.362(4)	C(6)-C(1)-C(7)	118.3(3)
O(4)—C(10)	1.443(4)	O(3)-C(2)-C(1)	117.1(3)
C(1)—C(2)	1.432(4)	O(3)-C(2)-C(3)	121.9(3)
C(1)—C(6)	1.393(4)	C(1)-C(2)-C(3)	121.03
C(1)—C(7)	1.465(4)	C(2)-C(3)-C(4)	119.8(3)
C(2)—C(3)	1.378(4)	O(4)-C(4)-C(3)	114.4(3)
C(3)—C(4)	1.406(4)	O(4)-C(4)-C(5)	125.1(3)
C(4)—C(5)	1.364(4)	C(3)-C(4)-C(5)	120.6(3)
C(5)—C(6)	1.402(5)	C(4)-C(5)-C(6)	119.7(3)
O(5)—C(6)	1.349(4)	O(5)-C(6)-C(1)	122.3(3)
		O(5)-C(6)-C(5)	115.7(3)
		C(1)-C(6)-C(5)	122.0(3)
		O(1)-C(7)-O(2)	120.7(3)
		O(1)-C(7)-C(1)	122.0(3)
		O(2)-C(7)-C(1)	117.3(3)

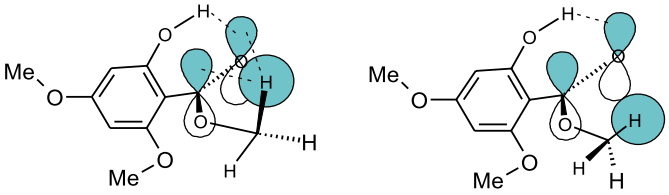
[a]Atom numbering is as in Fig. 1.

Scheme 3. Structure of **8**. Corresponding structures calculated by ab initio, AM1, and PM3 methods are available as Supplementary material.[2]



C=O double bond (in what we label a "bisected" conformation with C_s symmetry (Figs. 2*a* and 2*b*, and Scheme 4)). The orientations of the *o*-OMe and ester-OMe are such to minimize steric interactions. The structure of **8** was also calculated by semiempirical ab-initio, PM3, and AM1 methods, and data for bond lengths and angles, and the torsion angles match well the experimental ones (Tables S1–S3)[2], while the corresponding calculated H(1)···O(1) bond lengths were 1.57, 1.78, and 1.97 Å, respectively, and the calculated O(5)-H(1) values were 1.00, 0.980, 0.970 Å, respectively. The ab initio value for the weaker H-bonding interaction

Scheme 4. Diagrams showing the favored so-called bisected (left) and eclipsed (right) conformations of **8**.



was 2.574 Å. The ab initio calculation also revealed a 1.40 kcal (1 cal = 4.1868 J) higher energy, eclipsed conformation with C_1 symmetry (Figs. 2*c* and 2*d*, Scheme 4, Table 3) with an H(8)-carbonyl bond length of 2.14 Å.

The proposed mechanism for the formation of **8** is outlined in Scheme 5. The Lewis acid activates the carbonyl group of the tetrazole **1a** and initiates a nucleophilic aromatic substitution reaction with 1,3,5-trimethoxybenzene to form a resonance-stabilized intermediate (**9** ↔ **10**) and the tetrazolide anion (**B**:); this then reacts with the Me group of the 2-OMe of **10** (via a bimolecular nucleophilic substitution process) to produce intermediate **11** that isomerizes to **8**, a strongly resonance-stabilized compound (Scheme 6). That methyl-4-hydroxy-2,6-dimethoxy benzoate is not formed is a good indication that intermediate **10** is involved. Compound **8** is not sensitive to air, moisture, or heat, and could be converted easily to other useful derivatives such as 2-hydroxy-4,6-dimethoxybenzoic acid, methyl-2,4,6-trimethoxybenzoate, and 1,3,5-trimethoxybenzoic acid. The mechanism accounts nicely for the observed methyltetrazole co-products **3a** and **4a**, while **5** is a hydrolysis product (see Scheme 1). Corre-

[2]Supplementary data may be purchased from the Depository of Unpublished Data, Document Delivery, CISTI, National Research Council Canada, Ottawa, ON K1A 0S2, Canada (http://nrc.ca/cisti/irm/unpub_e.shtml for information on ordering electronically). CCDC 229696 contains the supplementary crystal data for this paper, and can be obtained, free of charge, via www.ccdc.cam.ac.uk/conts/retrieving.html (or from the Cambridge Crystallographic Data Centre, 12 Union Road, Cambridge, UK; fax +44 1223 336033; or deposit@ccdc.cam.ac.uk).

© 2004 NRC Canada

Fig. 2. Molecular structures for **8** from ab initio analysis (side view: bisected (**a**), eclipsed (**c**)), and front view: bisected (**b**), eclipsed (**d**)).

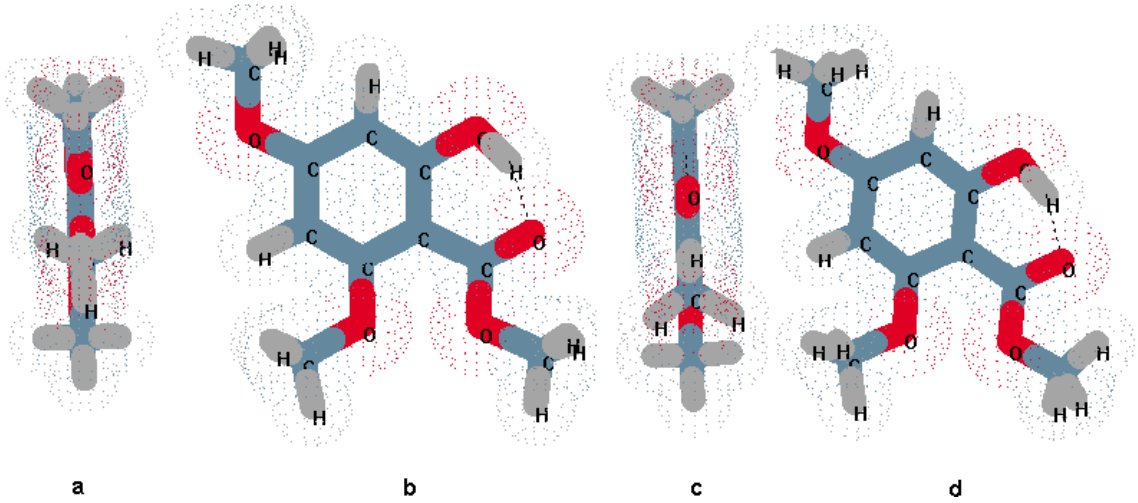
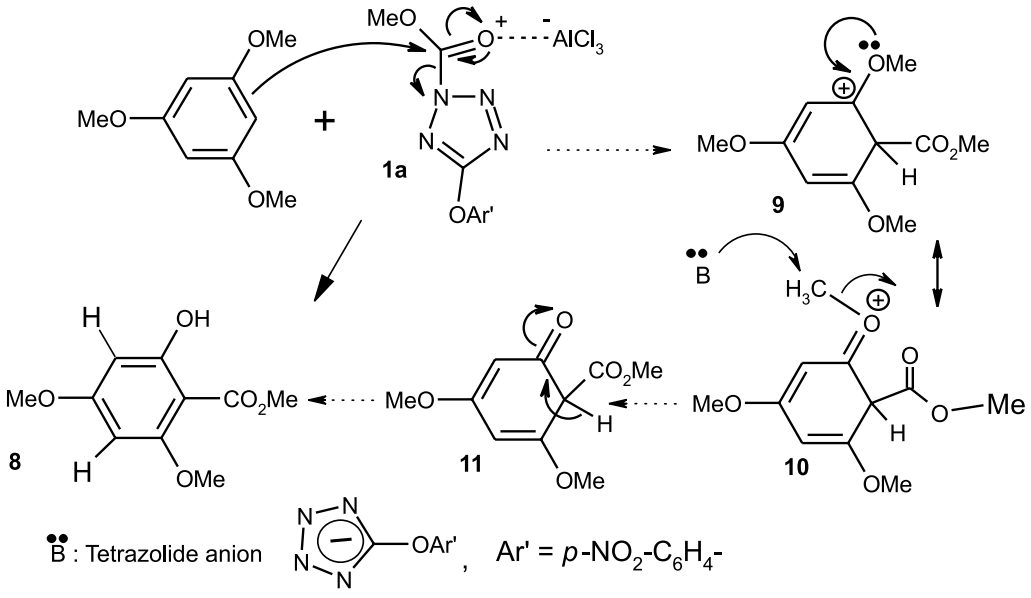


Table 3. Experimental and calculated[a] hydrogen bond lengths and energies (kcal/mol) for bisected and eclipsed structures of **8** (see Scheme 4 and Fig. 2).

	Bisected			Eclipsed			
Method	E_{total} (kcal/mol)	[C=O···H-C] (Å)	[C=O···H-O] (Å)	E_{total} (kcal/mol)	[C=O···H-C] (Å)	[C=O···H-O] (Å)	Relative energy ($E_{eclip} - E_{bist}$)
X-ray	—	2.535	1.68(4)	—	—	—	—
Ab initio	–470 792.80	2.574	1.565	–470 791.40	2.139	1.557	1.40
PM3	–2 812.50	2.647	1.780	–2 811.10	2.309	1.780	1.40
AM1	–2 813.50	2.554	1.974	–2 812.50	2.186	1.969	1.0

[a]Average of three calculations.

Scheme 5. Proposed mechanism for the formation of **8**.



sponding reactions with the tetrazoles **1b–1e** (containing weaker electron-donor substituents in the Ar′ moiety, Scheme 1) generate, respectively, the tetrazoles **3b–3e**, **4b–4e**, **5b–5e** and CO_2, but no **8**.

Comparison of the strength of the H-bond in **8** with those in the 2′-6′-dimethoxyflavone-carboxylic acid derivatives reported by Wallet and co-workers (4) allows for the determination of the pK_a of the flavone acid compounds (Fig. 3).

© 2004 NRC Canada

Scheme 6. Resonance forms for **8**.

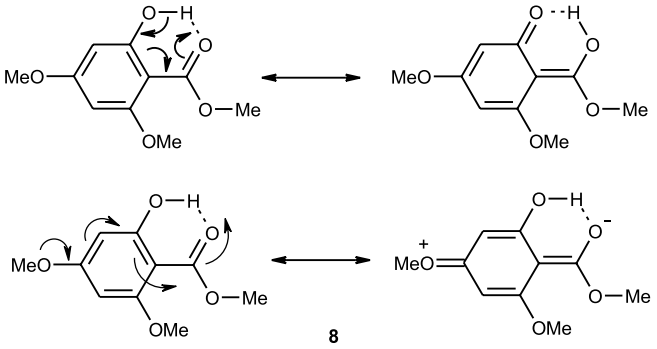
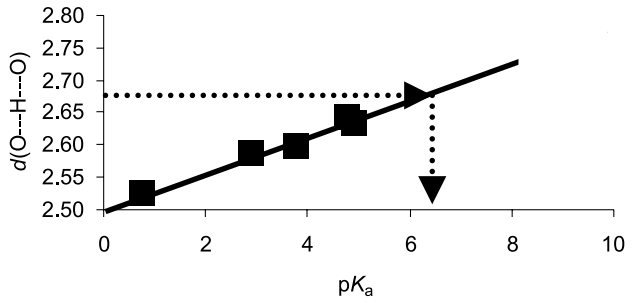


Fig. 3. Correlation of H-bond distances in 2′,6′-dimethoxyflavone-carboxylic acid adducts (O···H···O) with increasing pK_a values of trichloroacetic, chloroacetic, formic, acetic, and propionic acids (4*a*, 4*b*). Estimation of the pK_a value for **8** (···▸**).**



They used this method when the experimental pK_a determination was impractical. The estimated pK_a value for **8** is equal to ~6.4; an experimental value of 6.8 is in the range 6.5–7 determined for similar derivatives of **8** with anti-tumour properties (3).

Experimental

The key ^{1}H NMR and ^{13}C NMR data were recorded on a Bruker AV 300 (300 MHz) instrument, and the FT-IR spectra were obtained on a Shimadzu IR-470. MS data were measured on a GC–MS Fission Trio 1000 instrument (70 eV). Melting points (mp) (uncorrected) were taken on a Gallenkamp apparatus. The computational analyses were performed using HyperChem pro 6.0, with the ab initio, AM1, and PM3 calculations optimized using Polak–Ribiere or Fletcher–Reeves algorithms.

X-ray crystallographic analysis of 8

Data (see Table 1) were collected on a Rigaku/ADSC CCD instrument in 0.50° oscillations with 90.0 s exposures (with graphite-monochromated Mo-Kα radiation, 0.710 69 Å). A sweep of data was done using φ oscillations from 0.0 to 190.0° at χ = –90° and a second sweep was performed using ω oscillations between –17.0 and 23.0° at χ = –90.0°. The crystal-to-detector distance was 38.82 mm, with a detector swing angle of –5.5°. Data were corrected for Lorentz and polarization effects. Computing of data collection, cell refinement, and data reduction (see Table 1) were done using the d*TREK program (22*a*), and the structure was solved by direct methods (SIR97) (22*b*). All calculations were performed using the teXsan crystallographic software package (22*c*).

Synthesis of aryloxytetrazoles

2-Methoxycarbonyl-5-aryloxytetrazoles (aryl = 4-nitrophenyl (**1a**), 4-methylphenyl (**1b**), 4-methoxyphenyl (**1c**), 2,6-dimethylphenyl (**1d**), 2,6-dimethoxyphenyl (**1e**)) were synthesized by reported methods (21).[3]

Synthesis of methyl-2,4-dimethoxysalicylate (8)

Compound **1a** (3.8 mmol), 1,3,5-trimethoxy-benzene (3.8 mmol). and 1.5 mol equiv. of $AlCl_3$ were mixed and ground to a homogeneous powder, and heated at 100 °C for 20 min; the TLC spot for the trimethoxybenzene gradually disappeared. The mixture was then transferred to a separating funnel using 10 mL CH_2Cl_2, 10 mL H_2O, and 5 mL HCl (5%), and the organic phase was washed several times with brine. The orange organic phase was dried over $CaCl_2$ and the solvent evaporated off. The residue was passed through a silica gel column and elution with cyclohexane:ethyl acetate (95:5) gave **8** (30% yield, mp. 96–98 °C), **4a** (30% yield), **3a** (15% yield), and tetrazole **5** (25%). This procedure was repeated with tetrazoles **1b**–**1e**; the product tetrazoles **3b**–**3e** and **4b**–**4e** were detected, but there was no trace of **8**. The ^{1}H NMR and IR data for the **3b**–**4e** and **4b**–**4e** have been reported (19–21). For **8**: FT-IR (KBr, cm^{-1}): 3200–3600 (s), 2925 (m), 2800 (w), 1642 (s), 1615 (s), 1440 (m), 1380 (s), 1273 (s), 1250 (s), 1165 (s), 1119 (s), 1051 (m), 944 (w), 828 (m), 460 (s). ^{1}H NMR ($CDCl_3$): δ 3.73 (s, 3H, *p*-CH_3O), 3.74 (s, 3H, *o*-CH_3O), 3.83 (s, 3H, CH_3OCO), 5.89 (d, 1H^3, J = 8.0 Hz), 6.02 (d, 1H^5, J = 8.3 Hz), 11.91 (s, 1H, OH). ^{13}C NMR ($CDCl_3$): δ 53.48, 56.81, 57.43, 92.92, 94.88, 98.00, 163.56, 166.74, 167.22, 173.00. MS (70 eV): 212 (M^+, 40), 211.1 (72), 180.5 (92), 178.9 (100), 152.2 (36), 137.2 (40). A crystal of **8** was grown over 2 days at room temperature from a cyclohexane:CH_2Cl_2 (~4:1) solution of the compound.

Acknowledgements

We thank the Isfahan University of Technology Research Council (grant No. IUT-1CHI 821) and the Natural Sciences and Engineering Research Council of Canada (NSERC) for financial support.

References

1. (*a*) J.F.R. Epuran. French Patent 2 578 539, 1986; Chem. Abstr. **107**, 175 877w (1987); (*b*) D.W. Robertson, E.E. Beedle, J.H. Krushinski, G.D. Pollock, H. Wilson, V.L. Wyss, and J.H. Scott. J. Med. Chem. **28**, 717 (1985); (*c*) I. Leifertova and M. Lisa Folia. Pharm. (Prague), **10**, 53 (1988) [In Russian]; Chem. Abstr. **110**, 111 608p (1989); (*d*) S.A. Orysmonde. Belg. Patent, 653 214, 1965; Chem. Abstr. pc11 228a (1966).
2. T. Morimoto, Y. Hamaya, Y. Masaru, and K. Shigeo. JP Patent 63 302 513, 1988; Chem. Abstr. **110**, 224 077h (1989).

[3] H.A. Dabbagh, N. Noroozi-Pesyan, S. Takemoto, and H. Hayashi. Unpublished results.

© 2004 NRC Canada

3. K. Kreutz and A. Schlossberg. US Patent 6 395 720 B1, 2002.
4. (*a*) J.-C. Wallet, E. Molins, and C. Miravitlles. J. Phys. Org. Chem. **11**, 751 (1998); (*b*) E. Espinosa, E. Molins, and J.-C. Wallet. J. Phys. Org. Chem. **12**, 499 (1999); (*c*) J.-C. Wallet, E. Molins, and C. Miravitlles. Struct. Chem. **11**, 319 (2000).
5. (*a*) S.A. Telung. J. Org. Chem. **30**, 752 (1965); (*b*) F.E. King, J.W. Clark-Lewis, D.A.A. Kidd, and G.R. Smith. J. Chem. Soc. 4206 (1955); (*c*) S.G. Williams and F.E. Norrington. J. Am. Chem. Soc. **98**, 508 (1976).
6. L.C. King, M. McWhirter, and D.M. Barton. J. Am. Chem. Soc. **67**, 2089 (1945).
7. E. Puxeddu. Gazz. Chim. Ital. **59**, 10 (1929).
8. L.G. Shah, G.D. Shah, and R.C. Shah. J. Sci. Ind. Res. Sect. B, **15**, 159 (1956).
9. (*a*) D.S. Pratt and G.A. Perkins. J. Am. Chem. Soc. **40**, 198 (1918); (*b*) J.A. Pearl. J. Am. Chem. Soc. **68**, 2180 (1946).
10. O. Baine, G.F. Adamson, J.W. Barton, J.L. Fitch, D.R. Swayampati, and H. Jeskey. J. Org. Chem. **19**, 510 (1954).
11. A. Kreuchunas. J. Org. Chem. **21**, 910 (1956).
12. A. Kreuchunas and R. Mosher. J. Org. Chem. **21**, 589 (1956).
13. (*a*) F.S. Head and A. Robertson. J. Chem. Soc. 2434 (1930); (*b*) O.P. Jha. Indian J. Chem. **11**, 979 (1973).
14. Z. Horii, Y. Komiyama, K. Otsuki, and Y. Yamamura. J. Pharm. Soc. Jpn. **72**, 1520 (1952).
15. P. Holmes, D.E. White, and I.H. Wilson. J. Chem. Soc. 2810 (1950).
16. K.R. Hargreaves, A. McGookin, and A. Robertson. J. Appl. Chem. (London), **8**, 273 (1958).
17. K.G. Dave and K. Venkataraman. J. Sci. Ind. Res. India, **15B**, 183 (1956).
18. F.A. Carey. Organic chemistry. 2nd ed. McGraw- Hill, New York. 1992.
19. (*a*) H.A. Dabbagh and W. Lwowski. J. Org. Chem. **65**, 7284 (2000); (*b*) H.A. Dabbagh and A.R. Modarresi-Alam. J. Chem. Res. (S), 14 (2000).
20. H.A. Dabbagh and Y. Mansoori. Russ. J. Org. Chem. **37**, 1771 (2001).
21. H.A. Dabbagh, Y. Mansoori, M. Jafari, and M. Rostami. J. Chem. Res. (S), 442 (2000).
22. (*a*) d*TREK: Area detector software version 4.4 [computer program]. Molecular Structure Corporation, 3200 Research Forest Drive, The Woodlands, Tex. 1996–1998; (*b*) A. Altomare, M.C. Burla, G. Cammalli, M. Cascarano, C. Giacovazzo, A. Guagliardi, A.G.G. Moliterni, G. Polidori, and A.Spagna. J. Appl. Cryst. **32**, 115 (1999); (*c*) teXsan: Single crystal structure analysis software version 1.8 [computer program]. Molecular Structure Corporation, 3200 Research Forest Drive, The Woodlands, Tex. 1992–1997.

© 2004 NRC Canada

Fluorine chemistry — Wittig based synthesis of volatile organofluorine compounds

Pinaki S. Bhadury, Sapna Singh, Mamta Sharma, Meehir Palit, and Devendra K. Jaiswal

Abstract: A simple and practical method has been developed for the synthesis and characterization of several interesting classes of volatile organofluorine compounds from fluorophosphonium salts via their in situ generated corresponding ylides. The fluorinated phosphonium ylides react with hexafluoroacetone in DMF to generate perfluoroisobutylene, whereas in the presence of bromine or iodine containing electrophiles, tetrafluoroethylene, perfluoro-2-butene, perfluorocyclobutane, and 1*H*-heptafluoropropane are obtained.

Key words: difluoromethylene phosphonium ylides, perfluoroisobutylene, tetrafluoroethylene, perfluorocyclobutane, 1*H*-heptafluoropropane.

Résumé : On a développé une méthode simple et pratique pour synthétiser et caractériser plusieurs classes intéressantes de composés organofluorés volatils à partir de sels de fluorophosphonium, par le biais des ylures correspondants générés in situ. Les ylures de phosphonium fluorés réagissent avec l'hexafluoroacétone, dans le DMF, pour générer le perfluoroisobutylène alors que, en présence d'électrophiles contenant du brome ou de l'iode, on obtient le tétrafluoroéthylène, le perfluorobut-2-ène et le 1*H*-heptafluoropropane.

Mots clés : ylures de difluorométhylènephosphonium, perfluoroisobutylène, tétrafluoroéthylène, perfluorocyclobutane, 1*H*-heptafluoropropane.

[Traduit par la Rédaction]

Introduction

Fluorinated phosphonium salts can be generated by the reaction of tertiary phosphines and halogenated fluoroalkanes (1, 2). Metal dehalogenation of these quaternary phosphonium salts in dimethylformamide (DMF) generates in situ difluoromethylene phosphonium ylides which, on reaction with electrophilic carbonyl compounds, e.g., activated ketones and aldehydes, provide a practical route to terminal 1,1-difluoroolefins (3, 4). In the absence of suitable electrophilic substrates, the ylide decomposes into difluorocarbene ($:CF_2$) and in DMF can act as a source of fluoride ion or a combination of fluoride ion and proton (3–5). This property has been utilized by us to obtain several classes of organofluorine compounds, e.g., chlorofluorocarbon (CFC) substitutes (3), the HF addition product of fluoroolefins (6), *O*-(chlorodifluoroacylated) alcohols from fluorinated alcohols (7), and chlorohydrins from epoxides (8). Based on these results, a novel and practical procedure has been developed for the synthesis and characterization of several other interesting classes of volatile organofluorine compounds from fluorophosphonium salts and their in situ generated corresponding ylides. The compounds selected in our studies include perfluoroisobutylene, a Schedule 2 chemical under the Chemical Weapons Convention (9). We have also investigated the fate of the nucleophilic ylide in the presence of electrophiles containing positive iodine or bromine. The study has resulted in the synthesis of several synthetically and (or) industrially useful organofluorine compounds such as tetrafluoroethylene (TFE), perfluoro-2-butene (*E* and *Z*), perfluorocyclobutane, and 1*H*-heptafluoropropane (HFC-227ca). The synthesis and characterization, based on ^{1}H NMR (wherever applicable) and ^{19}F NMR and mass spectral studies, of the above-named organofluorine compounds are described in this communication.

Results and discussion

Perfluoroolefins are an important group of organofluorine compounds amongst which perfluoroisobutylene (1,1,1,3,3-pentafluoro-2-(trifluoromethyl)propene), commonly known as PFIB, has been used as a test compound for the determination of the protective properties of activated carbon in filters owing to its extreme respiratory toxicity and alleged mask-breaking properties (10, 11). Perfluoro-2-butene is an important isomer of PFIB, whereas perfluorocyclobutane has been reported as the immediate precursor of PFIB through thermal degradation (12). TFE finds several industrial appli-

Received 12 December 2003. Published on the NRC Research Press Web site at http://canjchem.nrc.ca on 25 September 2004.

P.S. Bhadury,[1] S. Singh, M. Sharma, M. Palit, and D.K. Jaiswal. Synthetic Chemistry Division, Defence Research & Development Establishment, Gwalior 474 002, India.

[1]Corresponding author (e-mail: drpsb2003@yahoo.co.in).

 doi: 10.1139/V04-058 © 2004 NRC Canada

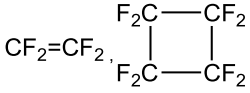
cations and has been employed as the starting monomer for the manufacture of numerous classes of commercially important organic fluoropolymers, including Teflon, Neoflon, and Viton (13). HFC-227ca can be employed as a potential CFC replacement under the Montreal Protocol (14). We have studied reactions for the preparation of the above-mentioned organofluorine compounds, for which simple and practical synthetic procedures were not readily available.

Highly volatile fluorinated olefins such as PFIB, TFE, and perfluoro-2-butene (*E* and *Z*) are, in general, known to be produced by high-temperature disproportionation of perfluorinated hydrocarbons and polymers (12, 15). While pyrolysis of fluorocarbons usually leads to complex mixtures, other methods reported require high temperature and use of corrosive materials (13). Therefore, alternate synthetic procedures to synthesize these fluoroolefins would be highly useful. In this context, the reactions of fluorinated phosphonium ylides generated in situ from quaternary salts in DMF with appropriate substrates have been investigated. Thus, difluoromethylene triphenylphosphonium ylide reacts with hexafluoroacetone (sesquihydrate) in a Wittig reaction to generate PFIB. Other compounds produced are tetrafluoroethylene from 1-bromo-2-iodotetrafluoroethane, tetrafluoroethylene and perfluorocyclobutane from 1-iodononafluorobutane, perfluoro-2-butene from 2-iodononafluorobutane, and HFC-227ca from 1-iodoperfluoropropane. We have also studied the formation of TFE from the quaternary phosphonium salt generated by the reaction of triphenylphosphine and 1-bromo-2-iodotetrafluoroethane. The syntheses of these highly volatile organofluorine compounds employing different reagent systems are summarized in Table 1. The compounds have been characterized by ^{1}H NMR, ^{19}F NMR, and mass spectral data, shown in Table 2, which were consistent with their structure and reported literature values (10, 13, 16).

The in situ ylide formation reaction in DMF has been carried out for the conversion of carbonyl compounds into the corresponding terminal 1,1-difluoroolefins. We have employed this reaction to convert several activated aromatic ketones and aldehydes into olefins (3). The Wittig reaction has now been successfully extended to yield yet another highly volatile aliphatic difluoroolefin, PFIB, a highly toxic Schedule 2 chemical.

Facile conversion of hexafluoroacetone (sesquihydrate) into PFIB has been achieved when the ketone is subjected to a Wittig reaction with difluoromethylene triphenylphosphonium ylide. The reaction is based on zinc metal dehalogenation of in situ generated (bromodifluoromethyl)triphenylphosphonium bromide salt (**I**, Scheme 1) in DMF (3). The salt was formed when an equimolar amount of dibromodifluoromethane was added all at once to a well-stirred solution of triphenylphosphine at room temperature in dry DMF. This was followed by the addition of 0.5 mol of hexafluoroacetone (sesquihydrate) to the salt solution at room temperature. Then 1 mol of zinc powder was added slowly into the reaction mixture. Within 1 to 2 min an exothermic reaction ensued due to the formation of organozinc bromide (**II**) in equilibrium with difluoromethylene triphenylphosphonium ylide (**III**). The PFIB generated was collected in a trap cooled by a liquid-nitrogen/methanol mixture. It should be noted that an initially attempted synthesis of PFIB via a Wittig reaction of the in situ generated ylide with hexafluoroacetone gas did not produce any significant amount of PFIB. This may presumably be due to the fact that anhydrous hexafluoroacetone (bp –26 °C), a low-boiling gaseous substance at ambient temperature, would have very low contact time with the reagents and may have escaped from the reaction mixture. A reported procedure in which hexafluoroacetone (sesquihydrate) was successfully used in place of anhydrous hexafluoroacetone in catalytic epoxidation of alkenes (17) led us to employ the sesquihydrate instead of hexafluoroacetone gas for generation of PFIB. This also meets the requirement that substrate be present before the addition of the zinc metal to the phosphonium salt. Although the sesquihydrate predominantly exists as a diol, presumably the equilibrium between thediol and the ketonic form is shifted towards the right in the aprotic solvent DMF. This enables the ylide to consume the ketone to yield PFIB at a rapid rate (Scheme 1). The synthetic route provides a convenient and safe method for the generation and isolation of the highly toxic compound PFIB.

Table 1. Ylide-based synthesis of organofluorine compounds.

Reagent system	Substrate	Product
$Ph_3P/CF_2Br_2/Zn$	$CF_3COCF_3 \cdot 1.5H_2O$	$(CF_3)_2C=CF_2$
$Ph_3P/CF_2Br_2/Zn$	CF_2BrCF_2I	$CF_2=CF_2$
Ph_3P/Zn	CF_2BrCF_2I	$CF_2=CF_2$
$Ph_3P/CF_2Br_2/Zn$	$CF_3CF_2CF_2CF_2I$	$CF_2=CF_2$, 
$Ph_3P/CF_2Br_2/Zn$	$CF_3CF_2CFICF_3$	$CF_3CF=CFCF_3$
$Ph_3P/CF_2Br_2/Zn$	$CF_3CF_2CF_2I$	$CF_3CF_2CF_2H$

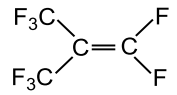
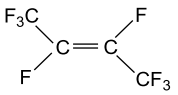
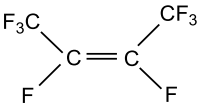
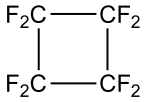
Note: GC yields are 84–96% based on starting compound; isolated yields are given in Experimental section.

For the synthesis of TFE, the substrate 1-bromo-2-iodotetrafluoroethane was added to a room temperature solution of the salt $[Ph_3P^+–CF_2Br]Br^–$, which had been generated in situ by the reaction of Ph_3P and CF_2Br_2 in DMF. This was followed by the addition of zinc metal, resulting in a highly exothermic reaction due to the formation of an organozinc halide/fluoromethylene ylide system. The nucleophilic ylide under the reaction conditions presumably abstracts the more labile positive iodine from the substrate to give a carbanion (**IV**, Scheme 2). Subsequent elimination of bromide ion from the adjacent carbon atom forms TFE. Alternatively, TFE could also be generated from the quaternary phosphonium salt $[Ph_3P^+–CF_2–CF_2Br]I^–$ (**V**, Scheme 2) obtained in situ by the reaction of Ph_3P and CF_2BrCF_2I. The organozinc halide **VI**, obtained after the addition of zinc metal, collapses spontaneously to yield TFE by the elimination of a molecule of Ph_3P from the carbon atom adjacent to the carbanion center (Scheme 2).

Similarly, when 1-iodononafluorobutane was added into a solution of the salt $[Ph_3P^+–CF_2Br]Br^–$ followed by zinc metal, a mixture of volatile products consisting of TFE and perfluorocyclobutane was generated. As the result of the nucleophilic attack of the ylide on the positive iodine of the substrate, the carbanion (**VII**, Scheme 3) is first generated. Fragmentation and fluoride ion elimination from the terminal carbon atom of the conjugated system lead to the formation of TFE. The nucleophilic attack by this carbanion on

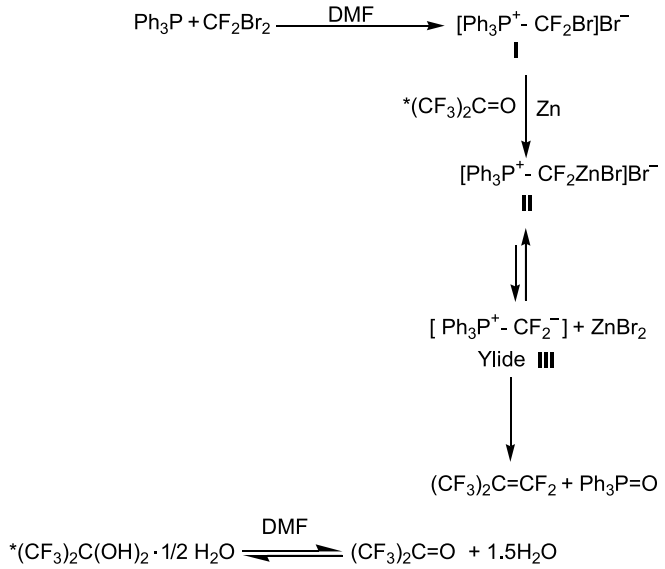
© 2004 NRC Canada

Table 2. NMR and mass spectral data of organofluorine compounds.

Compound	^{19}F NMR δ_F (ppm) Obs.	Lit.	EI-MS (*m/z*)
	–65.42 (CF_3, s, 6F) –65.39 (CF_2, s, 2F)	—	200 (M^+), 181, 150, 131, 100, 69
CF_2=CF_2	–133.8(CF_2, s, 4F)	–134.0	100 (M^+), 81, 50
	–71.1 (CF_3, m, 6F) –163.2 (F, m, 2F)	–72.0 –164.0	200 (M^+), 181, 131, 69
	–69.9 (CF_3, m, 6F) –146.3 (F, m, 2F)	–70.1 –147.3	200 (M^+), 181, 131, 69
	–135.5 (CF_2, s, 8F)	–136.0	200 (M^+), 181, 100, 81, 69
1 2 3 $CF_3CF_2CF_2H$[a]	–80.89 (CF_3, m, 3F); –133.88(CF_2, m, 2F); –140.06(CF_2H, m, 2F)	—	[b]151, 119, 101, 100, 69, 51

Note: The spectral data were consistent with the structure and reported literature values (10, 13, 16).
[a]^{1}H NMR 6.7 (CF_2H, tt, 1H, $^2J_{H-F}$ 50.84 Hz, $^3J_{H-F}$ 4.63 Hz).
[b]Negative chemical-ionization mass spectrometry (CI-MS) 169 (M – 1).

Scheme 1. Formation of perfluoroisobutylene (PFIB) from zinc dehalogenation of fluorinated phosphonium salt.



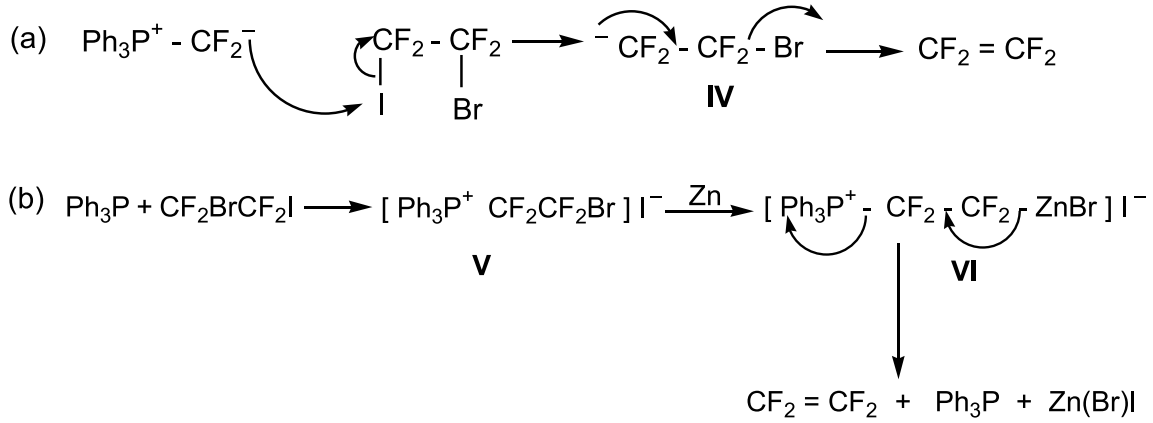
the terminal carbon atom in an S_Ni fashion can lead to the formation of perfluorocyclobutane. Fluoride ion elimination from the adjacent carbon atom generating terminal fluoroolefin (perfluoro-1-butene) seems unlikely in favor of the more stable cyclic saturated product (1). On the other hand, when the difluoromethylene triphenylphosphonium ylide was reacted with 2-iodononafluorobutane, perfluoro-2-butene (predominantly the *Z* isomer) was obtained. Here again, elimination of F^- from the carbanion (**VIII**) occurred to favor a stable internal olefin over a terminal isomer, as shown in Scheme 3.

When the ylide reaction was carried out with 1-iodoperfluoropropane, neither a perfluoroolefin nor a cyclic product was obtained. This is probably due to the fact that an S_Ni substitution would not produce a stable perfluorocycloalkane, and F^- elimination from the carbanion (**IX**, Scheme 4) would have resulted in a less stable terminal fluoroolefin, hexafluoropropene. The intermediate carbanion, therefore, instead abstracts a proton from the solvent to form a hydrofluorocarbon, 1*H*-heptafluoropropane (Scheme 4). As observed earlier (3, 6–8), the solvent DMF can provide a proton in the presence of :CF_2, which in turn is generated by the decomposition of excess ylide under the reaction conditions.

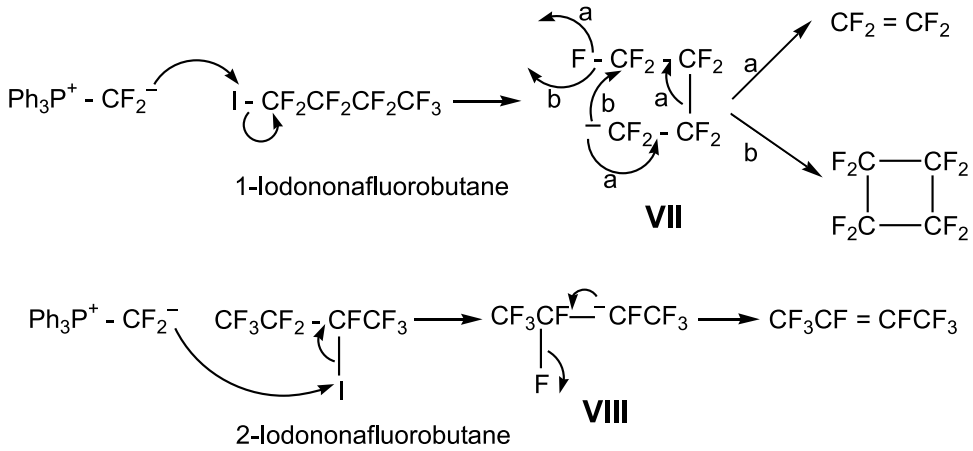
It should be noted further that control experiments involving the substrates (e.g., hexafluoroacetone (sesquihydrate), 1-bromo-2-iodotetrafluoroethane, 1-iodononafluorobutane, 2-iodononafluorobutane, and 1-iodoperfluoropropane) and CF_2Br_2 and Zn in the absence of Ph_3P did not lead to the formation of products. This shows that generation of the nucleophilic ylide Ph_3P^+–CF_2^- (**III**) is necessary either for a Wittig reaction (Scheme 1) or for the abstraction of positive iodine (Schemes 2*a*, 3, and 4) from the substrate. This observation rules out any possibility of participation by Zn in the reaction by the activation of dibromodifluoromethane. When CF_2BrCF_2I is used in place of CF_2Br_2, no ylide formation takes place, and quite understandably the inter-

© 2004 NRC Canada

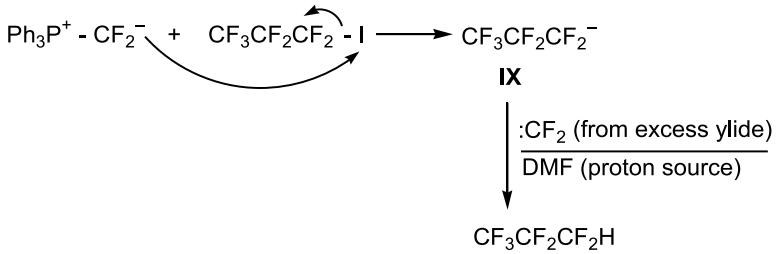
Scheme 2. Synthesis of tetrafluoroethylene (TFE) from (a) ylide and (b) quaternary phosphonium salt.



Scheme 3. Reaction of phosphonium ylides with 1- and 2-iodononafluorobutane.



Scheme 4. Formation of 1*H*-heptafluoropropane.



mediate organozinc halide (**VI**) collapses into CF_2=CF_2 (Scheme 2*b*).

It is thus observed that the above study has resulted in the synthesis of several useful organofluorine compounds. The reactions are facile and the products are generated in high yield under mild reaction conditions.

Conclusion

A facile synthesis of several interesting classes of volatile organofluorine compounds has been developed. The method essentially utilizes the Wittig based reaction of fluorophosphonium ylides generated in situ from their corresponding quaternary phosphonium salts in DMF with different substrates. Thus, facile conversion of hexafluoroacetone (sesquihydrate) into PFIB has been achieved. This synthetic route provides a convenient and safe method for the generation and isolation of the highly toxic PFIB. Other compounds prepared by this method are TFE from 1-bromo-2-iodotetrafluoroethane, perfluoro-2-butene from 2-iodononafluorobutane, TFE and perfluorocyclobutane from 1-iodononafluorobutane, and HFC-227ca from 1-iodoperfluoropropane. The procedure is simple and convenient, does not involve high-temperature reaction conditions, and is devoid of any significant side products.

Experimental

The volatile organofluorine compounds generated can be safely stored in 1- and 2-L capacity Tedlar® bags (3) procured from Supelco (Bellefonte, Pa.). Their analysis was effected either by gas-phase injection after drawing the sample

© 2004 NRC Canada

through the septum for mass spectrometry or by bubbling the gas into a NMR tube in deuterated solvent at low temperature. Reactions were monitored by gas chromatography – mass spectrometry (GC–MS), and the mass spectra were recorded on a TSQ 7000 mass spectrometer (Finnigan MAT) using a Varian 3400 GC inlet with a BP-5 column (30 m × 2.5 mm (i.d.) × 0.25 μm (film thickness)) with a temperature program of 30 °C (2 min), 120 °C at 5 °C/min, 200 °C at 200 °C/min, and 200 °C (5 min) using helium as the carrier gas at a flow rate of 1.2 mL/min. The injector temperature was 150 °C, and the transfer line was heated to 200 °C. Electron-impact ionization mass spectrometry (EI-MS) was performed at 70 eV with an ion source temperature of 150 °C and an emission current of 400 mA. Chemical-ionization mass spectrometry (CI-MS) experiments were performed using methane as a reagent gas at a pressure of 4 torr (1 torr = 133.322 Pa), a source temperature of 150 °C, and an emission current of 300 mA. The NMR spectra of fluoroolefins and fluorocarbons were recorded on a Bruker Avance DPX 400 spectrometer in acetone-d_6 solution using TMS and $CFCl_3$ as internal references for ^1H and ^{19}F NMR, respectively (3).

PFIB shows respiratory toxicity and alleged mask-breaking properties (11, 18). It is recommended that precautions taken in handling volatile toxic compounds should strictly be followed during its synthesis and handling.

Perfluoroisobutylene

Triphenylphosphine (25.2 g, 0.096 mol) was dissolved in 80 mL of dry DMF and placed in a three-necked 250-mL round-bottom flask, containing a stirring bar, at room temperature under positive nitrogen pressure. The middle neck of the flask was connected directly to a distillation device, downstream of the nitrogen flow, whose end was connected to a receiver cooled by a mixture of liquid nitrogen and methanol. Nitrogen gas was bubbled into the stirred mixture for 2 h, after which time dibromodifluoromethane (20.15 g, 0.096 mol) was added all at once and a mildly exothermic reaction occurred. The formation of (bromodifluoromethyl)triphenylphosphonium bromide salt was almost instantaneous. Then the substrate 1,1,1,3,3,3-hexafluoroacetone (sesquihydrate) (9.26 g, 0.048 mol) was added all at once into the reaction mixture at room temperature through the third neck of the flask. This was followed by slow addition of zinc powder (6.28 g, 0.096 mol) through a solid addition tube. As soon as the zinc powder addition started, an exothermic reaction began. The reaction mixture first assumed a green color; then all the zinc went into solution turning the reaction mixture colorless, and immediately after the excess zinc settled to the bottom of the flask, the reaction mixture became orange–yellow. The heat of reaction was sufficient to distill PFIB. The conversion of hexafluoroacetone (sesquihydrate) to PFIB was high under these experimental conditions as indicated by GC analysis. The product was collected in DMF at –30 to –40 °C at a purity > 98.0%.

Tetrafluoroethylene

From in situ generated ylide

Triphenylphosphine (12.6 g, 0.048 mol) was dissolved in 35 mL of dry DMF and placed in a three-necked 250-mL round-bottom flask, containing a stirring bar and equipped with a dry nitrogen inlet, at room temperature. The middle neck of the flask was connected to a condenser fitted with a $CaCl_2$ guard tube. Dibromodifluoromethane (10.08 g, 0.048 mol) was added all at once to the well-stirred solution, and a mildly exothermic reaction occurred. After stirring the mixture for another 30 min, 1-bromo-2-iodotetrafluoroethane (7.36 g, 0.024 mol) was added at room temperature. Nitrogen flow was stopped and the guard tube was replaced at this stage by an evacuated and preweighed Tedlar® bag by connecting the end of its valve stem to tubing (3/16 in. i.d.) fitted to an adapter. To open the valve, the tubing was pushed onto the stem to the appropriate overlap distance. Zinc powder (3.14 g, 0.048 mol) was then slowly added to the reaction mixture through a solid addition tube, and almost immediately a violent exothermic reaction occurred. Gaseous product could be seen evolving, and TFE gas was collected in the Tedlar® bag attached to the reaction system as described in our earlier work (3). The course of the reaction was followed by withdrawing the sample and subjecting it to GC–MS analysis. The isolated yield of TFE was 1.6 g (67%).

From quaternary phosphonium salt

In this procedure, instead of CF_2Br_2, 1-bromo-2-iodotetrafluoroethane (14.7 g, 0.048 mol) was added to a well-stirred solution of triphenylphosphine (12.6 g, 0.048 mol) dissolved in 35 mL of dry DMF. A mildly exothermic reaction occurred due to the formation of an in situ quaternary phosphonium salt. Zinc powder (3.14 g, 0.048 mol) was added through a solid addition tube. A highly exothermic reaction took place, and the volatile C_2F_4 was collected in a Tedlar® bag. Yield 3.07 g (64%).

Perfluoro-2-butene

Perfluoro-2-butene was prepared by the same procedure as described for the TFE by ylide method using the substrate 2-iodononafluorobutane (8.3 g, 0.024 mol). Yield 2.68 g (56%).

Perfluorocyclobutane along with tetrafluoroethylene

The volatile products $CF_2{=}CF_2$ and perfluorocyclobutane were generated by the same procedure as above but using the substrate 1-iodononafluorobutane (8.3 g, 0.024 mol) and were collected in a Tedlar® bag. GC yield 96% (ratio of perfluorocyclobutane:C_2F_4 = 51:49 by GC).

1*H*-Heptafluoropropane

For the synthesis of this hydrofluorocarbon, the substrate 1-iodoperfluoropropane (7.1 g, 0.024 mol) was added to the in situ generated quaternary phosphonium salt obtained by the reaction of Ph_3P and CF_2Br_2 in DMF. The gaseous product ($CF_3CF_2CF_2H$) generated after the addition of Zn metal was collected in a Tedlar® bag. Yield 2.57 g (63%).

Acknowledgements

We thank Mr. K. Sekhar, Director, Defence Research & Development Establishment (DRDE), Gwalior, for his keen interest in the work. Sapna Singh thanks the Defence

© 2004 NRC Canada

Research & Development Organisation (DRDO) for providing financial assistance in the form of a research fellowship.

References

1. D.J. Burton. Chem. Rev. **96**, 1641 (1996).
2. D.J. Burton. J. Fluorine Chem. **100**, 177 (1999).
3. P.S. Bhadury, M. Palit, M. Sharma, S.K. Raza, and D.K. Jaiswal. J. Fluorine Chem. **116**, 75 (2002).
4. P.S. Bhadury. Ph.D. thesis, Jiwaji University, Gwalior, India. 2002.
5. D.J. Burton and D.M. Wiemers. J. Am. Chem. Soc. **107**, 5014 (1985).
6. P.S. Bhadury, B.P. Pant, M. Palit, and D.K. Jaiswal. J. Fluorine Chem. **85**, 115 (1997).
7. P.S. Bhadury, M. Palit, M. Sharma, S.K. Raza, and D. K. Jaiswal. J. Fluorine Chem. **113**, 47 (2002).
8. S. Singh, P.S. Bhadury, and D.K. Jaiswal. 39th Annual Convention of Chemists, Nagarjunanagar, Andhra Pradesh, India. 22–26 December 2002.
9. W. Krutzsch and R. Trapp. *In* A commentary on the chemical weapons convention. Martinus Nijhoff, Dordrecht, The Netherlands. 1994. p. 255.
10. C.M. Erasmus, C.A. Barnardt, M. Wentzel, and E.H. Cowley. *In* Proceedings of the 5th international symposium for protection against chemical and biological agents. Stockholm, Sweden, 11–16 June 1995. p. 201.
11. M.C. Biesinger, N.S. McIntyre, S.J. Splinter, and S. Liang. Carbon, **35**, 463 (1997).
12. T.J. Brice, J.D. Lazerte, L.J. Hals, and W.H. Pearlson. J. Am. Chem. Soc. **75**, 2698 (1953).
13. M. Hudlicky and A.E. Pavlath. (*Editors*). Chemistry of organic fluorine compounds II: A critical review, American Chemical Society, Washington, D.C. 1995.
14. A. McCulloch. J. Fluorine Chem. **100**, 163 (1999).
15. J.S. Marhevka, G.D. Johnson, and D.F. Hagen. Anal. Chem. **54**, 2607 (1982).
16. V. Wray and G.A. Webb. (*Editors*). Annual reports on NMR spectroscopy. Vol. 10B. Academic Press, New York. 1980.
17. J. Biloski, R.P. Heggs, and B. Ganem. Synthesis, p. 810 (1980).
18. G.L. Kennedy, Jr., and R.J. Geisen. J. Occup. Med. **27**, 675 (1985).

© 2004 NRC Canada

Green preparation of quinoline derivatives through $FeCl_3 \cdot 6H_2O$ catalyzed Friedlander reaction in ionic liquids

Jianji Wang, Xuesen Fan, Xinying Zhang, and Lijun Han

Abstract: The preparation of substituted quinoline derivatives through a Friedlander condensation reaction utilizing the ionic liquid [bmim][BF_4] as the reaction medium and iron chloride hexahydrate ($FeCl_3 \cdot 6H_2O$) as a catalyst is described. The advantages in using this method include its environmental friendliness, simple operating process in both mild and neutral reaction conditions, and good yields.

Key words: ionic liquid, Friedlander reaction, quinoline derivatives, green chemistry.

Résumé : On décrit l'utilisation du [bmim][BF_4], un liquide ionique, comme milieu réactionnel et de l'hexahydrate du chlorure de fer ($FeCl_3 \cdot 6H_2O$) comme catalyseur pour la préparation de dérivés de quinoléines substituées par la réaction de condensation de Friedlander. Cette méthode présente l'avantage d'être bénigne pour l'environnement, d'impliquer un processus d'opération simple, de se faire dans des conditions douces et neutres et de donner de bons rendements.

Mots clés : liquide ionique, réaction de Friedlander, dérivés de la quinoléine, chimie verte.

[Traduit par la Rédaction]

Introduction

For many years, the synthesis of quinoline and its derivatives has been of considerable interest in organic and medicinal chemistry since a large number of natural products and drugs contain this heterocyclic nucleus (1). While versatile methods for the synthesis of the quinoline ring system have been developed (2), many of them suffer from harsh reaction conditions, poor yields, and (or) the use of expensive catalysts. Thus, simple, general, and efficient procedures for the synthesis of this important heterocycle are still in demand.

As one of the most frequently used pathways to prepare quinoline derivatives, Friedlander synthesis involves a condensation of 2-aminobenzaldehyde with an aldehyde, ketone, or polyfunctional carbonyl compound having a reactive α-methylene group (3). This classical process is usually carried out either by refluxing an aqueous or alcoholic solution of the reactants in the presence of a base or by heating a mixture of substrates at temperatures ranging from 150 to 220 °C in the absence of solvent and catalyst to produce the corresponding 2- and 3-substituted quinolines in moderate yields. Unfortunately, attempts to extend this method to the preparation of 4-substituted quinolines from 2-aminoaryl ketones appear to have met with very limited success. Subsequent studies showed that problems resulting from the classical Friedlander procedure can be overcome by using acid catalysis. For example, it has been reported that drops of concentrated sulfuric acid or 6 mol/L hydrochloric acid can be used as efficient catalysts in the Friedlander condensation procedure (4). With this method, various structurally varied substrates, including 2-aminobenzophenone, can give the corresponding quinolines in moderate to high yields. However, this method still has some drawbacks, notably use of very strong acids as the catalyst, use of excessive glacial acetic acid as the solvent, or even requiring the use of a metal bath that can maintain a reaction temperature as high as 200 °C, thus making this method unsuitable for scale up in an environmentally benign and economical way.

Room temperature ionic liquids based on the 1,3-dialkylimidazolium cation are attracting increasing interest as alternative reaction media. The desirable advantages of ionic liquids, include their lack of vapor pressure, wide liquid range, and thermal stability, have made them exceptional reaction media as well as environmentally benign solvents in organic synthesis (5). In line with our research program of using ionic liquids as novel reaction media in organic reactions (6), we wish to report here a novel and efficient procedure for the preparation of quinolines through a Friedlander reaction catalyzed by $FeCl_3 \cdot 6H_2O$ in an ionic liquid (Scheme 1).

Received 6 January 2004. Published on the NRC Research Press Web site at http://canjchem.nrc.ca on 25 September 2004.

J. Wang,[1] X. Fan, X. Zhang, and L. Han. School of Chemical and Environmental Sciences, Key Laboratory of Environmental Science and Engineering for Colleges and Universities of Henan Province, Henan Normal University, Xinxiang, Henan 453002, P. R. China.

[1]Corresponding author (e-mail: jwang@henannu.edu.cn).

Results and discussion

We set out to examine the Friedlander reaction in one of the most widely used ionic liquids, 1-butyl-3-methylimidazolium tetrafluoroborate ([bmim][BF_4]), using

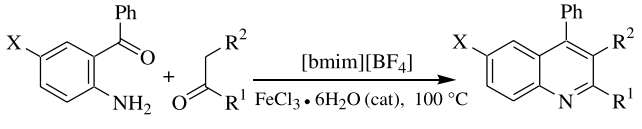
 doi: 10.1139/V04-066 © 2004 NRC Canada

Table 1. Friedlander reaction of 2-aminobenzophenone and acetophenone in different catalytic systems.

Entry	Solvent	Catalyst	Amount of catalyst (mmol)	Reaction temp. (°C)	Reaction time (h)	Isolated yield (%)
1	[bmim][BF_4]	None	0	RT	10	0
2	[bmim][BF_4]	None	0	100	10	9
3	[bmim][BF_4]	$FeCl_3{\cdot}6H_2O$	0.1	100	10	41
4	[bmim][BF_4]	$FeCl_3{\cdot}6H_2O$	0.3	100	10	65
5	[bmim][BF_4]	$FeCl_3{\cdot}6H_2O$	0.5	100	10	78
6	[bmim][BF_4]	$FeCl_3{\cdot}6H_2O$	0.5	100	6	75
7	[bmim][BF_4]	$FeCl_3$	0.5	100	6	74
8	Toluene	$FeCl_3{\cdot}6H_2O$	0.5	100	6	62
9	EtOAc	$FeCl_3{\cdot}6H_2O$	0.5	reflux	6	68
10	THF	$FeCl_3{\cdot}6H_2O$	0.5	reflux	6	8
11	Ethanol	$FeCl_3{\cdot}6H_2O$	0.5	reflux	6	26

Note: Reaction conditions: 1 mL solvent, 1 mmol 2-aminobenzophenone, and 1 mmol acetophenone.

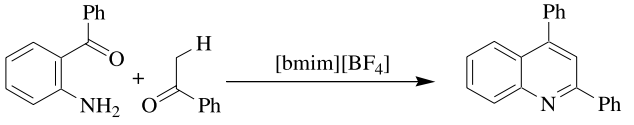
Scheme 1.



1 **2** **3**

(X = H, Cl)

Scheme 2.



1a **2a** **3a**

2-aminobenzophenone (Scheme 2, **1a**) and acetophenone (**2a**) as the starting materials.

Firstly, the mixture of **1a** (1 mmol) and **2a** (1mmol) in 1 mL of [bmim][BF_4] was stirred at room temperature for 10 h, but no reaction took place as indicated by TLC (Table 1, entry 1). Then, the mixture was heated at 100 °C. To our delight, the desired condensation reaction eventually took place but in a rather sluggish way. In fact, after being stirred at 100 °C for more than 10 h, the mixture produced the corresponding quinoline product in less than 10% yield (Table 1, entry 2). This means that while the ionic liquid [bmim][BF_4] itself possesses some catalytic activity for this condensation process, the activity is too low to give the product in a reasonable yield. Bearing in mind that $FeCl_3{\cdot}6H_2O$ has been successfully used as an environmentally benign and efficient Lewis acid catalyst for promoting several kinds of reactions (7), we then added catalytic amounts of $FeCl_3{\cdot}6H_2O$ to the reaction mixture. Fortunately, the expected product was obtained with a much improved yield (Table 1, entry 3). Further studies showed that the yield could be increased to as high as 75% within 6 h when 0.5 mmol of $FeCl_3{\cdot}6H_2O$ was used (Table 1, entry 6). However, any excess use of $FeCl_3{\cdot}6H_2O$ beyond this amount did not show any further increase in yield.

As for the possible mechanism of this catalytic reaction, we believe that the Lewis acidity of Fe(III) ion in $FeCl_3{\cdot}6H_2O$ has played an important role in the promotion of this condensation process. In order to clarify the role of Fe(III) ion and the hydration water of $FeCl_3{\cdot}6H_2O$, anhydrous $FeCl_3$ was also tried as the catalyst for this reaction, and it gave similar results compared with $FeCl_3{\cdot}6H_2O$ (Table 1, entry 7). At this stage, it may be safe to say that it is the Fe(III) ion rather than Fe(III) ion together with the hydration water in $FeCl_3{\cdot}6H_2O$ that acts as the real catalyst in this condensation process. Of the two Fe(III) salts used, although anhydrous $FeCl_3$ exhibited a similar catalytic activity for this reaction when compared with $FeCl_3{\cdot}6H_2O$, the latter is preferred because of its higher solubility in ionic liquid, ease in handling, and lower price.

In addition, the use of several conventional organic solvents, specifically toluene, tetrahydrofuran (THF), ethyl acetate (EtOAc), and ethanol, in this catalytic process were also studied for the sake of comparison with [bmim][BF_4]. The results are also shown in Table 1. It has been shown that of the five solvents used, [bmim][BF_4] gave the highest yield for the desired product under similar reaction conditions. Thus, the use of [bmim][BF_4] as the reaction medium not only avoids the disadvantages of conventional organic solvents, such as volatility, inflammability, and potential pollution hazards, but it also results in greatly enhanced reactivity.

Based on the above results, this process was then extended to other structurally varied substrates to investigate its scope and generality. The results collected are listed in Table 2. It can be seen that under similar conditions, a wide range of ketones containing a reactive α-methylene group can undergo easy condensation with 2-aminobenzophenones to give substituted quinolines with fast reaction times and in reasonably high yields. It is worthwhile noting that both aliphatic and aromatic-aliphatic ketones gave corresponding quinoline products in almost equally fair yields. With unsymmetrical ketone substrates of the type CH_3COCH_2R, from which two different modes of cyclization are theoretically possible, condensation occurred predominantly at the more highly substituted alpha position and thus only one product was obtained (Table 2, entry 13). In addition, higher

© 2004 NRC Canada

Table 2. Preparation of quinoline derivatives through Friedlander reaction catalyzed by $FeCl_3 \cdot 6H_2O$ in ionic liquid.

Entry	X	R^1	R^2	Reaction temp. (°C)	Reaction time (h)	Products	Isolated yield (%)
1	H	C_6H_5	H	100	6	**3a**	75
2	H	4-BrC_6H_4	H	100	6	**3b**	84
3	H	4-$NO_2C_6H_4$	H	100	6	**3c**	89
4	H	CH_3	H	40	8	**3d**	75
5	H	-$(CH_2)_3^-$		100	5	**3e**	74
6	H	-$(CH_2)_4^-$		100	5	**3f**	75
7	Cl	C_6H_5	H	100	6	**3g**	82
8	Cl	4-BrC_6H_4	H	100	6	**3h**	85
9	Cl	4-ClC_6H_4	H	100	6	**3i**	85
10	Cl	4-$CH_3C_6H_4$	H	100	6	**3j**	80
11	Cl	4-$NO_2C_6H_4$	H	100	6	**3k**	92
12	Cl	CH_3	H	40	8	**3l**	78
13	Cl	CH_3	CH_3	60	8	**3m**	73
14	Cl	C_2H_5	CH_3	60	8	**3n**	74
15	Cl	-$(CH_2)_3^-$		100	5	**3o**	70
16	Cl	-$(CH_2)_4^-$		100	5	**3p**	72

yields were obtained using 4-nitroacetophone (Table 2, entries 3 and 11), showing that the yields of quinolines are to some extent affected by the nature of the substituents attached to the aromatic ring of the ketone.

Our attention was then directed toward the possibility of recycling the reaction media since recovery and reuse of the catalyst and solvent are highly preferable for a greener process. At completion, the reaction mixture was diluted with water and extracted with diethyl ether to obtain the desired product. Meanwhile, due to its much higher solubility in water and ionic liquid than in diethyl ether, Fe(III) ion was left and immobilized in [bmim][BF_4]. After removal of water under reduced pressure, [bmim][BF_4] together with the catalyst could be recovered almost quantitatively. Then, their reusability was investigated by using 2-aminobenzophenone and acetophenone as model substrates. It was observed that even in the sixth recycle, reuse of the ionic liquid and the catalyst recovered from the fifth recycle still gave the corresponding product in fairly good yield (Table 3, Recycle no. 6).

In conclusion, [bmim][BF_4] was proved to be a useful and alternative reaction medium, and $FeCl_3 \cdot 6H_2O$ was found to be an efficient catalyst for the preparation of quinolines. The simple experimental and product isolation procedures, combined with ease of recovery and reuse of the catalyst and the reaction media, are expected to contribute to the development of greener and waste free chemical processes for the preparation of quinolines with biological activity. Further studies to develop other new uses for ionic liquid in the preparation of heterocyclic compounds are now in progress in our laboratory.

Experimental

Melting points were measured using a Kofler micro melting point apparatus and were uncorrected. IR spectra were recorded for KBr pellets on a Bruker Vector 22 spectrometer with absorptions given in cm^{-1}. ^1H NMR spectra were obtained with a Bruker AC 400 spectrometer using $CDCl_3$ as the solvent. Chemical shifts (δ) were expressed in ppm downfield from an internal tetramethylsilane standard and coupling constants (*J*) were given in Hz. Mass spectra were recorded on a HP-5989B mass spectrometer. Elemental analyses were performed on an EA-1110 (CE Instruments) instrument.

Table 3. Reusability of both [bmim][BF_4] and catalyst.

Recycle no.	Ionic liquid recovered (%)	Isolated yield of **3a** (%)[a]
1	99	75
2	98	78
3	99	77
4	99	75
5	98	73
6	97	69

[a]Reaction conditions: reaction time 6 h at 100 °C.

The ionic liquid [bmim][BF_4] was prepared and purified according to a literature procedure (8). All other reagents were reagent grade and were used without further purification.

General procedure for the preparation of quinoline derivatives

2-Aminobenzophenone (**1**, 1 mmol), ketone (**2**, 1 mmol) and $FeCl_3 \cdot 6H_2O$ (0.5 mmol) were added to a 10-mL round-bottom flask containing 1 mL of [bmim][BF_4]. The mixture was then stirred at 100 °C for a certain period of time to ensure complete reaction (monitored by TLC). At completion, the reaction mixture was diluted with water (5 mL) and ex-

© 2004 NRC Canada

tracted with ethyl ether (3 × 10 mL). After drying, the combined ether layers were concentrated under reduced pressure and the resulting residue was charged on a silica gel column and eluted with a mixture of ethyl acetate/*n*-hexane (1:8) to obtain product **3**. All products were fully characterized by IR, ^{1}H NMR, MS, and elemental analysis. The aqueous solution of ionic liquid and catalyst was concentrated at reduced pressure to recover the ionic liquid and catalyst for subsequent reuse.

2,4-Diphenylquinoline (3a)

mp 110–111 °C (lit. (9) 112–113 °C). ^{1}H NMR (400 MHz, $CDCl_3$) δ: 8.26 (d, 1H, J = 8.4 Hz), 8.19–8.22 (m, 2H), 7.91 (dd, 1H, J_1 = 8.4 Hz, J_2 = 1.2 Hz), 7.83 (s, 1H), 7.72–7.76 (m, 1H), and 7.47–7.59 (m, 9H). MS *m/z* (%): 281 (M^+, 70), 280 (M^+ – 1, 100), 202 (9), and 139 (8).

2-(4-Bromophenyl)-4-phenylquinoline (3b)

mp 128–129 °C. IR ν (cm^{-1}) : 3050, 1610, and 1590. ^{1}H NMR (400 MHz, $CDCl_3$) δ: 8.23 (d, 1H, J = 8.0 Hz), 8.08–8.11 (m, 2H), 7.90 (d, 1H, J = 8.0 Hz), 7.72–7.78 (m, 2H), 7.64–7.67 (m, 2H), and 7.47–7.59 (m, 6H). MS *m/z* (%): 361 (M^+ +2, 89), 359 (M^+, 100), 278 (40), 202 (17), and 139 (25). Anal. calcd. for $C_{21}H_{14}BrN$: C 70.01, H 3.92, and N 3.89; found: C 69.85, H 3.88, and N 3.73.

2-(4-Nitrophenyl)-4-phenylquinoline (3c)

mp 162–163 °C (lit. (9) 156–161 °C). IR ν (cm^{-1}): 3061, 1620, and 1595. ^{1}H NMR (400 MHz, $CDCl_3$) δ: 8.37–8.42 (m, 4H), 8.31 (d, 1H, J = 8.0 Hz), 7.96 (d, 1H, J = 8.0 Hz), 7.87 (s, 1H), 7.80 (t, 1H, J = 8.0 Hz), and 7.54 –7.59 (m, 6H). MS *m/z* (%): 326 (M^+, 100) and 202 (23). Anal. calcd. for $C_{21}H_{14}N_2O_2$: C 77.29, H 4.32, and N 8.58; found: C 77.15, H 4.48, and N 8.63.

2-Methyl-4-phenylquinoline (3d)

mp 93–95 °C (lit. (10) 92–94 °C). IR ν (cm^{-1}): 3057, 2971, 1617, and 1485. ^{1}H NMR (400 MHz, $CDCl_3$) δ: 8.09 (d, 1H, J = 8.4 Hz), 7.85 (dd, 1H, J_1 = 8.4 Hz, J_2 = 0.8 Hz), 7.66–7.70 (m, 1H), 7.45–7.55 (m, 5H), 7.40–7.45 (m, 1H), 7.22 (s, 1H), and 2.77 (s, 3H). MS *m/z* (%): 219 (M^+, 100), 204 (14), and 176 (10). Anal. calcd. for $C_{16}H_{13}N$: C 87.64, H 5.98, and N 6.39; found: C 87.48, H 6.12, and N 6.46.

2,3-Dihydro-9-phenyl-1H-cyclopenta[b]-quinoline (3e)

mp 104–105.5 °C (lit. (4) 134– 135 °C). IR ν (cm^{-1}) : 3011, 2968, 1610, and 1455. ^{1}H NMR (400 MHz, $CDCl_3$) δ: 8.06–8.08 (m, 1H), 7.60–7.64 (m, 2H), 7.45–7.55 (m, 3H), 7.35–7.40 (m, 3H), 3.24 (t, 2H, J = 8.0 Hz), 2.91 (t, 2H, J = 8.0 Hz), and 2.13–2.21 (m, 2H). MS *m/z* (%): 245 (M^+, 100), 217 (9), and 168 (14). Anal. calcd. for $C_{18}H_{15}N$: C 88.13, H 6.16, and N 5.71; found: C 88.18, H 6.02, and N 5.86.

1,2,3,4-Tetrahydro-9-phenylacridine (3f)

mp 131–133 °C (lit. (4) 142–143 °C). IR ν (cm^{-1}) : 3020, 2978, 1600, and 1495. ^{1}H NMR (400 MHz, $CDCl_3$) δ: 8.06 (d, 1H, J = 8.0 Hz), 7.59–7.64 (m, 1H), 7.43–7.55 (m, 3H), 7.28–7.34 (m, 4H), 3.23 (t, 2H, J = 8.0 Hz), 2.59 (t, 2H, J = 8.0 Hz), 1.94–2.00 (m, 2H), and 1.76–1.83 (m, 2H). MS *m/z* (%): 259 (M^+, 100), 230 (12), and 182 (6). Anal. calcd. for $C_{18}H_{17}N$: C 87.99, H 6.61, and N 5.40; found: C 88.07, H 6.52, and N 5.48.

6-Chloro-2,4-diphenylquinoline (3g)

mp 130–132 °C (lit. (11) 130–131 °C). IR ν (cm^{-1}): 3050, 1610, and 1589. ^{1}H NMR (400 MHz, $CDCl_3$) δ: 8.11–8.15 (m, 3H), 7.82 (d, 1H, J = 2.2 Hz), 7.76 (s, 1H), 7.59–7.60 (m, 2H), and 7.45–7.50 (m, 7H). MS *m/z* (%): 317 (M^+ + 2, 33), 315 (M^+, 100), and 280 (32). Anal. calcd. for $C_{21}H_{14}ClN$: C 79.87, H 4.47, and N 4.44; found: C 79.95, H 4.43, and N 4.35.

6-Chloro-2-(4-bromophenyl)-4-phenylquinoline (3h)

mp 174–176 °C (lit. (11) 174–175 °C). IR ν (cm^{-1}): 3061, 1600, and 1590. ^{1}H NMR (400 MHz, $CDCl_3$) δ: 8.14 (d, 1H, J = 8.8 Hz), 8.07 (d, 2H, J = 8.8 Hz), 7.85 (d, 1H, J = 2.2 Hz), 7.79 (s, 1H), 7.64–7.68 (m, 3H), and 7.54–7.58 (m, 5H). MS *m/z* (%): 397 (M^+ + 4, 26), 395 (M^+ + 2, 100), 393 (M^+, 79), and 358 (18). Anal. calcd. for $C_{21}H_{13}BrClN$: C 63.90, H 3.32, and N 3.55; found: C 63.85, H 3.21, and N 3.53.

6-Chloro-2-(4-chlorophenyl)-4-phenylquinoline (3i)

mp 164–166 °C (lit.(11) 159–160 °C). IR ν (cm^{-1}): 3058, 1605, and 1587. ^{1}H NMR (400 MHz, $CDCl_3$) δ: 8.26 (d, 1H, J = 8.4 Hz), 8.15 (d, 2H, J = 8 Hz), 7.87 (d, 1H, J = 2.2 Hz), 7.80 (s, 1H), 7.68–7.71 (m, 1H), and 7.50–7.59 (m, 7H). MS *m/z* (%): 353 (M^+ + 4, 12), 351 (M^+ + 2, 65), 349 (M^+, 100), and 314 (34). Anal. calcd. for $C_{21}H_{13}Cl_2N$: C 72.02, H 3.74, and N 4.00; found: C 72.07, H 3.71, and N 4.03.

6-Chloro-2-(4-methylphenyl)-4-phenylquinoline (3j)

mp 132–134 °C (lit.[1]1 132–133). IR ν (cm^{-1}): 3048, 1600, and 1580. ^{1}H NMR (400 MHz, $CDCl_3$) δ: 8.20 (d, 1H, J = 8.4 Hz), 8.09 (d, 2H, J = 8.0 Hz), 7.85 (d, 1H, J = 3.5 Hz), 7.82 (s, 1H), 7.67–7.64 (m, 1H), 7.57–7.52 (m, 5H), 7.33 (d, 2H, J = 8.0 Hz), and 2.43 (s, 3H). MS *m/z* (%): 331 (M^+ + 2, 34), 329 (M^+, 100), and 294 (23). Anal. calcd. for $C_{22}H_{16}ClN$: C 80.11, H 4.89, and N 4.25; found: C 80.25, H 4.78, and N 4.33.

6-Chloro-2-(4-nitrophenyl)-4-phenylquinoline (3k)

mp 218–220 °C. IR ν (cm^{-1}): 3038, 1610, and 1525. ^{1}H NMR (400 MHz, $CDCl_3$) δ: 8.34–8.38 (m, 4H), 8.20 (d, 1H, J = 8.0 Hz), 7.90 (d, 1H, J = 2.4 Hz), 7.88 (s, 1H), 7.23 (dd, 1H, J_1 = 9.2 Hz, J_2 = 2.4 Hz), and 7.54–7.60 (m, 5H). MS *m/z* (%): 362 (M^+ + 2, 34), 360 (M^+, 100), 314 (40), 278 (32), and 139 (20). Anal. calcd. for $C_{21}H_{13}ClN_2O_2$: C 69.91, H 3.63, and N 7.76; found: C 69.94, H 3.68, and N 7.59.

6-Chloro-2-methyl-4-phenylquinoline (3l)

mp 88–90 °C. IR ν (cm^{-1}): 3050, 2978, 1610, and 1496. ^{1}H NMR (400 MHz, $CDCl_3$) δ: 8.02 (d, 1H, J = 9.2 Hz), 7.82 (d, 1H, J = 2.4 Hz), 7.62 (dd, 1H, J_1 = 9.2 Hz, J_2 = 2.4 Hz), 7.46–7.57 (m, 5H), 7.24 (s, 1H), and 2.77 (s, 3H). MS *m/z* (%): 255 (M^+ + 2, 32), 253 (M^+, 100), 218 (40), and 176 (11). Anal. calcd. for $C_{16}H_{12}ClN$: C 75.74, H 4.77, and N 5.52; found: C 75.88, H 4.62, and N 5.63.

6-Chloro-2,3-dimethyl-4-phenylquinoline (3m)

mp 121–124 °C. IR ν (cm^{-1}): 3035, 2959, 1610, and 1459. ^{1}H NMR (400 MHz, $CDCl_3$) δ: 7.95 (d, 1H, J = 9.2 Hz),

© 2004 NRC Canada

7.47–7.56 (m, 4H), 7.27 (d, 1H, J = 2.4 Hz), 7.20–7.23 (m, 2H), 2.74 (s, 3H), and 2.17 (s, 3H). MS *m/z* (%): 269 (M^+ + 2, 33), 267 (M^+, 100), 232 (32), 217 (15), 189 (18), and 94 (6). Anal. calcd. for $C_{17}H_{14}ClN$: C 76.26, H 5.27, and N 5.23; found: C 76.38, H 5.32, and N 5.16.

6-Chloro-2-ethyl-3-methyl-4-phenylquinoline (3n)

mp 139–141 °C. IR ν (cm^{-1}): 3025, 2950, 1621, and 1493. ^1H NMR (400 MHz, $CDCl_3$) δ: 7.99 (d, 1H, J = 8.8 Hz), 7.46–7.55 (m, 4H), 7.22–7.26 (m, 3H), 3.05 (q, 2H, J = 7.2 Hz), 2.20 (s, 3H), and 1.41 (t, 3H, J = 7.2 Hz). MS *m/z* (%): 283 (M^+ + 2, 34), 281 (M^+, 100), 217 (9), 189 (7), and 115 (5). Anal. calcd. for $C_{18}H_{16}ClN$: C 76.72, H 5.72, and N 4.97; found: C 76.74, H 5.80, and N 4.88.

6-Chloro-2,3-Dihydro-9-phenyl-1H-cyclopenta[b]-quinoline (3o)

mp 94–96 °C. IR ν (cm^{-1}): 3035, 2970, 1610, and 1486. ^1H NMR (400 MHz, $CDCl_3$) δ: 7.99 (d, 1H, J = 8.8 Hz), 7.46–7.58 (m, 5H), 7.32–7.35 (m, 2H), 3.20 (t, 2H, J = 8.0 Hz), 2.90 (t, 2H, J = 8.0 Hz), and 2.13–2.20 (m, 2H). MS *m/z* (%): 281 (M^+ + 2, 33), 279 (M^+, 100), 244 (95), 202 (11), and 120 (12). Anal. calcd. for $C_{18}H_{14}ClN$: C 77.28, H 5.04, and N 5.01; found: C 77.40, H 5.02, and N 4.96.

6-Chloro-1,2,3,4-tetrahydro-9-phenylacridine (3p)

mp 163.5–165 °C. IR ν (cm^{-1}): 3038, 2975, 1605, and 1488. ^1H NMR (400 MHz, $CDCl_3$) δ: 7.95 (1H, d, J = 8.8 Hz), 7.48–7.56 (m, 4H), 7.28 (1H, d, J = 2.4 Hz), 7.20–7.22 (m, 2H), 3.18 (t, 2H, J = 6.4 Hz), 2.59 (t, 2H, J = 6.4 Hz), 1.93–1.98 (m, 2H), and 1.77–1.82 (m, 2H). MS *m/z* (%): 295 (M^+ + 2, 35), 293 (M^+, 100), 258 (59), 230 (9), and 121 (8). Anal. calcd. for $C_{19}H_{16}ClN$: C 77.68, H 5.49, and N 4.77; found: C 77.55, H 5.42, and N 4.68.

Acknowledgement

This work was financially supported by the National Natural Science Foundation of China under NSFC grant No. 20273019 and the Research Foundation of Henan Normal University (No. 200303).

References

1. (*a*) A.R. Katritzky and C.N. Rees. *In* Comprehensive heterocyclic chemistry. *Edited by* A.J. Boulton and A. McKillop. Vol. 2. Pergamon Press, Oxford. 1984; (*b*) T.L. Gilchist. Heterocyclic chemistry. Longmans, London. 1997.
2. (*a*) G. Jones. *In* Comprehensive heterocyclic chemistry. *Edited by* A.R. Katritzky, C.W. Rees, and R.F.V. Scriven. Vol. 5. Pergamon Press, Oxford. 1996. Chap. 5.05. p. 167; (*b*) H. Tokuyama, M. Sato, T. Ueda, and T. Fukuyama. Heterocycles, **54**, 105 (2001); (*c*) N.J. Ton and E.M. Ruel. Synthesis, 1351 (2001).
3. (*a*) P. Friedlander. Ber. **15**, 2572 (1882); (*b*) R.C. Elderfield. *In* The chemistry of heterocyclic compounds. *Edited by* R.C. Elderfield. Vol. 4. John Wiley & Sons, New York. 1952.
4. E.A. Fehnel. J. Org. Chem. **31**, 2899 (1966).
5. (*a*) J. Dupont, R.F. de Souza, and P.A.Z. Suarez. Chem. Rev. **102**, 3667 (2002); (*b*) D.B. Zhao, M. Wu, Y. Kou, and E.Z. Min. Catal. Today, **74**, 157 (2002); (*c*) H. Olivier-Bourbigou and L. Magna. J. Mol. Catal. A, **182**–**183**, 419 (2002); (*d*) T. Welton. Chem. Rev. **99**, 2071 (1999); (*e*) Z. Li and C.G. Xia. Tetrahedron Lett. **44**, 2069 (2003); (*f*) J.S. Yadav, B.V.B. Reddy, A.K. Basak, and A. Venkat Narsaiah. Tetrahedron Lett. **44**, 1047 (2003).
6. (*a*) X. Zhang, H. Niu, and J. Wang. J. Chem. Res. (S) 33 (2003); (*b*) X. Zhang, X. Fan, H. Niu, and J. Wang. Green Chem. **5**, 267 (2003).
7. (*a*) J. Christoffers. J. Chem. Soc., Perkin Trans. 1, 3141 (1997); (*b*) J. Lu, H.R. Ma, and W.H. Li. Chin. J. Org. Chem. **20**, 815 (2000).
8. J.D. Holbrey and K.R. Seddon. J. Chem. Soc., Dalton Trans. 2133 (1999).
9. R. Leardini, D. Nanni, A. Tundo, G. Zanardi, and F. Ruggieri. J. Org. Chem. **57**, 1842 (1992).
10. M. Al-Talib, J.C. Jochims, Q. Wang, A. Hamed, and A.E. Ismail. Synthesis, 875 (1992).
11. Y. Toi, K. Isagawa, Y. Fushizaki. Nippon Kagaku Zasshi, **89**, 1096 (1968); Chem. Abstr. **70**, 87508 (1969).

© 2004 NRC Canada

TMAH-pyrolysis – gas chromatography – mass spectrometry analysis of residual lignin changes in softwood kraft pulp during oxygen delignification

Shiyu Fu and Lucian A. Lucia

Abstract: The residual lignins from pulps and effluent lignins from oxygen delignification effluents were characterized using pyrolysis – gas chromatography – mass spectrometry in the presence of tetramethylammonium hydroxide. The results indicated that oxidation under alkali oxygen conditions can induce fragmentation in lignin and produce more acid groups, but the lignin maintains most of its C_6–C_3 units. Oxygen delignification also led to a decrease in diphenyl structures in the residual lignin and an enrichment in concentration of lignin carbohydrate complex structures.

Key words: residual lignin, pyrolysis, oxygen delignification.

Résumé : Faisant appel à la spectrométrie de masse couplée à la chromatographie en phase gazeuse avec pyrolyse en présence d'hydroxyde de tétraméthylammonium, on a caractérisé les lignines résiduelles de pulpes et d'effluents de lignines provenant de la délignification des effluents. Les résultats indiquent que l'oxydation dans des conditions impliquant de l'oxygène en milieu alcalin peut induire une fragmentation de la lignine et conduire à une production accrue de groupes acides, mais que la lignine maintient la plupart de ses unités C_6–C_3. La délignification à l'oxygène conduit aussi à une diminution des structures diphényles dans la lignine résiduelle et à une augmentation dans la concentration des structures « LCC ».

Mots clés : lignine résiduelle, pyrolyse, délignification à l'oxygène.

[Traduit par la Rédaction]

Introduction

Tetramethylammonium hydroxide (TMAH) thermochemolysis or pyrolysis in the presence of TMAH was developed by Challinor (1, 2) and has gained wide acceptance as a powerful means to characterize lignin (3–6). Online TMAH thermochemolysis programs are characterized by selective cleavage of β-aryl ether linkages, while online permethylated products indicate that the structural attributes of the β-aryl ether substructures have been retained (3). Filly found that the base-catalyzed reactions caused by TMAH thermochemolysis occurred mainly where propyl-aryl ether linkages were adjacent to hydroxyl groups on the alkyl side chain (7). This suggested that phenylpropane units linked by C—C bonds or without an adjacent hydroxyl group were not released as thermochemolysis products. The functional groups in raw lignin samples are, therefore, retained in the products of thermochemolysis.

Received 3 April 2003. Published on the NRC Research Press Web site at http://canjchem.nrc.ca on 28 September 2004.

S. Fu and L.A. Lucia.[1,2] Institute of Paper Science and Technology, Georgia Institute of Technology, 500 10th St. NW, Atlanta, GA 30332–0620, USA.

[1]Corresponding author (e-mail: lucian.lucia@ncsu.edu).

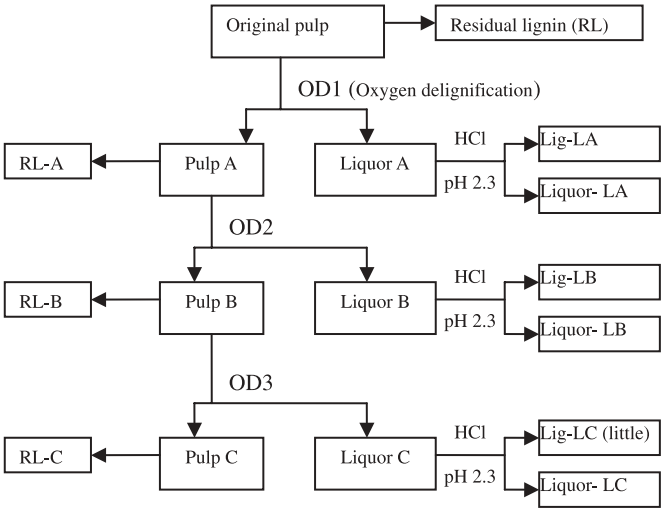
[2]Present address: North Carolina State University, Department of Wood and Paper Science, 3108 Biltmore Hall, Campus Box 8005, Raleigh, NC 27695–8005, USA.

Oxygen delignification has been recognized as an efficient method to remove the bulk of the residual lignin from pulps and is widely used in mills prior to bleaching. However, the degree of lignin removal for a single oxygen stage is about 50%; further delignification would lead to excessive damage of cellulose and result in a decrease in the pulp viscosity and a loss in pulp strength (8). Residual lignin in kraft pulp is a three-dimensional polymer linked by condensed bonds and some ether linkages between dihydrophenyl propionic diphenylmethane and stilbene units, most of which are not readily hydrolysable. The structure of residual lignin in kraft pulps is significantly different from that of lignin in wood and even from lignin dissolved in black liquors from kraft cooking. During kraft pulping, aryl ethers are depleted, condensed bonds are enriched, and new links to polysaccharides are formed. Heretofore, several methods have been used in the characterization of lignin in pulping and bleaching processes: NMR (9–11), nitrobenzene oxidation, manganate oxidation (12), and the derivatization followed by reductive cleavage (DFRC) method (13, 14).

To provide a greater understanding of the structural changes occurring in kraft pulp residual lignin during the oxygen delignification process, a mill softwood kraft pulp was oxygen delignified in three stages (O-O-O), as illustrated in Fig. 1. Residual lignins were extracted from the original and delignified pulps, as were the effluent lignins from oxygen delignified liquors and all were analyzed as appropriate by the following methods: the crystallinity of the

 doi: 10.1139/V04-085 © 2004 NRC Canada

Fig. 1. Flow diagram for the three stages in oxygen delignification and lignin isolation.



pulps, an elemental analysis of the chemical changes, NMR spectra, and the low molecular weight compounds were analyzed as in a previous report (15). This report will evaluate the molecular characterization of residual lignins from pulps and effluent lignins from oxygen delignification effluents using pyrolysis – gas chromatography – mass spectrometry (pyrolysis–GC–MS) in the presence of TMAH and will estimate the structural changes in lignin during the oxygen delignification process.

Experimental

Pulp and residual lignin preparations

Softwood kraft pulp with oxygen pretreatment from a North American paper mill was delignified with oxygen-alkaline in stages according to the following program. The oxygen delignification in each stage was done using the following conditions (final concentrations given): sodium hydroxide 2.5%, magnesium sulfate 1.5%, phenol 0.5%, consistency of pulp 12%, reaction in two phases; the first phase was under an oxygen pressure of 135 psi at 193°F (89.4 °C) for 30 min while the second phase was at 80 psi at 210°F (98.9 °C) for 60 min.

The residual lignins in the pulps were extracted with 0.1 mol/ L HCl in aqueous dioxane according to the method described by Chakar (9). The remaining lignin in the effluent after oxygen-alkaline delignification was precipitated by adding HCl until the final pH was 2.3. It was then washed with 0.002 mol/L HCl and freeze dried for thermochemolysis analysis.

Pyrolysis

Approximately 0.4 mg of the lignin sample was dissolved in 10 μL of 1 mol/L TMAH solution. The resulting lignin mixture solution was homogenously distributed on the glass fiber which had previously been inserted into a pyrolysis tube. The tube was then loaded into the pyrolysis probe (CDS Pyroprobe 1000, Chemical Data System Oxford, Pa.) and was preheated in the pyrolysis chamber at 150 °C for 10 min under purged helium gas. The lignin sample was degraded at a 360 °C pyrolysis temperature for 10 s and the pyrolysis products were immediately methylated because of the presence of 1 mol/L TMAH.

GC–MS analysis

The methylated lignin degradation products were separated and analyzed with a HP 5890 Series II gas chromatograph coupled to a HP 5971A mass selective detector. The gas chromatograph was equipped with a DB-1 column with dimensions of 15 m × 0.25 mm × 0.25 μm. The initial temperature was set at 50 °C for 1 min, and the oven temperature was then increased at a rate of 10 °C/min until a maximum temperature of 280 °C was achieved. Final time at the maximum temperature was 1 min. The solvent delay was set to 2 min. The compounds identified by GC–MS with major fragments are shown in Table 1.

Results and discussion

Analysis of pyrolysis products

The TMAH-pyrolysis method causes cleavage of β-aryl ether bonds in lignin samples followed by online methylation of degraded polyhydroxy products. The characteristics of these products can indicate the identity of lignin subunits in pulp, and can let us know the reason why residual lignins in pulp are stagnant during the oxygen alkali process and why more than 20% of residual lignins can not be removed even after three stages of delignification. The compounds identified from the pyrolysis of the lignin samples are illustrated in Fig. 2. Table 1 lists the retention times and major fragments of the corresponding components.

The isolated lignins were thermochemolysed in the presence of TMAH at 360 °C, and the main products were aromatics that contain the 3,4-dimethoxylphenyl group (veratryl units), i.e., methylated guaiacyl units (shown in Fig. 2). The major products include veratric aldehyde and acid, veratryl units with two or three carbon side chains, together with several phenols. Phenol from the identified compounds, which did not exist in the residual lignin from the original pulp, mainly originates from the residuals of the reaction system because phenol was used as an additive. The appearance of compounds **2, 4, 5, 6, 7,** and **13** (see Table 1 for a complete listing of identified compounds) was also attributed to impurities introduced during the oxygen delignification process. Compound **2** was formed through the cleavage of C_{α}—$C_{aromatic}$ bonds during thermochemolysis (16).

The glycerol backbone of the phenylpropane unit in lignins contains asymmetric carbons, which yield both a threo and an erythro form. Compounds **24** and **25** are the two diasteriomeric derivatives shown in the pyrogram through a β-O-4 ether cleavage, which is maintained as the glycerol hydroxyl group, while the other moiety of the ether linkage is lost as oxygen; therefore compound **10** was probably formed during pyrolysis. The aryl glycol compounds, **16**–**21** and **26**–**29** constituted most of the rest of the products. Compounds **17** and **19**, **20** and **21**, and, **28** and **29** were stereoisomeric pairs with identical mass spectra. Because the C_{γ}–C_{β} side chain cleavage took place during the kraft pulping process, the residual lignins of the pulp possessed two carbon side chains; therefore, a few of these products came from pyrolysis. Compounds **14**, **17**,**19**, and **22** had two carbon

© 2004 NRC Canada

Table 1. Major fragments of identified compounds as methyl derivatives in their mass spectra.

	Tentative assignment for the analyzed compounds	Retention time (min)	Molecular peak	Major fragments
1	Methoxyl benzene	2.3	108	65, 78, 93
2	Carboxylic benzene, methyl ester	4.7	136	105, 77, 51
3	1,2-Dimethoxyl benzene	5.5	138	95, 123, 77, 52
4	1,4-Dimethoxyl benzene	5.8	138	123, 95
5	1,2-Dihydroxy-3-methoxyl benzene	6.8	140	125, 97
6	2,6-Dimethoxyl phenol	8.4	154	139, 111, 95, 77
7	4-Methoxy benzoic acid, methyl ester	8.6	166	135, 77, 92, 105, 120
8	3,4-Dimethoxy benzaldehyde	10.8	166	95, 77, 151
9	1,3,4-Trimethoxybenzene	9.2	168	153, 125, 110, 95
10	3-Phenyl-2-propenoic acid, methyl ester	9.4	162	131, 103, 77, 51
11	1,3-Benzene dicarboxylic acid, methyl ester	10.4	194	163, 135, 77
12	3,4-Dimethoxybenzyl methyl ether	10.5	182	151, 166, 139, 107
13	1,4-Benzene dicarboxylic acid, dimethyl ester	11.3	194	163, 179, 135, 103
14	1-(3,4-Dimethoxyphenyl)ethanone	12.2	180	165, 77, 137
15	3,4-Dimethoxybenzoic acid, methyl ester	12.7	196	165, 181, 79, 51
16	1-(3,4-Dimethoxyphenyl)-2-methoxy propene-1	13.15	208	194, 179, 151, 91
17	1-(3,4-Dimethoxyphenyl)-2-methoxy-ethylene (*cis*)	13.06	194	151, 179, 91
18	1-(3,4-Dimethoxyphenyl)-3-methoxy-propane	13.245	210	151, 168, 107, 121,136
19	1-(3,4-Dimethoxyphenyl)-2-methoxy-ethylene (*trans*)	13.326	194	179, 148
20	1-(3,4-Dimethoxyphenyl)-1-methoxy-propene-1 (*cis*)	13.758	208	193, 165
21	1-(3,4-Dimethoxyphenyl)-1-methoxy-propene-1 (*trans*)	13.96	208	193, 165, 150, 77
22	1-(3,4-Dimethoxyphenyl)-1,2-dimethoxy ethane	14.473	226	181, 74, 87, 166
23	3-(3-Methoxy-4-hydroxyphenyl)-2-propenoic acid, methyl ester	14.689	208	177, 145
24	1-(3,4-Dimethoxyphenyl)-1,2,3-trihydroxy propane	15.62	270	181, 151, 166
25	1-(3,4-Dimethoxyphenyl)-1,2,3-trihydroxy propane	15.64	270	181, 151, 166
26	1-(3,4-Dimethoxyphenyl)-2, 3 -dimethoxy-propene-1	15.944	238	179, 74, 87, 223
27	1-(3,4-Dimethoxyphenyl)-2-propenoic acid, methyl ester	16.511	254	222, 191, 181, 207, 238
28	1-(3,4-Dimethoxyphenyl)-1,3-dimethoxy-propene-1 (*cis*)	15.957	238	179, 207, 74, 89
29	1-(3,4-Dimethoxyphenyl)-1,3-dimethoxy-propene-1 (*trans*)	16.065	238	207, 165, 192, 223

side chains. Dihydrogen conifer alcohol (17) and γ-carboxylic acid (18) are formed from the disproportionation reaction of coniferyl alcohol. The β-ether aryl-alkyl linkage units with α-hydroxyl groups form α-methoxyl veratryl propenyl products, such as compounds **20**, **21**, **28**, and **29**. The formation of compounds **16**, **17**, **19**, and **26** does not all come from α-ether aryl-alkyl linkage units, which were eliminated during the kraft pulping process, but from the enol ether structures. The chemistry of the pyrolysis of lignins in the presence of TMAH is very much akin to the chemistry of pulping. In non-phenolic lignin units, β-ether linkages are cleaved with the assistance of ionized neighboring hydroxyl groups (19). During pyrolysis, the oxidative reaction leads to 1,3-benzene dicarboxylic acid formation from the β-5 linkage of diphenyl methane structural units.

Quantitative analysis of products from pyrolysis

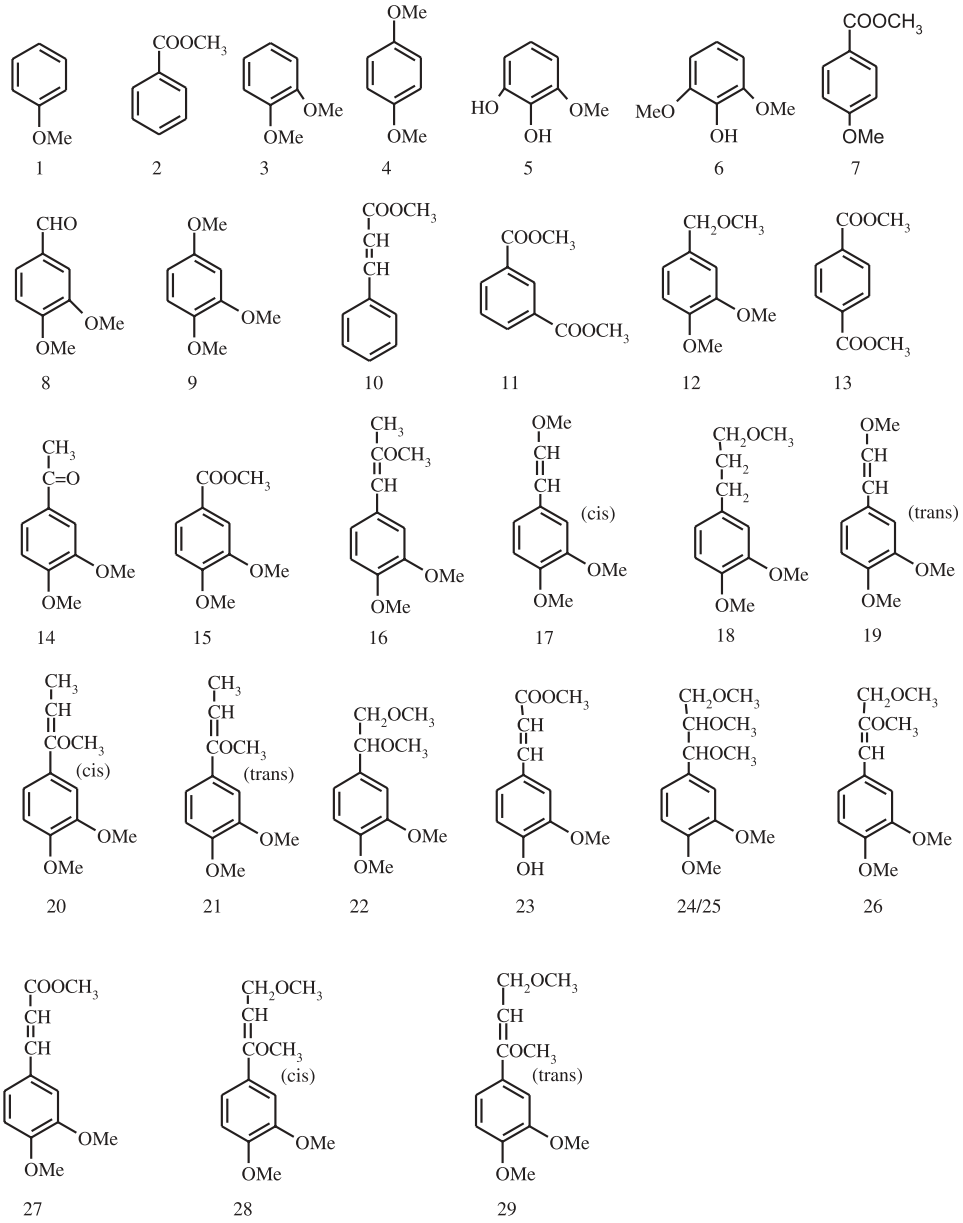
The operational conditions selected for the pyrolysis process appeared to be feasible for the study of residual lignin structures. Coupled with quantitative analysis, the procedure should be able to reveal the change of aryl ether linkages in lignin macromolecules during the different stages of oxygen delignification (shown in Table 2). The relative amount of products observed from lignin sample RL-B was different from the others because of contamination and therefore will not be discussed.

Vanillin, in our experiment, is responsible for 9% in the pyrograms of residual lignin from the original pulp and 7% from oxygen delignified pulp. Choi et al. (20) obtained 1.4%–2.3% vanillin in the pyrograms of residual lignin from spruce pulp. These differences in the pyrograms of residual lignin are most likely due to temperature differences in pyrolysis. It is found that the ratios of carboxylic acid to aldehyde are much different for residual lignins from the original pulp compared with the oxygen delignified pulp and effluent lignin compared with the oxygen delignified effluents (shown in Table 2). The carboxylic acid group from the residual lignin of the original pulp was less than that in residual lignin of oxygen delignified pulp and effluent lignin, which can be explained by the oxidation of lignin during oxygen delignification. Though oxidation of the side chains took place during pyrolysis (19) it is actually limited under a helium atmosphere. These results are consistent with our previous results from NMR determination (15).

In whole spruce milled wood lignin, 1-(3,4-dimethoxylphenyl)-1,2,3-trimethoxypropane constituted about 20% of all products for pyrolysis (19), but only about 4% was in our residual lignins from kraft pulp, oxygen delignified pulp, and effluent lignins. However, different pyrolysis conditions give rise to different product profiles. Pyrolysis at 600 °C in the presence of TMAH gave products including two carbon side chains containing 3,4 dimethoxybenzenes (3), whose reaction is similar to kraft pulping in inducing cleavage of the side chains in alkali. Pyrolysis at low temperatures of 310–360 °C does not cause cleavage of the phenylpropane side chains; the one carbon and two carbon

© 2004 NRC Canada

Fig. 2. Structure of compounds identified in pyrolysis of lignin samples.



side chain compounds arise mainly from the lignin samples used for pyrolysis. The C_3 side chain dimethoxybenzene units are responsible for about 34% of all products from thermochemolysis of lignin preparations, which indicates that residual lignins or effluent lignins dissolved from oxygen delignification still contain complete benzyl propane units.

Oxidation under alkali oxygen conditions can fragment lignin and produce more acid groups but the lignin can retain most of its C_6–C_3 units. The ratio of C_1 and C_2 side chain compounds to C_3 side chain compounds (shown in Table 2) demonstrates that residual lignin either from original pulp or from oxygen delignified pulps contained not many more short side chains than effluent lignins. The rationale is probable because of the loss of low molecular weight compounds from residual lignins during oxygen delignification.

The dicarboxylic acid that arises from diphenyl methane structures decreased after oxygen delignification which indicates that the diphenyl methane structures formed during the kraft process can be partly removed by oxygen delignification. Lai (21) demonstrated, using model compounds, that diphenyl methane structures subjected to oxidation under alkali oxygen conditions, led to a decrease in diphenyl methane structures in the residual lignin of oxygen delignified pulp.

Actually, it was found that the products in pyrograms of residual lignin from the 1st to the 3rd stage of oxygen delignified pulps were not much different in C_6–C_3 compounds except for 3,4-dimethoxy benzaldehyde and 3,4-dimethoxy benzoic acid methyl ester, which showed that oxidation of residual lignin in kraft pulp occurs through a peeling process. After each oxygen delignification step, the retained lignin is similar to the original residual lignin. The way to improve delignification in an alkali oxygen process would be to improve the active oxidative agents (22) and in-

© 2004 NRC Canada

Table 2. The relative abundance of identified compounds by pyrolysis–GC–MS for lignin preparations.

Tentative assignment for the analyzed compounds	RL	RL-A	RL-B	RL-C	Lig-LA	Lig-LB	Lig-LC
Methoxyl benzene	0	2.76	1.63	3.19	10.73	6.78	6.50
Carboxylic benzene, methyl ester	6.54	5.53	3.68	5.18	5.20	5.55	5.07
1,2-Dimethoxyl benzene	2.57	2.80	2.73	2.44	2.48	2.59	2.31
1,4-Dimethoxyl benzene	0	0.20	0.09	0.09	0.07	0.18	0.03
1,2-Dihydroxy-3-methoxyl benzene	0	0	0	2.06	2.58	2.00	2.10
2,6-Dimethoxy phenol	0	0.10	0	0.11	0.14	0.16	0.05
4-Methoxy benzoic acid, methyl ester	0	4.93	0	4.83	4.94	4.76	4.95
3,4-Dimethoxy benzaldehyde	9.09	9.91	1.90	7.59	2.53	4.84	4.23
1,3,4-Trimethoxybenzene	0.22	0.36	0.60	0.26	0.26	0.22	0.10
3-Phenyl-2-propenoic acid, methyl ester	3.78	3.24	2.32	3.13	3.24	3.08	3.23
1,3-Benzene dicarboxylic acid, methyl ester	11.12	7.34	53.5	7.32	5.08	4.84	5.07
3,4-Dimethoxybenzyl methyl ether	5.50	4.78	0	5.31	3.26	4.85	4.20
1,4-Benzene dicarboxylic acid, dimethyl ester	5.91	4.97	0	4.86	5.19	4.73	4.93
1-(3,4-Dimethoxyphenyl)ethanone	1.91	0	0	0	1.25	1.26	1.26
3,4-Dimethoxy benzoic acid, methyl ester	7.31	5.25	4.03	6.69	5.08	6.46	6.65
1-(3,4-Dimethoxyphenyl)-2-methoxy propene-1	3.82	3.40	2.32	3.23	3.40	3.39	3.31
1-(3,4-Dimethoxyphenyl)-2-methoxy-ethylene (*cis*)	3.82	3.51	2.35	3.45	3.21	3.07	3.28
1-(3,4-Dimethoxyphenyl)-3-methoxy-propane	3.88	3.71	2.43	3.14	3.62	3.39	3.49
1-(3,4-Dimethoxyphenyl)-2-methoxy-ethylene (*trans*)	3.91	3.51	2.34	3.38	3.38	3.21	3.28
1-(3,4-Dimethoxyphenyl)-1-methoxy-propene-1 (*cis*)	3.78	3.24	0	3.13	3.24	3.12	3.24
1-(3,4-Dimethoxyphenyl)-1-methoxy-propene-1 (*trans*)	3.78	3.20	0	3.12	3.21	3.07	3.21
1-(3,4-Dimethoxyphenyl)-1,2-dimethoxy ethane	0	0	0	1.21	1.35	1.28	1.37
3-(3-Methoxy-4-hydroxyphenyl)-2-propenoic acid, methyl ester	3.78	3.24	2.41	3.19	3.26	3.15	3.28
1-(3,4-Dimethoxyphenyl)-1,2,3-trimethoxy propane	4.10	3.83	2.96	3.72	4.18	4.09	4.18
1-(3,4-Dimethoxyphenyl)-2, 3 -dimethoxy-propene-1	4.00	4.18	2.97	3.75	3.92	4.57	4.51
3-(3,4-Dimethoxyphenyl)-2-propenoic acid, methyl ester	0	3.20	2.35	3.11	3.21	3.08	3.23
1-(3,4-Dimethoxyphenyl)-1,3-dimethoxy-propene-1 (*cis*)	3.72	3.20	2.35	3.13	3.21	3.08	3.23
1-(3,4-Dimethoxyphenyl)-1,3-dimethoxy-propene-1 (*trans*)	3.75	3.24	2.37	3.14	3.24	3.08	3.24
Acid/aldehyde	0.21	0.53	—	0.88	2.01	1.33	1.57
C_1C_2/C_3	0.99	0.86	0.66	0.92	0.63	0.81	0.76
C_3 side chain	34.6	34.44	20.16	32.66	34.49	34.02	34.92

Note: Quantitative estimation of the identified compounds was made based on the response factors of 1,2,3-trimethoxy benzene, vanillin, vanillic acid, and 1-(3,4-dimethoxyphenyl)ethanone. The response factors for peak area to the compounds weight were similar. The values of relative abundance were calculated according to the weight from quantitative estimation. The heading notation in this table is explained in Fig. 1.

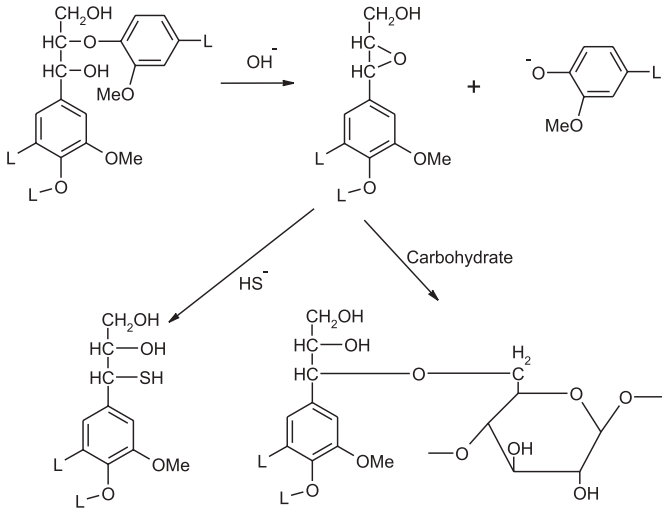
crease the penetrability of the reactive agent into the lignin matrix of the pulp fibers.

The possibility of lignin carbohydrate complexes (LCC)

The chemical linkages between lignin and sugars, known as lignin carbohydrate complexes (LCC) exist in native wood or are formed during the pulping process. The structural research on residual lignins in kraft pulp by Chen (18) suggested that LCC in pulp are difficult to oxidize by alkali oxygen delignification, which is one of the main reasons why residual lignin in pulps is difficult to completely remove by oxygen alkali. Gierer and Wannstrom proposed the formation of an ether linkage between a sugar moiety and a non-phenolic or phenolic lignin structure (see Fig. 3) using model compounds in kraft pulping (17, 23).

Hardell and Nilvebrant (19) have claimed that the glucose unit in model compound ***I***, which has the structure of linkage bonding lignin and carbohydrate, a model of LCC, would form 1,2,4-trihydroxy benzene under pyrolysis temperatures of 360 °C as indicated in Fig 4. When lignocellulosic materials were used, a typical pyrolysis temperature of 650 °C was required to cleave the glycosidic bonds to give this 1,2,4-trihydroxy benzene (19). However, the amount of

Fig. 3. Formation of a lignin and sugar linkage (23).



1,2,4-trimethoxy benzene for samples is relative to the carbohydrate content of the lignin samples as shown in Table 3. Therefore, detection of 1,2,4-trimethoxy benzene under low

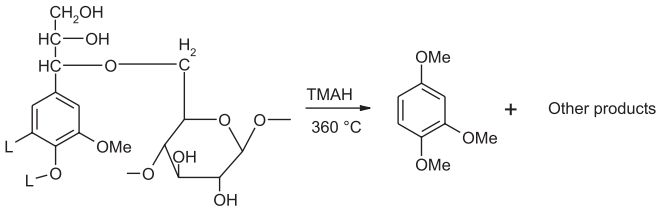
© 2004 NRC Canada

Table 3. The content of 1,2,4-trihydroxy benzene in the analyzed lignin samples.

Sample	Klason lignin[a] (%)	Lignin weight (μg)	Peak area	Area/lignin wt.[b]
Residual lignin	99.4	352.5	450 842	1291
RL-A	83.5	580.8	1 692 704	3510
RL -B	73.0	345.6	1 432 087	5676
RL -C	54.9	345.0	1 071 017	5644
Lig-LA	82.3	247.8	793 690	3906
Lig-LB	82.2	206.7	1 210 342	7140
Lig-LC	82.3	349.8	745 889	2600

[a]Klason lignin is undissolved lignin in 3% H_2SO_4, see TAPPI method T 222 om-98.
[b]Results were corrected for the carbohydrate content in the lignin samples.

Fig. 4. Possible mechanism leading to the formation of 1,2,4-trimethoxy benzene (19).



pyrolysis temperatures provides evidence for the existence of LCC in lignin samples.

The amount of 1,2,4-trihydroxy benzene in the pyrograms increased for the oxygen delignified lignin. This indicated that LCC might be enriched during the delignification process. This finding was in agreement with the proposal that the presence of LCC during oxygen delignification may constitute a barrier to delignification since LCC strongly resist degradation even under alkaline oxygen conditions.

Conclusions

Pyrolysis of lignin under 360 °C in the presence of TMAH led to cleavage in lignin aryl ether linkages and generated methyl derivatives. The results of pyrolysis indicated that oxidation under alkali oxygen conditions can fragment lignin and generate more acid groups, but lignin can retain most of its C_6–C_3 units. The step-wise degradation of lignin generated low molecular weight compounds and caused the dissolution of effluent lignin during oxygen delignification. Oxygen delignification led to a decrease in diphenyl structures in residual lignin, whereas the identification of 1,2,4-trihydroxy benzene may serve to indicate the presence of LCC in lignin. LCC also appear to be enriched during the oxygen delignification process.

Acknowledgement

The authors thank Dr. Rallming Yang for his pyrolysis–GC–MS analyses and gratefully acknowledge the United States Department of Energy for financial support (Contract DE-FC07–02ID14261), the member companies of the Institute of Paper Science and Technology, and the Georgia Institute of Technology for the use of their facilities. We dedicate this paper to the memory of Dr. Barry Crouse.

References

1. J.M. Challinor. J. Anal. Appl. Pyrol. **16,** 323 (1989).
2. J.M. Challinor. J. Anal. Appl. Pyrol., **61**, 3 (2001).
3. D.J. Clifford, D.M. Carson, D.E. Mckinney, et al. Org. Geochem. **23**(2), 169 (1995).
4. Ken-ichi Kuroda, N. Nishimura, A Izumi, and D. Dimmel. J. Agr. Food Chem. **50,** 1022 (2002).
5. Ken-ichi Kuroda, A. Izumi, B.B Mazumder, Y. Ohtani, and K. Sameshima. J. Anal. Appl. Pyrol. **64**, 453 (2002).
6. Ken-ichi Kuroda. J. Anal. Appl. Pyrol. **64,** 433 (2002).
7. T.R. Filly, R.D. Minard, and P.G. Hatcher. Org. Geochem. **30,** 607 (1999).
8. T.J. McDonough. *In* Pulp bleaching: principles and practice. *Edited by* C.W. Dence and D.W. Reeve. Tappi Press, Atlanta, Ga. 2000. pp. 215–237.
9. F.S. Chakar and A.J. Ragauskas. J. Wood Chem. Technol. **20**(2), 169 (2000).
10. Z.-H. Jiang and D.S. Argyropoulos. J. Pulp Pap. Sci. **25**(1), 25 (1999).
11. F.S. Chakar, L. Lucia, and A.J. Ragauskas. *In* International pulp bleaching conference. Halifax, N.S., 27–30 June 2000, Tappi Press, Atlanta, Ga. pp. 123–130.
12. C. L. Chen. Methods Enzymol. (Biomass, Pt. B) **161,** 110 (1988).
13. F. Lu and J. Ralph. J. Agric. Food Chem. **45**, 4655 (2002).
14. T. Ikeda, K. Holtman, J. Kadla, H.-m. Chang, and H. Jameel. J. Agric. Food Chem. **50,** 129 (2002).
15. S.Y. Fu and L.A. Lucia. Ind. Eng. Chem. Res. **42**, 4269 (2003).
16. T.C. Drage, C.H. Vane, and G.D. Abbott. Org. Geochem. **33,** 1523 (2002).
17. G. Gellerstedt. *In* Pulp bleaching: principles and practice. *Edited by* C.W. Dence and D.W. Reeve. Tappi Press, Atlanta, Ga. 1996. Chap. III-1. p. 103.
18. J.Y. Chen, Y. Shimizu, M. Takai, and J. Hayashi. Mokuzai Gakkaishi **42**(5), 497 (1996).
19. H.L. Hardell and N.O. Nilvebrant. Nord. Pulp Pap. Res. J. **11**(2), 121 (1996).
20. J.W. Choi, O. Faix, and D. Meier. Holzforschung, **55,** 1875 (2001).
21. Y.Z. Lai, R. Yang, and H. Xu. International Pulp Bleaching Conference, Halifax, N.S., 27–30 June 2000. pp. 301–305.
22. T. Yokoyama, Y. Matsumoto, and G. Meshitsuka. *In* Proceedings of the 2nd international symposium on emerging technologies of pulping and papermaking. South China University of Technology Press, Guangzhou, China. 2002. pp. 11–19.
23. J. Gierer and S. Wannstrom. Holzforschung, **40**(6), 347 (1986).

© 2004 NRC Canada

Voltammetric behavior and quantification of the anti-leukemia drug imatinib in bulk form, pharmaceutical formulation, and human serum at a mercury electrode

E. Hammam, H.S. El-Desoky, A. Tawfik, and M.M. Ghoneim

Abstract: Imatinib (Gleevec™, ST1571) exemplifies the successful development of a rationally designed molecularly targeted therapy for treatment of a specific cancer. It is a highly promising new drug for the treatment of chronic myelogenous leukemia in blast crisis, in the accelerated or chronic phase after interferon failure or intolerance. The electrochemical behavior of imatinib was studied in Britton–Robinson (B–R) buffers of pH 2 to 11 by means of cyclic voltammetry at a hanging mercury drop electrode. The voltammograms showed a single 2-electron irreversible cathodic peak, which may be attributed to reduction of the C=O double bond of the imatinib molecule. Imatinib exhibited a strong adsorption onto the electrode surface especially in B–R buffers of pH 6 and 7. The adsorptive response of the drug was optimized with respect to the pH of the electrolysis medium, accumulation variables, and instrumental parameters using a square-wave stripping voltammetry technique. A fully validated, simple, sensitive, precise, and selective square-wave adsorptive cathodic stripping voltammetric procedure is described for trace determination of imatinib. The limits of detection (LOD) and quantitation (LOQ) of the bulk imatinib, following preconcentration for 150 s onto the hanging mercury drop electrode, were found to be 2.6×10^{-10} and 8.7×10^{-10} mol/L, respectively. The proposed procedure was successfully applied for quantitation of imatinib in pharmaceutical formulation (Glivec®) and spiked human serum, without the necessity for sample pretreatment or time-consuming extraction or evaporation steps prior to analysis of the drug. LOD and LOQ of 4.6×10^{-10} and 1.5×10^{-9} mol/L, respectively, were achieved after 120 s of preconcentration of the drug spiked in human serum.

Key words: imatinib, Gleevec™, Glivec®, ST1571, cyclic voltammetry, square-wave stripping voltammetry, electrochemical behavior, quantification, pharmaceutical formulation, human serum.

Résumé : L'imatinib (Gleevec™, ST1571) est un exemple du développement avec succès d'une thérapie orientée d'une façon moléculaire du traitement d'un cancer spécifique mis au point d'une façon rationnelle. Il s'agit d'un nouveau médicament très prometteur pour le traitement de la leucémie myélogéneuse chronique en phase de crise, en phase accélérée ou en phase chronique, après l'échec d'un traitement ou une intolérance à l'interféron. On a étudié le comportement électrochimique de l'imatinib dans des tampons de Britton–Robinson, à des pH allant de 2 à 11, en faisant appel à la voltampérométrie cyclique à électrode avec goutte de mercure suspendue. Les voltampérogrammes présentent une seule vague cathodique irréversible à deux électrons qui peut être attribuée à la réduction de la double liaison C=O de la molécule d'imatinib. L'imatinib présente un fort caractère absorbant sur la surface de l'électrode, particulièrement dans le tampon de Britton–Robinson de pH 6 et 7. La réponse absorbante du médicament a été optimisée par rapport au pH du milieu électrolytique, des variables d'accumulation et des paramètres expérimentaux en faisant appel à la voltampérométrie à vague carrée. On décrit une méthode sélective, précise, sensible, simple et validée de voltampérométrie cathodique d'absorption à vague carrée pouvant être utilisée pour la détermination de traces d'imatinib. On a déterminé que les limites de détection (LDD) et de quantification (LDQ) du médicament global, suivant une préconcentration de 150 s sur l'électrode à goutte pendante de mercure, sont respectivement de $2{,}6 \times 10^{-10}$ et de $8{,}7 \times 10^{-10}$ mol/L. La méthode proposée a été appliquée avec succès à la quantification de l'imatinib dans la formulation pharmaceutique (Glivec®) et dans du sérum humain additionné d'imatinib, sans devoir soumettre les échantillons, avant l'analyse du médicament, à des prétraitements, de longues étapes d'extraction ou d'évaporation. Les valeurs obtenues pour les limites de détection et de quantification de sérum humain additionné du médicament, à la suite d'une préconcentration de 120 s, sont respectivement de $4{,}6 \times 10^{-10}$ et de $1{,}5 \times 10^{-10}$ mol/L.

Received 27 April 2003. Published on the NRC Research Press Web site at http://canjchem.nrc.ca on 29 September 2004.

E. Hammam, H.S. El-Desoky, A. Tawfik, and M.M. Ghoneim.[1] Department of Chemistry, Faculty of Science, Tanta University, 31527 Tanta, Egypt.

[1]Corresponding author (e-mail: mmghoneim@usa.net).

 doi: 10.1139/V04-060 © 2004 NRC Canada

Mots clés : imatinib, Gleevec™, Glivec®, ST1571, voltampérométrie cyclique, voltampérométrie à vague carrée, comportement électrochimique, quantification, formulation pharmaceutique, sérum humain.

[Traduit par la Rédaction]

Introduction

Imatinib mesylate (Scheme 1), also known as Gleevec™, Glivec® or ST1571, (4-[(4-methyl-1-piperazinyl) methyl]-*N*-[4-methyl-3-[[4-(3-pyridinyl)-2-pyrimidinyl] aminophenyl] benzamide methanesulfonate), is a protein-tyrosine kinase inhibitor that potently inhibits the Abelson (Abl) tyrosine kinase in vitro (1–3) and in vivo (4–8).

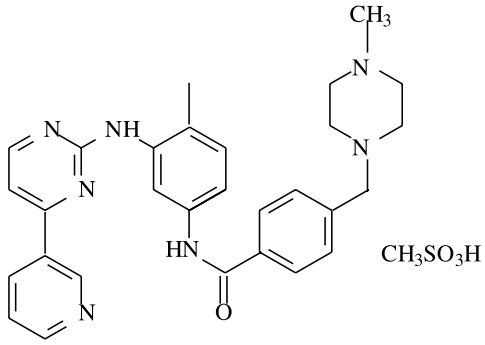
The drug selectively inhibits proliferation and induces apoptosis in Bcr-Abl positive cell lines as well as in fresh leukemia cells from Philadelphia chromosome positive chronic myelogeous leukemia (CML) and acute lymphoblastic leukemia (ALL) patients. In colony transformation assays using ex vivo peripheral blood and bone marrow samples, the drug shows selective inhibition of Bcr-Abl positive colonies from CML patients. In vivo, imatinib shows anti-tumor activity as a single agent in animal models using Bcr-Abl positive tumor cells. In addition, the drug is a potent inhibitor of the receptor tyrosine kinases for platelet-derived growth factor (PDGF) and stem cell factor (SCF), c-kit, and inhibits PDGF- and SCF-mediated cellular events. Imatinib has been shown to inhibit the growth of glioblastoma cells injected into the brains of nude mice, suggesting that this agent could have potential as a therapy for this currently incurable disease. Imatinib is used for the treatment of patients with CML in blast crisis, accelerated phase, or in chronic phase after failure of interferon-alpha therapy.

To date, six assays for the determination of imatinib in plasma including liquid chromatography tandem mass spectrometry (LC–MS–MS) (9, 10), liquid chromatography electro spray ionization mass spectrometry (11), isocratic reverse-phase liquid chromatography UV spectrometry (12), isocratic high-performance liquid chromatography tandem mass spectrometry (13), and capillary zone electrophoresis (14), have been published. While most of these assays provided the sensitivity and speed that were necessary for quantitation of imatinib in different samples, all necessitate sample pretreatment or time-consuming separation steps prior to analysis of the drug. Besides, most of the chromatographic methods use LC–MS–MS technology, which is expensive and not widely available.

In our opinion, the clinical and pharmacological studies of imatinib still require more facile, sensitive, simple, and low cost analytical methods for its determination in different samples. The remarkable sensitivity, broad scope, and low cost of stripping voltammetric analysis have led to its application in several analytical problems (15).

We describe here, for the first time, the electrochemical behavior of imatinib in Britton–Robinson (B–R) buffers of pH 2 to 11 at a hanging mercury drop electrode. In addition, a simple fully-validated, low cost square-wave adsorptive cathodic stripping voltammetric procedure for quantitation of imatinib in bulk, pharmaceutical formulation, and spiked in human serum is described. The procedure does not require sample pretreatment or time-consuming extraction or evaporation steps prior to analysis of the drug.

Scheme 1.



Experimental

Apparatus and software

The voltammetric measurements were carried out using the PAR (Princeton Applied Research, Princeton, N.J.) Electrochemical Analyzer Models 394 and 263A, interfaced with a personal computer loaded with the software package 270/250 (PAR). The electrode assembly (303A-PAR) and a micro-electrolysis cell incorporating a three electrode configuration system consisting of a hanging mercury drop electrode (HMDE) as a working electrode (area: 0.026 cm^2), an Ag/AgCl (saturated KCl) reference electrode, and a platinum wire auxiliary electrode were used in this study. The solution was stirred in the electrochemical cell, using a magnetic stirrer (305-PAR) and a stirring bar, to provide convective transport during the preconcentration step. All measurements were automated and controlled through the programming capacity of the apparatus.

A Mettler balance (Toledo–AB104, Switzerland) was used for weighing the solid materials. An Orion SA 720 pH-meter with combined glass and saturated calomel electrodes was used for the pH measurements. The de-ionized water was supplied from a Purite–Still Plus de-ionizer connected to an AquaMatic (Hamilton Laboratory Glass Ltd., Kent, UK) double-distillation water system.

Reagents and solutions

Bulk drug solutions

Standard stock solutions (10^{-3}–10^{-5} mol/L) of imatinib (Novartis, East Hanover, N.J.) were prepared in methanol (Merck) and were then stored in the dark at 4 °C. Working solutions were obtained by appropriate dilution of the standard stock solution with methanol, then kept in the dark immediately after preparation.

Glivec® solutions

The drug content of five capsules of Glivec® (Novartis Pharm. AG, Basle, Switzerland, labeled as containing 100 mg/capsule) were weighed and then ground to a homogeneous fine powder in a mortar. A portion of the powder equivalent to 50–100 mg of imatinib was accurately weighed

© 2004 NRC Canada

and transferred to a 100-mL calibrated flask, then made up to volume with methanol. The content of the flask was sonicated for at least 10 min to effect complete dissolution. The solution was next filtered through a 0.45-μm Millipore filter (Gelman, Germany) and then kept in the dark at 4 °C. The drug solutions were stable and their concentrations did not change with time.

Imatinib spiked in human serum

Serum samples collected from healthy volunteers were stored frozen until assay. An aliquot of the standard stock solution of imatinib was fortified with serum sample. A 100-μL aliquot of this solution was diluted to 1.0 mL with methanol (to precipitate the proteins originally present in the blood sample) in a small centrifuge tube. The precipitated proteins were removed by centrifugation for 5 min at 14 000 rpm. The clear supernatant layer was filtered through a 0.45-μm Millipore filter to produce protein-free spiked human serum solution, which was then stored in the dark at 4 °C.

Supporting electrolyte

B–R buffers of pH 2 to 11 were prepared by mixing equal volumes of 0.04 mol/L acetic, 0.04 mol/L boric, and 0.04 mol/L orthophosphoric acids (16) to serve as supporting electrolytes. The pH of the solution was adjusted with an appropriate amount of 0.2 mol/L sodium hydroxide solution.

All chemicals were analytical reagent grade and were used without further purification.

General analytical procedure

For stripping voltammetric measurements, an aliquot of the analyte solution was transferred quantitatively into a 10-mL calibrated flask and made up to volume with B–R buffer of the appropriate pH value. The solution was transferred into a dark electrolysis cell, then deoxygenated with pure nitrogen for 10 min. A selected accumulation potential was applied to the working electrode for a selected time period while the solution was stirred. At the end of the accumulation period the stirrer was stopped and a 5 s time period was allowed for the solution to become quiescent. Then the voltammograms were recorded by scanning the potential toward the negative direction using the square-wave waveform and the peak heights were measured. All data were obtained at room temperature.

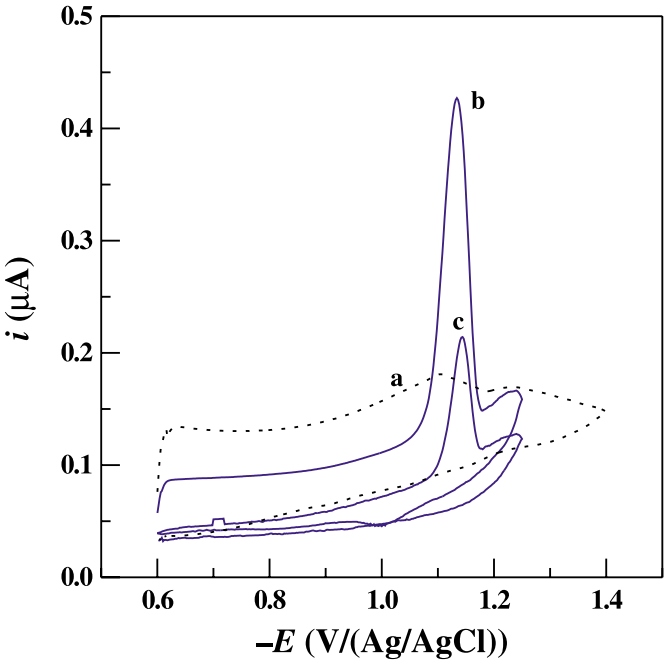
To study the reproducibility, accuracy, and precision of the proposed procedure in determining the drug in bulk, capsule, and human serum samples, recovery experiments were carried out using both the calibration curve and standard addition methods.

Results and discussion

Cyclic voltammetry

The cyclic voltammograms for 1×10^{-4} mol/L imatinib at the HMDE in B–R buffers of pH 2–11 exhibited a single 2-electron irreversible cathodic peak over the whole pH range. The peak current (i_p) was practically pH-independent. This peak may be attributed to reduction of the C=O double bond of the reactant molecule. The peak potential shifted to more negative values with increasing pH, indicating the involvement of protons in the electrode reaction and the proton-transfer reaction preceding the electrode process proper (17). Accordingly, the general sequence of the reduction process of imatinib is: proton, electron, proton, electron (H^+, e, H^+, e) (17). The irreversible nature of the cathodic reaction of imatinib at the HMDE was confirmed from the shift of peak potential (E_p) to more negative values upon increasing the scan rate (ν).

Fig. 1. Cyclic voltammograms for 5×10^{-7} mol/L imatinib: (*a*) without preconcentration for an accumulation time (t_{acc}) of 0 s, (*b*) following preconcentration for t_{acc} = 30 s at an accumulation potential (E_{acc}) = –0.6 V, and (*c*) the repetitive cycle at the same mercury drop; scan rate ν = 100 mV/s.



The adsorptive character of imatinib onto the HMDE was identified from the study of cyclic voltammograms for 5×10^{-7} mol/L imatinib in a B–R buffer of pH 6 (Fig. 1) without preconcentration (curve a) and following preconcentration for 30 s (curve b) at –0.6 V. In a repetitive cycle at the same mercury drop (curve c), the peak height significantly decreased, which may be attributed to desorption of the drug species from the mercury electrode surface. This behavior indicates the adsorption of imatinib onto the HMDE during the preconcentration step. The interfacial adsorptive character of imatinib onto the mercury electrode surface in B–R buffers of pH 2–11 was also identified from plots of log i_p (after preconcentration of the drug for 30 s) against log ν, at different pH values; straight lines were obtained. The slope values of 0.85–0.96 were obtained for the pH values of 6 and 7 and agree well with the theoretical value of 1.0 which is expected for an ideal reaction of surface species (18). The result confirms again the adsorptive character of imatinib onto the HMDE surface during the preconcentration step, especially in B–R buffers of pH 6 and 7.

The electrode surface coverage

The electrode surface coverage, Γ_o (the amount of reactant adsorbed onto the working electrode surface), was calculated from the total charge (Q_{total}) consumed by the surface pro-

© 2004 NRC Canada

cess, which was estimated by integration of the area under the peak of the cyclic voltammogram of 5×10^{-7} mol/L imatinib in a B–R buffer of pH 6, corrected for the residual current (19). The surface coverage Γ_o (mol cm^{-2}) was calculated according to the equation $\Gamma_o = Q/nFA$, where n is the number of electrons consumed in the reduction process (n = 2), F is Faraday's constant (96 487 C), and A is the electrode surface area (0.026 cm^2). On dividing the number of coulombs transferred, 0.91 μC, by the conversion factor (nFA), a Γ_o value of 1.8×10^{-10} mol cm^{-2} was obtained, and each adsorbed imatinib molecule therefore occupies an area of 0.93 nm^2.

A value for Γ_o was also estimated from chronocoulometry experiments for 10 mL of B–R buffer of pH 6 alone (blank) and in the presence of 1×10^{-5} mol/L imatinib. The Q_{total} versus square root of time ($t^{1/2}$) plots were obtained for the blank alone and in the presence of imatinib after its preconcentration for 30 s onto the HMDE. The amount of reactant adsorbed onto the mercury electrode surface in mol cm^{-2} was estimated by applying the following relation (20)

$$Q_{total} = Q_{diff} + Q_{ads} + Q_{dl}$$

$$Q_{total} = \int_0^t i\mathrm{d}t = \frac{2nFACD^{1/2}t^{1/2}}{\pi^{1/2}} + nFA\Gamma + Q_{dl}$$

where Q_{total} is the total charge, Q_{diff} is the charge required to reduce the reactant species in solution at a diffusion-controlled rate, Q_{ads} is defined below, Q_{dl} is the double layer charge (blank), C is the concentration (mol/L) of the reactant, and D is the diffusion coefficient (cm^2 s^{-1}) of the reactant species. The plot of the Q_{total} vs. $t^{1/2}$ has an intercept equal to ($nFA\Gamma_o + Q_{dl}$). Since Q_{dl} was measured in a separate experiment for the supporting electrolyte alone (blank), the contribution of the adsorbed species of the drug was determined and then the Γ_o was estimated.

$$Q_{dl} = 2.7920\ t^{1/2} + 0.0546 \text{ (blank)}$$

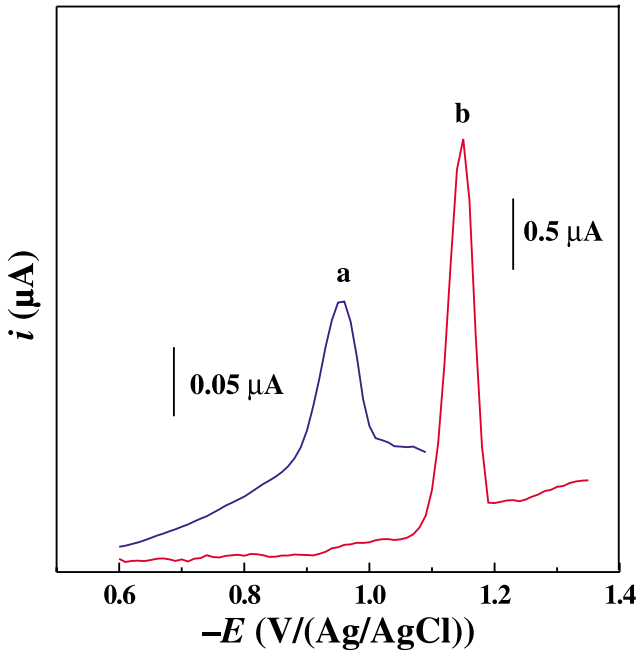
$$Q_{total} = 2.1825\ t^{1/2} + 0.8586 \text{ (imatinib)}$$

The difference between the intercepts of Q_{total} and Q_{dl} is the amount of charge required to reduce the adsorbed reactant species (Q_{ads}). Thus the Γ_o was found to equal 1.6×10^{-10} mol cm^{-2}, and each adsorbed imatinib molecule therefore occupies an area of 1.1 nm^2, which agrees well with the value obtained from cyclic voltammetry measurements. The diffusion coefficient ($D°$) of imatinib in a B–R buffer of pH 6 was also estimated from the slope of the Q_{total} vs. $t^{1/2}$ plot and found to equal 1.49×10^{-7} cm^2 s^{-1}.

Adsorptive stripping voltammetry

In order to develop a voltammetric methodology for determination of the drug, comparative voltammograms for 5×10^{-8} mol/L imatinib in a B–R buffer of pH 6 following preconcentration for 60 s at –0.6 V (vs. Ag/AgCl/KCl$_s$) were recorded applying: (*a*) differential-pulse (pulse-height a = 25 mV and ν = 10 mV/s) and (*b*) square-wave (scan increment ΔE = 10 mV, frequency f = 120 Hz, and a = 25 mV) waveforms. The square-wave peak signal (i_p = 2.5 μA and peak potential E_p = –1.14 V) was more developed compared to that of the differential pulse (i_p = 0.14 μA and E_p = –0.95 V) waveform (Fig. 2). Thus, the square-wave waveform was preferred for the present study, since the cathodic peak was sharper and its current more developed even for low concentrations of the drug.

Fig. 2. Adsorptive cathodic stripping voltammograms for 6×10^{-8} mol/L imatinib in a Britton–Robinson (B–R) buffer of pH 6 using: (*a*) Differential-pulse (pulse-height a = 25 mV and ν = 10 mV/s) and (*b*) square-wave (pulse-height a = 25 mV, frequency f = 120 Hz, and scan increment ΔE = 10 mV) waveforms; t_{acc} = 90 s, E_{acc} = –0.6 V, stirring rate = 400 rpm, and rest period = 5 s.



Operational parameters of square-wave procedure

Effect of pH

In general, the pH of the electrolysis medium is one of the variables that commonly and strongly influences the shape of voltammograms. Thus, it was important to investigate the effects of pH on the electrochemical behavior of imatinib. The square-wave adsorptive cathodic stripping (SWAdCS) voltammograms recorded for 1×10^{-7} mol/L imatinib in B–R buffers of pH 2–11, following preconcentration of the drug for 30 s onto the HMDE, exhibited a single irreversible peak over the whole pH range (Fig. 3). A more developed peak current was obtained in B–R buffers of pH 6 and 7.

Effect of accumulation time and potential

The effect of accumulation time (t_{acc}) on the peak current at a selected potential was studied. Four concentrations of bulk imatinib (3×10^{-9}, 7×10^{-9}, 2×10^{-8}, and 6×10^{-8} mol/L) were analyzed in a B–R buffer of pH 6 at different accumulation time periods, while the accumulation potential was kept constant at –0.6 V. As shown in Fig. 4, the response was linear up to about 150 or 120 s for imatinib concentrations lower or higher than 2×10^{-8} mol/L, respectively.

To determine the optimal accumulation potential, the potential range of 0 to –1.1 V was examined for 7×10^{-8} mol/L imatinib in B–R buffer of pH 6, following pre-

© 2004 NRC Canada

Fig. 3. Square-wave adsorptive cathodic stripping (SWAdCS) voltammograms for 1×10^{-7} mol/L imatinib in B–R buffers of different pH values 2–11; t_{acc} = 30 s, E_{acc} = –0.6 V, f = 120 Hz, ΔE = 10 mV, and a = 25 mV. Other operational parameters are as described in the caption of Fig. 2.

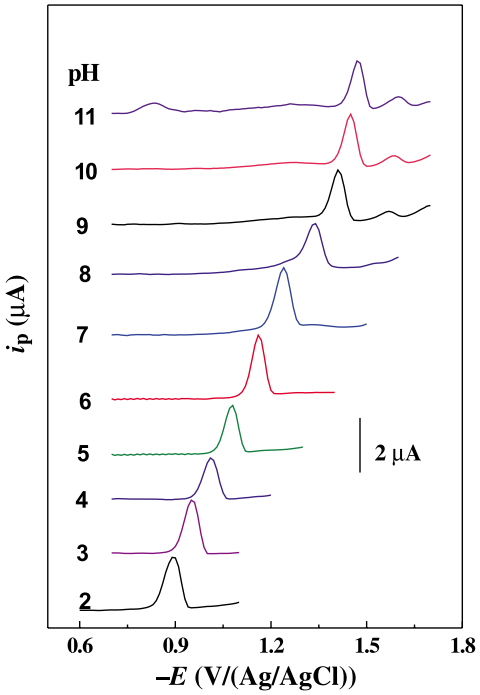
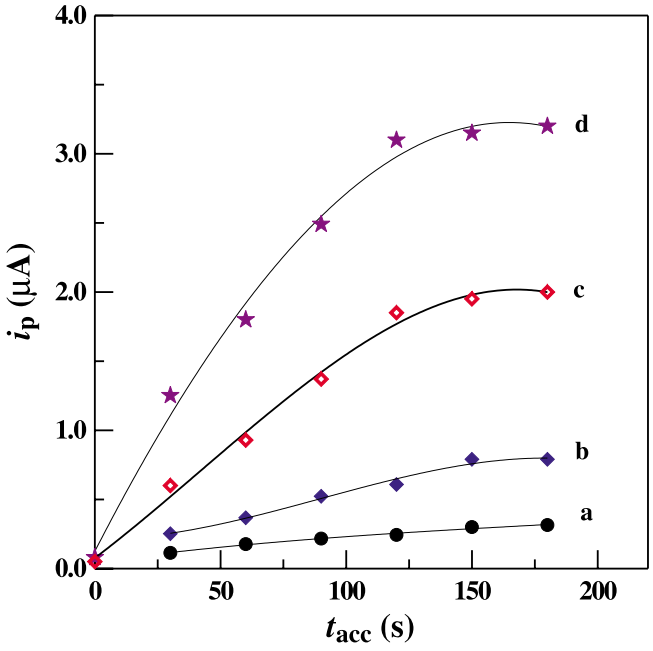
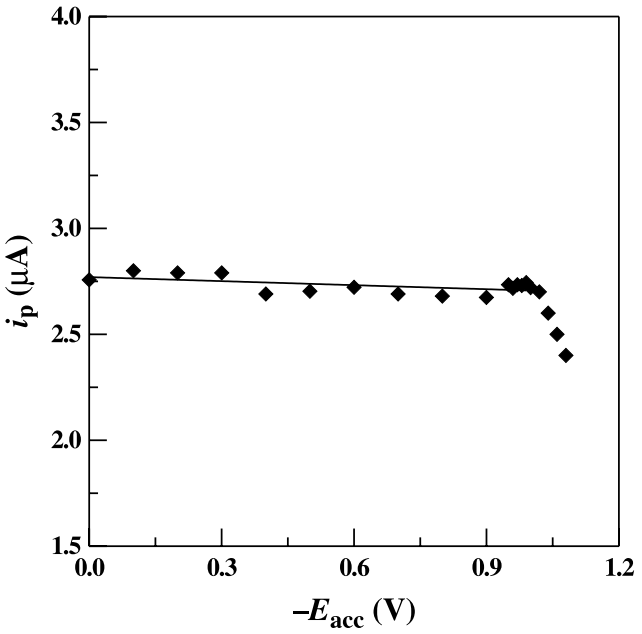


Fig. 4. Effect of t_{acc} on SWAdCS voltammetric peak current at different concentrations of imatinib: (*a*) 3×10^{-9}, (*b*) 7×10^{-9}, (*c*) 2×10^{-8}, and (*d*) 6×10^{-8} mol/L in a B–R buffer of pH 6; E_{acc} = –0.6 V. Other operational parameters are as described in the caption of Fig. 2.



concentration for 90 s. The accumulation potential had no obvious effect on the peak height over the range 0 to – 0.9 V (Fig. 5).

Fig. 5. Effect of E_{acc} on SWAdCS voltammetric peak current for 7×10^{-8} mol/L imatinib in a B–R buffer of pH 6; t_{acc} = 90 s. Other operational parameters are as described in the caption of Fig. 2.



The optimum instrumental conditions were identified from a study of the variation in peak current, for 5×10^{-8} mol/L imatinib in a B–R buffer of pH 6, with frequency, scan increment, and pulse-amplitude. A more developed peak current was achieved with high frequencies of the order 120 Hz. Higher peak current was also obtained by increasing the pulse-amplitude up to 25 mV and the scan increment up to 10 mV without loss of resolution, i.e., the peak half-width remains almost constant. According to the foregoing results, the following parameters were chosen as the optimal operational conditions for the proposed stripping procedure: an accumulation potential (E_{acc}) = –0.6 V, t_{acc} = 120–150 s, frequency (f) = 120 Hz, pulse amplitude = 25 mV, and scan increment 10 mV using a B–R buffer of pH 6 as the supporting electrolyte.

Validation of the analytical procedure

The SWAdCS voltammograms of different concentrations of bulk imatinib standard solutions following preconcentration onto the HMDE for different time periods (30–150 s) were recorded five times for each concentration under the optimized operational conditions of the proposed procedure. The corresponding calibration graphs were linear over the concentration ranges reported in Table 1. The limits of detection (LOD) and quantitation (LOQ) were calculated (Table 1) using the following equations: LOD = 3 s/m and LOQ = 10 s/m, respectively (21), where s is the standard deviation of the blank and m is the slope of the calibration curve.

The selectivity (22) of the optimized procedure for assays of imatinib was identified by studying the effect of various substances that often accompany the drug in various pharmaceutical preparations. An attractive feature of an analytical procedure is its relative freedom from interference by the usual occupants such as cellulose, magnesium searate, glu-

© 2004 NRC Canada

Table 1. Characteristics of calibration graphs of imatinib in a Britton–Robinson buffer of pH 6 using the proposed procedure at different accumulation times (t_{acc}).

t_{acc} (s)	Slope (*n*A/*n*mol/L)	Intercept (*n*A)	*r*	Linear range (mol/L)	LOD (mol/L)	LOQ (mol/L)
30	26.22	73.0	0.995	5×10^{-9} – 1×10^{-7}	5.7×10^{-10}	1.9×10^{-9}
60	27.20	120.0	0.995	2×10^{-9} – 8×10^{-8}	5.5×10^{-10}	1.8×10^{-9}
90	39.04	140.0	0.998	1×10^{-9} – 6×10^{-8}	3.8×10^{-10}	1.3×10^{-9}
120	48.94	300.0	0.997	1×10^{-9} – 5×10^{-8}	3.1×10^{-10}	1.0×10^{-9}
150	93.50	172.0	0.996	9×10^{-10} – 3×10^{-8}	2.6×10^{-10}	8.7×10^{-10}

Table 2. Quantification of imatinib in Glivec® capsules by the proposed procedure (t_{acc} = 90 s) using the standard addition method (n = 5).

Concn. of drug (taken) (ng)	Concn. of drug (found) (ng)	%R[a]	%RSD[b]
2.95	2.89	98.2	0.8
5.89	5.95	101.0	0.8
8.84	8.78	99.3	0.5
11.78	11.96	101.5	1.2

[a]Mean percentage recoveries.
[b]Mean percentage relative standard deviations.

cose, lactose, dextrose, and starch. Samples containing 5×10^{-8} mol/L bulk imatinib and different concentrations of the occupants under evaluation were analyzed by means of the proposed procedure. The obtained mean percentage recoveries (%R) and relative standard deviations (%RSD), based on three replicate measurements, (98.5 ± 1.6 – 100.1 ± 1, respectively) showed that there was no significant interference from occupants. Thus the procedure was able to assay imatinib in the presence of occupants and it can, therefore, be considered selective.

The proposed procedure analysis accuracy (22) was evaluated by calculating any systemic error involved. The estimated mean percentage recoveries of imatinib (97.8 ± 1.2 – 98.6 ± 1.5) indicated the high accuracy of the proposed analysis procedure.

The intra-day and inter-day precision (22) of the method was determined by analyzing different concentrations of imatinib for three times in one day and for five days over a period of one week. The intra-day and inter-day coefficients of variation of imatinib recovery (1.1–1.5) indicated good repeatability confirming the high precision of the proposed procedure.

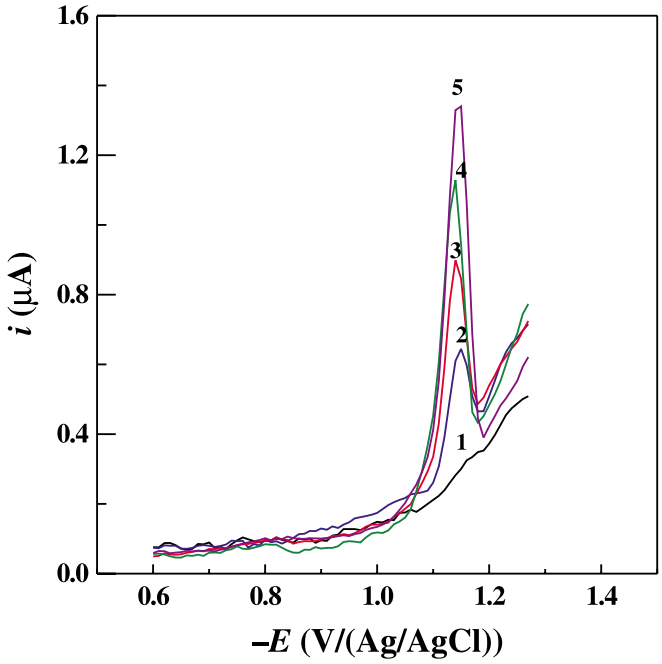
The robustness (22) of the proposed analysis procedure was also examined by evaluating the influence of small variations in some of the most important procedural conditions including pH, preconcentration time period, and preconcentration potential. The mean percentage recoveries obtained (97.7 ± 1.2 – 98.5 ± 1.3) were not significantly affected within the operational parameter variation range studied, and consequently the proposed analysis procedure was reliable for assay of imatinib and it can be deemed robust.

Application

Assay of imatinib in capsules

The proposed procedure was successfully applied for direct assay of imatinib in its pharmaceutical formulation (Glivec® capsules) without the necessity for sample pretreatment or any time-consuming extraction or evaporation steps prior to analysis of the drug The %R obtained using the standard addition method (Table 2) and the corresponding %RSD verified the accuracy of the proposed procedure for assay of the drug in capsules.

Fig. 6. Representative SWAdCS voltammograms for different concentrations of imatinib spiked in human serum in a B–R buffer of pH 6: (1) Background, (2) 4×10^{-9}, (3) 8×10^{-9}, (4) 1.2×10^{-8}, and (5) 1.6×10^{-8} mol/L; t_{acc} = 90 s. Other operational parameters are as described in the caption of Fig. 2.



Assay of imatinib spiked in human serum

The proposed procedure was also successfully applied for direct determination of the drug spiked in human serum, without the necessity for sample pretreatment or any time-consuming extraction or evaporation steps other than the centrifugal separation of precipitated proteins from the serum samples, prior to analysis of the drug. Representative voltammograms for different concentrations of imatinib spiked in human serum following preconcentration for 90 s at –0.6 V are shown in Fig. 6. The LOD and LOQ of 4.6×10^{-10} mol/L and 1.5×10^{-9} mol/L imatinib, respectively, were achieved in spiked human serum samples. The accuracy of the proposed procedure for analysis of the drug in serum samples was identified from the %R, based on av-

© 2004 NRC Canada

Table 3. Application of the proposed method to the determination of imatinib spiked in human serum (t_{acc} = 90 s) using the standard addition method (n = 5).

Concn. of drug (taken) (ng)	Concn. of drug (found) (ng)	%R	%RSD
2.36	2.38	101.0	0.7
3.53	3.52	99.6	0.4
4.71	4.73	100.3	0.1
5.89	5.83	99.0	0.7

erages of five replicate measurements, at different concentrations of imatinib spiked in human serum using the standard addition method (Table 3).

Conclusion

The electrochemical behavior of imatinib in B–R buffers of pH 2–11 at a HMDE was studied for the first time. The drug was found to exhibit strong adsorption onto the electrode surface over the pH values 6 and 7. A SWAdCS voltammetric procedure for quantification of imatinib in bulk form, pharmaceutical formulation, and spiked in human serum was described. The developed procedure was facile, fast, sensitive, selective, and inexpensive; as well it did not require sample pretreatment or any time-consuming extraction or evaporation steps prior to analysis of the drug. The procedure could possibly be adopted for use in clinical and quality control laboratories.

Acknowledgement

The authors express their gratitude to the Alexander von Humboldt Foundation (Bonn, Germany) for donating the Electrochemical Analyzer Model 263A-PAR and the Eppindorf centrifuge used in the present study to Prof. Dr. M.M. Ghoneim.

References

1. J. Zimmermann, E. Buchdunger, H. Mett, T. Meyer, and N.B. Lydon. Bioorg. Med. Chem. Lett. **7**, 187 (1997).
2. E. Buchdunger, J. Zimmermann, H. Mett, T. Meyer, M. Muller, B.J. Druker, and N.B. Lydon. Cancer Res. **56**, 100 (1996).
3. J. Tyler-Thiesing, S. Ohno-Jones, K.S. Kolibaba, and B.J. Druker. Blood, **96**, 3195 (2000).
4. M.E. O'Dwyer and B.J. Druker. Curr. Opin. Oncol. **12**, 594 (2000).
5. T.I. Mughal and J.M. Gholdman. Eur. J. Cancer **37**, 561 (2000).
6. M.J. Mauro and B.J. Druker. Oncologist, **6**, 233 (2001).
7. J.M. Goldman. Lancet, **355**, 1031 (2000).
8. B.J. Druker and N.B. Lydon. J. Clin. Invest. **105**, 3 (2000).
9. R. Bakhtiar, L. Khemani, M. Hayes, T. Bedman, and F. Tse. J. Pharm. Biomed. Anal. **28**, 1183 (2002).
10. R. Bakhtiar, J. Lohne, L. Ramos, L. Khemani, M. Hayes, and F. Tse. J. Chromatogr. B, **768**, 325 (2002).
11. R.A. Parise, R.K. Ramanathan, M. Hayes, and M.J. Egorin. J. Chromatog. B, **791**, 39 (2003).
12. V.V. Vivekanand, D.R. Sreenivas, G. Vaidyanathan, N.M. Sekhar, S. Avijit Kelkar, and P. P. Ramachandra. J. Pharm. Biomed. Anal. **33**, 879 (2003).
13. G. Guetens, G. De Boeck, M. Highley, H. Dumez, A.T. Van Oosterom, and E.A. De Bruijn. J. Chromatogr. A, **1020**, 27 (2003).
14. J.R. Flores, J. Berzas, G. Castaneda, and N. Rodriguez. J. Chromatogr. B, **794**, 381 (2003).
15. J. Wang. Analytical electrochemistry, 2nd ed. Wiley-VCH, New York. 2000. p. 75.
16. H.T.S. Britton. *In* Hydrogen ions, 4th ed. Chapman and Hall, London. 1952. p. 113.
17. P. Zuman. *In* The elucidation of organic electrode processes. Academic Press, New York. 1969. pp. 21–24.
18. E. Laviron. J. Electroanal. Chem. **112**, 11 (1980).
19. A. Webber, M. Shah, and J. Osteryoung. Anal. Chim. Acta **157**, 17 (1984).
20. W.R. Heineman and P.T. Kissinger. *In* Laboratory techniques in electroanalytical chemistry, Marcel Dekker, New York. 1984. Chap. 3. p. 62.
21. J.C. Miller and J.N. Miller. *In* Statistics for analytical chemistry, 4th ed. Ellis-Horwood, New York. 1984. p. 115.
22. The United States Pharmacopoeia, The National Formulary, USP 24, NF 19, USP Convention Inc. 2000. p. 2151.

© 2004 NRC Canada

Identification of glycerophospholipids in rapeseed, olive, almond, and sunflower oils by LC–MS and LC–MS–MS

Sadok Boukhchina, Khaled Sebai, Ammar Cherif, Habib Kallel, and Paul M. Mayer

Abstract: HPLC employing a thermostatted Lichrospher 100 diol column was used to separate mixtures of glycerophospholipids of rapeseed, olive, almond, and sunflower oils. Elution was performed with a binary gradient of two mixed solvents A: hexane – isopropanol – acetic acid – triethylamine (82:17:1.0:0.08 v/v/v/v) and B: isopropanol – water – acetic acid – triethylamine (85:14:1.0:0.08 v/v/v/v). The LC effluent was directly introduced into the mass spectrometer through an electrospray capillary. Information about the fatty acid composition of each glycerophospholipid class was given by tandem mass spectrometry (MS–MS). These techniques permitted a rapid separation and identification of complex mixtures of glycerophospholipids. The relative abundance of each lipid class in each oil was also determined. The resulting glycerophospholipid signature may provide an efficient means of identifying oil origin and possible adulteration.

Key words: glycerophospholipids, vegetable oils, tandem mass spectrometry, LC–MS.

Résumé : Faisant appel à la chromatographie liquide à haute performance et une colonne de diol Lichrospher 100 maintenue à température constante, on a séparé les mélanges de glycérophospholipides d'huiles de colza, d'olive, d'amande et de tournesol. On a effectué l'élution à l'aide de gradients binaires de deux solvants mixtes, A: hexane – isopropanol – acide acétique – triéthylamine (82:17:1,0:0,08 v/v/v/v) et B: isopropanol – eau – acide acétique – triéthylamine (85:14:1,0:0,08 v/v/v/v). Les effluents des chromatographies liquides ont été introduits directement dans un spectromètre de masse par le biais d'un capillaire à électronébulisation. On a obtenu l'information relative à la composition en acide gras de chaque classe de glycérophospholipide à partir d'un tandem de spectrométrie de masse (SM/SM). Ces techniques ont permis d'effectuer une séparation et une identification rapides de mélanges complexes de glycérophospholipides. On a aussi déterminé l'abondance relative de chaque classe de lipide dans chacune des huiles. Les signatures de glycérophospholipides résultantes pourraient fournir une méthode efficace d'identifier l'origine d'une huile et éventuellement de déterminer s'il y a eu adultération.

Mots clés : glycérophospholipides, huiles végétales, spectrométrie de masse en tandem, chromatographie liquide – spectrométrie de masse.

[Traduit par la Rédaction]

Introduction

Glycerophospholipids constitute a principal class of membrane lipids. They are comprised of a glycerol backbone in which two alcohol substituents have been replaced with fatty acid side chains and the third has been phosphorylated. They play a role in both the physical structure of the cell membrane and in the various phenomena linked to the functioning of these membranes such as selective permeability, active transportation, and electrical conductivity.

Received 6 January 2004. Published on the NRC Research Press Web site at http://canjchem.nrc.ca on 28 September 2004.

S. Boukhchina,[1] K. Sebai, A. Cherif, and H. Kallel. Faculté des Sciences de Tunis, El Manar, Tunisie.
P.M. Mayer.[2] Chemistry Department, University of Ottawa, Ottawa, ON K1N 6N5, Canada.

[1]Corresponding author (e-mail: sboukchina@yahoo.fr).
[2]Corresponding author (e-mail: pmayer@science.uottawa.ca).

The various classes of glycerophospholipids are derived from phosphatidate (diacylglycerol-3-phosphate) which itself is not usually a prominent membrane phospholipid but is involved in their biosynthesis. The phosphate group of the phosphatidate is esterified by the hydroxyl group of various alcohols such as ethanolamine, choline, inositol and glycerol (Fig. 1). This variety makes their separation and analysis with classical techniques difficult.

The conventional method for analysing glycerophospholipids required a preliminary separation by thin layer chromatography (TLC) (1) followed by enzymatic hydrolysis to permit their separation and detection by gas chromatography (GC) (2). To enhance the resolution of the often complex mixtures of lipids, high performance liquid chromatography (HPLC) has largely supplanted TLC (3–6). A combination of HPLC and GC methods has been proposed to resolve the complex mixtures of potato tuber and tobacco leaf glycerophospholipids into the various molecular species present in each lipid class (7). Liquid chromatography – mass spectrometry (LC–MS) employing a thermospray interface has

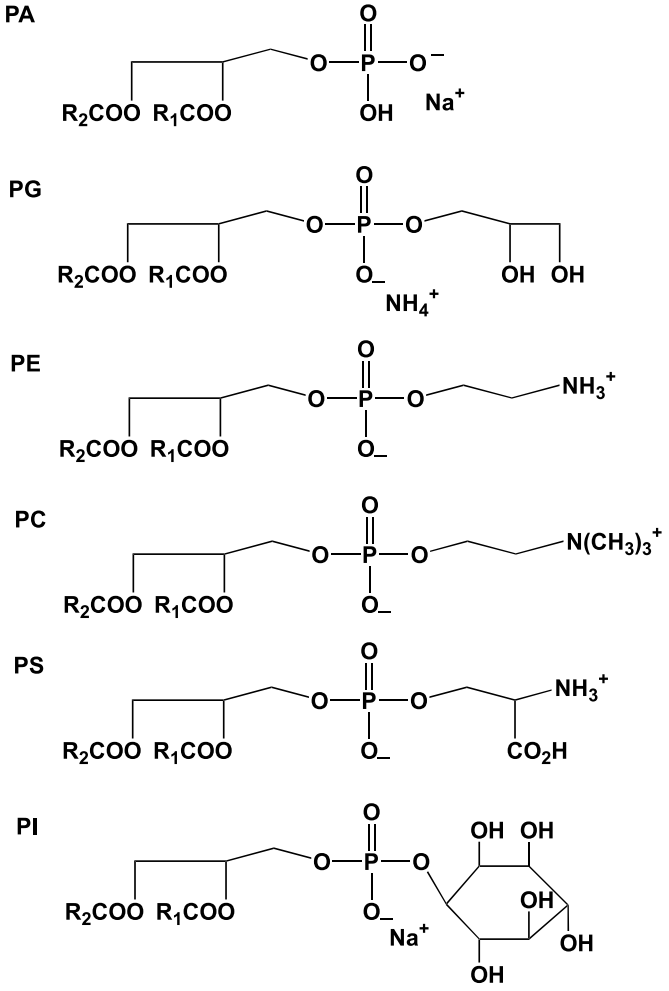
 doi: 10.1139/V04-094 © 2004 NRC Canada

Table 1. Glycerophospholipid classes, retention times, and observed ions.

Lipid class	Abbr.	Retention time (min)	Observed ion	Odd/even mass
Phosphatidic acid	PA	8–10	$[M - Na]^-$	Odd
Phosphatidylethanolamine	PE	10–12	$[M - H]^-$	Even
Phosphatidylglycerol	PG	11–13	$[M - NH_4]^-$	Odd
Phosphatidylcholine	PC	14–15	$[M - CH_3]^-$	Even
Phosphatidylserine[a]	PS	15–16	$[M - H]^-$	Even
Phosphatidylinositol	PI	16–18	$[M - Na]^-$	Odd

[a]No glycerophosphatidylserines were observed in the oil samples reported here.

Fig. 1. Chemical structures of glycerophospholipid classes: phosphatidic acid (PA), phosphatidylglycerol (PG), phosphatidylethanolamine (PE), phosphatidylcholine (PC), phosphatidylserine (PS), phosphatidylinositol (PI). Fatty acid groups R1 and R2 vary within each class and are typically denoted according to carbon chain length and number of double bonds (e.g., C18:1 denotes a fatty acid chain of length 18 carbons (including the carbonyl carbon) containing one double bond).



been used to determine the molecular species of several components of the lipid classes (8) but the procedure still required that the fatty acids be analysed by GC. Off-line coupling of HPLC separation with fast-atom bombardment (FAB) mass spectrometry has also been used in the analysis of phospholipids in peanuts (9). There have been considerable efforts in the last few years to identify glycerophospholipids by electrospray-tandem mass spectrometry (10) and all have focussed on the analysis of positive lipid ions (either protonated lipids or ones complexed by a metal ion). The tandem mass spectra obtained in positive ion mode, however, are quite complex and requiring extensive interpretation (10). Recently, a sensitive method has been described for the separation and identification of glycerophospholipids derived from fungi and pollen in air samples by negative ion LC–MS and tandem mass spectrometry (MS–MS) (11). The tandem mass spectra obtained for negatively charged lipids are very simple and typically contain only peaks due to the fatty acid side chains, thus allowing their identification.

In the present study, we have employed LC–MS and LC–MS–MS as a rapid separation and identification tool for the complex mixtures of glycerophospholipids found in five vegetable oils: the oils from two forms of rapeseeds (Hybridol and Pactol), olives, almonds, and sunflowers. Tandem mass spectrometry is used to aid in the identification of lipid class and fatty acid composition. The information provides a unique glycerophospholipid signature for each kind of oil, which may be used to improve purity tests for these oils that face frequent adulteration.

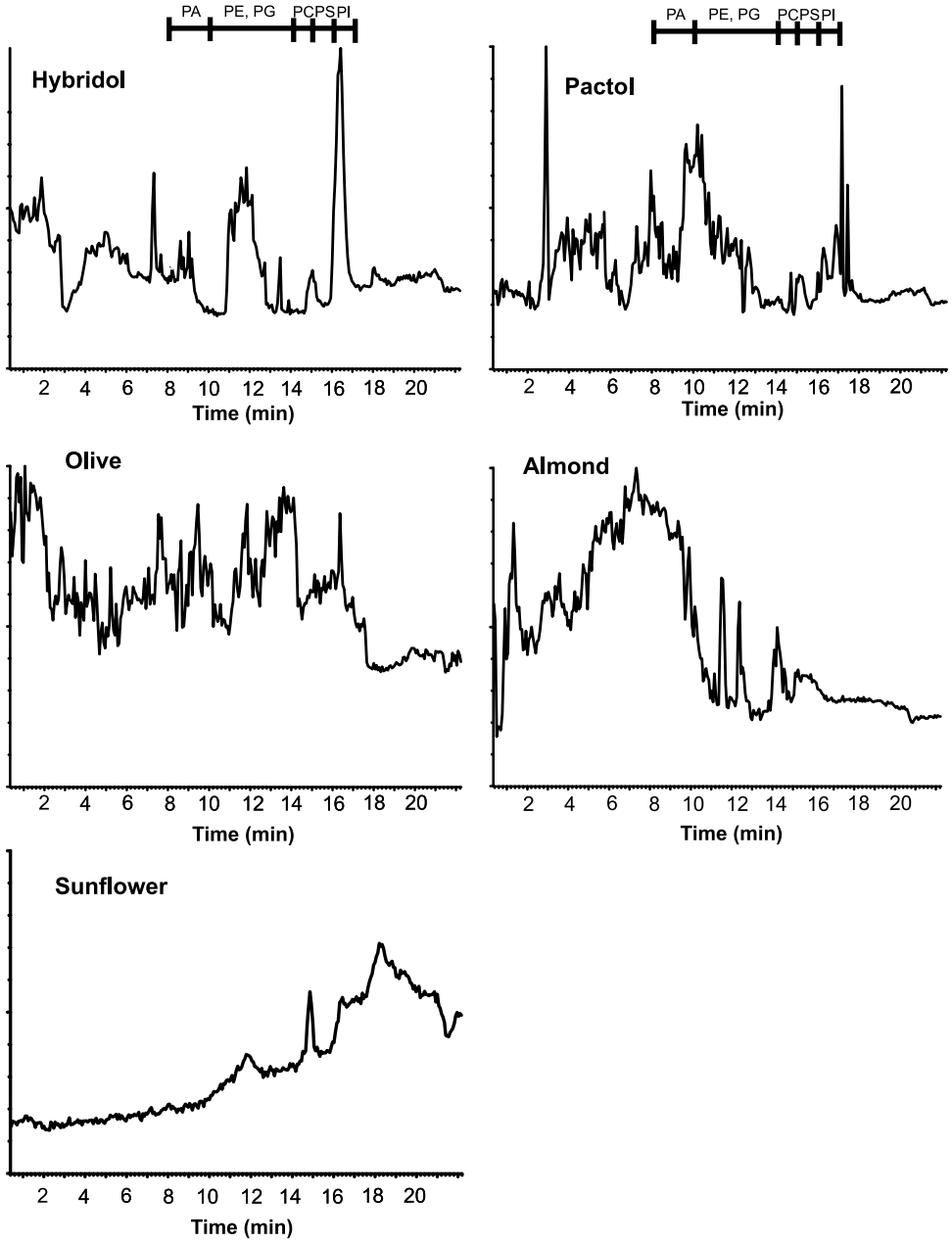
Experimental procedures

Olive oil was commercially obtained (Almoubaraka). Rapeseeds (*Brassica napus* L.) of the variety Pactol and Hybridol, almonds and sunflower seeds were provided by the Institut de Recherches Agronomiques de Tunis. Total lipids were extracted by a modified Bligh and Dyer method (12). The seeds were put in boiling water for 5 min to inactivate the phospholipases and were then finely crushed with a mortar and pestle. Lipids were extracted with a mixture of chloroform and methanol (1:1, v/v). Fixing water was added at the end of the extraction to eliminate nonlipid components. The extract was centrifuged at 3000 rpm for 15 min. The final chloroform extract was evaporated using a rotary evaporator at 35 °C and finally dried under a stream of nitrogen. The extracted was stored at –10 °C.

The LC-MS and LC-MS–MS procedures employed in this study have been discussed previously (11). Briefly, liquid chromatography was performed on an HP 1050 Ti series gradient pump having a 10 µL sample loop. A Lichrospher 100 diol column (250 mm × 4.6 mm, 5 µm particle size; Merck, Germany) was used to separate phospholipids according to class (see Table 1). The binary solvent gradient consisted of solvent mixture A: hexane – isopropanol – acetic acid – triethylamine (82:17:1.0:0.08 v/v/v/v) and mix-

© 2004 NRC Canada

Fig. 2. Total ion chromatograms for Hybridol, Pactol, olive, almond, and sunflower oil extracts. Superimposed on the top two chromatograms are the retention time windows for each glycerophospholipid class.



ture B: isopropanol – water – acetic acid – triethylamine (85:14:1.0:0.08 v/v/v/v). The gradient was started at 5% mixture B and its percentage was increased linearly to 80% over 25 min. This composition was maintained for 1 min before being returned to 5% B over 10 min and maintained at 5% for another 4 min (40 min total run time). The flow rate of 1 mL/min through the column was subsequently split to 100 µL/min using a micro-splitter valve (Upchurch Scientific, Oak Harbor, Wash.) before being introduced to the electrospray ionization source of the mass spectrometer.

Glycerophospholipids were detected with a Quattro-LC (Waters) electrospray ionization triple-quadrupole mass spectrometer (operating in negative ion mode) employing the MassLynx (ver. 3.5) control and processing software. The 100 µL/min flow of eluent was passed through the electrospray capillary, which was held at –3.8 kV. The source block temperature was 80 °C and the cone voltage was set at –70 V. N_2 drying gas was passed coaxially to the capillary with a flow rate of approximately 100 L/h. Tandem mass spectra were obtained by introducing argon collision gas into the central, RF-only hexapole to a recorded pressure of 2×10^{-4} mbar (1 bar = 100 kPa). Precursor ions were selected with unit mass resolution by the first quadrupole (Q1) and collision-induced dissociation (CID) mass spectra were obtained by scanning the last quadrupole (Q3) with slightly less than unit mass resolution.

Results and discussion

The total ion chromatograms for the five oils are shown in

© 2004 NRC Canada

Fig. 3. Mass spectra corresponding to each lipid class in the chromatogram of Pactol oil. Each spectrum is an average over the corresponding retention time window for that class.

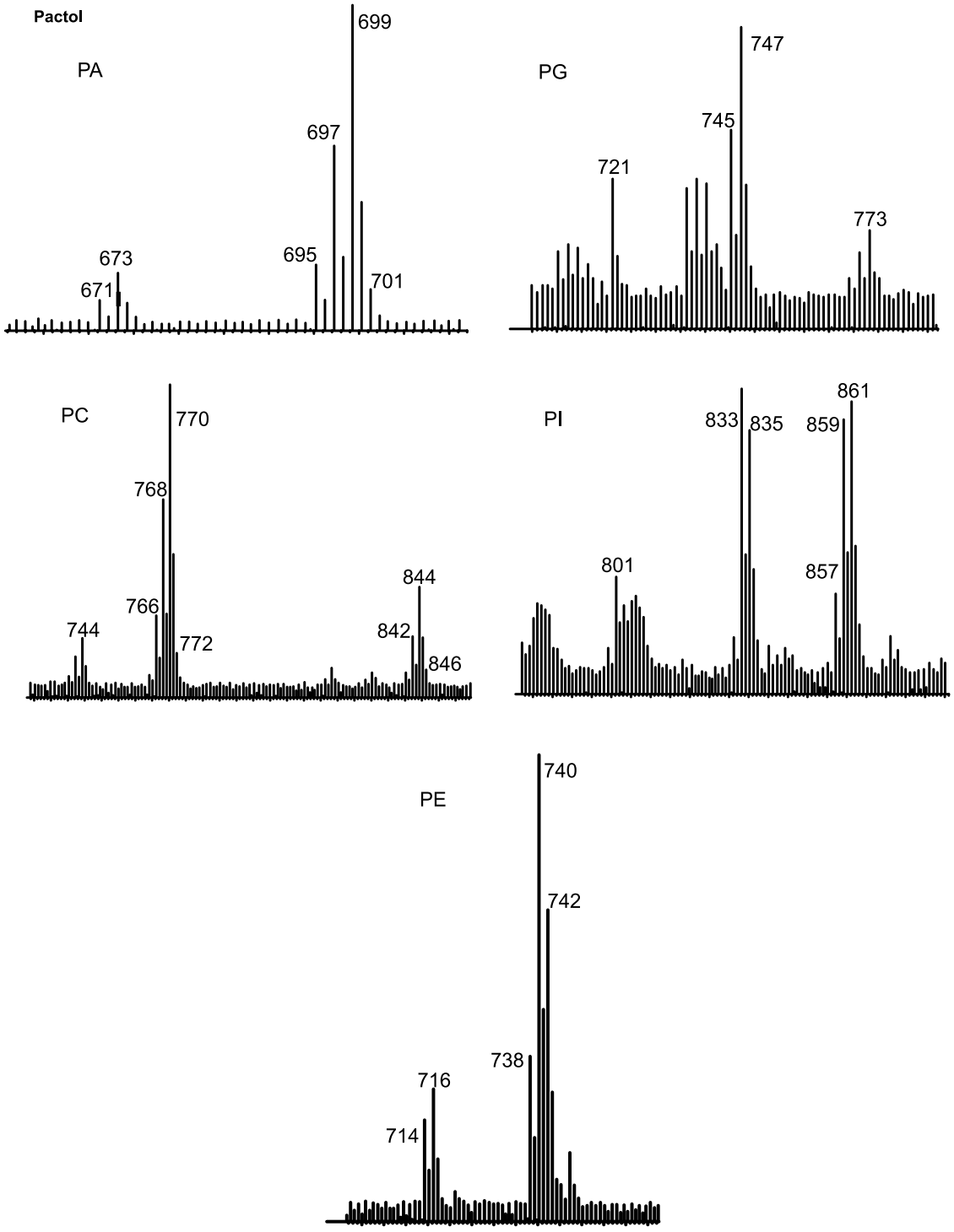


Fig. 2. Glycerophospholipid class identification was confirmed by summing the mass of each R group (Fig. 1) identified by MS–MS with that of the glycerol backbone (41 Da) and phosphoric acid (95 Da). The remaining mass is due to the polar head group. This was done once for the Pactol oil extract and the resulting retention time ranges used in the analyses of the other oils. No glycerophosphatidylserines were observed in the oil samples reported here. Figure 3 shows the averaged mass spectrum for each class of glycerophospholipid in Pactol. An example of the MS–MS data is shown in Fig. 4 for *m*/*z* 768, a PC class glycerophospholipid. Due to the small amounts of glycerophospholipids present in each sample, MS–MS identification of the R groups for all phospholipids in each oil could not be achieved. Those glycerophospholipids in Pactol oil that could be identified with respect to their fatty acid chains are summarized in Ta-

© 2004 NRC Canada

Fig. 4. Tandem mass spectrum for *m*/*z* 768 of Pactol oil (PC class). See text for experimental conditions.

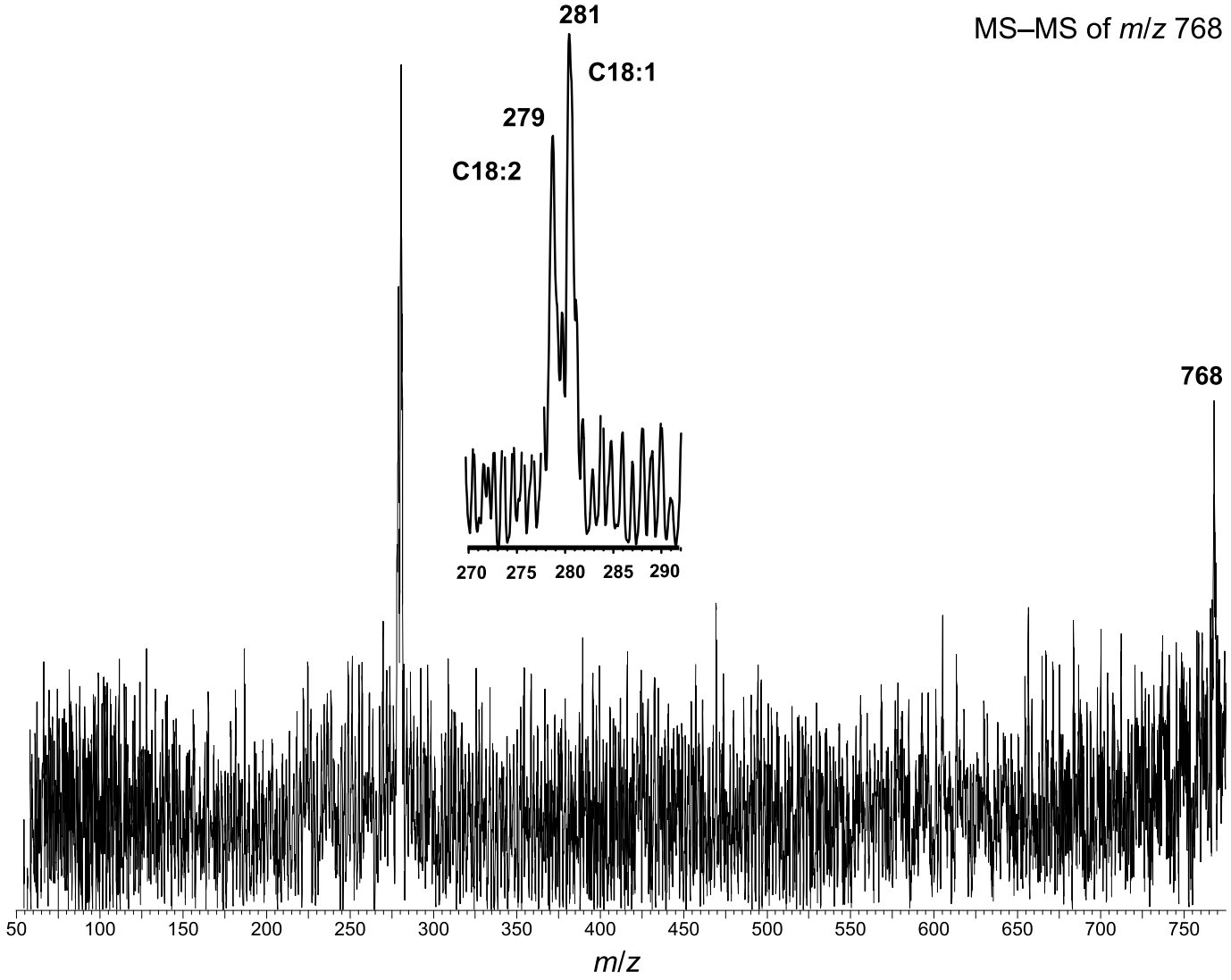


Table 2. Glycerophospholipids in Pactol oil identified by MS–MS.[a]

m/*z*	Class	R_1	R_2
699	PA	281 (C18:1)	281 (C18:1)
747	PG	281 (C18:1)	255 (C16:0)*
738	PE	279 (C18:2)	279 (C18:2)
740	PE	279 (C18:2)	281 (C18:1)
742	PE	281 (C18:1)	281 (C18:1)
766	PC	279 (C18:2)	279 (C18:2)
768	PC	279 (C18:2)	281 (C18:1)
770	PC	281 (C18:1)	281 (C18:1)
859	PI	279 (C18:2)	281 (C18:1)*

[a]Fatty acids for which peaks were not observed in the tandem mass spectrum, but whose presence was inferred from the molecular weight, are denoted with an asterisk.

ble 2. Fatty acid chains of C18 are predominant in the oils, which is consistent with the results from previous studies of a wide range of plant material (7–9, 11). One exception in Table 2 is for *m*/*z* 747, a PG class lipid that has both C18 and C16 side chains. This combination has also been observed by Demandre et al. (7) in potato tuber and tobacco leaf samples and by Womiloju et al. (11) in extracts from fungal spores.

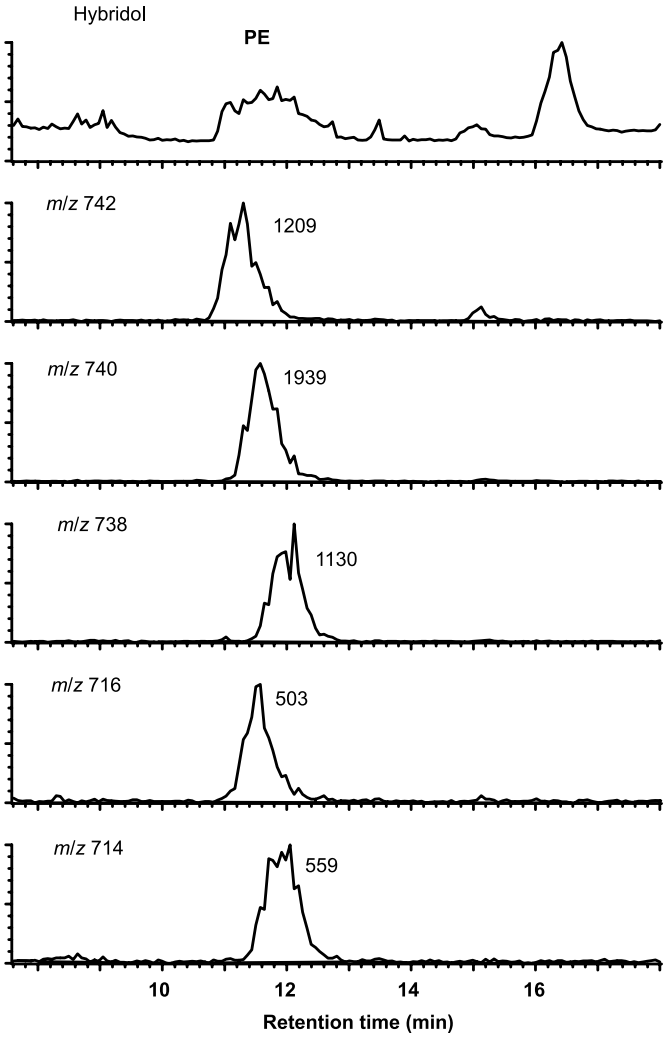
Table 3. Relative abundance of each glycerophospholipid class in each vegetable oil.

	Relative abundance (%)				
Oil	PA	PG	PE	PC	PI
Olive	12	63	9	5	11
Almond	0	2	45	45	8
Sunflower	0	11	34	46	8
Hybridol	1	0	38	6	55
Pactol	25	30	2	19	24

Relative abundances of each individual glycerophospholipid in each class were determined from the area of the ion chromatogram corresponding to the detected ion for that particular lipid (see Table 1). An example is shown in Fig. 5

© 2004 NRC Canada

Fig. 5. Selected ion chromatograms for individual glycerophosphatidylethanolamine lipids in Hybridol oil. Integrated peak areas are listed for each chromatogram (arbitrary units).



for the glycerophosphatidylethanolamines (PE) in Hybridol oil. The results for each oil are summarized in Table 3. Without a suitable internal standard, it was not possible to compare the absolute amounts of glycerophospholipids among oils, but provided that the extraction efficiencies were similar, the rapeseed oils had significantly more lipid content than olive, almond, or sunflower oils. Olive oil is characterized by a unique signature being comprised principally of PG class glycerophospholipids. It is the only oil that exhibits a single dominant class of lipids and is the only nonseed derived oil in this study. Almond and sunflower oils are poor in PG lipids, the profiles for both exhibiting primarily PE and PC class glycerophospholipids. Indeed, it would be difficult to distinguish these two oils based solely on their lipid profiles. Interestingly, rapeseed oils derived from the two varieties of seeds dealt with here, Pactol and Hybridol, display quite unique lipid abundances. Hybridol oil contains mainly PE and PI class lipids, while Pactol is more evenly distributed, except for a notable absence of PE class lipids.

Conclusions

The described LC–MS and MS–MS methods for the separation and identification of glycerophospholipids in vegetable oils (two types of rapeseed plus olive, almond, and sunflower) are simple and rapid alternatives to previous approaches that require chemical fictionalisation of the lipids and multiple-technique analyses. HPLC allows speed and reproducible separations of the main glycerophospholipid classes. Information about the fatty acid composition of each glycerophospholipid class was given by tandem mass spectrometry without the need to further chemically modify the phospholipids.

Each vegetable oil was found to have a characteristic glycerophospholipid composition, including significant differences between two rapeseed oils, which may be useful in the identification of the oil source in commercial applications.

Acknowledgments

PMM thanks the Natural Sciences and Engineering Research Council of Canada (NSERC) for continuing financial support and the Canadian Foundation for Innovation (New Opportunities), along with the Ontario Innovation Trust, for the funding for the Quattro-LC.

References

1. J.C. Touchstone. J. Chromatogr. B, **671**, 169 (1995).
2. C.V. Nwosu and L.C. Boyd. J. Am. Oil Chem. Soc. **74**, 293 (1997).
3. T.L. Mounts, S.L. Abidi, and K.A. Rennick. J. Am. Oil Chem. Soc. **69**, 438 (1992).
4. S.L. Melton. J. Am. Oil Chem. Soc. **69**, 784 (1992).
5. A.A. Carelli, M.I.V. Brevedan, and G.H. Crapiste. J. Am. Oil Chem. Soc. **74**, 511 (1997).
6. T. Nomicos, H.C. Karantonis, E. Fragopoulou, and C.A. Demopoulos. J. Liq. Chromatogr. Related Technol. **25**, 137 (2002).
7. C. Demandre, A. Tremolieres, A. Justin, and P. Mazliak. Phytochemistry, **24**, 481 (1985).
8. H.Y. Kim and N. Salem. Anal. Chem. **59**, 722 (1987).
9. J.A. Singleton, M. Ruan, J.H. Stanford, C.A. Haney, and L.F. Stikeleather. J. Am. Oil Chem. Soc. **76**, 49 (1999).
10. For examples see: F.-F. Hsu and J. Turk. J. Am. Soc. Mass Spectrom. **14**, 352 (2003); F.-F. Hsu, A. Boher, and J. Turk. J. Am. Soc. Mass Spectrom. **9**, 516 (1998); P. Domingues, F.M.L. Amado, M.G.O. Santana-Marques, and A.J. Ferrer-Correia. J. Am. Soc. Mass Spectrom. **9**, 1189 (1998); X. Han and R.W. Gross. J. Am. Soc. Mass Spectrom. **6**, 1202 (1995); P. Domingues, M.R.M. Domingues, F.M.L. Amado, and A.J. Ferrer-Correia. Rapid Commun. Mass Spectrom. **15**, 799 (2001); F.-F. Hsu and J. Turk. J. Mass Spectrom. **35**, 596 (2000).
11. T.O. Womiloju, J.D. Miller, P.M. Mayer, and J.R. Brook. Atmos. Environ.ment, **37**, 4335 (2003).
12. D.C. White, W.M. Davis, J.S. Nickels, J.D. King, and R.J. Bobbie. Oecologia, **40**, 51 (1979).

© 2004 NRC Canada

An ab initio study of the potential energy surfaces for the collision between a Cs atom and an I_2 molecule

Xiaomin Sun, Dacheng Feng, Zhengting Cai, and Wensheng Bian

Abstract: For the Cs + I_2 collision system, a systematic theoretical study is first reported using the ab initio method. Three of eight possible channels are considered. The nonadiabatic coupling between the covalent state and the ionic one is calculated from different angles, especially the T-shape collision. The complete ion-pair formation potential energy surfaces of the T-shape collision in two electronic states (ionic $^2B_2$ state and covalent $^2A_1$ state) and the reactive surface of the linear collision are constructed at the QCISD(T)/SDD level. The main features of potential energy surfaces, such as the minimum energy reaction path, the crossing radius (R_c), and energy minimum geometries, are analyzed. The cross section of this titled system is calculated based on the harpoon mechanism and compared with the available experimental data and those obtained for the M + I_2 (M = Li, Na) systems.

Key words: ab initio two-state potential energy surfaces, nonadiabatic coupling, ion-pair formation, cross section.

Résumé : Faisant appel à une méthode ab initio, on a réalisé la première étude théorique systématique du système de collision Cs + I_2. On a considéré trois des huit canaux possibles. Le couplage non adiabatique entre l'état covalent et l'état ionique a été calculé pour divers angles, particulièrement pour la collision en forme de T. Opérant au niveau QCISD(T)/SDD, on a construit l'ensemble des surfaces d'énergie potentielle conduisant à la formation de la paire d'ions de la collision en forme de T dans les deux états électroniques (état ionique $^2B_2$ et l'état covalent $^2A_1$) ainsi que la surface réactive de la collision linéaire. On a analysé les caractéristiques principales des surfaces d'énergies potentielles, telles que la voie réactionnelle d'énergie minimale, le rayon de croisement (R_c) et les géométries minimales d'énergie. La section droite du système mentionné dans le titre a été calculée sur la base du mécanisme du harpon et on l'a comparée avec les données expérimentales ainsi que celles obtenues pour les systèmes M + I_2 (M = Li, Na).

Mots clés : surfaces d'énergie potentielle à deux états ab initio, couplage non adiabatique, formation de paires d'ions, section droite.

[Traduit par la Rédaction]

Introduction

Potential energy surface (PES) is the key to the research of molecular reaction dynamics, and the main features of a PES could directly influence the energy distribution, the ratio of the products, the role that the translational and internal energy plays in a reaction, and so on. Theoretically, as long as the whole fine PES of a reaction system is provided, the foundation is laid for solving the Schrödinger equation of its nuclear motion. Thus, constructing a reliable PES is of great importance to the study of basic chemical dynamics.

The collision between an alkali metal atom M (M = Li, Na, K, Rb, Cs) and a halogen molecule X_2 (X = F, Cl, Br, I) has been widely investigated by a variety of techniques in the last 30 years, from which valuable information for collision-induced reaction dynamics can be obtained. For example, the crossed molecular beam (CMB) was adopted to provide considerable experimental data (1–3). For these collision systems, the main processes involved are as follows:

[1] $M + X_2 \rightarrow M + X_2$

[2] $\rightarrow M + X + X$

[3] $\rightarrow M^+ + X_2^-$

[4] $\rightarrow M^+ + X^- + X$

[5] $\rightarrow M^+X + X^-$

[6] $\rightarrow M^+ + X + X + e$

[7] $\rightarrow M^+X + X + e$

[8] $\rightarrow MX + X$

where rxn. [1] represents the nonreactive collision including elastic and inelastic collisions, rxn. [2] is the process of collisionally induced dissociation, and rxns. [3] to [7] involve the electron transfer and ion-pair formation. Among them, rxn. [4] includes the dissociation one, rxn. [5] consists

Received 23 September 2003. Published on the NRC Research Press Web site at http://canjchem@nrc.ca on 5 October 2004.

X. Sun, D. Feng, and Z. Cai.[1] Institute of Theoretical Chemistry, Shandong University, Jinan, Shandong Province 250100, China.
W. Bian. State Key Laboratory of Molecular Reaction Dynamics, Institute of Chemistry, Chinese Academy of Science, Beijing, 100080, China.

[1]Corresponding author (e-mail: zhtcai@sdu.edu.cn).

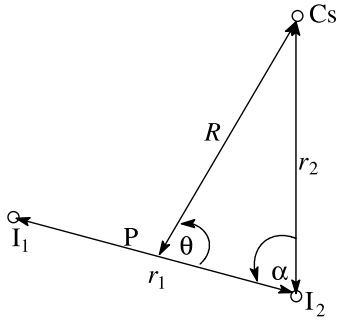
 doi: 10.1139/V04-025 © 2004 NRC Canada

of an association reaction, rxn. [6] is a Penning ionization, and rxn. [7] is a Penning ionization with an association reaction. Reaction [8] is a reactive collision. These eight channels are applicable to the Na + I_2 system (4). Research for these systems has been performed at a highly systematic level. There are comprehensive CMB studies and calculations of the classical trajectory (5, 6) and the quantum reaction scattering theory (7–9). Those calculations were performed on the semiempirical PESs (10). Various mechanisms and calculated models were proposed to interpret experimental phenomena. Among them, the most famous theory was the harpoon mechanism proposed by Polanyi (11) and Magee (12) and developed by Herschbach (13).

For the titled system, previous research results are mainly as follows: In 1971, Edelstein and Davidovits (14) obtained the reaction cross section of alkali metal atoms with an I_2 molecule by direct measurement of the Cs atom decay rates. In 1974, Tang et al. (15) used CMB to study the ionizing collision of energetic Cs atoms with I_2, and the cross section for formation of Cs^+, the intensity ratio I^-/I_2^-, and the electron affinity of the I_2 molecule were reported. In 1975, Anderson and Herschbach (16) performed the calculation of the orbiting scattering inversion from elastic collisions of reactive molecules; Gislason and Grobe Sachs (17) examined the reaction of a Cs atom with an I_2 molecule via an electron jump using the multiple-crossing formalism and obtained the reactive cross section from the already known properties of the Cs atom and the I_2 molecule. Howard and Andrews (18) measured the Raman spectra of cesium atom – iodine matrix reaction products and the resonance Raman spectrum of the iodine molecular anion I_2^-. In 1976, Andrews (19) found a strong 254/286 nm doublet absorption in the $Cs^+I_2^-$ spectrum. In 1977, Aten et al. (10, 20) measured the energy dependence of the differential cross section for ion-pair formation in the Cs + I_2 collision and proposed a semiempirical PES. Later, they carried out the calculation of trajectory surface hopping (TSH) (21). In 1999, Ma et al. (7–9) performed the quantum-scattering dynamics calculations using the extended linear combination of arrangement channels – scattering wavefunction (LCAC–SW) method (7) on Aten–Langting–Los PESs (10).

To the best of our knowledge, no ab initio PES for the Cs + I_2 collision system has been reported up to now. In the present paper, the quantum chemical study was performed for the Cs + I_2 collision system. Three channels (Cs + I_2, Cs^+ + I_2^-, and CsI + I) were mainly considered among the eight possible ones. The collision between the ionic state and covalent state was investigated from various angles with the equilibrium distance of the I_2 molecule fixed. The results indicated that the energy minimum geometry on each PES appears at θ = 90° and was called the T-shape configuration. The complete ab initio PESs of two electronic states (ionic $^2B_2$ state and covalent $^2A_1$ state) for the T-shape collision and the $^2\Sigma$ state for collinear collision were constructed at the QCISD(T) (22) level. Minimum energy reaction paths (MEPs) on each PES and the crossing curve of the two-state PESs were abstracted. Based on the crossing curve, the crossing radius (R_c) between the ionic and covalent states was determined, and the fine electronic structure on the crossing point was computed. The energy minimum geometry on each PES was optimized. The cross sections obtained in terms of the harpoon mechanism were compared with the available data of the title system and those of the M + I_2 (M = Li, Na) systems.

Fig. 1. Reaction coordinates (P represents the center of the I_2 molecule).



Calculation methods

Geometry optimization and the scanning of PESs were performed at the QCISD(T) level, and at the same time, the natural bond orbital (NBO) population was analyzed at the QCISD level. For the Cs and I atoms, a SDD (23) basis set (an effective core potential basis set), including the relativistic effect, was applied.

The Jacobi coordinate is illustrated in Fig. 1 where R is the distance from the Cs atom to the center of the I_2 molecule, r_1 is the I_2 bond distance, and θ is the angle between vectors $\boldsymbol{R}$ and $\boldsymbol{r_1}$. In the process of scanning PES, r_1 was fixed at the equilibrium distance, while θ and R were changing, and then the PES dependent of angle θ was obtained. With a similar method, the PES independent of angle θ (angle θ fixed) could also be obtained. It should be noted that the energy unit in the contours of the PES was a hartree. All the work was completed with the Gaussian 98 packet (24).

Results and discussion

Potential energy surfaces

The PESs dependent of angle θ in the ionic and covalent states are shown in Figs. 2 and 3. During scanning of the PESs, r_1 was fixed at 0.2922 nm (obtained at the QCISD(T)/SDD level), while R with a step-length of 0.01 nm and with the θ angle at 5° was changing. It should be noted that, for an atom plus a diatomic molecule, the total electronic wavefunction depends not only on the electronic species of M and X_2 (or M^+ and X_2^-), but also on the angle θ (17). For example, ground-state Cs (^2S_g) plus ground-state I_2 ($^1\Sigma_g$) combines to generate a $^2A_1$ state in C_{2v} symmetry (θ = 90°), while a $^2\Sigma$ state in $C_{\infty v}$ symmetry (θ = 0°or 180°) and a $^2A'$ state in C_s symmetry (0° < θ < 90°or 90° < θ < 180°) are also generated. By comparison, ground-state Cs^+ (^1S_g) and ground-state I_2^- ($^2\Sigma_u$) yield $^2B_2$, $^2\Sigma$, and $^2A'$ states for the same symmetries. From the PES, it is clearly seen that a potential well appears as R decreases at each θ value in Fig. 2. As θ increases, the depth of the potential well becomes deeper. When θ = 90°, the deepest potential well comes into being, which illustrates the existence of a long-lived geometry. A similar case emerges on the covalent PES in Fig. 3. From the above analysis, the long-lived geometry is formed

© 2004 NRC Canada

Fig. 2. The ionic collision PES with angle θ ranging from 0° to 180° (during scanning, r_1 is fixed at the equilibrium distance).

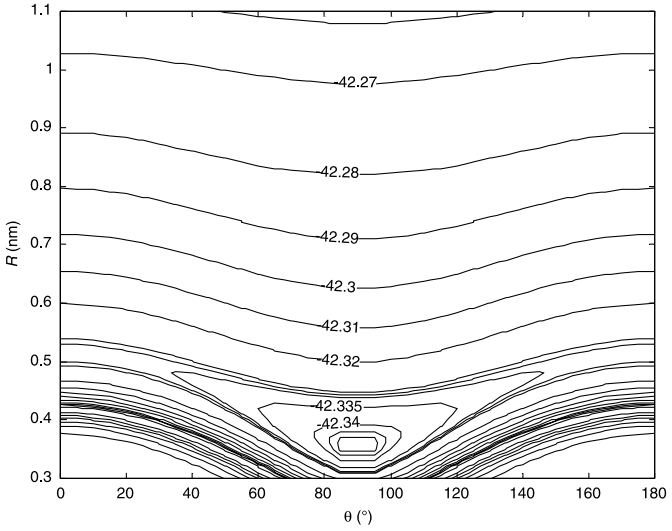


Fig. 3. The covalent collision PES with angle θ ranging from 0° to 180° (during scanning, r_1 is fixed at the equilibrium distance).

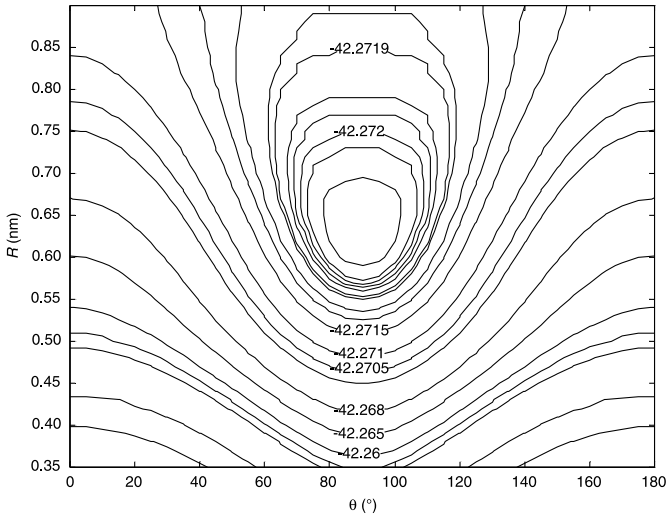


Fig. 4. The contour of the T-shape covalent collision PES with C_{2v} symmetry and the $^2A_1$ electronic state.

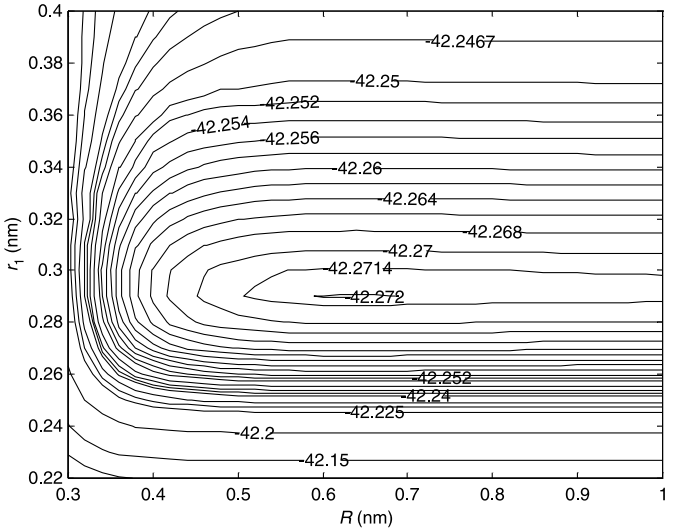
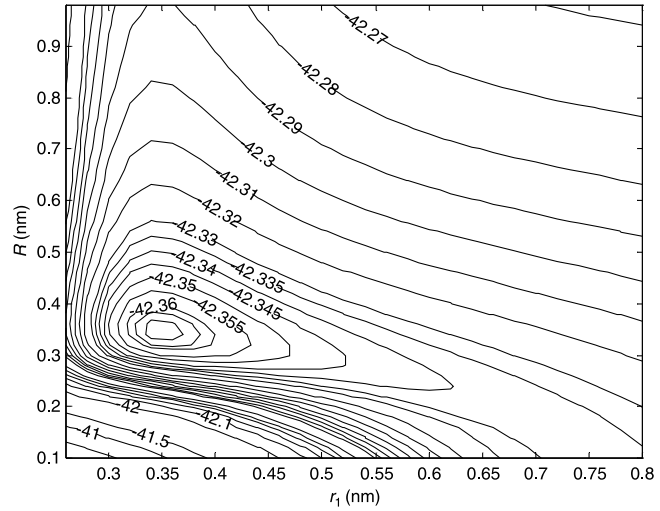


Fig. 5. The contour of the T-shape ionic collision PES with C_{2v} symmetry and the $^2B_2$ electronic state.



under the T-shape collision, and the electron is evenly distributed on two I atoms in the process of ion-pair formation. Hence, the T-shape collision is a very important case in the study of ion-pair formation.

The T-shape collision has C_{2v} symmetry with two electronic states (the ionic $^2B_2$ state and the covalent $^2A_1$ state). The PESs of the T-shape collision were calculated during scanning using r_1 at 0.01 nm in step-length, and R at 0.02 nm in step-length. Figures 4 and 5 show the contour of the whole two-state PESs.

Figure 4 shows the $^2A_1$ state PES of the T-shape structure with C_{2v} symmetry (the covalent state). The entrance point, which is also the exit point of a reaction path, at r_1 = 0.29 nm, R = 1.0 nm, is close to the reactant Cs + I_2 (or the product Cs + I_2), which corresponds to the elastic and inelastic collisions. Its energy is –42.27180 au, and the net charge is 0.00 for both Cs and I atoms. When the Cs atom gradually approaches and then departs from the I_2 molecule, the energy passes a small and shallow well that corresponds to the van der Waals intermediate A, then climbs up quickly, and finally returns back along the reaction path. This phenomenon is vividly demonstrated through the U-type curve on the equal-counter potential plot. It is worth mentioning that the net charge on each atom is almost zero for the $^2A_1$ state PES.

In Fig. 5, the point with r_1 = 0.34 nm and R = 1.0 nm for the $^2B_2$ state PES is close to the ion-pair species $Cs^+ + I_2^-$ and is located at the entrance to the reaction path. The total energy of the system is –42.28962 au. The electronic charge on Cs and on each I atom is +0.9995 and –0.49975, respectively. There is no potential barrier from the entrance to the long-lived geometry B and then to the exit. The potential energy first decreases and then increases smoothly along the reaction path.

© 2004 NRC Canada

Fig. 6. The main features of the collision PESs for the Cs + I_2 system. (*a*) The MEP on the $^2A_1$ state PES, (*b*) the MEP on the $^2B_2$ state PES, (*c*) the crossing curves between the two-state PESs at the crossing radius R_c, and (*d*) the MEP on the $^2\Sigma$ state PES.

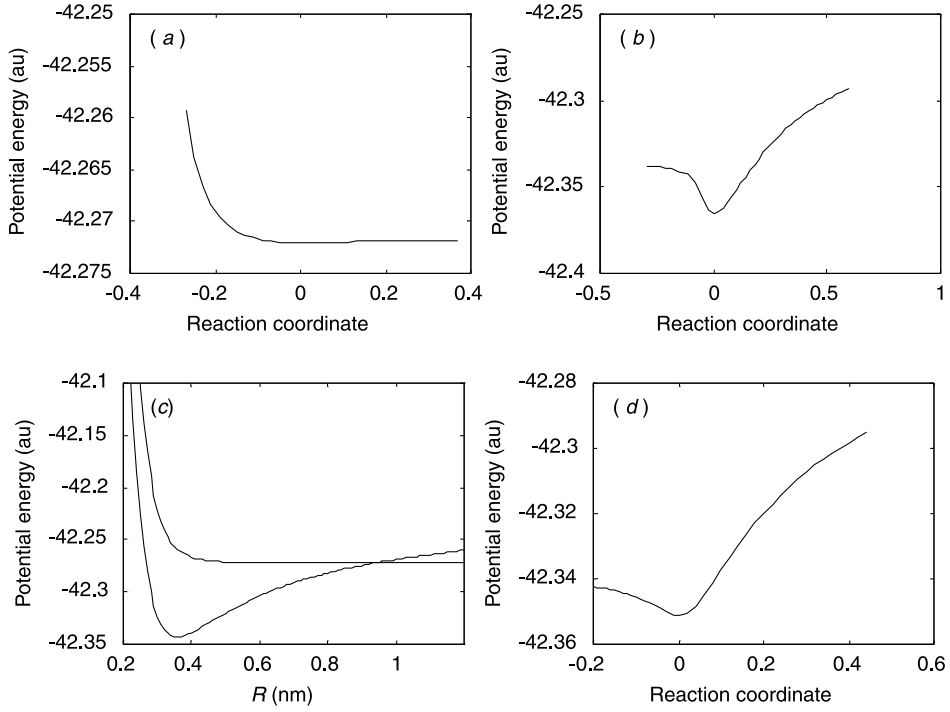


Figure 6 shows the main characteristics of the PESs. Curve (*a*) is the MEP on the $^2A_1$ state PES for the T-shape configuration, and curve (*b*) is the counterpart of (*a*) for the $^2B_2$ state PES. The crossing curve between the two-state PESs is represented by curve (*c*), where R_c is obtained step-by-step, and the value is 0.9427 nm, and at this point the system energy is –42.27188 au. The charge population analysis calculated at the QCISD level illustrates that about 99.9% of the electron transfers from the Cs atom to the I_2 molecule at the cross point. The process is very fast (even within several fs) according to the Cai study (25, 26). Curve (*d*) is the MEP on the $^2\Sigma$ state PES for the linear configuration.

From Figs. 4–6, the whole ion-pair formation process (the reaction path) can be described as follows: while the Cs atom is approaching the I_2 molecule along the $^2A_1$ state PES, the potential energy first mildly decreases. At about R_c = 0.9427 nm, the $^2A_1$ state PES crosses with the $^2B_2$ state PES where there are two alternative paths. Path one is moving continuously on the $^2A_1$ state PES and reaches the bottom of the potential well where van der Waals complex A is formed, and then the potential energy increases gradually and stably. The other path jumps to the $^2B_2$ state PES and electron transfer occurs, so Cs^+ and I_2^- are formed. Under the effect of the strong Coulomb force between Cs^+ and I_2^-, the potential energy drops sharply as Cs^+ continues to approach the I_2^- molecule anion and reaches the bottom of the second well. At that moment the strong polar geometry B appears. After Cs^+ departs from I_2^-, the ionizing collision is completed. Clearly, there are two interaction paths leading to ionization (10). The first interaction path is called covalent scattering. In this case, the first crossing is passed adiabatically and the second diabatically; the transition to the ionic state takes place at the second crossing. The larger part of the trajectory is located on the covalent potential surface. The second interaction path is called ionic scattering. Here, the first crossing is passed diabatically and the second adiabatically; the transition to the ionic state occurs at the first crossing. It should be noted that the ionizing process is different from that described for the M + $I_2 \rightarrow M^+ + I_2^-$ (M = Li, Na) system (4, 27, 28). In the latter, the van der Waals collision complex forms first and then crosses between the covalent and ionic state PES so that double-potential-well structure will be found, though one is very shallow. The result is similar to the Marcus electronic transfer theory (29, 30). The ionization potential of the Cs atom is smaller than that of the Li and Na atoms, thus the electron can be transferred easily, even at a larger R_c.

Under the collinear collision, the system has the $C_{\infty v}$ symmetry and the electronic state belongs to the $^2\Sigma$ state. In the process of scanning the reactive PES for Cs + $I_2 \rightarrow$ CsI + I, angle θ is fixed at 0°, while r_1 and r_2 are changing with the step-length at 0.01 and 0.02 nm, respectively. The PES is shown in Fig. 7, where an unstable geometry (configuration C) is found. The detailed structure is listed in Table 1.

This type of contour in Fig. 7 is referred to as a downhill attractive PES without barrier and Fig. 6*d* demonstrates the MEP on the collinear PES. The reaction is a topic exothermic one. Its reaction energy is released along the reaction path and is converted into vibrational energy of the newly formed CsI molecule. A similar case is found in the CMB experiment. It is widely accepted that the reaction M + $I_2 \rightarrow$ MI + I is a direct reactive collision via a stripping mechanism. But in collinear collision, they may mainly follow the rebound mechanism. In fact, it is difficult to retain the collinear collision, and the collinear configuration shows its in-

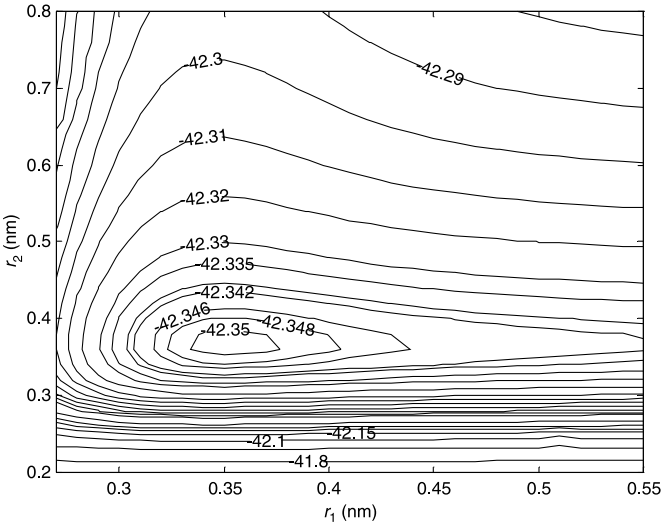
© 2004 NRC Canada

Table 1. The geometry-optimized results of the reactant, the product, and the minima on PESs.

	Sample	θ (°)	r_1 (nm)	r_2 (nm)	R (nm)	E_{total} (au)
1	$Cs + I_2$	—	0.2924 (0.2666)[a]	∞	∞	–42.27 184
2	Cs + I + I	—	∞	∞	∞	–42.23 960
3	$Cs^+ + I_2^-$	—	0.3465 (0.317)[b]	∞	∞	–42.23 750
4	$Cs^+ + I^- + I$	—	∞	∞	∞	–42.20 672
5	$Cs^+I + I^-$	—	∞	0.4562	∞	–42.20 964
6	$Cs^+ + I + I + e$	—	∞	∞	∞	–42.10 943
7	$Cs^+I + I + e$	—	∞	0.4562	∞	–42.11 235
8	CsI + I	—	∞	0.3658 (0.3315)[a]	∞	–42.34 006
A	$Cs^+I_2^-$	90	0.2924 (0.2670)[c]	—	0.6312 (0.2688)[c]	–42.27 210
B	CsI_2	90	0.3486 (0.3200)[c]	—	0.3458 (0.1884)[c]	–42.36 546
C	Cs-I-I	0	0.3514	0.3663	0.5420	–42.35 117

[a]The number in round brackets is quoted in ref. 32.
[b]The number in round brackets is quoted in ref. 16.
[c]The number in round brackets is quoted in ref. 10.

Fig. 7. The contour of the collinear reactive collision PES with $C_{\infty v}$ symmetry and the $^2\Sigma$ electronic state.



stability. So the reaction occurs easily via the stripping mechanism as long as the collinear geometry has a tiny variation (i.e., in the case of θ ≠ 0° or 180°).

The intensity contour maps for the atom–molecule CMB experiment show a symmetry about θ = 90°, which reflects the existence of a long-lived collision complex. The existence of a deep potential valley along the reaction path suggests the long-lived configuration is formed such that the collision pairs may be combined together long enough. The above two cases verify each other. In the experiment, whether the collision complex is measured or not is determined by the relationship among the collision time, the lifetime, and the rotational cycle of the collision complex; while in the ab inito method, the detailed geometry structure can be calculated. Of course, it was performed on the static PES.

Optimized geometry structures

The optimized results of all geometry structures including the eight channels are illustrated in Table 1, where the numeral ladder method is used to optimize the reactant, minimum configuration, and the product; meanwhile, the vibration analysis and zero-energy correction are also carried out on them. Configurations A, B, and C are the minimum energy ones for $^2A_1$, $^2B_2$, and $^2\Sigma$ state PESs, respectively.

Configuration A is a van der Waals complex in the very smooth and shallow potential valley of the $^2A_1$ state PES, whose frequencies are 5.0563 (A_1) cm^{-1}, 5.9021 (B_2) cm^{-1}, and 156.6694 (A_1) cm^{-1}. From the NBO population analysis on the QCISD level, it is known that the net charge on each atom is nearly zero. Similarly, configuration B is a long-lived complex in the deep potential valley of the $^2B_2$ state PES whose frequencies are 52.6047 (B_2) cm^{-1}, 69.2449 (A_1) cm^{-1}, and 96.6696 (A_1) cm^{-1}. The population analysis illustrates that this complex is a strong polar intermediate (the net charge on Cs and each I is +0.9147 and –0.4573, respectively).

As for configuration C, it lies at the potential valley of the $^2\Sigma$ state PES. It is interesting that configuration C has two virtual frequencies and another two frequencies are real. The concrete values are –6.6188(∏) cm^{-1}, –6.5563(∏) cm^{-1}, 55.8811(∑) cm^{-1}, and 101.6466(∑) cm^{-1}, respectively. The detailed interpretation is the same as that of the Na + I_2 system (31).

Cross section of ion-pair formation

According to the harpoon mechanism, the reaction occurs as a result of the electron transfer from the alkali atom to the halogen molecule. The rapid transfer or jump of the electron occurs in the region of crossing between the covalent M-X_2 and the ionic M^+-X_2^- potential energy curves. Coulomb attraction dominates the interaction in this region since the ion pair is formed and the internuclear distance is relatively large. The harpoon model yields a straightforward expression for the reaction cross section, and it is assumed that once colliding particles have reached the crossing point (R_c), the electron jump occurs and then the reaction proceeds to completion. Therefore, the reaction cross section for the collision of M with X_2 is simply πR_c^2. The longer R_c is, the larger the cross section will be. R_c for the Cs + I_2 ion-pair formation system is 0.943 nm. When the same process is applied to the M + $I_2 \rightarrow M^+ + I_2^-$ (M = Li, Na) system, R_c is 0.439 and 0.493 nm, respectively. The comparison of the cross sections for different systems and experimental groups is listed in Table 2. The ionization potential of the Cs atom

© 2004 NRC Canada

Table 2. The comparison of the present calculations and different results for the cross section and cross radius.

	Reaction cross section (nm^2)					Cross radii (nm)			
	a	*b*	*c*	Ab initio	*d*	*b*	*c*	Ab initio	*d*
Li	—	0.57	0.92	0.60	0.76	0.426	0.445	0.439	0.493
Na	0.95	0.66	0.99	0.70	0.84	0.458	0.472	0.493	0.516
Cs	1.95	1.81	1.91	2.79	3.58	0.759	0.780	0.943	1.068

Note: For *a*, the data is quoted in ref. 14; for b, the data is quoted in ref. 16; for *c* the data is quoted in ref. 17; for *d*, the data is calculated using the following empirical equation:

$$\Delta E_0 = I(\mathrm{M}) - \mathrm{EA}(\mathrm{X}_2)_{\mathrm{eV}}$$

$$R_c = \frac{e^2}{\Delta E_0} = \frac{14.35}{\Delta E_0}, \sigma = \pi R_c^2$$

where the electron affinity (EA) of the I_2 molecule is 2.55 eV and the ionization potentials (I) of the Li, Na, and Cs atoms are 5.3317, 5.1391, and 3.8939 eV, respectively.

is 3.544 eV obtained with the ab initio method, while the experimental value is 3.8939 eV (32). The electron affinity of the I_2 molecule in this work is 2.585 eV, whereas the experimental value varies from one experiment group to another with those values being $2.50^{+0.2}_{-0.1}$ eV (33), 2.55 ± 0.55 eV (34), 2.6 + 0.1 eV (35), 2.58 + 0.1 eV (36), and 2.42 + 0.2 eV (37). From Table 2, it is clear that the R_c and the cross section are getting larger and larger from Li to the Cs atom. The results are in accord qualitatively with those of the previous studies.

Conclusions

The two-state PESs of the ion-pair formation process for the $Cs + I_2 \rightarrow Cs^+ + I_2^-$ system were constructed for the first time at the QCISD(T)/SDD level. In scanning the PESs, the T-shape ion-pair formation and the linear reactive collision are mainly considered. In the former, the charge is evenly distributed on two I atoms, which is identical with the assumption in the Aten–Lanting–Los PES (10). The two-state PESs crosses and the crossing radius (R_c) is 0.9427 nm. Our calculation reveals that the ion-pair formation process is electronically nonadiabatic. The energy minimum geometry on each PES is given. According to the harpoon mechanism, the reaction cross section is calculated. The variation trend from Li, Na to the Cs atom is similar to those of previous studies.

Acknowledgements

This work is supported by the National Natural Science Foundation of China (Nos. 20173032 and 20073024) and the Ph.D. Special Research Foundation of Chinese Education Department.

References

1. Y.T. Lee. In State-to-state chemistry. ACS Symposium 56, Washington, D.C. 1977. p. 72.
2. A.J. Orr-Ewing and R.N. Zare. Annu. Rev. Phys. Chem. **45**, 315 (1994).
3. R.B. Bernstein. Chemical dynamics via molecular beam and laser techniques. Clarendon Press, Oxford. 1982.
4. D.C. Feng, C.M. Kang, C.S. Qi, and Z.T. Cai. Chem. Phys. Lett. **285**, 355 (2002).
5. J.C. Tully and R.K. Preston. J. Chem. Phys. **55**, 562 (1971).
6. Chr.W.A. Evers and A.E. De Vries. Chem. Phys. **15**, 201 (1976).
7. W.Y. Ma, Z.T. Cai, and C.H. Deng. Chem. Phys. Lett. **304**, 117 (1999).
8. W.Y. Ma, D.C. Feng, Z.T. Cai, and C.H. Deng. Chin. J. Chem. **17**, 331 (1999).
9. W.Y. Ma, D.C. Feng, Z.T. Cai, and C.H. Deng. Chem. J. Chin. Univ. **20**, 797 (1999).
10. J.A. Aten, G.E.H. Lanting, and J. Los. Chem. Phys. **19**, 241 (1977).
11. M. Polanyi. Atomic reactions. Williams and Norgate, London. 1932.
12. J.L. Magee. J. Chem. Phys. **8**, 687 (1940).
13. D.R. Herschbach. Adv. Chem. Phys. **10**, 319 (1966).
14. S.A. Edelstein and P. Davidovits. J. Chem. Phys. **55**, 5164 (1971).
15. S.Y. Tang, C.B. Leffert, and E.W. Rothe. J. Chem. Phys. **62**, 132 (1975).
16. R.W. Anderson and D.R. Herschbach. J. Chem. Phys. **62**, 2666 (1975).
17. E.A. Gislason and J. Grobe Sachs. J. Chem. Phys. **62**, 2678 (1975).
18. W.F. Howard, Jr. and L. Andrews. J. Am. Chem. Soc. **97**, 2956 (1975).
19. L. Andrews. J. Am. Chem. Soc. **98**, 2152 (1976).
20. J.A. Aten, G.E.H. Lanting, and J. Los. Chem. Phys. **22**, 333 (1977).
21. J.A. Aten, C.W.A. Evers, A.E. De Vries, and J. Los. Chem. Phys. **23**, 12 (1977).
22. J.A. Pople, M. Head-Gordon, and K. Raghavachari. J. Chem. Phys. **87**, 5968 (1987).
23. P. Fuentealba, H. Preuss, H. Stoll, and L. v. Szentpály. Chem. Phys. Lett. **89**, 418 (1982).
24. M.J. Frisch, G.W. Trucks, H.B. Schlegel, G.E. Scuseria, M.A. Robb, J.R. Cheeseman, V.G. Zakrzewski, J.A. Montgomery, Jr., R.E. Stratmann, J.C. Burant, S. Dapprich, J.M. Millam, A.D. Daniels, K.N. Kudin, M.C. Strain, O. Farkas, J. Tomasi, V. Barone, M. Cossi, R. Cammi, B. Mennucci, C. Pomelli, C. Adamo, S. Clifford, J. Ochterski, G.A. Petersson, P.Y. Ayala, Q. Cui, K. Morokuma, N. Rega, P. Salvador, J.J. Dannenberg, D.K. Malick, A.D. Rabuck, K. Raghavachari, J.B. Foresman, J. Cioslowski, J.V. Ortiz, A.G. Baboul, B.B. Stefanov, G. Liu, A. Liashenko, P. Piskorz, I. Komaromi, R. Gomperts, R.L. Martin, D.J. Fox, T. Keith, M.A. Al-Laham, C.Y. Peng, A. Nanayakkara, M. Challacombe, P.M.W. Gill, B. Johnson, W. Chen, M.W. Wong, J.L. Andres, C. Gonzalez, M. Head-

© 2004 NRC Canada

Gordon, E.S. Replogle, and J.A. Pople. Gaussian 98 [computer program]. Gaussian, Inc., Pittsburgh, Pa. 1998.
25. Z.T. Cai, W.Y. Ma, X.M. Sun, D.C. Feng, and D.H. Zhang. *In* Abstract book of second Worldwise Chinese Theoretical and Computational Chemistry Conference, Taipei, 2–7 September, 2002. p. 14.
26. Z.T. Cai, W.Y. Ma, X.M. Sun, D.C. Feng, and D.H. Zhang. J. Chin. Chem. Soc. **50**, 703 (2003).
27. X.M. Sun, Z.T. Cai, and D.C. Feng. Chin. J. Chem. **21**, 617 (2003).
28. X.M. Sun, J. Zhang, Z.T. Cai, D.C. Feng, and W.S. Bian. Acta Chim. Sin. (2004). In press.
29. R.A. Marcus. Can. J. Chem. **37**, 155 (1959).
30. R.A. Marcus. J. Chem. Phys. **39**, 1734 (1963).
31. X.M. Sun, D.C. Feng, and Z.T. Cai. Chin. Chem. Lett. (2004). In press.
32. D.R. Lide. *In* Handbook of chemistry and physics. 7th ed. *Edited by* D.R. Lide. CRC Press, Boca Raton, Fla. 1992
33. S.Y. Tang, C.B. Leffert, and E.W. Rothe. J. Chem. Phys. **62**, 132 (1975).
34. A.P.M. Beade. Physica (Utrecht), **59**, 541 (1972).
35. J.J. DeCorpo and J.L. Franklin. J. Chem. Phys. **54**, 1885 (1971).
36. W.A. Chupka, J. Berkowltz, and D. Gutman. J. Chem. Phys. **55**, 2724 (1971).
37. B.W. Hughes, C. Lifshitz, and T.O. Tiernan. J. Chem. Phys. **59**, 3162 (1973).

© 2004 NRC Canada

Micellar properties of zwitterionic surfactant – alkoxyethanol mixed micelles

Maria K. Mullally and D. Gerrard Marangoni

Abstract: The micelle formation process for a zwitterionic surfactant, *N*-dodecyl-*N*,*N*-dimethyl-3-ammonio-1-propanesulfonate (ZW3-12), has been investigated in a series of mixed solvents consisting of different concentrations of ethoxylated alcohols and polymers. The critical micelle concentrations (cmc values) of the aggregates were determined by fluorescence spectroscopy, and the surfactant aggregation numbers were obtained from luminescence probing experiments. The cmc values for ZW3-12 changed very little in the presence of increasing amounts of poly(ethyleneoxide) (PEO) in the mixed solvent. In the case of the ethoxylated alcohol – ZW3-12 systems, the cmc values and aggregation numbers decreased systematically with increasing alcohol concentration. However, the cmc values of the mixed micelles showed little dependence on the number of ethylene oxide (EO) groups at constant alcohol concentration. These results are compared with the well-studied sodium dodecylsulfate – ethoxylated alcohol, and dodecyltrimethylammonium bromide – ethoxylated alcohol mixed micellar systems and to SDS–PEO systems and are discussed in terms of the contribution of the EO groups to the hydrophobic interactions.

Key words: zwitterionic surfactant, alcohols, mixed micelles, luminescence probing.

Résumé : On a étudié le processus de formation de micelle pour un agent de surface zwitterionique, le *N*-dodécyl-*N*,*N*-diméthyl-3-ammonio-1-propanesulfonate (ZW3-12), dans une série de solvants mixtes formés de concentrations diverses d'alcools éthoxylés et de polymères. On a déterminé les concentrations micellaires critiques (valeurs des cmc) en faisant appel à la spectroscopie de fluorescence et on a obtenu les nombres d'agrégation de l'agent de surface à partir d'expériences de luminescence exploratoire. Les valeurs de cmc pour le ZW3-12 varient très peu en présence de quantités croissantes de poly(oxyde d'éthylène) (POE), dans le solvant mixte. Dans le cas des systèmes alcool éthoxylé – ZW3-12, les valeurs des cmc et les nombres d'agrégation diminuent d'une façon systématique avec une augmentation de la concentration d'alcool. Toutefois, les valeurs des cmc ne dépendent que faiblement sur le nombre de groupes d'oxyde d'éthylène (OE), à des concentrations constantes d'alcool. Ces résultats se comparent bien avec les systèmes micellaires mixtes bien étudiés dodécylsulfate de sodium – alcool éthoxylé et bromure de dodécyltriméthylammonium – alcool éthoxylé et aux systèmes SDS–POE et on les discute en fonction de la contribution des groupes OE aux interactions hydrophobes.

Mots clés : agent de surface zwitterionique, alcool, micelles mixtes, luminescence exploratoire.

[Traduit par la Rédaction]

Introduction

Zwitterionic surfactants are, to date, generally much less studied than other classes of surfactants. However, they are widely used in industry (1), and the interest in these surfactants as well as the amount of research into their fundamental micellar and solution properties is increasing. Their main applications are based on such properties as mildness to the skin and eyes (which is related to their low cmc values and the nonionic nature of the headgroups), excellent water solubility, broad isoelectric ranges, and resistance to hard water. They are also resistant to degradation by oxidizing and reducing agents, exhibit low toxicity, and are highly compatible with most of the main commercial surfactants and detergent additives.

When an alcohol with a sufficiently long chain is in solution with a surfactant, it is generally accepted that mixed micelles — incorporating both surfactant monomers and alcohol molecules — form (1–8). That is, the alcohol may solubilize preferentially in a micelle interior, rather than in the aqueous phase, facilitating mixed micelle formation. The interaction of alcohols with surfactants is widely studied, but has been mostly focused on mixtures of *n*-alkanols with ionic and nonionic surfactants (5). A number of papers have examined the mixed micelle formation process for typical anionic and cationic surfactants with a variety of alcohols and alkanediols (3, 6, 7).

Ethoxylated alcohols represent an interesting family of cosurfactants that may be considered as lower members of the alcohol ethoxylate, nonionic surfactant family. In the case of the nonionic surfactants, the ethoxylate (EO) group ($-CH_2CH_2O-$) is considered to be hydrophilic, whereas for the lower members of this family, the EO groups have been clearly shown to contribute to hydrophobic effects and to a

Received 28 May 2003. Published on the NRC Research Press Web site at http://canjchem@nrc.ca on 2 October 2004.

M.K. Mullally and D.G. Marangoni.[1] Department of Chemistry, St. Francis Xavier University, Antigonish, NS B2G 2W5, Canada.

[1]Corresponding author (e-mail: gmarango@stfx.ca).

 doi: 10.1139/V04-022 © 2004 NRC Canada

decrease in the Gibbs transfer energy of the alcohol from the aqueous phase to the micellar phase. The interactions between ethoxylated alcohols and the anionic surfactant sodium dodecylsulfate (SDS) and the cationic surfactant dodecyltrimethylammonium bromide (DTAB) have been examined by a number of authors and were found to be as follows (4, 7, 9–14). For SDS, critical micelle concentrations (cmc values) and surfactant aggregation number (N_s) values decreased as the number of EO groups was increased, suggesting that the EO group has a contribution to hydrophobic effects, whereas for DTAB, the cmc and N_s values did not vary with increasing numbers of EO groups at constant alcohol concentration. This suggested that the EO groups do not contribute to the hydrophobic interactions in mixed micelle formation for the cationic surfactants studied. In the case of the volumetric and other thermodynamic properties of carboxylate surfactants mixed with ethoxylated alcohols, the properties of the mixed micelles changed in a fashion consistent with the EO group contributing to the hydrophobic interactions (10, 11).

Surfactant–polymer mixtures are of widespread use in biochemical, pharmaceutical, paint, and cosmetic industries (15, 16). In the presence of certain polymers, surfactant molecules associate with the polymers to form polymer–surfactant aggregates at surfactant concentrations below the cmc value. In such cases, a plot of a surfactant physicochemical property, such as surface tension or fluorescence, vs. surfactant concentration exhibits two breaks. The first break is taken to be the concentration above which interaction between the two molecules begins and is called the critical aggregation concentration (CAC). At this concentration, the surfactant begins to adsorb on the polymer chain forming aggregates. Once the polymer is saturated with surfactant, free surfactant monomers form micelles and the second break in the curve is the cmc value. At concentrations above the cmc value, polymer-bound surfactant aggregates coexist in solution with free micelles. Intuitively, aggregation formation or binding between oppositely charged polyelectrolytes and surfactants can be rationalized in terms of the strong electrostatic forces. However, nonionic, water-soluble polymers and ionic surfactants are the most studied polymer–surfactant systems and the interaction between these polymers and surfactants is strong. Some of the explanations of this phenomenon that have been proposed are (15, 16): (*a*) the reduction of the hydrocarbon–water contact area of the alkyl chains of the surfactant; (*b*) an ion-dipole interaction between the surfactant head group and the polymer; and (*c*) a hydrophobic interaction between the polymer and the surfactant hydrocarbon chains.

For zwitterionic surfactants, there have been very few studies concerning interactions with polymer additives. Ribera and Velazquez (17) have studied the interactions of ZW3-12 (which they called DPS) in solution with poly(vinylpyrrolidone) (PVP), polyacrylic acid sodium salt (PAC), and poly(sodium 4-styrenesulfonate) (PSS). The only polymer that showed any significant interaction was PSS. PVP and PAC exhibited virtually no interaction with ZW3-12. The authors used surface tension measurements and determined the cmc values in the presence and absence of polymers. However, no explanation was offered for the observed interactions (or lack thereof).

This paper presents the micellar properties of the zwittergent ZW3-12 (cmc and N_s values) in aqueous solutions of *n*-butanol (C_4E_0), ethylene glycol mono-*n*-butyl ether (C_4E_1), diethylene glycol mono-*n*-butyl ether (C_4E_2), and triethylene glycol mono-*n*-butyl ether (C_4E_3), and also in a mixture with 35 000 g/mol poly(ethyleneoxide) (PEO). Both the cmc and the N_s values have been determined using luminescence probing techniques. The results are compared with the well-studied mixed micelles composed of ethoxylated alcohols and SDS and DTAB to examine whether or not the hydrophobic effects of the EO groups are evident in the zwitterionic surfactant micelles.

Experimental

Materials

ZW3-12 was received from Calbiochem and was used without further purification. C_4E_0, C_4E_1, and C_4E_2 were spectrophotometric grade solvents from Aldrich and were used as received. C_4E_3 was obtained from Tokyo Kasei and used without purification.

PEO with an average molecular weight of 35 000 g/mol was a 99% pure Fluka product and was used as received. Pyrene was received from Aldrich and purified by successive sublimations. Safranine T was a Tokyo Kasei product and was used without further purification. The quencher, cetylpyridinium chloride monohydrate (CPC), was also obtained from Aldrich and it was purified by repeated recrystallization from an acetone–ethanol mixture.

All solutions were prepared with deionized, conductance grade water from a Millipore ion-exchange system and all experiments were performed at room temperature.

Methods

Cmc value determination by fluorescence spectroscopy

Solutions of the surfactant (ZW3-12) and alcohols were prepared in volumetric flasks using the appropriate mass of surfactant and alcohol in deionized water. All surfactant and alcohol concentrations are expressed in molarity units, where the molarity is defined as the number of moles of surfactant per litre of mixed solvent. A stock solution of the fluorescence probe, safranine T, was prepared by dissolving the probe in water and this stock solution was used in the preparation of the surfactant solutions. Sample preparation was done by combining the appropriate volumes of the surfactant–alcohol–probe solution with the alcohol–probe solution so that the alcohol and probe concentrations were constant and the surfactant concentrations ranged above and below its cmc value. The surfactant–PEO solutions were prepared in the same way as the surfactant–alcohol solutions with the exception that the polymer concentrations are expressed as the weight percent of the polymer per volume of solution.

Fluorescence spectra were measured using the Aminco-Bowman Series 2 luminescence spectrometer. Slit widths were set at 2.0 nm and the excitation wavelength was set to 532 nm, scanning the emission from 550 to 625 nm. The cmc values of the surfactant–alcohol and surfactant–polymer systems were obtained from the break in the plot of

© 2004 NRC Canada

maximum fluorescence emission intensity against surfactant concentration.

Luminescence probing experiments

All the solutions for the luminescence probing experiments were made up on a molar basis. A small amount of a 0.025 mol L^{-1} pyrene–ethanol solution was placed in a beaker, and the ethanol was allowed to evaporate overnight, leaving a thin film of pyrene on the bottom of the beaker. A solution of 20 mmol L^{-1} surfactant with the desired concentration of alcohol was placed in the beaker and the solution was stirred vigorously for a minimum of 3 to 4 h to ensure complete solubilization of the pyrene by the micelles. A portion of the solution (≈half) was then used to make a solution of approximately 1.00×10^{-4} mol L^{-1} CPC. This quencher solution was stirred for 3 to 4 h to fully dissolve the CPC in the micelles. Solutions were prepared with varying amounts of quencher so that the concentration of quencher was between 0 and approximately 1.00×10^{-4} mol L^{-1}. Steady-state pyrene fluorescence emission spectra were recorded using an Aminco-Bowman Series 2 luminescence spectrometer with an excitation wavelength of 338 nm, and scanning the emission from 350 to 500 nm. The heights of the first (I_1) and third (I_3) emission peaks were recorded directly from the spectra. The intensities of the first emission peak (at 373 nm) were used in the plot of $\ln(I_0/I)$ vs. quencher concentration to determine the aggregation numbers for the mixed micellar systems.

Results and discussion

Cmc values for ZW3-12 – ethoxylated alcohol mixed micelles

A sample curve of the fluorescence intensity of the safranine T probe vs. the concentration of ZW3-12 is given in Fig. 1. The cmc values were obtained from the breaks in the plots of maximum fluorescence emission intensity vs. total surfactant concentration ($C_{surf,t}$). These values are presented in Table 1 and plotted in Figs. 2 and 3 as a function of total concentration for each of the ethoxylated alcohols investigated. The cmc value for ZW3-12 without added alcohol is 2.74 mmol L^{-1} ± 0.10 mmol L^{-1}, which is somewhat lower than the literature value (1, 17). This is consistent, however, with cmc values from spectroscopic methods being somewhat lower than cmc values obtained via other methods (e.g., surface tension, viscosities, and densities) (19).

From Figs. 2 and 3, it is seen that, in all cases, the cmc values decrease as the total concentration of added alcohol increases. This trend is consistent with the well-known decrease in the cmc values for several types of ionic and nonionic surfactants mixed with alcohols possessing at least a four-carbon chain (1, 3–9), and it is consistent with the formation of mixed micelles containing surfactant and alcohol molecules. The cmc values decrease because, though the favourable increase in entropy upon micellization is lowered, mixed micelle formation means alcohol molecules replace some surfactant monomers and so micelles can be formed at lower surfactant concentrations. The higher alcohol concentration at which the cmc value begins to increase often correlates with the concentration at which the number of alcohol molecules and the number of surfactant monomers in the mixed micelle are roughly equivalent.

It is also useful to look at the rates of cmc value decrease (the dcmc/dC_a values) for each one of the alcohols. From the slopes of the linear portions of the cmc value graphs in Figs. 2 and 3, the dcmc/dC_a values are –5.7 mmol L^{-1}/mol L^{-1} for C_4E_0, –4.9 mmol L^{-1}/mol L^{-1} for C_4E_1, –5.2 mmol L^{-1}/mol L^{-1} for C_4E_2, and –4.3 mmol L^{-1}/mol L^{-1} for C_4E_3. It is clear from Figs. 2 and 3 and the calculated dcmc/dC_a values that the formation of the mixed micelles between the zwittergent and the ethoxylated alcohols is insensitive to the number of EO groups in the alcohol at similar alcohol concentrations. This can be compared with the data of Marangoni and Kwak (4) and Marangoni et al. (9) for the

Fig. 1. Sample plot of fluorescence intensity of safranine T vs. concentration of ZW3-12 in a 0.10 mol L^{-1} C_4E_0 solution.

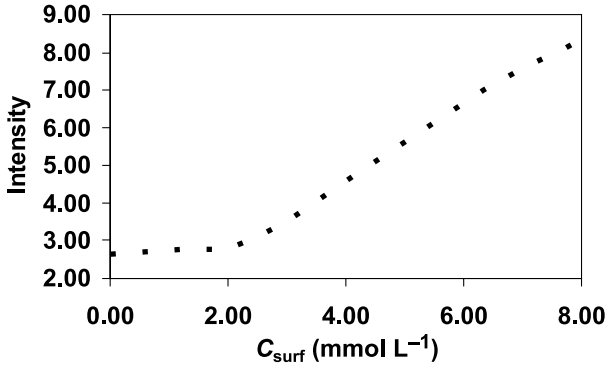
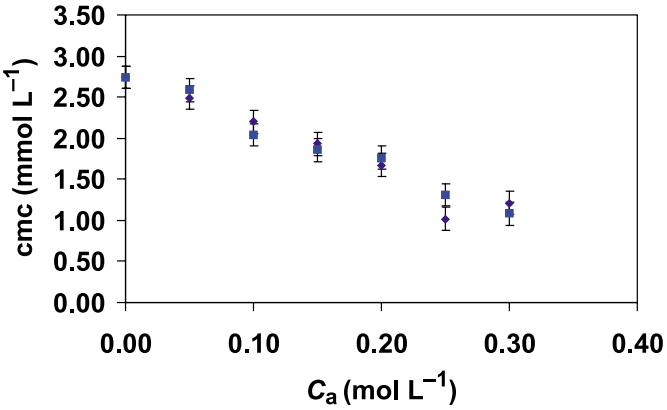


Table 1. Cmc values (±0.1 mmol L^{-1}) for ZW3-12 – ethoxylated alcohol mixed micelles as a function of the total concentration of added alcohol.

C_a (mol L^{-1})	C_4E_0	C_4E_1	C_4E_2	C_4E_3
0.00	2.74	2.74	2.74	2.74
0.05	2.49	2.59	2.68	2.62
0.10	2.20	2.04	2.40	2.49
0.15	1.93	1.86	1.96	2.06
0.20	1.67	1.76	1.85	1.98
0.25	1.02	1.31	1.54	1.87
0.30	1.21	1.08	2.42	2.54

Fig. 2. Cmc values (±0.1 mmol L^{-1}) for ZW3-12–C_4E_0 (■) and ZW3-12–C_4E_1 (◆) mixed micelles as a function of C_a.



© 2004 NRC Canada

Fig. 3. Cmc values (±0.1 mmol L^{-1}) for ZW3-12–C_4E_2 (●) and ZW3-12–C_4E_3 (▲) mixed micelles as a function of C_a.

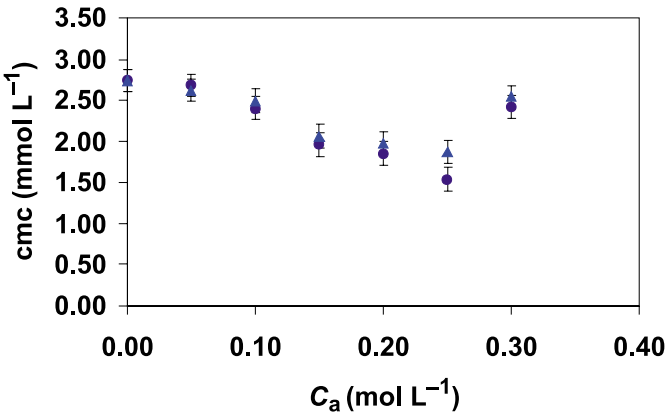
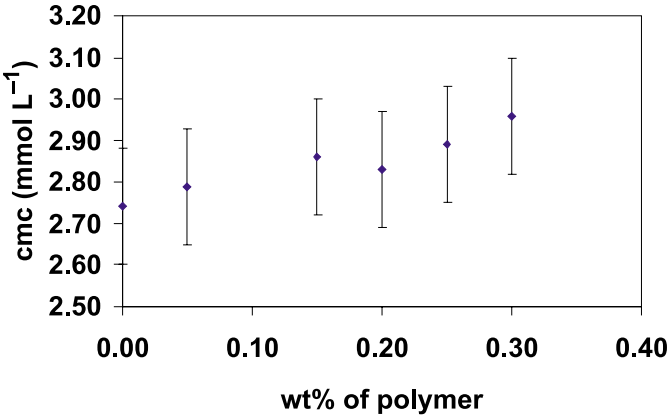


Fig. 4. Cmc values (±0.1 mmol L^{-1}) for ZW3-12–PEO-32 000 as a function of the wt% of polymer.



systems SDS–C_4E_n and DTAB–C_4E_n. In their study of ethoxylated alcohols with anionic and cationic micelles, it was clear that in the case of the cmc values of SDS – ethoxylated alcohol mixed micelles, at a constant alcohol concentration, the cmc values are observed to decrease in the direction of increasing number of alcohol ethoxylate groups. For the DTAB–C_4E_n series, these authors found that the cmc values are rather insensitive to the number of EO groups in the alcohol at constant alcohol concentration. In addition, the degree of solubilization of the ethoxylated alcohol (p-values) in the micellar phase was determined by NMR paramagnetic relaxation enhancement experiments. The p-values for the SDS micelles increased with an increase in the number of EO groups, suggesting that ethoxylated alcohols have a greater preference to be solubilized in the micellar interior with an increasing number of alcohol ethoxylate groups. In the case of DTAB – ethoxylated alcohols, the p-values were essentially constant for $C_4E_0 \rightarrow C_4E_3$. The authors proposed that the EO groups not only enhance micelle formation by a reduction of headgroup repulsion, they also drive micelle formation by a contribution to hydrophobic effects in the anionic surfactant systems, whereas they have little effect in the case of the cationic surfactants. As with the cationic surfactant – ethoxylated alcohol systems, Figs. 2 and 3 show that the rate of decrease of the cmc value is relatively insensitive to the number of EO groups in the alcohol. Thus, the ZW3-12 – ethoxylated alcohol systems are more comparable to the DTAB system because the increasing number of EO groups does not cause a drastic decrease in the cmc value of the mixed micelles at constant alcohol concentration. This suggests that EO groups in the alcohols do not contribute significantly to the hydrophobic effects or to the screening of electrostatic interactions when mixed micelles are formed. However, the magnitude of these interactions in a zwitterionic surfactant is not well known, as we have not yet measured the partition coefficients for ethoxylated alcohols in the ZW3-12, nor is there a reasonable picture of the charge distribution in the headgroups of these zwitterionic surfactants.

Cmc values for the ZW3-12–PEO system

Cmc values for the ZW3-12–PEO system were also obtained by fluorescence spectroscopy. All the fluorescence plots exhibited one break, indicating that no ZW3-12–PEO aggregates form in this system. The two main postulates for explaining the lack of interaction of cationic micelles with polymers have to do with the size of the headgroup and the polymer's hydration shell (13–16). In the first case, cationic surfactants are considered to have larger headgroups than anionic ones that reduce the access of the polymer to the micelles. In the second case, systematic alteration of the kind and size of headgroups in anionic surfactants has shown that interaction between ionic surfactants and polymers can depend on the polymer's hydration shell (the hydrogen-bonded water molecules that surround it). For surfactants, the amount of hydration of cationic head groups is much less than that for anionic ones. Thus, with anionic surfactant micelles, the polymer can associate with the water molecules that hydrate the headgroups and its ether oxygens can remain hydrogen bonded. This would occur less with a cationic surfactant micelle, and would thus contribute to the weaker interactions for these surfactants. Overall, the fluorescence data show no interaction with PEO and so ZW3-12 seems to mimic a cationic surfactant more than an anionic one.

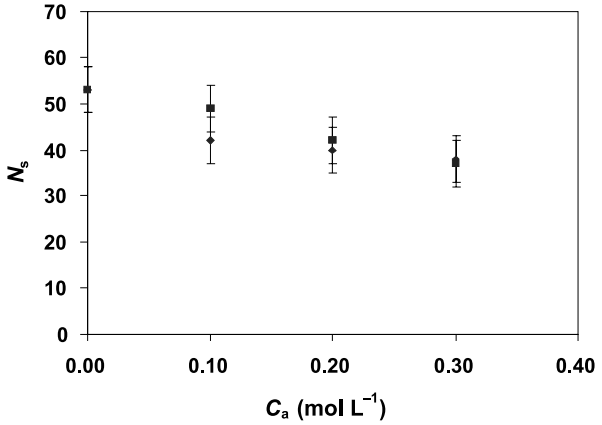
Table 2. Cmc values (±0.1 mmol L^{-1}) for ZW3-12–PEO systems as a function of the total weight percent of added PEO.

Total wt% of added PEO-35 000	Cmc value (mmol L^{-1})
0.00	2.74
0.05	2.79
0.15	2.86
0.20	2.83
0.25	2.89
0.30	2.96

Cmc values for the ZW3-12–PEO system are presented in Table 2 and are plotted in Fig. 4 as a function of the total added weight percent of PEO. We observe a slight increase in the cmc value as the weight percent of added PEO increases. This suggests that PEO acts as a net structure breaker in the system. That is, PEO breaks up the structure "icebergs" of water that form around the hydrocarbon chains

© 2004 NRC Canada

Fig. 5. N_s values (±5) for ZW3-12–C_4E_0 (■) and ZW3-12–C_4E_1 (◆) mixed micelles as a function of C_a.



of the surfactant monomers. This means that the entropy increase upon micellization is decreased and so a higher concentration of surfactant is required before micelles form. The increase in the cmc value confirms the lack of interaction between ZW3-12 and the polymer. This is because if surfactant–polymer aggregates were formed or if there were partitioning of the PEO inside the micelle, the cmc value would be expected to decrease as it did with the addition of the ethoxylated alcohols at low concentrations. It should be noted that higher molecular weight PEOs may have an interaction with the zwittergents, as it has been shown in the literature that anionic surfactants are known to interact more strongly with higher weight PEOs. Indeed, Gao et al. (20) have shown by a study of solubilization equilibria that the nature of the interaction between SDS and PEO depends strongly on the molecular weight of the polymer. As well, Weng and Olofsson (13, 14) have shown that the enthalpies of the interaction of PEO with various surfactants are strongly dependent on the polymer molecular weight.

Luminescence probing experiments

N_s values were calculated using the Turro–Yekta equation and the derived relationship:

$$[1] \qquad N_s = \frac{C_{surf,t} - cmc}{[M]}$$

where the cmc values are those for the mixed micelles, reported earlier; [M] is the micellar concentration; 1/[M] is the slope of the plot of $\ln(I_0/I)$ vs. quencher concentration (21, 22), and $C_{surf,t}$ is the total surfactant concentration. These N_s values are presented in Table 3 and are plotted in Figs. 5 and 6 as a function of the total alcohol concentration. The N_s value without added alcohol was found to be 53 ± 6, which is considerably lower than the literature value for ZW3-12 (1). However, several trends in the N_s values with increasing additive concentration are noteworthy, particularly keeping in mind the SDS – ethoxylated alcohol and DTAB – ethoxylated alcohol systems mentioned earlier. First, the N_s values decrease as the concentration of added alcohol increases. This is true for all four alcohols and is an expected trend. In a surfactant–alcohol mixture where mixed micelles are formed, N_s is expected to decrease and N_a, the alcohol aggregation number, is expected to increase as more alcohol is incorporated into the micelle. The decrease in the N_s values is due to the changes in the hydrophobic interactions and electrostatic interactions that occur when the alcohol is incorporated into the micelle.

Table 3. Aggregation numbers (±5) of surfactant and alcohol for 20 mmol L^{-1} ZW3-12 – ethoxylated alcohol mixed micelles as a function of the concentration of alcohol.

C_a (mol L^{-1})	C_4E_0	C_4E_1	C_4E_2	C_4E_3
0.00	53	53	53	53
0.10	49	42	41	41
0.20	42	40	32	34
0.30	37	38	34	29

Table 4. I_1/I_3 ratios (±0.01) of surfactant and alcohol for 20 mmol L^{-1} ZW3-12 – ethoxylated alcohol mixed micelles as a function of the concentration of alcohol.

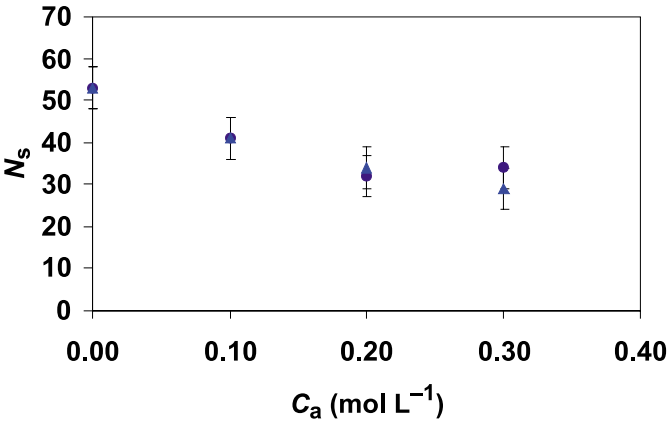
C_a (mol L^{-1})	C_4E_0	C_4E_1	C_4E_2	C_4E_3
0.0	1.55	1.55	1.55	1.55
0.1	1.53	1.54	1.55	1.53
0.2	1.49	1.53	1.52	1.51
0.3	1.47	1.52	1.53	1.49

If we examine the N_s values at a given alcohol concentration in Figs. 5 and 6, a decrease in N_s value is observed when the values for C_4E_0 are compared to those for the three other alcohols, but there are no significant differences noted within the ethoxylated alcohols themselves. This suggests again that the number of EO groups is not contributing to hydrophobic effects in these systems.

The I_1/I_3 ratios provide information on the polarity experienced by pyrene in these mixed micelles; these values are given in Table 4. In all cases, we observe a decrease with increasing concentration of added alcohol for all four alcohols. This suggests that pyrene is experiencing a progressively less polar environment as more alcohol is added to the mixed solvent system. This could be due to alcohol molecules blocking water penetration into the micelle (22). However, this trend is only subtle. Comparing the I_1/I_3 ratios at a given alcohol concentration, it is seen that the ratios are relatively insensitive to changing the alcohol from C_4E_0 to C_4E_3. This suggests that the pyrene experiences essentially the same microenvironment in all the ethoxylated alcohol – zwitterionic surfactant systems studied at the same alcohol concentration. An important point about these I_1/I_3 ratios is that they are comparable to the I_1/I_3 ratios of cationic surfactants such as DTAB, i.e., the ratio for ZW3-12 without added alcohol is 1.55, whereas the I_1/I_3 ratio for DTAB is 1.40, and that of SDS is 1.26 (22). For the ZW3-12 surfactants, a considerable nonpolar environment could be provided by the two methyl groups and the methylene groups of the intercharge arm. On the basis of this, the relatively high I_1/I_3 ratio for ZW3-12 both by itself and in the presence of the ethoxylated alcohols at all concentrations suggests that this affinity of the quaternary ammonium headgroup for pyrene could play a role, despite the nearby presence of an anionic functionality, the sulfonate group. Perhaps the affinity of the quaternary ammonium site could be due to the ob-

© 2004 NRC Canada

Fig. 6. N_s values (±5) for ZW3-12–C_4E_2 (●) and ZW3-12–C_4E_3 (▲) mixed micelles as a function of C_a.



servation that zwitterionic micelles are expected to bind anions electrostatically because the charge density due to the cationic ammonium centres is higher than that at the anionic sulfonate centres (24). In this case, although pyrene is not an anion, it acts as a Lewis base, and a polarization of its π-electron cloud could be caused by protons and positively charged groups. However, the interaction between pyrene and the quaternary ammonium groups is not thought to be strong (25). As well, in a zwitterionic surfactant, the possibility exists that the pyrene is repelled by the anionic sulfonate group.

A consideration that might explain these observations is that the sulfonate group can bend toward the ammonium group and the electrostatic interaction causes the formation of a six-member ring-like structure. The headgroups of these surfactants are already large, but this would make them very bulky. Thus, the longer ethoxylated alcohols might be too large for significant formation of mixed micelles because they are blocked from penetration into the micelle and any additional EO groups would not significantly decrease the cmc values. The bulkiness might also prevent aggregation with the polymer and if the positively and negatively charged centres essentially neutralize one another, the sulfonate group would not be expected to interact strongly with PEO. The subtle decrease of N_s values might also be explained by the idea of a six-member ring. We are currently undertaking NMR 2D-NOESY and ^{13}C chemical shift experiments of these systems to investigate the possibility of inter- and intramolecular correlations that would give us significant insights as to the conformation of the tail and headgroup moieties in the zwitterionic surfactant.

If the alcohols cannot penetrate the micelle very effectively as the micelles become larger, then N_a values would not be expected to increase and N_s values would not decrease significantly, at a constant total aggregation number ($N_a + N_s$). N_a values can be calculated if the partition constants for these alcohols in the zwitterionic surfactant are known; this will be the subject of a future paper.

The I_1/I_3 value might be observed to be large because the pyrene finds a significantly more polar environment in the region created by the ammonium–sulfonate interaction. The presence of alcohols and the ethoxylate groups likely would not alter this environment in any substantive way if they cannot penetrate significantly into the micellar interior. We note that most of these effects can be explained with the idea of a six-member ring-like structure, or some other conformation change that leads to subtle changes in the packing and charge distribution in the headgroup region of the ZW3-12 surfactant micelles. The aforementioned NMR 2D-NOESY and ^{13}C chemical shift experiments are expected to shed light into these areas.

Finally, in considering the results presented here, it is important to note the nature of the EO group in the alcohol. The hydroxyl group is hydrophilic and, as has been demonstrated for other alcohols by NMR 2D-NOESY experiments (26), it would be anchored at the micellar surface when mixed micelles form. The EO group is more complex. The oxygen is capable of hydrogen bonding and so may favour interactions with water in some cases. Indeed, Manabe et al. (3) have described EO as a hydrophilic group, though less so than the OH group. However, the two-carbon chain on the EO group is hydrophobic and may prefer the micellar interior environment if it is accessible. A strict definition of the behaviour of the EO group is difficult here. There may be binding of the alcohol groups and complex interactions with the micellar interior, the headgroup region, and (or) with water molecules at the micellar surface and in the bulk. This therefore limits any predictions of its behaviour. Marangoni and Kwak (4) and Marangoni et al. (9) have viewed the EO group as contributing in a small but significant manner to the hydrophobic effects in mixed micelles with SDS because there the cmc value decreased drastically with more EO groups. Since this is not observed with ZW3-12, it could be surmised that the EO group in this system behaves more as a hydrophilic group. This would be supported by the lack of interaction of ZW3-12 with PEO. With the large number of EO groups, the polymer prefers the bulk water solution, even though it has been shown by both NMR 2D-NOESY experiments (27, 28) and NMR ring-current effects (29) that for some surfactant systems, some of the PEO EO groups are penetrating the micelle palisade layer and are indeed solubilized in the micellar interior. Since the system also exhibits no CAC, interaction of PEO with surfactant monomers also seems unfavourable and may be due to a lack of an interaction between the EO groups and the micellar interior (in effect, the PEO seems to be blocked out of the micellar interior, much like the case of the cationic surfactants). The increase in the cmc value with increasing weight % of PEO also supports these poor interactions between ZW3-12 and PEO.

Conclusions

The interactions of ZW3-12, a zwitterionic surfactant, with ethoxylated alcohols and the polymer PEO were examined by luminescence probing experiments. The cmc values of the ZW3-12 – ethoxylated alcohol systems decreased with increasing added alcohol concentration. However, as the number of EO groups in the alcohol increased, at a constant concentration of added alcohol, the cmc values appeared to be insensitive to the addition of the EO groups to the alcohol. Surfactant aggregation numbers decreased with increasing added alcohol concentration, and again the EO group showed no significant influence on the magnitude of

© 2004 NRC Canada

the N_s value at a constant alcohol concentration. As well, I_1/I_3 values decreased with increasing added alcohol concentration but were relatively high, and again the number of EO groups did not cause significant variation in these ratios. The probe, therefore, consistently experienced a relatively nonpolar environment in these zwitterionic surfactants. Thus, it can be concluded from these measurements that mixed micelles are formed in these systems but the EO groups do not solubilize preferentially in the micellar interior, and hence do not appear to contribute to the hydrophobic effects. For the ZW3-12–PEO system (a polymer–surfactant system), no formation of complexes or penetration of PEO into the micellar interior was observed. By comparing these results to the case of SDS – and DTAB – ethoxylated alcohol mixed micellar systems, the ZW3-12 surfactant appears to behave more like the cationic DTAB surfactant. This suggests that the ammonium functionality of the headgroup defines the behaviour for this surfactant in these systems. Questions remain about the specifics of the interactions observed, especially regarding the sulfonate functionality of the headgroup, and the EO group. These will be the subject of future investigations.

Acknowledgements

The financial support of the Natural Sciences and Engineering Research Council of Canada (NSERC) (research grant, D.G.M.) and the St. Francis Xavier University Council for Research is greatly appreciated. M.M. wishes to acknowledge the grant of an NSERC Undergraduate Summer Research Award.

References

1. B. Sesta. J. Phys. Chem. **93**, 7677 (1989).
2. M. Manabe and M. Koda. Bull. Chem. Soc. Jpn. **51**, 1599 (1978).
3. M. Manabe, K. Shirahama, and M. Koda. Bull. Chem. Soc. Jpn. **49**, 2904 (1976).
4. D.G. Marangoni and J.C.T. Kwak. Langmuir, **7**, 2083 (1991).
5. J.C. Burrows, D.J. Flynn, S.M. Kutay, T.G. Leriche, and D.G Marangoni. Langmuir, **11**, 3388 (1995).
6. C.A. McMahon, B.E. Hawrylak, D.G. Marangoni, and R. Palepu. Langmuir, **15**, 429 (1999).
7. H. Høiland, E. Ljosland, and S. Backlund. J. Colloid Interface Sci. **101**, 467 (1984).
8. H. Høiland, A.M. Blokhus, O.J. Kvammen, and S. Backlund. J. Colloid Interface Sci. **107**, 576 (1985).
9. D.G. Marangoni, A.P. Rodenhiser, J.M. Thomas, and J.C.T. Kwak. ACS Symp. Ser. **45**, 194 (1992).
10. H. Huang and R.E. Verrall. Can. J. Chem. **75**, 1445 (1997).
11. H. Huang, R.E. Verrall, and B. Skalski. Langmuir, **13**, 4821 (1997).
12. D.J. Flynn, S.M. Kutay, B.E. Hawrylak, C.A. Kennedy, E.V. Alexander, J.A. Howard, and D.G. Marangoni. Colloid Polym. Sci. **280**, 848 (2002).
13. G. Wang and G. Olofsson. J. Phys. Chem. B, **102**, 9276 (1998).
14. G. Olofsson and G. Wang. Pure Appl. Chem. **66**, 527 (1994).
15. E.D. Goddard and K.P. Ananthapadmanaban. Interactions of surfactants and polymers and proteins. CRC Press, Boca Raton, Fla. 1993.
16. J.C.T. Kwak. Polymer-surfactant systems. Surf. Sci. Ser. Vol. 77. Marcel Dekker, New York. 1998.
17. R. Ribera and M.M. Velazquez. Langmuir, **15**, 6686 (1999).
18. F. Li, G.-Z. Li, and J.-B. Chen. Colloids and Surfaces A, **145**, 167 (1998).
19. B. Lindman and H. Wennerstron. Top. Curr. Chem. **23**, 1 (1979).
20. Z. Gao, R.E. Wasylishen, and J.C.T. Kwak. J. Phys. Chem. **95**, 462 (1991).
21. N.J. Turro and A. Yekta. J. Am. Chem. Soc. **100**, 5951 (1978).
22. M. Tachiya. Chem. Phys. Lett. **69**, 289 (1975).
23. A. Malliaris, J. Lang, and R. Zana. J. Colloid Interface Sci. **11**, 237 (1986).
24. K.K. Ghosh, A. Pandey, and S. Roy. Colloids and Surfaces A, **163**, 293 (2000).
25. P. Lianos, M.-L. Viriot, and R. Zana. J. Phys. Chem. **88**, 1098 (1984).
26. B.E. Hawrylak and D.G. Marangoni. Can. J. Chem. **77**, 1241 (1999).
27. M.I. Gjerde, W. Nerdal, and H. Høiland. J. Colloid Interface Sci. **183**, 285 (1996).
28. H.-C. Gao, S. Zhao, S.-Z. Mao, H.-Z. Yuan, J.-Y. Yu, L.-F. Shen, and Y.-R. Du. J. Colloid Interface Sci. **249**, 200 (2002).
29. Z. Gao, R.E. Wasylishen, and J.C.T. Kwak. J. Colloid Interface Sci. **13**, 137 (1990).

© 2004 NRC Canada

A simple biomimetic protocol for the oxidation of alcohols with sodium hypochlorite in the presence of β-cyclodextrin in water

K. Surendra, N. Srilakshmi Krishnaveni, and K. Rama Rao

Abstract: A simple and efficient protocol, which is inexpensive, convenient, clean, and facile, for oxidation of alcohols to carbonyl compounds has been developed using sodium hypochlorite in the presence of β-cyclodextrin with water as solvent. A series of alcohols were oxidized at room temperature in excellent yields.

Key words: oxidation, alcohols, sodium hypochlorite, KBr, β-cyclodextrin, biomimetic, water.

Résumé : On a mis au point un protocole simple et efficace d'oxydation des alcools en composés carbonylés qui est peu coûteux, pratique, propre, et facile et qui fait appel à l'utilisation d'hypochlorite de sodium en présence de β-cyclodextrine dans l'eau comme solvant. On a oxydé une série d'alcools, à la température ambiante, avec d'excellents rendements.

Mots clés : oxydation, alcools, hypochlorite de sodium, KBr, β-cyclodextrine, biomimétique, eau.

[Traduit par la Rédaction]

Introduction

Green chemistry is becoming a central issue in both academic and industrial research in the 21st century (1). Industrial chemistry is not sustainable without this approach. Hence, the goal of present-day industrial research is to develop environmentally benign and clean synthetic technologies, thereby minimizing the cost of waste disposal.

Among various reactions of industrial significance, oxidation of alcohols to carbonyl compounds is a pivotal reaction and is essential for the preparation of organic intermediates, fragrances, and food additives (2). Numerous methods have been developed for these oxidations (3–17). All these traditional methods involve the use of stoichiometric amounts of inorganic oxidants, e.g., Cr(VI), which generate copious amounts of waste heavy metals. Moreover, these methods involve the use of hazardous reagents and solvents, and sometimes expensive reagents and transition metal catalysts, which interfere and make the recovery of catalyst cumbersome. In some cases, overoxidation products have also been detected. The use of molecular O_2 for oxidation is often difficult to control and sometimes results in combustion, and the reaction is performed with low conversion to avoid overoxidation.

Among various oxidizing agents, sodium hypochlorite seems to be the most inexpensive with the highest potential for industrial application. The earliest application of NaOCl as a practical synthetic reagent for alcohol oxidation involved its use in a two-phase system with a phase-transfer catalyst (18). More recently, two improved methods for bleach oxidation of alcohols have been developed. One method employs acetic acid as a solvent in a monophasic system (19) while the other uses catalytic amounts of TEMPO in a buffered biphasic medium (20). All these methods involve the use of biphasic systems employing dichloromethane or toluene as the organic phase, a phase-transfer catalyst, and subsequent formation of overoxidation products. It is difficult to find a procedure that is selective, cheap, efficient, and easy to work up.

In a continuation of our work on supramolecular chemistry involving cyclodextrins (21), we have attempted the oxidation of alcohols with sodium hypochlorite in the presence of β-cyclodextrin in water to develop an environmentally viable process. Cyclodextrins, which are cyclic oligosaccharides, exert microenvironmental effects leading to selective reactions. They catalyze reactions by supramolecular catalysis through non-covalent bonding as seen in enzymes. Complexation depends on the size, shape, and hydrophobicity of the guest molecule. Thus, mimicking biochemical selectivity, where orientation of the substrate by complex formation positioning presents only certain regions for favorable attack, will be superior to chemical selectivity, which involves random attack at different regions due to the intrinsic reactivity of the substrate. These attractive features of cyclodextrins in the biomimetic modeling of chemical reactions prompted us to investigate a variety of oxidations us-

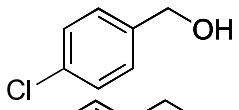
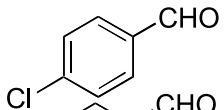
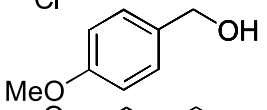
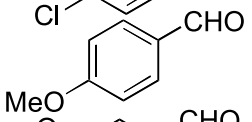
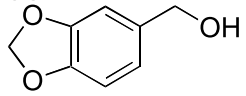
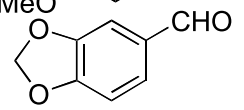
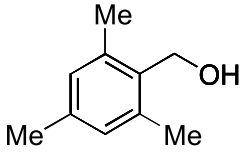
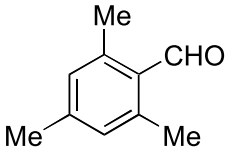
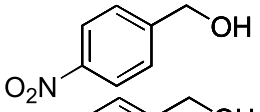
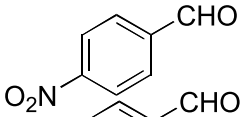
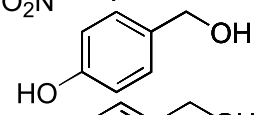
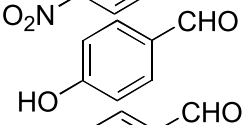
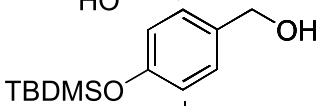
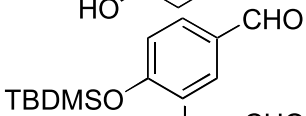
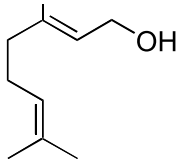
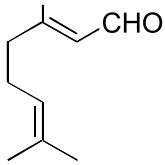
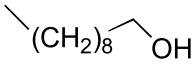
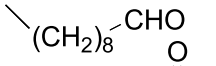
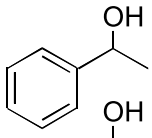
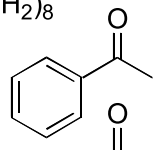
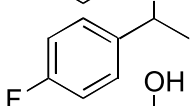
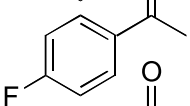
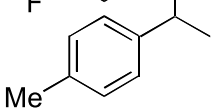
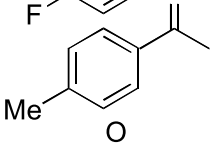
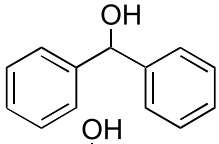
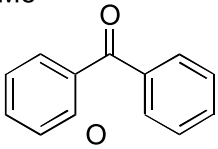
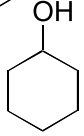
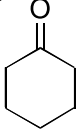
Received 19 December 2003. Published on the NRC Research Press Web site at http://canjchem@nrc.ca on 2 October 2004.

K. Surendra, N.S. Krishnaveni, and K.R. Rao[1]. Organic Chemistry Division-I, Indian Institute of Chemical Technology, Hyderabad-500 007, India.

[1]Corresponding author (e-mail: ramaraok@iict.res.in).

 doi: 10.1139/V04-065 © 2004 NRC Canada

Table 1. Oxidation of alcohols with NaOCl–KBr in the presence of β-CD in water.

Entry	Substrate	Product [a]	Time (h)	Yield (%)[b]
1			8	94
2			8	94
3			8	91
4			10	89
5			12	88
6			12	89
7			8	90
8			8	92
9			12	84
10			12	88
11			12	86
12			12	86
13			12	84
14			14	82

[a] All products were characterized by ^{1}H NMR, IR, and MS, and all physical characteristic comparisons were done with authentic samples.

[b] Isolated and unoptimized yields.

© 2004 NRC Canada

ing the substrate β-cyclodextrin complexes with sodium hypochlorite in water. The complexes were formed with β-cyclodextrin since it is easily accessible and the least expensive among the cyclodextrins.

There are reports of utilizing sodium hypochlorite in conjunction with cyclodextrins for certain oxidations such as for the chlorination of anisole at the para position (22), for asymmetric catalytic epoxidation (23), and sulfoxidation (24). To date, no alcohol oxidations to important carbonyl compounds have been carried out with sodium hypochlorite under supramolecular catalysis involving cyclodextrins.

Experimental

Materials

All reactions were carried out in an air atmosphere without any special precautions. Chemicals and solvents were purchased from Fluka and S. D. Fine Chemicals and used as received. ^{1}H NMR spectra were obtained on a Gemini-200 or 300 MHz spectrometer. IR spectra were recorded on a Nicolet Nexus 670 FT-IR spectrometer. Mass spectra were observed on a Micromass VG AutoSpec M spectrometer.

Typical procedure for oxidation

β-Cyclodextrin (1 mmol) was dissolved in water (15 mL) at 60 °C, then substrate (1 mmol) previously dissolved in methanol/acetone (1 mL) was added slowly with stirring and cooled to room temperature. Later, the reaction was cooled in an ice bath and sodium hypochlorite (5 mmol) was added slowly, followed by addition of KBr (1 mmol) and subsequent stirring at room temperature was continued until the reaction had gone to completion (Table 1). It was extracted with ethyl acetate and filtered. The organic layer was dried over anhydrous Na_2SO_4 and the solvent was removed in vacuum to obtain the crude product, which was purified by column chromatography using *n*-hexane : ethyl acetate (95:5) on silica gel.

Results and discussion

The reaction was carried out by the in situ formation of the β-cyclodextrin complex of the alcohol in water followed by addition of sodium hypochlorite and KBr at 0–5 °C and later stirring at room temperature until the reaction went to completion. A variety of alcohols have been oxidized to their corresponding carbonyl compounds in impressive yields using NaOCl–KBr under supramolecular catalysis in water (Scheme 1). This methodology is also compatible in the presence of other functionalities such as methoxy, methylenedioxy, nitro, hydroxy, and alkene double bonds. The yields of oxidation products of primary alcohols are comparatively better than secondary alcohols. Though inclusion complexation takes place in situ during the reaction, the complexes have been isolated and characterized by powder X-ray (25) and ^{1}H NMR studies (26). All the compounds were characterized by MS, ^{1}H NMR, and IR techniques followed by comparison of the collected data to known compounds (27).

The reaction has also been studied in detail for various ratios of β-cyclodextrin and KBr by taking 4-methoxybenzyl alcohol as an example (Table 2). It was observed that optimum yields were obtained when β-cyclodextrin and KBr were taken in equimolar ratios of 1 equiv. each. However, the yields were comparatively less with lower ratios of β-cyclodextrin and KBr. Another point of interest is that the yields were drastically reduced with lower equivalents of KBr in spite of higher ratios of β-cyclodextrin. Thus, it could be seen that KBr plays a major role in these oxidations and its function can be explained as follows.

Scheme 1.

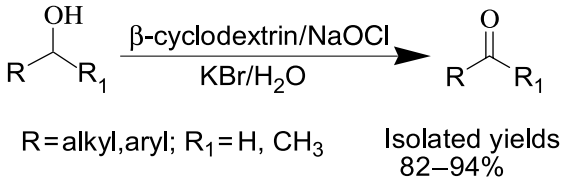


Table 2. Oxidation of 4-methoxybenzyl alcohol using NaOCl–KBr system.

Entry	β-CD [a] (mmol/L)	Hypo[b] (mmol/L)	KBr (mmol/L)	Alcohol (mmol/L)	Yield (%)
1	0.1	5.0	0.1	1.0	30
2	0.1	5.0	1.0	1.0	45
3	1.0	5.0	0.1	1.0	68
4	1.0	5.0	1.0	1.0	94

[a]β-Cyclodextrin.
[b]Sodium hypochlorite.

The oxidation of alcohols in the presence of β-cyclodextrin using sodium hypochlorite and KBr can take place through the initial formation of β-cyclodextrin–hypochlorite as observed by Breslow and co-workers (22) followed by the in situ generation of the more active β-cyclodextrin–hypobromite, which further increases the oxidation yields. This is substantiated by the fact that no oxidation was observed when the alcohol was reacted in the presence of β-cyclodextrin using hydrogen peroxide and KBr.

In conclusion, we have developed an inexpensive, eco-conscious chemical process for the oxidation of alcohols to carbonyl compounds in aqueous medium. This methodology is simple, inexpensive, and can be applied to a variety of substrates with high potential for industrial applications.

Acknowledgement

K. Surendra thanks the Council of Scientific and Industrial Research, New Delhi, India, for the award of a research fellowship. IICT communication no. 040116.

References

1. (*a*) P.T. Anastas and J.C. Warner. *In* Green chemistry, theory and practice. Oxford University Press, Oxford. 1998; (*b*) P.T. Anastas and T.C. Williamson (*Editors*). Green chemistry, frontiers in benign chemical synthesis and processes. Oxford University Press, Oxford. 1998; (*c*) P.T. Anastas, L.G. Heine, and T.C. Williamson (*Editors*). Green engineering. ACS Symposium Series. Vol. 766. American Chemical Society, Washington, D.C. 2000; (*d*) J. Clark and D. Macquarrie (*Editors*). Handbook of green chemistry & technology. Blackwell, Ox-

© 2004 NRC Canada

ford. 2002; (*e*) M. Eissen, J. O. Metzger, E. Schmidt, and U. Schneidewind. Angew. Chem. Int. Ed. **41**, 414 (2002).
2. (*a*) R.A. Sheldon, I.W.C.E. Arends, and A. Dijksman. Catal. Today, **57**, 157 (2000); (*b*) T. Mallat and A. Baiker. Catal. Today, **19**, 247 (1994).
3. M. Hudlicky. Oxidations in organic chemistry. American Chemical Society Monograph 186. American Chemical Society, Washington, D.C. 1990.
4. (*a*) J.D. Albright and L. Goldman. J. Am. Chem. Soc. **87**, 4214 (1965); (*b*) K.E. Pitzner and J.G. Moffatt. J. Am. Chem. Soc. **87**, 5661 (1965); (*c*) K.E. Pitzner and J.G. Moffatt. J. Am. Chem. Soc. **87**, 5670 (1965); (*d*) R.J. Parikh and W.E. Doering. J. Am. Chem. Soc. **89**, 5505 (1967); (*e*) W.W. Epstein and F.W. Sweat. Chem. Rev. **67,** 247 (1967); (*f*) K. Omura, A.K. Sharma, and D. Swern. J. Org. Chem. **41,** 957 (1976).
5. (*a*) G. Cainelli and G. Cardillo. Chromium oxidations in organic chemistry. Springer, New York. 1984; (*b*) S.V. Ley and A. Madin. *In* Comprehensive organic synthesis. *Edited by* B.M. Trost and I. Fleming. Pergamon Press, Oxford. 1991. pp. 7, 251; (*c*) E.J. Corey and G. Schmidt. Tetrahedron Lett. 399 (1979).
6. (*a*) R.A. Sheldon, I.W.C.E. Arends, and A. Dijksman. Catal. Today, **57**, 157 (2000); (*b*) M. Hayashi and H.J. Kawabata. Synth. Org. Chem. Jpn. **60,** 137 (2002); (*c*) M. Hayashi and H.J. Kawabata. Synth. Org. Chem. Jpn. **60,** 1625 (2002); (*d*) S.V. Ley, W.P. Griffith, and S.P. Marsden. Synthesis, 639 (1994).
7. M.R. Leanna, T.J. Sowin, and H.E. Morton. Tetrahedron Lett. **33**, 5029 (1992).
8. V.M. Dembitsky. Tetrahedron, **59**, 4701 (2003).
9. (*a*) K. Omura and D. Swern. Tetrahedron, **34**, 1651 (1978); (*b*) A.J. Mancuso and D. Swern. Synthesis, 165 (1981).
10. (*a*) D.B. Dess and J.C. Martin. J. Org. Chem. **48**, 4155 (1983); (*b*) D.B. Dess and J.C. Martin. J. Am. Chem. Soc. **113**, 7277 (1991); (*c*) J.B. Plumb and D.J. Harper. Chem. Eng. News, **68**(29), 3 (1990).
11. P.H.J. Carlsen, T. Katsuki, V.S. Martin, and K.B. Sharpless. J. Org. Chem. **46**, 3936 (1981).
12. R.G. Vaghei and A. Khazaei. Tetrahedron Lett. **44**, 7525 (2003).
13. (*a*) A.J. Fatiadi. Synthesis, 133 (1976); (*b*) L.A. Paquette (*Editor*). Encyclopedia of reagents for organic synthesis. Wiley, Chichester. 1995.
14. (*a*) J-i. Matsuo, D. Iida, H. Yamnaka, and T. Mukaiyama. Tetrahedron, **59**, 6739 (2003); (*b*) T. Mukaiyama, J-i. Matsuo, D. Iida, and H. Kitagawa. Chem. Lett. 846 (2001).
15. (*a*) R. Filler. Chem. Rev. **63**, 21 (1963); (*b*) J. Einhorn, C. Einhorn, F. Ratajczak, and J.L. Pierre. J. Org. Chem. **61**, 7452 (1996).
16. (*a*) J. Yoshida, R. Nakai, and N. Kawabata. J. Org. Chem. **45**, 5269 (1980); (*b*) C.R. Harrison and P. Hodge. J. Chem. Soc., Perkin Trans. 1, 509 (1982).
17. T. Mallat and A. Baiker. Catal. Today, **19**, 247 (1994).
18. (*a*) G.A. Lee and H.H. Freedman. Tetrahedron Lett. 1641 (1976); (*b*) S.L. Regen. J. Org. Chem. **42**, 875 (1997).
19. R.V. Stevens, K.T. Chapman, and H.N. Weller. J. Org. Chem. **45**, 2030 (1980).
20. P.L. Anelli, C. Biffi, F. Montanari, and S. Quici. J. Org. Chem. **52,** 2559 (1987).
21. (*a*) K. Surendra, N.S. Krishnaveni, Y.V.D. Nageswar, and K.R. Rao. J. Org. Chem. **68**, 4994 (2003); (*b*) K. Surendra, N.S. Krishnaveni, M.A. Reddy, Y.V.D. Nageswar, and K.R. Rao. J. Org. Chem. **68**, 2058 (2003); (*c*) N.S. Krishnaveni, K. Surendra, M.A. Reddy, Y.V.D. Nageswar, and K.R. Rao. J. Org. Chem. **68**, 2018 (2003); (*d*) N.S. Krishnaveni, K. Surendra, Y.V.D. Nageswar, and K.R. Rao. Synthesis, 1968 (2003).
22. R. Breslow. Acc. Chem. Rec. **13**, 170 (1980).
23. S. Banfi and S. Colonna. Synth. Commun. 1049 (1983).
24. K.R. Rao and P.B. Sattur. J. Chem. Soc. Chem. Commun. 342 (1989).
25. J. Szejtli and T. Osa. *In* Comprehensive supramolecular chemistry. Vol. 3. Pergamon Press, Oxford, UK. 1996. p. 253.
26. P.V. Demarco and A.L. Thakkar. J. Chem. Soc. Chem. Commun. 2 (1970).
27. C.J.P.J. Behnke (*Editor*). The Aldrich library of IR, ^{13}C and ^{1}H FT-NMR spectra. Aldrich, Milwaukee, Wis. 1985–1989.

© 2004 NRC Canada

ERRATUM / ERRATUM

Erratum: Canadian Journal of Chemistry, Volume 82, Issue 6

Ref.: Can. J. Chem. **82**: 673 (2004).

Because of the last-minute rescheduling of an article, pages 665–671 were inadvertently omitted from Volume 82. Hence, the June issue of Volume 82 began at page 673, rather than page 665.

NRC Research Press sincerely apologizes for any inconvenience this may cause.

Received 23 September 2004. Published on the NRC Research Press Web site at http://canjchem@nrc.ca on 2 October 2004.

 doi: 10.1139/V04-135 © 2004 NRC Canada

ERRATUM / ERRATUM

Erratum: Electronic spectroscopy of the nonlinear carbon chains $C_4H_4^+$ and $C_8H_4^+$

Mitsunori Araki, Pawel Cias, Alexey Denisov, Jan Fulara, and John P. Maier

Ref.: Can. J. Chem. **82**(6): 848–853 (2004).

Readers who accessed this paper online between 20 April 2004 and 15 September 2004 should take note of the following. The third sentence of the French abstract now reads:

Ces spectres ont été détectés par absorption directe par la technique CRDS (« cavity ringdown spectroscopy ») grâce à une décharge supersonique planaire.

NRC Research Press apologizes for any inconvenience this may have caused.

Réf. : Rev. Can. Chim. **82**(6) : 848–853 (2004).

Les lecteurs qui ont accédé à cet article en direct entre le 20 avril 2004 et le 15 septembre 2004 sont priés de prendre note que la troisième phrase du résumé contenait une erreur. Voici la version révisée de cette phrase :

Ces spectres ont été détectés par absorption directe par la technique CRDS (« cavity ringdown spectroscopy ») grâce à une décharge supersonique planaire.

Les Presses scientifiques du CNRC s'excusent de tout problème que cette situation aurait pu causer.

Received 15 September 2004. Published on the NRC Research Press Web site at http://canjchem.nrc.ca on 05 October 2004.

M. Araki, P. Cias, A. Denisov, J. Fulara,[1] and J.P. Maier.[2] Department of Chemistry, Klingelbergstrasse 80, CH-4056 Basel, Switzerland.

[1]Permanent address: Institute of Physics, Polish Academy of Science, Warsaw, Poland.
[2]Corresponding author (e-mail: J.P.Maier@unibas.ch).

 doi: 10.1139/V04-136 © 2004 NRC Canada

ANNOUNCEMENT / COMMUNIQUÉ



May 1929 marked the publication of Volume 1 Number 1 of the *Canadian Journal of Research* by the National Research Council of Canada. An introduction by NRC President H.M. Tory stated that, "While the Journal is intended primarily for the publication of results of work carried out under the auspices of the Council, it will also be open for suitable papers from Canadian research workers not connected with this organization" — little imagining that one day NRC research journals would be open to the world.

NRC Research Press (now part of the NRC Canada Institute for Scientific and Technical Information) is Canada's foremost publisher of scientific and technical information. The Press publishes 15 journals in fields as diverse as genomics, chemistry, zoology, and civil engineering.

A number of Research Press journals trace their origins back to the original volume in 1929 and, testament to growing specialization in the sciences, have undergone many name changes along the way. In recent years, new journals reflecting emerging areas of research have been added to the Research Press stable. The most recent addition is the 2002 launch of the *Journal of Environmental Engineering and Science*.

All Research Press journals are internationally respected, peer-reviewed journals, well rated in terms of impact factor (the number of times papers from specific publications are cited by other authors, divided by the number of scientific papers published, calculated over a two-year period). Research Press journals *Canadian Journal of Fisheries and Aquatic Sciences* and *Biochemistry and Cell Biology* have very high impact factors; in addition, the *Canadian Journal of Fisheries and Aquatic Sciences* and the *Canadian Journal of Forest Research* are listed among the top four publications in their fields.

NRC Research Press journals focus on critical, high-quality research from Canadian universities and industry and from international research centres. In 2003 the Press received 3941 research papers from authors in Canada and around the world, of which 1841 were accepted and published after rigorous peer review by international boards of associate editors and peer reviewers.

Once published, Research Press journals appear in print and on the Web. More than three quarters of the journals' subscriptions are sent to international subscribers such as academic libraries, research centres, and universities. The journals are now available on the Web free of charge to all Canadians through the support of the federal government's Depository Services Program.

Research Press also has developed an extensive program of scientific monographs and conference proceedings. It has recently launched a series of biographies of famous Canadian scientists and engineers, including physicist Gerhard

Mai 1929 a marqué la parution du numéro inaugural du *Canadian Journal of Research* par le Conseil national de recherches du Canada. En préface, le président du CNRC de l'époque, H.M. Tory, observait : « Bien que cette revue se veuille principalement un véhicule de diffusion des résultats de la recherche réalisée sous la bannière du Conseil, on y publiera volontiers des articles méritoires signés par des chercheurs canadiens non affiliés à notre organisme. » Jamais il n'aurait pu présager la place que se tailleraient un jour les revues du CNRC sur la scène mondiale.

Les Presses scientifiques du CNRC (aujourd'hui rattachées à l'Institut canadien de l'information scientifique et technique) constituent le plus important éditeur de publications scientifiques et techniques du pays. Elles publient quinze revues dans des domaines aussi variés que la génomique, la chimie, la zoologie et le génie civil, pour ne nommer que ceux-là.

Plusieurs des revues des Presses scientifiques tirent leur origine du premier numéro du *Journal*, en 1929, et ont revêtu de nouvelles dénominations au fil de la spécialisation de la science. Au cours des dernières années, de nouvelles revues reflétant des secteurs scientifiques naissants sont venues s'ajouter à la gerbe des Presses scientifiques du CNRC. La cadette, qui a vu le jour en 2002, est la *Revue du génie et de la science de l'environnement*.

Toutes les revues des Presses scientifiques sont arbitrées, mondialement respectées et déterminantes par leur facteur d'impact (soit le nombre de fois que des articles d'une publication sont cités par des auteurs externes, divisé par le nombre total d'articles publiés sur une période de deux ans). De fait, les revues des Presses scientifiques *Journal canadien des sciences halieutiques et aquatiques et Biochimie et biologie cellulaire* affichent des facteurs d'impact très élevés; de plus, le *Journal canadien des sciences halieutiques et aquatiques* et la *Revue canadienne de recherche forestière* font partie des quatre publications les plus reconnues dans leur domaine respectif.

Les revues des Presses scientifiques du CNRC ciblent principalement la recherche critique et supérieure réalisée par les universités et l'industrie canadienne de même que par les centres de recherche internationaux. En 2003, les Presses ont reçu 3941 articles en provenance du Canada et de l'étranger, parmi lesquels 1841 ont été publiés après un rigoureux examen par des comités de lecture internationaux composés de directeurs scientifiques associés et d'examinateurs spécialisés.

Toutes les revues des Presses paraissent sous forme imprimée et sur le Web. Plus des trois quarts des abonnements sont destinés à des organismes étrangers, y compris des bibliothèques savantes, des centres de recherche et des universités. Nos revues sur le Web sont maintenant accessibles

© 2004 NRC Canada

Herzberg and inventor George J. Klein. Since 1997, the Press has supported the research and scientific community in Canada by publishing 14 other journals on behalf of Canadian scientific societies such as the Agricultural Institute of Canada and the Mineralogical Association of Canada.

NRC Research Press has moved a long way in the past 75 years, but it cannot slow the pace. *Au contraire*: scientific communication is evolving quickly, and NRC Research Press is evolving with it. The need for speedy publication, new publishing technologies, new delivery formats, and new business models such as open access are the main drivers in scientific publishing today. To meet future needs, the Press is adopting new publishing technologies and standards such as XML, as well as exploiting the functionality of the Internet to launch a new submission and review system called **OSPR**EY. The Press has also allowed the popular search engine Google to "deep index" its Web-based publication, to assist users in gaining fast and precise access to valuable content. Articles will soon be available in full-text HTML on the Web, enabling reference linking and other functionality.

NRC Research Press continues to plan and work toward the future, but it cannot work alone. The Research Press is looking for partners and has recently undertaken joint projects with the Commonwealth Scientific and Industrial Research Organisation in Australia and CABI Publishing in the United Kingdom.

Finally, none of this illustrious 75 years of publishing would have been possible without the commitment and support of the researchers in the scientific community, the editors and reviewers who select and review the research, and the staff of the NRC Research Press who edit and publish it. My personal thanks to all of you, and my sincere wishes for another 75 years of scientific publishing leadership.

Bruce Dancik
Editor-in-Chief
NRC Research Press

à titre gratuit à tous les Canadiens, grâce à l'appui du Programme des services de dépôt du gouvernement du Canada.

Les Presses scientifiques administrent également un enviable programme de publication de monographies scientifiques et de comptes rendus de conférences. Par ailleurs, elles ont récemment donné le coup d'envoi à une collection de biographies de scientifiques et d'ingénieurs canadiens de renom, notamment le physicien Gerhard Herzberg et l'inventeur George J. Klein. Depuis 1997, les Presses ont prêté main-forte à la collectivité canadienne de la recherche et de la science en publiant quatorze autres revues au nom de sociétés scientifiques canadiennes telles que l'Institut agricole du Canada et l'Association minéralogique du Canada.

Les Presses scientifiques du CNRC ont certes fait de grandes enjambées au cours des 75 dernières années, mais elles ne peuvent pas s'endormir sur leurs lauriers. Il est un fait que la communication savante se transforme sans cesse et que les Presses scientifiques se doivent d'emboîter le pas. Ainsi, la publication accélérée, les nouvelles technologies d'édition, les modes de diffusion évolués et les nouveaux modèles commerciaux, notamment le libre accès, sont les tendances les plus influentes sur le secteur de l'édition savante. Conscientes de l'importance d'être « de leur temps », les Presses adoptent de nouvelles technologies et normes de publication, telles que le XML, et exploitent le plein potentiel d'Internet en lançant un nouveau système de soumission et d'examen de manuscrits en direct appelé **OSPR**EY. Les Presses ont également autorisé le moteur de recherche bien connu Google à réaliser un dépouillement approfondi de leurs publications Web, cela afin d'assurer le repérage rapide et efficace d'articles d'intérêt par les utilisateurs. À courte échéance, tous les articles intégraux seront offerts en format HTML sur le Web, ce qui permettra l'hyper-référençage et d'autres fonctions avancées.

Les Presses scientifiques du CNRC continuent à planifier l'avenir et à travailler en ce sens mais savent qu'elles ne peuvent pas s'exécuter en solitaire. Elles restent à l'affût des partenariats et, témoin, ont récemment lancé des coentreprises avec la Commonwealth Scientific and Industrial Research Organisation, en Australie, et CABI Publishing, au Royaume-Uni.

Nos 75 brillantes années d'édition sont étroitement tributaires de l'engagement et de l'appui des chercheurs de la collectivité scientifique, des directeurs scientifiques et examinateurs qui sélectionnent et évaluent les manuscrits, et du personnel des Presses scientifiques du CNRC, qui les pétrissent et les publient. Je tiens à remercier chacun de vous de votre apport et je nous souhaite à tous encore 75 ans d'excellence en édition scientifique.

Bruce Dancik
Directeur scientifique en chef
Presses scientifiques du CNRC

© 2004 NRC Canada

Gaussian basis sets for low-lying excited states of neutral atoms with $2 \leq Z \leq 36$

M.T. Barreto, A. Canal Neto, and F.E. Jorge

Abstract: The improved generator coordinate Hartree–Fock method is used to generate Gaussian basis sets for low-lying excited states of neutral atoms from He (Z = 2) to Kr (Z = 36). Then, excitation energies and orbital energies of the outermost orbitals of each symmetry are calculated and compared with the corresponding values obtained with numerical Hartree–Fock calculations. Besides this, the basis sets for Be (^{3}P) and F (^{2}P) are contracted by a standard procedure and, then, enriched with polarization functions. From these basis sets, total energies, dissociation energy, and bond length for BeF are calculated and compared with results obtained with other basis sets and with experimental values. The sets for He–Kr are useful in constructing basis sets for molecular calculations.

Key words: improved generator coordinate Hartree–Fock method, Gaussian basis sets, low-lying excited states, neutral atoms.

Résumé : On a utilisé la méthode améliorée de Hartree–Fock avec coordonnée génératrice pour générer des ensembles de base gaussiens pour les états excités de basse énergie des atomes neutres allant de He (Z = 2) à Kr (Z = 36). On a ensuite calculé les énergies d'excitation et les énergies orbitales des orbitales extérieures de chacune des symétries et on les a comparées aux valeurs correspondantes obtenues par des calculs de Hartree–Fock numériques. De plus, on a contracté les ensembles de base pour Be (^{3}P) et F (^{2}P) en faisant appel à une procédure standard suivie par l'enrichissement à l'aide de fonctions de polarisation. À partir de ces ensembles de base, on a calculé les énergies totales et l'énergie de dissociation de BeF ainsi que la longueur de la liaison BeF et on les a comparées aux résultats obtenus avec d'autres ensembles de base et avec les valeurs expérimentales. Les ensembles pour He–Kr sont utiles pour construire des ensembles de base pour faire des calculs moléculaires.

Mots clés : méthode améliorée de Hartree–Fock avec coordonnée génératrice, ensembles de base gaussiens, états excités de basse énergie, atomes neutres.

[Traduit par la Rédaction]

Introduction

Mohallem et al. (1) developed the generator coordinate Hartree–Fock (GCHF) method, which was used with success in the generation of universal basis sets of various atomic systems (2–5).

In 1999, Jorge and de Castro (6) presented the improved GCHF (IGCHF) method and applied it to generate Gaussian basis sets (GBSs) for first-row atoms. In the last 4 years, the IGCHF method has been applied with success to generate accurate GBSs for several atomic and molecular systems (7–10).

It is known that for some atoms (for example: Li, Be, Na, etc.) it is necessary to optimize uncontracted basis sets of some excited states to obtain reasonable descriptions of all valence orbitals, since these orbitals have a crucial importance to the chemical bond description of molecular systems. In this work, the IGCHF method was applied to generate GBSs of low-lying excited states of neutral atoms from He (Z = 2) to Kr (Z = 36). The excitation energies were evaluated and compared with those obtained with a numerical HF (NHF) method (11, 12). Besides this, the orbital energies of the outermost orbitals of each symmetry were also computed. To test the performance of the GBSs generated in this work, the basis sets of Be (^{3}P) and F (^{2}P) were contracted and enriched with polarization functions and, then, used at the restricted open-shell HF (ROHF) and RO Møller–Plesset second-order (ROMP2) levels to calculate energies, bond length, and dissociation energy of the BeF molecule. A comparison with results obtained with other approaches (13, 14) and with experimental values (15, 16) was done.

Received 31 July 2003. Published on the NRC Research Press Web site at http://canjchem.nrc.ca on 12 October 2004.

M.T. Barreto, A. Canal Neto, and F.E. Jorge.[1]
Departamento de Física, Universidade federal do Espírito Santo, 29060-900 Vitória, ES, Brazil.

[1]Corresponding author (e-mail: Jorge@cce.ufes.br).

Improved generator coordinate Hartree–Fock method

The GCHF approach (1) is based on choosing the one-electron functions as a continuous superposition, i.e.,

$$[1] \qquad \Psi_i(1) = \int \phi_i(1,\alpha)\, f_i(\alpha) \mathrm{d}\alpha \qquad i = 1,\ldots,n$$

where ϕ_i are the generator functions, f_i are the weight functions, and α is the generator coordinate. Using eq. [1] to build a Slater determinant for the multielectronic wave functions, and minimizing the total energy (E) with respect to the

 doi: 10.1139/V04-084 © 2004 NRC Canada

f_i, one arrives at the Griffin–Hill–Wheeler–HF (GHWHF) equations (1),

$$[2] \qquad \int [F(\alpha,\beta) - \varepsilon_i S(\alpha,\beta)]\, f_i(\beta)\mathrm{d}\beta = 0 \qquad i = 1,\ldots,n$$

where the ε_i are the HF eigenvalues, and the Fock ($F(\alpha, \beta)$) and overlap ($S(\alpha,\beta)$) kernels were defined by Mohallem et al. (1).

The GHWHF equations were integrated numerically through a technique called integral discretization (ID) (17). This technique was implemented through a relabelling of the generator coordinate space, i.e.,

$$[3] \qquad \Omega = \ln\alpha/A \qquad A > 1$$

where A is a scaling parameter determined numerically. The new generator coordinate space (Ω) was discretized for each s, p, d, and f symmetry in an equally spaced mesh $\{\Omega_i\}$ so that:

$$[4] \qquad \Omega_k = \Omega_{\min} + (k - 1)\Delta\Omega \qquad k = 1,\ldots,N$$

In eq. [4], N is the number of discretization points defining the basis set size, $\Omega_{\min}$ is the initial point, and $\Delta\Omega$ an increment. Thus, the original GCHF method (1) corresponds to the use of only one arithmetic sequence of equally spaced points $\{\Omega_i\}$ to generate single-optimized Gaussian basis sets.

Jorge and de Castro (6) have found a simple modification in the GCHF method that produces improvements in the HF atomic energy values without adding more functions (in our case, Gaussian-type functions (GTFs)); this methodology has been named the IGCHF method. In this new approach, the new generator coordinate space (Ω) was discretized for each s, p, d, and f symmetry in three independent arithmetic sequences,

$$[5] \qquad \Omega_k = \begin{cases} \Omega_{\min} + (k-1)\Delta\Omega & k = 1,\ldots,j \\ \Omega'_{\min} + (k-1)\Delta\Omega' & k = j+1,\ldots,M \\ \Omega''_{\min} + (k-1)\Delta\Omega'' & k = M+1,\ldots,N \end{cases}$$

For a given value of N, the number of parameters now to be optimized for each symmetry when one uses eq. [5] is three times that of the original GCHF method (see eq. [4]). The basis sets generated through eqs. [3] and [5] were called triple-optimized Gaussian basis sets (TOGBSs) (6).

We call attention to the fact that when eq. [5] is used, there is no longer an equally spaced mesh $\{\Omega_i\}$ because now there are three arithmetic sequences to generate the basis function exponents for each symmetry.

Results and discussion

Neutral atoms

The IGCHF method presented in the previous section was employed to generate TOGBSs for low-lying excited states of the neutral atoms from He to Kr. The scaling parameter A (see eq. [3]) utilized in the calculations is equal to 6.0. All calculations were carried out using a modified version of the ATOMSCF program (18). For all excited states studied, the optimization process was repeated until the total energies stabilized within 10 significant figures.

In this work, we considered all states arising from the following electronic configurations:

He ($1s^2$ and $1s^12p^1$), Li and Na (ns^1 and np^1), Be to F and Mg to Cl (ns^2np^m and ns^1np^{m+1}), Ne ($2s^22p^6$ and $2s^22p^53s^1$), Ar ($3s^23p^6$, $3s^23p^54s^1$, and $3s^23p^53d^1$), K ($4s^1$, $4p^1$, and $3d^1$), Ca ($4s^2$, $4s^14p^1$ and $4s^13d^1$), Sc to Cu ($4s^23d^m$ and $4s^13d^{m+1}$), Zn ($4s^2$, $4s^14p^1$, and $4s^14d^1$), Ga to Br ($4s^24p^m$ and $4s^14p^{m+1}$), and Kr ($4s^24p^6$, $4s^24p^55s^1$, and $4s^24p^54d^1$).

Although we have calculated 109 excited states arising from the above configurations, we give information about the ground states (6–8) for completeness here. Tables 1 (He to Ar) and 2 (K to Kr) display the excitation energies [E(excited state) – E(ground state)] of some states and the orbital energies (ε) of the outermost orbitals of each symmetry evaluated with the IGCHF (6) and NHF (11, 12) methods. The ground-state total HF energies are also presented. All values are given in hartrees (1 hartree = 4.3598×10^{-18} J).

From Table 1 one can verify that the total energy errors obtained with the TOGBSs for the atoms from He to Ar are always smaller than 1.3 mhartree. Colpa et al. (19) observed that within the same electronic configuration, the smallest mean electron–nucleus distance is associated with the state of the lowest total energy and maximum multiplicity. One particular example is the case of the ^{1}P and ^{3}P states of Be $2s^12p^1$. As discussed previously by other authors (20–23), the broadness of the $2p$ atomic orbital in Be ^{1}P arises from a repulsive exchange potential among the $2s$ and $2p$ electrons. In both the ^{1}P and ^{3}P states, the $2s$ orbital energies are lower than in the ground state (see Table 1). Thus, one can think that in excited states arising from $2s \rightarrow 2p$ transitions, the ε_{2s} should be lower than in the ground state, but Table 1 shows that this expectation does not hold in many cases. The $3p^53d^1$ ^{3}D and ^{1}D energy levels of Ar are degenerate in the restricted HF theory, since the two configuration state functions share the same energy expression. In general, in the same group of the Periodic Table, the excitation energies of each atom of the first row are larger than the corresponding ones of the second row. Here, it is also important to emphasize that for the atoms from He to Ar the excitation and orbital energies evaluated with the TOGBSs are in good agreement with the corresponding NHF results (11).

For the atoms from K to Kr (see Tables 2), the differences among the corresponding total energies computed with the IGCHF (6) and NHF (12) methods are in the range between 0.36 and 6.88 mhartree. The excitation energy from the $4s$ to $3d$ atomic orbital ($4s^23d^m \rightarrow 4s^13d^{m+1}$) decreases from Sc (0.036 604 6 hartree) to V (0.004 148 3 hartree). For Cr, the $4s^13d^5$ configuration becomes the ground state. For the next atom (Mn), the ground state is the $4s^23d^5$ configuration and the $4s \rightarrow 3d$ transition requires an excitation energy of 0.121 786 hartree. The excitation energy again decreases to 0.046 150 hartree for Ni. Then, for the Cu atom the $4s^13d^{10}$ configuration is the ground state. The symmetry of the ground states obtained with the IGCHF method (6) agrees with the experimental one (24). For the atoms displayed in Table 2, there is excellent agreement among corresponding excitation and orbital energies evaluated with the IGCHF and NHF (12) methods.

The BeF molecule

Basis sets for molecular calculations are usually devel-

© 2004 NRC Canada

Table 1. Excitation [E(excited state) – E(ground state)] and orbital (ε) energies (in hartrees) of some states of the atoms from He to Ar.

Z	Atom	Configuration	State	TOGBS (Size)	Excit. energy (This work)[a]	Excit. energy (NHF)[b]	$-\varepsilon_s$ (This work)[a]	$-\varepsilon_p$ (This work)[a]	$-\varepsilon_d$ (This work)[a]
2	He	$1s^2$	^{1}S	18s	–2.861 679 855[c]	–2.861 680 00[d]		0.917 955[c]	—
		$1s^12p^1$	^{3}P	20s11p	0.730 242 910	0.730 242 93	1.733 744	0.131 560	—
			^{1}P	20s11p	0.739 215 734	0.739 215 78	1.756 340	0.122 480	—
3	Li	[He]$2s^1$	^{2}S	18s	–7.432 723 753[c]	–7.432 726 93[d]	0.196 322[c]	—	—
		[He]$2p^1$	^{2}P	18s11p	0.067 654 635	0.067 657 27	2.530 726	0.128 672	—
4	Be	[He]$2s^2$	^{1}S	18s	–14.573 016 88[c]	–14.573 023 2[d]	0.309269[c]	—	—
		[He]$2s^12p^1$	^{3}P	18s11p	0.061 519 42	0.061 521 3	0.394 376	0.241 499	—
			^{1}P	18s11p	0.178 287 07	0.178 287 8	0.395 574	0.117 529	—
5	B	[He]$2s^22p^1$	^{2}P	20s11p	–24.529 057 06[c]	–24.529 060 7[d]	0.494 705[c]	0.309 855[c]	—
		[He]$2s^12p^2$	^{4}P	20s11p	0.078 403 00	0.078 403 1	0.642 267	0.354 554	—
			^{2}D	20s11p	0.217 189 95	0.217 191 8	0.573 185	0.276 479	—
			^{2}S	20s11p	0.280 968 16	0.280 970 1	0.594 255	0.222 960	—
			^{2}P	20s11p	0.350 017 01	0.350 017 5	0.427 311	0.244 385	—
6	C	[He]$2s^22p^2$	^{3}P	20s11p	–37.688 612 13[c]	–37.688 619 0[d]	0.705 623[c]	0.433 333[c]	—
			^{1}D	20s11p	0.057 284 79	0.057 287 7	0.718 673	0.381 336	—
			^{1}S	20s11p	0.139 005 51	0.139 008 1	0.739 674	0.310 058	—
		[He]$2s^12p^3$	^{5}S	20s11p	0.089 403 95	0.089 404 4	0.941 729	0.478 839	—
			^{3}D	20s11p	0.294 245 79	0.294 249 3	0.849 815	0.402 139	—
			^{3}P	20s11p	0.350 898 99	0.350 902 4	0.861 208	0.372 093	—
			^{1}D	20s11p	0.519 001 42	0.519 001 3	0.652 100	0.350 046	—
			^{3}S	20s11p	0.546 504 32	0.546 504 8	0.528 457	0.369 292	—
			^{1}P	20s11p	0.572 822 73	0.572 829 2	0.669 325	0.322 121	—
7	N	[He]$2s^22p^3$	^{4}S	20s11p	–54.400 922 41[c]	–54.400 93*4* 2[d]	0.945 324[c]	0.567 601[c]	—
			^{2}D	20s11p	0.104 758 01	0.104 764	0.963 670	0.508 653	—
			^{2}P	20s11p	0.172 828 32	0.172 832 3	0.976 336	0.471 292	—
		[He]$2s^12p^4$	^{4}P	20s11p	0.412 641 71	0.412 649 3	1.186 220	0.522 351	—
			^{2}D	20s11p	0.617 286 61	0.617 293 2	1.071 731	0.474 451	—
			^{2}S	20s11p	0.717 518 48	0.717 524 5	1.090 225	0.437 799	—
			^{2}P	20s11p	0.816 993 95	0.816 993 3	0.814 164	0.457 080	—
8	O	[He]$2s^22p^4$	^{3}P	20s11p	–74.809 378 67[c]	–74.809 398 5[d]	1.244 308[c]	0.631 867[c]	—
			^{1}D	20s11p	0.080 123 70	0.080 134 2	1.256 466	0.600 691	—
			^{1}S	20s11p	0.198 370 24	0.198 377 8	1.275 103	0.555 500	—
		[He]$2s^12p^5$	^{3}P	20s11p	0.625 482 22	0.625 489 9	1.441 623	0.601 196	—
9	F	[He]$2s^22p^5$	^{2}P	20s11p	–99.409 318 21[c]	–99.409 349 4[d]	1.572 522[c]	0.730 000[c]	—
		[He]$2s^12p^6$	^{2}S	20s11p	0.878 093 82	0.878 107 4	1.705 841	0.702 711	—
10	Ne	[He]$2s^22p^6$	^{1}S	20s11p	–128.547 051 6[c]	–128.547 098[d]	1.930 366	0.850 374	—
		[He]$2s^22p^53s^1$	^{3}P	20s11p	0.554 790 3	0.554 784	0.174 760	1.340 815	—
11	Na	[Ne]$3s^1$	^{2}S	18s11p	–161.858 571 2[c]	–161.858 912[d]	0.182 069[c]	1.517 832[c]	—
		[Ne]$3p^1$	^{2}P	18s11p	0.072 527 0	0.072 504	2.873 878	0.109 425	—
12	Mg	[Ne]$3s^2$	^{1}S	18s11p	–199.614 253 0[c]	–199.614 636[d]	0.252 962[c]	2.282 033[c]	—
		[Ne]$3s^13p^1$	^{3}P	18s11p	0.068 103 7	0.067 924	0.339 288	0.179 587	—
			^{1}P	18s11p	0.144 098 6	0.143 505	0.343 735	0.099 296	—
13	Al	[Ne]$3s^23p^1$	^{2}P	18s13p	–241.876 226 4[c]	–241.876 707[d]	0.393 245[c]	0.209 899[c]	—
		[Ne]$3s^13p^2$	^{4}P	18s13p	0.085 590 8	0.085 842	0.519 166	0.259 964	—
			^{2}D	18s13p	0.184 801 1	0.185 020	0.472 705	0.201 410	—
			^{2}S	18s13p	0.231 247 1	0.231 455	0.486 240	0.161 267	—
			^{2}P	18s13p	0.270 361 1	0.270 630	0.402 493	0.181 807	—
14	Si	[Ne]$3s^23p^2$	^{3}P	18s13p	–288.853 820 7[c]	–288.854 363[d]	0.539 691[c]	0.297 023[c]	—
		[Ne]$3s^23p^2$	^{1}D	18s13p	0.038 923 3	0.039 155	0.547 376	0.260 848	—

© 2004 NRC Canada

Table 1 (*concluded*).

Z	Atom	Configuration	State	TOGBS (Size)	Excit. energy (This work)[a]	Excit. energy (NHF)[b]	$-\varepsilon_s$ (This work)[a]	$-\varepsilon_p$ (This work)[a]	$-\varepsilon_d$ (This work)[a]
			^{1}S	18*s*13*p*	0.095 021 3	0.095 278	0.560 002	0.210 863	—
		[Ne]3$s^1$3p^3	^{5}S	18*s*13*p*	0.091 146 2	0.091 323	0.722 543	0.347 942	—
			^{3}D	18*s*13*p*	0.234 099 5	0.234 258	0.658 740	0.290 892	—
		[Ne]3$s^1$3p^3	^{3}P	18*s*13*p*	0.273 751 3	0.274 075	0.665 210	0.268 507	—
			^{1}D	18*s*13*p*	0.387 654 5	0.387 948	0.535 708	0.252 906	—
			^{3}S	18*s*13*p*	0.404 779 1	0.405 104	0.469 228	0.266 781	—
			^{1}P	18*s*13*p*	0.424 907 1	0.425 193	0.546 276	0.232 592	—
15	P	[Ne]3$s^2$3p^3	^{4}S	18*s*13*p*	–340.718 162 8[c]	–340.718 781[d]	0.696 267[c]	0.391 597[c]	—
			^{2}D	18*s*13*p*	0.069 578 5	0.069 910	0.706 297	0.350 503	—
			^{2}P	18*s*13*p*	0.115 184 1	0.115 477	0.713 242	0.324 251	—
		[Ne]3$s^1$3p^4	^{4}P	18*s*13*p*	0.301 915 7	0.302 263	0.874 807	0.375 847	—
			^{2}D	18s13p	0.440 768 6	0.441 136	0.798 380	0.340 508	—
			^{2}S	18*s*13*p*	0.509 160 3	0.509 447	0.808 533	0.313 308	—
			^{2}P	18*s*13*p*	0.575 473 5	0.575 775	0.637 375	0.327 909	—
16	S	[Ne]3$s^2$3p^4	^{3}P	18*s*13*p*	–397.504 163 6[c]	–397.504 896[d]	0.879 357[c]	0.437 224[c]	—
			^{1}D	18*s*13*p*	0.052 096 3	0.052 542	0.885 755	0.415 319	—
		[Ne]3$s^1$3p^5	^{1}S	18*s*13*p*	0.129 778 1	0.130 216	0.895 491	0.383 385	—
			^{3}P	18*s*13*p*	0.425 567 8	0.426 027	1.026 106	0.429 960	—
17	Cl	[Ne]3$s^2$3p^5	^{2}P	18*s*13*p*	–459.481 224 2[c]	–459.482 072[d]	1.072 744[c]	0.506 246[c]	—
		[Ne]3$s^1$3p^6	^{2}S	18*s*13*p*	0.564 779 2	0.565 307	1.175 681	0.500 575	—
18	Ar	[Ne]3$s^2$3p^6	^{1}S	18*s*13*p*	–526.816 542 1[c]	–526.817 513[d]	1.277 156[c]	0.590 840[c]	
		[Ne]3$s^2$3$p^5$4s^1	^{3}P	18*s*13*p*10*d*	0.401 025 0	0.400 768	0.142 499	0.837 437	—
		[Ne]3$s^2$3$p^5$3d^1	^{3}P	18*s*13*p*10*d*	0.478 238 9	0.478 817	1.546 160	0.883 457	0.064 376
			^{3}F	18*s*13*p*10*d*	0.481 793 5	0.482 443	1.568 215	0.903 636	0.060 594
			^{1}F	18*s*13*p*10*d*	0.483 892 8	0.484 550	1.583 714	0.918 236	0.058 435
			^{3}D	18*s*13*p*10*d*	0.485 706 9	0.486 365	1.588 866	0.923 021	0.056 616
			^{1}D	18*s*13*p*10*d*	0.485 706 9	0.486 365	1.588 866	0.923 021	0.056 616
			^{1}P	18*s*13*p*10*d*	0.485 815 2	0.486 486	1.598 151	0.932 415	0.056 495

[a]Excitation energies and energies of the outermost atomic orbitals obtained with our triple-optimized Gaussian basis sets (TOGBSs).
[b]Excitation energies obtained by Tatewaki et al. (11) with a numerical HF (NHF) method.
[c]Ground state total and orbital energies obtained with the TOGBSs of refs. 6 and 7.
[d]Ground state total energies obtained with an NHF method (11).

oped in three stages: (*i*) generation of extended basis sets in atomic calculations; (*ii*) construction of contracted basis sets using a segmented or general contraction scheme; and (*iii*) addition of supplementary functions of polarization and of diffuse character. The first stage in this work was done by employing the IGCHF method (6). The second stage was implemented by employing the segmented contraction scheme proposed by Dunning (25), instead of the general contraction scheme proposed by Raffenetti (26). The main reason for choosing the segmented contraction scheme is to minimize the time required to calculate the two-electron integrals and energy gradient when using a quantum chemistry code.

For Be (^{3}P) and F (^{2}P), our (18*s*11*p*) and (20*s*11*p*) TOGBSs were contracted to [6s5p] through the contraction schemes 10,2,2,2,1,1/7,1,1,1,1 and 12,2,2,2,1,1/7,1,1,1,1, respectively. The total energies of the selected states are minimized with the ATOMSCF program (18), modified by us to introduce the IGCHF method (6). This program uses the RO SCF procedure. For F, exponents for the inner and valence atomic orbitals were obtained by minimizing the total energy of the atomic ground state and, then, optimized contraction coefficients for the schemes presented above were calculated with the ATOMSCF program (18). For Be, optimization was carried out on the ^{3}P excited state to obtain a reasonable simultaneous description of both valence *s* and *p* orbitals.

To implement the contracted GBSs presented above in molecular calculations, it is necessary to include polarization functions to the basis sets to better describe the energy and other chemical and physical properties. The choice of *d*, *f*, *g*, and *h* polarization functions for Be (^{3}P) and F (^{2}P) was done using the minimum ROMP2 energy criterion in atomic calculations. These calculations were performed with the Gaussian 94 program (27) using pure *d*, *f*, *g*, and *h* functions.

Some comment should be made on the variational use of the second-order perturbation energy. The variational theorem does not apply to this energy, which is not an expectation value of the Hamiltonian. Nevertheless, practical computations have suggested that MP2 energy does approach a limiting value from above as the size of the basis set is increased (28).

In the above procedure, we have not included the full correlation energy correction, but have limited it to the valence atomic orbitals. This approximation is known as frozen core

© 2004 NRC Canada

Table 2. Excitation [E(excited state) – E(ground state)] and orbital (ε) energies (in hartrees) of some states of the atoms from K to Kr.

Z	Atom	Configuration	State	TOGBS (size)	Excit. energy (This work)[a]	Excit. energy (NHF)[b]	$-\varepsilon_s$ (This work)[a]	$-\varepsilon_p$ (This work)[a]	$-\varepsilon_d$ (This work)[a]
19	K	[Ar]4s^1	^{2}S	20s13p	–599.163 449 8[c]	–599.164 787[d]	0.147 384[c]	0.954 188[c]	—
		[Ar]4p^1	^{2}P	20s13p	0.052 645 1	0.051 642	1.797 669	0.095 204	—
		[Ar]3d^1	^{2}D	20s13p10d	0.088 105 4	0.089 075	1.835 697	1.042 793	0.058 132
20	Ca	[Ar]4s^2	^{1}S	21s13p	–676.757234 4[c]	–676.758 186[d]	0.195 253[c]	1.340 187[c]	—
		[Ar]4$s^1$4p^1	^{3}P	21s13p	0.040 368 4	0.039 418	0.258 735	0.152 314	—
			^{1}P	21s13p	0.103 742 1	0.101 849	0.248 539	0.085 836	—
		[Ar]4$s^1$3d^1	^{3}D	21s13p10d	0.080 706 5	0.080 925	0.190 970	1.250 020	0.125 725
			^{1}D	21s13p10d	0.107 111 5	0.107 24	0.154 908	1.226 812	0.121 705
21	Sc	[Ar]4$s^2$3d^1	^{2}D	20s13p10d	–759.734 183 6[c]	–759.735 718[d]	0.209 762[c]	1.573 877[c]	0.343 045[c]
		[Ar]4$s^1$3d^2	^{4}F	20s13p10d	0.036 604 6	0.036 932	0.195 496	1.435 307	0.214 770
			^{2}S	20s13p10d	0.162 794 8	0.163 133	0.206 372	1.513 470	0.118 255
22	Ti	[Ar]4$s^2$3d^2	^{3}F	20s13p10d	–848.404 236 7[c]	–848.405 997[d]	0.220 367[c]	1.794 236[c]	0.439 811[c]
			^{1}D	20s13p10d	0.047 143 1	0.047 497	0.221 970	1.805 045	0.393 969
		[Ar]4$s^1$3d^3	^{5}F	20s13p10d	0.019 488 5	0.019 843	0.204 891	1.636 096	0.272 498
23	V	[Ar]4$s^2$3d^3	^{4}F	20s13p10d	–942.882 319 6[c]	–942.884 338[d]	0.230 087[c]	2.018 228[c]	0.508 633[c]
			^{4}P	20s13p10d	0.063 666 3	0.064 119	0.231 473	2.028 973	0.469 852
		[Ar]4$s^1$3d^4	^{2}D	20s13p10d	0.202 671 9	0.199 636	0.197 583	1.892 757	0.257 738
			^{6}D	20s13p10d	0.004 148 3	0.004 555	0.214 296	1.843 357	0.319 818
24	Cr	[Ar]4$s^1$3d^5	^{7}S	20s13p10d	–1043.353 979[c]	–1043.356 38[d]	0.221 786[c]	2.049 434[c]	0.372 095[c]
			^{5}S	20s13p10d	0.038 716	0.039 04	0.178 494	2.062 060	0.386 446
		[Ar]4$s^2$3d^4	^{5}D	20s13p10d	0.045 956	0.046 56	0.239 287	2.247 885	0.568 227
25	Mn	[Ar]4$s^2$3d^5	^{6}S	20s13p10d	–1149.863 619[c]	–1149.866 25[d]	0.247 203[c]	2.478 070[c]	0.637 399[c]
			^{4}G	20s13p10d	0.142 236	0.142 87	0.249 393	2.497 123	0.591 433
		[Ar]4$s^1$3d^6	^{6}D	20s13p10d	0.121 786	0.122 29	0.226 920	2.297 738	0.382 067
26	Fe	[Ar]4$s^2$3d^6	^{5}D	20s13p10d	–1262.440 683[c]	–1262.443 67[d]	0.257 433[c]	2.740 611[c]	0.645 328[c]
			^{3}H	20s13p10d	0.098 685	0.099 43	0.258 887	2.753 289	0.620 611
		[Ar]4$s^1$3d^7	^{5}F	20s13p10d	0.065 455	0.066 05	0.230 078	2.544 519	0.405 636
27	Co	[Ar]4$s^2$3d^7	^{4}F	20s13p10d	–1381.411 190[c]	–1381.414 55[d]	0.266 697[c]	3.004 784[c]	0.673 986[c]
			^{4}P	20s13p10d	0.083 382	0.084 18	0.267 861	3.013 963	0.656 463
		[Ar]4$s^1$3d^8	^{4}F	20s13p10d	0.055 508	0.056 17	0.233 109	2.798 474	0.430 997
			^{2}S	20s13p10d	0.302 986	0.303 61	0.230 308	2.835 504	0.397 488
28	Ni	[Ar]4$s^2$3d^8	^{3}F	20s13p10d	0.000 000	0.000 00	0.275 436[c]	3.275 953[c]	0.705 241[c]
			^{1}D	20s13p10d	0.072 342	0.073 11	0.276 364	3.283 733	0.692 756
			^{1}S	20s13p10d	0.280 301	0.281 07	0.278 524	3.304 963	0.656 388
		[Ar]4$s^1$3d^9	^{3}D	20s13p10d	0.046 150	0.046 88	0.236 059	3.060 024	0.457 334
			^{1}D	20s13p10d	0.058 907	0.059 53	0.222 242	3.065 126	0.462 280
29	Cu	[Ar]4$s^1$3d^{10}	^{2}S	20s13p10d	–1638.959 169[c]	–1638.963 74[d]	0.238 156[c]	3.323 352[c]	0.489 814[c]
		[Ar]4$s^2$3d^9	^{2}D	20s13p10d	0.012 164	0.013 66	0.284 427	3.556 241	0.739 586
30	Zn	[Ar]3d^{10}4s^2	^{1}S	20s13p10d	–1777.843 481[c]	–1777.848 12[d]	0.291 879[c]	3.838 022[c]	0.781 235[c]
		[Ar]3d^{10}4$s^1$4p^1	^{3}P	21s14p10d	0.097 705	0.097 12	0.391 280	0.187 974	0.843 364
			^{1}P	21s15p10d	0.175 904	0.175 86	0.396 356	0.104 328	0.921 216
		[Ar]3d^{10}4$s^1$4d^1	^{3}D	21s14p11d	0.223 657	0.223 97	0.492 853	4.061 559	0.056 067
			^{1}D	21s14p11d	0.225 637	0.225 79	0.498 513	4.067 977	0.054 252
31	Ga	[Ar]3d^{10}4$s^2$4p^1	^{2}P	22s14p10d	–1923.255 079[c]	–1923.261 01[d]	0.422 333[c]	0.208 003[c]	1.190 241[c]
		[Ar]3d^{10}4$s^1$4p^2	^{4}P	22s14p10d	0.111 264	0.112 37	0.556 144	0.261 915	1.235 843
			^{2}D	22s14p10d	0.212 435	0.212 82	0.508 878	0.201 682	1.268 716
			^{2}P	22s14p10d	0.297 206	0.297 07	0.439 225	0.183 180	1.311 102
32	Ge	[Ar]3d^{10}4$s^2$4p^2	^{3}P	22s14p9d	–2075.353 405[c]	–2075.359 73[d]	0.551 538[c]	0.286 310[c]	1.632 261[c]
			^{1}D	22s14p9d	0.037 546	0.038 38	0.558 945	0.250 667	1.643 997

© 2004 NRC Canada

Table 2 (*concluded*).

Z	Atom	Configuration	State	TOGBS (size)	Excit. energy (This work)[a]	Excit. energy (NHF)[b]	$-\varepsilon_s$ (This work)[a]	$-\varepsilon_p$ (This work)[a]	$-\varepsilon_d$ (This work)[a]
			^{1}S	22*s*14*p*9*d*	0.093 280	0.093 35	0.570 571	0.200 914	1.661 671
		[Ar]3d^{10}4$s^1$4p^3	^{5}S	22*s*14*p*9*d*	0.113 366	0.114 46	0.735 753	0.340 372	1.669 874
			^{1}P	22*s*14*p*9*d*	0.438 264	0.438 26	0.565 212	0.225 613	1.751 096
33	A*s*	[Ar]3d^{10}4$s^2$4p^3	^{4}S	22*s*14*p*9*d*	–2234.232 429[c]	–2234.238 65[d]	0.684 259[c]	0.368 317[c]	2.110 323[c]
			^{2}D	22*s*14*p*9*d*	0.065 976	0.066 49	0.693 555	0.328 975	2.125 442
			^{2}P	22*s*14*p*9*d*	0.109 497	0.109 83	0.699 931	0.303 756	2.135 635
		[Ar]3d^{10}4$s^1$4p^4	^{4}P	22*s*14*p*9*d*	0.310 542	0.311 27	0.856 942	0.356 202	2.175 681
			^{2}P	22*s*14*p*9*d*	0.565 619	0.565 90	0.639 617	0.311 224	2.228 364
34	Se	[Ar]3d^{10}4$s^2$4p^4	^{3}P	22*s*14*p*9*d*	–2399.861 092[c]	–2399.867 61[d]	0.835 660[c]	0.401 411[c]	2.647 192[c]
			^{1}D	22*s*14*p*9*d*	0.047 969	0.048 65	0.843 438	0.382 581	2.659 434
			^{1}S	22*s*14*p*9*d*	0.120 085	0.120 59	0.850 336	0.351 102	2.673 058
		[Ar]3d^{10}4$s^1$4p^5	^{3}P	22*s*14*p*9*d*	0.415 274	0.416 09	0.974 907	0.397 801	2.716 554
35	Br	[Ar]3d^{10}4$s^2$4p^5	^{2}P	22*s*14*p*9*d*	–2572.434 622[c]	–2572.441 33[d]	0.990 979[c]	0.455 575[c]	3.217 837[c]
		[Ar]3d^{10}4$s^1$4p^6	^{2}S	22*s*14*p*9*d*	0.528 757	0.529 83	1.088 384	0.453 630	3.290 601
36	Kr	[Ar]3d^{10}4$s^2$4p^6	^{1}S	22*s*14*p*9*d*	–2752.048 102[c]	–2752.054 98[d]	1.151 273[c]	0.522 650[c]	3.822 966[c]
		[Ar]3d^{10}4$s^2$4$p^5$5s^1	^{3}P	22*s*14*p*9*d*	0.353 050	0.353 43	0.133 927	0.720 657	4.065 124
		[Ar]3d^{10}4$s^2$4$p^5$4d^1	^{3}P	23*s*16*p*12*d*	0.416 780	0.419 63	1.348 735	0.737 607	0.067 736
			^{1}P	23*s*16*p*12*d*	0.429 414	0.431 02	1.412 091	0.796 403	0.055 739

[a]Excitation energies and energies of the outermost atomic orbitals obtained with our triple-optimized Gaussian basis sets (TOGBSs).
[b]Excitation energies obtained by Tatewaki and Koga (12) with a numerical HF (NHF) method.
[c]Ground state total and orbital energies obtained with the TOGBSs of ref. 8.
[d]Ground state total energies obtained with an NHF method (12).

Table 3. Ground state (X $^2\Sigma^+$) energies (*E*), bond lengths (*r*), and dissociation energies (D_e) for the BeF molecule.

Method	Basis set	N^a	$-E^b$ (hartree)	*r* (Å)	$D_e{}^c$ (kJ/mol)	Reference
Expt.	—	—	—	1.361	577±42	(15,16)
ROHF	6-311++G(3df,3pd)	78	114.156 962 4	1.351	496	Calculated in this work
	Be(32s17p17d);F(30s15p15d)	318	114.171 508 2	—	—	(14)
	Be[6s5p4d3f2g1h];F[6s5p4d3f2g1h]	182	114.171 735 6	1.350	500	This work
	Be(32s17p17d17f);F(30s15p15d15f)	542	114.172 615 5	—	—	(14)
	HF limit	—	114.172 685 0	—	—	[14]
ROMP2	6-311++G(3df,3pd)	78	114.438 130 1	1.373	623	Calculated in this work
	Be[6s5p4d3f2g1h];F[6s5p4d3f2g1h]	182	114.485 262 8	1.369	604	This work

Note: In all ROMP2 calculations the frozen core approximation was used.
[a]Number of GTFs.
[b]The total energies were calculated using the experimental nuclear distance (1.361 Å).
[c]The dissociation energies were calculated using the experimental nuclear distance (1.361 Å).

for electron correlation. The reason for making this approximation is that the correlation energy associated with inner shell electrons varies little with chemical environment. Besides this, if this approximation were not used in deriving the basis sets, there would be an undesirable tendency for some of the functions to adjust themselves to give an improved description of inner shell at the expense of valence electron correlation.

Next, we considered *s* and *p* basis sets to be used in correlated calculations, that is, we reoptimized at the ROMP2 level the uncontracted exponents of the valence shell.

To obtain a preliminary assessment of the performance of the molecular basis sets constructed in this work, ROHF and ROMP2 energies (*E*), bond length (*r*), and energy dissociation (D_e) of the BeF open shell (X $^2\Sigma^+$) molecule (see Table 3) are computed and compared with results obtained with other approaches (13, 14) and with experimental values (15, 16). The calculations were performed with the Gaussian 94 program (27).

From Table 3, one can see that the 6-311++G(3df,3pd) basis set (13), the Be(32s17p17d);F(30s15p15d) basis set of primitive GTFs (14), the Be[6s5p4d3f2g1h];F[6s5p4d3f2g1h] basis set generated from the IGCHF method (6), and the Be(32s17p17d17f);F(30s15p15d15f) basis set generated by Kobus et al. (14) have associated errors of 15 723, 1177, 949, and 70 μhartree, respectively. From these results, one can verify that our total HF energy is only worse than the very large atom centered basis set of primitive GTFs of ref. 14. Here, it is important to say that this basis set has three times the number of functions of our set and that the number of two-electron integrals, which consumes a major part of the time needed in a SCF molecular orbital calcula-

© 2004 NRC Canada

tion, increases as N^4. At the MP2 level, the difference between the energies obtained with the correlated wave function of this work and the 6-311++G(3df,3pd) basis set (13) is 47 mhartree. The widely used correlation consistent basis sets of Dunning (29) are atom specific and, to our knowledge, have not been tabulated for the Be atom; thus, this is the reason that calculations with these basis sets were not included in Table 3.

At the HF level, our r and D_e results, when compared with the corresponding experimental values, are, respectively, as good as and better than those evaluated with the 6-311++G(3df,3pd) basis set (see Table 3). At the MP2 level, our r and D_e results are closer to the experimental values than those obtained with the 6-311++G(3df,3pd) basis set, and in good agreement with the corresponding experimental values.

Conclusions

The IGCHF method was employed to generate TOGBSs for low-lying excited states of neutral atoms from He to Kr. From these basis sets, excitation energies and orbital energies of the outermost atomic orbitals were calculated and compared with NHF results (11, 12). For all excited states studied here, the errors obtained with the TOGBSs are always smaller than 6.88 mhartree, and our excitation and orbital energies are in excellent agreement with the corresponding NHF results. Besides this, from the TOGBSs for Be (^{3}P) and F (^{2}P), contracted GBSs plus polarization functions are constructed and, then, used with success to study the electronic structure of the BeF molecule.

In summary, from the results presented in this work and those of refs. 6–8, we believe that the TOGBSs are useful for constructing basis sets for molecules containing any atom of the first, second, or third row of the Periodic Table.

The TOGBSs generated in this work are available as supplementary material.[2]

Acknowledgements

We would like to acknowledge the financial support of Conselho Nacional de Desenvolvimento Científico e Tecnológico (CNPq) and Coordenação de Aperfeiçoamento de Pessoal de Nível Superior (CAPES) (Brazil). We employed computational facilities at Universidade Federal do Espírito Santo and Universidade Estadual Paulista (IQ Araraquara)..

References

1. J.R. Mohallem, R.M. Dreizler, and M. Trsic. Int. J. Quantum Chem. Symp. **20**, 45 (1986).
2. A.B.F. da Silva and M. Trsic. Can. J. Chem. **74**, 1526 (1996).
3. H.F.M. da Costa, M. Trsic, and J.R. Mohallem. Mol. Phys. **62**, 91 (1987).
4. F.E. Jorge and M.L. Franco. Chem. Phys. **253**, 21 (2000).
5. F.E. Jorge and C.L. Barros. Comput. Chem. **26**, 387 (2002).
6. F.E. Jorge and E.V.R. de Castro. Chem. Phys. Lett. **302**, 454 (1999).
7. E.V.R. de Castro, F.E. Jorge, and J.C. Pinheiro. Chem. Phys. **243**, 1 (1999).
8. R. Centoducatte, E.V.R. de Castro, and F.E. Jorge. Can. J. Chem. **79**, 121 (2001).
9. A. Canal Neto, F.E. Jorge, and M. de Castro. Int. J. Quantum Chem. **82**, 126 (2002).
10. F.E. Jorge and A. Canal Neto. J. Mol. Struct. (THEOCHEM), **589–590**, 359 (2002).
11. H. Tatewaki, T. Koga, Y. Sakai, and A.J. Thakkar. J. Chem. Phys. **101**, 4945 (1994).
12. H. Tatewaki and T. Koga. Chem. Phys. Lett. **228**, 562 (1994).
13. M.J. Frisch, J.A. Pople, and J.S. Binkley. J. Chem. Phys. **80**, 3265 (1984).
14. J. Kobus, D. Moncrieff, and S. Wilson. Mol. Phys. **96**, 1559 (1999).
15. K.P. Huber and G. Herzberg. *In* Molecular spectra and molecular structure. Vol. VI. Van Nostrand, Princeton. 1979.
16. M. Faber and R.D. Srivastava. J. Chem. Soc. Faraday Trans. 1, **70**, 1581 (1974).
17. J.R. Mohallem. Z. Phys. D, **3,** 339 (1986).
18. S.J. Chakravorty, G. Corongiu, J.R. Flores, V. Sonnad, E. Clementi, V. Carravetta, and I. Cacelli. MOTECC – Modern techniques in computational chemistry. *Edited by* E. Clementi. ESCOM, Leiden. 1989.
19. J.P. Colpa, A.J. Thakkar, V.H. Smith, Jr., and P. Randle. Mol. Phys. **29**, 1861 (1975).
20. D.R. Hartree and W. Hartree. Proc. R. Soc. London Ser. A, **154**, 588 (1936).
21. C. Froese. J. Chem. Phys. **47**, 4010 (1968).
22. H. Tatewaki. Int. J. Quantum Chem. **7**, 97 (1973).
23. H. Tatewaki and K. Tanaka. J. Chem. Phys. **60**, 601 (1974).
24. C.E. Moore. Atomic energy levels. NSRDS-NBS Circular No. 35. Vols. 1 and 2. US GPO, Washington, D.C. 1971.
25. T.H. Dunning, Jr. J. Chem. Phys. **53**, 2823 (1970).
26. R.C. Raffenetti. J. Chem. Phys. **58**, 4452 (1973).
27. M.J. Frisch, G.W. Trucks, H.B. Schlegel, P.M.W. Gill, B.G. Johnson, M.A. Robb, J.R. Cheeseman, T.A. Keith, G.A. Peterson, J.A. Montgomery, K. Raghavachari, M.A. Al-Laham, V.G. Zakrzewski, J.V. Ortiz; J.B. Foresman, J. Cioslowski, B.B. Stefanov, A. Nanayakkara, M. Challacombe, C.Y. Peng, P.Y. Ayala, W. Chen, M.W. Wong, J.L. Andres, E.S. Replogle, R. Gomperts, R.L. Martin, D.J. Fox, J.S. Binkley, D.J. Defrees, J. Baker, J.P. Stewart, M. Head-Gordon, C. Gonzalez, and J.A. Pople. Gaussian 94. Revision A.I [computer program]. Gaussian Inc., Pittsburgh, Pa. 1995.
28. J.S. Binkley and J.A. Pople. Int. J. Quantum Chem. **9**, 229 (1975).
29. T.H. Dunning, Jr. J. Chem. Phys. **90**, 1007 (1989).

[2] Supplementary data may be purchased from the Depository of Unpublished Data, Document Delivery, CISTI, National Research Council Canada, Ottawa, ON K1A 0S2, Canada (http://www.nrc.ca/cisti/irm/unpub_e.shtml for information on ordering electronically).

© 2004 NRC Canada

The titanocene-catalyzed reduction of acetamides to tertiary amines by $PhMeSiH_2$

Kumaravel Selvakumar, Kesamreddy Rangareddy, and John F. Harrod

Abstract: A variety of acetamide derivatives are reduced in excellent yields to tertiary amines by $PhMeSiH_2$ in the presence of Cp_2TiX_2 (X = F or Me) catalysts. The reactions are very clean at 80 °C. At room temperature a secondary reaction, hydrogenolysis of the C(O)—N bond, intervenes and reduces the chemoselectivity. Nevertheless, this chemistry provides a simple methodology for the amide/alkylamine transformation using inexpensive, commercially available reagents.

Key words: amides, reduction, secondary amides, methylphenylsilane, titanocene, catalysis.

Résumé : Divers dérivés de l'acétamide sont réduits avec d'excellents rendements en amines tertiaires par le $PhMeSiH_2$ en présence de catalyseurs du type Cp_2TiX_2 (X = F ou Me). Les réactions sont très propres à 80 °C. À la température ambiante la chimiosélectivité est réduite par l'intervention d'une réaction secondaire, l'hydrogénolyse de la liaison C(O)—N. Néanmoins, cette chimie fournit une méthodologie simple pour la transformation d'amides en alkylamines faisant appel à des réactifs peu coûteux et commercialement disponibles.

Mots clés : amides, réduction, amides secondaires, méthylphénylsilane, titanocène, catalyse.

[Traduit par la Rédaction]

Introduction

The use of hydrosilation chemistry to achieve the reduction of carbonyl groups has received a great deal of attention (1–5). Many studies of ketone hydrosilation have been directed towards enantioselective synthesis of carbinols, and excellent results have been achieved with both later and early transition metal homogeneous catalysts (6, 7). Facile hydrosilations of esters and lactones have also been reported (8, 9). Among the early transition metal catalysts, titanocene derivatives are the most effective with respect to both rate and selectivity for all of these reactions.

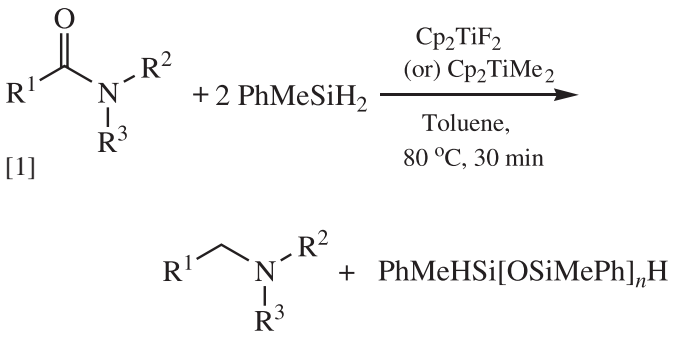
Carboxamides are generally more resistant to reduction than ketones and esters. Nevertheless, the conversion of amides to the corresponding amines is an important transformation in organic synthetic methodology. Catalytic hydrogenation of amides normally requires high pressures and elevated temperatures (10). Consequently, stoichiometric reduction using expensive reactive main group metal hydride complexes is the usual method of choice (11–15).

Literature on the hydrosilation of carboxamides is sparse (16–19). Kuwano et al. (17) and Igarashi and Fuchikami (18) reported efficient reduction of aliphatic amides to amines by catalytic hydrosilation, using late transition metal catalysts. In a preliminary communication (19), we described an unusal titanocene-catalyzed deoxygenation/coupling of aromatic amides to give 1,2-diaminoethanes. Classical hydrosilation products (i.e., those containing either Si—OR or Si—C bonds) have never been observed as products of the reaction of amides under hydrosilation conditions.

In the present paper, we report results for the catalytic reduction of acetamides, under hydrosilation conditions, using titanocene-based catalysts. Although there is still much scope for improving the specificity and yields of catalytic amide reduction reactions, the present work shows that appropriate catalytic hydrosilation conditions can be useful for reduction of tertiary amides to tertiary amines.

Results

The reaction of acetamide derivatives with $PhMeSiH_2$ at moderate temperature in the presence of catalytic amounts of Cp_2TiX_2 (Cp = η-C_5H_5; X = F or Me) takes place as shown in eq. [1].



[1]

Received 23 October 2003. Published on the NRC Research Press Web site at http://canjchem.nrc.ca on 19 October 2004.

K. Selvakumar, K. Rangareddy, and J.F. Harrod.[1] Chemistry Department, McGill University, 801 Sherbrooke St. W., Montreal, QC H3A 2K6, Canada.

[1]Corresponding author. (e-mail: john.harrod@mcgill.ca).

 doi: 10.1139/V04-063 © 2004 NRC Canada

Table 1. Results of Ti-catalyzed reduction of acetamides at 80 °C (reaction [1]).

Entry	R^1	R^2	R^3	Method	Yield (%)
1	Me	Me	Ph	A	93
	Me	Me	Ph	B	89
2	Me	Et	Ph	A	77
	Me	Et	Ph	B	83
3	Me	Bn	Ph	A	89
	Me	Bn	Ph	B	92
4	Me	Bn	Bn	A	91
5	Me	Me	3,4-$(OMe)_2$Ph	A	76[a]
6	Bn	Me	Ph	A	40
7	Me	Ph	4-(OMe)Bn	A	90
8	Me	Ph	Furfuryl	A	92
9	Me	Me	4-(NO_2)Ph	A	—[b]
10	1-Acetylindoline			A	88
11	1-Phenyl-2-pyrrolidinone			A	96
12	*N*,*N*′-Dimethylacrylamide				94 (polymer)

Note: Method A, Cp_2TiF_2 catalyst; method B, Cp_2TiMe_2 catalyst. Yields are given for isolated compounds.

[a]10% secondary amine formed as deacetylated product.

[b]No reaction.

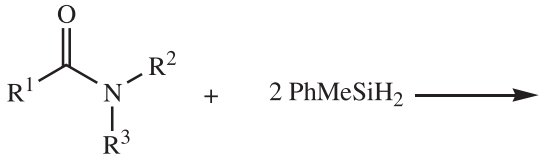
At 80 °C this reaction occurs rapidly and gives excellent yields of the tertiary amine, for a range of substituents R_1, R_2, and R_3. This product results from reduction and deoxygenation of the carbonyl group and contrasts with the coupling, to give vicinal diamines, observed with aromatic amides (19). The present results are very similar to those reported for reactions catalyzed by complexes of Rh (17) and Ru (18). There is, however, a considerable price advantage in using the relatively inexpensive Cp_2TiF_2.

The siloxane product was identified by ^{1}H NMR as a typical mixture of H-terminated oligo(phenylmethylsiloxanes). The resonances occur at 0.2–0.5 ppm (CH_3; broad massif or many singlet and doublet peaks), 4.6–4.8 ppm (Si–H; overlapping quartets), and 6.6–7.5 ppm (Ph; broad massif). The mass spectrum of a crude extract of the siloxane product recorded by chemical ionization mass spectrometry (CI-MS) showed the presence of oligomers of *n* up to a value of ca. 10. The siloxane product was not studied further.

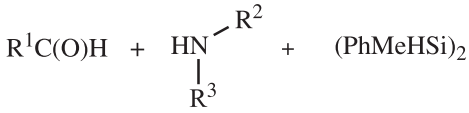
The reaction shows some tolerance for functional groups, as exemplified by entries 5, 7, and 9 in Table 1. Reduction of secondary amides is very slow compared to that of *N*,*N*-disubstituted acetamides. For example, under similar conditions, acetanilide undergoes reduction to give a small amount of *N*-ethylaniline and aniline along with unreacted acetanilide. Incomplete conversion is observed even after 15 h at 80 °C. *N*,*N*-Dimethylacrylamide underwent rapid polymerization under the conditions used in these experiments, probably due to free radical initiation, and there was no evidence for reduction of the amide function.

There is little difference in the performance of Cp_2TiF_2 and Cp_2TiMe_2, but given the long-term stability of the fluoride, its commercial availability (or ease of preparation from the commercially available Cp_2TiCl_2), and its insensitivity to air and humidity, it is the preferred catalyst (20).

At room temperature, reactivity remains high (Table 2), but a side reaction involving hydrogenolysis of the C(O)—N bond (eq. [2]) lowers the efficiency of the reaction in certain



[2]



cases and complicates purification of the tertiary amine product. In some cases, this reaction becomes a major consumer of reactant (Table 2, entries 1, 3, and 7), and in one case (Table 2, entry 10) it is the only reaction observed. In the latter case, if the reaction is carried out in a closed tube, ca. 1 equiv. of acetaldehyde is also detected in solution by ^{1}H NMR. In other cases, where secondary amine is produced in a significant amount, the characteristic quartet of acetaldehyde is also detected in the ^{1}H NMR spectrum.

Catalyst concentration also has a significant influence on the relative contributions of reactions [1] and [2] at room temperature (Table 2, entries 1–6). A similar effect was detected at 80 °C. At a catalyst loading of 10 mol%, the reduction of *N*-benzylacetanilide (Table 1, entry 3) to the tertiary amine occurs with high chemoselectivity. At 5 mol% catalyst concentration, both the rate of reduction and the chemoselectivity are similar to those at 10 mol% catalyst. However, at 2 mol% catalyst concentration, the reaction is slow (1.5 h for complete conversion) and *N*-benzylaniline (24%) is formed along with *N*-ethyl-*N*-benzylaniline (76%).

The reaction mechanism

Kuwano et al. (17) suggested a mechanistic cycle for the Rh(I)-catalyzed reaction [1] involving a series of conventional two-electron oxidative addition/elimination steps, in conjunction with a σ-bond metathesis step. In principle, the mechanism of the titanocene-catalyzed reaction could be analogous to that proposed for Rh. This would require a sequence in which the Ti cycles alternately through Ti(II) and Ti(IV). Although such a two-electron cycle is not unreasonable for titanocene, a cycle involving $Ti^{III}H$ and $Ti^{III}Si$ is, in our opinion, more likely. The facile disproportionation of titanocene(III) to titanocene(II) and titanocene(IV) and vice versa makes the distinction between these two possibilities very difficult to draw, but there is ample evidence that all three oxidation states are chemically available in Cp_2TiMe_2/silane reaction mixtures (21). A tentative set of pathways that explain the observed chemistry is shown in Scheme 1. In this scheme, the silane functions as a source of hydride to generate Ti–H (step **a**) and as a receptor for O) but does not give rise to silylated organic products. Addition of Ti–H across the C=O bond (step **b**) generates the highly functionalized alkoxytitanocene intermediate, **1**. This intermediate then undergoes reactions to the various observed products, whose relative importance depends on the substituents on the substrate, on the catalyst concentration, and on the temperature. The various titanocene derivatives produced in the reactions of Scheme 1 will be recycled by appropriate σ-bond metathesis reactions with $PhMeSiH_2$.

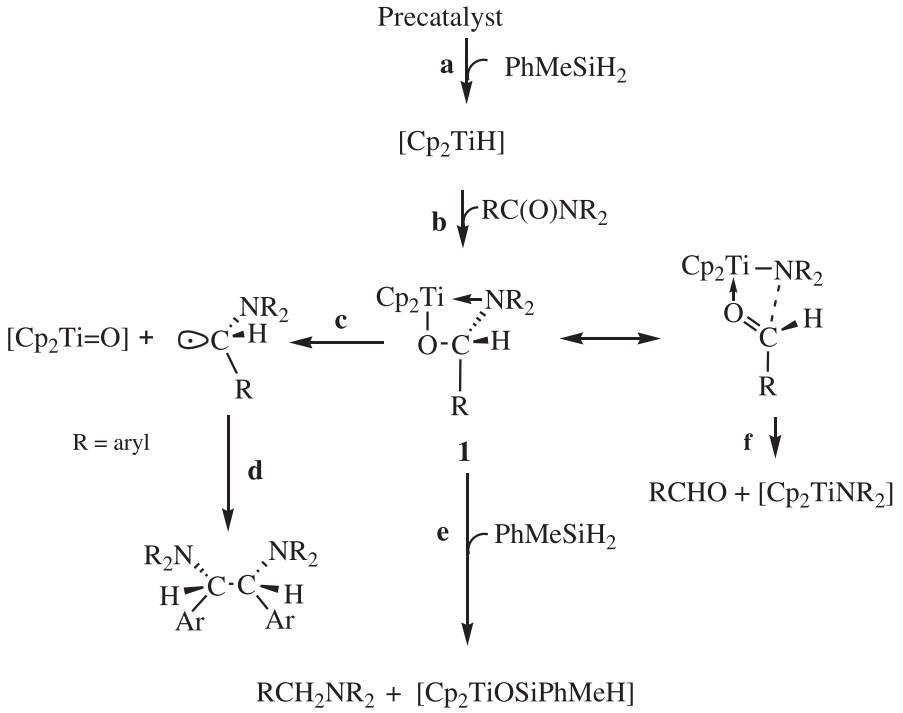
© 2004 NRC Canada

Table 2. Results of Ti-catalyzed reduction of acetamides at 25 °C.

Entry	R^1	R^2	R^3	Catalyst concn. (mol%)	Product distribution (%) Tertiary amine	Secondary amine
1	Me	Me	Ph	2	64	36
2	Me	Me	Ph	5	88	12
3	Me	Me	Ph	10	93	7
4	Me	Et	Ph	2	60	40
5	Me	Et	Ph	5	100	—
6	Me	Et	Ph	10	100	—
7	Me	Bn	Ph	10	68	32
8	Me	Bn	Bn	10	94	6
9	Me	Ph	Furfuryl	10	71	29
10	Me	Me	2-Py	10	—	100
11	Me	Ph	4-(OMe)Bn	10	77	23
12	Me	Me	3,4-$(OMe)_2$Ph	10	85	15
13	Me	Me	4-(NO_2)Ph	10	—[a]	—[a]
14	1-Acetylindoline			10	100	—
15	1-Phenyl-2-pyrrolidinone			2	100	—

Note: Ratios of the products were determined by ^{1}H NMR Products were not isolated. Amines were characterized by comparison of the NMR spectra with those of isolated products (Table 1) or commercial samples.
[a]No reaction.

Scheme 1. A $[Cp_2TiH]$-mediated reaction sequence for the reduction, deoxygenation, and coupling of amides in the presence of $PhMeSiH_2$.



A possible mechanism for C—N bond cleavage is shown in Scheme 1. The favoring of the C—N bond cleavage reaction, relative to that of the C—O bond cleavage, at lower catalyst concentrations (Table 2, entries 1–6) could be due to the former involving a rate law that is higher order in catalyst concentration than is the rate law for the latter. Such a situation could arise if the recycling reactions of the titanocene products of reactions **e** and **f** in Scheme 1 are slow enough to contribute to the overall rate. Given the known tendency of titanocene(III) species to form coordination complexes (21–23), intramolecular coordination of the amino group to the Ti is a reasonable possibility. The resulting complex could then decompose in a unimolecular process to give the aldehyde and Cp_2TiNR_2. The latter could then undergo a σ-bond metathesis with Si–H to generate Ti–Si and give the secondary amine product. Finally, Ti–Si can then be converted by a σ-bond metathesis step to Ti–H and the silane dimer.

© 2004 NRC Canada

Buchwald and co-workers (24) have described a synthesis of aldehydes from acetamide derivatives by reaction with $Ti(O\text{-}i\text{-}Pr)_4/Ph_2SiH_2$. In those reactions, the primary product was found to be the enamine, which was then converted to aldehyde by mild acid hydrolysis. With our system, the aldehyde is the direct product in entry 10 of Table 2, and no intermediate vinylamine was detected. In the other reactions where significant amounts of the secondary amine were produced, acetaldehyde was also detected, but not vinylamine. However, the complexity of the reaction products in the latter cases prevented the definitive exclusion of the possible presence of vinylamine.

We attribute the reactivity difference between aromatic amides and acetamide derivatives to the lower stability of the radical intermediate in step **d** when R is an alkyl, rather than an aromatic, substituent. Detailing the mechanisms of these interesting reactions is the subject of continuing studies.

Experimental

Materials

All of the reactant amides were either obtained commercially from Aldrich Chemical Co. or synthesized by standard methods. Cp_2TiF_2 (20) and Cp_2TiMe_2 (25) were prepared according to previously described methods.

A typical procedure for the synthesis of tertiary amines is the following (Table 1, method A). *N*-Methylacetanilide (149 mg, 1 mmol), Cp_2TiF_2 (21 mg, 0.1 mmol), methylphenylsilane (0.28 mL, 2 mmol), and toluene (1 mL) were heated at 80 °C for 30 min in a Schlenk tube. After the reaction mixture had cooled to room temperature, ether (10 mL) was added and the solution was extracted with 1 mol/L HCl solution. Evaporation of the depleted ether solution gave an oily residue, which was shown by ^{1}H NMR to consist of a mixture of oligo(phenyl-methylsiloxanes) and catalyst residues. The acid extract was neutralized with 3 mol/L KOH and extracted with ether. The ether layer was dried with anhydrous $MgSO_4$ and evaporated to give analytically pure *N*-methyl-*N*-ethylaniline. In method B of Table 1, Cp_2TiMe_2 was used instead of Cp_2TiF_2. The identity of all the products listed in Table 1 was determined by comparison of ^{1}H NMR data to literature values and to those of authentic samples.

***N*-Ethyl-*N*-methylaniline** (Table 1, entry 1) ^{1}H NMR (ppm): 1.13 (t, J = 7.2 Hz, 3H), 3.42 (q, J = 7.2 Hz, 2H), 2.91 (s, 3H), 6.70 (m, 2H), and 7.26 (m, 3H).

***N*,*N*-Diethylaniline** (Table 1, entry 2) ^{1}H NMR (ppm): 1.06 (t, J = 7.2 Hz, 6H), 3.26 (q, J = 7.2 Hz, 4H), 6.61 (m, 2H), and 7.14 (q, J = 4.8 Hz, 3H)

***N*-Benzyl-*N*-ethylaniline** (Table 1, entry 3) ^{1}H NMR: 1.30 (t, J = 9.6 Hz, 3H), 3.56 (q, J = 9.6 Hz, 2H), 4.6 (s, 2H), 6.76 (m, 4H), and 7.43 (m, 6H); ^{13}C NMR: 45.43 (CH_3), 54.19 (N–CH_2), 112.4, 116.31, 126.85, 129.5, and 139.58 (aromatic).

***N*,*N*-Dibenzylethylamine** (Table 1, entry 4) ^{1}H NMR: 1.07 (t, J = 9.2 Hz, 3H), 2.50 (q, J = 9.2 Hz, 2H), 3.57 (s, 4H), and 7.22–7.52 (m, 10H).

***N*-Methyl-*N*-ethyl-3,4-dimethoxyaniline** (Table 1, entry 5) ^{1}H NMR: 1.17 (t, J = 7.4 Hz, 3H), 2.79–3.18 (m, 6H), 3.78 (q, J = 7.4 Hz, 2H), 3.85 (t, J = 0.9 Hz, 3H), and 6.57–6.92 (m, 3H).

***N*-Methyl-*N*-(2-phenylethyl)aniline** (Table 1, entry 6) ^{1}H NMR: 2.82 (s, 3H), 2.78 (t, J = 10.04 Hz, 2H), 3.5 (t, J = 10.04 Hz, 2H), 6.64–6.69 (m, 4H), and 7.13–7.24 (m, 6H); ^{13}C NMR: 33.72 (N–CH_3), 38.02 (N–CH_2), 54.99 (CH_2), 112.33, 116.36, 126.43, and 129.04 (aromatic).

***N*-Ethyl-*N*-phenyl-(*p*-methoxy)benzylamine** (Table 1, entry 7) ^{1}H NMR: 1.19 (t, J = 6.8 Hz, 3H), 3.44 (q, J = 6.8 Hz, 2H) 3.79 (s, 3H), 4.56 (s, 2H), and 6.68–7.19 (m, 9H)

***N*-Ethyl-*N*-(2-furoylmethyl)aniline** (Table 1, entry 8) ^{1}H NMR: 1.18 (t, J = 7.1 Hz, 3H), 3.49 (q, J = 7.1 Hz, 2H), 4.58 (s, 2H), 6.69–6.81 (m, 3H), and 7.2–7.4 (m, 5H).

***N*-Ethylindoline** (Table 1, entry 10) ^{1}H NMR: 1.23 (t, J = 10.01 Hz, 3H), 3.02 (t, J = 10.01 Hz, 2H), 3.20 (t, J = 9.2 Hz, 2H), 3.37 (t, J = 9.2 Hz, 2H), 6.55 (d, J = 10.4 Hz, 1H), 6.72 (d, J = 10.4 Hz, 1H), and 7.09 (t, J = 9.2 Hz, 2H); ^{13}C NMR: 28.79 (CH_3), 43.50 (CH_2), 52.57 (N–CH_2), 97.76, 117.89, 124.6, and127.59 (aromatic).

***N*-Phenylpyrrolidine** (Table 1, entry 11): ^{1}H NMR 1.98–2.07 (m, 4H), 3.41 (t, J = 7.2 Hz, 4H), 6.58 (m, 2H), and 7.21 (m, 3H).

***N*,*N*′-Dimethylpolyacrylamide** (Table 1, entry 12): ^{13}C NMR (CP-MAS): 37.5 (CH_3), 69.02, 77.81, 84.27, 128.2, (CH(CO)), and 178.03 (CO).

Acknowledgements

We are grateful to the Natural Sciences and Engineering Research Council of Canada (NSERC) and to the Fonds FCAR (Québec) for their generous financial support.

References

1. I. Ojima. *In* The chemistry of organic silicon compounds. *Edited by* S. Patai and Z. Rappoport. John Wiley & Sons, New York. 1989. p. 1479, and refs. therein.
2. I. Ojima, Z. Li, and J. Zhu. *In* The chemistry of organic silicon compounds. *Edited by* Z. Rappoport and Y. Apeloig. John Wiley & Sons, New York. 1998. p. 1687.
3. J.F. Harrod. *In* Encyclopedia of inorganic chemistry. Vol. 3. *Edited by* R.B. King. John Wiley & Sons, London. 1994. p. 1486.
4. H. Brunner. *In* Transition metals in organic synthesis. Vol. 2. *Edited by* M. Beller and C. Bolm, Wiley-VCH, Weinheim. 1998. p. 131.
5. R.L. Halterman. Chem. Rev. **92**, 965 (1992).
6. (*a*) I. Ojima (*Editor).* Catalytic asymmetric synthesis. VCH Publishers, New York. 1993; (*b*) N. Clos and C. Bastos. Tetrahedron, **45**, 6901 (1989); (*c*) I. Ojima and K. Hirai. *In* Asymmetric synthesis. Vol. 5. *Edited by* J.D. Morrison. Academic Press, Orlando. 1985. p. 103; (*d*) I. Ojima, K. Yamamoto, and M. Kumada. *In* Aspects of homogeneous catalysis. Vol. 3. *Edited by* R. Ugo. Reidel, Dordrecht. 1977. p. 185.
7. (*a*) M.B. Carter, B. Schiøtt, A. Gutiérrez, and S.L. Buchwald. J. Am. Chem. Soc. **116**, 11 667 (1994); (*b*) S. Xin and J.F. Harrod. Can. J. Chem. **73**, 999 (1995).
8. (*a*) M.T. Reding and S.L. Buchwald. J. Org. Chem. **60**, 7884 (1995); (*b*) K.J. Barr, S.C. Berk, and S.L. Buchwald. J. Org. Chem. **59**, 4323 (1994).
9. X. Verdaguer, M.C. Hansen, S.C. Berk, and S.L. Buchwald. J. Org. Chem. **62**, 8522 (1997).
10. C. Hirosawa, N. Wakasa, and T. Fuchikami, Tetrahedron Lett. **37**, 6749 (1996).

© 2004 NRC Canada

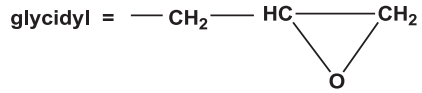
11. W.G. Brown. *In* Organic reactions. Vol. VI. *Edited by* R. Adams, H. Adkins, F.C. McGrew, A.H. Blatt, C. Niemann, A.C. Cope, and H.R. Snyder. John Wiley & Sons, New York. 1951. pp. 469–509.
12. A.C. Cope and E. Cieganek. *In* Organic synthesis. Vol. IV. *Edited by* N. Rabjohn, R.T. Arnold, N.J. Leonard, T.L. Cairns, C.C. Price, J. Cason, R.S. Schreiber, A.C. Cope, J.C. Sheehan, W.S. Johnson, and M. Tischle. John Wiley & Sons, New York. 1963. p. 339.
13. A.C. Cope and E. Cieganek. *In* Organic synthesis. Vol. IV. *Edited by* N. Rabjohn, R.T. Arnold, N.J. Leonard, T.L. Cairns, C.C. Price, J. Cason, R.S. Schreiber, A.C. Cope, J.C. Sheehan, W.S. Johnson, and M. Tischle. John Wiley & Sons, New York. 1963. p. 354.
14. W.G. Brown and P. Heim. J. Am. Chem. Soc. **86**, 3566 (1964).
15. Z.B. Papanastassiou and R.J. Brun. J. Org. Chem. **29**, 2870 (1964).
16. R.A. Benkeser, G.S. Li, and E.C. Mozdzen. J. Organometal. Chem. **178**, 21 (1979).
17. R. Kuwano, M. Takahashi, and Y. Ito. Tetrahedron Lett. **39**, 1017 (1998).
18. M. Igarashi and T. Fuchikami. Tetrahedron Lett. **42**, 1945 (2001).
19. K. Selvakumar and J.F. Harrod. Angew. Chem. Int. Ed. **40**(11), 2129 (2001).
20. X. Verdaguer, E.W. Udo, M.T. Reding, and S.L. Buchwald. J. Am. Chem. Soc. **118**, 6784 (1996).
21. J.F. Harrod. Coord. Chem. Rev. **206**, 493 (2000).
22. L. Hao, H.G. Woo, A.M. Lebuis, E. Samuel, and J.F. Harrod. J. Chem. Soc., Chem. Commun. 2013 (1998).
23. L. Hao and J.F. Harrod. Inorg. Chem. Commun. **2**, 191 (1999).
24. S. Bower, K.A. Kreutzer, and S.L. Buchwald. Angew. Chem. **108**, 1662 (1996); Angew. Chem. Int. Ed. **35**, 1515 (1996).
25. K. Claus and K. Bestian. Justus Liebigs Ann. Chem. **654**, 8 (1962).

© 2004 NRC Canada

Difluorocarbene induced facile synthesis of chlorohydrins from glycidyl ethers

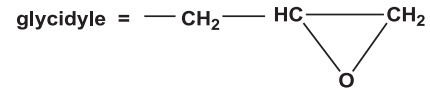
Sapna Singh, Pinaki S. Bhadury, Mamta Sharma, Meehir Palit, and Devendra K. Jaiswal

Abstract: A novel and unusual approach based on a $ClCF_2COONa$–DMF system has been developed for the synthesis of chlorohydrins via an unexpected mechanism. In a first ever report for the synthesis of chlorohydrins from glycidyl ethers, e.g., CH_2=CH-CH_2-O-Z, CH_3CH_2-O-Z, C_6H_5-O-Z, C_6H_4(*o*-CH_3)-O-Z, CH_2=C(CH_3)C(=O)-O-Z, etc., (where Z = glycidyl), difluorocarbene-induced facile regioselective ring opening of epoxides has generated the compound in high yield (70%–83%).

glycidyl = 

Key words: difluorocarbene, sodium chlorodifluoroacetate, chlorohydrins.

Résumé : On a mis au point une nouvelle approche inhabituelle à la synthèse de chlorohydrines qui est basée sur l'utilization du système $ClCF_2COONa$–DMF et qui implique un mécanisme inattendu. Dans ce travail, on en décrit la première application à la synthèse de chlorohydrines d'éthers glycidylés de la forme CH_2=CH-CH_2-O-Z, CH_3CH_2-O-Z, C_6H_5-O-Z, C_6H_4(*o*-CH_3)-O-Z, CH_2=C(CH_3)C(=O)-O-Z, etc., (dans lesquels Z = glycidyle) qui ont été générés avec des rendements élevés (70%–83%) par le biais d'une ouverture de cycle régiosélective et facile d'époxydes, induite par le difluorocarbène.

glycidyle = 

Mots clés : difluorocarbène, chlorodifluoroacétate de sodium, chlorohydrines.

[Traduit par la Rédaction]

Introduction

Difluorocarbene, a useful synthon (1–3), can be made by thermal decarboxylation of sodium chlorodifluoroacetate. In dimethyl formamide (DMF), this salt can act as a source of hydrogen fluoride (4–7). We showed that this property enabled the esterification of sodium chlorodifluoroacetate by fluoroalcohols (5). Here, we attempted to prepare *O*-(chlorodifluoroacylated) alcohols by treating various epoxides with sodium chlorodifluoroacetate in DMF. However, ring opening occurred to give chlorohydrins. Chlorohydrins are an important class of compounds that have several synthetic and industrial applications, including the manufacture of dye intermediates, pharmaceuticals, pesticides, and plasticizers. Routes to conventional chlorohydrins include hypochlorination, enzymatic methods, or reaction of chromyl chloride with simple aliphatic straight chain alkenes (8–11). The application of these reagents is further limited due to poor yield and the specific nature of the substrate. In this paper, we describe a new way to make them based on the special properties of the sodium chlorodifluoroacetate – DMF system. The difluorocarbene (**:**CF_2) induced regioselective ring opening of epoxides produces chlorohydrins in high yield with the chlorine atom almost exclusively located on the primary and (or) less-hindered carbon atom. This highly facile reaction works particularly well with electron deficient epoxides and has been successfully employed for the first time in the ring opening of glycidyl ethers.

Received 20 April 2004. Published on the NRC Research Press Web site at http://canjchem.nrc.ca on 22 October 2004.

S. Singh, P.S. Bhadury,[1] M. Sharma, M. Palit, and D.K. Jaiswal. Synthetic Chemistry Division, Defence Research and Development Establishment, Gwalior 474 002, India.

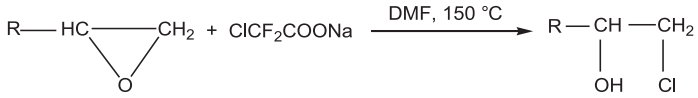
[1]Corresponding author (e-mail: drpsb2003@yahoo.co.in).

Results and discussion

We have achieved regioselective synthesis of chlorohydrins by the reaction of epoxides and sodium chlorodifluoroacetate in DMF. This highly facile reaction works particularly well with electron deficient epoxides (e.g., glycidyl ethers). Furthermore, the reaction proceeds in DMF only, and no significant product could be detected in other solvents such as diglyme, triglyme, acetonitrile, and dimethyl sulphoxide.

 doi: 10.1139/V04-093 © 2004 NRC Canada

Table 1. Synthesis of chlorohydrins.

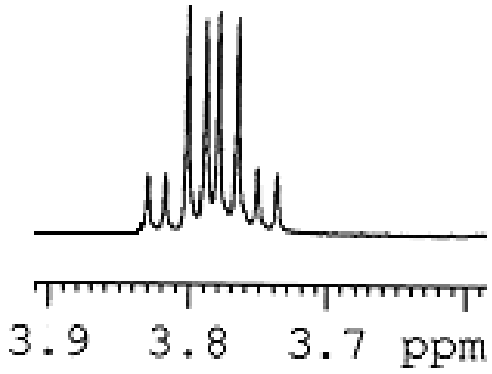


Compound no.	R	Isolated yield (%)
I	CH_2=CH-CH_2-O-CH_2	72
II	C_6H_5-O-CH_2	75
III	C_6H_4(*o*-CH_3)-O-CH_2	75
IV	C_6H_4(*p*-OCH_3)-O-CH_2	77
V	C_6H_4(*p*-NO_2)-O-CH_2	83
VI	CH_3CH_2-O-CH_2	70
VII	CH_2=C(CH_3)C(=O)-O-CH_2	81
VIII	$CH_3(CH_2)_2CH_2$	0
IX	$CH_3(CH_2)_4CH_2$	0
X	HO-CH_2	27

Synthesis of a series of chlorohydrins has been achieved by heating 1 mol of monoepoxides with 2 mol of sodium chlorodifluoroacetate in DMF under a nitrogen atmosphere at a temperature of 150 °C. The compounds synthesized are listed in Table 1. With diepoxide 1,4 butanediol diglycidyl ether, under similar conditions, the reaction required 4 mol of sodium chlorodifluoroacetate. The ring opening occurs at both epoxide centers giving rise to $ClCH_2CH(OH)CH_2O(CH_2)_4OCH_2CH(OH)CH_2Cl$ (**XI**) in 71% yield.

All compounds synthesized have been characterized on the basis of IR spectra, ^{1}H and ^{13}C NMR, and mass spectral data. Purity of the products (>98%) was confirmed by ^{1}H NMR and GC–MS studies. IR showed strong bands in the region 3360–3446 (OH) and 725–752 (C-Cl) cm^{-1}. ^{1}H NMR data were consistent with the assigned structures and chemical shift values were assigned on the basis of observed splitting patterns and shielding and (or) deshielding effects exerted by neighboring groups or atoms (Table 2). This assignment was further confirmed from two-dimensional homo correlation spectroscopy (^{1}H–^{1}H HOMOCOSY) by observing contours indicative of characteristic coupling among all nonequivalent protons. The characteristic pattern of the starting epoxide ring was absent in ^{1}H NMR, confirming the complete ring opening. The integration ratio for all the protons in their respective ^{1}H NMR corresponds to the assigned structures. The representative and distinctive patterns of two magnetically nonequivalent protons of CH_2Cl moiety in product chlorohydrin after ring opening is shown in Fig. 1. Mass spectral data were recorded both in electron ionization (EI) and chemical ionization (CI) modes. The spectra were also obtained on silyl derivatives of chlorohydrins obtained through silylation with *N*,*O*-bis(trimethylsilyl)trifluoroacetamide (BSTFA); these were particularly useful in cases where M^+ was not detectable in the original sample (Table 2). The presence of the chloromethyl moiety in the chlorohydrins is further supported by the fragmentation pattern showing the characteristic loss of CH_2Cl (*m*/*z* 49/51) from the molecular ion in their respective mass spectra. For unequivocal structural assessment of products, ^{13}C NMR data were obtained for all the chlorohydrins and described in Table 3. Physical characteristics (bp and (or) mp) of product chlorohydrins are also given in Table 3. Analytical data for elemental analysis (C and H for **I**–**IV**, **VI**, **VII**, and **XI**) and (C, H, and N for **V**) were found to be in agreement with calculated values.

Fig. 1. Representative ^{1}H NMR pattern of CH_2Cl in the product chlorohydrin.



Formation of difluorocarbene from the present system ($ClCF_2COONa$–DMF) and its participation in several synthetic transformations has been noted by several groups of workers (5, 12, 13). To account for the formation of chlorohydrins, we presume that under the influence of **:**CF_2, obtained by heating $ClCF_2COONa$, the solvent DMF probably generates an active fluoro Vilsmeier–Haack intermediate $[Me_2N–^+CHF]F^-$ (*i*, Scheme 1).

Proof of the formation of this strong Lewis acid intermediate (*i*) has been provided by Burton and Wiemers (4). It is probably that this coordinates with the epoxide oxygen atom. Any possibility of protonation on the β-oxygen (in the alkyl group R) and its subsequent participation in the reaction is ruled out on the ground that in the end, the product alkyl group has been found to remain intact. The S_N2 attack on the primary carbon atom by the chlorodifluoroacetate anion, electrophilically assisted by protonation of epoxide ring (14), generates the intermediates *O*-(chlorodifluoroacylated) alcohols (*ii*) (5). The nucleophilic attack occurs almost exclusively at the less-hindered carbon atom probably due to a

© 2004 NRC Canada

Table 2. ^{1}H NMR and mass spectral data of the chlorohydrins.[a]

Compound No.	^{1}H NMR δ (ppm), *J* (Hz)	Mass (*m*/*z*) EI (CI)
I	5.86 (1H, m, CH_2=C*H*-CH_2), 5.23, 5.10 (2H, m, CH_2=CH-CH_2), 4.27(1H, bs, OH), 4.0 (2H, td, *J* = 5.2, 1.2, CH-CH_2-O-), 3.88 (1H, m, C*H*-OH), 3.63, 3.61 (2H, m, CH_2Cl), 3.45 (2H, d, *J* = 5.6, O-CH_2-CHOH)	150/152, 109/111, 101, 93/95, 79/81,71, (151/153)
II	7.11 (5H, m, Ar), 4.55 (1H, bs, OH), 4.18 (1H, m, C*H*-OH), 4.06 (2H, d, *J* = 5.6, O-CH_2-CH), 3.79, 3.76 (2H, m, CH_2Cl)	186/188, 137, 109/111, 107, 93/95, 79/81,77, (187/189)
III	6.97 (4H, m, Ar), 4.23 (1H, m,C*H*-OH), 4.08, 4.06 (2H, m, Ar-O-CH_2-), 3.94 (1H, bs, OH), 3.76, 3.78 (2H, m, CH_2Cl), 2.21 (3H, s, CH_3)	200/202, 151, 109/111, 107, 93/95, 79/81,91, (201/203)
IV	6.80 (4H, m, Ar), 4.13 (1H, m, C*H*-OH), 4.0, 3.96 (2H, m, Ar-O-CH_2-), 3.66, 3.64 (2H, m, CH_2Cl), 3.72 (3H,s, OCH_3), 2.88 (1H, bs, OH)	As the silyl derivative: 288/290, 239, 181/183, 165/167, 151/153, 137, 123, 107, 73, (289/291)
V	7.0, 8.2 (4H, 2xd, Ar), 4.29 (1H, m, C*H*-OH), 4.20 (2H, d, *J* = 5.6, Ar-O-CH_2 -), 3.78, 3.76 (2H, m, CH_2Cl), 2.90 (1H, bs, OH)	As the silyl derivative: 303/305, 254, 181/183, 165/167, 152, 151/153, 138, 122, 73, (304/306)
VI	3.65 (1H, m,C*H*-OH), 3.56 (1H, bs, OH), 3.34, 3.32 (2H, m, CH_2Cl), 3.21 (4H, m, CH_2-O-CH_2), 0.82 (3H, t, CH_3CH_2)	138/140, 109/111, 93/95, 89, 79/81, 59, (139/141)
VII	6.03 (2H, m, =CH_2), 4.29 (2H, d, *J* = 5.8, -O-CH_2), 4.13 (1H, m, C*H*-OH), 3.75 (1H, bs, OH), 3.67, 3.65 (2H, m, CH_2Cl), 1.99 (3H, s, CH_3)	As the silyl derivative: 250/252, 235/237, 201, 181/183, 165/167,151/153, 99, 85, 73, 69, (251/253)
X	4.31 (2H, d, *J* = 5.6, CH_2OH), 4.13 (1H, m, CHOH), 3.77, 3.75 (2H, m, CH_2Cl)	As the silyl derivative: 182/184, 165/167, 151/153, 133, 73, (183/185)

[a]With 1,4 butanediol diglycidyl ether, a diepoxide, the ring opening occurs at both epoxide centers giving rise to $ClCH_2CH(OH)CH_2O(CH_2)_4OCH_2CH(OH)CH_2Cl$ (**XI**). ^{1}H NMR (ppm) δ: 3.92 (2H, m, C*H*OH), 3.57, 3.54 (4H, m, CH_2Cl), 3.48 (8H, m, CH_2-O-CH_2), 2.10 (1H, bs, OH), 1.60 (4H, m, CH_2-CH_2). Mass spectra EI (CI), *m*/*z* as the silyl derivative: 418/420/422, 369/371, 267/269, 253/255, 237/239,116,73 (419/421/423).

steric factor. However, the ester intermediate is short lived and in the presence of an electron attracting environment decarboxylates readily to generate chlorodifluoromethide ion (CF_2Cl^-), which decomposes to regenerate **:**CF_2 and Cl^- ions. The simultaneous attack of the Cl ion on the primary positive carbon yields the desired chlorohydrins. As with most other S_N2 displacements, the method works well with electron-poor epoxides like alkyl, allyl, and aryl glycidyl ethers and with glycidyl methacrylate and 1,4 butanediol diglycidyl ether, but fails to take place with 1,2-epoxyoctane and butyloxirane. A similar observation was noted earlier when *O*-(chlorodifluoroacylated) alcohols were formed from electron-deficient alcohols using this system (5). With moderately electron-deficient epoxides containing active alcoholic (-OH) functionality (e.g., glycidol), the yield of the desired chlorohydrin (**X**) is poor.

Taking *o*-cresyl glycidyl ether as the model epoxide, the reaction was carried out at different time intervals with sodium chlorodifluoroacetate in DMF. The intermediate *O*-(chlorodifluoroacylated) species (*ii*, Scheme 1) was detected (EI-MS *m*/*z*: 294/296 (M^+), 187/189,108, 85/87) along with the product chlorohydrin (*iii*), after heating the reaction mixture for 0.5 h at 150 °C. On further heating for 1 h, the intermediate disappeared and chlorohydrin was detected as the main product in solution. If the heating was continued further (e.g., after 3 h), the chlorodifluoroacylated derivative of chlorohydrin, (o-CH_3)$C_6H_4OCH_2CH(OCOCF_2Cl)CH_2Cl$, EI-MS *m*/*z*: 312/314/316 (M^+), 205/207/209, 91, δ CF_2 –61.6), similar to our earlier observation with fluoroalcohols (5), started appearing. A similar observation including in situ detection of an *O*-(chlorodifluoroacylated) intermediate was noted with other epoxides. These observations support our proposed mechanism as shown in Scheme 1.

Conclusion

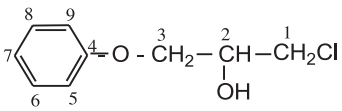
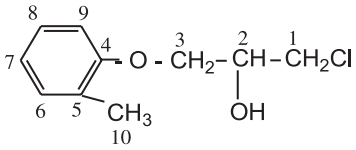
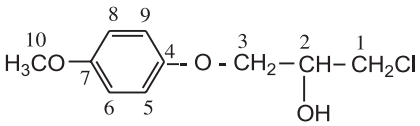
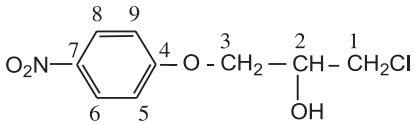
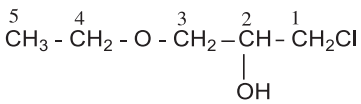
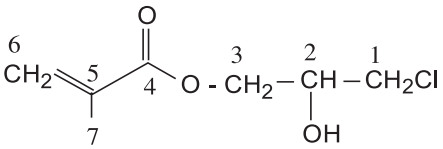
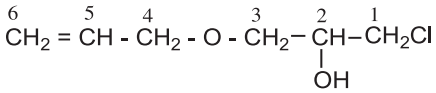
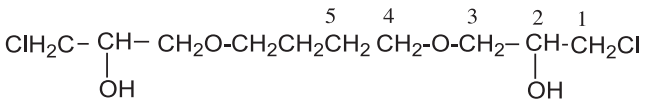
In summary, the $ClCF_2COONa$–DMF mixture works as a facile reagent system for the preparation of chlorohydrins from electron-deficient epoxides. The difluorocarbene (**:**CF_2) induced regioselective ring opening reported for the first time on glycidyl ethers is simple, facile, does not require any prior reagent preparation and is devoid of any appreciable side reaction products. Using a similar system, fluorohydrins, volatile CFC alternatives, and perfluoroolefins have been obtained, which wwill be subsequently communicated.

Experimental

Reactions were monitored by GC–MS and the mass spectra were recorded on a TSQ 7000 mass spectrometer

© 2004 NRC Canada

Table 3. ^{13}C NMR and physical characteristic data of the chlorohydrins.

Chlorohydrin	^{13}C NMR (δ ppm)	Boiling point or [melting point] (°C)
	157.2 (C4), 129.5 (C8 and C6), 120.0 (C7), 115.1 (C9 and C5), 69.7 (C3), 68.7 (C2), 46.0 (C1)	138–140 (2 mmHg)[a]
	156.4 (C4), 130.9 (C6), 127.0 (C8), 126.8 (C5), 121.4 (C7), 111.5 (C9), 69.4 (C3), 68.6 (C2), 46.1 (C1) 16.1 (C10)	143–145 (0.5 mmHg)[a]
	154.1 (C7), 151.6 (C4), 115.8 (C5 and C9), 114.5 (C8 and C6), 70.3 (C3), 68.9 (C2), 56.9 (C10), 46.4 (C1)	[68–70]
	165.3 (C4), 140.5 (C7), 125.3 (C8 and C6), 116.0 (C9 and C5), 70.8 (C3), 70.1 (C2), 47.0 (C1)	[97–99]
	68.6 (C3), 67.9 (C2), 61.8 (C4), 46.0 (C1), 14.2 (C5)	64–66 (4 mmHg)[a]
	164.5 (C4), 138.7 (C5), 122.0 (C6), 68.5 (C3), 67.9 (C2), 45.9 (C1), 17.9 (C7)	123–125 (16 mmHg)[a]
	137.2 (C5), 115.2 (C6), 69.0 (C3), 68.6 (C4), 68.2 (C2), 46.3 (C1)	110–112 (20 mmHg)[a]
	68.8 (C3), 67.6 (C4), 67.1 (C2), 46.2 (C1), 27.5 (C5)	119–121 (0.8 mmHg)[a]

[a]1 mmHg = 133.3224 Pa.

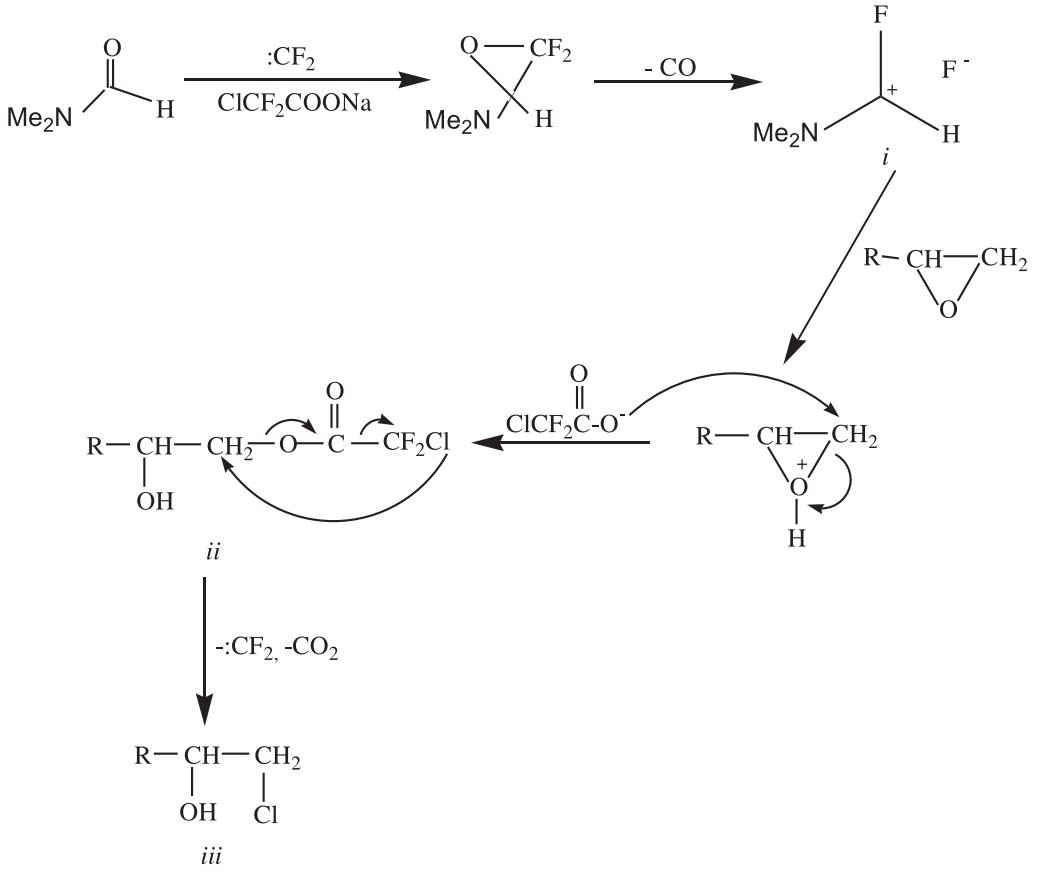
(Finigan MAT, USA) using a Varian 3400 GC inlet with a BP-5 column (30 m × 2.5 mm (i.d.) × 0.25 μm (film thickness) with a temperature program of 50 °C (2 min) – at 10 °C/min – 280 °C (5 min) using helium as carrier gas at a flow rate of 1.2 mL/min. The injector temperature was 250 °C and the transfer line was heated to 280 °C. EI-MS was performed at 70 eV with the ion source temperature 180 °C and an emission current of 400 mA. The CI-MS experiments were performed using methane as a reagent gas at pressure 2500 mtorr (1 torr = 133.3224 Pa), source temperature 200 °C, and emission current 300 mA. The ^{1}H and ^{13}C NMR spectra of the chlorohydrins were recorded on a Bruker Avance DPX-400 spectrometer in $CDCl_3$ solution for all except compound No. **I**, which was run in DMF-d_7, using TMS as the internal reference. ^{19}F NMR of the intermediate *O*-(chlorodifluoroacylated) derivatives was obtained using $CFCl_3$ as the internal standard. The epoxides were obtained commercially and distilled before use. DMF was dried by storing on a 4 Å Linde molecular sieve followed by distillation under vacuum.

Synthesis of chlorohydrins

Sodium salt of chlorodifluoroacetic acid (6.1 g, 0.04 mol for all cases; except for compound No. **XI**, 12.2 g, 0.08 mol) in 50 mL of dry DMF was placed in a 250 mL three-necked flask, containing a stirring bar and a dry nitrogen inlet, at room temperature. Epoxide (0.02 mol) was then added slowly through a dropping funnel to the well-stirred mixture. The temperature of the reaction mixture was raised to 150 °C and was further refluxed for 1 h. The course of the reaction was followed by withdrawing a small aliquot of the reaction mixture and subjecting it to GC–MS analysis. Initially the salt was soluble making a homogeneous solution in DMF. On heating, the reaction mixture turned brown with the deposition of a solid at the bottom of the flask, which in-

© 2004 NRC Canada

Scheme 1. A probable mechanism for the formation of chlorohydrins.



dicated completion of the reaction. The reaction mixture was then filtered and the bulk of DMF was removed by distillation under vacuum. The residue, which still contained some traces of solid, was separated by centrifugation. It was then washed with excess water to remove the remaining DMF and extracted into diethyl ether. The ether layer was dried and then removed by distillation. The chlorohydrins were obtained either by distillation under vacuum (compound Nos. **I–III**, **VI**, **VII**, **X**, and **XI**) or by crystallization from hexane (compound Nos. **IV** and **V**).

Acknowledgement

We thank Mr. K. Sekhar, Director, D.R.D.E., Gwalior for his keen interest in this work.

References

1. P. Crabbe, J.-L. Luche, J.-C. Damiano, M.-J. Luche, and A. Cruz. J. Org. Chem. **44**, 2929 (1979).
2. Y. Kobayashi, T. Taguchi, T. Morikawa, T. Takase, and H. Takanashi. J. Org. Chem. **47**, 3232 (1982).
3. T. Taguchi, T. Takigawa, Y. Tawara, T. Morikawa, and Y. Kobayashi. Tetrahedron Lett. **25**, 5689 (1984).
4. D.J. Burton and D.M. Wiemers. J. Am. Chem. Soc. **107**, 5014 (1985).
5. P.S. Bhadury, M. Palit, M. Sharma, S.K. Raza, and D.K. Jaiswal. J. Fluorine Chem. **113**, 47 (2002).
6. P.S. Bhadury, M. Palit, M. Sharma, S.K. Raza, and D.K. Jaiswal. J. Fluorine Chem. **116**, 75 (2002).
7. P.S. Bhadury. Ph.D. thesis, Jiwaji University, Gwalior, India, 2002.
8. Kirk-Othmer encyclopedia of chemical technology. 4th ed. Vol. 6. 1992. pp. 140–155, and refs. cited therein.
9. R.T. Morrison and R.N. Boyd. Organic chemistry. 5th ed. Allyn and Bacon Inc., Boston, Mass. 1987. p. 323.
10. J.M. Klunder and G.H. Posner. *In* Comprehensive organic synthesis. *Edited by* B.M. Trost. Pergamon Press, Oxford. 1991. p. 224.
11. J. Geigart and S.L. Neidleman. US Patent 4 587 217, 1986.
12. Y. Kobayashi, T. Taguchi, M. Mamada, H. Shimizu, and H. Murohashi. Chem. Pharm. Bull. **27**, 3123 (1979).
13. P.S. Bhadury, B.P. Pant, M. Palit, and D.K. Jaiswal. J. Fluorine Chem. **85**, 115 (1997).
14. D. Landini and M. Penso. Tetrahedron Lett. **31**, 7209 (1990).

© 2004 NRC Canada

Identification of complexes involving toxic heavy metals with amino acid ligands by electrospray ionization mass spectrometry

Neil Burford, Melanie D. Eelman, and Wesley G. LeBlanc

Abstract: Electrospray ionization mass spectra (ESI-MS) of reaction mixtures containing ions of the heavy metals, cadmium, mercury, thallium, lead, and bismuth with each of the naturally occurring amino acids allows for definitive identification of monocationic complexes in the gas phase. Prominent *m*/*z* peaks are assigned to ions of the type $[E(Am) - xH]^+$ (x = 0, 1, 2), $[E(Am)_2 - xH]^+$ (x = 0, 1, 2), $[E_2(Am) - xH]^+$ (x = 1, 2, 3), and (or) $[E_2(Am)_2 - xH]^+$ (x = 1, 3, 5) for all amino acids studied (Am) with all metals studied (E = Cd, Hg, Tl, Pb) except bismuth, which shows complexes with only seven amino acids (Am = His, Thr, Met, Cys, Hcys, Asn, Gln). The results demonstrate the potential application of ESI-MS as a versatile and efficient approach to study toxic heavy metals in biological systems.

Key words: heavy metals, amino acids, electrospray ionization mass spectrometry.

Résumé : La spectrométrie de masse par ionisation avec électronébulisation (SM-IEN) de mélanges réactionnels contenant des ions de métaux lourds, cadmium, mercure, thallium, plomb et bismuth, avec chacun des acides aminés qu'on retrouve dans la nature permet d'identifier d'une façon définitive les complexes monocationiques présents en phase gazeuse. Les pics *m*/*z* prédominants sont attribués aux ions du type $[E(Am) - xH]^+$ (x = 0, 1, 2), $[E(Am)_2 - xH]^+$ (x = 0, 1, 2), $[E_2(Am) - xH]^+$ (x = 1, 2, 3) et (ou) $[E_2(Am)_2 - xH]^+$ (x = 1, 3, 5) pour tous les acides aminés étudiés (Am), avec tous les métaux étudiés (E = Cd, Hg, Tl, Pb) à l'exception du bismuth qui ne donne des complexes qu'avec sept acides aminés (Am = His, Thr, Met, Cys, Hcys, Asn, Gln). Les résultats démontrent que l'application de la SM-IEN est une approche versatile et efficace pour étudier les métaux lourds toxiques dans les systèmes biologiques.

Mots clés : métaux lourds, acides aminés, spectrométrie de masse avec électronébulisation.

[Traduit par la Rédaction]

Introduction

The bioactivity of toxic heavy metals is likely governed by their interaction with biological molecules such as amino acids, peptides, proteins, or enzymes. The existence of specific complexes has been confirmed in a few cases by spectroscopic (1) or X-ray crystallographic studies (2–4), which shed light on potential mechanisms of bioactivity. Nevertheless, a deeper appreciation of heavy metal biochemistry requires a systematic and comprehensive assessment in terms of both the variety of metals and the vast array of biological molecules. To address this challenge, we have used electrospray ionization mass spectrometry (ESI-MS) to examine reaction mixtures containing each of the essential amino acids with ions of the toxic heavy metals (5), cadmium (human minimum lethal dose, MLD = 1 g), mercury (MLD = 0.5 g), thallium (MLD = 0.3 g), and lead (MLD = 10 g). ESI mass spectra show *m*/*z* peaks that are readily assigned to cationic complexes for all amino acid with all toxic heavy metals. In contrast, similar reaction mixtures involving the less-toxic and medicinally relevant (6, 7) heavy metal, bismuth (MLD = 15 g), exhibit complexes with only seven amino acids.

Received 27 February 2004. Published on the NRC Research Press Web site at http://canjchem.nrc.ca on 23 October 2004.

N. Burford,[1] M.D. Eelman, and W.G. LeBlanc. Department of Chemistry, Dalhousie University, Halifax, NS B3H 4J3, Canada.

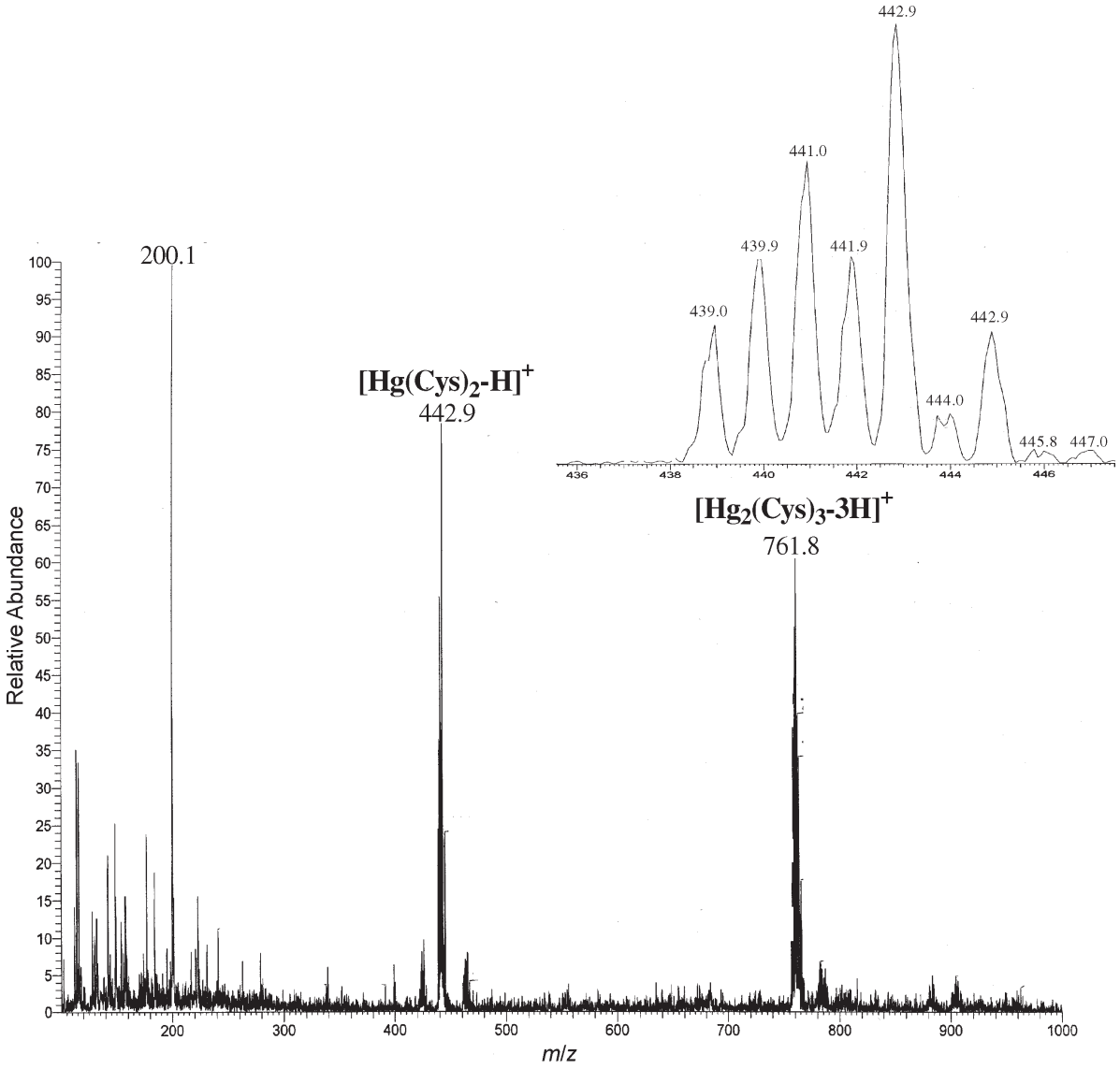
[1]Corresponding author (e-mail: neil.burford@dal.ca).

Experimental

All reagents were used as received from Aldrich. Equimolar mixtures (0.5 mmol) of $Cd(NO_3)_2{\cdot}4H_2O$, $Hg(NO_3)_2{\cdot}H_2O$, $Hg_2(NO_3)_2{\cdot}2H_2O$, $TlNO_3$, $Pb(NO_3)_2$, or $Bi(NO_3)_3{\cdot}5H_2O$ with each of 20 common L-amino acids (and DL-homocysteine) in 15 mL distilled water and 15 mL ethanol were stirred overnight (12 h) at room temperature (RT). Reactions involving cysteine or homocysteine were performed under an atmosphere of nitrogen. ESI mass spectra of the suction filtrate from each reaction were obtained using a Finnigan LCQ Duo ion trap mass spectrometer and (or) a Sciex Qtrap quadrupole/ion trap mass spectrometer. Samples were introduced directly into the electrospray source at a flow rate of 1.2 mL/h with a source temperature of 473 K, an applied voltage of 4 kV, and the in-source fragmentation off or a source temperature of 385 K and a declustering potential of 50 V, respectively. Tandem (MS–MS) spectra were obtained by introducing helium as the collision gas and the collision energy was optimized for each sample.

 doi: 10.1139/V04-095 © 2004 NRC Canada

Fig. 1. A positive ion ESI-MS of a reaction mixture containing $Hg(NO_3)_2$ and L-cysteine in 50% ethanol–water. Assignments are supported by MS–MS. The isotopic pattern observed for each peak corresponding to a metal containing cation is shown for the representative peak at *m/z* 442.9.



Results and discussion

Electrospray ionization mass spectrometry (ESI-MS) offers a sensitive and versatile technique to sample low volatility ionic species in the gas phase (8). The absence of high energies that are typically required with electron ionization (EI) and chemical ionization (CI) mass spectrometric techniques facilitates the observation of *m/z* peaks corresponding to molecular ions and minimizes fragmentation. Solutions can be readily sampled providing a convenient approach to study inorganic compounds, including systems containing complexes of metals and metalloids (8–17).

Reaction mixtures containing equimolar combinations of $Cd(NO_3)_2$, $Hg(NO_3)_2$, $Hg_2(NO_3)_2$, $TlNO_3$, $Pb(NO_3)_2$, or $Bi(NO_3)_3$ with each of 21 amino acids in 50% ethanol–water were analysed by positive ion ESI-MS. Most spectra exhibit few prominent *m/z* peaks. Most peaks are readily assigned (Table 1) to monocationic complexes of the metal with one or more amino acids (or conjugate base of the amino acid). Some *m/z* peaks are assigned to cations that contain additional solvent molecules or nitrate units. The observed spectra are essentially independent of reaction mixture stoichiometry (10:1 – 1:10) or reaction time (hours or days).

Characteristic isotopic patterns exhibited by some metals provide valuable "fingerprints" that enable definitive determination of the number of metal ions in the formulae that correspond to an *m/z* peak. A representative ESI-MS is shown in Fig. 1 for $Hg(NO_3)_2$ with L-cysteine. Two prominent peaks with *m/z* values of 443 and 762 are assigned to $[Hg(Cys)_2–H]^+$ and $[Hg_2(Cys)_3–3H]^+$, respectively, assuming retention of the 2+ oxidation state for Hg under these experimental conditions. Each peak exhibits an isotopic pattern consistent with the seven naturally occurring isotopes of Hg, as illustrated for *m/z* 443. Amino acids are given conventional three letter abbreviations.

Table 1 lists formula assignments involving metal and

© 2004 NRC Canada

Table 1. Assignments for *m*/*z* peaks observed in ESI-MS of 1:1 stoichiometry reaction mixtures containing $E(NO_3)_z$ (z = 1, 2, or 3) and an amino acid (Am) in 50% ethanol–water.

E	Gly	Ala	Val	Leu	Ile	Phe	Trp	Tyr	His	Ser	Thr
Bi									1:2–2		1:2–2
z = 3											
Hg	1:1		*1:1*[b]	*1:2*	*1:2*	1:1	*2:1–1*	1:1[b]	1:2	1:1[b]	1:1[b]
z = 1	1:1[b]		*2:1–1*[b]	2:3–1	2:3–1	1:2	*2:2*[c]	1:2	2:2–1		*2:3–1*
				2:4–1	2:4–1		3:3–2[c]		2:3–1		
				2:4[c]	3:4–2						
				3:4–2	4:4–3						
				4:4–3							
Pb	*1:1–1*	*1:1–1*	1:1–1	1:1–1	1:1–1	*1:1–1*	*1:1–1*	*1:1–1*	*1:1–1*	*1:1–1*	*1:1–1*
z = 2	2:3–2	1:1[c]	*1:1*[c]	1:2–1	1:2–1	1:2–1	1:2–1		2:2–3		2:2–3
		1:2–1	1:2–1	2:2–3	2:2–3	2:2–3	2:2–3		2:3–3		2:3–3
		2:2–3[b]	2:2–3[d]	*2:3–3*	*2:3–3*	*2:3–3*	2:3–3				3:3–5
Ref. 19		*2:3–3*	2:2–2[c]								
			2:3–3								
Tl	2:1–1	*1:1*	1:1	1:1	1:1	1:1	*1:1*	3:2–2	1:1	1:1	*1:1*
z = 1	3:2–2	2:1–1	*2:1–1*	*2:1–1*	*2:1–1*	*2:1–1*	2:1–1		*1:2*	*2:1–1*	2:1–1
			3:2–2						3:2–2		
Hg	*1:1–1*[b]	1:1–1[b]	*1:1–1*[b]	1:1–1	1:1–1	1:1–1	1:2–1	1:2–1	1:2–1	*1:2–1*	1:1–1
z = 2	*3:3–5*	1:2–1		1:1–1[b]	*1:1–1*[b]	1:1–1[d]		2:2–3	2:3–3	2:2–3	1:2–1
		2:2–3		1:2–1	*1:2–1*	1:2–1		2:3–3		*2:3–3*	*2:2–3*
		2:3–3		3:3–5	*3:3–5*	1:2–1[d]				3:2–5	*2:3–3*
		3:3–5				2:2–3				*3:3–5*	*3:3–5*
						2:3–3					
Cd	*1:1*[c]	*1:1*[c]	*1:1*[c]	*1:1*[c]	*1:1*[c]	*1:1*[c]	*1:1*[c]	*1:1*[c]	1:1–1	*1:1*[c]	*1:1*[c]
z = 2	3:3–4[c]		1:2–1	*2:3–3*	*2:3–3*	*1:2*[c]	*1:2–1*		*1:1*[c]		1:2[c]
	3:5–4[c]		*1:2*[c]	*4:6–6*[c]	*4:6–6*[c]	*2:3–3*	2:2–2[c]		*2:2–2*[c]		2:2–2[c]
			2:2–3				*2:3–3*		3:3–4[c]		
			2:3–3								
			3:3–5								
			3:4–4[c]								

Note: Amino acids are given traditional three letter abbreviations. Assignments are only given for monocations containing both metal (E) and amino acid (Am) units. Formulae are abbreviated as *n*:*m*–*x* corresponding to the generic formula $[E_n(Am)_m - xH + Y]^+$, where Y = Na, EtOH, H_2O, and (or) NO_3. Assignments for peaks with a relative intensity of greater than 50% are in italics.

[a] Y = Na.
[b] Y = EtOH.
[c] Y = NO_3.
[d] Y = H_2O.

amino acid components for observed *m*/*z* peaks that have been supported by tandem mass spectrometry (MS–MS) experiments. Assignments for peaks with a relative intensity of greater than 50% are italicized. Complexes involving each of the amino acids are observed for lead(II), thallium(I), mercury(II) (except for Hcys), and cadmium(II). Formulae are abbreviated as *n*:*m*–*x*, corresponding to the generic formula $[E_n(Am)_m - xH + Y]^+$, where Y = Na, EtOH, H_2O, and (or) NO_3. Almost all metals are observed to adopt (*n*:*m*–*x*) formulae of 1:1, 1:1–1, or 1:1–2, and most can accommodate two amino acid ligands (*n*:*m*–*x* = 1:2, 1:2–1, or 1:2–2). Formulae that do not involve the loss of a hydrogen atom (e.g., $[Tl(Ala)]^+$) can be considered complexes of the metal with a neutral amino acid ligand, while there are more examples of complexes involving an anionic conjugate base of the amino acid (e.g., $[Pb(Gly -H]^+$). Most numerous are

© 2004 NRC Canada

Table 1 (*concluded*).

Met	Cys	Hcys	Asp	Glu	Asn	Gln	Lys	Arg	Pro
1:1–2 *1:2–2* 1:2–3[a] 2:2–5 2:3–5 2:3–6[a]	*1:1–2* *1:2–2* 2:2–5 2:3–5	*1:1–2* *1:2–2* 2:2–5 2:3–5			1:2–2	1:2–2			
1:2 2:2–1 2:3–1	1:2				1:2 2:3–1		1:1 1:2 2:2–1 2:3–1 3:3–2	1:2 2:2–1 2:3–1 3:4–2	1:1[b] *2:3–1*
1:1–1 1:2–1 2:2–3 *3:2–5*	*1:1–1* *1:2–1* *2:2–3*	*1:1–1* 1:2–1 *2:2–3*	*1:1–1* *2:2–3* 3:2–3 3:3–5	*1:1–1* 2:1–3 2:1–2[d] 2:2–3	*1:1–1* 1:2–1 2:2–3 *2:3–3*	*1:1–1* *2:2–3* *2:3–3*	1:1–1 *2:3–3*	*1:1–1* 1:1[c] *1:2–1* 1:2[c] 1:3–1 1:3[c] 1:4[c] 1:5[c] 1:6[c]	1:1–1 *1:1*[c] *1:2–1* *2:3–3*
1:1 *2:1–1*	1:1	*1:1* *2:1–1*	2:1–1 3:1–2	1:1 *3:1–2*	*2:1–1*	*1:1* 2:1–1 2:2–1	1:1 2:1–1 3:2–2	*1:1* 1:2 1:3 1:4 1:5	1:1 2:1–1 3:2–2
1:1–1 1:2–1 2:2–3 2:3–3	*1:2–1* *2:3–3*		2:2–3[b]	2:2–3	1:1–1 1:2–1 1:3–1 2:2–3 2:3–3 3:3–5	2:2–3 2:3–3	1:1–1 1:2–1 2:2–3 2:3–3	1:1–1 1:2–1 2:2–3 2:3–3	1:1–1 2:3–3
1:1[c] 1:2–1 *2:2–2*[c] *2:3–3*	1:2	2:2–3 3:2–4[c]	*1:1–1*[d] *1:1*[c] 2:2–2[c]	*1:1*[c]	*1:1*[c] *2:2–2*[c] 2:3–3	*1:1*[c] 2:2–2[c] 2:3–3	*1:1*[c] *2:2–2*[c] *2:3–3*	*1:1*[c] 1:2–1 2:2–2[c]	*1:1*[c] 1:2[d]

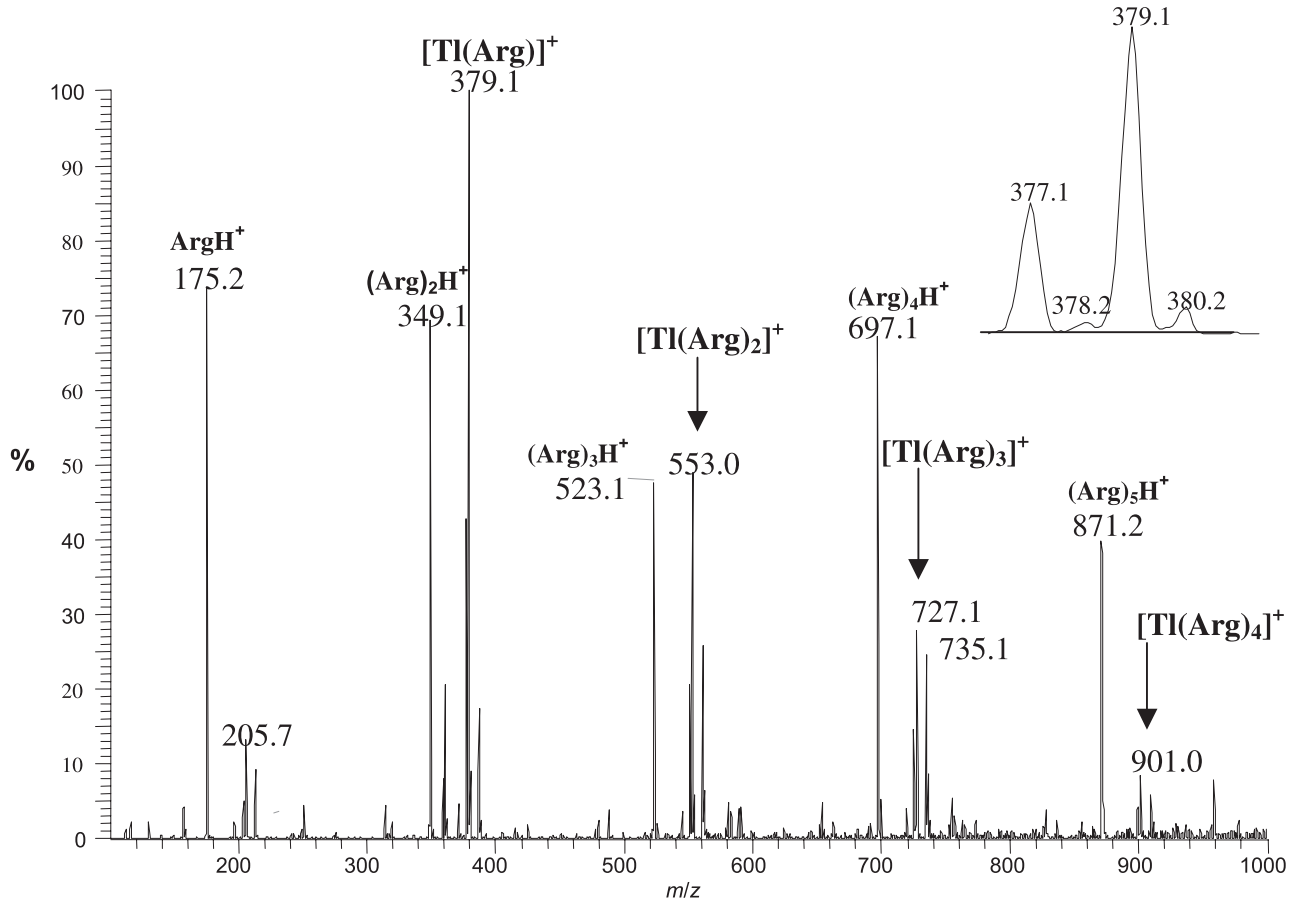
complexes involving both a neutral amino acid and a conjugate base(s) of the amino acid (e.g., $[Cd(Trp)_2 - H]^+$).

Amino acid rich ($m > n$) complexes are observed in some cases and are most pronounced for arginine with thallium ($m = 5$, $n = 1$) or lead ($m = 6$, $n = 1$). The representative ESI-MS for thallium(I) nitrate with L-arginine in Fig. 2 shows peaks with m/z values corresponding to proton bound clusters of general formula $[Arg_mH]^+$, up to $m = 5$. Of greater or comparable intensity are four peaks that are assigned to the $m = 1$, 2, 3, and 4 series with the general formula $[Tl(Arg)_m]^+$, on the basis of the distinct isotopic pattern corresponding to the presence of a single thallium atom. Metal-rich ($n > m$) complexes are evident for mercury, lead, and thallium (e.g., n:m–x = 2:1–1, 2:1–2, 2:1–3), but clusters of metals and ligands ($n > 1$; $m > 1$; x = 1–6) are more common.

Monocations containing amino acid ligand(s) on mer-

© 2004 NRC Canada

Fig. 2. A positive ion ESI-MS of a reaction mixture containing $TlNO_3$ and L-arginine in 50% ethanol–water. Assignments are supported by MS–MS. The isotopic pattern observed for each peak corresponding to a metal containing cation is shown for the representative peak at *m/z* 379.1.



cury(I) or bismuth(III) are only observed for 16 and seven amino acids, respectively. In the case of reaction mixtures of methionine with $Bi(NO_3)_3$, the charge on two of the observed cations is imposed by complexation with a sodium ion (e.g., $[Bi(Met)_2 - 3H + Na]^+$ and $[Bi_2(Met)_3 - 6H + Na]^+$). The *m/z* peaks corresponding to cations containing bismuth are generally of weak intensity relative to those for other heavy metals, but the assignments have been supported by MS–MS experiments. Bismuth exhibits a particular preference for complexes involving the sulfur-containing amino acids L-methionine, L-cysteine, or DL-homocysteine, consistent with the recognised thiophilicity of bismuth (18).

Conclusions

Complexes of amino acids with toxic heavy metals (Cd, Hg, Tl, Pb) as well as Bi have been definitively identified by ESI-MS. While this study is not comprehensive due to the inability of the technique to detect neutral complexes, this represents a systematic investigation into the chemistry of heavy metal – amino acid complexes and the first identification of most complexes in any phase. ESI-MS is demonstrated as a potentially powerful approach to evaluate and understand coordination chemistry. The gas-phase identification of complexes with peptides, proteins, and other biological molecules is in progress.

Acknowledgments

We thank the Natural Sciences and Engineering Research Council of Canada (NSERC), the Killam Program of the Canada Council for the Arts, the Canada Research Chairs program, the Canada Foundation for Innovation, the Nova Scotia Research and Innovation Trust Fund, and MDS Sciex for funding, the Maritime Mass Spectrometry Laboratories and the National Research Council of Canada (NRC), Institute for Marine Biosciences for use of instrumentation, and Dr. Devanand Pinto for helpful discussion.

References

1. D.L. Rabenstein and R.S. Reid. Inorg. Chem. **23**, 1246 (1984).
2. M.C. Corbeil and A.L. Beauchamp. Can. J. Chem. **66**, 2458 (1988).
3. N.J. Taylor, Y.S. Wong, P.C. Chieh, and A.J. Carty. J. Chem. Soc. Dalton Trans. 438 (1975).
4. H.C. Freeman and C.J. Moore. Acta. Crystallogr. Sect. B: Struct. Sci. **B33**, 2690 (1977).
5. J.M. Arena and R.H. Drew. Poisoning: Toxicology, symptoms, treatments. Thomas, Springfield, Ill., USA. 1986.
6. G.G. Briand and N. Burford. Chem. Rev. **99**, 2601 (1999).
7. P.J. Sadler, H. Li, and H. Sun. Coord. Chem. Rev. 1**85–186**, 689 (1999).

© 2004 NRC Canada

8. B.F.G. Johnson and J.S. McIndoe. Coord. Chem. Rev. **200–202**, 901 (2000).
9. S.M. Blair, J.S. Brodbelt, A.P. Marchand, K.A. Kumar, and H.-S. Chong. Anal. Chem. **72**, 2433 (2000).
10. N. Burford, M.D. Eelman, D. Mahony, and M. Morash. Chem. Commun. 146 (2003).
11. G.G. Briand, N. Burford, M.D. Eelman, T.S. Cameron, and K.N. Robertson. Inorg. Chem. **42**, 3136 (2003).
12. N. Burford, M.D. Eelman, and T.S. Cameron. Chem. Commun. 1402 (2002).
13. J.-Y. Salpin and J. Tortajada. J. Phys. Chem. A, **107**, 2943 (2003).
14. J.-Y. Salpin and J. Tortajada. J. Mass Spectrom. **37**, 379 (2002).
15. S. Colette, B. Amekraz, C. Madic, L. Berthon, G. Cote, and C. Moulin. Inorg. Chem. **42**, 2215 (2003).
16. P.J. Dyson and J.S. McIndoe. Inorg. Chim. Acta, **354**, 68 (2003).
17. J.C. Woodcock, W. Henderson, and C.O. Miles. J. Inorg. Biochem. **85**, 187 (2001).
18. G.G. Briand and N. Burford. Adv. Inorg. Chem. **50**, 285 (2000).
19. Preliminary communication: N. Burford, M.D. Eelman, W.G. LeBlanc, T.S. Cameron, and K.N. Robertson. Chem. Commun. 332 (2004).

© 2004 NRC Canada

Study of acid hydrolysis of bromazepam

Tatjana Damjanović, Gordana Popović, Srđan Verbić, and Lidija Pfendt

Abstract: Quantitative study of an acid hydrolysis of bromazepam, which in acidic solution simultaneously undergoes reversible 4,5-azomethine bond cleavage and protolytic reactions, was performed (t = 25 °C). When an equilibrium is established, four species are simultaneously present in solution. Two approaches, both based on theoretically derived dependence between the absorbance (A) and the solution acidity ($[H_3O^+]$), were used to determine appropriate equilibrium constants. In the first, the least-squares method was used to fit experimentally obtained (A, $[H_3O^+]$) value pairs to a derived function. With values obtained as fitting parameters, the probability distribution for equilibrium constants was calculated with the virtual experiments performed using Monte Carlo simulations. In the second one, spectrophotometric analysis indicated an existence of two distinct pH intervals, both with three dominant species involved. Spectral data were used to calculate equilibrium constants by a linear curve fitting analysis. Values obtained for equilibrium constants from the numerical and the experimental approaches are in good accordance and were used to calculate distribution of all the species as a function of pc_H.

Key words: bromazepam, acid hydrolysis, equilibrium constants.

Résumé : Opérant à 25 °C, on a effectué une étude quantitative de l'hydrolyse acide du bromazépam qui, en solution acide, subit simultanément des réactions protolytique ainsi que de coupure réversible de la liaison 4,5-azométhine. Une fois l'équilibre établit, la solution contient simultanément quatre espèces. Pour la détermination des constantes d'équilibre appropriées, on a utilisé deux approches, toutes deux basées sur la relation théorique entre l'absorbance (A) et l'acidité ($[H_3O^+]$). Dans le premier cas, on a utilisé la méthode des moindres carrés pour ajuster d'une façon expérimentale les paires de valeurs (A, $[H_3O^+]$) avec une fonction dérivée. À l'aide des valeurs obtenues à partir des paramètres d'ajustement, on a calculé la distribution de la probabilité des constantes à l'aide d'expériences virtuelles réalisées à l'aide de simulations de Monte Carlo. Dans le deuxième cas, l'analyse spectroscopique a indiqué l'existence de deux intervalles distincts de pH qui comprenaient toutefois trois espèces dominantes. On a utilisé les données spectrales pour calculer les constantes d'équilibre à l'aide d'une analyse de l'ajustement de la courbe linéaire. Les valeurs pour les constantes d'équilibre à partir des approches numériques et expérimentales sont en bon accord entre elles et on les a utilisées pour calculer la distribution de toutes les espèces en fonction du pc_H.

Mots clés : bromazépam, hydrolyse acide, constantes d'équilibre.

[Traduit par la Rédaction]

Introduction

Bromazepam (7-bromo-1,3-dihydro-5-(2′-pyridyl)-2*H*-1,4-benzodiazepin-2-one) belongs to the group of 1,4-benzodiazepines, drugs that are widely used in everyday medical practice to treat insomnia, anxiety, panic attacks, muscule spasms, and seizure disorders.

In aqueous solution, 1,4-benzodiazepines undergo acid–base reactions and hydrolytic degradation that cause changes in molecular structure (1–10). Study of these reactions, especially within the physiological pH range, is of great interest, particularly with respect to the study of the metabolism of these drugs, the analysis of the corresponding pharmaceutical preparations, and the pharmaceutical technology in connection with the choice of optimum conditions for the preparation of various dosage forms. The huge number of benzodiazepine analogues provide an excellent opportunity to study the relationship between the structure and chemical reactivity.

As with most of the 1,4-benzodiazepines, bromazepam has two sites potentially susceptible for nucleophilic hydration in acidic solution: the 1,2-amide and the 4,5-azomethine bond. According to newer NMR analysis (11), the 4,5-azomethine bond is the only site of the diazepine ring-opening reaction in the molecule of bromazepam.

The presence of the pyridine moiety in the molecule of bromazepam and the simultaneous occurrence of two processes, simple acid–base and hydrolytic reactions, make the system present in an acidic solution rather complicated. As the complex equilibria present in acidic solution of

Received 5 January 2004. Published on the NRC Research Press Web site at http://canjchem.nrc.ca on 23 October 2004.

T. Damjanović and L. Pfendt. Faculty of Chemistry, University of Belgrade, Studentski trg 16, P.O. Box 158, 11000 Belgrade, Serbia and Montenegro.
G. Popović.[1] Faculty of Pharmacy, University of Belgrade, Vojvode Stepe 450, P.O. Box 146, 11000 Belgrade, Serbia and Montenegro.
S. Verbić. Petnica Science Center, P.O. Box 6, 14104 Valjevo, Serbia and Montenegro.

[1]Corresponding author (e-mail: gpopovic@pharmacy.bg.ac.yu).

 doi: 10.1139/V04-091 © 2004 NRC Canada

bromazepam was not studied yet, the aim of this work was to quantitatively define the multiple equilibria between all the species actually present in the system.

Experimental

Apparatus and reagents

A GBC 911A Spectrophotometer (GBC Scientific Equipment Pty Ltd.) with 1 cm silica cells was used for spectrophotometric measurements. A PHM240 pH meter (Radiometer) with a combined GK2401B electrode (Radiometer) served for pH value measurements. Titrations were performed with a TTT-60 titrator with an ABU-12 auto burette (Radiometer). Measured pH values (pH > 2) were converted into pc_H according to relation (12): $pc_H = -\log[H_3O^+] = pH - A$. For $I = 0.1$ mol L^{-1} (NaCl) and $t = 25$ °C, the correction factor value was $A = 0.12$. For pH < 2, pc_H values were calculated according to HCl solution concentrations.

Bromazepam (Hoffmann La Roche) was of pharmaceutical purity grade, and other reagents, hydrochloric acid, sodium hydroxide, sodium chloride, sodium acetate, potassium dihydrogenphosphate, sodium hydrogenphosphate dihydrate, and ethanol were of analytical reagent grade (Merck). All solutions were prepared with double distilled water.

HCl and NaOH solutions were potentiometrically standardized. NaOH solution was standardized with potassium hydrogen phthalate. HCl solution was standardized in relation to the standard NaOH solution.

Estimation of the ring-opening reaction reversibility

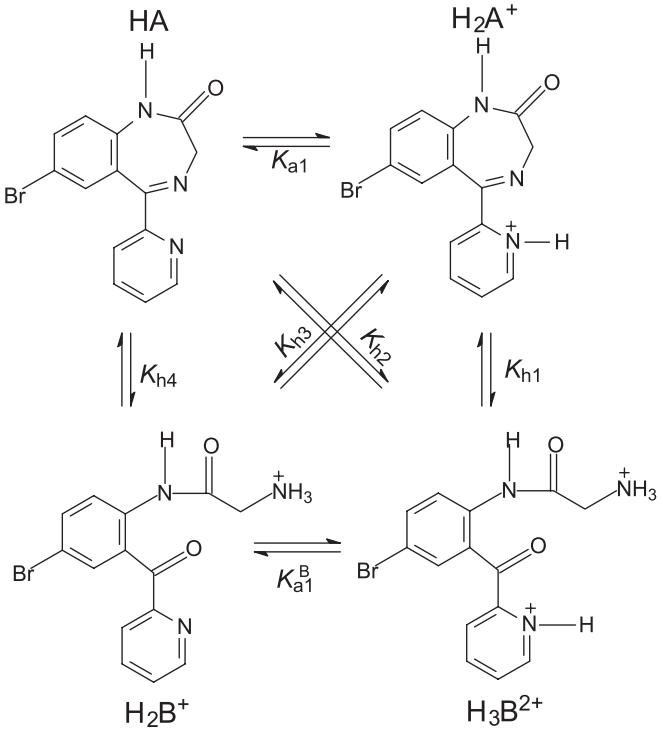
A stock solution of bromazepam (Bz) was prepared in ethanol ($c_{Bz} = 1.50 \times 10^{-2}$ mol L^{-1}). One mL aliquots of stock solution were transferred into 25 mL volumetric flasks and diluted to volume with HCl solutions of different concentrations (10^{-3}, 10^{-2}, 0.1, and 1 mol L^{-1}). Solutions were thermostated (light protected) for 4 h (until the equilibrium was established) at $t = 25.0 \pm 0.1$ °C (to determine the time needed for equilibrium to establish, time-dependent spectral changes in the absorption spectra of bromazepam were monitored; depending on solution acidity, equilibrium is established in 2–4 h). One mL aliquots of these solutions were rapidly transferred into 25 mL of phosphate buffer ($c = 0.5$ mol L^{-1}, pH 6.8, $c_{Bz} = 2.40 \times 10^{-5}$ mol L^{-1}). The time-dependent ring-closing reaction was spectrophotometrically monitored in the 200–400 nm wavelength range, with the appropriate blanks and the scan speed of 500 nm min^{-1}. For the comparison, a spectrum of bromazepam ($c_{Bz} = 2.40 \times 10^{-5}$ mol L^{-1}) in phosphate buffer (pH 6.8) was also recorded.

Equilibrium constants determination

Equilibrium constants K_{a1}^B, K_{h1}, and K_{h3} (Scheme 1) were determined spectrophotometrically at $t = 25.0 \pm 0.1$ °C.

K_{a1}^B was determined according to the following procedure: bromazepam was dissolved in 1.0 mol L^{-1} HCl ($c_{Bz} = 2.64 \times 10^{-3}$ mol L^{-1}) and hydrolyzed at 25 °C. After equilibration was completed (2 h), this solution served for the preparation of the following solutions (for all of them $c = 5.28 \times 10^{-5}$ mol L^{-1}): (*i*) solution of the H_3B^{2+} form prepared in 1.0 mol L^{-1} HCl, (*ii*) mixture of the H_3B^{2+} and H_2B^+ forms

Scheme 1.



prepared in pc_H range 1.2–2.0, (*iii*) and H_2B^+ solution in acetate buffer (pH 4.5). Solutions in the pc_H interval 1.2–2.0 and the solution of the H_2B^+ form were prepared with the fast working procedure to avoid a diazepine ring-closing reaction. The absorption spectra of all solutions were recorded immediately after preparation in the 200–400 nm wavelength range with the scanning speed of 1000 nm/min. For the K_{a1}^B determination measurements were done at 237 nm.

For the K_{h1} and K_{h3} determination, a stock solution of bromazepam was prepared in ethanol ($c_{Bz} = 2.64 \times 10^{-3}$ mol L^{-1}). Aliquots of 1 mL were transferred into 50 mL volumetric flasks and diluted to volume with HCl and NaCl solutions to reach pH in the 1.3–3.8 range and ionic strength $I = 0.1$ mol L^{-1}. These solutions ($c_{Bz} = 5.28 \times 10^{-5}$ mol L^{-1}) were hydrolyzed at 25 °C until complete equilibration was achieved (4 h). UV spectra were recorded in the 200–400 nm wavelength range. Spectra of "pure" bromazepam forms, protonated (H_2A^+) and molecular (HA), were recorded in 1 mol L^{-1} HCl and 0.1 mol L^{-1} NaCl (pH 6.8), respectively. The spectrum of the H_2A^+ form was recorded with a fast working procedure to minimize errors due to the hydrolytic changes in molecular structure. The preparation of the H_3B^{2+} form solution and recording of its spectrum obtaining are described within the K_{a1}^B determination procedure. All spectra were recorded against the corresponding blanks.

The acidity constant of the $-NH_3^+$ in the opened-ring form (K_{a2}^B) was estimated potentiometrically with a fast working procedure. Bromazepam was dissolved in 0.1 mol L^{-1} HCl ($c_{Bz} = 2.00 \times 10^{-3}$ mol L^{-1}) and hydrolyzed for 4 h at 25 °C. To 20 mL aliquots of this solution, a standard solution of NaOH ($c = 1.15$ mol L^{-1}) was rapidly added until pH 8.5–9.5 was reached and solutions were rapidly titrated with 0.02 mL increments of standard HCl solution ($c =$

© 2004 NRC Canada

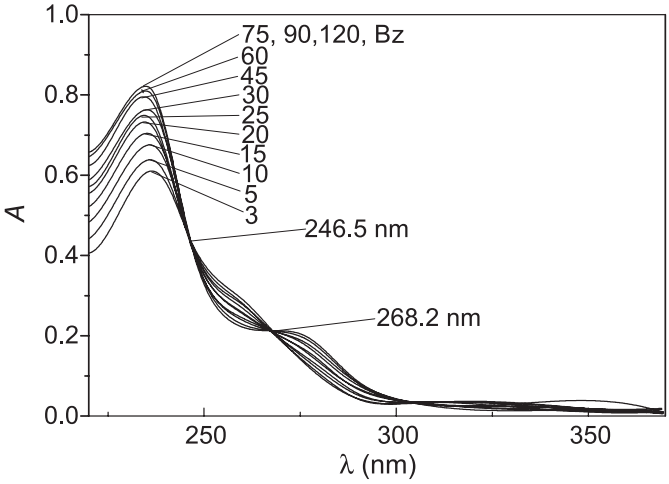
0.11 mol L^{-1}). Total titration times were 5–7 min. The equilibrium constant K_{a2}^{B} was calculated from the titration curve inflexion point (second derivative equals zero).

Results and discussion

Estimation of the ring-opening reaction reversibility

Bromazepam was hydrolyzed in HCl solutions of different concentrations (10^{-3}, 10^{-2}, 0.1, and 1 mol L^{-1}). When equilibrium was established, the solution pH values were adjusted to 6.8 (phosphate buffer) and the ring-closing reaction spectrophotometrically monitored. As for the comparison, the spectrum of bromazepam kept in phosphate buffer (pH 6.8) was also recorded. In all examined solutions, the final spectrum (after the ring-closing reaction was completed) overlapped with the spectrum of the intact bromazepam form. This draws the conclusion that in neutral solution the diazepine ring was completely restored (i.e., that bromazepam was not degraded with the glycine release). Furthermore, ring-closing time increases (within the time interval of 45–75 min) with the concentration of the HCl solution used for hydrolysis. For example, the ring-closing reaction of the bromazepam hydrolyzed in 1 mol L^{-1} HCl is shown in Fig. 1.

Fig. 1. Time-dependent changes of the absorption spectra of bromazepam during the ring-closing reaction in the phosphate buffer solution (pH 6.8). Previously, bromazepam was hydrolyzed in 1.0 mol L^{-1} HCl solution until equilibrium was established (4 h, $c_{Bz} = 2.40 \times 10^{-5}$ mol L^{-1}). Numbers on the spectra show the time (in min) after the reaction was initiated; Bz–bromazepam solution kept in a phosphate buffer solution.



Equilibrium constants determination

In acidic solution (pH < 6), two processes occur simultaneously, a simple acid–base reaction (fast process) and hydrolysis of the 4,5-azomethine bond (relatively slow process) (11). The simple acid–base reaction was previously studied (13), and it was found that the pyridine nitrogen is protonated in an acidic solution (pK_{a1} 2.83). As the acid–base reactions are much faster processes than the hydrolysis reactions are, with a fast working procedure, K_{a1} was determined independent on hydrolysis. In the alkaline solution, the amide group is deprotonated (pK_{a2} 11.60). If we summarize all the reactions that are occurring in an acidic solution of bromazepam, established equilibrium may be depicted as it is shown in Scheme 1.

In general, equilibrium constants of the processes shown in Scheme 1 are defined as follows:

$$[1] \qquad K_{al} = \frac{[HA][H_3O^+]}{[H_2A^+]}$$

$$[2] \qquad K_{al}^{B} = \frac{[H_2B^+][H_3O^+]}{[H_3B^{2+}]}$$

$$[3] \qquad K_{hl} = \frac{[H_3B^{2+}]}{[H_2A^+][H_3O^+]}$$

$$[4] \qquad K_{h2} = \frac{[H_3B^{2+}]}{[HA][H_3O^+]^2}$$

$$[5] \qquad K_{h3} = \frac{[H_2B^+]}{[H_2A^+]}$$

$$[6] \qquad K_{a4} = \frac{[H_2B^+]}{[HA][H_3O^+]}$$

In solutions with pH < 6, the amino group of the opened-ring form is mostly in its protonated form (its acidity constant (pK_{a2}^{B} 7.6) was determined with fast potentiometric titration as described in the Experimental).

After the equilibrium was established within the solutions of bromazepam in the pH range 0–7, absorption spectra were recorded and analyzed. Determination of the equilibrium constants is based on the fact that the absorbance is an additive value. In acidic solution, the total concentration of bromazepam is given through the mass balance equation:

$$[7] \qquad C = [H_2A^+] + [HA] + [H_3B^{2+}] + [H_2B^+]$$

and the absorbance, for the 1.0 cm cell length, is given by the following equation:

$$[8] \qquad A = \varepsilon_{H_2A^+}[H_2A^+] + \varepsilon_{HA}[HA] + \varepsilon_{H_3B^{2+}}[H_3B^{2+}] + \varepsilon_{H_2B^+}[H_2B^+]$$

where $\varepsilon_{H_2A^+}$, ε_{HA}, $\varepsilon_{H_3B^{2+}}$, and $\varepsilon_{H_2B^+}$ stand for molar absorptivities of the appropriate species. If the total concentration of bromazepam remains constant during all the measurements, combination of the eqs. [1]–[8] gives the following dependence:

$$[9] \qquad A = \frac{A_{H_2A^+}[H_3O^+] + A_{HA}K_{al} + A_{H_3B^{2+}}K_{hl}[H_3O^+]^2 + A_{H_2B^+}K_{h3}[H_3O^+]}{[H_3O^+] + K_{al} + K_{hl}[H_3O^+]^2 + K_{h3}[H_3O^+]}$$

which shows that the absorbance at the chosen wavelength is a nonlinear function of the solution acidity ($[H_3O^+]$) in the pH region in which the hydrolysis occurs (0–6). A_{HA}, $A_{H_2A^+}$, $A_{H_2B^+}$, and $A_{H_3B^{2+}}$ are the absorbances of the appropriate pure forms at the chosen wavelength.

Preliminary values of the equilibrium constants given in eq. [9] were determined by a nonlinear curve-fitting analysis. Two parameters (K_{a1} and A_{HA}) were experimentally obtained and their values introduced into eq. [9] as starting parameters (with no starting parameters nonlinear curve-

© 2004 NRC Canada

Table 1. Equilibrium constants calculated using Monte Carlo simulations (90% confidence level, I = 0.1 mol L^{-1} (NaCl), t = 25 °C).

Constant	Value ± σ	pK ± σ	Equation applied
K_{h1}	180^{+300}_{-70} [a]	$-2.26^{+0.22}_{-0.41}$ [a]	[9]
K_{h2}	$120^{+200}_{-50} \times 10^3$	$-5.09^{+0.22}_{-0.41}$	[10]
K_{h3}	3.2±0.7	–0.5±0.1	[9]
K_{h4}	(2.0±0.5) × 10^3	–3.3±0.1	[10]
K^B_{a1}	$1.6^{+2.4}_{-1.0} \times 10^{-2}$	1.8±0.4	[11]

[a]Distribution is considerably asymmetrical, thus the upper and lower interval limits are not equal.

fitting analysis would more likely give a mathematically correct, but for this case meaningless solution). The pK_{a1} value of 2.83 was previously (13) spectrophotometrically determined in the same experimental conditions (I = 0.1 mol L^{-1} (NaCl), t = 25 °C). Absorbance of the molecular form (HA) was relatively easily obtained, because the HA form is actually the only species present in the pH range 6–8, where bromazepam is quite stable. The least-squares method was used to fit the experimentally obtained (A, $[H_3O^+]$) value pairs (λ = 237 nm) to the dependence [9]. For the obtained function [9] parameter values, probability distributions were calculated with the virtual experiments performed using Monte Carlo simulations. Results are shown in Table 1. Equilibrium constants K^B_{a1}, K_{h2}, and K_{h4} were calculated with the K_{a1}, K_{h1}, and K_{h3} values according to relations derived from eqs. [1]–[6]:

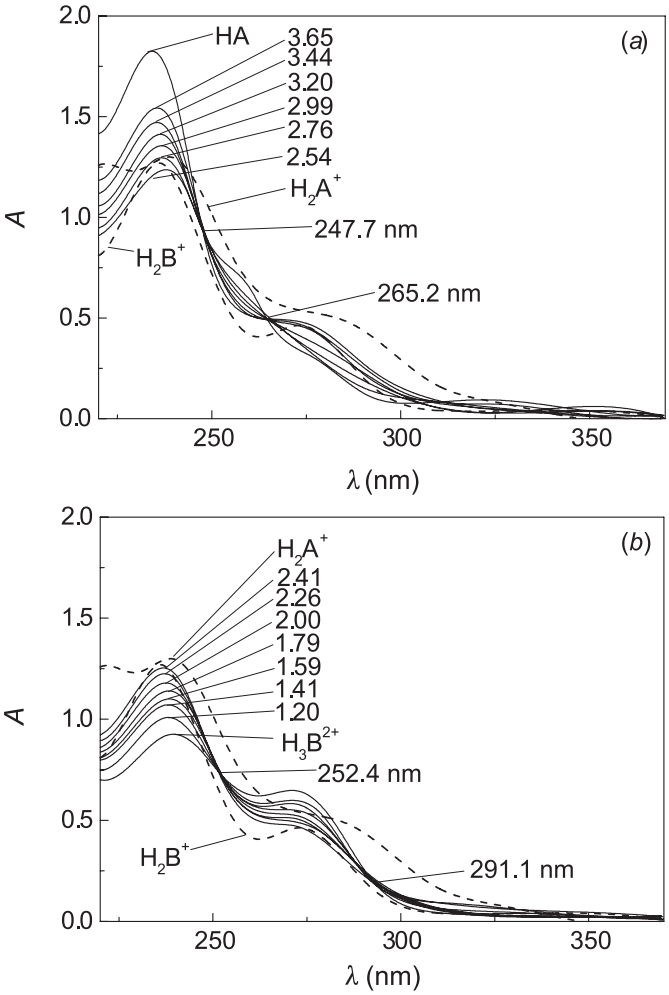
$$[10] \quad K_{al} = \frac{K_{h3}}{K_{h4}} = \frac{K_{h1}}{K_{h2}}$$

$$[11] \quad K^B_{al} = \frac{K_{h3}}{K_{h1}}$$

Distribution of the species present in the system, obtained according to calculated equilibrium constants, showed that at pH 0 the diazepine ring is practically completely opened and that H_3B^{2+} form is the dominant species present. Detailed analysis of the spectra obtained after the equilibrium was established in acidic solutions of bromazepam (Fig. 2) showed that two pH regions can be separated. These regions have clearly defined isosbestic points. Spectra of the solutions equilibrated within the pc_H > 2.4 region accompanied with the spectrum of the HA form have isosbestic points at 247.7 and 265.2 nm (Fig. 2*a*), and the spectra of the solutions equilibrated in the pc_H ≤ 2.4 region together with the H_3B^{2+} form have isosbestic points at 252.4 and 291.1 nm (Fig. 2*b*). Absorption spectra of the H_2A^+ and H_2B^+ forms do not pass through any of these isosbestic points. When all these facts are considered, existence of the less complicated systems (Scheme 2) with three species simultaneously present in an equilibrium, can be assumed.

The existence of the isosbestic points in these solutions where three species are present can be explained with the fact that an equilibrium between H_2A^+ and H_2B^+ forms is pH independent (eq. [5]). Their concentrations are pH dependent, but the molar ratio between H_2A^+ and H_2B^+ forms is constant and given through the K_{h3} value. Thus, it can be

Fig. 2. Absorption spectra of bromazepam in solutions of different acidity: (*a*) pc_H > 2.4; (*b*) pc_H ≤ 2.4 after the equilibrium was established. Numbers on the spectra show pc_H values; spectra of the pure forms are marked (c_{Bz} = 5.28 × 10^{-5} mol L^{-1}, pc_H = pH – 0.12).



assumed that when present in the solution, they formally act as one species.

When two separated pH regions are considered, from the following absorbances:

$$[12a] \quad A = \varepsilon_{H_2A^+}[H_2A^+] + \varepsilon_{HA}[HA] + \varepsilon_{H_2B^+}[H_2B^+] \qquad (pc_H > 2.4)$$

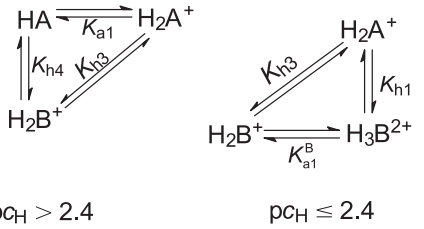
$$[12b] \quad A = \varepsilon_{H_2A^+}[H_2A^+] + \varepsilon_{H_3B^{2+}}[H_3B^{2+}] + \varepsilon_{H_2B^+}[H_2B^+] \qquad (pc_H \le 2.4)$$

and eqs. [1]–[6], follows:

$$[13a] \quad A = \frac{A_{H_2A^+}[H_3O^+] + A_{HA}K_{al} + A_{H_2B^+}K_{h3}[H_3O^+]}{[H_3O^+] + K_{al} + K_{h3}[H_3O^+]} \qquad (pc_H > 2.4)$$

© 2004 NRC Canada

Scheme 2.



$$[13b] \quad A = \frac{A_{H_2A^+} + A_{H_3B^{2+}} K_{h1}[H_3O^+] + A_{H_2B^+} K_{h3}}{1 + K_{h3} + K_{h1}[H_3O^+]} \qquad (pc_H \leq 2.4)$$

With the transformation of the eqs. [13*a*] and [13*b*], the following linear dependences are derived:

$$[14a] \quad \underbrace{A}_{Y} = \frac{A_{H_2A^+} + A_{H_2B^+} K_{h3}}{1 + K_{h3}} + \frac{K_{a1}}{1 + K_{h3}} \underbrace{\frac{1}{[H_3O^+]}(A_{HA} - A)}_{x} \qquad (pc_H > 2.4)$$

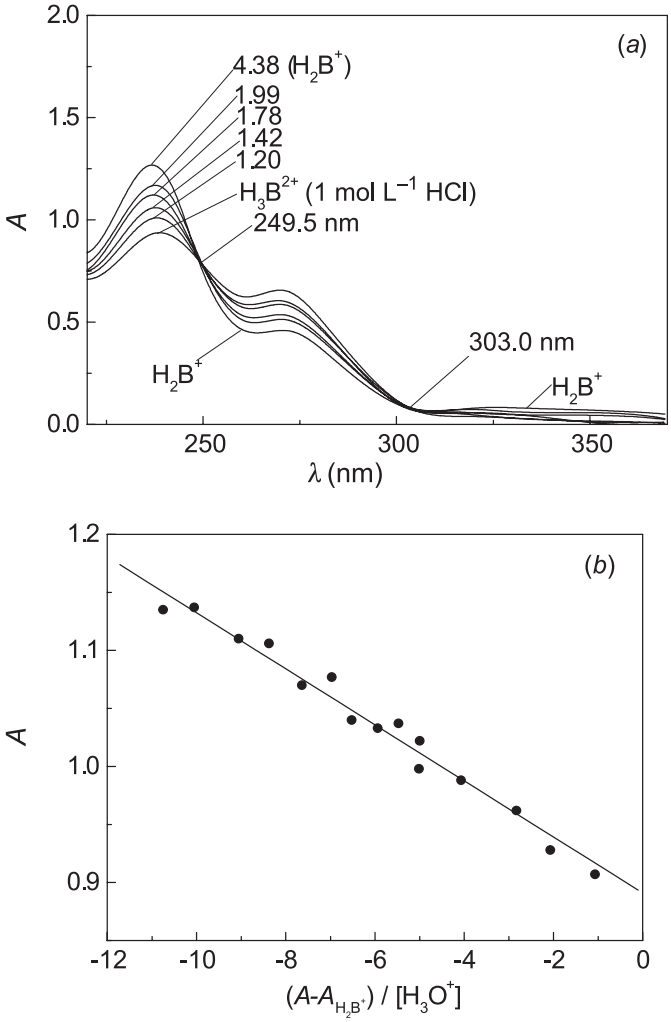
$$[14b] \quad \underbrace{A}_{Y} = \frac{A_{H_2A^+} + A_{H_2B^+} K_{h3}}{1 + K_{h3}} + \frac{K_{h1}}{1 + K_{h1} K^B_{a1}} \underbrace{[H_3O^+](A_{H_3B^{2+}} - A)}_{x} \qquad (pc_H \leq 2.4)$$

The set of (A, $[H_3O^+]$) data was used to determine K_{h3} and K_{h1} values according to these linear functions. It can be seen that acidity constants K_{a1} and K^B_{a1} and the spectra of HA and H_3B^{2+} forms are needed for this determination. To determine the value of K^B_{a1}, bromazepam dissolved and equilibrated in 1 mol L^{-1} HCl was used as a stock solution. The K^B_{a1} was spectrophotometrically determined according to the transformation of the classical spectrophotometric equation (14), which gives a linear dependence:

$$[15] \quad A = A_{H_3B^{2+}} - K^B_{a1} \frac{A - A_{H_2B^+}}{[H_3O^+]}$$

where $A_{H_3B^{2+}}$ and $A_{H_2B^+}$ represent absorbances of the appropriate pure opened-ring forms (Scheme 2) and A represents absorbance of their mixture at the specified wavelength (237 nm). The exact procedure is described in the Experimental partsection. Absorption spectra that served for the K^B_{a1} determination are shown in Fig. 3*a*. The K^B_{a1} was calculated by linear regression analysis from the slope of the corresponding line (pK^B_{a1} 1.62) (Fig. 3*b*). Values for $A_{H_3B^{2+}}$ found by linear regression analysis (as the interception with the ordinate, $A_{H_3B^{2+}} = 0.89$) and as the measured value (obtained in 1 mol L^{-1} HCl, $A_{H_3B^{2+}} = 0.91$) are in good accordance. When the K_{a1} and K^B_{a1} values are known, with the set of (A, pc_H) data, A_{HA} and $A_{H_3B^{2+}}$ values measured at 237 nm, and according to eqs. [14*a*] and [14*b*], constants K_{h3} and K_{h1} were calculated by linear regression analysis from the slope of the corresponding lines (Fig. 4). Constants K_{h2} and K_{h4} were calculated according to eq. [10].

Fig. 3. Spectrophotometric determination of K^B_{a1}: (*a*) absorption spectra of bromazepam used for K^B_{a1} determination. Numbers on the spectra show pc_H values; spectra of the pure forms are marked; (*b*) linear dependence given in eq. [15], λ = 237 nm (c = 5.28 × 10^{-5} mol L^{-1}, pc_H = pH – 0.12).



A compendium of all determined equilibrium constants is shown in Table 2. Values of equilibrium constants calculated by Monte Carlo computer simulations and those determined according to linear dependences are in quite good accordance. Thus, it can be concluded that the assumptions made to make the system less complicated and possible for experimental determinations, are correct.

Based on determined equilibrium constants, the distribution of all the species as a function of pc_H is calculated according to equations:

$$[16] \quad X_{H_2A^+} = \frac{1}{10^{pc_H - pK_{a1}} + 1 + 10^{-pK_{h3}} + 10^{-pc_H - pK_{h1}}}$$

$$[17] \quad X_{HA} = \frac{10^{pc_H - pK_{a1}}}{10^{pc_H - pK_{a1}} + 1 + 10^{-pK_{h3}} + 10^{-pc_H - pK_{h1}}}$$

$$[18] \quad X_{H_3B^{2+}} = \frac{10^{pc_H - pK_{h1}}}{10^{pc_H - pK_{a1}} + 1 + 10^{-pK_{h3}} + 10^{-pc_H - pK_{h1}}}$$

© 2004 NRC Canada

Fig. 4. Spectrophotometric determination of equilibrium constants: (*a*) K_{h1} according to eq. [14*b*]; (*b*) K_{h3} according to eq. [14*a*] (c_{Bz} = 5.28 × 10^{-5} mol L^{-1}, λ = 237 nm).

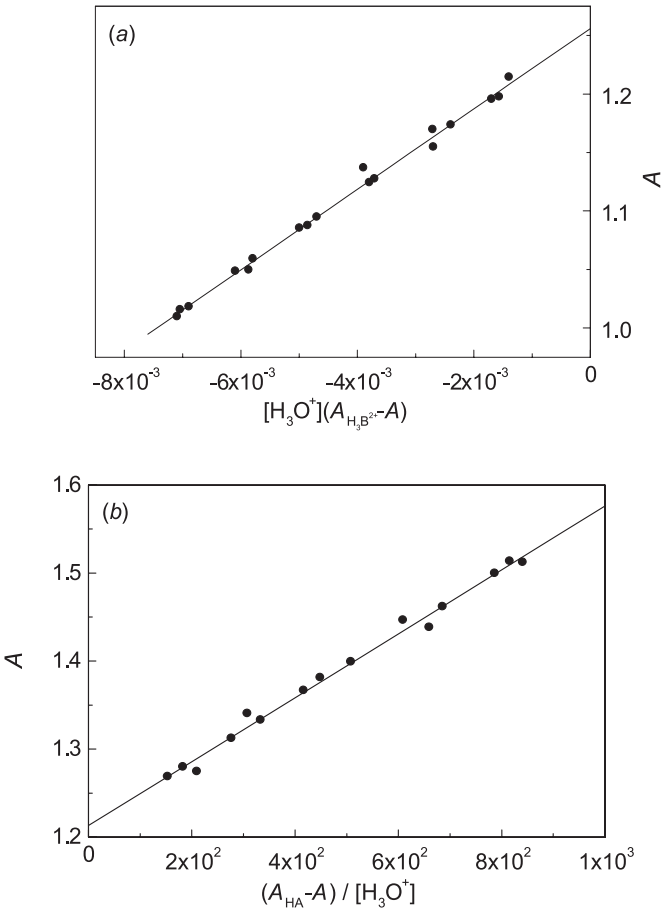


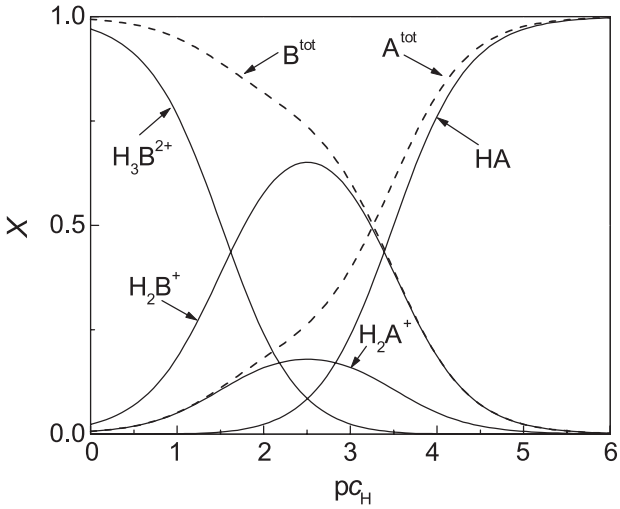
Table 2. Equilibrium constants determined in an acidic solution of bromazepam (I = 0.1 mol L^{-1} (NaCl), t = 25 °C).

Constant	Value ± s	pK ± s	Equation applied
K_{h1}	200^{+140}_{-60}	–2.3±0.2	[14*b*]
K_{h2}	130^{+90}_{-40} × 10^3	–5.1±0.2	[14*b*]
K_{h3}	3.05±0.40	–0.48±0.06	[14a]
K_{h4}	(2.1±0.8) × 10^3	–3.3±0.2	[14*a*]
K^{B}_{a1}	(2.4±0.2) × 10^{-2}	1.62±0.04	[15]
K_{a1}	(1.48±0.04) × 10^{-3}	2.83±0.01	Reference 13

$$[19] \quad X_{H_2B^+} = \frac{10^{-pK_{h3}}}{10^{pc_H - pK_{a1}} + 1 + 10^{-pK_{h3}} + 10^{-pc_H - pK_{h1}}}$$

A distribution diagram of the species present in the acidic solution of bromazepam after the equilibrium is established is shown in Fig. 5. It can be seen that the HA form of bromazepam is the dominant one in the 5 to 6 pH region. At pH 3.3, the concentrations of the intact form of bromazepam

Fig. 5. Distribution diagram of bromazepam as a function of pc_H (pc_H = pH – 0.12).



(C^{tot}_A = [HA] + [H_2A^+]) and the opened-ring form (C^{tot}_B = [H_2B^+] + [H_3B^{2+}]) are equal, and at pH < 1.0 opened-ring forms are dominant.

Acknowledgement

This work was performed within the framework of the research project supported by the Ministry for Science, Technology and Development of Serbia, contract No. 1713.

References

1. W.W. Han, G.J. Yakatan, and D.D. Maness. J. Pharm. Sci. **65**, 1198 (1976).
2. W.W. Han, G.J. Yakatan, and D.D. Maness. J. Pharm. Sci. **66**, 573 (1977).
3. W.W. Han, G.J. Yakatan, and D.D. Maness. J. Pharm. Sci. **66**, 795 (1977).
4. H.V. Maulding, J.P. Nazareno, J.E. Pearson, and A.F. Michaelis. J. Pharm. Sci. **64**, 278 (1975).
5. W.F. Smyth, M.R. Smyth, J.A. Groves, and S.B. Tan. Analyst (Cambridge, U.K.), **103**, 497 (1978).
6. W.F. Smyth and J.A. Groves. Anal. Chim. Acta, **139**, 227 (1982).
7. N. Inotsume and M. Nakano. J. Pharm. Sci. **69**, 1331 (1980).
8. J.C. Vire, G.J. Patriarche, and B.G. Hermosa. Anal. Chim. Acta, **196**, 205 (1987).
9. L.B. Pfendt and G.V. Popović. J. Chem. Soc. Perkin Trans. **2**, 1845 (1994).
10. M.J. Cho, T.A. Scahill, and J.B. Hester. J. Pharm. Sci. **72**: 356 (1983).
11. I. Panderi, H. Archontaki, E. Gikas, and M. Parissi-Poulou. J. Pharm. Biomed. Anal. **17**, 327 (1998).
12. L.B. Pfendt, D.M. Sladić, T.J. Janjić, and G.V. Popović. Analyst (Cambridge, U.K.), **115**, 383 (1990).
13. L.B. Pfendt, G.V. Popović, T.Ž. Damjanović, and D.M. Sladić, J. Serb. Chem. Soc. **67**, 187 (2002).
14. A. Albert, and E.P. Serjeant. *In* The determination of ionization constants. 2nd ed. Chapman and Hall, London. 1971. p. 44.

© 2004 NRC Canada

Synthesis of the tetranitro derivative of thiacalix[4]arene and its acid–base properties

Xiaojun Hu, Zhongliang Zhu, Tianxiang Shen, Xianfa Shi, Jie Ren, and Qiuhong Sun

Abstract: The tetranitro derivative **3** of thiacalix[4]arene was synthesized and characterized. Its acid–base properties in water solution were studied by UV spectroscopy. The four pK_a values of **3** were determined by target testing factor analysis (TTFA). The pure UV absorption curves and pH distribution curves of five forms of **3** presented in aqueous solution were also calculated by TTFA.

Key words: thiacalixarene, nitro derivative, acid–base properties.

Résumé : On a réalisé la synthèse et caractérisé le dérivé tétranitré **3** du thiacalix[4]arène. On a étudié ses propriétés acide–base, en solution aqueuse, à l'aide de la spectroscopie UV. Les quatre valeurs de pK_a du produit **3** ont été déterminées par « TTFA ». Les courbes d'absorption UV pures et les courbes de distribution de pH des cinq formes du produit **3** présentes en solution aqueuse ont aussi été calculées par TTFA.

Mots clés : thiacalixarène, dérivé nitré, propriétés acide–base.

[Traduit par la Rédaction]

Introduction

The calixarenes, which are typical excellent molecular receptors made up of phenol units linked via methylene bridges, have attracted much attention from chemists all over the world (1). By modification of the upper and lower rims of calixarenes, a variety of derivatives have been synthesized. Recently, thiacalixarenes, a class of new molecular receptors have caught the eyes of chemists. The properties of thiacalixarenes are different from calixarenes due to the substitution of the methylene bridge groups with sulfur atoms. Thiacalixarenes are therefore new types of building blocks and molecular scaffolds for molecular assembly.

A variety of thiacalixarene derivatives have been synthesized after Kumagai et al. (2) reported the facile synthesis of tetra(*p-tert*-butyl)tetrathiacalix[4]arene **1** (Fig. 1). For instance, the derivatives of thiacalix[4]arene with alkyl (3), ether (4), ester (4, 5), carboxylic acid (6), alcohol, and ketone (7) substituents, respectively, on the lower rims have been synthesized. Katagiri et al. (8) used several reaction steps to get a novel derivative in which the phenolic hydroxyls were replaced by amino groups. However, all of these modifications were on the lower rims of thiacalixarenes, with none having been reported on the upper rims to date.

Received 20 October 2003. Published on the NRC Research Press Web site at http://canjchem.nrc.ca on 23 October 2004.

X. Hu, Z. Zhu, T. Shen, and X. Shi.[1] Department of Chemistry, Tongji University, Shanghai 200092, P.R. China.
J. Ren. School of Material Science, Tongji University, Shanghai 200092, P.R. China.
Q. Sun. College of Information, Hebei University of Science & Technology, Shijiazhuang 050054, P.R. China.

[1]Corresponding author (e-mail: xfshi@mail.tongji.edu.cn).

The nitro-substituted derivative **3** of thiacalix[4]arene **2** is a desirable intermediate compound leading to the amino-substituted derivative of thiacalix[4]arene **4**, which in turn is an excellent platform for synthesizing larger molecular building blocks. The nitration of thiacalix[4]arene, however, easily leads to the corresponding sulphoxide or sulphone derivatives of thiacalix[4]arene other than the nitro derivative of thiacalix[4]arene, because the epithio atoms of thiacalix[4]arene would be oxidized during the nitration. Lhoták et al. (9) had tried to prepare the tetranitro derivative of thiacalix[4]arene **3** under various conditions (conc. HNO_3 or 100% HNO_3 – CH_2Cl_2 or acetic acid, 100% HNO_3 – CF_3COOH, $NaNO_3$–CF_3COOH), but all these attempts "lead only to the oxidation of the bridging sulphur atoms".

In this work, the tetranitro derivative of thiacalix[4]arene **3** was successfully synthesized without oxidation of the bridging sulfur, using nitric acid as the nitrating agent in glacial acetic acid as the regulating agent for the acidity. The acid–base properties of **3** were studied by UV spectroscopy and the four pK_a values of **3** as determined by target testing factor analysis (TTFA) (10) are also reported.

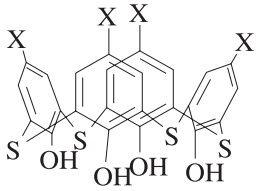
Experimental

Materials and methods

All reagents were obtained from commercial sources and were used without further purification. ^{1}H NMR spectra were measured using a Bruker NMR spectrometer (Avance 500 MHz model). Infrared spectra were obtained using a Nicolet FT-IR spectrometer (Nexus 912A0446 model). ESI-MS were measured using an Agilent spectrometer (1100/LC–MSD model). UV–vis were measured using an Agilent spectrometer (8453 model).

 doi: 10.1139/V04-090 © 2004 NRC Canada

Fig. 1. The structural formulas of **1–4**.



Synthesis and characterization of 3

Thiacalix[4]arene **2** (1.25 g, 0.0025 mol) was dissolved in $CHCl_3$ (200mL). Glacial acetic acid (7 mL) and aq.65%~68% HNO_3 (5 mL) were added with stirring, at room temperature. After 30 h, the precipitate was filtered from the reaction mixture and washed with water several times to afford **3** (1.31 g, 76%) as an orange solid.

Characterization: mp > 350 (dec.). IR (KBr) υ (cm^{-1}): 1521 and 1340 (Ar-NO_2), 3313 (Ar-OH), 1240 (C-N). ^1H NMR (DMSO-d_6, 500 Hz) δ: 8.42 ppm (s, Ar-H_β). ESI-MS *m/z* (rel. int.): –674.9 $[M - H]^-$ (100%). EA calcd for $C_{24}H_{12}N_4O_{12}S_4$: C 42.6, H 1.78, N 8.28, S 18.93; found: C 41.6, H 2.06, N 7.79, S 18.59.

The acid–base properties of 3 as determined by UV spectroscopy

The UV absorption spectra were recorded for aqueous solutions containing the tetranitro derivative of thiacalix[4]arene **3** (5×10^{-5}mol L^{-1}) at appropriate pH intervals and I = 0.2 mol L^{-1}.

The determination of four pK_{an} (n = 1–4) values of 3 by TTFA

Assume that spectra collected during a distribution profile can be arranged against measurement time and form a data matrix (**Y**). The size of the matrix is $nt \times w$, where nt denotes the number of measurement times and nw the number of the corresponding wavelengths. The data matrix **Y** is allowed to be decomposed to the pure absorption spectral matrix **S** and the distribution profiles matrix $\mathbf{D}^T$. The relationship can be described by:

$$[1] \qquad \mathbf{Y} = \sum_{i=1}^{nc} s_i \boldsymbol{d}_i^T + \mathbf{E}_1 = \mathbf{S}\mathbf{D}^T + \mathbf{E}_1$$

where nc is the number of the absorbing species, $\boldsymbol{d}_i^T$ (column vector) and $\boldsymbol{s}_i$ (row vector) represent the distribution profile and the absorption spectrum of the ith component, respectively. Superscript T denotes the transpose of a matrix or a vector. $\mathbf{E}_1$ is the residual matrix. Principal component analysis (PCA) is a widely used chemometric technique. By using it, the data matrix **Y** can be decomposed to two orthogonal matrices, a score matrix **T** and a loading matrix $\mathbf{P}^T$. That is,

$$[2] \qquad \mathbf{Y} = \mathbf{T}\mathbf{P}^T + \mathbf{E}_2$$

If the pure absorption spectra of components in the samples are unknown, the concentration distribution of the components can be calculated through a series of acid ionization constants according to the principle of material equilibrium. Denote the samples as H_nL, the corresponding acid ionization constants $K_1K_2...K_{n-1}$. The distribution coefficient model is as follows:

$$[3] \qquad \boldsymbol{d}_i = \frac{[H]^{n-i} \cdot K_1 \cdots K_i}{[H]^n + [H]^{n-1} \cdot K_1 + \cdots + K_1 K_2 \cdots K_{n-1}}$$

Now the question is calculating this distribution coefficient. Concerning the background conditions, we assume some experiential values to the series of K_i, and calculate the corresponding concentration distribution to get the test target $\mathbf{D}_{test}^T(nc \times ns)$. Then according to the following partial least-squares regression equation we get the target transformed matrix:

$$[4] \qquad \mathbf{R} = \mathbf{D}_{test}^T \mathbf{P}$$

Having the target transformed matrix, we get the corresponding pure absorption spectrum matrix $\mathbf{S}_{test}(nc \times ns)$ through the equation $\mathbf{S} = \mathbf{T}\mathbf{R}^{-1}$. The residual matrix $\mathbf{Y}_{res}$ of the original data is:

$$[5] \qquad \mathbf{Y}_{res} = \mathbf{Y} - \mathbf{S}_{test}\mathbf{D}_{test}^T$$

With the sum square of the matrix $\mathbf{Y}_{res}$ as the target function, denoted by SSQ, we can get the minimum value of SSQ after optimization of K_i.

When the value of SSQ is minimum, the corresponding $\mathbf{S}_{test}$ and $\mathbf{D}_{test}^T$ can be seen as the actual spectrum matrix and the concentration distribution matrix, therefore the concentration distribution model can be calculated. We used global search or the NGA algorithm (11) to optimize the parameters.

The key of this method is optimizing the test target through factor analysis, referred to as TTFA (10).

Results and discussion

Synthesis and characterization of 3

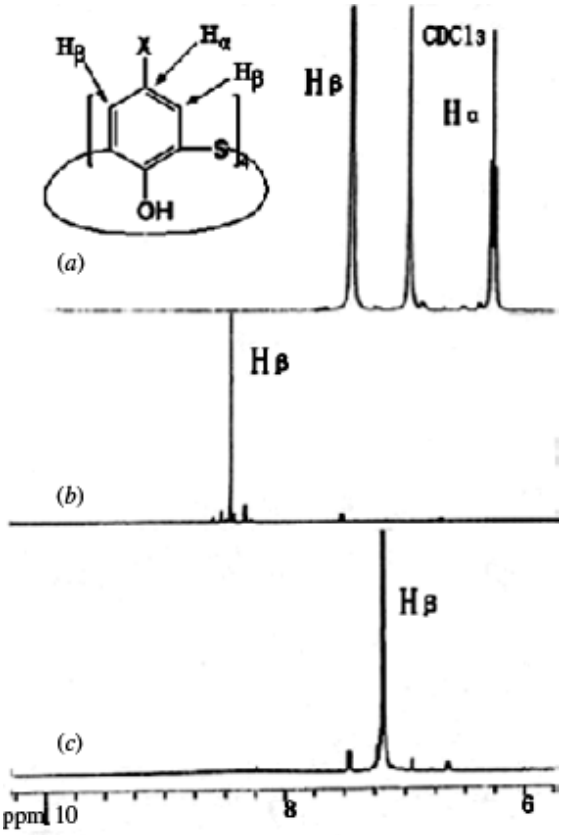
The tetranitro derivative **3** of thiacalix[4]arene **2** was synthesized under optimal conditions, which prevented the epithio atoms from being oxidized. Whether the bridging sulphur atoms are oxidized or not is partly dependent on the acidity of solution, therefore, glacial acetic acid was chosen as the regulating regent of acidity, rather than conc. H_2SO_4, which is preferred for the nitration of calixarenes. To ensure full tetranitro-substitution of the thiacalix[4]arene **2**, 65%~68% HNO_3 was used with vigorous stirring. An orange solid **3** slowly separated out after several hours, and after 30 h of reaction it was filtered from the solution. The ESI-MS spectrum of the orange product showed a peak at *m/z* = –674.9 (100%) corresponding to the $(M - 1)^-$ ion of **3**. Figure 2 shows the differences in the ^1H NMR spectra of **2** and **3**: the singlet due to H_β in **3** has been shifted to δ 8.42 ppm (see Fig. 2*b*) due to the electron-withdrawing effect of the nitro groups, while the corresponding signal in **2** shows up as a doublet at δ 7.64 and 7.62 ppm due to the spin coupling (observable in the $CDCl_3$ solvent) (see Fig. 2*a*).

The acid–base properties of 3 as studied by UV spectroscopy

Tetranitro thiacalix[4]arene **3** has strong acidic properties: in aqueous solution, the four hydrogen atoms of the phenolic

© 2004 NRC Canada

Fig. 2. (*a*) The ^{1}H NMR spectrum of **2** ($CDCl_3$, 500 Hz). (*b*) The ^{1}H NMR spectrum of **3** (DMSO-d_6, 500 Hz). (*c*) The ^{1}H NMR spectrum of **4** (DMSO-d_6, 500 Hz).



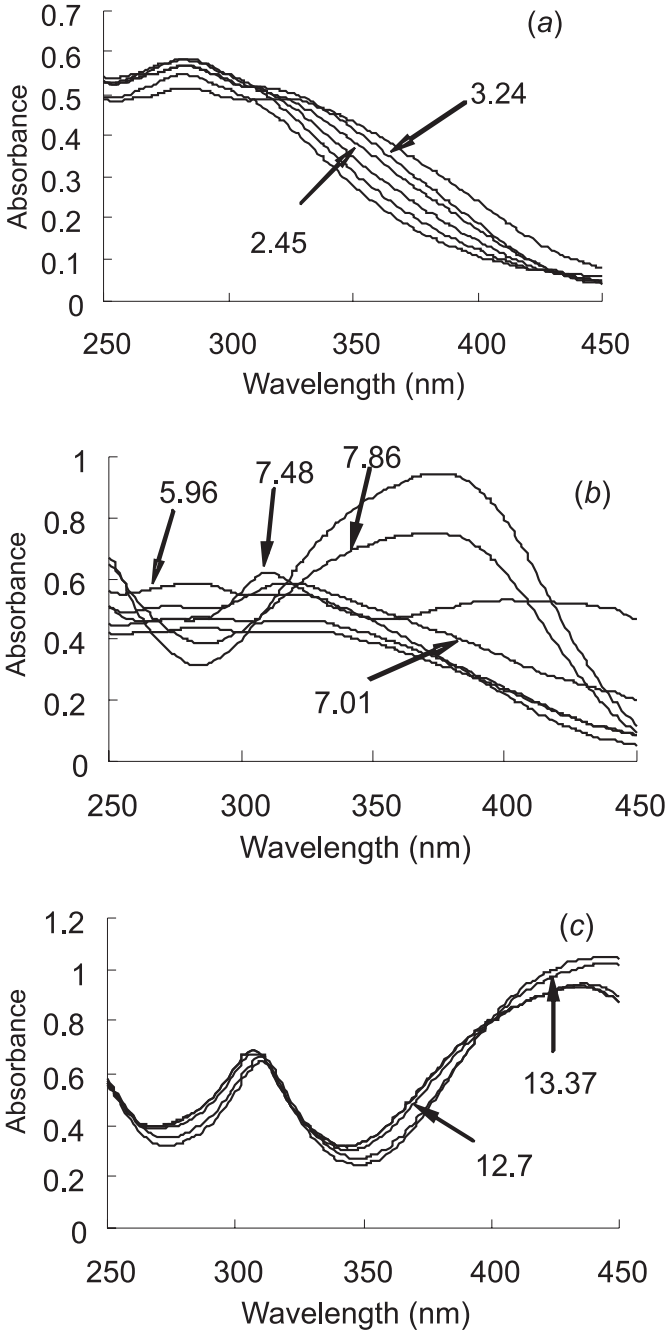
hydroxyl groups can be dissociated successively with an increase in the solution pH, and is therefore a tetraprotonic acid, and can be defined as H_4L. H_3L^-, H_2L^{2-}, HL^{3-}, and L^{4-} will correspond to the loss of one, two, three, and four H^+ ions, respectively, from **3**.

Figures 3*a*–3*c* show the UV absorption spectra of **3** in water solution at different pH conditions. As Fig. 3*a* shows, the absorption band around 285 nm increased with an increase in the solution pH from 0.43 to 2.05, and then declined with a further increase in the solution pH. There was an obvious difference in shape of the UV absorption curves, and a shift of the absorption peak observed in the solution pH > 2.45. That is to say, there is an isolated single-step acid dissociation that occurred in the pH region around 2.45. This change can be described by eq. [6]:

$$[6] \qquad H_4L \overset{K_{a1}}{\rightleftharpoons} H_3L^- + H^+$$

In Fig. 3*b*, an obvious red shift of the absorption peak from pH 5.96 to 7.01 shows that there is a second acid dissociation occurring in this pH region. When the pH value increased from 7.48 to 7.86, there was another acid dissociation of the third phenolic OH group in accordance with the apparent red shift of the absorption peak from 312 to 378 nm. These two acid dissociations can also be depicted by eqs. [7] and [8]:

Fig. 3. (*a*) UV absorbance spectra of **3** at solution pH 0.43, 1.55, 2.05, 2.45, 3.24, and 4.75. (*b*) UV absorbance spectra of **3** at solution pH 5.11, 5.41, 5.96, 7.01, 7.48, 7.86 and 8.73. (*c*) UV absorbance spectra of **3** at solution pH 11.82, 12.11, 12.7, 13.37, 8.98, and 13.62.



$$[7] \qquad H_3L^- \overset{K_{a2}}{\rightleftharpoons} H_2L^{2-} + H^+$$

$$[8] \qquad H_2L^{2-} \overset{K_{a3}}{\rightleftharpoons} HL^{3-} + H^+$$

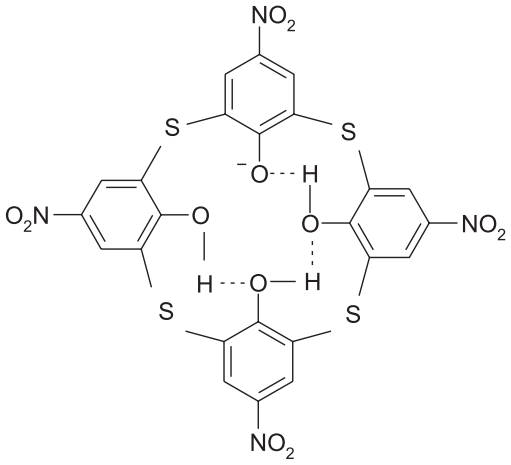
From pH 12.7 to 13.37 (Fig. 3*c*), the fourth acid dissociation of the phenolic OH group of **3** occurred corresponding to the

© 2004 NRC Canada

Table 1. The pK_a values of **3** determined by TTFA.

Compound	pK_{a1}	pK_{a2}	pK_{a3}	pK_{a4}
3	2.75	6.48	7.60	13.35
p-Nitrophenol	7.15			

Fig. 4. Schematic representation of a possible intramolecular hydrogen bonding mode.



isosbestic point at 402 nm. This fourth dissociation can be described by eq. [9]:

$$[9] \qquad HL^{3-} \overset{K_{a_4}}{\rightleftharpoons} L^{4-} + H^+$$

The determination of four pK_{an}(n = 1–4) values of 3 by TTFA

Table 1 shows the four pK_a values of **3** in aqueous solution. The pK_a1 = 2.75 of **3** is far lower than the subsequent pK_a values. This indicates that the first acid dissociation of **3** is far easier than the subsequent acid dissociations. As speculated by several researchers (11), these may be attributed to stabilization of the monophenolate species through the strong intramolecular hydrogen bonding between the phenolate O^- and its flanking OH groups (see Fig. 4). This stabilization effect also makes it possible that the first pK_a of **3** is far lower than the pK_a of *p*-nitrophenol (7.15).

On the other hand, the pure UV absorption curves (Fig. 5) and pH distribution curves (Fig. 6) of the five forms of **3** were also calculated by TTFA.

Conclusion

Tetranitro thiacalix[4]arene **3** was synthesized in good yield and characterized. The acid–base properties of **3** in aqueous solution were studied by UV spectroscopy. Four pK_a values in aqueous solution were determined by TTFA. The pure UV absorption curves and pH distribution curves for five occurring forms of **3** were also calculated by TTFA. The results presented here could be helpful for the further exploration of the complexation properties of thiacalixarene, such as its recognition of metal ions.

Fig. 5. Pure absorbance curves of five occurring forms of **3**: (*a*) H_4L, (*b*) H_3L^-, (*c*) H_2L^{2-}, (*d*) HL^{3-}, (*e*) L^{4-}.

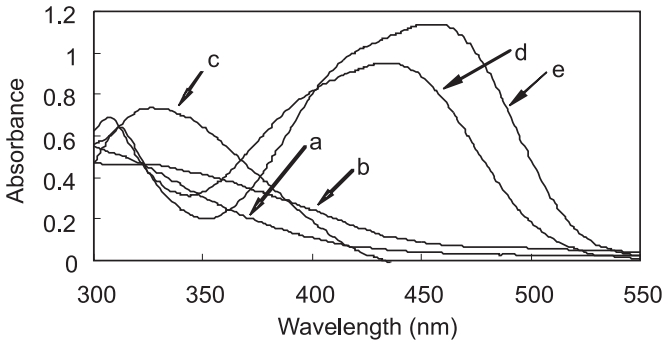
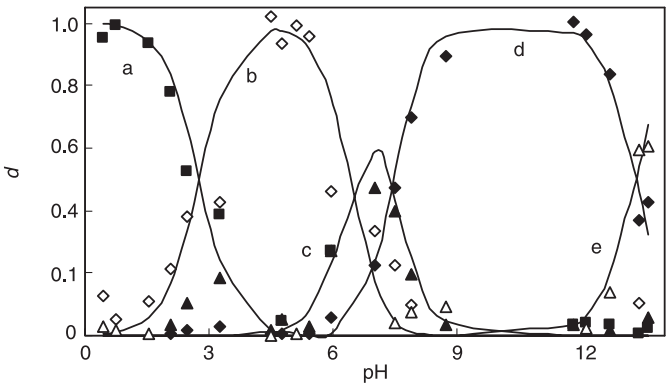


Fig. 6. The pH distribution curves of five occurring forms of **3**: (*a*) H_4L, (*b*) H_3L^-, (*c*) H_2L^{2-}, (*d*) HL^{3-}, (*e*) L^{4-}.



Acknowledgement

The authors thank the National Science Foundation of China for support of this research (Grant No.29971023).

References

1. C.D. Gustche. Calixarenes revisited. Monographs in supramolecular chemistry. *Edited by* J.F. Stoddart. The Royal Society of Chemistry, Cambridge, UK. 1998.
2. H. Kumagai, M. Hasegawa, S. Miyanari, Y. Sugawa, Y. Sato, T. Hori, S. Ueda, H. Kamiyama, and S. Miyano. Tetrahedron Lett. **38**, 3971 (1997).
3. P. Lhoták, M. Himl, S. Pakhomova, and I. Stibor. Tetrahedron Lett. **39**, 8915 (1998).
4. H. Akdas, W. Jaunky, E. Graf, M.W. Hosseini, J.M. Planeix, A.D. Cian, and J. Fischer. Tetrahedron Lett. **41**, 3601 (2000).
5. N. Iki, F. Narumi, T. Fujimoto, N. Morohashi, and S. Miyano. J. Chem. Soc. Perkin Trans. 2, 2745 (1998).
6. N. Iki, N. Morohashi, F. Narumi, T. Fujimoto, T. Suzuki, and S. Miyano. Tetrahedron Lett. **40**, 7337 (1999).
7. Z.F. Ye, Z.G. Pan, W.J. He, and X.F. Shi. J. Inclusion Phenom. Macrocyclic Chem. **40**, 89 (2001).
8. H. Katagiri, N. Iki, T. Hattori, C. Kabuto, and S. Miyano. J. Am. Chem. Soc. **123**, 779 (2001).
9. P. Lhoták, J. Morávek, and I. Stibor. Tetrahedron Lett. **43**, 3665–3668 (2002).

© 2004 NRC Canada

10. (*a*) E. Furusjo and L.G. Danielesson. Anal. Chim. Acta, **373**, 83 (1998); (*b*) Z.L. Zhu, J. Xia, S.G. Mi, and T.H. Li. Chem. J. Chin. Univ. **23**, 546 (2002).
11. P.S. Cong and T.H. Li. Anal. Chim. Acta, **293**, 191 (1994).
12. (*a*) P.D.J. Grootenhuis, P.A. Kollman, and L.C. Groenen. J. Am. Chem. Soc. **112**, 4165 (1990); (*b*) S. Shinkai, P.D.J. Grootenen, and D.N. Reinhoudt. J. Chem. Soc. Perkin Trans. 2, 1883 (1991); (*c*) H. Matsumuya, Y. Terazono, N. Iki, and S. Miyano. J. Chem. Soc. Perkin Trans. 2, 1166 (2002).

© 2004 NRC Canada

Thermodynamic properties of 1,1,1,2-tetrafluoroethane + polyether mixtures up to 60 MPa

M.J.P. Comuñas, C. Boned, A. Baylaucq, E.R. López, and J. Fernández

Abstract: In this work we report several derived thermodynamic properties, the isothermal compressibility (κ_T), the isobaric thermal expansion coefficient (α_p), and the internal pressure (π), and their excess functions (κ_T^E, α_p^E, and π^E) for the refrigerant + lubricant mixtures HFC-134a + triethylene glycol dimethyl ether and HFC-134a + tetraethylene glycol dimethyl ether. These properties have been determined in wide temperature (293.15–373.15 K) and pressure (10–60 MPa) ranges in an effort to better understand the behaviour of these kinds of mixtures and their thermophysical properties as functions of temperature, pressure, and composition. The analysis of the thermodynamic excess properties (negative values for κ_T^E and α_p^E, positive values for π^E) for both systems shows a high degree of interaction between the refrigerant and the synthetic lubricant molecules.

Key words: HFC-134a, high pressure, internal pressure, isobaric thermal expansion coefficient, isothermal compressibility, polyglycol ethers, refrigerant–lubricant mixtures.

Résumé : Dans ce travail nous rapportons plusieurs propriétés thermodynamiques, la compressibilité isotherme (κ_T) l'expansivité isobare (α_p) et la pression interne (π) et aussi leur fonction d'excès (κ_T^E, α_p^E et π^E) pour les systèmes binaires réfrigérant + lubrifiant HFC-134a + triethylene glycol dimethyl éther et HFC-134a + tetraethylene glycol dimethyl éther. Nous avons déterminé ces propriétés dans un large domaine de température (293.15–373.15 K) et de pression (10–60 MPa) avec l'objectif de comprendre le comportement de ces mélanges et des grandeurs d'excès en fonction de la température, de la pression et de la fraction molaire. L'analyse des propriétés d'excès (valeurs négatives de κ_T^E et α_p^E, valeurs positives de π^E) pour les deux mélanges étudiés, met en évidence l'existence d'interactions fortes entre les molécules du réfrigérant et celles du lubrifiant.

Mots clés : HFC-134a, haute pression, pression interne, expansivité isobare, compressibilité isotherme, polyglycol éthers, mélanges réfrigérant–lubrifiant.

Introduction

High-pressure, high-temperature thermodynamic measurements for refrigerant + lubricant mixtures are quite limited and a rapid accumulation of accurate data over wide temperature and pressure ranges is required. A literature review shows several studies concerning the measurement of solubility (1), miscibility (2), viscosity (2, 3), vapour–liquid equilibrium (4), and density (5, 6) of mixtures of selected refrigerants such as HFC-125, HFC-32, HFC-134a, and HFC-410A, and compatible lubricants (polyol esters or polyalkylene glycols) up to the region close to the critical point of the refrigerant. Among these properties, the density and its derived quantities, such as excess volume, are an essential tool to discuss the interactions between the components.

In recent work (5, 6) we have reported experimental densities in the compressed liquid phase for 1,1,1,2-tetrafluoroethane (HFC-134a), triethylene glycol dimethylether (TriEGDME), tetraethylene glycol dimethylether (TEGDME), for six mixtures HFC-134a + TriEGDME (818 experimental points) and for eight mixtures HFC-134a + TEGDME (1017 experimental points) from 293.15 to 373.15 K and at pressures up to 60 MPa. From the experimental results, the volumetric behaviour of HFC-134a + polyether systems has been analysed. In almost all the measurement range, the density of the refrigerant is greater than that of the polyether. Furthermore, the densities of the mixtures display a crossover phenomenon with composition at higher temperatures. The excess volumes for this kind of mixture are strongly negative and asymmetrical towards high refrigerant concentrations, becoming more negative when the temperature increases and

Received 14 January 2004. Published on the NRC Research Press Web site at http://canjchem.nrc.ca on 28 October 2004.

M.J.P. Comuñas. Laboratorio de Propiedades Termofísicas, Departamento de Física Aplicada, Facultad de Física, Universidad de Santiago de Compostela, E-15782 Santiago de Compostela, Spain and Laboratoire des Fluides Complexes, UMR CNRS 5150, Faculté des Sciences, BP 1155, F-64013 Pau, France.
C. Boned and A. Baylaucq. Laboratoire des Fluides Complexes, UMR CNRS 5150, Faculté des Sciences, BP 1155, F-64013 Pau, France.
E.R. López and J. Fernández.[1] Laboratorio de Propiedades Termofísicas, Departamento de Física Aplicada, Facultad de Física, Universidad de Santiago de Compostela, E-15782 Santiago de Compostela, Spain.

[1]Corresponding author (e-mail: fajferna@usc.es).

 doi: 10.1139/V04-087 © 2004 NRC Canada

the pressure decreases. The negative values of V_m^E are in agreement with the previous remarks regarding the high degree of interactions in the HFC-134a + polyether (1). Nevertheless, in this case free-volume or packing effects could give an important negative contribution.

The aim of the present work is to determine several thermodynamic properties: the isothermal compressibility (κ_T), the isobaric thermal expansion coefficient (α_p), and the internal pressure (π) for HFC-134a + polyether systems, and to analyze how the pressure and the temperature affect all these thermodynamic properties. We have also determined for these refrigerant + lubricant mixtures the corresponding excess properties κ_T^E, α_p^E, and π^E over wide temperature and pressure ranges. Furthermore, the study of these properties as a function of both pressure and temperature is of fundamental interest because theoreticians need experimental data to apply their models to these chemical species and their mixtures.

Derived properties

For each mol fraction, the density can be satisfactorily represented by the following modified Tait equation

$$[1] \qquad \rho(T, p) = \frac{\rho(T, p_{ref})}{1 - C \ln\left[\dfrac{B(T) + p}{B(T) + p_{ref}}\right]}$$

where $\rho(T, p_{ref})$ is the temperature dependence of the density at the reference pressure (p_{ref} = 10 MPa), for which we have used the following expression

$$[2] \qquad \rho(T, 10\ \text{MPa}) = \rho_0(T) = A_0 + A_1 T + A_2 T^2$$

In eq. [1], the parameter C was assumed to be temperature independent, and for $B(T)$ we have used the polynomial function

$$[3] \qquad B(T) = B_0 + B_1 T + B_2 T^2$$

Taking into account the previous expressions, the final Tait-like equation used for the density correlation at all temperatures and pressures is

$$[4] \qquad \rho(T, p) = \frac{A_0 + A_1 T + A_2 T^2}{1 - C \ln\left(\dfrac{B_0 + B_1 T + B_2 T^2 + p}{B_0 + B_1 T + B_2 T^2 + 10\ \text{MPa}}\right)}$$

The isothermal compressibility is obtained from eq. [4] using the equations

$$[5] \qquad \kappa_T = \left(\frac{1}{\rho}\right)\left(\frac{\partial \rho}{\partial p}\right)_T = \frac{C}{\left\{1 - C \ln\left[\dfrac{B(T) + p}{B(T) + 10\ \text{MPa}}\right]\right\}[B(T) + p]}$$

The isobaric thermal expansion coefficient is determined using the equations

$$[6] \qquad \alpha_p = -\left(\frac{1}{\rho}\right)\left(\frac{\partial \rho}{\partial T}\right)_p = -\frac{1}{\rho}\left[\frac{\rho_0'(T) F(T, p) - \rho_0(T) F'(T, p)}{F(T, p)^2}\right]$$

where $F(T, p)$ is the denominator of the right side of eq. [4] and $F'(T, p)$ is its temperature derivative given by

$$[7] \qquad F'(T, p) = \left[\frac{\partial F(T, p)}{\partial T}\right]_p = CB'(T)\left[\frac{1}{B(T) + 10\ \text{MPa}} - \frac{1}{B(T) + p}\right]$$

$\rho_0'(T) = d\rho_0/dT$ and $B'(T) = dB/dT$ are easily derived from eqs. [2] and [3] obtaining $\rho_0'(T) = A_1 + 2A_2T$ and $B'(T) = B_1 + 2B_2(T)$.

Finally, the internal pressure, is given by

$$[8] \qquad \pi = \left(\frac{\partial U}{\partial V}\right)_T = T\left(\frac{\partial p}{\partial T}\right)_V - p$$

Values of π were obtained from the Tait-like equation, first by expressing p as a function of T and ρ:

$$[9] \qquad p = [B(T) + 10\ \text{MPa}] \exp\left(\frac{\rho - \rho_0}{\rho C}\right) - B(T)$$

and then by performing the analytical differentiation of this expression

$$[10] \qquad \left(\frac{\partial p}{\partial T}\right)_V = B'(T) \exp\left(\frac{\rho - \rho_0}{\rho C}\right) - \frac{1}{\rho C}[B(T) + 10\ \text{MPa}]\rho_0'(T) \exp\left(\frac{\rho - \rho_0}{\rho C}\right) - B'(T)$$

Taking into account eqs. [8] and [10], the expression of the internal pressure can be easily derived.

Excess derived properties

The excess derived properties χ^E can be employed as a measure of the departure from ideal behaviour and are defined as

$$[11] \qquad \chi^E = \chi^{mix} - \chi^{id}$$

where χ^{mix} and χ^{id} stand for the derived property at the same temperature and pressure for the real and the ideal mixtures, respectively. The procedure commonly used in the literature is to calculate χ^{id} as the sum of the mol-fraction weighted contributions of the derived property of the pure components (χ_i)

$$[12] \qquad \chi^{id} = \sum_{i=1}^{N} x_i \chi_i$$

where x_i denotes the mol fraction of the component i in the mixture. However, based on the fundamental thermodynamic definition of the isothermal compressibility and of the isobaric thermal expansion coefficient, it can be shown that

© 2004 NRC Canada

Table 1. C, A_i, and B_j coefficients and standard deviations (σ) of eq. [4] for xHFC-134a + $(1 - x)$polyether systems.

x	A_0	$10^3 \times A_1$	$10^6 \times A_2$	C	B_0	B_1	B_2	σ
xHFC-134a + $(1 - x)$TriEGDME								
0	1.262 6	0.930 87	0.024 47	0.087 24	539.611	–1.977 14	0.001 95	0.0001
0.2030	1.325 78	–1.023 06	–0.002 83	0.088 59	524.495	–1.981 68	0.001 99	0.0001
0.3517	1.366 10	–0.996 10	–0.221 73	0.087 75	493.622	–1.910 57	0.001 94	0.0001
0.4596	1.409 44	–1.007 93	–0.379 30	0.087 75	465.302	–1.828 82	0.001 86	0.0001
0.6015	1.471 08	–0.983 55	–0.744 59	0.088 26	438.863	–1.798 99	0.001 88	0.0001
0.7784	1.525 52	0.548 80	–2.137 45	0.089 25	382.066	–1.656 16	0.001 79	0.0001
0.9295	1.425 13	1.127 81	–6.007 02	0.093 17	343.101	–1.601 97	0.001 84	0.0004
xHFC-134a + $(1 - x)$TEGDME								
0	1.315 53	–1.126 27	0.370 75	0.086 66	542.261	–1.907 55	0.001 81	0.0001
0.1114	1.323 92	–1.046 02	0.164 71	0.086 61	613.295	–2.386 24	0.002 54	0.0001
0.2896	1.360 61	–1.049 68	0.039 07	0.087 35	535.337	–2.012 54	0.002 02	0.0001
0.3648	1.391 10	–1.106 98	0.040 23	0.087 32	542.740	–2.112 71	0.002 20	0.0001
0.5702	1.471 74	–1.125 06	–0.288 95	0.086 63	473.078	–1.890 91	0.001 96	0.0001
0.6931	1.518 05	–1.010 13	–0.805 77	0.087 28	432.799	–1.782 22	0.001 87	0.0001
0.7288	1.503 33	–0.773 17	–1.315 26	0.087 22	417.581	–1.730 10	0.001 81	0.0001
0.8727	1.540 54	–0.181 55	–3.134 88	0.089 68	366.140	–1.630 97	0.001 80	0.0002
0.9290	1.464 70	0.813 78	–5.373 87	0.092 26	349.777	–1.619 38	0.001 84	0.0003

their rigorous expressions for an ideal mixture are obtained by taking into account the volume-fraction weighted contributions of the isothermal compressibility and of the isobaric thermal expansion coefficient (7–13). The volume-fraction ϕ_i is defined by

$$[13] \quad \phi_i = \frac{x_i V_{mi}}{\sum_{j=1}^{N} x_j V_{mj}}$$

where V_{mj} is the molar volume of the pure compound j. Finally, the excess thermal expansion coefficient α_p^E and the excess isothermal compressibility κ_T^E are obtained for a binary system by using the following equations

$$[14] \quad \alpha_p^E = \alpha_p^{mix} - \sum_{i=1}^{2} \frac{x_i V_{mi}}{x_1 V_{ml} + x_2 V_{m2}} \alpha_{pi}$$

$$[15] \quad \kappa_T^E = \kappa_T^{mix} - \sum_{i=1}^{2} \frac{x_i V_{mi}}{x_1 V_{ml} + x_2 V_{m2}} \kappa_{Ti}$$

where α_{pi} and κ_{Ti} are, respectively, the isobaric thermal expansion coefficient and the isothermal compressibility of pure compound i. There are large differences between the excess properties calculated with eqs. [14] and [15] and those evaluated by using the incorrect expression (eq. [12]) for an ideal mixture (14).

For the excess internal pressure of an ideal mixture, the additivity of this property in the mol fraction scale is often assumed (15, 16). With this assumption, the excess internal pressure can be calculated by using the relation

$$[16] \quad \Delta\pi = \pi^{mix} - \sum_{i=1}^{2} x_i \pi_i$$

However, this expression is not correct because the internal pressure is not an extensive property, and therefore the additivity based on the mol fraction for ideal mixtures is not accomplished. For this reason the quantity calculated from eq. [16] (i.e., $\Delta\pi$) is sometimes (17) called the "deviation internal pressure" or "quasi-excess internal pressure". Recently, Marczak has published a paper (18) concerning the correct expression for the internal pressure of a thermodynamically ideal mixture. Using this expression for the internal pressure of an ideal mixture that includes the "compression fraction", the excess internal pressure for a binary mixture must be obtained using the equation

$$[17] \quad \pi^E = \pi^{mix} - \sum_{i=1}^{2} \frac{x_i V_{mi} \kappa_{Ti}}{x_1 V_{ml} \kappa_{T1} + x_2 V_{m2} \kappa_{T2}} \pi_i$$

In this equation the compression fraction is used instead of the volume fraction that appears in eqs. [14] and [15] for the excess thermal expansion coefficient and the excess isothermal compressibility. It should be pointed out that eq. [17] can be obtained (19) using the expression of the isochoric pressure coefficient $\gamma_V = (\partial p/\partial T)_V$ for an ideal mixture, and taking into account the definition $\pi = T(\partial p/\partial T)_V - p$.

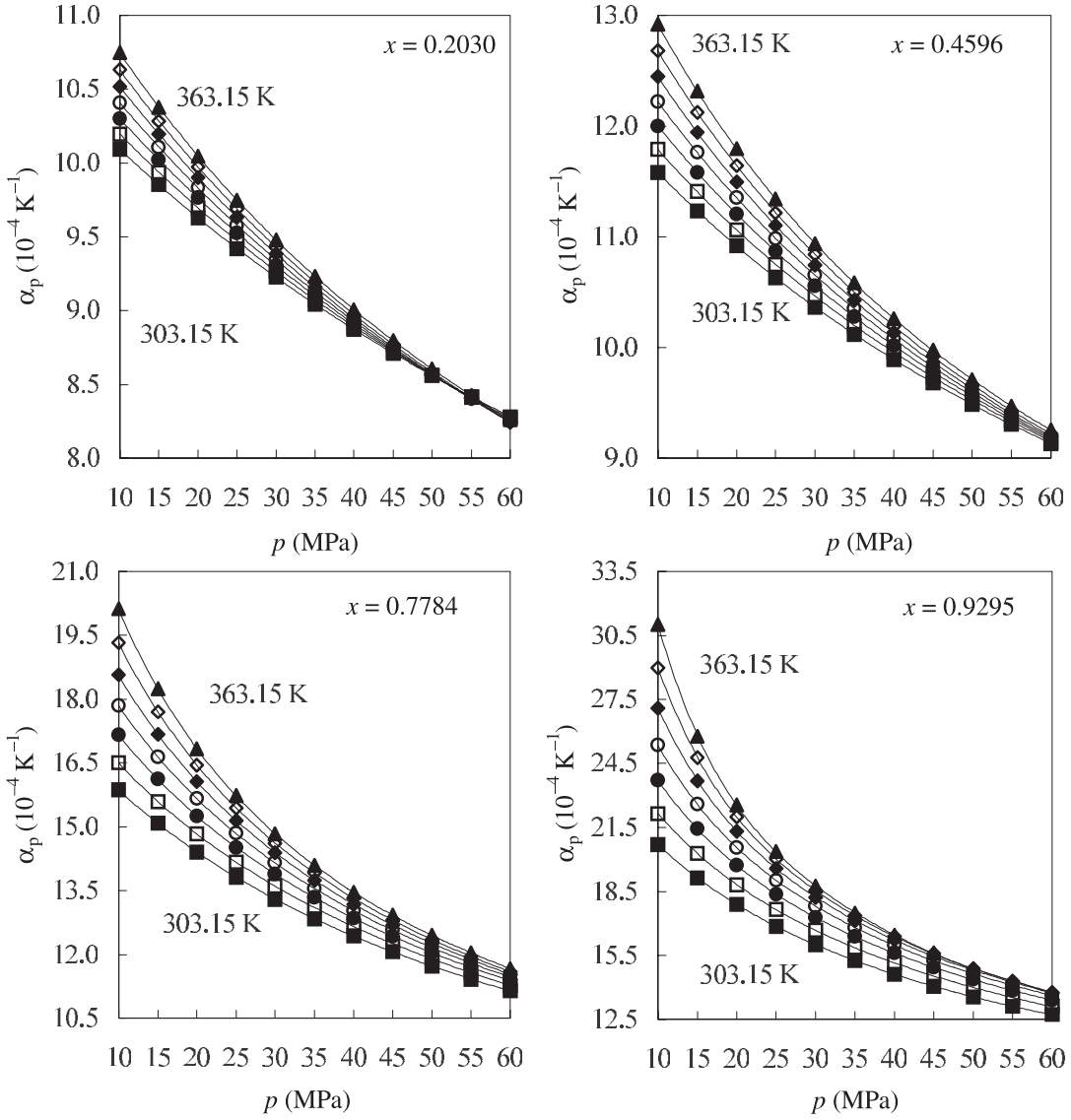
Results

The values of the A_i (i = 0, 1, 2), B_j (j = 0, 1, 2), and C coefficients for the Tait-like density correlation were determined for HFC-134a + TriEGDME and HFC-134a + TEGDME mixtures from our previously reported density data (5, 6) by fitting, at each fixed composition, the $p\rho T$ surface to eq. [4] using a Marquardt–Levenberg type algorithm. In Table 1 the values of these parameters are summarized for the HFC-134a + TriEGDME and HFC-134a + TEGDME systems. For pure HFC-134a, these parameters were reported in our previous paper (5). $B(T)$ increases when the temperature decreases and has a regular mol fraction dependence.

The estimated uncertainties of the isothermal compressibility (κ_T), the isobaric thermal expansion coefficient (α_p), and the internal pressure (π) calculated using eqs. [5]–[10] are $\pm 0.05 \times 10^{-4}$ MPa^{-1}, $\pm 0.02 \times 10^{-3}$ K^{-1}, and 1%, respec-

© 2004 NRC Canada

Fig. 1. Temperature and pressure dependence of the isobaric thermal expansion coefficient (α_p) for the *x*HFC-134a + (1 – *x*)TriEGDME mixtures: 303.15 K (■), 313.15 K (□), 323.15 K (●), 333.15 K (○), 343.15 K (◆), 353.15 K (◇), 363.15 K (▲). (—— Polynomial interpolation).

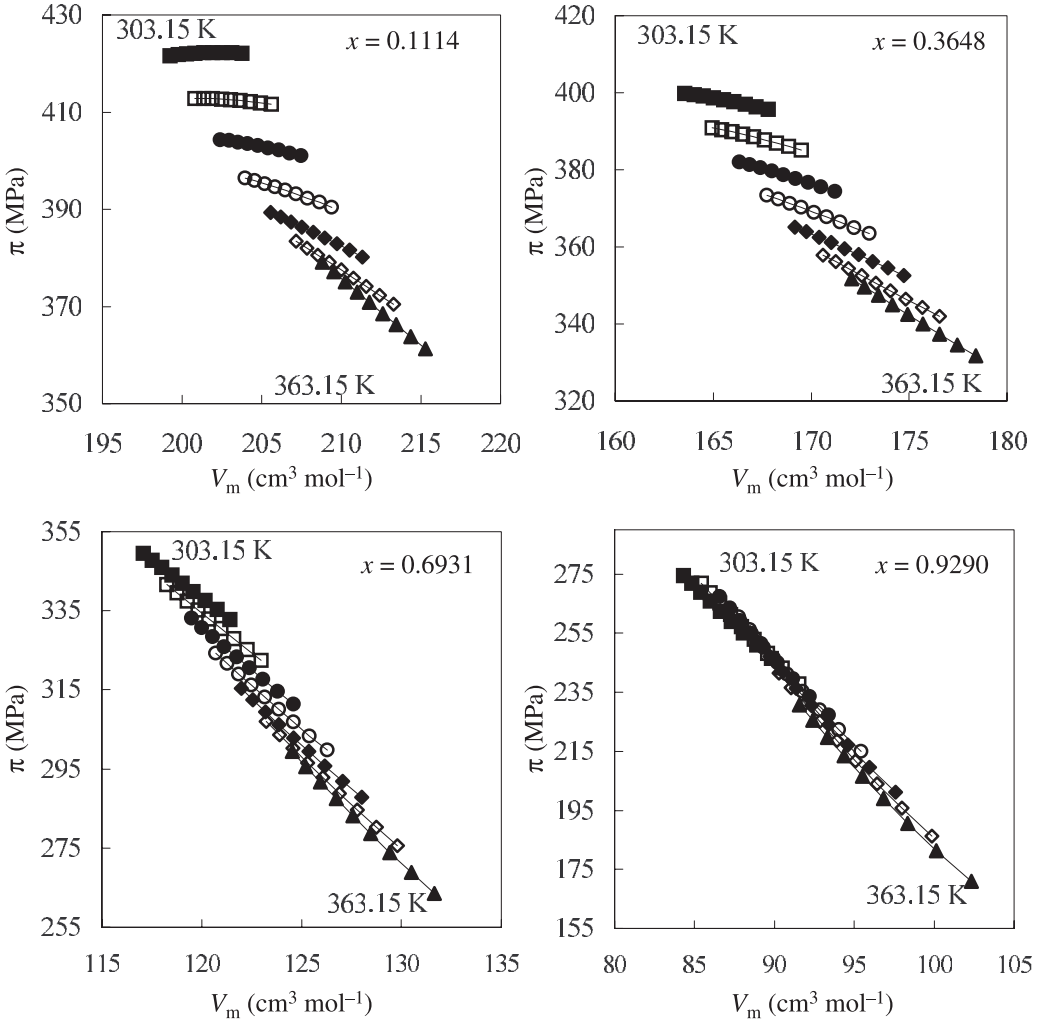


tively, over the entire temperature and pressure ranges. In a previous study (20), isothermal compressibility and isobaric thermal expansivity values have been reported for pure TriEGDME and TEGDME up to 353.15 K and 60 MPa. These values have been calculated from density data measured with the same apparatus and correlated also with the Tait equation, but using as the reference pressure 0.1 MPa instead of 10 MPa used in the present work. We have compared both sets of data for TEGDME obtaining an average absolute deviation of 0.2% for the isothermal compressibility and 0.8% for the isobaric thermal expansivity, along with maximum deviations of 0.4% and 2.5%. For TriEGDME, the previous corresponding deviations are 0.2%, 0.4%, 0.5%, and 0.7%, respectively.

For the isobaric thermal expansion coefficient, it is evident that its pressure dependence is higher for the pure refrigerant than for the pure polyether. For example, at 323.15 K, α_p for TEGDME decreases from 8.8×10^{-4} K^{-1} at 15 MPa to 7.6×10^{-4} K^{-1} at 55 MPa (i.e., a variation of 1.2×10^{-4} K^{-1} in this pressure range), whereas in the same pressure range, the variation of α_p for HFC-134a is 10.6×10^{-4} K^{-1}. Figure 1 shows the dependence of the isobaric thermal expansion coefficient on the temperature and on the pressure at different mol fractions. At fixed temperature and pressure, α_p increases when the refrigerant mol fraction increases. We can also observe in Fig. 1 that there is a crossover point of the isotherms (21–23). At the pressure of the crossing point, α_p is independent of temperature. Increasing the mol fraction of refrigerant increases the crossover pressure. For the *x*HFC-134a + (1 – *x*)TEGDME system at $x = 0$ (pure TEGDME), the crossing point appears near 30 MPa, as we reported in our previous study (20), at $x = 0.2030$ near 50 MPa, and at $x = 0.4596$ near 60 MPa. For higher mol fractions this crossover point is not visible in the pressure range used for the experiments. This intersection point of the isotherms is related to the existence of a minimum in the

© 2004 NRC Canada

Fig. 2. Internal pressure (π) plotted against the molar volume at different temperatures and pressures for the *x*HFC-134a + (1 – *x*)TEGDME mixtures at several refrigerant mol fractions: 303.15 K (■), 313.15 K (□), 323.15 K (●), 333.15 K (○), 343.15 K (◆), 353.15 K (◇), 363.15 K (▲).



plot of the isobaric heat capacity vs. temperature (21), where $(\partial^2\rho/\partial T^2) = 0$.

The isothermal compressibility for the pure refrigerant is also higher and more pressure dependent (with a variation of 22.7×10^{-4} MPa^{-1} at 323.15 K between 15 and 50 MPa) than that of the polyethers (with a variation of 1.5×10^{-4} MPa^{-1} for TriEGDME and 1.3×10^{-4} MPa^{-1} for TEGDME in the same pressure range). For both mixtures, the variation of α_p and κ_T as a function of the refrigerant mol fraction, at constant temperature and pressure, shows at low concentrations of the refrigerant a small increase, whereas for the higher concentrations a sharp increase can be observed.

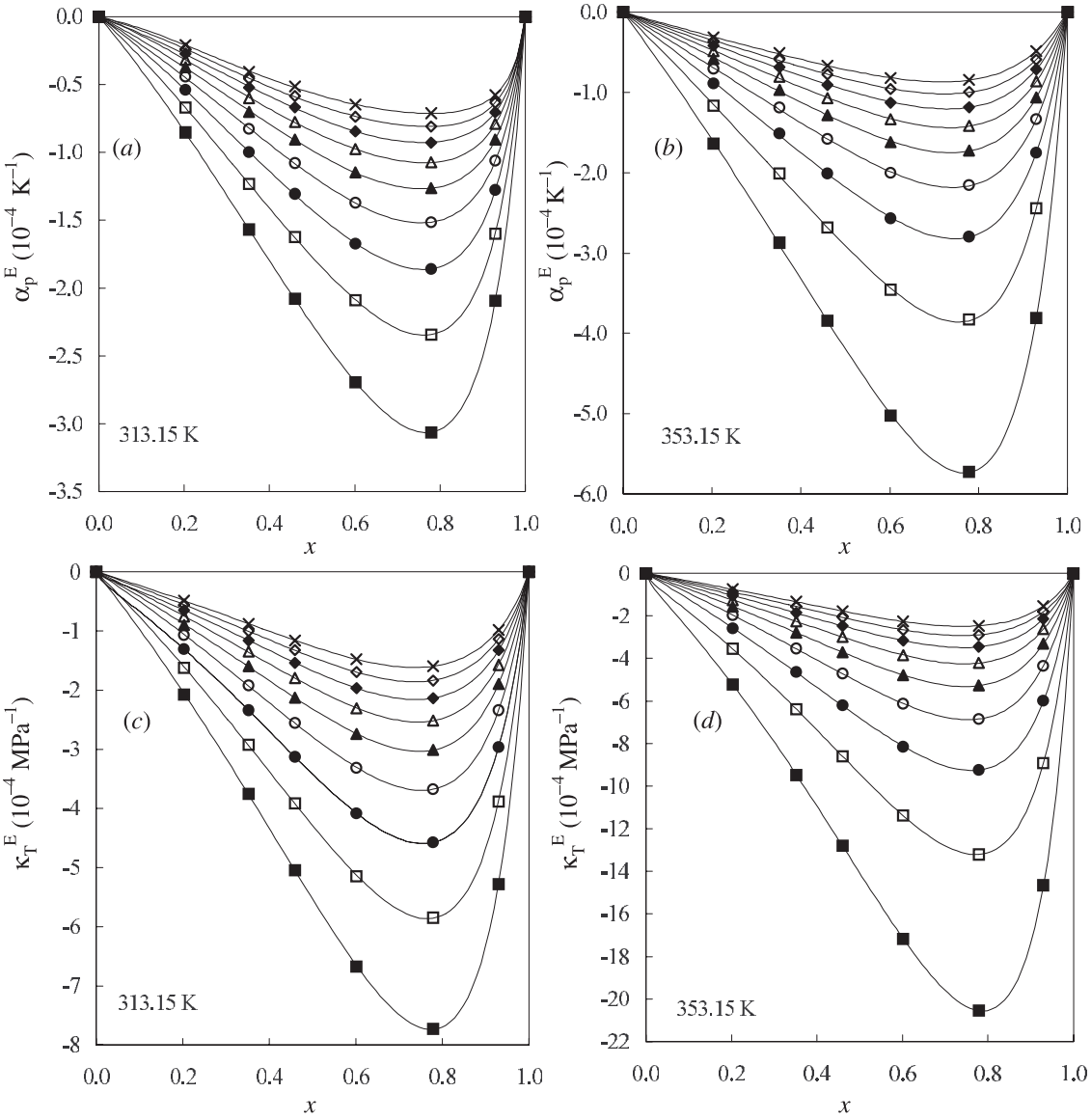
In Fig. 2, we have plotted the internal pressure against the molar volume at four refrigerant mol fractions 0.1114, 0.3648, 0.6931, and 0.9290 and at different temperatures for the binary system HFC-134a + TEGDME. When the refrigerant concentration in the mixture increases, the change of the internal pressure with the molar volume tends to the same slope (i.e., the internal pressure could be represented as a unique curve). To the knowledge of the authors no similar behaviour of the internal pressure has been reported.

Concerning the excess thermodynamic properties of liquid mixtures, we must point out that they are useful because their analysis can give information on the intermolecular interactions and of the packing and order effects. The first derivatives (excess molar volumes, enthalpies, and entropies) and the second derivatives (excess isothermal compressibility and thermal expansion coefficients) can provide information on the Gibbs energy of the mixtures.

In Figs. 3*a* and 3*b*, we present the variation of the excess thermal expansion coefficient with the mol fraction, and for nine pressures at two temperatures for the *x*HFC-134a + (1 – *x*)TriEGDME. This excess property is always negative and increases as the pressure rises. The behaviour of the binary mixture *x*HFC-134a + (1 – *x*)TEGDME is similar, but at 343.15 and 363.15 K for the highest pressures, α_p^E reaches small and positive values. Figures 3*c* and 3*d* show that the temperature, pressure, and mol fraction dependences of the excess isothermal compressibility for the binary system containing TriEGDME are similar to those of the excess thermal expansion coefficient. The same observation can be made for the mixture containing the other polyether (TEGDME).

© 2004 NRC Canada

Fig. 3. Variation of α_p^E (*a* and *b*) and κ_T^E (*c* and *d*) with composition and pressure at two different temperatures for the *x*HFC-134a + (1 – *x*)TriEGDME system: 15 MPa (■), 20 MPa (□), 25 MPa (●), 30 MPa (○), 35 MPa (▲), 40 MPa (△), 45 MPa (◆), 50 MPa (◇), 55 MPa (×). (—— Polynomial interpolation).



The excess internal pressure (Figs. 4*a* and 4*b*) contrary to the previously discussed excess properties, is positive as expected, and increases as the temperature increases and as the pressure decreases. This behaviour is similar for the two studied systems. In Figs. 5*a* and 5*b*, we compare the "deviation of the internal pressure" $\Delta\pi$ calculated with eq. [16] with the excess internal pressure π^E calculated by using eq. [17]. Both quantities are positive, but the excess internal pressure is twice as large as the deviation of the internal pressure. The main differences between these quantities are due to the fact that the isothermal compressibilities are much higher for HFC-134a than for the pure polyether. Marczak (18) using the data of Ogawa and Murakami (24) also reported large differences between π^E and $\Delta\pi$ in the methanol + 1-propanol systems at atmospheric pressure and at 298.15 K. The positive values of the excess internal pressure indicate that for these systems the variation of the internal energy during the expansion $((\partial U/\partial V)_T)$ is higher than that of the ideal mixture $((\partial U^{id}/\partial V^{id})_T)$. This could be interpreted by using the fact that new interactions appearing in the mixtures are more sensitive to changes in the intermolecular distance than those existing in the pure compounds (25).

In Fig. 6, we present a comparison between the excess isothermal compressibility, the excess thermal expansion coefficient, and the excess internal pressures for the HFC-134a + TriEGDME and HFC-134a + TEGDME mixtures. The values of α_p^E and κ_T^E are very similar for both binary systems. The values of π^E for the two systems are different; higher π^E values are found for the mixture containing TEGDME. The maxima of the $\pi^E(x)$ curves are located close to the equimolar mixtures, displaying shapes more symmetrical than those for the other excess properties ($\kappa_T^E(x)$ and $\alpha_p^E(x)$).

The results obtained in our previous studies (5, 6) and in

© 2004 NRC Canada

Fig. 4. Curves showing the variation of π^E with composition and pressure: (*a*) for the *x*HFC-134a + (1 – *x*)TriEGDME system, and (*b*) for the *x*HFC-134a + (1 – *x*) TEGDME system at 313.15 K: 15 MPa (■), 20 MPa (□), 25 MPa (●), 30 MPa (○), 35 MPa (▲), 40 MPa (△), 45 MPa (◆), 50 MPa (◇). (—— Polynomial interpolation).

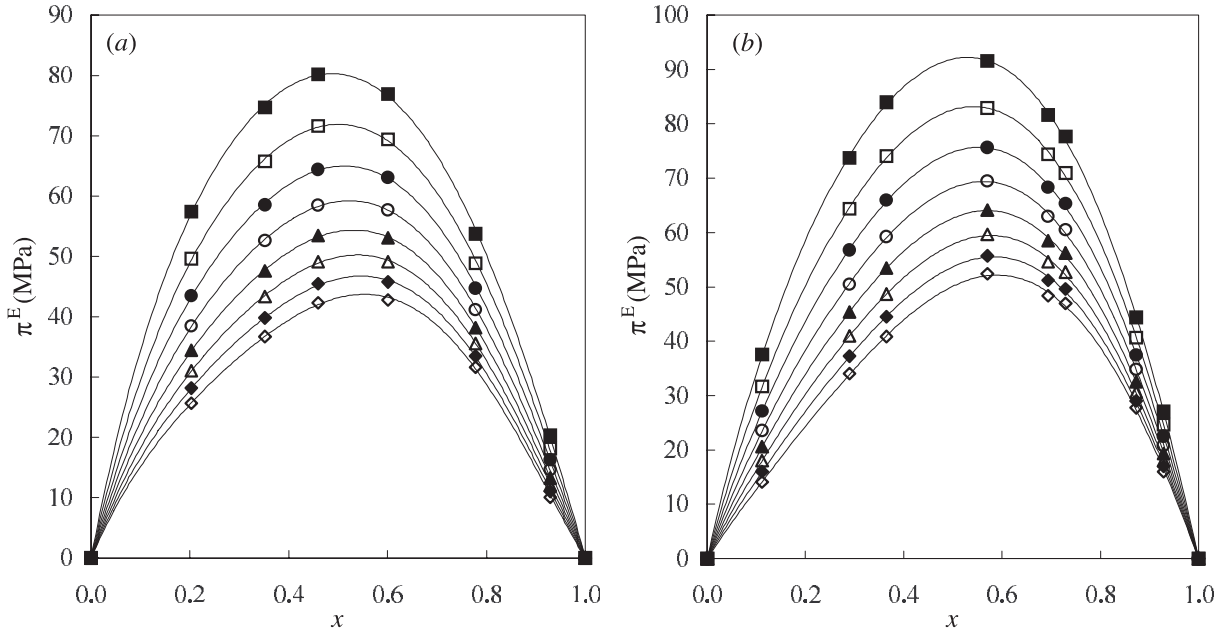
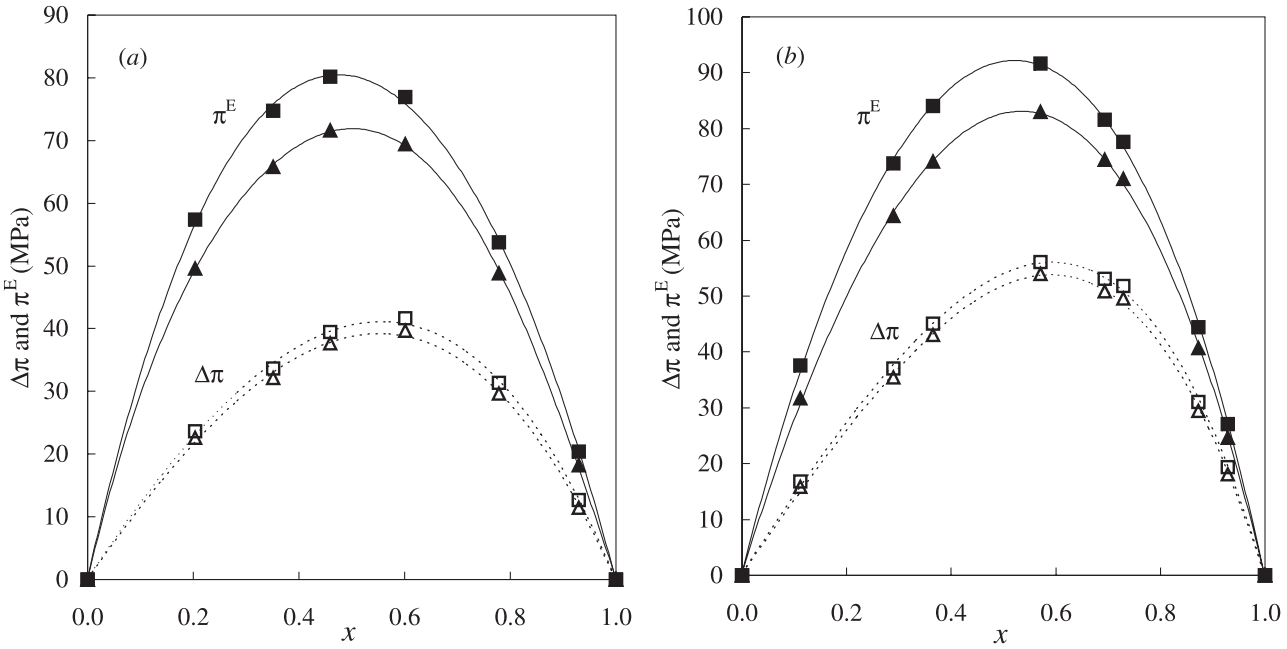


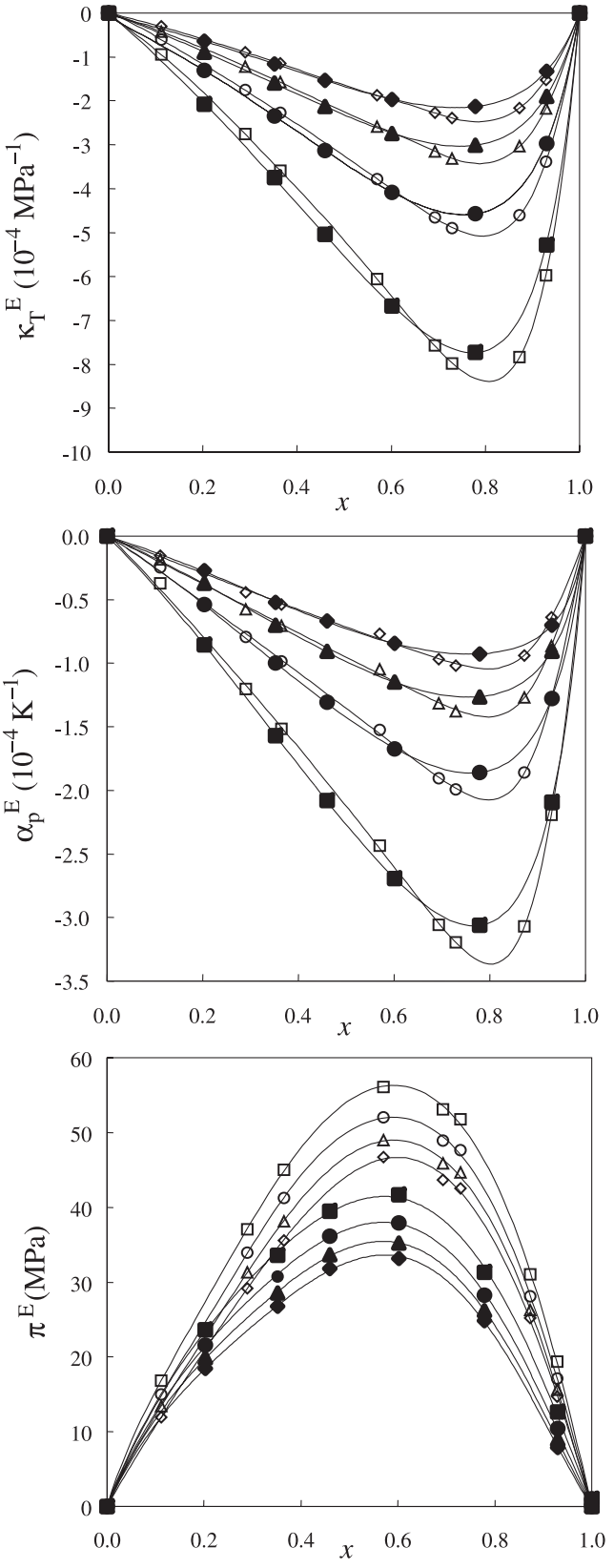
Fig 5. Comparison between the excess internal pressure and the deviations of the internal pressure: (*a*) for the *x*HFC-134a + (1 – *x*)TriEGDME system, and (*b*) for the *x*HFC-134a + (1 – *x*)TEGDME mixture at 313.15 K for two pressures (15 MPa (■, □) and 20 MPa (▲, △)). The filled symbols are calculated by using eq. [17] and the hollow symbols by using eq. [16]. (------; —— Polynomial fitting).



the present work for the two binary systems can be summarized as follows: both highlight negative values for the excess molar volumes ($V_m^E < 0$), for the excess isothermal compressibility ($\kappa_T^E < 0$), as well as for the excess thermal expansion coefficient ($\alpha_p^E < 0$), but positive values for the excess internal pressure ($\pi^E > 0$) in the entire temperature and pressure interval. The negative values of the excess molar volumes indicate that the mixtures are more closely packed that the pure components and can be explained by considering two effects. The first one is the existence of stronger interactions between unlike molecules (TriEGDME or TEGDME with HFC-134a) than between identical molecules. This effect implies a diminution in the volume because the intermolecular distances diminish. The second effect is that the smallest molecules (HFC-134a) occupy the free volume of the largest molecules (TriEGDME or

© 2004 NRC Canada

Fig. 6. Comparison between the excess properties of the *x*HFC-134a + (1 – *x*) polyether system: 15 MPa (□), 25 MPa (○), 35 MPa (△), 45 MPa (◇). The filled symbols are used for the mixture containing TriEGDME and the hollow symbols for the mixture containing TEGDME.



TEGDME). For the HFC-134a + polyether systems, the two contributions can be important, as can be deduced from the results for V_m^E and κ_T^E. Generally, these properties present negative values for systems in which there is hydrogen bonding or important electrostatic interactions between the unlike molecules (26, 27). The dependence of both excess properties with the mol fraction is similar, emphasizing an asymmetrical shape. The excess isothermal compressibility values are also affected by the existence of molecular aggregation due to the molecular interactions. The negative values of these excess properties show that during the mixing process there is a decrease of the volume and an increase of the rigidity (i.e., the mixture is less compressible than the ideal mixture). The negative values of α_p^E show that the mixtures are also less expansible than the ideal mixture, and this idea is compatible with the interpretation of the rigidity increase during the mixing process (28–30). Excess internal pressure and deviations of the internal pressure data are scarce in the literature. We have observed that, frequently, the sign of $\Delta\pi$ is opposite to the sign of the excess volumes (17, 31, 32).

The solubilities of HFC-134a in TriEGDME and in TEGDME have been recently measured (1, 33). These binary systems present negative deviations from Raoult's law ($G^E < 0$) and this also indicates strong interactions between the polyether and the refrigerant molecules. From the VLE data published by Tseregounis and Riley (1), we calculated the NRTL parameters for the HFC-134a + TEGDME mixtures, whereas the NRTL coefficients for the HFC-134a + TriEGDME system were reported by Coronas et al. (33). Taking into account these parameter values, we have estimated the excess enthalpies (H^E) for both systems. The extremely negative H^E values (indicating the exothermic character) of these systems, show again that the formation of new interactions during the mixing process is energetically more important than the rupture of existing interactions.

Our results are in agreement with those reported in refs. 34–36 for the vapour–liquid equilibrium values of several refrigerants + dimethyl ether for which the HFC molecules have active donor protons capable of strong H-bonding with proton acceptors. We must also take into account that in pure HFC-134a and in pure polyethers, strong interactions are also reported by several authors (37). Nevertheless, we can conclude that according to the values presented here and to those reported in refs. 1 and 33–36, the interactions in the mixture of HFC-134a and polyethers are stronger than those for the pure components. This behaviour is in contrast with that for HFC-134a + polyolester oil (POE) systems, which, according to the experimental activity coefficients at infinite dilution, do not present specific interactions between the unlike molecules (38).

Acknowledgements

This work was carried out under the Research Project PPQ2001-3022 and the Spanish–French Joint Actions 04238PG and HF2001-0101.

References

1. S.I. Tseregounis and M.J. Riley. AIChE J. **40**, 726 (1994).

© 2004 NRC Canada

2. P. Popovic, R.L. Shimon, M. Pate, and N.E. Schnur. ASHRAE Trans. **106**, 668 (2000).
3. R.C. Cavestri and W.R. Schafer. ASHRAE Trans. **106**, 277 (2000).
4. Y.R. Jeng, C.S. Chang, and C.C. Wang. Appl. Therm. Eng. **21**, 863 (2001).
5. M.J.P. Comuñas, J. Fernández, A. Baylaucq, X. Canet, and C. Boned. Fluid Phase Equilib. **199**, 185 (2002).
6. M.J.P. Comuñas, A. Baylaucq, C. Boned, X. Canet, and J. Fernández. J. Chem. Eng. Data, **47**, 233 (2002).
7. O. Kiyohara and G.C. Benson. J. Chem. Thermodyn. **11**, 861 (1979).
8. G. Douheret, C. Moreau, and A. Viallard. Fluid Phase Equilib. **22**, 277 (1985).
9. G.C. Benson and O. Kiyohara. J. Chem. Thermodyn. **11**, 1061 (1979).
10. W.E. Acree. J. Chem. Eng. Data, **28**, 215 (1983).
11. P. Picker, E. Tremblay, and C. Jolicoeur. J. Solution Chem. **3**, 377 (1974).
12. N.P. Rao and R.R. Verral. Can. J. Chem. **65**, 810 (1987).
13. J.C.R. Reis, M.J. Blandamer, M.I. Davis, and G. Douhéret. Phys. Chem. Chem. Phys. **3**, 1465 (2001).
14. B. Hawrylak, S.E. Burke, and R. Palepu. J. Solution Chem. **29**, 575 (2000).
15. L. Acevedo, G.C. Pedrosa, and M. Katz. J. Solution Chem. **19**, 911 (1990).
16. J.D. Pandey, N. Pant, and B.R. Chaturvedi. Chem. Scr. **18**, 224 (1981).
17. T.M. Aminabhavi, V.B. Patil, K. Banerjee, and R.H. Balundgi. Bull. Chem. Soc. Jpn. **72**, 1187 (1999).
18. W. Marczak. Phys. Chem. Chem. Phys. **4**, 1889 (2002).
19. G. Douhéret and A. Viallard. J. Chim. Phys. **80**, 809 (1983).
20. M.J.P. Comuñas, A. Baylaucq, C. Boned, and J. Fernández. Int. J. Thermophys. **22**, 749 (2001).
21. S.L. Randzio. Thermochim. Acta, **121**, 463 (1987).
22. M.S. Benson, P.S. Dynder, and J. Winnick. J. Chem. Thermodyn. **3**, 891 (1971).
23. R. Malhotra and L.A. Woolf. Int. J. Thermophys. **14**, 1153 (1993).
24. H. Ogawa and S. Murakami. J. Solution Chem. **16**, 315 (1987).
25. M.R.J. Dack. Aust. J. Chem. **28**, 1643 (1975).
26. G. Douheret and M.I. Davis. Chem. Soc. Rev. **22**, 43 (1993).
27. R.J. Fort and W.R. Moore. Trans. Faraday Soc. **61**, 2102 (1965).
28. J. Peleteiro, D. González-Salgado, C.A. Cerdeiriña, J.L. Valencia, and L. Romaní. Fluid Phase Equilib. **191**, 83 (2001).
29. H. Ohji, H. Ogawa, S. Murakami, K. Sachio, and J.P. Grolier. Fluid Phase Equilib. **156**, 101 (1999).
30. A.D. Matilla, G. Tardajos, and E.J. Aicart. J. Solution Chem. **19**, 1137 (1990).
31. R. Riggio, J.F. Ramos, and H.E. Martínez. Can. J. Chem. **79**, 50 (2001).
32. K. Malakondaiah, K. Subbarangaiah, and S.V. Subrahmanyam. Phys. Chem. Liq. **23**, 49 (1991).
33. A. Coronas, A.M. Mainar, K.R. Patil, A. Conesa, S. Shen, and S. Zhu. J. Chem Eng. Data, **47**, 56 (2002).
34. S. Bobbo, R. Camporese, and R. Stryjek. J. Chem. Thermodyn. **32**, 1647 (2000).
35. S. Bobbo, L. Fedele, R. Camporese, and R. Stryjek. Fluid Phase Equilib. **199**, 153 (2002).
36. S. Bobbo, L. Fedele, R. Camporese, and R. Stryjek. Fluid Phase Equilib. **174**, 3 (2000).
37. B.J. Costa-Cabral, R.C. Guedes, R.S. Pai-Panandiker, and C.A. Nieto-Castro. Phys. Chem. Chem. Phys. **3**, 4200 (2001).
38. R. Stryjek, S. Bobbo, R. Camporese and C. Zilio, J. Chem. Eng. Data, **44**, 568 (1999).

© 2004 NRC Canada

Spectroscopic and photophysical properties of carbazole-based triads

Michel Belletête, Mélanie Bédard, Jimmy Bouchard, Mario Leclerc, and Gilles Durocher

Abstract: A study of the spectroscopy and photophysics of four carbazole-based triads, namely, 1,4-bis(*N*-octylcarbazol-2-yl)phenylene (CPC), 2,5-bis(*N*-octylcarbazol-2-yl)thiophene (CTC), 2,7-bis(*N*-octylcarbazol-2-yl)-9,9-dihexylfluorene (CFC), and 2,7-bis(*N*-octylcarbazol-2-yl)-*N*-octylcarbazole (CCC) are reported. From ZINDO/S calculations performed on the optimized ground state geometries (HF/6-31G*), the $S_1 \leftarrow S_0$ and $S_2 \leftarrow S_0$ electronic transitions of CPC, CFC, and CCC are weakly allowed, whereas the $S_3 \leftarrow S_0$ electronic transition is dipole-allowed (*x* axis) and possesses a high value of the oscillator strength. On the other hand, for CTC, the dipole-allowed electronic transition is $S_1 \leftarrow S_0$. For the four derivatives, the dipole-allowed transition corresponds mainly to the promotion of an electron from the HOMO to the LUMO. The first absorption band of each derivative can be assigned to the dipole-allowed transition. The geometry optimization of the excited states has been done with RCIS/6-31G* ab initio calculations. For CPC, CFC, and CCC, S_3 is much more stabilized than S_1 and S_2, causing a crossing of the singlet excited states (S_3 becomes lower in energy than S_1 and S_2). Emission energies from the first relaxed excited states ($S_1 \rightarrow S_0$) have been obtained from ZINDO/S calculations performed on the optimized S_1 geometries (RCIS/6-31G*). It is found that these energies are in very good agreement with those determined from the fluorescence spectra. Going from CPC to CTC, the replacement of a phenylene ring by a thiophene unit induces a red shift in the absorption and fluorescence spectra. This behavior is interpreted in terms of the electron donor properties of the thiophene ring. The increase of the oligomer chain (CFC and CCC compared to CPC) also induces bathochromic shifts in the spectra because of a longer electronic delocalization along the molecular frame. From fluorescence data, it is observed that a more planar conformation is favored in the relaxed excited states. RCIS/6-31G* ab initio calculations performed on the S_1 relaxed excited states confirm this statement. Finally, the photophysical properties of CTC are mainly governed by nonradiative processes (k_{nr}), whereas the variation in the photophysics of CPC, CFC, and CCC mainly involves radiative processes (k_F).

Key words: electronic spectroscopy, fluorescence, photophysics, ab initio calculations, excited states.

Résumé : Une étude de la spectroscopie et de la photophysique de quatre dérivés du carbazole, soit 1,4-bis(*N*-octylcarbazol-2-yl)phenylene (CPC), 2,5-bis(*N*-octylcarbazol-2-yl)thiophene (CTC), 2,7-bis(*N*-octylcarbazol-2-yl)-9,9-dihexylfluorene (CFC), et 2,7-bis(*N*-octylcarbazol-2-yl)-*N*-octylcarbazole (CCC) est reportée. À partir de calculs ZINDO/S effectués sur les géométries à l'état fondamental optimisées (HF/6-31G*), il est démontré que les transitions électroniques $S_1 \leftarrow S_0$ et $S_2 \leftarrow S_0$ du CPC, du CFC et du CCC sont faiblement permises. Par contre, la transition électronique $S_3 \leftarrow S_0$ de ces molécules est fortement permise (axe *x*) et possède une valeur élevée de sa force oscillatrice. D'autre part, pour le CTC, la transition électronique fortement permise est très stabilisée et devient alors la transition $S_1 \leftarrow S_0$. Pour les quatre dérivés, la transition fortement permise correspond principalement à la promotion d'un électron de l'orbitale HOMO vers l'orbitale LUMO. La première bande d'absorption de chaque dérivé peut être assignée à la transition électronique fortement permise. L'optimisation de la géométrie des états excités a été effectuée à l'aide de la méthode RCIS/6-31G*. Pour les molécules CPC, CFC et CCC, il a été démontré que l'état S_3 est beaucoup plus stabilisé que les états S_1 et S_2 causant ainsi un croisement des états singulets excités (S_3 devient moins énergétique que S_1 et S_2). Les énergies d'émission provenant des premiers états excités relaxés ($S_1 \rightarrow S_0$) ont été obtenus à partir de calculs ZINDO/S effectués sur les géométries optimisées des états S_1 (RCIS/6-31G*). Il est démontré que ces énergies sont en très bon accord avec les énergies d'émission expérimentale déterminées à partir des spectres de fluorescence. En passant du CPC au CTC, le remplacement d'un groupe phénylène par un cycle thiophène induit un déplacement bathochrome dans les spectres d'absorption et de fluorescence. Il est suggéré que ce comportement est causé par les propriétés électro-donneur du groupe thiophène. L'augmentation de la longueur de la chaîne de l'oligomère (CFC et CCC comparés à CPC) induit aussi des déplacements bathochromes dans les spectres due à une délocalisation

Received 30 January 2004. Published on the NRC Research Press Web site at http://canjchem.nrc.ca on 29 October 2004.

M. Belletête and G. Durocher.[1] Laboratoire de photophysique moléculaire, Département de Chimie, Université de Montréal, C.P. 6128, Succ. Centre-Ville, Montréal, QC H3C 3J7, Canada.
M. Bédard, J. Bouchard, and M. Leclerc. Laboratoire des polymères photoactifs et électroactifs, Centre de recherche en sciences et ingénierie des macromolécules (CERSIM), Université Laval, Cité Universitaire, Québec, QC G1K 7P4, Canada.

[1]Corresponding author (e-mail: gilles.durocher@umontreal.ca).

 doi: 10.1139/V04-096 © 2004 NRC Canada

électronique accrue selon le grand axe moléculaire. À partir des données spectrales de fluorescence, il est observé qu'une conformation plus plane semble atteinte pour les oligomères dans leurs états excités relaxés. Les calculs RCIS/6-31G* effectués sur les états excités relaxés confirment cette observation. Finalement, il est démontré que les propriétés photophysiques du CTC sont principalement gouvernées par des processus non radiatifs (k_{nr}), tandis que la photophysique de CPC, CFC et CCC implique principalement des processus radiatifs (k_F).

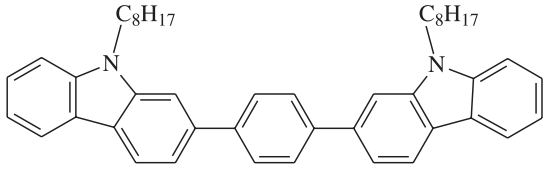
Mots cles : spectroscopie électronique, fluorescence, photophysique, calculs ab initio, états excités.

Introduction

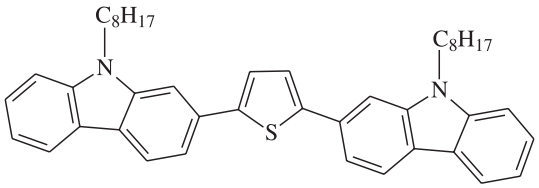
Conjugated polymers and oligomers have been investigated intensively in the past few decades because of their great potential for the development of electronic devices such as field-effect transistors (1–3), solar cells (4, 5), and light-emitting diodes (LEDs) (6–10). The advantages of organic electroactive and photoactive materials over inorganic systems are their ease of processing and the tunability of their properties through simple chemical modifications. Recently, the synthesis of various well-defined conjugated oligomers and polymers derived from phenylene, pyrrole, thiophene, and fluorene moieties has been achieved. However, the fabrication of novel materials from conjugated building blocks is still a challenge for future electronic devices.

Recently, novel well-defined 2,7-carbazole-based polymers have been synthesized by Leclerc's research group (11–14). Luminescent materials spanning the entire visible range have been prepared from these polymers (15), which can be useful as LEDs (16, 17). To learn more about the structure–property relationships in this new class of materials, we believe that it is important to study the optical and photophysical properties of the corresponding carbazole oligomers. Therefore, we report herein the spectroscopy and photophysics of four carbazole-based triads: 1,4-bis(*N*-octylcarbazol-2-yl)phenylene (CPC), 2,5-bis(*N*-octylcarbazol-2-yl)thiophene (CTC), 2,7-bis(*N*-octylcarbazol-2-yl)-9,9-dihexylfluorene (CFC), and 2,7-bis(*N*-octylcarbazol-2-yl)-*N*-octylcarbazole (CCC) in solution. The absorption and emission energies of these derivatives are correlated with their electronic transitions computed from ZINDO/S calculations performed on optimized ground state (HF/6-31G*) and first relaxed excited state (RCIS/6-31G*). A good agreement is obtained between the computed electronic transitions and the optical data. Moreover, the photophysical results are discussed in terms of the relative importance of the radiative and nonradiative processes occurring in these materials. The molecular structures of the compounds investigated in this paper are displayed in Fig. 1.

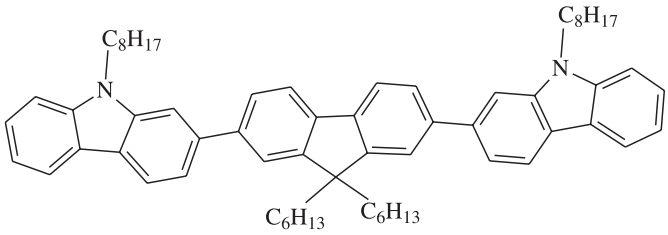
Fig. 1. Molecular structure of the carbazole-based triads.



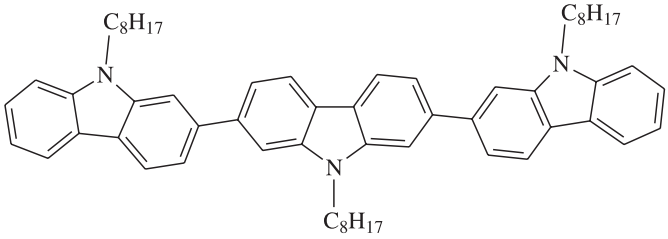
CPC



CTC



CFC



CCC

Experimental section

Materials

n-Hexane was purchased from Aldrich (spectrograde) and used as received. Prior to use, the solvent was checked for spurious emission in the region of interest and found to be satisfactory. All starting organic compounds were purchased from Aldrich Co. and used without further purification. *N*-Octyl-2,7-bis(4,4,5,5-tetramethyl-1,3,2-dioxaborolan-2-

© 2004 NRC Canada

yl)carbazole (12), $Pd(PPh_3)_4$ (18), *N*-octyl-2-(4,4,5,5-tetramethyl-1,3,2-dioxaborolan-2-yl)carbazole (19), 2-(4,4,5,5-tetramethyl-1,3,2-dioxaborolan-2-yl)-9,9-dioctylfluorene (20), and 2,7-bis(4,4,5,5-tetramethyl-1,3,2-dioxaborolan-2-yl)-9,9-dioctylfluorene (21) were synthesized following procedures reported in the literature.

Synthesis and characterization

The carbazole-based triads were synthesized by Suzuki coupling (22).

*1,4-Bis(*N*-octylcarbazol-2-yl)phenylene (CPC)*

Into a 10 mL flask was added 0.617 mmol (250 mg) of *N*-octyl-2-(4,4,5,5-tetramethyl-1,3,2-dioxaborolan-2-yl)carbazole, 0.339 mmol (80 mg) of 1,4-dibromobenzene, 2.5 mL of toluene, and 1.5 mL of a 2 mol L^{-1} solution of K_2CO_3 in water. The mixture was degassed under argon for 30 min. $Pd(PPh_3)_4$ (0.0123 mmol, 7 mg) was added to the mixture and the whole mixture was refluxed overnight. The whole mixture was extracted three times with chloroform and washed with water. The organic extracts were dried over magnesium sulfate and the solvent was removed under reduced pressure. The crude product was purified by column chromatography using 5% diethyl ether – hexanes as the eluent (R_f = 0.66) to provide 110 mg of a pale brown solid (mp = 172–178 °C) (yield = 51%). ^{1}H NMR (400 MHz, $CDCl_3$, ppm) δ: 8.18 (d, 2H, *J* = 8.1 Hz), 8.14 (d, 2H, *J* = 7.9 Hz), 7.87 (s, 4H), 7.66 (d, 2H, *J* = 1.1 Hz), 7.56 (dd, 2H, *J* = 8.1 and 1.5 Hz), 7.47 (m, 4H), 7.26 (t, 2H, *J* = 7.0 Hz), 4.38 (t, 4H, *J* = 7.0 Hz), 1.93 (qt, 4H, *J* = 7.1 Hz), 1.35 (m, 20H), 0.87 (t, 6H, *J* = 6.7 Hz). ^{13}C NMR (100 MHz, $CDCl_3$, ppm) δ: 144.87, 141.28, 141.09, 132.27, 125.93, 124.21, 122.89, 122.59, 120.94, 120.53, 119.24, 117.43, 108.97, 105.78, 43.30, 32.04, 29.60, 29.41, 29.20, 27.53, 22.84, 14.30. HR-MS calcd. for $C_{46}H_{52}N_2$: 632.4130; found: 632.4138.

*2,5-Bis(*N*-octylcarbazol-2-yl)thiophene (CTC)*

Into a 25 mL flask was added 1.95 mmol (0.22 mL) of 2,5-dibromothiophene, 3.70 mmol (1.5 g) of *N*-octyl-2-(4,4,5,5-tetramethyl-1,3,2-dioxaborolan-2-yl)carbazole, 5 mL of toluene, and 3 mL of a 2 mol L^{-1} solution of K_2CO_3 in water. The mixture was degassed under argon for 30 min. $Pd(PPh_3)_4$ (42 mg, 0.078 mmol) was added and the mixture was refluxed overnight. The whole mixture was extracted with chloroform three times and washed with water. The organic extracts were dried over magnesium sulfate and the solvent was removed under reduced pressure. The crude product was purified by column chromatography using 5% diethyl ether – hexanes as the eluent (R_f = 0.61) and the product was recrystallized in a minimum of chloroform in hexanes to provide 511 mg of a yellow solid (mp = 181 to 182 °C) (yield = 41%). ^{1}H NMR (400 MHz, $CDCl_3$, ppm) δ: 8.10 (d, 4H, *J* = 8.1 Hz), 7.66 (s, 2H), 7.57 (d, 2H, *J* = 8.1 Hz), 7.46 (m, 6H), 7.25 (t, 2H, *J* = 7.3 Hz), 4.35 (t, 4H, *J* = 7.4 Hz), 1.93 (q, 4H, *J* = 7.5 Hz), 1.36 (m, 20H), 0.87 (t, 6H, *J* = 6.8 Hz). ^{13}C NMR (75 MHz, $CDCl_3$, ppm) δ: 144.72, 141.13, 140.93, 132.11, 125.74, 124.01, 122.74, 122.43, 120.74, 120.34, 119.06, 117.27, 108.77, 105.60, 43.10, 31.84, 29.40, 29.20, 28.99, 27.33, 22.63, 14.07. HR-MS calcd. for $C_{44}H_{50}N_2S$: 638.3694; found: 638.3694.

*2,7-Bis(*N*-octylcarbazol-2-yl)-9,9-dihexylfluorene (CFC)*

Into a 5 mL flask was added 0.585 mmol (250 mg) of *N*-octyl-2-trifluoromethanesulfonylcarbazole, 0.278 mmol (163 mg) of 2,7-bis(4,4,5,5-tetramethyl-1,3,2-dioxaborolan-2-yl)-9,9-dioctylfluorene, 2 mL of THF and 1 mL of 2 mol L^{-1} K_2CO_3 in water. The mixture was degassed for 30 min under argon. $Pd(PPh)_3$ (0.0111 mmol, 6 mg) was added and the whole mixture was refluxed overnight. The mixture was extracted with chloroform three times and washed with water. The organic layer was dried over magnesium sulfate and the solvent was removed under reduced pressure. The crude product was purified by preparative TLC using 5% diethyl ether – hexanes as the eluent (R_f = 0.76). to provide 110 mg of a colorless rubbery solid (T_g = 19 °C) (yield = 44%). ^{1}H NMR (400 MHz, $CDCl_3$, ppm) δ: 8.21 (d, 2H, *J* = 8.1 Hz), 8.17 (d, 2H, *J* = 6.8 Hz), 7.88 (d, 2H, *J* = 7.5 Hz), 7.77 (d, 4H, *J* = 10.0 Hz), 7.69 (s, 2H), 7.60 (d, 2H, *J* = 7.8 Hz), 7.51 (t, 2H, *J* = 7.8 Hz), 7.46 (d, 2H, *J* = 8.1 Hz), 7.29 (t, 2H, *J* = 7.2 Hz), 4.41 (t, 4H, *J* = 6.8 Hz), 2.16 (m, 4H), 1.97 (q, 4H, *J* = 6.5 Hz), 1.39 (m, 20H), 1.17 (m, 12H), 0.90 (t, 10H, *J* = 7.2 Hz), 0.81 (t, 6H, *J* = 7.2 Hz). ^{13}C NMR (100 MHz, $CDCl_3$, ppm) δ: 152.01, 141.39, 141.29, 141.25, 140.18, 139.88, 126.78, 125.83, 122.92, 122.32, 122.28, 120.79, 120.62, 120.21, 119.13, 118.88, 108.96, 107.42, 55.56, 43.34, 40.70, 32.06, 31.74, 29.98, 29.64, 29.47, 29.29, 27.63, 24.14, 22.87, 22.83, 14.33, 14.26. HR-MS calcd. for $C_{40}H_{48}N_2$: 888.6321; found: 888.6339.

*2,7-Bis(*N*-octylcarbazol-2-yl)-*N*-octylcarbazole (CCC)*

Into a 10 mL flask was added 0.702 mmol (300 mg) of *N*-octyl-2-trifluoromethanesulfonylcarbazole, 0.351 mmol (186 mg) of *N*-octyl-2,7-bis(4,4,5,5-tetramethyl-1,3,2-dioxaborolan-2-yl)carbazole, 2 mL of THF and 1 mL of 2 mol L^{-1} K_2CO_3 in water. The mixture was degassed for 30 min under argon. $Pd(PPh)_3$ (0.0140 mmol, 8 mg) was added and the whole mixture was refluxed overnight. The mixture was extracted with chloroform three times and washed with water. The organic layer was dried over magnesium sulfate and the solvent was removed to dryness. The crude product was solubilized in hot hexanes and filtered to elimimate the catalyst residues. The solution was evaporated and recrystallized in a minimum of hexanes to provide 158 mg of an off-white powder (T_g = 20 °C) (yield = 54%). ^{1}H NMR (400 MHz, $CDCl_3$, ppm) δ: 8.23 (m, 4H), 8.17 (d, 2H, *J* = 8.0 Hz), 7.75 (s, 4H), 7.66 (m, 4H), 7.50 (m, 4H), 7.29 (t, 2H, *J* = 7.6 Hz), 4.48 (t, 2H, *J* = 7.6 Hz), 4.41 (t, 4H, *J* = 6.8 Hz), 1.99 (m, 6H), 1.40 (m, 30H), 0.88 (m, 9H). ^{13}C NMR (100 MHz, $CDCl_3$, ppm) δ: 141.84, 141.28, 141.23, 140.51, 140.48, 125.82, 122.94, 122.22, 122.09, 120.81, 120.80, 120.62, 119.50, 119.30, 119.13, 108.96, 108.01, 107.95, 43.36, 43.39, 32.08, 32.07, 29.69, 29.67, 29.50, 29.47, 27.69, 27.64, 22.87, 14.33, 14.32. HR-MS calcd. for $C_{60}H_{71}N_3$: 833.5648; found: 833.5640.

Instrumentation

^{1}H and ^{13}C NMR spectra were recorded on a Bruker AMX300 or on a Varian AS400 apparatus in deuterated solvent solutions at 298 K. Differential scanning calorimetry (DSC) analyses were performed on a PerkinElmer (DSC-7)

© 2004 NRC Canada

instrument, calibrated with ultrapure indium, at a scanning rate of 10 °C/min under a nitrogen flow.

Absorption spectra were recorded on a Varian Cary 1 Bio UV–vis spectrophotometer at room temperature using 1 cm quartz cells and solute concentrations of (1–3) × 10^{-5} mol L^{-1}. It has been verified that the Beer–Lambert law is well-respected in the region of the concentrations used. Fluorescence spectra corrected for the emission detection were recorded on a Spex Fluorolog-2 spectrophotometer with a F2T11 special configuration. Excitation and emission band passes used were 2.6 and 1.9 nm, respectively. Each solution was excited near the absorption wavelength maximum using a 1 cm path length quartz cell. Solution concentrations used were (1–3) × 10^{-6} mol L^{-1}, giving absorbances always less than 0.1 to avoid any inner-filter effects. For all molecules, a study of the concentration (*C*) effect has been done on the fluorescence intensity (I_F) and all measurements have been performed in the linear region of the I_F vs. *C* curve. All corrected fluorescence excitation spectra were found to be equivalent to their respective absorption spectra. Quantum yields of fluorescence were determined in argon-saturated solutions of the substrates at 298 K against 9,10-diphenylanthracene in cyclohexane (ϕ_f = 0.90) as a standard (23).

Fluorescence lifetimes were measured on a multiplexed time-correlated single-photon-counting fluorimeter (Edinburgh Instruments, model 299T) at 298 K. Details on the instrument have been published elsewhere (24). The instrument incorporates an all-metal coaxial hydrogen flashlamp. Reconvolution analysis was performed by fitting over all the fluorescence decay including the rising edge. The kinetic interpretation of the goodness-of-fit was assessed using plots of weighted residuals, reduced $\chi 2$ values, and Durbin–Watson (DW) parameters.

Calculation methodology

Ab initio calculations were performed on a Pentium 4 (2.53 Gz) personal computer with 1 Gb RAM using the Gaussian 98W program, version 5.2 (25). The geometries were optimized at the HF level with the 6-31G* basis set. The Berny analytical gradient method was used for the optimizations. The requested HF convergence on the density matrix was 10^{-8} and the threshold values for the maximum force and the maximum displacement were 0.00045 and 0.0018 au, respectively.

The ZINDO/S method including configuration interaction (CI) as employed in the HyperChem package (version 5.01) was used to calculate the singlet–singlet electronic transition energies of the optimized conformers. ZINDO/S is a modified INDO method parameterized to reproduce UV–vis spectroscopic transitions (26, 27). The electron-repulsion integrals were evaluated using the Mataga–Nishimoto formula. All singly excited configurations involving the 20 highest occupied and the 20 lowest unoccupied orbitals (CI = 20/20) were included in the energy calculation. The π-π* overlap weighting factor has been adjusted to 0.548 to reproduce the S_1 origin of fluorene (33 779 cm^{-1}) measured in a supersonic jet (28).

The excited state geometries were optimized with the restricted configuration interaction of singly excited states (RCIS) using 6-31G* basis sets. The optimized excited state geometries have been used as inputs for the ZINDO/S program to obtain the electronic transition energies from the relaxed excited states.

Fig. 2. Absorption (—) and fluorescence (----) spectra of CPC in *n*-hexane. The fluorescence intensity has been normalized relative to the absorption band.

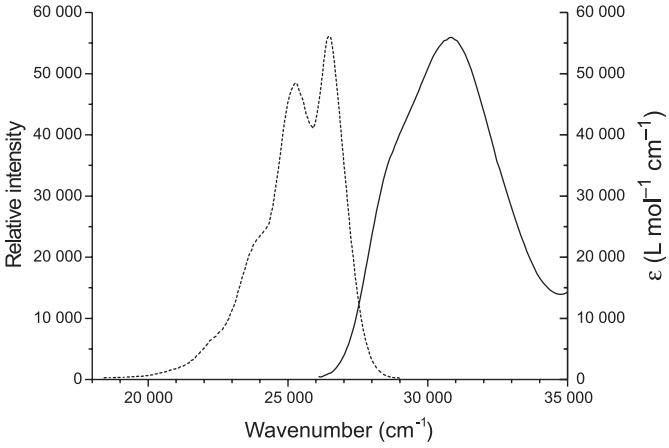
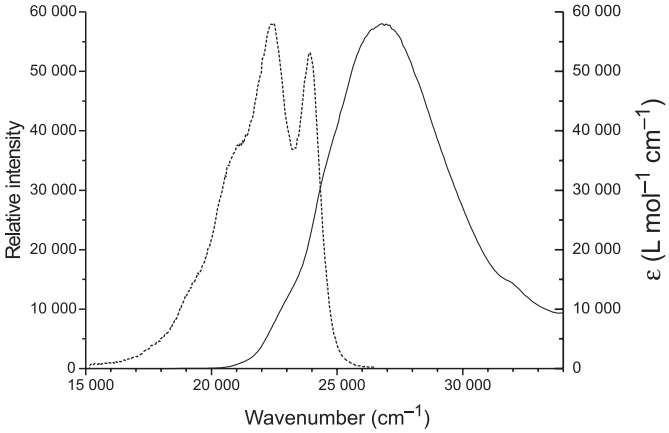


Fig. 3. Absorption (—) and fluorescence (----) spectra of CTC in *n*-hexane. The fluorescence intensity has been normalized relative to the absorption band.



Results and discussion

Optical properties

The absorption and fluorescence spectra of the carbazole-based triads have been recorded in *n*-hexane at room temperature and are shown in Figs. 2–5. Their spectral data are reported in Table 1.

The first absorption band of CPC is centered at 30 800 cm^{-1}. A shoulder is observed around 28 700 cm^{-1} showing that this molecule possesses a certain rigidity in its ground state. In contrast, the fluorescence spectrum of CPC shows two well-resolved vibronic peaks at 26 500 and 25 300 cm^{-1} and a shoulder at around 23 800 cm^{-1}. This indicates that the molecule is more rigid in its first relaxed excited state.

The replacement of the phenyl group by a thiophene ring provokes a large red shift of the absorption and fluorescence bands in CTC. Two effects might be responsible for this be-

© 2004 NRC Canada

Table 1. Spectroscopic parameters of carbazole-based triads in *n*-hexane at room temperature (298 K).

Molecule	λ_A[a] (nm)	ν_A[b] (cm^{-1})	ε[c] (L mol^{-1} cm^{-1})	$FWHM_A$[d] (cm^{-1})	λ_F[e] (nm)	ν_F[f] (cm^{-1})	$FWHM_F$[g] (cm^{-1})
CPC	325	30 800	55 900	4800	396	25 300	2700
CTC	374	26 900	58 000	5500	447	22 400	3945
CFC	348	28 700	78 800	4900	409	24 500	2800
CCC	352	28 400	80 000	4500	409	24 500	2600

[a]Absorption wavelengths taken at the maximum of the absorption band.
[b]Absorption wavenumbers taken at the maximum of the absorption band.
[c]Absorption coefficient at the maximum of the absorption band.
[d]Full width at half-maximum (FWHM) of the absorption band.
[e]Fluorescence wavelengths at the maximum of the 0–1 vibronic peak.
[f]Fluorescence wavenumbers at the maximum of the 0–1 vibronic peak.
[g]Full width at half-maximum (FWHM) of the fluorescence band.

Fig. 4. Absorption (—) and fluorescence (----) spectra of CFC in *n*-hexane. The fluorescence intensity has been normalized relative to the absorption band.

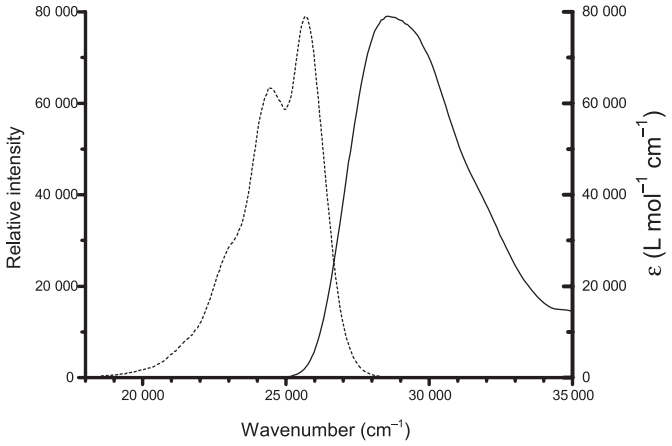
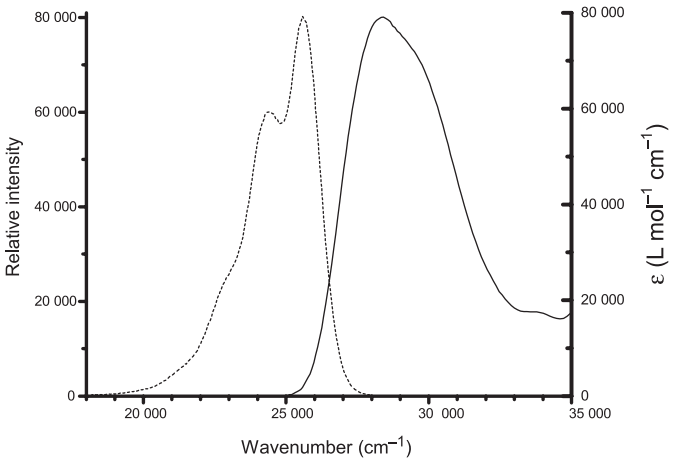


Fig. 5. Absorption (—) and fluorescence (----) spectra of CCC in *n*-hexane. The fluorescence intensity has been normalized relative to the absorption band.



havior: (*i*) a decrease in the twisting between thiophene and carbazole rings and (*ii*) a charge transfer interaction due to the electron donor properties of the thiophene ring. To distinguish between these two effects, HF/6-31G* ab initio calculations were performed on both molecules. To reduce the time scale of the calculations, the octyl chain on the nitrogen atom of each carbazole unit was replaced by an ethyl group. The dihedral angles between adjacent rings are summarized in Table 2. One can see that CTC is slightly less twisted than CPC in its ground state. This effect should contribute to the bathochromic shifts observed in the absorption spectrum of CTC. But in our opinion, the experimental shifts are too large to be explained solely by such small conformational changes. To confirm this statement, ZINDO/S calculations were performed for the conformers of CTC having dihedral angles of 45° and 37°, respectively. It was observed that the more planar conformer of CTC contributes to a red shift of about 800 cm^{-1}, whereas the experimental bathochromic shift observed between the absorption maxima of CPC and CTC is about 4000 cm^{-1} (see Table 1). One can then conclude that the presence of the thiophene ring in the CTC chromophore provokes significant charge transfer interactions. This was confirmed from atomic charges obtained from HF and RCIS calculations. Accordingly, the bandwidth of the absorption band of CTC is wider than that of CPC.

Compared to the absorption and fluorescence spectra of CPC, the optical transitions of CFC are red shifted (see Fig. 4 and Table 1). This is due to the increase of the conjugation length. Moreover, one can see in Table 2 that the torsional angles between adjacent rings of both molecules are very close. This indicates that increasing the conjugation length does not improve the molecular planarity of CFC. Accordingly, the absorption and fluorescence bandwidths of CPC and CFC are very similar.

Finally, Table 1 and Fig. 5 show that the absorption and fluorescence band maxima of CCC are very close to those obtained for CFC. Moreover, one can see that the bandwidths of the absorption and fluorescence spectra of both molecules are very similar. Along these lines, Table 2 shows that the dihedral angles and the inter-ring distances of CFC and CCC are very close. It thus seems that that the replacement of a fluorene ring by a carbazole moiety does not significantly affect the molecular structure and the optical properties of carbazole derivatives.

It is also observed that the fluorescence spectra of the four compounds are sharper and more structured compared to their respective absorption spectra (see Figs. 2–5 and Table 1). This suggests that these molecules, in the relaxed S_1 state, are characterized by more rigid conformations of the subunits. This is in agreement with the computed S_1 torsional potentials of carbazole-based dyads showing that the co-planar energy barrier is much reduced for all the derivatives in the S_1 state, whereas the energy barriers at the per-

© 2004 NRC Canada

Table 2. Dihedral angles and inter-ring distances of carbazole-based triads in the ground and relaxed S_1 excited states as obtained by HF/6-31G* and RCIS/6-31G* ab initio calculations.

	S_0		S_1	
Molecule	Dihedral angles (°)	Inter-ring distances (Å)	Dihedral angles (°)	Inter-ring distances (Å)
CPC	44.8	1.490	15	1.432
CTC	37.1	1.478	0	1.430
CFC	45.4	1.491	15	1.451
CCC	46.0	1.492	15	1.450

Fig. 6. Contour plots of the HOMO and LUMO of CPC as calculated by HF/6-31G* ab initio calculations.

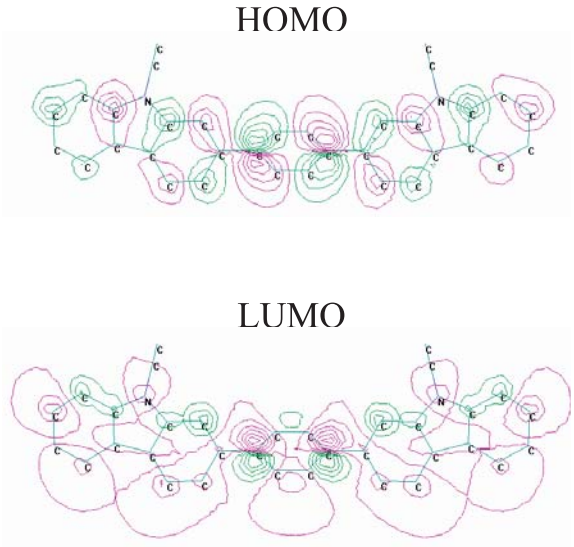


Table 3. HOMO, LUMO, and HOMO–LUMO energy gaps of carbazole-based triads as obtained from HF/6-31G* ab initio calculations.

Molecule	HOMO (eV)	LUMO (eV)	HOMO–LUMO (eV)
CPC	–7.12	2.37	9.49
CTC	–6.96	2.13	9.09
CFC	–6.93	2.22	9.15
CCC	–6.87	2.25	9.12

pendicular conformations are much larger when the molecules are excited to the S_1 state as compared to those in the ground state (29). Moreover, one can see in Fig. 3 that the 0–1 vibronic peak of the fluorescence spectrum of CTC is more intense than the 0–0 vibronic peak causing a broadening of the emission band. As discussed above, this is probably due to charge transfer interactions caused by the presence of the thiophene ring.

Frontier molecular orbitals

The nature and the energies of the HOMO and LUMO of these carbazole derivatives, which are mainly involved in the first allowed electronic excitation ($S_3 \leftarrow S_0$, see below), were investigated at the HF/6-31G* level. Both molecular orbitals of each derivative are delocalized along the long molecular axis and involve mainly p_z (out-of-plane axis) atomic orbitals. The nature of the molecular orbitals remains unchanged among the oligomers investigated. For each compound, we have found that the HOMO possesses an antibonding character between adjacent rings, which may explain the nonplanarity observed for these derivatives in their ground electronic state. On the other hand, the LUMO of all the derivatives shows a bonding character between adjacent rings. As an example, Fig. 6 shows the contour plots of the HOMO and LUMO of CPC. This implies that the promotion of an electron from the HOMO to the LUMO is indeed improving the molecular planarity of these derivatives as suggested above from the fluorescence spectra.

The energies of the HOMO and LUMO are given in Table 3. Compared to CPC, one can see that the HOMOs of CTC, CFC, and CCC are destabilized whereas their LUMOs are stabilized. Consequently, the HOMO–LUMO energy gaps are smaller for the latter molecules than that of CPC. Among the four carbazole-based triads investigated, the HOMO–LUMO energy gap of CTC is the smallest. This clearly shows that the thiophene ring possesses strong electron donor properties that can be more dominating than the conjugation length of the molecule. Indeed, CFC and CCC possess longer conjugation lengths than CTC but show larger energy gaps.

Electronic excitations

The ZINDO/S semiempirical method was used to obtain the nature and the energy of the first three electronic transitions in the oligomers. Optimized geometries (HF/6-31G*) were used in the calculations. The electronic excitation properties are summarized in Table 4.

The $S_1 \leftarrow S_0$ and $S_2 \leftarrow S_0$ electronic transitions (π-π^*) of CPC are very close in energy and possess oscillator strengths (f) of very small values. On the other hand, the $S_3 \leftarrow S_0$ electronic transition possesses a much larger oscillator strength and is mainly described by the promotion of one electron from the HOMO to the LUMO. ZINDO/S calculations also show that the $S_3 \leftarrow S_0$ electronic transition of CPC is dipole allowed and polarized along the long axis of the molecule (x) (see Table 4). This electronic transition is computed at 31 600 cm^{-1} and should correspond to the first absorption band of this molecule measured at 30 800 cm^{-1} in n-hexane and having a large absorption coefficient (55 900 L mol^{-1} cm^{-1}).

A small energy decrease is computed for the two weakly allowed electronic transitions of CTC compared to those of CPC. On the other hand, the strongly allowed electronic transition of CTC becomes the first electronic transition

© 2004 NRC Canada

Table 4. Singlet–singlet electronic transition data obtained by the ZINDO/S semiempirical method for the carbazole-based triads at the HF/6-31G* optimized geometry.

Molecule	Electronic transitions	Energy (cm^{-1})	f	Transition dipole moment (D)		
				X^a	Y	Z
CPC	$S_1 \leftarrow S_0$	30 200	0.012	0.455	–0.794	0.0394
	$S_2 \leftarrow S_0$	30 300	0.012	–0.779	–0.455	0.0222
	$S_3 \leftarrow S_0$	31 600	1.603	–10.4	–0.0003	0.0004
CTC	$S_1 \leftarrow S_0$	28 700	1.653	–11.1	0.0131	0.0007
	$S_2 \leftarrow S_0$	29 900	0.006	0.335	0.535	–0.247
	$S_3 \leftarrow S_0$	30 000	0.005	0.3611	–0.4509	0.2128
CFC	$S_1 \leftarrow S_0$	30 200	0.239	4.09	–0.173	0.0230
	$S_2 \leftarrow S_0$	30 300	0.020	0.724	0.948	–0.114
	$S_3 \leftarrow S_0$	30 500	2.056	12.0	–0.002	0.002
CCC	$S_1 \leftarrow S_0$	29 800	0.007	–0.0291	0.602	–0.389
	$S_2 \leftarrow S_0$	30 300	0.037	–1.36	0.840	0.0949
	$S_3 \leftarrow S_0$	30 400	2.09	12.2	–0.003	0.001

[a] X is the long molecular axis.

computed at 28 700 cm^{-1} (see Table 4). This electronic transition is lowered by 2900 cm^{-1} compared to the dipole-allowed transition of CPC ($S_3 \leftarrow S_0$). This indicates the effect of the electron donor properties of the thiophene ring along the x axis of the triad.

The first two electronic transitions of CFC are computed at exactly the same energies as those of CPC. On the other hand, the $S_3 \leftarrow S_0$ electronic transition of CFC is calculated at 30 500 cm^{-1}, which is lower in energy by 1100 cm^{-1} compared to that of CPC. This goes along with the conjugation length, which increases for the former molecule. Finally, Table 4 shows that the electronic transitions of CCC are computed at about the same energy as those of CFC. This shows that the replacement of the fluorene ring by a carbazole unit does not significantly affect the spectroscopy of these carbazole-based triads.

Finally, it is also observed that the excitation energies of the first allowed electronic transition of the four carbazole derivatives follow the relative values of their HOMO–LUMO energy gaps computed in Table 3.

Emission energies

The optimization (relaxation) of the singlet excited states was done using the RCIS/6-31G* method. As observed recently for carbazole-based dyads, a crossing of the excited states occurs such that the first electronic transition becomes dipole allowed, with a high value of its oscillator strength (29).

The RCIS/6-31G* inter-ring distances and the torsional angles (θ) of the molecules in the S_1 (optimized) state are listed in Table 2. For the four derivatives in the S_1 state, it was found that the inter-ring bond lengths are significantly shorter compared to the respective bond lengths computed for the molecules in their ground state (see Table 2). This indicates that, in the S_1 relaxed excited state, these derivatives possess much more quinoidic-like character. In other words, the conjugation along the long axis of the molecule is enhanced in the S_1 state. In these conditions, it is not surprising to observe that each derivative almost reaches coplanarity in the S_1 state.

The RCIS/6-31G*-optimized geometries have been used as input in the ZINDO/S program to obtain the electronic transition energies from the relaxed excited states. For the four carbazole derivatives, a crossing in the relaxed excited states is achieved such that the electronic transition from the first relaxed excited state ($S_1 \leftarrow S_0$) is dipole allowed. Thus, this transition taken at the minimum of the S_1 torsional potentials should correspond to the emission energy of the oligomers. Indeed, the absorption of a photon excites the molecules to a Franck–Condon state, in which they should possess the same torsional angle as the molecules in the S_0 state. After the excitation, the molecules should relax to their most stable geometry before the emission process can occur. The results are compiled in Table 5. As expected, the relative order of the emission energies is the same as that of the corresponding absorption energies. Indeed, the $S_1 \rightarrow S_0$ energy of CPC is the highest among the four carbazole derivatives investigated, whereas the emission transition of CTC is computed at the lowest energy. The energy of the 0–1 fluorescence peaks (near maxima) of the carbazole derivatives are reported in Tables 5. One can see that the fluorescence peaks of the carbazole derivatives are in very good agreement with the computed emission energies.

Molecular photophysics

The fluorescence quantum yields (ϕ_F) and lifetimes (τ_F) as well as the radiative ($k_F = \phi_F/\tau_F$) and nonradiative ($k_{nr} = k_F(1 - \phi_F)/\phi_F$) decay rate constants of all the compounds are reported in Table 6. For all fluorescence decay profiles, a single-exponential fit gives acceptable statistical parameters ($\chi^2 < 1.3$ and DW ≈ 1.7).

Table 6 shows that ϕ_F and τ_F of CTC are smaller than those of CPC giving rise to a much higher value of k_{nr}. For oligothiophenes, it is well-established that the main deactivation pathway of the S_1 state involves an intersystem crossing process (k_{isc}) because of the presence of the heavy sulphur atom (30, 31). The same behavior may also occur here for CTC and might contribute to the deactivation of the fluorescence. An internal conversion process could also contribute to the deactivation of the fluorescence of CTC. How-

© 2004 NRC Canada

Table 5. Electronic transition energies (E ($S_1 \rightarrow S_0$)) of the carbazole derivatives as obtained by ZINDO/S performed on the RCIS/6-31G* optimized geometries of S_1 relaxed excited states.

Molecule	Wavelength (nm)	E ($S_1 \rightarrow S_0$) (cm^{-1})	f	Transition dipole moment			E_f (nm)	ν_F (cm^{-1})
				X^a	Y	Z		
CPC	397	25 200	2.26	13.8	0.0057	–0.0006	396	25 300
CTC	463	21 600	1.83	13.4	0.0026	–0.0006	447	22 400
CFC	406	24 600	2.48	14.6	–0.011	0.0019	409	24 500
CCC	407	24 600	2.39	14.4	0.0068	0.0015	409	24 500

Note: Experimental wavenumbers (0–2 fluorescence peaks in *n*-hexane) are given in the last column.
[a]*X* is the long molecular axis.

Table 6. Photophysical properties of carbazole-based triads in *n*-hexane at room temperature (298 K).

Molecule	ϕ_F	τ_F (ns)	10^{-8} $k_F{}^a$ (s^{-1})	10^{-8} $k_{nr}{}^b$ (s^{-1})
CPC	0.52	1.74	3.0	2.8
CTC	0.23	0.57	4.0	14
CFC	0.66	0.84	7.9	4.0
CCC	0.62	0.88	7.1	4.4

[a]$k_F = \phi_F/\tau_F$ (radiative fluorescence decay rate constant).
[b]$k_{nr} = k_F(1 - \phi_F)/\phi_F$ (nonradiative fluorescence decay rate constant).

ever, we have reported recently that the S_1 torsional potential surfaces of the corresponding dyads (CT and CC) are very similar, suggesting that both molecules possess about the same flexibility in the S_1 excited state (29). Thus, these theoretical results strongly suggest that the internal conversion process does not play an important role in the deactivation pathway of CTC compared with that of CPC. It is also worth noting that the radiative decay constant of CTC is slightly larger than that of CPC. The electron donor properties of the thiophene group may be responsible for this behavior.

On the other hand, Table 6 shows that the fluorescence quantum yields of CFC and CCC are higher than that of CPC. Higher k_F values of CFC and CCC are mainly responsible for this behavior. This is surely due to a longer conjugation length experienced by CFC and CCC as shown by the ε and f values computed in Tables 1 and 4, respectively. Moreover, it is observed that the replacement of a fluorene ring by a carbazole unit does not affect much the photophysical parameters of these carbazole derivatives.

Concluding remarks

The first absorption band of each derivative can be assigned to the calculated electronic transition, which corresponds mainly to the promotion of an electron from the HOMO to the LUMO. The HOMO possesses an antibonding character between neighboring rings, which should contribute to the nonplanarity observed for these derivatives in their ground states. On the other hand, the LUMO shows bonding character between adjacent rings in agreement with more planar S_1 excited states. The overall shape of the absorption and fluorescence spectra suggests that the molecules are more planar in the first relaxed excited state than in the ground state. Ab initio calculations performed on the carbazole derivatives in their ground (HF/6-31G*) and excited states (CIS/6-31G*) confirm this statement.

The replacement of a phenyl group by a thiophene moiety causes a siginificant red shift of the absorption and fluorescence bands, which is mainly due to the electron donor properties of the thiophene ring. The increase of the conjugation length (CFC and CCC) also induces a red shift of the absorption and emission spectra. After relaxation of the excited states (optimization), a crossing of the excited states of the oligomers is achieved such that the first electronic transition of each derivative becomes dipole allowed, with a high value of the oscillator strength. The fluorescence spectrum of each derivative is well reproduced by ZINDO/S semiempirical calculations performed on the optimized S_1 geometries.

The fluorescence quantum yield and lifetime of CTC are smaller than those of CPC giving rise to a higher nonradiative decay rate constant for the former compound. These results are interpreted in terms of an intersystem crossing process (k_{isc}) because of the presence of the heavy sulphur atom. On the other hand, fluorescence quantum yields of CFC and CCC are slightly larger than that of CPC. An increase of the k_F values of CFC and CCC, caused by an increase in the conjugation length, is mainly responsible for this behavior. Moreover, it is observed that the replacement of a fluorene ring by a carbazole moiety does not significantly affect conformational, spectroscopic, and photophysical properties of carbazole-based triads.

Finally, we found a good agreement between theoretical electronic transitions (excitation and emission energies) and experimental spectra (absorption and fluorescence). Thus, we believe that this methodology can be used to design organic light-emitting diodes based on oligo- and polycarbazoles.

Acknowledgements

This work was supported by Natural Sciences and Engineering Research Council of Canada (NSERC) strategic and research grants.

References

1. C.D. Dimitrakopoulos and P.R.L. Malenfant. Adv. Mater. **14**, 99 (2002).
2. H.E. Katz and Z. Bao. J. Phys. Chem. B, **104**, 671 (2000).
3. G. Horowitz. Adv. Mater. **10**, 365 (1998).
4. C.J. Brabec, N.S. Sariciftci, and J.C. Hummelen. Adv. Funct. Mater. **12**, 192 (2002).
5. N.S. Sariciftci, D. Braun, C. Zhang, V.I. Srdanov, A.J. Heeger, G. Stucky, and F. Wudl. Appl. Phys. Lett. **62**, 585 (1993).
6. D. Neher. Macromol. Rapid Commun. **22**, 1365 (2001)

© 2004 NRC Canada

7. M. Leclerc. J. Polym. Sci. Part. A, Polym. Chem. **39**, 2867 (2001).
8. U. Mitschke and P. Bauerle. J. Mater. Chem. **10**, 1471 (2000).
9. A. Kraft, A.C. Grimsdale, and A.B. Holmes. Angew. Chem. Int. Ed. **37**, 402 (1998).
10. J.H. Burroughes, D.D.C. Bradley, A.R. Brown, R.N. Marks, K. MacKay, R.H. Friend, P.L. Burns, and A.B. Holmes. Nature (London), **347**, 539 (1990).
11. J. Bouchard, M. Belletête, G. Durocher, and M. Leclerc. Macromolecules, **36**, 4624 (2003).
12. G. Zotti, G. Schiavon, S. Zecchin, J.-F. Morin, and M. Leclerc. Macromolecules, **35**, 2122 (2002).
13. J.-F. Morin, P.-L. Boudreault, and M. Leclerc. Macromol. Rapid Commun. **23**, 1032 (2002).
14. J.-F. Morin and M. Leclerc. Macromolecules, **34**, 4680 (2001).
15. J.-F. Morin and M. Leclerc. Macromolecules, **35**, 8413 (2002).
16. J.-F. Morin, S. Beaupré, M. Leclerc, I. Lévesque, and M. D'Iorio. Appl. Phys. Lett. **80**, 341 (2002).
17. N. Drolet, S. Beaupré, J.-F. Morin, Y. Tao, and M. Leclerc. J. Opt. A: Pure Appl. Opt. **4**, S252 (2002).
18. D.R. Coulson. Inorg. Synth. **13**, 121 (1972).
19. M. Belletête, M. Bédard, M. Leclerc, and G. Durocher. Synth. Met. **146**, 99 (2004).
20. M. Belletête, S. Beaupré, J. Bouchard, P. Blondin, M. Leclerc, and G. Durocher. J. Phys. Chem. B, **104**, 9118 (2000).
21. M. Ranger, D. Rondeau, and M. Leclerc. Macromolecules, **30**, 7686 (1997).
22. M. Rehahn, A.D. Schlüter, G. Wegner, and W.J. Feast. Polymer, **30**, 1054 (1989).
23. D.F. Eaton. Pure Appl. Chem. **60**, 1107 (1988).
24. B. Zelent, T. Ganguly, L. Farmer, D. Gravel, and G. Durocher. J. Photochem. Photobiol. **56**, 165 (1991).
25. M.J. Frisch, G.W. Trucks, H.B. Schlegel, G.E. Scuseria, M.A. Robb, J.R. Cheeseman, V.G. Zakrzewski, J.A. Montgomery, Jr., R.E. Stratmann, J.C. Burant, S. Dapprich, J.M. Millam, A.D. Daniels, K.N. Kudin, M.C. Strain, O. Farkas, J. Tomasi, V. Barone, M. Cossi, R. Cammi, B. Mennucci, C. Pomelli, C. Adamo, S. Clifford, J. Ochterski, G.A. Petersson, P.Y. Ayala, Q. Cui, K. Morokuma, D.K. Malick, A.D. Rabuck, K. Raghavachari, J.B. Foresman, J. Cioslowski, J.V. Ortiz, B.B. Stefanov, G. Liu, A. Liashenko, P. Piskorz, I. Komaromi, R. Gomperts, R.L. Martin, D.J. Fox, T. Keith, M.A. Al-Laham, C.Y. Peng, A. Nanayakkara, C. Gonzalez, M. Challacombe, P.M.W. Gill, B. Johnson, W. Chen, M.W. Wong, J.L. Andres, C. Gonzalez, M. Head-Gordon, E.S. Replogle, and J.A. Pople. Gaussian 98W. Version 5.2 [computer program]. Gaussian, Inc., Pittsburgh, Pa. 1998.
26. J. Ridley and M.C. Zerner. Theor. Chim. Acta, **32**, 111 (1973).
27. C. Forber and M.C. Zerner. J. Am. Chem. Soc. **107**, 5884 (1985).
28. X. Zhang, J.D. Pitts, R. Nadarajah, and J.L. Knee. J. Chem. Phys. **107**, 8239 (1997).
29. M. Belletête, M. Bédard, M. Leclerc, and G. Durocher. J. Mol. Struct. (THEOCHEM), **679**, 9 (2004).
30. R.S. Becker, J. Seixas De Malo, A.L. Maçanita, and F. Elisei. Pure Appl. Chem. **87**, 9 (1995).
31. R. Rossi, M. Ciofalo, A. Carrita, and G. Ponterini. J. Photochem. Photobiol. A: Chem. **70**, 59 (1993).

© 2004 NRC Canada

A new efficient synthesis of α-methyl-β-ketoesters through an Eschenmoser sulfide reaction

Christian Bellec and Olivier Gaurat

Abstract: Various α-methyl-β-ketoesters were readily synthesized through Eschenmoser condensation of thioamides with a commercially available bromoester. β-Enaminoesters were easily prepared through this sulfide contraction reaction and were hydrolysed to afford the corresponding β-ketoesters in moderate to good yields.

Key words : α-alkylated-β-ketoesters, Eschenmoser, β-enaminoesters.

Résumé : Divers β-cétoesters-α-méthylés sont facilement préparés par condensation d'Eschenmoser de thioamides avec un bromoester commercial. Les β-énaminoesters, facilement préparés par cette réaction d'extrusion de soufre, sont hydrolysés pour conduire aux β-cétoesters correspondants avec des rendements bons à modérés.

Mots clés : β-cétoesters α-alkylés, Eschenmoser, β-énaminoesters.

Introduction

β-Ketoesters are widely recognized as very useful auxiliaries for several organic syntheses. Many synthetic approaches to α-unsubstituted compounds have been reported in the literature over the years (1–3). Conversely, investigations into reactions giving α-alkylated β-ketoesters directly have been more limited. Most often, these latter compounds have been obtained by alkylation of unsubstituted moieties, with the obvious disadvantages associated with this methodology (4, 5).

For some time, we have been interested in the synthesis of β-enaminoesters using the Eschenmoser coupling reaction (6, 7). Such enaminoesters are particularly suitable intermediates for the synthesis of various alkaloids (8, 9). More recently, we became interested in a new application of the efficient Eschenmoser alkylation sulfur contraction reaction for a short and convenient access to α-monoalkylated β-ketoesters that could take its place among other methodologies.

In the literature, various synthetic routes have been exploited for access to α-alkylated β-ketoesters. The direct alkylation method with aliphatic substrates, initially reported by Robinson (1), has been seldom used and leads generally to poor yields (10). Indeed, it is often difficult to avoid a double condensation or an *O*-alkylation process, although some recent modifications of the work-up procedure gave rise to better results (11, 12).

Received 10 December 2003. Published on the NRC Research Press Web site at http://canjchem.nrc.ca on 2 November 2004.

C. Bellec[1,2] and O. Gaurat. Laboratoire de Chimie des Hétérocycles (UMR 7611), Université Pierre et Marie Curie, 4 Place Jussieu, 75252 Paris CEDEX 05, France.

[1]Present address: Laboratoire de Chimie organique, Université Pierre et Marie Curie, Case courrier 64, 4 Place Jussieu, 75252 Paris CEDEX 05, France.

[2]Corresponding author (e-mail: bellec@ccr.jussieu.fr).

The preparation of β-ketoesters from malonic acid ester precursors has generally been rarely used for monoalkylated compounds (2, 4, 13). Other synthetic approaches, using a modified Reformatsky reaction (14–16), treatment of an acylpyrazole with an organozinc reagent (17), or α-diazo-β-hydroxyester rearrangment (18), have been described but do not have, on the whole, general applicability. Oxidation of β-hydroxyesters has most often been carried out with nonalkylated substrates (19, 20).

We wish to report herein a new methodology that provides direct access to α-substituted β-ketoesters from enaminoesters. These substrates are readily prepared through an Eschenmoser sulfide reaction involving condensation of thioamides with bromoesters and are then hydrolyzed, in a final step, to afford the desired ketoesters with moderate to good yields.

Results and discussion

Synthesis of thioamides

The synthesis of thioamides **2a–2f** was carried out by condensation of acyl chlorides **1a**–**1f** with pyrrolidine in the presence of pyridine. Amide moieties obtained in a first step were not isolated but were directly transformed into thioamides using P_4S_{10} (Scheme 1).

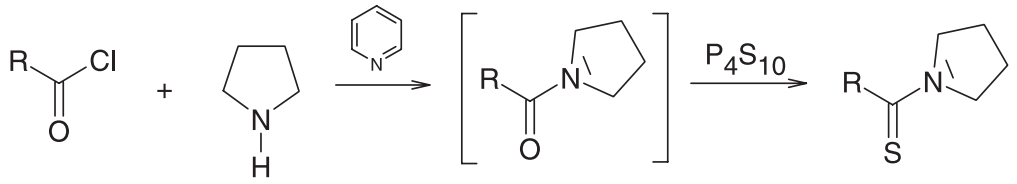
Synthesis of α-substituted β-ketoesters

Various α-substituted β-ketoesters were produced by hydrolysis of the corresponding enaminoesters, which were most often not isolated. The synthesis of these enaminoesters was first carried out by adapting the modified Eschenmoser coupling reaction previously described for thiolactams (6). Thus, a mixture of triethylamine and triphenylphosphine in dry acetonitrile was slowly added to a solution of thioamide **2** and commercially available 2-bromopropionic acid ethylester (**3**) in refluxing CH_3CN (Scheme 2).

The condensation was monitored by gas chromatography. Despite a good rate of thioamide transformation (except in

 doi: 10.1139/V04-088 © 2004 NRC Canada

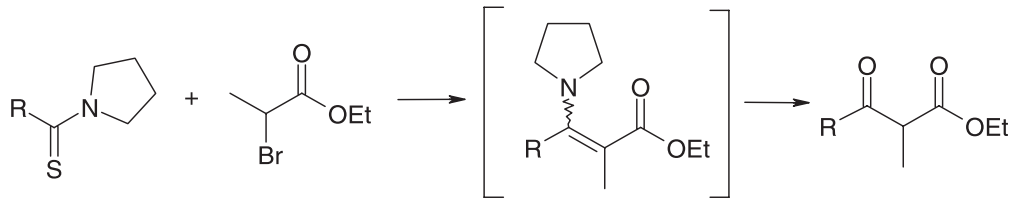
Scheme 1. Preparation of thioamides **2a**–**2f**.



1a – 1f **2a – 2f**

Compound	R
a	*n*-Pr
b	*i*-Bu
c	*t*-Bu
d	*n*-Pent
e	Ph
f	$(CH_2)_2COOMe$

Scheme 2. Preparation of β-enaminoesters **5a**–**5f**.



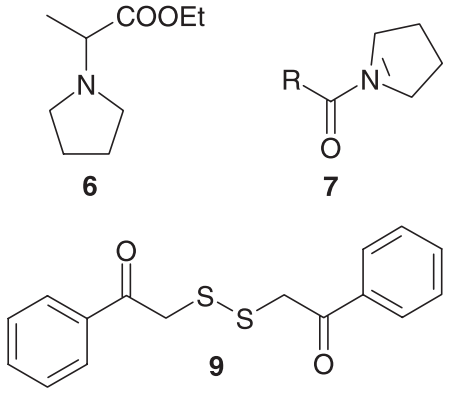
2a – 2f **3** **4a – 4f** **5a – 5f**

the case of **2c**, for which no reaction was observed), several by-products were observed in the crude reaction mixture. Besides the α-substituted β-ketoester **5** and the desulfuration product $Ph_3P=S$, the aminoester **6** (Scheme 3), amide **7**, and sulfide **8** ($EtOOC–CH(CH_3)–S–CH(CH_3)–COOEt$) were also detected.

Although the condensation was carried out under a nitrogen atmosphere and despite the use of an anhydrous solvent, some of the thioamide **2** was generally transformed in the reaction mixture to the corresponding amide **7**. Similarly, the presence of lactam as a by-product in the Eschenmoser sulfide contraction of thiolactams with halogenoesters has been reported by some authors (21, 22). The formation of the aminoester **6** could be explained by a nucleophilic substitution of pyrrolidine on the bromoester **3**. Indeed, pyrrolidine was formed in situ by hydrolysis of the enaminoester. Michael and co-workers reported, in a similar manner, the presence of the disulfide **9** in an Eschenmoser reaction with bromoacetophenone (23).

As several by-products were present in the crude reaction mixture, it was difficult to purify the β-ketoester **5** by chromatography on a silica gel column. With various eluents, the yield of the α-substituted β-ketoester was poor to moderate, and some fractions always contained $Ph_3P=S$ and Ph_3P. Therefore, it was necessary to modify the reaction conditions to minimize the formation of by-products in the condensation–extrusion process and to facilitate the elimination of these by-products in the experimental work-up. With Ph_3P as the thiophilic agent, the major difficulty was in eliminating the desulfuration product $Ph_3P=S$. In the case of thiolactam condensation, this problem was resolved by acidic extraction of the cyclic enaminoester with HCl (2 mol/L) (6), but with thioamides, the hydrolysis of the formed enaminoester, leading to the ketoester, was too rapid to permit a satisfactory extraction. So our idea was to mod-

Scheme 3.



6 **7** **9**

Table 1. Reaction conditions for transformation of **2a** to **3a**.

Thiophilic reagent	Reaction time (h)	Sulfide **8** (%)
Ph_3P	6	25
$P(OEt)_3$	3	11.5
$P(NR_2)_3$	1	Traces

© 2004 NRC Canada

Table 2. Comparative results for various thiophilic reagents.

Thioamide	Thiophilic reagent	Sulfide **8** (%)	Thioamide **2** transformed (%)	β-Ketoester **5** isolated yield[a] (%)	Yield from lit.[b] (%)
2a	Ph_3P	25	100	28	58[c], 64[d]
	$P(OEt)_3$	11	94	47	
	$P(NR_2)_3$	<1	100	60	
2b	$P(OEt)_3$	10	95	60	80[e]
	$P(NR_2)_3$	<1	80	70	
2d	$P(OEt)_3$	35	88	30	75[e]
	$P(NR_2)_3$	<1	86	72.5	
2e	Ph_3P	27	85	40	52[f], 71[g]
	$P(OEt)_3$	9	93	60	
	$P(NR_2)_3$	<1	100	67	

Note: For **2c**, no reaction was observed, irrespective of which desulfuration reagent was employed.
[a]After purification by chromatography.
[b]Obtained using other synthetic methods.
[c]From ref. 26.
[d]From ref. 27.
[e]From ref. 15.
[f]From ref. 4.
[g]From ref. 17.

ify the thiophilic reagent. The use of triethylphosphite ($P(OEt)_3$) in CH_3CN and the same work-up as with Ph_3P did not result in a significant modification of the sulfide yield. On the other hand, when the condensation was carried out without solvent (5 mL of CH_3CN being added in the desulfuration step to obtain a concentrated but homogeneous medium), the sulfide yield relative to the enaminoester–ketoester yield was substantially reduced. Unfortunately, the solubility of $(EtO)_3P{=}S$ in water is very low, and the work-up only led to its partial elimination. Hence, another thiophilic agent, $P(NR_2)_3$, was employed. Indeed, tris(alkylamino)phosphines have been reported to be good reagents for the transformation of disulfides to sulfides and for the reduction of thiiranes to olefins (24, 25). The same work-up as with $P(OEt)_3$ was carried out without solvent, but under a nitrogen atmosphere. In the same reaction time, a better transformation rate of the thioamide **2** was observed (Table 1), but, notably, only traces (<1% by gas chromatographic analysis) of the sulfide **8** were detected.

Nevertheless, purification of the β-ketoester on a silica gel column always resulted in some fractions that were contaminated with the desulfuration product $S{=}P(NE_2)_3$, no matter which elution solvent was employed. However, the presence of **8** in very small amounts permitted an appreciable improvement in the extraction yield of the α-substituted β-ketoester **5** in the chromatographic step. Table 2 shows comparative results for the various thiophilic agents employed. For comparison, we have also listed the yields reported in the literature for many different methods and experimental conditions.

Thus, with tris(dimethylamino)phosphine or tris(diethylamino)phosphine as the thiophilic reagent, α-alkylated β-ketoesters were synthesized via an Eschenmoser reaction in moderate to good yields. We have performed several other syntheses using different bromoesters, but no other series has been investigated in a systematic manner. However, even from these limited experiments, this method remains efficient and leads, after extraction, to similar yields to those in Table 2.

Conclusion

We have shown that several α-substituted β-ketoesters can be easily obtained by an efficient direct condensation of bromoesters with thiolactams through the Eschenmoser sulfur extrusion reaction. This strategy represents a quick and convenient route that can take its place among the available methodologies that provide access to these compounds.

Experimental

General procedure for thioamide synthesis

In a mixture of 150 mL of pyridine and about 0.2 mol of pyrrolidine, a slight excess (<1.1 equiv.) of acyl chloride **1** was added dropwise at room temperature. The stirred solution was refluxed for 30 min. After cooling, P_4S_{10} was added and the mixture was heated for 2 h and then poured into 500 mL of 1 mol/L HCl. The mixture was stirred for 1 h and was then extracted three times with 150 mL of dichloromethane (CH_2Cl_2). The combined organic layers were washed successively with 2 × 150 mL of 1 mol/L HCl, 2 × 150 mL of water, and 2 × 100 mL of a saturated solution of sodium hydrogen carbonate ($NaHCO_3$), then dried over magnesium sulfate ($MgSO_4$) and evaporated. The residue was purified by chromatography on a silica gel column.

1-Pyrrolidin-1-yl butan-1-thione (2a)

Condensation of 15.62 g (0.22 mol) of pyrrolidine and 25 g (0.235 mol, 1.07 equiv.) of butanoyl chloride **1a** gave, after chromatography using ethyl acetate (EtOAc)/cyclohexane (1/1), 28.76 g of **2a**. Yield 83%. Oil. ^{1}H NMR: 3.90 and 3.66 (t, J = 7 Hz, 4H), 2.70 (t, J = 7.5 Hz, 2H), 2.10–2.00 (m, 4H), 1.80 (m, 2H), and 1.05 (t, J = 7.5 Hz, 3H). ^{13}C NMR: 200.6, 50.9, 46.1, 26.6, 24.6, 22.5, and 14.1. IR

© 2004 NRC Canada

($CHBr_3$): 1480 cm^{-1}. Anal. calcd. (%) for $C_8H_{15}NS$: C 61.12, H 9.62, N 8.91; found: C 61.25, H 9.57, N 8.84.

3-Methyl-1-pyrrolidin-1-yl butan-1-thione (2b)

Using the same procedure, condensation of 6.39 g (0.09 mol) of pyrrolidine and 12.05 g (0.1 mol, 1.1 equiv.) of isobutyryl chloride **1b** gave, after chromatography using EtOAc/cyclohexane (1/1), 11.9 g of **2b**. Yield 77%. Yellow oil. ^{1}H NMR: 3.85 and 3.55 (2t, J = 7 Hz, 4H), 2.54 (d, J = 7.5 Hz, 2H), 2.30 (m, 1H), 2.02 and 1.85 (2t, J = 7 Hz, 4H), and 0.94 (d, J = 7.5 Hz, 6H). ^{13}C NMR: 199.7, 53.6, 51.1, 50.7, 28.9, 26.1, 24.0, and 22.1. IR ($CHBr_3$): 1480 cm^{-1}. Anal. calcd. (%) for $C_9H_{17}NS$: C 63.13, H 10.00, N 8.18; found: C 63.03, H 10.11, N 8.23.

2,2-Dimethylpyrrolidin-1-yl propan-1-thione (2c)

Using the same work-up, condensation of 14.2 g (0.2 mol) of pyrrolidine and 25 g (0.21 mol, 1.05 equiv.) of pivaloyl chloride **1c** gave, after chromatography using EtOAc/cyclohexane (1/1), 32.3 g of **2c**. Yield 94%. Oil. 1H NMR: 3.90 and 3.75 (2t, J = 7 Hz, 4H), 2.10 and 1.80 (2t, J = 7Hz, 4H), and 1.36 (s, 9H). ^{13}C NMR: 208.5, 57.6, 52.7, 43.5, 30.2, 27.3, and 22.9. IR ($CHBr_3$): 1430 cm^{-1}. Anal. calcd. (%) for $C_9H_{17}NS$: C 63.13, H 10.00, N 8.18; found: C 63.27, H 10.02, N 8.12.

1-Pyrrolidin-1-yl hexan-1-thione (2d)

Condensation of 12.6 g (0.177 mol) of pyrrolidine and 25 g (0.186 mol, 1.05 equiv.) of hexanoyl chloride **1d** gave, after chromatography with EtOAc/cyclohexane (1/1), 30.2 g of **2d**. Yield 92%. Oil. ^{1}H NMR: 3.80 and 3.50 (2t, J = 7 Hz, 4H), 2.62 (t, J = 7 Hz, 2H), 2.05 and 1.88 (2q, J = 7 Hz, 4H) 1.70 (m, 2H), 1.32–1.25 (m, 4H), and 0.84 (t, J = 7 Hz, 3H). ^{13}C NMR: 201.2, 54.3, 51.0, 44.6, 32.0, 29.1, 26.8, 24.8, 22.9, and 14.4. IR ($CHBr_3$): 1430 cm^{-1}. Anal. calcd. (%) for $C_{10}H_{19}NS$: C 64.83, H 10.34, N 7.56; found: C 64.90, H 10.28, N 7.51.

1-Thiobenzoyl pyrrolidine (2e)

Condensation of 5.32 g (0.075 mol) of pyrrolidine and 11.24 g (0.08 mol, 1 equiv.) of benzoyl chloride **1e** gave, after chromatography with EtOAc/cyclohexane (1/1), 14 g of a yellow solid **2e**. Yield 97.5%; mp 73 °C. ^{1}H NMR: 7.30–7.20 (m, 5H), 3.90 and 3.39 (2t, J = 7 Hz, 4H), and 2.00–1.90 (m, 4H). ^{13}C NMR: 197.4, 144.3, 129.0, 128.6, 126.0, 54.2, 53.8, 26.8, and 25.0. IR ($CHBr_3$): 1505, 1490, and 1475 cm^{-1}. Anal. calcd. (%) for $C_{11}H_{13}NS$: C 69.09, H 6.85, N 7.33; found: C 68.98, H 6.80, N 7.40.

4-Pyrrolidin-1-yl-4-thioxobutanoic acid methylester (2f)

For the synthesis of the intermediate amide, the following specific procedure was used: 6.39 g (0.09 mol) of pyrrolidine was condensed with 15.05 g (0.1 mol, 1.1 equiv.) of 3-carbomethoxy propanoyl chloride. After reaction, pyridine was evaporated under reduced pressure. Dichloromethane (200 mL) was added. The mixture was washed twice with 100 mL of water. The organic layer was dried (Na_2SO_4) and concentrated to give the crude amide (yield 79%), which was used directly without further purification in the next step. The thionation was achieved with a solution of 13 g (0.07 mol) of amide in 400 mL of dried tetrahydrofuran (THF). Following the addition of 15.5 g of P_4S_{10}, the mixture was heated for 4 h. Using the same work-up as described in the general procedure, 10.9 g of **2f** were obtained after chromatography with EtOAc/cyclohexane (1/2). Yield 60%. Oil. ^{1}H NMR: 3.80 and 3.60 (2t, J = 7 Hz, 4H), 3.63 (s, 3H), 2.90 and 2.80 (2t, J = 6 Hz, 4H), and 2.10–1.90 (m, 4H). ^{13}C NMR: 197.4, 172.6, 53.4, 51.2, 50.1, 36.3, 32.3, 25.8, and 23.7. IR ($CHBr_3$): 1725 and 1480 cm^{-1}. Anal. calcd (%) for $C_9H_{15}NO_2S$: C 53.73, H 7.46, N 6.96; found: C 53.82, H 7.38, N 6.93.

General procedure for an Eschenmoser coupling reaction with Ph_3P as the thiophilic agent

Typically, a mixture of thioamide **2** (6.3 mmol) and bromoester **3** (0.019 mol, 3 equiv.) in 50 mL of acetonitrile (CH_3CN) was heated for 30 min. A solution of 1.26 mmol (2 equiv.) of Ph_3P and 1.26 mmol (2 equiv.) of triethylamine (Et_3N) in CH_3CN (30 mL) was added dropwise. After addition, the mixture was refluxed for 4 h. The solvent was removed in vacuo and the resulting residue was dissolved in CH_2Cl_2 (150 mL). The organic layer was washed with a solution of 1 mol/L HCl (150 mL). The aqueous layers were extracted with CH_2Cl_2 (3 × 75 mL). The combined organic phases were successively washed with saturated $NaHCO_3$ solution (50 mL) and water (50 mL) and were then dried ($MgSO_4$). After evaporation of the solvent, crude β-ketoester **5** was obtained. In some cases, portions of phosphorated by-products were precipitated out in ethanol at –18 °C. Thus, purification of the ketoesters by chromatography on a silica gel column was facilitated.

General procedure for an Eschenmoser coupling reaction with triethylphosphite as the thiophilic agent

A mixture of 5.4 mmol of thioamide **2** and 8.11 mmol of bromoester **3** (1.5 equiv.) was heated at 80 °C for 30–45 min. Then a mixture of triethylamine (8.11 mmol, 1.5 equiv.) and 8.11 mmol (1.5 equiv.) of $P(OEt)_3$ was added. A precipitate of ammonium bromide was formed, and 5 mL of CH_3CN was added. The residue was refluxed until no further change in the ratio of the different compounds was observed by gas chromatography (2–5 h). After addition of CH_3CN (15 mL) and 1 mol/L HCl (1 mL) at room temperature, the resulting mixture was stirred and hydrolysis of the enaminoester was monitored by TLC. The solvent was removed and CH_2Cl_2 (50 mL) was added. The organic layer was washed with a saturated $NaHCO_3$ solution. The aqueous layer was extracted with CH_2Cl_2 (2 × 50 mL). The combined organic layers were dried ($MgSO_4$) and condensed to give crude β-ketoester **5**, which was chromatographed on a silica gel column using various mixtures of EtOAc/cyclohexane as eluant.

General procedure for an Eschenmoser coupling reaction with tris(dimethylamino)phosphine as the thiophilic agent

A mixture of 5 mmol of thioamide **2** and 7.5 mmol (1.5 equiv.) of bromoester **3** was heated at 80 °C for 30–45 min under a nitrogen atmosphere. A mixture of 6 mmol (1.2 equiv.) of Et_3N and 7.5 mmol (1.5 equiv.) of tris(dimethylamino)phosphine was then added, followed by the addition of dry CH_3CN (5 mL). The resulting mixture

© 2004 NRC Canada

was refluxed until no further change in the ratio of the different compounds was observed by gas chromatography. After addition of CH_3CN (10 mL) and 1 mol/L HCl (1 mL) the mixture was stirred for an additional 30 min and the same type of work-up as previously described in the second procedure was achieved. Thus, crude β-ketoester **5** was obtained and then chromatographed as above.

2-Methyl-3-oxo-hexanoic acid ethylester (5a)

Oil. ^{1}H NMR: 12.5 (broad s, weak), 4.12 (q, 2H), 3.40 (q, 1H), 2.5–2.4 (2dxt, ^3J = 7 Hz, ^2J = 26 Hz, 2H), 1.98 (t, 3H), 1.55 (m, 2H), 1.25 (d, 3H), and 0.84 (t, 3H). ^{13}C NMR: 205.6, 170.4, 61.0, 52.6, 43.0, 16.8, 13.8, 13.3, and 12.5. IR ($CHBr_3$): 1750 and 1720 cm^{-1}. Anal. calcd. (%) for $C_9H_{16}O_3$: C 62.76, H 9.36; found: C 62.71, H 9.41.

2,5-Dimethyl-3-oxo-hexanoic acid ethylester (5b)

Oil. ^{1}H NMR: 12.7 (broad s, weak), 4.10 (q, J = 7 Hz, 2H), 3.42 (q, J = 7 Hz, 1H), 2.40–2.30 (2dxd, ^3J = 6.5 Hz, ^2J = 22 Hz, 2H), 2.25 (d, J = 7 Hz, 3H), 2.10 (m, 1H), 1.19 (t, J = 7 Hz, 3H), and 0.85 (t, J = 7 Hz, 3H). ^{13}C NMR: 204.9, 170.1, 60.8, 51.7, 49.9, 23.8, 22.1, 22.0, 13.7, and 12.2. IR ($CHBr_3$): 1750 and 1720 cm^{-1}. Anal. calcd. (%) for $C_{10}H_{18}O_3$: C 64.48, H 9.74; found: C 64.55, H 9.71.

2-Methyl-3-oxo-octanoic acid ethylester (5d)

Oil. ^{1}H NMR: 12.8 (broad s, weak), 4.11 (q, J = 7 Hz, 2H), 3.43 (q, J = 7 Hz, 1H), 2.50–2.40 (2dxt, ^3J = 7 Hz, ^2J = 26 Hz, 2H), 1.52 (m, 2H), 1.27 (d, J = 7 Hz, 3H), 1.25–1.22 (m, 4H), 1.20 (t, J = 7 Hz, 3H), and 0.82 (t, J = 7 Hz, 3H). ^{13}C NMR: 207.5, 169.6, 61.1, 52.0, 41.2, 31.2, 23.2, 22.4, 14.5, 13.8, and 12.7. IR ($CHBr_3$): 1750 and 1720 cm^{-1}. Anal. calcd. (%) for $C_{11}H_{20}O_3$: C 65.97, H 10.96; found: C 66.07, H 10.11.

2-Methyl-3-oxo-3-phenyl propanoic acid ethylester (5e)

Oil. ^{1}H NMR: 12.5 (broad s, weak), 7.90–7.35 (m, 5H), 4.30 (q, J = 7.1 Hz, 1H), 4.05 (q, J = 7 Hz, 2H), 1.42 (d, J = 7.1 Hz, 3H), and 1.15 (t, J = 7 Hz, 3H). ^{13}C NMR: 196.0, 170.8, 134.2, 131.8, 127.1, 126.9, 61.3, 48.3, 13.9, and 13.7. IR ($CHBr_3$): 1740, 1680, and 1595 cm^{-1}. Anal. calcd. (%) for $C_{12}H_{14}O_3$: C 69.88, H 6.84; found: C 69.79, H 6.78.

2-Methyl-3-oxo-hexandioic acid-1-ethyl-6-methylester (5f)

Oil. ^{1}H NMR: 4.12 (q, J = 7 Hz, 2H), 3.60 (s, 3H), 3.50 (q, J = 7 Hz, 1H), 2.85–2.75 (t, J = 6.5 Hz, 2H), 2.56 (t, J = 6.5 Hz, 2H),), 1.30 (d, J = 7 Hz, 3H), and 1.21 (t, J = 7 Hz, 3H). ^{13}C NMR: 203.9, 172.6, 170.1, 61.1, 52.6, 51.5, 35.7, 27.5, 13.8, and 12.4. IR ($CHBr_3$): 1730 cm^{-1} (broad). Anal. calcd. (%) for $C_{10}H_{16}O_5$: C 55.54, H 7.46; found: C 55.62, H 7.53.

2-(1-Ethoxycarbonyl-ethylsulfanyl)-propanoic acid ethylester (8)

Oil. ^{1}H NMR: 4.15–4.05 (2q, J = 7 Hz, 4H), 3.60–3.45 (2q, J = 7.2 Hz, 2H), 1.55–1.45 (2d, J = 7.2 Hz, 6H), and 1.43–1.32 (2t, J = 7 Hz, 6H). ^{13}C NMR: 172.6, 172.5, 61.0, 60.9, 41.2, 41.1, 17.6, 16.8, 13.9, and 13.8. IR ($CHBr_3$): 1735 cm^{-1}. Anal. calcd. (%) for $C_{10}H_{18}O_4S$: C 51.26, H 7.74; found: C 51.19, H 7.71.

References

1. R. Robinson. J. Chem. Soc. **109**, 1038 (1916).
2. D.S. Breslow, E. Baumgarten, and C.R. Hauser. J. Am. Chem. Soc. **66**, 1286 (1944).
3. C.R. Hauser and B.E. Hudson. *In* Organic chemistry. Vol. 1. *Edited by* R. Adams. John Wiley and Sons, New York. 1942. p. 266.
4. R.E. Ireland and J.A. Marshall. J. Am. Chem. Soc. **81**, 2907 (1959).
5. E.C. Taylor, G.H. Hawks, and A. Mc Killop. J. Am. Chem. Soc. **90**, 2421 (1968).
6. P. Marchand, C. Bellec, M.-C. Fargeau-Bellasoued, and G. Lhommet. Synthesis, **11**, 1118 (1994).
7. A. Bardou, J.-P. Celerier, and G. Lhommet. Tetrahedron Lett. **38**, 8507 (1997).
8. J. Blot, A. Bardou, C. Bellec, M.-C. Fargeau-Bellasoued, J.-P. Celerier, and G. Lhommet. Tetrahedron Lett. **38**, 8511 (1997).
9. O. David, J. Blot, C. Bellec, M.-C. Fargeau-Bellassoued, J.-P. Celerier, G. Lhommet, and J.-C. Gramain. J. Org. Chem. **64**, 3122 (1999).
10. A. Doutheau and J. Gore. Tetrahedron, **32**, 2705 (1976).
11. P.L. Stotter and K.A. Hill. Tetrahedron Lett. **40**, 4067 (1972).
12. A. Choudary and A.L. Baumstark. Synthesis, **9**, 688 (1989).
13. W. Wierenga and H.L. Skulnick. J. Org. Chem. **44**, 310 (1979).
14. E.E. Blaise. C. R. Acad. Sci. Paris, **132**, 478 (1901).
15. H.B. Kagan and Y.-H. Suen. Bull. Soc. Chim. Fr. **6**, 1819 (1966).
16. S.M. Hannick and Y. Kishi. J. Org. Chem. **48**, 3833 (1983).
17. C. Kashima, L. Kita, K. Takahashi, and A. Hosomi. J. Heterocycl. Chem. **32**, 723 (1995).
18. K. Nagao, M. Chiba, and S.-W. Kim. Synthesis, **3**, 197 (1983).
19. A.B. Smith and P.A. Levenberg. Synthesis, **7**, 567 (1981).
20. S. Katayama, K. Fukuda, T. Watanabe, and M. Yamauchi. Synthesis, **3**, 178 (1988).
21. K. Shiosaki, G. Fels, and H. Rapoport. J. Org. Chem. **46**, 3230 (1981).
22. K. Shiosaki and H. Rapoport. J. Org. Chem. **50**, 1229 (1985).
23. R. Ghirlando, A.S. Howard, R.B. Katz, and J.P. Michael. Tetrahedron, **40**, 2879 (1984).
24. D.N. Harpp and J.G. Gleason. J. Org. Chem. **35**, 3259 (1970).
25. N.P. Neureiter and F.G. Bordwell. J. Am. Chem. Soc. **81**, 578 (1958).
26. K. Tsuzuki, M. Akeyoshi, and S. Omura. Bull. Chem. Soc. Jpn. **58**, 395 (1985).
27. H.J. Bestman, G. Graf, H. Hartung, and S. Kolewa. Chem. Ber. **103**, 2794 (1970).

© 2004 NRC Canada

Synthesis and characterization of a series of 1-methyl-4-[2-aryl-1-diazenyl]piperazines and a series of ethyl 4-[2-aryl-1-diazenyl]-1-piperazinecarboxylates[1]

Vanessa Renée Little and Keith Vaughan

Abstract: 1-Methylpiperazine was coupled with a series of diazonium salts to afford the 1-methyl-4-[2-aryl-1-diazenyl]piperazines (**2**), a new series of triazenes, which have been characterized by ^{1}H and ^{13}C NMR spectroscopy, IR spectroscopy, and elemental analysis. Assignment of the chemical shifts to specific protons and carbons in the piperazine ring was facilitated by comparison with the chemical shifts in the model compounds piperazine and 1-methylpiperazine and by a HETCOR experiment with the *p*-tolyl derivative (**2i**). A DEPT experiment with 1-methylpiperazine (**6**) was necessary to distinguish the methyl and methylene groups in **6**, and a HETCOR spectrum of **6** enabled the correlation of proton and carbon chemical shifts. Line broadening of the signals from the ring methylene protons is attributed to restricted rotation around the N2–N3 bond of the triazene moiety in **2**. The second series of triazenes, the ethyl 4-[2-phenyl-1-diazenyl]-1-piperazinecarboxylates (**3**), have been prepared by similar diazonium coupling to ethyl 1-piperazinecarboxylate and were similarly characterized. The chemical shifts of the piperazine ring protons are much closer together in series **3** than in series **2**, resulting in distortion of the multiplets for these methylenes. It was noticed that the difference between these chemical shifts in **3** exhibited a linear free energy relationship with the Hammett substituent constants for the substituents in the aryl ring.

Key words: triazene, piperazine, diazonium coupling, NMR, HETCOR, linear free energy relationship.

Résumé : On a procédé au couplage de la 1-méthylpipérazine avec une série de sels de diazonium qui conduit à la formation de 1-méthyl-4-[2-aryl-1-diazényl]pipérazines (**2**), une nouvelle série de triazènes qui a été caractérisée par spectroscopie RMN du ^{1}H et du ^{13}C, par spectroscopie IR ainsi que par analyse élémentaire. L'attribution des déplacements chimiques des protons et des atomes de carbone a été facilitée par une comparaison avec les déplacements chimiques de composés modèles, la pipérazine et la 1-méthylpipérazine, ainsi que par une expérience « HETCOR » avec le dérivé *p*-tolyle (**2i**). Il a fallu faire appel à une expérience de « DEPT » avec la 1-méthylpipérazine (**6**) pour distinguer les groupes méthylènes et le méthyle du composé **6** et un spectre « HETCOR » du composé **6** a permis d'établir une corrélation entre les déplacements chimiques du proton et du carbone. Un élargissement de la raie des signaux des protons méthylène du cycle est attribuée à la rotation empêchée autour de la liaison N2-N3 de la portion triazène du composé **2**. Une deuxième série de triazènes, les 4-[2-phényl-1-diazényl]pipérazine-1-carboxylates d'éthyle, a été préparée par un couplage semblable avec du pipérazine-1-carboxylate d'éthyle et elle a été caractérisée de la même manière. Les déplacements chimiques des protons du cycle pipérazine sont beaucoup plus rapprochés dans la série **3** que dans la série **2**; il en résulte une distorsion dans les multiplets de ces méthylènes. On a noté que la différence entre les déplacements chimiques des composés de la série **3** présente une corrélation d'énergie libre linéaire avec les constantes de substituant de Hammett des substituants du noyau aryle.

Mots clés : triazène, pipérazine, couplage de diazonium, RMN, HETCOR, relation d'énergie libre linéaire.

[Traduit par la Rédaction]

Introduction

The antitumour activity of 1-aryl-3,3-dimethyltriazenes has been known for many years (1), and at least one member of this family, dacarbazine (5-(3,3-dimethyl-1-triazeno)imidazole-4-carboxamide), is clinically useful in the treatment of malignant melanoma (2). More recently, the pro-drug approach to triazene design led to the discovery of temozolomide, an imidazolotetrazinone, which is a novel broad-spectrum antitumour agent (3). Although temozolomide itself is not an acyclic triazene, its mode of action is thought to involve hydrolysis of the tetrazinone ring to afford a cytotoxic monomethyltriazene. The contemporary chemistry of the antitumour triazenes has been reviewed (4), and the impor-

Received 3 February 2004. Published on the NRC Research Press Web site at http://canjchem.nrc.ca on 2 November 2004.

V.R. Little and K. Vaughan.[2] Department of Chemistry, Saint Mary's University, Halifax, NS B3H 3C3, Canada.

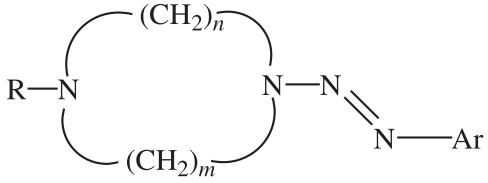
[1]Part I in a series of studies on triazene derivatives of (1,*x*)-diazacycloalkanes.

[2]Corresponding author (e-mail: keith.vaughan@smu.ca).

 doi: 10.1139/V04-081 © 2004 NRC Canada

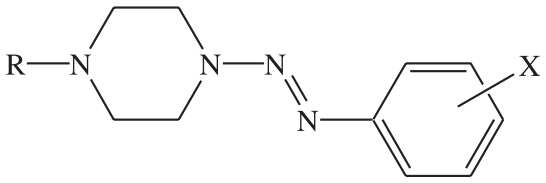
tance of triazenes as a versatile tool in organic synthesis has also been reviewed recently (5).

This paper is the start of a new series that will describe the synthesis of a wide variety of triazenes and bis-triazenes that fit the general classification of 1-aryldiazenyl-(1,*x*)-diazacycloalkanes described by the general structure **1**, where m = 1 or 2 and n = 2, 3, 4, or 5. In some of this series of compounds to be described, the R group will be a second triazenyl group, i.e., **1** will be a bis-triazene, and in others the R group will be a second diazacycloalkane moiety linked to the first by a one-carbon spacer. In this paper, we describe



1

the synthesis and characterization of 1-methyl-4-[(*E*)-2-aryl-1-diazenyl]piperazines (**2**) and a series of ethyl 4-[(*E*)-2-phenyl-1-diazenyl]-1-piperazine carboxylates (**3**). Most of these compounds are new to the triazene family and will serve as excellent model compounds for the characterization



2 R = CH_3
3 R = $CO_2C_2H_5$

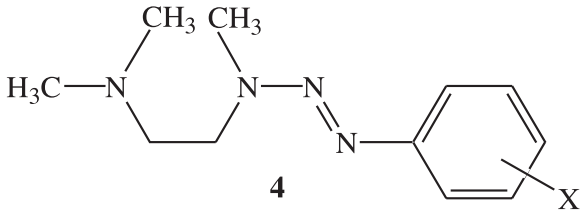
of bis-triazenes with the structure **2** (R = aryldiazenyl-) and similar compounds with larger heterocyclic rings.

Triazenes are generally synthesized by diazotization of an aromatic primary amine, followed by coupling of the diazonium salt to a secondary amine to provide the desired triazene in high yield as illustrated in eq. [1]:

[1] $ArN_2^+ + RR'NH \rightarrow ArN{=}NNRR'$

We previously used this approach successfully to synthesize *N,N*-dimethyl-*N*-2-[(*E*)-1-methyl-3-phenyl-2-triazenyl]ethylamines (**4**) by diazonium coupling with *N,N,N′*-trimethylethylenediamine (6); the type **4** triazene is actually the acyclic analogue of the type **2** triazene.

The potential biological activity of *N*-(aryldiazenyl)piperazines has attracted the attention of several previous investigators. Butkus and co-workers investigated a series of aminoazobenzenesulfonic acids for their potential anti-inflammatory activity (7); among this series is the piperazine derivative **2** (X = p-$SO_3^-K^+$). The analogous sulfonamides (**2**, X = p-SO_2NR_2, R = H, Me, or CH_2CH_2Cl) were prepared by Lalezari and Afghahi (8) as potential antitumour agents, but tests for biological activity were not reported. Two of the compounds that were prepared as part of the present study



4

have been reported previously (9), and several *N,N′*-bis-(aryldiazenyl)-piperazines have been reported (7, 10).

Experimental

All reagents were reagent-grade materials purchased from Sigma-Aldrich Canada and were used without further purification. Melting points were determined on a Fisher–Johns melting point apparatus and are uncorrected. Infrared spectra were obtained using Nujol mulls or KBr discs on a Bruker Vector 22 spectrometer. ^1H and ^{13}C NMR spectra were obtained with either (*i*) Bruker AC250 MHz and 500 MHz spectrometers at the Atlantic Regional Magnetic Resonance Center at Dalhousie University or (*ii*) the Anasazi 60 MHz EFT spectrometer at Saint Mary's University. Chemical shifts were recorded in $CDCl_3$ solutions at 20 °C (unless specified otherwise) and are relative to Me_4Si as the internal standard. Elemental analyses were performed by the Canadian Microanalytical Service Ltd. (Delta, B.C.). High-resolution electron-ionization mass spectral (EI-MS) data were obtained with the CEC 21–110B mass spectrometer at Dalhousie University. The standard deviation of the mass measurement is ±0.0008 amu, which is an average of 3.6 ppm over the mass range of 100–300 amu.

General procedure

1-Methyl-4-[(E)-2-aryl-1-diazenyl]piperazines (2a–2o)

The aromatic primary amine (0.01 mol) was dissolved in 10 mL of 3 mol/L HCl, with the aid of heat if necessary, and the resulting solution was cooled in an ice/salt bath to 0 °C. The solution was diazotized with a solution of sodium nitrite (0.76 g) in water (10 mL), with the temperature maintained below 5 °C, and then stirred for a further 30 min in the cold. The solution was then neutralized with a saturated sodium bicarbonate solution, after which the neat 1-methylpiperazine (1.2 mL, 0.011 mol) was added slowly to the mixture. After stirring for an additional 30 min, the mixture was further neutralized with a saturated sodium carbonate solution and then left to stir until precipitation was deemed to be complete (1–3 h). The solid product was filtered under suction, dried, and recrystallized from an appropriate solvent. In some cases, notably the ones with an ortho substituent in the aryl group, the product was an oil, in which case separation was achieved by extraction into dichloromethane. Physical data of the products (i.e., yield, mp, recrystallization solvent, and IR data) are listed in Table 1. Table 2 is a list of ^1H NMR chemical shift data, with appropriate assignments, and ^{13}C NMR data are listed in Table 3. The elemental analyses of selected compounds in this series are reported in Table 4. High-resolution EI-MS data of selected compounds of type **2** are given in Table 5.

© 2004 NRC Canada

Table 1. Physical data of the 1-methyl-4-[(*E*)-2-aryl-1-diazenyl]piperazines (**2**).

Compound	X	Yield (%)	mp (°C)	Recrystallization solvent	IR bands (cm^{-1})[a]
2a	*p*-CN	79	95–96	Hexane	2220 (CN) 844 (OOP)
2b	*p*-NO_2	80	106–107[b]	Hexane	1333, 1511 (NO_2) 852 (OOP)
2c	*p*-CO_2Me	85	81–82	Hexane	1718 (C=O) 824 (OOP)
2d	*p*-CO_2Et	87	49–51	Petroleum ether	1719 (C=O) 859 (OOP)
2e	*p*-$COCH_3$	68	69–71	Hexane	1673 (C=O) 832, 845 (OOP)
2f	*p*-$CONH_2$	89	212–214	EtOAc/EtOH	3161, 3298 (NH_2) 1667.5 (C=O) 863 (OOP)
2g	*p*-SO_2NH_2	39	115–127	—	3236, 3305 (NH_2) 840 (OOP)
2h	*p*-Br	86	78–81	Petroleum ether	830 (OOP)
2i	*p*-CH_3	75	42–44	EtOH/H_2O	828 (OOP)
2j	*m*-CF_3	59	Oil	—	697.5 (OOP)
2k	*o*-CN	78	Oil	—	2224.5 (CN) 761.5 (OOP)
2l	*o*-NO_2	72	Oil[c]	—	749, 775.5 (OOP)
2m	*o*-CO_2Me	66	Oil	—	1725 (C=O) 762 (OOP)
2n	*o*-Br	68	Oil	—	755 (OOP)
2o	H	63	45–48	—	692 (OOP)

[a]OOP, out-of-plane bending vibration.
[b]Lit. mp 113–114 °C (ether) (from ref. 9).
[c]Lit. bp 167–168 °C, 0.5 mm (from ref. 9).

Ethyl 4-[(E)-2-phenyl-1-diazenyl]-1-piperazinecarboxylates (3a–3m)

The general procedure described above for the *N*-methylpiperazines (**2**) was used exactly but with the substitution of ethyl 1-piperazinecarboxylate (1.6 mL) in place of the 1-methylpiperazine. Physical data of the products are listed in Table 6. Table 7 is a list of ^{1}H NMR chemical shift data, with appropriate assignments, and ^{13}C NMR data are listed in Table 8. The elemental analyses of selected compounds in this series are reported in Table 4. High-resolution EI-MS data of selected compounds of type **3** are given in Table 5.

Discussion

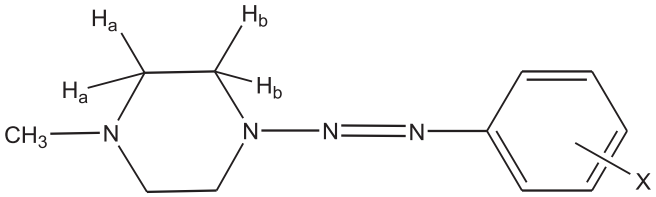
The reaction of 1-methylpiperazine with a series of diazonium salts proceeds, as expected, to give mostly excellent yields (60%–87%) of the 1-methyl-4-[2-aryl-1-diazenyl]-piperazines (**2**). Physical data of these triazenes are listed in Table 1. The solid triazenes of this series recrystallize from solvents of low polarity; several of these compounds were isolated as oils, which were found to be spectroscopically pure without further purification. The IR bands listed in Table 1 are all consistent with the particular aryl substituent, including the frequency of the out-of-plane (OOP) bending vibration bands.

The ^{1}H NMR data of the triazenes (**2a–2o**) are shown in Table 2 and are convincing evidence for the identity and purity of the products. The signals from the aromatic protons are consistent with the ortho-, meta-, or para-substitution pattern. The *N*-methyl group resonates at ca. 2.3 ppm as a sharp singlet except in the *p*-sulfonamide (**2g**), which shows an *N*-methyl resonance at 2.70 ppm. The protons of the ring methylene groups appear as two triplets at ca. 2.5–2.6 ppm and ca. 3.8–3.9 ppm, with a coupling constant universally of ca. 5.3 Hz. The lower-field triplet is assigned to the proton labeled H_b on the basis of comparison with model compounds and also from an unequivocal HETCOR NMR experiment with the *p*–tolyl derivative (**2i**) described below. The ^{1}H NMR spectra of triazenes **2c–2g**, **2i,** and **2m** display signals consistent with the protons present in the aryl substituent. A significant amount of line broadening of the methylene proton signals is observed in the spectra of compounds **2g** and **2k**, possibly because of the dynamic equilibrium (see **5A** $\leftrightarrows$ **5B**), which slows down the rotation around N_2–N_3 in the triazene moiety.

The ^{13}C NMR spectra of the triazene series **2** are given in Table 3. Assignment of the chemical shifts in these spectra was helped initially by examination of the ^{13}C NMR spectra of model compounds. Piperazine itself shows one ^{13}C NMR signal at 47.77 ppm; 1–methylpiperazine (**6**) has three signals at 56.6, 46.8, and 46.2 ppm. A DEPT experiment with **6** shows that the 46.8 ppm signal is from the *N*-methyl carbon and that the signals at 46.2 and 56.6 ppm are from methylene groups. Consideration of the 47.77 ppm chemical shift of the carbons in piperazine itself suggests very strongly that

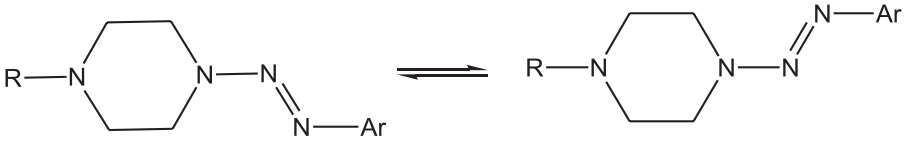
© 2004 NRC Canada

Table 2. ^{1}H NMR chemical shift data (ppm) in $CDCl_3$ of the 1-methyl-4-[(*E*)-2-aryl-1-diazenyl]piperazines (**2**).



Compound	X	Instrument[a]	Aromatic[b]	N-Me 3H	H_a 4H	H_b 4H	J_{ab} [b]	X
2a	*p*-CN	B	7.41 (d, 2H, *J* = 9) 7.59 (d, 2H, *J* = 9)	2.37(s)	2.56 (t)	3.91 (t)	5.3	—
2b	*p*-NO_2	A	7.51 (d, 2H, *J* = 7.2) 8.20 (d, 2H, *J* = 7.3)	2.38 (s)	2.58 (t)	3.94 (t)	5.2	—
2c	*p*-CO_2Me	A	7.47 (d, 2H, *J* = 8.55) 8.02 (d, 2H, *J* = 8.55)	2.36 (s)	2.56 (t)	3.88 (t)	5.2	3.90 (s) 3H
2d	*p*-CO_2Et	A	7.46 (d, 2H, *J* = 8.6) 8.03(d, 2H, *J* = 8.6)	2.37 (s)	2.56 (t)	3.88 (t)	5.2	1.39 (t, 3H), 4.37 (q, 2H) (*J* = 7.1)[b]
2e	*p*-$COCH_3$	C	7.48 (d, 2H, *J* = 8.6) 7.94 (d, 2H, *J* = 8.7)	2.37 (s)	2.57 (t)	3.90 (t)	5.3	2.57 (s, 3H)
2f	*p*-$CONH_2$	A	7.40 (d, 2H, *J* = 8.5) 7.88 (d, 2H, *J* = 8.5)	2.26 (s)	2.48 (t)	3.78 (t)	5.3	7.30, 7.94 (NH_2)
2g	*p*-SO_2NH_2	B	7.29 (d, 2H, *J* = 9) 7.855 (d, 2H, *J* = 9)	2.70 (s)	2.51 (t)	3.56 (br)	—	5.08 (br)
2h	*p*-Br	C	7.31 (d, 2H, *J* = 8.7) 7.44 (d, 2H, *J* = 8.8)	2.35 (s)	2.54 (t)	3.80 (t)	5.3	—
2i	*p*-CH_3	C	7.14 (d, 2H, *J* = 7.9) 7.345 (d, 2H, *J* = 8.4)	2.35 (s)	2.55 (t)	3.78 (t)	5.2	2.33 (s, 3H)
2j	*m*-CF_3	A	7.41 (m, 1H), 7.43 (t, 1H, *J* = 3.7) 7.60 (m, 1H), 7.71(s, 1H)	2.36 (s)	2.55 (t)	3.86 (t)	5.3	—
2k	*o*-CN	A	7.18 (dt, 1H, *J* = 1.3 & 7.3) 7.50 (dt, 1H, *J* = 1.3 & 7.3) 7.60 (m, 2H)	2.37 (s)	2.58 (br)	3.96 (br)	—	—
2l	*o*-NO_2	A	6.72 (m, 1H), 7.20 (m, 1H), 7.49 (m, 1H), 7.67 (dd, 1H, *J* = 1.1 & 8.0)	2.35 (s)	2.54 (t)	3.88 (t)	5.4	—
2m	*o*-CO_2Me	A	7.20 (m, 1H), 7.42 (m, 2H) 7.66 (dd, 1H, *J* = 1.0 & 7.3)	2.36 (s)	2.56 (t)	3.85 (t)	5.3	3.86 (s, 3H)
2n	*o*-Br	A	7.01 (dt, 1H, *J* = 1.5 & 8.4) 7.25 (dt, 1H, *J* = 1.4 & 8.3) 7.43 (dd, 1H, *J* = 1.6 & 8.1) 7.58 (dd, 1H, *J* = 1.3 & 7.9)	2.37 (s)	2.57 (t)	3.89 (t)	5.3	—
2o	H	B	7.12–7.51 (m)	2.36 (s)	2.55 (t)	3.82 (t)	5.3	—

[a]Spectrometer used for measurement: A, Bruker AC250 MHz; B, Anasazi 60 MHz; C, Bruker 500 MHz.
[b]Coupling constants (*J*) in Hz.



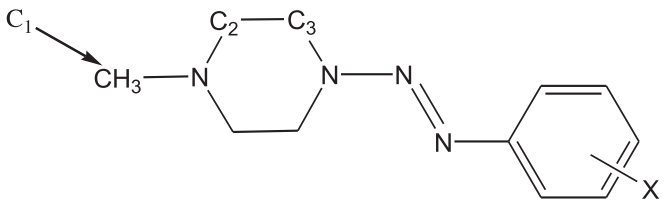
5A **5B**

C_3 in **6** is at 46.2 ppm. Thus, C_2 in **6** is assigned the 56.6 ppm signal.

The ^{1}H NMR spectrum of **6** has the *N*-methyl singlet at 2.22 ppm and triplets at 2.34 and 2.85 ppm. A HETCOR spectrum of **6** confirms that the *N*-methyl carbon at 46.8 ppm correlates with the proton signal at 2.22 ppm. The 56.5 ppm of C_2 correlates with the 2.3 ppm protons and the 46.2 ppm of C_3 correlates with the 2.85 ppm protons. Thus

© 2004 NRC Canada

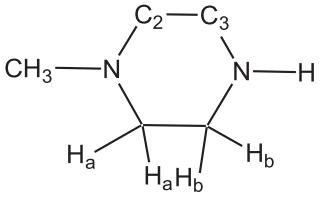
Table 3. ^{13}C NMR chemical shift data (ppm) in $CDCl_3$ of the 1-methyl-4-[(*E*)-2-aryl-1-diazenyl]piperazines (**2**).



Compound	X	Instrument[a]	Aromatic	C_1	C_2	C_3	X
2a	*p*-CN	B	119.1, 121.0 133.0, 153.6	45.8	54.1	~47 (br)	108.2 (CN)
2b	*p*-NO_2	B	120.6, 124.5 144.7, 155.5	45.9	54.2	~48 (v br)	—
2c	*p*-CO_2Me	A	120.3, 127.0 130.5, 153.9	46.0	54.3	~47 (br)	51.9 (CH_3) 166.9 (C=O)
2d	*p*-CO_2Et	A	120.3, 127.4 130.5, 153.8	46.0	54.25	~47 (br)	14.3 (CH_3) 60.7 (CH_2) 166.5 (C=O)
2e	*p*-$COCH_3$	C	120.6, 129.6 134.5, 154.2	46.1	54.4	—	26.6 (CH_3) 197.5 (C=O)
2h	*p*-Br	C	119.3, 122.4 131.9, 149.5	46.2	54.4	47.5 (br)	—
2i	*p*-CH_3	C	120.6, 129.5 135.9, 148.1	46.1	54.4	47.2 (br)	21.1 (Ar-CH_3)
2j	*m*-CF_3	A	117.4, 122.3 124.0, 129.3 131.0, 150.8	46.0	54.3	46.5 (br)	—
2k	*o*-CN	A	117.35 117.9, 125.5 133.1, 152.7	46.0	53.6	43.4 (w)	107.8 (CN)
2l	*o*-NO_2	A	118.7, 119.5, 123.6, 125.2, 132.2, 143.3	45.9	54.2 (br)	43.2 (w)	—
2m	*o*-CO_2Me	A	119.4, 125.4, 128.4 129.6, 131.7, 149.4	46.0	53.6	47 (br)	—
2n	*o*-Br	A	118.6, 120.15, 127.0, 127.8, 133.1, 147.7	46.1	54.3	47 (v br)	—
2o	H	B	120.7, 126.0 128.7, 150.4	45.9	54.2	47.1	—

[a]Spectrometer used for measurement: A, Bruker AC250 MHz; B, Anasazi 60 MHz; C, Bruker 500 MHz.

we conclude that the H_a protons in **6** resonate at 2.3 ppm and the H_b protons at 2.85 ppm, and that the assignment of the 2.5 ppm signal in the spectra of series **2** to the H_a protons is correct.



6

In the assignment of the ^{13}C NMR signals in Table 3, it follows that the *N*-methyl carbon (C_1) be assigned the 46.0 ppm signal and the 54 ppm signal is assigned to the C_2 methylene group in **2**. The signal from the other ring methylene, C_3, at ca. 47 ppm, is considerably broadened due to the dynamic equilibrium **5A** $\leftrightarrows$ **5B**. A HETCOR spectrum of the *p*-tolyl derivative (**2i**) shows that the 21.1 ppm carbon signal correlates with the proton shift at 2.33 ppm in the tolyl methyl group, and the 46.1 ppm carbon signal correlates with the *N*-methyl proton shift at 2.35 ppm. The 54.4 ppm signal of C_2 correlates with the 2.55 proton signal of H_a, leaving the H_b resonance at 3.78 ppm to correlate with the broad 47.2 ppm signal of C_3. The other important information recorded in Table 3 is the presence of the appropriate carbon signals from the substituents in the aromatic rings.

Comparison of the new NMR spectroscopic data of series **2** with the previously published data (6) of the acyclic series **4** is almost perfect. The *N*-methyl group in **2** resonates at

© 2004 NRC Canada

Table 4. Elemental analysis of selected examples of the triazene series **2** and **3**.

		Calcd. (%)			Found (%)		
Compound	Formula	C	H	N	C	H	N
2c	$C_{13}H_{18}N_4O_2$	59.5	6.9	21.4	59.7	7.1	21.2
2e	$C_{13}H_{18}N_4O$	63.4	7.3	22.8	62.9	7.2	22.6
2f	$C_{12}H_{17}N_5O$	58.3	6.9	28.3	58.1	7.1	28.0
2i	$C_{12}H_{18}N_4$	66.1	8.3	25.7	66.1	8.3	25.9
2h	$C_{11}H_{15}N_4Br$	46.7	5.3	19.8	47.0	5.2	19.7
3d	$C_{16}H_{22}N_4O_4$	57.5	6.6	16.8	57.6	6.5	16.85
3e	$C_{15}H_{20}N_4O_3$	59.2	6.6	18.4	60.1	6.9	18.3
3i	$C_{14}H_{20}N_4O_2$	60.9	7.2	20.3	60.8	7.0	20.2

Table 5. High-resolution electron-ionization mass spectral (EI-MS) data for selected compounds of series **2** and **3**.

Compound	Formula	Calcd. mass (amu)	Found mass (amu)
2a	$C_{12}H_{15}N_5$	229.1327	229.1322
2d	$C_{14}H_{20}N_4O_2$	276.1586	276.1579
2o	$C_{11}H_{16}N_4$	204.1375	204.1361
3a	$C_{14}H_{17}N_5O_2$	287.1382	287.1369
3b	$C_{13}H_{17}N_5O_4$	307.1280	307.1274
3c	$C_{15}H_{20}N_4O_4$	320.1484	320.1473
3e	$C_{15}H_{20}N_4O_3$	304.1535	304.1543
3h	$C_{13}H_{17}N_4O_2Br$	340.0535	340.0534
3k	$C_{14}H_{17}N_5O_2$	287.1382	287.1383
3m	$C_{13}H_{18}N_4O_2$	262.1429	262.1418

2.33 and 46 ppm, compared with 2.3 and 46 ppm for the analogous *N*-methyl group in **4**. The C_2 methylene in **2** resonates at ca. 2.5–2.6 and 54 ppm compared with 2.6 and 54 ppm for the analogous methylene group in **4**. The proton resonance of the H_b protons attached at C_3 in **2** occurs at ca. 3.8–3.9 ppm, which is exactly the same as the analogous protons in **4**. However, the carbon resonance of C_3 in **2** appearing at 47 ppm is very different from the assigned resonance of 58 ppm for the analogous carbon in **4.** The obvious explanation for this variance is the restricted rotation of the cyclic molecule **2** versus the acyclic equivalent **4**.

Corroboration of the structures of several compounds in series **2** was obtained by high-resolution EI-MS (Table 5). In addition to accurate mass measurement of the molecular ion, the fragmentation patterns give evidence to support the assigned structures. Fragmentation of the N1–N2 bond in the triazene is evident from the universal detection of a strong peak at *m*/*e* 99, corresponding to the *N*-methylpiperazine fragment, and the peak at the mass of the $ArN_2^{\cdot+}$ fragment. Also evident in these spectra is a strong peak from the Ar^+ fragment. Mass spectra of several compounds in series **3** also showed evidence of fragmentation of the N1–N2 bond from the universal presence of a fragment at *m*/*e* 157, which is the mass of the *N*-ethoxycarbonylpiperazine moiety. The $ArN_2^{\cdot+}$ fragment was also clearly evident in these spectra.

Following the complete elucidation of the spectroscopic data of the *N*-methylpiperazine triazene series (**2**), the synthesis of the carbamate series (**3**) was undertaken. Ethyl 1–piperazine carboxylate was coupled in aqueous solution with a series of diazonium salts to afford mostly excellent yields of 4–[2–aryl–1–diazenyl]–1-piperazine carboxylates (**3a–3m**). The physical data for this series of triazenes are given in Table 6. These are mostly solid, crystalline materials that can be recrystallized from hexanes; only compounds **3j** and **3l** were obtained as oils that did not crystallize over time. The carbonyl group of the *N*-ethoxycarbonyl moiety (the carbamate) gives rise to a strong absorption band in the IR spectrum, varying from 1685 to 1715 cm^{-1}. Compounds in this series with two carbonyl bands presented a challenge for the Bruker IR spectrometer to resolve, which it did with compounds **3c**, **3e,** and **3l**, but not with **3d** and **3f**.

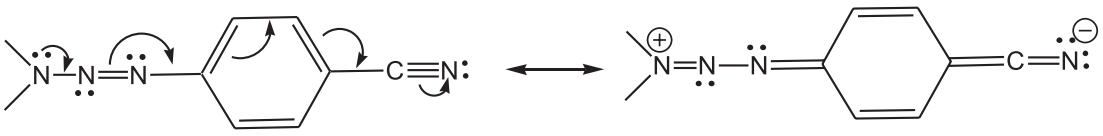
The ethyl aryldiazenylpiperazine carboxylates (**3**) were characterized by ^1H and ^{13}C NMR spectroscopy. The ^1H NMR chemical shift assignments are detailed in Table 7. The ethyl group of the *N*-ethoxycarbonyl group shows the typical triplet and quartet at ca. 1.29 and 4.19 ppm, respectively, and the protons of the substituent groups, X, are consistent with expectations, as are the aromatic proton resonances. The resonances of the heterocyclic ring protons are less easily interpreted than those of the *N*-methyl series (**2**) owing to the smaller separation between the chemical shift of the H_a and H_b proton signals and subsequent overlap of the multiplets. On average, the separation between H_a and H_b is only 0.05 ppm (3 Hz), which is less than the apparent coupling constant, J_{ab} (Table 7), which ranges from 3.9 to 9.8 Hz. Thus, the multiplets arising from H_a and H_b are severely distorted when the spectra are recorded at 60 MHz, and in some of the spectra of this series there are as many as

© 2004 NRC Canada

Table 6. Physical data of the ethyl 4-[(*E*)-2-aryl-1-diazenyl]-1-piperazinecarboxylates (**3**).

Compound	X	Yield (%)	mp (°C)	Recrystallization solvent	IR bands (cm^{-1})
3a	*p*-CN	71	108–109	Hexanes	2219 (CN) 1685 (C=O) 839/858 (OOP)
3b	*p*-NO_2	78	134–136	Hexanes	1690 (C=O) 1340, 1511 (NO_2) 852 (OOP)
3c	*p*-CO_2Me	95	107–109	Hexanes	1703.5 & 1710 (C=O) 856 (OOP)
3d	*p*-CO_2Et	89	68–70	Hexanes	1701 (br) (C=O)[a] 860.5 (OOP)
3e	*p*-$COCH_3$	87	77–79	Hexanes	1671 & 1700 (C=O) 839 (OOP)
3f	*p*-$CONH_2$	99	229–232	EtOH	3173.5 & 3387 (NH_2) 1681 (br) (C=O)[a] 861 (OOP)
3g	*p*-SO_2NH_2	48	142–150	—	3237 & 3306 (NH_2) 1687 (C=O) 838 (OOP)
3h	*p*-Br	64	59–60	Hexanes	1715 (C=O) 822 (OOP)
3i	*p*-CH_3	86	62–63	Hexanes	1714 (C=O) 822 (OOP)
3j	*m*-CF_3	86	Oil	—	1708 (C=O) 699 (OOP)
3k	*o*-CN	81	72–73	Hexanes	2218 (CN) 1708 (C=O) 766 (OOP)
3l	*o*-CO_2Me	86	Oil	—	1687 & 1725 (C=O) 762 (OOP)
3m	H	77	34–39	—	1706 (C=O) 766 (OOP)

[a]Carbonyl bands not resolved.



7A **7B**

12 lines in the multiplets. The assignment of the chemical shifts to the protons H_a and H_b has been resolved by analysis of a HETCOR spectrum (see below).

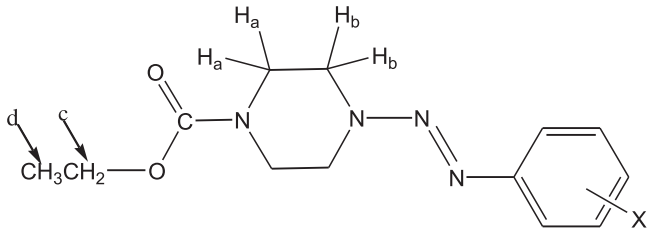
The ^{13}C NMR data of selected compounds in the carbamate series (**3**) are shown in Table 8. The three carbon atoms of the *N*-ethoxycarbonyl group are readily assigned at ca. 14.7 (CH_3), ca. 61.7 (O-CH_2), and ca. 155.2 ppm (carbonyl carbon). The carbon atoms of the piperazine ring occur at ca. 43 and 47 ppm; the 47 ppm signal is significantly broadened in the *p*-cyanophenyl (**3a**) and *p*-nitrophenyl (**3b**) derivatives. This observation is very useful in assigning the 47 ppm signal to C_5; the broadening of the C_5 signal is a direct consequence of the restricted rotation around the N—N bond of the triazene moiety (see **5A** ⇆ **5B**), which is more evident when a strongly electron-withdrawing substituent (CN or NO_2) is present in the para position of the aryl ring. The effect of through-conjugation resonance in the triazene moiety (**7A** ↔ **7B**) is to increase the bond order of the N2—N3 bond.

A ^{13}C NMR study by Axenrod et al. (11) of 1-aryl-3,3-dimethyltriazenes has established a rotational barrier around the N2—N3 bond consistent with some considerable double bond character between N2 and N3 of the triazene. In terms of the secondary orbital interactions within the molecule, overlap of the lone-pair *p*-orbital on N3 with the antibonding π* orbital between N1 and N2 gives rise to a degree of double bond character between N2 and N3.

Further consideration of the assignment of the carbon signals of C_4 and C_5 in the triazene series (**3**) concerns a comparison with the assignments in the *N*-methyl series (**2**),

© 2004 NRC Canada

Table 7. ^{1}H NMR chemical shift data (ppm) in $CDCl_3$ of the ethyl 4-[(*E*)-2-aryl-1-diazenyl]-1-piperazinecarboxylates (**3**).

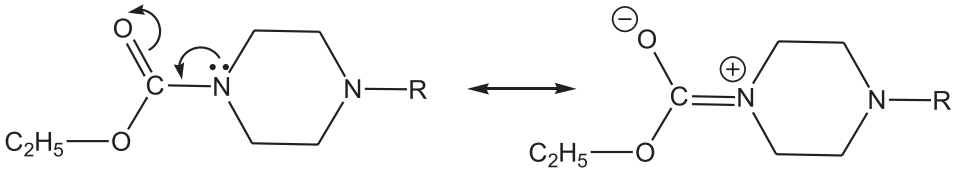


Compound	X	Instrument[a]	Aromatic[b]	H_a 4H	H_b 4H	H_c 2H (q)	H_d 3H (t)	J_{ab}[b]	X
3a	*p*-CN	A	7.50 (d, 2H, *J* = 9) 7.63 (d, 2H, *J* = 9)	3.89 (dd)	3.68 (dd)	4.20	1.30	5.8	—
3b	*p*-NO_2	B	7.50 (d, 2H, *J* = 9.2) 8.19 (d, 2H, *J* = 9.4)	3.86 (m)	3.77 (m)	4.20	1.30	8.1	—
3c	*p*-CO_2Me	B	7.46 (d, 2H, *J* = 8.9) 8.03 (d, 2H, *J* = 8.8)	3.79 (m)	3.72 (m)	4.19	1.29	6.5	3.90 (s, 3H) (O-Me)
3d	*p*-CO_2Et	B	7.46 (d, 2H, *J* = 8.9) 8.04 (d, 2H, *J* = 8.9)	3.79 (m)	3.72 (m)	4.19	1.29	6.6	1.38 (t, 3H) 4.36 (q, 2H) (*J* = 7.08)[b]
3e	*p*-$COCH_3$	B	7.48 (d, 2H, *J* = 8.8) 7.96 (d, 2H, *J* = 8.8)	3.80 (m)	3.74 (m)	4.19	1.29	6.6	2.57 (s, 3H) (acetyl Me)
3f	*p*-$CONH_2$[c]	B	7.40 (d, 2H, *J* = 8.5) 7.91 (d, 2H, *J* = 8.5)	3.77 (m)	3.66 (m)	4.10	1.22	7.2	3.37 (s)
3g	*p*-SO_2NH_2	B	7.50 (d, 2H, *J* = 8.5) 7.89 (d, 2H, *J* = 8.5)	3.82 (br)	3.73 (br)	4.19	1.29	—[d]	5.17
3h	*p*-Br	A	7.33 (d, 2H, *J* = 8.75) 7.46 (d, 2H, *J* = 8.75)	3.80 (dd)	3.66 (dd)	4.19	1.29	6.0	—
3i	*p*-CH_3	A	7.15 (d, 2H, *J* = 8.1) 7.35 (d, 2H, *J* = 8.2)	3.65 (dd)	3.76 (dd)	4.18	1.29	6.5	2.34 (s, 3H) (Ar-CH_3)
3j	*m*-CF_3	B	7.46–7.71 (m)	3.77 (br)	3.72 (br)	4.19	1.29	—[d]	—
3k	*o*-CN	B	7.31 (m, 1H), 7.57 (m, 2H) 7.69 (dt, 1H, *J* = 1.2 & 11.0)	3.88 (m)	3.76 (m)	4.19	1.29	9.8	—
3l	*o*-CO_2Me	B	7.18 (m, 1H), 7.37 (dt, 2H, *J* = 2,0 & 4.4), 7.66 (m,1H)	3.74 (m)	3.69 (m)	4.17	1.27	9.3	3.83 (s, 3H) (O-Me)
3m	H	B	7.10–7.56 (m, 5H)	3.63 (t)	3.60 (t)	4.13	1.23	8.4	—

[a]Spectrometer used for measurement: A Bruker AC250 MHz; B, Anasazi 60 MHz.
[b]Coupling constants (*J*) in Hz.
[c]Recorded in DMSO-d_6.
[d]Peaks are too broad to interpret quantitatively.

which shows that the analogous carbon (C_3 in **2**) has a chemical shift (ca. 46.0 ppm) very close to that of C_5 in **3**. However, C_4 in **3** occurs at ca. 43 ppm, which is quite different from C_2 in **2** at ca. 54 ppm. This difference must reflect the different character of the *N*-substituent in each case, i.e., the electron-releasing methyl group in **2** versus the electron-withdrawing ester group in **3**. The ultimate difference lies in the resonance in the carbamate group (**8A** ↔ **8B**).

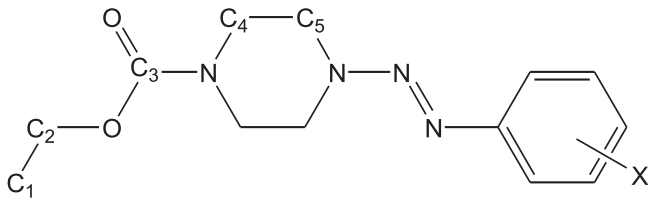
The assignment of chemical shifts in the carbamate series (**3**) is assisted by a HETCOR spectrum of the *p*-bromophenyl analogue (**3h**). In the HETCOR spectrum, the 14.6 ppm carbon (C_1) correlates with the proton triplet at



8A **8B**

© 2004 NRC Canada

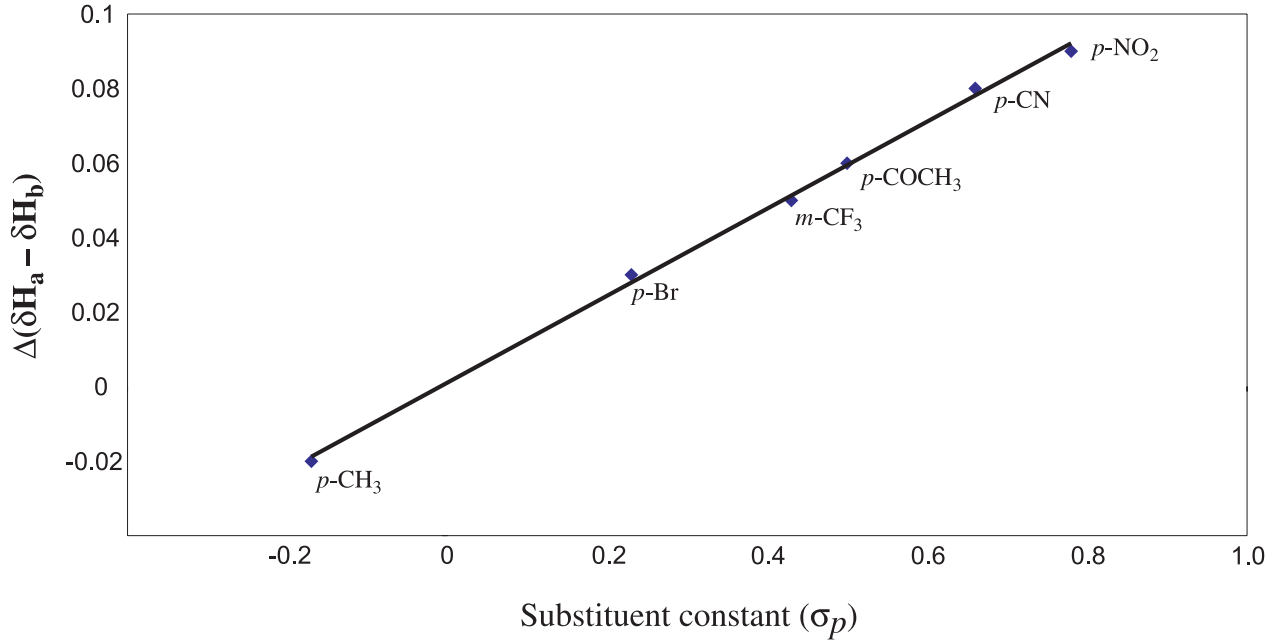
Table 8. ^{13}C NMR chemical shift data (ppm) in $CDCl_3$ of the ethyl 4-[(*E*)-2-aryl-1-diazenyl]-1-piperazinecarboxylates (**3**).



Compound	X	Instrument[a]	Aromatic	C_1	C_2	C_3	C_4	C_5	X
3a	*p*-CN	B	119.1, 121.2 132.9, 153.3	14.5	61.7	155	42.9	47 (br)	108.6 (CN)
3b	*p*-NO_2	B	120.9, 122.1 124.8, 145.3	14.7	61.8	155	43.0	47.3 (br)	—
3c	*p*-CO_2Me	B	120.8, 127.6 130.8, 153.7	14.9	61.9	155	43.3	47.4	52.0 (OCH_3) 169.9 (C=O)
3d	*p*-CO_2Et	B	120.7, 128.0 130.7, 153.8	14.5	61.7	155	43.0	47.2	14.8 (CH_3) 60.7 (CH_2) 166.4 (C=O)
3e	*p*-$COCH_3$	B	120.6, 129.3 134.5, 153.5	14.6	61.5	155	42.9	47.0	26.3 (CH_3) 196.8 (C=O)
3h	*p*-Br	B	119.4, 122.3 131.8, 148.9	14.6	61.6	155	42.9	47.0	—
3i	*p*-CH_3	B	120.7, 129.5 136.1, 147.9	14.7	61.6	156	43.0	47.2	21.0 (CH_3)
3k	*o*-CN	B	117.6, 125.9 133.1, 152.4	14.7	61.7	155	43.0	49.2	108.0 (CN)
3m	H	B	120.8, 126.3 128.8, 150.0	14.6	61.5	155	42.9	47.0	—

[a]Spectrometer used for measurement: B, Anasazi 60 MHz.

Fig. 1. Linear free energy relationship between the proton chemical shifts of H_a and H_b in series **3** and the Hammett constant of the aryl substituent (X).



© 2004 NRC Canada

1.29 ppm, the 61.6 ppm carbon (C_2) correlates with the proton quartet at 4.18 ppm, the 42.9 ppm carbon (C_4) correlates with the proton triplet at 3.70 ppm (H_a), and the 47.0 ppm carbon (C_5) correlates with the proton triplet at 3.73 ppm (H_b). This latter observation is the clearest evidence to assign the chemical shifts of H_a and H_b.

The similarity of the chemical shifts of the piperazine ring protons in the carbamates (**3**) may have implications in the physical organic chemistry of the *N*-substituents. This NMR observation would suggest that the electronic character of the two *N*-sustituents in **3** should be almost identical. The electronic character of the aryldiazenyl group, Ar-N=N–, is not well documented; Isaacs (12) gives a value for the substituent constant (σ_p) of the Ph-N=N group of 0.33, compared with 0.44 for the COOR group. The variation in the chemical shift difference between the H_a and H_b protons in the 60 MHz spectra of the compounds of series **3** has been measured and this difference has been plotted against the Hammett substituent constant (13) of the X substituent in the aryl group of **3** (Fig. 1), showing that there is a linear free energy relationship. It should be noted that the correlation exists for the *difference* in the chemical shift of the H_a and H_b protons, not for the H_b chemical shift itself. The significance of this correlation is not immediately obvious, and an explanation is not easy to formulate. It may indicate that there is a through-space interaction between the lone pairs on the piperazine nitrogen atoms. It certainly suggests that further study of the NMR properties of similar heterocyclic systems may be warranted.

Conclusion

The results reported here provide a comprehensive account of the synthesis and characterization of the *N*-methyl- (**2**) and the *N*-ethoxycarbonyl-*N′*-aryldiazenylpiperazines (**3**), which will provide a valuable resource of data for structure elucidation of related compounds.

Acknowledgements

The authors are grateful to the Natural Sciences and Engineering Council of Canada (NSERC) for a Discovery Grant to the principal author (K.V.) and an Undergraduate Summer Research Award (2003) to V.R.L. We are also grateful to the Atlantic Region Magnetic Resonance Centre at Dalhousie University for providing NMR spectra and to Dalhousie University for providing mass spectral data.

References

1. D.A. Clarke, R.K. Barclay, C.C. Stock, and C.S. Rondesvedt. Proc. Soc. Exp. Biol. Med. **90**, 484 (1955).
2. S.K. Carter and M.A. Friedman. Eur. J. Cancer, **8**, 85 (1972).
3. E.S. Newlands, M.F.G. Stevens, S.R.Wedge, R.T. Wheelhouse, and C. Brock. Cancer Treat. Rep. **23**, 35 (1997).
4. K. Vaughan. *In* The chemistry of antitumour agents. *Edited by* D.E.V. Wilman. Blackie, London. Chapman & Hall, New York. 1990. Chap. 5. pp. 159–186.
5. D.B. Kimball and M.M. Haley. Angew. Chem. Int. Ed. Engl. **41**, 3338 (2002).
6. D.L. Hooper, I.R. Pottie, M. Vacheresse, and K. Vaughan. Can. J. Chem. **76**, 125 (1998).
7. M. Kazemekaite, Z. Talaikyte, G. Niaura, and E. Butkus. Molecules, **7**, 706 (2002).
8. I. Lalezari and F. Afghahi. J. Pharm. Sci. **64**, 698 (1975).
9. M. Mazza, G. Pagani, G. Calderara, and L. Vicarini. Farmeco Ed. Sci. **28**, 846 (1973).
10. E. Yanarates, A. Disli, and Y. Yildirir. Org. Prep. Proced. Int. **31**, 429 (1999).
11. T. Axenrod, P. Mangiaracina, and P.S. Progosin. Helv. Chim. Acta, **59**, 1655 (1976).
12. N.S. Isaacs. Physical organic chemistry. Longman Scientific & Technical, Harlow, Essex, UK. 1987. p. 135.
13. B. Miller. *In* Advanced organic reactions: reaction and mechanism. Prentice Hall, Saddle River, N.J, 1998. p. 124; original source: H.H. Jaffe, Chem. Rev. **53**, 191 (1953).

© 2004 NRC Canada

Altering molecular weight distributions: Benzyl–phosphinimide titanium complexes as ethylene polymerization catalysts

Emily Hollink, Pingrong Wei, and Douglas W. Stephan

Abstract: The phosphines and corresponding phosphinimines $R_2BnPNSiMe_3$ (R = *t*-Bu, Cy), *p*-$C_6H_4(CH_2PR_2)_2$ (R = *t*-Bu (**1**), Cy (**2**)), and *p*-$C_6H_4(CH_2PR_2NSiMe_3)_2$ (R = *t*-Bu (**3**), Cy (**4**)) were prepared in high yields. Subsequent reaction with Ti precursors afforded $(R_2BnPN)TiCp^*Cl_2$ (Cp* = η-C_5Me_5; R = *t*-Bu (**5**), Cy (**6**)), $(R_2BnPN)TiCpCl_2$ (Cp = η-C_5H_5; R = *t*-Bu (**7**), Cy (**8**)), *p*-$C_6H_4(CH_2PR_2NTiCp^*Cl_2)_2$ (R = *t*-Bu (**9**), Cy (**10**)), and *p*-$C_6H_4(CH_2PR_2NTiCpCl_2)_2$ (R = *t*-Bu (**11**), Cy (**12**)). Methylation of the above complexes gave $(R_2BnPN)TiCp^*Me_2$ (R = *t*-Bu (**13**), Cy (**14**)), $(R_2BnPN)TiCpMe_2$ (R = *t*-Bu (**15**), Cy (**16**)), *p*-$C_6H_4(CH_2PR_2NTiCp^*Me_2)_2$ (R = *t*-Bu (**17**), Cy (**18**)), and *p*-$C_6H_4(CH_2PR_2NTiCpMe_2)_2$ (R = *t*-Bu (**19**), Cy (**20**)). The activity of these species as catalyst precursors in ethylene polymerization catalysis was evaluated using Schlenk line and Buchi reactor techniques using activation by methylaluminoxane (MAO) or $[Ph_3C][B(C_6F_5)_4]$. All these catalysts showed good activities and yield polymers with relatively broad molecular weight distributions. The bimodal polymers derived from catalysts generated using MAO are proposed to result from additional active species, possibly as a result of reaction of MAO with the benzylic fragments. X-ray data are reported for **1**, **4–8**, **10**, **12–14**, **16**, and **18–20**.

Key words: phosphinimides, polymerization, catalysis, polyethylene, titanium, polymer molecular weight distributions.

Résumé : On a préparé les phosphines et les phosphinimines correspondantes $R_2BnPNSMe_3$ (R = *t*-Bu, Cy), *p*-$C_6H_4(CH_2PR_2)_2$ (R = *t*-Bu (**1**), Cy (**2**)), et *p*-$C_6H_4(CH_2PR_2NSiMe_3)_2$ (R = *t*-Bu (**3**), Cy (**4**)) avec d'excellents rendements. Les réactions subséquentes avec des précurseurs de Ti ont conduit à la formation des composés $(R_2BnPN)TiCp^*Cl_2$ (Cp* = η-C_5Me_5; R = *t*-Bu (**5**), Cy (**6**)), $(R_2BnPN)TiCpCl_2$ (Cp = η-C_5H_5; R = *t*-Bu (**7**), Cy (**8**)), *p*-$C_6H_4(CH_2PR_2NTiCp^*Cl_2)_2$ (R = *t*-Bu (**9**), Cy (**10**)), et *p*-$C_6H_4(CH_2PR_2NTiCpCl_2)_2$ (R = *t*-Bu (**11**), Cy (**12**)). Une méthylation subséquente de ces complexes conduit à la formation des composés $(R_2BnPN)TiCp^*Me_2$, (R = *t*-Bu (**13**), Cy (**14**)), $(R_2BnPN)TiCpMe_2$ (R = *t*-Bu (**15**), Cy (**16**)), *p*-$C_6H_4(CH_2PR_2NTiCp^*Me_2)_2$ (R = *t*-Bu (**17**), Cy (**18**)), et *p*-$C_6H_4(CH_2PR_2NTiCpMe_2)_2$ (R = *t*-Bu (**19**), Cy (**20**)). On a évalué l'activité de ces espèces comme précurseurs de catalyseurs pour la polymérisation de l'éthylène à l'aide d'une ligne de Schlenk et un réacteur de Büchi et d'une activation par méthylaluminoxane (MAO) ou du $[Ph_3C][B(C_6F_5)_4]$. Tous ces catalyseurs présentent de bonnes activités et ils conduisent à la formation de polymères ayant des distributions de poids moléculaires relativement larges. Il est suggéré que les polymères à deux modes obtenus à l'aide de catalyseurs résultant d'une génération au MAO pourraient provenir d'espèces actives additionnelles résultant possiblement d'une réaction du MAO avec les fragments benzyliques. On rapporte les données cristallographiques pour les composés **1**, **4–8**, **10**, **12–14**, **16** et **18–20**.

Mots clés : phosphinimides, polymérisation, catalyse, polyéthylène, titane, distributions des poids moléculaires des polymères.

[Traduit par la Rédaction]

Introduction

Many of the developments in early-transition-metal chemistry in recent years have been prompted by attempts to uncover effective new homogeneous olefin polymerization catalysts. A number of studies have described non-metallocene systems based on a variety of novel ancillary ligands (1–3). Among such systems, we have described titanium catalysts that contain bulky phosphinimide ligands. The family of compounds of the form $CpTi(NPR_3)Cl_2$ (Cp = η-C_5H_5) yield active ethylene polymerization catalysts upon activation by methylaluminoxane (MAO) (4–8). Similarly, upon activation by $B(C_6F_5)_3$ or $Ph_3C[B(C_6F_5)_4]$, the species $(t\text{-}Bu_3PN)_2TiMe_2$ provides a remarkably active catalyst, producing polyethylene of narrow polydispersity and relatively high molecular weight (9).

Narrow polydispersities are typically observed for single-site or living polymerization catalysts; however, practical applications often require resins of broader molecular weight distribution for effective processing and manipulation (10, 11). There are a variety of methods employed to alter both the molecular weight and the molecular weight distributions of resins derived from single-site catalysts. These include controlled hydrogenolysis or hydrolysis of the polymeriza-

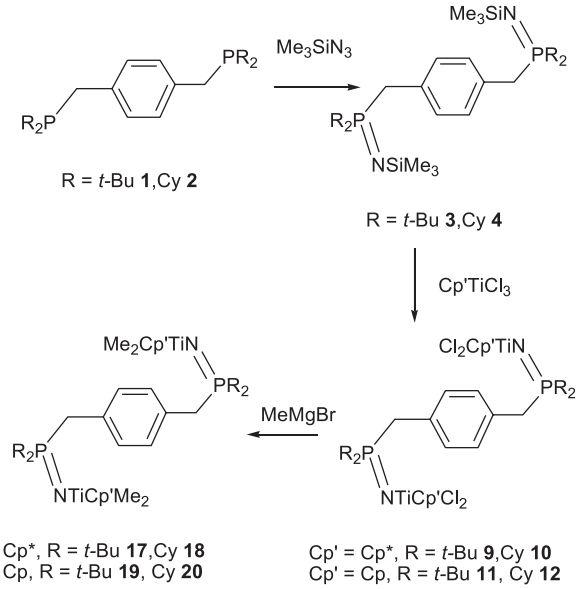
Received 31 December 2003. Published on the NRC Research Press Web site at http://canjchem.nrc.ca on 2 November 2004.

E. Hollink, P. Wei, and D.W. Stephan.[1] Department of Chemistry & Biochemistry, University of Windsor, Windsor, ON N9B 3P4, Canada.

[1]Corresponding author (e-mail: stephan@uwindsor.ca).

 doi: 10.1139/V04-062 © 2004 NRC Canada

Scheme 1.

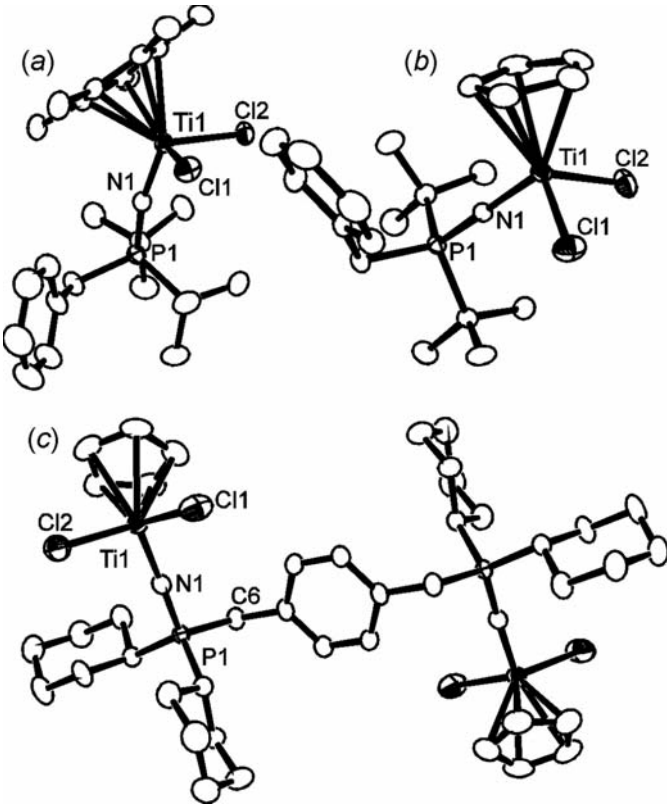


tion process (12, 13) or the use of sequential catalyst systems to produce the desired mixture of polymers (14–16). Academic studies and industrial developments continue in this area, with a particular emphasis on bimodal resins (7, 17–28). An alternative approach involves linking single-site catalysts together (16, 29–31), affording differing catalyst sites and thus broader molecular weight distributions (32). Synthetic routes to bimetallic catalyst precursors such as $C_6H_4((Me_3SiN)Zr(NMe_2)_2)_2$ (33), $C_6H_4(OMCpX_2)_2$ (M = Ti, Zr; X = Cl, Me), and $(CH_2PPh_2NCp^*TiX_2)_2$ and 2,6-$(C_5H_3N)(CH_2PPh_2NCp^*TiX_2)_2$ (Cp^* = η-C_5Me_5; X = Cl, Me) (34) have recently appeared, and some of these compounds were tested for their catalytic activity upon activation with MAO. However, very poor catalytic activity was observed, and thus the nature of the resulting polymers has not been explored. In this paper, we describe the facile synthesis of a series of bimetallic phosphinimide-based titanium precatalysts and show that these systems provide effective ethylene polymerization catalysts upon activation by MAO. Moreover, the influence of the nature of the precatalysts on the resulting polymer molecular weight distributions is probed. The implications and ramifications of these data are discussed.

Results and discussion

The phosphines and corresponding phosphinimines $R_2BnPNSiMe_3$ (R = *t*-Bu, Cy) were prepared via a modification of a literature procedure (35). The related diphosphines *p*-$C_6H_4(CH_2PR_2)_2$ (R = *t*-Bu (**1**) or Cy (**2**)) were prepared by a method analogous to that used for the related meta-substituted isomers (36). Thus, treatment of *p*-$C_6H_4(CH_2Br)_2$ with HPR_2 (R = *t*-Bu or Cy) followed by addition of the base NEt_3 afforded **1** and **2** in yields of 88% and 85%, respectively. X-ray data for **1** confirmed the formulation. These phosphines were oxidized in a conventional manner with Me_3SiN_3 to give the species *p*-$C_6H_4(CH_2PR_2NSiMe_3)_2$ (R = *t*-Bu (**3**), Cy (**4**)), also in high yields. Spectroscopic data, as well as X-ray data for compound **4**, were consistent

Fig. 1. ORTEP drawings of (*a*) **5**, (*b*) **8,** and (*c*) **12.** 30% thermal ellipsoids are shown. Hydrogen atoms are omitted for clarity.



with these formulations. The X-ray data revealed that in the solid state, **4** is centrosymmetric with typical P–N and Si–N bond lengths averaging 1.542(2) and 1.663(3) Å, respectively. The P–N–Si angle was found to range from 153.4(1)° to 163.5(1)°, which falls within the range of P–N–Si angles reported in a number of monodentate phosphinimines (37).

Subsequent thermal reaction of the above phosphinimines with 1 or 2 equiv. of Cp^*TiCl_3 or $CpTiCl_3$ resulted in the high-yield formation of $(R_2BnPN)TiCp^*Cl_2$ (R = *t*-Bu (**5**), Cy (**6**)), $(R_2BnPN)TiCpCl_2$ (R = *t*-Bu (**7**), Cy (**8**)), *p*-$C_6H_4(CH_2PR_2NTiCp^*Cl_2)_2$ (R = *t*-Bu (**9**), Cy (**10**)), and *p*-$C_6H_4(CH_2PR_2NTiCpCl_2)_2$ (R = *t*-Bu (**11**) or Cy (**12**)) upon liberation of Me_3SiCl (Scheme 1). While the compounds **9** and **11** were less soluble in benzene than the others, spectroscopic data in all cases were consistent with the formulations. X-ray data (Table 1, Fig. 1) were also acquired for **5–8**, **10,** and **12**. Key metric parameters are tabulated in Table 2. In all cases, the Ti–N distances fall within the range of 1.764(3)–1.786(2) Å. The P–N–Ti angles in these compounds are approximately linear, ranging from 157.1(3)° to 175.2(1)°. These values are similar to those of 155.4(2)° and 165.7(1)° reported for 2,6-$(C_5H_3N)(CH_2PPh_2NTiCp^*Cl_2)_2$ and are typical of titanium complexes of phosphinimide derivatives (5, 37). Variations in the metric parameters among these species are consistent with the steric and electronic differences between the Cp* and Cp ligands.

Methylation of the above complexes proceeded in a facile manner to give $(R_2BnPN)TiCp^*Me_2$ (R = *t*-Bu (**13**), Cy (**14**)), $(R_2BnPN)TiCpMe_2$ (R = *t*-Bu (**15**), Cy (**16**)), *p*-$C_6H_4(CH_2PR_2NTiCp^*Me_2)_2$ (R = *t*-Bu (**17**), Cy (**18**)), and

© 2004 NRC Canada

Table 1 Crystallographic data.

	1	**4**	**5**	**6**	**7**	**8**	**10**
Formula	$C_{24}H_{44}P_2$	$C_{38}H_{70}N_2P_2Si_2$	$C_{25}H_{40}NCl_2PTi$	$C_{29}H_{44}Cl_2NPTi$	$C_{26}H_{36}C_{l2}NPTi$	$C_{24}H_{34}Cl_2NPTi$	$C_{52}H_{82}N_2Cl_2P_2Ti_2$
Formula wt.	394.53	673.08	504.35	556.42	512.33	486.29	1034.74
a (Å)	6.1600(2)	9.453(6)	9.743(6)	11.359(7)	12.3260(18)	11.660(6)	15.218(9)
b (Å)	8.2564(3)	14.566(8)	17.528(11)	16.383(10)	11.6587(17)	13.481(7)	24.238(14)
c (Å)	13.5269(6)	17.616(10)	16.130(10)	16.443(10)	19.500(5)	15.984(8)	15.996(9)
α (°)	80.1900(10)	106.248(11)					
β (°)	79.0530(10)	104.112(9)	98.567(12)	102.672(12)	101.975(11)		110.387(10)
γ (°))	71.0740(10)	103.764(11)					
Crystal system	Triclinic	Triclinic	Monoclinic	Monoclinic	Monoclinic	Orthorhombic	Monoclinic
V (Å^3)	634.54(4)	2133(2)	2724(3)	2985(3)	2741.3(9)	2512(2)	5530(5)
Space group	$P\bar{1}$	$P\bar{1}$	$P2_1/c$	$P2_1/c$	$P2_1/c$	$P2_12_12_1$	$P2_1/c$
δ(calcd.) (g cm^{-1})	1.032	1.048	1.230	1.238	1.241	1.286	1.243
Z	1	2	4	4	4	4	4
μ(Mo Kα) (cm^{-1})	0.177	0.184	0.581	0.537	0.579	0.628	0.574
Data collected	3184	9172	11 282	12 502	13 075	10 691	22 618
Data $F_o^2 > 3\sigma(F_o^2)$	2131	6063	3860	4275	4767	3567	7876
Variables	124	397	271	307	280	262	559
R^a	0.0674	0.0372	0.0394	0.0330	0.0361	0.0233	0.0546
$R_w{}^b$	0.2067	0.0981	0.1213	0.0889	0.0711	0.0555	0.1515
GOF	0.913	0.903	1.114	0.965	0.840	0.981	0.859

Note: All data collected at 24 °C with Mo Kα radiation (λ = 0.71069 Å).
[a] $R = \Sigma (||F_o| - |F_c||)/ \Sigma|F_o|$.
[b] $R_w = [\Sigma (\omega(F_o^2 - F_c^2)^2)/\Sigma (\omega(F_o^2)^2)]^{1/2}$.

p-$C_6H_4(CH_2PR_2NTiCpMe_2)_2$ (R = *t*-Bu (**19**), Cy (**20**)) in isolated yields ranging from 46% to 83%. Each of these dimethyl derivatives was characterized spectroscopically. All of these species with the exception of compounds **15** and **17** were also characterized by crystallography (Table 2). In these structures, the Ti–N distances are slightly elongated in comparison to those in the corresponding dichloride derivatives. This is consistent with the increased electron density at the metal center as a result of methylation. The Ti–C bond lengths are typical, ranging from 2.119(7) to 2.228(3) Å. The remaining metric parameters of these compounds are unexceptional.

Olefin polymerization studies

Preliminary evaluation of these compounds as ethylene polymerization catalysts was performed in 50 mL of toluene in a Schlenk flask at 25 °C under 1 atm of ethylene and employing 1000 equiv. of MAO as co-catalyst. These experiments were allowed to run 30 min prior to quenching. The preliminary Schlenk screenings provided an indication of the relative polymerization activity (Table 3), revealing that among the bimetallic systems, precatalyst **19** afforded the best polymerization activity. While the activities were reproducible, the characteristics of the resulting polyethylene (MW and polydipersity index (PDI)) differed from those obtained subsequently, under the more controlled conditions in the Buchi reactor. Such inconsistencies were attributed to the effects of the heat of polymerization within the small volume of the Schlenk flask.

Subsequently, catalysts were tested in a 1-L Buchi reactor equipped with a temperature control bath and a stirring mechanism. The conditions in this case included 500 mL of toluene, 30 °C (±2 °C) and a much lower concentration of precatalyst (50 μmol/L). In initial screening experiments, low pressures of ethylene (1 atm or less) were used; nonetheless, the data was reproducible within acceptable experimental errors. The activities reported (Table 3) are averages of (at least) duplicate runs; however, insufficient saturation of the catalyst with ethylene may have resulted in an underestimation of the activity. Nonetheless, in general, the monometallic catalysts show higher activities, ranging from 200 to 280 g mmol^{-1} h^{-1} atm^{-1}. These activities fall within the range of those reported previously for a series of Ti–phosphinimide complexes (5). These values were significantly higher than those seen for catalysts derived from the previously reported bimetallic systems, where the activities ranged from 20 to 150 g mmol^{-1} h^{-1} atm^{-1}. In particular, these systems stand in contrast to those derived from the related species $(CH_2PPh_2NTiCp^*Cl_2)_2$, which was reported to exhibit extremely low activities for polymerization (34). The cause of such differences is not clear; however, the bimetallic systems are much less soluble than the corresponding monometallic systems. Similarly, this is true for systems incorporating Cp rather than Cp* ligands. It is also noteworthy that in all pairs of analogs, incorporation of the more sterically demanding substituents (Cp* in place of Cp or *t*-Bu in place of Cy) afforded higher catalyst activity. This observation is consistent with the previously suggested notion that steric protection of the phosphinimide N atom enhances activity (4, 38–40).

The monometallic catalysts derived from **5**, **7,** and **13** described herein yield polyethylene of molecular weights ranging from 239 800 to 628 400 g mmol^{-1} h^{-1} atm^{-1} with PDIs of 2.8–3.2 in the Buchi reactor. The corresponding bimetallic catalysts, in contrast, provided PE of molecular weights ranging from 143 300 to 1 416 000 g mmol^{-1} h^{-1} atm^{-1} depending on the precatalyst. These polymers showed broader bimodal molecular weight distributions (Fig. 2). The

© 2004 NRC Canada

12	13	14	16	18	19	20
$C_{42}H_{62}N_2Cl_4P_2Ti_2$ ($2CH_2Cl_2$)	$C_{27}H_{46}NPTi$	$C_{31}H_{50}NPTi$	$C_{26}H_{40}NPTi$	$C_{56}H_{94}N_2P_2Ti_2 \cdot 2C_6H_6$	$C_{38}H_{66}N_2P_2Ti_2$	$C_{52}H_{80}N_2P_2Ti_2$
1064.32	463.52	515.59	445.46	1109.29	708.67	890.92
8.974(5)	10.037(5)	11.613(6)	11.729(7)	16.526(10)	16.290(9)	8.794(5)
11.490(6)	19.055(10)	16.468(8)	13.616(8)	17.114(10)	16.455(9)	9.772(5)
14.905(8)	15.059(8)	16.287(8)	16.206(9)	24.453(14)	15.594(8)	16.678(9)
96.092(10)						77.211(10)
105.085(9)	104.047(10)	102.618(9)		106.280(10)	100.865(10)	79.909(10)
112.201(11)						68.500(9)
Triclinic	Monoclinic	Monoclinic	Orthorhombic	Monoclinic	Monoclinic	Triclinic
1337.4(12)	2794(3)	3040(3)	2588(3)	6639(7)	4105(4)	1293.4(12)
$P1$	$P2_1/c$	$P2_1/c$	$P2_12_12_1$	$P2_1/c$	$P2_1/c$	$P\bar{1}$
1.322	1.102	1.127	1.143	1.110	1.147	1.144
1	4	4	4	4	4	1
0.789	0.376	0.352	0.404	0.327	0.493	0.404
5717	11 755	12 862	10 620	27 145	17 348	5554
3790	3986	4376	3656	9431	5861	3672
262	271	307	262	667	397	262
0.0461	0.0408	0.0414	0.0595	0.0510	0.0378	0.0379
0.1317	0.1209	0.1248	0.1196	0.1084	0.1081	0.1080
1.062	1.056	0.570	1.199	0.693	1.008	1.033

Table 2. Selected metric parameters from X-ray structures.

Compd.	Ti—X (X = Cl, Me) (Å)	Ti—N (Å)	N—P (Å)	Ti–N–P (°)
5	2.322(1), 2.324(1)	1.786(2)	1.598(2)	167.6(1)
6	2.317(1), 2.309(1)	1.776(2)	1.594(2)	157.3(1)
7	2.3072(9), 2.3091(8)	1.760(2)	1.599(2)	175.2(1)
8	2.313(1), 2.314(1)	1.765(2)	1.607(2)	168.4(1)
10	2.312(2), 2.328(2)	1.786(5)	1.589(5)	157.1(3)
	2.305(2), 2.317(2)	1.768(5)	1.602(5)	162.6(3)
12	2.303(2), 2.323(1)	1.764(3)	1.608(3)	172.7(2)
13	2.165(3), 2.228(3)	1.830(2)	1.580(2)	172.6(2)
14	2.136(3), 2.152(3)	1.811(2)	1.570(2)	162.8(2)
16	2.131(6), 2.130(6)	1.804(4)	1.579(4)	168.1(3)
18	2.119(7), 2.145(6)	1.829(5)	1.573(5)	163.4(4)
	2.160(6), 2.155(6)	1.813(5)	1.582(5)	161.5(4)
19	2.137(3), 2.143(3)	1.806(2)	1.582(2)	171.0(1)
	2.124(3), 2.130(4)	1.802(2)	1.581(2)	173.9(2)
20	2.160(3), 2.191(3)	1.806(2)	1.580(2)	167.9(1)

separation of the peak molecular weights and the relative intensities of the two modes were catalyst and condition dependent. For example, the polymer derived from the precatalyst **9** (Fig. 2*a*) exhibited a bimodal distribution that was fit with two Gaussian curves of peak molecular weights 98 600 and 447 700 g mmol^{-1}. In contrast, the catalyst derived from **19** (Fig. 2*b*) gave rise to a polymer with clearly separated peaks at 19 700 and 537 000 g mmol^{-1}. These results stand in marked contrast to previous reports regarding compounds of the form $(R_3PN)TiCpCl_2$, which upon activation by MAO, behave as single-site catalysts providing polyethylene of high molecular weight with narrow polydispersities (5).

Related tests done using the monometallic catalyst precursor **5** showed that under 2 atm of constant ethylene pressure (Table 4), polymer with a broaden molecular weight distribution in which a lower molecular weight polymer fraction is similar to that derived from **9** (Fig. 3) was produced. This observation seemed to counter the notion that a bimodal polymer was a direct result of the bimetallic catalysts. Monitoring the polymerizations using **5** and **13** over 10-min intervals revealed the initial appearance of a higher molecular weight fraction that accumulated over time (Fig. 4). This suggests that the active catalyst undergoes some sort of transformation during the course of the polymerization, possibly via reaction of the benzylic protons. It is noteworthy that Bochmann and co-workers have observed metallation of the methylene protons of $(CH_2PPh_2NTiCp^*Cl_2)_2$ (34).

Using similar increased pressure conditions, activation of the bimetallic catalyst precursors **18** and **20** with 1, 2, or

© 2004 NRC Canada

Table 3. Ethylene polymerization data.

Precatalyst	T (°C)	Catalyst concn. (μmol L^{-1})	Activity	M_w[a] (g mol^{-1})	PDI[a,b]	MW[c] (g mol^{-1})
9	25	350	36	131 100	5.4	—
10	25	350	<1	—[d]	—[d]	—
11	25	350	20	15 200	4.8	—
12	25	350	<1	—[d]	—[d]	—
5	25	350	42	234 100	4.35	—
17	25	350	93	138 700	1.6	—
18	25	350	55	—[e]	—[e]	—
19	25	350	100	38 100	2.2	—
20	25	350	11	536 500	2.0	—
13	25	350	170	117 400	2.02	—
$ZrCp_2Cl_2$	25	350	200	35 600	2.5	—
9	30	50	150	319 200	3.2	98 600, 447 700
10	30	50	85	—[e]	—[e]	—
11	30	50	50	143 300	4.8	34 300, 653 100
12	30	50	25	1 104 000	1.9	684 200, 1 407 700
5	30	50	200	239 800	2.8	—
17	30	50	100	468 600	1.9	299 200, 1 425 600
18	30	50	92	—[e]	—[e]	—
19	30	50	60	195 200	10.0	19 700, 537 000
20	30	50	20	1 416 000	3.4	522 400, 1 710 000
13	30	50	280	628 400	3.2	—
$ZrCp_2Cl_2$	30	50	610	340 800	2.1	—

Note: Ti:Al ratio of 1:500, toluene solvent, 30 min, 1 atm ethylene Activities are in units of g $mmol^{-1}$ h^{-1} atm^{-1}. Limited ethylene supply may result in an underestimation of the activity.

[a]Values are overall averages observed.

[b]PDI, polydispersity index.

[c]Peak molecular weight from nonlinear Gaussian fit.

[d]Too little polymer to analyze.

[e]Polymer would not dissolve in solvent.

Table 4. Ethylene polymerization data.

Precatalyst	T (°C)	Co-catalyst[a]	Activity	M_n (g mol^{-1})	M_w (g mol^{-1})	PDI[b]
5	10	MAO	1510			
5	15	MAO	1190			
5	20	MAO	1050			
13	10	MAO	1580			
13	15	MAO	1260			
13	20	MAO	1140			
13	30	MAO	780			
$ZrCp_2Me_2$	10	MAO	1880			
$ZrCp_2Cl_2$	10	MAO	2030			
18	10	TB (1 equiv)	630	213 600	566 400	2.7
18	10	TB (2 equiv)	895	126 300	382 300	3.0
18	10	TB (4 equiv)	525	252 200	718 000	2.9
20	10	TB (1 equiv)	10	50 300	206 700	4.1
20	10	TB (2 equiv)	95	628 900	1 270 000	2.0
20	10	TB (4 equiv)	126	157 500	491 000	3.1
$ZrCp_2Me_2$[c]	10	TB (2 equiv)	1030	171 000	334 800	1.9

Note: Toluene solvent, 30 °C, 1.82 atm ethylene (constant). Activities are in units of g $mmol^{-1}$ h^{-1} atm^{-1}.

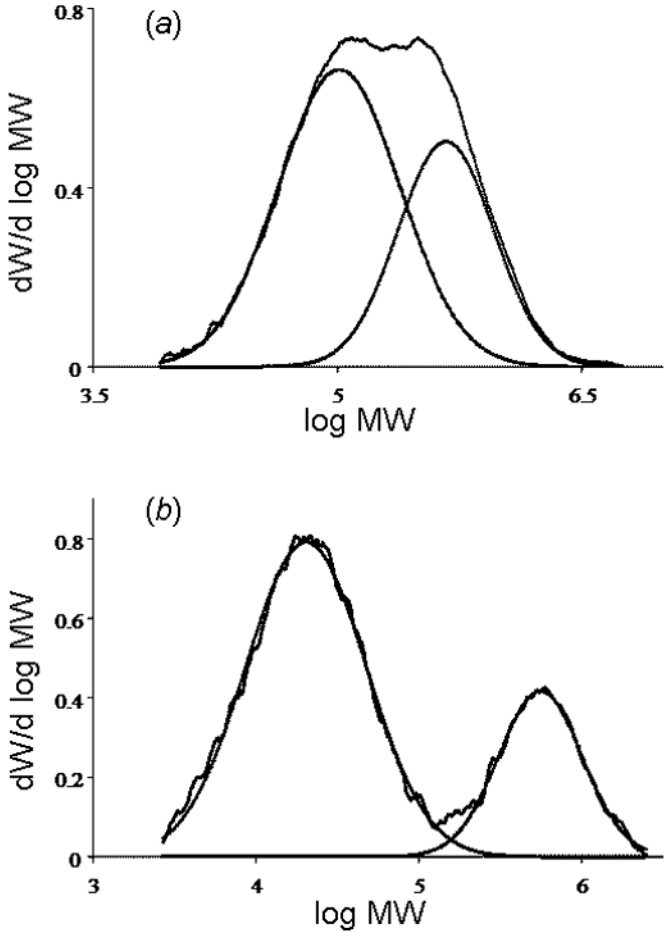
[a]For MAO activation, Ti:Al or Zr:Al ratio of 1:500; for TB ($[Ph_3C][B(C_6F_5)_4]$), Al(*i*-Pr)$_3$ scrubber, Ti:Al ratio of 1:5.

[b]PDI, polydispersity index.

[c]Zr:Al ratio of 1:20.

© 2004 NRC Canada

Fig. 2. Observed and two-Gaussian fit of GPC of polyethylene derived from the precatalysts (*a*) **9** and (*b*) **19**.



4 equiv. of $[Ph_3C][B(C_6F_5)_4]$ resulted in the efficient polymerization of ethylene (Table 4). In general, with an increase in the amount of activator from 1 to 2 equiv., polymerization activities also increased. The bulkier Cp* derivative showed 4 times the activity of the Cp analog when 4 equiv. of $[Ph_3C][B(C_6F_5)_4]$ were used, and ca. 60 times the activity when only 1 equiv. of activator was employed. The resulting polymers showed monodisperse GPC traces with PDI values less than 4. This is in contrast to the results obtained when MAO was used as an activator.

In conclusion, MAO or $[Ph_3C][B(C_6F_5)_4]$ activation of the monometallic and bimetallic benzyl-phosphinimide catalysts produced polyethylene with good activities. While all these catalyst systems gave relatively broad molecular weight distributions, catalysts generated using MAO gave bimodal polymers. Given that previous studies have shown that other phosphinimide catalysts give single-site activity, the present observations infer that MAO reacts with the present catalysts, probably at the benzylic fragment, to modify the active species, resulting in two (or more) catalyst sites. While this postulate remains unconfirmed, it is noteworthy that in related systems, Bochmann and co-workers (34) have observed metallation of methylene groups in phosphinimide ligands. While the precise cause remains a subject of investigation, it is clear that modification of the catalyst structure alters the nature of the resulting polymer. We are currently investigating strategies to other modified catalyst systems in an effort to understand the relationship between catalyst structure and polymer properties in more detail.

Fig. 3. GPC of polyethylene from catalysts derived from **9** (——) and derivative **5** (– – –).

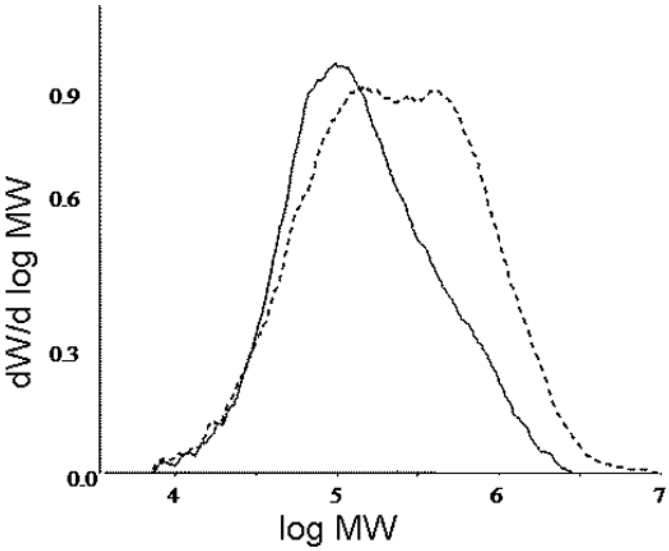
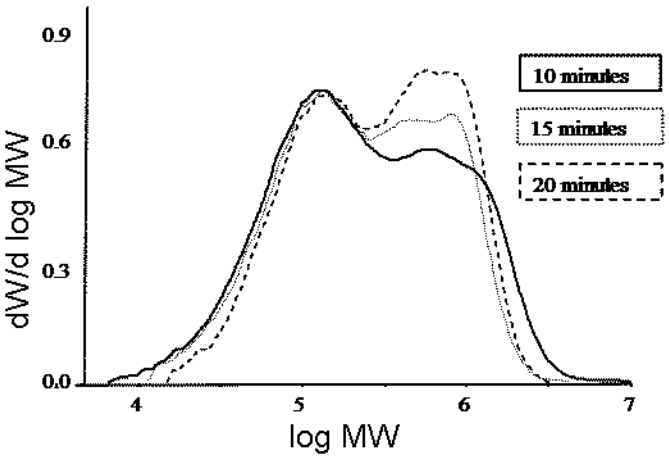


Fig. 4. GPC of polyethylene from catalysts derived from **5** as a function of time.



Experimental

General data

The syntheses were performed under an atmosphere of dry, oxygen-free nitrogen in a Vacuum Atmospheres (Hawthorne, Calif.) inert atmosphere glove box or by standard Schlenk techniques. Proton NMR data were acquired on a Bruker Avance 500-MHz spectrometer, and $^{13}C\{^1H\}$ and $^{31}P\{^1H\}$ NMR data on a Bruker Avance 300-MHz spectrometer. Proton and ^{13}C NMR chemical shifts are listed downfield from $SiMe_4$ in parts per million and were referenced to the residual proton or carbon peak of the solvent. Phosphorus-31 NMR data were referenced using an external standard relative to 85% H_3PO_4. All NMR spectra were recorded in C_6D_6 unless otherwise stated. Combustion analyses were performed by Galbraith Laboratories Inc. or in-

© 2004 NRC Canada

house elemental analysis services. In a very few cases, despite repeated analyses and the use of added oxidant, C analyses yielded deviations from calculated values. We attribute this to partial formation of Ti–C during combustion of the Ti-organometallic derivatives. Gel permeation chromatography (GPC) was performed employing a Waters 150C GPC using 1,2,4-trichlorobenzene as the mobile phase at 140 °C at NOVA Research and Technology Centre (Calgary, Alta.). The samples were prepared for GPC analyses by dissolving the polymer in the mobile-phase solvent in an external oven at 0.1% (*w*/*v*) and were filtered before injection. Molecular weights are expressed as polyethylene equivalents with a relative standard deviation of 2.9% and 5.0% for M_n and M_w, respectively. Reagent-grade solvents and NEt_3 were purchased from Aldrich Chemical Co. Benzene, toluene, and Et_2O were dried over Na, MeOH was dried over Mg, and NEt_3 was dried over KOH prior to distillation. C_6D_6 and CD_2Cl_2 were purchased from Cambridge Isotopes Laboratories (Andover, Mass.) and degassed by at least 4 freeze/pump/thaw cycles before storing over 4Å molecular sieves. The compounds R_2BnP and $R_2BnPNSiMe_3$ (Bn = benzyl; R = *t*-Bu, Cy) (35) and $CpTiCl_3$ (41) were prepared according to literature methods, and the phosphines were prepared via a modification of a literature procedure (36). The reagents MeMgBr, Me_3SiN_3, and *p*-$C_6H_4(CH_2Br)_2$ were purchased from Aldrich Chemical Co., and $HP(t\text{-}Bu)_2$, $HPCy_2$, and Cp^*TiCl_3 were purchased from Strem Chemical Co. (Newburyport, Mass.); all were used without further purification.

Synthesis of *p*-$C_6H_4(CH_2PR_2)_2$ (R = *t*-Bu, Cy)

Compounds **1** (R = *t*-Bu) and **2** (R = Cy) were prepared in a similar manner to a literature method for the related meta-substituted analogs (36). *p*-$C_6H_4(CH_2Br)_2$ (0.88 g, 3.3 mmol) was slurried in MeOH, and $HP(t\text{-}Bu)_2$ (1.08 g, 7.3 mmol) was added via syringe. The mixture was stirred at 25 °C for 16 h, during which time the mixture became a homogeneous solution. NEt_3 (0.74 g, 7.3 mmol) was added via syringe, and a fine white solid precipitated from solution. The solid was washed with MeOH (3 × 20 mL) and dried in vacuo for 5 h. A second crop was obtained by concentrating the mother liquor and precipitating the product with degassed water; no degradation in purity was evidenced by the ^1H NMR spectrum. Compound **1**: White solid. Yield 1.16 g (88%). ^1H NMR: 7.38 (s, 4H, C_6H_4), 2.73 (s, 4H, CH_2), 1.06 (d, 36H, J_{P-H} = 10 Hz, *t*-Bu). $^{13}C\{^1H\}$ NMR: 138.4 (s, C_6H_4), 130.1 (s, C_6H_4), 32.1 (d, J_{P-C} = 54 Hz, *t*-Bu), 30.1 (s, *t*-Bu), 29.0 (d, J_{P-C} = 48 Hz, CH_2). $^{31}P\{^1H\}$ NMR: 33.4 (s). Crystals suitable for X-ray diffraction were grown by slow evaporation from benzene. Anal. Calcd. for $C_{24}H_{44}P_2$: C 73.06, H 11.24; found: C 72.36, H 11.05. Compound **2**: White solid. Yield 4.23 g, 85%. ^1H NMR: 7.33 (s, 4H, C_6H_4), 2.72 (s, 4H, CH_2P), 1.80–1.51 (m, 18H, Cy), 1.25–1.12 (m, 26H, Cy). $^{13}C\{^1H\}$ NMR: 137.9 (s, C_6H_4), 129.7 (s, C_6H_4), 34.0 (d, J_{P-C} = 17 Hz, Cy), 30.3 (d, J_{P-C} = 14 Hz, CH_2P), 29.7 (d, J_{P-C} = 10 Hz, Cy), 27.6 (s, Cy), 26.9 (s, Cy). $^{31}P\{^1H\}$ NMR: 1.2 (s). Anal. Calcd. for $C_{32}H_{52}P_2$: C 77.07, H 10.51; found: C 76.42, H 10.68.

Synthesis of *p*-$C_6H_4(CH_2PR_2NSiMe_3)_2$ (R = *t*-Bu, Cy)

Compounds **3** (R = *t*-Bu) and **4** (R = Cy) were both prepared in a similar manner, and one sample preparation is detailed. Solid **1** (0.69 g, 1.7 mmol) and Me_3SiN_3 (1.00 g, 8.7 mmol) were combined to generate a slurry. The mixture was heated at reflux for 15 h, after which time the excess Me_3SiN_3 was removed in vacuo. The beige solid was crushed with a mortar and pestle into a fine powder, washed with hexanes (3 × 10 mL), and dried in vacuo for an additional 5 h. Compound **3**: Yield 0.88 g, 88%. Crystals suitable for X-ray diffraction were grown by slow evaporation from hexanes. ^1H NMR: 7.39 (s, 4H, C_6H_4), 2.73 (d, 4H, J_{P-H} = 10 Hz, CH_2), 0.99 (d, 36H, J_{P-H} = 13 Hz, *t*-Bu), 0.35 (s, 18H, Me). $^{13}C\{^1H\}$ NMR: 133.4 (s, C_6H_4), 130.4 (s, C_6H_4), 37.1 (d, J_{P-C} = 60 Hz, CH_2), 30.1 (d, J_{P-C} = 57 Hz, CH_2), 27.6 (s, *t*-Bu), 1.4 (s, Me_3). $^{31}P\{^1H\}$ NMR: 24.6 (s). Anal. Calcd. for $C_{30}H_{62}N_2P_2Si_2$: C 63.33, H 10.98, N 4.92; found: C 63.34, H 10.36, N 4.93. Compound **4**: Yield 2.77 g, 94%. ^1H NMR: 7.34 (s, 4H, C_6H_4), 2.67 (d, 4H, J_{P-H} = 12 Hz, CH_2P), 1.78–1.58 (m, 18H, Cy), 1.45–1.07 (m, 26H, Cy), 0.41 (s, 18H, Me). $^{13}C\{^1H\}$ NMR: 132.9 (s, C_6H_4), 130.1 (s, C_6H_4), 37.6 (d, J_{P-C} = 65 Hz, Cy), 33.7 (d, J_{P-C} = 60 Hz, CH_2P), 27.2 (d, J_{P-C} = 13 Hz, Cy), 26.5 (s, Cy), 26.2 (s, Cy), 5.2 (s, Me_3). $^{31}P\{^1H\}$ NMR: 13.5 (s). Anal. Calcd. for $C_{38}H_{70}N_2P_2Si_2$: C 67.81, H 10.48, N 4.16; found: C 68.08, H 10.85, N 3.89.

Synthesis of $(R_2BnPN)Cp'TiCl_2$ (Cp′ = Cp*, Cp; R = *t*-Bu, Cy)

Compounds **5** (Cp′ = Cp*; R = *t*-Bu), **6** (Cp′ = Cp*; R = Cy), **7** (Cp′ = Cp; R = *t*-Bu), and **8** (Cp′ = Cp; R = Cy) were all prepared in a similar manner, and thus only one preparation is detailed. Solid Cp^*TiCl_3 (1.12 g, 3.8 mmol) was dissolved in toluene (100 mL) to give a clear, red solution. Liquid $(t\text{-}Bu)_2BnPNSiMe_3$ (1.24 g, 3.8 mmol) was added dropwise at 25 °C, and the mixture was stirred for 24 h. The volatile products were removed in vacuo, and the bright orange solid was washed with hexanes (3 × 10 mL) and dried. Compound **5**: Yield 1.73 g, 91%. ^1H NMR: 7.39 (d, 2H, J_{H-H} = 8 Hz, C_6H_5), 7.19 (t, 2H, J_{H-H} = 8 Hz, Ph), 7.08 (t, 1H, J_{H-H} = 8 Hz, Ph), 2.92 (d, 2H, J_{P-H} = 12 Hz, CH_2), 2.21 (s, 15H, Cp*), 1.10 (d, 18H, J_{P-H} = 14 Hz, P*t*-Bu_2). $^{13}C\{^1H\}$ NMR: 140.8 (s, Ph), 131.2 (s, Ph), 128.7 (s, Ph), 127.1 (s, Ph), 125.9 (s, Cp*), 39.6 (d, J_{P-C} = 52 Hz, *t*-Bu), 30.9 (d, J_{P-C} = 48 Hz, CH_2), 27.8 (s, *t*-Bu), 13.1 (s, Cp*). $^{31}P\{^1H\}$ NMR: 35.3 (s). Anal. Calcd. for $C_{25}H_{40}Cl_2NPTi$: C 59.54, H 7.99, N 2.78; found: C 59.74, H 7.88, N 2.95. Crystals suitable for X-ray diffraction were grown by slow evaporation from benzene. Compound **6**: Bright orange solid. Yield 580 mg, 93%. ^1H NMR δ: 7.20 (d, 2H, $^3J_{H-H}$ = 8 Hz, Ph (*o*-H)), 7.15 (dd, 2H, $^3J_{H-H}$ = 8 Hz, Ph (*m*-H)), 7.04 (t, 1H, $^3J_{H-H}$ = 8 Hz, Ph (*p*-H)), 3.01 (d, 2H, $^2J_{P-H}$ = 14 Hz, CH_2P), 2.20 (s, 15H, Cp*), 1.71–0.96 (m, 22H, Cy). $^{13}C\{^1H\}$ NMR δ: 132.6 (d, $^2J_{P-C}$ = 7 Hz, Ph (*ipso*-C)), 130.5 (d, $^3J_{P-C}$ = 5 Hz, Ph (*o*-C)), 128.9 (s, Ph (*m*-C)), 127.2 (s, Ph (*p*-C)), 125.9 (s, Cp*), 37.2 (d, $^1J_{P-C}$ = 59 Hz, Cy (*ipso*-C)), 32.2 (d, $^1J_{P-C}$ = 52 Hz, CH_2P), 26.8 (d, $^2J_{P-C}$ = 12 Hz, Cy (*o*-C)), 26.7 (d, $^2J_{P-C}$ = 12 Hz, Cy (*o*-C)), 26.1 (s, Cy (*m*-C)), 26.0 (s, Cy (*p*-C)), 13.2 (s, Cp*). $^{31}P\{^1H\}$ NMR δ: 23.0 (s). Anal. Calcd. for $C_{29}H_{44}Cl_2NPTi$: C 62.60, H 7.97, N 2.52; found: C 62.29, H 8.27, N 2.45. Orange crystals suitable for X-ray diffraction were grown by slow diffusion of pentanes/hexanes into benzene. Compound **7**: Bright yellow solid. Yield

© 2004 NRC Canada

0.390 g, 77%. ^{1}H NMR δ: 7.26 (d, 2H, $^3J_{H–H}$ = 8 Hz, Ph), 7.20 (t, 2H, $^3J_{H–H}$ = 8 Hz, Ph), 7.07 (t, 1H, $^3J_{H–H}$ = 8 Hz, Ph), 6.22 (s, 5H, Cp), 2.61 (d, 2H, $^2J_{P–H}$ = 10 Hz, CH_2), 1.04 (d, 18H, $^3J_{P–H}$ = 15 Hz, *t*-Bu). ^{13}C{^{1}H} NMR δ: 131.5 (d, $^2J_{P–C}$ = 5 Hz, (*ipso*-C)), 128.7 (d, $^3J_{P–C}$ = 5 Hz, (*o*-C)), 128.6 (s, Ph), 128.3 (s, Ph), 115.5 (s, Cp), 39.3 (d, $^1J_{P–C}$ = 51 Hz, *t*-Bu), 28.9 (d, $^1J_{P–C}$ = 47 Hz, CH_2), 27.2 (s, *t*-Bu). ^{31}P{^{1}H} NMR δ: 34.9 (s). Anal. Calcd. for $C_{20}H_{30}Cl_2NPTi$: C 55.32, H, 6.96, N 3.23; found: C 55.49, H, 7.14, N 3.19. Crystals suitable for X-ray diffraction were grown by slow evaporation from benzene. Compound **8**: Bright yellow solid. Yield 685 mg, 92%. ^{1}H NMR δ: 7.27 (d, 2H, $^3J_{H–H}$ = 8 Hz, Ph (*o*-H)), 7.18 (dd, 2H, $^3J_{H–H}$ = 8 Hz, Ph (*m*-H)), 7.06 (t, 1H, $^3J_{H–H}$ = 8 Hz, Ph (*p*-H)), 6.38 (s, 5H, Cp), 2.65 (d, 2H, $^2J_{P–H}$ = 13 Hz, CH_2P), 1.74–0.84 (m, 22H, Cy). ^{13}C{^{1}H} NMR δ: 131.6 (d, $^2J_{P–C}$ = 8 Hz, Ph (*ipso*-C)), 130.8 (d, $^3J_{P–C}$ = 5 Hz, Ph (*o*-C)), 128.9 (s, Ph (*m*-C)), 128.5 (s, Ph (*p*-C)), 115.2 (s, Cp), 36.6 (d, $^1J_{P–C}$ = 58 Hz, Cy (*ipso*-C)), 30.9 (d, $^1J_{P–C}$ = 52 Hz, CH_2P), 26.6 (d, $^2J_{P–C}$ = 13 Hz, Cy (*o*-C)), 25.9 (s, Cy (*m*-C)), 25.7 (s, Cy (*p*-C)). ^{31}P{^{1}H} NMR δ: 24.3 (s). Anal. Calcd. for $C_{24}H_{34}Cl_2NPTi$: C 59.27, H 7.05, N 2.88; found: C 59.68, H 7.28, N 2.82. Yellow crystals suitable for X-ray diffraction were grown by slow diffusion of pentanes/hexanes into benzene.

Synthesis of *p*-$C_6H_4(CH_2PR_2NTiCp'Cl_2)_2$ (Cp′ = Cp*, Cp; R = *t*-Bu, Cy)

Compounds **9** (Cp′ = Cp*; R = *t*-Bu), **10** (Cp′ = Cp*; R = Cy), **11** (Cp′ = Cp; R = *t*-Bu), and **12** (Cp′ = Cp; R = Cy) were all prepared in a similar manner, and only one sample preparation is detailed. Compound **3** (0.81 g, 1.2 mmol) and Cp^*TiCl_3 (0.70 g, 2.4 mmol) were slurried in toluene (80 mL) to afford a bright orange, foggy solution. The mixture was heated at reflux for 15 h, after which time it was filtered. The filtrate was concentrated to ca. 20 mL, and the bright orange powder that precipitated was filtered, washed with benzene (3 × 15 mL), and dried in vacuo. Compound **10**: Yield 2.34 g, 95%. ^{1}H NMR (CD_2Cl_2): 7.48 (s, 4H, C_6H_4), 3.38 (d, 4H, $J_{P–H}$ = 12 Hz, CH_2), 2.14 (s, 30H, Cp*), 1.34 (d, 36H, $J_{P–H}$ = 15 Hz, *t*-Bu). ^{13}C{^{1}H} NMR (CD_2Cl_2): 133.4 (s, C_6H_4), 131.5 (s, C_6H_4), 123.2 (s, Cp*), 40.6 (s, CH_2), 39.8 (d, $J_{P–C}$ = 55 Hz, *t*-Bu), 28.3 (s, *t*-Bu), 8.9 (s, Cp*). ^{31}P{^{1}H} NMR (CD_2Cl_2): 37.2 (s). Anal. Calcd. for $C_{44}H_{74}Cl_4N_2P_2Ti_2$: C 56.79, H 8.02, N 3.01; found: C 54.92, H 8.16, N 3.35. Compound **10**: Bright orange solid. Yield 0.98 g, 79%. ^{1}H NMR: 7.36 (s, 4H, C_6H_4), 3.01 (d, 4H, $J_{P–H}$ = 13 Hz, CH_2P), 2.24 (s, 30H, Cp*), 1.71–1.45 (m, 18H, Cy), 1.18–1.03 (m, 26H, Cy). ^{13}C{^{1}H} NMR: 137.4 (s, C_6H_4), 131.0 (s, C_6H_4), 125.8 (s, Cp*), 37.2 (d, $J_{P–C}$ = 59 Hz, Cy), 31.9 (d, $J_{P–C}$ = 52 Hz, CH_2P), 26.8 (d, $J_{P–C}$ = 12 Hz, Cy), 26.1 (s, Cy (*m*-C)), 26.1 (s, Cy), 13.2 (s, Cp*). ^{31}P{^{1}H} NMR: 22.4 (s). Anal. Calcd. for $C_{52}H_{82}Cl_4N_2P_2Ti_2$: C 60.36, H 7.99, N 2.71; found: C 60.20, H 8.19, N 2.76. Crystals suitable for X-ray diffraction were grown by slow evaporation from toluene. Compound **11**: Yellow solid. Yield 2.34 g, 95%. ^{1}H NMR (CD_2Cl_2): 7.54 (s, 4H, C_6H_4), 6.29 (s, 10H, C_5H_5), 3.31 (d, 4H, $J_{P–H}$ = 10 Hz, CH_2), 1.40 (d, 36H, $J_{P–H}$ = 13 Hz, *t*-Bu). ^{13}C{^{1}H} NMR (CD_2Cl_2): 132.7 (s, C_6H_4), 132.0 (s, C_6H_4), 116.0 (s, Cp), 46.4 (s, CH_2), 40.0 (d, $J_{P–C}$ = 51 Hz, *t*-Bu), 27.8 (s, *t*-Bu). ^{31}P{^{1}H} NMR (CD_2Cl_2): 38.7 (s). Anal. Calcd. for $C_{34}H_{54}Cl_4N_2P_2Ti_2$: C 51.67, H 6.89, N 3.54; found: C 52.65, H 7.64, N 3.45. Compound **12**: Light yellow solid. Yield 1.36 g, 95%. ^{1}H NMR: 7.46 (s, 4H, C_6H_4), 6.39 (s, 10H, Cp), 3.21 (d, 4H, $J_{P–H}$ = 12 Hz, CH_2P), 1.96–1.27 (m, 44H, Cy). ^{13}C{^{1}H} NMR: 131.8 (s, C_6H_4), 131.5 (s, C_6H_4), 115.7 (s, Cp), 37.1 (d, $J_{P–C}$ = 58 Hz, Cy), 31.1 (d, $J_{P–C}$ = 53 Hz, CH_2P), 27.0 (d, $J_{P–C}$ = 13 Hz, Cy), 26.3 (s, Cy), 26.3 (s, Cy). ^{31}P{^{1}H} NMR: 27.0 (s). Anal. Calcd. for $C_{42}H_{62}Cl_4N_2P_2Ti_2$: C 56.40, H 6.99, N 3.13; found: C 56.23, H 7.00, N 3.36. Crystals suitable for X-ray diffraction were grown by slow evaporation from CH_2Cl_2.

Synthesis of (R_2BnPN)TiCp′Me_2 (Cp′ = Cp*, Cp; R = *t*-Bu, Cy)

Compounds **13** (Cp′ = Cp*; R = *t*-Bu), **14** (Cp′ = Cp*; R = Cy), **15** (Cp′ = Cp; R = *t*-Bu), and **16** (Cp′ = Cp; R = Cy) were all prepared in a similar manner, and thus only the preparation of **13** is detailed. Compound **5** (160 mg, 0.32 mmol) was slurried in Et_2O (15 mL), and a 3.0 mol L^{-1} solution of MeMgBr in the same solvent (2.24 mL, 0.67 mmol) was added dropwise via syringe at 25 °C. The heterogeneous solution was stirred for 15 h, after which time the solvent was removed in vacuo. Extraction with hexanes (3 × 10 mL) and filtration through Hyflo Super Cel® (Beaver Chemicals, Burlington, Ont.) afforded a bright yellow solution. Subsequent removal of the solvent in vacuo generated bright yellow crystals of **13**. Yield 122 mg, 83%. ^{1}H NMR δ: 7.38 (d, 2H, $^3J_{H–H}$ = 8 Hz, Ph (*o*-H)), 7.15 (dd, 2H, $^3J_{H–H}$ = 8 Hz, Ph (*m*-H)), 7.08 (t, 1H, $^3J_{H–H}$ = 8 Hz, Ph (*p*-H)), 2.90 (d, 2H, $^2J_{P–H}$ = 12 Hz, CH_2), 2.03 (s, 15H, Cp*), 1.16 (d, 18H, $^3J_{P–H}$ = 14 Hz, *t*-Bu), 0.39 (s, 6H, TiMe). ^{13}C{^{1}H} NMR δ: 135.0 (d, $^2J_{P–C}$ = 7 Hz, Ph (*ipso*-C)), 130.9 (d, $^3J_{P–C}$ = 5 Hz, Ph (*o*-C)), 128.3 (s, Ph (*m*-C)), 126.7 (s, Ph (*p*-C)), 118.5 (s, Cp*), 44.4 (s, TiMe), 39.0 (d, $^1J_{P–C}$ = 54 Hz, *t*-Bu), 31.6 (d, $^1J_{P–C}$ = 48 Hz, CH_2), 28.0 (s, *t*-Bu), 12.2 (s, Cp*). ^{31}P{^{1}H} NMR δ: 21.4 (s). Anal. Calcd. for $C_{27}H_{46}NPTi$: C 69.96, H 10.00, N 3.02; found: C 69.59, H 10.03, N 3.02. Yellow crystals suitable for X-ray diffraction were grown by slow evaporation from hexanes. Compound **14**: Light yellow solid. Yield 100 mg, 47%. ^{1}H NMR δ: 7.28 (d, 2H, $^3J_{H–H}$ = 8 Hz, Ph (*o*-H)), 7.17 (dd, 2H, $^3J_{H–H}$ = 8 Hz, Ph (*m*-H)), 7.06 (t, 1H, $^3J_{H–H}$ = 8 Hz, Ph (*p*-H)), 2.93 (d, 2H, $^2J_{P–H}$ = 13 Hz, CH_2P), 2.08 (s, 15H, Cp*), 1.91–1.03 (m, 22H, Cy), 0.45 (s, 6H, TiMe). ^{13}C{^{1}H} NMR δ: 134.2 (d, $^2J_{P–C}$ = 7 Hz, Ph (*ipso*-C)), 130.3 (d, $^3J_{P–C}$ = 5 Hz, Ph (*o*-C)), 128.6 (s, Ph (*m*-C)), 126.8 (s, Ph (*p*-C)), 118.5 (s, Cp*), 42.6 (s, TiMe), 38.1 (d, $^1J_{P–C}$ = 60 Hz, Cy), 34.4 (d, $^1J_{P–C}$ = 52 Hz, CH_2P), 27.0 (d, $^2J_{P–C}$ = 3 Hz, Cy), 26.8 (d, $^2J_{P–C}$ = 3 Hz, Cy), 26.4 (s, Cy), 26.3 (s, Cy), 12.3 (s, Cp*). ^{31}P{^{1}H} NMR δ: 8.4 (s). Anal. Calcd. for $C_{31}H_{50}NPTi$: C 72.22, H, 9.77, N 2.72; found: C 71.93, H, 10.10, N 2.52. Yellow–orange crystals suitable for X-ray diffraction were grown by slow evaporation from pentanes. Compound **15**: Beige solid. Yield 74 mg, 78%. ^{1}H NMR δ: 7.32 (d, 2H, $^3J_{H–H}$ = 7 Hz, Ph (*o*-H)), 7.16 (dd, 2H, $^3J_{H–H}$ = 7 Hz, Ph (*m*-H)), 7.05 (t, 1H, $^3J_{H–H}$ = 7 Hz, Ph (*p*-H)), 6.08 (s, 5H, Cp), 2.74 (d, 2H, $^2J_{P–H}$ = 11 Hz, CH_2), 1.06 (d, 18H, $^3J_{P–H}$ = 14 Hz, *t*-Bu), 0.70 (s, 6H, TiMe). ^{13}C{^{1}H} NMR δ: 134.0 (s, Ph (*ipso*-C)), 131.1 (d, $^3J_{P–C}$ = 4 Hz, Ph (*o*-C)), 128.4 (s, Ph (*m*-C)), 126.8 (s, Ph (*p*-C)), 111.1 (s, Cp), 41.4 (s, TiMe), 38.5 (d, $^1J_{P–C}$ = 54 Hz, *t*-Bu), 30.2 (d, $^1J_{P–C}$ = 48 Hz, CH_2), 27.5 (s, *t*-Bu).

© 2004 NRC Canada

$^{31}P\{^{1}H\}$ NMR (121.5 MHz, C_6D_6) δ: 21.6 (s). Anal. Calcd. for $C_{22}H_{36}NPTi$: C 67.17, H 9.22, N 3.56; found: C 67.09, H 9.03, N 3.02. Compound **16**: Beige solid. Yield 230 mg, 46%. ^{1}H NMR δ: 7.33 (d, 2H, $^{3}J_{H-H}$ = 8 Hz, Ph (*o*-H)), 7.18 (dd, 2H, $^{3}J_{H-H}$ = 8 Hz, Ph (*m*-H)), 7.06 (t, 1H, $^{3}J_{H-H}$ = 8 Hz, Ph (*p*-H)), 6.18 (s, 5H, Cp), 2.71 (d, 2H, $^{2}J_{P-H}$ = 13 Hz, CH_2P), 1.62–0.98 (m, 22H, Cy), 0.73 (s, 6H, TiMe). $^{13}C\{^{1}H\}$ NMR δ: 133.5 (d, $^{2}J_{P-C}$ = 7 Hz, Ph (*ipso*-C)), 130.5 (d, $^{3}J_{P-C}$ = 5 Hz, Ph (*o*-C)), 128.5 (s, Ph (*m*-C)), 127.0 (s, Ph (*p*-C)), 110.8 (s, Cp), 40.7 (s, TiMe), 37.6 (d, $^{1}J_{P-C}$ = 60 Hz, Cy (*ipso*-C)), 32.9 (d, $^{1}J_{P-C}$ = 53 Hz, CH_2P), 26.8 (d, $^{2}J_{P-C}$ = 12 Hz, Cy (*o*-C)), 26.3 (s, Cy (*p*-C)), 26.0 (d, $^{3}J_{P-C}$ = 8 Hz, Cy (*m*-C)). $^{31}P\{^{1}H\}$ NMR δ: 10.2 (s). Anal. Calcd. for $C_{26}H_{40}NPTi$: C 70.11, H 9.05, N 3.14; found: C 69.03, H 9.20, N 3.08. Yellow crystals suitable for X-ray diffraction were grown by slow evaporation from pentanes.

Synthesis of *p*-$C_6H_4(CH_2PR_2NTiCp'Me_2)_2$ (Cp′ = Cp*, Cp; R = *t*-Bu, Cy)

Compounds **17** (Cp′ = Cp*; R = *t*-Bu), **18** (Cp′ = Cp*; R = Cy), **19** (Cp′ = Cp; R = *t*-Bu), and **20** (Cp′ = Cp; R = Cy) were all prepared in a similar manner and one sample preparation is detailed. Compound **5** (0.21 g, 0.27 mmol) was slurried in Et_2O (25 mL), and a solution of MeMgBr in the same solvent (1.4 mmol) was added dropwise via syringe at 25 °C. The heterogeneous solution was stirred for 15 h, after which time the solvent was removed in vacuo. Extraction with hexanes (3 × 10 mL) and filtration through Hyflo Super Cel® afforded a colorless liquid. Removal of the solvent in vacuo generated a white solid. The yield increased when extraction was performed with toluene. Compound **17**: Yield 0.23 g, 77%. ^{1}H NMR: 7.50 (s, 4H, C_6H_4), 2.96 (d, 4H, J_{P-H} = 11 Hz, CH_2), 2.12 (s, 30H, Cp*), 1.17 (d, 36H, J_{P-H} = 14 Hz, *t*-Bu), 0.46 (s, 12H, TiMe). $^{13}C\{^{1}H\}$ NMR: 133.4 (s, C_6H_4), 130.8 (s, C_6H_4), 118.4 (s, Cp*), 44.4 (s, TiMe), 38.9 (d, J_{P-C} = 54 Hz, *t*-Bu), 31.6 (d, J_{P-C} = 48 Hz, CH_2), 28.0 (s, *t*-Bu), 12.3 (s, Cp*). $^{31}P\{^{1}H\}$ NMR: 22.0 (s). Anal. Calcd. for $C_{48}H_{86}N_2P_2Ti_2$: C 67.91, H 10.21, N 3.30; found: 67.51, H 9.96, N. 2.95. Compound **18**: White solid. Yield 0.41 g, 73%. ^{1}H NMR: 7.35 (s, 4H, C_6H_4), 2.92 (d, 4H, J_{P-H} = 13 Hz, CH_2P), 2.10 (s, 30H, Cp*), 1.81–1.10 (m, 44H, Cy), 0.43 (s, 12H, TiMe). $^{13}C\{^{1}H\}$ NMR: 132.5 (s, C_6H_4), 130.5 (s, C_6H_4), 122.3 (s, Cp*), 42.7 (s, TiMe), 38.2 (d, J_{P-C} = 61 Hz, Cy), 34.0 (d, J_{P-C} = 52 Hz, CH_2P), 27.1 (d, J_{P-C} = 12 Hz, Cy), 26.5 (d, J_{P-C} = 6 Hz, Cy), 26.4 (s, Cy), 11.9 (s, Cp*). $^{31}P\{^{1}H\}$ NMR: 8.0 (s). Anal. Calcd. for $C_{54}H_{94}N_2P_2Ti_2$: C 69.81, H, 10.20, N 3.02; found: 69.56, H, 9.94, N 2.94. **19**: Colorless block crystals. Yield 0.16 g, 83%. ^{1}H NMR: 7.48 (s, 4H, C_6H_4), 6.18 (s, 10H, Cp), 2.80 (d, 4H, J_{P-H} = 10 Hz, CH_2P), 1.06 (d, 36H, J_{P-H} = 14 Hz, *t*-Bu), 0.72 (s, 12H, TiMe). $^{13}C\{^{1}H\}$ NMR: 132.5 (s, C_6H_4), 130.8 (s, C_6H_4), 110.9 (s, Cp), 41.3 (s, CH_2P), 38.4 (d, J_{P-C} = 54 Hz, *t*-Bu), 31.7 (s, TiMe), 27.4 (s, *t*-Bu). $^{31}P\{^{1}H\}$ NMR: 22.6 (s). Anal. Calcd. for $C_{38}H_{66}N_2P_2Ti_2$: C 64.41, H 9.39, N 3.95; found: C 64.15, H 9.39, N 3.47. Crystals suitable for X-ray diffraction were grown by slow evaporation from toluene. Compound **20**: White solid. Yield 0.45 g, 77%. ^{1}H NMR δ: 7.48 (s, 4H, C_6H_4), 6.22 (s, 10H, Cp), 2.70 (d, 4H, J_{P-H} = 12 Hz, CH_2P), 1.65–1.06 (m, 44H, Cy), 0.74 (s, 12H, TiMe). $^{13}C\{^{1}H\}$ NMR: 132.1 (s, C_6H_4), 130.6 (s, C_6H_4), 110.8 (s, Cp), 40.8 (s, TiMe), 37.6 (d, J_{P-C} = 60 Hz, Cy), 32.4 (d, J_{P-C} = 53 Hz, CH_2P), 26.9 (d, J_{P-C} = 12 Hz, Cy), 26.3 (s, Cy), 26.1 (s, Cy). $^{31}P\{^{1}H\}$ NMR: 10.1 (s). Anal. Calcd. for $C_{52}H_{80}N_2P_2Ti_2$: C 70.10, H 9.05, N 3.14; found: C 70.30, H 9.45, N 3.06. Crystals suitable for X-ray diffraction were grown by slow evaporation from benzene.

Polymerization protocol

Two protocols were employed. In the first, a Schlenk flask was charged with toluene (50 mL) and MAO (1000 equiv., 10% in toluene), and the solution was presaturated with the monomer by briefly evacuating/backfilling (4×) and then stirring under an atmosphere of C_2H_4 for 5 min. A toluene, solution of the catalyst precursor (350 μmol) was injected, and the mixture was stirred at 25 °C for 30 min. The reaction was quenched with 1 mol/L HCl in MeOH, and the precipitated polymer was subsequently washed with HCl, HCl/MeOH, and toluene before drying at 50 °C for at least 48 h prior to weighing. In the second protocol, a 1-L Buchi reactor was dried in vacuo (10^{-2} mm Hg (1 mm Hg = 133.322 Pa)) for several hours. Toluene (500 mL) was transferred into the vessel under a positive pressure of N_2 and was heated to 30°C. The temperature was controlled (to ca. ±2 °C) with an external heating/cooling bath and was monitored by a thermocouple that extended into the polymerization vessel. The vessel was vented of N_2 and then pressurized with C_2H_4 (12 psig) while the solvent stirred at a rate of 150 rpm. A solution of MAO (1000 equiv., 10% in toluene) was injected and the mixture was stirred for 5 min. A toluene solution, of the precatalyst (50 μmol) was injected, the rate of stirring was increased to 1000 rpm, and the solution was stirred for 30 min. Any recorded exotherm was within the allowed temperature differential of the heating/cooling system. The quenching of the reaction and the collection/treatment of the polymer were as described above.

X-ray data collection and reduction

Crystals were manipulated and mounted in capillaries in a glove box, thus maintaining a dry, O_2-free environment for each crystal. Diffraction experiments were performed on a Siemens SMART System CCD diffractometer. The data were collected in a hemisphere of data in 1329 frames with 10-s exposure times. The observed extinctions were consistent with the space groups in each case. The data sets were collected ($4.5° < 2\theta < 45–50.0°$). A measure of decay was obtained by re-collecting the first 50 frames of each data set. The intensities of reflections within these frames showed no statistically significant change over the duration of the data collections. The data were processed using the SAINT and XPREP processing packages (Bruker AXS, Madison, Wis.). An empirical absorption correction based on redundant data was applied to each data set. Subsequent solution and refinement was performed using the SHELXTL solution package (Bruker AXS, Madison, Wis.).

Structure solution and refinement

Non-hydrogen atomic scattering factors were taken from the literature tabulations (42). The heavy-atom positions were determined using direct methods employing the SHELXTL direct methods routine. The remaining non-hydrogen atoms were located from successive difference

© 2004 NRC Canada

Fourier map calculations. The refinements were carried out by using full-matrix least-squares techniques on F^2, minimizing the function $\omega(|F_o| - |F_c|)^2$, where the weight ω is defined as $4F_o^2/2\sigma(F_o^2)$, and F_o and F_c are the observed and calculated structure factor amplitudes. In the final cycles of each refinement, all non-hydrogen atoms were assigned anisotropic temperature factors in the absence of disorder or insufficient data. In the latter cases, atoms were treated isotropically. C-H atom positions were calculated, and the hydrogens were allowed to ride on the carbon to which they are bonded assuming a C–H bond length of 0.95 Å. H-atom temperature factors were fixed at 1.10 times the isotropic temperature factor of the C-atom to which the hydrogens are bonded. The H-atom contributions were calculated but not refined. The locations of the largest peaks in the final difference Fourier map calculation as well as the magnitude of the residual electron densities in each case were of no chemical significance. Details are provided in Table 1 and the supplementary data.

Acknowledgements

Financial support from the Natural Sciences and Engineering Research Council of Canada (NSERC) and NOVA Chemicals Corporation is gratefully acknowledged. EH is grateful for the award of an Ontario Graduate Scholarship.

Supplementary data

Supplementary data may be purchased form the Depository of Unpublished Data, Document Delivery, CISTI, National Research Council Canada, Ottawa, ON K1A OS2, Canada (http://www.nrc.ca/cisti/irm/unpub_e.shtml for information on obtaining electronically). CCDC 223337–223350 contain the supplementary crystallographic data for this paper. These data can be obtained, free of charge, via www.ccdc.cam.ac.uk/conts/retrieving.html (or from the Cambridge Crystallographic Data Centre, 12 Union Road, Cambridge CB2 1EZ, UK; fax: +44 1233 336033; or deposit@ccdc.cam.ca.uk).

References

1. G.G. Hlatky. Coord. Chem Rev. **181,** 243 (1999).
2. G.G. Hlatky. Coord. Chem. Rev. **199,** 235 (2000).
3. G.J.P. Britovsek, V.C. Gibson, and D.F. Wass. Angew. Chem. Int. Ed. Engl. **38,** 428 (1999).
4. D.W. Stephan. Macromol. Symp. **173,** 105 (2001).
5. D.W. Stephan, J.C. Stewart, F. Guerin, R.E.v.H. Spence, W. Xu, and D.G. Harrison. Organometallics, **18,** 1116 (1999).
6. D.W. Stephan, J.C. Stewart, and D.G. Harrison. Eur. Pat. Appl. 1999. 21 pp.
7. S.J. Brown, X. Gao, D.G. Harrison, I. McKay, L. Koch, Q. Wang, W. Xu, R.E. Von Haken Spence, and D.W. Stephan. PCT Int. Appl. 2000. 33 pp.
8. I. McKay, D. Jeremic, Q. Wang, and S.P. Chisholm. PCT Int. Appl. 2000. 23 pp.
9. D.W. Stephan, F. Guerin, R.E.v.H. Spence, L. Koch, X. Gao, S.J. Brown, J.W. Swabey, Q. Wang, W. Xu, P. Zoricak, and D.G. Harrison. Organometallics, **18,** 2046 (1999).
10. H.H. Zabusky and R.F. Heitmiller. SPE Trans. **4,** 17 (1964).
11. R.B. Wilson, Jr. PCT Int. Appl. 1999. 54 pp.
12. A. Kunzel, M. Sokolow, F.-Q. Liu, H.W. Roesky, M. Noltemeyer, H.-G. Schmidt, and I. Uson. J. Chem. Soc., Dalton Trans. 913 (1996).
13. R. Blom and I.M. Dahl. Macromol. Chem. Phys. **202,** 719 (2001).
14. Z.J.A. Komon and G.C. Bazan. Macromol. Rapid Commun. **22,** 467 (2001).
15. J.D. Kim and J.B.P. Soares. J. Polym. Sci. A, **38,** 1427 (2000).
16. L. Li, M.V. Metz, H. Li, M.-C. Chen, T.J. Marks, L. Liable-Sands, and A.L. Rheingold. J. Am. Chem. Soc. **124,** 12 725 (2002).
17. I. Jaber and S.J. Brown. PCT Int. Appl. 2000. 32 pp.
18. P. Marechal. Eur. Pat. Appl. 2002.
19. E. Van Praet, P. Lehmus, and K. Kallio. International Conference on Polyolefins, Houston, Tex., February 2001. Society of Plastics Engineers, Brookfield, Conn. 2001. p. 236.
20. M. Vaehaelae, H. Salminen, and A. Lehtinen. PCT Int. Appl. 2001. 33 pp.
21. J.B.P. Soares and J.D. Kim. J. Polym. Sci. A, **38,** 1408 (2000).
22. R.I. Mink, T.E. Nowlin, S.D. Schregenberger, P.P. Shirodkar, and G.O. Tsien. PCT Int. Appl. 1997. 28 pp.
23. D.H. McConville, D.R. Loveday, M.W. Holtcamp, J.F. Szul, K.A. Erickson, S. Mawson, T.H. Kwack, F.J. Karol, D.J. Schreck, M.G. Goode, P.T. Daniell, M.G. McKee, and C.C. Williams. PCT Int. Appl. 2001. 100 pp.
24. W. Michalke, S. Kreitmeier, M. Lang, A. Buchner, and D. Goritz. Comput. Theor. Polym. Sci. **11,** 459 (2001).
25. P.J. Maddox, D. Pratt, and J.P. McNally. Eur. Pat. Appl. 1995. 11 pp.
26. A.K. Lindahl, H. Oysaed, and R. Goris. Eur. Pat. Appl. 2001. 9 pp.
27. A.K. Kulshreshtha and S.K. Awasthi. Pop. Plast. Packag. **45,** 53 (2000).
28. A. Follestad, V. Almquist, U. Palmqvist, and H. Hokkanen. PCT Int. Appl. 1999. 37 pp.
29. S.K. Noh, J. Lee, and D.-h. Lee. J. Organomet. Chem. **667,** 53 (2003).
30. Y. Tohi, H. Makio, S. Matsui, M. Orda, and T. Fujita. Macromolecules, **36,** 523 (2003).
31. L. Li, M.V. Metz, T.J. Marks, L. Laiable-Sands, and A.L. Rheingold. Polymer Preprints, **4**1 1912 (2000).
32. J.B.P.S. Jung Dae Kim, Garry L. Rempel. Macromol. Rapid Commun. **19,** 197 (1998).
33. S. Daniele, P.B. Hitchcock, and M.F. Lappert. Chem. Commun. 1909 (1999).
34. M.J. Sarsfield, M. Said, M. Thornton-Pett, L.A. Gerrard, and M. Bochmann. J. Chem. Soc., Dalton Trans. 822 (2001).
35. L. Birkofer, A. Ritter, and S.M. Kim. Ber. **96,** 3099 (1963).
36. D.G. Gusev, M. Madott, F.M. Dolgushin, K.A. Lyssenko, and M.Y. Antipin. Organometallics, **19,** 1734 (2000).
37. K. Dehnicke, M. Krieger, and W. Massa. Coord. Chem. Rev. **182,** 19 (1999).
38. N. Yue, E. Hollink, F. Guérin, and D.W. Stephan. Organometallics, **20,** 4424 (2001).
39. N.L.S. Yue and D.W. Stephan. Organometallics, **20,** 2303 (2001).
40. D.W. Stephan. Can. J. Chem. **80,** 125 (2002).
41. J.C. Brantley, E.L. Morehouse, and L. Parts. U.S. Patent 3 306 919. 1967. 4 pp.
42. D.T. Cromer and J.B. Mann. Acta Crystallogr. A, **A24,** 321 (1968).

© 2004 NRC Canada

A facile synthesis of 3,4-dialkyl-3,4-dihydro-2*H*-1,3-benzoxazin-2-ones and naphthoxazin-2-ones and their reactions with organolithium and Grignard reagents — Preparation of *N*-[1-(2′-hydroxyphenyl)alkyl]amides

Cristina Cimarelli, Gianni Palmieri, and Emanuela Volpini

Abstract: A facile and simple method for the preparation of 3,4-dialkyl-3,4-dihydro-2*H*-1,3-benzoxazin-2-ones or naphthoxazin-2-ones in high yields from aminoalkylphenols and aminoalkylnaphthols is described. The reactions of the products obtained with organolithium and Grignard reagents were studied, and a method for the preparation of *N*-[1-(2-hydroxyphenyl)alkyl]-*N*-alkylamides, which are of pharmaceutical interest, from benzoxazinones was developed. A possible reaction mechanism is also proposed. The relative configuration of chiral products was determined from conformational analysis of ^{1}H NMR spectra.

Key words: benzoxazinones, naphthoxazinones, organometallic reagents, amide preparation, aminoalkylphenols.

Résumé : On décrit une méthode simple et efficace de préparer avec des rendements élevés des 3,4-dialkyl-3,4-dihydro-2*H*-1,3-benzoxazin-2-ones ou naphtoxazin-2-ones à partir d'aminoalkylphénols ou d'aminoalkylnaphtols. On a étudié les réactions des produits avec les réactifs de Grignard et les organolithiens et on a mis au point une méthode de préparation de *N*-[1-(2-hydroxyphényl)alkyl]-*N*-alkylamides, des produits présentant un intérêt pharmaceutique, à partir de benzoxazinones. On propose une hypothèse de mécanisme réactionnel. La configuration relative des produits chiraux a été déterminée par une analyse conformationnelle appliquée aux spectres de résonance magnétique du proton.

Mots clés : benzoxazinones, naphtoxazinones, réactifs organométalliques, préparation d'amides, aminoalkylphénols.

[Traduit par la Rédaction]

Introduction

3,4-Dialkyl-3,4-dihydro-2*H*-1,3-benzoxazin-2-ones are a class of compounds studied because of their diverse biological properties as potential antimicrobial agents (1), as anti-inflammatory agents (2), as acetylcholinesterase inhibitors (3), and as analgesics, bactericides, and muscle relaxants (4). At the same time they are also known to originate from the photodegradation of pesticides such as ethiofencarb (5). Several synthesis methods for benzoxazinones have been reported in the literature (4, 6–9). All of these methods suffer from the same drawbacks, specifically the use of toxic solvents (benzene) or reagents (carbamyl chlorides, isocyanates, phosgene), or they require a two-step synthesis sequence.

On the other hand, 3,4-dialkyl-3,4-dihydro-2*H*-1,3-naphthoxazin-2-ones are known in the literature (10) for their activity against several bacterial species, and they have also been used as precursors in the preparation of phosphinic ligands for asymmetric catalysis (11); however, only very few methods for their preparation have been reported (10, 12).

Recently, we became interested in the synthesis of aminoalkylphenols (13) and aminoalkylnaphthols (14), two classes of compounds studied for their pharmaceutical properties (15) but also widely used as ligands in ligand-accelerated catalysis (LAC) (16), in particular in the asymmetric catalyzed addition of organozinc reagents to aldehydes (17). We have developed a series of synthetic procedures that lead to aminoalkylphenols and aminoalkylnaphthols in a simple and straightforward way.

Now we wish to report a new, direct, and mild method for the preparation of 3,4-disubstituted 3,4-dihydro-2*H*-1,3-benzoxazin-2-ones and naphthoxazin-2-ones that we have developed using aminoalkylphenols and aminoalkylnaphthols as precursors. Moreover, the results of the study of the reactions of these compounds with alkyllithium and Grignard reagents and a method for the preparation of *N*-[1-(2-hydroxyphenyl)alkyl]amides and of the corresponding naphthyl derivatives, which are known for their pharmaceutical properties (10, 18), are described.

Received 10 February 2004. Published on the NRC Research Press Web site at http://canjchem.nrc.ca on 2 November 2004.

C. Cimarelli,[1] G. Palmieri, and E. Volpini. Dipartimento di Scienze Chimiche, Università di Camerino, Via S. Agostino 1, I-62032 Camerino, Italy.

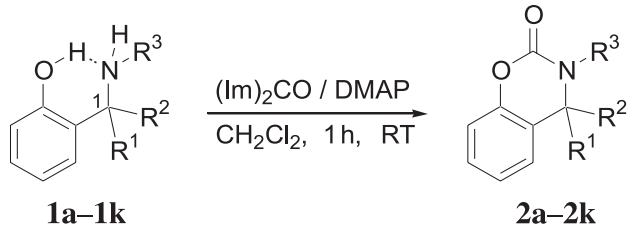
[1]Corresponding author (e-mail: cristina.cimarelli@unicam.it).

Results and discussion

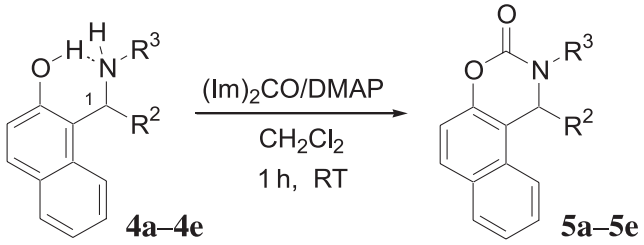
Aminoalkylphenols **(1)** and aminoalkylnaphthols **(4)**, when treated with carbonyldiimidazole (Im_2CO) in dichloro-

 doi: 10.1139/V04-100 © 2004 NRC Canada

Scheme 1.



Scheme 2.



methane, in the presence of dimethylaminopyridine (DMAP) (19), produce the desired 3,4-dialkyl-3,4-dihydro-2*H*-1,3-benzoxazin-2-ones (**2**) (Scheme 1) and naphthoxazin-2-ones (**5**) (Scheme 2), respectively, in reasonable reaction times and in good yields. This procedure allows the one-step preparation of cyclized products in a mild and straightforward way. It is very simple and quick and does not require dangerous or expensive chemicals. Moreover, when the reaction is complete, simple filtration of the reaction mixture on a thin pad of silica gel provides a quick and easy method for obtaining a high yield of purified product. The silica gel isolates the excess carbonyldiimidazole and DMAP and the basic by-products. The absolute configuration of chiral centres remains unaltered under these reaction conditions. The results obtained for several aminoalkylphenols and aminoalkylnaphthols are reported in Tables 1 and 2, respectively.

Cyclization with carbonyldiimidazole was previously reported in the literature (22) for the preparation of 1-benzyl-4-(2-oxo-3,4-dihydro-2*H*-1,3-benzoxazine-3-yl)piperidine from 1-benzyl-4-(2-hydroxyphenylmethyl)aminopiperidine, a product unsubstituted at the C-4 carbon atom. The described methodology, without DMAP, requires heating of the reaction mixture in THF to reflux and a longer reaction time.

The reactivity of the synthesized 3,4-dialkyl-3,4-dihydro-2*H*-1,3-benzoxazin-2-ones (**2**) towards organometallic reagents has been studied, in particular with alkyllithium and Grignard reagents. 3,4-Dialkyl-3,4-dihydro-2*H*-1,3-benzoxazin-2-ones (**2**) react with organolithiums at 0 °C in toluene in reasonable times and give satisfactory yields of *N*-[1-(2-hydroxyphenyl)alkyl]-*N*-alkylamides (**3**) (Scheme 3). Naphthoxazin-2-one (**5a**), under the same reaction conditions, reacts with *n*-butyllithium to afford the corresponding amide **(6ab)** but only in poor yield (28%). The reaction gives satisfactory yields with methyllithium, isopropyllithium, *n*-butyllithium, and phenyllithium. Only allyl- and benzyl-Grignard reagents are reactive towards the substrates studied, while MeMgBr and PhMgCl are nonreactive.

Alkyllithiums and Grignard reagents have been used in a slight excess (10%) with respect to the starting material. With a large excess, the double addition of organometallic

Table 1. Synthesis of benzoxazinones **2**.

Entry	**1**	R^1	R^2	R^3	**2**	Yield (%)[a]
1	**1a**[b]	H	H	R*[c]	**2a**	72
2	**1b**[d]	H	Me	Bn	**2b**	91
3	(*l*)[e]-**1c**[f]	H	Me	R*[c]	(*l*)[e]-**2c**	69
4	(*u*)[e]-**1c**[f]	H	Me	R*[c]	(*u*)[e]-**2c**	64
5	(*l*)[e]-**1d**[f]	H	Et	R*[c]	(*l*)[e]-**2d**	65
6	**1e**	H	*n*-Bu	Me	**2e**	98
7	**1f**	H	*n*-Bu	Bn	**2f**	78
8	(*l*)[e]-**1g**[g]	H	*n*-Bu	R*[c]	(*l*)[e]-**2g**	93
9	(*u*)[e]-**1g**[g]	H	*n*-Bu	R*[c]	(*u*)[e]-**2g**	88
10	**1h**[h]	H	Ph	Bn	**2h**	76
11	(*l*)[e]-**1i**[f]	H	Ph	R*[c]	(*l*)[e]-**2i**	84
12	(*u*)[e]-**1i**[f]	H	Ph	R*[c]	(*u*)[e]-**2i**	87
13	**1j**	Me	Ph	Me	**2j**	85
14	**1k**	*n*-Bu	Ph	Bn	**2k**	78

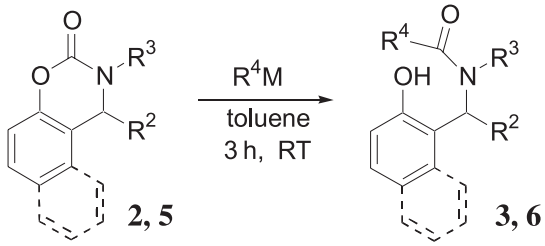
[a]Yields of the pure isolated compounds.
[b]Reference 20.
[c]R*–NH_2 = (±)-1-phenylethylamine.
[d]Reference 21.
[e](*l*) = like (*RR*, *SS*); (*u*) = unlike (*RS*, *SR*)
[f]Reference 13*a*.
[g]Reference 13*d*.
[h]Reference 17.

Table 2. Synthesis of naphthoxazinones **5**.

Entry	**4**	R^2	R^3	**5**	Yield (%)[a]
1	**4a**[b]	Ph	Bn	**5a**	98
2	(*l*)[c]-**4b**[d]	Ph	R*[e]	(*l*)[c]-**5b**	95
3	(*l*)[c]-**4c**[g]	Ph	R*[f]	(*l*)[c]-**5c**	95
4	(*l*)[c]-**4d**[h]	4-$MeOC_6H_4$	R*[e]	(*l*)[c]-**5d**	86
5	(*l*)[c]-**4e**[h]	2-Naphthyl	R*[e]	(*l*)[c]-**5e**	71

[a]Yields of the pure isolated compounds.
[b]Reference 22.
[c](*l*) = like (*RR*, *SS*); (*u*) = unlike (*RS*, *SR*).
[d]Reference 17.
[e]R*–NH_2 = (±)-1-phenylethylamine.
[f]R*–NH_2 = (±)-1-(1-naphthyl)ethylamine.
[g]Reference 13*a*.
[h]Reference 14*a*.

Scheme 3.



reagent to the carbonyl group of the starting benzoxazinone is observed, and the reaction produces the original aminoalkylphenol **1** and the corresponding symmetric ketone. In fact, GC–MS analysis of the crude mixtures of the reactions of **2b**, **2h**, and **2e** with 2.5 equiv. of phenyllithium and butyllithium reveals the chromatographic peaks and mass spectra of aminoalkylphenols **1b**, **1h**, and **1e** and of dibutylketone and benzophenone.

© 2004 NRC Canada

Scheme 4.

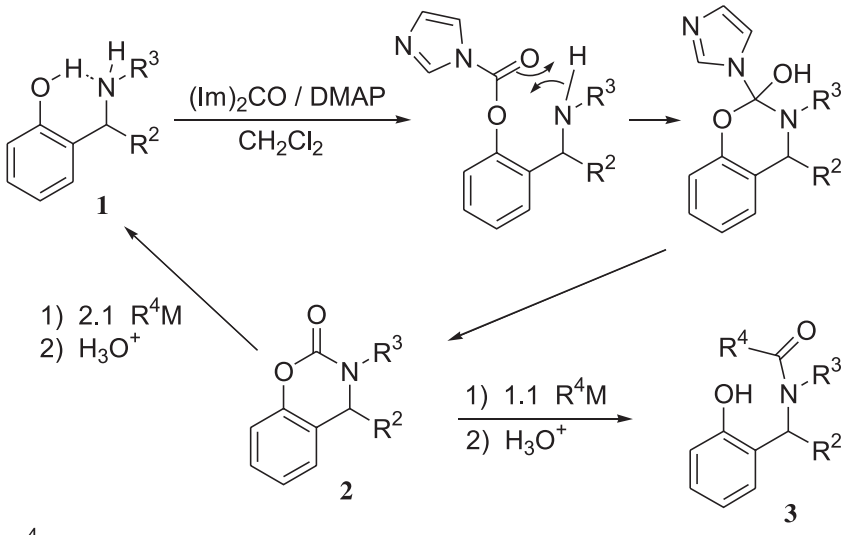


Table 3. Synthesis of *N*-[1-(2′-hydroxyphenyl)alkyl]amides.

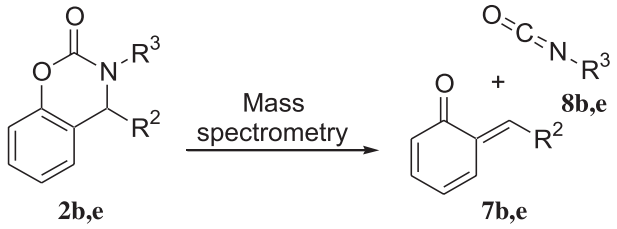
Entry	**2**	R^4M	**3**	Yield (%)[a]
1	**2b**	MeLi	**3ba**	69
2	**2b**	*n*-BuLi	**3bb**	90
3	**2b**	PhLi	**3bd**	75
4	**2b**	AllylMgCl	**3be**	79
5	**2b**	BnMgCl	**3bf**	50
6	(*l*)[b]-**2d**	*n*-BuLi	(*l*)[b]-**3db**	56
7	**2e**	*n*-BuLi	**3eb**	31
8	**2h**	*n*-BuLi	**3hb**	43
9	**2h**	*i*-PrLi	**3hc**	77
10	(*l*)[b]-**2i**	*n*-BuLi	(*l*)[b]-**3ib**	62
11	**5a**	*n*-BuLi	**6ab**	28

[a]Yields of the pure isolated compounds.
[b](*l*) = like (*RR*, *SS*); (*u*) = unlike (*RS*, *SR*).

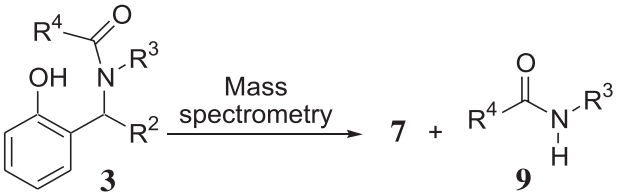
In several cases the reaction proceeds with comparable results in *n*-hexane, but when the starting materials are poorly soluble in this solvent, toluene gave the best results. The results obtained in the reactions of benzoxazinones **2b**, **2d**, **2e**, **2h**, and **2i** with some organolithiums and Grignard reagents are reported in Table 3.

A hypothesized mechanism for these reactions is presented in Scheme 4. Moreover, it is possible to make some observations for the behaviour of these compounds when they are subjected to GC–MS analysis. Within the mass spectra of pure benzoxazinones **2b** and **2e**, we observed the fragmentation pattern corresponding to the enone **7** and the isocyanate **8**, as depicted in Scheme 5. In a similar fashion, in 1,4-dihydro-2*H*-3,1-benzoxazin-2-one derivatives, under flash vacuum pyrolysis conditions, CO_2 extrusion was observed (23). Naphthoxazinones **5** under the same conditions decompose during the gas chromatographic analysis to give a complex mixture of unidentified products. The final amide **3** decomposes in a similar way, and it is possible to observe in the mass spectra the peaks corresponding to the enone **7**

Scheme 5.



Scheme 6.



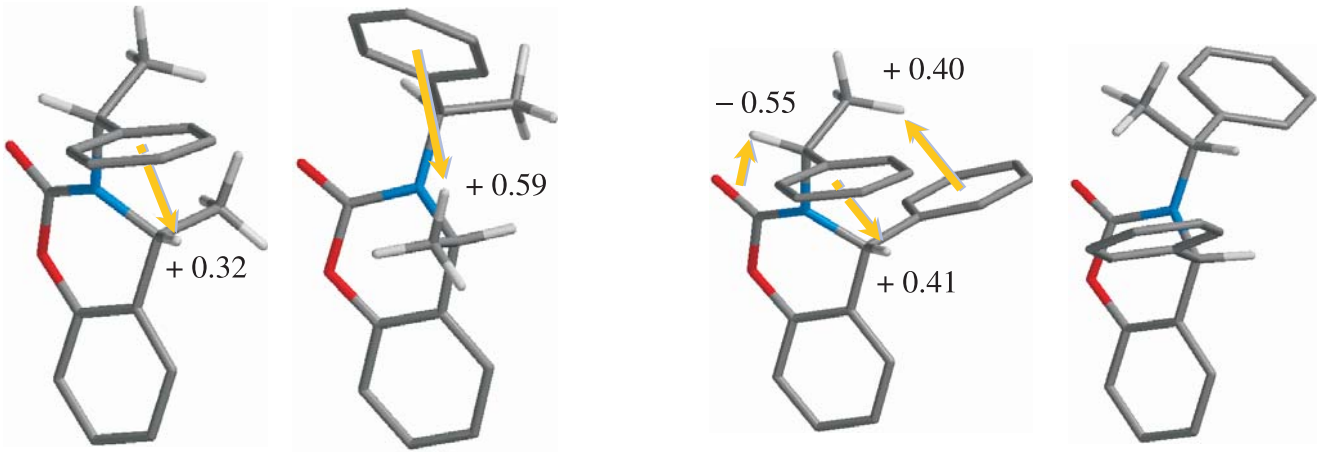
and the amide **9**, as depicted in Scheme 6 for **3bb**, **3db**, **3bd**, **3bf**, and **3eb**.

Stereochemistry

The relative configurations of benzoxazinones and naphthoxazinones were assigned by analogy with the chiral starting aminophenols. To confirm that cyclization took place with retention of configuration, the stereochemistry of the prepared oxazinones was confirmed by conformational analysis on the diastereomeric couples (*R*,*R*)-**2c**/(4*S*,1*R*)-**2c** and (*R*,*R*)-**2i**/(4*S*,1*R*)-**2i**. The more stable conformations for (*R*,*R*)- and (4*S*,1′*R*)-**2c** and (*R*,*R*)- and (4*S*,1′*R*)-**2i**, obtained by PM3 semi-empirical minimization, are reported in Fig. 1. A comparison of the differences in ^{1}H NMR chemical shifts ($\Delta\delta$) observed for the diastereomeric couples, resulting from the anisotropic effects of the phenyl and carbonyl groups, as indicated in Fig. 1, allowed us to assign relative configurations.

© 2004 NRC Canada

Fig. 1. Minimized conformations for the (*R,R*)- and (4*S*,1′*R*)-**2c** and the (*R,R*)- and (4*S*,1′*R*)-**2i** oxazinones with observed ^{1}H NMR Δδ (ppm) resulting from anisotropic effects.



(*R,R*)-**2c** (4*S*, 1′*R*)-**2c** (*R,R*)-**2i** (4*S*,1′*R*)-**2i**

Experimental

General methods

Proton and ^{13}C NMR spectra were recorded with a Varian VXR 300 instrument. Chemical shifts are given in ppm downfield from Me_4Si in $CDCl_3$ solution. Coupling constants are given in Hz. IR spectra were recorded with a Perkin-Elmer 257 spectrometer. GC–MS analyses were performed with a HP-59970 workstation consisting of a HP-5890 gas chromatograph equipped with a methyl silicone capillary column and a HP-5970 mass detector. All melting points are uncorrected. Toluene and hexane were dried by refluxing over sodium wires and then distilled into a dry receiver under a nitrogen atmosphere. All reagents were of commercial quality from freshly opened containers. Commercial alkyllithium and Grignard reagent solutions (Aldrich) were used in a dry atmosphere.

Preparation of starting aminoalkylphenols 1a–1i and aminoalkylnaphthols 4a–4e

Starting aminoalkylphenols and aminoalkylnaphthols were prepared according to previously reported procedures (11) using (±)-phenylethylamine as the chiral starting material instead of the (*R*) enantiomer. Spectral data for the unknown starting materials **1e, 1f**, **1j**, and **1k** follow.

2-[1-(Methylamino)pentyl]phenol (1e)

Yield 98%. Oil. IR ν_{max} (liquid film) (cm^{-1}): 2950, 2836, 1482, 1447, and 1270. ^{1}H NMR ($CDCl_3$) δ: 0.89 (t, 3H, *J* = 6.6 Hz), 1.10–1.50 (m, 4H), 1.60 (bs, 1H), 1.60–1.90 (m, 2H), 2.43 (s, 3H), 3.61 (t, 1H, *J* = 7.0 Hz), 6.70–7.30 (m, 4 H), and 9.00 (s, 1H). Anal. calcd. (%) for $C_{12}H_{19}NO$, MW 193.288: C 74.45, H 9.91, N 7.25; found: C 74.56, H 10.04, N 7.27.

2-[1-(Benzylamino)pentyl]phenol (1f)

Yield 80%. Oil. IR ν_{max} (liquid film) (cm^{-1}): 2968, 2943, 2870, 1527, 1488, and 1243. ^{1}H NMR (300 MHz, $CDCl_3$) δ: 0.83 (t, 3H, *J* = 7.0 Hz), 1.09–1.34 (m, 4H), 1.62–1.85 (m, 3H), 3.60 (d, 1H, *J* = 12.8 Hz), 3.74 (t, 1H, *J* = 7.2 Hz), 3.83 (d, 1H, *J* = 12.8 Hz), 6.80–7.20 (m, 9H), and 13.40 (bs, 1H). ^{13}C NMR (75 MHz, $CDCl_3$) δ: 13.9, 22.6, 28.4, 35.7, 51.8, 63.6, 116.8, 118.9, 127.5, 128.4, 128.5, 128.7, 129.2, 132.4, 157.4, and 165.6. Anal. calcd. (%) for $C_{18}H_{23}NO$, MW 269.386: C 80.26, H 8.61, N 5.20; found: C 80.21, H 8.86, N 5.37.

2-[1-(Methylamino)-1-phenylethyl]phenol (1j)

Yield 91%. Oil. IR ν_{max} (liquid film) (cm^{-1}): 3308, 2981, 1494, 1262, 820, 754, and 720. ^{1}H NMR (300 MHz, $CDCl_3$) δ: 1.86 (s, 3H), 2.29 (s, 3H), 2.65 (s, 1H), 6.66–7.44 (m, 9H), and 12.30 (s, 1H). ^{13}C NMR (75 MHz, $CDCl_3$) δ: 24.6, 28.9, 64.7, 117.4, 118.8, 126.7, 127.5, 128.5, 128.6, 129.1, 129.8, 144.7, and 158.3. Anal. calcd. (%) for $C_{15}H_{17}NO$, MW 227.30: C 79.26, H 7.54, N 6.16; found: C 79.48, H 7.32, N 6.27.

2-[1-(Benzylamino)-1-phenylpentyl]phenol (1k)

Yield 84%. Oil. IR ν_{max} (liquid film) (cm^{-1}): 2954, 1606, 1455, 1295, 753, and 699. ^{1}H NMR (300 MHz, $CDCl_3$) δ: 0.99 (t, 3H, *J* = 7.0 Hz), 1.20–1.60 (m, 4H), 2.30–2.70 (m, 3H), 3.62 (bs, 2H), 6.70–7.70 (m, 14H), and 12.20 (bs, 1H). ^{13}C NMR (75 MHz, $CDCl_3$) δ: 14.4, 23.3, 25.4, 36.1, 47.0, 55.8, 117.5, 118.9, 126.7, 127.1, 128.0, 128.4, 129.0, 129.1, 129.2, 139.0, 143.8, 158.1, 163.5, and 175.1. Anal. calcd. (%) for $C_{24}H_{27}NO$, MW 345.48: C 83.44, H 7.88, N 4.05; found: C 83.30, H 7.57, N 4.23.

Preparation of benzoxazinones 2a–2k and naphthoxazinones 5a–5e

Aminoalkylphenols **1b**–**1i** (2 mmol) or aminoalkylnaphthols **3a**–**3e** (2 mmol), in a 50-mL round-bottom flask equipped with a magnetic stirring bar, were dissolved in 10 mL CH_2Cl_2 at room temperature (RT) to which was added DMAP (0.2 mmol) and carbonyldiimidazole (3 mmol). The reaction mixture was allowed to stand at RT for 1 h and then the mixture was filtered on a thin pad of silica gel, affording almost pure **2a**–**2k** or **5a**–**5e.** When necessary, the final benzoxazinones or naphthoxazinones were purified further by recrystallization or chromatographic separation.

© 2004 NRC Canada

Spectral data for the products obtained follow. In the numerical designations of the compounds below, the prefixes *(l)* and *(u)* mean *like* (*RR*, *SS*) and *unlike* (*RS*, *SR*), respectively.

3-(1′-Phenylethyl)-3,4-dihydro-1,3-benzo[e][1,3]oxazin-2-one (2a)

White crystals; mp 98–100 °C (*n*-hexane/CH_2Cl_2). IR ν_{max} (Nujol) (cm^{-1}): 2930, 1712, 1500, 1415, 1238, 797, and 734. ^1H NMR (300 MHz, $CDCl_3$) δ: 1.68 (d, 3H, *J* = 7.0 Hz), 3.91 (d, 1H, *J* = 14.3 Hz), 4.30 (d, 1H, *J* = 14.6 Hz), 5.92 (q, 1H, *J* = 7.2 Hz), and 6.95–7.43 (m, 9H). ^{13}C NMR (75 MHz, $CDCl_3$) δ: 15.2, 41.3, 53.8, 116.3, 117.8, 124.3, 125.7, 127.6, 128.1, 128.9, 129.0, 138.8, 149.7, and 151.3. MS (EI) *m/z* (%): 253 (M^+, 10), 148 (7), 105 (100), and 77 (18). Anal. calcd. (%) for $C_{16}H_{15}NO_2$, MW 253.30: C 75.87, H 5.97, N 5.53; found: C 75.92, H 6.21, N 5.79.

3-Benzyl-4-methyl-3,4-dihydro-1,3-benzo[e][1,3]oxazin-2-one (2b)

White crystals; mp 110–112 °C (*n*-hexane). IR ν_{max} (Nujol) (cm^{-1}): 2924, 1709, 1497, 1423, 1371, 1253, 761, and 746. ^1H NMR (300 MHz, $CDCl_3$) δ: 1.44 (d, 3H, *J* = 6.6 Hz), 4.28 (d, 1H, *J* = 15.4 Hz), 4.39 (q, 1H, *J* = 6.6 Hz), 5.26 (d, 1H, *J* = 15.4 Hz), and 7.00–7.50 (m, 9H). ^{13}C NMR (75 MHz, $CDCl_3$) δ: 22.5, 50.1, 52.9, 116.7, 124.1, 124.5, 125.4, 128.1, 128.2, 129.0, 129.1, 136.2, 149.4, and 151.8. MS (EI) *m/z* (%): 253 (M^+, 9), 238 (20), 162 (11), 120 (48), and 91 (100). Anal. calcd. (%) for $C_{16}H_{15}NO_2$, MW 253.30: C 75.87, H 5.97, N 5.53; found: C 75.78, H 5.90, N 5.64.

(l)-(±)-4-Methyl-3-(1′-phenylethyl)-3,4-dihydro-1,3-benzo[e][1,3]oxazin-2-one ((l)-2c)

Oil. IR ν_{max} (liquid film) (cm^{-1}): 2932, 1715, 1503, 1423, 1369, 1248, 760, and 744. ^1H NMR (300 MHz, $CDCl_3$) δ: 1.43 (d, 3H, *J* = 6.6 Hz), 1.81 (d, 3H, *J* = 7.3 Hz), 4.15 (q, 1H, *J* = 6.6 Hz), 5.65 (q, 1H, *J* = 7.0 Hz), and 7.00–7.60 (m, 9H). ^{13}C NMR (75 MHz, $CDCl_3$) δ: 18.4, 29.9, 50.5, 55.7, 116.6, 124.4, 124.5, 126.5, 127.5, 128.0, 128.7, 128.9, 139.6, 149.8, and 152.2. Anal. calcd. (%) for $C_{17}H_{17}NO_2$, MW 267.322: C 76.38, H 6.41, N 5.24; found: C 76.29, H 6.54, N 5.18.

(u)-(±)-4-Methyl-3-(1′-phenylethyl)-3,4-dihydro-1,3-benzo[e][1,3]oxazin-2-one ((u)-2c)

Oil. IR ν_{max} (liquid film) (cm^{-1}): 2930, 1712, 1428, 1243, 763, and 748. ^1H NMR (300 MHz, $CDCl_3$) δ: 0.83 (d, 3H, *J* = 6.6 Hz), 1.66 (d, 3H, *J* = 7.0 Hz), 4.47 (q, 1H, *J* = 6.6 Hz), 5.70 (q, 1H, *J* = 7.1 Hz), and 7.00–7.60 (m, 9H). Anal. calcd. (%) for $C_{17}H_{17}NO_2$, MW 267.322: C 76.38, H 6.41, N 5.24; found: C 76.22, H 6.63, N 5.20.

(l)-(±)-4-Ethyl-3-(1′-phenylethyl)-3,4-dihydro-benzo[e][1,3]oxazin-2-one ((l)-2d)

Oil. IR ν_{max} (liquid film) (cm^{-1}): 2948, 1690, 1607, 1412, 1350, 760, and 695. ^1H NMR (300 MHz, $CDCl_3$) δ: 0.75 (t, 3H, *J* = 7.4 Hz), 1.79 (d, 3H, *J* = 7.3 Hz), 1.64–1.88 (m, 2H), 3.97 (dd, 1H, *J* = 3.7, 7.4 Hz), 5.62 (q, 1H, *J* = 7.3 Hz), and 6.78–7.60 (m, 9H). ^{13}C NMR (75 MHz, $CDCl_3$) δ: 8.5, 18.2, 30.7, 55.6, 55.9, 116.2, 123.7, 123.9, 125.5, 127.5, 127.9, 128.7, 128.8, 139.3, 150.2, and 152.4. MS (EI) *m/z* (%): 281 (M^+, 1), 252 (41), 148 (87), 105 (100), and 77 (18). Anal. calcd. (%) for $C_{18}H_{19}NO_2$, MW 281.349: C 76.84, H 6.81, N, 4.98; found: C 76.63, H 6.90, N, 5.14.

4-Butyl-3-methyl-3,4-dihydro-1,3-benzo[e][1,3]oxazin-2-one (2e)

White crystals; mp 127–129 °C (*n*-hexane/CH_2Cl_2). IR ν_{max} (Nujol) (cm^{-1}): 2924, 1712, 1463, 1230, and 757. ^1H NMR (300 MHz, $CDCl_3$) δ: 0.86 (t, 3H, *J* = 6.8 Hz), 1.00–1.40 (m, 4H), 1.65–2.00 (m, 2H), 3.12 (s, 3H), 4.41 (dd, 1H, *J* = 3.7, 6.2 Hz), and 7.00–7.40 (m, 4H). ^{13}C NMR (75 MHz, $CDCl_3$) δ: 14.1, 22.7, 25.5, 34.9, 35.3, 60.4, 116.4, 122.1, 124.2, 125.7, 129.0, 150.1, and 151.7. MS (EI) *m/z* (%): 219 (M^+, 1), 162 (100), 118 (7), and 91 (19). Anal. calcd. (%) for $C_{13}H_{17}NO_2$, MW 219.280: C 71.21, H 7.81, N 6.39; found: C 70.97, H 7.68, N 6.45.

3-Benzyl-4-butyl-3,4-dihydro-1,3-benzo[e][1,3]oxazin-2-one (2f)

White crystals; mp 48–50 °C (*n*-hexane/CH_2Cl_2). IR ν_{max} (Nujol) (cm^{-1}): 2982, 2914, 1741, 1438, 1255, 757, and 743. ^1H NMR (300 MHz, $CDCl_3$) δ: 0.79 (t, 3H, *J* = 6.7 Hz), 1.00–1.60 (m, 4H), 1.50–1.90 (m, 2H), 4.20 (d, 1H, *J* = 15.3 Hz), 4.28 (dd, 1H, *J* = 3.5, 6.9 Hz), 5.24 (d, 1H, *J* = 15.3 Hz), and 6.92–7.18 (m, 9H). ^{13}C NMR (75 MHz, $CDCl_3$) δ: 13.9, 22.4, 25.5, 34.6, 50.1, 56.7, 116.3, 122.3, 124.0, 125.6, 127.9, 127.9, 1278.0, 128.7, 128.8, 136.0, and 149.9. MS (EI) *m/z* (%): 295 (M^+, 2), 238 (100), 155 (17), and 91 (98). Anal. calcd. (%) for $C_{19}H_{21}NO_2$, MW 295.376: C 75.87, H 5.97, N 5.53; found: C 75.77, H 5.91, N 5.63.

(l)-(±)-4-Butyl-3-(1′-phenylethyl)-3,4-dihydro-1,3-benzo[e][1,3]oxazin-2-one ((l)-2g)

Oil. IR ν_{max} (liquid film) (cm^{-1}): 2930, 1718, 1500, 1429, 1364, 1251, 762, and 743. ^1H NMR (300 MHz, $CDCl_3$) δ: 0.82 (t, 3H, *J* = 6.2 Hz), 0.87–1.30 (m, 4H), 1.60–1.80 (m, 2H), 1.80 (d, 3H, *J* = 7.3 Hz), 4.01 (dd, 1H, *J* = 3.7, 8.0 Hz), 5.63 (q, 1H, *J* = 7.3 Hz), and 6.80–7.60 (m, 9H). Anal. calcd. (%) for $C_{16}H_{23}NO_2$, MW 309.402: C 77.64, H 7.49, N 4.53; found: C 77.63, H 7.61, N, 4.43.

(u)-(±)-4-Butyl-3-(1′-phenylethyl)-3,4-dihydro-1,3-benzo[e][1,3]oxazin-2-one ((u)-2g)

Oil. IR ν_{max} (liquid film) (cm^{-1}): 2935, 1720, 1432, 1231, and 762. ^1H NMR (300 MHz, $CDCl_3$) δ: 0.63 (t, 3H, *J* = 6.8 Hz), 0.87–1.30 (m, 4H), 1.60–1.80 (m, 2H), 1.65 (d, 3H, *J* = 7.3 Hz), 4.33 (d, 1H, *J* = 8.4 Hz), 5.66 (q, 1H, *J* = 7.0 Hz), and 6.80–7.60 (m, 9H). Anal. calcd. (%) for $C_{16}H_{23}NO_2$, MW 309.402: C 77.64, H 7.49, N 4.53; found: C 77.51, H 7.63, N 4.71.

3-Benzyl-4-phenyl-3,4-dihydro-1,3-benzo[e][1,3]oxazin-2-one (2h)

White crystals; mp 130–134 °C (*n*-hexane/CH_2Cl_2). IR ν_{max} (Nujol) (cm^{-1}): 2937, 1705, 1599, 1424, 1356, 745, and 698. ^1H NMR (300 MHz, $CDCl_3$) δ: 3.76 (d, 1H, *J* = 15.2 Hz), 5.26 (s, 1H), 5.40 (d, 1H, *J* = 15.2 Hz), and 6.83–7.45 (m, 14H). ^{13}C NMR (75 MHz, $CDCl_3$) δ: 49.7, 60.9, 116.7, 121.7, 124.6, 127.0, 127.3, 128.2, 128.6, 128.9, 129.1, 129.2, 129.5, 135.7, 140.7, 148.6, and 151.2. MS (EI) *m/z* (%): 315 (M^+, 7), 224 (9), 181 (100), 132 (13), 106 (14),

© 2004 NRC Canada

and 91 (34). Anal. calcd. (%) for $C_{21}H_{17}NO_2$, MW 315.365: C 79.98, H 5.43, N 4.44; found: C 80.05, H 5.62, N 4.64.

(l)-(±)-4-Phenyl-3-(1′-phenylethyl)-3,4-dihydro-1,3-benzo[e][1,3]oxazin-2-one ((l)-2i)

Oil. IR ν_{max} (liquid film) (cm^{-1}): 2944, 1689, 1610, 1404, 1352, 758, and 696. ^1H NMR (300 MHz, $CDCl_3$) δ: 1.28 (d, 3H, *J* = 7.2 Hz), 5.02 (s, 1H), 5.81 (q, 1H, *J* = 7.2 Hz), and 6.83–7.48 (m, 14H). ^{13}C NMR (75 MHz, $CDCl_3$) δ: 17.3, 56.1, 58.5, 116.7, 123.8, 124.6, 125.9, 126.3, 128.1, 128.3, 128.5, 128.9, 129.0, 129.4, 138.9, 143.6, 148.6, and 151.7. MS (EI) *m/z* (%): 329 (M^+, 11), 224 (7), 182 (40), 181 (85), 146 (27), 105 (100), and 77 (19). Anal. calcd. (%) for $C_{22}H_{19}NO_2$, MW 329.392: C 80.22, H 5.81, N 4.25; found: C 80.37, H 5.90, N 4.43.

(u)-(±)-4-Phenyl-3-(1′-phenylethyl)-3,4-dihydro-1,3-benzo[e][1,3]oxazin-2-one ((u)-2i)

Oil. IR ν_{max} (liquid film) (cm^{-1}): 2951, 1692, 1413, 1332, and 760. ^1H NMR (300 MHz, $CDCl_3$) δ: 1.67 (d, 3H, *J* = 7.3 Hz), 5.26 (q, 1H, *J* = 7.3 Hz), 5.43 (s, 1H), and 6.80–7.40 (m, 14H). MS (EI) *m/z* (%): 329 (M^+, 9), 182 (37), 181 (82), 105 (100), and 77 (16). Anal. calcd. (%) for $C_{22}H_{19}NO_2$, MW 329.392: C 80.22, H 5.81, N 4.25; found: C 80.31, H 5.69, N 4.15.

3,4-Dimethyl-4-phenyl-3,4-dihydro-1,3-benzo[e][1,3]oxazin-2-one (2j)

Oil. IR ν_{max} (liquid film) (cm^{-1}): 1710, 1414, 1377, 1232, 778, 745, and 700. ^1H NMR (300 MHz, $CDCl_3$) δ: 1.98 (s, 3H), 2.77 (s, 3H), and 6.60–7.20 (m, 9H). ^{13}C NMR (75 MHz, $CDCl_3$) δ: 26.6, 32.0, 64.8, 116.3, 124.5, 127.0, 127.3, 127.4, 128.3, 129.0, 129.1, 143.5, 147.9, and 150.9. MS (EI) *m/z* (%): 253 (M^+, 4), 238 (10), 195 (89), 181 (40), 165 (23), and 152 (29). Anal. calcd. (%) for $C_{16}H_{15}NO_2$, MW 253.30: C 75.87, H 5.97, N 5.53; found: C 75.24, H 5.72, N, 5.46.

3-Benzyl-4-butyl-4-phenyl-3,4-dihydro-1,3-benzo[e][1,3]oxazin-2-one (2k)

Oil. IR ν_{max} (liquid film) (cm^{-1}): 2957, 1713, 1455, 1389, 1231, 748, and 704. ^1H NMR (300 MHz, $CDCl_3$) δ: 0.67 (t, 3H, *J* = 6.4 Hz), 0.75–1.30 (m, 4H), 2.00–2.40 (m, 2H), 4.07 (d, 1H, *J* = 15.0 Hz), 4.62 (d, 1H, *J* = 15.0 Hz), and 6.50–7.42 (m, 14H). ^{13}C NMR (75 MHz, $CDCl_3$) δ: 13.9, 22.4, 25.4, 38.6, 49.1, 69.2, 115.8, 124.4, 125.5, 127.3, 128.0, 128.2, 128.3, 128.5, 128.6, 128.7, 129.3, 138.3, 144.1, 148.8, and 152.0. MS (EI) *m/z* (%): 371 (M^+, 1), 314 (100), 222 (13), and 91 (95). Anal. calcd. (%) for $C_{25}H_{25}NO_2$, MW 371.47: C 80.83, H 6.78, N 3.77; found: C 80.57, H 6.53, N 3.84.

2-Benzyl-1-phenyl-1,2-dihydro-naphtho[1,2-e][1,3]oxazin-3-one (5a)

Oil. IR ν_{max} (liquid film) (cm^{-1}): 3063, 3030, 1709, 1635, 1446, 1218, 1085, 994, 826, 743, and 703. ^1H NMR (300 MHz, $CDCl_3$) δ: 3.93 (d, 1H, *J* = 15.4 Hz), 5.40 (d, 1H, *J* = 15.4 Hz), 5.73 (s, 1H), and 7.20–7.90 (m, 16H). ^{13}C NMR (75 MHz, $CDCl_3$) δ: 49.3, 58.8, 114.4, 117.2, 122.5, 125.3, 127.6, 128.2, 128.3, 128.4, 129.1, 129.1, 129.2, 129.4, 129.8, 130.6, 131.1, 135.7, 139.5, 147.1, and 151.1. MS (EI) *m/z* (%): 365 (M^+, 11), 288 (6), 260 (5), 231 (100), 202 (14), and 91 (20). Anal. calcd. (%) for $C_{25}H_{19}NO_2$, MW 365.424: C 82.17, H 5.24, N 3.83; found: C 82.38, H 4.97, N 3.62.

(l)-(±)-1-Phenyl-2-(1′-phenylethyl)-1,2-dihydro-naphtho[1,2-e][1,3]oxazin-3-one ((l)-5b)

White crystals; mp 174–176 °C (*n*-hexane/CH_2Cl_2). IR ν_{max} (Nujol) (cm^{-1}): 3064, 3027, 1712, 1628, 1588, 1517, 1438, 1158, 1029, 959, 882, 768, and 614. ^1H NMR (300 MHz, $CDCl_3$) δ: 1.38 (d, 3H, *J* = 7.2 Hz), 5.69 (s, 1H), 5.86 (q, 1H, *J* = 7.2 Hz), and 7.20–7.80 (m, 16H). ^{13}C NMR (75 MHz, $CDCl_3$) δ: 16.9, 55.6, 56.4, 116.6, 117.1, 121.9, 125.0, 127.3, 127.4, 128.1, 128.3, 128.5, 128.6, 129.0, 129.1, 129.2, 130.1, 131.0, 138.6, 142.4, 146.8, and 151.5. Anal. calcd. (%) for $C_{26}H_{21}NO_2$; MW 379.45: C 82.30, H 5.58, N 3.69; found: C 82.28, H 5.72, N 3.40.

(l)-(±)-2-(1′-Naphthalen-2-yl-ethyl)-1-phenyl-1,2-dihydro-naphtho[1,2-e][1,3]oxazin-3-one ((l)-5c)

White crystals; mp 142–144 °C (*n*-hexane/CH_2Cl_2). IR ν_{max} (Nujol) (cm^{-1}): 3060, 1712, 1420, 1222, 1184, 804, and 730. ^1H NMR (300 MHz, $CDCl_3$) δ: 1.41 (d, 3H, *J* = 7.2 Hz), 5.37 (s, 1H), 6.46 (q, 1H, *J* = 7.2 Hz), and 7.20–8.00 (m, 18H). ^{13}C NMR (75 MHz, $CDCl_3$) δ: 17.2, 53.2, 55.1, 116.1, 116.8, 121.6, 123.1, 124.6, 124.7, 126.1, 126.2, 126.9, 127.2, 127.3, 127.5, 128.4, 128.7, 128.8, 129.0, 129.7, 129.8, 130.7, 131.9, 133.2, 133.9, 142.4, 146.1, and 152.0. Anal. calcd. (%) for $C_{30}H_{23}NO_2$, MW 429.51: C 83.89, H 5.40, N 3.26; found: C 83.72, H 5.28, N 3.35.

(l)-(±)-1-(4-Methoxy-phenyl)-2-(1′-phenylethyl)-1,2-dihydro-naphtho[1,2-e][1,3]-oxazin-3-one ((l)-5d)

White crystals; mp 151–153 °C (*n*-hexane/CH_2Cl_2). IR ν_{max} (Nujol) (cm^{-1}): 3061, 2935, 1716, 1512, 1223, 1183, 1032, 814, 736, and 699. ^1H NMR (300 MHz, $CDCl_3$) δ: 1.38 (d, 3H, *J* = 7.3 Hz), 3.71 (s, 3H), 5.62 (s, 1H), 5.81 (q, 1H, *J* = 7.3 Hz), and 6.75–7.80 (m, 15H). ^{13}C NMR (75 MHz, $CDCl_3$) δ: 17.1, 55.2, 55.4, 56.5, 114.6, 116.9, 117.0, 117.1, 122.0, 125.1, 127.5, 128.2, 128.4, 128.7, 129.1, 129.4, 130.1, 131.1, 134.6, 138.8, 146.7, 151.6, and 159.7. Anal. calcd. (%) for $C_{27}H_{23}NO_3$, MW 409.476: C 79.20, H 5.66, N 3.42; found: C 79.02, H 5.43, N, 3.15.

(l)-(±)-1-Naphthalen-2-yl-2-(1′-phenylethyl)-1,2-dihydro-naphtho[1,2-e][1,3]oxazin-3-one ((l)-5e)

White crystals; mp 139–141 °C (*n*-hexane/CH_2Cl_2). IR ν_{max} (Nujol) (cm^{-1}): 3058, 1712, 1717, 1634, 1517, 1222, 1184, 814, 739, and 699. ^1H NMR (300 MHz, $CDCl_3$) δ: 1.31 (d, 3H, *J* = 7.3 Hz), 5.81 (s, 1H), 5.85 (q, 1H, *J* = 7.3 Hz), and 7.30–7.90 (m, 18H). ^{13}C NMR (75 MHz, $CDCl_3$) δ: 17.1, 55.9, 55.4, 56.6, 116.4, 117.2, 122.0, 125.0, 125.1, 126.4, 126.7, 129.8, 127.5, 127.9, 128.2, 128.3, 128.4, 128.7, 129.1, 129.1, 129.7, 130.3, 131.1, 133.3, 138.7, 139.7, 146.9, and 151.6. Anal. calcd. (%) for $C_{30}H_{23}NO_2$, MW 429.509: C 83.89, H 5.40, N 3.26; found: C 83.67, H 5.58, N 3.44.

Reaction of oxazinones 2b, 2d, 2e, 2h, 2i, and 5a with organolithiums and Grignard reagents

Oxazinones **2** or **5** (3 mmol) in a three-necked round-bottom flask, equipped with a magnetic stirring bar and rub-

© 2004 NRC Canada

ber septum, were dissolved in anhydrous toluene (10 mL) under a nitrogen atmosphere at 0 °C and were then treated with 3.3 mmol of a commercial solution of alkyllithium or Grignard reagent. The reaction was monitored by TLC using *n*-hexane/ethyl acetate (80/20) as an eluent. After a variable time (2–3 h) at RT, when the starting material was consumed, the reaction was quenched with a NH_4Cl saturated solution (5 mL) and the brine was extracted with CH_2Cl_2 (2 × 20 mL). The solution was dried with anhydrous Na_2SO_4 then filtered, and the solvent was evaporated under reduced pressure. Chromatographic separation of the crude oil obtained, with cyclohexane/ethyl acetate (80/20) as an eluent afforded products **3** and **6** in yields of 28% and 90%, respectively. Spectral data follow.

N-*Benzyl*-N-*[1-(2-hydroxyphenyl)ethyl]acetamide (3ba)

Oil. IR ν_{max} (liquid film) (cm^{-1}): 3138, 2966, 1630, 1484, 1445, 1223, and 758. ^1H NMR (300 MHz, $CDCl_3$) δ: 1.49 (d, 3H, *J* = 7.1 Hz), 2.04 (s, 3H), 4.47 (s, 2H), 6.11 (q, 1H, *J* = 7.1 Hz), 6.80–7.40 (m, 9H), and 9.20 (bs, 1H). ^{13}C NMR (75 MHz, $CDCl_3$) δ: 17.4, 22.5, 27.1, 47.3, 47.5, 117.9, 119.6, 125.9, 126.8, 127.6, 129.1, 129.8, 137.4, 156.0, and 174.9. Anal. calcd. (%) for $C_{17}H_{19}NO_2$, MW 269.34: C 75.81, H 7.11, N 5.20; found: C 75.58, H 7.38, N 5.32.

N-*Benzyl*-N-*[1-(2-hydroxyphenyl)ethyl]pentanamide (3bb)

Oil. IR ν_{max} (liquid film) (cm^{-1}): 3165, 2948, 1620, 1493, 1448, 1238, and 740. ^1H NMR (300 MHz, $CDCl_3$) δ: 0.81 (t, 3H, *J* = 7.1 Hz), 1.12–1.34 (m, 2H), 1.46 (d, 3H, *J* = 7.0 Hz), 1.50–1.68 (m, 2H), 2.21 (dt, 2H, *J* = 3.2, 15.0 Hz), 4.45 (s, 2H), 6.12 (q, 1H, *J* = 7.2 Hz), 6.80–7.20 (m, 9H), and 9.10 (bs, 1H). ^{13}C NMR (75 MHz, $CDCl_3$) δ: 14.1, 22.6, 22.7, 26.2, 42.7, 51.9, 58.7, 117.1, 119.4, 125.9, 127.8, 128.5, 128.6, 128.9, 129.0, 129.8, 138.8, and 157.5. Anal. calcd. (%) for $C_{20}H_{25}NO_2$, MW 311.42: C 77.14, H 8.09, N 4.50; found: C 77.11, H 8.06, N 4.49.

N-*Benzyl*-N-*[1-(2-hydroxyphenyl)ethyl]benzamide (3bd)

White crystals; mp 160–162 °C (*n*-hexane/CH_2Cl_2). IR ν_{max} (Nujol) (cm^{-1}): 3138, 2966, 1630, 1484, 1445, 1223, and 758. ^1H NMR (300 MHz, $CDCl_3$) δ: 1.71 (d, 3H, *J* = 7.3 Hz), 4.50 (s, 2H), 6.03 (q, 1H, *J* = 7.3 Hz), 6.60–7.40 (m, 14H), and 9.50 (bs, 1H). ^{13}C NMR (75 MHz, $CDCl_3$) δ: 17.9, 27.1, 49.4, 117.7, 119.6, 125.3, 126.9, 127.0, 127.2, 127.4, 127.8, 128.5, 128.5, 128.7, 129.9, 130.1, 156.1, and 175.4. Anal. calcd. (%) for $C_{22}H_{21}NO_2$, MW 331.41: C 79.73, H 6.39, N, 4.23; found: C 79.48, H 5.58, N 4.32.

N-*Benzyl*-N-*[1-(2-hydroxyphenyl)ethyl]but-3-enamide (3be)

Oil. IR ν_{max} (liquid film) (cm^{-1}): 3138, 2966, 1630, 1484, 1445, 1223, and 758. ^1H NMR (300 MHz, $CDCl_3$) δ: 1.49 (d, 3H, *J* = 7.1 Hz), 2.90–3.20 (m, 2H), 4.47 (s, 2H), 4.96 (d, 1H, *J* = 17.2 Hz), 5.11 (d, 1H, *J* = 9.9 Hz), 5.77–6.03 (m, 1H), 6.12 (q, 1H, *J* = 7.1), 6.80–7.40 (m, 9H), and 9.10 (bs, 1H). ^{13}C NMR (75 MHz, $CDCl_3$) δ: 17.4, 39.3, 46.8, 47.6, 117.8, 118.5, 119.7, 125.4, 125.9, 126.9, 127.8, 129.1, 129.9, 131.0, 137.4, 155.8, and 175.2. Anal. calcd. (%) for $C_{19}H_{21}NO_2$, MW 295.38: C 77.26, H 7.17, N 4.74; found: C 79.43, H 7.28, N 4.51.

N-*Benzyl*-N-*[1-(2-hydroxyphenyl)ethyl]-2-phenylacetamide (3bf)

Oil. IR ν_{max} (liquid film) (cm^{-1}): 3138, 2966, 1630, 1484, 1445, 1223, and 758. ^1H NMR (300 MHz, $CDCl_3$) δ: 1.51 (d, 3H, *J* = 7.2 Hz), 3.54 (d, 1H, *J* = 15.4 Hz), 3.66 (d, 1H, *J* = 15.4 Hz), 4.46 (s, 2H), 6.16 (q, 1H, *J* = 7.2 Hz), 6.70–7.40 (m, 14H), and 9.13 (bs, 1H). ^{13}C NMR (75 MHz, $CDCl_3$) δ: 17.4, 41.4, 46.8, 47.8, 117.8, 119.6, 125.9, 126.9, 127.3, 127.7, 128.9, 129.0, 129.2, 129.9, 134.3, 137.5, 142.8, 156.0, and 175.3. Anal. calcd. (%) for $C_{23}H_{23}NO_2$, MW 345.434: C 79.97, H 6.71, N 4.05; found: C 79.78, H 6.90, N 4.23.

(l)-(±)-[1-(2-Hydroxyphenyl)propyl]-(1′-phenylethyl)-pentanamide ((l)-3db)

Oil. IR ν_{max} (liquid film) (cm^{-1}): 3138, 2965, 1624, 1487, 1451, 1232, and 760. ^1H NMR (300 MHz, $CDCl_3$) δ: 0.70 (t, 3H, *J* = 6.8 Hz), 0.90–1.14 (m, 2H), 1.02 (t, 3H, *J* = 7.1 Hz), 1.36–1.58 (m, 2H), 1.66–1.90 (m, 2H), 1.85 (d, 3H, *J* = 7.0 Hz), 1.94–2.34 (m, 2H), 4.80 (m, 1H), 5.90 (bs, 1H), 6.60–7.40 (m, 9H), and 9.45 (bs, 1H). ^{13}C NMR (75 MHz, $CDCl_3$) δ: 11.8, 13.8, 19.5, 22.4, 24.3, 27.6, 35.8, 51.1, 55.3, 117.6, 119.6, 124.0, 125.9, 126.4, 127.2, 128.6, 129.7, 141.3, 156.8, and 178.0. Anal. calcd. (%) for $C_{22}H_{29}NO_2$, MW 339.471: C 77.84, H 8.61, N 4.13; found: C 77.58, H 8.34, N 3.92.

N-*[1-(2-Hydroxyphenyl)pentyl]*-N-*methylpentanamide (3eb)

Oil. IR ν_{max} (liquid film) (cm^{-1}): 3172, 2957, 1603, 1488, 1457, 1242, and 754. ^1H NMR (300 MHz, $CDCl_3$) δ: 0.92 (t, 3H, *J* = 7.0 Hz), 0.93 (t, 3H, *J* = 7.0 Hz), 1.18–1.50 (m, 6H), 1.56–1.74 (m, 2H), 1.78–2.16 (m, 2H), 2.36 (dt, 2H, *J* = 3.7, 7.5 Hz), 2.79 (s, 3H), 5.79 (dd, 1H, *J* = 6.2, 9.5 Hz), 6.80–6.98 (m, 2H), 7.16–7.29 (m, 2H), and 9.22 (s, 1H). ^{13}C NMR (75 MHz, $CDCl_3$) δ: 14.0, 14.2, 22.6, 22.7, 27.3, 28.8, 29.1, 29.2, 33.8, 50.7, 117.7, 119.3, 124.7, 126.8, 129.5, 156.4, and 176.4. MS (EI) *m/z* (%): 277 (M^+, 27), 220 (12), 162 (40), 136 (100), 133 (60), 116 (35), and 107 (43). Anal. calcd. (%) for $C_{17}H_{27}NO_2$, MW 277.402: C 73.61, H 9.81, N 5.05; found: C 73.48, H 9.47, N 5.24.

N-*Benzyl*-N-*[(2-hydroxyphenyl)phenylmethyl]pentanamide (3hb)

Oil. IR ν_{max} (liquid film) (cm^{-1}): 3142, 2956, 1626, 1487, 1454, 1229, and 761. ^1H NMR (300 MHz, $CDCl_3$) δ: 0.85 (t, 3H, *J* = 7.3 Hz), 1.22–1.38 (m, 2H), 1.53–1.75 (m, 2H), 2.22–2.38 (m, 1H), 2.42–2.56 (m, 1H), 4.57 (d, 1H, *J* = 16.9 Hz), 4.84 (d, 1H, *J* = 16.9 Hz), 6.65–7.40 (m, 15H), and 8.90 (bs, 1H). ^{13}C NMR (75 MHz, $CDCl_3$) δ: 14.0, 22.7, 27.6, 34.09, 50.5, 58.0, 118.1, 119.9, 124.3, 126.2, 127.4, 127.8, 128.2, 128.7, 129.0, 130.0, 130.4, 136.9, 137.8, 156.7, and 177.5. Anal. calcd. (%) for $C_{25}H_{27}NO_2$, MW 373.487: C 80.40, H 7.29, N 3.75; found: C 80.18, H 7.43, N 3.57.

N-*Benzyl*-N-*[(2-hydroxyphenyl)phenylmethyl]isobutyramide (3hc)

White crystals; mp 166–167 °C (*n*-hexane/CH_2Cl_2). IR ν_{max} (Nujol) (cm^{-1}): 3138, 2966, 1630, 1484, 1445, 1223, and 758. ^1H NMR (300 MHz, $CDCl_3$) δ: 0.92 (d, 3H, *J* = 6.1 Hz), 1.26 (d, 3H, *J* = 7.0 Hz), 2.67–2.82 (m, 1H), 4.61

© 2004 NRC Canada

(d, 1H, *J* = 17.5 Hz), 4.84 (d, 1H, *J* = 17.5 Hz), 6.60–7.40 (m, 15H), and 9.00 (bs, 1H). ^{13}C NMR (75 MHz, $CDCl_3$) δ: 18.9, 20.8, 32.3, 50.2, 57.5, 118.2, 119.9, 124.0, 126.0, 127.4, 127.7, 128.6, 128.7, 129.3, 130.1, 130.3, 137.4, 137.7, 157.0, and 182.0. Anal. calcd. (%) for $C_{24}H_{25}NO_2$, MW 359.46: C 80.19, H 7.01, N 3.90; found: C 79.97, H 7.23, N 3.69.

(l)-(±)*-N-*[(2-Hydroxyphenyl)phenylmethyl]*-N-*(1-phenylethyl)pentanamide ((l)-3ib)

Oil. IR ν_{max} (liquid film) (cm^{-1}): 3140, 2961, 1626, 1486, 1451, 1229, and 761. ^{1}H NMR (300 MHz, $CDCl_3$) δ: 0.96 (t, 3H, *J* = 7.3 Hz), 1.38–1.60 (m, 2H), 1.65–1.87 (m, 2H), 1.81 (d, 3H, *J* = 7.0 Hz), 2.68 (t, 2H, *J* = 7.5 Hz), 5.50 (q, 1H, *J* = 7.0 Hz), 5.60 (m, 1H) 6.30–7.40 (m, 14H), and 9.85 (bs, 1H). ^{13}C NMR (75 MHz, $CDCl_3$) δ: 14.0, 18.0, 22.8, 27.7, 35.2, 56.7, 62.2, 118.9, 124.6, 126.2, 126.5, 126.9, 128.0, 128.4, 128.8, 129.4, 129.6, 133.0, 138.5, 139.36, 156.3, and 174.8. Anal. calcd. (%) for $C_{26}H_{29}NO_2$, MW 387.514: C 80.59, H 7.54, N 3.61; found: C 80.32, H 7.76, N 3.48

N-*Benzyl-[(2-hydroxynaphthalen-1-yl)phenylmethyl]-pentanamide (6ab)*

Oil. IR ν_{max} (liquid film) (cm^{-1}): 3138, 2966, 1630, 1484, 1445, 1223, and 758. ^{1}H NMR (300 MHz, $CDCl_3$) δ: 0.89 (t, 3H, *J* = 7.1 Hz), 1.26–1.43 (m, 2H), 1.60–1.78 (m, 2H), 2.38–2.67 (m, 2H), 4.54 (d, 1H, *J* = 16.8 Hz), 4.91 (d, 1H, *J* = 16.8), 6.90–7.70 (m, 17H), and 8.63 (bs, 1H). ^{13}C NMR (75 MHz, $CDCl_3$) δ: 14.1, 22.7, 27.7, 34.3, 51.7, 57.4, 114.4, 120.6, 122.3, 123.0, 126.5, 126.6, 127.0, 127.5, 127.6, 128.6, 129.1, 129.1, 129.3, 131.3, 134.3, 136.4, 137.9, 155.2, and 176.2. Anal. calcd. (%) for $C_{29}H_{29}NO_2$, MW 423.55: C 82.24, H 6.90, N 3.31; found: C 79.47, H 5.78, N 3.54.

Acknowledgement

Financial support from the Ministero del l'Università e della Ricerca Scientifica e Tecnologica, Rome and the University of Camerino (National Project "Stereoselezione in Sintesi Organica. Metodologie ed applicazioni") is gratefully acknowledged.

References

1. H. A. El-Shafei, S. M. Badr-Eldin. Egypt. J. Microbiol. **27**, 353 (1994).
2. J. Shavel, Jr. and G. Bobowski. U.S. Patent 3 446 804, 1969; Chem. Abstr. **71**, 61 400t (1969).
3. H. Sugimoto, M. Yonaga, N. Karibe, Y. Iimura, S. Nagato, A. Sasaki, Y. Yamanishi, H. Ogura, T. Kosasa, K. Uchikoshi, and K. Yamatsu. Eur. Patent Appl. EP 468 187, 1992; Chem. Abstr. **116**, 235 643 (1992).
4. (*a*) E. Merck. A.-G. Neth. Appl. 297 368, 1965; Chem. Abstr. **64**, 3563a (1966); (*b*) E. Merck. A.-G. Neth. Appl. 6 511 478, 1966; Chem. Abstr. **65**, 10 596f (1966).
5. J. Sanz-Asensio, M. Plaza-Medina, M.T. Martinez-Soria, and M. Perez-Clavijo. J. Chromatogr. A **840**, 235 (1999).
6. E. Merck. A.-G. French Patent M2933, 1964; Chem. Abstr. **62**, 14 689g (1965).
7. R.E. Strube and F.A. Mackellar. Recl. Trav. Chim. Pays–Bas, **83**, 1191 (1964).
8. N.M. Yousef, A.F.M. Fahmy, M.S. Amine, F.A. Gad, and H.H. Sayed. Indian. J. Heterocycl. Chem. **7**, 119 (1997).
9. (*a*) J. Mindl, O. Hrabik, V. Sterba, and J. Kavalek. Collect. Czech. Chem. Commun. **65**, 1262 (2000). (*b*) A.S. Girgis. Pharmazie, **55**, 426 (2000). (*c*) Jpn. Kokai Tokkyo Koho, Japanese Patent 60 081 182, 1985; Chem. Abstr. **103**, 215 305 (1985).
10. N. Latif, N. Mishriky, and F.M. Assad. Aust. J. Chem. **35**, 1037 (1982).
11. Y. Wang, X. Li, and K. Ding. Tetrahedron: Asymmetry, **13**, 1291 (2002).
12. K. Ikeda, T. Morimoto, and M. Sekyia. Chem. Pharm. Bull. 1178 (1980).
13. (*a*) G. Palmieri. Eur. J. Org. Chem. 805 (1999). (*b*) C. Cimarelli, G. Palmieri, and E. Volpini. Tetrahedron, **57**, 6089 (2001). (*c*) C. Cimarelli, G. Palmieri, and E. Volpini. Tetrahedron, **57**, 6809 (2001). (*d*) C. Cimarelli, G. Palmieri, and E. Volpini. J. Org. Chem. **68**, 1200 (2003).
14. (*a*) C. Cimarelli, A. Mazzanti, G. Palmieri, and E. Volpini. J. Org. Chem. **66**, 4759 (2001). (*b*) C. Cimarelli, G. Palmieri, and E. Volpini. Tetrahedron: Asymmetry, **13**, 2417 (2002).
15. (*a*) G.B. Barlin, S.J. Ireland, T.M.T. Nguyen, B. Kotecka, and K.H. Rieckmann. Aust. J. Chem. **47**, 1143 (1994). (*b*) G.B. Barlin, S.J. Ireland, T.M.T. Nguyen, B. Kotecka, and K.H. Rieckmann. Aust. J. Chem. **47**, 1553 (1994). (*c*) L. Jurd, R.L. Fye, and J. Morgan, Jr. J. Agric. Food Chem. **27**, 1007 (1979). (*d*) P.A. Langley, M.A. Trewern, and L. Jurd. Bull. Entomol. Res. **72,** 473 (1982). (*e*) L. Jurd. J. Heterocycl. Chem. **22**, 993 (1985). (*f*) V.N. Komissarov, L.Y. Ukhin, V.A. Kharlanov, V.A. Lokshin, and E.Y. Bulgarevich. Bull. Acad. Sci. USSR, Div. Chem. Sci. **41**, 1875 (1992).
16. D.J. Berrisford, C. Bolm, and K.B. Sharpless. Angew. Chem. Int. Ed. Engl. **34**, 1059 (1995).
17. (*a*) G. Palmieri. Tetrahedron: Asymmetry, **11**, 3361 (2000). (*b*) C. Cardellicchio, G. Ciccarella, F. Naso, F. Perna, and P. Tortorella. Tetrahedron, **55**, 14685 (1999).
18. J.R. Geigy Akt.-Ges. British Patent 811 130, 1959; Chem. Abstr. **54**, 2270e (1960).
19. H. Ohtake, Y. Imada, and S. Murahashi. J. Org. Chem. **64**, 3790 (1999).
20. K. Hiroi, S. Sato, and R. Kitayama. Chem. Pharm. Bull. **31**, 3471 (1983).
21. K. Neuvonen and K. Pihlaja. Magn. Reson. Chem. **28**, 239 (1990).
22. H. Takai, H. Obase, N. Nakamizo, M. Teranishi, K. Kubo, K. Shuto, and T. Hashimoto. Chem. Pharm. Bull. **33**, 1104 (1985).
23. R. Consonni, P. Dalla Croce, R. Ferraccioli, and C. La Rosa. J. Chem. Soc., Perkin Trans. 1, 1809 (1996).

© 2004 NRC Canada

A simple synthesis of benzimidazole *N*-oxides from 2-nitroaniline derivatives — Scope and limitations

Elba I. Buján and María Laura Salum

Abstract: Several benzimidazole *N*-oxide derivatives were synthesized in very good yield by heating at reflux the corresponding *N*-alkyl-2-nitroaniline derivative with NaOH in 60% 1,4-dioxane–water. The effect of substituents on the aromatic ring and amino group on the reaction is discussed.

Key words: synthesis, benzimidazole *N*-oxides.

Résumé : On a réalisé la synthèse de plusieurs dérivés de *N*-oxydes de benzimidazole avec de très bons rendements en chauffant au reflux le dérivé *N*-alkyl-2-nitroaniline correspondant avec du NaOH dans un mélange à 60 % de 1,4-dioxane/eau. On discute de l'effet sur la réaction des substituants présents sur le noyau aromatique ainsi que sur le groupe amino.

Mots clés : synthèse, *N*-oxydes de benzimidazole.

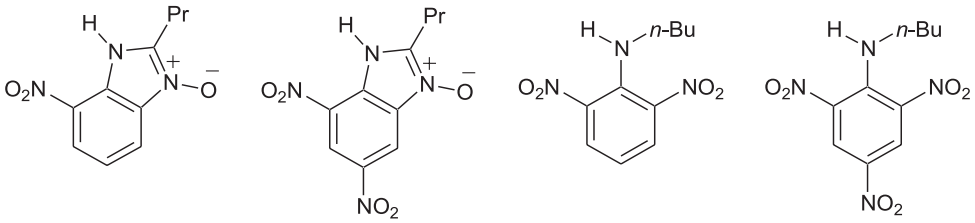
[Traduit par la Rédaction]

Introduction

Benzimidazole and benzimidazole *N*-oxides have biological activity. Some benzimidazole derivatives are known as antivirals, antifungals, and antibacterials (1). Fluorinated benzimidazoles are insecticides or herbicides (2). *N*-Oxides derived from purines have antitumoral, antimicrobial, or antiviral activity (3, 4). Some 1-alkoxy-2-alkylbenzimidazoles derived from 2-nitroanilines also exhibit activity against HIV-1 (5).

Although several classes of amines are oxidized to their corresponding *N*-oxides (6), we could find no reports on direct oxidation of benzimidazoles to benzimidazole *N*-oxides. Synthetic methods known to give benzimidazole *N*-oxides include Pt-catalyzed hydrogenation of 2′-nitro-*N*-phenylacetanilide in EtOH–HCl (7), cyclization of 2-nitroaniline derivatives having electron-withdrawing substituents β to the amino group in basic media (3, 8, 9), photolysis in aqueous methanolic hydrochloric acid of 1-amino-2-nitrobenzene and 1-amino-4-chloro-2-nitrobenzene with pyrrolidine, piperidine, or morpholine as the amino group (10), and photolysis in 0.5% acetic acid of *N*-(2′,6′-dinitro-4′-trifluoromethylphenyl)-2-aminobutyric acid (11). Recently, examples of cyclization of *N*-alkyl-2,4-dinitro-6-trifluoromethylanilines in 50% EtOH–H_2O with $KHCO_3$ resulting in 2-alkyl-substituted benzimidazole *N*-oxides have been reported (12).

We have previously reported on the synthesis of benzimidazole *N*-oxides by cyclization of two 2-nitroaniline derivatives having electron-donating groups β to the amino group; namely, 7-nitro-2-*n*-propyl-1*H*-benzimidazole-3-oxide (**1**) and 5,7-dinitro-2-*n*-propyl-1*H*-benzimidazole-3-oxide (**2**) were synthesized by cyclization of *N*-*n*-butyl-2,6-dinitroaniline (**3**) and *N*-*n*-butyl-2,4,6-trinitroaniline (**4**), respectively (13). The method that we proposed was superior to all others because shorter reaction times were required, there was no need for a substituent in the *N*-alkyl group, generally



1 **2** **3** **4**

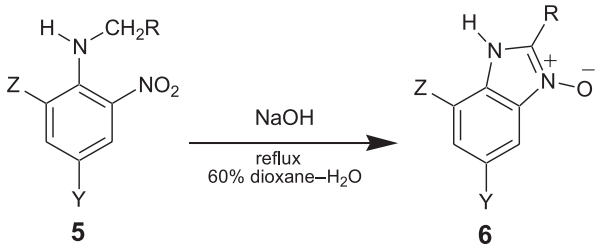
Received 2 December 2003. Published on the NRC Research Press Web site at http://canjchem.nrc.ca on 2 November 2004.

E.I. Buján[1] and M.L. Salum. Instituto de Investigaciones en Fisicoquímica de Córdoba (INFIQC), Dpto. de Química Orgánica, Facultad de Ciencias Químicas, Universidad Nacional de Córdoba, Ciudad Universitaria, 5000, Córdoba, Argentina.

[1]Corresponding author (e-mail: elba@dqo.fcq.unc.edu.ar).

 doi: 10.1139/V04-083 © 2004 NRC Canada

Scheme 1.



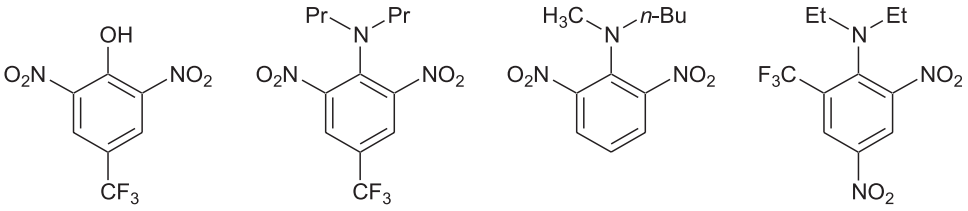
5 **6**

a R = *n*-Pr, Y = CF_3, Z = NO_2
b R = *n*-Pr, Y = NO_2, Z = CF_3
c R = Et, Y = H, Z = NO_2
d R = Et, Y = CF_3, Z = NO_2

Table 1. Synthesis of benzimidazole *N*-oxides **6**.

Substrate	[NaOH] (mol/L)	Time (min)	Product	Yield[a] (%)	pK_{a1}	pK_{a2}
5a	0.20	10	**6a**[b]	62	2.02	5.91
5a	0.20[c]	10	**6a**[b]	72		
5a	0.11	10	**6a**[b]	75		
5a	0.05	10	**6a**[b]	89		
5a	0.01	15	**6a**[b]	94		
5b	0.20	40	**6b**	74	1.59	5.39
5c	0.20	30	**6c**	76	2.46	7.02
5d	0.05	20	**6d**[b]	69	1.92	5.74
5d	0.01	35	**6d**[b]	74		

[a]Percentage yield of isolated product.
[b]Phenol **7** was formed but could not be isolated.
[c]The reaction was carried out under N_2.



7 **8** **9** **10**

better yields were obtained, and the reaction could be carried out in a solvent with high water content.

To determine the scope of the method in regard to the derivatives that can be prepared, we carried out a study on the reaction of substrates **5a**–**5d** and the results are reported here.

Results and discussion

When compounds **5a**–**5d** were heated at reflux in 60% (*v*/*v*) 1,4-dioxane–H_2O with NaOH, they afforded the corresponding benzimidazole *N*-oxides **6a–6d** in very good yields (Scheme 1, Table 1). The structures of **6a**–**6d** were confirmed by their ^{1}H NMR, ^{13}C NMR, and IR spectra. In some cases, substitution of the amino group competed with *N*-oxide formation. For instance, in the reaction of *N*-*n*-butyl-2,6-dinitro-4-trifluoromethylaniline (**5a**) and *N*-*n*-propyl-2,6-dinitro-4-trifluoromethylaniline (**5d**), 2,6-dinitro-4-trifluoromethylphenol (**7**) was also formed (Table 1). The substitution product was also found in the reaction of **3** in 10% 1,4-dioxane–H_2O at 25 °C (14) and in the reaction of **4** in 60% 1,4-dioxane–H_2O at reflux (13). In all cases, the yield of the phenol decreased with decreasing NaOH concentration.

When the reaction of **5a** was performed under a N_2 atmosphere with 0.2 mol/L NaOH, the yield of **6a** increased approximately 10% (Table 1). This is consistent with the mechanism previously proposed (14).

An *N,N*-disubstituted derivative of **5d,** namely, *N,N*-di-*n*-propyl-2,6-dinitro-4-trifluoromethylaniline (trifluralin) (**8**), yielded the phenol **7** along with unreacted substrate after 18 h at reflux with 0.01 mol/L NaOH in 60% 1,4-dioxane–H_2O. It was previously reported that with other *N,N*-dialkylated anilines, namely, *N*-*n*-butyl-*N*-methyl-2,6-dinitroaniline (**9**) (14) and *N,N*-diethyl-2,4-dinitro-6-trifluoromethylaniline (**10**) (12), cyclization requires the presence of the NH proton. This is in agreement with the mechanism proposed for cyclization that requires ionization of the amino group as the initial step (14).

In the reactions of compounds **5b** and **5c**, the only products isolated were benzimidazole *N*-oxides **6b** and **6c**, respectively. Although the yield of both reactions was ~75%, neither the corresponding phenol nor the unreacted substrate or any other product was observed by TLC so the actual yield was probably higher, with some product being lost during work-up. Benzimidazole *N*-oxide was also the only product found in the reaction of **3** in 60% 1,4-dioxane–H_2O at 25 °C (14) or at reflux (13). These results indicate that the formation of benzimidazole *N*-oxide is not dependent on the length of the alkyl chain (3 or 4 carbon atoms).

Another derivative of 2-nitroaniline, namely, *N*-*n*-butyl-4-cyano-2,6-dinitroaniline (**5e**), was also tested as a precursor for an *N*-oxide. In this case, with NaOH concentrations of both 0.20 and 0.01 mol/L, four products were detected by TLC, but they could not be isolated. While one of them seemed to be the *N*-oxide, the others may have originated from the reaction of base with the cyano group, as was observed for other cyanobenzenes (15).

The substituents on the aromatic ring have an important effect on the competition between substitution and cyclization. The absence of a second group *ortho* to the amino group prevents cyclization, as was observed with *N*-*n*-butyl-2,4-dinitroaniline, which gave 2,4-dinitrophenol in 100% yield after 24 h at reflux with 0.01 mol/L NaOH (13). When both of the substituents *ortho* to the amino group are NO_2, the yield of the cyclization product increases as the electron-

© 2004 NRC Canada

Table 2. UV–visible data for 2,4,6-trinitroaniline (**11**),[a] *N*-*n*-butyl-2,6-dinitro-4-trifluoromethylaniline (**5a**), *N*-*n*-butyl-2,4-dinitro-6-trifluoromethylaniline **(4b),** and *N*-*n*-butyl-2,4,6-trinitroaniline (**4**).

Compound	λ (nm)	ε (L mol^{-1} cm^{-1})	λ (nm)	ε (L mol^{-1} cm^{-1})
11	318	12 000	408	7800
4	338	16 588	413	6336
5a	416	7 026	325	1893
5b	340	16 507		

[a] Data from ref. 16.

withdrawing ability of the *para* substituent decreases. This is evident from the fact that with an NaOH concentration of 0.20 mol/L, the yield of *N*-oxide is 95.6%, 61.6%, and 0% for **3** (13), **5a**, and **4** (13), respectively. The replacement of an *o*-NO_2 group by an *o*-CF_3 completely inhibits the substitution reaction (compare the results for **5a** and **5b**). Because of this and the fact that the absence of a second *ortho* substituent inhibits cyclization (12–14), we believe that the substituent on C(6) plays a very important role in the reaction. We propose that the conformation of compounds having two *ortho* substituents may favour the cyclization reaction.

To investigate the conformation of compounds **5a**, **5b,** and **4** in solution, we analyzed their UV–visible spectra in methanol; the spectral data are summarized in Table 2. The spectrum of 2,4,6-trinitroaniline (**11**) in methanol shows two absorption bands: one at 318 nm (band 1) and the other at 408 nm (band 2). These bands correspond to electronic transitions from the amino group to the *p*-nitro (band 1) and *o*-nitro (band 2) groups, respectively (16). In compound **4,** bathochromic displacements of bands 1 and 2 relative to those of **11** were observed. Similar bathochromic displacements in related 2,4-dinitroaniline and 2,4,6-trinitroaniline derivatives were interpreted as a consequence of destabilization of the ground state of the molecule due to rotation around the C(1)–N bond or to steric enhancement of resonance caused by rotation around the C(2)–N and (or) the C(6)–N bond or by a combination of both factors (16–19). In related nitroanilines, hypsochromic and hypochromic displacement of band 2 was attributed to rotation around the C(2)–N and (or) the C(6)–N bond, while a decrease in the intensity of band 1 was attributed to rotation around the C(1)–N bond (16–19). Compound **5a** shows a bathochromic and hypochromic displacement of band 1 as well as a hypsochromic and hypochromic displacement of band 2 when compared to **11**. These observations indicate nonplanarity of the two *o*-nitro groups and the amino group with the aromatic ring. The bathochromic displacement and increased intensity (increase in ε due to steric effects) of band 1 and the complete disappearance of band 2 in **5b** point to nonplanarity of the *o*-nitro group with the aromatic ring.

Analysis of the ^{1}H NMR chemical shifts of the methylene protons α to the nitrogen was performed to confirm the nonplanarity of the amino group (Table 3). The chemical shifts of the methylene protons α to the amino group in **5a**, **5b,** and **4** were calculated by computational methods (20). The difference between the calculated and observed values shows shielding of the protons of the butylamine moiety in **4** and **5a**, which could be attributed to the ring current produced by the electrons of benzene (21). Therefore, the butylamine moiety must be out-of-plane with respect to the plane of the aromatic ring in these compounds. The fact that the chemical shift of the α-methylene protons in **5b** is nearly the same as the calculated value could mean that there is no rotation around the C(1)–N bond. However, considering that CF_3 is sterically more bulky than the NO_2 group as evidenced by its steric substituent constant E_S or ν (22), it is reasonable to think that there must be some loss of coplanarity between the lone pair of electrons on nitrogen and the π electrons of the benzene ring.

Table 3. Experimental and calculated ^{1}H NMR chemical shifts for aliphatic protons in compounds **5a**, **5b**, and **4**.

	5a		**5b**		**4**	
Atom	Exptl.	Calcd.	Exptl.	Calcd.	Exptl.	Calcd.
H(1′)	3.03	3.48	3.37	3.30	3.11	3.48
H(2′)	1.69	1.59	1.71	1.59	1.73	1.59
H(3′)	1.42	1.43	1.45	1.43	1.44	1.43
H(4′)	0.94	0.95	0.97	0.95	0.97	0.95

Note: Chemical shifts were calculated with ACD/Chem Sketch (20).

Table 4. C(1)–N(7) bond length (Å) and selected torsion angles (°) for **5a**, **5b,** and **4**.

	5a	5b	4
C(1)–N(7)	1.356	1.363	1.352
C(3)–C(2)–N(8)–O(9)	–41.06	– 46.05	–40.63
C(3)–C(2)–N(8)–O(10)	136.36	131.56	136.95
C(6)–C(1)–N(7)–H	–17.32	–7.468	–16.51
C(6)–C(1)–N(7)–C(1′)	152.95	153.47	156.53
C(5)–C(6)–C(1)–N(7)	–168.72	–175.014	–165.95
C(3)–C(2)–C(1)–N(7)	172.55	166.52	163.85

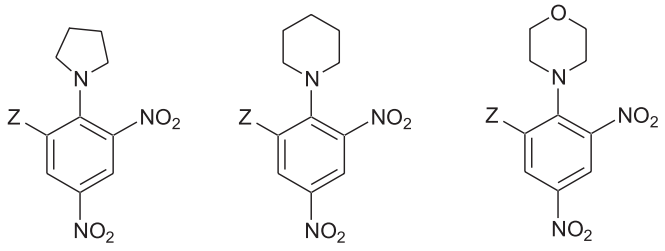
Note: Calculated with MOPAC program (23).

We have also performed geometry optimization of the structures of compounds **5a**, **5b,** and **4** using the quantum chemistry program MOPAC (23); some of the results are shown in Table 4. The length of the C(1)–N bond varies in the order **5b > 5a > 4**, indicating the greatest double bond character in **4**. The rotation around the C(2)–N bond is greater in **5b** than in the other compounds, in agreement with the UV–visible spectra. Rotation around the C(1)–N bond can be inferred by comparing the dihedral angles defined by C(6)–C(1)–N–H (**5a > 4 > 5b**) or C(6)–C(1)–N–C(1′) (**5a ≈ 5b > 4**). In addition, the bending of the amino nitrogen out of the aromatic plane is evidenced by the dihedral angles C(5)–C(6)–C(1)–N and C(3)–C(2)–C(1)–N; the deviation from planarity is 6.5°, 12.5°, and 15° for **5b**, **5a,** and **4**, respectively.

These results indicate that rotation of the *ortho* substituents favours cyclization while nonplanarity of the amino group favours the substitution reaction. We have shown in previous work that in 2,4,6-trinitro-1-pyrrolidinobenzene (**12a**), 2,4,6-trinitro-1-piperidinobenzene (**13a**)**,** and 1-morpholino-2,4,6-trinitrobenzene (**14a**) (17), in 2,4-dinitro-1-piperidinobenzene (**13b**) (18), and in 2,4-dinitro-1-pyrrolidinobenzene (**12b**) and 1-morpholino-2,4-dinitrobenzene (**14b**) (19), nonplanarity of the *o*-nitro groups and the amino

© 2004 NRC Canada

group relative to the aromatic ring occurs both in the solid state and in solution. The decrease of the interaction of the lone pair of electrons of the amino nitrogen with the π system due to nonplanarity and the formation of σ complexes



by addition of a nucleophile to an unsubstituted position on the aromatic ring favours substitution of the amino group (24).

The UV–visible spectra of **6a**–**6d** change with the pH of the solution (in the range 1.00 < pH < 8.00) as shown for **6a** in Fig. 1. These spectra are attributed to acid–base equilibria as shown in Scheme 2 (25). Spectrophotometric titration gave two inflection points corresponding to two pK_as; the values are summarized in Table 1 and are similar to those reported for **1** (13) and 6-nitro-3*H*-benzimidazole-1-oxide (8).

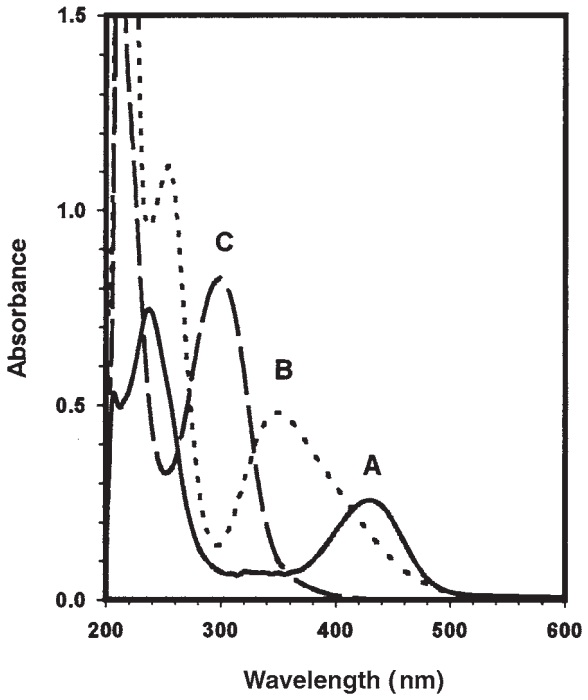
We conclude that benzimidazole *N*-oxides can be obtained in a very simple way and with good yields starting with *N*-alkylanilines that have two *ortho* substituents, one of them being a nitro group. Several new derivatives have been prepared and isolated. The method offers advantages over previously reported procedures since easily available materials can be used, shorter reaction times are required, and compounds with a nitro group at the C(7) position of benzimidazole can be obtained.

Experimental

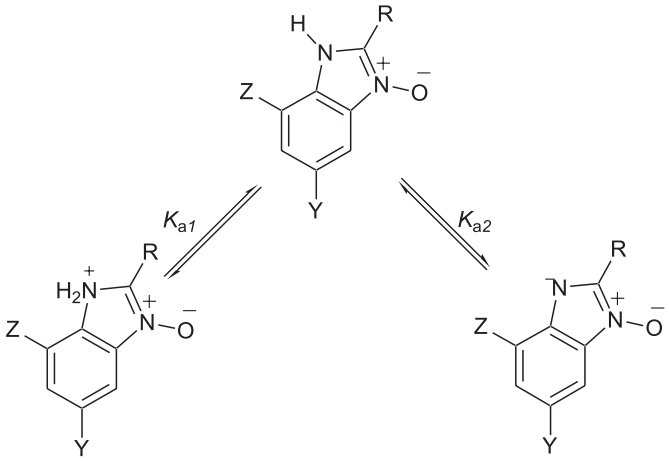
1,4-Dioxane was purified as described previously (26). Water purified in a Millipore Milli-Q apparatus was used throughout. All of the inorganic reagents were of analytical-reagent grade and were used without further purification. NaOH concentrations are expressed in terms of total solvent volume (1,4-dixane–H_2O). Melting points were determined on an electrothermal apparatus. Proton (200 MHz) and ^{13}C (50 MHz) NMR spectra were recorded on a Bruker ACE 200 spectrometer. Chemical shifts in $CDCl_3$ are reported as δ values downfield from Me_4Si, and those in $(CD_3)_2SO$ are referenced to the solvent signal. The mass spectra (EI) and HRMS (EI) were done at Unidad de Espectrometría de Masas, Universidad de Santiago de Compostela, Spain. IR spectra in KBr were obtained on a Nicolet 5SXC FT-IR spectrometer. UV–visible spectra in 10% (*v*/*v*) 1,4-dioxane–H_2O or methanol were obtained on a Shimadzu UV 2101 spectrophotometer. TLC was carried out using silica gel 60 F_{254} (Merck), and spots were visualized by UV or I_2. Silica gel, 60 mesh size (0.063–0.200 nm) (Merck), was used for column chromatography.

The second product formed in the reaction of **5a** and **5d** was identified as 2,6-dinitro-4-trifluoromethylphenol (**7**) by

Fig. 1. (A) Spectrum of **5a** in 10% 1,4-dioxane–H_2O at pH 7.22 (Na_2HPO_4/KH_2PO_4 buffer); $[\mathbf{5a}]_0 = 3.91 \times 10^{-5}$ mol/L. (B, C) Spectra of **6a** in 10% 1,4-dioxane–H_2O at different pHs; $[\mathbf{6a}]_0 = 1.00 \times 10^{-4}$ mol/L: (B) pH 7.22 (Na_2HPO_4/KH_2PO_4 buffer); (C) pH 1.11 (HCl 0.1 mol/L).



Scheme 2.



TLC comparison with an authentic sample. It was contaminated with solvent, and no further attempts to purify it were made. The phenol **7** was synthesized in DMSO–H_2O by following a reported method (27); the reaction mixture was subjected to liquid–liquid extraction with Et_2O, the solvent was evaporated, and the solid obtained was recrystallized in $CHCl_3$ (mp 49–51 °C (lit. (27) 46–48 °C)). ^1H NMR ($(CD_3)_2SO$, 200 MHz): δ = 8.10.

The pK_as of compounds **6a**–**6d** were determined by spectrophotometric titration in 10% 1,4-dioxane–H_2O at 25 °C. Solutions for the various pH ranges were prepared using HCl (0.7–3.0 mol/L), acetic acid/sodium hydroxide (3.5–5.5 mol/L), and Na_2HPO_4/KH_2PO_4 (5.8–8.0 mol/L).

© 2004 NRC Canada

Synthesis of *N*-alkyl-2-nitroanilines

Compounds **5a–5c** were synthesized and isolated by the methods previously described (28) from the corresponding 1-chloro derivative and *n*-butylamine or *n*-propylamine in DMF. Compound **5d** was synthesized as described elsewhere (11) and recrystallized from MeOH.

N-n-*Butyl-2,6-dinitro-4-trifluoromethylaniline* (5a)

Yellow solid; mp 35.5–37.5 °C. Yield 81%. ^{1}H NMR ($CDCl_3$, 200 MHz) δ: 0.94 (t, 3H, J = 7.2 Hz, CH_3), 1.42 (m, 2H, J = 7.2 Hz, CH_2CH_3), 1.69 (m, 2H, J = 7.1 Hz, $CH_2CH_2CH_3$), 3.03 (td, 2H, J = 6.9 Hz, 4.7 Hz, $CH_2CH_2CH_2CH_3$), 8.38 (s, 2H, Ar), and 8.62 (s, 1H, NH). ^{13}C NMR ($CDCl_3$, 50 MHz) δ: 13.47, 19.83, 31.94, 46.38, 115.98 (q, J_{CF} = 36 Hz, C-CF_3), 122.45 (q, J_{CF} = 270 Hz, CF_3), 128.99, 137.16, and 141.44. MS *m/z*: 308.1 ([M+1]$^+$, 10.3), 307.0 (M$^+$, 17.6), 264.0 (100), 218.2, 201.4, 248.2, 218.2, 202.1, 70.9, 68.9, 43.0, 41.0, and 30.2. HRMS (EI): *m/z* calcd. for $C_{11}H_{12}N_3O_4F_3$: 307.0780; found: 307.0784.

N-n-*Butyl-2,4-dinitro-6-trifluoromethylaniline* (5b)

Yellow oil. ^{1}H NMR ($CDCl_3$, 200 MHz) δ: 0.97 (t, 3H, J = 7.2 Hz, CH_3), 1.45 (m, 2H, J = 7.3 Hz, CH_2CH_3), 1.71 (m, 2H, J = 7.1 Hz, $CH_2CH_2CH_3$), 3.37 (q, 2H, J = 5.8 Hz, $CH_2CH_2CH_2CH_3$), 7.74 (s, 1H, NH), 8.63 (d, 1H, J = 2.5 Hz, Ar), and 9.05 (d, 1H, J = 2.9 Hz, Ar). MS *m/z*: 309.1 ([M+1]$^+$, 12.1), 307.8 (M$^+$, 88.8), 264.1 (100), 218.4, 201.4, 247.9, 218.4, 202.2, 70.9, 68.8, 42.9, 40.9, and 30.2. HRMS (EI): *m/z* calcd. for $C_{11}H_{12}N_3O_4F_3$: 307.0780; found: 307.0773.

N-n-*Propyl-2,6-dinitroaniline* (5c)

Yellow solid; mp 79–80 °C. Yield: 83%. ^{1}H NMR ($CDCl_3$, 200 MHz) δ: 0.99 (t, 3H, J = 7.2 Hz, CH_3), 1.71 (m, 2H, J = 7.2 Hz, CH_2CH_3), 2.96 (td, 2H, J = 6.9 Hz, 4.7 Hz, $CH_2CH_2CH_3$), 6.74 (t, 1H, J = 8.2 Hz, Ar), 8.17 (d, 2H, J = 8.0 Hz, Ar), and 8.35 (s, 1H, NH). MS *m/z*: 226.2 ([M+1]$^+$, 16.3), 225.0 (M$^+$, 54.4), 196.0 (100), 179.8, 150.1, 134.1, 132.9, 56.9, 40.9, 29.1, and 28.1. HRMS (EI): *m/z* calcd. for $C_9H_{11}N_3O_4$: 225.0749; found: 225.0748.

N-n-*Propyl-2,6-dinitro-4-trifluoromethylaniline* (5d)

Yellow solid; mp 61–62 °C (lit. (11) 62.5–63.0 °C). Yield: 85%. ^{1}H NMR ($CDCl_3$, 200 MHz) δ: 1.02 (t, 3H, J = 7.3 Hz, CH_3), 1.74 (m, 2H, J = 7.2 Hz, CH_2CH_3), 3.01 (td, 2H, J = 6.9 Hz, 4.8 Hz, $CH_2CH_2CH_3$), 8.40 (s, 1H, Ar), and 8.65 (s, 1H, NH).

Synthesis of benzimidazole *N*-oxides; general procedure

The corresponding *N*-alkyl-2-nitroaniline derivative was heated at reflux in 60% (*v*/*v*) 1,4-dioxane–H_2O with NaOH. The reaction was followed by TLC; when no remaining reactant was observed, the heating was stopped; the solution was cooled to room temperature and acidified to pH ≤ 4 with 3.2 mol/L HCl.

***7-Nitro-2*-n-*propyl-5-trifluoromethyl-1*H-*benzimidazole 3-oxide* (6a)**

A solution prepared by dissolving 200 mg (0.65 mmol) of **5a** in 100 mL of solvent was heated at reflux with NaOH (0.20–0.01mol/L) for 10–15 min. The reaction mixture was acidified to pH 4 and the solvent was evaporated in a rotary evaporator. The salts were separated from the products by column chromatography on silica gel by eluting with variable amounts of hexane–EtOAc. The products were treated with acetone, in which the phenol is completely soluble while the *N*-oxide precipitates. The *N*-oxide was isolated by vacuum filtration as a yellow powder that decomposed at 196 °C.

^{1}H NMR ((CD_3)$_2$SO, 200 MHz) δ: 1.02 (t, 3H, J = 7.3 Hz, CH_3), 1.86 (m, 2H, J = 7.5 Hz, CH_2CH_3), 2.98 (t, 2H, J = 7.3 Hz, $CH_2CH_2CH_3$), 8.25 (s, 1H, Ar), 8.26 (s, 1H, Ar), and 12.52 (s, 1H, NH). ^{13}C NMR ((CD_3)$_2$SO, 50 MHz) δ: 13.40, 19.68, 27.26, 111.99 (q, J_{CF} = 4.0 Hz, CHAr), 114.58 (q, J_{CF} = 4.0 Hz, CHAr), 121.41 (q, J_{CF} = 33.5 Hz, C-CF_3), 123.43 (q, J_{CF} = 270 Hz, CF_3), 133.12, 134.77, 137.36, and 158.08. IR (KBr, ν_{max} cm^{-1}): 1539.4 (s), 1337.4 (s, 1288.9 (s), and 1258.2 (s). MS *m/z*: 291.2 ([M+1]$^+$, 20.4%), 289.8 (M$^+$, 82.2), 272.1, 260.8, 244.5, 226.1, 199.3, 142.8, 70.9 (100), 68.8, 42.9, and 41.0. HRMS (EI): *m/z* calcd. for $C_{11}H_{10}N_3O_3F_3$: 289.0674; found: 289.0676.

***5-Nitro-2*-n-*propyl-7-trifluoromethyl-1*H-*benzimidazole 3-oxide* (6b)**

A solution prepared by dissolving 50 mg (0.16 mmol) of **6b** in 25 mL of solvent was heated at reflux with NaOH (0.20 mol/L) for 40 min. Only the *N*-oxide was formed; it precipitated upon acidification of the solution with HCl and was separated by vacuum filtration. It decomposed at 183 °C (lit. (12) 213 °C).

^{1}H NMR ((CD_3)$_2$SO, 200 MHz) δ: 1.01 (t, 3H, J = 7.4 Hz, CH_3), 1.85 (m, 2H, J = 7.4 Hz, CH_2CH_3), 2.98 (t, 2H, J = 7.6 Hz, $CH_2CH_2CH_3$), 8.31 (d, 1H, J = 2.0 Hz, Ar), and 8.57 (d, 1H, J = 2.0 Hz, Ar). ^{13}C NMR ((CD_3)$_2$SO, 50 MHz) δ: 13.67, 19.95, 27.63, 109.33, 114.31 (q, J_{CF} = 4.9 Hz, CHAr), 118.29 (q, J_{CF} = 33.0 Hz, C-CF_3), 122.93 (q, J_{CF} = 271 Hz, CF_3), 132.69, 138.60, 141.34, and 158.65. IR (KBr, ν_{max} cm^{-1}): 1540.8 (s), 1362.4 (s), 1287.2 (s), and 1254.9 (s). MS *m/z*: 291.1 ([M+1]$^+$, 18.4%), 289.7 (M$^+$, 64.7), 272.1, 260.8, 244.3 (100), 226.1, 199.1, 143.0, 68.6, 71.1, 43.1, and 40.9. HRMS (EI): *m/z* calcd. for $C_{11}H_{10}N_3O_3F_3$: 289.0674; found: 289.0681.

***2-Ethyl-7-nitro-1*H-*benzimidazole 3-oxide* (6c)**

A solution prepared by dissolving 50 mg (0.22 mmol) of **5c** in 25 mL of solvent was heated at reflux with NaOH (0.20 mol/L) for 30 min. The only product formed was isolated by column chromatography over silica gel by eluting with variable amounts of hexane–EtOAc. The solid decomposed at 163 °C.

^{1}H NMR ((CD_3)$_2$SO, 200 MHz) δ: 1.36 (t, 3H, J = 7.4 Hz, CH_3), 2.96 (q, 2H, J = 7.6 Hz, CH_2CH_3), 7.41 (t, 1H, J = 8.04 Hz, Ar), 7.88 (d, 1H, J = 7.66 Hz, Ar), 8.02 (d, 1H, J = 8.02 Hz, Ar), and 12.23 (s, 1H, NH). ^{13}C NMR ((CD_3)$_2$SO, 50 MHz) δ: 10.98, 18.93, 115.09, 117.87, 120.94, 130.86, 134.82, 137.54, and 155.95. IR (KBr, ν_{max} cm^{-1}): 1526.1 (s), 1338.7 (s), 1321.2 (s), and 1251.5 (s). MS *m/z*: 208.1 ([M+1]$^+$, 5.1%), 207.3 (M$^+$, 85.1), 193.2, 189.9 (100), 178.1, 143.8, 132.1, 74.9, 56.9, 41.1, and 29.1. HRMS (EI): *m/z* calcd. for $C_9H_9N_3O_3$: 207.0644; found: 207.0645.

***2-Ethyl-7-nitro-5-trifluoromethyl-1*H-*benzimidazole 3-oxide* (6d)**

A solution prepared by dissolving 100 mg (0.34 mmol) of

© 2004 NRC Canada

1d in 50 mL of solvent was heated at reflux with NaOH (0.05 or 0.01 mol/L) for 20–35 min. The reaction mixture was acidified to pH 2 and the products were extracted with CH_2Cl_2. The combined extracts were dried over anhydrous Na_2SO_4, filtered, and the solvent evaporated in a rotary evaporator. The solid obtained was a mixture of **6d** and **7**; the *N*-oxide **6d** was isolated as described for **6a**. The solid decomposed at 196 °C (lit. (11) 215–216 °C).

^{1}H NMR ($(CD_3)_2SO$, 200 MHz) δ: 1.38 (t, 3H, J = 7.5 Hz, CH_3), 3.02 (q, 2H, J = 7.5 Hz, CH_2CH_3), 8.24 (s, 1H, Ar), 8.25 (s, 1H, Ar), and 12.48 (s, 1H, NH). ^{13}C NMR ($(CD_3)_2SO$, 50 MHz) δ: 10.65, 19.06, 111.81 (q, J_{CF} = 4.0 Hz, CHAr), 114.47 (q, J_{CF} = 4.0 Hz, CHAr), 121.43 (q, J_{CF} = 33.5 Hz, C-CF_3), 123.41 (q, J_{CF} = 270 Hz, CF_3), 133.04, 134.85, 137.36, and 159.11

Acknowledgements

This research was supported in part by Consejo Nacional de Investigaciones Científicas y Técnicas (CONICET), Argentina; Agencia Córdoba Ciencia; Agencia Nacional de Promoción Científica y Tecnológica (FONCYT); Fundación Antorchas, Argentina; and Secretaría de Ciencia y Tecnología, Universidad Nacional de Córdoba, Argentina. M.L.S. is a FONCYT doctoral fellow. We thank Dr. Alejandro Granados for helpful suggestions.

References

1. D.J. Cundy and G.W. Sympson. Aust. J. Chem. **49,** 199 (1996).
2. M. Kobayashi and K. Uneyama. J. Org. Chem., **61**, 3902 (1996).
3. F. Nohara, M. Nishii, K. Ogawa, K. Isono, M. Ubukata, T. Fujii, T. Itaya, and T. Saito. Tetrahedron Lett. **28**, 1287 (1987).
4. T. Fujii, T. Itaya, and K. Ogawa. Heterocycles, **44**, 573 (1997).
5. J.M. Gardiner, C.R. Loyns, C.H. Schwalbe, G.C. Barrett, and P.R. Lowe. Tetrahedron, **51**, 4101 (1995).
6. (*a*) Tertiary amines: K. Bergstad and J.E. Backvall. J. Org. Chem. **63**, 6650 (1998); S. Colonna, N. Gaggero, J. Drabowicz, P. Lyzwa, and M. Mikolajczyk. Chem. Commun. 1787 (1999); S. Dayan, M. Kol, and S. Rozen. Synthesis, 1427 (1999); (*b*) Pyridines: C. Copéret, H. Adolfsson, T-A.V. Khuong, A.K. Yudin, and K.B. Sharpless. J. Org. Chem. **63**, 1740 (1998). (*c*) Alkyl benzotriazoles: A.R. Katritzky, R. Maimait, S.N. Denisenko, P.J. Steel, and N.G. Akhmedov. J. Org. Chem. **66**, 5585 (2001).
7. J.W. Schulenberg and S. Archer. J. Chem. Soc. **30**, 1279 (1965).
8. L.A. Ljublinskaya and V.M. Stepanov. Tetrahedron Lett. **12**, 4511 (1971).
9. (*a*) I.W. Harvey, M.D. McFarlane, D.J. Moody, and D.M. Smith. J. Chem. Soc., Perkin Trans. I, 681 (1988). (*b*) P.A. Collins Cafiero, C.S. French, M.D. McFarlane, R.K. Mackie, and D.M. Smith. J. Chem. Soc., Perkin Trans. I, 1375 (1997).
10. R. Fielden, O. Meth-Cohn, and H. Suschitzky. Tetrahedron Lett. **15**, 1229 (1970).
11. E. Leitis and D.G. Crosby. J. Agric. Food Chem. **22**, 842 (1974).
12. P. Szczecinski and D. Bartusik. J. Chem. Res. (S) 84 (2002).
13. E. Buján de Vargas and A.I. Cañas. Tetrahedron Lett. **37**, 767 (1996).
14. E.I. Buján, A.I. Cañas, and R.H. de Rossi. J. Chem. Soc., Perkin Trans. 2, 1973 (2001).
15. P.C.M. Castilho, M.R. Crampton, and J. Yerwood. J. Chem. Res. (S) 370 (1989).
16. M.J. Kamlet, H.G. Adolph, and J.C. Hoffsommer. J. Am. Chem. Soc. **86**, 4018 (1964).
17. R. Baggio, M.V. Remedi, M.T. Garland, and E.I. Buján. J. Chem. Crystallogr. **27**, 499 (1997).
18. J. Ellena, G. Punte, B.E. Rivero, M.V. Remedi, E.B. de Vargas, and R.H. de Rossi. J. Chem. Crystallogr. **25**, 801 (1995).
19. M.V. Remedi, E.I. Buján, R. Baggio, and M.T. Garland. J. Phys. Org. Chem. **11**, 895 (1998).
20. ACD/Chem Sketch. Version 5.09 [computer program]. ACD/Labs, Toronto, Ont., Canada. 2001.
21. H. Gunther. NMR spectroscopy, an introduction. Wiley, New York. 1979. p. 77.
22. F. Ruff and I.G. Csizmadia. Organic reactions: equilibria, kinetics and mechanism, Elsevier, Amsterdam. 1994. p. 182.
23. These calculations were done with the software included in Chem3D Pro. Version 4.0. CambridgeSoft Corp., Cambridge, Mass. 1997.
24. (*a*) E.I. Buján, M.V. Remedi, and R.H. de Rossi. J. Chem. Soc., Perkin Trans 2, 969 (2000); (*b*) E. Buján de Vargas, M.V. Remedi, and R.H. de Rossi. J. Phys. Org. Chem. **8**, 113 (1995).
25. S.O. Chua, M.J. Cook, and A.R. Katritzky. J. Chem. Soc. B, 2350 (1971).
26. R.H. de Rossi and E.B. de Vargas. J. Am. Chem. Soc. **103**, 1533 (1981).
27. R.L. Jacobs. J. Org. Chem. **36**, 242 (1971).
28. E.B. de Vargas and R.H. de Rossi. J. Org. Chem. **49**, 3978 (1984).

© 2004 NRC Canada

AWARD LECTURE / CONFÉRENCE D'HONNEUR

Prospects for controlling plant fungal diseases — Alternatives based on chemical ecology and biotechnology[1]

M. Soledade C. Pedras

Abstract: Plants produce a diverse array of secondary metabolites associated with important defence and resistance mechanisms. In general, within the same plant family the chemical structures of these metabolites are related and suggest common biogenetic precursors. Crucifers are known to produce constitutive and induced tryptophan derived metabolites. Pathogenic fungi can resist such defences utilizing a variety of processes, as for example, enzymatic detoxification. On the other hand, to facilitate their penetration and colonization of the plant tissues, fungal phytopathogens can produce phytotoxic metabolites, some of which are selectively toxic to host-plants. However, plants may be resistant to these pathogens partly due to their ability to detoxify these selective phytotoxins. Nonetheless, the outcome of these interactions frequently favours the pathogen and can lead to enormous yield losses or even major plant epidemics. An overview of some of the most recent studies of metabolic pathways and stress responses in crucifers and several of their pathogens is presented. Potential strategies to prevent and control plant microbial diseases based on chemical ecology studies and biotechnology will be discussed.

Key words: phytoalexin, phytotoxin, chemical defence, metabolic detoxification, destruxin B.

Résumé : Les plantes produisent une variété de métabolites secondaires associés à d'importants mécanismes de défense et de résistance. En général, dans une même famille de plantes, les structures chimiques de ces métabolites sont apparentées, ce qui suggère des précurseurs biogénétiques communs. Les crucifères sont bien connus pour produire des métabolites à base de ou apparentés au tryptophane. Les champignons pathogènes peuvent résister à de telles défenses en faisant appel à une grande variété de processus, tels que la détoxification enzymatique. Par ailleurs, afin de faciliter leur pénétration et leur colonisation des tissus des plantes, les phytopathogènes fongiques peuvent produire des métabolites phytotoxiques dont quelques-uns sont sélectivement toxiques aux plantes hôtes. Toutefois, les plantes peuvent être résistantes à ces pathogènes en raison de leur habilité à détoxifier ces phytotoxines sélectives. Malgré tout, le résultat de ces interactions favorise fréquemment le pathogène et peut conduire à des pertes énormes de rendement ou même à des épidémies majeures pour les plantes. On présente une revue de quelques études récentes sur les voies métaboliques et les réponses au stress dans les crucifères ainsi que sur plusieurs de leurs pathogènes. On discute aussi de stratégies potentielles, basées sur des études d'écologie chimique et de biotechnologie, pour prévenir et contrôler les maladies microbiennes des plantes.

Mots clés : phytoalexine, phytoxine, défense chimique, détoxification métabolique, dextruxine B.

[Traduit par la Rédaction]

Introduction

Plant diseases caused by fungi are responsible for about 50% of the worldwide losses (1). Through the ages, examples of devastating fungal disease epidemics causing complete depletion of staple crops such as potatoes, rice, and maize have demonstrated the critical need to control phytopathogenic fungi. In general, plants show resistance to certain fungal species and susceptibility to others, suggesting that effective control of fungal infections requires a combination of structurally diverse compounds. Thus, it is not surprising to find that plants produce a vast array of

Received 27 October 2003. Published on the NRC Research Press Web site at http://canjchem.nrc.ca on 23 October 2004.

M.S.C. Pedras. Department of Chemistry, University of Saskatchewan, 110 Science Place, Saskatoon, SK S7N 5C9, Canada. (e-mail: s.pedras@usask.ca).

[1]Based on the Clara Benson Award Lecture presented at the 86th CSC Conference and at the 39th IUPAC Congress on 12 August 2003.

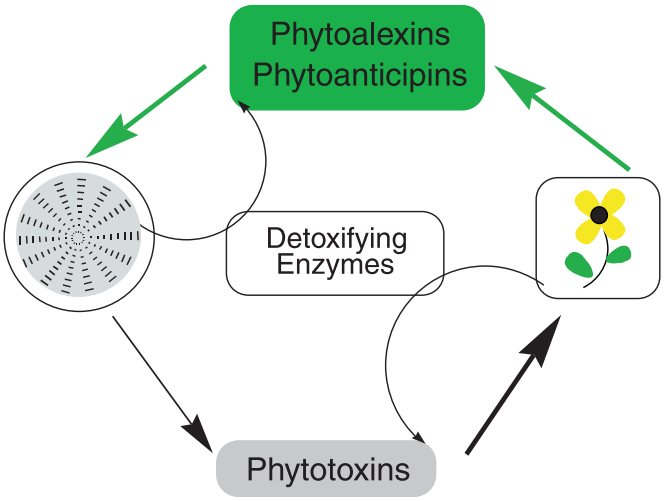
 doi: 10.1139/V04-105 © 2004 NRC Canada

products with very diverse roles in defence against microorganisms and other pests, generally known as secondary metabolites (2). The importance of secondary metabolites in plant defence and fungal attack has been shown in numerous situations through the use of transgenic and (or) mutant organisms (3).

Fungal infection of plants is a complex process, which starts with fungal penetration of plant tissues mediated by secretion of enzymes such as cutinases, cellulases, pectinases, and polygalacturonases, to degrade the protective barriers covering the aerial plant organs and (or) cell wall polymers (4). After penetration, to colonize plant tissues many fungal pathogens produce secondary metabolites that can damage the plant cells irreversibly, phytotoxins. Some phytotoxins cause plant disease symptoms similar to the fungus and affect only host plants, thus they are named host-selective toxins (HST); others affect a much broader range of hosts than the fungus and are known as nonselective toxins (5). The importance of HSTs has been shown in a few important fungal diseases where resistance or susceptibility to the pathogen correlated positively with susceptibility to the HST. On the other hand, plants detect the fungal invader through elicitors, small compounds generated during the penetration of the tissues by fungi, and respond with a sophisticated arsenal of secondary metabolites and enzymes. However, when constitutive (e.g., phytoanticipins) and induced (e.g., phytoalexins) defences (6) are insufficient to deter the invader, the outcome may favour the pathogen. Frequently, fungal pathogens can overcome the plant chemical defences (phytoanticipins and phytoalexins) and plants can overcome fungal phytotoxins through detoxifying enzymes. While phytoalexins are an important part of the plants' defence mechanism, phytotoxins are virulence and (or) pathogenicity factors of phytopathogenic fungi. Overall, the interaction of plants with their pathogens involves an array of chemical reactions, some of which transform highly bioactive secondary metabolites into harmless products, (i.e., detoxification). A simplistic overview of the chemical interaction between plants and fungal pathogens is summarized in Fig. 1.

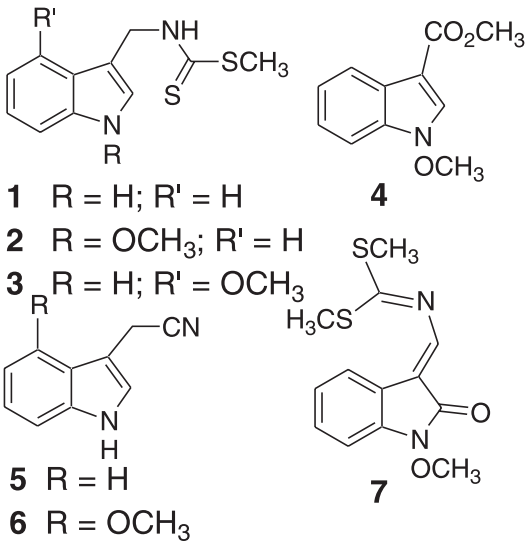
The family Cruciferae comprises a number of major crops, including the oilseeds canola, rapeseed, and mustard, and the vegetables cauliflower, broccoli, cabbage, rutabaga, turnip, etc. Oilseed crucifers (mainly *Brassica* species) constitute the third largest source of edible vegetable oils. A number of cruciferous weeds are well-known for their negative effects on cultivated systems. Besides their economic importance, crucifers are also interesting plant model systems, containing the first example of a completely sequenced plant genome (7). Interestingly, a number of epidemiological studies suggest that cruciferous vegetables protect against cancer by modulating carcinogen metabolism (8). My research group has been investigating the secondary metabolites of both cultivated and wild crucifers in connection with some of the main fungal diseases of economically important crops. Our approach to design strategies to control plant fungal diseases requires a chemical–ecological understanding of the plant and the pathogen secondary metabolism. Here, I attempt to give a glimpse of how we are using chemistry to decipher and control metabolic processes underlying important plant fungal diseases.

Fig. 1. Chemical interaction between plant and fungal pathogens.



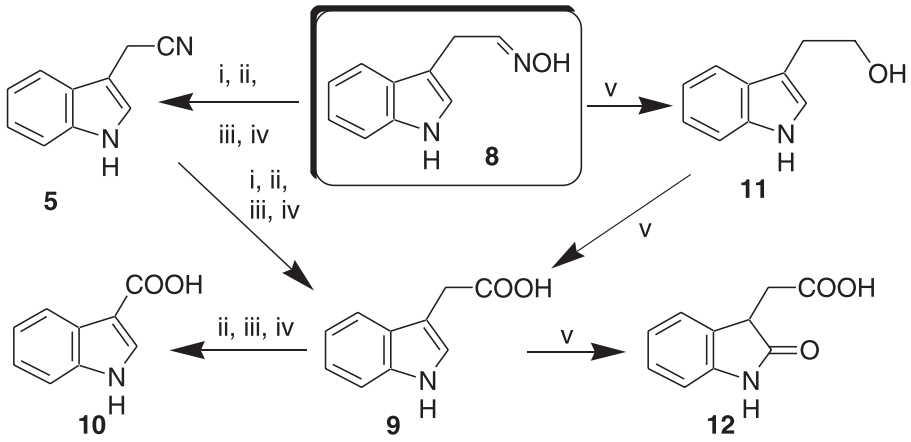
Crucifer phytoalexins and phytoanticipins

Crucifers are the only plants known to produce compounds containing a dithiocarbamate group (e.g., **1**–**3**), although some of the important pesticides and herbicides developed in the 1960s are dithiocarbamates (9). Except for methyl 1-methoxyindole-3-carboxylate (**4**) (10), indolyl-3-acetonitrile (**5**) (11), and arvelexin (**6**) (12), all cruciferous phytoalexins reported thus far contain sulfur. We found that indolyl-3-acetonitrile (**5**) is a phytoalexin in brown mustard (*B. juncea*) but a phytoanticipin in canola (*B. rapa* and *B. napus*) (11). Recently, our search for phytoalexins from cruciferous plants resistant to economically important fungal diseases led us to examine stinkweed (*Thlaspi arvense*) (12), a potential source of disease resistance to the virulent blackleg fungus, and wasabi (*Wasabia japonica*, syn. *Eutrema wasabi*) (13), a perennial plant widely cultivated in Japan. Unexpectedly, we have discovered that both wasabi and stinkweed produce wasalexin A (**7**), although these plants are from rather different genera. Wasalexin A (**7**) production might suggest that it has a role



© 2004 NRC Canada

Scheme 1. Metabolism of indole-3-acetaldoxime (**8**) by fungi: (*i*) *P.* lingam virulent to canola; (*ii*) *P. lingam* virulent to brown mustard; (*iii*) *S. sclerotiorum* virulent to canola and mustard; (*iv*) *R. solani* virulent to canola and mustard; (*v*) *B. bassiana*, insect pathogen.



in the resistance and (or) defence of these two unrelated species against virulent blackleg isolates. It is anticipated that the "design" of plants producing desirable phytoalexin blends active against a range of pathogens can become a feasible strategy as phytoalexins from unrelated cruciferous species are discovered and biological activities established. Such a strategy could be applicable through either classic or biotechnological plant breeding techniques.

Overcoming plant chemical defences

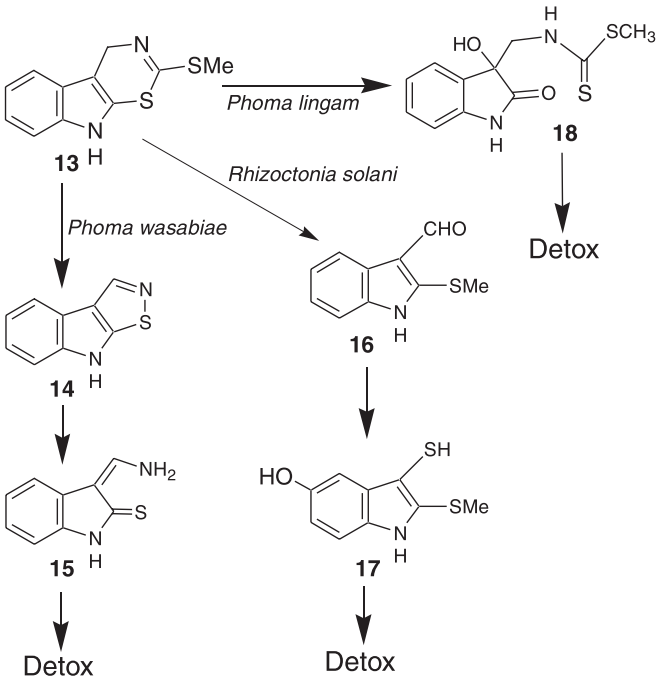
Despite producing multiple chemical defences, crucifers are susceptible to numerous pests and diseases. The susceptibility of crucifers to infection by a wide range of fungi appears to be related with an effective detoxification of their chemical defences by these phytopathogens. Phytopathogenic fungi are able to circumvent some of the plant chemical defences through metabolism and detoxification; to date, our work demonstrates that cruciferous phytoalexins and precursors can be detoxified efficiently by some of their fungal pathogens. For example, because indole-3-acetaldoxime (**8**) is a key precursor of most of the cruciferous defences (11), it was important to establish if common fungal pathogens can metabolize it, as such a process could be highly detrimental to the plant. Towards this end, we investigated the metabolism of **8** by fungi that cause important plant diseases in crucifers: *Leptosphaeria maculans* (Desm.) Ces. et Not. asexual stage *Phoma lingam* (Tode ex Fr.) Desm., the causative agent of blackleg disease, *Rhizoctonia solani* Kuhn, the causative agent of root rot disease, and *Sclerotinia sclerotiorum* (Lib.) de Bary, causative agent of stem rot disease (14). As well, we examined the metabolism of **8** by a fungus pathogenic to insects (*Beauveria bassiana*) but not to plants, to determine if these transformations were common to non-plant pathogenic fungi. As summarized in Scheme 1, the cruciferous pathogens and the insect pathogen metabolized indolyl-3-acetaldoxime (**8**) to the corresponding carboxylic acid **9**; however, while the plant pathogens transformed **8** via indolyl-3-acetonitrile (**5**), transformation of **8** by the insect pathogen occurred via tryptophol (**11**) (14). It could be suggested that the enzymes responsible for this transformation might be specific to crucifers and to their pathogens, especially considering that the biotransformation of **8** by a non-phytopathogen (*B. bassiana*) yielded indole-3-acetic acid via a different intermediate, tryptophol (**11**) (14). Due to the central biogenetic role played by intermediate **8** in crucifer metabolism, it is of interest to establish if the fungal enzymes involved in these transformations are related with currently known plant enzymes; these data should provide a better understanding of the plant–pathogen co-evolution. Interestingly, the antifungal activity of indole-3-acetaldoxime (**8**) to both types of *P. lingam* and to *R. solani* was lower that that of indole-3-acetonitrile (**5**). By contrast, oxime **8** was more inhibitory to *S. sclerotiorum* than nitrile **5**, whereas indole-3-acetic acid (**9**) had no substantial inhibitory effect on any of the species. Neither indole-3-acetaldoxime (**8**) nor indole-3-ethanol (**11**) showed inhibitory activity against *B. bassiana*.

Detoxifying reactions

In cases where phytopathogenic fungi can effectively disarm the plant by detoxifying chemical defences such as phytoalexins, it is expected that the isolation of fungal enzymes involved in crucial detoxification steps will assist the biorational design of antifungal agents selective against cruciferous phytopathogens. Current work with plant pathogenic fungi suggests that such detoxification mechanisms are both substrate and pathogen specific (15). We have analyzed the reactions of cruciferous pathogens to several phytoalexins and found that each fungal species metabolizes and detoxifies phytoalexins via different pathways. For example, as shown in Scheme 2, cyclobrassinin (**13**) a phytoalexin produced by canola, rapeseed, mustards, etc., was metabolized by *P. wasabiae* to brassilexin (**14**) and to a mixture of 3-aminomethylen-2,3-dihydroindole-2-thione (**15**), and (or) related tautomers (16). Two days after incubation of the avirulent isolate with cyclobrassinin, no brassilexin or other phytoalexins or putative metabolites were detected in any of the cultures or their extracts. Similar experiments carried out with virulent isolates of *P. lingam* incubated with cyclobrassinin (**13**) afforded yet another known phytoalexin, dioxibrassinin (**18**), which was further transformed into nontoxic products. Additional biotransformation studies with *R.*

© 2004 NRC Canada

Scheme 2. Metabolism of cyclobrassinin (**13**) by virulent fungi: *P. lingam*, *P. wasabiae*, and *R. solani*.

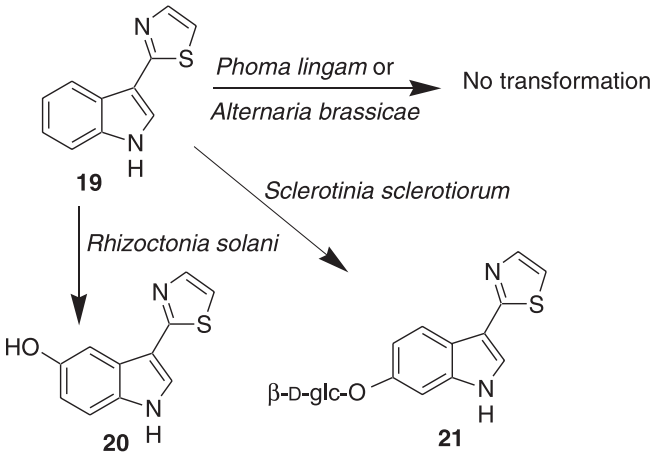


solani established that this pathogen metabolized and detoxified cyclobrassinin via the phytoalexin brassicanal A (**16**), which was further metabolized into nontoxic products. These results demonstrated that cyclobrassinin (**13**) was detoxified via the phytoalexins dioxibrassinin (**18**), brassilexin (**14**), or brassicanal A (**16**), depending on the fungal species, as shown in Scheme 2 (16).

None of the fungal isolates of *P. lingam* or *Alternaria brassicae* metabolized camalexin (**19**) to a detectable level; however, both *R. solani* (17), a pathogen of a plant that produces camalexin (*Camelina sativa*, false flax), and *S. sclerotiorum* (18) metabolized **19** as shown in Scheme 3. While *R. solani* oxidized the C-5 of the indole moiety of camalexin to a more polar and substantially less-toxic metabolite, *S. sclerotiorum* oxidized and glucosylated C-6 to yield a derivative devoid of antifungal activity.

To probe the selectivity of the fungal enzymes involved in detoxification of phytoalexins such as brassinin (**1**) and camalexin (**19**), the metabolism and antifungal activity of analogs was investigated (15, 18). The much slower rates of transformation of some analogs were partly attributed to the specificity of the enzymes involved in the detoxification steps. Further work to better understand phytoalexin detoxification mechanisms employed by plant pathogens, particularly where the outcome of the plant–pathogen interaction is highly detrimental to the plant, should lead to new strategies to control plant fungal diseases. In this connection, a new term coined "paldoxin" has been proposed to designate potential phytoalexin detoxification inhibitors (19). By design, paldoxins are nontoxic selective inhibitors that could be used as a mixture against a variety of plant pathogens, according to crop and region. Upon optimization, such mixtures might have the advantage of acting synergistically with the natural

Scheme 3. Metabolism of camalexin (**19**) by fungi virulent to canola: *P. lingam, A. brassicae*, and *R. solani*.



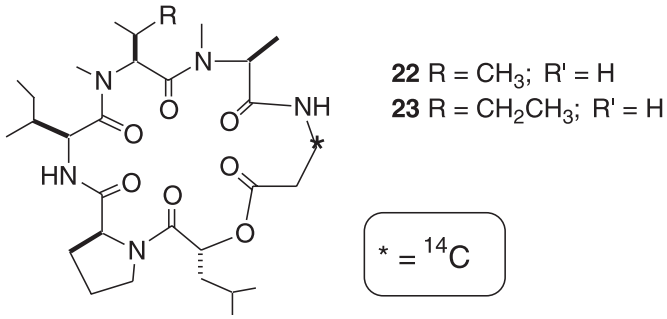
disease resistance factors of plants and be very effective crop protection agents.

Overcoming fungal attack

Necrotrophic fungal phytopathogens are known to produce phytotoxins to damage plant tissues and facilitate colonization, while in response to this attack plants may synthesize detoxifying enzymes. Plants may be resistant to a particular pathogen if they produce enzyme(s) that catalyze detoxification of the pathogen's toxin(s) (20). Consequently, such detoxification traits are desirable and of much importance in classic plant breeding or in engineering disease resistance. While a number of phytoalexin detoxifying reactions have been shown to occur in various plant pathogenic fungi (15, 21),[2] detoxification of phytotoxins were reported in only a few plant species (22).

Plant reactions to the Alternaria blackspot pathogen

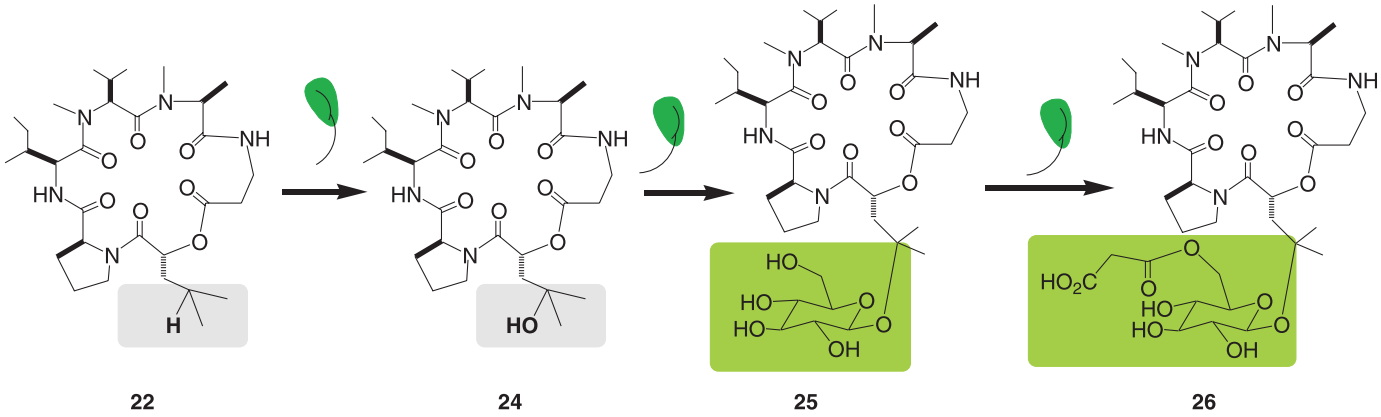
Alternaria blackspot is one of the most damaging and widespread fungal diseases of rapeseed (*B. napus* and *B. rapa*), an oilseed crop of great economic importance worldwide (23). *Alternaria brassicae* (Berk.) Sacc., the blackspot causing fungus, produces the cyclic depsipeptide toxins destruxin B (**22**) and homodestruxin B (**23**), both in vitro (24) and in planta (25). Ultrastructural studies have shown that destruxin B causes tissue damage similar to that observed in plants naturally infected with *A. brassicae*, that is, destruxin B showed selective phytotoxicity. We proposed that this apparent selectivity might be due to detoxification



[2] For a review of the detoxification of crucifer phytoalexins see ref. 15.

© 2004 NRC Canada

Fig. 2. Metabolism of the phytotoxin destruxin B (**22**) by cruciferous plant leaves.



reactions occurring in tissues of plant species resistant to *A. brassicae*. Considering that no sources of Alternaria blackspot resistance are known within *Brassica* species, such information would be of great importance to generate blackspot resistant plant lines. Consequently, we became interested in investigating the metabolism of destruxins in plants susceptible and resistant to *A. brassicae*. Sources of blackspot resistance within the family Cruciferae include cultivars of *Sinapis alba*, a mustard used as a condiment and vegetable.

Recently, using ^{14}C-labelled synthetic compounds, we demonstrated that complete detoxification of destruxin B (**22**) in plants resistant to *A. brassicae* is a two-step process involving sequential hydroxylation to **24** and glucosylation to **25** (26). The chemical structure of the nontoxic destruxin B product (β-D-glucosyl hydroxydestruxin B (**25**)) was determined by a combination of spectroscopic analyses and chemical synthesis of both the β- and α-glucosides of **25**, as well as the tetracetyl derivative. The chemical synthesis of ^{14}C-labelled hydroxydestruxin B (**24**), and results of phytotoxicity assays (27) of hydroxydestruxin B (**22**), hydroxyhomodestruxin B (**24**), and β-D-glucosyl hydroxydestruxin B (**25**) have been described (28). Interestingly, although the hydroxylation and glucosylation reactions occur in both resistant and susceptible species, hydroxylation was the rate-limiting step in the susceptible species, whereas glucosylation was the rate-limiting step in the resistant species (Fig. 2). Remarkably, it was established that hydroxydestruxin B (**24**) induced the biosynthesis of phytoalexins in the resistant white mustard (*S. alba*) but not in the susceptible canola or brown mustard. Taken together our studies suggest that white mustard can overcome the fungal invader through detoxification of destruxin B (**22**) coupled with production of phytoalexins (26).

Further investigation of the metabolism of ^{14}C-destruxin B (**22**) and ^{14}C-hydroxydestruxin B (**24**) in additional crucifers showed that three resistant cultivars of white mustard metabolized destruxin B (**22**) to hydroxydestruxin B (**24**) substantially faster than cultivars of any other species. Among the *Brassica* species, a cultivar of brown mustard (Cutlass, *B. juncea*) appeared to metabolize destruxin B (**22**) to hydroxydestruxin B (**24**) faster. On the other hand, a contrasting trend was observed for the metabolism of hydroxydestruxin B (**24**) to β-D-glucosyl hydroxydestruxin B (**25**); cultivars of canola (susceptible) appeared to transform hydroxydestruxin B (**24**) to **25** substantially faster than cultivars of white mustard, while brown mustard Cutlass showed an intermediate rate. Importantly, leaf and cell culture assays showed that hydroxydestruxin B (**24**) was substantially less toxic to the susceptible species than destruxin B (**22**), and β-D-glucosyl hydroxydestruxin B (**25**) showed no toxicity at all. In summary, these studies indicated that the rate of hydroxylation of destruxin B in cruciferous plants correlated with species resistance to *A. brassica.* Furthermore, we observed that during this detoxification process the phytoalexins sinalexin and sinalbin A were produced in white mustard, however no phytoalexins were detected in canola or brown mustard (26). Although it is well-known that phytoalexins can be biosynthesized in response to a variety of elicitors, including phytotoxins, to the best of my knowledge this is the first and only example of phytoalexin elicitation by a detoxification product of a phytotoxin. Thus, the relatively slower glucosylation rate of hydroxydestruxin B (**24**) in resistant white mustard may be favourable since **24** also elicits biosynthesis of phytoalexins in this species, but not in susceptible species. β-D-Glucosyl hydroxydestruxin B (**25**) was further metabolized to the malonyl derivative **26**, as shown in Fig. 2 (29).

Our results of destruxin B (**22**) detoxification suggest that resistance of mustard to blackspot might be due to detoxification of destruxin B and be amplified by well-synchronized phytoalexin elicitation. This hypothesis, however, does not imply that all blackspot resistant species have the same resistance mechanism. Since the resistance to *A. brassicae* of the cruciferous weeds false flax (*Camelina sativa*) and shepherd's purse (*Capsella bursa-pastoris*) was proposed to be due to production of the phytoalexin camalexin (**19**), we have investigated destruxin B metabolism in these species as well (29). This work showed that *C. bursa-pastoris* metabolized ^{14}C-destruxin B to ^{14}C-hydroxydestruxin B glucoside substantially faster than *C. sativa*, even though uptake of toxin solutions by *C. bursa-pastoris* was slower. Furthermore, *Eruca sativa* transformed hydroxydestruxin B glucoside to the malonylated derivative substantially faster than *C. sativa* or *C. bursa-pastoris.* Comparison of these results with our previous work (26) demonstrates that the transformation of destruxin B in *C. sativa* (69% in 168 h) was much slower than in *S. alba* (ca. 100% in 48 h). Although *C. sativa* and

© 2004 NRC Canada

C. bursa-pastoris produce the phytoalexin camalexin, which is highly inhibitory to *A. brassicae,* these wild species still metabolize destruxin B similar to cultivated species. Phytoalexins did not appear to be elicited by destruxin B or hydroxydestruxin B either in *C. sativa* and *C. bursa-pastoris*. In conclusion, since the destruxin B detoxification pathway present in *S. alba* is also present in three other unrelated species, it was suggested a conservation of this pathway across crucifers. Considering that *C. sativa* and *C. bursa-pastoris* detoxify destruxin B and produce the phytoalexins camalexins, it appears that these wild crucifers represent unique sources of Alternaria blackspot resistance (29).

Conclusions and future prospects

Our work on the biotransformation of cruciferous phytoalexins indicated that different pathogens utilized different pathways to transform the same phytoalexin, and that those processes might contribute to successful plant colonization (15–18). On the other hand, work on the biotransformation of phytotoxins demonstrated that different plants transformed a pathogen's HST using identical pathways (26, 29). These results suggest that such plant pathways are conserved across species and genera; however, the rates of such transformations are substantially different. It would be important to establish if such differences exist among other taxa and between monocotyledons and dicotyledons, to better understand the co-evolution of plant–pathogen populations.

Over the past 50 years, the control of plant pests and diseases has relied mainly on chemical pesticides. However useful and necessary, it is clear that sustainable agriculture practices demand control strategies other than massive application of pesticides. It is anticipated that future approaches to control pests and diseases will rely on more selective and environmentally friendly control methods. Such methods require a much better understanding of the ecological roles of secondary metabolites of plants and their pathogens. Ultimately, systematic modification of metabolite profiles will demonstrate their significance in plant defence and disease resistance. For example, glucosinolates play a role in plant defence as attractants and deterrents against herbivorous insects. A key step in glucosinolate biosynthesis is the conversion of amino acids to the corresponding aldoximes, which is catalyzed by cytochromes P 450 belonging to the CYP79 family. Expression of a CYP79 from cassava in Arabidopsis resulted in the production of new glucosinolates. Metabolically engineered plants producing these new glucosinolates have acquired novel properties with great potential for improvement of resistance to herbivores (30).

In conclusion, considering the diversity of strategies that fungal pathogens use as well as their ability to quickly adapt, it is difficult to predict which developments will lead to durable and broad-spectrum disease resistance. No matter what sophisticated methodologies may be discovered, it is clear that effective plant protection will require a better understanding of the ecological roles of secondary metabolites, their metabolic pathways, and the integration of the various agricultural practices and control procedures.

Acknowledgements

I am very grateful to the Canadian Society for Chemistry (CSC) for having chosen me to receive the Clara Benson Award. It is a great honor and particularly meaningful to be the recipient of this award in 2003, the year celebrating the centenary of the Ph.D. award to Clara Benson, at the University of Toronto.

I have a number of people whom I owe my deepest gratitude for their immense support and trust in my abilities. First and foremost, I thank Dale and João (Tuco) for their unrelenting faith in me. I wish to acknowledge the support of my early collaborators from whom I learned so much about fungi and plants, in particular my "blacklegger" colleague Ginette Séguin-Swartz, and my senior colleagues in the Department of Chemistry of the University of Saskatchewan.

I am in debt to a group of hard working and talented young researchers with whom I have worked during the past 9 years. While a number of these people worked on chemistries not referenced herein, their contributions remain very important to our program progress and success. These include the postdoctoral fellows and technical associates: Farooq Biabani, Corinne Biesenthal, Vera Cekic, Ashlesha Deshpande, Ravi Gadagi, Nargis Ismail, Yanqiu Jiang, Abdul Khan, Iwona Kowalczyk, Ali Loukaci, Sabine Montaut, Oladapo Okeola, Soroush Sardari, Kevin Smith, Mojmir Suchy, Venkat Uppala, Yiming Xu, Dongfeng Zhan, Yifa Zhou; as well as the graduate and undergraduate students: Pearson Ahiahonu, Keith Block, Paulos Chumala, Claudia Erosa-Lopez, Heather Filson, Mohammad Hossain, Mukund Jha, Mohammad Kabir, Soong Lee, Jun Liu, Tyler Norsten, Corwin Nycholat, Francis Okanga, Denis Owiti, Gopal Sarwar, John Sorensen, Shawndra Sttetner, and Irina Zaharia.

In addition, financial support from the Natural Sciences and Engineering Research Council of Canada (NSERC), The Canada Foundation for Innovation (CFI), the Government of Saskatchewan (Saskatchewan Agricultural Development Fund), the University of Saskatchewan, the Canola Research Council of Canada, the Saskatchewan Canola Development Commission, and the Saskatchewan Wheat Pool, is very gratefully acknowledged.

References

1. M.B. Thomas. Proc. Natl. Acad. Sci. U.S.A. **96**, 5944 (1999).
2. M. Wink. Phytochemistry, **64**, 3 (2003).
3. J.P. Morrissey and A.E. Osbourn. Microbiol. Mol. Biol. Rev. **63**, 708 (1999).
4. K.E. Hammond-Kosack and J.D.G. Jones. Plant Cell, **8**, 1773 (1996).
5. A. Ballio and A. Graniti (*Editors*). Experientia, **47**, 751 (1991).
6. (*a*) C.J. Smith. New Phytol. **132**, 1 (1996); (*b*) R.A. Dixon, Nature, **411**, 843 (2001).
7. The Arabidopsis Genome Initiative. Nature, **408**, 796 (2000).
8. P. Talalay and J.W. Fahey. J. Nutr. **131**, 3027S (2001).
9. G.D. Thorn and R.A. Ludwig. The dithiocarbamates and related compounds. Elsevier Publishing Company, New York. 1962. pp. 169–276.
10. M.S.C. Pedras and J.L. Sorensen. Phytochemistry, **49**, 1959 (1998).

© 2004 NRC Canada

11. M.S.C. Pedras, C.M. Nycholat, S. Montaut, Y. Xu, and A.Q. Khan. Phytochemistry, **59**, 611 (2002).
12. M.S.C. Pedras, P.B. Chumala, and M. Suchy. Phytochemistry, **64**, 949 (2003).
13. M.S.C. Pedras, J.L. Sorensen, F.I. Okanga, and I.L. Zaharia. Bioorg. Med. Chem. Lett. **9**, 3015 (1999).
14. M.S.C. Pedras and S. Montaut. Bioorg. Med. Chem. **11**, 3115 (2003).
15. M.S.C. Pedras, F.I. Okanga, I.L. Zaharia, and A.Q. Khan. Phytochemistry, **53**, 161 (2000).
16. M.S.C. Pedras and F.I. Okanga. J. Agric. Food Chem. **47**, 1196 (1999).
17. M.S.C. Pedras and A.Q. Khan. Bioorg. Med. Chem. Lett. **7**, 2255 (1997).
18. M.S.C. Pedras and P.W.K. Ahiahonu. Bioorg. Med. Chem. **10**, 3307 (2002).
19. M.S.C. Pedras, M. Jha, and P.W.K. Ahiahonu. Curr. Org. Chem. **7**, 1635 (2003).
20. J.D. Walton. Plant Cell, **8**, 1723 (1996).
21. (*a*) H.D. VanEtten, R.W. Sandrock, C.C. Wasmann, S.D. Soby, K. McCluskey, and P. Wang. Can. J. Bot. **73**(Suppl. 1), S518 (1995); (*b*) R.P. Purkayastha. *In* Handbook of phytoalexin metabolism and action. *Edited by* M. Daniel and R.P. Purkayastha. Marcel Dekker, Inc., New York. 1995. pp. 1–39.
22. P. Karlovski. Nat. Toxins, **7**, 1 (1999).
23. G.S. Saharan. *In* Breeding oilseed brassicas. *Edited by* K.S. Labana, S.S. Banga, and S. K. Banga. Springer-Verlag, Berlin. 1993. pp. 181–205.
24. W.A. Ayer and L.M. Peña-Rodriguez. J. Nat. Prod. **50**, 400 (1987).
25. (*a*) L. Buchwaldt and J.S. Jensen. Phytochemistry, **30**, 2311 (1991); (*b*) M.S.C. Pedras and K.C. Smith. Phytochemistry, **46**, 833 (1997).
26. M.S.C. Pedras, I.L. Zaharia, Y. Gai, Y. Zhou, and D.E. Ward. Proc. Nat. Acad. Sci. U.S.A. **98**, 747 (2001).
27. M.S.C. Pedras, C.J. Biesenthal, and I.L. Zaharia. Plant Sci. **156**, 185 (2000).
28. D.E. Ward, Y. Gai, R. Lazny, and M.S.C. Pedras. J. Org. Chem. **66**, 7832 (2001).
29. M.S.C. Pedras, S. Montaut, I.L. Zaharia, Y. Gai, and D.E. Ward. Phytochemistry, **64**, 957 (2003).
30. M.D. Mikkelsen and B.A. Halkier. Plant Physiol. **131**, 773 (2003).

© 2004 NRC Canada

Kinetic evidence for the importance of solvent-separated ion pairs during the solvolyses of adamantylideneadamantyl derivatives

Xicai Huang and Andrew J. Bennet

Abstract: The aqueous ethanolysis reactions of adamantylideneadamantyl tosylate, -bromide, and -iodide (**1-OTs**, **1-Br** and **1-I**) were monitored as a function of ionic strength. Special salt effects are observed during the solvolyses of both homoallylic halides, but not in the case of the tosylate **1-OTs**. The measured α-secondary deuterium kinetic isotope effects for the solvolysis of **1-Br** in 80:20 and 60:40 v/v ethanol–water mixtures at 25 °C are 1.110 ± 0.018 and 1.146 ± 0.009, respectively. The above results are consistent with the homoallylic halides reacting via a virtual transition state in which both formation and dissociation of a solvent-separated ion pair are partially rate-determining. While the corresponding transition state for adamantylideneadamantyl tosylate involves formation of the solvent-separated ion pair.

Key words: salt effects, kinetic isotope effect, internal return, solvolysis, ion pairs.

Résumé : On a examiné les réactions d'éthanolyse aqueuse du tosylate, du bromure et de l'iodure d'adamantylidène-adamantyle (**1-OTs**, **1-Br** et **1-I**) en fonction de la force ionique. On a observé des effets de sel spéciaux au cours des solvolyses de chacun des halogénures homoallyliques, mais ce n'est pas le cas pour le tosylate **1-OTs**. On a déterminé que les effets isotopiques cinétiques du deutérium secondaire en α sur la solvolyse du **1-Br** dans des mélanges 80:20 et 60:40 v/v d'éthanol et d'eau, à 25 °C, sont respectivement de 1,110 ± 0,018 et 1,146 ± 0,009. Ces résultats sont en accord avec un mécanisme par lequel les halogénures homoallyliques réagissent par le biais d'un état de transition virtuel dans lequel la formation ainsi que la dissociation d'une paire d'ions séparés par le solvant sont toutes les deux partiellement cinétiquement déterminantes. Dans le cas du tosylate d'adamantylidèneadamantyle, l'état de transition correspondant implique toutefois une paire d'ions séparés par le solvant.

Mots clés : effets de sel, effet isotopique cinétique, retour interne, solvolyse, paires d'ions.

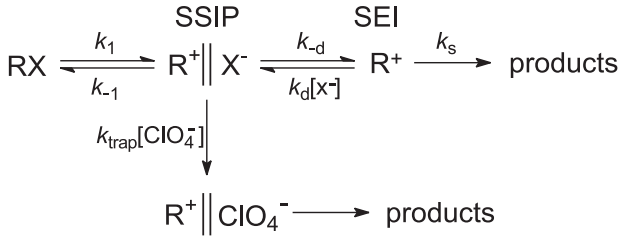
[Traduit par la Rédaction]

Introduction

In 1956, Winstein reported that addition of $LiClO_4$ to the solvolytic reactions of several structurally diverse arylsulfonates resulted in a nonlinear correlation between the rate constant for acetolysis and the ionic strength of the solution (1–4). These observations were rationalized within the mechanism shown in Scheme 1. In this scheme, a simplified version of Winstein's ion-pair mechanism (5–7), two separate carbenium ion intermediates are incorporated: (*i*) the solvent-separated ion pair (SSIP); and (*ii*) the solvent-equilibrated ion (SEI). Furthermore, the observed nonlinearity is a consequence of SSIP trapping by the added perchlorate with the result that "external" ion-pair return is prevented (1, 2).

In 1994, Huang and Bennet reported that in 80% v/v ethanol–water the homoallylic adamantylideneadamantyl tosylate (**1-OTs**) solvolyzed 4×10^5 faster than did 2-adamantyl tosylate (**2-OTs**) at 25 °C (8). This observation led to the conclusion that at the solvolytic transition state π-electron delocalization was occurring into the developing carbenium ion *p*-orbital (8). In a separate study, it was shown that the corresponding halides (**1-Br** and **1-I**) displayed the phenomenon of common-ion rate depression during their solvolyses. Thus, it was inferred that these reactions entail formation of the solvent-equilibrated homoallylic carbenium ion **3**, an intermediate that has a lifetime of $\geq 6.4 \times 10^{-9}$ s in 60:40 v/v EtOH–H_2O at 25 °C (9).

Scheme 1.

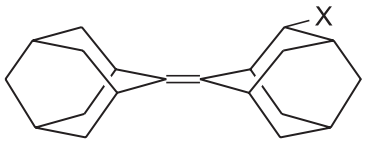


Received 16 January 2004. Published on the NRC Research Press Web site at http://canjchem.nrc.ca on 23 October 2004.

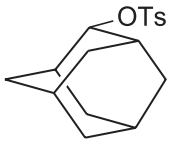
X. Huang and A.J. Bennet.[1] Department of Chemistry, Simon Fraser University, 8888 University Drive, Burnaby, BC V5A 1S6, Canada.

[1]Corresponding author (e-mail: bennet@sfu.ca).

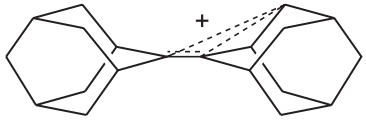
 doi: 10.1139/V04-101 © 2004 NRC Canada



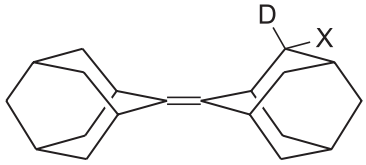
1-X: X = OTs, Br or I



2-OTs



3



4-X: X = OH, OTs or Br

Given that one of the substrates on which Winstein reported observing a special salt effect was cholesteryl tosylate (4), a homoallylic system, it seemed appropriate to investigate the kinetic behavior of adamantylideneadamantyl derivatives upon addition of perchlorate to the solvolytic medium. Thus, this report addresses several questions concerning the solvolysis reactions of adamantylideneadamantyl tosylate, -bromide, and -iodide (**1-OTs**, **1-Br** and **1-I**). For example, are solvent-separated ion pairs (SSIPs) kinetically important intermediates in these dissociative reactions? How does modification of the nucleofuge perturb the transition-state structure in these reactions?

Materials and methods

Flash column chromatography was performed using Merck silica gel 60 (230–400 mesh). All reagents were used as purchased. NMR spectra were recorded on a Bruker AMX-400 NMR spectrometer operating at 400.13 MHz and 100.61 MHz for ^{1}H and ^{13}C, respectively. Chemical shifts (δ) for all compounds are listed in ppm downfield from TMS using residual $CHCl_3$ (δ 7.24 ppm) as the internal reference for ^{1}H spectra and $CDCl_3$ (δ 77.0 ppm) as the internal reference for ^{13}C spectra. Synthesis of adamantylidene adamantyl compounds **1-OTs**, **1-Br**, and **1-I** were accomplished by following the published procedures (8, 9).

(1*R,2*R**)-1-Bromo-2-*deuterio*-4-tricyclo[3.3.1.1^{3,7}]dec-2-ylidene tricyclo[3.3.1.1^{3,7}]-decane (4-Br)**

The deuterated alcohol **4-OH** (10) (0.16 g) was added to a solution of HBr (1.08 g) in CH_2Cl_2 (30 mL), made by the in situ reaction of acetyl bromide (1.0 mL) and methanol (0.54 mL). This solution was stirred at 0 °C for 60 min, followed by the removal of volatile components under reduced pressure. Purification of the residue by flash column chromatography on silica gel with hexane as the eluent gave **4-Br** as a white solid (0.18 g, 90%), mp 121 to 122 °C (lit. value for **1-Br** (8) mp 129 to 130 °C). EI-MS *m*/*z* **4-Br**: 347 (M^+, 10.7), 348 (2.6), 349 (12.0), and 350 (2.5); data for **1-Br**: 346 (M^+, 10.5), 347 (2.7), 348 (10.0), and 349 (2.4). The ^{1}H NMR spectrum for **4-Br** is essentially identical to that of **1-Br** except that the broad singlet for the secondary bromide (δ 4.4) is absent in the spectrum of **4-Br**.

Kinetics

Solvolysis kinetics were monitored as previously described (8, 10).

Results

To investigate whether significant external ion-pair return (Scheme 1) occurs during the solvolysis of **1-OTs**, **1-Br**, and **1-I** rate constants were measured as a function of sodium perchlorate concentration. The measured values are listed in Tables S1 and S2 of the supporting information.[2] Two typical plots of the measured solvolysis reaction rate constant vs. ionic strength data are displayed in Fig. 1.

In contrast to the expected behavior for a normal salt effect (3, 11), the observed rate constants for the solvolyses of **1-Br** and **1-I** in both 60:40 and 80:20 v/v EtOH–H_2O mixtures varies in a nonlinear fashion at low ionic strength.

For reactions that exhibit a special salt effect, the addition of "common ion" can cause a reduction in the importance of the perchlorate ion-containing SSIP ($R^+ \parallel ClO_4^-$), thereby reducing the observed "special salt" effect (12). Therefore, the effect of ionic strength on the rate constant for solvolysis of **1-I** was measured in the presence of the common ion ([NaI] = 0.02 mol/L) and these measured rate constants are catalogued in Table S3.[2] Shown in Fig. 2 is the kinetic data for solvolysis of **1-I** (60:40 v/v, EtOH–H_2O) measured in the presence and absence of the common ion.

Additionally, secondary deuterium kinetic isotope effects (α-SDKIEs: $k_{\mathbf{1\text{-}Br}}/k_{\mathbf{4\text{-}Br}}$) were measured for the solvolysis of the homoallylic bromide in 60:40 and 80:20 v/v EtOH–H_2O at 25 °C. The calculated α-SDKIEs are listed in Table 1. Also, listed in Table 1 are the previously reported α-SDKIEs for the solvolysis reactions of **1-OTs** ($k_{\mathbf{1\text{-}OTs}}/k_{\mathbf{4\text{-}OTs}}$) (10).

Discussion

The curvature seen in the plots of solvolysis reaction rate constant vs. ionic strength data (e.g., Fig. 1) is modest. However, such nonlinearity is still evidence that the addition of the non-nucleophilic ClO_4^- anion to the reaction mixture can

[2] Supplementary data may be purchased from the Depository of Unpublished Data, Document Delivery, CISTI, National Research Council Canada, Ottawa, ON K1A 0S2, Canada (http://www.nrc.ca/cisti/irm/unpub_e.shtml for information on ordering electronically).

© 2004 NRC Canada

Table 1. Observed α-secondary deuterium isotope effects for the solvolysis of **1-Br** and **1-OTs** in ethanol–water mixtures, no added salt at 25 °C.[a,b]

Solvent (EtOH–H_2O)	$10^3 \times k_H$ (s^{-1})	$10^3 \times k_D$ (s^{-1})	$(k_H/k_D)_{\mathbf{1\text{-}Br}}$	$(k_H/k_D)_{\mathbf{1\text{-}OTs}}$
80:20	0.141±0.002	0.127±0.001	1.110±0.018	1.158±0.012
60:40	1.96±0.01	1.71±0.01	1.146±0.009	1.149±0.022

[a]The quoted values are the mean and standard deviation from at least three independent kinetic runs.
[b]The reported values for **1-OTs** are taken from ref. 10.

Fig. 1. Plot of k_{obs} vs. [$NaClO_4$] for the solvolysis of **1-OTs** (○) and **1-Br** (△) in 80% v/v aqueous ethanol at 25 °C. The line through the data points (**1-OTs**) is the best linear fit for all data and the second line is the best linear fit for the **1-Br** data where [$NaClO_4$] ≥ 0.1 mol/L. Error limits are encompassed within the symbol diameter except where shown explicitly.

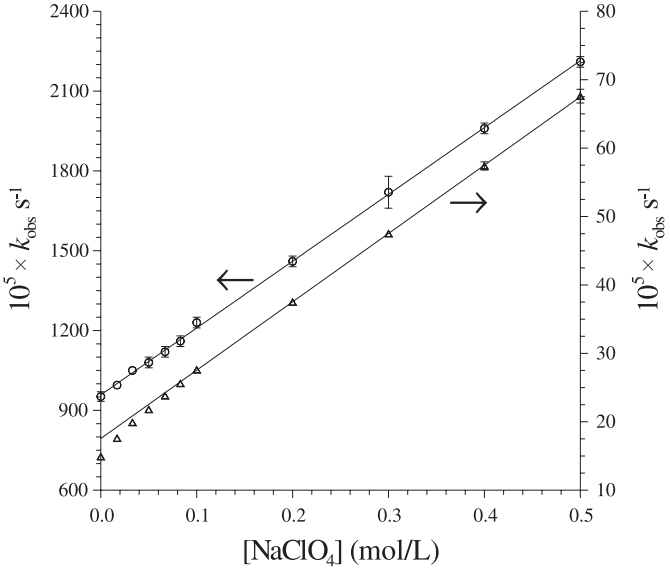
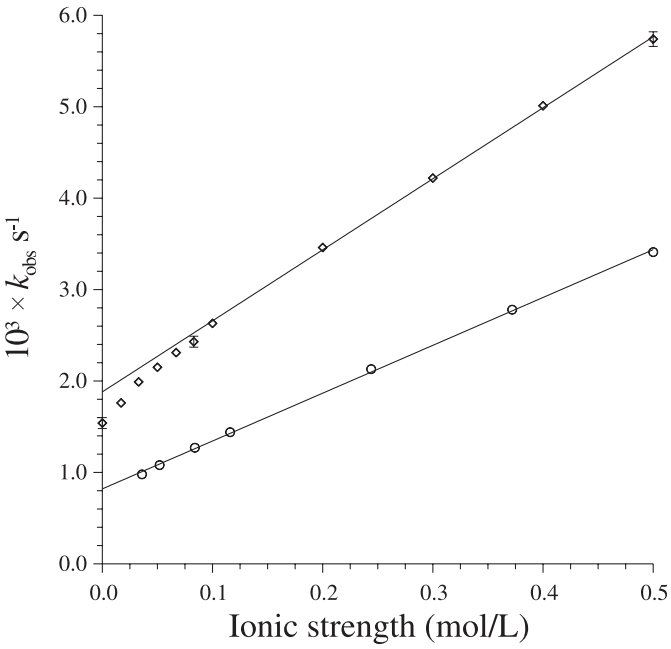


Fig. 2. Plot of k_{obs} vs. ionic strength for the solvolysis of **1-I** in 60% v/v aqueous ethanol at 25 °C. The line through the data points (**1-I**, [NaI] = 0.02 mol/L (○)) is the best linear fit for all data and the second line is the best linear fit for the **1-I** ([NaI] = 0.0 mol/L: (◇)) data where [$NaClO_4$] ≥ 0.1 mol/L. Error limits are encompassed within the symbol diameter except where shown explicitly.

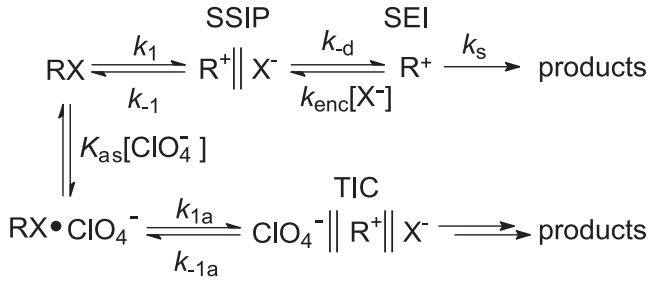


result in a reduction of external ion return (k_{-1}, Scheme 1) from the SSIP ($R^+ \parallel X^-$).

The mechanistic scheme utilized by Winstein and others (Scheme 1) to analyze their observed special salt effects must be modified in the present case. That is, because the current reactions were performed in aqueous solutions it is possible to rule out certain mechanistic pathways based on literature precedent. Specifically, the rate constant for SSIP dissociation to give SEI (Scheme 1, $k_{-d} = 1.6 \times 10^{10}$ s^{-1} (13) is much faster than the maximal rate for the second-order interception of $R^+ \parallel X^-$ by ClO_4^- (Scheme 1, $k_{trap}[ClO_4^-] \leq 5 \times 10^8$ s^{-1}, when $[ClO_4^-] = 0.1$ mol/L). It can therefore be concluded that perchlorate is incapable of trapping the SSIP as depicted in Scheme 1. As a consequence, the modified reaction mechanism for aqueous solvolyses includes a "preassociation" pathway (Scheme 2).

The rate and equilibrium constants shown in Scheme 2 are: (*a*) ionization of the starting material to the SSIP (k_1); (*b*) reformation of starting material by collapse of the SSIP intermediate (k_{-1}); (*c*) dissociation of the SSIP to form the SEI (k_{-d}); (*d*) capture of the SEI by solvent (k_s); (*e*) encounter of the SEI with the common ion to regenerate the $R^+ \parallel X^-$ SSIP (k_{enc}); (*f*) formation of a preassociation complex between R–X and ClO_4^- (K_{as}); (*g*) ionization of the preassociation complex (k_{1a}); and (*h*) capture of the triple ion complex (TIC) to give, after several steps, the reaction products.

Scheme 2.



The degree of curvature apparent in Figs. 1 and 2 is much less than that reported in many other studies on special salt effects, such as those of Allen et al. (14, 15). Therefore, in the interpretation of the present data, a simple first-order analysis was employed using eq. [1].

$$[1] \qquad k_{obs} = k^0(1 + b[salt])$$

© 2004 NRC Canada

In eq. [1], k^0 is the rate constant extrapolated from the linear portion of the solvolytic rate constant data ($I \geq 0.1$, $NaClO_4$) to zero ionic strength, and b is the magnitude for the normal salt effect.

In mainly aqueous solutions, the value of K_{as} should be <<1.0 mol/L^{-1} (16, 17), therefore, the curvature in the rate vs. ionic strength plots is not caused by complete formation of the preassociation complex. On the contrary, the observed nonlinearity is consistent with the degree of reversion back to starting material being greater when the solvolyses are performed at low ionic strength (reaction proceeds via SSIPs) than at high ionic strength (where TICs are implicated).

In addition, when the solvolysis of **1-I** is performed in the presence of added common ion ([I^-] = 0.02 mol/L) the reaction rate is about 50% of that in the absence of iodide ion (Fig. 2, Tables S1 and S3[2]). While the corresponding figure at high ionic strength is around 60% (μ = 0.5 mol/L). In other words, common-ion rate depression is less prevalent at high ionic strength (TIC pathway) than at low ionic strength (SSIP pathway).

Of note, compound **1-OTs** shows no detectable special salt effect (Fig. 1) and therefore, formation of the SSIP is irreversible. In contrast, the non-zero special salt effect observed for both **1-Br** and **1-I** (Figs. 1 and 2) requires that in the absence of salt no single step is entirely rate-limiting and that the virtual transition state for solvolysis incorporates both the formation and the breakdown of the SSIP.

Secondary deuterium kinetic isotope effects

For many years, the magnitude of an observed α-secondary deuterium kinetic isotope effect (α-SDKIE) in solvolysis reactions has been used as a transition-state structure probe (18). For instance, in $D_N + A_N$ reactions (19), the predominant factor for the generation of an observed α-SDKIE is the weakening of the out-of-plane C-H bending vibration as the hybridization of the reacting center changes from sp^3 to an sp^2-like transition state (18). The predicted maximal values for α-SDKIEs at 25 °C for solvolysis of secondary alkyl tosylates and bromides are approximately 1.225 and 1.125, respectively (20, 21). Indeed, two separate research groups reported α-SDKIEs for solvolyses of two different 2-adamantyl sulfonates at 25 °C that are indistinguishable from the predicted maximal value (22, 23). In contrast, the documented α-SDKIE values for the aqueous ethanolysis of **1-OTs** fall in the range of 1.14–1.17 at 25 °C (10). Mechanistically, the observed α-SDKIEs for the reactions of **1-OTs** are indicative of an earlier solvolytic transition state, one which involves a smaller decrease in the C-H bending force constant at the reaction centre, than at the corresponding TS for the solvolysis of 2-adamantyl tosylate (**2-OTs**). In contrast, the observed α-SDKIEs for solvolysis of **1-Br** (Table 1) are identical to the predicted maximal value for reaction of a secondary alkyl bromide. This indicates that the rate-limiting TS for the S_N1 ($D_N + A_N$) solvolyses of **1-Br** is "later" than that for the reactions of **1-OTs**. An interpretation that is in agreement with the conclusions reached above concerning the observed special salt effects. Thus, the rate-limiting TS for reaction of **1-OTs** occurs prior to dissociation of the SSIP (Fig. 1 displays a strict linear correlation of rate constant and ionic strength), but the corresponding solvolysis of **1-Br** proceeds via a virtual TS that incorporates components of SSIP formation and dissociation (vide supra).

Differences between 1-OTs and cholesteryl tosylate

As a final point, a comment is warranted on the different salt effects observed during the solvolyses of **1-OTs** and cholesteryl tosylate (4). In their salt effect study on cholesteryl tosylate solvolysis, Winstein and Clippinger (4) used the poorly ionizing solvent acetic acid (Y_{OTs} = –0.61 (24)), but in the current study the solvents employed are more polar (e.g., Y_{OTs} (80% v/v EtOH–H_2O) = 0.00 (24)). Therefore, it is likely that in the less polar solvent the associated slower rates for ion-pair dissociation give rise to the observed special salt effect phenomenon (4).

Acknowledgments

The authors are grateful to the Natural Sciences and Engineering Research Council of Canada (NSERC) for financial support.

References

1. A.H. Fainberg and S. Winstein. J. Am. Chem. Soc. **78**, 2767 (1956).
2. A.H. Fainberg, G.C. Robinson, and S. Winstein. J. Am. Chem. Soc. **78**, 2777 (1956).
3. A.H. Fainberg and S. Winstein. J. Am. Chem. Soc. **78**, 2780 (1956).
4. S. Winstein and E. Clippinger. J. Am Chem. Soc. **78**, 2784 (1956).
5. S. Winstein, B. Appel, R. Baker, and A. Diaz. Chem. Soc. Spec. Publ. **19**, 109 (1965).
6. D.J. Raber, J.M. Harris, and P.v.R. Schleyer. Ions and ion pairs in organic reactions. Vol. 2. *Edited by* M. Szwarc. Wiley-Interscience, New York. 1972.
7. J.M. Harris. Prog. Phys. Org. Chem. **11**, 89 (1974).
8. X. Huang and A.J. Bennet. J. Chem. Soc. Perkin Trans. 2, 1279 (1994).
9. X. Huang, K.S.E. Tanaka, and A.J. Bennet. J. Am. Chem. Soc. **120**, 1405 (1998).
10. X. Huang and A.J. Bennet. J. Chem. Soc. Perkin Trans. 2, 1027 (1997).
11. A.H. Fainberg and S. Winstein. J. Am. Chem. Soc. **78**, 2763 (1956).
12. S. Winstein, P.E.J. Klinedinst, and G.C. Robinson. J. Am. Chem. Soc. **83**, 885 (1961).
13. J.P. Richard and W.P. Jencks. J. Am. Chem. Soc. **106**, 1373 (1984).
14. A.T. Allen, T.T. Tidwell, and O.S. Tee. J. Am. Chem. Soc. **115**, 10 091 (1993).
15. A.D. Allen, M. Fujio, O.S. Tee, T.T. Tidwell, Y. Tsuji, Y. Tsuno, and K.-I. Yatsugi. J. Am. Chem. Soc. **117**, 8974 (1995).
16. C.W. Davies. Ion association. Butterworths, Washington, D.C. 1962. pp. 162–167.
17. J.P. Richard. Tetrahedron, **51**, 1535 (1995).

© 2004 NRC Canada

18. L.C.S. Melander and W.H.J. Saunders. Reaction rates of isotopic molecules. Wiley, New York. 1980. pp. 170–174.
19. R. Guthrie and W.P. Jencks. Acc. Chem. Res. **22**, 343 (1989).
20. V.J. Shiner, Jr., M.W. Rapp, E.A. Halevi, and M. Wolfsberg. J. Am. Chem. Soc. **90**, 7171 (1968).
21. V.J. Shiner, Jr. and W. Dowd. J. Am. Chem. Soc. **93**, 1029 (1971).
22. J.M. Harris, R.E. Hall, and P.v.R. Schleyer. J. Am. Chem. Soc. **93**, 2551 (1971).
23. V.J. Shiner, Jr. and R.D. Fisher. J. Am. Chem. Soc. **93**, 2553 (1971).
24. T.W. Bentley and G.E. Carter. J. Org. Chem. **48**, 579 (1983).

© 2004 NRC Canada

Growth and morphological evolution of hexapod-shaped cuprous oxide microcrystals at room temperature

Xu Zhang, Yi Xie, Fen Xu, Di Xu, and Huarong Liu

Abstract: Growth and morphological evolution of hexapod-shaped Cu_2O microcrystals is carefully studied via a γ-irradiation reduction route at room temperature and under ambient pressure. The products are examined by means of XRD patterns and FE-SEM images. The as-obtained hexapod-shaped Cu_2O microcrystal is composed of six legs, whose adjacent legs are perpendicular to each other and each leg is composed of two perpendicular cross blades. A simple reaction system, excluding the influence of surfactant and thermal disturbance, would favor revelation of the inherent growth habit of Cu_2O microcrystals under relatively mild experimental conditions. Furthermore, the effects of several factors on the final product and morphology are investigated.

Key words: hexapod-shaped, γ-irradiation, cuprous oxide, morphological evolution.

Résumé : Faisant appel à une réduction de l'irradiation γ, à la température et à la pression ambiante, on a étudié avec soin la croissance et l'évolution morphologique de microcristaux de Cu_2O en forme d'hexapode. Les produits ont été examinés par le biais de patrons XRD et d'images FE-SEM. Le microcristal de Cu_2O en forme d'hexapode tel qu'il est obtenu est formé de six membres dans lesquels les membres adjacents sont perpendiculaires les uns aux autres alors que chaque membre est composé de deux lames qui leur sont perpendiculaires. Un système réactionnel simple, qui exclurait l'influence de l'agent de surface et les perturbations thermiques, favoriserait la façon de croissance inhérente des microcristaux de Cu_2O dans des conditions expérimentales relativement douces. On a étudié de plus les effets de plusieurs facteurs sur la nature et la morphologie du produit final.

Mots clés : en forme d'hexapode, irradiation γ, oxyde cuivreux, évolution morphologique.

Introduction

Among the numerous transition metal semiconductor oxides, cuprous oxide is of intense interest and has been investigated extensively for its distinctive properties. Firstly, cuprous oxide (Cu_2O) is an important metal-oxide *p*-type semiconductor (1–3) with a direct band gap of 2 eV, which makes it a promising material for the conversion of solar energy into electrical or chemical energy (4, 5). Moreover, Cu_2O has also been widely exploited for use in coloring of glass, in catalysts (6, 7) and antifouling coatings (8), or for killing snails to prevent schistosomiasis. Recently, it has also been found that Cu_2O submicrospheres can be used as the negative electrode material for lithium ion batteries (9).

Received 16 November 2003. Published on the NRC Research Press Web site at http://canjchem.nrc.ca on 23 October 2004.

X. Zhang, Y. Xie,[1] F. Xu, and D. Xu. Structure Research Laboratory and Department of Chemistry, University of Science and Technology of China, Hefei, Anhui 230026, P. R. China.
H. Liu. Department of Polymer Science and Engineering, University of Science and Technology of China, Hefei, Anhui 230026, P. R. China.

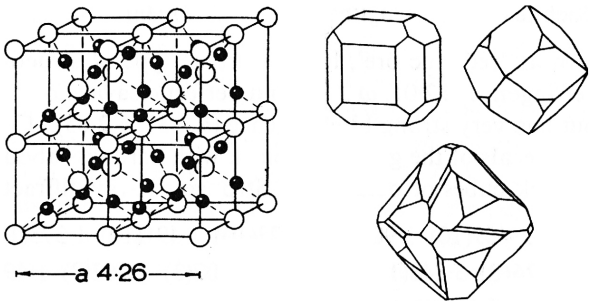
[1]Corresponding author (e-mail: yxielab@ustc.edu.cn).

Cuprous oxide (Cu_2O) crystallizes in the cuprite structure. It belongs to an isometric system and its space symmetry is expressed as *Pn*3*m* (Fig. 1). The coordination of the copper atoms is twice that of the oxygen atoms in the unit cell. The structure can be described as a cubic close packing of copper atoms, some of the tetrahedral sites of which are situated by oxygen atoms (10, 11). Cuprous oxide microcrystals are usually octahedral, less often dodecahedral or cubic, occasionally elongated along the <001> directions into capillary fibers.

It is well-known that some chemical and physics properties of materials are dependent, to a large extent, on their shapes and textures. Thus, several methods have been developed to prepare Cu_2O microcrystals with different shapes, including electrodeposition (12, 13), reduction of metal salts in solution (14–20), and vacuum evaporation (21) most of which employed either template or surfactant or thermal disturbance and the products belong to the final growth stage. Therefore, it is difficult to trace the growth history of the product and further reveal the inherent growth habit of Cu_2O for lack of the detailed information on the evolution sequence from the initial nuclei to the intermediate geometries to the final product. It is meaningful to investigate the morphological evolution of Cu_2O, especially the multipod-shaped microcrystals, which can provide important information to the fields of crystal growth, design, and morphology-

 doi: 10.1139/V04-108 © 2004 NRC Canada

Fig. 1. Structure and microcrystal form of cuprous oxide.



controlled synthesis of Cu_2O, and further other inorganic building blocks. Therefore, it is necessary to find another simple, relatively mild approach to investigate the whole growth process of multipod-shaped Cu_2O.

In the latest decades, the γ-irradiation technique has been developed as a novel method to prepare nanoscale materials, including metal, metal oxides, chalcogenides, and inorganic–polymer nanocomposite (22–27). It is well-known that γ-irradiation can induce solvated electrons (e^-_{aq}) at room temperature and under ambient pressure, which are totally clean reductive agents from the green chemistry point of view because it can avoid the by-products coming from chemical reducing agents and the pollution to the environment. Moreover, it is technologically important for solvated electrons to make metal ions reduce gradually to lower valence ions (28). It is the virtue of slow reduction that gives us an inspiration that γ-irradiation may be an ideal method to trace the morphological evolution of multipod-shaped Cu_2O in the whole growth process.

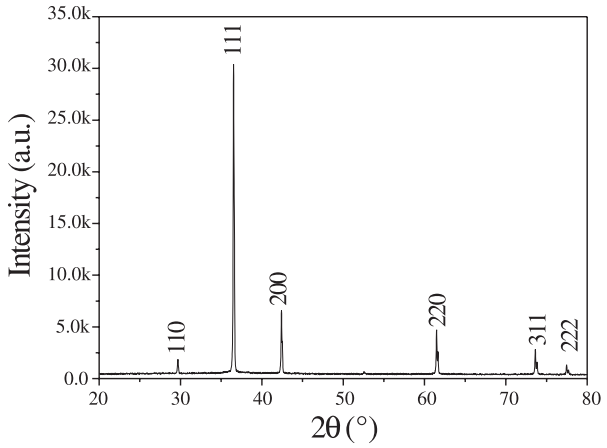
In this paper, we firstly apply the relatively mild γ-irradiation reduction route to prepare pure cubic phase Cu_2O microcrystals with special morphology at room temperature and under ambient pressure. The whole growth process of Cu_2O microcrystals has been carefully studied through a series of detailed pictures taken at different radiation times. Our experimental results are different from that of a previous study (29), which may be attributed to the difference of the detailed experimental parameters employed.

Experimental section

All reagents were of analytical grade and were purchased from Shanghai Chemical Co. Ltd. All of the reactions were conducted at room temperature and under ambient pressure. In a typical procedure, 0.50 g of cupric acetate ($Cu(CH_3COO)_2{\cdot}H_2O$) was dissolved in 50 mL distilled water. Isopropanol (10 mL) was added into the above solution as a scavenger for hydroxyl radicals. After deaeration by bubbling with pure nitrogen for 30 min to remove oxygen, the solution was irradiated in the field of 2.59×10^{15} Bq of ^{60}Co γ-ray source for 8 h at room temperature. After γ-irradiation, the precipitate was separated from solution, washed with distilled water and absolute ethanol several times, then dried in vacuum at 25 °C for 5 h. In the controlled experiments, different radiation times and different precursors were applied.

The purity of the products was determined by X-ray powder diffraction (XRD) with a Philips X' Pert PRO SUPER

Fig. 2. Typical XRD pattern of the as-prepared product.



X-ray diffractometer with Cu Kα radiation (λ = 1.541 8 Å). The scan rate of $0.06°{\cdot}s^{-1}$ was applied to record the patterns in the 2θ range of 20°–80°. Field emission scanning electron microscopy (FE-SEM) was performed on a JEOL JSM-6700F scanning electron microanalyzer.

Results and discussion

Figure 2 shows the typical XRD pattern of the as-prepared product. All of the reflections in Fig. 2 can be indexed to a pure cubic phase of cuprous oxide with the lattice constant a = 4.264 5 Å, compatible with the literature value of a = 4.269 6 Å (JCPDS file No. 05-0667). No other peaks of impurities were detected.

The morphology of the Cu_2O products was observed by FE-SEM. Figure 3*a* shows that a large number of hexapod-shaped microcrystals are obtained and Fig. 3*b* presents a high-magnification image of a single microcrystal, in which the average length of each leg is about 15 μm. Observed along a leg growth direction (as shown in the inset of Fig. 3*b*), is that each leg is composed of two perpendicular-cross blades and some stacking faults were also observed, which may be attributed to the heterogeneous crystal growth under static conditions during the growth process.

In the present approach, γ-irradiation is a prerequisite for the synthesis of hexpod-shaped Cu_2O microcrystals and the observation of morphological evolution at room temperature. If the reaction is conducted with the same reaction conditions without γ-irradiation, no solid phase is obtained, and no hexapod-shaped Cu_2O particles were found, which was also confirmed by a previous study (18).

In addition, it was also found that the in situ formed acetic acid and acetate ion buffer pair had a crucial influence on the final product in this approach. The formation of Cu_2O involves the reduction reactions of cupric ions with solvated electrons when the solution is γ-irradiated, which may be easily understood as follows:

$$[1] \quad H_2O \xrightarrow{\text{irradiation}} e^-_{aq}, H_3O^+, H_2, H_2O_2, \cdot H, \cdot OH$$

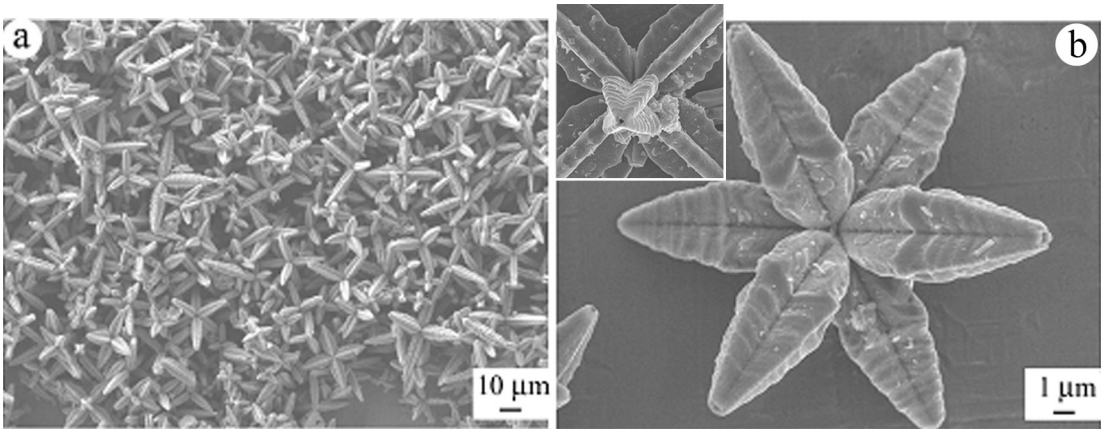
$$[2] \quad e^-_{aq} + Cu^{2+} \rightarrow Cu^+$$

$$[3] \quad 2Cu^+ \rightarrow Cu^0 + Cu^{2+}$$

$$[4] \quad 2Cu^+ + 2OH^- \rightarrow 2CuOH \rightarrow Cu_2O + H_2O$$

© 2004 NRC Canada

Fig. 3. FE-SEM images of hexapod-shaped Cu_2O microcrystals: (*a*) a panorama image, (*b*) showing a single microcrystal and the inset is the view of a leg along its growth direction.



As can be seen from eq. [1], hydrogen ion can be produced gradually in the process of the irradiation, and the acidity of the solution increases with the progress of the rxn. [1]. The formed oxidative hydroxyl radicals (·OH) have been scavenged by isopropanol. Pure Cu_2O can only be obtained in the pH range of 4.0–5.6 as is observed experimentally. Therefore, cupric acetate is selected to be an effective reagent because a buffer system can be in situ formed by the cooperation of acetate ion (CH_3COO^-) and the hydrogen ion (H_3O^+), which can keep the pH value of the reaction system in the range of 4.0 ~ 5.6. Moreover, the appropriate pH value was confirmed by the pH meter: the pH value of the solution was ~5.6 before the reaction and the pH value decreased to ~4.0 after the reaction finished. Under this pH value range, the reduction and dismutation (rxn. [3]) of cuprous ions are completely suppressed. In addition, the unstable cuprous hydroxide (CuOH) can also decompose rapidly to cuprous oxide, which can guarantee the formation of a large quantity of pure Cu_2O. In the controlled experiments, if $Cu(CH_3COOH)_2$ was replaced by $CuSO_4$ or $CuCl_2$ in the reactions, the product was the mixture of copper and cuprous oxide, which should be attributed to the absence of the in situ formed buffer pair. Because the pH value cannot be kept in the range of 4.0 ~ 5.6 under such conditions, the reduction and dismutation of cuprous ions (rxn. [3]) predominates in the reaction system, while the formation and the decomposition of cuprous hydroxide (CuOH) (rxn. [4]) is subsidiary.

To study the morphological evolution and further know the inherent growth habit of Cu_2O at room temperature, different radiation times were used in the experimental process by keeping the other experimental parameters constant. A set of FE-SEM images (shown in Fig. 4) taken at different radiation times clearly illustrates the nucleation and growth processes of the hexapod-shaped microcrystals. In our experimental process, the Cu_2O octahedra are found as the initial nuclei, while the legs grow from the six corners of the octahedral nuclei. Moreover, it was found that the remarkable transformation of morphology occurs when the radiation time was in the range of 2 ~ 4 h. When the reaction system was irradiated for 2 h, a large quantity of Cu_2O octahedral first-order structures formed initially. As a cubic structure, Cu_2O has a growth habit of an octahedral morphology enclosed by lowest-energy (111) facets, which can be used as the core for the following growth (Fig. 4*a*). After the Cu_2O cores are formed, new reactants are continuously arriving at the site. When the radiation time increases from 2.5 to 3 to 3.5 h, the emerged octahedral first-order structures nucleate secondary microcrystals and begin to develop their legs on their six corners along six directions according to the symmetry of the Cu_2O octahedron (Figs. 4*b*–*4d*), then eight intracrystal holes on the centers of (111) planes are generated. After irradiation for 4 h, secondary octahedral structures were formed, resulting in a face-centered close packing of crystal octahedra where the interconnectivity is generated by edge sharing (shown in Fig. 4*e*). Because the (001) face is dipolar and unstable (18), such anisotropic growth along the energetically favorable <001> direction progressed gradually with the increase of the radiation time from 5 to 6 h (Figs. 4*f* and 4*g*) and meanwhile, four edges also elongated along the <001> direction and obtained two perpendicular-cross blades in one leg. Finally, the hexapod-shaped Cu_2O microcrystals were formed after the reaction system was irradiated for 8 h (Fig. 4*h*). In the growth process, some symmetrical stacking faults occured at the surface of each blade, which may be attributed to the existence of the concentration gradient of some reactants (i. e. Cu^+ and OH^-) in the static growth process. Since the nucleus takes an exact octahedron form, the inter-leg angles are kept at precise angles as the legs continued to grow. The growth scheme of Cu_2O particles is summarized in Fig. 5. The angle between the adjacent two legs of the final hexapod-shaped microcrystal is 90°, which corresponds to the angle between the body diagonals of the initial octahedron.

Conclusion

In summary, hexapod-shaped cuprous oxide microcrystals were prepared via a γ-irradiation reduction route at relatively mild conditions. As a relatively mild reduction process, the γ-irradiation route not only makes the as-grown Cu_2O microcrystal fully exhibit its anisotropism at room temperature, but also provides us a simple means to study the morphological evolution of Cu_2O microcrystals. The phase and morphology of the as-prepared products are investigated by XRD and FE-SEM, respectively. This work shows that complex structures and morphologies can be derived from the

© 2004 NRC Canada

Fig. 4. Illustration of the nucleation and growth process of the hexapod-shaped Cu_2O microcrystals at different radiation times: (*a*) 2 h, the primary octahedral microcrystals; (*b*), (*c*), (*d*) the early stages of leg growth that had a tendency to develop legs on their six corners along the <001> direction with the increase of the radiation time from 2.5 to 3 to 3.5 h; (*e*) 4 h, the secondary octahedral microcrystals; (*f*), (*g*) the formation of two perpendicular-cross blades with the increase of the radiation time from 5 to 6 h; and (*h*) 8 h, a hexapod-shaped microcrystal.

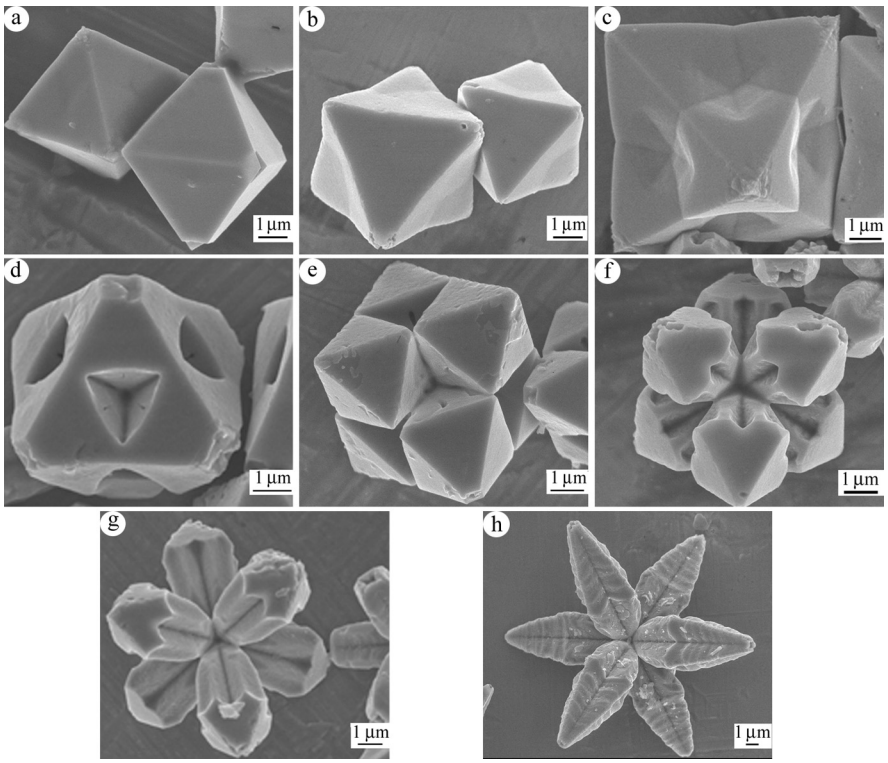
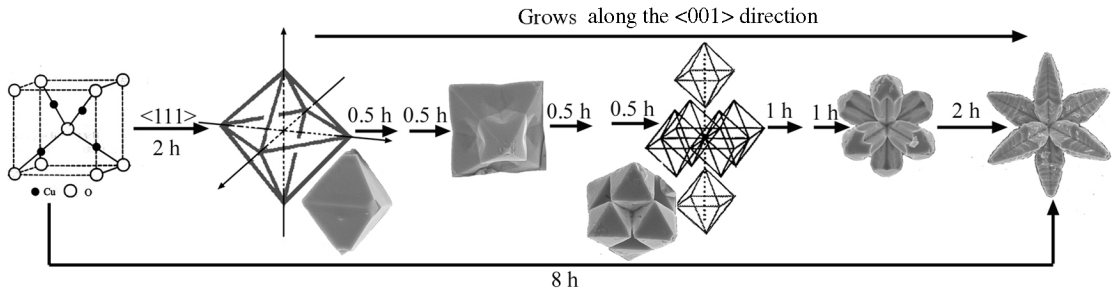


Fig. 5. Schematic diagram for the growth process of the hexapod-shaped Cu_2O microcrystal.



fundamental microscopic building units, and the final morphologies are correlated with the structure and shape of the basic microcrystal. This method may be extended to study the growth process of some special materials and prepare different materials with interesting morphology for special practical applications.

Acknowledgments

Financial support from the Chinese National Foundation of Natural Sciences and the Chinese Ministry of Education is gratefully acknowledged.

References

1. I. Grozdanov. Mater. Lett. **19**, 281 (1994).
2. M.Y. Shen, T. Yokouchi, S. Koyama, and T. Goto. Phys. Rev. B, **56**, 13 066 (1997).
3. A.E. Rakhshani. J. Appl. Phys. **69**, 2290 (1991).
4. R.N. Briskman. Sol. Energ. Mat. Sol. Cells, **27**, 361 (1992).
5. M. Smith, V. Gotovac, L. Aljinovic, and M. Luciclavcevic. Surf. Sci. **335**, 171 (1995).
6. S. Ikeda, T. Takata, T. Kondo, G. Hitoki, M. Hara, J.N. Kondo, K. Domen, H. Hosono, H. Kawazoe, and A. Tanaka. Chem. Commun. 2185 (1998).
7. P.E. de Jongh, D. Vanmaekelbergh, and J.J. Kelly. Chem. Commun. 1069 (1999).
8. V.J.D. Rascio. Corros. Rev. **18**, 133 (2000).
9. P. Poizot, S. Laruelle, S. Grugeon, L. Dupont, and J.M. Tarascon. Nature (London), **407**, 496 (2000).
10. I. Kostov. *In* Mineralogy. *Edited by* P.G. Embrey and J. Phemister. Oliver and Boyd, Edinburgh and London. 1968. p. 257.

© 2004 NRC Canada

11. L.G. Berry and B. Mason. *In* Mineralogy: Concepts, descriptions, determinations. *Edited by* J. Gilluly and A.O. Woodford. W.H. Freeman and Company, San Francisco and London. 1959. p. 349.
12. J.K. Barton, A.A. Vertegel, E.W. Bohannan, and J.A. Switzer. Chem. Mater. **13**, 952 (2001).
13. L.M. Huang, H.T. Wang, Z.B. Wang, A.P. Mitra, D. Zhao, and Y.H. Yan. Chem. Mater. **14**, 876 (2002).
14. S.J. Chen, X.T. Chen, Z.L. Xue, L.H. Li, and X.Z. You. J. Cryst. Growth, **246**, 169 (2002).
15. L.F. Gou and C.J. Murphy. Nano Lett. **3**, 231 (2003).
16. Y.J. Dong, Y.D. Li, C. Wang, A.L. Cui, and Z.X. Deng. J. Colloid Interface Sci. **243**, 85 (2001).
17. P. Mcfadyen and E. Matijević. J. Colloid Interface Sci. **44**, 95 (1973).
18. Z.Z. Chen, E.W. Shi, Y.Q. Zheng, W.J. Li, B. Xiao, and J.Y. Zhuang. J. Cryst. Growth, **249**, 294 (2003).
19. Y. Chang and H.C. Zeng. Cryst. Growth Design, **4**, 273 (2004).
20. X. Zhang, Y. Xie, F. Xu, X.H. Liu, and D. Xu. Inorg. Chem. Commun. **6**, 1390 (2003).
21. H. Yanagimoto, K. Akamatsu, K. Goto, and S. Deki. Eur. Phys. J. D, **16**, 313 (2001).
22. Y.J. Zhu, Y.T. Qian, M.W. Zhang, Z.Y. Chen, M. Chen, and G.E. Zhou. J. Mater. Sci. Lett. **13**, 1243 (1994).
23. Y.P. Liu, Y.T. Qian, Y.H. Zhang, M.W. Zhang, Z.Y. Chen, L. Yang, C.S. Wang, and Z.W. Chen. Mater. Lett. **28**, 357 (1996).
24. Z.P. Qiao, Y. Xie, J.G. Xu, Y.J. Zhu, and Y.T. Qian. J. Colloid Interface Sci. **214**, 459 (1999).
25. F. Wang, Z.C. Zhang, and Z.Q. Chang. Mater. Lett. **55**, 27 (2002).
26. Y. Xie, Z.P. Qiao, M. Chen, X.M. Liu, and Y.T. Qian. Adv. Mater. **11**, 1512 (1999).
27. F. Xu, X. Zhang, J. Lu, W. Xi, J. Hong, and Y. Xie. Can. J. Chem. **81**, 381(2003).
28. J.L. Marignier, J. Belloni, M.O. Delcourt, and J.P. Chevalier. Nature (London), **317**, 344 (1985).
29. Y.J. Zhu, Y.T. Qian, M.W. Zhang, Z.Y. Chen, and D.F. Xu. Mater. Res. Bull. **29**, 377 (1994).

© 2004 NRC Canada

Synthesis and structural characterization of *m*-terphenyl Schiff base ligands and their aluminum complexes

Diane A. Dickie, Hanifa Jalali, Rahul G. Samant, Michael C. Jennings, and Jason A.C. Clyburne

Abstract: 2,4,6-Triphenylbenzaldehyde **1** undergoes a condensation reaction with 2-aminophenol to give *N*-(2′,4′,6′-triphenylbenzylidene)-2-iminophenol (TPIP) **2**. The imine **2** can be reduced with $NaBH_4$ in ethanol to form *N*-(2′,4′,6′-triphenylbenzyl)-2-aminophenol (TPAP) **3**. Addition of trimethylaluminum to **2** or **3** results in the formation of the complexes TPIP-$AlMe_2$·$AlMe_3$ (**4**) or TPAP-$AlMe_2$ (**5**). Compounds **2**, **3**, and **4** have been crystallographically characterized.

Key words: N,O ligands, aluminum, *m*-terphenyl, Schiff bases, X-ray crystallography.

Résumé : Le 2,4,6-triphénylbenzaldéhyde **1** subit une réaction de condensation avec le 2-aminophénol qui conduit à la formation du *N*-(2′,4′,6′-triphénylbenzylidène)-2-iminophénol (TPIP, **2**). L'imine **2** peut être réduite à l'aide de $NaBH_4$, dans l'éthanol, pour conduire à la formation du *N*-(2′,4′,6′-triphénylbenzyl)-2-aminophénol (TPAP, **3**). L'addition de triméthylaluminium aux composés **2** ou **3** conduit à la formation de complexes TPIP-$AlMe_2$·$AlMe_3$ (**4**) ou TPAP-$AlMe_2$ (**5**). Les composés **2**, **3** et **4** ont été caractérisés par cristallographie par diffraction des rayons X.

Mots clés : ligands N,O, aluminium, *m*-terphényle, bases de Schiff, cristallographie par diffraction des rayons X.

[Traduit par la Rédaction]

Introduction

The chemistry of *m*-terphenyl ligands is a rapidly developing field of research (1, 2). These molecules feature a central phenyl ring with two meta-aryl substituents that twist out of the plane of the central ring to form a bowl-shaped pocket into which numerous metals or functional groups can be placed (Fig. 1). The steric demands of the ligand can be tuned by varying the substituents of the aryl groups. Synthetically, the steric demands of *m*-terphenyl ligands have been used to stabilize unusual coordination environments and multiple bonds between heavy main group elements (3–6).

Organoaluminum compounds are widely used as catalysts or co-catalysts in numerous polymerization reactions (7–10). When developing a new homogeneous catalyst, it is important to have the ability to control the coordination environment around the metal centre (11). *m*-Terphenyl ligands, because of their ability to protect the space around the metal centre, have the potential to be useful in the field of catalysis. We have previously used amidine-substituted *m*-terphenyl ligands for the preparation of robust aluminum complexes (12, 13) and related compounds have been used as olefin polymerization catalysts (14). As a continuation of our studies on *m*-terphenyl substituted compounds, we decided to incorporate other catalytically active functional groups into the *m*-terphenyl pocket. An ideal candidate for the pocket appeared to be a Schiff base. We chose phenyl as the aryl substituent because it is less bulky than other substituted aryls, and it is also affordably and reliably synthesized.

Multidentate ligands such as Schiff bases, which contain both an imino (C=N) and a phenolic (OH) functional group, are potentially useful monoanionic ligands. While they can exhibit two different structural isomers (Fig. 2), the isomer featuring a three-carbon bridge (**A**) between the heteroatoms is much more common, with only a few published examples of main group Schiff base complexes containing a bridge of only two carbons (**B**) (15–18). Schiff bases are useful for varying the coordination number of the metal centre as the heteroatoms can bind in a monodentate fashion, chelate the metal, or bridge multiple metal centres (Fig. 3) (19). The tetradentate Salen family of ligands are perhaps the best known Schiff bases, and the coordination chemistry of main group elements with this class and the saturated Salan-type ligands has been extensively reviewed (20, 21).

In an attempt to incorporate Schiff bases onto an *m*-terphenyl ligand, we have prepared and structurally charac-

Received 3 September 2003. Published on the NRC Research Press Web site at http://canjchem.nrc.ca on 23 October 2004.

D.A. Dickie, H. Jalali, R.G. Samant, and J.A.C. Clyburne.[1] Department of Chemistry, Simon Fraser University, 8888 University Dr., Burnaby BC V5A 1S6, Canada.
M.C. Jennings.[2] Department of Chemistry, University of Western Ontario, 1151 Richmond Street, London ON N6A 5B7, Canada.

[1]Corresponding author (e-mail: clyburne@sfu.ca).
[2]Corresponding author (crystallography) (e-mail: mjenning@uwo.ca).

 doi: 10.1139/V04-110 © 2004 NRC Canada

Scheme 1. Synthesis of **1** and **2**.

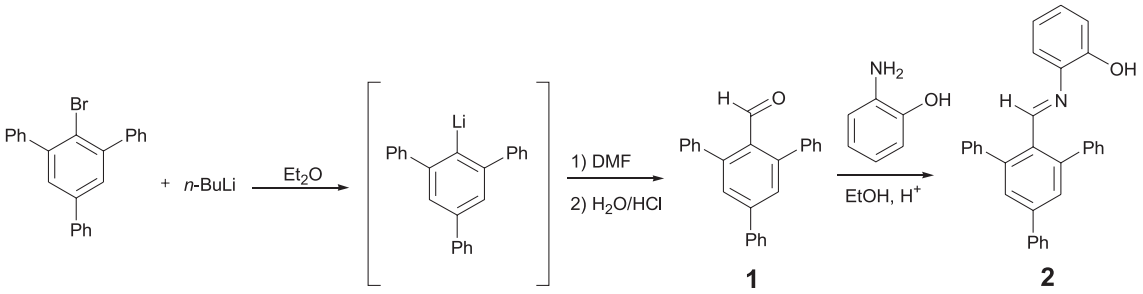


Fig. 1. Space-filling model of a *m*-terphenyl, 1,3-diphenylbenzene. Note the bowl-shaped cavity formed by the flanking rings. For clarity, only the hydrogen in the *m*-terphenyl pocket is shown.

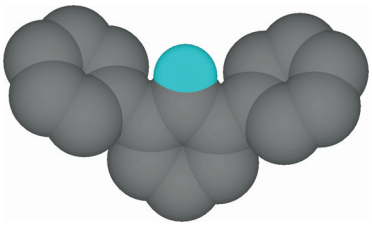
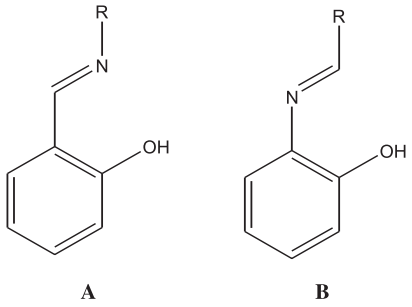


Fig. 2. Structural isomers of a Schiff base.



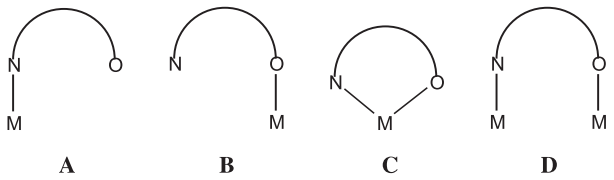
terized two ligands as well as a complex with aluminum. These molecules are related to bulky Schiff base ligands and complexes reported by Chisholm et al. (22), Gibson and co-workers (23), and Grubbs and co-workers (24).

Results and discussion

2,4,6-Triphenylbenzaldehyde **1** is readily synthesized on a large scale with good yield (80%) according to a variation of literature procedures (25) (Scheme 1). The white crystalline product was characterized by NMR spectroscopy. The aldehyde *H* resonance is observed at 10.0 ppm in the ^{1}H NMR spectrum. In the ^{13}C NMR, the aldehyde carbon signal appears at 193 ppm. Further confirmation of the assigned structure was provided by IR spectroscopy (ν C=O 1698 cm^{-1}; ν C-H 2747 cm^{-1}).

Aldehyde **1** was treated with 2-aminophenol in ethanol solution to form *N*-(2′,4′,6′-triphenylbenzylidene)-2-iminophenol (TPIP) **2** (Scheme 1). The product was isolated in high yield (>90%) as a yellow crystalline compound. Characterization of **2** was achieved by ^{1}H and ^{13}C NMR spectroscopy. The imine functionality was indicated by the peak at 8.59 ppm in the ^{1}H NMR spectrum as well as by the C=N stretch at

Fig. 3. Schiff base coordination patterns.



1625 cm^{-1} in the IR spectrum. These values are consistent with those reported by Yamamoto and co-workers (26) for the related 2-(phenylmethylene)aminophenol (δ N*H* 8.68 ppm, ν C=N 1630 cm^{-1}). The alcohol functionality was observed as a sharp singlet at 5.49 ppm in the ^{1}H NMR spectrum and at 3419 cm^{-1} in the IR. The value of the OH stretch in **2**, while higher than that of Yamamoto and co-workers at 3130 cm^{-1}, is comparable to other molecules that feature *intramolecular* [O-H···π] interactions, such as 2,6-diphenylphenol with an OH stretch of 3565 cm^{-1} (27).

X-ray crystallographic studies of a single crystal of **2** were performed and the results are presented in Table 1. As is typical in terphenyl molecules, the ortho phenyls are twisted out of the plane of the central phenyl ring to form a protective bowl around the imino functional group (Fig. 4). As expected from the spectroscopic data, an [O-H···π] interaction is observed between the phenolic proton and the centroid of one phenyl ring.

Reduction of the C=N double bond in TPIP was achieved by the addition of $NaBH_4$ in ethanol solution to give TPAP **3** (Scheme 2). The ^{1}H NMR spectrum showed a peak for the methylene protons at 4.05 ppm. This is consistent with data presented by Endo et al. (28) for the related *N*-benzyl-2-aminophenol where the methylene resonance is observed at 4.37 ppm. In the IR spectrum, the NH stretch appeared as a sharp peak at 3321 cm^{-1} while the OH appeared as a weak signal at 3391 cm^{-1}. X-ray crystallographic studies of a single crystal of **3** (Fig. 5) showed that the $C_{terphenyl}$—N bond length increased from 1.222(4) Å in TPIP to 1.448(3) Å in TPAP while the C_{phenol}—N bond shortened slightly from 1.427(4) to 1.394(3) Å. The [O-H···π] interaction noted in **2** is not observed in **3**.

TPIP **2** reacts with 2 equiv. of trimethylaluminum to give TPIP-$AlMe_2$·$AlMe_3$ (**4**) (Scheme 2), which features one aluminum chelated by the two heteroatoms as well as a second aluminum coordinated in Lewis acid–base fashion to the oxygen atom. In the presence of only 1 equiv. of $AlMe_3$, compound **4** is still formed, along with a yellow powder that was not further characterized because of its insolubility in conventional solvents.

© 2004 NRC Canada

Table 1. Crystal data.

	TPIP (**2**)	TPAP (**3**)	TPIP-$AlMe_2$·$AlMe_3$ (**4**)
Empirical formula	$C_{31}H_{23}NO$	$C_{31}H_{25}NO$	$C_{36}H_{37}Al_2NO$
Formula weight	425.50	427.52	553.63
Crystal system	Monoclinic	Monoclinic	Triclinic
Space group	*P*2(1)/*c*	*P*2(1)/*n*	*P*-1
Temperature (K)	297(2)	296(2)	150(2)
a (Å)	17.490 3(4)	12.418 4(3)	10.060 5(2)
b (Å)	5.702 9(1)	10.637 4(2)	12.418 5(4)
c (Å)	23.349 2(6)	17.993 2(5)	13.886 3(5)
α (°)	90	90	100.619(1)
β (°)	99.234(1)	101.353(1)	97.415(1)
γ (°)	90	90	110.549(2)
Volume ($Å^3$)	2298.79(9)	2330.38(10)	1560.91(8)
Z	4	4	2
D_{calcd} (Mg m^{-1})	1.229	1.219	1.178
μ (mm^{-1})	0.074	0.073	0.121
R (2σ)	0.069 0	0.052 6	0.052 9
R_w^2 (2σ)	0.191 0	0.141 3	0.120 1

Scheme 2. Synthesis of TPAP (**3**) and aluminum complexes TPIP-$AlMe_2$·$AlMe_3$ (**4**) and TPAP-$AlMe_2$ (**5**).

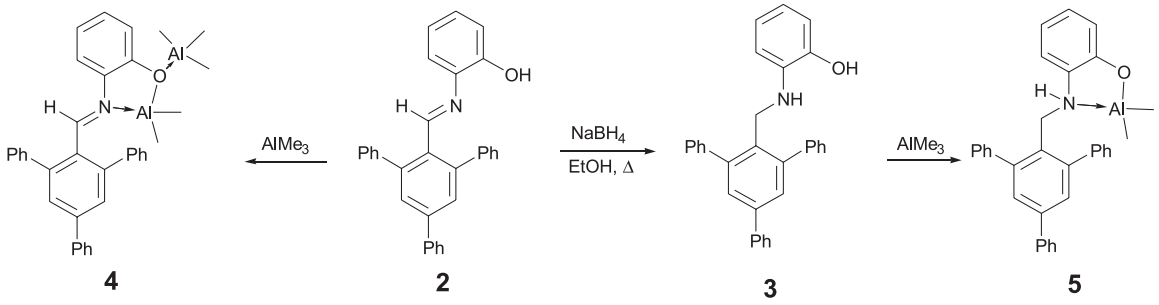
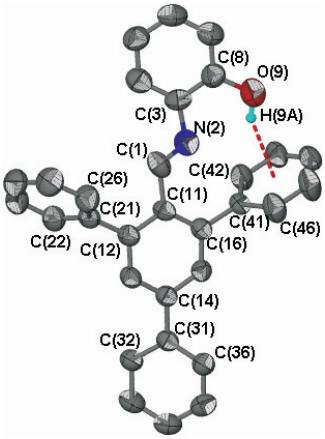


Fig. 4. The structure of TPIP (**2**) showing the numbering scheme. Hydrogen atoms, except the phenolic H, have been removed for clarity. Selected bond lengths (Å): C(1)—N(2) 1.222(4), C(1)—C(11) 1.505(5), N(2)—C(3) 1.427(4), C(8)—O(9) 1.393(5), H(9a)···centroid 2.986, O(9)···centroid 3.562. Selected bond angles (°): C(11)-C(1)-N(2) 123.2(4), C(1)-N(2)-C(3) 119.0(3), O(9)-H(9a)···centroid 139.73.



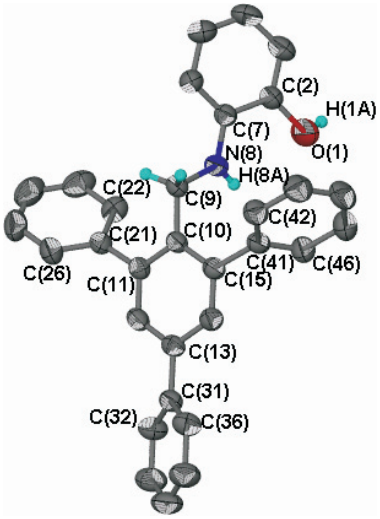
^{1}H NMR data indicated the presence of two different aluminum methyl environments with resonances observed at –1.31 and –0.89 ppm, with relative integrated intensities of 2:3. These signals were assigned to a *N*,*O*-chelated dimethylaluminum centre and the *O*-coordinated trimethylaluminum centre, respectively. Noticeably absent from the IR spectrum of **4** was the OH stretch observed in **2**. X-ray crystallographic studies confirmed the proposed structure (Fig. 6).

The coordination pattern observed in **4**, while unexpected, is not unprecedented (Fig. 7). Similar five-membered N-Al-O heterocycles with a second trialkylaluminum coordinated to the oxygen atom have been reported by Atwood et al. (17), Barron and co-workers (29), and van Koten and co-workers (30, 31). The Al—N and both Al—O bond lengths of **4** are consistent with the literatures values (Table 2). The environment around each aluminum centre in **4** is that of a distorted tetrahedron, with bond angles ranging from 84.13°–120.30° in the chelated aluminum, Al(13), and 102.02°–115.47° for the other, Al(4). The large distortions seen in the chelated centre are likely due to the steric constraints imposed by the formation of a five-membered ring, as well as the presence of the bulky *m*-terphenyl fragment.

The aluminum complex TPIP-$AlMe_2$·$AlMe_3$ (**4**) was tested as a catalyst in the ring-opening polymerization of ε-

© 2004 NRC Canada

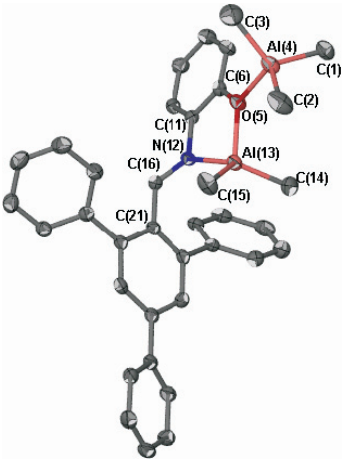
Fig. 5. The structure of TPAP (**3**) showing the numbering scheme. Aryl hydrogen atoms have been removed for clarity. Selected bond lengths (Å): C(10)—C(9) 1.517(3), C(9)—N(8) 1.448(3), N(8)—C(7) 1.394(3), C(2)—O(1) 1.375(3). Selected bond angles (°): C(10)-C(9)-N(8) 112.14(17), C(9)-N(8)-C(7) 118.91(18).



caprolactone (9) and propylene oxide (7). Complex **4** was found to give poly(caprolactone) with M_w = 10 964 and polydispersity of 1.50. Under similar conditions, the bulky alkylaluminum catalysts described by Okuda and co-workers (9) produced polymers with M_w in the range of 50 000 with polydispersities between 1.8–3.3. Complex **4** was not active in the polymerization of propylene oxide. This is poor compared with other alkylaluminum compounds featuring nitrogen and oxygen donors (7).

Finally, when TPAP **3** was combined with trimethylaluminum, the anticipated product TPAP-AlMe·$AlMe_3$ was not detected. To our surprise, the mononuclear complex TPAP-$AlMe_2$ (**5**) was isolated (Scheme 2). Complex **5** was characterized by IR, ^{1}H and ^{13}C NMR spectroscopy. The IR spectrum showed a peak assigned to an NH stretch at 3321 cm^{-1} (cf. TPAP N-H observed at 3291 cm^{-1}). In the ^{1}H NMR spectrum, the signal for the methylene protons was resolved into a doublet ($^3J_{H-H}$ = 7 Hz) and the N*H* signal appeared as a triplet at 3.08 ppm ($^3J_{H-H}$ = 7 Hz). Also observed in the ^{1}H NMR spectrum was a sharp singlet at –1.35 ppm that integrated to six hydrogens. This signal was assigned to six aluminum methyl hydrogen atoms. Similarly, the signal at –8.1 ppm in the ^{13}C NMR spectrum was assigned to the two aluminum methyl carbons. These spectroscopic observations, specifically the decreased frequency of ν_{N-H} in the IR spectrum and the N*H*-C*H* $^3J_{H-H}$ coupling constant in the ^{1}H NMR spectrum, are consistent with our suggested structure **5** and this structure is reminiscent of trialkylaluminum-dialkylamine adducts previously reported by Bradley et al. (32). Elemental analyses was performed on samples of **5**, and the results agree more closely with the suggested structure of **5** than any of the other likely reaction products. Unfortunately, despite numerous attempts in various solvents and conditions, we were not able to grow crystals suitable for X-ray crystallographic studies.

Fig. 6. Structure of TPIP-$AlMe_2$·$AlMe_3$ (**4**) showing the numbering scheme. Hydrogen atoms have been removed for clarity. Selected bond lengths (Å): C(21)—C(16) 1.470(3), C(16)—N(12) 1.289(3), N(12)—Al(13) 2.013(2), N(12)—C(11) 1.430(3), C(6)—O(5) 1.386(3), O(5)—Al(4) 1.936(2), O(5)—Al(13) 1.870(2), Al(13)—C(15) 1.939(3), Al(13)—C(14) 1.932(3), Al(4)—C(3) 1.972(3), Al(4)—C(1) 1.977(3), Al(4)—C(2) 1.970(3). Selected bond angles (°): C(21)-C(16)-N(12) 122.5(2), C(16)-N(12)-C(11) 120.3(2), N(12)-Al(13)-O(5) 84.13(8), N(12)-Al(13)-C(15) 108.27(12), N(12)-Al(13)-C(14) 115.13(12), C(15)-Al(13)-C(14) 120.30(15), O(5)-Al(13)-C(15) 116.83(14), O(5)-Al(13)-C(14) 106.74(12), C(6)-O(5)-Al(13) 112.72(16), C(6)-O(5)-Al(4) 123.28(16), O(5)-Al(4)-C(1) 106.45(11), O(5)-Al(4)-C(2) 102.01(12), O(5)-Al(4)-C(3) 105.25(12), C(1)-Al(4)-C(2) 112.31(15), C(1)-Al(4)-C(3) 115.47(15), C(2)-Al(4)-C(3) 113.82(17), Al(13)-O(5)-Al(4) 123.50(9).



Polymerization of ε-caprolactone and propylene oxide were attempted under similar conditions to those described for **4** but no reaction was observed. The reasons for this difference in activity are not immediately clear.

Summary

Two new aminophenol *m*-terphenyl derivatives were synthesized and characterized. The aluminum complexes of these ligands were also synthesized. The activity of TPIP-$AlMe_2$·$AlMe_3$ as a ring-opening polymerization catalyst was examined. Poly(caprolactone) with M_w = 10 964 and polydispersity of 1.50 was produced, however the molecule was not catalytically active in the presence of propylene oxide.

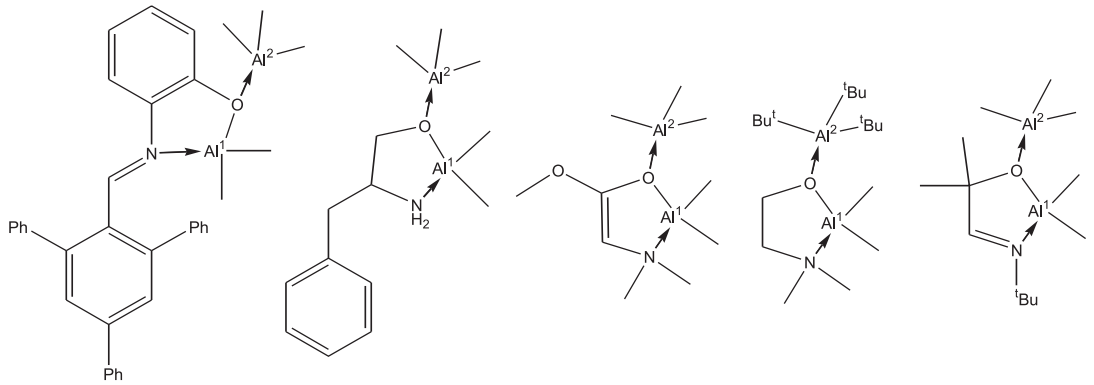
Experimental

General

An MBraun UL-99–245 dry box and standard Schlenk techniques on a double manifold vacuum line were used in the manipulation of air and moisture sensitive compounds. NMR spectra were recorded on a Bruker AMX 400 or a Varian AS 500 spectrometer in 5 mm quartz tubes. ^{1}H and ^{13}C chemical shifts are reported in parts per million (ppm) downfield from tetramethylsilane (TMS) and are calibrated to the residual signal of the solvent. Infrared spectra were obtained using a Bomem MB spectrometer with the % trans-

© 2004 NRC Canada

Fig. 7. Coordination of aluminum in **4**, **6** (17), **7** (29), **8** (30), and **9** (31).



4 **6** **7** **8** **9**

Table 2. Comparison of bond lengths in structurally characterized C_2NOAl rings exhibiting O-AlR_3 complexation.

	4	6	7	8	9
Bond lengths (Å)					
Al^1—N	2.013(2)	2.005(9)	2.039(2)	2.013(6)	2.002(6)
Al^1—O	1.870(2)	1.807(9)	1.870(2)	1.837(4)	1.825(5)
Al^2—O	1.936(2)	1.895(8)	1.895(2)	1.929(4)	1.910(5)
Bond angles (°)					
N-Al^1-O	84.13(8)	85.6(3)	85.65(9)	74.4(2)	84.6(2)
Al^1-O-Al^2	123.50(9)	126.4(3)	126.6(1)	135.5(2)	120.3(3)
Reference	This work	17	29	30	31

mittance values reported in cm^{-1}. Melting points were measured using a Mel-Temp apparatus and are uncorrected. Elemental analysis were obtained by M.K. Yang on a Carlo Erba Model 1106 CHN analyzer.

2,4,6-Triphenylbenzaldehyde (25) (1)

2,4,6-Triphenylbromobenzene (20 g, 52 mmol) was suspended in ca. 200 mL anhydrous ether and *n*-butyllithium (1.6 mol L^{-1} in hexane, 36 mL, 57 mmol) was added dropwise. The reaction was stirred at room temperature for 3 h and an excess of DMF (17 mL) was then added dropwise. After 2 h, the reaction was quenched with H_2O and extracted with ether. The combined ether portions were dried with $MgSO_4$, concentrated under vacuum, and stored at −20 °C. Yellow crystals were isolated and characterized as 2,4,6-triphenylbenzaldehyde (13.8 g, 41 mmol, 80%), mp 128 to 129 °C. IR (Nujol): 2747 (m), 1698 (s), 1590 (s), 1343 (s), 1198 (s), 892 (m), 764 (vs). ^{1}H NMR (400 MHz, $CDCl_3$) δ: 7.40–7.71 (m, 17H), 10.00 (s, 1H). ^{13}C NMR (100 MHz, $CDCl_3$) δ: 127.4, 127.7, 128.2, 128.5, 129.0, 129.1, 129.6, 131.6, 139.4, 139.8, 144.2, 145.2, 193.0.

N-*(2′,4′,6′-Triphenylbenzylidene)2-iminophenol (TPIP) (2)*

2,4,6,-Triphenylbenzaldehyde (10.0 g, 29.9 mmol) and 2-aminophenol (3.7 g, 29.9 mmol) were suspended in ca. 200 mL of anhyd. EtOH and heated to reflux. Glacial acetic acid (5 mL) was then added and reflux continued for 3 h. The mixture was allowed to cool to room temperature and bright yellow needle-like crystals were filtered off (11.5 g, 26.9 mmol, 90%), mp 158 to 159 °C. IR (Nujol): 3417 (m), 1625 (m), 1584 (m), 1297 (m), 1249 (m), 1212 (m), 887 (m), 699 (s). ^{1}H NMR (400 MHz, $CDCl_3$) δ: 5.49 (s, 1H, O*H*), 6.68–6.72 (m, 1H), 6.76–6.79 (m, 2H), 7.01–7.06 (m, 1H), 7.38–7.53 (m, 15H), 7.65 (s, 2H), 8.59 (s, 1H, N=C*H*). ^{13}C NMR (100 MHz, $CDCl_3$) δ: 119.7, 127.2, 127.4, 127.7, 128.0, 128.2, 128.4, 128.9, 129.0, 129.4, 129.5, 193.0 (quaternary carbons not observed). Anal. calcd. for $C_{31}H_{23}NO$: C 87.50, H 5.45, N 3.29; found: C 87.42, H 5.47, N 3.41.

N-*(2′,4′,6′-Triphenylbenzyl)-2-aminophenol (TPAP) (3)*

TPIP (4.05 g, 9.52 mmol) and sodium borohydride (0.90 g, 23.8 mmol) were suspended in ca. 200 mL of anhyd. EtOH. The mixture was heated slowly to reflux over 1 h and then allowed to cool to room temperature. The reaction was quenched with H_2O and extracted with CH_2Cl_2. The organic layer was washed with H_2O and a saturated sodium chloride solution and dried with $MgSO_4$. The solvent was removed under vacuum to give a brown powder that was recrystallized from Et_2O at room temperature (2.54 g, 5.94 mmol, 62.4%), mp 174–176 °C. IR (Nujol): 3391 (w), 3321 (m), 1595 (m), 1493 (m), 1480 (s), 1275 (m), 1251 (m), 886 (m), 702 (s). ^{1}H NMR (400 MHz, $CDCl_3$) δ: 4.06 (s, 2H, CH_2), 5.06 (br s, 1H, O*H*), 6.24 (s, 1H, N*H*), 6.63 (s, 4H), 7.38–77.67 (m, 17H). ^{13}C NMR (125 MHz) δ: 44.6, 114.2, 115.4, 119.5, 120.9, 127.1, 127.4, 127.5, 128.3, 128.8, 129.1, 132.8, 135.6, 139.9, 140.1, 141.3, 144.0, 145.5. Anal. calcd. for $C_{31}H_{25}NO$: C 87.09, H 5.89, N 3.28; found: C 87.13, H 5.97, N 3.21.

TPIP-$AlMe_2AlMe_3$ (4)

TPIP (0.5 g, 1.18 mmol) was dissolved in ca. 15 mL of anhydrous toluene under a N_2 atmosphere. Trimethyl-

© 2004 NRC Canada

aluminum (2.0 mol L^{-1} in toluene, 1.4 mL, 2.8 mmol) was added dropwise to the stirred TPIP solution. Evolution of methane was observed immediately but ceased after the halfway point of the addition. The solution was allowed to stir for 15 min and then the solvent was removed under vacuum. The resulting yellow powder was recrystallized by slow evaporation of a CH_2Cl_2 solution to give yellow crystals (0.58 g, 1.05 mmol, 89%), mp 276 °C (dec.). IR (Nujol): 3058 (w), 3029 (w), 1596 (vs), 1575 (s), 1556 (m), 1485 (s). ^{1}H NMR (400 MHz, CD_2Cl_2) δ: –1.31 (s, 6H), –0.89 (s, 9H), 7.19–7.54 (m, 17H), 7.73–7.82 (m, 4H), 8.98 (s, 1H). ^{13}C NMR (100 MHz, CD_2Cl_2) δ: –10.5, –7.2, 25.6, 117.5, 119.2, 120.8, 127.6, 127.7, 128.7, 128.9, 129.2, 129.4, 129.5, 130.3, 131.8, 138.8, 129.5, 143.7. Anal. calcd. for $C_{36}H_{37}Al_2NO$: C 78.10, H 6.74, N 2.53; found: C 77.80, H 6.70, N 2.26.

TPAP-AlMe$_2$ (5)

TPAP (250 mg, 0.58 mmol) was dissolved in ca. 5 mL anhyd. CH_2Cl_2. Trimethylaluminum (2.0 mol L^{-1} in hexane, 0.32 mL, 0.64 mmol) was added dropwise to the stirred TPAP solution. Evolution of methane was observed and the solution turned reddish brown. Upon completion of the addition, stirring was stopped and the flask was left to sit at room temperature to allow slow evaporation of solvent to give a pale brown powder (230 mg, 0.47 mmol, 82%), mp > 260 °C. IR (Nujol): 3291 (w), 1595 (s), 1574 (m), 1564 (m), 1493 (s). ^{1}H NMR (400 MHz, CD_2Cl_2) δ: –1.35 (s, 6H, Al(CH_3)$_2$), 3.08 (t, $J_{H\text{-}H}$ = 7 Hz, 1H, N*H*), 4.01 (d, $J_{H\text{-}H}$ = 7 Hz, 2H, CH_2), 6.17 (d of d, $J_{H\text{-}H}$ = 8 Hz, 1 Hz, 1H), 6.54 (t of d, $J_{H\text{-}H}$ = 8 Hz, 1 Hz, 1H), 6.80 (d of d, $J_{H\text{-}H}$ = 8 Hz, 1 Hz, 1H), 7.02–7.73 (m, 15H), 7.56 (s, 2H). ^{13}C NMR (100 MHz) δ: –8.1, 50.6, 118.7, 120.7, 127.3, 128.9, 129.5, 129.6, 129.7, 129.9, 130.6, 130.7, 130.8, 133.1, 133.5, 141.7, 142.0, 142.5, 145.8, 154.1. Anal. calcd. for $C_{33}H_{30}AlNO$: C 81.96, H 6.25, N 2.90; found: C 80.57, H 6.40, N 2.65.

Polymerization studies

TPIP-$AlMe_2$·$AlMe_3$ (**4**) (0.1 g, 0.2 mmol) was dissolved in 5 mL of warm anhydrous toluene. ε-Caprolactone (1.21 g, 0.011 mol) was added to the toluene solution. Over the course of 1 h, the solution became noticeably more viscous. The reaction was quenched with ca. 50 mL of methanol and the resulting yellow powder was filtered off. The solid poly(caprolactone) (0.48 g, 40%) was characterized by GPC as a THF solution.

X-ray crystallography

Crystals of **2** and **3** were grown from concentrated ethanol solutions. Crystals of **4** were grown from a concd. CH_2Cl_2 solution. Single crystals of **2**, **3**, and **4** were mounted on a glass fibre and data were collected at room temperature (**2**, **3**) or –123 °C (**4**) on a Nonius Kappa-CCD diffractometer with COLLECT (33). The unit cell parameters were calculated and refined from the full data set. Crystal cell refinement and data reduction were carried out using DENZO (34). The data were scaled using SCALEPACK (35). The SHELXTL/PC for Windows-NT Version 6.12 (36) suite of programs was used to solve the structure by direct methods. Subsequent difference Fouriers allowed the remaining atoms to be located. The molecule was very well behaved. All of the non-hydrogen atoms were refined with anisotropic thermal parameters. The hydrogen atom positions were calculated geometrically and were included as riding on their respective carbon atoms. The crystal data and refinement parameters are listed in Table 1. Thermal ellipsoids in Figs. 4–6 are shown at 50% probability.

Acknowledgements

Funding for this research was provided by the Natural Sciences and Engineering Research Council of Canada (NSERC), Simon Fraser University, and the University of Western Ontario. The authors would like to thank Zhiqing (Ken) Shi and Marianne Rodgers for help with the polymerization study, and Marcy Tracey and Madhvi Ramnial for the collection of NMR data.

References

1. B. Twamley, S.T. Haubrich, and P.P. Power. Adv. Organomet. Chem. **44**, 1 (1999).
2. J.A.C. Clyburne and N. McMullen. Coord. Chem. Rev. **210**, 73 (2000).
3. P.P. Power. Chem. Rev. **99**, 3463 (1999).
4. G.H. Robinson. Acc. Chem. Res. **32**, 773 (1999).
5. G.H. Robinson. Chem. Commun. 2175 (2000).
6. G.H. Robinson. Adv. Organomet. Chem. **47**, 283 (2001).
7. L.S. Baugh and J.A. Sissano. J. Polym. Sci. Part A: Polym. Chem. **40**, 1633 (2002).
8. D. Chakraborty and E.Y.-X. Chen. Organometallics, **22**, 769 (2003).
9. I. Taden, H.-C. Kang, W. Massa, T.P. Spaniol, and J. Okuda. Eur. J. Inorg. Chem. 441 (2000).
10. M.P. Coles and R.F. Jordan. J. Am. Chem. Soc. **119**, 8125 (1997).
11. G.W. Coates. Chem. Rev. **100**, 1223 (2000).
12. D. Abeysekera, K.N. Robertson, T.S. Cameron, and J.A.C. Clyburne. Organometallics, **20**, 5532 (2001).
13. H.A. Jenkins, D. Abeysekera, D.A. Dickie, and J.A.C. Clyburne. J. Chem. Soc. Dalton Trans. 3919 (2002).
14. J.A.R. Schmidt and J. Arnold. Organometallics, **21**, 2306 (2002).
15. D.W. Norman, J.P. Edwards, C.M. Vogels, A. Decken, and S.A. Westcott. Can. J. Chem. **80**, 31 (2002).
16. D.A. Lewis, D.J. Williams, A.M. Slawin, and J.D. Woollins. Polyhedron, **15**, 555 (1996).
17. D.A. Atwood, F.P. Gabbaï, J. Lu, M.P. Remington, D. Rutherford, and M.P. Sibi. Organometallics, **15**, 2308 (1996).
18. M.S.J. Briggs, J.S. Fossey, C.J. Richards, B. Scott, and J. Whateley. Tetrahedron Lett. **43**, 5169 (2002).
19. J. Lewinski, J. Zachara, and T. Kopec. Inorg. Chem. Commun. **1**, 182 (1998).
20. D.A. Atwood and M.J. Harvey. Chem. Rev. **101**, 37 (2001).
21. D.A. Atwood. Coord. Chem. Rev. **165**, 267 (1997).
22. M.H. Chisholm, J.C. Gallucci, H. Zhen, and J.C. Huffman. Inorg. Chem. **40**, 5051 (2001).
23. P.A. Cameron, V.C. Gibson, C. Redshaw, J.A. Segal, G.A. Solan, A.J.P. White, and D.J. Williams. J. Chem. Soc. Dalton Trans. 1472 (2001).
24. C. Wang, S. Friedrich, T.R. Younkin, R.T. Li, R.H. Grubbs, D.A. Bansleben, and M.W. Day. Organometallics, **17**, 3149 (1998).

© 2004 NRC Canada

25. K.S. Suslick and M.M. Fox. J. Am. Chem. Soc. **105**, 3507 (1983).
26. S. Saito, K. Hatanaka, and H. Yamamoto. Tetrahedron, **57**, 875 (2001).
27. S. Ueji, N. Ueda, and T. Kinugasa. J. Chem. Soc. Perkin Trans. 2, 178 (1976).
28. Y. Endo, K. Shudo, and T. Okamoto. Synthesis, **6**, 471 (1983).
29. C.N. McMahon, S.G. Bott, and A.R. Barron. J. Chem. Soc. Dalton Trans., 3301 (1998).
30. F.H. van der Steen, G.P.M. van Mier, A.L. Spek, J. Kroon, and G. van Koten. J. Am. Chem. Soc. **113**, 5742 (1991).
31. M.R.P. van Vliet, G. van Koten, M.A. Rotteveel, M. Schrap, K. Vrieze, B. Kojic-Prodic, A.L. Spek, and A.J.M. Duisenberg. Organometallics, **5**, 1389 (1986).
32. D.C. Bradley, G. Coumbarides, I.S. Harding, G.E. Hawkes, I.A. Maia, and M. Motevalli. J. Chem. Soc. Dalton Trans. 3553 (1999).
33. COLLECT [computer program]. Nonius BV, Delft, The Netherlands. 1997–2001.
34. Z. Otwinowski and W. Minor. DENZO-SM [computer program]. *In* Methods in enzymology. Vol. 276, Part A. *Edited by* C.W. Carter and R.M. Sweet. Academic Press, New York. pp. 307–326.
35. Z. Otwinowski and W. Monor. HKL-SCALEPACK [computer program]. 1997.
36. G.M. Sheldrick. SHELXTL/PC for Windows-NT. Version 6.12 [computer program]. University of Göttingen, Göttingen, Germany. 2002.

© 2004 NRC Canada

Solubility of crystalline nonelectrolyte solutes in organic solvents — Mathematical correlation of 2-methoxybenzoic acid and 4-methoxybenzoic acid solubilities with the Abraham solvation parameter model

Kaci R. Hoover, Dawn M. Stovall, Eric Pustejovsky, Rodrick Coaxum, Krisztina Pop, William E. Acree, Jr., and Michael H. Abraham

Abstract: The Abraham solvation parameter model is used to calculate the numerical values of the solute descriptors for 2-methoxybenzoic acid and 4-methoxybenzoic acid from experimental solubilities in organic solvents. The mathematical correlations take the form of

$$\log(C_S/C_W) = c + e\mathbf{E} + s\mathbf{S} + a\mathbf{A} + b\mathbf{B} + v\mathbf{V}$$

$$\log(C_S/C_G) = c + e\mathbf{E} + s\mathbf{S} + a\mathbf{A} + b\mathbf{B} + l\mathbf{L}$$

where C_S and C_W refer to the solute solubility in the organic solvent and water, respectively, C_G is a gas phase concentration, **E** is the solute excess molar refraction, **V** is the McGowan volume of the solute, **A** and **B** are measures of the solute hydrogen-bond acidity and hydrogen-bond basicity, **S** denotes the solute dipolarity–polarizability descriptor, and L is the logarithm of the solute gas phase dimensionless Ostwald partition coefficient into hexadecane at 298 K. The remaining symbols in the above expressions are known solvent coefficients, which have been determined previously for a large number of gas–solvent and water–solvent systems. The Abraham solvation parameter model was found to describe the experimental solubility data and published literature partitioning data of 2-methoxybenzoic acid and 4-methoxybenzoic acid to within overall standard deviations of 0.146 log units and 0.114 log units, respectively.

Key words: 2-methoxybenzoic acid solubilities, 4-methoxybenzoic acid solubilities, partition coefficients, molecular solute descriptors, solubility predictions.

Résumé : On a utilisé le modèle du paramètre de solvatation d'Abraham pour calculer les valeurs numériques des descripteurs de soluté des acides 2-méthoxybenzoïque et 4-méthoxybenzoïque à partir de leurs solubilités expérimentales dans des solvants organiques. Les corrélations mathématiques sont de la forme

$$\log(C_S/C_W) = c + e\mathbf{E} + s\mathbf{S} + a\mathbf{A} + b\mathbf{B} + v\mathbf{V}$$

$$\log\ (C_S/C_G) = c + e\mathbf{E} + s\mathbf{S} + a\mathbf{A} + b\mathbf{B} + l\mathbf{L}$$

dans lesquelles C_S et C_W se réfèrent à la solubilité du soluté respectivement dans le solvant organique et dans l'eau, C_G se réfère à la concentration en phase gazeuse, **E** est la réfraction molaire en excès du soluté, **V** est le volume de McGowan du soluté, **A** et **B** sont des mesures de l'acidité et de la basicité de la liaison hydrogène du soluté, **S** correspond au descripteur du caractère dipolaire–polarisabilité du soluté et L est le logarithme du coefficient de partage sans dimension d'Ostwald du soluté en phase gazeuse, dans l'hexadécane, à 298 K. Les autres symboles des expressions présentées plus haut sont des coefficients connus du solvant qui ont été déterminés antérieurement pour un grand nombre de systèmes gaz–solvant et eau–solvant. On a trouvé que le modèle du paramètre de solvatation d'Abraham permet de décrire les données expérimentales de solubilité ainsi que les valeurs publiées dans la littérature relatives aux données de partition des acides 2-méthoxybenzoïque et 4-méthoxybenzoïque avec des déviations standard globales respectivement de 0,146 et 0,114 unités logarithmiques.

Received 5 April 2004. Published on the NRC Research Press Web site at http://canjchem.nrc.ca on 23 October 2004.

K.R. Hoover, D.M. Stovall, E. Pustejovsky, R. Coaxum, K. Pop, and W.E. Acree, Jr.[1] Department of Chemistry, P.O. Box 305070, University of North Texas, Denton, TX 76203-5070, USA.
M.H. Abraham. Department of Chemistry, University College London, 20 Gordon Street, London, WC1H 0AJ, UK.

[1]Corresponding author (e-mail: acree@unt.edu).

 doi: 10.1139/V04-112 © 2004 NRC Canada

Mots clés : solubilités de l'acide 2-méthoxybenzoïque, solubilités de l'acide 4-méthoxybenzoïque, coefficients de partage, descripteurs de solutés moléculaires, prédictions de la solubilité.

[Traduit par la Rédaction]

Introduction

This work continues a systematic application of the Abraham solvation parameter model for describing the solubility behavior of both inert and self-associating crystalline organic solutes dissolved in neat organic solvents of varying polarity and hydrogen-bonding characteristics. The basic model relies on two linear free energy relationships, one for processes within condensed phases (1–10)

$$[1] \qquad SP = c + e\mathbf{E} + s\mathbf{S} + a\mathbf{A} + b\mathbf{B} + v\mathbf{V}$$

and one for processes involving gas to condensed phase transfer

$$[2] \qquad SP = c + e\mathbf{E} + s\mathbf{S} + a\mathbf{A} + b\mathbf{B} + l\mathbf{L}$$

The dependent variable in eqs. [1] and [2] (SP) is some property of a series of solutes in a fixed phase. The independent variables, or descriptors, are solute properties as follows: **E** and **S** refer to the excess molar refraction and dipolarity–polarizability of the solute, respectively, **A** and **B** denote the overall solute hydrogen-bond acidity and basicity, **V** is the McGowan volume of the solute, and L is the logarithm of the solute gas-hexadecane partition coefficient at 298.15 K. The first four descriptors can be regarded as measures of the tendency of a solute to undergo various solute–solvent interactions, all of which are energetically favorable. The L and **V** descriptors are both measures of the size of the solute, and will be measures of the cavity term that will accommodate the solute, plus will describe general solute–solvent interactions. The equation coefficients (*c*, *e*, *s*, *a*, *b*, *v*, and *l*) depend upon the process or solvent system under consideration. In the case of partition coefficients, where two solvent phases are involved, the equation coefficients represent differences in the solvent phase properties.

To date we have shown that eqs. [1] and [2] are capable of mathematically correlating the observed solubility behavior of anthracene (11), fluoranthene (12), pyrene (12), benzil (13), ferrocene (14), buckminsterfullerene (15), monuron (16), diuron (16), *trans*-stilbene (17), acetylsalicylic acid (18), 3-methylbenzoic acid (19), 4-chlorobenzoic acid (19), 4-nitrobenzoic acid (20), and 2-methylbenzoic acid (21) in a large number of organic solvents. Differences between the experimental and back-calculated SP values (SP calculated as the logarithm of the solute molar solubility in the organic solvent divided either by the solute molar solubility in water or by the solute gas phase concentration) were on the order of 0.12 log units or less for most of the fore-mentioned solutes. In the case of the five carboxylic acid solutes, the studies were limited to organic solvents in which the solute was believed to exist almost entirely in monomeric form. Alkane and aromatic hydrocarbon solvents were excluded from consideration, except in the case of a few published practical partition coefficients where the reported values had been corrected to account for dimerization effects. Carboxylic acids are known to dimerize in saturated hydrocarbons and in nonpolar aromatic hydrocarbons.

Presently, we are in the process of updating the numerical values of previously calculated molecular descriptors of carboxylic acid solutes. The calculated values that we have in our database for carboxylic acid solutes were derived almost entirely from "practical" partitioning data. For some of the carboxylic acid solutes there was only very limited experimental partitioning data, and one or two incorrect data points could lead to the calculation of incorrect values for the molecular descriptors, as was the case in a recently completed solubility study involving acetylsalicylic acid (18). To better characterize the carboxylic acid solutes that we plan to use in future studies, we have measured the solubilities of both 2-methoxybenzoic acid and 4-methoxybenzoic acid in several alcohol, ether, and alkylacetate solvents. Results of these measurements are interpreted using the Abraham solvation parameter model.

Materials and methods

2-Methoxybenzoic acid (Aldrich, 99%) and 4-methoxybenzoic acid (Aldrich, 99%) were purchased from a commercial source and were used as received. The purity of both samples was 99.8% (±0.3%), as determined by nonaqueous titration with freshly standardized sodium methoxide solution to the thymol blue endpoint according to the method of Fritz and Lisicki (22) except that toluene was substituted for benzene. Methanol (Aldrich, 99.8%, anhydrous), ethanol (Aaper Alcohol and Chemical Company, absolute), 1-propanol (Aldrich, 99+%, anhydrous), 1-butanol (Aldrich, HPLC, 99.8+%), 1-pentanol (Aldrich, 99+%), 1-hexanol (Alfa Aesar, 99+%), 1-heptanol (Alfa Aesar, 99+%), 1-octanol (Aldrich, 99+%, anhydrous), 2-propanol (Aldrich, 99+%, anhydrous), 2-butanol (Aldrich, 99+%, anhydrous), 2-methyl-1-propanol (Aldrich, 99+%, anhydrous), 3-methyl-1-butanol (Aldrich, 99%, anhydrous), 1-decanol (Alfa Aesar, 99+%), 2-pentanol (Acros, 99+%), 2-methyl-2-propanol (Arco Chemical Company, 99+%), 4-methyl-2-pentanol (Acros, 99+%), 2-methyl-1-pentanol (Aldrich, 99%), 2-methyl-1-butanol (Aldrich, 99%), tetrahydrofuran (Aldrich, 99.9%, anhydrous), methyl acetate (Aldrich, 99.5%, anhydrous), ethyl acetate (Aldrich, HPLC, 99.9%), pentyl acetate (Aldrich, 99%), butyl acetate (Aldrich, HPLC, 99.7%), diethyl ether (Aldrich, 99+%, anhydrous), diisopropyl ether (Aldrich, 99%, anhydrous), dibutyl ether (Aldrich, 99.3%, anhydrous), propylene carbonate (Aldrich, 99.7%, anhydrous), and 1,4-dioxane (Aldrich, 99.8%, anhydrous) were stored over molecular sieves and distilled shortly before use. Gas chromatographic analysis showed solvent purities to be 99.7 mol % or better.

Excess solute and solvent were placed in amber glass bottles and allowed to equilibrate in a constant temperature water bath at 25.0 ± 0.1 °C for at least 24 h (often longer) with periodic agitation. After equilibration, the samples stood

© 2004 NRC Canada

Table 1. Experimental 2-methoxybenzoic acid mol fraction solubilities (X_S) in selected organic solvents at 25 °C.

Organic solvent	X_S
Methanol	0.0911
Ethanol	0.0765
1-Propanol	0.0596
1-Butanol	0.0534
1-Pentanol	0.0519
1-Hexanol	0.0467
1-Heptanol	0.0478
1-Octanol	0.0477
1-Decanol	0.0416
2-Propanol	0.0463
2-Butanol	0.0474
2-Methyl-1-propanol	0.0383
2-Methyl-2-propanol	0.0498
3-Methyl-1-butanol	0.0400
2-Methyl-1-butanol	0.0427
2-Pentanol	0.0427
2-Methyl-1-pentanol	0.0438
4-Methyl-2-pentanol	0.0409
Diethyl ether	0.0243
Diisopropyl ether	0.00838
Dibutyl ether	0.00603
Tetrahydrofuran	0.1774
1,4-Dioxane	0.1441
Methyl acetate	0.0733
Ethyl acetate	0.0655
Butyl acetate	0.0445
Pentyl acetate	0.0379
Propylene carbonate	0.0895

Table 2. Experimental 4-methoxybenzoic acid mol fraction solubilities (X_S) in selected organic solvents at 25 °C.

Organic solvent	X_S
Ethanol	0.01185
1-Propanol	0.01008
1-Butanol	0.01088
1-Pentanol	0.01130
1-Hexanol	0.01190
1-Heptanol	0.01234
1-Octanol	0.01275
1-Decanol	0.01278
2-Propanol	0.01060
2-Butanol	0.01175
2-Methyl-1-propanol	0.00740
2-Methyl-2-propanol	0.01561
3-Methyl-1-butanol	0.00916
2-Pentanol	0.01156
Diethyl ether	0.00952
Diisopropyl ether	0.00377
Dibutyl ether	0.00275
Tetrahydrofuran	0.05811
1,4-Dioxane	0.03476
Ethyl acetate	0.01308
Butyl acetate	0.01087
Pentyl acetate	0.00949

unagitated for several hours in the constant temperature bath to allow any finely dispersed solid particles to settle. Attainment of equilibrium was verified both by repetitive measurements the following day (or sometimes after 2 days) and by approaching equilibrium from supersaturation by pre-equilibrating the solutions at a slightly higher temperature. Aliquots of saturated methoxybenzoic solutions were transferred through a coarse filter into a tared volumetric flask to determine the amount of sample and diluted quantitatively with methanol for spectrophotometric analysis at 295 nm (2-methoxybenzoic acid) and 273 nm (4-methoxybenzoic acid) on a Bausch and Lomb Spectronic 2000. Concentrations of the dilute solutions were determined from a Beer–Lambert law absorbance vs. concentration working curve.

Experimental molar concentrations were converted to (mass/mass) solubility fractions by multiplying by the molar mass of carboxylic acid solute, volume(s) of volumetric flask(s) used, and any dilutions required to place the measured absorbances on the Beer–Lambert law absorbance vs. concentration working curve, and then dividing by the mass of the saturated solution analyzed. Mol fraction solubilities were computed from solubility mass fractions using the molar masses of the solute and solvent. Experimental 2-methoxybenzoic acid and 4-methoxybenzoic acid solubilities (X_S) in the organic solvents studied are listed in Tables 1 and 2, respectively. Numerical values represent the average of between four and eight independent determinations, and were reproducible to within ±1.5%.

Results and discusion

Correlation of the measured solubility data using eqs. [1] and [2] is relatively straightforward. We start with the set of equations that have been constructed for the partition of solutes between water and a given solvent. Table 3 gives the coefficients in eq. [1] for the condensed phase processes we shall consider. Note that in the case of the organic solvents, the process may pertain to either the "wet" practical partition of the solute between water (saturated with the organic solvent) and organic solvent (saturated with water) or to the hypothetical "dry" partition, which for a solid solute, is calculated as

$$[3] \qquad SP = \log P = \log C_S - \log C_W$$

the ratio of the molar solute solubility in the organic solvent (C_S), divided by the molar solute solubility in water (C_W). Hence, if C_W is known predicted SP values based upon eq. [1] will lead to predicted molar solublities through eq. [3]. For solutes that are ionized in aqueous solution, C_W refers to the solubility of the neutral form. The correction for ionization should be fairly small, provided that the carboxylic acid solute is not highly insoluble or has a large acid dissociation constant. We use the solubilities of 2-methoxybenzoic acid, log C_W = –1.554 (23, 24) (corrected for ionization), and 4-methoxybenzoic acid, log C_W = –2.800 (23, 25) (corrected for ionization), to convert the predicted partition coefficients to saturation solublities, which

© 2004 NRC Canada

Table 3. (A) Water to solvent coefficients in eq. [1] and (B) gas to solvent coefficients in eq. [2] for various processes.[a]

(A) Water to solvent (eq. [1]).

Process and solvent	*c*	*e*	*s*	*a*	*b*	*v/l*
1-Octanol (wet)	0.088	0.562	–1.054	0.034	–3.460	3.814
Diethyl ether (wet)	0.248	0.561	–1.016	–0.226	–4.553	4.075
Hexane	0.361	0.579	–1.723	–3.599	–4.764	4.344
Benzene	0.142	0.464	–0.588	–3.099	–4.625	4.491
Toluene	0.143	0.527	–0.720	–3.010	–4.824	4.545
Diethyl ether (dry)	0.330	0.401	–0.814	–0.457	–4.949	4.320
1,4-Dioxane (dry)	0.098	0.350	–0.083	–0.556	–4.826	4.172
Tetrahydrofuran (dry)	0.207	0.372	–0.392	–0.236	–4.934	4.447
Methanol (dry)	0.329	0.299	–0.671	0.080	–3.389	3.512
Ethanol (dry)	0.208	0.409	–0.959	0.186	–3.645	3.928
1-Propanol (dry)	0.148	0.436	–1.098	0.389	–3.893	4.036
2-Propanol (dry)	0.063	0.320	–1.024	0.445	–3.824	4.067
1-Butanol (dry)	0.152	0.438	–1.177	0.096	–3.919	4.122
1-Pentanol (dry)	0.080	0.521	–1.294	0.208	–3.908	4.208
1-Hexanol (dry)	0.044	0.470	–1.153	0.083	–4.057	4.249
1-Heptanol (dry)	–0.026	0.491	–1.258	0.035	–4.155	4.415
1-Octanol (dry)	–0.034	0.490	–1.048	–0.028	–4.229	4.219
1-Decanol (dry)	–0.062	0.754	–1.461	0.063	–4.053	4.293
2-Butanol (dry)	0.106	0.272	–0.988	0.196	–3.805	4.110
2-Methyl-1-propanol (dry)	0.177	0.335	–1.099	0.069	–3.570	3.990
2-Methyl-2-propanol (dry)	0.197	0.136	–0.916	0.318	–4.031	4.113
Ethyl acetate (dry)	0.358	0.362	–0.449	–0.668	–5.016	4.155
ALTDB-2 (k′)	–0.560	0.000	–0.480	–0.669	–2.782	3.854
SDS	1.201	0.542	–0.400	–0.133	–1.580	2.793
IN-1/IN-2 (k′)	–0.101	0.324	–0.807	0.000	–2.989	2.923
(Gas to water)	–0.994	0.577	2.549	3.813	4.841	–0.869

(B) Gas to solvent (eq. [2]).

Process and solvent	*c*	*e*	*s*	*a*	*b*	*v/l*
1-Octanol (wet)	–0.198	0.002	0.709	3.519	1.429	0.858
Diethyl ether (wet)	0.206	–0.169	0.873	3.402	0.000	0.882
Hexane	0.292	–0.169	0.000	0.000	0.000	0.979
Benzene	0.107	–0.313	1.053	0.457	0.169	1.020
Toluene	0.121	–0.222	0.938	0.467	0.099	1.012
Diethyl ether (dry)	0.288	–0.347	0.775	2.985	0.000	0.973
Tetrahydrofuran (dry)	0.189	–0.347	1.238	3.289	0.000	0.982
1,4-Dioxane (dry)	–0.034	–0.354	1.674	3.021	0.000	0.919
Methanol	–0.004	–0.215	1.173	3.701	1.432	0.769
Ethanol (dry)	0.012	–0.206	0.789	3.635	1.311	0.853
1-Propanol (dry)	–0.028	–0.185	0.648	4.022	1.043	0.869
2-Propanol (dry)	–0.060	–0.335	0.702	4.017	1.040	0.893
1-Butanol (dry)	–0.039	–0.276	0.539	3.781	0.995	0.934
1-Pentanol (dry)	–0.042	–0.277	0.526	3.779	0.983	0.932
1-Hexanol (dry)	–0.035	–0.298	0.626	3.726	0.729	0.936
1-Heptanol (dry)	–0.062	–0.168	0.429	3.541	1.181	0.927
1-Octanol (dry)	–0.119	–0.203	0.560	3.576	0.702	0.940
1-Decanol (dry)	–0.136	–0.038	0.325	3.674	0.767	0.947
2-Butanol (dry)	–0.013	–0.456	0.780	3.753	1.064	0.906
2-Methyl-1-propanol (dry)	0.012	–0.407	0.670	3.645	1.283	0.895
2-Methyl-2-propanol (dry)	0.071	–0.538	0.818	3.951	0.823	0.905
Ethyl acetate (dry)	0.203	–0.335	1.251	2.949	0.000	0.917
(Gas to water)	–1.271	0.822	2.743	3.904	4.814	–0.213

[a]The solvents denoted as dry are those for which partitions refer to transfer to the pure dry solvent. The other partitions are from water (more correctly water saturated with solvent) to the solvent saturated with water (see text).

© 2004 NRC Canada

Table 4. Comparison between observed and back-calculated partitions and molar solubilities of 2-methoxybenzoic acid based upon eqs. [1] and [2] and calculated molecular solute descriptors.[a]

		Equation [1]			Equation [2]		
Solvent	log C_S	log P^{exp}	log P^{calc}	log C_S^{calc}	log L^{exp}	log L^{calc}	log C_S^{calc}
1-Octanol (wet)		1.590	1.292		8.390	8.109	
Hexane		–1.360	–1.207		5.440	5.658	
Benzene		0.750	0.549		7.550	7.370	
Toluene		0.450	0.398		7.250	7.219	
Diethyl ether (wet)		0.780	1.005		7.580	7.787	
Diethyl ether (dry)	–0.638	0.916	1.118	–0.436	7.716	7.896	–0.458
Tetrahydrofuran (dry)	0.299	1.853	1.854	0.300	8.653	8.637	0.283
1,4-Dioxane (dry)	0.197	1.751	1.773	0.219	8.551	8.547	0.193
Methanol (dry)	0.267	1.821	1.560	0.006	8.621	8.344	–0.010
Ethanol (dry)	0.074	1.628	1.491	–0.063	8.428	8.196	–0.158
1-Propanol (dry)	–0.120	1.434	1.319	–0.235	8.234	8.037	–0.317
2-Propanol (dry)	–0.392	1.162	1.337	–0.217	7.962	8.114	–0.240
1-Butanol (dry)	–0.247	1.307	1.163	–0.391	8.107	8.058	–0.296
1-Pentanol (dry)	–0.327	1.227	1.155	–0.399	8.027	8.014	–0.340
1-Hexanol (dry)	–0.430	1.124	1.170	–0.384	7.924	7.984	–0.370
1-Heptanol (dry)	–0.471	1.083	1.076	–0.478	7.883	7.942	–0.412
1-Octanol (dry)	–0.518	1.036	1.067	–0.487	7.836	7.824	–0.530
1-Decanol (dry)	–0.658	0.896	0.928	–0.626	7.696	7.754	–0.600
2-Butanol (dry)	–0.299	1.255	1.336	–0.218	8.055	8.132	–0.222
2-Methyl-1-propanol (dry)	–0.392	1.162	1.260	–0.294	7.962	8.071	–0.283
2-Methyl-2-propanol (dry)	–0.286	1.268	1.323	–0.231	8.068	8.130	–0.224
Ethyl acetate (dry)	–0.187	1.367	1.340	–0.214	8.168	8.161	–0.193
ALTDB-2 (k)		1.380[b]	1.097				
Gas to water		6.800	6.853		6.800	6.877	

[a]Numerical values of the descriptors used in these calculations are: **E** = 0.899, **S** = 1.410, **A** = 0.450, **B** = 0.620, **V** = 1.1313 and **L** = 5.636.
[b]Experimental data taken from ref. 29.

can then be compared with the experimentally determined values. Ionization is not a concern in the organic solvents that have dielectric constants much smaller than water.

Equation [2] is used for processes involving gas phase transfers. Equation coefficients are given in Table 3 for several organic solvents. Predicted SP values can also be converted to saturation molar solubilities, provided that the solid saturated vapor pressure at 298.15 K (VP^o), is available. VP^o can be transformed into the gas-phase concentration (C_G), and the gas–water and gas–solvent partitions (L_W and L_S) can be obtained through eqs. [4] and [5], respectively.

$$[4] \qquad SP = \log L_W = \log C_W - \log C_G$$

$$[5] \qquad SP = \log L_S = \log C_S - \log C_G$$

If one is unable to find an experimental vapor pressure for the given solute molecule, an estimated value can be used in the preliminary computations. The value can be adjusted then, if necessary, to reduce the log L deviations and to make the log P and log L predictions internally consistent.

To determine the solute descriptors for 2-methoxybenzoic acid and 4-methoxybenzoic acid, we first convert the experimental mol fractions in Tables 1 and 2 into molar solubilities by dividing X_S by the ideal molar volume of the saturated solution (i.e., $C_S \approx X_S/[X_S V_{Solute} + (1 - X_S)V_{Solvent}]$). A value of V_{Solute} = 124.1 cm^3 mol^{-1} was used for the molar volume of the two hypothetical subcooled liquid methoxybenzoic acids. Any errors resulting from the estimation of the hypothetical liquid molar volumes of the carboxylic acids (V_{Solute}) or from the ideal molar volume approximation should have only a very small effect on the calculated C_S values. 2-Methoxybenzoic acid and 4-methoxybenzoic acid are not overly soluble in many of the solvents considered, and the $X_S V_{Solute}$ term contributes very little to the molar volume of the saturated solutions. Dibutyl ether was excluded from the solubility analysis because we felt that dimerization of carboxylic acids was inevitable in this larger ether solvent. Carboxylic acids are known to dimerize in saturated hydrocarbon and aromatic hydrocarbon solvents. It was noted when the equation coefficients for dibutyl ether were calculated that the derived equations did not describe the solubility behavior of several carboxylic acids (benzoic acid, 2-hydroxybenzoic acid, 4-hydroxybenzoic acid, and 3-nitrobenzoic acid) (6). The calculated log P values were always less than observed log P values by the solubility method, as would be expected if dimerization did occur in dibutyl ether. Solubility measurements determine the total carboxylic acid concentration in the organic solvent, and unlike in the case of practical partition measurements, there is no convenient experimental means to correct the measured value for dimerization effects. Correlation equations for diethyl ether, tetrahydrofuran, and 1,4-dioxane did describe the solubility behavior of benzoic acid, 2-hydroxybenzoic acid, and 4-hydroxybenzoic acid (4). The latter three ether

© 2004 NRC Canada

Table 5. Comparison between observed and back-calculated partitions and molar solubilities of 4-methoxybenzoic acid based upon eqs. [1] and [2] and calculated molecular solute descriptors.[a]

		Equation [1]			Equation [2]		
Solvent	log C_S	log P^{exp}	log P^{calc}	log C_S^{calc}	log L^{exp}	log L^{calc}	log C_S^{calc}
1-Octanol (wet)		1.960	1.812		8.560	8.541	
Benzene		0.460	0.578		7.160	7.369	
Toluene		0.540	0.484		7.240	7.245	
Diethyl ether (wet)		1.490	1.585		8.190	8.318	
Diethyl ether (dry)	–1.043	1.757	1.688	–1.112	8.457	8.381	–1.119
Tetrahydrofuran (dry)	–0.162	2.638	2.370	–0.430	9.338	9.101	–0.399
1,4-Dioxane (dry)	–0.401	2.399	2.174	–0.626	9.099	8.889	–0.611
Ethanol (dry)	–0.702	2.098	2.041	–0.759	8.798	8.646	–0.854
1-Propanol (dry)	–0.875	1.925	1.950	–0.850	8.625	8.641	–0.859
2-Propanol (dry)	–0.864	1.936	1.959	–0.841	8.636	8.674	–0.826
1-Butanol (dry)	–0.929	1.871	1.759	–1.041	8.571	8.613	–0.887
1-Pentanol (dry)	–0.984	1.816	1.788	–1.012	8.516	8.571	–0.929
1-Hexanol (dry)	–1.022	1.778	1.774	–1.026	8.478	8.542	–0.958
1-Heptanol (dry)	–1.060	1.740	1.699	–1.101	8.440	8.455	–1.045
1-Octanol (dry)	–1.093	1.707	1.653	–1.147	8.407	8.370	–1.130
1-Decanol (dry)	–1.174	1.626	1.578	–1.222	8.326	8.350	–1.150
2-Butanol (dry)	–0.898	1.902	1.908	–0.892	8.602	8.634	–0.866
2-Methyl-1-propanol (dry)	–1.100	1.700	1.805	–0.995	8.400	8.549	–0.951
Ethyl acetate (dry)	–0.879	1.921	1.800	–1.000	8.621	8.558	–0.942
SDS		3.490[b]	3.444				
IN-1/IN-2 (k′)		2.330[c]	2.065				
Gas to water		6.700	6.609		6.700	6.598	

[a]Numerical values of the descriptors used in these calculations are: **E** = 0.899, **S** = 1.250, **A** = 0.620, **B** = 0.520, **V** = 1.1313, and **L** = 5.741.
[b]Experimental value taken from ref. 26.
[c]Experimental value taken from ref. 30.

solvents are included in the solubility analysis. Equation coefficients for dry diisopropyl ether have not been determined yet, and the solubility data for both 2-methoxybenzoic acid and 4-methoxybenzoic acid will be added to our existing data base for use in subsequent studies.

Available practical partition coefficient (26–28) and chromatographic retention (29, 30) data are retrieved from the chemical literature. Combining the two sets of linear free-energy relationships, we have a total of 47 equations for 2-methoxybenzoic acid and a total of 44 equations for 4-methoxybenzoic acid, for which partition data and equation coefficients are available. The McGowan volume of 2-methoxybenozic acid (**V** = 1.1313) and 4-methoxybenzoic acid (**V** = 1.1313) are calculated from the individual atomic sizes and number of bonds in each molecule (31). The excess molar refraction of both solutes is estimated as **E** = 0.899. The sets of 47 and 44 equations were then solved, using Microsoft Solver, to yield the numerical values of the remaining solute descriptors that best described the experimental log P and log L values. The two log C_G values were also calculated to give an internally consistent set of log P and log L values. The vapor concentration corresponds to a gas-to-water partition of log L_W = 6.80 (2-methoxybenzoic acid) and log L_W = 6.70 (4-methoxybenzoic acid), which is in good agreement with the calculated values based upon eqs. [1] and [2] (last numerical entries in Tables 4 and 5). Numerical values of the solute descriptors are given in Table 6. Molecular descriptors reproduce the experimental log P and log L values for 2-methoxybenzoic and 4-methoxybenzoic acid to within an overall standard deviation of 0.146 log units and 0.114 log units, respectively, as shown in Tables 4–6. Based on our past experience with the Abraham solvation parameter model, we expect that one could use the molecular descriptors in Table 6 to predict both the solubility and practical organic solvent–water partition coefficients of the two methoxybenzoic acids to within 0.20 log units for organic solvents in which carboxylic acid dimerization does not occur.

Table 6. Molecular descriptors and input properties for 2-methoxybenzoic acid and 4-methoxybenzoic acid.

Descriptor	2-Methoxybenzoic acid	4-Methoxybenzoic acid
Molecular descriptors		
E	0.899	0.899
S	1.410	1.250
A	0.450	0.620
B	0.620	0.520
V	1.1313	1.1313
L	5.636	5.741
Input properties		
log C_W	–1.554	–2.800
log C_G	–8.354	–9.500
Statistical information		
Log P standard deviation	0.146	0.119
Log L standard deviation	0.146	0.110

Calculated descriptors account very well for the experimental data on solubilities and partition coefficients; how-

© 2004 NRC Canada

ever, the values must reflect chemical properties of the solute, otherwise, the descriptors are simply "fitting parameters". The hydrogen-bond acidity (**A** = 0.620) and basicity (**B** = 0.520) descriptors of 4-methoxybenzoic acid are slightly larger than the known acidity (**A** = 0.590) and basicity (**B** = 0.400) values for benzoic acid. The two lone electron pairs on the oxygen atom of the methoxy-substituent group provide additional donor sites, and increase the electron density of the aromatic ring. The calculated descriptors reflect this effect. The lower calculated hydrogen-bond acidity value (**A** = 0.450) of 2-methoxybenzoic acid is likely due to intramolecular hydrogen-bond formation, which is indicated by both solution IR, and proton, ^{13}C, and ^{17}O NMR measurements (32–36). Spectroscopic studies further suggest that a substituent at the 6-ring position inhibited the formation of hydrogen bonding, and that a substituent at the 3-ring position had some unfavorable steric effects (37). Interestingly, the hydrogen-bond basicity of 2-methoxybenzoic acid (**B** = 0.62) is larger than that of 4-methoxybenzoic acid (**B** = 0.52). However, whilst internal hydrogen bonding will reduce the basicity of the methoxy oxygen atom, it will actually increase the basicity of the oxygen atom in the carboxylic -OH group. A similar effect is found in 2-nitrophenol and 4-nitrophenol. The former has a very strong intramolecular hydrogen-bond (**A** = 0.05 and **B** = 0.37), whereas 4-nitrophenol (**A** = 0.82, **B** = 0.26) has no internal hydrogen-bond at all. Just as for the methoxybenzoic acids, the hydrogen-bond basicity of the internally hydrogen-bonded 2-nitrophenol is larger than that of 4-nitrophenol. Future studies will examine steric substituent effects in greater detail. Intramolecular hydrogen-bond formation is also suggested in molecular orbital computations. (36, 38) The degree of intramolecular hydrogen-bond formation is, of course, solvent dependent, and the solute descriptors that have been calculated for 2-methoxybenzoic acid do not correspond to a single geometric conformation, but rather correspond to an average of the different conformations that the molecule adopts in the solvents studied.

Readers will note that while the Abraham solvation parameter model has been employed to mathematically describe the solubility of 2-methoxybenzoic acid and 4-methoxybenzoic acid in organic solvents, the computational methodology can be applied to other molecules of interest. The computational methodology requires experimental solubility data of the solute molecule in water and in a dozen or solvents for which equation coefficients are known. The solute descriptors, after they have been calculated, can be used to predict the solute solubility in any of the organic solvents for which equation coefficients are known. To date we have derived equation coefficients for 40 or so dry organic solvents and have calculated molecular descriptors for over 3000 common organic and pharmaceutical compounds. In addition, the solvation descriptors can be estimated from the structure of a compound ((39), thus increasing the number of compounds whose log *P* and log *L* values can be predicted.

Acknowledgements

Research supported in part by the University of North Texas Research Council. Kaci Hoover thanks the University of North Texas and the US Department of Education for support provided under the Ronald E. McNair Post-baccalaureate Achievement Program.

References

1. M.H. Abraham. Chem. Soc. Rev. **22**, 73 (1993), and refs. therein.
2. M.H. Abraham, J.A. Platts, A. Hersey, A.J. Leo, and R.W. Taft. J. Pharm. Sci. **88**, 670 (1999).
3. M.H. Abraham, G.S. Whiting, W.J. Shuely, and R.M. Doherty. J. Chem. Soc. Perkin Trans. 2, 1851 (1990).
4. M.H. Abraham, A.M. Zissimos, and W.E. Acree, Jr. New J. Chem. **27**, 1041 (2003).
5. M.H. Abraham, A.M. Zissimos, J.G. Huddleston, H.D. Willauer, R.D. Rogers, and W.E. Acree, Jr. Ind. Eng. Chem. Res. **42**, 413 (2003).
6. M.H. Abraham, A.M. Zissimos, and W.E. Acree, Jr. Phys. Chem. Chem. Phys. **3**, 3732 (2001).
7. M.H. Abraham, J. Le, W.E. Acree, Jr., P.W. Carr, and A.J. Dallas. Chemosphere, **44**, 855 (2001).
8. M.H. Abraham, G.S. Whiting, P.W. Carr, and H. Ouynag. J. Chem. Soc. Perkin Trans. 2, 1777 (1994).
9. M.H. Abraham, G.S. Whiting, W.J. Shuely, and R.M. Doherty. Can. J. Chem. **76**, 703 (1998).
10. M.H. Abraham, J. Andonian-Haftvan, J.P. Osei-Owusu, P. Sakellariou, J.S. Urieta, M.C. Lopez, and R. Fuchs. J. Chem. Soc. Perkin Trans. 2, 299 (1993).
11. W.E. Acree, Jr. and M.H. Abraham. Can. J. Chem. **79**, 1466 (2001).
12. W.E. Acree, Jr. and M.H. Abraham. Fluid Phase Equilib. **201**, 245 (2002).
13. W.E. Acree, Jr. and M.H. Abraham. J. Solution Chem. **31**, 293 (2002).
14. M.H. Abraham, N. Benjelloun-Dakhama, J.M.R. Gola, W.E. Acree, Jr., W.S. Cain, and J.E. Cometto-Muniz. New J. Chem. **24**, 825 (2000).
15. M.H. Abraham, C.E. Green, and W.E. Acree, Jr. J. Chem. Soc. Perkin Trans. 2, 281 (2000).
16. C.E. Green, M.H. Abraham, W.E. Acree, Jr., K.M. DeFina, and T.L. Sharp, Pest. Manag. Sci. **56**, 1043 (2000).
17. M.H. Abraham, C.E. Green, W.E. Acree, Jr., C.E. Hernandez, and L.E. Roy. J. Chem. Soc. Perkin Trans. 2, 2677 (1998).
18. A.K. Charlton, C.R. Daniels, W.E. Acree, Jr., and M.H. Abraham. J. Solution Chem. **32**, 1087 (2003).
19. C.R. Daniels, A.K. Charlton, R.M. Wold, W.E. Acree, Jr., and M.H. Abraham. Can. J. Chem. **81**, 1492 (2003).
20. K.R. Hoover, R. Coaxum, E. Pustejovsky, D.M. Stovall, W.E. Acree, Jr., and M.H. Abraham. Phys. Chem. Liq. 42, 339 (2004).
21. R. Coaxum, K.R. Hoover, E. Pustejovsky, D.M. Stovall, W.E. Acree, Jr., and M.H. Abraham. Phys. Chem. Liq. **42**, 313 (2004).
22. J.S. Fritz and N.M. Lisicki. Anal. Chem. **23**, 589 (1951).
23. R. Thuaire. Bull. Soc. Chim. Fr. 3815 (1971).
24. P.A. Ongley. J. Chem. Soc. 3634 (1954).
25. A. Apelblat and E. Manzurola. J. Chem. Thermodyn. **29**, 1527 (1997).
26. M.H. Abraham, H.S. Chadha, J.P. Dixon, C. Rafols, and C. Treiner. J. Chem. Soc. Perkin Trans. 2, 887 (1995).
27. A.J. Leo. The medicinal chemistry project. Pomona College, Claremont, Calif. USA 2002.
28. A. Seidell. Solubilities of organic compounds. 3rd ed. Van Nostrand, New York. 1941.

© 2004 NRC Canada

29. C. Altomare, S. Cellamare, A. Carotti, and M. Ferappi. Quant. Struct.-Act. Relat. **12**, 261 (1993).
30. C. Altomare, S. Cellamare, A. Carotti, and M. Ferappi. Il Farmaco, **49**, 393 (1994).
31. M.H. Abraham and J.C. McGowan. Chromatographia, **23**, 243 (1987).
32. M.C. Etter, Z. Urbanczyk-Lipkowska, P.A. Fish, T.W. Panunto, P.W. Baures and J.S. Frye, J. Crystallog. Spectrosc. Res. **18**, 311 (1988).
33. O. Exner, P. Fiedler, M. Budesinsky, and J. Kulhanek. J. Org. Chem. **64**, 3513 (1999).
34. H.A. Lloyd, K.S. Warren, and H.M. Fales. J. Am. Chem. Soc. **88**, 5544 (1966).
35. L.A. Schmiedekamp-Schneeweis and J.O. Payne. Int. J. Quantum Chem. **70**, 863 (1998).
36. M. Kondo. Bull. Chem. Soc. Jpn. **45**, 2790 (1972).
37. M. Oki and M. Hirota. Bull Chem. Soc. Jpn. **37**, 213 (1964).
38. G. Jaccard, P.A. Carrupt, and J. Lauterwein. Magn. Reson. Chem. **26**, 239 (1988).
39. ADME. Version 2.2 [computer program]. Pharma Algorithms, Inc., 591 Indian Road, Toronto, ON M6P 2C4, Canada. 2004.

© 2004 NRC Canada

Synthesis and biological evaluation of a bicyclo[4.1.0]heptyl analogue of glucose-1-phosphate

Veedeeta Dookhun and Andrew J. Bennet

Abstract: The synthesis of a bicyclo[4.1.0]heptyl analogue of glucose-1-phophate, (1*R*,2*R*,3*S*,4*S*,5*S*,6*S*)-3,4,5-trihydroxy-6-(hydroxymethyl)-bicyclo[4.1.0]heptan-2-yl dihydrogen phosphate (**5**) is reported. The synthetic route chosen started with methyl α-D-glucopyranoside and was accomplished in 11 steps with an overall yield of 3%. Compound **5** was tested as a potential substrate of UTP:α-D-glucose-1-phosphate uridylyltransferase, the enzyme that converts glucose-1-phosphate into UDP-glucose. However, the conformationally restricted glucose-1-phosphate analogue **5** was found to be a weakly binding inhibitor, rather than a substrate, of the yeast transferase (12% inhibition at a concentration of 0.1 mmol L^{-1}).

Key words: glucose 1-phosphate, inhibition, UTP:α-D-glucose-1-phosphate uridylyltransferase.

Résumé : On a réalisé la synthèse d'un analogue bicyclo[4.1.0]heptyle du 1-phosphate de glucose, le dihydrogène phosphate de (1*R*,2*R*,3*S*,4*S*,5*S*,6*S*)-3,4,5-trihydroxy-6-(hydroxyméthyl)bicyclo[4.1.0]heptan-2-yle (**5**). La voie de synthèse choisie utilise l'α-D-glucopyranoside de méthyle comme produit de départ et implique onze étapes avec un rendement global de 3 %. Le composé **5** a été évalué comme substrat potentiel de l'uridylyltransférase UTP:1-phosphate d'α-D-glucose, l'enzyme qui transforme le 1-phosphate de glucose en UDP-glucose. On a toutefois trouvé que, en raison de ses restrictions conformationnelles, l'analogue **5** un faible inhibiteur de fixation plutôt qu'un substrat de la transférase de la levure (12 % d'inhibition à une concentration de 0,1 mmol L^{-1}).

Mots clés : 1-phosphate de glucose, inhibition, uridylyltransférase UTP:1-phosphate d'α-D-glucose.

[Traduit par la Rédaction]

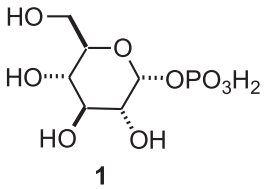
Introduction

Complex glycoconjugates are involved in numerous biochemical recognition processes, examples include fertilization, immune defense, viral and parasitic infections, cell growth, cell adhesion, and inflammation (1, 2). The assembly of oligosaccharides in living systems requires sugar nucleotide donors, compounds that are biosynthesized from glycosyl phosphates (3). For example, uridine 5′-(α-D-glucopyranosyl diphosphate) (UDP-Glc), a key intermediate in many biochemical pathways including that of glycogen formation, is made enzymatically from α-D-glucopyranosyl phosphate (Glc1P) and uridine 5′-triphosphate (UTP) (Scheme 1) (3).

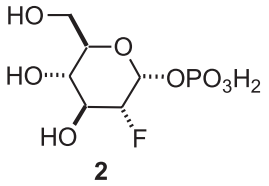
The biological importance of glycosyl phosphates has resulted in many researchers investing considerable effort to synthesize analogues of this important class of compounds. In the specific case of α-D-glucopyranosyl phosphate (**1**), analogues that have been reported include: (*i*) **2** a compound in which the C-2 hydroxyl group has been replaced by a fluorine atom (4); (*ii*) **3** an analogue that is hydrolytically stable (5, 6); and (*iii*) **4** a mimic where O-5 has been substituted by a phosphate group (7–9).

Scheme 1. Reaction catalyzed by UTP:α-D-glucose-1-phosphate uridylyltransferase.

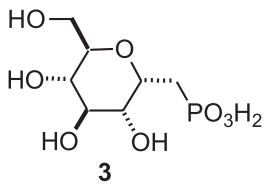




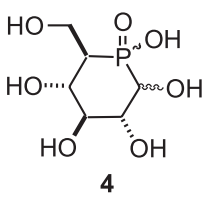
1



2



3



4

The synthesis and characterization of a novel, conformationally rigid, carbocyclic analogue of Glc1P is described. The target compound (**5**) was chosen on the basis of the potent α-glucosidase inhibition reported by Tanaka et al.

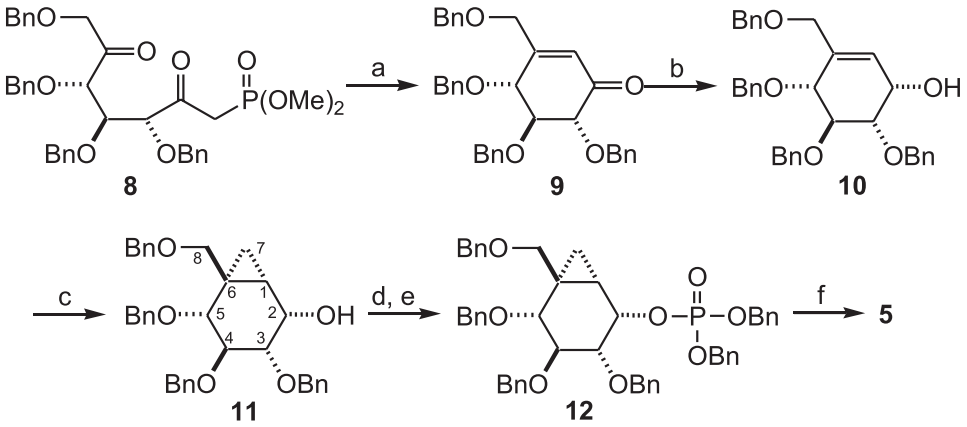
Received 13 April 2004. Published on the NRC Research Press Web site at http://canjchem.nrc.ca on 23 October 2004.

V. Dookhun and A.J. Bennet.[1] Department of Chemistry, Simon Fraser University, 8888 University Drive, Burnaby, BC V5A 1S6, Canada.

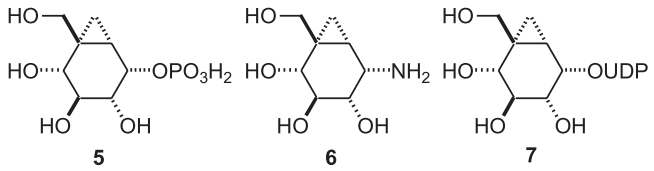
[1]Corresponding author (e-mail: bennet@sfu.ca).

 doi: 10.1139/V04-109 © 2004 NRC Canada

Scheme 2. Synthesis of **5**, a bicyclo[4.1.0]heptyl analogue of glucose-1-phosphate: (*a*) $LiCl{\cdot}H_2O$, Et_3N, CH_2Cl_2; (*b*) L-selectride, THF, 0 °C; (*c*) $(Me)_2Zn$, CH_2I_2, toluene, –10 °C; (*d*) dibenzyl diisopropylphosphoramidate, tetrazole, CH_2Cl_2; (*e*) bleach, THF at RT; (*f*) 10% Pd-C, MeOH.



(10) of the compound **6**, which is a rigid carbocyclic analogue of α-D-glucopyranosylamine. In compound **6** the fused cyclopropane ring forces the six-membered ring into a half-chair conformation (10). In addition, **5** was examined with the yeast UTP:α-D-glucose-1-phosphate uridylyltransferase (Scheme 1) to test whether the UDP-analogue **7** could be made by a chemoenzymatic approach.



Results and discussion

Enone **9** was synthesized from methyl α-D-glucopyranoside in seven steps according to a literature procedure (11) except that triethylamine and LiCl were used to cyclize compound **8** (see Experimental section for full details). This modification was made because the cyclization of **8** proceeded faster with these reagents than it did when the combination of 18-crown-6 and K_2CO_3 (11) was used. As a consequence of this modification, it was observed that the enone product was less prone to aromatize. Attempted reduction of enone **9** with several reagents such as $LiAlH_4$, $LiAl(OBu\text{-}t)_3H$, and $ZnBH_4$ resulted in the formation of mixtures, of varying ratio, of two diastereomeric alcohols. However, the use L-selectride in THF at 0 °C gave a stereospecific reduction that produced only the pseudo-axial allylic alcohol **10** in 78% yield (Scheme 2). The stereochemistry of **10** was assigned based on the smaller coupling constant observed between H-1 and H-6 in the ^1H NMR spectrum in comparison to the reported value for the pseudo-equatorial diastereomer (11). Alcohol **10** was then reacted using Furakawa et al.'s protocol (12) to afford compound **11** as the only observable diastereomer in a 62% yield. The stereochemistry of bicyclo-[4.1.0]heptane **11** was confirmed by an nOe experiment to be equivalent to that of D-glucose rather than L-idose. Specifically, a strong nOe contact was observed between H-7*S* and H-4 (see numbering labels in Scheme 2).

Reaction of **11** with reagents such as diphenylphosphochloridate (13, 14) and tetraphenylpyrophosphate (15) in the presence of various bases failed to yield any phosphorylated products. However, the use of the phosphitylation method gave the expected phosphite product (16–18). The phosphite was immediately oxidized using a solution of bleach in THF–water. Standard work up procedures when followed by column chromatography afforded analytically pure **12** in a yield of 52%. Subsequent removal of the benzyl protecting groups was realized, in a quantitative yield, by hydrogenation in the presence of 10% Pd-C.

Enzymatic studies

Compound **5** was tested as a potential substrate for Baker's yeast UTP:α-D-glucose-1-phosphate uridylyltransferase (EC 2.7.7.9). Formation of the UDP-glucose analogue (**7**) would be accompanied by the simultaneous production of pyrophosphate (Scheme 1). The production of pyrophosphate was monitored by use of a commercial assay (19). Unfortunately, compound **5** was shown not to be a substrate for the Baker's yeast uridylyltransferase as no pyrophosphate was detected. Moreover, addition of **5** (0.1 mmol L^{-1}) to a UTP:α-D-glucose-1-phosphate uridylyltransferase-catalyzed reaction containing Glc1P (0.1 mmol L^{-1}) and UTP (0.1 mmol L^{-1}) resulted in a 12% reduction in the rate of pyrophosphate production. Therefore, it can be concluded that **5**, a conformationally rigid Glc1P analogue, is a weakly binding inhibitor of the yeast uridylyltransferase enzyme.

Experimental

General

Toluene and dichloromethane were distilled from CaH_2 prior to use. THF was dried over sodium in the presence of benzophenone. NMR spectra were recorded on Varian 500 MHz spectrometer. Chemical shifts (δ in ppm) are given relative to tetramethylsilane for (^1H and ^{13}C) and external 85% H_3PO_4 (for ^{31}P). Only definitive ^1H and ^{13}C assignments, which were made using standard 1D, ^1H–^1H COSY, and HMQC NMR experiments, are listed. All glassware was flame-dried before use. Dibenzyl diisopropylphosphor-

© 2004 NRC Canada

amidite was stored as a 50 mg/mL solution in anhydrous dichloromethane under an atmosphere of nitrogen.

(4*R*,5*S*,6*R*)-4,5,6-Tris(benzyloxy)-3-((benzyloxy)methyl)-2-cyclohexen-1-one (9)

To a stirred solution of 3,4,5,7-tetra-*O*-benzyl-1-deoxy-1-(dimethoxyphosphoryl)-D-*xylo*-2,6-heptodiulose **8** (11) (9.4 g, 14 mmol) in dry CH_2Cl_2 (300 mL) was added $LiCl{\cdot}H_2O$ (0.30 g, 0.5 equiv.) and Et_3N (2.18 mL, 1.1 equiv.). The reaction mixture was stirred for about 6 h. The organic phase was washed with aq. H_2SO_4 (100 mL, 5% v/v), satd. aq. $NaHCO_3$ (100 mL), brine (100 mL) and concentrated at aspirator pressure to afford a yellow syrup. The crude product material was purified by flash column chromatography (hexanes–EtOAc, 2:1) to give the product (4.17 g, 60%) as a colorless syrup. This material exhibited identical ^1H and ^{13}C NMR data to those reported in the literature (11).

(1*S*,4*R*,5*S*,6*S*)-4,5,6-Tris(benzyloxy)-3-((benzyloxy)methyl)-2-cyclohexen-1-ol (10)

A 1 mol L^{-1} solution of L-selectride in THF (11.7 mL, 1.5 equiv.) was added in a dropwise manner to a stirred and cooled (0 °C) solution of enone **9** (4.17 g, 7.8 mmol) in THF (200 mL) under a nitrogen atmosphere. The mixture was stirred for 18 h as it warmed to room temperature gradually. A saturated solution of NH_4Cl (50 mL) was added and the resulting mixture was stirred for 15 min after which water (100 mL) was added. Then the aqueous solution was extracted with EtOAc (2 × 150 mL), the organic extracts were washed with brine and dried over Na_2SO_4. A pale yellow syrup was obtained upon removal of the volatiles under reduced pressure. The resultant crude product was purified by column chromatography (hexanes–EtOAc, 2:1 v/v) to afford allylic alcohol **12** as a colourless syrup (3.22 g, 77%). $[\alpha]_D^{20}$ –39.0 (*c* 1.00, CH_2Cl_2). ^1H NMR ($CDCl_3$) δ: 2.57 (bs, 1H, OH), 3.59 (dd, 1H, $J_{6,5}$ = 9.3 Hz, $J_{6,1}$ = 4.1 Hz, H-6), 3.94 (d, 1H, $J_{7a,7b}$ = 12.3 Hz, CH_{7a}H$_{7b}$OBn), 4.05 (dd, 1H, $J_{5,4}$ = 6.8 Hz, H-5), 4.16 (dd, 1H, $J_{4,2}$ = 1.0 Hz, H-4), 4.23 (dd, 1H, $J_{7b,2}$ = 1.0 Hz, CH$_{7a}$$H_{7b}$OBn), 4.30 (t, 1H, $J_{1,2}$ + $J_{1,6}$ = 8.9 Hz, H-1), 4.46 (d, 1H, $J_{A,B}$ = 11.9 Hz, CH_ACH$_B$C$_6$H$_5$), 4.48 (d, 1H, CH$_A$CH_BC$_6$H$_5$), 4.66 (d, 1H, $J_{C,D}$ = 10.3 Hz, CH_CH$_D$C$_6$H$_5$), 4.68 (d, 1H, $J_{E,F}$ = 11.5 Hz, CH_EH$_F$C$_6$H$_5$), 4.74 (d, 1H, $J_{G,H}$ = 11.2 Hz, CH_GH$_H$C$_6$H$_5$), 4.78 (d, 1H, CH$_C$$H_DC_6H_5$), 4.79 (d, 1H, CH$_E$$H_FC_6H_5$), 4.87 (d, 1H, CH$_G$$H_HC_6H_5$), 5.91 (dd, 1H, $J_{2,1}$ = 4.9 Hz, $J_{2,6}$ = 1.4 Hz, H-2) 7.10–7.52 (m, 20H, H-Ar). ^{13}C NMR ($CDCl_3$) δ: 65.1 (C-1), 70.2 (C-7), 72.6 (*C*H$_A$H$_B$C$_6$H$_5$), 72.9 (*C*H$_E$H$_F$C$_6$H$_5$), 74.0 (*C*H$_C$H$_D$C$_6$H$_5$), 74.7 (*C*H$_G$H$_H$C$_6$H$_5$), 78.7 (C-4), 78.8 (C-6), 79.1 (C-5), 124.6 (C-2), 127.5, 127.6, 127.7, 127.9 (2 C), 128.0, 128.3 (2 C), 128.4, 128.5, 137.9, 138.1, 138.5, 138.6. Anal. calcd. for $C_{35}H_{37}O_5$: C 78.33, H 6.76; found: C 78.17, H 6.65.

(*1S*,2*S*,3*S*,4*S*,5*R*,6*R*)-3,4,5-Tris(benzyloxy)-6-((benzyloxy)methyl)-bicyclo[4.1.0]heptan-2-ol (11)

To rigorously dried allylic alcohol **12** (500 mg, 0.9 mmol) in dry toluene (100 mL) under nitrogen at –10 °C was added a 2 mol L^{-1} solution of Me_2Zn in toluene (4.00 mL, 8 mmol) dropwise. The mixture was stirred for 15 min, following which CH_2I_2 (1.4 mL, 18 mmol) was added dropwise and the resulting mixture was stirred overnight as the solution was allowed to warm up to room temperature. A saturated solution of NH_4Cl (50 mL) was added and the mixture was stirred for another 30 min. The resulting solution was then diluted with water (100 mL) and extracted with EtOAc (3 × 100 mL). The combined organic extracts were washed with 10% H_2SO_4 (150 mL), $NaHCO_3$ (150 mL), and brine (150 mL), and then dried over Na_2SO_4. Removal of the volatiles gave a yellow oil that was purified by column chromatography (hexanes–EtOAc, 2:1 v/v) to afford the cyclopropanated allylic alcohol **11** as a colourless syrup (317 mg, 62%). $[\alpha]_D^{20}$ +24.5 (*c* 1.10, CH_2Cl_2). ^1H NMR ($CDCl_3$) δ: 0.52 (dd, 1H, $J_{7R,1}$ = 9.5 Hz, $J_{7R,7S}$ = 5.8 Hz, H-7*R*), 1.14 (t, 1H, $J_{7S,7R}$ + $J_{7S,1}$ = 11.4 Hz, H-7*S*), 1.34 (m, 1H, H-1), 2.55 (bs, 1H, OH), 2.67 (d, 1H, $J_{8a,8b}$ = 10.0 Hz, H-8a), 3.42 (dd, 1H, $J_{4,3}$ = 9.6 Hz, $J_{2,3}$ = 4.6 Hz, H-3), 3.60 (dd, 1H, $J_{4,5}$ = 7.8 Hz, 1H, H-4), 3.81 (d, 1H, H-8b), 4.18 (d, 1H, H-5), 4.31 (d, 1H, $J_{A,B}$ = 12.1 Hz, CH_AH$_B$C$_6$H$_5$), 4.38 (d, 1H, CH$_A$$H_BC_6H_5$), 4.43 (dd, 1H, $J_{1,2}$ = 7.9 Hz, H-2), 4.61 (d, 1H, $J_{C,D}$ = 11.4 Hz, CH_CH$_D$C$_6$H$_5$), 4.63 (d, 1H, $J_{E,F}$ = 11.5 Hz, CH_EH$_F$C$_6$H$_5$), 4.70 (d, 1H, $J_{G,H}$ = 10.8 Hz, CH_GH$_H$C$_6$H$_5$), 4.78 (d, 1H, CH$_C$$H_DC_6H_5$), 4.82 (d, 1H, CH$_G$$H_HC_6H_5$), 4.84 (d, 1H, CH$_E$$H_FC_6H_5$), 7.18–7.42 (m, 20H, H-Ar). ^{13}C NMR ($CDCl_3$) δ: 8.8 (C-7), 22.3 (C-1), 28.3 (C-6), 64.6 (C-2), 72.7 (*C*H$_A$H$_B$C$_6$H$_5$), 73.1 (*C*H$_C$H$_D$C$_6$H$_5$), 74.5 (*C*H$_E$H$_F$C$_6$H$_5$), 74.9 (2 C, C-8, *C*H$_G$H$_H$C$_6$H$_5$), 78.6 (C-4), 79.2 (C-5), 80.9 (C-3), 127.4, 127.6 (2 C), 127.7, 127.8, 128.2, 128.3, 128.4 (2 C), 138.0, 138.2, 138.6, 139.0. Anal. calcd. for $C_{36}H_{39}O_5$: C 78.52, H 6.95; found: C 78.40, H 6.95.

(1*S*,2*S*,3*R*,4*S*,5*R*,6*R*)-3,4,5-Tris(benzyloxy)-6-((benzyloxy)methyl)-bicyclo[4.1.0]heptan-2-yl dibenzyl phosphate (12)

Dibenzyl diisopropylphosphoramidite (358 mg, 1.03 mmol) and tetrazole (105 mg, 1.50 mmol) were mixed vigorously in dry CH_2Cl_2 (30 mL) under nitrogen for about 30 min after which time the tetrazole had partially dissolved. A solution of alcohol **11** (275 mg, 0.5 mmol), which had previously been co-evaporated with dry toluene (3 × 50 mL), in dry CH_2Cl_2 (20 mL) was added to the above reaction mixture via a syringe. The resulting reaction mixture was stirred until the starting material had disappeared (monitored by TLC, hexanes – ethyl acetate, 2:1 v/v). Then the solution was concentrated under reduced pressure and the resulting residue was purified by column chromatography (hexanes–EtOAc, 2:1 v/v) to give the expected phosphite. After this material had been dissolved in THF (75 mL), a 5% v/v bleach solution (2 mL) was added and this mixture was stirred for about 1 h. The solvent was removed under reduced pressure, and then water (100 mL) was added and the aqueous solution was extracted with CH_2Cl_2 (3 × 50 mL). The combined organic extracts was washed with water (100 mL) and dried over $MgSO_4$. After removal of the solvent under reduced pressure, the residue was purified by column chromatography (toluene–acetone, 8:1 v/v) to afford a colorless oil (213 mg, 52%). $[\alpha]_D^{20}$ +58.0 (*c* 1.00, CH_2Cl_2). ^1H NMR ($CDCl_3$) δ: 0.53 (dd, 1H, $J_{7R,1}$ = 9.5 Hz, $J_{7R,7S}$ = 5.8 Hz, H-7*R*), 1.12 (t, 1H, $J_{7S,7R}$ + $J_{7S,1}$ = 11.4 Hz, H-7*S*), 1.41 (m, 1H, H-1), 2.60 (d, 1H, $J_{8a,8b}$ = 10.0 Hz, H-8a), 3.44 (m, 1H, H-3), 3.56 (dd, 1H, $J_{4,5}$ = 8.1 Hz, $J_{3,4}$ = 10.1 Hz, H-4), 3.72 (d, 1H, H-8b), 4.16 (d, 1H, H-5), 4.30 (d, 1H, $J_{A,B}$ =

© 2004 NRC Canada

12.3 Hz, CH_ACH_BC$_6$H$_5$), 4.31 (d, 1H, CH$_A$CH_BC$_6$H$_5$), 4.57–4.64 (m, 3H, CH_CH$_D$C$_6$H$_5$, CH_EH$_F$C$_6$H$_5$, CH_GH$_H$C$_6$H$_5$) 4.75–4.88 (m, 3H, CH$_C$CH_DC$_6$H$_5$, C$_E$H$_F$C$_6$H$_5$, CH$_G$CH_HC$_6$H$_5$), 4.94–5.08 (m, 4H, 2P(O)OCH_2OPh), 5.33 (td, 1H, $J_{2,3}$ = 4.5 Hz, $J_{1,2}$ + $J_{2,P}$ = 15.4 Hz, H-2) 7.18–7.40 (m, 30H, H-Ar). ^{13}C NMR (CDCl$_3$) δ: 10.0 (C-7), 22.1 (C-1), 29.1 (C-6), 69.3 (2 C, P(O)OCH$_2$OPh), 72.7 (C-2), 72.6 (CH_AH$_B$C$_6$H$_5$), 72.6$_4$ (CH_CH$_D$C$_6$H$_5$), 74.2 (C-8), 74.7 (CH_EH$_F$C$_6$H$_5$), 74.9(CH_GH$_H$C$_6$H$_5$), 78.2 (C-4), 78.4 (C-3) 127.4, 127.5, 127.6, 127.7, 128.0, 128.1, 128.2, 128.3, 128.4, 128.5, 128.7, 135.5, 135.6, 136.1, 138.1, 138.5, 138.9. ^{31}P NMR (CDCl$_3$) δ: –0.53. Anal. calcd. for C$_{50}$H$_{52}$O$_8$P: C 74.06, H 6.34; found: C 73.76, H 6.49.

(1*R*,2*R*,3*S*,4*S*,5*S*,6*S*)-3,4,5-Trihydroxy-6-(hydroxymethyl)-bicyclo[4.1.0]heptan-2-yl dihydrogen phosphate (5)

To a solution of **12** (200 mg) in dry methanol (20 mL) was added 10% Pd on carbon (84 mg). The mixture was stirred under an atmosphere of hydrogen for 24 h. The solution was filtered and the residue was washed thoroughly with MeOH. The combined filtrate was evaporated to dryness and dried under vacuum to afford a colourless solid (66.4 mg, 99% yield). $[\alpha]_D^{20}$ +23 (c = 1.00, H$_2$O). ^{1}H NMR (D$_2$O) δ: 0.58 (dd, 1H, $J_{7R,1}$ = 9.5 Hz, $J_{7R,7S}$ = 5.9 Hz H-7*R*), 0.91 (t, 1H, $J_{7S,7R}$ + $J_{7S,1}$ = 11.3 Hz, H-7*S*), 1.50 (m, 1H, H-1), 2.84 (d, 1H, $J_{8a,8b}$ = 11.9 Hz, H-8), 3.29–3.39 (m, 2H, H-3, H-4), 3.94 (d, 1H, H-8b), 4.00 (d, 1H, $J_{4,5}$ = 7.6 Hz, H-5), 4.71 (td, 1H, $J_{2,3}$ = 4.5 Hz, $J_{2,1}$ + $J_{2,P}$ = 15.4 Hz, H-2). ^{13}C NMR (D$_2$O) δ: 12.0 (C-7), 24.7 (C-1), 33.4 (C-7), 68.3 (C-8), 72.3 (C-3), 73.9 (C-4), 74.7 (C-5), 74.9 (C-2). ^{31}P NMR (D$_2$O) δ: –0.59.

Biological activity assays

To a solution of 2-amino-6-mercapto-7-methylpurine riboside (0.2 mmol L^{-1}) in 50 mmol L^{-1} Tris HCl buffer pH 7.5 (1 mL) was added pyrophosphorylase (1 × 10^{-3} units), purine nucleoside phosphorylase (PNP) (1 × 10^{-2} units), compound **5** (0.1 mmol L^{-1}), glucose-1-phosphate (0.1 mmol L^{-1}), and UTP (0.1 mmol L^{-1}). This mixture was equilibrated at 22 °C for 10 min. The reaction was then initiated by the addition of UTP:glucose-1-phosphate uridylyltransferase (1 × 10^{-4} units) and the production of 2-amino-6-mercapto-7-methylpurine was monitored using a Cary 3E spectrophotometer at a wavelength of 360 nm. Similar assays were performed in the absence of either glucose-1-phosphate or compound **5**.

Acknowledgements

The authors wish to thank the Natural Sciences and Engineering Research Council of Canada (NSERC) for funding this research.

References

1. R.A. Dwek. Chem. Rev. **96**, 683 (1996).
2. A. Varki. Glycobiology, **3**, 97 (1993).
3. D. Voet and J.G. Voet. Biochemistry. 2nd. ed. John Wiley and Sons Inc., New York. 1995. pp. 608–617.
4. I.P. Street, K. Rupitz, and S.G. Withers. Biochemistry, **28**, 1581 (1989).
5. F. Nicotra, F. Ronchetti, and G. Russo. J. Chem. Soc., Chem. Commun. 470 (1982).
6. F. Nicotra, F. Ronchetti, and G. Russo. J. Org. Chem. **47**, 4459 (1982).
7. H. Yamamoto, T. Hanaya, H. Kawamoto, S. Inokawa, M. Yamashita, M.A. Armour, and T.T. Nakashima. J. Org. Chem. **50**, 3516 (1985).
8. T. Richter, P. Luger, T. Hanaya, and H. Yamamoto. Carbohydr. Res. **193**, 9 (1989).
9. T. Hanaya and H. Yamamoto. Helv. Chim. Acta, **85**, 2608 (2002).
10. K.S.E. Tanaka, G.C. Winters, R.J. Batchelor, F.W.B. Einstein, and A.J. Bennet. J. Am. Chem. Soc. **123**, 998 (2001).
11. H. Fukase and S. Horii. J. Org. Chem. **57**, 3651 (1992).
12. J. Furukawa, N. Kawabata, and J. Nishimura. Tetrahedron, **24**, 53 (1968).
13. M. Inage, H. Chaki, S. Kusumoto, and T. Shiba. Chem. Lett. 1281 (1982).
14. H. Yuasa, O. Hindsgaul, and M.M. Palcic. J. Am. Chem. Soc. **114**, 5891 (1992).
15. H.G. Khorana and A.R. Todd. J. Chem. Soc. 2257 (1953).
16. K.L. Yu and B. Fraser-Reid. Tetrahedron Lett. **29**, 979 (1988).
17. W. Bannwarth and A. Trzeciak. Helv. Chim. Acta, **70**, 175 (1987).
18. D.J.R. Massy and P. Wyss. Helv. Chim. Acta, **73**, 1037 (1990).
19. M.R. Webb. Proc. Natl. Acad. Sci. U.S.A. **89**, 4884 (1992).

© 2004 NRC Canada

Synthesis of phosphonium salts under microwave activation — Leaving group and phosphine substituents effects

Ján Cvengros, Stefan Toma, Sylvain Marque, and André Loupy

Abstract: The specific nonpurely thermal effects of microwaves were evidenced according to neutral or charged leaving groups during nucleophilic substitution of benzylic electrophiles with triphenylphosphine and tributylphosphine. Microwave (MW) irradiation considerably enhanced the reactions with charged alkylating agents, especially under solvent-free conditions. Results are interpreted considering the magnitude of MW effects according to the position of the transition state along the reaction coordinates.

Key words: microwave irradiation, specific effects, phosphonium salts, leaving group effects.

Résumé : Des effets spécifiques non purement thermiques des micro-ondes ont été mis en évidence. Ils dépendent de la nature neutre ou chargée des groupes partants au cours de la substitution nucléophile par la triphénylphosphine ou la tributylphosphine sur des agents benzylants. L'irradiation micro-onde augmente considérablement les vitesses de réaction avec les agents alkylants chargés, particulièrement dans des conditions sans solvant. Les résultats sont interprétés en considérant les effets des micro-ondes en fonction de la position de l'état de transition sur les coordonnées réactionnelles.

Mots clés : irradiation aux micro-ondes, effets spécifiques, sels de phosphonium, effets de groupes partants.

[Traduit par la Rédaction]

Introduction

Application of microwave (MW) irradiation in organic synthesis is well documented (1–10). Most of the publications describe significant accelerations for a wide range of organic reactions especially when carried out under solvent-free conditions. They can find their origins in either thermal effects and (or) specific nonpurely thermal effects. Therefore, a vivid discussion was going on the possible intervention of any specific microwave effect resulting from decrease in the free energy of activation or if the enhancement of the reactions is due to a local overheating of the reaction mixture (11–13) (a hot spot effect as advocated in sonochemistry) (14).

Microwaves consist of electromagnetic waves generated by an alternating electric field of high frequency. The energy associated with a MW photon (1 J mol^{-1} by application of Planck's law $E = h\nu$ with $\nu = 2450$ MHz) is by far too small to induce any excitation of molecules. It can, however, provoke thermal effects because of some internal friction among polar molecules during their changes in orientation with each alternation of the electric field. In addition, they can induce some electrostatic interactions with polar materials by dipole–dipole interactions, rather similar to the behaviour of a dipolar solvent. It was, for instance, shown that the regioselectivity of phenacylation of 1,2,4-triazole is the same under conventional heating in a dipolar aprotic solvent (DMF) and under MW irradiation in a non-polar medium (xylene), or even in the absence of any solvent (15). By analogy and extension of the interpretation of solvent effects, the carbon–halogen bond breaking in S_N2 reactions can be facilitated by an increase in the polarity of the system during the reaction progress from the ground state to its transition state and could depend on the leaving group ability.

A working hypothesis was therefore advanced very recently according to which it is possible to predict (according to the type of reaction) if a significant specific (non-purely thermal) MW effect can be observed (15, 16). It considers medium and mechanism influences on the MW-assisted reactions. MW stabilizations by electrostatic dipole–dipole interactions between materials and the electromagnetic field are foreseen to be increased if the polarity of the systems are increased when the reaction is progressing. From a reactivity point of view, a decrease in the energy of activation by extending stabilization from the ground state can be expected towards the transition state can be expected (15–17). It would be the case when polar mechanisms are concerned, i.e., when there is a development of charge during the course of the reaction. It would also be the case if the position of

Received 20 February 2004. Published on the NRC Research Press Web site at http://canjchem.nrc.ca on 23 October 2004.

J. Cvengros and S. Toma. Faculty of Natural Sciences, Comenius University, SK-842 15 Bratislava, Slovakia.
S. Marque and A. Loupy.[1] Laboratoire des Réactions Sélectives sur Supports, Université de Paris-Sud, Institut de Chimie Moléculaire et des Matériaux d'Orsay, CNRS UMR 8615, building 410, F-91405, Orsay, France.

[1]Corresponding author (e-mail: aloupy@icmo.u-psud.fr).

 doi: 10.1139/V04-103 © 2004 NRC Canada

Table 1. Reaction of triphenylphosphine **1b** with benzylating agents **2a**–**2c**.

Entry	X	Solvent	*t* (min)	*T* (°C)	Yield for **3** using MW (%)[a,b]	Yield for **3** using CH (%)[a,c]
1	Br (**2a**)	No	10	100	99 (**3ba**)	99
2		No	2	100	99	98
3	Cl (**2b**)	Xylene	30	140	33 (**3bb**)	11
4		No	10	150	94	91
5		No	10	100	78	24
6	$N^+Me_3Cl^-$ (**2c**)	No	10	150	70 (**3bb**)	0
7		No	10	250	95	70

[a]Yields in isolated products.
[b]MW = microwave irradiation inside a monomode S 402 reactor.
[c]CH = conventional heating inside a thermostatted oil bath under similar conditions.

the transition state lies later along the reaction coordinates (Hammond's postulate) (18).

MW syntheses of several triphenylalkylphosphonium salts were recently described by Kiddle (19–21). Several representative organic halides were treated with triphenylphosphine to afford phosphonium salts in excellent yields. The reaction times were reduced to 4 min or less from conventional heating times ranging from 30 min to 14 days. However, owing to the lack of accurate control of the temperature and to strict comparisons with conventional heating under similar conditions, the real intervention of MW activation is questionable and needs more detailed experiments for better understanding (22). This prompted us to publish our results on the study and interpretation of the microwave effects on the S_N2 reactions of alkylating agents (neutral or charged) with neutral nucleophiles (phosphines) (eq. [1]). This kind of experiment was synthetically exploited for the preparation of imidazolium and ephedrinium salts as ionic liquids by the alkylation of imidazole (23–26) or *N*-methylephedrine (27). Some preliminary results were previously presented at an international microwave chemistry meeting (28).

$$PR_3 \;(\mathbf{1}) + PhCH_2X \;(\mathbf{2}) \longrightarrow PhCH_2{}^+PR_3X^- \;(\mathbf{3}) \quad [1]$$

1 (**a**) R = *n*-C_4H_9 (**b**) R = C_6H_5

2 (**a**) X = Br (**b**) X = Cl (**c**) X = $N^+Me_3Cl^-$

3aa R = *n*-C_4H_9, X = Br
3ab R = *n*-C_4H_9, X = Cl
3ba R = C_6H_5, X = Br
3bb R = C_6H_5, X = Cl

Results

Reactions of benzyl halides and benzyl trimethylammonium chloride with triphenyl-phosphine **1b** were carried out either in xylene (a non-polar solvent, i.e., transparent to MW) or under solvent-free conditions. To check the possible intervention of specific (non-purely thermal) MW effects, control experiments were performed using conventional heating (CH) in a thermostated oil bath at the same temperature for the same time. Identical profiles for increasing temperature were maintained for both types of activation mode, allowing for the elimination of the purely thermal contribution of MW radiation (Fig. 1).

Table 1 gives the main results for the reaction of **1b** with the benzylating electrophiles **2a**–**2c**.

Solvent-free conditions were by far the most convenient and efficient ones (entry 3). With benzyl bromide at 100 °C, no special microwave effects were observed (entries 1 and 2).

When using benzyl chloride, similar yields (>90%) of product **3** were obtained both under MW and CH within 10 min at 150 °C. Although the MW effect is not appreciable at 150 °C, it was however possible to put into evidence an important specific MW effect by lowering the temperature to 100 °C (entry 5).

When benzyl trimethylammonium chloride **2c** was used as the electrophile, no reaction took place under thermal heating at 150 °C whereas 70% of the product was formed after 10 min at 150 °C under MW irradiation. A very noticeable specific MW is therefore clearly revealed in this case. The yield reached 95% at 250 °C under MW and remained limited to 70% by CH.

By comparing the magnitude of the specific MW effects according to electrophile, we have thus established the sequence: **2c** >> **2b** > **2a**.

In Table 2, we give the main results obtained for the reaction of tributylphosphine with **2a**–**2c** under solvent-free conditions.

In the case of the reaction with benzyl bromide, yields are quite similar whatever the mode of activation (entries 8 and 9).

Using benzyl chloride, a quite important specific MW effect was revealed by shortening the reaction time at 100 °C (entry 11). These observations are in agreement with some

© 2004 NRC Canada

Table 2. Solvent-free reaction of tributylphosphine **1a** with benzylating agents **2a**–**2c**.

Entry	X	*t* (min)	*T* (°C)	Yield for **3** using MW (%)[a,b]	Yield for **3** using CH (%)[a,c]
8	Br (**2a**)	0.75	100	94 (**3aa**)	92
9		2	80	78	73
10	Cl (**2b**)	10	100	92 (**3ab**)	87
11		0.75	100	91	64
12	$N^+Me_3Cl^-$ (**2c**)	10	100	100 (**3ab**)	0

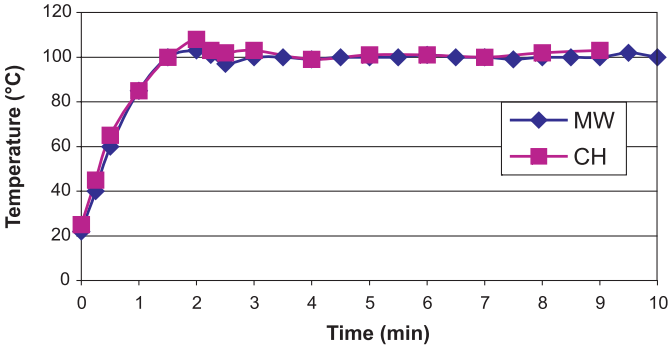
[a]Yields in isolated products.
[b]MW = microwave irradiation inside a monomode S 402 reactor.
[c]CH = conventional heating inside a thermostatted oil bath under similar conditions.

Table 3. Solvent-free alkylation of PR_3 by hexyl halides n-$C_6H_{13}X$.

Entry	R	X	*t* (min)	*T* (°C)	Yield for **5** using MW (%)[a,b]	Yield for **5** using CH (%)[a,c]
13	n-C_4H_9 (**1a**)	Br	5	100	95 (**5aa**)	78
14			1	60	30	2
15		Cl	90	150	81[d] (**5ab**)	40
16	C_6H_5 (**1b**)	Br	10	120	65 (**5ba**)	11
17			10	150	72	70
18		Cl	120	150	72[d] (**5bb**)	11

[a]Yields in isolated products.
[b]MW = microwave irradiation inside a monomode S 402 reactor.
[c]CH = conventional heating inside a thermostatted oil bath under similar conditions.
[d]Using a CEM Discover microwave device in closed vessels and under magnetical stirring.

Fig. 1. Profiles for the rise in temperature for the MW and CH methods.



previous ones. To find any evidence of specific MW effects, a reduction in the temperature and (or) reaction time under CH is needed to start from a rather poor yield to have the possibility of observing any specific MW effects. These cases have been revealed in some studies where MW effects appeared at lower temperatures. They can be masked at higher temperatures when yields of CH reactions are high (29–32).

With the charged electrophile **2c**, a very decisive specific effect is evidenced within 10 min at 100 °C; the reaction only occurred under MW and not at all by CH (entry 12).

The order of relative magnitude of specific MW effects leads to the same sequence as with **1b**: **2c** >> **2b** > **2a.** By comparing the two phosphines, it can be established that the specific MW effects are: **1b** > **1a** (compare entries 5 and 11 with **2b**).

We finally examined the reaction of the two phosphines with *n*-hexyl halides (eq. [2]). The main results are given in Table 3.

$$\underset{\mathbf{1}}{PR_3} + \underset{\mathbf{4}}{n\text{-}C_6H_{13}} \longrightarrow \underset{\mathbf{5}}{n\text{-}C_6H_{13}{}^+PR_3X^-} \quad [2]$$

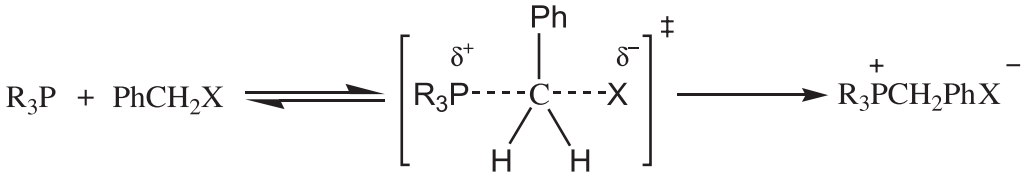
1 (**a**) R = n-C_4H_9 (**b**) R = C_6H_5

4 (**a**) X = Br (**b**) X = Cl

5aa R = n-C_4H_9, X = Br
5ab R = n-C_4H_9, X = Cl
5ba R = n-C_6H_5, X = Br
5bb R = n-C_6H_5, X = Cl

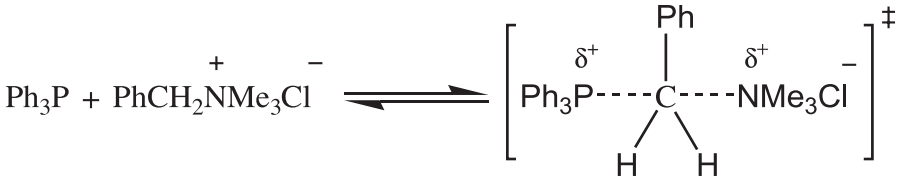
© 2004 NRC Canada

Scheme 1.



(GS) (Dipolar TS)

Scheme 2.



(Tight ion pair) (Loose ion pair)

In the case of **1a**, within 5 min at 100 °C, the reaction essentially occurred with hexyl bromide and with only slight MW effects (entry 13). With hexyl chloride at 150 °C within 90 min in closed vessels, a yield of 81% was obtained under MW and only 40% via CH. The magnitude of specific MW effects is clearly **4b** > **4a**.

With **1b**, satisfactory yields were obtained as well with bromide and chloride. Important MW specific effects were revealed (entries 16 and 18). The magnitude of these specific MW effects are clearly **1b** > **1a**.

Discussion

If the problem of thermal homogeneity can be taken into account, essentially when the reaction gave a solid during the reactions of triphenylphosphine **1b** (Table 1, most of the products are solids), this is not the case for the reactions of tributylphosphine **1a** (Table 2, most of the products are liquids). These problems are, however, largely minimized due to efficient mechanical stirring and accurate measurement of the temperature with an optical fiber inside the mixture.

In recent reviews (15, 16, 33), a lot of specific MW effects were explained and foreseen by considering the enhancement in polarity during the progress of the reaction. It is stated, from numerous experiments from our laboratory and the literature that they can be observed in a reaction if the transition state (TS) is more polar than its ground state (GS). It thus results in an increase in its stabilization by dipole–dipole electrostatic interactions and, consequently, a decrease in the activation energy.

Another important rule for the observation of MW effects is connected to the position of the TS along the reaction coordinates. In a polar mechanism, the later the TS (more product-like) the most important the MW effects; they will be weak if the TS is more reactant-like.

Benzyl halides

It was shown in both cases that benzyl chloride is more prone to lead to MW effects. The mechanism of the reaction concerns two neutral reagents leading to a dipolar TS (Scheme 1).

Concerning the leaving group ability, it is clear that chloride is a poorer electrofugal group when compared to the bromide equivalent, if we consider, for instance, the bond energies (C-Br, 66 kcal mol^{-1} and C-Cl 79 kcal mol^{-1}) (34). Therefore, the TS involving C—Cl bond breaking will occur later on the reaction coordinates than the one involving C-Br. It, therefore, can justify the increase in the magnitude of MW effects according to the sequence **2b** > **2a**.

Charged electrophiles

When benzyl trimethylammonium chloride **2c** was used as the reagent no reaction took place under thermal heating at 150 °C, whereas 70% of the product was formed after 10 min at 150 °C under MW irradiation. The magnitude of the specific MW effect is strongly amplified. It can be readily attributed to the very loose structure of the ion pairs in the TS (additionally involving the phenyl groups of the phosphine) and which are therefore far more polar than the initial tight ion pairs in the GS (positive charge is localized on the nitrogen atom) (Scheme 2).

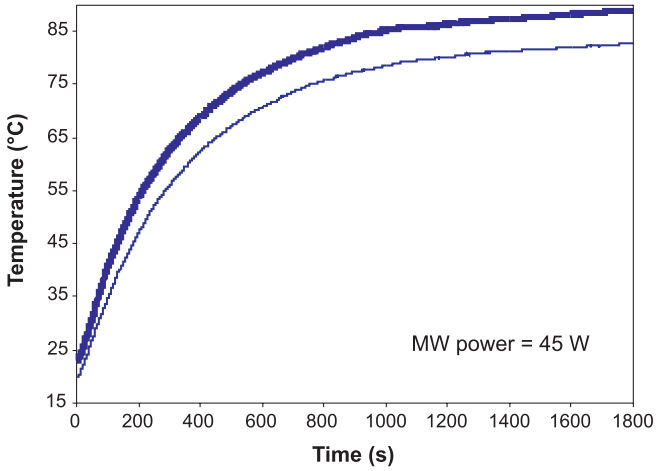
This behavior can also be foreseen if one considers the poor leaving ability of the ammonium moiety and which induces a late TS along the reaction coordinates, and consequently, important MW effects.

Phosphine substituent effects

Effects are more important with triphenylphosphine **1b**. If one considers the reaction between two neutral reagents (Scheme 1), the polarity of the TS may be deeply affected by the substituent on the phosphorous atom. Triphenylphosphine is less nucleophilic than tributylphosphine and the phenyl ring being able to delocalize the δ^+ charge, the structure of the transition state is shifted to the product (late transition state), which results in the increase of the polarity of the TS when compared to an alkyl group. The consequence is that the MW effects are increased according to **1b** > **1a**,

© 2004 NRC Canada

Fig. 2. Profiles for the rise in temperature for the MW absorption of **1a** (▬) and **1b** (–) in toluene.



essentially due to the extended polarity of the TS when an aromatic ring is concerned.

This interpretation is corroborated by the fact the two phosphines in their initial states have similar polarities if one considers their rises in temperature during MW irradiation (Fig. 2). A careful comparison between the two phosphines needs the addition of toluene for solubility (**1a** being liquid and **1b** solid).

Conclusions

We have observed specific MW effects depending essentially on the leaving group. Whereas they are rather weak with benzyl bromide, they are increased with chloride and even more with benzyl trialkylammonium salts. This behavior is compatible with the consideration of the position of the TS along the reaction coordinates, which induces an increase in the MW effects. The effects are more pronounced with triphenylphosphine **1b** due to the partial positive charge delocalization in the phenyl ring in the TS. The result is an enhancement in the polarity of the TS and consequently an improvement in the MW effects' magnitude. They could be perhaps better quantitatively understood in the future by consideration of some theoretical approaches including quantification of the polarity of the transition state when compared to the ground state (17, 35, 36).

Experimental

Microwave equipment

We have used a monomode reactor Synthewave® 402 from Prolabo (France) (37). The temperature was measured all along the reaction by IR detection, which indicates the surface temperature after previous calibration of emissivity in each case using an optical fibre inside the reaction mixture. The representative given temperatures are therefore accurate measurements of bulk homogeneous temperatures. The reactions were conducted using a cylinder tube in Pyrex under mechanical stirring to allow homogeneity inthe temperature. The power was monitored during irradiation to maintain a constant temperature. Occasionally, when reactions under closed vessels were necessary (entries 15 and 18), a CEM Discover microwave device was used.

Typical MW reactions

A mixture of 10 mmol of benzylating or alkylating electrophiles with 10 mmol of phosphine (**1a** (2.49 mL), **1b** (2.62 g)) was homogenized by stirring and shaking. It was irradiated in the Synthewave® monomode MW reactor for the times and the temperatures indicated in the tables. After cooling down to room temperature, the solid materials were filtered off, washed with toluene, and dried. They were analyzed by ^{1}H and ^{13}C NMR and the spectra were in agreement with authentic samples and the literature (38). They were also characterized by their melting points.

In the case where products are ionic liquids, they were washed with organic solvents to remove starting materials: cold diethyl ether for **5aa** and **5ab**, cold diethyl ether then hot toluene for **5ba** and **5bb**.

Experiments with xylene as the solvent (20 mL) were performed with 20 mmol of both starting materials. The product (phosphonium salts) were insoluble in xylene and were isolated by filtration followed by washing of the solid materials with fresh portions of xylene and diethyl ether.

Control experiments under conventional heating (Fig. 1)

In a thermostated oil bath at the same temperature as for MW irradiation, inside identical vessels and mechanical stirring, the two reactants were independently heated and mixed together. Temperature was evaluated inside the reaction mixture using the same optical fibre as for the MW evaluation (FISO, Universal Fiber Optic Sensor, FT1-10). Then the reaction was pursued for the same reaction time. The treatment and analysis remained identical.

Benzyltriphenylphosphonium bromide (3ba) (21, 38)

White crystals, mp 296 to 297 °C. ^{1}H NMR ($CDCl_3$, 300 MHz) δ: 5.44 (d, 2H, $^{2}J_{Hgem}$ = 14.56 Hz, -CH_2), 7.11–7.13 (m, 4H, -Ph), 7.60–7.66 (m, 6H, -Ph), 7.72–7.79 (m, 10H, -Ph). ^{1}H NMR (DMSO-d_6, 200 MHz) δ: 5.25 (d, 2H, $^{2}J_{Hgem}$ = 15.6 Hz, -CH_2), 7.0 (d, 2H, ^{3}J = 6.8 Hz, -Ph), 7.24 (m, 2H, -Ph), 7.6–7.8 (m, 14H, -Ph), 7.8–8.0 (m, 2H, -Ph). ^{13}C NMR (DMSO-d_6, 200 MHz) δ: 28.0 (d, $^{1}J_{CP}$ = 46.7 Hz), 117.8 (d, $^{1}J_{CP}$ = 85.1 Hz), 127.8 (d, $^{2}J_{CP}$ = 8.5 Hz), 128.2, 128.7, 130.0 (d, $^{3}J_{CP}$ = 12.2 Hz), 130.7, 133.9 (d, $^{2}J_{CP}$ = 8.9 Hz), 135.0.

Benzyltriphenylphosphonium chloride (3bb) (38)

White crystals, mp 333–337 °C. ^{1}H NMR ($CDCl_3$, 300 MHz) δ: 5.59 (d, 2H, $^{2}J_{Hgem}$ = 14.40 Hz, -CH_2), 7.10–7.12 (m, 4H, -Ph), 7.59–7.65 (m, 6H, -Ph), 7.71–7.78 (m, 10H, -Ph).

Benzyltributylphosphonium bromide (3aa) (39):

White crystals, mp 149 °C. ^{1}H NMR ($CDCl_3$, 300 MHz) δ: 0.93 (t, 9H, $^{3}J_{HH}$ = 6.96 Hz, 3 × -CH_3), 1.42–1.50 (m, 12 H, 3 × -CH_2CH_2), 2.38–2.47 (m, 6H, 3 × -CH_2P), 4.28 (d, 2H, $^{2}J_{Hgem}$ = 15.02 Hz, -CH_2P), 7.33–7.39 (m, 3H, -Ph), 7.45–7.49 (m, 2H, -Ph). ^{1}H NMR (DMSO-d_6, 200 MHz) δ: 0.90 (t, 9H, $^{3}J_{HH}$ = 6.6 Hz, 3 × -CH_3), 1.30–1.50 (m, 12H, 3 × -CH_2CH_2), 2.10–2.30 (m, 6H, 3 × -CH_2P), 3.95 (d, 2H,

© 2004 NRC Canada

$^2J_{Hgem}$ = 15.6 Hz, -CH_2P), 7.30–7.50 (m, 5H, -Ph). ^{13}C NMR (DMSO-d_6, 200 MHz) δ: 13.1, 16.9 (d, $^1J_{CP}$ = 46.7 Hz), 22.5 (d, $^2J_{CP}$ = 4.2 Hz), 23.3 (d, $^3J_{CP}$ = 15.5 Hz), 25.4 (d, $^1J_{CP}$ = 44.2 Hz), 127.8, 129.0, 129.3, 129.9.

Benzyltributylphosphonium chloride (3ab) (40, 41)

White crystals, mp 163 to 164 °C. ^{1}H NMR ($CDCl_3$, 300 MHz) δ: 0.92 (t, 9H, $^3J_{HH}$ = 6.59 Hz, 3 × -CH_3), 1.43–1.48 (m, 12H, 3 × -CH_2CH_2), 2.38–2.48 (m, 6H, 3 × -CH_2P), 4.31 (d, 2H, $^2J_{Hgem}$ = 15.38 Hz, -CH_2P), 7.33–7.39 (m, 3H, -Ph), 7.45–7.49 (m, 2H, -Ph). ^{1}H NMR (DMSO-d_6, 200 MHz) δ: 0.90 (t, 9H, $^3J_{HH}$ = 6.75 Hz, 3 × -CH_3), 1.30–1.50 (m, 12H, 3 × -CH_2CH_2), 2.10–2.30 (m, 6H, 3 × -CH_2P), 3.90 (d, 2H, $^2J_{Hgem}$ = 15.6 Hz, -CH_2P), 7.30–7.50 (m, 5H, -Ph). ^{13}C NMR (DMSO-d_6, 200 MHz) δ: 13.0, 17.5 (d, $^1J_{CP}$ = 46.8 Hz), 22.5 (d, $^2J_{CP}$ = 5 Hz), 23.5 (d, $^1J_{CP}$ = 15.7 Hz), 25.5 (d, $^1J_{CP}$ = 80 Hz), 128.0, 129.0, 129.5, 130.0

Hexyltriphenylphosphonium bromide (5ba) (42, 43)

mp 195–198 °C. ^{1}H NMR ($CDCl_3$, 300 MHz) δ: 082 (t, 3H, ^3J = 6.78 Hz, -CH_3), 1.19–1.28 (m, 4H, 2 × -CH_2), 1.57–1.69 (m, 4H, 2 × -CH_2), 3.80 (m, 2H, -CH_2P), 7.68–7.89 (m, 15H, 3 × -Ph). Insoluble in diethyl ether or toluene at their respective boiling points; soluble in acetone.

Hexyltriphenylphosphonium chloride (5bb)

mp 209 to 210 °C. ^{1}H NMR ($CDCl_3$, 300 MHz) δ: 0.82 (t, 3H, ^3J = 6.87 Hz, -CH_3), 1.18–1.28 (m, 4H, 2 × -CH_2), 1.57–1.68 (m, 4H, 2 × -CH_2), 3.92 (m, 2H, -CH_2P), 7.67–7.92 (m, 15H, 3 × –Ph). ^{13}C NMR ($CDCl_3$, 200 MHz) δ: 13.0, 21.2, 21.5 (d, $^2J_{CP}$ = 3.7 Hz), 21.5 (d, $^1J_{CP}$ = 49.6 Hz), 29.1 (d, $^3J_{CP}$ = 15.3 Hz), 30.2, 117.3 (d, $^1J_{CP}$ = 82.5 Hz), 129.6 (d, $^3J_{CP}$ = 12.3 Hz), 132.6 (d, $^2J_{CP}$ = 9.8 Hz), 134.2. Insoluble in diethyl ether or toluene at their respective boiling points; soluble in acetone.

Hexyltributylphosphonium bromide (5aa)

^{1}H NMR ($CDCl_3$, 300 MHz) δ: 0.87–1.01 (m, 12H, 4 × –CH_3), 1.29–1.35 (m, 4H, 2 × –CH_2), 1.47–1.60 (m, 16H, 8 × –CH_2), 2.40–2.53 (m, 8H, 4 ×-CH_2P). The product behaves like an ionic liquid and becomes solid upon freezing (–18 °C); insoluble in diethyl ether at room temperature.

Hexyltributylphosphonium chloride (5ab)

^{1}H NMR ($CDCl_3$, 250 MHz) δ: 0.90 (t, 3H, ^3J = 6.96 Hz, -CH_3), 1.00 (t, 9H, ^3J = 6.79 Hz, 3 × -CH_3), 1.20–1.40 (m, 4H, 2 × -CH_2), 1.40–1.70 (m, 16H, 8 × -CH_2), 2.30–2.60 (m, 8H, -CH_2P). ^{13}C NMR ($CDCl_3$, 250 MHz) δ: 13.2, 13.7, 18.7 (d, $^1J_{CP}$ = 47.4 Hz), 18.9 (d, $^1J_{CP}$ = 47.0 Hz), 21.5 (d, $^2J_{CP}$ = 5 Hz), 22.1, 23.6, 23.7 (d, $^3J_{CP}$ = 15.2 Hz), 30.2 (d, $^3J_{CP}$ = 14.7 Hz), 30.8. The product behaves like an ionic liquid and becomes solid upon freezing (–18 °C); insoluble in diethyl ether at room temperature.

Acknowledgments

This work was supported by Slovak grant agency VEGA grant No. 1/7348/20 and was carried out under the auspices of COST D10, project No. 00014/98.

References

1. D.R. Baghurst amd D.M.P. Mingos. Chem. Soc. Rev. **20**, 1 (1991).
2. S. Toma. Chem. Listy, **87**, 627 (1993).
3. S. Caddick. Tetrahedron, **51**, 10 403 (1995).
4. C.R. Strauss and R.W. Trainor. Aust. J. Chem. **48**, 1665 (1995).
5. F. Langa, P. de la Cruz, A. de la Hoz, A. Diaz-Ortiz, and E. Diez-Barra. Contemp. Org. Synth. 373 (1997).
6. A. Loupy, A. Petit, J. Hamelin, F. Texier-Boullet, P. Jacquault, and D. Mathé. Synthesis, 1213 (1998).
7. R.N. Gedye and J.B. Wei. Can. J. Chem. **76**, 525 (1998).
8. S. Deshayes, M. Liagre, A. Loupy, J.L. Luche, and A. Petit. Tetrahedron, **55**, 10 851 (1999).
9. P. Lidström, J. Tierney, B. Wathey, and J. Westman. Tetrahedron, **57**, 9225 (2001).
10. A. Loupy (*Editor*). Microwaves in organic synthesis. Wiley-VCH, Weinheim. 2002.
11. D.A.C. Stuerga and P. Gaillard. J. Microwave Power Electromagn. Energy, **31**, 87 (1996); **31**, 101 (1996).
12. R. Maoz, H. Cohen, and J. Sagiv. Langmuir, **14**, 5988 (1998).
13. D. Bogdal, M. Lukasiewicz, J. Pielichowski, and Sz. Bednarz. Tetrahedron, **59**, 649 (2003).
14. J. Berlan, P. Giboreau, S. Lefeuvre, and C. Marchand. Tetrahedron Lett. **32**, 2363 (1991).
15. A. Loupy, L. Perreux, M. Liagre, K. Burle, and M. Moneuse. Pure Appl. Chem. **73**, 161 (2001).
16. L. Perreux and A. Loupy. Tetrahedron, **57**, 9199 (2001).
17. F. Langa, P. de la Cruz, A. de la Hoz, E. Espildora, F. Cossio, and B. Lecea. J. Org. Chem. **65**, 2499 (2000).
18. G.S. Hammond. J. Am. Chem. Soc. **77**, 334 (1955).
19. J.J. Kiddle. Tetrahedron Lett. **41**, 1339 (2000).
20. J.J. Kiddle and A.F. Gurley. Phosphorus Sulfur Silicon Relat. Elem. **160**, 195 (2000).
21. J.J. Kiddle. Synth. Commun. **31**, 3377 (2001).
22. A. Stadler and C.O. Kappe. Eur. J. Org. Chem. 919 (2001).
23. B.M. Khadilkar and G. Ribeiro. Org. Process Res. Dev. **6**, 374 (2002).
24. R.S. Varma and V.V. Namboodiri. Chem. Commun. 643 (2001); Pure Appl. Chem. **73**, 1309 (2001); Tetrahedron Lett. **43**, 5381 (2002).
25. M.C. Law, K.W. Wong, and T.H. Chan. Green Chem. **4**, 181 (2002).
26. M. Deetlefs and K.S. Seddon. Green Chem. **5**, 328 (2003).
27. G. Vo Thanh, B. Pégot, and A. Loupy. Eur. J. Org. Chem. 1112 (2004).
28. B. Gotov, J. Cvengros, S. Toma, and A. Loupy. Proceedings of International Conference on Microwave Chemistry, Antibes – Juan-les-Pins, France, 4–7 September 2000. pp. 87–90.
29. M.T. Radoiu, J. Kurfustova, and M. Hajek. J. Mol. Catal. **160**, 383 (2000).
30. S. Chatti, M. Bortolussi, and A. Loupy. Tetrahedron, **56**, 5877 (2000).
31. A. Loupy, S. Chatti, S. Delamare, D.Y. Lee, J.H. Chung, and C.H. Jun. J. Chem. Soc. Perkin Trans. 1, 1280 (2002).
32. L. Perreux and A. Loupy. Org. Prep. Proced. Int. **35**, 361 (2003).
33. L. Perreux and A. Loupy. *In* Microwaves in organic synthesis. *Edited by* A. Loupy. Wiley-VCH, Weinheim. 2002. pp. 61–114.
34. L. Pauling. *In* The chemical bond. Cornell University Press, London. 1967.
35. S. Kalhori, B. Minaev, S. Stone-Elander, and N. Elander. J. Phys. Chem. A, **106**, 8516 (2002).

© 2004 NRC Canada

36. A. Loupy, F. Maurel, and A. Sabatié-Gogova. Tetrahedron, **60**, 1683 (2004).
37. R. Commarmot, R. Didenot, and J.F. Gardais. Fr. Patent 84/03496, 1986; Chem. Abstr. **105**, 17 442 (1986).
38. W.E. McEwen, W.I. Shiau, Y.I. Yeh, D.N. Schulz, R.U. Pagibagan, J.B. Levy, C. Symmes, Jr., G.O. Nelson, and I. Granoth. J. Am. Chem. Soc. **97**, 1787 (1975).
39. J.P. Cheng, B. Liu, Y. Zhao, and X.M. Zhang. J. Org. Chem. **63**, 7072 (1998).
40. C.E. Griffin and M. Gordon. J. Organomet. Chem. **3**, 414 (1965).
41. R.G. Barnhardt and W.E. McEwen. J. Am. Chem. Soc. **89**, 7009 (1967).
42. I. Bidd, D.W. Holdup, and M.C. Whiting. J. Chem. Soc. Perkin Trans. 1, 2455 (1987).
43. C.F. Hauser, T.W. Brooks, M.L. Miles, M.A. Raymond, and G.B. Butler. J. Org. Chem. **28**, 372 (1963).

© 2004 NRC Canada

The kinetics and the mechanism of oxidative decarboxylation of benzilic acid by acidic permanganate (stopped-flow technique) — An autocatalytic study

Sairabanu A. Farokhi and Sharanappa T. Nandibewoor

Abstract: The kinetics of the oxidation of benzilic acid by potassium permanganate in an acidic medium were studied spectrophotometrically. The reaction followed a two-stage process, wherein both stages of the reaction followed first-order kinetics with respect to permanganate ion and benzilic acid. The rate of the reaction increased with an increase in acid concentration. Autocatalysis was observed by one of the products, i.e., manganese(II). A composite mechanism involving autocatalysis has been proposed. The activation parameters of the reaction were calculated and discussed and the reaction constants involved in the mechanisms were calculated. There is a good agreement between the observed and calculated rate constants under different experimental conditions.

Key words: oxidation, autocatalysis, benzilic acid, two-stage kinetics.

Résumé : Faisant appel à la spectrophotométrie, on a étudié la cinétique de l'oxydation de l'acide benzilique par le permanganate de potassium en milieu acide. La réaction se produit en deux étapes et chacune d'elles est du premier ordre par rapport aux concentrations de l'ion permanganate et de l'acide benzilique. La vitesse de la réaction augmente avec une élévation de la concentration d'acide. On a observé de l'autocatalyse par l'un des produits, soit le manganèse(II). On propose un mécanisme composé impliquant de l'autocatalyse. On a calculé et on discute des paramètres d'activation de la réaction; on a aussi calculé les constantes de réaction impliquées dans les mécanismes. On a observé un bon accord entre les constantes de vitesses observées et calculées dans différentes conditions expérimentales.

Mots clés : oxydation, autocatalyse, acide benzilique; cinétique à deux étapes.

[Traduit par la Rédaction]

Introduction

It is evident that manganese(VII) is reduced to various oxidation states in acidic, alkaline, and neutral media during oxidation by permanganate. Out of the six oxidation states of manganese (1), from 2^+ to 7^+, permanganate Mn(VII), is the most powerful oxidant in a dilute acid medium with reduction potentials of 1.69 V for the Mn(VII)/Mn(IV) couple and 1.51 V for the Mn(VII)/Mn(II) couple.

Oxidations by permanganate ion are applied extensively in organic syntheses (2–8), especially since the advent of phase-transfer catalysis (4, 5, 7). Kinetic studies are important sources of mechanistic information on the reactions, as demonstrated by the results for unsaturated acids both in aqueous (2, 4, 8) and nonaqueous media (9).

Furthermore, the mechanism by which this multivalent oxidant oxidizes a substrate depends not only on the substrate but also on the medium (10, 11) used for the study. In some cases the mechanistic approach is based on the intermediate complex formation, and in others, the results are interpreted by a free radical mechanism. The mechanisms suggested by various authors are not uniform, indicating that a wide variety of mechanisms are possible depending on the nature of the reactive species of permanganate as well as the substrate.

Several studies have been reported on the oxidation of benzilic acid by other oxidants such as cerium(IV) (12, 13), ferricyanide (14), chromic acid (15), thallium(III) (16), persulphate (17), and *N*-bromosacharin (18). Even though the oxidation product of benzilic acid is the same in both acidic and alkaline media, the reactions differ in many kinetic parameters. Interest in kinetic studies, in particular of α-hydroxy acids (19), has developed and no attempts have been made to correlate the rate data with the structural differences in these acids.

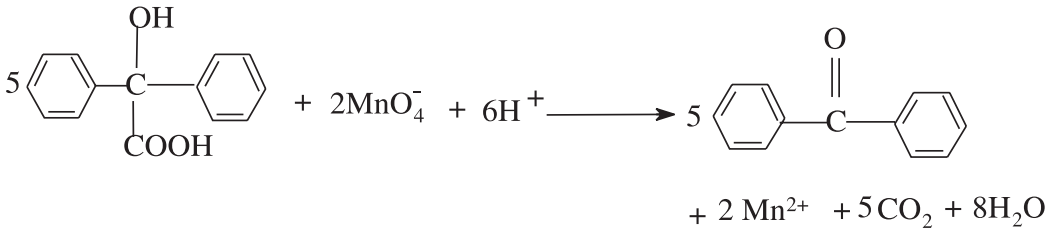
In view of the lack of reports in the literature on the oxidation of benzilic acid by acidic $KMnO_4$, we have selected it as a substrate for study. The present study deals with the ki-

Received 20 February 2004. Published on the NRC Research Press Web site at http://canjchem.nrc.ca on 23 October 2004.

S.A. Farokhi and S.T. Nandibewoor.[1] P.G. Department of Studies in Chemistry, Karmatak University, Dharwad, 580 003, India.

[1]Corresponding author (e-mail: stnandibewoor@yahoo.com).

 doi: 10.1139/V04-102 © 2004 NRC Canada

[1] 

netics of the oxidation of benzilic acid by $KMnO_4$ in an acidic medium to arrive at a plausible mechanism and to determine the active species of permanganate in such media.

Experimental

Since the initial reaction was too fast to monitor by the usual method, kinetic measurements were performed on a Hitachi 150-20 spectrophotometer connected to a rapid kinetic accessory (HI-TECH SFA-12).

Materials and methods

All chemicals used were of BDH Analar specifications. Potassium permanganate (BDH) was prepared in doubly distilled water and its strength was ascertained (20*a*) by titrating against standard $H_2(CO_2)_2$ solution in hot acidic medium. The solubility of benzilic acid (Merck) (BA) is low and it was prepared in water by warming. Perchloric acid (Merck) and sodium perchlorate (BDH) were used to provide the required acidity and ionic strength, respectively. Mn(II) was prepared by dissolving manganese(II) sulphate (Riedel). Doubly distilled conductivity water was used to prepare all the solutions.

The optical density vs. concentration plot for acidified permanganate ion showed that Beer's law, under the reaction conditions in 6.0×10^{-5} to 2.0×10^{-4} mol dm^{-3} in 0.01 mol dm^{-3} $HClO_4$, was obeyed at a wavelength of 526 nm and the molar absorptivity of permanganate was found to be 2300 ± 50 dm^3 mol^{-1} cm^{-1}, which was in good agreement with previous results (21, 22).

Kinetic measurements

All kinetic measurements were performed under pseudo-first-order conditions where [benzilic acid] was always in excess over [MnO_4^-] at a constant ionic strength of 5.0×10^{-3} mol dm^{-3} in acidic medium at a constant temperature of 21 ± 0.1 °C.

The progress of the reaction was followed by monitoring the decrease in MnO_4^- in a 1 cm quartz cell of a Hitachi model 150-20 spectrophotometer at its absorption maximum (526 nm) as a function of time. Earlier, it was verified that there is negligible interference from other reaction species at this wavelength. The pseudo-first-order rate constants were obtained from the plots of log $(A_t - A_\infty)$ vs. time and the plot of log $[(A_t - A_\infty) - (A_{t'} - A_\infty)]$ vs. time, where A_t and A_∞ represent the absorbance at time t and ∞, respectively. $A_{t'}$ represents the absorbance for the extrapolated point at time t'. The plots of log $(A_t - A_\infty)$ vs. time and of log $[(A_t - A_\infty) - (A_{t'} - A_\infty)]$ vs. time indicate that there was a two-stage process and that both stages were linear. In the first slow process, the linearity was observed up to 60% completion of the reaction and in the second fast process, linearity was observed from 60% to 80% completion of the reaction. k_{obs} values were reproducible within ±5%, where the first slow stage is followed by a second fast stage process (Fig. 1). This type of two-stage process has been observed in a few cases (23, 24). During the progress of the reaction, the colour of the solution changed from violet to colourless, indicating the formation of Mn(II), which was verified by a spot test (20 *b*). The formation of Mn(II) is shown spectrally in Fig. 2.

Results

Stoichiometry and product analysis

Different sets of reaction mixtures containing excess [MnO_4^-] over [benzilic acid] were mixed in the presence of 1.0×10^{-3} mol dm^{-3} perchloric acid, adjusted to an ionic strength of 5.0×10^{-3} mol dm^{-3}, and kept for 12 h in an inert atmosphere at 21 °C. After completion of the reaction, the remaining permanganate was then determined spectrophotometrically. The results indicated that 5 mol of benzilic acid were consumed by 2 mol of permanganate as in eq. [1].

The main oxidation products were identified as benzophenone, CO_2, and manganese(II). The product, manganese(II) in acid medium, was analyzed using EDTA solution with Erichrome black-T as the indicator (20*b*). The formation of benzophenone was confirmed by its IR and NMR spectra (25). Further, the yield was quantitatively estimated to ca. 85%, evidence for which is provided by isolation of its 2,4-DNP derivative (26), with a mp of 236 °C. Benzophenone did not undergo further oxidation under the stated kinetic conditions. The test for the probable oxidation product of the ketone, i.e., benzoic acid, was negative.

Reaction orders

The reaction order for benzilic acid and perchloric acid was investigated by varying one of these concentrations while keeping all other concentrations and conditions constant and studying the effect of its concentration on the rate of the reaction.

Kinetic data were collected for initial [MnO_4^-] in the $(0.40–4.0) \times 10^{-4}$ mol dm^{-3} range. In an acid medium, the reaction followed a two-stage process (Fig. 1). All the experiments exhibited an identical pattern, with the initial slow reaction followed by a faster one. The plots of log $(A_t - A_\infty)$ vs. time and log $[(A_t - A_\infty) - (A_{t'} - A_\infty)]$ vs. time ($r > 0.9355$, $s \leq 0.0144$ for stage 1, $r > 0.9951$, $s \leq 0.4480$ for stage 2) for different initial concentrations of MnO_4^- exhibit two distinct straight lines for the slow and fast stages of the reaction (Fig. 1). The fairly constant k_s (s^{-1}) values for the slow stage and k_f (s^{-1}) values for the fast stage confirms that slow and fast depletions in MnO_4^- follow first-order kinetics. The concentration of benzilic acid was varied in the range of $(0.40–4.0) \times 10^{-3}$ mol dm^{-3}, keeping all other reactant con-

© 2004 NRC Canada

Fig. 1. Plot of (*a*) $\log(A_t - A_\infty)$ vs. time and (*b*) $\log[(A_t - A_\infty) - (A_{t'} - A_\infty)]$ vs. time in an acidic medium ($[MnO_4^-]$ = 2 × 10^{-4} mol dm^{-3}, [BA] = 2 × 10^{-3} mol dm^{-3}, $[H^+]$ = 1.0 ×10^{-3} mol dm^{-3}, and I = 5.0 × 10^{-3} mol dm^{-3}.

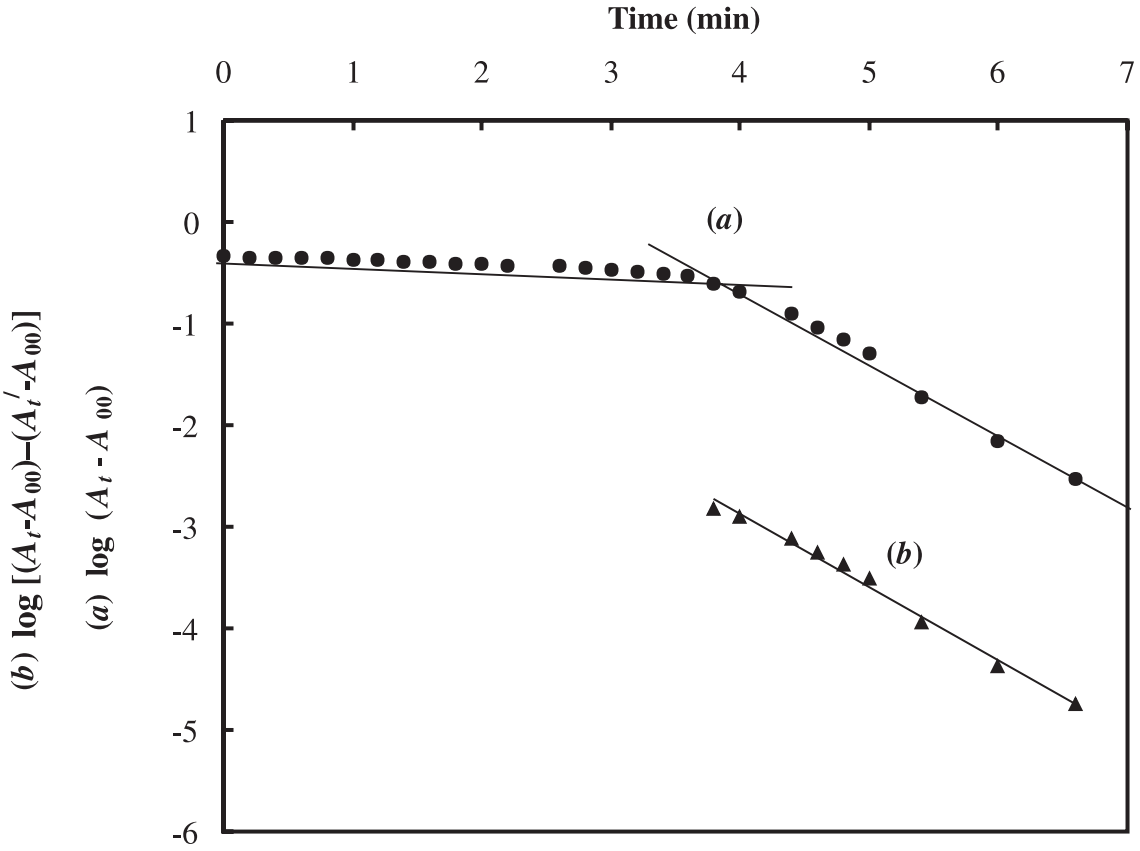
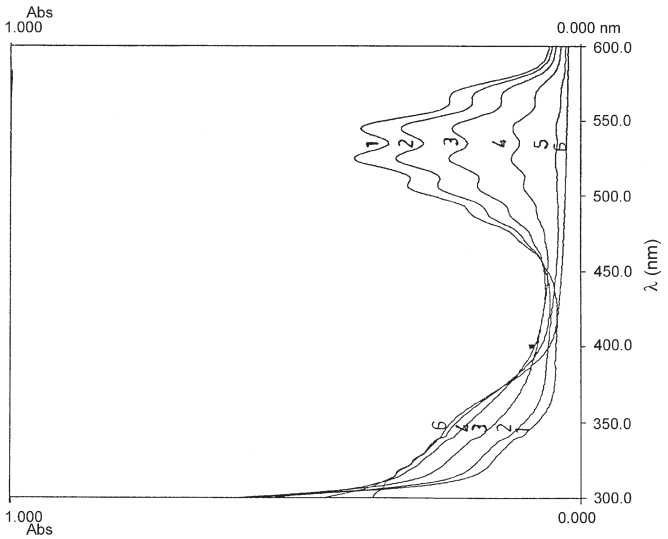


Fig. 2. Spectroscopic changes occurring in the oxidation of benzilic acid by permanganate with $[MnO_4^-]$ = 2.0 × 10^{-4} mol dm^{-3}, [BA] = 2.0 × 10^{-3} mol dm^{-3}, $[H^+]$ = 1.0 × 10^{-3} mol dm^{-3}, and I = 5.0 × 10^{-3} mol dm^{-3} at 21 °C (scanning time interval = 1 min).



centrations and conditions constant. In an acidic medium, the k_s and k_f values (Table 1) increased with increasing concentration of benzilic acid indicating first-order dependence on the [substrate] in both the stages. To study the effect of $[H^+]$ on the rate of the reaction, the $[H^+]$ was varied from (0.50–5.0) × 10^{-2} mol dm^{-3} at a constant concentration of MnO_4^- and benzilic acid, maintaining a constant ionic strength of 5.0 × 10^{-3} mol dm^{-3}. It was found that in both stages the rate increased with an increase of $[H^+]$. The order in both stages was less than unity (Table 1). It was found that the ionic strength and dielectric constant of the medium have no significant effect on the rate of reaction.

Effect of added products

The addition of the product benzophenone did not show any significant effect on the rate of the reaction. However, the initial addition of the product Mn(II) in the range of (0.20–2.0) × 10^{-4} mol dm^{-3}, keeping other conditions constant, had an appreciable increasing effect on the rate of the reaction. As the initial concentration of Mn(II) was increased, the rate progressively increased at an order of around 0.62 and 0.26 in the slow and fast stages, respectively. This illustrates the autocatalytic nature of the product (Table 2), which is also evident from the concentration vs. time plot (Fig. 3) and the linear plot of k_{obs} vs. k_{cal} for manganese(II) variation (Fig. 3, inset), as observed in earlier cases (27).

Polymerization study

To test for free radical intervention, the reaction mixture containing $[MnO_4^-]$ = 2 × 10^{-4} mol dm^{-3} and [BA] = 2 × 10^{-3} mol dm^{-3} were taken, and the pH of the solution was adjusted to 3.0 The solution was then degassed with nitrogen

© 2004 NRC Canada

Table 1. Effect of [benzilic acid], [MnO_4^-], and [H^+] on the oxidation of benzilic acid by acidified permanganate at 21 °C, $I = 5.0 \times 10^{-3}$ mol dm^{-3}.

[BA] ($\times 10^3$ mol dm^{-3})	[MnO_4^-] ($\times 10^4$ mol dm^{-3})	[H^+] ($\times 10^3$ mol dm^{-3})	k_s ($\times 10^3$ s^{-1}) (Expt.)	k_s ($\times 10^3$ s^{-1}) (Calcd.)	k_f ($\times 10^3$ s^{-1}) (Expt.)	k_f ($\times 10^3$ s^{-1}) (Calcd.)
0.4	2.0	1.0	0.41	0.42	5.21	5.01
1.0	2.0	1.0	1.12	1.05	13.2	12.5
2.0	2.0	1.0	2.07	2.10	27.5	25.1
3.0	2.0	1.0	3.10	3.16	37.2	37.6
4.0	2.0	1.0	4.23	4.22	51.3	50.1
2.0	0.4	1.0	2.08	2.10	27.3	25.1
2.0	1.0	1.0	2.03	2.10	27.5	25.1
2.0	2.0	1.0	2.07	2.10	27.5	25.1
2.0	3.0	1.0	2.16	2.10	27.9	25.1
2.0	4.0	1.0	2.12	2.10	28.0	25.1
2.0	2.0	0.5	1.15	1.16	14.3	14.5
2.0	2.0	0.8	1.81	1.75	21.0	21.2
2.0	2.0	1.0	2.07	2.10	27.5	25.1
2.0	2.0	2.0	3.60	3.57	36.4	39.0
2.0	2.0	5.0	5.85	6.11	60.2	60.2

Table 2. Effect of product Mn(II) on the oxidation of benzilic acid by acidified $KMnO_4$ at 294 K ([BA] = 2.0×10^{-3} mol dm^{-3}, [MnO_4^-] = 2.0×10^{-4} mol dm^{-3}, [H^+] = 1.0×10^{-3} mol dm^{-3}, and $I = 5.0 \times 10^{-3}$ mol dm^{-3}).

[Mn(II)] ($\times 10^4$ mol dm^{-3})	k_s ($\times 10^3$ s^{-1})	k_f ($\times 10^3$ s^{-1})
0.0	2.07	27.5
0.2	2.75	28.4
0.6	6.13	34.0
1.0	8.11	43.4
1.5	10.2	48.3
2.0	11.3	49.1

and acrylonitrile (5 mL, 20% v/v) was added to the solution at room temperature and was kept for 24 h. On diluting the reaction mixture with methanol, no precipitate resulted indicating no polymerization of acrylonitrile. This observation indicates that the oxidation of benzilic acid by acidic potassium permanganate proceeds through the absence of polymer formation and, as well, any intervention of free radicals. There is evidence of polymerization with acrylonitrile in the earlier studies (28).

Effect of temperature

The effect of temperature on the reaction was studied at four different temperatures. The rate increased with an increase in temperature. The $\Delta H^{\ddagger}$ and $\Delta S^{\ddagger}$ values were obtained from a $\log(k_{obs}/T)$ vs. $1/T$ plot ($r > 0.9719$, $s \leq 0.01298$ for stage 1, $r > 0.9839$, $s \leq 0.07748$ for stage 2). The activation parameters $\Delta H^{\ddagger}$ (kJ mol^{-1}), $\Delta S^{\ddagger}$ (J K^{-1} mol^{-1}), and $\Delta G^{\ddagger}$ (kJ mol^{-1}) were found to be 64 ± 2, –79 ± 6, and 87 ± 4 for stage 1 and 28 ± 2, –181 ± 16, and 81 ± 4 for stage 2, respectively.

Discussion

Oxidation of benzilic acid by permanganate in a $HClO_4$ medium is a noncomplementary reaction in which the oxidant undergoes five equivalent changes. In this experiment, the reaction between benzilic acid and MnO_4^- had a stoichiometry of 5:2 with first-order dependence on [MnO_4^-] and [BA] and fractional order dependence on both [H^+] and [Mn(II)]. Stoichiometric studies revealed 5-equivalent changes in Mn(VII). Hence, the formation of Mn(IV) as a reduced product of Mn(VII) in the reaction was excluded, although formation of Mn(IV) had been observed in earlier studies (29, 30). The strong reducing character of benzilic acid was evident in the reduction of Mn(VII) to Mn(II) in the $HClO_4$ medium.

The active species of permanganate in an aqueous acid medium may be deduced from the dependence of the rate on [H^+] in the reaction medium. The apparent order of less than unity in [H^+] may be an indication of the permanganate species as permanganic acid. In an acidic medium, permanganic acid ($HMnO_4$) is a more efficient oxidant species of manganese(VII) than permanganate ion (29–31). In addition, it was observed that the reaction rate increased with an increase in [H^+] and tended to attain a limiting value at high acidities. The plot of k_{obs} vs. [H^+] in an acidic medium is a curve of decreasing slope (convex to the rate axis) and passing through the origin (Fig. 4) from which it can be inferred (32) that a rapid equilibrium between the protonated and unprotonated form is involved. At higher acidities protonation is almost complete, leading to the limiting rate, which indicates that only the protonated form is active. The negligible ionic strength effect on the rate of the reaction also confirms $HMnO_4$ as the active species of MnO_4^-. Thus, the acid permanganate equilibrium is represented as

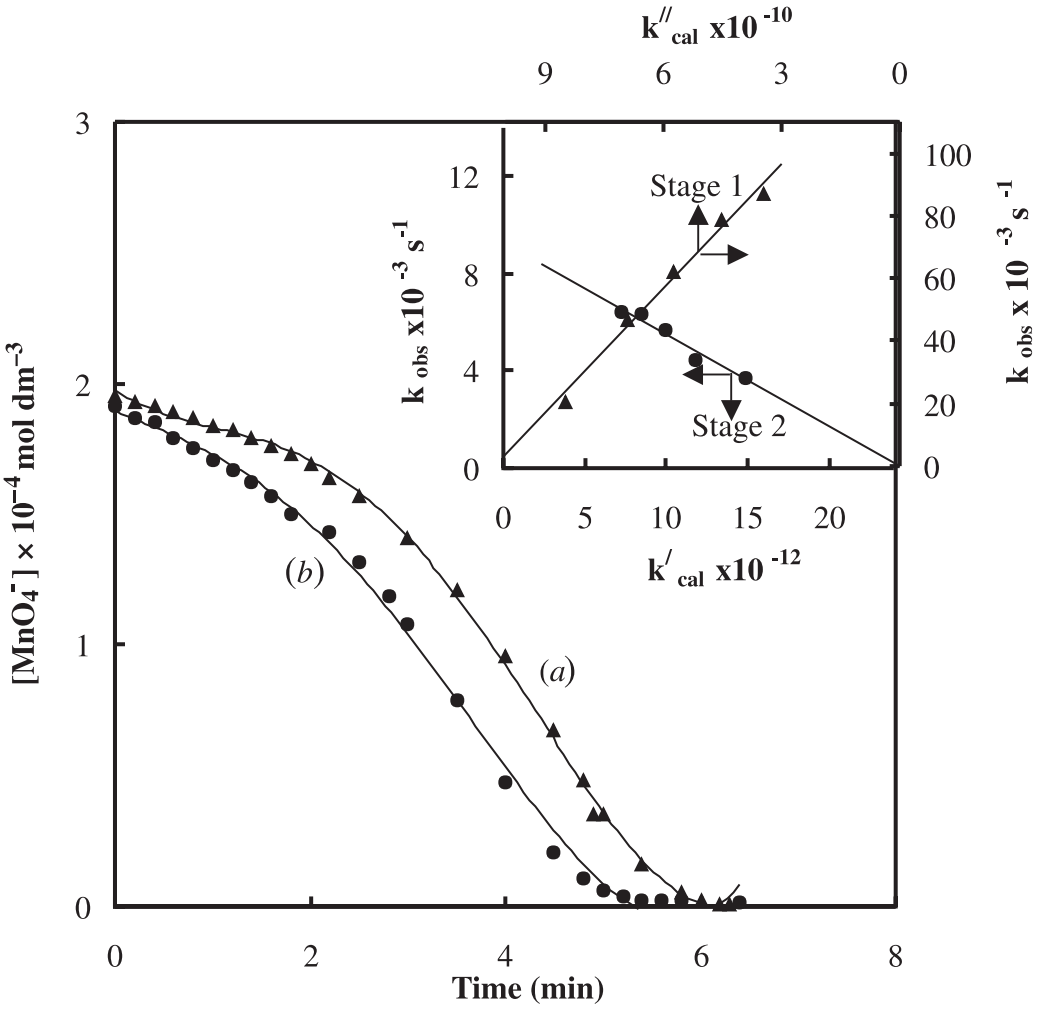
$$[2] \qquad H^+ + MnO_4^- \overset{K_1}{\rightleftharpoons} HMnO_4$$

where K_1 is the formation constant of $HMnO_4$.

Based on the experimental results, the following mechanism can be proposed in which all the observed orders with respect to each constituent such as [oxidant], [reductant], and [H^+] may be well accommodated. The results suggest the formation of a protonated form of permanganate as the

© 2004 NRC Canada

Fig. 3. Concentration vs. time plots to show autocatalysis. (*a*) [BA] = 2.0×10^{-3} mol dm^{-3}, [MnO_4^-] = 2.0×10^{-4} mol dm^{-3}, [H^+] = 1.0×10^{-3} mol dm^{-3}, $I = 5.0 \times 10^{-3}$ mol dm^{-3} (*b*) [BA] = 3.0×10^{-3} mol dm^{-3}, [MnO_4^-] = 2.0×10^{-4} mol dm^{-3}, [H^+] = 1.0×10^{-3} mol dm^{-3}, $I = 5.0 \times 10^{-3}$ mol dm^{-3}. Inset: plot of k_{expt} vs $k'_{cal} = [BA]^1[Mn(II)]^{0.62}[H^+]^{0.70}[MnO_4^-]^1$ for stage 1 and $k''_{cal} = [BA]^1[Mn(II)]^{0.26}[H^+]^{0.6}[MnO_4^-]^1$ for stage 2 for the variation of manganese(II) (Table 2).



active species of MnO_4^- in a prior equilibrium, which reacts with 1 mol of benzilic acid in a rate-determining step to give a complex (C_1) that further decomposes in a fast step to give benzophenone and the intermediate Mn(V). The intermediate Mn(V), being unstable in an acidic medium, reacts with another mol of benzilic acid in a fast step to Mn(III), which is subsequently reduced to the end product Mn(II) in further fast steps satisfying stoichiometric observations. The spectral evidence for the formation of complex C_1 was obtained from UV–vis spectra of both benzilic acid and the mixture of benzilic acid and permanganic acid, which indicated a bathochromic shift from 325 to 347 nm. The steps proposed are shown in Scheme 1.

Since none of the intermediates of Mn(VII) could be detected, Scheme 1 is only one of the possible mechanisms for the reaction in the absence of free radicals. Attempts were made to allow spectrophotometric detection (in terms of wavelengths) of Mn^{5+} and Mn^{3+} intermediates as the reaction proceeded in the oxidation of benzilic acid by $HMnO_4$. Unfortunately, the low concentration of Mn^{3+} and Mn^{5+} intermediates obtained under our experimental conditions made the detection unsuccessful. However, there are reports of their existence in the earlier literature (33, 34). Scheme 1 leads to the rate law (eq. [3] that explains all the observed orders except autocatalysis.

$$[3] \qquad -\frac{d[Mn(VII)]}{dt} = \frac{k_1K_1[H^+]_T[Mn(VII)]_T[BA]}{(1+K_1[H^+])(1+K_1[Mn(VII)])}$$

$$[4] \qquad = \frac{k_1K_1[H^+][BA][Mn(VII)]}{1+K_1[H^+]+K_1[Mn(VII)])+K_1^2[H^+][Mn(VII)]}$$

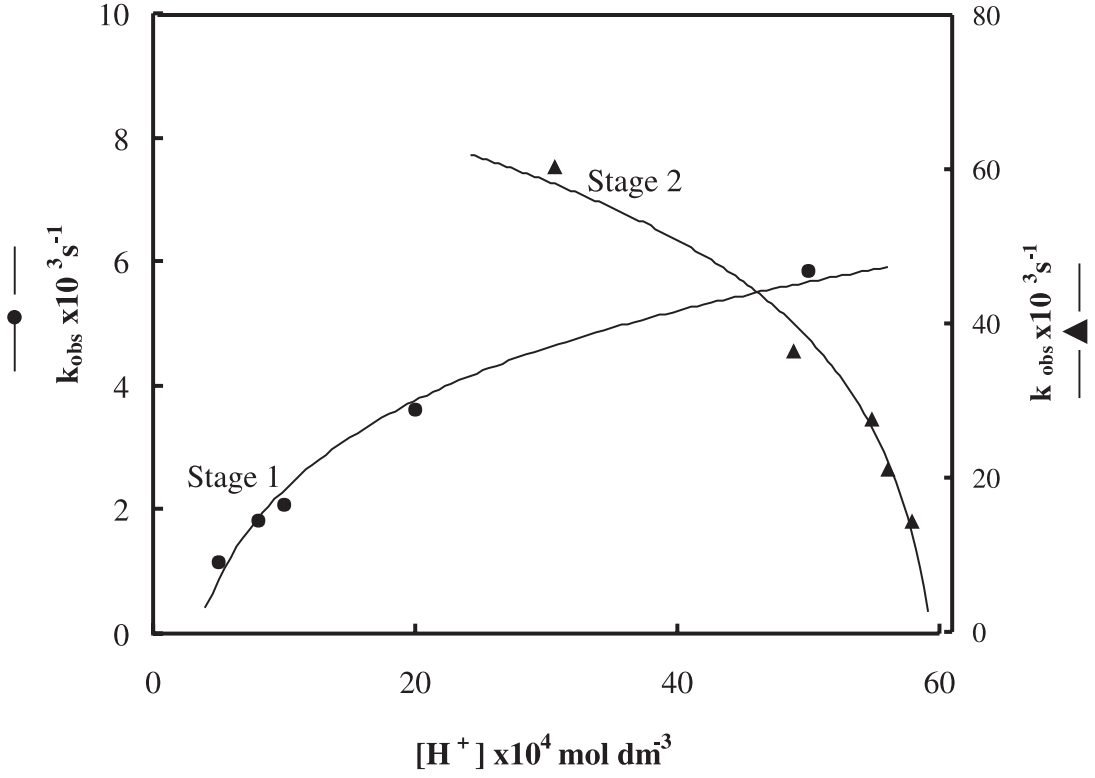
The terms such as $K_1[Mn(VII)]$ and $K_1^2[H^+][Mn(VII)]$ in the denominator of eq. [4] are negligibly small compared with unity, in view of the low concentration of [Mn(VII)] used in the experiments. Hence, eq. [4] becomes eq. [5]

$$[5] \qquad k_{obs} = \frac{\text{Rate}}{[Mn(VII)]} = \frac{k_1K_1[H^+][BA]}{1+K_1[H^+]}$$

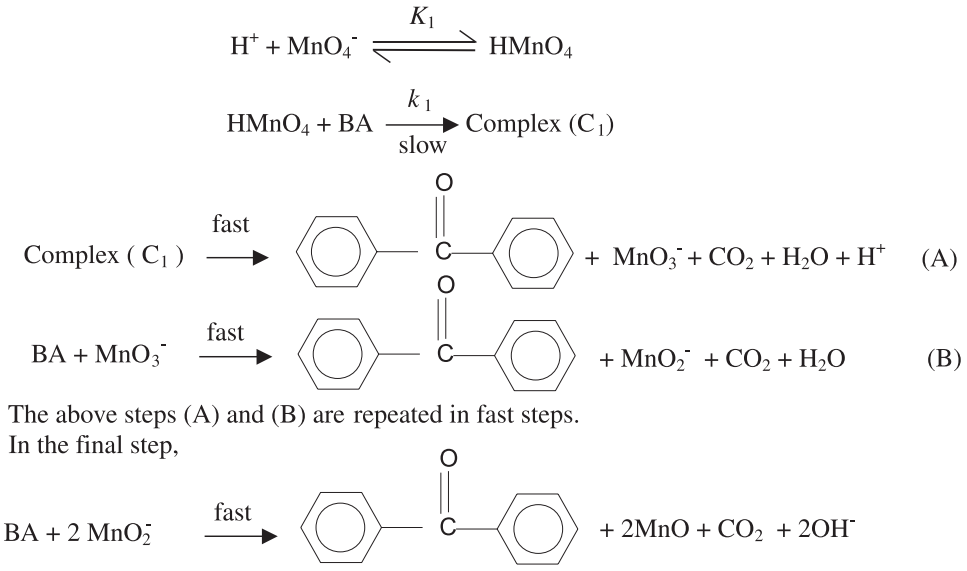
The mechanism of Scheme 1 and rate law (eq. [3]) may be verified by rearranging to the form

© 2004 NRC Canada

Fig. 4. The plot of k_{obs} vs. [H^+] (a curve of decreasing slope (convex to the rate axis)).



Scheme 1.

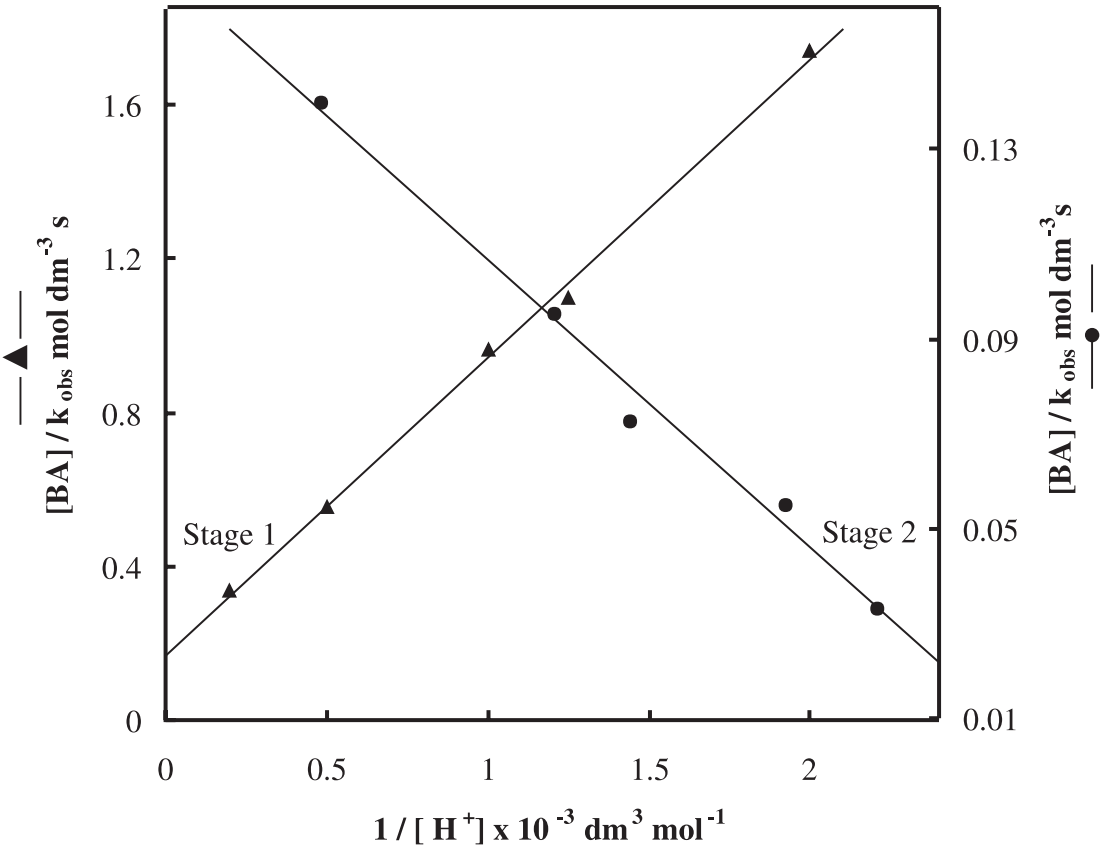


$$[6] \qquad \frac{[BA]}{k_{obs}} = \frac{1}{k_1 K_1 [H^+]} + \frac{1}{k_1}$$

where k_{obs} is first-order rate constant. According to eq. [6], the plot of $[BA]/k_{obs}$ vs. $1/[H^+]$ ($r > 0.999$, $s \leq 0.06990$ for stage 1, $r > 0.9946$, $s \leq 0.06993$ for stage 2) is expected to be linear, which is verified in Fig. 5. The slope and intercept of this plot lead to values of K_1 and k_1 at 21 °C of 221 ± 9 dm^3 mol^{-1}, 5.8 ± 0.3 dm^3 mol^{-1} s^{-1} for stage 1 and 371 ± 13 dm^3 mol^{-1}, 46 ± 2 dm^3 mol^{-1} s^{-1} for the fast stage 2, respectively. The experimental rate constants can be computed for both stages using these values. There is a reasonable agreement between the calculated and experimental rate constants (Table 1). The negligible effect of ionic strength

© 2004 NRC Canada

Fig. 5. The plot of [BA]/k_{obs} vs. 1/[H^+] (verification of rate law (eq. [3])).

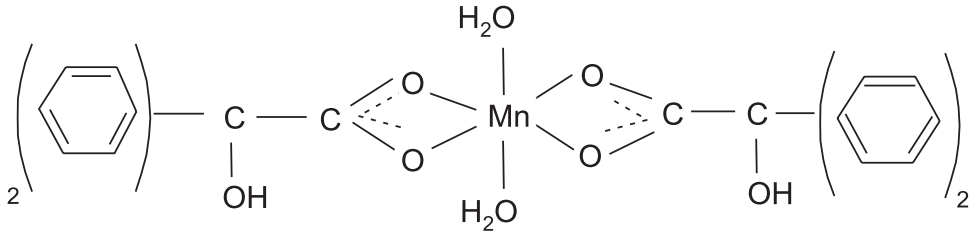


Scheme 2.

$$Mn(II) + 2BA \underset{}{\overset{K_2}{\rightleftharpoons}} Complex\ (C_2)$$

$$C2 + HMnO_4 \xrightarrow[slow]{k_2} Products$$

The probable structure of the complex (C_2) is given below



and relative permitivity on rate is qualitatively consistent with the reaction between two neutral molecules as in Scheme 1.

Autocatalysis by Mn(II) in an acidic medium

The autocatalysis by one of the products (Mn(II)) is interesting. The effect of Mn(II) as a catalyst in the case of the oxidation of permanganate is well-known (35–37). In the present case, Mn(II) was found to catalyse the rate of oxidation of benzilic acid (Table 2).

The apparent order of less than unity with respect to the Mn(II) ion may be attributed to a complex formation between benzilic acid and Mn(II). The complex (C_2) is then subsequently involved in the interaction with $HMnO_4$. These steps shown in Scheme 2 will form a part of Scheme 1.

The evidence for complex formation (C_2) was obtained from UV–vis spectra of both benzilic acid and mixtures of

© 2004 NRC Canada

benzilic acid and Mn(II), which indicated a hypsochromic shift of about 4 nm from 338 to 334 nm and a new band appeared at 372 nm. Indeed, such complex formation between substrates such as styrene and Mn(II) has been observed in the literature (38, 39).

Thus, when Mn(II) is initially present, a composite scheme involving all the steps of Schemes 1 and 2 operates and the rate law becomes

$$k_{gross} = k_{obs} + k_{autocat}$$

$$[7] \quad k_{gross} = \frac{k_1 K_1 [BA][H^+]}{1 + K_1[H^+]} + \frac{k_2 K_2 [Mn(II)][BA]^2}{\{1 + K_2[BA]^2\}\{1 + K_2[Mn(II)][BA]\}^2}$$

$$k_{autocat} = k_{gross} - k_{obs}$$

$$[8] \quad k_{autocat} = \frac{k_2 K_2 [Mn(II)][BA]^2}{\{1 + K_2[BA]^2\}\{1 + K_2[Mn(II)][BA]\}^2}$$

where k_{gross} and $k_{autocat}$ refer to the rate paths of the overall and autocatalytic paths, respectively. At constant concentrations of oxidant and substrate, a plot of $[BA]^2/k_{autocat}$ in eq. [8] vs. 1/[Mn(II)] ($r > 0.9987$, $s \leq 0.1566$ for stage 1, $r > 0.9596$, $s \leq 0.1574$ for stage 2) for both stages was found to be linear. Indeed, it is to be noted that the plot shows an intercept that is in agreement with the complex formation as shown in Scheme 2. The high negative values of $\Delta S^{\ddagger}$ indicate that complex (C_1) is more ordered than the reactants (40).

Reason for the two stages

Details regarding the occurrence of two successive stages, slow and fast, might be due to the creation of an optimum concentration of some intermediates (41–43). It might be possible that up to a certain range of MnO_4^- concentration (first slow stage), the active species of the oxidant (i.e., the protonated form of MnO_4^- ($HMnO_4$) is reactive) while in the second stage of the reaction, autocatalysis due to one of the products (Mn(II)) is operative. The product Mn^{2+} ions formed in the first slow stage, after achieving an optimum concentration, start reducing MnO_4^- ions to Mn^{3+} and or Mn^{4+} ions (44), ($MnO_4^- + 3Mn^{2+} + 8H^+ = 3Mn^{3+} + Mn^{4+} + 4H_2O$) indicating that the intermediate manganese ions are the active oxidizing species. On addition of Mn^{2+}, the acceleration of rate is due to the existence of Mn^{3+} or Mn^{4+} as the principal reactive species in the second fast stage. But the oxidation of benzilic acid by Mn(III), as well as the continuous increase in the oxidation rate with increasing Mn^{2+} added to the MnO_4^- – benzilic acid reaction mixture, indicates that Mn^{3+}, but not Mn^{4+}, is the sole oxidant throughout the auto acceleration stage.

Conclusions

In an acidic medium, the reaction exhibits an autocatalytic nature and follows two stages, as one of the products (Mn(II)) enhances the rate of the reaction. Mn(II) as the reduced product of Mn(VII) in the reaction may suggest that benzilic acid shows a strong reducing character in a $HClO_4$ medium. The overall mechanistic sequences described in the media are consistent with product, mechanistic, and kinetic studies.

Acknowledgement

One of the authors, Sairabanu A. Farokhi, would like to acknowledge the University Grants Commission (UGC), Southwestern Regional Office, Bangalore, for providing a Fellowship.

References

1. T.A. Zordan and LG. Hepler. Chem. Rev. **68**, 737 (1968).
2. R. Stewart. *In* Oxidation in organic chemistry. Part A. *Edited by* K.B. Wiberg. Academic Press, New York. 1965. Chap. 1.
3. F. Freeman. Rev. React. Species Chem. React. **1**, 179 (1976).
4. D.G Lee. The oxidations of organic compounds by permanganate ion and hexavalent chromium. Open Court, La Salle, Ill. 1980.
5. D.G. Lee. *In* Oxidation in organic chemistry. Part D. *Edited by* W.S. Trahanovsky. Academic Press, New York. 1982. p. 147.
6. L.I. Simandi. *In* The chemistry of functional groups. *Edited by* S. Patai and Z. Rappoport. Suppl. Wiley, Chichester, UK. 1983. Chap. 13.
7. D.G. Lee, E.J. Lee, and K.C. Brown. Phase transfer catalysis, new chemistry, catalysts and applications. ACS Symp. Ser. No. 326. Am. Chem. Soc., Washington, D.C. 1987. p. 82.
8. A.J. Fatiadi. Synthesis, **106**, 85 (1987).
9. J.F. Perez-Benito and D.G Lee. J. Org. Chem. **52**, 3239 (1987).
10. R. Stewart. *In* Oxidation in organic chemistry. Part A. *Edited by* K.B. Wiberg. Academic Press, New York. 1965.
11. K.A. Gardner, L.L. Kuehnert, and J.M. Mayer. Inorg. Chem. **36**, 2069 (1997).
12. V.K. Grover, Y.K. Gupta, and K.J. Yugul. J. Inorg. Nucl. Chem. **31**, 1403 (1969).
13. S.B. Hanna and S.A. Sarac. J. Org. Chem. **42**, 2063 (1977).
14. N.C. Khandual. J. Indian Chem. Soc. **67**, 561 (1990).
15. K.K. Sengupta, A.K. Chatterjee, and S.P. Moulik. Bull. Chem. Soc. Jpn. **43**, 3841 (1970).
16. P.S. Radha Krishnamurthi, R.K. Panda, and J.C. Panigrahi. Indian J. Chem. **26A**, 124 (1987).
17. H. Singh, J.C. Govil, and S.C. Saksena. J. Indian Chem. Soc. **58**, 951 (1981).
18. U. Mishra, K. Sharma, and V.K. Sharma. J. Indian Chem. Soc. **63**, 586 (1986).
19. J.R. Jones, W.A. Waters, and J.S. Littler. J. Chem. Soc. 630 (1961).
20. (*a*) G.H. Jeffery, J. Bassett, J. Mendham, and R.C. Denney. Vogel's textbook of quantitative chemical analysis. 5th ed. ELBS Longman, Essex, UK. 1996. p. 371; (*b*) p. 334.
21. K.W. Hicks and J.R. Sutter. J. Phys. Chem. **75**, 1107 (1971).
22. R.M. Hassan, M.A Mousa, and M.H. Wahdan. J. Chem. Soc. Dalton Trans. 605 (1988).
23. R.M. Hassan. Can. J. Chem. **69**, 2018 (1991).
24. N.N. Halligudi, S.M. Desai, and S.T. Nandibewoor. Transition Met. Chem. (Dordrecht, Neth.), **26**, 28 (2001).
25. L.J. Bellamy. The IR spectra of complex organic molecules. 2nd ed. Methuen and Co., London. 1958. p. 425.
26. A.I. Vogel. A textbook of practical organic chemistry including qualitative organic analysis. 3rd ed. Longman, Essex UK. 1973. p. 332.
27. S.T. Nandibewoor, and V.A. Morab. J. Chem. Soc. Dalton Trans, 483 (1995).

© 2004 NRC Canada

28. I.M. Kolthoff, E.J. Meehan, and E.M. Carr. J. Am. Chem. Soc. **72**, 1439 (1953); S.Bhattacharya and P. Banerjee. Bull. Chem. Soc. Jpn. **69**, 3475 (1996).
29. S.A. Chimatadar, S.C. Hiremath, and J.R Raju. Indian. J. Chem. **30A**, 190. (1991).
30. K.B. Wiberg. Oxidation in organic chemistry. Part A. Academic Press, New York. 1965. p. 6.
31. K.B. Wiberg. Oxidation in organic chemistry. Part A. Academic Press, New York. 1965. p. 57.
32. K.S. Gupta and Y.K. Gupta. J. Chem. Ed. **61**, 1972 (1964).
33. J.C. Bailar, H.J. Emeleus, R. Nyholm, and A.F.T. Dickenson. Comprehensive inorganic chemistry. Vol. 3. Pergamon. Press Ltd., New York. 1975. p. 771.
34. A. Carrington and M.C.R. Symons. Chem. Rev. **63**, 443 (1963).
35. J.M. Malcom and R.M. Noyes. J. Am. Chem. Soc. **74**, 2769 (1952).
36. G.R. Waterbury, A.M. Hayes, and D.S. Martin. J. Am. Chem. Soc. **74**, 15 (1952).
37. R.S. Verma, M.J. Reddy, and V.R. Shastry. J. Chem. Soc. Perkin Trans. 2, 469 (1976).
38. S.S. Kim, W. Zhang, and T.J. Pinnavaia. Catal. Lett. **43**, 149 (1997).
39. B.Z. Zahn and X.Y. Li. Stud. Surf. Sci. Catal. **105A**, 615 (1997).
40. P.S. Radha Krishnamurti and M.D.P. Rao. Indian J. Chem. **15A,** 524 (1977).
41. L.S. Levitte and E.R.J Melinovski. J. Am. Chem. Soc. **77**, 4517 (1955).
42. S.R. Sahu, V.R. Chourey, S. Pandey, and V.R. Shastry. Oxid. Commun. **21**, 574 (1998).
43. P.D. Pol, R.T. Mahesh, and S.T. Nandibewoor. J. Chem. Res. Synop. 533 (s), 1145 (m) (2002).
44. W.A. Waters. Q. Rev. Chem. Soc. **12**, 277 (1958).

Appendix

According to Scheme 1,

$$[A1] \quad \text{Rate} = k_1[HMnO_4][BA] = k_1K_1[Mn(VII)]_f[BA]_f[H^+]_f$$

The total concentration of MnO_4^- is given by (where "T" and "f "stand for total and free)

$$[Mn(VII)]_T = [Mn(VII)]_f + [HMnO_4] = [Mn(VII)]_f(1 + K_1[H^+])$$

Therefore,

$$[A1a] \quad [Mn(VII)]_f = [MnO_4^-]_T/1 + K_1[H^+]$$

Similarly,

$$[A1b] \quad [H^+]_f = [H^+]_T/1 + K_1[Mn(VII)]$$

Substituting eqs. [A1*a*]and [A1*b*] in eq. [A1]

$$[A1c] \quad \text{Rate} = -d[Mn(VII)]/dt = \frac{k_1K_1[H^+][BA][Mn(VII)]_T}{(1 + K_1[H^+])\,(1 + K_1[Mn(VII)])}$$

The term $(1 + K_1[Mn(VII)])$ in the denominator of eq. [A1*c*] approximates unity in view of the low concentration of Mn(VII) used.

Autocatalysis

According to Scheme 2,

$$[A1d] \quad \text{Rate} = k_2[C_2][HMnO_4] = k_2K_2[Mn(II)]_f[BA]_f^2[HMnO_4]$$

$$[Mn(II)]_T = [Mn(II)]_f + [C_2] = [Mn(II)]_f(1 + K_2[BA]^2)$$

Therefore,

$$[A1e] \quad [Mn(II)]_f = [Mn(II)]_T/1 + K_2[BA]^2$$

Similarly,

$$[A1f] \quad [BA]_f = [BA]_T/1 + K_2[Mn(II)][BA]$$

Substituting eqs. [A1*e*] and [A1*f*] in eq. [A1*d*]

$$[A1g] \quad \text{Rate} = \frac{k_2K_2[Mn(II)][BA]^2[HMnO_4]}{\{1 + K_2[BA]^2\}\{1 + K_2[Mn(II)][BA]\}^2}$$

© 2004 NRC Canada

Fluorine chemistry. Part 2. Synthesis and characterization of 2*H*-heptafluoropropane (HFC-227ea)

Pinaki S. Bhadury, Sapna Singh, Mamta Sharma, Ramesh C. Malhotra, and Krishnamurthy Sekhar

Abstract: A facile method has been developed for the synthesis and characterization of volatile 1,1,1,2,3,3,3-heptafluoropropane (HFC-227ea), a potential non-ozone depleting hydrofluorocarbon substitute for Halon 1301 (CF_3Br). The method involves hydrofluorination of hexafluoropropene using in situ generated onium bifluoride obtained from the decomposition of anhydrous tetrabutylammonium fluoride. The reagent acts as an excellent equivalent to hydrogen fluoride and permits the use of normal glassware.

Key words: 2*H*-heptafluoropropane, hydrofluorocarbon, hexafluoropropene, tetrabutylammonium fluoride, hydrofluorination.

Résumé : On a développé une méthode simple de synthèse et de caractérisation du 1,1,1,2,3,3,3-heptafluoropropane (HFC-227ea), un hydrofluorocarbone volatil sans effet nocif sur la couche d'ozone qui pourrait éventuellement remplacer le Halon 1301 (CF_3Br). La méthode implique l'hydrofluoration de l'hexafluoropropène en faisant appel à bifluorure d'onium généré in situ par décomposition du fluorure de tétrabutylammonium anhydre. Le réactif agit comme un excellent équivalent pour le fluorure d'hydrogène et permet d'utiliser de la verrerie normale.

Mots clés : 2*H*-heptafluoropropane, hydrofluorocarbone, hexafluoropropène, fluorure de tétrabutylammonium, hydrofluoration.

[Traduit par la Rédaction]

Introduction

Chlorofluorocarbons (CFCs) and bromine-containing halons are recognized as potent contributors to the depletion of earth's stratospheric ozone layer. In accordance with the Montreal Protocol, consumption of CFCs and halons is prohibited (to be phased out over the period 1996–2030) (1, 2). According to the United States Environmental Protection Agency (USEPA), 2*H*-heptafluoropropane (HFC-227ea) does not deplete stratospheric ozone. In addition, HFC-227ea is the most effective of the proposed hydrofluorocarbon (HFC) substitutes for Halon 1301 (CF_3Br) in fire protection applications (3).

Although various synthetic procedures for chlorofluorocarbons and hydrochlorofluorocarbons have been reported in the literature, those actually used in manufacturing processes are limited. By far the most important is the original Swarts reaction, which has the limitation of employing corrosive reagents (anhyd. HF, SbF_3, and SbF_5) and is associated with poor yield with a number of side reaction products (4). The specific information on the synthesis of HFC-227ea and related chemicals is again very limited and involves either reaction of elemental fluorine gas with 2-trifluoromethyl-3,3,3-trifluoropropionic acid (5) or high-temperature, vapour-phase addition of corrosive HF on hexafluoropropene (HFP) in the presence of a fluorination catalyst (6).

Anhydrous hydrogen fluoride as such or its equivalent such as Olah's reagent (pyridinium poly(hydrogen fluoride)) (4, 7), essentially employs free HF. These reagents are highly toxic, corrosive to the skin, and readily attack glass. In addition, owing to the strong H-bond and the relatively weak acidic nature of HF, they possess poor fluoride activity and are not suitable for conversion of HFP into HFC-227ea.

Earlier, we developed methodologies for the synthesis of hydrofluorocarbons such as CF_2ClH, CF_2BrH, $CFBr_2H$, CF_2H_2, and $CF_3CF_2CF_2H$ (HFC-227ca, isomer of HFC-227ea) based on in situ generated reactive fluorinated phosphonium ylide and the related Wittig reaction (8, 9). This methodology has now been extended to HFC-227ea. Another useful and facile method developed utilizes the reaction of HFP with anhydrous tetrabutylammonium fluoride (TBAF) at higher temperature with the latter serving as a potential source for hydrogen fluoride. The results of this interesting finding are summarized in this communication.

Results and discussion

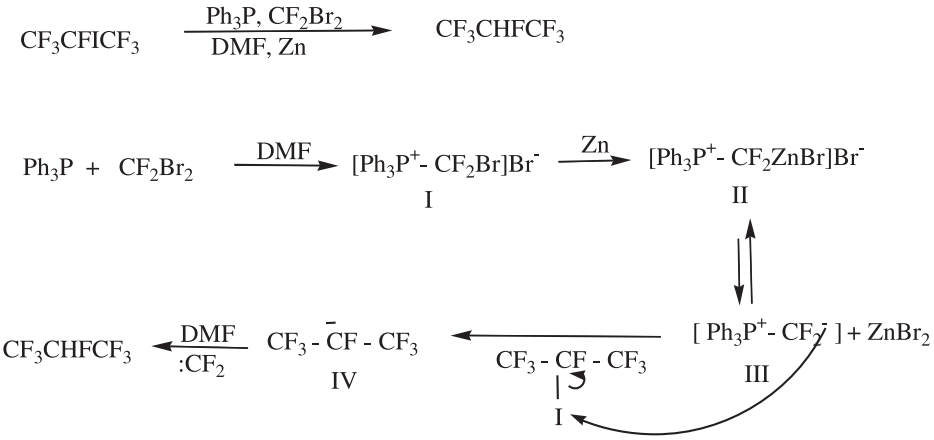
A Wittig reaction involving in situ difluoromethylene triphenylphosphonium ylide [$Ph_3P^+–^-CF_2$] in DMF has been successfully employed by us to convert several activated aromatic ketones and aldehydes into their corresponding termi-

Received 23 March 2004. Published on the NRC Research Press Web site at http://canjchem.nrc.ca on 23 October 2004.

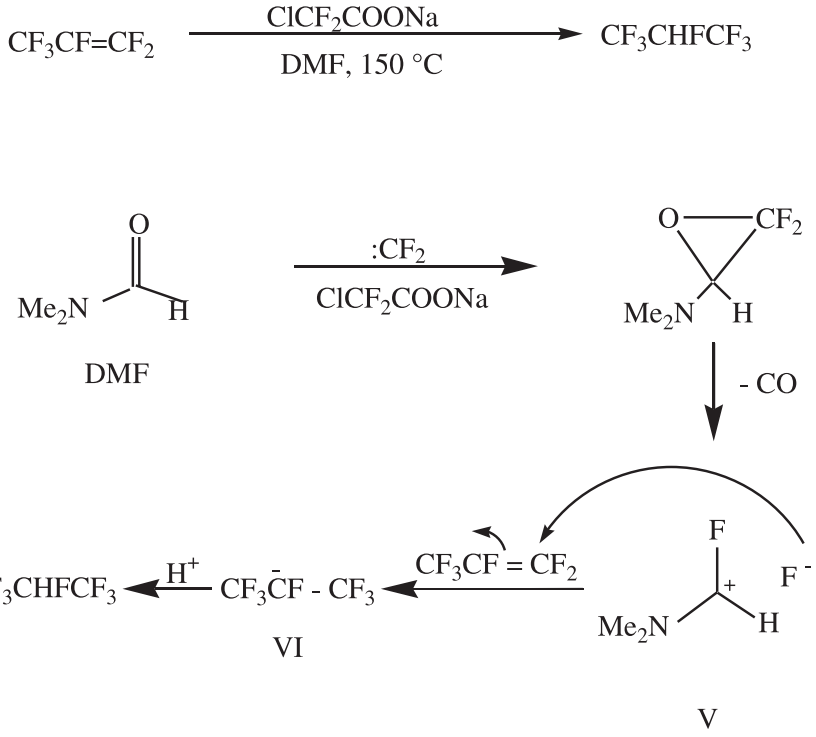
P.S. Bhadury,[1] S. Singh, M. Sharma, R.C. Malhotra, and K. Sekhar. Synthetic Chemistry Division, Defence Research and Development Establishment, Gwalior 474 002, India.
[1]Corresponding author (e-mail: drpsb2003@yahoo.co.in).

 doi: 10.1139/V04-111 © 2004 NRC Canada

Scheme 1. Formation of HFC-227ea from zinc dehalogenation of fluorinated phosphonium salt.



Scheme 2. Proposed mechanism for the formation of HFC-227ea by the salt method.



nal 1,1-difluoroolefins (8, 10, 11). The study has recently been extended to yield perfluoroisobutylene (PFIB), a Schedule 2 higly toxic chemical (9). The fate of this highly reactive nucleophilic ylide in the presence of a non-carbonyl moiety, e.g., positive iodine- or bromine-containing electrophiles has further been studied to yield volatile organofluorins such as CF_2=CF_2, perfluorocyclobutane, CF_3CF=$CFCF_3$, and HFC-227ca (9). The formation of [Ph_3P^+–$^-CF_2$] by zinc metal dehalogenation of in situ generated (bromodifluoromethyl) triphenylphosphonium bromide salt has now been utilized for the synthesis of HFC-227ea.

The (bromodifluoromethyl) triphenylphosphonium bromide salt (**I**, Scheme 1) was formed when an equimolar amount of CF_2Br_2 was added in one installment to a well-stirred solution of triphenylphosphine at room temperature in dry DMF. This was followed by the addition of a half molar equivalent of 2-iodoheptafluoropropane to the salt solution at room temperature. Then 1 g atom equivalent of Zn powder was added slowly into the reaction mixture. Within 1 to 2 min an exothermic reaction ensued owing to the formation of organozinc bromide (**II**) in equilibrium with difluoromethylene triphenylphosphonium ylide (**III**). Volatile HFC-227ea was generated and directly collected in a tedlar bag attached to the reaction system. The nucleophilic ylide (**III**) under the reaction conditions can abstract labile positive iodine from the substrate 2-iodoheptafluoropropane to give a carbanion (**IV**). The intermediate carbanion, stabilized largely by negative hyperconjugation because of the presence of six β fluorine atoms, abstracts a proton from the solvent to form 2*H*-heptafluoropropane. As observed earlier, the solvent DMF can provide a proton in the presence of difluorocarbene (**:**CF_2), which in turn is generated by the de-

© 2004 NRC Canada

Table 1. Spectral data of HFC-227ea (CF_3CHFCF_3).

^{1}H NMR δ (ppm)	6.05 (1H, sd, CHF,^{3} $J_{H\text{-}F}$ = 5.75 Hz, $^2J_{H\text{-}F}$ = 42.4 Hz)
^{19}F NMR δ_F (ppm)	–77.44 (6F, dd, CF_3, $^3J_{F\text{-}F}$ = 11.08 Hz, $^3J_{H\text{-}F}$ = 5.75 Hz)
	–217.19 (1F, sd, CF, $^3J_{F\text{-}F}$ = 11.08 Hz, $^2J_{H\text{-}F}$ = 42.4 Hz)
^{13}C NMR δ (ppm)	82.5 (1C, sd, CF, $^1J_{C\text{-}F}$ = 197.5 Hz, $^2J_{C\text{-}F}$ = 36.1 Hz)
	120 (2C, dq, CF_3, $^1J_{C\text{-}F}$ = 281 Hz, $^2J_{C\text{-}F}$ = 25.75 Hz)
GC–MS (EI)	151 (M – F), 101, 69
GC–MS (NCI)	169 (M – 1)

composition of excess ylide under reaction conditions (8, 10). A similar observation was noted during the synthesis of HFC-227ca, the other isomer of HFC-227ea, when 1-iodoheptafluoropropane was subjected to reaction with in situ generated [Ph_3P^+–$^-CF_2$] ylide in DMF (9).

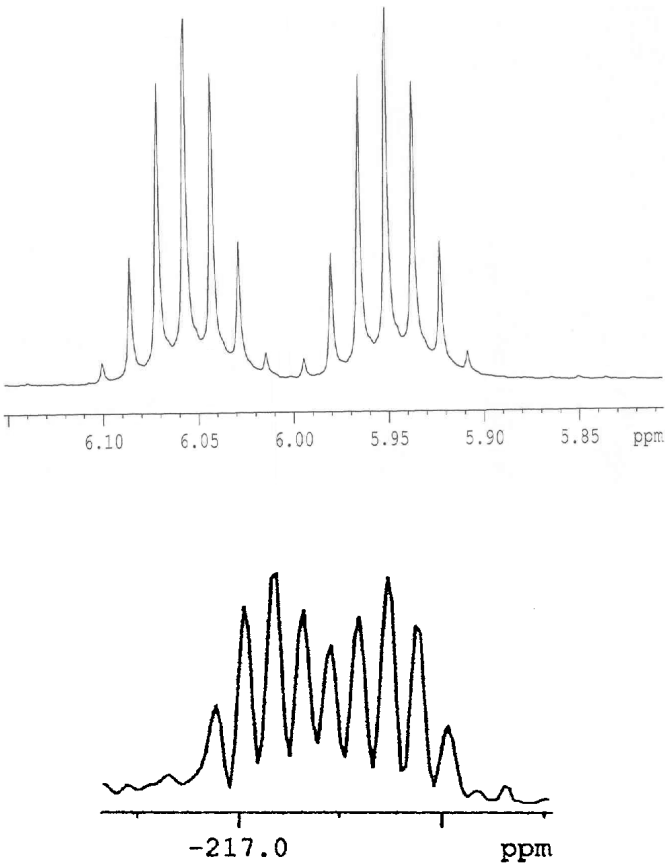
The ylide method, despite being facile, is highly expensive. Therefore, an alternative method using in situ hydrofluorination of hexafluoropropene has been developed.

The difluorocarbene intermediate can be generated in situ at high temperature by the decarboxylation of sodium chlorodifluoroacetate (12, 13). When this decarboxylated salt is reacted with HFP at 150 °C in the solvent DMF, HFC-227ea is formed. Under the influence of difluorocarbene obtained by heating $ClCF_2COONa$, the solvent DMF generates an active fluoro Vilsmeier–Haack intermediate (**V**, Scheme 2). Proof of the formation of this strong Lewis acid intermediate [Me_2N–$^+$CHF]F^- has been provided by Burton et al. (14). This intermediate can act not only as a source of H^+ but also for F^- ion. The S_N2 attack by F^- ion on the terminal carbon atom of fluoroolefin HFP generates carbanion (**VI**), which is stabilized by negative hyperconjugation. Abstraction of a proton by the carbanion results in the formation of the desired product. However, the yield of the final product is low due to the formation of side reaction products including free HF from the decomposition of salt and (or) a Vilsmeier–Haack intermediate.

Onium fluorides such as tetrabutylammonium fluoride ($(Bu)_4N^+F^-$, (TBAF)), tetrabutylammonium bifluoride ($(Bu)_4N^+HF_2^-$, (TBABF)), etc., if free from water, can be employed as a potential fluorinating agent in nucleophilic fluoride exchange reactions on different substrates (15–18). Unfortunately, these salts are invariably associated with water and the presence of water molecules largely diminishes fluoride activity because of hydrogen bonding. To overcome this limitation we have earlier worked on in situ generated onium fluorides by using a semi-molten mixture of onium bromide and alkali metal fluoride for studying fluorodehalogenation reactions (19, 20). We further believe that in situ generated and largely unsolvated TBABF should act not only as a strong source of F^- ion, but also as an equivalent to HF for hydrofluorination reaction. Therefore, we have employed anhydrous tetrabutylammonium fluoride at high temperature as a possible in situ source of hydrogen fluoride and studied its reaction with HFP for the synthesis of HFC-227ea.

Commercially available TBAF·$3H_2O$ was heated on a boiling water bath under high vacuum until a highly viscous oil was obtained. The oil was immediately diluted with DMF and heated on an oil bath up to 150 °C. The mixture was then cooled to 130 °C and the required amount of HFP was bubbled into the solution when almost instantaneously

Fig. 1. ^{1}H and ^{19}F NMR patterns of the central hydrogen and fluorine atoms of HFC-227ea.



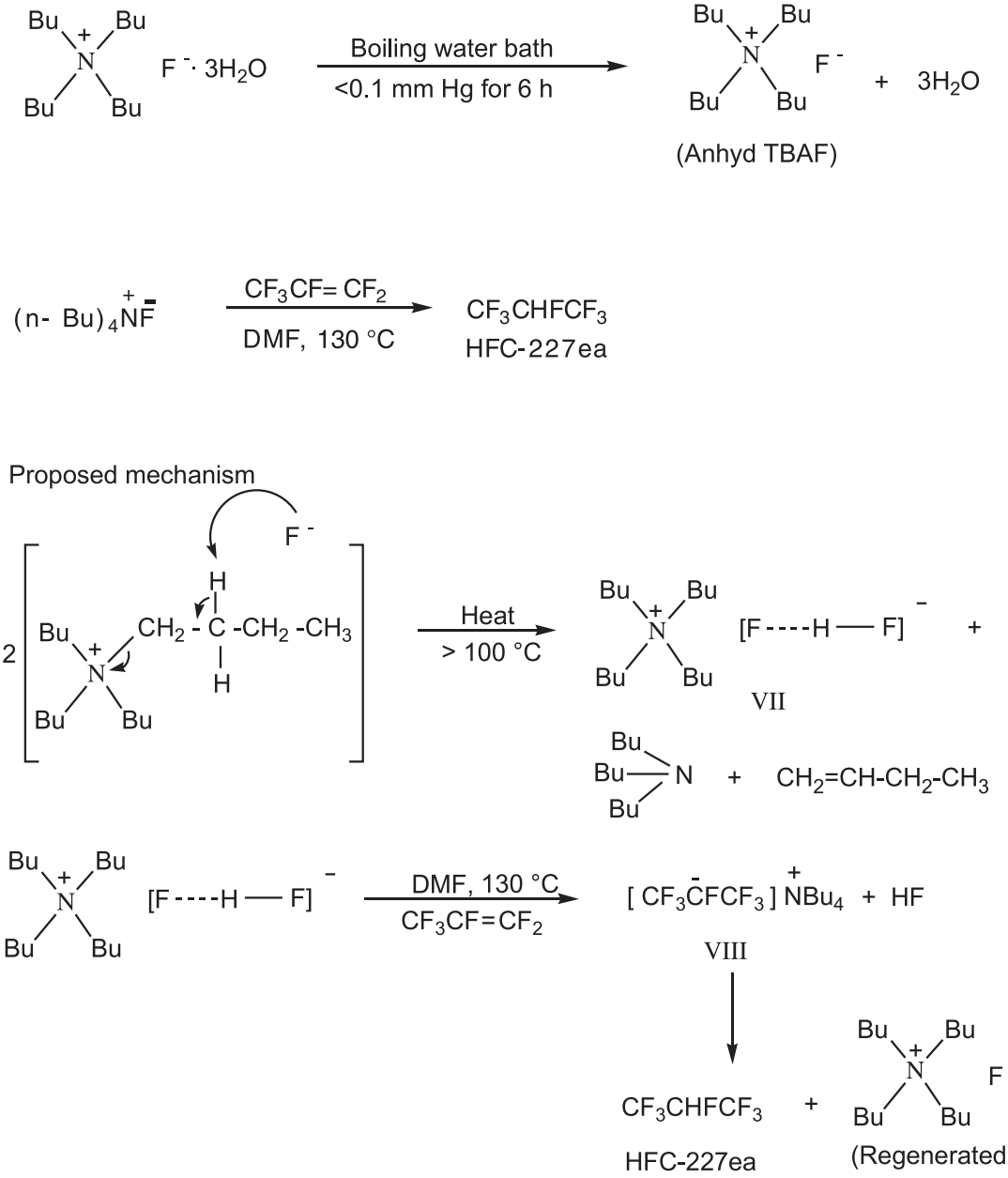
an exothermic reaction ensued. The highly volatile HFC-227ea evolved was directly collected in a tedlar bag attached to the reaction system. Toxic HFP was not been detected in the tedlar bag (confirmed by ^{19}F, ^{13}C NMR and GC–MS studies). The product was successfully collected up to the 5 g level and completely characterized by spectral data (Table 1). The distinctive and interesting NMR pattern of the central hydrogen and fluorine atom of HFC-227ea in their respective proton and fluorine spectrums is depicted in Fig. 1.

The spectral results have been compared and completely found to match with that of a standard sample supplied by Great Lakes Chemical Corporation, USA.

Presumably, extensively dried, largely unsolvated "naked" in situ source of F^- ion in TBAF loses its H-bonded stabilizing force and can behave as a base (21). Abstraction of a proton by F^- ion from a second molecule of TBAF in a β-elimination reaction generates higly reactive in situ

© 2004 NRC Canada

Scheme 3. Formation of HFC-227ea by the TBAF method.



hydrofluorinating agent tetrabutylammonium bifluoride ($(Bu)_4N^+HF_2^-$) (**VII**, Scheme 3) along with tributylamine and 1-butene. This type of F^- ion induced β-elimination of onium salts has earlier been noted by Sharma and Fry (22) but has never been utilized in synthetic transformations. Fluoride ion attack on the terminal carbon atom of HFP generates intermediate (**VIII**), which after abstracting a proton from generated HF leads to the formation of HFC-227ea. The mechanism is further supported by the fact that liquid tributylamine and volatile 1-butene (in the tedlar bag) have been detected during the process. Pure HFC-227ea was obtained after removal of butene (see Experimental).

Thus, reaction of HFP with in situ generated TBABF obtained from the decomposition of commercial TBAF·$3H_2O$ appears to be the most practical method for the synthesis of 2*H*-heptafluoropropane.

Conclusion

Of the various methods developed for the synthesis of 2*H*-heptafluoropropane, the one using anhydrous onium fluoride at high temperature holds considerable promise. The in situ generated and largely unsolvated hydrofluorination agent acts as an excellent equivalent to hydrogen fluoride. The reagent is highly reactive, easy to handle, noncorrosive, and permits the use of normal glass apparatus for storage of the agent and execution of the reaction.

Experimental

The volatile HFC-227ea generated can be safely stored in 1 and 2 L capacity tedlar bags procured from Supelco, USA. The analysis was effected either by bubbling the gas into a

© 2004 NRC Canada

NMR tube in deuterated solvent at low temperature or by gas phase injection after drawing the sample through the septum for MS. The NMR spectra were recorded on a Bruker Avance DPX 400 spectrometer in acetone-d_6 solution using TMS for ^{1}H NMR and $CFCl_3$ for ^{19}F NMR as internal references, respectively. Mass spectra were recorded on a TSQ 7000 mass spectrometer (Finnigan MAT, USA) as described earlier (8, 9).

Synthesis of HFC-227ea

TBAF method

Commercial tetrabutylammonium fluoride trihydrate ($TBAF{\cdot}3H_2O$) (20 g, 0.063 mol) was transferred into a round-bottomed flask and heated on a boiling water bath under vacuum (<0.1 mmHg, 1 mmHg = 133.322 4 Pa) for 6 h when a highly viscous liquid (anhyd. TBAF; about 13 mL) was obtained; 20 mL of dry DMF was then added to this oil. The resultant homogenous solution was heated up to 150 °C in a two-necked 100 mL round-bottomed flask containing a stirring bar and a dry nitrogen inlet for 45 min. The flask was connected to a condenser fitted with a $CaCl_2$ guard tube. The solution was then cooled to 130 °C and hexafluoropropene (5 g, 0.033 mol) from a tedlar bag was bubbled into the flask. At this stage, nitrogen flow was stopped and the guard tube was replaced by an evacuated and preweighed tedlar bag by connecting the end of its valve stem to a 3/16 in (1 in = 25.4 mm) i.d. tubing fitted to an adapter. To open the valve, the tubing was pushed onto the stem to the appropriate overlap distance. As soon as HFP was bubbled into the mixture, a highly exothermic reaction occurred and gaseous product (volatile HFC-227ea along with 1-butene) was collected in the tedlar bag (total 4.5 g) attached to the reaction system. To close the valve of the tedlar bag, the stem was pulled outward until it stopped. To disconnect the tubing, it was pulled upward or was cut off just above the stem as described in our earlier work (8, 9). The mixture of volatile products from the tedlar bag was passed into another round-bottomed flask containing a solution of bromine (3 g in 6 mL of chloroform) at 0 °C. Butene was completely consumed by bromine and pure gaseous HFC-227ea was collected in another tedlar bag (4.01 g, 70%).

Ylide method

Triphenylphosphine (12.6 g, 0.048 mol) was dissolved in 35 mL of dry DMF and placed in a dried three-necked 250 mL round-bottomed flask containing a stirring bar and a dry nitrogen inlet, at room temperature. The middle neck of the flask was connected to a condenser fitted with a $CaCl_2$ guard tube. Dibromodifluoromethane (10.08 g, 0.048 mol) was added in one installment to the well-stirred solution, when a mildly exothermic reaction occurred. After stirring the mixture for another 30 min, 2-iodoheptafluoropropane (7.1 g, 0.024 mol) was added at room temperature. Nitrogen flow was stopped and the guard tube at this stage was replaced by an evacuated and preweighed tedlar bag as described above. Zinc powder (3.14 g, 0.048 mol) was then slowly added to the reaction mixture through a solid addition tube when almost immediately a violent exothermic reaction occurred. Gaseous product could be seen evolving and HFC-227ea was collected in the tedlar bag (2.61 g, 64%).

Acknowledgement

We thank Dr. D.K. Jaiswal, former Associate Director, DRDE, Gwalior for his keen interest in the work.

References

1. R.E. Banks. J. Fluorine Chem. **67**, 193 (1994).
2. A. McClloch. J. Fluorine Chem. **100**, 163 (1999).
3. US Federal Register. **58**, 12 May 1993.
4. M. Hudlicky and A.E. Pavlath (*Editors*). Chemistry of organic fluorine compounds II: A critical review. ACS, Washington, D.C. 1995.
5. T. Otsuka and H. Aoyama. US Pat. 6 191 326, 20 February 2001.
6. M.J. Nappa, V.N.M. Rao, and A.C. Sievert. Chem. Abstr. **135**, 182 382n (2001).
7. G.A. Olah, J.T. Welch, Y.D. Vankar, M. Nojima, I. Kerekes, and J.A. Olah. J. Org. Chem. **44**, 3872 (1979).
8. P.S. Bhadury, M. Palit, M. Sharma, S.K. Raza, and D.K. Jaiswal. J. Fluorine Chem. **116**, 75 (2002).
9. P.S. Bhadury, S. Singh, M. Sharma, M. Palit, and D.K. Jaiswal. Can. J. Chem. In press.
10. P.S. Bhadury, B.P. Pant, M. Palit, and D.K. Jaiswal. J. Fluorine Chem. **85**, 115 (1997).
11. P.S. Bhadury. Ph.D. thesis, Jiwaji University, Gwalior, India, 2002.
12. P.S. Bhadury, M. Palit, M. Sharma, S.K. Raza, and D.K. Jaiswal. J. Fluorine Chem. **113**, 47 (2002).
13. S. Singh, P.S. Bhadury, and D.K. Jaiswal. 39th Annual Convention of Chemists, Nagarjunanagar, A.P., India, 22–26 December 2002.
14. D.J. Burton and D.M. Wiemers. J. Am. Chem. Soc. **107**, 5014 (1985).
15. J.A. Wilkinson. Chem. Rev. **92**, 505 (1992).
16. O.A. Mascaretti. Aldrichim. Acta, **26**, 47 (1993).
17. P. Bosch, F. Camps, E. Chamorro, V. Gasol, and A. Guerrero. Tetrahedron Lett. **28**, 4733 (1987).
18. D.P. Cox, J. Terpinski, and W. Lawrynowicz. J. Org. Chem. **49**, 3216 (1984).
19. P.S. Bhadury, M. Pandey, and D.K. Jaiswal. J. Fluorine Chem. **73**, 185 (1995).
20. P.S. Bhadury, S.K. Raza, and D.K. Jaiswal. J. Fluorine Chem. **99**, 115 (1999).
21. J. Cousseau and P. Albert. J. Org. Chem. **54**, 5380 (1989).
22. R.K. Sharma and J.L. Fry. J. Org. Chem. **48**, 2112 (1983).

© 2004 NRC Canada

Three validated stripping voltammetric procedures for determination of the anti-prostate cancer drug flutamide in tablets and human serum at a mercury electrode

E. Hammam, H.S. El-Desoky, K.Y. El-Baradie, and A.M. Beltagi

Abstract: Flutamide is a nonsteriodal anti-androgen drug, which is commonly used in the treatment of advanced prostate cancer. Based on the reduction of the nitro organic moiety of the drug molecule in acetate buffer of pH 5 at the hanging mercury drop electrode, three adsorptive cathodic stripping voltammetric procedures were optimized for determination of flutamide in bulk, tablets, and human serum applying linear-sweep, differential-pulse, and square-wave waveforms. The achieved limits of detection of the bulk drug were 1.9×10^{-7}, 8.7×10^{-8}, and 9.7×10^{-9} mol L^{-1} by using the optimized differential-pulse, linear-sweep, and square-wave adsorptive stripping voltammetric procedures, respectively. Repeatability of the results was studied for 1×10^{-6} mol L^{-1} of the drug and the recoveries obtained were 98.51 ± 1.56% (LSV), 98.89 ± 0.87% (DPV), and 99.21 ± 1.03% (SWV). The proposed procedures were successfully applied to the determination of the drug in pharmaceutical formulation (Eulexin® tablets) and human serum. The detection limits of the drug in bulk, pharmaceutical formulation, and human serum achieved by means of the proposed procedures showed that the square-wave mode was more reliable for determination of the drug especially in its low concentration levels.

Key words: flutamide, linear-sweep, differential-pulse, square-wave, cathodic adsorptive stripping voltammetry, determination, Eulexin® tablets, human serum.

Résumé : Le flutamide est un médicament antiandrogène non-stéroïdal qui est couramment utilisé dans le traitement du cancer avancé de la prostate. En se basant sur la réduction de la portion nitro de la molécule, dans un tampon acétate à un pH de 5, à une électrode à goutte de mercure pendante, on a optimisé trois méthodes voltampérométriques à redissolution cathodique absorbante pour la détermination du flutamide en vrac, dans des comprimés et dans le sérum humain en appliquant un des formes d'onde à balayage linéaire, à pulsation différentielle et en ondes carrées. Les limites de détection réalisées pour le médicament en vrac ont été de $1{,}9 \times 10^{-7}$, $8{,}7 \times 10^{-8}$ et $9{,}7 \times 10^{-9}$ mol L^{-1} pour les méthodes voltampérométriques à redissolution cathodique absorbante optimisées respectivement avec une pulsation différentielle (PD), un balayage linéaire (BL) et des ondes carrées (OC). On a étudié la répétabilité des résultats à l'aide d'une solution 1×10^{-6} mol L^{-1} du médicament et les degrés de récupération obtenus ont été de 98,51 ± 1,56 % (BL), 98,89 ± 0,87 % (PD) et 99,21 ± 1,03 % (OC). Les méthodes proposées ont été appliquées avec succès à la détermination de la quantité de médicament présente dans la formulation pharmaceutique (cachets d'Eulexin®) et dans le sérum humain. Les limites de détection du médicament en vrac, dans la formulation pharmaceutique et dans le sérum humain à l'aide des méthodes proposées ont montré que le mode des ondes carrées est le plus fiable pour la détermination du médicament, particulièrement aux concentrations les plus faibles.

Mots clés : flutamide, balayage linéaire, pulsation différentielle, onde carrée, voltampérométrie à redissolution cathodique absorbante, détermination, cachets d'Eulexin®, sérum humain.

[Traduit par la Rédaction]

Introduction

Flutamide (FM), 2-methyl-*N*-[4-nitro-3-(trifluoromethyl) phenyl] propanamide (Scheme 1), is a nonsteroidal anti-androgen drug that blocks androgen receptor sites. It is commonly used in the treatment of advanced prostate cancer (1–3). FM is reported to be rapidly and completely metabolized with the major metabolite 2-hydroxyflutamide, which also possesses active anti-androgenic properties.

The half-life of both FM and the major metabolite, 2-hydroxy flutamide, is about 5 to 6 h. Excretion is predominantly in urine with only minor amounts appearing in the

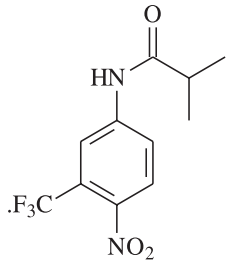
Received 20 April 2003. Published on the NRC Research Press Web site at http://canjchem.nrc.ca on 23 October 2004.

E. Hammam, H.S. El-Desoky, K.Y. El-Baradie. Department of Chemistry, Faculty of Science, Tanta University, 31527 Tanta, Egypt. **A.M. Beltagi.**[1] Department of Chemistry & Physics, Faculty of Education, Tanta University, 33516 Kafr El-Sheikh, Egypt.

[1]Corresponding author (e-mail: ambeltagi@hotmail.com).

 doi: 10.1139/V04-104 © 2004 NRC Canada

Scheme 1.



faeces (4). Analysis of flutamide in serum samples collected from 16 healthy volunteers following an oral administration of a 250 mg flutamide single dose provided the following pharmacokinetic data: C_{max} = 776–400 ng mL^{-1} (2.8 × 10^{-6} – 1.5 × 10^{-6} mol L^{-1}), T_{max} = 2.6–1.6 h, and elimination half-life k_{el} = 5.2–2.0 1/h (5, 6).

Many analytical methods were described in the literature for determination of FM in bulk form, pharmaceutical formulations, and human plasma. These methods include: spectrophotometry (7–12), high-performance liquid chromatography (HPLC) (5, 12–14), polarography (15), and differential-pulse polarography (12). No stripping voltammetric procedures for determination of flutamide have been reported in the literature yet.

We demonstrate here the electrochemical behavior of the FM drug at the hanging mercury drop electrode. Based on the reduction of the nitro group of the drug molecule, three stripping voltammetric procedures were optimized for determination of FM in bulk drug, pharmaceutical formulation (Eulexin® tablets), and human serum, using the linear-sweep, differential-pulse, and square-wave waveforms.

Experimental

Instrumentation

Electrochemical analyzer models 394 and 263A-PAR (Princeton Applied Research, Oak Ridge, Tenn., USA) were used for the voltammetric measurements. The electrode assembly model 303A-PAR incorporated with a dark micro-electrolysis cell of a three-electrode system comprised of a hanging mercury drop electrode (HMDE) as a working electrode (area = 0.026 cm^2), an Ag/AgCl (saturated KCl) reference electrode, and a platinum wire counter electrode was used. Stirring of the solution in the micro-electrolysis cell was performed using a magnetic stirrer (model 305-PAR) with a star-shaped magnet to provide the convective transport during the preconcentration step. The whole measurements were automated and controlled through the programming capacity of the apparatus. Recovery and quantification of the drug in different samples were performed by means of calibration curve and standard addition methods. The data were treated through a personal computer connected to the potentiostat and loaded with the Analytical voltammetry software (16).

The deionized water used throughout the present study was supplied from a Purite-Still Plus deionizer connected to a Hamilton-AquaMatic bidistillation water system.

A Mettler balance (Toledo-AB104, Greifensee, Switzerland) was used for weighing the solid materials. An Orion SA-720 pH meter incorporated with combined glass and saturated calomel electrodes was used for the pH measurements. A centrifuge (Eppendorf-5417 C, Hamburg, Germany) was used for separation of the precipitated proteins from human serum samples prior to assay of the drug. A micopipetter (Eppendorf-Multipette® plus) was used for transfer of the reactant solutions throughout the present experimental work. All data were obtained at room temperature.

Materials and reagents

Bulk flutamide drug was kindly supplied from the Egyptian International Pharmaceutical Industries Company (EIPICO). A standard stock solution of 1 × 10^{-3} mol L^{-1} flutamide was prepared in methanol (Merck) and stored in the dark at 4 °C. A more dilute solution of 1 × 10^{-5} mol L^{-1} FM was prepared daily in methanol just before use. Eulexin® tablets (Schering-Plough, Kenilworth, N.J., USA), labeled to contain 250 mg FM per tablet, were used for the present analytical application.

Britton-Robinson (B-R) buffers of pH 2–11 (17) and acetate buffers of pH 4–6 (18) were prepared then used as supporting electrolytes. All chemicals and reagents were of analytical grade.

Procedures

General analytical procedure

A 10 mL volume of the supporting electrolyte was introduced into a dark micro-electrolysis cell then deaerated with pure nitrogen for 10 min. A selected preconcentration potential was then applied to the hanging mercury drop electrode for a selected preconcentration time period, while the solution was stirred at 400 rpm. The stirring was then stopped, and after a 15 s rest period, the voltammogram was recorded by applying a negative-going scan. After the background voltammogram was recorded, an aliquot of the drug solution was introduced into the micro-electrolysis cell, deaerated again with pure nitrogen for 3 min, then the voltammogram was recorded at a new mercury drop.

Analysis of Eulexin® tablets

The drug content of five tablets was weighed, finely powdered, then mixed. The average mass per tablet was determined. A quantity of the homogenous powder equivalent to 250 mg FM was transferred accurately into a 100 mL volume calibrated flask contained 70 mL of methanol. The content of the flask was shaken for about 15 min and then made up to volume with methanol. The solution was then filtered through a 0.45 μm millipore filter (Gelman, Germany), to separate the insoluble excipients, rejecting the first portion of the filtrate. The desired concentration of the drug was obtained by accurate dilution with methanol and the analysis was followed up as indicated in the general analytical procedure.

Analysis of human serum samples

Serum samples, obtained from healthy volunteers, were collected and stored frozen until assay. Aliquots of human serum sample (each of 100 μL) were fortified with FM in a

© 2004 NRC Canada

small tube to achieve serum samples spiked with different concentrations of FM ($1 \times 10^{-8} - 1 \times 10^{-5}$ mol L^{-1}), then the volume of each sample was made up to 1 mL with methanol (as a protein precipitating agent). After vortexing each serum sample for 30 s, the precipitated proteins were separated by centrifugation for 3 min at 14 000 rpm. The clear supernatant layer was filtered through a 0.45 μm millipore filter to obtain protein-free human serum samples, which were used as standard solutions. Then the analysis was followed up as indicated in the general analytical procedure.

Results and discussion

Effect of type and pH of the supporting electrolyte

The influence of pH on the linear-sweep voltammetric response of 1×10^{-6} mol L^{-1} FM was examined in B-R buffers (pH 2–11) and acetate buffers (pH 4–6) following preconcentration for 30 s at a scan rate of 100 mV s^{-1}. The voltammograms showed a single well-defined irreversible peak over the whole pH range of both B-R and acetate buffers. This peak may be attributed to the reduction of the aromatic nitro group of the drug molecule to the amine stage via the consumption of six electrons. The peak potential shifted to more negative values on the increase of pH of the medium, denoting the involvement of H^+ ions in the electrode reaction process and that the proton-transfer reaction precedes the electrode process proper (19). As shown in Fig. 1, the linear-sweep voltammogram of the drug in the acetate buffer of pH 5 at the HMDE showed a single cathodic peak (E_p = – 0.37 V) with a more developed peak current intensity compared to that obtained in a B-R buffer of the same pH value. Therefore, the acetate buffer of pH 5 was chosen as a supporting electrolyte in the rest of the present work.

Cyclic voltammetry

The interfacial adsorptive character of FM onto the HMDE was studied by means of cyclic voltammetry in an acetate buffer of pH 5. A single well-defined irreversible cathodic peak was obtained (E_p = –0.41 V vs. $Ag/AgCl/KCl_s$). Figure 2 shows the cyclic voltammograms of 1×10^{-5} mol L^{-1} bulk FM recorded in the acetate buffer of pH 5 without preconcentration of the drug, t_{acc} = 0 s (dashed curve), after preconcentration onto the HMDE for 30 s (curve 1), and then its repetitive cycle at the same mercury drop (curve 2). A more developed peak current intensity was achieved following preconcentration of the bulk drug onto the electrode surface, whereas the repetitive cycle at the same mercury drop exhibited a lower peak current intensity, which may be attributed to the desorption of drug species out of the mercury electrode surface. This behavior indicated the interfacial adsorptive accumulation of the drug onto the mercury electrode surface. The cycles carried out for increased values of the scan rate (ν) gave rise to a cathodic peak with current intensities that showed a linear increase with the scan rate between 20–200 mV s^{-1}, following the relation: $\log i_{pc} = 0.84 \log \nu - 1.85$ (r = 0.996 and n = 8). Its slope value (0.84) was close to that expected for an ideal reaction of surface species (20).

Fig. 1. Linear-sweep adsorptive cathodic stripping voltammograms of 1×10^{-6} mol L^{-1} FM recorded in B-R buffers of different pH values: (*a*) 3, (*b*) 5, (*c*) 7, (*d*) 9, and (*e*) in an acetate buffer of pH 5. Scan rate = 100 mV s^{-1} and t_{acc} = 30 s.

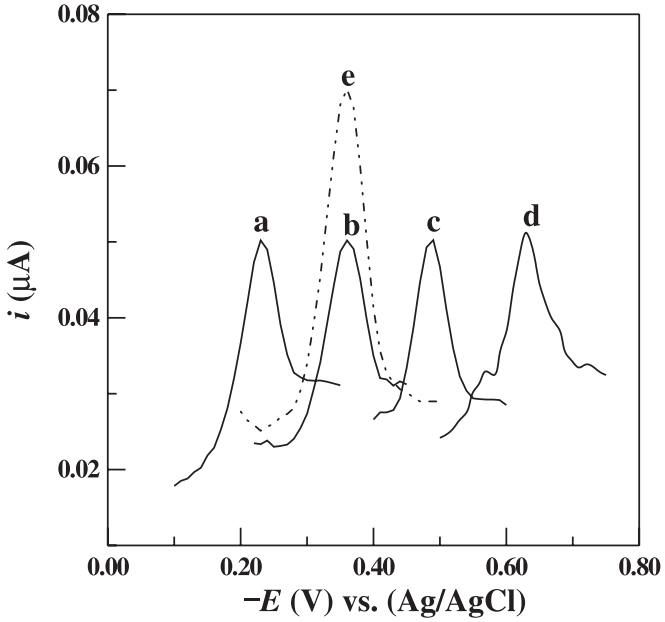
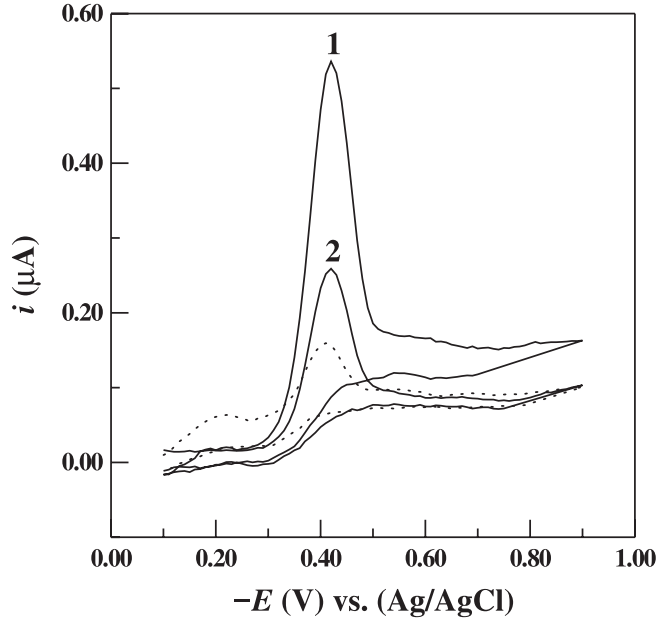


Fig. 2. Cyclic voltammograms of 1×10^{-5} mol L^{-1} FM in an acetate buffer of pH 5: without preconcentration (t_{acc}= 0 s, dashed curve), following preconcentration for 30 s (curve 1), and then its repetitive cycle at the same mercury drop (curve 2). Scan rate ν = 100 mV s^{-1} and E_{acc} = –0.10 V.



For a totally irreversible electrode reaction, the relationship between the peak potential (E_p) and scan rate (ν) was expressed as (21):

$$E_p = (2.303RT/\alpha n_a F) \log(RTk_f^0/\alpha n_a F) - (2.303RT/\alpha n_a F) \log \nu$$

© 2004 NRC Canada

Fig. 3. Effect of preconcentration potential (E_{acc}) on the adsorptive cathodic stripping peak current (i_p) of 1×10^{-6} mol L^{-1} FM in an acetate buffer of pH 5 using different waveforms: (*a*) linear-sweep (ν = 10 mV s^{-1} and E_{dp} = 25 mV), (*b*) differential-pulse (ν = 10 mV s^{-1} and E_{dp} = 25 mV), and (*c*) square-wave (f = 60 Hz, Δs = 10 mV, and E_{sw} = 25 mV). t_{acc} = 30 s.

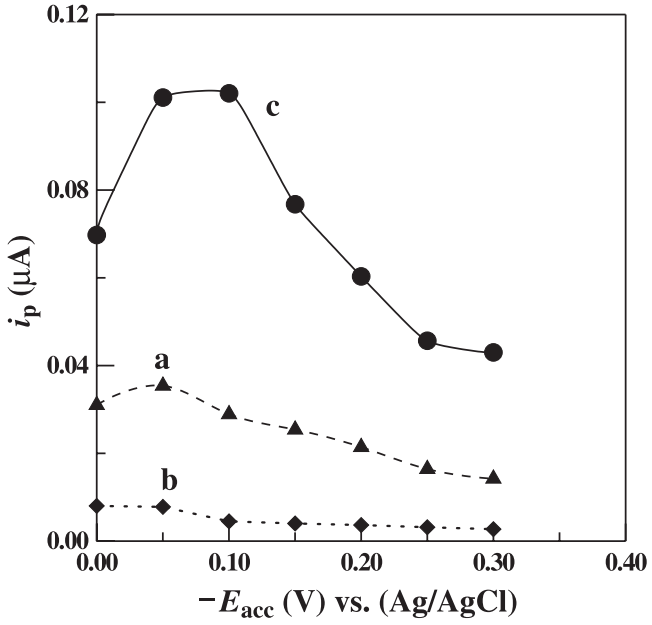
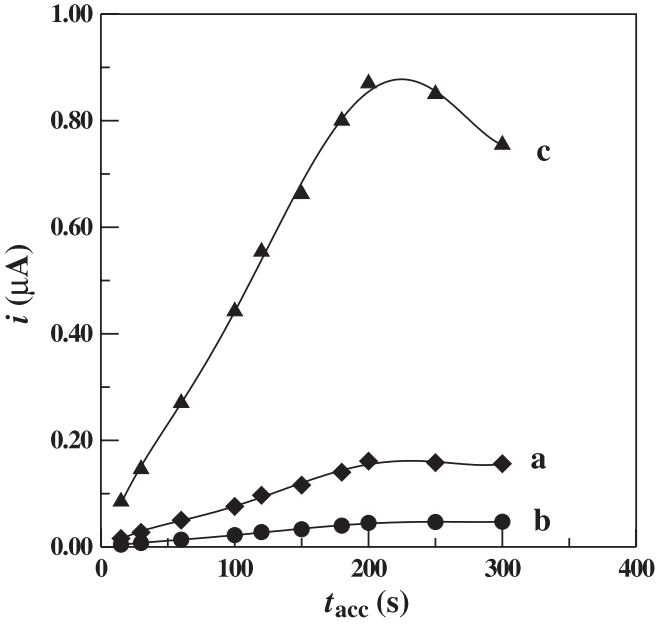


Fig. 4. Effect of preconcentration time (t_{acc}) on the adsorptive cathodic stripping peak current (i_p) of 1×10^{-6} mol L^{-1} FM in an acetate buffer of pH 5 using different waveforms: (*a*) linear-sweep, (*b*) differential-pulse, and (*c*) square-wave. Other operational parameters are as those given in Fig. 3.



The dependence of the peak potential (E_p) of bulk FM on the decimal logarithm of the scan rate (ν) was linear, following the relationship:

$$E_p \text{ (V)} = 0.058 \log \nu - 0.416$$

From its slope, a value of αn_a = 1.02 was obtained. Accordingly, the number of electrons (n_a) transferred in the rate-determining step should be two (n_a = 2). Hence, the estimated value of the transfer coefficient (α) was 0.51.

Optimization of the electroanalytical procedures

Linear-sweep voltammetry procedure

The linear-sweep adsorptive cathodic stripping (LSAdCS) voltammograms of the drug in an acetate buffer (pH 5) at the HMDE showed a single cathodic peak (E_p = – 0.37 V). The effect of scan rate (ν) on the linear-sweep peak current of 1×10^{-6} mol L^{-1} FM was studied within the range 25–200 mV s^{-1}. Although the peak current intensity increased with an increase of scan rate, the peak morphology was sharper at a scan rate of 100 mV s^{-1}. The effect of preconcentration potential on the linear-sweep peak current was also studied over the potential range 0.0 to –0.30 V (vs. Ag/AgCl/KCl_s). As shown in Fig. 3, a higher peak current intensity was achieved at a preconcentration potential of –0.05 V (curve a). The effect of the preconcentration time on the peak current of 1×10^{-6} mol L^{-1} FM in the acetate buffer of pH 5 (E_{acc} = –0.05 V) was studied and a linear relation up to 200 s preconcentration time was obtained. At longer preconcentration time, saturation of the mercury surface was achieved (Fig. 4, curve a). Therefore, the optimal conditions used throughout the rest of the present linear-sweep measurements were: scan rate (ν) = 100 mV s^{-1}, pulse amplitude (E_{ls}) = 25 mV, preconcentration potential (E_{acc}) = –0.05 V, and preconcentration time = 60–150 s.

Differential-pulse voltammetry procedure

The differential-pulse adsorptive cathodic stripping (DPAdCS) voltammogram of bulk FM in an acetate buffer of pH 5 showed a single cathodic stripping peak (E_p = –0.4 V). The effect of scan rate showed a gradual increase of the differential-pulse peak current intensity within the range 2–20 mV s^{-1}. A scan rate of 10 mV s^{-1} was chosen where a sharper peak was obtained. As 25 mV pulse-height gave rise to the best peak morphology; it was chosen for the further investigations. Figure 3 (curve b) shows the effect of the preconcentration potential on the peak current of 1×10^{-6} mol L^{-1} bulk FM (t_{acc} = 30 s) over the potential range 0.0 to –0.3 V. There was almost no change in the peak current over the potential range 0.0 to –0.05 V. Therefore, a preconcentration potential (E_{acc}) of –0.05 V (vs. Ag/AgCl/KCl_s) was considered throughout the present differential-pulse measurements. Figure 4 (curve b) shows the plot of the peak current of 1×10^{-6} mol L^{-1} bulk FM vs. preconcentration time (t_{acc}) in the acetate buffer of pH 5. A straight line was obtained and the magnitude of the peak current increased with an increase of preconcentration time. Saturation of the mercury surface with the drug was achieved after preconcentration for about 200 s. Therefore, the optimal conditions used throughout the rest of the present differential-pulse measurements were: scan rate (ν) = 10 mV s^{-1}, pulse amplitude (E_{dp}) = 25 mV, preconcentration potential (E_{acc}) = –0.05 V, and preconcentration time (t_{acc}) = 60–150 s.

Square-wave voltammetry procedure

The square-wave adsorptive cathodic stripping (SWAdCS) voltammogram of bulk FM at the HMDE in an acetate

© 2004 NRC Canada

Table 1. Characteristics of the calibration curves of the determination of bulk FM in an acetate buffer of pH 5 by means of the three proposed stripping voltammetric procedures.

AdCSV procedure	t_{acc} (s)	Linearity range (mol L^{-1})	Least-squares equation[a] Intercept (nA)	Slope (nA/μmol L^{-1})	Corr. coefficient (r)	LOD (mol L^{-1})	LOQ (mol L^{-1})
LS	60	$6 \times 10^{-7} - 6 \times 10^{-6}$	2.78	12.11	0.996	1.4×10^{-7}	4.7×10^{-7}
	150	$4 \times 10^{-7} - 5 \times 10^{-6}$	3.40	27.80	0.998	8.7×10^{-8}	2.9×10^{-7}
DP	60	$8 \times 10^{-7} - 8 \times 10^{-6}$	1.78	5.87	0.996	4.2×10^{-7}	1.4×10^{-6}
	150	$5 \times 10^{-7} - 6 \times 10^{-6}$	2.41	7.82	0.998	1.9×10^{-7}	6.3×10^{-7}
SW	0	$5 \times 10^{-7} - 5 \times 10^{-6}$	37.91	43.16	0.997	3.2×10^{-7}	1.1×10^{-6}
	60	$1 \times 10^{-7} - 3 \times 10^{-6}$	21.46	116.8	0.995	5.5×10^{-8}	1.8×10^{-7}
	150	$5 \times 10^{-8} - 1 \times 10^{-6}$	20.11	282.3	0.996	9.7×10^{-9}	3.2×10^{-8}

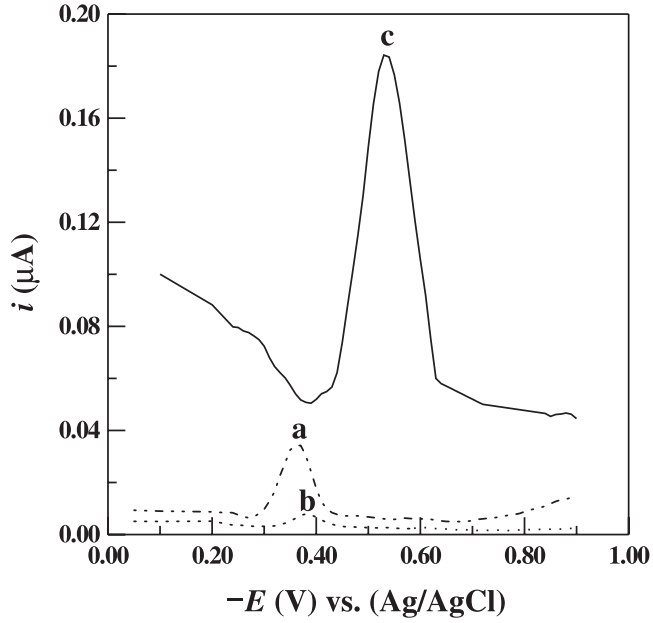
[a]Average of three determinations.

buffer of pH 5 gave rise to a single well-defined cathodic peak (E_p = –0.56 V). The optimum instrumental conditions (such as frequency f, scan increment Δs, and pulse-amplitude E_{sw}) were achieved from study of the variation of the peak current of 5×10^{-7} mol L^{-1} FM in the acetate buffer of pH 5, following preconcentration for 30 s. At a scan increment of 10 mV and a pulse amplitude of 25 mV, the peak current increased gradually with an increase in frequency up to 60 Hz. At a frequency higher than 60 Hz, a peak with poorer resolution was obtained. At a frequency of 60 Hz and 25 mV pulse amplitude, the peak current increased linearly with the scan increment up to 10 mV. At f = 60 Hz and Δs = 10 mV, although the peak current increased linearly with the increase of the pulse amplitude from 25 to 100 mV, peak distortion resulted in a poorer resolution observed over 25 mV. Thus, a pulse amplitude of 25 mV was applied in the rest of the study, as it was better for analytical purposes.

The effect of varying the preconcentration potential (E_{acc}) over the range 0.0 to –0.3 V on the peak current intensity of the square-wave adsorptive cathodic stripping voltammogram of 1×10^{-6} mol L^{-1} FM in an acetate buffer of pH 5 following preconcentration for 30 s was also evaluated under the optimized conditions (Fig. 3, curve c). A more developed peak current intensity was achieved over the potential range –0.05 to –0.10 V (f = 60 Hz, Δs = 10 mV, and E_{sw} = 25 mV). The observed gradual decrease in the peak current intensity may be attributed to the consequence of desorption of the drug at more higher or lower potential values than the zero charge potential, where a maximum adsorption of uncharged organic molecules can be expected. Hence, a preconcentration potential of –0.10 V was applied throughout the present analytical study. On the other hand, a linear relationship between peak current (i_p) intensity and preconcentration time up to 200 s was obtained (Fig. 4, curve c). Therefore, the optimal experimental conditions of the present proposed square-wave adsorptive cathodic stripping voltammetry procedure were: frequency (f) = 60 Hz, scan increment (Δs) = 10 mV, pulse amplitude (E_{sw}) = 25 mV, preconcentration potential (E_{acc}) = –0.10 V, and preconcentration time (t_{acc}) = 60–150 s.

The ability to readily assay nanomolar concentrations was attributed not only to both the effective preconcentration potential and time, but also to the improved sensitivity of the applied voltammetric waveform for monitoring of the preconcentrated drug. Figure 5 shows the adsorptive cathodic stripping (AdCS) voltammograms recorded for 1×10^{-6} mol L^{-1} FM in an acetate buffer of pH 5 following preconcentration for 60 s using three different waveforms: (*a*) linear-sweep (LS), (*b*) differential-pulse (DP), and (*c*) square-wave (SW). The signal intensity obtained by means of the proposed SWAdCS voltammetric procedure was found to be 20 and 5 times higher than those obtained by means of the proposed LSAdCS and DPAdCS voltammetric procedures, respectively.

Fig. 5. Adsorptive cathodic stripping voltammograms of 1×10^{-6} mol L^{-1} FM drug recorded in an acetate buffer of pH 5 following preconcentration for 30 s using different voltammetric waveforms: (*a*) linear-sweep (ν = 100 mV s^{-1} and E_{acc} = –0.05 V), (*b*) differential-pulse (ν = 10 mV s^{-1}, E_{dp} = 25 mV, and E_{acc} = –0.05 V), and (*c*) square-wave (f = 60 Hz, Δs = 10 mV, E_{sw} = 25 mV, and E_{acc} = –0.10 V).



The calibration curves within the concentration levels of 10^{-8} and 10^{-5} mol L^{-1} FM were attempted following different preconcentration time periods. The regression equations associated with the calibration plots exhibited a good linearity (r = 0.995–0.998) that supported the validation of the proposed procedures (Table 1). Limits of detection (LOD) and quantitation (LOQ) were calculated using the relation

© 2004 NRC Canada

Table 2. Recovery of FM drug in Eulexin® tablets (250 mg FM per tablet) by means of the proposed voltammetric procedures in comparison to a reported HPLC method (13).

	Calibration curve			Standard addition		
Proposed procedures[a]	(% R±SD)	*F*	*t*	(% R±SD)	*F*	*t*
LSV	98.7±1.1	1.62	0.24	98.1±1.2	1.95	1.12
DPV	97.5±1.6	3.27	1.64	97.9±1.7	3.60	1.17
SWV	99.53±0.7	1.73	1.33	98.8±0.5	2.66	0.04
Reported HPLC method (13): 98.9±0.9%						

Note: Theoretical values of the *F* and *t* test at the 95% confidence limit (for $n_1 = 5$, and $n_2 = 5$) are 6.39 and 2.30, respectively.
[a]Average of five determinations.

Table 3. Characteristics of the calibration curves of the voltammetric determination of FM spiked in human serum following preconcentration for 150 s.

	Least-squares equation[a]				
AdCSV procedure	Intercept (*n*A)	Slope (*n*A/μmol L^{-1})	Corr. coefficient (*r*)	LOD (mol L^{-1})	LOQ (mol L^{-1})
LS	14.26	24.09	0.996	3.5×10^{-7}	1.2×10^{-6}
DP	2.05	6.43	0.998	4.9×10^{-7}	1.6×10^{-6}
SW	61.54	87.77	0.998	1.2×10^{-7}	4.0×10^{-7}

[a]Average of three determinations.

kSD_a/b (22), where $k = 3$ for LOD and 10 for LOQ, SD_a is the standard deviation of the intercept, and *b* is the slope of the calibration curve. LOD and LOQ values, shown in Table 1, confirmed the sensitivity of the proposed procedures compared with those obtained by means of the reported polarographic methods (12, 15).

Validation of the present proposed procedures for the quantitative assay of FM was examined via repeatability, recovery, selectivity, robustness, and ruggedness (22). The obtained results confirmed the reliability of the proposed procedures for the trace quantitation of FM.

Application

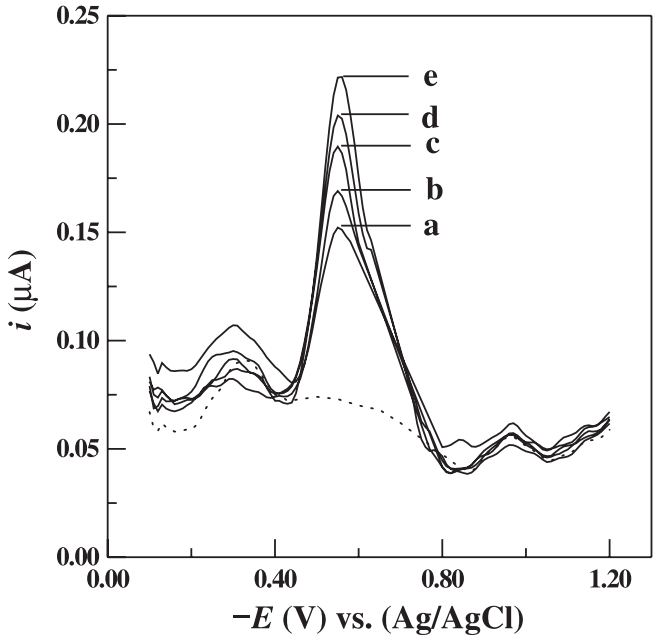
Analysis of Eulexin® tablets

The three proposed stripping voltammetric procedures were successfully applied to the determination of the FM drug in tablets (Eulexin®, 250 mg FM per tablet) following preconcentration onto the HMDE for 60 s, without the necessity for sample pretreatment or time-consuming extraction steps prior to analysis of the drug. The mean recoveries of FM, based on the average of five replicate measurements using both the calibration curve and the standard addition (23) methods, are reported and statistically compared with those obtained by a reported HPLC method (13) in Table 2. Values of *F*-calculated, *F*-theoretical, *t*-calculated and *t*-theoretical are also included in Table 2. Since the calculated value of *F* did not exceed the theoretical value, there was no significant difference between the proposed and reported methods with respect to reproducibility. Also, no significant difference was noticed between the proposed and reported methods regarding accuracy and precision as revealed by the *t* value (24).

Analysis of human serum

Voltammograms of different concentrations of the drug spiked in human serum were recorded using the three proposed voltammetric procedures. Figure 6 illustrates the

Fig. 6. SWAdCS voltammograms of different concentrations of FM spiked in human serum in an acetate buffer of pH 5: (*a*) 2×10^{-7}, (*b*) 4×10^{-7}, (*c*) 6×10^{-7}, (*d*) 8×10^{-7}, and (*e*) 1×10^{-6} mol L^{-1} FM. The dotted curve represents the blank solution. $E_{acc} = -0.10$ V and $t_{acc} = 150$ s. Other operational parameters are as those given in Fig. 3.



SWAdCS voltammograms of successive additions of spiked human serum following preconcentration onto the HMDE for 150 s. The variations of the peak current vs. the drug concentrations applying the three proposed voltammetric procedures were represented by straight lines, their characteristics are reported in Table 3. Mean recoveries of the drug in human serum, based on the average of five replicate measurements of 96.51 ± 3.67%, 95.57 ± 2.88%, and 98.24 ±

© 2004 NRC Canada

1.54% were achieved using LSAdCS, RPAdCS, and SWAdCS voltammetric procedures, respectively. The LOD and LOQ of the drug in spiked human serum samples using the three proposed voltammetric procedures were calculated (Table 3). Although, the achieved LOD and LOQ of the drug using the three proposed stripping voltammetric procedures were low enough to allow determination of the FM drug in serum samples of a volunteer who administrated an oral 250 mg FM single dose, the square-wave adsorptive cathodic stripping voltammetric procedure was preferred due to its high sensitivity and precision; also, it is the faster procedure compared with both DPAdCS and LSAdCS voltammetric procedures.

Conclusion

Linear-sweep, differential-pulse, and square-wave adsorptive cathodic stripping voltammetric procedures were optimized for the determination of the FM drug based on the reduction of its nitro aromatic moiety and its strong adsorptive character onto the mercury electrode surface. The three optimized procedures were successfully applied for determination of the drug in bulk, pharmaceutical formulation, and human serum. The results showed that the SWAdCS voltammetric procedure was more sensitive and precise compared with LSAdCS and DPAdCS voltammetric procedures. The three proposed procedures were simple, sensitive, fast, and selective. Unlike most of the reported methods, the optimized procedures for assay of flutamide did not require sample pretreatment or time-consuming extraction steps prior to assay of the drug.

Acknowledgements

The authors express their gratitude to the Alexander von Humboldt Foundation (Bonn, Germany) for donating the electrochemical analyzer model 263A-PAR, the Eppendorf centrifuge 5417 C, the digital micropipette, and the personal computer used in the present study to Dr. M.M. Ghoneim, Chemistry Department, Faculty of Science, Tanta University, Egypt.

References

1. P. Schellhammer, R. Sharifi, and N. Block. Urology, **45**, 745 (1995).
2. D.K. Ornstein, G.S. Rao, B. Johnson, E.T. Charlton, and G.L. Andriole, Urology, **48**, 901 (1996).
3. C. Mahler, J. Verhelst, and L. Denism. Clin. Pharmacokinet. **34**, 405 (1998).
4. S. Sweetman (*Editor*). Martindale. 31st ed. Pharmaceutical Press (Royal Pharmaceutical Society), London. 1996. p. 1400.
5. I. Niopas and A.C. Daftsios. J. Chromatogr. B, **75**9 179 (2001).
6. S. Anjum, S.K. Swan, L.J. Lambrecht, E. Radwanski, D.L. Cutler, M.B. Affrime, and C.E. Halstenson. Brit. J. Clin. Pharmaco. **47**, 43 (1999).
7. P. Nagaraja, K.R. Sunitha, and M.F. Silwadi. J. Pharm. Biomed. Anal. **23**, 617 (2000).
8. M.N. Reddy, T.K. Murthy, K. Rajita, M.D. Reddy, and D.G. Shankar. Asian J. Chem. **13**, 241 (2001).
9. T.K. Murthy, M.N. Reddy, M.D. Reddy, and D.G. Shankar. Asian J. Chem. **13**, 915 (2001).
10. K.S. Rangappa, P. Nagaraja, and K.C.S. Murthy. Anal. Sci. **16**, 637 (2000).
11. P. Nagaraja, H.R.A. Kumar, and R.A. Vasantha. Int. J. Pharm. **235**, 113 (2002).
12. A. Alvarez-Lueje, C. Pena, L.J. Nunez-Vergara, and J.A. Squella. Electroanal. **10**, 1043 (1998).
13. D. Farthing, D. Sica, I. Fakhry, D.L. Walters, E.A. Cefali, and G. Allan. Biomed. Chromatogr. **8**, 251 (1994).
14. J. Leibinger and M. Kapas. J. Pharm. Biomed. Anal. **14**, 1377 (1996).
15. A. Snycerski. J. Pharm. Biomed. Anal. **7**, 1513 (1989).
16. Analytical software. Version 2.01 [computer program]. Princeton Applied Research, Oak Ridge, Tenn., USA. 1994.
17. H.T.S. Britton. Hydrogen ions. 4th ed. Chapman and Hall, London. 1952. p. 113.
18. J. Lurie. Handbook of analytical chemistry. Mir Publishers, Moscow. 1975. p. 262.
19. P. Zuman. The elucidation of organic electrode processes. Academic Press Inc., New York. 1969. p. 21.
20. E. Laviron. J. Electroanal. Chem. **112**, 11 (1980).
21. E. Laviron. J. Electroanal. Chem. **52**, 255 (1974).
22. USP–NF, USP 24. The United States Pharmacopoeial Convention Inc., Rockville, Md. 2000. p. 2151.
23. G.W. Ewing. Instrumental methods of chemical analysis. 5th ed. Lippincott-Raven, Philadelphia, Penn., USA. 1995. p. 464.
24. G.D. Christian. Analytical chemistry. 5th ed. John Wiley and Sons Inc., New York. 1994. p. 36.

© 2004 NRC Canada

Multi-armed, TEMPO-functionalized unimolecular initiators for starburst dendrimer synthesis via stable free radical polymerization. 1. Tri azo-functionalized unimer

Dalia Abdallah, Mohmad Asri Abd Ghani, Michael F. Cunningham, Peter M. Kazmaier, Barkev Keoshkerian, and Erwin Buncel

Abstract: The synthesis of azobenzene-functionalized multi-armed unimolecular initiators or "*unimers*" that can be polymerized using styrene or styrenic derivatives via TEMPO (2,2,6,6-tetramethylpiperidenyl-1-oxyl) mediated stable free radical polymerization (SFRP) is described. The unimers are composed of an azobenzene-functionalized core and a TEMPO-modified unit. Homopolymers and copolymers of styrene and acetoxystyrene were synthesized using the mono-and trifunctionalized unimers as initiators under bulk conditions with average molecular weights and polydispersities reported. The studies lay the groundwork for further investigations involving SFRP towards building a light harvesting system by introducing chromophores onto the polymer chains for capturing light and thence transferring it to the azobenzene core.

Key words: azo-functionalized unimolecular initiator, stable free radical polymerization, starburst dendrimer.

Résumé : On décrit la synthèse d'initiateurs unimoléculaires tentaculaires à base d'azobenzènes, dénommés unimères, qui peuvent être polymérisés à l'aide de styrène ou de ses dérivés par le biais d'une polymérisation avec un radical libre stable catalysée par le 2,2,6,6-tétraméthylpipéridinyl-1-oxyle (TEMPO). Les unimères sont formés d'un noyau azobenzène fonctionnalisé et d'une unité TEMPO modifiée. On a synthétisé des homopolymères et des copolymères du styrène et de l'acétoxystyrène en utilisant des unimères mono- et trifonctionnalisés comme initiateurs, dans des conditions globales, et on rapporte des poids moléculaires et des polydispersités moyennes. Les études posent les fondements pour des études ultérieures, impliquant des polymérisations avec un radical libre stable, dans l'élaboration d'un système permettant de recueillir la lumière en introduisant sur les chaînes de polymère des chromophores qui pourraient capter la lumière et par la suite la transmettre au noyau azobenzène.

Mots clés : initiateur unimoléculaire à base d'azobenzène fonctionnalisé, polymérisation avec un radical libre stable, dendrimère en « éclatement d'étoile ».

[Traduit par la Rédaction]

Introduction

The synthesis of macromolecules with "complex" and controlled architecture is becoming increasingly important in the field of polymer chemistry (1). There are two categories of complexity that one can introduce: functional complexity and architectural complexity. Azo moieties are an example of functional complexity since they can operate as optical transducers, i.e., through light absorption, energy transfer, and cis/trans isomerism. The second category, architectural complexity, can be achieved by introducing branches into the polymer backbone, which leads to the formation of graft or star polymer systems. In our study, we would like to couple these two categories of complexity in a single system to enable the investigation of the unique properties of this system.

Traditional methods of synthesizing well-defined macromolecular architectures involve *living* polymerization techniques such as anionic (2), cationic (3), group transfer polymerization (4), and transition-metal catalysis (5). However, as a result of work over the past decade living free radical polymerization is now possible where there is control over the molecular weight, the end group, and the ability to synthesize block copolymers.

Georges et al. (6) were the first to report the synthesis of low polydispersity polystyrene using free radical polymer-

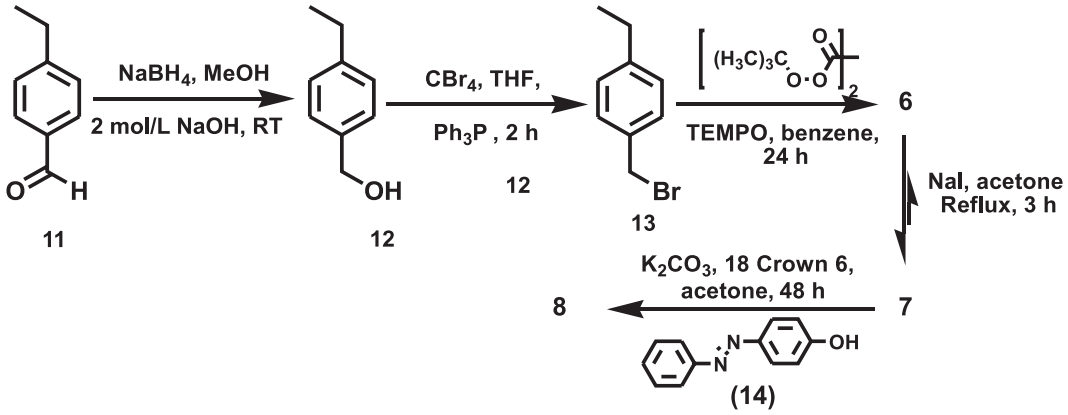
Received 2 February 2004. Published on the NRC Research Press Web site at http://canjchem.nrc.ca on 9 November 2004.

D. Abdallah, M.A.A. Ghani, and E. Buncel.[1] Department of Chemistry, Queen's University, Kingston, ON K7L 3N6, Canada.
M.F. Cunningham. Department of Chemical Engineering, Queen's University, Kingston, ON K7L 3N6, Canada.
P.M. Kazmaier and B. Keoshkerian. The Xerox Research Centre of Canada, 2660 Speakman Drive, Mississauga, ON L5K 2L1, Canada.

[1]Corresponding author (e-mail: buncele@chem.queensu.ca).

 doi: 10.1139/V04-107 © 2004 NRC Canada

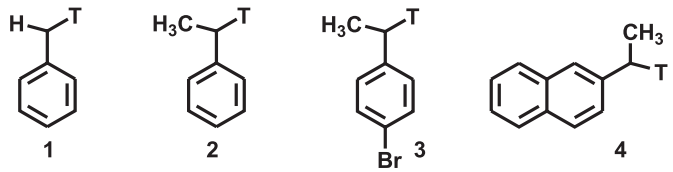
Scheme 1.

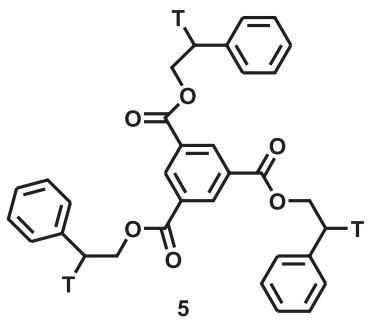


ization, based on use of the stable nitroxide radical 2,2,6,6-tatramethylpiperdinyloxy (TEMPO) in combination with benzoyl peroxide (BPO) as a *bimolecular* initiating system. The TEMPO unit acts as a "capping" agent for the growing polymer chain and controls the polymerization (7). The use of stable nitroxides to control free radical polymerization was originally stimulated by the work of Moad and Rizzardo (8) who employed TEMPO to reversibly terminate a growing polymer chain.



During the past decade much work has been done on designing and synthesizing functionalized *unimolecular* initiators that contain the TEMPO unit. Some examples of unimolecular initiators synthesized by Hawker and coworkers (9, 10) are shown below. Compounds **1**, **2**, **3**, and **4** are *monofunctionalized* unimolecular initiators that form linear polymers upon polymerization, while compound **5** is a *trifunctionalized* unimolecular initiator that forms a star polymer upon polymerization, where T stands for the TEMPO moiety.





The work described in this paper focuses on the synthesis of *multiazofunctionalized* azo unimolecular initiators, which we call "unimers", for stable free radical polymerization (SFRP). The structures of the unimers are shown below, where **6** and **7** are used in the synthesis of **8**, **9**, and **10**, i.e., monoazofunctionalized, diazofunctionalized, and triazofunctionalized unimers, respectively. The mono- and trifunctionalized unimers were used in the polymerization of styrene and acetoxystyrene to form homopolymers, block copolymers, and random copolymers, where we report the average molecular weights and polydispersities based on GPC analysis.

We are specifically interested in azobenzene-modified polymers to study and compare cis/trans isomerization of the azobenzene units of the mono-, di-, and trifunctionalized polymers upon irradiation. It is anticipated that cis/trans isomerism of the azo core should have a profound effect on the overall tertiary structure of the molecules.

The present work continues our studies with azo, azoxy, and hydrazo arenes, encompassing various structure reactivity studies, such as rearrangements (Wallach, benzidine), spiropyran-merocyanine interconversion systems, and periphery-modified dendrimers, with applications in optical data storage, holography and drug delivery, as well as light harvesting properties (11).

Results and discussion

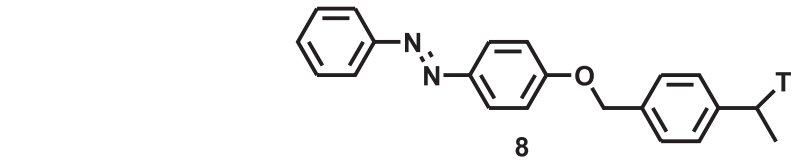
Our strategy is to develop the chemistry on a monoazofunctionalized unimer **8** and then extend this chemistry to the more complex difunctionalized **9** and trifunctionalized **GEN 0** unimer systems.

Monoazofunctionalized unimolecular initiator 8

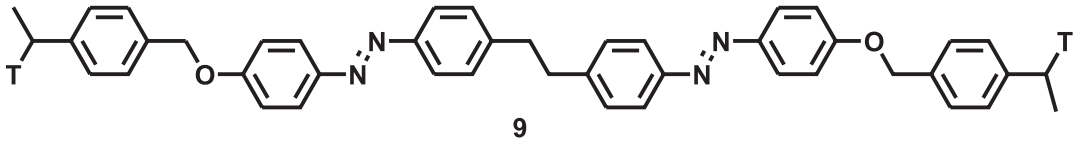
The monoazofunctionalized unimer **8** is composed of two parts, the core, *p*-hydroxyazobenzene **14** and the TEMPO-containing unit, TEMPO modified 4-ethylbenzyl iodide **7**. Scheme 1 shows the preparation of TEMPO-modified 4-ethylbenzyl iodide **7** starting from commercially available 4-ethylbenzaldehyde **11**.

To introduce a TEMPO unit and form the TEMPO-modified derivative of compound **13**, a carbon-centered radical must be generated in the presence of TEMPO. Hawker et al. (9) used di-*tert*-butyl peroxide to generate the carbon-

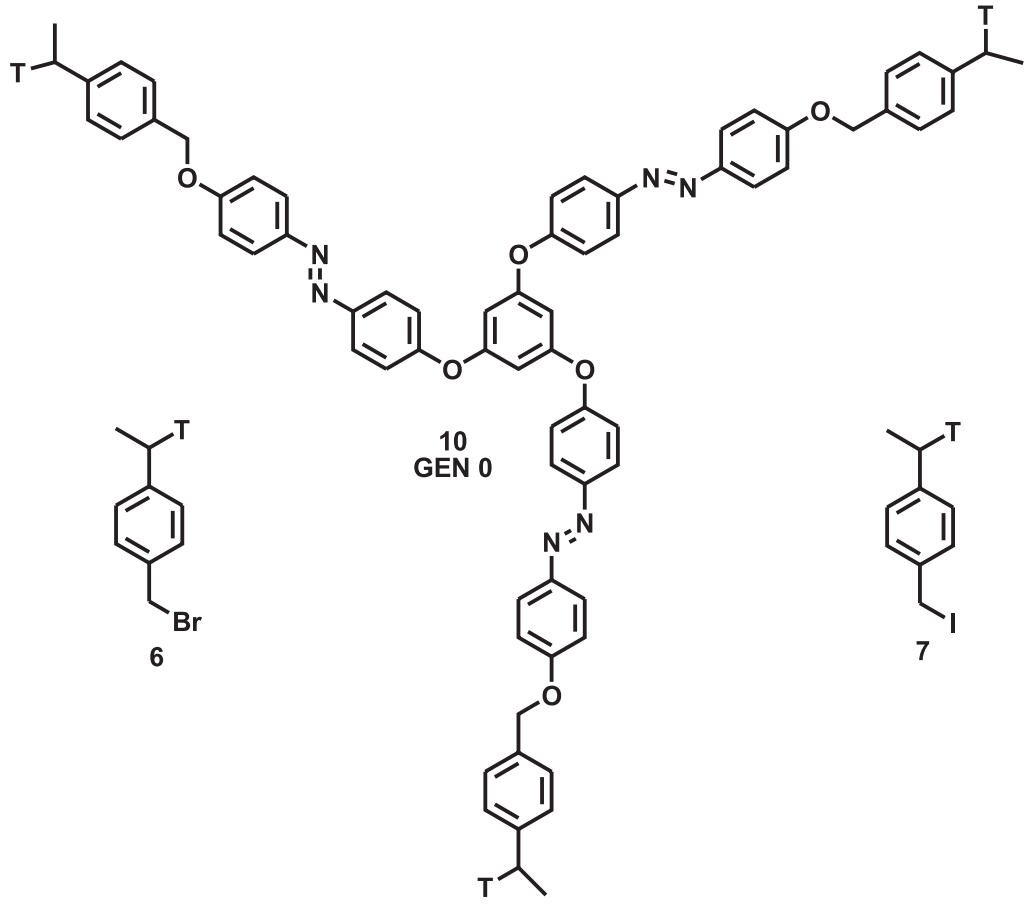
© 2004 NRC Canada



8



9



10
GEN 0

6

7

centered radicals at ca. 125 °C. We used di-*tert*-butyl peroxyoxalate instead since it undergoes facile decomposition in solvents such as benzene below 50 °C to give *tert*-butoxy radicals.

Coupling of the azobenzene core with the TEMPO-containing unit was first attempted using the bromo derivative **6** with poor yield (9%) (12). To optimize the yield, the iodo derivative **7** was synthesized using the Finkelstein reaction.

The monofunctionalized azobenzene unimer was synthesized as shown in Scheme 1 in 75% yield (16). The proton NMR spectrum confirms that the azobenzene core became attached to the TEMPO-containing unit. The aromatic protons on the azobenzene unit appear at 7 to 8 ppm and the TEMPO unit protons at 0.5–0.6 ppm.

Diazofunctionalized unimolecular initiator 9

The difunctionalized azobenzene unimer **9** is composed of a core containing two azobenzene units and two TEMPO-modified units attached to the ends of the core. The synthesis of **9** was accomplished in 62% yield as shown in Scheme 2.

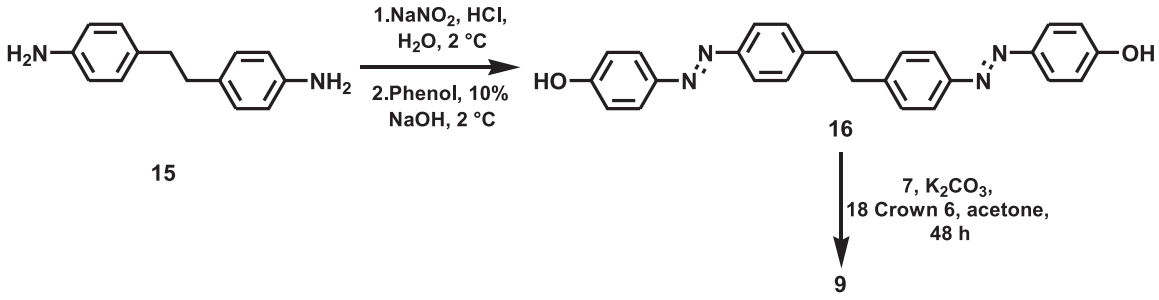
Coupling of the TEMPO units onto bis(4-aminophenyl)-1,2-ethane **16** to form the difunctionalized azobenzene-modified unimer was effected by reaction with **7** (Scheme 1) (18% yield).

Triazofunctionalized unimolecular initiator 10, GEN 0

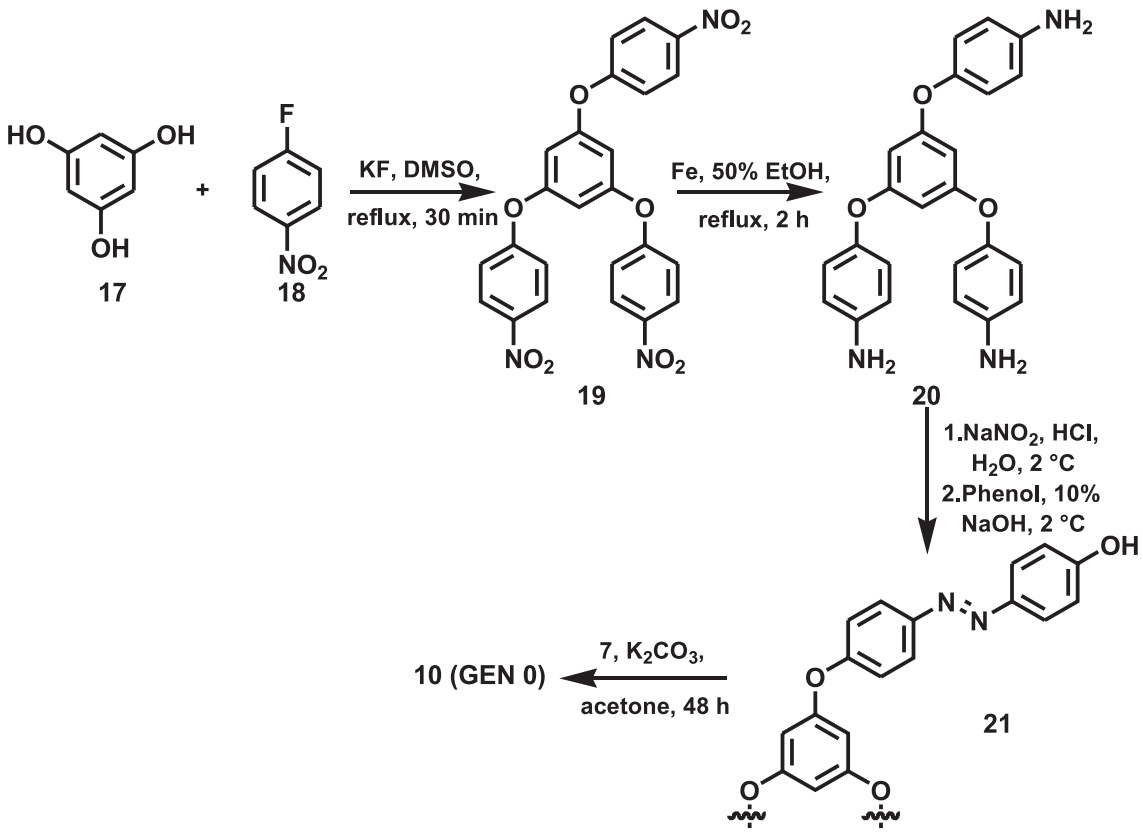
The trifunctionalized unimer is the zeroth generation of a dendrimer, i.e., **GEN 0**, a star-shaped unimer composed of a

© 2004 NRC Canada

Scheme 2.



Scheme 3.



core with three azobenzene units and three TEMPO-modified units attached to the ends of the core.

The preparation of **GEN 0** (Scheme 3) involved first the synthesis of the core **21** in three steps:

(1) Nucleophilic aromatic substitution yielded **19**.

(2) Reduction of **19** gave **20** in 94% yield.

(3) Diazotization and coupling gave **21** in 73% yield.

Introduction of the TEMPO units to form **GEN 0** was effected by Williamson ether coupling between the azobenzene core and the TEMPO-modified 4-ethylbenzyl iodide **7** (Scheme 1) in 22% yield (12). **Gen 0** is readily soluble in halogenated solvents such as dichloromethane or chloroform, and can be distinguished from the starting compound **21**, which dissolves only in acetone or DMSO. ^{1}H NMR shows the TEMPO moiety between 0.7 and 1.7 ppm and the aromatic protons between 7 and 8 ppm.

Controlled free radical polymerizations

We now describe polymerization studies that have been performed towards synthesis of polymers having an azobenzene unit at the core. The studies entailed the mono- and trifunctionalized azobenzene unimers that were used in the polymerization of styrene and acetoxystyrene, to give homopolymers, block and random copolymers.

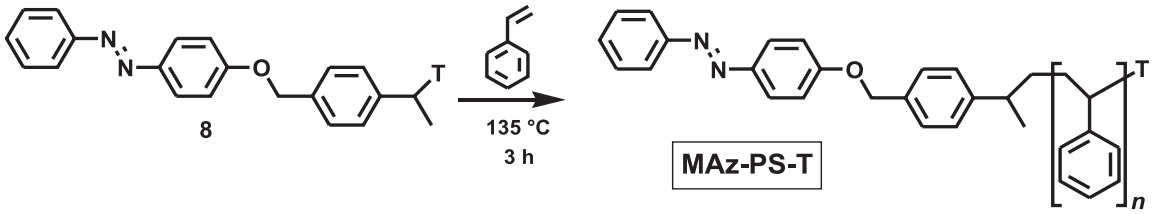
Controlled free radical polymerization of monoazo-functionalized unimer

Monoazo-functionalized polystyrene ***MAz-PS-T***

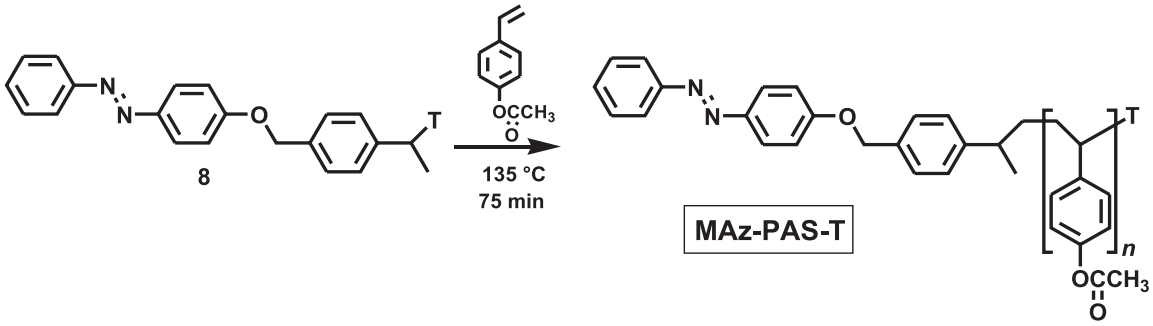
Polymerization of styrene with monofunctionalized azobenzene unimer **8** was effected under bulk conditions (Scheme 4) at 135 °C. The polymerization was stopped after 2 h by cooling to room temperature. The polymer **MAz-PS-T** was dissolved in THF and precipitated from methanol to give a yellow powder (26%) with an average molecular weight of 13 500 g/mol and a narrow polydispersity of 1.26

© 2004 NRC Canada

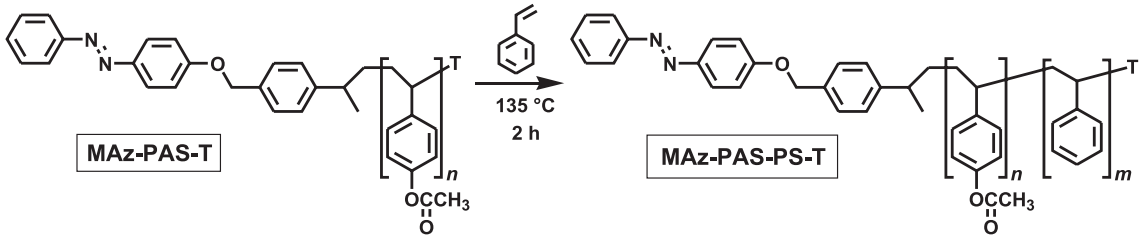
Scheme 4.



Scheme 5.



Scheme 6.



based on GPC analysis. The ^{1}H NMR shows broad peaks at 1.4 and 1.8 ppm representing the aliphatic hydrogens of the polystyrene, the methylene and methine protons, respectively. Aromatic hydrogens of polystyrene appear as broad peaks between 6.4 and 7.2 ppm. The ^{13}C NMR shows a peak at 145.6 ppm for the quaternary carbon of the aromatic moiety of polystyrene while the other carbons of the aromatic moiety appear at 128.4, 128.1, and 126.1 ppm. Aliphatic carbons appear at 44.3 and 40.7 ppm. The UV–vis absorption spectrum of **MAz-PS-T** in THF showed distinct π–π* and *n*–π* absorption bands of azobenzene appearing at ca. 350 and 450 nm, respectively, confirming that the polymer sample contains the azobenzene unit.

*Monoazofunctionalized polyacetoxystyrene **MAz-PAS-T***

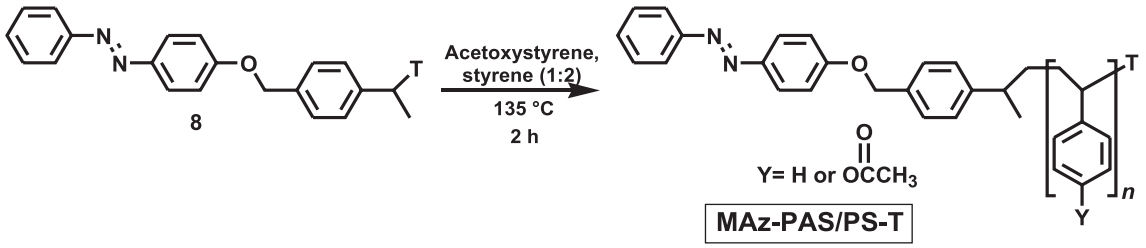
The polymerization of acetoxystyrene with **8** was effected under the same conditions as for **MAz-PS-T**, in bulk, under nitrogen and heating at 135 °C as illustrated in Scheme 5. The polymerization was stopped after 75 min at which point the mixture became too viscous for stirring. A yellow powder (**MAz-PAS-T**) with an average molecular weight of 35 300 g/mol and a polydispersity of 1.34 formed upon dissolving the reaction mixture in THF and precipitating from methanol (49%). The ^{1}H NMR shows two broad peaks between 1.2 and 2.0 ppm representing the aliphatic protons of polyacetoxystyrene and a broad peak between 6.2 and 6.9 ppm for the aromatic protons of polyacetoxystyrene. The methyl protons of the acetoxy group appear as a singlet at 2.3 ppm. The ^{13}C NMR shows a peak at 169.5 ppm representing the carbonyl carbon of the acetate group. Peaks at 149.1 and 142.6 ppm represent the quaternary carbons of the aromatic moiety of the polyacetoxystyrene while peaks at 128.8, 127.6, 122.0, and 121.5 represent the rest of the aromatic carbons. Aliphatic carbons of polyacetoxystyrene appear at 44.1 and 40.5 ppm representing the methylene and methine protons, respectively. The methyl carbon of the acetate group appears at 21.6 ppm.

*Monoazofunctionalized block (acetoxystyrene–styrene) copolymer **MAz-PAS-PS-T***

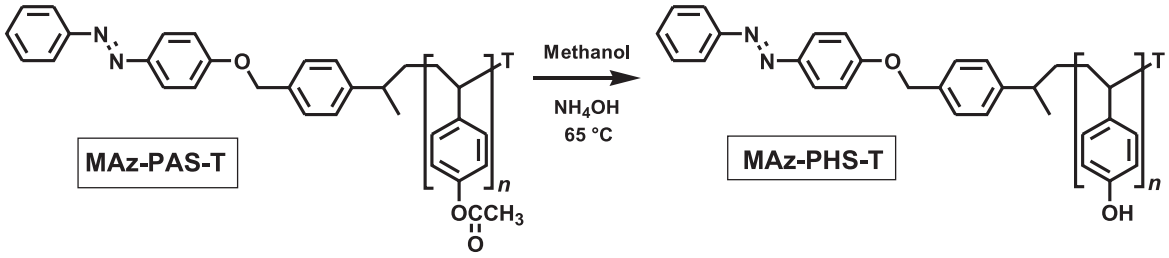
Chain extension of **MAz-PAS-T** with styrene under bulk conditions yielded **MAz-PAS-PS-T**, a block copolymer of acetoxystyrene and styrene, as illustrated in Scheme 6. The polymerization was stopped after 2 h and the reaction mixture was dissolved in THF and precipitated from methanol to give an off-white – yellow powder with an average molecular weight of 40 400 g/mol and 1.54 polydispersity. The ^{1}H NMR shows the aliphatic protons of the polymer chain between 1.2 and 2.2 ppm and the aromatic protons between 6.2 and 7.5 ppm. The methyl protons of the acetate group appear as a singlet at 2.3 ppm. The ^{13}C NMR shows the carbonyl carbon of the acetate group at 169.5 ppm, the quaternary aromatic carbons of the polyacetoxystyrene at 149.1 and 142.6 ppm and the quaternary aromatic carbon of polysty-

© 2004 NRC Canada

Scheme 7.



Scheme 8.



rene at 145.7 ppm. The rest of the aromatic carbons of the polymer chain appear at 128.4, 128.1, 126.0, and 121.5 ppm. The aliphatic carbons appear at 46.2, 44.0, 43.2, and 40.8 ppm. The methyl carbon of the acetoxy group appears at 21.6 ppm consistent with the block copolymer structure.

*Monoazofunctionalized random (acetoxystyrene–styrene) copolymer **MAz-PAS/PS-T***

Contrasting with the design for block copolymer **MAz-PAS-PS-T**, where the strategy is to begin with polymer **MAz-PAS-T** and under SFRP react that with acetoxystyrene, the second monomer was reacted simultaneously to give a random copolymer.

Thus, polymerization of acetoxystyrene, styrene (1:2 volume ratio), and monofunctionalized azobenzene unimer **8** under bulk conditions yielded the random copolymer **MAz-PAS/PS-T** as shown in Scheme 7. The polymer was dissolved in THF and precipitated from methanol, filtered and dried to give a yellow solid with an average molecular weight of 16 400 g/mol and a polydispersity of 1.24.

*Monoazofunctionalized poly(4-hydroxystyrene) **MAz-PHS-T***

The hydrolysis of **MAz-PAS-T** was effected by adding ammonium hydroxide to a solution of **MAz-PAS-T** in methanol under reflux conditions as shown in Scheme 8. The polymer was precipitated from water, filtered and dried to give yellow crystals in 40% yield. The absence of a ^{13}C carbonyl peak at 165.9 ppm confirms that the hydrolysis is complete. The aromatic quaternary carbon attached directly to the hydroxy group appears at 155.3 ppm while the other aromatic quaternary carbon appears at 137.0 ppm. The other aromatic carbons of the polymer chain appear at 128.8 and 115.1 ppm. Aliphatic carbons of the polymer chain appear between 28.6 and 39.7 ppm.

Controlled free radical polymerization of a triazo-functionalized unimer

*Polyacetoxystyrene starburst azo dendrimer **TAz-PAS-3T***

Polymerization of acetoxystyrene with triazofunctionalized unimer **GEN 0** was done under bulk conditions by heating the reaction mixture at 135 °C as illustrated in Scheme 9. The polymerization was stopped after 75 min. The polymer was dissolved in THF and precipitated from methanol, filtered and dried to give a yellow powder (**TAz-PAS-3T**) a star polymer, with an average molecular weight of 74 400 g/mol and a polydispersity of 1.49 based on light scattering detector analysis.

*Starburst block (acetoxystyrene–styrene) azo dendrimer **TAz-PAS-PS-3T***

The block copolymer **TAz-PAS-PS-3T** was synthesized by polymerizing **TAz-PAS-3T** with styrene under bulk conditions at 135 °C, as shown in Scheme 10. The polymerization was stopped after 45 min and the reaction mixture was dissolved in THF and precipitated from methanol, filtered and dried to give an off-white – yellow solid with an average molecular weight of 126 000 g/mol and a polydispersity of 1.64 based on light scattering detector analysis.

Conclusions

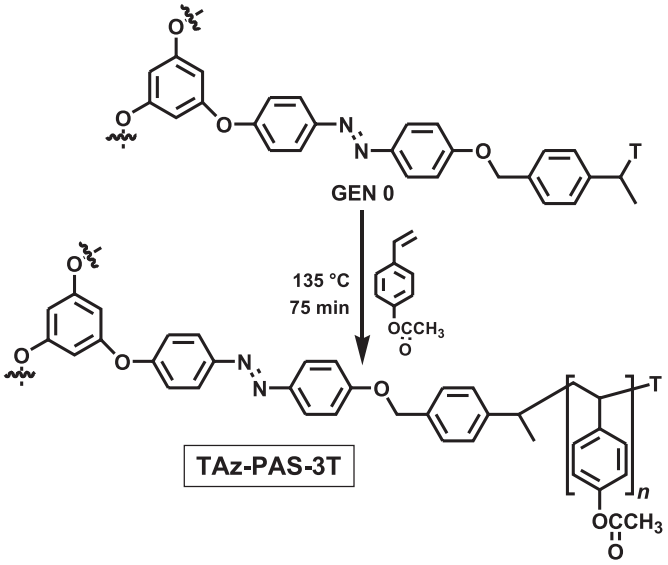
In conclusion, it has been shown in this work that functionally and architecturally dendritic structures with azo cores can be synthesized using controlled radical polymerization.

The synthesis of mono-, di-, and triazofunctionalized unimers was accomplished by coupling of the azobenzene cores, **14**, **16**, and **21**, with TEMPO-modified 4-ethylbenzene **7**. A combination of ^{1}H and ^{13}C NMR and mass spectra was used for full characterization of the unimers.

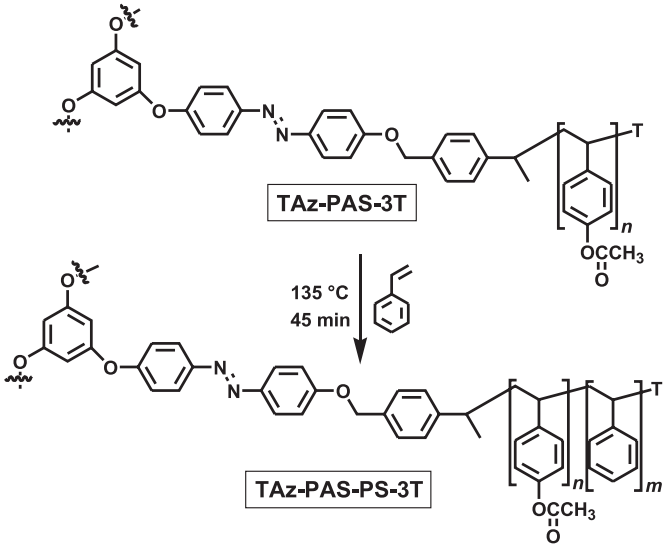
The mono- and trifunctionalized unimers were used in polymerization reactions with styrene and acetoxystyrene. Structures of the azobenzene-modified polymers were characterized by means of a combination of ^{1}H and ^{13}C NMR and UV–vis spectra. The monoazofunctionalized unimer **8** was polymerized with styrene to form a homopolymer, **MAz-PS-T**, with M_n value 13 500 and PD 1.26. Polymerization with acetoxystyrene yielded a polymer, **MAz-PAS-T**, with M_n 35 300 and PD 1.34. Copolymers of styrene and acetoxystyrene were also synthesized, where a block copolymer, **MAz-PAS-PS-T**, with M_n 40 400 and a PD 1.54 and a

© 2004 NRC Canada

Scheme 9.



Scheme 10.



random copolymer, **MAz-PAS/PS-T**, with M_n 16 400 and PD 1.24 were obtained.

The trifunctionalized unimer, **GEN 0**, was also polymerized with acetoxystyrene to yield a polymer, **TAz-PAS-3T**, with M_n 74 400 and PD 1.49. This polymer was copolymerized with styrene to give a block copolymer, **TAz-PAS-PS-3T**, with an M_n value of 126 000 and a PD of 1.64.

It is anticipated that the present polymers would have to be modified at the periphery to achieve light harvesting properties by functionalization with naphthyl moieties. The studies predict the formation of an *on*/*off* molecular switch through trans to cis isomerization of the azobenzene unit by irradiation of the naphthyl moieties and then energy transfer to the azo core.

Experimental section

IR spectra were recorded on a Bomen MB-120 spectrophotometer as KBr disks. ^{1}H and ^{13}C NMR spectra were recorded on Bruker AM300 spectrophotometer (^{1}H 300.1 MHz, ^{13}C 75.5 MHz). Chemical shifts are reported in parts per million (ppm) relative to the peaks for residual $CHCl_3$ in $CDCl_3$ (δ 7.28 ppm) and acetone-d_5H in acetone-d_6 (δ 2.05 ppm). Mass spectrometry results were recorded on a Fisons VG Quattro (triple-quadropole MS–MS). Several techniques were used to identify the mass of the parent ion, such as electron ionization (EI), chemical ionization (CI), fast atom bombardment (FAB), and electrospray (ES). High-resolution mass spectrometry (HR-MS) to establish molecular weights of new compounds was performed by the University of Ottawa Mass Spectrometry Service and University of Alberta Mass Spectrometry Service. Melting points were determined on a Mel-Temp capillary melting point apparatus and were not corrected.

4-Ethylbenzyl alcohol 12 (13)

12 was prepared by reduction of **11** as outlined in Scheme 1. To a stirred solution of **11** (13.1 g, 97.8 mmol) in methanol (100 mL) was added a solution of sodium borohydride (1.4 g, 37.0 mmol) in sodium hydroxide (2 mL, 2 mol/L) and water (18 mL) dropwise while maintaining the temperature at 23 °C. After removing the solvent on a rotary evaporator, the residue was dissolved in water (200 mL) and extracted with CH_2Cl_2 (3 × 100 mL). Drying ($MgSO_4$), filtration, and solvent removal on a rotary evaporator followed by column chromatography using hexanes – ethyl acetate (2:1) as the eluant yielded **12** as a pale yellow oil (10.0 g, 82%). IR (KBr disk, cm^{-1}): 3340, 2969, 2933, 2868, 1417, 1032, 813. ^{1}H NMR ($CDCl_3$) δ: 7.28 (4H, dd), 4.61 (2H, s), 1.06 (1H, d), 2.73 (2H, q), 1.33 (3H, t). ^{13}C NMR ($CDCl_3$) δ: 143.34, 138.03, 127.75, 127.00, 64.57, 28.39, 15.48.

4-Ethylbenzyl bromide 13 (12)

Triphenyl phosphine (11.8 g, 45.0 mmol) was added in two parts to a mixture of **12** (5.0 g, 36.8 mmol) and CBr_4 (14.8 g, 44.6 mmol) in dry THF (75 mL) and stirred under argon for 2 h. After removing the solvent by rotary evaporation, the residue was dissolved in water (100 mL) and extracted with CH_2Cl_2 (3 × 50 mL), dried over $MgSO_4$,

© 2004 NRC Canada

filtered, and the solvent was evaporated on a rotary evaporator. Column chromatography using CH_2Cl_2 as the eluant yielded a pale yellow oil (7.0 g, 95%). IR (KBr disk, cm^{-1}): 3062, 2962, 2926, 2868, 1898, 1618, 1510, 1438, 1222, 827. ^1H NMR ($CDCl_3$) δ: 7.40, 7.26 (4H, dd), 4.58 (2H, s), 2.74 (2H, q), 1.34 (3H, t). ^{13}C NMR ($CDCl_3$) δ: 144.72, 135.08, 129.11, 128.36, 33.81, 28.66, 15.49. EI-MS *m/z*: 198.4 and 199.9 (calcd. for $C_9H_{11}Br$: 198.0 and 200.0).

Di-*tert*-butylperoxyoxalate (14)

A solution of oxalyl chloride (2.5 mL) in petroleum ether (25 mL) was added slowly to a stirred cold solution of anhydrous pyridine (4 mL) and 5.5 mol/L solution of *tert*-butyl hydroperoxide (5 mL) in petroleum ether (50 mL) over 20 min while maintaining the temperature at –4 °C. The reaction mixture was then warmed to 15 °C where the white precipitate formed was filtered and the filtrate was cooled for 15 min in dry ice – acetone (–78 °C) to allow crystallization of peroxyoxalate as fine white crystals. The solvent was decanted and the peroxyoxalate crystals, 4.01 g (69%), dried under argon and stored in the refrigerator.

TEMPO-modified 4-ethylbenzyl bromide 6 (15)

As outlined in Scheme 1, a mixture of **13** (5 g, 25.1 mmol), TEMPO (3 g, 19.2 mmol) and di-*tert*-butylperoxyoxalate (4 g, 1.59 mmol) in benzene (40 mL) was stirred and heated to 35 °C under argon for 24 h. After removing the solvent by rotary evaporation the product was purified by column chromatography using hexanes–dichloromethane (1:1) as the eluant to give the TEMPO modified 4-ethylbenzyl bromide **6** as a white solid (1.78 g, 20%), mp 63 to 64 °C. IR (KBr disk, cm^{-1}): 3013, 2969, 1509, 1442, 1227, 1056, 842, 697. ^1H NMR ($CDCl_3$) δ: 7.36 (4H, dd), 4.80 (1H, q), 4.52 (2H, s), 1.50 (3H, d), 1.41–1.11 (6H, m), 1.31, 1.27, 1.09, 1.05 (18H, each br s). ^{13}C NMR ($CDCl_3$) δ: 146.20, 136.17, 128.79, 126.98, 82.71, 59.69, 40.35, 34.19, 33.72, 23.51, 20.36, 17.22. CI-MS *m/z*: 354.144 548 and 356.141 660 (1:1) (calcd. for $C_{18}H_{28}NOBr$: 353.135 41 and 355.133 54).

TEMPO-modified 4-ethylbenzyl iodide 7 (16)

Following the Finkelstein reaction outlined in Scheme 1, **6** (0.90 g, 2.91 mmol) was added to a stirred solution of sodium iodide (7.5 g, 50 mmol) in dry acetone (20 mL), which was refluxed under argon for 3 h. After filtering and removal of the solvent by rotary evaporation, the solid was dissolved in CH_2Cl_2 (50 mL) and extracted with water (50 mL) and CH_2Cl_2 (2 × 50 mL) where the extracts were dried over $MgSO_4$, filtered and the solvent evaporated to yield a white solid (**7**) (1.1 g, 94%), mp 72 °C. IR (KBr disk, cm^{-1}): 3004, 2922, 1506, 1446, 1280, 1055, 874, 836, 699. ^1H NMR ($CDCl_3$) δ: 7.36, 7.27 (4H, dd,), 4.77 (1H, q), 4.49 (2H, s), 1.61–1.18 (6H, m), 1.47 (3H, d), 1.23, 1.18, 1.04, 0.68 (12H, each br s). ^{13}C NMR ($CDCl_3$) δ: 145.51, 137.51, 128.35, 126.92, 82.55, 59.57, 40.23, 34.33, 23.26, 20.30, 17.10, 5.96. CI-MS *m/z*: 402.131 155 (calcd. for $C_{18}H_{28}NOI$: 401.121 6).

Monoazofunctionalized unimer 8 (12)

8 was synthesized by the coupling of **7** and *para*-hydroxyazobenzene **14** as illustrated in Scheme 1. A mixture of **7** (1.0 g, 2.49 mmol), **14** (0.60 g, 3.03 mmol), anhyd. K_2CO_3 (0.54 g, 3.91 mmol), and crown ether (0.24 g, 0.91 mmol) in dry acetone (50 mL) was refluxed (60 °C) under argon for 48 h. After removal of the solvent by rotary evaporation, the residue was dissolved in CH_2Cl_2 (50 mL) and extracted with water (3 × 50 mL). The organic layer was dried over $MgSO_4$, filtered, and the solvent was removed by rotary evaporation. Column chromatography using CH_2Cl_2 as the eluant yielded an orange solid **7** (0.75 g, 75%), mp 125 to 126 °C. IR (KBr disk, cm^{-1}): 3064, 2968, 1497, 1457, 1251, 1145, 930, 836, 687. ^1H NMR ($CDCl_3$) δ: 7.94 (2H, d), 7.90 (2H, d), 7.55–7.32 (3H, m), 7.40 (4H, d), 7.12 (2H, d), 5.16 (2H, s), 4.83 (1H, q), 1.51 (3H, d), 1.58–1.26 (6H, m), 1.26, 1.19, 1.06, 0.70 (12H, each br s). ^{13}C NMR ($CDCl_3$) δ: 160.10, 158.30, 145.92, 130.77, 129.44, 127.75, 127.29, 125.14, 122.97, 115.53, 83.21, 70.70, 59.97, 40.76, 30.83, 23.60, 20.44, 17.26. CI-MS *m/z*: 472.294 317 (calcd. for $C_{30}H_{37}N_3O_2$: 471.2885).

Diazofunctionalized core 16 (16)

16 was synthesized from 4,4′-ethylenedianiline **15** via diazotization and coupling as shown in Scheme 2. The diazonium salt solution resulting when a solution of stirred sodium nitrite (4.16 g, 60.3 mmol) in water (5 mL) was added slowly to a solution of **15** (5.0 g, 23.6 mmol) in aq. HCl (17 mL of HCl in 5 mL of water) cooled below 2 °C in an ice-water bath, was coupled with phenol as follows. The diazonium salt solution was added slowly with stirring to a solution of phenol (5.6 g, 59.6 mmol) in 10% sodium hydroxide (12.8 g NaOH in 120 mL water) while maintaining the reaction temperature below 2 °C and was allowed to stand in an ice-water bath for 1 h with stirring. After the solution was acidified slowly with concd. HCl, the resultant precipitate was filtered, washed with cold water several times, recrystalized from ethanol, and precipitated with ice to give a diazofunctionalized core **16** as a light orange solid (6.2 g, 62%), mp 245 to 246 °C. ^1H NMR (acetone-d_6) δ: 9.10 (2H, s), 7.84 (4H, d), 7.79 (4H, d), 7.41 (4H, d), 7.01 (4H, d), 3.08 (4H, s). ^{13}C NMR (acetone-d_6) δ: 37.60, 116.14, 122.73, 125.09, 129.72. EI-MS *m/z*: 422.174 20 (calcd. for $C_{26}H_{22}N_4O2$ 422.174 28).

Diazofunctionalized unimer 9 (12)

9 was synthesized by the coupling of **7** with **16** as illustrated in Scheme 2. A mixture of **7** (0.50 g, 1.41 mmol), diazofunctionalized core **16** (0.24 g, 0.57 mmol), anhyd. K_2CO_3 (0.040 g, 0.30 mmol), and crown-ether (0.030 g, 0.11 mmol) in dry acetone (20 mL) was refluxed (60 °C) under argon for 48 h. After removal of solvent by rotary evaporation, the residue was dissolved in CH_2Cl_2 (50 mL) and extracted with water (3 × 50 mL), dried over $MgSO_4$, filtered, and the solvent was removed by rotary evaporation. Column chromatography using hexanes – ethyl acetate (3:2) as the eluent yielded an orange solid **9** (0.1 g, 18%). ^1H NMR ($CDCl_3$) δ: 7.90 (4H, d), 7.80 (4H, d), 7.38 (8H, d), 7.29 (4H, d), 7.09 (4H, d), 5.13 (4H, s), 4.82 (2H, q), 3.04 (4H, s), 1.48 (6H, d), 1.60–0.60 (12H, m), 1.29, 1.18, 1.03, 0.68 (24H, each br s). ^{13}C NMR ($CDCl_3$) δ: 124.47, 122.49, 127.59, 126.87, 126.87, 114.88, 82.67, 69.74, 37.39, 23.38, 34.06, 29.51, 28.44, 20.77, 20.23, 20.20. EI-MS *m/z*: 969.600 22 (calcd. for $C_{62}H_{76}N_6O4$: 969.600 08).

© 2004 NRC Canada

1,3,5-Tris(4′-nitrophenoxy)benzene 19 (17)

1,3,5-Tris(4′-nitrophenoxy)benzene was prepared via S_NAr displacement as outlined in Scheme 3. A mixture of 1,3,5-trihydroxybenzene dihydrate (phloroglucinol) **17** (12.40 g, 76.50 mmol), 4-fluoronitrobenzene **18** (24.4 mL, 230 mmol), potassium fluoride (26.70 g, 460.0 mmol), and 150 mL of DMSO was heated to reflux temperature for 30 min. The reaction mixture was then cooled to room temperature (r.t.), and the precipitate was filtered, washed with water (150 mL), and allowed to dry to give a crude product as a tan flaky solid, which was recrystallized from ethyl acetate – charcoal and followed by chloroform–hexanes to give 1,3,5-tris(4′-nitrophenoxy)benzene **19** as a creamy white solid (25.0 g, 50%), mp 203 to 204 °C (lit. value (7) 203.5–205.5 °C). IR (KBr disk, cm^{-1}): 3091, 2840, 2448, 1918, 1591, 1561, 1468, 1340, 1230, 1114, 994, 848, 741, 632. ^1H NMR ($CDCl_3$) δ: 8.27 (6H, d), 7.15 (6H, d), 6.67 (3H, s). ^{13}C NMR ($CDCl_3$) δ: 161.30, 157.77, 143.60, 126.09, 118.21, 107.60. EI-MS *m/z*: 489.081 9 (calcd. for $C_{24}H_{15}N_3O9$ 489.080 1).

1,3,5-Tris(4′-aminophenoxy)benzene 20 (18)

The synthesis of **20** is outlined in Scheme 3. To a stirred solution of **19** (8.0 g, 16 mmol) and Fe powder (8.10 g, 145 mmol) in 50% ethanol (100 mL) was added slowly HCl (0.6 mL concd. HCl in 10 mL of 50% ethanol) and the reaction mixture was refluxed for 2 h. After the reaction mixture was made alkaline by addition of 15% KOH, the iron was filtered quickly and washed with 95% ethanol (2 × 50 mL). The solvent was removed by rotary evaporation and the residue was dissolved in chloroform (100 mL) and extracted with water (3 × 500 mL). The organic layer was dried over $MgSO_4$, filtered, and the solvent was evaporated on a rotary evaporator. The residue was dried under vacuum for 48 h to give 1,3,5-tris(4′-aminophenoxy)benzene **20** as a light purple solid (6.10 g, 94%), mp 88–90 °C (lit. value (8) 88 to 89 °C). IR (KBr disk, cm^{-1}): 3424, 3352, 3212, 1606, 1503, 1451, 1214, 1113, 1003, 8.31. ^1H NMR ($CDCl_3$) δ: 6.86 (6H, d), 6.65 (6H, d), 6.18 (3H, s), 3.67 (6H, br s). ^{13}C NMR ($CDCl_3$) δ: 160.77, 147.84, 142.90, 121.23, 116.17, 99.97. EI-MS *m/z*: 399.157 3 (calcd. for $C_{24}H_{21}N_3O3$ 399.158 4).

Triazofunctionalized core 21 (13)

The trifunctionalized core **21** was synthesized from **20** via diazotization and coupling as illustrated in Scheme 3. A diazonium salt solution resulted when sodium nitrite (1.56 g, 22.6 mmol) in water (12 mL) was added slowly with stirring to a solution of **20** (3 g, 7.52 mmol) in aq. HCl (5 mL of HCl in 12 mL of water) cooled below 2 °C in an ice-water bath. The diazonium salt was added slowly with stirring to phenol (2.1 g, 22.3 mmol) in 10% sodium hydroxide (48 mL) while maintaining the reaction temperature below 2 °C and was allowed to stand in an ice-water bath for 1 h with stirring. After the solution was acidified with HCl the resultant precipitate was filtered, washed with cold water several times, and air-dried for a few days to give the trifunctionalized azobenzene core (**21**) as a dark red solid (4.50 g, 84%), mp 190 °C. IR (KBr disk, cm^{-1}): 3405, 3168, 1451, 1312, 1225, 1146, 999, 685. 638. ^1H NMR (acetone-d_6) δ: 7.89 (6H, d), 7.81 (6H, d), 7.24 (6H, d), 6.99 (6H, d), 6.63 (3H, br s), 6.62 (3H, s). ^{13}C NMR (acetone-d_6) δ: 160.85, 159.55, 158.52, 149.35, 146.54, 125.17, 124.60, 119.72, 116.10, 105.45. EI-MS: 714.222 683 (calcd. for $C_{42}H_{31}N_6O6$ 714.222 7).

Triazofunctionalized unimer 10 (GEN 0) (12)

GEN 0 was synthesized by coupling of **7** with **21** as illustrated in Scheme 3. A mixture of **7** (0.15 g, 0.37 mmol), the azo core **21** (0.11 g, 0.15 mmol), and anhyd. K_2CO_3 (0.050 g, 0.58 mmol) in dry acetone (20 mL) was heated at reflux (60 °C) under argon for 48 h. After removal of the solvent by rotary evaporation, the residue was purified by column chromatography using CH_2Cl_2 as the eluant to give **GEN 0** (0.05 g, 22%) as an orange thick oil. IR (KBr disk, cm^{-1}): 2968, 2926, 2868, 2362, 2335, 1584, 1496, 1455, 1370, 1225, 1095, 1005, 838. ^1H NMR ($CDCl_3$) δ: 7.91 (12H, d), 7.40 (12H, d), 7.18 (12H, d), 7.10 (2H, d), 6.58 (3H, s), 5.15 (6H, s), 4.84 (3H, apparent d), 1.51 (9H, d), 1.66–1.00 (18H, m), 1.32, 1.20, 1.07, 0.71 (36H, each br s). ^{13}C NMR ($CDCl_3$) δ: 161.28, 159.07, 158.13, 149.12, 145.95, 134.85, 127.39, 126.93, 124.69, 124.47, 119.33, 115.18, 105.09, 82.86, 70.34, 59.76, 40.41, 34.50, 23.64, 20.37, 17.28. ES-MS: $(M + H)^+$ 1535.2 (calcd. for $C_{96}H_{111}N_9O9$ 1533.85).

Polymerization of styrene with monoazofunctionalized unimer (MAz-PS-T)

MAz-PS-T was synthesized by polymerizing styrene with **8** under bulk conditions as illustrated in Scheme 4. A mixture of monofunctionalized unimer **8** (0.10 g, 0.20 mmol) and styrene (18.2 g, 17 5mmol) was heated at 135 °C under nitrogen for 3 h. The polymerization mixture was dissolved in 50 mL of THF and precipitated from 750 mL of methanol, filtered and dried in a vacuum oven at 70 °C resulting in a yellow powder (4.69 g, 26%). M_n = 13 500, M_w/M_n = 1.26.

Polymerization of acetoxystyrene with monoazofunctionalized unimer (MAz-PAS-T)

MAz-PAS-T was synthesized by polymerizing acetoxystyrene with **8** under bulk conditions as illustrated in Scheme 5. A mixture of monofunctionalized unimer **8** (0.10 g, 0.20 mmol) and acetoxystyrene (26.6 g, 164 mmol) was heated at 135 °C under nitrogen for 75 min. The polymerization mixture was dissolved in 50 mL of THF and precipitated from 750 mL of methanol, filtered and dried in a vacuum oven at 70 °C resulting in a yellow powder (12.9 g, 49%). M_n = 35 300, M_w/M_n = 1.34.

Block copolymer of acetoxystyrene–styrene with monoazofunctionalized unimer (MAz-PAS-PS-T)

MAz-PAS-PS-T was synthesized by polymerizing **MAz-PAS-T** with styrene under bulk conditions as illustrated in Scheme 6. A mixture of **MAz-PAS-T** (3.00 g) and styrene (18.2 g, 175 mmol) was heated at 135 °C under nitrogen for 2 h. The polymerization mixture was dissolved in 50 mL of THF and precipitated from 750 mL of methanol, filtered and dried in a vacuum oven at 70 °C resulting in an off-white – yellow powder (5.49 g). M_n = 40 400, M_w/M_n = 1.54.

Random copolymer of acetoxystyrene–styrene with monoazofunctionalized unimer (MAz-PAS/PS-T)

MAz-PAS/PS-T was synthesized by polymerizing

© 2004 NRC Canada

acetoxystyrene and styrene with monofunctionalized unimer **8** under bulk conditions as illustrated in Scheme 7. A mixture of **8** (0.1 g, 0.20 mmol), styrene (12.7 g, 123 mmol) and acetoxystyrene (7.45 g, 45.0 mmol) was heated at 135 °C under nitrogen for 2 h. The polymerization mixture was dissolved in 50 mL of THF and precipitated from 750 mL of methanol, filtered and dried in a vacuum oven at 70 °C resulting in a yellow powder (4.36 g). M_n = 16 400 g/mol, M_w/M_n = 1.24.

Synthesis of monofunctionalized azobenzene poly(4-hydroxystyrene) (MAz-PHS-T) (19)

MAz-PHS-T was synthesized by hydrolysis of **MAz-PAS-T** as illustrated in Scheme 8. Concd. ammonium hydroxide (1.5 mL) in 5 mL of water was added dropwise to a 0.5 g solution of **MAz-PAS-T** in 20 mL of methanol. The reaction mixture was refluxed at 65 °C under nitrogen and was stopped after 24 h and was left to cool at room temperature. The polymer was precipitated from 200 mL of water, filtered and dried in an oven at 50 °C to yield yellow crystals (0.20 g, 40%).

Polymerization of acetoxystyrene with triazofunctionalized unimer (TAz-PAS-3T)

TAz-PAS-3T was synthesized by polymerizing acetoxystyrene with **10** under bulk conditions as illustrated in Scheme 9. A mixture of trifunctionalized unimer **10** (0.10 g, 0.07 mmol) and acetoxystyrene (26.6 g, 164 mmol) was heated at 135 °C under nitrogen for 75 min. The polymerization mixture was dissolved in 50 mL of THF and precipitated from 750 mL of methanol, filtered and dried in a vacuum oven at 70 °C resulting in a yellow powder (13.66 g, 51%). M_n = 74 400, M_w/M_n = 1.49.

Block copolymer of acetoxystyrene–styrene with triazofunctionalized unimer (TAz-PAS-PS-3T)

TAz-PAS-PS-3T was synthesized by polymerizing **TAz-PAS-3T** with styrene under bulk conditions as illustrated in **Scheme 10**. A mixture of **TAz-PAS-3T** (3.00 g) and styrene (18.2 g, 175 mmol) was heated at 135 °C under nitrogen for 45 min. The polymerization mixture was dissolved in 50 mL of THF and precipitated from 750 mL of methanol, filtered and dried in a vacuum oven at 70 °C resulting in an off-white – yellow powder (6.13 g). M_n = 126 000, M_w/M_n = 1.64.

Acknowledgements

We thank the Natural Sciences and Engineering Research Council of Canada (NSERC) for financial support.

References

1. (*a*) J.M.J. Fréchet. Science, **263**, 1710 (1994); (*b*) K.S. Cheon, P.M. Kazmaier, S.R. Keum, K.T. Park, and E. Buncel. Can. J. Chem **82**, 551 (2004); (*c*) K.S. Cheon, Y.S. Park, P.M. Kazmaier, and E. Buncel. Dyes Pigm. **53**, 3 (2002).
2. P.J. Lutz, G. Beinert, and P.F. Rempp. Macromol. Chem. (Oxford), **183**, 2787 (1982).
3. H.A. Nguyen and J.P. Kennedy. Polym. Bull. **10**, 74 (1983).
4. D.Y. Sogah, W.R. Hertler, O.W. Webster, and G.M. Cohen. Macromolecules, **20**, 1473 (1987).
5. C.B. Gorman, E.J. Ginsburg, and R.H. Grubbs. J. Am. Chem. Soc. **115**, 1397 (1993).
6. M.K. Georges, R.P.N. Veregin, P.M. Kazmaier, and G.K. Hamer. Macromolecules, **26**, 2987 (1993).
7. C.J. Hawker. J. Am. Chem. Soc. **116**, 11 185 (1994).
8. G. Moad and E. Rizzardo. Macromolecules, **28**, 8722 (1995), references therein.
9. C.J. Hawker, G.G. Barclay, A. Orellana, J. Dao, and W. Devenport. Macromolecules, **29**, 16 (1996).
10. C.J. Hawker. Angew. Chem. Int. Ed. Engl. **34**, 1456 (1995).
11. (*a*) E. Buncel. Can. J. Chem. **78**, 1251 (2000); (*b*) S. Swansberg, E. Buncel, and R.P. Lemieux. J. Am. Chem. Soc. **122**, 6594 (2000); (*c*) J.T.C Wojtyk, P.M. Kazmaier, and E. Buncel. J. Chem. Soc. Chem. Commun. 1703 (1998); (*d*) E. Buncel and K.S. Cheon. J. Chem. Soc. Perkin Trans. 2, 1241 (1998); (*e*) R.A. Cox, E. Buncel, and S. Patai (*Editors*). The chemistry of hydrazo, azo, and azoxy groups. Vol. 2. Wiley Interscience, New York. 1997; (*f*) S.-R. Keum, K.-B. Lee, P.M. Kazmaier, and E. Buncel. Tetrahedron Lett. **35**, 1015 (1994); (*g*) R.A. Cox, I. Onyido, and E. Buncel. J. Am. Chem. Soc. **114**, 1358 (1992); (*h*) E. Buncel and S. Rajagopal. Acc. Chem. Res. **23**, 226 (1990); (*i*) D.L.H. Williams and E. Buncel. *In* Isotopes in organic chemistry. Vol. 5. *Edited by* E. Buncel and C.C. Lee. Elsevier, Amsterdam. 1980. pp. 184–197; (*j*) R.A. Cox and E. Buncel. *In* The chemistry of the hydrazo, azo, and azoxy groups. *Edited by* S. Patai. Wiley, London. 1975. pp. 775–859; (*k*) A.J. Dolenko and E. Buncel. *In* The chemistry of the hydrazo, azo, and azoxy groups. *Edited by* S. Patai. Wiley, London. 1975. pp. 725–773; (*l*) E. Buncel. Acc. Chem. Res. **8**, 132 (1975); (*m*) E. Buncel. *In* Mechanisms of molecular migrations. Vol. 1. *Edited by* B.S. Thyagarajan. Wiley, New York. 1968. pp. 61–119.
12. C.J. Hawker and J.M.J. Fréchet. J. Am. Chem. Soc. **112**, 7638 (1990).
13. B.S. Furniss, A.J. Hannaford, P.W.G. Smith, and A.R. Tatchell. Vogel's textbook of practical organic chemistry. 5th ed. 1996.
14. P.D. Bartlett, E.P. Benzing, and R.E. Pincock. J. Am. Chem. Soc. **82**, 1762 (1960).
15. Y. Miura, K. Hirota, H. Moto, and B. Yamada. Macromolecules, **18**, 4659 (1998).
16. B.S. Furniss, A.J. Hannaford, P.W.G. Smith, and A.R. Tatchell. Vogel's textbook of practical organic chemistry. 5th ed. 1996. p. 572.
17. T. Takeichi and J.K. Stille. Macromolecules, **19**, 2093 (1986).
18. S.A. Mahood and P.V.L. Schaffner. Org. Synth. Coll. Vol. **II**, 160 (1967).
19. G.G. Barclay, C.J. Hawker, H. Ito, A. Orellana, P.R.L. Malenfant, and R.F. Sinta. Macromolecules, **31**, 1024 (1998).

© 2004 NRC Canada

Multi-armed, TEMPO-functionalized unimolecular initiators for starburst dendrimer synthesis via stable free radical polymerisation. 2. Tris (1,3,5)benzyloxy unimers[1]

Mohmad Asri Abd Ghani, Dalia Abdallah, Peter M. Kazmaier, Barkev Keoshkerian, and Erwin Buncel

Abstract: The synthesis of the trifunctionalized TEMPO-modified unimolecular initiators, unimers I, II, and III is described. Unimer I was prepared via an S_N2 type Williamson ether coupling of 1,3,5-tris(iodomethyl)benzene with a TEMPO-containing ethylbenzene hydroxy derivative. The synthesis of unimer II, however, was accomplished through S_N1 reaction of 1,3,5-tris(bromomethyl)benzene with the hydroxy-ethylbenzene TEMPO derivative in the presence of silver triflate. Synthesis of unimer III started from phloroglucinol and an S_NAr reaction with 1-fluoro-4-nitrobenzene, followed by reduction to the amino compound and Schiff base formation with the TEMPO-derivatized aromatic aldehyde. Stable free radical polymerisation (SFRP) of styrene and acetoxystyrene with unimer I are also described with molecular weights and polydispersities reported. It is concluded that the SFRP of styrene with a triradical initiator meets the requirements of a living system.

Key words: stable free radical polymerisation, starburst dendrimer, multi-armed unimolecular initiators.

Résumé : On décrit la synthèse d'initiateurs unimoléculaires trifonctionnalisés à base de 2,2,6,6-tétraméthylpipéridinyloxyle (TEMPO), les unimères I, II et III. L'unimère I a été préparé par le biais d'une réaction S_N2, de type formation d'éther de Williamson, par le couplage du 1,3,5-tris(iodométhyl)benzène avec un dérivé hydroxylé de l'éthylbenzène portant le radical TEMPO. Toutefois, la synthèse de l'unimère II a été réalisée par le biais d'une réaction S_N1 du 1,3,5-tris(iodométhyl)benzène avec le dérivé hydroxylé de l'éthylbenzène portant le radical TEMPO, en présence de triflate d'argent. La synthèse de l'unimère III a été réalisée à partir du phloroglucinol et une réaction S_NAr avec le 1-fluoro-4-nitrobenzène, suivie d'une réduction en dérivé amino et de la formation d'une base de Schiff avec un aldéhyde aromatique portant le radical TEMPO. On décrit aussi la polymérisation avec un radical libre stable du styrène et de l'acétoxystyrène catalysée par l'unimère I et on rapporte les poids moléculaires et les polydispersités moyennes. On conclut que la polymérisation avec un radical libre stable du styrène catalysée par un initiateur triradicalaire satisfait les besoins d'un système vivant.

Mots clés : polymérisation avec un radical libre stable, dendrimère en « éclatement d'étoile », initiateur unimoléculaire tentaculaire.

[Traduit par la Rédaction]

Introduction

The achieving of controlled architecture in macromolecules is at the forefront in the synthesis of novel materials with improved properties. In the realm of polymers, profound changes in properties accompany the introduction of branches into the polymer backbone, which leads to the formation of graft or star polymer systems.

The present work forms part of a series of investigations where controlled architecture in a star polymer is achieved through stable free radical polymerisation (SFRP) using the stable nitroxide radical 2,2,6,6-tetramethylpiperidinyloxy (TEMPO) (1). Our approach is to synthesize unimolecular initiators containing the TEMPO unit, termed unimers, which are then employed in synthesis of star polymers and copolymers. We describe here the synthesis of three trifunctionalized unimers (I, II, III). The polymerisations of styrene and acetoxystyrene with unimer I to form homopolymers and co-

Received 2 February 2004. Published on the NRC Research Press Web site at http://canjchem.nrc.ca on 9 November 2004.

M.A.A. Ghani, D. Abdallah, and E. Buncel.[2]. Department of Chemistry, Queen's University, Kingston, ON K7L 3N6, Canada.
P.M. Kazmaier and B. Keoshkerian. The Xerox Research Centre of Canada, 2660 Speakman Drive, Mississauga, ON L5K 2L1, Canada.

[1]Part 1, ref. 1.
[2]Corresponding author (e-mail: buncele@chem.queensu.ca).

 doi: 10.1139/V04-106 © 2004 NRC Canada

polymers are also described. This work is a continuation of our structure-property studies of functionalized dendrimers (2).

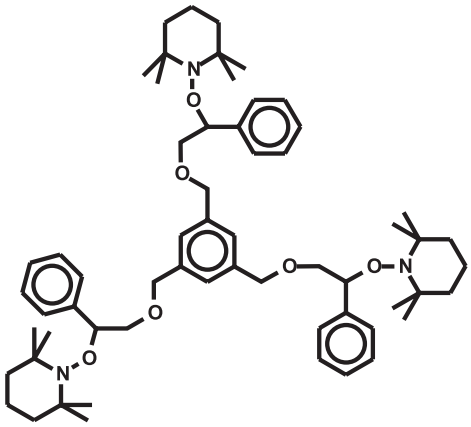
Results and discussion

Unimolecular initiator I synthesis

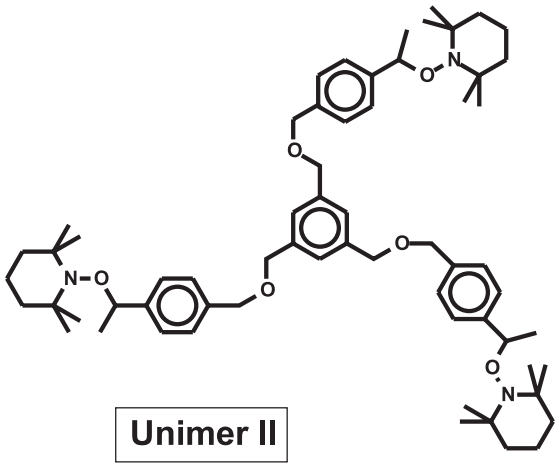
The synthesis of unimer I consisted of a three-step sequence (Scheme 1): (*i*) The benzyloxyamine ester **1** was first prepared by a modification of the method reported by Veregin (3), Hawker (4), Kobatake (5), and their co-workers, by heating benzoyl peroxide and TEMPO with excess styrene at 80 °C for 30 min (82% yield after recrystallization from 2-propanol). (*ii*) Saponification of **1** (4, 6) by heating at reflux with 2 mol L^{-1} KOH in ethanol and flash chromatography gave the alcohol **2** as a light yellow oil (97%). (*iii*) Williamson ether coupling of **2** with 1,3,5-tris(iodomethyl)benzene in THF under reflux (24 h) in the presence of sodium hydride, after flash chromatographic separation, gave unimer I as a light yellow thick syrup (97%).

Unimolecular initiator II synthesis

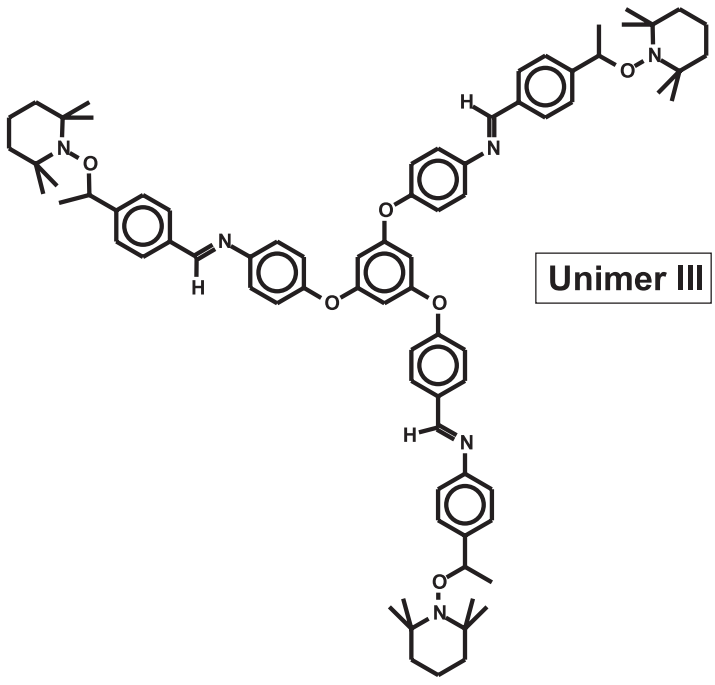
The unimer II was prepared by the following sequence (Scheme 2): (*a*) Initially the benzyloxamine derivatives **3** (X = H, CH_2Cl, CH_2Br, CH_2I, CH_2OH) were synthesized starting with commercially available ethylbenzene derivatives and using modifications of the methods of Georges and co-workers (7), Hawker et al. (8), Priddy and co-workers (9), and Miura et al. (10). In our hands the highest yield of **3** (X = H), 93% after crystallization from ethanol, was obtained by reacting ethylbenzene with *tert*-butyl peroxyoxalate and TEMPO (10); (*b*) in an alternative method, use of Jacobson's catalyst (Salem (10, 11)) with the ethylbenzene derivatives in the presence of di-*tert*-butyl peroxide, sodium



Unimer I



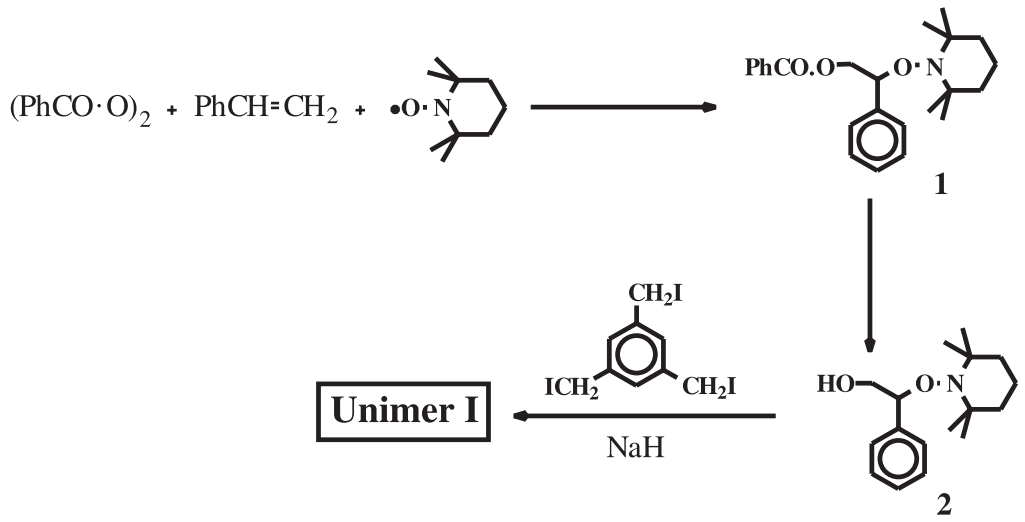
Unimer II



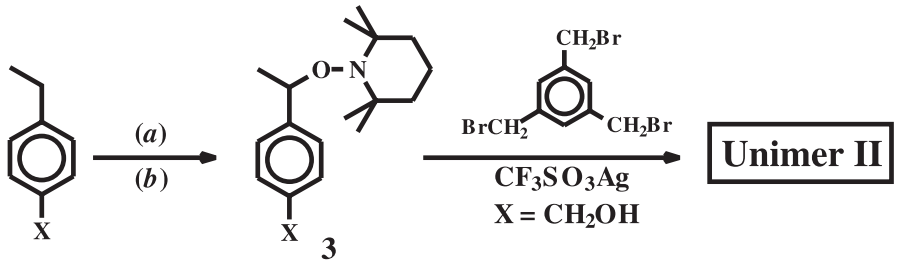
Unimer III

© 2004 NRC Canada

Scheme 1.



Scheme 2.



X = H, CH_2Cl (Br, I, OH)

(*a*) (*t*-BuO·O·CO)$_2$, TEMPO
(*b*) Salen, *t*-BuO·O·Bu-*t* , $NaBH_4$, TEMPO

borohydride, and TEMPO (12) gave alkoxyamines **3** in yields ranging over 20% (X = CH_2Cl), 41% (X = H), and 51% (X = CH_2OH). Attempted formation of unimer II through S_N2 Williamson ether coupling of **3** (X = CH_2OH) with 1,3,5-tris(iodomethyl)benzene as in the case of unimer I, was unsuccessful in our hands. The preparation of unimer II was then accomplished via an S_N1 type reaction of 1,3,5-tris(bromomethyl)benzene with **3** (X = CH_2OH) in the presence of silver triflate (17% after column chromatographic separation).

Unimolecular initiator III synthesis

The reaction scheme followed the sequence shown in Scheme 3.

(1) The triamine core **4** was obtained in two steps: an S_NAr reaction between 1,3,5-trihydroxy-benzene and 1-fluoro-4-nitrobenzene in the presence of KF in DMSO produced the 1,3,5-tris(4-nitrophenyl)benzene derivative **4**-NO_2 in 50% yield. The triamino core **4**-NH_2 was then obtained through Fe–HCl reduction in 94% yield after purification.

(2) Unimer III was obtained as the Schiff base adduct on reaction of the triamino core compound **4**-NH_2 with the benzyloxyamine derivative **3** (X = CHO) (85% yield after column chromatographic purification).

Controlled free radical polymerisation of unimolecular initiator I

Polystyrene starburst dendrimer I

Two polymerisations of styrene were performed with Unimer I under bulk conditions at 135 °C, **SFRP 1** and **SFRP 2**. The progress of the SFRP processes was monitored by withdrawal of aliquots from the reaction mixture at different times for % conversion and molecular weight determinations.

In the first polymerisation (**SFRP 1**), 1200 equiv. of styrene to 1 equiv. of unimer I were used under the above conditions for 3 h. The polymer was precipitated from methanol to give star polystyrene with terminal TEMPO end groups (**PS-3T1**), as a white solid (15 g), average molecular weight (M_n) 34 200 and polydespersity (PD) 1.29.

The second polymerisation (**SFRP 2**) was performed using 400 equiv. of styrene to 1 equiv. of unimer I for 4 h to give **PS-3T2** (8.70 g) after precipitation from methanol. The polystyrene had a M_n value of 12 700 and a PD of 1.34.

The ^{1}H NMR for both polymer samples showed broad peaks between 1.50 and 1.87 ppm representing the methylene and methine protons. Aromatic protons of polystyrene appear as a broad multiplet between 6.49 and 7.10 ppm.

The polymerisation results are shown in Table 1. The conversion-time relationship is plotted for the formation of

© 2004 NRC Canada

Scheme 3.

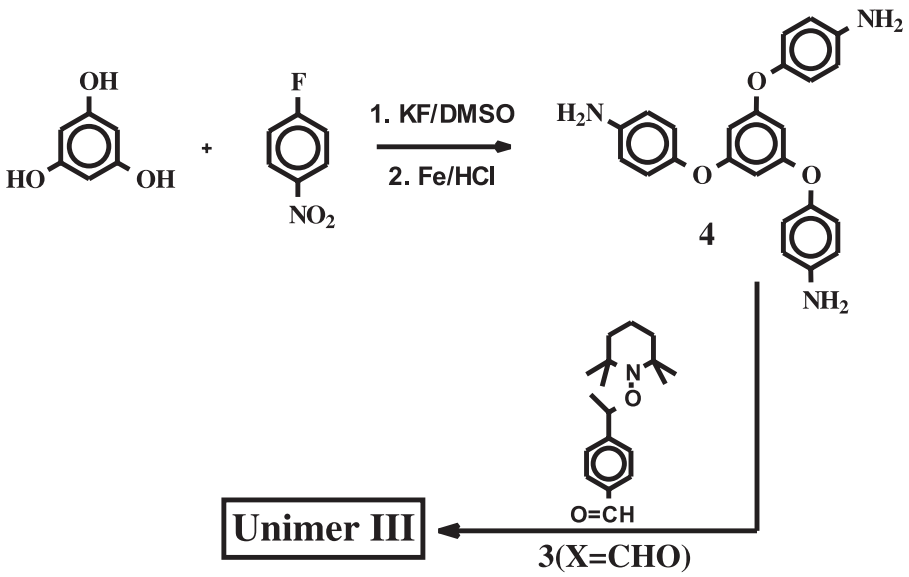


Table 1. Polymerisation results with unimer I.

Method	Time	Conversion[a] (%)	M_n[b] (Theo.)	M_n[c] (Exptl., GPC)	PD[d] (GPC)
SFRP 1					
	30	10	12 320	12 390	1.20
	60	18	21 290	21 040	1.17
	120	45	54 180	28 080	1.28
	180	51	60 760	34 150	1.29
SFRP 2					
	30	12	4 800	5 685	1.25
	60	24	9 600	8 951	1.23
	120	38	15 200	11 690	1.27
	180	48	19 200	14 350	1.27
	240	53	21 200	12 710	1.34

[a]Based on TGA.
[b]Calculation of M_n (Theo.): (*i*) for **SFRP 1**: M_n (Theo.) = conversion (%) × molecular weight (monomer) × 1200 (ratio of styrene to unimer I); (*ii*) for **SFRP 2**: M_n (Theo.) = conversion (%) × molecular weight (monomer) × 400 (ratio of styrene to unimer I).
[c]Estimated by GPC based on polystyrene standards.
[d]PD = M_n/M_w estimated by polystyrene standards.

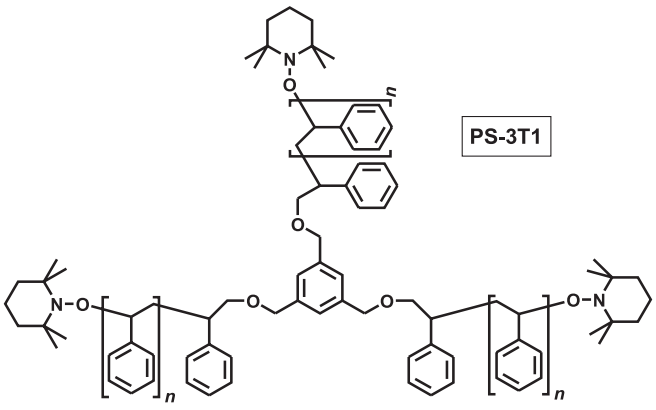
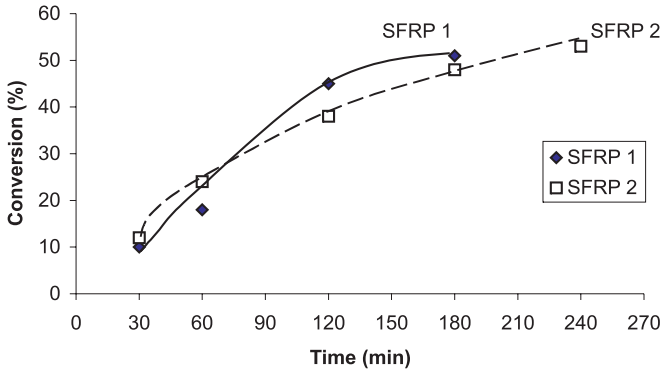


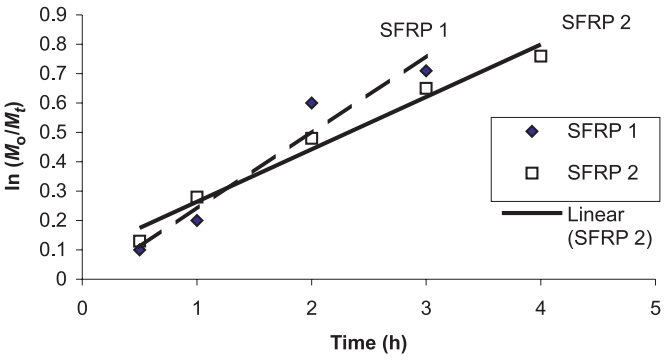
Fig. 1. Plot of % conversion vs. time for **SFRP 1** and **SFRP 2** with unimer I.



PS-3T1 and **PS-3T2** in Fig. 1. As the polymerisation time increases, monomer conversion also increases. Even though the ratio of styrene : unimer I for **SFRP 1** and **SFRP 2** is 3:1, the rate of conversion is almost constant for the two polymerisations. Thus, the polymerisation rate is independent of unimer I concentration.

© 2004 NRC Canada

Fig. 2. Semilogarithmic plot of conversion with reaction time for the SFRP processes with varying initial concentration for **SFRP 1** and **SFRP 2**.



A kinetic plot in semilogarithmic coordinates showing the variation of monomer consumption with time is presented in Fig. 2. M_o represents the initial monomer concentration while M_t is the concentration after time t. Thus, the SFRP of styrene at 135 °C with a triradical initiator (unimer I) meets the requirement of a living system.

Number average molecular weights (M_n) and polydispersities were determined by GPC with polystyrene standards. The plot of the theoretical and experimental M_n data against % conversion are shown in Figs. 3 and 4 for **SFRP 1** and **SFRP 2**, respectively. The experimental M_n data are very close to the calculated theoretical values at the early stages of the polymerisation, which indicates that the formed styryl radicals initiated all growing chains at the same time. There are large deviations of M_n compared with the theoretical values after 40% conversion, which suggests that determination of molecular weight using polystyrene standards (linear chains) is not suitable for star polystyrene. At higher molecular weights the multi-armed polystyrene has a totally different structure and properties compared to the linear analog and will have less hydrodynamic volume. In a related SFRP study with a trifunctionalized unimer, Hawker (13) found that the experimental M_n = 16 500 of the star polymer was lower than the theoretical value (M_n = 21 000). However, when the star polymer was hydrolyzed and the molecular weight of the individual arms measured it was fully consistent with the proposed structure and that each arm of the initiator can actively initiate the monomer similar to the monoinitiator system.

Polyacetoxystyrene starburst dendrimer I

The polymerisation of acetoxystyrene (400 equiv. to 1 equiv. of unimer I) was effected under bulk conditions at 135 °C for 3 h. The polymer was precipitated from methanol to give 5.0 g of a white solid (**PAS-3T**) with an average molecular weight of 21 100 and a PD of 1.30. The ^{1}H NMR shows broad peaks between 1.78 and 1.40 ppm representing the aliphatic protons and a broad multiplet between 7.08 and 6.33 ppm for the aromatic protons of polyacetoxystyrene. The methyl protons of the acetoxy group appear as a singlet at 2.81 ppm. The ^{13}C NMR shows a peak at 169.2 ppm for the carbonyl carbon and 21.23 ppm for the methyl carbon of the acetate group.

Fig. 3. Theoretical and experimental molecular weights for **SFRP 1** plotted against % conversion.

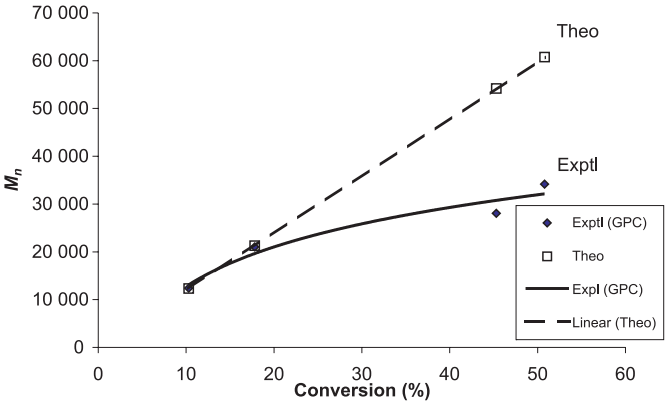
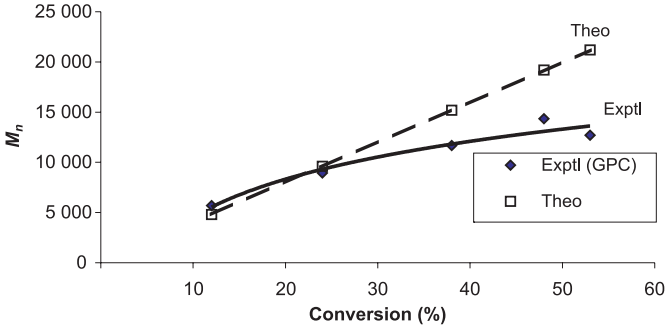


Fig. 4. Theoretical and experimental molecular weights for **SFRP 2** plotted against % conversion.



Hydrolysis of polyacetoxystyrene starburst dendrimer I

Removal of the acetyl group from **PAS-3T** was carried out in methanol by treatment with ammonium hydroxide (15) to give a light yellow solid with an average molecular weight of 16 500 and a PD of 1.23. The decrease in average molecular weight in comparison to **PAS-3T** (M_n = 21 100) is in good agreement with calculated values for deacetylation. The ^{1}H NMR shows the disappearance of the singlet at 2.81 ppm for the methyl protons of the acetoxy group; also, the disappearance of the carbonyl carbon and the methyl group carbon peaks at 196.2 and 21.23 ppm, respectively, confirming that the hydrolysis is complete.

Starburst block copolymer (styrene–acetoxystyrene) dendrimer I

The synthesis of block copolymer was undertaken from **PS-3T1**. A diblock copolymer was obtained via the SFRP technique using 4-acetoxystyrene (25 mL) as the feed monomer at 135 °C for 4 h. A white powder precipitated from methanol (26 g, M_n 95 500, and PD 1.23). The ^{1}H NMR shows two broad peaks at 7.10 and 6.25 ppm corresponding to the protons of the aromatic rings of polystyrene and polyacetoxystyrene, while an intense peak at 2.25 ppm represents the methyl protons of the acetyl group.

Conclusions

The synthesis of unimers I, II, and III was accomplished by reaction sequences outlined in Schemes 1, 2, and 3. Each

© 2004 NRC Canada

unimer contains one stereogenic center at the TEMPO junction and the products are obtained as complex diastereomeric mixtures.

The polymerisation of styrene and acetoxystyrene was effected with unimer I to form homopolymers and copolymers. For styrene, two polymerisations (**SFRP 1** and **SFRP 2**) were done using different ratios of unimer I to styrene. A polymer with a M_n of 34 200 and a PD of 1.29 was produced from **SFRP 1** while **SFRP 2** yielded a polymer with a M_n of 12 700 and a PD of 1.34. Conversion-time relationships for **SFRP 1** and **SFRP 2** were plotted and an equivalent rate of polymerisation in both cases was obtained, i.e., the rate is independent of unimer I concentration. Linear semilogarithmic kinetic plots of monomer consumption vs. time were obtained, which meets the requirements of a living system. On plotting the theoretical and experimental M_n data against % conversion, the experimental data correlate with theoretical at low M_n while a variance at higher M_n values is in accord with the star-shaped structure of the polymer.

With acetoxystyrene, unimer I gave a polymer (**PAS-3T**) with a M_n of 21 100 and a PD of 1.30. This was hydrolyzed to yield the hydroxystyrene polymer (**PHS-3T**) with a M_n of 16 500 and a PD of 1.23.

A star block copolymer of styrene and acetoxystyrene was obtained from polymerisation of **PS-3T** with acetoxystyrene to give a polymer with a M_n of 95 500 and of PD 1.23.

Experimental section

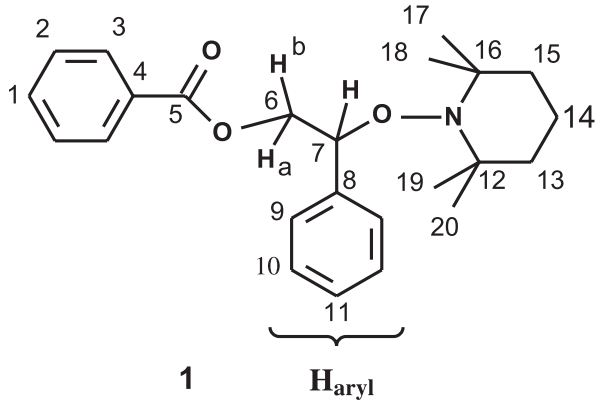
Unimer I

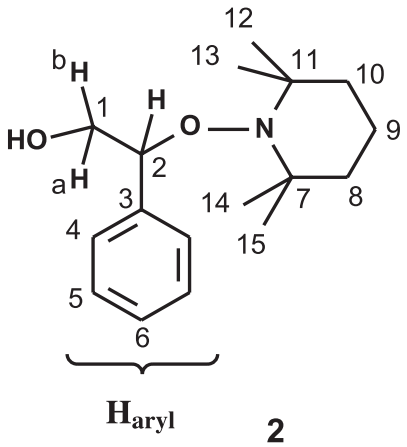
Phenethyloxy(2,2,6,6-tetramethylpiperidino)benzoate 1

A solution of TEMPO (3.43 g, 22.0 mmol) and BPO (8.0 g, 33.0 mmol) in repurified styrene (150 mL) in a round-bottomed (RB) flask was heated under argon at 80 °C for 30 min while stirring, during which period the solution changed from red to light yellow. After cooling, excess styrene was removed under reduced pressure at ca. 50 °C and the residue was purified by flash column chromatography using CH_2Cl_2 as the eluant to give a pale yellow oil. Recrystallization from 2-propanol yielded **1** as a white solid (7.0 g, 82%), mp 72 °C (lit. value (5) mp 72.2–72.6 °C). IR (KBr disk, cm^{-1}): 2928, 1713, 1460, 1371, 1264, 1129, 1100, 997, 700. ^{1}H NMR ($CDCl_3$) δ: 7.95 (2H, d, $J_{H\text{-}H}$ ortho = 6.9, H_3), 7.57–7.26 (8H, m, H_{aryl}, $H_{1,2}$), 5.09 (1H, app. t (overlapping d, d), J_{6b7} = 6.3, J_{6a7} = 5.1, H_7), 4.85 (1H, d, d, J_{6a6b} = 11.1, J_{6a7} = 5.1, H_{6a}), 4.55 (1H, d, d, J_{6a6b} = 11.1, J_{6b7} = 6.3, H_{6b}), 1.66–1.02 (6H, m, $H_{13,14,15}$), 1.39, 1.23, 1.09, 0.78 (12H, br s, $H_{17,18,19,20}$). ^{13}C NMR ($CDCl_3$) δ: 166.38 (C_5), 140.76 (C_8), 132.88 (C_9), 130.24 (C_4), 129.63 (C_3), 128.33, 128.10 ($C_{1,11}$), 127.68 ($C_{2,10}$), 84.01 (C_7), 66.83 (C_6), 60.16 ($C_{12,16}$), 40.48 ($C_{13,15}$), 34.11 ($C_{17,18}$ or $C_{19,20}$), 20.37 ($C_{19,20}$ or $C_{17,18}$), 17.21 (C_{14}). CI-MS *m/z*: 382.3 (calcd. for $C_{24}H_{31}NO_3$ 381.2).

Benzyloxyamine of styrenic alcohol 2

The reaction mixture consisting of ester **1** (4.0 g, 10 mmol) in ethanol (ca. 150 mL) and 2 mol L^{-1} KOH (25 mL) was heated under reflux for 3 h. After removal of ethanol on a rotary evaporator, the residue was dissolved in CH_2Cl_2 (100 mL), which was extracted with water (3 × 100 mL). The residual CH_2Cl_2 solution was dried over anhyd. $MgSO_4$. After removal of the solvent, the product was purified by flash column chromatography using CH_2Cl_2 as the eluant to give **2** as a light yellow oil (2.70 g, yield 97%). IR (neat, cm^{-1}): 3421–3302, 2930, 1739; 1721, 1606, 1458, 1360, 1248, 1125, 1027, 920, 762, 703. ^{1}H NMR ($CDCl_3$) δ: 7.43–7.32 (5H, m, H_{aryl}), 5.92 (1H, br s, H_{OH}), 1.64–1.46 (6H, m, $H_{8,9,10}$), 1.58, 1.39, 1.30, 1.22 (12H, br s, $H_{12,13,14,15}$). The signals for H_{1a}, H_{1b}, and H_2 could not be fully resolved, however, the ^{13}C NMR signals were in satisfactory agreement with the reported data (15) and the MS is also satisfactory. ^{13}C NMR ($CDCl_3$) δ: 138.31 (C_3), 127.72 (C_5), 127.27 (C_6), 126.17 (C_4), 83.02 (C_2), 69.05 (C_1), 61.04 (C_7 or C_{11}), 59.76 (C_7 or C_{11}), 39.78, 39.60 ($C_{8,10}$), 33.99, 32.45 ($C_{12,13}$ or $C_{14,15}$), 20.11, 19.79 ($C_{14,15}$ or $C_{12,13}$), 16.53 (C_9). CI-MS *m/z*: 278.2 (calcd. for $C_{17}H_{27}NO_2$ 277.20).



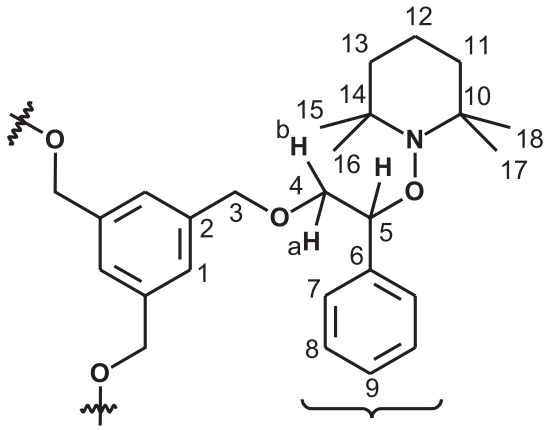


Williamson ether coupling of 2 and 1,3,5-tris(iodomethyl)benzene

A solution of alcohol **2** (2.50 g, 10 mmol) in dry THF (50 mL) in a RB flask fitted with a reflux condenser was treated with dry sodium hydride (1.10 g, 5 mmol) and the reaction mixture was stirred under argon at room temperature for 4 h. The iodo compound (1.25 g, 2.50 mmol) in dry THF (20 mL) was added slowly to the reaction mixture that was then heated at reflux for 24 h. On cooling, the resultant precipitate was filtered and the filtrate was evaporated to dryness. The residue in CH_2Cl_2 (100 mL), was washed with water (3 × 100 mL), and purified by flash column chromatography using ethyl acetate – hexanes – CH_2Cl_2 (1:3:6) as

© 2004 NRC Canada

the eluant to give unimer I as a light yellow thick syrup (2.30 g, 97%). IR (neat, cm^{-1}): 2925, 2854, 1605, 1458, 1376, 1242, 1183, 957, 858, 761. ^1H NMR ($CDCl_3$) δ: 7.33–7.25 (15H, m, H_{aryl}), 6.78 (3H, s, H_1), 4.85 (3H, app t (overlapping d, d), J_{4b5} = 6.6, J_{4a5} = 5.1, H_5), 4.31 (6H, q, $J_{H\text{-}H}$ = 12.3, H_3), 3.94 (3H, d, d, J_{4a4b} = 9.6, J_{4a5} = 5.1, H_{4a}), 3.64 (3H, d, d, J_{4a4b} = 9.6, J_{4b5} = 6.6, H_{4b}), 1.61–1.13 (18H, m, $H_{11,12,13}$), 1.33, 1.19, 1.05, 0.66 (36H, each br s, $H_{15,16,17,18}$). ^{13}C NMR ($CDCl_3$) δ: 141.91 (C_2), 138.28 (C_6), 127.80, 127.72 ($C_{7,8}$), 127.15 (C_9), 125.21 (C_1), 85.36 (C_5), 72.72 ($C_{3,4}$), 60.03 ($C_{10,14}$), 40.40 ($C_{11,13}$), 33.82 ($C_{15,16}$ or $C_{17,18}$), 20.26 ($C_{17,18}$ or $C_{15,16}$), 17.09 (C_{12}). HR-MS (FAB+) calcd. for $C_{60}H_{88}N_3O_6$: 946.667 7; found: 946.692 7. Anal. calcd. for $C_{60}H_{87}N_3O_6$ (%): C 76.15, H 9.27, N 4.44; found: C 76.47, H 9.27, N 4.47.



Unimer I H_{aryl}

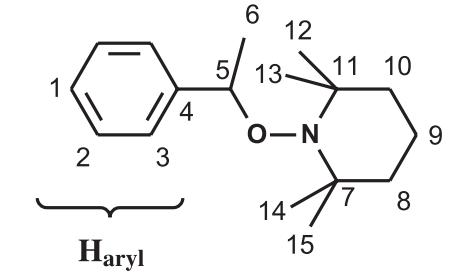
Unimer II

Illustrative synthesis of the benzyloxyamine of ethylbenzene (3 (X = H)) via the peroxyoxalate method

Di-*tert*-butylperoxyoxalate (2.21 g, 9.6 mmol), prepared by a modification of Bartlett's method (16) in 25 mL of ethylbenzene was treated with TEMPO (1.0 g, 6.4 mmol) and the mixture was stirred under argon at 35 °C. The red colour of the solution disappeared to give a light yellow solution within 30 min. Excess ethylbenzene was removed under reduced pressure at r.t. to give a viscous oil that solidified on standing in the refrigerator. The solid was repeatedly recrystallized from ethanol to provide the benzyloxyamine of 4-ethylbenzene (**3** (X = H)) (1.55 g, 93%) as colourless needles, mp 44 °C (lit. value (16) mp 44–46 °C). IR (KBr disk, cm^{-1}): 2977, 2936, 1461, 1366, 1283, 1244, 1218, 1126, 1064, 980, 927, 778, 699. ^1H NMR ($CDCl_3$) δ: 7.36–7.25 (5H, m, H_{aryl}), 4.82 (1H, q, $J_{H\text{-}H}$ = 6.6, H_5), 1.52 (3H, d, $J_{H\text{-}H}$ = 6.6 H_6), 1.42–1.28 (6H, m, $H_{8,9,10}$), 1.36, 1.21, 1.07, 0.700 (12H, each br s, $H_{12,13,14,15}$). ^{13}C NMR ($CDCl_3$) δ: 145.86 (C_4), 128.02 (C_2), 126.77 (C_1), 126.61 (C_3), 83.13 (C_5), 59.67 ($C_{7,11}$), 40.39 ($C_{8,10}$), 34.19 ($C_{12,13}$ or $C_{14,15}$), 23.58 (C_6), 20.32 ($C_{14,15}$ or $C_{12,13}$), 17.25 (C_9). CI-MS *m/z*: 262.3 (calcd. for $C_{17}H_{27}NO$ 261.2).

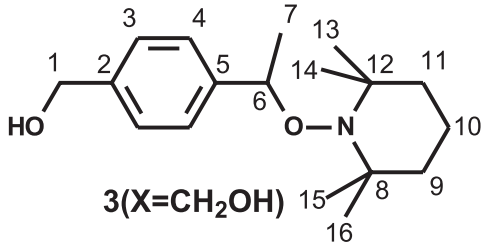
Illustrative synthesis of the benzyloxyamine of 4-ethylbenzyl alcohol (3 (X = CH_2OH)) via Jacobson's method

The Jacobson reaction (11, 12) was carried out with 4-vinylbenzyl alcohol (2.0 g, 15 mmol), TEMPO (3.51 g, 23 mmol), [salen]MnCl (1.90 g, 3 mmol), di-*tert*-butyl peroxide (2.20 g, 15 mmol), sodium borohydride (1.14 g, 30 mmol) in toluene–ethanol (1:1) (300 mL) medium at r.t. for 30 h. Removal of solvent under vacuo, extraction (CH_2Cl_2), H_2O wash, drying ($MgSO_4$), followed by flash column chromatography (CH_2Cl_2 eluant) yielded **3** (X = CH_2OH) as a light yellow solid (2.20 g., 51%), mp 40 °C. IR (neat, cm^{-1}): 3326 (broad), 2932, 1457, 1365, 1250, 1199, 1128, 1055, 944, 829, 732. ^1H NMR ($CDCl_3$) δ: 7.33 (4H, s, $H_{3,4}$), 4.81 (1H, q, $J_{H\text{-}H}$ = 6.6, H_5), 4.70 (2H, s, H_1), 2.20 (1H, br s, H_{OH}), 1.49 (3H, d, $J_{H\text{-}H}$ = 6.9, H_7), 1.48–1.10 (6H, m, $H_{9,10,11}$), 1.33, 1.21, 1.07, 0.71 (12H, each br s, $H_{13,14,15,16}$). ^{13}C NMR ($CDCl_3$) δ: 144.95 (C_5), 138.99 (C_2), 126.45, 126.35 ($C_{3,4}$), 82.52 (C_6), 64.80 (C_1), 59.32($C_{8,12}$), 39.94 ($C_{9,11}$), 34.08, 33.84 ($C_{13,14}$ or $C_{15,16}$), 23.34 (C_7), 19.99 ($C_{15,16}$ or $C_{13,14}$), 16.84 (C_{10}). CI-MS *m/z*: 292.3 (calcd. for $C_{18}H_{29}NO2$ 291.2).



H_{aryl}

3(X=H)



3(X=CH_2OH)

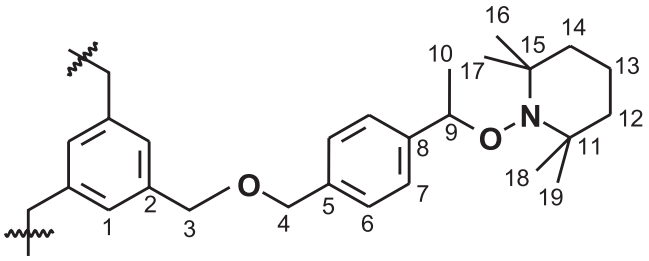
Silver-assisted S_N1 reaction for the formation of unimer II

Silver trifluoromethanesulfonate (silver triflate, $CF_3SO_3^-Ag^+$) was employed for the etherification of **3** (X = CH_2OH) with the core (1,3,5-tris(bromoethyl)benzene).

A solution of the alcohol **3** (X = CH_2OH) (0.47 g, 1.60 mmol) and silver triflate (0.33 g, 1.60 mmol) in dichloromethane (10 mL) at 0 °C was stirred for 1 h following which the tris bromide (0.15 g, 0.42 mmol) was added and stirring was continued for another 6 h. The solution was then diluted with CH_2Cl_2 (20 mL), filtered through a plug of Celite, and the filtrate was washed with 1 mol L^{-1} HCl (50 mL), then satd. $NaHCO_3$ (50 mL), brine (50 mL), dried ($MgSO_4$), and finally concentrated by rotary evaporation. The crude product was purified by flash column chromatography using hexanes – ethyl acetate (3:1) as the eluant to give unimer II as a light yellow thick syrup (70 mg, 17%) and other complex by-products that could not be assigned. IR (neat): 2972, 2930, 2869, 1449, 1360, 1259, 1209, 1131, 1064, 1019, 935, 821, 680 cm^{-1}. ^1H NMR ($CDCl_3$) δ: 7.33

© 2004 NRC Canada

(12H, s, $H_{6,7}$ and H_1), 4.80 (3H, q, $J_{H\text{-}H}$ = 6.6, H_9), 4.58 (12H, app. d, d, $H_{3,4}$), 1.70–1.30 (18H, m, $H_{12,13,14}$), 1.49 (12H, d, $J_{H\text{-}H}$ = 7.2, H_{10}), 1.32, 1.19, 1.05, 0.70 (36H, each br s, $H_{16,17,18,19}$). ^{13}C NMR ($CDCl_3$) δ: 145.29 (C_8), 138.73 (C_5), 136.53 (C_2), 128.00 ($C_{6,7}$), 126.60 (C_1), 82.87 (C_9), 72.17, 71.92 ($C_{3,4}$), 59.63 ($C_{11,15}$), 40.32 ($C_{12,14}$), 34.20 ($C_{16,17}$ or $C_{18,19}$), 23.57 (C_{10}), 20.31 ($C_{18,19}$ or $C_{16,17}$), 17.19 (C_{13}). FAB-HR-MS: $(M + H)^+$ calcd. for $C_{63}H_{94}N_3O_6$: 988.7143; found: 988.7141.



Unimer II

Unimer III

1,3,5-Tris(4′-nitrophenoxy)benzene (4-NO_2)

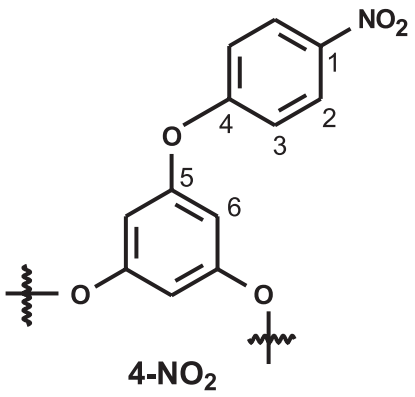
1,3,5-Tris(4′-nitrophenoxy)benzene (**4**-NO_2) was prepared via S_NAr displacement according to the method of Takeichi and Stille (17).

A mixture of 1,3,5-trihydroxybenzene dihydrate (phloroglucinol) (12.40 g, 76.50 mmol), 4-fluoronitrobenzene (24.4 mL, 230 mmol), potassium fluoride (26.70 g, 460.0 mmol), and 150 mL of DMSO was heated under reflux for 30 min. After cooling the precipitate that formed was filtered, washed with water (150 mL), and allowed to dry to give a crude product as a tan flaky solid. The supernatant of the initial filtrate on adding water (100 mL) gave more precipitate, which was filtered, washed with water (400 mL), and allowed to dry to give additional crude product. The combined crude products were recrystallized from ethyl acetate – charcoal and followed by chloroform–hexanes to give 1,3,5-tris(4′-nitrophenoxy)benzene (**4**-NO_2) as a creamy white solid (25.0 g, 50%), mp 203 to 204 °C (lit. value (17) mp 203.5–205.5 °C). IR (KBr disk, cm^{-1}): 3091, 2840, 2448, 1918, 1591, 1561, 1468, 1340, 1230, 1114, 994, 848, 741, 632. ^{1}H NMR ($CDCl_3$) δ: 8.27 (6H, d, $J_{H\text{-}H}$ ortho = 9.3, H_2), 7.15 (6H, d, $J_{H\text{-}H}$ ortho = 7.2, H_3), 6.67 (3H, s, H_6). ^{13}C NMR ($CDCl_3$) δ: 161.30 (C_4), 157.77 (C_5), 143.60 (C_1), 126.09 (C_2), 118.21 (C_3), 107.60 (C_6). HR-MS (EI) *m*/*z* calcd. for $C_{24}H_{15}N_3O_9$: 489.0801; found: 489.0819.

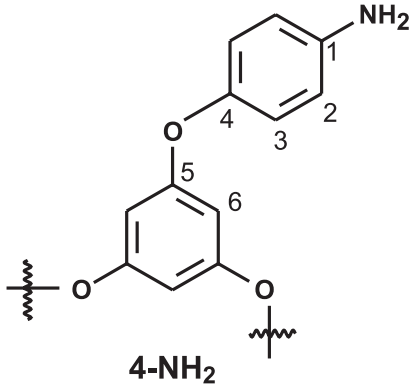
1,3,5-Tris(4′-aminophenoxy)benzene (4-NH_2)

Reduction of **4**-NO_2 was performed according to an experimental procedure adapted from the synthesis of 2,4-toluenediamine as described by Mahood and Schaffner (18).

To a stirred solution of **4**-NO_2 (8.0 g, 16 mmol) and Fe powder (8.10 g, 145 mmol) in 50% ethanol (100 mL) was added slowly HCl (0.6 mL concd. HCl in 10 mL of 50% ethanol). The reaction mixture was heated at reflux for 2 h and was then made alkaline to litmus with 15% aq. KOH. Without allowing the mixture to cool, the iron was filtered quickly and washed with 95% ethanol (2 × 50 mL). The solvent was removed by rotary evaporation and the residue was redissolved in chloroform (100 mL) and extracted with water (3 × 500 mL). The organic layer was dried ($MgSO_4$), filtered from the desiccant, evaporated to dryness, and further dried in vacuo for 48 h to give 1,3,5-tris(4′-aminophenoxy)benzene (**4**-NH_2) as a light purple solid (6.10 g, 94%), mp 88–90 °C (lit. value (18) mp 88 to 89 °C). IR (KBr disk, cm^{-1}): 3424, 3352, 3212 (NH_2), 1606, 1503, 1451, 1214 (C-O), 1113, 1003, 8.31 (C-N). ^{1}H NMR ($CDCl_3$) δ: 6.86 (6H, d, $J_{H\text{-}H}$ ortho = 8.7, H_3), 6.65 (6H, d, $J_{H\text{-}H}$ ortho = 8.7, H_2), 6.18 (3H, s, H_6), 3.67 (6H, br s, (H_{amino})). ^{13}C NMR ($CDCl_3$) δ: 160.77 (C_5), 147.84 (C_4), 142.90 (C_1), 121.23 (C_3), 116.17 (C_2), 99.97 (C_6). HR-MS (EI) *m*/*z* calcd. for $C_{24}H_{21}N_3O_3$: 399.1584; found: 399.1573.



4-NO_2



4-NH_2

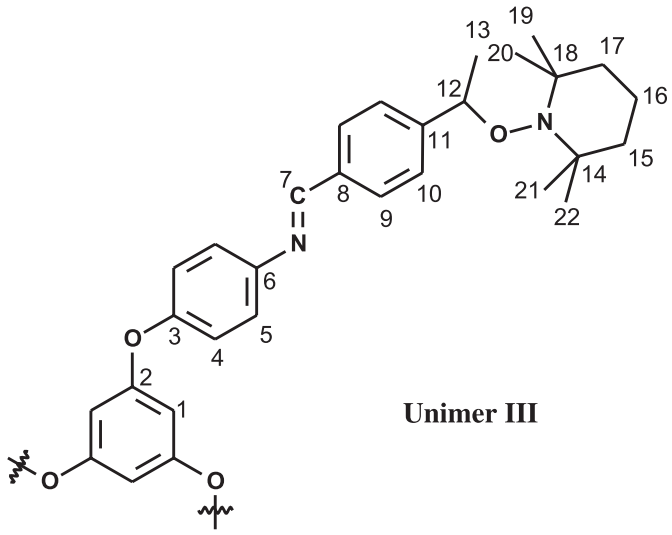
Synthesis of the Schiff base adduct (unimer III)

Unimer III was prepared by the reaction of aldehyde **3** (X = CHO) with amine **4**-NH_2 via a method modified from Furniss et al. (19).

A solution of **3** (X = CHO) (0.60 g, 2.10 mmol) and **4**-NH_2 (0.25 g, 0.63 mmol) in 95% ethanol (10 mL) was stirred at reflux for 30 min after which water (3 mL) was added until cloudy and the solution was allowed to cool and induced to crystallize. The product was filtered, rinsed with cold aqueous ethanol, and purified by flash column chromatography using CH_2Cl_2 as the eluant to give unimer III, as a light yellow rubber-like solid (0.675 g, 85%). IR (KBr disk, cm^{-1}): 3435, 2969, 2928, 2869, 1614, 1497, 1453, 1366, 1218, 1121, 1064, 1003, 937, 836, 700. ^{1}H NMR ($CDCl_3$) δ: 8.47 (3H, s, H_7), 7.86 (6H, d, $J_{H\text{-}H}$ ortho = 8.1, H_9), 7.43 (6H, d, $J_{H\text{-}H}$ ortho = 8.1, H_{10}), 7.23 (6H, d, $J_{H\text{-}H}$

© 2004 NRC Canada

ortho = 8.7, H_5), 7.09 (6H, $J_{H\text{-}H}$ ortho = 8.7, H_4), 6.43 (3H, s, H_1), 4.85 (3H, q, $J_{H\text{-}H}$ = 6.6, H_{12}), 1.68–1.39 (18H, m, $H_{15,16,17}$), 1.52 (9H, d, $J_{H\text{-}H}$ = 6.6, H_{13}), 1.32, 1.20, 1.06, 0.69 (36H, each br s, $H_{19,20,21,22}$). ^{13}C NMR ($CDCl_3$) δ: 159.92 (C_7), 159.84 (C_2), 154.28 (C_8), 149.63 (C_{11}), 148.25 (C_6), 134.84 (C_3), 128.69 (C_9), 127.00 (C_{10}), 122.35 (C_5), 120.18 (C_4), 102.99 (C_1), 83.17 (C_{12}), 59.76 ($C_{14,18}$), 40.39 ($C_{15,17}$), 34.50 ($C_{19,20}$ or $C_{21,22}$), 23.64 (C_{13}), 20.37 ($C_{21,22}$ or $C_{19,20}$), 17.23 (C_{16}). ES-MS *m/z* calcd. for $C_{78}H_{96}N_6O_6$: 1213.7: found: 1214.3.



Synthesis of PS-3T1

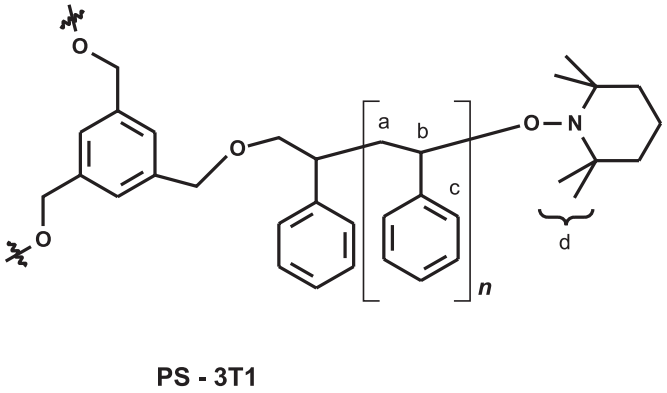
SFRP 1 polymerisation of styrene (50 mL, 0.44 mol) using unimer I (0.36 g, 0.38 mmol) was carried out at 135 °C under nitrogen via bulk polymerisation (no solvent added) for 4 h. As the reaction proceeded, the clear solution became viscous over time. Intermediate samples (0.5 mL) were withdrawn at times 0.5 h, 1 h, 2 h, 3 h, and 4 h to follow the progress of polymerisation. Each intermediate sample was transferred into two small vials for thermal gravimetric analysis (TGA) and gel permeation chromatography (GPC) purposes. To determine conversion, the sample was transferred directly from the vial to the TGA apparatus. The second vial was evaporated to remove the excess styrene, diluted with THF (ca. 1 mL), and analyzed by GPC. Polymerisation was stopped after 4 h. The polymer was precipitated from methanol (500 mL), redissolved in dichloromethane (100 mL), and finally polystyrene with a terminal TEMPO group (**PS-3T1**) was isolated as a white powder, after drying in a vacuum oven at 50 °C for 12 h, yield 15.0 g. M_n = 34 200, M_n/M_w = 1.29.

Synthesis of PS-3T2

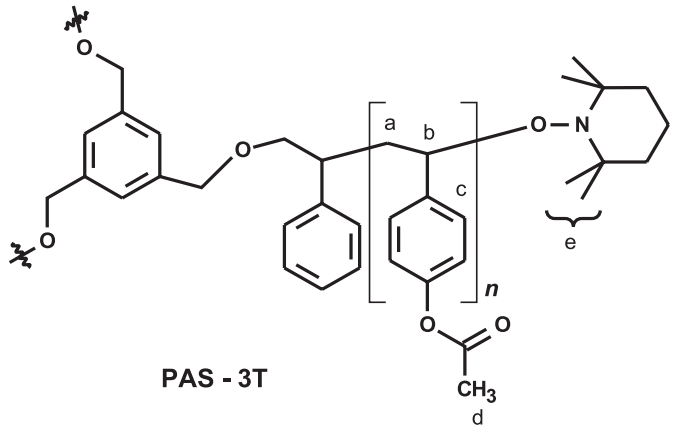
SFRP 2 polymerisation of styrene (25 mL, 0.22 mol) using unimer I (0.418 g, 0.500 0 mmol) was repeated in the identical manner as described above, forming **PS-3T2** as a white solid, 8.70 g. M_n = 12 700, M_n/M_w = 1.34.

Synthesis of PAS-3T

Bulk polymerisation of acetoxystyrene (25 mL, 0.164 mol) using unimer I (0.18 g, 0.38 mmol) was performed in an identical manner to the synthesis of **PS-3T1**. The product

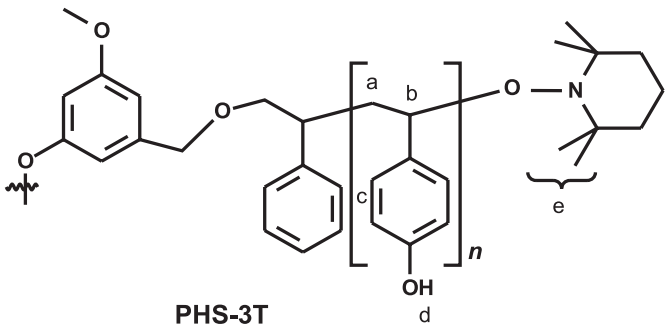


PAS-3T was obtained as a white powder (5.0 g). M_n = 21 100, M_n/M_w = 1.30.



Synthesis of PHS-3T

To a solution of **PAS-3T** (0.50 g) in methanol (20 mL) at reflux under nitrogen was added dropwise ammonium hydroxide (1.5 mL in 5 mL water). After the addition, heating of the reaction mixture was continued at reflux for 24 h. The reaction mixture was then cooled to room temperature, the polymer was isolated by precipitation in water (200 mL), filtered, and washed several times with water. The polymer was dried in a vacuum oven at 50 °C for 12 h to give star polyhydroxystyrene (**PHS-3T**) as a light yellow solid (0.3 g). Molecular weights and polydispersities of **PHS-3T** were estimated by GPC. M_n = 16 400, M_n/M_w = 1.23.

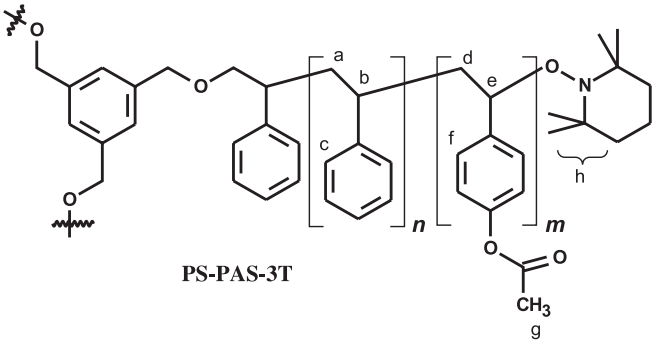


Synthesis of block copolymer PS-PAS-3T

To a solution of acetoxystyrene (25.00 mL, 0.164 mmol) was added **PS-3T1** (10.0 g) and the reaction mixture was de-

© 2004 NRC Canada

gassed under nitrogen for 30 min. The reaction mixture was then stirred and heated at 135 °C for 4 h. During this time the polymerisation mixture became progressively more viscous. The reaction mixture was cooled to room temperature, redissolved in dichloromethane (200 mL), and precipitated with methanol (1000 mL). The product was dried in a vacuum oven at 60 °C for 12 h to give **PS-PAS-3T** as a white powder (26.0 g). Molecular weights and polydispersities of **PS-PAS-3T** were estimated by GPC. M_n = 95 500, M_n/M_w = 1.21.



PS-PAS-3T

Acknowledgements

We thank the Natural Sciences and Engineering Research Council of Canada (NSERC) for financial support.

References

1. D. Abdallah, M.A.A. Ghani, M.F. Cunningham, P.M. Kazmaier, B. Keoshkerian, and E. Buncel. Can. J. Chem. **82**, 1393 (2004).
2. K.S. Cheon, Y.S. Park, P.M. Kazmaier, and E. Buncel. Dyes Pigm. **53**, 3 (2002).
3. R.P.N. Veregin, M.K. Georges, G.K. Hamer, and P.M. Kazmaier. Macromolecules, **28**, 4391 (1995).
4. C.J. Hawker. J. Am. Chem. Soc. **116**, 11 185 (1994).
5. L. Leclercq, I. Cazaux, and C. Caze. J.M.S.-Pure Appl. Chem. **A33**, 1123 (1996).
6. S. Kobatake, H.J. Horwood, R.P. Quirk, and D.B. Priddy. Macromolecules, **30**, 4238 (1997).
7. K.A. Moffat, G.K. Hamer, and M.K. Georges. Macromolecules, **32**, 1004 (1999).
8. C.J. Hawker, G.G. Barclay, A. Orellana, J. Dao, and W. Devonport. Macromolecules, **29**, 5245 (1996).
9. I.Q. Li, B.A. Howell, A. Ellaboudy, P.E. Kastl, and D.B. Priddy. Polym. Prepr. (Am. Chem. Soc. Div. Polym. Chem.), **36**, 469 (1995).
10. Y. Miura, K. Hirota, H. Moto, and B. Yamada. Macromolecules, **18**, 4659 (1998).
11. W. Zhang, J.L. Leobach, S.R. Wilson, and E.N. Jacobsen. J. Am. Chem. Soc. **112**, 2801 (1990).
12. J. Dao, D. Benoit, and C.J. Hawker. J. Polym. Sci. Part A: Polym. Chem. **36**, 2161 (1998).
13. C.J. Hawker. Angew. Chem. Int. Ed. Engl. **34**, 1456 (1995).
14. G.G. Barclay, C.J. Hawker, H. Ito, A. Orellana, P.R.L. Malenfant, and R.F. Sinta. Macromolecules, **31**, 1024 (1998).
15. U. Jahn. J. Org. Chem. **63**, 7130 (1998).
16. P.D. Bartlett, E.P. Benzing, and R.E. Pincock. J. Am. Chem. Soc. **82**, 1762 (1960).
17. T. Takeichi and J.K. Stille. Macromolecules, **19**, 2093 (1986).
18. S.A. Mahood and P.V.L. Schaffner. Org. Synth. Coll. Vol. **II**, 160 (1967).
19. B.S. Furniss, A.J. Hannaford, P.W.G. Smith, and A.R. Tatchell. Vogel's textbook of practical organic chemistry. 5th ed. Longman, London. 1989.

© 2004 NRC Canada

Liaison hydrogène des arylamines : compétition des sites π et N

Eric Marquis, Jérôme Graton, Michel Berthelot, Aurélien Planchat et Christian Laurence

Résumé : L'étude infrarouge, dans la région ν(OH), d'un donneur de liaison hydrogène de référence, le 4-fluorophénol, en présence d'arylamines primaires, secondaires et tertiaires différemment substituées sur le noyau et sur l'azote, montre la formation de deux complexes de stœchiométrie 1 : 1 en solution dans CCl_4, un complexe OH···π et un complexe OH···N. Une méthode est proposée pour décomposer la constante globale (K_t) de complexation en une composante K_π pour le complexe π et une composante K_N pour le complexe sur l'azote. Cette méthode est validée par comparaison des valeurs K_π et K_N obtenues avec des descripteurs calculés théoriquement, géométriques (direction de la paire libre de l'azote), électrostatiques (potentiels électrostatiques) et énergétiques (enthalpie de complexation avec HF). Les principaux facteurs stériques, inductifs et de résonance modifiant le pouvoir accepteur de liaison hydrogène des sites π et N sont analysés. La meilleure base π est la julolidine, et la meilleure base azotée est la base de Tröger. La triphénylamine, base de Brønsted azotée, se comporte essentiellement comme une base π de liaison hydrogène. Cette molécule constitue un exemple instructif des différences importantes existant entre les échelles de basicité de liaison hydrogène et de basicité de Brønsted.

Mots clés : liaison hydrogène, arylamines, échelle pK_{HB}, compétition de sites π et N.

Abstract: An IR study, in the region of OH stretching, of a reference hydrogen-bond donor, 4-fluorophenol, hydrogen bonded to primary, secondary, and tertiary arylamines differently substituted on the ring and on the nitrogen, shows the formation of two kinds of 1:1 complexes in CCl_4 solution: an OH···π and an OH···N hydrogen-bonded complex. The IR method gives only access to a global complexation constant K_t. A method is proposed for separating K_t into a K_π component for hydrogen bonding to the π system and a K_N component for hydrogen bonding to the nitrogen atom. This method is validated by comparing the estimated K_π and K_N values to theoretically calculated descriptors of basicity: the nitrogen lone pair orientation towards the aromatic ring, the molecular electrostatic potentials around the nitrogen and the π cloud, and the enthalpy of hydrogen bonding of hydrogen fluoride with the π system of selected arylamines. The main electronic and steric factors governing the competition between π and N sites are analysed. The strongest π and N bases among the arylamines are julolidine and Tröger's base, respectively. Triphenylamine and diphenylamine, which are nitrogen Brønsted bases, become π bases in hydrogen bonding. Moreover, there is no correlation between the pK_{HB} and the pK_{BH^+} scales of basicity of arylamines. The use of the pK_{BH^+} scale is therefore not recommended in hydrogen-bonding studies.

Key words: hydrogen bonding, arylamines, pK_{HB} scale, competition of π and N hydrogen-bonded sites.

Introduction

Les arylamines se comportent comme des bases de Brønsted azotées et non pas carbonées en solution aqueuse. Par exemple, le pK_{BH^+} de l'acide conjugué de l'aniline $PhNH_2$ (4,61) (1) dérive de celui de la méthylamine (10,65) (2) par l'effet électroattracteur et donc réducteur de basicité du phényle, et non de celui de l'hexaméthylbenzène (–14,65) (3). En phase gazeuse l'azote reste généralement le site de protonation, mais le noyau aromatique a été proposé comme site de protonation de certaines anilines (4–7). L'azote est également généralement considéré comme le site de liaison hydrogène (liaison H) des anilines (8–10). Cependant quelques travaux en spectrométrie infrarouge (IR) ont remarqué qu'un phénol en présence d'arylamine montre deux bandes de complexe dans la région de la vibration d'élongation OH (11, 12), qu'ils attribuent aux vibrations ν(OH···π) pour la moins large et la moins déplacée et ν(OH···N) pour la plus large et la plus déplacée. Ces bandes démontrent l'existence de deux types de complexes que nous appellerons π et N (Schéma 1). Cette dualité est générale pour tout accepteur de liaison H comprenant un hétéroatome (N, O, S, P, As, Sb) fixé sur un noyau aromatique (11–14).

Ces travaux anciens (11, 12) n'ont étudié que le déplacement de fréquence OH par liaison H, et seulement pour quelques arylamines simples. Ils n'ont pas effectué d'étude

Reçu le 12 mai 2004. Publié sur le site Web des Presses scientifiques du CNRC à http://revcanchim.cnrc.ca, le 15 novembre 2004.

E. Marquis, J. Graton, M. Berthelot, A. Planchat et C. Laurence[1]. Université de Nantes, Laboratoire de Spectrochimie et Modélisation, Faculté des Sciences et des Techniques, 2, rue de la Houssinière, B.P. 92208, 44322 Nantes CEDEX 3, France.

1. Auteur correspondant (courriel : Christian.Laurence@chimie.univ-nantes.fr).

 doi: 10.1139/V04-128 © 2004 CNRC Canada

Schéma 1.



thermodynamique sur les stabilités respectives des complexes π et N. Lorsque des constantes de complexation ont été déterminées (9), elles ont été attribuées uniquement, et donc de manière erronée, au complexe N.

Dans le cadre de nos travaux sur la construction d'une échelle thermodynamique de basicité de liaison H des bases organiques, notée pK_{HB} et définie par les équations [1]–[3],

[1] base + 4-FC_6H_4OH ⇌ 4-FC_6H_4OH···base

[2] $$\frac{K_c}{\mathrm{dm^3\ mol^{-1}}} = \frac{[\text{4-FC}_6\text{H}_4\text{OH···B}]}{[\text{B}][\text{4-FC}_6\text{H}_4\text{OH}]}$$

[3] $$pK_{HB} = \log_{10} K_c = -\Delta G^\circ_{298}/5{,}7\ \mathrm{kJ\ mol^{-1}}$$

et après avoir déterminé l'échelle pK_{HB} des bases π (15) et des amines aliphatiques primaires (16), secondaires (17) et tertiaires (18), nous rapportons dans ce travail la mesure des constantes de complexation par liaison H du 4-fluorophénol avec des arylamines dans CCl_4 à 25 °C, par spectrométrie IR à transformée de Fourier (IRTF) sur la bande ν(OH) à 3614 cm^{-1} du 4-fluorophénol. Toutes les arylamines forment deux complexes de stœchiométrie 1 : 1 en solution diluée (un excès d'amine empêche la formation de complexes 2 : 1 (2 phénols : 1 amine)) selon les équilibres [4] et [6] de constantes d'équilibre K_π (équation [5]) et K_N (équation [7]). La

[4] ArNRR′ + 4-FC_6H_4OH ⇌ 4-FC_6H_4OH···ArNRR′

[5] K_π = [complexe π]/[ArNRR′][4-FC_6H_4OH]

[6] ArNRR′ + 4-FC_6H_4OH ⇌ 4-FC_6H_4OH···N(Ar)RR′

[7] K_N = [complexe N]/[ArNRR′][4-FC_6H_4OH]

diminution d'absorbance, par ajout d'amine à la solution de 4-FC_6H_4OH, de la bande OH du 4-fluorophénol libre est due à la formation simultanée de complexes π et N. La méthode IRTF ne permet donc de déterminer que la constante apparente K_t (équation [8]) qui est évidemment égale à $K_\pi + K_N$.

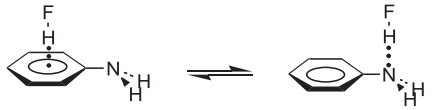
[8] K_t = ([complexe π] + [complexe N])/[ArNRR′][4-FC_6H_4OH]

Si l'arylamine possède *m* noyaux aromatiques équivalents et *n* atomes d'azote équivalents, la correction statistique (19) conduit à l'équation générale [9].

[9] $K_t = mK_\pi + nK_N$

Contrairement aux valeurs pK_{HB} (équation [3]) des bases monofonctionnelles, proportionnelles à une énergie de Gibbs, la quantité log K_t n'a aucune signification thermodynamique. Nous proposons donc d'abord une méthode pour déterminer séparément K_π et K_N. Les valeurs $pK_{HB}(\pi) = \log K_\pi$ et $pK_{HB}(N) = \log K_N$ pourront alors être comparées aux valeurs pK_{HB} des bases monofonctionnelles, bases π (15), amines aliphatiques (16–18) ou toute autre base organique (20).

Puis, pour valider notre méthode et les valeurs K_π et K_N obtenues, nous effectuerons une étude théorique des arylamines et de leurs complexes de liaison H, de trois manières différentes. Premièrement nous comparerons $pK_{HB}(\pi)$ et $pK_{HB}(N)$ aux potentiels électrostatiques à la surface moléculaire autour de l'azote ($V_{S,min}(N)$ (minimum absolu)), et sur le nuage aromatique ($V_S(\pi)$). Ce premier test se justifie par le fait que la liaison H est principalement électrostatique et que des relations satisfaisantes sont observées entre pK_{HB} et $V_{S,min}$ pour les bases monofonctionnelles, à condition de considérer des familles de bases homogènes, par exemple les nitriles (21), les amines aliphatiques (16, 17) ou les pyridines (22). Deuxièmement nous calculerons l'énergie de Gibbs de la réaction [10], c'est-à-dire la proportion de complexes π

[10] 

et N pour le système aniline – fluorure d'hydrogène. Nous avons sélectionné une seule et la plus simple des arylamines, l'aniline, et remplacé le 4-fluorophénol par HF, le plus petit donneur de liaison H, car le calcul des énergies de Gibbs de complexation du 4-fluorophénol sur les sites π et N ne peut actuellement être envisagé à un niveau de calcul satisfaisant pour un si grand nombre de complexes avec des molécules de si grande taille. Une étude récente (23) a montré que HF pouvait constituer un modèle raisonnable du pouvoir donneur de liaison H du 4-fluorophénol. Troisièmement nous calculerons l'enthalpie de complexation de HF sur le site π du benzène et de quelques arylamines (réaction [11]); depuis

[11] HF + C_6H_6 ou ArNRR′ ⇌ FH···π

la plus faible (3-chloroaniline) jusqu'à la plus forte (julolidine) valeur de $pK_{HB}(\pi)$. Nous avons ici choisi de calculer ΔH plutôt que ΔG à cause des calculs imprécis des fréquences de vibration intermoléculaires, et donc de l'entropie de vibration, et du fait de l'existence de relations $\Delta G/\Delta H$ pour de nombreuses familles de complexes de liaison H (24).

Enfin nous mettrons en évidence les principaux facteurs structuraux qui déterminent la sélectivité du site de fixation de liaison H des arylamines. Pour cela nous avons étudié un échantillon de 26 arylamines primaires, secondaires et tertiaires, où peuvent s'exprimer les principaux effets stériques et électroniques (inductif et de résonance) de la chimie organique. Un facteur évident de la compétition des sites π et N est la conjugaison de la paire libre de l'azote avec le(s) noyau(x) aromatique(s) : une augmentation de conjugaison diminue la basicité de l'azote et augmente la basicité π et vice-versa. Cette conjugaison dépend en particulier de l'orientation de la paire libre par rapport au noyau. Nous étudierons avec soin la géométrie des arylamines autour de

© 2004 CNRC Canada

l'azote et essaierons de localiser la paire libre par la méthode NBO (« natural bond orbital ») (25, 26).

Partie expérimentale

Produits

Toutes les amines étudiées sont des composés commerciaux purifiés par les méthodes usuelles puis contrôlés par chromatographie gazeuse sur colonne SE30 ou chromatographie sur couche mince. Les solvants CCl_4 et C_2Cl_4 (pour deux amines qui semblaient réagir avec CCl_4) sont de qualité spectroscopique; ils sont stockés sur tamis moléculaire 4 Å (1 Å = 0,1 nm) avant d'être soutirés. Le 4-fluorophénol est purifié par sublimation. Les produits sont manipulés en boîte sèche pour préparer les solutions et remplir la cellule IR.

Spectres IR

Ils sont enregistrés sur des spectromètres Bruker IFS48 ou Vector22 avec une résolution de 1 cm^{-1}. La cellule en quartz possède un trajet optique de 1 cm. Elle est thermorégulée à 25,0 ± 0,2 °C à l'aide d'un système thermoélectrique à effet Peltier.

Constantes K_t

Elles sont définies par l'équation [12] dans laquelle C_c est la somme $C_\pi + C_N$ des concentrations en complexes π et N; C_a, la concentration du 4-fluorophénol et C_b,

$$[12] \quad K_t = \frac{C_c}{C_a C_b} = \frac{C_a^\circ - C_a}{C_a(C_b^\circ - C_a^\circ + C_a)}$$

la concentration d'amine non complexés (à l'équilibre et en mol dm^{-3}). C_a° et C_b° sont les concentrations initiales déterminées par pesées. C_a° est de l'ordre de 4 mmol dm^{-3} pour éviter l'autoassociation du 4-fluorophénol. C_b° est ajustée de manière à ce que 20 % à 80 % de phénol soit complexé et varie de 0,01 à 0,6 mol dm^{-3} selon la basicité de l'amine. La concentration C_a en phénol non complexé est déterminée à partir de l'absorbance de la bande ν(OH) à 3614 cm^{-1} par la loi de Beer–Lambert. Cinq déterminations de K_t sont effectuées à cinq concentrations différentes d'amine. L'erreur relative sur K_t est estimée à ±8 % (27).

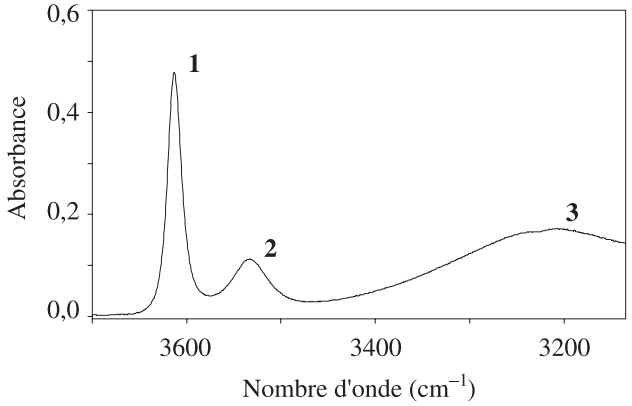
Déplacements de fréquence Δν(OH)

Le déplacement de la fréquence d'élongation ν(OH) du 4-fluorophénol par formation d'un complexe de liaison H sur le site π est défini par la différence [13]. La précision sur Δν(OH···π) est estimée à ±1 cm^{-1} (car la bande ν(OH···π) est peu élargie par rapport à ν(OH)).

$$[13] \quad \Delta\nu(OH\cdots\pi) = \nu(OH, \text{phénol libre}) - \nu(OH\cdots\pi)$$

Pour le complexe OH···N le déplacement ne peut être mesuré facilement, car la bande ν(OH···N) est très large et peut être recouverte par les bandes ν(NH) de l'amine et les bandes ν(CH) du 4-fluorophénol et de l'amine. Ce déplacement ne sera donné qu'à titre indicatif (il est cependant souvent meilleur que ±10 cm^{-1}).

Fig. 1. Spectre IR dans la région ν(OH) d'une solution dans CCl_4 de 4-fluorophénol (4 mmol dm^{-3}) et de *N*,*N*-diméthylaniline (en large excès) montrant (**1**) la bande ν(OH) du 4-fluorophénol libre à 3614 cm^{-1}, (**2**) la bande ν(OH···π) d'un premier complexe 1 : 1, déplacée de 80 cm^{-1} et (**3**) la bande ν(OH···N) d'un second complexe 1 : 1 déplacée de 394 cm^{-1}.



Un spectre IR représentatif de la région ν(OH) des complexes des arylamines avec le 4-fluorophénol est montré sur la figure 1.

Calculs

Ils ont été effectués avec Gaussian 98 (28), le programme NBO (29) et, pour les potentiels électrostatiques, Molden (30), sur des ordinateurs bi-processeurs Xeon 2,2 GHz ou sur les calculateurs du Centre informatique national de l'enseignement supérieur et de l'Institut du développement et des ressources en informatique scientifique. Nous avons sélectionné 13 arylamines (composés **1**, **6–8**, **9–11**, **14**, **16**, **20**, **22**, **25**, **26** du tableau 1) couvrant toute la gamme de basicité π et N pour limiter le coût des calculs.

Géométrie des amines

Elles ont été totalement optimisées au niveau B3LYP/6-31+G(d,p). La conformation trouvée la plus stable par ce niveau de calcul est toujours en accord avec celle, expérimentale, des bases de données MOGADOC (31) pour la phase gazeuse ou CSD (32) pour l'état solide (la comparaison a pu être effectuée pour les composés **1**, **6**, **8**, **11**, **15**, **16**, **20**, **25** et **26** du tableau 1).

Potentiels électrostatiques

Ils sont calculés au niveau B3LYP/6-31+G(d,p)//B3LYP/6-31+G(d,p) sur la surface moléculaire définie, selon Bader et al. (33), par la surface d'isodensité électronique 0,001 e $bohr^{-3}$. Les premiers minima sont trouvés soit autour de l'azote soit au-dessus du nuage π. Ils sont notés $V_S(N)$ et $V_S(\pi)$.

Complexes de liaison H avec HF

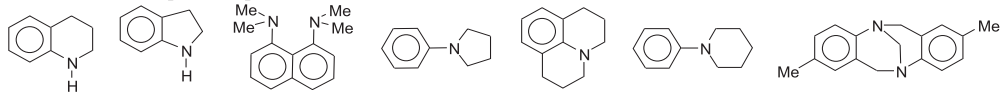
Leur géométrie est optimisée au niveau B3LYP/6-31+G(d,p). Un calcul de fréquences confirme que la géométrie trouvée est un vrai minimum. L'énergie électronique de complexation est calculée au niveau MP2/6-31+G(d,p) par la méthode de la super-molécule (34). Elle doit donc être corrigée de l'erreur de superposition des bases (BSSE) (34).

© 2004 CNRC Canada

Tableau 1. Constantes (dm^3 mol^{-1}) de complexation de liaison H totales (K_t), sur le site π (K_π) et sur le site N (K_N), des arylamines avec le 4-fluorophénol dans CCl_4 (C_2Cl_4) à 25 °C; logarithmes décimaux $pK_{HB}(\pi)$ et $pK_{HB}(N)$; déplacements de la bande ν(OH), $\Delta\nu$(OH···π) et $\Delta\nu$(OH···N) (cm^{-1}); pourcentage de complexe π ($\%C_\pi$); valeurs pK_{BH^+} pour la protonation aqueuse.

				Site π				Site N			
N°	Arylamines	Formule	K_t	$\Delta\nu_{(OH\cdots\pi)}$	K_π	$pK_{HB}(\pi)$	% C_π	$\Delta\nu_{(OH\cdots N)}$	K_N	$pK_{HB}(N)$	pK_{BH^+}
Primaires											
1	3-Chloroaniline	$3\text{-}ClC_6H_4NH_2$	1,71	54	0,37	–0,43	22	327	1,34	0,13	3,52
2	2,4,6-Tri-*tert*-butylaniline	$2,4,6\text{-}t\text{-}Bu_3C_6H_2NH_2$	1,84	bm[a]	—	—	—	373	—	—	
3	3-Fluoroaniline	$3\text{-}FC_6H_4NH_2$	2,01	59	0,42	–0,38	21	326	1,59	0,20	3,59
4	2,6-Diisopropylaniline	$2,6\text{-}i\text{-}Pr_2C_6H_3NH_2$	3,30	92	0,96	–0,02	29	407	2,34	0,37	
5	2,6-Diéthylaniline	$2,6\text{-}Et_2C_6H_3NH_2$	3,41	91	0,94	–0,03	28	393	2,47	0,39	
6	Aniline	$C_6H_5NH_2$	3,46	70	0,55	–0,26	16	361	2,91	0,46	4,61
7	2,6-Diméthylaniline	$2,6\text{-}Me_2C_6H_3NH_2$	3,78	86	0,83	–0,08	22	381	2,95	0,47	3,95
8	4-Toluidine	$4\text{-}MeC_6H_4NH_2$	4,33	77	0,66	–0,18	15	386	3,67	0,56	5,08
Secondaires											
9	Diphénylamine	Ph_2NH	1,09	66	0,50[b]	–0,30[b]	92	nm[c]	0,09	–1,05	0,79
10	4-Chloro-*N*-méthylaniline	$4\text{-}ClC_6H_4NHMe$	1,50	56	0,39	–0,41	26	375	1,11	0,05	3,90
11	*N*-Méthylaniline	C_6H_5NHMe	2,49	79	0,69	–0,16	28	410	1,80	0,26	4,85
12	*N*-Méthyl-4-toluidine	$4\text{-}MeC_6H_4NHMe$	3,47	84	0,79	–0,10	23	425	2,68	0,43	5,36
13	1,2,3,4-Tétrahydroquinoléine	Voir schéma[d]	5,82	85	0,81	–0,09	14	492	5,01	0,70	5,03
14	2,3-Dihydroindole	Voir schéma[d]	6,87	82	0,75	–0,13	11	455	6,12	0,79	
Tertiaires											
15	Triphénylamine	Ph_3N	1,00	67	vt[e]	vt[e]	vt[e]	227	vt[e]	vt[e]	–3,91
16	Éponge à proton	Voir schéma[d]	1,44	72	0,58[b]	–0,24[b]	81	nm[c]	0,28[f]	–0,55	12,10
17	4-Bromo-*N*,*N*-diméthylaniline	$4\text{-}BrC_6H_4NMe_2$	1,85	55	0,38	–0,42	21	374	1,47	0,17	4,23
18	*N*,*N*-Diéthylaniline	$C_6H_5NEt_2$	1,90	84	0,79	–0,10	42	nm[c]	1,11	0,05	6,61
19	*N*-Phénylpyrrolidine	Voir schéma[d]	2,26	86	0,83	–0,08	37	377	1,43	0,16	4,30
20	*N*,*N*-Diméthylaniline	$C_6H_5NMe_2$	3,16	80	0,71	–0,15	22	394	2,45	0,39	5,07
21	*N*,*N*-Diméthyl-3-toluidine	$3\text{-}MeC_6H_4NMe_2$	3,45	89	0,89	–0,05	26	381	2,56	0,41	5,34
22	Julolidine	Voir schéma[d]	3,48	95	1,04	0,02	30	nm[c]	2,44	0,39	
23	*N*-Phénylpipéridine	Voir schéma[d]	5,28	69	0,54	–0,27	10	nm[c]	4,74	0,68	
24	*N*,*N*-Diméthyl-4-toluidine	$4\text{-}MeC_6H_4NMe_2$	5,71	87	0,85	–0,07	15	381	4,86	0,69	5,63
25	*N*,*N*,*N*′,*N*′-Tétraméthylbenzène-1,4-diamine	$4\text{-}Me_2NC_6H_4NMe_2$	27,70	92	0,96	–0,02	3	nm[c]	13,37[f]	1,13	6,05
26	Base de Tröger	Voir schéma[d]	29,07	70	0,55[b]	–0,26[b]	4	nm[c]	13,99[f]	1,15	

[a]Bande ν(OH···π) masquée par $\nu_{as}(NH_2)$.
[b]Pour un seul sextet π.
[c]Non mesurable (voir partie expérimentale).
[d]

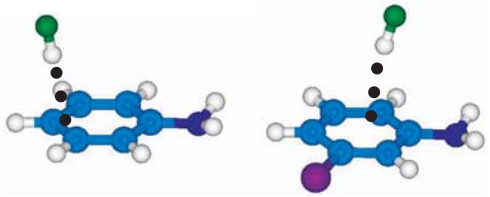


13 **14** **16** **19** **22** **23** **26**

[e]Voir texte.
[f]Pour un seul atome d'azote.

© 2004 CNRC Canada

Fig. 2. Géométries B3LYP/6-31+G(d,p) des complexes π de liaison H du fluorure d'hydrogène avec (*a*) l'aniline et (*b*) la 3-chloroaniline.



(***a***) (***b***)

Nous avons estimé cette correction par la méthode de Xantheas (35).

Pour la fixation de HF sur l'azote, la géométrie de départ choisie correspond à celle du complexe eau–aniline déterminée par spectrométrie micro-ondes (36). Pour la fixation sur le nuage π, nous avons placé HF perpendiculairement au noyau et pointant soit au centre, soit sur chacun des six carbones et nous avons considéré les deux faces du noyau (soit 14 géométries de départ). Pour l'aniline nous aboutissons sur chaque face à trois minima très proches en énergie, au niveau des carbones para et ortho (soit six minima au total). Le minimum absolu est trouvé au niveau du carbone para sur la face ne contenant pas la paire libre (fig. 2*a*). Pour les autres arylamines le minimum absolu est trouvé autour d'un carbone en ortho du groupe amino (fig. 2*b*) sur la même face.

Analyse NBO

Nous avons calculé au niveau MP2/6-31+G(d,p)//B3LYP/6-31+G(d,p), par la théorie de perturbation du second ordre, l'énergie d'interaction $E^{(2)}_{n\rightarrow\pi^*}$ entre la paire libre de l'azote et les orbitales antiliantes π* du cycle aromatique. Cette grandeur mesure la conjugaison de la paire libre de l'azote avec le nuage π du cycle.

De plus la localisation de la paire libre de l'azote permet de connaître son orientation à partir de deux angles θ et φ (fig. 3). L'angle θ (C_{ar}-N*n*) est défini par l'axe de la paire libre (*n*) et la liaison C_{ar}—N, tandis que l'angle de torsion φ (C_{ar}-C_{ar}-N*n*) est défini par l'axe de la paire libre (*n*) et le plan aromatique (C_{ar}-C_{ar}-N). L'orientation idéale pour une conjugaison maximum correspond à θ = 90° et φ = 90°.

Résultats et discussion

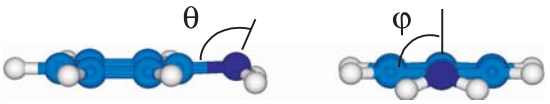
Détermination des constantes K_π et K_N

La détermination de K_π repose sur une relation (équation [14]) que nous avons établie

[14] $$pK_{HB}(\pi) = 1{,}09[\Delta\nu(OH)/100] - 1{,}02$$

dans un travail précédent (15) entre les valeurs pK_{HB} (pour un sextet π) et Δν(OH) de 17 bases π aromatiques (coefficient de corrélation r = 0,978 ; écart type s = 0,02). Cette relation entre l'énergie de Gibbs de complexation (c'est-à-dire pK_{HB} au facteur 2,303*RT* près) et le déplacement de la fréquence ν(OH) naît de la combinaison de la relation de Badger–Bauer (24) entre l'enthalpie de complexation et le déplacement Δν(OH) avec la relation de compensation entre

Fig. 3. Représentation des angles θ et φ mesurant l'orientation de la paire libre de l'azote de l'aniline.



l'enthalpie et l'entropie de complexation (24). Son domaine de validité est limité aux bases π dont le nuage π ne subit pas l'effet stérique de substituants encombrants (15). À partir des valeurs Δν(OH···π) expérimentales reportées dans le tableau 1 et de l'équation [14], on obtient donc K_π. Ces valeurs K_π ainsi que leur logarithme décimal $pK_{HB}(\pi)$ sont rassemblées dans le tableau 1.

La valeur K_N se déduit au moyen de l'équation [9] par différence entre la valeur K_t déterminée expérimentalement et la valeur K_π calculée ci-dessus.

Connaissant K_π (pour un sextet π) et K_N (pour un atome d'azote), on peut calculer les pourcentages de complexes π et N par les équations [15] et [16].

[15] $$\%C_\pi = 100mK_\pi/K_t$$

[16] $$\%C_N = 100 - \%C_\pi$$

Le tableau 1 rassemble (*i*) les valeurs expérimentales K_t, Δν(OH···π) et, à titre indicatif, Δν(OH···N), (*ii*) les valeurs calculées K_π et K_N, et le pourcentage de complexe π ($\%C_\pi$) et (*iii*) pour comparaison, les valeurs pK_{BH^+} de la littérature (1, 37) pour la protonation en phase aqueuse sur l'azote (en général à 25 °C).

Validation des constantes K_π et K_N

Notre méthode de séparation de la valeur expérimentale K_t en valeurs estimées K_π et K_N repose lourdement sur les qualités des déterminations expérimentales de K_t et Δν(OH···π) et de la relation [14] entre pK_{HB} (π) et Δν(OH···π), puisque nous n'avons pas trouvé de méthode pour estimer indépendamment K_N et que nous ne pouvons donc pas vérifier si la somme des valeurs estimées K_π et K_N (relation [9]) est bien égale à K_t.

Il est donc important de confronter les valeurs K_π et K_N estimées dans le paragraphe précédent à des descripteurs théoriques reconnus de la basicité de liaison H. Nous avons donc calculé (*i*) les potentiels électrostatiques autour de l'azote et du nuage π (tableau 2), (*ii*) l'enthalpie de complexation de HF avec le nuage π des arylamines (tableau 2) et (*iii*) l'énergie de Gibbs de l'échange de HF entre les sites π et N de l'aniline (réaction [10]).

Nous trouvons :

1° Une relation [17] satisfaisante entre les valeurs de K_π et le potentiel électrostatique minimum du nuage π, depuis l'arylamine de plus faible valeur K_π (3-chloroaniline **1**) jusqu'à celle de plus forte valeur K_π (julolidine **22**) :

[17] $$pK_{HB}(\pi) = 0{,}97(-V_S(\pi)/100) - 1{,}06$$

$$n = 13\ (\mathbf{1}, \mathbf{6}–\mathbf{11}, \mathbf{14}, \mathbf{16}, \mathbf{20}, \mathbf{22}, \mathbf{25}, \mathbf{26}),$$

$$r^2 = 0{,}885, \qquad s = 0{,}05$$

© 2004 CNRC Canada

Tableau 2. Arylamines : potentiels électrostatiques (kJ mol^{-1}) autour de l'azote ($V_{S,min}$(N)) et du nuage π ($V_S(\pi)$) et enthalpie de complexation (kJ mol^{-1}) de HF sur leur site π (réaction [11]).

N°	Arylamine	$-V_{S,min}(N)^a$	$-V_S(\pi)^a$	$-\Delta H^\circ_{298}$ [11]^b
1	3-Chloroaniline	109,2	63,6	9,9
6	Aniline	130,2	92,2	12,3
7	2,6-Diméthylaniline	126,4	100,4	
8	4-Toluidine	135,7	93,7	13,3
9	Diphénylamine	55,3	79,6	
10	4-Chloro-*N*-méthylaniline	86,7	65,2	
11	*N*-Méthylaniline	108,2	97,2	13,5
14	2,3-Dihydroindole	130,6	95,7	
16	Éponge à proton	49,7	85,7	
20	*N*,*N*-Diméthylaniline	91,1	99,8	
22	Julolidine	99,2	105,5	15,9
25	*N*,*N*,*N*′,*N*′-Tétraméthylbenzène-1,4-diamine	128,4	98,7	
26	Base de Tröger	129,5	84,1	

[a]Calculs au niveau B3LYP/6-31+G(d,p)//B3LYP/6-31+G(d,p).
[b]Calculs au niveau MP2/6-31+G(d,p)// B3LYP/6-31+G(d,p), avec correction de BSSE.

2° De bonnes relations entre les valeurs K_N des arylamines primaires [18], secondaires [19] et tertiaires [20] et le potentiel électrostatique minimum autour de l'azote :

[18] $pK_{HB}(N) = 1{,}63(-V_S(N)/100) - 1{,}63$

$n = 4$ (**1**, **6**–**8**), $r^2 = 0{,}970$, $s = 0{,}04$

[19] $pK_{HB}(N) = 2{,}36(-V_S(N)/100) - 2{,}23$

$n = 4$ (**9**–**11**, **14**), $r^2 = 0{,}956$, $s = 0{,}20$

[20] $pK_{HB}(N) = 2{,}12(-V_S(N)/100) - 1{,}61$

$n = 5$ (**16**, **20**, **22**, **25**, **26**), $r^2 = 0{,}992$, $s = 0{,}07$

La séparation des arylamines en trois sous-familles (primaires, secondaires et tertiaires, fig. 4) est conforme à ce que nous avons déjà observé pour les amines aliphatiques (27).

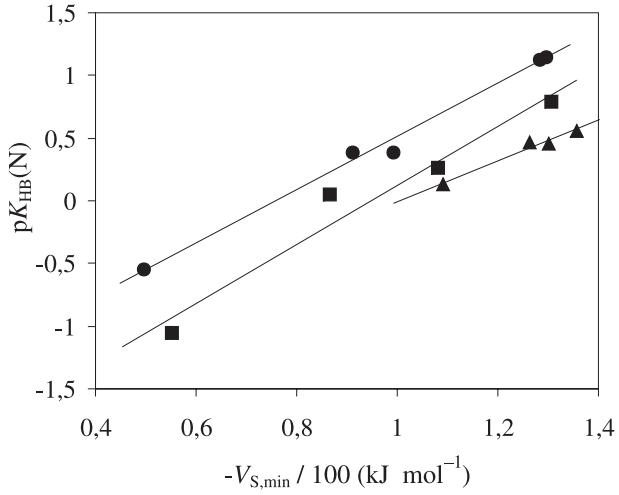
3° Une excellente relation [21] entre les valeurs K_π d'arylamines et l'enthalpie de complexation de HF sur leur site π (la géométrie de ces complexes est illustrée par la fig. 2). À titre de comparaison nous avons calculé l'enthalpie de complexation de HF avec une base π monofonctionnelle, le benzène. Nous trouvons une valeur de –9,5 kJ mol^{-1}. Il est satisfaisant de remarquer (fig. 5) que le benzène, de $pK_{HB}(\pi)$ égal à –0,49 (15), vérifie la relation [21].

[21] $pK_{HB}(\pi) = 0{,}078(-\Delta H^\circ_{298}\ [11]) - 1{,}22$

$n = 6$ (**1**, **6**, **8**, **11**, **22** et C_6H_6), $r^2 = 0{,}998$, $s = 0{,}01$

4° Un pourcentage de complexe π de 6 % (donc 94 % de complexe N) pour la liaison H de l'aniline avec HF. Ce pourcentage est obtenu à partir des paramètres thermodynamiques calculés au niveau MP2/6-31+G(d,p)//B3LYP/6-31+G(d,p) (avec correction de BSSE) pour la réaction d'isomérie de complexation [10], c'est-à-dire d'échange de HF entre les sites π et N de l'aniline :

Fig. 4. Relations entre le logarithme décimal des valeurs estimées K_N, $pK_{HB}(N)$, et le potentiel électrostatique minimum sur la surface moléculaire autour de l'azote ($V_{S,min}$(N)) pour des arylamines primaires (▲), secondaires (■) et tertiaires (●).



ΔH°_{298} [10] = –15,83 kJ mol^{-1}

ΔS°_{298} [10] = –29,8 J K^{-1} mol^{-1}

ΔG°_{298} [10] = –6,96 kJ mol^{-1}

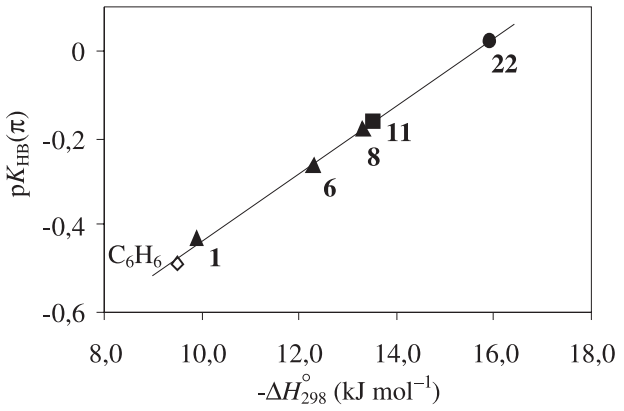
K [10] = 16,3

Cette constante d'équilibre est égale à K_N/K_π, c'est-à-dire C_N/C_π. Le calcul de ΔS°_{298} [10] tient compte d'un facteur statistique R ln 6 correspondant aux six complexes π d'énergies très proches (vide supra).

Ce pourcentage de complexe π est en accord qualitatif satisfaisant avec la valeur de 16 % (K = 5,3) trouvée pour le complexe π de l'aniline avec le 4-fluorophénol. Il n'y a en effet aucun espoir de calculer avec précision les paramètres thermodynamiques, et en particulier l'entropie, de la réac-

© 2004 CNRC Canada

Fig. 5. Relation entre le logarithme décimal des valeurs estimées K_π, $pK_{HB}(\pi)$, et l'enthalpie de complexation de HF sur le site π d'arylamines primaires (▲), secondaire (■) et tertiaire (●), et du benzène (◇). Pour ce dernier la valeur K_π est une valeur expérimentale (15).



tion [10] (même si certaines erreurs de calcul peuvent se compenser dans cette réaction d'échange), ni aucune raison pour que les liaisons H avec l'aniline de HF in vacuo et du 4-fluorophénol en solution dans CCl_4 conduisent au même rapport de complexes π et N. Les calculs théoriques indiquent seulement, en accord avec les observations expérimentales, que si l'aniline accepte la liaison H majoritairement sur l'azote, le site π ne peut cependant pas être négligé.

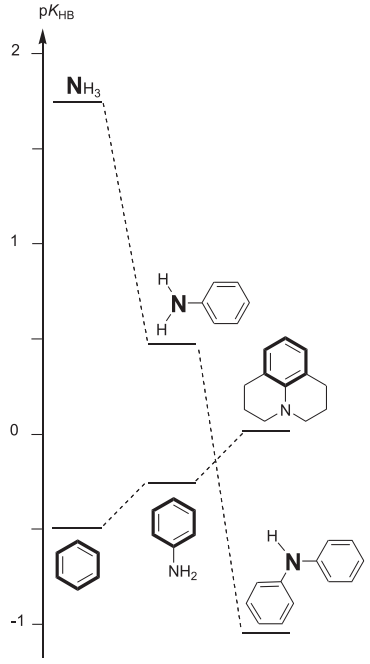
Effets structuraux sur la compétition des sites π et N

Le chef de file des arylamines, l'aniline, est, en liaison H, une base π plus forte que le benzène ($pK_{HB}(\pi)$ = –0,26 et –0,49 respectivement) et une base azotée beaucoup plus faible que l'ammoniac ($pK_{HB}(N)$ = 0,46 et 1,74). Ces variations de basicité proviennent principalement de l'effet de résonance électrodonneur du groupe NH_2, pour la basicité π, et, pour la basicité N, des effets inductif et de résonance électroattracteurs du groupe C_6H_5. L'optimisation de ces effets, ainsi que l'introduction d'autres effets structuraux, peut conduire à des liaisons H plus fortes sur le site π que sur le site N dans certaines arylamines. Ainsi le nuage π de la julolidine ($pK_{HB}(\pi)$ = 0,02) est un meilleur accepteur de liaison H que l'atome d'azote de la diphénylamine ($pK_{HB}(N)$ = –1,05), par plus d'une unité de p*K*, c'est-à-dire plus de 6 kJ mol^{-1} en énergie de Gibbs. La figure 6 illustre ces effets sur l'échelle pK_{HB} de liaison H.

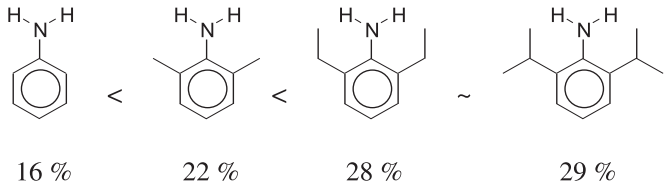
Dans une même molécule, il est ainsi possible de beaucoup moduler la basicité relative de liaison H des sites π et N, puisque la proportion de complexe π de l'aniline, qui est de 16 % vis-à-vis du 4-fluorophénol, peut monter à 92 % pour la diphénylamine (et probablement plus pour la triphénylamine) et descendre à 3 % ou 4 % pour la base de Tröger et la diamine 4-$Me_2NC_6H_4NMe_2$.

Certains effets structuraux influencent les basicités π et N dans le même sens et n'ont donc pas un effet décisif sur la compétition des sites π et N. C'est le cas de l'effet inductif électroattracteur des halogènes 3-F, 3-Cl, 4-Cl, 4-Br qui diminuent à la fois les basicités π et N. Ainsi $\%C_\pi$ de la 4-bromo-*N*,*N*-diméthylaniline (21 %) est pratiquement le même que celui de la *N*,*N*-diméthylaniline (22 %). De même

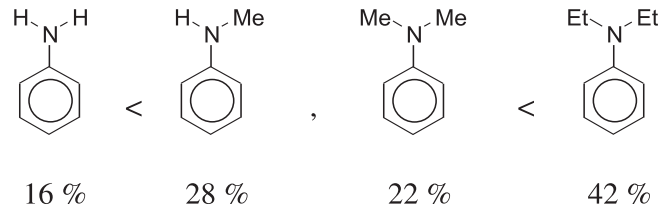
Fig. 6. Variations du pouvoir accepteur de liaison H des sites π du benzène, de l'aniline et de la julolidine et des sites N de l'ammoniac, de l'aniline et de la diphénylamine sur l'échelle pK_{HB}. La valeur pK_{HB} = 1,74 de l'ammoniac provient de la référence 27.



une alkylation du noyau aromatique augmente à la fois les basicités π et N et la 4-toluidine a un $\%C_\pi$ (15 %) très voisin de celui de l'aniline (16 %). Cependant une dialkylation en ortho de l'azote diminue la basicité de l'azote par effets stériques tout en augmentant la basicité π par effets électroniques, et on observe la séquence suivante de $\%C_\pi$:

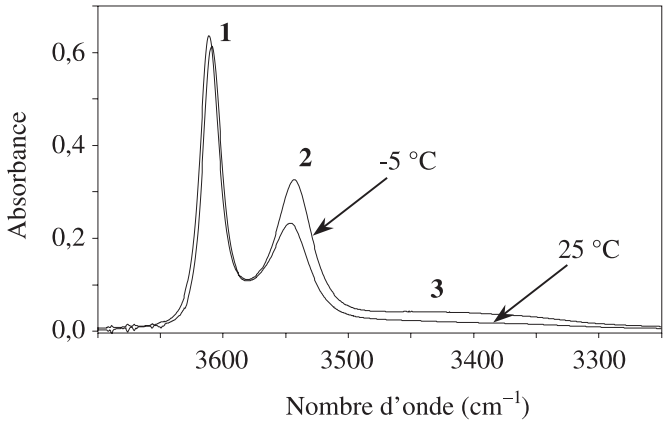


L'alkylation de l'azote entraîne des effets stériques et électroniques complexes qui peuvent se contrarier. La séquence ci-dessous n'est donc pas régulière, bien qu'une alkylation croissante augmente généralement $\%C_\pi$. Les effets stériques d'encombrement de l'azote ont un effet spectaculaire dans l'éponge à proton qui devient très majoritairement (81 %) une base π de liaison H.



© 2004 CNRC Canada

Fig. 7. Spectres IR dans la région ν(OH) d'une solution de 4-fluorophénol (4 mmol dm^{-3}) et de triphénylamine (0,45 mol dm^{-3}) dans C_2Cl_4 à –5 et 25 °C montrant (**1**) la bande ν(OH) de 4-fluorophénol libre à 3614 cm^{-1}, (**2**) la bande ν(OH···π) d'un premier complexe 1 : 1 déplacée de 67 cm^{-1} et (**3**) la bande ν(OH···N) d'un second complexe 1 : 1 déplacée de 227 cm^{-1}.



La phénylation de l'azote augmente considérablement $\%C_\pi$ comme le montre le passage de l'aniline (16 %) à la diphénylamine (92 %). Le facteur statistique (deux phényles) s'ajoute ici aux autres effets structuraux. Nous n'avons pu calculer ce pourcentage de complexe π pour la triphénylamine, car cette molécule n'obéit pas à la relation [14]. En effet en multipliant par trois (trois phényles) la valeur de K_π calculée par [14] on aboutit à une valeur sensiblement supérieure à K_t, ce qui est impossible. Nous avons déjà observé (15) la même anomalie avec le triphénylméthane. Elle résulte probablement d'une non-équivalence des trois sites π et (ou) d'effets stériques qui sont bien connus (15) être un facteur limitant la validité de la relation [14]. La question se pose cependant de l'existence de complexes N pour la triphénylamine. Nous avons vérifié expérimentalement que la constante K_N de complexation sur l'azote n'est pas complètement nulle. Avec une solution concentrée en triphénylamine (0,5 mol dm^{-3}) et en diminuant la température jusqu'à –5 °C pour déplacer les équilibres vers la formation des complexes, nous voyons en effet apparaître (fig. 7) une très faible bande vers 3387 cm^{-1} que nous attribuons au complexe sur l'azote ($\Delta\nu$(OH···N) = 227 cm^{-1}).

La conjugaison de la paire libre de l'azote avec le système π du cycle aromatique constitue un facteur décisif dans la compétition entre sites π et N des arylamines, puisqu'elle fait varier les basicités π et N dans des sens opposés; la délocalisation de la paire libre vers le système π augmente la densité électronique π (38) (donc la basicité π) et diminue la densité électronique de l'azote (38) (donc la basicité N). Plus la conjugaison $n \rightarrow \pi^*$ est importante plus l'azote devient trigonal. Il est donc possible de mesurer cette conjugaison par (*i*) l'angle dièdre τ entre le plan NH_2 et le plan C_6H_5N (schéma 2) ou (*ii*) la somme Σα des angles autour de l'azote (schéma 3). Pour un azote tétraédrique τ = 54,7° et Σα = 328,4° et pour un azote trigonal τ = 0° et Σα = 360°. Il est aussi possible de localiser la paire libre de l'azote par la méthode NBO (25, 26) et de définir l'orientation de l'axe de cette paire par rapport au noyau aromatique par les angles θ et φ définis dans la figure 3. La conjugaison $n \rightarrow \pi^*$ est

Schéma 2.

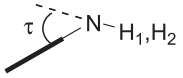


Schéma 3.

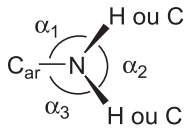
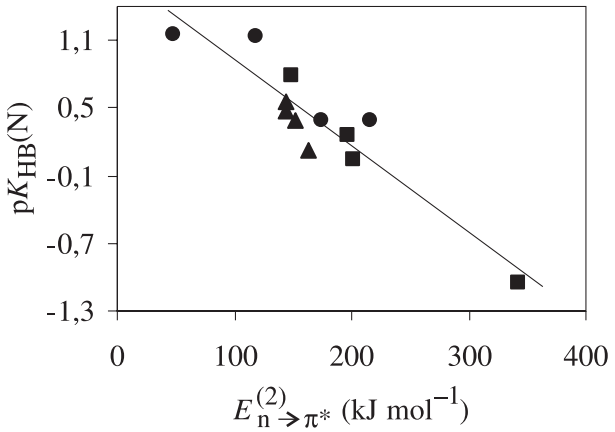


Fig. 8. Relation entre le pouvoir accepteur de liaison H de l'azote d'arylamines primaires (▲), secondaires (■) et tertiaires (●), mesuré par pK_{HB}(N), et l'énergie d'interaction $E^{(2)}_{n\rightarrow\pi^*}$: l'azote est d'autant plus basique que sa paire libre est moins conjuguée.



maximale quand θ et φ sont tous les deux égaux à 90°. La conjugaison augmente également comme l'énergie d'interaction calculée au second ordre ($E^{(2)}_{n\rightarrow\pi^*}$) entre l'orbitale (*n*) de la paire libre de l'azote et les orbitales π* du cycle aromatique. Nous avons calculé la géométrie B3LYP/6-31+G(d,p) de 13 amines et effectué leur analyse NBO au niveau MP2/6-31+G(d,p)//B3LYP/6-31+G(d,p). Les valeurs des angles τ, θ, φ et Σα, et de l'énergie ($E^{(2)}_{n\rightarrow\pi^*}$) sont reportées dans le tableau 3.

Ces valeurs permettent de montrer que la conjugaison $n \rightarrow \pi^*$ constitue un facteur significatif de la basicité π. L'énergie d'interaction $E^{(2)}_{n\rightarrow\pi^*}$ explique 41 % de la variance de $pK_{HB}(\pi)$ (r = +0,642, corrélation positive) pour neuf arylamines. Les amines chlorées **1** et **10** et celles ayant sur le noyau deux méthyles (**7**) ou deux méthylènes résidus de cycles (**22**) sont écartées de la corrélation, car leurs effets électroniques propres modifient fortement $pK_{HB}(\pi)$ et diluent l'effet de conjugaison de l'azote.

La conjugaison $n \rightarrow \pi^*$ est surtout déterminante pour la basicité N. L'énergie d'interaction $E^{(2)}_{n\rightarrow\pi^*}$ explique 86 % de la variance de pK_{HB}(N) (r = –0,930, corrélation négative) pour 12 arylamines (l'éponge à proton est écartée à cause des effets stériques) (fig. 8). Ainsi l'atome d'azote de la base de Tröger constitue-t-il le meilleur accepteur de liaison H, car la cyclisation contraint la paire libre à une orientation très défavorable à la conjugaison (θ = 108°, φ = 41°); les angles τ = 49,6° et Σα = 332,7° montrent également qu'il se rapproche de l'azote tétraédrique des amines aliphatiques.

© 2004 CNRC Canada

Tableau 3. Paramètres géométriques (τ, θ, φ et Σα, (°)), et énergétique ($E^{(2)}_{n\rightarrow\pi^*}$, kJ mol^{-1}) pouvant décrire la conjugaison de la paire libre de l'azote avec le noyau aromatique dans les arylamines.

N°	Arylamine	τ	θ	φ	Σα	$E^{(2)}_{n\rightarrow\pi^*}$
1	3-Chloroaniline	37,0	105	89	345,2	163,2
6	Aniline	38,7	106	89	343,9	152,3
7	2,6-Diméthylaniline	38,5	106	88	343,9	144,3
8	4-Toluidine	40,0	106	89	342,6	143,9
9	Diphénylamine	0	90	64	360,0	171,5[a]
10	4-Chloro-*N*-méthylaniline	26,8	100	84	352,4	201,7
11	*N*-Méthylaniline	27,6	101	86	351,9	196,2
14	2,3-Dihydroindole	44,4	107	83	340,3	149,0
16	Éponge à proton	36,5	104	49	345,3	90,0
20	*N*,*N*-Diméthylaniline	20,9	98	90	355,5	215,5
22	Julolidine[b]	27,5	100	89	351,9	174,1
25	*N*,*N*,*N*′,*N*′-Tétraméthylbenzène-1,4-diamine[b]	35,7	103	60	346,1	118,8[c]
26	Base de Tröger	49,6	108	41	332,7	48,5

[a]À multiplier par 2 pour la corrélation avec pK_{HB}(N).
[b]Conformère le plus stable.
[c]À multiplier par 2 pour la corrélation avec pK_{HB} (π).

La cyclisation et la benzofusion contraignent également la paire libre de l'azote du 2,3-dihydroindole à une mauvaise orientation pour sa conjugaison (θ = 107°, φ = 83°), ce qui en fait l'azote secondaire le plus basique. Au contraire, la double cyclisation de la julolidine oriente favorablement la paire libre pour une conjugaison (θ = 100°, φ = 89°), ce qui rend l'azote peu basique (au contraire la julolidine est la meilleure base π par synergie de cette conjugaison et de l'effet donneur des deux méthylènes résidus de cycle).

Il est enfin intéressant de remarquer que chaque azote de la diamine 4-$Me_2NC_6H_4NMe_2$ est beaucoup plus tétraédrique (τ = 35,7°) que celui de la monoamine correspondante $C_6H_5NMe_2$ (τ = 20,9°), et que les paires libres de 4-$Me_2NC_6H_4NMe_2$ sont beaucoup moins bien orientées pour la conjugaison (θ = 103°, φ = 60°) que celles de $C_6H_5NMe_2$ (θ = 98°, φ = 90°). Il s'agit de la manifestation géométrique de l'effet de saturation de résonance observée sur les pK_{BH^+} des anilines substituées par un donneur π en para (39). Les effets que chaque groupe NMe_2 exerce sur l'autre dans 4-$Me_2NC_6H_4NMe_2$ conduisent à un azote pratiquement aussi bon accepteur de liaison H (pK_{HB}(N) = 1,13) que chaque azote de la base de Tröger (pK_{HB}(N) = 1,15).

Comparaison des échelles pK_{HB}(N) et pK_{BH^+}

Même pour des composés structuralement voisins comme les arylamines, nous n'observons pas de corrélation utile (n = 19, r^2 = 0,004, r^2 = 0,606 en excluant l'éponge à proton) entre les valeurs pK_{BH^+} et pK_{HB}(N) des amines pour lesquelles à la fois pK_{BH^+} et pK_{HB}(N) ont pu être déterminés. Nous avions déjà noté cette absence de corrélation pour les amines aliphatiques secondaires (17) et tertiaires (18).

Nous notons également dans ce travail des différences importantes entre sites de protonation et sites de liaison H : la liaison H se forme majoritairement sur le(s) nuage(s) π de l'éponge à proton, de la diphénylamine et de la triphénylamine, alors que ces composés sont des bases de Brønsted azotées. Ils rejoignent la tribenzylamine (18) et la 2,6-di-*tert*-butylpyridine (40) comme exemples supplémentaires de bases azotées aromatiques qui se protonent sur l'azote mais acceptent majoritairement la liaison H sur les électrons π.

L'usage de l'échelle pK_{BH^+} pour prévoir la basicité de liaison H doit donc cesser. C'est l'échelle pK_{HB} qui est l'échelle de choix pour étudier le comportement accepteur de liaison H des bases organiques.

Remerciements

Les auteurs remercient le Professeur Frank Weinhold (Université du Wisconsin, Madison) pour son aide dans l'analyse NBO et l'Institut du développement et des ressources en informatique scientifique (IDRIS, Orsay, France) et le Centre informatique national de l'enseignement supérieur (CINES, Montpellier France) pour l'attribution d'heures de calculs.

Bibliographie

1. D.D. Perrin. Dissociation constants of organic bases in aqueous solution. (Pure and applied chemistry). Butterworths, Londres, R.-U. 1965; Supplément 1972.
2. F.M. Jones, III et E.M. Arnett. Prog. Phys. Org. Chem. **11**, 263 (1974).
3. A. Bagno, G. Scorrano, R.A. More O'Ferrall. Rev. Chem. Intermed. **7**, 313 (1987).
4. S.K. Pollack, J.L. Devlin, III, K.D. Summerhays, R.W. Taft et W.J. Hehre. J. Am. Chem. Soc. **99**, 4583 (1977).
5. K.D. Summerhays, S.K. Pollack, R.W. Taft et W.J. Hehre. J. Am. Chem. Soc. **99**, 4585 (1977).
6. Y.K. Lau, K. Nishizawa, A. Tse, R.S. Brown et P. Kebarle. J. Am. Chem. Soc. **103**, 6291 (1981).
7. S.G. Lias, J.A.A. Jackson, H. Argentar et J.F. Liebman. J. Org. Chem. **50**, 333 (1985).
8. T. Zeegers-Huyskens et T. Zeegers-Huyskens. Spectrochim. Acta, Part A, **23**, 855 (1967).
9. G. Lichtfus, F. Lemaire et T. Zeegers-Huyskens. Spectrochim. Acta, Part A, **28**, 2069 (1972).
10. G. Lichtfus et T. Zeegers-Huyskens. Spectrochim. Acta, Part A, **28**, 2081 (1972).
11. E. Osawa, T. Kato et Z. Yoshida. J. Org. Chem. **32**, 2803 (1967).
12. M. Berthelot, C. Laurence et B. Wojtkowiak. J. Mol. Struct. **18**, 435 (1973).

© 2004 CNRC Canada

13. B.B. Wayland et R.S. Drago. J. Am. Chem. Soc. **86**, 5240 (1964).
14. G. Broekmans et T. Zeegers-Huyskens. Spectrosc. Lett. **15**, 515 (1982).
15. F. Besseau, C. Laurence et M. Berthelot. Bull. Soc. Chim. Fr. **133**, 381 (1996).
16. J. Graton, C. Laurence, M. Berthelot, J.-Y. Le Questel, F. Besseau et E.D. Raczynska. J. Chem. Soc. Perkin Trans. 2, 997 (1999).
17. J. Graton, M. Berthelot et C. Laurence. J. Chem. Soc. Perkin Trans. 2, 2130 (2001).
18. J. Graton, F. Besseau, M. Berthelot, E.D. Raczynska et C. Laurence. Can. J. Chem. **80**, 1375 (2002).
19. J. Hine. Structural effects on equilibria in organic chemistry. Wiley, New York. 1975.
20. C. Laurence et M. Berthelot. Perspect. Drug Discovery Des. **18**, 39 (2000).
21. J.-Y. Le Questel, M. Berthelot et C. Laurence. J. Phys. Org. Chem. **13**, 347 (2000).
22. J. Graton, M. Berthelot, J.F. Gal, C. Laurence, J. Lebreton, J.Y. Le Questel, P.C. Maria et R. Robins. J. Org. Chem. **68**, 8208 (2003).
23. O. Lamarche et J.A. Platts. Chem. Eur. J. **8**, 457 (2002).
24. M.D. Joesten et L.J. Schaad. Hydrogen bonding. Dekker, New York. 1974.
25. A.E. Reed, R.B. Weinstock et F. Weinhold. J. Chem. Phys. **83**, 735 (1985).
26. A.E. Reed, L.A. Curtiss et F. Weinhold. Chem. Rev. **88**, 899 (1988).
27. J. Graton. Thèse de doctorat, Université de Nantes, Nantes, France, 2001.
28. M.J. Frisch, G.W. Trucks, H.B. Schlegel, G.E. Scuseria, M.A. Robb, J.R. Cheeseman, V.G. Zakrzewski, J.A.J. Montgomery, R.E. Stratmann, J.C. Burant, S. Dapprich, J.M. Millam, A.D. Daniels, K.N. Kudin, M.C. Strain, O. Farkas, J. Tomasi, V. Barone, M. Cossi, R. Cammi, B. Menucci, C. Pomelli, C. Adamo, S. Clifford, J. Ochterski, G.A. Petersson, P.Y. Ayala, Q. Cui, K. Morokuma, D.K. Malick, A.D. Rabuck, K. Raghavachari, J.B. Foresman, J. Cioslowski, J.V. Ortiz, A.G. Baboul, G. Liu, A. Liashenko, P. Piskorz, I. Komaromi, R. Gomperts, R.L. Martin, D.J. Fox, T. Keith, M.A. Al-Laham, C.Y. Peng, A. Nanayakkara, M. Challacombe, P.M.W. Gill, B. Johnson, W. Chen, M.W. Wong, J.L. Andres, C. Gonzalez, M. Head-Gordon, E.S. Replogle et J.A. Pople. Gaussian 98. Revision A,9 [programme d'ordinateur]. Gaussian, Inc., Pittsburgh Penn. 1998.
29. E.D. Glendening, A.E. Reed, J.E. Carpenter et F. Weinhold. NBO. Version 3.1 [programme d'ordinateur]. Theoretical Chemistry Institute, University of Wisconsin, Madison.
30. G. Schaftenaar et J.H. Noordik. J. Comput. Aided Mol. Des. **14**, 123 (2000).
31. J. Vogt, B. Mez-Starck, N. Vogt et W. Hutter. J. Mol. Struct. **485–486**, 249 (1999).
32. F.H. Allen, J.E. Davies, J.J. Galloy, O. Johnson, O. Kennard, C.F. Macrae, E.M. Mitchell, G.F. Mitchell, J.M. Smith et D.G. Watson. J. Chem. Inf. Comput. Sci. **31**, 187 (1991).
33. R.F.W. Bader, M.T. Carroll, J.R. Cheeseman et C. Chang. J. Am. Chem. Soc. **109**, 7968 (1987).
34. S. Scheiner. Hydrogen bonding: A theoretical perspective. Oxford University Press, New York. 1997.
35. S.S. Xantheas. J. Chem. Phys. **104**, 8821 (1996).
36. U. Spoerel et W. Stahl. J. Mol. Spectrosc. **190**, 278 (1998).
37. A.J. Hoefnagel, M.A. Hoefnagel et B.M. Wepster. J. Org. Chem. **46**, 4209 (1981).
38. P.M. Wojciechowski, W. Zierkiewicz, D. Michalska et P. Hobza. J. Chem. Phys. **118**, 10 900 (2003).
39. A.J. Hoefnagel, M.A. Hoefnagel et B.M. Wepster. J. Am. Chem. Soc. **98**, 6194 (1976).
40. A. Chardin, C. Laurence et M. Berthelot. J. Chem. Res. Synop. 332 (1996).

© 2004 CNRC Canada

Tetraphosphinitoresorcinarene complexes — A new structural form of a rhodium(I) diphosphine complex[1]

Dana J. Eisler and Richard J. Puddephatt

Abstract: Tetrakis(diphenylphosphinito)resorcinarene ligands are shown to react with $[Rh_2(\mu\text{-}Cl)_2(CO)_4]$ to give tetrarhodium(I) complexes in which there are two dirhodium units, each having the unprecedented structure *syn*-$[Rh_2(\mu\text{-}Cl)_2(CO)_2P_2]$, P = phosphinite donor.

Key words: rhodium, resorcinarene, tetraphosphinite, carbonyl.

Résumé : On démontre que les ligands tétrakis(diphénylphosphinito)résorciranène réagissent avec le $[Rh_2(\mu\text{-}Cl)_2(CO)_4]$ pour conduire à la formation de complexes tétrarhodium(I) dans lesquels on retrouve deux unités dirhodiium de structure *syn*-$[Rh_2(\mu\text{-}Cl)_2(CO)_2P_2]$ inconnue jusqu'à maintenant et dans lesquelles P = donneur phosphinite.

Mots clés : rhodium, résorcinarène, tétraphosphinite, carbonyle.

[Traduit par la Rédaction]

Introduction

Rhodium complexes with phosphorus-donor ligands often display useful catalytic activity and so there has been intense interest in the synthesis and chemistry of such compounds. Some examples of chloro carbonyl complexes of rhodium(I) with phosphine ligands are illustrated in Chart 1 (1–4). For monodentate phosphine ligands, structures **A** and **B** are observed when the rhodium to phosphine ligand stoichiometry is 1:1, while the mononuclear structure **C** is formed when this ratio is 1:2 (1). In the case of diphosphine ligands, the chelate structure (**D**) and, more commonly, the bridged structure (**E**) have been observed when Rh:PP = 1:1 (2).

There is also much current interest in the development of ligands derived from calixarenes or resorcinarenes, which are bowl-shaped macrocyclic molecules that have a rich host–guest chemistry (4, 5). If the host–guest chemistry can be introduced adjacent to a catalytically active metal, it may be possible to discover size- and shape-selective catalysis. In this context, there have been several studies of rhodium complexes of calixarene based phosphorus-donor ligands, but there are no reports of similar complexes of resorcinarenes (4, 5). This article reports the first such rhodium(I) complexes, derived from the recently reported tetraphosphinitoresorcinarene ligands (6), and shows that they contain the structural type **F** (Chart 1), which is unprecedented for a diphosphine ligand (2).

Received 9 March 2004. Published on the NRC Research Press Web site at http://canjchem.nrc.ca on 21 October 2004.

This article is dedicated to the memory of Don E. Irish for his distinguished contributions to chemistry in Canada, especially using Raman spectroscopy.

D.J. Eisler and R.J. Puddephatt.[2] Department of Chemistry, University of Western Ontario, London, ON N6A 5B7, Canada.

[1]This article is part of a Special Issue dedicated to the memory of Professor Don Irish.

[2]Corresponding author (e-mail: pudd@uwo.ca).

Results and discussion

Synthesis of the complexes

The new chemistry is shown in Scheme 1. The tetrakis (diphenylphosphinito)resorcinarene compounds, **1**–**3**, tend to adopt a boat conformation and, if the phosphinite groups are in the equatorial positions, the compounds can act as bis(diphosphinite) ligands, with well-separated pairs of phosphorus donors (6).

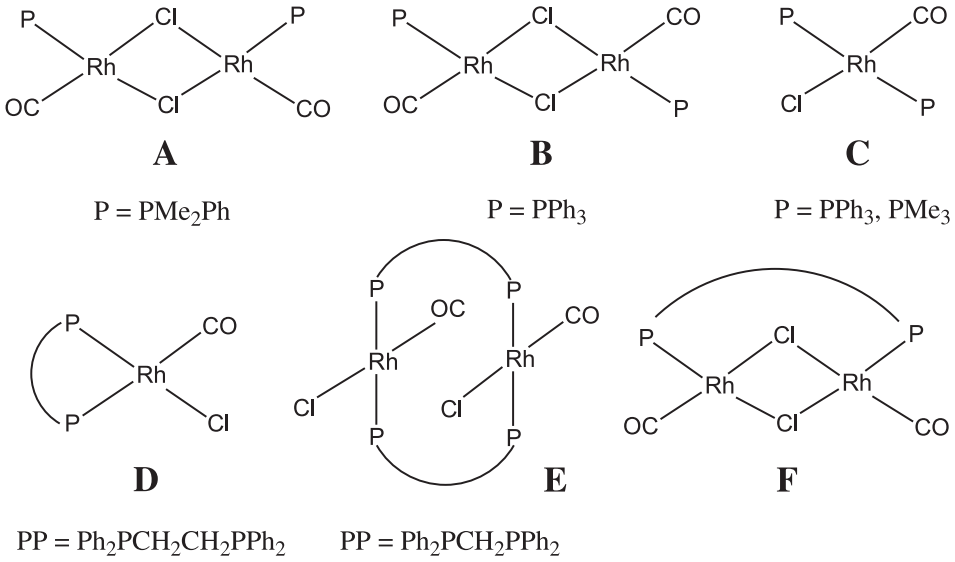
Reaction of the tetrakis(diphenylphosphinito)resorcinarene compounds **1**–**3** with 2 equiv. of $[Rh_2(\mu\text{-}Cl)_2(CO)_4]$ gave the tetrarhodium(I) complexes **4**–**6**, as outlined in Scheme 1, in high yield. In these complexes, the ratio Rh:P = 1:1. Attempts to prepare complexes with ratio Rh:P = 1:2, as found in the known diphosphine complexes **D** and **E** (Chart 1), were unsuccessful. The complexes **4**–**6** were isolated as yellow solids, which were characterized spectroscopically and, in the case of complex **4**, by an X-ray structure determination.

Structural characterization of complex 4

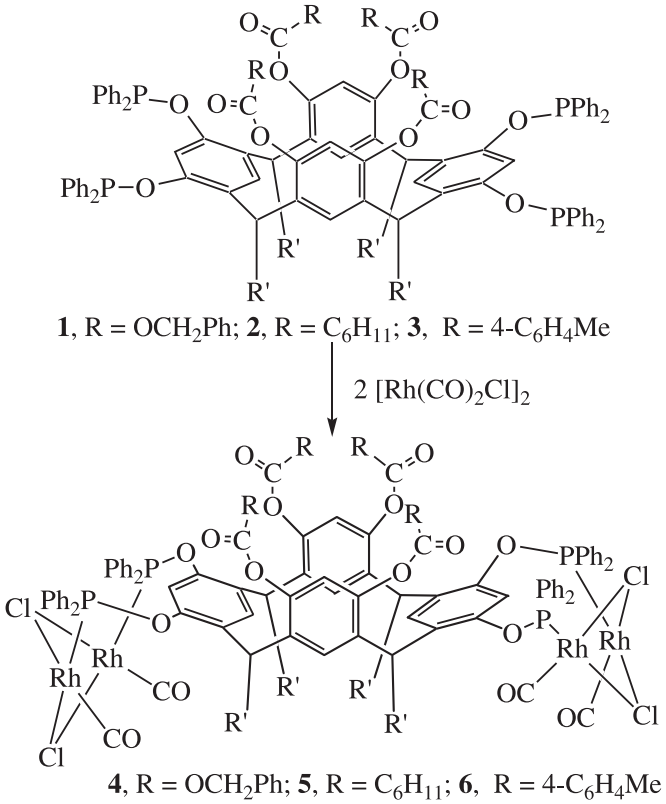
The structure of complex **4** was determined crystallographically and is illustrated in Fig. 1, with selected bond distances and angles listed in Table 1. The resorcinarene skeleton of **4** adopts a boat conformation, with the phosphinite-derivatized arene rings in the flattened position and the acylated arene rings in the upright position. The angle between the planes made by the upright arene rings is 28° while the angle between the planes of the flattened arene rings is 154°. The resorcinarene skeleton is considerably twisted, as seen by the dihedral angles between opposing arene rings (upright 23°, flattened 22°).

 doi: 10.1139/V04-099 © 2004 NRC Canada

Chart 1.



Scheme 1.



Each phosphorus donor (P) of the tetraphosphinito-resorcinarene ligand is involved in forming a *syn*-[$Rh_2(\mu\text{-}Cl)_2(CO)_2P_2$] unit. The type of dinuclear rhodium(I) unit present in **4** has been observed previously with monodentate phosphine ligands such as PMe_2Ph (**A**, Chart 1) and even for a monodentate calixarene-based phosphite ligand (4*b*). However, for diphosphine ligands, only chelate structures (**D**, Chart 1) or bridged structures (**E**, Chart 1), each with ratio Rh:P = 1:2, have been observed (2). No other diphosphine complex containing the binuclear $Rh_2(CO)_2(\mu\text{-}Cl)_2$ unit (**F**, Chart 1) has been structurally characterized, though a similar structure has been considered for a 1,4-bis(diphenylphosphino)butane derivative, based only on analytical data (2*c*). The unusual architecture of the resorcinarene ligands **1**–**3** is evidently suited for the selective formation of structure **F**. In particular, the P.P separations P1···P2 = 5.46 Å and P3···P4 = 5.44 Å are ideal for spanning the $Rh_2(\mu\text{-}Cl)_2$ unit, while the phosphorus donors are too far apart to chelate to a single rhodium atom as in **D** (Chart 1). Steric effects prevent formation of structure **E**. There is potential to form dirhodium complexes with similar structures by using simpler ligands of the type 1,3-$C_6H_4(CH_2PR_2)_2$.

The rhodium(I) centers have the usual square-planar stereochemistry in each case, and the angles between the planes of the adjacent $PRh(CO)Cl_2$ units (the fold angles) are 117° for each of the two [$Rh_2(CO)_2(\mu\text{-}Cl)_2P_2$] groups. The Rh—Cl bonds that are trans to the CO are all significantly shorter (2.377(1)–2.386(1) Å) than the Rh—Cl bonds trans to the phosphorus atoms (2.421(2)–2.424(1) Å).

For each molecule **4** there are 6.5 molecules of CH_2Cl_2 in the lattice. Most of these are in the voids between molecules, but two solvates can be considered as guest molecules, as illustrated in Fig. 2. One is in the cavity of the bowl structure, sandwiched between the benzylcarbonate groups, while the second is in the cavity beneath the bowl sandwiched between the phenethyl groups. This second dichloromethane solvate is loosely attached to one of the rhodium atoms, with the associated distance Rh(4)···Cl(1Q) = 3.90 Å.

Spectroscopic characterization and reactivity studies of the complexes

The ^1H and ^{31}P NMR spectra of complexes **4**–**6** were, in each case, consistent with the presence of a single species with effective C_{2v} symmetry. For example, in the ^1H NMR spectra, only single resonances were observed for the bridging methine protons and for the arene protons of the macrocyclic skeleton. The ^{31}P NMR spectra of the complexes each contained a single resonance, which appeared as a 1:1 doublet because of the coupling $^1J(^{103}Rh^{31}P)$, indicating equivalence of all four phosphorus atoms. For example,

© 2004 NRC Canada

Fig. 1. A view of the structure of complex **4**. The phenyl substituents on phosphorus are omitted for clarity.

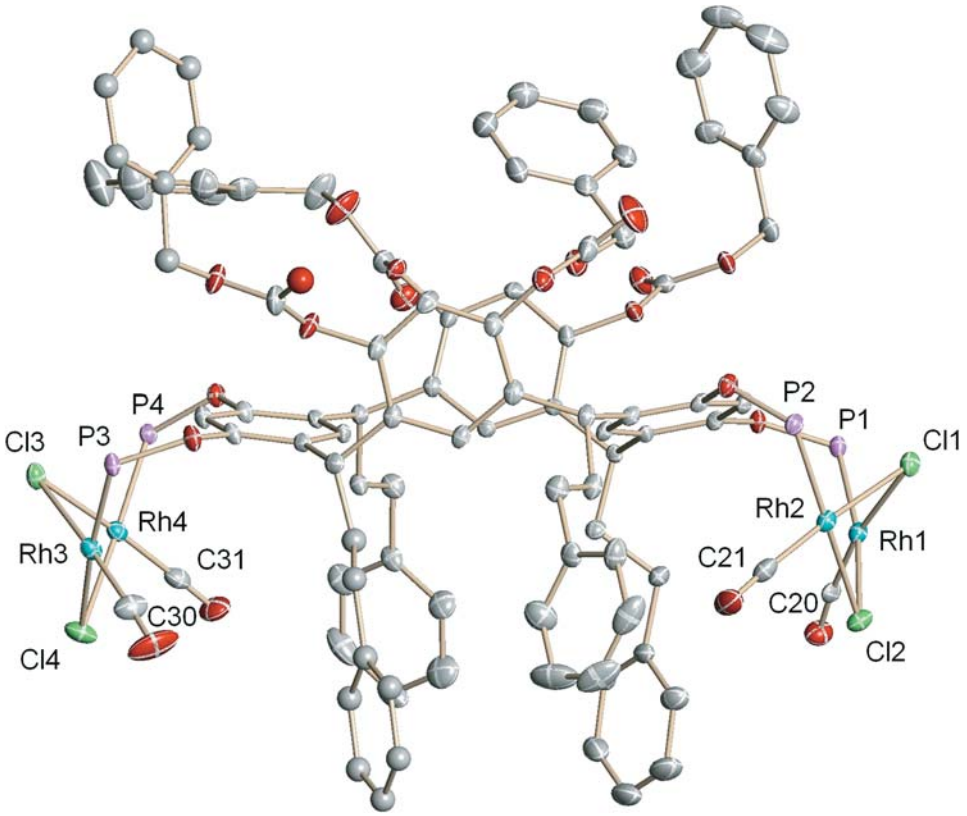
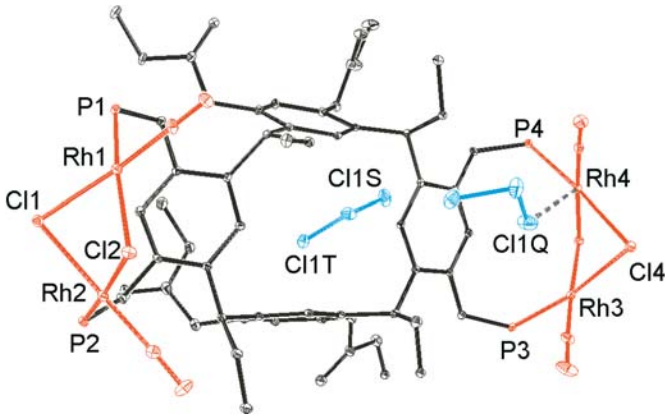


Table 1. Selected bond distances (Å) and angles (°) for complex **4**.

Bond distances (Å)		Bond angles (°)	
Rh1—P1	2.203(2)	P1-Rh1-C20	88.9(2)
Rh2—P2	2.202(1)	P1-Rh1-Cl1	95.27(5)
Rh3—P3	2.194(2)	C20-Rh1-Cl2	94.1(2)
Rh4—P4	2.202(1)	Cl1-Rh1-Cl2	83.41(5)
Rh1—C20	1.830(6)	P2-Rh2-C21	91.2(2)
Rh2—C21	1.820(7)	P2-Rh2-Cl1	92.41(5)
Rh3—C30	1.796(7)	C21-Rh2-Cl2	93.1(2)
Rh4—C31	1.819(7)	Cl1-Rh2-Cl2	83.33(5)
Rh1—Cl1	2.382(1)	P3-Rh3-C30	88.9(2)
Rh1—Cl2	2.424(1)	P3-Rh3-Cl3	93.67(5)
Rh2—Cl1	2.386(1)	C30-Rh3-Cl4	94.9(2)
Rh2—Cl2	2.424(1)	Cl3-Rh3-Cl4	82.72(5)
Rh3—Cl3	2.377(1)	P4-Rh4-C31	94.4(2)
Rh3—Cl4	2.421(2)	P4-Rh4-Cl3	93.13(5)
Rh4—Cl3	2.384(1)	C31-Rh4-Cl4	94.4(2)
Rh4—Cl4	2.421(2)	Cl3-Rh4-Cl4	82.56(5)

Fig. 2. A view of the structure of complex **4** showing the positions of the two "guest" molecules of dichloromethane. The $Rh_2(\mu\text{-}Cl)_2(CO)_2P_2$ units are shown in red and the heavy atoms of the CH_2Cl_2 molecules are shown in blue. All phenyl groups are omitted for clarity.



complex **4** gave $\delta(^{31}P)$ = 126.0 (d, $^1J_{RhP}$ = 197 Hz). It has previously been shown that the conformation of the tetraphosphinitoresorcinarene ligand can be determined from the ^1H-, ^{13}C gHMBC-, and ^1H-, ^{31}P gHMBC-correlated NMR spectra (6). From similar studies, it was established that the resorcinarene skeleton in complexes **4** and **5** adopts the same boat conformation as found in the solid state structure of complex **4**, with the phosphinite-derivatized rings in the flattened position. The IR spectra of the complexes each showed two bands in the carbonyl region, separated by ca. 10 cm^{-1}, which is consistent with the cis arrangement of the rhodium dinuclear unit observed in the solid state structure of complex **4** (1*a*–1*k*).

The tetrarhodium(I) complexes **4**–**6** were stable to air in both solid and solution states, and they displayed low reactivity towards oxidative addition reactions. Thus, complex **4** failed to react with dihydrogen at 10 atm (1 atm = 101.325 kPa) pressure over 2 days. Complex **4** was found to react very slowly with excess methyl iodide, apparently mostly by halogen exchange. Thus, when monitored by the ^{31}P NMR spectrum, the doublet due to complex **4** at $\delta(^{31}P)$ = 126.0 (d, $^1J_{RhP}$ = 197 Hz) was replaced over a 10 day period

© 2004 NRC Canada

at room temperature by a new doublet at $\delta(^{31}P)$ = 120.7 (d, $^1J_{RhP}$ = 201 Hz). The similarity in these parameters suggests a very similar structure as **4**, but several minor products were formed that could not be separated. The reaction of complex **4** with excess trimethylphosphine led to complete displacement of the rhodium atoms to give the known complex *trans*-[RhCl(CO)$(PMe_3)_2$] (1) and the free resorcinarene ligand **1**. The low reactivity of complex **4** compared with analogous rhodium(I) complexes with simpler phosphorus-donor ligands (1, 2) is most easily rationalized in terms of the high steric hindrance at the rhodium(I) centers. Although dihydrogen is small, the required cis stereochemistry of oxidative addition will lead to unfavorable steric effects between the other substituents.

In summary, the tetraphosphinitoresorcinarene ligands **1**–**3** have given the first examples of dirhodium(I) complexes with the *syn*-[$Rh_2(\mu\text{-}Cl)_2(CO)_2P_2$] stereochemistry and it is shown that the new geometrical form is favoured by the natural bite distance of pairs of phosphinite donors of the ligands. The dirhodium(I) units are sterically shielded, and therefore, exhibit only low reactivity.

Experimental

All reactions were performed under a nitrogen atmosphere using standard Schlenk techniques. Solvents were freshly distilled, dried, and degassed prior to use. NMR spectra were recorded using a Varian Inova 400 NMR spectrometer. The tetraphosphinite resorcinarene ligands **1**–**3** were prepared as reported elsewhere (6*a*). In the following formulae, the resorcinarene skeleton $(C_6H_2CH\{CH_2CH_2Ph\})_4$ is represented as Resorcinarene

[Resorcinarene$(OC(O)OCH_2Ph)_4(OPPh_2\{Rh(CO)Cl\})_4$] (4)

A mixture of ligand **1** (0.100 g, 0.046 mmol) and [$Rh(CO)_2\mu$-Cl]$_2$ (0.036 g, 0.093 mmol) in CH_2Cl_2 (10 mL) was stirred for 16 h. The resulting yellow solution was filtered through Celite and a yellow solid was precipitated with *n*-hexane. The solid was collected and washed with diethyl ether (5 mL). Yield 0.095 g, 73%. FT-IR ν(CO) (cm^{-1}): 2007, 1997. ^{1}H NMR (CD_2Cl_2) δ: 2.04, 2.19 (m, 8H, $CHCH_2CH_2Ph$), 2.30, 2.40 (m, 8H, $CHCH_2CH_2Ph$), 4.85 (m, 8H, $^2J_{HH}$ = 12 Hz, OCH_2Ph), 4.89 (t, 4H, $^3J_{HH}$ = 5 Hz, $CHCH_2CH_2Ph$), 6.53 (s, 2H, Ar-*H*, meta to *C*$OPPh_2$), 7.08 (s, 2H, Ar-*H*, ortho to *C*$OC(O)OCH_2Ph$), 7.76 (s, 2H, Ar-*H*, meta to *C*$OC(O)OCH_2Ph$), 7.77 (s, 2H, Ar-*H*, ortho to *C*$OPPh_2$), 6.61–8.12 (m, 80H, Ar-*H*, *Ph*). 31P NMR δ: 126.0 (d, $^1J_{RhP}$ = 197 Hz). Anal. calcd. for $C_{144}H_{116}Cl_4O_{20}P_4Rh_4$ (%): C 60.82, H 4.11; found: C 60.65, H 4.00.

[Resorcinarene$(OC(O)C_6H_{11})_4(OPPh_2\{Rh(CO)Cl\})_4$] (5)

This was prepared similarly from ligand **2** (0.100 g, 0.048 mmol) and [$Rh(CO)_2\mu$-Cl]$_2$ (0.038 g, 0.098 mmol). Yield 0.088 g, 67%. FT-IR ν(CO) (cm^{-1}): 2008, 1996. ^{1}H NMR (CD_2Cl_2) δ: 1.22–2.08 (m, 48H, $CHCH_2CH_2Ph$, C_6H_{11}), 2.29 (m, 4H, $CHCH_2CH_2Ph$), 2.51, 2.65 (m, 8H, $CHCH_2CH_2Ph$), 4.72 (m, 4H, $CHCH_2CH_2Ph$), 6.46 (s, 2H, Ar-*H*, meta to *C*$OPPh_2$), 6.84 (s, 2H, Ar-*H*, ortho to *C*$OC(O)C_6H_{11}$), 7.74 (s, 2H, Ar-*H*, meta to *C*$OC(O)C_6H_{11}$), 7.80 (s, 2H, Ar-*H*, ortho to *C*$OPPh_2$), 6.20–7.20 (m, 60H, Ar-*H*, *Ph*). ^{31}P NMR δ: 128.7 (d, $^1J_{RhP}$ = 199 Hz). Anal. calcd. for $C_{140}H_{132}Cl_4O_{16}P_4Rh_4$ (%): C 61.19, H 4.84; found: C 60.93, H 4.76.

[Resorcinarene$(OC(O)C_6H_4CH_3)_4(OPPh_2\{Rh(CO)Cl\})_4$] (6)

This was prepared similarly from ligand **3** (0.100 g, 0.047 mmol) and [$Rh(CO)_2\mu$-Cl]$_2$ (0.037 g, 0.095 mmol). Yield 0.094 g, 72%. ^{1}H NMR (CD_2Cl_2) δ: 1.92, 2.12 (m, 8H, $CHCH_2CH_2Ph$), 2.52 (s, 12H, $C_6H_4CH_3$), 2.61 (m, 8H, $CHCH_2CH_2Ph$), 4.94 (m, 4H, H^i), 6.26–8.04 (m, 84H, Ar-*H*, *Ph*, $C_6H_4CH_3$). ^{31}P NMR δ: 128.3 (d, $^1J_{RhP}$ = 200 Hz). FT-IR ν(CO) (cm^{-1}): 2007, 1995. Anal. calcd. for $C_{144}H_{116}Cl_4O_{16}P_4Rh_4$ (%): C 62.22, H 4.21; found: C 62.16, H 4.41.

X-ray structure determination

Crystals of [Resorcinarene$(OC(O)OCH_2Ph)_4(OPPh_2\{Rh(CO)Cl\})_4$] (**4**) as the dichloromethane solvate ($[C_{144}H_{116}Cl_4O_{20}P_4Rh_4]\cdot 6.5(CH_2Cl_2)$) were grown by diffusion of *n*-hexane into a dichloromethane solution. A crystal was mounted on a glass fiber, and data were collected using a Nonius-Kappa CCD diffractometer using COLLECT software (7). The unit cell parameters were calculated and refined from the full data set. Crystal cell refinement and data reduction were carried out using the Nonius DENZO package (7). The data were scaled using SCALEPACK (7). The SHELXTL V6.1 program package was used to solve and refine the structure (7). The structure was solved by direct methods. The hydrogen atoms were calculated geometrically and were riding on their respective carbon atoms. Except as mentioned, all non-hydrogen atoms were refined with anisotropic thermal parameters. Crystal data are summarized in Table 2.[3] The thermal ellipsoid diagram is shown at 30% probability.

Table 2. Crystallographic data for complex **4**.

Formula	$C_{150.5}H_{129}Cl_{17}O_{20}P_4Rh_4$
Fw	3395.71
Space group	*Pbca*
a (Å)	38.569(8)
b (Å)	29.011(6)
c (Å)	26.587(5)
Volume (Å^3)	29 749(1)
Z	8
$D_{calcd.}$ (Mg/m^3)	1.516
μ (mm^{-1})	0.849
*R*1, *wR*2 [$I > 2\sigma(I)$]	0.0650, 0.1799
R indices (all data)	0.1255, 0.2092

[3] Supplementary data may be purchased from the Directory of Unpublished Data, Document Delivery, CISTI, National Research Council Canada, Ottawa, ON K1A 0S2, Canada (http://www.nrc.ca/cisti/irm/unpub_e.shtml for information on ordering electronically). CCDC 233321 contains the crystallographic data for this paper (compound **4**). These data can be obtained, free of charge, via www.ccdc.cam.ac.uk/conts/retrieving.html (or from the Cambridge Crystallographic Data Centre, 12 Union Road, Cambridge, CB2 1EZ, UK; fax +44 1223 336033; or deposit@ccdc.cam.ac.uk).

© 2004 NRC Canada

There was some disorder of the molecules, as follows. One of the O*CH$_2$Ph* groups was modeled as a 55:45 isotropic mixture, and one of the phenethyl substituents was modeled as a 50:50 isotropic mixture; in both cases geometric restraints were applied. The carbon–chlorine bond lengths of the solvent molecules were fixed at the standard distance. The largest residual electron density peak (3.053 e/Å^3) was associated with one of these solvent molecules.

Acknowledgments

We thank the the Natural Sciences and Engineering Research Council of Canada (NSERC) for financial support. RJP thanks the Government of Canada for a Canada Research Chair.

References

1. (*a*) D.F. Steele and T.A. Stephenson. J. Chem. Soc. Dalton Trans. 2161 (1972); (*b*) J. Gallay, D.D. Montauzon, and R. Poilblanc. J. Organomet. Chem. **38**, 179 (1972); (*c*) J.F. Nixon and J.R. Swain. J. Chem. Soc. Dalton Trans. 1044 (1972); (*d*) A. Maisonnat, P. Kalck, and R. Poilblanc. Inorg. Chem. **13**, 661 (1974); (*e*) J.J. Bonnet, Y. Jeannin, P. Kalck, A. Maisonnat, and R. Poilblanc. Inorg. Chem. **14**, 743 (1975); (*f*) J. Browning, P.L. Goggin, R.J. Goodfellow, M.G. Norton, J.M. Rattray, B.F. Taylor, and J. Mink. J. Chem. Soc. Dalton Trans. 2061 (1977); (*g*) M.J. Doyle, A. Mayanza, J.-J. Bonnet, P. Kalck, and R. Poilblanc. J. Organomet. Chem. **146**, 293 (1978); (*h*) F.R. Hartley, S.G. Murray, and D.M. Potter. J. Organomet. Chem. **254**, 119 (1983); (*i*) C.G. Arena, F. Faraone, M. Lanfranchi, E. Rotondo, and A. Tiripicchio. Inorg. Chem. **31**, 4797 (1992); (*j*) E. Rotondo, G. Battaglia, G. Giordano, and F.P. Cusmano. J. Organomet. Chem. **450**, 245 (1993); (*k*) E. Fernández, A. Ruiz, C. Claver, S. Castillón, J.F. Piniella, and A. Alvarez-Larena. Organometallics, **17**, 2857 (1998).
2. (*a*) A.R. Sanger. J. Chem. Soc. Dalton Trans. 120 (1977); (*b*) M. Cowie and S.K. Dwight. Inorg. Chem. **19**, 2500 (1980); (*c*) F. Faraone, G. Bruno, S.L. Schiavo, G. Tresoldi, and G. Bombieri. J. Chem. Soc. Dalton Trans. 433 (1983); (*d*) M. Inga, S. Kenney, and J.W. Kenney. Organometallics, **5**, 230 (1986); (*e*) A.L. Balch, M. Ghedini, D.E. Oram, and P.E. Reedy, Jr. Inorg. Chem. **26**, 1223 (1987); (*f*) M.A. Garralda and L. Ibarlucea. J. Organomet. Chem. **377**, 367 (1989); (*g*) C.L. Thurner, M. Barz, M. Spiegler, and R.T. Werner. J. Organomet. Chem. **541**, 39 (1997); (*h*) J.R. Dilworth, Y. Zheng, and D.V. Griffiths. J. Chem. Soc. Dalton Trans. 1877 (1999); (*i*) T.W. Graham, A. Llamazares, R. McDonald, and M. Cowie. Organometallics, **18**, 3502 (1999); (*j*) M. Laly, R. Broussier, and B. Gautheron. Tetrahedron Lett. **41**, 1183 (2000); (*k*) A.D. Burrows, M.F. Mahon, M.T. Palmer, and M. Varrone. Inorg. Chem. **41**, 1695 (2002).
3. (*a*) P. Kalck and R. Poilblanc. Inorg. Chem. **14**, 2779 (1975); (*b*) P.D. Bartlett and J.S. McKennis. J. Am. Chem. Soc. **99**, 5334 (1977); (*c*) Y.-W. Ge and P.R. Sharp. Inorg. Chem. **30**, 1671 (1991); (*d*) T.E. Bitterwolf, D.L. Kline, J.C. Linehan, C.R. Yonker, and R.S. Addleman. Angew. Chem. Int. Ed. **40**, 2692 (2001); (*e*) R. Goikhman and D. Milstein. Angew. Chem. Int. Ed. **40**, 1119 (2001); (*f*) C. Krug and J.F. Hartwig. J. Am. Chem. Soc. **124**, 1674 (2002); (*g*) V. Circu, M.A. Fernandes, and L. Carlton. Inorg. Chem. **41**, 3859 (2002).
4. (*a*) M. Stolmàr, C. Floriani, A. Chiesi-Villa, and C. Rizzoli. Inorg. Chem. **36**, 1694 (1997); (*b*) C.J. Cobley, D.D. Ellis, A.G. Orpen, and P.G. Pringle. J. Chem. Soc. Dalton Trans. 1109 (2000); (*c*) F.J. Parlevliet, C. Kiener, J. Fraanje, K. Goubitz, M. Lutz, A.L. Spek, P.C.J. Kamer, and P.W.N.M. van Leeuwen. J. Chem. Soc. Dalton Trans. 1113 (2000); (*d*) M. Vézina, J. Gagnon, K. Villeneuve, M. Drouin, and P.D. Harvey. Chem. Commun. 1073 (2000); (*e*) C. Kunze, D. Selent, I. Neda, R. Schmutzler, A. Spannenberg, and A. Börner. Heteroatom Chem. **12**, 577 (2001); (*f*) C. Dieleman, S. Steyer, C. Jeunesse, and D. Matt. J. Chem. Soc. Dalton Trans. 2508 (2001); (*g*) S. Steyer, C. Jeunesse, D. Matt, R. Welter, and M. Wesolek. J. Chem. Soc. Dalton Trans. 4264 (2002); (*h*) Y. Ishii, K. Onaka, H. Hirakawa, and K. Shiramizu. Chem. Commun. 1150 (2002); (*i*) C. Kunze, D. Selent, I. Neda, M. Freytag, P.G. Jones, R. Schmutzler, W. Baumann, and A. Börner. Z. Anorg. Allg. Chem. **628**, 779 (2002).
5. (*a*) C. Wieser, C.B. Dieleman, and D. Matt. Coord. Chem. Rev. **165**, 93 (1997); (*b*) Z. Asfari, V. Böhmer, V. Harrowfield, and J. Vicens (*Editors*). Calixarenes 2001. Kluwer Academic Publishers, Dordrecht, The Netherlands. 2001.
6. (*a*) D.J. Eisler and R.J. Puddephatt. Can. J. Chem. **82**, 185 (2004); (*b*) D.J. Eisler, C.W. Kirby, and R.J. Puddephatt. Inorg. Chem. **42**, 7626 (2003); (*c*) D.J. Eisler and R.J. Puddephatt. Inorg. Chem. **42**, 6352 (2003); (*d*) D.J. Eisler and R.J. Puddephatt. Inorg. Chem. **42**, 8192 (2003).
7. (*a*) COLLECT, DENZO, SCALEPACK [computer programs]. Bruker Nonius B.V., Delft, The Netherlands, 1998. (*b*) SHELXTL, Version 6.1 [computer program]. Bruker AXS, Madison, Wis. 2000.

© 2004 NRC Canada

Coordination arrays — Synthesis and characterization of tetranuclear complexes of grid-type[1]

Garry S. Hanan, Dirk Volkmer, and Jean-Marie Lehn

Abstract: A series of tetranuclear metal complexes of grid-type consisting of four bis-tridentate ligands and four divalent transition metal ions were synthesized and characterized. The ^{1}H NMR spectra of diamagnetic complexes containing Zn(II), Cd(II), Fe(II), and Ru(II) was correlated to the radius of the metal ion. The UV–vis and electrochemical results indicated that the bridging ligand π^* orbital and the d_π metal orbital are stabilized by complexation of more than one metal ion. Furthermore, the Co(II) and Fe(II) grids exhibit metal–metal interaction mediated by the bis-tridentate ligands as indicated by electrochemical and spectroscopic methods. These results provide guidelines for the design of larger grids bearing several metal centres in a square arrangement, which also represent potential components of molecular electronic devices.

Key words: complexes with nitrogen ligands, octahedral metal ions, self-assembly, supramolecular chemistry.

Résumé : Des complexes tetramétalliques composés de métaux de transitions et des ligands bis-tridentates ont été synthétisés et caractérisés. Les interactions métales-métales de ces « grilles moléculaires » ont été mesurées par des méthodes spectroscopiques et électrochimiques et ont indiqué des fortes interactions entre les métaux pour les grilles de Co(II) et Fe(II). Les spectres de rmn ^{1}H des complexes diamagnétiques du Zn(II), Cd(II), Fe(II) et Ru(II) ont été corrélées au rayons des ions métalliques. Ces résultats permettent le design de nouvelles grilles carrées comme éléments des appareils électroniques moléculaires.

Mots clés : complexes avec des ligands azotés, ions métalliques octaédriques, autoassemblage, chimie supramoléculaire.

Introduction

Polynuclear metal complexes can perform useful functions that mononuclear metal complexes cannot, such as multi-electron redox (1) and light-harvesting processes (2). Our early work concerned the assembly of inorganic architectures based on tetrahedral metal ions, exemplified by the formation of helicates (3, 4), rods (5), and cylinders (6). The thermodynamic and entropic factors involved in the assembly of these polynuclear complexes have also been studied (7, 8). We previously established that structures of defined nuclearity, *coordination arrays*, could be assembled (9). Rack- (10, 11), ladder- (12), and grid-type (13–15) molecules are ordered inorganic architectures comprising one- or two-dimensional geometries of $[m \times n]$ nuclearity and presenting — in sequence of increasing complexity — basic geometries that may be termed *racks* $[n]$R, *ladders* $[2n]$L, and *grids* $[m \times n]$G (Fig. 1), where the nuclearity of the R, L, and G species is given by $[n]$, $[2n]$, and $[m \times n]$, with n (for a square grid) representing their rank.

Although metal ions that prefer a tetrahedral coordination environment are well suited for the assembly of ladder- and grid-like molecules (12, 13), their response to electrochemical and photonic stimuli are of limited interest as they may change coordination geometry during redox processes. Metal ions with octahedral coordination environments are better suited for building up coordination arrays due to their stability under a range of redox and excitation conditions. The complexes of octahedrally coordinated metal ions also present a much richer palette of physical and chemical properties than tetrahedrally coordinated metal ions such as Ag(I) and Cu(I).

In this paper, we describe the general synthesis and properties of [2 × 2] grids incorporating bis-tridentate ligand **1a** and two paramagnetic metal ions ($[Co(\mathbf{1a})]_4[PF_6]_8$ (**2a**), $[Ni(\mathbf{1a})]_4[PF_6]_8$ (**3a**)) and four diamagnetic metal ions ($[Zn(\mathbf{1a})]_4[PF_6]_8$ (**4a**), $[Cd(\mathbf{1a})]_4[PF_6]_8$ (**5a**), $[Fe(\mathbf{1a})]_4[PF_6]_8$ (**6a**), and $[Ru(\mathbf{1a})]_4[PF_6]_8$ (**7a**)). The synthesis and properties of the Co(II) complex of ligand **1b** $[Co(\mathbf{1b})]_4[PF_6]_8$ (**2b**) are also described.

Received 29 February 2004. Published on the NRC Research Press Web site at http://canjchem.nrc.ca on 21 October 2004.

G.S. Hanan,[2,3] D. Volkmer,[4] and J.-M. Lehn. ISIS, 8 allée Gaspard Monge, BP-70028 F-67083 Strasbourg CEDEX, France.

[1]This article is part of a Special Issue dedicated to the memory of Professor Don Irish.

[2]Present address: Département de chimie, Université de Montréal, 2900 Edouard-Montpetit, Montréal, QC H3T 1J4, Canada.
[3]Corresponding author (email: garry.hanan@umontreal.ca).
[4]Present address: Faculty of Chemistry, AC1, University of Bielefeld, Bielefeld, Germany.

 doi: 10.1139/V04-092 © 2004 NRC Canada

Table 1. ^{1}H NMR chemical shifts in metal complexes of ligand **1a** in CD_3CN at 200 MHz.[a]

Compound	$H_{6''}$	$H_{5''}$	$H_{4''}$	$H_{3''}$	$H_{5'}$	$H_{4'}$	$H_{3'}$	H_5	H_2
1a	8.75	7.39	7.89	8.79	8.61	8.05	8.57	9.78	9.40
4a, Zn	7.28	7.23	8.02	8.35	9.16	8.86	8.78	9.40	7.40
5a, Cd	7.70	7.32	8.06[b]	8.41	9.10	8.74[b]	8.74[b]	9.36	8.06[b]
6a, Fe	6.61	6.82	7.67	8.85	9.28[c]	8.93	8.22[c]	9.09	5.14
7a, Ru	7.11	6.95	7.77	8.33	10.08[c]	8.59	8.73[c]	10.56	5.75

[a]Ligand **1a** in $CDCl_3$.
[b]Coincidental overlap of peaks.
[c]$H_{3'}$ and $H_{5'}$ are not distinguished.

Fig. 1. Schematic representations of racks, ladders, and grids.

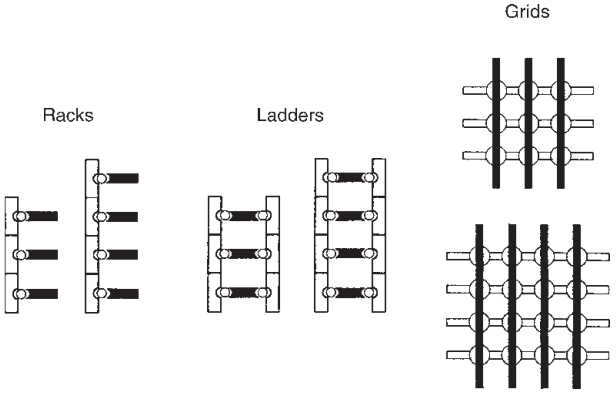
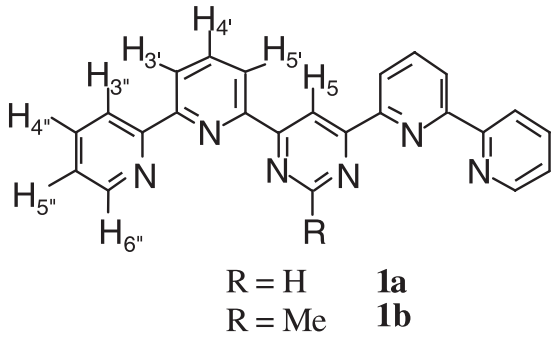


Fig. 2. Proton labelling scheme for ligands **1a** and **1b**.



Results and discussion

The synthetic strategy follows that previously reported for [2 × 2] grid-type structures (15) and the one established for polypyridyl helicates (16, 17). The metal salt and the ligand are combined in equimolar amounts in protic solvents (or a mixture of protic solvent and water), heated to reflux, and precipitated by the addition of NH_4PF_6. For Zn(II), Cd(II), Co(II), and Ni(II), analytically pure complexes are obtained by treating an acetonitrile solution of the isolated solid with activated charcoal, filtration, and recrystallization. The yields varied between 48% and 82% for reactions with **1a** with the various metal ions. The reaction of **1b** with Co(II) gave **2b** in 28% yield. For the reactions of **1a** with Fe(II) or Ru(II), **6a** and **7a** were only isolable in small quantities. Purification was afforded by repeated chromatography on Sephadex CM-25 (18). The use of alumina or silica as for other polynuclear metal complexes led to complete adsorption of the cations to the chromatographic support. The low yield of the Ru complex (2%) precluded its complete characterization.

^{1}H NMR spectra

The ^{1}H NMR chemical shifts of ligand **1a** and the diamagnetic complexes **4a**–**7a** are reported in Table 1. The proton labelling scheme is given in Fig. 2. The symmetric nature of the grids is demonstrated by the relative simplicity of the ^{1}H NMR spectra of **4a**–**7a**. A total of 64 protons are accounted for by nine peaks, seven of which integrate to eight protons each, and are ascribed to the protons on the bipyridyl moieties. The coupling constants (J (H_5H_6) ≈ 5; J (H_3H_4) = J (H_4H_5) ≈ 7; J (H_3H_5) ≈ 1 Hz) are typical for pyridyl protons. Decoupling experiments reveal the locations of $H_{3''}$ relative to the $H_{3'}$–$H_{5'}$ pair. $H_{6''}$ is evident from its upfield shift and coupling constant. The pyrimidine protons stand out either as doublets with J (H_2H_5) ≈ 1 Hz or as broadened singlets. One of the pyrimidinyl protons is shifted upfield relative to its position in uncoordinated ligand **1a** and is ascribed to the pyrimidine H_2 proton, which is found in a shielding environment upon metal complexation.

The radius of the coordinated metal ion plays an important role in the amount of pinching found in metal bis–tpy complexes in the solid state. In general, the smaller the cation, the more the ligands distort as they "pinch in" around the metal ions (19). Solid state structural information was related to solution ^{1}H NMR results and gave a general idea of the solution structure of a complex by the relative shifts of H_2, $H_{4'}$, and $H_{6''}$ (11, 20). By relating the proton NMR chemical shifts to cation size a qualitative degree of pinching in can be determined for the grids.

Two pairs of metals from the same group can be compared (Table 2). The chemical shifts of H_2 and $H_{6''}$ are less shielded in the cadmium complex relative to the zinc complex. The iron and ruthenium pair show similar effects; the larger Ru(II) cation causes less shielding of H_2 and $H_{6''}$ relative to the Fe(II) cation (Table 2). The opposite effect is noted for $H_{4'}$: for each pair of metal ions, the larger cation causes less deshielding of $H_{4'}$ as the ligand pinches in less, moving the deshielding zone of the terminal pyridine farther away from $H_{4'}$. The metal ion is farther away from $H_{4'}$ than H_2 and $H_{6''}$, and contributes little to shielding factors at this position.

When a larger cation is coordinated, $H_{6''}$ is farther away from the shielding effects of the orthogonal ligand (less pinching-in). The shielding of H_2, therefore, is not as pronounced when a larger cation is coordinated. This is clearly evident in the larger shielding of H_2 and $H_{6''}$ by coordination of the d^6 metals relative to the d^{10} metals. Since the d^6 metal

© 2004 NRC Canada

Table 2. Differences in ^{1}H NMR chemical shifts for H_2, $H_{4'}$, and $H_{6''}$ owing to shielding and deshielding effects in complexes **4a**–**7a**.[a,b]

Compound	H_2 (ppm)	$\Delta\partial$ H_2 (ppm)	$H_{6''}$ (ppm)	$\Delta\partial$ $H_{6''}$ (ppm)	∂ $H_{4'}$ (ppm)	$\Delta\partial$ $H_{4'}$ (ppm)
4a, Zn	7.28	+0.42	7.40	+0.66	8.86	–0.12
5a, Cd	7.70		8.06		8.74	
6a, Fe	5.14	+0.65	6.61	+0.50	8.93	–0.34
7a, Ru	5.75		7.11		8.59	

[a]In CD_3CN.
[b]Proton assignments in Fig. 2.

Table 3. Electronic absorption of **1a** and grids **2a**–**7a**.[a]

Compound	Electronic absoption bands (λ_{max} (nm); ε ($\times 10^{-4}$ L mol^{-1} cm^{-1})
1a	236 (3.8), 286 (3.3), 308 (sh, 2.6), 320 (sh, 3.2)[b]
2a, Co	274 (8.0), 342 (7.3), 275 (12), 325 (8.9), 338 (9.0),[c] 446 (1.6), 443 (1.7), 530 (sh, 1.1)[c]
3a, Ni	230 (11) 278 (6.3), 307 (sh, 3.4), 347 (6.5), 361 (sh, 5.0), 511 (0.20)
4a, Zn	233 (23), 276 (11), 331 (sh, 14), 341 (sh, 16), 356 (9.5)
5a, Cd	234 (21), 273 (12), 331 (9.5), 341 (16)
6a, Fe	230 (20), 276 (10), 341 (12), 490 (2.7), 616 (2.9)

[a]All solutions 10^{-5} – 10^{-6} mol L^{-1} in acetonitrile unless otherwise noted.
[b]In DCM.
[c]In DMF.

ions in low-spin configuration have smaller atomic radii than d^{10} metal ions in the same row (21), they should cause a greater convergence of the ancillary ligands, and hence, greater shielding of H_2 and $H_{6''}$. The greater charge density on the smaller cation may also contribute to the greater shielding of H_2 and $H_{6''}$ (22).

The assignment of $H_{3'}$ — $H_{5'}$ and H_2 — H_5 for the zinc complex **4a** was made by nOe experiments. In the free ligand, $H_{3'}$, $H_{5'}$, and H_5 do not interact with neighbouring protons on the adjacent rings via nOe owing to ligand preference for a transoid conformation. However, upon complexation the ligand lines up in cisoid conformation, allowing nOe interactions between heterocycles. Distinct nOe interactions occur along the ligand backbone with selective irradiation of **4a**. The relative positions of $H_{3'}$, $H_{5'}$, and H_5 for the other complexes may be inferred from these results (i.e., downfield position of $H_{5'}$ relative to $H_{3'}$, and downfield position of H_5 relative to H_2).

Infrared spectroscopy and mass spectrometry

All of the complexes exhibited ligand-based IR bands near 1600, 1450, and 560 cm^{-1}. Very strong bands near 845 cm^{-1} associated with the $[PF_6]^-$ counteranions were also present. The presence of both the $[PF_6]^-$ and the ligand bands is indicative of metal-to-ligand coordination (16).

Positive-ion FAB-MS was informative about the nature of these complexes, particularly for complexes of paramagnetic metal ions. The parent ion minus one counteranion was found in all cases. After the loss of the first $[PF_6]^-$ anion, successive losses of $[PF_6]^-$ counterions ensued, with losses of up to five $[PF_6]^-$ anions. The zinc and cadmium complexes (**4a** and **5a**) fragmented under FAB conditions. Losses of ligand **1a** from **4a**, and **1a** and two Cd(II) from **5a** were observed. In both cases, the peaks at the corresponding masses could be ascribed with certainty to a fragmentation since a M_4L_3 complex would exhibit a less symmetric ^{1}H NMR spectrum.

UV–vis spectroscopy

The UV–vis band maxima (λ_{max}) and molar absorptivities (ε) for the complexes and the free ligands **1a** and **1b** are listed in Table 3. Two types of bands, those involving pyridine and pyrimidine transitions, are observed in the UV region. The intensities of the ligand-centered (LC) transitions increase upon complexation by metal ions as the relative concentration of ligand increases in the complex compared to the free ligand. In the spectra of the metal complexes, these bands generally appear at slightly lower energies, but with greater intensities. Similar LC transitions have been described as roughly additive in other polypyridyl complexes (23). Metal complexes of **1a** and **1b** all exhibit a red-shift in the lower energy pyrimidine π–π^* transitions. The λ_{max} for the higher energy pyridine π–π^* transitions shift only slightly, whereas their intensity increases considerably (Table 3).

The orange nickel complex **3a** exhibits a single band in the visible region at 511 nm (ε = 2020 L mol^{-1} cm^{-1}). The relatively strong molar absorptivity for **3a** is unusual as the ε values for metal-centred (MC) transitions in Ni(II) octahedral complexes are normally lower (21). Distortions in the coordination environment of Ni(II) in **3a** may account for the greater ε value. A sterically strained Ni(II) catenate was reported and the orange complex was found to exhibit a MC transition in the visible region (λ_{max} ~ 480 nm, ε ~ 450 L mol^{-1} cm^{-1}) (24).

The green iron complex **6a** exhibits two distinct absorption maxima in the visible region at 490 and 616 nm, respectively (Fig. 3). The bands are attributed to MLCT transitions to the bipyridyl and pyrimidinyl moieties of **1a**, respectively, as the pyrimidine LUMO should be at lower energy than the

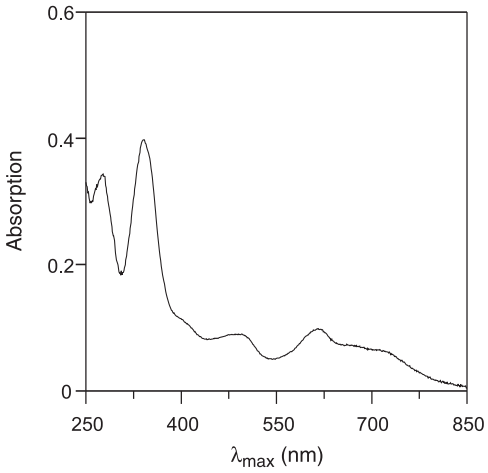
© 2004 NRC Canada

Table 4. Electrochemical potentials of the grids (vs. SCE).[a]

Compound	$\Delta E^{\circ\prime}$
1a	–1.44 [70], –2.07 [irrev]
2a, Co in DMF	+0.91 [80], +0.66 [110][b], +0.46 [70], –0.14 [50], –0.24 [50], –0.44 [60][b], –0.83 [60], –1.09 [60], –1.33 [60], –1.54 [70][b], –1.77 [60], –1.94 [100]
3a, Ni	+2.03 [irrev][c], –0.40 [50][bc], –0.52 [50][bc], –0.98 [irrev], –1.18 [irrev], –1.32 [irrev], –2.0 [ads], –1.22 [strip]
4a, Zn	–0.28 [50], –0.38 [50], –0.48 [70][b], –0.90 [60], –1.09 [60], –1.25 [ads], –1.56 [80], –2.08 [ads], –1.09 [strip]
5a, Cd	–0.46 [80][b], –0.58 [irrev], –1.26 [ads], –2.12 [ads], –1.16 [strip], –0.40 [strip]
6a, Fe	+1.83 [60], +1.71 [80], +1.52 [70], +1.39 [60], –0.19 [60][b], –0.31 [60], –0.45 [60], –1.00 [120], –1.18 [90], –1.42 [irrev], –1.55 [irrev]

[a]In acetonitrile unless otherwise noted.
[bc]Four one-electron processes.
[b]Two one-electron processes.

Fig. 3. Electronic absorption spectrum of tetranuclear Fe(II) complex **6a** in acetonitrile.



pyridine LUMO. This is further supported by electrochemical studies of **6a** (vide infra).

The visible absorption spectra of the brown cobalt complexes **2a** and **2b** exhibit a broad band near 445 nm that was ascribed to the bipyridyl MLCT transition. A broad, lingering band out to approximately 550 nm was attributed to the pyrimidinyl MLCT transition.

Electrochemical measurements

In general, the complexes exhibit several metal- and ligand-based reductions, and in a few cases, reversible metal-based oxidations are observed. In dinuclear ruthenium complexes, ligands **1a** and **1b** mediate significant metal–metal electronic communication (11). In the grids, owing to the D_{2d} symmetry of the complexes, each metal and ligand coordination environment is identical and, thus, different reduction potentials for the bridging ligand and oxidation potentials for the metals are an indication of electronic communication (23, 25). The redox potentials vs. SCE for the complexes and ligands **1a** and **1b** are given in Table 4.

Nickel complex **3a** displays an irreversible [Ni^{II}–Ni^{III}] oxidation at +2.17 V, at the edge of the solvent potential window. On scanning the potential past the oxidation at +2.03 V, upon return, irreversible waves are observed at +0.43, –0.16, and 0 V. These waves are not observed if the scans return before +1.90 V. As Ni(III) complexes are generally highly reactive (21), oxidation of **1a** and the return to a Ni(II) state may be occurring. The first two reductions may be associated with reduction of previously oxidized ligands. It was previously shown that various divalent metals (i.e., Ni, Fe, and Co) in phenanthroline catenates do not oxidize to their trivalent state, instead, ligand-based oxidations occur at $E^{\circ} >$ +1.4 V (26).

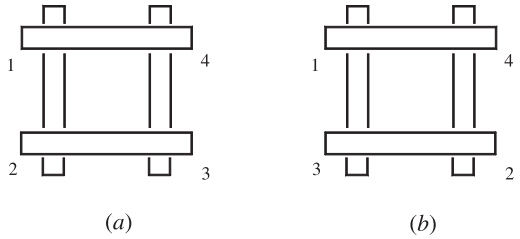
In the negative potential region, the first two reductions occur at –0.40 and –0.52 V and are ascribed to the reduction of the four pyrimidines in **3a**. Each reduction involves two electrons and is fully reversible. These reduction potentials are quite positive compared to Ni(II) bis–tpy metal-based reductions (–1.53 V) (27), which supports their assignment as ligand-based processes. Four irreversible reductions occur thereafter (–0.98, –1.18, –1.32, –2.00 V) with adsorption of the formally neutral complex to the electrode, as exemplified by a stripping peak at –1.22 V.

The zinc **4a** and cadmium **5a** complexes exhibit neither metal- nor ligand-based oxidations, as expected for d^{10} metal ions. The ligand-based reductions in **4a** were grouped in two sections: two reversible one-electron processes at –0.28 and –0.38 V, followed by a two simultaneous and reversible one-electron process at –0.48 V. At more negative potentials, two reversible one-electron processes at –0.90 and –1.09 V are followed by adsorption of the complex to the electrode at –1.25 V, and a stripping peak at –2.08 V. Complex **5a** undergoes a single ligand-based reversible reduction at –0.46 V upon scanning to –0.5 V. Scanning to further negative potentials renders the first reduction irreversible. The reduction is assigned to a ligand-based process rather than a cadmium-based reduction by analogy to the zinc case. An irreversible process at –0.58 V is followed by a succession of adsorptions and stripping peaks at similar potentials to those of the zinc complex.

Iron complex **6a** displays four reversible one-electron oxidation processes at +1.39 V, +1.52 V, +1.71 V, and +1.83 V, and are considerably more positive than those reported for $Fe(tpy)_2$ (+1.18 V) and are similar to those reported for the dinuclear helicate Fe_2(2,2′:6′,2″:6″,2‴:6‴,2⁗:6⁗,2⁗′:6⁗′,2⁗″-sexipyridine)$_2$ (+1.35, +1.50 V) (16). The $\Delta E^{\circ\prime}$ values between successive oxidations have previously been used as a measure of metal–metal communication (28–33). The four one-electron oxidations in **6a** occur most likely by the successive oxidations of opposing metal centres ($\Delta E^{\circ\prime}$ (Fe(1)–Fe(2)) = 0.13 V; $\Delta E^{\circ\prime}$ (Fe(2)–Fe(3)) = 0.19 V; $\Delta E^{\circ\prime}$ (Fe(3)–Fe(4)) = 0.12 V). The postulated order of metal oxidations maintains a maximum distance between oxidized species to

© 2004 NRC Canada

Fig. 4. Possible order of Fe(II) oxidations in the tetranuclear Fe(II) grid **6a**: (*a*) sequential adjacent Fe(II) centres; (*b*) double diagonal Fe(II) centres.



minimize electrostatic repulsion between them (Fig. 4). The greater difficulty in oxidizing the third Fe(II), with two adjacent Fe(II), relative to the second Fe(II), with no adjacent Fe(II), supports the diagonal oxidation pathway (Fig. 4*b*). The difference in the Fe(II) oxidation potentials can be explained by direct electronic communication through the pyrimidine–Fe(II)–pyrimidine bridge and the increase in positive charge on the complex as it is oxidized.

In the negative potential region, a reversible two-electron reduction occurred at –0.19 V, followed by two reversible one-electron reductions at –0.31 and –0.45 V. These four ligand-based reductions are ascribed to the reduction of the central pyrimidines in each strand of **1a**. The coincidental positioning of the first two reductions supports the diagonally opposed metal oxidation route; two adjacent pyrimidines should not reduce at the same potential. The next four one-electron reductions are irreversible.

The oxidation of cobalt complex **2a** in DMF was similar to that of **7**, except that it occurred at less positive values. This is in accord with potentials reported for $M(tpy)_2$ complexes (M = Fe(II), Co(II), Ni(II)) (28). However, the metal-based oxidations are not strictly reversible. The first oxidation at +0.46 V vs. SCE is quasireversible with $\Delta E1/2$ = 70 mV. For the following two-electron oxidation, $\Delta E1/2$ = 110 mV, which is ascribed to the close proximity of two oxidation waves, and not to the irreversibility of the wave. These values are lower than the values for $Co_2(sexipy)_2$, which show metal oxidation at +0.84 and +1.17 V (16). The $\Delta E°'$ values for the [Co^{III}–Co^{II}] and [Co^{II}–Co^{I}] processes in DMF are (0.20, 0, and 0.25 V) and (0.10, 0.20, and 0.41 V), respectively.

The [Co^{II} – Co^{I}] reduction in **2a** was more positive than that of $Co_2(sexipy)_2$ (–0.51 and –0.67 V), which is consistent with earlier work (16). The difference in formal potentials for the four metal-based reductions is greater than those of the metal-based oxidations. There are four reversible one-electron reductions at –0.83, –1.09, –1.33, and –1.77 V, as well as a reversible two-electron reduction at –1.54 V and an irreversible one-electron reduction at –1.94 V, attributable to ligand-localized reductions.

Conclusion

The grid-like complexes described herein exhibit several interesting features: (1) highly symmetric ^{1}H NMR spectra for the diamagnetic complexes; (2) successive loss of $[PF_6]^-$ counterions from the parent molecular ions in FAB-MS; and (3) intermetallic electronic communication for oxidation and reduction processes in electrochemical measurements. Indeed, single site redox processes are possible with these highly symmetric complexes. The best example ($[Fe(\mathbf{1a})]_4[PF_6]_8$, (**7**)) exhibits total communication among the metal centres electrochemically, yet has high symmetry in solution on the NMR timescale. The rigid nature of these ligands is well suited for the synthesis of tetrametallic grids. The assembly of larger grids using longer rigid polytridentate ligands (31) and by the stringing together of smaller 2 × 2 grids via hydrogen bonding (32) has led to novel applications for grid-like complexes, such as their surface ordering as models of molecular-level information storage devices (33).

Experimental

Reagent solvents, chromatographic supports, TLC supports, and analytical instrumentation were as described previously (34). Unless otherwise noted, materials were obtained from commercial suppliers and used without further purification. Ligands **1a** and **1b** were synthesized as described (34). ^{1}H and ^{13}C NMR spectra were measured in CD_3CN locked to the deuterated solvent and calibrated to the residual solvent peak. The proton labelling is as shown in Fig. 2. Brief synthetic details for complexes **2a** and **2b** were given previously (15).

Preparation of $[Co(\mathbf{1a})]_4[PF_6]_8$ (2a)

To a suspension of **1a** (0.0510 g, 0.131 mmol) in methanol (15 mL) was added cobalt acetate tetrahydrate (0.0080 g, 0.0278 mmol) in methanol (5 mL). The reaction mixture was heated at reflux for 1.5 h. The colourless suspension gave way to a dark brown solution. Excess methanolic ammonium hexafluorophosphate was added to the hot reaction mixture leading to immediate precipitation of a brown solid. The solid was washed with methanol (2 × 10 mL) and water (2 × 10 mL) and was filtered. The solid was dissolved in acetone and was reprecipitated by the addition of diethyl ether giving **2a** (0.0796 g, 82%) as a brown solid; mp > 300 °C. IR (cm^{-1}): 1606, 1466, 844, 559. *m/z* (FAB): 2802 (M – 145 (-PF_6)), 2659 (M – 288 (-2PF_6)), 2516 (M – 431 (-3PF_6)), 2369 (M – 578 (- PF_6)). Anal. calcd. for $C_{96}H_{64}F_{48}N_{24}P_8Co_4$: C (39.09), H (2.19), N (11.40); found: C (38.78), H (2.63), N (11.01).

Preparation of $[Co(\mathbf{1b})]_4[PF_6]_8$ (2b)

To a suspension of **1b** (0.0402 g, 0.100 mmol) in methanol (15 mL) was added cobalt acetate tetrahydrate (0.0177 g, 0.100 mmol) in methanol (5 mL). The reaction mixture was heated at reflux for 1.5 h. The colourless suspension gave way to a pale brown solution. Excess methanolic ammonium hexafluorophosphate was added to the hot reaction mixture leading to immediate precipitation of a brown solid. The solid was washed with methanol (2 × 10 mL) and water (2 × 10 mL) and was filtered. The solid was dissolved in acetone and was reprecipitated by the addition of diethyl ether giving **2b** (0.0213 g, 28%) as a pale brown solid. *m/z* (FAB): 2861 (M – 145 (-PF_6)), 2716 (M – 290 (-2PF_6)), 2571 (M – 435 (-3PF_6)), 2426 (M – 580 (-4PF_6)).

Preparation of $[Ni(\mathbf{1a})]_4[PF_6]_8$ (3a)

To a suspension of **1a** (0.0210 g, 0.0541 mmol) in ethanol–water (12 mL, 1:1) was added nickel acetate tetrahydrate (0.0135 g, 0.0541 mmol) dissolved in ethanol–

© 2004 NRC Canada

water (2 mL, 1:1). The mixture was heated at reflux for 16 h. The colourless suspension gave way to a dark red brown homogeneous solution. Excess aqueous ammonium hexafluorophosphate was added to the hot mixture leading to immediate precipitation of an orange solid. Recrystallization from acetonitrile–ether gave **3a** (0.0265 g, 66%) as an orange solid. mp > 300 °C. IR (cm^{-1}): 1619, 1606, 1466, 1450, 847, 559. *m/z* (FAB): 2804 (M – 145 (-PF_6), 5%), 2675 (M – 274 (-2PF_6 + O), 24%), 2529 (M – 419 (-3PF_6 + O), 70%), 2384 (M – 564 (-4PF_6 + O), 70%), 2239 (M – 710 (-5PF_6 + O), 32%), 2093 (M – 856 (-6PF_6 + O), 8%), 1265 ([M – 419]$^{2+}$ (-3PF_6 + O), 50%), 1192 ([M – 564]$^{2+}$ (-4PF_6 + O), 100%), 1120 ([M – 710]$^{2+}$ (-5PF_6 + O), 80%), 1047 ([M – 856]$^{2+}$ (-6PF_6 + O), 36%). Anal. calcd. for $C_{96}H_{64}F_{48}N_{24}P_8Ni_4$: C (39.10) H (2.19), N (11.40); found: C (40.60), H (2.30), N (11.88).

Preparation of [Zn(1a)]$_4$[PF$_6$]$_8$ (4a)

To a suspension of **1a** (0.0875 g, 0.225 mmol) in methanol (20 mL) was added zinc acetate dihydrate (0.0495 g, 0.225 mmol) in water (2 mL). The reaction mixture was heated at reflux for 5 h. The colourless suspension gave way to a clear solution. Excess aqueous ammonium hexafluorophosphate was added to the hot reaction mixture leading to immediate precipitation of a white solid. The solid was washed with methanol (2 × 10 mL) and water (2 × 10 mL), and was reprecipitated from acetone with diethyl ether. The solid was isolated and dried. Recrystallization from acetonitrile–ether gave **4a** (0.0799 g, 48%) as an off-white solid. mp dec. 290 °C. ^{1}H NMR (300 MHz, ppm) δ: 9.40 (s, H_5, 1H), 9.16 (d, $H_{5'}$, *J* = 7.7 Hz, 2H), 8.86 (t, $H_{4'}$, *J* = 7.9 Hz, 2H), 8.78 (d, $H_{3'}$, *J* = 7.7 Hz, 2H), 8.35 (d, $H_{3''}$, *J* = 8.1 Hz, 2H), 8.02 (dt, $H_{4''}$, *J* = 7.8, 1.7 Hz, 2H), 7.40 (s, H_2, 1H), 7.28 (d, $H_{6''}$, *J* = 4.0 Hz, 2H), 7.23 (ddd, $H_{5''}$, *J* = 7.4, 5.2, 0.8 Hz, 2H). ^{13}C NMR (DEPT, ppm) δ: 159.9, 151.8, 148.9, 146.2, 142.5, 128.9, 128.1, 126.8, 124.5. *m/z* (FAB): 2832 (M – 143 (-PF_6)), 2686 (M – 290 (-2PF_6)), 2557 (M – 418 (-3PF_6 + O)), 2540 (M – 435 (-3PF_6)), 2395 (M – 580 (-4PF_6)), 2250 (M – 725 (-5PF_6)), 1732 (M – 1243 (-**1a**, 5PF_6 + O)), 1586 (M – 1389 (-**1a**, 6PF_6 + O)), 1441 (M – 1534 (-**1a**, 7PF_6 + O)), 1270 ([M – 435]$^{2+}$ (-3PF_6)), 1198 ([M – 580]$^{2+}$ (-4PF_6), 1125 ([M – 725]$^{2+}$ (-5PF_6). Anal. calcd. for $C_{96}H_{64}F_{48}N_{24}P_8Zn_4$: C 38.75, H 2.17, N 11.30; found: C 38.72, H 2.61, N 11.60.

Preparation of [Cd(1a)]$_4$[PF$_6$]$_8$ (5a)

To a suspension of **1a** (0.0108 g, 0.0278 mmol) in methanol (10 mL) was added cadmium acetate dihydrate (0.0080 g, 0.0278 mmol) in methanol (1 mL). The reaction mixture was heated at reflux for 1.5 h. The colourless suspension gave way to a clear solution. Excess aqueous ammonium hexafluorophosphate was added to the hot reaction mixture leading to immediate precipitation of a white solid. The solid was washed with methanol and recrystallized from acetonitrile–ether giving **5a** (0.0131 g, 60%) as an off-white solid. mp > 300 °C. IR (cm^{-1}): 1601, 1580, 1464, 1447, 1024, 843, 558. ^{1}H NMR (ppm) δ: 9.36 (s, H_5, 1H), 9.10 (dd, $H_{5'}$, *J* = 6.9, 1.5 Hz, 2H), 8.74 (m, $H_{3',4'}$, 4H), 8.41 (d, $H_{3''}$, *J* = 8.0 Hz, 2H), 8.06 (m, $H_{4'',5}$, 3H), 7.70 (d, $H_{6''}$, *J* = 4.0 Hz, 2H), 7.32 (dd, $H_{5''}$, *J* = 6.9, 5.1 Hz, 2H). ^{13}C NMR (ppm) δ: 159.6 (CH), 151.6, 150.4 (CH), 145.0 (CH), 142.3 (CH), 128.5 (CH), 127.9 (CH), 127.8, 127.5, 127.2, 127.1 (CH), 124.7 (CH), 118.4 (CH). *m/z* (FAB): 3018 (M – 144 (-PF_6)), 2873 (M – 290 (-2PF_6)), 2728 (M – 435 (-3PF_6)), 2395 (M – 581 (-4PF_6)), 1824 (M – 1339 (- **1a**, 2Cd, 5PF_6)), 1680 (M – 1483 (-**1a**, 2Cu, 6PF_6)). Anal. calcd. for $C_{96}H_{64}F_{48}N_{24}P_8Cd_4$: C 36.45, H 2.04, N 10.63; found: C 36.32, H 2.33, N 10.40.

Preparation of [Fe(1a)]$_4$[PF$_6$]$_8$ (6a)

To a suspension of **1a** (0.0108 g, 0.0278 mmol) in chloroform–acetonitrile (10 mL, 1:1) was added iron tetrafluoroborate (0.0080 g, 0.0278 mmol) in MeCN (1 mL). The reaction mixture was heated at reflux for 5 h. The colourless suspension gave way to a deep green solution. The solvent was removed under reduced pressure and the remaining solid dissolved in acetone. Addition of excess ammonium hexafluorophosphate in acetone afforded a green precipitate. After anion exchange with tetrabutylammonium chloride in acetonitrile, the green solid was dissolved in a minimum of water and was chromatographed on Sephadex with increasingly concentrated NaCl solutions. A green band was collected with 0.4 mol L^{-1} NaCl and was treated with ammonium hexafluorophosphate giving **6a** (0.0013 g, 6.0%). IR (cm^{-1}): 1605, 846, 558. ^{1}H NMR (ppm) δ: 9.28 (d, $H_{3'\text{ or }5'}$, *J* = 7.6 Hz, 2H), 9.09 (s, H_5, 1H), 8.93 (t, $H_{4'}$, *J* = 7.9 Hz, 2H), 8.85 (td, $H_{3''}$, *J* = 8.0, 1.0 Hz, 2H), 8.22 (d, $H_{3'\text{ or }5'}$, *J* = 7.8 Hz, 2H), 7.67 (dt, $H_{4''}$, *J* = 7.8, 1.3 Hz, 2H), 6.82 (ddd, $H_{5''}$, *J* = 7.6, 5.6, 1.1 Hz, 2H), 6.61 (d, $H_{6''}$, *J* = 4.0 Hz, 2H), 5.14 (d, H_2, *J* = 0.5 Hz, 1H). *m/z* (FAB): (M – 144 (-PF_6), 10%), (M – 288 (-2PF_6), 30%), (M – 333 (-3PF_6), 20%). Anal. calcd. for $C_{96}H_{64}F_{48}N_{24}P_8Fe_4$: C 39.26, H 2.20, N 11.45; found: C 39.36, H 2.52, N 11.17.

Preparation of [Ru(1a)]$_4$[PF$_6$]$_8$ (7a)

To a suspension of **1a** (0.0210 g, 0.0541 mmol) in ethylene glycol (12 mL, 1:1) was added ruthenium trichloride trihydrate (0.0141 g, 0.0541 mmol). The reaction mixture was heated at reflux for 16 h. The colourless suspension gave way to a dark purple-black homogeneous solution. Excess aqueous ammonium hexafluorophosphate was added to the hot reaction mixture leading to immediate precipitate formation. The solid was isolated by filtration, was dissolved in acetone and the chloride salt was recipitated by the addition of tetrabutylammonium chloride in acetone. The purple-black solid was dissolved in a minimum of water and was chromatographed on Sephadex with increasingly concentrated NaCl solutions. A purple-black band was collected (0.4 mol L^{-1} NaCl) and was treated with ammonium hexafluorophosphate giving **7a** (0.008 g, 2%). ^{1}H NMR (ppm) δ: 10.56 (s, H_5, 1H), 10.08 (d, $H_{3'\text{ or }5'}$, *J* = 7.8 Hz, 2H), 8.73 (d, $H_{3'\text{ or }5'}$, *J* = 8.1 Hz, 2H), 8.59 (t, $H_{4'}$, *J* = 8.0 Hz, 2H), 8.33 (d, $H_{3''}$, *J* = 8.0 Hz, 2H), 7.77 (dt, $H_{4''}$, *J* = Hz, 2H), 7.11 (d, $H_{6''}$, *J* = 4.5 Hz, 2H), 6.95 (m, $H_{5''}$, 2H), 5.75 (s, H_2, 1H). *m/z* (FAB): 2866 (M – 252 (-2PF_6 + 2H + Cl)), 2719 (M – 399 (-3PF_6 + Cl)), 2572 (M – 546 (-4PF_6 – 2H + Cl)), 2426 (M – 692 (-5PF_6 + Cl)).

Acknowledgements

GSH thanks the Natural Sciences and Engineering Research Council of Canada (NSERC) for a post-graduate

© 2004 NRC Canada

fellowship. DV thanks the Alexander-von-Humboldt foundation for a Feodor Lynen post-doctoral fellowship.

References

1. A. Gelasco, A. Askenas, and V.L. Pecoraro. Inorg. Chem. **35**, 1419 (1996).
2. R.V. Slone, J.T. Hupp, C.L. Stern, and T.E. Albrecht-Schmitt. Inorg. Chem. **35**, 4096 (1996).
3. J.-M. Lehn, A. Rigault, J. Siegel, J. Harrowfield, B. Chevrier, and D. Moras. Proc. Natl. Acad. Sci. U.S.A. **84**, 2565 (1987).
4. (*a*) B. Hasenknopf, J.-M. Lehn, N. Boumediene, A. Dupont-Gervais, A. Van Dorsselaer, B. Kneisel, and D. Fenske. J. Am. Chem. Soc. **119**, 10 956 (1997); (*b*) B. Hasenknopf, J.-M. Lehn, N. Boumediene, E. Leize, and A. Van Dorsselaer. Angew. Chem. Int. Ed. **37**, 3265 (1998).
5. H. Sleiman, P.N.W. Baxter, J.-M. Lehn, and K. Rissanen. J. Chem. Soc. Chem. Commun. 715, (1995).
6. P. Baxter and J.-M. Lehn. Angew. Chem. Int. Ed. Engl. **32**, 69 (1993).
7. A. Pfeil and J.-M. Lehn. J. Chem. Soc. Chem. Commun. 838 (1992).
8. A. Marquis-Rigault, A. Dupont-Gervais, P.N.W. Baxter, A. Van Dorsselaer, and J.-M. Lehn. Inorg. Chem. **35**, 2307 (1996).
9. J.-M. Lehn. Supramolecular chemistry — Concepts and perspectives. VCH, Weinheim. 1995.
10. G.S. Hanan, C.R. Arana, J.-M. Lehn, and D. Fenske. Angew. Chem., Int. Ed. Engl. **34**, 1122 (1995).
11. G.S. Hanan, C.R. Arana, J.-M. Lehn, G. Baum, and D. Fenske. Chem. Eur. J. **2**, 1292 (1996).
12. P.N. Baxter, G.S. Hanan, and J.-M. Lehn. Chem. Commun. 2019 (1996).
13. (*a*) M.-T. Youinou, N. Rahmouni, J. Fischer, and J.A. Osborn. Angew. Chem. Int. Ed. Engl. **31**, 733 (1992); (*b*) P. Baxter, J.-M. Lehn, J. Fischer, and M.-T. Youinou. Angew. Chem. Int. Ed. Engl. **33**, 2284 (1994).
14. (*a*) A.M. Garcia, F.J. Romero-Salguero, D.M. Bassani, J.-M. Lehn, G. Baum, and D. Fenske. Chem. Eur. J. **5**, 1803 (1999); (*b*) L. Zhao, C.J. Matthews, L.K. Thompson, and S.L. Heath. Chem. Commun. 265 (2000); (*c*) D.M. Bassani, J.-M. Lehn, K. Fromm, and D. Fenske. Angew. Chem. Int. Ed. **37**, 2364 (1998); (*d*) T. Bark, M. Duggeli, H. Stoeckli-Evans, and A. von Zelewsky. Angew. Chem. Int. Ed. **40**, 2848 (2001); (*e*) E. Breuning, G.S. Hanan, F.J. Romero-Salguero, A.M. Garcia, P.N.W. Baxter, J.-M. Lehn, E. Wegelius, K. Rissanen, H. Nierengarten, and A. Van Dorsselaer. Chem. Eur. J. **8**, 3458 (2002); (*f*) M. Ruben, E. Breuning, M. Barboiu, J.-P. Gisselbrecht, and J.-M. Lehn. Chem. Eur. J. **9**, 291 (2003); (*g*) M. Ruben, E. Breuning, J.-M. Lehn, V. Ksenofontov, F. Renz, P. Guetlich, and G.B.M. Vaughan. Chem. Eur. J. **9**, 4422 (2003).
15. G.S. Hanan, D. Volkmer, U.S. Schubert, J.-M. Lehn, G. Baum, and D. Fenske. Angew. Chem. Int. Ed. Engl. **36**, 1842 (1997).
16. (*a*) R. Chotalia, E.C. Constable, M. Neuburger, D.R. Smith, and M. Zehnder. J. Chem. Soc. Dalton Trans. 4207 (1996); (*b*) E.C. Constable, M.D. Ward, and D.A. Tocher. J. Chem. Soc. Dalton Trans. 1675 (1991).
17. E.C. Constable. *In* Progress in Inorganic Chemistry. *Edited by* K.D. Karlin. Vol. 42. John Wiley and Sons, Inc., New York. 1994. p. 67.
18. G. Denti, S. Campagna, S. Serroni, M. Ciano, and V. Balzani. J. Am. Chem. Soc. **114**, 2944 (1992).
19. C.A. Bessel, R.F. See, D.L. Jameson, M.R. Churchill, and K.L. Takeuchi. J. Chem. Soc. Dalton Trans. 3223 (1992).
20. R.P. Thummel and Y. Jahng. Inorg. Chem. **25**, 2527 (1986).
21. F.A. Cotton and G. Wilkinson. Advanced inorganic chemistry. John Wiley and Sons, Toronto. 1988.
22. H. Elsbernd and J.K. Beattie. J. Inorg. Nucl. Chem. **34**, 771 (1972).
23. G. Denti, S. Campagna, L. Sabatino, S. Serroni, M. Ciano, and V. Balzani. Inorg. Chem. **29**, 4750 (1990).
24. C. Dietrich-Buchecker, J. Guilhem, J.-M. Kern, C. Pascard, and J.-P. Sauvage. Inorg. Chem. **33**, 3498 (1994).
25. G. Giuffrida and S. Campagna. Coord. Chem. Rev. **135/136**, 517 (1994).
26. C. Dietrich-Buchecker, J.-P. Sauvage, and J.-M. Kern. J. Am. Chem. Soc. **111**, 7791 (1989).
27. R. Prasad and D.B. Scaife. J. Electroanal. Chem. **84**, 373 (1977).
28. S. Campagna, G. Denti, M. Ciano, and V. Balzani. Inorg. Chem. **30**, 3728 (1991).
29. V. Balzani and F. Scandola. Supramolecular photochemistry. Ellis Horwood, Chichester, UK. 1991.
30. P.J. Steel. Coord. Chem. Rev. **106**, 227 (1990).
31. M. Barboiu, G. Vaughan, R. Graff, and J.-M. Lehn. J. Am. Chem. Soc. **125**, 10 257 (2003).
32. E. Breuning, U. Ziener, J.-M. Lehn, E. Wegelius, and K. Rissanen. Eur. J. Inorg. Chem. 1515 (2001).
33. (*a*) C.A. Mirkin. Inorg. Chem. **39**, 2258 (2000); (*b*) A. Semenov, J.P. Spatz, M. Möller, J.-M. Lehn, B. Sell, D. Schubert, C. H. Weidl, and U. S. Schubert. Angew. Chem. Int. Ed. **38**, 2547 (1999).
34. G.S. Hanan, U.S. Schubert, D. Volkmer, E. Riviere, J.-M. Lehn, N. Kyritsakas, and J. Fischer. Can. J. Chem. **75**, 169 (1997).

© 2004 NRC Canada

Surface-enhanced Raman spectroscopy with a laser pointer light source and miniature spectrometer[1]

Matthew A. Young, Douglas A. Stuart, Olga Lyandres, Matthew R. Glucksberg, and Richard P. Van Duyne

Abstract: The initial steps toward a miniature, field portable sensor based on surface-enhanced Raman spectroscopy (SERS) are presented. It is demonstrated that a low-cost miniaturized Raman system can be used in place of a larger, higher-cost conventional Raman system. This system was developed by sequentially replacing components of a laboratory scale Raman spectroscopy system with smaller, lower-cost, commercially available components. For example, a green laser pointer was used as the excitation source, a reflectance probe fiber-optic cable was used for laser delivery and collection, and a compact card-based spectrometer was used for dispersion and detection. Spectra, collected with the laser pointer Raman system, are presented of a resonant (Rhodamine 6G) and a non-resonant (*trans*-1,2-bis(4-pyridyl)ethylene) molecule as well as a self-assembled monolayer (1-decanethiol). Small, low-cost sensors are in demand for a variety of applications, and SERS is positioned to contribute significantly with its remarkable sensitivity and molecular specificity.

Key words: Raman, SERS, fiber-optics, sensor.

Résumé : On présente les étapes initiales dans le développement d'une sonde miniature, à base de spectroscopie Raman de surface améliorée (SERS), qui serait utilisable sur le terrain. On a démontré qu'un système Raman miniaturisé et peu coûteux pourrait être utilisé à la place d'un système Raman conventionnel, plus volumineux et de coût plus élevé. Ce système a été mis au point en remplaçant successivement des composants d'un système de spectroscopie Raman normal de laboratoire par des composants plus petits et moins coûteux et commercialement disponibles. Par exemple, on a utilisé un laser vert pointeur comme source d'excitation, un câble en fibre optique d'une sonde de réflectance pour distribution et la collection du laser ou un spectromètre compact à base de carte pour la dispersion et la détection. Utilisant le système Raman à laser pointeur, on a recueilli les spectres de molécules résonante (Rhodamine 6G) et non résonante [*trans*-1,2-bis(4-pyridyl)éthylène] ainsi que d'une monocouche autoassemblée (décane-1-thiol). Les petites sondes peu coûteuses sont très en demande pour un grand nombre d'applications et la technique SERS est en bonne position pour faire des contributions importantes en raison de sa sensibilité remarquable et de sa spécificité moléculaire.

Mots clés : Raman, SERS, fibre optique, sonde.

[Traduit par la Rédaction]

Introduction

In the past few years, surface-enhanced Raman spectroscopy (SERS) has generated significant interest as a method for various sensing applications (1–10). Most chemical sensors rely on properties such as mass, fluorescence, or refractive index, which are often not specific for the substance in question. In contrast, Raman spectroscopy offers rich molecular information, and thus often provides unequivocal identification of chemical and biological materials of interest. Unfortunately, Raman spectroscopy is limited in its applicability to sensing schemes that require trace analysis because of the inefficiency of the Raman scattering process. Since 1977, it has been known that significant enhancement of the Raman scattering, and subsequent improvement in the detection, can be realized from molecules adsorbed on specifically roughened metal surfaces (11), and tremendous effort has been expended to explore and exploit this property. Generally, in ensemble averaged systems, SERS enhancement factors as large as 10^8 have been realized (12). Under certain

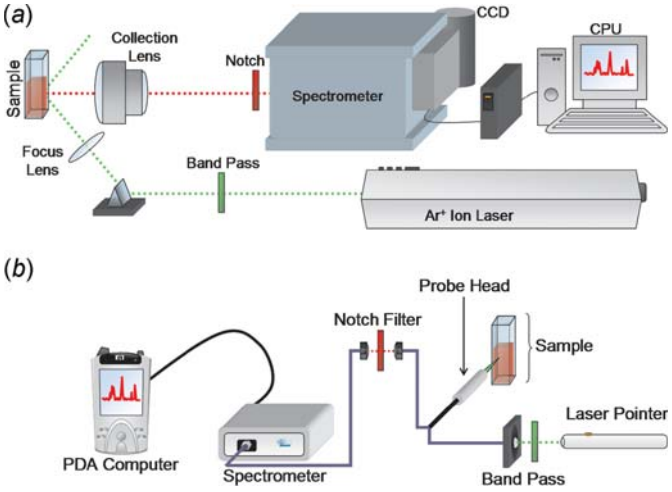
Received 19 March 2004. Published on the NRC Research Press Web site at http://canjchem.nrc.ca on 21 October 2004.

M.A. Young, D.A. Stuart, and R.P. Van Duyne.[2] Department of Chemistry, Northwestern University, Evanston, IL 60208-3113, USA.
O. Lyandres and M.R. Glucksberg. Department of Biomedical Engineering, Northwestern University, Evanston, IL 60208-3113, USA.

[1]This article is part of a Special Issue dedicated to the memory of Professor Don Irish.
[2]Corresponding author (e-mail: vanduyne@chem.northwestern.edu).

 doi: 10.1139/V04-098 © 2004 NRC Canada

Fig. 1. Experimental set-ups. (*a*) Conventional Raman system and (*b*) miniaturized system assembled with available lab equipment. Most of the cumbersome and expensive elements have been replaced with compact, off-the-shelf components to realize a savings in cost, size, and weight.



experimental conditions, enhancement factors of ~10^{14} have been achieved (13, 14), making SERS the only vibrational spectroscopy capable of both detecting and identifying single molecules under ambient conditions. With this enhancement, SERS provides exquisite sensitivity, which is complemented by the molecular specificity inherent to vibrational spectroscopy. SERS has been employed in the development of a myriad of sensors, including those detecting chemical and biological agents (15–18), explosives (19, 20), glucose (9, 10, 21), aromatics (22, 23), proteins (24, 25), and DNA (26–29).

In addition to being highly sensitive and selective, attractive properties for sensors include rapid response, ease of use, reliability, and low cost. Raman spectroscopy has taken several steps in this direction. The developments of sensitive charge-coupled device (CCD) detectors and holographic notch filters have allowed the rapid and facile implementation of Raman spectroscopy in a range of applications. The development of the silver film over nanosphere (AgFON) surface (30, 31), with reproducible nanoscale roughness features, has enabled stable and consistent SERS measurements to be taken. In addition, Ag colloids have proven to be reliable SERS active substrates and are used by a large number of researchers. Thus, SERS has become a relatively fast, simple, and reliable spectroscopy.

There remains a major limiting factor for the implementation of Raman spectroscopy to widespread sensing applications. This drawback is that for Raman (and SERS) experiments, large and expensive equipment is required. The major components of a typical Raman instrument are the laser, the delivery optics, the sample, the collection optics, the spectrograph, and the detector (Fig. 1*a*). Each component can take up significant space, be extremely expensive, and be difficult to assemble, align, and maintain. These factors, particularly the physical dimensions and cost, are important obstacles for the realization of Raman spectroscopy for use in critical routine situations such as blood glucose monitoring, drinking water testing, forensics, remote field defense sensing, and environmental sampling. Several small Raman systems have been recently developed to address these issues. These include systems from InPhotonics (Norwood, Mass.), Digilab (Randolph, Mass.), Enwave Optronics (Irvine, Calif.), and Delta Nu (Laramie, Wyo.). Towards this same end, the present work focuses on decreasing the cost and size of the typical Raman setup. Replacing many of the classic elements of the Raman setup listed above with smaller, lower-cost alternatives will be an important step in the realization of simple, field-worthy spectrometers and sensors based on the SERS phenomenon.

The work presented in this paper describes the first steps towards replacing the most cumbersome and costly elements of a traditional Raman system with significantly smaller and cheaper components (Fig. 1*b*). AgFON surfaces are used as SERS active substrates because they have been shown to be reproducible and stable in electrochemical, ultrahigh vacuum, and ambient experimental conditions (30, 32, 33) Thus, AgFONs are well-suited to the wide range of environments in which SERS sensors would be deployed. This work adds substantially to the growing literature demonstrations that SERS is feasible utilizing low-cost, compact, and readily available components while retaining the necessary sensitivity for sensing applications.

Experimental

Materials and equipment

Ag wire (99.99%, 0.04″ diameter (1 inch = 25.4 mm)) was purchased from D.F. Goldsmith (Evanston, Ill.). The Ag disk electrodes consisted of a Ag rod sealed with an epoxy (Torr Seal, Varian) into a Teflon® frame. The glass substrates were 18 mm diameter, No. 2 cover slips from Fisher Scientific (Pittsburgh, Penn.). Pretreatment of glass substrates required H_2SO_4, H_2O_2, and NH_4OH, all purchased from Fisher Scientific (Pittsburgh, Penn.). Surfactant-free white carboxyl-substituted polystyrene latex nanospheres with diameters of 410 nm were obtained from Interfacial Dynamics Corp. (Portland, Ore.). Tungsten vapor deposition boats were purchased from R.D. Mathis (Long Beach, Calif.). Rhodamine 6G (98%) was purchased from Sigma (St. Louis, Mo.) and was used as received. *trans*-1,2-Bis(4-pyridyl)ethylene (97%), 1-decanethiol (96%), and benzene (99%) were purchased from Aldrich (Milwaukee, Wis.) and used as received.

AgFON surface preparation

AgFON surfaces were fabricated with the use of a modified Consolidated Vacuum Corporation vapor deposition system. The steps included: (1) polishing an electrode surface with 0.3 and 0.05 μm alumina; (2) coating the smooth electrode surface with 410 nm diameter surfactant-free white carboxyl-substituted polystyrene latex nanospheres and allowing to dry; (3) masking off the area where deposited metal is not desired; (4) depositing 200 nm Ag; and (5) removing the mask after metal deposition. When glass was used instead of the electrode surfaces, the same procedure was followed, but without the polishing and masking. The glass also required a pretreatment consisting of: (1) piranha etch, H_2SO_4 – 30% H_2O_2 (3:1) at 80 °C for 1 h to clean the substrate; and (2) base treatment, H_2O – NH_4OH – 30%

© 2004 NRC Canada

Table 1. Comparison of cost, size, and weight between the conventional and miniaturized Raman systems.

Component	Cost (US dollars)	Size (cm)	Weight (kg)	Manufacturer	Model No.
Standard					
Ion laser	50 000	150×25×25	45	Spectra Physics	2060
Optics	200	10×6	0.3	Edmund	—
Notch filter	895	2.5×35	0.1	Semrock	NF01-532U-25
Spectrograph	15 000	55×40×40	23	Acton	VM-505
CCD	34 000	20×10×5	2	Roper Scientific	Spec-10:400B
Computer	600	50×50×20	4	Dell	—
Monitor	100	30×30×20	9	Dell	—
Total	100 795	250 810 cm^3	83.4	—	—
Miniature					
Laser pointer	99	15×1.5	72	JD Photonics	Green-GLP
Fiber probe	549	1000×0.5	100	Ocean Optics	R200-REF
Long pass filter	420	2.5×0.35	25	Semrock	LP01-532RU-25
Spectrometer	2 000	14.1×10.49×4.09	390	Ocean Optics	SD2000
CCD	Integrated	—	—	—	—
PDA	600	13.8×8.4×1.59	200	HP	iPAQ n5555
Total	3 668	1313 cm^3	787	—	—

Note: The miniaturized system is about 4% the cost and 0.5% the size of the standard system.

H_2O_2 (5:1:1) with sonication for 1 h to render the surface hydrophilic.

Raman spectroscopy

Sequential instrumental configurations were implemented to evaluate the efficiency and performance characteristics of the miniature Raman system. A variety of molecules were probed to establish the applicability and utility of the instrument to the detection of molecules differing in chemical structure and scattering cross sections. In the first series of experiments, the AgFON substrates were incubated in both resonant and non-resonant molecules. The first instrumental configuration closely approximates that used in conventional, lab-scale Raman spectroscopy. The first step taken in this work was to replace the excitation Argon ion laser (Spectra-Physics, Mountain View, Calif.) with an inexpensive CW green laser pointer (JD Photonics, Renton, Wash.). The battery powered green laser pointer consists of a high power IR laser diode at 808 nm pumping a tiny block of Nd:YVO_4, which generates light at 1064 nm. This feeds a KTP intracavity frequency doubling crystal to produce the green beam at 532 nm. The Raman instrument was further modified by replacing the bulky collection and focusing optics with a low profile 200 μm core reflection fiber-optic probe (Ocean Optics, Dunedin, Fla.). Raman spectra for the resonant and non-resonant molecules were collected by focusing the output of the fiber onto the entrance slit of the large scale Acton VM-505 dispersion spectrograph (Acton, Mass.) with a Roper Scientific (Trenton, N.J.) Spec-10:400B liquid N_2 cooled CCD detector. Finally, we evaluated the use of a compact, off the shelf, card-based, USB interface Ocean Optics (Dunedin, Fla.) model SD2000 spectrometer as a replacement for the critical dispersion and detection components. The dual channel spectrometer is configured with a 600 lines mm^{-1} grating and a 1200 lines mm^{-1} grating. Conveniently, the fiber-optic bearing the Raman scattered light can be coupled directly into this spectrometer, allowing for quick and simple alignment.

Results and discussion

Clearly, experimental Raman spectroscopy has traditionally been an expensive endeavor. In addition to being costly, the large components have prevented an easily portable system. Figure 1 depicts our miniaturized (and lower cost) Raman setup and compares it to a traditional system. Table 1 summarizes the approximate cost, size, and weight of the components for both the conventional and miniature Raman instruments. This does not depict the lowest-cost or highest-cost systems that one could construct. It is an estimate based on the systems used in our lab. Readily available components have been used to demonstrate the feasibility of performing SERS experiments with a small and relatively inexpensive setup. Obviously, conventional setups have many advantages (e.g., wavelength selection, more power, higher sensitivity, and high resolution) over the presented low-cost prototype. However, for many applications this approach presents an attractive alternative. The significant savings in resources and space generously offsets the compromise in resolution and sensitivity. Additionally, a miniaturized system will increase the use of Raman and SERS for portable environmental testing and in undergraduate teaching laboratories.

We have used an *aufbau* approach to demonstrate the concept of an economical, miniaturized SERS instrument. We have systematically built up this system by consecutively replacing components of a conventional system with lower-cost, smaller items. The project began with the replacement of the traditional excitation source (Ar^+, Ti:S, HeNe, or dye laser) with a simple green laser pointer (GLP), λ_{ex} = 532 nm. Figures 2 and 3 show the applicability of the GLP as a SERS excitation source for both resonant and non-resonant molecules. While Rhodamine 6G (R6G) is resonant at 532 nm, *trans*-1,2-bis(4-pyridyl)ethylene (BPE) is not. BPE is a relatively strong Raman scatterer and it has been a molecule of interest for many SERS studies (34–38). For the R6G experiment, the AgFON on a polished electrode was

© 2004 NRC Canada

Fig. 2. SER spectrum of R6G on a AgFON electrode (dry). λ_{ex} = 532 nm (GLP). (*a*) *P* = 0.25 mW, acquisition time = 300 ms. (*b*) Laser delivered and collected with reflectance probe fiber-optic. *P* = 10 μW, acquisition time = 10 s.

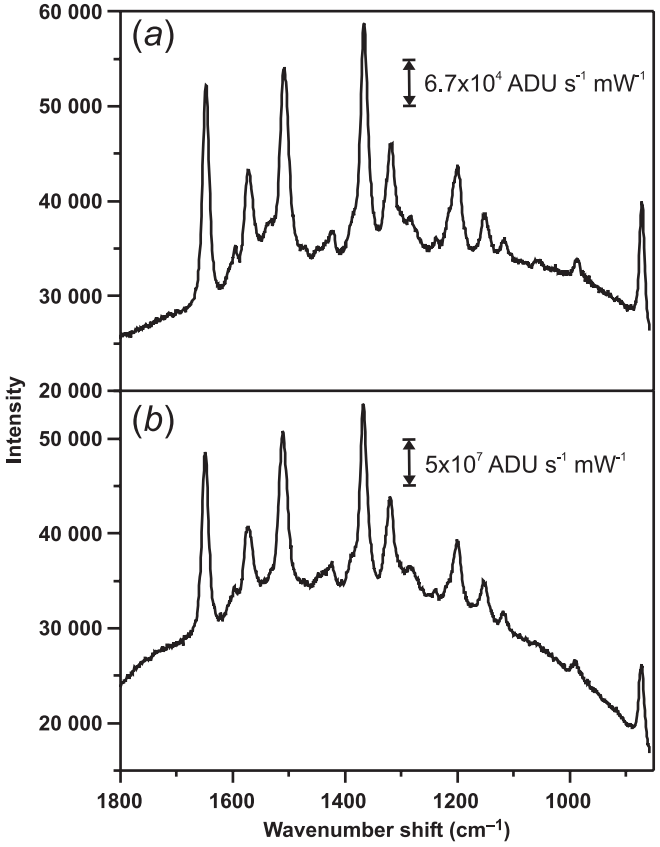
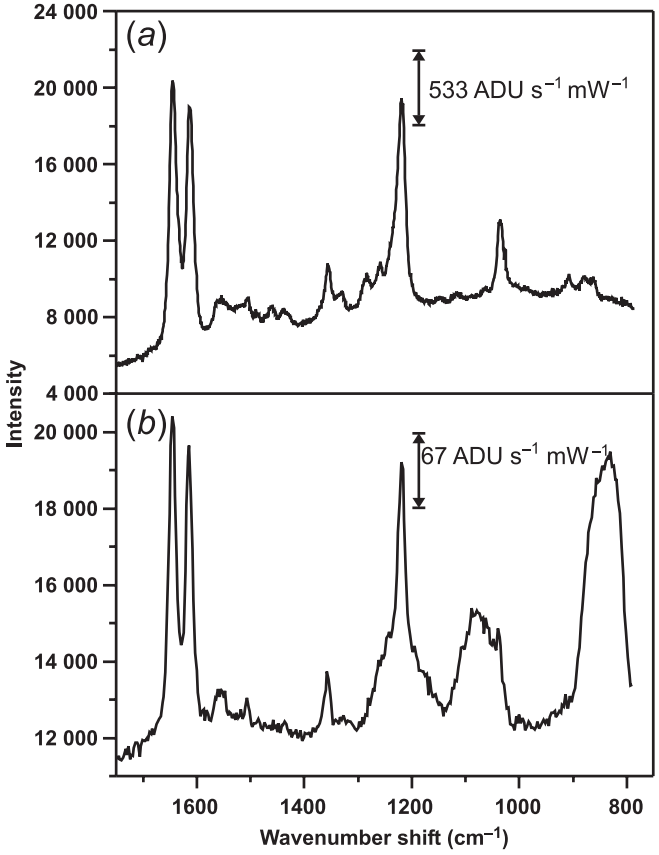


Fig. 3. SER spectrum of BPE on a AgFON electrode in flow cell. λ_{ex} = 532 nm (GLP). (*a*) *P* = 1.5 mW, acquisition time = 5 s. (*b*) Laser delivered and collected with reflectance probe fiber-optic. *P* = 0.25 mW, bin 3, acquisition time = 40 s.



incubated in 2.4 μmol L^{-1} R6G solution for 10 min., then rinsed carefully with water and allowed to dry. In the case of BPE, a 0.5 mmol L^{-1} solution was introduced into a flow cell containing a AgFON on a polished Ag electrode. Figures 2*a* and 3*a* show high quality SER spectra acquired using the GLP as the excitation source. The spectra exhibit intense, well-defined peaks characteristic of the given molecule.

A second set of experiments was conducted to determine the effect of altering the collection optics and light delivery of the system. Figures 2*b* and 3*b* show the case where the light delivery, focusing, and collection optics are replaced by a fiber-optic probe. The light was delivered from the GLP to the sample through the probe, and the scattered light was collected by the probe and focused onto the slit of the Acton spectrometer. The spectra compare quite favorably to those using conventional delivery and collection optics. In the case of R6G, little to no signal intensity is lost with the fiber-based delivery and collection. For BPE, the signal is slightly attenuated, but an ample amount of Raman scattered light is transmitted back through the fiber to generate a strong SER spectrum in a short collection time. The broad featureless peaks on the right side of the BPE spectrum (~1225, ~1075, and ~840 cm^{-1}) are due to Raman scattering generated inside the fiber itself. Altering the filter design of the fiber-optic probe can eliminate these broad peaks. They could also be removed by background subtraction since they are constant at a given excitation power.

In addition to strong scatterers such as R6G and BPE, it is important to demonstrate the acquisition of spectra of molecules with smaller Raman scattering cross sections. Many analytes of interest in sensing applications are not strong scatterers. Figure 4 depicts an SER spectrum with a laser pointer utilizing a self-assembled monolayer (SAM) of 1-decanethiol (1-DT). SAMs have generated enormous interest in many areas of chemistry, including SERS; and they are vital for many sensing applications including their use as species selective partition layers (9, 10, 27, 39–42). 1-DT is a relatively poor Raman scatterer, but a SER spectrum was readily obtained using the GLP as the excitation source.

The final components to be replaced in the conventional Raman apparatus are the spectrograph and detector. We replaced these components by coupling the collection fiber directly into an SD2000 spectrometer from Ocean Optics. Because these spectrometers are designed for UV–vis spectroscopy, it was necessary to determine if the sensitivity of the detector would be adequate for the low level of radiated photons generated by SERS and if the grating would provide sufficient dispersion to adequately resolve the narrow Raman peaks. While small laser diodes are available with adequate power (e.g., >10 mW), the GLP used in the above experiments supplies only 3 to 4 mW. Therefore, for this experi-

© 2004 NRC Canada

Fig. 4. SER spectrum of 1-DT on a AgFON on clean glass (dry). λ_{ex} = 532 nm (GLP). P = 0.5 mW, acquisition time = 60 s.

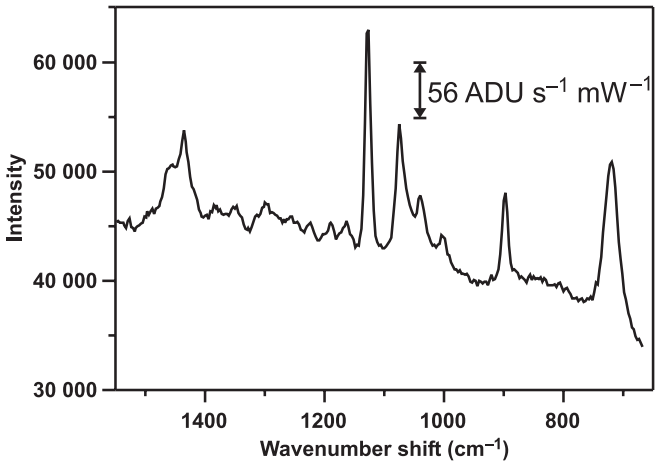
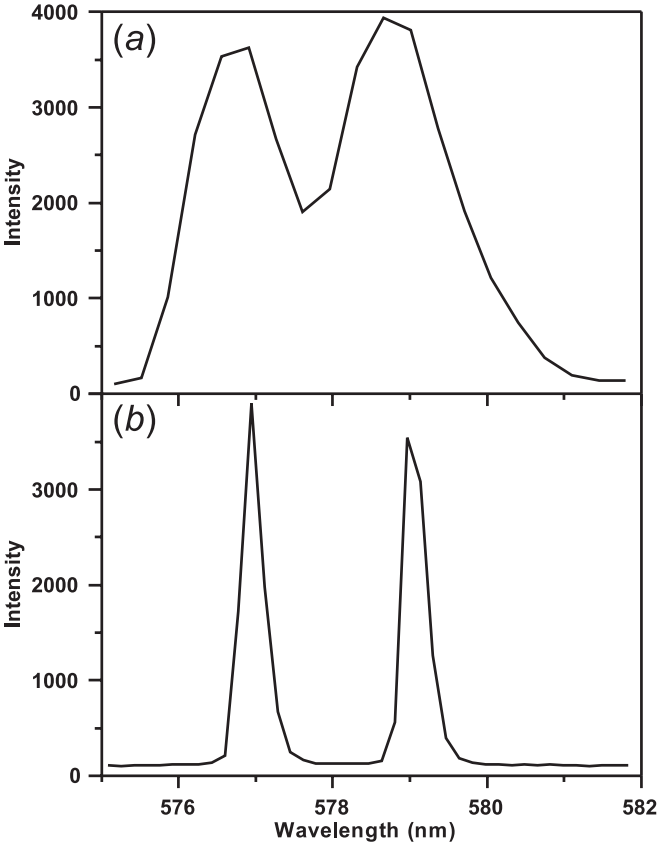
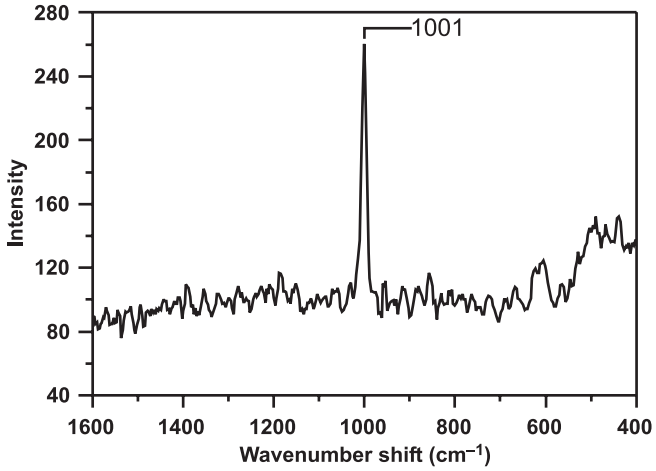


Fig. 5. Mercury emission lines recorded with SD2000 spectrometer. (*a*) Grating 1 (600 lines/mm) and (*b*) grating 2 (1200 lines/mm).



ment ~20 mW of laser light was coupled into the fiber using a Coherent (Santa Clara, Calif.) model 590 dye laser operating at λ_{ex} = 632.8 nm. This was done simply to allow more power to be coupled into the fiber, and to decrease the acquisition time. The SD2000 spectrometer used here is configured with two different gratings. Figure 5 shows a comparison of the two gratings using mercury emission

Fig. 6. Raman spectrum of neat benzene recorded with SD2000 spectrometer. λ_{ex} = 632.8 nm. Acquisition time = 30 s. S/N ~ 7.



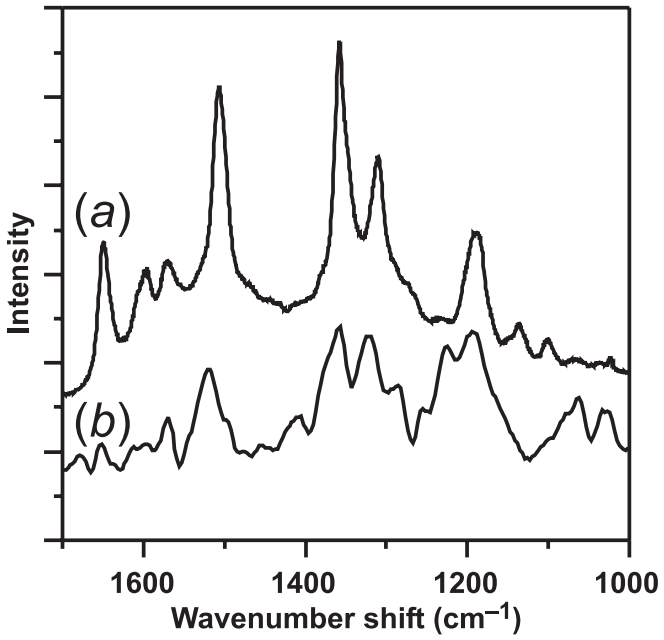
lines. It is clear that grating 2 has significantly higher resolution. Following Sommer and Stewart (43), band fitting of the 577 and 579 emission lines of the Hg lamp gave values of 0.32 nm and 0.37 nm at FWHM. These values were used to determine that the spectral resolution of this instrument is ~10 cm^{-1} at 632.8 nm excitation. Although the spectrometer was not originally optimized for the high resolution generally demanded for Raman spectroscopy, it gives sufficient resolution for identification of Raman signatures. This is clearly demonstrated in Fig. 6, which shows a normal Raman spectrum of benzene, with an estimated signal-to-noise ratio of ~7. While this is certainly less than ideal relative to spectra obtained on a commercial FT-Raman instrument, it is a positive step in the development of the miniaturized system. The measurement of a Raman spectrum of neat benzene is, however, substantially different than in a typical SERS experiment, in which the concentration of the analyte is significantly lower. Figure 7 directly compares SER spectra collected with the Acton spectrograph and the SD2000 spectrograph with R6G on a dried AgFON as the analyte. Figure 7*a* corresponds to the SER spectrum recorded on the Acton and Fig. 7*b* to the SER spectrum recorded on the SD2000 spectrograph. The intensity of the 7*a* spectrum was significantly reduced so that 7*a* and 7*b* could be on the same scale. The spectra compare quite favorably. While there is much room for improvement, this demonstration of SERS utilizing such a small and low-resolution piece of equipment is significant. The signature of R6G is clear and represents a considerable step towards the miniaturization of SERS instrumentation.

Conclusions

Here, we demonstrated that a low-cost miniaturized Raman system could be used in place of a larger, higher-cost conventional Raman system. There are clearly several advantages that remain with the larger and more expensive components of a Raman setup. In addition, the components that have been used in this work as a technology demonstration test-bed are far from optimized. While the ability to obtain adequate SERS spectra with small and cheap equipment has been clearly shown, the components used were selected

© 2004 NRC Canada

Fig. 7. SER spectrum of R6G on a AgFON on clean glass (dry). λ_{ex} = 632.8 nm. (*a*) Acton VM-505 spectrometer, *P* = 1.8 mW, acquisition time = 10 s. (*b*) Ocean Optics SD2000 spectrometer, acquisition time = 30 s.



primarily for being convenient, readily available, off the shelf components. Vast improvements in sensitivity and resolution can be made by carefully selecting each component (e.g., using smaller filters, altering the probe configuration, more sensitive detector, etc.). With continued optimization, smaller and less expensive equipment will allow SERS to enter into a variety of field-sensing applications that will contribute to public safety and improved quality of life.

Acknowledgements

The authors gratefully acknowledge Amanda J. Haes, Adam D. McFarland, and Chanda R. Yonzon for helpful comments and technical assistance. Funding for this work was provided by the Institute for Bioengineering and Nanoscience in Advanced Medicine at Northwestern University, the National Institutes of Health (EY13002, EY13015, and DK066990), the National Science Foundation (DMR-0076097), and the Air Force Office of Scientific Research MURI program (F49620-02-1-0381).

References

1. Y.W.C. Cao, R.C. Jin, and C.A. Mirkin. Science, **297**, 1536 (2002).
2. Y.C. Cao, R.C. Jin, J.M. Nam, C.S. Thaxton, and C.A. Mirkin. J. Am. Chem. Soc. **125**, 14 676 (2003).
3. W.E. Doering and S.M. Nie. Anal. Chem. **75**, 6171 (2003).
4. A. Tao, F. Kim, C. Hess, J. Goldberger, R. He, Y. Sun, Y. Xia, and P. Yang. Nano Lett. **3**, 1229 (2003).
5. A. McCabe, W.E. Smith, G. Thomson, D. Batchelder, R. Lacey, G. Ashcroft, and B.F. Foulger. Appl. Spectrosc. **56**, 820 (2002).
6. K. Kneipp, A.S. Haka, H. Kneipp, K. Badizadegan, N. Yoshizawa, C. Boone, K.E. Shafer-Peltier, J.T. Motz, R.R. Dasari, and M.S. Feld. Appl. Spectrosc. **56**, 150 (2002).
7. K. Kneipp and H. Kneipp. Can. J. Anal. Sci. Spect. **48**, 125 (2003).
8. R. Sulk, C. Chan, J. Guicheteau, C. Gomez, J.B.B. Heyns, R. Corcoran, and K. Carron. J. Raman. Spectrosc. **30**, 853 (1999).
9. K.E. Shafer-Peltier, C.L. Haynes, M.R. Glucksberg, and R.P. Van Duyne. J. Am. Chem. Soc. **125**, 588 (2003).
10. C.R. Yonzon, C.L. Haynes, X.Y. Zhang, J.T. Walsh, and R.P. Van Duyne. Anal. Chem. **76**, 78 (2004).
11. D.L. Jeanmaire and R.P. Van Duyne. J. Electroanal. Chem. **84**, 1 (1977).
12. C.L. Haynes and R.P. Van Duyne. J. Phys. Chem. B, **107**, 7426 (2003).
13. S.M. Nie and S.R. Emery. Science, **275**, 1102 (1997).
14. K. Kneipp, Y. Wang, H. Kneipp, L.T. Perelman, I. Itzkan, R. Dasari, and M.S. Feld. Phys. Rev. Lett. **78**, 1667 (1997).
15. S. Christesen, B. MacIver, L. Procell, D. Sorrick, B. Carrabba, and J. Bello. Appl. Spectrosc. **53**, 850 (1999).
16. S. Farquharson, L. Grigely, V. Khitrov, W. Smith, J.F. Sperry, and G. Fenerty. J. Raman. Spectrosc. **35**, 82 (2004).
17. S. Farquharson, W.W. Smith, V.Y.-H. Lee, S. Elliott, and J.F. Sperry. Proc. SPIE, **4575**, 62 (2002).
18. W.R. Premasiri, R.H. Clarke, and M.E. Womble. Proc. SPIE, **4577**, 205 (2002).
19. J.M. Sylvia, J.A. Janni, J.D. Klein, and K.M. Spencer. Anal. Chem. **72**, 5834 (2000).
20. J.A. Janni, J.M. Sylvia, S.L. Clauson, and K.M. Spencer. Proc. SPIE, **4577**, 230 (2002).
21. M.F. Mrozek and M.J. Weaver. Anal. Chem. **74**, 4069 (2002).
22. W. Hill, V. Fallourd, and D. Klockow. J. Phys. Chem. B, **103**, 4707 (1999).
23. B. Wehling, W. Hill, and D. Klockow. Int. J. Environ. Anal. Chem. **73**, 223 (1999).
24. M.H. Chowdhury, B. Atkinson, T. Good, and G.L. Cote. Proc. SPIE, **4965**, 111 (2003).
25. S. Habuchi, M. Cotlet, R. Gronheid, G. Dirix, J. Michiels, J. Vanderleyden, F.C. De Schryver, and J. Hofkens. J. Am. Chem. Soc. **125**, 8446 (2003).
26. T. Vo-Dinh, L.R. Allain, and D.L. Stokes. J. Raman. Spectrosc. **33**, 511 (2002).
27. M. Culha, D. Stokes, L.R. Allain, and T. Vo-Dinh. Anal. Chem. **75**, 6196 (2003).
28. D. Graham, L. Fruk, and W. Ewen Smith. Analyst (U.K.), **128**, 692 (2003).
29. D. Graham, B.J. Mallinder, and W.E. Smith. Biopolymers, **57**, 85 (2000).
30. L.A. Dick, A.D. McFarland, C.L. Haynes, and R.P. Van Duyne. J. Phys. Chem. B, **106**, 853 (2002).
31. R.P. Van Duyne, J.C. Hulteen, and D.A. Treichel. J. Chem. Phys. **99**, 2101 (1993).
32. M. Litorja, C.L. Haynes, A.J. Haes, T.R. Jensen, and R.P. Van Duyne. J. Phys. Chem. B, **105**, 6907 (2001).
33. P. Freunscht, R.P. Van Duyne, and S. Schneider. Chem. Phys. Lett. **281**, 372 (1997).
34. R.G. Freeman, R.M. Bright, M.B. Hommer, and M.J. Natan. J. Raman. Spectrosc. **30**, 733 (1999).
35. L. He, M.J. Natan, and C.D. Keating. Anal. Chem. **72**, 5348 (2000).
36. R. Aroca, P. Corio, and J.C. Rubim. Ann. Chim-Rome **87**, 1 (1997).
37. W.H. Yang, J. Hulteen, G.C. Schatz, and R.P. Van Duyne. J. Chem. Phys. **104**, 4313 (1996).

© 2004 NRC Canada

38. S. Bernard, N. Felidj, S. Truong, P. Peretti, G. Levi, and J. Aubard. Biopolymers, **67**, 314 (2002).
39. A. Loren, J. Engelbrektsson, C. Eliasson, M. Josefson, J. Abrahamsson, and K. Abrahamsson. Nano Lett. **4**, 309 (2004).
40. R.A. Sulk, R.C. Corcoran, and K.T. Carron. Appl. Spectrosc. **53**, 954 (1999).
41. L.A. Dick, A.J. Haes, and R.P. Van Duyne. J. Phys. Chem. B, **104**, 11 752 (2000).
42. D.H. Murgida and P. Hildebrandt. J. Phys. Chem. B, **105**, 1578 (2001).
43. A.J. Sommer and S.A. Stewart. Appl. Spectrosc. **53**, 483 (1999).

© 2004 NRC Canada

A vibrational spectroscopic study of the thermal behavior of $Re_2(CO)_{10}$ on zeolite Y[1]

Robert R. Poissant and Yining Huang

Abstract: This work describes the thermal decomposition of $Re_2(CO)_{10}$ in zeolite Y, which generates the zeolite-supported complex $Re^0(CO)_3(O\text{-}Z)_3$, where (O-Z) represents a framework oxygen. The adsorption and thermal decomposition of $Re_2(CO)_{10}$ was performed on dehydrated and hydrated zeolite NaY. The conversion to $Re^0(CO)_3(O\text{-}Z)_3$ was not significantly affected by the presence of water within the supercages as the supported complex formed at around 200 °C no matter what the initial water content of the zeolite was. However, when the zeolite sample was treated at ≥200 °C for long periods, the adsorbed H_2O became involved in the reactivity, playing a role as an oxidant. The subcarbonyl complex $Re^0(CO)_3(O\text{-}Z)_3$ was oxidized, generating isolated Re_2O_7 or $HReO_4$, or a mixture of both, which was dispersed inside the zeolite host. This result suggests that thermal decomposition of $Re_2(CO)_{10}$ on a hydrated zeolite under mild conditions can be a convenient route for preparation of zeolite-supported Re_2O_7 catalysts. $Re^0(CO)_3(O\text{-}Z)_3$ was also formed in siliceous zeolite Y (SiY) upon heating. But it quickly decomposes into metal Re at around 200 °C, suggesting that the tricarbonyl species is destabilized in the almost natural zeolite framework. The present study also shows that FT-Raman spectroscopy is a useful technique for monitoring the behavior of the metal carbonyl species in zeolitic hosts.

Key words: Raman spectroscopy, zeolite Y, rhenium carbonyl, rhenium oxide.

Résumé : Ce travail décrit la décomposition thermique de $Re_2(CO)_{10}$ dans du zéolite Y qui génère le complexe $Re^0(CO)_3(O\text{-}Z)_3$ déposé sur le zéolite et dans lequel (O-Z) représente un oxygène du squelette. On a procédé à l'adsorption et la décomposition thermique du $Re_2(CO)_{10}$ sur du zéolite NaY hydraté ainsi que déshydraté. Quelle que soit la quantité d'eau contenue initialement sur le zéolite, la conversion en $Re^0(CO)_3(O\text{-}Z)_3$ n'est pas affectée d'une façon significative par la présence d'eau dans les supercages du complexe déposé qui se forment aux environs de 200 °C. Toutefois, quand l'échantillon de zéolite est traité, pour de longues périodes, à des températures égales ou supérieures à 200 °C, l'eau adsorbée devient impliquée dans la réactivité alors qu'elle joue un rôle d'oxydant. On a oxydé le complexe de sous-carbonyle, $Re^0(CO)_3(O\text{-}Z)_3$, et on a pu isoler du Re_2O_7 ou du $HReO_4$ ou un mélange des deux qui était dispersé à l'intérieur du zéolite hôte. Ce résultat suggère que la décomposition thermique, dans des conditions douces, du $Re_2(CO)_{10}$ sur un zéolite hydraté est une méthode pratique de préparer des catalyseurs de Re_2O_7 déposés sur du zéolite. Le $Re^0(CO)_3(O\text{-}Z)_3$ se forme aussi par chauffage dans le zéolite Y (SiY). Toutefois, il se décompose rapidement en Re métallique aux environs de 200 °C, ce qui suggère que l'espèce tricarbonyle est déstabilisée dans le squelette d'un zéolite pratiquement naturel. Dans le présent travail, on montre aussi que la spectroscopie FT-Raman est une technique utile pour suivre le comportement des espèces carbonyles des métaux dans des hôtes zéolites.

Mots clés : spectroscopie Raman, zéolite Y, rhénium carbonyle, oxyde de rhénium.

[Traduit par la Rédaction]

Introduction

Rhenium complexes supported on metal oxide surfaces have been of technological interest for some time because they can be easily prepared, are generally stable, and can catalyze several reactions (1, 2). For example, the supported complex Re_2O_7–Al_2O_3, has been extensively studied with respect to the activity it shows as an alkene metathesis catalyst (3, 4). One of the difficulties in gaining a better understanding of these type of systems lies in the fact that the dispersed metal complexes are typically very small and nonuniform, making characterization difficult. Metal complexes grafted to the internal walls of zeolites have the potential to offer the same catalytic activity observed on other metal oxide supports, but offer the additional advantage of providing shape-selectivity (5). Gallezot et al. (6) first examined the

Received 8 March 2004. Published on the NRC Research Press Web site at http://canjchem.nrc.ca on 21 October 2004.

A tribute to Don Irish.

R.R. Poissant and Y. Huang.[2] Department of Chemistry, The University of Western Ontario, London, ON N6A 5B7, Canada.

[1]This article is part of a Special Issue dedicated to the memory of Professor Don Irish.

[2]Corresponding author (yhuang@uwo.ca).

 doi: 10.1139/V04-119 © 2004 NRC Canada

adsorption of $Re_2(CO)_{10}$ on the surface of acidic zeolite Y (HY). When $Re_2(CO)_{10}$ was adsorbed on HY and treated at 110 °C, the authors suggested that $Re_2(CO)_{10}$ was located inside the supercages of HY. After heating near 300 °C, the FT-IR spectra pointed towards the presence of a $Re(CO)_3$ moiety. Dossi et al. (7) also examined the thermal decomposition of $Re_2(CO)_{10}$ on HY. Their temperature-programmed decomposition studies suggested that $Re_2(CO)_{10}$ first decomposed to generate $Re(CO)_3$ at 207 °C and the rhenium tricarbonyl species underwent further decomposition, yielding metal Re at 351 °C. $Re_2(CO)_{10}$ has also been adsorbed on non-acidic zeolite Y. Zecchina et al. (8) used FT-IR to obtain evidence for several different types of $Re_2(CO)_{10}$ molecules upon mild thermal activation in NaY. The authors briefly examined the thermal decomposition of the metal carbonyl after adsorption onto the zeolite. However, the IR spectrum in the ν(CO) region obtained after heating the $Re_2(CO)_{10}$/zeolite sample at 250 °C displayed an overall very broad band profile, which little information could be extracted from. The observation of low-frequency ν(CO) absorption bands suggested the presence of subcarbonylic entities. However, owing to the broad bands, the structural nature of these subcarbonyls could not be unambiguously identified by the IR spectra alone. All the above-mentioned literature work was carried out by using dehydrated zeolite Y.

To gain a better understanding of the adsorption and thermal decomposition of rhenium carbonyl on zeolite Y, we have carefully examined the reactivity of $Re_2(CO)_{10}$ in both hydrated and dehydrated NaY, as well as siliceous zeolite Y. Our work shows that the hydrated zeolite NaY can actually be used to prepare Re_2O_7 supported in a zeolite via thermal decomposition using $Re_2(CO)_{10}$ as a precursor. In the present study, we have used FT-Raman in combination with FT-IR spectroscopy to follow the behavior of various surface-bound species.

In the past, the IR method has been extensively employed to obtain the structural information on the metal carbonyl species formed or adsorbed in zeolitic hosts by monitoring the ν(CO) vibrations. It has been recently shown that Fourier transform (FT)-Raman spectroscopy is also a useful technique for investigation of organometallic compounds supported on the zeolites (9). Because zeolite frameworks exhibit very weak Raman signals owing to their small scattering cross sections (10), the behavior of the guest species can be easily probed by observing the Raman spectra of the guest molecules. The Raman spectra can provide information on the metal carbonyl species not only from the ν(CO) bands, but also from the ν(M-C) and δ(M-CO), ν(M-X) and ν(M-M) modes, which appear in the region below 700 cm^{-1}. In the corresponding mid-IR spectra, the very strong bands owing to zeolitic framework appearing in the region of 1300–300 cm^{-1} usually mask the signals from the guest molecules in this region. For metal carbonyl – zeolite systems, FT-Raman is advantageous compared to conventional visible Raman. This is because FT-Raman instrumentation uses the 1064 nm excitation line from a near-IR laser, which largely minimizes laser-induced photodecomposition and significantly reduces fluorescence background (a problem often associated with zeolites (11)). In the present study, we wish to show that the combination of FT-Raman and FT-IR methods can furnish unambiguous information on the behavior of metal carbonyl species inside zeolites.

Experimental

$Re_2(CO)_{10}$ (98%) was purchased from Strem Chemical Inc., and used without further purification. NaY (Si/Al = 2.35) and siliceous zeolite Y (Si/Al = 300) were obtained from Strem Chemical Inc. and Degussa, respectively. The crystallinity and identification of zeolite Y were checked by powder X-ray diffraction. The typical experimental procedure for the dehydrated zeolite samples was the following: zeolite Y was first dehydrated at 550 °C under vacuum. The dehydrated zeolite was then mixed mechanically with crystalline $Re_2(CO)_{10}$ under nitrogen (1.8 molecules/super cage) in a Schlenk tube. After heating the mixture at a desired temperature under nitrogen flow, the sample was cooled down to room temperature and taken out from the Schlenk tubes under a nitrogen atmosphere for IR and Raman studies. The samples for Raman study were sealed in the capillary tubes. For the samples prepared using the hydrated form of NaY, the hydrated zeolite (water content 25% wt) was directly loaded into a Schlenk tube without any prior thermal treatment. Crystalline $Re_2(CO)_{10}$ was then added (1.8 molecules/super cage) and the sample was heated at a desired temperature. All Raman spectra were recorded on a Bruker RFS 100/S FT-Raman spectrometer equipped with a Nd^{3+}:YAG laser operating at a wavelength of 1064.1 nm and a liquid-nitrogen-cooled Ge detector. The laser power was typically 80 mW at the sample. We varied the laser power level and found that laser-induced photodecomposition only occurs when the power level is above 160 mW. The IR spectra were obtained on a Bomem MB-100 FT-IR spectrometer equipped with a DTGS detector, using the standard KBr method. The resolution for both the Raman and IR measurements was 4 cm^{-1}.

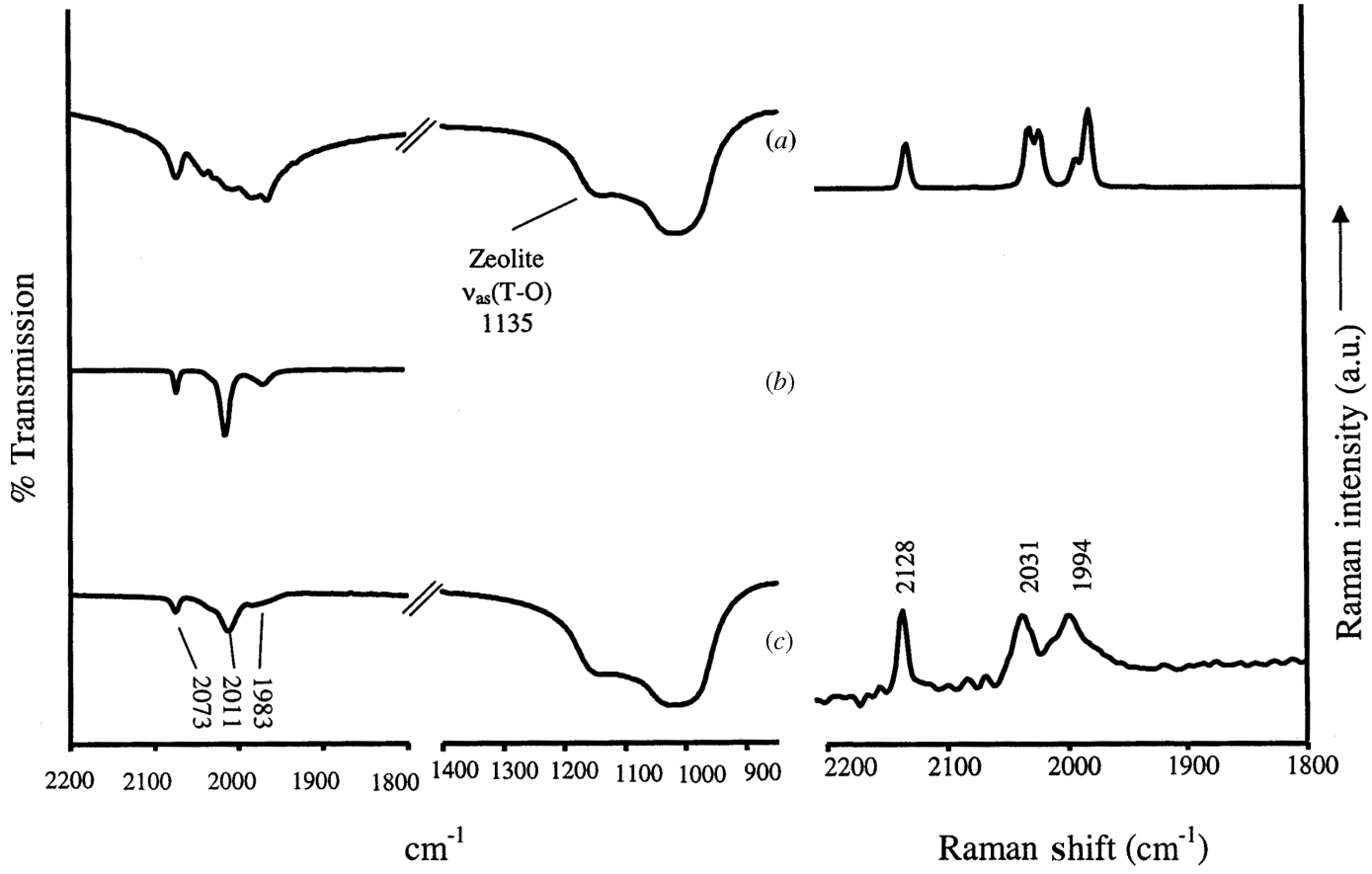
Results and discussion

$Re_2(CO)_{10}$ / hydrated NaY

The mixture of $Re_2(CO)_{10}$ and hydrated NaY was heated at several temperatures to examine the thermal stability of $Re_2(CO)_{10}$. When the sample was heated at 60 °C, the resulting IR spectrum (Fig. 1*a*) closely resembled that of pure $Re_2(CO)_{10}$ in the solid state (Fig. 2*b*), which contains very broad and closely overlapping and featureless bands in the ν(CO) region. When the same sample was washed with excess chloroform, the IR spectrum of the washing (Fig. 1*b*) was identical to that of pure $Re_2(CO)_{10}$ in solution (Fig. 2*c*), which exhibits three ν(CO) bands corresponding to the $2b_2$ and e_1 modes expected for an isolated $Re_2(CO)_{10}$ molecule with D_{4d} symmetry. In addition, upon washing of the sample $Re_2(CO)_{10}$/NaY heated at 60 °C, the overall band intensity in the ν(CO) region decreased significantly relative to that of the 1135 cm^{-1} band, which is assigned to the asymmetric zeolite T-O (T= Si, Al) stretching mode (ν_{as}(T-O)) (Figs. 1*a* and 1*c*). These results suggest that after heating at 60 °C, a significant portion of the metal carbonyl species was still located on the external surface of NaY as small crystallites, which can be easily removed by washing with $CHCl_3$. The

© 2004 NRC Canada

Fig. 1. IR and Raman spectra of: (*a*) $Re_2(CO)_{10}$/NaY heated at 60 °C for 1 h; (*b*) $CHCl_3$ washing solution resulting from treatment of sample (*a*); (*c*) $Re_2(CO)_{10}$/NaY heated at 60 °C for 1 h and then washed with $CHCl_3$.



IR spectrum of the resulting washed solid (Fig. 1*c*) exhibited three ν(CO) bands at 2073, 2011, and 1983 cm^{-1}, which match those of pure $Re_2(CO)_{10}$ in solution (Fig. 2*c*) very well (2071 (b_2), 2013 (e_1), and 1968 (b_2) cm^{-1}) (12*a*). This indicates that after washing with $CHCl_3$, the sample contained metal carbonyl species in the form of isolated $Re_2(CO)_{10}$ molecules that had retained D_{4d} symmetry. Examination of the Raman spectra of the same sample before and after washing, provides further evidence for the presence of the isolated $Re_2(CO)_{10}$ species. Before washing with $CHCl_3$, the Raman spectrum (Fig. 1*a*) was identical to that of pure crystalline $Re_2(CO)_{10}$ (Fig. 2*b*), where the splitting because of the solid-state effect (factor group splitting) is clearly evident. After washing, the Raman spectrum of the washed solid (Fig. 1*c*) displayed three principal ν(CO) bands at 2128, 2031, and 1994 cm^{-1}, which are in excellent agreement with those observed for pure $Re_2(CO)_{10}$ in solution (12) at 2127 (a_1), 2030 (e_2), and 1989 (a_1) cm^{-1} (Fig. 2*c*). All these results suggest that before washing with chloroform, $Re_2(CO)_{10}$ is present in the solid sample in two different forms: (*i*) $Re_2(CO)_{10}$ crystallites and (*ii*) isolated $Re_2(CO)_{10}$ molecules located both on the exterior and the interior of zeolite Y. Washing with $CHCl_3$ removes the metal carbonyl species located on the exterior of the zeolite surface, leaving only isolated $Re_2(CO)_{10}$ molecules located inside the supercages of NaY.

After treatment of the sample at 150 °C, the IR spectrum of the sample contains a relatively sharp band (2074 cm^{-1}), and a broad, featureless envelope centered near 2000 cm^{-1} (Fig. 2*a*). The most striking feature of the IR spectrum is a broad, low-frequency ν(CO) band, positioned at 1891 cm^{-1} (Fig. 2*a*), which is also present in the corresponding Raman spectrum with much weaker intensity (Fig. 2*a*). In addition to a sharp peak at 2127 cm^{-1}, the Raman spectrum in Fig. 2*a* also contains four sharp ν(CO) bands, which are sitting on top of a rather broad base. It appears that after treatment at 150 °C, the Raman spectrum of the $Re_2(CO)_{10}$/zeolite sample (Fig. 2*a*) is the superposition of the Raman spectra of $Re_2(CO)_{10}$ in the solid state (Fig. 2*b*) and in solution (Fig. 2*c*). This indicates that the sample contains $Re_2(CO)_{10}$ in the form of isolated molecules as well as crystallites. The broad IR band near 1891 cm^{-1} indicates that some $Re_2(CO)_{10}$ molecules had started to decompose.

Heating at 200 °C facilitated a dramatic change in the spectra of the resulting sample. The IR spectrum in the ν(CO) region now consisted of two overlapping bands centered at 2013 and 2003 cm^{-1}, and an extremely broad band centered around 1895 cm^{-1} (Fig. 3*a*). The band at 2013 cm^{-1} is positioned very similar to that of pure $Re_2(CO)_{10}$ in solution (Fig. 2*c*). However, the overall broad profile of the IR spectrum does not allow one to definitively conclude if $Re_2(CO)_{10}$ is still present in the sample after treatment at 200 °C. The corresponding Raman spectrum is much more informative. It contains several ν(CO) bands at 2128, 2033,

© 2004 NRC Canada

Fig. 2. (*a*) IR and Raman spectra of $Re_2(CO)_{10}$/NaY heated at 150 °C for 1 h; (*b*) IR and Raman spectra of pure solid $Re_2(CO)_{10}$; (*c*) IR and Raman spectra of pure $Re_2(CO)_{10}$ in $CHCl_3$.

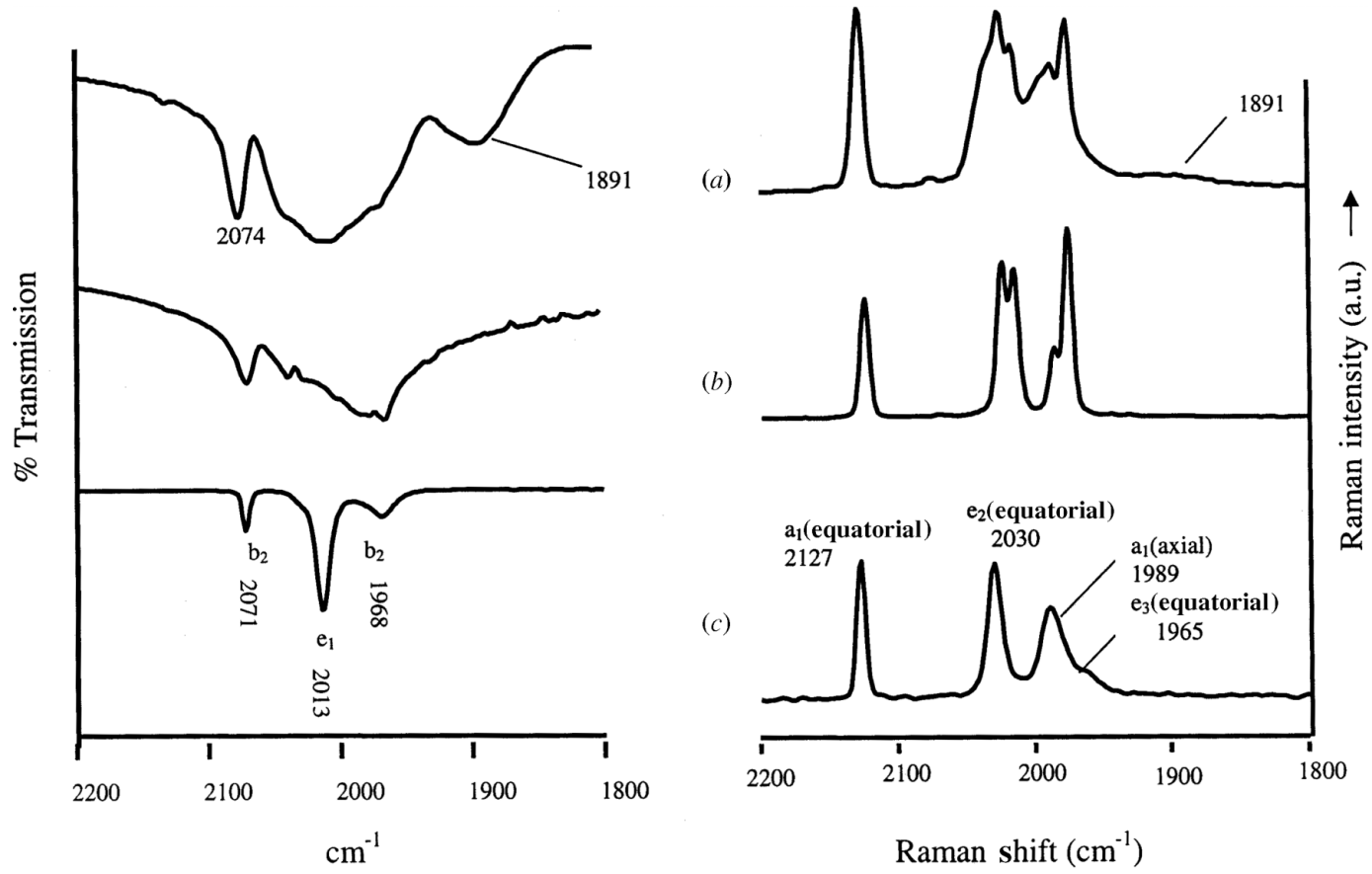
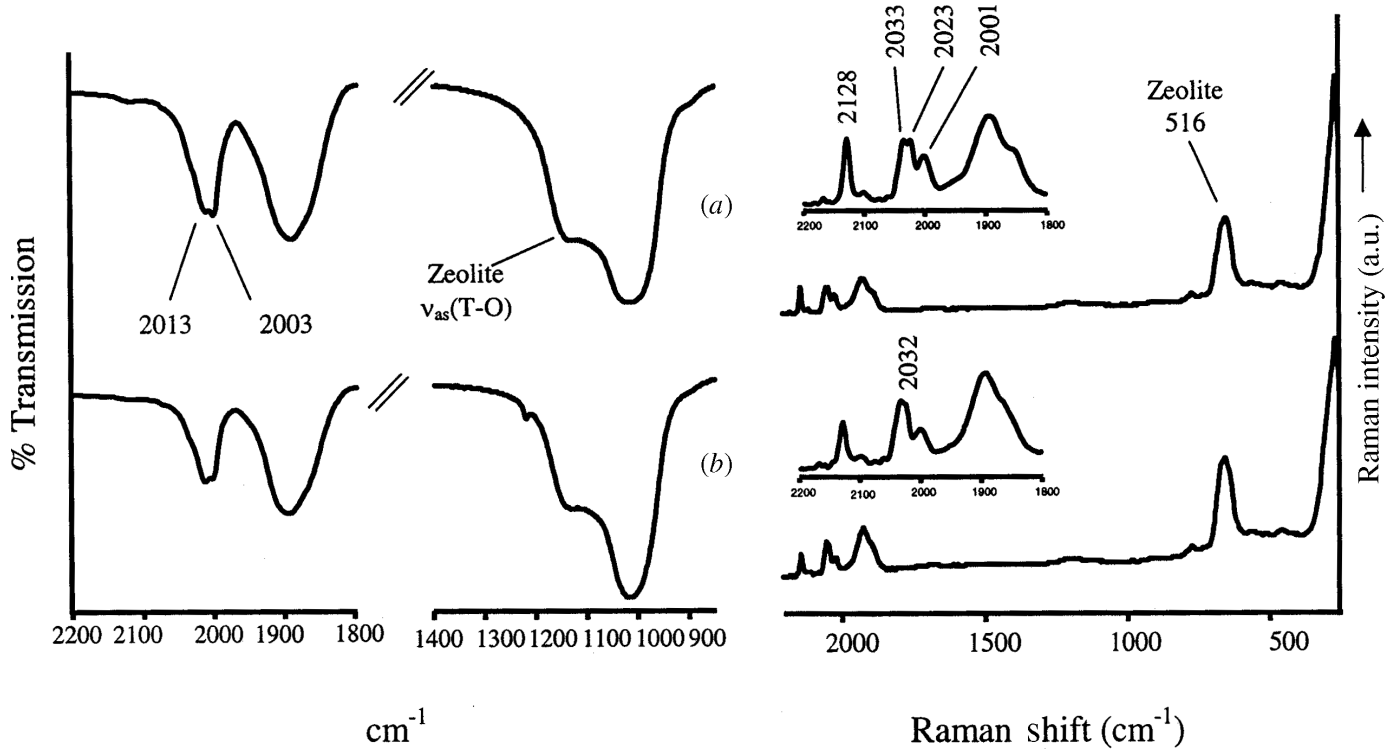
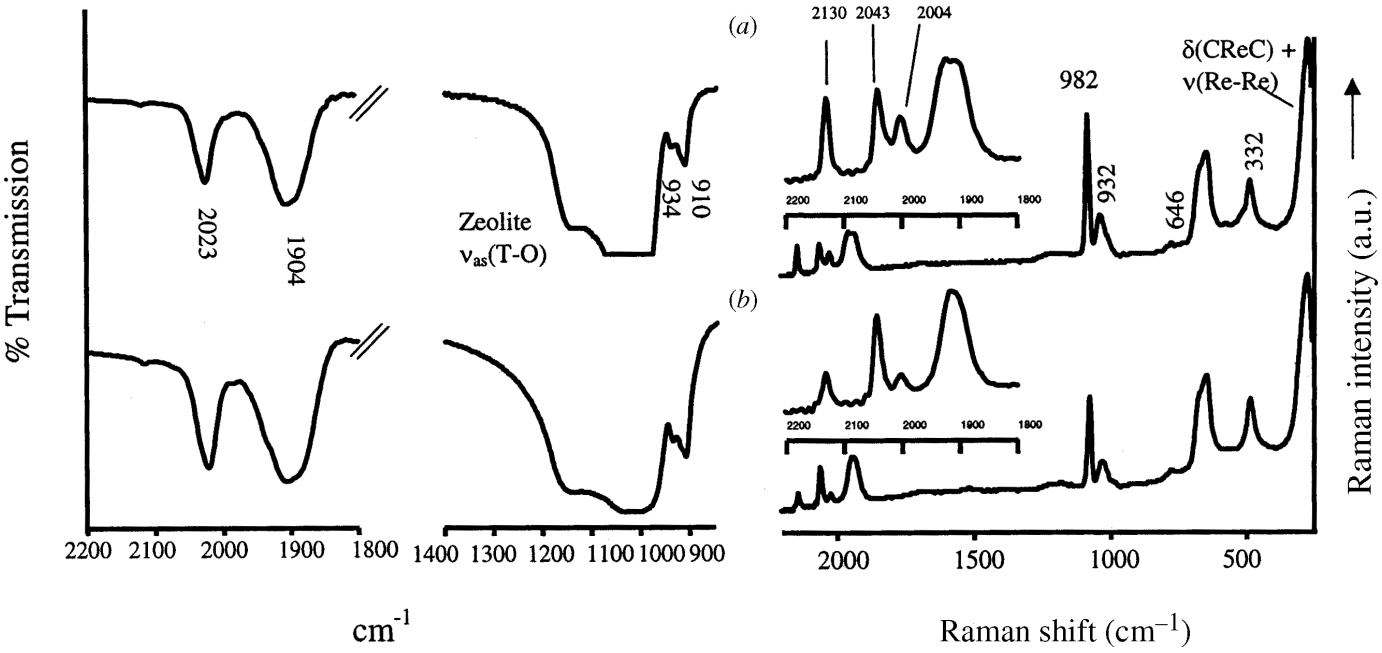


Fig. 3. IR and Raman spectra of: (*a*) $Re_2(CO)_{10}$/NaY heated at 200 °C for 1 h; and (*b*) sample (*a*) after extraction with $CHCl_3$.



© 2004 NRC Canada

Fig. 4. IR and Raman spectra of: (*a*) $Re_2(CO)_{10}$/NaY heated at 200 °C for 4 h; and (*b*) $Re_2(CO)_{10}$/NaY heated at 200 °C for 4 h and then washed with $CHCl_3$.



2023, 2001, and 1900 (broad) cm^{-1} (Fig. 3*a*). The band at 2128 cm^{-1} is the characteristic a_1 ν(CO)(eq) mode of $Re_2(CO)_{10}$ in solution, indicating that, indeed, $Re_2(CO)_{10}$ is still present after treatment at 200 °C. After extraction with excess $CHCl_3$, the IR spectrum of the solution (not shown) did not display any bands in the ν(CO) region, indicating that very little, if any, carbonyl species were extracted from the solid sample. This is confirmed upon inspection of the overall IR band intensity in the ν(CO) region, before and after washing (relative to the ν_{as}(T-O) zeolite band), which remained approximately constant (Figs. 3*a* and 3*b*). Once again, the corresponding Raman spectrum exhibits better resolution. Examination of the Raman spectrum of the washed solid revealed three peaks at 2128, 2023, and 2001 cm^{-1} corresponding to those of pure $Re_2(CO)_{10}$ in solution, clearly indicating the presence of $Re_2(CO)_{10}$. The Raman peak at 2033 cm^{-1} and the broad peak around 1900 cm^{-1} did not decrease in intensity relative to the zeolite symmetric (T-O) stretching mode at 516 cm^{-1} (Figs. 3*a* and 3*b*), suggesting that these bands are due to a second metal carbonyl species within NaY. Thus, the Raman spectrum of the sample $Re_2(CO)_{10}$/NaY treated at 200 °C consists of two sets of bands: (*i*) three peaks at 2128, 2023, and 2001 cm^{-1} are assigned to the a_1(eq), e_2(eq), and a_1(ax) ν(CO) modes, respectively, of isolated $Re_2(CO)_{10}$ and (*ii*) two other bands at 2033 and 1894 cm^{-1} (very broad) are representative of a new rhenium subcarbonyl species (the nature of which will be discussed below).

After the $Re_2(CO)_{10}$/NaY sample was heated at 200 °C for longer periods (4 h), the IR spectrum of the sample displayed a significant reduction in the overall ν(CO) intensity, relative to the ν_{as}(T-O) zeolite band (Fig. 4*a*). The ν(CO) region of the IR spectrum consisted of two main bands at 2023 and 1904 cm^{-1}. Two new IR bands were observed at 934 and 910 cm^{-1} (Fig. 4*a*). In the corresponding Raman spectrum (Fig. 4*a*), three new bands appeared positioned at 982, 932, and 332 cm^{-1}. The regions 900–1200 cm^{-1} and 200–400 cm^{-1} coincide with that observed for Re=O stretching ν(Re=O), and bending δ(O=Re=O) vibrations (13), respectively, suggesting the possible formation of rhenium oxides. It appears that a large portion of the metal carbonyl had converted to a new species, possibly a rhenium oxide, which gave rise to new bands in the IR and Raman spectra. It seems that after prolonged treatment at 200 °C (4 h), the sample $Re_2(CO)_{10}$/NaY consists of three different rhenium species: (*i*) isolated $Re_2(CO)_{10}$ molecules, (*ii*) rhenium subcarbonyl species, and (*iii*) rhenium species containing Re=O bonds.

Structural nature of the rhenium subcarbonyl species

An obvious choice for the subcarbonyl species formed in zeolite is a $Re(CO)_3$ fragment (6). An isolated $Re(CO)_3$ fragment possessing C_{3v} point symmetry should exhibit two vibrational modes (a_1 + e) in the ν(CO) region, which are both IR and Raman active (14). The IR spectrum of the sample treated at 200 °C for 4 h does principally exhibit two ν(CO) bands at 2023 and 1904 cm^{-1} (Fig. 4*a*). These frequencies agree well with several reports in the literature of similar rhenium tricarbonyls formed on magnesium oxide powder (15). Upon washing of the sample $Re_2(CO)_{10}$/NaY heated at 200 °C (4 h) with $CHCl_3$, the two bands at 2043 and 1900 cm^{-1} in the corresponding Raman spectra remain unchanged in intensity (Figs. 4*a* and 4*b*). These two bands are close in frequency, relative intensity, and bandwidth to the corresponding ν(CO) bands in the IR spectrum. Therefore, these bands are assigned to the a_1 and e modes of the species *fac*-$Re(CO)_3(O\text{-}Z)_3$, where (O-Z) represents a framework oxygen. The Raman spectrum (Fig. 4*a*) also contains a weak band at 646 cm^{-1}. The Raman spectrum of pure $Re_2(CO)_{10}$ in either the solid or solution does not contain any band in this region. However, this is the region where Re-CO bend-

© 2004 NRC Canada

ing vibrations (δ(ReCO)) occur in species containing a $Re(CO)_3$ fragment (15*a*,16), providing further evidence that the new carbonyl species has a $Re(CO)_3$ moiety. Our results are in agreement with those of previous studies of $Re_2(CO)_{10}$ adsorbed in NaY by Dossi et al. (7) and Gallezot et al. (6), and similar studies reported in the literature describing $Re_2(CO)_{10}$ adsorbed on magnesium oxide powder. The fact that the species containing the $Re(CO)_3$ moiety cannot be extracted from the zeolite sample with $CHCl_3$, suggests that the supported complex is tightly bonded to the internal zeolite surface.

Structural nature of the rhenium oxide species

When considering the structure of the species responsible for the new bands observed in the IR and Raman spectra in the 900–1000 cm^{-1} and 200–400 cm^{-1} region, several possibilities must be entertained. For example, when $Re_2(CO)_{10}$ is thermally decomposed in air, the oxides Re_2O_7, ReO_3, and ReO_2 have all been identified upon heating between the temperatures 200–300 °C (17). To help discriminate between these and other possible metal oxides, magnetic susceptibility measurements were performed. The gram susceptibility of a physical mixture of $Re_2(CO)_{10}$/NaY prior to heating is diamagnetic ($\chi_g = -1.9 \times 10^{-7}$ cgs units). The same measurement on the sample $Re_2(CO)_{10}$/NaY after treatment at 200 °C for 4 h revealed that this sample is also diagmagnetic ($\chi_g = -5.4 \times 10^{-8}$ cgs units). Since ReO_3 (18) and ReO_2 (19) both exhibit temperature-independent paramagnetism, it is unlikely that either of these species could be predominantly responsible for the new peaks observed in our spectra. Therefore, Re_2O_7 is a viable possibility, since Re(VII) does not contain any 5*d* electrons. Interestingly, in a study by Nakamura et al. (20), the IR spectrum obtained of Re_2O_7 supported on Al_2O_3 exhibited ν(Re=O) bands, which are close in frequency to those observed in our study. Depending on the ratio Re/Al, the authors found that upon deposition of Re_2O_7 on Al_2O_3, the adsorbed rhenium oxide species displayed two different structural forms: (*i*) a species of the type Re_2O_7 (925 and 915 cm^{-1}) and (*ii*) a species of the type $H^+(ReO_4)^-$ (915 cm^{-1}). We have observed similar IR bands at 934 and 910 cm^{-1} (Fig. 4). Our Raman spectrum (Fig. 4) exhibits two bands at 982 and 932 cm^{-1} and a low-frequency band at 332 cm^{-1}. The frequencies and relative intensities of these bands are similar to those of the Raman spectrum of pure gaseous Re_2O_7 (21). Another possible form of the oxide present in our samples is $HReO_4$ (also diamagnetic) since the Raman spectrum of ReO_4^-(aq) also has three bands at 970, 916, and 332 cm^{-1} (22). Based on the above information, we believe that the most likely form of the rhenium oxide formed in our samples is Re_2O_7, but $HReO_4$ cannot be ruled out.

To determine other possible decomposition reactions of rhenium carbonyl, we further heated the sample $Re_2(CO)_{10}$/NaY at 270 °C for 3 h. The IR spectrum of this sample (supplementary material Fig. S1A)[3] did not differ significantly from those obtained after treatment at lower temperatures. The corresponding Raman spectrum exhibited significant fluorescence as indicated by the sloping baseline (supplementary material Fig. S1A).[3] The bands owing to $Re_2(CO)_{10}$ were still observed at 2129 and 2006 cm^{-1}, which exhibited intensities comparable to the other ν(CO) bands present. The bands owing to the rhenium oxide species clearly dominated the spectrum. Instead of chloroform, this sample was washed with a more polar solvent (water) and the IR and Raman spectra of the resulting solid were taken (supplementary material Fig. S1B).[3] The peaks owing to the metal oxide have essentially disappeared in both the IR and Raman spectra. The Raman bands at 2129 and 2006 cm^{-1}, owing to $Re_2(CO)_{10}$, also disappeared upon washing with H_2O (supplementary material Fig. S1B)[3], leaving only two ν(CO) Raman bands at 2042 and 1915 cm^{-1}. Therefore, the intensity of the ν(CO) Raman bands at 2043 and ~1900 cm^{-1} remain unchanged upon extraction with $CHCl_3$ and H_2O, suggesting that the grafted complex $Re(CO)_3(O\text{-}Z)_3$ is tightly bound to the zeolite wall.

$Re_2(CO)_{10}$ / *dehydrated* NaY

To investigate the possible involvement of water in the reactivity of $Re_2(CO)_{10}$ on zeolite Y, we performed the same experiments using NaY, which had been carefully dehydrated before the introduction of rhenium carbonyl. Figure 5*a* shows the IR and Raman spectra after heating the sample $Re_2(CO)_{10}$ / dehydrated NaY at 200 °C. The spectra are virtually identical to those obtained using the hydrated analogue of NaY (Fig. 3*a*). This indicates that upon treatment at 200 °C, the reactivity of $Re_2(CO)_{10}$ in NaY is not affected by the presence of H_2O, and that the solid sample contained a mixture of $Re_2(CO)_{10}$ and $Re(CO)_3(O\text{-}Z)_3$. Upon heating for longer periods at 200 °C (Figs. 5*b* and 5*c*) the IR spectra did not change significantly. However, the corresponding Raman spectra showed a gradual decrease in the intensity of the ν(CO) peaks owing to $Re_2(CO)_{10}$ at 2129, 2022, and 2003 cm^{-1}. Interestingly, the bands in the regions 900–1000 cm^{-1} and 200 – 400 cm^{-1} in the IR and Raman spectra, owing to the rhenium oxides, are barely visible even after prolonged treatment at 200 °C (Fig. 5*c*).

To further mimic the conditions used in the experiments with hydrated NaY, we heated the sample $Re_2(CO)_{10}$ / dehydrated NaY at 270 °C for 3 h (Fig. 6*a*). Even after this heat treatment, the intensity of the bands owing to the rhenium oxide species still remained very weak. In addition, the ν(CO) bands owing to $Re_2(CO)_{10}$ continued to decrease in intensity, essentially leaving those of $Re(CO)_3(O\text{-}Z)_3$ (Fig. 6*a*). These results confirm that in the absence of water, the majority of the original $Re_2(CO)_{10}$ is converted to the subcarbonyl species $Re(CO)_3(O\text{-}Z)_3$; this process is not accompanied by the formation of rhenium oxide. A sample of hydrated NaY contains approximately 25% water by weight, as indicated by thermogravimetric analysis. This amount of water was added to the sample $Re_2(CO)_{10}$ / dehydrated NaY treated at 270 °C for 3 h, and then the sample was subsequently heated another hour at 270 °C, and the IR and Raman spectra were taken. The spectra indicate a dramatic increase in the amount of rhenium oxide species present in the sample. This is evidenced by the growth of bands at 982, 931, and 332 cm^{-1} in the Raman spectrum and 937 and

[3] Supplementary data may be purchased from the Directory of Unpublished Data, Document Delivery, CISTI, National Research Council Canada, Ottawa, ON K1A 0S2, Canada (http://www.nrc.ca/cisti/irm/unpub_e.shtml for information on ordering electronically).

© 2004 NRC Canada

Fig. 5. IR and Raman spectra of: (*a*) $Re_2(CO)_{10}$ / dehydrated NaY heated at 200 °C for 2 h; (*b*) 3h; and (*c*) 4 h.

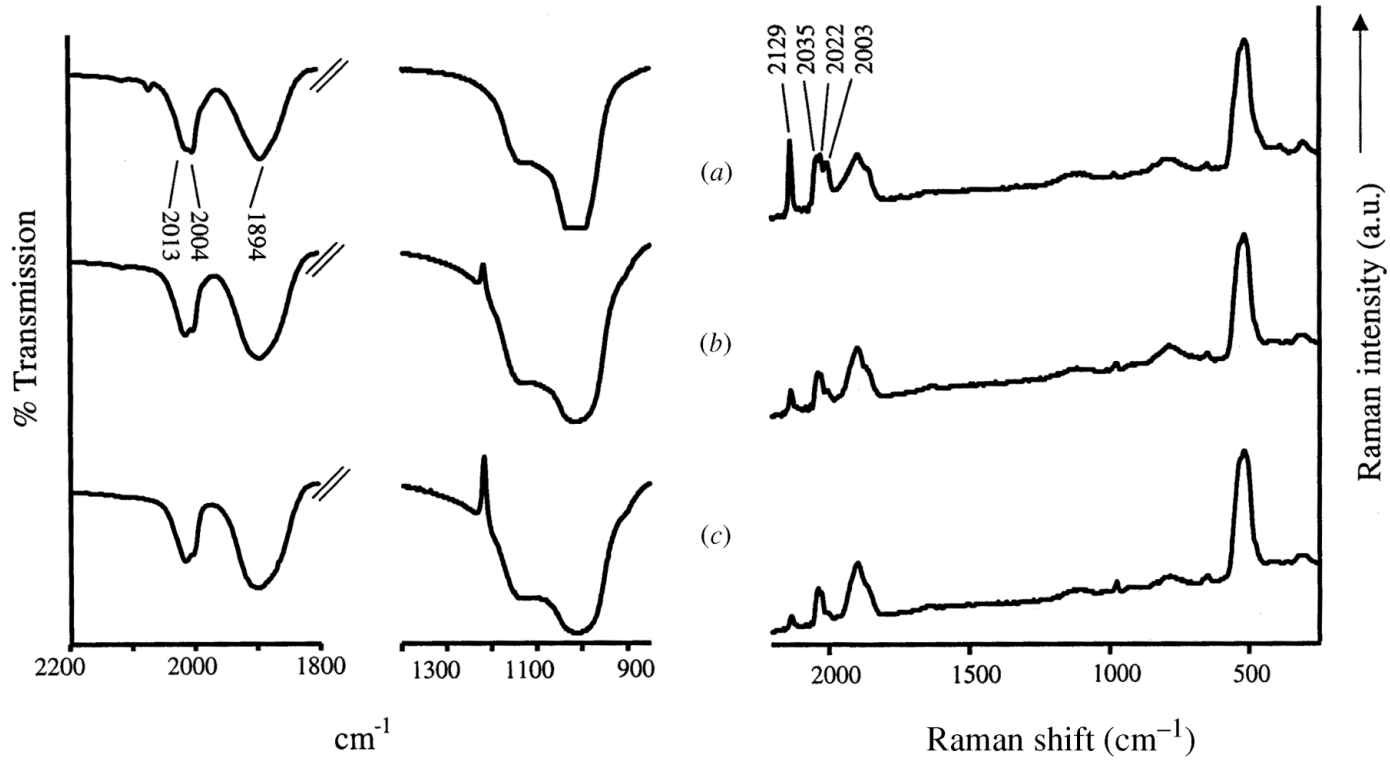
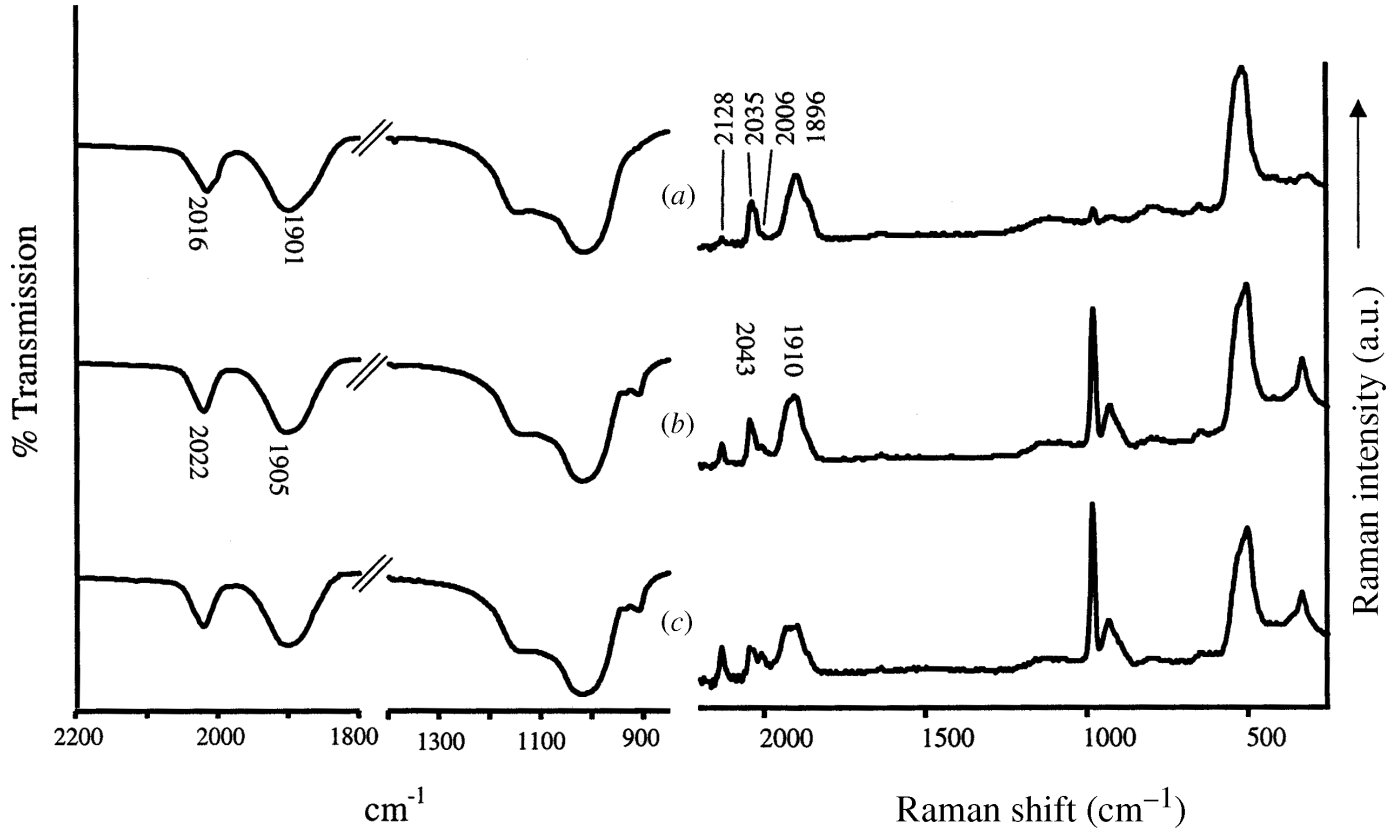
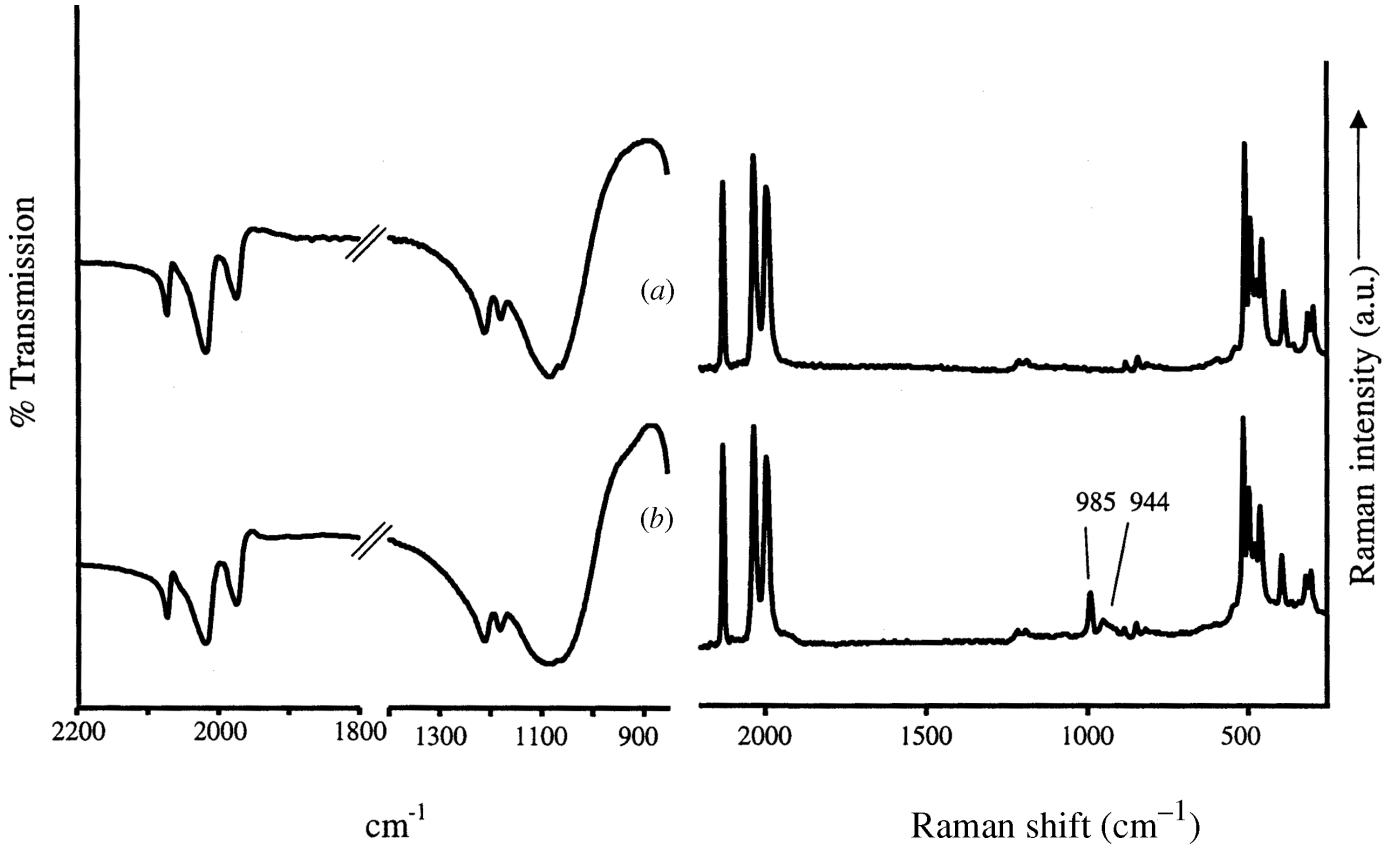


Fig. 6. IR and Raman spectra of: (*a*) $Re_2(CO)_{10}$ / dehydrated NaY heated at 270 °C for 3 h; (*b*) the same sample after addition of 25% H_2O and then heated at 270 °C for 1 h; (*c*) 2 h.



© 2004 NRC Canada

Fig. 7. IR and Raman spectra of: (*a*) $Re_2(CO)_{10}$ /SiY heated at 130 °C for 1 h; (*b*) 200 °C for 1 h.



910 cm^{-1} in the corresponding IR spectrum (Fig. 6*b*). At the same time, the bands at 2129 and 2008 cm^{-1} grew in intensity, suggesting that a portion of the metal carbonyl species $Re(CO)_3(O\text{-}Z)_3$ had converted back to $Re_2(CO)_{10}$. Further treatment at 270 °C confirmed this trend (Fig. 6*c*), as evidenced by the continued growth of the bands at 2129 and 2008 cm^{-1}. At the same time, a slight growth in the Raman bands owing to the rhenium oxide was observed (Fig. 6*c*). All these results indicate that in the absence of water, heating the sample $Re_2(CO)_{10}$ / dehydrated NaY results in an almost complete conversion of rhenium carbonyl:

[1] $$Re_2(CO)_{10} + 3(O\text{-}Z) \rightarrow 2Re(CO)_3(O\text{-}Z)_3 + 4CO$$

Upon addition of water, a portion of the $Re(CO)_3(O\text{-}Z)_3$ species is converted into the metal oxide Re_2O_7. This is accompanied by a slight reformation of $Re_2(CO)_{10}$.

Reaction schemes

Our experimental data provide some new insight concerning the adsorption and thermal reactivity of $Re_2(CO)_{10}$ on zeolite Y. Upon mild treatment at 60 °C, the hydrated NaY – carbonyl sample consists mostly of rhenium carbonyl, which is located on the exterior of the zeolite as crystallites, although some $Re_2(CO)_{10}$ molecules had already diffused into the supercages of NaY. Decomposition begins to occur near 150 °C. The development of a broad band near 1891 cm^{-1} suggests the onset of the decarbonylation reaction outlined in eq. [1]. Treatment at 200 °C facilitates the conversion of a significant portion of the subcarbonyl species into the rhenium oxide Re_2O_7. Photo-oxidation of $Re_2(CO)_{10}$ with O_2, generating the metal oxide Re_2O_7, has been reported (23). However, in our case, hydrated NaY contains primarily sorbed H_2O. Our results indicate that the adsorbed water plays an important role in the formation of the rhenium oxide and is responsible for the oxidation of the rhenium carbonyl species present in our samples. The hydroxyl groups present on Al_2O_3 were shown to oxidize the zero valent carbonyl species of Cr, W, and Mo to various metal oxides (24). Following these reports, a very thorough study was conducted by Hucul and Brenner (25), who examined this redox behaviour for alumina-supported complexes of many known transition metals that form stable carbonyls. The authors concluded that upon thermal reaction with alumina, all of the zero valent metal carbonyls underwent partial oxidation:

[2] $$M(CO)_j + n(Z\text{-}OH) \rightarrow (O^-)_nM^{n+} + (n/2)H_2 + jCO$$

(Z-OH) represents a surface hydroxyl group. In the case of $Re_2(CO)_{10}$, the oxidation began to occur at 200 °C, the same temperature that we first observed the formation of metal oxide on hydrated NaY (Fig. 4*a*). Hucul and Brenner (25) determined that after the thermal reaction of $Re_2(CO)_{10}$ with alumina was complete, the final average oxidation number of the rhenium atom was approximately +5.4. In view of this redox behaviour, we suggest that the oxidation observed in our study is the result of the presence of H_2O molecules inside the supercages of NaY. Since the interactions between the Na^+ ions and H_2O molecules polarize the O—H bonds, the polarized H_2O molecules exhibit similar oxidizing char-

© 2004 NRC Canada

acteristics to that of the surface hydroxyl groups present on metal oxides such as Al_2O_3.

When H_2O was added to the sample $Re_2(CO)_{10}$ / dehydrated NaY treated at 270 °C, we observed a partial reformation of $Re_2(CO)_{10}$, in addition to the formation of rhenium oxide (Figs. 6*b* and 6*c*). This is attributed to the carbonylation of the species $Re(CO)_3(O\text{-}Z)_3$. Upon thermal decomposition of $Re_2(CO)_{10}$ in NaY, Zecchina et al. (8) detected the presence of subcarbonyl species. Exposure to CO was shown to result in a recarbonylation of the subcarbonyls, leading to the partial reformation of $Re_2(CO)_{10}$. Figure 6*a* shows that upon prolonged treatment at 270 °C, the sample $Re_2(CO)_{10}$ / dehydrated NaY consists mainly of the species $Re(CO)_3(O\text{-}Z)_3$. Upon the introduction of H_2O into the sample and further heating, the rhenium tricarbonyl species undergoes oxidation, which can be approximated as:

$$[3]\qquad 2Re(CO)_3(O\text{-}Z)_3 + 7[H_2O\cdots Na^+] \rightarrow Re_2O_7 + 6CO + 7H_2 + 6(O\text{-}Z) + 7Na^+$$

The CO released from the reaction is responsible for the recarbonylation of $Re(CO)_3(O\text{-}Z)_3$, leading to the partial reformation of the original metal carbonyl ($Re_2(CO)_{10}$). It is worth noting that the Raman spectra of Re_2O_7 formed inside zeolite Y are very similar to those of Re_2O_7 in solution, liquid as well as gas phase, but distinctly different from that of crystalline Re_2O_7, which exhibits more than 20 bands owing to factor group splitting (21).

$Re_2(CO)_{10}$ / *siliceous* zeolite Y

To investigate the role played by the Na^+ cations on the reactivity of $Re_2(CO)_{10}$ within zeolite Y, we performed similar experiments using siliceous Y (SiY), which had been dehydrated before introduction of $Re_2(CO)_{10}$. Figure 7*a* shows the IR and Raman spectra of the sample $Re_2(CO)_{10}$/SiY heated at 130 °C. Both the IR and Raman spectra in the ν(CO) region look very similar to those of pure $Re_2(CO)_{10}$ in solution, indicating that the solid sample consists mainly of isolated $Re_2(CO)_{10}$ molecules. Treatment of the sample at 200 °C did not result in significant changes in the appearances of either the IR or Raman spectra in the ν(CO) region (Fig. 7*b*). However, weak bands at 985 and 944 appeared in the Raman spectrum (Fig. 7*b*). These results suggest that the same rhenium oxide species that formed in the $Re_2(CO)_{10}$/NaY sample had also formed in the $Re_2(CO)_{10}$/SiY sample, albeit in a much smaller amount. This is likely due to a small concentration of hydroxyl groups (Si-OH) present within SiY.

Further treatment of the $Re_2(CO)_{10}$/SiY sample at 200 °C resulted in the solid sample turning from a white to a grey solid. The Raman spectrum of this sample (not shown) exhibited intense fluorescence, rendering any peak identification virtually impossible. The corresponding IR spectrum in the ν(CO) region still exhibited an overall profile that was indicative of isolated $Re_2(CO)_{10}$ molecules (supplementary material Fig. S2A).[3] A weak, broad IR band at 1931 cm^{-1} was also evident, suggesting a decomposition reaction had started to occur. This was accompanied by a slight overall reduction in the total ν(CO) band intensity relative to the various ν_{as}(T-O) modes of SiY (supplementary material Fig. S2A).[3] Treatment at 200 °C for a total of 3 h resulted in a further decrease in the overall ν(CO) IR band intensity, which was accompanied by another colour change from a grey to a dark black solid (supplementary material Fig. S2B).[3] The Raman spectrum of this sample (not shown) also exhibited intense fluoresence. The corresponding IR spectrum now consisted of two sets of bands: (*i*) bands at 2072, 2020, and 1974 cm^{-1} are indicative of isolated $Re_2(CO)_{10}$ molecules and (*ii*) two bands at 2030 and 1932 cm^{-1} are assigned to the complex $Re(CO)_3(O\text{-}Z)_3$.

Heating the $Re_2(CO)_{10}$/SiY sample at 200 °C (4 h total) facilitated the almost complete decomposition of the metal carbonyl species present as indicated by the very weak ν(CO) bands in the IR spectrum of the resulting sample (supplementary material Fig. S2C).[3] The ν(CO) region did not display any of the characteristic bands owing to isolated $Re_2(CO)_{10}$ molecules. Only two bands were observed at 2032 and 1931 cm^{-1} indicating that the only metal carbonyl species present in the solid sample was $Re(CO)_3(O\text{-}Z)_3$. The same sample was extracted with $CHCl_3$. The IR spectra of the solid sample before and after washing were identical (supplementary material Figs. S2C and S2D),[3] indicating that a very small amount of residual $Re(CO)_3(O\text{-}Z)_3$ is tightly bound to the zeolite wall.

The ν(CO) IR frequencies of $Re(CO)_3(O\text{-}Z)_3$ supported in SiY at 2032 and 1931 cm^{-1} are shifted considerably to a higher frequency relative to those observed for the same complex in NaY (Si/Al = 2.35) at 2023 and 1904 cm^{-1} (Fig. 4*a*). The lower ν(CO) frequencies observed in NaY (Si/Al = 2.35) are reflective of the presence of Na^+ ions, which interact with the carbonyl ligands of the supported complex $Re(CO)_3(O\text{-}Z)_3$ [Re-CO···Na^+], causing a weakening of the C—O bonds.

Summary

In the absence of water, $Re_2(CO)_{10}$ supported in NaY (Si/Al = 2.35) undergoes the decomposition reaction outlined in eq. [1]. The decomposition begins near 150 °C and is essentially complete at 270 °C. In the presence of H_2O, $Re_2(CO)_{10}$ is first converted to $Re(CO)_3(O\text{-}Z)_3$ and the latter is partially converted to the metal oxide Re_2O_7. The study suggests that thermal decomposition of $Re_2(CO)_{10}$ on hydrated zeolite under mild conditions may serve as a convenient route to form highly dispersed Re_2O_7 in a zeolite host for catalysis. $Re_2(CO)_{10}$ adsorbed in SiY decomposes to metal Re almost completely at 200 °C, indicating that zerovalent rhenium carbonyl species are considerably destabilized within the supercages of the highly siliceous SiY relative to the same species present in NaY.

In the present work, we have shown that the FT-Raman spectra have been more informative in terms of providing structural data, whereas the corresponding IR spectra often contain rather broad peaks, which can be difficult to interpret.

Acknowledgements

YH acknowledges the financial assistance from the Natural Sciences and Engineering Research Council of Canada (NSERC) for a research and an equipment grant. Funding from the Canada Research Chair (CRC) and Premier's Re-

© 2004 NRC Canada

search Excellence Award (PREA) programs and an Academic Development Funds (ADF) grant from UWO is also gratefully acknowledged. RRP thanks the government of Ontario for an OGSST scholarship.

References

1. F.P.J.M. Kerkhof, J.A. Moulin, and R.J. Thomas. J. Catal. **56**, 279 (1979).
2. J.H. Sinfelt. Bimetallic catalysis: Discoveries, concepts, and applications. John Wiley, New York. 1983.
3. A.A. Olsthoorn and C. Boelhouwer. J. Catal. **44**, 197 (1976).
4. L. Wang and W.K. Hall. J. Catal. **82**, 177 (1983).
5. For important reviewers see: (*a*) A. Zecchina and C. Otero Arean. Catal. Rev. – Sci. Eng. **35**, 261 (1993); (*b*) R. Psaro and S. Recchia. Catal. Today, **41**, 139 (1998); (*c*) N. Herron and D.R. Corbin (*Editors*). Inclusion chemistry with zeolites: Nanoscale materials by design. Kluwer Academic Publishers, Dordtrecht, The Netherlands.1995; (*d*) G.A. Ozin and C. Gil. Chem. Rev. **89**, 1749 (1989); (*e*) C. Bremard. Coord. Chem. Rev. **180**, 1647 (1998); (*f*) T. Bein. *In* Comprehensive supramolecular chemistry. Vol. 7. Pergamon, Oxford. 1996. Chap. 20; (*g*) B.C. Gates, L. Guczi, and H. Knozinger. Metal clusters in catalysis. Elsevier, Amsterdam. 1986.
6. P. Gallezot, G. Coudurier, M. Primet, and B. Imelik. ACS Symp. Ser. **40**, 144 (1977).
7. C. Dossi, J. Schaefer, and W.M.H. Sachtler. J. Mol. Catal. **52**, 193 (1989).
8. A. Zecchina, S. Bordiga, C. Otero Arean, and E. Escalona Platero. J. Mol. Catal. **70**, 43 (1991).
9. (*a*) Y. Huang, R.R. Poissant, and P. Qiu. Langmuir, **16**, 889 (2000); (*b*) Y. Huang and R.R. Poissant. Langmuir, **18**, 5487 (2002).
10. C.L. Angell. J. Phys. Chem. **77**, 222 (1973).
11. P.K. Dutta and R.E. Zaykoski. Zeolites, **8**, 179 (1988).
12. (*a*) D.M. Adams, M.A. Hooper, and A. Squire. J. Chem. Soc. A, 71 (1971); (*b*) D.M. Adams, M.A. Hooper, and A. Squire. Chem. Comm. 1188 (1970).
13. B. Jezowska-Trzebiatowska, J. Hanuza, and M. Baluka. Spectrochim. Acta Part A, **27A**, 1753 (1971).
14. D.M. Adams. Metal-ligand and related vibrations: A critical survey of the infrared and Raman spectra of metallic and organometallic compounds. Edward Arnold, London. 1967.
15. (*a*) P.S. Kirlin, F.A. DeThomas, J.W. Bailey, H.S. Gold, C. Dybowski, and B.C. Gates. J. Phys. Chem. **90**, 4882 (1986); (*b*) J.C. Papile and B.C. Gates. Lanmuir, **8**, 74 (1992); (*c*) S.K. Purnell, X. Xu, D.W. Goodman, and B.C. Gates. J. Phys. Chem. **98**, 4076 (1994).
16. M. Herberhold, G. Süss, J. Ellermann, and H. Gabelein. Chem. Ber. **111**, 2931 (1978).
17. P. Lemoine, and M. Gross. J. Therm. Anal. **6**, 159 (1974).
18. J.D. Greinerand H.R. Shanks. J. Solid State Chem. **5**, 262 (1972).
19. P. Gibart. Compt. Rend. **259**, 4237 (1964).
20. R. Nakamura, F. Abe, and E. Echigoya. Chem. Lett. **51** (1981).
21. I.R. Beattie and G.A. Ozin. J. Chem. Soc. A, 2615 (1969).
22. I.R. Beattie, T.R. Gilson, and P.J. Jones. Inorg. Chem. **35**, 1301 (1996).
23. M.J. Almond and R.H. Orrin. J. Chem. Soc. Dalton Trans. 1229 (1992).
24. See: (*a*) A. Brenner, D.A. Hucul, and S.J. Hardwick. Inorg. Chem. **18**, 1478 (1979); (*b*) A. Brenner and D.A. Hucul. J. Catal. **61**, 216 (1980); (*c*) A. Brenner and R.L. Burwell. J. Catal. **52**, 353 (1978).
25. D.A. Hucul and A. Brenner. J. Phys. Chem. **85**, 496 (1981).

© 2004 NRC Canada

New insights about the host–guest chemistry of the tungsten oxo complex of calix[4]arene, and novel "one pot" difunctionalizations of calix[4]arene using tetrachlorometal(VI) oxide (M = Mo, W)[1]

Pascal Mongrain, Jasmin Douville, Jonathan Gagnon, Marc Drouin, Andreas Decken, Daniel Fortin, and Pierre D. Harvey

Abstract: The strong Lewis acid tungsten oxo complex of calix[4]arene can be obtained in both hydrated and non-hydrated forms. This complex coordinates a water molecule inside the cavity via strong O···W interactions with relatively short distances of 2.284(4) and 2.329(2) Å for the tungsten oxo complex of calix[4]arene··H_2O·aniline (**1**), and the tungsten oxo complex of calix[4]arene·H_2O·toluene (**2**·toluene), respectively. The strong interactions are also deduced by the relatively high H_2O elimination temperature observed by TGA and DSC (above 200 °C). The coordinated water molecule inside the calix[4]arene cavity is characterized by a strong IR absorption at 3616 cm^{-1}, and a narrow resonance at ~1.2 ppm (the chemical shifts of the uncoordinated water are 1.55 and 1.60 ppm in C_6D_6 and $CDCl_3$, respectively). This water molecule gives rise to H-bonds with aniline in **1**. The tungsten oxo complex of 5,11,17,23-tetrabromocalix[4]arene (**4**), also binds H_2O as the characteristic signatures are observed. The successful removal of H_2O in **2**, is performed under mild conditions using bis(tetrahydrofuran)-uranyl nitrate as a competitive Lewis acid. When this reaction is performed in acetonitrile, butyronitrile or *tert*-butylnitrile, the corresponding tungsten oxo complexes of calix[4]arene·acetonitrile (**3**), ·butyronitrile (**5**), and ·*tert*-butylnitrile (**6**) are obtained. The use of uranyl as a H_2O abstractor is unprecedented. The X-ray structure of **3** consists of a tungsten oxo complex of calix[4]arene coordinated by an acetonitrile molecule (d(W···N = 2.412(2) Å). The tetra-5,11,17,23-choromethyl-25,26,27,28-tetrahydroxycalix[4]arene reacts with $M(O)Cl_4$ (M = Mo, W) in a 1:1 stoichiometry, via a tetra Friedel–Crafts addition of benzene or toluene, followed by a lower-rim complexation of the metal oxide, to form "flower-shaped" calix[4]arenes. This "one pot" double functionalization is unprecedented.

Key words: calix[4]arene, tungsten, molybdenum, X-ray, host–guest, Friedel–Crafts, Lewis acid, uranyl, DSC, TGA.

Résumé : Le complexe très fort de l'oxo tungstène avec calix[4]arène peut être obtenu sous les formes hydratée et non hydratée. Ce complexe donne lieu à une coordination avec une molécule d'eau à l'intérieur de la cavité, par le biais d'interactions O···W relativement courtes de 2,284(4) et 2,329(2) Å respectivement pour le complexe de l'oxo tungstène avec calix[4]arène··H_2O·aniline (**1**) et le complexe de l'oxo tungstène avec calix[4]arène·H_2O·toluène (**2**·toluène). On peut aussi déduire le caractère très fort des interactions de la température relativement élevée (supérieure à 200 °C) de l'élimination de l'eau observée par analyse thermogravimétrique et par calorimétrie à balayage différentiel. La molécule d'eau coordinée à l'intérieur de la cavité du calix[4]arène est caractérisée par une forte bande d'absorption IR à 3616 cm^{-1} et par une résonance étroite à environ 1,2 ppm (les déplacements chimiques de l'eau qui n'est pas coordinée absorbant à 1,55 et 1,60 ppm respectivement dans le C_6D_6 et le $CDCl_3$). Cette molécule d'eau donne aussi lieu à des liaisons hydrogènes avec l'aniline dans le composé **1**. Le complexe de l'oxo tungstène du 5,11,17,23-tétrabromocalix[4]arène (**4**) fixe aussi une molécule d'eau observée par les signatures caractéristiques. On peut réussir à enlever la molécule d'eau du composé **2** dans des conditions douces en utilisant du nitrate de bis(tétrahydrofurane)-uranyle comme acide de Lewis compétitif. Lorsqu'on effectue cette réaction dans l'acétonitrile, le butyronitrile ou le *tert*-butylnitrile, on obtient les

Received 6 January 2004. Published on the NRC Research Press Web site at http://canjchem.nrc.ca on 26 October 2004.

This paper is dedicated to Professor Don Irish.

P. Mongrain, J. Douville, J. Gagnon,[2] M. Drouin, D. Fortin, and P.D. Harvey.[3] Université de Sherbrooke, Département de chimie, 2500, boul. de l'Université, Sherbrooke, QC J1K 2R1, Canada.
A. Decken. University of New Brunswick, Department of Chemistry, PO Box 4400, Fredericton, NB E3B 6E2, Canada.

[1]This article is part of a Special Issue dedicated to the memory of Professor Don Irish.
[2]Present address: Département de chimie, Université du Québec à Rimouski, 300, allée des Ursulines, C.P. 3300, Rimouski, QC G5L 3A1, Canada.
[3]Corresponding author (e-mail: p.harvey@usherbrooke.ca).

 doi: 10.1139/V04-097 © 2004 NRC Canada

complexes de l'oxo tungstène de calix[4]arène·acétonitrile (**3**), ·butyronitrile (**5**) et de ·*tert*-butylnitrile (**6**). Il n'existe pas de précédent pour l'utilisation de l'uranyle pour l'enlèvement d'une molécule d'eau. La structure cristalline du complexe **3**, telle que déterminée par diffraction des rayons X, est formée d'un complexe de l'oxo tungstène du calix[4]arène comportant une coordination à une molécule d'acétonitrile (d(W···N) = 2,412(2) Å). Le 5,11,17,23-tétra(chlorométhyl)-25,26,27,28-tétrahydroxycalix[4]arène réagit avec le $M(O)Cl_4$ (M = Mo, W) suivant une stoechiométrie 1:1 par le biais d'une tétraaddition de Friedel–Crafts du benzène ou du toluène, qui est suivie d'une complexation de l'oxyde métallique à la ceinture inférieure, qui conduit à la formation de calix[4]arènes en forme de fleur. Cette double fonctionnalisation monotope n'a pas non plus de précédent.

Mots clés : calix[4]arène, tungstène, molybdène, rayons X, hôte–invité, Friedel–Crafts, acide de Lewis, uranyle, calorimétrie à balayage différentiel, analyse thermogravimétrique.

[Traduit par la Rédaction]

Introduction

The syntheses and investigations of calix[4]arene macrocycles and derivatives continue to be very active fields (1). Applications for cation extractions, biomimetics, luminescence probes, sensors, nuclear waste treatment, and catalysis are well-known (1, 2). Among these species, calix[4]arene is certainly the most investigated compound. The cyclic structure composed of four aryl groups exhibits four conformations (cone, partial cone, and 1,2- and 1,3- alternated), where the first, may allow host–guest interactions between a substrate, ordinarily a neutral organic molecule, and the cavity formed by the cone. This property is highly variable, as empty flattened structures often exist because of the relative flexibility of the macrocycles (3). The coordination of a metal atom such as Nb(V) (4–6), Mo(VI) (7, 8), and W(VI) (9–11) for example, in the calix[4]arene narrow rim has been used to secure the cone conformation and to open the hydrophobic cavity wide enough to allow guest molecules such as benzene, tetrahydrofuran, dimethylamine, pyridine, acetic acid, and even water, to penetrate. The common point in these reported systems is that the wide rim is functionalized by four tert-butyl groups, thus enhancing the cavity size. The use of larger groups such as -N=NR can even let another calix[4]arene compound penetrate the cavity (12, 13). Numerous questions arise such as what happens when the wide rim is unfunctionalized, what other organic substrates can interact with the calix[4]arene's cavity, and can one take advantage of the presence of a water molecule at the bottom of the cavity.

In the first section of this paper, we wish to report the preparation of the tungsten oxo complexes of calix[4]arene that is not functionalized at the wide rim, along with three X-ray structures in which a water or an acetonitrile molecule is held inside the cavity with W···O or W···N interactions. In one structure, H-bonds with the aniline molecule are observed, and supramolecular construction is possible above the cavity. In the other case, the coordination of a nitrile molecule also indicates that the calix[4]arene cavity can also be functionalized at the upper and lower rims. The water molecule can be removed by the use of the Lewis acid UO_2^{2+}, or by heating the solid samples at temperatures of about 200 °C. In the second section, we wish to report an unprecedented reactivity in the calix[4]arene chemistry, which consists of tetra Friedel–Craft additions of an aromatic to tetra-5,11,17,23-chloromethyl-25,26,27,28-tetrahydroxycalix[4]arene (**1**), hence expanding the cavity, followed by the coordination of the metal oxide.

Experimental section

Materials

Calix[4]arene (14), tungsten oxo complex of calix[4]arene (8), bis(tetrahydrofuran)uranyl nitrate (15), and tetra-5,11,17,23-chloromethyl-25,26,27,28-tetrahydroxycalix[4]arene (16) (**7**) were prepared according to procedures reported in the literature. The tetrachloride(oxo)tungsten(VI) and uranyl nitrate were purchased from Aldrich and were used as received.

Tungsten oxo complex of calix[4]arene·H_2O·aniline (1)

The tungsten oxo complex of calix[4]arene (0.1 g, 0.16 mmol) was treated with 3 mL of aniline in 20 mL of benzene and 0.2 mL of water. The solution was refluxed for 8 h and cooled to room temperature. The solution was evaporated until it reached 2 mL. The solute was precipitated by diffusion of diethyl ether. Yellow crystals were obtained in 70% yield (79.9 mg). IR (solid) (cm^{-1}): ~3600, br (ν(OH···N)). ^{1}H NMR ($CDCl_3$): 7.13 (d, 8H, meta H Ph_{calix}, $J_{H\text{-}H}$ = 7.45), 7.05 (t, 3H, meta and para H of aniline, $J_{H\text{-}H}$ = 7.70), 7.71 (t, 4H, para H Ph_{calix}, $J_{H\text{-}H}$ = 7.63), 6.34 (d, 2H, ortho H of aniline, $J_{H\text{-}H}$ = 7.91), 4.68 (d, 4H, Ar-CH_2-Ar, $J_{H\text{-}H}$ = 12.71), 3.34 (d, 4H, Ar-CH_2-Ar, $J_{H\text{-}H}$ = 12.71), 2.35 (NH_2), 1.21 (s, 2H, H_2O···W). ^{13}C NMR (CD_3Cl): 156.2, 130.3, 129.2, 128.3, 123.9, 119.1, 115.4, 32.2. EI-MS: 620 M^+.

Tungsten oxo complex of calix[4]arene·H_2O·toluene (2·toluene)

A solution of calix[4]arene (0.5 g, 1.18 mmol) and 40 mL of toluene was treated with $WOCl_4$ (400 mg, 1.18 mmol). The solution was refluxed for 48 h. Then, the solution was filtered and was extracted with toluene. The solution was evaporated with a flux of argon and a purple crystalline material identified as the tungsten oxo complex of calix[4]arene·H_2O (**2**) was obtained in 72% yield (60.5 mg). IR (solid) (cm^{-1}): 3616, s (ν(OH)). ^{1}H NMR (C_6D_6): 6.80 (d, 8H, ortho H Ph, $J_{H\text{-}H}$ = 7.57), 6.55 (t, 4H, para H Ph, $J_{H\text{-}H}$ = 7.57), 4.62 (d, 4H, Ar-CH_2-Ar, $J_{H\text{-}H}$ = 12.71), 2.94 (d, 4H, Ar-CH_2-Ar, $J_{H\text{-}H}$ = 12.71), 1.10 (s, 2H, H_2O···W). EI-MS: 620 M^+. Anal. calcd. for $C_{28}H_{20}O_5W{\cdot}H_2O$: C 52.69, H 3.47; found: C 52.33, H 3.57. Compound **2**·toluene obtained when

© 2004 NRC Canada

the product was dissolved in toluene and acetonitrile was slowly vapour diffused through it, and crystals suitable for X-ray analysis were obtained.

Tungsten oxo complex of calix[4]arene·acetonitrile (3)

A solution containing 28 mg (0.045 mmol) of **2**, 3.5 mL of CH_2Cl_2, and 3.5 mL of acetonitrile was treated with 31 mg (0.068 mmol) of $(UO_2)(NO_3)_2(THF)_2$. The solution was stirred for 24 h and a precipitate was formed. The solution was filtered and yellow crystals were obtained in 62% yield (18 mg). IR (solid) (cm^{-1}): 2285, s (ν(CN)). ^1H NMR (C_6D_6): 6.80 (d, 8H, Ph, J_{H-H} = 7.57 Hz), 6.55 (t, 4H, Ph, J_{H-H} = 7.57 Hz), 4.62 (d, 4H, Ar-CH_2-Ar, J_{H-H} = 12.71Hz), 2.93 (d, 4H, Ar-CH_2-Ar, J_{H-H} = 12.71Hz), 1.21 (s, 3H, N=C-CH_3). EI-MS: 620 M^+.

Tungsten oxo complex of 5,11,17,23-tetrabromocalix[4]arene·H_2O (4)

A solution of **2** (47 mg, 0.076 mmol) with 10 mL of $CHCl_3$ was treated with 0.02 mL of Br_2. The solution was stirred for 24 h. The reaction was quenched twice with $Na_2S_2O_3$ and washed with H_2O. A yellow solid was obtained in 99% yield (70.7 mg). IR (solid) (cm^{-1}): 3616, s (ν(OH)). ^1H NMR ($CDCl_3$): 7.28 (s, 8H, Ph), 4.59 (d, 4H, Ar-CH_2-Ar, J_{H-H} = 12.70 Hz), 3.37 (d, 4H, Ar-CH_2-Ar, J_{H-H} = 12.70 Hz), 1.25 (2H, H_2O···W). EI-MS: 936 M^+.

Tungsten oxo complex of calix[4]arene·butyronitrile (5)

This compound was prepared according to the same procedure described for **3** using butyronitrile as the solvent. A yellow solid was obtained in 59% yield. IR (solid) (cm^{-1}): 2283, s (ν(CN)). ^1H NMR ($CDCl_3$): 7.14 (d, 8H, meta Ph, J_{H-H} = 7.61), 6.72 (t, 4H, ortho H Ph, J_{H-H} = 7.49) 4.68 (d, 4H, Ar-CH_2-Ar, J_{H-H} = 12.50), 3.65 (t, 2H, N=C-CH_2-, J_{H-H} = 7.18) 3.37 (d, 4H, Ar-CH_2-Ar, J_{H-H} = 12.52), 1.25 (m, 2H, -CH_2-CH_3) 0.86 (m, 3H, -CH_2-CH_2-CH_3). EI-MS: 620 M^+.

Tungsten oxo complex of calix[4]arene·*tert*-butylnitrile (6)

This compound was prepared according to the same procedure described for **3** using *tert*-butylnitrile as the solvent. A yellow solid was obtained in 64% yield. IR (solid) (cm^{-1}): 2263, s (ν(CN)). ^1H NMR ($CDCl_3$): 7.14 (d, 8H, meta Ph, J_{H-H} = 7.53), 6.72 (t, 4H, ortho H Ph, J = 7.51) 4.68 (d, 4H, Ar-CH_2-Ar, J_{H-H} = 12.55), 3.33 (d, 4H, Ar-CH_2-Ar, J_{H-H} = 12.87), 1.37 (s, 9H, -C-(CH_3)$_3$, J = 6.86). EI-MS: 620 M^+.

5,11,17,23-Tetrabenzyl-25,26,27,28-oxomolybdenum(VI)calix[4]arene (8)

A benzene (15 mL) suspension of $MoOCl_4$ (0.070 g, 0.27 mmol) was reacted with **7** (0.100 g, 0.16 mmol). The suspension was refluxed overnight. The solvent was evaporated in vacuo and the residue was dissolved in CH_2Cl_2 (40 mL). The solution was washed three times with water. The organic phase was separated, dried with $MgSO_4$, and filtered. The solvent was evaporated to afford a dark blue solid. Yield: 53% (0.076 g). ^1H NMR ($CDCl_3$): 7.29–6.87 (m, 28H, Ar), 4.39 (d, 4H, J_{H-H} = 12.7, ArCH_2Ar), 3.80 (s, $C_6H_5CH_2$Ar), 3.17 (d, 4H, J_{H-H} = 12.5, ArCH_2Ar). ^{13}C NMR ($CDCl_3$): 156.88, 140.86, 137.10, 129.73, 128.71, 128.45, 126.17, 41.09, 32.50. EI-MS *m*/*e*: 892 (M^+). Anal. calcd. for $C_{56}H_{40}O_5Mo·H_2O$: C 74.17, H 4.67; found: C 73.23, H 5.40.

5,11,17,23-Tetrabenzyl-25,26,27,28-oxotungsten(VI)calix[4]arene (9)

First method

A benzene (15 mL) suspension of $WOCl_4$ (0.160 g, 0.47 mmol) was reacted with **7** (0.200 g, 0.32 mmol). The suspension was refluxed overnight. The solvent was evaporated in vacuo and the residue was dissolved in CH_2Cl_2 (40 mL). The solution was washed three times with water. The organic phase was separated, dried with $MgSO_4$, and filtered. The solvent was evaporated to produce a black solid. Yield: 52% (0.17 g). ^1H NMR ($CDCl_3$): 7.29–6.89 (m, 28H, Ar), 4.58 (d, 4H, J_{H-H} = 12.8, ArCH_2Ar), 3.80 (s, $C_6H_5CH_2$Ar), 3.20 (d, 4H, J_{H-H} = 12.9, ArCH_2Ar). ^{13}C NMR ($CDCl_3$): 154.33, 140.87, 136.71, 130.82, 128.64, 128.45, 126.19, 41.02, 32.21. EI-MS: 980 (M^+). Anal. calcd. for $C_{56}H_{40}O_5W·H_2O$: C 67.21, H 4.83; found: C 67.07, H 5.07.

Second method

The procedure was identical to that used for the first method, except that **12** was used instead of **7**.

5,11,17,23-Tetra(4-methylbenzyl)-25,26,27,28-oxomolybdenum(VI)calix[4]arene (10)

A toluene (20 mL) suspension of $MoOCl_4$ (0.029 g, 0.11 mmol) was reacted with **7** (0.040 g, 0.06 mmol). The suspension was refluxed overnight. The solvent was evaporated in vacuo and the residue was dissolved in CH_2Cl_2 (50 mL). The solution was washed three times with water. The organic phase was separated, dried with $MgSO_4$ and filtered. The solvent was evaporated to afford a golden brown solid. Yield: 92% (0.052 g). ^1H NMR ($CDCl_3$): 7.18–6.80 (m, 24H, Ar), 4.39 (d, 4H, J_{H-H} = 12.5, ArCH_2Ar), 3.78 (d, 8H, J_{H-H} = 11.2, $C_6H_4CH_2$Ar), 3.15 (d, 4H, J_{H-H} = 12.6, ArCH_2Ar), 2.36 (s, 12H, $CH_3C_6H_4$). ^{13}C NMR ($CDCl_3$): 156.93, 138.86, 137.92, 137.46, 136.48, 136.35, 135.70, 130.36, 129.75, 129.21, 129.00, 128.74, 126.99, 126.57, 126.08, 40.76, 38.61, 32.56, 21.11, 19.76. EI-MS: 949 (M^+). Anal. calcd. for $C_{60}H_{52}O_5Mo·H_2O$: C 74.52, H 5.63; found: C 74.46, H 5.12.

5,11,17,23-Tetrakis(methylbenzyl)-25,26,27,28-oxotungsten(VI)calix[4]arene (11)

A toluene (20 mL) suspension of $WOCl_4$ (0.192 g, 0.56 mmol) was reacted with **7** (0.250 g, 0.40 mmol). The suspension was refluxed overnight. The solvent was evaporated in vacuo and the residue was dissolved in CH_2Cl_2 (50 mL). The solution was washed three times with water. The organic phase was separated, dried with $MgSO_4$, and filtered. The solvent was evaporated to give the product as a dark blue solid. Yield: 98% (0.041 g). ^1H NMR ($CDCl_3$): 7.17–6.89 (m, 24H, Ar), 4.56 (d, 4H, J_{H-H} = 12.6, ArCH_2Ar), 3.78 (d, 8H, J_{H-H} = 12.3, $C_6H_4CH_2$Ar), 3.15 (d, 4H, J_{H-H} = 12.6, ArCH_2Ar), 2.34 (s, 12H, $CH_3C_6H_4$). ^{13}C NMR ($CDCl_3$): 154.25, 138.79, 137.88, 136.99, 135.88, 135.69, 130.77, 130.31, 129.60, 129.15, 128.57, 126.55, 126.03, 40.62, 38.44, 32.18, 21.04, 19.72. EI-MS: 1036

© 2004 NRC Canada

(M^+). Anal. calcd. for $C_{60}H_{52}O_5W{\cdot}H_2O$: C 68.31, H 5.16; found: C 68.51, H 5.23.

5,11,17,23-Chloromethyl-25,26,27,28-oxotungsten(IV)calix[4]arene (12)

2 (0.050 g, 0.083 mmol) and chloromethyl octyl ether (0.3 mL, 2.4 mmol) were dissolved in CH_2Cl_2 (15 mL). The solution was cooled to –5 °C and $SnCl_4$ (0.2 mL, 1.7 mmol) was added dropwise over 15 min under agitation. The solution was then warmed up to room temperature and was further stirred for 1 h. Water (15 mL) was slowly added to the solution and the organic phase was separated. The organic phase was washed twice with brine (20 mL), then dried with $MgSO_4$ and filtered. The solvent was evaporated until a yellow paste formed. The residue was washed with cooled hexane (50 mL; 4 °C) to afford a yellow powder. Yield: 79% (0.053 g). ^{1}H NMR ($CDCl_3$): 7.19 (s, 8H, Ar), 4.66 (d, 4H, $J_{H\text{-}H}$ = 12.9, Ar*CH*$_2$Ar), 4.46 (s, 8H, Ar*CH*$_2$Cl), 3.35 (d, 4H, $J_{H\text{-}H}$ = 13.0, Ar*CH*$_2$Ar). ^{13}C NMR ($CDCl_3$): 141.32, 131.18, 128.87, 45.44, 32.15. EI-MS: 672 (M^+ – 4Cl). Anal. calcd. for $C_{32}H_{24}O_5Cl_4W{\cdot}H_2O$: C 46.18, H 3.15; found: C 46.11, H 3.08.

Apparatus

The NMR spectra were acquired on a 300 MHz Bruker instrument (^{1}H, 300.15 MHz). The chemical shifts (δ) are reported with respect to tetramethylsilane (TMS = 0 ppm) (^{1}H). The chemical shifts and coupling constants are reported in ppm and Hz, respectively. The FT-IR data were obtained on a PerkinElmer spectrometer Model 1600. The mass spectra (EI) were measured on a ZAB-1F instrument (VG model). The TGA analyses were performed using a PerkinElmer TGA 7 apparatus operating between 50 and 700 °C scanning at the rate of 3 °C/min. under N_2 atmosphere. The glass transition temperatures (Tg) were measured using a PerkinElmer 5A DSC7 equipped with a thermal controller 5B TAC 7/DS. The temperature calibrations were done with water and metallic indium as standards. The accuracy is ±0.1 °C and ±0.1% for the temperature and heat capacity, respectively. The sample weights ranged from 5 to 10 mg, and the scan rate was 10°/min.

Crystallography

Tungsten oxo complex of calix[4]arene·H_2O·aniline (1)

Intensity data were collected at 293 K on an Enraf Nonius CAD-4 automatic diffractometer at the Université de Sherbrooke. Table 1 provides crystallographic and data collection details. The NRCCAD programs were used for centering, indexing, and data collection (17). The structure was solved by the application of direct methods using the NRCVAX (18) program and refined by least-squares using SHELXL-93 (19). Hydrogen atoms were geometrically placed at idealized positions and not refined except for those of the water molecule, which were located by Δ*F*. The aniline molecule was disordered and occupancy refinement showed a 0.316(7)/0.684(7) ratio. The ORTEP diagram (20) includes only the aniline with higher occupancy factor.

Tungsten oxo complex of calix[4]arene·H_2O·toluene (2·toluene) and of calix[4]arene·acetonitrile (3)

Crystals of **2**·toluene and 3 were grown by a slow evaporation method using toluene and acetonitrile, respectively, at 25 °C. Single crystals were coated with Paratone-N oil, mounted using a glass fibre and frozen in the cold nitrogen stream of the goniometer. A hemisphere of data was collected on a Bruker AXS P4/SMART 1000 diffractometer at the University of New Brunswick, using ω and θ scans with a scan width of 0.3° and 10 s exposure times. The detector distance was 6 cm. The data were reduced (SAINT) (21) and corrected for absorption (SADABS) (22). The structures were solved by direct methods and refined by full-matrix least-squares on F^2 (SHELXTL) (23). All non-hydrogen atoms were refined anisotropically. For calix[4]arene·H_2O·toluene (2·toluene), the hydrogen atoms were found in Fourier difference maps and refined isotropically. For calix[4]arene·acetonitrile (**3**), the hydrogen atoms were included in calculated positions and refined using a riding model.

5,11,17,23-Tetrabenzyl-25,26,27,28-oxotungsten(VI)calix[4]arene (9)

Crystals of **9** were obtained from the evaporation of an acetonitrile–hexane solution. Single crystals were coated with Paratone-N oil, mounted using a glass fibre and frozen in the cold nitrogen stream of the goniometer at 198 K. A hemisphere of data was collected on a Bruker AXS P4/SMART 1000 diffractometer at the University of New Brunswick, using ω and θ scans. The detector distance was 6 cm. The data were analyzed at the Université de Sherbrooke. The data were reduced with Bruker SHELXTL but not corrected for absorption, solved by direct methods with SHELXS-86 (24) and refined by full-matrix least-squares on F^2 with SHELXL-93 (19). All the hydrogen atoms were placed at idealized calculated geometric positions and refined using a riding model. The phenyl groups were disordered on two positions (1) C10-C15 and (2) C10′-C15′ with 50.8% relative occupation for (1) that were kept fixed in the ORTEP drawing. All non-hydrogen atoms included of the calix[4]arene molecule were refined anisotropically with FLAT 66, DELU and SIMU (all included in SHELXL-93), with constrains on the phenyls (1) and (2) groups. One oxygen atom belonging to a water molecule trapped inside the calix[4]arene cavity and one oxygen outside (W=O) were given a fixed occupation factor of 100%. The crystallization acetonitrile molecule was refined isotropically with fixed bond lengths and thermal restrains. The occupation factor was 0.51. The remaining electronic density found above the cavity was assigned to water crystallization molecules based on ^{1}H NMR and IR data. These water molecules (O4, O5, O6) were refined isotropically with fixed thermal parameters. The total refined occupation factors for these were approximately 1.48 water molecules per assymetric unit.

Results and discussion

Host–guest chemistry

The tungsten oxo complex of calix[4]arene is very hydroscopic as it picks up water readily when synthesized or handled in air or in the presence of wet solvents as described

© 2004 NRC Canada

Table 1. Crystal data for **1**, **2**·toluene, **3**, and **9**.

	1	**2**·Toluene	**3**	**9**
Empirical formula	$C_{34}H_{29}NO_6W$	$C_{35}H_{30}O_6W$	$C_{30}H_{23}NO_5W$	$C_{56}H_{46}O_6W{\cdot}0.5CH_3CN{\cdot}1.5H_2O$
Formula weight	731.46	730.44	661.34	1041.29
Colour, habit	Yellow prism	Orange, parallelepiped	Red, parallelepiped	Red, irregular
Crystal dimension (mm^3)	0.15×0.25×0.30	0.23×0.30×0.35	0.23×0.38×0.40	0.30×0.35×0.35
Crystal system	Monoclinic	Monoclinic	Orthorhombic	Cubic
Space group	*P*21/*n*	*P*21/*n*	*Pnma*	*Im*-3
Z	4	4	4	12
a (Å)	10.8224(12)	10.3446(7)	16.4878(9)	25.317(4)
b (Å)	17.350(2)	17.0079(12)	13.4789(7)	25.317(4)
c (Å)	15.2482(15)	15.6971(11)	10.8745(6)	25.317(4)
α (°)	90	90	90	90
β (°)	98.058(8)	99.247(1)	90	90
γ (°)	90	90	90	90
Temperature (K)	293(2)	198(1)	198(1)	198(2)
Volume ($Å^3$)	2 834.8(5)	2725.9(3)	2416.7(2)	16 227(4)
Calculated density (Mg m^{-3})	1.714	1.780	1.818	1.279
Radiation (Å)	0.710 73	0.710 73	0.710 73	0.710 73
Absorption coeff., μ (mm^{-1})	4.207	4.287	4.823	2.184
F(000)	1448	1448	1296	6300
θ-range (°)	1.78–24.90	1.78–25.00	2.24–27.50	1.61–20.15
Limiting indices	$-12 \le h \le 12$	$-11 \le h \le 12$	$-21 \le h \le 20$	$-24 \le h \le 24$
	$0 \le k \le 20$	$-20 \le k \le 20$	$-17 \le k \le 17$	$-22 \le k \le 24$
	$0 \le l \le 17$	$-17 \le l \le 16$	$-13 \le l \le 12$	$-24 \le l \le 23$
Reflections collected	4897	13 330	16 098	26 514
Independent refletions	4897	4608	2872	1424
Data/restraints/parameters	4897/26/374	4608/0/499	2872/2/229	1424/190/195
Goodness-of-fit on F^2	1.028	1.050	1.114	1.136
Final *R* indices [$I > 2\sigma(I)$] (*R*1, *wR*2)	0.0339, 0.0743	0.0157, 0.0401	0.0141, 0.0367	0.0671, 0.1716
R indices (all data) (*R*1, *wR*2)	0.0489, 0.0787	0.0185, 0.0410	0.0153, 0.0372	0.1325, 0.2090
Min/max trans. ratio	0.803	0.623	0.640	—
Largest diff. peak and hole (e $Å^{-3}$)	1.490, –0.872	0.637, –0.308	0.365, –0.621	0.759, –0.531

Note: $R1 = \Sigma||F_o| - |F_c||/\Sigma|F_o|$, $wR2 = (\Sigma[w(F_o^2 - F_c^2)2]/\Sigma[F_o^4])^{1/2}$, weight (**1**) = $1/[\sigma^2(F_o^2) + (0.0463P)^2 + (1.7267P)]$, weight (**2**·toluene) = $1/[\sigma2(F_o^2) + (0.0214P)^2 + (2.0738P)]$, weight (**3**) = $1/[\sigma^2(F_o^2) + (0.0164P)^2 + (1.839P)]$, weight (**9**) = $1/[\sigma^2(F_o^2) + (0.0987P)^2 + (165.9406P)]$, where $P = (\max(F_o^2, 0) + 2F_c^2)/3$.

in the Experimental section for compounds **1** and **2**. This behaviour is not uncommon (8, 10, 11). The coordinated water molecule inside the tungsten oxo complex of calix[4]arene is characterized by a strong narrow IR absorption at 3616 cm^{-1}, and a narrow resonance at ~1.2 ppm in the ^1H NMR spectra (the chemical shifts of the uncoordinated water are 1.55 and 1.60 ppm for C_6D_6 and $CDCl_3$, respectively). This water molecule can be removed by heating the samples under vacuum, or at room pressure at temperatures approaching 200 °C (see AGT/DSC data).

The tungsten oxo complex of 5,11,17,23-tetrabromocalix[4]arene (**4**) was prepared taking advantage of the potential H-bonding network between the Br lone pairs and the H_2O protons, and to investigate the inductive effect on the W···OH_2 binding strength. The spectroscopic IR and ^1H NMR W···OH_2 signatures are clearly observed in this product, but all attempts to obtain crystals suitable for crystallography failed, as low diffracting, very thin rectangular green plates were always obtained.

Recently, we demonstrated that the strongly bonded halide ions on the unsaturated face of the $Pd_3(dppm)_3(CO)^{2+}$ cluster (25–27) could be removed with the use of another Lewis acid such as Cu^+ and Ag^+ (28, 29). In this work, anhydrous uranyl compound $(THF)_2(UO_2)(NO_3)_2$ is successfully used to abstract water from **2** (rxn. 1). Because of the strong ionic character of this reactant, acetonitrile, butyronitrile, and *tert*-butylnitrile were used as solvents, while the co-solvent dichloromethane dissolves the calix[4]arene complex. The uranyl compound shows affinity for calix[4]arene derivatives only if O atoms containing residues are present in the macrocycle forming multi-dentate ligand structures (see ref. 30 as an example) to form stable chelates. This is not the case here. The identity of **3** has been confirmed on the basis of crystallography, and **5** and **6** from IR and ^1H NMR spectroscopy. In all three cases, the nitrile molecule coordinates to the W atom in the final products (rxn. 2).

[1] $$\text{Calix(W=O)}{\cdot}H_2O + \text{“}UO_2^{2+}\text{”} \rightarrow \text{Calix(W=O)} + \text{“}UO_2{\cdot}(H_2O)^{2+}\text{”}$$

[2] $$\text{Calix(W=O)} + RC{\equiv}N \rightarrow \text{Calix(W=O)}{\cdot}N{\equiv}CR \quad (R = Me, Pr, t\text{-}Bu)$$

© 2004 NRC Canada

Table 2. Selected bond distances (Å) and angles (°) for **1**, **2**·toluene, **3**, and **9**.

	1	**2**·Toluene	**3**	**9**
d(W=O) (Å)	1.698(4)	1.706(2)	1.7039(19)	1.727(19)
d(W···X) (Å)	2.284 (4)	2.329(2)	2.412(2)	2.424(17)
d(W-O) (Å)	1.910(4), 1.926(4)	1.911(2), 1.923(2)	1.9076(13)	1.901(11)
	1.905(3), 1.926(4)	1.894(2), 1.922(2)	1.9156(13)	
∠(O=W-X) (°)	179.8(5)	179.1(8)	179.61(9)	180.000(1)
∠(O-W-X) (°)	81.5(2), 81.2(2)	80.99(7), 80.82(7)	80.89(5),	80.2(3)
	81.7(2), 81.1(2)	80.66(8), 79.50(7)	80.09(5)	
∠(O-W=O) (°)	98.4(2), 99.0(2)	99.60(8), 99.10(8)	99.39(6),	99.8(3)
	99.1(2), 98.1(2)	99.11(8), 100.24(8)	99.63(6)	

Fig. 1. ORTEP diagram of **1**. The ellipsoids are shown at 50% probability and the H atoms are not shown for clarity.

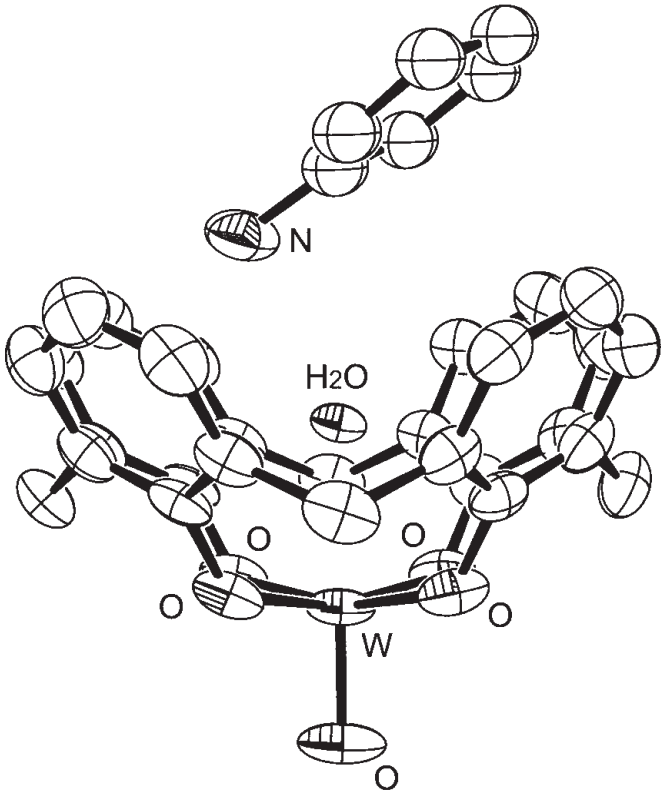
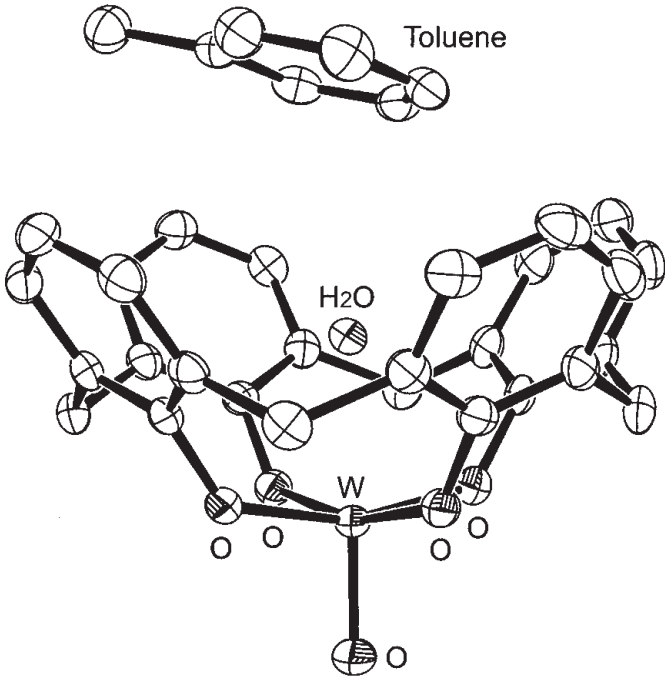


Fig. 2. ORTEP diagram of **2**·toluene. The ellipsoids are shown at 30% probability and the H atoms are not shown for clarity.



X-ray structure of 1, 2·toluene, and 3

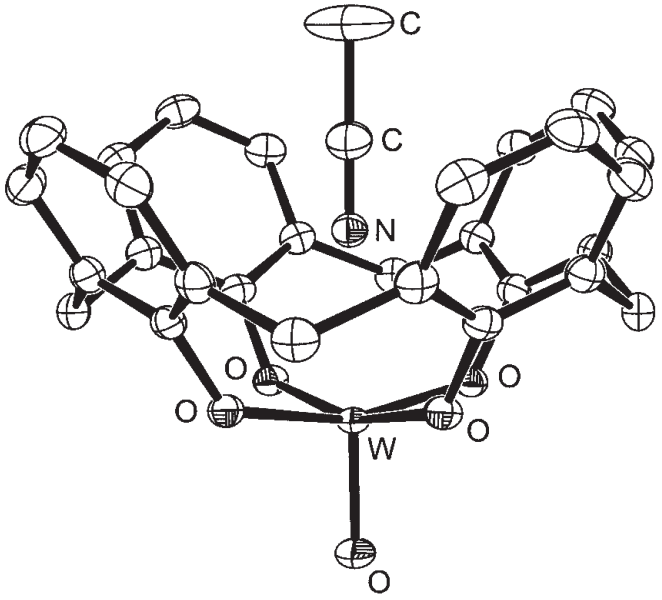
Tables 1 and 2, and Figs. 1–3 present the X-ray data for the three investigated compounds. **1** exhibits a H_2O molecule inside the cavity strongly interacting with the W atom. The short W···O contact (2.284 Å) is the shortest ever to be reported for this family of complexes (Table 3). This distance is still longer by about ~0.3 Å than what it is expected for a covalent W—O single bond (1.89–1.92 Å, see Tables 2 and 3). The O=W···O angle is linear, certainly because of the constraint imposed by the cavity. The key feature is the presence of an aniline molecule held by H-bonds. The aniline is disordered as described in the Experimental section and two nonbonding distances are depicted for the two occupancies (d(O···N) = 2.625 and 2.740 Å). The supramolecular structure bears similarities with the structure reported for (*t*-Bu)$_4$calix[4]arene(Mo=O)·H_2O·$C_6H_5NO_2$ where the H-bonds retain the nitrobenzene over the calix[4]arene·H_2O moiety (8).

Compound **2**·toluene is similar to **1**, where a toluene crystallization molecule is found in the crystal lattice, also located on top of the cavity. A short W···O distance is observed (2.329 Å). The WO_5 core remains identical to that found for **1** where the bond distances and angles are identical within the experimental uncertainties. The toluene molecule is found tilted towards the cavity where the phenyl group exhibits the closest carbon–oxygen distances (3.079 (para from CH_3), 3.301 and 3.418 Å), suggesting some weak O-H···C interactions.

Compound **3** does not exhibit a water molecule inside the cavity, indicating that the H_2O abstraction was successful, consistent with the ^{1}H NMR and IR data. Instead, an acetonitrile molecule is located inside the cavity with the N atom directed towards the W metal with a short distance of 2.412(5) Å. Host–guest assemblies of the type calix[4]arene–acetonitrile are rare with respect to other organic substrates (31–34). Amoung these examples, some cases involve interactions of the N atom with a metal, which

© 2004 NRC Canada

Fig. 3. ORTEP diagram of **3**. The ellipsoids are shown at 30% probability and the H atoms are not shown for clarity.



are even more unusual (34). Again the molecular skeleton of this metallated host remains unchanged by these interactions.

Table 3 allows a number of comparisons. The O=W···OH_2 distance is found to be shorter for the unfunctionalized metallated macrocycles (2.284(4) and 2.329(2) Å for **1** and **2**·toluene, respectively) than that of the *tert*-butylated species (2.370(1) Å for (*t*-Bu)$_4$calix[4]arene-(W=O)·H_2O). The *tert*-butyl groups render the phenolate fragments more electron rich, such that the W atom is also richer, promoting weaker W···OH_2 interactions. An examination of the O-W=O angles also shows a slightly smaller cone angle of ~0.5° for the *tert*-butylated derivatives (in comparison with the unfunctionalized systems). In addition, the M···NCMe distances reported for the related compounds (*t*-Bu)$_4$calix[4]arene(Mo=$NCMe_3$)·NCMe (2.343(9)) (33), (*t*-Bu)$_4$calix[4]arene(Mo=NC-Mes)·NCMe (2.303(3)) (33), (*t*-Bu)$_4$calix[4]arene(W=NCMes)·NCMe (2.314(3)) (33), and (*t*-Bu)$_4$calix[4]arene(Mo=NCAr)·NCMe (2.324(7) Å) (Ar = 2-$C_6H_4CH_2CH_2C_6H_4$N-2´-CHC_5H_5N) (32), are also shorter than that found in **3** (2.412(2) Å).

TGA/DSC data

These measurements were performed to determine the relative binding strength of the water inside the cavity (Figs. 4 and 5). The weight loss observed for **1** in the 180–210 °C window corresponds to the loss of aniline and water. The assignment is confirmed with a sample that contains only a tungsten oxo complex of calix[4]arene·H_2O·toluene (**2**·toluene). In this case, a small weight loss (~3%) is observed at ~200–220 °C corresponding to the loss of H_2O. On the other hand, the loss of toluene occurs slowly between 100 and 200 °C. The examination of the first derivative of the weight loss curves indicates a maximum at 184 and 200, and 205 °C for **1** and **2**, respectively. By DSC, the latter decomposition process is observed in the 180–220 °C window as anticipated for **2**·toluene. Indeed, a heat absorption maximum at 197 °C exhibiting an exothermic change in heat capacity (ΔCp) of –116 J/g is observed. The cyclic thermogram of the sample between 25 and 300 °C results in the disappearance of the DSC signal, consistent with the water loss. **1** and **2** decompose at temperatures exceeding 380–400 °C.

Fig. 4. TGA traces for compounds **1** and **2**·toluene.

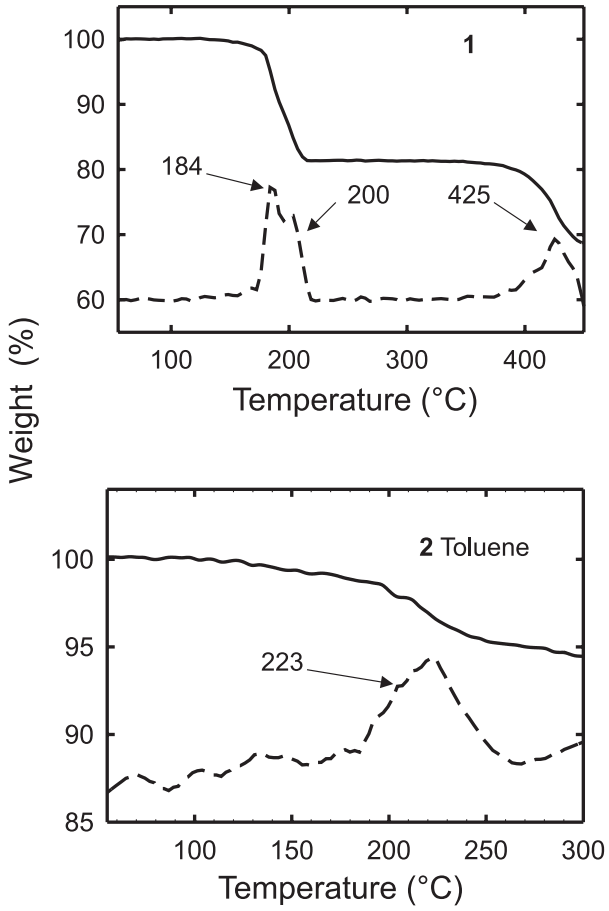
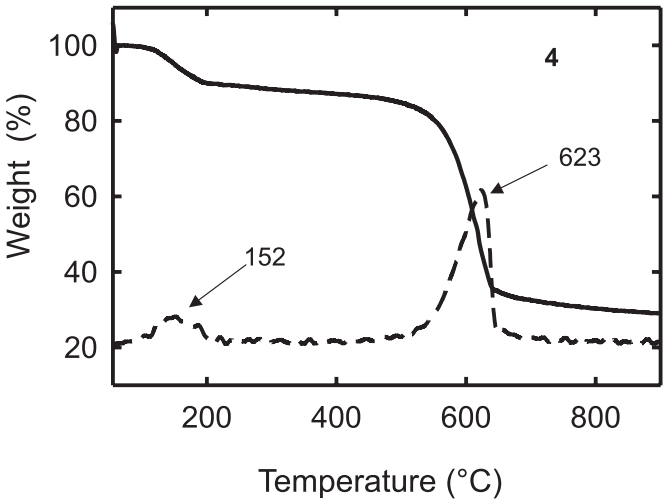


Fig. 5. TGA traces for compound **4**.



For **4**, the first weight loss occurs in the 180–200 °C window, but the corresponding mass (10%) is exactly the mass

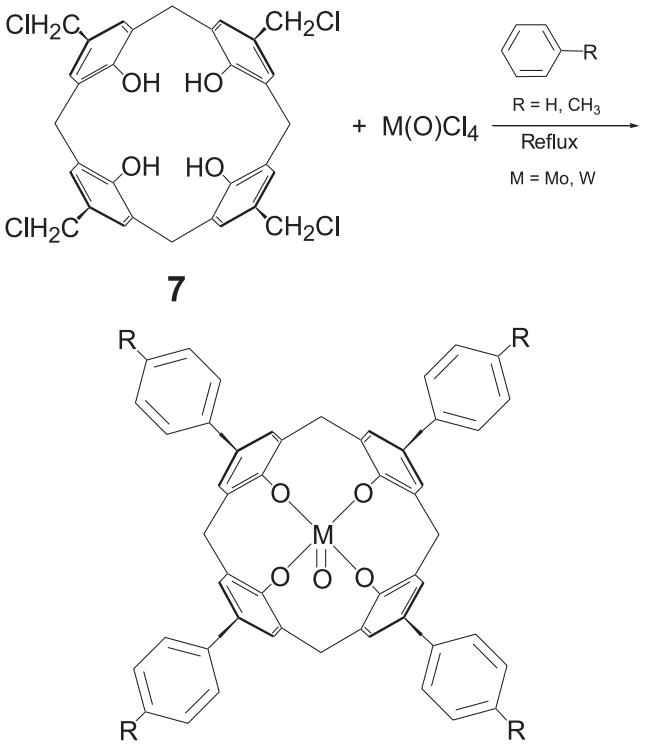
© 2004 NRC Canada

Table 3. Comparison of selected bond distances and angles among metal oxo calix[4]arene complexes.[a]

	Calix[4]arene(W=O)·H_2O·$H_2NC_6H_5$ (**1**)	Calix[4]arene(W=O)·H_2O·toluene (**2**)	(*t*-Bu)$_4$calix[4]arene(W=NCMe$_3$)·H_2O
d(W=X) (Å)	1.698(4) (X=O)	1.706(2) (X=O)	1.718(5) (X=N)
d(W···O) (Å)	2.284(4)	2.329(2)	2.303(4)
d(O···N) (Å)	2.68(6)	—	—
d(W-O) (Å)	1.917(10)	1.912(15)	1.940(4)
∠(X=W-O) (°)	179.8(5) (X=O)	179.1(8) (X=O)	179.9(2) (X=N)
∠(O-W···O) (°)	81.4(3)	80.5(7)	81.8(2)
∠(O-W=X) (°)	98.6(5) (X=O)	99.5(7) (X=O)	98.2(2) (X=N)
	(*t*-Bu)$_4$calix[4]arene(W=O)·H_2O	(*t*-Bu)$_4$calix[4]arene(W=O)·CH_3CO_2H	(*t*-Bu)$_4$calix[4]arene(Mo=O)·H_2O·$C_6H_5NO_2$
d(M=O) (Å)	1.690(1)	1.698(4)	1.673(16)
d(M-OH$_2$) (Å)	2.370(1)	2.386(4)	2.408(16)
d(O···O) (Å)	—	—	3.190(3)
d(M-O) (Å)	1.910(6)	1.888(3)	1.901(5)
∠(O=M-OH$_2$) (°)	180.0(2)	180.0(4)	180.0(4)
∠(O-M-OH$_2$) (°)	80.3(2)	80.9(1)	79.8(3)
∠(O-M=O) (°)	99.7(2)	99.2(1)	100.2(4)

[a]Average values. The data for (*t*-Bu)$_4$calix[4]arene(W=NCMe$_3$)·H_2O, (*t*-Bu)$_4$calix[4]arene(W=O)·H_2O, (*t*-Bu)$_4$calix[4]arene(W=O)·CH_3CO_2H, and (*t*-Bu)$_4$calix[4]arene(Mo=O)·H_2O·$C_6H_5NO_2$ are from refs. 33, 11, 10, and 8, respectively.

Scheme 1.



8 (R = H; M = Mo), **9** (R = H; M = W)
10 (R = Me; M = Mo), **11** (R = Me; M = W)

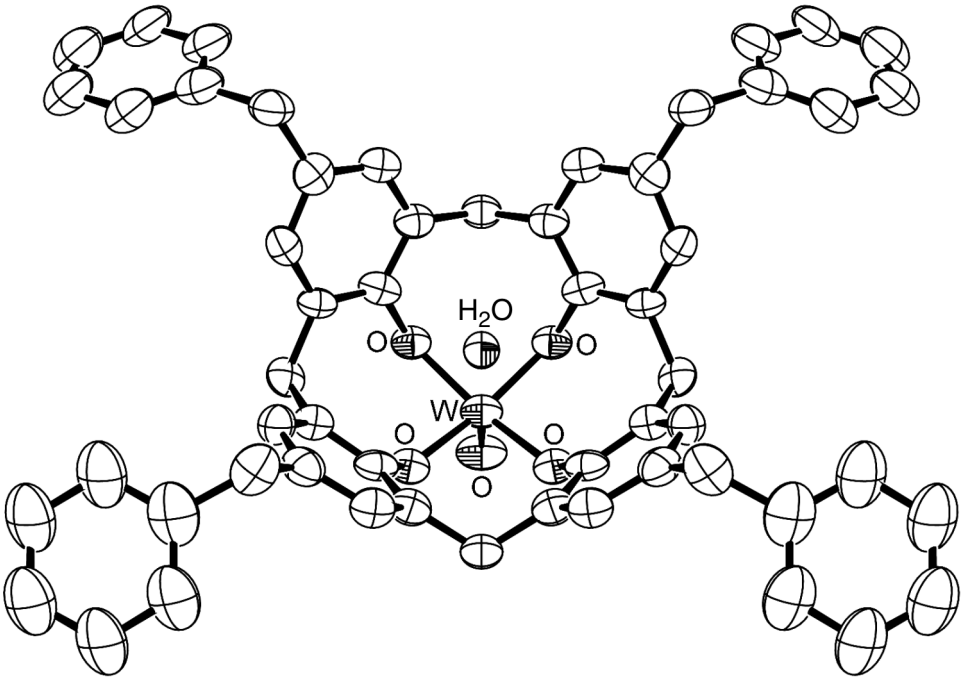
of Br and H_2O, indicating the facile Br elimination in this compound. It is not possible to tell whether the C-Br scission induces a simultaneous H_2O loss, or if both occur simultaneously yet independently. Examination of the first derivative of the ATG traces indicates a maximum at 160 ± 5 °C, which also corroborates the DSC data that exhibit an irreversible exothermic process at 171 °C. The TGA traces exhibit a smooth weight loss, from which it is not possible to say which thermal event occurs first. A long plateau with a slope indicating a second but slower weight loss is observed in the traces between 200 and 500 °C, but a third but rapid weight loss occurs about 550–610 °C. The residual mass corresponds to about 30%, which indicates the presence of C remaining in the samples.

Double functionalization

7 reacts with a slight excess of M(O)Cl_4 (M = Mo, W) in benzene or toluene to afford in moderate (benzene) to good yields (toluene) the corresponding metal oxide complexes of the tetra-5,11,17,23-benzyl- and *para*-methylbenzyl-25,26,27,28-tetrahydroxycalix[4]arene (compounds **8**–**11**, Scheme 1). The identities of the compounds have been unambiguously demonstrated by ^{1}H NMR spectroscopy, mass spectrometry, and by chemical analysis. In addition, X-ray data for **9** have been obtained (Fig. 6). Because of the poorer quality of the crystal, and the presence of disorder and partial occupancies of the molecules of crystallization, the *R*1 and *wR*2 values are somewhat large (Table 1). In this case, a water molecule is also found inside the cavity because the crystallization solutions were handled in the presence of air.

© 2004 NRC Canada

Fig. 6. ORTEP diagram of **9**. The ellipsoids are shown at 30% probability. The H atoms and acetonitrile and other water molecules of crystallization are not shown for clarity. Only one orientation of the phenyl groups is shown.

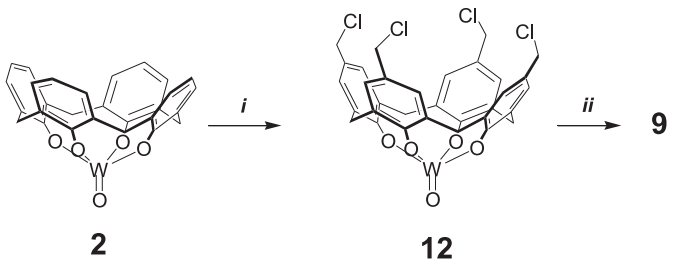


In addition, an acetonitrile molecule is found in the lattice, where no obvious interaction, such as H-bonding, is observed. The key feature is that H_2O binds the W centre selectively over acetonitrile. Both the d(W=O) (1.732(19) Å) and d(W···O) (2.423(18) Å) values are greater than that found for **1** and **2**, while d(W-O) is shorter (1.904(11) Å). The phenyl groups are disordered, where two orientations of the aromatic planes are depicted in the structure. The dihedral angles about the calix-CH_2-Ph single bonds are 110(2)° and 95(3)° for conformation 1, and 92(2) and 139(2)° for conformation 2, with occupancies of 51 and 49, respectively.

These products (**8**–**11**) result from a tetra Friedel–Crafts reaction followed by a coordination of the metal oxide. This tetra Friedel–Crafts reactivity on the calix[4]arene is unique for two reasons. First, the use of the $M(O)Cl_4$ complexes (M = Mo, W) as Friedel–Crafts catalysts is to our knowledge, unprecedented (35). Second, and more importantly, the catalyst completes these reactions by coordinating the lower rim, hence leading to the one-step functionalization of both the lower and upper rim. This strategy differs from the common cyclisation of a prefunctionalized unit (36). The structure exhibits a "flower-shape" geometry similar to that reported for the unmetallated analogue tetra-5,11,17,23-benzyl-25,26,27,28-tetrahydroxycalix[4]arene (36), but differs from the tetra-5,11,17,23-benzylhydroxy-25,26,27,28-tetra-*n*-propoxycalix[4]arene compound for which host–guest interactions and H-bonds promote the formation of a cage structure (37).

For comparison purposes, compound **9** has also been prepared in two steps from the unfunctionalized tungsten oxo complex of calix[4]arene (**2**) (10) (Scheme 2). The first step uses the $ROCH_2Cl$ reactant (R = octyl) with **2** to produce the tungsten oxo complex of tetra-5,11,17,23-chloromethylcalix[4]arene (**12**) cleanly and in good yield. The upper-rim functionalization of **2** or a related complex is novel

Scheme 2.



i = $CH_3(CH_2)_7OCH_2Cl$ / $SnCl_4$ / -5 °C; *ii* = $W(O)Cl_4$, reflux / benzene

(4–6, 8, 10, 11). The reaction proceeds without the loss of the W=O group. Then, the tetra Friedel–Crafts addition of benzene proceeds as described for **8** and **9**. The overall yield for the two reactions going from **2** to **12** (i.e., **2** → **12** → **9**) is 42%. By considering the 60% yield reported for the synthesis of tetra-5,11,17,23-benzyl-25,26,27,28-tetrahydroxycalix[4]arene from *p*-benzylphenol (36), and the 68% yield for the metallation of unfunctionalized calix[4]arene by W=O (6), the predicted yield for this two-step synthesis of **9** would be 41%. The "one pot" methodology described above is obviously more convenient and less expensive than the two step procedures.

Concluding remarks

This work shows that the title complex coordinates water and nitrile molecules strongly. The removal of water can be performed by extraction with another strong Lewis acid, or by heating the solid samples at about 200 °C. This information is important when the use of a rigid cavity is necessary, for example in the preparation of mesophasic-containing ma-

© 2004 NRC Canada

terials (13), the probing of guest molecules by UV–vis and luminescence spectroscopy (12), and catalysis (38). On the other hand, the presence of coordinated water offers the possibility of H-bond interactions and supramolecular architecture (8) Similarly, the use of nitrile-containing substrates is convenient for the same purpose, since the nitrile residue can anchor a molecule bearing a desired function. This area has surprisingly been neglected in the literature, and the reported reactions in Schemes 1 and 2 open the door to new "cavity extensions" of calix[4]arene derivatives. Further research in this area is anticipated.

Acknowledgment

PDH thanks the Natural Sciences and Engineering Research Council of Canada (NSERC) and FCAR (Fonds Concertés pour l'Avancement de la Recherche) for funding.

Supporting information

X-ray crystallographic files are available for **1**, **2**·toluene, **3**, and **9** in CIF format.[4]

References

1. (*a*) Z. Asfari, V. Börner, J Harrowfield, and J Vicens. Calixarenes. Kluwer Academic Publishers, Dordrecht, The Netherlands. 2001; (*b*) C.D. Gutsche. Calixarene revisited. Royal Society of Chemistry, Cambridge, UK. 1998.
2. See, for example: (*a*) C. Kunze, D. Selent, I. Neda, R. Schmutzler, A. Spannenberg, and A. Börner. Heteroat. Chem. **12**, 577 (2001); (*b*) F.J. Parlevliet, C. Kiener, J. Fraanje, K. Goubitz, M. Lutz, A.L. Spek, P.C.J. Kramer, and P.W.N.M. van Leeuwen. J. Chem. Soc. Dalton Trans. 1113 (2001); (*c*) C.J. Cobley, D.D. Ellis, A.G. Orpen, and P.G. Pringle. J. Chem. Soc. Dalton Trans. 1109 (2000); (*d*) C. Dieleman, S. Steyer, C. Jeunesse, and D. Matt. J. Chem. Soc. Dalton Trans. 2508 (2001); (*e*) S. Steyer, C. Jeunesse, D. Matt, R. Welter, and M. Wesolek. J. Chem Soc. Dalton Trans. 4264 (2002).
3. P.D. Harvey. Coord. Chem. Rev. **233–234**, 289 (2002).
4. A. Zanotti-Gerosa, E. Solari, L. Giannini, C. Floriani, A. Chiesi-Villa, and C. Rizzoli. J. Am. Chem. Soc. **120**, 437 (1998).
5. A. Caselli, E. Solari, R. Scopelliti, and C. Floriani. J. Am. Chem. Soc. **121**, 8296 (1999).
6. A. Caselli, E. Solari, R. Scopelliti, C. Floriani, N. Re, C. Rizzoli, and A. Chiesi-Villa. J. Am. Chem. Soc. **122**, 3652 (2000).
7. M.H. Chisholm, K. Folting, W. E. Streib, and D.-D. Wu. Inorg Chem. **38**, 5219 (1999).
8. F. Corazza, C. Floriani, A. Chiesi-Villa, and C. Guastini. J. Chem. Soc. Chem. Commun. 640 (1990).
9. S. Dovesi, E. Solari, R. Scopelliti, and C. Floriani. Angew. Chem. Int. Ed. **38**, 16, (1999).
10. F. Corazza, C. Floriani, A. Chiesi-Villa, and C. Rizzoli. Inorg. Chem. **30**, 4465 (1991).
11. M. Brown and C. Jablonsky. Can. J. Chem. **79**, 463 (2001).
12. P.D. Harvey, J. Gagnon, R. Provencher, Bing Xu, and T.M. Swager. Can. J. Chem. **74**, 2279 (1996).
13. B. Xu, and T.M. Swager. J. Am. Chem. Soc. **115**, 1159 (1993).
14. C.D. Gusche and L.G. Lin. Tetrahedron, **42**, 1633 (1986).
15. J.G. Reynolds, A. Zalkin, and D.H. Templeton. Inorg. Chem. **16**, 3357 (1977).
16. M. Almi, A. Arduini, A. Casnati, and R. Ungaro. Tetrahedron, **45**, 2177 (1989).
17. Y. Le Page, P.S. White, and E.J. Gabe. NRCCAD. An Enhanced CAD-4 Control Program, Proc. Am. Crystallogr., Hamilton Meeting, Abstract PA 23 (1986).
18. E.J. Gabe, Y. Le Page, J.-P. Charland, F. L. Lee, and P.S. White. J. Appl. Crystallogr. **22**, 384 (1989).
19. G.M. Sheldrick. SHELXL-93 [computer program]. Institut für Anorg. Chemie, Trammannstranne 4, D-370077 Göttingen, Germany.
20. C.K. Johnson. ORTEP-A [computer program]. Technical Report ORNL-5138, Oak Ridge National Laboratory, Oak Ridge, Tenn. 1976.
21. SAINT. Version 6.02 [computer program]. Bruker AXS, Inc., Madison, Wis. USA. 1997–1999.
22. G. Sheldrick. SADABS [computer program]. Bruker AXS, Inc., Madison, Wis. USA. 1999.
23. G. Sheldrick. SHELXTL. Version 5.1 [computer program]. Bruker AXS, Inc., Madison, Wis. USA. 1997.
24. G. Sheldrick. SHELXS-83 [computer program]. Institüt für Anorg. Chemie, Trammannstranne 4, D-37077, Göttingen, Germany.
25. R. Provencher, K.T. Aye, M. Drouin, J. Gagnon, N. Boudreault, and P.D. Harvey. Inorg. Chem. **33**, 3689 (1994).
26. T. Zhang, M. Drouin, and P.D. Harvey. Chem. Commun. 877 (1996).
27. P.D. Harvey, K. Hierso, P. Braunstein, and X. Morise. Inorg. Chim. Acta, **250**, 337 (1996).
28. F. Lemaître, D. Lucas, K. Groison, P. Richard, Y. Mugnier, and P.D. Harvey. J. Am. Chem. Soc. **125**, 5511 (2003).
29. F. Lemaître, D. Lucas, Y. Mugnier, and P.D. Harvey. J. Org. Chem. **67**, 7537 (2002).
30. P.D. Beer, M.G.B. Drew, D. Hesek, M. Kan, G. Nicholson, P. Schmitt, P.D. Sheen, and G. Williams. Dalton Trans. 2783 (1998).
31. A. Moser, G.P.A. Yap, and C. Detelier. J. Chem. Soc. Dalton Trans. 428 (2002).
32. A.F. Danil de Namor, S. Chahine, D. Kowalska, E.E. Castellino, and O.E. Piro. J. Am. Chem. Soc. **124**, 12 824 (2002).
33. V.C. Gibson, C. Redshaw, and R.J. Elsegood. New J. Chem. **16**, 26 (2002).
34. U. Radius and J. Attner. Eur. J. Inorg. Chem. 2221 (1999).
35. A. Arduini, A. Pochini, A. Rizzi, A.R. Sicuri, F. Ugozzoli, and R. Ungaro. Tetrahedron, **48**, 905 (1992).
36. M. Makha and C.L. Raston. Chem. Commun. 2470 (2001).
37. A. Arduini, G. Giorgi, A. Pochini, A. Secchi, and F. Ugozzoli. J. Org. Chem. **66**, 8302 (2001).
38. F. Plourde, K. Gilbert, J. Gagnon, and P.D. Harvey. Organometallics, **22**, 2862 (2003).

[4] Supplementary data may be purchased from the Directory of Unpublished Data, Document Delivery, CISTI, National Research Council Canada, Ottawa, ON K1A 0S2, Canada (http://www.nrc.ca/cisti/irm/unpub_e.shtml for information on ordering electronically). CCDC 240808 to 240811 contain the crystallographic data for this manuscript. These data can be obtained, free of charge, via www.ccdc.cam.ac.uk/conts/retrieving.html (or from the Cambridge Crystallographic Data Centre, 12 Union Road, Cambridge CB2 1EZ, U.K.; fax +44 1223 336033; or deposit@ccdc.cam.ac.uk).

© 2004 NRC Canada

New method of energy–mass dispersion applied to mass spectral data from positively charged water vapor clusters[1]

George E. Walrafen and Hugh R. Carlon

Abstract: A new method is presented by which energy–mass, volume–mass, and enthalpy–mass dispersion curves may be determined for charged water vapor clusters. This method involves two closely spaced partial pressures at a fixed temperature. The method is exemplified by using mass spectral data from positively charged water vapor clusters ($H^+(H_2O)_M$) where $6 \leq M \leq 45$. A ΔG–mass dispersion was also determined using the ΔH–mass dispersion for comparison. ΔG displays an enormous minimum, which is of signal importance because it indicates that a size of maximum stability (SMS) exists. The SMS corresponds to $M = 13$ for pressures between 0.056 and 0.151 bar (1 bar = 100 kPa) at 373.15 K, and to $M = 32 \pm 1$ for pressures between 0.473 and 0.556 bar at 372.15 K. The free energy corresponding to $M = 45$ occurs far above that corresponding to the SMS. The resultant instability leads to condensation for pressures above 0.556 bar at 372.15 K.

Key words: clusters, mass spectrometry, thermodynamics, water vapour.

Résumé : On présente une nouvelle méthode de déterminer les courbes de dispersion énergie–masse, volume–masse et enthalpie–masse d'agrégats de vapeur d'eau chargés. Cette méthode implique deux pressions partielles rapprochées dans l'espace à une température donnée. On donne un exemple de la méthode à l'aide de données de spectres de masse d'agrégats de vapeur d'eau portant des charges positives partielles ($H^+(H_2O)_M$) dans lesquels $6 \leq M \leq 45$. On a aussi déterminé une dispersion ΔG–masse en utilisant une dispersion ΔH–masse pour fins de comparaison. Le ΔG présente un immense minimum qui peut être très important comme signal puisqu'il indique l'existence d'une taille de stabilité maximale (TSM). La TSM correspond à $M = 13$ pour des pressions allant de 0,056 à 0,151 bar (1 bar = 100 kPa), à 373,15 K, et à $M = 32 \pm 1$ pour des pressions allant de 0,473 à 0,556 bar, à 372,15 K. L'énergie libre correspondant à $M = 45$ est beaucoup plus élevée que celle qui correspond à la TSM. L'instabilité qui en résulte conduit à une condensation à des pressions supérieures à 0,556 bar, à 372,15 K.

Mots clés : agrégats, spectrométrie de masse, thermodynamique, vapeur d'eau.

[Traduit par la Rédaction]

Introduction

Carlon and Harden (1) examined mass spectra from positively charged water vapor clusters ($H^+(H_2O)_M$), produced by intense β irradiation of moist air. The mass spectra consist of a series of very sharp peaks, whose amplitude-mass envelope is roughly bell-shaped. The peaks are distributed over a range of cluster sizes, e.g., from 6 to 17 at 373.15 K and partial pressures between 0.056 to 0.151 bar (1 bar = 100 kPa), or from 21 to 45 at 372.15 K and partial pressures between 0.473 and 0.556 bar. The M value corresponding to the average of the distribution decreases with rising temperature at constant partial pressure (1, 2) or rises with increasing partial pressure at constant temperature (1, 2).

Walrafen et al. (2) presented a thermodynamic analysis of the above-described mass spectral data (2). This analysis involved solution of simultaneous equations of the form $\ln \langle c \rangle = A/T + B \times P$ for various partial pressures (P) at a fixed T. The form of the equation relates to the temperature and pressure dependence of the Gibbs free energy, and $\langle c \rangle$ is the most probable cluster size determined by the method described in ref. 2. Values of the H-bond energy, and of the volume change related to condensation of gaseous water on the clusters resulted (2).

The dispersion of the H-bond energy as a function of Raman frequency (ω) was recently reported for liquid water (3). Values of the H-bond energy (more exactly enthalpy) were obtained from $\partial[\ln(I_i/I_{REF})/\partial(1/T)]_P$, where I_i is the Raman contour height at $i = \omega$, and I_{REF} is the contour height at some suitable reference frequency, usually the isosbestic frequency (3). This method of obtaining the H-bond energy–frequency dispersion curve inspired the current work, in

Received 30 March 2004. Published on the NRC Research Press Web site at http://canjchem.nrc.ca on 26 October 2004.

This article is presented in memory of Professor Donald E. Irish — a trusted friend and valued colleague for more than 40 years.

G.E. Walrafen.[2] Department of Chemistry, University of Kansas, Lawrence, KS 66045-0046, USA.
H.R. Carlon. 133 North Main, Port Deposit, MD 21904, USA.

[1]This article is part of a Special Issue dedicated to the memory of Professor Don Irish.

[2]Corresponding author (e-mail: gwalrafen@chem.ku.edu).

 doi: 10.1139/V04-114 © 2004 NRC Canada

which energy–mass and volume–mass dispersion curves were calculated.

The current method is different from the energy–frequency dispersion method in that two simultaneous equations are solved for each mass point on the dispersion curve, as opposed to obtaining a least-squares fit of Raman intensities at a series of temperatures for each ω in the Raman spectrum (3). However, both methods employ a reference point. In the instant case a normalization factor was used that required scaling of the high and low pressure peak amplitudes at some convenient M at which the signal-to-noise of the mass peaks was large.

Minima were observed in the energy, enthalpy, and free energy for different sets of mass spectral data obtained at different partial pressures. Such minima indicate that a size of maximum stability (SMS) exists. This is a very important finding because the SMS increases with increasing partial pressure at constant temperature. This increase leads to large instability at the high mass end of the distribution (M = 45) for a partial pressure of 0.556 bar at 372.15 K, finally resulting in condensation for partial pressures above 0.556 bar.

The method of calculation for ΔE, ΔV, and ΔH is described in the next section. This is followed by results presented in various figures. The article ends with a discussion section in which the method of calculating the free energy is presented and discussed.

Method of calculation

The calculation method used for the mass spectral data of Carlon and Harden (1) employs two equations related to two closely spaced partial pressures at a fixed temperature. Mass spectral data are not available for the parallel calculation involving the temperature dependence of the peak amplitudes at a fixed partial pressure. The two equations used for each M in the mass spectrum are:

$$[1] \qquad \ln H_E = A/T + BP_E$$

and

$$[2] \qquad \ln H_F = A/T + BP_F$$

$P_E > P_F$ and A and B are constants at a specific T and P, and for a given M. H_E and H_F are heights for peaks whose Ms range over the entire mass distribution. Normalization may be employed, if desired, as described by the following. Subtraction of eq. [2] from eq. [1] gives

$$[3] \qquad \ln H_E - \ln H_F = B(P_E - P_F)$$

Substitution of the resulting B value into either eq. [1] or eq. [2] with the appropriate partial pressure yields A. ΔE and ΔV were then obtained from $\Delta E = -AR$, and $\Delta V = -BRT$.

ΔE and ΔV were calculated for each mass peak throughout the entire distribution, except for peaks whose amplitudes were so small that accurate calculation was precluded. Plots were then made of ΔE vs. M and of ΔV vs. M. These plots were not continuous functions because the M values were integers. Nevertheless, curves were drawn through the data points as an aid in visualization.

Several methods of referencing the data, i.e., of normalization may be employed. A simple method, used here, involves choosing two mass peaks from different mass spectra whose amplitudes are nearly the same.

The amplitude of one mass peak, corresponding to M = 33 at P_F = 0.4733 bar was chosen as the reference. A normalization factor (NF) was then determined from $H_E(33)/H_F(33)$ = NF. All peak amplitudes of the E spectrum were then multiplied by NF. This yielded two sets of amplitude vs. M data, for which $H_E(33) = H_F(33)$. This normalization condition means that B = 0 at M = 33 (see eq. [3]).

The choice of the reference mass peak is completely arbitrary. Any choice involving reasonably large signal-to-noise ratios for H_E and for H_F is suitable. Moreover, it should be emphasized that the shapes of the ΔE vs. M and ΔV vs. M dispersion curves are invariant relative to the reference mass peak employed, as well as to no choice of reference mass peak. The various reference choices simply translate the dispersion curves up or down on the ordinate.

The ΔH–mass dispersion curve may be obtained after the ΔEs and ΔVs have been calculated for a range of Ms. This calculation involved the use of the average $P_{av} = (P_E + P_F)/2$. The average P is a property of the simultaneous solution, just as ΔE and ΔV are averages over the pressure range of the simultaneous solution ($\Delta H = \Delta E + P_{av}\Delta V$). This allows an enthalpy–mass dispersion curve to be constructed. Note also that $\Delta H = -AR + P_{av}(-BRT)$. Moreover, both A and B are functions of M, T, and P.

The free energy–mass dispersion does not result from the simultaneous equations. It was determined by comparing $\Delta G = -RT\ln H(M)$ with ΔH, where $H(M)$ is the peak height for mass M.

The calculated dispersion curves

The dispersion curves corresponding to the smaller partial pressures are shown first in Figs. 1, 2, and 3. A reference mass of M = 13 was chosen for these three curves. ΔE is not zero at M = 13 because the normalization makes $\ln H_E(M = 13) = \ln H_F(M = 13) = A/T$, when $BP = 0$. T = 373.15 K for Figs. 1–3. (A = 182 at M = 13, $\Delta E = -AR$ = –362 cal/mol, $\Delta H = \Delta E$ = –362 cal/mol, and ΔV = 0; B = 0, P_E = 0.1507 bar and P_F = 0.056 bar.

From Fig. 1 it is evident that a pronounced minimum occurs in the ΔE–mass dispersion at $M = 11\pm1$. This minimum is very important because it is the first indication of a SMS. This minimum suggests that the stability decreases as M increases or decreases compared to the M value of the SMS (see ΔG discussion).

The average ΔE per M increment was obtained from the data of Fig. 1, namely, ≈453 cal/mol. This value, and the maximum difference per M increment (904 cal/mol) are too small to refer to the H-bond energy per se (2). They refer to changes in the H-bond energy with the change in cluster size and structure.

The ΔV–mass dispersion curve is shown in Fig. 2. The average volume change per M increment is ≈140 000 cm^3/mol. This average volume change is roughly one-half of the ideal gas molal volume of water vapor at 373.15 K and P_{av} = 0.1033 bar, ≈300 000 cm^3/mol. The ΔV–mass dispersion curve displays a maximum at $M = 8\pm1$; not far from the SMS of Fig. 1, at which $M = 11\pm1$.

© 2004 NRC Canada

Fig. 1. Energy–mass dispersion for positively charged water vapor clusters containing from 6 to 17 water molecules. The partial pressures were 0.056 and 0.151 bar (1 bar = 100 kPa).

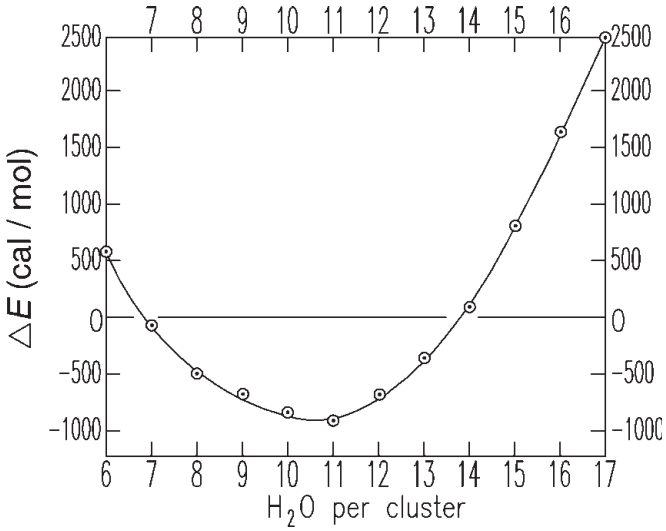


Fig. 2. Volume–mass dispersion for positively charged water vapor clusters containing from 6 to 17 water molecules. The partial pressures are the same as for Fig. 1.

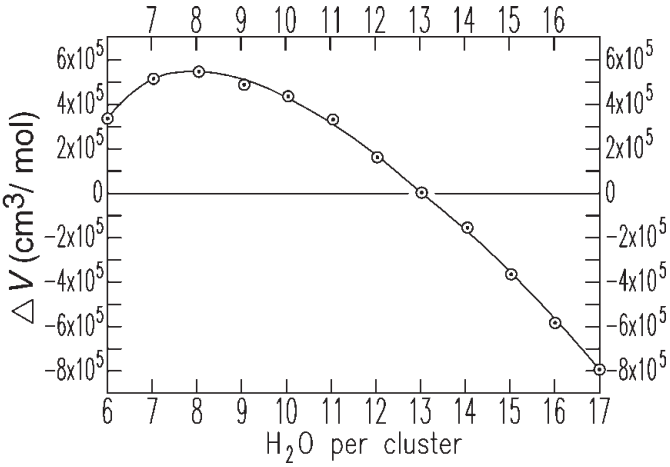


Fig. 3. Enthalpy–mass dispersion for positively charged water vapor clusters containing from 6 to 17 water molecules. The partial pressures are the same as for Fig. 1.

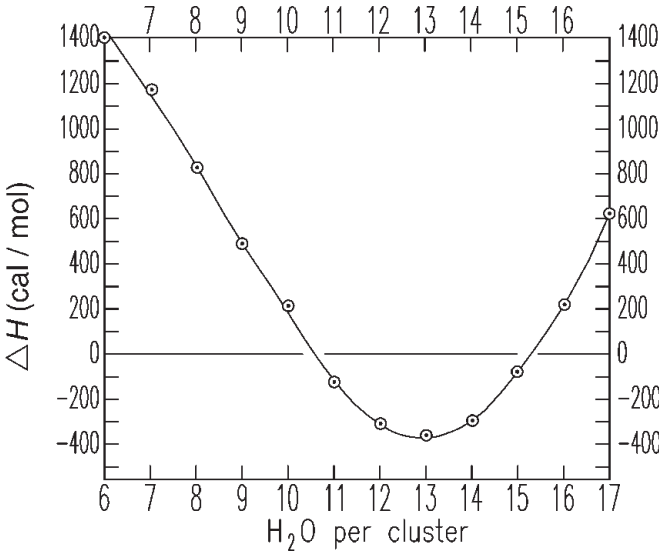
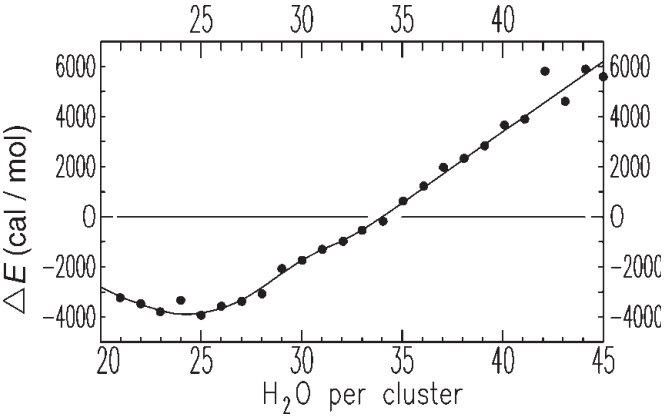


Fig. 4. Energy–mass dispersion for positively charged water vapor clusters containing from 21 to 45 water molecules. The partial pressures were 0.4733 and 0.5560 bar (1 bar = 100 kPa).



The ΔH–mass dispersion curve is shown in Fig. 3. It displays a pronounced minimum near $M = 13\pm1$, which is about $2M$ units above that for ΔE (Fig. 2). The ΔH–mass dispersion curve also displays an average value of ≈250 cal/mol between M increments.

The ΔH–mass dispersion curve is shown in the Discussion section to be extremely important because it is used, by comparison, to calibrate the free energy–mass dispersion curve.

Dispersion curves are displayed in Figs. 4–6 for $21 \leq M \leq 45$ at $P_E = 0.5560$ bar, $P_F = 0.4733$ bar, $P_{av} = 0.5146$ bar, and $T = 372.15$ K. The reference mass is $M = 33$.

Figure 4 indicates that an energy minimum occurs at $M = 24\pm2$. The rise in the mass corresponding to the minimum compared to the minimum of Fig. 1 suggests that the SMS rises with partial pressure.

The magic number peaks observed in the original mass spectra occur at $M = 21$ (very obvious) and $M = 28$ (less prominent). The $M = 29$ mass peak also seems too small in amplitude, as opposed to too large for $M = 21$ and $M = 28$. The minimum in Fig. 4 is not well-correlated with the magic number peaks.

The minimum of Fig. 4 is important because partial pressures above 0.5560 bar are known to lead to condensation (1). Condensation is shown in the following to be related to the fact that the $M = 45$ peak is far removed from the SMS (1), a separation which corresponds to instability.

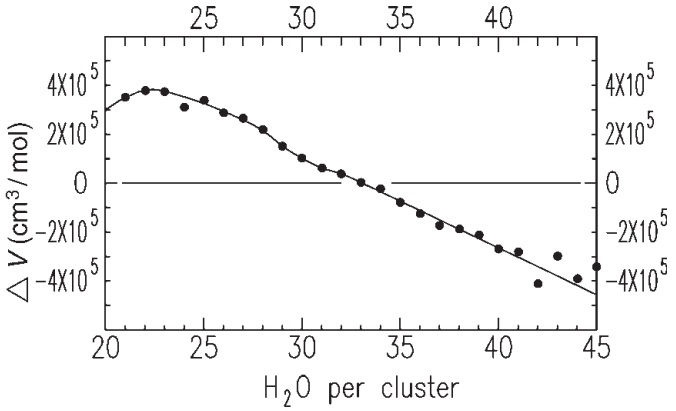
The average ΔE per M increment is $(\Delta E_{45} - \Delta E_{26})/19 \approx$ 9900 cal/19 mol ≈ 520 cal/mol. This value has roughly the same magnitude as the ≈453 cal/mol value obtained from Fig. 1.

Figure 5 indicates a maximum in the ΔV–mass dispersion curve at $M = 22$ that is experimentally the same as the $M = 24\pm2$ value, which corresponds to the minimum of Fig. 4.

Figure 5 also indicates that the average volume change per M increment is $(\Delta V_{45} - \Delta V_{25})/20 = -749\,000$ cm^3/20 mol = $-39\,500$ cm^3/mol. This value has the same approximate magnitude and sign as those reported previously (2), which

© 2004 NRC Canada

Fig. 5. Volume–mass dispersion for positively charged water vapor clusters containing from 21 to 45 water molecules. The partial pressures are the same as for Fig. 4.



averaged –31,300 cm^3/mol H-bond for the same partial pressures and the same T.

The ΔH–mass dispersion curve is shown in Fig. 6 ($\Delta H_{45} - \Delta H_{36}$)/9 ≈ 180 cal/mol. A large minimum occurs in Fig. 6 at $M = 31 \pm 2$. This minimum is directly related to the SMS, as shown below because it agrees with the minimum in free energy.

The ΔH–mass dispersion curve of Fig. 6 is only roughly symmetrical about its minimum. But the ΔH–mass dispersion curve of Fig. 3, truncated at $M = 17$, is very nearly symmetrical (about $M = 13$) from $M = 9$ to $M = 17$. The curve of Fig. 3 fits $\Delta H \approx$ constant × $(M - 13)^2$ within experimental error between $M = 9$ and $M = 17$ when it is translated upward to make $\Delta H = 0$ at $M = 13$.

$M = 13$ *might* correspond to H_3O^+ surrounded by three nearest-neighbors, i.e., Eigen's structure, $H_9O_4^+$, plus nine second-nearest (tetrahedrally H-bonded) neighbors. This would be an especially stable structure. See the minimum in the free energy in the following.

Discussion

Relation to the equilibrium constant and free energy

Equation [3] refers to constant temperature. Substitution of $\Delta V = -BRT$ into eq. [3] gives

$$[4] \qquad [\Delta \ln H(M)/\Delta P]_T = -\Delta V/RT$$

where $\Delta \ln H(M) = \ln H_E(M) - \ln H_F(E)$, and $\Delta P = P_E - P_F$. But eq. [4] is simply the difference equation analog of

$$[5] \qquad (\partial \ln K/\partial P)_T = -\Delta V/RT$$

Hence,

$$[6] \qquad K(M) = \text{constant} \times H(M)$$

Substitution of eq. [6] into eq. [1] yields

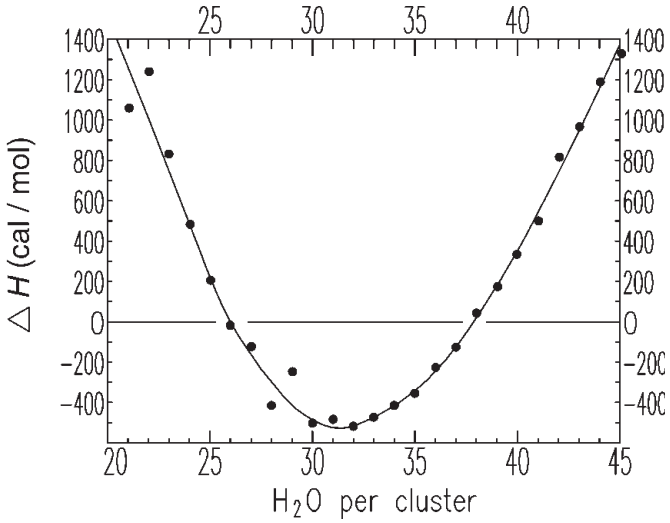
$$[7] \qquad \ln K_E - \ln \text{constant} = A/T + BP_E$$

Then from the thermodynamic relation

$$[8] \qquad \ln K_E = -\Delta E/RT - P_E/RT + \Delta S/R$$

one identifies the constant in eq. [6] as

Fig. 6. Enthalpy–mass dispersion for positively charged water vapor clusters containing from 21 to 45 water molecules. The partial pressures are the same as for Fig. 4.



$$[9] \qquad \text{constant} = \exp(\Delta S/R)$$

Hence,

$$[10] \qquad K(M) = H(M)\exp(\Delta S/R)$$

or

$$H(M) = \exp(-\Delta S/R)K(M)$$

Because of the relation between $H(M)$ and $K(M)$ and $\Delta G = -RT \ln K$, it was possible to construct a ΔG–mass dispersion curve from the data used for Figs. 4–6. The same normalization was employed, viz., $M = 33$, i.e., the same normalized amplitude values were used without further scaling.

The results of the calculations for partial pressures $P_E = 0.5560$ bar and $P_F = 0.4733$ bar are compared with the ΔH–mass dispersion curve obtained from simultaneous equations in Fig. 7. The solid curve, without experimental points, is the same curve drawn through the ΔH data of Fig. 6. The curve drawn through the filled circles refers to the partial pressure $P_E = 0.5560$ bar. The curve drawn through the open circles refers to $P_F = 0.4733$ bar.

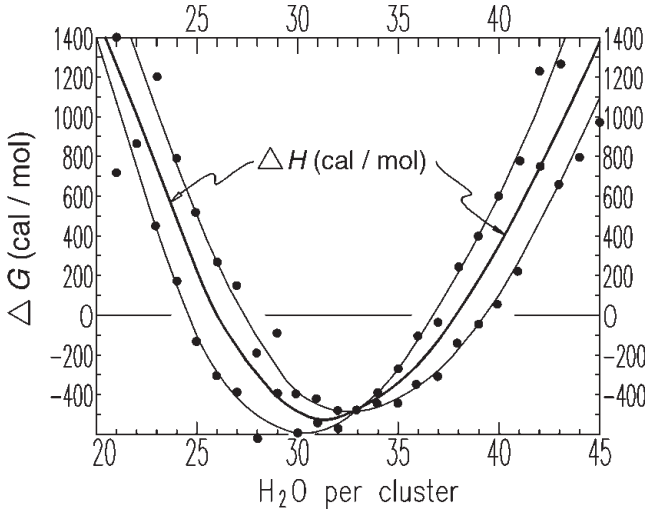
It is obvious from examination of Fig. 7 that the ΔH–mass dispersion curve, labelled ΔH, is the *average* of the curves corresponding to P_E and P_F. The curve related to P_F lies to the left, below, and to the right, above, the ΔH curve, whereas the curve related to P_E lies to the left, above, and to the right, below, the ΔH curve. The fact that the ΔH–mass curve is the average of the individual ΔG dispersion curves is to be expected because ΔH is an average over the partial pressure range of P_F to P_E.

Accretion of water by the clusters

Water vapor clusters in the mass range of say, 6–45, exist in a sea of smaller charged clusters, as well as a range of neutral clusters and neutral monomers (1). The neutral monomer concentration is large (1). Moreover, an H_2O mass balance exists for a fixed and confined volume of moist air at a given water partial pressure.

© 2004 NRC Canada

Fig. 7. Comparison of the ΔH–mass dispersion obtained from Fig. 6 (solid center curve without experimental points) to $\Delta G = -RT \ln H(M)$. The ΔG–mass dispersion for $P_F = 0.4733$ bar (1 bar = 100 kPa) is displayed by open circles. The ΔG–mass dispersion for $P_E = 0.5560$ bar is displayed by filled circles. Note that the ΔH–mass dispersion is, within experimental error, the average of the two ΔG–mass dispersion curves. The points that appear to lie on or near the solid heavy line corresponding to ΔH actually refer to scattered points from the two sets of ΔG data.



The mass balance is epitomized by the reaction

[11] $(H_2O)_N(g) + H^+(H_2O)_L = H^+(H_2O)_M$ with $L >> N$

which constitutes a mechanism for increase, in the forward direction, of the M numbers of the clusters. Note that the forward reaction refers to two-body collisions. Such two-body collisions are much more probable than three-body or higher-body collisions.

Successive two-body collisions with water monomers, dimers, or with other neutral water clusters increase the M of a positively charged cluster.

It is known that condensation occurs when the partial pressure of water vapor rises above 0.5560 bar at 372.15 K (1). A scheme in which a positively charged cluster of M = 45 may lose its proton and condense, as well as simultaneously lower the free energy, is as follows

[12] $(H_2O)_{32} + H^+(H_2O)_{45} = H^+(H_2O)_{32} + (H_2O)_{45}$

This equation amounts to a proton transfer occuring as a result of a two-body collision between a charged M = 45 species and an uncharged M = 32 species. Note that the free energy of the charged M = 32 species corresponds to the minimum value, and to the SMS, which lowers the free energy of the charged product cluster.

Equation [12] is tantamount to the formation of an extremely small droplet of liquid water, because a neutral cluster of M = 45 is beginning to have the physical properties of the liquid as explained in the next section.

What cluster size is needed to mimic the physical properties of liquid water?

The size of a water cluster that assumes the properties of bulk liquid water may be estimated from the wavelength of the transverse acoustic (TA) phonon which gives rise to the 50–60 cm^{-1} Raman peak from pure liquid water (4). This TA wavelength is about 9 Å (4) and it corresponds to the structural correlation length that refers to the O-third-O or O-fourth-O distance in the X-ray pair correlation function of water (5). The corresponding number of water molecules has been estimated to be 53 for the O-third-O neighbors (4).

The point is that a cluster having M = 45 is just barely beginning to reach a size capable of sustaining a TA phonon of the required 9 Å length. The properties of the cluster should be similar to those of bulk liquid water once this 9 Å length has been attained or exceeded.

The above considerations are approximate. Most of the water molecules in a cluster of 45 water molecules are near the surface, and thus the structure differs from the bulk liquid.

Smallness of the ΔE and ΔH values per M increment

Values of the average ΔE per M increment are ≈453 cal/mol (Fig. 1) and ≈520 cal/mol (Fig. 4). Values of the average ΔH per M increment are ≈250 cal/mol (Fig. 3) and ≈180 cal/mol (Fig. 6). None of these values is large enough to correspond to the H-bond energy because the maximum H-bond energy for liquid water is 5100 ± 500 cal/mol H-bond (3), and the average H-bond energy for liquid water is 2830 ± 50 cal/mol H-bond (3).

The average ΔV per M increment is –39 500 cm^3/mol (Fig. 5). This value has roughly the same magnitude and it has the same sign as the ΔV from previous work, which is –31 300 cal/mol.

The above described energy and enthalpy values are only a few % of the maximum H-bond energy for liquid water. Such values probably refer to changes of H-bond energy in clusters of different size and structure.

The H-bond strength in the M = 6 cluster, which probably refers to $H_3O^+(H_2O)_5$, is unlikely to be the same as the H-bond strength in the M = 21 cluster, which probably refers to a hydrogen-bonded pentagonal dodecahedron with H_3O^+ included.

Addendum on mechanism

One H_2O per cluster necessarily separates all of the adjoining peaks in the mass spectrum. But the consecutive ΔV differences observed here are equivalent to the volume of ≈0.5 mol of monomers, or to roughly 0.5 mol of (ideal) gas, both at low and at high partial pressures. This difficulty presents a serious problem.

One conceivable solution to the problem results if dimers react with the clusters as follows:

[13] $0.5(H_2O)_2 + H^+(H_2O)_M = H^+(H_2O)_{M+1}$

Reaction [13] adds one H_2O to the cluster M yielding the cluster M + 1, but the volume change per increment is equivalent to the volume of 0.5 mol of *monomers* or 0.5 mol of an ideal gas of dimers.

The above mechanism fits the present experimental facts. However, it raises new questions. For example, why should

© 2004 NRC Canada

dimers constitute the primary reactant that increases the mass of the charged clusters? And, because reaction [13], when multiplied by 2, must refer to a three-body reaction, why should it be so important?

Other currently unknown mechanisms may ultimately resolve the difficulties presented above. In any case, the addition of one water to a cluster increases the *M* value by one unit, and this produces a redistribution that results in a new structure having somewhat different H-bond energies than the parent structure.

References

1. H.R. Carlon and C.S. Harden. Appl. Opt. **19**, 1776 (1980).
2. G.E. Walrafen, Y.C. Chu, and H.R. Carlon. J. Phys. Chem. **106**, 933 (2002).
3. G.E. Walrafen. J. Chem. Phys. **120**, 4868 (2004).
4. G.E. Walrafen. J. Phys. Chem. **94**, 2237 (1990).
5. A.H. Narten and H.A. Levy. *In* Water a comprehensive treatise. Vol. 1. *Edited by* F. Franks. Plenum, New York. 1972. Chap. 8.

© 2004 NRC Canada

A Raman study of aqueous DMF and DMA solutions at low temperatures[1]

K. Tomikawa, H. Kanno, and H. Kimoto

Abstract: Hydrogen bonding in aqueous *N*,*N*-dimethylformamide (DMF) and *N*,*N*-dimethylacetamide (DMA) solutions was studied by Raman spectroscopy of the OH-stretching spectra of water as functions of solute concentration and temperature (from –50 to 50 °C). The Raman spectra were decomposed successfully into two components (the low- and high-frequency components). The peak area ratio of the low-frequency component to the high-frequency component increases exponentially with decreasing temperature. The frequency of the low-frequency component decreases linearly with lowering temperature down to –50 °C at all solute concentrations (solute mol fraction from 0.3 to 0.7). It is shown that the hydrogen bonds in the clathrate structures around DMA molecules are stronger than those around DMF molecules.

Key words: Raman spectrum, DMF, DMA, aqueous solution, low temperature.

Résumé : On a étudié la formation de liaisons hydrogènes dans des solutions aqueuses de *N*,*N*-diméthylformamide (DMF) et de *N*,*N*-diméthylacétamide (DMA) en faisant appel à la spectroscopie Raman et examinant la bande d'élongation du OH de l'eau en fonction de la concentration du soluté et de la température (de –50 à 50 °C). On a pu décomposer le spectre Raman en deux composantes, l'une de basse fréquence et l'autre de fréquence plus élevée. Le rapport des pics de la composante de basse fréquence à celui de la composante de haute fréquence augmente d'une façon exponentielle avec une diminution de la température. À toutes les concentrations de soluté (allant d'une fraction molaire de soluté de 0,3 jusqu'à 0,7), la fréquence de la composante de basse fréquence diminue d'une façon linéaire avec une diminution de la température jusqu'à –50 °C. On montre que les liaisons hydrogènes dans les structures de clathrate autour des molécules de DMA sont plus fortes que celles autour des molécules de DMF.

Mots clés : spectre Raman, DMF, DMA, solution aqueuse, basse température.

[Traduit par la Rédaction]

Introduction

Raman spectroscopy is one of the best spectroscopic methods for probing structural changes in aqueous solutions (1). There have been a number of reports devoted to structural studies of aqueous solutions (1–4). Early Raman studies of aqueous electrolyte solutions by Walrafen (2, 5, 6) demonstrated that both Raman OH-stretching and low-frequency (<600 cm^{-1}) spectra are very sensitive to the nature of the electrolyte. There is a clear trend that structure-breaking ions weaken the strength of hydrogen bonds, thereby shifting the frequency of the Raman OH-stretching spectrum to a higher frequency region while structure-making ions strengthen hydrogen bonds in aqueous solution, moving the OH-stretching spectrum to lower frequencies.

Kanno and Hiraishi (7) reported that the characteristic nature of dissolved ions is well-represented in the Raman spectrum for solutions at low temperatures, especially for glassy solutions. There have been many Raman studies on water at various temperatures (3, 8–12). From these studies, it is clear that hydrogen bonds become stronger with decreasing temperature. In view of these Raman studies, it would be interesting and important to study aqueous solutions of molecular solutes to see how hydrogen bonds are perturbed by dissolved molecular solutes as functions of solute concentration and temperature since Raman studies of aqueous solutions of molecular solutes are scarce as compared with those of electrolytes.

In this study we have measured Raman OH-stretching spectra of aqueous *N*,*N*-dimethyl formamide (DMF) and *N*,*N*-dimethyl acetamide (DMA) solutions as functions of solute concentration and temperature to investigate how hydrogen bond strength changes with solute concentration and temperature.

Experimental

All aqueous DMF and DMA solutions were prepared by dissolving DMF or DMA in distilled water by weight. Guaranteed grade DMF and DMA were purchased from Wako and used as received.

Raman spectra were measured with a JASCO NR-1800 Raman spectrometer equipped with a microscope and a CCD detector. The spectra were excited with about 100 mW of

Received 15 March 2004. Published on the NRC Research Press Web site at http://canjchem.nrc.ca on 26 October 2004.

This paper is dedicated to Professor Don Irish.

K. Tomikawa, H. Kanno,[2] and H. Kimoto. Department of Applied Chemistry, National Defense Academy, Yokosuka 239-8686, Japan.

[1]This article is part of a Special Issue dedicated to the memory of Professor Don Irish.

[2]Corresponding author (e-mail: hkanno@nda.ac.jp).

 doi: 10.1139/V04-116 © 2004 NRC Canada

Fig. 1. Raman OH-stretching spectra of the XDMF·$(1 - X)H_2O$ solutions. The Raman intensity increase below 3200 cm^{-1} with an increase in DMF content is due to the intensity increase of the C-H stretching Raman bands of DMF.

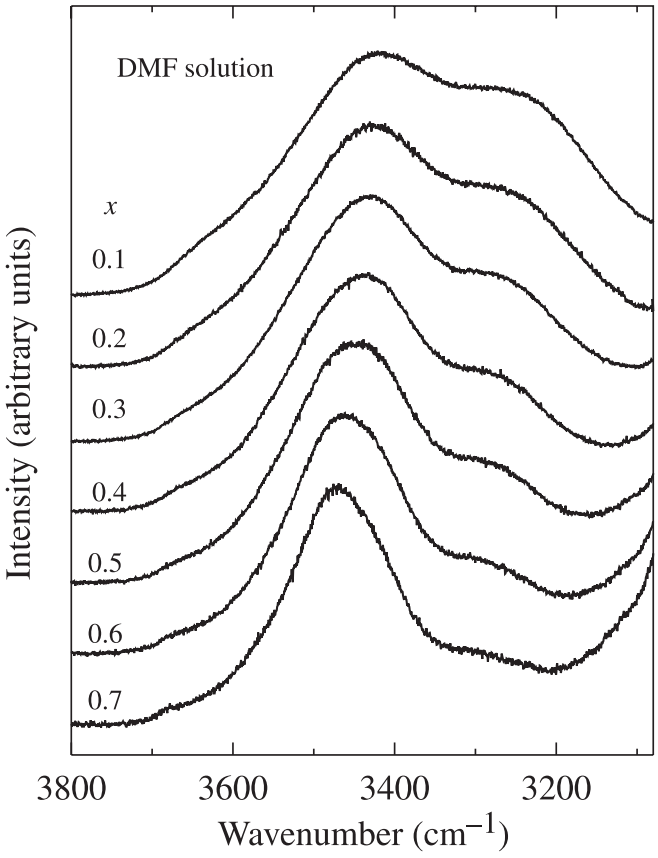
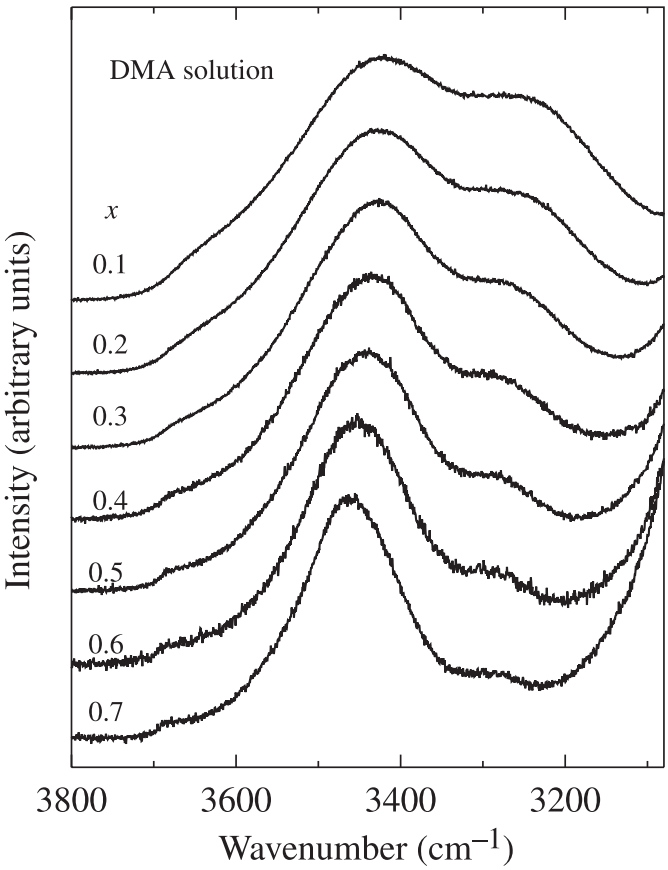


Fig. 2. Raman OH-stretching spectra of the XDMA·$(1 - X)$ H_2O solutions. The Raman intensity increase below 3200 cm^{-1} with an increase in DMA content is due to the intensity increase of the C-H stretching Raman bands of DMA.



the 514.5 nm line from a Lexcel argon ion laser. When Raman spectra of the aqueous DMF and DMA solutions were measured, we used a Japan High-Tech model LK-600PH temperature controller with which the temperature of the sample solution was maintained at a specified temperature (between –196 °C and 200 °C) to within ±2 °C.

Results and discussion

First of all, we present the OH-stretching Raman spectra of aqueous DMF and DMA solutions as a function of the organic solute concentration in Figs. 1 and 2. As expected from literature data for various aqueous solutions, the entire OH-stretching spectrum gradually shifts to the higher frequency side with an attendant decrease in the low-frequency region. These spectral changes indicate that the addition of DMF or DMA to water results in the weakening of hydrogen bonds in the resulting aqueous solution. This trend is rather general and is observed in many aqueous systems (1, 3, 8). The existence of foreign particles (ions) generally interferes or prohibits the formation of strong hydrogen bonds among water molecules.

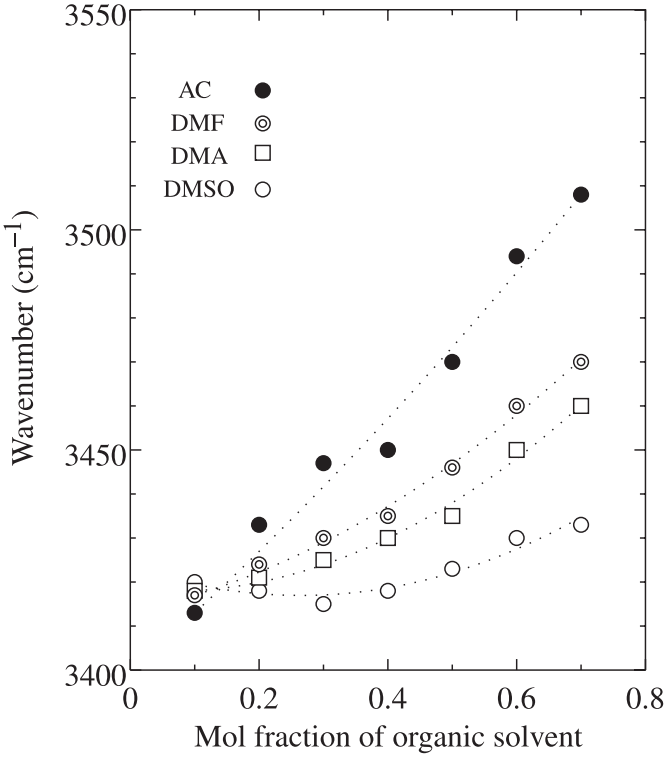
At low concentrations of DMF or DMA, the shape of the OH-stretching spectrum is similar to that of liquid water. The spectrum appears to consist of three component bands. They are centered at about 3250, 3450, and 3650 cm^{-1} (8). The ~3250 cm^{-1} component can be ascribed mainly to the collective OH-stretching vibrations of water molecules in the intrinsic tetrahedral structures of liquid water. The ~3450 cm^{-1} component becomes progressively larger with increasing DMF or DMA concentration and is mainly due to the OH-stretching vibrations of water molecules coordinating to DMF or DMA molecules and of water molecules in the deformed tetrahedral structures. It must be stressed that this component is dominant even in liquid water. The ~3650 cm^{-1} component is usually assigned to the OH-stretching vibrations of the weakly hydrogen-bonded water molecules in strongly deformed tetrahedral structures of liquid water and of imperfect hydration spheres surrounding DMF or DMA molecules.

In the intermediate to higher solute concentration range, the component at ~3250 cm^{-1} progressively gets smaller and smaller. On the other hand, the component at about 3450 cm^{-1} becomes more dominant and shifts to higher frequency with an increase in solute concentration. It appears that the ~3650 cm^{-1} component becomes a part of the ~3450 cm^{-1} component and therefore, the spectrum can be approximated by the combination of the two components.

Figure 3 gives the frequency variations of the high-frequency peaks of the OH-stretching spectra for aqueous DMF and DMA solutions together with other solute solutions (other solutes are acetone (AC) and dimethyl sulfoxide (DMSO)) as a function of solute concentration. As is easily

© 2004 NRC Canada

Fig. 3. Variation of the high-frequency peak of the OH-stretching spectrum for the $XA\cdot(1 - X)H_2O$ solution (X = 0.1~0.7, A = Ac, DMF, DMA, and DMSO). The Raman results for aqueous acetone and DMSO solutions are from unpublished data from this laboratory.

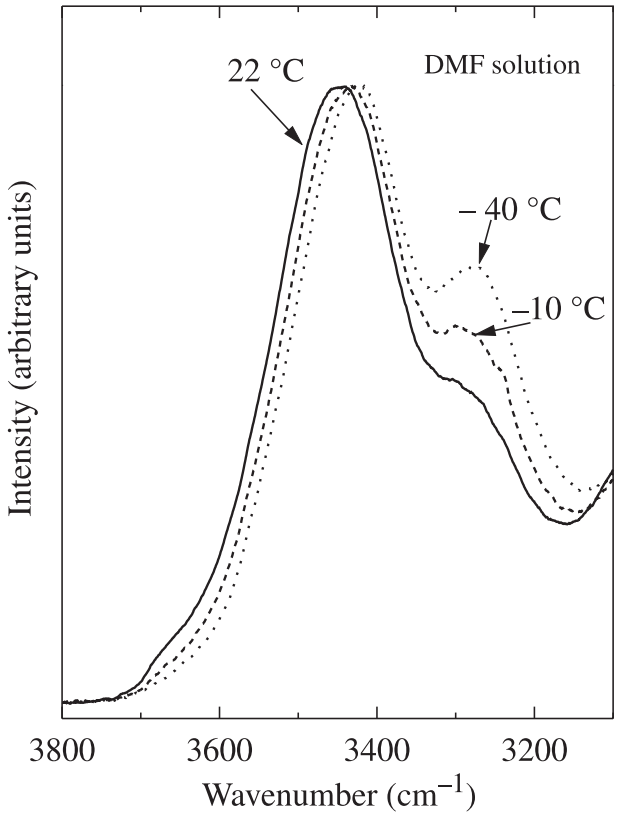


noticed, the peak frequency rapidly increases with increasing solute concentration. The intensity of the high-frequency region is also increased with an increase in solute concentration. These changes are a clear manifestation of the weakening of hydrogen bonds because of the breaking of strong hydrogen bonds in water and to rearrangements of water molecules in the solution.

The frequency increase at X = 0.6 is in the order: AC > DMF > DMA > DMSO. This order is in good correlation with the decreasing order of the donor number: DMSO (29.8) > DMA (27.8) > DMF (26.6) > AC (17.0) (the numerical value in parentheses is the donor number of the solute) (13, 14), although the order of DMF and DMA does not follow the order of donor number. Thus, it is considered that with increasing solute concentration of the hydrogen bonds between water molecules are gradually replaced with the hydrogen bonds between water molecules and solute molecules and those in the hydration spheres of solute molecules.

The viscosity of aqueous solutions of these solutes shows a maximum at the mol fraction of ~0.2 (AC), ~0.25 (DMA and DMF) and ~0.33 (DMSO) (15, 16). Since our Raman measurements are not made at very small intervals of solute concentration, the peak frequency increase with solute concentration looks rather smooth so that the average hydrogen bond strength in each solution appears to become weaker with increasing solute concentration. Therefore, the appearance of the maximum in viscosity at the mol fraction of ~0.25 appears to be irrelevant to the variation of hydrogen

Fig. 4. Raman OH-stretching spectra for the $DMF\cdot H_2O$ solution at 22, –10, and –40 °C.



bond strength, but may be related to the structural changes of the solution.

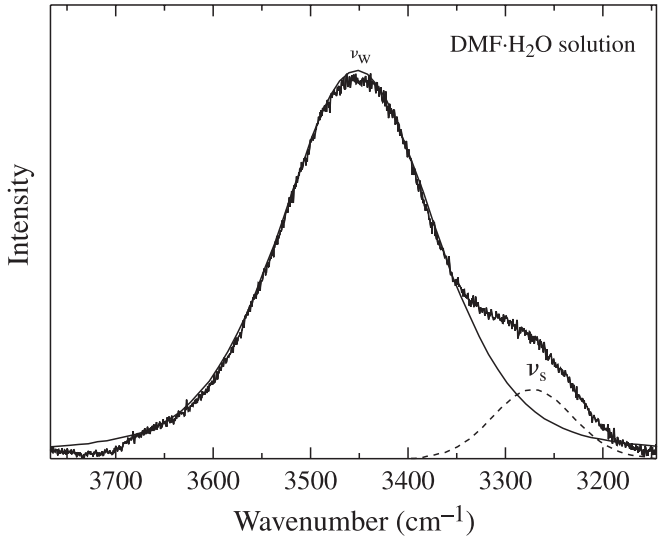
Next, we examined the spectral changes with temperature. Special emphasis is placed in the temperature region below 0 °C since characteristic features of the solution should appear at low temperatures. Figure 4 shows the spectral changes of the DMF solution at three different temperatures. The low-frequency component below 3350 cm^{-1} increases rapidly and the whole spectrum moves to the lower frequency side with decreasing temperature. These spectral changes are a clear indication that the hydrogen bonds become stronger with decreasing temperature. Although the spectra are not shown here, similar spectral changes were also observed for the DMA solution.

Scherer et al. (8, 17) reported in their Raman study of pure water and aqueous DMSO solutions that there are two kinds of water molecules: one involves two strong symmetric hydrogen bonds and the other has one strong and one weak hydrogen bond. They also assumed that the strongly hydrogen bonded OHs of both types of water molecules have distributions of hydrogen bond strengths. The broadness of the OH-stretching spectra suggests that the strength of hydrogen bonds in aqueous solution has a wide distribution, depending on temperature and solute concentration, not to mention the nature of the solute. They decomposed the spectrum into four Raman components and interpreted their temperature dependencies.

Kanno et al. (18) reported that hydrogen bonds whose strength is clearly manifested in the frequency of the OH-stretching spectrum become stronger with decreasing tem-

© 2004 NRC Canada

Fig. 5. Decomposition of the OH-stretching spectrum into two components. Solid curve: the high-frequency component (peak wavenumber: ν_w, peak area: $S(\nu_w)$). Dotted curve: the low-frequency component (peak wavenumber: ν_s, peak area: $S(\nu_s)$).

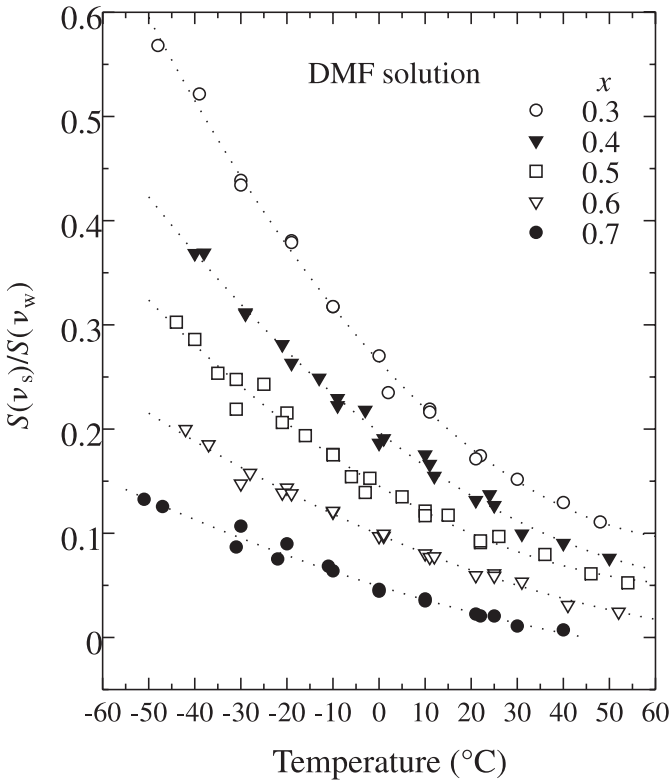


perature in aqueous tetraalkylammonium chloride solutions. They considered that water molecules around alkyl groups form clathrate-like structures with strong hydrogen bonds, especially at low temperatures. In fact, the intensity of the low-frequency region of the OH-stretching spectrum in glassy state solutions is dramatically large at low solute concentrations. The spectral features of the glassy Y = 24 tetrapropylammonium chloride solution (Y = mol of water / mol of salt) are very similar to those of low density amorphous solid water in which the strength of the hydrogen bonds is only a few wavenumbers weaker than that in crystalline ice (19).

On the other hand, the strength of hydrogen bonds in aqueous inorganic salt solutions is generally weakened as compared with that in pure liquid water. In particular, large anions such as ClO_4^- and PF_6^- ions exert large structure-breaking effects on water, thereby weakening hydrogen bonds (20, 21). Molecules such as urea and large ions such as ClO_4^- and I^- are regarded as structure breakers, whereas molecules such as sucrose and hydrophobic ions such as tetraalkylammonium ions are considered as structure makers (1).

To investigate the structural changes associated with the addition of DMF or DMA in more detail, the OH-stretching spectrum was decomposed into two components by a least-squares curve fitting method. After subtracting the background spectrum from the observed OH spectrum, the resulting OH spectrum was decomposed into two components. It is assumed to be represented by Gaussian and Lorentzian mixed curves. A typical example is shown in Fig. 5. The peak frequency of each component (the low- and the high-frequency components) is denoted as ν_s and ν_w, respectively, and the peak area is designated as $S(\nu_s)$ and $S(\nu_w)$, respectively. As our main objective was the observation of overall changes in the OH-stretching spectrum in the solution with solute concentration or temperature, we considered that the present method is sufficiently reliable and sensitive to probe

Fig. 6. Variation of the $S(\nu_s)/S(\nu_w)$ ratio for the XDMF·$(1 - X)H_2O$ solution with temperature.



structural changes in these aqueous solutions. Although only one case is shown in Fig. 5, all of the spectra were successfully decomposed into two components.

First, we see how the $S(\nu_s)/S(\nu_w)$ ratio changes with decreasing temperature. The $S(\nu_s)/S(\nu_w)$ results are shown in Figs. 6 and 7. An important aspect is that the ratio increases exponentially with decreasing temperature, although the trend becomes weaker with increasing solute concentration and shifts to the low-temperature side. These features are in common with many thermodynamic and transport properties observed in water and aqueous solutions at low temperatures. Angell and co-workers (22, 23) showed that many thermodynamic and transport properties of water give divergent behavior at the expected singularity temperature of −45 °C.

These features are closely connected with the cooperative increase of strong hydrogen bonds with decreasing temperature. Oguni and Angell (24) measured heat capacities (Cp) of aq. H_2O_2 and N_2H_4 solutions as a function of solute concentration and reported that the anomalous increase in Cp was eliminated by addition of about 20% (by mol fraction) of the solute (H_2O_2 or N_2H_4). On the other hand, an interesting point is that the increases in the $S(\nu_s)/S(\nu_w)$ ratio at lower temperatures in the DMF and DMA solutions remain qualitatively unchanged even at very high solute concentrations (up to X = 0.7), but seem to shift to lower temperatures. In fact, similar increases in $S(\nu_s)/S(\nu_w)$ at lower temperatures were observed even in aqueous electrolyte solutions at very high salt concentrations. Thus, it is evident that the rapid $S(\nu_s)/S(\nu_w)$ increases at low temperatures is a common phenomenon in aqueous solutions.

© 2004 NRC Canada

Fig. 7. Variation of the $S(\nu_s)/S(\nu_w)$ ratio for the XDMA·(1 – X)H_2O solution with temperature.

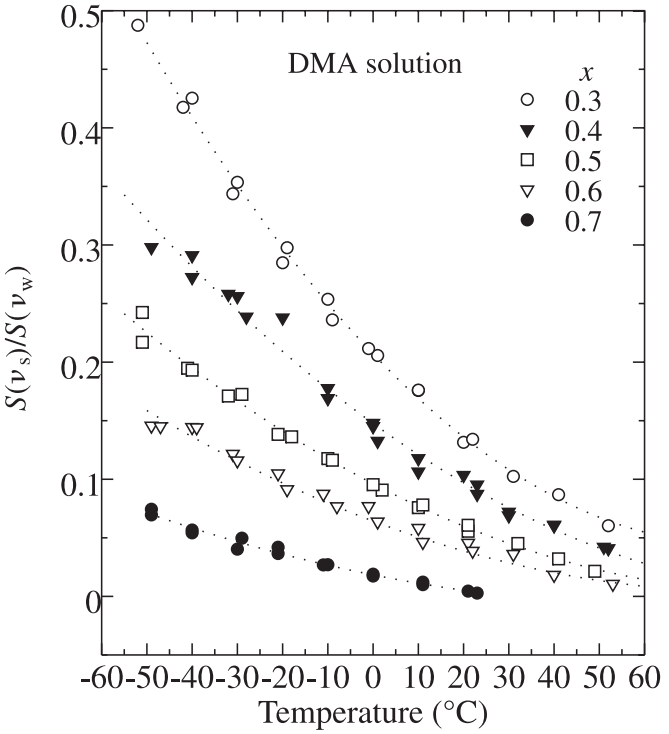
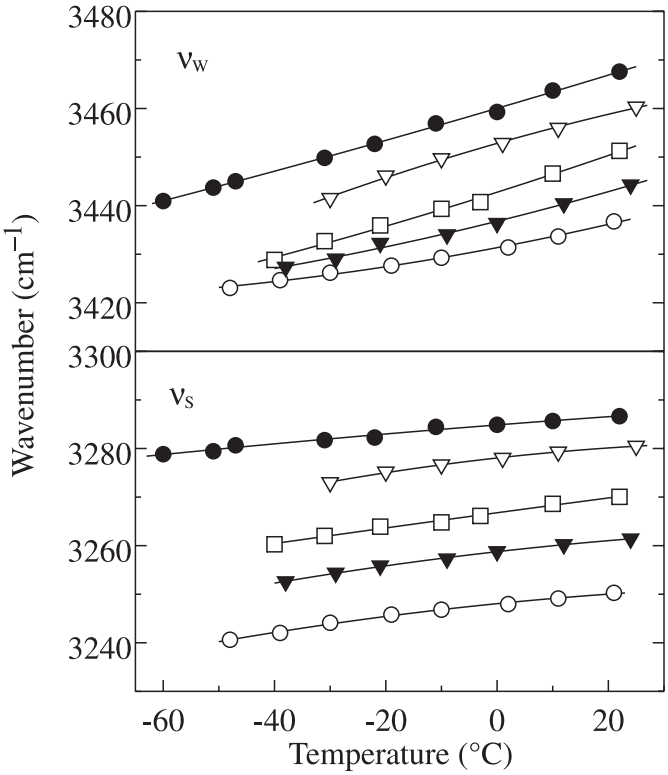


Fig. 8. Frequency variations of the ν_s and ν_w components for the XDMF·(1 – X)H_2O solution with temperature (X = 0.7 (●), X = 0.6 (▽), X = 0.5 (□), X = 0.4 (▼), X = 0.3 (○)).



Next, we compare the frequency changes of the ν_s and ν_w components with temperature. Figures 8 and 9 show the frequency changes of the ν_s and ν_w components with decreasing temperature. Both ν_s and ν_w decrease linearly in most cases with decreasing temperature, indicating that the strength of the hydrogen bonds increases linearly with decreasing temperature. Considering the fact that the $S(\nu_s)/S(\nu_w)$ value increases exponentially with decreasing temperature, it is evident that the average strength of the hydrogen bonds in both the DMF and DMA solutions increases rapidly with decreasing temperature.

Both DMF and DMA have two methyl groups and therefore, hydrophobic hydration around two methyl groups exerts an important effect on the hydrogen bond strengths in the solutions. Although they are structurally similar and their liquid properties such as donor and acceptor numbers are also similar, it is interesting to see the differences in their aqueous solutions. We can point out the following differences from Figs. 6–9.

(1) The $S(\nu_s)/S(\nu_w)$ ratio is always larger for the DMF solution than for the DMA solution, implying that DMA is more destructive to water hydrogen bonds.

(2) The ν_s frequency of the DMF solution is always lower than that of the DMA solution while the reverse is the case for the ν_w frequency.

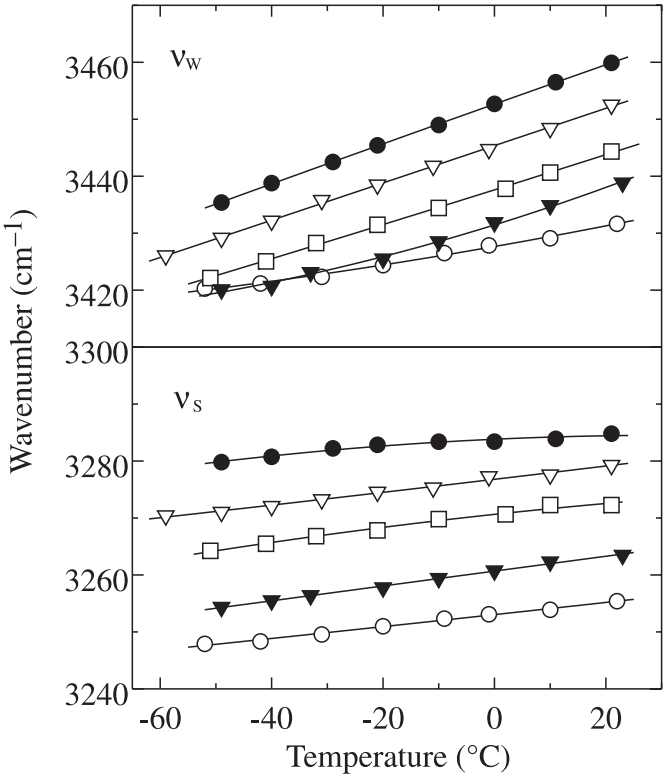
The first result can be ascribed to the fact that DMA molecules are larger than DMF molecules. On the other hand, the fact that the ν_w frequency is lower for the DMA solution than for the DMF solution suggests that the water molecules around DMA molecules have stronger hydrogen bonds than those around DMF molecules. Therefore, clathrate structures around DMA molecules are more stable than those around DMF molecules. This feature is consistent with the view that hydrophobic hydration is important in aqueous solutions of solutes having alkyl group(s). There are number of organic substances that form stable clathrate hydrates. Among tetraalkylammonium ions, tetrabutylammonium and tetraamylammonium ions form very stable clathrate hydrates while tetraalkylammonium ions of small alkyl groups (methyl, ethyl, and propyl) rarely form stable clathrate hydrates (25–27). Although both DMF and DMA are structure breakers in water, DMA is considered to be more suitable in size for clathrate formation.

An interesting aspect is that at low solute concentrations (less than X = 0.4), the ν_w frequency decreases with decreasing temperature, reaching a plateau value at around −30 °C, indicating that solvation structure around a DMA molecule becomes a more stable structure at low temperatures.

Comparing the temperature variations of the ν_s and ν_w frequencies, the lowering rate of the frequency with decreasing temperature is larger for the ν_w component than the ν_s component at most solute concentrations. In the case of the X = 0.5 solution, the ν_w frequency decrease from 20 to −40 °C is ~21 °C for the DMF solution and ~19 °C for the DMA solution, while the ν_s frequency decrease is ~7 °C and ~7 °C for the DMF and DMA solutions, respectively. Therefore, the frequency decrease with decreasing temperature is almost the same for the two solutions at X = 0.5. A remarkable point is that the $(d\nu_s/dT)$ value is almost invariant with the change in solute concentration while the $(d\nu_w/dT)$ value becomes larger with an increase in solute concentration. This feature may indicate that at higher temperatures (higher than

© 2004 NRC Canada

Fig. 9. Frequency variations of the ν_s and ν_w components for the XDMA·$(1 - X)H_2O$ solution with temperature (X = 0.7 (●), X = 0.6 (▽), X = 0.5 (□), X = 0.4 (▼), X = 0.3 (○)).



room temperature) clathrate-like structures are destabilized and that at lower temperatures (lower than 0 °C) they regain their stability with decreasing temperature. In fact, most clathrates are stable only at temperatures lower than room temperature (25, 26).

Finally, it is worth mentioning that there have been several reports on the solvated complex formation between water molecules and organic solute molecules (28, 29). The observation of no irregular variations in the $S(\nu_s)/S(\nu_w)$ ratio and ν_s and ν_w frequencies with temperature suggests that solvated complex formation, if any, is not important in aqueous DMF and DMA solutions.

References

1. D.E. Irish and M.H. Brooker. *In* Advances in infrared and Raman spectroscopy. Vol. 2. *Edited by* R.J.H. Clark and R.E. Hester. Heydon, London. 1976. Chap. 6.
2. G.E. Walrafen. *In* Water, a comprehensive treatise. Vol. 1. *Edited by* F. Franks. Plenum Press, New York. 1972. Chap. 5.
3. M.H. Brooker. *In* The chemical physics of solvation. *Edited by* J. Ulstrup, R.R. Dogonadze, E. Kálmán, and A.A. Karnyshev. Elsevier, Amsterdam. 1985. Chap. 4.
4. R.E. Verrall. *In* Water, a comprehensive treatise. Vol. 3. *Edited by* F. Franks. Plenum, New York. 1973.
5. G.E. Walrafen. J. Chem. Phys. **40**, 3249 (1964).
6. G.E. Walrafen and Y.C. Chu. J. Phys. Chem. **99**, 10 635 (1995).
7. H. Kanno and J. Hiraishi. J. Phys. Chem. **87**, 3664 (1983).
8. J.R. Scherer, M.K. Go, and S. Kint. J. Phys. Chem. **77**, 2108 (1973).
9. Y. Yeh, J.H. Bilgram, and W. Känzig. J. Chem. Phys. **77**, 2317 (1982).
10. C.I. Ratcliffe and D.E. Irish. J. Phys. Chem. **86**, 4397 (1982).
11. C.I. Ratcliffe and D.E. Irish. Can. J. Chem. **62**, 1134 (1984).
12. D.M. Carey and G.M. Korenowski. J. Chem. Phys. **108**, 2669 (1998).
13. V. Gutmann. *In* The donor-acceptor approach to molecular interactions. Plenum, New York. 1978. Chap. 2.
14. V. Gutmann and E. Wychera. Inorg. Nucl. Chem. Lett. **2**, 257 (1966).
15. T.M. Ahrinabhavi and B. Gopalakrishna. J. Chem. Eng. Data, **40**, 856 (1995).
16. R.J. Fort and W.R. Moore. Trans. Faraday Soc. **62**, 1112 (1966).
17. J.R. Sherer, M.K. Go, and S. Kint. J. Phys. Chem. **78**, 1304 (1973).
18. H. Kanno, A. Ohnishi, K. Tomikawa, and Y. Yoshimura. J. Raman Spectrosc. **30**, 705 (1999).
19. D.D. Klug, O. Mishima, and E. Whalley. Physica B, **139/140**, 475 (1986).
20. G.E. Walrafen. J. Chem. Phys. **52**, 4176 (1970).
21. H. Kanno and J. Hiraishi. Chem. Phys. Lett. **83**, 452 (1981)
22. R.J. Speedy and C.A. Angell. J. Chem. Phys. **65**, 851 (1976).
23. C.A. Angell. Annu. Rev. Phys. Chem. **34**, 593 (1983).
24. M. Oguni and C.A. Angell. J. Chem. Phys. **73**, 1948 (1980).
25. F. Franks and D.S. Reid. *In* Water: A comprehensive treatise. Vol. 2. *Edited by* F. Franks. Plenum, New York. 1973. pp. 323–380.
26. W.-Y. Wen. *In* Water and aqueous solutions: Structure, thermodynamics and transport processes. *Edited by* R.A. Horne. Wiley-Interscience, New York. 1972. Chap. 15.
27. R.K. McMullan, T.C.W. Mak, and G.A. Jeffrey. J. Chem. Phys. **44**, 2338 (1966).
28. S.S.N. Murthy. J. Phys. Chem. B, **101**, 6043 (1997).
29. J.G. Dawber. J. Chem. Soc. Faraday Trans. 1, **78**, 1127 (1982).

© 2004 NRC Canada

Surface-enhanced Raman scattering (SERS) from a silver electrode modified with oxazine 720[1]

Alexandre G. Brolo and Aaron C. Sanderson

Abstract: Electrochemical and spectroelectrochemical data was obtained for a silver electrode modified with oxazine 720 immersed in 0.2 mol L^{-1} KCl solution. A quasi-reversible redox behaviour was observed for the modified electrode. The electrochemical charges, obtained during either the anodic or the cathodic processes, were higher than expected for a monolayer of flat-adsorbed oxazine 720. Surface-enhanced Raman scattering (SERS) was recorded in situ for different applied potentials. Although the tilt angle was not determined, the analysis of the most enhanced vibrational modes in the SERS data, in conjunction with results of a DFT calculation, suggest that the molecule is adsorbed with its ring perpendicular to the electrode surface. This adsorption mode allows a higher surface packing than for flat-adsorbed molecules, consistent with the electrochemically estimated surface coverage. The potential dependence of the SERS signal is consistent with the redox process observed from cyclic voltammetry. The SERS intensities remain relatively constant between –200 and –500 mV (vs. Ag | AgCl | Cl^-_{sat}), but decrease drastically as the applied potential is made more negative than the onset of oxazine 720 reduction at –500 mV. The spectroelectrochemical data indicate that the molecule remains adsorbed at the SERS active sites even in its reduced form.

Key words: phenoxazine electrochemistry, oxazine 720, modified electrodes, surface-enhanced Raman scattering, SERS, molecular orientation.

Résumé : On a obtenu des données électrochimiques et spectroélectrochimiques pour une électrode d'argent modifiée avec de l'oxazine 720, immergée dans une solution 0,2 mol L^{-1} de KCl. On a observé un comportement redox quasi-réversible pour l'électrode modifiée. Les charges électrochimiques, obtenues durant les processus tant anodique que cathodique, sont plus élevés que ceux attendus pour une monocouche d'oxazine 720 adsorbée à plat. On a enregistré in situ des spectres améliorés de diffraction Raman de la surface (« SERS ») pour différents potentiels appliqués. Même si l'angle d'inclinaison n'a pas été déterminé, l'analyse de la plupart des modes vibrationnels améliorés des données SERS en relation avec les résultats d'un calcul selon la théorie de la densité fonctionnelle suggère que la molécule est adsorbée avec son cycle perpendiculaire à la surface de l'électrode. Avec ce mode d'adsorption, l'empilement est plus facile qu'avec des molécules adsorbées à plat et ceci est en accord avec la surface de couverture évaluée d'une façon électrochimique. La dépendance du signal SERS sur le potentiel est en accord avec le processus redox observée à l'aide de la voltampérométrie cyclique. Les intensités SERS demeurent relativement constantes entre –200 et –500 mV (vs. Ag | AgCl | Cl^-_{sat}), mais elles diminuent d'une façon drastique lorsque le potentiel appliqué est rendu plus négatif que celui nécessaire pour le début de la réduction de l'oxazine 720, à –500 mV. Les données spectroélectrochimiques indiquent que la molécule demeure adsorbée sur les sites actifs en SERS, même dans sa forme réduite.

Mots clés : électrochimie de la phénoxazine, oxazine 720, électrodes modifiées, spectres améliorés de diffraction Raman de la surface, SERS, orientation moléculaire.

[Traduit par la Rédaction]

Introduction

Oxazine 720 (alternatively called oxazine 170) is a typical laser dye used in the production of coherent radiation in the range 660–730 nm. Oxazine 720 contains a phenoxazine ring in its chemical structure, which is responsible for the strong photoabsorption band in the visible range (λ_{max} at ca. 620 nm) and its reversible electrochemistry at metallic (1) and semiconducting surfaces (2). These physical properties make phenoxazine compounds suitable to applications in several industrial fields, including electrocatalysis (3) and energy conversion (4). The hydrophobic phenoxazine ring promotes molecular aggregation in aqueous solution (5), and such dye aggregates are important for several photoconversion applications such as photography (6), solar energy collection (4), and photocatalytic remediation of groundwater (7). Phenoxazines can also be used as a mediator in charge transfer involving biological molecules (1, 8). For instance,

Received 16 March 2004. Published on the NRC Research Press Web site at http://canjchem.nrc.ca on 28 October 2004.

A.G. Brolo.[2] Department of Chemistry, University of Victoria, P.O. Box 3065, Victoria, BC V8W 3V6, Canada.
A.C. Sanderson. Department of Physics and Astronomy, University of Victoria, P.O. Box 3055, Victoria, BC V8W 3P6, Canada.

[1]This article is part of a Special Issue dedicated to the memory of Professor Don Irish.
[2]Corresponding author (e-mail: agbrolo@uvic.ca).

 doi: 10.1139/V04-117 © 2004 NRC Canada

the oxidation of NADH occurs at +1.1 V (vs. SCE) on carbon electrodes, but this oxidation potential is shifted to a region between −200 and –600 mV when the carbon surface is modified by phenoxazines (8). The electrocatalytic behaviour of the oxidation of NADH for several phenoxazines adsorbed on different electrode materials has been widely investigated (1, 8). Electrodes modified by polymeric phenoxazine compounds have also shown electrocatalytic activity, and, for example, can be used for the voltammetric determination of dissolved molecular oxygen in water at the μmol L^{-1} level (9).

Although the electrochemistry of electrodes modified by phenoxazines is regularly reported in the contexts mentioned above, there are few reports in the literature on the application of spectroelectrochemical methods to elucidate the electrochemical behaviour. This is particularly true for oxazine 720, where the utilization of in situ electronic spectroscopy to evaluate the redox potential of manganese(III) reconstituted mioglobin (10) is among the few examples available. Surface-enhanced Raman scattering (SERS) is an ideal tool to investigate this class of compounds adsorbed on gold, silver, or copper electrodes because adsorbed phenoxazines yield a very large enhancement of their Raman signal, especially when excited with radiation within their electronic resonance (in this condition the effect is termed surface-enhanced resonance Raman scattering (SERRS)) (11). In fact, the SERRS signal from dyes adsorbed on aggregated silver nano particles are capable of producing Raman signals up to 10^{15} times larger than the free molecule. This spectacular increase in the Raman cross section has allowed the observation of extremely low concentrations and even the detection of single dye molecules (11). This high sensitivity has recently led to the exploration of the use of dyes as SERS (and SERRS) labels for the detection of minute amounts of biological species (12).

Although there are no reports in the literature related to the SERS of oxazine 720 adsorbed on electrode surfaces under potential control (in situ SERS), the SERS spectra of oxazine 720 adsorbed on silver colloids were reported by Schneider et al. (13). It was noted that the relative SERS intensities of several dyes (including oxazine 720) adsorbed on silver colloids were dependent on the nature of the anion presented in the aqueous environment (13). Two processes could explain the origin of this phenomenon as reported in ref. 13: Firstly, the dependence can be related to the "chemical" contribution to the overall SERS effect (13). This enhancing mechanism may be related to a charge transfer (CT) between the metal and the adsorbed molecule in a resonance Raman-like process (14). According to ref. 13, the coupling between the electronic states of the metal and the dye depends on the strength of the interaction between the co-adsorbed anion and the dye. Therefore, the anions can tune the resonance and provoke spectral shifts and changes in relative SERS intensities. On the other hand, the observed difference in the SERS spectra of oxazine 720 obtained in media containing different anions could also be explained by anion-induced reorientation (13). The relative contribution of the CT mechanism to the overall SERS signal can easily be manipulated in an electrochemical environment since the energy of the Fermi level is related to the applied electrical potential (14). Therefore, in situ spectroelectrochemical SERS measurements would be useful to clarify some of these aspects discussed in ref. 13.

In this paper, we present electrochemical and SERS results from a silver surface modified with oxazine 720 in a 0.2 mol L^{-1} KCl solution. The electrochemical data show that oxazine 720 undergoes reduction at ca. –500 mV (vs. Ag | AgCl | Cl^-_{sat}). The dependence of the SERS intensities on the applied potential provides insights into the molecular orientation and the role of the CT mechanism (14). It will also be demonstrated that the reduced form of oxazine 720 remains adsorbed at the SERS active sites on the silver surface even at potentials as negative as –1000 mV.

Experimental

Solutions

Solutions for electrochemical and spectroelectrochemical measurements were prepared using KCl 99% (ACP) and ultra-pure water (18.2 MΩ.cm) from a Barnstead NANOpure Diamond water purification system. Analyte solutions were prepared with oxazine 720 (Lambdachrome) and HPLC grade methanol (Aldrich).

Cell, electrodes, and electrochemical equipment

The working electrode was fabricated using a 99.99% silver rod (Premion – Alfa Aesar), machined into a silver disk of ca. 6.35 mm diameter and mounted in a Teflon holder. Electrical contact was made to the silver electrode by an externally threaded stainless-steel rod. The silver electrode was polished before each experiment with emery paper, and then with progressively finer grades of alumina powder down to 0.05 μm. After the surface polishing treatment, the silver electrode was rinsed with copious amounts of ultra-pure water and then transferred to the appropriate cell. The reference electrode was a saturated silver–silver chloride electrode, and all potentials in this work are quoted against this reference. A 0.3 mm platinum wire (Alfa Aesar) was used as the counter electrode. The spectroelectrochemical cell used for the SERS measurements has been described in a previous publication (15). A Hokuto Denko potentiostat–galvanostat (HAB-151) was used to control the potential applied to the silver surface. The assembled cell was purged with prepurified nitrogen for 30 min prior to taking measurements, and a gentle stream of nitrogen was maintained to blanket the solution during data acquisition.

Activation procedure

The "activation procedure" used to prepare the SERS active (rough) silver surface consisted of a sequence of oxidation–reduction cycles (ORCs) performed on the polished silver electrode immersed in a 0.2 mol L^{-1} KCl aqueous solution. A triangular potential sweep program was applied, changing the surface potential from –700 to +250 mV and back to –700 mV at a scan rate of 5 mV s^{-1}. Typically, three such cycles were performed to produce the desired roughness. The metallic silver oxidizes in this medium at potentials more positive than +50 mV, producing an insoluble salt (AgCl). During the reverse scan, the AgCl film is reduced back to metallic silver at ca. –100 mV. The freshly formed silver surface obtained during the reduction

© 2004 NRC Canada

is naturally rough, and sustains significant enhancement of the Raman signal for adsorbed molecules (16, 17).

The modified electrode was prepared using a droplet evaporation procedure. After the activation procedure, the rough silver electrode was removed from the cell and a drop of a ca. 10 μmol L^{-1} solution of the dye in methanol was added to the electrode surface. The solvent was allowed to evaporate, after which the surface was rinsed with ultra-pure water. The modified electrode was then placed back into the cell. Electrochemical control was resumed and the desired potential was applied. The objective of this procedure was to adsorb a single monolayer of the dye on the surface. The high quality of the SERS spectra obtained from oxazine 720 adsorbed using this procedure indicates that an extremely large enhancement of the Raman cross section was achieved for these molecules.

The silver electrode was never oxidized in the presence of oxazine 720. This ensured that the dye molecules were neither trapped nor electrochemically degraded by the activation ORC (18).

Raman instrumentation

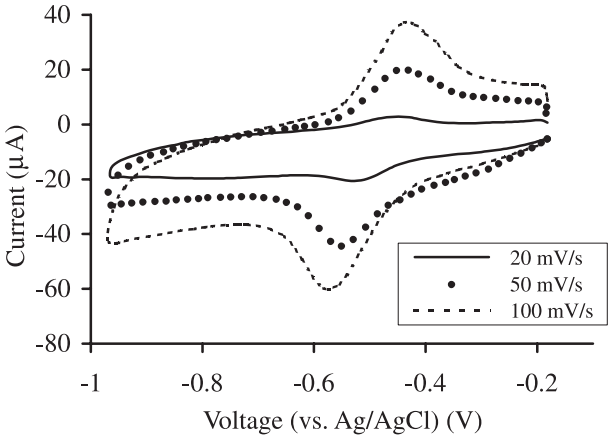
SERS spectra were collected using a Dilor OMARS89 spectrometer coupled to an optical multichannel analyzer. The detector was a thermoelectricaly cooled (ca. –15 °C) intensified diode array (512 diodes) interfaced to a computer for data collection. Excitation at 514.5 nm was provided by a Spectra-Physics model 2020 argon ion laser with the power set to less than 40 mW at the laser head. Excitation at 632.8 nm was provided by a Melles Griot He–Ne laser at similar power levels. The acquisition time for each measurement was 1 s and a minimum of 10 accumulations were summed for each spectrum. The laser light was chopped to allow background spectra to be obtained and subtracted during each accumulation. The resulting spectra were then baseline corrected during analysis.

The normal Raman spectra of solid oxazine 720 were collected with a Renishaw inVia microscope Raman spectrometer system utilizing a Spectra-Physics argon ion laser to produce excitation at 514.5 nm.

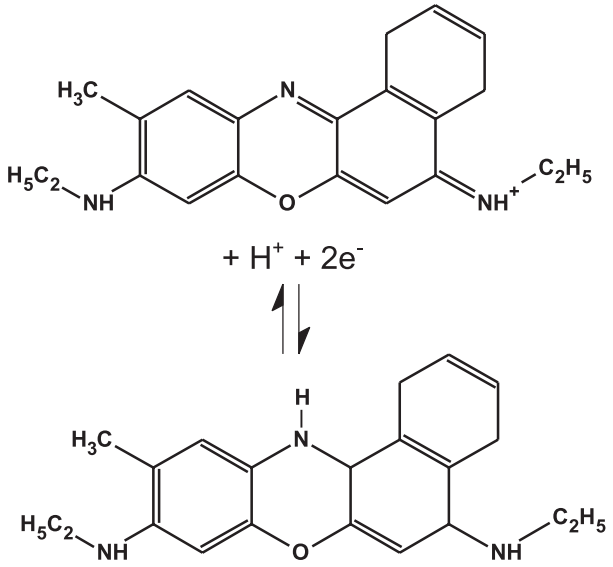
Results

Figure 1 shows cyclic voltammograms at different scan rates for a silver electrode modified with oxazine 720 immersed in a 0.2 mol L^{-1} KCl solution. The cathodic and anodic peaks are related to the redox of the phenoxazine ring as proposed elsewhere (19). At neutral pH, the electrochemical process (depicted in Scheme 1) involves the transfer of two electrons and one proton. The process is pH-dependent and two protons should be exchanged in acidic medium (19). The electrochemical mechanism may involve the formation of a radical cation intermediate (20). Both the cathodic and the anodic peaks presented in Fig. 1 shift with the scan rate, but this effect is more pronounced for the reductive process. The cathodic peak moves from ca. –525 mV at 20 mV s^{-1} to ca. –590 mV at 200 mV s^{-1} (not shown) and the anodic peak shifts from –460 to –430 mV at 20 mV s^{-1} and 200 mV s^{-1} (not shown), respectively, (all potentials are reported against a Ag | AgCl | Cl^-_{sat} reference electrode). The redox potential observed here is more negative than the formal redox potential of –325 mV reported for the reduction of oxazine 720 (10), although the redox potential of surface-confined phenoxazines may differ significantly from that observed for the molecule in solution (8). The peak currents presented a linear relationship with the square root of the scan rate. A direct relationship with the scan rate is expected for strongly bound species (21), and the dependence with $v^{1/2}$ indicates that diffusion from solution is playing a significant role in the electrochemical mechanism. This is not surprising considering that protons are involved in the electrochemical reaction. The cathodic charge (Q_c) is ca. 40% higher than the anodic charge (Q_a) at slow scan rates. This difference decreases as the scan rate increases and a Q_c/Q_a ratio equal to one is observed for sweep rates faster than 100 mV s^{-1}. The electrochemical charges were corrected for the surface roughness (19) and used to estimate the amount of oxazine 720 at the solid–liquid interface. The calculated values depend on the sweep rate and on the nature of the process (cathodic or anodic), with the amounts ranging between 3 and 8×10^{-10} mol cm^{-2}. The expected coverage for a monolayer of a phenoxazine species adsorbed flat on the metallic

Fig. 1. Cyclic voltammograms of oxazine 720 on a silver electrode in a 0.2 mol L^{-1} KCl solution.



Scheme 1.



© 2004 NRC Canada

surface is estimated to be between 1 and 2×10^{-10} mol cm^{-2} (22). Therefore, if oxazine 720 is flat-adsorbed on the modified surface, multilayers must be present. On the other hand, the higher surface coverage reported here may also indicate that the molecule is adsorbed end-on, probably attached by the nitrogens from the amino groups. Finally, oxazine 720 is known to form dimers in aqueous solution (5). In fact, second-harmonic generation measurements have demonstrated that oxazine 720 dimers are the main species present at a liquid–air interface (23). Therefore, the discrepancy in the expected and experimental surface coverage may also be related to the preferential adsorption of the dimer.

The normal Raman spectrum of solid oxazine 720 is compared to the SERS signal from the modified electrode in Fig. 2. These spectra were obtained using 514.5 nm laser excitation, which is away from the visible-range absorption maximum for oxazine 720 (ca. 620 nm). The vibrational assignment of selected oxazine 720 modes (presented in Table 1 and shown in Fig. 3) was performed using previous work for other dyes that contains the phenoxazine ring (19, 24) and our own DFT calculations using Gaussian 98W®, carried out at the B3LYP level using the 6-31G(d)5D basis set. Figure 2 shows that there are two regions that contain a wealth of vibrational information in both the solid and the adsorbed molecule spectra: the region between 500 and 700 cm^{-1} and the region between 1100 and 1700 cm^{-1}. A specific set of bands are enhanced under adsorption and appear in the SERS spectrum at 546, 585, 675, 1339, 1395, and 1644 cm^{-1}. The vibrational frequencies from the adsorbed molecule are similar to the ones observed for the solid, suggesting a relatively weak adsorption to the surface. Representations of the normal modes of the most surface-enhanced bands are presented in Fig. 3.

Further analysis of the SERS spectrum shows the lack of enhanced out-of-plane ring vibrations (Fig. 3), which, according to the SERS selection rules, are expected to show significant intensity if the ring is adsorbed flat to the surface (18). It is known that the breathing mode of benzene shifts to lower frequency as the flat-adsorbed molecule interacts with the surface (25), and although the multi-ring oxazine 720 system is much more complex than benzene, some shift to lower frequency should be observed for vibrations that are dominated by ring modes if the molecule is adsorbed flat. All these pieces of evidence indicate that the oxazine 720 ring is not completely flat-adsorbed, but is interacting with the surface through the aliphatic amino groups. The tilt angle between the molecule and the surface normal cannot be evaluated solely from the data presented in Fig. 2, but it suggests that the oxygen–nitrogen axis is in an upright position, with the ring in a position perpendicular to the surface. Since such an orientation allows more molecules to be packed on the silver surface, the spectroscopic data is in agreement with the high surface coverage obtained from the electrochemical data presented in Fig. 1, where cyclic voltammetry suggested coverage in excess of a monolayer of flat-adsorbed oxazine 720. This upright orientation was also suggested by Schneider et al. (13) for high coverage of oxazine 720 adsorbed on silver colloidal particles. The end-on orientation is also consistent with the tendency of oxazine 720 to form H-aggregates in aqueous environments (5). Spectroelectrochemical SERS studies involving other phenoxazine rings, such as nile blue, also suggest the end-on orientation for the adsorption from acidic solutions (19).

Fig. 2. (*a*) The SERS spectra of oxazine 720 on a rough silver electrode compared to (*b*) the Raman spectra of solid oxazine 720. Six vibration bands with significant SERS enhancement are labelled.

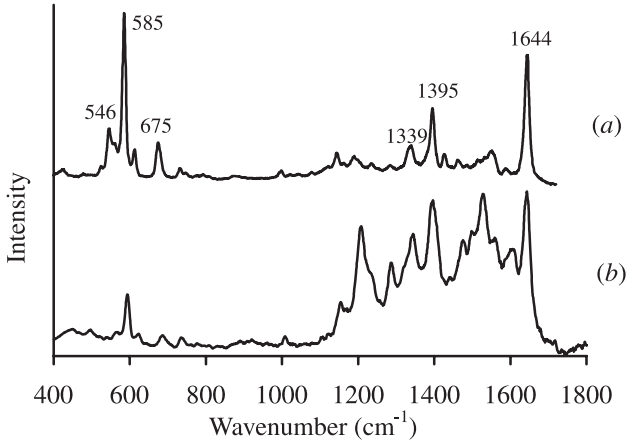


Table 1. Calculated vibrational wavenumbers (B3LYP/6-31G(d)5D), along with the measured SERS and Raman band positions for oxazine 720.

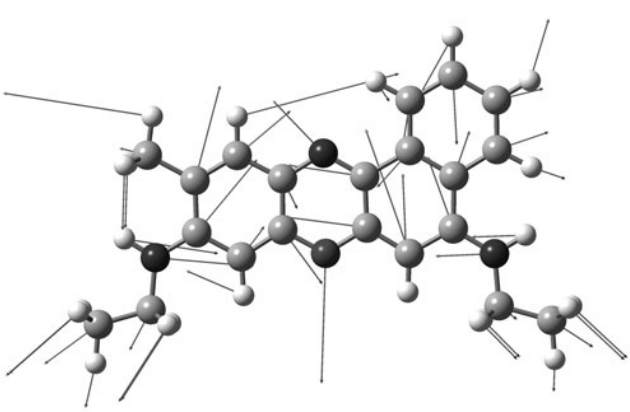
ν_{cal} (cm^{-1})	ν_{SERS} (cm^{-1})	ν_{solid} (cm^{-1})	ν_{cresyl} (cm^{-1})[a]
547.3	546		548
607.5	585	594	589
701.6	675	687	673
1386.0	1339	1343	1330
1452.3	1395	1395	1401
1696.7	1644	1642	1641

Note: The last column contains measured SERS bands of cresyl violet, a similar phenoxazine dye.
[a]From ref. 24.

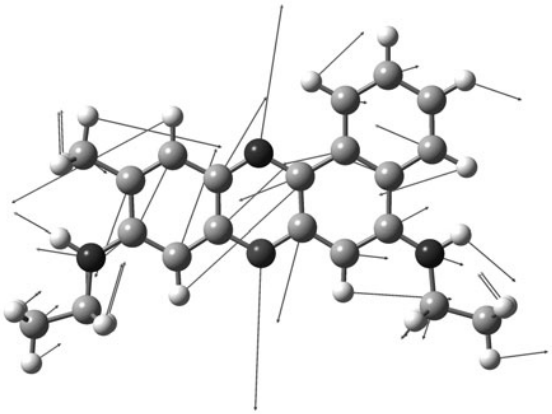
SERS spectra from a silver electrode modified with oxazine 720, obtained at different applied potentials, are shown in Fig. 4. The spectra in Fig. 4 were collected using green excitation at 514.5 nm. Experiments using red (632.8 nm) excitation (not shown), which is within the absorption band of the free molecule, were also performed, but no significant differences in the relative intensities of the main modes indicated in Fig. 3 and Table 1 were observed. A plot of the intensities of selected peaks from Fig. 4 vs. the applied potential (potential profile) is presented in Fig. 5. The intensities of most of the SERS bands did not change significantly when the applied potentials were more positive than –500 mV. This can be clearly observed in the potential profile for the 1644 and 1545 cm^{-1} bands shown in Fig. 5. On the other hand, a band at 1475 cm^{-1} was absent in the SERS spectrum for applied potential more positive than –250 mV, while the intensity of this mode increased as the potential was scanned more negative, reaching a maximum at around −450 mV. Figure 5 indicates that the SERS intensities for all modes of adsorbed oxazine 720 decreased sharply as the potential is made more negative than –500 mV. This behaviour can be correlated to the electrochemical curves presented in Fig. 1, demonstrating that the SERS intensities decrease as

© 2004 NRC Canada

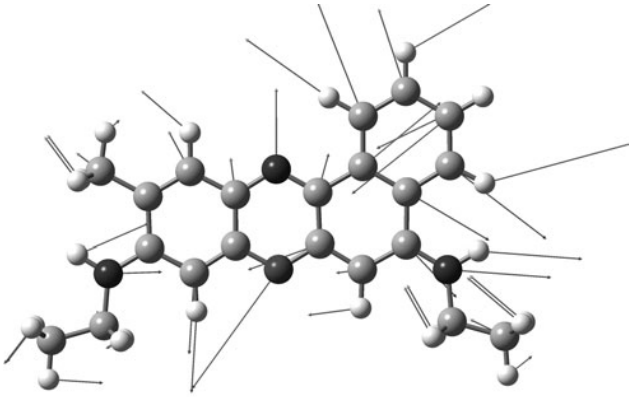
Fig. 3. Normal coordinates of the six oxazine 720 bands labelled in Fig. 2. The mode number and calculated wavenumber from Guassian 98W as well as the measured SERS wavenumber (in brackets) are given for each mode.



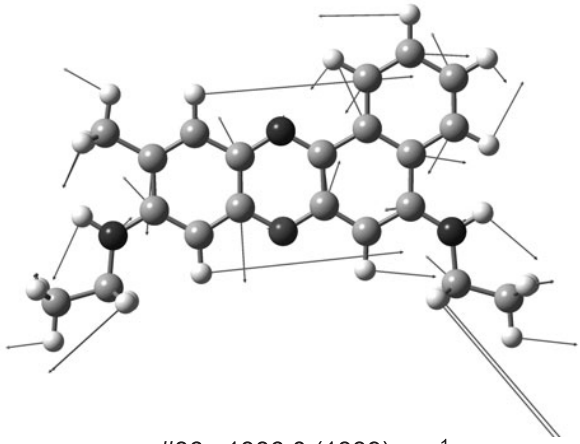
#34, 547.3 (546) cm^{-1}



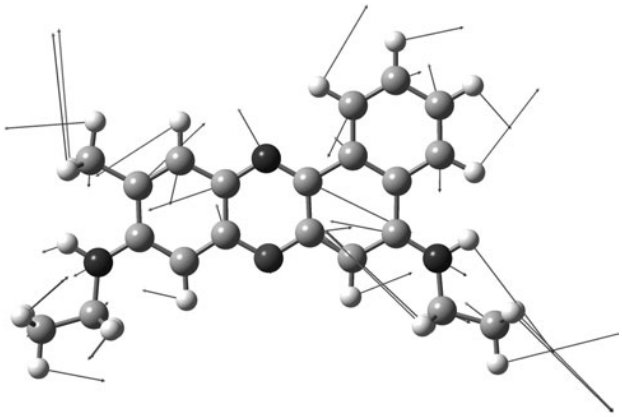
#37, 607.5 (585) cm^{-1}



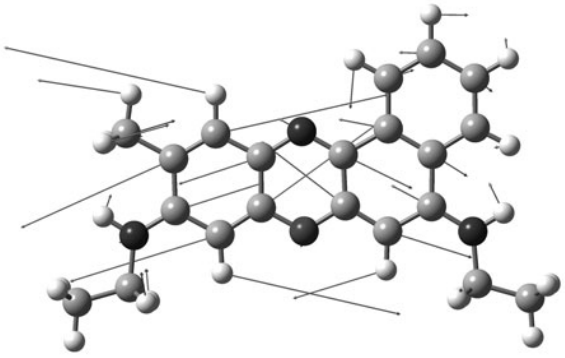
#41, 701.6 (675) cm^{-1}



#86, 1386.0 (1339) cm^{-1}



#92, 1452.3 (1395) cm^{-1}



#113, 1695.7 (1644) cm^{-1}

the onset of oxazine 720 reduction is reached. Two explanations can be considered for the transient nature of the 1475 cm^{-1} band. Firstly, this mode may indicate some sort of molecular rearrangement that occurs just before reduction or, alternatively, the increase in the 1475 cm^{-1} band can be explained using charge transfer (CT) arguments. The CT theory of electrochemical SERS explains the potential dependence of the SERS intensities as an electron transfer res-

© 2004 NRC Canada

Fig. 4. SERS spectra of oxazine 720 on a rough silver electrode at various applied potentials.

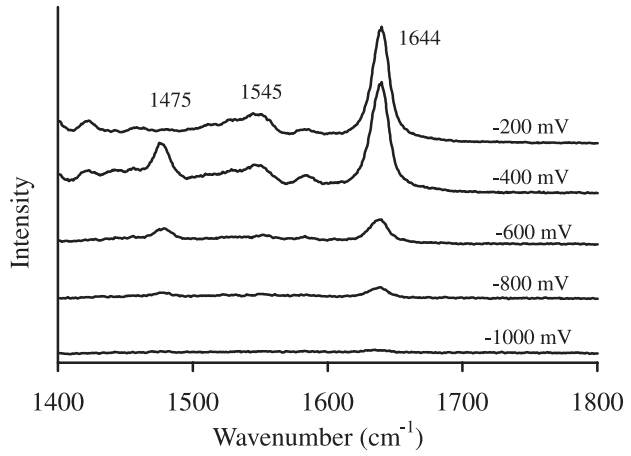
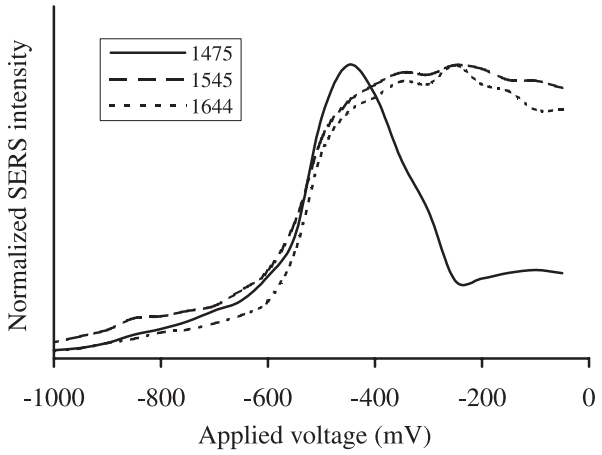
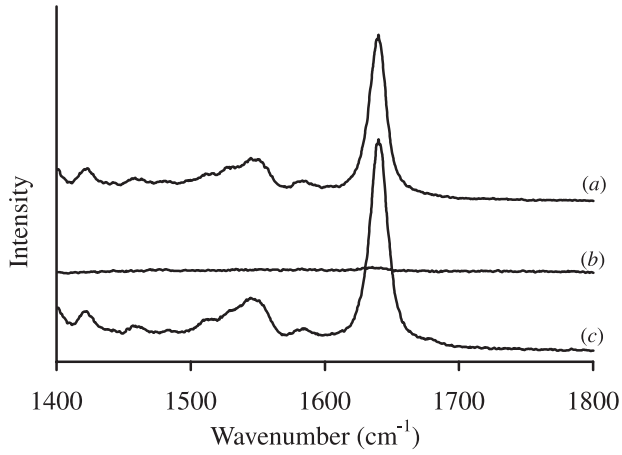


Fig. 5. Potential profiles (see text) of the three oxazine 720 bands labelled in Fig. 4.



onance between the metal and the molecular orbitals of the adsorbed species (14, 15). This resonance is modulated by the applied potential, which controls the position of the Fermi level. The CT contribution can then be probed in electrochemical SERS by obtaining the potential profile at different excitation wavelengths and observing the shift in the potential where the SERS intensity is maximized (15). The SERS spectra from a silver electrode modified with oxazine 720 using 632.8 nm excitation presented potential profiles similar to those observed in Fig. 5 for most of the bands, including the ones at 1644 and 1545 cm^{-1}. In these cases, the SERS intensity remained almost constant for potentials between –200 and –500 mV and then decreased as the applied voltages became more negative than –500 mV. The potential-transient 1475 cm^{-1} band was not observed at any applied potential for experiments using red excitation. This behaviour shows that this mode is not related to reorientation. The intensity of the 1475 cm^{-1}-mode has been reported to be sensitive to the nature of the anion in solution for oxazine 720 adsorbed on colloidal silver (13). This was interpreted as an indication that this vibration could be tuned in and out of resonance by the anion-induced modification

Fig. 6. SERS spectra of oxazine 720 showing the recoverability of the SERS signal. (*a*) The initial spectrum was collected with an applied potential of –200 mV. (*b*) The potential was then changed to –1000 mV, where the SERS signal is no longer visible. (*c*) The applied potential was then returned to –200 mV, and the SERS signal was recovered.



of the electronic properties of the silver particles (13). The results reported here confirm the role of the CT mechanism for this specific mode.

As discussed above, the decrease in intensity of the SERS bands as the potential is made more negative than –500 mV is obviously related to the reduction of oxazine 720. Interestingly, however, the SERS signal is recovered when the potential is returned to values more positive than –500 mV. This process is illustrated in Fig. 6. The initial SERS spectrum was collected with an applied potential of –200 mV (Fig. 6*a*), after which the potential was gradually swept to –1000 mV, where the SERS signal completely vanished because of the reduction (Fig. 6*b*). The potential was then returned to –200mV, where a good quality SERS signal was recovered (Fig. 6*c*). Figure 1 indicates that the electrochemical behaviour of oxazine 720 adsorbed on silver is quasi-reversible, in agreement with the observations from Fig. 6. It is well-established, however, in the SERS literature that the active sites that support the enhancement are lost during incursions to highly negative potentials (26). This is due to potential-induced morphological changes related to molecular (or anionic) desorption followed by surface diffusion and incorporation of the roughness features (26). The fact that the SERS signal is recovered in Fig. 6*c* is the result of the molecule remaining adsorbed at the SERS active sites in its reduced form. This is in agreement with the observed Raman bands of the reduced form of other phenoxazine dyes adsorbed at negative potentials (19). It is important to stress, however, that SERS signals originate only from specific active sites. The observation that the molecule stays adsorbed at highly negative potentials (Fig. 6) may not represent an average behaviour that would be observed from a smooth surface. The weak SERS signal from the reduced form of oxazine 720 reported here is not related to molecular desorption: the reduction populates the low-lying LUMO, shifting the CT resonance to higher energies not accessible using the laser excitations used in this work.

© 2004 NRC Canada

Conclusions

The redox behaviour of a silver electrode modified by oxazine 720 was investigated by SERS and cyclic voltammetry. The combination of electrochemical and spectroelectrochemical data indicate that oxazine 720 adsorbs in an upright position, interacting with the surface by the nitrogens from the amino side chains. A quasi-reversible redox was observed around –500 mV, and the reduced molecule was shown to remain adsorbed to the surface down to an applied potential of –1000 mV. The role of the CT mechanism on the overall SERS intensity was explored and specific SERS bands were found to be significantly enhanced only over a short potential window, indicating a resonant behaviour. This resonant characteristic was confirmed by collecting SERS spectra using different excitation energies. These results should help in understanding the role of phenoxazines in electrocatalysis and photon conversion applications.

Acknowledgements

This work was supported by operating grants from the University of Victoria (Start Up grant) and the Natural Sciences and Engineering Research Council of Canada (NSERC) and by equipment grants from the Canada Foundation for Innovation (CFI–New Opportunities) and the British Columbia Knowledge and Development Fund (BCKDF). We would like to thank Anderson P. Smith and Yanhong Yang for their assistance with data collection, and Kelly Akers for supplying us access to the Renishaw inVia system.

We also thank Dr. Donald E. Irish for the donation of the Raman equipment. Don Irish was a mentor and a friend to one of us (AGB). He will certainly be greatly missed.

References

1. A.S. Santos, L. Gorton, and L.T. Kubota. Electrochim. Acta, **47**, 3351 (2002).
2. I. Bedja, S. Hotchandani, and P.V. Kamat J. Phys. Chem. **97**, 11 064 (1993).
3. L. Gorton. J. Chem. Soc. Faraday Trans. **82**, 1245 (1986).
4. A. Hagfeldt and M. Gratzel. Chem. Rev. **95**, 49 (1995).
5. D.A. Steinhurst and J.C. Owrutsky. J. Phys. Chem. B, **105**, 3062 (2001).
6. J. Bourdon. J. Phys. Chem. **69**, 705 (1965).
7. P.V. Kamat. Chem. Rev. **93**, 267 (1993).
8. A. Malinauskas, T. Ruzgas, and L. Gorton. J. Electroanal. Chem. **484**, 55 (2000).
9. H. Ju and C. Shen. Electroanalysis, **13**, 789 (2001).
10. I. Taniguchi, C.-Z. Li, M. Ishida, and Q. Yao. J. Electroanal. Chem. **460**, 245 (1999).
11. K. Kneipp, H. Kneipp, I. Itzkan, R.R. Dasari, and M.S. Feld. Chem. Rev. **99**, 2957 (1999).
12. Y.-W.C. Cao, R. Jin, and C.A. Mirkin. Science, **297**, 1536 (2002).
13. S. Schneider, H. Grau, P. Halbig, P. Freunscht, and U. Nickel. J. Raman Spectrosc. **27**, 57 (1996).
14. J.R. Lombardi, R.L. Birke, T. Lu, and J. Xu. J. Chem. Phys. **84**, 4174 (1986).
15. A.G. Brolo, D.E. Irish, and B.D. Smith. J. Mol. Struct. **405**, 29 (1997).
16. J. Pemberton and M.M. Girand. J. Electroanal. Chem. **217**, 79 (1987).
17. D.D. Tuschel, J.E. Pemberton, and J.E. Cook. Langmuir, **2**, 380 (1986).
18. A.G. Brolo and D.E. Irish. J. Electroanal. Chem. **414**, 183 (1996).
19. F. Ni, H. Feng, L. Gorton, and T.M. Cotton. Langmuir, **6**, 66 (1990).
20. S.H.A Nicolai, P.R.P. Rodrigues, S.M.L. Agostinho, and J.C. Rubim. J. Electroanal. Chem. **527**, 103 (2002).
21. A. Bard and L.R. Faulkner. Electrochemical methods — Fundaments and applications. 2nd ed. Wiley, Toronto. 2001.
22. L. Gorton, A. Tortensson, J. Jaegfeldt, and G. Johansson. J. Electroanal. Chem. **161**, 103 (1984).
23. D.A. Steinhurst, A.P. Baronavski, and J.C. Owrutsky. J. Phys. Chem. B, **106**, 3160 (2002).
24. E. Vogel, A. Gbureck, and W. Kiefer. J. Mol. Struct. **550–551**, 177 (2000).
25. M. Moskovits and D.P. DiLella. J. Chem. Phys. **73**, 6068 (1980).
26. R.L. Sobocinski and J.E. Pemberton. Langmuir, **4**, 836 (1988).

© 2004 NRC Canada

In situ ATR-SEIRAS study of adsorption and phase formation of trimesic acid on Au(111-25 nm) film electrodes[1]

B. Han, Z. Li, S. Pronkin, and Th. Wandlowski

Abstract: The adsorption and phase formation of 3 mmol L^{-1} trimesic acid (TMA) on Au(111-25 nm) film electrodes in contact with aq. 0.1 mol L^{-1} $HClO_4$ electrolyte have been investigated by in situ ATR-SEIRAS, cyclic voltammetry, chronoamperometry, and STM measurements. Depending on the applied electrode potential, TMA molecules assemble in three distinctly different 2D ordered adlayers. In the range $0.10 < E < 0.50$ V, planar-oriented molecules form an open ring honeycomb pattern (phase I) stabilized by directional hydrogen bonds. Interfacial water molecules are being replaced. A close-packed, physisorbed adlayer II forms at higher potentials in the range $0.58 < E < 0.75$ V. Further increase of the electrode potential causes an orientation change. An initially disordered phase transforms into an ordered, stripe-like chemisorbed adlayer III of perpendicularly oriented TMA molecules ($0.90 < E < 1.20$ V). One *carboxylate* group per molecule is bound to the electrode surface, while the two other *protonated carboxyl* groups are directed toward the electrolyte, and act as structure-determining components of a hydrogen-bonded molecular ladder network. Strongly hydrogen-bonded and isolated water species are co-adsorbed. The potential-induced formation of chemisorbed TMA proceeds in two steps: (*i*) orientation change from planar to a disordered tilted and (or) perpendicular phase III_a ($\tau < 5$ ms) according to a Langmuir-type kinetics; (*ii*) subsequently, the chemisorbed TMA molecules align into a highly ordered, stripe-like phase III_b with co-adsorbed water species.

Key words: ATR-SEIRAS, trimesic acid, Au(111), supramolecular assembly.

Résumé : Faisant appel à des mesures in situ d'ATR-SEIRAS, de voltampérométrie cyclique, de chronoampérométrie et de STM, on a étudié l'adsorption et la formation de la phase de 3 mmol L^{-1} d'acide trimésique (ATM) sur des électrodes en film de Au(111-25 nm) en contact avec une solution aqueuse 0,1 mol L^{-1} de $HClO_4$ agissant comme électrolyte. Suivant le potentiel d'électrode applique, les molécules d'ATM s'assemblent dans trois couches d'adsorption différentes organisées en deux dimensions. Dans la plage de $0{,}10 < E < 0{,}50$ V, les molécules orientées dans un plan forment une structure alvéolée à cycle ouvert (la phase I) stabilisée par des liaisons hydrogènes orientées. Les molécules d'eau interfaciales sont déplacées. À des potentiels plus élevés, dans la plage de $0{,}58 < E < 0{,}75$ V, il se forme une couche d'adsorption physique serrée, II. Une augmentation du potentiel d'électrode provoque un changement d'orientation. Une phase initialement désordonnée se transforme en une phase d'adsorption chimique (III) bien ordonnée et en forme de rayure avec des molécules d'ATM orientées perpendiculairement ($0{,}90 < E < 1{,}20$ V). Un groupe carboxylate par molécule est attaché à la surface de l'électrode alors que les deux autres groupes carboxyles protonés sont orientés vers l'électrolyte et agissent comme composants déterminants la structure d'un réseau en escabeau moléculaire formé par des liaisons hydrogènes. La formation induite par le potentiel de l'ATM s'effectue en deux étapes: (*i*) un changement d'orientation de la phase planaire vers une phase désordonnée et inclinée et (ou) une phase perpendiculaire III_a ($\tau < 5$ ms) qui suit une cinétique de type Langmuir; (*ii*) et, subséquemment, les molécules d'ATM chimisorbées s'alignent dans la phase bien orientée et en forme de rayure, III_b, coadsorbées avec des molécules d'eau.

Mots clés : ATR-SEIRAS, acide trimésique, Au(111), assemblage supramoléculaire.

[Traduit par la Rédaction]

Introduction

J.M. Lehn describes supramolecular chemistry as the "Chemistry of the inter-molecular bonds, which involves recognition, transformation, and translocation of information" (1). Basic ordering motifs comprise hydrogen bonding, electrostatic interactions, such as dipole or π-stacking, and metal ion | ligand coordination. In the case of an electro-

Received 28 March 2004. Published on the NRC Research Press Web site at http://canjchem.nrc.ca on 2 November 2004.

We dedicate this paper to the memory of Don Irish. His breadth, depth, and productivity as well as his engaging personality made him an outstanding member of our community.

B. Han, Z. Li, S. Pronkin, and Th. Wandlowski.[2] Institute of Thin Films and Interfaces ISG 3, Research Centre Jülich, 52425 Jülich, Germany.

[1]This article is part of a Special Issue dedicated to the memory of Professor Don Irish.

[2]Corresponding author (e-mail: th.wandlowski@fz-juelich.de).

 doi: 10.1139/V04-118 © 2004 NRC Canada

chemical system, the electrode surface acts as an electron (charge) source or sink and additional coordination center. The electrode potential assumes the role of an universal tuning source to fabricate and address nano-structures (2). The selectivity and directional nature of hydrogen bonding has led to its extensive use in the construction and stabilization of non-covalently bonded molecular and supramolecular structures (3–5). Hydrogen bonds are formed when a donor (D) with an available acidic hydrogen atom is brought into contact with an acceptor (A). Hydrogen bonding is not random, but controlled by the directional strength of intermolecular interactions and can be used to tune spatial arrangement of functional molecules and ions in bulk systems and on surfaces (2, 5–8).

Carboxylic acids are commonly used as pattern-controlling functional groups for the purpose of crystal engineering. They can form hydrogen-bonded structures that contain a center of symmetry (dimer motif) and also aggregate in acentric one-dimensional chains (catemer motif) resulting from the formation of hydrogen bonds to two or more neighboring acids (5). The dimer synthon has been used to assemble a variety of super-molecules. For example, terephthalic or 1,4-benzenedicarboxylate acid (TA) (9), isophthalic or 1,3-benzenedicarboxylate acid (IA) (10), and a wide variety of their derivatives (11) are known to form one-dimensional tapes and ribbons. Trimesic or 1,3,5-tricarboxylic acid (TMA), which is composed of a phenyl ring and three trigonal exodentate carboxyl groups, arranges in two-dimensional networks with characteristic honeycomb units (12, 13). TMA and its metal and inclusion complexes represent prototype materials for supramolecular assemblies involving directional hydrogen bonding and (or) metal ion | ligand coordination (13–24).

The assembly of TMA on surfaces was recently studied under UHV conditions (25, 26) as well as at electrified solid–liquid interfaces (27, 28) employing scanning tunneling microscopy (STM). Griessl et al. (25) reported on highly oriented pyrolytic graphite (HOPG), the coexistence of two hexagonal ring structures composed of TMA with hydrogen bonds formed either between two ("chicken wire" or "honeycomb" motif) or between three ("flower" motif) adjacent molecules. Dmitriev et al. (26) reported in a temperature-dependent study on Cu(100) two different 2D structures: a honeycomb structure at low temperature (200 K), and a more densely packed stripe arrangement at room temperature. The latter was assigned to upright standing TMA molecules, which are adsorbed on Cu(100) via one or two deprotonated carboxylate groups. Under electrochemical conditions, Ishikawa et al. (27) found for Au(111) – 0.1 mol L^{-1} $HClO_4$ a honeycomb-type (8 × 8) two-dimensional network of flat oriented TMA molecules, which transforms at higher potentials into a close-packed structure of dimers. Under similar experimental conditions, Su et al. (28) found three ordered adlayers: a quasi-hexagonal (4 × 4) phase of planar-oriented molecules at low coverage, a mixed (5 × 2√3) adlayer, and a striped phase represented by (2√3 × 4√3) or (7 × 2√3). The latter was tentatively ascribed to perpendicularly adsorbed molecules. Despite the detailed structure information, the reported results do not provide direct insight into the chemical composition and formation kinetics of the TMA-modified electrochemical interfaces. This knowledge can be developed from surface spectroscopic experiments employing classical (IRAS) or surface-enhanced IR reflection absorption spectroscopy (SEIRAS) (29, 30). Both techniques were already used to study the adsorption and phase formation of simple carboxylic acids, such as benzoic acid (BA) (31–33), *p*-nitrobenzoic acid (34, 35), fluorobenzoic acid (36), terephthalic acid (37), and fumaric acid (38) on Au(*hkl*), Ag(*hkl*), or Pt(*hkl*). The application of in situ SEIRAS in an attenuated total reflection configuration (ATR-SEIRAS) has several advantages in comparison to IRAS studies employing the so-called thin layer configuration (29, 39): (*i*) high and specific surface sensitivity with an enhancement of the IR response up to ca. 100 times stronger; (*ii*) dominant first layer effect (Helmholtz region) with a short decay length of the locally enhanced field of 3 to 4 nm towards the bulk electrolyte; (*iii*) signals from the interface and the solution background are of comparable magnitude and can be separated by applying the potential difference tactics; (*iv*) no severe limitations because of mass transport and advanced potential perturbations allowing a time resolution of up to 50 μs in in situ step-scan experiments (limited by the time constant of double layer charging).

In this paper, we are presenting a comprehensive in situ ATR-SEIRAS study of the vibrational properties of TMA and co-adsorbed water species on quasi-single crystalline Au(111-25 nm) film electrodes in contact with aq. 0.1 mol L^{-1} $HClO_4$. First, we report on the steady state properties of the potential dependent adlayer structures with special emphasis on the role of interfacial water. The second part of this contribution is focused on exploring the kinetics of phase formation employing time-resolved measurements in the rapid-scan and step-scan regimes, respectively. The IR spectroscopic results will be compared with in situ STM and electrochemical experiments employing well-defined single crystal electrodes.

Experimental

Spectroscopic setup

The SEIRAS experiments were carried out in a vertical spectroelectrochemical cell in the Kretschmann ATR configuration (39, 40). The working electrode was prepared by electron beam evaporation (deposition rate 0.005–0.007 nm s^{-1}, base pressure < 2 × 10^{-7} mbar (1 bar = 100 kPa)) of a thin gold film (25 nm mass thickness) onto the (111)-plane of a highly refractive Si hemisphere. The geometrical area of the electrode in direct contact with the electrolyte solution was 1.53 cm^2. The gold films were electrochemically annealed by cycling the potential in the double layer region at 50 mV s^{-1} for 1.5 h after deaeration. The primary reference electrode (RE) was either a trapped hydrogen electrode (RHE) or a mercury sulfate electrode (MSE). The counter electrode (CE) was a large-area platinum spiral. The electrode potential was controlled and synchronized with a HEKA potentiostat PG 310. All potentials in this paper are quoted with respect to the trapped hydrogen electrodes (0.310 V vs. SCE).

The IR spectra were measured with a Bruker IF66 V/s Fourier transform spectrometer. The spectral resolution was 4 cm^{-1} in slow-scan or rapid-scan experiments, and 8 cm^{-1} in the step-scan regime. Unpolarized IR radiation from a

© 2004 NRC Canada

globar source was focused onto the electrode | electrolyte interface by passing through the back of the Si prism. The incident angle was typically 70° referred to the surface normal. The IR radiation totally reflected at the interface was measured with a liquid-nitrogen-cooled MCT detector (Model Colmar Technologies MCT 317). The spectroelectrochemical experiments were carried out under potential sweep or potential step conditions. In the potential sweep experiments (10 mV s^{-1}), the spectrometer was operated in the slow-scan mode. 160 sequentially acquired interferograms were co-added into each single beam spectrum. The potential step experiments were carried out either in the rapid-scan mode (28 ms time resolution, average of 256 traces) or in the step-scan regime (200 μs time resolution, 10 traces averaged, 1000 time slices). The spectra were plotted in absorbance units defined as $A = -\log (I/I_o)$, where I and I_o represent the intensities of the reflected radiation at the sample and the reference potentials, respectively. Positive (negative) going bands indicate accumulation (decay) of the species with respect to the reference.

Single crystal experiments

The ideal Au(111) or stepped Au(n n n-2) = Au [n(111)-110] electrodes were single crystal cylinders of 4 mm height and 4 mm diameter. The massive gold single crystals were flame-annealed in a butane flame at red heat and then cooled in high purity argon before immersion into ultrapure water. Contact with the electrolyte was established under potential control. A detailed description of the custom-made electrochemical setup being employed in these experiments was given in ref. 41.

In situ STM setup

The in situ STM experiments were carried out with a Molecular Imaging Pico-SPM on disc-shaped Au(111) massive single crystal electrodes in 0.1 mol L^{-1} $HClO_4$ or 0.1 mol L^{-1} H_2SO_4. The STM tips were electrochemically etched W tips (0.25 mm diameter), coated with polyethylene. Pt wires served as reference and counter electrodes. All STM images were recorded at room temperature in constant current mode with tunneling currents ranging between 3 and 200 pA.

Electrolyte solution

The solutions were prepared with Milli-Q water (18 MΩ cm, 1 to 2 ppb TOC), $HClO_4$ (suprapure, Merck), TMA (for synthesis, Lancaster, twice recrystallized in water), benzoic acid (standard for element analysis, Merck), and isophthalic acid (for synthesis, Merck, twice recystallized in water). All electrolytes (EC, SEIRAS) were deareated with argon before and during the experiments. The measurements were carried out at 20 ± 0.5 °C.

The glassware was cleaned either in a 1:1 mixture of hot H_2SO_4 and HNO_3, or by soaking in caroic acid, followed by rinsing cycles with Milli-Q water.

Results and discussions

Steady-state voltammetry

Figure 1*a* shows typical cyclic voltammograms of Au(111) in 0.1 mol L^{-1} $HClO_4$ solution in the absence (dotted) and in the presence (full, dashed curve) of 3 mmol L^{-1}

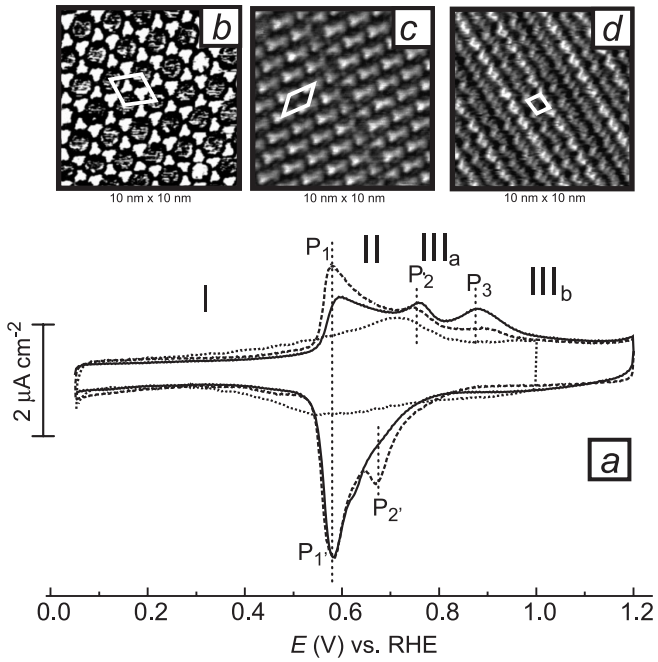


Fig. 1. (*a*) Cyclic voltammograms of an ideal Au(111) electrode (miscut angle <0.2°) in 3 mmol L^{-1} TMA – 0.1 mol L^{-1} $HClO_4$, scan rate of 10 mV s^{-1}. The solid curve represents the steady-state curve recorded after three complete potential cycles, the dashed curve was obtained after 10 min cycling from 0.85 to 1.20 V. The base electrolyte voltammogram is plotted as a dotted curve. The various adlayer regions are labeled I, II, III_a, and III_b. (*b*), (*c*), and (*d*) represent high-resolution, in situ STM images of the ordered phases recorded at 0.10, 0.70, and 1.0 V, respectively (42).

TMA. The experiment started with a thermally reconstructed Au(111) electrode immersed in the electrolyte at 0.30 V. The trace represented by the solid line was recorded after three subsequent cycles in the double layer region. The dashed curve was obtained after 10 min of cycling the potential from 0.85 to 1.20 V. Four characteristic potential regions (labeled I, II, III_a, and III_b), which are separated by the current peaks $P_1/P_{1'}$, $P_2/P_{2'}$, and P_3, can be readily distinguished. Based on previous in situ STM experiments, the following tentative assignment is suggested (28, 42): a physisorbed adlayer develops in region I during the positive potential scan, followed by a transition phase II ($E > P_1$ = 0.59 V), which transforms into a chemisorbed adlayer at $E >$ 0.76 V (P_2). The chemisorbed region III is further separated into III_a and III_b by a broad current peak P_3 ~0.88 V indicating a slow disorder–order transformation (42). Extended potential cycling in region III facilitates the formation of a long-range ordered chemisorbed adlayer. The subsequent dissolution upon a negative potential excursion gives rise to a characteristic cathodic current peak P_2'.

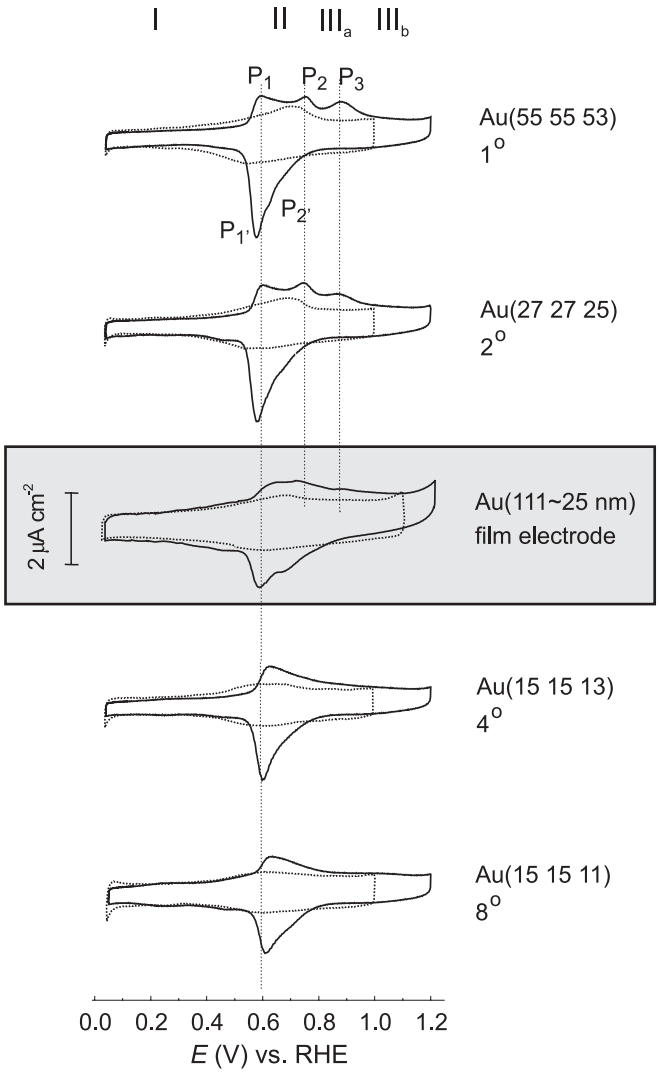
The in situ STM images in Figs. 1*b*–1*d* illustrate the molecular arrangements of TMA in the three ordered phases I, II, and III_b, respectively (42). Figure 1*b* shows the open honeycomb pattern of planar-oriented, physisorbed TMA molecules, which are connected by symmetrical hydrogen bonds between neighboring carboxyl groups (dimer motif). The rhombohedral unit cell with a = (1.65 ± 0.08) nm and α =

© 2004 NRC Canada

(60 ± 6)° contains two molecules, which gives rise to a coverage of Γ_{mI} = (1.4 ± 0.2) 10^{-10} mol cm^{-2} or an area per molecule of A_I = (1.18 ± 0.06) nm^2. Similar structures were reported previously under UHV conditions as well as in solution on HOPG, Cu(100), and Au(111) (25–28, 42). At higher electrode potentials, in region II (Fig. 1*c*), an assembly of physisorbed, quasi-linear rows is observed. Within the rows adjacent molecules appear to be connected by hydrogen bonds in an alternating arrangement of centrosymmetric and macrocyclic dimers (42). The unit cell, composed of two TMA molecules, is represented by a parallelogram with a = (1.47 ± 0.05) nm, b = (1.22 ± 0.20) nm, and α = (57 ± 5)°. The corresponding coverage and area per molecule are estimated to be Γ_{mII} = (2.2 ± 0.2) 10^{-10} mol cm^{-2} and A_{II} = (0.75 ± 0.05) nm^2 (42). At more positive electrode potentials, in region III_b, STM experiments revealed a close-packed, striped TMA phase with a suggested unit cell of a = (1.15 ± 0.05) nm, b = (0.95 ± 0.06) nm, α = (80 ± 5)°, Γ_{mIIIb} = (3.1 ± 0.2) 10^{-10} mol cm^{-2}, and A_{IIIb} = (0.54 ± 0.05) nm^2 (42). This tentative assignment is based only on the assumption that TMA molecules are perpendicularly adsorbed on the positively charged electrodes, similar to behaviour reported for other aromatic carboxylic acids (31–33, 35, 36, 38). A comprehensive structural analysis of the interfacial adlayer will be given in the following.

We also compared the voltammetric profiles of TMA on the Au(111-25 nm) film electrodes with the corresponding response obtained from a series of monatomically stepped single crystals Au[n(111)-110] for internal calibration. Figure 2 shows that, with higher step density, the characteristic phase transition peaks decrease in magnitude, broaden, and finally merge. These trends indicate the increasing disorder within the TMA adlayers. The cyclic voltammogram of an electrochemically annealed Au(111-25 nm) film electrode (shaded panel in Fig. 2) exhibits all the characteristic potential-dependent features of an Au(111)-oriented surface, except that the current peaks are broader than on an ideally smooth single crystalline electrode. The comparison demonstrates that the response of carefully prepared Au(111-25 nm) film electrodes is comparable to that of a stepped Au(111) electrode with an equivalent miscut angle ranging between 2° and 4°. Therefore, the film electrodes employed in the present ATR-SEIRAS study represent a rather good approximation to an ideal Au(111) single crystal electrode. Similar conclusions were also reported in our previous studies for sulfate and uracil on Au(111-20 nm) in aqueous electrolytes (39, 40).

Fig. 2. Steady-state cyclic voltammograms of a series of stepped single crystals Au(n n n-1) = Au[n(111)-(110)] in 0.1 mol L^{-1} $HClO_4$ without (dashed curves) and with (solid curves) 3 mmol L^{-1} TMA, scan rate 10 mV s^{-1}. The miscut angles are indicated in the figure. The shaded frame shows the corresponding cyclic voltammograms of an Au(111–25 nm) film electrode for comparison.



Steady-state ATR-SEIRAS

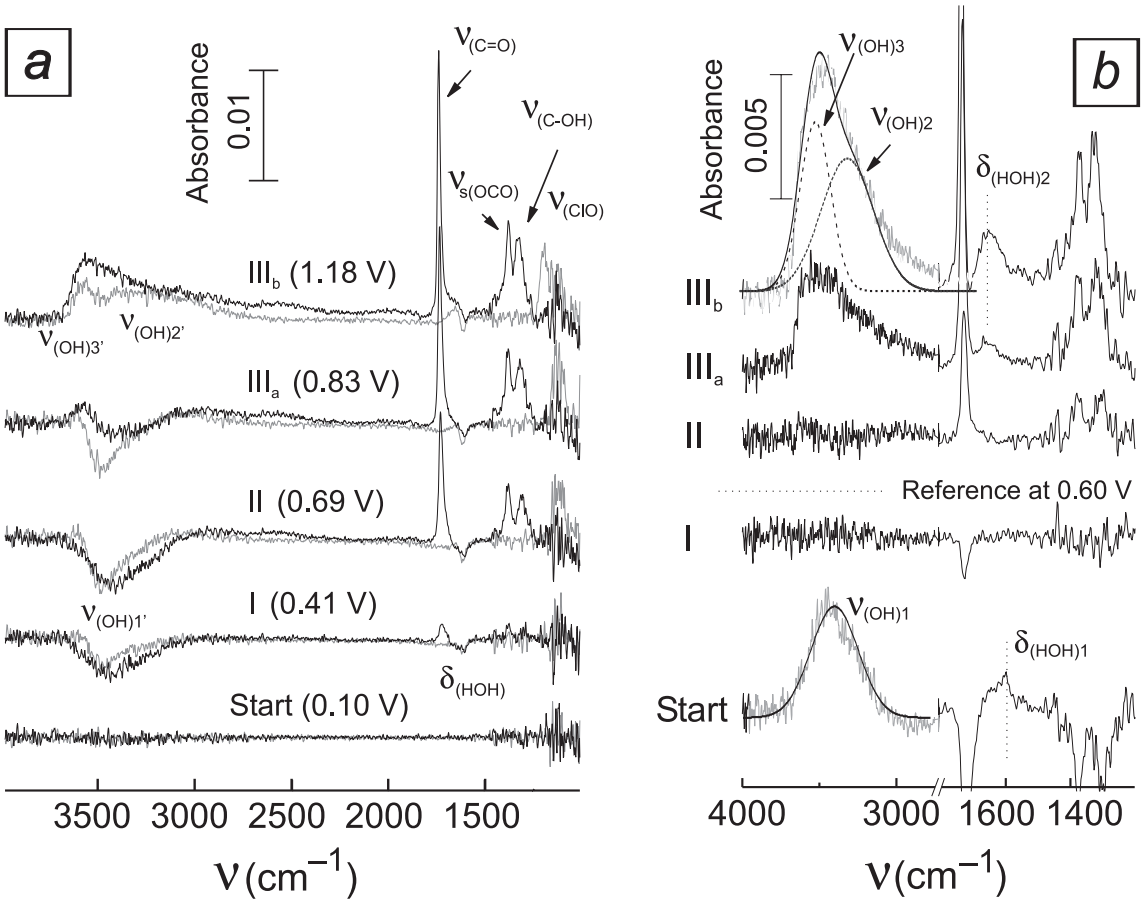
Overview and band assignments

Figure 3 shows selected slow-scan SEIRA spectra of 3 mmol L^{-1} TMA in 0.1 mol L^{-1} $HClO_4$ on Au(111-25 nm) acquired simultaneously with the potentiodynamic cyclic voltammogram (scan rate 10 mV s^{-1}). The corresponding data of the TMA-free "blank" electrolyte are also plotted as gray traces. Each set of spectra represents one of the characteristic adlayer phases (I, II, III_a, and III_b) aquired during a positive potential scan. A set of single beam spectra recorded at E = 0.10 V was chosen as the reference. For reasons of clarity, the continuous evolution of the spectral features during a complete potential cycle is shown separately in Fig. 4 for the two intervals 1200 < ν < 1800 cm^{-1} and 2750 < ν < 4000 cm^{-1}. The spectra in the OH-stretching region are plotted choosing either E = 0.10 V (Fig. 4*b*) or E = 0.60 V (Fig. 4*c*) as the reference.

As the potential increases from 0.10 V to more positive values, three sharp positive-going IR bands appear in the presence of 3 mmol L^{-1} TMA at 1720–1735 cm^{-1}, around 1375 cm^{-1}, and at 1300–1320 cm^{-1} (black traces in Fig. 3*a*). Comparison with the solid-state and solution spectra of BA, IA, and TMA as well as their potassium salts supports the assignment of these spectral features to the following TMA vibrations: the stretching mode of C=O in COOH ($\nu_{(C=O)}$), the symmetric stretching mode of O-C-O in COO^- ($\nu_{s(OCO)}$), e.g., a deprotonated carboxylate group, and the stretching mode of C-OH in COOH (ν(C-OH)), respectively (43, 44).

© 2004 NRC Canada

Fig. 3. (*a*) Selected SEIRA spectra of Au(111-25 nm) | 0.1 mol L^{-1} $HClO_4$ in the absence (gray traces) and in the presence of 3 mmol L^{-1} TMA (black traces) recorded simultaneously during a positive-going potential from 0.10 to 1.20 V, scan rate 10 mV s^{-1}. The background spectra were measured at 0.10 V. The data represent different potential regions of the various adlayer phases of TMA: Start (0.10 V), I (0.41 V), II (0.69 V), III_a (0.83 V), and III_b (1.18 V). (*b*) Selected SEIRA spectra of the characteristic potential regions, I, II, III_a, and III_b from 4000 to 2750 cm^{-1} and 1800 to 1200 cm^{-1} with the reference voltage chosen at E = 0.60 V. A typical result of the deconvolution of the OH-stretching region is illustrated in the top of panel (*b*).



A correlation analysis suggests that both sets of vibration modes originate from the same molecule. The intensities of these TMA bands increase with positive potential, reach their maximum in the chemisorbed region III, and decrease during the subsequent negative potential scan.

Simultaneously, broad IR bands are observed between 3000 and 3600 cm^{-1} corresponding to $\nu_{(OH)}$ stretching vibrations of interfacial water molecules (39, 45, 46). The potential-dependent evolution of the OH-stretching modes ($\nu_{(OH)}$) and of the HOH-bending mode ($\delta_{(HOH)}$) is plotted in Figs. 3 and 4. The reference spectrum was either recorded at E = 0.10 V (most negative potential) or at E = 0.60 V (close to the potential of zero charge for the present system). Qualitatively, the spectra in Figs. 3*a* and Fig. 4*b* illustrate that the intensity of a broad negative-going band centered around 3410 cm^{-1}, which starts to grow in phase I, reaches its maximum at 0.65 V. This band is labeled $\nu_{(OH)1}$, and corresponds to the replacement of weakly hydrogen-bonded interfacial water by physisorbed TMA molecules (40, 45). At more positive potentials, a new, positive-going water stretching mode centered at 3500 cm^{-1}, which is labeled $\nu_{(OH)2}$, starts to evolve. This vibration is attributed to water species coadsorbed with the chemisorbed TMA adlayer.

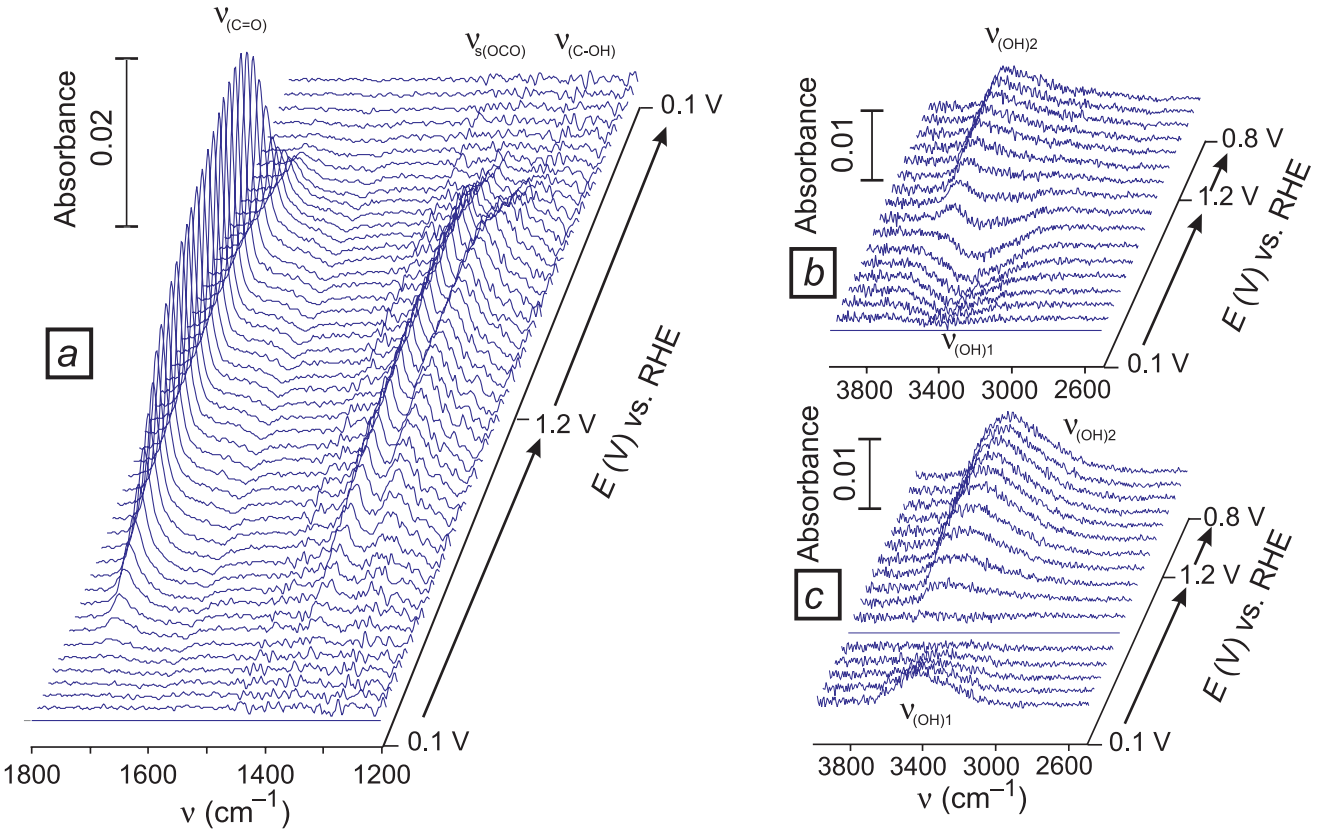
The SEIRA spectra of the supporting electrolyte (0.1 mol L^{-1} $HClO_4$, gray traces in Fig. 3*a*) show the existence of weakly hydrogen bonded water at $E < 0.60$ V as indicated by $\nu_{(OH)1'}$, a negative-going band centered around 3500 cm^{-1}. At $E > 0.60$ V, a broad positive-going $\nu_{(OH)2'}$ band centered at 3400 cm^{-1} starts to grow, followed at $E >$ 0.80 V by a rather sharp feature $\nu_{(OH)3'}$ with a center at 3600 cm^{-1}. The former is assigned to strongly hydrogen-bonded interfacial water while the later indicates the presence of non-hydrogen-bonded OH species caused by the onset of specific adsorption of the structure breaking perchlorate ion ($\nu_{(ClO)}$) at 1100–1130 cm^{-1} (45).

Local structure of chemisorbed TMA molecules

Both calculations and experimental evidence support that a deprotonated carboxylate group has a strong preference for the occupation of a bridge site with the carbon atom positioned midway between two neighboring metal atoms via chemical bonds including two oxygen atoms (47–49). At sufficient positive potentials, perpendicularly oriented TMA molecules could be chemisorbed onto the electrode surface via one or two deprotonated carboxylate groups (26, 28, 50). To resolve the issue on surface coordination, we carried out

© 2004 NRC Canada

Fig. 4. Typical set of 3D SEIRA spectra measured simultaneously with a slow-scan voltammogram (10 mV s^{-1}) during a potential cycle from E = 0.10 to E = 1.20 V and back to E = 0.10 V. Each spectrum represents the average of 160 single traces within a potential interval of 50 mV. (*a*) Shows the wavenumber region from 1800 to 1200 cm^{-1} with a single beam at 0.10 V as the reference; (*b*) and (*c*) represent the $\nu_{(OH)}$ region from 4000 to 2750 cm^{-1} choosing the reference spectra at E = 0.10 V (*b*) and E = 0.60 V (*c*), respectively. For clarity, the spectra in panels (*b*) and (*c*) do not show the complete sets of data for the negative-going potential cycle.



a comparative study with BA, IA, and TMA in the high coverage region III. These carboxylic acids have different numbers of identical carboxyl groups but similar conjugated structures. Figure 5 shows SEIRA equilibrium spectra of the three molecules at E = 1.1 V, as recorded during slow potential scanning experiments. The symmetric mode $\nu_{s(OCO)}$ at 1370–1390 cm^{-1} (FWHM ~ 2 cm^{-1}) was observed in all three spectra (labeled as A_3, B_3, and C_3 in Fig. 5), indicating that these three acids are coordinated to the positively charged electrode by at least one deprotonated carboxylate group. The spectrum of IA shows the $\nu_{s(OCO)}$ mode (B_3) and two additional vibrations, $\nu_{(C=O)}$ at 1715 cm^{-1} (B_1) and $\nu_{s(COOH)}$ at 1290 cm^{-1} (B_2), which originate from a protonated -COOH group. This signature indicates that IA is coordinated to the electrode surface with one carboxylate group, while the other (protonated) carboxyl group faces the electrolyte.

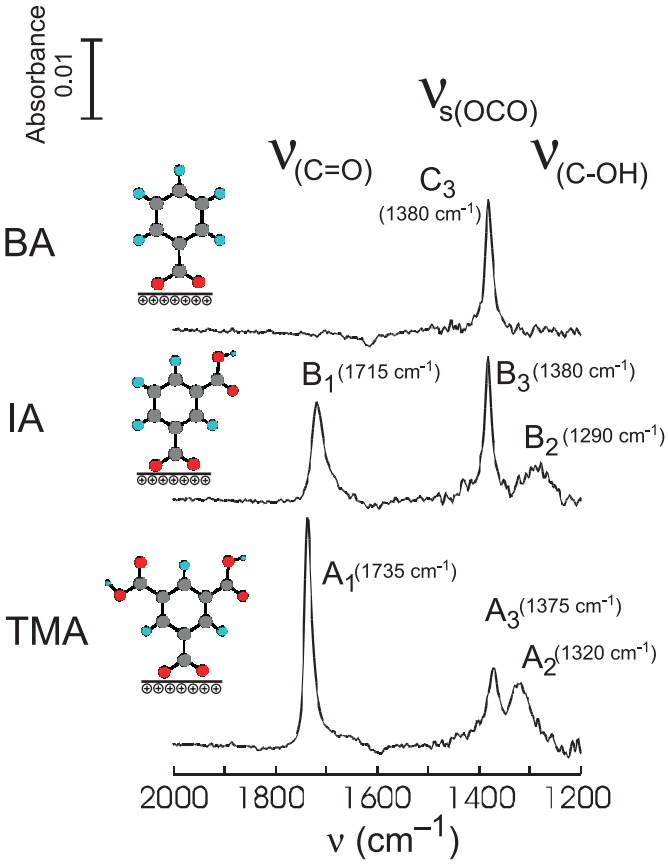
One may assume that position and surface coordination of carboxylate and carboxyl groups should be constant after adsorption equilibrium has been established. Therefore, we can conclude from the approximately identical ratio of the integrated intensities $I_{B1}/I_{B2} \approx I_{A1}/I_{A2} \approx 1.40$ that the chemisorbed adlayers of IA and TMA exhibit structural similarities. With I_{A3} and I_{B3} as an internal standard, one obtains $I_{A1}/I_{A3} \approx 2 \times I_{B1}/I_{B3}$ indicating that the TMA adlayer exhibits two protonated -COOH groups while IA has only one. This quantitative estimation also implies that both acids are coordinated via one carboxylate group to the positively charged electrode in the chemisorbed phase under equilibrium conditions.

Adlayer structure

The slow-scan SEIRA spectra plotted in Fig. 4 indicate that the adsorption and surface orientation of TMA are potential dependent and major changes occur upon the transition from physisorption to chemisorption. Based on the surface selection rule of SEIRAS, only those molecular vibrations that induce dipole moments normal to the local surface give enhanced IR absorption (29, 30). No vibration modes related to TMA adsorption were observed at E < 0.35 V. The absence of the characteristic TMA bands $\nu_{(C=O)}$, $\nu_{s(OCO)}$, and $\nu_{(C-OH)}$, which induce dipole moments parallel to the plane of the phenyl ring, indicates that TMA molecules are oriented with the phenyl ring parallel to the electrode surface. Locally, the organic molecules appear to change their orientation at E > 0.35 V. To describe this structural transition in detail, we plotted in Fig. 6 the potential dependence of intensity, peak position, and full-width at half maximum (FWHM) of $\nu_{(C=O)}$, $\nu_{s(OCO)}$, and $\nu_{(C-OH)}$. These three characteristic IR bands are related to the -COOH side groups ($\nu_{(C=O)}$ and $\nu_{(C-OH)}$) and to the coordinating carboxylate group ($\nu_{s(OCO)}$), respectively.

© 2004 NRC Canada

Fig. 5. Equilibrium SEIRA spectra of TMA (3 mmol L^{-1}), isophthalic acid (IA, saturated solution), and benzoic acid (BA, 3 mmol L^{-1}) in 0.1 mol L^{-1} $HClO_4$ obtained at 1.10 V in region III_b, reference spectrum taken at E = 0.10 V. The inset illustrates the derived molecular orientations of the three molecules chemisorbed on a positively charged Au(111-25 nm) film electrode.



$\nu_{(C=O)}$ *and* $\nu_{(C\text{-}OH)}$

The intensities of $\nu_{(C=O)}$ and $\nu_{(C\text{-}OH)}$ are directly influenced by the TMA orientation and the number of uncoordinated -COOH side groups. The rapid intensity increase upon changing the potential from region I to region II indicates the onset of an orientation change from planar to tilted or perpendicular. The intensity of $\nu_{(C=O)}$ and $\nu_{(C\text{-}OH)}$ increases only moderately in region III_a and reaches a plateau in region III_b, indicating the formation of a stable chemisorbed adlayer III_b. Reversing the direction of the potential scan exhibits a distinct hysteresis in $1.00 > E > 0.40$ V, which suggests a rather slow structural transition in this potential range. We notice further that in situ STM experiments of TMA on ideally smooth Au(111) single crystal electrodes show long-range ordered physisorbed adlayers of hydrogen-bonded and still planar-oriented molecules in region II (e.g., up to $E \sim 0.80$ V) (42). The more negative onset of the structural transition of TMA on the Au(111-25 nm) electrodes is most probably related to the surface morphology of the gold film. The latter is composed of 20–30 nm size, interconnected islands with a preferential (111) surface orientation, which have inherently a higher defect density and larger grain boundaries than an ideal Au(111) single crystal surface (39). In consequence, the molecular film appears to be more disordered in the physisorbed regions I and II, and the uneven potential distribution near defect sites might facilitate localized orientation changes at lower potentials, as observed in the in situ ATR-SEIRA spectra.

Both bands ($\nu_{(C=O)}$ and $\nu_{(C\text{-}OH)}$) shift to higher wavenumbers with increasing electrode potential. A plateau is reached after establishing an equilibrated chemisorbed phase in III, the most pronounced change occurs in region II. This evolution is reversible, but shows a distinct hysteresis. Potential-dependent peak shifts of vibration modes may be attributed to three different factors: Stark tuning effect, metal–adsorbate electron back donation, and lateral interactions such as dipole–dipole coupling (51, 52). There is no strong experimental evidence for a predominant Stark tuning effect because the potential-dependent peak shifts are not as linear as expected (40, 51), and the electric field around the -COOH side groups is rather weak. Peak shifts preferentially attributed to strong dipole–dipole coupling have been suggested for the adsorption of several organic molecules capable of forming close-packed adlayers, such as cytosine (53), 4,4′-bipyridine (54), BA (31, 32), and uracil (40). For the present system, the ladder-type network of chemisorbed TMA appears to be still too open to support strong interactions between the oscillating dipoles of adjacent -COOH groups. Although a direct substrate | -COOH side group electron donation can be ruled out, an indirect electron transfer via the π-electron system of TMA appears to be possible. The molecule represents a perfectly conjugated system. In consequence, changes in the electron (charge) density in one -COOH group can be partly "transferred" to the other two -COOH or $-COO^-$ groups, respectively. An electron back donation to the coordinating carboxylate group at positive potentials may generate a simultaneous electron donation to both -COOH side groups, which results in a shift of $\nu_{(C=O)}$ and $\nu_{(C\text{-}OH)}$ to higher wavenumbers. A similar blue shift of the $\nu_{(C=O)}$ and $\nu_{(C\text{-}OH)}$ bands is observed in the potential-dependent SEIRA spectra of IA. An additional contribution to the observed blue shift in phase III could be induced due to directional hydrogen bonding between the -COOH side groups, which should increase the stretching constant of the in-phase $\nu_{(C=O)}$ and $\nu_{(C\text{-}OH)}$ vibrations. Table 1 compares the peak shifts $\Delta\nu$ for the characteristic vibrations of BA, IA, and TMA. The smaller values of $\Delta\nu$ of the $\nu_{(C=O)}$ and $\nu_{(C\text{-}OH)}$ vibrations of IA could be attributed to the weaker hydrogen-bonding interactions when compared to TMA.

Simultaneously, the FWHM of $\nu_{(C=O)}$ and $\nu_{(C\text{-}OH)}$ decrease from phase I to III_b, and reaches a minimum in the potential region III. This trend suggests an increasing long-range lateral order with the establishment of the chemisorbed phase III_b. The present SEIRAS experiment demonstrates, in combination with an in situ STM study (42), that TMA molecules form a highly ordered two-dimensional ladder network. The molecules are coordinated via one $-COO^-$ group to the electrode surface, while the two remaining -COOH side groups give rise to rows of hydrogen-bonded dimers (42).

$\nu_{s(OCO)}$

The three carboxyl groups of TMA are protonated in 0.1 mol L^{-1} $HClO_4$ (pH = 1 and pK_a = 2.12, 4.10, and 5.18, respectively (55)). The $\nu_{s(OCO)}$ vibration appears only when TMA molecules are deprotonated and chemisorbed onto the

© 2004 NRC Canada

Fig. 6. Potential dependencies of integrated intensity (■, □), peak position (●, ○), and the FWHM (▲, △) of the $\nu_{(C=O)}$ (~1725 cm^{-1}), $\nu_{s(OCO)}$ (~1375 cm^{-1}), and $\nu_{s(C\text{-}OH)}$ (~1315 cm^{-1}) bands of TMA as obtained from the data plotted in Figs. 3 and 4. The solid (open) symbols represent the positive- (negative-) going potential scan.

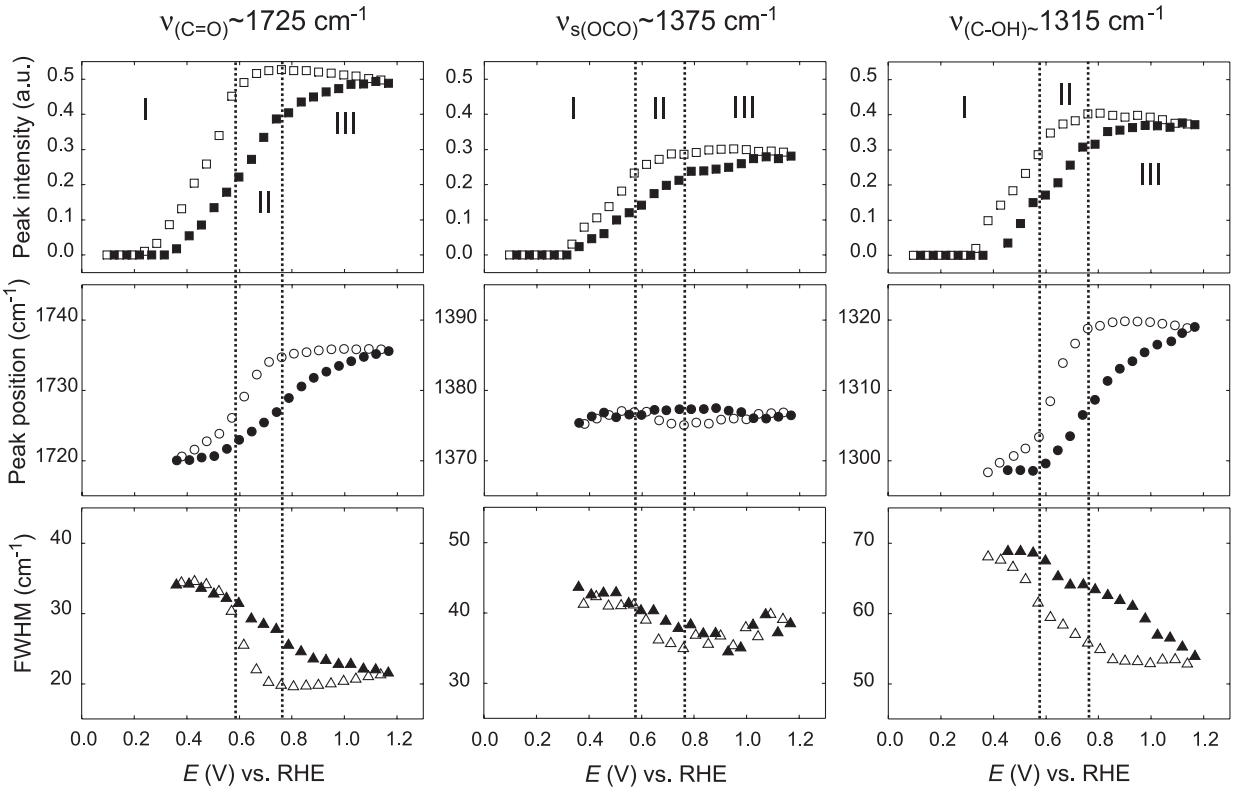


Table 1. Peak shift value of different carboxylic acids.

Carboxylic acid	$\Delta\nu_{s(OCO)}$ (cm^{-1})	$\Delta\nu_{a(C=O)}$ (cm^{-1})	$\Delta\nu_{(C\text{-}OH)}$ (cm^{-1})	Γ_m (10^{-10} mol cm^{-2})
Fumaric acid (38)	16	—	—	4.0 (38)
Benzoic acid (31)	15	—	—	7.3 (32)
				7.2[a]
Isophthalic acid	8	11	14	—
Trimesic acid	~0	15	20	3.3

Note: Δν values were calculated from the subtraction of spectra at 0.64 and 1.18 V.

[a]Z. Li and Th. Wandlowski. Unpublished. 2004.

surface via one carboxylate group. Similar $\nu_{s(OCO)}$ vibrational bands were observed for chemisorbed benzoic acid (31, 32, 36, 47), fumaric acid (35), fluorobenzoic acid (33), and *p*-nitrobenzoic acid (35) on various gold electrodes.

As illustrated in Fig. 6, the plot of the intensity of $\nu_{s(OCO)}$ shows a similar potential dependence as $\nu_{(C=O)}$ and $\nu_{(C\text{-}OH)}$: It grows slowly with increasing potential in phase I, and reaches a constant value in phase III_b. This intensity increase in region II suggests deprotonation and a change in molecular orientation. Similar trends were observed for benzoic acid on Au(111) (31, 32).

The frequency of the $\nu_{s(OCO)}$ band is almost potential independent. We notice that $\nu_{s(OCO)}$ shows a strong potential dependence and a characteristic blue shift with Δν up to 16 cm^{-1} for closely packed carboxylic acids such as BA (31, 32) and fumaric acid (38). This observation was attributed to strong dipole–dipole coupling at high surface coverages. STM experiments (Fig. 1*d*) (42) revealed that the packing of TMA in the chemisorbed phase III appears to be less compact resulting in rather large distances between the oscillating dipoles of neighboring carboxylate groups. Table 1 illustrates that Δν changes in the following sequence: fumaric acid > BA > IA > TMA. One also needs to consider a strong adsorbate substrate interaction between the surface-coordinated carboxylate group and the positively charged gold electrode, which should result in a red shift of $\nu_{s(OCO)}$. This trend appears to be compensated by a Stark shift in the opposite direction.

Interfacial water

The high sensitivity of ATR-SEIRAS enables us to monitor structural properties of electrolyte species in the electrochemical double layer associated with the adsorption of TMA (39, 40, 45, 46). Figures 3 and 4 demonstrate the strong potential-dependence of the vibrational signatures of interfacial water species.

© 2004 NRC Canada

As discussed in the Overview and band assignements section, the overlap of positive- and negative-going OH-stretching modes ($\nu_{(OH)}$) complicates the analysis. To deconvolute the contributions of different interfacial water species, we adapted a strategy proposed in ref. 45 and have chosen the spectrum at $E = 0.60$ V, which is close to the potential of zero charge for the present system, as the new reference spectrum. The recalculated spectra are plotted in Figs. 3*b* and 4*c*. At $E < 0.60$ V, a broad band ($\nu_{(OH)1}$) centered at 3410 cm^{-1} and a weak band ($\delta_{(HOH)1}$) at 1600 cm^{-1} are observed. The shape of the $\nu_{(OH)1}$ band is rather symmetric, suggesting the preference of only one type of water species. At more positive potentials, in regions II and III, an asymmetric band with a distinct shoulder at higher wavenumber evolves. The deconvolution allows the identification of two contributions: one broad band ($\nu_{(OH)2}$) centered at 3320 cm^{-1} and a sharper band ($\nu_{(OH)3}$) around 3520 cm^{-1} (Fig. 3*b*). The stretching mode ($\nu_{(OH)2}$) as well as a weak bending mode ($\delta_{(HOH)2}$) at 1650 cm^{-1}, indicate the existence of strongly H-bonded water species in phase III_b.

Based on the above analysis, at least three different co-adsorbed water species appear during a slow scan from negative to positive potentials accompanied with the formation of the various TMA adlayers. Figure 7 shows the potential-dependence of peak intensity, peak position, and FWHM of the OH-stretching modes $\nu_{(OH)1}$, $\nu_{(OH)2}$, and $\nu_{(OH)3}$. $\nu_{(OH)1}$ corresponds to weakly hydrogen-bonded water species that are adsorbed on the surface at negative charge densities and in the absence of TMA. They are subsequently replaced by physisorbed TMA molecules in phase I giving rise to a decreasing spectroscopic feature. $\nu_{(OH)2}$ and $\nu_{(OH)3}$ start to grow in phase III_a simultaneously with the physisorption | chemisorption transition and the formation of a chemisorbed TMA adlayer, indicating that interfacial water is co-adsorbed within or next to the ordered TMA adlayer. Their intensities increase until a maximum is reached in the potential regions of an equilibrium phase III_b, and subsequently decrease upon the onset of TMA desorption. Weakly hydrogen-bonded water appears again as indicated by an increase of the intensity of $\nu_{(OH)1}$ in phase I at negative charge densities.

Additional knowledge has been obtained from the potential-dependence of the respective peak positions. The vibration mode indicating strongly hydrogen-bonded water ($\nu_{(OH)2}$) appears in region III_a and shifts to a higher wavenumber ($\Delta\nu \approx 50$ cm^{-1}) with increasing potential. Such water molecules could be hydrogen-bonded to the oxygen atoms of the -COOH side groups of TMA, which are directed toward the electrolyte. The small blue shift shows that the hydrogen-bonding interaction between interfacial water and the -COOH groups is weakened upon the formation of the long-range ordered ladder network between adjacent TMA molecules in III_b. Simultaneously, the FWHM of $\nu_{(OH)2}$ decreases in phase III_a and reaches a minimum in phase III_b.

Compared to $\nu_{(OH)2}$, $\nu_{(OH)3}$ is less synchronized with the formation | dissolution of the chemisorbed TMA adlayer. Peak position and FWHM are almost potential-independent. The integrated intensity of $\nu_{(OH)3}$ increases towards phase III_b. The high wavenumbers and narrow bands suggest attributing $\nu_{(OH)3}$ to weakly hydrogen-bonded or isolated water species next to the chemisorbed TMA adlayer and (or) at defect sites not being in direct contact with the electrode surface. The location of these water species appears to be different from those discussed for blank supporting electrolytes such as $HClO_4$ (45), where a direct contact to the electrode surface is proposed.

Fig. 7. Potential dependencies of integrated intensity, peak position, and FWHM of the OH-stretching modes for 3 mmol L^{-1} TMA – 0.1 mol L^{-1} $HClO_4$ on Au(111-25 nm) film electrodes: $\nu_{(OH)1}$ (■, □), $\nu_{(OH)2}$ (●, ○), and $\nu_{(OH)3}$ (▲, △) as obtained from the data plotted in Figs. 3 and 4. The solid (open) symbols represent the positive- (negative-) going potential scan.

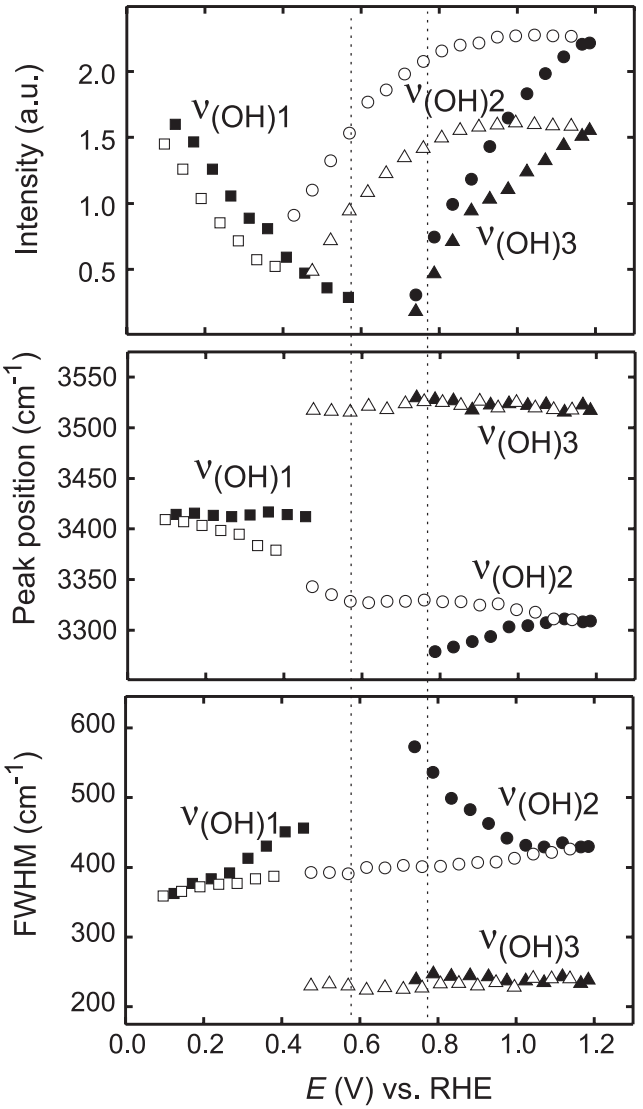


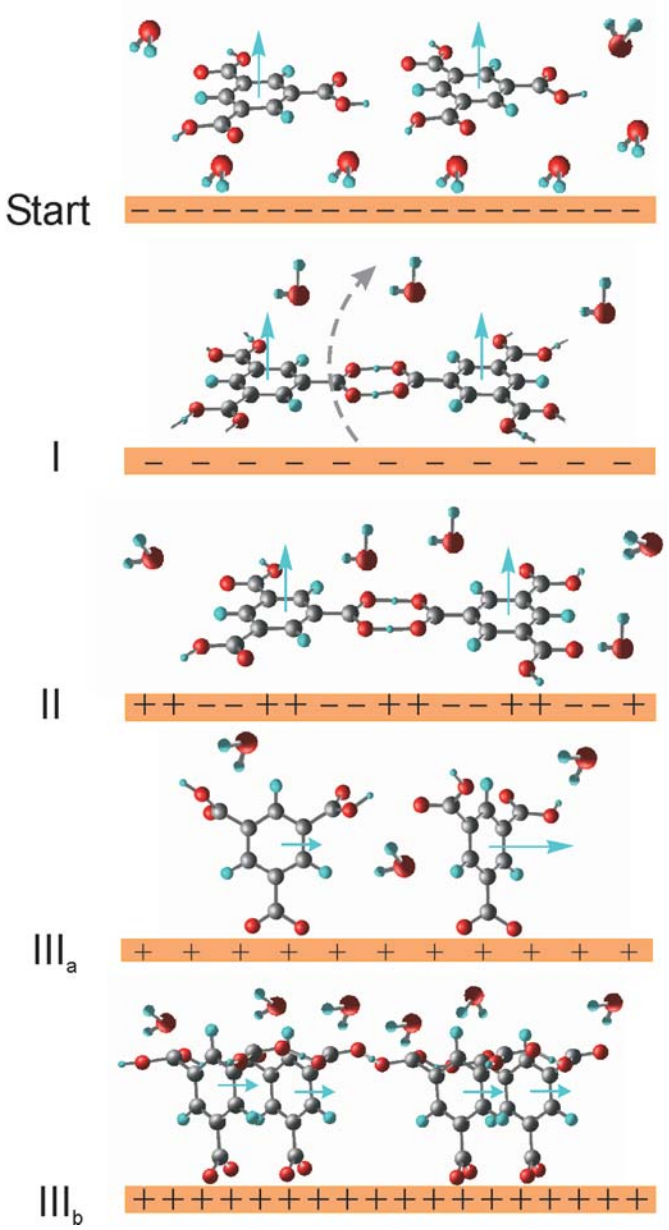
Figure 8 summarizes schematically the potential-dependent evolution of the TMA adlayer structures on Au(111-25 nm) film electrodes in contact with 0.1 mol L^{-1} $HClO_4$ aqueous electrolyte.

2D phase formation kinetics

After the discussion of the potential-dependent, steady-state TMA adlayer structures, we focus next on the kinetics of structural transitions between the different adlayer phases. Data acquisition modes such as rapid-scan and step-scan enable us to study potential-induced structural changes with high time resolution. Potential steps from the physisorbed

© 2004 NRC Canada

Fig. 8. Model of steady-state TMA adlayer structures in the potential regions I, II, III_a, and III_b.

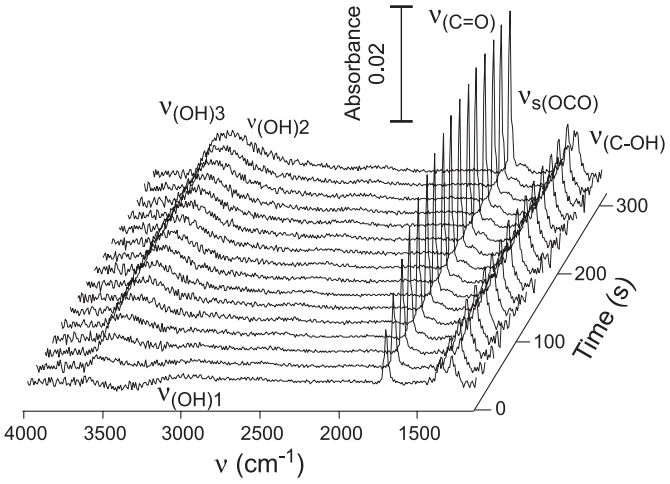


phase I into the chemisorbed phase III_b were applied to monitor the formation kinetics of the chemisorbed TMA adlayer. The corresponding current transients are recorded simultaneously. We have chosen the following regime: E_i = 0.45 V (10 s) → E_f = 0.90 V for rapid-scan experiments and E_i = 0.50 (250 ms) → E_f = 0.90 V for the step-scan studies. The reference spectra were measured at each starting potential before stepping the potential.

Rapid scan

Figure 9 shows selected SEIRAS spectra recorded in rapid-scan mode for a single potential step from E_i = 0.45 (10 s) to E_f = 0.90 V. The three characteristic bands of chemisorbed TMA start to grow immediately after the potential step, indicating an orientation change from planar to perpendicular within << 5 s. Subsequently, these bands become gradually stronger and sharper until a maximum is reached, suggesting a rather slow increase of surface coverage and two-dimensional long-range order in region III_b. The time dependencies of intensity, peak position, and FWHM are plotted in Fig. 10. The evolution of the simultaneously co-adsorbed water species is shown in Fig. 11.

Fig. 9. Time-resolved SEIRA spectra for the formation of a chemisorbed TMA adlayer III_b on Au(111-25 nm) – 0.1 mol L^{-1} $HClO_4$ + 3 mmol L^{-1} TMA, recorded in a rapid-scan regime after a single potential step from E_i = 0.45 to E_f = 0.90 V. The waiting time at E_i was 10 s. Each spectrum plotted was acquired in intervals of 9.7 s and represents the average of 256 individual traces.



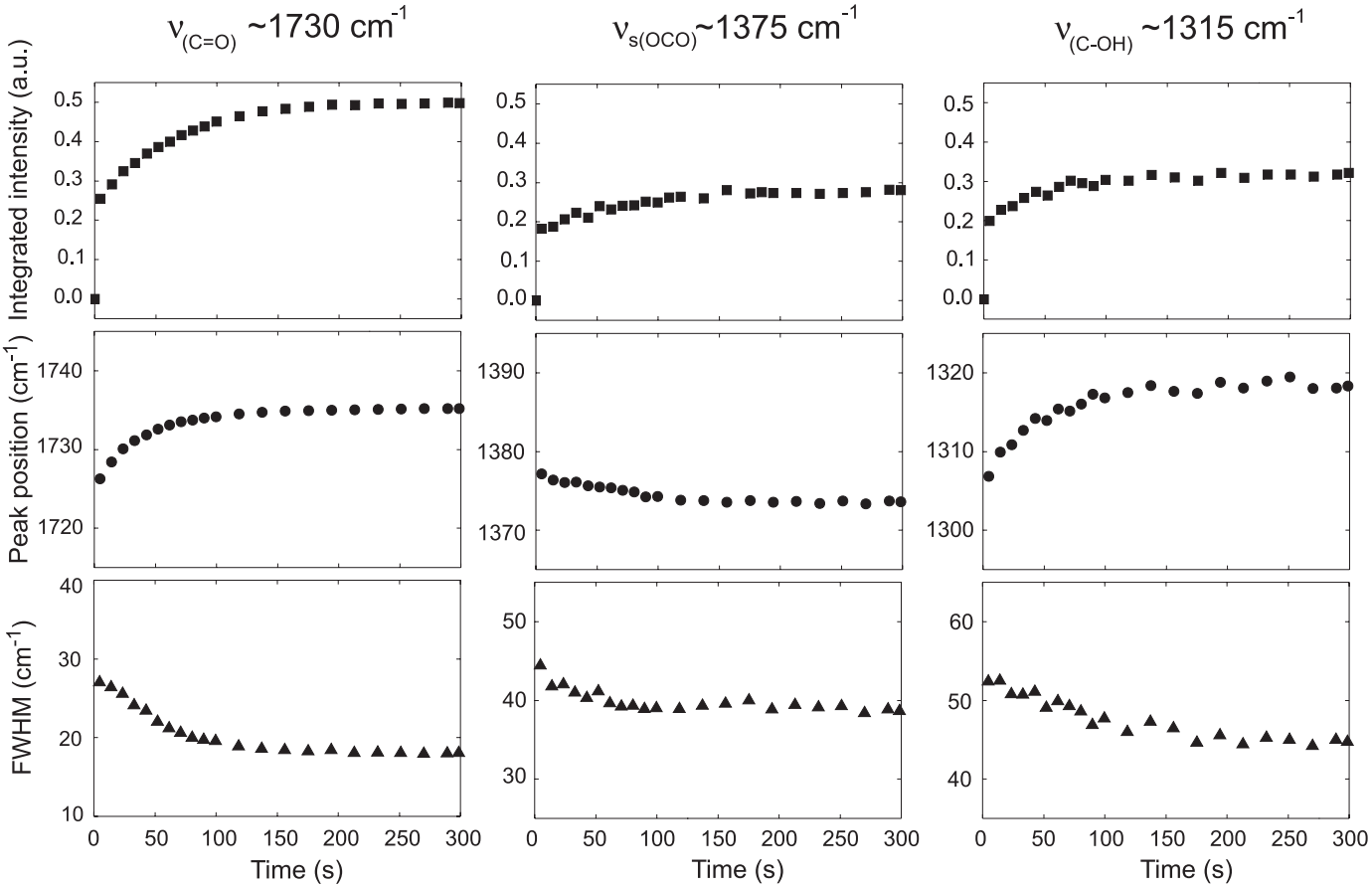
The intensities of $\nu_{(C=O)}$, $\nu_{s(OCO)}$, and $\nu_{(C\text{-}OH)}$ indicate that a final steady state is reached approximately 150 s after triggering the potential step. The lateral alignment of TMA to establish the long-range ordered, hydrogen-bonded, and surface-coordinated molecular network is rather slow, which is consistent with the result of our recent in situ STM measurements (42). Further insight into the kinetics of ordering can be provided by the analysis of the time dependencies of the FWHM and the peak positions of the TMA modes, as well as of the structural feature of co-adsorbed water.

The FWHM values of $\nu_{(C=O)}$, $\nu_{s(OCO)}$, and $\nu_{(C\text{-}OH)}$ decrease with time and reach a steady state after 150 s, indicating the formation of a long-range ordered adlayer (Fig. 10). The simultaneously recorded time dependencies of the peak positions of $\nu_{(C=O)}$ and $\nu_{(C\text{-}OH)}$ exhibit a slow shift to higher wavenumbers ($\Delta\nu$ ~ 10 cm^{-1}). This is partly due to the increasing lateral interactions as a result of directional hydrogen bonds formed between neighboring TMA molecules. The electron donation may also contribute to the blue shift representing an increase of substrate | adsorbate interactions upon the formation of a long-range ordered adlayer at the positively charged electrode surface.

Compared with the blue shift of $\nu_{(C=O)}$ and $\nu_{(C\text{-}OH)}$, the $\nu_{s(OCO)}$ band shifts to lower wavenumbers ($\Delta\nu \approx 5$ cm^{-1}) reaching a constant position at 1373 cm^{-1}. As described in the Overview and band assignments section, $\nu_{s(OCO)}$ is related to carboxylate co-ordinated in a perpendicular position to the positively charged electrode surface. The red shift of the $\nu_{s(OCO)}$ band can be attributed to the increase of electron back-donation when the substrate | adlayer interaction increases with surface order.

© 2004 NRC Canada

Fig. 10. Time dependence of integrated intensity (■), peak position (●), and FWHM (▲) of the ν(C=O) (~1730 cm^{-1}), $\nu_{s(OCO)}$ (~1375 cm^{-1}), and $\nu_{s(C\text{-}OH)}$ (~1315 cm^{-1}) bands of TMA as obtained from the data plotted in Fig. 9.



The appearance of the negative going band $\nu_{(OH)1}$, immediately after application of the potential step (<< 5 s, Fig. 9), represents the displacement of weakly hydrogen-bonded water molecules from the electrode surface by additionally adsorbed TMA. Its intensity is small because the experiment starts from a rather positive potential with a significant amount of TMA adsorbed in a planar orientation. The intensities of $\nu_{(OH)2}$ and $\nu_{(OH)3}$ increase simultaneously with the evolution of the characteristic bands for perpendicularly adsorbed TMA (Fig. 10) indicating co-adsorption with the organic molecules in phase III_b. Interestingly, the peak position and FWHM of the $\nu_{(OH)3}$ band reach steady state values somewhat faster (~100 s) than the $\nu_{(OH)2}$ band (~150 s). Such a delay between $\nu_{(OH)2}$ and $\nu_{(OH)3}$ shows that the isolated water species are co-adsorbed with the TMA adlayer before the equilibrated ordered TMA structure is formed, while the strongly hydrogen-bonded water forms simultaneously with the ordered TMA structure.

Step scan

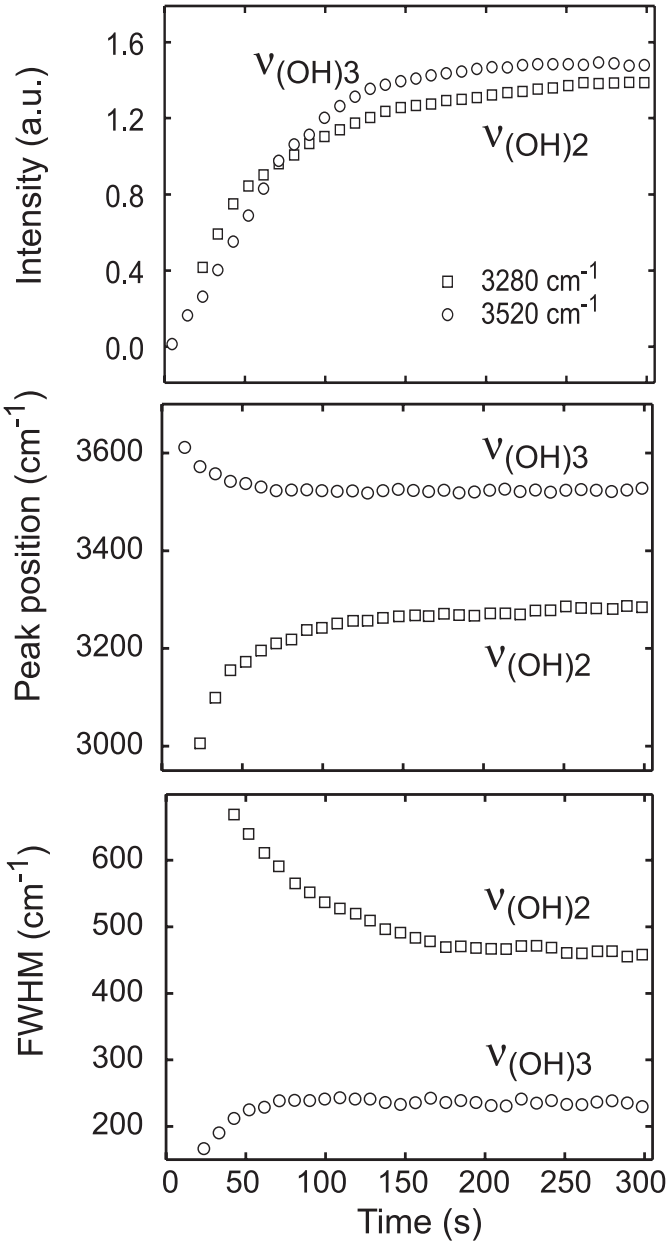
To explore the kinetics of the structural transition within the TMA adlayer when stepping the potential from E_i = 0.50 to E_f = 0.90 V at very short times, we carried out simultaneous electrochemical and spectroscopic step-scan experiments. This regime enables us to increase the time resolution with our current setup to 10^{-5} s. Figure 12*a* shows a 3D plot for the evolution of the TMA marker band $\nu_{(C=O)}$ after application of a single potential step from E_i = 0.50 to E_f = 0.90 V. The time dependence of the integrated intensity of the $\nu_{(C=O)}$ TMA marker band, as calculated from time slices of 0.2 ms, is plotted in Fig. 12*b*. A similar time dependence was observed for $\nu_{s(OCO)}$ and $\nu_{(C\text{-}OH)}$. For clarity, we plotted as an inset of Fig. 12*a* only one typical spectrum recorded after 8 ms in $1200 < \nu < 1800$ cm^{-1}.

The electrochemical current transient, as monitored after the potential step, is characterized by a single exponential decay (cf. solid line in Fig. 12*b*). This macroscopic response may contain several different contributions such as double layer charging, deprotonation of -COOH groups, reorientation of the organic molecule, and (or) co-adsorbed water species. However, the chronoamperometric experiment does not provide direct information on structural changes within the adlayer. To address this issue we carried out electrochemical measurements with synchronized step-scan SEIRAS experiments.

Figure 12*b* demonstrates that the intensity of the $\nu_{(C=O)}$ mode increases rapidly and reaches its maximum after 8 ms, which is much longer than the time constant of our IR cell (ca. 50 μs (39)). This result suggests a fast orientation change of TMA from planar to randomly oriented perpendicular molecules. The simultaneous evolution of $\nu_{s(OCO)}$ also indicates the deprotonation of the carboxyl group. The observed transition is significantly faster than the establishment of a two-dimensional order within the organic adlayer. The

© 2004 NRC Canada

Fig. 11. Time dependence of integrated intensity, peak position, and FWHM of the OH-stretching modes $\nu_{(OH)2}$ (□) and $\nu_{(OH)3}$ (○) of co-adsorbed water species as obtained from the rapid-scan spectra plotted in Fig. 9 after deconvolution.

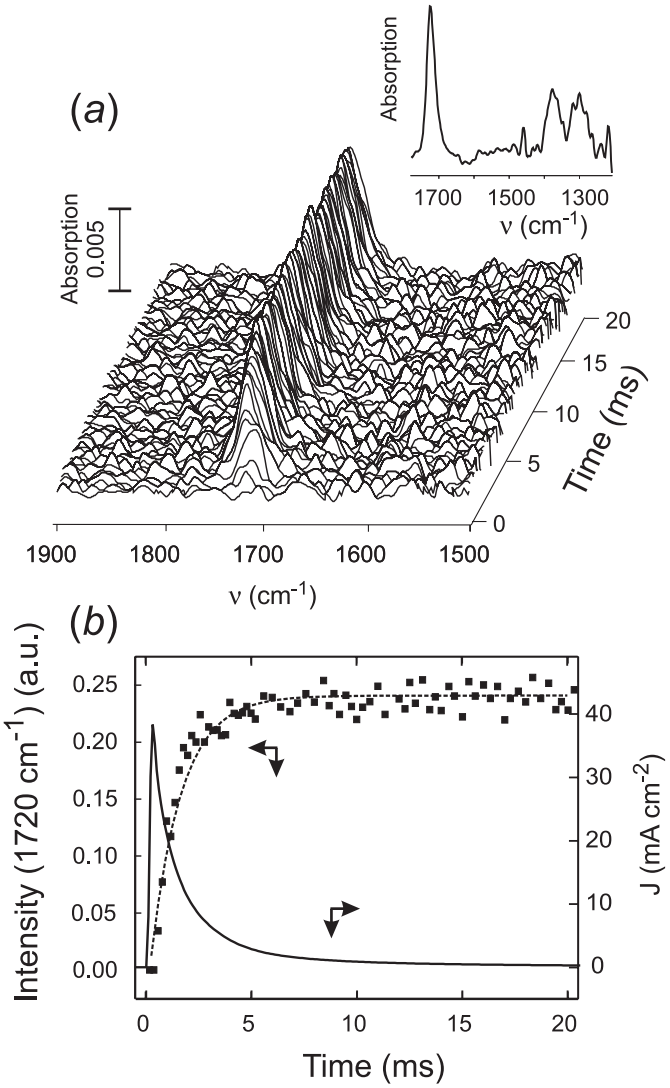


intensity vs. time curve in Fig. 12*b* is represented by a first-order, Langmuir-type rate equation

$$[1] \qquad I = I_\infty \{1 - \exp[-K(t - t_0)]\}$$

with I_∞ as the integrated intensity at $t \to \infty$, K is the rate coefficient, and t_0 an induction time (dotted line in Fig. 12*b*). The model suggests that the reorientation of TMA molecules is initialized at randomly distributed defect sites, and no long-range order of the chemisorbed TMA phase is established within the short time scale of 20 ms. Similar transitions were reported previously in kinetic SEIRAS studies with fumaric acid (38), which give rises to a completely disordered adlayer, and for *p*-nitrobenzoic acid on Au(111-20 nm) film electrodes (35).

Fig. 12. (*a*) Series of time-dependent SEIRAS spectra for the formation of a chemisorbed TMA adlayer on Au(111-25 nm) in 0.1 mol L^{-1} $HClO_4$ + 3 mmol L^{-1} TMA after a single potential step from E_i = 0.50 (t_w = 0.25 s) to E_f = 0.90 V as measured in the step-scan regime. The inset shows a typical extended spectrum recorded after 8 ms in 1200 < ν < 1800 cm^{-1}. (*b*) Time dependence of the integrated intensity of the TMA marker band $\nu_{(C=O)}$ (■) as calculated from the spectra shown in panel (*a*). The dotted line represents the fit of eq. [1] to the spectroelectrochemical transients with the following parameters: I_∞ = 0.237, K = 0.686 ms^{-1}, t_0 = 0 ms. The experimental time resolution is 200 μs. The simultaneously measured current transient is shown as a solid curve.



Such a two-step scenario and the disorder | order evolution of chemisorbed TMA are consistent with our STM results (42).

Summary and conclusions

We have investigated the adsorption and phase formation of TMA on Au(111) single crystal and Au(111-25 nm) film electrodes in 0.1 mol L^{-1} $HClO_4$ by combining in situ ATR-SEIRAS with simultaneous electrochemical experiments.

© 2004 NRC Canada

At 0.10 V (starting potential), TMA molecules are randomly adsorbed on the negatively charged gold surface in a planar orientation together with weakly hydrogen-bonded interfacial water molecules. In phase I, $0.10 < E < 0.50$ V, planar-oriented TMA molecules form a two-dimensionally ordered physisorbed adlayer. STM experiments show that the TMA molecules are interconnected by centrosymmetric hydrogen bonds giving rise to a honeycomb network of open rings. Weakly hydrogen-bonded water species are displaced by the organic molecules. At more positive potentials, but still in phase I ($E > 0.30$ V), TMA molecules at grain boundaries and defect sites start to tilt and break apart the long-range, hydrogen-bonded network. At higher potentials, in $0.58 < E < 0.75$ V (phase II), a close-packed physisorbed adlayer composed of linear dimers forms slowly, but only on ideally smooth spots of the electrode surface (42), accompanied by the replacement of additional interfacial water species. Further increase of the electrode potential, $0.75 < E < 0.88$ V (phase III_a), causes an orientation change from planar to perpendicular, accompanied by the deprotonation of one -COOH group that is chemically bonded to the positively charged electrode surface. Each TMA molecule is chemisorbed via one deprotonated carboxylate group in the "atop" model leaving the two -COOH side groups available for further hydrogen bonding between neighboring TMA molecules (42). Simultaneously, two types of water species start to co-adsorb, weakly hydrogen-bonded water at intermolecular defect sites and strongly hydrogen-bonded water interacting with the noncoordinated -COOH side groups. The chemisorbed TMA molecules are still mobile and not yet incorporated into an ordered two-dimensional network. Phase III_a represents a "disordered chemisorption" phase. At $E > 0.90$ V, in region III_b, almost all surface-coordinated TMA molecules are interconnected via intermolecular hydrogen bonds between adjacent -COOH side groups, resulting in a stable and highly ordered ladder network.

The formation kinetics of the chemisorbed TMA adlayer was explored by electrochemical transient experiments and time-resolved ATR-SEIRAS employing rapid-scan and step-scan acquisition modes. The analysis of the SEIRAS transients shows that the formation of chemisorbed TMA in phase III_b proceeds in two steps: (*i*) TMA molecules change their orientation from planar to tilted or perpendicular accompanied by the deprotonation of one carboxyl group immediately after a potential step in region III. This process involves the breakdown of the hydrogen-bonded network of the physisorbed phase I and a fast incorporation of additional TMA molecules from the bulk electrolyte into the interfacial region. The process follows a Langmuir-type kinetics indicating randomly triggered orientation changes with rather weak lateral interactions between the active species; (*ii*) In a subsequent and much slower process, the chemisorbed TMA molecules start to gradually align into a highly ordered two-dimensional network III_b. At the same time, small amounts of TMA molecules appear to be co-adsorbed with strongly hydrogen-bonded and isolated water species.

Based on a detailed analysis of carboxyl and carboxylate vibration modes and OH-stretching modes, the present ATR-SEIRAS study reveals a comprehensive understanding of steady-state structures and dynamic changes as triggered by the electrode potential for TMA and co-adsorbed water species on a Au(111-25 nm) film electrode in 0.1 mol L^{-1} $HClO_4$. The combination of macroscopic electrochemical experiments (in situ STM and SEIRAS) provided details of structural changes and of the chemical composition of TMA adlayers on well-defined gold–electrolyte interfaces.

Acknowledgements

The work was supported by the Volkswagen Stiftung under grant No. I77-116 and the Research Center Jülich. The authors would also like to acknowledge the skilful preparation of stepped gold single crystals by U. Linke and the help of H. Bierfeld in preparing the gold film electrodes.

References

1. J.M. Lehn. *In* Supramolecular chemistry — Concept and perspectives. VCH, Weinheim. 1995. p. 139.
2. Th. Dretschkow and Th. Wandlowski. Top. Appl. Phys. **85**, 259 (2003).
3. G.R. Desiraju. Crystal engineering. Elsevier, Amsterdam. 1989.
4. J.G. MacDonald and G.M. Whiteside. Chem. Rev. **94**, 2383 (1994).
5. R. Melendres and A.D. Hamilton. Top. Curr. Chem. **197**, 97 (1998).
6. J.V. Barth, J. Weckesser, C. Cai, P. Günter, L. Bürgi, O. Jeandupeux, and K. Kern. Angew. Chem. Int. Ed. **39**, 1230 (2000).
7. S.J. Sowerby and W.M. Heckl. Origins Life Evol. Biosph. **28**, 283 (1998).
8. S. de Feyter, A. Gesquiere, M. Klapper, K. Müllen, and F.C. De Shryver. Nano Lett. **3**, 1485 (2003).
9. M. Bailey and C.J. Brown. Acta. Crystallogr. **B22**, 387 (1967).
10. R. Alcala and S. Martinez-Carrera. Acta. Crystallogr. **B25**, 1671 (1972).
11. S. de Feyter, A. Gesquiere, M.M. Abdel-Mottaleb, P.C.M. Grim, F.C. De Shryver, C. Meiners, M. Sieffert, S. Valiyaveettil, and K. Müllen. Acc. Chem. Res. **33**, 520 (2000).
12. D.J. Duchamp and R.E. March. Acta Crystallogr. **B25**, 5 (1969).
13. F.H. Herbstein. *In* Comprehenive supramolecular chemistry. Vol. 6. *Edited by* J.L. Atwood, D.D. MacNico, D.D. Vögtle, and J.M. Lehn. Pergamon, New York. 1996. p. 61.
14. S.V. Kolotuchin, P.A. Thiessen, E.E. Fenlon, S.R. Wilson, C.J. Loweth, and S.C. Zimmerman. Chem. Eur. J. **5**, 2537 (1999).
15. S. Chatterjee, V.R. Pedireddi, A. Ranganathan, and C.N.R. Rao. J. Mol. Struct. **520**, 107 (2000).
16. J.V. Barth, J. Wechesser, N. Lin, A. Dmitriev, and K. Kern. Appl. Phys. A, **76**, 645 (2003).
17. O. Ermer and J. Neudörfl. Chem. Eur. J. **7**, 4961 (2001).
18. J.C. Dai, S.M. Hu, X.T. Wu, Z.Y. Fu, W.X. Du, H.H. Zhang, and R.Q. Sun. New J. Chem. **27**, 94 (2003).
19. L. Yang, H. Naruke, and T. Yamase. Inorg. Chem. Commun. **6**, 1020 (2003).
20. S.V. Kolotuchin, E.E. Fenlon, S.R. Wilson, C.J. Loweth, and S.C. Zimmerman. Angew. Chem. Int. Ed. Engl. **34**, 2654 (1995).
21. R.E. Melendez, C.V.K. Shrama, M.J. Zaworotko, C. Bauer, and R.D. Rogers. Angew. Chem. Int. Ed. Engl. **35**, 2213 (1996).
22. C.V.K. Shrama and M.J. Zaworotko. Chem. Commun. 2655 (1996).
23. N. Lin, A. Dmitriev, J. Weckesser, J.V. Barth, and K. Kern. Angew. Chem. Int. Ed. **41**, 4779 (2002).

© 2004 NRC Canada

24. P. Messina, A. Dmitriev, N. Lin, H. Spillmann, M. Abel, J.V. Barth, and K. Kern. J. Am. Chem. Soc. **124**, 14 000 (2002).
25. S. Griessl, M. Lackinger, M. Edelwirth, M. Hietschold, and W.M. Heckl. Single Mol. **3**, 25 (2002).
26. A. Dmitriev, N. Lin, J. Weckesser, J.V. Barth, and K. Kern. J. Phys. Chem. B, **106**, 6907 (2002).
27. Y. Ishikawa, A. Ohira, M. Sakata, C. Hirayama, and M. Kunitake. J. Chem. Soc. Chem. Commun. 2652 (2002).
28. G.J. Su, H.M. Zhang, L.J. Wan, C.L. Bai, and Th. Wandlowski. J. Phys. Chem. B, **108**, 1931 (2004).
29. M. Osawa. Bull. Chem. Soc. Jpn. **70**, 2861 (1997).
30. M. Osawa. *In* Handbook of vibrational spectroscopy. Vol. 1: Theory and instrumentation. *Edited by* J.M. Chalmers and P.R. Griffiths. Wiley, Chichester. 2002. p. 785.
31. Y. Ikezawa, R. Sekiguchi, and T. Kitazume. Electrochim. Acta, **46**, 731 (2000).
32. H.Q. Li, S.G. Roscoe, and J. Lipkowski. J. Electroanal. Chem. **478**, 67 (1999).
33. Y. Ikezawa, R. Sekiguchi, and T. Kitazume. Electrochim. Acta, **45**, 1089 (1999).
34. M. Osawa and M. Ikeda. J. Phys. Chem. **95**, 9914 (1991).
35. H. Noda, L.J. Wan, and M. Osawa. Phys. Chem. Chem. Phys. **3**, 3336 (2001).
36. Y. Ikezawa, A. Yoshida, and R. Sekiguchi. Electrochim. Acta, **46**, 769 (2000).
37. M.W. Lee, M.S. Kim, and K. Kim. J. Mol. Struct. **415**, 93 (1997).
38. H. Noda, K. Ataka, L.J. Wan, and M. Osawa. Surf. Sci. **427–428**, 190 (1999).
39. Th. Wandlowski, K. Ataka, S. Pronkin, and D. Diesing. Electrochim. Acta, **49**, 1233 (2004).
40. S. Pronkin and Th. Wandlowski. J. Electroanal. Chem. **550–551**, 131 (2003).
41. T. Pajkosy, Th. Wandlowski, and D.M. Kolb. J. Electroanal. Chem. **414**, 209 (1996).
42. Z. Li, B. Han, Th. Wandlowski, G. Su, and L.J. Wan. In preparation, 2004.
43. J.F. Arenas and J.I. Marcos. Spectrochim. Acta, **35A**, 355 (1979).
44. F. Gonzalez-Sanchez. Spectrochim. Acta, **12**, 17 (1957).
45. K. Ataka, T. Yotsuyanagi, and M. Osawa. J. Phys. Chem. **100**, 10 664 (1996).
46. K. Ataka and M. Osawa. Langmuir, **14**, 951 (1998).
47. D.S. Corrigan and M.J. Weaver. Langmuir, **4**, 599 (1988).
48. B.G. Frederick, Q. Chen, S.M. Barlow, N.G. Condon, F.M. Leibsle, and N.V. Richardson. Surf. Sci. **352–354**, 238 (1996).
49. B.G. Frederick, Q. Chen, F.M. Leibsle, M.B. Lee, K.J. Kitching, and N.V. Richardson. Surf. Sci. **394**, 1 (1997).
50. S. De Feyter and F.C. De Schryver. Chem. Soc. Rev. **32**, 139 (2003).
51. R. Nichols. *In* Adsorption of molecules at electrodes. *Edited by* J. Lipkowski and P.N. Ross. VCH, New York. 1992. p. 347.
52. D.K. Lambert. Electrochim. Acta, **41**, 623 (1996).
53. K. Ataka and M. Osawa. J. Electroanal. Chem. **460**, 188 (1999).
54. Th. Wandlowski, K. Ataka, and D. Mayer. Langmuir, **18**, 4331 (2002).
55. J.A. Dean. *In* Lange's handbook of chemistry. 13th ed. McGraw-Hill, New York. 1985. pp. 5–42.

© 2004 NRC Canada

Distribution of oxides on iron materials used for remediation of organic groundwater contaminants — Implications for hydrogen evolution reactions[1]

M.S. Odziemkowski and R.P. Simpraga

Abstract: The distribution of oxides on commercial iron materials used for remediation of organic groundwater contaminants was studied using confocal Raman microspectroscopy. Raman microprobe mapping experiments revealed that commercial iron materials used for the construction of permeable reactive barriers are covered with an oxide film consisting of an inner film of magnetite Fe_3O_4 and an outer film of Fe_2O_3. The calculated probability of the charge transfer process (i.e., electron tunnelling probability) at commercial Fe | Fe_2O_3 (semiconductor) | solution interfaces approaches zero, indicating that "as received" commercial iron materials should not be reactive towards both organic contaminants and water. The combination of OCP (corrosion potential) – time measurements with in situ Raman spectroscopy demonstrated that the breakdown of the protective Fe_2O_3 oxide film followed by autoreduction of Fe_2O_3 is a requirement for the commercial materials to be chemically active towards both water and organic contaminants. Hydrogen evolution reactions on metals and oxide-covered iron were also investigated. In particular, spectroscopic evidence for adsorption of atomic hydrogen on polycrystalline Pt is presented. The possibility of adsorption of H on magnetite-covered iron was considered using thermodynamic calculations after Marcus and Protopopoff. The evolution of hydrogen on commercial iron materials is described. It is suggested that the separation of the anodic and cathodic sites because of opening of pores in the bulk metallic Fe and the involvement of spill-over hydrogen may play a crucial role in the catalytic hydrogenation of groundwater contaminants.

Key words: Raman microprobe confocal spectroscopy, iron oxides, hydrogen evolution, remediation of organic groundwater contaminants.

Résumé : Faisant appel à la microspectroscopie Raman confocale, on a étudié la distribution des oxydes présents sur les produits commerciaux du fer utilisés pour remédier aux contaminants organiques des eaux de puits. Des expériences de relevés à l'aide de microsondes Raman ont permis d'observer que les produits commerciaux du fer utilisés pour la construction de barrières réactives perméables sont couverts d'un film d'oxyde formé d'une couche intérieure de magnétite, Fe_3O_4, et d'un film extérieur de Fe_2O_3. La probabilité d'un processus de transfert de charge (c'est-à-dire la probabilité d'un effet tunnel d'un électron) aux interfaces Fe commercial | Fe_2O_3 (semiconducteur) | solution est pratiquement nulle, ce qui indique que les produits du fer utilisés tels que reçus ne devraient pas être réactifs vis-à-vis des contaminants organiques ou de l'eau. La combinaison de la spectroscopie Raman in situ avec des mesures de potentiel de corrosion (OCP) en fonction du temps a permis de démontrer que la détérioration complète du film protecteur d'oxyde de fer, Fe_2O_3, suivie d'une autoréduction du Fe_2O_3 est un prérequis à la transformation des produits commerciaux en entités chimiquement actives vis-à-vis de l'eau et des contaminants organiques. On a aussi étudié les réactions des métaux et du fer couvert d'oxydes qui conduisent à l'évolution d'hydrogène. En présente en particulier des données spectroscopiques relatives à l'adsorption d'hydrogène atomique sur du Pt polycristallin. Faisant appel à des calculs de Marcus et Protopopoff, on a considéré la possibilité d'adsorption de H sur du fer couvert de magnétite. On décrit l'évolution d'hydrogène de produits commerciaux du fer. On suggère que la séparation des sites anodique et cathodique qui résulte d'une ouverture des pores de la masse du fer métallique et l'implication d'hydrogène qui se répand jouent un rôle crucial dans l'hydrogénation catalytique des contaminants de l'eau de puits.

Mots clés : microspectroscopie Raman confocale, oxydes de fer, évolution d'hydrogène, remédiation des contaminants organiques de l'eau de puits.

[Traduit par la Rédaction]

Received 27 February 2004. Published on the NRC Research Press Web site at http://canjchem.nrc.ca on 2 November 2004.

This manuscript is a tribute to Professor Donald E. Irish, our friend, teacher, and mentor. He is and will be greatly missed.

M.S. Odziemkowski[2] and R.P. Simpraga. Department of Earth Sciences, University of Waterloo, Waterloo, ON N2L 3G1, Canada.

[1]This article is part of a Special Issue dedicated to the memory of Professor Don Irish.
[2]Corresponding author (e-mail: marek@sciborg.uwaterloo.ca).

 doi: 10.1139/V04-120 © 2004 NRC Canada

Introduction

Over the past few decades, the development of methods for remediation of groundwater contaminated with various organic or inorganic compounds has emerged as a significant environmental priority. The growing awareness of the limitations of pump-and-treat technologies has shifted attention to in situ treatment methods such as permeable reactive barrier (PRB) technology. PRB technology combines subsurface fluid-flow management with contaminant treatment by chemical, physical, or biological processes, or by combinations of those processes. The concept is remarkably simple, involving the construction of a permeable curtain containing appropriate reactive material across the path of a contaminant plume. PRB methodology has advantages over traditional pump-and-treat systems in that it is passive and a large plume can be treated in a cost-effective manner (1).

Granular iron is most often used as a reactive medium in full-scale site remediation efforts using PRB technology. The prevalent use of scrap iron mainly stems from its low cost, availability, and documented ability to degrade a wide variety of organic contaminants (1). The first environmental application of iron for removal of chlorinated organic contaminants from aqueous solution was reported in the patent literature by Sweeny and Fischer (2) and later by Sweeny (3). Both inventions addressed the removal of organic compounds from wastewater streams. To the best of the authors' knowledge, these methods have not been applied on a broad industrial scale. One possible reason could be the mismatch of the relatively low degradation rates and the requirement for high 5 up to 150 gallon/min (1 gallon (US) = 3.78 dm^3) water flow rates in modern wastewater treatment systems.

In the late 1980s, Gillham and and co-workers (4), unaware of the earlier work of Sweeny, observed sampling bias caused by the use of inexpensive steel (i.e., unalloyed steel) wells to monitor halocarbons in groundwater. Interestingly, this bias was removed by using stainless steel (i.e., highly alloyed steel) or plastic wells. These empirical observations prompted Gillham and O'Hannesin (5) to extend the work to a broad range of halogenated aliphatic compounds. They confirmed the degradation of many halogenated aliphatic compounds in the presence of metallic iron with half-lives from 0.13 to 400 h (5). For normal groundwater velocities (5–50 cm/day), they proposed the use of scrap iron materials in the form of a permeable reactive barrier for in situ removal of a wide range of organic contaminants (6).

Over the past decade, a number of research groups confirmed the degradation of several chlorinated solvents by metallic iron (7–9) and the technology has since been evaluated for degradation of nitroaromatic compounds (10–12), nitramines (13, 14), azo dyes (15, 16), nitrate (17), and removal of arsenate, arsenite, and radionuclides (18) from groundwater.

The first proposal of possible dechlorination mechanisms was given by Matheson and Tratnyek (7). Three possible dechlorination mechanisms have been proposed: (A) direct electron transfer from iron metal to the adsorbed alkyl halide; (B) reduction by Fe^{2+} resulting from corrosion of metal; and (C) catalysed hydrogenolysis by the H_2 that is formed by reduction of H_2O during anaerobic corrosion. According to these authors (7), dissolved Fe^{2+} is a reductant capable of causing dehalogenation of some alkyl halides, although these reactions are generally quite slow. It was also noted (7) that the inner-sphere complexation of Fe^{2+} to metal oxides can create more reducing species, but at the time of publication it was uncertain whether these species could significantly influence the rate of dechlorination. With regards to the third mechanism (C), it was noted (7) that excessive H_2 accumulation at the metal surface could inhibit the corrosion and reduction of organic contaminants. According to the authors, rapid dehalogenation is still possible if an effective catalyst is available; the surface of iron, its defects, or other solid phases present in the system could provide this catalysis (7). Using spectroelectrochemical measurements, Bonin et al. (19) modified the latter conceptual model of the reaction, suggesting that the reduction of CCl_4 is controlled by electron transfer through an oxide film such as magnetite. With regard to catalysed hydrogenolysis (mechanism C), Bonin et al. (19) suggested involvement of atomic H in the hydrogenation reaction rather than molecular hydrogen H_2. The work of Matheson and Tratnyek (7) prompted researchers to apply so-called bi-metals (i.e., metals partially deposited with electrocatalytically active Pd, Pt, or Ni), Fe/Pd (20, 21), Pt/Fe (21), and Fe/Ni (22) for the degradation of organic groundwater contaminants.

It is beyond the scope of the present work to discuss hundreds[3] of publications regarding the use of iron in the remediation of groundwater contaminants. Instead, one of the objectives of this study is to address issues related to the mechanism of degradation of organic contaminants, which have not been addressed in previous publications and those which remain controversial, such as hydrogen evolution reactions on metals or oxide-covered metal surfaces.

Experimental

Materials

The granular iron samples used in the experiments were obtained from three suppliers of commercial iron materials used for PRB field installations: Connelly-GPM (Chicago, Illinois); Peerless Metal Powder and Abrasive (Detroit, Michigan); Master Builders (Cleveland, Ohio). All solutions were prepared from Milli-Q water unless stated otherwise and analytical reagent grade KOH (Aldrich), $NaHCO_3$ (Baker), H_2SO_4, and $HClO_4$ (Aldrich). D_2O (purity 99%) was obtained from CIL Isotopes. Hydrogen adsorption studies were performed using 6.0 mm Pd (99.95%), Pt (99.99%), and 5 mm Ni (99.999%) polycrystalline rods (Johnson Matthey).

Methods

Ex situ Raman spectral studies of the distribution of oxides on "as received" commercial iron

Raman spectra were obtained with a Renishaw 1000 microscope system with a CCD detector (400 pixels × 600 pixels) using a 30 mW HeNe (632.8 nm) laser. The optical throughput of the instrument is high (≥30%), as is the sensitivity. The detection of a very weak signal (1 photon/s) is

[3] Database available at http://cgr.ese.ogi.edu/ironrefs/Process.pl.

© 2004 NRC Canada

possible. Raman spectra of as received iron materials were obtained using a 100× magnification objective and the confocal mode of instrument operation. Raman results were analysed based on available literature data and (or) compared with Raman spectra of standards.

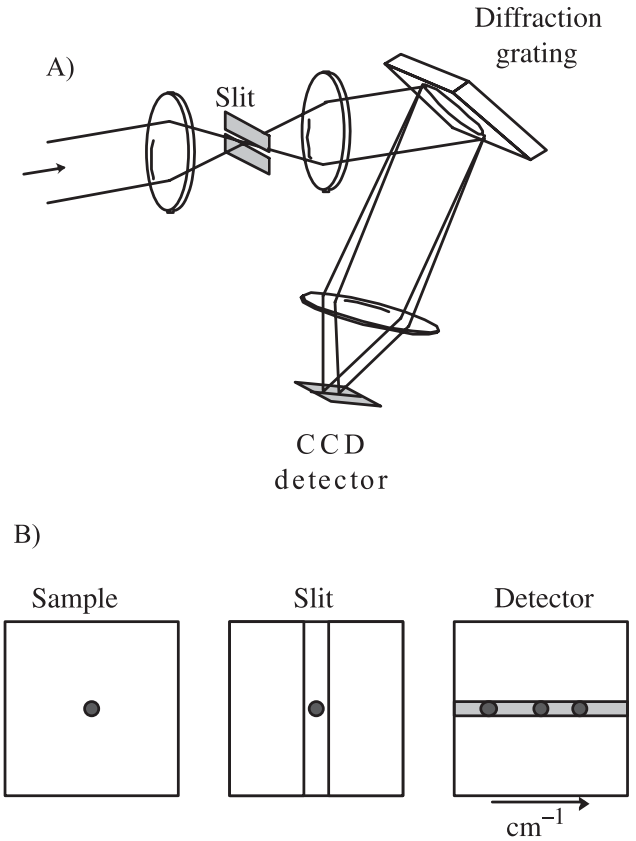
The confocal mode of operation was achieved by decreasing the slit width to 15 μm and the area of the CCD detector to 4 pixels × 600 pixels, as demonstrated in Fig. 1. The slit is used as the primary aperture in the system and, as such, provides an additional spatial filter for the confocal measurements. The optical design of the system produces an image spot size of ca. 15 μm (depending on objective used) at the slit, and thus, it discriminates against the out-of-focus sample region. The optical alignment of the instrument was optimized using the 521 cm^{-1} Raman signal from a silicon wafer. The confocal setting and 100× magnification objective should give a 2 μm sampling depth (23). The proper confocal optical alignment and the depth of field was confirmed by plotting the Si signal intensity as a function of position through focus (Z distance profile) of the silicon wafer. The use of confocal Raman microspectroscopy was important for two reasons: (*i*) it dramatically diminishes undesirable fluorescence and (*ii*) allows for the filtration of the signal from the nearest neighbouring species in the sequential mapping of the iron surface with 1 μm resolution (for the 100× objective). All in situ studies presented in this work were carried out using the non-confocal setting of the Raman instrument.

Electrochemical measurements (cells and electrode preparation)

The open-circuit potential (OCP) of a single grain of Connelly™ iron was measured in a simple two-electrode cell with a $Ag/AgCl/Cl_{sat}$ or Hg/HgO/0.1 mol/L OH^- electrode used as an external reference electrode. The cell was purged with ultra-pure argon and filled with Milli-Q water containing 25 mg/L of *N*-nitrosodimethylamine (NDMA) or, in the second experiment, with 0.12 mol/L $NaHCO_3$ + 0.1 mol/L KOH. The solution was introduced into the cell and deaerated for 30 min. To simulate the batch–column kinetic experiments, 150–200 g of sieved granular Connelly™ iron was added at the bottom of the cell. All OCP data were converted to the standard hydrogen electrode (SHE) as a common reference scale.

Hydrogen adsorption experiments were carried out in a three-electrode spectroelectrochemical cell described in detail in an earlier publication (24). A double-junction $Ag|AgCl|Cl_{sat.}$ reference electrode was used. The Luggin capillary was terminated with a second glass-sealed asbestos frit to avoid possible contamination of the electrolyte by Cl^- ions. The cell construction unfortunately did not allow the use of a reversible hydrogen electrode (RHE) as the reference electrode, which would be preferred for this type of study. A platinum mesh sealed into glass was used as the counter electrode. The working electrodes were mechanically polished with 0.3 and 0.05 μm alumina powder to a mirror finish followed by ultrasonic cleaning in Milli-Q water. The Pt and Pd electrodes underwent 24 h of electrochemical polishing by potential cycling between –0.20 and 1.20 or 1.25 V (vs. $Ag|AgCl|Cl_{sat.}$). Pt, Pd, and Ni are not surface-enhanced Raman active metals. Therefore, to observe very weak signals from adsorbates the Raman scattering cross-section needs to be increased. In practice this can be achieved by creation of roughness at the metal electrode surface. The roughening procedure was adapted from Ariva and co-workers (25) and successfully applied to Raman spectroscopic studies of hydrogen adsorption by Tian and co-workers (26). Namely, potential steps from –0.20 up to 2.45 V with a frequency of 2 kHz were applied to the electrodes in deaerated 0.1 mol/L H_2SO_4 or 0.1 mol/L $HClO_4$ for 10 min. After roughening, the electrodes underwent further potential cycling at a sweep rate of 20 mV/s between –0.20 and 1.20 or 1.25 V depending on the electrolyte. The cycling was continued until all unstable atoms or metal clusters were removed, as indicated by a reproducible cyclic voltammogram (CV), which was usually achieved after the third cycle.

Fig. 1. The optical configuration of the Renishaw 1000 system — confocal mode. (*a*) Confocal optics. (*b*) CCD pixel binning. Slit width 15 μm (or less), CCD area 4 pixels (or less) by 600 pixels.



All OCP and CV measurements were carried out using an AutoLab PGSTAT 30 potentiostat interfaced to a personal computer. Electrochemical roughening of the Pt and Pd electrodes was performed using an EG&G PAR model 273 potentiostat and a Wavetek Model 142 high frequency wave generator.

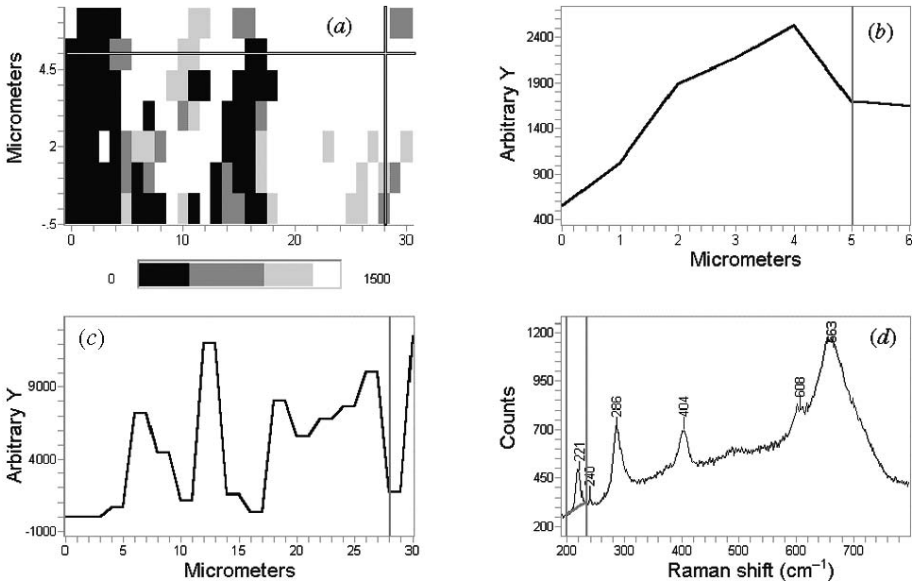
Results and discussion

Raman confocal mapping of commercial iron materials

Literature data on the remediation of groundwater contaminants by iron filings lack comprehensive studies of the

© 2004 NRC Canada

Fig. 2. (*a*) Raman map of the integrated 221 cm^{-1} α-Fe_2O_3 signal. (*b*) Signal along the Y axis at X = 28 μm. (*c*) Signal along the X axis at Y = 5 μm. (*d*) Raman spectrum at X = 28 μm, Y = 5 μm. The scale at the bottom of Fig. 2*a* represents the integrated area of the α-Fe_2O_3 peak.



distribution of various oxides on the surface of the commercial materials used for PRB construction, or at the best are limited to maximum of nine arbitrary chosen points at the surface (27).

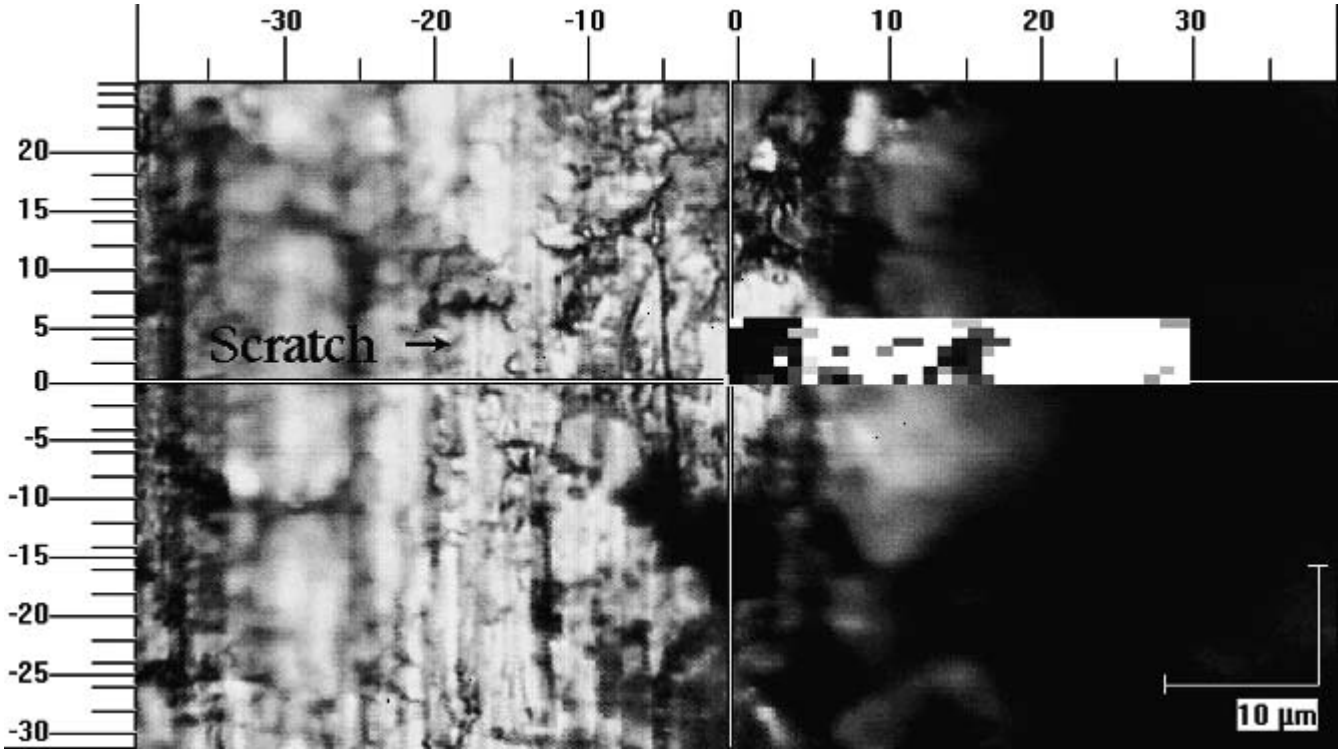
During production of commercial materials used for construction of PRBs, the low alloy scrap steel and (or) cast iron undergo high-temperature thermal treatment in rotary kiln ovens. The temperature and partial pressures of gases maintained in the rotary kilns are considered proprietary by the suppliers and therefore, are not readily available. A randomly chosen, but relatively flat, grain of Connelly™ iron was scratched to reveal the underlying material. In the mapping experiment, Raman spectra were taken over a 30 μm × 6 μm area covering both scratched and unscratched grain regions. In total, this corresponds to 217 Raman spectra taken over 12 h of measurements. The mapping process was fully automated by using a computer-controlled XYZ motorized stage. For XY movement, a 1 μm × 1 μm scan step pattern was chosen. To account for surface height changes (i.e., scratch, roughness, etc.), the autofocussing spectra acquisition mode was chosen with Z-direction step movements of 1 μm. The Raman map of hematite (α-Fe_2O_3) is presented in Fig. 2. It was generated using the signal to baseline calculation method, where the Raman peak at 221 cm^{-1} (A_{1g} mode of α-Fe_2O_3) was used as the fingerprint of hematite. Figure 3 represents the overlay of the α-Fe_2O_3 Raman map with the white light image of a grain of the Connelly™ iron. Raman mapping of maghemite (γ-Fe_2O_3) and magnetite (F_3O_4) are presented in Figs. 4*a* and 5*a*, respectively. The fingerprint Raman signals for γ-Fe_2O_3 and F_3O_4 do not exist because the strongest A_{1g} mode of F_3O_4 at 663–673 cm^{-1} overlaps very broad complex Raman bands of γ-Fe_2O_3 at 643, 671, and 718 cm^{-1} (see Fig. 4*b*). Therefore, the simple method of signal to background calculation cannot be applied. In this case, the map components calculation method was used. This method searches for the best match of the combination of the differential of the component spectrum (Raman spectrum of γ-Fe_2O_3 standard in Fig. 4*b*) to the differentials of the spectrum taken at each X-Y coordinate (Fig. 4*c*). This method effectively compares the shape of the component spectra to the unknown at different XY positions. The comparison of the Raman spectrum of the γ-Fe_2O_3 standard with Raman spectra obtained at X = 28 μm, Y = 5 μm (Fig. 2*d*), and X = 12 μm, Y = 0 μm (Fig. 4*c*) indicates that at these locations the Raman band at 663–665 cm^{-1} should not be attributed to γ-Fe_2O_3, but rather to the A_{1g} mode of Fe_3O_4. The mapping of Fe_3O_4 was performed using many different calculation methods, including peak half-width mapping, mapping data by curve fitting, and component mapping. The most reliable results were obtained using component mapping with the background offset correction. The Fe_3O_4 mapping results are presented in Fig. 5*a*. The latter calculation method generates an extra map of the background offset (Fig. 5*b*), which is in fact the map of underlying fluorescence.

The same mapping procedure was used to study oxide distribution on both the Peerless™ and Master Builder™ samples. The white light image of a grain of Peerless™ iron is presented in Fig. 6. The distribution of hematite (α-Fe_2O_3) on the surface of Peerless™ iron is shown in Fig. 7. The entire surface of Peerless™ iron is covered by a thick layer of hematite. Because of space constraints, the distribution of oxides for Master Builder™ is not shown in this work.

Raman microprobe mapping experiments revealed that the commercial iron materials used for the construction of permeable reactive barriers are covered with an inner film of magnetite Fe_3O_4 (scratched area) and an outer film of Fe_2O_3. The majority of the outer film (unscratched area) consists of hematite (α-Fe_2O_3). Maghemite γ-Fe_2O_3 was only observed at a few locations and was accompanied by very strong fluorescence as indicated by comparison of the γ-Fe_2O_3 map in Fig. 4*a* with the map of fluorescence in Fig. 5*b*. Wüstite, which can be nominally written as FeO, is characterized by a very broad single Raman band at 652 cm^{-1} (28). The

© 2004 NRC Canada

Fig. 3. The overlay of the α-Fe_2O_3 Raman signal map with the white light image of a grain of the Connelly™ iron. White areas in Figs. 2*a* and 3 indicate a strong Raman signal of α-Fe_2O_3.



wüstite phase is unstable below 570 °C and was not observed in our experiments. The Raman results are in very good agreement with the high-temperature oxidation model of ferric materials (29).

The charge transfer processes at the metal | oxide | solution interface

Oxide-covered metals represent intermediate systems that have similarities to metal and semiconductors. According to the charge transfer theory of Gerischer (30), charge transfer proceeds at constant electronic energy and can be described using a diagram of electron terms at the interface. With regard to the reduction of chlorinated solvents by iron, the elements of Gerischer's theory of charge transfer were used by Balko and Tratnyek (31) to explain the effects of light on the reduction of CCl_4 by high purity iron. This interesting work prompted us to make similar considerations for the commercial Fe materials.

The probability of charge transfer at an oxide-covered metal can be estimated using the Gamov formula (30)

$$[1] \qquad \ln W = -4\pi d(2m_e \Delta E)^{0.5}/h$$

where m_e is rest mass of the electron and h is Planck's constant. W is the electron-tunnelling probability, which depends strongly on the thickness (d) and the height of the semiconductor energy barrier (ΔE). Using the known value of the complex part of the refractive index for the high-temperature grown Fe_2O_3, $k = 0.326$ (32), the laser penetration depth can be estimated using the following formula (33)

$$[2] \qquad d = c/2k\nu = \lambda/2k$$

where ν, λ, and c are the frequency, wavelength, and velocity of light in a vacuum, respectively. In the case of the commercial iron materials, the Raman signal of the inner Fe_3O_4 layer was not visible, indicating that the thickness of the outer Fe_2O_3 is greater than 970 nm, the calculated laser penetration depth for the outer oxide.

For a typical energy barrier $\Delta E = 1$ eV for a semiconductor film on iron (30) and 970 nm thick Fe_2O_3, the probability of charge transfer by tunnelling is $W = 10^{-4307}$. Therefore, as received commercial iron materials for the construction of permeable reactive barriers should not be reactive towards not only chlorinated solvents but also chemically inert towards groundwater. The calculation assumed the inner Fe_3O_4 to be electronically conducting. The tunnelling probability calculation might be slightly misleading since the calculation assumes an ideal passive film, free of local defects. The reason behind the effectiveness of commercial iron materials in the reductive destruction of organic contaminants is considered in the next section.

Autoreduction of the outer protective Fe_2O_3 film

In the earlier stages of PRB technology development, research was directed towards identification of precipitates formed during solvent remediation. This is understandable considering the fact that the activity of a PRB must be maintained for 10 to 20 years to be economically superior over pump-and-treat groundwater systems. In this way, the reactions that are responsible for the effectiveness of the technology have been largely neglected (34). These are autoreduction reactions that can be written as (35*a*)

$$[3] \qquad Fe_2O_3 + 6H^+ + 2e^- \rightarrow 2Fe^{2+} + 3H_2O$$

© 2004 NRC Canada

Fig. 4. (*a*) Raman signal map of γ-Fe_2O_3. (*b*) Raman spectrum of the γ-Fe_2O_3 standard. (*c*) Raman spectrum at X = 12 μm, Y = 0 μm. The scale at the bottom of Fig. 4*a* represents the quality of the match between standard and unknown; a ratio of 1 represents the best match.

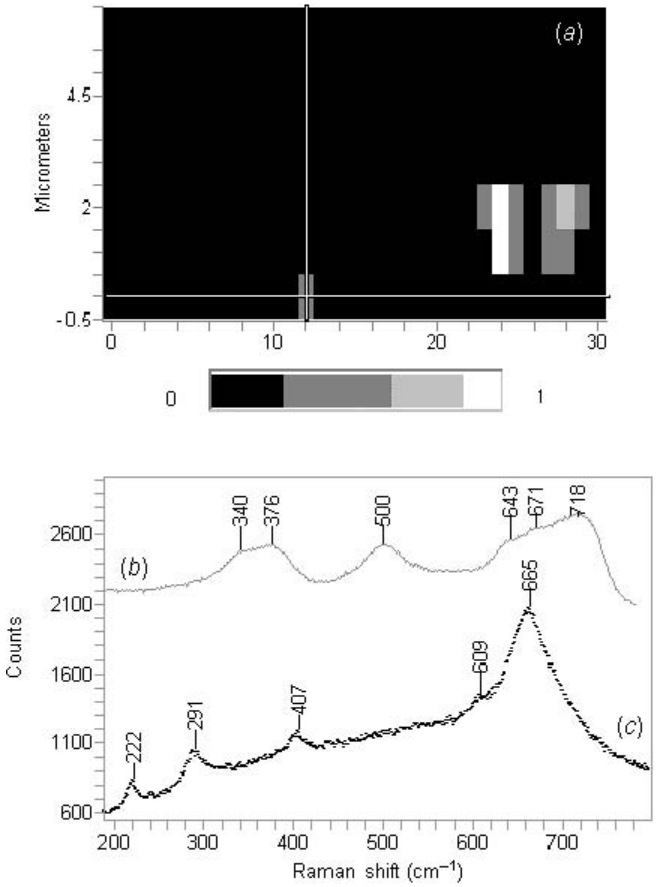
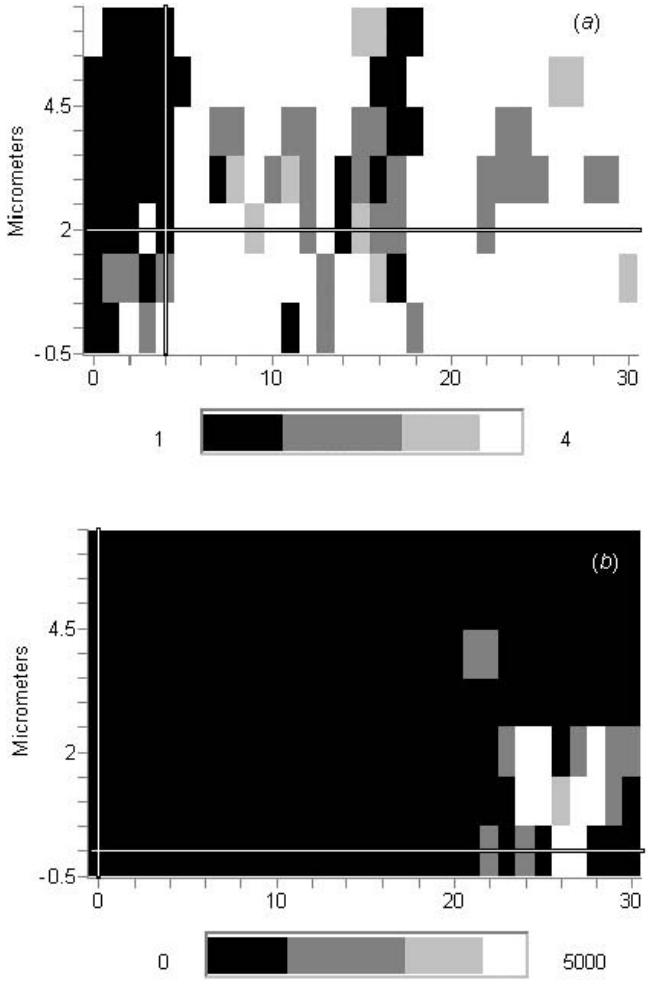


Fig. 5. (*a*) Raman signal map of Fe_3O_4. The scale at the bottom represents the quality of the match between the standard and unknown. A ratio of 1 represents the best match. (*b*) Map of the offset background (map of fluorescence). The scale 0–5000 indicates the offset background intensity.



or (35*b*)

[4] $Fe_2O_3 + 2H^+ + 2e^- \rightarrow 2Fe_3O_4 + H_2O$

PRB reactive barriers are passive treatment methods, and hence, operate under OCP conditions. At the OCP, electrons for reductive dissolution of the protective oxides (rxns. [3] and [4]) are supplied by the anodic corrosion process (12, 35, 36).

[5] $Fe \rightarrow Fe^{2+} + 2e^-$

Over several years we have collected considerable experimental evidence that confirms the occurrence of these reactions in both pure water and groundwater solutions. The experimental evidence includes: (*i*) colour changes of the commercial materials from reddish to black when exposed to deaerated aqueous solutions; (*ii*) in situ Raman spectroscopic data confirming the disappearance of Fe_2O_3 from the surface with simultaneous occurrence of the Fe_3O_4 Raman signal (27, 35c); and (*iii*) OCP-time potential transients (see, for example, Fig. 8).

The potential-time transient presented in Fig. 8 is in good agreement with OCP-time transients measured for low alloy pipeline steel covered with a thick layer of millscale oxides in groundwater solutions (36). The millscale-covered pipeline steel most closely resembles the commercial iron materials used for PRB construction. Therefore, the most recent electrochemical impedance and potential-time transients measurements of Qin et al. (36) are particularly important for understanding the processes occurring on Fe used in PRBs. According to Qin et al. (36), three regions of OCP-time transients can be observed, which correspond to: (*i*) the initial attempts at breakdown of the millscale (positive potentials in this first region indicate that only the millscale is exposed to the solution); (*ii*) coupling of the dissolution of underlying iron to the reductive dissolution of the millscale oxides in the intermediate potential range; (*iii*) active corrosion of the material at the base of the pores in the film supported by water reduction either on the metal or on the conducting (i.e., magnetite) millscale at the most negative potentials (36).

The white light image of the cross section of the grain of Connelly^{TM} iron used in the mapping experiment is presented in Fig. 9. The as received material is cracked. The cracks penetrate deep into the bulk material. The cracking of commercial Fe is evidently the result of the thermal treat-

© 2004 NRC Canada

Fig. 6. The white light image of a grain of the Peerless™ iron.

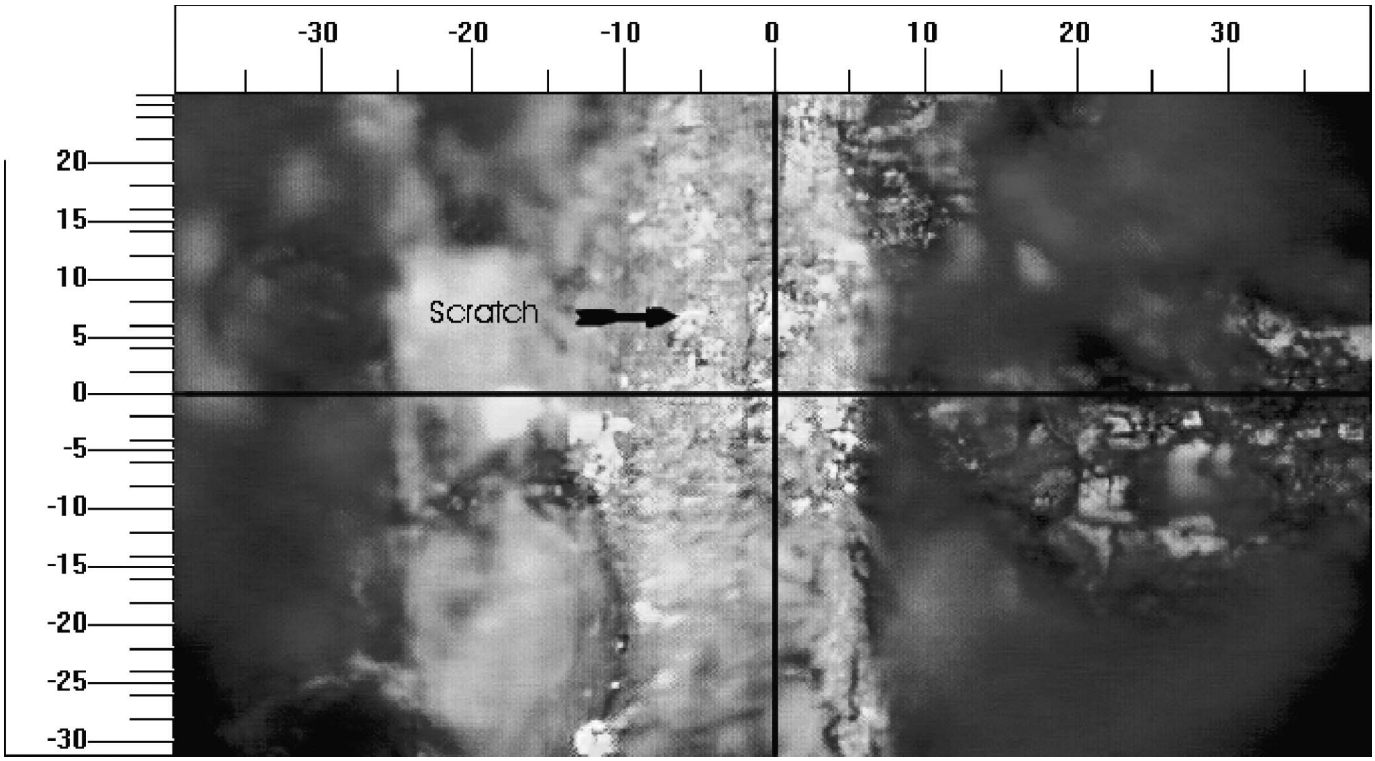
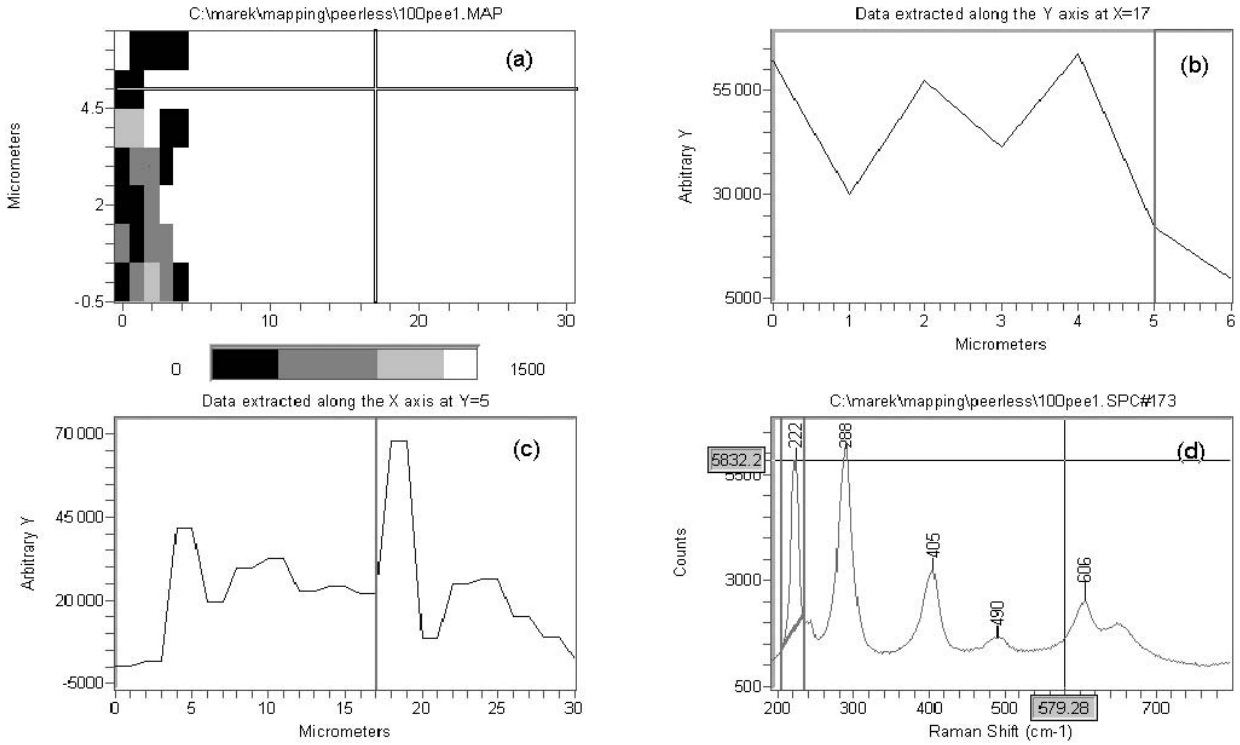


Fig. 7. (*a*) Raman map of the integrated 221 cm^{-1} α-Fe_2O_3 signal for Peerless™ iron. (*b*) Signal along the Y axis at X = 17 μm. (*c*) Signal along the X axis at Y = 5 μm. (*d*) Raman spectrum at X = 17 μm, Y = 5 μm. The scale at the bottom of Fig. 7*a* represents the integrated area of the α-Fe_2O_3 peak.



ment of the scrap material in the kiln ovens. Raman microspectroscopy of the different areas inside the cracks revealed (data not illustrated) the presence of graphite, carbides, and stressed α-Fe_2O_3 oxide. The stress in the oxide was evident from the shift of the A_{1g} mode of α-Fe_2O_3 from 225 cm^{-1} to as low as 217 cm^{-1}. Sometimes the splitting of

© 2004 NRC Canada

Fig. 8. OCP-time dependence of a single grain of Connelly^{TM} iron immersed in distilled water containing 25 mg/L NDMA. The potential arrest after ca. 1100 min (see inset) represents autoreduction of the outer protective Fe_2O_3 oxide film. The dotted lines indicate the equilibrium potentials for hydrogen evolution for the pH range observed in the column experiment during degradation kinetic studies of NDMA. The broken lines indicate potentials required for the electroreduction of NDMA, obtained from differential pulse voltammetry on mercury electrodes. Further experimental details can be found in our earlier publication on mechanistic studies of the reduction of NDMA in the presence of granular iron (37). The potential spike at ca. 1700 min is an experimental artifact. Its occurrence does not influence the interpretation of the present results.

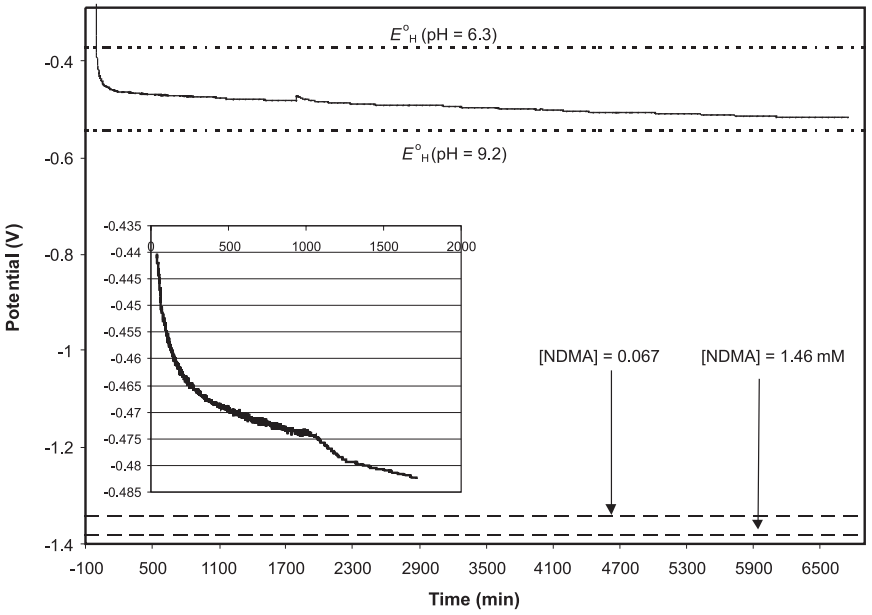
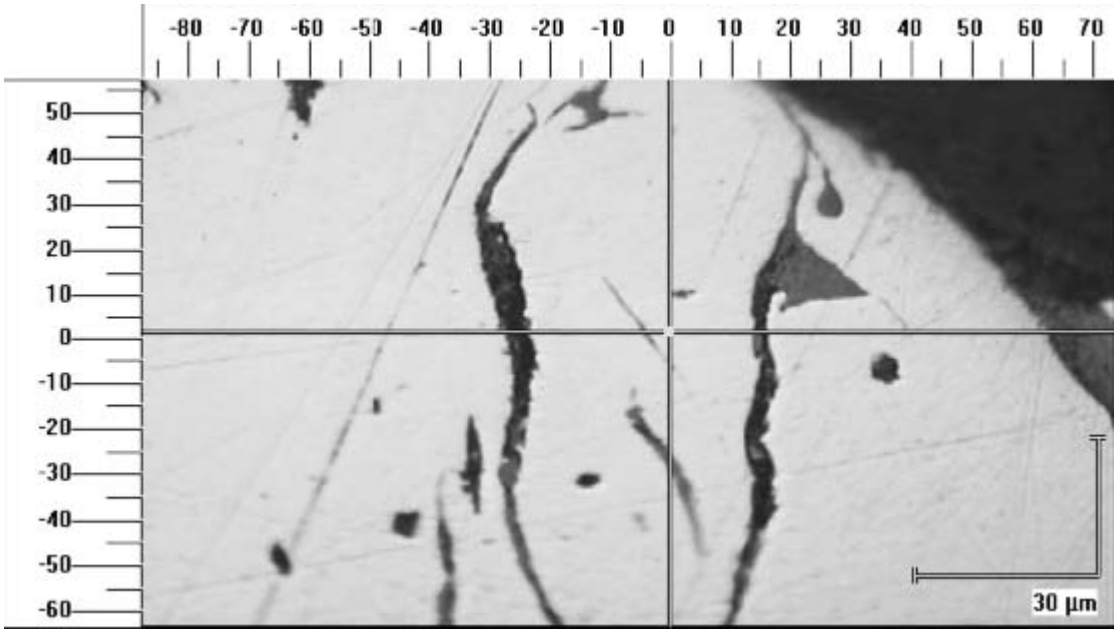


Fig. 9. The white light image of the cross section of the grain of the Connelly^{TM} iron used for the Raman mapping experiment. Cracks penetrate from the oxide layer (right upper corner) deep into bulk of the material.



this band was observed. Cracking and stressing create ideal conditions for the autoreduction processes described by Qin et al. (36).

The potential in the intermediate potential region (see Fig. 8) never reaches a steady-state value but decreases continuously. This would suggest that the autoreduction process opens up the porous structure of the oxide (36) and possibly the underlying metal as the oxide dissolves. The deeply cracked structure of the commercial iron materials increases the possibility of local separation of anodic and cathodic sites, which would promote localized corrosion and, as a consequence, the degradation of organic contaminants.

© 2004 NRC Canada

Hydrogen evolution reactions (HER) on metals and oxide cover iron

Processes involving hydrogen evolution are important in many applications, such as catalysis, electrocatalysis, metallurgy, and corrosion engineering. With regards to degradation of organic contaminants by scrap iron materials, these processes have received very little attention. In the environmental literature, for example, the corrosion reaction for iron in water is frequently written as $Fe + H_2O \rightarrow Fe^{2+} + H_2 + 2OH^-$. The work of Wang and Farrell (38) is the rare exception. Wang and Farrell (38) addressed the issue of atomic hydrogen only in low pH environments (see rxns. [1]–[3] in ref. 38). However, the low pH environment is not typical for PRB operation. We believe that the hydrogen evolution reactions on metals such as Pt, Pd, Fe, and Ni are more complex and strongly pH dependent.

It is commonly agreed that the HER on metals such as Pt, Pd, Fe, and Ni takes place in several steps and the mechanism strongly depends upon the pH of the solution (39).

At low pH (i.e., pH < 5), the first reaction step involves the discharge of hydrated protons

[6] First step $Me + H_3O^+ + e^- \rightleftarrows MeH_{ads} + H_2O$ (Volmer reaction)

followed by electrochemical desorption

[7] Second step (*a*) $MeH_{ads} + H_3O^+ + e^- \rightleftarrows H_2 + H_2O + Me$ (Heyrovsky reaction)

or by chemical desorption (also called catalytic recombination)

[8] Second step (*b*) $MeH_{ads} + MeH_{ads} \rightleftarrows 2Me + H_2$ (Tafel reaction)

In alkaline solutions (pH > 5), the first reaction step involves the electrolysis of water

[9] First step $Me + H_2O + e^- \rightleftarrows MeH_{ads} + OH^-$ (Volmer reaction)

followed by electrochemical desorption

[10] Second step (*a*) $MeH_{ads} + H_2O + e^- \rightleftarrows H_2 + OH^- + Me$ (Heyrovsky reaction)

or by chemical desorption

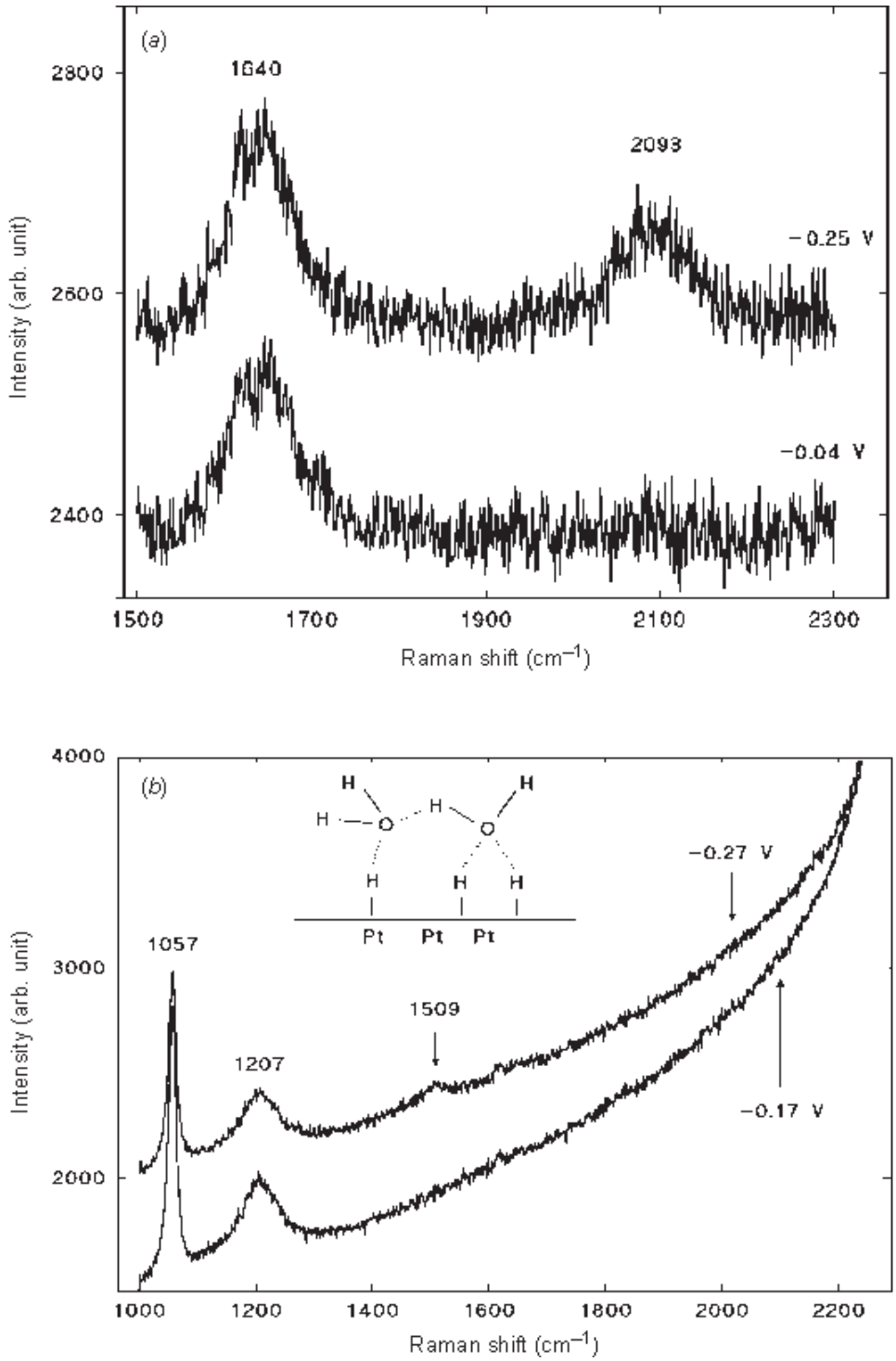
[11] Second step (*b*) $MeH_{ads} + MeH_{ads} \rightleftarrows 2Me + H_2$ (Tafel reaction)

It is important to note that the formation of adsorbed hydrogen changes the free energy of the electron transfer step by an amount equal to the free energy of the bond formation between the hydrogen atom and the surface of the metal. The consecutive rxns. [6]–[9] for many metals, including Fe, Ni, Pt, Pd, etc., can occur at potentials more positive than the equilibrium potential for the hydrogen evolution reaction (39). The spectroscopic evidence for adsorption of atomic hydrogen on Pt is presented in Fig. 10*a*. Our results are in good agreement with those of Tian and co-workers (26) who observed singly coordinated H on the surface of Pt at 2088 cm^{-1}. The confirming evidence that the presently observed band at 2093 cm^{-1} indeed arises from adsorbed H is provided by an experiment carried out in heavy water. Namely, the band at 2093 cm^{-1} shifts by a factor of 1.39 (see Fig. 10*b*), which is expected for the isotopic shift. Changing the anion in the electrolyte from SO_4^{2-} to ClO_4^- (not specifically adsorbable) shifted the hydrogen band from 2093 to 2098 cm^{-1}, suggesting that a stronger bond was created in the electrolyte free of specifically adsorbable anions. The other bands in Fig. 10 at 1640, 1207, and 1057 cm^{-1} arise from the bending mode of water and heavy water and the stretching mode of the SO_4^{2-} anion, respectively. In our studies, we carefully scrutinized the potential region for hydrogen adsorption. In agreement with Tian and co-workers (26), we could observe adsorbed hydrogen at potentials just before the onset of formation of molecular hydrogen by rxns. [7] and [8]. This indicates that we observed both "strongly" (first cathodic peak-cycling voltamograms for Pt (not presented) can be found in ref. 39) and "weakly" (second cathodic peak) adsorbed hydrogen. Distinguishing these different species will be difficult using normal Raman spectroscopy (NRS). Until now, attempts to obtain Raman spectra of adsorbed H on Pd, Ni, and Fe were not successful. The success of NRS in the research on hydrogen adsorption will depend upon finding the suitable roughening procedure that would increase the intrinsically weak Raman signal of adsorbates. Furthermore, the use of vibrational spectroscopy based on nonlinear optics, for example, visible-IR sum-frequency generation providing more surface sensitivity, should be considered as a better method for detection of atomic hydrogen on Pd, Ni, and Fe.

While there exists a considerable amount of spectroscopic and electrochemical evidence concerning adsorption of atomic hydrogen on transition metals such as Fe, Co, and Ni, the adsorption of H on magnetite-covered Fe surfaces is more speculative and requires confirmation by independent spectroscopic experiments. Thermodynamic calculations by Marcus and Protopopoff (40), however, indicate such a possibility. The thermodynamic stability region of H_{ads} (i.e., under-potential deposited (UPD) H) on Fe overlaps the region of Fe_3O_4 stability. Calculations in ref. 40 assume a simplified model of competitive Langmuir adsorption of H and O atoms. In the case where adsorbed O has a strong blocking effect, the domain of FeH_{ads} would be shifted to more cathodic potentials, outside the stability region of Fe_3O_4 (see Fig. 11). While the latter may be true in normal aqueous solutions, in column experiments on the kinetics of degradation of organic contaminants, O_2 is consumed at the inlet of the column. Thus, it is not available as a competitor for hydrogen adsorption. Furthermore, the stress induced during thermal treatment of commercial scrap iron in kiln ovens induces nano-cracks both in the oxide layer and in the matrix of the metal (see Fig. 9). Hydrogen evolution in occluded cells such as cracks, pits, and crevices can take place even at anodic potentials (i.e., potentials more positive than the measured OCP) (41). The latter is the result of the acidification of the solution inside the local defect. Moreover, hydrogen evolution is further supported by the shift of the potential inside the crack in the negative direction because of the ohmic potential drop. All of the above factors increase the probabil-

© 2004 NRC Canada

Fig. 10. Potential dependent surface Raman spectra of: (*a*) hydrogen adsorption in 0.1 mol/L H_2SO_4 in water and (*b*) deuterium adsorption in 0.1 mol/L H_2SO_4 in heavy water. The insert in Fig. 10*b* represents possible coordination of atomic hydrogen at the interface.



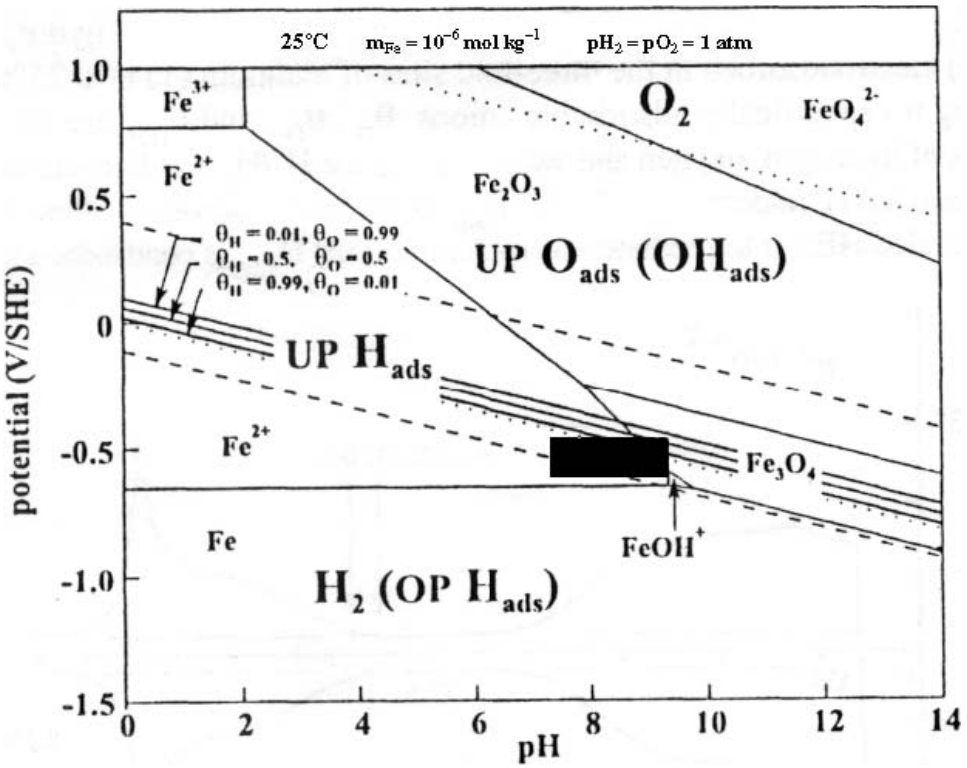
ity of the local separation of anodic and cathodic sites, which are known in the corrosion literature as Evans cells. In earlier work (7) on the dehalogenation of chlorinated methanes by iron, the separation of local anodes and cathodes was questioned.

Further supporting evidence for the existence of atomic hydrogen, despite the presence of a thick layer of magnetite at pH > 5, comes from hydrogen permeation experiments in neutral and alkaline solutions (41). Note here that only hydrogen in the atomic form can enter the lattice of iron metal.

In recent years there is growing evidence (12, 37) that despite the existence of a thick layer of magnetite on the commercial iron, many groundwater organic contaminants can be destroyed by catalytic action of atomic hydrogen. The

© 2004 NRC Canada

Fig. 11. Equilibrium potential – pH diagrams for the strongly bonded hydrogen and oxygen species electroadsorbed in the high coordination sites of iron at 25 °C in an electrolyte containing no specifically adsorbable anions. θ_H and θ_O are the fractional surface coverages of adsorbed hydrogen and oxygen, respectively. UP H_{ads} denotes the strongly bonded H electroadsorbed at underpotential, i.e., above the equilibrium line (dotted line) for hydrogen evolution. Below this line, the weakly bonded, overpotential (OP) H_{ads} is coadsorbed. The dashed lines are the lines for the hypothetical case where H and O species would be electrosorbed independently (for $\theta = 0.5$). *Reproduced by permission of The Electrochemical Society.* Details of the calculations are provided in ref. 40. The black area superimposed on the equilibrium diagram represents a collection of published (27, 37) and unpublished experimental data for the pH and OCP observed during batch or column experiments on the degradation of organic contaminants by commercial iron materials. The pH and OCP are given after autoreduction of Fe_2O_3 and confirmed by Raman microspectroscopy of the existence of magnetite on the surface of the commercial materials.



separation of the anodic and cathodic sites and spillover atomic hydrogen can play a crucial role in these processes.

Conclusions

Raman microprobe mapping experiments reveal that commercial iron materials used for the construction of permeable reactive barriers are covered with an inner film of magnetite Fe_3O_4 (scratched area) and an outer film of Fe_2O_3 (unscratched area). This observation is in good agreement with the high-temperature oxidation model of ferric materials.

The charge transfer process at Fe | iron oxide (semiconductor) | solution interfaces has been briefly discussed. In particular, it was estimated that the probability of charge transfer process (by electron tunnelling) at commercial Fe | Fe_2O_3 (semiconductor) | solution interfaces approaches zero. It was concluded that as received commercial iron materials should not be reactive towards both organic contaminants and water.

The combination of OCP (corrosion potential)-time measurements with in situ Raman spectroscopy demonstrated that the breakdown of the protective Fe_2O_3, oxide film, followed by autoreduction of Fe_2O_3, is a required step to make the commercial materials chemically active towards both water and organic contaminants. Based on OCP-time behaviour and available literature data, it was suggested that the autoreduction process opens up the porous structure of the oxide and cracks in the underlying metallic iron. The opening of defects in the bulk iron metal creates conditions for the local separation of anodic and cathodic sites and the formation of so-called Evans galvanic cells.

Hydrogen evolution reactions on metals and oxide-covered iron was also described. In particular, spectroscopic evidence for adsorption of atomic hydrogen on polycrystalline Pt was presented. The possibility of adsorption of H on magnetite-covered iron was considered using thermodynamic calculations of Marcus and Protopopoff (40). The evolution of hydrogen on the commercial iron materials was described. It was suggested that the separation of the anodic and cathodic sites and involvement of spillover hydrogen may play a crucial role in the catalytic hydrogenation of groundwater contaminants.

Acknowledgements

The authors wish to thank Dr. D. Shoesmith (University

© 2004 NRC Canada

of Western Ontario) for providing us access to ref. 36 prior to publication. Our thanks also go to Greg Friday who introduced us to the history of the development of "iron technology" at the University of Waterloo. We also would like to thank Dr. David F. Tessier for proofreading the manuscript.

Funding for this study was provided in part by the Natural Sciences and Engineering Research Council of Canada (NSERC) research grant of the late Dr. D.E. Irish and in part by the NSERC, DuPont, ETI Industrial Research Chair held by Dr. R.W. Gillham. Part of this work was presented at The Electrochemical Society Meeting, Toronto, May 2000.

References

1. R.T. Wilkin and R.W. Puls. Capstone report on the application monitoring, and performance of permeable reactive barriers for ground-water remediation. Vol. 1. Office of Research and Development US EPA, Cincinnati, Ohio. August 2003. p. 1.
2. K.H. Sweeny and J.R. Fischer. Reductive degradation of halogenated pesticides. US Patent 3 640 821, February 1972.
3. K.H. Sweeny. Treatment of reducible hydrocarbon containing aqueous stream. US Patent 4 219 419, August 1980.
4. G.W. Reynolds, J.T. Hoff, and RW. Gillham. Environ. Sci. Technol. **24**, 135 (1990).
5. R.W. Gillham and S.F. O'Hannesin. Ground Water, **32**, 958 (1994).
6. R.W. Gillham and S.F. O'Hannesin. Metal-catalysed abiotic degradation of halogenated organic compounds. IAH Conference Proceedings, Hamilton, Ontario, 10–13 May 1992. pp 94–103.
7. L.J. Matheson and P.G. Tratnyek. Environ. Sci. Technol. **28**, 2045 (1994).
8. A.L. Roberts, L.A. Totten, W.A. Arnold, D.R. Burris, and T.J. Campbell. Environ. Sci. Technol. **30**, 2654 (1994).
9. B. Deng, S. Hu, and D.R. Burris. *In* Physical, chemical, and thermal technologies: remediation of chlorinated and recalcitrant compounds. *Edited by* G.B. Wickramanayake and R.E. Hinchee. Battelle Press, Columbus, Ohio. 1998. pp. 341–346.
10. A. Agrawal and P.G. Tratnyek. Environ. Sci. Technol. **30**, 153 (1996).
11. J.F. Devlin, J. Klausen, R.P. Schwarzenbach. Environ. Sci. Technol. **32**, 1941 (1998).
12. O.H. Seok-Young, D.K. Cha, and P.C. Chiu. Environ. Sci. Technol. **36**, 2178 (2002).
13. J. Singh, S.D. Comfort, and P.J. Shea. J. Environ. Qual. **27**, 1240 (1998).
14. J. Singh, S.D. Comfort, and P.J. Shea. Environ. Sci. Technol. **33**, 1488 (1999).
15. E.J. Webber. Environ. Sci. Technol. **30**, 716 (1996).
16. S. Nam and P.G. Tratnyek. Water Res. **34**, 1837 (2000).
17. C.P. Huang, H.W. Wang, and P.C. Chiu. Water Res. **32**, 2257 (2000).
18. (*a*) D.W. Blowes, C.J. Ptacek, and J.L. Jambor. Environ. Sci. Technol. **31**, 3348 (1997); (*b*) J.A. Lackovic, N.P. Nikolaidis, and G.M. Dobbs. Environ. Eng. Sci. **17**, 29 (2000); (*c*) R.W. Puls and C. Su. Environ. Sci. Technol. **35**, 3348 (2001); (*d*) S.J. Morrison, D.R. Metzler, and B.P. Dwyer. J. Contam. Hydrol. **56**, 99 (2002).
19. P.M.L Bonin, M.S. Odziemkowski, and R.W. Gillham. Corros. Sci. **40**, 1391 (1998).
20. R. Muftikian, Q. Fernando, and N. Korte. Water Res. **29**, 2434 (1995).
21. W.-X. Zhang, C.-B. Wang, and H.-L. Lien. Catal. Today, **40**, 387 (1998).
22. M.S. Odziemkowski, R.W. Gillham, and R. Focht. *In* Environmental issues in the electronic/semiconductor industries and electrochemical/photo-chemical methods for pollution abatement. Vol. 98. *Edited by* C.R. Simpson, L. Mendicino, K. Rajeshwar, and J.M. Fenton. Electrochemical Society, Pennington, New Jersey. 1999. pp. 91–102.
23. K.P.J. Williams, G.D. Pitt, D.N. Batchelder, and B.J. Kip. Appl. Spectrosc. **48**, 232 (1994).
24. M. Odziemkowski, M. Krell, and D.E. Irish. J. Electrochem. Soc. **139**, 3052 (1992).
25. (*a*) A.C. Chialvo, W.E. Triaca, and A.J. Ariva. J. Electroanal. Chem. **146**, 93 (1983); (*b*) A. Visinitin, W.E. Triaca, and A.J. Ariva. J. Electroanal. Chem. **221**, 239 (1987).
26. B. Ren, Q.J. Huang, W.B. Cai, B.W. Mao, F.M. Liu, and Z.Q. Tian. J. Electroanal. Chem. **221**, 239 (1987).
27. K. Ritter, M. Odziemkowski, R. Simpraga, R.W. Gillham, and D.E. Irish. J. Contam. Hydrol. **65**, 121 (2003).
28. D.L.A. de Faria, S.V. Silva, and M.T. de Oliveira. J. Raman. Spectrosc. **28**, 879 (1997).
29. P. Kofstad. *In* High temperature corrosion. Elsevier Applied Science, New York. 1988.
30. J.W. Schultze. *In* Passivity of metals. *Edited by* R.P. Frankenthal and J. Kruger. Electrochemical Society, Princeton, New Jersey. 1978. p. 82.
31. B.A. Balko and P.G. Tratnyek. J. Phys. Chem. B, **102**, 1459 (1998).
32. T. Ohtsuka, K. Kubo, and N. Sato. Corrosion (Houston), **42**, 476 (1986).
33. J. Dünnwald and A. Otto. Corros. Sci. **29**, 1167 (1989).
34. M.S. Odziemkowski and R.W. Gillham. 213th National Meeting, American Chemical Society, San Francisco, Calif. Preprint Extended Abstracts, Division of Environmental Chemistry, **37**, No. 1. 1997. pp. 177–180.
35. (*a*) H.G. Oswin and M.Cohen. J. Electrochem. Soc. **104**, 9 (1957); (*b*) K. Ogura, S. Haruyama, and K. Nagasaki. J. Electrochem. Soc. Jpn. **37**, 102 (1969); (*c*) K. Ritter, M. Odziemkowski, and R.W. Gillham. J. Contam. Hydrol. **55**, 87 (2002).
36. Z. Qin, B. Demko, J. Noël, D. Shoesmith, F. King, R. Worthingham, and K. Keith. Corrosion. **60**, 906 (2004).
37. M.S. Odziemkowski, L. Gui, and R.W. Gillham. Environ. Sci. Technol. **34**, 3495 (2000).
38. J. Wang and J. Farrell. Environ. Sci. Technol. **37,** 3891 (2003).
39. (*a*) G. Jerkiewicz. Prog. Surf. Sci. **55**, 137 (1998); (*b*) T. Zakroczymski. *In* Hydrogen degradation of ferrous alloys. *Edited by* R.A. Oriani, J.P. Hirth, and M. Smialowski. Noyes Publications, Park Ridge, New Jersey. 1985. p. 215; (*c*) P.M.L. Bonin, W. Jedral, M.S. Odziemkowski, and R.W. Gillham. Corros. Sci. **42**, 1921, (2000).
40. P. Marcus and E. Protopopoff. *In* Electrochemical surface science of hydrogen adsorption and absorption. Vol. 97-16. *Edited by* G. Jerkiewicz and P. Marcus. Electrochemical Society, Pennington, New Jersey. 1997. pp. 211–224.
41. J. Flis and T. Zakroczymski. Corrosion (Houston), **48**, 530 (1992).

© 2004 NRC Canada

Synthesis and transformations of 60-, 62-, and 64-electron $Co_4(CO)_x(PNR_2)_2$ (x = 8, 9, 10) clusters[1]

Javier Sánchez-Nieves, Brian T. Sterenberg, Konstantin A. Udachin, and Arthur J. Carty

Abstract: A unique family of bis-(amino)phosphinidene Co_4 clusters with electron counts in the 60–64 e regime is described. The 62-electron (5 Co–Co) butterfly compound $[Co_4(CO)_8(\mu\text{-}CO)\{\mu_3\text{-}P(TMP)\}_2]$ (TMP = 2,2,6,6-tetramethylpiperidyl) (**1a**) is obtained via condensation of the bridged (amino)phosphinidene complex $[Co_2(CO)_6\{\mu\text{-}P(TMP)\}]$. Further heating and removal of CO gives the 60-electron (6 Co–Co) tetrahedral compound $[Co_4(CO)_6(\mu\text{-}CO)_2\{\mu_3\text{-}P(TMP)\}_2]$ (**3a**). The reaction of $K[Co(CO)_4]$ with $PCl_2(N\text{-}i\text{-}Pr_2)$ gives the 64-electron (4 Co–Co) square-planar derivative $[Co_4(CO)_8(\mu\text{-}CO)_2(\mu_4\text{-}PN\text{-}i\text{-}Pr_2)_2]$ (**2**), which loses one carbonyl ligand to form the 62-electron (5 Co–Co) butterfly compound $[Co_4(CO)_8(\mu\text{-}CO)(\mu_3\text{-}PN\text{-}i\text{-}Pr_2)_2]$ (**1b**). Complex **1b** releases another carbonyl to form the 60-electron (6 Co–Co) tetrahedral compound $[Co_4(CO)_6(\mu\text{-}CO)_2(\mu_3\text{-}PN\text{-}i\text{-}Pr_2)_2]$ (**3b**). X-ray structural analyses of compounds **1a**, **1b**, **2**, and **3a** have been carried out. The reversibility of the CO elimination reactions and the structural rearrangements accompanying changes in electron count in this series are discussed.

Key words: cobalt, cluster compounds, phosphinidene, skeletal rearrangement.

Résumé : On décrit une famille unique d'agrégats de la famille du bis-(amino)phosphinidène Co_4 comportant de 60 à 64 électrons. Le composé en forme de papille comportant 62 électrons (5 Co–Co), le $[Co_4(CO)_8(\mu\text{-}CO)\{\mu_3\text{-}P(TMP)\}_2]$ (TMP = 2,2,6,6-tétraméthylpipéridyl) (**1a**) est obtenu par condensation du complexe (amino)phosphinidène ponté $[Co_2(CO)_6\{\mu\text{-}P(TMP)\}]$. Un chauffage additionnel avec élimination du CO conduit au composé tétraédrique à 60 électrons (6 Co–Co) $[Co_4(CO)_6(\mu\text{-}CO)_2\{\mu_3\text{-}P(TMP)\}_2]$ (**3a**). La réaction du $K[Co(CO)_4]$ avec le $PCl_2(N\text{-}i\text{-}Pr_2)_2$ conduit au dérivé plan carré à 64 électrons (4 Co–Co) $[Co_4(CO)_8(\mu\text{-}CO)_2(\mu_4\text{-}PN\text{-}i\text{-}Pr_2)_2]$ (**2**) qui perd un ligand carbonyle pour former le composé en forme de papillon comportant 62 électrons (5 Co–Co), le $[Co_4(CO)_8(\mu\text{-}CO)(\mu_3\text{-}PN\text{-}i\text{-}Pr_2)_2]$ (**1b**). Le composé **1b** perd un autre ligand carbonyle pour former le composé tétraédrique à 60 électrons (6 Co–Co) $[Co_4(CO)_6(\mu\text{-}CO)_2(\mu_3\text{-}PN\text{-}i\text{-}Pr_2)_2]$ (**3b**). On a déterminé les structures des composés **1a**, **1b**, **2** et **3a** par diffraction des rayons X. On discute de la réversibilité des réactions d'élimination du CO et des réarrangements de structure qui accompagnent les changements dans les nombres d'électrons dans ces séries.

Mots clés : cobalt, agrégats, phosphinidène, réarrangement des squelettes.

[Traduit par la Rédaction]

Introduction

One of the most interesting regimes of low nuclearity metal cluster chemistry is that involving four metal atoms where structural changes in the M_4 skeletal framework accompany variations in cluster valence electron counts. Neither of the two principal models for bonding and structure, namely the effective atomic number rule (EAN) and the polyhedral skeletal electron pair theory (PSEPT) (1), satisfactorily account for all of the diverse structural features of molecules with 60–64 valence electrons. Thus, for example, the EAN rule, which describes the metal–metal interaction as a 2-centre 2-electron bond, predicts $E = (18n - N)/2$ metal–metal bonds between n transition metal atoms when the number of valence electrons is N e, leading to 6 M—M bonds in a 60 e tetrahedral framework, 5 M—M bonds (butterfly, 62 e), and 4 M—M bonds (square, rectangle, spiked triangle, 64 e). Exceptions to these rules include several electron deficient 62 e "square" M_4 frameworks such as $[Ru_4(CO)_{10}(\mu\text{-}CO)(\mu_4\text{-}PR)_2]$ (2) and a class of "electron-rich" butterfly 64 e molecules (3) such as $[Ru_4(CO)_{13}(\mu\text{-}PR_2)_2]$, which exhibit one or more elongated metal–metal

Received 8 February 2004. Published on the NRC Research Press Web site at http://canjchem.nrc.ca on 2 November 2004.

Dedicated to the late Dr. Donald G. Irish in memory of his contributions to Canadian chemistry.

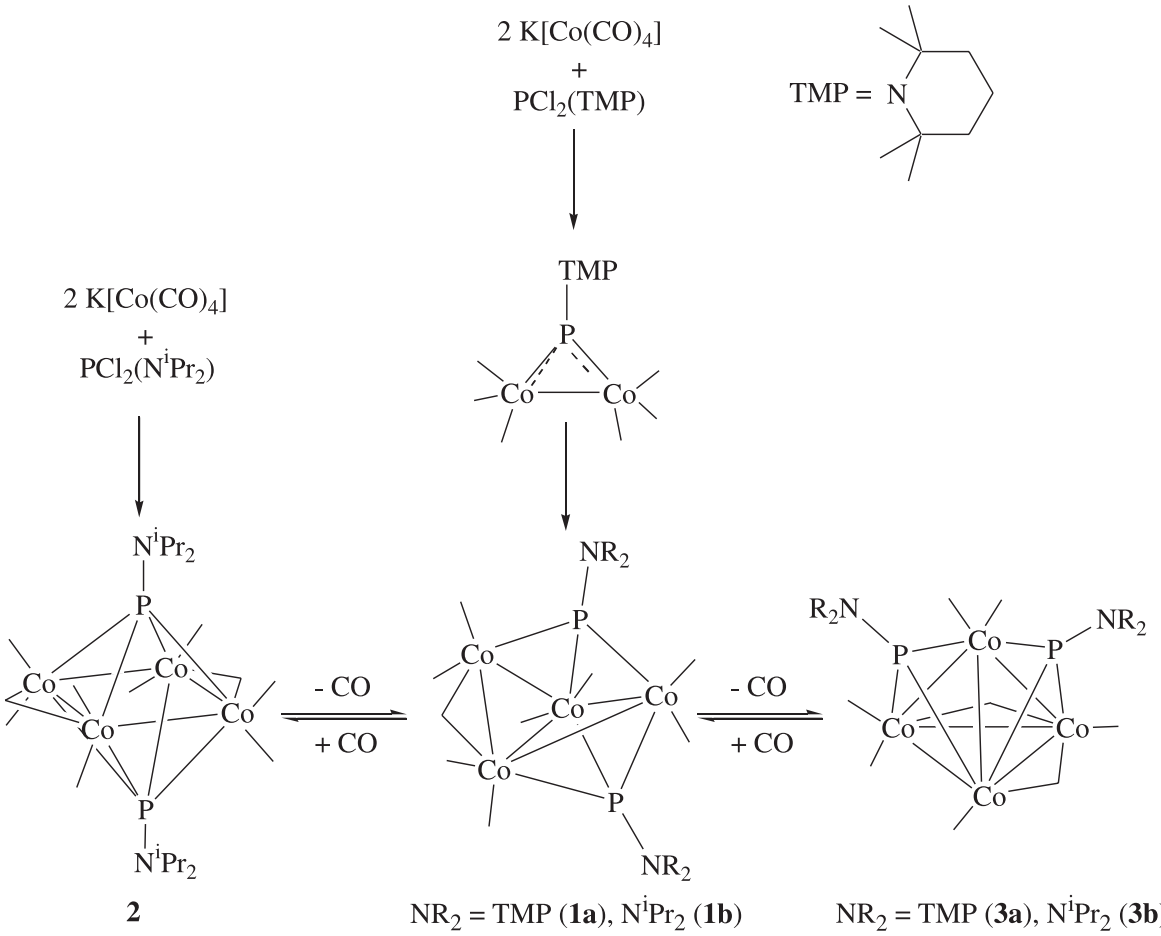
J. Sánchez-Nieves, B.T. Sterenberg,[2] K.A. Udachin, and A.J. Carty.[3] Steacie Institute for Molecular Sciences, National Research Council Canada, 100 Sussex Drive, Ottawa, ON K1A 0R6, Canada and the Ottawa-Carleton Chemistry Research Institute, Department of Chemistry, University of Ottawa, Ottawa, ON K1N 6N5, Canada.

[1]This article is part of a Special Issue dedicated to the memory of Professor Don Irish.

[2]Present address: Department of Chemistry and Biochemistry, University of Regina, 3737 Wascana Parkway, Regina, SK S4S 0A2, Canada.
[3]Corresponding author (e-mail: acarty@pco-bcp.gc.ca).

 doi: 10.1139/V04-124 © 2004 NRC Canada

Scheme 1.



bonds. On the other hand, in the PSEPT framework, the 7 skeletal electron pair (SEP) count of $[Ru_4(CO)_{10}(\mu\text{-CO})(\mu_4\text{-PPh})_2]$ is consistent with the square M_4 (or closo M_4P_2) polyhedron, whereas the 8 SEP molecules $[Co_4(CO)_{10}(\mu_4\text{-PR})_2]$ with a similar square Co_4 structure are electron rich (4). There are other anomalies within the 60–64 e regime including a 64-electron (8 SEP) puckered square framework in $[Ru_4(CO)_{12}(\mu_4\text{-PNR}_2)_2]$ where the nonconical nature of the ligands contributes to metal framework distortions (2*c*, 5). EHMO and DFT calculations have provided satisfactory answers to some of these structural features (3*e*, 3*f*, 5, 6). Although examples of single-step transformations (tetrahedron (60 e) ↔ butterfly (62 e) and butterfly ↔ square (64 e)) via 2 e donor additions or eliminations have been described (1*b*, 7), there are very few instances of sequential electronic and structural changes within a single family of compounds. Reversible transformations are even scarcer (1*b*, 3*b*–3*d*, 7*a*–7*b*, 8). One example is the spiked triangular osmium cluster $[Os_4(CO)_{15}(PMe_3)]$, which loses carbonyl ligands to give the planar butterfly (or rhomboidal) cluster $[Os_4(CO)_{14}(PMe_3)]$ and tetrahedral $[Os_4(CO)_{13}(PMe_3)]$ (9). The 64–60 e conversion has also been reported for the electron-rich (64 e) rhomboidal cluster $[Ru_4(CO)_{13}\{\mu\text{-P(N-}i\text{-Pr}_2)_2\}_2]$ (3*f*, 3*g*), although in this case, the reactions involved CO loss and μ_4-η^2-CO coordination to afford 62 e $[Ru_4(CO)_9(\mu\text{-CO})(\mu_4\text{-}\eta^2\text{-CO})\{\mu\text{-P(N-}i\text{-Pr}_2)_2\}]$ and hydrogenolysis of a phosphido bridge to afford 60 e $[(\mu_3\text{-H})Ru_4(CO)_9(\mu\text{-CO})\{\mu\text{-}P(N\text{-}i\text{-Pr}_2)_2\}(\mu_3\text{-PN-}i\text{-Pr}_2)]$.

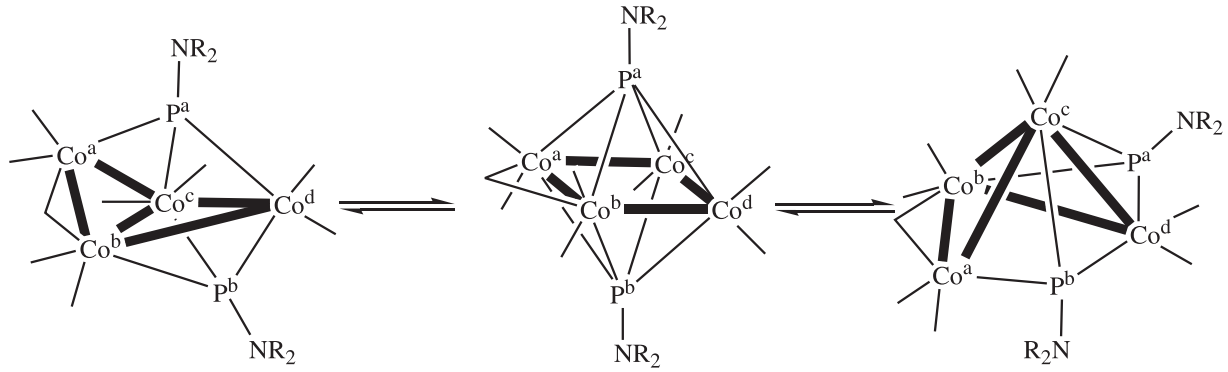
Through our recent synthetic work on stable Fischer type electrophilic terminal phosphinidene complexes (10), we prepared the unstable, doubly bridged phosphinidene compound $[Co_2(CO)_6\{\mu\text{-P(TMP)}\}]$ (TMP = 2,2,6,6-tetramethylpiperidyl) (11). This binuclear complex and its μ-PN-*i*-Pr_2 analogue undergo facile condensation reactions and CO loss to afford a unique family of 60, 62, and 64 e clusters whose structures and interconversions are described herein.

Results and discussion

We have reported that the reaction of $K[Co(CO)_4]$ with $PCl_2(TMP)$ in THF affords the unstable μ-(amino)phosphinidene complex $[Co_2(CO)_6\{\mu\text{-P(TMP)}\}]$, which can be stabilized by disubstitution with the bridging bis-diphenylphosphinomethane ligand (dppm) to form $[Co_2(CO)_4\{\mu\text{-P(TMP)}\}(dppm)]$ (11). In the absence of stabilizing ligands, the (amino)phosphinidene complex $[Co_2(CO)_6\{\mu\text{-P(TMP)}\}]$ loses carbonyl ligands in solution to give the tetracobalt cluster $[Co_4(CO)_8(\mu\text{-CO})\{\mu_3\text{-P(TMP)}\}_2]$ (**1a**) after 36 h of stirring in hexane (Scheme 1). The compound **1a** was identified by IR and NMR spectroscopies, X-ray diffraction studies, and elemental analysis. In the IR spectrum both terminal and bridging carbonyl bands were

© 2004 NRC Canada

Scheme 2.



observed. In the ^{31}P NMR spectrum at room temperature two broad resonances were found at δ 542.4 and δ 471.8. No coupling was observed between the phosphorus nuclei, probably as a result of broadening of the resonances via quadrupolar coupling to ^{59}Co and ^{14}N but also perhaps because of the onset of exchange (vide infra). We measured the ^{31}P NMR spectrum of **1a** at –40 °C and observed that each resonance was split into a doublet (J(PP) = 213 Hz) at this temperature. The formation of compound **1a** can be rationalised as the condensation of two $[Co_2(CO)_6\{\mu\text{-}P(TMP)\}]$ molecules with the loss of three CO groups. This process likely leads in a first step to the 64-electron cluster $[Co_4(CO)_{10}\{\mu_3\text{-}P(TMP)\}_2]$, which would possess a Co_4 rectangular framework (vide infra). Then, probably because of the bulky TMP group, it loses one carbonyl ligand to give the 62-electron compound $[Co_4(CO)_9\{\mu_3\text{-}P(TMP)\}_2]$ (**1a**).

We were not able to observe the proposed intermediate, though compounds of the type $[Co_4(CO)_{10}(\mu_4\text{-}PR)_2]$ with a planar Co_4 core are well-known in the literature (4). They can be prepared via reaction of $[Co(CO)_4]^-$ with dichlorophosphines (4*a*–4*c*), so we decided to carry out the reaction of $[Co(CO)_4]^-$ with the less bulky phosphinidene source $PCl_2(N\text{-}i\text{-}Pr_2)$ in an attempt to synthesize the analogous 64-electron cluster $[Co_4(CO)_{10}(\mu_4\text{-}PN\text{-}i\text{-}Pr_2)_2]$ to study whether this compound would release a carbonyl ligand to afford the 62-electron butterfly cluster $[Co_4(CO)_9(\mu_3\text{-}PN\text{-}i\text{-}Pr_2)_2]$.

Fast addition of a $K[Co(CO)_4]$ solution in THF to a solution of $PCl_2(N\text{-}i\text{-}Pr_2)$ in THF gave the expected 64-electron (8 SEP) cluster $[Co_4(CO)_8(\mu\text{-}CO)_2(\mu_4\text{-}PN\text{-}i\text{-}Pr_2)_2]$ (**2**) (Scheme 1), identified by means of IR and NMR spectroscopies, single-crystal X-ray diffraction, and elemental analysis. In this reaction we did not observe the parent compound $[Co_2(CO)_6(\mu\text{-}PN\text{-}i\text{-}Pr_2)]$, although we believe it should be formed as a necessary intermediate prior to the formation of compound **2**. The ^{31}P NMR spectrum of **2** showed a single resonance at δ 258 typical of *closo* octahedral $[Co_4(CO)_{10}(\mu_4\text{-}PR)_2]$ clusters (4), with both phosphorus atoms in apical positions in a Co_4P_2 framework, and in the IR spectrum we observed bands for both terminal and bridging carbonyl ligands again as expected for this type of complex.

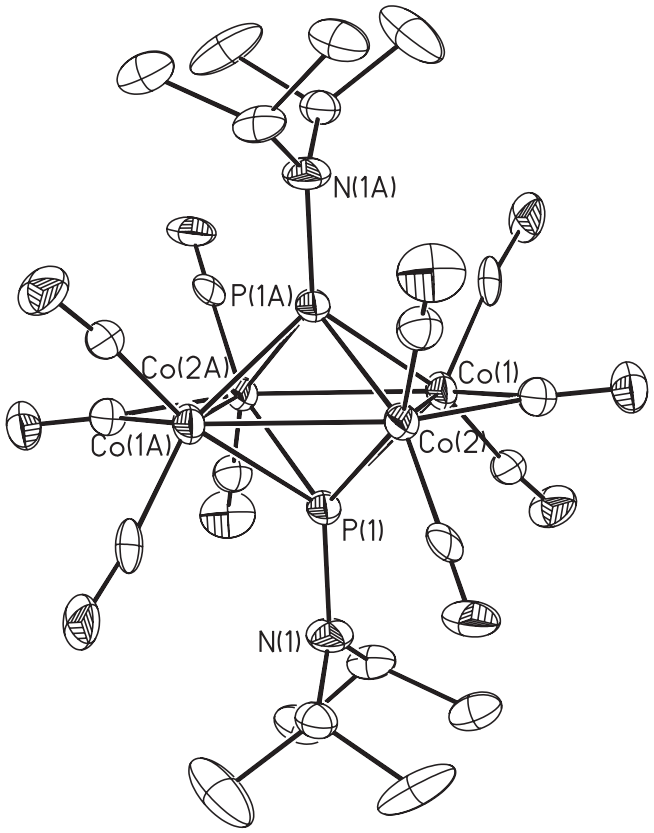
Once we had obtained the pure cluster $[Co_4(CO)_{10}(\mu_4\text{-}PN\text{-}i\text{-}Pr_2)_2]$ (**2**), we proceeded to charge an NMR tube equipped with a valve containing a solution of complex **2** in C_6D_6 and heated the contents at 60 °C with frequent removal of the inner atmosphere. We followed the course of the reaction by NMR spectroscopy and observed in the ^{31}P NMR spectrum the slow growth of a new broad resonance at δ 524 and in the ^1H NMR spectrum new resonances for the N-*i*-Pr_2 groups. We isolated the new compound by repeating the experiment in toluene and characterized it as the 62-electron butterfly cluster $[Co_4(CO)_8(\mu\text{-}CO)(\mu_3\text{-}PN\text{-}i\text{-}Pr_2)_2]$ (**1b**) (Scheme 1). In the IR spectrum we observed stretching bands for both terminal and bridging carbonyl ligands. As in compound **1a**, two different μ_3-phosphinidene ligands are present in the molecule, but in the ^{31}P NMR spectrum of compound **1b** only one broad resonance was observed for both phosphorus atoms. We carried out a variable-temperature ^{31}P NMR experiment of a solution of **1b** in CH_2Cl_2 and observed that the broad resonance was split into two new resonances upon cooling the sample, although we were unable to observe coupling between the two phosphorus nuclei even at –85 °C. At ambient temperature, both phosphorus atoms are equivalent on the NMR timescale presumably because of a dynamic process that essentially results in a "flapping of the wings" of the butterfly with Co–Co bond cleavage and reformation, which renders the two phosphinidene ligands equivalent on the NMR timescale (Scheme 2). The energy barrier for this process was estimated as 9.6 ± 0.5 kcal/mol (T_c = –27 °C). A possible intermediate in the dynamic process converting **A** to **C** in Scheme 2 is the octahedral cluster Co_4P_2 **B** with equivalent phosphinidene ligands. It is clear from the variable-temperature ^{31}P spectra described above that the barrier to the fluxional process in **1a** is considerably higher than in **1b**. Indeed, the fluxionality of **1b** even at –85 °C is sufficient to prevent the observation of any P–P coupling.

The loss of one carbonyl ligand from an octahedral $M_4(\mu_4\text{-}PR)_2$ cluster compound with 64 MVEs (8 SEP) has been reported previously (12), but in such cases the $M_4(\mu_4\text{-}PR)_2$ octahedral core is retained and the product is an unsaturated 62 MVE cluster according to the EAN rule.

When the same procedure as above was applied to solutions of the 62-electron butterfly clusters $[Co_4(CO)_9(\mu_3\text{-}PNR_2)_2]$ (NR_2 = TMP (**1a**), N-*i*-Pr_2 (**1b**)) in C_6D_6 new resonances appeared in the ^1H and ^{31}P NMR spectra. The same experiment was then carried out in toluene allowing

© 2004 NRC Canada

Fig. 1. ORTEP diagram of $[Co_4(CO)_8(\mu\text{-}CO)_2(\mu_4\text{-}PN\text{-}i\text{-}Pr_2)_2]$ (**2**). Hydrogen atoms have been omitted and thermal ellipsoids are shown at the 50% level.



isolation of the new tetrahedral 60-electron compound $[Co_4(CO)_6(\mu\text{-}CO)_2\{\mu_3\text{-}P(TMP)\}_2]$ (**3a**), while for the less bulky phosphinidene ligand PN-*i*-Pr_2 a mixture of **1b** and $[Co_4(CO)_6(\mu\text{-}CO)_2(\mu_3\text{-}PN\text{-}i\text{-}Pr_2)_2]$ (**3b**) was obtained (Scheme 1). In an attempt to obtain the derivative **3b** as the sole product, we added an equivalent of Me_3NO to a solution of **1b** in hexane. This procedure did not lead to the formation of compound **3b** and instead led to the precipitation of a dark solid. The remaining solution contained the cluster compounds **1b** and **2**. Thus, it seems that the presence of the bulky TMP group helps to stabilize the tetrahedral core in **3a**. In the ^{31}P NMR spectra, a single resonance was observed at δ 521 for **3a** and at δ 522 for **3b**. In the IR spectra, bands for terminal and bridging carbonyl ligands were observed. Suitable crystals for X-ray diffraction studies were obtained for **3a**. The carbonylation–decarbonylation processes described above are reversible and the cycle of loss and addition can be repeated, but eventually a dark decomposition product precipitated.

X-ray structural analyses

The X-ray structure of $[Co_4(CO)_8(\mu\text{-}CO)_2(\mu_4\text{-}PN\text{-}i\text{-}Pr_2)_2]$ (**2**) is shown in Fig. 1 and selected bond distances and angles are given in Table 1. The Co_4 framework forms a rectangle capped by two μ_4-(amino)phosphinidene ligands to give a Co_4P_2 octahedral core. Each Co atom is bound to two terminal carbonyl ligands and there are two μ_2-carbonyl ligands bridging opposite Co–Co edges, resulting in a total electron count of 64 e. This stereochemistry is typically

Table 1. Selected bond distances (Å) and angles (°) for $[Co_4(CO)_8(\mu\text{-}CO)_2(\mu_4\text{-}PN\text{-}i\text{-}Pr_2)_2]$ (**2**).

Bond distances (Å)	
Co(1)—Co(2)	2.5319(9)
Co(1)—Co(2A)	2.7046(8)
Co(1)—P(1)	2.2609(9)
Co(1)—P(1A)	2.266(1)
Co(2)—P(1)	2.2599(9)
Co(2)—P(1A)	2.271(1)
P(1)—N(1)	1.671(2)
P(1)—P(1A)	2.605(1)
Bond angles (°)	
Co(1)-P(1)-Co(2)	68.12(3)
Co(1)-P(1)-Co(2A)	73.27(3)
Co(1A)-P(1)-Co(2)	73.40(2)
Co(1A)-P(1)-Co(2A)	67.84(3)
N(1)-P(1)-Co(1)	125.34(9)
N(1)-P(1)-Co(2)	125.2(1)
N(1)-P(1)-Co(1A)	124.92(9)
N(1)-P(1)-Co(2A)	124.96(9)
C(6)-N(1)-C(9)	122.6(3)
C(6)-N(1)-P(1)	119.6(2)
C(9)-N(1)-P(1)	116.3(2)

found in complexes of the type $[Co_4(CO)_{10}(\mu_4\text{-}PR_2)_2]$ (4), and no distortion in the planar M_4 core is observed, in contrast to the isoelectronic 8-skeletal electron pair bis-(amino)phosphinidene compounds $[Ru_4(CO)_{12}(\mu_4\text{-}PNR_2)_2]$ (2*c*, 5) where the Ru_4 skeleton is significantly distorted from planarity and the phosphinidene ligands have two short and two long bonds to the ruthenium atoms. In the present case, it appears that the presence of a nonconical, electron releasing amino group bound to the phosphorus atom does *not* induce changes in the Co_4P_2 framework when compared with the analogous complexes $[Co_4(CO)_{10}(\mu_4\text{-}PR_2)_2]$ where $R \neq NR_2$. The P–P distance in **2** of 2.605(1) Å is similar to those found in other clusters $[Co_4(CO)_{10}(\mu_4\text{-}PR)_2]$, where the phosphinidene bears a bulky substituent (e.g., R = *t*-Bu, 2.608 Å (4*d*); $CH(SiMe_3)_2$, 2.627 Å (4*c*)) or where a less bulky aryl or alkyl phosphinidene is present (e.g., Ph, 2.533 Å (4*b*) and 2.544 Å (4*a*); *i*-Pr, 2.553 Å (4*e*)). These distances can be compared with twice the covalent radius of phosphorus (2.20 Å) indicating that there is a weak bonding interaction "through the cluster" between the two phosphorus atoms (4*a*, 6*a*). The value of the P—N bond length in **2** (1.671(2) Å) and the planar environment at the nitrogen atom (Σ = 358.5°) indicate π donation from the nitrogen atom to the phosphinidene phosphorus atom (11, 13).

The X-ray structures of $[Co_4(CO)_8(\mu\text{-}CO)(\mu_3\text{-}PNR_2)_2]$ (NR_2 = TMP (**1a**), N-*i*-Pr_2 (**1b**)) are shown in Figs. 2 and 3, respectively, and selected bond distances and angles are given in Table 2. The compounds **1a** and **1b** have a Co_4-butterfly framework with two different types of μ_3-phosphinidene ligands, one of which caps a closed Co_3 triangular face while the other is bound to an open Co_3 face consisting of two wing-tip cobalt atoms and one of the hinge cobalt atoms. All Co atoms have two terminal carbonyls and there is one bridging carbonyl between the two Co atoms bound to only one phosphorus atom, resulting in a total electron count of

© 2004 NRC Canada

Fig. 2. ORTEP diagram of $[Co_4(CO)_8(\mu\text{-}CO)\{\mu_3\text{-}P(TMP)\}_2]$ (**1a**). Hydrogen atoms have been omitted and thermal ellipsoids are shown at the 50% level.

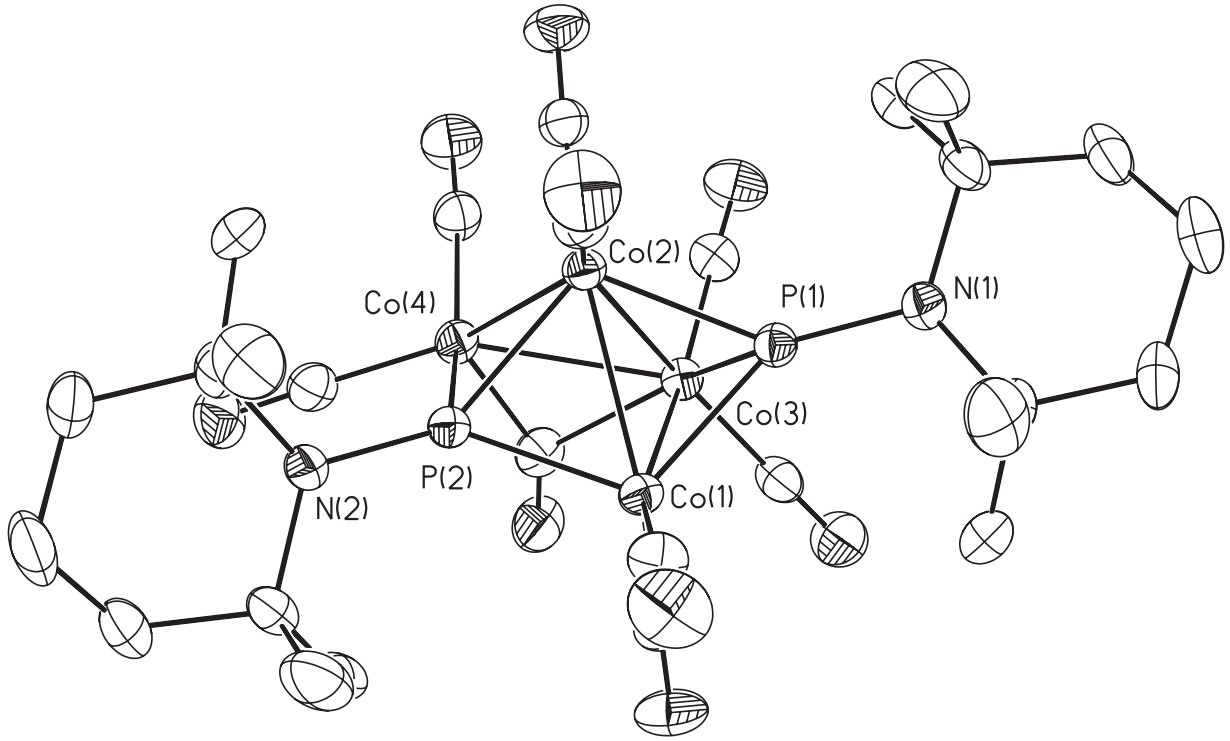
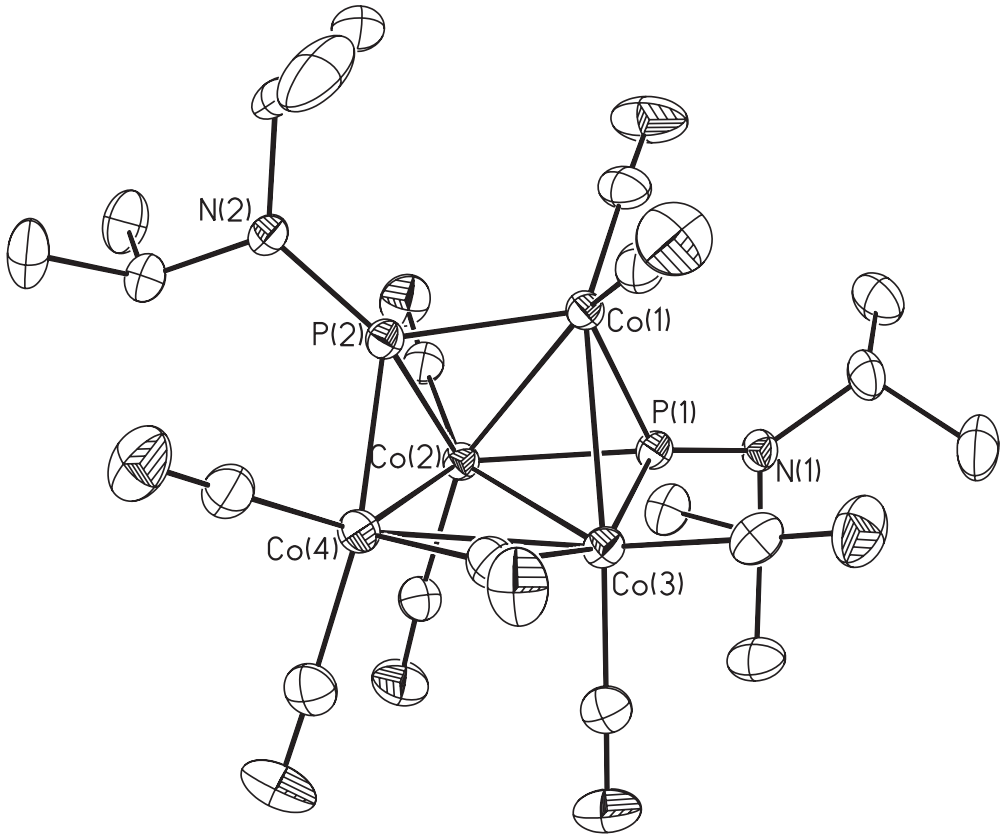


Fig. 3. ORTEP diagram of $[Co_4(CO)_8(\mu\text{-}CO)(\mu_3\text{-}PN\text{-}i\text{-}Pr_2)_2]$ (**1b**). Hydrogen atoms have been omitted and thermal ellipsoids are shown at the 50% level.



© 2004 NRC Canada

Table 2. Selected bond distances (Å) and angles (°) for $[Co_4(CO)_8(\mu\text{-}CO)(\mu_3\text{-}PNR_2)_2]$ (NR_2 = TMP (**1a**), N-*i*-Pr_2 (**1b**)).

	1a	**1b**
Bond distances (Å)		
Co(1)—Co(2)	2.4585(4)	2.4889(5)
Co(1)—Co(3)	2.5494(5)	2.5741(6)
Co(2)—Co(3)	2.5566(4)	2.5547(5)
Co(2)—Co(4)	2.6670(5)	2.6474(5)
Co(3)—Co(4)	2.5770(5)	2.5944(5)
Co(1)—P(1)	2.1472(7)	2.1191(8)
Co(2)—P(1)	2.1832(6)	2.1472(8)
Co(3)—P(1)	2.1597(7)	2.1471(8)
Co(1)—P(2)	2.1798(6)	2.1650(8)
Co(2)—P(2)	2.2118(7)	2.2258(8)
Co(4)—P(2)	2.1626(7)	2.1486(8)
P(1)—N(1)	1.655(2)	1.637(2)
P(2)—N(2)	1.682(2)	1.658(2)
Bond angles (°)		
Co(1)-P(1)-Co(2)	69.18(2)	71.37(3)
Co(1)-P(1)-Co(3)	72.59(2)	74.22(3)
Co(2)-P(1)-Co(3)	72.13(2)	73.01(3)
Co(1)-P(2)-Co(2)	68.08(2)	69.05(2)
Co(1)-P(2)-Co(4)	106.82(3)	106.97(3)
Co(2)-P(2)-Co(4)	75.12(2)	74.46(3)
N(1)-P(1)-Co(1)	138.62(8)	132.69(9)
N(1)-P(1)-Co(2)	138.62(8)	138.22(9)
N(1)-P(1)-Co(3)	135.90(8)	138.9(1)
N(2)-P(2)-Co(1)	130.27(8)	128.82(9)
N(2)-P(2)-Co(2)	134.85(8)	128.92(9)
N(2)-P(2)-Co(4)	120.83(8)	123.56(9)
C(10)-N(1)-C(14)	119.9(2)	117.6(2)
C(10)-N(1)-P(1)	118.9(2)	119.4(2)
C(14)-N(1)-P(1)	119.8(2)	122.3(2)
C(19)-N(2)-C(23)	118.9(2)	116.2(2)
C(19)-N(2)-P(2)	122.0(2)	119.5(2)
C(23)-N(2)-P(2)	117.8(2)	124.2(2)

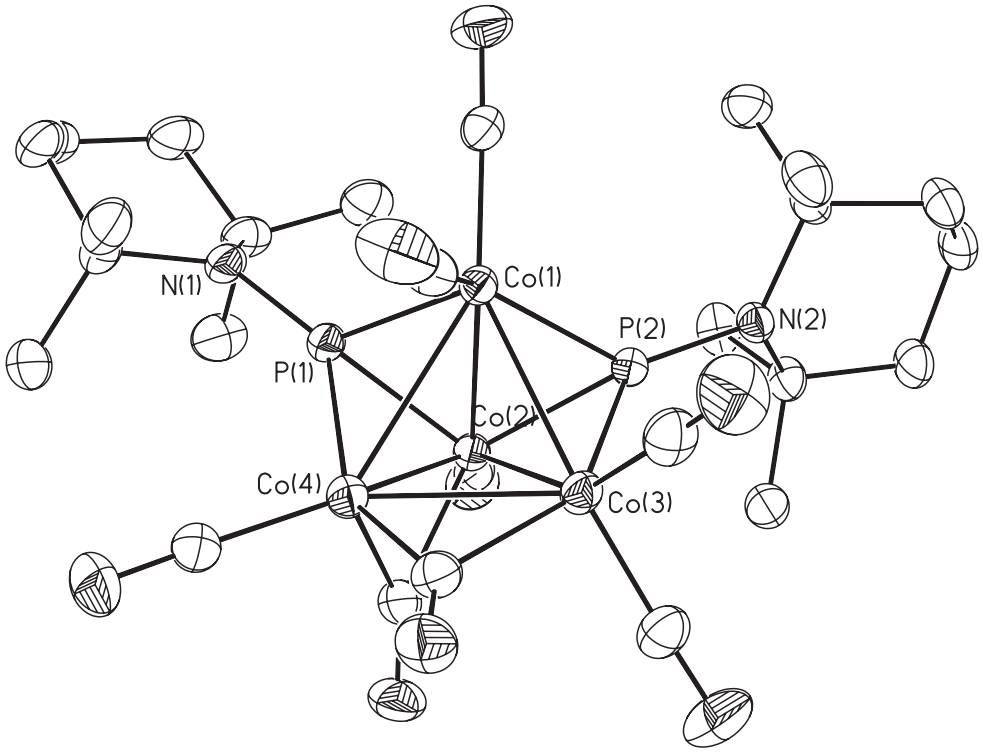
62 e or 7-skeletal electron pairs. This result is somewhat surprising since all of the structures known for complexes of the type $[Co_4(PR)_2]$ have an octahedral core as previously discussed for compound **2**. There are, however, well-known clusters of the type $[Co_4L_2]$ (L_2 = alkyne (14, 15), Al_2 (16), B_2 (17)) in which the tetracobalt core has a butterfly configuration, but these molecules, which have only 60 MVEs and are therefore electron deficient according to the EAN rule, are probably best described within the PSEPT framework as *closo* Co_4L_2 octahedra in which each main group fragment contributes three electrons to a 6-skeletal pair count.

The unsymmetrical disposition of the two phosphinidene ligands gives rise to an asymmetrical butterfly core, as reflected in the four Co—Co bond lengths between the hinge and wing-tip Co atoms. The shortest Co—Co bond distance (Co(1)—Co(2) = 2.4585(4) Å (**1a**), 2.4889(5) Å (**1b**)) lies between the two cobalt atoms supporting both μ_3-phosphinidene ligands, and is in the range of bond lengths found in cobalt carbonyl butterfly clusters of the type $[Co_4(CO)_{10}L_2]$ (L_2 = alkyne) (14). The longest bond (Co(2)—Co(4) = 2.6670(5) Å (**1a**), 2.6474(5) Å (**1b**)) is that between the wing-tip cobalt atom bound to only one μ_3-phosphinidene ligand (Co(4)) and the hinge cobalt atom bound to both μ_3-phosphinidene ligands (Co(2)). The other two Co—Co bond lengths are intermediate between the previous two (Co(1)—Co(3) = 2.5494(5) Å (**1a**), 2.5741(6) Å (**1b**); Co(3)—Co(4) = 2.5770(5) Å (**1a**), 2.5944(5) Å (**1b**)). The hinge Co(2)—Co(3) bond length (2.5566(4) Å (**1a**), 2.5547(5) Å (**1b**)) is a typical one, but the nonbonding wing-tip Co(1)—Co(4) distance (3.487 Å (**1a**), 3.467 Å (**1b**); dihedral angle = 103.5° (**1a**), 101.5° (**1b**)) is shorter than in the butterfly carbonyl clusters $[Co_4(CO)_{10}L_2]$ (L_2 = alkyne) (3.541–3.575 Å) (14) and longer than in the cyclopentadienyl butterfly molecules $[(\eta^5\text{-}C_5H_5Co)_4L_2]$ (L_2 = alkyne) (3.306–3.401 Å) (15). From the values of the Co—P bond distances it is clear that one stands out. This is the bond between the hinge Co atom bound to both phosphorus atoms and the phosphorus atom located between the wings (Co(2)—P(2) = 2.2118(7) Å (**1a**), 2.2258(8) Å (**1b**)), which is considerably longer than the remainder of the Co—P bond distances undoubtedly because this phosphorus atom is bound to an open Co_3 face with one nonbonding Co···Co contact. Although the two clusters **1a** and **1b** are very similar, all of the Co—P distances in **1a**, with the exception of Co(2)—P(2), are slightly longer than the corresponding values in **1b**, possibly because of the steric requirements imposed by the more bulky TMP ligand. Overall, the Co—P bond lengths lie within the range of values found in other cobalt μ_3-phosphinidene complexes (11, 13, 18). The N—P bond distances do not differ significantly from those in related μ_3-(amino)phosphinidene complexes, where π donation from the nitrogen atom to phosphorus atom is proposed (11, 13, 18). Accordingly the sums of angles at both nitrogen atoms indicate a planar environment (358.5° and 358.7° (**1a**), 359.9° and 359.3° (**1b**)).

The X-ray structure of the cluster $[Co_4(CO)_6(\mu\text{-}CO)_2\{\mu_3\text{-}P(TMP)\}_2]$ (**3a**) is shown in Fig. 4 and selected bond distances and angles are given in Table 3. This molecule consists of a tetrahedral Co_4 metallic core with two μ_3-(amino)phosphinidene ligands on two faces of the tetrahedron. There are two Co atoms that bear two terminal carbonyl ligands and two bound to only one terminal carbonyl ligand. Another two bridging carbonyl ligands are present in the molecule, sharing one Co atom, for a total electron count of 60 e. The Co_4 tetrahedral framework is distorted with one Co—Co bond distance being clearly shorter (Co(2)—Co(4) = 2.3847(4) Å) than the others, which range from 2.5323(4) to 2.6797(3) Å. The shortest bond is associated with the two cobalt atoms that share a bridging carbonyl ligand and a μ_3-phosphinidene ligand. The remainder of the values, except for the longest one (Co(1)—Co(4) = 2.6797(3) Å), are close to the Co—Co distances in the related tetrahedral μ_3-phosphinidene clusters $[Co_4(\mu_3\text{-}PPh)_4(PPh_3)_4]$ (2.571(3)–2.586(2) Å) (19) and $[Co_4(\mu_3\text{-}PPh)_4(PPh_3)_4][CoCl_3(PPh_3)]$ (2.527(6)–2.611(6) Å) (19), the only other reported tetrahedral phosphinidene Co_4 compounds. The Co—P bond lengths are within the normal range for μ_3-phosphinidene compounds (2.1412(5)–2.1788(5) Å) (11, 13, 18). The environments around both nitrogen atoms are close to planarity (357.97° and 357.23°) and the P—N bonds are typical of μ_3-(amino)phosphinidene clusters (1.658(2) and 1.664(1) Å) (11, 13, 18).

© 2004 NRC Canada

Fig. 4. ORTEP diagram of $[Co_4(CO)_6(\mu\text{-}CO)_2\{\mu_3\text{-}P(TMP)\}_2]$ (**3a**). Hydrogen atoms have been omitted and thermal ellipsoids are shown at the 50% level.



An examination of structural parameters for the entire set of clusters that were structurally characterized, namely **1a**, **1b**, **2**, and **3b**, reveals some interesting trends. Thus, for example, the average Co—Co bond length decreases from **2**, which has a 64 e count and square Co_4 framework (Co—Co avg. 2.618 Å), to **1a** (2.562 Å) and **1b** (2.572 Å), which have 62 e counts and butterfly Co_4 cores, to **3a** (2.553 Å), with a 60 e count and tetrahedral Co_4 skeleton. The metal–metal connectivity (i.e., the number of M—M bonds per metal atom) increases in the opposite sense from two in cluster **2** to two and three in clusters **1a** and **1b** to three in cluster **3b**. The difference in these values is small for the compounds **1a**, **1b**, and **3a**, where the phosphinidene ligands are of the μ_3-type. In the case of the tetrahedral compound **3a**, the average Co—Co bond length is rather similar to that found in the non-carbonyl cluster compounds $[Co_4(\mu_3\text{-}PPh)_4(PPh_3)_4]$ (2.578 Å) (19) and $[Co_4(\mu_3\text{-}PPh)_4(PPh_3)_4]^+$ (2.565 Å) (19), but longer than that in the homoleptic carbonyl $[Co_4(CO)_{12}]$ (2.490 Å) (20), where there are no ligands capping a face of the tetrahedral core. A shortening of the average Co—P bond distance is observed as expected when changing the coordination number of phosphorus from μ_4- (2.235 Å in **2**) to μ_3-phosphinidene (2.174 Å in **1a**, 2.159 Å in **1b**, and 2.159 Å in **3a**), these values being close to those in $[Co_4(\mu_3\text{-}PPh)_4(PPh_3)_4]$ (2.164 Å) (19) and $[Co_4(\mu_3\text{-}PPh)_4(PPh_3)_4]^+$ (2.160 Å) (19).

Conclusion

We have succeeded in synthesizing an entire family of tetracobalt clusters, namely 64 e square $[Co_4(CO)_{10}(\mu_4\text{-}PN\text{-}i\text{-}Pr_2)_2]$ (**2**), 62 e butterfly $[Co_4(CO)_9(\mu_3\text{-}PN\text{-}i\text{-}Pr_2)_2]$ (**1b**), and 60 e tetrahedral $[Co_4(CO)_8(\mu_3\text{-}PN\text{-}i\text{-}Pr_2)_2]$ (**3b**) via the reaction of $K[Co(CO)_4]$ and the dichloroaminophosphine $PCl_2N\text{-}i\text{-}Pr_2$. When the amino group is 2,2,6,6-tetramethylpiperidinyl (TMP), the intermediate observed en route to 62 e $[Co_4(CO)_9\{\mu_3\text{-}P(TMP\}_2]$ (**1a**) is the binuclear μ-P(TMP) phosphinidene complex $[Co_2(CO)_6\{\mu\text{-}P(TMP)\}]$. The clusters **1b**, **2**, and **3b** bearing diisopropylaminophosphinidene ligands undergo facile interconversion via a sequence of 2 e additions or eliminations of carbon monoxide. Similarly, **1a** and **3a** can be interconverted. The skeletal frameworks of this family of clusters are all in accord with the predictions of the EAN rule and provide a textbook illustration not only of electron count, structure, and bonding relationships within the 60–64 e regime, but also of the interconversion between structures through 2 e ligand gain or loss.

Experimental section

All procedures were carried out under a nitrogen atmosphere using standard Schlenk techniques or a glovebox. THF was distilled from Na–benzophenone and hexane was purified using solvent purification columns containing alumina and copper catalyst. Deuterated chloroform was vacuum distilled from P_2O_5. The compound $[Co_2(CO)_6\{\mu_2\text{-}P(TMP)\}]$ was prepared and used in situ from the reaction of $K[Co(CO)_4]$ and $PCl_2(TMP)$ (11). $PCl_2(N\text{-}i\text{-}Pr_2)$ and $PCl_2(TMP)$ were prepared according to published procedures (21) as was KC_8 (22) and $[Co_2(CO)_8]$ was purchased from Fluka. The NMR spectra were recorded on a Bruker Avance 400 spectrometer at 400 MHz (^1H) or 161.975 ($^{31}P\{^1H\}$).

© 2004 NRC Canada

Table 3. Selected bond distances (Å) and angles (°) for $[Co_4(CO)_6(\mu\text{-}CO)_2\{\mu_3\text{-}P(TMP)\}_2]$ (**3a**).

Bond distances (Å)	
Co(1)—Co(2)	2.5509(3)
Co(1)—Co(3)	2.5389(3)
Co(1)—Co(4)	2.6797(3)
Co(2)—Co(3)	2.6306(3)
Co(2)—Co(4)	2.3847(4)
Co(3)—Co(4)	2.5323(4)
Co(1)—P(2)	2.1764(5)
Co(2)—P(2)	2.1429(5)
Co(3)—P(2)	2.1788(5)
Co(1)—P(1)	2.1526(5)
Co(2)—P(1)	2.1412(5)
Co(4)—P(1)	2.1618(5)
P(1)—N(1)	1.658(2)
P(2)—N(2)	1.663(1)
Bond angles (°)	
Co(1)-P(1)-Co(2)	72.90(2)
Co(1)-P(1)-Co(4)	76.79(2)
Co(2)-P(1)-Co(4)	67.31(2)
Co(1)-P(2)-Co(2)	72.39(2)
Co(1)-P(2)-Co(3)	71.32(2)
Co(2)-P(2)-Co(3)	74.98(2)
N(1)-P(1)-Co(1)	130.03(6)
N(1)-P(1)-Co(2)	139.18(6)
N(1)-P(1)-Co(4)	141.91(6)
N(2)-P(2)-Co(1)	137.26(5)
N(2)-P(2)-Co(2)	138.49(5)
N(2)-P(2)-Co(3)	134.15(6)
C(13)-N(1)-P(1)	119.3(1)
C(9)-N(1)-P(1)	117.5(1)
C(13)-N(1)-C(9)	121.3(1)
C(22)-N(2)-C(18)	119.9(1)
C(18)-N(2)-P(2)	117.7(1)
C(22)-N(2)-P(2)	119.6(1)

$[Co_4(CO)_8(\mu\text{-}CO)\{\mu_3\text{-}P(TMP)\}_2]$ (1a)

A solution of $[Co_2(CO)_6\{\mu_2\text{-}P(TMP)\}]$ (1.46 mmol) in hexane (15 mL) was stirred at room temperature for 36 h. The solution was filtered, concentrated to 3 mL, and cooled to –40 °C, yielding **1a** as black needles (0.24 g, 40%). Spectral data for **1a**: IR (hexane, ν(CO), cm^{-1}): 1862 w, 2017 m, 2028 s, 2067 w. ^1H NMR (C_6D_6, δ): 1.34 (s, 12H, CH_2), 1.60 (s, 24H, Me). ^{31}P NMR (C_6D_6, δ): 471.8 (bs), 542.4 (bs). Anal. calcd. for $C_{27}H_{36}Co_4N_2O_9P_2$ (830.27): C 39.06, H 4.37, N 3.37; found: C 38.53, H 3.99, N 3.06.

$[Co_4(CO)_8(\mu\text{-}CO)(\mu_3\text{-}PN\text{-}i\text{-}Pr_2)_2]$ (1b)

A solution of $[Co_4(CO)_8(\mu\text{-}CO)_2(\mu_4\text{-}PN\text{-}i\text{-}Pr_2)_2]$ (**2**) (1.46 mmol, prepared in situ) in toluene (10 mL) was heated at 50 °C under vacuum for 14 h. Afterwards, the solvent was removed and the residue was extracted with hexane (10 mL). The solution was concentrated to approximately 4 mL and cooled to –40 °C, yielding **1b** as black crystals (0.19 g, 35%). Spectral data for **1b**: IR (hexane, ν(CO), cm^{-1}): 1866 w, 1990 w, 2009 m, 2026 s, 2062 w. ^1H NMR (C_6D_6, δ): 1.15 (d, ^3J(HH) = 6.55 Hz, 24H, CHMe_2), 3.86 (sept., ^3J(HH) = 6.55 Hz, 4H, CHMe$_2$). ^{31}P NMR (C_6D_6, δ): 526. Anal. calcd. for $C_{21}H_{28}Co_4N_2O_9P_2$ (750.14): C 33.62, H 3.76, N 3.73; found: C 33.56, H 3.51, N 3.64.

$[Co_4(CO)_8(\mu\text{-}CO)_2(\mu_4\text{-}PN\text{-}i\text{-}Pr_2)_2]$ (2)

$[Co_2(CO)_8]$ (0.50 g, 1.46 mmol) and KC_8 (0.45 g, 0.33 mmol) were stirred in THF (20 mL) for 45 min. The solution was filtered and added dropwise (10 min) to a solution of PCl_2(N-i-Pr_2) (0.21 mL, 1.46 mmol) in THF (10 mL) at room temperature. When the addition was complete, the solvent was removed. The residue was extracted with hexane (10 mL), concentrated to approximately 4 mL, and cooled to –40 °C, yielding **2** as black crystals (0.27 g, 48%). Spectral data for **2**: IR (hexane, ν(CO), cm^{-1}): 1867 w, 2000 m, 2030 s, 2089 w. ^1H NMR ($CDCl_3$, δ): 1.42 (d, ^3J(HH) = 6.92 Hz, 24H, CHMe_2), 3.86 (sept., ^{3}(HH) = 6.92 Hz, 4H, CHMe$_2$). ^{31}P NMR ($CDCl_3$, δ): 258. Anal. calcd. for $C_{22}H_{28}Co_4N_2O_{10}P_2$ (778.15): C 33.96, H 3.63, N 3.60; found: C 33.57, H 3.57, N 3.41.

$[Co_4(CO)_6(\mu\text{-}CO)_2\{\mu_3\text{-}P(TMP)\}_2]$ (3a)

A solution of $[Co_2(CO)_6\{\mu\text{-}P(TMP)\}]$ (1.46 mmol) in toluene (10 mL) was heated at 50 °C under vacuum for 16 h. Afterwards, the solvent was removed and the residue was extracted with hexane (10 mL). The solution was concentrated to 3 mL and cooled to –40 °C, yielding **3a** as black crystals (0.22 g, 38%). Spectral data for **3a**: IR (hexane, ν(CO), cm^{-1}): 1872 w, 2005 s, 2016 w, 2026 w, 2038 w. ^1H NMR (C_6D_6, δ): 1.19 (s, 12H, CH_2), 1.55 (s, 24H, Me). ^{31}P NMR (C_6D_6, δ): 521. Anal. calcd. for $C_{26}H_{36}Co_4N_2O_8P_2$ (802.26): C 38.93, H 4.52, N 3.49; found: C 38.43, H 4.23, N 3.06.

$[Co_4(CO)_6(\mu\text{-}CO)_2(\mu_3\text{-}PN\text{-}i\text{-}Pr_2)_2]$ (3b)

A solution of $[Co_4(CO)_8(\mu\text{-}CO)_2(\mu_4\text{-}PN\text{-}i\text{-}Pr_2)_2]$ (**2**) in C_6D_6 was introduced into an NMR tube sealed with a valve. The atmosphere was removed and the tube was heated at 50 °C. After 16 h, the ^{31}P and ^1H NMR spectra showed that the starting product **2** had disappeared and resonances for **1b** were observed. The sample was heated for another 16 h and a 1:1 mixture of **1b** and **3b** was observed. NMR data for **2** (C_6D_6, δ): ^1H: 1.10 (d, ^3J(HH) = 6.84 Hz, 24H, CHMe_2), 3.80 (sept., ^3J(HH) = 6.84 Hz, 4H, CHMe$_2$). ^{31}P: 257.0. NMR data for **1b** (C_6D_6, δ): ^1H: 1.15 (d, ^3J(HH) = 6.69 Hz, 24H, CHMe_2), 3.93 (sept., ^3J(HH) = 6.69 Hz, 4H, CHMe$_2$); ^{31}P: 527.1 broad. NMR data for **3b** (C_6D_6, δ): ^1H: 1.07 (d,^3J(HH) = 6.76 Hz, 24H, CHMe_2), 3.69 (sept., ^3J(HH) = 6.76 Hz, 4H, CHMe$_2$); ^{31}P: 523.8.

X-ray crystallographic study

Crystals of compounds **1a**, **1b**, **2**, and **3a** were mounted on glass fibres. Intensity data were collected on a Siemens SMART CCD diffractometer using graphite-monochromated Mo K_α radiation. Unit cells were determined from randomly selected reflections obtained using the SMART CCD automatic search, centre, index, and least-squares routines. Integration was carried out using SAINT and empirical absorption corrections were applied using SADABS. The structure solution and refinement were carried out using the SHELXTL 5.1 suite of programs. Initial solutions were ob-

© 2004 NRC Canada

Table 4. Crystal data for complexes **1a**, **1b**, **2**, and **3a**.

	1a	**1b**	**2**	**3a**
Formula	$C_{27}H_{36}Co_4N_2O_9P_2$	$C_{21}H_{28}Co_4N_2O_9P_2$	$C_{22}H_{28}Co_4N_2O_{10}P_2$	$C_{26}H_{36}Co_4N_2O_8P_2$
M_w	830.24	750.11	778.12	802.23
T (K)	173(2)	150(1)	125(2)	173(2)
λ (Å)	0.710 73	0.710 73	0.710 70	0.710 73
Crystal system	Monoclinic	Orthorhombic	Monoclinic	Triclinic
Space group	$P2_1$	$Pbca$	$P2_1/c$	$P\bar{1}$
Z	2	8	2	2
a (Å)	12.082 4(7)	12.537 8(8)	10.102(3)	9.824 7(7)
b (Å)	11.029 4(7)	15.941(1)	8.370(3)	10.019(7)
c (Å)	12.795 2(8)	29.486(2)	17.384(6)	18.595(1)
α (°)	90	90	90	83.630(1)
β (°)	95.593(1)°	90	94.406(5)	82.142(1)
γ (°)	90	90	90	64.582(1)
V (Å^3)	1 691.0(2)	5 893.2(6)	1 465.6(8)	1 634.9(2)
D (Mg/m^3)	1.625	1.691	1.763	1.630
μ (mm^{-1})	2.065	2.369	2.387	2.138
Reflections collected (unique)	20 299, 8536	70 405, 8282	17 732, 4085	20 648, 9092
R_1, $wR_2[I > 2\sigma(I)]$	0.024 4, 0.062 6	0.042 3, 0.081 0	0.035 9, 0.082 6	0.029 0, 0.071 1
Largest diff. peak and hole (e Å^{-3})	0.538, –0.279	1.052, –0.414	0.788, –0.974	0.677, –0.424

tained by direct methods and refined by successive least-squares cycles. Full matrix least-squares refinements minimized the function $\Sigma_{hkl}\,\omega(|Fo| - |Fc|)^2$ where $w = 1/\sigma(Fo^2)$, $\sigma(Fo) = \sigma(Fo^2)/2Fo$, and $\sigma(Fo^2) = [\sigma(I_{raw})^2 + (0.02I_{net})^2]^{1/2}/Lp$. Crystal data and collection parameters are listed in Table 4.[4]

Acknowledgments

We are grateful to the Natural Sciences and Engineering Research Council of Canada (NSERC) and the National Research Council Canada (NRC) for financial support of this work.

References

1. (*a*) K. Wade. Transition metal clusters. *Edited by* B.F.G. Johnson. Wiley and Sons, Chichester. 1980; (*b*) D.M.P. Mingos and D.J. Wales. Introduction to cluster chemistry. Prentice-Hall, Englewood Cliffs, New Jersey. 1990.
2. (*a*) J.S. Field, R.J. Haines, and D.N. Smit. J. Organomet. Chem. **224**, C29 (1982); (*b*) J.S. Field, R.J. Haines, and D.N. Smit. J. Chem. Soc. Dalton Trans. 1315 (1988); (*c*) W. Wang, J.F. Corrigan, G.D. Enright, N.J. Taylor, and A.J. Carty. Organometallics, **17**, 427 (1998).
3. (*a*) M.R. Churchill, C. Bueno, and D.A. Young. J. Organomet. Chem. **213**, 139 (1981); (*b*) R.D. Adams and L.W. Yang. J. Am. Chem. Soc. **105**, 235 (1983); (*c*) R.D. Adams, I.T. Horvath, and P. Mathur. J. Am. Chem. Soc. **106**, 6296 (1984); (*d*) R.D. Adams and I.T. Horvath. Inorg. Chem. **25**, 2534 (1986); (*e*) W.P. Mul, C.J. Elsevier, M. van Leijen, K. Vrieze, W.J.J. Smeets, and A.L. Spek. Organometallics, **11**, 1877 (1992); (*f*) J.F. Corrigan, S. Doherty, N.J. Taylor, and A.J. Carty. Organometallics, **12**, 993 (1993); (*g*) J.F. Corrigan, Y. Sun, and A.J. Carty. New J. Chem. **18**, 77 (1994); (*h*) J.F. Corrigan, M. Dinardo, S. Doherty, G. Hogarth, Y. Sun, N.J. Taylor, and A.J. Carty. Organometallics, **13**, 3572 (1994); (*i*) H.G. Ang, S.-G. Ang, and S. Du. J. Organomet. Chem. **590**, 1 (1999); (*j*) H.-C. Böttcher, M. Graf, K. Merzweiler, and C. Wagner. Polyhedron, **19**, 2593 (2000).
4. (*a*) R.C. Ryan and L.F. Dahl. J. Am. Chem. Soc. **97**, 6904 (1975); (*b*) R.C. Ryan, C.V. Pittman, and J.P. O'Connor. J. Organomet. Chem. **193**, 241 (1980); (*c*) A.M. Arif, A.H. Cowley, M. Pakulski, M.B. Hursthouse, and A. Karauloz. Organometallics, **4**, 2227 (1985); (*d*) J. Queisser and D. Fenske. Z. Anorg. Allg. Chem. **620**, 58 (1994); (*e*) D. Fenske, J. Queisser, and H. Schottmüller. Z. Anorg. Allg. Chem. **622**, 1731 (1996).
5. S. Kahlal, K.A. Udachin, L. Scoles, A.J. Carty, and J.-Y. Saillard. Organometallics, **19**, 2251 (2000).
6. (*a*) J.-F. Halet, R. Hoffmann, and J.-Y. Saillard. Inorg. Chem. **25**, 1695 (1985); (*b*) J.-F. Halet. Coord. Chem. Rev. **635**, 637 (1995).
7. (*a*) E. Sappa, A. Tiripicchio, A.J. Carty, and G.E. Toogood. Prog. Inorg. Chem. **35**, 437 (1987); (*b*) M.D. Vargas and J.N. Nicolls. Adv. Inorg. Chem. Radiochem. **30**, 123 (1986); (*c*) J.F. Corrigan, S. Doherty, N.J. Taylor, and A.J. Carty. J. Am. Chem. Soc. **116**, 9799 (1994); (*d*) S.P. Tunik, V.R. Krym, G.L. Stanova, A.B. Nikolskii, I.S. Podkorytov, S. Ooi, M. Yamasaki, and M. Shiro. J. Organomet. Chem. **481**, 83 (1994); (*e*) C.K. Schamer, S. Harris, M. Sabat, E.J. Voss, and D.F. Shriver. Inorg. Chem. **34**, 5017 (1995); (*f*) V. Ferrand, G. Süss-Fink, A. Neels, and H. Stoeckli-Evans. J. Chem. Soc. Dalton Trans. 3825 (1998); (*g*) H.G. Ang, S.-G. Ang, and S. Du. J. Chem. Soc. Dalton Trans. 2963 (1999); (*h*) S. Haak, A.

[4] Supplementary data may be purchased from the Directory of Unpublished Data, Document Delivery, CISTI, National Research Council Canada, Ottawa, ON K1A 0S2, Canada (http://www.nrc.ca/cisti/irm/unpub_e.shtml for information on ordering electronically). CCDC 229625–229628 contain the crystallographic data for this manuscript. These data can be obtained, free of charge, via www.ccdc.cam.ac.uk/conts/retrieving.html (or from the Cambridge Crystallographic Data Centre, 12 Union Road, Cambridge CB2 1EZ, UK; fax +44 1223 336033; or deposit@ccdc.cam.ac.uk).

© 2004 NRC Canada

Neels, H. Stoeckli-Evans, G. Süss-Fink, and C.M. Thomas. J. Chem. Soc. Chem. Commun. 1959 (1999); (*i*) V. Ferrand, G. Süss-Fink, A. Neels, and H. Stoeckli-Evans. Eur. J. Inorg. Chem. 853 (1999); (*j*) E.G.A. Notaras, N.T. Lucas, J.P. Blitz, and M.G. Humphrey. J. Organomet. Chem. **631**, 143 (2001); (*k*) A. Choualeb, P. Braunstein, J. Rosé, S.-E. Bouaoud, R. Welter. Organometallics **22**, 4405 (2003); (*l*) J.P. Canal, G.P.A. Yap, and R.K. Pomeroy. Organometallics, **22**, 3439 (2003); (*m*) Y. Li and W.-T. Wong. J. Chem. Soc. Dalton Trans. 398 (2003).

8. (*a*) V. Riaz, O. Curnow, and M.D. Curtis. J. Am. Chem. Soc **113**, 1416 (1991); (*b*) J.T. Park, Y. Chi, J.R. Shapley, M.R. Churchill, and J.W. Ziller. Organometallics, **13**, 813 (1994); (*c*) Y. Chi, P.C. Su, G.H. Lee, and S.-M. Peng. Organometallics, **14**, 5483 (1995); (*d*) J.T. Park, J.H. Chung, H. Song, K. Lee, J.H. Lee, J.-R. Park, and I.-H. Suh. J. Organomet. Chem. **526**, 215 (1996); (*e*) R.D. Adams, B. Captain, and W. Fu. Organometallics, **19**, 3670 (2000); (*f*) Y. Chi, S.-M. Peng, G.-H. Lee, and C.-J. Su. Organometallics, **20**, 1102 (2001).
9. L.R. Martin, F.W.B. Einstein, and R.K. Pomeroy. Organometallics, **7**, 294 (1988).
10. J. Sánchez-Nieves, B.T. Sterenberg, K.A. Udachin, and A.J. Carty. J. Am. Chem. Soc. **125**, 2404 (2003).
11. J. Sánchez-Nieves, B.T. Sterenberg, K.A. Udachin, and A.J. Carty. J. Cluster Sci. 15, 151 (2004).
12. (*a*) H. Vahrenkamp and D. Wolters. Organometallics, **1**, 874 (1982); (*b*) H.H. Ohst and J.K. Kochi. Organometallics, **5**, 1359 (1986).
13. (*a*) L. Markó and B. Markó. Inorg. Chim. Acta, **14**, L39 (1975); (*b*) H. Beurich, T. Madach, F. Richter, and H. Vahrenkamp. Angew. Chem. Int. Ed. Engl. **18**, 690 (1979); Angew. Chem. **91**, 690 (1979); (*c*) R.B. King, W.-K. Fu, and E.M. Holt. Inorg. Chem. **25**, 2390 (1986); (*d*) A.M. Arif, A.H. Cowley, M. Pakulski, M.B. Hursthouse, and A. Karauloz. Organometallics, **4**, 2227 (1986).
14. (*a*) G. Gervasio, R. Rossetti, and P.L. Stanghellini. Organometallics, **4**,1612 (1985); (*b*) R. Rumin, P. Courtot, J.E. Guerchais, F.Y. Petillon, L. Manojlovic-Muir, and K.W. Muir. J. Organomet. Chem. **301**, C1 (1986); (*c*) A.A. Pasynskii, Yu.V. Torubayev, A.Yu. Lyakina, R.I. Valiullina, and K.A. Lyssenko. Zh. Neorg. Khim. (Russ. J. Inorg. Chem.), **45**, 934 (2000); (*d*) D. Osella, M. Ravera, C. Nervi, C.E. Housecroft, P.R. Raithby, P. Zanello, and F. Laschi. Organometallics, **10**, 3253 (1991); (*e*) H.-P. Wu, Z.-Y. Zhao, S.-M. Liu,E.-R. Ding, Y.-Q. Yin, X.-Y. Huang, and K.-B. Yu. Polyhedron, **15**, 4117 (1996); (*f*) L.F. Dahl, D.L. Smith. J. Am. Chem. Soc. **84**, 2450 (1962); (*g*) S. Li-Cheng, S. Jin-Yu, H. Qing-Mei, and H. Xiao-Ying. Jiegou Huaxue, **14**, 281 (1995).
15. (*a*) H. Wadepohl, T. Borchert, and H. Pritzkow. Chem. Ber. **130**, 593 (1997); (*b*) C.E. Barnes, W.D. King, and J.A. Orvis. J. Am. Chem. Soc. **117**, 1855 (1995).
16. J.J. Schneider, C. Kruger, M. Nolte, I. Abraham, T.S. Ertel, and H. Bertagnolli. Angew. Chem. Int. Ed. Engl. **33**, 2435 (1994); Angew. Chem. **106**, 2537 (1994).
17. J. Feilong, T.P. Fehlner, and A.L. Rheingold. J. Am. Chem. Soc. **109**, 1860 (1987).
18. J. Sánchez-Nieves, B.T. Sterenberg, K.A. Udachin, and A.J. Carty. Can. J. Chem. **81**, 1149 (2003).
19. D. Fenske, R. Basogl, J. Hachgenei, and F. Rogel. Angew. Chem., Int. Ed. Engl. **23**, 160 (1984); Angew. Chem. **96**, 160 (1984).
20. L.J. Farrugia, D. Braga, and F. Grepioni. J. Organomet. Chem. **573**, 60 (1999).
21. R.B. King and N.D. Sadanani. Synth. React. Inorg. Met.-Org. Chem. **15**, 149 (1985).
22. A. Fűrstner. Angew. Chem. Int. Ed. Engl. **32**, 164 (1993).

© 2004 NRC Canada

Phase behaviour and dynamics in ethylammonium halide salts[1]

Christopher I. Ratcliffe

Abstract: ^{1}H and ^{2}H NMR spin-lattice relaxation times (T_1) have been studied as a function of temperature to obtain activation energies for the threefold reorientations of CH_3 groups (Ea = 22.83, 18.95, and 18.39 kJ mol^{-1}) and NH_3 groups (Ea = 47.64, 45.31, and 28.74 kJ mol^{-1}) in the β-phases of ethylammonium chloride, -bromide, and -iodide, respectively, for comparison with barriers determined from Raman torsional frequencies. T_1, ^{2}H NMR lineshapes, and DSC studies have been used to clarify the existence of a $\beta \rightarrow \alpha$ phase transition above room temperature in all three salts, and the absence of a transition at low temperature. ^{2}H NMR lineshape analysis indicates a rapid *n*-fold (probably fourfold) reorientation of the whole molecule in the α-phase. This motion occurs about an axis in the molecular CCN mirror plane in the bromide and iodide. In the chloride, the axis is in the plane perpendicular to the bisector of the DCD bond angle.

Key words: ethylammonium halides, solid state ^{1}H and ^{2}H NMR, molecular dynamics, rotational barriers, phase behaviour.

Résumé : On a mesuré les temps de relaxation spin-réseau (T_1) en RMN du ^{1}H et du ^{2}H, en fonction de la température, dans les phases β respectivement du chlorure, du bromure et de l'iodure d'éthylammonium afin de déterminé les énergies d'activation des réorientations ternaires des groupes CH_3 (Ea = 22,83, 18,95 et 18,39 kJ mol^{-1}) et des groupes NH_3 (Ea = 47,64, 45,31 et 28,74 kJ mol^{-1}) et de pouvoir les comparer avec les valeurs des barrières déterminées à partir des fréquences de torsion Raman. On a utilisé les valeurs des T_1, les formes des raies en RMN du ^{2}H et des études d'analyse calorimétrique différentielle (ACD) pour clarifier l'existence d'une transition de phase $\beta \rightarrow \alpha$ au-dessus de la température ambiante, dans chacun des trois sels, et de l'absence d'une transition à basse température. L'analyse de la forme des raies de la résonance du ^{2}H indique qu'il se produit une réorientation rapide, probablement quaternaire, de l'ensemble de la molécule dans la phase α. Dans le bromure et l'iodure, ce mouvement se produit autour d'un axe dans le plan miroir CCN. Dans le chlorure, l'axe se trouve dans un plan perpendiculaire à la bissectrice de l'angle de liaison DCD.

Mots clés : halogénures d'éthylammonium, RMN du ^{1}H et du ^{2}H à l'état solide, dynamique moléculaire, barrières à la rotation, comportement des phases.

[Traduit par la Rédaction]

Introduction

The ethylammonium halide salts $C_2H_5NH_3^+X^-$, where X = Cl, Br, or I, form a series that is unusual in that all three salts have the same crystal structure, generally referred to as the β-phase, at room temperature and below (1–3). The NH_3^+ group is surrounded by and has hydrogen-bonding interactions with three halide ions in a roughly threefold arrangement. This environment gives rise to a fairly large external contribution to the barrier to rotation about the threefold axis of the group. The fact that the structures are alike thus makes possible a fairly direct comparison of the hydrogen-bonding strengths from measurements of the rotational barriers. In previous work, barriers were determined from values of the torsional mode frequencies obtained from IR and Raman spectroscopy (4). Another method, employed in the current study, is to obtain activation energies for the NH_3^+ and CH_3 group reorientations by measuring NMR spin-lattice relaxation times (T_1) as a function of temperature. It is then of great interest to be able to compare the NMR activation energies with the IR and Raman barrier values, since it is found that when hydrogen bonding occurs there is generally an appreciable difference between the two, which might be explained by a larger sixfold term in the barrier potential (5–7). The strengths of the external interactions of each group are also reflected in the results of high pressure Raman studies of the bromide up to several kilobars (8), where the torsional mode and barrier were found to have a strong pressure dependence for CH_3 (in a soft environment), but not for NH_3 (in a hard environment).

Received 20 May 2004. Published on the NRC Research Press Web site at http://canjchem.nrc.ca on 1 December 2004.

Dedicated to the memory of Professor Donald E. Irish.

C.I. Ratcliffe. Steacie Institute for Molecular Sciences, National Research Council of Canada, 100 Sussex Drive, Ottawa, ON K1A 0R6, Canada. (e-mail: chris.ratcliffe@nrc-cnrc.gc.ca).

[1]This article is part of a Special Issue dedicated to the memory of Professor Don Irish.

 doi: 10.1139/V04-126 © 2004 NRC Canada

Also of interest are the phase transitions, to which NMR is often quite sensitive, and the changes in the dynamics of the ethylammonium ion associated with these. ^{2}H NMR lineshape studies are particularly useful with regard to the latter. There seems to be some conflicting information regarding phase transitions in the chloride and bromide. Phase transitions from the room temperature β-phase to a high temperature α-phase in the bromide and iodide are well-established (3, 9, 10), though a similar transition for the chloride has only been reported in one study (10) and was not detected in DSC and TGA studies (11, 12). IR and Raman studies of all three salts (4, 8–10, 13, 14) and NQR studies of the bromide and iodide (15) all seem to indicate that the room temperature β-phase is stable down to liquid nitrogen temperatures. However, the DSC results of Rao et al. (10) on the chloride and bromide show thermal events at 221 and 236 K, respectively, which they suggest are phase transitions. They also reported a larger thermal change in the chloride at 345 K, which they interpreted as a $\beta \rightarrow \alpha$ transition, though other studies have suggested that the chloride remains in the β-phase up to its melting point at 369 K (3, 9).

Experimental

The salts were prepared by neutralization of a solution of ethylamine, $C_2H_5NH_2$ (Aldrich) or $C_2D_5NH_2$ (MSD Isotopes), by the appropriate acids followed by evaporation to dryness and several hours pumping under vacuum. The deuterated materials $C_2H_5ND_3X$ were prepared by dissolving the $C_2H_5NH_3X$ salts in D_2O (MSD Isotopes) and evaporating to dryness and repeating this twice.

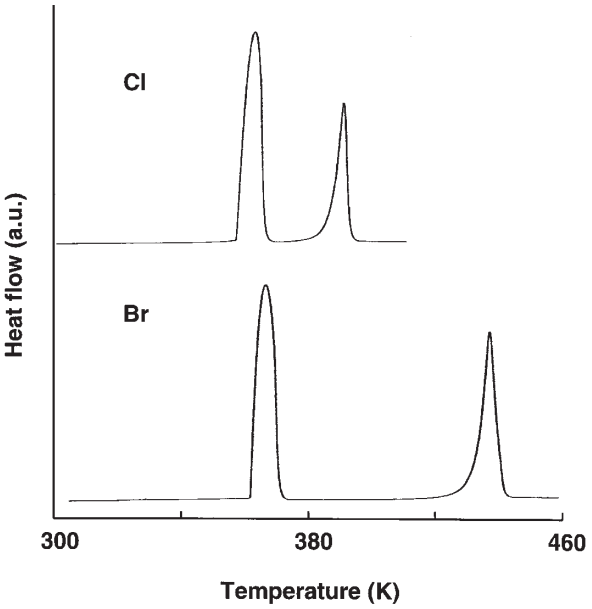
^{1}H T_1 measurements on $C_2H_5NH_3I$ and $C_2H_5ND_3I$ were obtained at 31 MHz using a Bruker BKR-322s spectrometer and temperature control as previously described (16, 17). All other measurements of ^{1}H T_1 of $C_2H_5NH_3^+$ chloride and bromide at 18 MHz and ^{2}H T_1 of $C_2H_5ND_3^+$ in all three salts at 9.2 MHz were obtained on a Bruker SXP spectrometer and electromagnet with temperature controlled in an Andonian cryostat. The ^{1}H T_1 values were generally measured with a $\pi - \tau - \pi/2$ pulse sequence. For $T_1 > 3$ s, a saturation sequence ($(\pi/2)_n - \tau - \pi/2$) was used. The ^{1}H spin-lattice relaxation was quite exponential on the low temperature side of the low-temperature T_1 minimum in all cases, but for the chloride and bromide around the minimum and to higher temperatures there was marked nonexponential behaviour (in both cases in the approximate temperature range 220–295 K). This problem became much less pronounced as T_1 began to decrease again towards the high-temperature T_1 minimum. In the problem region, a nominal "T_1" was estimated from a linear fit to the initial magnetization recovery, over about $2 \times T_1$, since this gave less scatter of points than estimates made from null times or forced linear fits over longer times.

To obtain more reliable values of the activation energies for the $-NH_3^+$ motion, without the complications of an overlapping relaxation process for the $-CH_3$ group and the nonexponential relaxation behaviour described above, ^{2}H T_1 measurements were obtained for the $C_2H_5ND_3^+$ salts. $\pi/2 - \tau - \pi/2$ or $\pi - \tau - \pi/2$ pulse sequences were used followed by generation of a quadrupolar echo using a 90° phase-shifted $\pi/2$ pulse after a delay of ~40 μs. It is known from T_1 measurements based on anisotropic ^{2}H lineshapes that T_1 values vary slightly across the spectrum (18). One assumes that this small variation is averaged in obtaining a T_1 from measurements of the quadrupolar echo amplitudes. Indeed, in the experiments reported here the measured relaxation was found to be exponential within experimental error. In both $C_2H_5NH_3Cl$ and $C_2H_5ND_3Cl$, the T_1 measurements were restricted somewhat at the high-temperature end approaching the melting point, by the appearance of a much longer free-induction decay component. This might be associated with the suggested phase transition at ~345 K (10) or possibly due to a trace of highly concentrated solution as the salt is very hygroscopic and difficult to dry.

^{2}H NMR lineshapes were obtained on a Bruker CXP-180 NMR spectrometer at 27.63 MHz using quadrupole echo techniques (19), with 90° pulse lengths of 2.7–3.0 μs and recycle times of 0.25–60 s, using a variable-temperature N_2 gas-flow probe with a Bruker B-VT-1000 temperature controller.

DSC traces for the chloride and bromide were obtained using a Tian-Calvet (Setaram model BT) heat flow calorimeter.

Fig. 1. DSC plots for $C_2H_5NH_3Cl$ and $C_2H_5NH_3Br$.



Results and analysis

Calorimetry

Figure 1 shows the DSC scans for the chloride and bromide above room temperature. Both are very similar in appearance and show two major thermal events that correspond to the known $\beta \rightarrow \alpha$ and melting transitions. The enthalpies for the $\beta \rightarrow \alpha$ transitions are almost identical. A comparison of these and previous results is given in Table 1. A scan on the chloride starting at 200 K showed no trace of the thermal event at 221 K reported earlier (10), also the $\beta \rightarrow \alpha$ and melting temperatures for the chloride in the current study are also significantly higher, suggesting that perhaps the earlier measurements were influenced by impurities.

© 2004 NRC Canada

Table 1. Phase transition information.

Ion	$\gamma \rightarrow \beta$? (K)	$\beta \rightarrow \alpha$ (K)	mp (K)	Method	Reference
Cl	221(0.3)[a]	345(7.4)	369	DSC	10
			381(9.79)	DSC	11
			382	DTA	12
		357.4(11.56)	383.4(5.52)	DSC	This work
		362±5		^{1}H NMR	This work
		362±2 (ND_3)		^{2}H NMR	This work
		363±2 (C_2D_5)		^{2}H NMR	This work
Br	236(0.3)	363(9.6)		DSC	10
		363w 357c[b]	434(8.37)	DSC	11
		365		?	3
		362	423	DTA	12
		362(11.55)	428.2(8.27)	DSC	This work
		367±5		^{1}H NMR	This work
		362±2w 353±2c(ND_3)		^{2}H NMR	This work
		363±2(C_2D_5)		^{2}H NMR	This work
I		328		?	3
		330±5		^{1}H NMR	This work
		325±2 (ND_3)		^{2}H NMR	This work
		329±2 (C_2D_5)		^{2}H NMR	This work

[a]Values in brackets are enthalpies (kJ mol^{-1}) for the phase change.
[b]Values on warming and cooling.

^{1}H and ^{2}H spin-lattice relaxation

Log plots of T_1 vs. 1000/T are shown in Figs. 2–4. All three $C_2H_5NH_3^+$ salts show two overlapping relaxation processes corresponding to threefold reorientation of NH_3^+ and CH_3 and the results for the deuteriated materials very clearly show that NH_3^+ reorientation is the higher temperature process, as expected based on the barriers calculated from the Raman torsional frequencies (4).

The BPP theory (20) as extended and modified by others (21, 22) forms the basis for understanding the ^{1}H T_1 results. Relaxation is effected by reorientation of the internuclear dipole–dipole vectors in the applied field. The general expression for threefold reorientation of an equilateral triangle of protons is given by

$$[1] \quad (1/T_1)_{H-H} = (9/20)(\gamma_H^4\hbar^2/r^6_{H-H})\{\tau_c/(1 + \omega_H^2\tau_c^2) + 4\tau_c/(1 + 4\omega_H^2\tau_c^2)\}$$

where γ_H = ^{1}H magnetogyric ratio, $\hbar = h/2\pi$, $r_{H\text{-}H}$ = interproton distance, ω_H = ^{1}H Larmor frequency, and τ_c = correlation time for the motion. τ_c is generally assumed to have an Arrhenius dependence on the activation energy for the motion (Ea) and on temperature (T)

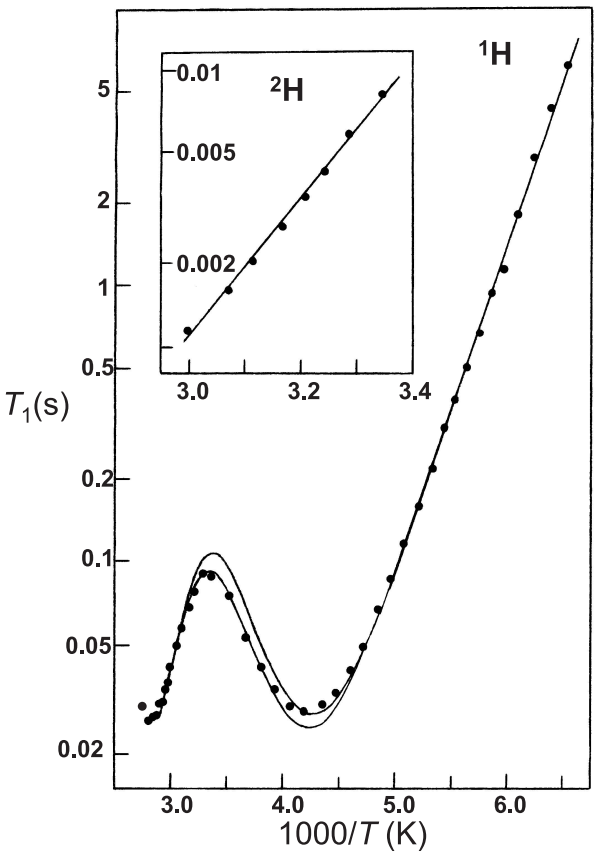
$$[2] \quad \tau_c = \tau_c^0 \exp(Ea/RT)$$

For NH_3^+, the expression must be modified to account for the ^{14}N–^{1}H dipolar interactions, which make a small but significant contribution to the relaxation (about 14% at the T_1 minimum (23)). The effective T_1 is given to a good approximation by

$$[3] \quad 1/T_1 = [1/T_1]_{H\text{-}H} + [1/T_1]_{N\text{-}H}$$

where the first term is the same as eq. [1] and the modifying term is given by

Fig. 2. ^{1}H (18 MHz) T_1 plot for $C_2H_5NH_3Cl$. Inset: ^{2}H (9.2 MHz) T_1 plot for $C_2H_5ND_3Cl$. The solid lines correspond to the fits described in the text. The two minima for the CH_3 BPP curve correspond to set values of 25 and 28 ms.



© 2004 NRC Canada

Fig. 3. ^{1}H (18 MHz) T_1 plot for $C_2H_5NH_3Br$. Inset: ^{2}H (9.2 MHz) T_1 plot for $C_2H_5ND_3Br$. The solid lines correspond to the fits described in the text. The minimum for the CH_3 BPP curve corresponds to a set value of 27 ms.

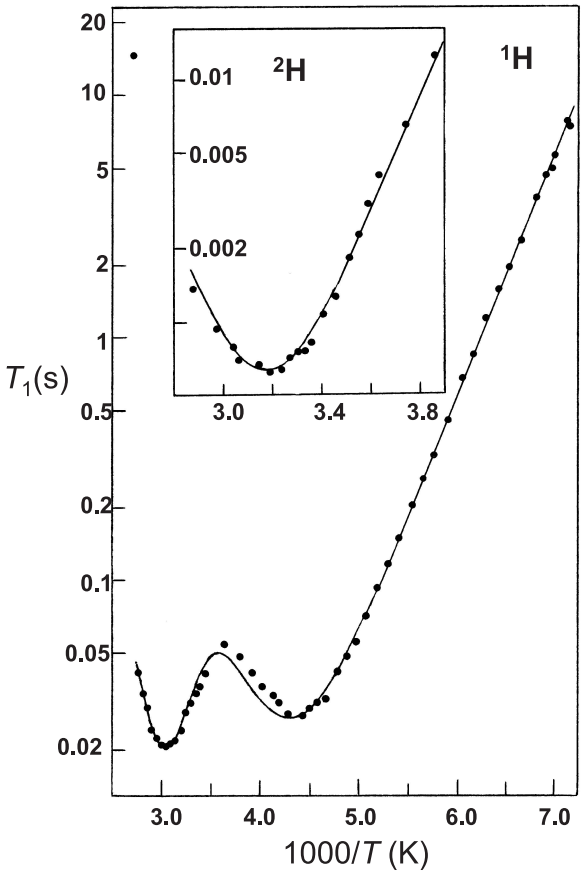
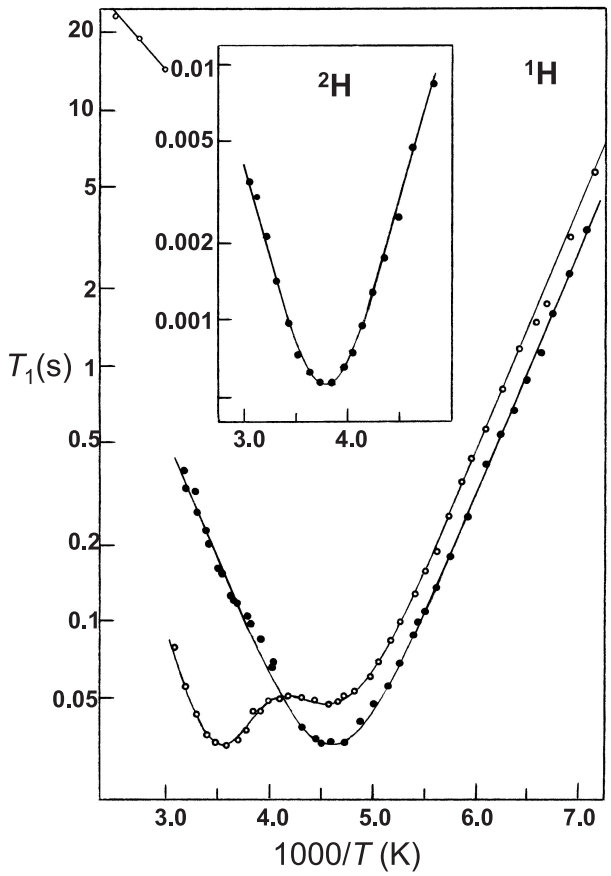


Fig. 4. ^{1}H (31 MHz) T_1 plots for $C_2H_5NH_3I$ (open circles) and $C_2H_5ND_3I$ (filled circles). Inset: ^{2}H (9.2 MHz) T_1 plot for $C_2H_5ND_3I$. The solid lines correspond to the fits described in the text.



[4] $$[1/T_1]_{N\text{-}H} = [2\gamma_H^2\gamma_N^2\hbar^2 g(\Delta)/r^6_{N\text{-}H}]\{\tau_c/(1 + \omega_H^2\tau_c^2)\}$$

[5] $$g(\Delta) = (\sin^2(2\Delta) + \sin^4\Delta)$$

and Δ = the angle between the N-H vector and the threefold rotation axis.

T_1 minima are predicted from eq. [1] when $\omega_H\tau_c = 0.616$ and, assuming $\Delta = (180 - Td)$ for the NH_3^+ group (where Td = tetrahedral angle), from eq. [4] when $\omega_H\tau_c = 0.663$ (23). Assuming values of C-H = 1.10 Å and N-H = 1.04 Å and tetrahedral bond angles, one can calculate theoretical T_1 minima. In the case of $C_2H_5NH_3^+$, the motion of three protons effects relaxation of all eight protons (via spin diffusion) and hence, for CH_3 motion at 31 MHz one calculates 48.00 ms and for $-NH_3^+$ motion 29.33 ms. Equivalent empirical values are 52–63.5 ms (for CH_3) (24) and 32–38 ms (for NH_3) (25). It is almost invariably found that the calculated values are less than experimental values. Thus, the observed depths of the T_1 minima for the iodide (51 and 38 ms) are quite consistent with threefold reorientation of CH_3 and NH_3^+, respectively. The minimum of 22 ms observed for NH_3^+ for the bromide at 18 MHz, which scales to 38 ms at 31MHz, is also consistent. Although accurate values for the minima for CH_3 for the chloride and bromide cannot be obtained because of the problems with nonexponential relaxation, the results are nevertheless quite close to the expected value (51 ms converts to 30 ms at 18 MHz). ^{1}H T_1 measurements have previously been obtained for ethylammonium nitrate (26) and ethylammonium tetrabromomercurate(II) (27). In the former, CH_3 group reorientation again occurs at lower temperatures than for NH_3 and the T_1 minimum for $C_2H_5ND_3NO_3$ is consistent with the numbers above for CH_3 after correction for frequency and spin diffusion. The $HgBr_4$ salt is different in that the relaxation is clearly due to whole molecule reorientation.

Deuterium spin-lattice relaxation is effected by reorientation of the ^{2}H nuclear quadrupolar coupling tensor in the applied field. For the threefold reorientation of a $-ND_3^+$ group, the relaxation behaviour can be expressed as (22, 28, 29)

[6] $$(1/T_1)_D = (9\pi^2/40)C_Q^2(1 + \eta^2/3)g(\Delta)\{\tau_c/(1 + \omega_D^2\tau_c^2) + 4\tau_c/(1 + 4\omega_D^2\tau_c^2)\}$$

where C_Q and η are the quadrupole coupling constant and asymmetry parameters for the deuteron when the ND_3^+ group is static. Strictly speaking, Δ is the angle between the threefold rotation axis and the unique component of the electric field gradient tensor (q_{zz}), which in the present case is reasonably assumed to be along the N—D bond. Based on the static ^{2}H quadrupolar coupling constants observed for the bromide and iodide at low temperatures (see the following) the T_1 minimum calculated using eq. [6] is ~0.485 ms.

© 2004 NRC Canada

Table 2. Activation energies and correlation times for CH_3 and ND_3 reorientation in the β-phases of the ethylammonium halides from ^1H and ^2H T_1 results.

Ethylammonium halides	Ea (kJ mol^{-1})	τ_c^0 (s)[a]	R^b
$CH_3CH_2ND_3Cl$	47.64±1.20	(~1.7×10^{-15})	0.9980
$CH_3CH_2NH_3Cl$	22.83±0.23	(~4.3×10^{-14})	0.9994
$CH_3CH_2ND_3Br$	45.31±0.87	$3.23 \pm 1.33\times10^{-16}$	0.9981
$CH_3CH_2NH_3Br$	18.95±0.09	(~2.8×10^{-13})	0.9998
$CH_3CH_2ND_3I$	28.74±0.22	$2.17 \pm 0.23\times10^{-14}$	0.9995
$CH_3CH_2ND_3I$	18.39±0.10	$1.18 \pm 0.07\times10^{-13}$	0.9994

[a] τ_c^0 values in brackets are estimates calculated using an assumed value for the T_1 minimum.
[b] R factor for linear least-squares fit of $\ln(\omega_o\tau_c)$ or $\ln(T_1)$ vs. T.

Table 3. Comparison of NMR activation energies and potential barriers calculated from Raman torsional modes (cm^{-1}).

Group	Halide	V_3	Δν	$V_3 - 0.5\Delta\nu$	Ea	$V_3 - 0.5\Delta\nu$ – Ea
NH_3	Cl	4534	464	4297	3980	317
	Br	3948	441	3728	3785	–57
	I	3255	399	3056	2401	655
CH_3	Cl	2158	308	2004	1908	96
	Br	2068	301	1918	1583	335
	I	1895	287	1752	1518	234

Note: V_3 = sum of internal and external barriers. Zero point energy estimated at half the fundamental Raman B_g torsional frequency Δν/2. From Raman data at 77 K.

This compares reasonably well with experimental values 0.63 ms (bromide) and 0.56 ms (iodide).

All the T_1 results for the β-phase of the iodide can be fit consistently with one set of parameters (Table 2). Not surprisingly, however, there are difficulties for the chloride and bromide for those results that are most affected by the nonexponential behaviour, as these points do not fall on the expected BPP curves. Consequently the analysis for the chloride and bromide proceeded as follows: (*i*) the results on the low-temperature slopes of the plots ($\omega_H\tau_c >> 1$) are well-behaved and give a good linear correlation from which an activation energy for CH_3 reorientation can be determined; (*ii*) the ^2H results are also well-behaved and give activation energies for NH_3 reorientation; (*iii*) these Ea parameters were then used to calculate the solid curves shown in the ^1H T_1 plots with the constant factors simply adjusted to give the T_1 minima shown. Thus, although there is clearly a problem in the mid-region, good values for the activation energies can be obtained. Values of Ea are given in Table 2.

Phase behaviour from the T_1 results

The bromide and iodide show very sudden and drastic increases (greater than two orders of magnitude) in their ^1H T_1 between 364 and 370 K and 324 and 335 K, respectively, corresponding quite well with the $\beta \rightarrow \alpha$ phase transition temperatures from DSC and indicative of a dramatic change in the dynamics of the ethylammonium ion. The chloride is less definitive, though there is a small but rapid increase between 357 and 367 K. (The transition temperatures indicated are listed in Table 1 for comparison). An estimate of the activation energy for a motion in the α-phase of $C_2H_5NH_3I$ (Ea = 8.8 ± 0.5 kJ/mol) was obtained from the three T_1 points obtained (Fig. 4). This is significantly smaller than for the CH_3 and NH_3 group motions in the β-phases and it is clear that the motion is rapid since the points are on the high-temperature slope of the relaxation curve.

It is interesting to note that the relaxation begins to show nonexponentiality at ~210 K, which happens to be just a little below the small thermal anomalies seen by Rao et al. (10). This could just be coincidence or some connection might be inferred. Although it is not possible to offer any concrete explanation for this behaviour, one possibility that comes to mind is that trace water may cause some unusual phase behavior. This is not unprecedented and one example is the case of tetramethylammonium chloride (30). However, a counter argument is the absence of thermal events in this region in the DSC scan of the chloride.

Barriers vs. activation energies

The comparison between NMR Ea values and barriers calculated from torsional mode frequencies is summarized in Table 3. The parameters being compared are ($V_3 - \Delta\nu/2$), which is the sum of the internal and external threefold potential barriers minus the zero point energy, estimated as half the Raman fundamental torsional frequency vs. Ea, the NMR activation energy. Overall, the values compare quite favourably and the general trends are reproduced. As can be seen from the differences, however, Ea is generally smaller (the only exception is a small negative value for NH_3 for the bromide). It is also clear that it would not be reasonable to make conclusions about the premise of sizeable sixfold terms in the potential in cases of strong hydrogen bonding, since the differences for CH_3, with no hydrogen bonding, are of the same magnitude as for NH_3. The barriers from torsional frequencies rely on models of the potential surface, which in the case of the ethylammonium halides is complicated by interactions between rotor groups on adjacent molecules. Furthermore, the torsional modes do not sample the

© 2004 NRC Canada

Fig. 5. ^{2}H NMR lineshapes of $C_2D_5NH_3Cl$ in the α-phase (bottom) and β-phase (top).

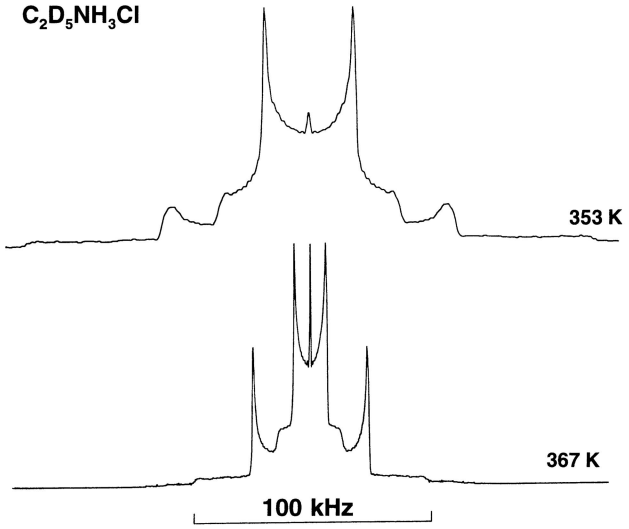
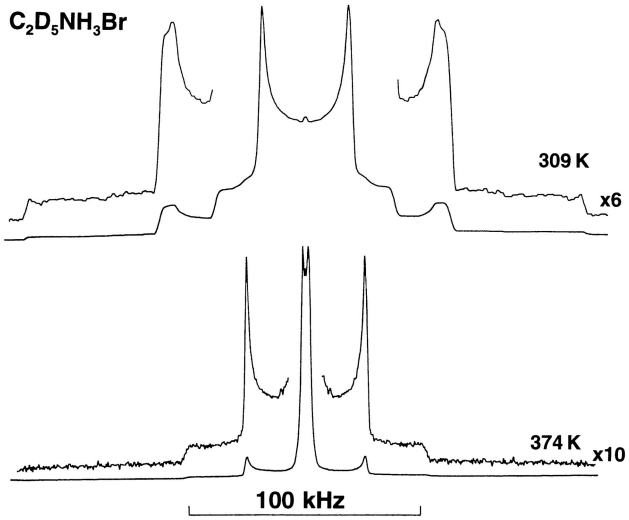


Fig. 6. ^{2}H NMR lineshapes of $C_2D_5NH_3Br$ in the α-phase (bottom) and β-phase (top).



higher parts of the potential surfaces and thus, the calculated barriers reflect the quality of the model, whereas the Eas are a more direct measurement and should give a reasonable and more reliable value for the barrier (minus the zero point energy).

Dynamics in the α-phase

^{2}H NMR lineshapes

^{2}H NMR lineshapes are shown in Figs. 5–9. The lineshapes at *RT* and up to the $\beta \rightarrow \alpha$ transition for all three salts confirm that threefold reorientation of the CD_3 and ND_3 groups occur in the β-phases. They also show well-defined changes at the phase transition, from which it is possible to develop a dynamic model for the α-phase.

^{2}H NMR in solids is dominated by first-order perturbation of the Zeeman interaction by the nuclear quadrupolar coupling between the nuclear electric quadrupole moment and the electric field gradient (EFG), usually denoted by the tensor ***V*** (31, 32). There are two transitions, displaced equally on either side of the Zeeman frequency, whose frequencies depend on the orientation of the quadrupolar coupling tensor with respect to the magnetic field. The ^{2}H NMR powder lineshape has either two or three pairs of characteristic features (edges, shoulders, and peaks) separated by frequencies

Fig. 7. ^{2}H NMR lineshapes of $C_2D_5NH_3I$ in the α-phase (bottom) and β-phase (top).

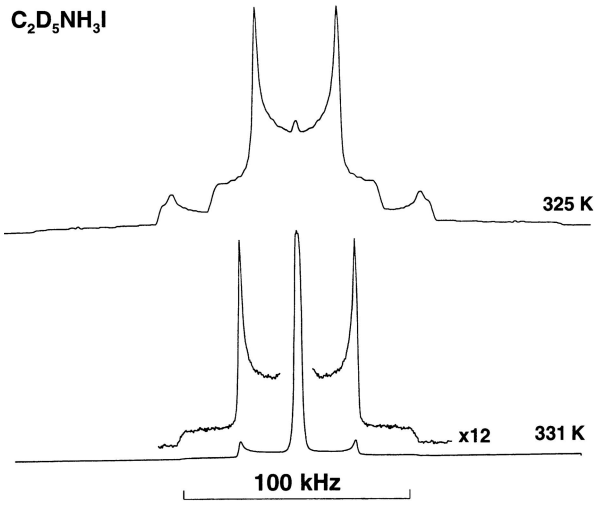
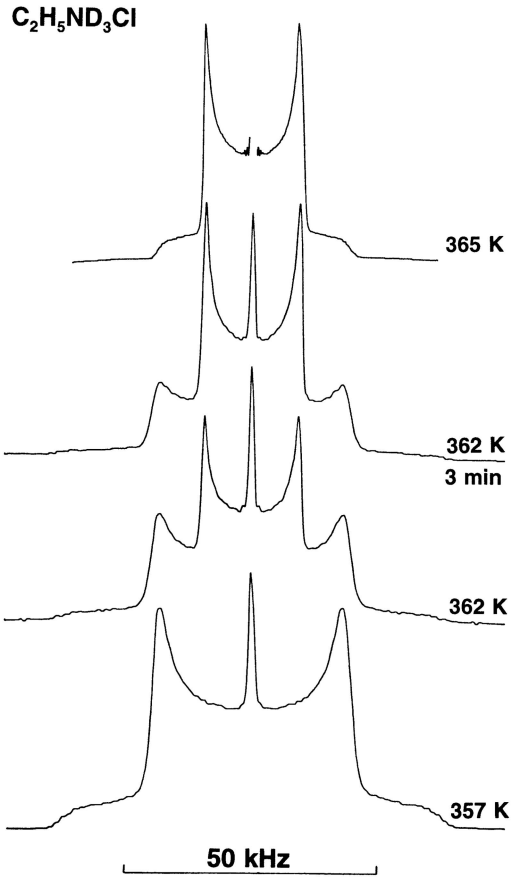
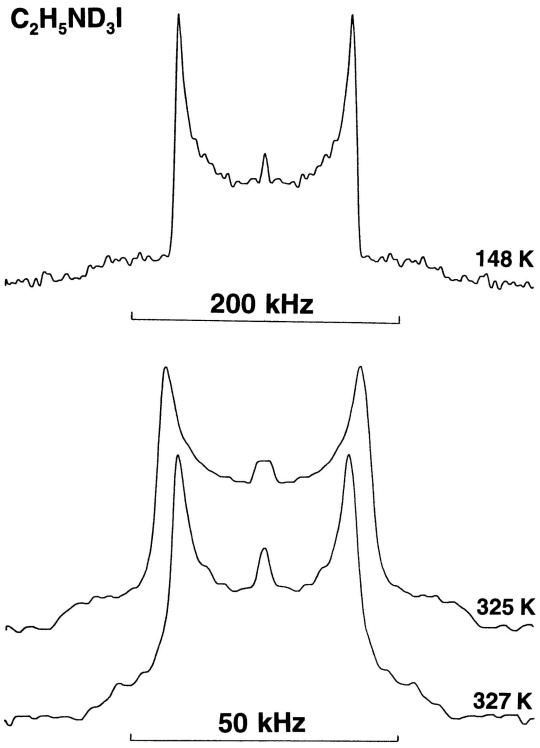


Fig. 8. ^{2}H NMR lineshapes of $C_2H_5ND_3Cl$ showing transformation from the β-phase (bottom) to the α-phase (top).



© 2004 NRC Canada

Fig. 9. ^{2}H NMR lineshapes of $C_2H_5ND_3I$ showing the β-phase at 148 and 325 K and the α-phase at 327 K.



[7] $\Delta\nu_{zz} = 3C_Q/2$

[8] $\Delta\nu_{yy} = 3C_Q(1 + \eta)/4$

[9] $\Delta\nu_{xx} = 3C_Q(1 - \eta)/4$

where $\eta = (\Delta\nu_{yy} - \Delta\nu_{xx})/\Delta\nu_{zz}$. These $\Delta\nu_{ii}$ are proportional to the magnitudes of the principal axis components V_{ii} of the effective quadrupolar coupling tensor. These values can thus be read from the spectra and are important because they reflect the dynamic behaviour of the molecule. Any motion that causes a change in the orientation of the tensor can bring about changes in the ^{2}H NMR lineshape. Once the reorientational rates are about 10^7 jumps s^{-1} or faster (i.e., the fast motion limit, FML), the line takes on a shape that can be described by an averaged effective tensor. Such lineshapes are very sensitive to specific details of the motion and may be used to determine models for the molecular motion, since analytical expressions for the parameters governing the FML lineshapes are relatively easy to obtain (33–35). The orientation of the EFG tensor must first be described in a final reference frame in terms of the Euler angles α, β, γ

[10] $V(\alpha, \beta, \gamma) = \mathbf{R}V_{pas}\mathbf{R}^{-1}$

where **R** is the Euler angle rotation matrix describing the coordinate transformation and $\boldsymbol{V}_{pas}$ is the tensor in its principal axis system. The FML lineshape then represents the effective tensor $\boldsymbol{V}_{eff}$, which is the population weighted average of the tensor components in the final frame for all the sites (orientations) visited during the motion:

[11] $$\boldsymbol{V}_{eff} = \frac{\sum_{i=1}^{n} V_i(\alpha, \beta, \gamma)p_i}{\sum_{i=1}^{n} p_i}$$

with p_i the population factor of site *i*. Note that to understand and calculate the dynamically averaged lineshapes it is necessary to have some knowledge of the quadrupolar parameters for the starting tensor.

The observed lineshapes can now be examined in light of this background.

Parameters derived from the spectra at various temperatures are given in Table 4.

β-*Phase*

The β-phases of the $C_2H_5ND_3$ salts below 200 K show static ^{2}H lineshapes characteristic of axially symmetric tensors, but by room temperature (in fact by 268 K for the iodide) dynamic averaging produces FML axial tensor lineshapes reduced in width by a factor of ~3. This is quite characteristic for threefold reorientation of the ND_3 group. Both the bromide and iodide show ~0.4 kHz reduction in these FML linewidths over 50°, typically seen in all ^{2}H spectra and believed to be due to additional averaging from small amplitude librational motions. The static tensor coupling constants for the bromide (173.9 kHz) and iodide (177.8 kHz) are in agreement with a value of 168–177 kHz measured for the chloride by NQR at 77 K (36).

For the $C_2D_5NH_3$ salts at room temperature the CD_2 group is effectively static and the nonaxially symmetric tensors of its two D give rise to the broad component of the lineshape, whereas threefold averaging of the CD_3 group produces an FML axial component, which is narrowed by a factor of ~3. The observed parameters are typical for both (32). Furthermore, the relaxation behaviour and intensities confirm this assignment: Long recycle times (~60 s) are required to observe the broad lineshape at its full intensity, in which case a 2:3 (broad: narrow) intensity ratio is observed. If a short recycle time of 1 s is used instead, the narrow lineshape is observed selectively, since the dynamics of the CD_3 group make its ^{2}H T_1 considerably shorter.

α-*Phase*

Of greater interest, however, is that the ^{2}H NMR gives information about the behaviour at and above the $\beta \rightarrow \alpha$ phase transition: Over a very short temperature range, the $C_2D_5NH_3$ lineshapes show some dramatic changes. The component owing to CD_2 narrows somewhat and becomes axial and the CD_3 component narrows (drastically in the cases of Br and I) and remains axial. Likewise the $C_2H_5ND_3$ lineshapes also narrow, though much less dramatically, and remain axial, over a very short temperature range (The transition temperatures indicated by these changes are listed in Table 1). These all appear to be FML lineshapes as might have been anticipated from the T_1 results. One cooling run for the bromide showed a marked hysteresis, since reversion to the β-phase did not begin until about 353 K. The phase transition is accompanied by a sudden change in ^{2}H T_1: typically for the $C_2H_5ND_3^+$ salts the recycle times were changed from 0.5 s or less in the β-phase to 4–10 s in the α-phase, and in the

© 2004 NRC Canada

Table 4. ^{2}H NMR quadrupolar coupling constants, asymmetry parameters, and lineshape splittings for the ^{2}H spectra in the β- and α-phases.

Species	Phase	T (K)	C_Q (kHz)	η	$\Delta\nu_{xx}$ (kHz)	$\Delta\nu_{yy}$ (kHz)	$\Delta\nu_{zz}$ (kHz)
$CD_3CD_2NH_3Cl$	β	353	51.5	0	38.6	—	77.2
	α	367	18.4	0	13.8	—	27.6
$CD_3CD_2NH_3Cl$	β	353	159.9	0.037	115.5	124.4	239.9
	α	367	65.1	0	48.8	—	97.6
$CH_3CH_2ND_3Cl$	β	357	50.9	0	38.15	—	76.3
	α	365	25.4	0	19.1	—	38.2
$CD_3CD_2NH_3Br$	β	309	51.5	0	38.6	—	77.2
	α	374	4.5	0	3.4	—	6.8
$CD_3CD_2NH_3Br$	β	309	160.4	0.046	114.7	125.9	240.6
	α	374	69.8	0	52.35	—	104.7
$CH_3CH_2ND_3Br$	β	188	173.9	0	130.4	—	260.8
	β	362	52.1	0	39.1	—	78.2
	α	362	40.7	0	30.5	—	61.0
$CD_3CD_2NH_3I$	β	325	49.9	0	37.4	—	74.8
	α	331	2.8	0	2.1	—	4.2
$CD_3CD_2NH_3I$	β	325	154.9	0.050	110.4	121.9	232.3
	α	331	69.8	0	52.35	—	104.7
$CH_3CH_2ND_3I$	β	148	177.8	0	133.3	—	266.7
	β	325	51.1	0	38.3	—	76.7
	α	327	44.4	0	33.3	—	66.7

$C_2D_5NH_3^+$ salts, the recycle time could be decreased from 16 s or more in the β-phase to about 8 s in the α-phase.

^{2}H NMR lineshape analysis

The fact that the averaged lineshapes indicate axial tensors in the α-phase is a crucial observation, since it implies a new rotation of the whole molecule about an n-fold axis with $n > 2$. Following from the theory behind eqs.[10] and [11] for n-fold reorientation ($n > 2$), the averaged tensor components are given by

$$[12]\quad V_{xx}' = V_{yy}' = 0.5[(\cos^2\alpha\cos^2\beta + \sin^2\alpha)V_{xx} + (\sin^2\alpha\cos^2\beta + \cos^2\alpha)V_{yy} + (\sin^2\beta)V_{zz}]$$

$$[13]\quad V_{zz}' = (\cos^2\alpha\sin^2\beta)V_{xx} + (\sin^2\alpha\sin^2\beta)V_{yy} + (\cos^2\beta)V_{zz}$$

Note, this always gives an axial averaged tensor. For an axial starting tensor the dependence on α is lost ($V_{xx} = V_{yy}$ and $V_{zz} = -2V_{xx}$) and these equations reduce to

$$[14]\quad V_{zz}' = 0.5[3\cos^2\beta - 1]V_{zz}$$

$$[15]\quad V_{xx}' = V_{yy}' = -0.5V_{zz}$$

The threefold averaged CD_3 or ND_3 groups have axial averaged tensors in the β-phase with V_{zz} aligned along the threefold axis. Thus, we can readily calculate the β angles for the n-fold rotation in the α-phase using eq. [14] where β is the angle between the threefold axis of the CD_3 or ND_3 group and the n-fold axis (Table 5).

The CD_2 groups are more of a challenge since (*i*) the static β-phase tensors are nonaxial and (*ii*) the orientations of V_{xx} and V_{yy} are not determined by any symmetry elements. Thus, we must use the more general eqs. [12] and [13].

From eq. [13] we can derive

$$[16]\quad \cos^2\beta = [\cos^2\alpha(V_{yy} - V_{xx}) - V_{yy} \pm V_{zz'}]/[V_{zz} - V_{yy} + \cos^2\alpha(V_{yy} - V_{xx})]$$

From known starting and averaged tensor values we can then calculate the possible values of β for α = 0°–90°. The ranges of β values obtained turn out to be quite small (Table 5).

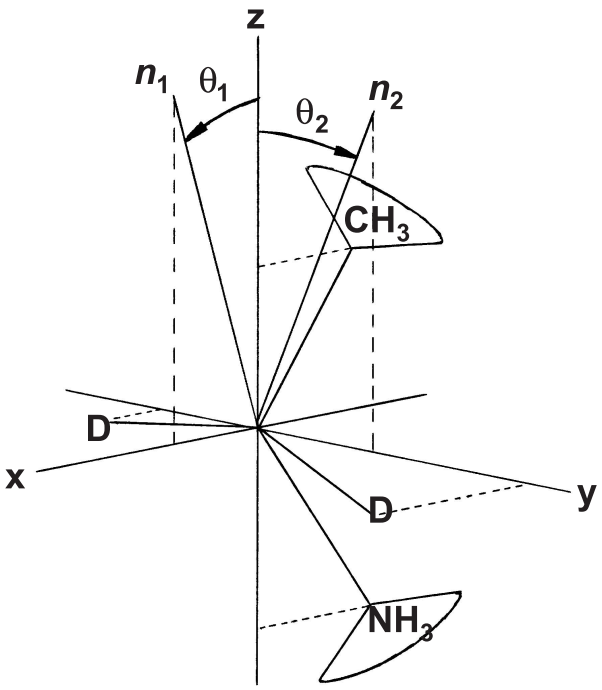
So far this determination of the β angles has made no assumptions; it is based strictly on the theoretical background. However, it will be seen from Table 5 that in some cases two solutions are possible and one must then decide which values are physically reasonable. Ultimately one wants to be able to decide on the position of the n-fold axis with respect to the molecule such that it is consistent both with the deter-

© 2004 NRC Canada

Table 5. β-Angles of the ^2H quadrupolar coupling tensors with respect to the *n*-fold rotation axis in the α-phases.

Ion	ND_3	CD_3	CD_2
Cl	**35.3** or 89.6	**41** or 72	38.7–39.3 or **74.3–77.0**
Br	**22.5**	**51.2** or 58.4	37.5–38.2 or **76.1–80.3**
I	**17.2**	**52.5** or **57.1**	36.9–37.6 or **77.3–82.6**

Fig. 10. Molecular reference frame and orientation of *n*-fold axes.



mined angles and the geometry of the molecule. In this regard, another important observation is that the averaged lineshapes of the CD_2 groups in the α-phase indicate that both C-D behave identically. There are two general situations where this can happen under an *n*-fold reorientation and here the description refers to the reference frame indicated in Fig. 10:

(1) Where the *n*-fold axis is in the plane containing the CCN backbone of the molecule, i.e., the xz reference plane.

(2) Where the *n*-fold axis is in the yz reference plane.

If the *n*-fold axis departs from either of these two planes then the two D of CD_2 will no longer behave identically. A special case of (1) is if the motion incorporates a rotation about the CD_2 bisector (coincident with the reference x axis), but with bond angles close to the tetrahedral angle (Td), this would require *n*-fold rotation of the tensors at an angle β ~ Td/2 (i.e., close to the magic angle) resulting in very considerable narrowing for CD_2, ND_3, and CD_3. In fact, the averaged CD_2 and ND_3 lineshapes are still quite large for all the salts and so this case can be ruled out. A special case of (2) is when the *n*-fold axis coincides with the reference y axis, but then CD_2 will have β ~ (90 – Td/2) and thus, reduce by a factor of ~2, which is significantly more than observed, and CD_3 and ND_3 will rotate in a plane that also produces a reduction factor of 2, which in their cases is not enough. So this case can also be ruled out. Another special case of both (1) and (2) is when the *n*-fold axis coincides with the reference z axis, but the CD_2 would then average by a factor of 2, which again is more than observed. Note model (2) will require CD_3 and ND_3 to have very similar β values, which means that the chloride might fit this model, but the bromide and iodide probably will not.

Table 6. Closest fits for the two models.[a]

Ion	θ	CCN angle	Inter-bisector angle
Cl	*16.0 (Model 2)*	*109.8*	*176.8*
	22.9 (Model 1)	103.7	160.0
Br	*17.0 (Model 1)*	*106.3*	*177.4*
	17.1 (Model 2)	108.4	159.0
I	*17.7 (Model 1)*	*110.3*	*180.0*
	9.08 (Model 2)	108.7	159.0

[a]The best fit for each salt is in italics.

It then remains to decide which of the determined angles (where there were more than one solution) are consistent with either of these models. In either model (1) or (2) one must first determine the angle θ by which the *n*-fold axis has to be rotated away from the reference z axis in either the xz or yz planes to give the correct β-angle for the CD_2 deuterons. One can then calculate other relevant angles and use two criteria to judge how well the model fits:

(*a*) The sum of the angle between the CD_3 axis and the z axis plus the angle between the ND_3 axis and the z axis when subtracted from 180° gives a value for the CCN bond angle. This must be quite comparable to the XRD-determined angle of 109.25°.

(*b*) The angle between the CD_2 bisector and the CCN bisector should be close to 180° if all bond angles are to be close to tetrahedral.

Table 6 gives the solutions with the closest fits for both models. It is quite clear that the bromide and iodide fit model (1) quite well but not model (2), whereas the chloride gives a much better fit with model (2). This suggests that the bromide and iodide probably have identical α-phases, while the chloride may be different. Alternatively, it could be that the structural arrangement of halide anions and molecular cations are basically the same in all three, but that packing constraints (largely owing to the different sizes of and interactions with the anions) force the molecules to orient differently.

Unfortunately, the crystal structures of the α-phases are not known. However, they are probably related to the room-temperature phases of methylammonium chloride (37) and -bromide (38) and of *n*-propylammonium chloride, -bromide, and -iodide (39), which are tetragonal (*P*4/*nmm*). The common feature of these structures is that the molecules sit on a fourfold crystal axis and must, therefore, be disordered. The mismatch of molecular and crystal site symmetries also usually means that the barrier to rotation is low and the disorder is dynamic. All have low-temperature phase transitions and the NH_3 rotational barriers in these phases are generally high, indicative of threefold H-bonding situations (40, 41). The structure of *n*-propylammonium chloride is monoclinic (*C*2/*m*) (42), as is ethylammonium bromide β-

© 2004 NRC Canada

phase at room temperature ($P2_1/m$) (3). Thus, the α-phases of the halides of ethylammonium may be structurally similar to the room-temperature phases of these other alkylammonium halides, in which case the rotational axis in the α-phase would be fourfold.

Conclusions

^{1}H and ^{2}H NMR and DSC studies have been used to study the phase behaviour and molecular dynamics in ethylammonium chloride, -bromide, and -iodide. It has been firmly established that all three salts exhibit a $\beta \rightarrow \alpha$ phase transition above room temperature and that the previously reported low-temperature transitions are probably related to impurities or trace water. It has been found that static or very slow motion prevails below 180 K, followed by reorientation, first of CH_3 then NH_3 groups, which are rapid by at least room temperature. After the $\beta \rightarrow \alpha$ phase transition, in addition to these group motions, the whole molecule rotates rapidly about an n-fold axis ($n > 2$), which by analogy with structures of other alkylammonium halides is probably fourfold. ^{2}H NMR lineshape analysis has allowed the determination of the orientation of this n-fold axis with respect to the molecular frame. In the cases of the bromide and iodide, the axis is in the molecular mirror plane, but in the chloride it is in the plane perpendicular to the bisector of the DCD bond angle. The activation energies for CH_3 and NH_3 group motions in the β-phase compare quite favourably with barriers determined from torsional mode frequencies. Eas for NH_3 reorientation reflect decreasing hydrogen bond strength in the order Cl > Br > I.

Acknowledgements

I would like to thank Dr. Paul Handa for obtaining the DSC scans of the chloride and bromide and Prof. B.A. Dunell in whose lab the ^{1}H T_1 measurements of the iodide were obtained.

References

1. P. Groth. Chem. Krystallogr. **1**, 186 (1906).
2. S.B. Hendricks. Z. Kristallogr. **67**, 119 (1928).
3. F. Jellinek. Acta Crystallogr. **11**, 626 (1958).
4. C.I. Ratcliffe, W.F. Sherman, and G.R. Wilkinson. J. Raman Spectrosc. **13**, 189 (1982).
5. S. Forss, G. Bergstrom, N. Meinander, and F. Stenman. Commentat. Phys. Maths. Soc. Sci. Fenn. **48**, 115 (1978).
6. T.C. Waddington. Faraday Disc. Chem. Soc. **13**, 191 (1979).
7. C.I. Ratcliffe, W.F. Sherman, and G.R. Wilkinson. J. Raman Spectrosc. **11**, 199 (1981).
8. C.I. Ratcliffe, W.F. Sherman, and G.R. Wilkinson. J. Raman Spectrosc. **11**, 205 (1981).
9. P. Chevalier and C. Sandorfy. Symposium on molecular structure and spectra. Tokyo, Japan, 1962. A109-1.
10. C.N.R. Rao, S. Ganguly, H.R. Swamy, and I.A. Oxton. J. Chem. Soc. Faraday Trans. 2, **77**, 1825 (1981).
11. J. Tsau, and D.F.R. Gilson. J. Phys. Chem. **72**, 4082 (1968).
12. N.I. Singh and S. Mitra. Thermochim. Acta, **197**, 341 (1992).
13. S.D. Hamann and M. Linton. High Temp. High Pressure, **7**, 177 (1975).
14. H. Hagemann and H. Bill. J. Chem. Phys. **80**, 111 (1984).
15. G. Jugie and J.A.S.Smith. J. Chem. Soc. Faraday Trans. 2, **74**, 994 (1978).
16. T.T. Ang and B.A. Dunell. J. Chem. Soc. Faraday Trans. 2, **68**, 1331 (1972).
17. C.I. Ratcliffe and B.A. Dunell. J. Chem. Soc. Faraday Trans. 2, **73**, 493 (1977).
18. B.A. Pettitt, J.S. Lewis, R.E. Wasylishen, W. Danchura, and E. Tomchuk. J. Magn. Reson. **44**, 508 (1981).
19. J.H. Davis, K.R. Jeffrey, M. Bloom, M.I. Valic, and T.P. Higgs. Chem. Phys. Lett. **42**, 390 (1976).
20. N. Bloembergen, E.M. Purcell, and R.V. Pound. Phys. Rev. **73**, 679 (1948).
21. R. Kubo and K. Tomita. J. Phys. Soc. Jpn. **9**, 888 (1954).
22. D.E. Woessner. J. Chem. Phys. **36**, 1 (1962).
23. C.I. Ratcliffe. J. Magn. Reson. **38**, 283 (1980).
24. C.I. Ratcliffe and B.A. Dunell. J. Chem. Soc. Faraday Trans. 2, **77**, 2181 (1981).
25. C.I. Ratcliffe. J. Chem. Soc. Faraday Trans. 2, **76**, 1196 (1980).
26. H. Ishida and A. Weiss. Ber. Bunsenges. Phys. Chem. **92**, 511 (1988).
27. H. Terao, Y. Furukawa, M. Hashimoto, K. Yamada, and T. Okuda. Z. Naturforsch. **57a**, 369 (2002).
28. A. Abragam. The principles of nuclear magnetism. Oxford University Press, London. 1961. p. 314.
29. J.A. Ripmeester, R.E. Hawkins, and D.W. Davidson. J. Chem. Phys. **71**, 1889 (1979).
30. S. Albert and J.A. Ripmeester. J. Chem. Phys. **58**, 2870 (1973).
31. M.H. Cohen and F. Reif. Solid State Phys. **5**, 321 (1957).
32. R.G. Barnes. Adv. Nucl. Quadrupole Reson. **1**, 335 (1974).
33. M.S. Greenfield, A.D. Ronemus, R.L. Vold, R.R. Vold, P.D. Ellis, and T.E. Raidy. J. Magn. Reson. **72**, 89 (1987).
34. R.J. Wittebort, E.T. Olejniczak, and R.G. Griffin. J. Chem. Phys. **86**, 5411 (1987).
35. C.I. Ratcliffe. J. Phys. Chem. **91**, 6464 (1987).
36. M.J. Hunt and A.L. Mackay. J. Magn. Reson. **15**, 402 (1974).
37. E.W. Hughes and W.N. Lipscomb. J. Am. Chem. Soc. **68**, 1970 (1946).
38. E.J. Gabe. Acta Crystallogr. **14**, 1296 (1961).
39. M. Vernon King and W.N. Lipscomb. Acta Crystallogr. **3**, 222 (1950).
40. S. Albert and J.A. Ripmeester. J. Chem. Phys. **58**, 541 (1973).
41. C.J. Ludman, C.I. Ratcliffe, and T.C. Waddington. J. Chem. Soc. Faraday Trans. 2, **72**, 1759 (1976).
42. M. Vernon King and W.N. Lipscomb. Acta Crystallogr. **3**, 227 (1950).

© 2004 NRC Canada

Insertion of acetone molecules in the nanostructured tunnels of palygorskite[1]

Wenxing Kuang and Christian Detellier

Abstract: The insertion of acetone molecules in the nanostructured tunnels of palygorskite (PFl-1) was studied by thermal gravimetric analysis connected with mass spectrometry and ^{29}Si and ^{13}C solid-state NMR techniques. In comparison with palygorskite, new weight losses appear at 130 and 340 °C for palygorskite previously heated at 150 °C for 20 h then exposed to acetone for a week. Two types of water molecules occupy the palygorskite tunnels: weakly bound zeolitic water and structural water molecules coordinated to Mg(II) cations at the edge of the octahedral sheets. Acetone molecules that intercalate in the nanostructured tunnels replace the zeolitic water and are H-bonded to structural water. The mass loss at 130 °C is accounted for by the release of structural water and acetone. The loss at 340 °C is due to the release of acetone molecules that coordinate directly to terminal cations in the nanostructured tunnels and to residual structural water. A nanostructured hybrid material, with a structure similar to the parent palygorskite, can be formed through the direct coordination of acetone molecules to the terminal cationic coordination sites in the nanostructured tunnels of palygorskite. There is evidence for the fixation of two different types of acetone on palygorskite: mobile acetone molecules on the external surface and acetone molecules more rigidly fixed inside the nanotunnels. The former ones are detected by the ^{13}C magic-angle spinning NMR experiment and can be easily removed by gentle heating at 60 °C, while the latter ones are detected by ^{13}C cross-polarization magic-angle spinning NMR. It is also demonstrated that nearly complete recovery of the original structure is achieved by exposing palygorskite previously dehydrated at 150 or 300 °C to acetone vapor at room temperature.

Key words: insertion, intercalation, nanostructured tunnels, palygorskite, acetone, nanocomposite materials, nanohybrid.

Résumé : Faisant appel à une analyse gravimétrique thermique reliée à de la spectrométrie de masse et à des techniques de RMN à l'état solide du ^{29}Si et du ^{13}C, on a étudié l'insertion de molécules d'acétone dans les tunnels nanostructurés de la palygorskite (PFl-1). Par comparaison avec la palygorskite, de nouvelles pertes de poids sont observées à 130 et à 340 °C pour de la palygorskite qui a déjà été portée à 150 °C, pendant 20 h, puis exposée à l'acétone pendant une semaine. Deux types de molécules occupent les tunnels de la palygorskite, de l'eau zéolitique faiblement liée et des molécules d'eau structurales coordinées aux cations Mg(II) à la périphérie des feuillets octaédriques. Les molécules d'acétone qui s'intercalent dans les tunnels nanostructurés remplacent l'eau zéolitique et sont rattachées à l'eau structurale par des liaisons hydrogènes. On peut expliquer la perte de masse à 130 °C par la perte d'eau structurale et d'acétone. La perte à 340 °C est due à la perte d'eau structurale résiduelle et de molécules d'acétone coordinées directement aux cations terminaux dans les tunnels nanostructurés. Un matériau hybride nanostructuré, ayant une structure similaire à celle de la palygorskite parente, peut se former par une coordination directe de molécules d'acétone aux sites de coordination cationiques terminaux dans les tunnels nanostructurés de la palygorskite. Il existe des données qui suggèrent la fixation de deux types différents d'acétone sur la palygorskite, des molécules d'acétone mobiles sur la surface externe et des molécules d'acétone fixées d'une façon plus rigide à l'intérieur des nanotunnels. Les premières sont détectées par l'expérience de RMN du ^{13}C avec rotation à l'angle magique et elles peuvent être facilement enlevées par un chauffage à 60 °C alors que le deuxième type est détecté par RMN du ^{13}C avec polarisation croisée à l'angle magique. On a aussi démontré que, une palygorskite qui aurait été déshydratée antérieurement à 150 ou 300 °C peut récupérer pratiquement complètement sa structure originale en l'exposant à de l'acétone à la température ambiante.

Mots clés : insertion, intercalation, tunnels nanostructurés, palygorskite, acétone, matériaux nanocomposites, nanohybride.

Received 11 May 2004. Published on the NRC Research Press Web site at http://canjchem.nrc.ca on 3 December 2004.

This paper is dedicated to the memory of Professor Donald E. Irish.

W. Kuang and C. Detellier.[2] Centre for Catalysis Research and Innovation, and Department of Chemistry, University of Ottawa, Ottawa, ON K1N 6N5, Canada.

[1]This article is part of a Special Issue dedicated to the memory of Professor Don Irish.

[2]Corresponding author (e-mail: dete@science.uottawa.ca).

Introduction

Palygorskite is a naturally occurring, fibrous magnesium and aluminum silicate clay mineral with important sorptive, colloidal-rheological, and catalytic properties (1). It is a 2:1 phyllosilicate the hormite group that forms with sepiolite. In the past decades, the structure of palygorskite was studied by powder X-ray diffraction, TEM, IR, NMR, and Mössbauer spectroscopy. Two main structural models were proposed for palygorskite, i.e., monoclinic (2) and orthorhombic (3). In both models, talc-like tetrahedral-octahedral-tetrahedral

 doi: 10.1139/V04-130 © 2004 NRC Canada

(T-O-T) ribbons expand along the axis of the fibers, resulting in the fibrous morphology. Each T-O-T ribbon is connected to the next through an inverted Si-O-Si bond, which produces a staggered talc layer with a continuous tetrahedral sheet and a discontinuous octahedral sheet. Terminal cations (mainly Mg(II)) located at the edges of the ribbons complete their coordination shell with two structural water molecules, which are in turn hydrogen bonded to zeolitic water molecules occupying the channels and tunnels that run parallel to the fiber axis. These nanostructured tunnels have a cross section of approximately 3.7 Å × 6.4 Å. They account in large part for the high specific surface area and excellent sorptive properties of palygorskite once the zeolitic water molecules have been removed by thermal treatment that does not exceed 150 °C (1*b*).

The nitrogen adsorption–desorption isotherm of palygorskite (PFl-1), is of type I at lower relative pressures, characteristic of microporous solids, and of type IV at higher relative pressures, indicative of the presence of interparticle mesopores (4). The BET surface area is 196 m^2/g, with a micropore area of 93 m^2/g, a micropore volume of 47 mm^3/g, and an external surface area of 103 m^2/g. The differential pore volume plot of palygorskite reveals a median micropore equivalent spherical diameter of 6.1 Å. Similar results were also reported for palygorskite samples of other origins (5). The high external surface area, micropore area and micropore volume result in the high sorptive properties of palygorskite.

Currently, palygorskite is used in several industrial applications on the basis of its high absorption capacity. The sorption can occur either in the nanostructured tunnels or on the external surfaces. Compounds with a small molecular size have a possibility of penetrating the nanostructured tunnels, while larger molecules can just access the external surfaces. It was previously reported (5*a*, 6) that small organic molecules with high polarity (i.e., alcohol), could penetrate into the tunnels and interact with structural water molecules through H-bonding. This leads to the possibility of the design of highly structured nanohybrid materials based on naturally occurring magnesio-silicates.

In the present work, the insertion of acetone molecules in the nanostructured tunnels of palygorskite was studied by using thermal gravimetric analysis and multinuclear solid-state NMR. It is demonstrated that the original palygorskite structure is recovered by exposing a previously dehydrated sample at 150 or 300 °C to acetone vapor at room temperature, acetone molecules replacing zeolitic water molecules, and consequently filling the nanostructured tunnels.

Experimental section

Materials

Palygorskite (PFl-1) from Gadsden County, Florida, was obtained from the Source Clays Repository of the Clay Minerals Society (Purdue University), with a chemical composition (%) of SiO_2 (60.35), Al_2O_3 (11.13), Fe_2O_3 (3.74), TiO_2 (0.48), MgO (10.58), CaO (1.89), Na_2O (0.05), K_2O (0.87), P_2O_5 (0.92) (7). As reported by Güven et al. (2*f*), palygorskite makes up about 85% of the fine (<2 μm) fraction. Smectite (10%), quartz (1%–3%), apatite (2%), carbonates (1%), and mica (<1%) were identified as the main impurities in the fine fraction. These data are close to those given by Chipera and Bish (8). Acetone (>99.5%) was obtained from BDH Inc. Acetone-d_6 (>99%), was obtained from Aldrich Chemical Co.

Preparation of the samples

Palygorskite was heated with a ramp rate of 1 °C/min to 150 °C (or 300 °C) and then kept at 150 °C (or 300 °C) for 20 h under air in a baffle furnace to selectively eliminate the surface-bound water and zeolitic water (and partially structural water) from the nanoporous tunnels. The vials containing approximately 0.1 g of the partially dehydrated palygorskite were immediately transferred from the furnace into capped bottles containing a few mL of acetone or acetone-d_6. The partially dehydrated samples were then kept in contact with acetone vapor for various amounts of time at room temperature.

Thermal analysis

Differential thermal analysis (DTA), thermal gravimetric analysis (TGA), and derivative thermal gravimetric analysis (DTG) were performed on a TA SDT 2960 instrument. Approximately 10–20 mg of the sample was placed in a platinum crucible on the pan of a microbalance and then heated from room temperature to 1000 °C at a heating rate of 10 °C/min while being purged with helium at a flowing rate of 100 mL/min and constantly weighed. The gases were drawn down a capillary in the SDT furnace. MS spectra were recorded on a Pfeiffer GSD 301 instrument. The mass spectrum was run in the scanning mode from mass 10 to mass 80, at a scan rate of 0.2 s per mass.

NMR spectroscopy

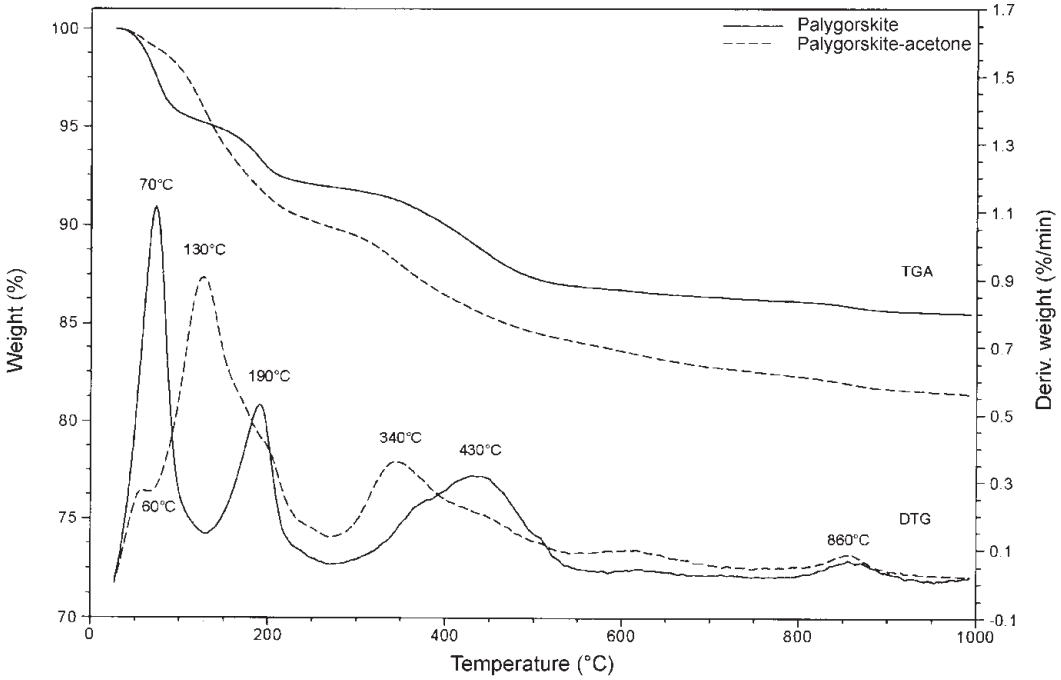
Solid-state ^{29}Si magic-angle spinning (MAS) and cross-polarization (CP)/MAS NMR and ^{13}C MAS and CP/MAS NMR spectra were recorded at 39.75 and 50.32 MHz, respectively, at room temperature on a Bruker ASX-200 spectrometer. Typical spinning rates of 4 kHz (^{29}Si) and 5 kHz (^{13}C) were used. As many of the NMR runs were long, a ramped CP sequence (9) using an X (^{13}C, ^{29}Si) ramp varying in field strength from 59 to 66 KHz was used to compensate for potential drift in probe tuning or amplifier output over the long data acquisition times. The recycle delay time was 2 s and the proton 90° pulse was 4 μs. The contact time to allow the transfer of magnetization between protons and ^{29}Si (and ^{13}C) nuclei was 10 ms for ^{29}Si and 2 ms for ^{13}C NMR. All MAS and CP/MAS experiments employed a 63 KHz CW decoupling field during the acquisition times. The ^{29}Si NMR signals were externally referenced to the $-Si(CH_3)_3$ resonance of tetrakis(trimethylsilyl)silane at –9.9 ppm, corresponding to tetramethylsilane (TMS) at 0 ppm. The ^{13}C NMR signals were externally referenced to the high frequency signal of adamantane at 38.4 ppm, corresponding to TMS at 0 ppm.

Results and discussion

Palygorskite (PFl-1) is progressively dehydrated in the range of temperatures from room temperature to 1000 °C

© 2004 NRC Canada

Fig. 1. TGA and DTG of palygorskite (—) and of palygorskite previously heated at 150 °C for 20 h then exposed to acetone (-----).



(1*b*). As shown in Fig. 1, the TGA curve of PFl-1 can be divided into four major weight losses at maxima of 70, 190, 430 (with a shoulder at 370 °C), and 860 °C under He flow. These steps were previously assigned, respectively, to the release of zeolitic water, the partial release of structural water, the release of the residual structural water, and the dehydroxylation of the Mg-OH groups (10). Since the terminal cations are plausibly coordinated to two water molecules to complete their coordination shell, the two steps corresponding to the loss of structural water can be attributed to the release of a first structural water leading to a distorted tunnel-like structure where the terminal cations are coordinated to one water molecule (the terminal cations may complete its coordination with the oxygen of the neighboring silica surface), and the second loss of water corresponds to the complete dehydration accompanied by the collapse of the tunnel structure. Frost and Ding (11) recently reported the thermal behavior of PFl-1 under nitrogen flow. They speculated that the weight losses at 370 and 430 °C (357 and 415 °C in their experiment) could be due to the dehydroxylation of the OH units from octahedral Fe(III) and Al(III) sites, respectively. However, they indicated that another more likely interpretation is that these two temperatures represent the irreversible dehydration of residual bound water and the folding of the tunnels (at 370 °C) and partial dehydroxylation (at 430 °C).

Consequently, heating palygorskite from room temperature to 130 °C selectively removes water adsorbed on the external surfaces and the zeolitic water from the nanostructured tunnels, while leaving the structural water and the hydroxyl groups unaffected. The elimination of the first coordinated, structural water starts above 130 °C. Folding of the palygorskite crystals occurs when partial structural water has been removed, which plausibly allow terminal cations to complete their coordination shell with oxygens from the neighboring silica surface (2*b*). Structural folding is nearly completely reversible provided that the treatment temperature does not exceed 350 °C (1*b*), but becomes irreversible once all the structural water molecules are removed and partial dehydroxylation has occurred forming an anhydride form. Finally, the remaining Mg-OH hydroxyl groups are released at about 860 °C (11, 12).

The TGA and DTG curves of palygorskite previously heated at 150 °C for 20 h then exposed to acetone for a week are also shown in Fig. 1. Weight losses appear now at 130 and 340 °C, with several shoulders approximately at 60, 190, 430, and 600 °C. Finally the peak at 860 °C characteristic of the dehydroxylation of Mg-OH groups is also observed. Similar results were obtained for TGA and DTG when the nature of the flux gas was changed from He to air. The observed major weight losses at 130 and 340 °C are an indication that acetone molecules were intercalated into the nanotunnels of palygorskite.

Figure 2 shows the mass detection of water (*m*/*e* = 18) in the released gases for palygorskite and for palygorskite previously heated at 150 °C for 20 h then exposed to acetone. For palygorskite, the water mass trace is almost identical to the DTG curve (Fig. 1). In the case of the palygorskite–acetone sample, the water mass trace is similar to the DTG curve but the relative intensity of the peak at 130 °C has decreased. Figure 3 gives the corresponding mass trace for acetone (*m*/*e* = 58). It shows a major loss of acetone at 120 °C, accounting mainly for the DTG peak maximum observed at 130 °C, and a minor loss at 330 °C. Consequently, the two maxima observed on the TGA and DTG curves at 130 and 340 °C are partially due to the release of acetone molecules that intercalate in the nanotunnels of palygorskite. Their loss at these temperatures is accompanied by the loss of structural water molecules. In addition, the loss of some structural water molecules is also observed at temperatures

© 2004 NRC Canada

Fig. 2. Mass spectrometry of water (*m/e* = 18) for palygorskite (—) and for palygorskite previously heated at 150 °C for 20 h then exposed to acetone (----).

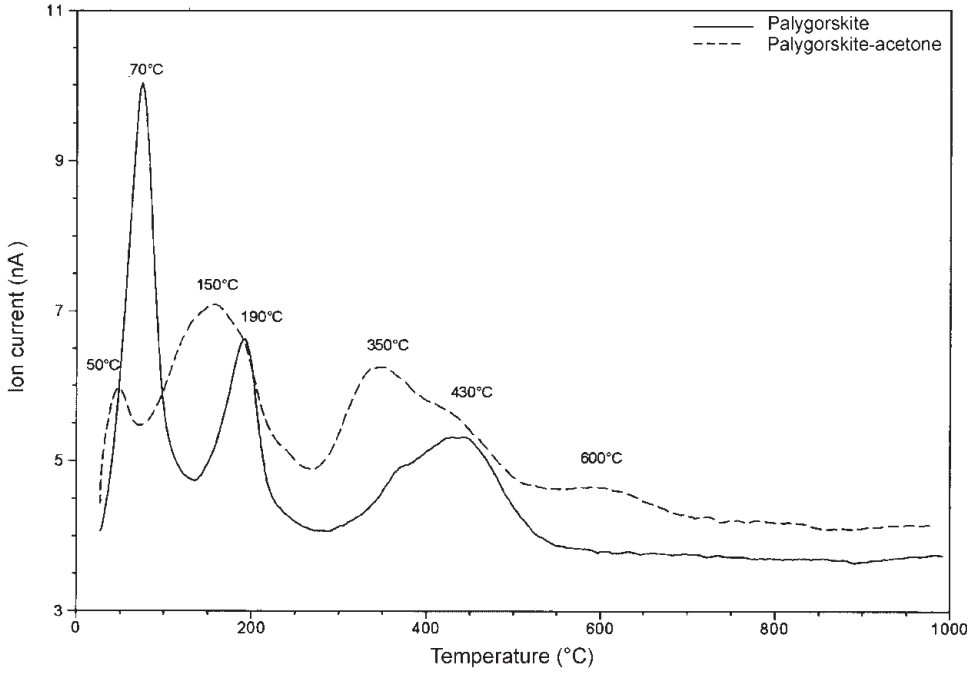
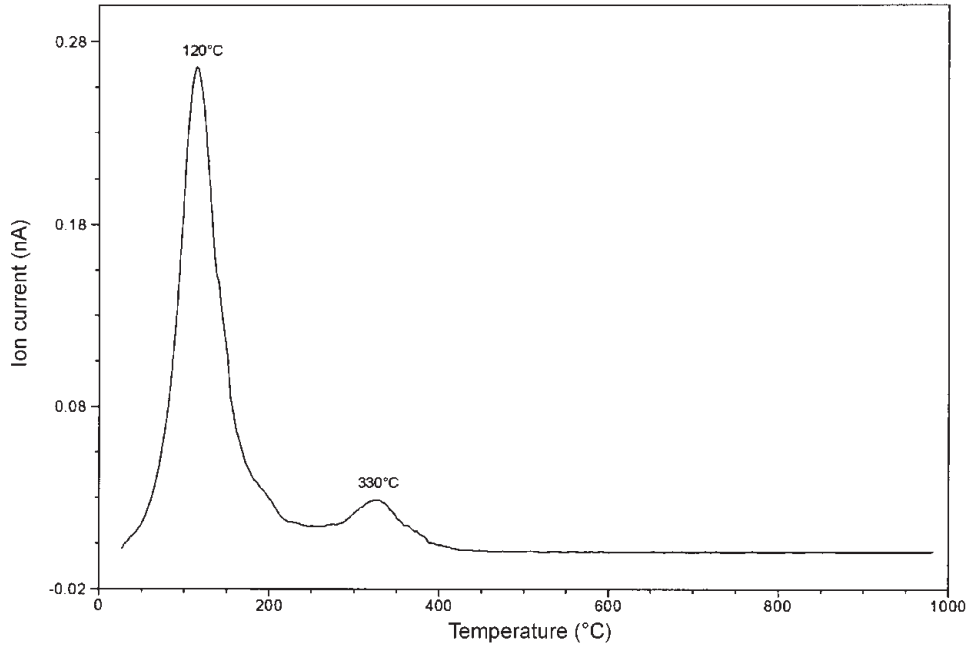


Fig. 3. Mass spectrometry of acetone (*m/e* = 58) for palygorskite previously heated at 150 °C for 20 h then exposed to acetone.

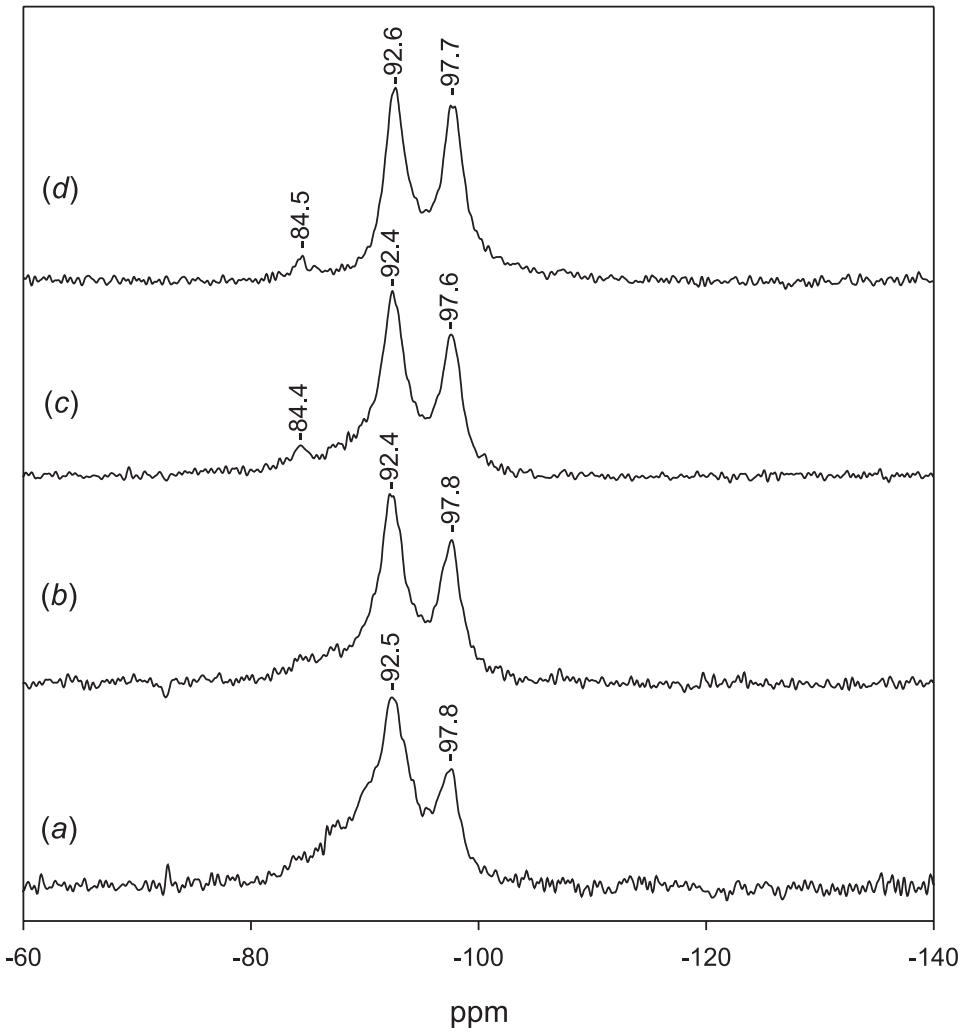


similar to palygorskite (190 and 430 °C). When the TGA–DTA analysis is performed in air, two major weight losses also appear at 130 and 370 °C, with a strong exothermic peak at 340 °C on the DTA, indicating the combustion of acetone molecules at this temperature.

The results of Figs. 1–3 permit an interpretation of the thermal behaviour of the palygorskite-acetone nanohybrid. When acetone is inserted in the nanotunnels of palygorskite, the release of the first structural water starts at a lower temperature than in the case of palygorskite (a broad peak maximum is observed at 150 °C compared to 190 °C). This water loss is accompanied by the partial release of acetone molecules (peak maximum at 120 °C). The loss of some first structural water molecules is still observed as a shoulder at 190 °C indicating the presence of zones in the nanotunnels that were not perturbed by the insertion of acetone. When this step is completed (around 260 °C), there are still acetone molecules in the nanotunnels. It is plausible that at this

© 2004 NRC Canada

Fig. 4. ^{29}Si MAS NMR spectra of palygorskite heated at 150 °C for 20 h then exposed to acetone-d_6 for (*a*) 4 h; (*b*) 1 day; (*c*) 5 days; (*d*) 1 month (exposed to acetone).



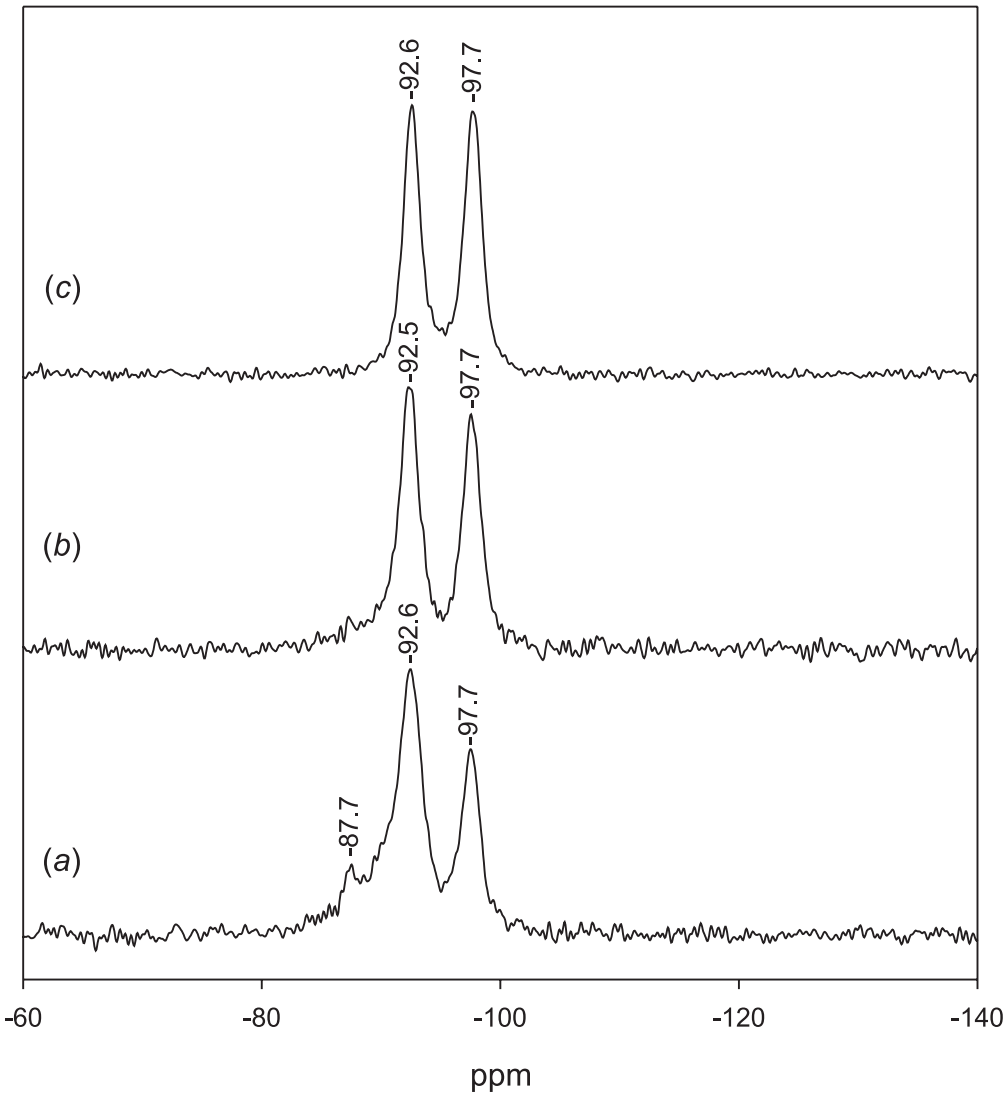
stage the terminal cations are coordinated either by acetone or residual structural water molecules. This is in agreement with the observation that the remaining acetone molecules are released only at 330 °C, accompanied by the residual structural water molecules (seen as a broad peak with a maximum at 350 °C on the water trace in Fig. 2). The shoulder at 430 °C corresponds to zones of palygorskite not affected by the insertion of acetone, as seen above for the loss at 190 °C. These results are similar to those obtained in the case of a sepiolite–pyridine nanohybrid material reported recently (13).

Figure 4 shows the ^{29}Si MAS NMR spectra of palygorskite heated at 150 °C for 20 h then exposed to acetone-d_6 (or acetone) for various amounts of time, from 4 h to 1 month. In a previous study (4), the two main resonances at –92.0 and –97.5 ppm in the ^{29}Si NMR spectra of palygorskite were attributed to the central silicon position and to the edge silicon sites, respectively. A minor resonance at –84.3 ppm was attributed to Q^2(Si-OH) silicon nuclei, and the integral ratio is approximately 1:7:6 for the resonances at –84.4, –92.0, and –97.5 ppm, respectively. Upon heating at 150 °C for 20 h, the two main resonances shift to –93.1 and –96.9 ppm, respectively. As shown in Fig. 4, the characteristic ^{29}Si NMR spectrum of palygorskite is gradually recovered over time when heated palygorskite is exposed to acetone. After 5 days, the recovery is almost complete, and three well-resolved signals at –84.4, –92.4, and –97.6 ppm are obtained. These results are an indication that acetone molecules do intercalate into the nanotunnels and that the original structure of palygorskite is recovered. Similar results were recently reported in the case of sepiolite–acetone samples (14). The same experiment was performed under CP/MAS conditions with similar results (shown in Fig. 5). In comparison with the ^{29}Si CP/MAS NMR spectrum of palygorskite (4), the signal of the edge silicium atoms at –97.7 ppm is stronger. This is attributed to a strong H-bonding directed organization of water and acetone molecules in the nanotunnels.

Figure 6*a* presents the ^{13}C MAS NMR spectra of palygorskite previously heated at 150 °C for 20 h then exposed to acetone. The signals at 205.8 and 29.5 ppm can be assigned to the carbonyl and methyl carbons, respectively.

© 2004 NRC Canada

Fig. 5. ^{29}Si CP/MAS NMR spectra of palygorskite heated at 150 °C for 20 h then exposed to acetone-d_6 for (*a*) 4 h; (*b*) 1 day; (*c*) 1 month (exposed to acetone).

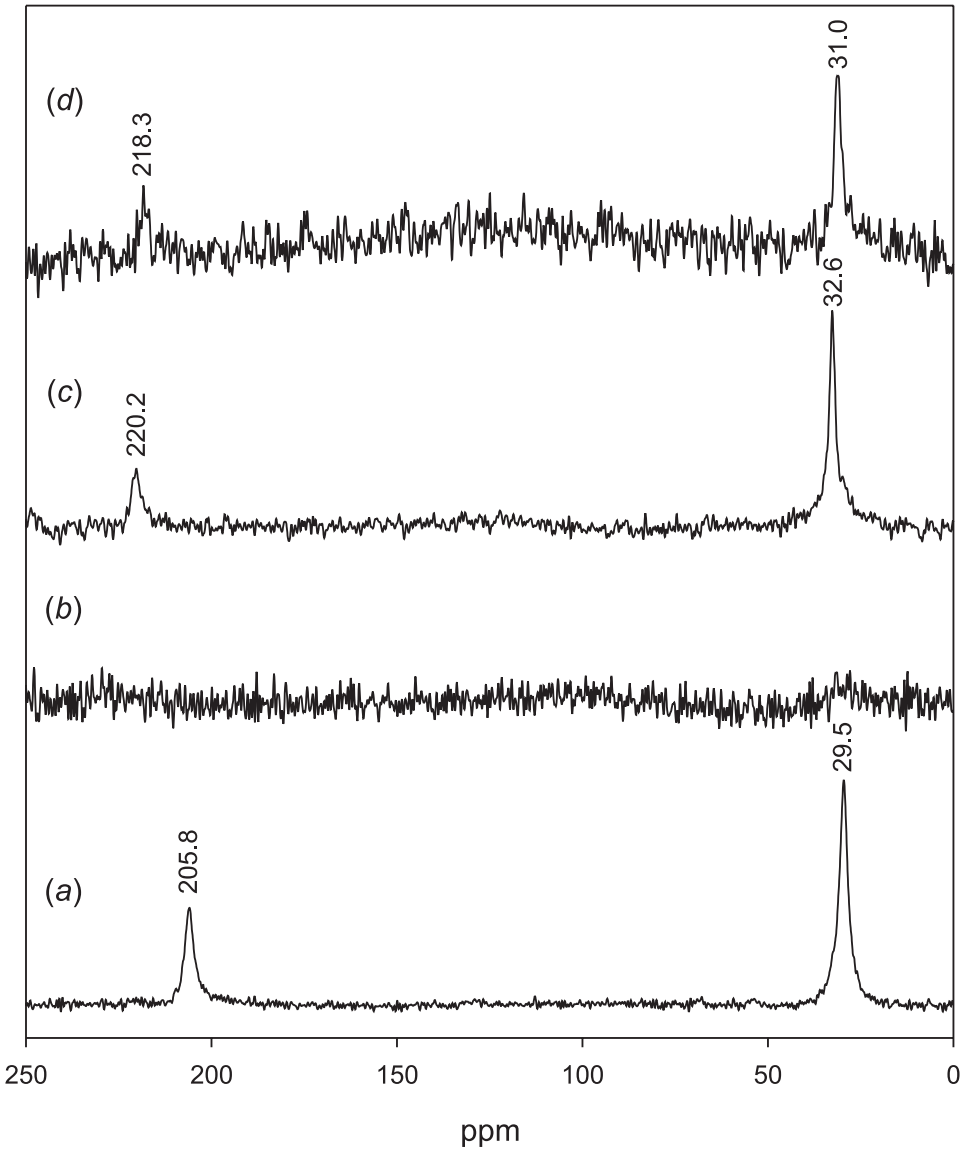


These chemical shift values are almost identical to the chemical shifts observed for the pure solvent. These peaks can be attributed to liquid-like acetone on the surface of the clay. This liquid-like acetone moves essentially isotropically and does not cross polarize very efficiently because of the motionally averaged dipolar coupling. This accounts for the very low intensity of these two peaks under CP/MAS conditions (Fig. 6*c*). However, under these conditions, two other peaks appear at 220.2 and 32.6 ppm. These signals can be attributed to acetone molecules intercalated into the congested space of the nanotunnels of palygorskite where they interact with the structural water molecules and cross polarize efficiently. As shown in Figs. 6*b* and 6*d*, gentle heating of the sample at 60 °C for 1 day leads to the removal of the liquid-like acetone molecules, while the intercalated acetone is kept in the nanotunnels. The intercalated acetone peaks are barely detectable in the MAS spectra because of the very small amounts present. Also the MAS measurements provide no sensitivity enhancement for the detection of intercalated acetone. These results can be interpreted as evidence for the fixation of two different types of acetone on palygorskite: mobile acetone molecules on the external surface and acetone molecules more rigidly fixed inside the nanotunnels. The former ones are detected by the MAS NMR experiment, while the latter ones are detected by CP/MAS.

Figure 7 presents the ^{29}Si MAS and CP/MAS NMR spectra of palygorskite heated at 300 °C for 20 h then exposed to acetone-d_6. As mentioned above, heating at 300 °C for 20 h could produce a folding of the structure because of the partial removal of the structural water molecules. As shown in Figs. 7*c* and 7*d*, the ^{29}Si MAS and CP/MAS NMR spectra of palygorskite after treatment at 300 °C for 20 h show several broad signals, with a peak maximum around –92.4 ppm for MAS and –92.8 ppm for CP/MAS, in agreement with a loss of symmetry and folding of the structure (4). However, the spectra of the same sample exposed to acetone vapor (Figs. 7*a* and 7*b*) are very similar to that of the original

© 2004 NRC Canada

Fig. 6. ^{13}C NMR spectra of samples: (*a*) MAS of palygorskite heated at 150 °C for 20 h then exposed to acetone (sample A); (*b*) MAS of sample A but after heating at 60 °C for 1 day; (*c*) CP/MAS of sample A; (*d*) CP/MAS of sample A but after heating at 60 °C for 1 day.



palygorskite and to that of the restored structure after heating at 150 °C (see Fig. 4*d* and ref. 4). Consequently, exposure to acetone vapor restores the original structure even when palygorskite was previously heated to 300 °C. This implies that the acetone molecules can still access the interior of the folded structure, restoring the nanotunnel structure. Nearly complete recovery is achieved by exposing palygorskite samples, which have been partially dehydrated at 300 °C, to acetone vapor at room temperature.

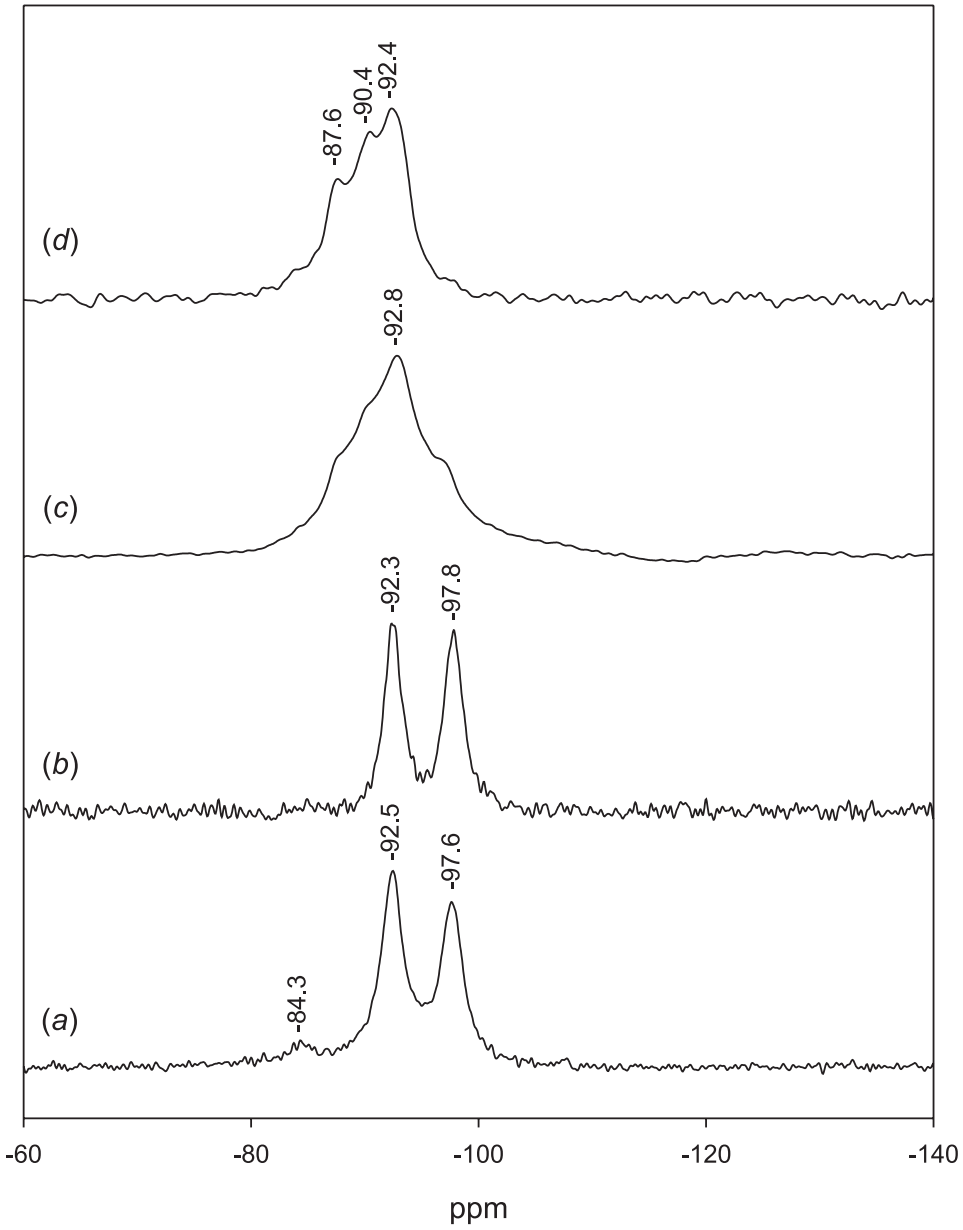
This study confirms that the structural changes of palygorskite are reversible when it is heated at temperatures up to 300 °C, even if, at that temperature, approximately 50% of the structural water molecules have been removed, causing the folding of the tunnel structure with an associated loss in microporosity. In a previous study (4), the ^{29}Si and ^{1}H NMR spectra indicated that exposure to D_2O or water vapor at room temperature restored the original structure when palygorskite was previously heated at 150 or 300 °C. Since the molecular dimensions of acetone are 6.6 Å × 4.1 Å × 5.2 Å (15), much larger than that of D_2O or water (3.2 Å × 2.9 Å × 3.9 Å), it is of great interest that acetone molecules can be inserted in the nanostructured tunnels of palygorskite, even after their folding at 300 °C. Moreover, similarly to what was reported in the case of the sepiolite–pyridine system (13), a nanohybrid material with a structure similar to the parent palygorskite can be formed through the direct coordination of acetone molecules to the terminal cation coordination sites in the tunnels of palygorskite.

Acknowledgements

The Natural Sciences and Engineering Research Council of Canada (NSERC, discovery grant program) is gratefully

© 2004 NRC Canada

Fig. 7 ^{29}Si (*a*) MAS and (*b*) CP/MAS NMR spectra of palygorskite heated at 300 °C for 20 h then exposed to acetone-d_6, in comparison with the ^{29}Si (*c*) MAS and (*d*) CP/MAS NMR spectra of palygorskite heated at 300 °C for 20 h.



acknowledged for financial support. Dr. Glenn Facey is thanked for his help in the NMR experiments.

References

1. (*a*) J.M. Serratosa. *In* Proc. Intern. Clay Conf. 1978. *Edited by* M.M. Mortland and V.C. Farmer. Elsevier Sci. Publ., Amsterdam, 1979. pp. 99–109; (*b*) B.F. Jones and E. Galán. *In* Reviews in mineralogy. Vol. 19. *Edited by* S.W. Bailey. Mineralogical Society of America, Washington D.C. 1988. pp. 631–674; (*c*) E. Galán. Clay Miner. **31**, 443 (1996); (*d*) H.H. Murray. Appl. Clay Sci. **17**, 207 (2000).
2. (*a*) W.F. Bradley. Am. Mineral, **25**, 405 (1940); (*b*) A. Preisinger. Clays Clay Miner. **10**, 365 (1963); (*c*) V.A. Drits and G.V. Sokolova. Sov. Phys.Crystallogr. **16**, 183 (1971); (*d*) S.W. Bailey. *In* Crystal structures of clay minerals and their X-ray identification. Monograph 5. *Edited by* G.W. Brindley and G. Brown. Mineralogical Society, London. 1980. pp. 1–123; (*e*) A.C.D. Newman and G. Brown. *In* Chemistry of clays and clay minerals. Monograph 6. *Edited by* A.C.D. Newman. Mineralogical Society, London. 1987. pp. 109–112; (*f*) N. Güven, J.-B. d'Espinose de la Caillerie, and J.J. Fripiat. Clays Clay Miner. **40**, 457 (1992); (*g*) E. Galán and M.I. Carretero. Clays Clay Miner. **47**, 399 (1999); (*h*) A. Chahi, S. Petit, and A. Decarreau. Clays Clay Miner. **50**, 306 (2002).
3. (*a*) J.E. Chisholm. Can. Mineral. **28**, 329 (1990); (*b*) J.E. Chisholm. Can. Mineral. **30**, 61 (1992); (*c*) G. Artioli and E. Galli. Mater. Sci. Forum **166–169**, 647 (1994); (*d*) G. Artioli, E. Galli, E. Burattini, G. Cappuccio, and S. Simeoni. Neues Jahrbuch fuer Mineralogie, Monatshefte, issue 5, 217 (1994); (*e*) M.E. Fernandez, J.A. Ascencio, D. Mendoza-Anaya, V. Rodriguez Lugo, and M. Jose-Yacaman. J. Mater. Sci. **34**,

© 2004 NRC Canada

5243 (1999); (*f*) G. Chiari, R. Giustetto, and G. Ricchiardi. Eur. J. Mineral. **15**, 21 (2003).
4. W. Kuang, A. Facey, and C. Detellier. Clays Clay Miner. **52**, 635 (2004).
5. (*a*) R.M. Barrer and N. Mackenzie. J. Phys. Chem. **58**, 560 (1954); (*b*) C. Serna, G.E. VanScoyoc, and J.L. Ahlrichs. Am. Mineral. **62**, 784 (1977); (*c*) F. Gonzalez, C. Pesquera, C. Blanco, I. Benito, S. Mendioroz, and J.A. Pajares. Appl. Clay Sci. **4**, 373 (1989); (*d*) M. Suárez Barrios, L.V. Flores González, M.A. Vicente Rodríguez, and J.M. Martín Pozas. Appl. Clay Sci. **10**, 247 (1995).
6. (*a*) R.M. Barrer, N. Mackenzie, and D.M. MacLeod. J. Phys. Chem. **58**, 568 (1954); (*b*) C.J. Serna and G.E. VanScoyoc. *In* Proc. Intern. Clay Conf. 1978. *Edited by* M.M. Mortland and V.C. Farmer. Elsevier, Amsterdam. 1979. pp. 197–206; (*c*) R.M. Barrer. Clays Clay Miner. **37**, 385 (1989).
7. A.R. Mermut and A.F. Cano. Clays Clay Miner. **49**, 381 (2001).
8. S.J. Chipera and D.L. Bish. Clays Clay Miner. **49**, 398 (2001).
9. G. Metz, X. Wu, and S.O. Smith. J. Magn. Reson. **A110**, 219 (1994).
10. U. Shuali, S. Yariv, M. Steinberg, M. Muller-Vonmoos, G. Kahr, and A. Rub. Thermochim. Acta, **135**, 291 (1988).
11. R.L. Frost and Z. Ding. Thermochim. Acta, **397,** 119 (2003).
12. G.E. VanScoyoc, C.J. Serna, and J.L. Ahlrichs. Am. Mineral. **64**, 215 (1979).
13. W. Kuang, G.A. Facey, C. Detellier, B. Casal, J.M. Serratosa, and E. Ruiz-Hitzky. Chem. Mater. **15**, 4956 (2003).
14. M.R. Weir, G.A. Facey, and C. Detellier. Stud. Surf. Sci. Catal. **129**, 551 (2000).
15. C.E. Webster, R.S. Drago, and M.C. Zerner. J. Am. Chem. Soc. **120**, 5509 (1998).

© 2004 NRC Canada

The reductive deposition of quaternary pyridinium corrosion inhibitor multilayers on glassy carbon electrodes[1]

Rick P.C. Wong, Jennifer E. Wong, and Viola I. Birss

Abstract: The redox behaviour of several quaternary pyridinium corrosion inhibitors ("Quats") at glassy carbon (GC) electrodes has been investigated in neutral aqueous solutions. The primary emphasis is on *n*-butyl-3-(*N*-octylcarbamyl)pyridinium bromide, one of the Quats determined to have very good corrosion inhibition properties based on parallel weight loss experiments. It is demonstrated that the reduction of the Quats, which occurs in a two-electron reaction at potentials negative of –1.0 V vs. SSCE, results in the formation of a neutral product. This forms a porous film on the electrode surface, with clusters that expand and thicken as more Quat deposits, as confirmed by atomic force microscopy. The film charge density reaches a maximum of ~4 mC/cm^2, equivalent to more than 100 monolayers of Quat, after which no further Quat can be deposited, suggesting full surface coverage by a nonconducting product. The Quat multilayer can then be redissolved at potentials positive of ~ –0.2 V, during its oxidation back to its original solution-soluble form.

Key words: quaternarized pyridinium compounds, reductive film deposition, glassy carbon, multilayer, corrosion inhibitors, cyclic voltammetry, AFM.

Résumé : Opérant dans des solutions aqueuses neutres, on a étudié le comportement redox, au niveau d'électrodes de carbone vitreux (CV), de plusieurs sels de pyridinium quaternaires, des inhibiteurs de la corrosion (« Quats »). L'accent a principalement été mis sur le bromure de *n*-butyl-3-(*N*-octylcarbamyl)pyridinium, un des quatre Quats qui, sur la base d'expériences parallèles de pertes de poids, devrait présenter de très bonnes propriétés d'inhibition de la corrosion. Il a été démontré que la réduction du Quats, une réaction à deux électrons à des potentiels négatifs de –1,0 V vs. SSCE, conduit à la formation d'un produit neutre. Tel que confirmé par une microscopie de forces atomiques, celui-ci forme un film poreux sur la surface de l'électrode, avec des agrégats qui conduisent à une expansion et un épaississement avec les dépôts additionnels de Quats. La densité de charge du film atteint un maximum de ~4 mC/cm^2, équivalent à plus de 100 monocouches de Quat, après quoi il ne peut plus se déposer de Quat, ce qui suggère que la surface totale est couverte par un produit qui ne conduit pas l'électricité. La multicouche de Quat peut alors être redissoute à des potentiels positifs de ~ –0.2 V, durant sa réoxydation à sa forme originale soluble dans la solution.

Mots clés : dérivés pyridinium quaternaires, dépôt d'un film de réduction, carbone vitreux, multicouche, inhibiteurs de corrosion, voltampérométrie cyclique, AFM.

[Traduit par la Rédaction]

Introduction

Quaternary pyridinium compounds ("Quats", Fig. 1*a*) are a class of cationic organic corrosion inhibitors used for the protection of metals such as carbon steel in pipeline and drilling equipment. These inhibitors are relatively low in cost and are especially effective in environments that contain brine and high concentrations of H_2S or CO_2. While the mechanism of the corrosion protection of metals by Quats remains essentially unknown, it has been surmised that Quats adsorb strongly, thus blocking local anodic and cathodic surface sites.

We have recently examined (1)[3,4] the impact of the addition of Quats to aqueous neutral and weakly alkaline solutions on Pt electrochemistry. It was demonstrated that Pt oxide formation and reduction, as well as hydrogen adsorption and evolution, could be essentially fully suppressed by the presence of certain Quats in solution, at concentrations >40 μmol/L (1). Quats that showed a high propensity for adsorption on Pt also served to protect carbon steel from corro-

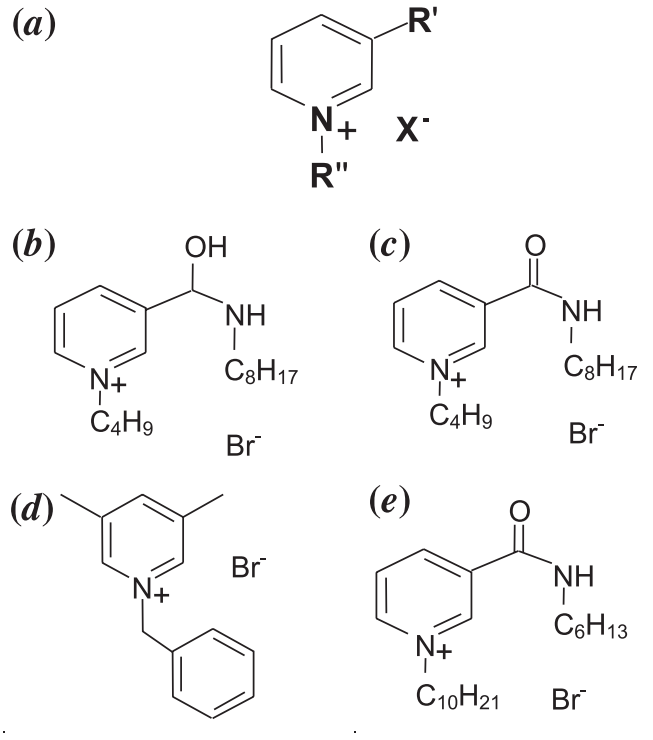
Received 7 June 2004. Published on the NRC Research Press Web site at http://canjchem.nrc.ca on 3 December 2004.

R.P.C. Wong, J.E. Wong, and V.I. Birss.[2] Department of Chemistry, University of Calgary, 2500 University Drive N.W., Calgary, AB T2N 1N4, Canada.

[1]This article is part of a Special Issue dedicated to the memory of Professor Don Irish.
[2]Corresponding author (e-mail: birss@ucalgary.ca).
[3]J.E. Wong, D.T. Cramb, and V.I. Birss. Article in preparation.
[4]J.E. Wong, D.T. Cramb, and V.I. Birss. Article in preparation.

 doi: 10.1139/V04-127 © 2004 NRC Canada

Fig. 1. (*a*) Generic structure of quaternary pyridinium compounds (Quats) and structures of (*b*) *n*-butyl-3-[hydroxy(octylamino)methyl] pyridinium bromide (Quat 1); (*c*) *n*-butyl-3-(*N*-octylcarbamyl)pyridinium bromide (Quat 2); (*d*) *n*-benzyl-3,5-dimethyl pyridinium bromide (Quat 3); (*e*) *n*-decyl-3-(*N*-hexylcarbamyl) pyridinium bromide (Quat 4).



sion in parallel tests in brine solutions. It was generally observed (1) that Quats containing alkyl chains of C-8 or longer, either in the meta position or attached to the pyridinium nitrogen (Fig. 1*a*), were most effective in decreasing the corrosion rate of carbon steel. Corresponding quartz crystal microbalance (QCMB) results (1) showed a mass increase equivalent to about two monolayers of adsorbed molecules in these experiments. It was also shown that (1), once Pt electrochemistry was blocked by Quat adsorption, the normal potential window could be widened well beyond the normal limit defined by hydrogen evolution, allowing potentials to be reached at which the Quats can be reduced. This led to the deposition of a Quat multilayer.

The reduction of related compounds (e.g., 4-cyano-1-methyl pyridinium) has been reported previously, and it has been suggested that they can be reductively dimerized, forming the viologen form of the compound (2). Nicotinamide, another compound with a closely related structure, has also been shown to reduce electrochemically (3–5), forming a neutral hydropyridine monomer or dimer, while dimerization is proposed during reduction in acidic environments. 2-Vinyl pyridine has also been shown to reduce on a steel electrode (6), possibly forming a polymeric surface product.

In the present work, the behavior of Quats at a stable electrode surface, not susceptible to dissolution, was examined using a combination of cyclic voltammetry and constant potential methods, as well as atomic force microscopy (AFM). Glassy carbon (GC) was chosen for this purpose, primarily because of its high overpotential for hydrogen evolution, allowing easy access to negative potentials. Also, GC electrodes are not readily oxidized and display only minimal surface electrochemistry.

In this paper, the primary focus is on the electrochemical behavior of a specific Quat, namely *n*-butyl-3-(*N*-octylcarbamyl)pyridinium bromide (Quat 2, Fig. 1*c*), chosen because of the high degree of protection it offers carbon steel from corrosion in weight loss experiments in brine solutions (7). A pure form of this Quat was synthesized to avoid the impurities commonly encountered in the commercial Quat mixtures. Three other Quats (Quats 1, 3, and 4, Figs. 1*b*–1*e*) were also examined for comparison purposes. Cyclic voltammetric studies show that all of the Quats (8) can be reduced, resulting in the deposition of a Quat multilayer on the GC surface. The properties of this layer and its impact on the corrosion inhibition properties of Quats will also be discussed.

Experimental methods

Electrodes and surface preparation

The working electrode consisted of an 11 mm diameter glassy carbon (GC) rod, electrically connected to a copper wire using conducting silver epoxy (Allied Electronics, 2400 Circuit Works). To ensure a high quality connection and good adhesion, a layer of standard epoxy was applied on top of the conducting silver epoxy. The GC rod was then imbedded in an inert resin (Scandia, 58 Hagen), exposing only its cross-sectional end (0.95 cm^2). All current and charge densities in this paper are calculated on the basis of this apparent electrode area.

Prior to use, the GC electrode was hand-polished on a flat surface using 600 grit silicon carbide emery paper. The electrode was then polished using a coarse suspension of alumina (Metaserv, 7.0 μm) on a Rayfinal polishing cloth (Micro-Metallurgical Ltd.). Progressively finer alumina powder (E.T. Enterprises, 1.0, 0.3, and 0.05 μm) was then used, until a mirror-like surface was obtained (9, 10). The polished electrode was then cleaned with triply distilled water in an ultrasonic bath for at least 10 min to remove any alumina powder left on the surface.

The counter electrode (CE) was a large surface area Pt gauze electrode, embedded in soft glass tubing. A saturated sodium calomel electrode (SSCE, 0.235 V vs. SHE) was used as the reference electrode (RE) and all potentials are referred to the SSCE in this paper.

Instrumentation, cells, and solutions

All CV measurements were performed using an EG&G PARC 273 potentiostat/galvanostat and all data were recorded on a Hewlett-Packard 7045B X-Y recorder. A two-compartment electrochemical cell was employed, with the RE in one compartment joined to the main compartment containing the WE and CE, via a Luggin capillary. The GC electrode was suspended face-downwards in this cell configuration. Nitrogen bubbling, either through or above the cell solution, served to deaerate the cell solutions.

Water was triply distilled using a Corning Mega-Pure-6A system. A 0.05 mol/L KH_2PO_4 + 0.03 mol/L NaOH pH 7.2 phosphate buffer solution was prepared according to the CRC Handbook (11). All reagents were Fisher Certified or

© 2004 NRC Canada

ACS grade and were used as received. The temperature of the solutions ranged from 20 to 22 °C. Quaternary pyridinium compounds (Quats) were provided by Brenntag Canada (formerly Travis Chemicals), either in solution or in crystalline form, and their general structure is presented in Fig. 1*a*. The primary emphasis of this paper is on the *n*-butyl-3-(*N*-octylcarbamyl)pyridinium bromide (Quat 2), as shown in Fig. 1*c*, but *n*-butyl-3-[hydroxy(octylamino)methyl] pyridinium bromide (Quat 1, Fig. 1*b*), *n*-benzyl-3,5-dimethyl pyridinium bromide (Quat 3, Fig. 1*d*), and *n*-decyl-3-(*N*-hexylcarbamyl) pyridinium bromide (Quat 4, Fig. 1*e*) were also investigated. Stock solutions of these Quats of 100 mmol/L were used in this work.

Atomic force microscopy (AFM)

Samples were prepared using a lithographically deposited (for ease of positioning of the AFM tip) Pt sputtered coated glass working electrode (apparent area 0.75 cm^2), cleaned electrochemically in stirred, deaerated 1 mol/L H_2SO_4 until a steady-state CV was observed. The potential was then cycled between –0.6 and 1.0 V vs. SSCE in a stirred, deaerated pH 7.2 phosphate buffer solution. An aliquot of the 100 mmol/L Quat stock solution was added such that the final solution concentration was 0.25 mmol/L and after a period of potential cycling, the potential was held at –0.9 V to deposit the Quat multilayer. The electrode was then rinsed, allowed to air-dry, and imaged using a Molecular Imaging, Inc. Nanoscope II instrument in MacMode in air. The cantilever used had a force constant ranging from 2 to 5 N/m.

Results and discussion

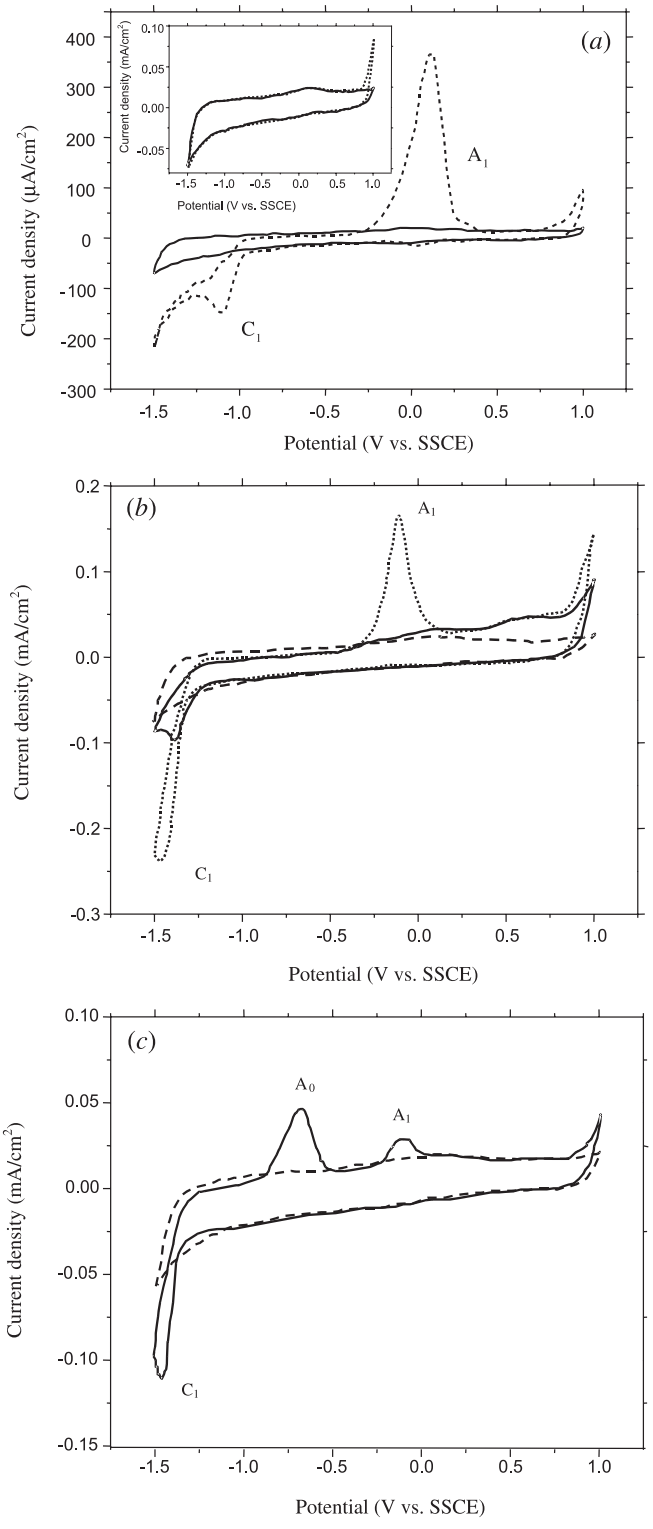
General electrochemical behaviour of Quats at GC in neutral phosphate buffer solutions

After 30 min of cycling in a pH 7.2 phosphate buffer solution in the range of –1.5 to 1.0 V vs. SSCE, the bare, polished GC electrode reveals an almost featureless cyclic voltammetric (CV) response (Fig. 2*a*), as previously reported in the literature (12–17). Only capacitive current is seen over the entire potential range from –1.5 to 1.0 V, with no evidence for the onset of the HER until potentials below –1.2 V.

Upon the addition of an aliquot (2 mmol/L in cell) of *n*-butyl-3-(*N*-octylcarbamyl)pyridinium bromide (Quat 2) to the phosphate buffer solution, the magnitude of the charging current does not change significantly, suggesting that Quat 2 does not adsorb on the GC surface (Fig. 2*a*). However, at more negative potentials, an obvious set of redox peaks (A_1 and C_1) are seen. Notably, these features are quite similar to those observed at Pt (1), although the anodic peak potential is more positive on Pt (0.3 V) than on GC (0.1 V) under otherwise the same conditions. Also, previous work on Pt in pH 7.2 phosphate buffer demonstrated that the Quat reduction peak was sometimes difficult to resolve from the currents because of hydrogen evolution, which is the main reason that GC electrodes were chosen for the present work.

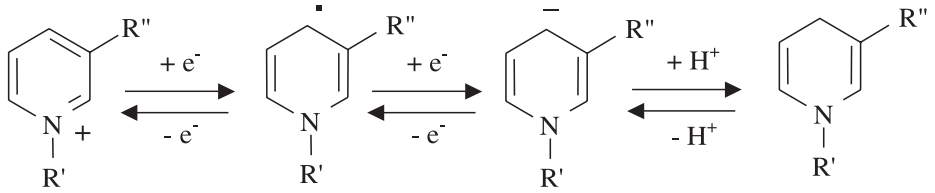
In the case of the addition of Quats 1 and 3 to the phosphate buffer solution, Figs. 2*b* and 2*c*, respectively, show very similar results, except that the anodic peak A_1 is actually composed of two peaks in the first few cycles of potential. The origin of these two anodic peaks is still unclear.

Fig. 2. (*a*) CV of GC in deaerated pH 7.2 phosphate buffer solution at 100 mV/s, before (—) and after (----) the addition of 2 mmol/L Quat 2. Inset: CV response of GC before (—) and after (····) the addition of 1.6 mmol/L KBr. (*b*) CV of GC in deaerated pH 7.2 phosphate buffer solution at 100 mV/s before (– – – –) and after the addition of 0.32 mmol/L (—) and 1.6 mmol/L (···) Quat 1. (*c*) CV of GC in deaerated pH 7.2 phosphate buffer solution at 100 mV/s before (– – – –) and after (—) the addition of 0.32 mmol/L Quat 3.



© 2004 NRC Canada

Scheme 1. Proposed redox mechanism of a typical Quat monomer.



However, based on the discussion below, it is possible that the two anodic peaks often observed for the Quats reflects the stabilization of the one-electron oxidation product (Scheme 1), such that the transfer of each of the electrons is seen in a separate peak. Notably, their appearance separately seems to be related to the cycling time (exposure time) and the scan rate employed. Also, the size of the two anodic peaks decreases slightly and their potential shifts positively with increased time of cycling. Earlier published work with similar compounds, employing the dropping mercury electrode, showed two peaks during the reduction step, an example being the work of Carelli and Cardinali (2) for 4-cyano-1-methyl pyridinium in aqueous solutions of varying pH. Galvin and co-workers (4, 5) also observed two peaks during the reduction of nicotinamide under similar conditions and attributed the first reduction peak to the dimerization of the pyridinium rings, while the second peak was considered to be due to the reduction of the radical to form a neutral hydropyridine monomer.

The anodic current observed at potentials greater than ca. 0.85 V vs. SSCE, after the addition of the Quats to the cell solution (Fig. 2*a*), is due to the oxidation of bromide ions (rxn. [1]) (17), as was confirmed by the addition of 2 mmol/L KBr alone to the buffer solution (Fig. 2 inset).

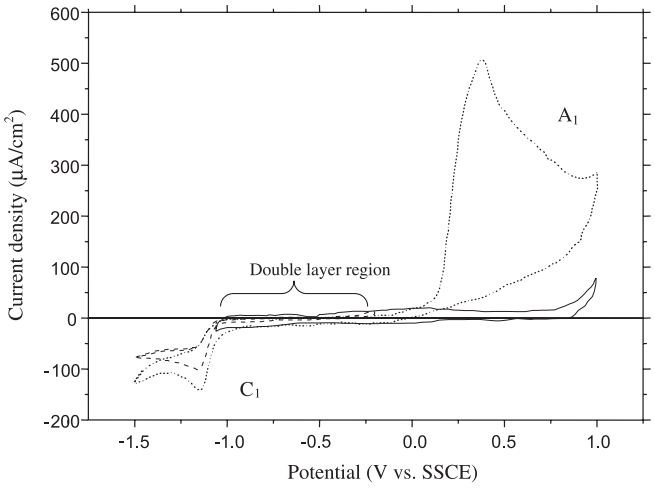
[1] $2Br^- \rightarrow Br_2(aq) + 2e^-$

$E^0 = 0.863$ V (vs. SSCE)

To study Quat redox chemistry further, the lower potential limit (E_-) was changed from –1.5 V vs. SSCE to a less negative value of –1.0 V, as shown in Fig. 3 for Quat 2 (curve a). Both the C_1 and A_1 peaks have now disappeared, confirming that these peaks are coupled and that it is essential to first reduce the Quat to then allow its reoxidation. In another experiment, E_+ was lowered to –0.2 V, to prevent the oxidation process, while retaining an E_- of –1.5 V. The size of the C_1 peak decreases with each cycle of potential, as shown in Fig. 3 (curve b). The currents owing to double layer charging, between the A_1 and C_1 peaks, also then decrease with each cycle. Both of these results indicate that the C_1 peak reflects the deposition of a product on the electrode surface. Hence, when the potential is maintained negative of the A_1 peak, more Quat can be deposited on the GC surface with time. This appears to serve to increasingly block the electrode surface, reducing the activity of the surface towards further Quat reduction and also decreasing the capacitance of the double layer.

When E_+ was then increased back to its original value (from –0.2 to 1.0 V), a very large anodic peak was seen in the next anodic cycle, as shown in Fig. 3 (curve c). The potential of the A_1 peak is also shifted positively, implying that a more resistive (e.g., thicker) surface layer is now present.

Fig. 3. Effect of potential limits on CV response of GC electrode in 2 mmol/L Quat 2 in deaerated pH 7.2 phosphate buffer solution at 100 mV/s: steady-state response for $E_+ = 1.0$ V and $E_- = -1.0$ V, curve a (—); fifth cycle for $E_+ = -0.2$ V and $E_- = -1.5$ V, curve b (– – – –); first cycle with $E_+ = 1.0$ V and $E_- = -1.5$ V, curve c (·····).



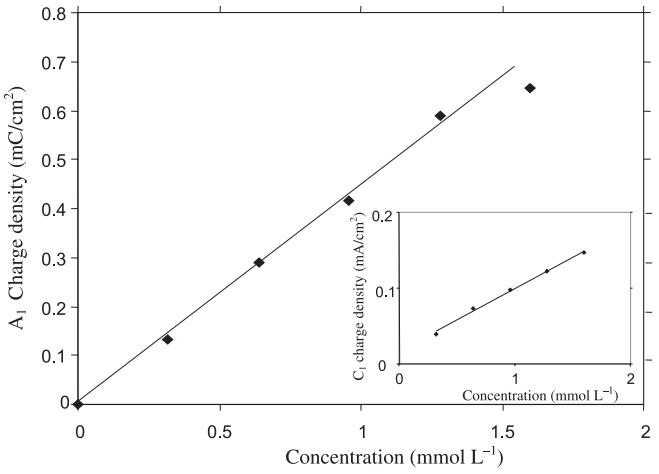
This likely indicates that the surface product, formed at negative potentials, is not very conductive. The reappearance of both redox peaks after extension of the potential limits beyond both the A_1 and C_1 peaks shows clearly that the A_1 peak depicts the removal of the surface product, allowing more Quat to be reduced and deposited in the following cathodic scan.

As a final confirmation of the deposition of a surface film in peak C_1, the GC electrode was removed from the Quat containing solution at $E_- = -1.5$ V, rinsed and blotted carefully with a tissue to remove any adhering solution, and then placed in a fresh phosphate buffer solution (without any added Quat). When the potential of this electrode was scanned positively from –1.5 V, the A_1 peak was clearly observed. However, the C_1 peak at –1.0 V was not seen in the following cathodic scan, and only a very small A_1 peak was seen in the next few anodic cycles. These results show clearly that the deposition of a reduced surface film occurs at negative potentials in the Quat-containing solution, and that it is oxidized and concurrently lost from the surface in the A_1 peak.

Overall, the results of Figs. 2 and 3 confirm that the Quats can be reduced at potentials negative of ca. –1.0 V, forming a surface product. However, this material is not oxidized at the GC electrode until a potential of ca. –0.3 V is reached. These electrochemical characteristics, seen for all of the Quats studied here, are very similar to those reported previously for NADH (3–5, 18), as discussed above (16). It

© 2004 NRC Canada

Fig. 4. Anodic peak (A_1) charge density as a function of Quat 2 concentration in stirred, deaerated pH 7.2 phosphate buffer solution after scanning negatively to –1.5 V at 100 mV/s. Inset: cathodic peak (C_1) charge density as a function of Quat 2 concentration in deaerated pH 7.2 phosphate buffer solution after scanning negatively to –1.5 V at 100 mV/s.



should be noted that the formation of a poorly conducting surface product at relatively negative potentials may be related to the corrosion inhibiting nature of the Quats at carbon steel electrodes, at which the corrosion potential can be quite negative at neutral pH.

Kinetics of Quat deposition

To determine the dependence of the Quat multilayer formation rate on Quat concentration, different volumes of the Quat stock solutions were added to the cell solution during continuous potential cycling, all at 100 mV s^{-1}. The CVs were recorded after a steady state was reached ~2 min after each addition. Figure 4 shows that the A_1 and A_2 (Fig. 4, inset) peak charge densities are linearly dependent on the Quat 2 concentration in the phosphate buffer solution. The results of Fig. 4 suggest that the rate of the C_1 deposition process, and hence, also of the A_1 oxidation reaction, is controlled by the rate of diffusion of Quat 2 to the electrode surface.

It is notable that the peak currents also increased significantly in size with solution stirring, consistent with this hypothesis. To test this further, the effect of the scan rate on the peak currents was examined. The zero current baseline for the C_1 peak was estimated consistently at each scan rate, assuming that the rate of the HER would be the same in each experiment. The results reveal that the C_1 peak current density exhibits a square root dependence on the scan rate, as shown in Fig. 5, again indicative of the control of Quat 2 reduction and deposition (peak C_1) rate by the transport of the Quat from solution to the electrode. Similar results were seen with Quats 1, 3, and 4, and also for Quats 1 and 2 at Pt.

Characteristics of Quat film at GC electrodes

The effect of holding the potential for various periods of time at –1.5 V in the presence of 4 mmol/L Quat 1 in the pH 7.2 phosphate buffer solution (stirred) was then examined. The results showed that the A_1 peak in the following anodic scan initially increased in size, at a rate proportional

Fig. 5. Dependence of the C_1 peak current density on the square rate of the sweep rate for 2 mmol/L Quat 2 in deaerated pH 7.2 phosphate buffer solution.

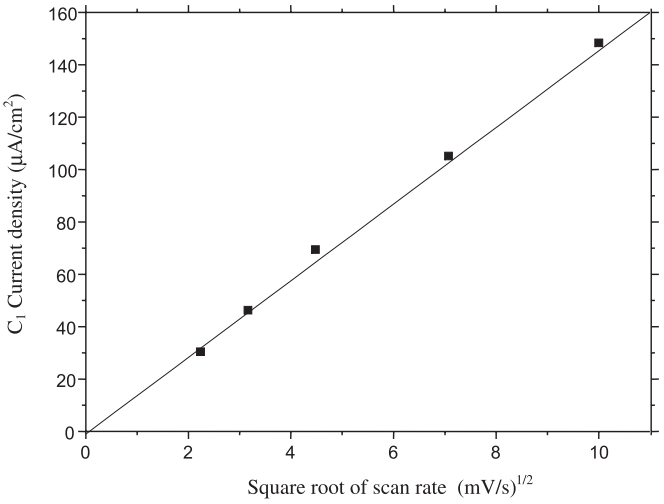
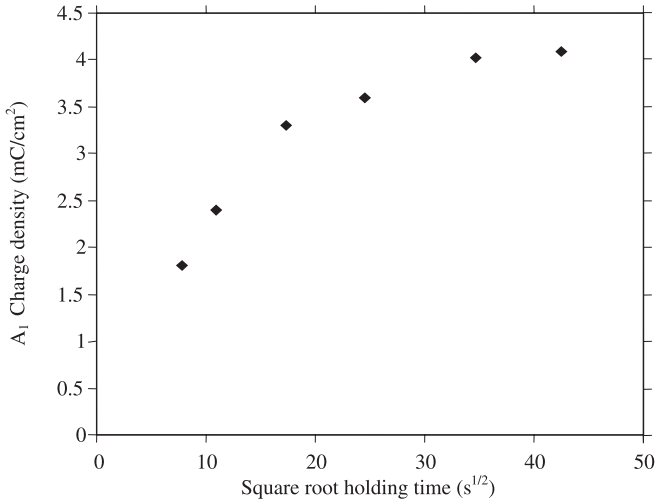


Fig. 6. Charge density of A_1 peak at GC as a function of holding time at –1.5 V vs. SSCE for 4 mmol/L Quat 2 in deaerated pH 7.2 phosphate buffer solution (100 mV/s).

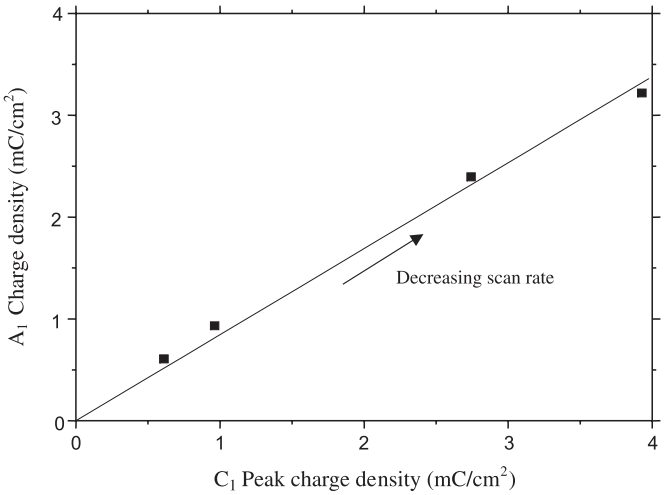


to the square root of the holding time. As shown in Fig. 6, the A_1 charge density appears to reach a threshold value of ca. 4 mC/cm^2 after about 30–40 min under these conditions (note that the dependence of the amount of deposited Quat is linear with the square root of holding time at earlier times, again indicative of diffusion-controlled Quat film deposition). In our earlier work with Pt substrates (1), the highest charge densities seen during Quat 2 deposition (at constant potential) and subsequent stripping at 2 mV/s were in the range of 2 to 5 mC/cm^2.

A parallel set of experiments in the 4 mmol/L Quat 1 solution, aimed at reaching an upper limit to the amount of Quat deposited by sweeping more slowly through the –1.5 to 1.0 V range, was then carried out. Figure 7 shows that the charge increases at slower sweep rates, which is expected if the rate of Quat deposition is diffusion controlled. At 5 mV/s, a charge of ca. 3 mC/cm^2 is seen, and it appears that

© 2004 NRC Canada

Fig. 7. Anodic vs. cathodic charge density obtained from 4 mmol/L Quat 2 in deaerated pH 7.2 phosphate buffer solution at different scan rates.



the plot would taper off at a somewhat higher charge density. Figure 7 also shows that the anodic and cathodic charges are very similar, especially at high scan rates, confirming that essentially all of the reduced product can be reoxidized under these conditions and also that the current baselines beneath the C_1 and A_1 peaks are being appropriately selected.

It is also possible that, as more Quat is deposited (higher concentrations, slower reduction sweep rates), not all of it is fully removed in the anodic scan. This would then lead to the curvature developing at high charge densities in Fig. 7. This is also consistent with the fact that with long times of continuous potential cycling at slow sweep rates, both the A_1 and C_1 peaks decrease in size somewhat, consistent with some residue building up on the electrode surface with time.

Based on the fact that an upper limit to Quat deposition is seen (Fig. 6), this suggests that further Quat reduction is limited by the film thickness and (or) resistance. Even so, for film quantities below 4 mC/cm^2 on GC, there is clearly sufficient conductivity present for film reoxidation to occur, although the large separation of the A_1 and C_1 peaks may also be an indication of the presence of some film resistance.

It is clear that the charge densities observed in these experiments are significantly greater than expected for monolayer coverage. Rahman and Ghosh (15) reported that an unsubstituted pyridine molecule occupies ca. 24 Å^2 on various oxide surfaces, based on the analysis of adsorption data using the Langmuir equation. Assuming that the reduction of the Quat involves a two-electron process (see the following section) and that each Quat molecule occupies a minimum area of 24 Å^2 (expected to be larger than this because of the attached groups (Fig. 1)), this yields 4×10^{14} molecules/cm^2 for a single monolayer of reduced Quat 1 (i.e., 130 μC/cm^2 for a two-electron reaction (19)). Therefore, 4 mC/cm^2 would be equivalent to at least 30 monolayers of the reduced Quat film. In fact, it is likely that the film is much thicker than this, even up to the equivalent of 100 monolayers, allowing for a variety of surface configurations, more open packing, and porosity for ion transport during film growth and oxidation.

To understand what the limitations might be in terms of charge transport through the Quat multilayer, the film morphology was examined using AFM, using a lithographically deposited Pt surface to facilitate the positioning of the AFM tip. Figure 8 shows that the Quat film deposits in the form of clusters, and that at longer deposition times, the clusters grow and coalesce. These images are of two different Quat 4 multilayer samples in air. The sample shown in Fig. 8*a* was prepared by holding at –0.9 V for 10 min in a 0.25 mmol/L Quat 4 solution, while the sample shown in Fig. 8*b* was held at –0.9 V for 60 min. The observed morphology of the Quat multilayer, together with the electrochemistry discussed above and the anticipated poor electronic conductivity of the multilayer (see below), suggests that charge transfer during multilayer formation and oxidative dissolution involves the transfer of the cationic Quat monomer to and (or) from the GC substrate via the pores between the Quat clusters. A more detailed discussion of Quat multilayer formation and removal from Pt is presented elsewhere.[5]

Proposed mechanism of Quat reduction–oxidation

As indicated above, the A_1 and C_1 peaks were observed for all quaternary pyridinium compounds examined electrochemically at the GC electrode, indicating that the redox reaction is associated with the pyridinium ring itself, rather than of any of the functional groups attaching the side chain to the meta-position to the ring or of the chains themselves. Indeed, within the group of Quats studied at GC, Table 1 shows that, when the pyridinium charge is more positive because of the electron-withdrawing nature of the attached groups, the C_1 peak potential is less negative under otherwise identical conditions. These data again demonstrate that the C_1 peak is associated with the reduction of the pyridinium nitrogen of the ring.

Scheme 1 shows a possible mechanism for the reduction of the Quat monomer. Previous workers (15, 20) have suggested a similar mechanism for the reduction of NADH (3–5, 18), which has a very similar structure to that of the Quats studied here. Others (3–5) have proposed a series of possible reaction routes for the reduction of nicotinamide under varying pH conditions. Also, a similar reduction mechanism to that in Scheme 1 for analogous substituted pyridinium compounds, but in aprotic solvents, has been suggested (18, 21). In addition, it has been reported that dialkylcarbamoylpyridinium could be reduced to form 1,4-dihydropyridine in an aqueous solution (22). Further, polypyridinium cations of very high molecular weight (> 30 000 g/mol) have been shown to be reduced in nonaqueous solutions on bismuth by the reduction of the pyridinium ring (23). Interestingly, in a separate paper by the same group, it was shown that monopyridinium and polypyridinium cations can cross-link on the bismuth surface to form dimers after the pyridinium ring has been reduced (24).

This proposed two-electron mechanism shown in Scheme 1 demonstrates that the reduced product can be reoxidized, forming the original structure and hence, that the reaction should be reversible, consistent with our observations. When

[5] J.E. Wong, V.I. Birss, and D.T. Cramb. Article in preparation.

© 2004 NRC Canada

Fig. 8. AFM images of Quat 4 multilayer coated Pt electrode in air (*a*) after holding for 20 min and (*b*) after holding for 60 min at –0.9 V vs. SSCE. The line on the image indicates the location of cross section.

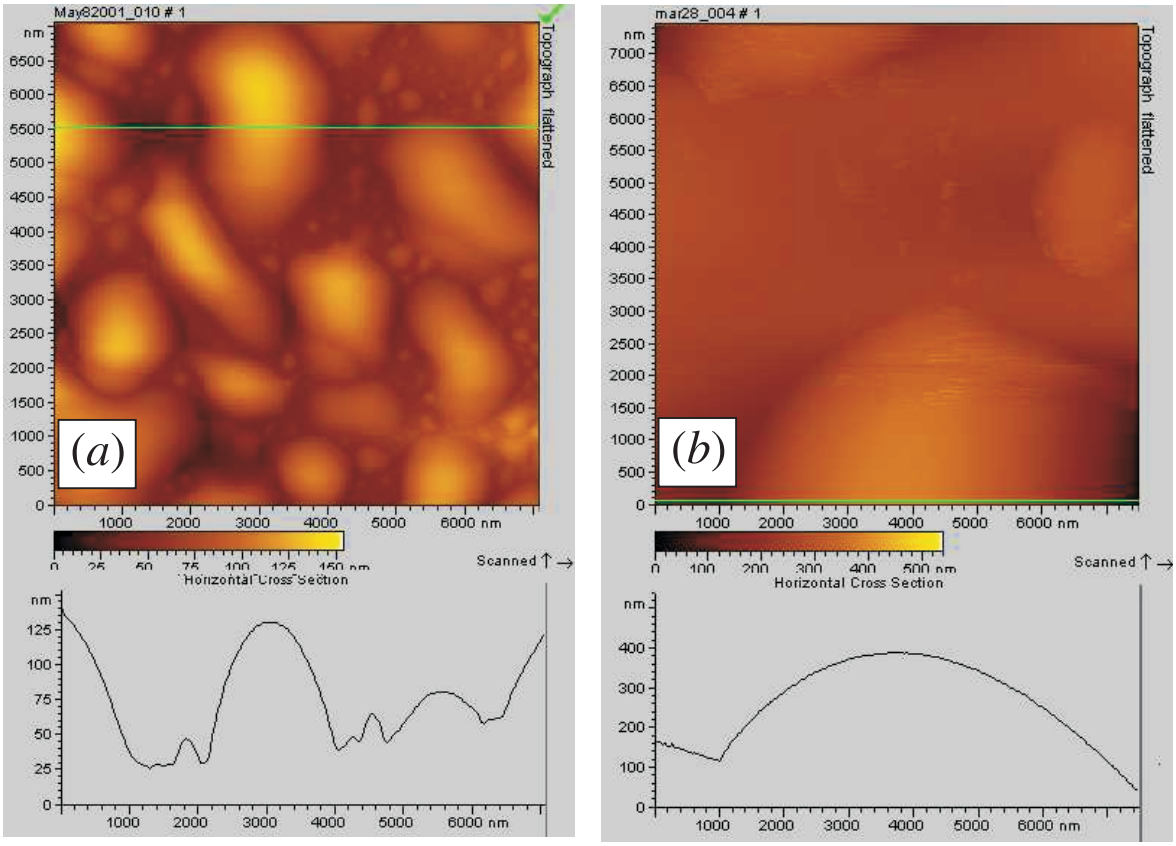


Table 1. Summary of observed peak potentials of Quats 1–3 (1.25 mmol/L Quat in stirred, deaerated pH 7.2 phosphate buffer solution, E_{-} = –1.5 V, E_{+} = 1.0 V, 100 mV/s).

Quat	Reduction peak potential (V)	Oxidation peak potential (V)
1	–1.1	0.1
2	–1.35	–0.2
3	–1.45	–0.55 and –0.1

the Quat is reduced, its positive charge is lost so that a neutral species is generated. This neutral organic molecule would tend to come out of the polar aqueous solution employed in the present work and deposit on the GC electrode surface. When reoxidized, the Quat would regain its positive charge and, therefore, should readily redissolve into the aqueous medium.

Two electrons and one proton are required to reduce the positively charged pyridinium compound to a neutral species, according to this mechanism. This would predict a shift of the reaction redox potential negatively by –29.5 mV per pH unit. It was not possible to test this prediction in this study, as the peak potentials varied with the experimental variables employed, related also to the rate of the concurrent hydrogen evolution reaction on GC.

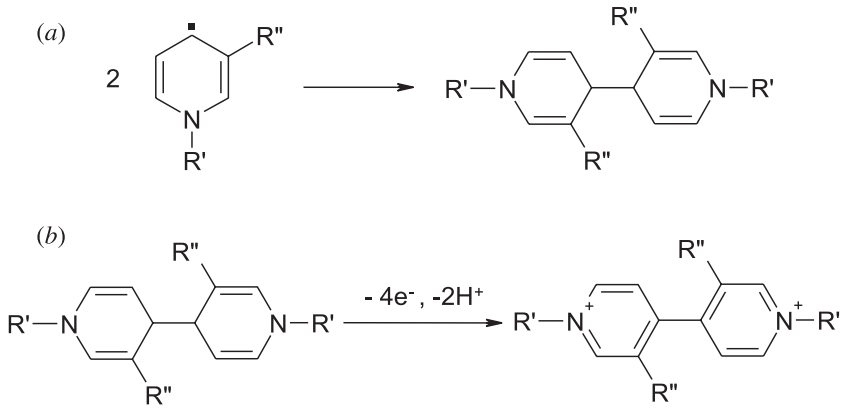
The radical intermediate suggested in Scheme 1 could potentially initiate the formation of other products. For example, when two of these species react together, a dimer (Scheme 2*a*) could be formed if steric hindrance is not a factor (21). Each dimer would then undergo a two-electron reduction process, not involving protons. However, cleavage of the joining bond in the reoxidation step is not likely and therefore, the reaction in Scheme 2*a* would be irreversible. Instead, a dimeric oxidation product could be formed, as shown in Scheme 2*b*. This redox mechanism would result in an anodic to cathodic charge ratio of two. One electron would be required to form each radical (two electrons per dimer molecule), while four would be required in the oxidation step. As shown in Fig. 7, the charge density in the A_1 and C_1 peaks are very similar, and thus, the formation of this dimeric compound as a primary reaction product is not considered likely in the present case.

After long times of potential cycling, a nonoxidizable residue did seem to build up on the electrode surface, which could be related to the formation of a small amount of the dimeric product. Discrimination between a monomeric vs. dimeric product turned out to be very difficult when GC–MS and NMR analyses were attempted. This is due, in part, to the similarities of the responses of these two products. Also, the ex-situ analysis of this film product was complicated by the possibility of air oxidation of the reduced product once the film-covered electrode was removed from solution.

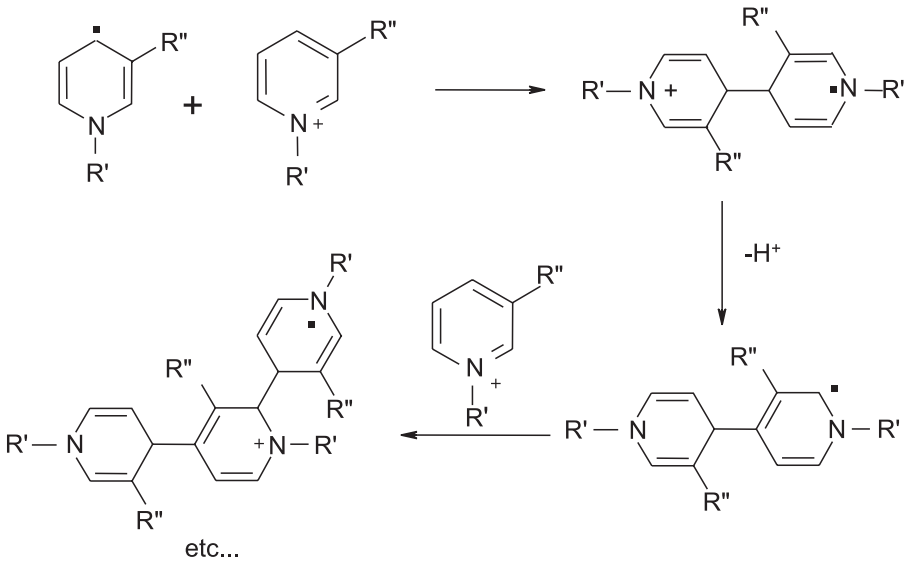
The radical intermediate shown in Scheme 2*a* could also initiate a nonelectrochemical polymerization process, as depicted in Scheme 3. This polymerization reaction would require the loss of one proton per Quat for its propagation and

© 2004 NRC Canada

Scheme 2. (*a*) Dimerization of two radical intermediate species and (*b*) possible reoxidation of the dimer.



Scheme 3. Possible non-electrochemical polymerization route of a typical Quat.



would be expected to occur to a more significant extent in basic solutions, assuming that the OH^- ion will react with the proton to initiate this propagation. Indeed, in exploratory experiments carried out in 0.1 mol/L NaOH solutions, a yellow product was often seen to deposit on the electrode surface (K. Dang, Personal communication, 1998). This may reflect the formation of some polymeric product under these conditions. However, as in the case of the dimeric product, a polymeric product is not likely to be electrochemically oxidizable and is, therefore, inconsistent with the results of Fig. 5. The formation of a polymeric product could potentially explain the slow build-up of nonreactive residue on the GC electrode surface with long times of cycling and as more Quat is deposited (slow sweep rates and long times at E_-).

Summary

In this paper, we have examined the reductive behaviour primarily of *n*-butyl-3-(*N*-octylcarbamyl)pyridinium bromide (Quat 2), but also of *n*-butyl-3-[hydroxy(octylamino)methyl] pyridinium bromide (Quat 1), *n*-benzyl-3,5-dimethyl pyridinium bromide (Quat 3), and *n*-decyl-3-(*N*-hexylcarbamyl) pyridinium bromide (Quat 4) on a glassy carbon (GC) in neutral phosphate buffer solutions. While there is no evidence for the adsorption of the Quats on GC in the normal range of potential, we have demonstrated that all of these Quats can be reduced at potentials more negative that –1.0 V vs. SSCE and that the product deposits as a film on the electrode surface. The corresponding oxidation process, which is seen at ca. –0.2 or –0.3 V, sometimes in two anodic peaks, involves the oxidative dissolution of the film, reforming the original cationic monomer form of the Quat. In general, the amount of Quat that is reduced and deposited is equal to the charge density that passes during its oxidation, although after long times of potential cycling, not all of the surface film can be electrochemically removed.

We have also shown that under the conditions of our experiments, the rate of Quat reduction is likely diffusion controlled, at least initially. At higher Quat concentrations, using slow potential sweep rates, or long times of potential holding, a limit to the amount of Quats that deposits is reached (ca. 4 mC/cm^2), equivalent to ca. 100 monolayers of film. This result, together with the anticipated poor electronic conductivity of the film, argues for a porous film structure. Indeed, AFM studies have shown that the Quat multilayer is composed of clusters, which aggregate together

© 2004 NRC Canada

as more Quat is deposited, thus, ultimately preventing access to the cationic Quat starting material and blocking further multilayer formation.

In terms of the mechanism of Quat reduction, it is shown that the redox chemistry is associated with the pyridinium ring itself, and not with the attached functional groups or side chains. Further, the formation of reduced, neutral monomers is the mostly likely process occurring. Products such as dimers or oligomers may also form, but only after long cycling times, when not all of the Quat reduced can be reoxidized and a residue is observed to build up on the GC electrode surface.

Acknowledgements

We are grateful to the Natural Sciences and Engineering Research Council of Canada (NSERC) Industrial Postgraduate Scholarship program and Brenntag Canada (formerly Travis Chemicals) for the financial support of R.P.C. Wong and J.E. Wong. The authors would also like to thank Dr. Neil Warrender and John Cossar, both formerly of Brenntag Canada, for provision of the Quats and for many helpful discussions. We would also like to acknowledge very useful discussions with Professor Jean Lessard, University of Sherbrooke, in relation to this work.

References

1. V.I. Birss, K. Dang, J.E. Wong, and R.P.C. Wong. J. Electroanal. Chem. **550–551**, 67 (2003).
2. I. Carelli and M.E. Cardinali. J. Electroanal. Chem. **124**, 147 (1981).
3. R.M. Galvin and J.M. Rodriguez-Mellado. J. Electroanal. Chem. **265**, 195 (1989).
4. R.M. Galvin and J.M. Rodriguez-Mellado. J. Electroanal. Chem. **283**, 337 (1990).
5. R.M. Galvin, J.M. Rodriguez-Mellado, and F.G. Blanco. J. Electroanal. Chem. **251**, 163 (1988).
6. X. Ling, J.J. Byerley, M.D. Pritzker, and C.M. Burns. J. Appl. Electrochem. **27**, 1343 (1997).
7. N. Warrender. Travis Chemicals Research Symposium, 1999, Calgary, Alberta.
8. R.P.C. Wong. M.Sc. Thesis, University of Calgary, Calgary, Alberta, 1998.
9. M.M. Ficquelmont-Loizos, H. Takenouti, and W. Kante. J. Electroanal. Chem. **428**, 129 (1997).
10. A.M.O. Brett and F.M. Matysik. J. Electroanal. Chem. **429**, 95 (1997).
11. Robert C. Weast. CRC Handbook of chemistry and physics. 62nd ed. CRC Press, Inc., Boca Raton, Florida. 1981. p. D-126.
12. R.L. McCreery. Carbon electrodes. *In* Electroanalytical chemistry. Vol. 17. *Edited by* A.J. Bard. Marcel Dekker, Inc, New York. 1991.
13. P. Heiduschka, A.W. Munz, and W. Gopel. Electrochim. Acta, **39**, 2207 (1994).
14. Y. Wang, J. Zhang, G. Zhu, and E. Wang. J. Electroanal. Chem. **419**, 1 (1996).
15. M.A. Rahman and A.K. Ghosh. J. Colloid Interface Sci. **77**, 50 (1980).
16. B. Persson. Surface electrochemistry. Plenum, New York. 1993.
17. D.C. Harris. Quantitative chemical analysis. 3rd ed. W.H. Freeman and Company, New York. 1991.
18. J. Volke, L. Dunsch, V. Voleova, A. Petr, and J. Urban. Electrochim. Acta, **42**, 1771 (1997).
19. L. Stolberg, J. Richer, J. Lipkowski, and D.E. Irish. J. Electroanal. Chem. **207**, 213 (1986).
20. S. Sampath and O. Lev. J. Electroanal. Chem. **446**, 57 (1998).
21. J. Volke, J. Urban, and V. Volkeova. Electrochim. Acta, **39**, 13 (1994).
22. J.C. Lepretre, D. Limosin, and G. Pierre. J. Electroanal. Chem. **324**, 115 (1991).
23. G.Y. Vyaseleva, R.K. Sabirov, V.A. Golovin, and M.A. Chizhova. J. Anal. Chem. **49**, 890 (1994).
24. G.Y. Vyaseleva, R.K. Sabirov, I. R. Manyuro, A.E. Gvodeva-Karelina, and V.P. Barabanov. Russ. J. Electrochem. **33**, 126 (1997).

© 2004 NRC Canada

Bovine serum albumin adsorption on passivated porous silicon layers[1]

L. Tay, N.L. Rowell, D. Poitras, J.W. Fraser, D.J. Lockwood, and R. Boukherroub

Abstract: Hydrogen-terminated porous silicon (pSi-H) films were fabricated through electrochemical anodization of crystalline silicon in hydrofluoric-acid-based solutions. The pSi-H surface was chemically functionalized by thermal reaction with undecylenic acid to produce an organic monolayer covalently attached to the silicon surface through Si—C bonds and bearing an acid terminal group. Bovine serum albumin (BSA) was adsorbed onto such surface-modified pSi structures. The resulting surfaces were characterized using scanning electron microscopy (SEM), reflection FT-IR spectroscopy, and ellipsometry. SEM showed that the porous films were damaged and partially lifted off the silicon substrate after a prolonged BSA adsorption. Ellipsometry analysis revealed that the BSA penetrated ~1.3 μm into the porous structure. The film damage is likely a result of BSA anchoring itself tightly through strong electrostatic interaction with the acid-covered Si sidewalls. A change in surface tension during BSA film formation then causes the pSi layer to buckle and lift off the underlying Si substrate. FT-IR results from the undecylenic-acid-modified pSi surfaces before and after BSA adsorption showed the presence of strong characteristic amide I, II, and III vibrational bands after BSA adsorption. The surface properties of the pSi matrix and its interactions with BSA are examined in this study.

Key words: ellipsometry, porous silicon, protein adsorption, surface passivation.

Résumé : Des films de silicium poreux se terminant par de l'hydrogène (pSi-H) ont été préparés par une anodisation électrochimique de silicium cristallin à l'aide de solutions à base d'acide fluorhydrique. La surface des pSi-H a été fonctionnalisée par le biais d'une réaction thermique avec de l'acide undécylénique qui a conduit à la formation d'une monocouche organique qui est liée à la surface de silicium par des liaisons Si—C covalentes et qui porte un groupe acide terminal. On a absorbé de l'albumine de sérum bovin (ASB) sur de telles surfaces à structures de pSi modifiées et on a caractérisé les surfaces qui en résultent par microscopie électronique à balayage (MEB), spectroscopie IR à transformée de Fourier (FT-IR) et ellipsométrie. Les données de la microscopie électronique à balayage montrent que les films poreux ont été endommagés et soulevés du substrat de silicium après une absorption prolongée de l'ASB. L'ellipsométrie révèle que l'ABS pénètre environ ~1,3 μm dans la structure poreuse. Il est probable que le dommage au film résulte du fait que l'ASB se lie fortement aux côtés du Si couvert d'acide par le biais d'une interaction électrostatique. Un changement dans la tension au cours de la formation du film d'ASB provoque alors déformation de la couche pSi et le soulèvement du substrat Si qui se trouve en dessous. Les résultats de la spectroscopie FT-IR sur des surfaces de pSi modifiées par de l'acide undécylénique, avant et après l'absorption d'ASB permettent de mettre en évidence, après l'adsorption de l'ASB, la présence de bandes fortes caractéristiques de vibrations amides I, II et III. Dans ce travail, on a aussi examiné les propriétés de la surface de la matrice pSi et ses interactions avec l'ASB.

Mots clés : ellipsométrie, silicium poreux, adsorption de protéine, passivation de la surface.

[Traduit par la Rédaction]

Introduction

Porous silicon (pSi) films fabricated through chemical or electrochemical etching of crystalline silicon in hydrofluoric acid solution have attracted much attention owing to their strong room-temperature photoluminescence (PL) properties (1). The origin of the PL has been attributed to quantum confinement effects within the silicon nanocrystallites comprising pSi (2). A freshly prepared pSi surface is covered with Si—H_x bonds. A slow oxidation takes place when pSi is exposed to ambient air and this results in the degradation of its optical and electronic properties. A significant research effort has been directed towards passivating the hydrogen-terminated pSi surface, thereby stabilizing the PL for potential use in optoelectronic applications (3). Organic modification of the pSi-H surfaces through Si—C bond formation has emerged as a feasible solution towards pSi surface passivation and prohibiting its oxidation. Various methods (such as, photochemical, electrochemical, thermal, and catalytic reactions) have all been successfully demon-

Received 29 February 2004. Published on the NRC Research Press Web site at http://canjchem.nrc.ca on 3 December 2004.

L. Tay,[2] N.L. Rowell, D. Poitras, J.W. Fraser, and D.J. Lockwood. National Research Council, Ottawa, ON K1A 0R6, Canada.
R. Boukherroub. Interdisciplinary Research Institute, IRI-IEMN, Avenue Poincaré – BP 69, 59652 Villeneuve d'Ascq, France.

[1]This article is part of a Special Issue dedicated to the memory of Professor Don Irish.
[2]Corresponding author (e-mail: lilin.tay@nrc-cnrc.gc.ca).

 doi: 10.1139/V04-129 © 2004 NRC Canada

strated for covalently attaching monolayers of simple and functional alkenes, and aldehydes to both porous and planar Si surfaces through Si—C and Si—O—C bonds, respectively (4, 5). We have used a thermal treatment to functionalize the pSi surface with a high coverage and to introduce different functional groups (ester and acid) on the surface (6–10). We have successfully used this approach to stabilize the photoluminescent properties of the pSi surfaces (11), as well as the electroluminescence (EL) efficiency and EL output intensity of a pSi-based diode under continuous operation (12). The selection of the terminal functional group in the alkyl chain plays an important role on the wetting properties of the functionalized surface and subsequent functionalization processes.

The enormously large surface area within a small volume is an attractive advantage in pSi for other potential applications. It has been employed as a substrate for matrix-free biomolecular mass spectrometry based on a pulsed-laser desorption–ionization technique. In the study carried out by Wei et al. (13), analyte molecules trapped in the chemically modified pSi were vaporized and ionized by laser pulses and their fragments analyzed by mass spectroscopy. Sailor and co-workers (14) have demonstrated pSi optical interferometric biosensors by detecting the change in the film refractive index caused by the analyte binding at the functionalized pSi surface. In addition, its biocompatibility is an important issue to be considered in the biosensor application. Earlier studies have shown that silicon material does not exhibit a significant amount of cytotoxicity (15). Hence, pSi material has the distinct advantage over the other semiconductor-based materials such as III-V-, SiC-, and SiN-based materials. In fact, Bayliss et al. (16) have investigated the adherence and viability of rat neuronal (B50) cells cultured directly on the pSi structure and Canham et al. (17) studied the lifetime of derivatized pSi in a simulated human blood plasma environment. Biocompability can be either active or passive (16). A bioactive material encourages the wanted species and prohibits the production of unwanted species, whereas a biopassive substrate would not interfere with the local or remote functionality of the biosystem. It has been shown that while low-porosity pSi films promoted bioactivities such as hydroxyapatite growth in-vitro, the high-porosity pSi films exhibited substantial dissolution abilities implying its biodegradability in-vivo (18). Hence, pSi has a higher biocompatibility compared with other bulk polycrystalline or amorphous silicon-based substrates.

The binding of protein to solid surfaces has an important function in the chemical and pharmaceutical industries. More specifically, in many biosensor-related applications, the pSi surfaces must be functionalized with highly specific biological or chemical recognition species. Hence, an understanding of the protein–solid substrate interaction and diffusion of protein inside the pSi matrix has a great impact on pSi-based biosensors. Here, we investigate the interaction between carboxylic acid functionalized pSi surfaces and a protein molecule, bovine serum albumin (BSA). The resulting surfaces were characterized using ellipsometry, Fourier transform infrared spectroscopy (FT-IR), and scanning electron microscopy (SEM). We also compare and contrast the results obtained from pSi surfaces to those of planar Si surfaces, both being functionalized with identical chemical species.

Experimental

All cleaning and etching reagents were clean room grade and all other reagents were of the highest purity available from Aldrich.

Sample preparation

Double-side polished Si(100) oriented p-type silicon wafers (boron-doped, 1–15 Ω cm resistivity) were first cleaned in 3:1 concd. H_2SO_4 – 30% H_2O_2 for 15 min at 80 °C and then rinsed copiously with Milli-Q water. The clean wafers were immersed in 5% aq. HF solution for 1 min at room temperature to remove the native oxide. The hydrogen-terminated surfaces were electrochemically etched in a 1:1 (v/v) solution of pure ethanol and 48% aq. HF for 2 min at a current density of 40 mA/cm^2. After etching, the samples were rinsed with pure ethanol and were dried under a stream of dry nitrogen prior to use. SEM showed that pSi films prepared in this way are 3.8 μm thick with an average pore diameter of ca. 10 nm.

pSi functionalization

The freshly prepared pSi surface was placed under argon gas in a Schlenk tube containing deoxygenated neat undecylenic acid and allowed to react at 95 °C for 16 h. The excess of unreacted and physisorbed reagent was removed by rinsing with tetrahydrofuran and 1,1,1-trichloroethane at room temperature and then the sample was dried under a stream of nitrogen.

Acid-terminated monolayer on Si(111)-H

Single side polished silicon crystals were cleaned with piranha solution (H_2SO_4:H_2O_2, 3:1) at 100 °C for 30 min then hydrogen terminated by etching in ammonium fluoride. The resulting hydrogen-terminated surfaces Si(111)-H were placed under argon gas in a Schlenk tube containing a previously deoxygenated neat or toluene solution of undecylenic acid and irradiated in a photochemical reactor at 300 nm for 3 h. The excess of unreacted and physisorbed reagent was removed by rinsing with tetrahydrofuran and 1,1,1-trichloroethane at room temperature and the sample was dried under a stream of nitrogen.

BSA functionalization

BSA was obtained from Sigma (Sigma, B4287-1G, USA). The BSA solution was prepared by dissolving 2 mg of BSA in 1 mL of deionized water (18 MΩ). The resulting solution had a pH value of 6.4. The undecylenic-acid-modified planar and pSi samples were immersed in the BSA solution for 4 days at room temperature. At the end of the incubation period, both silicon surfaces were removed from the BSA solution and rinsed with copious amounts of deionized water and dried under a steady stream of nitrogen gas. In a separate experiment, an incubation solution was prepared with concentration of 0.02 mg of BSA per 1 mL of water. An undecylenic-acid-functionalized pSi surface was immersed in this solution for 3 days at room temperature.

© 2004 NRC Canada

FT-IR spectroscopy

Oblique angle IR external reflectance spectroscopy was performed on the samples with p-polarized radiation from 580 to 4000 cm^{-1} at a 60° angle of incidence using an evacuated Fourier transform spectrometer (Model DA3, ABB Bomem Inc., Québec, Quebec). An angle of incidence near Brewster's angle for silicon and in-plane polarization were employed to enhance the method's sensitivity to the surface layers in the structure. We also obtained results for the BSA adsorption on the planar silicon in an attenuated total reflection (ATR) FT-IR configuration using a single-bounce Ge internal reflection hemisphere.

Ellipsometry

Ellipsometric measurements were performed in air with a variable-angle spectroscopic ellipsometer (VASE, J.A. Woollam Co., Lincoln, Nebraska) from 300 to 800 nm and at three different angles of incidence (55°, 65°, and 75°). Ellipsometry provided a measurement of the complex reflectance ratio:

$$\rho \equiv \frac{R_p}{R_s} = \tan(\Psi)\exp(i\Delta)$$

where R_p and R_s represent the complex reflection coefficients of the light polarized parallel and perpendicular to the plane of incidence, respectively, and Ψ and Δ are the ellipsometric angles. Optical models including parameters such as the refractive indices and thicknesses of the materials involved were used for analyzing the data (using the WVASE32 software package). Some of these models included birefringent porous layers modeled by Bruggeman effective medium approximation (BEMA) layers and graded interfaces, as described by quintic transition layers (19).

SEM

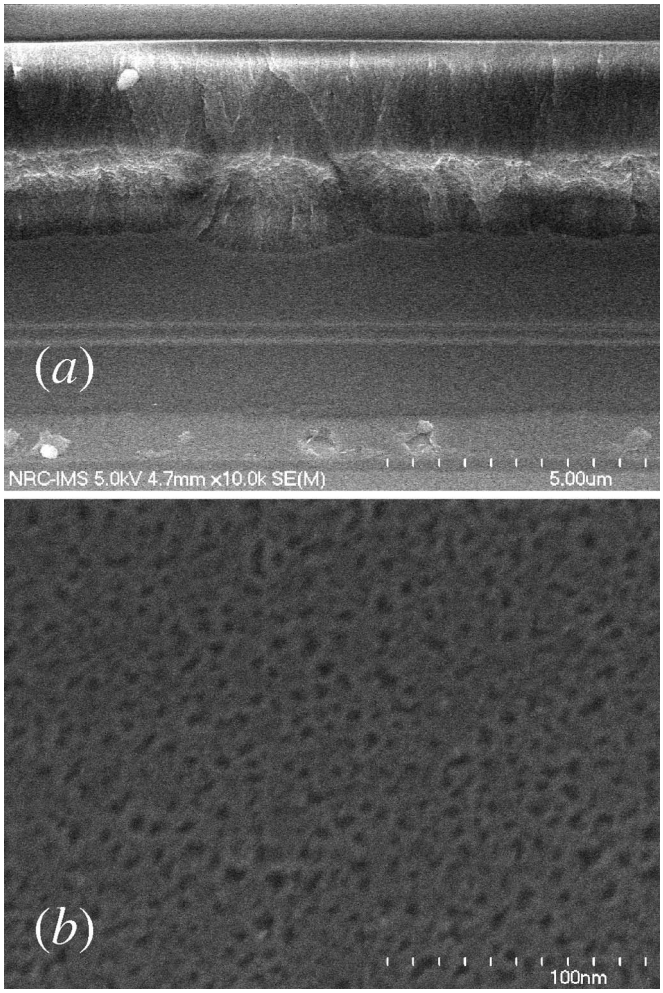
SEM was carried out with a Hitachi (S4700) field emission SEM with an image resolution of 2.1 nm at 1 kV and 1.5 nm at 15 kV at the analytical working distance. Both planar and pSi samples were cleaved through their center to provide clean edges to determine the layer thickness of the BSA and pSi films. The topography and cross-sectional SEM images of a reference pSi sample, which was anodized under the same conditions as the acid-modified pSi sample, were also obtained. It provided a reference for the porous layer thickness and average pore diameter of the acid-modified sample.

Results

SEM

Cross-sectional SEM analysis of the hydrogen-terminated pSi sample (reference sample), prepared under the same experimental condition as the pSi films modified with organic acid, indicated the porous layer thickness to be of the order of 3.8 μm (see Fig. 1*a*). The average pore diameter of the reference pSi sample was found to be approximately 10 nm (see inset Fig. 1*b*). The porosity of films prepared with this process is estimated to be ~70%. Owing to the BSA build up and the damage it produced in the acid-modified pSi film, the pore diameter and porous layer thickness for such films had to be inferred from the reference pSi material.

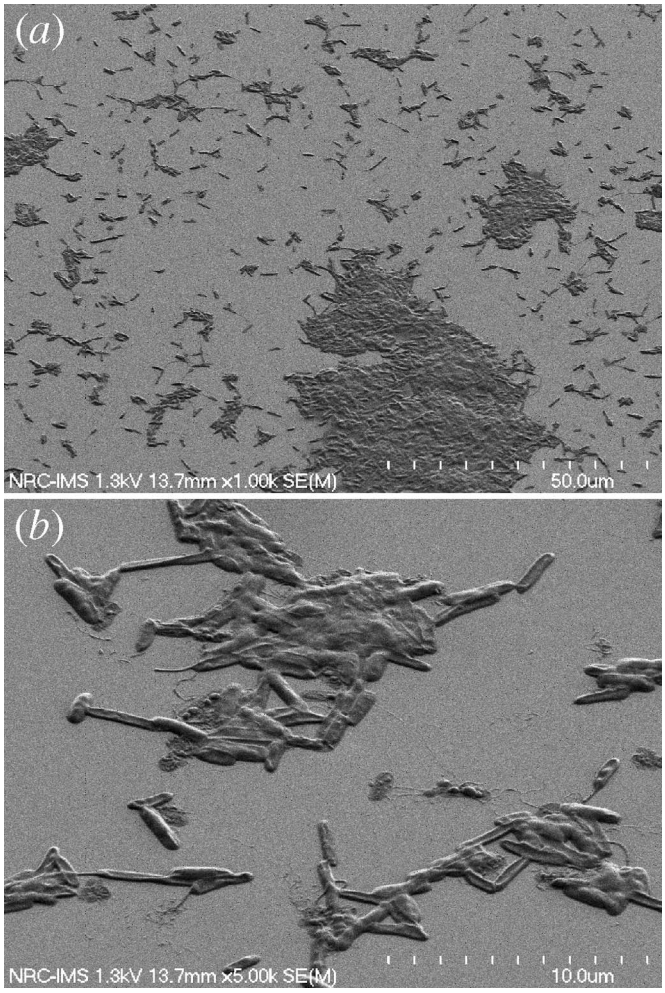
Fig. 1. (*a*) Cross-sectional SEM image of the reference pSi film. The average thickness of the porous film is approximately 3.8 μm. (*b*) Planar view of the pSi film.



A planar Si(111) sample modified with undecylenic acid was functionalized with BSA according to the procedure described in the Experimental section. Topographical SEM images in Fig. 2 showed an interesting topology on the acid-modified surfaces. As Fig. 2*a* shows, there are islands of BSA distributed all over the planar Si surfaces. Though some aggregates form large islands, as shown in the bottom images of Fig. 2*a*, most of the aggregates have a rod-like structure with an average length of 25 μm and width of 2 μm. At higher magnifications, the rod-like structures are actually comprised of two parallel ridges separated by a distance of ~2 μm. This observation is consistent with the formation of BSA thin films through solvent evaporation (20). Figure 2*b* shows interesting fiber-like features among the rod-like BSA aggregates. It is important to point out that the seemingly flat and featureless areas between the BSA aggregates are actually covered with a very thin layer of BSA film. This is confirmed by cross-sectional SEM imaging and ellipsometry. The film thickness in these flat regions is estimated to be of the order of 7~10 nm.

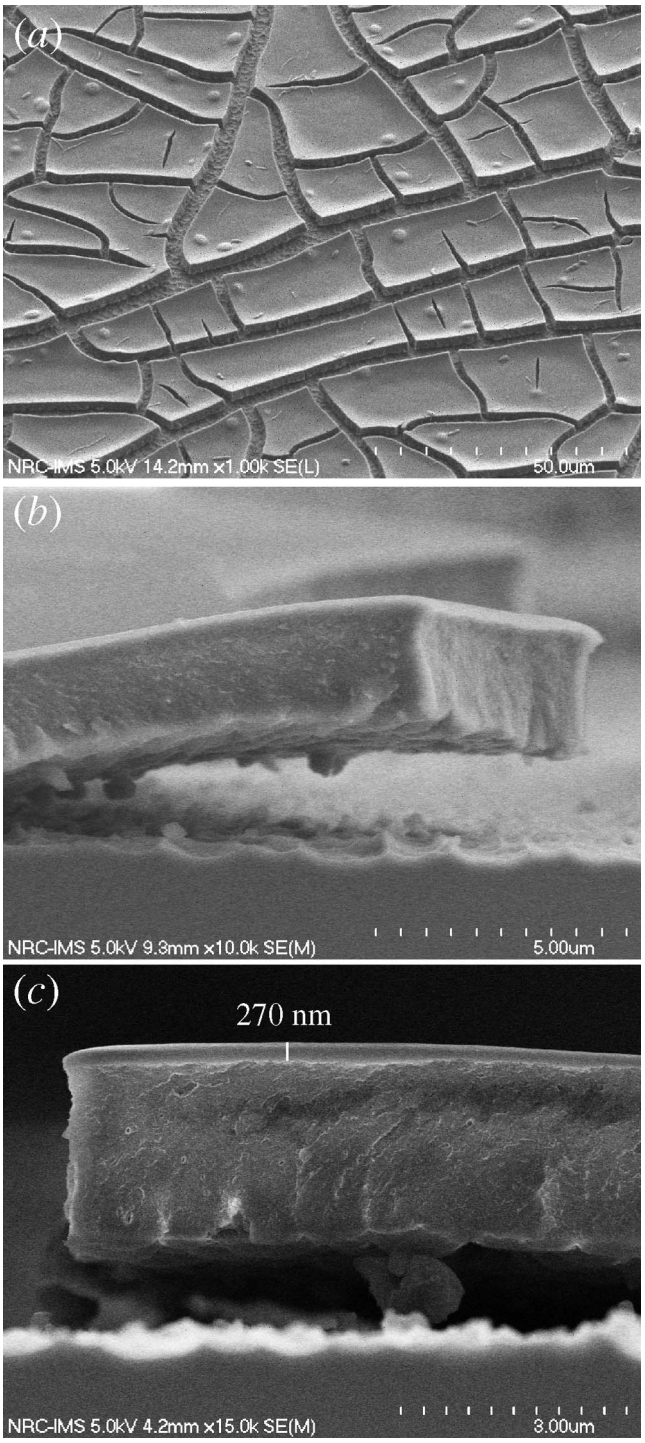
© 2004 NRC Canada

Fig. 2. SEM images of the BSA film formed on top of the undecylenic-acid-modified planar Si surfaces. The seemingly flat area between the protein aggregates are covered with an ~10 nm thick smooth layer of BSA film.



Results from the acid-modified pSi sample present the most intriguing information. The topographic SEM image shown, for example, in Fig. 3*a* indicate that the film was cracked over the entire pSi sample and in many areas was partially detached from the substrate. Within the cracks in the broken films, one can clearly see a sponge-like pSi layer lying underneath. At higher magnification, one can, again, observe the rod-like BSA aggregates and the fiber-like linkage lying on top of the BSA films. These are similar to the structures observed on the BSA films formed on the planar Si samples (Fig. 2*a*). This implies that the fiber-like features are due to the inherent nature of BSA film formation and not a consequence of the surface morphology of the pSi samples. It is likely that the BSA aggregates observed on both planar and porous substrates are the result of the lengthy incubation time and incubation using a relatively high BSA concentration in solution. SEM images of the sample incubated at a concentration of 0.02 mg/mL showed only minor BSA aggregation with most of the aggregates ranging from 100 to 800 nm in size. By cleaving the sample and examining its cross section, it was confirmed that most of the broken pSi film has lifted off the substrate, as can be seen in

Fig. 3. (*a*) SEM image of BSA adsorption on pSi film. The pSi film is broken into many pieces. The cross-sectional image in (*b*) shows the broken film lifting off the crystalline Si substrate. The porous structure can be seen on the sidewall and underneath of the lifted-off film pieces. The image also shows that only a small portion of the porous film still remains intact with the crystalline substrate. Part (*c*) shows a layer of BSA film 270 nm in thickness formed on top of the lifted-off pSi structure.



Figs. 3*b* and 3*c*. More importantly, the porous structures are clearly observed at the sidewall of the lifted-off film. The sponge-like porous structure left intact on top of the crystal-

© 2004 NRC Canada

Fig. 4. (*a*) The modeled refractive indices n_x and n_z at 550 nm are shown. Room temperature experimental (dashed lines) and modeled (solid lines) ellipsometry for (*b*) Ψ and (*c*) Δ results obtained at 65°, 70°, and 75° for the pSi sample.

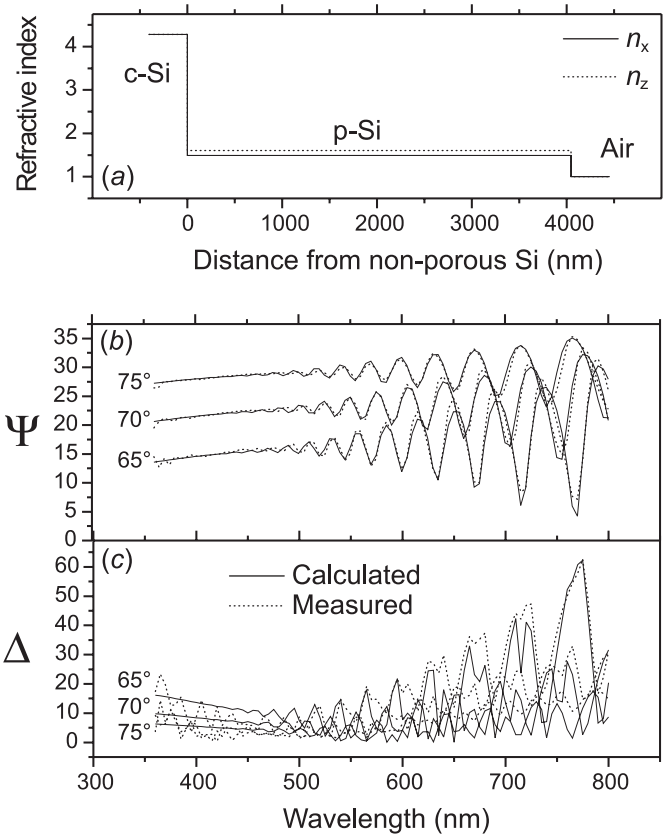
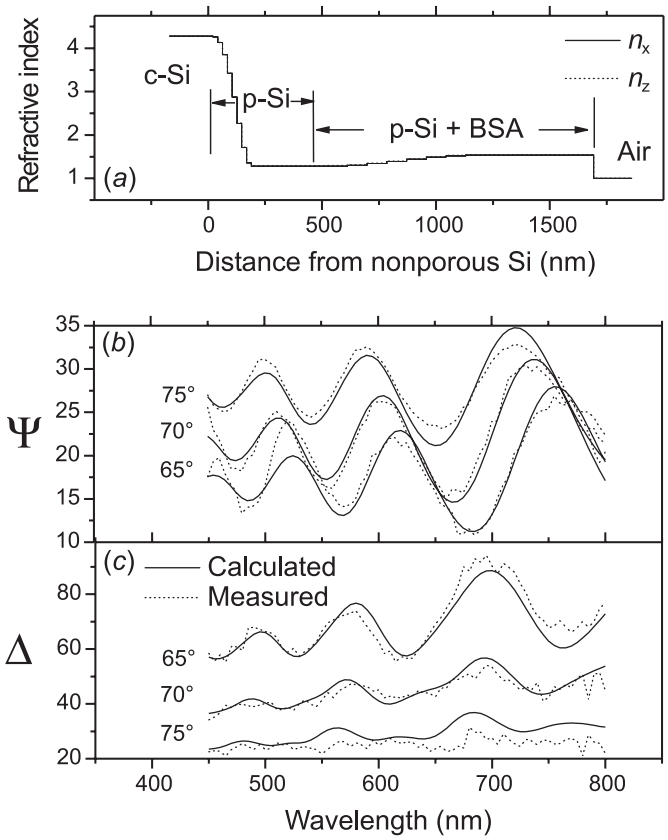


Fig. 5. (*a*) The modeled refractive indices n_x and n_z at 550 nm are shown. Room temperature experimental (dashed lines) and modeled (solid lines) ellipsometry for (*b*) Ψ and (*c*) Δ results obtained at 65°, 70°, and 75° for the pSi:BSA sample.



line Si substrate is estimated by SEM cross-section imaging to be less than 1 μm thick. It is not obvious what has led to the loss of the ~2.8 μm of porous film from the surface, however, the surface tension from the formation of the BSA film in and on top of the pSi layer during the drying phase is a likely cause for such film damage. In many of the lifted-off pSi pieces, there were small portions of the pSi that remained in contact with the rest of the substrate. The attachment is usually through a small piece of pSi structure, as shown underneath the lifted-off films in Fig. 3*b*. In both Figs. 3*b* and 3*c*, one can also observe a layer of smooth and homogeneous BSA film deposited on top of the pSi structure. From the cross-sectional images, we estimate the thickness of this smooth BSA film on top of the porous structure to range between 160 and 270 nm.

Ellipsometry

The results obtained from the ellipsometric study of the reference pSi sample are shown in Fig. 4. The best fit to the observed reflectivity through the visible wavelength region was obtained with a single birefringent porous layer on top of the crystalline Si substrate. For good fits, it was essential to include the weak birefringent nature of the porous layer. The calculated refractive indices are shown in Fig. 4*a* and these indicate an abrupt substrate – porous layer interface and a film thickness of 4.05 ± 0.02 μm. The pSi layer porosity was found to be 75.9 ± 0.1% and the refractive indices at 550 nm are $n_x = n_y = 1.474$ and $n_z = 1.579$ (perpendicular to the plane of the layer). The refractive indices exhibit dispersion varying from $n_x = 1.58$ and $n_z = 1.73$ at 360 nm to $n_x = 1.43$ and $n_z = 1.48$ at 800 nm. The birefringence is quite small ($\Delta n = n_z - n_x = 0.105$). Overall, these ellipsometry results confirm the data obtained by SEM from this air-oxidized sample.

The ellipsometry results for the BSA protein covered pSi sample look quite different from those of untreated pSi (compare Figs. 4 and 5). The spacing between fringes is greater for pSi:BSA indicating a thinner pSi layer. A two-layer model is required to fit this data, including a pSi and pSi plus adsorbed BSA protein layer. In addition it was necessary to include the birefringence of the pSi, a concentration gradient at each interface, and a nonuniformity of overall thickness across the layer (to account for the pSi layer delamination). From the model fit to Δ and Ψ (see Figs. 5*b* and 5*c*), we find a pSi:BSA layer thickness of 388 ± 202 nm, a pSi:BSA graded composition layer of thickness of 867 ± 333 nm, a pSi layer thickness of 226 ± 183 nm, and a pSi graded composition layer thickness of 211 ± 28 nm, giving a total pSi layer thickness of 1.7 ± 0.7 um. The large uncertainties in the fitted parameters are attributed to the fractured nature of the film. This may also explain why the ellipsometry determined layer thickness is smaller than the value measured by SEM. The thickness nonuniformity was found to be 12.1 ± 0.7%, and the pSi porosity was deter-

© 2004 NRC Canada

Fig. 6. (*a*) The modeled refractive indices n_x and n_z at 550 nm are shown. Room temperature experimental ellipsometry results (dashed lines) measured at 55°, 65°, and 75° for (*b*) Ψ and (*c*) Δ for BSA adsorbed on planar Si. The modeled fits are shown by the solid lines.

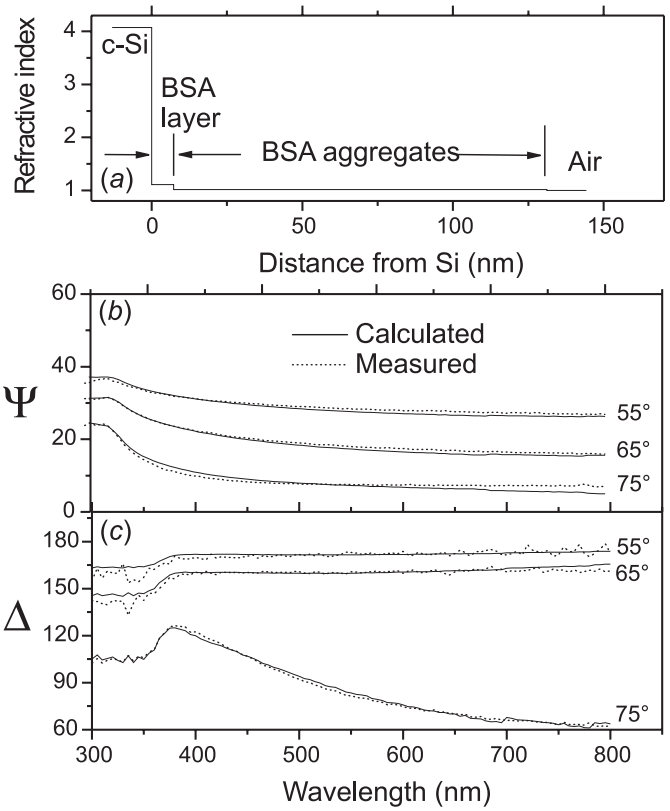
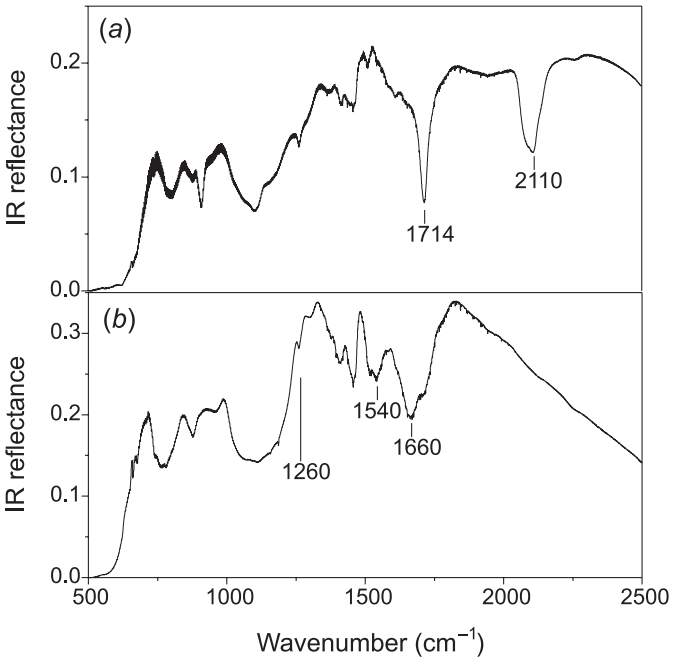


Fig. 7. Oblique incidence FT-IR spectra of the undecylenic-acid-modified pSi substrate (*a*) prior to the BSA incubation and (*b*) after incubating in 2 mg/mL of BSA for 4 days.



mined to be 83% with a large uncertainty (~100%). The calculated refractive indices are given in Fig. 5*a*. At 550 nm, n_x = 1.283 and n_z = 1.291. The pSi refractive index is lower than that for the pSi reference sample shown in Fig. 4, which is consistent with the higher porosity of this BSA treated sample. Also, the birefringence Δn = 0.008 is smaller. The graded composition layer between the c-Si substrate and the p-Si layer accounts for the film peeling shown in Fig. 3. The ellipsometry results confirm the penetration of the BSA protein deep into the pSi layer. The BSA concentration slowly decreases to zero through the film, but appears to fill the pores down to about 400 nm from the surface. The lack of an abrupt interface explains why it is difficult to observe the BSA penetration by SEM.

Ellipsometric data from the BSA protein treated planar Si sample are shown in Fig. 6. Here, a best fit was obtained with a two-layer model on top of a crystalline Si substrate. Such a model was necessary to reproduce the strong variation in Δ at high angle of incidence: a fit with a single homogeneous layer of BSA proved to be quite inappropriate for this data. The model comprised a Bruggeman effective medium approximation for the inner layer (assuming n = 1.57) and a Cauchy dispersion relation for the outer layer. The layer thicknesses determined from the model fits (see Fig. 6) were 124 ± 4 and 7.3 ± 4.2 nm for the outer and inner layers, respectively. The thickness of the inner layer is in accord with the SEM determination of ~10 nm. Its porosity was determined to be 80 ± 7%. The top layer thickness represents an average value for the conglomerated lumps of BSA protein. The scattering of light produced by the BSA conglomerates had to be accounted for in the model by fixing, artificially, the extinction coefficient k at a small value (0.02). The refractive indices for these layers exhibit dispersion and were determined at 550 nm to be 1.016 ± 0.002 for the outer layer (corresponding to a porosity of 97.9 ± 0.1%) and 1.097 for the inner layer, which are smaller than the value of 1.57 found by Arwin (21). Arwin obtained this value from thin BSA protein layers (2–3 nm thick) on substrates other than Si, as he was not successful in obtaining high-density layers on Si. We believe a large part of the difference in these two determinations can be attributed to film morphology: our films grown on Si are less dense than those of Arwin, which were grown on HgCdTe.

FT-IR

Figures 7*a* and 7*b* show the oblique incidence FT-IR spectrum of the pSi samples before and after the BSA incubation, respectively. Prior to BSA incubation, the pSi spectrum is dominated by a strong absorption at 1714 cm^{-1} because of the carbonyl (C=O) stretching. The stretching and deformation of CH_2 of the alkyl chain at 2922 and 1460 cm^{-1}, respectively, are also observed. In addition to the vibrational modes related to the undecylenic acid, the broad peak located at 2110 cm^{-1} showed three different Si-H stretching modes. It is due to the presence of unreacted Si—H bonds remaining after the thermal modification of the pSi surfaces. Indeed, the steric hindrance of the organic molecule limits the surface coverage during the grafting process. The ob-

© 2004 NRC Canada

served spectrum is in agreement with previously published data (9). The spectrum after BSA incubation shows the characteristic IR bands of BSA: the amide I (C=O stretching) and the amide II (N-H bending) and the less obvious amide III (C-N) peaks are observed at 1660, 1540, and 1260 cm^{-1}, respectively. It is important to point out that the enormous surface area in the pSi samples contributes positively towards the observation of the vibrational signatures in the surface modification species (undecylenic acid). As for observation of the BSA vibrational signal, the extra volume provided by the porous medium essentially increased the effective sampling volume of the BSA molecules and hence made the detection possible. Although there appeared to be a smooth ~200 nm thick BSA film formed on top of the damaged and partially peeled-off pSi layer, its presence is unlikely to be the sole contribution to the intense amide vibrational bands observed. On the contrary, as demonstrated in the ellipsometry results, it is likely the appreciable amount of BSA, which slipped into the pores utilizing the natural advantage of a porous medium that produced a strong and thus easily detectable vibrational signature. Similar amide I and II bands were also observed on the pSi sample, which was incubated in the 0.02 mg/mL BSA solution for 3 days. Since a BSA vibrational signature is not likely from such sparse BSA aggregates in the oblique angle reflectance FT-IR measurement, the presence of the amide bands suggests there are BSA molecules in the pSi matrix.

In contrast with the pSi sample, the IR spectra obtained from the acid-terminated planar Si sample did not show any signature of either undecylenic acid or protein when measured under oblique-angle reflectance FT-IR. SEM characterization showed that the smooth continuous layer of BSA formed on the planar surface is ~10 nm thick. A similar BSA vibrational signature from planar Si samples was detected by variable-angle single-bounce ATR-FT-IR. The spectrum of the BSA on planar Si showed the characteristic amide I and II bands at 1660 and 1533 cm^{-1}.

Discussion

The interaction between the protein molecule and the pSi layer is a complex matter. Many factors contribute to the protein adsorption in pSi substrates: the size of the protein, the protein conformation, the protein's overall charge, the pore diameter of pSi, its porosity and surface state (hydrophobicity–hydrophilicity), and the chemical functionality of the surface-modified layer all play very important roles. With an average pore diameter of 10 nm and layer thickness of 3.2–4.1 μm (as determined from the reference sample), the irregularity and depth of the pores in pSi present quite a challenge for the large albumin molecules (14 nm × 4 nm in globular form) to penetrate them. Several prior studies (21–23) have investigated the protein adsorption in either a bare pSi substrate terminated with hydrogen or its oxidized surface. In these ellipsometry based studies, the porous film thickness ranges from 240 to 370 nm. In all three cases, the ellipsometry analysis indicated protein penetration deep into the pores, reaching 90% of the overall film thickness. Of course, the amount of protein mass appeared to be higher closer to the surface of the porous layer and the albumin mass percentage in the porous layer drops closer to the crystalline silicon. Our ellipsometry results similarly echo the tapering-off of the protein penetration behavior despite the presence of the carboxyl terminal group covering the pSi sidewalls and the presence of a much thicker porous layer (~3.8 μm).

Penetration of protein into the porous layer is likely to play an important role in the break up of the porous film. It is well-established that the structural integrity of the porous film is fragile (2) and that the entire film can be removed from the crystalline Si substrate by electropolishing with a high current density. Also, for films with relatively high porosity, the film can peel-off the supporting crystalline Si substrate simply from the capillary effect of the water during the film's fabrication process (2, 24). Control experiments performed on our samples showed no film damage after soaking both acid- and hydrogen-terminated pSi films in water for 3 days and drying them with nitrogen gas. It is likely that the presence of the BSA film was responsible for the damage to the porous film. A possible explanation is that when the protein molecules penetrated deep into the pores they tightly anchored themselves to the acid-covered sidewalls of the pSi matrix (through strong electrostatic interaction) during the BSA film formation and caused a ~2.8 μm thick layer of pSi to peel off the substrate. The damage incurred on the pSi film is likely a result of the prolonged (4 days) incubation period in a solution of relatively high BSA concentration causing a substantial amount of BSA build-up on and inside the porous layer. Other studies on unmodified pSi substrates incubated in a similar albumin protein medium over a time period of several hours did not show such pSi film damage (22). Experiments performed here at 1/100th of the initial BSA concentration also showed no film damage.

There are several factors that favor the penetration of albumin into pSi pores. First, we consider the hydrophilicity of the binding surfaces. As discussed earlier, the electrochemical fabrication of pSi in HF leaves the pSi surfaces covered with hydrophobic Si—H bonds. The hydrophobicity is reduced by surface modification with undecylenic acid coating the porous walls. This reduction of hydrophobicity allows aqueous solvents to wet the pores better and help to transport albumin molecules deeper into the pores. Second, it is important to point out that BSA has a high affinity towards the acid-ligands. In fact, a BSA molecule contains several high affinity acid-binding sites (25). It is well-known that a protein will modify its conformational structure to adapt to the substrate that it interacts with (26). The acid-modified pSi surface, no doubt, presents lots of active binding sites for the albumin and quite possibly prompted such structural changes of the BSA to aid the surface-protein interaction. Arwin et al. (23) have examined the penetration of human serum albumin (HSA), a protein that is very similar to BSA both structurally and in its dimensions, into unmodified pSi structures. In their studies, albumin protein was found to reach ~200 nm into the pore structure. In addition, Arwin et al. found that the penetration of HSA depends on both a critical porosity of pSi and the acidity of the incubating medium. More protein adsorption on the interior surfaces was found on the high porosity (~70%) samples, while

© 2004 NRC Canada

the adsorbed protein mass is substantially higher at lower pH (pH 4) as supposed to the physiological pH of 7.4. At low porosity, Arwin et al. observed that adsorption of the protein occurs mainly on top of the porous layer or in the outer most region of the porous medium. They pointed out that a minimum porosity (~70% in the case of HSA) is necessary to stimulate the penetration deep into the porous layer. The estimated porosity of our pSi samples found from X-ray reflectivity and ellipsometry studies is 70% and 76%, respectively. Although the surface properties of our chemically modified surfaces differ from the hydrogen terminated pSi films, it is likely that the high porosity still played a favourable role in the penetration of the protein into the porous medium.

In addition to the porosity, the overall pH value of the incubation solution plays an important role in the protein interaction with the porous layer. The isoelectric point of BSA is 4.7 and this implies that the BSA molecules will carry overall negative charges in the pH 6.4 incubating medium. The pK_a of the surface-bound carboxylic acids are in the range of 4–6, hence, in the pH of 6.4 incubation medium, the acid terminal group is present mostly in the deprotonated conjugated base (COO^-) form. In addition, it is unlikely that BSA will accept the proton from the carboxylic acid unless the overall incubating medium has a pH below the isoelectric point. This means that both the BSA molecules and pSi surfaces are both negatively charged. The similar charge on both mediums may not necessarily hamper the interaction between the two molecules. In fact, an ellipsometry-based study (27) has found that regardless of the cationic or anionic nature of the surface functional group, the intake of BSA mass is higher in the coated pSi matrix compared to the bare (hydrogen-terminated) pSi matrix. Studies have shown that proteins that carry the same net charge as the surface might still bind through local patches of opposite charges (26). In addition, the binding can be dominated by electrostatic interaction between polar group interactions such as hydrogen bonding or ligand-like interactions (28). It is likely that the interaction between the protein and the surface COO^- group is dominated by hydrogen bonding or through electrostatic interactions of specific groups in the BSA molecule (e.g., lysines, arginine, and tyrosines), which have high binding affinity for the carboxylate group (29). Serum albumin contains multiple fatty acid binding sites. For most of the binding sites, the carboxylate moieties of the fatty acids are strongly anchored by electrostatic interactions to the polar side chains (often through hydrogen bonding) and the methylene tails are accommodated within hydrophobic cavities (30). In the case of the carboxylate covered sidewalls, the electrostatic interaction and hydrogen bonding between the surface and protein is likely to overcome the charge repulsion between them and dominate the bonding mechanism of the albumin to the sidewall of the porous matrix. It is not impossible that some acid binding sites become available through structural changes of the protein and this allows the oppositely charged protein and carboxylate-covered surfaces to form chemical bonds. To address the interaction between the protein molecule and the functionalized surfaces, we intend to carry out pH dependent protein adsorption studies in future. In addition, investigation of a pSi matrix terminated with other functional groups such as long chain alkyl molecules or amines will provide valuable information in the study of the protein and porous matrix interaction.

Conclusion

We have presented the first results of BSA adsorption on undecylenic-acid-modified planar Si and pSi layers. Cross-sectional SEM images show damages in the porous film with a layer of BSA (160–280 nm thick) formed on top of the damaged porous layer. Ellipsometry confirmed the penetration of BSA molecules (~1.3 μm into the porous layer). The presence of the BSA penetration into the porous structure probably caused the porous film to buckle and peel off the Si substrate possibly because of the change in surface tension during the drying phase. We have examined interactions between BSA and the carboxyl terminal groups in aiding the penetration of protein into the porous structure. In future work, protein adsorption on other functional groups (e.g., amide- or alkyl-terminated surfaces) as well as the pH dependent adsorption need to be examined in more detail. This will help to elucidate the role played by the hydrophobicity, surface charge, and the interaction of BSA molecules with the porous structure.

References

1. L.T. Canham. Appl. Phys. Lett. **57**, 1046 (1990).
2. A.J. Cullis, L.T. Canham, and P.D.J. Calcott. J. Appl. Phys. **82**, 909 (1997).
3. J.-N. Chazalviel and F. Ozanam. MRS Conf. Proc. **536**, 155 (1999).
4. J.M. Buriak. Chem. Rev. **102**, 1272 (2002).
5. D.D.M. Wayner and R.A. Wolkow. J. Chem. Soc. Perkin Trans. 2, 23 (2002).
6. R. Boukherroub, S. Morin, D.D.M. Wayner, F. Bensebaa, G.I. Sproule, J.-M. Baribeau, and D.J. Lockwood. Chem. Mater. **13**, 2002 (2001).
7. R. Boukherroub, S. Morin, D.D.M. Wayner, and D.J. Lockwood. Phys. Status Solidi A, **182**, 117 (2000).
8. R. Boukherroub, D.D.M. Wayner, G.I. Sproule, D.J. Lockwood, and L.T. Canham. Nano Lett. **1**, 713 (2001).
9. R. Boukherroub, J.T.C. Wojtyk, D.D.M. Wayner, and D.J. Lockwood. J. Electrochem. Soc. **149**, H59 (2002).
10. R. Boukherroub, A. Petit, A. Loupy, J.-N. Chazalviel, and F. Ozanam. J. Phys. Chem. B, **107**, 13459 (2003).
11. R. Boukherroub, D.D.M. Wayner, and D.J. Lockwood. Appl. Phys. Lett. **81**, 601 (2002).
12. B. Gelloz, H. Sano, R. Boukherroub, D.D.M. Wayner, D.J. Lockwood, and N. Koshida. Appl. Phys. Lett. **83**, 2342 (2003).
13. J. Wei, J.M. Buriak, and G. Siuzdak. Nature (London), **399**, 243 (1999).
14. A. Janshoff, K.P.S. Dancil, C. Steinem, D.P. Greiner, V.S.Y. Lin, C. Gurtner, K. Motesharei, M.J. Sailor, and M.R. Ghadiri. J. Am. Chem. Soc. **120**, 12 108 (1998).
15. S.C. Bayliss, P.J. Harris, L. Buckberry, and C. Rousseau. J. Mater. Sci. Lett. **16**, 737 (1997).
16. S.C. Bayliss, L.D. Buckberry, I. Fletcher, and M.J. Tobin. Sensor Actuator. **74**, 139 (1999).
17. L. Canham, C. Reeves, J. Newey, M. Houlton, T. Cox, J.M. Buriak, and M.P. Stewart. Adv. Mater. **11**, 1505 (1999).
18. L.T. Canham. Adv. Mater. **7**, 1033 (1995).
19. W.H. Southwell. Opt. Lett. **8**, 584 (1983).

© 2004 NRC Canada

20. C.C. Annarelli, L. Reyes, J. Fornazero, J. Bert, R. Cohen, and A.W. Coleman. Cryst. Eng. **3**, 173 (2000).
21. H. Arwin. Appl. Spectrosc. **40**, 313 (1986).
22. R. Boukherroub, J.T.C. Wojtyk, D.D.M. Wayner, and D.J. Lockwood. J. Electrochem. Soc. **149**, H59 (2002).
22. L.M. Karlsson, P.Tengvall, I. Lundstrom, and H. Arwin. Phys. Status Solidi A, **197**, 326 (2003).
23. H. Arwin, M. Gavutis, J. Gustafsson, M. Schultzberg, S. Zangooie, and P. Tengvall. Phys. Stat. Solidi A, **182**, 515 (2000).
24. D. Bellet. Properties of porous silicon. *Edited by* L.T. Canham. Inspec Publication, London. 1997. p. 38.
25. A. Bhattacharya, T. Grune, and S. Cury. J. Mol. Biol. **303**, 721 (2000).
26. M. Wahlgren and T. Arnebrant. Trends Biotechnol. **9**, 201 (1991).
27. A. Tsargorodskaya, A.V. Nabok, and A.K. Ray. Nanotech. **15**, 703 (2004).
28. J.S. Parks, D.P. Cistola, D.M. Small, and J.A. Hamilton. J. Bio. Chem. **258**, 9262 (1983).
29. J.B.Szaney and I.M. Klotz. Biochemistry, **9**, 2570 (1970).
30. A.A. Bhattacharya, T. Grune, and S. Curry. J. Mol. Biol. **303**, 721 (2000).

© 2004 NRC Canada

A solid-state NMR investigation of orexin-B[1]

Guy M. Bernard, Mark Miskolzie, George Kotovych, and Roderick E. Wasylishen

Abstract: Some key aspects of the secondary structure of solid orexin-B, a 28 amino-acid peptide, have been investigated by solid-state NMR spectroscopy. The $^{13}C–^{15}N$ dipolar coupling between the carbonyl carbon of Leu^{11} and the nitrogen of Leu^{15}, as determined by rotational echo double resonance (REDOR) experiments, is 35 Hz, indicating that these nuclei are separated by approximately 4.5 Å. This distance is consistent with the α-helical structure determined for this segment of orexin-B by solution NMR measurements. REDOR measurements of the dipolar coupling between the carbonyl carbon of Ala^{17} and the nitrogen of Ala^{22} support the contention in an earlier solution NMR study that a bend exists between the two α helices of orexin-B. However, in the solid state the internuclear distance (6.4 Å) is significantly greater than that observed for orexin-B in aqueous solution. In addition to the distance measurements, the principal components of the amide carbonyl carbon chemical shift (CS) tensors for Leu^{11} and Ala^{17} and of the amide nitrogen CS tensors for Leu^{15} and Ala^{22} are reported. There are only minor differences between the amide carbonyl carbon CS tensors for Leu^{11} and Ala^{17} and between the nitrogen CS tensors for Leu^{15} and Ala^{22}.

Key words: orexin-B, solid-state NMR, REDOR, chemical shift tensors.

Résumé : Faisant appel à la spectroscopie RMN à l'état solide, on a étudié quelques aspects de la structure secondaire de l'orexine-B solide, un peptide comportant 28 acides aminés. Le couplage dipolaire $^{13}C–^{15}N$ entre le carbone du carbonyle de la Leu^{11} et l'azote de la Leu^{15}, tel que déterminé par des expériences de double résonance avec écho rotationnel (REDOR), est égal à 35 Hz et cette valeur indique que ces noyaux sont séparés par environ 4,5 Å. Cette distance est en accord avec la structure α-hélicoïdale déterminée pour ce segment de l'orexine-B sur la base d'expériences de RMN en solution. Des mesures REDOR du couplage dipolaire entre le carbone du carbonyle du Ala^{17} et l'azote du Ala^{22} est aussi en accord avec l'hypothèse émise antérieurement, sur la base d'une étude RMN en solution, à l'effet qu'il existe une déviation entre les deux hélices α de l'orexine-B. Toutefois, à l'état solide, la distance internucléaire de 6,4 Å est significativement plus élevée que celle observée pour l'orexine-B en solution. En supplément aux mesures de distances, on rapporte aussi les principaux composants des tenseurs des déplacements chimiques (DC) du carbone du carbonyle de l'amide pour les Leu^{11} et Ala^{17} et pour les tenseurs des DC de l'azote de l'amide des Leu^{15} et Ala^{22}. On n'observe que des différences mineures entre les tenseurs des DC du carbone du carbonyle de l'amide des Leu^{11} et Ala^{17} et entre les tenseurs des DC de l'azote de l'amide des Leu^{15} et Ala^{22}.

Mots clés : orexine-B, RMN à l'état solide, REDOR, tenseurs des déplacements chimiques.

[Traduit par la Rédaction]

Introduction

Orexin-B, together with its closely related analogue orexin-A, were first identified in 1998 (1). The orexins have been implicated in numerous physiological processes. For example, they coordinate the complex behaviour in sleep and (or) wakefulness and in feeding (2) and also control several functions outside the central nervous system (3).

Orexins A and B are 33 and 28 amino-acid peptides, respectively. Orexin-B, also known as hypocretin-2 (1, 4), whose primary sequence is linear, shares 46% sequence homology with orexin-A; both are C-terminally amidated. The amino acid sequence for orexin-B is:

H-Arg-Ser-Gly-Pro-Pro-Gly-Leu-Gln-Gly-Arg-Leu^{11}-Gln-Arg-Leu-Leu^{15}-Gln-Ala^{17}-Ser-Gly-Asn-His-Ala^{22}-Ala-Gly-Ile-Leu-Thr-Met-NH_2

The amino acids of importance in this study have been numbered. The conformation of Phe^{1}-orexin-B has been determined by Lee and co-workers (5) from an analysis of two-dimensional NMR data for the peptide dissolved in water at a pH of 3.5 and in water–trifluoroethanol mixtures. They reported that in both solvent systems, Phe^{1}-orexin-B consists of two α helices (helix I, spanning Leu^{7} to Gly^{19} and helix II, spanning Ala^{23} to Met^{28}). These helices are connected by a short flexible region containing a bend, such

Received 10 August 2004. Published on the NRC Research Press Web site at http://canjchem.nrc.ca on 4 December 2004.

Dedicated to the memory of Professor Donald E. Irish.

G.M. Bernard, M. Miskolzie, G. Kotovych, and R.E. Wasylishen.[2] Gunning-Lemieux Chemistry Centre, University of Alberta, Edmonton AB T6G 2G2, Canada.

[1]This article is part of a Special Issue dedicated to the memory of Professor Don Irish.

[2]Corresponding author (email: roderick.wasylishen@ualberta.ca).

 doi: 10.1139/V04-131 © 2004 NRC Canada

that the axis of helix I is oriented 60°–80° relative to that of helix II (Fig. 1). In a more recent solution NMR study, Miskolzie et al. (6) investigated orexin-B dissolved in aqueous solutions of sodium dodecylsulphate (SDS). These authors confirmed the presence of the two α helices but found that in aqueous SDS solution, helix I spans Leu^{7} to Ser^{18} and helix II spans Ala^{22} to Leu^{26}. They did not have sufficient data to confirm the bend reported by Lee and co-workers. Overall, the results of the two studies are in qualitative agreement; the minor differences in the secondary structure were attributed to the choice of solvent (6). Analogous solvent effects on secondary structure have been found for other peptides (7).

Solid-state NMR spectroscopy is becoming an important technique to elucidate the secondary structure of proteins and peptides (8–16), particularly when obtaining crystallites of suitable size or quality for X-ray diffraction studies is impractical. For example, diffraction data is not available for orexin-B; hence we have undertaken a solid-state NMR investigation to further characterize its secondary structure. Rather than reinvestigating the entire molecule, we undertook rotational echo double resonance (REDOR) (10, 17–26) measurements of two distances that might help define important fragments of the secondary structure for orexin-B. First, we investigated the internuclear separation between the amide carbonyl carbon of Leu^{11} and the amide nitrogen of Leu^{15} ($r_{C11,N15}$). This separation was selected to investigate whether the α helix, an important structural unit observed in both previous solution NMR studies of orexin-B (5, 6), is also present in the solid state. Second, we used the REDOR technique to measure $r_{C17,N22}$; if the bend between the two helices is present in the solid state, there should be a measurable dipolar interaction between the carbonyl carbon of Ala^{17} and the nitrogen of Ala^{22}. Based on the structure deposited in the Protein Data Base (pdb, access code 1CQ0) by Lee et al. (5), the internuclear separation between the amide carbonyl carbon of Ala^{17} and the amide nitrogen of Ala^{22} ($r_{C17,N22}$) is approximately 4 Å. Since peptides and proteins naturally exist in an aqueous environment, an important issue is whether secondary structure determined for solids via X-ray crystallography or solid-state NMR correspond to those found for the same molecule when it is solvated (27). Because solution NMR data is available for orexin-B (5, 6), another objective of this study is to determine whether distances measured for the molecule in the solid state correspond to those determined for the molecule in solution.

Since the REDOR experiment was first proposed (17), the technique has been used to elucidate structures for numerous peptides. Recent examples include investigations of: the antibiotic peptide KIAGKIA-KIAGKIA-KIAGKIA (28, 29), the elasticity in an elastin-mimetic peptide (30), derivatives of β-amyloid (31), *Staphylococcus aureus* (32), a model peptide for the silkworm *Samia cynthia ricini* (33), the role of proline residues in the photo cycle of bacteriorhodopsin (34), the arrangement of peptide strands in HIV-1 (35), a bisubstrate inhibitor (36), and a ^{13}C–^{2}H REDOR study of the silk fibroins from *Bombyx mori* (37). As well, Vogt et al. (38) have recently investigated triply labelled uracil and glycine using θ-REDOR (39) to demonstrate that the technique may also provide the angle between two internuclear vectors.

Fig. 1. Molecular structure of orexin-B deposited in the Protein Data Bank (pdb, access code 1CQ0) (5). The horizontal helix (helix I) spans Leu^{7} to Gly^{19} while the vertical helix (helix II) spans Ala^{23} to Met^{28}.



Isotropic NMR chemical shifts generally are sensitive to hydrogen bonding, a key factor controlling the secondary structure of peptides (40, 41). In solution NMR studies of peptides, one often obtains a trial structure based on a comparison of measured chemical shifts with those for samples with a known structure (42). To facilitate these studies, extensive databases summarizing isotropic ^{1}H, ^{13}C, and ^{15}N chemical shifts measured in solution have been compiled (43–45). While isotropic chemical shifts measured for peptides in solution are a weighted average of the various rotational isomers, this is generally not a factor in the solid state, particularly for micro-crystalline samples. One benefit of solid-state NMR measurements is that chemical shift (CS) tensors may in principle be characterized (vide infra). Such measurements can be challenging, particularly when only small amounts of sample are available, as is often the case for NMR studies of solid peptides. However, the three-dimensional nature of the CS tensor (46) can provide significant information about secondary structure (12, 47, 48). A wide range of CS tensor data for peptides with known secondary structure is required to determine reliable relationships between secondary structure and CS tensors. Hence, as part of our solid-state NMR investigation of orexin-B, the CS tensors for the isotopically enriched samples used for the REDOR measurements, the amide carbonyl carbons of Leu^{11} and Ala^{17}, and the amide nitrogens of Leu^{15} and Ala^{22}, are presented.

Background

REDOR

For spin-1/2 nuclei in an applied magnetic field ($\mathbf{B}_0$) typically used in NMR experiments, the Zeeman interaction dominates, but spin-spin interactions with neighbouring magnetically active nuclei may also manifest themselves in the NMR spectra of solid samples. These are the direct dipolar interaction (**D**) transmitted through space and the indirect interaction (**J**) transmitted via the intervening electrons (49). Both spin-spin interactions are described by second-rank tensors. In the absence of molecular symmetry, six parameters are required to fully characterize the symmetric part of these tensors: three principal components and three angles that orient the principal axis system in the molecular axis system. The indirect spin-spin interaction is usu-

© 2004 NRC Canada

ally described by its isotropic value (J_{iso} = (1/3)Tr**J**), while the dipolar interaction is characterized by the dipolar coupling constant (R_{DD}), which depends on the inverse cube of the internuclear separation (r_{AB}):

$$[1] \qquad R_{DD} = \left(\frac{\mu_0}{4\pi}\right)\left(\frac{\hbar}{2\pi}\right)\gamma_A\gamma_B\left\langle r_{AB}^{-3}\right\rangle$$

where μ_0 is the permeability constant and $\hbar$ is Planck's constant divided by 2π, while γ_A and γ_B are the magnetogyric ratios for nuclei A and B, respectively. Rapid molecular motion, such as that which occurs for molecules dissolved in isotropic solutions, leads to an averaging of the values for **D** and **J**. The direct spin-spin interaction is not directly observed in isotropic fluids, since the trace of **D** is zero (49); averaging of **J** manifests itself as the so-called scalar coupling (J_{iso}).

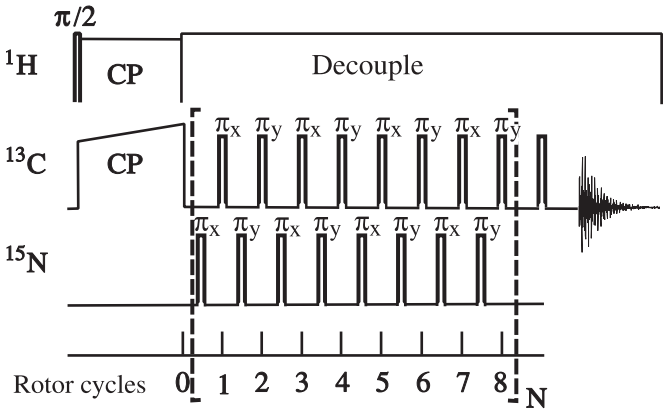
NMR spectra of spin-1/2 nuclei in solid samples are complicated not only by spin-spin interactions, but also by anisotropic magnetic shielding. Rapid magic-angle spinning (MAS) of the sample leads to "solution-like" NMR spectra by averaging to zero both **D** and the anisotropic magnetic shielding. Since the direct relationship between R_{DD} and the internuclear separation renders knowledge of R_{DD} very desirable for structure elucidation, numerous dipolar recovery techniques (17, 25, 26, 50, 51, 52) have been developed. These techniques reintroduce the dipolar interaction while still averaging the magnetic shielding to its isotropic value through MAS. Such techniques are particularly useful when the magnetic shielding anisotropy is much greater than the dipolar interaction. Experimentally, one reintroduces the effective dipolar coupling (R_{eff}) equal to $R_{DD} - 1/3\Delta J$, where the latter term is the anisotropy in **J** (53). Because indirect spin-spin interactions are transferred through the electrons, ΔJ is not significant when there are several intervening bonds between the interacting nuclei, as for the systems considered here. Hence, in the ensuing discussion, R_{eff} is assumed to be equal to R_{DD} (54).

The REDOR technique (10, 17–26) is the most frequently used method for the recovery of heteronuclear dipolar interactions in MAS experiments. Although described as a double resonance technique, typically three rf fields are employed for REDOR experiments, since ^{1}H irradiation is generally used for cross-polarization (CP) and for ^{1}H decoupling. The typical ^{13}C{^{15}N} experiment (22) entails CP from ^{1}H to ^{13}C under the Hartmann–Hahn match condition (55), insertion of rotor-synchronized ^{15}N π pulses to reintroduce $R_{DD}(^{13}C,^{15}N)$, insertion of a refocusing ^{13}C π pulse, and ^{1}H-decoupled data acquisition. In the absence of the ^{15}N π pulses, dephasing arising from $R_{DD}(^{13}C,^{15}N)$ is refocused by the π pulse on the observed ^{13}C nucleus. With the ^{15}N π pulses, the magnetization is not completely refocused, resulting in reduced signal intensity. The REDOR difference ($\Delta S = S_0 - S$) is the difference in signal intensity obtained without S_0, and with, S, ^{15}N dephasing pulses. Regardless of the magnitude of the dipolar interaction, the ratio $\Delta S/S_0$ has the same dependence on the parameter λ_D (23), where:

$$[2] \qquad \lambda_D = N_c T_r R_{DD}$$

In eq. [2], N_c is the number of rotor cycles and T_r is the rotor period. The dependence of $\Delta S/S_0$ on λ_D is described by the universal REDOR curve (22). Knowledge of a few values of $\Delta S/S_0$ yields λ_D. Since N_c and T_r are known, R_{DD} (22) may be determined; the internuclear separation follows from eq. [1]. In the work presented here, $\Delta S/S_0$ is plotted vs. the dephasing time (N_cT_r). Since this is equal to λ_D/R_{DD}, the universal curve can be fit to the experimental points by scaling λ_D by the magnitude of the dipolar interaction.

Fig. 2. REDOR-*xy*8 pulse sequence (56) preceded by CP with a ramped ^{13}C mixing pulse. Note that the $\pi/2$ and π pulses are not drawn to scale.



For the measurement of small heteronuclear interactions and to compensate for possible fluctuations in rf power during the experiment, a modified REDOR pulse sequence has been developed (22, 56). In this pulse sequence (REDOR-*xy*8), phase-alternating π pulses are applied to both ^{13}C and ^{15}N, followed by a refocusing ^{13}C π pulse; this is usually preceded by CP from ^{1}H (Fig. 2). As for most REDOR experiments on peptides, in the present work the ^{1}H-decoupled ^{13}C NMR signal, modified by ^{15}N dephasing pulses, is observed; however readers should recognize that REDOR experiments may in principle be performed between any isolated heteronuclear spin pair (22, 36) and that the technique may also be applied to more complex spin systems (39).

A significant REDOR difference signal will be measured if the dephasing time is equal to or greater than $1/R_{DD}$ (57). Distance measurements based on a smaller REDOR difference are expected to be qualitatively correct but have a greater relative uncertainly. The dephasing time is limited by the effective spin-spin relaxation time and by limits imposed by the hardware, particularly if high-power proton decoupling is required during the dephasing period.

All possible contributions to S or S_0 must be considered when assessing REDOR data. For example, contributions from ^{13}C nuclei present at natural abundance from other residues must be considered when determining the REDOR difference for a ^{13}C NMR signal from a specific residue (20). A more detailed discussion of the corrections required for our data is presented with the results. An article by Naito and Saitô (58) discussing the factors affecting the accuracy of REDOR measurements is highly recommended.

^{13}C and ^{15}N NMR spectroscopy of solid stationary samples

The ^{13}C and ^{15}N NMR line shapes of stationary solid sam-

© 2004 NRC Canada

ples are defined by the span (Ω) and the skew (κ) (59) of the CS tensor:

$$[3] \qquad \Omega = \delta_{11} - \delta_{33}$$

and

$$[4] \qquad \kappa = \frac{3(\delta_{22} - \delta_{iso})}{\Omega}$$

where the δ_{ii} (i = 1–3) are the principal components of the chemical shift tensor, defined such that $\delta_{11} \geq \delta_{22} \geq \delta_{33}$ and $\delta_{iso} = (1/3)(\delta_{11} + \delta_{22} + \delta_{33})$. For a sample containing isolated ^{13}C or ^{15}N nuclei, the principal components of the CS tensor may be obtained directly from the NMR powder pattern (55, 60–62). While these experiments provide the principal components of CS tensors, they do not yield information about the orientations of the CS tensors in the molecular framework. For the data presented here, CS tensor orientations will be proposed based on those determined for closely related compounds.

Experimental details

Sample preparation

Samples of orexin-B, either at natural abundance or doubly enriched at Leu^{11}-1-^{13}C, Leu^{15}-^{15}N, or at Ala^{17}-1-^{13}C, Ala^{22}-^{15}N, were synthesized by the Alberta Peptide Institute of the University of Alberta from enriched samples of *N*-fmoc-L-leucine and *N*-fmoc-L-alanine; the latter samples were obtained commercially (Cambridge Isotope Laboratories, 99% 1-^{13}C or 98% ^{15}N) and characterized by high-performance liquid chromatography (HPLC). The purity of the orexin-B samples was also confirmed by HPLC. Following purification, the orexin-B samples were lyophilized and stored at 0 °C.

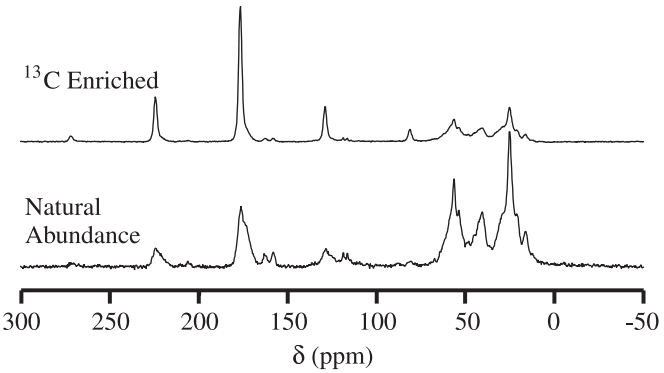
NMR Spectroscopy

Spectra were acquired on a Bruker Avance 500 NMR spectrometer operating at 500.3, 125.8, and 50.7 MHz for ^{1}H, ^{13}C, and ^{15}N, respectively. Samples were packed into 4 mm o.d. zirconia rotors; teflon spacers were placed at the top and bottom of the rotor to ensure that the samples (approximately 20 mg) were centred in the NMR coil.

One-dimensional ^{13}C NMR spectra were acquired using RAMP CP (63) under the Hartmann–Hahn matching condition (55), with a 4.0 μs ^{1}H $\pi/2$ pulse, a 1.0 ms contact time, and 3.0–5.0 s recycle delays. A Hahn echo preceded by CP from ^{1}H was used to acquire ^{15}N NMR spectra of stationary samples. A 3.5 μs ^{1}H $\pi/2$ pulse, 3.0 ms contact time, 70 μs delay before a 13 μs refocusing π pulse and 3–5 s recycle delays were used to acquire these spectra. All spectra were acquired with the two-pulse phase modulation (TPPM) decoupling scheme of Bennett et al. (64). Carbon-13 NMR spectra were referenced to TMS (δ_{iso} = 0) by setting the high-frequency isotropic peak of an external solid adamantane sample to 38.56 ppm (65); those for ^{15}N were referenced to a neat liquid of CH_3NO_2 (δ_{iso} = 0) by setting the isotropic peak for an external NH_4Cl sample to –341.2 ppm (66).

REDOR-*xy*8 (56), with the pulse sequence illustrated in Fig. 2, was used to acquire REDOR data. CP from ^{1}H to ^{13}C was obtained using the same parameters as was used for the one-dimensional ^{13}C NMR spectra. The π pulses were 9.0 and 8.5 μs, respectively, for ^{15}N and ^{13}C. These pulses were optimized by observing the minimum and maximum signals in spectra of a glycine sample that was 10% 1-^{13}C,^{15}N enriched, acquired with the REDOR-*xy*8 pulse sequence using a dephasing time of 1.5 ms. For the orexin-B sample enriched at Leu^{11} and Leu^{15}, 20 points were acquired with an increment of eight rotor cycles between points, corresponding to a maximum dephasing time of 26.7 ms for the sample spinning at 6.0 kHz. For the sample enriched at Ala^{17} and Ala^{22}, three points, with dephasing times of 21.3, 24.0, and 26.7 ms, were acquired; the spinning frequency was also 6.0 kHz. Spectra with short dephasing times contained first- and second-order spinning sidebands; the intensity of these were added to that of the isotropic peak before analysis of the data. The universal REDOR curve was obtained using data generated by the program SIMPSON (67). The program ORIGIN, Version 3.0, was used to fit the universal curve to the experimental points.

Fig. 3. Carbon-13 NMR spectra for orexin-B obtained at 11.75 T with ν_{rot} = 6.0 kHz. The upper trace is that for the sample enriched in ^{13}C at the Leu^{11} carbonyl site and in ^{15}N at Leu^{15}. The lower trace is that for the sample at natural abundance. 13 020 and 13 600 transients were added for the upper and lower traces, respectively.



Results and discussion

REDOR

Determination of $r_{C11,N15}$

Before presenting the data used to extract R_{DD}, spectra of MAS samples and corrections to the data because of ^{13}C nuclei present at natural abundance are considered. Figure 3 illustrates the ^{13}C NMR spectra of orexin-B, obtained at 11.75 T with a rotor frequency (ν_{rot}) of 6 kHz. The spectrum of the sample that is ^{13}C enriched at the amide carbonyl of Leu^{11} contains an isotropic peak at δ_{iso} = 176.3 ± 0.5 ppm, typical of values observed for amide carbonyl carbons (16, 45, 68). The peak width at half height ($\Delta\delta_{1/2}$) is slightly more than 2 ppm at B_0 = 11.75 T, normal for carbonyl carbons of lyophilized peptide samples (15). Residual dipolar coupling to the neighbouring ^{14}N nucleus (I = 1) is expected to only contribute approximately 0.2 ppm to the line width of the isotropic amide carbonyl peak of a spectrum acquired at 11.75 T (69, 70). Furthermore, the line broadening is not

© 2004 NRC Canada

thought to be a consequence of variations in the secondary structure. However, variations in the conformations of the side chains, leading to a distribution of values for δ_{iso}, have been suggested as a cause for broad isotropic peaks in spectra of lyophilized samples (15). DePristo et al. (71) have recently provided a comprehensive discussion of heterogeneity in protein structures. The intensity of the peaks centred at approximately 176 ppm in the spectrum of the natural-abundance sample demonstrates that most amide carbonyl ^{13}C nuclei of orexin-B appear near the position of the Leu^{11} carbonyl carbon and must be considered in the analysis of the REDOR data. However, because these do not all have exactly the same isotropic chemical shift as does the carbonyl carbon of Leu^{11}, the correction cannot be based solely on the number of natural-abundance amide carbonyl carbons in orexin-B. To determine the correction required for the intensity of the peak at 176 ppm, the sharp peaks at 25 ppm are considered, since these arise solely from ^{13}C present at natural abundance in either spectrum. Since the spectra of the labelled and unlabelled samples were acquired under identical experimental conditions, the small difference in intensity at this shift must arise from different sample masses and the difference in the number of scans. By normalizing the intensities of these peaks, the contribution to the peak at 176.3 ppm from ^{13}C nuclei at natural abundance was determined to be 11%, suggesting that 10 ^{13}C nuclear sites in each molecule contribute intensity to the peak at 176.3 ± 0.5 ppm. Other amide carbonyl carbons of orexin-B also appear near 176.3 ppm, but they are sufficiently different to avoid affecting the peak intensity; the broadening of the base of the isotropic peak is attributed to these nuclei. Since one of the 10 carbonyl carbons appearing at 176.3 ppm in the spectrum of the natural-abundance sample is that from Leu^{11}, nine carbonyl carbon atoms present at natural abundance contribute to the signal intensity of the isotropic peak for the spectrum of the ^{13}C-enriched sample. Hence, 9.9% of the peak intensity observed for the peak at δ = 176.3 ppm was subtracted from the values of S_0 in the calculation of the REDOR data.

Most amide carbonyl carbon nuclei present at natural abundance are distant from the site of ^{15}N enrichment and hence are unaffected by ^{15}N dephasing pulses. Thus, for these nuclei, $S_0 - S = 0$ and a correction is not required for ΔS. Exceptions are the natural-abundance carbonyl ^{13}C for Leu^{15} and the backbone carbonyl ^{13}C for Gln^{16}, which are one- and two-bonds distant, respectively, from the site of ^{15}N enrichment, Leu^{15}. If these nuclei appear at the same frequency as the carbonyl ^{13}C of Leu^{11}, a correction to the ΔS term is required. The initial points of the REDOR data (Fig. 4*a*) do indeed show stronger than expected dephasing, since the intercept of the points at the ordinate axis is greater than zero and a fit to the universal REDOR curve is not possible. Based on the structure for DL-alanine (72), ^{13}C–^{15}N dipolar interactions of approximately 900 and 200 Hz, respectively, are expected for the carbonyl carbons of Leu^{15} and Gln^{16} present at natural abundance. By correcting for the dephasing of these nuclei (Fig. 4*b*), the fit to the curve is much better and the intercept is near the origin as expected. This confirms that the isotropic resonances for the carbonyl ^{13}C nuclei for Leu^{15} and Gln^{16} are at approximately 176.3 ppm. In their investigation of glutamine-binding protein, Hing et al. (73) found that the contribution to the observed dephasing from neighbouring carbons present at natural abundance reaches a maximum of 2% after a dephasing period of 4.25 ms, but is negligible after 8.5 ms; similar results are observed here.

The ^{15}N nuclei present at natural abundance (0.366%) are subject to the dephasing pulses and could in principle affect the ^{13}C signal, but Naito et al. (74) have shown that the effect on ΔS is negligible; hence, no corrections to the data were made for this factor. Likewise, the data were not corrected for intermolecular dipolar interactions, since these are not expected to be significant for a large molecule such as orexin-B. In REDOR investigations of (Phe-Leu-Ala)$_6$, Kimura et al. (75) found that intermolecular effects are negligible when measuring distances within α helices.

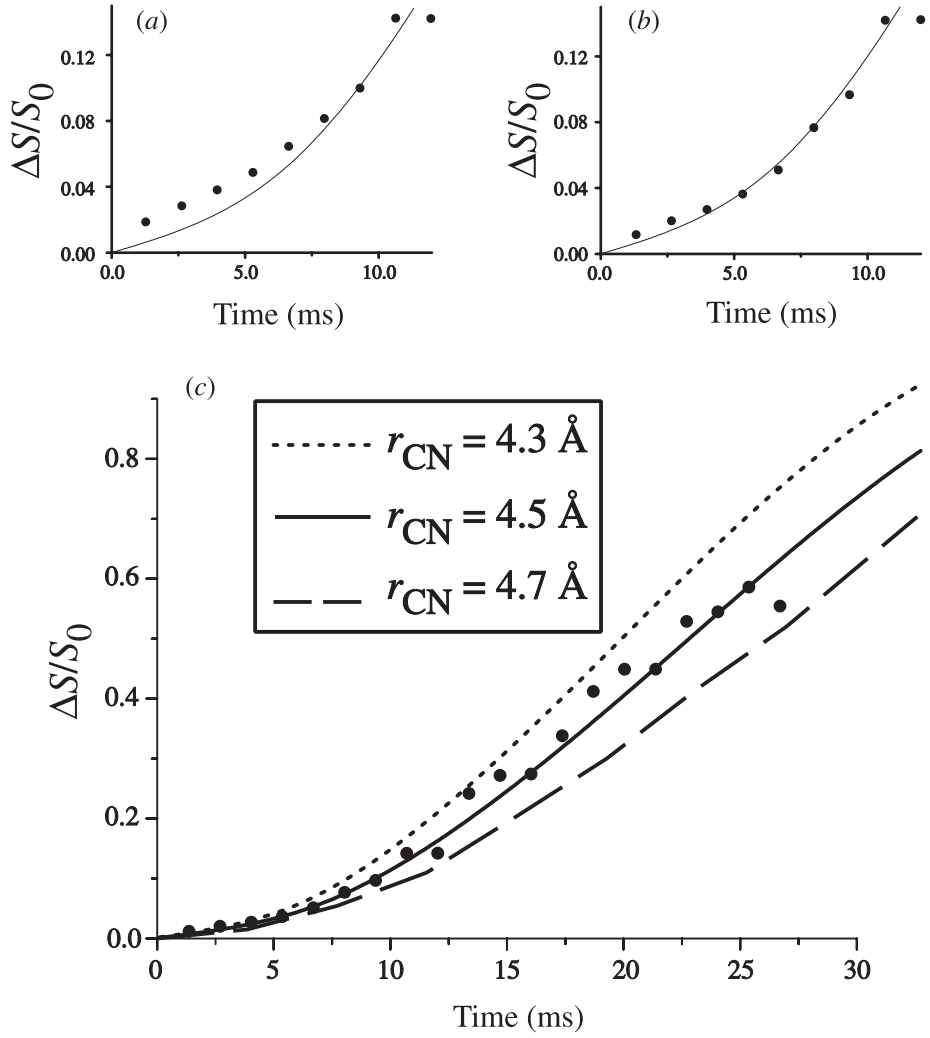
Figure 4*c* illustrates a plot of $\Delta S/S_0$ as a function of dephasing time for orexin-B ^{13}C and ^{15}N enriched at Leu^{11} and Leu^{15}, respectively. Data used to prepare this plot were corrected as already discussed. The fit of the data yields a value of 35 ± 3 Hz for $R_{DD}(^{15}N,^{13}C)$, corresponding to $r_{C11,N15}$ = 4.5 ± 0.2 Å. This value has not been corrected for librational averaging (76); at 20 °C, this may lead to dipolar coupling constants that are approximately 10% less than that expected for a rigid lattice (20). This leads to an error in the internuclear distance of approximately 2%, which is much smaller than the value of ±0.2 Å arising from other sources. The value for $r_{C11,N15}$ is in agreement with those reported for other α helices (75) and is within the range of values (3.6 Å (5) and 5.1 Å (6)) measured in the solution NMR studies of orexin-B. The distance between the corresponding nuclei of an idealized structure consisting of seven alanine residues is 4.12 Å for the nuclei in an α helix, but 12.1 Å if the polyalanine is extended. Therefore, our data strongly suggests that the α helix for the Leu^{11} to Leu^{15} fragment of orexin-B found in solution studies (5, 6) is also present in the solid state.

Determination of $r_{C17,N22}$

To investigate the relative orientations of the two α helices of orexin-B (5, 6), we undertook a REDOR experiment on solid orexin-B with ^{13}C and ^{15}N enrichment at Ala^{17} and Ala^{22}, respectively. Within experimental error, the isotropic peak for the amide carbonyl carbon is the same as for Leu^{11} (176.1 ± 1.0 ppm), but it is considerably broader ($\Delta\delta_{1/2} \approx$ 6.4 ppm, Fig. 5). Broad peaks (>6 ppm) have been observed for other amide carbonyl carbons in lyophilized peptides (77). Because this line width is three times greater than that observed for the amide carbonyl carbon for Leu^{11}, the possibility that this is a consequence of sample preparation was considered. The sample was redissolved and lyophilized; the line widths were unchanged. The purity was verified by acquiring a ^{13}C NMR spectrum of the sample dissolved in aqueous SDS solution — a single peak was observed for the carbonyl carbon of Ala^{17}. To further verify that all samples of orexin-B were the same, apart from the sites of enrichment, other peaks in the ^{13}C NMR spectrum of the sample enriched at Ala^{17} were compared with those for orexin-B ^{13}C enriched at Leu^{11} and at natural abundance. A peak at 158 ppm, attributed to C_ε of one of the arginine residues of orexin-B (78), has the same line width in spectra of the natural abundance sample and of the sample enriched at Ala^{17};

© 2004 NRC Canada

Fig. 4. Dependence of $\Delta S/S_0$ on the dephasing time (points) for the Leu[11] carbonyl carbon. The solid lines are the universal REDOR curve for a dipolar interaction of 35 Hz. The data arising from the first 11 ms of dephasing time, calculated *without* (*a*) and *with* (*b*) the correction for dephasing of the amide carbonyl ^{13}C nuclei of Leu[15] and Gln[16] are shown at the top. The complete plot (*c*) is shown at the bottom; the dashed and dotted lines indicate the uncertainty in the data.



the peaks at 25 ppm for all three samples also have the same line widths. In addition, the isotropic ^{15}N peak of the sample ^{15}N enriched at Leu[15] has the same line width as that for this sample, which is ^{15}N enriched at Ala[22]. Hence, the broad line width for the carbonyl carbon of Ala[17] is indeed specific to that site, suggesting a greater degree of disorder in this portion of orexin-B than is found about Leu[11]. Belton et al. (79) have presented a detailed discussion of factors affecting ^{13}C NMR line widths in the spectra of solid proteins.

Considering the broad peaks in the ^{13}C NMR spectra for Ala[17], acquiring multiple points for a REDOR curve as was done for the sample enriched at Leu[11] and Leu[15] was impractical. Three points, with dephasing times of 21.3, 24.0, and 26.7 ms, were collected yielding dipolar coupling constants of 12, 14, and 10 Hz, respectively. As for the data used in the determination of $r_{C11,N15}$, these data were corrected for the effects of ^{13}C nuclei present at natural abundance. Because of the broad peaks and the long dephasing time, spectra had lower signal-to-noise than those for the sample enriched at Leu[11]. Figure 5 illustrates the spectra obtained with and without the ^{15}N dephasing pulses for a dephasing time of 24 ms. From these spectra, a dipolar interaction of 12 ± 3 Hz is determined. This corresponds to an internuclear separation of 6.4 ± 0.5 Å, but considering the broad isotropic carbonyl ^{13}C peak, the possibility of multiple relative orientations for the two α helices cannot be discounted. Hence, the value of 6.4 Å may be a weighted average. For example, similar REDOR data would be obtained if 90% of the sample had a structure such that $r_{C17,N22}$ = 8 Å and 10% had a structure such that $r_{C17,N22}$ = 4 Å. Experiments to resolve this issue are not practical with the limited sample available. Although dynamic disorder would also reduce the measured dipolar coupling, this may be discounted since the spans of the ^{13}C and ^{15}N NMR spectra (vide infra) of a stationary sample are typical of these samples in the absence of motion (80). Finally, we note that a distance of 6.0 Å is expected for a nitrogen five residues distant from a carbonyl carbon in an idealized polyalanine α helix, within error of the value for $r_{C17,N22}$. However, considering the solution NMR data (5), a bend between two helices in

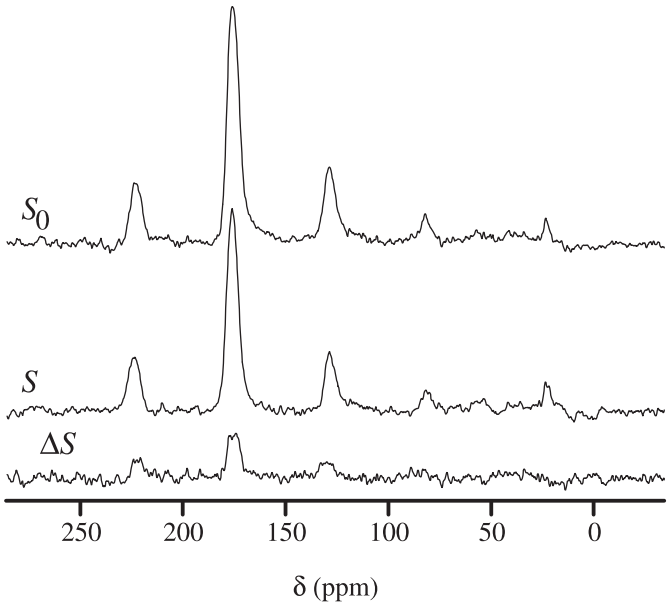
© 2004 NRC Canada

Table 1. Principal components of the amide carbonyl carbon CS tensors for Leu[11] and Ala[17] and of the amide nitrogen CS tensors for Leu[15] and Ala[22] in orexin-B.[a]

CS tensor	δ_{11}	δ_{22}	δ_{33}	δ_{iso}[b]	Ω[c]	κ[d]
Carbon						
L-Leu[11]	243(3)	193(2)	93(3)	176.3(5)	150	0.33
L-Ala[17]	243(3)	187(3)	97(3)	176.1(10)	146	0.22
Nitrogen						
L-Leu[15]	–158(3)	–303(3)	–322(3)	–260.7(15)	164	–0.77
L-Ala[22]	–159(5)	–296(4)	–319(5)	–258.2(15)	160	–0.71

[a]Data are in ppm, apart from κ, which has no units; estimated uncertainties in the last digits are in parentheses.
[b]Measured from spectra of MAS samples. δ_{iso} may not be exactly equal to the average of the principal components because of the greater uncertainty in the values of the latter.
[c]$\Omega = \delta_{11} - \delta_{33}$.
[d]$\kappa = 3(\delta_{22} - \delta_{iso})/\Omega$.

Fig. 5. Carbon-13 NMR spectra for orexin-B ^{13}C enriched at the amide carbonyl of Ala[17] and ^{15}N enriched at Ala[22] obtained at 11.75 T with ν_{rot} = 6.0 kHz. Traces S_0 and S, respectively, were acquired without and with ^{15}N dephasing pulses in the REDOR-*xy*8 pulse sequence. 15 120 transients were acquired for each spectrum. The REDOR difference (ΔS) is shown in the lower trace.



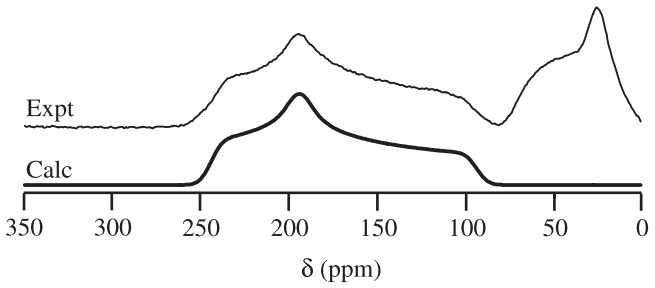
orexin-B is thought to be the more likely explanation for the relative proximity of Ala[17] and Ala[22].

Summarizing, our REDOR experiments are consistent with the presence of an α helix that incorporates Leu[11] and Leu[15]; the dipolar coupling between the carbonyl carbon of Ala[17] and the nitrogen of Ala[22] suggests a value of 6.4 Å for $r_{C17,N22}$. Although the latter value may be a weighted average, it is compatible with a bend between the two α helices of orexin-B. Examination of the solution NMR data (6) indicates that a bend could lead to a value for $r_{C17,N22}$ between 5 and 9 Å.

Chemical shift tensors

The carbon and nitrogen CS tensors for the nuclei involved in the REDOR investigation discussed above were determined via the analyses of NMR spectra of stationary samples. The spin systems were assumed to be isolated — the small ^{13}C–^{15}N dipolar interactions amount to less than 1 ppm at 11.75 T and hence are negligible.

Fig. 6. Experimental and calculated ^{13}C NMR spectra for the carbonyl carbon nucleus of the Leu[11] residue of a stationary sample of orexin-B acquired at 11.75 T. The peaks in the 0–80 ppm region of the experimental spectrum arise from aliphatic ^{13}C nuclei at natural abundance; 21 875 transients were acquired.



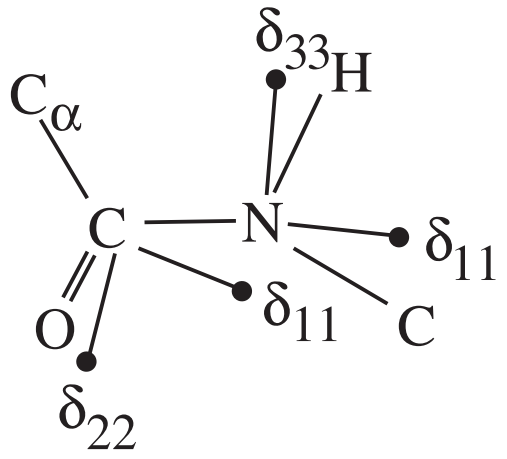
Carbon CS tensors

The ^{13}C NMR spectra of MAS samples of orexin-B have been discussed above. These consist of relatively broad isotropic peaks for Leu[11] (Fig. 3) and for Ala[17] (Fig. 5) with first- and second-order spinning side bands at ν_{rot} = 6 kHz, suggesting significant spans. Figure 6 illustrates the ^{13}C NMR spectra of the carbonyl ^{13}C nuclei of Leu[11] for a stationary sample of orexin-B; those for Ala[17] are similar. The principal components of the CS tensors derived from simulations of these spectra are listed in Table 1. These are within the range of values reported in previous studies of carbonyl carbon CS tensors for leucine (68, 81–83) and alanine (68, 81, 84–86) residues in various peptides.

Before proceeding with a comparison of the CS tensor data, consideration of the CS tensor orientations is important. Those for the nuclei of orexin-B were not determined directly, since they are not thought to vary significantly for amide carbonyl carbons in peptides. Calculations (81, 83) and experiment (83, 87, 88), including a single-crystal NMR study of Gly containing peptides (89), suggest that the CS tensors are oriented such that δ_{11} and δ_{22} are in the peptide plane, with the latter component approximately along the C—O bond and with δ_{33} perpendicular to this plane, as shown in Fig. 7.

© 2004 NRC Canada

Fig. 7. General orientation of amide carbonyl carbon and amide nitrogen CS tensors in peptides. The δ_{33} component for the carbonyl carbon and the δ_{22} component for the nitrogen are perpendicular to the page.



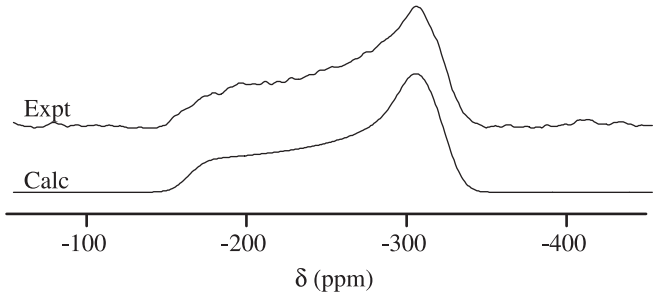
The carbon CS tensors for Leu[11] and for Ala[17] (Table 1) are very similar; only the shielding in the direction of δ_{22} has a difference greater than the experimental error. Although magnetic shielding in this direction is particularly sensitive to hydrogen bonding (48, 81, 90, 91), the difference observed here is too small to draw any conclusions about hydrogen bonding. The similarity of the CS tensors is not surprising, since solution NMR studies (5, 6) suggest that both Leu[11] and Ala[17] form part of the α helix I.

Nitrogen CS tensors

Nitrogen-15 NMR spectra for MAS samples of orexin-B ^{15}N-enriched at Leu[15] and Ala[22] (not shown) are relatively broad ($\Delta\delta_{1/2}$ = 8 ppm); within error, they have the same isotropic values. Figure 8 illustrates the ^{15}N NMR spectra for the Leu[15] residue of a stationary sample of orexin-B; similar spectra were obtained for the Ala[22] residue. The principal components of the nitrogen CS tensors, obtained from fits to these spectra, are listed in Table 1. These data fall within the standard deviation of a compilation of nitrogen CS tensors for 61 amides (68). Likewise, the isotropic chemical shifts are in the range of solution NMR values obtained for Leu and Ala residues in peptides (45) and also for these residues in ubiquitin, measured in the solid state (92). The ^{15}N NMR properties for the Leu residues of solid gramicidin A have been investigated by several groups (93–95); our results for Leu[15] are similar. Likewise, those for the amide nitrogen of Ala[22] are similar to those reported for other Ala residues (88, 93–100). A summary of solid-state ^{15}N NMR studies of peptides has recently been published (101).

The nitrogen CS tensor orientation for glycyl-[^{15}N]glycine hydrochloride monohydrate was determined from a single-crystal NMR study (102). An axially symmetric CS tensor was determined, with the unique component in the peptide plane, approximately orthogonal to the carbonyl carbon-to-nitrogen bond. Later powder NMR (69, 95, 103–106) and quantum chemical studies (83) found similar orientations; for non-axially symmetric CS tensors, the δ_{11} and δ_{33} components lie approximately in the peptide plane, as illustrated in Fig. 7.

Fig. 8. Experimental and calculated ^{15}N NMR spectra for the Leu[15] residue of a stationary sample of orexin-B acquired at 11.75 T; 27 400 transients were acquired.



There are no significant differences between the nitrogen CS tensors for Leu[15] and Ala[22]. This is consistent with the data of Miskolzie et al. (6), who reported that both residues form part of the α helices and therefore are expected to have similar local environments. A complex relationship between isotropic ^{15}N chemical shifts and hydrogen bonding, depending on the orientation of the hydrogen bond, has been suggested (81). Considering the similar nitrogen CS tensors for Leu[15] and Ala[22], it is not possible to surmise any differences in the hydrogen bonding environments between these two sites.

Conclusions

REDOR experiments were undertaken on orexin-B to investigate the secondary structure in the solid state. Measurement of the internuclear distance between the carbonyl carbon of Leu[11] and the nitrogen of Leu[15] yields a value of 4.5 ± 0.2 Å, consistent with an α helix for this segment of orexin-B, as reported by Lee and co-workers (5) and by Miskolzie et al. (6). Distance measurements between the carbonyl carbon of Ala[17] and the amide nitrogen of Ala[22] yield an effective value of 6.4 ± 0.5 Å. This distance is compatible with a bend between two α helices in orexin-B, but other structures, such as that of an α helix that includes Ala[17] and Ala[22], would also yield the same value.

To obtain more information about the secondary structure of orexin-B in the solid state, it would be desirable to prepare other samples of orexin-B containing selectively labelled ^{13}C and ^{15}N spin pairs. Because the REDOR technique works best for isolated spin pairs, a separate sample must be prepared for every distance required. Obviously future experiments must be planned carefully since the cost of preparing selectively ^{13}C, ^{15}N enriched samples is significant.

We have also determined the amide carbonyl carbon and amide nitrogen CS tensors for the labelled residues of orexin-B. There is no significant variation between the amide carbonyl carbon CS tensors for Leu[11] or Ala[17], nor between the amide nitrogen CS tensors for Leu[15] and Ala[22].

This study has demonstrated the value of REDOR to complement solution NMR data. It is hoped that this work will encourage researchers to consider these or related techniques when investigating the secondary structure of peptides.

© 2004 NRC Canada

Acknowledgments

We thank the members of the solid-state NMR group at the University of Alberta for many helpful comments and suggestions. We are grateful to Dr. Anil Mehta of Washington University for his advice on the REDOR experiments. We acknowledge Robert Parker and the Alberta Peptide Institute, as well as Richard Tomski of the machine shop, for their assistance. R.E.W. and G.K. acknowledge funding from the Natural Sciences and Engineering Research Council of Canada (NSERC). R.E.W. thanks the Government of Canada for a Canada Research Chair in physical chemistry at the University of Alberta. Finally, R.E.W. is grateful to the late Professor Don Irish who introduced him to spectroscopy in an undergraduate class at the University of Waterloo.

References

1. T. Sakurai, A. Amemiya, M. Ishii, I. Matsuzaki, R.M. Chemelli, H. Tanaka, S.C. Williams, J.A. Richardson, G.P. Kozlowski, S. Wilson, J.R.S. Arch, R.E. Buckingham, A.C. Haynes, S.A. Carr, R.S. Annan, D.E. McNulty, W.-S. Liu, J.A. Terrett, N.A. Elshourbagy, D.J. Bergsma, and M. Yanagisawa. Cell, **92**, 573 (1998).
2. J.T. Willie, R.M. Chemelli, C.M. Sinton, and M. Yanagisawa. Annu. Rev. Neurosci. **24**, 429 (2001).
3. T. Voisin, P. Rouet-Benzineb, N. Reuter, and M. Laburthe. Cell. Mol. Life Sci. **60**, 72 (2003).
4. L. De Lecea, T.S. Kilduff, C. Peyron, X.-B. Gao, P.E. Foye, P.E. Danielson, C. Fukuhara, E.L.F. Battenberg, V.T. Gautvik, F.S. Bartlett II, W.N. Frankel, A.N. Van Den Pol, F.E. Bloom, K.M. Gautvik, and J.G. Sutcliffe. Proc. Natl. Acad. Sci. U.S.A. **95**, 322 (1998).
5. J.-H. Lee, E. Bang, K.-J. Chae, J.-Y. Kim, D.W. Lee, and W. Lee. Eur. J. Biochem. **266**, 831 (1999).
6. M. Miskolzie, S. Lucyk, and G. Kotovych. J. Biomol. Struct. Dyn. **21**, 341 (2003).
7. R. Bader, A. Bettio, A.G. Beck-Sickinger, and O. Zerbe. J. Mol. Biol. **305**, 307 (2001).
8. S.O. Smith and O.B. Peersen. Annu. Rev. Biophys. Biomol. Struct. **21**, 25 (1992).
9. D. Sitkoff and D.A. Case. Prog. Nucl. Magn. Reson. Spectrosc. **32**, 165 (1998).
10. R. Fu and T.A. Cross. Annu. Rev. Biophys. Biomol. Struct. **28**, 235 (1999).
11. J.H. Davis and M. Auger. Prog. Nucl. Magn. Reson. Spectrosc. **35**, 1 (1999).
12. F.M. Marassi. Concepts Magn. Reson. **14**, 212 (2002).
13. C.M. Rienstra, L. Tucker-Kellogg, C.P. Jaroniec, M. Hohwy, B. Reif, M.T. McMahon, B. Tidor, T. Lozano-Pérez, and R.G. Griffin. Proc. Natl. Acad. Sci. **99**, 10 260 (2002).
14. S. Luca, H. Heise, and M. Baldus. Acc. Chem. Res. **36**, 858 (2003).
15. R.W. Martin and K.W. Zilm. J. Magn. Reson. **165**, 162 (2003).
16. T.I. Igumenova, A.E. McDermott, K.W. Zilm, R.W. Martin, E.K. Paulson, and A.J. Wand. J. Am. Chem. Soc. **126**, 6720 (2004).
17. T. Gullion and J. Schaefer. J. Magn. Reson. **81**, 196 (1989).
18. T. Gullion and J. Schaefer. Adv. Magn. Reson. **13**, 57 (1989).
19. Y. Pan, T. Gullion, and J. Schaefer. J. Magn. Reson. **90**, 330 (1990).
20. J.R. Garbow and T. Gullion. *In* Carbon-13 NMR spectroscopy of biological systems. *Edited by* N. Beckmann. Academic Press, San Diego. 1995. Chap. 3.
21. J.N.S. Evans. Biomolecular NMR spectroscopy. Oxford University Press, Oxford. 1995.
22. J. Schaefer. *In* Encyclopedia of nuclear magnetic resonance. Vol. 6. *Edited by* D.M. Grant and R.K. Harris. John Wiley and Sons, Chichester. 1996. p. 3977.
23. T. Gullion. Magn. Reson. Rev. **17**, 83 (1997).
24. R. Tycko. Annu. Rev. Phys. Chem. **52**, 575 (2001).
25. D.D. Laws, H.-M.L. Bitter, and A. Jerschow. Angew. Chem. Int. Ed. **41**, 3096 (2002).
26. M.J. Duer. *In* Solid-state NMR spectroscopy principles and applications. *Edited by* M.J. Duer. Blackwell Science, Oxford. 2002. Chap. 3.
27. (*a*) H. Kessler, G. Zimmermann, H. Förster, J. Engel, G. Oepen, and W.S. Sheldrick. Angew. Chem. Int. Ed. Eng. **20**, 1053 (1981); (*b*) H. Kessler, G. Zimmermann, H. Förster, J. Engel, G. Oepen, and W.S. Sheldrick. Angew. Chem. **93**, 1085 (1981).
28. O. Toke, W.L. Maloy, S.J. Kim, J. Blazyk, and J. Schaefer. Biophys. J. **87**, 662 (2004).
29. O. Toke, R.D. O'Connor, T.K. Weldeghiorghis, W.L. Maloy, R.W. Glaser, A.S. Ulrich, and J. Schaefer. Biophys. J. **87**, 675 (2004).
30. X.L. Yao and M. Hong. J. Am. Chem. Soc. **126**, 4199 (2004).
31. D.J. Gordon, J.L. Balbach, R. Tycko, and S.C. Meredith. Biophys. J. **86**, 428 (2004).
32. A.K. Mehta, L. Cegelski, R.D. O'Connor, and J. Schaefer. J. Magn. Reson. **163**, 182 (2003).
33. Y. Nakazawa and T. Asakura. J. Am. Chem. Soc. **125**, 7230 (2003).
34. J.C. Lansing, J.G. Hu, M. Belenky, R.G. Griffin, and J. Herzfeld. Biochemistry, **42**, 3586 (2003).
35. J. Yang and D.P. Weliky. Biochemistry, **42**, 11 879 (2003).
36. L.M. McDowell, D.R. Studelska, B. Poliks, R.D. O'Connor, and J. Schaefer. Biochemistry, **43**, 6606 (2004).
37. T. Gullion, R. Kishore, and T. Asakura. J. Am. Chem. Soc. **125**, 7510 (2003).
38. F.G. Vogt, J.M. Gibson, S.M. Mattingly, and K.T. Mueller. J. Phys. Chem. B, **107**, 1272 (2003).
39. T. Gullion and C.H. Pennington. Chem. Phys. Lett. **290**, 88 (1998).
40. G.A. Jeffrey. An introduction to hydrogen bonding. Oxford University Press, New York. 1997. Chap. 10.
41. H.-H. Limbach (*Editor*). Special issue of Magn. Reson. Chem. **39**, S1 (2001).
42. K. Wüthrich. NMR of proteins and nucleic acids. John Wiley and Sons, New York. 1986.
43. D.S. Wishart, B.D. Sykes, and F.M. Richards. Biochemistry, **31**, 1647 (1992).
44. B.R. Seavey, E.A. Farr, W.M. Westler, and J.L. Markley. J. Biomol. NMR, **1**, 217 (1991).
45. H. Zhang, S. Neal, and D.S. Wishart. J. Biomol. NMR, **25**, 173 (2003).
46. K. Schmidt-Rohr and H.W. Spiess. Multidimensional solid-state NMR and polymers. Academic Press, London. 1994.
47. For a discussion of various solid-state ^{15}N NMR techniques, see: R.J. Pugmire. *In* Encyclopedia of nuclear magnetic resonance. Vol. 9. Advances in NMR. *Edited by* D.M. Grant and R.K. Harris. John Wiley and Sons, Chichester. 2002. p. 298.
48. A.C. de Dios and E. Oldfield. J. Am. Chem. Soc. **116**, 11 485 (1994).

© 2004 NRC Canada

49. R.E. Wasylishen. *In* Encyclopedia of nuclear magnetic resonance. Vol. 3. *Edited by* D.M. Grant and R.K. Harris. John Wiley and Sons, Chichester. 1996. p. 1685.
50. M. Auger. J. Chim. Phys. Phys.-Chim. Biol. **92**, 1751 (1995).
51. D.L. Bryce and R.E. Wasylishen. *In* Encyclopedia of spectroscopy and spectrometry. Vol. 3. *Edited by* J.C. Lindon, G.E. Tranter, and J.L. Holmes. Academic Press, San Diego. 2000. p. 2136.
52. R.G. Griffin. Nat. Struct. Biol. **5**, 508 (1998).
53. J. Vaara, J. Jokisaari, R.E. Wasylishen, and D.L. Bryce. Prog. Nucl. Magn. Reson. Spectrosc. **41**, 233 (2002).
54. D.L. Bryce and R.E. Wasylishen. J. Biomol. NMR, **25**, 73 (2003).
55. A. Pines, M.G. Gibby, and J.S. Waugh. J. Chem. Phys. **56**, 1776 (1972).
56. T. Gullion, D.B. Baker, and M.S. Conradi. J. Magn. Reson. **89**, 479 (1990).
57. J.J. Balbach, Y. Ishii, O.N. Antzutkin, R.D. Leapman, N.W. Rizzo, F. Dyda, J. Reed, and R. Tycko. Biochemistry, **39**, 13 748 (2000).
58. A. Naito and H. Saitô. *In* Encylclopedia of nuclear magnetic resonance. Vol. 9. Advances in NMR. *Edited by* D.M. Grant and R.K. Harris. John Wiley and Sons, Chichester. 2002. p. 283.
59. J. Mason. Solid State Nucl. Magn. Reson. **2**, 285 (1993).
60. A. Pines, W.-K. Rhim, and J.S. Waugh. J. Chem. Phys. **54**, 5438 (1971).
61. D.M. Grant. *In* Encyclopedia of nuclear magnetic resonance. Vol. 2. *Edited by* D.M. Grant and R.K. Harris. John Wiley and Sons, Chichester. 1996. p. 1298.
62. D.L. Bryce, G.M. Bernard, M. Gee, M.D. Lumsden, K. Eichele and R.E Wasylishen. Can. J. Anal. Sci. Spectrosc. **46**, 46 (2001).
63. G. Metz, X. Wu, and S.O. Smith, J. Magn. Reson. A, **110**, 219 (1994).
64. A.E. Bennett, C.M. Rienstra, M. Auger, K.V. Lakshmi, and R.G. Griffin. J. Chem. Phys. **103**, 6951 (1995).
65. W.L. Earl and D.L. VanderHart. J. Magn. Reson. **48**, 35 (1982).
66. S. Hayashi and K. Hayamizu. Bull. Chem. Soc. Jpn. **64**, 688 (1991).
67. M. Bak, J.T. Rasmussen, and N.C. Nielsen, J. Magn. Reson. **147**, 296 (2000).
68. For a summary of the CS tensor data to 1994, see: T.M. Duncan. Principal components of chemical shift tensors: a compilation. 2nd ed. Farragut Press, Chicago. 1994.
69. K. Eichele, M.D. Lumsden, and R.E. Wasylishen. J. Phys. Chem. **97**, 8909 (1993).
70. M. Strohmeier, D. Stueber, and D.M. Grant. J. Phys. Chem. A, **107**, 7629 (2003), and refs. cited therein.
71. M.A. DePristo, P.I.W. de Bakker, and T.L. Blundell. Structure, **12**, 831 (2004).
72. M.S. Nandhini, R.V. Krishnakumar, and. S. Natarajan. Acta Crystallogr. **C57**, 614 (2001).
73. A.W. Hing, N. Tjandra, P.F. Cottam, J. Schaefer, and C. Ho. Biochemistry, **33**, 8651 (1994).
74. A. Naito, K. Nishimura, S. Tuzi, and H. Saitô. Chem. Phys. Lett. **229**, 506 (1994).
75. S. Kimura, A. Naito, H. Saitô, K. Ogawa, and A. Shoji. J. Mol. Struct. **562**, 197 (2001).
76. K. Saalwächter and I. Fischbach. J. Magn. Reson. **157**, 17 (2002).
77. Y. Tomita, E. J. O'Connor, and A. McDermott. J. Am. Chem. Soc. **116**, 8766 (1994).
78. C. Ye, R. Fu, J. Hu, H. Hou, and S. Ding. Magn. Reson. Chem. **31**, 699 (1993).
79. P.S. Belton, A.M. Gil, and S.F. Tanner. Magn. Reson. Chem. **31**, 1001 (1993).
80. A. Naito, A. Fukutani, M. Uitdehaag, S. Tuzi, and H. Saitô. J. Mol. Struct. **441**, 231 (1998).
81. N. Asakawa, T. Kameda, S. Kuroki, H. Kurosu, S. Ando, I. Ando, and A. Shoji. Annu. Rep. NMR Spectrosc. **35**, 55 (1998).
82. T. Kameda, N. Takeda, S. Kuroki, H. Kurosu, S. Ando, I Ando, A. Shoji, and T. Ozaki. J. Mol. Struct. **384**, 17 (1996).
83. M. Strohmeier and D.M. Grant. J. Am. Chem. Soc. **126**, 966 (2004).
84. N. Asakawa, S. Kuroki, H. Kurosu, I. Ando, A. Shoji, and T. Ozaki. J. Am. Chem. Soc. **114**, 3261 (1992).
85. K. Tsuchiya, A. Takahashi, N. Takeda, N. Asakawa, S. Kuroki, I. Ando, A. Shoji, and T. Ozaki. J. Mol. Struct. **350**, 233 (1995).
86. Q. Teng, M. Iqbal, and T.A. Cross. J. Am. Chem. Soc. **114**, 5312 (1992).
87. R.E. Stark, L.W. Jelinski, D.J. Ruben, D.A. Torchia, and R.G. Griffin. J. Magn. Reson. **55**, 266 (1983).
88. C.J. Hartzell, M. Whitfield, T.G. Oas, and G.P. Drobny. J. Am. Chem. Soc. **109**, 5966 (1987).
89. N. Takeda, S. Kuroki, H. Kurosu, and I. Ando. Biopolymers, **50**, 61 (1999).
90. G. Zheng, L. Wang, J. Hu, X. Zhang, L. Shen, C. Ye, and G.A. Webb. Magn. Reson. Chem. **35**, 606 (1997).
91. Y. Wei, D.-K. Lee, and A. Ramamoorthy. J. Am. Chem. Soc. **123**, 6118 (2001).
92. T.I. Igumenova, A.J. Wand, and A.E. McDermott. J. Am. Chem. Soc. **126**, 5323 (2004).
93. Q. Teng and T.A. Cross. J. Magn. Reson. **85**, 439 (1989).
94. L.K. Nicholson and T.A. Cross. Biochemistry, **28**, 9379 (1989).
95. W. Mai, W. Hu, C. Wang, and T.A. Cross. Protein Sci. **2**, 532 (1993).
96. C.J. Hartzell, T.K. Pratum, and G. Drobny. J. Chem. Phys. **87**, 4324 (1987).
98. G.B. Fields, C.G. Fields, J. Petefish, H.E. Van Wart, and T.A. Cross. Proc. Natl. Acad. Sci. U.S.A. **85**, 1384 (1988).
99. A. Shoji, T. Ozaki, T. Fujito, K. Deguchi, S. Ando, and I. Ando. Macromolecules, **22**, 2860 (1989).
100. A. Shoji, T. Ozaki, T. Fujito, K. Deguchi, S. Ando, and I. Ando. J. Am. Chem. Soc. **112**, 4693 (1990).
101. E.Y. Chekmenev, Q. Zhang, K.W. Waddell, M.S. Mashuta, and R.J. Wittebort. J. Am. Chem. Soc. **126**, 379 (2004).
102. G.S. Harbison, L.W. Jelinski, R.E. Stark, D.A. Torchia, J. Herzfeld, and R.G. Griffin. J. Magn. Reson. **60**, 79 (1984).
103. M.D. Lumsden, R.E. Wasylishen, K. Eichele, M. Schindler, G.H. Penner, W.P. Power, and R.D. Curtis. J. Am. Chem. Soc. **116**, 1403 (1994).
104. C.W. Kirby, M.D. Lumsden, and R.E. Wasylishen. Can. J. Chem. **73**, 604 (1995).
105. C.H. Wu, A. Ramamoorthy, L.M. Gierasch, and S.J. Opella. J. Am. Chem. Soc. **117**, 6148 (1995).
106. D.K. Lee, R.J. Wittebort, and A. Ramamoorthy. J. Am. Chem. Soc. **120**, 8868 (1998).

© 2004 NRC Canada

TRIBUTE / HOMMAGE

This issue of the *Canadian Journal of Chemistry* contains papers dedicated to the memory of Professor Donald Edward Irish. It was with great sadness that we heard that Don had passed away on 26 October 2002 in Waterloo, Ontario, after a two-year battle with cancer. Don had many friends and colleagues across the scientific community, both at home in Canada and abroad, and it is fitting that we have been able to put together in the *Canadian Journal of Chemistry* a tribute to his life and career.

Don was born on 14 June 1932 in Uxbridge, Ontario, and grew up in Port Elgin, Ontario. He obtained his B.Sc. in 1955 with Honours in Chemistry and Physics at the University of Western Ontario and then went on to a obtain a Master's degree under R.H. Tomlinson at McMaster University in 1956, for which he studied yields in the thermal neutron fission of ^{233}U. He earned his Ph.D. in 1962 under T.F. Young at the University of Chicago, where he began his lifelong interest in Raman spectral studies of electrolyte solutions.

After a short spell as a chemistry teacher at the Central Technical School in Toronto, Don's long association with Waterloo began on 1 July 1957, when he was appointed Lecturer in the Waterloo College Associate Faculties (which shortly thereafter became the University of Waterloo). He was the first Lecturer in Chemistry to be hired at the fledgling university. He became Assistant Professor in 1962 and reached the level of Full Professor in 1971. He served as Chairman of the Department of Chemistry from 1977 to 1983. He also served the university on numerous committees at the university, provincial, and national levels. Don was an avid international traveler and spent time at laboratories in several countries, including Bell Laboratories in New Jersey, the University of Newcastle-upon-Tyne, CNRS Laboratories in Thiais, the University of Karlsruhe, DSIR New Zealand, the University of Queensland, and the University of Geneva. Not one to sit back, he stayed active as Adjunct Professor Emeritus upon his retirement on 1 July 1996 and was named Distinguished Professor Emeritus in 1999.

Don will be remembered by his many former undergraduate and graduate students as a great science teacher, a facet of his abilities for which he was honoured with three awards: the University of Waterloo Distinguished Teacher Award in 1987, the Ontario Confederation of University Faculty Associations' Teaching Award in 1988, and The Union Carbide Award of the Chemical Institute of Canada for Chemical Education in 1990.

As a member of the broader scientific community, Don was a very active member of the Chemical Institute of Canada (CIC) and the Canadian Society for Chemistry (CSC), serving on committees both at the national and local levels, and he became a Fellow of the CIC in 1974. He was on the organizing committees of several international conferences and served on the editorial board of the *Journal of Solution Chemistry* for many years. A special symposium was arranged for the 82nd CSC Congress held in Toronto in 1999 to honour Don on his retirement, and the proceedings fittingly were published in a special issue of the *Journal of Solution Chemistry* (Vol. 29, No. 10, October 2000). This symposium, and the dinner that followed, was a testimonial to Don's high standing amongst his colleagues both nationally and internationally and amongst his former students.

Don was primarily a physical chemist, specializing in Raman and IR spectroscopy of electrolyte solutions, probing both solvent and solute. By observing the various species as

Ce numéro de la *Revue canadienne de chimie* réunit des articles dédiés à la mémoire du professor Donald Edward Irish. C'est avec une profonde émotion que nous avons appris le décès de Don, le 26 octobre 2002, à Waterloo, en Ontario, au terme d'une lutte de deux ans contre le cancer. Don comptait de très nombreux amis et collègues dans la collectivité scientifique, tant au Canada qu'à l'étranger. La publication d'un numéro spécial de la *Revue canadienne de chimie* nous a donc paru une élégante façon d'honorer sa vie et son oeuvre.

Don est né le 14 juin 1932 à Uxbridge, en Ontario, et a grandi à Port Elgin, dans cette même province. Il a obtenu un baccalauréat *ès* sciences spécialisé en chimie et en physique à l'Université Western Ontario (1955), puis une maîtrise à l'Université McMaster (1956), où il a analysé la puissance de la fission induite par neutron thermique de l'uranium 233, sous la direction de R.H. Tomlinson. Il a obtenu son doctorat aux côtés de T.F. Young, en 1962, dans les laboratoires de la University of Chicago, point de départ d'un intérêt pour les études par spectroscopie Raman de solutions électrolytiques que Don cultivera toute sa vie.

Après une brève période comme professeur de chimie à la Central Technical School de Toronto, Don a amorcé sa longue carrière à Waterloo, le 1er juillet 1957, à titre de chargé de cours aux Waterloo College Associate Faculties, appelées à devenir l'Université de Waterloo. De fait, il a été le premier chargé de cours en chimie dans les effectifs de la nouvelle université. Il a ensuite gravi les échelons : professeur adjoint (1962), professeur titulaire (1971) et président du département de chimie (1977–1983). Don a aussi représenté l'Université auprès de nombreux comités universitaires, provinciaux et nationaux. « Globe-trotter » invétéré, Don a exercé son art dans des laboratoires des quatre coins du monde, y compris aux laboratoires Bell (New Jersey, É.-U.), à la University of Newcastle-upon-Tyne (R.-U.), aux laboratoires du CNRS (Thiais, France), à la Universität Karlsruhe (Allemagne), au DSIR (Nouvelle-Zélande), à la University of Queensland (Australie) et à l'Université de Genève (Suisse). D'un caractère énergique, il a continué à contribuer activement au domaine à titre de professeur émérite adjoint après sa retraite, le 1er juillet 1996, et a été reçu professeur émérite distingué en 1999.

Ses anciens étudiants de premier et de deuxième cycles se souviendront toujours de Don comme d'un enseignant doué. De fait, son talent de pédagogue a été confirmé par trois honneurs : le prix du mérite en enseignement de l'Université de Waterloo (1987), le prix d'excellence en enseignement de l'Union des associations des professeurs des universités de l'Ontario (1988) et le Prix Union Carbide pour l'enseignement de la chimie de l'Institut de chimie du Canada (1990).

Au sein de la collectivité scientifique, Don a été un membre assidu de l'Institut de chimie du Canada (ICC) et de la Société canadienne de chimie (SCC), auprès desquels il a participé à plusieurs comités nationaux et locaux. Il a notamment été reçu Fellow de l'ICC en 1974. Il a siégé au comité organisateur de nombreux congrès internationaux et a été membre du comité de rédaction du *Journal of Solution Chemistry* pendant plusieurs années. Incidemment, un symposium en son honneur a été organisé en 1999, dans le cadre du 82e congrès de la SCC, à Toronto, à l'occasion de sa retraite. Les actes de ce symposium ont fait l'objet, fort opportunément, d'un numéro spécial du *Journal of Solution*

© 2004 NRC Canada

a function of concentration and temperature he was able to determine, often in minute detail, the various processes that can occur and thereby extract equilibrium constants and other thermodynamic parameters. Over the years he made invaluable contributions to our understanding of species and processes in solution, such as complex formation, acid dissociation, hydrated proton species, solvation, ion–ion interactions, solvent structure making and breaking, and the structure of water and solutions at high temperature. His high-temperature work was of great interest to Canada's energy industries. Also, in the early days of computers, Don was a strong proponent of their use in the collection and analysis of spectral data. As time went by he became more involved in surface enhanced Raman spectroscopy (SERS) for the study of adsorbates at electrode surfaces, both in understanding the phenomenon itself and the processes occurring at the electrode–electrolyte interface and in the potential application of SERS in areas such as corrosion and electrocatalysis.

Throughout his career Don authored about 170 publications, including eight monographs. His scientific work earned him an outstanding international reputation in physical chemistry. He supervised 16 Ph.D. and 13 M.Sc. students and his lab hosted 18 visiting scientists and post-doctoral fellows. These graduates and fellows went on to positions in universities, colleges, industry, NRC, AECL, and NSF. He gave much help to these and many other individuals over the years in their scientific careers. One of us (DJL) experienced this first hand when Don visited Canterbury University in 1969 and responded to a request for help in a way that significantly and positively altered his eventual Postdoctoral fellow's life and career. In all this he was characteristically modest and unassuming, enjoying a love for science with an enthusiasm that infected all who worked with him.

Don was not just a one-track scientist: he had many other interests and hobbies. He and his wife, Shirley, loved to travel, and they visited most of the world together over the years, with Don recording these events with his trusty camera that was always at hand. These trips were regaled with a slide show to his current crop of graduate students at the frequent pleasant dinner evenings he and Shirley graciously hosted for them. He ensured his own physical fitness mainly through the ritual of walking the family dog each evening, but he also firmly encouraged his graduate students to maintain a regime of regular physical activity. Don thoroughly enjoyed hiking in the countryside and observing nature and he shared this enthusiasm with anyone who was willing to accompany him on his frequent expeditions. He took an active role in the movement to preserve the Bruce Trail and the Niagara Escarpment in Southern Ontario. Don and Shirley eventually purchased a cottage overlooking Georgian Bay so that they could be closer to this significant life-long interest. He was interested in reading, music, and drama, and was a keen sailor. Don was also a profoundly religious man and was an active member of the United Church of Canada, serving on many committees. He was closely involved with St. Paul's United College from its founding as an Affiliated College of the University of Waterloo. Those of us who knew him well marveled at how Don managed to fit so many activities into a normal day; he was always moving on from one event to another without missing a beat!

We celebrate Don's life, which was dedicated to his family, his friends, his community, and to science and education and the beneficial influence he has had on our own lives that will not be forgotten.

Chris I. Ratcliffe
David J. Lockwood

Chemistry (vol. 29, n° 10, octobre 2000). Ce symposium et les agapes qui ont suivi ont mis en lumière l'énorme respect qu'inspirait Don à ses anciens disciples de même qu'à ses collègues du Canada et du monde entier.

Don était avant tout un physicochimiste, spécialisé en spectroscopie Raman et infrarouge appliquée aux solvants et aux solutés de solutions électrolytiques. En observant diverses espèces chimiques en fonction de leur concentration et de leur température, Don est arrivé à définir, souvent très précisément, les processus chimiques susceptibles de se manifester et, par conséquent, à dégager des constantes d'équilibre et d'autres paramètres de thermodynamique. Au fil des ans, il a sensiblement enrichi notre connaissance des espèces chimiques et des phénomènes en présence dans les solutions, tels que la formation de complexes, la dissociation des acides, les espèces à protons hydratés, la solvatation, les interactions ion–ion, l'élaboration et la fragmentation des structures de solvant ainsi que la structure de l'eau et des solutions à température élevée. Ses travaux à température élevée ont d'ailleurs fait date dans l'industrie énergétique canadienne. En outre, dès l'apparition des ordinateurs, Don a loué haut et fort l'efficacité de ces appareils pour la collecte et l'analyse des données spectrales. Ultérieurement, Don a eu recours à la spectrométrie laser de l'effet Raman exalté de surface (SERS) pour étudier les adsorbats à la surface des électrodes, ceci en vue de comprendre non seulement le phénomène en tant que tel mais encore les processus qui se produisent à l'interface électrode–électrolyte de même que l'utilité de la SERS pour l'étude de mécanismes tels que la corrosion et l'électrocatalyse.

Au cours de sa carrière, Don a signé environ 170 publications, dont huit monographies. Ses recherches scientifiques lui ont permis d'acquérir des lettres de noblesse dans la collectivité mondiale de la chimie physique. Il a supervisé 16 doctorants et 13 mastères, et son laboratoire a accueilli 18 chercheurs invités et boursiers postdoctoraux. Les étudiants et confrères qu'il a encadrés oeuvrent aujourd'hui auprès d'universités, de collèges, de l'industrie, du CNRC, d'EACL et de la NSF. Don n'hésitait pas à épauler ses protégés et ses collègues au cours de leur carrière. Un de nous, DJL, peut en attester : Don, alors en visite à la Canterbury University, en 1969, lui a prêté une aide bénéfique et déterminante pour ses études postdoctorales, voire pour sa carrière. En dépit de sa vaste influence, Don a toujours fait preuve de modestie et de simplicité, conjuguées à une passion communicative pour la science.

Pour autant, Don ne restait pas claquemuré dans les laboratoires : il se consacrait à de nombreux intérêts et passe-temps. Ainsi, Don et son épouse Shirley adoraient voyager et ont sillonné le monde pendant leur vie commune. Don, sa caméra fétiche au cou, se faisait un devoir de croquer sur le vif les moments passés outre frontière en vue de projections souvenir qui concluaient souvent les soirées gourmandes qu'il organisait avec Shirley pour ses étudiants. Il gardait la forme surtout par des promenades avec son chien dans l'air du soir et ne se lassait pas de rappeler à ses étudiants l'importance de l'exercice physique. Don affectionnait aussi les promenades en campagne et la communion avec la nature. Il partageait cette passion avec quiconque daignait l'accompagner dans ses nombreuses expéditions. Don a fait partie du mouvement de préservation du sentier Bruce et de l'escarpement de Niagara, dans le sud de l'Ontario. Pour étancher leur soif d'immersion dans la nature, Don et Shirley se sont acheté un chalet sur la Baie Georgienne. Don passait aussi beaucoup de temps à la lecture, la musique et le théâtre. Il était également un mordu de la voile. Don était un homme foncièrement croyant : il servait activement son

© 2004 NRC Canada

église, l'Église unie du Canada, autant comme fidèle que comme membre de divers comités. Il a étroitement contribué à la fondation du St. Paul's United College et à son affiliation avec les collèges de l'Université de Waterloo. Ceux d'entre nous qui le connaissaient bien s'émerveillaient de la façon dont il arrivait à sertir ses journées de si nombreuses activités. Il semblait passer d'un rôle à l'autre sans jamais perdre son souffle!

Nous sommes fiers de pouvoir célébrer ici la vie de Don, qu'il a su pleinement investir dans sa famille, ses amis, sa communauté, la science et l'enseignement, et de souligner l'enrichissante et l'inoubliable influence que Don Edward Irish aura eue sur nos vies.

Chris I. Ratcliffe
David J. Lockwood

© 2004 NRC Canada

This special issue is dedicated to the memory of

Professor Donald Edward Irish

to honour his outstanding contributions to chemistry, especially using Raman spectroscopy.

Associate Editors: Chris Ratcliffe, Ross Hill, Derek Leaist, Chris Orvig, and Rod Wasylishen

Ce numéro spécial est dédié à la mémoire du

Professeur Donald Edward Irish

en reconnaissance de ses inestimables contributions au domaine de la chimie, notamment les applications de la spectrométrie Raman.

Directeurs scientifiques associés : Chris Ratcliffe, Ross Hill, Derek Leaist, Chris Orvig et Rod Wasylishen

© 2004 NRC Canada



Professor Donald Edward Irish

© 2004 NRC Canada

AWARD LECTURE / CONFÉRENCE D'HONNEUR

2003 Fred Beamish Award Lecture — Exploring the dynamics of biological systems by mass spectrometry

Lars Konermann

Abstract: This review describes the use of electrospray ionization mass spectrometry (ESI-MS) in conjunction with on-line rapid mixing techniques. This combination, termed "time-resolved" ESI-MS, provides a powerful approach for studying solution-phase reactions on timescales as short as a few milliseconds. Of particular interest is the application of this technique for monitoring protein folding reactions. Time-resolved ESI-MS can provide detailed information on structural changes of the polypeptide chain, while at the same time probing the occurrence of noncovalent ligand–protein interactions. Especially when used in combination with hydrogen–deuterium pulse labeling, these measurements yield valuable structural information on short-lived folding intermediates. Similar approaches can be used to monitor the dynamics of proteins under equilibrium conditions. Another important application of time-resolved ESI-MS are mechanistic studies on enzyme-catalyzed processes. These reactions can be monitored under presteady-state conditions, without requiring artificial chromophoric substrates or radioactive labeling. We also discuss the use of ESI-MS for monitoring noncovalent ligand–protein interactions by diffusion measurements. In contrast to conventional MS-based techniques, this approach does not rely on the preservation of noncovalent interactions in the gas phase. It appears that diffusion measurements by ESI-MS could become an interesting alternative to existing methods for the high throughput screening of compound libraries in the context of drug discovery.

Key words: reaction intermediate, rapid mixing, kinetics, protein conformation, protein function.

Résumé : Cette revue décrit l'utilisation de la spectrométrie de masse avec ionisation par électronébulisation (SM-IEN) en relation avec les techniques de mixage rapide en ligne. Cette combinaison, à laquelle on se réfère comme SM-IEN résolue en fonction du temps, fournit une approche puissante à l'étude des réactions en solution, à des échelles de temps aussi rapides que quelques millisecondes. Il est particulièrement intéressant que cette technique puisse être appliquée au monitoring des réactions de repliement des protéines. La SM-IEN résolue en fonction du temps peut fournir des informations détaillées sur les changements structuraux de la chaîne polypeptidique tout en examinant l'apparition d'interactions non covalentes ligand–protéine. Lorsqu'on les utilise en combinaison avec un marquage pulsé hydrogène–deutérium, ces mesures fournissent en particulier des informations importantes relatives à la structures des intermédiaires de repliement de courte vie. On peut utiliser des approches semblables pour suivre la dynamique des protéines dans des conditions équilibrantes. Les études mécanistiques des processus catalysés par les enzymes correspondent à un autre champ d'application important pour la SM-IEN résolue en fonction du temps. On peut suivre ces réactions dans des conditions antérieures à l'état d'équilibre, sans avoir besoin de substrats chromophoriques artificiels ou de marquages radioactifs. On discute aussi de l'utilisation de la SM-IEN pour détecter et suivre les interactions ligand–protéine non covalentes par des mesures de diffusion. Par opposition aux techniques conventionnelles de SM, cette approche ne repose pas sur la préservation d'interactions non covalentes en phase gazeuse. Il semble que les mesures de diffusion par SM-IEN pourraient devenir une alternative intéressante aux méthodes actuelles pour l'évaluation à grand volume de librairies de composés dans le contexte de la découverte de nouveaux médicaments.

Mots clés : intermédiaire réactionnel, mélange rapide, cinétique, conformation des protéines, fonction des protéines.

[Traduit par la Rédaction]

Received 24 June 2004. Published on the NRC Research Press Web site at http://canjchem.nrc.ca on 21 December 2004.

L. Konermann. Department of Chemistry, The University of Western Ontario, London, ON N6A 5B7, Canada. (e-mail: konerman@uwo.ca).

Introduction

The following is a written account of the Fred Beamish Award Lecture, which was given in August 2003 at the 86th Canadian Society for Chemistry Conference and Exhibition in Ottawa, Ontario. It is the aim of this article to provide an overview of recent developments in the area of biological

 doi: 10.1139/V04-132 © 2004 NRC Canada

mass spectrometry (MS), with focus on work from the author's laboratory. Modern MS-based techniques represent some of the most powerful analytical tools for a wide range of quantitative and qualitative applications. Traditional MS studies are usually carried out under the premise that the chemical composition of the sample under consideration does not change during the time required for the analysis, i.e., from injection of the sample until ionization takes place. The information obtained from these measurements is *static* in nature. In contrast, the work in our laboratory focuses on the use of MS for studying the *dynamics* of biological systems. We will describe methods that permit the detection of short-lived reaction intermediates and that allow measuring of the rates at which individual species are formed or consumed. The results of these studies can provide a detailed understanding of (bio)chemical reaction mechanisms.

The entire area of biological MS has experienced explosive growth since the early 1990s. This process was triggered by the development of two novel ionization methods, namely electrospray ionization (ESI) (1) and matrix-assisted laser desorption/ionization (MALDI) (2, 3). Besides their versatility, the most important feature of both ionization techniques is their "softness", a term often used to describe the fact that little or no fragmentation occurs during ion formation. Consequently, both ESI-MS and MALDI-MS are powerful tools for studying a wide range of analytes, including biological macromolecules and other large nonvolatile species. This is in contrast to more traditional MS-based approaches, which can only be used for the analysis of relatively small molecular species, and where extensive fragmentation of covalent bonds is the norm. ESI-MS is particularly well-suited for studies on biologically relevant reactions because it allows the direct on-line coupling of solution-phase processes with gas phase analysis and detection methods. The softness of ESI-MS is best demonstrated in experiments involving the ionization of intact noncovalent assemblies, such as ligand–protein complexes (4), cell organelles (5), or even whole viruses (6). Another important factor for the rapidly growing popularity of MS-based techniques are recent dramatic improvements of the mass analyzers used, leading to ever-increasing sensitivity, accuracy, resolution, and mass range. In particular, the development of quadrupole-time-of-flight (Q-TOF) (7) and Fourier transform ion cyclotron resonance (FT-ICR) mass spectrometers (8) has had a major impact.

One of the major driving forces behind the technological advances in the area of MS was the need to identify and characterize large numbers of proteins in a high throughput fashion, resulting in the emergence of a new field of research termed "proteomics" (9). Initially, this term almost exclusively encompassed the MS analysis of proteins separated by two-dimensional gel electrophoresis. Today, proteomics has grown into a much broader research area that also uses numerous non-MS approaches and that heavily relies on bioinformatics for data mining (10). The goal of proteomics research is the characterization of the entire protein complement of selected organisms, and to understand the dependence of this "proteome" on factors such as environmental stress, diseases, drugs, etc. These global approaches undoubtedly hold great promise for unraveling some of the complexity of biological systems, and for developing new therapeutic agents. However, it appears that this kind of research is not always well-suited to provide a detailed understanding of molecular structure–function relationships, which hold the key for deciphering many of the intricate processes taking place in living organisms. There definitely remains an urgent need for novel biophysical and bioanalytical approaches that can be used for exploring the molecular features of smaller subsystems. Accordingly, work in the author's laboratory is *not* geared towards the development of large scale protein identification strategies. Instead, ESI-MS is used for gaining a better understanding of protein dynamics, folding, catalysis, and binding.

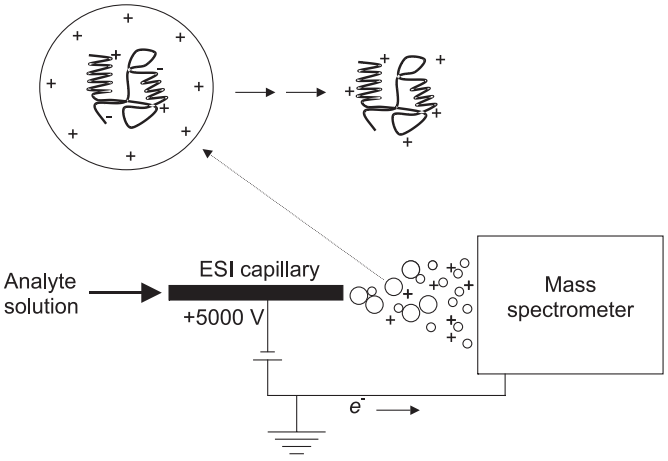


Fig. 1. Schematic depiction of the electrospray ionization (ESI) process. Analyte solution is injected into a metal capillary to which a positive potential has been applied. At the tip of this ESI capillary the solution is turned into a mist of small and highly charged droplets. Gas-phase analyte ions are generated from these droplets as indicated in the inset, where the analyte is assumed to be a protein. Further details are given in the text.

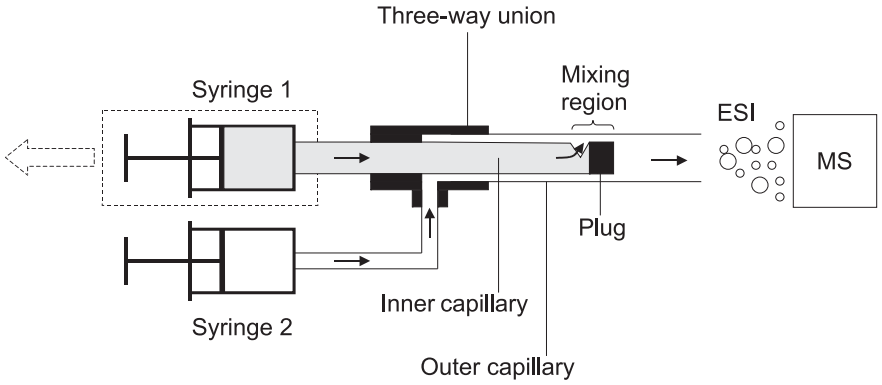
Kinetic studies by time-resolved ESI-MS

The ESI process

A typical ESI-MS setup is schematically depicted in Fig. 1 (11). Analyte solution is continuously infused into a metal capillary that is held at a high electric potential (typically 2–5 kV). The polarity of this electrospray voltage can be positive or negative. We will focus our discussion on the commonly used positive ion mode, where the applied potential is positive. Highly charged solvent droplets are emitted from the capillary tip. The excess charge on these droplets is primarily due to protons that are spread across the droplet surface. One important proton source is the electrolytic oxidation of water within the ESI capillary ($H_2O \rightarrow 2H^+ + 2e^- + 1/2O_2$) (12). Electrons generated by this reaction (or by other charge-balancing redox processes) flow to the mass spectrometer, thus completing a series circuit. The droplets sprayed from the tip of the ESI capillary undergo shrinkage because of rapid solvent evaporation. This process leads to the so-called Rayleigh limit, where the surface tension is balanced by the electrostatic repulsion of the charges within a droplet. At this point fission events start to occur, thus causing the formation of smaller offspring droplets. The continuation of this evaporation–fission cycle generates

© 2004 NRC Canada

Fig. 2. Schematic representation of a continuous-flow mixing setup for kinetic measurements by time-resolved ESI-MS. Syringes 1 and 2 deliver a continuous-flow of reactants; mixing of the two solutions initiates the reaction of interest. The plug at the end of the inner capillary ensures that all the liquid from syringe 1 is expelled through a notch at the capillary end into the narrow inter-capillary space. The inner capillary can be automatically pulled back, together with syringe 1 (as indicated by the dashed arrow). This provides a means to control the "age" (reaction time) of the mixture at the capillary outlet. Arrows indicate the direction of liquid flow.



smaller and smaller droplets, and eventually leads to the formation of gas phase ions from the solution phase analytes that were contained within the droplets. At present, many aspects of this ionization process are not fully understood and the mechanism(s) of ESI are a very active field of research (13). Ion formation during ESI occurs at atmospheric pressure. A suitable ion sampling interface is required to capture the ions and to inject them into the vacuum chamber of the mass spectrometer where they are analyzed according to their mass to charge (m/z) ratio. A wide array of different mass analyzers can be used for this purpose. The experiments described in the following were mostly performed on quadrupole instruments.

As mentioned previously, ESI is an extremely gentle process that allows the formation of intact gas phase ions even from large biomolecules in solution. Another important feature of ESI is that it tends to result in the formation of multiply charged ions, an effect that is especially pronounced for proteins. Typically, not all analyte ions acquire exactly the same number of protons, thus leading to the formation of several charge states that can be observed in the mass spectrum. The m/z values at which multiply protonated ions appear in the spectrum are given by $(M + 1.008 \times z)/z$, where M is the mass of the neutral analyte, 1.008 is the mass of a proton (in Da), and z is the number of protons attached to the analyte.

ESI-MS as a tool for studying solution-phase kinetics

Kinetic studies are of fundamental importance for the understanding of biochemical processes. They provide information on reaction mechanisms, intermediate species, reaction rates, thermodynamic parameters, etc. Many physiologically important reactions occur on fairly rapid timescales. This often represents a problem when attempting to study these processes by traditional analytical approaches. Therefore, techniques capable of providing kinetic data with a time resolution of milliseconds (or even sub-milliseconds) are of particular importance for addressing a wide range of issues (14). Kinetic experiments require a trigger that perturbs an equilibrium situation, thus defining a zero time point where all the molecules within the sample start to undergo a certain process simultaneously. One of the most common kinetic triggers is the mixing of two solutions, which can routinely be achieved within milliseconds; even microsecond mixing techniques have been reported (15).

Biochemical kinetics can be monitored by exposing the reaction mixture to a suitable quenching agent (e.g., acid, base, liquid nitrogen, etc.) after selected time intervals. Various analytical methods including MS or NMR can be used for the off-line analysis of the quenched reaction mixture. Problems encountered with this approach include the possible degradation or chemical modification of labile species in the reaction mixture prior to or during the analysis (16). These limitations can be avoided when using on-line detection methods. Optical stopped-flow spectroscopy is probably the most common tool for experiments of this kind. One major drawback of this approach is the poor selectivity of optical detection techniques, and the fact that numerous biochemical processes are not associated with any significant chromophoric changes. The use of ESI-MS as a highly selective and sensitive detection technique for on-line kinetic studies represents an obvious and attractive solution to these problems (16–18). ESI-MS allows the relative concentrations of multiple reactive species to be recorded as a function of time, without any need for chromophoric changes during the reaction. Transient intermediates may be identified based on their mass-to-charge ratio and (or) their MS–MS characteristics (19). One possible approach for on-line kinetic experiments by ESI-MS is the direct coupling of a stopped-flow instrument to a mass spectrometer (20–23). An alternative method, which is conceptually much simpler, is the use of continuous-flow methods in conjunction with ESI-MS.

A continuous-flow setup for "time-resolved" ESI-MS is depicted in Fig. 2 (24). This system represents a concentric capillary mixer with adjustable reaction chamber volume. In contrast to previously described rapid mixing devices (25), this instrument operates under laminar flow conditions, a fact that has to be taken into account for the data analysis (24). Reactant solutions are continuously expelled from two syringes. The first of these syringes is connected to the inner capillary, whereas the solution delivered by the second syringe flows through the outer capillary. The reaction of interest is initiated by mixing the two solutions at the end of the

© 2004 NRC Canada

inner capillary. The reaction then proceeds, while the mixture flows towards the outlet of the apparatus, where ESI takes place. The reaction time is determined by the solution flow rate, the diameter of the outer tube and, most importantly, by the distance between the mixing point and the outlet. This distance can be modified by adjusting the position of the inner capillary, as indicated in Fig. 2. Kinetic experiments are typically performed by initially positioning the mixer directly at the outlet of the apparatus, corresponding to a reaction time of zero. The mass spectrometer then continuously monitors the ions emitted from the capillary outlet, while the mixer is slowly pulled back. These experiments provide data in three dimensions; the time axis is determined by the mixer position, the *m*/*z* axis provides information on the identity of the species in the reaction mixture, and the intensity axis is related to the concentration of each of these species. The kinetic data obtained can be visualized by either displaying mass spectra for specific reaction times or by plotting intensity–time profiles for selected ionic species. The time resolution of this system is suitable for measuring rate constants in the range of ca. 1 min^{-1} up to at least 100 s^{-1} (24). In the following sections we will discuss several applications of this on-line ESI-MS rapid mixing system.

Monitoring protein folding and ligand binding kinetics

The protein folding problem

The three-dimensional structure adopted by the polypeptide chain of a protein depends on its solvent environment. Under physiological conditions of pH and temperature and in the absence of chemical denaturants, many proteins fold into a unique, highly ordered, and compact structure. This "native" conformation usually represents the biologically active state of a protein. Denaturing agents such as acid or heat can induce a transition to a largely disordered conformation (26). Many unfolded proteins can spontaneously refold to their native structures once the denaturant is removed. This remarkable observation implies that all of the information required to attain the native structure is contained within the amino acid sequence of the polypeptide chain. The native state of a protein corresponds to the conformation with the lowest overall free energy, taking into account the contributions from the polypeptide chain and the surrounding solvent (27). Although a lot of progress has been made in protein folding research over the last 40 years, the question of how and why proteins fold remains one of the major unsolved problems in biophysical chemistry (28). The "protein folding problem" is not only a fascinating challenge from an intellectual point of view, it also has important biomedical implications. For example, misfolding and aggregation are related to diseases like Alzheimer's, Parkinson's, Creutzfeldt–Jakob syndrome, type II diabetes, BSE ("mad cow disease"), and many others (29).

Folding processes involve conformational ensembles of proteins that undergo a biased diffusion on a multidimensional energy landscape. The global minimum of this landscape corresponds to the native conformation, thus resulting in a "folding funnel". Because of the enormous conformational space that is available to an unfolded polypeptide chain, every protein may start its folding process from a different point on the rim of the funnel, and thus follow a different trajectory to the native state (30). The topologic features of the energy landscape that govern the overall folding mechanism are determined by various enthalpic and entropic contributions such as hydrogen bonding, polar interactions, hydrophobic interactions, etc. Despite its complexity, the description of protein folding in terms of simple pathway models is often very helpful. However, it has to be understood that individual reactive species used in these models represent ensembles of polypeptide chains that can exhibit a fair amount of structural heterogeneity (31).

Of particular importance for the mechanistic understanding of folding processes is the detection and structural characterization of transient folding intermediates. This task is not straightforward, mostly because the lifetimes of these species are often very short, spanning a range from submilliseconds to seconds, which prevents the use of X-ray or NMR methods for direct structural studies (32–36). Another important aspect that has received surprisingly little attention is the fact that many proteins adopt their biologically active conformation only after binding metal ions, prosthetic groups, or other proteins. Very little is known about the interplay of folding and binding, and about the interactions of noncovalent binding partners with short-lived folding intermediates. Only very recently have these important questions come to the forefront of research (37–39). In the following sections we hope to demonstrate that time-resolved ESI-MS has the potential to address these and other questions, thus contributing to a better understanding of protein folding in general.

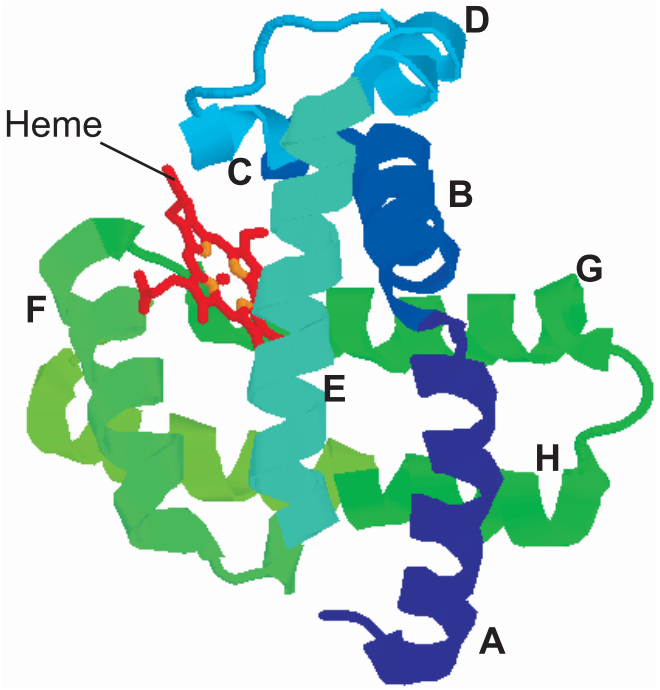
Protein folding and ligand binding monitored by time-resolved ESI-MS

As outlined above, ESI produces intact and multiply charged protein ions in the gas phase. The charge states observed in ESI-MS depend critically on the protein conformation in solution. Unfolded proteins form higher protonation states than those with tightly folded structures, thus providing a highly sensitive probe for protein conformational changes in solution (40–42). A particularly attractive feature of this approach is that it can be used to probe structural features of the protein, while at the same time providing information on noncovalent protein–ligand and protein–protein interactions through the direct observation of these complexes in the gas phase (43–46). Using the on-line rapid mixing setup of Fig. 2, it thus becomes possible to monitor structural changes and binding events as a function of time.

Myoglobin is a convenient model protein for studying the interplay between folding and ligand binding. Holomyoglobin (hMb) is an oxygen storage protein of 17.5 kDa. The native protein has eight α-helices, and forms a hydrophobic pocket into which a heme group is bound (Fig. 3). Unfolding of the protein leads to a disruption of the heme–protein interactions. The reverse process ("reconstitution") involves refolding of the polypeptide chain and rebinding of the heme group. The mechanism of reconstitution can be studied by recording mass spectra at different times after mixing acid-unfolded apo-myoglobin (heme-free protein, aMb) with basic heme solution (47). The spectrum of acid-unfolded aMb is depicted in Fig. 4*a*. It shows a wide distribution of peaks with a maximum at fairly high charge

© 2004 NRC Canada

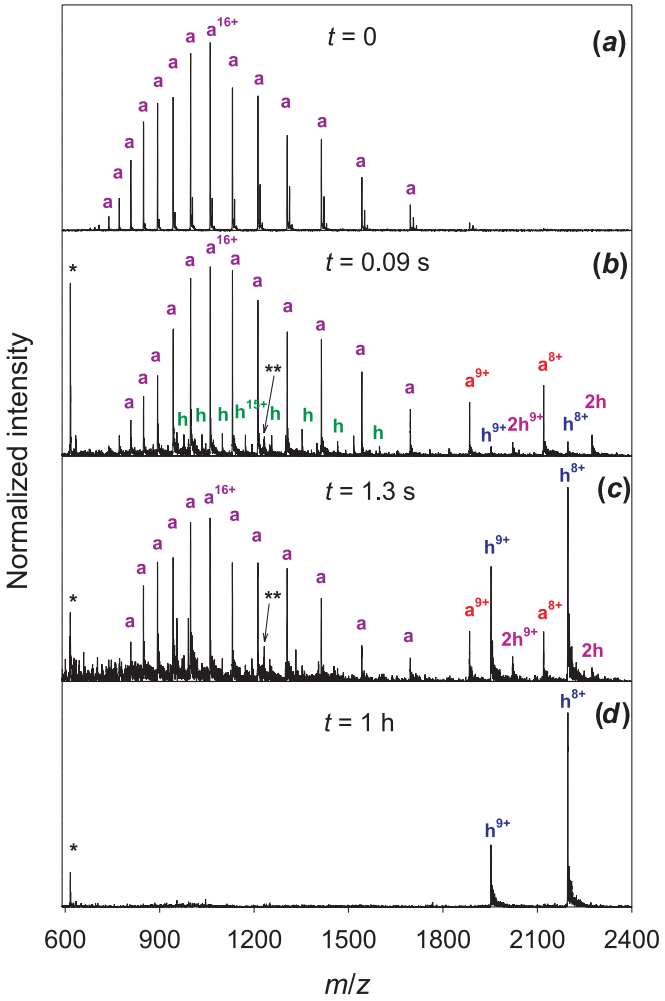
Fig. 3. Structure of native holo-myoglobin based on Brookhaven data file 1wla.pdb. The eight α-helices of this protein are labeled as A–H. The protein forms a hydrophobic pocket into which a heme group is bound.



states, around aMb^{16+} (labeled as a). The spectrum shown in Fig. 4*b* was recorded 90 ms after initiation of reconstitution, and it shows a more complex pattern of ionic signals. The observation of highly charged hMb ions (around hMb^{15+}, labeled as h) indicates the formation of an intermediate that is bound to a heme group, but still retains a largely unfolded conformation. The spectrum also shows strong signals for aMb ions in low charge states (aMb^{9+}, aMb^{8+}) that indicate the formation of a compact apo-protein intermediate. In addition, there is a subpopulation of proteins that adopt a compact conformation, while being bound to two heme groups (labeled as 2h). Tandem MS experiments showed this species to be bound to heme dimers, not to two separate heme moieties. The observation of hMb^{9+} and hMb^{8+} ions in Fig. 4*a* indicates that even after 90 ms a subpopulation of proteins has already reached a native-like conformation. With increasing reaction time, the relative abundance of protein ions in high charge states decreases as more and more proteins adopt tightly folded conformations (Fig. 4*c*). Eventually, for $t \approx 1$ h (Fig. 4*d*), hMb^{9+} and hMb^{8+} are the only protein ions observed. The spectrum depicted in Fig. 4*d* is virtually indistinguishable from that of native (unreconstituted) hMb.

Based on the time-resolved mass spectra depicted in Fig. 4, an overall model for the myoglobin reconstitution process can be proposed (Fig. 5) (45, 47). Unfolded aMb (top row, purple) represents a conformationally heterogeneous ensemble. Individual protein chains can undergo one of three different processes, all of which result in the formation of a transient intermediate. Folding into a compact conformation without heme binding leads to a "folded" aMb species (red). Alternatively, the protein can bind to a heme

Fig. 4. Time-resolved mass spectra recorded at selected times during myoglobin reconstitution. (*a*) Spectrum of acid-unfolded aMb prior to initiation of reconstitution; (*b*) 90 ms; (*c*) 1.3 s; and (*d*) 1 h. The spectrum depicted in panel (*d*) was obtained with manual mixing. Notation: (a) apo-myoglobin (aMb); (h) holo-myoglobin (hMb); (2h) myoglobin with two heme groups attached (2hMb); (*) heme; (**) heme dimer. The charge states of selected protein ions are as indicated. The occurrence of residual heme in panel (*d*) stems from the use of a slight heme excess in the reconstitution experiment. Adapted from ref. 47. Copyright 2002 American Chemical Society.



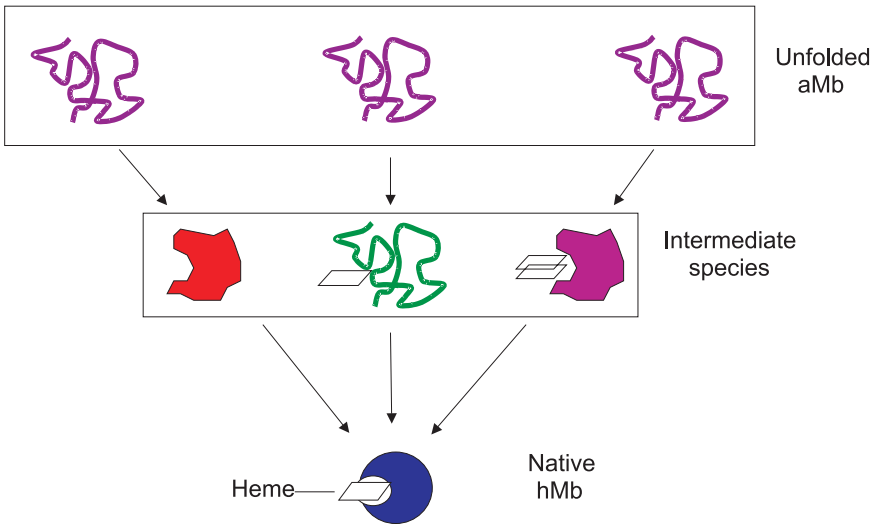
group, while maintaining a largely unfolded conformation (green). The third alternative involves the formation of proteins that are transiently bound to a heme dimer (pink). Time-resolved ESI-MS allows the detection of all of these three short-lived species in parallel, although none of them becomes strongly populated during reconstitution. The schematic representation in Fig. 5 suggests that all three intermediates are "productive", in a sense that they are direct precursors of the native state (blue). However, based on the data that are presently available we cannot strictly rule out the possible occurrence of off-pathway intermediates during myoglobin reconstitution (48).

Time-resolved ESI-MS with on-line pulse labeling

The hydrogen atoms in the NH, OH, and SH groups of a

© 2004 NRC Canada

Fig. 5. Proposed reaction mechanism for the reconstitution of holo-myoglobin from acid-unfolded apo-protein and free heme. The color coding used matches that of Fig. 4; heme is represented as a white trapezoid. Details are given in the text.



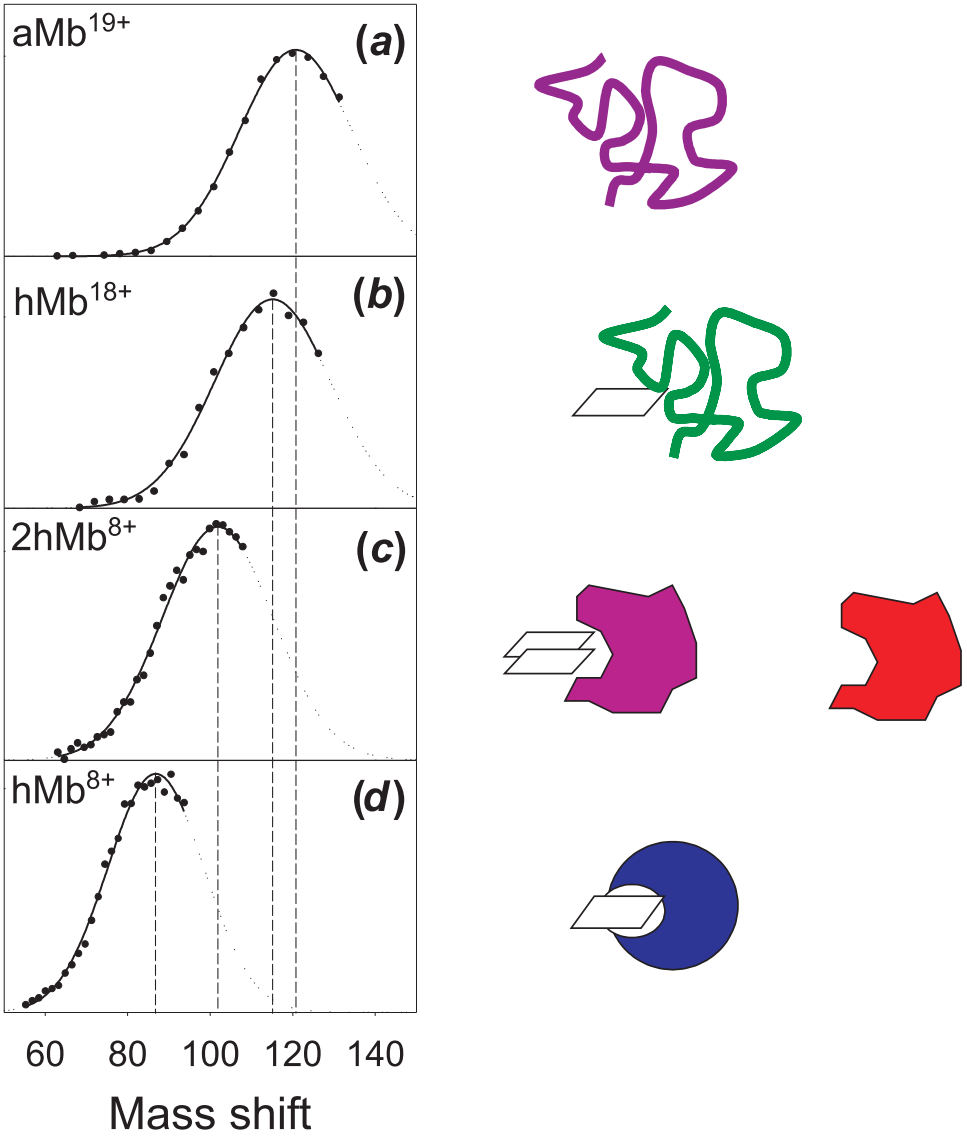
protein are labile, i.e., these sites can undergo hydrogen–deuterium exchange (HDX) when the protein is exposed to D_2O. Of particular importance for isotope exchange studies are the amide hydrogens located along the polypeptide backbone. A labile hydrogen can only undergo exchange (*i*) if it is accessible to the solvent, and (*ii*) if it is not involved in a stable hydrogen bond. Therefore, the HDX pattern of a protein depends strongly on its solution-phase conformation. The properties of short-lived folding intermediates can be probed by using pulse-labeling strategies. In these experiments, the protein is allowed to refold for a controlled period of time until it is briefly exposed to a large excess of labeling solvent. Conventionally, the labeling pulse is terminated by a rapid pH change that quenches exchange. The quenched reaction mixture can then be analyzed off-line by multidimensional NMR spectroscopy (49, 50) or by MS (31, 51). NMR measurements are based on the different nuclear spins of H (spin 1/2) and D (spin 1), while MS relies on the different mass of the two isotopes (1.0078 vs. 2.0141 Da). NMR provides spatially resolved information on the proton occupancy of individual exchangeable sites. However, the information obtained is averaged over all the protein molecules within the sample. In contrast, MS allows the detection of coexisting protein populations, such that their HDX properties can be monitored individually. Spatially resolved information can be obtained by MS when the off-line analysis of the experiment is coupled with proteolytic digestion and liquid chromatography (52), or with gas phase fragmentation techniques (53). The conventionally performed off-line analysis of pulse-labeled proteins after quenching has an inherent limitation. The conformation and ligand-binding state of individual protein molecules at the time of analysis is *not* correlated with the protein's H–D exchange pattern. As a result, ESI mass spectra of proteins that were pulse-labeled in quench-flow experiments show the same mass distribution for all charge states.

Recently, our group has shown that time-resolved ESI-MS can be used to analyze pulse-labeled proteins on-line, in a "quasi-instantaneous" fashion (47). Instead of quenching isotope exchange through a rapid mixing step, the protein solution is injected directly into the ESI source of the mass spectrometer. Here, the labeling pulse is terminated by desolvation within less than 1 ms (11). With this approach, the different charge- and ligand-binding states in the ESI mass spectrum are directly correlated with the HDX levels observed for each peak. Therefore, this technique allows the exchange behavior of different protein conformations and different ligand-binding states to be monitored with extremely high selectivity. This type of experiment requires a setup similar to that shown in Fig. 2, but with an additional on-line mixing step added immediately upstream from the ion source. Protein refolding is initiated at the first mixer, and labeling occurs at the second mixer. The refolding time is varied by changing the distance between the two mixers, while the duration of the labeling pulse is held constant at a few milliseconds.

The described on-line pulse-labeling approach was applied to study the reconstitution of acid-induced myoglobin under the conditions of Fig. 4. Selected peaks of pulse-labeled myoglobin for a reconstitution time of 240 ms are depicted in Fig. 6. As expected, the greatest extent of HDX was observed for unfolded apo-protein (e.g., aMb^{19+}, Fig. 6*a*). Ions corresponding to unfolded holo-myoglobin species in solution (Fig. 6*b*) show exchange levels slightly lower than the unfolded apo-protein. Much of this effect may be due to the steric protection of labile sites by the heme group. Ions corresponding to compact apo-protein species and those that are bound to two heme groups show a very similar exchange behavior (Fig. 6*c*). Based on their ESI charge state distributions, the two underlying solution-phase conformations are expected to have an overall compactness close to that of the native protein. However, the HDX level in Fig. 6*c* is evidently higher than that observed for native hMb (Fig. 6*d*), thus indicating that these two compact folding intermediates must exhibit a significantly perturbed structure. The fact that compact conformations can show dramatically different HDX levels demonstrates that ESI charge state distribution and HDX behavior represent com-

© 2004 NRC Canada

Fig. 6. Selected peaks observed in the mass spectrum of myoglobin that was pulse-labeled 240 ms after initiation of reconstitution. The x-axis shows the mass shift relative to the unlabeled protein. (*a*) aMb^{19+}; (*b*) hMb^{18+}; (*c*) $2hMb^{8+}$; (*d*) hMb^{8+}. Solid lines represent Gaussian fits to the experimental data. A limited number of data points on the high-mass side of the peaks could not be taken into account for the analysis because of adduct formation; these points have been omitted for clarity. Adapted with permission from ref. 47. Copyright 2002 American Chemical Society.



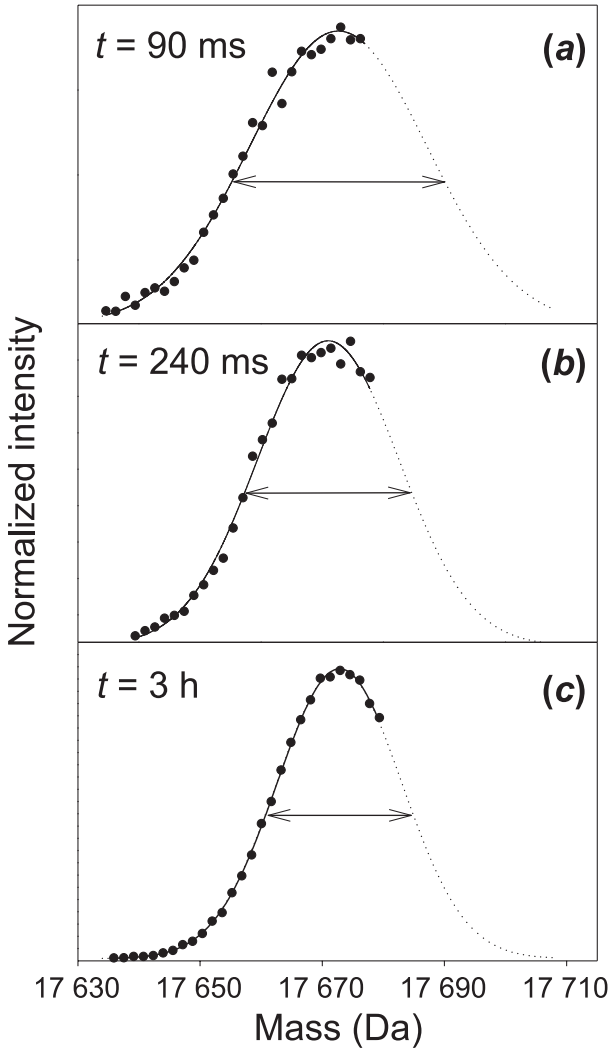
plementary, rather than redundant probes of protein structure in solution.

Figure 7 shows the peak shape of hMb^{8+} ions after pulse labeling for three different reconstitution times. As discussed previously, these ions are derived from holo-proteins in a native-like conformation. The observed peak width decreases notably as time proceeds. We attribute this observation to changes in the structural heterogeneity of the protein conformation. Following pulse labeling, a structurally heterogeneous protein ensemble will show a wider mass distribution than a homogeneous ensemble. Consequently, the data in Fig. 7 indicate that hMb^{8+} ions observed early during reconstitution are derived from solution-phase proteins in somewhat different conformations, presumably because some of them have not reached the global energy minimum of the folding funnel yet. Structural relaxation processes eventually allow all proteins to fold into the fully native state. This interpretation is consistent with the view that the energy landscapes of proteins exhibit a certain "roughness", giving rise to multiple local energy minima in the vicinity of the native conformation that can act as conformational traps (54, 55).

It is worth noting that the mass shift distributions for all the different protein species obtained after pulse labeling show a significant overlap (see Fig. 6). It is only because of the quasi-instantaneous nature of the on-line labeling–analysis strategy used that the distributions of individual species can be discerned. Different protein species appear in distinct ESI charge- and ligand-binding states, thus providing additional structural dimensions that allow the determination of individual HDX levels in a straightforward manner. In contrast, conventional quench-flow studies would have resulted

© 2004 NRC Canada

Fig. 7. Mass spectral data and Gaussian fits (solid lines) measured after pulse labeling for hMb^{8+} (*a*) 90 ms, (*b*) 240 ms, (*c*) and 3 h after initiation of reconstitution. Horizontal arrows represent FWHMs of the fitted peaks.



in broad unstructured mass distributions, and it would have been impossible to assign mass shifts to individual protein species.

Monitoring protein conformational dynamics under equilibrium conditions

HDX methods for monitoring protein dynamics

Many proteins are known to adopt partially folded conformations when they are exposed to mildly denaturing solvent conditions. These semi-denatured species are structurally heterogeneous ensembles, undergoing conformational fluctuations on various time scales. Studies on partially folded proteins are of great importance for understanding a wide range of biological processes such as amyloid formation, signal transduction, ligand binding, and protein transport across membranes (56). Interestingly, partially folded proteins under equilibrium conditions often resemble intermediates formed in kinetic experiments (57). Recent work has shown that some proteins exhibit a significant degree of disorder, even under physiological conditions where they are biologically active (58).

Experimental techniques capable of probing the dynamic nature of partially folded proteins are crucial for obtaining a better understanding of their biophysical properties. Once again, the most powerful approaches for studies in this area are based on HDX techniques (59, 60). In contrast to the pulse-labeling strategies introduced in the previous section, studies on conformational dynamics require the use of continuous-labeling approaches. For these experiments, a protein is incubated in an isotopic labeling buffer and its HDX properties are probed as a function of labeling time. For exchangeable sites that are sterically shielded from the solvent and (or) involved in stable hydrogen bonds, HDX is mediated by structural fluctuations of the protein. Therefore, the exchange kinetics are related to the conformational dynamics of the polypeptide chain. Opening–closing events mediating exchange may correspond to global or subglobal unfolding–refolding transitions, or to local fluctuations (61–63). The exchange mechanism is commonly described by Scheme 1 (64)

$$[1] \qquad X-H_{closed} \underset{k_{cl}}{\overset{k_{op}}{\rightleftharpoons}} X-H_{open} \xrightarrow[D_2O]{k_{ch}} \text{exchanged}$$

where k_{op} and k_{cl} are the rate constants for the opening and closing, respectively, of a particular exchangeable site. The intrinsic exchange rate constant (k_{ch}) represents the kinetics that would be expected for a fully unprotected hydrogen. For amide hydrogens, the k_{ch} value of any individual site depends on its neighboring amino acids and on pD. Reference data are available that allow the estimation of amide k_{ch} values for any set of solvent conditions (65). Two different exchange regimes can be distinguished, depending on whether the conformational dynamics are fast (EX2) or slow (EX1) compared to k_{ch}. In the EX2 limit, characterized by $k_{cl} >> k_{ch}$, the overall exchange rate constant (k_{ex}) is given by $k_{ex} = K_{op}k_{ch}$, where $K_{op} = (k_{op}/k_{cl})$ is the equilibrium constant of the opening reaction. Under EX2 conditions, most sites have to visit the open conformation many times before exchange occurs. Conversely, if $k_{ch} >> k_{cl}$ (EX1 regime), complete labeling will occur with the first opening event, such that $k_{ex} = k_{op}$.

NMR spectroscopy has traditionally been the method of choice for analyzing proteins in continuous-labeling experiments. However, in recent years, the use of ESI-MS for this purpose has become increasingly popular (42). One particularly attractive feature of ESI-MS is the possibility to clearly distinguish EX1 from EX2 exchange events. In the former case, spectra recorded at different times exhibit peaks corresponding to the fully labeled and the unlabeled protein, respectively. As time proceeds, the intensity ratio of these peaks changes, but not their individual mass values. In contrast, EX2 kinetics give rise to a single peak that gradually moves to higher mass as HDX proceeds (66, 67).

Conformational dynamics of semi-denatured myoglobin

In a recent study, our group has described continuous-labeling experiments by time-resolved ESI-MS on the millisecond timescale (56). These experiments employed a rapid mixing setup similar to that depicted in Fig. 2. The studies

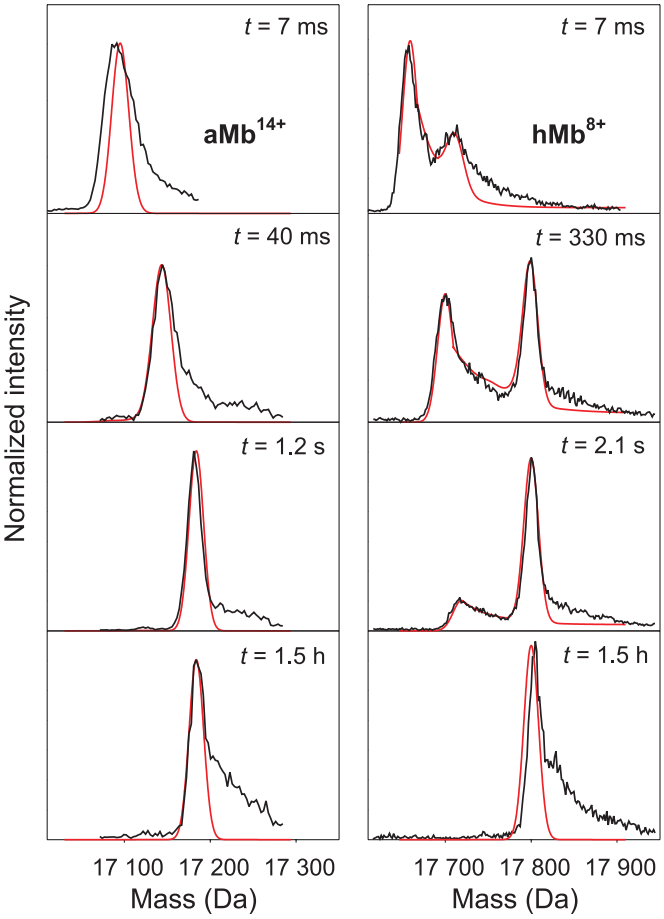
© 2004 NRC Canada

were carried out at slightly basic pD, where k_{ch} for amide hydrogens is around 650 s^{-1}. Once again, Mb was used as the model system. The formation of partially folded Mb conformations under equilibrium conditions can be promoted through the presence of an organic cosolvent. The Mb ESI mass spectrum recorded at pH 9.3 in the presence of 27% acetonitrile resembles the reconstitution spectra depicted in Figs. 4*b* and 4*c* (data not shown). Mass distributions obtained in continuous-labeling experiments for two representative ions are shown in Fig. 8. aMb^{14+} represents a semi-unfolded apo-protein species in solution. With increasing labeling time these ions shift to higher mass, indicating EX2 exchange, i.e., the occurrence of rapid unfolding–refolding events with closing rate constants $k_{cl} >> 650$ s^{-1}. A more complex exchange behavior is exhibited by hMb^{8+}, which represents a native-like conformation of the holo-protein. For labeling times up to roughly 2 s, these protein ions show bimodal mass distributions. The relative intensity of the low mass peak decreases and that of the high mass peak increases (EX1 behavior). This observation shows that the corresponding solution-phase proteins are involved in slow unfolding–refolding processes with $k_{cl} << 650$ s^{-1}. In addition, a gradual shift to higher mass is observed for both peaks, which shows that the proteins also undergo more rapid structural fluctuations (EX2 exchange).

Upon combining the data obtained in these HDX experiments with previous results from the literature, we were able to develop a detailed kinetic model for the conformational dynamics of myoglobin under the conditions of ref. 56. The HDX peak shapes predicted by this model for different exchange times are shown as red curves in Fig. 8. A simplified version of the model is shown in Fig. 9. It assumes that the Mb structure can be dissected into three distinct folding–unfolding units (48, 62). It is proposed that unit 1 encompasses the heme binding region (68), unit 3 includes the folding core (A-G-H helices) (69), while the remaining structural elements of the protein are assigned to unit 2. Each unit can be in an open (O) or in a closed (C) conformation. The two major species observed in the spectrum, semi-unfolded aMb and native-like hMb, are assigned to the structures (O,C,C) and ^{Heme}(C,C,C), respectively. The EX1 process seen for hMb^{8+} is attributed to slow opening–closing events of unit 1, presumably in conjunction with heme loss–binding. These transitions are associated with the crossing of a major free energy barrier. Rapid opening–closing events on both sides of this major barrier involve all three units and give rise to EX2 kinetics. It has been suggested that proteins may cross major free energy barriers not by surmounting them, but by circumventing them through a long diffusive journey on a multidimensional energy landscape (70). Accordingly, slow conformational transitions could be mediated by rapid, thermally activated dynamics. Such a view is consistent with the model suggested in Fig. 9, where rapid structural fluctuations on each side of a major barrier may represent conformational sampling processes that on rare occasions result in barrier crossing.

In summary, ESI-MS used in conjunction with rapid mixing techniques and on-line HDX provides an extremely powerful tool for monitoring the folding and structural dynamics of proteins. The on-line approaches described in the previous sections allow the correlation of three complementary

Fig. 8. Conformational dynamics of semi-denatured myoglobin (in water:acetonitrile, 73:27 v/v, pD 9.3) studied in continuous-labeling HDX experiments. The data show the HDX behavior for the protein ions aMb^{14+} (left) and hMb^{8+} (right) for selected time points. Noisy black lines represent experimental data. Smooth red lines are simulated peak shapes based on the kinetic model outlined in Fig. 9.



structural probes: ESI charge state distribution, ligand-binding state, and isotope exchange kinetics. All of this information is obtained simultaneously for coexisting protein conformations in solution. One limitation of the described experimental strategies is the lack of direct insights into the spatial hydrogendeuterium distribution within the protein. However, this type of information should be obtainable by on-line fragmentation of gas-phase protein ions in tandem MS experiments (53). Another important aspect are improvements of the time resolution; this goal should be achievable through the use of microfluidic devices that allow reactions to be initiated by ultra-rapid mixing (15, 71). Modifications of this kind could allow detailed studies on even the very earliest events in protein folding. Efforts in these directions are currently underway in our laboratory.

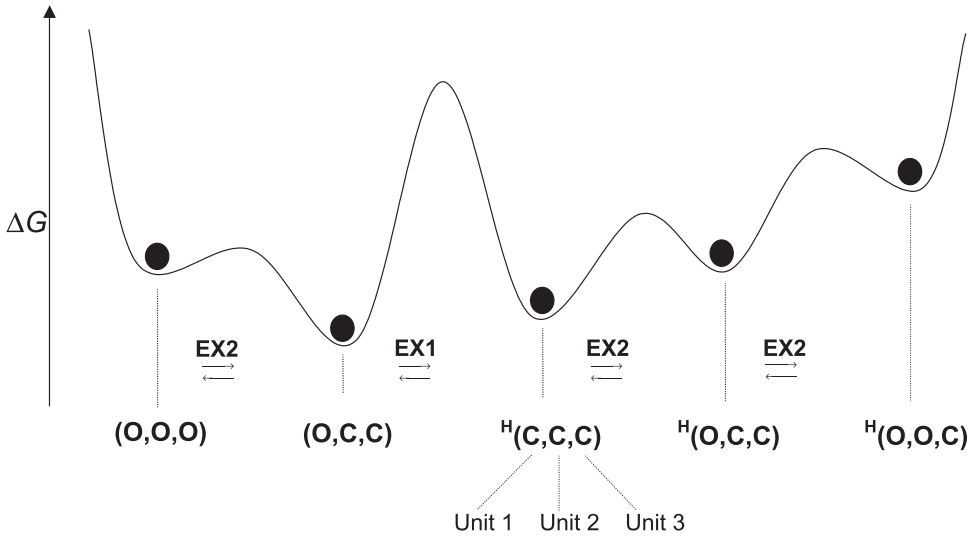
Mechanistic studies on enzyme reactions by time-resolved ESI-MS

Why study enzymes?

Enzyme catalysis is a vital component of all biological systems. Enzyme mechanisms range from simple two-step

© 2004 NRC Canada

Fig. 9. Simplified energy profile used for modeling the conformational dynamics of myoglobin under mildly denaturing conditions. Different protein conformations are represented in "vector notation", where each of the three structural units of the protein can be either open (unfolded, O) or closed (folded, C). The presence of a heme group is denoted as a superscript H.



processes to complex multistep reactions. Kinetic experiments are among the most important tools for elucidating these reaction mechanisms. Most of these studies are carried out under steady-state conditions where high time resolution is usually not required. However, kinetic experiments in the *pre*steady-state regime often provide more mechanistic information. These studies focus on the short period of time immediately following the initiation of an enzymatic reaction. It is during this period that reaction intermediates become successively populated, such that the rate constants of individual steps can be measured (16, 72, 73). Rapid mixing experiments with optical detection are a well-established tool for presteady-state kinetic experiments. However, most reactions of enzymes with their "natural" substrates cannot be studied in this way because there are no associated chromophoric changes. For this reason, kineticists often use artificial substrate analogs that undergo a color change upon turnover. Obviously, this approach is problematic because the kinetics observed with these analogs may be different from those that would be observed with the natural substrate(s). In some cases, the use of radioactively labeled substrates provides an alternative approach (74). However, radiochemical methods are somewhat cumbersome, and problems can arise due to nonspecific entrapment of the label. Kinetic studies by time-resolved ESI-MS do not require chromophoric substrates or radioactive labeling and, therefore, the application of this approach to enzymatic systems seems very attractive (17–19, 22, 75). The time resolution of this approach should be sufficient for exploring the presteady-state of a wide array of different enzyme systems.

Kinetics of chymotrypsin-catalyzed reactions

We explored the application of our rapid mixing system (Fig. 2) in experiments on chymotrypsin (76). This enzyme is a serine protease, with Ser_{195} representing the reactive nucleophile (77). Although the physiological role of chymotrypsin is to serve as an endopeptidase, it also catalyzes the hydrolysis of esters including numerous synthetic substrate analogs. The generally accepted reaction mechanism for chymotrypsin-catalyzed hydrolysis is depicted in Scheme 2 (72, 73, 78).

$$[2]\quad E_{free} + S \underset{}{\overset{K_d}{\rightleftharpoons}} ES \xrightarrow{k_2} EP_2 \xrightarrow{k_3} E_{free} + P_2$$
$$\qquad\qquad\qquad\qquad\qquad\qquad\quad \downarrow$$
$$\qquad\qquad\qquad\qquad\qquad\qquad\quad P_1$$

In the first step of this reaction sequence, the free enzyme E_{free} and the substrate S form a noncovalent enzyme–substrate complex (ES) that is characterized by the dissociation constant K_d. Subsequently, Ser_{195} forms a covalent bond with the carbonyl carbon of the substrate, thus releasing the first hydrolysis product P_1. The rate constant of this acylation step is denoted as k_2. The subsequent deacylation has a rate constant of k_3 and it leads to regeneration of the free enzyme by hydrolysis of the Ser_{195}–ester bond, through release of the second hydrolysis product P_2. For conditions where S is present in large excess, it can be shown that the concentration of EP_2 as a function of time t in the presteady-state regime is given by (72, 73)

$$[3]\quad [EP_2](t) = A(1 - \exp(-k_{obs}t))$$

Consequently, the sum of the concentrations of E_{free} and ES are given by

$$[4]\quad ([E_{free}] + [ES])(t) = B\exp(-k_{obs}t) + C$$

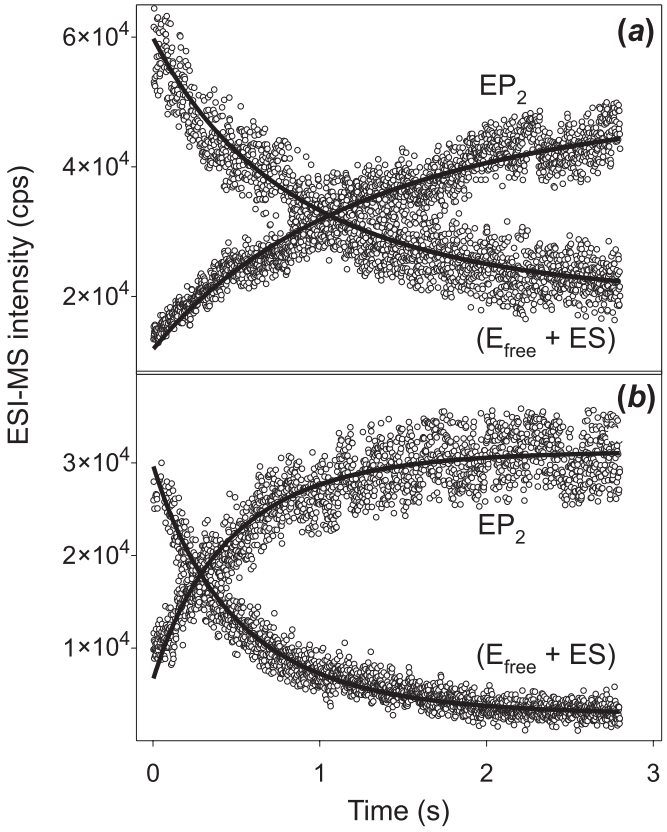
A, B, and C in these expressions are constants and k_{obs} can be expressed as

$$[5]\quad k_{obs} = k_3 + \frac{k_2[S]}{K_d + [S]}$$

where [S] is the substrate concentration. Measurements of k_{obs} as a function of substrate concentration should allow the determination of the parameters k_2, k_3, and K_d in Scheme 2. For $t >> 1/k_{obs}$, the exponential terms in eqs. [3] and [4] become negligible, thus marking the transition from the presteady-state to the steady-state regime.

© 2004 NRC Canada

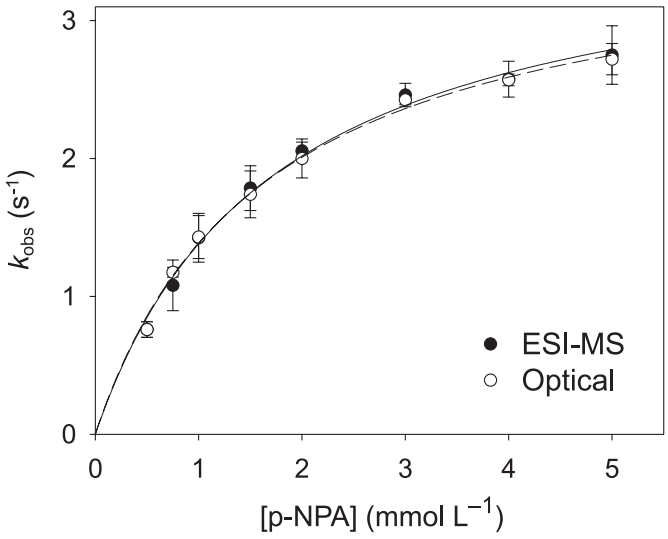
Fig. 10. Presteady-state kinetics of *p*-NPA hydrolysis by chymotrypsin monitored by ESI-MS. The two panels depict the depletion of unmodified enzyme (E_{free} + ES), and the formation of acetylated chymotrypsin (EP_2), at substrate concentrations of (*a*) 1 mmol L^{-1} and (*b*) 5 mmol L^{-1}. The data were obtained by monitoring the 12^+ charge state of free and acetylated enzyme at *m*/*z* 2103 and 2107, respectively. Solid lines are fits to the experimental data based on eqs. [3] and [4]. Adapted with permission from ref. 76. Copyright 2004 American Chemical Society.



For testing the applicability of our rapid mixing ESI-MS setup to studies on chymotrypsin kinetics, a two-step strategy was used (76). We initially monitored the hydrolysis of the chromophoric substrate *para*-nitrophenyl acetate (*p*-NPA) to *para*-nitrophenol (*p*-NP) and acetate. In the framework of Scheme 2, *p*-NP corresponds to P_1, and acetate corresponds to P_2. *p*-NPA was chosen as the substrate because the released *p*-NP has an intense yellow color, thus providing a way to compare the ESI-MS-based kinetic experiments with the results of optical control experiments. Subsequently, we studied the chymotrypsin-catalyzed hydrolysis of a peptide that cannot be monitored by optical means.

Figure 10 shows ESI-MS presteady-state kinetics obtained for two different *p*-NPA concentrations. The signals monitored in these experiments correspond to the accumulation of the acetylated enzyme (EP_2) and the decay of the free- and substrate-bound chymotrypsin (E_{free} + ES). The kinetics obtained for a *p*-NPA concentration of 1 mmol L^{-1} (Fig. 10*a*) are notably slower than those for a substrate concentration of 5 mmol L^{-1} (Fig. 10*b*). The dependence of the measured k_{obs} values on the *p*-NPA concentration is depicted in Fig. 11. These data can be fitted according to eq. [5], resulting in a

Fig. 11. Measured k_{obs} values for *p*-NPA hydrolysis by chymotrypsin as a function of substrate concentration. Solid circles represent ESI-MS measurements; open circles depict values determined by optical stopped-flow spectroscopy. Fits to these k_{obs} values based on eq. [5] are given as a solid line for the ESI-MS kinetics and as a dashed line for the optical data. Adapted with permission from ref. 76. Copyright 2004 American Chemical Society.



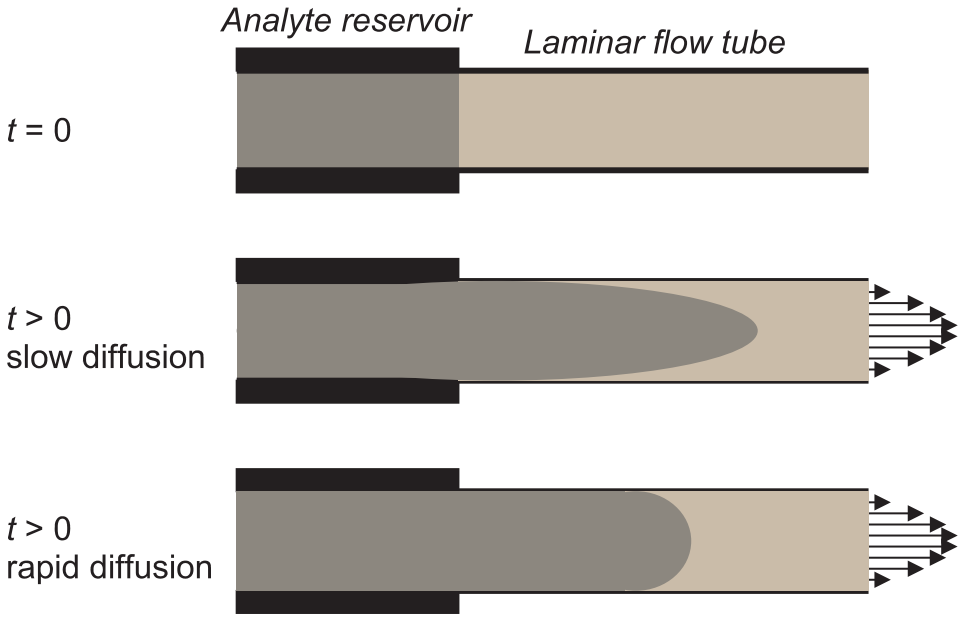
K_d value of (1.6 ± 0.2) mmol L^{-1} and a rate constant k_2 of (3.5 ± 0.3) s^{-1}. Unfortunately, k_3 is too small to be determined by this method (the y-axis intercept of the curves in Fig. 11 is close to zero). These results show the deacylation step (k_3) to be rate limiting for the hydrolysis of *p*-NPA by chymotrypsin. Also shown in Fig. 11 are the results of control experiments where the release of *p*-NP was monitored by optical stopped-flow spectroscopy. The corresponding values of K_d and k_2 are very close to those obtained by ESI-MS, (1.6 ± 0.1) mmol L^{-1} and (3.6 ± 0.2) s^{-1}, respectively.

The chymotrypsin-catalyzed hydrolysis of the non-chromophoric peptide bradykinin results in the release of the N-terminal arginine residue. In contrast to the *p*-NPA data described above, acylation (k_2) was found to be rate limiting for the hydrolysis of this peptide bond, such that the EP_2 complex in Scheme 2 cannot accumulate. Because this scenario precludes a presteady-state analysis of the reaction, time-resolved ESI-MS was used to monitor the production of the hydrolysis products under steady-state conditions, resulting in a Michaelis constant of K_M = (0.51 ± 0.08) mmol L^{-1} and a k_{cat} value of (43 ± 2) s^{-1} (data not shown) (76).

These results clearly demonstrate the feasibility of kinetic measurements on enzymatic systems by time-resolved ESI-MS. One limitation of the current on-line method is its incompatibility with high concentrations of salts, buffers, and other solvent additives that have detrimental effects on the ionization process (79). Currently, this factor does not permit MS experiments to be carried out at physiological salt concentrations. The development of rapid desalting devices (79), fused droplet ESI (80), or on-line MALDI-MS methods (81) is likely to provide ways to overcome this limitation in the foreseeable future.

© 2004 NRC Canada

Fig. 12. Diagram illustrating how solution-phase diffusion coefficients can be determined by ESI-MS. A thin capillary tube is initially filled with solution having a low analyte concentration. The tube inlet is then connected to a reservoir that contains analyte solution at a higher concentration, thus generating a sharp boundary between the two solutions (top panel). Subsequently, solution is pumped from the reservoir into the tube. Laminar flow leads to a parabolic flow velocity distribution within the tube, i.e., the flow velocity in the capillary center is highest, whereas it is zero at the tube walls (indicated by the arrows in the middle and bottom panels). This velocity distribution leads to a dispersion of the initially sharp boundary between the two solutions. However, radial diffusion of analyte molecules counteracts this dispersion, because the molecules constantly migrate between zones of different flow velocity. This compensating effect is relatively small in the case of slow diffusion (middle panel), but it is large in the case of rapid diffusion (bottom panel). Diffusion coefficients can thus be determined by monitoring the analyte signal intensity at the tube outlet by ESI-MS. All of the dispersion profiles obtained in this way have a sigmoidal appearance. Analytes with small diffusion coefficients D show more extended profiles than those with larger values of D. It is noted that the effects of *axial* diffusion are negligible under typical operating conditions (99).



Noncovalent ligand–protein interactions probed by ESI-MS-based diffusion measurements

Noncovalent interactions

The previous chapters of this review have described various strategies for studying rapid processes in biochemical systems. The key to observing events in the range of milliseconds to seconds was the use of ESI-MS in conjunction with on-line rapid mixing techniques. This final chapter will focus on measurements that take place on somewhat longer timescales. It will be demonstrated how ESI-MS can be used for monitoring the diffusion behavior of biological molecules, and how measurements of this type can provide information on how these molecules interact with each other in solution.

Numerous physiological processes are mediated by noncovalent interactions involving biological macromolecules; examples include signaling and regulation, immune response, protein biosynthesis, and enzyme catalysis. Many drugs act by noncovalently binding to proteins or other biopolymers, often mimicking structural features of naturally occurring ligands (82). Experimental methods capable of monitoring these interactions are of great importance. Of particular interest is the identification of high-affinity ligands for macromolecular drug targets in high-throughput screening tests of compound libraries (83, 84).

The myoglobin studies summarized previously attest to the fact that ESI-MS is a sensitive and highly selective approach for monitoring ligand–protein interactions. This is in line with a large number of other studies, all confirming that numerous noncovalent complexes can survive the ESI process, thus making them amenable to direct mass spectrometric analysis (4, 43, 85). However, it is well-known that the presence of noncovalent complexes in solution is *not always* correlated with the observation of the corresponding species in the mass spectrum. "False-negative" results are obtained when solution-phase complexes dissociate prior to detection. Noncovalent binding partners that are held together primarily by hydrophobic interactions are thought to be particularly prone to dissociation during ESI, whereas electrostatic complexes are often considered to be more stable (86). On the other hand, extensive dissociation during ESI is also observed for some electrostatically stabilized complexes, even under the most gentle ionization conditions (87). ESI-MS can also produce "false-positive" results, as some analytes tend to form noncovalent gas-phase assemblies during ESI, despite the nonexistence of the corresponding complexes in solution (88–90). These considerations imply that the pres-

© 2004 NRC Canada

ence or absence of noncovalent complex ions in an ESI mass spectrum does not always allow conclusions to be drawn regarding specific solution-phase interactions. It appears that this issue is at least partly responsible for the limited acceptance of ESI-MS as a general tool for "mix and measure" experiments in the context of high-throughput screening tests (84). Not surprisingly, the development of alternative techniques for monitoring ligand–protein interactions is an area of great interest (91–93).

Noncovalent interactions and diffusion

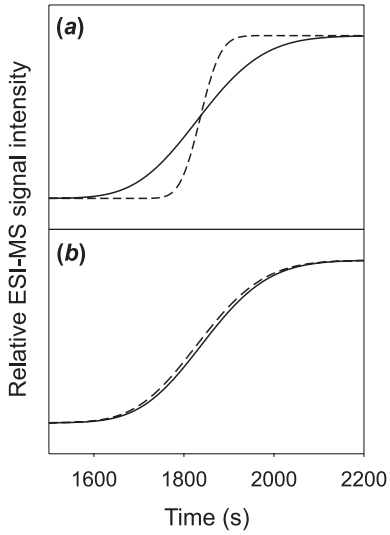
A number of optical and NMR-based techniques make use of the fact that noncovalent interactions affect the diffusion behavior of ligands that bind to a target macromolecule. Typically, the potential ligands used in screening assays are relatively small compounds that have large diffusion coefficients, as long as they are free in solution. However, once a ligand is bound to a protein or nucleic acid target, its translational motions will be governed by the slow diffusion of the macromolecule. In other words, *noncovalent binding will drastically reduce the diffusion coefficient of the ligand*. This phenomenon can be exploited for the screening of compound libraries by fluorescence correlation spectroscopy (94, 95) and diffusion-ordered nuclear magnetic resonance spectroscopy (DOSY-NMR) (83).

Unfortunately, many of the existing screening methods suffer from certain limitations. Fluorescence-based approaches are only applicable in cases where suitable chromophores are available. The selectivity of NMR techniques may be limited by overlapping analyte resonances, especially when studying mixtures of structurally related compounds (83). In addition, analyte concentrations in the millimolar range are often required for NMR. Not only does this result in large sample consumption, but also nonspecific aggregation may become an issue. Other methods for studying noncovalent interactions, such as affinity chromatography and surface-plasmon resonance-based assays require the chemical immobilization of ligand or target molecules on a solid support, which may impede binding because of restrictions in the orientation of the immobilized molecules. Furthermore, nonspecific binding to carrier materials may occur (96). Our group has devised an approach for monitoring noncovalent interactions that may help to overcome these limitations. It is based on diffusion measurements of analytes in solution by ESI-MS.

Measuring diffusion coefficients by ESI-MS

Initially, we will contemplate a single analyte species in solution to illustrate how solution-phase diffusion coefficients can be measured by ESI-MS (Fig. 12). The extension of this approach to studies on noncovalent interactions will be straightforward. Consider the case where analyte solution is infused into a capillary tube that has previously been filled with another solution containing the same analyte, but at a different concentration. Because of the laminar flow conditions within the tube, the flow velocity distribution is parabolic. This leads to a dispersion of the initially sharp boundary between the two solutions as liquid flows through the tube. However, diffusion causes a constant radial mixing of analyte molecules, thereby counteracting the dispersion because of laminar flow (97, 98). The outlet of the tube is connected to the ESI source of a mass spectrometer, where the signal intensity of the analyte is monitored as a function of time. The resulting dispersion profile shows a sigmoidal intensity transition from low to high or from high to low, depending on the concentrations of the two solutions used. The diffusion coefficient of the analyte can be determined from a fit to the measured profile. Analytes with large diffusion coefficients will show relatively steep transitions, whereas smaller diffusion coefficients result in more extended dispersion profiles (99). Figure 13*a* represents simulated profiles for a small molecule and a ligand that do not interact with each other in solution, such that the diffusion behavior of the two species is independent. In contrast, Fig. 13*b* depicts the situation expected for tight noncovalent binding between the two species. In the latter case, the diffusion of the (small) ligand is governed by the Brownian motion of the (large) protein. The profile of the ligand will become more extended upon complex formation and it will approach the profile exhibited by the protein. Unlike conventional ESI-MS studies on noncovalent complexes, this approach does *not* rely on the preservation of solution-phase interactions in the gas phase. In fact, very harsh conditions are employed at the ion source to disrupt any residual interactions, thereby ensuring that the dispersion profiles of individual analytes can be monitored separately (100).

Fig. 13. Simulated dispersion profiles, representing the ESI-MS signal intensity of two analytes at the end of a laminar flow tube under different conditions. (*a*) Dispersion profiles expected for a protein ($D = 1 \times 10^{-10}$ m^2/s, solid curve) and a small molecule ($D = 10 \times 10^{-10}$ m^2/s, dashed curve). It is assumed that the two analytes do *not* interact in solution. (*b*) Dispersion profiles as in panel *a*, but under the assumption of tight noncovalent binding between the two analytes. Under these conditions the profiles measured for the two species will be identical (for better visualization, one of the profiles has been slightly shifted).



Screening of libraries for binding to a protein target

The described approach was tested in experiments that monitored the noncovalent binding of mono-, di-, and trisaccharides to lysozyme (101). This 129 amino acid protein (MW 14.3 kDa) hydrolyzes polysaccharides containing *N*-

© 2004 NRC Canada

Fig. 14. Dispersion profiles of NAG_3 recorded (*a*) in the absence and (*b*) in the presence of lysozyme. Solid lines represent fits to the experimental based on eq. [17] of ref. 99. Close inspection reveals that the profile depicted in panel *b* is more extended than that in panel *a*. Adapted with permission from ref. 101. Copyright 2004 American Chemical Society.

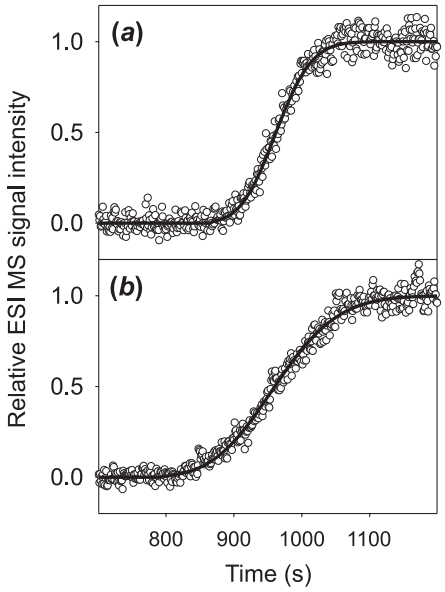
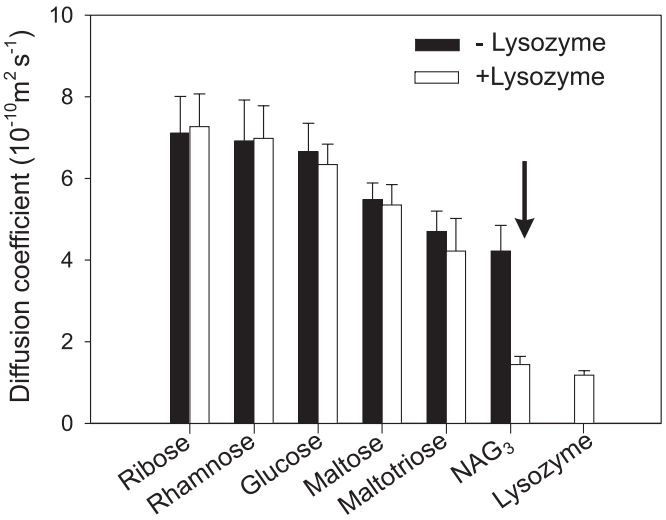


Fig. 15. Diffusion coefficients of saccharides determined from ESI-MS dispersion profiles measured in the absence (black bars) and in the presence (white bars) of lysozyme. Only NAG_3 shows a significant change upon addition of the protein, as indicated by the arrow. The diffusion coefficient of lysozyme is shown for comparison. Adapted with permission from ref. 101. Copyright 2004 American Chemical Society.



acetylated monomers (102). Short oligomers of *N*-acetyl glucosamine (NAG) represent competitive inhibitors of lysozyme. In our experiments, we monitored the diffusion behavior of six different saccharides (ribose, rhamnose, glucose, maltose, maltotriose, and NAG_3) in parallel. In an initial run, the dispersion profiles of all these compounds were monitored in the absence of the protein receptor; subsequently, they were repeated in the presence of lysozyme. For five of the saccharides, dispersion profiles recorded with and without the protein were indistinguishable, thus indicating that their diffusion behavior is independent of the presence of lysozyme. Only for NAG_3, the profile recorded in the presence of the protein was significantly more extended than that observed in a protein-free solution (Fig. 14). This result shows that of the six compounds tested, only NAG_3 forms a noncovalent complex with lysozyme. The results of this screening experiment are summarized in Fig. 15, where the diffusion coefficients of all compounds measured with and without lysozyme are depicted.

The successful application of this approach for screening a small "compound library" strongly indicates that this experimental technique might become an interesting alternative to existing methods for monitoring noncovalent interactions. Automation of the described diffusion-based method could provide a new and powerful tool for the high-throughput screening of compound libraries, with possible applications in the area of drug discovery. ESI-MS dispersion measurements are not necessarily restricted to water-soluble proteins; studies on nucleic acids, solubilized membrane receptors, or on entire organelles may also be feasible. Another interesting aspect is the determination of dissociation constants directly from the measured dispersion profiles (103). These and other research directions are currently being explored in our laboratory.

Conclusions

This review has summarized some recent developments in the area of biological MS. The combination of on-line rapid mixing with ESI-MS provides a unique opportunity to probe the structure and function of biological systems as a function of time. These *dynamic* studies are in contrast to most traditional MS-based approaches that provide a static picture of the system under investigation. Time-dependent changes of proteins and other biological molecules include folding and unfolding processes, structural fluctuations, and transient chemical modifications. The diffusion behavior of biological molecules in solution also represents a dynamic feature. It has been demonstrated how diffusion measurements can reveal the occurrence of intermolecular binding events. Much remains to be learned and explored, and it may take researchers considerable time to fully understand the intricate factors determining the structure and function of biological molecules and assemblies. In any case, MS-based approaches are certain to play an ever increasing role for these endeavors, not only in bioanalytical and biophysical chemistry, but also in many other areas.

Acknowledgments

Over the last couple of years, the author has had the privilege of working with a number of extremely talented undergraduates, graduate students, and post-doctoral fellows. In particular, the contributions of Sonya M. Clark, Beata M. Kolakowski, Douglas A. Simmons, and Derek J. Wilson deserve special recognition. We gratefully acknowledge financial support of our work by the Natural Sciences and

© 2004 NRC Canada

Engineering Research Council of Canada (NSERC), the Canada Foundation for Innovation, the Provincial Government of Ontario, The University of Western Ontario, and by the Canada Research Chairs Program.

References

1. J.B. Fenn. Angew. Chem. Int. Ed. **42**, 3871 (2003).
2. M. Karas and F. Hillenkamp. Anal. Chem. **60**, 2299 (1988).
3. K. Tanaka. Angew. Chem. Int. Ed. **42**, 3861 (2003).
4. J.A. Loo. Int. J. Mass Spectrom. **200**, 175 (2000).
5. A.A. Rostom, P. Fucini, D.R. Benjamin, R. Juenemann, K.H. Nierhaus, F.U. Hartl, C.M. Dobson, and C.V. Robinson. Proc. Natl. Acad. Sci. U.S.A. **97**, 5185 (2000).
6. S.D. Fuerstenau, W.H. Benner, J.J. Thomas, C. Brugidou, B. Bothner, and G. Siuzdak. Angew. Chem. Int. Ed. **40**, 542 (2001).
7. M. Guilhaus, D. Selby, and V. Mlynski. Mass Spectrom. Rev. **19**, 65 (2000).
8. A.G. Marshall, C.L. Hendrickson, and G.S. Jackson. Mass Spectrom. Rev. **17**, 1 (1998).
9. R. Aebersold and M. Mann. Nature (London), **422**, 198 (2003).
10. M.S. Boguski and M.W. McIntosh. Nature (London), **422**, 233 (2003).
11. P. Kebarle and Y. Ho. *In* Electrospray ionization mass spectrometry. *Edited by* R.B. Cole. John Wiley and Sons, Inc., New York. 1997. pp. 3–63.
12. L. Konermann, E.A. Silva, and O.F. Sogbein. Anal. Chem. **73**, 4836 (2001).
13. T.L. Constantopoulos, G.S. Jackson, and C.G. Enke. Anal. Chim. Acta, **406**, 37 (2000).
14. M. Gruebele. Annu. Rev. Phys. Chem. **50**, 485 (1999).
15. J.B. Knight, A. Vishwanath, J.P. Brody, and R.H. Austin. Phys. Rev. Lett. **80**, 3863 (1998).
16. L. Konermann and D.J. Douglas. Methods Enzymol. **354**, 50 (2002).
17. D.B. Northrop and F.B. Simpson. Bioorg. Med. Chem. **5**, 641 (1997).
18. D.L. Zechel, L. Konermann, S.G. Withers, and D.J. Douglas. Biochemistry, **37**, 7664 (1998).
19. E.D. Lee, W. Mück, J.D. Henion, and T.R. Covey. J. Am. Chem. Soc. **111**, 4600 (1989).
20. B.M. Kolakowski, D.A. Simmons, and L. Konermann. Rapid Commun. Mass Spectrom. **14**, 772 (2000).
21. B.M. Kolakowski and L. Konermann. Anal. Biochem. **292**, 107 (2001).
22. A.A. Paiva, R.F. Tilton, G.P. Crooks, L.Q. Huang, and K.S. Anderson. Biochemistry, **36**, 15 472 (1997).
23. H. Ørsnes, T. Graf, and H. Degn. Anal. Chem. **70**, 4751 (1998).
24. D.J. Wilson and L. Konermann. Anal. Chem. **75**, 6408 (2003).
25. H. Roder and M.C.R. Shastry. Curr. Opin. Struct. Biol. **9**, 620 (1999).
26. L. Konermann. *In* Encyclopedia of life sciences [online]. Available from http://www.els.net. Nature Publishing Group, London. 2003.
27. C.B. Anfinsen. Science (Washington, D.C.), **181**, 223 (1973).
28. R.H. Pain. Mechanisms of protein folding. 2nd ed. Oxford University Press, New York. 2000.
29. C.M. Dobson. Nature (London), **426**, 884 (2003).
30. K.A. Dill and H.S. Chan. Nat. Struct. Biol. **4**, 10 (1997).
31. L. Konermann and D.A. Simmons. Mass Spectrom. Rev. **22**, 1 (2003).
32. K.W. Plaxco, K.T. Simons, I. Ruczinski, and D. Baker. Biochemistry, **39**, 11 177 (2000).
33. R.L. Baldwin and G.D. Rose. Trends Biochem. Sci. **24**, 77 (1999).
34. A. Bachmann and T. Kiefhaber. J. Mol. Biol. **306**, 375 (2001).
35. Y. Bai. Biochem. Biophys. Res. Comm. **305**, 785 (2003).
36. S.W. Englander, T.R. Sosnick, L.C. Mayne, M. Shtilterman, P.X. Qi, and Y. Bai. Acc. Chem. Res. **31**, 737 (1998).
37. B.A. Shoemaker, J.J. Portman, and P.G. Wolynes. Proc. Natl. Acad. Sci. U.S.A. **97**, 8868 (2000).
38. G.M. Verkhivker, D. Bouzida, D.K. Gehlhaar, P.A. Rejto, S.T. Freer, and P.W. Rose. Proc. Natl. Acad. Sci. U.S.A. **100**, 5148 (2003).
39. P. Wittung-Stafshede. Acc. Chem. Res. **35**, 201 (2002).
40. S.K. Chowdhury, V. Katta, and B.T. Chait. J. Am. Chem. Soc. **112**, 9012 (1990).
41. L. Konermann, B.A. Collings, and D.J. Douglas. Biochemistry, **36**, 5554 (1997).
42. I.A. Kaltashov and S.J. Eyles. Mass Spectrom. Rev. **21**, 37 (2002).
43. V. Katta and B.T. Chait. J. Am. Chem. Soc. **113**, 8534 (1991).
44. H. Vis, U. Heinemann, C.M. Dobson, and C.V. Robinson. J. Am. Chem. Soc. **120**, 6427 (1998).
45. V.W.S. Lee, Y.-L. Chen, and L. Konermann. Anal. Chem. **71**, 4154 (1999).
46. D.R. Gumerov, A.B. Mason, and I.A. Kaltashov. Biochemistry, **42**, 5421 (2003).
47. D.A. Simmons and L. Konermann. Biochemistry, **41**, 1906 (2002).
48. V. Tsui, C. Garcia, S. Cavagnero, G. Siuzdak, H.J. Dyson, and P.E. Wright. Protein Sci. **8**, 45 (1999).
49. H. Roder, G.A. Elöve, and S.W. Englander. Nature (London), **335**, 700 (1988).
50. J.B. Udgaonkar and R.L. Baldwin. Nature (London), **335**, 694 (1988).
51. A. Miranker, C.V. Robinson, S.E. Radford, R. Aplin, and C.M. Dobson. Science (Washington, D.C.), **262**, 896 (1993).
52. H. Yang and D.L. Smith. Biochemistry, **36**, 14 992 (1997).
53. J.K. Hoerner, H. Xiao, A. Dobo, and I.A. Kaltashov. J. Am. Chem. Soc. **126**, 7709 (2004).
54. G.U. Nienhaus, J.D. Müller, B.H. McMahon, and H. Frauenfelder. Physica D: (Amsterdam), **107**, 297 (1997).
55. H. Frauenfelder, S.G. Sligar, and P.G. Wolynes. Science (Washington, D.C.), **254**, 1598 (1991).
56. D.A. Simmons, S.D. Dunn, and L. Konermann. Biochemistry, **42**, 5896 (2003).
57. T.M. Raschke and S. Marqusee. Nat. Struct. Biol. **4**, 298 (1997).
58. P.E. Wright and H.J. Dyson. J. Mol. Biol. **293**, 321 (1999).
59. S.W. Englander, L.M. Bai, and T.R. Sosnick. Protein Sci. **6**, 1101 (1997).
60. J.R. Engen and D.L. Smith. Anal. Chem. **73**, 256A (2001).
61. R. Li and C. Woodward. Protein Sci. **8**, 1571 (1999).
62. S.W. Englander, L. Mayne, and J.N. Rumbley. Biophys. Chem. **101–102**, 57 (2002).
63. H. Maity, W.K. Lim, J.N. Rumbley, and S.W. Englander. Protein Sci. **12**, 153 (2003).
64. A. Hvidt and S.O. Nielsen. Adv. Protein Chem. **21**, 287 (1966).
65. Y. Bai, J.S. Milne, L. Mayne, and S.W. Englander. Proteins: Struct. Funct. Genet. **17**, 75 (1993).
66. A. Miranker, C.V. Robinson, S.E. Radford, and C.M. Dobson. FASEB J. **10**, 93 (1996).
67. D.M. Ferraro, N.D. Lazo, and A.D. Robertson. Biochemistry, **43**, 587 (2004).

© 2004 NRC Canada

68. D. Eliezer, J. Yao, H.J. Dyson, and P.E. Wright. Nat. Struct. Biol. **5**, 148 (1998).
69. F.M. Hughson, P.E. Wright, and R.L. Baldwin. Science (Washington, D.C.), **249**, 1544 (1990).
70. K. Döring, T. Surrey, S. Grunewald, E. John, and F. Jähnig. Protein Sci. **9**, 2246 (2000).
71. R.D. Oleschuk and D.J. Harrison. Trends Anal. Chem. **19**, 379 (2000).
72. A. Fersht. Structure and mechanism in protein science. W.H. Freeman and Co., New York. 1999.
73. K. Hiromi. Kinetics of fast enzyme reactions: Theory and practice. John Wiley and Sons, New York, Chichester, Brisbane, Toronto. 1979.
74. K.S. Anderson, J.A. Sikorski, and K.A. Johnson. Biochemistry, **27**, 7395 (1988).
75. Z. Li, A.K. Sau, S. Shen, C. Whitehouse, T. Baasov, and K.S. Anderson. J. Am. Chem. Soc. **125**, 9938 (2003).
76. D.J. Wilson and L. Konermann. Anal. Chem. **76**, 2537 (2004).
77. D.M. Blow. Acc. Chem. Res. **9**, 145 (1976).
78. G. Zubay. Biochemistry. 4th ed. Wm. C. Brown, Dubuque, Iowa. 1998.
79. N. Xu, Y. Lin, S.A. Hofstadler, D. Matson, C.J. Call, and R.D. Smith. Anal. Chem. **70**, 3553 (1998).
80. D.-Y. Chang, C.-C. Lee, and J. Shiea. Anal. Chem. **74**, 2465 (2002).
81. M. Brivio, R.H. Fokkens, W. Verboom, D.N. Reinhoudt, N.R. Tas, M. Goedbloed, and A. van den Berg. Anal. Chem. **74**, 3972 (2002).
82. S.R. George, B.F. O'Dowd, and S.P. Lee. Nat. Rev. Drug Discovery **1**, 808 (2002).
83. P. Hajduk, R.P. Meadows, and S.W. Fesik. Q. Rev. Biophys. **32**, 211 (1999).
84. J. Wölcke and D. Ullmann. Drug Discovery Today, **6**, 637 (2001).
85. M.G. McCammon and C.V. Robinson. Curr. Opin. Chem. Biol. **8**, 60 (2004).
86. C.V. Robinson, E.W. Chung, B.B. Kragelund, J. Knudsen, R.T. Aplin, F.M. Poulsen, and C.M. Dobson. J. Am. Chem. Soc. **118**, 8646 (1996).
87. M.R. Mauk, A.G. Mauk, Y.-L. Chen, and D.J. Douglas. J. Am. Soc. Mass Spectrom. **13**, 59 (2002).
88. J.B. Cunniff and P. Vouros. J. Am. Soc. Mass Spectrom. **6**, 437 (1995).
89. R. Juraschek, T. Dulcks, and M. Karas. J. Am. Soc. Mass Spectrom. **10**, 300 (1999).
90. P. Hu, Q.-Z. Ye, and J. A. Loo. Anal. Chem. **66**, 4190 (1994).
91. P.A. Wabnitz and J.A. Loo. Rapid Commun. Mass Spectrom. **16**, 85 (2002).
92. D.C. Schriemer, D.R. Bundle, L. Li, and O. Hindsgaul. Angew. Chem. Int. Ed. **37**, 3383 (1998).
93. M. Entzeroth. Curr. Opin. Pharmacol. **3**, 522 (2003).
94. G. Gradl, R. Guenther, and S. Sterrer. BioMethods (Basel), **10**, 331 (1999).
95. R. Rigler. J. Biotechnol. **41**, 177 (1995).
96. G. Fassina. *In* Encyclopedia of life sciences [online]. Available from http://www.els.net. Nature Publishing Group, London. 2001.
97. G. Taylor. Proc. R. Soc. London Ser. A, **219**, 186 (1953).
98. L. Konermann. J. Phys. Chem. A, **103**, 7210 (1999).
99. S.M. Clark, D.G. Leaist, and L. Konermann. Rapid. Commun. Mass Spectrom. **16**, 1454 (2002).
100. S.M. Clark and L. Konermann. J. Am. Soc. Mass Spectrom. **14**, 430 (2003).
101. S.M. Clark and L. Konermann. Anal. Chem. **76**, 1257 (2004).
102. B. Ganem, Y.-T. Li, and J.D. Henion. J. Am. Chem. Soc. **113**, 7818 (1991).
103. S.M. Clark and L. Konermann. Anal. Chem. **76**, 7077 (2004).

© 2004 NRC Canada

The synthesis of some mechanistic probes for sialic acid processing enzymes and the labeling of a sialidase from *Trypanosoma rangeli*

Andrew G. Watts and Stephen G. Withers

Abstract: Sialyl hydrolases, *trans*-sialidases, and sialyl transferases are biologically important enzymes that are responsible for the incorporation and removal of sialic acid residues, which decorate many cell surface glycocongugates. Two fluorinated sialic acid derivatives have been synthesized as mechanism-based inactivators, to probe the catalytic mechanisms through which sialidases and *trans*-sialidases operate. Both compounds are known to be covalent inactivators of a *trans*-sialidase from *Trypanosoma cruzi*. Here, 3-fluorosialosyl fluoride has been found to covalently label the catalytic nucleophile of a sialidase from *T. rangeli*, and the residue involved is shown to be Tyr346 within the sequence DENSGYSSVL. This is the first demonstration that sialidases operate through a covalent glycosyl-enzyme intermediate, strongly suggesting a common catalytic mechanism amongst all members of the sialidase superfamily. CMP-3-fluorosialic acid is a competitive inhibitor of sialyl transferases and was synthesized via a two-step enzymatic process from commercially available *N*-acetyl mannosamine, 3-fluoropyruvic acid, and cytidine triphosphate in around 84% yield.

Key words: sialidase, mechanism, labeling, nucleophile, inhibitor.

Résumé : Les hydrolases de sialyle, les sialidases *trans* et les transférases de sialyle, sont des enzymes biologiquement importants qui sont responsables de l'incorporation et de l'élimination des résidus d'acide sialique qui décorent plusieurs glycoconjugués de la surface des cellules. Dans le but d'étudier les mécanismes catalytiques par lesquels les sialidases et les sialidases *trans* opèrent, on a synthétisé deux dérivés fluorés de l'acide sialique à utiliser comme inactivateurs basés sur le mécanisme. Il est connu que les deux composés sont des inactivateurs covalents d'une sialase trans issue de *Trypanosoma cruzi*. Dans notre cas, on a trouvé que le fluorure de 3-fluorosialosyle marquent d'une façon covalente le nucléophile catalytique d'une sialidase issue de *T. rangeli* et on a montré que le résidu impliqué est la Tyr346 de la séquence DENSGYSSVL. Il s'agit de la première démonstration que les lialidases opèrent par le biais d'un intermédiare covalent glycosyle-enzyme, ce qui suggère fortement l'existence d'un mécanisme catalytique commun pour tous les membres de la superfamille des sialidases. L'acide CMP-3-fluorosialique est un inhibiteur compétitif des transférases de sialyle et on l'a synthétisé en deux étapes, avec un rendement de 84 %, à partir de la *N*-acétyl mannosamine disponible commercialement, de l'acide 3-fluoropyruvique et du triphosphate de cytidine.

Mots clés : sialidase, mécanisme, marquage, nucléophile, inhibiteur.

[Traduit par la Rédaction]

Introduction

Sialic acids are considered as very important biomolecules since they are commonly displayed as the terminal sugar residues on cell surface glycocongugates and macromolecules (1–3). These nine-carbon sugars, which bear a negative charge at physiological pH, are known to be involved in many important ligand-receptor interactions that can greatly affect specific cell–cell, pathogen–cell, or drug–cell communications (4–6). Consequently, the enzymes responsible for the synthesis and hydrolysis of sialic acid linkages (sialyl transferases and sialidases, respectively) are of great medical interest and a number of such enzymes are considered to be potential targets for the therapeutic treatment of various diseases (7, 8). This has inspired a great deal of work into the synthesis of sialic acids and their analogues (9, 10), resulting in the development of at least two competitive sialidase inhibitors, Zanamivir® (GlaxoSmithKline) and Oseltamivir® (Roche), which are currently being prescribed for the treatment of influenza virus A and B. Yet, despite the obvious importance of these enzymes, the mechanisms through which sialyl transferases and hydrolases operate have remained relatively unexplored. To generate new classes of inhibitors a better understanding of these mechanisms is needed, as well as structural studies on complexes of these enzymes with their substrates and reaction intermediates.

Sialidases (EC: 3.2.1.18) catalyze the hydrolytic cleavage of sialosidic linkages with a net retention of anomeric configuration and have been assigned to CAZy (11) families GH

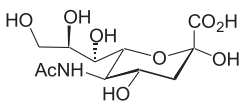
Received 26 November 2003. Published on the NRC Research Press Web site at http://canjchem.nrc.ca on 1 December 2004.

Dedicated to Professor Ed Piers on the occasion of his 65th birthday.

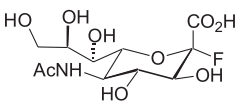
A.G. Watts and S.G. Withers.[1] Department of Chemistry, University of British Columbia, 2036 Main Mall, Vancouver, BC V6T 1Z1, Canada.

[1]Corresponding author (e-mail: withers@chem.ubc.ca).

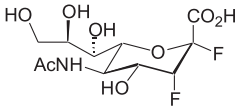
 doi: 10.1139/V04-125 © 2004 NRC Canada



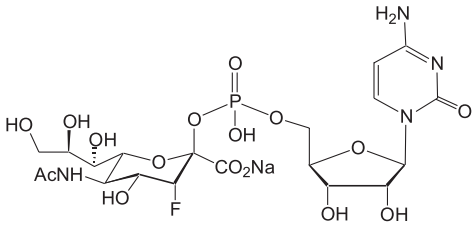
(**1**)



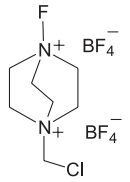
(**2**)



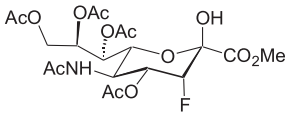
(**3**)



(**4**)



(**9**)



(**10**)

33, 34, and 83. Kinetic studies (12) and recent trapping experiments (13, 14) performed on a *trans*-sialidase from family GH 33 have shown that these enzymes use an analogous mechanism to that of other retaining glycosidases, involving a covalent glycosyl-enzyme intermediate, but utilizing a tyrosine as the catalytic nucleophile. Sialyl transferases (EC: 2.4.99.–.) are responsible for the transfer of the sialic acid moiety from CMP-sialic acid to the terminal carbohydrate of various glycoconjugates with an inversion of anomeric configuration. They have been assigned to CAZy families GT 29, 42, and 52 yet, to date, little is known about the catalytic mechanism of these enzymes with only one X-ray crystal structure so far reported (15).

Small molecule inhibitors that interact with enzyme active sites, either competitively or through the generation of a covalent linkage, have proven to be valuable tools for gaining insights into the catalytic mechanisms of various enzymes. Carbohydrate derivatives with an electronegative fluorine atom adjacent to the anomeric center have proved particularly useful in this regard and have been used successfully to label the catalytic nucleophiles of several retaining glycosidases via the formation of stable, covalent glycosyl-enzyme intermediates (16–18). The electronegative substituent destabilizes the oxocarbenium ion-like transition state, slowing both glycosylation (k_1) and deglycosylation steps (k_2). However, the presence of a good leaving group, fluoride, allows glycosylation to proceed efficiently and results in accumulation of the intermediate. Since sialic acid itself (**1**) bears no electronegative substituent at C-3, adjacent to the anomeric center, the introduction of a fluorine atom or even a hydroxyl group at C-3 might serve the same end, while incorporation of a fluoride leaving group should render the intermediate kinetically accessible. Based on previous studies, the fluorinated derivatives **2** and **3** were considered suitable targets for attempts to label the catalytic nucleophile of retaining sialidases (16–18). Inhibitors for glycosyl transferases can be designed on a similar basis, with a fluorine substituent dramatically slowing turnover. However, since the requirement for nucleotide phosphate leaving groups appears to be absolute, it has not proved possible to trap intermediates with such analogues since the initial step of glycosyl-enzyme formation remains rate-limiting. These analogues have, therefore, best served as inert substrate analogues. Through mechanistic and crystallographic analysis, these analogues have yielded important information on active site architecture and substrate binding interactions (15, 19–21).

This article describes the synthesis of the fluorinated sialic acid derivatives **2** and **3**, which are known mechanism-based inactivators of *Trypanosoma cruzi trans*-sialidase (13, 14). Further, compound **3** is shown here to label the catalytic nucleophile of a sialidase from *T. rangeli*. Also, a convenient two-step synthesis of a non-hydrolysable, competitive inhibitor of sialyl transferases (15, 21), namely **4**, is described.

Results and discussion

Covalent inactivators of sialidases and *trans*-sialidases

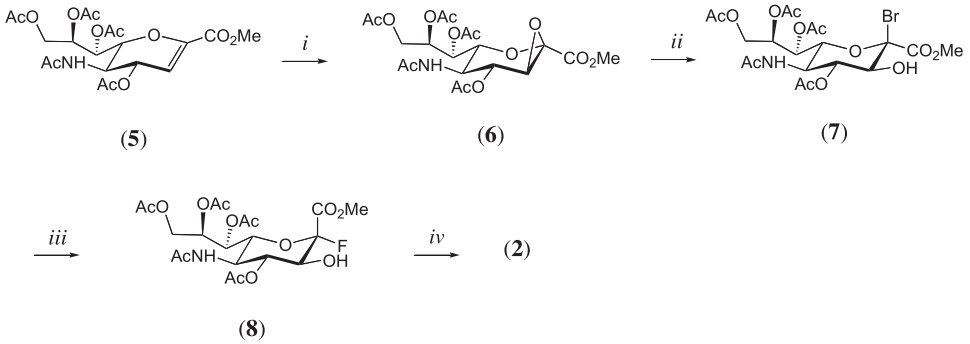
The 3-hydroxy sialic acid derivative **2** was synthesized from the easily accessible 2,3-dehydro derivative **5** (Scheme 1) (22). Treatment of **5** with dimethyl dioxirane for 3 h gave the epoxide **6**, which was directly opened using titanium(IV) bromide to give the known 3-hydroxy-sialyl bromide **7**. Treatment of the β-bromide **7** with AgF according to the procedure of Okomato et al. (23), then gave the α-sialyl fluoride **8** in moderate yield. The epoxide **6** was also isolated from this reaction, owing to participation by the 3-hydroxyl group. In an attempt to overcome the formation of **6**, the bromide **7** was acetylated prior to fluorination with AgF. This resulted in a slightly higher yield for the fluorination reaction, though there was little difference in the overall yield. Deacetylation of **8** with sodium methoxide in methanol, followed by saponification with aqueous sodium hydroxide, afforded the target fluoride **2**.

The synthesis of 3-fluorosialosyl fluoride **3** requires incorporation of a fluorine at C-3 and several methods currently exist for such a reaction. Treatment of the 2,3-dehydro derivative **5** with Selectfluor™ (**9**), in the presence of water, has been reported to give the 3-fluoro derivative **10** (24). However, in our hands this method was found to be sluggish and ineffective, owing to the unreactive nature of this alkene. Xenon difluoride is known to react with **5** in good yield (25). Unfortunately, owing to the acidity of the reaction conditions, only the thermodynamically more stable β-anomer was ever isolated, rather than the desired α-anomer.

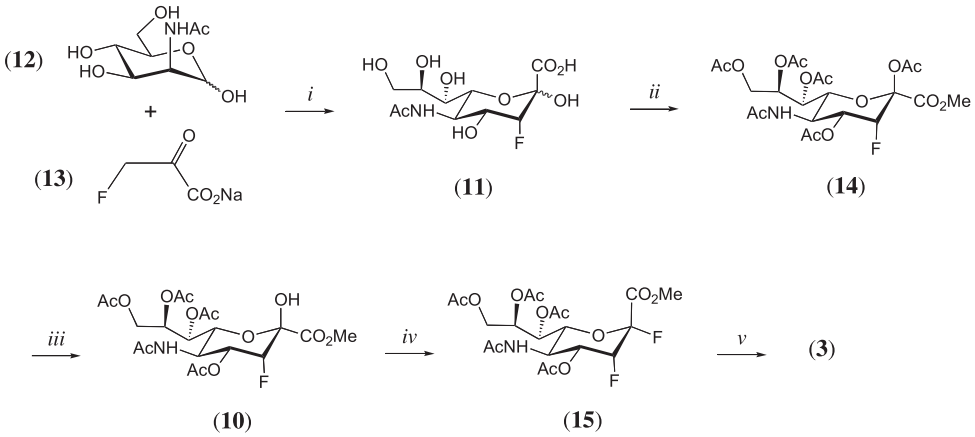
An alternative approach to the synthesis of sialic acid derivatives involves the use of the biosynthetic enzymes. *N*-Acetylneuraminic acid aldolase (Neu5Ac aldolase, EC: 4.1.3.3) catalyses the biosynthesis of sialic acid, from *N*-

© 2004 NRC Canada

Scheme 1. (*i*) DMDO, acetone; (*ii*) $TiBr_4$, CH_2Cl_2; (*iii*) AgF, MeCN; (*iv*) (*a*) NaOMe, MeOH, (*b*) aq. NaOH.



Scheme 2. (*i*) NeuAc aldose, H_2O; (*ii*) (*a*) Ac_2O, pyridine; (*b*) TMS diazomethane, MeOH, Et_2O; (*iii*) hydrazine acetate, MeOH, CH_2Cl_2; (*iv*) DAST, CH_2Cl_2, –30 °C; (*v*) (*a*) NaOMe, MeOH, (*b*) aq. NaOH.



acetyl mannosamine and pyruvic acid. A recent patent describes the use of Neu5Ac aldolase of high specific activity (>24 U/mL), to synthesize **11** in high yield, directly from *N*-acetyl mannosamine (**12**) and 3-fluoropyruvic acid (**13**) (Scheme 2) (26). The aldolase was found to be active for several days at room temperature, in the absence of buffer, and could be used in multiple reaction cycles (26). In our hands, Neu5Ac aldolase (>24 U/mL) effectively catalyzed the synthesis of **11**, from **12** and **13**, as described in ref. 26. Further, we also found that this reaction could be efficiently monitored by ^{19}F NMR spectroscopy, following the disappearance of **13**.

3-Fluorosialic acid (**11**) was acetylated with acetic anhydride in pyridine, then converted to its methyl ester using tetramethylsilyl diazomethane, to give **14** in high yield (Scheme 2). Selective deacetylation at the anomeric position was then achieved using hydrazine acetate, yielding the hemi-acetal **10**. Compound **10** was treated with diethylamino sulfurtrifluoride at –30 °C to give the α-fluoride **15** in good yield. The anomeric stereochemistry of **15** was assigned on the basis of the small ^{19}F NMR coupling constant for $J_{F2,F3}$ (11 Hz), which is indicative of an equatorial–axial configuration (27). The opposite anomeric configuration would place the two fluorine atoms in a trans-diaxial arrangement, which is known to give large F–F couplings (20 Hz) (28). Deacetylation of **15** with sodium methoxide, followed by saponification with aqueous sodium hydroxide, afforded the target compound **3**. Compound **3** has been shown to react with wild type *T. cruzi trans*-sialidase (13, 14), further supporting the stereochemical assignment of the anomeric fluoride.

Labeling of the catalytic nucleophile of a sialidase from *T. rangeli*

A wild-type sialidase from *T. rangeli* (TrSA) was inactivated upon incubation with the 3-fluorosialosyl fluoride derivative **3**. Mass spectral analysis of the inactivated protein revealed a single species of mass 71 380 ± 6 Da, greater in mass by 318 ± 12 Da than the wild-type protein (71 062 ± 6 Da), as shown in Fig. 1. This increase of 318 ± 12 Da is that expected for the covalent attachment of one 3-fluorosialosyl moiety (310 Da). To identify the site of covalent attachment, TrSA was incubated with **3** and then immediately subjected to peptic digestion at pH 2, in parallel with a sample of unlabeled protein. The peptic digests from both labeled and unlabeled enzymes were then purified by RP-HPLC coupled with on-line MS analysis. Comparison of the two LC–MS elution profiles revealed that a peptide of mass 1379 Da was observed only in the chromatogram for the labeled sample, with a corresponding peptide of m/z = 1069 present in the unlabeled sample. Daughter-ion fragmentation analysis of this 1379 Da peptide revealed a sequence of DENSGYSSVL – 3-fluorosialic acid, and identified Tyr 346 as the site of sialic acid attachment (Fig. 2). This is the first evidence to confirm that sialidase-catalyzed hydrolysis proceeds through a covalent glycosyl-enzyme intermediate in-

© 2004 NRC Canada

Fig. 1. ESI mass spectra of *T. rangeli* sialidase. (*a*) Wild-type enzyme; (*b*) wild-type enzyme incubated with **3**.

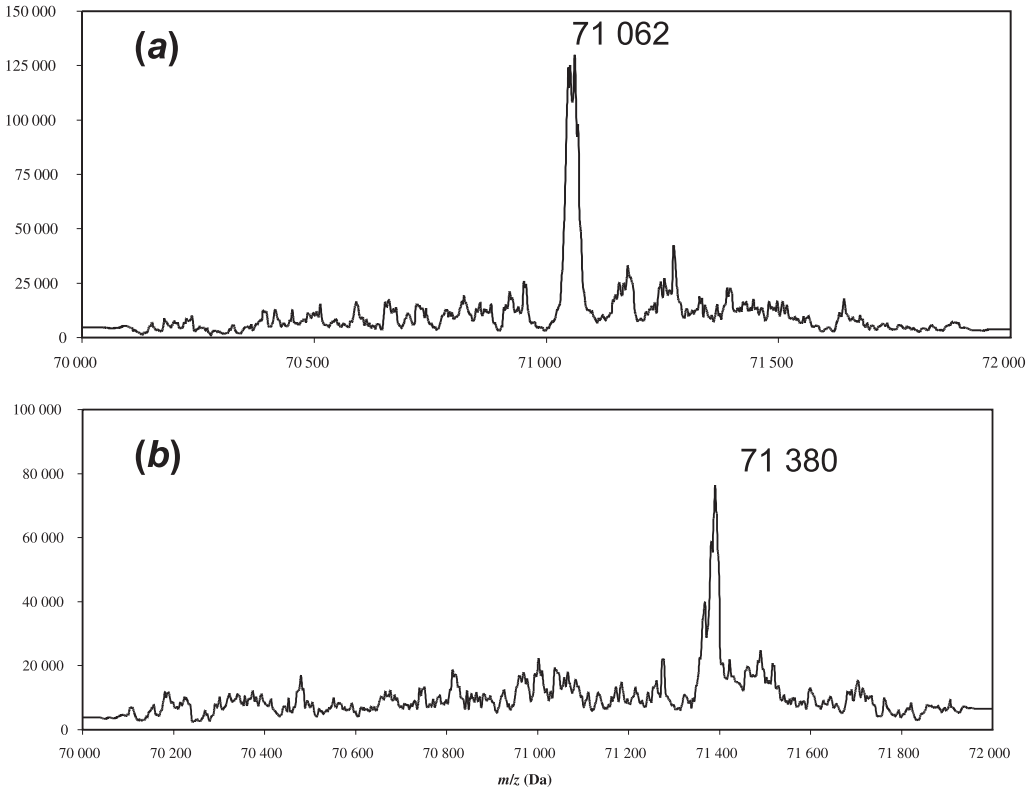
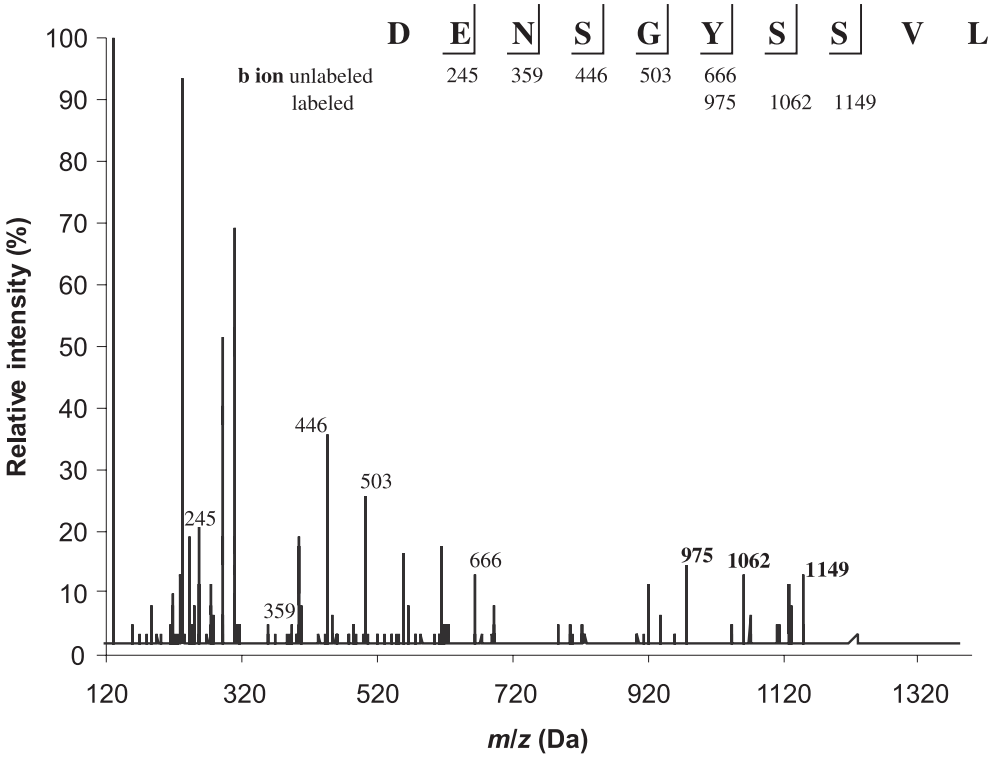
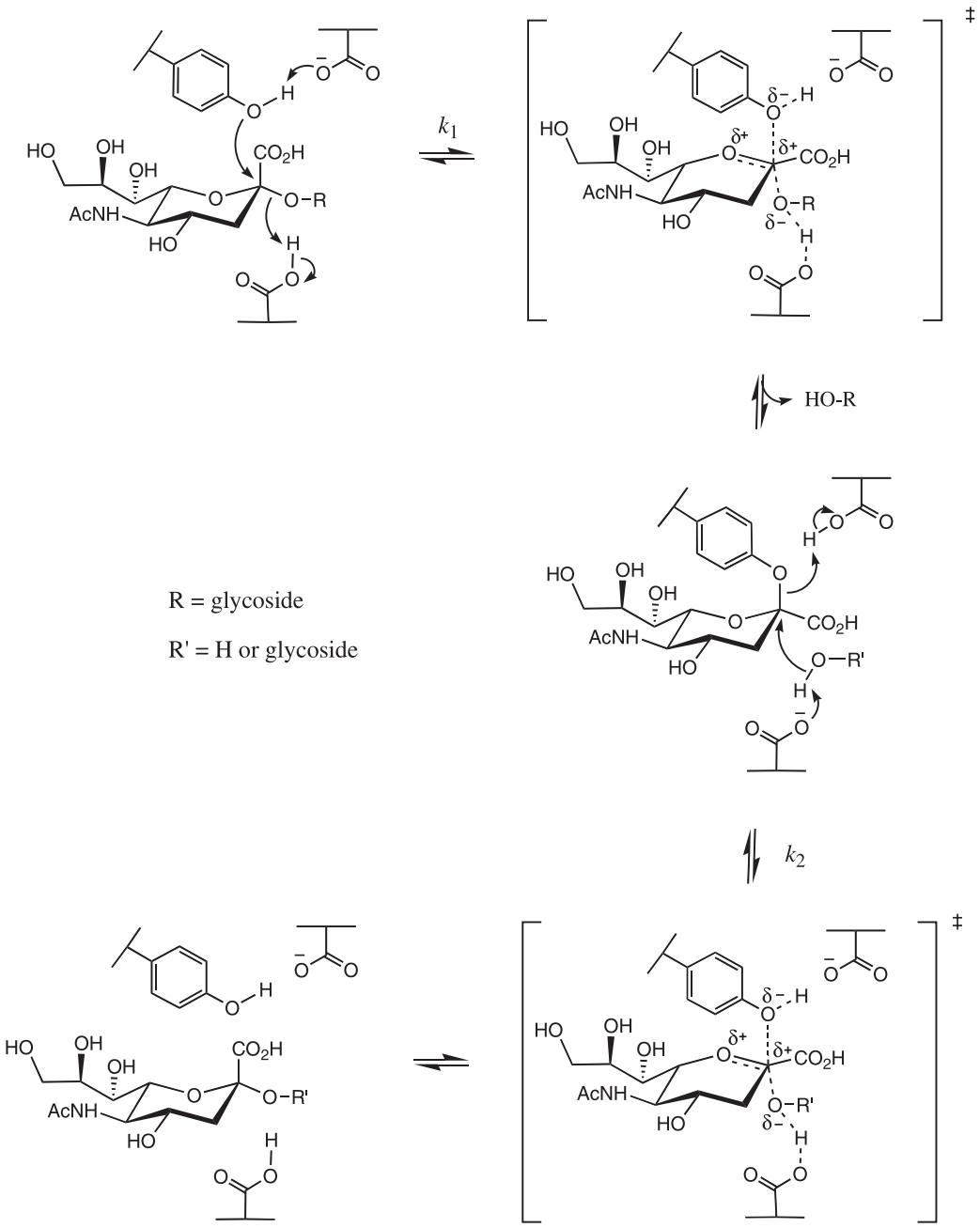


Fig. 2. ESI tandem MS daughter-ion spectrum of the 3-fluorosialyl peptide. Observed b ion series fragments are shown below the peptide sequence.



© 2004 NRC Canada

Scheme 3. The proposed catalytic mechanism for retaining sialyl hydrolases. R′ = H for sialidases, while R′ = glycoside for *trans*-sialidases.



volving a tyrosine residue (Scheme 3), and supports earlier findings that a *trans*-sialidase from *T. cruzi* operates through a similar mechanism (12–14).

Enzymatic synthesis of the competitive sialyl transferase inhibitor 4

The fluorinated CMP-sialic acid derivative **4** is known to be a noncleavable, competitive inhibitor of sialyl transferases, having a K_i = 5.1 μmol/L for an α-(2,6)-sialyltransferase (21). This value compares well to the K_m value for the natural substrate CMP-sialic acid (K_m = 15 μmol/L) (29). Compound **4** is also a competitive inhibitor for the sialyl transferase CstII from *Campylobacter jejuni* (K_i = 657 μmol/L compared to a K_m = 460 μmol/L for CMP-sialic acid) (15). Recent crystallographic studies of CstII with **4** bound in the active site provide unique insights into the catalytic mechanism of sialyl transferases (15). For this reason, a convenient synthesis of **4** would be desirable. However, the only synthesis of **4** reported is both lengthy (10 steps from sialic acid) and low yielding (27% from the alkene **5**) (29).

Here, we find that CMP-sialic acid synthetase (30) efficiently catalyzes the synthesis of **4** directly from 3-fluorosialic acid (**11**) and CTP, in high yield (91%). This is

© 2004 NRC Canada

in contrast to a previous report that the enzymatic synthesis of **4** using CMP-sialic acid synthetase is not viable as 3-fluorosialic acid (**11**) is not a substrate for CMP-sialic acid synthetase (29). Coupled with the one-step enzymatic synthesis of **11** using NeuAc aldolase, we report here the total enzymatic synthesis of **4** from *N*-acetyl mannosamine (**12**), 3-fluoropyruvic acid (**13**), and CTP in only two steps, in around 84% yield.

Conclusion

Facile and efficient chemoenzymatic syntheses are described for three useful probes of enzymes involved in sialic acid biotransformations. The two mechanism-based inactivators **2** and **3** have recently been used to label the catalytic nucleophile of *T. cruzi trans*-sialidase (13, 14), while **3** has been shown here to covalently label a sialidase from *T. rangeli*, allowing identification of Tyr346 as the catalytic nucleophile. This is the first report describing the labeling of the catalytic nucleophile of a sialidase, and supports earlier mechanistic studies on the closely related *T. cruzi trans*-sialidase. Combined, these labeling studies suggest that all members of the sialidase superfamily may operate through a similar catalytic mechanism, one that proceeds through the transient formation of a covalent glycosyl-enzyme intermediate (Scheme 3). An efficient synthesis is described for CMP-3-fluorosialic acid **4**, which has been used in the structural analysis of Cst-II to provide important insights into the catalytic mechanism of this enzyme (15).

Experimental

Moisture-sensitive reactions were carried out under an atmosphere of dry nitrogen. HPLC grade solvents (acetonitrile, pyridine, ethyl acetate, hexane, diethyl ether, and dichloromethane) were used without further purification. All reagents were purchased from Sigma-Aldrich unless otherwise stated, and used without further purification. *N*-Acetyl neuraminic acid aldolase (Neu5Ac aldolase, 4.1.3.3) was purchased from Jülich Fine Chemicals (Germany) and used without further purification. CMP-sialic acid synthetase was expressed and purified as described previously (30). HPLC purification was carried out using an Amide-80 column (TosoHaas, 20 cm × 2.5 cm) on a Waters 2400 System. Thin layer chromatography was performed using 0.25 mm silica gel F_{254} (EM Science-Merck) and visualized by charring with 10% sulfuric acid in ethanol. Flash chromatography was performed using silica gel Kieselgel 60 (230–400 mesh ASTM).

All NMR spectra were acquired on a Bruker AV-300 or Bruker AV-400. Chemical shifts are reported in ppm (δ) relative to tetramethylsilane (^{1}H NMR), $CDCl_3$ (^{13}C NMR), or trifluoroacetic acid (^{19}F NMR).

Methyl 5-acetamido-4,7,8,9-tetra-*O*-acetyl-5-deoxy-2-bromo-D-*erythro*-α-L-gluco-2-nonulopyranosonate (7)

The alkene **5** (22) (500 mg, 1.06 mmol) was dissolved in a solution of DMDO in acetone (20 mL, 0.1 mol/L) and allowed to react at room temperature (3 h). The solution was then concentrated in vacuo to give the epoxide **6** as a colorless oil, which was used without further purification. The oil was dissolved in dry CH_2Cl_2 (10 mL) and treated with $TiBr_4$ (0.47 g, 1.3 mmol) with vigorous stirring (10 min). The mixture was then concentrated in vacuo, dissolved in EtOAc and washed with saturated aq. Na_2SO_4, 5% aq. $NaHCO_3$, and then brine. The organic phase was then concentrated in vacuo and the residue purified by flash chromatography (EtOAc) to give the title compound as a colourless oil (510 mg, 86%). The ^{1}H NMR spectrum was consistent with that reported in the literature (23).

5-Acetamido-5-deoxy-2-fluoro-D-*erythro*-β-L-gluco-2-nonulopyranosonic acid (2)

The β-bromide (**7**) (980 mg, 1.8 mmol) was treated with AgF (330 mg, 2.6 mmol) according to the procedure of Okomato et al. (23) gave the α-fluoride **8** as a colorless oil (483 mg, 54%). A small amount of sodium metal (2 mg) was added to a solution of the fluoride **8** (140 mg, 0.28 mmol) in dry methanol (4 mL) at 0 °C and the mixture allowed to stir for 1 h at this temperature. The mixture was then neutralized (Amberlite IR120, H^+ form) and concentrated in vacuo. The resultant oil was then dissolved in water (2 mL), 1 mol/L NaOH (280 μL) added and then allowed to stand at room temperature until no starting material remained (TLC). The solution was neutralized (Amberlite IR120, H^+ form) and lyophilized to give the title compound **2** as a colorless solid (90 mg). ^{1}H NMR (400 MHz, $CDCl_3$) δ: 1.92 (s, 3H, Ac), 3.48 (br d, 1H, $J_{7,8}$ = 9.8 Hz, H-7), 3.57 (br dd, 1H, $J_{8,9}$ = 6.9, $J_{9,9'}$ = 12.1 Hz, H-9), 3.67 (br d, 1H, $J_{5,6}$ = 10.0 Hz, H-6), 3.73–3.83 (m, 3H, H-3, 8, 9′), 3.95 (dd, 1H, $J_{3,4}$ = 9.5, $J_{4,5}$ = 10.5 Hz, H-4), 4.14 (t, 1H, H-5). ^{13}C NMR (100.6 MHz, $CDCl_3$) δ: 22.45 (Me), 47.10 (C-5), 64.10 (C-9), 68.14 (C-7), 69.49 (d, 1C, $J_{4,F2}$ = 4 Hz, C-4), 70.23 (d, 1C, $J_{3,F2}$ = 18 Hz, C-3), 71.02 (C-8), 72.99 (d, 1C, $J_{6,F2}$ = 4 Hz, C-6), 105.32 (d, 1C, $J_{2,F2}$ = 220 Hz, C-2), 169.03 (d, 1C, $J_{1,F2}$ = 24 Hz, C-1), 175.36 (C=O). ^{19}F NMR (282.4 MHz, $CDCl_3$) δ: –40.5 (d, $J_{3,F2}$ = 12 Hz, F-2). LR-MS calcd. for $C_{11}H_{17}FNO_9$: 326.1; found: 326.0.

5-Acetamido-3,5-dideoxy-3-fluoro-D-*erythro*-L-manno-2-nonulopyranosonic acid (11)

A solution of Neu5Ac aldolase (15 mg, 23 U/mg) in water (4 mL) was added to a solution of 3-fluoropyruvic acid (150 mg, 1.2 mmol) and *N*-acetyl-D-mannosamine monohydrate (1.0 g, 4.2 mmol) in water (8 mL) and the mixture was left to stand at 25 °C (10 h). The mixture was then filtered (Amicon, 30 kDa) to remove small molecule substrates and products, and the protein used again with 3-fluoropyruvic acid and *N*-acetyl mannosamine as described above. After three such cycles, the filtrates were combined and then purified by ion exchange chromatography (Dowex, formate form) eluting with 0 → 1 mol/L formic acid. Lyophilisation gave 3-fluorosialic acid (**11**) as a colorless hygroscopic solid (1.1 g). ^{1}H and ^{13}C NMR spectra were consistent with those reported in the literature (31). ^{19}F NMR (282.4 MHz) δ: –131.9 (dd, $J_{3,F}$ = 43, $J_{4,F}$ = 31 Hz, F-3).

Methyl 5-acetamido-2,4,7,8,9-penta-*O*-acetyl-3,5-dideoxy-3-fluoro-D-*erythro*-α-L-manno-2-nonulopyranulosate (14)

Ac_2O (5 mL) was added to a solution of the 3-fluorosialic acid (**11**) (890 mg, 2.8 mmol) in pyridine (6 mL) at 0 °C, and the solution left to warm to room temperature (12 h).

© 2004 NRC Canada

The mixture was then concentrated in vacuo, and residual pyridine removed by azeotropic distillation with toluene (3 × 10 mL) to give a pale yellow oil (1.6 g). A solution of ethereal TMS–diazomethane (1.5 mol/L) was then added dropwise to a solution of the yellow oil (1.6 g) in MeOH–Et_2O (2:1, 15 mL) at –10 °C until a darker yellow color persisted (≈3 mL). The mixture was left to stir at this temperature for 10 min then concentrated in vacuo and the residue subjected to a standard work up (EtOAc) to give a light yellow oil. Purification of the yellow oil by flash chromatography (EtOAc) gave **14** as a colorless oil (1.4 g, 90%). ^{1}H NMR (300 MHz, $CDCl_3$) δ: 5.60 (br d, 1H, $J_{NH,5}$ = 9.3 Hz, NH), 5.51 (ddd, 1H, $J_{4,F}$ = 27.8, $J_{3,4}$ = 2.3, $J_{4,5}$ = 10.6 Hz, H-4), 5.33 (dd, 1H, $J_{6,7}$ = 1.8, $J_{7,8}$ = 5.0 Hz, H-7), 5.07 (ddd, 1H, $J_{8,9}$ = 2.3, 6.6 Hz, H-8), 4.88 (dd, 1H, $J_{F,3}$ = 49 Hz, H-3), 4.52 (dd, 1H, $J_{9,9}$ = 12.5 Hz, H-9), 4.15–4.24 (m, 2H, H-5,6), 4.12 (dd, 1H, H-9), 3.78 (s, 3H, OMe), 2.14, 2.12, 2.07, 1.98, 1.94 (5 s, 15H, OAc), 1.85 (s, 3H, NHAc). ^{13}C NMR (75.5 MHz, $CDCl_3$) δ: 20.28–23.07 (5 s, 6C, Ac), 45.21 (C-5), 53.41 (OMe), 62.02 (C-9), 67.85 (C-7), 71.43 (C-8), 71.85 (C-6), 71.87 (d, 1C, $J_{4,F}$ = 32 Hz, C-4), 87.18 (d, 1C, $J_{3,F}$ = 185 Hz, C-3), 95.01 (d, 1C, $J_{2,F}$ = 29 Hz, C-2), 165.02 (C-1), 167.02–170.53 (5 s, 6C, C=O). ^{19}F NMR (282.4 MHz) δ: –132.2 (dd, F-3).

Methyl 5-acetamido-4,7,8,9-tetra-*O*-acetyl-3,5-dideoxy-3-fluoro-D-*erythro*-α-L-manno-2-nonulopyranulosate (10)

A solution of hydrazine acetate (550 mg, 6.0 mmol) in MeOH (10 mL) was added to a solution of the 3-fluorosialic acid (**14**) (1.1 g, 2.0 mmol) in CH_2Cl_2 (10 mL) at 0 °C and the mixture left to stand at this temperature (3 h). The mixture was then concentrated in vacuo, subjected to a standard work up (EtOAc), and the residue purified by flash chromatography (EtOAc) to give the hemiacetal (**10**) as a colourless oil (850 mg, 84%). ^{1}H and ^{13}C NMR spectra were consistent with those reported in the literature (24). ^{19}F NMR (282.4 MHz, $CDCl_3$) δ: –128.9 (dd, $J_{F,3}$ = 48, $J_{F,4}$ = 28 Hz, F-3).

Methyl 5-acetamido-4,7,8,9-tetra-*O*-acetyl-3,5-dideoxy-3-fluoro-D-erythro-β-L-manno-2-nonulopyranosyl fluoride (15)

DAST (95 µL, 0.70 mmol) was added dropwise to a stirred solution of the hemiacetal (**10**) (240 mg, 0.47 mmol) in CH_2Cl_2 (10 mL) at –30 °C and the mixture held at this temperature with stirring (30 min). The reaction was quenched by the addition of methanol (20 µL) then subjected to a standard work up (CH_2Cl_2) and the resultant residue purified by flash chromatography (EtOAc) to give the difluorosialic acid derivative (**15**) as a colorless oil (197 mg, 82%). Crystallization (EtOAc–*i*-Pr_2O) gave **15** as long white needles, mp 68–70 °C. ^{1}H NMR (300 MHz, $CDCl_3$) δ: 5.55 (br d, 1H, $J_{NH,5}$ = 9.0 Hz, NH), 5.41 (br dd, 1H, $J_{F,4}$ = 27.1, $J_{4,5}$ = 10.5 Hz, H-4), 5.33 (ddd, 1H, $J_{7,8}$ = 5.1, $J_{8,9}$ = 2.5, $J_{8,9}$ = 7.7 Hz, H-8), 5.28 (br d, 1H, H-7), 5.08 (dt, 1H, $J_{F2,3}$ = $J_{3,4}$ = 2.5, $J_{F3,3}$ = 51 Hz, H-3), 4.28–4.35 (m, 2H, H-6, 9), 4.03–4.15 (m, 2H, H-5, 9′), 3.88 (s, 3H, OMe), 2.13, 2.08, 2.07, 2.00 (4 s, 12H, OAc), 1.89 (s, 3H, NHAc). ^{13}C NMR (282.4 MHz, $CDCl_3$) δ: 21.93, 22.06, 22.23, 22.40 (OAc), 24.53 (NHAc), 46.63 (C-5), 55.13 (OMe), 63.31 (C-9), 68.43 (C-7), 69.2–70.1 (m, C-4), 70.54 (C-8), 73.54 (d, $J_{F3,6}$ = 4 Hz, C-6), 86.92 (dd, $J_{F2,3}$ = 19, $J_{F3,3}$ = 194 Hz, C-3), 106.06 (dd, $J_{F3,2}$ = 18, $J_{F2,2}$ = 226 Hz, C-2), 166.02 (br d, $J_{F2,1}$ = 21 Hz, C-1), 171.25, 171.35, 171.553, 171.745, 171.976 (CO). ^{19}F NMR (282.4 MHz, $CDCl_3$) δ: –46.7 (br d, $J_{F2,F3}$ = 11 Hz, F-2), –140.2 (ddd, $J_{F3,3}$ = 50, $J_{F3,4}$ = 25 Hz, F-3). LR-MS calcd. for $C_{20}H_{28}F_2NO_{12}$: 512.8; found: 512.2.

5-Acetamido-3,5-dideoxy-3-fluoro-D-*erythro*-β-L-manno-2-nonulopyranosonic acid (3)

A small amount of sodium metal (2 mg) was added to a solution of the difluoride (**15**) (180 mg, 0.35 mmol) in dry methanol (5 mL) at 0 °C and the mixture allowed to stir at this temperature (2 h). The mixture was then neutralized (Dowex IR120, H^+ form) and concentrated in vacuo. The resultant oil was dissolved in water (2 mL), treated with 1 mol/L NaOH (360 µL) and allowed to stand at room temperature until no starting material remained (TLC). The solution was neutralized (Amberlite IR120, H^+ form) and lyophilized to give the title compound (**3**) as a colorless solid (120 mg). ^{1}H NMR (400 MHz, $CDCl_3$) δ: 5.10 (br dt, 1H, $J_{3,4}$ = 2.5, $J_{3,F2}$ = 2.5, $J_{3,F3}$ = 51 Hz, H-3), 4.15 (t, 1H, $J_{4,5}$ = 10.5 Hz, H-5), 4.04 (br dd, 1H, $J_{4,F3}$ = 28.5 Hz, H-4), 3.73–3.78 (m, 2H, H-8, 9′), 3.68 (br d, 1H, $J_{5,6}$ = 10.5 Hz, H-6), 3.53 (br dd, 1H, $J_{8,9}$ = 6.9, $J_{9,9'}$ = 12.1 Hz, H-9), 3.45 (br d, 1H, $J_{F,4}$ = 9.8 Hz, H-7), 1.93 (s, 1H, Ac). ^{13}C NMR (100.6 MHz, $CDCl_3$) δ: 22.39 (Me), 47.17 (d, 1C, $J_{5,F3}$ = 3 Hz, C-5), 63.22 (C-9), 68.16 (C-7), 69.40 (dd, 1C, $J_{4,F2}$ = 6, $J_{4,F3}$ = 18 Hz, C-4), 70.85 (C-8), 72.92 (d, 1C, $J_{6,F2}$ = 4 Hz, C-6), 89.05 (dd, 1C, $J_{3,F2}$ = 19, $J_{3,F3}$ = 184 Hz, C-3), 107.03 (dd, 1C, $J_{2,F2}$ = 220, $J_{2,F3}$ = 15 Hz, C-2), 169.78 (dd, 1C, $J_{1,F2}$ = 26, $J_{1,F3}$ = 3 Hz, C-1), 175.36 (C=O). ^{19}F NMR (282.4 MHz, $CDCl_3$) δ: –45.5 (br d, $J_{F2,F3}$ = 11 Hz, F-2), –141.3 (br ddd, F-3). LR-MS calcd. for $C_{11}H_{16}F_2NO_8$: 328.1; found: 328.0.

Cytidine 5′-phosphate, *P*′-(5-acetamido-3,5-dideoxy-3-fluoro-2-D-*erythro*-α-L-manno-2-nonulopyranosonic acid (4)

A 20 mL solution of 3-fluorosialic acid (**11**) (130 mg, 0.37 mmol), 20 mmol/L CTP, 25 mmol/L $MgCl_2$, CMP-Neu5Ac synthetase (30) (10 U, 109 U/mL), and pyrophosphatase (5 U) in 50 mmol/L Tris-HCl (pH 8.5) was left to stand overnight at room temperature. The mixture was purified by HPLC (30% H_2O–MeCN, 6 mL/min), then lyophilized to give the title compound (**4**) as a white solid (210 mg, 91%). ^{1}H NMR was consistent with that reported (21). ^{19}F NMR (282.4 MHz, $CDCl_3$) δ: –131.5 (dd, $J_{3,F3}$ = 42, $J_{4,F3}$ = 28 Hz, F-3).

Labeling and proteolysis of wild-type *T. rangeli* sialidase

Labeling of wild-type *T. rangeli* sialidase (2.1 mg/mL) was accomplished by incubating the enzyme (40 µL) in pH 7.1, 50 mmol/L phosphate buffer, containing 50 mmol/L 3-fluorosialosyl fluoride (**3**) (30 µL) for 30 min at room temperature. After this time, digestion buffer (120 µL, pH 2.0) containing pepsin (0.3 mg/mL) was added. Proteolytic digestion was performed for 1 h and the sample was frozen prior to mass spectrometric analysis. A sample of unlabeled enzyme for comparison was also prepared in the same manner.

© 2004 NRC Canada

ES-MS analysis of the proteolytic digest

Mass spectra were recorded on a PE-Sciex API 300 triple-quadrupole mass spectrometer and a PE-Sciex API QSTAR pulsar i (Sciex, Thornhill, Ontario, Canada) equipped with an Ionspray ion source. Peptides were separated by reverse-phase HPLC on a LC Packing UltiMate Micro HPLC system (Dionex, Sunnyvale, California) directly interfaced with the mass spectrometer. In each of the MS experiments, the proteolytic digest was loaded onto a C-18 column (LC Packing, 100 Å pepMap, 1 mm × 150 mm) equilibrated with solvent A (solvent A: 0.05% trifluoroacetic acid – 2% acetonitrile in water). Elution of the peptides was accomplished using a gradient (0%–60%) of solvent B over 60 min followed by 85% solvent B over 20 min (solvent B: 0.045% trifluoroacetic acid – 80% acetonitrile in water). Solvents were pumped at a constant flow rate of 50 μL/min. Spectra were recorded in the single quadrupole scan mode (LC–MS) or the tandem MS product-ion scan mode. In the single-quadrupole mode (LC–MS), the quadrupole mass analyzer was scanned over a mass-to-charge ratio (m/z) range of 100–2200 Da with a step size of 0.5 Da and a dwell time of 1.5 ms per step. The ion source voltage (ISV) was set at 5.5 kV and the orifice energy (OR) was 45 V. In the tandem MS daughter-ion scan mode, the spectra were obtained in a separate experiment by selectively introducing the labeled (m/z = 1379) or unlabeled (m/z = 1069) parent ion from the first quadrupole (Q1) into the collision cell (Q2) and observing the product ions in the third quadrupole (Q3). The scan range of Q3 was 100–1400, the step size was 0.5 Da, the dwell time was 1 ms, ISV was 5 kV, OR was 45 V, Q0 = –10, IQ2 = –48.

Acknowledgements

We thank the Human Frontiers Science Program for their generous financial assistance. We thank Dr. W. Wakarchuck for his kind gift of CMP-sialic acid synthetase and Dr. Carlos Frasch and Dr. Pedro Alzari for the *T. rangeli* sialidase. Shouming He is thanked for performing the MS analysis.

References

1. R. Schauer. Trends Glycosci. Glycotechnol. **9**, 315 (1997).
2. A. Varki. Glycobiology, **3**, 97 (1993).
3. R. Schauer. Glycoconjugate J. **17**, 485 (2000).
4. C. Traving and R. Schauer. Cell Mol. Life Sci. **54**, 1330 (1998).
5. E. Vimr and C. Lichtensteiger. Trends Microbiol. **10**, 254 (2002).
6. T. Feizi. Immunol. Rev. **173**, 79 (2000).
7. F. Dall'Olio and M. Chiricolo. Glycoconjugate J. **18**, 841 (2001).
8. O.T. Keppler, P. Stehling, M. Herrmann, H. Kayser, D. Grunow, W. Reutter, and M. Pawlita. J. Biol. Chem. **270**, 1308 (1995).
9. G.-J. Boons and A.N. Demenchenko. Carbohydr.-Based Drug Discovery, **1**, 55 (2003).
10. M.J. Kiefel and M. von Itzstein. Chem. Rev. **102**, 471 (2002).
11. The Carbohydrate-Active Enzymes (CAZy) database describes the families of structurally related catalytic and carbohydrate-binding modules (or functional domains) of enzymes that degrade, modify, or create glycosidic bonds. P.M. Coutinho and B. Henrissat. Carbohydrate-Active Enzymes (CAZy) database [online]. Available from http://afmb.cnrs-mrs.fr/~cazy/CAZY/index.html. 1999.
12. J. Yang, S. Schenkman, and B.A. Horenstein. Biochemistry, **39**, 5902 (2000).
13. M.F. Amaya, A.G. Watts, I. Damager, A. Wehenkel, T. Nguyen, A. Buschiazzo, G. Paris, A.C. Frasch, S.G. Withers, and P.M. Alzari. Structure, **12**, 775 (2004).
14. A.G. Watts, I. Damager, M.L. Amaya, A. Buschiazzo, P. Alzari, A.C. Frasch, and S.G. Withers. J. Am. Chem. Soc. **125**, 7533 (2003).
15. C.P.C. Chiu, A.G. Watts, L. Lairson, D. Lim, S.G. Withers, W.W. Wakarchuk, and N.C.J. Strynadka. Nat. Struct. Mol. Biol. **11**, 163 (2004).
16. J. Wicki, D.R. Rose, and S.G. Withers. Methods Enzymol. **354**, 84 (2002).
17. J.D. McCarter and S.G. Withers. J. Am. Chem. Soc. **118**, 241 (1996).
18. D.L. Zechel and S.G. Withers. Acc. Chem. Res. **33**, 11 (2000).
19. H.D. Ly, B. Lougheed, W.W. Wakarchuk, and S.G. Withers. Biochemistry, **41**, 5075 (2002).
20. M.D. Burkart, S.P. Vincent, A. Duffels, B.W. Murray, S.V. Ley, and C.-H. Wong. Bioorg. Med. Chem. **8**, 1937 (2000).
21. K. Persson, H.D. Ly, M. Dieckelmann, W.W. Wakarchuk, S.G. Withers, and N.C.J. Strynadka. Nat. Struct. Biol. **8**, 166 (2001).
22. A. Marra and P. Sinay. Carbohydr. Res. **190**, 317 (1989).
23. K. Okamoto, T. Kondo, and T. Goto. Bull. Chem. Soc. Jpn. **60**, 631 (1987).
24. M.D. Burkart, Z. Zhang, S.-C. Hung, and C.-H. Wong. J. Am. Chem. Soc. **119**, 11 743 (1997).
25. C.R. Petrie III, M. Sharma, O.D. Simmons, and W. Korytnyk. Carbohydr. Res. **186**, 326 (1989).
26. J. Beliczey, U. Kragl, A. Liese, C. Wandrey, K. Hamacher, H.H. Coenen, and T. Tierling. US Patent 6 355 453 B1, 12 March 2002.
27. M.N. Sharma and R. Eby. Carbohydr. Res. **127**, 201 (1984).
28. L.D. Hall, R.N. Johnson, J. Adamson, and A.B. Foster. Can. J. Chem. **49**, 118 (1971).
29. M.D. Burkart, S.P. Vincent, and C.-H. Wong. Chem. Comm. 1525 (1999).
30. M.-F. Karwaski, W.W. Wakarchuck, and M. Gilbert. Protein Expression Purif. **25**, 237 (2002).
31. T. Nakajima, H. Hori, H. Ohrui, H. Meguro, and T. Ido. Agric. Biol. Chem. **52**, 1209 (1988).

© 2004 NRC Canada

Exo selectivity and the effect of disubstitution in the Diels–Alder reactions of butadiene with 3,3-disubstituted cyclopropenes

Tammy L. Gosse and Raymond A. Poirier

Abstract: A density functional computational study was performed to accomplish two tasks: to examine the endo–exo selectivity in the Diels–Alder reactions of 3,3-disubstituted cyclopropenes with *s-cis*-butadiene, and to study the effect of disubstitution on the reactivity of the cyclopropene dienophile. Cyclopropene is substituted at C-3 with CH_3, SiH_3, NH_2, PH_2, OH, SH, F, and Cl; both 3-substituted and 3,3-disubstituted ground states are examined to determine relative reactivities. The exo transition-state structures are consistently lower in energy than the endo transition-state structures for the 3,3-disubstituted cyclopropene – butadiene system, and surprisingly, both modes of addition have lower activation barriers than the syn 3-substituted cyclopropene – butadiene system. Through a series of isodesmic reactions, we have concluded that there is an additional stabilization in the transition-state structures of the 3,3-disubstituted system that can account for the lowering of the activation barriers below that of the 3-substituted cases. This stabilization is a combination of the anomeric effect and the ring relaxation that occurs in the transition-state structure.

Key words: Diels–Alder reaction, cyclopropene, exo selectivity, anomeric effect.

Résumé : On a réalisé une étude théorique à l'aide de la théorie de la densité fonctionnelle pour examiner la sélectivité endo–exo des réactions de Diels–Alder de cyclopropènes 3,3-disubstitués avec le *s-cis*-butadiène ainsi que pour étudier l'effet de la disubstitution sur la réactivité du cyclopropène diénophile. Le cyclopropène est substitué en position C-3 avec des CH_3, SiH_3, NH_2, PH_2, OH, SH, F et Cl et, dans le but de déterminer leurs réactivités relatives, on a examiné les états fondamentaux produits tant mono- que disubstitués en position C-3. Pour le système cyclopropène 3,3-disubstitué – butadiène, les structures de l'état de transition exo ont systématiquement des énergies plus faibles que celles de l'état de transition endo et, à notre grande surprise, les barrières d'activation pour les deux modes d'addition sont plus faibles que celles du système cyclopropène 3-monosubstitué syn – butadiène. Par le biais d'une série de réactions isodesmiques, on en est venu à la conclusion qu'il y a une stabilisation additionnelle dans les structures de l'état de transition du système 3,3-disubstitué qui permet d'expliquer l'abaissement des barrières d'activation à des niveaux inférieurs à celles observées dans les cas 3-substitués. Cette stabilisation est une combinaison d'effet anomère et de relaxation du cycle qui se produit dans l'état de transition.

Mots clés : réaction de Diels–Alder, cyclopropène, sélectivité exo, effet anomère.

[Traduit par la Rédaction]

Introduction

It has been demonstrated both experimentally and theoretically that the majority of Diels–Alder cycloadditions show a preference for the formation of endo products (1, 2). This preponderance for endo selectivity has been shown in a variety of studies involving cyclopropene and its 3-substituted derivatives (3). There have been some specific instances of exo selectivity encountered for this family of cyclic dienophiles with various dienes (4), however, this phenomenon is typically not seen and no explanation exists for the exo selectivity.

Received 25 March 2004. Published on the NRC Research Press Web site at http://canjchem.nrc.ca on 1 December 2004.

T.L. Gosse[1] and R.A. Poirier. Department of Chemistry, Memorial University of Newfoundland, St. John's, NL A1B 3X7, Canada.

[1]Corresponding author (e-mail: u36tlg@mun.ca).

The endo preference of chemical systems has been explained mainly by the argument of favourable "secondary orbital interactions" (SOI) in the endo geometry, first suggested by Woodward and Hoffmann (5); these interactions are defined as the overlap of the frontier molecular orbitals at the nonreacting π centers of the diene and dienophile at the transition state. In the case of the cyclopropene and butadiene reaction, this interaction would occur between the syn methylene hydrogen at C-3 of cyclopropene and the π system of butadiene. While SOI has been the most popular argument discussed in terms of explaining endo selectivity, there are an increasing number of studies providing evidence that lessens its significance. Xidos et al. (6) deduced that these "H–π" interactions were not energetically significant enough to be a deciding factor of endo-exo selectivity and Salvatella and co-workers (7) also disputed the importance of SOI in Diels–Alder reactions; both groups state that steric interaction arguments may be invoked to explain endo–exo selectivity. A recent paper by Ogawa and Fujimoto (8) employed numerical analysis in the examination of the endo

 doi: 10.1139/V04-115 © 2004 NRC Canada

transition state of butadiene and maleic anhydride; they deduced that SOI is much less significant than previously thought.

In recent literature, we have not encountered a theoretical examination of the 3,3-disubstituted cyclopropene and butadiene system and this is the focus of the present study. An extensive analysis of the facial and endo–exo selectivity of the 3-substituted cyclopropene and butadiene addition reaction (6) suggested that the disubstituted system should show considerable preference for exo addition. Latypova et al. (9) examined the Diels–Alder reactions of 3-methyl-3-cyanocyclopropene with a variety of dienes experimentally, and all cases were shown to be stereospecific with the cyano group in the syn position of the transition state; exo selectivity was found for the furan-type dienes. Apeloig et al. (10) determined the stereoselectivity of three different cyclopropene derivatives (none of which were 3,3-disubstituted as in the present study) with a series of substituted dienes by using X-ray and NOE studies; one of the cyclopropene reactants, 1,2,3,3-tetrachlorocyclopropene, was shown to be exo selective when reacted with some 1-substituted-1,3-dienes. This group predicted at that time that 3,3-disubstituted cyclopropenes would yield exo selective products with open-chain dienes. Boger and Brotherton (11) studied the Diels–Alder reactions of cyclopropenone ketals with electron-rich, electron-poor, and neutral dienes; nearly all of the reactions produced the exo cycloadduct only, and it was concluded that this exo preference was a result of steric factors in the transition state.

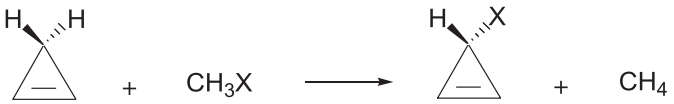
Cyclopropene is the simplest cyclic dienophile and its reactivity can be easily modified by substitution at the C-3 position. The cycloaddition reaction of 3,3-disubstituted cyclopropene to butadiene is an ideal system for studying reactivity and steric effects on the endo–exo selectivity. Herein we examine a series of these reactions, and where applicable, compare the results with those obtained for the previously studied 3-substituted cyclopropene – butadiene system (6).

Computational methods

Ground-state minima for cyclopropene and its derivatives, disubstituted at C-3 by CH_3, SiH_3, NH_2, PH_2, OH, SH, F, and Cl, and *s-cis*-butadiene, as well as transition-state structures for the endo and exo Diels–Alder cycloadditions were initially obtained using MUNgauss (12) at the HF/6-31++G(*d*) level of theory. All subsequent calculations were performed with Gaussian 98 (13). The ground-state and transition-state structures were further optimized using B3LYP/6-31++G(d). All probable rotational minima were determined for those 3,3-disubstituted cyclopropene ground states with conformational mobility; the ground-state cyclopropenes reported here refer to the rotational global minimum determined at B3LYP/6-31++G(d), unless otherwise noted. Likewise, all probable rotational minima for the endo and exo transition states with CH_3, SiH_3, NH_2, PH_2, OH, and SH disubstituted at C-3 on the dienophile, were obtained. In all cases, the *s-cis*-butadiene with a four-carbon torsion of 31.9° was used as the ground-state minimum for the diene. Gaussian 98 confirmed that all ground-state minima had no imaginary frequencies and all transition-state structures had a single imaginary frequency.

All ground-state and transition-state structures for the previously studied 3-substituted cyclopropene – butadiene system (6) were updated to the B3LYP/6-31++G(*d*) level of theory to allow for comparison to the present 3,3-disubstituted system.

Scheme 1.



Scheme 2.



Results and discussion

Ground-state cyclopropenes

The stabilization of the various 3-substituted cyclopropene ground states was quantified in a previous examination via an isodesmic reaction, which quantified the effect of substitution at C-3 of cyclopropene relative to a similarly substituted methane derivative. These isodesmic energies showed a good correlation with the electronegativity (14) of the substituent atom or group. The examined substituents, with the exception of SiH_3, showed a stabilization of the cyclopropene ring upon substitution and that the degree of stabilization increased with increasing electronegativity, suggesting that the stabilization of cyclopropene is strongly influenced by the strength of σ-withdrawal by the substituent.

A similar investigation was conducted in the present study for the 3,3-disubstituted cyclopropenes and the results then compared with those obtained for the updated 3-substituted cyclopropenes. Schemes 1 and 2 show the isodesmic reactions considered here and Table 1 includes the isodesmic stabilization energies (ΔE^{X}_{stab} and ΔE^{XX}_{stab}) for both reactions.

Scheme 1 represents the effect (stabilization or destabilization) on the cyclopropene ring that results from the addition of one substituent (X) to C-3 of cyclopropene relative to a similarly substituted methane. The X substituents of these methane derivatives all have a staggered conformation. Scheme 2 represents the stabilization – destabilization of 3-substituted cyclopropene resulting from the addition of the second X to C-3 of the 3-substituted cyclopropene relative to a similarly monosubstituted methane derivative.

Table 1 shows that upon the addition of the first X to C-3 of cyclopropene, we see a stabilization of the cyclopropene ring for all examined substituents except SiH_3, which is only slightly destabilized. These results are comparable to the previous energies obtained at the Hartree–Fock level. The value of ΔE^{X}_{stab} increases with the electronegativity of X, suggesting a gradual reduction in the reactivity of the dienophile with increasing electronegativity. The energies of Scheme 2 show a further stabilization upon the addition of the second X to 3-substituted cyclopropene for all examined

© 2004 NRC Canada

Table 1. Energetic data (kJ mol^{-1}) and ground-state bond lengths (Å) for 3-substituted and 3,3-disubstituted cyclopropenes at B3LYP/6-31++G(d).

	Ground-state conformation			Isodesmic stabilization energies				3-Substituted cyclopropene		3,3-Disubstituted cyclopropene	
Substituent[a]	3-Sub	3,3-Disub[b]	Group electronegativity[c]	ΔE^{X}_{stab}	$\Delta E^{XX,d}_{stab}$ (anom-ring)	ΔE_{anom}[e]	$\Delta\Delta E_{ring}$[f]	C1-C3, C2-C3	C1=C2	C1-C3, C2-C3	C1=C2
SiH_3	stag	**1C**	1.91	3.06	4.70	–5.68	10.38	1.528	1.292	1.546	1.289
PH_2	stag	**2B**	2.17	–10.76	–5.66	–4.29	–1.37	1.515	1.294	1.515, 1.518	1.295
H	—	—	2.20	0.00	0.00	0.00	0.00	1.511	1.296	1.511	1.296
CH_3	stag	**1A**	2.56	–14.40	–11.88	–12.08	0.20	1.511	1.299	1.513	1.300
SH	gauche	**3A**	2.63	–23.82	–14.09	–10.14	–3.96	1.498, 1.494	1.298	1.488	1.301
Cl	—	—	3.05	–39.46	–4.04	4.25	–8.28	1.471	1.306	1.456	1.310
NH_2	gauche	**2D**	3.10	–34.22	–44.78	–34.15	–10.63	1.508, 1.490	1.306	1.493	1.313
OH	stag	**3A**	3.64	–48.46	–57.73	–69.54	11.81	1.486	1.311	1.468	1.312
F	—	—	4.00	–57.48	–43.09	–39.09	–4.00	1.466	1.309	1.445	1.321

Note: Isodesmic energetic data for the 3,3-disubstitution of cyclopropane and the results of Scheme 4 are also included.
[a]Substituents are placed in order of increasing electronegativity.
[b]Conformations for 3,3-disubstituted cyclopropenes as per Figs. 1–3.
[c]Group electronegativities as per ref. 14.
[d]Results from Scheme 2.
[e]Results from Scheme 3*b*.
[f]Calculated as ΔE^{XX}_{stab} (anom-ring) – ΔE_{anom} (Scheme 4).

Scheme 3.

substituents with the exception of SiH_3, which is further destabilized upon disubstitution.

It is clear that the addition of X to unsubstituted cyclopropene and the addition of the second X to the 3-substituted cyclopropene are not equivalent. Generally, the greatest degree of stabilization (or destabilization) of the cyclopropene ring comes with the addition of the first X. The most electronegative substituents (X = NH_2, OH, and F) show significantly larger stabilization energies, especially NH_2 and OH, upon the addition of the second X to the 3-substituted cyclopropene. This can be explained by the occurrence of the anomeric effect (15), which measures the extent to which two substituents bonded to the same sp^3-hybridized carbon interact with each other. For NH_2, OH, and F, this large stabilizing interaction results from the lone pair of one substituent donating electron density to the σ system of the other substituent and vice versa. As a means of expressing this effect quantitatively for the most basic molecular system of 3,3-disubstituted methane, we considered the isodesmic reaction in Scheme 3*a*.

The result obtained at B3LYP/6-31++G(*d*) for X = OH (ΔE = –63.6 kJ mol^{-1}) clearly shows a significant anomeric stabilization. The two other electronegative substituents, NH_2 (ΔE = –31.9 kJ mol^{-1}) and F (ΔE = –46.6 kJ mol^{-1}) gave similar results; however, the remaining substituents in this study showed significantly less stabilization upon disubstitution.

The other substituent worthy of note here is Cl, which generally shows a slightly destabilizing anomeric effect (Scheme 3*a*, calculated ΔE of CH_2Cl_2 = 4.9 kJ mol^{-1}). As can be seen from Table 1, the addition of the second Cl to C-3 of 3-Cl-cyclopropene results in little stabilization (ΔE^{XX}_{stab} = –4.04 kJ mol^{-1}) compared to the addition of the first Cl to cyclopropene, which is very stabilizing. This indicates that the second Cl should have very little effect on the stability and reactivity of the 3-Cl-cyclopropene.

An examination of the 3,3-disubstituted cyclopropene ground-state geometries (Table 1) reveals trends similar to that of the 3-substituted cyclopropenes as the electronegativity of the substituents increase. Table 1 includes the C—C single bonds and the C=C double bonds of both types of dienophiles with the various substituents. As shown, the addition of increasingly electronegative substituents results in a longer, and thus more electron deficient, C=C double bond, as well as generally shorter C—C single bonds of the cyclopropene ring, in comparison to cyclopropene itself. In comparing the 3-substituted to the 3,3-disubstituted cyclopropenes for each substituent, we see the effect of disubstitution on the geometry. The C=C bonds are generally longer in the 3,3-disubstituted cyclopropenes, and the degree of elongation increases upon the disubstitution of stronger electron-withdrawing groups. An exception is SiH_3, which

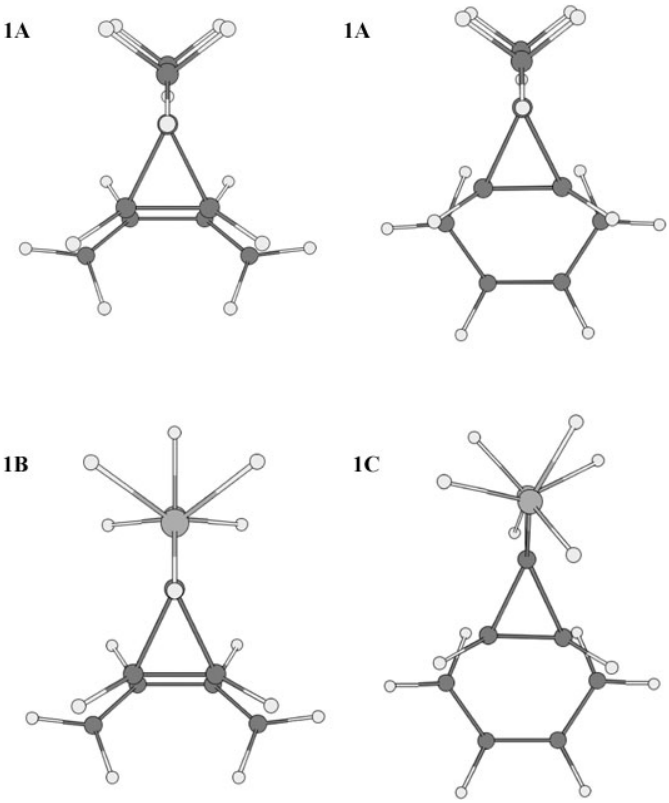
© 2004 NRC Canada

Table 2. Conformations of substituents for endo and exo addition and $\Delta E_{endo\text{-}exo}$ (kJ mol^{-1}) for the transition-state structures for 3,3-disubstituted cyclopropene with butadiene.

	Conformation		
Substituent	endo Addition	exo Addition	$\Delta E_{endo\text{-}exo}$
SiH_3	**1B**	**1C**	2.8
PH_2	**2B**	**2B**	10.0
CH_3	**1A**	**1A**	7.2
SH	**3B**	**3B**	13.0
Cl	—	—	12.0
NH_2	**2D**	**2B**	12.4
OH	**3A**	**3A**	14.2
F	—	—	12.2

exhibits a further shortening of the C=C bond. This geometric trend supports the energetic data; the cyclopropenes with the longer, more electron-deficient C=C bonds are also the more stable structures. In addition, the C—C single bonds get substantially shorter upon disubstitution of electron-withdrawing groups and generally longer for electron-donating groups. In relation to the unsubstituted cyclopropene, it can be seen that 3,3-disubstitution has similar effects on the ring as 3-substitution. The nature of the substituent (electron-withdrawing or -donating) affects the geometry and stabilization energies in a similar way; however, the anomeric effect that results from 3,3-disubstitution can also contribute to the geometrical changes in the ring as well as the stabilization energies.

Fig. 1. Transition-state structures for 3,3-CH_3-cyclopropene with butadiene, endo and exo addition (**1A**); 3,3-SiH_3-cyclopropene with butadiene, endo addition (**1B**); and 3,3-SiH_3-cyclopropene with butadiene, exo addition (**1C**).



Transition-state structures

Because the dienophile of the present reaction is disubstituted at the C-3 position, we are removing the possibility of facial selectivity and are thus dealing with endo–exo selectivity only. In ref. 6, plots of activation energies of the four modes of addition (endo-syn, endo-anti, exo-syn, and exo-anti) of 3-substituted cyclopropene to butadiene against electronegativities show that the syn transition states are higher in energy than the anti transition states in all cases. However, in looking solely at the syn additions, we see that additions take place more favourably in the exo geometry than in the endo geometry. This suggested that if the Diels–Alder reactions could occur via syn addition only, as would be the case with 3,3-disubstituted cyclopropene and butadiene, the exo geometry would be favoured.

The transition-state structures of disubstituted CH_3-, SiH_3-, F-, and Cl-cyclopropenes with butadiene each have one endo and one exo structure that are first-order saddle points. In the case of the two halogens examined, we see 100% exo selectivity with $\Delta E_{endo\text{-}exo}$ of 12.2 and 12.0 kJ mol^{-1} at B3LYP/6-31++G(*d*) for F and Cl, respectively (Table 2). The conformations of the CH_3 substituents in the transition states for endo and exo addition are the same (conformation **1A**). However, the SiH_3 groups in the endo transition state are in a staggered conformation (**1B**) and for exo addition, in a slightly skewed conformation (**1C**) (Fig. 1). In addition, the $\Delta E_{endo\text{-}exo}$ value for the 3,3-SiH_3-cyclopropene – butadiene case is small; the exo addition is favoured by a mere 2.8 kJ mol^{-1}, indicating no real preference for either mode of addition. The $\Delta E_{endo\text{-}exo}$ for the CH_3 substituent is calculated to be 7.2 kJ mol^{-1}.

For the Diels–Alder reactions of disubstituted NH_2-, PH_2-, OH-, and SH-cyclopropenes with butadiene, there were multiple first-order saddle points. Figure 2 illustrates examples of the four possible conformations for 3,3-NH_2- and 3,3-PH_2-cyclopropene addition to butadiene, and Table 2 lists the lowest energy conformer for each mode. Conformations **2A**, **2B**, and **2D** were identified for 3,3-NH_2-cyclopropene – butadiene endo and exo addition; **2C** is a confirmed second-order saddle point for exo addition, but no such conformation was found for endo addition. For the 3,3-PH_2-cyclopropene – butadiene cases, conformations **2A**–**2D** were found for both endo and exo addition. All, except for **2D** endo addition, which is second-order, are first-order saddle points. The exo geometries are favoured over the endo forms for each conformation. The lowest energy conformation for 3,3-NH_2-cyclopropene – butadiene endo addition is **2D**, unlike the other additions for NH_2 and PH_2, in which **2B** is the preferred conformer.

For both OH and SH substituents, two different first-order conformations (**3A** and **3B**) were obtained for both endo and exo addition, as shown in Fig. 3. The **3A** and **3B** exo transition-state structures for both OH and SH are favoured over their endo counterparts. Interestingly, the same conformation (**3A**) is preferred for both endo and exo addition for 3,3-OH-cyclopropene – butadiene, and the other conformation (**3B**) is the lowest in energy for both endo and exo addition for

© 2004 NRC Canada

Fig. 2. Examples of transition-state structures obtained for 3,3-NH_2(or PH_2)-cyclopropene with butadiene; NH_2 endo addition (**2A**), PH_2 endo addition (**2B**), PH_2 exo addition (**2C**), and NH_2 exo addition (**2D**).

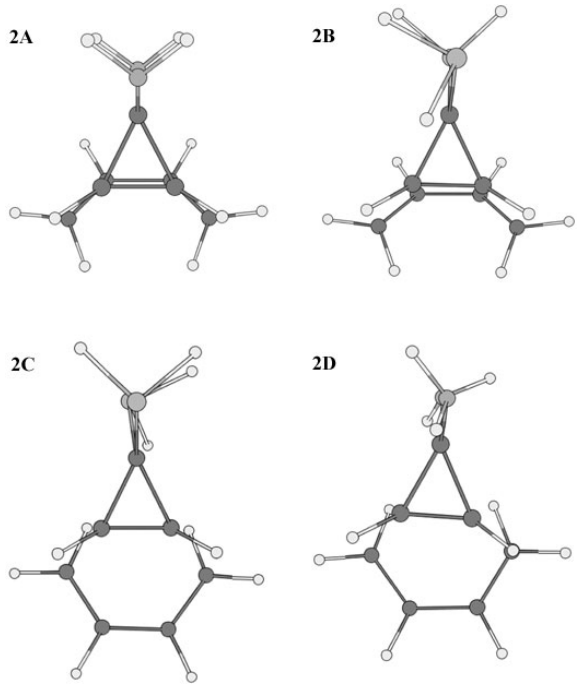
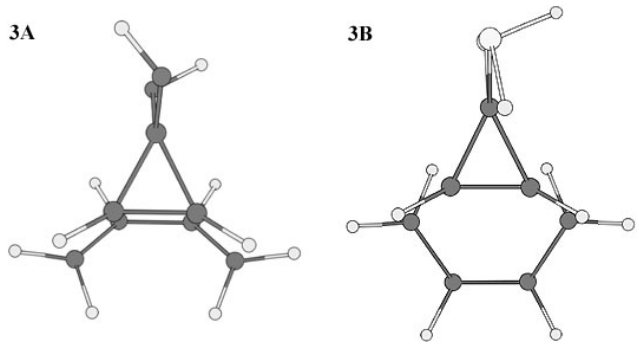


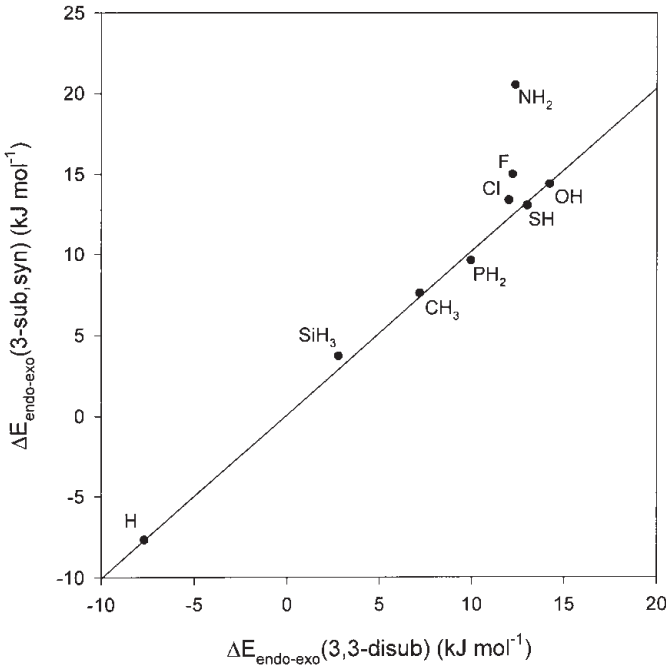
Fig. 3. Examples of transition-state structures obtained for 3,3-OH(or SH)-cyclopropene with butadiene; OH endo addition (**3A**) and SH exo addition (**3B**).



3,3-SH-cyclopropene – butadiene. These reactions exhibit 100% exo selectivity with $\Delta E_{\text{endo-exo}}$ of 14.2 and 13.0 kJ mol^{-1} at B3LYP/6-31++G(*d*) for OH and SH, respectively (Table 2). In both conformers, the H of the syn substituent is pointing away from the π bond (in endo addition) and away from the Hs of C-1 and C-4 of butadiene (in exo addition). The OH and SH substituents in both of their **3A** and **3B** conformations are positioned so as to minimize steric interactions with one another.

The 3-substituted cyclopropene with butadiene syn transition states from ref. 6 were optimized at B3LYP/6-31++G(*d*) to investigate the effects of disubstitution on energetics and structure. Figure 4 is a plot of $\Delta E_{\text{endo-exo}}$ of 3-substituted cyclopropene (syn) with butadiene vs. $\Delta E_{\text{endo-exo}}$ of 3,3-disubstituted cyclopropene with butadiene, illustrating

Fig. 4. Plot of $\Delta E_{\text{endo-exo}}$(3-substituted, syn, kJ mol^{-1}) vs. $\Delta E_{\text{endo-exo}}$(3,3-disubstituted, kJ mol^{-1}) at B3LYP/6-31++G(d).



the effect on the selectivity of adding the second substituent to the anti position of the monosubstituted syn transition state. The negative values of both Δ*E*s for cyclopropene are a result of the endo preference in the cyclopropene–butadiene parent system. As indicated in Table 3, many of the values for ΔΔ*E* between the 3-substituted and 3,3-disubstituted cases are essentially zero. Since the addition of the substituent to the anti position of the syn transition state has very little effect on the endo–exo selectivity in general, it may be deduced that the change in the nature of the dienophile (from monosubstituted to disubstituted) does not play as important a role when the steric interactions in the transition state are very similar, as is the case here. These similar steric interactions (syn substituent positioned over the diene) translate into very similar selectivities. In addition, it can be stated that, for this system, if there is a substituent *other than H* at the syn position of the transition state, exo selectivity will prevail irrespective of the electron-withdrawing or electron-donating nature of the group.

In Fig. 4, the one substituent worthy of note is NH_2 with a ΔΔ*E* of 8.2 kJ mol^{-1}. An examination of the ground-state and transition-state structures reveal that for both the mono- and disubstituted NH_2 dienophiles, there is a change in conformation of the substituent(s) from the ground state to the *exo* transition state. The NH_2 group of 3-NH_2-cyclopropene changes from the preferred gauche conformation in the ground state to a staggered conformation in the exo-syn transition-state structure, with the nitrogen lone pair pointing down towards the C-1 and C-4 Hs of butadiene. Based on

© 2004 NRC Canada

Table 3. A comparison of the calculated selectivities of 3-substituted cyclopropenes with butadiene (syn, endo and exo addition) with 3,3-disubstituted cyclopropenes with butadiene (endo and exo addition).

		3-Substituted cyclopropene		3,3-Disubstituted cyclopropene	
Substituent	$\Delta\Delta E^a$	Conf change from GS / mode of addition	GS ΔE_{conf}	Conf change from GS / mode of addition	GS ΔE_{conf}
SiH_3	0.9	Yes / endo	2.6	Yes / endo	1.1
PH_2	–0.4	No	0	No	0
H	0.0	No	0	No	0
CH_3	0.4	No	0	No	0
SH	0.0	No	0	Yes / endo, exo	1.4
Cl	1.4	No	0	No	0
NH_2	8.2	Yes / exo	2.2	Yes / exo	8.9
OH	0.2	Yes / exo	1.9	No	0
F	2.8	No	0	No	0

Note: All (Δ)ΔEs are in kJ mol^{-1}.
[a]Calculated as $\Delta E_{endo\text{-}exo}$(3-substituted, syn) – $\Delta E_{endo\text{-}exo}$(3,3-disubstituted).

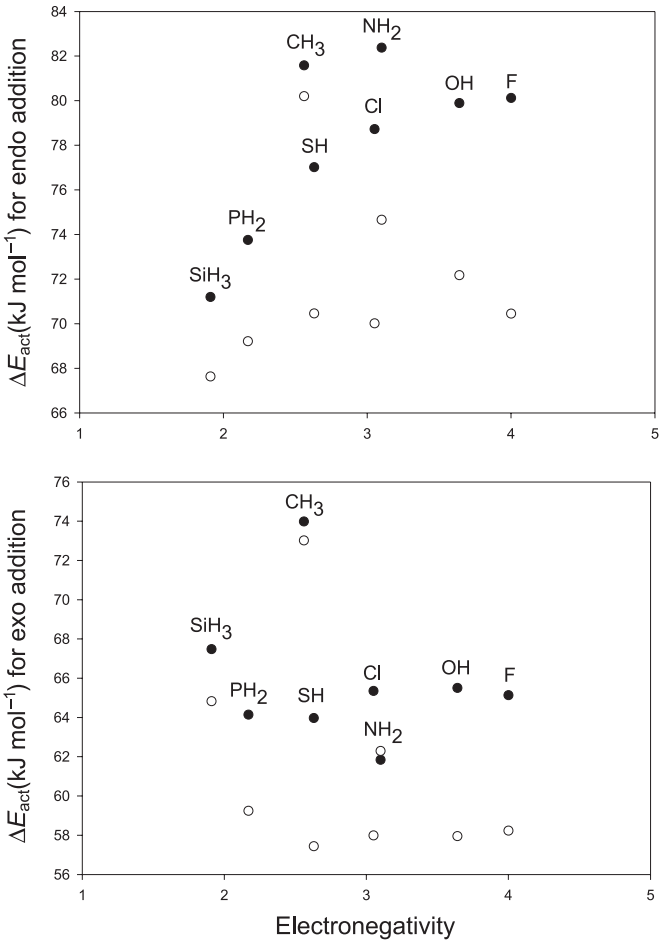
computed ground-state energies, the energy cost of this conformational change (ΔE_{conf}) is estimated to be 2.2 kJ mol^{-1}. Likewise, we see a change in conformation for the 3,3-NH_2-cyclopropene from the **2D** conformation in the ground state to **2B** in the exo transition state. This involves a rotation of the NH_2 group syn to the butadiene, which becomes staggered in the exo transition-state structure much like the NH_2 group of the 3-NH_2-cyclopropene in its exo-syn structure. However, we see that there is no conformational change of the anti NH_2 substituent from the ground state to the exo transition state, and it is likely that this introduces steric interactions between the two NH_2 groups. The ΔE_{conf} for the ground-state 3,3-NH_2-cyclopropene is 8.9 kJ mol^{-1}; thus, the estimated energy cost for the change in conformation for the 3,3-NH_2-cyclopropene system is about 6.7 kJ mol^{-1} greater than for the 3-substituted case, which compares favourably with the $\Delta\Delta E$ of 8.2 kJ mol^{-1}. It is concluded that while the presence of the second substituent at the anti position generally has very little effect on the endo–exo selectivity (Fig. 4), a *change in conformation* of one or more substituents in the transition state can have a significant effect on the selectivity if the conformational changes introduce unfavourable steric interactions. In this case, the activation energy required for the exo addition of 3,3-NH_2-cyclopropene to butadiene increases because of the energy cost of conformational change, resulting in a smaller endo–exo selectivity.

The effect of disubstitution on activation energy

Figure 5 depicts the plots of activation energies (ΔE_{act}) of the endo and exo modes of addition vs. electronegativities for the 3-substituted (syn) and 3,3-disubstituted cyclopropene with butadiene Diels–Alder reactions. As shown, for both endo and exo addition, the 3,3-disubstituted system has activation energies that are consistently *lower* than for the 3-substituted system for all substituents examined, with the single exception of NH_2 exo addition, where the 3-NH_2-cyclopropene with butadiene activation energy is lower than that of the 3,3-disubstituted analog ($\Delta\Delta E_{act}$ is approximately 0.5 kJ mol^{-1}).

It has been previously established that the 3,3-disubstitution of the cyclopropene ground state yields an additional stabilization of the ring and therefore should be less reactive. In view of this, one would expect an increase in activation energy for the disubstituted system above that for

Fig. 5. Plots of ΔE_{act} for endo (top) and exo (bottom) addition (kJ mol^{-1}) vs. the electronegativity of the substituent at B3LYP/6-31++G(d). For each plot, the filled circles represent the ΔE_{act} for the 3-substituted cyclopropene – butadiene syn addition, and the open circles represent the ΔE_{act} for the 3,3-disubstituted cyclopropene – butadiene addition.



© 2004 NRC Canada

Scheme 4.



the 3-substituted case; however, we see that the opposite is true. This implies that there is a significant stabilization component in the transition-state structure of 3,3-disubstituted cyclopropene and butadiene that enables an overall decrease in the activation barrier for the reaction. In Scheme 2, the addition of the second substituent to the ground-state 3-substituted cyclopropene results in a total stabilization–destabilization that is composed of two effects: the anomeric effect and the overall effect on the cyclopropene ring itself (represented as ΔE^{XX}_{stab} (anom-ring)). Scheme 3*b* illustrates a similar isodesmic reaction using cyclopropane.

The 3-substituted and 3,3-disubstituted cyclopropanes have the same substituent conformations as the corresponding substituted cyclopropenes, with the exception of SiH_3; the 3,3-SiH_3-cyclopropene has a slightly skewed conformation whereas the 3,3-SiH_3-cyclopropane has an eclipsed conformation. The cyclopropane isodesmic reaction (cyclopropane closely resembling the molecule of interest, cyclopropene) is a measure of the anomeric effect only (ΔE_{anom}). Assuming that the anomeric effect is energetically similar in both 3,3-disubstituted cyclopropenes and cyclopropanes for the same substituent, the difference between these reactions represents the degree to which the ring is affected upon disubstitution (Scheme 4), represented as $\Delta\Delta E_{ring}$.

Table 1 contains the ground-state cyclopropene and cyclopropane energetic data. The ΔE_{anom} of Scheme 3*b* compares favourably with the calculated values of the anomeric effect in a system of similarly substituted methanes and thus has no effect on the ring itself. The anomeric effect is stabilizing for all substituents except Cl, which is slightly destabilizing. The values for $\Delta\Delta E_{ring}$ are intended to show the degree of stabilization–destabilization that occurs because of the changes in the ring upon 3,3-disubstitution; these values are supported by observing the *actual* geometric changes that occur in the ground state upon substitution. Many of the substituents yield small negative values for $\Delta\Delta E_{ring}$ and these correlate well with the degree of elongation that occurs in the C=C bond of the ground-state cyclopropene upon addition of the second substituent (Table 1). The CH_3 substituent has almost zero $\Delta\Delta E_{ring}$ and likewise exhibits virtually no change in C=C bond length; the SiH_3 group, however, is substantially destabilizing ($\Delta\Delta E_{ring}$ = 10.38 kJ mol^{-1}) and shows a shortening of the C=C bond. The actual amount of ring stabilization–destabilization, given by $\Delta\Delta E_{ring}$ that results from the 3,3-disubstitution of cyclopropene is significantly less than the stabilization–destabilization observed for the first substitution represented in Scheme 1. In other words, the 3-substituted cyclopropenes exhibit a large stabilization (destabilization for SiH_3) as compared to cyclopropene itself; this is evident in both the stabilization energies as well as the geometrical changes that occur in the ring (Table 1). While the ground-state 3,3-disubstituted cyclopropenes show greater stabilities overall (again, greater destabilization for SiH_3) as compared with the 3-substituted analogs, the majority of this stability is a consequence of the anomeric effect, not the ring stabilization–destabilization. In some cases, the ring effect upon 3,3-disubstitution is actually destabilizing ($\Delta\Delta E_{ring}$ is positive for SiH_3, CH_3, and OH).

The question to address now is, what produces the drop in activation energy for the 3,3-disubstituted system below that of the 3-substituted case? It is assumed that the anomeric effect in the ground-state cyclopropenes and the transition-state structures for the 3,3-disubstituted system remain constant during the reaction. The 3,3-disubstituted cyclopropene–butadiene transition state must be stabilized due to the substantial relief of ring strain as the cyclopropene ring becomes more like cyclopropane. Therefore, the remaining stabilization (after accounting for the anomeric effect) is mostly due to the relaxation of the ring. This further stabilization of the cyclopropene ring produces a drop in the transition-state energy and an overall lowering of the energy barrier.

As an example and because it deserves comment, the OH substituent has a $\Delta\Delta E_{ring}$ that is destabilizing ($\Delta\Delta E_{ring}$ = 11.81 kJ mol^{-1}). Disubstitution with OH has a huge stabilizing anomeric effect (Table 1, ΔE_{anom}), and although there is the expected shortening of the C—C single bonds of 3,3-OH-cyclopropene upon disubstitution, there is no change in the C=C bond length. Normally, the C=C bond would lengthen to relieve bond–bond repulsion that derives from the increased electron density in the C—C bonds. As a consequence, the 3,3-OH-cyclopropene is destabilized by a large ring strain, which is relieved in the transition-state structure and corresponds to a large drop in activation energy.[2]

Conclusions

We have shown in the present computational study that for the Diels–Alder reactions of 3,3-disubstituted cyclopropenes with butadiene:

- The analysis of the 3-substituted and 3,3-disubstituted cyclopropene ground states shows the important role that the second substituent plays in the stability and reactivity of the dienophile. The anomeric effect produces an increased stability upon disubstitution, the consequence of which can be seen in the geometry of the ring.
- For all substituents examined, the transition-state structures of 3,3-disubstituted cyclopropene with butadiene is shown to prefer the exo isomer.
- The comparison of selectivities ($\Delta E_{endo\text{-}exo}$) between the syn 3-substituted cyclopropenes with butadiene and the 3,3-disubstituted cyclopropenes with butadiene correlated well with each other, and conformational analysis can be used to explain the deviation of the NH_2 substituent. It is concluded that for this system, the presence of a substituent *other than H* at the syn position of the transition state will result in exo selectivity, irrespective of the

[2] Supplementary data may be purchased from the Directory of Unpublished Data, Document Delivery, CISTI, National Research Council Canada, Ottawa, ON K1A 0S2, Canada (http://www.nrc.ca/cisti/irm/unpub_e.shtml for information on ordering electronically).

© 2004 NRC Canada

electron-withdrawing or electron-donating nature of the substituent.

- Interestingly, the activation energy barriers of the 3,3-disubstituted cyclopropene systems were lower than the syn 3-substituted cyclopropene systems, despite the expectant lower reactivity of the disubstituted analogs. Isodesmic reactions using ground-state cyclopropenes and cyclopropanes indicate that the anomeric effect accounts for the majority of the stabilization in the 3,3-disubstituted cyclopropenes, and only a small portion can be attributed to ring stabilization–destabilization.
- In summary, the effect of 3-substitution of an electron-withdrawing or -donating group on cyclopropene can be rationalized based on simple arguments; however, 3,3-disubstitution complicates matters considerably when investigating reactivity in the Diels–Alder reaction, and at times energetics and geometric changes need to be examined on a case-by-case basis.

Acknowledgments

We thank the Natural Sciences and Engineering Research Council of Canada (NSERC) for financial support as well as the Memorial University of Newfoundland Advanced Computation and Visualization Centre for computing resources.

References

1. K. Alder and G. Stein. Angew. Chem. **50**, 514 (1937).
2. Some recent examples: (*a*) M. Avalos, R. Babiano, J.L. Bravo, P. Cintas, J.L. Jiménez, J.C. Palacios, and M.A. Silva. J. Org. Chem. **65**, 6613 (2000); (*b*) J.L. García Ruano, C. Alemparte, A.M. Martín Castro, H. Adams, and J.H. Rodriguez Ramos. J. Org. Chem. **65**, 7938 (2000); (*c*) S. Kong and J.D. Evanseck. J. Am. Chem. Soc. **122**, 10 418 (2000); (*d*) M. Ge, B.M. Stoltz, and E.J. Corey. Org. Lett. **2**, 1927 (2000); (*e*) A.G. Leach and K.N. Houk. J. Org. Chem. **66**, 5192 (2001); (*f*) A. Arrieta and F.P. Cossío. J. Org. Chem. **66**, 6178 (2001); (*g*) P. Caramella, P. Quadrelli, and L. Toma. J. Am. Chem. Soc. **124**, 1130 (2002).
3. (*a*) K.B. Wiberg and W.J. Bartley. J. Am. Chem. Soc. **82**, 6375 (1960); (*b*) J.E. Baldwin and V.P. Reddy. J. Org. Chem. **54**, 5264 (1989); (*c*) Y. Apeloig and E. Matzner. J. Am. Chem. Soc. **117**, 5375 (1995); (*d*) B.S. Jursic. J. Org. Chem. **62**, 3046 (1997); (*e*) M. Sodupe, R. Rios, V. Branchadell, T. Nicholas, A. Oliva, and J.J. Dannenberg. J. Am. Chem. Soc. **119**, 4232 (1997); (*f*) B.S. Jursic. J. Mol. Struct. **454**, 117 (1998); (*g*) M. Imade, H. Hirao, K. Omoto, and H. Fujimoto. J. Org. Chem. **64**, 6697 (1999).
4. (*a*) R. Breslow and M. Oda. J. Am. Chem. Soc. **94**, 4787 (1972); (*b*) M. Oda, R. Breslow, and J. Pecoraro. Tetrahedron Lett. **13**, 4419 (1972); (*c*) P. Binger, P. Wedemann, R. Goddard, and U.H. Brinker. J. Org. Chem. **61**, 6462 (1996); (*d*) B.S. Jursic. Tetrahedron Lett. **38**, 1305 (1997).
5. R.B. Woodward and R. Hoffmann. The conservation of orbital symmetry. Verlag Chemie, Weinheim, Germany. 1971.
6. J.D. Xidos, T.L. Gosse, E.D. Burke, R.A. Poirier, and D.J. Burnell. J. Am. Chem. Soc. **123**, 5482 (2001).
7. J.I. Garcia, J.A. Mayoral, and L. Salvatella. Acc. Chem. Res. **33**, 658 (2000).
8. A. Ogawa and H. Fujimoto. Tetrahedron Lett. **43**, 2055 (2002).
9. M.M. Latypova, V.V. Plemenkov, V.N. Kalinina, and I.G. Bolesov. Zh. Org. Khim. **20**, 542 (1984).
10. Y. Apeloig, D. Arad, M. Kapon, and M. Wallerstein. Tetrahedron Lett. **28**, 5917 (1987).
11. D.L. Boger and C.E. Brotherton. Tetrahedron, **42**, 2777 (1986).
12. R.A. Poirier. MUNgauss. Fortran 90 version [computer program]. Department of Chemistry, Memorial University of Newfoundland, St. John's, Newfoundland, Canada. 2001. With contributions from S.D. Bungay, A. El-Sherbiny, T.L. Gosse, D. Keefe, C.C. Pye, D. Reid, M. Shaw, Y. Wang, and J.D. Xidos.
13. M.J. Frisch, G.W. Trucks, H.B. Schlegel, G.E. Scuseria, M.A. Robb, J.R. Cheeseman, V.G. Zakrzewski, J.A. Montgomery, Jr., R.E. Stratmann, J.C. Burant, S. Dapprich, J.M. Millam, A.D. Daniels, K.N. Kudin, M.C. Strain, O. Farkas, J. Tomasi, V. Barone, M. Cossi, R. Cammi, B. Mennucci, C. Pomelli, C. Adamo, S. Clifford, J. Ochterski, G.A. Petersson, P.Y. Ayala, Q. Cui, K. Morokuma, N. Rega, P. Salvador, J.J. Dannenberg, D.K. Malick, A.D. Rabuck, K. Raghavachari, J.B. Foresman, J. Cioslowski, J.V. Ortiz, A.G. Baboul, B.B. Stefanov, G. Liu, A. Liashenko, P. Piskorz, I. Komaromi, R. Gomperts, R.L. Martin, D.J. Fox, T. Keith, M.A. Al-Laham, C.Y. Peng, A. Nanayakkara, M. Challacombe, P.M.W. Gill, B. Johnson, W. Chen, M.W. Wong, J.L. Andres, C. Gonzalez, M. Head-Gordon, E.S. Replogle, and J.A. Pople. Gaussian 98. Revision A.11.3 [computer program]. Gaussian, Inc., Pittsburgh, Penn. 2002.
14. R.J. Boyd and K.E. Edgecombe. J. Am. Chem. Soc. **110**, 4182 (1988).
15. W.J. Hehre, L. Radom, P.v.R. Schleyer, and J.A. Pople. Ab initio molecular orbital theory. Wiley-Interscience, New York. 1986.

© 2004 NRC Canada

Liquid-phase oxidation of benzene to phenol by copper catalysts in aqueous solvent with a high acetic acid concentration

Takahiro Kitamura, Hiroshi Kanzaki, Rei Hamada, Satoru Nishiyama, and Shigeru Tsuruya

Abstract: The liquid-phase catalytic oxidation of benzene was carried out under mild reaction conditions over Cu-impregnated zeolite catalysts (Cu/NaX, Cu/HX, Cu/NaY, Cu/HY, Cu/NaZSM-5, Cu/HZSM-5, Cu/Namordenite, Cu/Hmordenite, and Cu/Hbeta) using both molecular oxygen and ascorbic acid as the oxidant and the reducing reagents, respectively. Phenol was exclusively produced as the oxidation product and no other product was detected. Among the catalysts tested in this study, the Cu/HY catalyst had the highest activity for phenol formation. H-type zeolites were more effective supports for phenol formation than the corresponding Na-type ones. The yield of phenol was found to increase with the simultaneous increase in the amounts of both the supported Cu and the added ascorbic acid. The Cu species supported on HY began to elute as Cu^{2+} species in the solvent from the HY support with the initiation of the oxidation of benzene. The dissolved Cu^{2+} species were reduced to form precipitated Cu^{1+} species during the benzene oxidation. The homogeneous Cu species dissolved from the Cu/HY catalyst were thus suggested as mainly contributing to the phenol formation. The precipitated Cu^{1+} species that had no activity for the benzene oxidation were found to be regenerated in their oxidation activity toward phenol formation by calcination of the Cu^{1+} species in flowing air, although parts of the Cu species were found to be converted to aggregated CuO during the calcination.

Key words: supported copper catalysts, zeolite, oxidation, benzene, phenol, oxygen, ascorbic acid.

Résumé : On a effectué l'oxydation catalytique du benzène en phase liquide, dans des conditions douces, sur des catalyseurs de zéolite imprégnée de cuivre (Cu/NaX, C/HX, Cu/NaY, Cu/HY, Cu/NaZSM-5, Cu/HZSM-5, Cu/Namordenite, Cu/Hmordenite et Cu/Hbeta), en utilisant de l'oxygène moléculaire et de l'acide ascorbique respectivement comme agents oxydant et réducteur. Le seul produit d'oxydation est le phénol et aucun autre produit n'a été détecté. Parmi les catalyseurs évalués dans cette étude, le catalyseur Cu/HY présente l'activité la plus élevée pour la formation de phénol. Les zéolites du type H sont des supports plus efficaces que les supports correspondants de type Na pour la formation de phénol. On a observé que le rendement en phénol augmente avec une augmentation simultanée dans les quantités à la fois du Cu supporté et de l'acide ascorbique ajouté. Les entités de Cu supportées sur HY commencent à s'éluer du support HY vers le solvant, sous la forme de cations Cu^{2+}, dès le début de l'oxydation de benzène. Au cours de l'oxydation du benzène, les cations Cu^{2+} sont réduits en espèces Cu^{1+} qui précipitent. On suggère donc que les espèces Cu homogènes, dissoutes du catalyseur Cu/HY, sont les principales à contribuer à la formation du phénol. On a observé que, si on soumet les espèces Cu^{1+} qui ont précipité à une calcination avec circulation d'air, elles peuvent être partiellement régénérées dans leur activité oxydante conduisant à la formation de phénol, même si une certaine partie de ces entités est transformée en CuO agrégé au cours de cette calcination.

Mots clés : catalyseurs de cuivre supportés, zéolite, oxydation, benzène, phénol, oxygène, acide ascorbique.

[Traduit par la Rédaction]

Introduction

Phenol, one of the key chemicals that serve as a precursor for resins, synthetic fibers, agrochemicals, and dyestuffs, has been mostly produced using the cumene process developed by BP Chemicals and Hercules (1). This process consists of three steps in which each step is highly selective and produces acetone as a by-product, in addition to phenol. The production of phenol using the toluene process (2) that consisted of two steps and produced no acetone has been carried out at a few plants. One-step synthesis of phenol by a direct oxygenation of benzene must have an advantage in the sim-

Received 9 November 2003. Published on the NRC Research Press Web site at http://canjchem.nrc.ca on 1 December 2004.

T. Kitamura, H. Kanzaki, and R. Hamada. Division of Molecular Science, Graduate School of Science and Technology, Kobe University, Nada, Kobe 657-8501, Japan.
S. Nishiyama and S. Tsuruya.[1] Department of Chemical Science and Engineering, Faculty of Engineering, Kobe University, Nada, Kobe 657-8501, Japan.

[1]Corresponding author (e-mail: tsuruya@cx.kobe-u.ac.jp).

 doi: 10.1139/V04-123 © 2004 NRC Canada

plicity of the process and the saving of production costs. From an organic synthetic chemical point of view, the direct insertion of an oxygen atom into the benzene ring is one of the most difficult and challenging steps among a variety of oxidation steps. The liquid-phase oxidation of benzene to phenol was reported using a ferric sulfate – hydrogen peroxide system (3) (Fenton reagent) and a Fe^{3+}–H_2O_2–catechol system (4) (Hamilton reagent). More recently, phenol syntheses from benzene utilizing the activation of molecular oxygen with various reducing reagents have been studied under relatively mild reaction conditions. The oxidation of benzene to phenol using a $Pt/V_2O_5/SiO_2$ (5) or $Pd/V_2O_5/SiO_2$ (6) catalyst in the presence of both O_2 and H_2, and using a $EuCl_3$-$TiO(acac)_2$ catalyst (7) in an aqueous acetic acid solvent in the presence of both O_2 and Zn^0 has been reported. The catalytic activities for hydroxylation of benzene in the presence of aq. H_2O_2 were examined using site-substituted vanadium(V) heteropolyacids (8). The oxidation of benzene to phenol at 130 °C using molecular oxygen was reported (9) in the presence of palladium and heteropolyacids, which is used as a promoter for the reoxidation of the palladium (the yield of phenol: 10.5%). Further, titanium silicalite (TS-1) was studied (10) as the catalyst for phenol production by the benzene oxidation under solvent-free, triphase conditions using aq. H_2O_2 as an oxidant. More recently, direct oxidation of benzene to phenol in sulfolane solvent at 100 °C with hydrogen peroxide was reported (11) using a titanium silicate catalyst modified with NH_4HF_2 and H_2O_2 (the yield of phenol: 8.1%). We have also attempted the liquid-phase oxidation of benzene to phenol using Cu ion-exchanged zeolites (12), Cu catalysts impregnated on some amorphous oxide supports (13), Cu catalysts supported on MCM-41 (14), Cu catalysts prepared by coprecipitation of both Cu and Al nitrates (15), and Cu catalysts supported on Al_2O_3 (16) in the presence of both O_2 and ascorbic acid. The vanadium catalysts supported on SiO_2 (17) (the yield of phenol: 4.1%) and Al_2O_3 (18) (the yield of phenol: 8.4%) have been reported to function as catalysts for the phenol formation in the presence of O_2 and ascorbic acid. An aqueous solution with high acetic acid concentration has been found to be an effective solvent for phenol formation, irrespective of the supported Cu (15, 16) (the yield of phenol: 3.0%) or V (18) catalysts. We have been interested in the liquid-phase oxidation of benzene to phenol using gaseous O_2 as an oxidant, rather than H_2O_2, because of its economical and safety point of views, although the yield of phenol using O_2, in place of H_2O_2, was rather low. The liquid-phase oxidation of benzene to phenol over supported Cu catalysts using molecular O_2 as an oxidant has hardly been reported, although the reports on the corresponding oxidation using H_2O_2 as an oxidant have been so far published.

In this study, the liquid-phase oxidation of benzene to phenol in an aqueous solvent with high acetic acid concentration was investigated using the Cu catalysts supported on zeolites, mainly HY zeolite. A variety of reaction conditions were attempted to promote the phenol production. The fate and the oxidation states of the Cu species supported on HY zeolite were followed during the oxidation of benzene to phenol to seek the cause of deactivation of the supported Cu catalysts in the initial stage of the benzene oxidation. Homogeneous Cu species that were dissolved in the solvent from the Cu-supported HY catalyst were suggested to be the main active Cu species for phenol formation.

Experimental

Catalysts

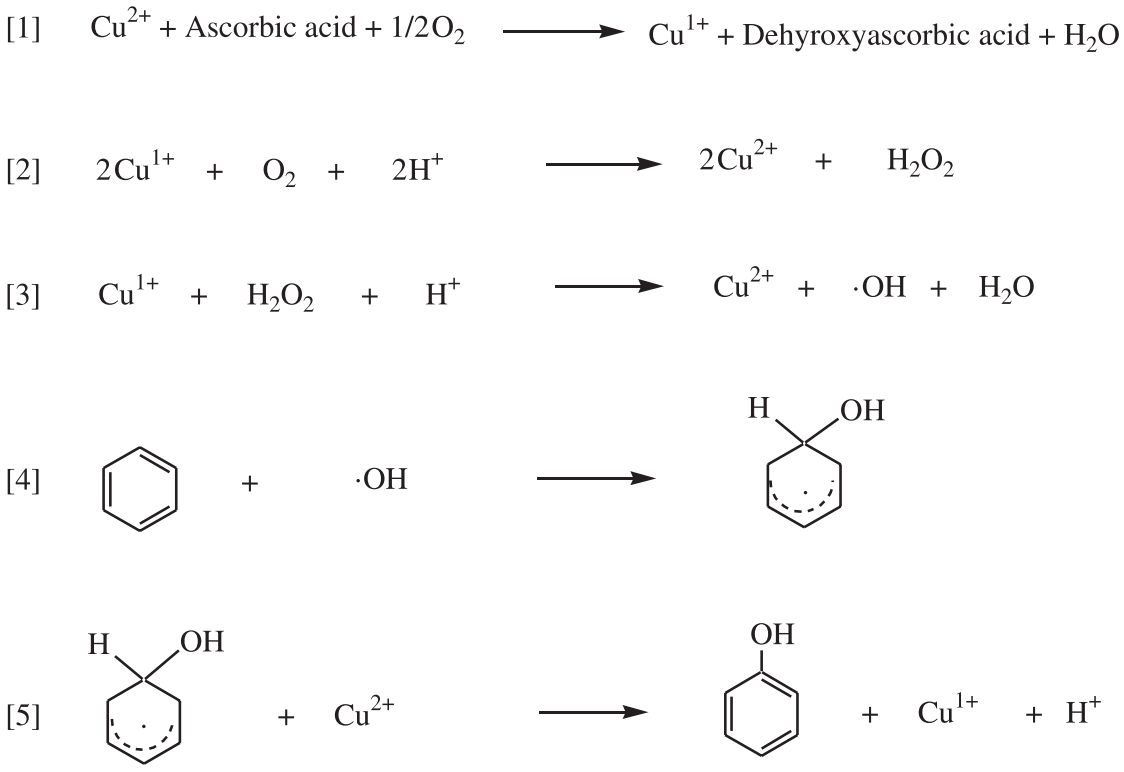
NaX (Tosoh, Si/Al = 1.25), NaY (Tosoh, Si/Al = 2.85), and mordenite (JRC-Z-M2O, Si/Al = 13) were used as supports after washing in water, drying at 393 K overnight, and calcining at 773 K for 5 h. NaZSM-5 was prepared according to a patent (19). The prepared ZSM-5 zeolite (Si/Al = 58) was treated twice with aq. 1 mol/L $NaNO_3$ solution at 353 K for 1 h, dried at 393 K overnight, and calcined at 773 K for 5 h in flowing air. HX, HY, H-mordenite, and HZSM-5 zeolites were prepared by treating the corresponding Na-zeolites three times with aq. 1 mol/L NH_4NO_3 solution at 343–353 K for 6 h, drying at 393 K overnight, and calcining at 773 K for 5 h in flowing air. HBeta support was used as received (JRC-Z-HB25, Si/Al = 16). The corresponding Cu-impregnated zeolites (Cu/zeolite) were prepared by the usual impregnation method using $Cu(CH_3COO)_2 \cdot H_2O$ (Nacalai, guaranteed reagent). The Cu/zeolite was dried at 393 K overnight and calcined at 773 K for 5 h in flowing air. In the case of the HY support, Cu ion-exchanged HY (Cu/HY) was also prepared by the usual ion-exchange method at 353 K for 2 h. The Cu/Y was dried at 393 K overnight and calcined at 773 K for 5 h in flowing air. The alkali metal-added Cu/HY catalysts were prepared by impregnating the alkali metal acetate on the Cu/HY, drying at 393 K overnight, and calcining at 773 K for 5 h. The Fe- and the Sn-added Cu/HY catalysts were prepared by impregnating $Fe(NO_3)_2 \cdot 9H_2O$ (Nacalai, guaranteed reagent) and $SnCl_2 \cdot 2H_2O$ (Nacalai, guaranteed reagent) on the Cu/HY, respectively, drying at 393 K overnight, and calcining at 773 K for 5 h in flowing air. The amounts of the various metals supported on the zeolites were determined using an atomic absorption spectrometer (Shimazu type AA-6200) after the catalyst was dissolved homogeneously by adding a few drops of hydrogen fluoride (Sterachemifer, guaranteed reagent 46%–48%).

Liquid-phase oxidation of benzene

All the reagents, except CuCl, were used as received without further purification. CuCl (Nacalai, guaranteed reagent) was treated with aqueous ascorbic acid and dried at 373 K for 3 h in flowing N_2. The liquid-phase oxidation of benzene was carried out using a 50 cm^3 flat-bottomed flask with a magnetic stirrer under the standard conditions of 20 cm^3 aqueous acetic acid solvent, 0.1 MPa O_2, a reaction temperature of 303 K, and a reaction time of 24 h. After removing the solid catalyst by centrifuging the reaction mixture mixed with 2-propanol as an internal standard, the reaction solution was analyzed at 463 K under a N_2 carrier (44 cm^3/min) using a gas chromatograph (Shimazu type GC-8A) with a 3 m stainless column packed with silicon OV-17. No 2-propanol was confirmed to be oxidized during the analytical treatment. The quantitative analyses of the amount of the "apparent" (see the Results and discussion section) Cu leaching were carried out by measuring the Cu amount dissolved in the filtrate using atomic absorption equipment after separating the solid catalyst from the reaction solution by centrifugation.

© 2004 NRC Canada

Scheme 1.



Instrumental analyses

The X-ray diffraction (XRD) patterns of both the fresh and the used Cu/HY catalysts were observed at room temperature using a Rigaku RINT 2000 XRD instrument with an X-ray source of Cu Kα. The used catalyst, before the XRD measurement, was separated from the reaction solution by centrifuging, washed with acetone, and dried at 393 K overnight or calcined at 773 K for 5 h in flowing air.

UV–vis ray absorption spectra of the Cu species in the solution were measured in an air atmosphere using a Shimazu UV-240 spectrophotometer.

Diffuse reflectance (DR) spectra of the fresh, the used, and the reduced Cu/HY catalysts were measured at room temperature using a Hitachi type U-3210 spectrophotometer equipped with an integral sphere. The obtained data were transformed to the corresponding Kubelka–Munk (K-M) function using an applied program. Before the DR measurement, the used catalyst was washed several times with acetone and dried at 393 K overnight or calcined at 773 K for 5 h. The reduced catalyst was prepared by treating the Cu/HY catalyst with 100 torr H_2 (1 torr = 133.322 4 Pa) at 573 K for 1 h followed by degassing at the same temperature for 30 min.

The fluorescence spectra of the fresh, the used, and the reduced Cu/HY catalyst were measured at room temperature using a Nihon Bunkoh type FP-750 spectrophotometer with an excitation energy source of 267.0 nm. All the catalysts were treated in the same manner as those in the DR measurement.

The electron spin resonance (ESR) spectra of the catalysts were measured at room temperature using a JEOL type JES-TE-300 instrument. The fresh catalyst was degassed at 473 K for 2 h before the ESR measurement. The used catalysts, which were centrifuged from the reaction solution and washed with acetone several times and dried at 393 K overnight or calcined at 773 K for 5 h in flowing air, were also degassed at 473 K for 2 h before the ESR measurement.

Results and discussion

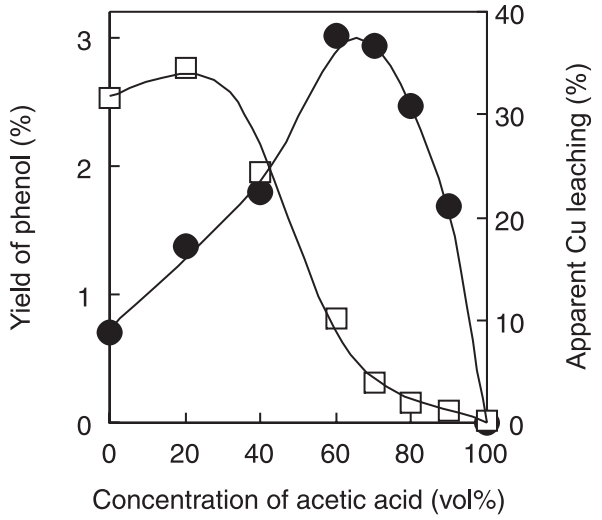
Liquid-phase oxidation of benzene to phenol with supported Cu catalysts

No other product except phenol was detected using the Cu catalysts supported on various zeolites under the reaction conditions (thus, the selectivity toward phenol is 100%). A plausible catalytic scheme of the phenol formation over the Cu catalysts supported on zeolites using both oxygen and ascorbic acid as an oxidant and a reducing reagent, respectively, will be substantially similar to the previously proposed one (Scheme 1) (3, 15). The proposed scheme includes H_2O_2 as an intermediate, although the catalysts deactivate at the initial stage of the benzene oxidation because of the irreversible reduction of the Cu^{2+} species to Cu^{1+} ones, as discussed afterward.

The amount of Cu dissolved from the Cu/HY catalyst during the benzene oxidation was obtained by measuring the Cu amount dissolved in the filtrate of the reaction solution after separating the solid catalyst by centrifugation. However, some of the dissolved Cu species are considered to become insoluble Cu^{1+} species during the benzene oxidation (14, 15). We observed Cu^{1+} species on the recovered Cu/HY catalyst as described in the redox behavior of the Cu species of the Cu/HY catalyst during benzene oxidation section. Thus, the solid catalyst separated by centrifugation seems to con-

© 2004 NRC Canada

Fig. 1. Dependence of both the yield of phenol and the percentage of apparent Cu leaching on the volumetric concentration of acetic acid. Catalyst (0.4 g of Cu(2)/HY, Cu amount (2 wt%)), benzene (22.5 mmol), reducing reagent (4 mmol of ascorbic acid), solvent (20 cm^3 of aqueous acetic acid), 0.1 MPa of O_2, reaction temperature (303 K), reaction time (24 h), yield of phenol (●), percentage of apparent Cu leaching (□).



tain the insoluble Cu^{1+} species originated from the Cu (possibly Cu^{2+} species) species leached from the Cu/HY catalyst. Owing to these quite complex situations of the Cu species in the measurement of dissolved Cu species, the amount of leached Cu measured will underestimate the amount actually leached from the Cu/HY catalyst. This is the reason why the term apparent was used in both the amount and the percentage of the leached Cu thereinafter.

The dependence of both the yield of phenol and the percentage of apparent Cu leaching on the concentration of acetic acid using the Cu(2)/HY (Cu amount, 2 wt%) catalyst are illustrated in Fig. 1. The yield of phenol obtained over the Cu/HY catalyst was comparable to the one over the Cu catalyst supported on Al_2O_3 (15). The yield of phenol, being 0.7% in H_2O solvent, increased with the increase in the amount of acetic acid and had a maximum value at an acetic acid concentration of around 60 vol%. A further increase in the volumetric concentration of acetic acid caused a sharp decline in the yield of phenol, and no phenol was obtained in pure acetic acid. If the medium is too acidic, reduction of Cu^{2+} to Cu^{1+} will be difficult (20). The Cu^{1+} ions are necessary for the formation of H_2O_2 that is used in the phenol formation (15). The high yield of phenol in the aqueous solvent with the higher acetic acid concentration was due to the fact that H_2O_2 has been reported (21) to be stable in acid media. The maximum yield of phenol at the acetic acid concentration of around 60 vol% is thought to be due to the trade-off between the easiness of the reduction of Cu^{2+} species and both the effective production and the stability of the produced H_2O_2, which is crucial for phenol formation. Similar results were obtained using other supported Cu (15) and V (17, 18) catalysts.

The percentage of the apparent Cu leaching was significantly inhibited with increasing acetic acid volumetric concentration and fell to less than 2% at an acetic acid concentration of more than 80 vol% (Fig. 1). Hereafter, aqueous 80 vol% acetic acid solvent was used because of both the low apparent Cu leaching and the comparatively high yield of phenol.

Table 1. Effect of zeolite support on both the yield of phenol and the apparent Cu leaching.[a]

Catalyst	Phenol yield (%)	Apparent Cu leaching (%)
Cu/NaX	2.0	6.5
Cu/HX	2.3	1.5
Cu/NaY	2.2	0.5
Cu/HY	2.5	2.0
Cu/NaZSM-5	1.5	0.1
Cu/HZSM-5	1.7	0.1
Cu/Namordenite	0.8	Trace
Cu/Hmordenite	0.9	0.4
Cu/Hbeta	1.8	0.3

[a]Cu content (2 wt% (0.31 mmol/g-cat)), catalyst (0.4 g), benzene (22.5 mmol), solvent (20 cm^3 of aqueous solution containing 80 vol% acetic acid), reducing reagent (4 mmol ascorbic acid), oxidant (0.1 MPa O_2), reaction temperature (303 K), reaction time (24 h).

The effect of the zeolite support on the yield of phenol and the apparent Cu leaching was investigated as summarized in Table 1. H-type zeolite had a higher yield of phenol than the Na-type zeolite in comparison with the same structural zeolites, though the Cu species supported on the H-type zeolite tended to leach more easily. Hereafter, the liquid-phase oxidation of benzene using the Cu/HY catalyst in aqueous solvent containing 80 vol% acetic acid was investigated in detail.

Some reducing reagents, $SnCl_2 \cdot H_2O$, Zn powder, $Zn(CH_3COO)_2$, Na_2SO_3, sodium thiosulfate, hydroquinone, and pyrocatechol, were tried in the place of ascorbic acid (0.4 g of Cu/HY (Cu, 2 wt%), benzene (22.5 mmol), 20 mL of aqueous acetic acid (80 vol%) solvent, reducing reagent (4 mmol), 0.1 MPa of O_2, reaction temperature (303 K), reaction time (24 h)). However, all these reagents have no activity for phenol formation, except $SnCl_2 \cdot H_2O$, the use of which as a reducing reagent produced a low yield of phenol (0.4%). Alkali metal, Fe, or Sn added to the Cu/HY (Cu, 2 wt%; added metal/Cu atomic ratio = 2) catalyst hardly promoted the catalytic activity for the phenol formation using ascorbic acid as a reducing reagent.

The dependence of the yield of phenol on the amount of impregnated Cu using 0.4 g of the Cu/HY catalyst is illustrated in Fig. 2. The yield of phenol obtained using the Cu ion-exchanged HY catalyst (Cu-HY) is also shown in Fig. 2. The yield of phenol had a maximum value at the amount of supported Cu of around 2.5 wt% (Cu, around 0.19 mmol), irrespective of the supported method of Cu, though the yield of phenol catalyzed by the Cu-HY considerably decreased at a higher amount of supported Cu. The dependence of the yield of phenol on the amount of the Cu(2)/HY catalyst was investigated (Fig. 3). The yield of phenol had a maximum value at an amount of the Cu(2)/HY catalyst of around 0.6 g, of which Cu corresponds to 0.19 mmol. All the results of Figs. 1–3 were obtained under the condition of a constant amount of ascorbic acid. The dependence of the amount of ascorbic acid on the phenol yield using a 0.4 g Cu(2)/HY catalyst is illustrated in Fig. 4. The yield of phenol increased

© 2004 NRC Canada

Fig. 2. Dependence of the yield of phenol on the amount of supported Cu. Benzene (22.5 mmol), reducing reagent (4 mmol of ascorbic acid), solvent (20 cm^3 of aqueous acetic acid), 0.1 MPa of O_2, reaction temperature (303 K), reaction time (24 h), 0.4 g of Cu/HY (impregnated Cu) catalyst (●), 0.4 g of Cu-HY (ion-exchanged Cu) catalyst (■).

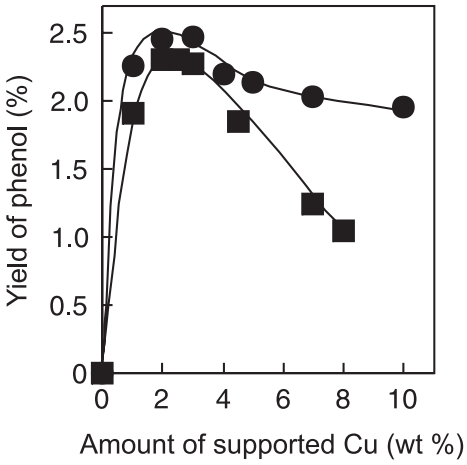
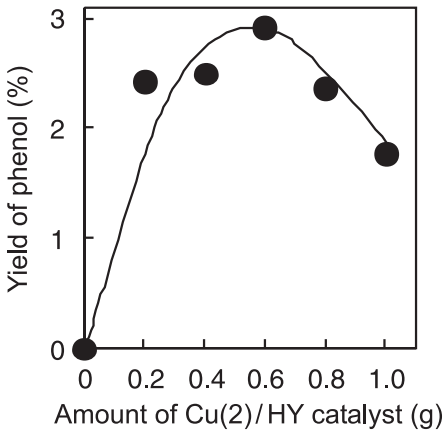


Fig. 3. Dependence of the yield of phenol on the amount of Cu(2)/HY catalyst. Benzene (22.5 mmol), reducing reagent (4 mmol of ascorbic acid), solvent (20 cm^3 of aqueous acetic acid), 0.1 MPa of O_2, reaction temperature (303 K), reaction time (24 h).



with the increase in the amount of ascorbic acid and passed through a maximum. A further increase in ascorbic acid tended to cause a decrease in the yield of phenol. The H_2O_2 produced during the oxidation, which is necessary for phenol formation, may be consumed by excess ascorbic acid. The dependence of the yield of phenol on the amount of supported Cu under the condition of constant supported Cu/ascorbic acid ratios is illustrated in Fig. 5. The yield of phenol increased almost linearly with the amount of supported Cu at a constant ascorbic acid/Cu ratio.

Contribution of the leached Cu species to phenol formation

The relationships between both the phenol yield and the percentage of apparent Cu leaching, and the reaction time were investigated using the Cu(2)/HY catalyst (Fig. 6). The yield of phenol sharply increased up to an initial reaction

Fig. 4. Dependence of the yield of phenol on the amount of ascorbic acid. Catalyst (0.4 g of Cu(2)/HY), benzene (22.5 mmol), reducing reagent (4 mmol of ascorbic acid), solvent (20 cm^3 of aqueous acetic acid), 0.1 MPa of O_2, reaction temperature (303 K), reaction time (24 h).

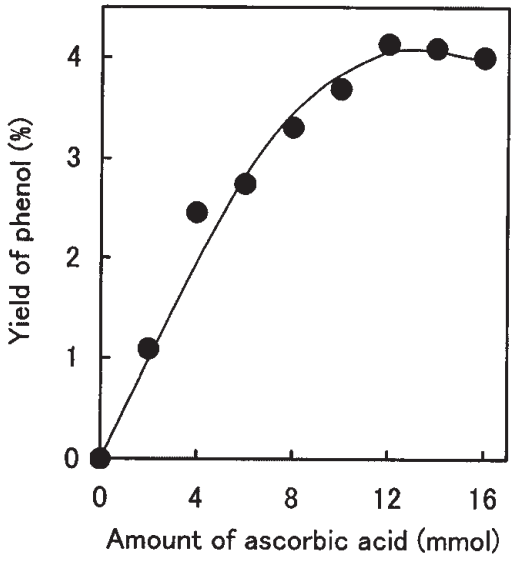
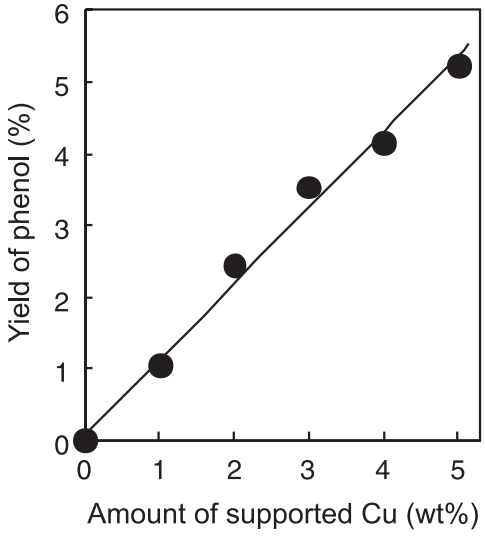


Fig. 5. Dependence of the yield of phenol on the amount of impregnated Cu at constant impregnated Cu/ascorbic acid ratios. Catalyst (0.4 g of Cu(2)/HY), benzene (22.5 mmol), solvent (20 cm^3 of aqueous acetic acid), 0.1 MPa of O_2, reaction temperature (303 K), reaction time (24 h).



time of around 5 h followed by an almost leveling off of the phenol production. The percentage of the apparent Cu leaching abruptly increased up to a reaction time of around 5 h followed by a significant decline in the apparent Cu leaching and the retention of a low percentage of Cu leaching. This observation will be interpreted as follows: the Cu species are eluted from the Cu/HY catalyst in the initial stage of the reaction, and afterward the eluted Cu species are rapidly precipitated followed by an apparently low percentage of Cu leaching (apparent Cu leaching). The combined results between the yield of phenol and the apparent Cu leaching in

© 2004 NRC Canada

Fig. 6. Dependence of both the yield of phenol and the percentage of the apparent Cu leaching on the reaction time. Catalyst (0.4 g of Cu(2)/HY, Cu amount, 2 wt%)), benzene (22.5 mmol), reducing reagent (4 mmol of ascorbic acid), solvent (20 cm^3 of aqueous acetic acid), 0.1 MPa of O_2, reaction temperature (303 K), reaction time (24 h), yield of phenol (●), percentage of apparent Cu leaching (□).

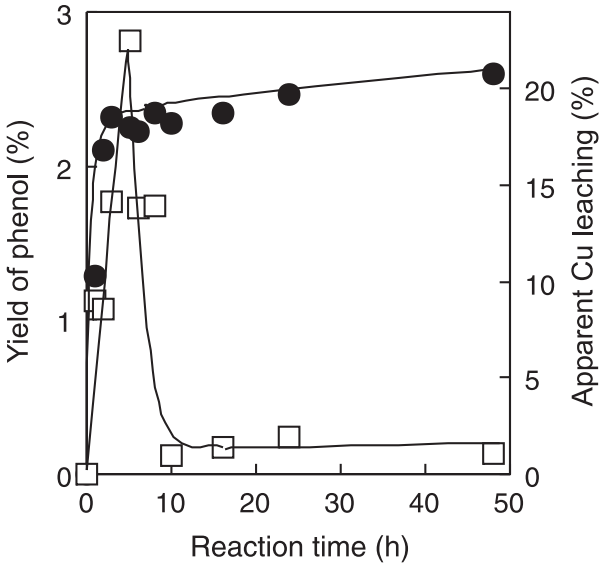


Fig. 6 suggest that the Cu species leached into the reaction solution in the initial stage are responsible for the phenol formation and are rapidly deactivated to form an insoluble Cu species during the oxidation of benzene to phenol. Thus, the soluble Cu species will be the main active species for phenol formation. To confirm the behavior of the Cu species during the reaction, the oxidation of benzene was attempted using unsupported $Cu(CH_3COO)_2{\cdot}H_2O$, instead of the Cu(2)/HY catalyst (Fig. 7). The concentration of soluble Cu species decreased rapidly with the reaction time, together with a sharp increase in the yield of phenol in the initial stage of the benzene oxidation. To investigate the activity of the Cu species supported on the zeolite for phenol formation, rather than the eluted Cu species, the time dependence of both the yield of phenol and the apparent Cu leaching were observed using the Cu(2)/NaM catalyst, of which the apparent Cu leaching was very low (Fig. 8). The yield of phenol sharply increased in the initial stage and almost leveled off after a reaction time of around 5 h similar to that demonstrated in Figs. 6 and 7. However, the percentage of the apparent Cu leaching remained very low irrespective of the reaction time. Thus, the amount of phenol detected (Fig. 8) will be mainly formed by the Cu species supported on the NaM zeolite, rather than by the eluted Cu species. The Cu species supported on a zeolite were also found to be active for the phenol formation, though the intrinsic activity of the supported Cu species is lower than that of the eluted Cu species.

Deactivation and regeneration of the Cu/HY catalyst in benzene oxidation

As evidenced from the dependence of the yield of phenol on the reaction time illustrated in Figs. 6–8, the Cu/HY catalyst (including the eluted Cu species) was quickly deactivated in the initial stage of the benzene oxidation. Both the supported and the eluted Cu species may be irreversibly reduced to the Cu^{1+} species accompanying the formation of phenol in the initial stage, of which the reduced Cu^{1+} species are precipitated and cause the low apparent Cu leaching as illustrated in Fig. 6. To attempt regeneration of the used Cu/HY catalyst, the catalyst was retrieved by centrifugation from the reaction solution after a reaction time of 24 h, washed with acetone, and dried at 393 K overnight. The used catalyst calcined at 773 K for 5 h after drying was also

Fig. 7. Liquid-phase oxidation of benzene with unsupported $Cu(CH_3COO)_2{\cdot}H_2O$ catalyst. Catalyst (25.1 mg of $Cu(CH_3COO)_2{\cdot}H_2O$, benzene (22.5 mmol), reducing reagent (4 mmol of ascorbic acid), solvent (20 cm^3 of aqueous acetic acid), 0.1 MPa of O_2, reaction temperature (303 K), reaction time (24 h), yield of phenol (●), mmol of soluble Cu/mmol of total Cu fed) ×100 (□).

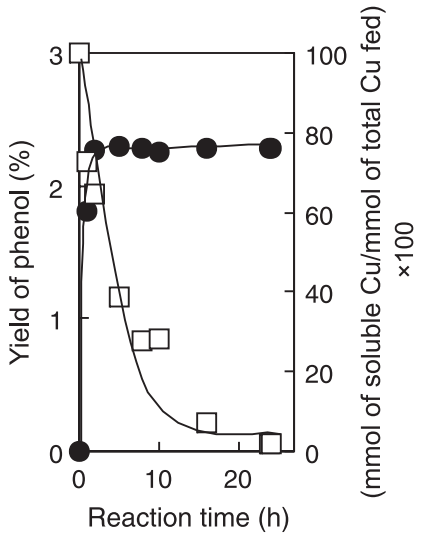
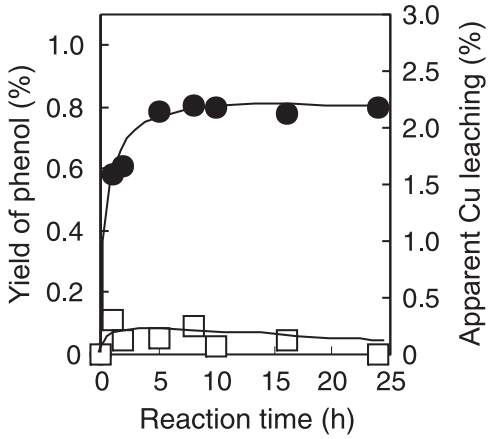


Fig. 8. Yield of phenol and apparent Cu leaching vs. reaction time using the Cu/NaM catalyst. Catalyst (0.4 g of Cu(2)/NaM (0.31 mmol Cu/g-cat)), benzene (22.5 mmol), solvent (20 cm^3 of aqueous 80 vol% acetic acid solution), ascorbic acid (4 mmol), O_2 (0.1 MPa), reaction temperature (303 K), yield of phenol (●), percentage of apparent Cu leaching (□).



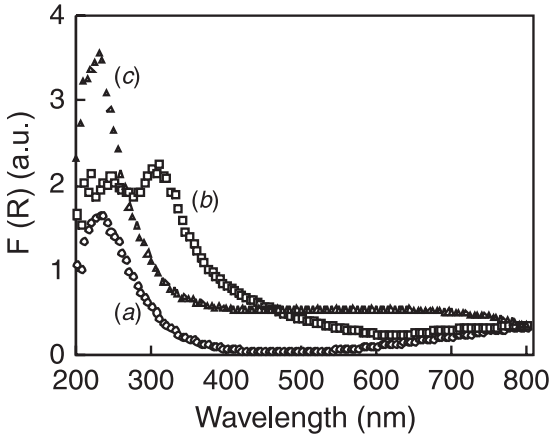
© 2004 NRC Canada

Table 2. Benzene oxidation to phenol using the used Cu/HY catalysts.[a]

Catalyst	Phenol yield (%)
Fresh Cu/HY[b]	2.5
Used Cu/HY (without calcination)[c]	1.1
Used Cu/HY (with calcination)[d]	2.3

[a]Benzene (22.5 mmol), solvent (20 cm^3 of aqueous 80 vol% acetic acid), ascorbic acid (4 mmol), O_2 (0.1 MPa), reaction time (303 K), reaction time (24 h).
[b]Catalyst (0.4 g of Cu(2)/HY).
[c]Only dried at 303 K overnight.
[d]Calcined at 773 K for 5 h in flowing air.

Fig. 9. DR spectra of the fresh Cu/HY catalyst and both the recovered counterparts with and without calcination. (*a*) Fresh Cu(2)/HY catalyst (○); (*b*) recovered catalyst without calcination (□); (*c*) recovered catalyst calcined at 773 K for 1 h in flowing air (△).

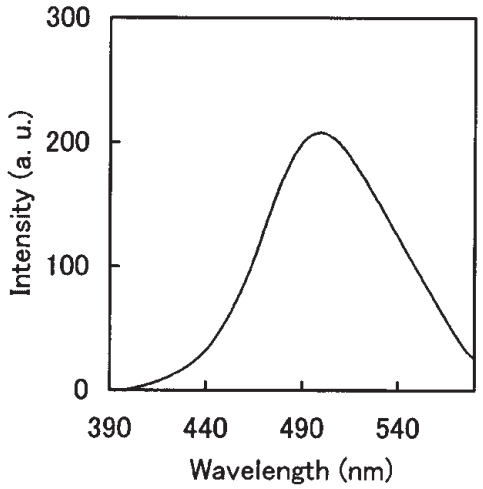


tried as the catalyst for the benzene oxidation (Table 2). The yield of phenol with the used catalyst being treated only by drying was significantly lower than that with the fresh one. On the other hand, the used Cu/HY calcined at 773 K for 5 h after the recovery was found to have an activity for phenol formation almost similar to that of the fresh one. The inactive reduced Cu species is thought to be thoroughly oxidized by the calcinations to reform the active Cu species for the phenol formation.

Redox behavior of the Cu species of the Cu/HY catalyst during benzene oxidation

The DR spectra of the fresh catalyst showed a broad band at around 800 nm that is due to a *d–d* transition of an octahedral Cu^{2+} and a band appeared at around 230 nm, which will be identified (20) as one based on the charge transfer from the zeolite framework O species to Cu^{2+} (Fig. 9*a*). The recovered catalyst without calcination (Fig. 9*b*) showed a new band at around 305 nm, in addition to the bands of 220–240 nm and around 800 nm. The corresponding catalyst with calcination (Fig. 9*c*) showed a very broad absorption in the visible region in addition to the peak at around 230 nm (22). The presence of CuO was reported (23) to show the DR absorption over the visible region. A DR band at around 305 nm observed in the recovered catalysts without calcination disappeared during calcination. To clarify the identification of the DR band at around 305 nm of the recovered catalyst without calcination, the fluorescence emission spectrum of the fresh Cu(2)/HY catalyst reduced at 573 K for 1 h in H_2 was measured (Fig. 10). H_2 treatment of Cu ion-exchanged Y (Cu-Y) zeolite at 573 K was reported (24) to produce Cu^{1+}. A broad band was observed at around 500 nm as illustrated in Fig. 10. It was reported (25) that the bands based on the Cu^{1+} of the H_2-reduced Cu-Y zeolites with the Cu ion-exchanged percentage of 2% and 60% were observed at around 480 and 523 nm, and that the fluorescence band based on the Cu^{1+} shifted to a longer wavelength with an increase in the percentage of the Cu ion exchange of the reduced Cu-Y zeolite. Because the present Cu(2)/HY (Cu, 2 wt%) catalyst corresponds to the percentage of Cu ion-exchange of about 18%, it will be reasonable that the fluorescence band observed at around 500 nm is identified to be Cu^{1+}. Accordingly, a band at around 300 nm appearing in the DR spectrum of the H_2-reduced Cu(2)/HY catalyst is due to reduced Cu^{1+} (Fig. 11). From these results, the DR band at 305 nm of the recovered Cu/HY catalyst without calcination was confirmed to be due to Cu^{1+}.

Fig. 10. Fluorescence emission spectrum of the reduced Cu/HY catalyst. Cu(2)/HY catalyst reduced at 573 K for 1 h in flowing H_2.



The ESR spectrum of the fresh Cu(2)/HY catalyst (Fig. 12*a*) is similar to one in which the Cu^{2+} species are mainly aggregated and undergo Cu^{2+} spin-spin interaction with each other (26). The ESR intensity of the recovered catalyst not precalcined was lower than the unused catalyst and a new sharp peak appeared at the position of a *g* value of around 2 (Fig. 12*b*). The calcination of the recovered catalyst caused the disappearance of the sharp ESR peak at g = ca. 2.0 (Fig. 12*c*), together with the reappearance of the broad peak based on aggregated Cu^{2+}. However, the intensity of the ESR peak based on aggregated Cu^{2+} was much smaller than that (Fig. 12*a*) of the fresh Cu/HY catalyst. This can be interpreted in that the calcination of the recovered catalyst produced CuO, which is apparently undetectable by ESR, in agreement with the results of the very broad DR spectrum in the visible region of the corresponding catalyst (Fig. 9*c*). The ESR peak at g = ca. 2.0 appearing in the ESR spectrum of the recovered catalyst without calcination almost completely disappeared on calcining of the recovered

© 2004 NRC Canada

Fig. 11. DR spectrum of the reduced Cu/HY catalyst. Cu(2)/HY catalyst reduced at 573 K for 1 h in flowing H_2.

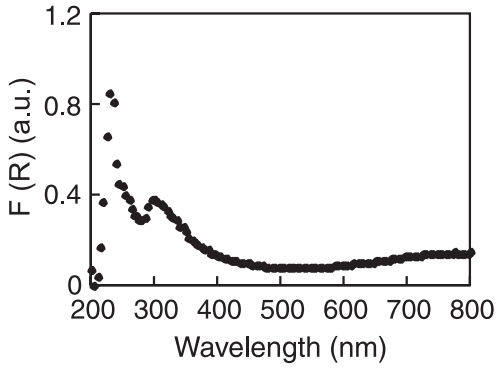
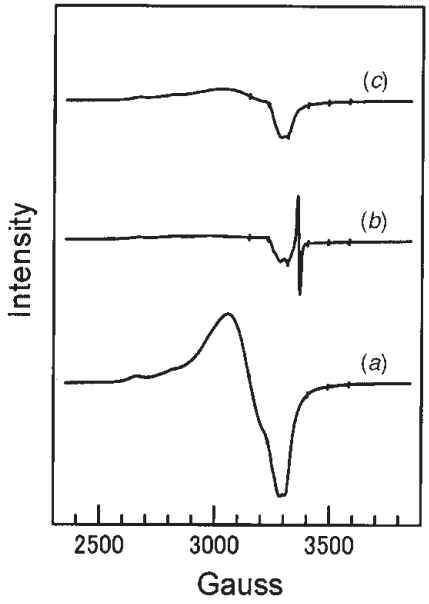


Fig. 12. ESR spectra of the fresh Cu/HY catalyst and both the recovered counterparts with and without calcination. Mn^{2+} used as a g-marker. (*a*) Fresh Cu(2)/HY catalyst; (*b*) recovered catalyst without calcination; (*c*) recovered catalyst calcined at 773 K for 1 h in flowing air.



catalyst (Fig. 12*b* → Fig. 12*c*). This result suggests that the sharp ESR peak at g = ca. 2.0 (Fig. 12*b*) might be due to organic radical(s) and (or) carbonaceous radical(s), though we have no idea of the definite structure.

Based on the obtained DR and ESR spectral data, Cu^{2+} species on the Cu/HY catalyst are dissolved into the reaction solution and reduced to Cu^{1+} species during the benzene oxidation. The almost insoluble Cu^{1+} species are collected together with the Cu/HY catalyst through centrifugation to form the recovered Cu/HY catalyst. The Cu^{1+} species in the recovered catalyst is reoxidized to the Cu^{2+} species and in part, CuO, because of the disappearance of the DR band based on Cu^{1+} and the appearance of the very broad absorption over visible region based on CuO by calcination of the recovered Cu/HY catalyst. We are currently investigating the identity of the insoluble Cu^{1+} species formed during the benzene oxidation to phenol.

Conclusions

The liquid-phase catalytic oxidation of benzene to phenol with Cu catalysts supported on zeolites was attempted using gaseous oxygen as an oxidant and ascorbic acid as a reducing reagent. Only phenol was selectively obtained. The usage of an aqueous solvent containing a high acetic acid concentration of around 80 vol% caused both enhancement of the yield of phenol and inhibition of apparent Cu leaching from the Cu/HY catalyst. The simultaneous increase in both the amount of Cu and the concentration of ascorbic acid caused an increase in the yield of phenol. Both the yield of phenol and the percentage of the apparent Cu leaching of the Cu species impregnated on HY (Cu/HY) had a correlation during the initial stage of the benzene oxidation. The eluted Cu species was thought to be the main active species for the phenol formation. The irreversible reduction of the Cu^{2+} species to Cu^{1+} ones was suggested as causing the deactivation of the catalyst for the benzene oxidation to phenol. The calcination of the recovered Cu catalyst caused the regeneration of the catalyst for phenol formation.

Acknowledgments

The authors thank Mr Kenji Nomura of Kobe University for his technical assistance during this study.

References

1. R.A. Sheldon and J.K. Kochi. Metal-catalyzed oxidations of organic compounds. Academic Press, New York. 1981. Chap. 10.
2. S. Itho and K. Sasaki. J. Synth. Org. Chem. (Jpn.), **41**, 839 (1983).
3. W.T. Dixon and R.C.O. Norman. J. Chem. Soc. 4857 (1964).
4. G.A. Hamilton and J.P. Friedmann. J. Am. Chem. Soc. **88**, 5269 (1966).
5. M. Hamada, Y. Sasaki, and T. Miyake. Japanese Patent H5-4935, 1993.
6. T. Miyake, M. Hamada, Y. Sasaki, and M. Oguni. Appl. Catal. A, **131**, 33 (1995).
7. T. Nabeta, I. Yamanaka, and K. Ohtsuka. Preprint of the 2nd Symposium on selective oxidation. P31. 1998. [In Japanese].
8. K. Nomiya, H. Yanagibayashi, C. Nozaki, K. Kondoh, E. Hiramatsu, and Y. Shimizu. J. Mol. Catal. A: Chem. **114**, 181 (1996).
9. L.C. Passoni, A.T. Cruz, R. Buffon, and U. Schuchardt. J. Mol. Catal. A: Chem. **120**, 117 (1997).
10. A. Bhaumilk, P. Mukhherjee, and R. Kumar. J. Catal. **178**, 101 (1998).
11. L. Balducci, D. Bianchi, R. Bortolo, R. D'Aloisio, M. Ricci, R. Tassinari, and R. Ungarelli. Angew. Chem. Int. Ed. **42**, 4937 (2003).
12. T. Ohtani, S. Nishiyama, S. Tsuruya, and M. Masai. *In* Proc. 10th Inter. Cong. Catal. Budapest, 1992. *Edited by* L. Guczi, F. Solymosi, and P. Tetenyi. Elsevier, Amsterdam. 1993. p. 1999.
13. T. Ohtani, S. Nishiyama, S. Tsuruya, and M. Masai. J. Catal. **155**, 158 (1995).
14. J. Okamura, S. Nishiyama, S. Tsuruya, and M. Masai. J. Mol. Catal. A: Chem. **135**, 133 (1998).
15. T. Miyahara, H. Kanzaki, R. Hamada, S. Kuroiwa, S. Nishiyama, and S. Tsuruya. J. Mol. Catal. A: Chem. **176**, 141 (2001).

© 2004 NRC Canada

16. H. Kanzaki, T. Kitamura, R. Hamada, S. Nishiyama, and S. Tsuruya. J. Mol. Catal. A: Chem. **208**, 203 (2004).
17. M. Ishida, Y. Masumoto, R. Hamada, S. Nishiyama, S. Tsuruya, and M. Masai. J. Chem. Soc. Perkin Trans. 2, 847 (1999).
18. Y. Masumoto, R. Hamada, K. Yokota, S. Nishiyama, and S. Tsuruya. J. Mol. Catal. A: Chem. **184**, 215 (2002).
19. N.Y. Chenn, S.J. Lucki, and W.E. Garwood. US Patent 3 700 585, 1972.
20. E.V. Shtamm, A.P. Purmal, and Y.I. Skurlatov. Int. J. Chem. Kinet. **XI**, 461 (1974).
21. S. Nagakura, H. Iguchi, H. Ezawa, I. Iwamura, F. Satoh, and R. Kubo (*Editors*). Rikagaku Jiten. Iwanami-Shoten, Tokyo. 1981. p. 13.
22. G. Genti, F. Fazzini, and A. Galli. Res. Chem. Intermed. **24**, 541 (1998).
23. M.L. Jacono, G. Fierro, R. Dragone, X. Feng, J. d'Itri, and W.K. Hall. J. Phys. Chem. B, **101**, 1979 (1997).
24. C. Torre-Abreu, C. Henriques, F.R. Ribeiro, G. Delaahay, and M.F. Ribeiro. Catal. Today, **54**, 407 (1999).
25. J. Dedecek, Z. Sobalik, Z. Tvarukova, D. Kaucky, and B. Wichterlova. J. Phys. Chem. **99**, 16 327 (1995).
26. R.G. Hermann, J.H. Lunsford, H. Beyer, P.A. Jacobs, and J.B. Uytterhoeven. J. Phys. Chem. **79**, 2388 (1975).

© 2004 NRC Canada

Multinuclear magnetic resonance studies of the aqueous products of the complexes *cis*- and *trans*-Pt(amine)$_2$(NO$_3$)$_2$

Fernande D. Rochon and Viorel Buculei

Abstract: The hydrolyis or the aquation reactions of the compounds *cis*- and *trans*-Pt(amine)$_2$(NO$_3$)$_2$ were studied in D$_2$O in different conditions of pH. The products were characterized by multinuclear (^{195}Pt, ^{13}C, and ^{1}H) magnetic resonance spectroscopy. In acidic medium, the product was [Pt(amine)$_2$(D$_2$O$_2$)]$^{2+}$ and for a few amines, *trans*-[Pt(amine)$_2$(D$_2$O)(NO$_3$)]$^{+}$ was detected. The ^{195}Pt NMR resonances of the diaqua complexes were observed at higher fields for the cis compounds (avg. –1727 ppm) than for the trans isomers (avg. –1560 ppm). At basic pH, Pt(amine)$_2$(OD)$_2$ was formed and for ethylamine, *trans*-Pt(EtNH$_2$)$_2$(OD)(NO$_3$) was detected. The cis compounds were also observed at higher fields than the trans isomers (–1706 ppm vs. –1574 ppm). The coupling constants with ^{195}Pt were geometry dependent. The avg. ^{2}J(^{195}Pt-^{1}H) values for the diaqua species were 66 (cis) and 57 (trans) Hz, while the avg. ^{3}J(^{195}Pt-^{1}H) were 43 (cis) and 34 (trans) Hz for the diaqua compounds, and 43 and 37 Hz, respectively, for the dihydroxo species. The ^{2}J(^{195}Pt-^{13}C) avg. values were 18 (cis) and 12 (trans) Hz and the avg. ^{3}J(^{195}Pt-^{13}C) were 31 (cis) and 23 (trans) Hz for both the diaqua and dihydroxo compounds. For the cis isomers, at neutral pH, the monoaqua–monohydroxo species (avg. –1721 ppm) and the dihydroxo-bridged dimer (avg. –1353 ppm) were observed. For a few amines, the monohydroxo-bridged dimer was observed (avg. –1684 ppm) and its concentration increased with time. For the trans compounds, the monoaqua–monohydroxo species was observed at –1563 ppm (avg.). For a few amines, the hydroxo-bridged dimer was present. For methylamine, a third species assigned to a higher oligomer was observed after 6 months.

Key words: platinum, amine, nitrato, hydrolysis, NMR, aquation.

Résumé : Les réactions d'hydrolyse ou d'aquation des composés *cis*- et *trans*-Pt(amine)$_2$(NO$_3$)$_2$ ont été étudiées dans D$_2$O à plusieurs pH. Les produits ont été caractérisés par résonance magnétique multinucléaire (^{195}Pt, ^{13}C et ^{1}H). En milieu acide, le produit est [Pt(amine)$_2$(D$_2$O)$_2$]$^{2+}$ et pour quelques amines, *trans*- [Pt(amine)$_2$(D$_2$O)(NO$_3$)]$^{+}$ a été détecté. En RMN du ^{195}Pt, les résonances des composés diaqua ont été observées à champ plus élevé pour les composés cis (moy. –1727 ppm) que pour les isomères trans (moy. –1560 ppm). En milieu basique, Pt(amine)$_2$(OD)$_2$ se forme et *trans*-Pt(amine)$_2$(OD)(NO$_3$) a été détecté pour éthylamine. Les composés cis ont aussi été observés à plus haut champ que les analogues trans (–1706 ppm vs. –1574 ppm). Les constantes de couplage dépendent de la géométrie du complexe. Les valeurs moyennes ^{2}J(^{195}Pt-^{1}H) pour les espèces diaqua sont 66 (cis) et 57 (trans) Hz, tandis que celles de ^{3}J(^{195}Pt-^{1}H) sont 43 (cis) et 34 (trans) Hz pour les composés diaqua et 43 et 37 Hz pour les espèces dihydroxo. Les valeurs moyennes ^{2}J(^{195}Pt-^{13}C) sont 18 (cis) and 12 (trans) Hz tandis que les ^{3}J(^{195}Pt-^{13}C) sont 31 (cis) et 23 (trans) Hz pour les complexes diaqua et dihydroxo. Pour les isomères *cis* en milieu neutre, les espèces monoaqua–monohydroxo (moy. –1721 ppm) et les dimères à double ponts hydroxo (moy. –1353 ppm) ont été caractérisés. Pour quelques amines, le dimère à simple pont hydroxo a été observé (moy. –1684 ppm) et sa concentration augmente avec le temps. Pour les composés trans, l'espèce monoaqua–monohydroxo a été observé à –1563 ppm (moy.). Pour quelques amines, le dimère à pont hydroxo est présent. Pour méthylamine, une troisième espèce attribuée à un plus grand oligomère a été observée après 6 mois.

Introduction

The antitumor properties of diamine Pt(II) compounds have been known for a few decades. The drug *cisplatin* (*cis*-Pt(NH$_3$)$_2$Cl$_2$) is still the most widely used in chemotherapy. A good review of the influence of the structure on the activity of Pt drugs has been published (1). The drug remains mainly unchanged in the plasma because of the presence of a large chloride concentration (103 mmol L^{-1}) and can cross the cell membrane because of its neutrality. Inside the cells, the chloride ion concentration is much lower (4 mmol L^{-1}) and in these conditions, *cis*-Pt(NH$_3$)$_2$Cl$_2$ can produce differ-

Received 13 February 2004. Published on the NRC Research Press Web site at http://canjchem.nrc.ca on 15 December 2004.

F.D. Rochon[1] and V. Buculei. Département de chimie, Université du Québec à Montréal, C.P. 8888, Succ. Centre-ville, Montréal, QC H3C 3P8, Canada.

[1]Corresponding author (e-mail: rochon.fernande@uqam.ca).

 doi: 10.1139/V04-121 © 2004 NRC Canada

ent ionic species. Its mechanism of action seems extremely complex (2, 3) and involves aquation or hydrolysis reactions, which have been studied in a few laboratories. One of the ionic species is the aqua-chloro complex *cis*-$[Pt(NH_3)_2(OH_2)Cl]Cl$, which can either bind to DNA (4) leading to the eventual destruction of the cell, or react with water to produce the diaqua species. At neutral pH, the latter compound will exist mainly in the form of the monoaqua–monohydroxo complex (4–7) *cis*-$[Pt(NH_3)_2(OH)(OH_2)]^+$, which can also bind to DNA (4). It has also been shown in laboratories to produce different oligomeric species, which have been characterized by ^{195}Pt NMR (8) and by crystallographic methods (9, 10). Some of these compounds are toxic to humans and could be partially responsible for the toxicity of cisplatin (11). It is, therefore, very important to study the aquation and hydrolysis reactions of a complex prior to its development as an antitumor drug.

It has been observed that when NH_3 is replaced by primary amines, the antitumor properties can increase, especially with cyclic amines (12, 13), but the latter compounds have often a more limited activity spectrum. Furthermore, several very active compounds are too insoluble to become useful anticancer drugs (14). In the amine system, the most active compounds usually have the cis geometry, although a few trans compounds have been shown to possess some antitumor properties. Our research group has recently undertaken a systematic study on complexes of the types *cis*- and *trans*-$Pt(amine)_2I_2$ with 10 different amines (15). We have transformed these complexes into *cis*- and *trans*-$Pt(amine)_2(NO_3)_2$, which have also been studied in the solid state by IR and in solution in acetone by ^{195}Pt, ^{1}H, and ^{13}C NMR spectroscopy (16). The results have shown that all these compounds were pure except for $Pt(Et_2NH)_2X_2$, which was a mixture of the cis and trans isomers. Conductivity measurements in acetone have shown that the dinitrato complexes are not dissociated. We have characterized these dinitrato complexes to subsequently study their aquation and hydrolysis reactions. The solubility of the dichloro and the diiodo complexes in water is very low, but substitution of the halides by nitrato ligands leads to a greater aqueous solubility. We have now completed our NMR study on the cis and trans dinitrato compounds and the results are reported in this paper. We have studied the aqueous reactions at three different conditions of pH (acidic, neutral, and basic). Although a few studies in the literature were made on cis compounds (8, 17–23) (especially *cis*-$Pt(NH_3)_2Cl_2$), only one study has been reported on a trans compound, namely on *trans*-$Pt(NH_3)_2Cl_2$ (24). A tentative preliminary study has also been reported (22) on *trans*-$Pt(Ypy)_2(NO_3)_2$ where Ypy = pyridine derivative.

Experimental

$K_2[PtCl_4]$ was purchased from Johnson–Matthey and was recrystallized in water before use. The amines were bought from Aldrich, while silver nitrate was purchased from Analar. D_2O was obtained from CDN Isotopes.

The NMR spectra were measured on a Varian Gemini 300BB in D_2O. The fields were 300.070, 75.460, and 64.395 MHz for ^{1}H, ^{13}C, and ^{195}Pt, respectively. For the ^{195}Pt NMR spectra, $K_2[PtCl_4]$ (–1628 ppm in D_2O with KCl) was the external standard. The pH values were measured on a Fisher Scientific Accumet-15 pH meter, using a combined electrode Ag/AgCl (Fisher Scientific) at room temperature. For the pD values, the pH values were increased by 0.4 (25).

The NaOD solution was prepared by dissolving NaOH in D_2O to make a 0.4 mol L^{-1} solution. The complexes *cis*- and *trans*-$Pt(amine)_2(NO_3)_2$ were prepared and characterized as reported in our recent publication (16). The aquation or hydrolysis of the dinitrato complexes were studied in three different conditions of pH. The dinitrato complexes (12–15 mg) were dissolved in 1 mL of D_2O with slight heating (40°–45°). The concentration of the solution was about 0.03 mol L^{-1} and the pH was acidic (2.0–2.4 or pD = 2.4–2.8). The ^{195}Pt, ^{1}H, and ^{13}C NMR were measured directly on these fresh D_2O solutions. The pD of another fresh solution was adjusted to about 7 with NaOD and the NMR spectra were measured immediately. The pD of a third fresh D_2O solution of the dinitrato complex was adjusted between 9.9 and 10.4 just before recording the NMR spectra. In a typical experiment, the dinitrato compound was dissolved in D_2O with heating in a hot water bath. For the products in acidic and basic pH, the ^{195}Pt NMR spectrum was measured immediately during about 1–3 h, the ^{1}H spectrum was then recorded for 30–60 min, and the ^{13}C spectrum was measured overnight (~15 h). At neutral pH, where the number of species in solution is usually greater, the accumulation time was 2 to 3 times longer. A few NMR tubes were left standing at about 4° and the ^{195}Pt NMR spectra were later remeasured to see the evolution of the different species with time.

Results and discussion

The dinitrato complexes were prepared by the reaction (in the dark around 5 °C) of the diiodo complexes with a slight excess (10%) of silver nitrate in acetone, as recently described (16).

$$Pt(amine)_2I_2 + 2Ag(NO_3) \rightarrow Pt(amine)_2(NO_3)_2 + 2AgI\downarrow$$

Compounds (cis and trans) with amine = methylamine ($MeNH_2$), ethylamine ($EtNH_2$), *n*-propylamine (*n*-$PrNH_2$), *n*-butylamine (*n*-$BuNH_2$), isopropylamine (iso-$PrNH_2$), iso-butylamine (iso-$BuNH_2$), *sec*-butylamine (*sec*-$BuNH_2$), dimethylamine (Me_2NH), and trans compounds with *tert*-butylamine and diethylamine were synthesized and characterized by multinuclear magnetic resonance in acetone. For the chiral molecule *sec*-butylamine, the racemate mixture was used. The *tert*-butylamine dinitrato complex could not be dissolved in D_2O and the diethylamine compound contained some cis complex that could not be well separated. These two amines were therefore not included in the present study. The other dinitrato complexes were pure and were not dissociated in acetone as shown by conductivity measurements. The aquation and hydrolysis reactions of the eight cis and eight trans dinitrato compounds were studied in three different conditions of pH (acidic, neutral, and basic).

Aquation in acidic pH

When the dinitrato compounds are dissolved in water or D_2O (~0.03 mol L^{-1}), heating in a water bath is required by

© 2004 NRC Canada

Table 1. $\delta(^{195}Pt)$ and $\Delta\delta = \delta_{cis} - \delta_{trans}$ (ppm) of the complexes $[Pt(amine)_2(D_2O)_2](NO_3)_2$ and some results from the literature.

Amine	Proton affinity	pK_a	cis	trans	$\Delta\delta$
$MeNH_2$	914	10.62	–1749	–1588 (–1622[a])	–161
$EtNH_2$	930	10.67	–1736	–1554 (–1589[a])	–182
				–1552[b]	
n-$PrNH_2$	933	10.708	–1733	–1548	–185
n-$BuNH_2$	924	10.777	–1720	–1550	–170
iso-$PrNH_2$		10.63	–1716	–1528	–188
iso-$BuNH_2$		10.72	–1729	–1548	–181
sec-$BuNH_2$		10.56	–1699	–1515	–184
Me_2NH		10.732	–1731	–1650	–81
NH_3			–1584 (–1598[a]) (24)	–1374 (24)	–210
			–1588 (8)		
			–1590 (17)		
$EtNH_2$ (18)			–1721		
Pyridine (22)			–1514	–1425	–89
3-Picoline (22)			–1525	–1430	–95

[a](Aqua)(nitrato) species.
[b]Aquation of *trans*-$Pt(EtNH_2)_2(ClO_4)_2$.

most samples (especially the trans isomers), and the pH of the solution is acidic (pH = 2.0–2.4 or pD = 2.4–2.8). In these conditions, the diaqua species are formed.

$$Pt(amine)_2(NO_3)_2 + 2D_2O \rightarrow [Pt(amine)_2(D_2O)_2](NO_3)_2$$

These D_2O solutions were characterized by multinuclear (^{195}Pt, ^{1}H, and ^{13}C) magnetic resonance spectroscopy.

For the cis isomers, the ^{195}Pt NMR spectra of these solutions showed the presence of only one signal, corresponding to the diaqua species. The chemical shifts of the complexes varied between –1699 and –1749 ppm. Surprisingly, the secondary amine complex was not observed at lower fields than the others. These results are shown in Table 1 along with some published values on similar compounds. The chemical shifts of the NH_3 (8, 17, 24) and pyridine (22) complexes are usually found at lower fields than those of amine complexes. Our values are at much lower fields than those reported for Pt(II) compounds with ethylenediamine and its derivatives (–1867 to –1999 ppm) (19, 20) or with 1,2-diaminocyclohexane (–1998 ppm) (23). Complexes containing five-membered chelate rings produce signals at much higher fields than those containing monodentate ligands.

The trans diaqua compounds were observed at lower fields (avg. –1547 ppm) than the cis isomers (avg. –1727 ppm) with an avg. $\Delta\delta$ ($\delta_{cis} - \delta_{trans}$) = –179 ppm for the primary amines and –81 ppm for Me_2NH. There are not many results in the literature for trans compounds. Only the NH_3 and some pyridine derivatives Pt(II) complexes are known (included in Table 1). Our results on the primary amines are close to the $\Delta\delta$ value (–210 ppm) observed for the NH_3 system (8, 17, 24), while our results on the secondary amine are closer to those observed with pyridine derivatives ($\Delta\delta$ = –90 ppm) (22).

The *trans*-$MeNH_2$ and -$EtNH_2$ compounds showed a second signal of lower intensity (about 10%) at slightly higher field than the diaqua species (35 ppm). We have assigned this signal to the presence of *trans*-$[Pt(amine)_2(NO_3)(D_2O)](NO_3)$. This type of compound has not been observed yet on trans complexes, but the group of Appleton (17) has studied the aquation of *cis*-$Pt(NH_3)_2(NO_3)_2$ and have suggested the presence of *cis*-$[Pt(NH_3)_2(NO_3)(H_2O)](NO_3)$ to a signal found at higher field (14 ppm) than the one of the diaqua species. Their ratio of the monoaqua–mononitrato to the diaqua compounds was about 0.1, as we have observed. Monoaqua–mononitrato species were also reported for some ethylenediamine derivatives at slightly higher fields (about 20 ppm) than the diaqua system in about the same ratio (19). To confirm the identity of the monoaqua–mononitrato species, we synthesized *trans*-$Pt(EtNH_2)_2(ClO_4)_2$ and studied its aquation products at the same pH. Only one species was observed at –1552 ppm, where the signal of the trans diaqua complex was found, which confirmed our hypothesis. This monoaqua–mononitrato complex was not observed for any of the cis compounds.

Although the chemical shift of the cis compound with the secondary amine Me_2NH was not different from the others, it was found at higher field in the trans series. Its δ(Pt) was observed at –1650 ppm compared to an avg. value of –1547 ppm for the primary amine complexes. This result was quite surprising and it was repeated to ascertain it. The δ(Pt) of secondary amine complexes were expected to be found at lower fields than primary amine compounds because of the solvent effect. For square-planar complexes, the molecules of solvent can normally approach and weakly bind to the Pt atom on both sides of the coordination plane. When the amines are more bulky, the approach of the molecules of solvent is more limited, which decreases the electronic density around the Pt atom, causing a deshielding effect in ^{195}Pt NMR. This solvent effect is particularly important in a coordinating solvent like water. The solvent effect is probably more different in the cis compounds where the steric hindrance is a more important factor than in the

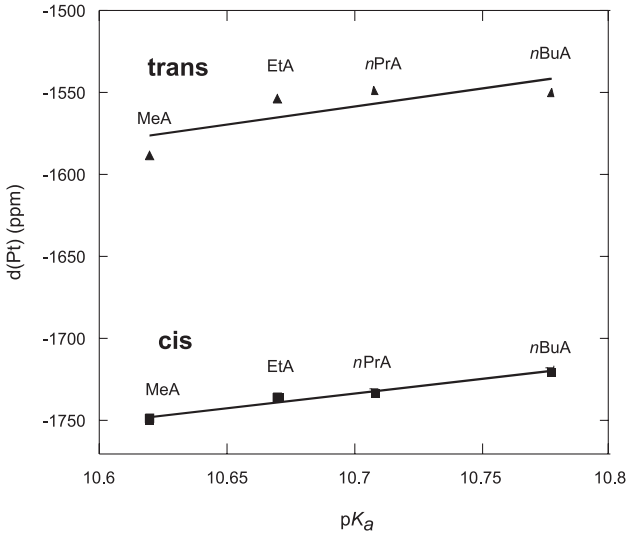
© 2004 NRC Canada

trans configuration. In the trans isomers, the solvation of the Pt atom should be more uniform, unless the amines are very sterically demanding. Downfield ^{195}Pt NMR shifts were thus observed for the Pt cis and trans diaqua (22) and the cis dinitrato complexes (26) with pyridine derivatives that have ortho substituents, and also for the complexes K[Pt(pyridine)Cl_3] (27). In the diamine systems, downfield shifts were also observed for the diiodo complexes (15) and some dichloro compounds (28). But for the dinitrato diamine complexes (16) that we have recently reported, opposite results were observed. The δ(Pt) of cis secondary amine complexes were observed at the same fields as the primary amine compounds, while for the trans isomers, the δ(Pt) of the secondary amine complexes were found at slightly higher fields than the primary amine compounds. It seems that the dinitrato and diaqua systems behave in a similar fashion. In the trans configuration, the electron density on the Pt atom is larger for the secondary amine complex than primary amine compounds. It might be attributed to the larger basicity of the secondary amines or to different conformations of the molecules in solution, but more data are needed before a sound conclusion can be made. In the *trans*-Pt(pyridine)$_2I_2$ series (29), the compounds with ortho methyl substituents were also observed at higher fields than the others.

All these ^{195}Pt NMR studies are difficult to compare, since the neutral dihalo compounds and the dinitrato complexes have been reported in an organic solvent, while the diaqua systems and the ionic compounds K[Pt(pyridine)Cl_3] have been studied in water. The solvation of the Pt atom is a very important factor and is quite dependent on the solvent. Therefore, several factors are responsible for these different results. The solvent plays probably a very important role. Water, which can coordinate to platinum, can be responsible for the solvent effect discussed previously in this work. The charge on the complex might also be an important factor, but is difficult to evaluate at the moment, since the ionic compounds are normally studied in D_2O, while the spectra of the neutral complexes are measured in organic solvents. For pyridine ligands, the orientation of the pyridine ring is also an important factor and free rotation around the Pt—N bond will be limited in the presence of ortho substituents on the pyridine ligand, especially in the cis geometry. For diamine compounds, there is almost free rotation about the Pt—N bond in most of the trans compounds, but in the cis geometry, the rotation might be more limited, especially with more bulky ligands. The two cis amine ligands are probably mostly in the anti conformation as observed in the solid state for *cis*-Pt($MeNH_2$)I_2 (15), or the alkyl groups are far from each other as observed in the solid state for *cis*-Pt(Et_2NH)I_2 (15), where the amine H of the two ligands face each other in the Pt coordination plane, pushing the ethyl groups far from each other. The second type of ligand is also an important factor. For example, nitrato ligands are more bulky than iodo ligands, which are also further away from the Pt atom. Since the amines studied in this project are quite different, all these factors contribute to their ^{195}Pt chemical shifts, especially since the second ligand in this project (D_2O) is the same as the solvent.

Attempts were made to correlate the δ(Pt) of the diaqua complexes to the basicity of the amine, since amines cannot form multiple bonding with Pt. The pK_a of the protonated amines are shown in Table 1 (30). If we use all the data, there is no correlation. If we use only the linear amines, we can see a linear relationship, but not as expected. An increase in the basicity of the ligand should produce a stronger σ bond with Pt, resulting in a shielding effect in ^{195}Pt NMR. Figure 1 shows the reverse, although the differences in pK_a are not very large (from 10.56 to 10.78). The pK_a values are measured in a solvent and are sensitive to the environment of the protonated atom. Furthermore, the errors are probably quite large. The proton affinity of the amines, which are measured in the gas phase, might be a better indicator of the basicity of the ligands. But these data are not easily available in the literature. Figure 2 shows the correlation between the δ(Pt) vs. the proton affinity of the amines (31) for the cis and trans compounds. Again, a linear correlation was found, but not in the expected direction. These results indicate that the most important factor for these diamine compounds is not the basicity of the amine. Other factors like the solvent effect and the different conformations of the ligands in solution are probably more important.

Fig. 1. δ(Pt) (ppm) of $[Pt(amine)_2(D_2O)_2]^{2+}$ vs. pK_a of the protonated linear amine.



The ^{1}H NMR chemical shifts of the diaqua complexes are listed in Table 2, as well as the Δδ values ($\delta_{complex} - \delta_{amine}$). The NMR spectra of the amines were also measured in D_2O. Although the NH protons in the free amines are not detected in D_2O because of fast exchange, they were observed in the complexes. Their chemical shifts are at much lower fields for the cis isomers, which is in agreement with the ^{195}Pt NMR results, where the cis compounds were observed at higher fields than the trans isomers. An increase of electron density on the Pt atom (shielding effect) will correspond to a decrease of electron density on the ligands (deshielding effect). Furthermore, the $^2J(^{195}Pt\text{-}^1HN)$ coupling constants could be calculated and they are larger for the cis isomers, with an average value of 66 Hz, while it is 57 Hz for the trans complexes.

Surprisingly, most of the H-1 signals (in the α position to the amine group) were found at higher fields that the corresponding protons in the free ligand, except for the secondary amine compound (Table 2). This table also shows the ΣΔδ,

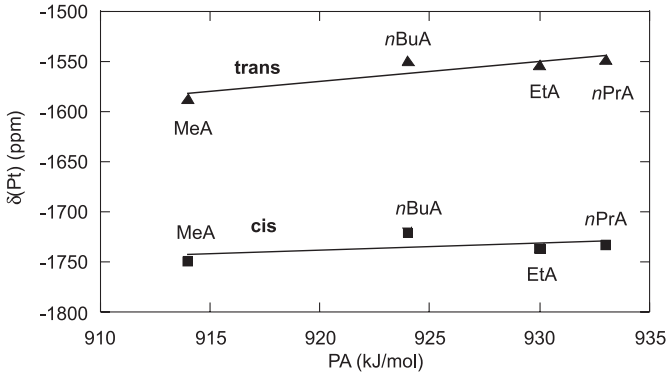
© 2004 NRC Canada

Table 2. ^{1}H NMR chemical shifts, ($\Delta\delta$), $\Sigma\Delta\delta$ (ppm), and $J(^{195}\text{Pt-}^1\text{H})$ coupling constants (Hz) for the complexes $[\text{Pt(amine)}_2(\text{D}_2\text{O})_2](\text{NO}_3)_2$.

Amine	NH	H-1	H-2	H-3	H-4 or H-2′	$^2J(^{195}\text{Pt-}^1\text{H})$	$^3J(^{195}\text{Pt-}^1\text{H})$	$\Sigma\Delta\delta$
$MeNH_2$								
cis	5.230	2.261(0.016)				67	47	0.016
trans	4.661	2.247(0.002)				58	34	0.002
	4.717[a]	2.195(–0.050)[a]						–0.050
$EtNH_2$								
cis	5.255	2.577(–0.022)	1.238(0.222)			67	42	0.200
trans	4.718	2.608(0.009)	1.299(0.283)			57	35	0.292
	4.736[a]	Not observed	1.265(0.249)[a]					0.249[a]
n-$PrNH_2$								
cis	5.241	2.489(–0.031)	1.669(0.275)	0.908(0.064)		65	38	0.308
trans	4.729	2.510(–0.010)	1.752(0.358)	0.922(0.078)		56		0.426
n-$BuNH_2$								
cis	5.239	2.531(–0.040)	1.664(0.278)	1.346(0.055)	0.878(0.149)	65		0.442
trans	4.694	2.687(0.116)	1.632(0.246)	1.355(0.064)	0.891(0.162)	56		0.588
iso-$PrNH_2$								
cis	5.248	2.882(–0.105)	1.313(0.321)			66		0.216
trans	4.702	2.929(–0.058)	1.345(0.353)			57		0.295
iso-$BuNH_2$								
cis	5.276	2.387(–0.001)	2.001(0.425)	0.907(0.054)		67		0.478
trans	4.695	2.426(0.038)	2.036(0.460)	0.924(0.071)		56		0.569
sec-$BuNH_2$								
cis	5.218	2.614(–0.115)	1.464(0.156)	0.908(0.062)	1.315(0.325)	65		0.428
trans	4.703	2.665(–0.064)	1.533(0.226)	0.924(0.078)	1.348(0.358)	57		0.598
Me_2NH								
cis	6.048	2.467(0.239)				67	45	0.239
trans	5.411	2.417(0.189)				56	33	0.189

[a]Monoaqua–mononitrato species.

Fig. 2. δ(Pt) (ppm) vs. proton affinity of the amine for the complexes $[\text{Pt(amine)}_2(\text{D}_2\text{O})_2]^{2+}$.



which is the sum of the $\Delta\delta$ for all the protons, except those on the amine. For most of the diamine complexes, this value is larger for the trans compounds, except for the secondary amine complex. For a few compounds, the $^3J(^{195}\text{Pt-}^1\text{H})$ coupling constants were calculated. They are greater for the cis compounds (avg. 43 Hz) than for their trans analogues (avg. 34 Hz). These coupling constants depend on the geometry of the compounds as observed for other similar Pt(II) compounds (15, 16, 22, 26, 29).

For the trans monoaqua–mononitrato species, the signal of the NH proton was found at slightly lower fields than the one of the diaqua compound as expected from the ^{195}Pt NMR results. The other H signals were observed at slightly higher fields. No $J(^{195}\text{Pt-}^1\text{H})$ coupling could be detected for this species because of its low concentration.

The ^{13}C NMR chemical shifts, the $\Delta\delta$ values ($\delta_{\text{complex}} - \delta_{\text{free amine}}$), the $\Sigma\Delta\delta$, as well as the $J(^{195}\text{Pt-}^{13}\text{C})$ coupling constants are listed in Table 3. The $\Delta\delta$ values for C-1 are quite large and are greater for the cis compounds as expected from the ^{195}Pt NMR results, where the cis compounds were observed at higher fields. Again, an increase of electron density on Pt (shielding effect) will correspond to a deshielding effect on the ligand as observed also in ^{1}H NMR for the NH protons. Most of the other C atoms were observed at higher fields than in the free amines ($\Delta\delta$ is negative). The $\Sigma\Delta\delta$ values are all greater for the cis compounds because of the larger values for C-1. The coupling constants $^2J(^{195}\text{Pt-}^{13}\text{C}_1)$ are larger in the cis configuration (avg. 18 vs. 13 Hz). These values are quite small probably due to inadequate orientation of the orbitals. Similar values were observed for other Pt(II) complexes (15, 16, 27). The $^3J(^{195}\text{Pt-}^{13}\text{C})$ values are larger in the cis configuration (avg. 31 Hz) than in the trans geometry (avg. 23 Hz) as observed for other related compounds (15, 16, 22, 26, 29).

Hydrolysis in basic pH

When the pH of the diaqua complex is raised with NaOD to about 10, the dihydroxo species *cis*-$\text{Pt(amine)}_2(\text{OD})_2$ are formed. The ^{195}Pt NMR spectra of these solutions have shown the presence of a single signal, except for the *trans*-

© 2004 NRC Canada

Table 3. ^{13}C NMR chemical shifts, ($\Delta\delta$), $\Sigma\Delta\delta$ (ppm), and $J(^{195}Pt\text{-}^{13}C)$ (Hz) for the complexes $[Pt(amine)_2(D_2O)_2](NO_3)_2$.

Amine	C-1	C-2	C-3	C-4 or C-2′	$^2J(^{195}Pt\text{-}^{13}C)$	$^3J(^{195}Pt\text{-}^{13}C)$	$\Sigma\Delta\delta$
$MeNH_2$							
cis	33.045(6.405)				19		6.405
trans	31.481(4.841)				15		4.841
$EtNH_2$							
cis	42.121(6.769)	14.907(–1.941)			17	32	4.828
trans	40.391(5.039)	15.059(–1.852)			12	24	3.187
n-$PrNH_2$							
cis	48.511(5.980)	23.270(–1.624)	10.293(–0.380)		18	32	3.976
trans	47.084(4.553)	23.422(–1.472)	10.384(–0.289)		13	23	2.792
n-$BuNH_2$							
cis	47.327(7.058)	32.448(–1.401)	19.315(–0.145)	12.997(0.759)	18	31	6.271
trans	46.431(6.162)	32.771(–1.078)	19.400(–0.060)	13.101(0.863)	14	24	5.887
iso-$PrNH_2$							
cis	49.330(7.482)	22.314(–1.821)			19	30	5.661
trans	48.799(6.951)	22.845(–1.290)			13	22	5.661
iso-$BuNH_2$							
cis	54.127(5.556)	28.745(–1.279)	19.283(–0.117)		17	32	4.160
trans	53.094(4.523)	28.947(–1.077)	19.233(–0.167)		12	23	3.279
sec-$BuNH_2$							
cis	54.506(6.936)	29.417(–1.776)	9.595(–0.273)	19.385(–2.064)	16	29, 26	2.823
trans	53.231(5.661)	29.781(–1.412)	9.580(–0.288)	19.810(–1.639)	12	23, 20	2.322
Me_2NH							
cis	43.654 (7.043)				16		7.043
trans	41.817(5.206)				10		5.206

Table 4. $\delta(^{195}Pt)$, $\Delta\delta = \delta_{cis} - \delta_{trans}$, and $\Delta\delta_a = \delta_{diaqua} - \delta_{dihydroxo}$ (ppm) for the complexes $Pt(amine)_2(OD)_2$ and some results from the literature.

Amine	cis	trans	$\Delta\delta$	$\Delta\delta_a$ cis	$\Delta\delta_a$ trans
$MeNH_2$	–1716	–1591	–125	–33	3
$EtNH_2$	–1718	–1573 (–1590)[a] –1574[b]	–145	–18	19
n-$PrNH_2$	–1710	–1571	–139	–23	23
n-$BuNH_2$	–1709	–1570	–139	–11	20
iso-$PrNH_2$	–1708	–1561	–147	–8	33
iso-$BuNH_2$	–1711	–1573	–181	–18	25
sec-$BuNH_2$	–1697	–1550	–184	–2	35
Me_2NH	–1681	–1602	–79	–50	–48
NH_3 (24)	–1572	–1385	–187	–12	11
$EtNH_2$ (18)	–1695			–26	
Pyridine(22)	–1505	–1478	–27	–10	53
3-Picoline (22)	–1517	–1473	–44	–8	43

[a](Hydroxo)(nitrato) species.
[b]Hydrolysis of *trans*-$Pt(EtNH_2)_2(ClO_4)_2$.

$EtNH_2$ complex, which showed a second weaker signal at slightly higher field (Table 4). The latter was assigned to the presence of *trans*-$Pt(EtNH_2)_2(OD)(NO_3)$. To verify the hypothesis, *trans*-$Pt(EtNH_2)_2(ClO_4)_2$ was synthesized and its hydrolysis studied at the same pH. Only one peak corresponding to the dihydroxo species was observed at –1574 ppm, which confirmed our assignments.

Similarly to the diaqua species, the cis dihydroxo compounds with primary amines were observed at higher fields (avg. –1706 ppm) than the trans analogues (avg. –1574 ppm). The cis secondary amine compound is at slightly lower fields than the primary amine complexes, but again surprisingly, the secondary amine trans compound was found at higher field than the primary amine analogues. The difference between the two isomers $\Delta\delta_{cis\text{-}trans}$ is larger for the primary amines (avg. –140 ppm) than for the secondary amine (–79 ppm) as observed for the diaqua species. The pertinent data found in the literature are included in Table 4. Our $\Delta\delta$ values on the primary amine compounds are close to the one reported for the $Pt(NH_3)_2$ system (24), while our value on

© 2004 NRC Canada

the secondary amine is close to those reported for complexes containing pyridine ligands (22).

Table 4 also shows the $\Delta\delta_a$ ($\delta_{diaqua} - \delta_{dihydroxo}$) values for the cis and trans compounds. For the cis analogues, all the dihydroxo compounds were observed at lower fields than the diaqua compounds. The average $\Delta\delta_a = -16$ ppm for the primary amines and –50 ppm for Me_2NH. Our results on the primary amine compounds are in agreement with those of the $Pt(NH_3)_2$ system (24), and our results on the secondary amine complexes agree with those published for the pyridine system (22) as shown in Table 4.

All the trans dihydroxo compounds with primary amines were observed at slightly higher fields than the diaqua species (avg. $\Delta\delta_a = 23$ ppm) as observed for the NH_3 and pyridine series. For the secondary amine Me_2NH, the trans dihydroxo complex was found at lower field ($\Delta\delta_a = -48$ ppm), which is very different from all other works. We have repeated our experiments on the Me_2NH complexes with similar results.

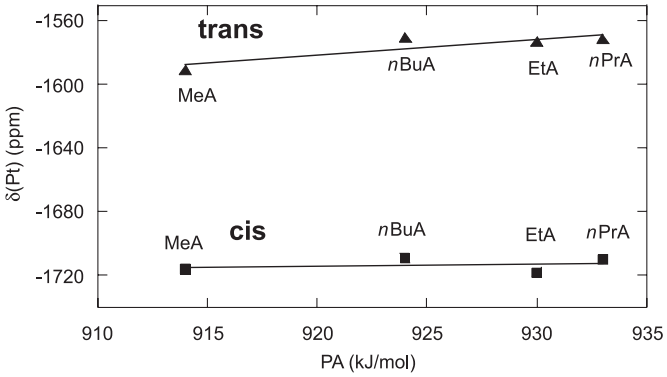
For all the cis compounds, the signals of the dihydroxo complexes are observed at slightly lower fields than the corresponding diaqua compounds ($\Delta\delta_a$ is negative). The shielding of a heavy atom like the ^{195}Pt nucleus has been expressed in the Ramsey equation, which contains some C terms representing the metallic coefficients of the platinum *d* orbitals. A more covalent bond will result in a decrease in the C terms and hence a shielding of the ^{195}Pt signals. D_2O is a more polarizable molecule than OD^-, leading to a more covalent Pt—OD_2 bond (in the diaqua system) compared to the Pt—OD bond in the dihydroxo complex. A greater covalency leads to a reduction of the C terms on the Pt atom and therefore, an increase in the shielding in the Ramsey equation. Therefore, the diaqua compounds should be observed at higher fields than the dihydroxo complexes, as observed in the literature cited previously and in our cis diamine complexes.

In the trans series, except for Me_2NH, which behaves like a cis compound, the reverse was observed. The trans dihydroxo complexes were observed at higher fields than the diaqua compounds as observed in the pyridine series (22). The solvent effect probably plays a more important role in the trans geometry, where the bulkiness of the amine is less important and the molecules of solvent can more easily approach the Pt atom. It might also be quite different for an ionic complex like $[Pt(amine)_2(D_2O)_2]^{2+}$ and for a neutral compound such as $Pt(amine)_2(OD)_2$. The different conformations of the molecules in solution might also be an important factor.

When the pH is acidic, the monoaqua–mononitrato species were observed for the *trans*-$MeNH_2$ and -$EtNH_2$ complexes. At basic pH, the monohydroxo–mononitrato was observed only for the *trans*-$EtNH_2$ compound, which was found at slightly higher field (17 ppm) than the dihydroxo complex. Monohydroxo–mononitrato species have not been reported yet in the literature for either cis or trans Pt(II) amine compounds.

Correlations of the δ(Pt) of the dihydroxo compounds with the basicity of the amines were studied. There is no general trend, but if only the linear amines are chosen, there is a tendency towards lower fields as the pK_a of the protonated amine increases. The same trend is observed for the proton affinity in the gas phase. Figure 3 shows the δ(Pt) vs. the proton affinity of the linear amines. For the cis compounds, the chemical shifts δ(Pt) are constant, while for the trans isomers, it slightly increases towards lower fields as the proton affinity increases. Again, this correlation is not as expected. These results seem to indicate that the basicity of the amine is not a very large factor in the ^{195}Pt chemical shifts. The basicity of the different amines are quite close to each other and the solvent effect is a more important factor for these diamine complexes.

Fig. 3. δ(Pt) (ppm) vs. proton affinity of the amine for the complexes $Pt(amine)_2(OD)_2$.



The ^1H NMR spectra of the dihydroxo complexes are shown in Table 5, as well as the $\Delta\delta$ values ($\delta_{complex} - \delta_{amine}$). In basic solution, the NH protons exchange rapidly and are not detected. Similarly to the diaqua species, the resonances of the C protons in the trans compounds are observed at lower field than those of the cis isomers. Table 5 shows that the $\Sigma\Delta\delta$ values are larger for the trans isomers, except for the secondary amine compounds. The $^3J(^{195}Pt\text{-}^1H)$ couplings were observed only for the $MeNH_2$ and Me_2NH complexes. As for similar compounds, this constant is larger in the cis geometry (43 vs. 36 Hz). The proton chemical shifts in the trans monohydroxo–mononitrato $EtNH_2$ complex were found at slightly higher fields than in the corresponding dihydroxo species.

The ^{13}C NMR spectra of the dihydroxo complexes are shown in Table 6. The signals of C-1 of the trans compounds were observed at higher fields than those of the corresponding cis complexes as expected from the ^{195}Pt NMR results. No correlation with the pK_a or the proton affinity was found. The $^2J(^{195}Pt\text{-}^{13}C)$ coupling constants could be measured. The average value is 18 Hz for the cis compounds and 11 Hz for the trans isomers. These values are relatively small, probably because of inadequate orientations of the orbitals. The $^3J(^{195}Pt\text{-}^{13}C)$ coupling constants are larger, with average values of 31 Hz for the cis complexes and 22 Hz for the trans isomers. For *sec*-$BuNH_2$, the ^{195}Pt coupling with the terminal C-2′ atoms is smaller (20–22 Hz) than with the other C-2 atoms (23–29 Hz).

sec-Butylamine is a chiral molecule and for the cis dihydroxo complex, the two enantiomers could be detected. Only one series of signals was found for the corresponding diaqua species and in the trans complexes.

The ^{13}C chemical shifts of the trans monohydroxo–mononitrato $EtNH_2$ complex were found at slightly higher fields than the corresponding dihydroxo species. No $J(^{195}Pt\text{-}$

© 2004 NRC Canada

Table 5. ^{1}H NMR chemical shifts, ($\Delta\delta$), $\Sigma\Delta\delta$ (ppm), and $J(^{195}Pt-^1H)$ coupling constants (Hz) for the complexes $Pt(amine)_2(OD)_2$.

Amine	H-1	H-2	H-3	H-4 or H-2′	$^3J(^{195}Pt-^1H)$	$\Sigma\Delta\delta$
$MeNH_2$						
cis	2.359(0.114)				44	0.114
trans	2.359(0.114)				39	0.114
$EtNH_2$						
cis	2.611(0.012)	1.189(0.173)				0.185
trans	2.680(0.081)	1.254(0.238)				0.319
	2.639(0.040)[a]	1.229(0.213)[a]				0.253[a]
n-$PrNH_2$						
cis	2.563(0.043)	1.625(0.231)	0.898(0.054)			0.328
trans	2.612(0.092)	1.691(0.297)	0.912(0.068)			0.457
n-$BuNH_2$						
cis	2.594(0.023)	1.594(0.208)	1.323(0.032)	0.881(0.152)		0.415
trans	2.675(0.104)	1.618(0.232)	1.347(0.056)	0.902(0.173)		0.565
iso-$PrNH_2$						
cis	2.848(–0.139)	1.282(0.290)				0.151
trans	2.981(–0.006)	1.323(0.331)				0.325
iso-$BuNH_2$						
cis	2.409(0.021)	1.892(0.316)	0.895(0.042)			0.379
trans	2.495(0.107)	1.970(0.394)	0.914(0.061)			0.562
sec-$BuNH_2$						
cis	2.604(–0.125)	1.430(0.123)	0.899(0.053)	1.292(0.302)		0.353
trans	2.739(0.010)	1.474(0.167)	0.917(0.071)	1.328(0.338)		0.586
Me_2NH						
cis	2.556(0.328)				41	0.328
trans	2.519(0.291)				34	0.291

[a]Monohydroxo–mononitrato species.

^{1}H) coupling could be detected for this species because of its low concentration.

Hydrolysis of the cis complexes at neutral pH

The study on the cis compounds at neutral pH was made only by Pt NMR spectroscopy. The ^{195}Pt NMR spectra of these fresh solutions were recorded immediately. For all the complexes, the spectra have shown two or three species in solution. The results are shown in Table 7 with the proportion of each species. The percentage values are very approximate. Our assignments for the different signals are based on the results published in the literature, especially for the *cis*-$Pt(NH_3)_2$ system (17, 24) and the dipyridine complexes (22). The reported results are also shown in Table 7.

For all the amines, the signal observed at highest field (between –1714 and –1734 ppm) was assigned to the monoaqua–monohydroxo complex, *cis*-$[Pt(amine)_2(D_2O)(OD)]^+$, which is found close to the diaqua and the dihydroxo species. In fresh solutions, the proportion of this species varied between 13% and 75%. The δ(Pt) of the secondary amine complex was found at the same field as the other diamine compounds. No correlation could be found between the ^{195}Pt chemical shifts of these species with either the pK_a of the protonated amines or the proton affinity.

The signals observed at lowest fields (avg. –1355 ppm) were assigned to the dihydroxo-bridged species *cis*-$[Pt(amine)_2(\mu\text{-}OD)_2Pt(amine)_2]^{2+}$ (Scheme 1), at 371 ppm (avg.) from the diaqua compounds. These results are in agreement with those reported for a few similar studies (17, 18, 22). In the *cis*-$Pt(NH_3)_2$ system, this dimer was observed at 423 ppm from the diaqua complex (8, 17). The crystal structures of several compounds of this type have been published (9, 10, 20). The chemical shifts for these species are found at much lower fields than the other compounds because of the important strain inside the four-membered ring. The proportion of this species varied between 25% and 73% in fresh solutions.

A third signal was observed in fresh solutions of the *cis*-$MeNH_2$, *n*-$BuNH_2$, and *sec*-$BuNH_2$ compounds at –1684 ppm (avg.). It was assigned to the monohydroxo-bridged dimer *cis*-$[Pt(amine)_2(D_2O)(\mu\text{-}OD)Pt(amine)_2(OD)]^{2+}$ (Scheme 1), which is probably in equilibrium with its diaqua analogue *cis*-$[Pt(amine)_2(D_2O)(\mu\text{-}OD)Pt(amine)_2(D_2O)]^{3+}$ and its dihydroxo analogue. The monohydroxo-bridged dimer was found at lower field (avg. 39 ppm) than the *cis*-$[Pt(amine)_2(D_2O)_2]^{2+}$ species. This dimer has been reported for $EtNH_2$ at –1680 ppm (18) and for *cis*-$[Pt(NH_3)_2(D_2O)(\mu\text{-}OD)Pt(NH_3)_2(D_2O)]^{3+}$,at 47 ppm (17) from the diaqua monomer *cis*-$[Pt(NH_3)_2(D_2O)_2]^{2+}$. It was also reported for the dipyridine systems (22).

No hydroxo-bridged trimers or tetramers could be detected in this study. Trimers have been reported for the ligands NH_3 (8, 9), ethylenediamine and its methyl derivatives (20), and diaminocyclohexane (23). The structure of a cyclic hydroxo-bridged tetramer was also reported with ethylenediamine (32). These species are usually formed after a longer time in solution. Our study was done mostly on fresh solutions.

© 2004 NRC Canada

Table 6. ^{13}C NMR chemical shifts, ($\Delta\delta$), $\Sigma\Delta\delta$ (ppm), and $J(^{195}Pt\text{-}^{13}C)$ coupling constants (Hz) for the complexes $Pt(amine)_2(OD)_2$.

Amine	C-1	C-2	C-3	C-4 or C-2′	$^2J(^{195}Pt\text{-}^{13}C)$	$^3J(^{195}Pt\text{-}^{13}C)$	$\Sigma\Delta\delta$
$MeNH_2$							
cis	33.455(6.815)				18		6.815
trans	31.906(5.226)				11		5.226
$EtNH_2$							
cis	41.666(6.314)	15.636(–1.275)			19	34	5.039
trans	40.558(5.206)	15.560(–1.351)			12	23	3.855
	40.300(4.948)[a]	15.332(–1.579)[a]			9[a]	19[a]	3.369[a]
n-$PrNH_2$							
cis	48.617(6.086)	23.938(–0.956)	10.369(–0.304)		18	34	4.826
trans	47.388(4.857)	23.771(–1.123)	10.430(–0.243)		11	21	3.491
n-$BuNH_2$							
cis	46.553(6.284)	31.952(–1.897)	19.294(–0.116)	13.025(0.787)	18	35	5.008
trans	46.219(5.950)	32.605(–1.244)	19.415(–0.045)	13.116(0.878)	13	24	5.539
iso-$PrNH_2$							
cis	48.021(6.173)	23.314(–0.821)			16	29	5.352
trans	47.524(5.676)	23.073(–1.062)			11	21	4.614
iso-$BuNH_2$							
cis	53.894(5.323)	29.016(–1.008)	19.105(–0.295)		18	30	4.020
trans	53.094(4.523)	28.947(–1.077)	19.233(–0.167)		13	22	3.279
sec-$BuNH_2$							
cis	53.535(5.965)	29.888(–1.305)	9.625(–0.243)	19.764(–1.685)	16	29, 22C-2′	1.732
	53.504(5.934)	28.857(–2.336)	9.625(–0.243)	19.764(–1.685)	15	28, 21C-2′	1.670
trans	52.715(5.145)	29.994(–1.199)	9.519(–0.349)	19.977(–1.472)	10	23, 20C-2′	2.125
Me_2NH							
cis	43.381(6.770)				17		6.770
trans	42.151(5.540)				10		5.206

[a]Monohydroxo–mononitrato species.

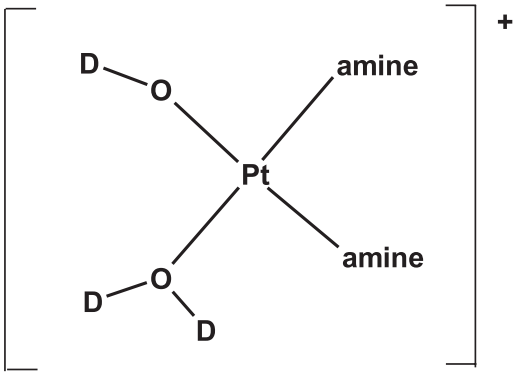
Table 7. $\delta(^{195}Pt)$ (ppm) of the different species at neutral pD of the cis complexes and some results from the literature.

Amine	$[Pt(amine)_2(D_2O)(OD)]^+$	Monohydro-bridged dimer	Dihydro-bridged dimer
$MeNH_2$	–1719 (19%)	–1697 (9%)	–1347 (72%)
	–1719 (11%)[a]	–1697 (17%)[a]	–1347 (72%)[a]
$EtNH_2$	–1734 (40%)		–1347 (60%)
n-$PrNH_2$	–1723 (27%)		–1369 (73%)
n-$BuNH_2$	–1714 (13%)	–1683 (20%)	–1341 (67%)
iso-$PrNH_2$	–1727 (75%)		–1344 (25%)
	–1720 (12%)[b]	–1683 (27%)[b]	–1347 (61%)[b]
iso-$BuNH_2$	–1723 (56%)		–1374 (44%)
sec-$BuNH_2$	–1721 (25%)	–1671 (19%)	–1332 (56%)
	(0%)[c]	–1668 (49%)[c]	–1333 (51%)[c]
Me_2NH	–1718 (55%)		–1373 (45%)
NH_3 (17, 24)		–1547	–1161
$EtNH_2$ (18)		–1680	–1326
iso-$PrNH_2$ (18)			–1322
Pyridine (22)	–1507	–1453	–1121
3- or 4-Picoline (22)	–1514	–1459	–1136
3,5-Lutidine (22)	–1524	–1456	

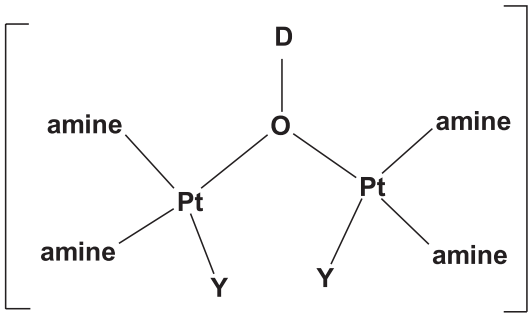
[a]After 5 days.
[b]After 1 week.
[c]After 3 months.

© 2004 NRC Canada

Scheme 1.

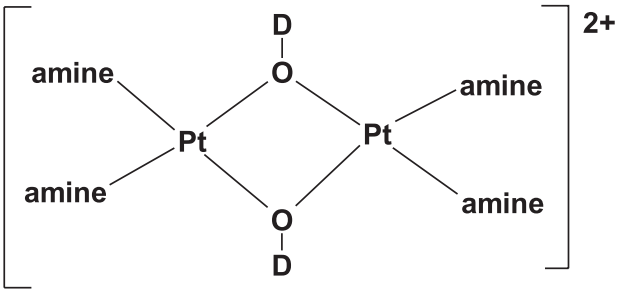


cis(Monoaqua)(monohydroxo) monomer

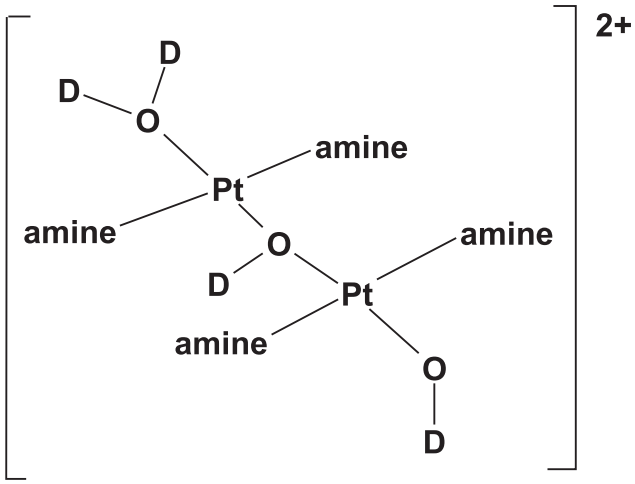


Monohydroxo-bridged dimer

$Y = H_2O$ or OH^-



Dihydroxo-bridged dimer



trans Dimer

The ^{195}Pt NMR spectrum of the $MeNH_2$ complex was remeasured after 5 days. The same three signals were observed, but the intensity of the monomer was lower (19% to 11%), while the monohydroxo-bridged dimer increased from 9% to 17%. The concentration of the dihydroxo-bridged dimer was about the same. The iso-$PrNH_2$ solution was also remeasured after standing in the refrigerator for 1 week. Three species were again detected. The concentration of the monomers had decreased from 75% to 12%, the monohydroxo-bridged dimer increased from 0% to 27%, while the concentration of the dihydroxo-bridged dimer also increased from 25% to 61%. Finally, the *sec*-$BuNH_2$ solution was remeasured after standing in the cold for 3 months. The monomers were absent (25% in the fresh solution), the monohydroxo-bridged dimer increased from 19% to 49%, while the concentration of the dihydroxo-bridged dimer slightly decreased from 56% to 51%.

These preliminary results on the changes of these solutions with time show that the monomer is rapidly formed and its concentration decreases with time, while the formation on the monohydroxo-bridged dimer is much slower. The dihydroxo-bridged dimer is also formed quite rapidly and stays in the solution for a long time. The proportions of the different species depend also on the pH, which might vary slightly for the different compounds.

Study of the trans isomers at neutral pH

A similar study on the trans complexes was performed by ^{195}Pt and ^{1}H NMR spectroscopy. For most compounds, only one ^{195}Pt NMR signal was observed (Table 8). For the primary amine systems, the avg. value is –1555 ppm, an intermediate value between the diaqua compounds (avg. –1547 ppm) and the dihydroxo species (avg. –1574 ppm). The signal was assigned to the monoaqua–monohydroxo monomers *trans*-$[Pt(amine)_2(D_2O)(OD)]^+$. For $MeNH_2$, *n*-$PrNH_2$, and Me_2NH, a second weak signal (5%–8% concentration) was observed. It was assigned to the monohydroxo-bridged dimer (Scheme 1), which has been suggested for the *trans*-$Pt(NH_3)_2$ system (24) and for the trans pyridine compounds (22). This signal was observed at slightly lower field than the one of the monomer and it has been suggested (24) (for the *trans*-$Pt(NH_3)_2$ system) that the concentration of this species increases with time. We have remeasured the ^{195}Pt NMR spectrum of the $MeNH_2$ com-

© 2004 NRC Canada

Table 8. $\delta(^{195}Pt)$ (ppm) of the different species at neutral pD of the trans complexes and some results from the literature.

Amine	$[Pt(amine)_2(D_2O)(OD)]^+$	trans-Dimer	Other signal
$MeNH_2$	–1585 (92%)	–1563 (8%)	
	–1592 (49%)[a]	–1564 (45%)[a]	–1541 (7%)[a]
$EtNH_2$	–1560		
n-$PrNH_2$	–1554 (95%)	–1540 (5%)	
n-$BuNH_2$	–1553		
iso-$PrNH_2$	–1542		
iso-$BuNH_2$	–1557		
sec-$BuNH_2$	–1534		
Me_2NH	–1623 (92%)	–1601 (8%)	
NH_3 (24)	–1377	–1394 (Acid pH)	
		–1340 (Basic pH)	
Pyridine (22)	–1474	–1369	–1355
3-Picoline (22)	–1471	–1360	–1344

[a]After 6 months.

Table 9. $\delta(^1H)$, $(\Delta\delta)$, $\Sigma\Delta\delta$ in ppm, and $^3J(^{195}Pt\text{-}H^1)$ (Hz) for the complexes *trans*-$[Pt(amine)_2(D_2O)(OD)]^+$.

L	H-1	H-2	H-3	H-4 or (H-2′)	$^3J(^{195}Pt\text{-}H_1)$	$\Sigma\Delta\delta$
$MeNH_2$	2.286 (0.041)				36	0.041
	2.301 (0.056)[a]					0.056[a]
$EtNH_2$	2.664 (0.065)	1.288 (0.272)				0.337
n-$PrNH_2$	2.599 (0.079)	1.523 (0.174)	0.934 (0.090)			0.343
n-$BuNH_2$	2.693 (0.122)	1.647 (0.261)	1.374 (0.083)	0.907 (0.178)		0.644
iso-$PrNH_2$	2.996 (0.009)	1.352 (0.360)				0.369
iso-$BuNH_2$	2.469 (0.081)	2.004 (0.428)	0.916 (0.063)			0.572
sec-$BuNH_2$	2.764 (0.035)	1.659 (0.352)	0.914 (0.068)	1.372 (0.382)		0.837
Me_2NH	2.351 (0.123)				33	0.123
	2.364 (0.136)[a]					0.136[a]

[a]Hydroxo-bridged dimer.

pound after 3 months, and the weak signal had now increased to 45%, which seemed to confirm our assignments. The old $MeNH_2$ compound solution also showed a third weak signal at –1541 ppm, which was assigned to a longer chain hydroxo-bridged oligomer or polymer, which could be linear or cyclic. For the *trans*-$Pt(NH_3)_2$ system, Appleton et al. (24) have isolated a solid that formed at pH = 5 to 6, after the solution was allowed to stand. The authors have formulated the solid as containing hydroxo-bridged polymeric cations ($[\{trans\text{-}Pt(NH_3)_2(\mu\text{-}OH)\}_n]^{n+}$), which could be linear or cyclic. The published work on pyridine complexes also suggested this type of polymer in small concentration in fresh solutions (about 5%), but its formation increased with time to about 30% after 7 months (22).

No correlation could be found between the δ(Pt) of the complexes *trans*-$[Pt(amine)_2(D_2O)(OD]^+$ with the pK_a or the proton affinity values.

The chemical shifts in ^1H NMR and the $\Delta\delta$ values of the fresh solutions are shown in Table 9. The amine protons were not detected. In general, the δ(H-1) are between those of the corresponding dihydroxo and diaqua compounds. Only one series of peaks was observed for the chiral ligand *sec*-$BuNH_2$. The $^3J(^{195}Pt\text{-}^1H)$ were detected for the $MeNH_2$ and Me_2NH complexes. They are about 35 Hz.

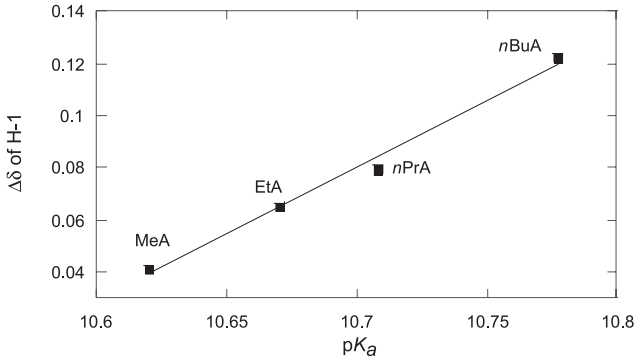
An attempt was made to correlate the $\Delta\delta$(H-1) with the pK_a of the protonated amines. Figure 4 shows the results with the linear amines. An increase in the basicity of the amine leads to a greater $\Delta\delta(H_1)$ value as expected. This is the first time that such a correlation is observed. If we use all the primary amines in this study, we have the same correlation, although the fit is not as perfect.

Conclusion

When the complexes $Pt(amine)_2(NO_3)_2$ were dissolved in D_2O, the diaqua complexes were observed in acidic media, while hydrolysis occurs at basic pH to produce the dihydroxo compounds. In acid solution, the monoaqua–mononitrato species were detected for the trans complexes of $MeNH_2$ and $EtNH_2$, while in basic medium the monohydroxo–mononitrato compound was found only for the *trans*-$EtNH_2$ complex. This is the first report on the presence of monohydroxo–mononitrato compounds in solution.

© 2004 NRC Canada

Fig. 4. Δδ(H-1) (ppm) vs. pK_a of the protonated linear amine for the complexes $[Pt(amine)_2(D_2O)(OD)]^+$.



In ^{195}Pt NMR spectroscopy, the cis diaqua complexes were observed at higher fields than the trans analogues. The difference in δ(Pt) is probably due to differences in the Δ*E* values for the two isomers in the Ramsey equation (33) as suggested in the literature (24). For complexes of the type $Pt(amine)_2X_2$, the Δ*E* difference will be larger when the two ligands (amines and X) are far from each other in the trans influence series (34). The trans influence difference between amine and aqua ligands is quite large (35), resulting in a much lower shielding for the trans complexes than for the cis isomers (Δδ(Pt) ~ 180 ppm). The same is true for the diamine dihydroxo complexes, although the difference is slightly smaller (Δδ(Pt) ~ 140 ppm). This might suggest that the trans influence of the hydroxo ligand is closer to the one of amines than the one of the aqua ligand.

At neutral pH, two or three species were found for the cis isomers. The concentration of these varies with time. We have not made a systematic study of the different species, but a few compounds were remeasured later in time. The presence of the monoaqua–monohydroxo compound is important in fresh solutions and decreases with time. Two oligomeric ionic species were detected. The dihydroxo-bridged dimers are observed at very low fields and they are present in fresh solutions and in older solutions. The second oligomer is the monohydroxo-bridged dimers, which are present in only three of the eight amine complexes in fresh solutions. The concentration of this species increases with time. After 6 months, its concentration is about 50% for the *sec*-butylamine complex. No cyclic trimers or tetramers could be detected. A more systematic study of the different species present in solution as a function of time might show the presence of these species in small concentration.

For the trans compounds at neutral pH, the monoaqua–monohydroxo compound is the only species found in fresh solutions for five of the eight complexes. For $MeNH_2$, *n*-$PrNH_2$, and Me_2NH, a second species identified as the hydroxo-bridged dimer was observed in low concentration in fresh solution. After 6 months, the concentration of the latter increased to about 50% for the $MeNH_2$ complex and a new weak signal (7%) was found at slightly lower field. It was assigned to a larger hydroxo-bridged cyclic or linear oligomer.

The species in solution vary slightly with concentration and the time of heating to dissolve the dinitrato complexes. The latter complexes are not very soluble and must be heated in hot water and it was difficult to reproduce the exact experimental conditions of sample preparation. Furthermore, there sometimes was a residue at the bottom of the NMR tube after the experiment was completed, especially for the cis complexes. Therefore, there were some variations in the proportions of each species when the experiments were repeated.

Acknowledgements

The authors are grateful to the Natural Sciences and Engineering Research Council of Canada (NSERC) for financial support of the project.

References

1. T.W. Humbley. Coord. Chem. Rev. **166**, 181 (1997).
2. B. Lippert. Chemistry and biochemistry of a leading anticancer drug. Wiley-VCH, Weinheim. 1999.
3. P.M. Takahara, A.C. Rosenzweig, C.A. Frederick, and S.J. Lippard. Nature (London), **377**, 649 (1995).
4. S.E. Miller and D.A. House. Inorg. Chim. Acta, **173**, 53 (1990).
5. B.K. Kepler. Metal complexes in cancer chemotherapy. VCH, New York. 1993.
6. W. Kaim and B. Schwedersky. Bioinorganic chemistry, inorganic elements in the chemistry of life. John Wiley and Sons, Inc., New York. 1994.
7. M.J. Cleare and J.D. Hoeschele. Bioinorg. Chem. **2**, 187 (1974).
8. B. Rosenberg. Biochimie, **60**, 859 (1978); B. Rosenberg. Cancer Chemother. Rep. **63**, 1433 (1979); C.J. Boreham, J.A. Broomhead, and D.P. Fairlie. Aust. J. Chem. **34**, 659 (1981).
9. R. Faggiani, B. Lippert, C.J.L. Lock and B. Rosenberg. J. Am. Chem. Soc. **99**, 777 (1977); B. Lippert, C.J.L. Lock, B. Rosenberg, and M. Zvagulis. Inorg. Chem. **17**, 2971 (1978); R. Faggiani, B. Lippert, C.J.L. Lock, and B. Rosenberg. Inorg. Chem. **16**, 1192 (1977); R. Faggiani, B. Lippert, C.J.L. Lock, and B. Rosenberg. Inorg. Chem. **17**, 1941 (1978).
10. J.A. Stanko, L.S. Hollis, J.A. Schreifels, and J.D. Hoeschele. J. Clin. Hematol. Oncol. **7**, 138 (1977).
11. J.A. Broomhead, D.P. Fairlie, and M.W. Whitehouse. Chem. Biol. Interact. **31**, 113 (1980); S.K. Aggarwal, J.A. Broomhead, D.P. Fairlie, and M.W. Whitehouse. Cancer Chemother. Pharmacol. **4**, 249 (1980).
12. M.J. Cleare. Coord. Chem. Rev. **12**, 349 (1974); M.J. Cleare, P.C. Hydes, B.W. Malerbi, and D.M. Watkins. Biochimie, **60**, 835 (1978); P.D. Braddock, T. Connors, M. Jones, A.R. KhorHar, D.H. Melzack, and M.L. Tobe. Chem. Biol. Interactions **11**, 145 (1975).
13. F.D. Rochon and R. Melanson. Acta Crystallogr. **C42**, 1291 (1986).
14. M. Nicolini. Platinum and other metal coordination compounds in cancer chemotherapy. University of Padua, Padua, Italy. 1987.
15. F.D. Rochon and V. Buculei. Inorg. Chim Acta, **357**, 2218 (2004).
16. F.D. Rochon and V. Buculei. Can. J. Chem. **82**, 524 (2004).
17. T.G. Appleton, R.D. Berry, C.A. Davis, J.R. Hall, and H.A. Kimlin. Inorg. Chem. **23**, 3514 (1984).
18. S. Al-Baker and J.C. Dabrowiak. Inorg. Chem. **26**, 613 (1987); S. Al-Baker, J.F. Vollano, and J.C. Dabrowiak. J. Am. Chem. Soc. **108**, 5643 (1986).

© 2004 NRC Canada

19. F.D. Rochon and A. Morneau. Magn. Reson. Chem. **29**, 120 (1991).
20. F.D. Rochon and A. Morneau. Magn. Reson. Chem. **30**, 697 (1992).
21. S. Wimmer, P. Castan, F.L. Wimmer, and N.P. Johnson. J. Chem. Soc. Dalton Trans. 403 (1989).
22. F.D. Rochon and C. Tessier. Can. J. Chem. **80**, 379 (2002).
23. D.S. Gill and B. Rosenberg. J. Am. Chem. Soc. **104**, 4598 (1982).
24. T.G. Appleton, A.J. Baily, K.G. Barnham, and J.R. Hall. Inorg. Chem. **31**, 3077 (1992).
25. P.K. Glasoe and F.A. Long. J. Phys. Chem. **64**, 188 (1960).
26. C. Tessier and F.D. Rochon. Inorg. Chim. Acta, **322**, 37 (2001).
27. F.D. Rochon, A.L. Beauchamp, and C. Bensimon. Can. J. Chem. **74**, 2121 (1996).
28. F.D. Rochon, M. Doyon, and I.S. Butler. Inorg. Chem. **32**, 2717 (1993).
29. C. Tessier and F.D. Rochon. Inorg. Chim. Acta, **295**, 25 (1999).
30. D.D. Derrin. Dissociation constants of organic bases in aqueous solution. Butterworths, London. 1965. pp. 140–183; B.A. Karolev, M.A. Mal'tseva, A.I. Tarasov, and V.A. Vasnev. J. Gen. Chem. **44**, 4, 864 (1974).
31. G. Bouchoux, J.Y. Salpin, and D. Leblanc. J. Phys. Chem. **110**, 16 555 (1996); J.P. Tollenaere and H. Moereels. Tetrahedron Lett. **15**, 1347 (1978); A. Baeten, F. De Proft, and P. Geerlings. Chem. Phys. Lett. **235**, 17 (1995); M.G. Hutchings and J. Gasteiger. Tetrahedron Lett. **24**, 2541 (1983); K. Hiraoka. Can. J. Chem. **65**, 1258 (1987).
32. F.D. Rochon, A. Morneau, and R. Melanson. Inorg. Chem. **27**, 10 (1988).
33. W. McFarlane. J. Chem. Soc. Dalton Trans. 324 (1974).
34. P.L. Goggin, R.J. Goodfellow, S.P. Haddock, B.F. Tayler, and I.R.H. Marshall. J. Chem. Soc. Dalton Trans. 459 (1976).
35. T.G. Appleton, H.C. Clark, and L.E. Manzer. Coord. Chem. Rev. **10**, 335 (1973).

© 2004 NRC Canada

Molecular modeling utilizing purple acid phosphatase biomimetic models

Lilian W. Paes, Roberto B. Faria, Juan O. Machuca-Herrera, Ademir Neves, and Sérgio P. Machado

Abstract: Purple acid phosphatases (PAPs) constitute a new class of metalloenzymes that catalyze the hydrolysis of certain phosphate esters, including nucleoside di- and triphosphates and aryl phosphates, under acidic conditions. To provide some insight into these metalloenzymes we have performed quantum chemical and molecular mechanics calculations based on the mixed-valence $[Fe^{II}Fe^{III}(BPBPMP)(OAc)_2]^+$ model complex (**1**) (H_2BPBPMP = 2-bis[{(2-pyridylmethyl)-aminomethyl}-6-{(2-hydroxybenzyl)-(2-pyridylmethyl)}-aminomethyl]-4-methylphenol). The geometric and the vibrational parameters calculated by molecular mechanics show that the force fields established in this work reproduce the binuclear iron core with μ-phenoxo or μ-alkoxo and di-μ-acetate bridges presented in the PAPs model complexes. The atomic orbital analysis of the SOMO contributions indicated that the Fe^{III} atom and the terminal phenolate are involved in the phenolate to Fe^{III} charge transfer electronic transition in **1** as argued from electronic spectroscopic data in the PAPs.

Key words: mixed-valence $Fe^{II}Fe^{III}$ complex, purple acid phosphatases, molecular modeling.

Résumé : Les phosphatases acides violettes (PAV) constituent une nouvelle classe de métalloenzymes qui catalysent, en milieu acide, l'hydrolyse de certains esters de l'acide phosphorique, y compris des di- et des triphosphates de nucléoside et des phosphates d'aryle. Afin de mieux comprendre ces métalloenzymes, des calculs théoriques de mécanique moléculaire et de chimie quantique ont été effectués sur le complexe modèle de valence mixte $[Fe^{II}Fe^{III}(BPBPMP)(OAc)_2]^+$ (**1**) (H_2BPBPMP = 2-bis[{2-pyridylméthyl)-aminométhyl}-6-{(2-hydroxybenzyl)(2-pyridylméthyl)}aminométhyl]-4-méthylphénol). Les paramètres géométriques et vibrationnels calculés sur la base de la mécanique moléculaire montrent que les champs de force établis dans ce travail correspondent au noyau binucléaire de fer avec des ponts μ-phénoxo ou μ-alkoxo et di-μ-acétatate qui ont été présentés dans les complexe du modèle de PAV. L'analyse de l'orbitale atomique des contributions SOMO indique que l'atome de Fe^{III} et le phénolate terminal sont impliqués dans la transition électronique detransfert de charge du phénolate au Fe^{III} du composé **1**, tel qu'il avait été suggéré à partir des données de spectroscopie électronique des PAV.

Mots clés : complexe $Fe^{II}Fe^{III}$ de valence mixte, phosphatases acide violettes, modélisaton moléculaire.

[Traduit par la Rédaction]

Introduction

Purple acid phosphatases (PAP) represent a new class of non-heme proteins, which catalyze the hydrolysis of a wide range of phosphate esters and anhydrides including nucleoside di- and triphosphates under acidic conditions. The active site of these PAPs from mammalian sources consists of a binuclear center with two accessible oxidation states of $Fe^{III}M^{II}$ and $Fe^{III}M^{III}$ (M = Fe) (1). The reduced form of the enzyme is active for hydrolysis while the oxidized form is inactive. The PAPs have been isolated from a variety of mammalian, plant, and microbial sources. In mammalian PAPs there is a Fe^{III}–Fe^{II} center, while plant PAPs from red kidney bean have a Fe^{III}–Zn^{II} center in their enzymatically active form (2, 3).

Crystal structures (4, 5) of PAPs show that seven conserved protein residues, including a monodentate bridging carboxylate, occupy eight coordination sites on the two metals, leaving four possible sites for the exogenous ligands. The presence of a hydroxy bridge occupying two of the exogenous ligand sites has been proposed on the basis of spectroscopic and magnetic measurements of the active mixed valence $Fe^{III}Fe^{II}$ enzyme. Their purple color originates from the tyrosinate-to-Fe^{III} charge-transfer band. In both reduced and oxidized forms, the iron atoms are antiferromagnetically spin coupled giving rise to S = 1/2 and S = 0 ground states, respectively. Magnetic susceptibility measurements (6) of the reduced form have revealed that the Fe^{II} and Fe^{III} centers are weakly coupled with *J* values in the range of –5 to –15 cm^{-1}. The binuclear iron center of purple acid phosphatases (PAPs) has been studied extensively using various spectroscopic techniques (7–10). It seems that the pres-

Received 18 March 2004. Published on the NRC Research Press Web site at http://canjchem.nrc.ca on 15 December 2004.

L.W. Paes, R.B. Faria, J.O. Machuca-Herrera, and S.P. Machado.[1] Departamento de Química Inorgânica, Instituto de Química, Laboratório de Química Inorgânica Computacional, Universidade Federal do Rio de Janeiro, Caixa Postal 68563, Rio de Janeiro, RJ, 21945-970, Brazil. **A. Neves.** Departamento de Química, LABINC – Universidade Federal de Santa Catarina, Florianópolis, SC, Brazil.

[1]Corresponding author (e-mail: sergiopm@iq.ufrj.br).

 doi: 10.1139/V04-134 © 2004 NRC Canada

ence of at least one terminal phenolate ligand bound to the Fe^{III} center is required to obtain suitable dinuclear biomimetic complexes. Moreover, the stabilization of these complexes in the reduced and oxidized forms, displaying reversible redox properties, appears to be essential to the biological activity of these metalloproteins.

The initial goal in modeling the active site of the purple acid phosphatases is to synthesize an inorganic compound having structural and spectroscopic features as similar as possible to the active site in stable states. The biomimetic synthesis and characterization of new binuclear complexes with relevant N,O-donor ligands (amines, phenolate, imidazole, and pyridine), therefore, offers a useful contribution to the understanding of the electronic and structural properties of these metalloproteins. These ligands must induce unsymmetrical M–L environments and vacant or labile sites for reactivity, and must be capable of stabilizing both $Fe^{III}Fe^{III}$ and $Fe^{II}Fe^{III}$. Recently, various model complexes have been synthesized with polypodal ligands (11–18) such as 2-bis[{(2-pyridylmethyl)-aminomethyl}-6-{(2-hydroxybenzyl)-(2-pyridylmethyl)}-aminomethyl]-4-methylphenol (H_2BPBPMP). Also, effective computational methods have emerged that provide some insight into bioinorganic systems. Accurate and efficient approaches combining quantum chemical and molecular mechanics models have been developed, complementing experimental work, to study these metalloproteins. Molecular mechanics is an efficient approach to optimizing molecular structures with generally high accuracy and comparably little computational expense (19–22). The choice of the force field and its parameterization, is dictated by the problem to be solved and the available experimental data. In the last decade, various papers have discussed the application of molecular mechanics programs in many chemistry areas showing the efficiency of the empirical force field calculations, and the variety of force fields developed.

Despite the increase in computer power, modeling of large molecules continues to depend on the evolution of simplified representations at all levels. Considering the size of most bioinorganic systems, semiempirical models and molecular mechanics still seem to be the tools of choice in the description of relevant systems, allowing a large number of atoms to be worked with, giving reductions in the cost:performance ratio of the computational hardware. However, in the last few years high-level, large-scale computational models of diiron complexes have been developed (23, 24).

To provide some insight into this class of metalloenzymes, in this study we performed molecular mechanics, quantum chemical and semiempirical calculations for some PAPs model compounds to complement experimental studies of these metalloenzymes. The calculation consisted firstly of the use of molecular mechanics, with the FORCES program (25, 26). After the molecular mechanics optimized structures were obtained, the ab initio "single point" calculations were carried out using the GAMESS program with the ECP-SBK basis set (27). This basis has been shown to be a good choice in treating heavier elements and to be useful for the lower transition metal series as well (28). The semiempirical extended Hückel (EHT) (29) calculations were carried out with the EXTEN program developed in our laboratory, which considers the Pearson's atomic local hardness (30, 31) following the Dronskowski (32) approach, to calculate the reactivity of the metal centers.

Computational details

All the calculations were carried out on a Pentium 200 MHz computer with 256 Mb RAM and a 10 Gb HD under the Windows operational system for the FORCES and EXTEN programs, and an Athlon 1 GHz PC, with 512 Mb RAM and a 20 Gb HD running under UNIX Free BSD 4.X operational system for the GAMESS program.

The methodology adopted for the calculations consisted firstly of the use of molecular mechanics with the FORCES program developed in the Laboratory of Computational Inorganic Chemistry, for the geometry optimization of the model complexes. The force field employed was developed specifically for diiron core centers. The optimized structures were submitted to the ab initio ROHF (Restrict Open Hartree Fock) MO single point calculations performed by the GAMESS program with the ECP-SBK basis set, with multiplicity equals 2 for electronic analysis. The semiempirical molecular orbital calculation was made considering Pearson's atomic local hardness following the Dronskowski approach, using the extended Hückel method approximations given by the EXTEN program developed in our laboratory.

Results and discussion

The MM, EHT, and QM theory (ab initio – single point) calculations were performed on a series of model complexes, according to the experimentally available information (11–18). The model complexes are shown in Fig. 1. These compounds have an asymmetric binuclear structure with two iron atoms in the oxidation states (Fe^{II}, Fe^{III}), and each iron center with a six-coordinated octahedral environment. The iron ions are bridged by alkoxo or phenoxo groups and two carboxylate ligands, nitrogen's amine and phenolate or alkoxo groups complete the coordination environment.

Table 1 shows the bonds, angles, and dihedral angles force constants that were used in this work, and Table 2 presents the experimental and calculated structural parameters.

Comparison between the geometric parameters of the model with the experimental data shows that the force field adopted for these binuclear iron complexes performed very well, although some calculated angles did not present values close to the experimental data. This difference is due to the fact that the model complexes present some free dihedral angles, supplying lesser rigidity to the system when compared with experimental parameters.

It is important to note that the experimental and calculated (Fe^{II}-O_b-Fe^{III}) bridging angle presented very close values, indicating a good reproduction of the binuclear core. The oxygen bridge was coordinated asymmetrically with the two metallic centers, as has been observed in other iron mixed valence complexes (13).

Table 3 shows the experimental and vibrational frequencies analysis calculated by the FORCES program for the model complexes.

© 2004 NRC Canada

Fig. 1. Structure of the model complexes.

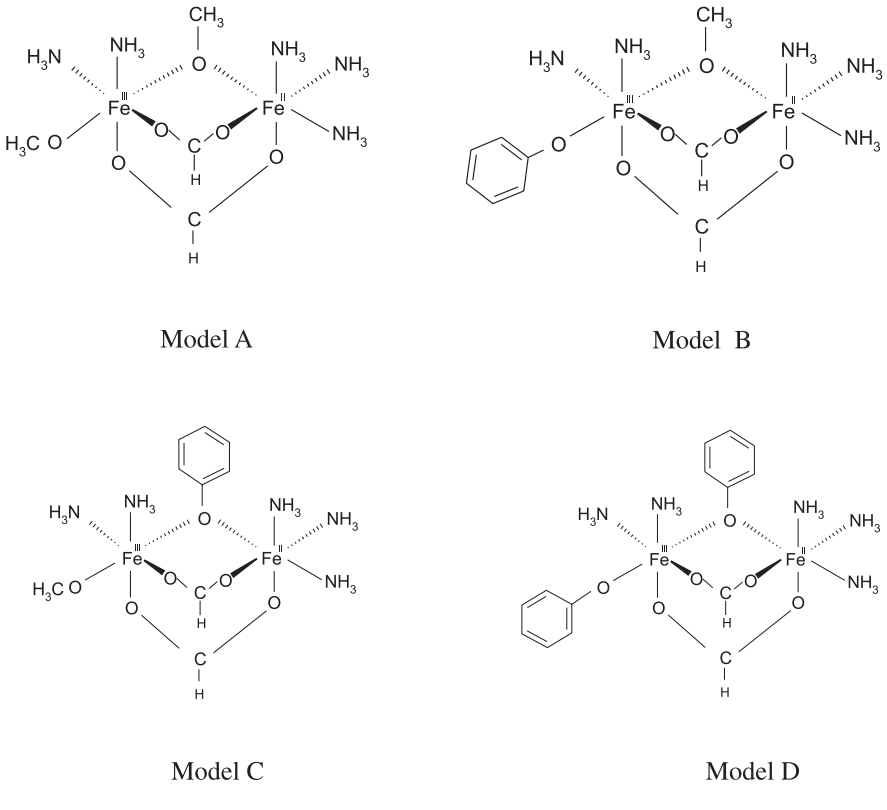


Table 1. Select bonds, angles and dihedral angle force constants.

Bond	K_h (mydna/Å)
Fe—O_b	1.30
Fe—O_t	1.50
N_p—C_{ar}	3.00
C—O_p	6.0
Angle and dihedral	K_θ (mydnaÅ/rad^2)
Fe-O_b-Fe	0.80
Fe-O_p-C_{ar}	0.90
O_p-Fe-O_b	0.80
Fe-O_p-C_{ar}-C_{ar}	0.07
Fe-O_c-C-H	0.08
Fe-O_c-C-O_c	0.09

Note: O_b = bridge oxygen, O_t = terminal oxygen (-CH_3), O_c = carboxylate oxygen, O_p = phenolate oxygen, C_{ar} = aromatic carbon, N_{am} = amine nitrogen, N_p = pyridyl nitrogen.

Many IR and Raman studies of the Fe–O fragment have been published (33–36). In a recent paper (37), the band in the Raman spectra at approximately 340 cm^{-1} was tentatively assigned to the ν_s (Fe–O_{bridge}). Such assignment was based on standard coordination analysis of compounds such as M_2X_{10} that indicated the following relative energy order: δ (M–X–M) < ν_s (M–X_{bridge}) < ν (M–$X_{terminal}$) < ν_{as} (M–X_{bridge}). This assignment was reinforced by the density functional theory (DFT) that indicated a ν_s Fe–O vibration chelate band at approximately 320 cm^{-1}.

The same order was established in this work, where the region of lower frequency was at 300 cm^{-1} (ν_s M–O_{bridge}) and the region of higher frequency was at 600 cm^{-1} (ν_{as} M–O_{bridge}), while the ν(M–$O_{terminal}$) was in the intermediate region. Based on these results, we assign the band at ~314 cm^{-1} to Fe–O_{bridge} stretching. To analyze the electronic structure, quantum chemical calculations were performed on the optimized structure of the model complexes. Figure 2 presents the graphic representation of the frontier orbitals SOMO in the ground state for the model complexes. The calculated single occupied higher molecular orbitals (SOMO) show only the participation of the d_{xy} iron(III) atomic orbital together with the p_y oxygen atomic orbital of the phenolate ligands in all of the model complexes. The atomic orbital d_{xy} of Fe^{II} and the atomic orbital of the oxygen bridge do not contribute to this molecular orbital.

The characteristic electronic absorption spectrum of the PAPs consists of a broad band centered at 555 nm; this band is assigned to a tyrosinate-to-iron(III) charge transfer transition. The ground state graphical representations calculated for the SOMO show that the Fe^{III} atom from the metal center and the terminal phenolate are involved in this electronic transition. For a better analysis, a configuration interaction (CI) calculation was attempted, but the model complexes present a large number of atoms, making the calculation impossible.

The Mulliken population analyses of the SOMO for the oxygen atoms are shown in Table 4.

In recent years, many studies of magnetic properties on binuclear iron complexes have been carried out (38–44). This class of binuclear iron complexes can be divided into two groups: the strong, antiferromagnetically coupled oxo-

© 2004 NRC Canada

Table 2. Selected bond lengths and bond angles of the optimized and experimental structures.

Model complexes	Fe^{II}—O_b (Å)	Fe^{III}—O_b (Å)	Fe^{III}—$O_{p\ or\ t}$ (Å)	Fe^{II}-O_b-Fe^{III} (°)	Fe^{II}···Fe^{III} (Å)
A	2.050	2.023	1.916	116.95	3.47
B	2.057	2.024	1.925	116.24	3.46
C	2.138	2.105	1.911	112.60	3.52
D	2.051	2.030	1.935	117.62	3.49
Experimental[a]	2.102	2.005	1.902	117.14	3.50

Note: O_b = bridge oxygen, $O_{p\ or\ t}$ = phenolate oxygen or terminal (-CH_3).
[a]For [$Fe^{II}Fe^{III}$(BPBPMP)$(OAc)_2$](ClO_4) (ref. 18).

Table 3. Experimental and calculated vibrational frequencies for the model complexes.

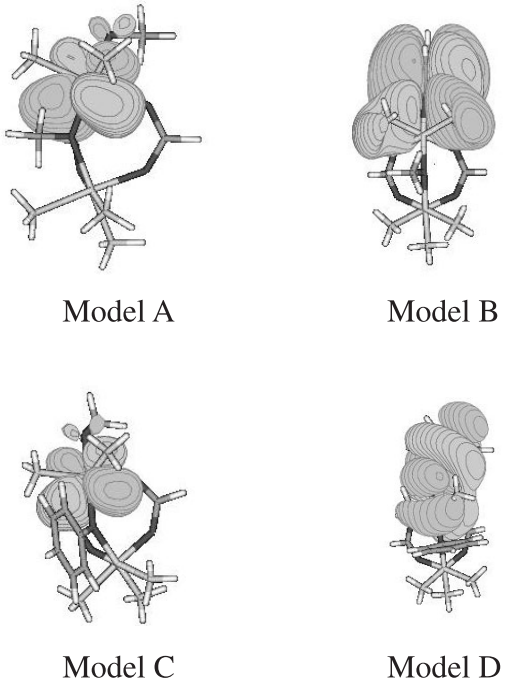
Model complex	ν Fe–O (cm^{-1})	ν $C_{phenolate}$–O (cm^{-1})
A	361.6/579.8/651.8	—
B	319.4/591.8/651.7	1358.9
C	302.4/548.0/639.8	1323.6
D	314.6/586.4/656.1	1211.6/1378.8
Experimental[a]	567.05/649.79	1200–1343

[a]For [$Fe^{II}Fe^{III}$(BPBPMP)$(OAc)_2$](ClO_4) (ref. 18).

Table 4. Mulliken population analyses of the SOMO.

Model complex	O_{bridge}	$O_{terminal}$
A	0.0057	0.017
B	0.00013	0.149
C	0.0038	0.018
D	0.00005	0.889

Fig. 2. Surface representation of the SOMO obtained from the ab initio calculation by the ECP-SBK basis set for models A–D.



bridged complexes and weak, antiferromagnetically coupled hydroxy-, alkoxo-, and phenoxo-bridge complexes. It has been suggested, on the basis of semiquantitative MO theory, that the strength of antiferromagnetic interaction should increase since the higher electron density of the oxo-bridge leads to a much stronger antiferromagnetic coupling (~–55 > J > ~–135 cm^{-1}) when compared with hydroxy-, alkoxo-, or phenoxo-bridged iron compounds (+1.2 > J > ~–30 cm^{-1}). The electron density of the bridging oxygen atom should increase in the series Ph < H < R. It was observed that the electronic effect of the ligand in the trans position must be considered in the antiferromagnetic interaction. In Scheme 1, we show the charge density and bond order for the A and C models.

Analyzing the data in the Scheme 1, we note that the model A presents a higher electronic density on the oxygen bridge. The aromatic substituents show a weak negative inductive effect while aliphatic substituents show a weak positive inductive effect, causing a decrease in the J values. The Fe—O bond order for model A is higher than that for model C, showing that the electronic density on the oxygen bridge in model A is higher than that of model C.

Scheme 2 shows that the electronic density on the oxygen bridge for model D is smaller than the oxygen bridge for model B, which can be explained by the phenoxo bridge and the Fe—O bond order that show the same tendency.

Although we show another effect on the charge density when comparing models A and B, the oxygen bridge is the same, but the terminal ligands in the trans position are different. We expected the same electronic density on the oxygen bridge for models A and B because of the CH_3 substitute on the oxygen bridge, but the electronic density on the oxygen bridge in model A is higher than that in model B. In other words, when the ligand in the trans position is a phenolate group, the electronic density on the oxygen bridge decreases. The same tendency was observed for models C and D. The less electronegative atoms in the trans position result in a somewhat stronger magnetic interaction, and this electronic effect might be responsible for the decrease in the magnitude of antiferromagnetic interaction on substitution that was also observed in this work (45).

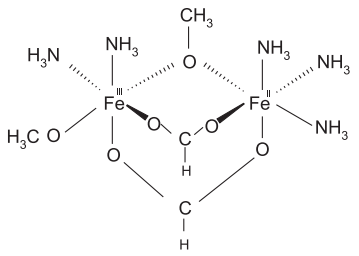
The semiempirical calculated reactivity indices for models A–D are listed in Table 5.

The reactivity indices calculated by the semiempirical MO program (EXTEN) for the Fe^{II} and Fe^{III} were 0.341 and 0.00 eV, respectively, indicating that the Fe^{II} presents higher reactivity than the Fe^{III} in agreement with one of the hydrolysis mechanisms proposed (46, 47), where the dianionic

© 2004 NRC Canada

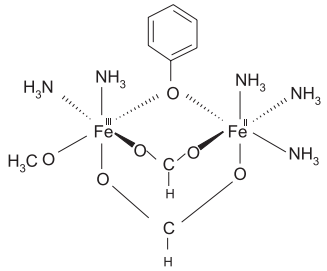
Scheme 1.

Model A



BO $Fe^{III} - O_{bridge} = 0.392$
BO $Fe^{II} - O_{bridge} = 0.110$
Charge density $O_{bridge} = 0.0057$
Charge density $O_{terminal} = 0.017$

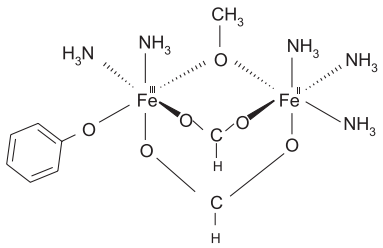
Model C



BO $Fe^{III} - O_{bridge} = 0.310$
BO $Fe^{II} - O_{bridge} = 0.051$
Charge density $O_{bridge} = 0.0038$
Charge density $O_{terminal} = 0.018$

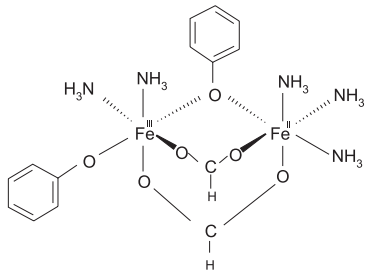
Scheme 2.

Model B



OL $Fe^{III} - O_{bridge} = 0.433$
OL $Fe^{II} - O_{bridge} = 0.120$
Charge density $O_{bridge} = 0.00013$
Charge density $O_{phenolate} = 0.149$

Model D



OL $Fe^{III} - O_{bridge} = 0.172$
OL $Fe^{II} - O_{bridge} = 0.133$
Charge density $O_{bridge} = 0.00005$
Charge density $O_{phenolate} = 0.889$

Table 5. Reactivity indices calculated by the EXTEN program.

	Reactivity indices (eV)	
Model complex	Fe(III)	Fe(II)
A	0.000	0.316
B	0.000	0.439
C	0.282	0.000
D	0.000	0.341

phosphate monoester substrate preferentially binds the Fe^{II}, which is subsequently attacked by the Fe^{III}–OH nucleophile.

Conclusions

The geometric and the vibrational parameters calculated by molecular mechanics show that the force fields established in this work reproduce very well the binuclear iron core, with μ-phenoxo and μ-alkoxo bridges present in the PAPs model complexes.

The ab initio single point (SP) calculated for the SOMO shows the participation of the d_{xy} iron(III) atomic orbital together with the p_y oxygen atomic orbital of the phenolate ligands (terminal) for all models. Therefore, the atomic orbital analysis of the SOMO contributions indicated that the Fe^{III} atom from the dinuclear $Fe^{II}Fe^{III}$ center and the terminal phenolate may be involved in the tyrosinate-to-iron(III) charge transfer electronic transition in PAPs.

The reactivity indices calculated for Fe^{II} and Fe^{III} indicate that the Fe^{II} presents an atomic local hardness higher than Fe^{III}, in agreement with one of the mechanisms proposed.

The results above reflect the progress that has been made in modeling metalloprotein active sites. The agreement between the experimental data and calculated results validates the methodology used in this work.

Acknowledgments

The authors would like to thank the Brazilian agencies Conselho Nacional de Desenvolvimento Científico e Tecnológico (CNPq), Coordenação de Aperfeiçoamento de

© 2004 NRC Canada

Pessoal de Nível Superior (CAPES), Fundação Carlos Chagas de Amparo à Pesquisa do Estado do Rio de Janeiro (FAPERJ), Fundação Universitária José Bonifácio (FUJB), and Fundação José Pelúcio Ferreira.

To Ary Machado Borges in memoriam.

References

1. B.A. Averill, J.C. Davis, S. Burman, T. Zirino, J. Sanders-Loehr, T.M. Loehr, T. Sage, and P.G. Debrunner. J. Am. Chem. Soc. **109**, 3760 (1987).
2. E.D. Wilcox. Chem. Rev. **96**, 2435 (1996).
3. T. Klabunde, N. Sträter, B. Krebs, and H. Witzel. FEBS Lett. **367**, 56 (1995).
4. J. Uppenberg, F. Lindqvist, C. Svensson, B. Ek-Rylander, and G. Andersson. J. Mol. Biol. **290**, 201 (1999).
5. L.W. Guddat, A.S. McAlpine, D. Hume, S. Hamilton, J. Jersey, and J.L. Martin. Structure, **7**, 757 (1999).
6. S. Gehring, P. Fleischhauer, M. Behlendorf, M. Hüber, J. Lorösch, W. Haase, M. Dietrich, H. Witzel, R. Löcke, and B. Krebs. Inorg. Chim. Acta, **252**, 13 (1996).
7. R.P. Gaber, J.P. Sheridan, F.W. Bazer, and R.M. Roberts. J. Biol. Chem. **254**, 8340 (1979).
8. B.C. Antanaitis and P. Aisen. J. Biol. Chem. **257**, 5330 (1982).
9. R.C. Holz, L. Que, Jr., and J.L. Ming. J. Am. Chem. Soc. **114**, 4434 (1992).
10. S.S. David and L. Que, Jr. J. Am. Chem. Soc. **112**, 6455 (1990).
11. A. Neves, M.A. Brito, V. Drago, K. Griesar, and W. Haase. Inorg. Chim. Acta, **237**, 131 (1995).
12. M.A. Brito, A. Neves, and L.R. Zilli. Quim. Nova, **20**, 154 (1997).
13. E. Lambert, B. Chabut, S. Chardon-Noblat, A. Deronzier, G. Chottard, A. Bousseksou, J.-P. Tuchagues, J. Laugier, M. Bardet, and J.-M. Latour. J. Am. Chem. Soc. **119**, 9424 (1997).
14. A. Neves, L.M. Rossi, I. Vencato, W. Haase, and R. Werner. J. Chem. Soc. Dalton Trans. **5**, 707 (2000).
15. M. Scarpellini, A. Neves, A.J. Bortoluzzi, D. Vencato, W.A. Ortiz, and C. Zucco. J. Chem. Soc. Dalton Trans. **18**, 2616 (2001).
16. M. Lanznaster, A. Neves, A.J. Bortoluzzi, B. Szpoganicz, and E. Schwinge. Inorg. Chem. Commun. **41**, 5641 (2002).
17. P. Karsten, A. Neves, A.J. Bortoluzzi, M. Lanznaster, and V. Drago. Inorg. Chem. **41**, 4624 (2002).
18. A. Horn, Jr. Ph.D thesis, Universidade Federal de Santa Catarina, Florianópolis, SC, Brazil, 2000.
19. P. Comba, A. Lledos, F. Maseras, and R. Remenyi. Inorg. Chim. Acta, **324**, 21 (2001).
20. P. Comba and R. Remenyi. Coord. Chem. Rev. **238–239**, 9 (2003).
21. R.A. Friesner, M.-H. Baik, B.F. Gherman, V. Guallar, M. Wirstam, R.B. Murphy, and S.J. Lippard. Coord. Chem. Rev. **238–239**, 267 (2003).
22. L.W. Coelho, G.M.A. Junqueira, J.O. Machuca-Herrera, S. de P. Machado, and B.D. Machado. Quim. Nova, **22**, 396 (1999).
23. B.D. Dunietz, M.D. Beachy, Y. Cao, D.A. Whittington, S.T. Lippard, and R.A. Friesner. J. Am. Chem. Soc. **122**, 2828 (2000).
24. G.A. Papoian, W.F. DeGrado, and M.L. Klein. J. Am. Chem. Soc. **125**, 560 (2003)
25. J.O. Machuca-Herrera. Ph.D thesis, Universidade Estadual de Campinas, Campinas, SP, Brazil, 1988.
26. C.H.F. Almeida, J.O. Machuca-Herrera, and S.P. Machado. Quim. Nova, **25**, 957 (2002).
27. W.J. Stevens, H. Bash, and M. Krauss. J. Chem. Phys. **81**, 6026 (1984).
28. L.W. Paes, R.B. Faria, J.O. Machuca-Herrera, and S.P. Machado. Inorg. Chim. Acta, **321**, 22 (2001).
29. R.E. Hoffmann. J. Chem. Phys. **39**, 1397 (1963).
30. R.G. Pearson and R.R.G. Parr. J. Am. Chem. Soc. **105**, 7512 (1983).
31. R.G. Pearson. J. Chem. Ed. **64**, 561 (1987).
32. R. Dronskowski. J. Am. Chem. Soc. **114**, 7230 (1992).
33. L. Montri and R. D. Cannon. Spectrochim. Acta, **41A**, 643 (1985).
34. L. Öhrström and I. Michaud-Soret. J. Phys. Chem. A, **103**, 256 (1999).
35. R. Wu, A.J. Upali, and R.D. Cannon. Spectrochim. Acta A, **56**, 575 (2000).
36. C.J. Carrano, M.W.Carrano, K. Sharma, G. Backes, and J. Sanders-Loehr. Inorg. Chem. **29**, 1865 (1990).
37. N.S. Gonçalves, L.M. Rossi, L.K. Noda, P.S. Santos, A.J. Bortoluzzi, A. Neves, and I. Vencato. Inorg. Chim. Acta, **329**, 141 (2002).
38. J.P. Hay, J.C. Thibeault, and R. Hoffmann. J. Am. Chem. Soc. **20**, 4884 (1975).
39. S.M. Gorun and S.J Lippard. Inorg. Chem. **30**, 1625 (1991).
40. J.R. Hart, A.K. Rappe, S.M. Gorun, and T.H. Upton. J. Phys. Chem. **96**, 6264 (1992).
41. C. Saal, C.M. Böhm, and W. Haase. Inorg. Chim. Acta, **291**, 82 (1999).
42. E.Q. Gao, L.H. Yin, J.K. Tang, P. Cheng, D.Z. Liao, Z.H. Jiang, and S.P. Yan. Polyhedron, **20**, 669 (2001).
43. R. Werner, S. Ostrovsky, K. Griesar, and W. Haase. Inorg. Chim. Acta, **326**, 78 (2001).
44. Z. Chen, Z. Xu, L. Zhang, F.Yan, and Z. Lin. J. Phys. Chem. A, **105**, 9710 (2001).
45. A. Escuer, R. Vicente, J. Ribas, and B. Raynaud. Inorg. Chim. Acta, **216**, 139 (1994).
46. Y. Lindqvist, E. Johansson, H. Kaija, P. Vihko, and G. Schneider. J. Mol. Biol. **291**, 135 (1999).
47. T. Klabunde, N. Sträter, R. Fröhlich, H. Witzel, and B. Krebs. J. Mol. Biol. **259**, 737 (1996).

© 2004 NRC Canada

The chiral oxime of 13*H*-dibenzo(*a*,*i*)fluoren-13-one

Sean Higgins, David G. Morris, Kenneth W. Muir, and Karl S. Ryder

Abstract: On the basis of single crystal diffraction analyses it is shown that conversion of 13*H*-dibenzo(*a*,*i*)fluoren-13-one into its oxime causes distortion of the aromatic framework because of steric crowding. The oxime is, in consequence, chiral.

Key words: oxime, crystal structure, chirality.

Résumé : Sur la base d'analyses de diffraction de rayons X par un cristal unique, on montre que la conversion de la 13*H*-dibenzo(*a*,*i*)fluorén-13-one en son oxime provoque une distorsion du squelette aromatique en raison d'un encombrement stérique. En conséquence, l'oxime est chiral.

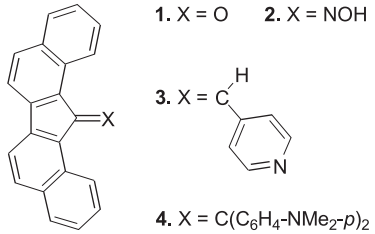
Mots clés : oxime, structure cristalline, chiralité.

[Traduit par la Rédaction]

Introduction

We have recently shown that the carbon skeleton of the aromatic ketone (**1**) is almost exactly planar: the angle between the two naphthalene residues is only 1.9(1)° (1). This has led us to consider overcrowding in derivatives of **1**, such as its oxime **2**. For steric reasons **2** cannot adopt a planar structure. A major departure from planarity in **2** would render the molecule chiral, with the proviso that the oxime is configurationally stable. Previous work indicates that this is certainly the case; thus, the barrier to in-plane nitrogen inversion for methanal oxime has been estimated to be greater than 160 kJ mol^{-1} and the barrier to rotation around the >C=N bond in an oxime is even larger — a value of ca. 210 kJ mol^{-1} has been suggested (2). Optical isomerism of this type has not previously been demonstrated in oximes. There appears to be no *published* discussion of distortions of the 13*H*-dibenzo(*a*,*i*)fluoren-9-one skeleton induced by sterically demanding substituents. However, the structures of **3** and **4**, both of which contain such substituents, have recently been deposited in the Cambridge Structural Database (hereinafter CSD) (3) by Scherschlicht et al. (4) (Scheme 1).

Scheme 1.



Results and discussion

A sample of **2** was made from **1** by established methods (5). X-ray analysis[2] of a twinned crystal reveals a structure built from pairs of hydrogen-bonded molecules (Fig. 1). This $R_2^2(6)$ motif is typical of oxime structures, though other patterns of hydrogen bonding are also found (6), and it underlies their use as well-defined crystalline derivatives of carbonyl compounds.

Conversion of **1** into its oxime **2** distorts the central C1-C2-C11-C12-C21 cyclopentadiene ring into an envelope

Received 6 May 2004. Published on the NRC Research Press Web site at http://canjchem.nrc.ca on 20 December 2004.

S. Higgens, D.G. Morris,[1] and K.W. Muir.[1] Department of Chemistry, University of Glasgow, Glasgow G12 8QQ, UK.
K.S. Ryder. Department of Chemistry, Loughborough University, Loughborough LE11 3TU, UK.

[1]Corresponding authors (e-mail: ken@chem.gla.ac.uk).

[2]Structure analysis of **2**. Crystal data: $C_{21}H_{13}NO$, M_r = 295.32, orange plate 0.40 mm × 0.23 mm × 0.02 mm, monoclinic, $P2_1/n$, a = 12.882(3), b = 3.763 5(10), c = 28.633(6) Å, β = 99.797(10)°, V = 1367.9(6) $Å^3$, Z = 4, D_x = 1.434 Mg/m^3, T = 100(2) K, λ(Mo-K_α) = 0.710 73 Å, μ = 0.088 mm^{-1}, crystallization from hot toluene. Data collection: Nonius KappaCCD, thick slice ω scans, 19 967 reflections collected over 33 h, 3895 independent reflections, R_{int} = 0.043, θ range 1.4°–30.2°, $-18 \le h \le 17$, $0 \le k \le 5$, $-12 \le l \le 40$, no absorption correction. Refinement: full-matrix on F^2, data / parameters 3895 / 213, $R(F$, all data) = 0.085, $wR(F^2$, all data) = 0.203, Δρ +0.41 to –0.34 e $Å^{-3}$. Complete X-ray data are available as supplementary material and may be purchased from the Directory of Unpublished Data, Document Delivery, CISTI, National Research Council Canada, Ottawa, ON K1A 0S2, Canada (http://www.nrc.ca/cisti/irm/unpub_e.shtml for information on ordering electronically). CCDC 237830 contains the crystallographic data for this manuscript. These data can be obtained, free of charge, via www.ccdc.cam.ac.uk/conts/retrieving.html (or from the Cambridge Crystallographic Data Centre, 12 Union Rd., Cambridge CB2 1EZ, UK; fax +44 1223 336033; or deposit@ccdc.cam.ac.uk).

 doi: 10.1139/V04-133 © 2004 NRC Canada

Fig. 1. A view of two centrosymmetrically related molecules of **2** linked by O1-H···N1^{i} hydrogen bonds (O1-H1 (0.97(4) Å), H1···N1^{i} (1.85(4) Å), and O1···N1^{i} (2.786(3) Å)); O1-H1···N1^{i} 161(4)°; $i = 1 - x, -y, -z$]. Probability ellipsoids at 50% are shown. Selected bond lengths and angles : O(1)—N(1) (1.396(2) Å), N(1)—C(1) (1.293(3) Å), C(1)—C(21) (1.488(3) Å), C(1)—C(2) (1.485(3) Å), C(11)—C(12) (1.475(3) Å), C(1)-N(1)-O(1) (114.9(2)°), N(1)-C(1)-C(2) (132.9(2)°), N(1)-C(1)-C(21) (117.5(2)°), O(1)-N(1)-C(1)-C(2) (9.0(4)°), N(1)-C(1)-C(2)-C(3) (–30.5(5)°), and N(1)-C(1)-C(21)-C(20) (24.0(4)°).

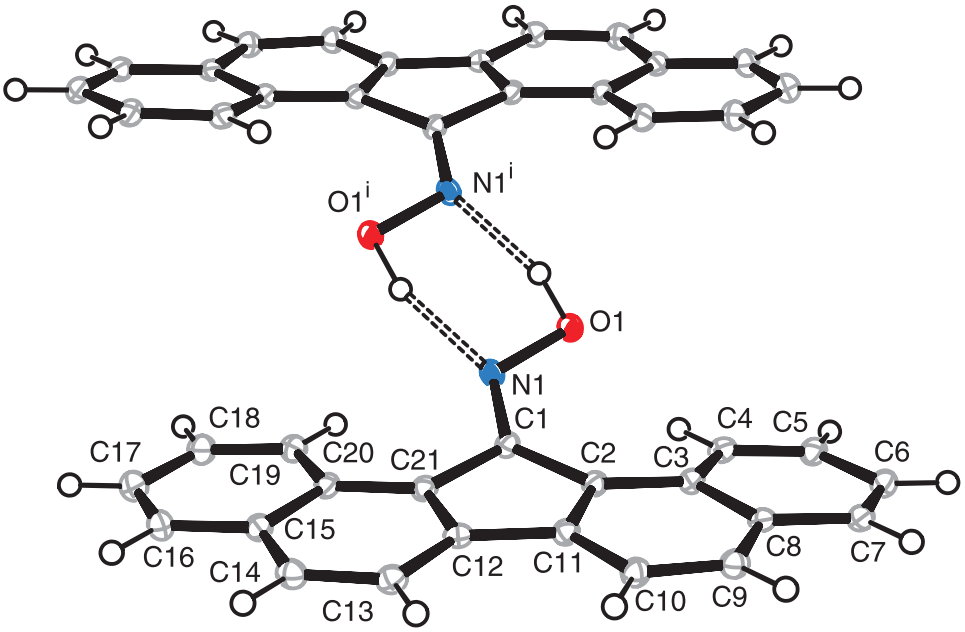
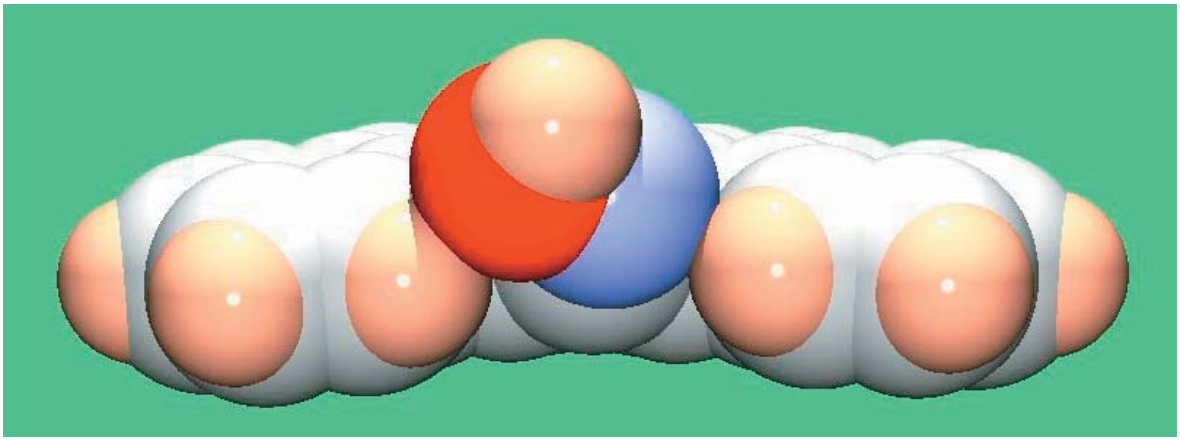


Fig. 2. View of a space-filling model of a molecule of **2**.

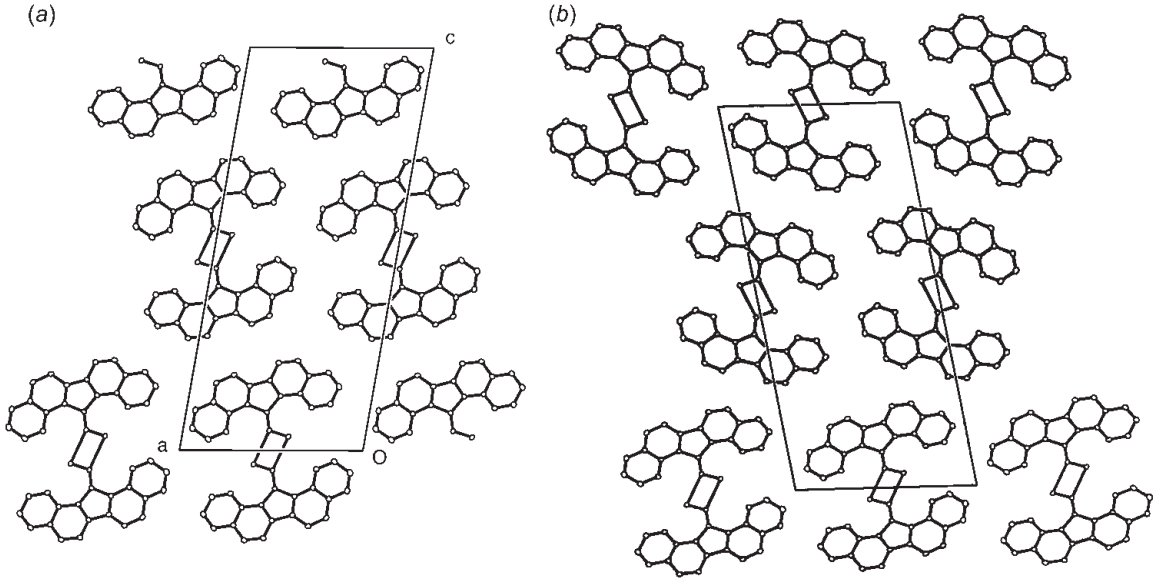


with C1 at the flap: successive endocyclic torsion angles, starting with that across C1-C2, are –11.9(2), 7.9(2), –0.8(3), –6.8(3), and 11.5(2)° in **2**, whereas the corresponding angles in **1** do not exceed 0.4(2)°. This distortion reflects intramolecular overcrowding of the oxime substituent (Fig. 2): the O1···H4 contact of 2.24 Å is particularly short, but that of 2.54 Å between H19 and N1 should also be noted. These interactions are relieved by folding the cyclopentadiene ring across the C2-C21 flap by 11.9(2)° and by a further bending of the C1-N1 vector by 13.9(2)° from the C1-C2-C21 plane. In consequence, the N1-C1-C2-C3 and N1-C1-C21-C20 sequences (respective torsion angles –30.5(5)° and 24.0(4)°) are appreciably nonplanar. From Figs. 1 and 2, it is apparent that the intramolecular overcrowding causes the atom sequence O1-N1-C1-C2-C3-C4 to define a helix and that there is no low energy path between enantiomeric forms of this helix.

The CSD contains 354 ketoxime structures with mean N-O and N=C distances (1.399(1) and 1.282(1) Å), which agree well with values in **2** (1.396(2) and 1.293(3) Å). In **2** the cisoid N1-C1-C2 angle (132.9(2)°) is appreciably more obtuse than the N1-C1-C21 angle (117.5(2)°); this difference is greater than that between the corresponding average values in ketoximes (125.3(1)° and 116.6(1)°) and may reflect the overcrowding in **2**. An unusual feature of **2** is the nonplanarity of the oxime function (O(1)-N(1)-C(1)-C(2) = 9.0(4)°); the average value of this angle in ketoximes is only 1.4(1)° and it exceeds 6° in only three published structures: the largest previously reported value is that of 7.9° for 2′,5′-bis(*O*-trityl)-oximinouridine (7). It should be noted that the

© 2004 NRC Canada

Fig. 3. (*a*) The packing viewed down the *b*-axis. Hydrogen atoms are omitted, but the formation of dimers through N-OH···N hydrogen bonds is indicated. These dimers are repeated by translation along *a* and *b* to form layers parallel to the (001) cell faces. Along *b*, the stacking involves π–π interactions; of these C3···C4 (*x*, *y* – 1, *z*) = 3.313(3) Å is the shortest. Packing between layers is fairly loose; an H7···H7 contact of 2.46 Å represents the closest interlayer interaction. (*b*) A hypothetical composite packing showing how twinning might arise. The bottom layer of molecules is the same as in the previous diagram and the twin boundary is roughly at *z* = 1/4.



direction of this distortion in **2** takes O1 *closer* to C4. **3** contains an envelope-shaped central ring like **2**, though the torsion angle across the exocyclic C=C bond is near zero (2.5(4)°). In **4** there is a twist of nearly 40° about the C=C bond (C-C=C-C torsion angles 37.6(4)° and 42.0(4)°).

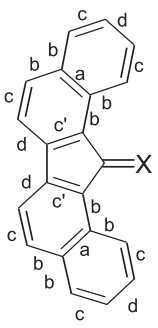
Corresponding bond lengths in the naphthalene nuclei of **1**–**4** are compared in Table 1 with those in naphthalene **5** itself (8). The *c′* bonds in the five-membered rings of **1**–**4** are 0.02–0.03 Å longer than other bonds of type *c*. In **2** the nucleus containing C2 through to C11, where steric strain is greater, is less planar (rmsΔ 0.050 Å) than the C12-C21 nucleus (rmsΔ 0.028 Å); these planes define a dihedral angle (τ) of 6.2(1)°.

Table 1. Mean bond lengths (Å) and the dihedral angle (τ°) between the mean naphthalene planes in **1**–**4** (see bond key). Mean bond lengths for naphthalene (**5**) are given for comparison.

Bond	**1**	**2**	**3**	**4**	**5**
a	1.426(2)	1.432(2)	1.430(3)	1.428(2)	1.426
b	1.417(2)	1.422(2)	1.414(2)	1.410(3)	1.426
c	1.366(1)	1.373(1)	1.358(4)	1.356(4)	1.378
c′	1.385(2)	1.394(7)	1.390(2)	1.390(3)	1.378
d	1.401(3)	1.411(3)	1.402(2)	1.399(3)	1.415
τ	1.9(1)	6.2(1)	17.7(1)	20.3(1)	—
Ref.	1	This work	3	3	8

Note: (1) Results for **2** and **5** refer to 100 K whereas those for **1**, **3**, and **4** were measured at room temperature and are more likely to be affected by thermal shrinkage. (2) The individual *c′* bonds in **2** differ significantly (see Fig. 1).

Bond key



Nature of the twinning

The crystal structure analysis was based on KappaCCD diffractometric data measured at 100(2) K. Standard computational procedures were used (9). As noted above, crystals of **2** are non-merohedral twins, the separate components being related by rotation about the *a*-axis by 180°. In the final refinement F^2calc = $\alpha F^2(hkl)+(1-\alpha)F^2(h'k'l')$ where $h' = h$, $k' = -k$ and $l' = -0.757h - l$ and $\alpha = 0.634(2)$. Exact overlap occurs only when *h* is divisible by 4. The 982 reflections meeting this condition were used in a preliminary refinement; the resulting F^2calc values were then used to decide whether both twin components contributed to F^2obs of other reflections: specifically, a SHELXL HKLF 5 file was prepared on the basis that all reflections with modulo(*h*,4) = 0 contained contributions from both twin components, all those with modulo(*h*,4) = 2 contained contributions only from the major component, while those with modulo(*h*,4) = 1 or 3 were deemed to contain contributions from both components only if a lower Δ*F* was thereby obtained. This approach allowed 96% of the unique reflections with θ(Mo-*K*α) < 30.2° to be used in a final refinement. The results, not significantly different from the preliminary refinement, have internally consistent bond lengths (Table 1) and thermal parameters that give a satisfactory rigid body analysis: $R(\Delta U^2) = 0.10$ and a maximum difference in the

© 2004 NRC Canada

Hirshfeld rigid bond test of 0.0023(13) $Å^2$ (10). We conclude that systematic error arising from uncertainties in modelling the twinning is probably not significant.

Inspection of the packing down the short *b* axis (Fig. 3) allows the nature of the twinning to be tentatively and qualitatively described. Layers of hydrogen-bonded dimers run parallel to the (001) planes. Successive glide-related layers, rather loosely bound together, propagate the structure in the *c* direction. Figure 3*a* shows the actual structure. Figure 3*b* is a composite, showing the twin boundary. We have previously noted that tertiary alcohols crystallize with unusual frequency in tetragonal and trigonal space groups and often with two or more crystallographically independent molecules. These features help them to saturate their capacity for hydrogen bonding (11). The space groups and crystal systems adopted by the 354 CSD oxime structures show no unusual features, being distributed in much the same way as the contents of the database as a whole.

Conclusions

Previously, certain oximes have been shown to be chiral although their molecules lack stereogenic centres; this was first demonstrated for the oxime of cyclohexanone-4-carboxylic acid (12). The present work indicates that a second class of oxime, exemplified by **2**, which also lacks a stereogenic centre and in which all carbon atoms are sp^2 hybridized, will be chiral by virtue of the nonplanarity of the molecule brought about by steric crowding. However, we have not been able to resolve **2** because insufficient material was available to us.

Acknowledgement

We thank the Engineering and Physical Sciences Research Council (EPSRC) and Glasgow University for support.

References

1. D.G. Morris, S. Higgins, K.S. Ryder, R.A. Howie, and K.W. Muir. Acta Crystallogr. **C56**, 570 (2000).
2. J.M. Lehn. Fortschr. Chem. Forsch. **15**, 311 (1970).
3. F.H. Allen and O. Kennard. Chemical Design Automation News, **8**, 1 (1993); **8**, 31 (1993). QUEST and CONQUEST search programs were used with Version 5.25 (November 2003) of the Cambridge Structural Database (CSD).
4. K.H. Scherschlicht, R.Gompper, and K. Polborn. Reference codes MUDYAL and VADHEO in the CSD (see ref. 3) (2002).
5. P.M.G. Bavin. Can. J. Chem. **38**, 1148 (1960); M.P. Cava and R.H. Schlessinger. Tetrahedron Lett. **5**, 2109 (1964).
6. M. Lutz, A.L. Spek, R. Dabirian, C.A. van Walree, and L.W. Jenneskens. Acta Crystallogr. **C60,** O127 (2004).
7. P. Agback, A. Papchikhin, S. Neidle, and J. Chattopadhyaya. Nucleosides Nucleotides, **12**, 605 (1993).
8. C.P. Brock and J.D. Dunitz. Acta Crystallogr. **B38**, 2218 (1982).
9. (*a*) L.J. Farrugia. J. Appl. Crystallogr. **30**, 565 (1997); (*b*) L.J. Farrugia. J. Appl. Crystallogr. **32**, 837 (1999); (*c*) KappaCCD control software [computer program]. BV. Nonius, Delft, The Netherlands. 2000; (*d*) Z. Otwinowski and W. Minor. Methods in enzymology. Vol. 276. Macromolecular crystallography, Part A. *Edited by* C.W. Carter, Jr. and R.M. Sweet. Academic Press, New York. 1997. pp. 307–326; (*e*) G.M. Sheldrick. SHELXS97 and SHELXL97 [computer programs]. University of Göttingen, Göttingen, Germany. 1997.
10. (*a*) F.L. Hirshfeld. Acta Crystallogr. **A32**, 239 (1976); (*b*) V. Schomacher and K.N. Trueblood. Acta Crystallogr. **B24**, 63 (1968).
11. A.G. Fraile, D.G. Morris, A.G. Martinez, S. de la Moya Cerero, K.W. Muir, K.S. Ryder, and E.T. Vilar. Org. Biomol. Chem. **1**, 700 (2003).
12. W.H. Mills and A.M. Bain. J. Chem. Soc. **97**, 1866 (1910). See also E.L. Eliel. Stereochemistry of carbon compounds. McGraw-Hill, New York. 1962. p. 309.

© 2004 NRC Canada

Syntheses and electropolymerization behavior of ethylenedioxythiophene-substituted silanes

M'hamed Chahma and Robin G. Hicks

Abstract: Silicon-bridged thiophene oligomers have been prepared via the reactions of lithiated (3,4-ethylenedioxy)thiophene (EDOT) (**1**) or 2,2′-bis-(3,4-ethylenedioxy)thiophene (biEDOT) (**2**) with dichlorodimethylsilane to afford bis-(2,3-dihydro-thieno[3,4-*b*][1,4]dioxin-5-yl)-dimethylsilane (**3**) and dimethyl-bis-(2,3,2′,3′-tetrahydro-[5,5′]bi[thieno[3,4-*b*][1,4]dioxinyl]-7-yl)silane (**4**). Products **3** and **4** were characterized and show good stability in organic solvent and in air. The electropolymerization of these monomers affords stable and highly conducting polymers. The conductivity was found to be 25 and 60 S/cm for **Poly3** and **Poly4**, respectively. Characterization data for the polymers suggested that the resulting materials have a backbone identical to p(EDOT), which formed through cleavage of the silicon–carbon (Si—C) bonds during electropolymerization.

Key words: polythiophenes, EDOT, silicon, electropolymerization, Si—C bond cleavage, conductivity.

Résumé : Faisant appel à des réactions de (3,4-éthylènedioxy)thiophène (EDOT) (**1**) ou de 2,2′-bis-(3,4-éthylènedioxy)thiophène (biEDOT) avec du dichlorodiméthylsilane, on a préparé des oligomères de thiophène avec pont de silicium, les bis-(2,3-dihydro-thiéno[3,4-*b*][1,4]dioxin-5-yl)diméthylsilane (**3**) et diméthyl-bis-(2,3,2′,3′-tétrahydro-[5,5′]bi[thiéno[3,4-*b*][1,4]dioxinyl]-7-yl)silane (**4**). Les produits **3** et **4** ont été caractérisés et présentent une bonne stabilité dans les solvants organiques et dans l'air. L'électropolymérisation de ces monomères conduit à des polymères stables et très bons conducteurs. On a trouvé que les conductivités respectives des **Poly3** et **Poly4** sont de 25 et 60 S/cm. Les données de caractérisation des polymères suggèrent que les produits obtenus possèdent un squelette identique à celui du p(EDOT) qui se forme par clivage des liaisons silicium–carbone (Si—C) au cours de l'électropolymérisation.

Mots clés : polythiophènes, EDOT, silicium, électropolymérisation, clivage de la liaison Si—C, conductivité.

[Traduit par la Rédaction]

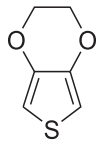
Introduction

Polythiophene and its derivatives are widely used in transistors (1–3), light emitting diodes (4), electroluminescent devices (5, 6), photovoltaic cells (7), and bioelectrochemical sensors (8, 9). Despite the existence of a wide variety of thiophene monomers, the preparation of novel thiophene motifs remains a quest for many scientists as part of the search for new materials with properties such as low band gaps, electrochromism ranges, etc. One derivative of thiophene that has become immensely popular is 3,4-ethylenedioxy)thiophene (EDOT) (**1**) (10). The corresponding polymer, p(EDOT), is exceptionally stable in its doped state and highly conducting. It also exhibits a low oxidation potential with respect to classical polythiophene derivatives (11). Recently, Wudl and co-workers reported that p(EDOT) have promising applications in the field of "plastic electronics" (12, 13).

Received 30 April 2004. Published on the NRC Research Press Web site at http://canjchem.nrc.ca on 21 December 2004.

M. Chahma and R.G. Hicks.[1] Department of Chemistry, University of Victoria, PO Box 3065, STN CSC, Victoria, BC V8W 3V6, Canada.

[1]Corresponding author (e-mail: rhicks@uvic.ca).



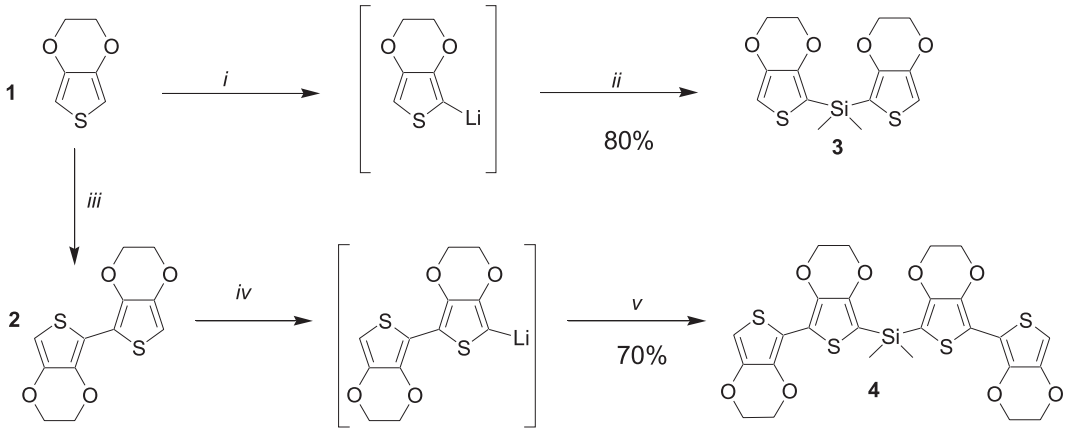
1

Different strategies have been used to synthesize new polymers incorporating EDOT. For example, the incorporation of alkyl chains in the ethylene moiety increases the solubility and conductivity of the corresponding polymers (14). Another approach involves polymers consisting of alternating EDOT with aryl groups (e.g., benzene, furan, carbazole) to provide a large range of redox and optical properties (15–17). Hybrid conjugated organic EDOT – metal-containing polymers have also been explored (18, 19). Another recent approach has been the incorporation of main group elements. We recently synthesized a monomer bis(3,4-ethylenedioxy-2-thienyl)sulfide in which two EDOT moieties are connected to a divalent sulfur atom; its corresponding polymer exhibits high electrochemical stability in its oxidized and reduced states and good conductivity for a nonconjugated polymer (20).

Other main group elements have been introduced into conducting polymer systems, including silicon. Ferraris and co-workers (21) prepared bridged bithiophenes linked by

 doi: 10.1139/V04-139 © 2004 NRC Canada

Scheme 1. (*i*) *n*-BuLi, RT, 1 h; (*ii*) –78 °C, $(Me)_2SiCl_2$, 24 h; (*iii*) see ref. 29; (*iv*) *n*-BuLi, RT, 1 h, –78 °C; (*v*) –78 °C, $(Me)_2SiCl_2$, 24 h.



dimethylsilyl units for which the corresponding polymers exhibited interesting electrochromic properties, and silicon has also been incorporated into oligo- and poly(siloles) (22–24). We became interested in the possibility of preparing EDOT-based polymers linked by simple (nonheterocyclic) silane groups. To this end, herein we present the synthesis of new monomers based on EDOT and biEDOT motifs linked via silicon.

Result and discussion

Synthesis and characterization of "monomers"

The lithiated salt of EDOT **1** and biEDOT **2** reacts with Me_2SiCl_2 to afford silicon-bridged thiophenes **3** and **4** in high yield (Scheme 1). Product **3** was purified via column chromatography on silica gel, but product **4** decomposed on attempted chromatography and so was purified by precipitation using pentane. Products **3** and **4** are air-stable in the solid state and solution, in air and in the presence of organic solvents.

In CH_2Cl_2, compounds **1**–**4** exhibit single irreversible oxidation waves at potentials of +1.60, 1.04, 1.63, and 1.02 V (vs. Ag/AgCl*),* respectively, as shown in Fig. 1 for monomers **1** and **3**. No significant differences in oxidation potentials were observed between **1** and **3** and similar behavior was observed in the case of **2** and **4**. The presence of the silicon element, therefore, does not strongly affect the oxidation peak potential of thiophenes. The oxidation peak potential of the monomers and the oxidation potential of the corresponding polymers are summarized in Table 1. Also shown in Table 1 are the solution λ_{max} from the electronic spectra of the monomers. In comparing each "parent" EDOT and bi EDOT with their corresponding silicon derivatives (**1** vs. **3** and **2** vs. **4**), it can be seen that the absorption maxima are identical (25).[2] These results are in agreement with the electrochemical data; silanes do not effect the electronic configurations of these monomers.

Fig. 1. Oxidation of **1** (solid line) and **2** (dashed line) in CH_2Cl_2 at 100 mV/s.

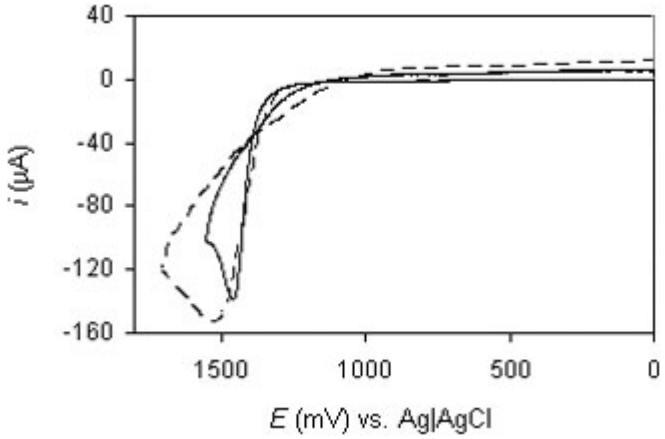


Table 1. Oxidation potentials and UV–vis maxima of **1**–**4**.

Monomer	E_{ox} (V) (vs. Ag/AgCl)[a]	$E_{1/2}$ (V) (vs. Ag/AgCl)[b]	λ_{max} (nm)[c]
1	1.600	–0.100	260
2	1.04	—	330, 350
3	1.630	0.150	260
4	1.020	0.000	330, 350

[a]Oxidation peak potential determined from the first scan.
[b]Average of the oxidation and reduction potential of the corresponding polymer.
[c]λ_{max} of the monomer.

Electrochemcial polymerization and polymer properties

The electrochemical polymerizations of monomers **1**, **3**, and **4** (0.01 mol/L) were carried out in CH_2Cl_2 (the low solubility of **3** and **4** precluded performing these experiments in more polar solvents) containing 1 mol/L $(n\text{-Bu})_4NBF_4$ via repeated electrochemical cycling at the oxidation potential of the monomers using a scan rate of 0.1 V/s. The relatively

[2]The absorption maxima for **2** differ from the literature values of 313, 319, and 305nm in ref. 29. This may be due to solvent effects; the previous literature spectrum was obtained in chloroform while ours was obtained in dichloromethane. In support of this we note that a *a*,*w*-dihexyl-substituted biEDOT has been reported (25) that has a nearly identical UV–vis solution spectrum (λ_{max} 333, 349 nm) to our data of of **2** in CH_2Cl_2. The hexyl groups are not expected to exert a measurable electronic effect on the electronic spectrum.

© 2004 NRC Canada

Scheme 2.

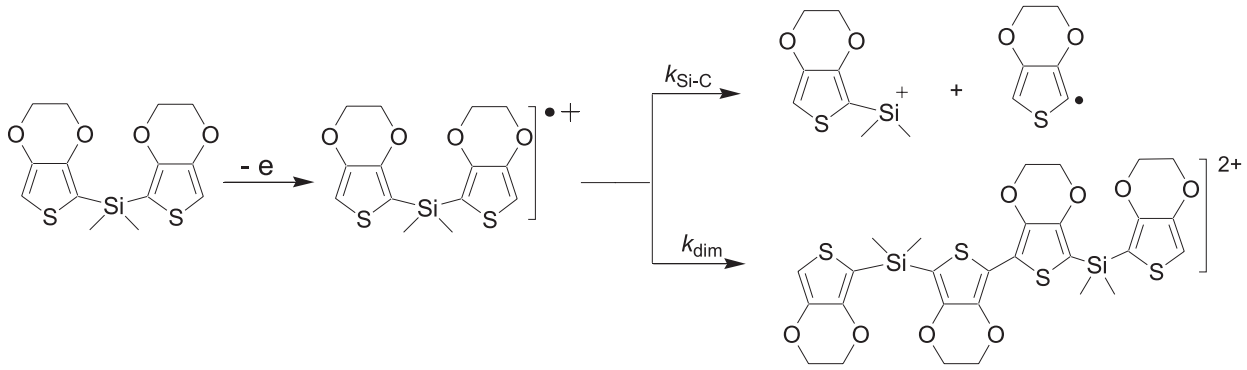


Fig. 2. Electropolymerization of **4** in CH_2Cl_2 at a 100 mV/s scan rate.

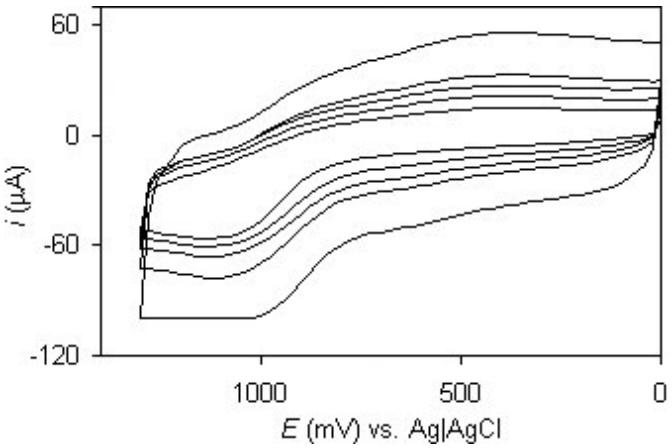
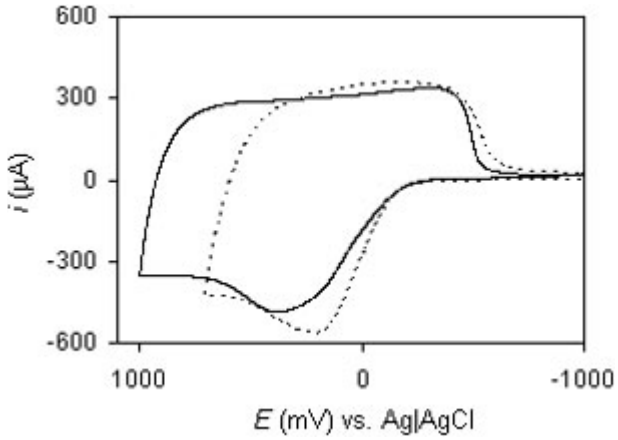


Fig. 3. CV of **Poly1** (solid line) and **Poly4** (dashed line) on a Pt electrode at 100 mV/s in CH_2Cl_2.



high supporting electrolyte concentration of 1 mol/L was employed for the electropolymerization process because at this concentration, the current of the platinum-modified electrode remained constant after 100 scans, which shows a good adhesion and stability of the polymer on the surface of the electrode. Figure 2 shows a typical cyclic voltammetry (CV) curve for the electropolymerization of **4**. A new reversible wave appears at a more negative potential, which corresponds to the formation and deposition of the polymer onto the surface of the platinum electrode.

The electrochemical properties of the platinum-modified electrodes were studied in monomer-free solutions. Cyclic voltammograms of **Poly1** and **Poly4** are shown in Fig. 3. **Poly1**-, **Poly3**-, and **Poly4**-modified platinum electrodes all exhibit a broad reversible wave and are qualitatively very similar. The oxidation potentials ($E_{1/2}$ is the average of peak oxidation and reduction potentials) of **Poly1**, **Poly3**, and **Poly4** were similar and were found to be in the range –0.100 and +0.150 V (vs. Ag/AgCl). The electropolymerization of **1** follows an *E*(CE)n mechanism in which the first step is the formation of the radical cation (26, 27), which is further engaged in a chain process that leads to **Poly1** after the expulsion of protons. Following the oxidation of **3** (shown in Scheme 2) and **4**, the resulting carbocations $\mathbf{3}^{\cdot+}$ and $\mathbf{4}^{\cdot+}$ will further be engaged either in a Si—C bond cleavage or a dimerization process. The putative dimer $[\mathbf{3}–\mathbf{3}]^{2+}$ (to the extent that it is formed) is also susceptible to Si—C bond cleavage reactions. Ultimately, all of the silicon is extruded during the electropolymerization, leading to **Poly3** whose identity is very likely similar in structure to pEDOT (see the following).

Hapiot et al. (28) have reported the dimerization of the carbocation resulting from bithiophene substituted by a trimethylsilyl group in position 2, 2′ (Me_3Si-2T-$SiMe_3$) to afford a dimer $(Me_3Si\text{-}4T\text{-}SiMe_3)^{2+}$. They also reported that the desilylation depends on the nature of the solvent and on the number of thiophenes end-capped by the silyl group (28). The electrochemical properties of the polymers derived from **3** and **4** do not, in and of themselves, permit an assessment of their chemical composition.

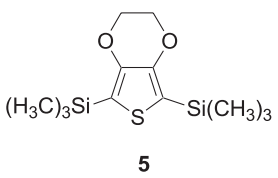
Reynolds and co-workers (29) reported the electropolymerization in acetonitrile for related silane-substituted EDOT compounds **5** and **6**. They found that after the formation of the radical cation, the electropolymerization is initiated by a Si—C cleavage and the leaving group was the trimethylsilyl cation. The loss of a trimethyl silyl group is identical to the loss of a proton in the conventional polymerizations of EDOT and thiophenes. Moreover, they reported that the film resulting from desilylation had a rapid response time in optical switching rates and better adhesion on the surface of the electrode than the resulting polymer from the direct electropolymerization of naked EDOT (29).

© 2004 NRC Canada

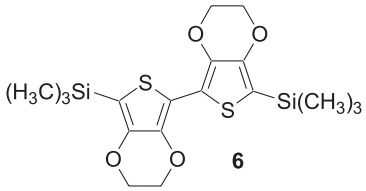
Table 2. Characterization of polymers derived from **1**, **3**, and **4**.

Polymer	E (V)[a]	λ_{max} (nm)	σ (S/cm)
Poly1	1.600	431, 460, 493	53.65±0.35
Poly3	1.600	430, 460, 490	25.25±0.15
Poly4	1.000	432, 460, 485, 520	60.15±1.25

[a]Potential electrolysis.



5



6

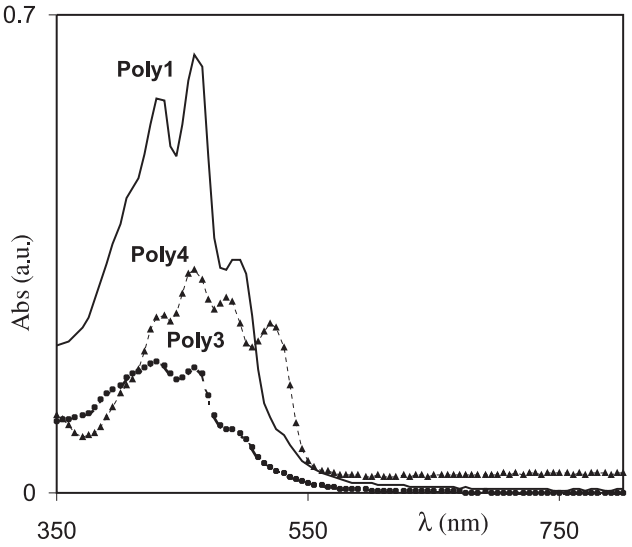
Other characterization data point to a common structure for all polymers. The UV–vis spectra for the neutral films of **Poly1**, **Poly3**, and **Poly4** on indium tin oxide (ITO) are tabulated in Table 2 and shown in Fig. 4. All spectra possess absorption peaks in the range 400–500 nm for all undoped polymers, which proves that the backbones of **Poly1**, **Poly3**, and **Poly4** are very similar in nature. No significant differences were observed in the IR spectra of **Poly1**, **Poly3**, and **Poly4**. Most telling is the fact that the elemental analyses of **Poly3** and **Poly4** shows that the amount of silicon present in the polymers is negligible (<0.3%).

The electrical conductivity was measured using a four-point method on a pellet. As shown in Table 2, **Poly1**, **Poly3**, and **Poly4** are highly conducting in comparison to others formed via other chemical polymerizations, i.e., $FeCl_3$ (12, 30), or by solid state polymerization (13). The maximum conductivity was found to be 60 S/cm for **Poly4**. On the other hand, the conductivity of **Poly3**, (25 S/cm) was ranging by half of that and may be due to less ordering in the backbone of the polymer after the Si—C bond cleavage of the $\mathbf{3}^{\cdot+}$.

Conclusions

We have reported the synthesis of organosilanes based on (3,4-ethylenedioxy)thiophene and 2,2′-bis-(3,4-ethylenedioxy)thiophene. The presence of silicon does not perturb the fundamental electrochemical and optical properties of the EDOT chromophores. Electrochemical polymerizations of **3** and **4** proceed via Si—C bond cleavage to afford stable, highly conducting polymers that are in all likelihood p(EDOT). Subtle differences in the properties of the polymers derived from the different monomers are probably due to chain length and (or) morphological effects. This is consistent with previously reported work on EDOT-silanes (29) and reinforces the observation that the silane – aromatic carbon bond in EDOT is highly reactive under the conventional electropolymerization conditiaions. This provides an interesting contrast to silanes containing unsubistuted thiophenes, which appear to be electropolymerizable with retention of the thiophene–silicon skeleton in the resulting polymers (21).

Fig. 4. UV–vis of different polymers reduced by hydrazine hydrate in CH_2Cl_2.



Experimental section

Materials and reagents

All reagents were purchased from Aldrich and used as received. biEDOT (2) was prepared according to a literature method (29). Solvents were dried and distilled under argon prior to use (CH_2Cl_2, CaH_2, THF, Na–benzophenone).

Physical methods

NMR spectra (^1H, ^{13}C, ^{29}Si NMR) were obtained on an AMX 300 MHz Bruker. IR spectra were recorded on a PerkinElmer FT-IR spectrometer. UV–vis data were collected on a Cary 100 SCAN spectrophotometer. The electrochemical experiments were performed using a CV-50 W voltammetric analyzer (BAS) at room temperature (22 ± 2 °C). Voltammetric measurements were performed in CH_2Cl_2 containing 1 mol/L of n-Bu_4NBF_4. The platinum electrode (BAS, diameter 1.6 mm) was used as working electrode. Platinum wire and Ag/AgCl were used as auxiliary and reference electrodes, respectively. The reference electrode was calibrated vs. the ferrocene/ferrocenium redox (E^0 = 0.580 vs. Ag/AgCl) internal reference. The working electrode was polished on alumina before use. *iR* compensations were applied for all experiments. The bulk electrolyses were performed using a controlled potential in a cell with one compartment using a platinum plate (3 cm^2) as the cathode and anode. The electrical conductivity was estimated using a four-point method.

Synthesis of bis-(2,3-dihydro-thieno[3,4-*b*][1,4]dioxin-5-yl)-dimethylsilane (3)

To a solution of EDOT (2.10 g, 14.8 mmol) dissolved in 50 mL of THF under argon was added 7.4 mL (14.8 mmol) of *n*-BuLi (2 mol/L) dropwise. After stirring for 1 h at room temperature, the mixture was cooled to –78 °C. Dichlorodimethylsilane (0.98 g, 7.6 mmol) was added dropwise and the mixture was stirred for a further 3 h at –78 °C followed by 21 h at room temperature. The mixture was then poured

© 2004 NRC Canada

into 100 mL of water and the product was extracted using 2 × 100 mL portions of CH_2Cl_2. The organic layers were combined and dried over $MgSO_4$. After evaporation of the solvent, the product was purified by chromatography on silica gel using CH_2Cl_2 as the eluent. The product was colorless and crystallized slowly after a few weeks affording a yield of 75% (1.9 g, 5.6 mmol). ^{1}H NMR (CD_2Cl_2, 300 MHz) (ppm) δ: 0.60 (s, 6H), 4.20 (m, 8H), 6.60 (s, 2H). ^{13}C NMR (CD_2Cl_2, 75 MHz) (ppm) δ: –1.20, 64.7, 64.8, 106.1, 109.1, 142.8, 148.2. ^{29}Si NMR ($CDCl_3$, 100 MHz) (ppm) δ: –16.83. MS LSI-MS *m*/*z*: 340 (M^+, 100%). HR-MS (EI) calcd. for $C_{14}H_{16}S_2O_4Si$ [M^+]: 340.0259; found: 340.0262.

Synthesis of dimethyl-bis-(2,3,2′,3′-tetrahydro-[5,5′]bi[thieno[3,4-*b*][1,4]dioxinyl]-7-yl)-silane (4)

To a solution of biEDOT (1.52 g, 5.4 mmol) dissolved in 50 mL of THF under argon was added 2.7 mL (5.40 mmol) of *n*-BuLi (2 mol/L) dropwise. After stirring for 1 h at room temperature, the mixture was cooled at –78 °C. Dichlorodimethylsilane (0.38 g, 2.9 mmol) was added dropwise and the mixture was stirred for a further 3 h at –78 °C and then for 21 h at room temperature. Following that, the mixture was poured in 100 mL of water and the product was extracted using 2 × 100 mL portions of diethyl ether. The organic layers were combined and dried over $MgSO_4$. After evaporation of ether, the crude was dissolved in acetone, and precipitated by adding pentane and freezing the mixture overnight. A pale yellow solid was formed (1.2 g, 1.9 mmol) in a 70% yield. ^{1}H NMR ($CDCl_3$, 300 MHz) (ppm) δ: 0.60 (s, 6H), 4.30 (m, 16H), 6.20 (s, 2H). ^{13}C NMR ($CDCl_3$, 75 MHz) (ppm) δ: –0.9, 64.6, 64.8, 64.9, 65.2, 97.9, 106.4, 110.4, 115.8, 137.5, 138.0, 141.4, 147.5. ^{29}Si NMR ($CDCl_3$, 100 MHz) (ppm) δ: –17.12. MS LSI-MS *m*/*z*: = 620 (M^+, 100%). HR-MS (EI) calcd. for $C_{26}H_{24}S_4O_8Si$ [M^+]: 620.0123; found: 620.0116.

Electrosynthesis of the polymers

Poly1, **Poly3**, and **Poly4** were prepared by controlled potential electrolysis in CH_2Cl_2 containing 1 mol/L of *n*-Bu_4NBF_4. The concentration of the monomer was 0.01 mol/L. At the end of the electrolysis, a dark film formed on the surface of the electrode. The film was removed from the electrode and washed with 500 mL of CH_2Cl_2 and dried under vacuum for 30 h. **Poly1**: yield 80%. Anal. calcd. for $C_6H_4O_2S_1B_{0.67}F_{2.8}$ (%): C 36.36, H 2.04, S 16.18; found (%): C 36.90, H: 2.64, S 18.08. **Poly3**: yield 76%. Anal. calcd. for $C_6H_4O_2S_1B_{0.40}F_{1.6}$ (%): C 41.24, H 2.31, S 18.35; found: C 41.13, H 2.71, S 18.14. **Poly4**: yield 85%. Anal. calcd. for $C_6H_4O_2S_1B_{0.45}F_{1.8}$ (%): C 40.24, H 2.25, S 17.91; found: C 40.07, H 2.56, S 18.41.

Acknowledgements

We thank the University of Victoria, the Natural Sciences and Engineering Research Council of Canada (NSERC), and Defence R and D Canada-Atlantic for support.

References

1. G. Horowitz. Adv. Mater. **10**, 365 (1990).
2. A. Dodabalapur, L. Torsi, and H.E. Katz. Science, **268**, 270 (1995).
3. A. Dodabalapur, L. Torsi, H.E. Katz, and R.C. Haddon. Science, **269**, 1560 (1995).
4. A. Kraft, A.C. Grimsdale, and A.B. Holmes. Angew. Chem. Int. Ed. **37**, 402 (1998).
5. T. Noda, H. Ogawa, and Y. Shirota. Adv. Mater. **11**, 283 (1999).
6. T. Noda and Y. Shirota. J. Am. Chem. Soc. **120**, 9714 (1998).
7. N. Noma, T. Tsuzuki, and Y. Shirota. Adv. Mater. **7**, 647 (1995).
8. D.T. McQuade, A.E. Pullen, and T.M. Swager. Chem. Rev. **100**, 2537 (2000).
9. J. Roncali. J. Mater. Chem. **9**, 1875 (1999).
10. B.L. Groenendaal, F. Jonas, D. Freitag, H. Pierlatzik, and J.R. Reynolds. Adv. Mater. **12**, 481 (2000).
11. J. Roncali. Chem. Rev. **92**, 711 (1992).
12. H. Meng, D.F. Perepichka, and F. Wudl. Angew. Chem. Int. Ed. **6**, 658 (2003).
13. H. Meng, D.F. Perepichka, M. Bendikov, F. Wudl, G.Z. Pan, W.J. Yu, W.J. Dong, and S. Brown. J. Am. Chem. Soc. **125**, 15 151 (2003).
14. L. Groenendal, G. Zotti, P-H. Aubert, S.M. Waybright, and J.R. Reynolds. Adv. Mater. **15**, 855 (2003).
15. G.A. Sotzing and J.R. Reynolds. Chem. Mater. **8**, 882 (1996).
16. A.L. Gaupp and J.R. Reynolds. Macromolecules, **36**, 6305 (2003).
17. A.A. Argun, A. Cirpan, and J.R. Reynolds. Adv. Mater. **15**, 1338 (2003).
18. S.S. Zhu and T.M. Swager. J. Am. Chem. Soc. **119**, 12 568 (1997).
19. R.P. Kingsborough and T.M. Swager. J. Am. Chem. Soc. **121**, 8825 (1999).
20. M. Chahma, R.G. Hicks, and D.J.T. Myles. Macromolecules, **37**, 2010 (2004).
21. D.S.K. Mudigonda, J.L. Boehme, I.D. Brotherson, D.L. Meeker, and J.P. Ferraris. Chem. Mater. **12**, 1508 (2000).
22. K. Tamao, S. Yamagushi, M. Shiozaki, Y. Najagawa, and Y. Ito. J. Am. Chem. Soc. **114**, 5867 (1992).
23. K. Tamao, S. Yamagushi, and M. Shiro. J. Am. Chem. Soc. **116**, 11 715 (1994).
24. Y. Lee, S. Sadki, B. Tsuie, and J.R. Reynolds. Chem. Mater. **13**, 2234 (2001).
25. M. Turbiez, P. Frere, and J. Roncali. J. Org. Chem. **68**, 5357 (2003).
26. P. Audebert, J.-M. Catel, G. Le Coustumer, V. Duchenet, and P. Hapiot. J. Phys. Chem. **99**, 11 923 (1995).
27. P. Hapiot, P. Audebert, K. Monnier, J.-M. Pernaut, and P. Garcia. Chem. Mater. **6**, 1549 (1994).
28. P. Hapiot, L. Gaillon, J.J.E. Moreau, J.-P. Lere-Porte, and M. Wong Chi Man. J. Electroanal. Chem. **435**, 85 (1997).
29. A. Sotzing, J.R. Reynolds, and P.J. Steel. Adv. Mater. **9**, 795 (1997).
30. R. Corradi and S.P. Armes. Synthetic Metals, **84**, 453 (1997).

© 2004 NRC Canada

Group IV phosphinimide amide complexes

Emily Hollink, Pingrong Wei, and Douglas W. Stephan

Abstract: Complexes of formula $TiCp(NPR_3)(NMe_2)_2$ (R = *t*-Bu **1**, Ph **2**) were prepared via salt metathesis of $TiCp(NPR_3)Cl_2$ with a slight excess of $LiNMe_2$. The species $Ti(NP\text{-}t\text{-}Bu_3)(NMe_2)_3$ (**3**) was obtained as a by-product. The related derivative $ZrCp(NP\text{-}t\text{-}Bu_3)(NMe_2)_2$ (**4**) was also prepared. Reaction of $TiCp(NP\text{-}t\text{-}Bu_3)Cl_2$ with $LiNHC_6H_3(2,6\text{-}i\text{-}Pr_2)$ afforded $TiCp(NP\text{-}t\text{-}Bu_3)(NHC_6H_3(2,6\text{-}i\text{-}Pr_2))Cl$ (**5**) and $Ti(NP\text{-}t\text{-}Bu_3)(NHC_6H_3(2,6\text{-}i\text{-}Pr_2))_3$ (**6**). In a similar manner, the Zr analogs $ZrCp(NP\text{-}t\text{-}Bu_3)(NHC_6H_3(2,6\text{-}i\text{-}Pr_2))Me$ (**7**) and $ZrCp(NP\text{-}t\text{-}Bu_3)(NHC_6H_3(2,6\text{-}i\text{-}Pr_2))_2$ (**8**) were also prepared. X-ray structural data for compounds **5**, **6**, and **8** are reported. Reactivity of these phosphinimide–amide derivatives was explored. While these species do not yield imide derivatives upon thermolysis, reaction of **5** with excess $AlMe_3$ afforded $TiCp(NP\text{-}t\text{-}Bu_3)Me_2$ while reaction with 1 equiv. of $AlMe_3$ gave $TiCp(NP\text{-}t\text{-}Bu_3)MeCl$ (**9**) and $Al_2(m\text{-}NHC_6H_3(2,6\text{-}i\text{-}Pr_2))_2Me_4$ (**10**).

Key words: titanium, zirconium, phosphinimide, amide, ligand metathesis.

Résumé : On a préparé des complexes de formule $TiCp(NPR_3)(NMe_2)_2$ (R = *t*-Bu **1**, Ph **2**) par la métathèse du sel de $TiCp(NPR_3)Cl_2$ avec un léger excès de $LiNMe_2$. On a obtenu l'espèce $Ti(NP\text{-}t\text{-}Bu_3)(NMe_2)_3$ (**3**) comme sous-produit. On a aussi préparé le dérivé apparenté $ZrCp(NP\text{-}t\text{-}Bu_3)(NMe_2)_2$ (**4**). La réaction du $TiCp(NP\text{-}t\text{-}Bu_3)Cl_2$ avec du $LiNHC_6H_3(2,6\text{-}i\text{-}Pr_2)$ conduit à la formation de $TiCp(NP\text{-}t\text{-}Bu_3)(NHC_6H_3(2,6\text{-}i\text{-}Pr_2))Cl$ (**5**), et de $Ti(NP\text{-}t\text{-}Bu_3)(NHC_6H_3(2,6\text{-}i\text{-}Pr_2))_3$ (**6**). Opérant de la même façon, on a aussi préparé les analogues $ZrCp(NP\text{-}t\text{-}Bu_3)(NHC_6H_3(2,6\text{-}i\text{-}Pr_2))Me$ (**7**) et $ZrCp(NP\text{-}t\text{-}Bu_3)(NHC_6H_3(2,6\text{-}i\text{-}Pr_2))_2$ (**8**). On a déterminé les structures des composés **5**, **6** et **8** par diffraction des rayons X. On a examiné la réactivité de ces dérivés phosphinimide–amides. Alors que la thermolyse de ces espèces ne conduit pas à des dérivés imides, la réaction de **5** avec un excès de $AlMe_3$ conduit à la formation de $TiCp(Np\text{-}t\text{-}Bu_3)Me_2$ alors que la réaction avec un équivalent de $AlMe_3$ fournit les composés $TiCp(Np\text{-}t\text{-}Bu_3)MeCl$ (**9**) et $Al_2(\mu\text{-}NHC_6H_3(2,6\text{-}i\text{-}Pr_2))_2Me_4$ (**10**).

Mots clés : titane, zirconium, phosphinimide, amide, métathèse de ligand.

[Traduit par la Rédaction]

Introduction

Group IV amide complexes have received enormous attention because of their remarkable diversity, serving as precursors for imido derivatives (1–5), olefin polymerization catalysts (6–11), precursors in chemical vapour deposition processes (12–18), and as hydroamination (pre)catalysts (19–22). In addition, the propensities of Ti- (23–25) or Zr- (2, 3, 26, 27) imide complexes to effect C-H activation and hydroamination (21) are the subject of theoretical (28, 29) and experimental interest. In our own work, we have demonstrated that phosphinimide ligands can replace cyclopentadienyl ligand derivatives to give highly active olefin polymerization catalysts (30–32). Studies of the structure–reactivity relationship have shown that a range of sterically demanding phosphinimide ligands provide effective catalysts (33–38), whereas sterically less-demanding ligands prompt novel reactivity with Lewis acids including C-H activation processes (39–41). In an effort to broaden the range of reactivity of group IV phosphinimide complexes, we undertook the syntheses of phosphinimide–amide complexes. In this manuscript we describe the syntheses, characterization, and our initial studies of the reactivity of the group IV phosphinimide–amide complexes. These systems are compared with the metallocene analogs.

Received 1 April 2004. Published on the NRC Research Press Web site at http://canjchem.nrc.ca on 21 December 2004.

E. Hollink, P. Wei, and D.W. Stephan.[1] Department of Chemistry and Biochemistry, University of Windsor, Windsor, ON N9B 3P4, Canada.

[1]Corresponding author (e-mail: stephan@uwindsor.ca).

Experimental

All syntheses were performed employing an atmosphere of dry, oxygen-free nitrogen in a Vacuum Atmospheres inert atmosphere glove box or standard Schlenk techniques using oven-dried (140 °C) glassware unless otherwise stated. ^1H NMR data were acquired on a Bruker Avance 500 MHz spectrometer, while ^{13}C and ^{31}P NMR data were obtained from a Bruker Avance 300 MHz spectrometer. ^1H and ^{13}C chemical shifts are listed relative to $SiMe_4$ in ppm and were referenced to the residual proton or carbon peak of the solvent. ^{31}P NMR data were referenced using 85% H_3PO_4 as an external standard. All NMR spectra were recorded in C_6D_6 unless otherwise noted. University of Windsor Analytical Services, using a Perkin Elmer 2400 Series II instrument, performed the combustion analyses. Despite repeated attempts, carbon analyses for Zr complexes consistently gave systematically low values as a result of the formation of ZrC (i.e., incomplete combustion). Reagent grade solvents were purchased from Aldrich Chemical Co. and were predried using Grubbs' column systems, manufactured by Innovative

 doi: 10.1139/V04-141 © 2004 NRC Canada

Technologies, Inc. (42). Deuterated benzene, toluene, and methylene chloride were purchased from Canadian Isotopes Laboratories and degassed by at least four freeze–pump–thaw cycles before storing over 4 Å molecular sieves. The reagents *n*-BuLi (2.0 mol L^{-1} in hexanes), Al_2Me_6, $TiCp_2Cl_2$, $LiNMe_2$, and $NH_2C_6H_3(2,6\text{-}i\text{-}Pr_2)$ were purchased from Aldrich Chemical Co. $NH_2C_6H_3(2,6\text{-}i\text{-}Pr_2)$ was vacuum distilled from KOH, and all other reagents were used without further purification. The compounds $Ti(NP\text{-}t\text{-}Bu_3)Cl_3$ (37) and $TiCp(NP\text{-}t\text{-}Bu_3)Cl_2$ (32) were prepared according to literature methods, and $LiNHC_6H_3(2,6\text{-}i\text{-}Pr_2)$ was prepared via a modification of a literature procedure (43).

Synthesis of $TiCp(NP\text{-}t\text{-}Bu_3)(NMe_2)_2$ (1) and $TiCp(NPPh_3)(NMe_2)_2$ (2)

These compounds were prepared in a similar fashion and thus one preparation is detailed. Solid $LiNMe_2$ (46 mg, 0.90 mmol) was added in several portions to a clear solution of $TiCp(NP\text{-}t\text{-}Bu_3)Cl_2$ (179 mg, 0.45 mmol) in benzene (20 mL). The slurry was stirred for 20 h, after which time the mixture was filtered through Celite. The solvent was removed in vacuo affording a bright orange solid. The residue was washed with pentanes (3 × 5 mL) and dried to afford a fine, orange powder (126 mg, 67%). Small quantities (typical yields ca. 10%–15%) of the by-product $Ti(NP\text{-}t\text{-}Bu_3)(NMe_2)_3$ (**3**) were isolated from the pentane washings (**1**). For **1**: ^{1}H NMR δ: 6.18 (s, 5H, Cp), 3.28 (s, 12H, NMe_2), 1.24 (d, 27H, $^3J_{P\text{-}H}$ = 13 Hz, *t*-Bu). ^{13}C NMR δ: 109.7, 50.5, 40.6 (d, $^1J_{P\text{-}C}$ = 28 Hz), 29.7. ^{31}P NMR δ: 28.9. Anal. calcd. for $C_{21}H_{44}N_3PTi$ (%): C 60.42, H 10.62, N 10.07; found: C 60.34, H 10.52, N 9.67. For **2**: yellow solid (312 mg, 77%). ^{1}H NMR δ: 7.75 (m, 6H, Ph), 7.06 (m, 9H, Ph), 5.99 (s, 5H, Cp), 3.34 (s, 12H, NMe_2). ^{13}C NMR δ: 135.9 (d, $^1J_{P\text{-}C}$ = 58 Hz), 132.4 (d, $^2J_{P\text{-}C}$ = 6 Hz), 128.3, 128.6 (d, $^3J_{P\text{-}C}$ = 7 Hz), 109.8, 50.1. ^{31}P NMR δ: –9.3. Anal. calcd. for $C_{27}H_{32}N_3PTi$ (%): C 67.93, H 6.76, N 8.80; found: C 67.67, H 6.54, N 8.52.

Synthesis of $Ti(NP\text{-}t\text{-}Bu_3)(NMe_2)_3$ (3)

A slurry of $LiNMe_2$ (44 mg, 0.87 mmol) in benzene (1 mL) was added to a suspension of $Ti(NP\text{-}t\text{-}Bu_3)Cl_3$ (105 mg, 0.28 mmol) in the same solvent (10 mL). After stirring for 12 h at 25 °C, the mixture was filtered through Celite. Removal of the solvent in vacuo afforded an orange crystalline solid (83 mg, 75%). ^{1}H NMR δ: 3.40 (s, 18H, NMe_2), 1.27 (s, 27H, $^3J_{P\text{-}H}$ = 13 Hz, *t*-Bu). ^{13}C NMR δ: 46.3, 39.9 (d, $^1J_{P\text{-}C}$ = 48 Hz), 29.5. ^{31}P NMR δ: 29.8. Anal. calcd. for $C_{18}H_{45}N_4PTi$ (%): C 54.54, H 11.44, N 14.13; found: C 54.74, H 11.63, N 13.78. Deep orange-red crystals suitable for X-ray diffraction were grown by slow evaporation from hexanes–pentanes.

Synthesis of $ZrCp(NP\text{-}t\text{-}Bu_3)(NMe_2)_2$ (4)

Solid $LiNMe_2$ (193 mg, 3.6 mmol) was added in several portions at 25 °C to a clear solution of $ZrCp(NP\text{-}t\text{-}Bu_3)Cl_2$ (411 mg, 0.90 mmol) in benzene (50 mL). The slurry was stirred for 18 h and was subsequently filtered through Celite. The solvent was removed in vacuo affording **4** as a fine, white powder (340 mg, 82%). ^{1}H NMR δ: 6.32 (s, 5H, Cp), 3.14 (s, 12H, NMe_2), 1.21 (s, 27H, $^3J_{P\text{-}H}$ = 12 Hz, *t*-Bu). ^{13}C NMR δ: 109.6, 46.3, 39.9 (d, $^1J_{P\text{-}C}$ = 48 Hz), 29.6. ^{31}P NMR δ: 31.4. Anal. calcd. for $C_{21}H_{44}N_3PZr$ (%): C 54.74, H 9.62, N 9.12; found: C 53.73, H 9.64, N 8.49.

Synthesis of $TiCp(NP\text{-}t\text{-}Bu_3)(NHC_6H_3(2,6\text{-}i\text{-}Pr_2))Cl$ (5)

Solid $LiNHC_6H_3(2,6\text{-}i\text{-}Pr_2)$ (1.51 g, 12.2 mmol) was added in small portions at 25 °C over a 1 h period to a clear solution of $TiCp(NP\text{-}t\text{-}Bu_3)Cl_2$ (4.91 g, 12.2 mmol) in benzene (150 mL). The slurry was stirred for 20 h, after which time the mixture was filtered through Celite. The solution was concentrated in vacuo to ca. 20 mL, during which time a bright yellow solid precipitated. The solid was filtered, washed with pentanes (3 × 20 mL), and dried to afford a fine, yellow powder (5.94 g, 89%). ^{1}H NMR δ: 9.65 (br, 1H, NH), 7.23 (br, 2H, C_6H_3 (*m*-H)), 7.05 (t, 1H, $^3J_{H\text{-}H}$ = 7 Hz, C_6H_3 (*p*-H)), 6.21 (s, 5H, Cp), 3.26 (sep, 2H, $^3J_{H\text{-}H}$ = 7 Hz, *i*-Pr), 1.39 (d, 12H, $^3J_{H\text{-}H}$ = 7 Hz, *i*-Pr), 1.19 (d, 27H, $^3J_{P\text{-}H}$ = 13 Hz, *t*-Bu). ^{13}C NMR δ: 153.9, 128.3, 123.3, 123.1, 112.8, 41.5 (d, $^1J_{P\text{-}C}$ = 27 Hz), 29.5, 28.1, 22.6. ^{31}P NMR δ: 39.0. Anal. calcd. for $C_{29}H_{50}ClN_2PTi$ (%): C 64.38, H 9.32, N 5.18; found: C 63.95, H 9.06, N 4.74. Bright yellow crystals suitable for X-ray diffraction were grown by slow evaporation from benzene.

Synthesis of $Ti(NP\text{-}t\text{-}Bu_3)(NHC_6H_3(2,6\text{-}i\text{-}Pr_2))_3$ (6)

A slurry of $LiNHC_6H_3(2,6\text{-}i\text{-}Pr_2)$ (591 mg, 4.8 mmol) in benzene (20 mL) was added over a 0.5 h period at 25 °C to a clear solution of $TiCp(NP\text{-}t\text{-}Bu_3)Cl_2$ (380 mg, 0.96 mmol) in the same solvent (25 mL). The slurry was stirred for an additional 10 h, then filtered through Celite. The solvent was removed in vacuo, and the residue was washed with hexanes (3 × 10 mL) to afford a yellow solid (586 mg, 77%). ^{1}H NMR δ: 7.80 (br, 3H, NH), 7.11 (d, 6H, $^3J_{H\text{-}H}$ = 8 Hz, C_6H_3 (*m*-H)), 6.96 (t, 3H, $^3J_{H\text{-}H}$ = 8 Hz, C_6H_3 (*p*-H)), 3.70 (sep, 6H, $^3J_{H\text{-}H}$ = 7 Hz, *i*-Pr), 1.28 (d, 36H, $^3J_{H\text{-}H}$ = 7 Hz, *i*-Pr), 1.06 (d, 27H, $^3J_{P\text{-}H}$ = 13 Hz, *t*-Bu). ^{13}C NMR δ: 150.9, 137.6, 123.0, 120.8, 40.6 (d, $^1J_{P\text{-}C}$ = 46 Hz), 29.4, 29.2, 24.1. ^{31}P NMR δ: 37.4. Anal. calcd. for $C_{48}H_{81}N_4PTi$ (%): C 72.70, H 10.30, N 7.06; found: C 72.49, H 10.60, N 7.28. Deep red crystals suitable for X-ray diffraction were grown by slow evaporation from benzene.

Synthesis of $ZrCp(NP\text{-}t\text{-}Bu_3)(NHC_6H_3(2,6\text{-}i\text{-}Pr_2))Me$ (7)

$NH_2C_6H_3(2,6\text{-}i\text{-}Pr_2)$ (58 mL, 0.31 mmol) was added dropwise to a clear solution of $ZrCp(NP\text{-}t\text{-}Bu_3)Me_2$ (125 mg, 0.31 mmol) in benzene (20 mL) at 25 °C. After stirring for 12 h, the volatile products were removed in vacuo to afford a beige solid (162 mg, 92%). ^{1}H NMR δ: 7.21 (d, 2H, $^3J_{H\text{-}H}$ = 8 Hz, C_6H_3 (*m*-H)), 7.04 (t, 1H, $^3J_{H\text{-}H}$ = 8 Hz, C_6H_3 (*p*-H)), 6.51 (br, 1H, NH), 6.20 (s, 5H, Cp), 3.45 (sep, 2H, $^3J_{H\text{-}H}$ = 7 Hz, *i*-Pr), 1.36 (d, 6H, $^3J_{H\text{-}H}$ = 7 Hz, *i*-Pr), 1.35 (d, 6H, $^3J_{H\text{-}H}$ = 7 Hz, CMe_2H), 1.13 (d, 27H, $^3J_{P\text{-}H}$ = 13 Hz, *t*-Bu), 0.47 (s, 3H, ZrMe). ^{13}C NMR δ: 150.9, 137.7, 122.7, 120.1, 110.0, 40.0 (d, $^1J_{P\text{-}C}$ = 47 Hz), 29.0, 27.9, 27.9, 23.8, 22.8. ^{31}P NMR δ: 34.3. Anal. calcd. for $C_{30}H_{53}N_2PZr$ (%): C 63.89, H 9.47, N 4.97; found: C 62.84, H 9.43, N 4.90.

Synthesis of $ZrCp(NP\text{-}t\text{-}Bu_3)(NHC_6H_3(2,6\text{-}i\text{-}Pr_2))_2$ (8)

A slurry of $LiNHC_6H_3(2,6\text{-}i\text{-}Pr_2)$ (527 mg, 2.9 mmol) in benzene (20 mL) was added over a 15 min period at 25 °C to a solution of $ZrCp(NP\text{-}t\text{-}Bu_3)Cl_2$ (320 mg, 0.72 mmol) in

© 2004 NRC Canada

the same solvent (25 mL). The slurry was stirred for an additional 10 h, after which time it was filtered through Celite. The solvent was removed in vacuo, and the residue was washed with hexanes (3 × 5 mL) to afford a beige solid (486 mg, 93%). ^{1}H NMR δ: 7.18 (d, 4H, $^3J_{H-H}$ = 8 Hz, C_6H_3 (*m*-H)), 7.02 (t, 2H, $^3J_{H-H}$ = 8 Hz, C_6H_3 (*p*-H)), 6.34 (s, 5H, Cp), 5.75 (s, 2H, NH), 3.73 (sep, 4H, $^3J_{H-H}$ = 7 Hz, *i*-Pr), 1.34 (d, 24H, $^3J_{H-H}$ = 7 Hz, *i*-Pr), 1.04 (d, 27H, $^3J_{P-H}$ = 13 Hz, *t*-Bu). ^{13}C NMR δ: 151.9, 138.7, 122.9, 120.2, 111.4, 39.9 (d, $^1J_{P-C}$ = 47 Hz), 29.5, 28.7, 24.3. ^{31}P NMR δ: 35.8. Anal. calcd. for $C_{41}H_{68}N_3PZr$ (%): C 67.90, H 9.45, N 5.79; found: C 66.62, H 9.84, N 5.86. Colourless crystals suitable for X-ray diffraction were grown by slow evaporation from benzene (Scheme 1).

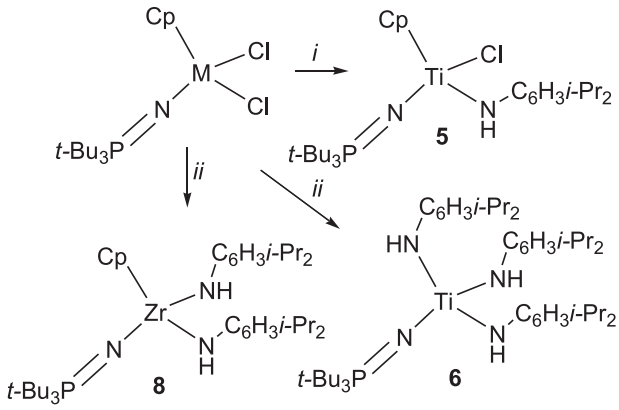
Generation of TiCp(NP-*t*-Bu$_3$)MeCl (9) and Al$_2$(*m*-NHC$_6$H$_3$(2,6-*i*-Pr$_2$))$_2$Me$_4$ (10)

Neat Al_2Me_6 (0.14 mL, 0.14 mmol) was added dropwise at 25 °C to a clear orange solution of **5** (153 mg, 0.28 mmol) in benzene (15 mL). The solution became deeper yellow in colour and was stirred for an additional 2 h, after which time the solvent was removed in vacuo. The residue was recrystallized from pentanes to afford yellow and colourless crystals (combined yield: 162 mg, 94%). X-ray analysis of the crystals isolated from the mixture confirmed the presence of **9** and **10**, although because of their similar solubility properties, they could not be adequately separated. Thus, microanalysis was performed on the mixture, confirming a 1:1 ratio of the two products. Anal. calcd. for $C_{32}H_{59}AlClN_2PTi$ (%): C 64.50, H 9.83, N 4.85; found: C 65.19, H 10.25, N 5.01. Both, however, were identified spectroscopically. **9**: ^{1}H NMR δ: 6.27 (s, 5H, Cp), 1.20 (s, 3H, TiMe), 1.04 (d, 27H, $^3J_{P-H}$ = 20 Hz, *t*-Bu). ^{13}C NMR δ: 113.3, 41.4 (d, $^1J_{P-C}$ = 45 Hz), 29.4, 25.2. ^{31}P NMR δ: 42.0. **10**: ^{1}H NMR: 7.06 (d, 2H, $^3J_{H-H}$ = 8 Hz, C_6H_3 (*m*-H)), 6.98 (t, 1H, $^3J_{H-H}$ = 8 Hz, C_6H_3 (*p*-H)), 4.58 (br, 1H, NH), 3.40 (sep, 2H, $^3J_{H-H}$ = 7 Hz, *i*-Pr), 1.26 (d, 12H, $^3J_{H-H}$ = 7 Hz, *i*-Pr), –0.32 (s, 6H, AlMe). ^{13}C NMR δ: 139.2, 137.7, 124.6, 123.8, 29.0, 25.0, –7.2. The spectroscopic and crystallographic data for Al$_2$(*m*-NH(2,6-*i*-Pr$_2$)C$_6$H$_3$)$_2$Me$_4$ were consistent with literature data.

X-ray data collection and reduction

Crystals were manipulated and mounted in capillaries in a glove box, thus maintaining a dry, O_2-free environment for each crystal. Diffraction experiments were performed on a Siemens SMART System CCD diffractometer. The data were collected in a hemisphere of data in 1329 frames with 10 s exposure times. The observed extinctions were consistent with the space groups in each case. The data sets were collected ($4.5° < 2q < 45°$–$50.0°$). A measure of decay was obtained by recollecting the first 50 frames of each data set. The intensities of reflections within these frames showed no statistically significant change over the duration of the data collections. The data were processed using the SAINT and XPREP processing packages. An empirical absorption correction based on redundant data was applied to each data set. Subsequent solution and refinement was performed using the SHELXTL solution package operating on a Pentium-3 computer (Table 1).

Scheme 1. Synthesis of **5**–**8**: (*i*) 1 equiv. of LiNHC$_6$H$_3$(2,6-*i*-Pr$_2$); (*ii*) 2 equiv. of LiNHC$_6$H$_3$(2,6-*i*-Pr$_2$).



Structure solution and refinement

Non-hydrogen atomic scattering factors were taken from the literature tabulations (44). The heavy atom positions were determined using direct methods employing the SHELXTL direct methods routine. The remaining non-hydrogen atoms were located from successive difference Fourier map calculations. The refinements were carried out by using full-matrix least-squares techniques on *F*, minimizing the function $\omega(|F_o| - |F_c|)^2$ where the weight ω is defined as $4F_o^2/2s$ (F_o^2) and F_o and F_c are the observed and calculated structure factor amplitudes. In the final cycles of each refinement, all non-hydrogen atoms were assigned anisotropic temperature factors in the absence of disorder or insufficient data. In the latter cases atoms were treated isotropically. C-H atom positions were calculated and allowed to ride on the carbon to which they are bonded assuming a C—H bond length of 0.95 Å. H-atom temperature factors were fixed at 1.10 times the isotropic temperature factor of the C atom to which they are bonded. The H-atom contributions were calculated, but not refined. The locations of the largest peaks in the final difference Fourier map calculation as well as the magnitude of the residual electron densities in each case were of no chemical significance. Additional details are provided in the supplementary data.[2]

Results and discussion

Complexes of formula TiCp(NPR$_3$)(NMe$_2$)$_2$ (R = *t*-Bu **1**, Ph **2**) were prepared via salt metathesis of TiCp(NPR$_3$)Cl$_2$ with a slight excess of LiNMe$_2$ affording the desired products in 67% and 77% yields, respectively. In the case where R = *t*-Bu, the by-product Ti(NP-*t*-Bu$_3$)(NMe$_2$)$_3$ (**3**) was also

[2] Supplementary data may be purchased from the Directory of Unpublished Data, Document Delivery, CISTI, National Research Council Canada, Ottawa, ON K1A 0S2, Canada (http://www.nrc.ca/cisti/irm/unpub_e.shtml for information on ordering electronically). CCDC 235292–235294 contain the crystallographic data for this manuscript. These data can be obtained, free of charge, via www.ccdc.cam.ac.uk/conts/retrieving.html (or from the Cambridge Crystallographic Data Centre, 12 Union Road, Cambridge CB2 1EZ, UK; fax +44 1223 336033; or deposit@ccdc.cam.ac.uk).

© 2004 NRC Canada

Table 1. Crystallographic data.[a]

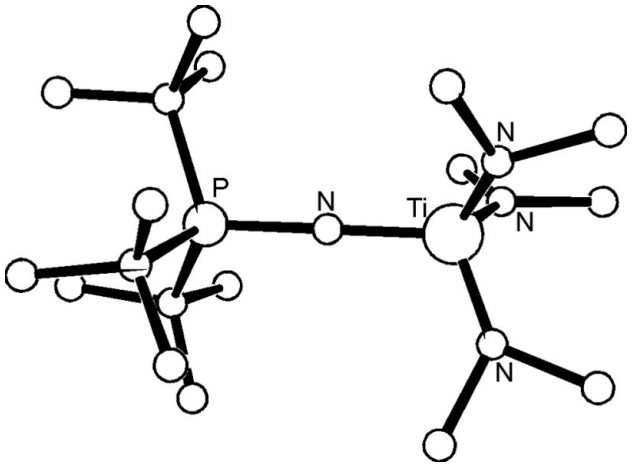
	5·0.5C_6H_6	**6**	**8**
Formula	$C_{32}H_{53}ClN_2PTi$	$C_{48}H_{81}N_4PTi$	$C_{41}H_{68}N_3PZr$
Formula wt.	580.08	793.04	725.17
Crystal syst.	Triclinic	Monoclinic	Orthorhombic
Space group	*P*-1	$P2_1/c$	*Pbca*
a (Å)	11.334(6)	11.476(2)	19.38(2)
b (Å)	11.891(6)	42.136(8)	19.77(2)
c (Å)	13.769(7)	20.590(4)	21.92(2)
α (°)	100.315(9)		
β (°)	101.464(9)	92.248(5)	
γ (°)	107.256(9)		
V (Å^3)	1680(1)	9 949(3)	8 400(2)
D(calcd.) (g cm^{-1})	1.147	1.059	1.147
Z	2	8	8
Abs coeff (μ, cm^{-1})	0.403	0.233	0.329
Data collected	7162	47 974	34 645
Data $F_o^2 > 3\sigma(F_o^2)$	4078	14 448	3 049
Variables	343	973	415
R	0.036 5	0.090 7	0.041 6
R_w	0.101 8	0.224 8	0.062 9
GOF	1.028	1.040	1.022

[a]All data collected at 24 °C with Mo Kα radiation (λ = 0.710 69 Å), $R = \Sigma||F_o| - |F_c|| / \Sigma|F_o|$, $R_w = [\Sigma[\omega(F_o^2 - F_c^2)^2] / \omega F_o^2)^2]]^{0.5}$.

generated in low yields (ca. 10%–15%). While the formation of **3** was unexpected as it requires Cp–M cleavage, such reactions are not unprecedented (45–48). This by-product **3** was prepared in a more conventional manner by a metathesis route in 75% yield from Ti(NP-*t*-Bu_3)Cl_3 and an excess of the lithium amide reagent. The related Zr derivative ZrCp(NP-*t*-Bu_3)$(NMe_2)_2$ (**4**) was also prepared in 82% yield from the dichloride precursor using an excess of the Li amide. Similarly the preparation of the related complexes TiCp′$(NMe_2)_3$ (Cp′ = Cp, C_5Me_5, indenyl) have been previously reported (9, 49). The ^{1}H NMR chemical shift of the amido-methyl groups for **3** and TiCp*$(NMe_2)_3$ were observed at 3.40 and 3.09 ppm, respectively. Preliminary X-ray data[3] for **3** was obtained from rather poor quality crystals. While these data confirmed the connectivity and inferred that **3** exhibits threefold symmetry in the solid state (Fig. 1), the poor quality of the crystals precludes a discussion of the metric parameters.

Similarly, reaction of TiCp(NP-*t*-Bu_3)Cl_2 with Li-NHC_6H_3(2,6-*i*-Pr_2) afforded TiCp(NP-*t*-Bu_3)(NHC_6H_3(2,6-*i*-Pr_2))Cl (**5**) and Ti(NP-*t*-Bu_3)$(NHC_6H_3(2,6\text{-}i\text{-}Pr_2))_3$ (**6**). However, unlike the dialkyl amide reaction, preparation of TiCp(NP-*t*-Bu_3)$(NHC_6H_3(2,6\text{-}i\text{-}Pr_2))_2$ could not be achieved cleanly, presumably a result of excessive steric crowding about the metal centre. The room-temperature ^{1}H NMR spectrum of **5** exhibited broad resonances attributed to the methine protons on the isopropyl groups and a doublet signal originating from the methyl groups. Variable-temperature studies confirmed restricted rotation about the Ti—N amide bond with coalescence of the methine protons of the isopropyl groups at 308 K. The free energy of activation

Fig. 1. PLUTO drawing of **3** (30% thermal ellipsoids are shown). Hydrogen atoms are omitted for clarity.



($\Delta G^{\ddagger}$) for rotation of the N—C_{ipso} bond was determined to be 58.1(5) kJ mol^{-1} at 298 K. This value is greater than those reported for Ti$(NR_2)_3$Cl (R = Me, Et) (<42 kJ mol^{-1}), but compares well with an estimation of 55.6 kJ mol^{-1} obtained for rotation of the N—C_{ipso} bond in the related complex Zr($(NC_6H_3(2,6\text{-}i\text{-}Pr_2)CH_2]_2CH_2)Me_2$ (50). The higher activation energies reflect the greater steric crowding around the metal center (51, 52). Compounds **5** and **6** were also characterized crystallographically (Figs. 2 and 3, Table 2). In both cases, the Ti—N bond for the phosphinimide ligands were significantly shorter than the Ti—N amide bonds, con-

[3]Preliminary X-ray data for **3**: $C_{18}H_{45}N_4PTi$, trigonal, *R*3, *a* = 14.066(6), *c* = 11.023(7), *V* = 1888.9(7). **9**: $C_{18}H_{35}ClNPTi$, orthorhombic, *Pbca*, *a* = 10.294(5), *b* = 14.828(8), *c* = 28.49(1), *V* = 4348(5). **10**: $C_{28}H_{46}N_2Al_2$, orthorhombic, $Pna2_1$, *a* = 18.810(8), *b* = 10.160(4), *c* = 15.902(7), *V* = 3039(2).

© 2004 NRC Canada

Table 2. Metric parameters.[a]

Cmpd	M—N (NR_2)	M—N (NPR_3)	N—P	M-N-P
5	1.946(2)	1.790(2)	1.604(7)	167.1(3)
6	1.931(5), 1.934(5)	1.782(6)	1.592(6)	170.3(3)
	1.933(5), 1.914(6)	1.796(6)	1.576(6)	167.0(4)
	1.927(5), 1.937(5)			
8	2.107(4), 2.110(3)	1.939(3)	1.592(3)	176.5(2)

[a]Bond distance in Å, angles in °.

Fig. 2. ORTEP drawing of **5** (30% thermal ellipsoids are shown). Hydrogen atoms are omitted for clarity.

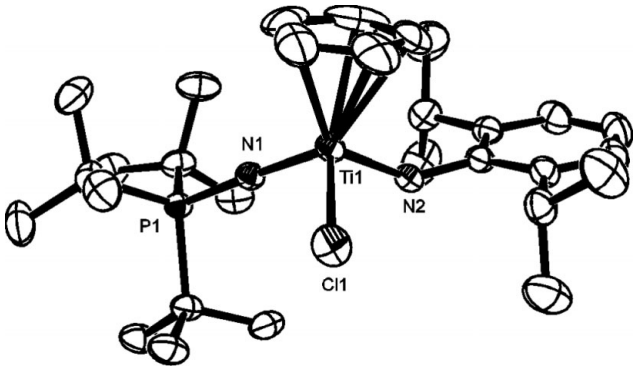
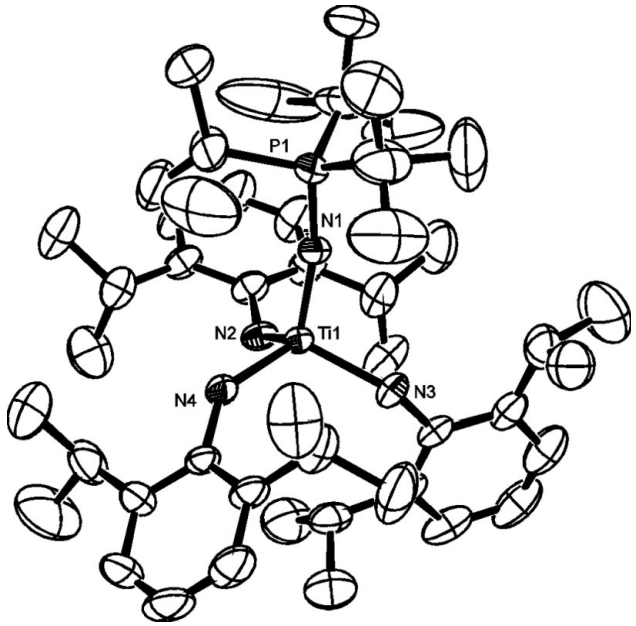
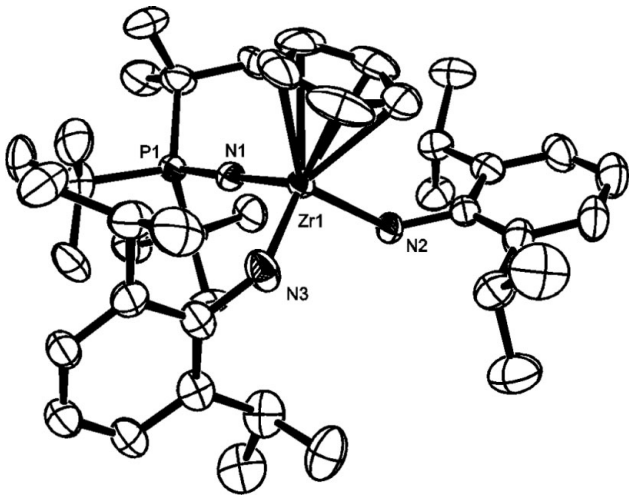


Fig. 3. ORTEP drawing of **6** (30% thermal ellipsoids are shown). Hydrogen atoms are omitted for clarity.



sistent with the strength of the Ti—phosphinimide bond. The related compound ZrCp(NP-*t*-Bu_3)(NHC_6H_3(2,6-*i*-Pr_2))Me (**7**) was prepared in 92% yield via a stoichiometric protonolysis reaction of ZrCp(NP-*t*-Bu_3)Me_2 with NH_2(2,6-*i*-Pr_2)C_6H_3. In contrast, the bis-amido analog ZrCp(NP-*t*-Bu_3)(NHC_6H_3(2,6-*i*-Pr_2))$_2$ (**8**) was prepared in 93% yield via metatheses of the chloride ligands of ZrCp(NP-*t*-Bu_3)Cl_2 with $LiNHC_6H_3$(2,6-*i*-Pr_2). The crystallographic data for **8**

Fig. 4. ORTEP drawing of **8** (30% thermal ellipsoids are shown). Hydrogen atoms are omitted for clarity.



revealed that the Zr—N bond distances were slightly longer than those in the Ti complexes as expected (Fig. 4, Table 2).

Reactivity of these phosphinimide–amide derivatives was explored. Attempts to effect the thermolytic formation of group IV phosphinimide imide complexes (1–3, 5, 53–56) were unsuccessful, affording instead the elimination of both free amine and phosphinimine. Similarly, attempts to prepare imido derivatives directly employing Mountford's precursor Ti(N-*t*-Bu)Cl_2(*t*-BuPy)$_2$ (57) were also unsuccessful.

In other chemistry, reaction of **5** with excess $AlMe_3$ resulted in the clean, near-quantitative isolation of TiCp(NP-*t*-Bu_3)Me_2. However, when 1 equiv. of $AlMe_3$ was used, TiCp(NP-*t*-Bu_3)MeCl (**9**) and the dimer Al_2(*m*-$NH(C_6H_3$(2,6-*i*-Pr_2))$_2Me_4$ (**10**) were obtained. The formation of **9** and **10** were confirmed via preliminary crystallographic data.[3] Similar methylations using $AlMe_3$ have been previously reported to replace alkoxide (58) or amide (59) ligands.

We noted the work of Doye and co-workers (60) who reported moderate conversion of 3-hexyne and 4-methylaniline to the secondary amine using TiCp($NPPh_3$)Me_2 as a catalyst. Efforts to effect similar transformations using **6**–**8** as catalyst precursors were unsuccessful resulting again in liberation of amine and phosphinimine ligands. It is interesting to note that while the phosphinimide ligand is an effective replacement for Cp in olefin polymerization catalysts, the present data imply that this is not the case for hydroamination catalysts. Intuitively, this may be related to the Lewis basicity of the phosphinimide N and its affinity for small Lewis acids such as protons. Nonetheless, efforts are continuing to ex-

© 2004 NRC Canada

plore the utility and limitations of phosphinimide-ligands as ancillary ligands.

References

1. P.J. Walsh, F.J. Hollander, and R.G. Bergman. J. Am. Chem. Soc. **110**, 8729 (1988).
2. C.C. Cummins, S.M. Baxter, and P.T. Wolczanski. J. Am. Chem. Soc. **110**, 8731 (1988).
3. P.J. Walsh, F.J. Hollander, and R.G. Bergman. Organometallics, **12**, 3705 (1993).
4. A.M. Baranger, F.J. Hollander, and R.G. Bergman. J. Am. Chem. Soc. **115**, 7890 (1993).
5. C.P. Schaller, C.C. Cummins, and P.T. Wolczanski. J. Am. Chem. Soc. **118**, 591 (1996).
6. J.D. Scollard, D.H. McConville, N.C. Payne, and J.J. Vittal. Macromolecules, **29**, 5241 (1996).
7. J.D. Scollard, D.H. McConville, J.J. Vittal, and N.C. Payne. J. Mol. Catal. A: Chem. **128**, 201 (1998).
8. L.-C. Liang, R.R. Schrock, W.M. Davis, and D.H. McConville. J. Am. Chem. Soc. **121**, 5797 (1999).
9. B. Rhodes, M.D. Rausch, and J.C.W. Chien. J. Polym. Sci. Part A: Polym. Chem. **39**, 313 (2000).
10. P. Mehrkhodavandi, P.J. Bonitatebus, Jr., and R.R. Schrock. J. Am. Chem. Soc. **122**, 7841 (2000).
11. P. Mehrkhodavandi, R.R. Schrock, and P.J. Bonitatebus, Jr. Organometallics, **21**, 5785 (2002).
12. R.M. Fix, R.G. Gordon, and D.M. Hoffman. Chem. Mater. **2**, 235 (1990).
13. H.R. Stock, H. Berndt, and P. Mayr. Surf. Coat. Technol. **46**, 15 (1991).
14. M. Janovska and Z. Bastl. Infrared Phys. Technol. **37**, 727 (1996).
15. M. Galakhov, P. Gomez-Sal, A. Martin, M. Mena, and C. Yelamos. Eur. J. Inorg. Chem. 1319 (1998).
16. J. Cheon, M. Guile, P. Muraoka, and J.I. Zink. Inorg. Chem. **38**, 2238 (1999).
17. J.B. Cross and H.B. Schlegel. Chem. Mater. **12**, 2466 (2000).
18. S. Akram. US Patent, 6 338 880, 2002.
19. P.J. Walsh, A.M. Baranger, and R.G. Bergman. J. Am. Chem. Soc. **114**, 1708 (1992).
20. L. Ackermann and R.G. Bergman. Org. Lett. **4**, 1475 (2002).
21. I. Bytschkov and S. Doye. Eur. J. Org. Chem. 935 (2003).
22. Y. Shi, C. Hall, J.T. Ciszewski, C. Cao, and A.L. Odom. Chem. Commun. 586 (2003).
23. J.L. Bennett and P.T. Wolczanski. J. Am. Chem. Soc. **119**, 10 696 (1997).
24. A. Bashall, P.E. Collier, L.H. Gade, M. McPartlin, P. Mountford, and D.J.M. Trosch. Chem. Commun. 2555 (1998).
25. T.R. Cundari, T.R. Klinckman, and P.T. Wolczanski. J. Am. Chem. Soc. **124**, 1481 (2002).
26. S.Y. Lee and R.G. Bergman. J. Am. Chem. Soc. **117**, 5877 (1995).
27. R.L. Zuckerman, S.W. Krska, and R.G. Bergman. J. Am. Chem. Soc. **122**, 751 (2000).
28. B.F. Straub and R.G. Bergman. Angew. Chem. Int. Ed. **40**, 4632 (2001).
29. F. Pohlki and S. Doye. Angew. Chem. Int. Ed. **40**, 2305 (2001).
30. D.W. Stephan, J.C. Stewart, F. Guerin, S. Courtenay, J. Kickham, E. Hollink, C. Beddie, A. Hoskin, T. Graham, P. Wei, R.E.v.H. Spence, W. Xu, L. Koch, X. Gao, and D.G. Harrison. Organometallics, **22**, 1937 (2003).
31. D.W. Stephan, F. Guerin, R.E.v.H. Spence, L. Koch, X. Gao, S.J. Brown, J.W. Swabey, Q. Wang, W. Xu, P. Zoricak, and D.G. Harrison. Organometallics, **18**, 2046 (1999).
32. D.W. Stephan, J.C. Stewart, F. Guerin, R.E.v.H. Spence, W. Xu, and D.G. Harrison. Organometallics, **18**, 1116 (1999).
33. N. Yue, E. Hollink, F. Guerin, and D.W. Stephan. Organometallics, **20**, 4424 (2001).
34. N.L.S. Yue and D.W. Stephan. Organometallics, **20**, 2303 (2001).
35. D.W. Stephan. Macromol. Symp. **173**, 105 (2001).
36. F. Guerin, C.L. Beddie, D.W. Stephan, R.E.v.H. Spence, and R. Wurz. Organometallics, **20**, 3466 (2001).
37. F. Guerin, J.C. Stewart, C. Beddie, and D.W. Stephan. Organometallics, **19**, 2994 (2000).
38. F. Guerin and D.W. Stephan. Angew. Chem. Int. Ed. **39**, 1298 (2000).
39. J.E. Kickham, F. Guerin, J.C. Stewart, E. Urbanska, C.M. Ong, and D.W. Stephan. Organometallics, **20**, 1175 (2001).
40. J.E. Kickham, F. Guerin, J.C. Stewart, and D.W. Stephan. Angew. Chem. Int. Ed. **39**, 3263 (2000).
41. J.E. Kickham, F. Guerin, and D.W. Stephan. J. Am. Chem. Soc. **124**, 11 486 (2002).
42. A.B. Pangborn, M.A. Giardello, R.H. Grubbs, R.K. Rosen, and F.J. Timmers. Organometallics, **15**, 1518 (1996).
43. S. Daniele, C. Drost, B. Gehrhus, S.M. Hawkins, P.B. Hitchcock, M.F. Lappert, P.G. Merle, and S.G. Bott. Dalton Trans. 3179 (2001).
44. D.T. Cromer and J.B. Mann. Acta Crystallogr. Sect. A, **A24**, 321 (1968).
45. G. Erker, C. Sarter, M. Albrecht, S. Dehnicke, C. Kruger, E. Raabe, R. Schlund, R. Benn, A. Rufinska, and R. Mynott. J. Organomet. Chem. **382**, 89 (1990).
46. J.S. Johnson and R.G. Bergman. J. Am. Chem. Soc. **123**, 2923 (2001).
47. R.D. Gorsich. J. Am. Chem. Soc. **82**, 4211 (1960).
48. J.S. Brantley, E.L. Morehouse, and L. Parts. US Patent, 3 306 919, 1967.
49. G. Chandra and M.F. Lappert. J. Chem. Soc. A, 1940 (1968).
50. J.D. Scollard, D.H. McConville, and J.J. Vittal. Organometallics, **16**, 4415 (1997).
51. R.A. Andersen. Inorg. Chem. **18**, 1724 (1979).
52. D.G. Dick, R. Rousseau, and D.W. Stephan. Can. J. Chem. **69**, 357 (1991).
53. A.M. Baranger, P.J. Walsh, and R.G. Bergman. J. Am. Chem. Soc. **115**, 2753 (1993).
54. B.R. Jagirdar, R. Murugavel, and H.G. Schmidt. Inorg. Chim. Acta, **292**, 105 (1999).
55. C. Yelamos, M.J. Heeg, and C.H. Winter. Organometallics, **18**, 1168 (1999).
56. Z.K. Sweeney, J.L. Salsman, R.A. Andersen, and R.G. Bergman. Angew. Chem. Int. Ed. **39**, 2339 (2000).
57. S.C. Dunn, A.S. Batsanov, and P. Mountford. Chem. Commun. 2007 (1994).
58. W. Kaschube, K.R. Porschke, and G. Wilke. J. Organomet. Chem. **355**, 525 (1988).
59. V.C. Gibson, B.S. Kimberley, A.J.P. White, D.J. Williams, and P. Howard. Chem. Commun. 313 (1998).
60. F. Pohlki, A. Heutling, I. Bytschkov, T. Hotopp, and S. Doye. Synlett, **5**, 799 (2002).

© 2004 NRC Canada

Total synthesis of (–)-xyloketal D and its enantiomer — Confirmation of absolute stereochemistry

Jeremy D. Pettigrew, Rebecca P. Freeman, and Peter D. Wilson

Abstract: The total synthesis of (–)-xyloketal D and its enantiomer have been achieved by the reaction of an *ortho*-quinone methide with (4*R*)- and (4*S*)-4,5-dihydro-2,4-dimethylfuran via a diastereoselective inverse electron demand Diels–Alder reaction. This total synthesis confirmed the absolute stereochemistry of the natural product. The *ortho*-quinone methide was generated by reaction of an appropriately functionalized Mannich base with methyl iodide. The Mannich base was prepared in one step from 2,4-dihydroxyacetophenone, formaldehyde, and morpholine. The enantiomeric dihydrofurans were prepared from (2*R*)- and (2*S*)-2-methylpent-4-ynoic acid via a three-step reaction sequence. These chiral nonracemic synthetic precursors were prepared from the corresponding (*R*)-phenylglycinol-derived diastereomeric amides of the readily available racemic carboxylic acid. The absolute stereochemistry of these carboxylic acids was firmly established by conversion to a known compound that had been previously prepared from a chiral pool starting material.

Key words: xyloketal D, inverse electron demand Diels–Alder reaction, *ortho*-quinone methide, dihydrofuran.

Résumé : Faisant appel à une réaction de Diels–Alder diastéréosélective, avec une demande d'électron inversée, on a réalisé une synthèse totale de (–)-xylocétal D et de son énantiomère par réaction d'une *ortho*-quinone méthide avec les (4*R*)- et (4*S*)-4,5-dihydro-2,5-diméthyfurane. Cette synthèse totale confirme la stéréochimie absolue du produit naturel. L'*ortho*-quinone méthide a été générée par réaction de l'iodure de méthyle avec une base de Mannich portant une fonctionnalisation appropriée. La base de Mannich a été préparée en une étape à partir de la 2,4-dihydroxyacétophénone, du formaldéhyde et de la morpholine. On a préparé les dihydrofuranes énantiomères en trois étapes par une série de réactions à partir des acides (2*R*)- et (2*S*)-2-méthylpent-4-ynoïque. On a préparé ces précurseurs de synthèse chiraux non racémiques à partir des amides diastéréomères correspondants dérivés du (*R*)-phénylglycinol et de l'acide carboxylique racémique commercialement disponible. La configuration absolue de ces acides carboxyliques a été fermement établie par conversion en un composé connu qui avait précédemment été préparé à partir d'un produit appartenant à un ensemble chiral.

Mots clés : xylocétal D, réaction de Diels–Alder avec demande d'électron inversée, *ortho*-quinone méthide, dihydrofurane.

[Traduit par la Rédaction]

Introduction

The natural products xyloketal A (**1**), B (**2**), C (**3**), D (**4**), and E (**5**) were isolated from a mangrove fungus of the *Xylaria* species (Fig. 1) (1). The molecular structures of these novel secondary metabolites were determined by extensive spectroscopic methods and by X-ray crystallography. In addition, the absolute stereochemistry of xyloketal A (**1**) and D (**4**) were determined by interpretation of their CD spectra. Xyloketal A (**1**) has a unique chiral, C_3-symmetric molecular structure and was shown to be an inhibitor of acetylcholine esterase (1, 2). Xyloketal D (**4**) is the simplest member of this family of natural products. We have previously reported the synthesis of (±)-11-norxyloketal D, the first total synthesis of (±)-xyloketal D (±)-**4** and model studies towards the total synthesis of xyloketal A (**1**) (3).[2] These syntheses featured the cycloaddition reactions of appropriately functionalized *ortho*-quinone methides and dihydrofurans as a key step (4).

The synthesis of (±)-11-norxyloketal D (**10**) (43% yield), via the *ortho*-quinone methide **9**, was achieved by heating the Mannich base **7** and commercially available 4,5-dihydro-2-methylfuran (**8**) (3 equiv.) with methyl iodide (1.05 equiv.) in benzene at reflux for 5 days (Fig. 2) (4–6). The Mannich

Received 25 May 2004. Published on the NRC Research Press Web site at http://canjchem.nrc.ca on 21 December 2004.

J.D. Pettigrew, R.P. Freeman, and P.D. Wilson.[1] Department of Chemistry, Simon Fraser University, 8888 University Drive, Burnaby, BC V5A 1S6, Canada.

[1]Corresponding author (e-mail: pwilson@sfu.ca).

[2]The numbering scheme provided for (–)-xyloketal D (**4**) by Lin and co-workers is employed throughout this paper. See ref. 1.

 doi: 10.1139/V04-138 © 2004 NRC Canada

Fig. 1. Molecular structures of xyloketal A (**1**), B (**2**), C (**3**), D (**4**), and E (**5**).

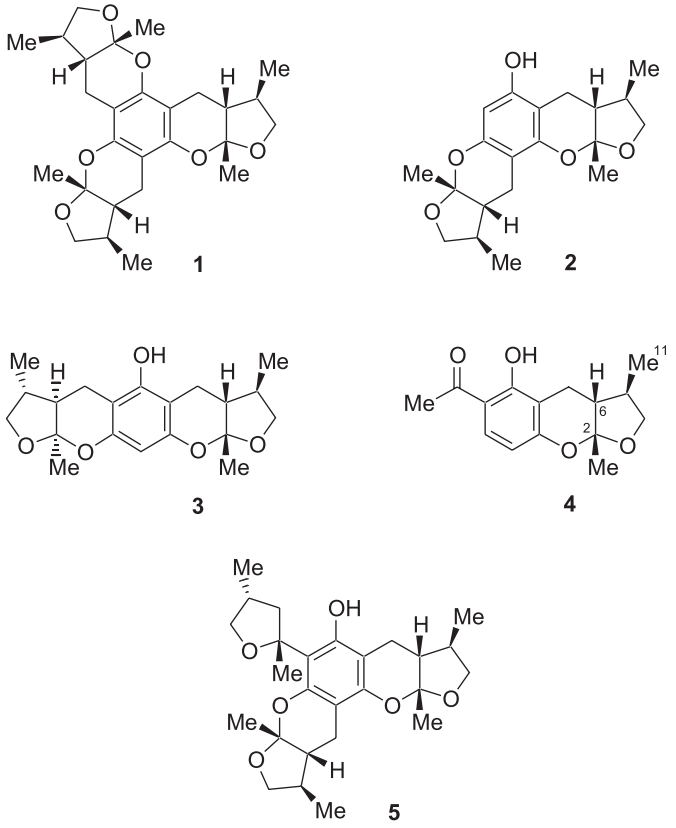
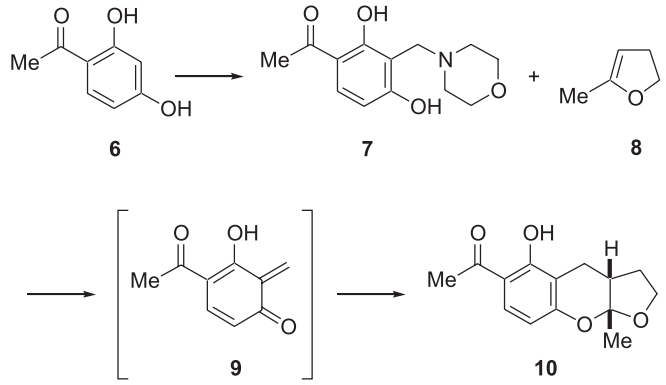


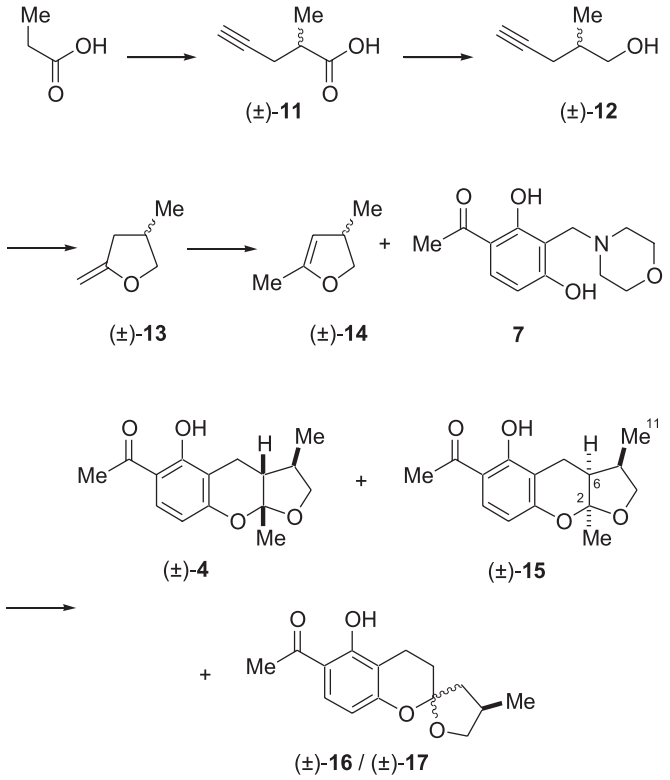
Fig. 2. Synthesis of (±)-11-norxyloketal D ((±)-**10**) (3).



base **7** was prepared as a single regioisomeric product from 2,4-dihydroxyacetophenone (**6**), formaldehyde, and morpholine in 83% yield (7).

The total synthesis of (±)-xyloketal D ((±)-**4**) involved a new synthesis of the known racemic dihydrofuran (±)-**14** (Fig. 3) (8). The racemic carboxylic acid (±)-**11** was prepared by alkylation of propionic acid with propargyl bromide, which in turn was reduced with lithium aluminum hydride to afford the racemic alcohol (±)-**12** (9, 10). Heating this alcohol with a sub-stoichiometric amount of sodium amide afforded the exocyclic dihydrofuran (±)-**13**, which was isomerized thermally to afford the required dihydrofuran (±)-**14** (8). The cycloaddition reaction of the Mannich base **7** with the dihydrofuran (±)-**14** (3 equiv.), under the reaction

Fig. 3. Total synthesis of (±)-xyloketal D ((±)-**4**), (±)-2,6-*epi*-xyloketal D ((±)-**15**), and the diastereomeric spiroacetals (±)-**16** and (±)-**17** (3).

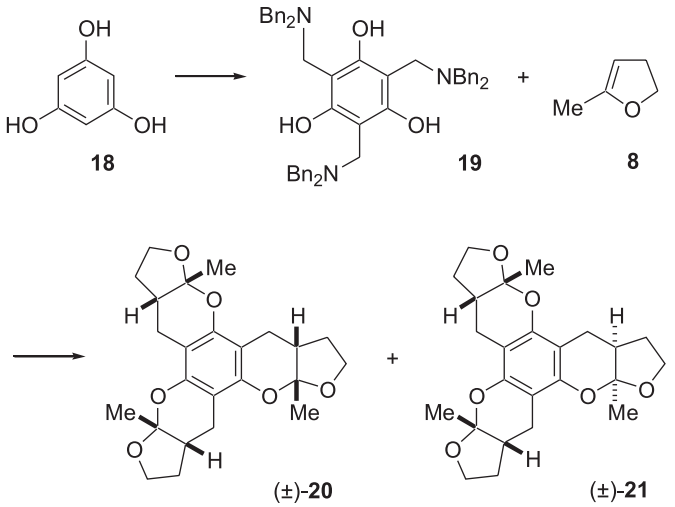


conditions described above, afforded (±)-xyloketal D ((±)-**4**), (±)-2,6-*epi*-xyloketal D ((±)-**15**), and the diastereomeric spiroacetals (±)-**16** and (±)-**17** as a mixture of products (11:1:3:3) in a combined yield of 54%. The spectral data for synthetic (±)-xyloketal D ((±)-**4**) were in agreement with those reported for the natural product (1). This diastereoselective cycloaddition reaction (11:1 dr) was controlled by the C4-methyl substituent of the dihydrofuran (±)-**14**. We attributed the formation of the isomeric spiroacetal reaction products (±)-**16** and (±)-**17** to the isomerization and subsequent cycloaddition reaction of the corresponding exocyclic dihydrofuran (±)-**13**. Of note, related spiroacetal reaction products were not isolated from the cycloaddition reaction of the dihydrofuran **8** that was employed in the synthesis of (±)-11-norxyloketal D (**10**). We concluded that the additional methyl substituent of dihydrofuran (±)-**14** decreased the reactivity of this endocyclic dihydrofuran in the cycloaddition reaction.

The preliminary model studies towards the total synthesis of (±)-xyloketal A ((±)-**1**) involved the reaction of the Mannich base **19**, the dihydrofuran **8** (9 equiv.), and methyl iodide (3 equiv.) (Fig. 4). This afforded a mixture (1:4) of the desired C_3-symmetric xyloketal A analogue (±)-**20** and the diastereoisomer (±)-**21** in 19% combined yield. This unprecedented and direct synthetic process involved nine individual reactions (three alkylation reactions, three elimination reactions, and three subsequent cycloaddition reactions). Of additional note, the Mannich base **19** was prepared in one step by adaptation of a literature procedure from phloro-

© 2004 NRC Canada

Fig. 4. Synthesis of xyloketal A analogues (±)-**20** and (±)-**21** (3).



glucinol (**18**), *N*,*N*-dibenzylamine, and formaldehyde (11, 12).

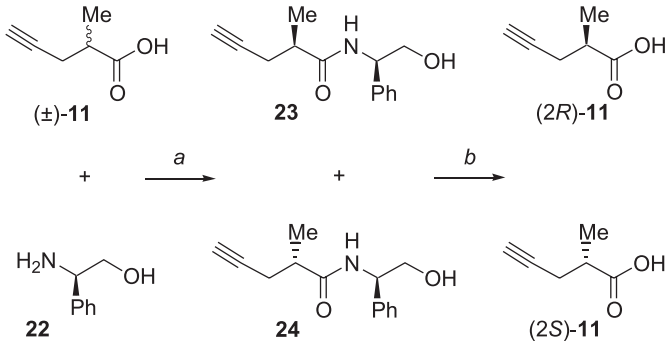
We have subsequently attempted to prepare (±)-xyloketal A ((±)-**1**) from the dihydrofuran (±)-**14** and the Mannich base **19**. However, it was not possible to isolate the desired target compound from a complex mixture of reaction products. Presumably, this process was complicated by the formation of diastereomeric as well as spirocyclic reaction by-products.

In this paper, we report an efficient resolution procedure for the racemic carboxylic acid (±)-**11**, a proof of the absolute stereochemistry, and the asymmetric synthesis of (–)-xyloketal D (**4**) as well as its enantiomer. This study was also undertaken to confirm the absolute stereochemistry of the natural product. Recently, Krohn and co-workers (13) have reported an alternative asymmetric synthesis of (–)-xyloketal D (**4**) and the C2,C6-epimer (8.5:1.5 dr) from (3*R*)-3-methylbutyrolactone (93% ee) and 2,4-dihydroxyacetophenone (**6**), as well as model studies towards the total synthesis of xyloketal A (**1**).

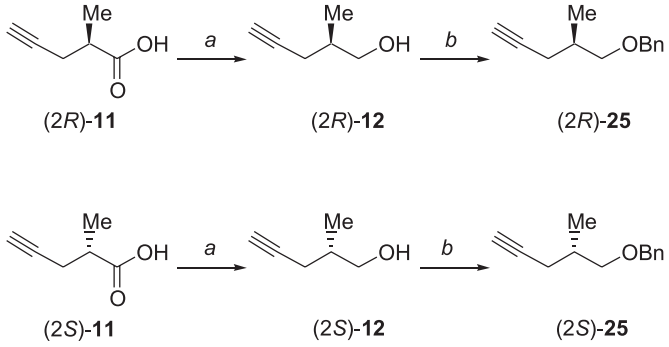
Results and discussion

A variety of methods were investigated to identify an efficient resolution procedure for the racemic carboxylic acid (±)-**11** (3).[3] It was not possible to separate the diastereomeric salts that were formed between the carboxylic acid and (*R*)-methylbenzylamine or (*R*)-(1-naphthyl)-ethylamine by fractional recrystallization. The racemic carboxylic acid (±)-**11** was also converted to the corresponding acid chloride and condensed with a series of commercially available chiral nonracemic alcohols.[4] All of the diastereomeric esters that were prepared could not be separated by fractional recrystallization or by chromatographic methods. The corresponding acid chloride of the carboxylic acid was also condensed with an extensive series of chiral nonracemic amines.[5] It was found that the diastereomeric amides **23** and **24** prepared from (*R*)-phenylglycinol (**22**) could be separated readily by flash chromatography on a multigram scale (Scheme 1) (14, 15).[6,7] The chiral nonracemic carboxylic acids (2*R*)-**11** and (2*S*)-**11** were then prepared by hydrolysis of the diastereomeric amides **23** and **24** under acidic reaction conditions (14, 16).

Scheme 1. Resolution of (±)-2-methylpent-4-ynoic acid ((±)-**11**). Reagents and conditions: (*a*) $(COCl)_2$, CH_2Cl_2, DMF (cat.), 0 °C to room temperature, 2 h; (*R*)-phenylglycinol (**22**), NEt_3, CH_2Cl_2, 0 °C to room temperature, 16 h, 36% (**23**), 34% (**24**); (*b*) 3 mol L^{-1} H_2SO_4, *p*-dioxane, reflux, 7 h, 76% ((2*R*)-**11**), 86% ((2*S*)-**11**).



Scheme 2. Synthesis of (2*R*)-2-methylpent-4-yn-1-ol ((2*R*)-**12**) and (2*S*)-2-methylpent-4-yn-1-ol ((2*S*)-**12**): confirmation of absolute stereochemistry. Reagents and conditions: (*a*) $LiAlH_4$, THF, 0 °C to room temperature, 16 h, 89% ((2*R*)-**12**), 85% ((2*S*)-**12**); (*b*) NaH, BnBr, DMF, THF, 6 h, 90% ((2*R*)-**25**), 90% ((2*S*)-**25**).

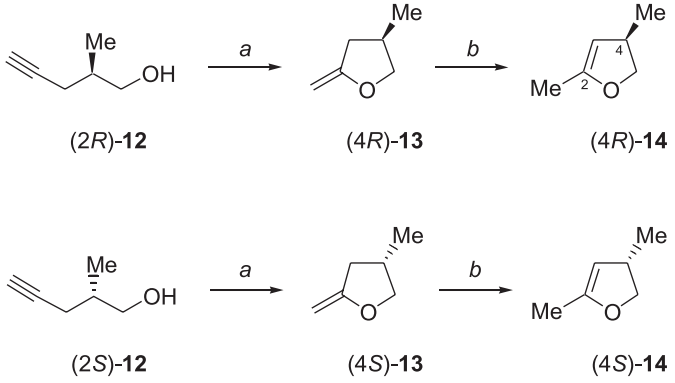


The chiral nonracemic carboxylic acid (2*R*)-**11** was reduced with lithium aluminum hydride to afford the corresponding alcohol (2*R*)-**12** (Scheme 2) (17). A sample of this alcohol was then converted to the benzyl ether (2*R*)-**25**. The latter compound has been prepared previously from an expensive chiral pool starting material and the optical rotation

[3] A full experimental procedure for the preparation of the racemic carboxylic acid (±)-**11** is provided in the supplementary material.[10]
[4] For example, the diastereomeric esters prepared from menthol, isomenthol, and (2*R*)-butan-2-ol were copolar by TLC.
[5] The chiral nonracemic amines that were employed in these reactions included: (*R*)-methylbenzylamine and (*R*)-(1-naphthyl)-ethylamine, the methyl esters of (*S*)-alanine, isoleucine, leucine, phenylalanine, proline, tryptophan, and (*R*)-phenylglycine, as well as (*S*)-valinol and (1*S*,2*R*)-norephedrine.
[6] The diastereomeric amides that were prepared from (*S*)-valinol were also chromatographically separable.
[7] Attempts, albeit unsuccessful, were also made to resolve the racemic alcohol (±)-**12** on condensation with a series of commercially available chiral nonracemic carboxylic acids and sulfonyl chlorides.

© 2004 NRC Canada

Scheme 3. Synthesis of (4*R*)-4,5-dihydro-2,4-dimethylfuran ((4*R*)-**14**) and (4*S*)-4,5-dihydro-2,4-dimethylfuran ((4*S*)-**14**). Reagents and conditions: (*a*) $NaNH_2$, reflux, 2 h; (*b*) reflux, 2 h, 44% (over two steps) ((4*R*)-**14**), 36% (over two steps) ((4*R*)-**14**).

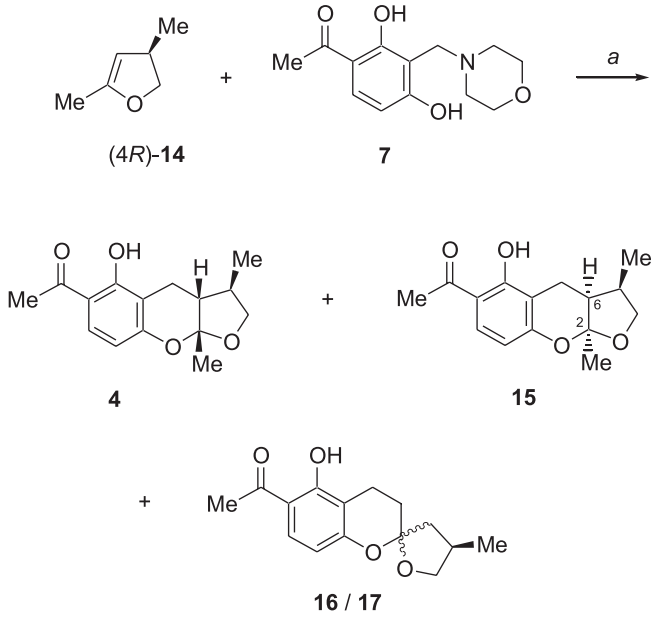


has been reported (18). Thus, the absolute stereochemistry and high optical purity of the resolved carboxylic acid (2*R*)-**11** was firmly established (see Experimental section). To complete the total synthesis of (–)-xyloketal D (**4**) and its nonnatural enantiomer, the carboxylic acid (2*S*)-**11** was reduced with lithium aluminum hydride to afford the alcohol (2*S*)-**12**. A sample of this compound was also converted to the corresponding benzyl ether (2*S*)-**25**, which proved to be the enantiomer of a known compound (18).

The chiral nonracemic alcohol (2*R*)-**12** was then used to prepare the dihydrofuran (4*R*)-**14** as described earlier for the racemic compound (Scheme 3).[8] This compound would serve as the precursor of (–)-xyloketal D (**4**) and would allow for the confirmation of the absolute stereochemistry of the natural product. In an identical fashion, the alcohol (2*S*)-**12** was used to prepare the dihydrofuran (4*S*)-**14**. This compound would serve as the precursor of the nonnatural enantiomer of xyloketal D.

The chiral nonracemic dihydrofuran (4*R*)-**14** (3 equiv.) and the Mannich base **7** were heated in benzene at reflux with methyl iodide (1 equiv.) (Scheme 4).[9] This reaction afforded a mixture (8:1:2:2) of (–)-xyloketal D (**4**), 2,6-*epi*-xyloketal D (**15**), and the diastereomeric spiroacetals **16** and **17** in a combined yield of 40%. The reaction was also repeated using dimethyl sulfate instead of methyl iodide. This reaction proceeded at a faster rate and afforded a mixture of reaction products (16:1:4:4) in a similar combined yield. A diastereomerically and analytically pure sample of the synthetic natural product, (–)-xyloketal D (**4**), was obtained by repeated chromatography and recrystallization. An analytically pure sample of the diastereomeric spiroacetals **16** and **17** was also isolated as a mixture (4:5) by repeated chromatography and recrystallization.

Scheme 4. Synthesis of (–)-xyloketal D (**4**), 2,6-*epi*-xyloketal D (**15**), and the diastereomeric spiroacetals **16** and **17**. Reagents and conditions: (*a*) dihydrofuran (4*R*)-**14** (3 equiv.), MeI (1 equiv), benzene, reflux, 8 days, 40% (**4**, **15**, **16**, and **17** (8:1:2:2)) *or* dihydrofuran (4*R*)-**14** (3 equiv.), Me_2SO_4 (1 equiv.), benzene, reflux, 3 days, 37% (**4**, **15**, **16**, and **17** (16:1:4:4)).

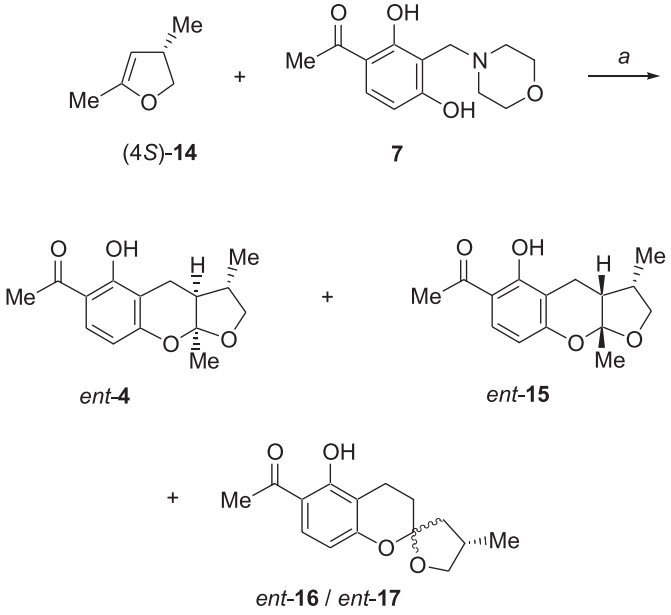


The ^1H NMR spectrum and ^{13}C NMR data of synthetic (–)-xyloketal D (**4**) were identical to those of the natural product[10] (1).[11] The sign of the optical rotation of synthetic (–)-xyloketal D (**4**) was in agreement with that reported for the natural product. This confirmed the absolute stereochemistry of the natural product that had been assigned previously by the interpretation of CD data (1, 13). However, the magnitude of the rotation was slightly lower than reported for the natural product (92% ee based on the optical rotation of the natural product) (1). To determine the enantiomeric purity of synthetic (–)-xyloketal D (**4**), efforts were also made to separate the enantiomers of a sample of racemic xyloketal D ((±)-**4**) (3). This was not possible by analytical chiral HPLC (Daicel Chiracel OD column) or by GC (Cyclosil-B column). Similarly, ^1H NMR spectroscopy using a chiral shift reagent ($Eu(hfc)_3$) was unsuccessful. Derivatization of the phenol moiety of racemic xyloketal D ((±)-**4**) with (*S*)-(+)-α-methoxy-α-trifluoromethyl-phenylacetyl chloride afforded the corresponding Mosher's esters (19). The ^1H NMR (600 MHz) signals of the methoxy substituents were clearly resolved.[12] Subsequent derivatization of synthetic (–)-xyloketal D (**4**) afforded the corresponding Mosher's ester as a single diastereoisomer. This confirmed

[8] The lower yield for the preparation of the chiral nonracemic dihydrofuran (4*R*)-**14** than that reported for the racemic compound is reflective of the smaller scale that this reaction was performed on. See ref. 3.
[9] We have previously reported full experimental procedures for the preparation of Mannich base **7**. See ref. 3.
[10] Detailed experimental procedures and complete product characterization data for all of the additional compounds synthesized, as well as ^1H and ^{13}C NMR spectra for compounds (±)-**11**, **23**, **24**, (2*R*)-**12**, (2*R*)-**25**, (4*R*)-**14**, **4**, **16**, **17**, and the Mosher's ester derivatives of (±)-xyloketal D ((±)-**4**) and synthetic (–)-xyloketal D (**4**) may be purchased from the Directory of Unpublished Data, Document Delivery, CISTI, National Research Council Canada, Ottawa, ON K1A 0S2, Canada (http://www.nrc.ca/cisti/irm/unpub_e.shtml for information on ordering electronically).
[11] Of note, the ^1H NMR signal of natural (–)-xyloketal D (**4**) centred at 2.15 ppm should have been reported at 2.08 ppm.
[12] The ^{19}F NMR (470 MHz) signals of the Mosher's ester derivatives were separate but poorly resolved.

© 2004 NRC Canada

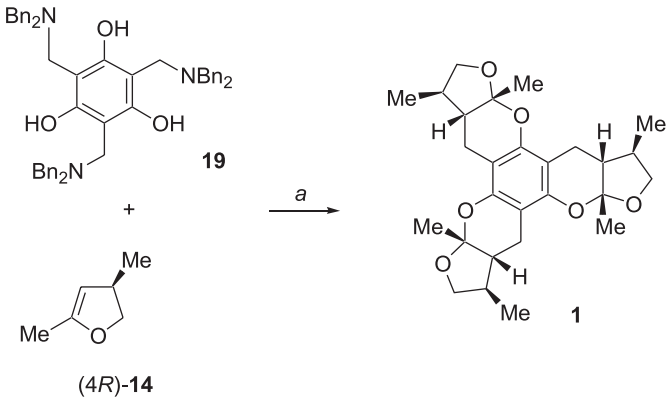
Scheme 5. Synthesis of (+)-xyloketal D (*ent*-**4**), *ent*-2,6-*epi*-xyloketal D (*ent*-**15**), and the diastereomeric spiroacetals *ent*-**16** and *ent*-**17**. Reagents and conditions: (*a*) dihydrofuran (4*S*)-**14** (3 equiv.), MeI (1 equiv.), benzene, reflux, 6 days, 46% (*ent*-**4**, *ent*-**15**, *ent*-**16** and *ent*-**17** (13:1:3:3)) *or* dihydrofuran (4*S*)-**14** (3 equiv.), Me_2SO_4 (1 equiv.), benzene, reflux, 3 days, 36% (*ent*-**4**, *ent*-**15**, *ent*-**16**, and *ent*-**17** (20:1:3:3)).



that the synthetic material was enantiomerically pure.[10] The melting point of synthetic (–)-xyloketal D (**4**) (71–73 °C) was, however, significantly lower than that reported for the natural product (111–113 °C). We were unable to increase the melting point of our synthetic material by repeated recrystallization from petroleum ether. Krohn et al. (13*b*) have reported that synthetic (–)-xyloketal D (**4**) (93% ee calculated from optical rotation and 93% ee based on the enantiomeric purity of a synthetic precursor) also had a lower melting point (87 °C, ether–pentane). They also reported that subsequent recrystallization from ether–pentane afforded the natural product, which had a melting point of 110 to 111 °C. We have also recrystallized our synthetic material from this solvent system. However, in our hands this procedure did not increase the melting point. We have concluded that our sample is either contaminated with a trace amount of the enantiomer, which has significantly depressed the melting point, or that we have isolated the natural product in a different crystal form.[13]

The Mannich base **7** was also reacted with the chiral nonracemic dihydrofuran (4*S*)-**14** using the two procedures described previously (Scheme 5). These reactions afforded mixtures of (+)-xyloketal D (*ent*-**4**), *ent*-2,6-*epi*-xyloketal D (*ent*-**15**), and the diastereomeric spiroacetals *ent*-**16** and *ent*-**17**. A diastereomerically and analytically pure sample of the enantiomeric natural product, (+)-xyloketal D (*ent*-**4**), was also prepared and fully characterized following repeated chromatography and recrystallization.

Scheme 6. Attempted synthesis of (–)-xyloketal A (**1**). Reagents and conditions: (*a*) dihydrofuran (4*R*)-**14** (9 equiv.), MeI (3 equiv.), benzene, reflux, or dihydrofuran (4*R*)-**14** (9 equiv.), Me_2SO_4 (3 equiv.), benzene, reflux.



The total synthesis of (–)-xyloketal A (**1**) was also attempted (Scheme 6). The Mannich base **19** and a large excess of the chiral nonracemic dihydrofuran (4*R*)-**14** were heated in benzene at reflux with methyl iodide and with dimethyl sulfate.[14] The natural product was not isolated from the complex mixtures of products that were produced in these reactions.

It was anticipated that the stereochemistry of this attempted cycloaddition reaction would have been directed efficiently by the C4-methyl substituent of the chiral nonracemic dihydrofuran (4*R*)-**14**. However, it appears that the competing isomerization reaction of the dihydrofuran (4*R*)-**14** and the subsequent nonstereoselective cycloaddition reaction of the exocyclic dihydrofuran (4*R*)-**13** is a dominant complicating factor.

Conclusions

The racemic carboxylic acid (±)-**11** was resolved by the chromatographic separation of the corresponding diastereomeric amides **23** and **24** that were prepared from (*R*)-phenylglycinol (**22**). The absolute stereochemistry and the enantiomeric purity of the chiral nonracemic carboxylic acid (2*R*)-**11** were determined by conversion to the benzyl ether (2*R*)-**25**, which had been prepared previously from a chiral pool starting material. The total synthesis of (–)-xyloketal D (**4**) and its enantiomer were completed from the chiral nonracemic dihydrofurans (4*R*)-**14** and (4*S*)-**14**. These dihydrofurans, which were prepared in three steps from the carboxylic acids (2*R*)-**11** and (2*S*)-**11**, were reacted with an appropriately functionalized *ortho*-quinone methide **9** that was generated from the Mannich base **7**. These results confirmed the absolute stereochemistry of the natural product that was reported by Lin and co-workers (1, 13). The synthesis of (–)-xyloketal A (**1**) from the chiral nonracemic dihydrofuran (4*R*)-**14** and the Mannich base **19** was unsuccessful. Thus, alternative synthetic routes are actively being

[13]Professor Krohn has informed us that he has recently checked the melting point of a sample of natural (–)-xyloketal D (**4**), which was kindly provided by Professor Lin, and found it to be 107 to 108 °C (Büchi SMP-20 melting point apparatus).
[14]We have previously reported full experimental procedures for the preparation of Mannich base **19**. See ref. 3.

© 2004 NRC Canada

pursued to complete the total synthesis of this unique and biologically relevant natural product.

Experimental section

For general experimental details refer to the supplementary material.[10]

(2*R*)-*N*-[(1*R*)-1-Phenyl-2-hydroxyethyl]-2-methyl-4-pentynamide (23) and (2*S*)-*N*-[(1*R*)-1-phenyl-2-hydroxyethyl]-2-methyl-4-pentynamide (24)

To a solution of the racemic carboxylic acid (±)-**11** (3) (5.40 g, 48.2 mmol) in dichloromethane (100 mL) at 0 °C were added oxalyl chloride (5.5 mL, 58 mmol) and *N*,*N*-dimethylformamide (2 drops). The resultant solution was allowed to warm to room temperature over 2 h and then was concentrated in vacuo to afford the corresponding acid chloride. A solution of this acid chloride in dichloromethane (50 mL) was then added to a stirred solution of (*R*)-phenylglycinol (**22**) (6.60 g, 48.2 mmol) and triethylamine (8.0 mL, 58 mmol) in dichloromethane (150 mL) at 0 °C. The resultant solution was allowed to warm to room temperature over 16 h and then water (50 mL) was added. The reaction mixture was extracted with ethyl acetate (3 × 50 mL) and the combined organic layers were washed with brine (50 mL), dried over anhydrous sodium sulfate, and concentrated in vacuo. Purification by flash chromatography using petroleum ether – ethyl acetate (1:2) as the eluant afforded the title compounds **23** (4.01 g, 36%) and **24** (3.82 g, 34%) as white solids. Amide **23**: R_f = 0.37 (petroleum ether – ethyl acetate, 1:2), mp 78–82 °C, petroleum ether – ethyl acetate. $[\alpha]_D^{24}$ = –63 (*c* 1.31, $CHCl_3$). IR (ef, cm^{-1}): 3314, 3286, 2936, 1650, 1544, 1052, 758, 702. ^1H NMR (400 MHz, $CDCl_3$) δ: 1.25 (d, *J* = 6.5 Hz, 3H), 2.07 (t, *J* = 2.6 Hz, 1H), 2.30 (broad s, 1H), 2.38 (m, 1H), 2.51 (m, 2H), 3.91 (d, *J* = 4.6 Hz, 2H), 5.10 (dt, *J* = 7.0, 4.8 Hz, 1H), 6.32 (broad d, *J* = 4.9 Hz, 1H), 7.34 (m, 5H). ^{13}C NMR (126 MHz, $CDCl_3$) δ: 17.1, 23.1, 40.4, 55.6, 66.2, 70.2, 82.1, 126.6, 127.7, 128.7, 138.9, 175.0. MS (CI) *m*/*z* (rel. intensity): 232 (M + H, 100). Anal. calcd. for $C_{14}H_{17}NO_2$: C 72.70, H 7.41, N 6.06; found: C 72.86, H 7.35, N 5.87. Amide **24**: R_f = 0.27 (petroleum ether – ethyl acetate, 1:2), mp 90–93 °C, petroleum ether – ethyl acetate. $[\alpha]_D^{23}$ = –33 (*c* 0.80, $CHCl_3$). IR (ef, cm^{-1}): 3282, 2938, 1645, 1545, 1038, 699. ^1H NMR (400 MHz, $CDCl_3$) δ: 1.29 (d, *J* = 6.7 Hz, 3H), 2.01 (t, *J* = 2.7 Hz, 1H), 2.25 (broad s, 1H), 2.39 (ddd, *J* = 15.8, 6.2, 2.8 Hz, 1H), 2.51 (m, 2H), 3.90 (m, 2H), 5.08 (dt, *J* = 6.8, 4.8 Hz, 1H), 6.37 (d, *J* = 4.3 Hz, 1H), 7.32 (m, 5H). ^{13}C NMR (126 MHz, $CDCl_3$) δ: 17.2, 23.1, 40.4, 55.8, 66.4, 70.4, 82.0, 126.7, 127.8, 128.8, 138.8, 175.1. MS (CI) *m*/*z* (rel. intensity): 232 (M + H, 100). Anal. calcd. for $C_{14}H_{17}NO_2$: C 72.70, H 7.41, N 6.06; found: C 72.45, H 7.54, N 5.77.

(2*R*)-2-Methylpent-4-ynoic acid ((2*R*)-11)

To a solution of the amide **23** (5.44 g, 23.5 mmol) in *p*-dioxane (60 mL) at room temperature was added sulfuric acid (3 mol L^{-1}, 60 mL). The resultant solution was heated at reflux for 7 h and then was cooled to 0 °C. The reaction mixture was basified to pH ~10 with an aqueous solution of sodium hydroxide (50 wt. %), then diluted with water (50 mL) and extracted with dichloromethane (3 × 50 mL). The aqueous layer was acidified to pH ~2 with sulfuric acid (3 mol L^{-1}) and then extracted with dichloromethane (3 × 50 mL). The combined organic layers were dried over anhydrous sodium sulfate and concentrated in vacuo. Purification by distillation at reduced pressure afforded the title compound (2*R*)-**11** (2.01 g, 76%) as a colourless oil. R_f = 0.48 (hexanes – ethyl acetate, 1:2), bp 103–106 °C, 5 mmHg (1 mmHg = 133.322 Pa) (lit. value (9) bp 106.5–109.5 °C, 14–15 mmHg (1 mmHg = 133.322 4 Pa)) for the racemic carboxylic acid (±)-**11**)). $[\alpha]_D^{20}$ = +6.5 (*c* 1.50, $CHCl_3$). All other spectroscopic data were identical to those reported for the racemic carboxylic acid (±)-**11**.[10]

(2*S*)-2-Methylpent-4-ynoic acid ((2*S*)-11)

The title compound (2*S*)-**11** (1.91 g, 86%) as a colourless oil was also prepared from the corresponding amide **24** (4.56 g, 19.7 mmol). $[\alpha]_D^{20}$ = –6.1 (*c* 1.52, $CHCl_3$). All other spectroscopic data were identical to those reported for the racemic carboxylic acid (±)-**11**.[10]

(2*R*)-2-Methylpent-4-yn-1-ol ((2*R*)-12)

To a suspension of lithium aluminum hydride (0.79 g, 20.8 mmol) in tetrahydrofuran (35 mL) at 0 °C was added a solution of the carboxylic acid (2*R*)-**11** (1.17 g, 10.4 mmol) in tetrahydrofuran (10 mL) and the resultant suspension was stirred at room temperature for 16 h. Water (0.8 mL), an aqueous solution of sodium hydroxide (2 mol L^{-1}, 0.8 mL), and water (2.4 mL) were then added in succession and the resultant mixture was filtered. The filter cake was rinsed with ether (100 mL) and the combined organic filtrates were concentrated in vacuo. Purification by distillation at reduced pressure afforded the title compound (2*R*)-**12** (0.91 g, 89%) as a colourless oil. R_f = 0.55 (hexanes – ethyl acetate, 1:2), bp 61–66 °C, ~20 mmHg (1 mmHg = 133.322 4 Pa) (lit. value (9) bp 64–64.5 °C, 10 mmHg (1 mmHg = 133.322 4 Pa) (for the racemic alcohol (±)-**12**)). $[\alpha]_D^{20}$ = +10.9 (*c* 1.10, $CHCl_3$). IR (ef, cm^{-1}): 3409, 2961, 2922, 1641, 2117, 1461, 1430, 1037, 651. ^1H NMR (400 MHz, $CDCl_3$) δ: 1.01 (d, *J* = 6.9 Hz, 3H), 1.56 (broad s, 1H), 1.90 (m, 1H), 1.98 (t, *J* = 2.7 Hz, 1H), 2.21 (ddd, *J* = 16.8, 6.4, 2.7 Hz, 1H), 2.29 (ddd, *J* = 16.8, 6.2, 2.7 Hz, 1H), 3.59 (d, *J* = 6.1 Hz, 2H). ^{13}C NMR (126 MHz, $CDCl_3$) δ: 16.0, 22.2, 34.8, 66.8, 69.6, 82.6. MS (CI) *m*/*z* (rel. intensity): 99 (M + H, 100).

(2*R*)-Benzyl-(2-methylpent-4-ynyl) ether ((2*R*)-25)

To a suspension of sodium hydride (60 wt. % in mineral oil, 81.3 mg, 2.03 mmol, prewashed with hexanes) in *N*,*N*-dimethylformamide (4.0 mL) at 0 °C were added a solution of the alcohol (2*R*)-**12** (181 mg, 1.85 mmol) in tetrahydrofuran (1 mL) and benzyl bromide (230 µL, 1.93 mmol). The resultant mixture was stirred at room temperature for 6 h. The reaction mixture was then diluted with ether (10 mL) and washed with water (3 × 10 mL) and brine (10 mL). The organic layer was dried over anhydrous magnesium sulfate and concentrated in vacuo. Purification by flash chromatography using hexanes–ether (50:1) as the eluant afforded the title compound (2*R*)-**25** (313 mg, 90%) as a colourless oil. R_f = 0.77 (hexanes–ether, 4:1). $[\alpha]_D^{20}$ = +16.1 (*c* 1.40, $CHCl_3$) (lit. value (18*a*) $[\alpha]_D^{20}$ = +16 (*c* 1.20,

© 2004 NRC Canada

$CHCl_3$) and lit. value (18*b*) $[\alpha]_D^{20}$ = +16.3 (*c* 0.95, $CHCl_3$)). IR (ef, cm^{-1}): 3289, 3031, 2857, 2117, 1609, 1496, 1454, 1112, 749. ^1H NMR (400 MHz, $CDCl_3$) δ: 1.03 (d, *J* = 6.8 Hz, 3H), 1.95 (t, *J* = 2.6 Hz, 1H), 2.02 (m, 1H), 2.21 (ddd, *J* = 16.7, 6.9, 2.6 Hz, 1H), 2.35 (ddd, *J* = 16.7, 5.5, 2.7 Hz, 1H), 3.39 (d, *J* = 6.5 Hz, 2H), 4.52 (s, 2H), 7.33 (m, 5H). ^{13}C NMR (126 MHz, $CDCl_3$) δ: 16.3, 22.5, 32.8, 69.3, 73.0, 74.1, 82.7, 127.48, 127.51, 128.3, 138.5. MS (CI) *m*/*z* (rel. intensity): 189 (M + H, 78), 171 (17), 111 (M – Ph, 100).

(2*S*)-2-Methylpent-4-yn-1-ol ((2*S*)-12)

The title compound (2*S*)-**12** (1.17 g, 85%) as a colourless oil was also prepared from the corresponding carboxylic acid (2*S*)-**11** (1.57 g, 14.0 mmol). $[\alpha]_D^{20}$ = –11.1 (*c* 1.83, $CHCl_3$). All other spectroscopic data were identical to those reported for the enantiomeric alcohol (2*R*)-**12**.

(2*S*)-Benzyl-(2-methylpent-4-ynyl) ether ((2*S*)-25)

The title compound (2*S*)-**25** (248 mg, 90%) as a colourless oil was also prepared from the corresponding alcohol (2*S*)-**12** (144 mg, 1.47 mmol). $[\alpha]_D^{20}$ = –15.9 (*c* 1.05, $CHCl_3$). All other spectroscopic data were identical to those reported for the enantiomeric ether (2*R*)-**25**.

(4*R*)-4,5-Dihydro-2,4-dimethylfuran ((4*R*)-14)

The alcohol (2*S*)-**12** (0.91 g, 9.28 mmol) and sodium amide (50 mg, 1.28 mmol) were heated, without solvent, at reflux for 2 h. Direct distillation of the reaction mixture at atmospheric pressure afforded the exocyclic dihydrofuran (4*R*)-**13** and a small amount of the endocyclic dihydrofuran (4*R*)-**14** as a colourless oil. ^1H NMR (500 MHz, C_6D_6, ~90% pure) δ: 0.58 (d, *J* = 6.2 Hz, 3H), 1.80 (m, 2H), 2.27 (m, 1H), 3.27 (dd, *J* = 8.1, 6.5 Hz, 1H), 3.77 (dd, *J* = 8.1, 6.0 Hz, 1H), 3.92 (m, 1H), 5.46 (m, 1H). This material was heated at reflux for 2 h and then distilled at atmospheric pressure to afford the title compound (4*R*)-**14** (0.40 g, 44%) as a colourless oil, bp 97–103 °C, ~760 mmHg (1 mmHg = 133.322 4 Pa) (lit. value (3) bp ~100 °C, ~760 mmHg (1 mmHg = 133.322 4 Pa) for the racemic dihydrofuran (±)-**14**)). $[\alpha]_D^{24}$ = +11.8 (*c* 0.82, $CHCl_3$). IR (ef, cm^{-1}): 2961, 2875, 1674, 1453, 1383, 1243, 1043, 1008, 886. ^1H NMR (400 MHz, C_6D_6) δ: 0.86 (d, *J* = 6.6 Hz, 3H), 1.68 (apparent t, *J* = 1.5 Hz, 3H), 2.76 (m, 1H), 3.71 (dd, *J* = 8.7, 6.5 Hz, 1H), 4.21 (dd, *J* = 9.5, 8.6 Hz, 1H), 4.43 (m, 1H). ^{13}C NMR (101 MHz, C_6D_6) δ: 13.6, 20.9, 37.9, 77.2, 101.4, 155.0. MS (CI) *m*/*z* (rel. intensity): 99 (M + H, 100).

(4*S*)-4,5-Dihydro-2,4-dimethylfuran ((4*S*)-14)

The title compound (4*S*)-**14** (0.42 g, 36%) as a colourless oil was also prepared from the corresponding alcohol (2*S*)-**12** (1.17 g, 11.9 mmol). $[\alpha]_D^{20}$ = –12 (*c* 0.44, $CHCl_3$). All other spectroscopic data were identical to those reported for the enantiomeric dihydrofuran (4*R*)-**14**.

(–)-Xyloketal D (4), 2,6-*epi*-xyloketal D (15), and the diastereomeric spiroacetals (16) and (17)

Method A

To a solution of the dihydrofuran (4*R*)-**14** (295 mg, 3.01 mmol) in benzene (10 mL) at room temperature were added the Mannich base **7** (251 mg, 1.00 mmol) and methyl iodide (65.0 μL, 1.05 mmol). The resultant solution was then heated at reflux until the Mannich base **7** had completely reacted (8 days, TLC analysis). The reaction mixture was then cooled to room temperature, filtered, and concentrated in vacuo. Purification by flash chromatography using dichloromethane as the eluant afforded a mixture (8:1:2:2) of (–)-xyloketal D (**4**), 2,6-*epi*-xyloketal D (**15**), and the diastereomeric spiroacetals **16** and **17** (105 mg, 40%) as a yellow solid. Repeated flash chromatography using hexanes–ether (4:1) as the eluant on TLC grade silica gel (5–25 μm) afforded a mixture (20:1) of (–)-xyloketal D (**4**) and 2,6-*epi*-xyloketal D (**15**) as a pale cream solid and a separate mixture (4:5) of the two diastereomeric spiroacetals **16** and **17** as a pale cream solid. An analytically pure sample of synthetic (–)-xyloketal D (**4**), as pale pink prisms, was prepared by recrystallization from petroleum ether. An analytically pure sample of a mixture (4:5) of the diastereomeric spiroacetals **16** and **17**, as white needles, was also prepared by recrystallization from petroleum ether.

Method B

To a solution of the dihydrofuran (4*R*)-**14** (121 mg, 1.23 mmol) in benzene (5 mL) at room temperature were added the Mannich base **7** (103 mg, 0.41 mmol) and dimethyl sulfate (41 μL, 0.43 mmol). The resultant solution was heated at reflux until the Mannich base **7** had completely reacted (3 days, TLC analysis). The reaction mixture was then cooled to room temperature and decanted. The remaining solid residue was extracted with dichloromethane (3 × 5 mL) and the combined organic extracts were concentrated in vacuo. Purification by flash chromatography using dichloromethane–ether (19:1) as the eluant afforded a mixture (16:1:4:4) of (–)-xyloketal D (**4**), 2,6-*epi*-xyloketal D (**15**), and the diastereomeric spiroacetals **16** and **17** (40 mg, 37%) as a yellow solid. (–)-Xyloketal D **4**: R_f = 0.24 (hexanes–ether, 4:1), mp 71–73 °C as pale pink prisms from petroleum ether (lit. value (1) mp 111–113 °C) and mp 68–70 °C as white crystals on recrystallization from ether–pentane (lit. value (13) mp 110 to 111 °C, ether–pentane). $[\alpha]_D^{20}$ = –110.1 (*c* 0.102, $CHCl_3$) (lit. value (1) $[\alpha]_D^{25}$ = –119.5 (*c* 0.113, $CHCl_3$)). IR (ef, cm^{-1}): 3399, 2967, 2927, 2884, 1620, 1491, 1421, 1382, 1370, 1332, 1272, 1117, 1070, 1006. ^1H NMR (500 MHz, $CDCl_3$) δ: 1.07 (d, *J* = 6.5 Hz, 3H), 1.53 (s, 3H), 1.98 (ddd, *J* = 11.3, 6.5, 1.1 Hz, 1H), 2.08 (m, 1H), 2.55 (s, 3H), 2.72 (dd, *J* = 17.9, 6.5 Hz, 1H), 2.97 (d, *J* = 18.0, 1H), 3.57 (apparent t, *J* = 8.4 Hz, 1H), 4.20 (apparent t, *J* = 8.3 Hz, 1H), 6.36 (d, *J* = 8.9 Hz, 1H), 7.52 (d, *J* = 8.9 Hz, 1H), 13.12 (s, 1H). ^{13}C NMR (101 MHz, $CDCl_3$) δ: 15.8, 18.0, 22.7, 26.1, 35.1, 47.0, 74.3, 106.2, 108.3, 108.8, 113.1, 130.0, 159.5, 162.9, 202.6. MS (CI) *m*/*z* (rel. intensity): 263 (M + H, 100). Anal. calcd. for $C_{15}H_{18}O_4$: C 68.68, H 6.92; found: C 68.52, H 6.98. Diastereomeric spiroacetals **16** and **17** (4:5 mixture): R_f = 0.32 (hexanes–ether, 4:1), mp 60 to 61 °C, petroleum ether. $[\alpha]_D^{20}$ = +26.9 (*c* 0.71, $CHCl_3$). IR (ef, cm^{-1}): 3423, 2958, 2878, 1626, 1488, 1419, 1369, 1331, 1270, 1247, 1136, 1060, 1018, 853. ^1H NMR (400 MHz, $CDCl_3$) δ: 1.10 (d, *J* = 6.6 Hz, 3H), 1.18 (d, *J* = 6.6 Hz, 3H), 1.55 (dd, *J* = 12.8, 9.5 Hz, 1H), 2.00 (m, 5H), 2.27 (dd, *J* = 13.4, 9.4, 1H), 2.36 (dd, *J* = 12.9, 7.3, 1H), 2.46 (m, 1H), 2.54 (s, 3H), 2.55 (s, 3H), 2.78 (m, 5H),

© 2004 NRC Canada

3.54 (t, *J* = 7.7 Hz, 1H), 3.64 (t, *J* = 8.4 Hz, 1H), 4.09 (t, *J* = 7.9 Hz, 1H), 4.21 (t, *J* = 7.9 Hz, 1H), 6.34 (d, *J* = 8.9 Hz, 1H), 6.37 (d, *J* = 9.0 Hz, 1H), 7.50 (d, *J* = 8.9 Hz, 1H), 7.51 (d, *J* = 8.9 Hz, 1H), 13.01 (s, 1H), 13.02 (s, 1H). ^{13}C NMR (126 MHz, $CDCl_3$) δ: 16.3, 16.5, 17.6, 18.0, 26.2, 29.3, 29.6, 31.9, 33.0, 45.2, 45.3, 75.0, 75.4, 108.1, 108.9, 109.0, 110.0, 110.1, 113.16, 113.24, 129.58, 129.62, 159.6, 162.2, 202.7, 202.8. MS (CI) *m/z* (rel. intensity): 263 (M + H, 100), 111 (12). Anal. calcd. for $C_{15}H_{18}O_4$: C 68.68, H 6.92; found: C 68.58, H 6.99.

ent-Xyloketal D (*ent*-4), *ent*-2,6-*epi*-xyloketal D (*ent*-15), and the diastereomeric spiroacetals (*ent*-16) and (*ent*-17)

Method A

A solution of the dihydrofuran (4*S*)-**14** (237 mg, 2.42 mmol), the Mannich base **7** (202 mg, 0.804 mmol), and methyl iodide (52 µL, 0.84 mmol) in benzene (8 mL) was heated at reflux for 6 days. Isolation and purification of the reaction products, as described previously, afforded a mixture (13:1:3:3) of *ent*-xyloketal D (*ent*-**4**), *ent*-2,6-*epi*-xyloketal D (*ent*-**15**), and the diastereomeric spiroacetals *ent*-**16** and *ent*-**17** (96 mg, 46%) as a yellow solid. Additional purification and recrystallization of these reaction products, as described previously, afforded an analytically pure sample of *ent*-xyloketal D (*ent*-**4**) as pale pink prisms and an analytically pure mixture (4:5) of the diastereomeric spiroacetals *ent*-**16** and ent-**17** as white needles.

Method B

The procedure described in the previous section was also used to prepare a mixture (20:1:3:3) of *ent*-xyloketal D (*ent*-**4**), *ent*-2,6-*epi*-xyloketal D (*ent*-**15**), and the diastereomeric spiroacetals *ent*-**16** and *ent*-**17** (64 mg, 36%) as a yellow solid. *ent*-Xyloketal D (*ent*-**4**): mp 70 to 71 °C as pale pink crystals from petroleum ether and mp 68–71 °C as white crystals from ether–pentane. $[\alpha]_D^{20}$ = +113.1 (*c* 0.122, $CHCl_3$). All other spectroscopic data were identical to those reported previously for (–)-xyoketal D (**4**). Diastereomeric spiroacetals *ent*-**16** and *ent*-**17** (4:5): mp 59–61 °C, petroleum ether. $[\alpha]_D^{20}$ = –26.7 (*c* 1.05, $CHCl_3$). All other spectroscopic data were consistent with that reported for the diastereomeric spiroacetals **16** and **17**.

Acknowledgments

We are grateful to the Natural Sciences and Engineering Research Council of Canada (NSERC) and Simon Fraser University (SFU) for financial support. We also wish to acknowledge the Canadian Foundation for Innovation (CFI) and AstraZeneca Canada Inc. for support of our research program. J.D.P. thanks SFU for an entrance scholarship and NSERC for a PGSA award. We thank Mr. Jason A. Bexrud for preliminary investigations. We are also grateful to Professor Yongcheng Lin for kindly providing a copy of the ^{1}H NMR spectrum of xyloketal D (**4**) for comparison purposes.

References

1. Y. Lin, X. Wu, S. Feng, G. Jiang, J. Luo, S. Zhou, L.L.P. Vrijmoed, E.B.G. Jones, K. Krohn, K. Steingröver, and F. Zsila. J. Org. Chem. **66**, 6252 (2001).
2. R.A. Hill and M.C. Parker. Nat. Prod. Rep. **18**, *iii* (2001).
3. J.D. Pettigrew, J.A. Bexrud, R.P. Freeman, and P.D. Wilson. Heterocycles, **62**, 445 (2004).
4. For a recent review on the chemistry of *ortho*-quinone methides, see: R.W. Van De Water and T.R.R. Pettus. Tetrahedron, **58**, 5367 (2002).
5. Alkylation, oxidation, and photochemical reactions have been used to generate *ortho*-quinone methides from the Mannich bases of phenols. See, for example: (*a*) E. Modica, R. Zanaletti, M. Freccero, and M. Mella. J. Org. Chem. **66**, 41 (2001); (*b*) P.D. Gardner, H.S. Rafsanjani, and L. Rand. J. Am. Chem. Soc. **81**, 3364 (1959); (*c*) K. Nakantani, N. Higashida, and I. Saito. Tetrahedron Lett. **38**, 5005 (1997).
6. For related examples of this regio- and stereoselective inverse electron demand Diels–Alder reaction, see: (*a*) M. Anniyappan, D. Muralidharan, and P.T. Perumal. Tetrahedron, **58**, 10 301 (2002); (*b*) J.S. Yadav, B.V.S. Reddy, M. Aurna, C. Venugopal, T. Ramalingam, S.K. Kumar, and A.C. Kunwar. J. Chem. Soc. Perkin Trans. 1, 165 (2002); (*c*) L. Diao, C. Yang, and P. Wan. J. Am. Chem. Soc. **117**, 5369 (1995); (*d*) J.D. Chambers, J. Crawford, H.W.R. Williams, C. Dufresne, J. Scheigetz, M.A. Bernstein, and C.K. Lau. Can. J. Chem. **70**, 1717 (1992).
7. We also prepared a corresponding Mannich base from *N*,*N*-dibenzylamine, 2,4-dihydroxyacetophenone (**6**), and formaldehyde. However, this substrate proved to be less suitable for subsequent cycloaddition reactions. The synthesis of a corresponding Mannich base derived from diethylamine, 2,4-dihydroxyacetophenone (**6**), and paraformaldehyde has been previously reported. See: Y. Omura, Y. Taruno, Y. Irisa, M. Morimoto, H. Saimoto, and Y. Shigesasa. Tetrahedron Lett. **42**, 7273 (2001).
8. (*a*) J. Colonge and R. Gelin. Bull. Soc. Chim. Fr. 799 (1954); (*b*) G. Eglinton, E.R.H. Jones, and M.C. Whiting. J. Chem. Soc. 2873 (1952).
9. V.E. Buchta and H. Schlesinger. Liebigs Ann. Chem. **598**, 1 (1955).
10. B.B. Snider, A.J. Allentoff, and M.B. Walner. Tetrahedron, **46**, 8031 (1990).
11. We also prepared a corresponding Mannich base from morpholine, phloroglucinol (**18**), and formaldehyde. However, this substrate was less suitable for subsequent cycloaddition reactions. For preparative details, see: F.F. Blicke and F.J. McCarty. J. Org. Chem. **24**, 1061 (1959).
12. A number of related Mannich bases of phloroglucinol **18** have also been prepared, see: A.P. Terent'ev, E.G. Rukhadze, and S.F. Zapuskalova. Probl. Org. Sint. 122 (1965); Chem. Abstr. **64**, 8065 (1966).
13. (*a*) K. Krohn and M. Riaz. Tetrahedron Lett. **45**, 293 (2004). Of note, there is an error in the title of this paper as the natural product, xyloketal D (**4**), is levorotatory; (*b*) K. Krohn, M. Riaz, and U. Flörke. Eur. J. Org. Chem. 1261 (2004).
14. (*a*) D.J. Baek, S.B. Daniels, P.E. Reed, and J.A. Katzenellenbogen. J. Org. Chem. **54**, 3963 (1989); (*b*) G. Helmchen, G. Nill, D. Flockerzi, and M.S.K. Youssef. Angew. Chem. Int. Ed. Engl. **18**, 63 (1979).
15. The racemic carboxylic acid (±)-**11** was also condensed with (*R*)-phenylglycinol (**22**) to afford the corresponding diastereomeric oxazolines. See: M.J. Kurth, O.H.W. Decker, H. Hope, and M.D. Yanuck. J. Am. Chem. Soc. **107**, 443 (1985). Unfortunately, these derivatives were chromatographically inseparable.
16. A.G. Myers, B.H. Yang, H. Chen, L. McKinstry, D.J. Kopecky, and J.L. Gleason. J. Am. Chem. Soc. **119**, 6496 (1997).

© 2004 NRC Canada

17. The chiral nonracemic alcohol (2*R*)-**12** is a known compound and has been prepared in six steps from commercially available (2*R*)-methyl-3-hydroxy-2-methylpropanoate. However, the optical rotation of this compound was not reported. See: (*a*) M. Christmann, U. Bhatt, M. Quitschalle, E. Claus, and M. Kalesse. Angew. Chem. Int. Ed. **39**, 4364 (2000); (*b*) R. Baker and M.A. Brimble. Tetrahedron Lett. **27**, 3311 (1986).
18. The chiral nonracemic benzyl ether (2*R*)-**25** has been prepared from commercially available (2*R*)-methyl-3-hydroxy-2-methylpropanoate. See: (*a*) A. Takle and P. Kocienski. Tetrahedron, **46**, 4503 (1990); (*b*) P.J. Kocienski, S.D.A. Street, C. Yeates, and S.F. Cambell. J. Chem. Soc., Perkin Trans. 1, 2189 (1987).
19. (*a*) G.J. Kang and T.H. Chan. J. Org. Chem. **50**, 452 (1985); (*b*) J.A. Dale, D.L. Dull, and H.S. Mosher. J. Org. Chem. **34**, 2543 (1969).

© 2004 NRC Canada

Lithiation of 1-arylimidazol-2(1*H*)-ones and 1-aryl-4,5-dihydroimidazol-2(1*H*)-ones

Carme Cantos Llopart, Conchita Ferrer, and John A. Joule

Abstract: 1-Arylimidazol-2(1*H*)-ones are shown to be readily lithiated, using 2 mol equiv. of *n*-butyllithium, on the benzene ring, ortho to the heterocycle. 1-Aryl-4,5-dihydroimidazol-2(1*H*)-ones also undergo metalation on the aromatic substitutuent ortho to the heterocycle, but less efficiently. 1-Aryl-3-methylimidazol-2(1*H*)-ones are lithiated on the heterocyclic ring and then on the benzene ring ortho to the heterocycle. No ortho-directing effect was found for 1-aryl-4,5-dihydro-3-methylimidazol-2(1*H*)-ones.

Key words: ortho-lithation, ureas for directed ortho metalation, 1-arylimidazol-2-ones, 1-arylimidazolidin-2-ones.

Résumé : On a démontré que les 1-arylimidazol-2(1*H*)-ones, sous l'action de 2 équivalents molaires de *n*-butyllithium, subissent facilement une réaction de lithiation sur le noyau benzénique, en position ortho par rapport à l'hétérocycle. Les 1-aryl-4,5-dihydroimidazol-2(1*H*)-ones subissent aussi une métallation sur le substituant aromatique ortho par rapport à l'hétérocycle, mais la réaction est moins efficace. Les 1-aryl-3-méthylimidazol-2(1*H*)-ones subissent une réaction de lithiation sur le noyau hétérocyclique avant de procéder à une lithiation sur le noyau benzénique en ortho de l'hétérocycle. On n'a pas observé d'effet d'orientation vers la position ortho avec les 1-aryl-4,5-dihydro-3-méthylimidazol-2(1*H*)-ones.

Mots clés : lithiation en ortho, urées pour des métallations orientées en ortho, 1-arylimidazol-2-ones, 1-arylimidazolidin-2-ones.

[Traduit par la Rédaction]

Introduction

We have described (1) our investigations into the use of the heterocyclic substituent in 1-arylpyrimidin-2(1*H*)-ones and in 1-aryl-3,4,5,6-tetrahydropyrimidin-2(1*H*)-ones to assist lithiation at an ortho position (2, 3). In the former case, the use of the pyrimidinone as a directing group was foiled by its strong tendency to undergo addition of the lithiating reagent. In the case of the six-membered cyclic ureas (1-aryl-3,4,5,6-tetrahydropyrimidin-2(1*H*)-ones), we showed that the substituent has a weak ortho directing effect (1). Our study was designed to produce intermediates for a route (4), alternative to those (5–7) previously described, to the biologically active variolin group (8) of alkaloids. The route will allow flexibility and easy introduction of diverse analogues for subsequent biological assessment. We have now examined the analogous five-membered compounds as a further element of eventual diversity in this context.

In the work described here, we have demonstrated the formation and exploitation of intermediates that are summarized as **1** and **2**, formed from **3** and **4**, implying significant ortho-directing effects in these cyclic ureas, which we believe have considerable potential in synthesis. We have also examined the lithiation of *N*-methyl analogues, **5** and **6**, and found no ortho assistance in the case of the latter; the former underwent lithiation in the heterocyclic ring and then ortho to the heterocycle. We are aware of no other attempts to use imidazolones or 4,5-dihydroimidazolones as ortho-directing groups in this way.

Aside from our own work (1), there are only two reports of the use of ureas as ortho-directing substituents, and in both of these, the urea was acyclic. Quéguiner and co-workers (9) lithiated *N*,*N*-dimethyl-*N*′-(quinolin-3-yl)urea with lithium di-isopropylamide leading to the 2-lithio derivative as the thermodynamic product. Smith et al. (10) used 2.5 equiv. of *n*-butyllithium or *tert*-butyllithium at 0 °C to deprotonate *N*-aryl-*N*′,*N*′-dimethylureas ortho to the urea unit; in some cases, the use of *tert*-butyllithium led to lithiation at *N*-methyl as well as, or instead of, ring lithiation.

Carpenter and Chadwick (11) examined the lithiation of five-membered aromatic heterocycles carrying a 1,3-dimethylimidazolidin-2-yl substituent at an α-position and found a weak ortho-directing effect. Earlier, it had been shown that in 1,3-dimethyl-2-phenylimidazolidine, efficient ortho lithiation of the phenyl ring is possible with *n*-butyllithium at room temperature (12). Simig and co-workers (13) demonstrated ortho lithiation in 2-aryl-2-methyl-1,3-dioxolanes; when a meta-chlorine was present on the benzene ring, lithiation took place at the carbon between the chlorine and the ketal-directing groups.

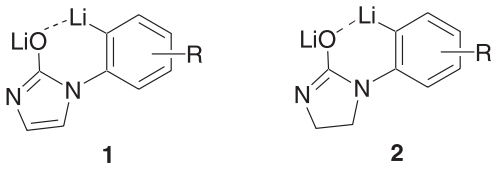
Following the efficient ortho lithiation of 2-phenylimidazoline (14), Chadwick and Ennis (15) examined 2-(2-heteroaryl)imidazolines and confirmed a strong ortho-directing effect. With an appropriate choice of lithiating agent (*sec*-BuLi–TMEDA at –78 °C) ortho lithiation of 2-(2-

Received 6 May 2004. Published on the NRC Research Press Web site at http://canjchem.nrc.ca on 23 December 2004.

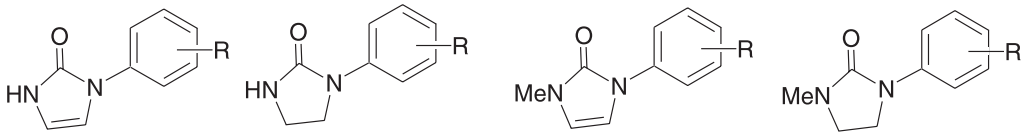
C.C. Llopart, C. Ferrer, and J.A. Joule.[1] Chemistry Department, The University of Manchester, Manchester M13 9PL, UK.

[1]Corresponding author (e-mail: john.joule@manchester.ac.uk).

 doi: 10.1139/V04-137 © 2004 NRC Canada



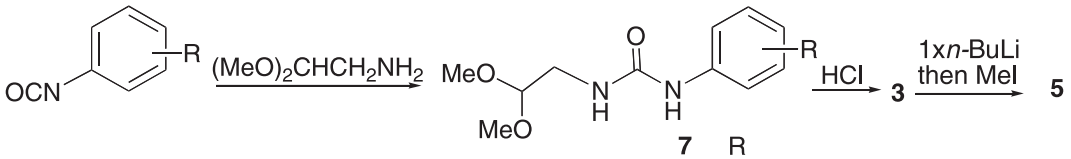
1 **2**



3 **4** **5** **6**

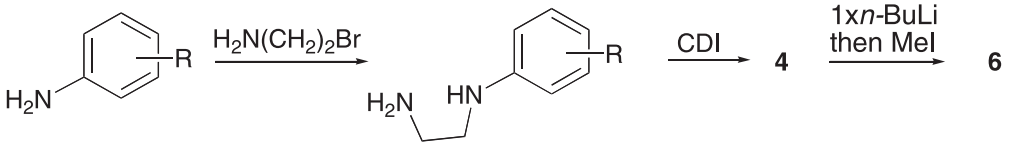
	R
a	H
b	2-OMe
c	3-OMe
d	4-OMe

Scheme 1.



	R
7	
a	H
b	2-OMe
c	3-OMe
d	4-OMe

Scheme 2.



	R
8	
a	H
b	2-OMe
c	3-OMe
d	4-OMe

methylphenyl)-4,4-dimethyloxazolidine can be made to compete with lithiation of the methyl group (16). The ortho-directing strength of a 1*H*-tetrazol-5-yl-substitutent was shown to be more than that of a methoxyl but less than that of diethylaminocarbonyl and this in turn less than that of a 2-(triphenylmethyl)-2*H*-tetrazol-5-yl substituent (17).

Syntheses of 1-arylimidazol-2(1*H*)-ones (3a–3d and 5a–5d) and 1-aryl-4,5-dihydro-imidazol-2(1*H*)-ones (4a–4d and 6a–6d)

The commercially available phenyl and 2-, 3-, and 4-methoxyphenyl isocyanates were each reacted with amino-acetaldehyde dimethyl acetal (18) and the resulting ureas **7** cyclised (19) by treatment with acid producing the imidazolones **3a**–**3d**. Reaction of each of these with 1 mol equiv. of *n*-butyllithium and then iodomethane cleanly gave their *N*-methyl derivatives, **5a**–**5d** (Scheme 1).

1-Aryl-4,5-dihydroimidazol-2(1*H*)-ones **4a**–**4d** were prepared following the method reported (20) for the synthesis of **4b**, namely cyclising *N*-aryl-1,2-diamines **8**, obtained by reaction of the aromatic amines with 2-bromoethanamine, using carbonyl diimidazole (CDI). The imidazolidinones **4a**–**4d** reacted smoothly with 1 mol equiv. of *n*-butyllithium and then iodomethane giving their *N*-methyl derivatives, **6a**–**6d** (Scheme 2).

© 2004 NRC Canada

Lithiation of 1-arylimidazol-2(1*H*)-ones 3a–3d and 5a–5d

Treatment of the *N*-hydrogen imidazolones **3a**–**3d** with 2.5 mol equiv. of *n*-butyllithium and then excess iodomethane proceeded smoothly and gave rise to *N*- and benzene-ring-dimethylated products in good yields (Table 1). Noteworthy are: (*i*) the absence of products of nucleophilic addition to the unsaturated five-membered ring (cf. 1-arylpyrimidin-2(1*H*)-ones in ref. 1); (*ii*) the clean nature of the transformations, even in the substrate **3a** with no electron-withdrawing methoxyl on the benzene ring (→ **5e**); (*iii*) the regiochemistry of lithiation of the meta-methoxy substrate **3c** — between the methoxyl group and the imidazolone (→ **5h**) — the combined effect of the two groups producing this result; (*iv*) the formation from the ortho-methoxy substrate **3b** of a mixture of dimethylated products (**5f** and **5g**) from lithiation either ortho to the heterocycle (18%) or ortho to the methoxyl (25%); and (*v*) the regiochemistry of lithiation of the para-methoxy substrate **3d** in which there was no trace of lithiation ortho to the methoxyl group — the influence of the imidazolone being the greater (→ **5i**). Where there was ambiguity regarding the position of the introduced aromatic methyl, nOe experiments were employed. Thus, in **5g** the proximity of the methoxyl methyl and the ring methyl was established, and for **5i** there was no nOe on the methyl (δ 2.23) on irradiation of the methoxyl methyl (δ 3.83) and conversely, irradation at 2.23 had no effect on the methoxyl but did show an nOe to the imidazolone signal at δ 6.27. We interpret the trapping results as involving the double methylation of dilithio species **1**, the formation of which are favoured by the aromatic character of the five-membered ring in these.

Experiments with **3a**–**3d** again using 2.5 mol equiv. of *n*-butyllithium, but with phenyl isocyanate as the trapping electrophile, produced *N*- and *C*-disubstituted, biuret-anilide products **9b**–**9e** and **9h**, with exactly comparable regioselectivity, but only in moderate yields, and in some cases accompanied by minor amounts of the mono-*N*-substituted biuret (**9a**, **9f**, **9g**) (Table 1).

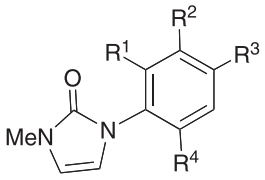
To determine whether an imidazolone that is not capable of *N*-deprotonation could act as an ortho-directing group, in partial analogy to the use of an *N*,*N*-dialkylamide as an ortho-directing group, we treated the *N*-methyl imidazolones **5a**–**5d** with *n*-BuLi and quenched with iodomethane. Here, there was a complete reversal of selectivity and a total preference for lithiation of the five-membered heterocycle when using approximately 1 equiv. of the strong base, though not very efficiently. Both 4- and 5-methylated products were formed — **5j/5k**, **5l/5m**, **5n/5o** — with the 4-methylated isomers predominating (Table 1). The regiochemistry of the methylation was established by nOe experiments — for the 3,4-dimethylimidazolones, e.g., **5k**, irradation of the *N*-methyl signal (δ 3.26) gave an effect with the *C*-methyl (δ 2.11), but not the remaining imidazolone ring proton (δ 6.33).

Even more intriguingly, when 2.5 mol equiv. of *n*-butyllithium were employed for the lithiation of **5a**–**5d**, dimethylated products were obtained in which one methyl had been introduced onto the benzene ring ortho to the imidazolone, presumably with its assistance, and the other at

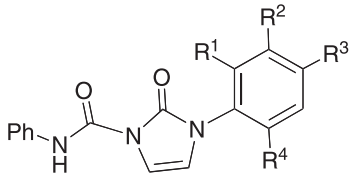
Table 1. Products and yields from lithations.

Substrate	*n*-BuLi (mol equiv.)	Electrophile	Product (% yield)	Product (% yield)
3a	2.5	MeI	**5e** (88)	
3b	2.5	MeI	**5f** (18)	**5g** (25)
3c	2.5	MeI	**5h** (60)	
3d	2.5	MeI	**5i** (96)	
4a	2.5	MeI	**6e** (34)	
4b	2.5	MeI	**6f** (28)	**6g** (37)
4c	2.5	MeI	**6h** (22)	
4d	2.5	MeI	**6i** (9)	**6j** (12)
3a	2.5	PhNCO	**9a** (3)	**9b** (86)
3b	2.5	PhNCO	**9c** (15)	**9d** (18)
3c	2.5	PhNCO	**9e** (36)	**9f** (21)
3d	2.5	PhNCO	**9g** (6.5)	**9h** (30)
5a	1.2	MeI	**5j** (12)	**5k** (46)
5b	1.2	MeI	**5l** (12)[a]	**5m** (36)[a]
5d	1.1	MeI	**5n** (49)	**5o** (16)
5a	2.5	MeI	**5p** (95)	
5b	2.5	MeI	**5q** (88)	
5c	2.5	MeI	**5r** (24)	
5d	2.5	MeI	**5s** (97)	

[a]Estimate from the ^{1}H NMR spectrum of the mixture.

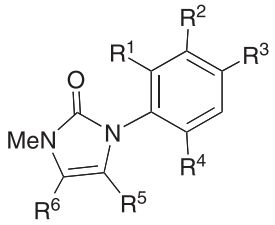


5	R^1	R^2	R^3	R^4
e	Me	H	H	H
f	Me	H	H	OMe
g	OMe	Me	H	H
h	Me	OMe	H	H
i	Me	H	OMe	H



9	R^1	R^2	R^3	R^4
a	H	H	H	H
b	C(O)NHPh	H	H	H
c	C(O)NHPh	H	H	OMe
d	OMe	C(O)NHPh	H	H
e	C(O)NHPh	OMe	H	H
f	H	OMe	H	H
g	H	H	OMe	H
h	C(O)NHPh	H	OMe	H

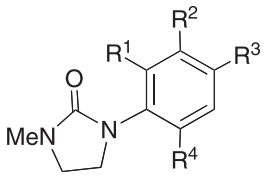
© 2004 NRC Canada



5	R^1	R^2	R^3	R^4	R^5	R^6
j	H	H	H	H	Me	H
k	H	H	H	H	H	Me
l	OMe	H	H	H	Me	H
m	OMe	H	H	H	H	Me
n	H	H	OMe	H	H	Me
o	Me	H	OMe	H	Me	H
p	Me	H	H	H	H	Me
q	OMe	H	H	Me	H	Me
r	Me	OMe	H	H	H	Me
s	Me	H	OMe	H	H	Me

C-4 of the imidazolone, with no C-5-methylation. Products **5p**, **5q**, and **5s** were formed very efficiently, but **5r** only in poor yield (Table 1). Again, nOe experiments involving irradiation of the *N*-methyl signals in the products **5p**–**5s** caused nOe enhancement of the *C*-methyl signal in each case, but had no effect on the imidazole C-5-proton signals.

The results described above in the lithiations of **5a**–**5d** were unexpected and a full understanding will require further experimentation. We offer the following explanation (Scheme 3) as a speculative rationalization for the observations. We suggest that initial lithiation of **5a**–**5d** takes place at C-4 of the imidazolone ring, giving **A** and that trapping of this species in the experiments using 1 mol equiv. of *n*-BuLi leads to the 3,4-dimethylated products **5k**, **5m**, and **5n**. We further speculate that **A** can undergo ring opening to generate an alkyne, rather as has been reported for lithiated isoxazoles (21) and oxazoles (22), generating **B**, which after conversion to the *C*-lithiated species **C** gives rise to the 3,5-dimethylated products **5j**, **5l**, and **5o** via alkyne *C* methylation then ring closure of **D**. In the experiments where 2.5 mol equiv. of the base were employed, benzene ring C lithiation of **B** using the second equivalent of base with ortho assistance, would give **E** and thence benzene-ring-methylated **F**, final closure of which would lead specifically



6	R^1	R^2	R^3	R^4
e	Me	H	H	H
f	Me	H	H	OMe
g	OMe	Me	H	H
h	Me	OMe	H	H
i	Me	H	H	OMe
j	H	Me	OMe	H

to the trimethylated 3,4-dimethylimidazolones **5p**–**5s** as shown.

Lithiation of 1-arylimidazolidin-2(1*H*)-ones (4a–4d) and attempted lithiation of 6a–6d

The use of 2.5 mol equiv. of *n*-butyllithium and then excess iodomethane gave rise to products **6e**–**6j** dimethylated on nitrogen and the benzene ring; when the *N*-hydrogen imidazolidinones **4a**–**4d** were examined (Table 1), however, these transformations were not as efficient as those involving the imidazolones **3a**–**3d**. Noteworthy are: (*i*) benzene ring lithiation ortho to the heterocycle (→ **6e**), even in the substrate **4a** with no electron-withdrawing methoxyl; (*ii*) the regiochemistry of lithiation of the meta-methoxy-substrate **4c** — between the methoxyl group and the imidazolidinone (→ **6h**); and (*iii*) the regiochemistry of lithiation of the ortho-**4b** and para-methoxy **4d** substrates — alternative lithiations ortho to either methoxyl or imidazolidinone groups being observed in both cases, giving **6f/6g** (ortho to the heterocycle 28% and ortho to the methoxyl 37%) and **6i/6j** (ortho to the heterocycle 9% and ortho to the methoxyl 12%), respectively.

The significantly more facile ortho lithiations observed with the *N*-arylimidazolones **3** as opposed to the *N*-arylimidazolidinones **4** seem unlikely to reside in their relative ease of *N*-deprotonation, even though in the former case, an aromatic alkoxide anion is generated. Rather, we suggest that subtle stereochemical factors, that influence the ease with which ortho assistance can be conveyed, are at play. We hope to be able to comment further on this aspect in future publications.

Attempted lithiation ortho to the *N*-methylimidazolidinone unit in substrates **6a**–**6d** failed.

Experimental

General

See ref. 1.

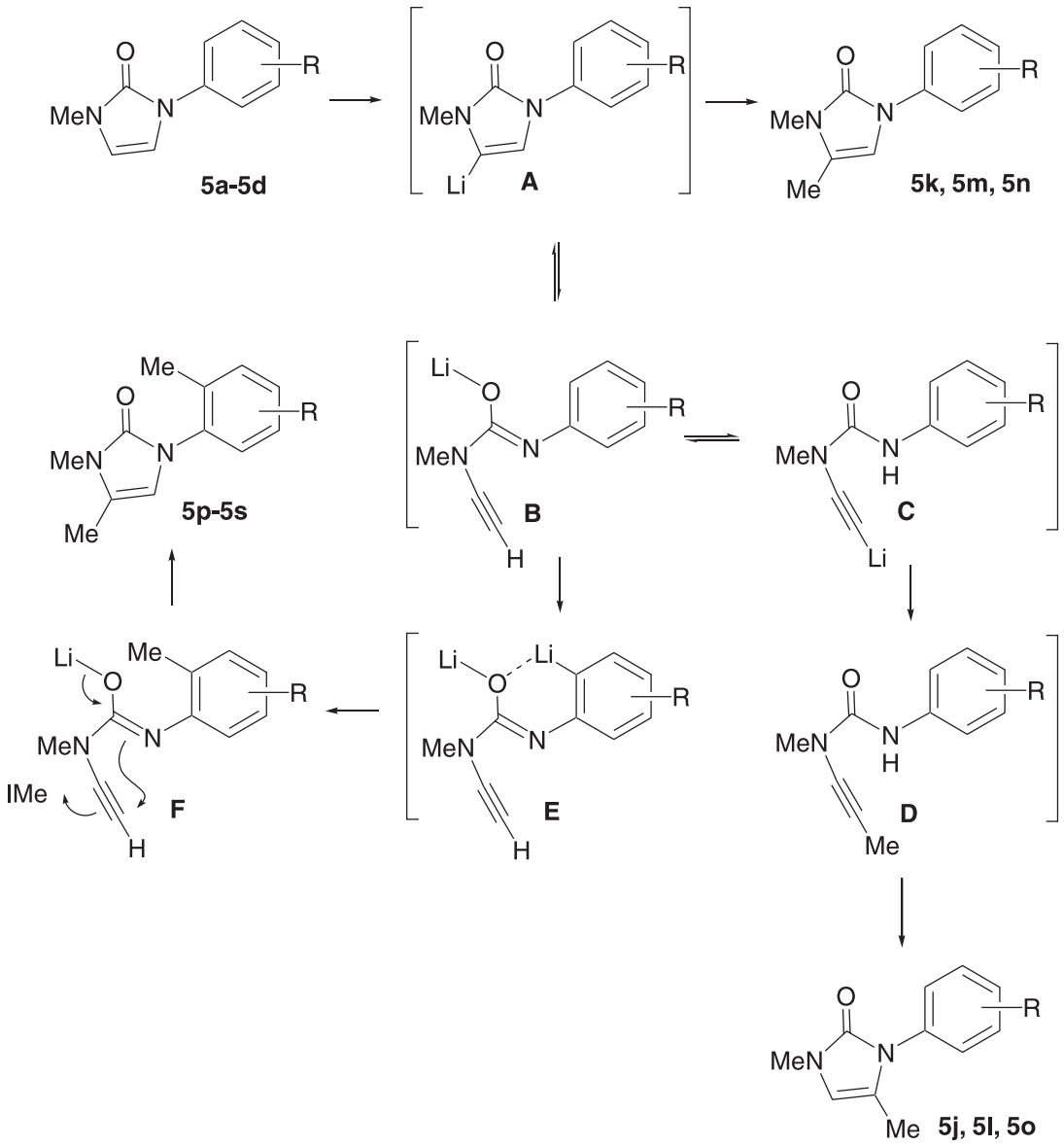
Typical procedure for synthesis of ureas (7)

N-*(2-Methoxyphenyl)*-N′-*(2,2-dimethoxyethyl)*urea *(7b)*

2-Methoxyphenyl isocyanate (4.77 g, 31.98 mmol) was added over a period of 5 min to aminoacetaldehyde dimethyl acetal (3.36 g, 31.98 mmol, 1 equiv.) while cooling in an ice bath. The reaction was allowed to warm up to rt for 1 h during which time a yellow crystalline mass was formed. The solid was washed with petroleum ether, dissolved in CH_2Cl_2, and the solution evaporated. Column SiO_2 chromatography (50% EtOAc in hexane) gave *N*-(2-methoxyphenyl)-*N′*-(2,2-dimethoxyethyl)urea **7b** as white crystals (6.98 g, 85%), mp 92–94 °C. ^{1}H NMR (300 MHz, $CDCl_3$) δ: 3.42 (2H, m, CH_2CH), 3.48 (6H, s, 2 × OCH_3), 3.88 (3H, s, OCH_3), 4.47 (1H, t, J = 5.2, CH_2CH), 5.05 (1H, bt, J = 5.5, NH), 6.86–7.06 (4H, m, Ar-H), 8.05 (1H, m, Ar-NH). ^{13}C NMR (75 MHz, $CDCl_3$) δ: 41.8, 54.4, 55.5, 103.4, 110.0, 119.5, 121.0, 122.3, 128.5, 142.1, 155.6. *m*/*z* (CI): 255 (MH^+, 100%), 223 (95), 75 (30). Anal. calcd. for $C_{12}H_{18}N_2O_4$ (M): 254.126 65; found (M^+): 254.126 9.

© 2004 NRC Canada

Scheme 3.



N-*(Phenyl)*-N′-*(2,2-dimethoxyethyl)urea (7a)*

N-(Phenyl)-*N′*-(2,2-dimethoxyethyl)urea (**7a**) was prepared as above from phenyl isocyanate (5 g, 41.9 mmol) and aminoacetaldehyde dimethyl acetal (4.5 mL, 41.9 mmol, 1 equiv.) giving **7a** as a white crystalline solid (9.53 g, 89%), mp 89–91 °C, lit. value (18) mp 86–89 °C. IR ν_{max} (film, cm^{-1}): 755, 1070, 1130, 1238, 1311, 1441, 1499, 1555, 1597, 1654, 3340. ^{1}H NMR (300 MHz, $CDCl_3$) δ: 3.41 (6H, s, OCH_3), 3.41 (2H, m, CH_2CH), 4.43 (1H, t, *J* = 5.1, CH_2CH), 5.82 (1H, t, *J* = 5.8, NH), 7.03 (1H, m, ArH), 7.28 (4H, m, ArH), 7.58 (1H, s, NH). ^{13}C NMR (75 MHz, $CDCl_3$) δ: 41.7, 54.5, 103.5, 120.1, 123.1, 128.9, 138.8, 156.3. *m/z* (CI): 225 (MH^+, 74%), 193 (100), 75 (92). Anal. calcd. for $C_{11}H_{16}N_2O_3$ (M): 224.116 1; found (M^+): 224.115 9.

N-*(3-Methoxyphenyl)*-N′-*(2,2-dimethoxyethyl)urea (7c)*

N-(3-Methoxyphenyl)-*N′*-(2,2-dimethoxyethyl)urea (**7c**) was prepared as above from 3-methoxyphenyl isocyanate (1 g, 6.7 mmol) and aminoacetaldehyde dimethyl acetal (0.7 g, 6.7 mmol, 1 equiv.) giving **7c** as a white crystalline solid (1.615 g, 95%) pure enough for its subsequent use. An analytical sample was recrystallized from EtOAc–hexane, mp 102 °C. IR ν_{max} (film, cm^{-1}): 1556, 1606, 1653, 2875, 2958. ^{1}H NMR (300 MHz, d_6-DMSO) δ: 3.44 (2H, m, CH_2CH), 3.44 (6H, s, 2 × OCH_3), 3.72 (3H, s, OCH_3), 4.39 (1H, t, *J* = 5.1, CH_2CH), 6.49 (1H, apparent dd, *J* = 8.2, 2.9, ArH), 6.84 (1H, apparent dd, *J* = 8.2, 2.9, ArH), 7.12 (1H, bs, ArH), 7.14 (1H, bs, NH), 7.15 (1H, t, *J* = 8.2, ArH), 8.6 (1H, s, NH). ^{13}C NMR (75 MHz, d_6-DMSO) (DEPT) δ: 41.0 (d), 53.7 (q), 55.2 (q), 102.9 (d), 103.7 (d), 106.9 (d), 110.3 (d), 129.7 (d), 141.9 (s), 155.4 (s), 160.0 (s). *m/z* (CI): 255 (MH^+, 7%), 208 (25), 191 (100). Anal. calcd. for $C_{12}H_{18}N_2O_4$ (%): C 56.68, H 7.13, N 11.02; found (%): C 57.07, H 7.00, N 10.99. Anal. calcd. for $C_{12}H_{18}N_2O_4$ (M): 254.1267; found (M^+): 254.1272.

© 2004 NRC Canada

N-*(4-Methoxyphenyl)*-N′-*(2,2-dimethoxyethyl)urea (7d)

N-(4-Methoxyphenyl)-*N′*-(2,2-dimethoxyethyl)urea (**7d**) was prepared from 4-methoxyphenyl isocyanate (5 g, 33.5 mmol) and aminoacetaldehyde dimethyl acetal (3.61 mL, 33.5 mmol, 1 equiv.) giving **7d** as a white crystalline solid (7.9 g, 92%), mp 112–114 °C. IR ν_{max} (film, cm^{-1}): 1240, 1509, 1551, 1560, 1638, 1654, 3400. ^{1}H NMR (300 MHz, $CDCl_3$) δ: 3.40 (6H, s, OCH_3), 3.40 (2H, d, *J* = 5.0, C*H*$_2$CH), 3.78 (3H, s, $ArOCH_3$), 4.41 (1H, t, *J* = 5.0, CH_2C*H*), 6.82 (1H, d, *J* = 6.9, ArH), 7.19 (2H, d, *J* = 6.9, ArH), 7.21 (1H, s, NH). ^{13}C NMR (75 MHz, $CDCl_3$) δ: 41.7, 54.4, 55.4, 103.4, 114.3, 123.2, 131.4, 156.2, 156.7. *m/z* (CI): 255 (MH^+, 100%), 223 (90), 75 (100). Anal. calcd. for $C_{12}H_{18}N_2O_4$ (%): C 56.68, H 7.13, N 11.02; found (%): C 57.07, H 7.00, N 10.99. Anal. calcd. for $C_{12}H_{18}N_2O_4$ (M): 254.126 7; found (M^+): 254.126 4.

Typical procedure for the synthesis of imidazolones (3)

1-(2-Methoxyphenyl)imidazol-2(1H)-one (3b)

N-(2-Methoxyphenyl)-*N′*-(2,2-dimethoxyethyl)urea (**7b**) (1.12 g, 4.4 mmol) was dissolved in aq. 2 mol L^{-1} HCl (10 mL). The solution was stirred at rt for 20 h. The resulting clear solution was made basic with aq. 2 mol L^{-1} NaOH, extracted with CH_2Cl_2, then the extract was dried over $MgSO_4$ and evaporated, yielding 1-(2-methoxyphenyl)imidazol-2(1*H*)-one **3b** as a white crystalline solid (0.92 g, 82%), mp 160–162 °C. IR ν_{max} (film, cm^{-1}): 764, 1024, 1244, 1283, 1431, 1465, 1510, 1684, 2934. ^{1}H NMR (300 MHz, $CDCl_3$) δ: 3.88 (s, 3H, OCH_3), 6.39 (1H, apparent t, *J* = 2.6, ImH), 6.44 (1H, apparent t, *J* = 2.6, ImH), 7.07 (2H, m, ArH), 7.37 (1H, m, ArH), 7.49 (1H, dd, *J* = 7.6, 1.6, ArH). ^{13}C NMR (75 MHz, $CDCl_3$) δ: 55.7, 108.5, 112.2, 113.5, 120.8, 125.0, 128.2, 129.0, 154.2, 154.4. *m/z* (CI): 191 (MH^+, 100%). Anal. calcd. for $C_{10}H_{10}N_2O_2$ (%): C 63.15, H 5.30, N 14.73; found (%): C 63.23, H 5.40, N 14.55. Anal. calcd. for $C_{10}H_{10}N_2O_2$ (M): 190.074 2; found (M^+): 190.074 5.

1-Phenylimidazol-2(1H)-one (3a)

1-Phenylimidazol-2(1*H*)-one (**3a**) was prepared as above from *N*-(phenyl)-*N′*-(2,2-dimethoxyethyl)urea **7a** (7 g, 31.2 mmol) in aq. 2.5 mol L^{-1} HCl (60 mL) giving **3a** as a white crystalline solid (3.27 g, 65%), mp 127 °C, lit. value (19) mp 123–126 °C. IR ν_{max} (film, cm^{-1}): 756, 1424, 1503, 1598, 1667, 3061, 3156. ^{1}H NMR (300 MHz, $CDCl_3$) δ: 6.45 (1H, apparent t, *J* = 2.5, ImH), 6.57 (1H, apparent t, *J* = 2.5, ImH), 7.31 (1H, m, ArH), 7.48 (2H, m, ArH), 7.61 (2H, m, ArH), 11.1 (1H, bs, NH). ^{13}C NMR (75 MHz, $CDCl_3$) δ: 109.6, 111.0, 122.3, 126.1, 129.2, 136.9, 153.8. *m/z* (CI): 178 (MNH_4^+, 100%), 161 (MH^+, 99). Anal. calcd. for $C_9H_8N_2O$: (M): 160.063 7; found (M^+): 160.063 8.

1-(3-Methoxyphenyl)imidazol-2(1H)-one (3c)

1-(3-Methoxyphenyl)imidazol-2(1*H*)-one (**3c**) was prepared as above from *N*-(3-methoxyphenyl)-*N′*-(2,2-dimethoxyethyl)urea **7c** (1.2 g, 4.7 mmol) in aq. 2.5 mol L^{-1} HCl (20 mL) giving **3c** as a white crystalline solid (0.87 g, 97%), pure enough for its subsequent use, mp 136 °C. IR ν_{max} (film, cm^{-1}): 1230, 1497, 1687. ^{1}H NMR (300 MHz, $CDCl_3$) δ: 3.88 (s, 3H, OCH_3), 6.50 (1H, d, *J* = 2.5, ImH), 6.62 (1H, d, *J* = 2.5, ImH), 6.86 (1H, dd, *J* = 8.1, 2.5, ArH), 7.17 (1H, apparent d, *J* = 8.1, ArH), 7.23 (1H, bs, ArH), 7.38 (1H, t, *J* = 8.1, ArH). ^{13}C NMR (75 MHz, $CDCl_3$) δ: 55.4, 108.3, 109.6, 111.0, 111.8, 114.4, 129.9, 138.0, 153.8, 160.2. *m/z* (CI): 208 (MNH_4^+, 30%), 191 (MH^+, 100). Anal. calcd. for $C_{10}H_{10}N_2O_2$ (M): 190.074 2; found (M^+): 190.073 8.

1-(4-Methoxyphenyl)imidazol-2(1H)-one (3d)

1-(4-Methoxyphenyl)imidazol-2(1*H*)-one (**3d**) was prepared as above from *N*-(4-methoxyphenyl)-*N′*-(2,2-dimethoxyethyl)urea **7d** (7 g, 27.5 mmol) in aq. 2.5 mol L^{-1} HCl (60 mL) giving **3d** as a white crystalline solid (4.69 g, 89%), mp 158 °C. IR ν_{max} (film, cm^{-1}): 1234, 1247, 1512, 1667. ^{1}H NMR (300 MHz, $CDCl_3$) δ: 3.86 (s, 3H, OCH_3), 6.42 (1H, apparent t, *J* = 2.5, ImH), 6.49 (1H, apparent t, *J* = 2.5, ImH), 7.00 (2H, d, *J* = 6.9, ArH), 7.48 (2H, d, *J* = 6.9, ArH), 11.1 (1H, s, NH). ^{13}C NMR (75 MHz, $CDCl_3$) δ: 55.5, 109.2, 111.5, 114.4, 124.3, 129.9, 157.9. *m/z* (CI): 208 (MNH_4^+, 2%), 191 (MH^+,100). Anal. calcd. for $C_{10}H_{10}N_2O_2$ (%): C 63.15, H 5.30, N 14.73; found (%): C 63.20, H 5.38, N 14.79. Anal. calcd. for $C_{10}H_{10}N_2O_2$ (M): 190.074 2; found (M^+): 190.073 9.

Typical procedure for synthesis of 1-aryl-3-methylimidazolones (5)

1-(2-Methoxyphenyl)-3-methylimidazol-2(1H)-one (5b)

A solution of 1-(2-methoxyphenyl)imidazol-2(1*H*)-one **3b** (0.26 g, 1.37 mmol) in anhyd. THF at –78 °C was treated with *n*-BuLi (1.6 mol L^{-1}, 0.89 mL, 1.1 equiv.) over 30 min under N_2. The solution was warmed up to 0 °C for 2 h and then cooled to –78 °C for the addition of iodomethane (0.09 mL, 1.43 mmol, 1.1 equiv.). The reaction mixture was allowed to warm up to rt and after 20 h the reaction was quenched with satd. aq. NH_4Cl and evaporated to remove the THF. The organic residue was dissolved in CH_2Cl_2, the solution washed with brine, dried and evaporated to give 1-(2-methoxyphenyl)-3-methylimidazol-2(1*H*)-one **5b** as a clear yellow oil (0.25 g, 94%). IR ν_{max} (film, cm^{-1}): 1045, 1224, 1270, 1405, 1461, 1497, 1605, 1687. ^{1}H NMR (300 MHz, $CDCl_3$) δ: 3.35 (3H, s, NCH_3), 3.87 (3H, s, OCH_3), 6.31 (1H, d, *J* = 2.9, ImH), 6.47 (1H, d, *J* = 2.9, ImH), 7.04 (2H, apparent t, *J* = 8.0, ArH), 7.34 (1H, m, ArH), 7.47 (1H, dd, *J* = 8.0, 1.6, ArH). ^{13}C NMR (75 MHz, $CDCl_3$) δ: 30.5, 55.7, 107.2, 110.1, 111.3, 112.1, 112.2, 120.8, 127.9, 128.6, 154.0. *m/z* (CI): 222 (MNH_4^+, 22%), 205 (MH^+, 100). $C_{11}H_{12}N_2O_2$ (M): 204.089 9; found (M^+): 204.090 0.

3-Methyl-1-phenylimidazol-2(1H)-one (5a)

3-Methyl-1-phenylimidazol-2(1*H*)-one (**5a**) was prepared as above from 1-phenylimidazol-2(1*H*)-one **3a** (0.5 g, 3.12 mmol) and *n*-BuLi (1.6 mol L^{-1}, 2.15 mL, 1.1 equiv.) then iodomethane (0.29 mL, 4.7 mmol, 1.5 equiv.) giving **5a** as a white solid (0.52 g, 96%). An analytical sample was prepared by column SiO_2 chromatography (50% EtOAc in hexane), mp 119–121 °C, lit. value (23) mp 119 °C. IR ν_{max} (film, cm^{-1}): 766, 1266, 1344, 1402, 1452, 1459, 1507, 1600, 1672, 3060, 3135. ^{1}H NMR (300 MHz, $CDCl_3$) δ: 3.35 (3H, s, NCH_3), 6.35 (1H, d, *J* = 3.0, ImH), 6.59 (1H, d, *J* = 3.0, ImH), 7.26 (1H, m, ArH), 7.44 (2H, apparent t, *J* = 8.0 ArH), 7.63 (2H, m, ArH). ^{13}C NMR (75 MHz, $CDCl_3$) δ:

© 2004 NRC Canada

30.4, 109.1, 112.6, 111.06, 121.5, 125.6, 129.1, 137.3, 155.4. *m/z* (CI): 192 (MNH_4^+, 32%), 175 (MH^+, 100).

1-(3-Methoxyphenyl)-3-methylimidazol-2(1H)-one (5c)

1-(3-Methoxyphenyl)-3-methylimidazol-2(1*H*)-one (**5c**) was prepared as above from 1-(3-methoxyphenyl)imidazol-2(1*H*)-one **3c** (0.8 g, 4.2 mmol) and *n*-BuLi (1.6 mol L^{-1}, 2.9 mL, 1.1 equiv.) then iodomethane (0.29 mL, 4.6 mmol, 1.1 equiv.) giving **5c** as a clear yellow oil (0.73 g, 86%). ^1H NMR (300MHz, $CDCl_3$) δ: 3.35 (3H, s, NCH_3), 3.87 (3H, s, OCH_3), 6.35 (1H, d, *J* = 3.0, ImH_a), 6.59 (1H, d, *J* = 3.0, ImH_b), 6.81 (1H, dd, *J* = 8.1, 3.0, ArH), 7.15 (1H, dd, *J* = 8.1, 3.0, ArH), 7.29 (1H, s, ArH), 7.34 (1H, t, *J* = 8.1, ArH). ^{13}C NMR (75 MHz, $CDCl_3$) δ: 30.4, 55.3, 107.2, 109.1, 111.6, 111.7, 112.6, 113.3, 129.7, 138.5, 160.2. *m/z* (CI): 222 (MNH_4^+, 22%), 205 (MH^+, 100). Anal. calcd. for $C_{11}H_{12}N_2O_2$ (M): 204.089 9; found (M^+): 204.090 5.

1-(4-Methoxyphenyl)-3-methylimidazol-2(1H)-one (5d)

1-(4-Methoxyphenyl)-3-methylimidazol-2(1*H*)-one (**5d**) was prepared as above from 1-(4-methoxyphenyl)imidazol-2(1*H*)-one **3d** (0.5 g, 2.6 mmol) and *n*-BuLi (1.6 mol L^{-1}, 1.8 mL, 1.1 equiv.) then iodomethane (0.24 mL, 3.9 mmol, 1.5 equiv.) giving **5d** as a white solid (0.516 g, 96%), mp 116–118 °C, lit. value (23) mp 114 °C. IR ν_{max} (film, cm^{-1}): 1248, 1458, 1514, 1678, 2360. ^1H NMR (300 MHz, $CDCl_3$) δ: 3.32 (3H, s, NCH_3), 3.83 (3H, s, OCH_3), 6.31 (1H, d, *J* = 2.9, ImH), 6.50 (1H, d, *J* = 2.9, ImH), 6.95 (2H, d, *J* = 6.9, ArH), 7.48 (2H, d, *J* = 6.9, ArH). ^{13}C NMR (75 MHz, $CDCl_3$) δ: 30.4, 55.4, 109.7, 111.8, 112.2, 114.2, 123.4, 130.5, 157.5. *m/z* (CI): 222 (MNH_4^+, 22%), 205 (MH^+, 100). Anal. calcd. for $C_{11}H_{12}N_2O_2$ (M): 204.089 9; found (M^+): 204.089 7.

Typical procedure for the synthesis of aryldiamines (8)

N-*(2-Methoxyphenyl)-1,2-diaminoethane (8b)*

A mixture of freshly distilled *o*-anisidine (19.7 g, 160 mmol) and 2-bromoethylamine hydrobromide (19.7 g, 160 mmol, 1 equiv.) in dry toluene (40 mL) was heated at reflux temperature for 18 h, and then cooled. A solution of 50% aq. NaOH and CH_2Cl_2 were added and the layers separated. The aqueous layer was saturated with NaCl and extracted with CH_2Cl_2. The combined organic layers were dried over $MgSO_4$, filtered and evaporated to dryness. Dry flash column SiO_2 chromatography (40%–100% of CH_2Cl_2 in hexane) yielded *N*-(2-methoxyphenyl)-1,2-diaminoethane **8b** (9.99 g, 75%) as a light brown low oil. ^1H NMR (24) (300 MHz, $CDCl_3$) δ: 1.98 (2H, bs, NH_2), 3.02 (2H, t, *J* = 5.6, CH_2), 3.24 (2H, t, *J* = 5.6, CH_2), 3.5 (1H, bs, NH), 3.9 (3H, s, $ArOCH_3$), 6.70 (2H, m, ArH), 6.80 (1H, m, ArH), 6.90 (1H, m, Ar). ^{13}C NMR (75 MHz, $CDCl_3$) δ: 41.3, 46.5, 55.4, 109.7, 110.2, 116.5, 121.4, 138.0, 146.8. *m/z* (CI): 167 (MH^+, 100%). Anal. calcd. for $C_8H_{11}N_2O$ (M – Me): 151.082 1; found: 151.063 7.

N-*Phenyl-1,2-diaminoethane (8a)*

N-Phenyl-1,2-diaminoethane (**8a**) was prepared as above from aniline (5 g, 53 mmol) and 2-bromoethylamine hydrobromide (5.5 g, 26 mmol, 0.5 equiv.) giving **8a** (1.5 g, 42%) as a clear oil (23). IR ν_{max} (film, cm^{-1}): 749, 1320, 1506, 1602, 2862, 2937, 3024, 3048, 3343. ^1H NMR (300 MHz, d_6-DMSO) δ: 2.85 (2H, t, *J* = 6.3, CH_2), 3.16 (2H, m, CH_2), 5.07 (2H, bs, NH_2), 5.75 (1H, bs, NH), 6.57 (3H, m, ArH), 7.10 (2H, m, ArH). ^{13}C NMR (75 MHz, d_6-DMSO) δ: 39.7, 44.3, 112.8, 116.6, 129.7, 149.4. *m/z* (CI): 137 (MH^+, 100%).

N-*(3-Methoxyphenyl)-1,2-diaminoethane (8c)*

N-(3-Methoxyphenyl)-1,2-diaminoethane (**8c**) was prepared as above from *m*-anisidine (20 g, 0.16 mmol) and 2-bromoethylamine hydrobromide (16.6 g, 0.8 mol, 0.5 equiv.) giving **8c** (9.78 g, 73%) as a brown semi-solid, lit. value (24) mp 45 to 46 °C. ^1H NMR (300 MHz, $CDCl_3$) δ: 1.42 (2H, bs, NH_2), 2.98 (2H, m, CH_2), 3.17 (2H, m, CH_2), 3.80 (3H, s, OCH_3), 6.20–6.35 (3H, m, ArH), 7.12 (1H, t, *J* = 8.1, ArH). ^{13}C NMR (75 MHz, $CDCl_3$) δ: 41.1, 46.4, 54.9, 98.8, 102.4, 106.0, 129.8. *m/z* (CI): 167 (MH^+, 100%), 136 (20).

N-*(4-Methoxyphenyl)-1,2-diaminoethane (8d)*

N-(4-Methoxyphenyl)-1,2-diaminoethane (**8d**) was prepared as above from *p*-anisidine (5 g, 40 mmol) and 2-bromoethylamine hydrobromide (4.15 g, 20 mmol, 0.5 equiv.) giving **8d** (1.35 g, 40%) as a brown solid, mp 60–62 °C, lit. value (25) mp 64 °C. IR ν_{max} (film, cm^{-1}): 823, 1034, 1236, 1512, 1668, 2932. ^1H NMR (300 MHz, CD_3OD) δ: 2.78 (2H, t, *J* = 6.1, CH_2), 3.07 (2H, t, *J* = 6.1, CH_2), 3.26 (1H, bs, NH), 4.83 (1H, bs, NH_2), 6.60 (2H, d, *J* = 9.0, ArH), 6.81 (2H, d, *J* = 9.0, ArH). ^{13}C NMR (75 MHz, $CDCl_3$) δ: 41.6, 47.8, 56.1, 114.6, 115.2, 126.0, 142.9. *m/z* (CI): 167 (M^+, 100%), 136 (20), 124 (65).

Typical procedure for the synthesis of *N*-arylimidazolidinones (4)

4,5-Dihydro-1-(2-methoxyphenyl)imidazol-2(1H)-one (4b)

To a solution of *N*-(2-methoxyphenyl)-1,2-diaminoethane **8b** (9.97 g, 0.06 mol) in anhyd. THF (50 mL), 1,1-carbonyldiimidazole (18.44 g, 0.145 mol, 2.4 equiv.) was added under N_2. The solution was refluxed for 21 h and then evaporated to dryness to remove the THF. The yellow residue was taken up with EtOAc, the solution washed with brine, dried over $MgSO_4$ and evaporated. Column SiO_2 chromatography (25% of EtOAc in hexane) yielded 4,5-dihydro-1-(2-methoxyphenyl)imidazol-2(1*H*)-one **4b** as a white crystalline solid (2.77 g, 25%), mp 150–152 °C, lit. value (26) mp 151–153 °C. ^1H NMR (300 MHz, $CDCl_3$) δ: 3.60 (2H, t, *J* = 8.2, ImH), 3.85 (2H, t, *J* = 8.2, ImH), 3.90 (3H, s, OCH_3), 5.18 (1H, bs, NH), 6.99 (2H, m, ArH), 7.26 (1H, m, ArH), 7.39 (1H, dd, *J* = 7.7, 1.6, ArH). ^{13}C NMR (75 MHz, $CDCl_3$) δ: 38.7, 47.3, 55.5, 111.9, 120.9, 127.7, 127.8, 128.6, 155.2, 162.0. *m/z* (CI): 193 (MH^+, 100%). Anal. calcd. for $C_{10}H_{12}N_2O_2$ (M): 192.089 9; found (M^+): 192.090 0.

4,5-Dihydro-1-phenylimidazol-2(1H)-one (4a)

4,5-Dihydro-1-phenylimidazol-2(1*H*)-one (**4a**) was prepared as above from *N*-phenyl-1,2-diaminoethane **8a** (1.5 g, 11 mmol) and 1,1-carbonyldiimidazole (7.2 g, 47 mmol, 4.3 equiv.) giving **4a** as a white crystalline solid (1.35 g, 76%), mp 159 °C, lit. value (27) mp 162 to 163 °C. IR ν_{max} (film, cm^{-1}): 748, 1150, 1484, 1680, 2906, 3424. ^1H NMR (300 MHz, $CDCl_3$) δ: 3.41 (2H, t, *J* = 7.9, ImH), 3.85 (2H, apparent t, *J* = 7.9, ImH), 6.94 (1H, bs, NH), 7.06 (1H, apparent t, *J* = 8.6, ArH), 7.35 (2H, apparent t, *J* = 8.6, ArH),

© 2004 NRC Canada

7.56 (2H, apparent d, J = 8.6, ArH). ^{13}C NMR (75 MHz, $CDCl_3$) δ: 42.0, 49.9, 122.4, 126.9, 134.0.

*4,5-Dihydro-1-(3-methoxyphenyl)imidazol-2(1*H*)-one (4c)*

4,5-Dihydro-1-(3-methoxyphenyl)imidazol-2(1*H*)-one (**4c**) was prepared as above from *N*-(3-methoxyphenyl)-1,2-diaminoethane **8c** (6 g, 0.036 mol) and 1,1-carbonyldiimidazole (25 g, 0.18 mol, 5.2 equiv.) giving **4c** as a white crystalline solid (4.35 g, 63%), mp 123 °C, lit. (20). IR ν_{max} (film, cm^{-1}): 662, 1259, 1411, 1482, 1601, 1705, 2923, 3257. ^{1}H NMR (300 MHz, $CDCl_3$) δ: 3.60 (2H, apparent t, J = 7.8, ImH), 3.80 (s, 3H, OCH_3), 3.98 (2H, apparent t, J = 7.8, ImH), 6.67 (1H, dd, J = 8.2, 2.5, ArH), 7.09 (1H, dd, J = 8.2, 2.06, ArH), 7.26–7.32 (2H, m, ArH). ^{13}C NMR (75 MHz, $CDCl_3$) δ: 41.3, 42.2, 55.3, 118.4, 129.5, 129.8, 138.4, 148.5, 151.09, 160.1. *m*/*z* (CI): 210 (MNH_4^+, 25%), 193 (100). Anal. calcd. for $C_{10}H_{12}N_2O_2$ (M): 192.089 9; found (M^+): 192.089 4.

*4,5-Dihydro-1-(4-methoxyphenyl)imidazol-2(1*H*)-one (4d)*

4,5-Dihydro-1-(4-methoxyphenyl)imidazol-2(1*H*)-one (**4d**) was prepared as above from *N*-(4-methoxyphenyl)-1,2-diaminoethane **8d** (1 g, 6 mmol) and 1,1′-carbonyldiimidazole (3.9 g, 52 mmol, 3.9 equiv.) giving **4d** as a white crystalline solid (0.45 g, 44%), mp 205–207 °C, lit. value (28) mp 211 °C. IR ν_{max} (film, cm^{-1}): 830, 1034, 1251, 1519, 1679, 3476, 3583. ^{1}H NMR (300 MHz, $CDCl_3$) δ: 3.90 (3H, s, OCH_3), 3.97 (2H, t, J = 7.9, ImH), 4.17 (2H, t, J = 7.9, ImH), 7.01 (2H, d, J = 7.8, ArH), 7.41 (2H, d, J = 7.8, ArH). ^{13}C NMR (75 MHz, $CDCl_3$) δ: 37.9, 46.2, 55.8, 114.3, 120.3, 141.6, 142.2, 158.7. *m*/*z* (CI): 210 (MNH_4^+, 10%), 193 (MH^+, 100).

Typical procedure for the synthesis of 1-aryl-3-methylimidazolidinones (6)

*4,5-Dihydro-1-(2-methoxyphenyl)-3-methylimidazol-2(1*H*)-one (6b)*

A solution of 4,5-dihydro-1-(2-methoxyphenyl)imidazol-2(1*H*)-one **4b** (0.250 g, 1.3 mmol) in anhyd. THF was treated with *n*-BuLi (1.6 mol L^{-1}, 0.9 mL, 1.1 equiv.) at –78 °C over 30 min under N_2. The solution was warmed then maintained at 0 °C for 2 h and cooled down to –78 °C again for the addition of iodomethane (0.09 mL, 1.43 mmol, 1.1 equiv.). The reaction mixture was warmed up to rt and after 20 h quenched with satd. aq. NH_4Cl and evaporated to remove the THF. The colourless residue was dissolved with CH_2Cl_2, the solution washed with brine, dried over $MgSO_4$ and evaporated to yield 4,5-dihydro-1-(2-methoxyphenyl)-3-methylimidazol-2(1*H*)-one **6b** (0.26 g, 95%) as a dark yellow oil. ^{1}H NMR (300 MHz, $CDCl_3$) δ: 2.92 (3H, s, NCH_3), 3.48 (2H, t, J = 7.7, ImH), 3.78 (2H, t, J = 7.7, ImH), 3.88 (3H, s, OCH_3), 6.92 (2H, m, ArH), 7.25 (1H, m, ArH), 7.38 (1H, dd, J = 7.8, 1.6, ArH). ^{13}C NMR (75 MHz, $CDCl_3$) δ: 31.5, 44.6, 45.4, 55.5, 111.8, 120.8, 127.4, 128.4, 129.3, 155.1, 160.0. *m*/*z* (CI): 207 (MH^+, 100%). Anal. calcd. for $C_{11}H_{14}N_2O_2$ (M): 206.105 5; found (M^+): 206.105 5.

*4,5-Dihydro-3-methyl-1-phenylimidazol-2(1*H*)-one (6a)*

4,5-Dihydro-3-methyl-1-phenylimidazol-2(1*H*)-one (**6a**) was prepared as above from 4,5-dihydro-1-phenylimidazol-2(1*H*)-one **4a** (0.162 mg, 1 mmol), *n*-BuLi (1.6 mol L^{-1}, 0.68 mL, 1.1 equiv.) then iodomethane (0.06 mL, 1.1 mmol, 1.1 equiv.) giving **6a** as a white crystalline solid (126 mg, 71%). An analytical sample was prepared by column SiO_2 chromatography (50% of EtOAc in hexane), mp 99 °C, lit. value (29) mp 110 to 111 °C. IR ν_{max} (film, cm^{-1}): 742, 899, 1275, 1387, 1404, 1439, 1476, 1504, 1598, 1702, 2826, 2887, 2917, 2952. ^{1}H NMR (300 MHz, $CDCl_3$) δ: 2.93 (3H, s, NCH_3), 3.48 (2H, t, J = 8.3, ImH), 3.80 (2H, t, J = 8.3, ImH), 7.05 (1H, dt, J = 7.3, 1.0, ArH), 7.32 (1H, m, ArH), 7.60 (1H, m, ArH). ^{13}C NMR (75 MHz, $CDCl_3$) δ: 31.4, 42.5, 44.3, 117.4, 122.4, 129.0, 140.9, 158.4. *m*/*z* (CI): 177 (MH^+, 100%), 105 (2).

*4,5-Dihydro-1-(3-methoxyphenyl)-3-methylimidazol-2(1*H*)-one (6c)*

4,5-Dihydro-1-(3-methoxyphenyl)-3-methylimidazol-2(1*H*)-one (**6c**) was prepared as above from 4,5-dihydro-1-(3-methoxyphenyl)imidazol-2(1*H*)-one **4c** (200 mg, 1.04 mmol, 1 equiv.) and *n*-BuLi (1.6 mol L^{-1}, 0.875 mL) then iodomethane (0.60 mL, 1.04 mmol, 1 equiv.) giving **6c** (200 mg, 93%) as white solid, mp 95 °C, lit. value (29) mp 97–99 °C. IR ν_{max} (film, cm^{-1}): 1221, 1452, 1500, 1601, 1703. ^{1}H NMR (300 MHz, $CDCl_3$) δ: 2.93 (3H, s, NCH_3), 3.50 (2H, apparent t, J = 7.9, ImH), 3.83 (2H, m, ImH), 3.85 (3H, s, OCH_3), 6.63 (1H, dd, J = 8.2, 2.2, ArH), 7.04 (1H, dd, J = 8.2, 2.2, ArH), 7.25 (1H, t, J = 8.2, ArH), 7.41 (1H, m, ArH). ^{13}C NMR (75 MHz, $CDCl_3$) δ: 31.1, 42.3, 43.9, 55.2, 103.1, 108.1, 109.1, 109.7, 129.3, 141.9, 159.9. *m*/*z* (CI): 207 (M^+, 100). Anal. calcd. for. $C_{10}H_{12}N_2O_2$ (M): 206.105 5; found (M^+): 206.105 5.

*4,5-Dihydro-1-(4-methoxyphenyl)-3-methylimidazol-2(1*H*)-one (6d)*

4,5-Dihydro-1-(4-methoxyphenyl)-3-methylimidazol-2(1*H*)-one (**6d**) was prepared as above from 4,5-dihydro-1-(4-methoxyphenyl)imidazol-2(1*H*)-one **4d** (0.25 g, 1.3 mmol) and *n*-BuLi (1.6 mol L^{-1}, 0.89 mL, 1.1 equiv.) then iodomethane (0.085 mL, 1.43 mmol, 1.1 equiv.) giving **6d** (180 mg, 68%) as a solid, mp 56 to 57 °C. IR ν_{max} (film, cm^{-1}): 828, 1038, 1252, 1686, 2948. ^{1}H NMR (300 MHz, $CDCl_3$) δ: 2.83 (3H, s, NCH_3), 3.39 (2H, apparent t, J = 7.6, ImH), 3.71 (2H, apparent t, J = 7.6, ImH), 3.73 (3H, s, OCH_3), 6.82 (2H, d, J = 8.9, ArH), 7.39 (2H, d, J = 8.9, ArH). ^{13}C NMR (75 MHz, $CDCl_3$) δ: 31.6, 43.1, 44.6, 55.8, 114.4, 119.5, 134.4, 146.2, 155.6. *m*/*z* (CI): 207 (MH^+, 100). Anal. calcd. for. $C_{10}H_{12}N_2O_2$ (M): 206.105 5; found (M^+): 206.105 8.

Typical procedure for reaction of imidazolones (3a–3d) and imidazolidinones (4a–4d) with 2.5 equiv. of *n*-BuLi then trapping with MeI

*1-(2-Methoxy-3-methylphenyl)-3-methylimidazol-2(1*H*)-one (5g) and 1-(2-methoxy-6-methylphenyl)-3-methylimidazol-2(1*H*)-one (5f)*

A solution of 1-(2-methoxyphenyl)imidazol-2(1*H*)-one **3b** (0.26 g, 1.3 mmol) in anhyd. THF was treated with *n*-BuLi (1.6 mol L^{-1}, 2 mL, 2.5 equiv.) at –78 °C over 30 min under N_2. The solution was warmed up to then maintained at 0 °C for 2 h and cooled down to –78 °C again for the addition of iodomethane (0.2 mL, 3.25 mmol, 2.5 equiv.). The reaction

© 2004 NRC Canada

mixture was allowed to warm up to rt and after 20 h quenched with satd. aq. NH_4Cl, and evaporated to remove the THF. The organic residue was taken up with CH_2Cl_2, the solution washed with brine, dried and evaporated. Column SiO_2 chromatography (50% of EtOAc in petroleum ether) yielded firstly 1-(2-methoxy-3-methylphenyl)-3-methylimidazol-2(1*H*)-one **5g** (70 mg, 25%), secondly 1-(2-methoxy-6-methylphenyl)-3-methylimidazol-2(1*H*)-one **5f** (50 mg, 18%) as yellow oils. Spectroscopic data for **5g**: ^{1}H NMR (300 MHz, $CDCl_3$) δ: 2.25 (3H, s, $ArCH_3$), 3.27 (3H, s, NCH_3), 3.57 (3H, s,OCH_3), 6.24 (2H, d, *J* = 3.0, ImH), 6.45 (1H, d, *J* = 3.0, ImH), 7.07 (1H, d, *J* = 8.2, ArH), 7.15 (1H, d, *J* = 8.2, ArH), 7.35 (1H, t, *J* = 8.2, ArH). ^{13}C NMR (75 MHz, $CDCl_3$) δ: 15.9, 30.5, 55.7, 111.4, 111.8, 111.9, 124.0, 125.4, 128.7, 129.6, 130.2, 156.0. *m*/*z* (CI): 219 (MH^+, 100%). Anal. calcd. for. $C_{12}H_{14}N_2O_2$ (M): 218.105 5; found (M^+): 218.105 6. Spectroscopic data for **5g**: ^{1}H NMR (300 MHz, $CDCl_3$) δ: 2.22 (3H, s, $ArCH_3$), 3.37 (3H, s, NCH_3), 3.82 (3H, s, OCH_3), 6.23 (2H, d, *J* = 2.9, ImH), 6.32 (1H, d, *J* = 2.9, ImH), 6.84 (1H, d, *J* = 7.9, ArH), 6.91 (1H, d, *J* = 7.9, ArH), 7.27 (1H, t, *J* = 7.9, ArH). ^{13}C NMR (75 MHz, $CDCl_3$) δ: 18.2. 31.2, 55.8, 109.2, 111.8, 111.9, 113.3, 122.4, 125.9, 129.1, 138.0, 155.9. *m*/*z* (CI): 233 (MNH_4^+, 10%), 219 (MH^+, 100), 205 (20). Anal. calcd. for. $C_{12}H_{14}N_2O_2$ (M): 218.105 5; found (M^+): 218.105 4.

*1-(2-Methylphenyl)-3-methylimidazol-2(1**H**)-one (5e)*

1-(2-Methylphenyl)-3-methylimidazol-2(1*H*)-one (**5e**) was prepared as above from 1-phenylimidazol-2(1*H*)-one **3a** (0.18 g, 1.12 mmol) giving 1-(2-methylphenyl)-3-methylimidazol-2(1*H*)-one **5e** as a yellow oil (189 mg, 88%). An analytical sample was prepared by column SiO_2 chromatography (50% EtOAc in hexane). IR ν_{max} (film, cm^{-1}): 1460, 1499, 1686. ^{1}H NMR (300 MHz, $CDCl_3$) δ: 2.27 (3H, s, $ArCH_3$), 3.35 (3H, s, NCH_3), 6.31 (1H, d, *J* = 2.9, ImH), 6.34 (1H, d, *J* = 2.9, ImH), 7.27 (4H, m, ArH). ^{13}C NMR (75 MHz, $CDCl_3$) δ: 17.9, 30.6, 115.6, 112.11, 126.6, 127.4, 128.2, 131.0, 135.5, 137.0, 156.7. *m*/*z* (CI): 236 (MNH_4^+, 76%), 489 (MH^+, 100). Anal. calcd. for. $C_{11}H_{12}N_2O$ (M): 188.094 5; found (M^+): 188.094 8.

*1-(3-Methoxy-2-methylphenyl)-3-methylimidazol-2(1**H**)-one (5h)*

1-(3-Methoxy-2-methylphenyl)-3-methylimidazol-2(1*H*)-one (**5h**) was prepared as above from 1-(3-methoxyphenyl)imidazol-2(1*H*)-one **3c** (0.5 g, 2.6 mmol, 1 equiv.) giving **5h** as a yellow oil (317 mg, 60%). IR ν_{max} (film, cm^{-1}): 1260, 1435, 1476, 1694. ^{1}H NMR (300 MHz, $CDCl_3$) δ: 2.11 (3H, s, $ArCH_3$), 3.34 (3H, s, NCH_3), 3.86 (3H, s, OCH_3), 6.31 (1H, d, *J* = 3.0, ImH), 6.33 (1H, d, *J* = 3.0, ImH), 6.87 (2H, d, *J* = 8.1, ArH), 7.22 (1H, t, *J* = 8.1, ArH). ^{13}C NMR (75 MHz, $CDCl_3$) δ: 11.0, 30.5, 55.7, 109.0, 110.0, 111.7, 112.9, 119.5, 126.5, 126.6, 136.6, 158.4. *m*/*z* (CI): 219 (MH^+, 100%), 102 (30). Anal. calcd. for. $C_{12}H_{14}N_2O_2$ (MH): 219.113 3; found (MH^+): 219.113 7.

*1-(4-Methoxy-2-methylphenyl)-3-methylimidazol-2(1**H**)-one (5i)*

1-(4-Methoxy-2-methylphenyl)-3-methylimidazol-2(1*H*)-one (**5i**) was prepared from 1-(4-methoxyphenyl)imidazol-2(1*H*)-one **3d** (0.2 g, 1.05 mmol) giving **5i** (0.22 g, 96%); an analytical sample was prepared by column SiO_2 chromatography (50% of EtOAc in hexane). IR ν_{max} (film, cm^{-1}): 1242, 1458, 1508, 1677. ^{1}H NMR (300 MHz, $CDCl_3$) δ: 2.23 (3H, s, $ArCH_3$), 3.35 (3H, s, NCH_3), 3.83 (3H, s, OCH_3), 6.27 (1H, d, *J* = 2.9, ImH), 6.32 (1H, d, *J* = 2.9, ImH), 6.79 (1H, dd, *J* = 8.5, 2.9, ArH), 6.83 (1H, d, *J* = 2.9, ArH), 7.15 (1H, d, *J* = 8.5, ArH). ^{13}C NMR (75 MHz, $CDCl_3$) δ: 18.2, 30.6, 55.4, 111.9, 116.0, 128.5, 128.8, 130.7, 137.0, 159.2, 152.7, 166.7. *m*/*z* (CI): 236 (MNH_4^+, 13%), 219 (MH^+, 100). Anal. calcd. for. $C_{12}H_{14}N_2O_2$ (M): 218.105 5; found (M^+): 218.105 4.

4,5-Dihydro-1-(2-methylphenyl)-3-methylimidazol-2(1H)-one (6e)

4,5-Dihydro-1-(2-methylphenyl)-3-methylimidazol-2(1*H*)-one (**6e**) was prepared from 4,5-dihydro-1-phenylimidazol-2(1*H*)-one **4a** (0.162 mg, 1 mmol) giving 4,5-dihydro-1-(2-methylphenyl)-3-methylimidazol-2(1*H*)-one **6e** (64 mg, 34%) as a yellow oil. IR ν_{max} (film, cm^{-1}): 756, 1265, 1400, 1431, 1494, 1701, 2871, 2933. ^{1}H NMR (300 MHz, $CDCl_3$) δ: 2.30 (3H, s, $ArCH_3$), 2.91 (3H, s, NCH_3), 3.49 (2H, t, *J* = 7.9, ImH), 3.81 (2H, t, *J* = 7.9, ImH), 7.21 (4H, m, ArH). ^{13}C NMR (75 MHz, $CDCl_3$) δ: 18.3, 31.9, 42.6, 45.7, 117.5, 126.9, 127.4, 129.0, 131.4, 136.5, 158.4. *m*/*z* (CI): 208 (MH^+, 50%), 191 (MH^+, 100), 177 (20). Anal. calcd. for. $C_{11}H_{14}N_2O$ (M): 190.110 6; found (M^+): 190.110 8.

*4,5-Dihydro-1-(2-methoxy-3-methylphenyl)-3-methylimidazol-2(1**H**)-one (6g) and 4,5-dihydro-1-(2-methoxy-6-methylphenyl)-3-methylimidazol-2(1**H**)-one (6f)*

4,5-Dihydro-1-(2-methoxy-3-methylphenyl)-3-methylimidazol-2(1*H*)-one (**6g**) and 4,5-dihydro-1-(2-methoxy-6-methylphenyl)-3-methylimidazol-2(1*H*)-one (**6f**) were prepared as above from 4,5-dihydro-1-(2-methoxy)phenylimidazol-2(1*H*)-one **4b** (0.4 g, 2.1 mmol) giving from the column firstly **6g** (0.168 g, 37%), then **6f** (0.130 g, 28%) as yellow oils. Spectroscopic data for **6g**: ^{1}H NMR (300 MHz, $CDCl_3$) δ: 2.29 (3H, s, $ArCH_3$), 2.90 (3H, s, NCH_3), 3.47 (2H, t, *J* = 7.3, ImH), 3.73 (3H, s, OCH_3), 3.77 (2H, t, *J* = 7.3, ImH), 7.04 (2H, m, ArH), 7.23 (1H, m, ArH). ^{13}C NMR (75 MHz, $CDCl_3$) δ: 15.8, 31.4, 44.5, 45.5, 59.9, 123.9, 124.0, 125.6, 128.8, 131.9, 154.0, 159.9. *m*/*z* (CI): 221 (M^+,100%). Anal. calcd. for. $C_{12}H_{16}N_2O_2$ (M): 206.121 2; found (M^+): 220.121 4. Spectroscopic data for **6f**: ^{1}H NMR (300 MHz, $CDCl_3$) δ: 2.17 (3H, s, $ArCH_3$), 2.73 (3H, s, NCH_3), 3.42 (2H, m, ImH), 3.62 (2H, m, ImH), 3.76 (3H, s, OCH_3) 6.85 (1H, apparent d, *J* = 8.0, ArH), 6.90 (1H, apparent d, *J* = 8.0, ArH), 7.20 (1H, apparent t, *J* = 8.0, Ar). ^{13}C NMR (75 MHz, $CDCl_3$) δ: 17.6, 31.6, 44.6, 45.8, 55.7, 109.2, 122.5, 128.1, 129.0, 139.2, 156.7, 160.1. *m*/*z* (CI): 221 (MH^+, 100%), 207 (70). Anal. calcd. for. $C_{12}H_{16}N_2O_2$ (M): 206.121 2; found (M^+): 220.121 4.

4,5-Dihydro-1-(3-methoxy-2-methylphenyl)-3-methylimidazolidin-2-one (6h)

4,5-Dihydro-1-(3-methoxy-2-methylphenyl)-3-methylimidazolidin-2-one (**6h**) was prepared as above from 4,5-dihydro-1-(3-methoxyphenyl)imidazol-2(1*H*)-one **4c** (0.1 g, 5.2 mmol) giving **6h** (0.08 g, 22%) as a yellow oil. ^{1}H NMR (300 MHz, $CDCl_3$) δ: 2.16 (3H, s, $ArCH_3$), 2.92 (3H, s, NCH_3), 3.51 (2H, t, *J* = 7.9, ImH), 3.68 (2H, t, *J* = 7.9,

© 2004 NRC Canada

ImH), 3.87 (3H, s, OCH_3), 6.80 (1H, d, J = 7.9, ArH), 6.85 (1H, d, J = 7.9, ArH), 7.19 (1H, t, J = 7.9, ArH). ^{13}C NMR (75 MHz, $CDCl_3$): 10.9, 31.5, 42.3, 42.5, 55.2, 103.1, 108.8, 118.7, 125.2, 129.3, 141.9, 159.9. *m/z* (CI): 221 (M^+, 100%), 207 (87). Anal. calcd. for. $C_{12}H_{16}N_2O_2$ (M): 220.121 2; found (M^+): 220.121 0.

4,5-Dihydro-1-(4-methoxy-2-methylphenyl)-3-methylimidazol-2(1H)-one (6i) and 4,5-dihydro-1-(4-methoxy-3-methylphenyl)-3-methylimidazol-2(1H)-one (6j)

4,5-Dihydro-1-(4-methoxy-2-methylphenyl)-3-methylimidazol-2(1*H*)-one (**6i**) and 4,5-dihydro-1-(4-methoxy-3-methylphenyl)-3-methylimidazol-2(1*H*)-one (**6j**) were prepared from 4,5-dihydro-1-(4-methoxyphenyl)imidazol-2(1*H*)-one **4d** (30 mg, 0.16 mmol) giving firstly from the column **6i** (3 mg, 9%) as a foamy yellow solid, and secondly, **6j** (4 mg, 12%) as a yellow oil. Spectroscopic data for **6i**: IR ν_{max} (film, cm^{-1}): 1030, 1106, 1244, 1400, 1433, 1505, 1700, 2923. ^{1}H NMR (300 MHz, $CDCl_3$) δ: 2.22 (3H, s, $ArCH_3$), 2.90 (3H, s, NCH_3), 3.45 (2H, apparent t, J = 7.9, ImH), 3.75 (2H, apparent t, J = 7.9, ImH), 3.80 (3H, s, OMe), 6.80 (1H, d, J = 7.7, ArH), 7.25 (1H, s, ArH), 7.57 (1H, m, ArH). *m/z* (CI): 238 (MNH_4^+, 20%), 221 (MH^+, 100). Anal. calcd. for $C_{12}H_{16}N_2O_2$ (M): 220.121 2; found (M^+): 220.121 6. Spectroscopic data for **6j**: IR ν_{max} (film, cm^{-1}): 1046, 1097, 1241, 1401, 1433, 1505, 1698, 3424. ^{1}H NMR (300 MHz, $CDCl_3$) δ: 2.30 (3H, s, $ArCH_3$), 2.80 (3H, s, NCH_3), 3.48 (2H, t, J = 7.9, ImH), 3.65 (2H, t, J = 7.9, ImH), 3.82 (3H, s, OMe), 6.76 (1H, m, ArH), 6.80 (1H, m, ArH), 7.12 (1H, d, J = 7.8, ArH). ^{13}C NMR (75 MHz, $CDCl_3$) δ: 18.4, 31.9, 46.8, 46.0, 55.7, 112.4, 116.4, 128.5, 131.7, 138.1, 146.8, 158.7. *m/z* (CI): 238 (MNH_4^+, 20%), 221 (MH^+, 100). Anal. calcd. for. $C_{12}H_{16}N_2O_2$ (M): 220.121 2; found (M^+): 220.121 1.

Typical procedure for lithiation of imidazolones (3a–3d) with 2.5 equiv. *n*-BuLi and then reaction with phenyl isocyanate

These experiments followed exactly the method described previously for trapping with iodomethane, but used phenyl isocyanate as the electrophile.

1-Phenyl-3-(phenylaminocarbonyl)imidazol-2(1H)-one (9a) and 3-(phenylaminocarbonyl)-1-[(2-phenylaminocarbonyl)phenyl]imidazol-2(1H)-one (9b)

1-Phenyl-3-(phenylaminocarbonyl)imidazol-2(1*H*)-one (**9a**) and 3-(phenylaminocarbonyl)-1-[(2-phenylaminocarbonyl)phenyl]imidazol-2(1*H*)-one (**9b**) were made from 1-phenylimidazol-2(1*H*)-one **3a** (0.2 g, 1.25 mmol) with *n*-BuLi (1.6 mol L^{-1}, 1.95 mL, 2.5 equiv.), then phenyl isocyanate (0.34 mL, 3.12 mmol, 2.5 equiv.) was added giving from chromatography firstly **9a** as a yellow solid (12 mg, 3%), mp 122 °C, lit. value (18) mp 123 °C, and secondly, **9b** as a white solid (300 mg, 86%), mp 150 °C. Spectroscopic data for **9a**: IR ν_{max} (film, cm^{-1}): 755, 1077, 1236, 1259, 1412, 1502, 1555, 1598, 1690, 1730. ^{1}H NMR (300 MHz, $CDCl_3$) δ: 6.81 (1H, d, J = 3.2, ImH), 7.20 (1H, m, ArH), 7.28 (1H, d, J = 3.2, ImH), 7.40 (4H, m, ArH), 7.59 (5H, m, ArH), 10.91 (1H, bs, NH). ^{13}C NMR (75 MHz, $CDCl_3$) δ: 108.6, 111.7, 120.0, 122.4, 124.4, 127.1, 129.0, 129.4, 136.9, 147.3, 150.3, 162.7. *m/z* (CI): 297 (MNH_4^+, 20%), 280 (MH^+, 100). Anal. calcd. for. $C_{16}H_{13}N_3O_2$ (M): 279.100 8; found (M^+): 279.100 5. Spectroscopic data for **9b**: IR ν_{max} (film, cm^{-1}): 754, 1234, 1320, 1411, 1443, 1495, 1553, 1601, 1678, 1730. ^{1}H NMR (300 MHz, $CDCl_3$) δ: 6.59 (1H, d, J = 3.2, ImH,), 7.12 (2H, m, ArH), 7.22 (1H, d, J = 3.2, ImH), 7.35 (5H, m, ArH), 7.58 (6H, m, ArH), 7.79 (1H, d, J = 7.3, ArH), 8.49 (1H, bs, NH), 10.65 (1H, bs, NH). ^{13}C NMR (75 MHz, $CDCl_3$) δ: 109.1, 113.9, 119.9, 120.1, 124.5, 124.7, 127.7, 128.3, 129.0, 129.3, 129.4, 131.5, 132.0, 135.0, 136.7, 137.6, 146.7, 151.4, 164.7. *m/z* (CI): 416 (MNH_4^+, 5%), 399 (MH^+, 8), 297 (20), 280 (100). Anal. calcd. for. $C_{23}H_{18}N_4O_3$ (M): 398.137 9; found (M^+): 398.137 5.

3-(Phenylaminocarbonyl)-1-[6-methoxy-2-(phenylaminocarbonyl)phenyl]imidazol-2(1H)-one (9c) and 3-(phenylaminocarbonyl)-1-[2-methoxy-3-(phenylaminocarbonyl)phenyl]-imidazol-2(1H)-one (9d)

3-(Phenylaminocarbonyl)-1-[6-methoxy-2-(phenylaminocarbonyl)phenyl]imidazol-2(1*H*)-one (**9c**) and 3-(phenylaminocarbonyl)-1-[2-methoxy-3-(phenylaminocarbonyl)phenyl]imidazol-2(1*H*)-one (**9d**) were made from a solution of 1-(2-methoxyphenyl)imidazol-2(1*H*)-one **3b** (0.23 g, 1.2 mmol) with *n*-BuLi (1.6 mol L^{-1}, 1.95 mL, 2.5 equiv.), then phenyl isocyanate (0.34 mL, 3.12 mmol, 2.5 equiv.) was added giving firstly from chromatography **9c** (80 mg, 15%, slightly contaminated by a phenyl isocyanate derivative), and secondly, **9d** (97 mg, 18%) as low mp yellow solids. Spectroscopic data for **9c**: IR ν_{max} (film, cm^{-1}): 754, 1055, 1233, 1409, 1440, 1492, 1550, 1599, 1680, 1707, 1728. ^{1}H NMR (300 MHz, $CDCl_3$) δ: 3.85 (3H, s, OCH_3), 6.42 (1H, d, J = 3.2, ImH), 7.01–7.81 (14H, m, ArH + ImH), 8.54 (1H, s, NH), 10.63 (1H, s, NH). ^{13}C NMR (75 MHz, $CDCl_3$) δ: 56.4, 102.9, 108.7, 113.9, 115.4, 120.0, 120.4, 120.7, 124.8, 124.9, 126.6, 128.6, 129.0, 129.3, 131.4, 138.0, 156.0, 163.3, 164.8. *m/z* (CI): 446 (MNH_4^+, 25%), 429 (MH^+, 40), 310 (100). Anal. calcd. for. $C_{24}H_{20}N_4O_4$ (M): 428.148 4; found (M^+): 428.149 3. Spectroscopic data for **9d**: IR ν_{max} (film, cm^{-1}): 753, 1441, 1598, 1710, 3329. ^{1}H NMR (300 MHz, $CDCl_3$) δ: 3.75 (3H, s, OCH_3), 6.24 (1H, bs, ImH), 6.30 (1H, bs, ImH), 7.03 (3H, m, ArH), 7.21 (4H, apparent t, J = 8.0, ArH), 7.29 (2H, apparent d, J = 7.7, ArH), 7.43 (2H, t, J = 8.0, ArH), 7.60 (2H, d, J = 7.7, ArH), 9.60 (1H, s, NH), 9.97 (1H, s, NH). ^{13}C NMR (75 MHz, $CDCl_3$) δ: 56.3, 109.4, 113.6, 115.0, 115.5, 120.2, 120.6, 121.1, 122.5, 124.5, 128.1, 129.1, 130.9, 131.9, 138.5, 138.7, 142.2, 154.8, 156.0, 165.3. *m/z* (CI): 446 (MNH_4^+, 2%), 429 (MH^+, 4), 327 (8), 310 (100), 217 (5), 102 (5). Anal. calcd. for. $C_{24}H_{20}N_4O_4$ (M): 428.148 4; found (M^+): 428.149 2.

1-[(3-Methoxy-2-phenylaminocarbonyl)phenyl]-3-phenylaminocarbonylimidazol-2(1H)-one (9e) and 1-(3-methoxyphenyl)-3-(phenylaminocarbonyl)imidazol-2(1H)-one (9f)

1-[(3-Methoxy-2-phenylaminocarbonyl)phenyl]-3-phenylaminocarbonylimidazol-2(1*H*)-one (**9e**) and 1-(3-methoxyphenyl)-3-(phenylaminocarbonyl)imidazol-2(1*H*)-one (**9f**) were made from 1-(3-methoxyphenyl)imidazol-2(1*H*)-one **3c** (0.27 g, 1.42 mmol) with *n*-BuLi (1.6 mol L^{-1}, 2.2 mL, 2.5 equiv.) then phenyl isocyanate (0.39 mL, 3.5 mmol, 2.5 equiv.) giving from chromatography firstly **9e** as a white solid (160 mg, 36%), mp 101 °C, and secondly, **9f** as a white solid (95 mg, 21%), mp 180 °C. Spectroscopic data for **9e**:

© 2004 NRC Canada

IR ν_{max} (film, cm^{-1}): 735, 1233, 1410, 1440, 1474, 1554, 1601, 1679, 1729. ^1H NMR (300 MHz, $CDCl_3$) δ: 3.91 (3H, s, OCH_3), 6.60 (1H, d, *J* = 3.3, ImH), 7.03 (2H, t, *J* = 7.8, ArH), 7.12 (1H, d, *J* = 3.3, ImH), 7.14 (2H, m, ArH), 7.33 (4H, m, ArH), 7.52 (3H, m, ArH), 7.58 (2H, apparent d, *J* = 8.4, ArH), 8.41 (1H, s, NH), 10.73 (1H, s, NH). ^{13}C NMR (75 MHz, $CDCl_3$) δ: 56.3, 108.5, 111.9, 113.9, 119.6, 119.9, 120.1, 124.4, 124.6, 128.9, 129.0, 131.4, 133.0, 133.4, 136.8, 137.6, 146.9, 151.3, 157.2, 162.4. *m/z* (CI): 429 (MH^+, 3%), 310 (12), 217 (100), 119 (10). Anal. calcd. for. $C_{24}H_{20}N_4O_4$ (M): 428.148 4; found (M^+): 428.148 5. Spectroscopic data for **9f**: IR ν_{max} (film, cm^{-1}): 758, 1263, 1441, 1474, 1597, 1680. ^1H NMR (300 MHz, $CDCl_3$) δ: 3.94 (3H, s, OCH_3), 6.47 (1H, d, *J* = 3.0, ImH), 6.58 (1H, d, *J* = 3.0, ImH), 7.07 (1H, m, ArH), 7.13 (1H, m, ArH), 7.21 (2H, d, *J* = 8.1, ArH), 7.32 (2H, m, ArH), 7.55 (3H, apparent t, *J* = 8.1, ArH). ^{13}C NMR (75 MHz, $CDCl_3$) δ: 55.3, 108.9, 111.0, 113.6, 119.5, 119.9, 124.0, 124.1, 125.0, 128.3, 130.6, 132.1, 138.2, 156.0, 157.2. *m/z* (CI): 310 (MH^+, 35%), 217 (100). Anal. calcd. for. $C_{17}H_{15}N_3O_3$ (M): 309.1113; found (M^+): 309.110 9.

1-(4-Methoxyphenyl)-3-(phenylaminocarbonyl)imidazol-2(1H)-one (9g) and 1-[(4-methoxy-2-phenylaminocarbonyl)phenyl]-3-phenylaminocarbonylimidazol-2(1H)-one (9h)

1-(4-Methoxyphenyl)-3-(phenylaminocarbonyl)imidazol-2(1*H*)-one (**9g**) and 1-[(4-methoxy-2-phenylaminocarbonyl)phenyl]-3-phenylaminocarbonylimidazol-2(1*H*)-one (**9h**) were made from 1-(4-methoxyphenyl)imidazol-2(1*H*)-one **3d** (0.24 g, 1.25 mmol) with *n*-BuLi (1.6 mol L^{-1}, 1.95 mL, 2.5 equiv.), then phenyl isocyanate (0.34 mL, 3.12 mmol, 2.5 equiv) was added giving from chromatography firstly **9g** as a white foam (20 mg, 6.5%), and secondly, **9h** as a white solid (0.091 g, 30%), mp 167–169 °C. Spectroscopic data for **9g**: ^1H NMR (300 MHz, $CDCl_3$) δ: 3.77 (3H, s, OCH_3), 6.52 (1H, d, *J* = 3.2, ImH), 6.92 (2H, m, ArH), 7.06 (1H, m, ArH), 7.13 (1H, d, *J* = 3.2, ImH), 7.28 (2H, m, ArH), 7.35 (2H, m, ArH), 7.49 (2H, m, ArH), 10.61 (1H, bs, NH). ^{13}C NMR (75 MHz, $CDCl_3$) δ: 55.9, 108.6, 112.6, 114.9, 120.3, 120.9, 124.6, 124.7, 129.3, 130.7, 137.3, 156.0, 158.9. *m/z* (CI): 310 (MH^+, 100%), 191 (70), 94 (25). Anal. calcd. for. $C_{17}H_{15}N_3O_3$ (M): 309.113 3; found (M^+): 309.113 1. Spectroscopic data for **9h**: ^1H NMR (300 MHz, $CDCl_3$) δ: 3.92 (3H, s, OCH_3), 6.54 (1H, d, *J* = 3.2, ImH), 7.14 (2H, m, ArH), 7.17 (1H, d, *J* = 3.2, ImH), 7.31 (4H, m, ArH), 7.39 (3H, apt, *J* = 7.4, ArH), 7.56 (4H, m, ArH), 8.61 (1H, bs, NH), 10.70 (1H, bs, NH). ^{13}C NMR (75 MHz, $CDCl_3$) δ: 55.8, 108.7, 110.0, 114.0, 114.4, 117.3, 119.8, 120.1, 124.5, 124.6, 124.7, 129.0, 129.4, 136.5, 137.4, 137.9, 146.7, 152.0, 160.1, 164.5. *m/z* (CI): 429 (MH^+, 5%), 310 (100), 217 (14), 119 (14). Anal. calcd. for. $C_{24}H_{20}N_4O_4$ (M): 428.148 4; found (M^+): 428.149 6.

Typical procedure for the reaction of 1-aryl-3-methylimidazolones (5a–5d) with 1 equiv. of *n*-BuLi and trapping with iodomethane

1-Phenyl-3,5-dimethylimidazol-2(1H)-one (5j) 1-phenyl-3,4-dimethylimidazol-2(1H)-one (5k)

A solution of 3-methyl-1-phenyl-imidazol-2(1*H*)-one **5a** (0.2 g, 1.15 mmol, 1 equiv.) in anhyd. THF was treated with *n*-BuLi (1.6 mol L^{-1}, 0.79 mL, 1.1 equiv.) at –78 °C over 30 min under N_2. The solution was warmed up to then maintained at 0 °C for 2 h and cooled down to –78 °C again for the addition of iodomethane (0.1 mL, 1.72 mmol, 1.5 equiv.). The reaction mixture was allowed to warm up to rt and after 20 h quenched with satd. aq. NH_4Cl, and evaporated to remove the THF. The white organic residue was taken up with CH_2Cl_2, the solution washed with brine, dried over $MgSO_4$ and evaporated. Column SiO_2 chromatography (50%–70%–100% of EtOAc in hexane) yielded firstly 1-(2-methylphenyl)-3,5-dimethylimidazol-2(1*H*)-one **5j** (28 mg, 12%) as a low mp solid, and secondly, 1-(2-methylphenyl)-3,4-methylimidazol-2(1*H*)-one **5k** (96 mg, 46%) as a solid mp 130 °C. Spectroscopic data for **5j**: IR ν_{max} (film, cm^{-1}): 1401, 1500, 1638, 1655, 1676, 1685. ^1H NMR (300 MHz, $CDCl_3$) δ: 1.84 (3H, s, $ImCH_3$), 3.19 (3H, s, NCH_3), 5.94 (1H, bs, ImH), 7.21 (2H, m, ArH), 7.28 (1H, apparent d, *J* = 7.2, ArH), 7.37 (1H, apparent t, *J* = 7.2, ArH). ^{13}C NMR (75 MHz, $CDCl_3$) δ: 10.9, 30.1, 108.5, 118.5, 127.3, 127.5, 129.0, 134.7, 152.7. *m/z* (CI): 206 (MNH_4^+, 15%), 189 (MH^+, 100). Anal. calcd. for. $C_{11}H_{12}N_2O$ (M): 188.095 0; found (M^+): 188.094 9. Spectroscopic data for **5k**: IR ν_{max} (film, cm^{-1}): 760, 1400, 1430, 1455, 1503, 1595, 1639, 1680, 1717. ^1H NMR (300 MHz, $CDCl_3$) δ: 2.11 (3H, s, $ImCH_3$), 3.26 (3H, s, NCH_3), 6.33 (1H, bs, ImH), 7.21 (1H, m, ArH), 7.41 (1H, apparent t, *J* = 7.5, ArH), 7.37 (1H, apparent t, *J* = 7.5, ArH). ^{13}C NMR (75 MHz, $CDCl_3$) δ: 10.2, 27.1, 104.9, 120.2, 121.1, 125.1, 125.6, 128.9, 137.3, 153.3. *m/z* (CI): 206 (MNH_4^+, 20%), 189 (MH^+, 100), 175 (42). Anal. calcd. for. $C_{11}H_{12}N_2O$ (M): 188.095 0; found (M^+): 188.094 8.

1-(2-Methoxyphenyl)-3,5-dimethylimidazol-2(1H)-one (5l) and 1-(2-methoxyphenyl)-3,4-dimethylimidazol-2(1H)-one (5m)

1-(2-Methoxyphenyl)-3,5-dimethylimidazol-2(1*H*)-one (**5l**) and 1-(2-methoxyphenyl)-3,4-dimethylimidazol-2(1*H*)-one (**5m**) were prepared from 1-(2-methoxyphenyl)-3-methylimidazol-2(1*H*)-one **5b** (0.25 g, 1.2 mmol) with *n*-BuLi (1.6 mol L^{-1}, 1.3 mL, 1.5 equiv.), then iodomethane (0.15 mL, 2.4 mmol, 2 equiv.) was added giving from chromatography a mixture (129 mg) (Anal. calcd. for $C_{12}H_{14}N_2O_2$ (M): 218.105 5; found (M^+): 218.204 9) of **5l** (12%, estimated by ^1H NMR) and its isomer **5m** (36%, estimated by ^1H NMR) as yellow oils. Spectroscopic data for **5l**: ^1H NMR (300 MHz, $CDCl_3$) δ: 2.20 (3H, s, $ImCH_3$), 3.30 (3H, s, NCH_3), 3.81 (3H, s, OCH_3), 5.95 (1H, bs, ImH), 6.86–7.50 (4H, m, ArH). *m/z* (CI): 233 (MNH_4^+, 51%), 219 (MH^+, 100). Spectroscopic data for **5m**: ^1H NMR (300 MHz, $CDCl_3$) δ: 2.12 (3H, bs, $ImCH_3$), 3.28 (3H, s, NCH_3), 3.87 (3H, s, OCH_3), 6.21 (1H, s, ImH), 7.01–7.50 (4H, m, ArH). *m/z* (CI): 233 (MNH_4^+, 51%), 219 (MH^+, 100).

1-(4-Methoxyphenyl)-3,4-dimethylimidazol-2(1H)-one (5n) and 1-(4-methoxyphenyl)-3,5-dimethylimidazol-2(1H)-one (5o)

1-(4-Methoxyphenyl)-3,4-dimethylimidazol-2(1*H*)-one **5n** and 1-(4-methoxyphenyl)-3,5-dimethylimidazol-2(1*H*)-one **5o** were prepared from 1-(4-methoxyphenyl)-3-methylimidazol-2(1*H*)-one **5d** (0.2 g, 0.98 mmol) with *n*-BuLi (1.6 mol L^{-1}, 0.67 mL, 1.1 equiv.), then iodomethane

© 2004 NRC Canada

(0.09 mL, 1.47 mmol, 1.5 equiv.) was added giving from chromatography firstly **5n** as yellow oil (104 mg, 49%), and secondly, **5o** as a yellow solid, mp 118–120 °C (33 mg, 16%). Spectroscopic data for **5n**: IR ν_{max} (film, cm^{-1}): 1251, 1516, 1678. ^1H NMR (300 MHz, $CDCl_3$) δ: 2.12 (3H, s, $ImCH_3$), 3.27 (3H, s, NCH_3), 3.83 (3H, s, OCH_3), 6.26 (1H, bs, ImH), 6.94 (2H, d, J = 9.1, ArH), 7.48 (2H, d, J = 9.1, ArH). ^{13}C NMR (75 MHz, $CDCl_3$) δ: 10.1, 30.4, 55.4, 105.5, 109.7, 112.2, 114.2, 123.0, 130.7, 157.1. *m/z* (CI): 236 (MNH_4^+, 10%), 219 (MH^+, 100), 205 (90). Anal. calcd. for $C_{12}H_{14}N_2O_2$ (M): 218.105 5; found (M^+): 218.105 6. Spectroscopic data for **5o**: IR ν_{max} (film, cm^{-1}): 1248, 1402, 1461, 1514, 1638, 1684, 2361. ^1H NMR (300 MHz, $CDCl_3$) δ: 1.91 (3H, s, $ImCH_3$), 3.30 (3H, s, NCH_3), 3.85 (3H, s, OCH_3), 6.02 (1H, bs, ImH), 6.98 (2H, d, J = 8.9, ArH), 7.22 (2H, d, J = 8.9, ArH). ^{13}C NMR (75 MHz, $CDCl_3$) δ: 10.8, 30.1, 55.0, 108.1, 114.4, 118.9, 127.9, 128.7, 153.3, 158.9. *m/z* (CI): 236 (MNH_4^+,10%), 219 (MH^+, 100). Anal. calcd. for $C_{12}H_{14}N_2O_2$ (M): 218.105 5; found (M^+): 218.105 2.

Typical procedure for dilithiation of (5a–5d) with 2.5 equiv. *n*-BuLi and trapping with iodomethane

*1-(2-Methylphenyl)-3,4-dimethylimidazol-2(1*H*)-one (5p)*

A solution of 3-methyl-1-phenylimidazol-2(1*H*)-one **5a** (0.1 g, 0.57 mmol) in anhyd. THF was treated with *n*-BuLi (1.6 mol L^{-1}, 0.89 mL, 2.5 equiv.) at –78 °C over 30 min under N_2. The solution was warmed up to then maintained at 0 °C for 2 h and cooled down to –78 °C again for the addition of iodomethane (0.09 mL, 1.43 mmol, 2.5 equiv.). The reaction mixture was allowed to warm up to rt and after 20 h quenched with satd. aq. NH_4Cl, and evaporated to remove the THF. The organic residue was taken up with CH_2Cl_2, the solution washed with brine, dried over $MgSO_4$, and evaporated to give the title compound **5p** as a yellow oil (109 mg, 95%). IR ν_{max} (film, cm^{-1}): 716, 757, 1401, 1432, 1463, 1497, 1689, 1718, 2922. ^1H NMR (300 MHz, $CDCl_3$) δ: 2.15 (3H, s, $ImCH_3$), 2.30 (3H, s, $ArCH_3$), 3.30 (3H, s, NCH_3), 6.07(1H, s, ImH), 7.25 (4H, m, ArH). ^{13}C NMR (75 MHz, $CDCl_3$) δ: 10.6, 18.4, 27.7, 107.8, 119.8, 126.8, 127.7, 128.3, 129.3, 131.3, 135.7, 152.6. *m/z* (CI): 220 (MNH_4^+, 37%), 203 (MH^+, 100). Anal. calcd. for $C_{12}H_{14}N_2O$ (M): 202.110 6; found (M^+): 202.110 2.

*1-(2-Methoxy-6-methylphenyl)-3,4-dimethylimidazol-2(1*H*)-one (5q)*

1-(2-Methoxy-6-methylphenyl)-3,4-dimethylimidazol-2(1*H*)-one **5q** was prepared from 1-(2-methoxyphenyl)-3-methylimidazol-2(1*H*)-one **5b** (0.1 g, 0.49 mmol) with *n*-BuLi (1.6 mol L^{-1}, 0.76 mL, 2.5 equiv.), then iodomethane (0.08 mL, 1.22 mmol, 2.5 equiv.) was added giving **5q** as a yellow oil (0.1 g, 88%). IR ν_{max} (film, cm^{-1}): 776, 1080, 1271, 1399, 1433, 1464, 1475, 1495, 1687, 2928. ^1H NMR (300 MHz, $CDCl_3$) δ: 2.11 (3H, s, $ImCH_3$), 2.17 (3H, s, $ArCH_3$), 3.29 (3H, s, NCH_3), 3.78 (3H, s, OCH_3), 5.97 (1H, s, ImH), 6.80 (1H, d, J = 8.0, ArH), 6.87 (1H, d, J = 8.0, ArH), 7.23 (1H, t, J = 8.0, ArH). ^{13}C NMR (75 MHz, $(CD_3)_2CO$) δ: 9.7, 17.5, 30.0, 55.5, 107.8, 109.6, 112.5, 119.2, 120.7, 122.3, 128.9, 134.4, 156.4. *m/z* (CI): 250 (MNH_4^+18, 4%), 232 (MH^+, 100), 219 (30). Anal. calcd. for $C_{13}H_{16}N_2O_2$ (M): 232.121 2; found (M^+): 232.121 5.

*1-(3-Methoxy-2-methylphenyl)-3,4-dimethylimidazol-2(1*H*)-one (5r)*

1-(3-Methoxy-2-methylphenyl)-3,4-dimethylimidazol-2(1*H*)-one **5r** was prepared from 1-(3-methoxyphenyl)-3-methylimidazol-2(1*H*)-one **5c** (0.17 g, 0.83 mmol) with *n*-BuLi (1.6 mol L^{-1}, 1.3 mL, 2.5 equiv.), then iodomethane (0.09 mL, 1.5 mmol, 1.9 equiv.) was added giving **5r** as a clear oil (0.43 mg, 24%). IR ν_{max} (film, cm^{-1}): 1140, 1261, 1402, 1433, 1475, 1589, 1638, 1686. ^1H NMR (300 MHz, $CDCl_3$) δ: 2.11 (3H, s, $ArCH_3$), 2.12 (3H, bs, $ImCH_3$), 3.28 (3H, s, NCH_3), 3.86 (3H, s, OCH_3), 6.04 (1H, bs, ImH), 6.86 (2H, d, J = 8.1, ArH), 7.20 (1H, t, J = 8.1, ArH). ^{13}C NMR (75 MHz, $CDCl_3$) δ: 10.3, 11.1, 27.3, 55.6, 107.6, 109.5, 119.35, 119.5, 124.6, 126.4, 136.7, 152.5, 158.4. *m/z* (CI): 250 (MNH_4^+, 7%), 233 (MH^+, 100), 219 (25). Anal. calcd. for $C_{13}H_{16}N_2O_2$ (M): 232.121 2; found (M^+): 232.121 0.

*1-(4-Methoxy-2-methylphenyl)-3,4-dimethylimidazol-2(1*H*)-one (5s)*

1-(4-Methoxy-2-methylphenyl)-3,4-dimethylimidazol-2(1*H*)-one **5s** was prepared from 1-(4-methoxyphenyl)-3-methylimidazol-2(1*H*)-one **5d** (0.1 g, 0.49 mmol, 1 equiv.) with *n*-BuLi (1.6 mol L^{-1}, 0.76 mL, 2.5 equiv.), then iodomethane (0.076 mL, 1.22 mmol, 2.5 equiv.) was added giving **5s** as a yellow oil (0.107 g, 97%). IR ν_{max} (film, cm^{-1}): 1044, 1096, 1161, 1252, 1401, 1432, 1463, 1508, 1686, 2932. ^1H NMR (300 MHz, $CDCl_3$) δ: 2.11 (3H, s, $ArCH_3$), 2.18 (3H, s, $ArCH_3$), 3.28 (3H, s, NCH_3), 3.81 (3H, s, OCH_3), 6.01 (1H, s, ImH), 6.80 (2H, m, ArH), 7.12 (1H, d, J = 8.6, ArH). ^{13}C NMR (75 MHz, $CDCl_3$) δ: 10.6, 18.5, 27.7, 55.7, 108.0, 112.0, 116.2, 119.4, 128.7, 129.1, 137.2, 142.2, 159.2. *m/z* (CI): 250 (MNH_4^+, 26%), 233 (MH^+, 100), 146.2, 164.5. *m/z* (CI): 163 (MH^+, 100%). Anal. calcd. for $C_{13}H_{16}N_2O_2$ (M): 232.121 2; found (M^+): 232.121 7.

References

1. J.-P. Meigh, M. Álvarez, and J.A. Joule. J. Chem. Soc. Perkin Trans. 1, 2012 (2001).
2. H.W. Gschwend and H.R. Rodriguez. Org. React. **26**, 1 (1979); K. Undheim and T. Benneche. Heterocycles, **30**, 1155 (1990); V. Snieckus. Chem. Rev. **90**, 879 (1990); G. Quéguiner, F. Marsais, V. Snieckus, and J. Epsztajn. Adv. Heterocycl. Chem. **52**, 187 (1991).
3. DoM the movie [online]. Available from http://www.chem.queensu.ca/people/faculty/snieckus/movie.WMV.
4. J.-P. Meigh. Ph.D thesis, University of Manchester, Manchester, UK, 2000.
5. A. Ahaidar, D. Fernandez, G. Danelon, C. Cuevas, I. Manzanares, F. Albericio, J.A. Joule, and M. Álvarez. J. Org. Chem. **68**, 10 020 (2003).
6. R.J. Anderson and J.C. Morris. Tetrahedron Lett. **42**, 8679 (2001).
7. P. Molina, P.M. Fresneda, and S. Delgado. J. Org. Chem., **68**, 489 (2003).
8. N.B. Perry, L. Ettouati, M. Litaudon, J.W. Blunt, M.H.G. Munro, S. Parkin, and H. Hope. Tetrahedron, **50**, 3987 (1994); G. Trimurtulu, D.J. Faulkner, N.B. Perry, L. Ettouati, M. Litaudon, J.W. Blunt, M.H.G. Munro, and G.B. Jameson. Tetrahedron, **50**, 3993 (1994).
9. A. Godard, J.-M. Jacquelin, and G. Quéguiner. J. Organomet. Chem. **354**, 273 (1988).

© 2004 NRC Canada

10. K. Smith, G. El-Hiti, and A.P. Shukla. J. Chem. Soc. Perkin Trans. 1, 2305 (1999).
11. A.J. Carpenter and D.J. Chadwick. Tetrahedron, **41**, 3803 (1985).
12. T.D. Harris and C.P. Roth. J. Org. Chem. **44**, 2004 (1979).
13. G. Lukacs, M. Porcs-Makkay, and G. Simig. Tetrahedron Lett. **44**, 3211 (2003).
14. W.J. Houlihan and V.A. Parrino. J. Org. Chem. **47**, 5177 (1982).
15. D.J. Chadwick and D.S. Ennis. Tetrahedron, **47**, 9901 (1991).
16 N. Tahara, T. Fukuda, and M. Iwao. Tetrahedron Lett. **43**, 9069 (2002).
17. P. Rhonnstad and D. Wensbo. Tetrahedron Lett. **43**, 3137 (2002).
18. T.P. Forrest, G.A. Danphinee, and F.M.F. Chen. Can. J. Chem. **52**, 2725 (1974).
19. V.V. Golovko, A.I. Statsenskaya, Yu.A. Baskakov, and Y.G. Putsykin. Chem. Heterocycl. Compd. (N.Y.), **22**, 1084 (1986).
20. F. Heidempergher, A. Pillan, V. Pinciroli, F. Vaghi, C. Arrigoni, G. Bolis, C. Caccia, L. Dho, R. McArthur, and M. Varasi. J. Med. Chem. **40**, 3369 (1997).
21. E.J. Hessler. J. Org. Chem. **41**, 1828 (1976).
22. E. Crowe, F. Hossner, and M.J. Hughes. Tetrahedron, **51**, 8889 (1995).
23. R.W. Luckenbaugh. US Patent 3 216 816; Chem. Abstr. **64**, 8195 (1966).
24. J.P. Fourneau and Y. de Lestrange. Bull. Chim. Soc. Fr. 827 (1947).
25. G.S. Poindexter. Synthesis, 541 (1981).
26. C. Banzatti, A. Della Torre, P. Melloni, D. Pieraccioli, and P. Salvadori. J. Heterocycl. Chem. **20**, 139 (1983).
27. T.K. Kim and G.-J. Lee. J. Org. Chem. **64**, 2941 (1999).
28. A.F. McKay, W.R.R. Park, and S.J. Viron. J. Am. Chem. Soc. **72**, 3659 (1950).
29. W.B. Wright and H.J. Brabander. J. Org. Chem. **26**, 4051 (1961).

© 2004 NRC Canada

The complex photochemistry of 2,3-dibenzylidenesuccinates

Tokouré Assoumatine, Brigitte L. Yvon, and James L. Charlton

Abstract: The photochemistry of diethyl *E,E*-2,3-(3,4,5-trimethoxybenzylidene)succinate (**8**) is solvent dependent. In both protic and aprotic solvents, there is a photoequilibrium established between **8** and its *E,Z*-isomer (**9**). In chloroform at high light intensity, very little **9** is formed and the main product is 1,4-dihydronaphthalene (**10**), formed via photoinduced intramolecular [1,3]-sigmatropic hydrogen shift within an intermediate 1,8a-dihydronaphthalene (**11**). In protic solvents, irradiation of either **8** or **9** ultimately gives primarily the *cis*-1,2-dihydronaphthalene product (**13**), along with smaller amounts of the trans isomer (**14**). By using deuterated solvents, it was shown that **13** and **14** are formed by solvent protonation (or deuteration) of the 1,8a-dihydronaphthalene intermediate (**11** or **12**).

Key words: 2,3-dibenzylidenesuccinate, photocyclization, dihydronaphthalene, lignan.

Résumé : La photochimie du *E,E*-2,3-(3,4,5-triméthoxybenzylidène)succinate de diéthyle (**8**) dépend de la nature du solvant. Dans les solvants tant protique qu'aprotique, il s'établit un photoéquilibre entre le composé **8** et son isomère *E,Z* (**9**). Dans le chloroforme, à une intensité lumineuse intense, il se forme très peu de composé **9** et le produit principal est le 1,4-dihydronaphtalène (**10**) qui se forme, à partir de l'intermédiaire 1,8a-dihydronaphtalène (**11**), par un déplacement photoinduit d'hydrogène [1,3]-sigmatropique. Dans les solvants protiques, l'irradiation des composés **8** ou **9** conduit toujours à des quantités importantes du produit *cis*-1,2-dihydronaphtalène (**13**) aux côtés de plus faibles quantités de l'isomère trans (**14**). En utilisant des solvants deutérés, il a été possible de démontrer que les composés **13** et **14** se forment par protonation (ou deutération) d'un intermédiaire 1,8a-dihydronaphtalène (**11** ou **12**) par le solvant.

Mots clés : 2,3-dibenzylidènesuccinate, photocyclisation, dihydronaphtalène, lignane.

[Traduit par la Rédaction]

Introduction

There is a rich literature on the photochemistry of *E,E*-2,3-dibenzylidenesuccinate derivatives (1–23). Although the majority of the work deals with the photochemical cyclization of fulgides (the cyclic anhydrides of *E,E*-dibenzylidenesuccinic acids; **1**, X = O), there are also examples of photoreactions of fulgimides (the cyclic imides of *E,E*-dibenzylidenesuccinic acids; **1**, X = NR), dibenzylidenebutyrolactones, and acyclic derivatives. Heller and co-workers (6) have provided a general mechanistic scheme to explain the photochemistry that has been observed for various fulgides and fulgimides (Scheme 1, where R represents various aromatic substitution patterns).

Although the results of irradiation vary with substituents R and solvents, photoinduced isomerization between the *E,E*- and *E,Z*-isomers **1** and **2** is generally observed. Isomers **1** and **2** also undergo photochemical conrotatory ring closure to form the *cis*- and *trans*-1,8a-dihydronaphthalenes (1,8a-DHNs) **3** and **4,** respectively. The thermal disrotatory opening of **3** and **4** to give **2** and **1,** respectively, is assumed to be the mechanism for the photoinduced isomerization of **1** and **2**. The 1,8a-DHNs **3** and **4** are seldom isolated owing to their thermal and photochemical instability, and the final isolated products (other than **1** and **2**) are more often the 1,4-DHN **5** and (or) the 1,2-DHNs **6** and **7** (or the corresponding naphthalenes if oxygen is present). On the basis of temperature and pH effects, Heller and co-workers (6) tentatively concluded that 1,4-DHN **5** was formed photochemically from **3** and **4** (a [1,3]-intramolecular sigmatropic H-shift) and that 1,2-DHNs **6** and **7** were formed by an acid-catalysed rearrangement of **3** and **4,** respectively, rather than by a thermal intramolecular [1,5]-sigmatropic shift (Scheme 1) (6). In previous papers by Heller's group, it had been assumed that the latter rearrangement involved an intramolecular [1,5]-sigmatropic H-shift (17, 18, 20).

While there have been many published studies of the photochemistry of cyclic derivatives of dibenzylidenesuccinates, such as the fulgides and fulgimides discussed above, there have been fewer published examples of the study of the photochemistry of the corresponding acyclic succinate derivatives. In an earlier paper (23), we reported the first example of the photolysis of a dibenzylidenesuccinate diester. In that preliminary study, we reported that the photolysis of *E,E*-2,3-(3,4,5-trimethoxybenzylidene)succinate (**8**) in ethanol acidified with trifluoroacetic acid (TFA), followed by column chromatography of the photolysis product, gave the dihydronaphthalene esters **13** (34% yield) and **14** (2% yield) (Scheme 2) (23). We have now conducted a more detailed study of the photochemical behaviour of **8** in various solvents and observed that the products depend quite strongly

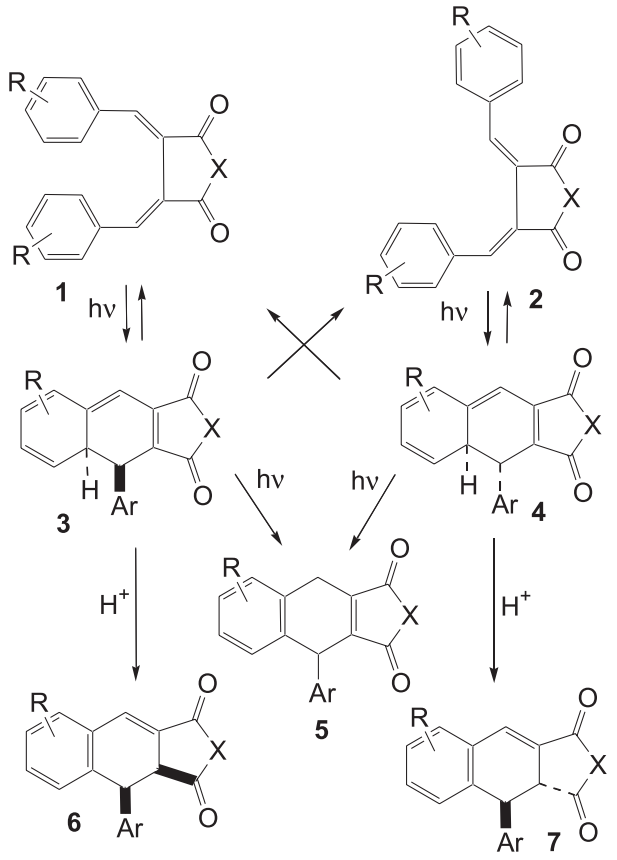
Received 31 January 2004. Published on the NRC Research Press Web site at http://canjchem.nrc.ca on 12 January 2005.

T. Assoumatine, B.L. Yvon, and J.L. Charlton.[1]
Department of Chemistry, University of Manitoba, Winnipeg, MB R3T 2N2, Canada.

[1]Corresponding author (e-mail: charltn@cc.umanitoba.ca).

 doi: 10.1139/V04-143 © 2004 NRC Canada

Scheme 1. Photoreactions of fulgides (X = O) and fulgimides (X = NH, NR, or NAr).



on the solvent and reaction conditions. By using deuterated solvents, we have established the mechanisms of the various prototropic rearrangements.

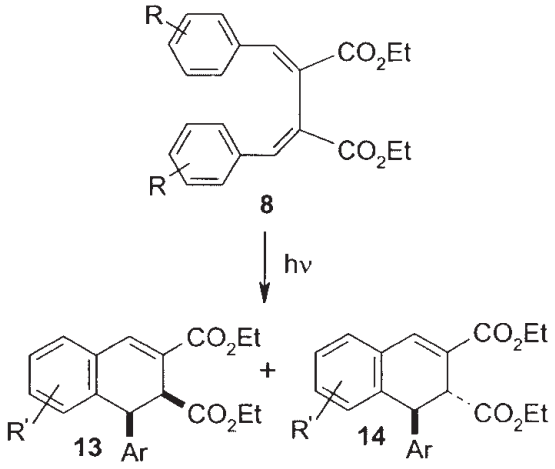
It is hoped that a better understanding of the photochemistry of 2,3-dibenzylidenesuccinates will make their photochemical reactions more useful for the synthesis of lignans, particularly the aryltetralin and aryldihydronaphthalene types. This goal has been partially achieved with the recent publication of an asymmetric synthesis of (+)-lyoniresinol dimethyl ether from a derivative of compound **8** (24).

Results and discussion

Diethyl *E,E*-2,3-(3,4,5-trimethoxybenzylidene)succinate (**8**) was prepared as previously described (23). Although **8** is shown in Scheme 2 in an *s*-cis conformation, it should be noted that this molecule does not have a planar butadiene system. Molecular mechanics calculations show that it exists as an equilibrating mixture of twisted *s*-cis and *s*-trans conformers. A fuller discussion of its conformation can be found in our previous publication (24). In the synthesis (23), **8** is formed in an *E,E* configuration as the sole product. This product is easily distinguished from the corresponding *E,Z* and *Z,Z* isomers by NMR (17).

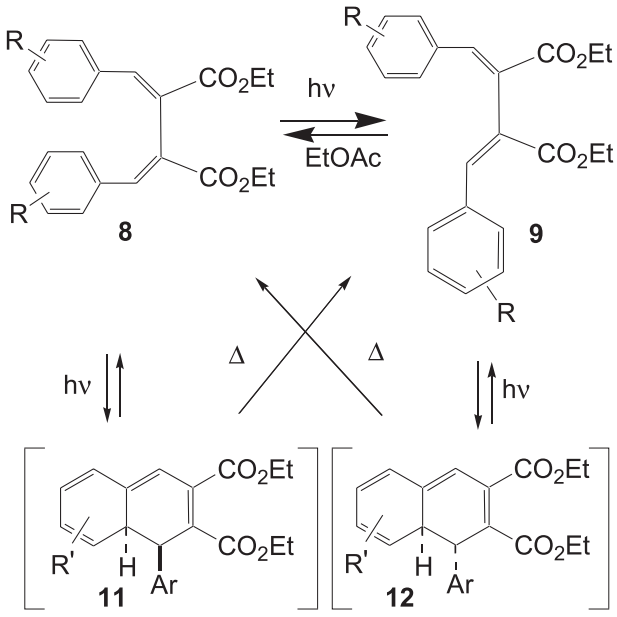
Irradiation of **8** in ethyl acetate with a medium-pressure mercury lamp through Pyrex glass gave only a slow and incomplete conversion of **8** to the corresponding *E,Z*-isomer **9** (Scheme 3). Further irradiation of the mixture resulted in the formation of several products (including **10**; see below). It

Scheme 2. Previous study of photolysis of *E,E*-2,3-(3,4,5-trimethoxybenzylidene)succinate (**8**).



R = 3,4,5-trimethoxy R' = 6,7,8-trimethoxy
Ar = 3,4,5-trimethoxyphenyl

Scheme 3. Irradiation of **8** in ethyl acetate.



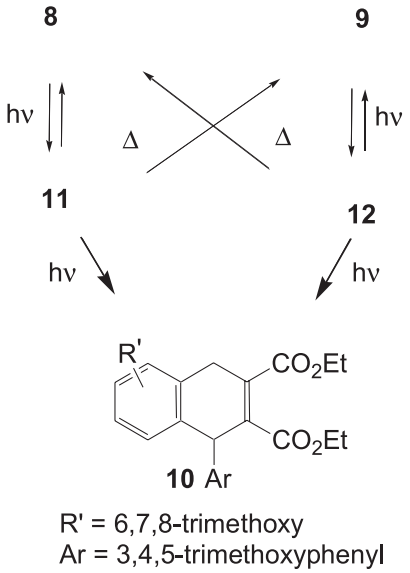
R = 3,4,5-trimethoxy R' = 6,7,8-trimethoxy
Ar = 3,4,5-trimethoxyphenyl

was possible to separate **9** from **8** by HPLC and to characterize **9** by ^{1}H and ^{13}C NMR. A possible mechanism for the conversion of **8** to **9** is photochemical cyclization to the 1,8a-DHN **11** followed by thermal disrotatory opening to **9**. It is also possible that there is a direct photoisomerization of the double bond. The irradiation of isolated **9** in ethyl acetate gave the same mixture of **8** and **9**, and the conversion of **9** to **8** may pass through intermediate **12**.

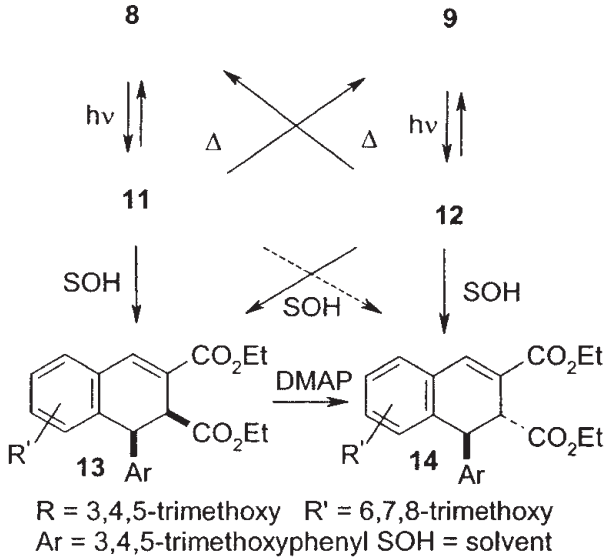
Surprisingly, irradiation of **8** in chloroform gave the 1,4-DHN **10** almost exclusively (Scheme 4). The reaction was most efficient if low concentrations of **8** were irradiated in tubes placed very close to the lamp (higher light intensity).

© 2004 NRC Canada

Scheme 4. Irradiation of **8** in chloroform.



Scheme 5. Irradiation of **8** in alcoholic solvents.



On moving the sample further from the lamp (30 cm), it was possible to detect the concurrent formation of the *E,Z*-isomer **9,** which, although it appeared early in the reaction, also slowly disappeared to form the 1,4-DHN **10**. When **8** was irradiated in deuterochloroform (that had been washed with D_2O to prevent any possibility that traces of water would protonate an intermediate), there was no incorporation of deuterium into the 1,4-DHN **10**. The lack of any deuterium incorporation when the reaction was run in D_2O-washed deuterochloroform confirmed that the proposed conversion of **11** to **10** was an intramolecular 1,3-sigmatropic hydrogen shift, an allowed photochemical pericyclic reaction. It thus appears that **11** (or **12**) is photochemically converted to **10** and that this allowed photochemical sigmatropic reaction competes very well with thermal opening of **11** (or **12**) to **9** (or **8**). The intermediate formation of *E,Z*-isomer **9** during irradiation in chloroform at lower light intensities, and its ultimate conversion to **10**, suggests that this is also a two-step photochemical conversion via the 1,8a-DHN **12**.

Irradiation of **8** in alcoholic solvents (methanol, ethanol, or 2-propanol), until the disappearance of **8**, gave primarily the *cis*-1,2-DHN **13** accompanied by the *trans*-1,2-DHN **14** in a 4:1 ratio (Scheme 5). Similar results were reported in a preliminary publication (23). However, irradiation for shorter periods of time showed that the *E,Z*-isomer **9** was initially formed along with the two DHN derivatives **13** and **14**. When **9** reached about 80% of the concentration of **8,** it ceased to increase and both **8** and **9** subsequently diminished as **13** and **14** formed. It therefore appears that a photoequilibrium between **8** and **9** also takes place in alcoholic solvents. A similar irradiation of **9** in methanol produced **8** and thereafter a slow conversion to a mixture of **13** and **14** in a 4:1 ratio.

Cis-1,2-DHN **13** could be quantitatively converted to *trans*-1,2-DHN **14** by warming with a trace of *N,N*-dimethyl-4-aminopyridine (DMAP) in ethanol, confirming that the trans ester **14** is thermodynamically more stable than **13**. When the irradiation of **8** was conducted in perdeuteromethanol (CD_3OD), a mass spectrum revealed that the 1,2-DHN product **13** was monodeuterated. This shows that rearrangement of **8** to **13** involves protonation by solvent. It seems likely that the 1,8a-DHN **11** (or **12**) is thermally protonated at the 2-position followed by the loss of a proton at carbon 8a. This mechanism is consistent with that proposed by Heller and co-workers for the acid-catalysed reactions of 1,8a-DHN formed from fulgides (6).

It was not possible to conclusively determine whether dihydronaphthalenes **13** and **14** were being formed via solvent protonation of both **11** and **12**, although it seems likely. In any event, an earlier suggestion by Heller and co-workers that the *trans*-DHN **14** is coming exclusively from irradiation of the *E,Z*-isomer seems incorrect for this series of compounds (6).

In summary, we have provided the first detailed study of the photochemistry of an *E,E*-2,3-dibenzylidenesuccinate diester and proposed a mechanism for the products formed in various solvents. In aprotic solvents, there is an equilibrium between **8** and **9**, in competition with the two-step photochemical conversion to the 1,4-DHN **10**. It is proposed that the isomerization between the *E,E*-isomer and the *E,Z*-isomer occurs by disrotatory closure to 1,8a-DNH **11** (or **12**) followed by conrotatory thermal opening to **9** (or **8**). In protic solvents, there is also an equilibrium between **8** and **9,** but solvent protonation of **11** (and (or) **12**) produces primarily (but not exclusively) the *cis*-1,2-DHN **13**. The possibility that **13** is formed via an intramolecular thermal [1,5]-sigmatropic hydrogen shift was ruled out by the fact that deuterium is incorporated from deuterated solvents.

Experimental

General methods

Proton and ^{13}C-NMR spectra were recorded on a Bruker AM-300 FT instrument using residual $CHCl_3$ in the $CDCl_3$ as internal standard, unless otherwise specified. Silica gel (40–63 μm) (Silicycle, Quebec City, Que.) was used for all chromatography. High-resolution mass spectra (HRMS) were obtained on a VG Analytical 7070E-HF instrument. Irradiations were conducted with a 450-W medium-pressure mercury lamp housed in a Pyrex water-cooled jacket or with

© 2004 NRC Canada

a circular set of low-pressure mercury lamps (254 nm, 100 W). In all cases, the temperature of the solutions being irradiated was 25 ± 5 °C. HPLC was conducted on a reverse-phase C_{18} column using methanol (50–80%) in water as eluent. Literature references for known compounds are: **8** (23)**, 13** (23), and **14** (25).

Diethyl *E,Z*-2,3-(3,4,5-trimethoxybenzylidene)succinate (9)

A solution of diethyl *E,E*-2,3-(3,4,5-trimethoxybenzylidene)succinate (**8**) (0.020 g, 0.040 mmol) in EtOAc (4 mL) in a Pyrex test tube was purged with N_2 for 5 min. The test tube was sealed, fixed at 24 cm from the medium-pressure mercury lamp, and irradiated for 6 h. The solvent was evaporated to leave a mixture of the *E,E*- and *E,Z*-isomers, **8** and **9** (approximately 57:43 as determined by ^{1}H NMR). The *E,Z*-isomer **9** was separated from the mixture by HPLC. ^{1}H NMR ($CDCl_3$) δ 1.17 (t, *J* = 7.1 Hz, 3H), 1.33 (t, *J* = 7.1 Hz, 3H), 3.78 (s, 6H), 3.81 (s, 6H), 3.84 (s, 3H), 3.85 (s, 3H), 4.18 (q, *J* = 7.1 Hz, 2H), 4.29 (q, *J* = 7.1 Hz, 2H), 6.63 (s, 2H), 6.73 (s, 1H), 6.91 (s, 2H), 7.75 (s, 1H). ^{13}C NMR ($CDCl_3$) δ 14.0, 14.3, 56.0 (2C), 56.1 (2C), 60.9, 60.9 (2C), 61.3, 106.5 (2C), 107.8 (2C), 127.8, 129.9, 130.3, 130.7, 140.8, 141.9, 152.8 (3C), 153.0 (3C), 166.9, 167.5.

Diethyl 1-(3,4,5-trimethoxyphenyl)-6,7,8-trimethoxy-1,4-dihydronaphthalene-2,3-dicarboxylate (10)

A solution of **8** (0.138 g, 0.260 mmol) in $CHCl_3$ (26 mL) in a Pyrex test tube was purged with N_2 for 5 min. The test tube was sealed, fixed at 7 cm from the medium-pressure Hanovia mercury lamp, and irradiated for 3 h. The solvent was evaporated, and the residue mixture was purified by flash chromatography on silica gel using 50% EtOAc in hexanes to give the product (0.464 g, 33% yield). ^{1}H NMR ($CDCl_3$) δ 1.18 (t, *J* = 7.1 Hz, 3H), 1.30 (t, *J* = 7.1 Hz, 3H), 3.63 (dd, *J* = 2.6 and 21.5 Hz, 1H), 3.87 (dd, *J* = 4.2 and 21.5 Hz, partly obscured by OMe signal at 3.85 Hz, 1H), 3.51 (s, 3H), 3.75 (s, 6H), 3.76 (s, 3H), 3.79 (s, 3H), 3.85 (s, 3H), 4.08–4.25 (m, 2H), 4.25 (q, *J* = 7.1 Hz, 2H), 5.21 (dd, *J* = 2.6 and 4.3 Hz, 1H), 6.37 (s, 2H), 6.52 (s, 1H). ^{13}C NMR ($CDCl_3$) δ 14.16, 14.22, 31.9, 43.5, 56.1, 56.3 (2C), 60.5, 60.9, 61.0, 61.3, 61.5, 105.8 (2C), 106.3, 123.0, 127.7, 131.5, 137.2, 138.4, 138.6, 141.3, 151.0, 153.0, 153.2 (2C), 167.7 (*C*=O), 167.8 (*C*=O). MS *m/z* (relative intensity): 530 (M^+, 64), 484 (60), 456 (35), 411 (56), 380 (27), 362 (26), 317 (100), 289 (66), 245 (12), 181 (28), 168 (21); HRMS calcd. for $C_{28}H_{34}O_{10}$: 530.2152; found: 530.2148.

Diethyl *cis*- and *trans*-1-(3,4,5-trimethoxyphenyl)-6,7,8-trimethoxy-1,2-dihydronaphthalene-2,3-dicarboxylate (13 and 14)

The characterizations of **13** and **14** are reported elsewhere (23, 24) but are included here for completeness.

13. ^{1}H NMR ($CDCl_3$) δ 0.89 (t, *J* = 7.2 Hz, 3H), 1.24 (t, *J* = 7.2 Hz, 3H), 3.46 (s, 3H), 3.71 (s, 3H), 3.72 (s, 6H), 3.82 (s, 3H), 3.86 (s, 3H), 4.08 (dd, *J* = 2.8, 9.1 Hz, 1H), 4.17 (m, 2H), 4.76 (d, *J* = 9.1 Hz, 1H), 6.32 (s, 2H), 6.63 (s, 1H), 7.36 (d, *J* = 2.8 Hz, 1H). ^{13}C NMR ($CDCl_3$) δ 13.8, 14.3, 40.5, 48.1, 56.10, 56.13 (2C), 60.4, 60.5, 60.7, 60.8 (2C), 106.4 (2C), 108.0, 123.7, 126.2, 127.1, 135.4, 136.4, 137.2, 144.2, 151.1, 152.6 (2C), 152.9, 167.3, 171.5; MS *m/z* (relative intensity): 530 (M^+, 100), 484 (44), 456 (62), 411 (65), 384 (33), 358 (69); HRMS calcd. for $C_{28}H_{34}O_{10}$: 530.2151; found: 530.2139.

14. ^{1}H NMR (300 MHz, $CDCl_3$) δ 1.19 (t, *J* = 7.2 Hz, 3H), 1.31 (t, *J* = 7.1 Hz, 3H), 3.67 (s, 3H), 3.72 (s, 6H), 3.77 (s, 3H), 3.88 (s, 3H), 3.89 (s, 3H), 4.06 (d, *J* = 1.2 Hz, 1H), 4.12 (2 overlapping quartets, *J* = 7.2 Hz, 2H), 4.23 (2 overlapping quartets, *J* = 7.1 Hz, 2H), 5.00 (d, *J* = 1.2 Hz, 1H), 6.28 (s, 2H), 6.71 (s, 1H), 7.62 (s, 1H). ^{13}C NMR ($CDCl_3$, 75 MHz) δ 14.1, 14.3, 39.4, 46.2, 56.0 (4C), 60.71, 60.77 (one quaternary carbon not observed). EIMS *m/z* = 530 [M^+], 456 (base), 411, 384, 196; HRMS calcd. for $C_{28}H_{34}O_{10}$: 530.2152; found: 530.2129.

Acknowledgements

We are grateful to the Natural Sciences and Engineering Research Council of Canada and the University of Manitoba for financial support of this project.

References

1. S.-T. Chang, S.-Y. Wang, U.C. Su, S.-L. Hunag, and Y.-H. Kuo. Hozforschung, **53**, 142 (1999).
2. A.S.R. Anjaneyulu, D. Santikumar, and U.V. Mallavadhani. Indian J. Chem., Sect. B,. **31B**, 401 (1992).
3. J.C.A. Boeyens, L. Denner, and G.W. Perold. J. Chem. Soc., Perkin Trans. 2, 1749 (1988).
4. A.S.R. Anjaneyulu, P. Raghu, and K.V.R. Rao. Indian J. Chem., Sect. B, **19B**, 511 (1980).
5. A.S.R. Anjaneyulu, P. Raghu, and K.V.R. Rao. Indian J. Chem., Sect. B, **18B**, 535 (1979).
6. O. Crescente, H.G. Heller, and S. Oliver. J. Chem. Soc., Perkin Trans. 1, 150 (1979).
7. T. Momose, T. Nakamura, and K. Kanai. Chem. Pharm. Bull. **26**, 3186 (1978).
8. T. Momose, K. Kanai, and K. Hayashi. Chem. Pharm. Bull. **26**, 3195 (1978).
9. T. Momose, K. Kanai, and T. Nakamura. Chem. Pharm. Bull. **26**, 1592 (1978).
10. T. Momose, K. Kanai, T. Nakamura, and Y. Kuni. Chem. Pharm. Bull. **25**, 2755 (1977).
11. T. Momose, T. Nakamura, and K. Kanai. Heterocycles, **6**, 277 (1977).
12. T. Momose, K. Kanai, and T. Nakamura. Heterocycles, **4**, 1481 (1976).
13. H.G. Heller and P.J. Strydom. J. Chem. Soc., Chem. Commun. 50 (1976).
14. R.J. Hart, H.G. Heller, R.M. Megit, and M. Szewczyk. J. Chem. Soc., Perkin Trans. 1, 2227 (1975).
15. J.S. Hastings, H.G. Heller, and K. Salisbury. J. Chem. Soc., Perkin Trans. 1, 1995 (1975).
16. H.G. Heller and M. Szewczyk. J. Chem. Soc., Perkin Trans. 1, 1487 (1974).
17. R.J. Hart and H.G. Heller. J. Chem. Soc., Perkin Trans. 1, 1321 (1972).
18. H.G. Heller and K. Salisbury. J. Chem. Soc. C, 873 (1970).
19. M.D. Cohen, H.W. Kaufman, D. Sinnreich, and G.M.J. Schmidt. J. Chem. Soc. B, 1035 (1970).
20. R.J. Hart, H.G. Heller, and K. Salisbury. J. Chem. Soc., Chem. Commun. 1627 (1968).
21. H.G. Heller and B. Swinney. J. Chem. Soc. C, 2452 (1967).

© 2004 NRC Canada

22. D.C. Ayres, B.G. Carpenter, and R.C. Denney. J. Chem. Soc. 3578 (1965).
23. P.K. Datta, C. Yau, T.S. Hooper, B.L. Yvon, and J.L. Charlton. J. Org. Chem. **66**, 8606 (2001).
24. T. Assoumatine, P.K. Datta, T.S. Hooper, B.L. Yvon, and J.L. Charlton. J. Org. Chem. **69**, 4140 (2004).
25. C. Cow, C. Leung, and J.L. Charlton. Can. J. Chem. **78**, 553 (2000).

© 2004 NRC Canada

Comparison of the free radical scavenger activities of quercetin and rutin — An experimental and theoretical study

Carolina Aliaga and Eduardo A. Lissi

Abstract: Natural radical scavengers have recently received considerable interest owing to the role of free radicals in causing oxidative stress in living organisms. Flavonoids constitute one of the most important families of molecules with antioxidant activities, a characteristic associated with the presence in their structure of hydroxyl groups bound to aromatic rings. Quercetin is a potent antioxidant whose high reactivity could be associated with the presence of the OH group in the C ring. To address the role of this group in quercetin's free radical scavenging capacity, we have carried out experimental determinations and theoretical calculations regarding the reactivity of quercetin and rutin. The reactivity of both compounds towards free radicals was assessed employing the radical anion 2,2′-azinobis(3-ethylbenzothiazoline-6-sulfonate) and peroxyl radicals. These measurements indicate that quercetin is more reactive and has more reactive centers than rutin, suggesting that the extra OH group located in the C ring could directly contribute to reactivity of quercetin. This conclusion is in agreement with the evaluation of local reactivity indexes, such as the Fukui function.

Key words: quercetin, rutin, antioxidant activity, $ABTS^{\bullet-}$, peroxyl radicals, Fukui function, local reactivity index.

Résumé : Les pièges naturels de radicaux ont récemment fait l'objet de beaucoup d'attention en raison du rôle que jouent les radicaux libres dans les réactions oxydantes dans les organismes vivants. Les flavonoïdes forment l'une des plus importantes familles de molécules ayant des activités antioxydantes, une caractéristique associée à la présence dans leur structure de groupes hydroxyles liés à des noyaux aromatiques. La quercétine est un puissant antioxydant dont la grande réactivité peut être liée à la présence d'un groupe hydroxyle dans le cycle C. Afin de pouvoir étudier le rôle de ce groupe dans les capacités de la quercétine à piéger les radicaux libres, nous avons effectué des déterminations expérimentales et des calculs théoriques concernant la réactivité de la quercétine et de la rutine. Pour évaluer la réactivité de ces deux composés vis-à-vis des radicaux libres, on a utilisé l'anion radical 2,2′-azinobis-(3-éthylbenzothiazoline-6-sulfonate) et les radicaux peroxyles. Ces mesures indiquent que la quercétine est plus réactive et possède plus de centres réactifs que la rutine, ce qui suggère que le groupe hydroxyle additionnel sur le cycle C peut contribuer directement à la réactivité de la quercétine. Cette conclusion est en accord avec l'évaluation des indices de réactivité locale, telle que la fonction Fukui.

Mots clés : quercétine, rutine, antioxydant, $ABTS^{\bullet-}$, radicaux peroxyles, fonction de Fukui, indice de réactivité locale.

[Traduit par la Rédaction]

Introduction

Flavonoids are one of the most abundant families of natural compounds with antioxidant activity (1–5). This antioxidant activity is mostly related to their ability to act as free radical scavengers due to the presence of one or several phenolic groups (6). These groups can react according to:

[1] $R\bullet + XOH \rightarrow RH + XO\bullet$

The antioxidant activity of the phenols is then promoted by the lability of the O–H bond in phenols (7) and the low reactivity of the phenoxyl radical, which favors termination reactions, thereby reducing the length of free radical chains.

Most flavonoids bear more than one potentially reactive group (8, 9), and their antioxidant activity mainly functions on the basis of an efficient hydrogen transfer capacity. However, a role for their metal-chelating potential towards iron- and copper-induced free radical reactions has also been associated with the presence of vicinal phenol groups (1, 10). The polyfunctional property of these molecules makes it difficult to establish which is the primary target for free radical attack. Two approaches can be employed to address this issue. Experimentally, the reactivity of the parent compound can be compared with that of derivatives in which some of the reactive centers are blocked (11). The second approach relies on the evaluation of local reactivity indexes, such as

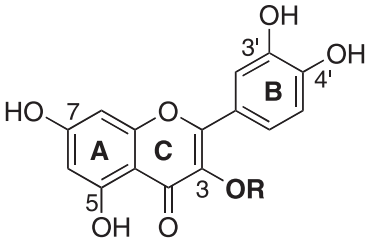
Received 6 July 2004. Published on the NRC Research Press Web site at http://canjchem.nrc.ca on 12 January 2005.

C. Aliaga and E.A. Lissi.[1] Facultad de Química y Biología, Universidad de Santiago de Chile, Casilla 40, correo 33, Santiago, Chile.

[1]Corresponding author (e-mail: carolina@photo.chem.uottawa.ca).

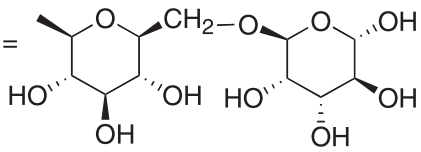
 doi: 10.1139/V04-151 © 2004 NRC Canada

Scheme 1.



Quercetin; R = H

Rutin; R =



the Fukui function, one of the most commonly used descriptors of site reactivity. In the case of flavonoids, the latter approach has been only scarcely employed (12, 13).

Rutin and quercetin (Scheme 1) are two closely related polyphenols that differ only in the substitution at the C3 position of the C ring. To establish which is the more reactive locus in quercetin and, in particular, if the reactivity towards free radicals is dominated by a reaction involving the OH group located at the C3 position, we have compared the reactions of rutin and quercetin with peroxyl radicals and with the radical anion derived from 2,2′-azinobis(3-ethylbenzothiazoline-6-sulfonate) (ABTS). To further investigate whether the OH located at the C3 position of the C ring would be the most reactive center in quercetin, local reactivity indexes have been obtained by semiempirical AM1 and ab initio HF/3-21G** level calculations.

Experimental

All experiments were carried out in phosphate buffer solutions, 100 mmol/L, pH 7.0.

Bleaching of pre-formed ABTS-derived radical anion ($ABTS^{\bullet-}$)

The methodology employed was similar to that described previously (14–16). The main difference is the method employed to produce the radical. In the present study, the ABTS-derived radicals were produced by the MnO_2-promoted oxidation of ABTS. The addition of 2 mg of MnO_2 to 25 mL of a 100 mol/L solution of ABTS instantaneously produces a blue color characteristic of the radical anion. After centrifugation and filtering to remove the excess oxide, the absorbance of the solution remains stable for several hours. The incorporation of an aliquot of a polyphenol solution produces a decrease in absorbance (measured at 734 nm) that is directly related to the capacity of the polyphenol to bleach the pre-formed radical. We have evaluated the fast absorbance decay at 734 nm, measured ca. 10 s after polyphenol addition, and the total bleaching, measured 15 min after polyphenol addition. A comparison of these values with that obtained instantaneously after Trolox addition provides an estimation of the total number of groups that react instantaneously and the number of groups that react slowly with the pre-formed radical. Thus, the number of equivalents reacting during the fast step of the reaction (ERF) and the total number of equivalents reacting towards the end of the reaction (ERT) are evaluated according to eqs. [2] and [3], respectively:

$$[2] \qquad \mathrm{ERF} = \frac{\Delta A[\mathrm{Trolox}]}{\Delta A^{0}[\mathrm{additive}]}$$

$$[3] \qquad \mathrm{ERT} = \frac{\Delta A[\mathrm{Trolox}]}{\Delta A^{15}[\mathrm{additive}]}$$

where ΔA represents the change in absorbance measured after addition of the corresponding Trolox concentration, and ΔA^0 and ΔA^{15} represent the decrease in ABTS-derived radical absorbance measured at 734 nm at 10 s and 15 min, respectively, after addition of quercetin or rutin.

All experiments were carried out at room temperature (21 ± 1 °C).

Protection against c-phycocyanin fluorescence bleaching

The methodology applied follows that described by Cao et al. (17), with c-phycocyanin employed as the target molecule in place of β-phycoerythrin (18). All experiments were carried out at 37 °C employing 2,2′-azobis(2-amidinopropane) dihydrochloride (AAPH, 10 mmol/L) as free radical source. Consumption of c-phycocyanin was monitored by the decrease in fluorescence intensity (excitation 620 nm; emission 640 nm) measured in a Spex Fluorolog spectrofluorimeter.

Theoretical calculations

All calculations were performed with a Gaussian94 program (19) that included a short routine added to the Mulpop link 601 of the main program (20). This added routine permits, through a single-point calculation, an evaluation of the overlap term that takes into account the interaction between orbitals. Optimization of the structures of the investigated polyphenols was carried out at the semiempirical AM1 and ab initio HF/3-21G** levels. The ab initio calculation was carried out after optimization at the AM1 level. This type of calculation has proven to be useful in the theoretical treatment of simple phenols (21).

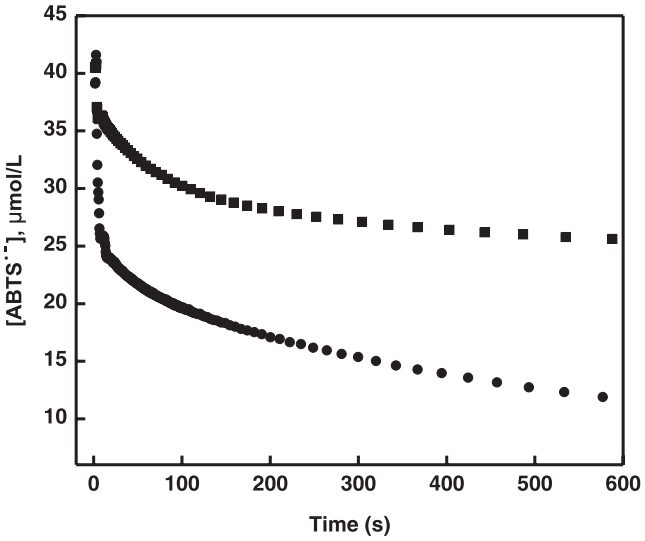
Results and discussion

The structures of quercetin and rutin are shown in Scheme 1. Both compounds are frequently present in plants, fruits, and beverages (22, 23) and contribute to their antioxidant activity (24, 25). As may be seen in Scheme 1, the only difference between the two compounds is the substitution of the OH group at position C3 in quercetin with a rutinose group in rutin. As such, the comparisons of these two compounds provide information regarding the role of the OH group at position C3 in the antioxidant capacity and free radical scavenging reactions of quercetin.

The reactivity of quercetin and rutin towards free radicals was evaluated in two in vitro systems, comprising the radi-

© 2004 NRC Canada

Fig. 1. Decrease of ABTS radical anion absorbance, measured at 734 nm, after addition of 10 μmol/L of quercetin (●) and rutin (■).



cals derived from ABTS (26) and peroxyl radicals generated in the aerobic decomposition of AAPH (27).

Reactivity of quercetin and rutin towards ABTS radical anions

ABTS-derived radicals in additive-free solutions are stable over a period of ca. 30 min. Addition of quercetin or rutin readily bleaches the absorbance of the radical. Typical profiles of the decay of the absorbance, measured at 734 nm, are shown in Fig. 1. These profiles reveal a biphasic behavior, characteristic of complex samples and (or) compounds bearing several potentially reactive groups (28). The fast decay, which is nearly complete after ca. 10 s, correlates with the number of centers of high reactivity. The extent of the bleaching observed after a relatively long reaction time (15 min) is determined by the total number of potentially reactive groups. The analysis of the curves given in Fig. 1 shows that both the number of groups of high reactivity and the total number of reactive groups are larger in quercetin than in rutin. It has been shown that, in spite of the fact that the ABTS radical consumption can be influenced by stoichiometric factors (14), the extent of bleaching correlates with the total number of phenolic groups in complex mixtures and in polyfunctional compounds (29).

The efficiency of bleaching of ABTS radical anions by each of the flavonoid molecules, "instantaneously" (during the first 10 s) and after 15 min incubation, is shown in Table 1. These data show that an extra Trolox equivalent participates in quercetin and that this extra reaction occurs very quickly. This would indicate that quercetin has one more group of high reactivity than rutin, suggesting that the OH group located in the C ring is able to readily bleach the ABTS-derived radical. Nearly two more Trolox equivalents in quercetin than in rutin have also been found in the classical Trolox equivalent antioxidant capacity (TEAC) assay involving myoglobin as a source of ABTS-derived radicals (2).

Table 1. Efficiency of rutin and quercetin in bleaching ABTS radical anion absorbance.

Additive	Concn. (μmol/L)	ΔA^0	ΔA^{15}	ERF	ERT
Trolox	2.5	0.418±0.01	—	1	1
Rutin	1.9	0.081±0.016	0.247±0.01	1.5	4.3
Quercetin	2.5	0.192±0.05	0.398±0.015	2.4	4.9

Note: Values tabulated are the decrease in ABTS radical anion absorbance (measured at 734 nm) evaluated at 10 s (ΔA^0) and 15 min (ΔA^{15}) reaction times and the number of equivalents reacting during the fast step of the reaction (ERF) and the total number of equivalents reacting towards the end of the reaction (ERT) (given in Trolox equivalents) measured after 10 s and 15 min reaction times, respectively.

The fact that the "fast" reaction takes place in a few seconds prevents an evaluation of its decay kinetics, which would require the use of fast stop-flow techniques (30). To gain some insight into the reactivity of the OH group at the C ring, relative to the phenolic groups present in the A and B rings, we carried out measurements in the c-phycocyanin–AAPH–additive system.

Protection against peroxyl-promoted bleaching of c-phycocyanin by quercetin and rutin

c-Phycocyanin fluorescence is readily bleached when the protein is incubated in the presence of a free radical source, such as AAPH (Fig. 2). The bleaching process follows nearly first-order kinetics (Fig. 3). The addition of micromolar concentrations of quercetin or rutin partially protects against the bleaching process (Fig. 2). The data in Fig. 2, obtained at equal concentrations of the two flavonoids, show that more protection is afforded by quercetin. The origin of this extra protection becomes clear when the data are plotted according to first-order kinetics (Fig. 3). The data given in Fig. 3 show that the extra protection provided by quercetin lasts for ca. 20 min, after which the bleaching rates in the presence of quercetin or rutin are similar. This suggests the presence of an extra group in quercetin that is consumed after ca. 20 min incubation. In fact, a comparison of this induction time with that elicited by the same amount of Trolox indicates that this extra protection can be assigned to a single extra group of very high reactivity towards peroxyl radicals.

The above results clearly show that, as in other free radical models (31), the reactivity of quercetin towards free radicals is greater than that of rutin. Three explanations can be given to account for this difference. First, substitution at the O3 position in the C ring may introduce a steric hindrance that reduces the coplanarity of the whole conjugated system, thereby reducing the reactivity of the phenol groups localized in the B ring. The second possibility could be a faster reaction of the catechol-like group located at the B ring of quercetin, due to its lower redox potential, as suggested in other systems (32, 33). The third explanation could be a high and dominant reactivity of the OH group at position C3 of the C ring in quercetin. Blocking of this group, as in rutin, would then reduce the compound's free radical scavenging capacity. The results given in Table 1 and Fig. 3, which suggest the presence of an "extra" very reactive center in quercetin, would support this last proposal. To test these

© 2004 NRC Canada

Fig. 2. Decrease of c-phycocyanin fluorescence elicited by AAPH-derived peroxyl radicals. ◆, Control; ■, 10 μmol/L rutin; ●, 10 μmol/L quercetin.

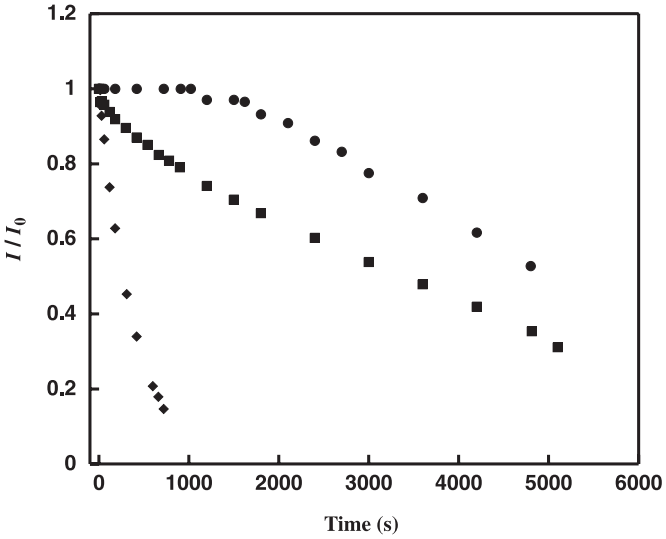
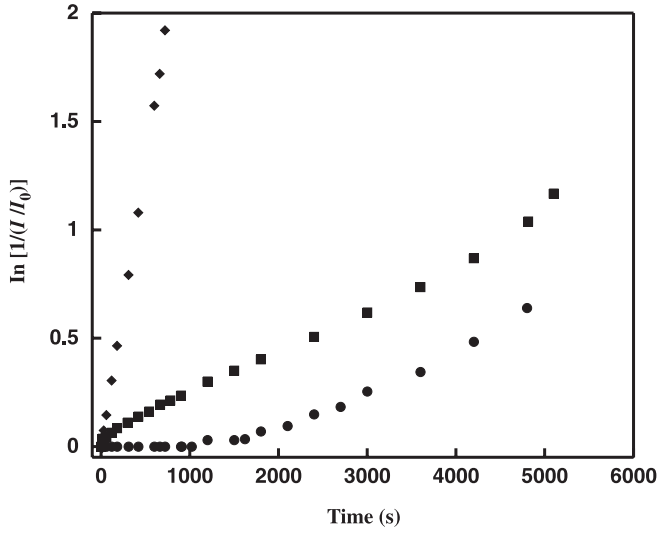


Fig. 3. Data of Fig. 2 plotted according to a first-order process.



possibilities, theoretical calculations of geometry and local reactivity indexes in both compounds were performed.

Theoretical framework

AM1 and HF/3-21G** level calculations were performed to obtain the radical Fukui index ($f_k^{\bullet}$) and the regional local softness ($s_k^{\bullet}$) centered on oxygen atoms of all the OH groups. The theoretical treatment also provided the geometry of the molecule.

Reactivity indexes were calculated using density functional theory (DFT) as the starting point. This theory provides a series of electronic descriptors that correlate with a variety of molecular properties, such as acidity/basicity and reactivity of various organic compounds. The Fukui function is a local quantity that has been formally defined as the derivative of electronic density $\rho(r)$ with respect to the total number of electrons N in the system, under adiabatic conditions (constant external potential $\upsilon(r)$):

$$[4] \qquad f(r) = \left[\frac{\partial \rho(r)}{\partial N}\right]_{\upsilon(r)}$$

Thus, this index represents and provides information regarding changes in the electronic density at the reaction locus at the initial part of the reaction coordinate. This function is normalized to unity by its integration over the entire molecular space. The Fukui function will be used here to analyze locally the radical activity on the oxygen atoms linked to the active hydrogen atom of the polyphenols for hydrogen atom transfer reactions. The value at a given atom can be considered to be a measure of the specific reactivity at that reaction center (i.e., O3). An exact definition for this index is derived from the electronic density of the HOMO and (or) LUMO orbitals of a particular center. In general, the molecular frontier function is given by

$$[5] \qquad f^{\alpha}(r) = \left|\Phi^{\alpha}(r)\right|^2$$

where $|\Phi^{\alpha}(r)|^2$ represents the electronic density on the frontier orbital. A negative value of α (i.e., $\Delta N < 0$) identifies an electrophilic process, and a positive α value (i.e., $\Delta N > 0$) identifies a nucleophilic attack. Expansion of the molecular frontier function according to a linear combination of atomic orbitals (LCAO) allows an evaluation of the orbital component of the Fukui function. Finally, the amount condensed to the site k can be obtained by the summation over all the orbitals of the k center (20).

For radical processes such as those considered in the present work, the radical Fukui function was equated to the average of the functions corresponding to nucleophilic and electrophilic reactions:

$$[6] \qquad f_k^{\bullet} = \frac{f_k^{+} + f_k^{-}}{2}$$

Another quantity that can be employed to estimate the reactivity at a given center is the regional local softness, $s_k^{\bullet}$. This parameter evaluates the electronic or spin polarizability at the site k (34, 35). The value of $s_k^{\bullet}$ is obtained from the product of the Fukui function at the site k and the global softness of the system (S):

$$[7] \qquad s_k^{\bullet} = f_k^{\bullet} S$$

The global softness corresponds to the inverse of the molecular global hardness (η) and hence, at the level of Koopman's aproximation (36), is given by:

$$[8] \qquad \eta = \frac{1}{S} = \frac{\varepsilon_L - \varepsilon_H}{2}$$

where ε_L and ε_H are *eigenvalues* corresponding to LUMO and HOMO orbitals, respectively.

Theoretical calculations

Computational time was reduced by carrying out optimizations for rutin with a methyl group in place of the R group bound to the oxygen in the C3 position. It was found that the most stable structure is obtained when the three

© 2004 NRC Canada

Table 2. Regional Fukui functions and local softness for quercetin and rutin.

		$f_k^\bullet$		$s_k^\bullet$	
Molecule	(k)-Site[a]	AM1	HF/3-21G	AM1	HF/3-21G
Quercetin	O3′	0.016	0.0219	0.1123	0.1244
	O4′	0.0397	0.0309	0.2786	0.1755
	O7	0.0073	0.0069	0.0513	0.0392
	O5	0.0085	0.0118	0.0597	0.067
	O3	0.0407	0.0316	0.2857	0.1795
Rutin	O3′	0.0201	0.0242	0.1387	0.1326
	O4′	0.0479	0.0333	0.3301	0.1825
	O7	0.0003	0.0056	0.0021	0.0115
	O5	0.0069	0.0115	0.0476	0.063
	O3	0.0214	0.0201	0.1476	0.1101

Note: The values for global softness S obtained by AM1 methods (and by ab initio methods, in parentheses) are 7.02 (5.68) and 6.90 (5.48) atomic units for quercetin and rutin, respectively.

[a]Numbering of the atoms corresponds to that in Scheme 1.

rings remain coplanar. Partial optimization employing the whole rutin molecule provided the same answer, with the substituent at the C3 position displaced out of the molecular plane.

The values of the $f_k^\bullet$ and $s_k^\bullet$ indexes for all of the oxygen atoms in OH moieties present in quercetin and rutin are given in Table 2. The data in this table show that:

(*i*) In quercetin, both methods assign the highest index to the oxygen at the C3 position. This applies both to the $f_k^\bullet$ and $s_k^\bullet$ indexes. This may indicate that this OH group is the most reactive. However, it should be noted that this value is only marginally different from that assigned to the oxygen located at the C4′ position, which could explain the contribution of 2.4 groups to the ERF index (see Table 1).

(*ii*) All the reactivity indexes of the remaining OH groups in rutin are similar to those of the corresponding atoms in quercetin. This is the result expected if the molecule remains nearly planar, in spite of the substitution at the O3 position. Furthermore, this indicates that the reduced reactivity of rutin mainly results from the blocking of the O3 position and is not due to a change in reactivity of the remaining OH groups. The observed reduction from 2.4 (in quercetin) to 1.5 Trolox equivalents for rutin during the fast step of the reaction with ABTS-derived radicals could be ascribed to the absence of this key reactive site. Interestingly, the presence of this OH group in the C ring has been considered to increase the antioxidant activity of flavonols (37).

Conclusions

Taken together, the experimental data and the theoretical calculations presented in this paper suggest that the high reactivity of quercetin is primarily due to reaction of the OH group located at the C ring, and not to an increased reactivity of the vicinal OH groups located at the B ring (28, 32, 33, 38). This proposal is in agreement with conclusions reached by Erkoç et al. (13) based on electronic properties of the radical isomers derived from quercetin. This would lead initially to a radical centered in the C ring that could decay, by inter- and (or) intramolecular processes, to the "classical" radical mostly localized in the B ring (32). Blocking of the O3 position in the C ring in rutin accounts then for the reduced reactivity of this compound, both towards ABTS-derived radicals and towards peroxyl radicals. Conflicting results showing that blocking of the C4′ position in the B ring reduces the antioxidant activity of quercetin more than blocking at the O3 position of the C ring (39) can be related to a reduction in the chelating activity of the former compound (40).

The high reactivity of quercetin has usually been explained by considering that the hydroxyl group in the C ring increases the reactivity of the catechol-like structure of the B ring (2, 32, 33, 41, 42). However, we consider that the data obtained in this work, suggesting the presence of an "extra" very reactive center in quercetin, points to a preferential reactivity of the hydroxyl group located in the C ring. This proposal is compatible with the theoretical calculations that show that this OH group is at least as reactive as the catechol-like group located at the B ring. In any case, it must be considered that the main locus of reaction must depend on the attacking radical, the pH, and the solvent, rendering generalizations of the present results unwarranted.

Acknowledgements

We gratefully acknowledge Dr. Renato Contreras for helpful discussion and support on the theoretical study. C.A. thanks Fondecyt Projects nos. 2980002 and 4990029.

References

1. C.A. Rice-Evans, N.J. Miller, G.P. Bolwell, P.M. Bramley, and J.B. Pridjam. Free Rad. Res. **22**, 375 (1995).
2. C.A. Rice-Evans, N.J. Miller, and G. Paganga. Free Rad. Biol. Med. **20**, 933 (1996).
3. N. Salah, N.J. Miller, G. Paganga, L. Tijburg, and C.A. Rice-Evans. Arch. Biochem. Biophys. **322**, 339 (1995).
4. N.J. Miller, J. Sampson, L.P. Candeiras, P.M. Bramley, and C.A. Rice-Evans. FEBS Lett. **384**, 240 (1996).
5. N.J. Miller, C. Castelluccio, L. Tijburg, and C.A. Rice-Evans. FEBS Lett. **392**, 40 (1996).
6. O. Benavente-Garcia, J. Castillo, J. Lorente, A. Ortuno, and J.A. del Rio. Food Chem. **68**, 457 (2000).
7. R. Bosque and J. Sales. J. Chem. Inf. Comput. Sci. **43**, 637 (2003).
8. S.S. Pekkarinen, I.M. Heinonen, and A.I. Hopia. J. Sci. Food Agric. **79**, 499 (1999).
9. D.P. Makris and J.T. Rossiter. J. Agric. Food. Chem. **48**, 3830 (2000).
10. A. Damianaki, E. Bakogeorgou, M. Kampa, G. Notas, A. Hatzoglou, S. Panagiotou, C. Gemetzi, E. Kouroumalis, P.M. Martin, and E. Castanas. J. Cell Biochem. **78**, 429 (2000).
11. J.S. Wright, E.R. Johnson, and G.A. DiLabio. J. Am. Chem. Soc. **123**, 1173 (2001).
12. I. Vedernokova, E. Propynov, D. Salanub, and A. Haemers. Int. J. Quantum Chem. **77**, 161 (2000).
13. S. Erkoç, F. Erkoç, and N. Keskin. J. Mol. Struct. THEOCHEM, **631**, 141 (2003).
14. C. Romay, C. Pascual, and E.A. Lissi. Braz. J. Med. Biol. Res. **29**, 175 (1996).
15. A.M. Campos and E.A. Lissi. Int. J. Chem. Kinet. **29**, 219 (1996).
16. C. Aliaga and E.A. Lissi. Can. J. Chem. **78**, 1052 (2000).

© 2004 NRC Canada

17. G. Cao, H.M. Alessio, and R.G. Cutler. Free Rad. Biol. Med. **14**, 303 (1993).
18. R.L. Atanasiu, D. Stea, M.A. Mateescu, C. Vergely, F. Dalloz, F. Briot, V. Maupoil, and L. Rochette. Mol. Cell. Biochem. **189**, 127 (1998).
19. M.J. Frisch, G.W. Trucks, W.B. Schlegel, P.M.W. Gill, B.G. Johnson, M.A. Robb, J.R. Cheeseman, T.A. Keith, G.A. Peterson, J.A. Montgomery, K. Raghavachari, M. Al-Laham, V.G. Zahrzewski, J.V. Ortiz, J.B. Foresman, J. Cioslowski, B.B. Stefanov, A. Nanayakkara, M. Challencombe, C.Y. Peng, P.Y. Ayala, W. Chen. M.W. Wong, J.L. Andres, E.S. Replogle, R. Gomperts, R.L. Martin, D.J. Fox, J.S. Binkley, D.J. Defrees, J. Baker, J.P. Stewar, M. Head-Gordon, C. Gonzalez, and J.A. Pople. Gaussian94 [computer program]. Gaussian Inc., Pittsburgh, Pa. 1995.
20. R.R. Contreras, P. Fuentealba, M. Galván, and P. Pérez. Chem. Phys. Lett. **304**, 405 (1999).
21. F. Méndez, M.L. Romero, F. DeProft, and P. Geerlings. J. Org. Chem. **63**, 5774 (1998).
22. M.B. Arnao, A. Cano, J. Hernandez-Ruiz, F. Garcia-Canovas, and M. Acosta. Anal. Biochem. **236**, 255 (1996).
23. P. Pietta, P. Simonetti, and P. Mauri. J. Agric. Food. Chem. **46**, 4487 (1998).
24. N.J. Miller, A.T. Diplock, and C.A. Rice-Evans. J. Agric. Food. Chem. **43**, 1794 (1995).
25. G. Paganga, N. Miller, and C.A. Rice-Evans. Free Rad. Res. **30**, 153 (1999).
26. I.I. Koleva, H.A.G. Niederlander, and T.A. van Beek. Anal. Chem. **73**, 3373 (2001).
27. Y.M. Naguib. Anal. Biochem. **284**, 93 (2000).
28. D.P. Makris and J.T. Rossiter. J. Agric. Food Chem. **49**, 3370 (2001).
29. Y.S. Velioglou, G. Mazza, L. Gao, and B.D. Oomah. J. Agric. Food Chem. **43**, 4113 (1998).
30. P.H. Daum and P. Zanie. Anal. Chem. **46**, 1347 (1974).
31. B. Alluis and O. Dangles. Helv. Chim. Acta, **84**, 1133 (2001).
32. S.V. Jovanovic, S. Steenken, Y. Hara, and M.G. Simic. J. Chem. Soc., Perkin Trans. 2, 2497 (1996).
33. S.V. Jovanovic, S. Steenken, M. Tosic, B. Marjanovic, and M.G. Simic. J. Am. Chem. Soc. **116**, 4846 (1994).
34. P. Fuentealba. J. Mol. Struct. THEOCHEM, **433**, 113 (1998).
35. P.K. Chattaraj and S.J. Segupta. Phys. Chem. **100**, 16 126 (1996).
36. B.O. Koopman. Proc. Natl. Acad. Sci. U.S.A. **17**, 315 (1931).
37. E.J. Lien, S. Ren, H.H. Bul, and R. Wang, Free Rad. Biol. Med. **26**, 285 (1999).
38. A. Arora, M.G. Nair, and G.M. Strasburg. Free Rad. Biol. Med. **24**, 1355 (1998).
39. J.-H. Moon, T. Tsushida, K. Nakahara, and J. Terao. Free Rad. Biol. Med. **30**, 1274 (2001).
40. J.E. Brown, H. Khodr, R.C. Hider, and C. Rice-Evans. Biochem. J. **330**, 1173 (1998).
41. W. Bors, C. Michel, and S. Schikora. Free Rad. Biol. Med. **19**, 45 (1995).
42. P.-G. Pietra. J. Nat. Prod. **63**, 1035 (2000).

© 2004 NRC Canada

Effect of cyclodextrins on iron-mediated dechlorination of trichloroethylene — A proposed new mechanism[1]

Salma Shirin, Erwin Buncel, and Gary W. vanLoon

Abstract: This paper evaluates the possibility of using cyclodextrins (CDs) as solubility-enhancing agents that could be employed to increase the rate of the mass delivery of trichloroethylene (TCE) to an iron wall where dechlorination will occur. Dechlorination of TCE by zero-valent iron was performed in the absence and in the presence of CDs in batch (*static*) and column (*dynamic*) systems. The presence of CDs slowed the overall degradation of TCE. The effect of various concentrations of different CDs on the rate of TCE degradation was evaluated, and it was found that as the CD concentration increased, reaction rate decreased. However, the overall decrease in reaction rate could not be explained solely on the basis of TCE:CD host-guest complexation. A novel mechanism involving CD binding to the iron surface, in addition to TCE:CD complexation, was proposed, and this enabled satisfactory interpretation of the kinetic data. A central feature of the proposal is that Fe:CD binding impedes electron transfer from the underlying iron metal to the TCE molecule. The overall rate of TCE degradation by zero-valent Fe in the presence of CDs is governed by several factors: the extent of binding of CD with the iron surface, the binding constant between CD and TCE, and the degradation of complexed TCE (TCE:CD), where CD is, in turn, associated with the iron surface. It appeared that CD binding to the iron surface depends largely on the type of substituent groups present in the β-CD derivatives as well as their degree of substitution. Association constants for the Fe:CD interaction were determined. The new hypothesis explained well both batch and column data, and the magnitude of Fe:CD binding constants was found to be similar in the two systems.

Key words: cyclodextrin, trichloroethylene, zero-valent iron, reductive dechlorination.

Résumé : Dans ce travail, on a évalué la possibilité d'utiliser les cyclodextrines (CD) comme agents d'augmentation de la solubilité pour augmenter la vitesse de distribution du trichloroéthylène (TCE) vers un mur de fer où une déchloruration se produira. On a réalisé la déchloruration du TCE par du fer zérovalent, en présence et en l'absence de CD, dans des systèmes par lots (*statiques*) et sur des colonnes (*dynamiques*). La présence de CD a ralenti la dégradation globale du TCE. On a évalué l'effet de diverses concentrations de différentes CD sur la vitesse de dégradation du TCE et on a observé qu'une augmentation de concentration de CD abaisse la vitesse de réaction. Toutefois, la diminution globale de la vitesse de réaction ne peut pas être expliquée uniquement sur la base d'une complexation hôte-invité TCE:CD. On propose un nouveau mécanisme impliquant une fixation de la CD sur la surface du fer, en plus de la complexation TCE:CD. La caractéristique centrale de cette proposition est que la fixation de la CD sur le Fe inhibe le transfert d'électron du fer métallique sous-jacent vers la molécule de TCE. La vitesse de dégradation du TCE sous l'influence du Fe zérovalent est déterminée par plusieurs facteurs: le taux de fixation de la CD sur la surface du Fe, la constante de fixation entre la CD et le TCE et la dégradation du TCE complexé (TCE:CD) où la CD est, à son tour, associée à la surface du fer. Il semble que la combinaison de la CD sur la surface du fer dépend beaucoup sur le type de substituants qu'on retrouve sur les dérivés de la CD ainsi que sur leur degré de substitution. On a déterminé les constantes d'interaction Fe:CD. La nouvelle hypothèse permet d'expliquer les données relatives aux systèmes statique et dynamique et on a trouvé que l'amplitude des constantes de fixation Fe:CD sont semblables dans les deux systèmes.

Mots clés : cyclodextrine, trichloroéthylène, fer zérovalent, déchloruration réductrice.

[Traduit par la Rédaction]

Received 7 May 2004. Published on the NRC Research Press Web site at http://canjchem.nrc.ca on 20 January 2005.

S. Shirin,[2] E. Buncel, and G.W. vanLoon.[3] Department of Chemistry, Queen's University, Kingston, ON K7L 3N6, Canada.

[1]Part 8 in a series on "Mechanisms of abiotic degradation and soil-water interactions of pesticides and other hydrophobic organic compounds". For the previous paper in this series, see ref. 35.

[2]Present address: Department of Chemistry, McGill University, Montreal, QC H3A 2K6, Canada.
[3]Corresponding author (e-mail: vanloon@chem.queensu.ca).

 doi: 10.1139/V04-140 © 2004 NRC Canada

Introduction

Subsurface contamination by hazardous organic chemicals and the associated risks to humans and to the environment have become issues of global importance. According to the United States Environmental Protection Agency (US EPA), there are approximately 330 000 hazardous waste sites in the United States where the groundwater may be contaminated (1). Chemicals can enter the subsurface environment from accidental spills, leaks in the storage tanks, industrial waste pits, and municipal and industrial landfills. Trichloroethylene (TCE) is listed as being among the most frequently detected groundwater contaminants across North America (1, 2). The major industrial uses of this compound are in the automotive, metal, and dry cleaning industries.

The aqueous solubility of TCE is approximately 1100 ppm, and, when released into the subsurface, it does not dissolve completely in groundwater but remains as a separate dense, nonaqueous phase liquid (DNAPL). A plume of dissolved contaminants forms in groundwater when the water contacts either small residual ganglia or a larger pool of DNAPL. The slow release of dissolved TCE creates a persistent source of groundwater contamination. The safe limit for TCE in drinking water, set by the US EPA, is 0.005 ppm (3) whereas in Canada it is 0.05 ppm (4), both limits being much smaller than the aqueous solubility. Trichloroethylene has been described as being potentially carcinogenic and mutagenic (5).

It is known that TCE is resistant to biotic and abiotic degradation under natural environmental conditions (6). However, in anaerobic environments, TCE can undergo partial biodegradation, with vinyl chloride (VC) being identified as one of the degradation products. The VC, a known carcinogen, does not undergo further biotic degradation and can therefore accumulate in the environment (5). Since TCE and other polychlorinated compounds are not rapidly removed by either dissolution or degradation, their life span in the soil/groundwater system can be of the order of several decades, perhaps even centuries. As a result of the environmental persistence and potential harmful effects on living organisms, removal of these compounds from the subsurface has become a priority, and numerous studies have focused on their environmental remediation.

Among various subsurface remediation technologies, pump-and-treat remediation is currently the most widely used, but its limitations have led to the ongoing development of complementary new treatment remediation techniques, including the "iron wall" methodology (1, 2, 7–26). This technology consists of placing a reactive permeable barrier of finely divided zero-valent iron in the path of the groundwater flow in such a way that it will interact with the organic pollutants in the contaminated groundwater and degrade them while they are passing through the treatment zone. Spontaneous reduction of halo-aliphatic compounds, including TCE, by zero-valent iron metal occurs owing to the differences in the reduction potential of the individual half-cell reactions that favour dechlorination (6).

The mechanism for dechlorination of TCE on the zero-valent iron surface has not yet been definitively described. The most recent mechanism proposed by Arnold and Roberts (24) postulated that reduction of TCE by zero-valent iron proceeds via two different but parallel mechanisms: reductive β-elimination (departure of two Cl atoms from the adjacent carbons leading to the formation of a new π-bond between the adjacent carbons) and hydrogenolysis (replacement of Cl by H). In both cases, the TCE was shown to initially form a surface complex with iron followed by dechlorination via either of the mechanisms mentioned above.

It is widely accepted that the degradation of chlorinated aliphatic compounds by Fe^0 is a surface-mediated reaction; i.e., it is necessary that the compound be in close contact with the reactive site of the iron for electron transfer to occur (11, 12, 15, 24, 27). It is, in fact, assumed by many researchers that an initial TCE–Fe^0 precursor complex is formed which leads to dechlorination. The existence of the precursor complex has been inferred from the observation that the quantity of product formed was always markedly smaller than the amount expected based on the quantity of reactant degraded (9, 13, 14, 22). Consequently, the amount of compound that could not be accounted for in the observed mass balance was assumed to be located on the surface, where it continued to undergo dechlorination. Moreover, it has been shown that the rate of TCE degradation increases upon increasing the amount of iron, which further supports the argument that TCE dechlorination by iron is a surface-mediated reaction (9, 24).

Alongside the dechlorination process on the iron surface, corrosion products develop at the Fe^0–H_2O interface owing to the thermodynamic oxidative instability of Fe^0 in the presence of H_2O and O_2. As a consequence, a passive layer is formed that may affect the rate of reductive dechlorination. Electron diffraction and X-ray absorption near-edge spectroscopy of an electrochemically generated oxide film showed that the passive coating consists of an inner layer of magnetite (Fe_3O_4) and an outer layer of maghemite (γ-Fe_2O_3) (28–30). Other than iron oxide formation, siderite ($FeCO_3$) and pyrite (FeS_2) were also detected during the dechlorination process where the carbonate and sulfide species (9, 13, 21) were present in the system. A mixed-valence iron (hydr)oxide salt (with an interlayer containing anions such as Cl^-, CO_3^{2-}, and SO_4^{2-}), known as green rust, is another commonly found aqueous product of corrosion (30, 31). Thus, the passive layer on the oxide surface is essentially a complex mixture of iron oxides and hydroxides, iron oxyhydroxide salts, and other mineral precipitates. The structure and mineralogy of the passive film can be variable depending on the experimental conditions.

Formation of this mixed layer in the course of Fe^0-mediated dechlorination reactions has been observed in many cases (9, 13, 15, 21). When present, this coating may inhibit the dechlorination process by acting as a physical barrier between the underlying metal and the dissolved chlorinated compound. Scherer et al. (30) have suggested that the reduction process remains operative when an oxide layer is present on the iron surface. Gaspar et al. (32) have recently shown, however, that where a passive layer is present, to a significant extent the reduction takes place at pits where zero-valent iron is exposed, rather than on the oxide layer itself.

The effectiveness of using an iron wall as a reactive barrier in groundwater treatment is limited by the low aqueous solubility of chlorinated compounds. Thus, the complete

© 2004 NRC Canada

treatment of a DNAPL-contaminated zone by an emplaced iron wall barrier could require decades owing to the slow mass delivery to the treatment zone.

Cyclodextrins (CDs), which are six-, seven-, or eight-membered cyclic glucose oligosaccharides, are able to increase the aqueous solubility of a range of nonpolar to low-polarity organic compounds, including TCE (33–35). Solubility enhancement occurs by means of host–guest complexation. To overcome the limitations associated with low aqueous solubility in the iron wall remediation technology, researchers have explored the idea of using CDs to increase mass delivery to the treatment facility (16, 36, 37).

This paper evaluates the dechlorination of TCE by Fe^0 both in the absence and in the presence of various amounts of different substituted β-CDs. Since TCE:CD complexation occurs in parallel with TCE degradation by Fe^0, the effect of complexation on the degradation kinetics requires exploration. A number of substituted β-CDs, having varying degrees of substitution, have been considered since variously substituted CDs have shown different abilities to enhance the aqueous solubility of TCE (35); this feature could also affect the Fe^0-mediated dechlorination process. Additionally, the performance of individual β-CD derivatives (considering the types and number of substituent groups) on the degradation kinetics is evaluated. Kinetic results obtained from both batch (static) and column (dynamic flow-through) experiments are compared.

Experimental

TCE, perchloroethylene (PCE), *cis*-dichloroethylene (*cis*-DCE), *trans*-dichloroethylene (*trans*-DCE), and HPLC-grade acetonitrile were obtained from Aldrich Chemicals. All chemicals were analytical grade at 99.99% purity and were used as received. The iron was 100-mesh (0.145 mm particle size) zero-valent electrolytic iron powder, obtained from Fisher Scientific. Reported purity was 99.99%, and it was used as received without any pretreatment.

The specific surface area ($m^2\ g^{-1}$) of the iron powder was determined by Micromeritics Co. (Norcross, Ga.) to be 0.3158 $m^2\ g^{-1}$, using single-point nitrogen gas adsorption Brunauer–Emmett–Teller (B.E.T.) analysis (38). The fractional porosity of the zero-valent iron powder was determined gravimetrically and was found to be 0.496 ± 0.009.

The substituted β-cyclodextrins (β-CDs) used in this study were a hydroxypropyl-β-CD (HPβ-CD, D.S.[4] 5.5) (Aldrich), two sulfated β-CDs (Sβ-CD1, D.S. 4: Sβ-CD2, D.S. 14), a methyl-β-CD (Mβ-CD, D.S. 12), and a carboxymethyl-β-CD (CMβ-CD1, D.S. 3.0), all supplied by Cerester, and a second carboxymethyl-β-CD (CMβ-CD2), synthesized in the laboratory of Professor G.R. Thatcher at Queen's University. Further characteristics of these CDs are provided in ref. 35. All CDs were used as received; the aqueous solubility of each was determined to be >50% (*w*/*v*).

Batch experiments

For each set of experiments, 9.0-g portions of Fe^0 powder were added to 40-mL Pyrex glass vials. The vials were completely filled with aqueous solution of TCE without or with CDs, taking care that no headspace remained, and then were closed immediately using a Teflon-lined cap equipped with a MININERT™ valve. For the experiments that involved CDs, the required amount of CD had been added to the TCE stock solution and mixed completely before transferring to the vials. Each experiment included two vials, one containing Fe^0 and an aqueous solution of TCE (without or with CD) and the other containing an aqueous solution of TCE without any Fe^0. The vials were placed into the head-over-head mixer (30 rpm) at room temperature (maintained at 23 ± 2 °C) to allow for continuous mixing. At different time intervals, vials were withdrawn from the mixer and centrifuged, and a portion of aqueous sample (ca. 40 μL) was withdrawn using a gas-tight syringe for analysis. For each measurement, a sample from the control vial was analyzed along with one from the reaction vial to confirm that there had been no loss of TCE due to volatility or sorption on the container walls. By measuring changes in concentration of TCE over time, degradation kinetics were followed for at least 3–5 half-lives.

Column experiments

The glass column constructed for use in this study was 30 cm long with an i.d. of 2.85 cm. Twelve sample ports were located along the column: port 1, in the glass-bead portion at the base of the column, and ports at distances of 1.4, 3.4, 6.4, 9.4, 12.5, 15.4, 18.5, 21.3, 24.3, 27, and 30 cm from the bottom of the column. Iron powder was poured into the column in small portions with careful tapping so that no gaps remained in the column packing. After the column had been packed with iron powder, it was purged with argon for 16 h to remove oxygen that could contribute to rusting of the iron. The deaerated influent solution (aqueous TCE or aqueous TCE + CD) was then pumped at the rate of 1.2 mL min^{-1} from an air-free collapsible Teflon bag through the column using a peristaltic pump. All connections in the column system were made with Teflon tubing. The TCE degradation profile was determined by analyzing samples taken from different ports along the column under steady-state conditions (39). For sampling, a Luer-lock stainless steel needle (point style 5) was inserted through the septum of the open cap of the Teflon-lined sampling port to withdraw ~100 μL of sample. The initial concentration of TCE in any given experiment was determined by removing the sample from port 1. This measurement also served as control and was checked periodically throughout each experiment.

Using procedures described previously (35), liquid chromatography (LC) was employed for analysis of the samples from both batch and column systems. Direct analysis of samples was carried out immediately following withdrawal.

Results

In both batch and column systems, the concentrations of TCE were found to decrease as the reaction proceeded while the TCE concentration in the control remained constant (within 3%–6%) throughout the experimental period. Observed pseudo-first-order rate constants (k_{obs}) were obtained graphically using the following equation:

$$[1] \qquad \ln C_t = \ln C_0 - k_{obs}\, t$$

[4] D.S., degree of substitution.

© 2004 NRC Canada

where C_t is the concentration of analyte (TCE) at time t and C_0 is the initial concentration of analyte at time 0. Linear plots of eq. [1] produced good fits with correlation coefficient ranging from 0.965 to 0.997.

To represent the kinetic data for the dechlorination of TCE by Fe^0 in a more general way, the k_{obs} values were normalized to 1.00 m^2 of iron surface per liter of solution, giving a normalized rate constant, k_{SA}, as follows (12):

$$[2] \qquad \ln C_t = \ln C_0 - k_{SA}\rho_a t$$

where ρ_a is the surface area concentration of zero-valent iron.

Batch results

In experiments performed in the absence of CD, linear kinetic plots (eq. [1]) were obtained for each TCE concentration (ranging from 35 to 325 ppm). Correlation coefficients (R^2) ranged between 0.985 and 0.998. The observed rate constants (k_{obs}), the normalized rate constants (k_{SA}), and half-lives are listed in Table 1; the k_{obs} values remained relatively constant over the range of TCE concentrations used in this study.

The effect of CD on the zero-valent iron-mediated dechlorination of TCE was evaluated with each of HPβ-CD, Mβ-CD, CMβ-CD1, and CMβ-CD2 at five different CD concentrations ranging from 0.5% to 5% (*w*/*v*) (corresponding to ca. 0.0033 to 0.033 mol L^{-1}). In the case of Sβ-CD2, TCE degradation was investigated at only three different concentrations because there appeared to be very little change in rate when higher CD concentrations were used. Only one concentration for Sβ-CD1 was used because of the limited amount available. In all experiments where CDs were present, the TCE concentration was kept constant at 0.0019 mol L^{-1} (250 ppm). The degradation of TCE was inhibited by the presence of each of the CDs. Values of k_{obs} are listed in Table 2.

When the degradation of TCE (with or without CD) was followed using LC analysis, peaks corresponding to *cis*-DCE and *trans*-DCE (as reaction products) were observed. These compounds accumulated at a very low rate as the reaction proceeded and reached a final value, with no further decay being observed. Without CDs, the concentrations of the cis and trans isomers observed at completion of the various experiments were 4–5 and 2–3 ppm, respectively, whereas with CDs the corresponding values were 2–3 and ~1 ppm, respectively. The maximum concentration of the products represented ≤8% of the initial concentration of parent compound.

Column results

To obtain a kinetic trace from the column system, the distance of each port along the column was converted to time units employing Darcy's law (39). Linear plots using eq. [1] resulted; the correlation coefficient ranged from 0.978 to 0.994 for all TCE concentrations (38.5–250 ppm). The observed rate constants (k°_{obs}), the normalized rate constants (k_{SA}), and half-lives are listed in Table 3.

Using the column system, the kinetics of TCE degradation was evaluated by varying the concentration of two CDs, HPβ-CD and CMβ-CD2, from 0.5% to 3.0% (*w*/*v*) (corresponding to 0.0030 to 0.020 mol L^{-1}). In these experiments, the TCE concentration was kept constant at 0.00050 mol L^{-1} (66 ppm). In each experiment, the linear plot obtained from eq. [1] produced a satisfactory fit (correlation coefficient of 0.975–0.996). Kinetic data are presented in Table 4.

Table 1. Observed rate constants (k°_{obs}),[a] half-lives ($t_{1/2}$), and normalized rate constants (k_{SA}) for degradation of TCE in presence of zero-valent 100-mesh electrolytic iron powder in batch systems.

Initial [TCE] (ppm)	$10^2 \times k^\circ_{obs}$ (h^{-1})[b,c]	$t_{1/2}$ (h)	$10^4 \times k_{SA}$ (L m^{-2} h^{-1})[d]
35.0	4.24±0.01	16.3	5.97
65	4.83±0.16	14.3	6.58
110	4.61±0.42	15.0	6.48
165	3.47±0.12	20.0	4.88
220	4.22±0.03	16.4	5.95
250	3.88±0.03	17.9	5.46
325	3.36±0.01	20.6	4.73

Note: Iron surface area concentration (ρ_a) = 71.1 m^2 L^{-1}, T = (23.0 ± 2.0) °C, mixing rate = 30 rpm.

[a]Observed rate constant for TCE degradation with Fe^0 without any CD is termed as k°_{obs}.

[b]Error in k°_{obs} values is the deviation from the mean of two values.

[c]Average k°_{obs} = (4.09 ± 0.55) × 10^{-2} h^{-1}.

[d]Average k_{SA} = (5.75 ± 0.79) × 10^{-4} L m^{-2} h^{-1}.

In the column experiments without CDs, *cis*-DCE and *trans*-DCE were observed as reaction products and reached a final value, as in the batch experiments, with 2–3 ppm *cis*-DCE and 1–2 ppm *trans*-DCE being observed in various experiments. However, in the column system, only the cis isomer (0.2–0.6 ppm) was observed when reactions were performed in the presence of CDs.

In this study, these were the only products observed during both batch and column experiments. The formation and the proportions of the *cis*- and *trans*-DCE products are in agreement with literature values (9, 13, 21). While other products (such as ethylene, acetylene, vinyl chloride, and ethane) have been reported in the literature when GC was used as an analytical technique (9, 13, 20, 21, 24), these could not be detected using the HPLC techniques employed in this study.

Discussion

This paper explores issues surrounding the use of CDs as solubility-enhancing agents to increase the rate of mass delivery of TCE to an iron wall where dechlorination can occur. To date, however, there have been no published works to study the consequences of using solubility-enhancing agents regarding rates and mechanisms of zero-valent iron-mediated TCE dechlorination. As part of a remediation protocol, the effects of CDs both on solubilization and on dechlorination must be considered together.

Based on results obtained in the batch experiments, two mechanistic approaches will be employed in an attempt to account for the dechlorination kinetic behavior. Rate reductions in the presence of CDs were obtained in all cases, and these will first be examined by attributing inhibition as due exclusively to TCE:CD host–guest binding (mechanism I). Secondly, a novel possibility will be considered, namely, the possible interaction between the added CD and the iron surface (mechanism II). This interaction, if it occurs, could par-

© 2004 NRC Canada

Table 2. Observed rate constants (k_{obs}) for degradation of TCE with Fe^0 in presence of various concentrations of different CDs in batch systems.[a]

	$10^2 \times k_{obs}$ (h^{-1})					
% CD (*w*/*v*)	HPβ-CD (60)[a]	Mβ-CD (120)[a]	CMβ-CD1 (31)[a]	CMβ-CD2 (20)[a]	Sβ-CD1 (44)[a]	Sβ-CD2 (3.0)[a]
0.5	1.45±0.20	2.17±0.17	1.49±0.02	2.98±0.24		
1.0	0.90±0.04	1.39±0.12	1.27±0.01	2.10±0.04		2.73±0.04
2.0	0.65±0.01	1.15±0.04	1.11±0.04	1.97±0.02		
3.0	0.53±0.01	0.52±0.03	0.85±0.03	1.78±0.01		2.31±0.03
4.0	0.46±0.01	0.77±0.05	0.73±0.01	2.02±0.02		
5.0	0.35±0.01	0.38±0.01	0.49±0.02	1.66±0.05	0.70±0.01	1.86±0.03

Note: Iron surface area concentration (ρ_a) = 71.1 m^2 L^{-1}, T = (23.0 ± 2.0) °C, mixing rate = 30 rpm. Error in k_{obs} values is the deviation from the mean of two values.

[a]Numbers in parentheses are binding constant (K_{11}) values of TCE with CDs, taken from ref. 35.

Table 3. Observed rate constants (k°_{obs}),[a] half-lives ($t_{1/2}$), and normalized rate constants (k_{SA}) for degradation of TCE at various initial concentrations in the zero-valent-iron-filled column.

Initial [TCE] (ppm)	k°_{obs} (h^{-1})[b]	$t_{1/2}$ (min)	$10^4 \times k_{SA}$ (L m^{-2} h^{-1})[c]
38.5	1.02	40.8	4.77
54.4	0.873	47.6	4.08
60.3	0.996	41.7	4.65
200	1.14	36.5	5.37
221	1.02	40.8	4.77
250	1.20	34.7	5.60

Note: Iron surface area concentration (ρ_a) = 2140 m^2 L^{-1}, T = (23.0 ± 2.0) °C, flow rate = 1.2 mL min^{-1}.

[a]Observed rate constant for TCE degradation without any CD is termed as k°_{obs}.

[b]Average k°_{obs} = 1.04 ± 0.12 h^{-1}.

[c]Average k_{SA} = (4.86 ± 0.56) × 10^{-4} L m^{-2} h^{-1}.

tially block access to the surface, limiting the extent to which the TCE molecule would make contact and be reduced by the zero-valent iron. Kinetic equations and schemes that incorporate the dual possibilities of CD binding either with TCE or with iron will then be used to rationalize the experimental data; both thermodynamic and kinetic parameters will be determined from these equations. Finally, a similar approach will be used to explain the results of the continuous-flow column experiments, and the parameters derived from these will be compared with those determined from batch studies.

Kinetic measurements of dechlorination using Fe^0

In this study, relatively high initial concentrations of TCE were used since one practical goal was to deliver a greater quantity of the contaminant to a reactive iron wall. Although the degradation process is generally considered to be pseudo-first-order with respect to the substrate, it is also known to be a surface-mediated process (9–11, 15, 24) as mentioned in the Introduction. Thus, one would anticipate that, at some upper limit in contaminant concentration, the reactive sites would be saturated and the reaction rate would become concentration-independent with respect to substrate. However, since changing the initial TCE concentration over one order of magnitude did not result in any change in observed rate constant (k°_{obs}) values in both batch and column systems (Tables 1 and 3), it appears that all experiments were, in fact, conducted under pseudo-first-order conditions.

Table 4. Observed rate constants (k_{obs}) for degradation of TCE with Fe^0 in presence of various amounts of different CDs in column systems.

	$10^2 \times k_{obs}$ (h^{-1})	
% CD (*w*/*v*)	HPβ-CD (60)	CMβ-CD2 (20)
0.5	1.45±0.20	2.98±0.24
1.0	0.90±0.04	2.10±0.04
2.3	0.65±0.01	1.97±0.02
3.0	0.53±0.01	1.78±0.01

Note: Iron surface area concentration (ρ_a) = 2140 m^2 L^{-1}, T = (23.0 ± 2.0)°C, flow rate = 1.2 mL min^{-1}. Numbers in parentheses are binding constant (K_{11}) values of TCE with CDs, taken from ref. 35. Error in k_{obs} values is the deviation from the mean of two values.

TCE was found to degrade faster in the column system (half-life = 40 min, Table 3) compared to the batch system (half-life = 17 h, Table 1) because the iron surface area concentration (ρ_a) was much higher in the column system (2140 m^2 L^{-1}) than in the batch system (71.1 m^2 L^{-1}). However, when the rate constants were expressed as k_{SA} values (rate constant normalized to 1 m^2 surface area of iron per liter of solution) for each system, they agreed rather well ((5.75 ± 0.79) × 10^{-4} m^{-2} L h^{-1} and (4.86 ± 0.56) × 10^{-4} m^{-2} L h^{-1} (Tables 1 and 3 for batch and column, respectively)).

Batch experiments: Dechlorination of TCE in the presence of CD

Since the rate constant for the TCE degradation was independent of initial concentrations between 35.0 and 325 ppm, TCE degradation in the presence of CDs was carried out using an initial TCE concentration of 0.0019 mol L^{-1} (250 ppm) and varying the CD concentration. In every case, the rate of TCE degradation was inhibited by the presence of CD, and the extent of inhibition was greater with increased concentration of CD (Table 2). The inhibitory effect has been attributed to the fact that the TCE:CD host–guest complexation shields the TCE molecule, making it less available for reaction at the iron surface.

Rate reduction due to host–guest binding (mechanism I)

To test this explanation for rate reduction, the extent of host–guest binding of TCE was determined using known binding constant (K_{11}·L mol^{-1}) values, and the kinetic equations were modified accordingly. Binding constants of TCE

© 2004 NRC Canada

with the CDs used in this work have been reported elsewhere (35). Because stronger binding means reduced availability for dechlorination, one would expect greatest inhibition to be associated with CDs having the largest binding constants.

Following ref. 16, a quantitative treatment can be deduced from Scheme 1, where the rate reduction is attributed solely to TCE:CD complexation. The rate equation corresponding to Scheme 1 is given by:

$$[3] \qquad -\frac{d[TCE]}{dt} = k^{\circ}_{obs}[TCE]_{free} + k_c[TCE:CD]$$

According to Scheme 1, in addition to TCE being directly degraded on the iron surface, TCE molecules are also in rapid equilibrium with CD, forming the TCE:CD complex. The decrease in the observed rate constants for the TCE degradation in the presence of CDs (Table 2) implies that an inhibitory effect arises due to formation of the unreactive host–guest complex between TCE and CD. It has been shown that when the substrate is included inside the CD cavity, reaction does not proceed via attack from an external agent (40). Since the dechlorination of TCE is known to be a surface-mediated process, electron transfer to the TCE:CD complex present in solution is unfavourable. Thus, the k_c[TCE:CD] term in eq. [3] can be ignored and the equation rewritten as

$$[4] \qquad -\frac{d[TCE]}{dt} = k^{\circ}_{obs}[TCE]_{free}$$

The rate of TCE degradation in the presence of CD can then be expressed as

$$[5] \qquad \text{Rate} = k_{obs}[TCE]_{total}$$

$$[6] \qquad = k_{obs}([TCE]_{free} + [TCE:CD])$$

$$= k_{obs}([TCE]_{free} + K_{11}[TCE]_{free}[CD])$$

$$[7] \qquad = k_{obs}[TCE]_{free}(1 + K_{11}[CD])$$

Now

$$-\frac{d[TCE]}{dt} = \text{Rate}$$

Hence, from eqs. [4] and [5],

$$[8] \qquad k^{\circ}_{obs}([TCE]_{free} = k_{obs}[TCE]_{free}(1 + K_{11}[CD])$$

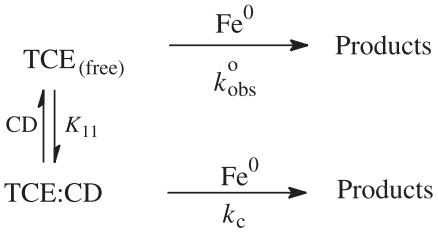
$$[9] \qquad k_{obs} = \frac{k^{\circ}_{obs}}{(1 + K_{11}[CD])}$$

where k_{obs} is the observed rate constant for TCE degradation in the presence of CD and k°_{obs} is the rate constant in the absence of CD.

Using eq. [9], the theoretical observed rate constant values for TCE degradation in the presence of CD can be calculated since the binding constant (K_{11}) and the rate constant for the TCE degradation in the absence of CD (k°_{obs}) are known independently (Table 1). For comparison, both theoretical and experimentally obtained k_{obs} values from Table 2 are plotted together for each CD in Fig. 1.

It is seen from Fig. 1 that large differences between the theoretical (open circles) and experimental (solid circles)

Scheme 1. Mechanism I for TCE degradation.



k_{obs} values were found in all cases with the exception of Mβ-CD, where the differences were considerably smaller. In each case, experimental k_{obs} values were lower than theoretically calculated values. This suggests that, apart from inhibition arising from complexing with the CD, other factors operating in the system contribute to additional lowering of the rate of TCE degradation. With most of the CDs, the difference between the theoretical and experimental k_{obs} value is greater at lower CD concentration.

Enhanced rate depression due to Fe–CD surface binding (mechanism II)

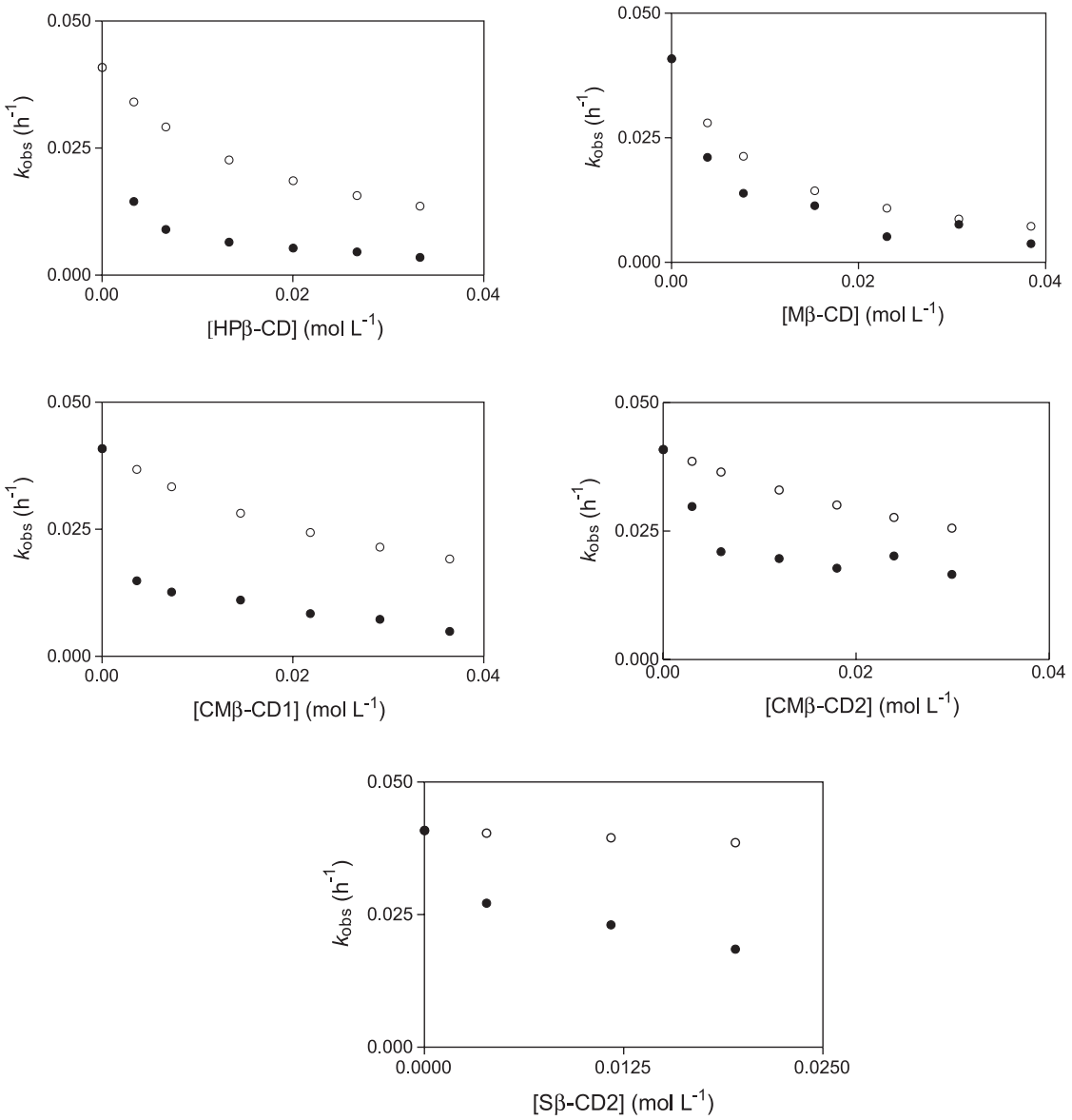
To explain the enhanced inhibition of dechlorination in the presence of CD, we propose that the CD (which is present in large excess in the solutions) may itself undergo interaction with the iron surface (which may contain an oxide or hydroxide surface layer). When this occurs, the surface area occupied by CD molecules becomes unavailable as a site for contact between iron and TCE molecules, which reduces the probability of surface-mediated electron transfer that leads to reductive dechlorination.

It has been shown that surface oxide and hydroxide groups on iron (hydr)oxide can take part in forming coordination complexes with a variety of organic ligands containing functional groups such as –OH and –COOH (41, 42). In a study of the dechlorination of CCl_4 by zero-valent iron, it was similarly shown that the presence of ligands, including borate, catechol, ascorbate, and acetate, slowed the observed rate of reaction (43). This was ascribed to specific binding between surface hydroxyls on the iron and the oxygen-containing ligands. The authors suggested that CCl_4 could be sorbed both at reactive and at nonreactive sites by weak hydrophobic or induced-dipole interactions. The strongly bound specific complex involving borate or other ligands blocks the reactive surface, reducing the probability of forming the weak Fe:CCl_4 precursor complex essential for dehalogenation. In another study (44), Tratnyek et al. have shown that the reduction of TCE and CCl_4 by Fe^0 was inhibited in the presence of natural organic matter (NOM). The authors concluded that NOM, which contains a variety of redox-active functional groups, competes with TCE and CCl_4 for the iron oxide surface, causing depression in the rate of reduction of chlorinated compounds.

Native CD molecules possess primary and secondary –OH groups, and, upon derivatization, some of these groups are replaced by the substituents, including $–CH_2CH(OH)CH_3$, $–CH_3$, $–CH_2COO^-$, and $–SO_4^-$. Additionally, through the –OH of the glucose molecules that make up the CDs, similar types of coordination with iron (hydr)oxide can be predicted. Since derivatization to form Mβ-CD replaces –OH groups by neutral substituents, it would be expected that the formation

© 2004 NRC Canada

Fig. 1. Effect of various CDs on the observed rate constant for TCE degradation by Fe^0 in batch system (ρ_a = 71.1 m^2 L^{-1}, 30 rpm, 23 ± 2 °C). Open and solid circles represent rate constants calculated using eq. [9] and experimental rate constant values, respectively.



of coordination complexes with (hydr)oxide layers would be less effective in these CDs compared to the free and otherwise substituted CDs.

Partially blocking access to the iron surface as a result of CD–iron (hydr)oxide complexation would limit the extent to which the TCE molecule could make contact with the iron as the first step in the reductive dechlorination process. One would anticipate a preferential interaction of CD with the iron surface, compared with TCE, owing both to its large excess as well as to the ability of its functional groups to form coordinate or covalent bonds with the iron surface.

Proposal of a new model for degradation of TCE in the presence of CDs

To account for the effect arising from formation of complexes between CD and the iron surface (the various Fe^0, Fe–O, and Fe–OH species being represented as Fe^*), and the subsequent effect on the rate of degradation of TCE, a competitive surface complexation model is now proposed. In this model, the processes operating in the TCE–CD–Fe^* system can be depicted as shown in Scheme 2. Considering the processes described in Scheme 2, the rate equation can be expressed as follows (refer to the Supplementary material[5] for full derivation):

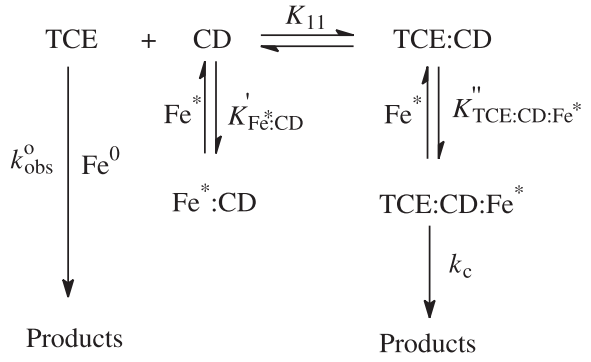
$$[10] \qquad k_{obs} = \frac{k^{\circ}_{obs} + k' K_{Fe^*:CD} K_{11}[CD]}{1 + K_{11}[CD] + K_{Fe^*:CD}[CD] + K_{Fe^*:CD} K_{11}[CD]^2}$$

From eq. [10], on plotting k_{obs} for degradation of TCE in the presence of various concentrations of CD against [CD], one

[5] Supplementary data may be purchased from the Directory of Unpublished Data, Document Delivery, CISTI, National Research Council Canada, Ottawa, ON K1A 0S2, Canada (http://www.nrc.ca/cisti/irm/unpub_e.shtml for information on ordering electronically).

© 2004 NRC Canada

Scheme 2. Proposed new mechanism II for TCE degradation.



can calculate the parameters $K_{Fe^*:CD}$ (association or binding constant of CD (free CD or CD complexed with TCE) on iron surface) and k' (rate constant for the degradation of complexed TCE, i.e., TCE:CD, where CD is in turn, associated with the iron surface) using nonlinear regression analysis and minimizing the sums of the squares of the residuals. Note that dechlorination of complexed TCE:CD was not considered in mechanism I, while in mechanism II the TCE-complexed CD is also taken as a degrading species. In the latter mechanism, TCE is assumed to be in close proximity to the iron surface through CD:Fe binding; this situation might facilitate electron transfer from iron metal to the bound TCE molecule.

Duplicate experimental data sets for TCE degradation in the presence of various concentrations of several CDs (Table 2) were fitted to eq. [10] and analyzed for the two unknowns, $K_{Fe^*:CD}$ and k'. Figure 2 illustrates the fitting of an experimental data set for each CD, and Table 5 lists the $K_{Fe^*:CD}$ and k' values obtained from the curve fitting. It is apparent from Fig. 2 that there is close agreement between the observed and calculated rate constants for degradation as described by mechanism II, which is consistent with the argument of CD binding to the iron surface shown in Scheme 2.

The k' values (rate constant for the degradation of complexed TCE, i.e., TCE:CD, where CD, in turn, is associated with the iron surface) listed in Table 5 range from 1% to ca. 15% of the k°_{obs} (rate constant for TCE in the absence of CD; Table 1). This may be explicable on the basis of the following: (*a*) most of the CD molecules bound to the Fe surface do not contain TCE and (or) (*b*) electron transfer from iron to complexed TCE is less favourable than that involving free TCE. One additional noteworthy observation from Table 5 is the generally inverse relationship between K_{11} (values obtained from ref. 35) and k'; a higher K_{11} value means stronger binding, thus leading to smaller k'.

The model as elaborated in Scheme 2 for the Fe^0-mediated degradation of TCE in the presence of CDs can be further analyzed in terms of the reaction sequence given by eqs. [11]–[15], where eq. [15] represents the overall hydrodehalogenation and eq. [11] represents initiation via the half-cell process $Fe^0 \rightarrow Fe^{2+} + 2e^-$ (E = –0.771 V). In this scheme, eq. [12], representing electron transfer from Fe^0 to the antibonding C–Cl σ* orbital of TCE, is the rate-limiting step, which is followed by fast expulsion of Cl^-, though the latter process could occur concertedly with electron transfer. The radical R• will then accept an electron and a proton from the aqueous medium, completing the hydrodehalogenation.

[11] $Fe^0 \rightarrow Fe^{2+} + 2e^-$

[12] $R–Cl + e^- \rightarrow R–Cl^-$

[13] $R–Cl^- \rightarrow R\bullet + Cl^-$

[14] $R\bullet + H^+ + e^- \rightarrow R–H$

[15] $R–Cl + H^+ + 2e^- \rightarrow R–H + Cl^-$

Reactions [12] and [13] find analogy with the radical $S_{RN}1$ mechanism of nucleophilic substitution of aryl and alkyl halides (45, 46). While similar mechanisms for dechlorination of related halogen compounds have been proposed by other workers (12, 13), the present study differs from previous ones through the role imparted by the presence of CDs. Previously, a di-σ-bonded Fe-surface-bound chlorinated alkene intermediate was postulated in the rate-determining step (24); however, in the present study, the formation of such an intermediate would be precluded by the CD, which effectively covers the iron surface through Fe*:CD binding. This would then account for a substantial reduction in the rate of dechlorination. At the same time, where TCE is encapsulated within the CD, it is envisaged that electron transfer to the analyte from Fe^0 could occur, up to a separation of approximately 10 Å.

Factors affecting extent of surface binding of CDs

There is considerable variation in the extent to which each CD inhibits degradation of TCE, and this is reflected in the differing $K_{Fe^*:CD}$ values. The $K_{Fe^*:CD}$ parameter measures the strength of binding between iron (hydr)oxide and CD. In these CD molecules, both unsubstituted –OH groups and the derivatized ones are available for complexation with the iron surface. Ideally, one could anticipate the relative order of $K_{Fe^*:CD}$ values amongst the different substituted CDs to be related to the type and number of substituent groups present. Accordingly, one would expect that, among the CDs employed here, Mβ-CD would be the least effective in forming complexes with the oxidized iron surface since there would be less tendency for the methyl substituents to complex with the polar surface (hydr)oxide groups. This would leave only the remaining unsubstituted –OH groups on the CD molecule (9 for Mβ-CD) to participate in bonding. This is borne out in that the $K_{Fe^*:CD}$ value for Mβ-CD is smaller than the others except that for Sβ-CD2, and there is correspondingly less inhibition of the reduction process, as shown in Table 2.

An interesting feature in Table 2 merits further consideration. It appears that $K_{Fe^*:CD}$ is directly correlated with the average number of underivatized –OH groups in the CD molecule. In the native β-CD molecule, there are 21 –OH groups where substitution can take place (33). The average D.S. of the substituted β-CDs used in this work are listed in Table 5, and it appears that as the average D.S. decreases (i.e., higher number of unsubstituted –OH groups), the $K_{Fe^*:CD}$ parameter increases. This correlation supports the earlier argument regarding the important role played by the –OH group in binding of CD to iron oxide surface.

If –OH groups play the dominant role in forming complexes between iron oxide and CD, one might then expect that HPβ-CD would have the highest $K_{Fe^*:CD}$ value since

© 2004 NRC Canada

Fig. 2. Fitting of the data sets from Table 2 according to eq. [10] for the dechlorination of TCE with various CDs using a batch system.

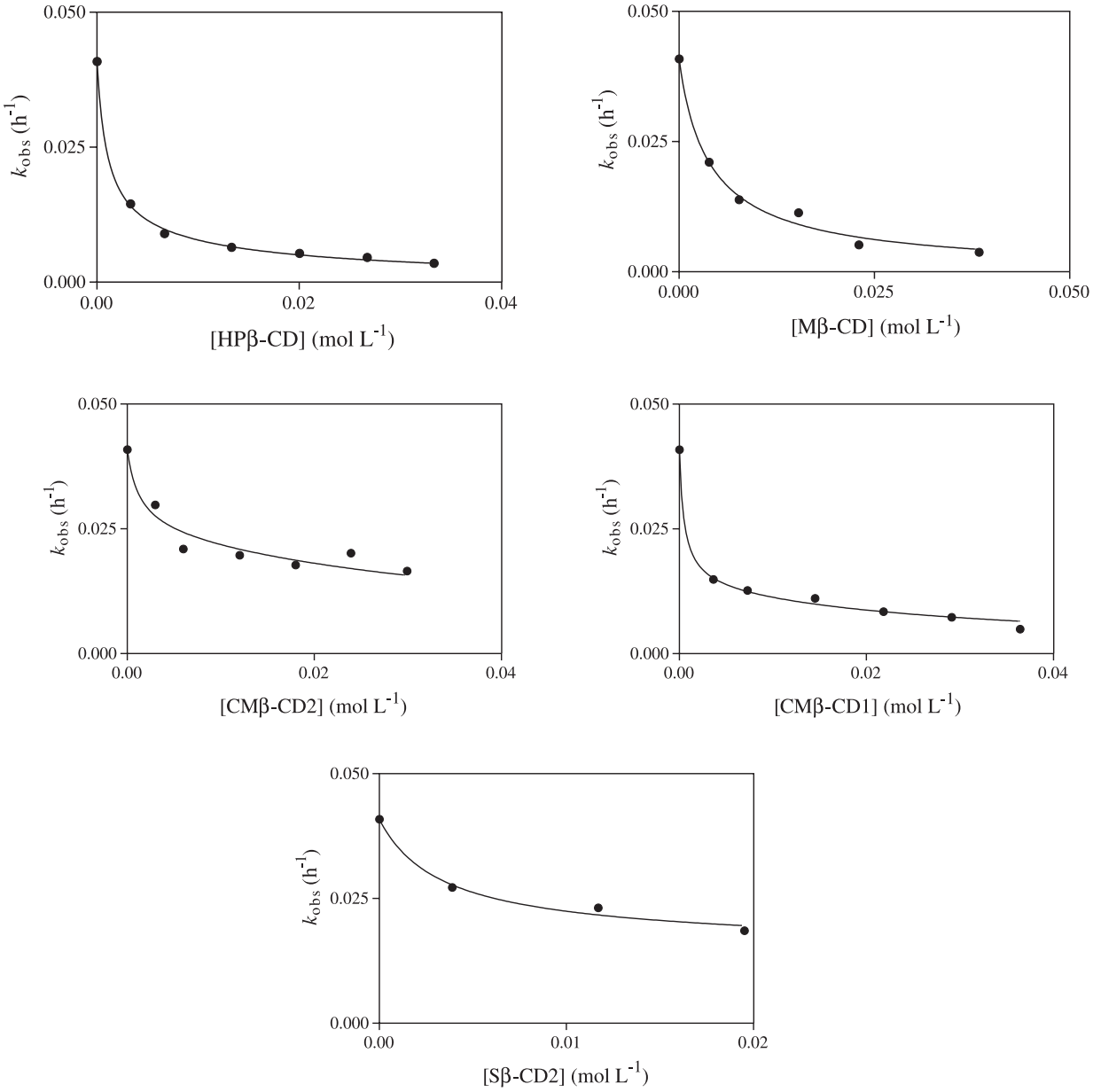


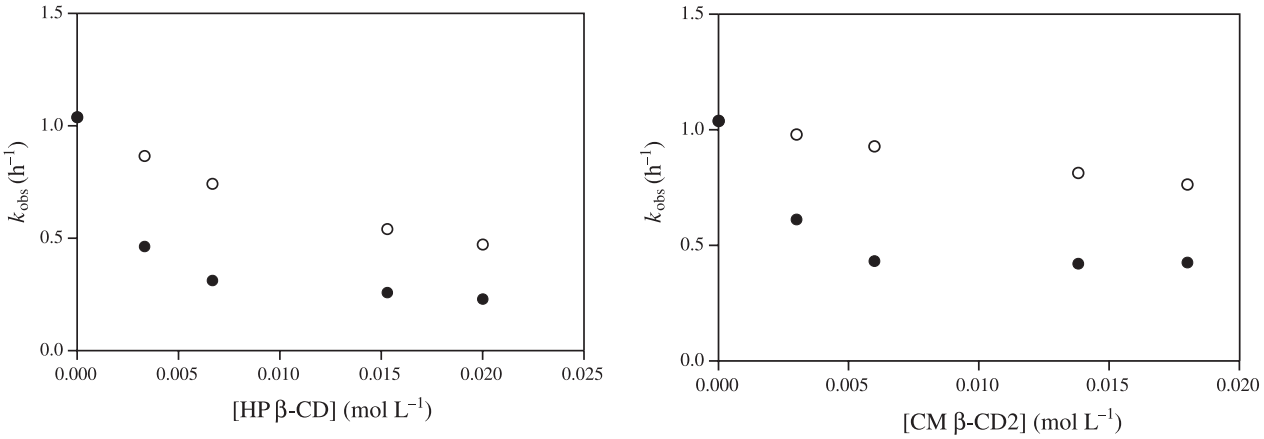
Table 5. Parameters ($K_{Fe^*:CD}$ and k') obtained from the reaction of TCE with zero-valent iron in presence of CDs in batch system by nonlinear regression analysis of the data sets from Table 2 using eq. [10].

CD (average D.S.)[a]	$K_{Fe^*:CD}$ (L mol^{-1})[b]	$10^4 \times k'$ (h^{-1})[b]	K_{11} (L mol^{-1})[c]
HPβ-CD (5.5)	1240±590	1.60±0.20	60.0
Mβ-CD (12)	630±370	2.10±0.03	120
CMβ-CD1 (3.0)	1950±180	4.30±0.02	31.0
CMβ-CD2 (7.0)	1050±550	12.0±0.2	20.0
Sβ-CD2 (14)	310±40	58.0±3.1	3.00

[a]Average D.S. out of total 21. Substitutions are random (ref. 35).
[b]Associated error represents the deviation from the mean of duplicate data set analyses.
[c]Values obtained from ref. 35.

© 2004 NRC Canada

Fig. 3. Effect of two CDs on the observed rate constant for TCE degradation by Fe^0 in column system (ρ_a = 2140 m^2 L^{-1}, flow rate = 1.2 mL min^{-1}, 23 ± 2 °C). Open and solid circles represent rate constants calculated using eq. [9] and experimental rate constant values, respectively.



HPβ-CD contains 21 –OH groups arising from either native –OH or $–CH_2CH(OH)CH_3$ substitution. However, it is clear from Table 5 that this is not the case, since CMβ-CD1 has in fact the highest $K_{Fe^{*}:CD}$ value, and. one can then speculate that the contribution from native CD–OH groups predominates. Given that CD–OH appears to be the key group responsible for the binding of CD to iron, thereby blocking the surface, one might expect that the observed differences between the theoretical and experimental k_{obs} values should be similar in situations involving CDs containing a similar number of unsubstituted –OH groups. Therefore, Sβ-CD2 and Mβ-CD would show similar differences between the theoretical and experimental k_{obs} values, since both contain a similar number of native –OH groups (on average 7 for Sβ-CD2 and 9 for Mβ-CD). However, based on Fig. 1 this is clearly not the case. As seen in the figure, Sβ-CD2 exhibited greater differences between theoretical and experimental k_{obs} values than did Mβ-CD. This discrepancy can be rationalized in that k_{obs} is a composite of the terms $K_{Fe^{*}:CD}$, K_{11}, and k', and, in this instance, the inhibitory effect associated with Mβ-CD on TCE degradation is substantially due to complexation of TCE; this in turn is evidenced by the large K_{11} value observed for Mβ-CD.

The average association constant (K_s) between TCE and Fe has been determined previously and was found to be 191 L mol^{-1} (47). In all cases, it is seen that the $K_{Fe^{*}:CD}$ values are substantially higher than K_s. For this reason and because the concentration of CD present in solution is manyfold greater than that of TCE, the number of Fe sites occupied by surface-bound CD will be much greater than sites occupied by TCE, and binding of TCE itself to the iron surface can be neglected. For this reason, such binding is omitted from Scheme 2, and K_s does not appear in the equation describing k_{obs}.

Column experiments: Dechlorination of TCE in the presence of CD

Following degradation of TCE by Fe^0 in a flowing system allows for further testing of the proposed mechanism to describe inhibition by CDs. For the column kinetic experiments, only two derivatized β-CDs, HPβ-CD (with a neutral substituent group) and CMβ-CD2 (with a charged substituent group), were studied.

As previously found in the batch system, the rate of TCE degradation was inhibited by the presence of both CDs (Table 4). This finding agrees with the literature report that the relative extent of PCE degradation in the column system decreased as the HPβ-CD concentration increased from 0.1% to 7.0% (16). In this work, the TCE degradation rate decreased as the CD concentration increased, attaining a minimum at 1% CD. Above this concentration, the rate of TCE degradation remained nearly constant for CMβ-CD2, and very little change was observed for HPβ-CD. However, the relative overall decrease in the rate of TCE degradation is greater with HPβ-CD than with CMβ-CD2, in agreement with results obtained in batch experiments. As with the batch systems, theoretical rate constants could be calculated to compare with experimental results in the column experiments. When mechanism I was considered to be operative, in both cases the experimental values were again found to be smaller than those determined by calculation (Fig. 3). However, when mechanism II was used as the basis for calculations, agreement between theory and experiment was much better (Fig. 4). In a similar manner as for the batch system, values for $K_{Fe^{*}:CD}$ and k' were obtained from nonlinear regression analysis, and these are listed in Table 6. Good fits were obtained in all cases as shown in Fig. 4.

As in the batch experiments, k' values are smaller than the rate constant for free TCE (k°_{obs} = 1.04 h^{-1}) in the absence of CD. The k' value range from ≤1% to ≤3% of the average k°_{obs} value obtained from the column experiments.

The $K_{Fe^{*}:CD}$ values reported in Table 6 for HPβ-CD and CMβ-CD2 for the column experiments are also similar in magnitude to the corresponding values measured in batch systems. Interestingly, the associated errors (deviations from the mean) in $K_{Fe^{*}:CD}$ values for HPβ-CD and CMβ-CD2 obtained from the column system are smaller than in the case of the batch system (Table 5). Recall that with HPβ-CD and CMβ-CD2 in the batch system, data points in the region of steepest slope (lowest concentration) displayed significant deviations between the two data sets. As a result, the deviation from the mean value of $K_{Fe^{*}:CD}$ was significant in those cases. However, this type of experimental scatter in data

© 2004 NRC Canada

Fig. 4. Fitting of the data sets from Table 4 according to eq. [10], for the dechlorination of TCE with two CDs using a column system.

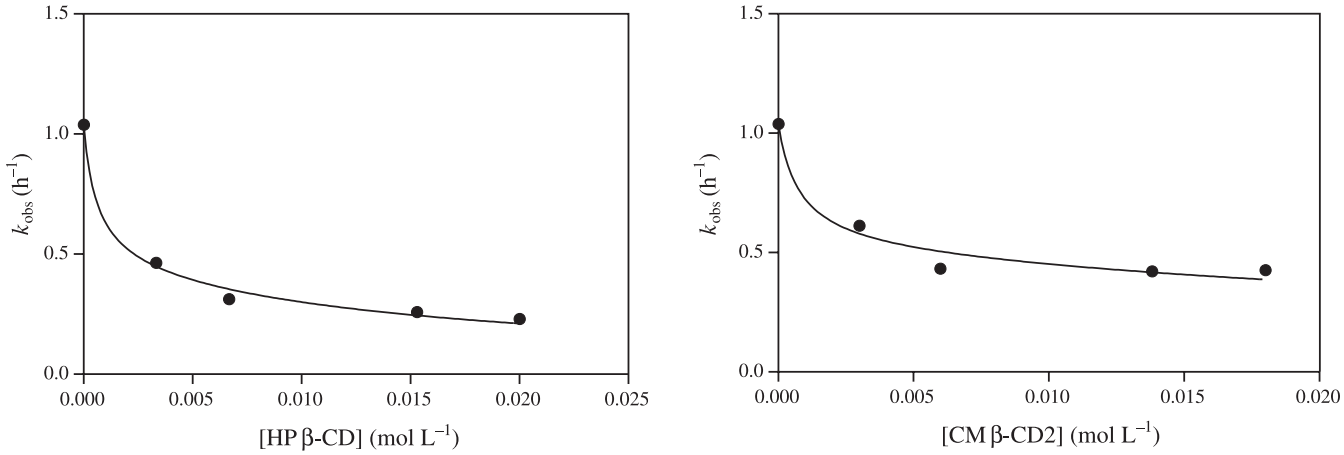


Table 6. Parameters ($K_{Fe^*:CD}$ and k') obtained from reaction of TCE with Fe^0 in presence of CDs in column system by nonlinear regression analysis of the data sets from Table 4 using eq. [10].

CD[a]	$K_{Fe^*:CD}$ (L mol^{-1})[b]	$10^3 \times k'_{obs}$ (h^{-1})[b]
HPβ-CD	1500±140	7.50±0.02
CMβ-CD2	1150±140	24.00±0.02

[a]Refer to Table 5 for D.S.
[b]Associated error represents the deviation from the mean of duplicate data set analyses.

points was not significant in the column system, and this may be one factor leading to a lower associated error for $K_{Fe^*:CD}$.

Acknowledgements

The authors wish to thank Cerestar Co. Ltd. for gifts of CDs used in this work. Financial support for the project was provided by the Environmental Science and Technology Alliance Canada (ESTAC), the Natural Sciences and Engineering Research Council of Canada (NSERC), and Queen's University.

References

1. National Academy of Science. Alternatives for ground water cleanup. Report of the National Academy of Science Committee of Groundwater Cleanup Alternatives. National Academy Press, Washington, D.C. 1994.
2. J.F. Pankow and J.A. Cherry. Dense chlorinated solvents and other DNAPLs in groundwater. Waterloo Press, Portland, Ore. 1996.
3. U.S. Environmental Protection Agency. National priority drinking water regulations [online]. Available from http://www.epa.gov/safewater/dwh/c-voc/tetrachl.html [updated 26 November 2002] and http://www.epa.gov/safewater/dwh/c-voc/trichlor.html [updated 26 November 2002].
4. Priority Substances List Assessment Report. Trichloroethylene. Canadian Environmental Protection Act, Environment Canada, Ottawa, 1993.
5. C.P. Gerba. *In* Pollution science. *Edited by* I.L. Pepper, C.P. Gerba, and M.L. Brusseau. Academic Press, San Diego. 1996. pp. 117–187.
6. T.M. Vogel, C.S. Criddle, and P.L. McCarty. Environ. Sci. Technol. **21**, 722 (1987).
7. J.P. Richardson and J.W. Nicklow. Soil Sediment Contam. **11**(2), 241 (2002).
8. Anon. *In* Groundwater and soil cleanup. National Academy Press, Washington, D.C. 1999. pp. 129–201.
9. R.W. Gillham and S.F. O'Hannesin. Ground Water, **32**, 958 (1994).
10. L.J. Matheson and P.G. Tratnyek. Environ. Sci. Technol. **28**, 2045 (1994).
11. D.R. Burris, T.J. Campbell, and V, Manoranjan. Environ. Sci. Technol. **29**, 2850 (1995).
12. T.L. Johnson, M.M. Scherer, and P.G. Tratnyek. Environ. Sci. Technol. **30**, 2634 (1996).
13. W.S. Orth and R.W. Gillham. Environ. Sci. Technol. **30**, 66 (1996).
14. A.L. Roberts, L.A. Totten, W.A. Arnold, D.A. Burris, and T.J. Campbell. Environ. Sci. Technol. **30**, 2654 (1996).
15. J. Gotpagar, E. Grulke, T. Tsang, and D. Bhattacharyya. Environ. Prog. **16**, 137 (1997).
16. G.O. Bizzigotti, G.W. Reynolds, and B.H. Kueper. Environ. Sci. Technol. **31**, 472 (1997).
17. P.G. Tratnyek, T.L. Johnson, M.M. Scherer, and G.R. Eykholt. Ground Water Monit. Rem. 108 (1997).
18. S.F. O'Hannesin and R.W. Gillham. Ground Water, **36**, 164 (1998).
19. D.R. Burris, R.M. Allen-King, V. Manoranjan, T.J. Campbell, G.A. Loraine, and B. Deng. J. Environ. Eng. 1012 (1998).
20. C. Su and R.W. Puls. Environ. Sci. Technol. **33**, 163 (1999).
21. J. Farrell, M. Kason, N. Melitas, and T. Li. Environ. Sci. Technol. **34**, 514 (2000).
22. T. Li and J. Farrell. Environ. Sci. Technol. **34**, 173 (2000).
23. J. Farrell, N. Meltias, M. Kason, and T. Li. Environ. Sci. Technol. **34**, 2549 (2000).
24. W.A. Arnold and A.L. Roberts. Environ. Sci. Technol. **34**, 1794 (2000).
25. E.C. Butler and K.F. Hayes. Environ. Sci. Technol. **35**, 3884 (2001).
26. U.S. Environmental Protection Agency. Field applications of in situ remediation technologies: permeable reactive barriers [online]. Available from http://www.epa.gov/cgi-bin [updated 26 August 2003].

© 2004 NRC Canada

27. E.J. Weber. Environ. Sci. Technol. **30**, 716 (1996).
28. M. Nagayama and M. Cohen. J. Electrochem. Soc. **109**, 781 (1962).
28. (*a*) A.J. Davenport, J.A. Bardwell, and C.M. Vitus. J. Electrochem. Soc. **142**, 721 (1995); (*b*) A.J. Davenport and M. Sansone. J. Electrochem. Soc. **142**, 725 (1995).
30. M.M Scherer, B.A. Balko, and P.G. Tratnyek. *In* Kinetics and mechanism of reactions at the mineral–water interface. *Edited by* T. Grundl and D. Sparks. American Chemical Society Symposium Series 715. American Chemical Society, Washington, D.C. 1999. Chap. 15.
31. K. Ritter, M.S. Odziemkowski, and R.W. Gillham. J. Contam. Hydrol. **55**, 87 (2002).
32. D.J. Gaspar, A.S. Lea, H. Engelhard, D.R. Bear, R. Miehr, and P.G. Tratnyek. Langmuir, **18**, 7688 (2002).
33. M.L. Bender and M. Komiyama. Cyclodextrin chemistry. Springer-Verlag, Berlin. 1978.
34. X. Wang and M.L. Brusseau. Environ. Sci. Technol. **27**, 2821 (1993).
35. S. Shirin, E. Buncel, and G.W. vanLoon. Can. J. Chem. **81**, 45 (2003), and refs. cited therein.
36. G. Grant. M.Sc. thesis, Queen's University, Kingston, Ont. 2000.
37. S.N. Taylor. M.Sc. thesis, Queen's University, Kingston, Ont. 2001.
38. S. Brunauer, P.H. Emmett, and E. Teller. J. Am. Chem. Soc. **60**, 309 (1938).
39. R.A. Freeze and J.A. Cherry. Groundwater. Prentice Hall, Englewood Cliffs, N.J. 1994. Chap. 2.
40. (*a*) E. Iglesias. J. Org. Chem. **65**, 6583 (2000), and refs. cited therein; (*b*) M.A. Fernandez and R.H. de Rossi. J. Org. Chem. **62**, 7554 (1997); (*c*) M.A. Fernandez and R.H. de Rossi. J. Org. Chem. **66**, 4399 (2001); (*d*) O.S. Tee. Adv. Phys. Org. Chem. **29**, 1 (1993).
41. G.W. vanLoon and S.J. Duffy. Environmental chemistry: a global perspective. Oxford University Press, Oxford, U.K. 2000. Chap. 14.
42. R.P. Schwarzenbach, P.M. Gschwend, and D.M. Imboden. Environmental organic chemistry. John Wiley & Sons, New York, N.Y. 1993. Chap. 11.
43. T.J. Johnson, W. Fish, W.A. Gorby, and P.G. Tratnyek. J. Contam. Hydrol. **29**, 379 (1998).
44. P.G. Tratnyek, M.M. Scherer, B. Deng, and S. Hu. Water Res. **35**, 4435 (2001).
45. J.F. Bunnett. Acc. Chem. Res. **11**, 413 (1978).
46. R.A. Rossi, A.B. Pierini, and S.M. Palacios. *In* Advances in free radical chemistry. Vol. 1. JAI Press, Greenwich, Conn. 1990. pp. 193–252.
47. S. Shirin. Ph.D. thesis, Queen's University, Kingston, Ont. 2002.

© 2004 NRC Canada

Asymmetric formal synthesis of (–)-cryptosporiopsin, a metabolite of *Phialophora asterris*, and its 3-deschloro congener

David I. MaGee, Tammy Mallais, and George M. Strunz

Abstract: An asymmetric formal synthesis of the fungal metabolites (–)-cryptosporiopsin and (–)-3-deschlorocryptosporiopsin has been accomplished. The asymmetry was introduced via a diastereoselective [2+2]-cycloaddition between an enoxy-ester, bearing a bulky chiral auxiliary, and dichloroketene. Diastereomeric ratios of 10:1 were obtained from the reaction mixture, but this could be increased by simple crystallization. Completion of the synthesis was only accomplished after the serendipitous discovery of a base-catalyzed rearrangement to furnish the requisite 3-chloroenone moiety.

Key words: diastereoselective [2+2]-cycloaddition, rearrangement, chiral auxiliary.

Résumé : On a effectué une synthèse asymétrique formelle des métabolites de champignons, les (–)-cryptosporiopsine et (–)-3-deschlorocryptosporiopsine. L'asymétrie a été introduite par le biais d'une cycloaddition diastéréosélective [2+2] entre le dichlorocétène et un ester énoxy portant un auxiliaire chiral auxiliaire volumineux. On a obtenu des rapports de diastéréomères de 10:1 à partir du mélange réactionnel, mais il a été possible de les augmenter par cristallisation simple. On n'a complété la synthèse qu'après la découverte fortuite d'une transposition catalysée par les bases qui permet d'obtenir la portion 3-chloroénone requise.

Mots clés : cycloaddition diastéréosélective [2+2], transposition, auxiliaire chiral.

[Traduit par la Rédaction]

Introduction

Cryptosporiopsin (**1**, Fig 1) and chlorinated cyclopentenone congeners were isolated in 1969, independently from *Sporormia affinis* (1), *Cryptosporiopsis* sp. (2), and *Periconia macrospinosa* (3). Several biogenetically related dihydroisocoumarins from *P. macrospinosa* (e.g., **2**) had been reported previously (4), and new members of the group, including the enantiomeric (–)-cryptosporiopsin (**3**) from *Phialophora asterris* (5), were subsequently disclosed (6). The antibiotic activity of cryptosporiopsin against an array of plant pathogenic fungi and other microorganisms was described (7) and this, together with its intriguing richly functionalized structure, provided the impetus for development of a synthetic route to the metabolite.

Total synthesis of cryptosporiopsin, in racemic form, was first accomplished in 1973 via a biomimetic pathway (8). The key step in this synthesis, ring contraction of a phenolic precursor through the action of alkaline hypochlorite, though providing access to advanced intermediate in a single operation, was a capricious and low-yield process. A later synthesis involving ring contraction of a pre-formed quinonoid intermediate provided a somewhat more efficient route to cryptosporiopsin (9).

Following elucidation of the interesting chemistry associated with dichloroketene cycloaddition with olefins (10), the important synthetic potential of this reaction allowing ready access, inter alia, to a variety of substituted four- and five-membered ring systems (see, e.g., refs. 10 and 11) was recognized.

In 1999, a highly efficient racemic synthesis of 3-deschlorocryptosporiopsin (**4**), a metabolite of *S. affinis* (1), was reported from our laboratories (12), in which the pivotal step was cycloaddition of dichloroketene with methyl 2-trimethylsilyloxy-2-hexenoate (**5**) (Fig. 2). Whereas the original biomimetic route to cryptosporiopsin via contraction of a six-membered ring was not readily amenable to chiral modification, the dichloroketene cycloaddition process can be conducted diastereoselectively, e.g., when the olefin bears a suitable chiral auxiliary (13).

In the present paper we report application of this strategy in an enantioselective synthesis of (–)-cryptosporiopsin, a product of *Phialophora asterris* (5), as well as that of an enantiomer of the *S. affinis* metabolite, 3-deschlorocryptosporiopsin (1).

Greene et al. (14) have shown that diastereoselectivities of around 16:1 can be realized in the cycloaddition of dichloroketene with a chiral enol ether such as **7** in Fig. 3. We considered that the most effective chiral induction for our purposes might be realized if the cycloaddition of dichloroketene was conducted with a cyclic precursor, such

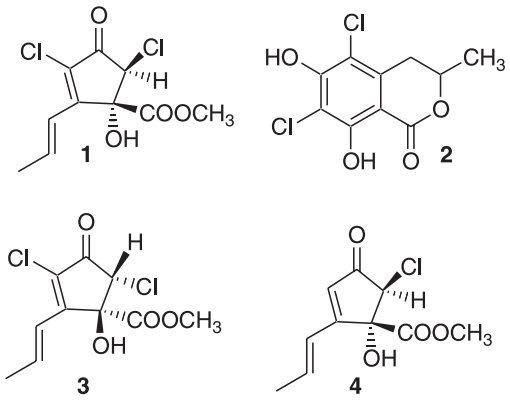
Received 7 May 2004. Published on the NRC Research Press Web site at http://canjchem.nrc.ca on 2 February 2005.

D.I. MaGee[1] and T. Mallais. Department of Chemistry, University of New Brunswick, Fredericton, NB E3B 6E2, Canada.
G.M. Strunz. Department of Chemistry, University of New Brunswick, Fredericton, NB E3B 6E2, Canada and Canadian Forest Service–Atlantic Forestry Centre, Natural Resources Canada, P.O. Box 4000, Fredericton, NB E3B 5P7, Canada.

[1]Corresponding author (e-mail: dmagee@unb.ca).

 doi: 10.1139/V04-145 © 2004 NRC Canada

Fig. 1. Various fungal chlorinated metabolites.



as the dioxolanone **8** or lactone **9** (15). In any event, the failure of both of these olefins to undergo satisfactory cycloaddition with dichloroketene led us to explore instead the diastereoselectivity of dichloroketene cycloaddition with a series of simple chiral 2-silyloxy-2-hexenoic esters (15), of which **10** (which has a (*t*-butyldimethylsilyl (TBS) group) proved to be functional. Useful enantioselectivity has not been observed in conjugate addition of nucleophilic reagents to conjugated chiral esters or during their reaction with diazomethane to give pyrazolines (16). It was reasoned, however, that the presence of a moderately, but not excessively,[2] sterically demanding silyloxy group in the 2-position of a suitable conjugated chiral ester might exert conformational effects resulting in enhanced asymmetric induction during a cycloaddition process.

This hypothesis was substantiated, and optimum diastereoselectity (>10:1) was, in fact, observed in dichloroketene cycloadditions with the 2,2-diphenylcyclopentane esters of 2-silyloxy-2-hexenoic acids (15). Molecular mechanics calculations[3] suggested that the preferred conformation of the (–)-2,2-diphenylcyclopentane ester of 2-*t*-butyldimethylsilyloxy-2-hexenoic acid (**10**), a candidate synthetic precursor, should favour a *Si* approach of the dichloroketene (Fig. 4). This ester thus emerged as the precursor of choice for the enantioselective synthesis of the *P. asterris* metabolite, (–)-cryptosporiopsin.

Cycloaddition of **10** (17) with dichloroketene afforded, after crystallization from hexanes, cyclobutanone **11** (Scheme 1) in 69% yield with 11.5:1 diastereoselectivity. Treatment of **11** with diazomethane (12) effected regiospecific ring expansion to produce diastereometrically enriched cyclopentanone **12** in 90% yield.[4]

This was deemed an appropriate point in the projected synthetic sequence for removal of the chiral auxiliary, preferably concomitant with direct transesterification. Familiar synthetic terrain, traversed previously (though with trimethylsilyloxy rather than *t*-butyldimethylsilyloxy protection) (12), would thus be attained. In any event, attempts at direct transesterification of **12** to the corresponding methyl ester using conventional methodology (see, e.g., ref. 15) were unsuccessful, undoubtedly as a result of the considerable steric encumbrance in the vicinity of the ester group. (In many cases the dimethyl acetal of the ketone resulted.) The chiral auxiliary could, however, be successfully removed by treatment of **12** with neat trifluoroacetic acid (TFA) (18) under reflux which, not surprisingly also removed the *t*-butyldimethylsilyl alcohol protecting group. The product, **13,** without purification, was directly esterified with diazomethane to afford the methyl hydroxy ester **14** in an overall yield of 53%.[5]

Difficulties were encountered in attempts at resilylation of the free hydroxyl group of **14** (including formation of an acyclic product by a retro-aldol process when basic conditions were used), suggesting that the silylation step might be better conducted following desaturation of the ring. Accordingly, **14** was converted to cyclopentenone **16** (54% yield, based on consumed starting material) by treatment with excess selenium dioxide (12). Reaction of **16** with trimethylsilyl trifluoromethanesulfonate (TMSOTf) then afforded **17**, identical in all respects, other than optical rotation, with its racemic counterpart, prepared in the course of the earlier synthesis (12). Preparation of **17** thus constitutes a formal total synthesis of the enantiomer of natural 3-deschlorocryptosporiopsin (cf. refs. 1 and 12).

In the racemic synthesis, the cyclopentenone was next transformed to the corresponding trimethylsilyl (TMS)-dienol ether **20** prior to introduction of the side-chain unsaturation. Under somewhat modified conditions, **17** with chlorotrimethylsilane in refluxing triethylamine afforded, to our pleasant surprise, not the expected TMS-dienol ether but the rearranged product **18** in modest yield. Further investigation revealed that the rearrangement occurred simply on heating **17** at reflux in THF with 2 mole equivalents of triethylamine alone, in the absence of chlorotrimethylsilane!

A rigorous explanation for the rearrangement of **17** to **18** requires additional mechanistic studies, beyond the scope of the present synthetic project. It may be noted, however, that the *gem*-dichloroketone (**17**) can be expected to be a rela-

[2] Cycloaddition failed when attempted with the excessively bulky 2-*t*-butyldiphenylsilyloxy-2-hexenoic diphenylcyclopentyl ester.

[3] Molecular mechanics calculations were performed using the MMFF94 program. No restrictions on bond rotations were imposed. Although there were approximately 20 low-energy conformations within 2.5 kcal/mol, 15 of them adopted the *s*-cis conformation (the lowest-energy *s*-cis conformation had a calculated potential energy of 89.1 kcal/mol). Each of these conformations indicated that the *Si*-face was more accessible for cycloaddition. The remaining low-energy conformations had the *s*-trans arrangement (the lowest-energy *s*-trans conformation had a calculated potential energy of 91.2 kcal/mol), again with the *Si*-face appearing more accessible. Of particular note was that a dihedral angle much less than 180°, and in some instances as low as 139°, between the carbonyl and the carbon–carbon double bond (O=C–C=C) was observed. This helps to corroborate our rationale as to why [2+2]-cycloadditions with these alkenes proceed while those with **8** and **9** do not.

[4] The absolute configurations depicted in **11** and **12** and subsequent structures were, in fact, only rigorously confirmed on completion of the synthesis.

[5] The free acid could, in fact, be obtained without removal of the TBS group by degradation of **12** to **15**, through the agency of ruthenium trichloride in the presence of sodium periodate (19), followed by decarboxylative elimination using 1,8-diazabicyclo[5.4.0]undec-7-ene (DBU). The yield of the desired silyloxy carboxylic acid, however, was not competitive with that from the TFA procedure adopted and described in the text.

© 2004 NRC Canada

Fig. 2. Attempted Kabanyane route to the synthesis of cryptosporiopsin.

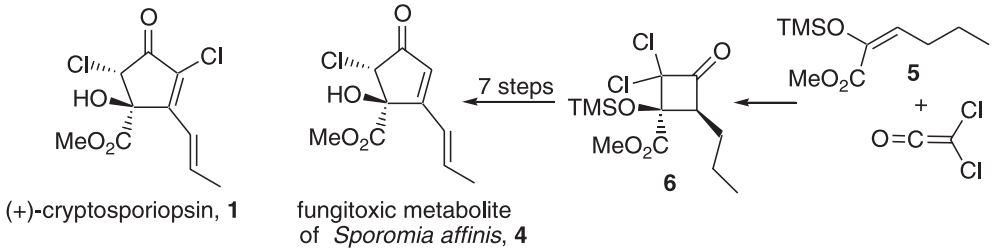
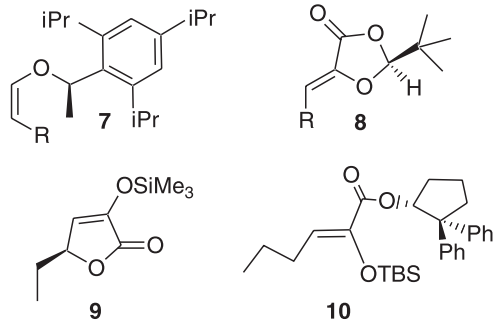


Fig. 3. Greene's enol ether and various other enol ethers investigated.



tively efficient source of electrophilic chlorine, perhaps capable of chlorinating triethylamine to a reactive triethylchloroammonium cationic species, as in Scheme 2. The dienolate **ii** formed from **i** via prototropic shifts could then undergo α-chlorination by the latter reactive species, affording the observed product **18**. The fact that the putative intermediate **ii** undergoes α-chlorination, in contrast to the *gem*-dichlorosilyl enol ether **20** (which reacts with electrophiles at the γ-position) (12), may be due to steric differences and the possible existence of **ii** as a tight ion pair. That said, one cannot rule out the possibility that enolate **ii**, in contrast to Kabanyane's TMS-dienol ether **20**, is simply more susceptible to α-chlorination owing to the increased electron density, or higher HOMO, on the α-carbon.

A slight permutation on the above mechanism may also be considered, in which **17**, as its dienolate (or dienol), undergoes direct chlorination by a second molecule of **17**, to furnish trichloro and monochloro intermediates. The monochloro species, as its conjugated dienolate (or dienol, following prototropic shifts), could then undergo halogenation at its free α-position by transfer of one of the geminal chlorine atoms of the trichloro product. In our experience (12), *gem*-dichloroenones such as **17** tend to react with electrophiles at the γ- rather than the α-position, so one might expect the latter mechanism to produce a mixture of α- and γ-chlorinated products. As only the α-chlorination product **18** was observed, we are inclined to favour the former mechanism. That the chlorine at C5 assumes the correct configuration relative to the functionality at C1 under the equilibrating conditions employed has much precedent (6, 12).

Finally, an alternate pathway to account for the rearrangement of **17** to **18** is shown in Scheme 3.[6] Initially, enone **17** may undergo γ-deprotonation with triethyamine to produce dienolate **i**; if this then suffers an S_N1 type solvolysis of one of the chlorine atoms, oxyallyl cation **ii** is produced. Trapping of **ii** with in situ chloride would generate enolate **iii**, which after protonation and conjugation of the alkene, produces **18**. Unlike the two aforementioned mechanistic proposals, the product formed via this pathway is produced by a nucleophilic chlorine source. This mechanistic rationale is also attractive since base-induced oxyallyl cation formations are well documented (20).

The formal synthesis of (+)-cryptosporiopsin was completed by removal of the TMS protecting group using known methodology (12). The product, **19**, obtained in a modest 41% yield from **18** via base-induced (K_2CO_3) desilylation was identical in all respects, other than its opposite optical rotation, with (–)-dihydrocryptosporiopsin, obtained by catalytic hydrogenation of (+)-cryptosporiopsin (2). The optical rotation of the dihydro derivative obtained from the natural product was +187° and that of synthetic **19**, –160°. This represents an enantiomeric excess of 85%. As desaturation of racemic dihydrocryptosporiopsin to racemic cryptosporiopsin has been accomplished previously (8), the present work constitutes a formal total synthesis of the *P. asterris* metabolite (–)-cryptosporiopsin (5).

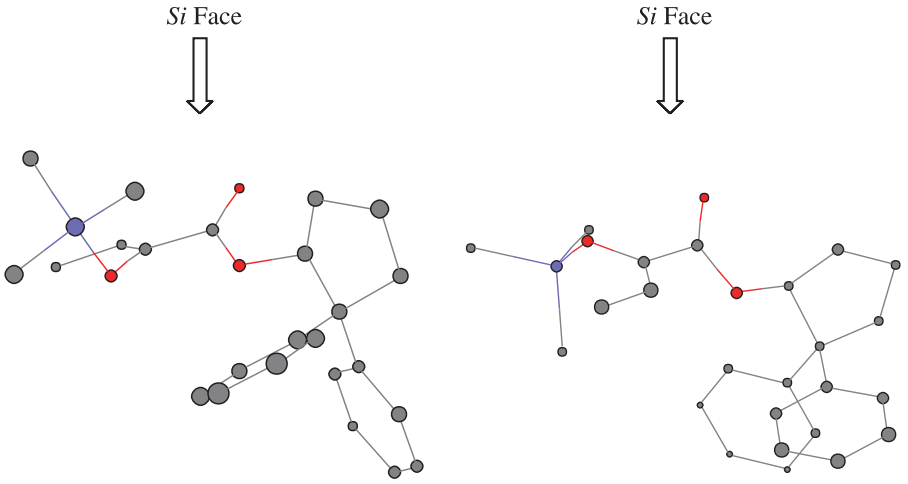
Experimental procedures

All reactions, unless stated otherwise, were performed under inert atmospheres of either argon or nitrogen in flame-dried glassware (Pyrex). Solvents, such as ether, tetrahydrofuran, xylenes, benzene, and toluene, were distilled over sodium, using benzophenone as an indicator, prior to use. Other solvents such as dichloromethane, triethylamine, and acetonitrile were freshly distilled over calcium hydride. Standard techniques were used in handling air-sensitive reagents. Silica gel chromatography (TLC) was performed with DC-Fertigplatten SIL G-25 UV_{254} glass plates (purchased from Aldrich Chemicals, Mississauga, Ont.) or by flash chromatography using Silicycle Ultra Pure Silica Gel for chromatography (Silicycle, Quebec City, Que.). All ^1H and ^{13}C NMR spectra were recorded on a Varian UNITY 400-MHz spectrometer using $CDCl_3$ as solvent. Optical rotations were recorded on a Perkin-Elmer 241 polarimeter using the Na lamp. All IR spectra were recorded on a Bruker IFS 25 instrument using NaCl windows. All high-resolution mass spectra (HR-MS) were run on a Kratos MS50 instrument.

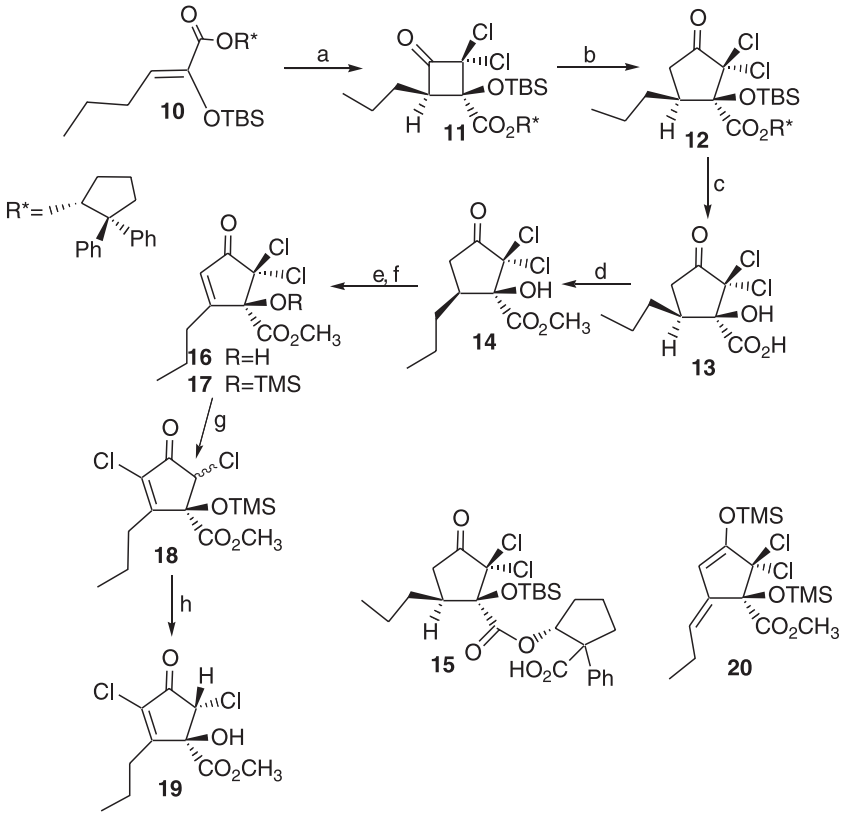
[6] The authors wish to thank one of the referees for suggesting and pointing out the possibility of this mechanism.

© 2004 NRC Canada

Fig. 4. Molecular mechanics (MMFF94) calculated structures for a model diphenylcyclopentyl TMS-enol ester.



Scheme 1. Steps in the enatioselective synthesis of (–)-cryptosporiopsin. a: Cl_3CCOCl, Zn, Et_2O; b: CH_2N_2, MeOH, Et_2O; c: TFA, Δ, 12 h; d: CH_2N_2, Et_2O; e: SeO_2, $C_6H_5CH_3$, Δ; f: TMSOTf, NEt_3, THF; g: NEt_3, Δ; h: K_2CO_3, MeOH.



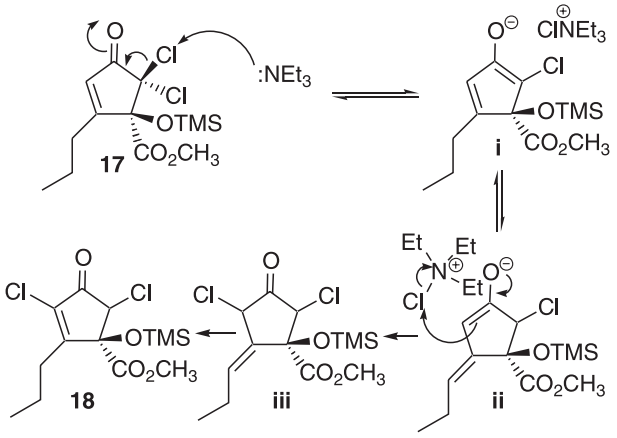
1-*t*-Butyldimethylsilyloxy-2,2-dichloro-3-oxo-4-propylcyclobutanecarboxylic acid (*S*)-(2,2-diphenyl)cyclopentyl ester (11)

Activated Zn dust[7] (1.12 g, 17.1 mmol) was flame-dried in a flask under argon. After cooling to room temperature, ether (10 mL) was added followed by dropwise addition over 4–5 h of a mixture of trichloroacetyl chloride (1.53 mL, 13.7 mmol) and silyl enol ether **10** (3.20 g, 6.9 mmol) (18). The heterogenous solution was stirred for 16 h at RT, diluted with diethyl ether, and filtered through Celite®. The

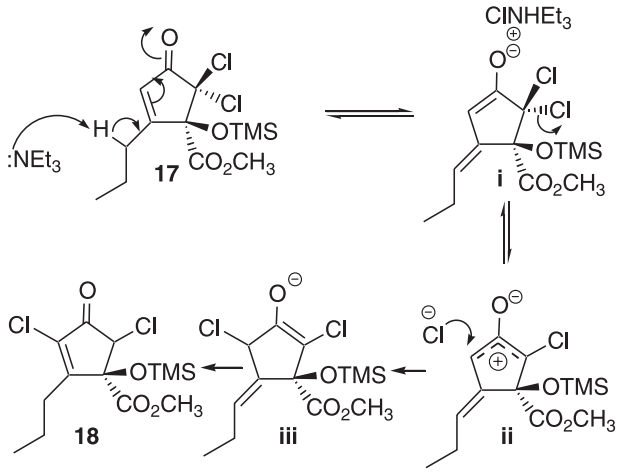
[7] Zn dust was activated by vigorously stirring with 10% HCl for 1–2 min, filtered, and then washed with H_2O (3×) followed by acetone (3×). Zinc activated in this manner was stored in an oven at 140 °C until it was needed.

© 2004 NRC Canada

Scheme 2. A proposed mechanism for the rearrangement of **17** and **18**.



Scheme 3. An alternate mechanism for the rearrangement of **17** and **18**.



filtrate was concentrated to 1–5 mL by rotary evaporation, diluted with pentane (15 mL), and then vigorously stirred for 5 min to induce precipitation of Zn salts. After the precipitate had been allowed to settle, the pentane solution was decanted from the Zn salts. This decanting/washing protocol was repeated twice more. The combined pentane extracts were washed with cold saturated $NaHCO_3$ (5%, 2×), H_2O (1×), and brine (1×) and dried over Na_2SO_4. The solvent was evaporated, and the crude residue was purified by filtration through a short column of SiO_2 (20:1 hexane:ethyl acetate) followed by recrystallization from hexanes to furnish cycloadduct **11** (2.68 g, 69% yield) as a colorless solid; mp 76–78 °C. ^{1}H NMR ($CDCl_3$) δ: 0.22 (s, 3H), 0.36 (s, 3H), 0.73 (t, J = 7.3 Hz, 3H), 0.92 (s, 9H), 1.29 (m, 2H), 1.51 (m, 3H), 1.87 (m, 1H), 2.04 (m, 1H), 2.31 (m, 1H), 2.47 (m, 1H), 2.65 (m, 1H), 2.95 (t, J = 7.7 Hz, 1H), 6.24 (d, J = 4.8 Hz, 1H), and 7.23 (m, 10H). ^{13}C NMR δ: –2.8, 14.1, 19.9, 20.7, 21.2, 26.3, 26.7, 28.8, 30.3, 35.2, 59.9, 64.3, 83.9, 126.3, 126.5, 126.7, 126.8, 127.6, 128.4, 128.5, 128.7, 128.8, 144.5, 145.1, 168.2, and 194.8. IR (cm^{-1}): 3030, 2878, 1818, 1735, 1518, 1460, 1225, and 920. $[\alpha]_D^{25}$ = –65.2° (c = 2.5, CH_2Cl_2).

1-*t*-Butyldimethylsilyloxy-2,2-dichloro-3-oxo-5-propylcyclopentanecarboxylic acid (*S*)-(2,2-diphenyl)cyclopentyl ester (12)

Dichlorocyclobutanone **11** (2.65 g, 4.69 mmol) was dissolved in diethyl ether (20 mL) and cooled to 0 °C, and then diazomethane in ether (0.2 mol/L, 28 mL, 5.6 mmol) was carefully added dropwise. Anhydrous methanol (5 mL) was subsequently added and the reaction mixture was stirred at 0 °C for 5–10 min. The excess diazomethane was quenched with glacial acetic acid (2 drops) and then the solvent was removed in vacuo. (*Note*: The reaction mixture can be left overnight at RT before removal of the solvent to ensure that all the diazomethane has been quenched or evaporated.) The residue was purified by SiO_2 chromatography (30:1 hexane:ethyl acetate) to provide dichlorocyclopentanone **12** (2.50 g, 90% yield) as a colorless oil. ^{1}H NMR ($CDCl_3$) δ: 0.14 (s, 3H), 0.39 (s, 3H), 0.74 (m, 3H), 0.82 (s, 9H), 0.96 (m, 4H), 1.65 (m, 1H), 1.97 (m, 3H), 2.17 (m, 1H), 2.46 (m, 3H), 2.75 (m, 1H), 6.35 (d, J = 4.4 Hz, 1H), 7.15 (m, 2H), 7.26 (m, 6H), and 7.37 (d, J = 7.69 Hz, 2H). ^{13}C NMR ($CDCl_3$) δ: –2.8, –2.2, 14.0, 19.4, 20.2, 20.5, 26.1, 26.2, 30.7, 31.6, 34.6, 36.4, 39.9, 59.3, 83.4, 86.8, 126.1, 126.2, 127.3, 128.0, 128.2, 128.4, 128.5, 128.6, 144.3, 144.9, 168.0, and 197.8. IR (cm^{-1}): 3030, 2404, 1776, 1738, 1518, 1424, 1218, and 926. HR-MS: $(C_{32}H_{42}Cl_2O_4Si - C_4H_9)_{obs.}$ = 531.15287; $(C_{32}H_{42}Cl_2O_4Si - C_4H_9)_{calcd.}$ = 531.15252. $[\alpha]_D^{25}$ = –42.4° (c = 2.5, CH_2Cl_2).

Methyl 2,2-dichloro-1-hydroxy-3-oxo-5-*n*-propylcyclopentane carboxylate (14)

Cyclopentanone **12** (2.47 g, 4.2 mmol) and trifluoroacetic acid (150 mL) were heated at reflux for 15 h. Upon cooling, the solvent was removed in vacuo to give **13** as a black oil. The oil was dissolved in ether (100 mL) and cooled to 0 °C, and diazomethane (0.2 mol/L, 33.5 mL, 5.0 mmol) was added dropwise. The reaction mixture was allowed to stir at 0 °C for 5 min, then warmed to RT, and stirred for 30 min. The dark reaction mixture was quenched with glacial acetic acid (10 drops) and the solvent evaporated. The residue was purified by SiO_2 chromatography (10:1 hexane:ethyl acetate) to furnish cyclopentanone **14** (0.602 g, 53% yield) as a colorless oil. ^{1}H NMR ($CDCl_3$) δ: 0.94 (t, J = 7.2 Hz, 3H), 1.31 (m, 2H), 1.52 (m, 2H), 2.21 (dd, J_1 = 9.1, J_2 = 18.9 Hz, 1H), 2.85 (dd, J_1 = 9.2, J_2 = 19.0 Hz, 1H), 3.11 (m, 1H), 3.69 (d, J = 1.88 Hz, 1H), and 3.94 (s, 3H). ^{13}C NMR ($CDCl_3$) δ: 14.1, 20.7, 31.5, 36.5, 37.2, 53.4, 83.5, 87.0, 169.0, and 198.0. IR (cm^{-1}): 3480, 2958, 2874, 1778, 1728, 1450, 1156, and 820. HR-MS: $(C_{10}H_{14}Cl_2O_4)_{obs.}$ = 268.02769; $(C_{10}H_{14}Cl_2O_4)_{calcd.}$ = 268.02692. $[\alpha]_D^{25}$ = +40° (c = 2.0, EtOH).

Methyl 5,5-dichloro-1-hydroxy-4-oxo-2-*n*-propyl-2-cyclopentene carboxylate (16)

Selenium dioxide (0.70 g, 6.4 mmol) was added to a solution of cyclopentanone **14** (0.57 g, 2.13 mmol) in toluene (20 mL). The solution was heated at reflux for 24 h, cooled to room temperature, then diluted with hexane and filtered through Celite®, and the solvent was evaporated. After purification by SiO_2 chromatography (5:1 hexane:ethyl acetate), cyclopentenone **16** (0.25 g, 63% yield based on consumed cyclopentanone **14**) was obtained as a colorless oil. ^{1}H NMR

© 2004 NRC Canada

($CDCl_3$) δ: 0.98 (t, J = 7.3 Hz, 3H), 1.58 (m, 2H), 2.23 (m, 1H), 2.47 (m, 1H), 3.82 (s, 3H), 4.47 (s, 1H), and 6.28 (s, 1H). ^{13}C NMR ($CDCl_3$) δ: 13.6, 19.7, 30.9, 54.6, 86.7, 87.0, 127.2, 169.8, 173.3, and 189.4. IR (cm^{-1}): 3480, 2952, 1736, 1640, 1464, 1272, 1176, 952, and 840. HR-MS: $(C_{10}H_{12}Cl_2O_4 - Cl)_{obs.}$ = 231.04094; $(C_{10}H_{12}Cl_2O_4 - Cl)_{calcd.}$ = 231.04248. $[\alpha]_D^{25}$ = –143° (c = 0.65, EtOH).

Methyl 5,5-dichloro-4-oxo-2-*n*-propyl-1-trimethylsilyloxy-2-cyclopentene carboxylate (17)

Trimethylsilyl trifluoromethanesulfonate (0.03 mL, 0.14 mmol) was added dropwise to a solution of alcohol **16** (18.8 mg, 0.07 mmol), triethylamine (0.03 mL, 0.17 mmol), and diethyl ether (1 mL). The reaction mixture was stirred at RT for 30 min, then quenched with saturated NH_4Cl (1 mL). The organic layer was separated, washed with brine (1×), and dried over $MgSO_4$, and the solvent was evaporated. Preparative TLC (5:1 hexane:ethyl acetate) provided **17** (14.5 mg, 61% yield) as a colorless oil. ^{1}H NMR ($CDCl_3$) δ: 0.35 (s, 9H), 0.99 (t, J = 7.3 Hz, 3H), 1.61 (m, 2H), 2.20 (m, 2H), 2.41 (m, 2H), 3.73 (s, 3H), and 6.19 (s, 1H). ^{13}C NMR ($CDCl_3$) δ: 2.1, 13.7, 19.8, 30.8, 53.4, 90.6, 125.3, 168.8, 175.5, and 189.9. IR (cm^{-1}): 3000, 1752, 1640, 1448, 1224, 894, and 856. HR-MS: $(C_{13}H_{20}Cl_2O_4Si - CH_3)_{obs.}$ = 323.02643; $(C_{13}H_{20}Cl_2O_4Si - CH_3)_{calcd.}$ = 323.02731. $[\alpha]_D^{25}$ = –109° (c = 0.97, EtOH).

Methyl 3,5-dichloro-4-oxo-2-*n*-propyl-1-trimethylsilyloxy-2-cyclopentene carboxylate (18)

A mixture of enone **17** (16.9 mg, 0.049 mmol) and triethylamine (0.014 mL, 0.099 mmol) was heated at reflux in THF and monitored by TLC. When the starting material was completely consumed, the solvent was removed in vacuo and the residue was purified by SiO_2 chromatography (10:1 hexane:ethyl acetate) to furnish **18** (10.5 mg, 62% yield) as a colorless oil. ^{1}H NMR ($CDCl_3$) δ: 0.27 (s, 9H), 0.97 (t, J = 7.4 Hz, 3H), 1.51 (m, 2H), 2.40 (m, 1H), 2.50 (m, 1H), 3.71 (s, 3H), and 4.44 (s, 1H). ^{13}C NMR ($CDCl_3$) δ: 2.1, 14.2, 20.4, 29.3, 53.2, 66.4, 86.1, 132.5, 168.2, 168.8, and 188.2. IR (cm^{-1}): 2961, 2877, 1769, 1622, 1436, 1253, 878, and 761. HR-MS: $(C_{13}H_{20}Cl_2O_4Si - CH_3)_{obs.}$ = 323.02695; $(C_{13}H_{20}Cl_2O_4Si - CH_3)_{calcd.}$ = 323.02731. $[\alpha]_D^{25}$ = –75° (c = 0.6, EtOH).

(–)-Dihydrocryptosporiopsin (19)

Chloroenone **18** (11.8 mg, 0.03 mmol) was dissolved in methanol (1 mL) and cooled to 0 °C. Potassium carbonate (6 mg, 0.04 mmol) was added in one portion, and the reaction mixture was stirred at 0 °C. When TLC showed complete consumption of the starting material, the mixture was poured into cold H_2O and extracted with ether (3×). After drying with $MgSO_4$, the solvent was removed in vacuo and the residue was purified by SiO_2 chromatography (5:1 hexane:ethyl acetate) to give (–)-dihydrocryptosporiopsin (**19**) as a colorless solid (4 mg, 41% yield), which had identical spectroscopic properties, except rotation, with a sample derived from the natural compound. ^{1}H NMR ($CDCl_3$) δ: 0.98 (t, J = 7.4 Hz, 3H), 1.52 (m, 2H), 2.42 (ddd, J_1 = 6.6 Hz, J_2 = 9.6 Hz, J_3 = 13.3, 1H), 2.55 (ddd, J_1 = 6.0 Hz, J_2 = 9.3 Hz, J_3 = 13.2 Hz, 1H), 3.82 (s, 3H), 4.40 (bs, 1H), and 4.55 (s, 1H). ^{13}C NMR ($CDCl_3$) δ: 14.4, 20.6, 29.4, 54.6, 65.6, 83.7, 133.9, 166.5, 170.8, and 188.0. IR (cm^{-1}): 3504, 3040, 3008, 1736, 1620, 1524, 1420, 1216, and 932. HR-MS: $(C_{10}H_{12}Cl_2O_4)_{obs.}$ = 266.01014; $(C_{10}H_{12}Cl_2O_4)_{calcd.}$ = 266.01126. $[\alpha]_D^{25}$ = –160° (c = 0.1, $CHCl_3$). Comparison with spectral data of the authentic sample of (+)-dihydrocryptosporiopsin: ^{1}H NMR ($CDCl_3$) δ: 0.98 (t, J = 7.3 Hz, 3H), 1.50 (m, 2H), 2.42 (ddd, J_1 = 6.6 Hz, J_2 = 9.6 Hz, J_3 = 13.3, 1H), 2.55 (ddd, J_1 = 6.0 Hz, J_2 = 9.3 Hz, J_3 = 13.2 Hz, 1H), 3.82 (s, 3H), 4.40 (s, 1H), and 4.57 (s, 1H). ^{13}C NMR ($CDCl_3$) δ: 14.4, 20.6, 29.4, 54.6, 65.7, 83.7, 133.9, 166.5, 170.7, and 188.0. $[\alpha]_D^{25}$ = +187° (c = 0.5, $CHCl_3$).

References

1. W.J. McGahren, J.H. van den Hende, and L.A. Mitscher. J. Am. Chem. Soc. **91**, 157 (1969).
2. G.M. Strunz, A.S. Court, J. Komlossy, and M.A. Stillwell. Can. J. Chem. **47**, 2087 and 3700 (1969).
3. D. Giles and W.B. Turner. J. Chem. Soc. C, 2187 (1969).
4. W.J. McGahren and L.A. Mitscher. J. Org. Chem. **33**, 1577 (1968).
5. R.J.J. Ch. Lousberg, Y. Tirilly, and M. Moreau. Experientia, **32**, 331 (1976).
6. G.M. Strunz, P.I. Kazinoti, and M.A. Stillwell. Can. J. Chem. **52**, 3623 (1974).
7. M.A. Stillwell, F.A. Wood, and G.M. Strunz. Can. J. Microbiol. **15**, 501 (1969).
8. G.M. Strunz and A.S. Court. J. Am. Chem. Soc. **95**, 3000 (1973).
9. G.B. Henderson and R.A. Hill. J. Chem. Soc., Perkin Trans. 1, 2595 (1983).
10. W.T. Brady. Tetrahedron, **37**, 2949 (1981).
11. A.E. Greene and J.P. Deprés. J. Am. Chem. Soc. **101**, 4003 (1979).
12. S. Kabanyane, A. Decken, C.-M. Yu, and G.M. Strunz. Can. J. Chem. **78**, 270 (2000).
13. P. Nebois and A.E. Greene. J. Org. Chem. **61**, 5210 (1996).
14. A.E. Greene, A. Kanazawa, and S. Gillet. Tetrahedron, **63**, 4660 (1998).
15. T.C. Mallais. Ph.D. thesis, Department of Chemistry, University of New Brunswick, Fredericton, N.B. 2003.
16. F.S. Impastato, L. Barash, and H.M. Walborsky. J. Am. Chem. Soc. **81**, 1514 (1959).
17. D.I. MaGee, T.C. Mallais, and M. Eic. Tetrahedron: Asymmetry, **14**, 3177 (2003).
18. F.X. Webster, J. Rivas-Enterrios, and R.M. Silverstein. J. Org. Chem. **52**, 689 (1987).
19. P.H.J. Carlsen, T. Katsuki, V.S. Martin, and K.B. Sharpless. J. Org. Chem. **46**, 3936 (1981).
20. For a review on oxyallyl cation formation, see: J. Mann. Tetrahedron, **42**, 4611 (1986).

© 2004 NRC Canada

Platinum pyridinecarboxaldimine complexes containing boronate esters

Hanni A. Darwish, Stephen J. Scales, Jennifer L. Horton, Liliya G. Nikolcheva, Haiwen Zhang, Christopher M. Vogels, Mazen T. Saleh, Robert J. Ireland, Andreas Decken, and Stephen A. Westcott

Abstract: Condensation of 2-pyridinecarboxaldehydes with 2-, 3-, and 4-$H_2NC_6H_4Bpin$ (pin = 1,2-$O_2C_2Me_4$) gave the corresponding boron-containing pyridinecarboxaldimines (N–N_{Bpin}). Addition of these ligands to $[PtCl_2(coe)]_2$ (coe = *cis*-cyclooctene) gave complexes of the type *cis*-$PtCl_2(N–N_{Bpin})$ in moderate yields. The platinum complexes have been examined for their potential cytotoxicities against OV2008 (human ovarian carcinoma) and the analogous cisplatin-resistant cell line C13.

Key words: boronate esters, pyridinecarboxaldimines, cytotoxicity, platinum, boron.

Résumé : La condensation des pyridine-2-carboxaldéhydes avec les 2-, 3- et 4-$H_2NC_6H_4Bpin$ (pin = 1,2-$O_2C_2Me_4$) conduit à la formation des pyridinecarboxaldimines contenant du bore (N–N_{Bpin}). L'addition de ces ligands au $[PtCl_2(coe)]_2$ (coe = *cis*-cyclooctène) conduit à la formation de complexes du type *cis*-$PtCl_2(N–N_{Bpin})$, avec des rendements modérés. On a étudié les cytotoxicités potentielles des complexes du platine vis-à-vis du OV2008 (carcinome ovarien humain) et la série de cellules C13 apparentées, qui est résistante au cisplatine.

Mots clés : esters de l'acide boronique, pyridinecarboxaldimines, cytotoxicité, platine, bore.

[Traduit par la Rédaction]

Introduction

Interest in compounds containing boronic acids $[RB(OH)_2]$ or boronate esters $[RB(OR')_2]$ arises from their remarkable versatility in catalysed carbon–carbon bond formation reactions, solid-phase synthesis, macrocyclic chemistry, organometallic and organic syntheses, and as glucose sensors for diabetes therapy (1). Interest in these compounds also arises from their potent biological activities (2–11). For instance, α-aminoboronic acids are effective and reversible inhibitors of serine proteases, a diverse group of proteolytic enzymes whose numerous physiological functions include digestion, growth, differentiation, and apoptosis. Proteases are also vital in the generation of most disease processes and, as a result, much effort has focused on the synthesis of α-aminoboronic acids for possible applications as enzyme inhibitors. Indeed, the boron compounds boromycin (12) and aplasmomycin (13) are powerful antibiotics and analogous amino acids containing boronic acids, such as L-4-boronophenylalanine, have also been investigated for their use in boron neutron capture therapy (BNCT) for the treatment of cancer (14–16). BNCT is a bimodal form of therapy, which depends on selectively depositing boron-10 atoms into the cancerous tumour prior to irradiation by slow (thermal) neutrons. These known biological activities, along with their ability to transport water insoluble reagents through membranes (17, 18), prompted us to investigate the use of boronate ester compounds as carrier ligands for biologically-active metal complexes.

Cisplatin, *cis*-$[PtCl_2(NH_3)_2]$, and a few related platinum-based complexes are currently used as anticancer agents against testicular and ovarian malignancies (19–25). However, there are several limitations to platinum therapy such as neural and kidney toxicity as well as intrinsic and acquired resistance of tumor cells to the drugs (19). These complications have provided incentive for further research in the development of platinum-based complexes with increased solubility and enhanced specificity towards cancer cells. Recent studies have shown that *cis*-amminedichloro(2-methylpyridine)platinum(II) (AMD473 or ZD0473, **1** in Fig. 1) shows considerable cytotoxicity in cisplatin-resistant cell lines (26, 27). Steric crowding from the methyl group is

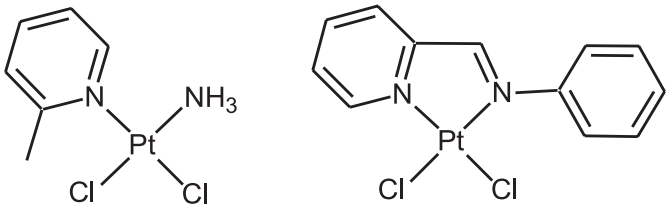
Received 5 June 2004. Published on the NRC Research Press Web site at http://canjchem.nrc.ca on 14 January 2005.

H.A. Darwish, **S.J. Scales**, **J.L. Horton**, **L.G. Nikolcheva**, **H. Zhang**, **C.M. Vogels**, **and S.A. Westcott.**[1] Department of Chemistry, Mount Allison University, Sackville, NB E4L 1G8, Canada.
M.T. Saleh and R.J. Ireland. Department of Biology and Biochemistry, Mount Allison University, Sackville, NB E4L 1G7, Canada.
A. Decken.[2] Department of Chemistry, University of New Brunswick, Fredericton, NB E3B 5A3, Canada.

[1]Corresponding author (e-mail: swestcott@mta.ca).
[2]Corresponding author regarding X-ray crystallography (e-mail: adecken@unb.ca).

 doi: 10.1139/V04-147 © 2004 NRC Canada

Fig. 1. Structure of AMD473 (**1**) and complex **2**.



1 **2**

believed to decrease the rates of hydrolysis, and substitution reactions of AMD473 thereby permit high selectivity in binding with DNA (28). The primary mechanism of action in these platinum drugs is believed to arise from the interaction of the metal with DNA.

We have begun to develop AMD473 analogues by replacing the NH_3 group with a pendant imine group. Previous studies have shown that the platinum complex derived from aniline, **2** (Fig. 1), has shown considerable activity against the hormone independent human mammary carcinoma cell line MDA-MB 231 (29). Varying the aniline functionality allows us to design compounds with a wide range of physical and chemical properties that may provide steric congestion around the platinum atom (29). As well, the use of bidentate ligands prevents trans labilization and undesired displacement of the ligands by sulfur and nitrogen donors in biomolecules, interactions believed responsible for some of the adverse side effects associated with cisplatin (19). We report herein our results on the synthesis and initial cytotoxic testing of *cis*-dichloro(pyridin-2-ylcarboxaldimine)platinum(II) compounds containing boronate esters.

Experimental

General

Reagents and solvents used were obtained from Aldrich Chemicals. K_2PtCl_4 was purchased from Precious Metals Online Ltd. (Melbourne, Australia) and $[PtCl_2(coe)]_2$ (coe = *cis*-cyclooctene) was made following an established procedure (30). 2-APBpin (pin = 1,2-$O_2C_2Me_4$) was synthesized by modification of a reported synthesis (31). Pyridinecarboxaldimine ligands were prepared as described elsewhere (32) and (6-methyl-pyridin-2-ylmethylene)-[4-(4,4,5,5-tetramethyl-[1,3,2]-dioxaborolan-2-yl)phenyl]amine was synthesized under a nitrogen atmosphere and used in situ. NMR spectra were recorded on a JEOL JNM-GSX270 FT or a Varian Mercury Plus 200 NMR spectrometer. ^{1}H NMR chemical shifts are reported in ppm and are referenced to residual protons in a deuterated solvent at 270 and 200 MHz. ^{11}B NMR chemical shifts are referenced to external $BF_3{\cdot}OEt_2$ at 87 MHz. ^{13}C NMR chemical shifts are referenced to solvent carbon resonances as internal standards at 68 and 50 MHz. Multiplicities are reported as singlet (s), doublet (d), triplet (t), multiplet (m), broad (br), and overlapping (ov). Infrared spectra were obtained using a Mattson Genesis II FT-IR spectrometer and are reported in cm^{-1}. Melting points were measured uncorrected with a Mel-Temp apparatus. Microanalyses for C, H, and N were carried out at Guelph Chemical Laboratories Ltd. (Guelph, Ont.).

Compound 3a

Under a nitrogen atmosphere, a THF (2 mL) solution of pyridin-2-ylmethylene-[2-(4,4,5,5-tetramethyl-[1,3,2]-dioxaborolan-2-yl)phenyl]amine (0.09 g, 0.29 mmol) was added to $[PtCl_2(coe)]_2$ (0.10 g, 0.13 mmol) in THF (3 mL). The reaction mixture was stirred for 18 h at which point a precipitate was collected by suction filtration and washed in turn with cold THF (3 × 1 mL) and Et_2O (3 × 5 mL) to afford **3a** (0.06 g, 39%) as a yellow-orange solid; mp 270–272 °C (decomposition). Spectroscopic NMR data (in DMSO-d_6): ^{1}H δ: 9.50 (d, $J_{H\text{-}H}$ = 7 Hz, $J_{H\text{-}Pt}$ = 62 Hz, 1H, Ar), 9.35 (s, $J_{H\text{-}Pt}$ = 92 Hz, 1H, C(*H*) = N), 8.47 (t, $J_{H\text{-}H}$ = 7 Hz, 1H, Ar), 8.22 (d, $J_{H\text{-}H}$ = 7 Hz, 1H, Ar), 8.01 (t, $J_{H\text{-}H}$ = 7 Hz, 1H, Ar), 7.74 (d, $J_{H\text{-}H}$ = 7 Hz, 1H, Ar), 7.60 (t, $J_{H\text{-}H}$ = 7 Hz, 1H, Ar), 7.42 (t, $J_{H\text{-}H}$ = 7 Hz, 1H, Ar), 7.34 (d, $J_{H\text{-}H}$ = 7 Hz, 1H, Ar), 1.21 (s, 6H, $O_2C_2(CH_3)_4$), and 1.15 (s, 6H, $O_2C_2(CH_3)_4$). ^{11}B{^{1}H} δ: 29.1 (br). ^{13}C{^{1}H} δ: 173.0, 157.7, 152.7, 149.7, 141.2, 135.4, 131.5, 130.1, 130 (br, *C*-B), 129.7, 128.3, 124.9, 84.5, 25.4, and 25.1. IR (cm^{-1}) (Nujol): 2926, 2856, 1601 (C=N), 1462, 1377, 1300, 1240, 1200, 1144, 1076, 964, 860, 779, and 654. Anal. calcd. (%) for $C_{18}H_{21}N_2BCl_2O_2Pt$, C 37.64, H 3.69, N 4.88; found: C 37.94, H 3.33, N 4.84.

Compound 3b

Pyridin-2-ylmethylene-[3-(4,4,5,5-tetramethyl-[1,3,2]-dioxaborolan-2-yl)phenyl]amine (0.09 g, 0.29 mmol) in CH_2Cl_2 (5 mL) was added to $[PtCl_2(coe)]_2$ (0.10 g, 0.13 mmol) in CH_2Cl_2 (5 mL) and the reaction mixture was stirred for 1 h at which point solvent was removed under vacuum to give an oil. Following trituration with hexane (3 × 10 mL) an orange solid was recovered and recrystallized from THF (5 mL) at room temperature to afford **3b** (0.08 g, 54%) as a red-orange solid; mp 316 °C (decomposition). Spectroscopic NMR data (in $CDCl_3$): ^{1}H δ: 9.76 (d, $J_{H\text{-}H}$ = 7 Hz, $J_{H\text{-}Pt}$ = 60 Hz, 1H, Ar), 8.88 (s, $J_{H\text{-}Pt}$ = 84 Hz, 1H, C(*H*) = N), 8.19 (t, $J_{H\text{-}H}$ = 7 Hz, 1H, Ar), 7.97 (d, $J_{H\text{-}H}$ = 7 Hz, 1H, Ar), 7.83 (d, $J_{H\text{-}H}$ = 7 Hz, 1H, Ar), 7.81–7.72 (ov m, 2H, Ar), 7.66 (d, $J_{H\text{-}H}$ = 7 Hz, 1H, Ar), 7.43 (t, $J_{H\text{-}H}$ = 7 Hz, 1H, Ar), and 1.27 (s, 12H, $O_2C_2(CH_3)_4$). ^{11}B{^{1}H} δ: 32.5 (br). ^{13}C{^{1}H} δ: 168.3, 156.5, 150.0, 146.1, 139.5, 135.6, 129.0, 129 (br, *C*-B), 128.9, 128.4, 127.5, 127.4, 84.0, and 24.7. IR (cm^{-1}) (Nujol): 2895, 2856, 1610 (C=N), 1462, 1377, 1329, 1234, 1151, 933, 854, 816, 777, and 706. Anal. calcd. (%) for $C_{18}H_{21}N_2BCl_2O_2Pt$, C 37.64, H 3.69, N 4.88; found: C 37.25, H 3.62, N 4.73.

Compound 3c

Pyridin-2-ylmethylene-[4-(4,4,5,5-tetramethyl-[1,3,2]-dioxaborolan-2-yl)phenyl]amine (0.18 g, 0.58 mmol) in CH_2Cl_2 (5 mL) was added to $[PtCl_2(coe)]_2$ (0.20 g, 0.26 mmol) in CH_2Cl_2 (5 mL) and the reaction mixture was stirred for 7 h at which point solvent was removed under vacuum to give an oil. Following trituration with hexane (3 × 10 mL) an orange solid was recovered and recrystallized from THF (5 mL) at room temperature to afford **3c** (0.19 g, 64%) as an orange solid; mp 304 °C (decomposition). Spectroscopic NMR data (in DMSO-d_6): ^{1}H δ: 9.48 (d,

© 2004 NRC Canada

$J_{H\text{-}H}$ = 7 Hz, $J_{H\text{-}Pt}$ = 65 Hz, 1H, Ar), 9.33 (s, $J_{H\text{-}Pt}$ = 84 Hz, 1H, C(*H*) = N), 8.45 (t, $J_{H\text{-}H}$ = 7 Hz, 1H, Ar), 8.24 (d, $J_{H\text{-}H}$ = 7 Hz, 1H, Ar), 8.00 (t, $J_{H\text{-}H}$ = 7 Hz, 1H, Ar), 7.77 (d, $J_{H\text{-}H}$ = 7 Hz, 2H, Ar), 7.46 (d, $J_{H\text{-}H}$ = 7 Hz, 2H, Ar), and 1.32 (s, 12H, $O_2C_2(CH_3)_4$). $^{11}B\{^1H\}$ δ: 33.1 (br). $^{13}C\{^1H\}$ δ: 173.1, 157.6, 149.8, 149.6, 141.2, 134.8, 130.4, 130.2, 129.5 (br, *C*-B), 124.4, 84.5, and 25.2. IR (cm^{-1}) (Nujol): 2941, 2914, 2858, 1601 (C=N), 1460, 1377, 1356, 1315, 1263, 1144, 1084, 1018, 968, 858, 764, 723, and 656. Anal. calcd. (%) for $C_{18}H_{21}N_2BCl_2O_2Pt$, C 37.64, H 3.69, N 4.88; found: C 37.31, H 3.50, N 4.69.

Compound 4a

Under an atmosphere of nitrogen, a THF (1 mL) solution of (6-methyl-pyridin-2-ylmethylene)-[2-(4,4,5,5-tetramethyl-[1,3,2]-dioxaborolan-2-yl)phenyl]amine (0.09 g, 0.28 mmol) was added to $[PtCl_2(coe)]_2$ (0.09 g, 0.12 mmol) in THF (3 mL). The reaction mixture was stirred for 8 h at which point a precipitate was collected by suction filtration and washed with Et_2O (3 × 5 mL) to afford **4a** (0.06 g, 42%) as an orange solid; mp 285 °C (decomposition). Spectroscopic NMR data (in $CDCl_3$): ^1H δ: 8.77 (s, $J_{H\text{-}Pt}$ = 84 Hz, 1H, C(*H*) = N), 8.02 (t, $J_{H\text{-}H}$ = 7 Hz, 1H, Ar), 7.86 (d, $J_{H\text{-}H}$ = 7 Hz, 1H, Ar), 7.68 (d, $J_{H\text{-}H}$ = 7 Hz, 1H, Ar), 7.56 (d, $J_{H\text{-}H}$ = 7 Hz, 1H, Ar), 7.50 (t, $J_{H\text{-}H}$ = 7 Hz, 1H, Ar), 7.36 (t, $J_{H\text{-}H}$ = 7 Hz, 1H, Ar), 7.29 (d, $J_{H\text{-}H}$ = 7 Hz, 1H, Ar), 3.25 (s, 3H, CH_3), and 1.25 (br s, 12H, $O_2C_2(CH_3)_4$). $^{11}B\{^1H\}$ δ: 29.3 (br). $^{13}C\{^1H\}$ δ: 161.9, 159.5, 155.2, 138.4, 136.8, 133.1, 129.1, 128.5, 126 (br, *C*-B), 119.6, 115.6, 114.8, 83.7, 25.2, and 24.3. IR (cm^{-1}) (Nujol): 2924, 2854, 1603 (C=N), 1462, 1377, 1348, 1144, 1072, 1018, 962, 858, 725, 654, and 596. Anal. calcd. (%) for $C_{19}H_{23}N_2BCl_2O_2Pt$, C 38.79, H 3.95, N 4.76; found: C 38.95, H 4.05, N 4.78.

Compound 4b

(6-Methyl-pyridin-2-ylmethylene)-[3-(4,4,5,5-tetramethyl-[1,3,2]-dioxaborolan-2-yl)phenyl]amine (0.08 g, 0.25 mmol) in CH_2Cl_2 (5 mL) was added to $[PtCl_2(coe)]_2$ (0.08 g, 0.11 mmol) in CH_2Cl_2 (5 mL) and the reaction was heated at reflux for 24 h. Removal of solvent under vacuum gave an oil which was triturated with hexane (3 × 10 mL) to afford a red-orange solid which was dissolved in a CH_2Cl_2:Et_2O (5:5 mL) solution and stored at 0 °C for 18 h. The resulting precipitate was collected by suction filtration to afford **4b** (0.08 g, 62%) as an orange solid; mp 264 °C (decomposition). Spectroscopic NMR data (in $CDCl_3$): ^1H δ: 8.91 (s, $J_{H\text{-}Pt}$ = 80 Hz, 1H, C(*H*) = N), 7.97 (t, $J_{H\text{-}H}$ = 7 Hz, 1H, Ar), 7.81–7.77 (ov m, 2H, Ar), 7.70 (s, 1H, Ar), 7.59–7.51 (ov m, 2H, Ar), 7.40 (t, $J_{H\text{-}H}$ = 7 Hz, 1H, Ar), 3.21 (s, 3H, CH_3), and 1.33 (s, 12H, $O_2C_2(CH_3)_4$). $^{11}B\{^1H\}$ δ: 29.6 (br). $^{13}C\{^1H\}$ δ: 168.6, 167.9, 157.6, 146.5, 138.8, 136.0, 131.8, 129 (br, *C*-B), 128.7, 127.8, 127.7, 126.3, 84.3, 28.1, and 25.0. IR (cm^{-1}) (Nujol): 2927, 2856, 1599 (C=N), 1568, 1462, 1428, 1377, 1319, 1252, 1228, 1166, 1144, 1101, 970, 924, 854, 798, 731, 704, and 606. Anal. calcd. (%) for $C_{19}H_{23}N_2BCl_2O_2Pt$, C 38.79, H 3.95, N 4.76; found: C 38.97, H 3.90, N 4.73.

Compound 4c

(6-Methyl-pyridin-2-ylmethylene)-[4-(4,4,5,5-tetramethyl-[1,3,2]-dioxaborolan-2-yl)phenyl]amine (0.08 g, 0.25 mmol) in CH_2Cl_2 (5 mL) was added to $[PtCl_2(coe)]_2$ (0.08 g, 0.11 mmol) in CH_2Cl_2 (5 mL) and the reaction was heated at reflux for 24 h. Removal of solvent under vacuum gave an oil which was triturated with hexane (3 × 10 mL) to afford a red-orange solid which was dissolved in a CH_2Cl_2:Et_2O (5:5 mL) solution and stored at 0 °C for 18 h. The resulting precipitate was collected by suction filtration to afford **4c** (0.10 g, 77%) as an orange solid; mp 277 °C (decomposition). Spectroscopic NMR data (in $CDCl_3$): ^1H δ: 8.94 (s, $J_{H\text{-}Pt}$ = 78 Hz, 1H, C(*H*) = N), 7.94 (t, $J_{H\text{-}H}$ = 7 Hz, 1H, Ar), 7.86 (d, $J_{H\text{-}H}$ = 7 Hz, 1H, Ar), 7.79 (d, $J_{H\text{-}H}$ = 7 Hz, 2H, Ar), 7.47 (d, $J_{H\text{-}H}$ = 7 Hz, 1H, Ar), 7.41 (d, $J_{H\text{-}H}$ = 7 Hz, 2H, Ar), 3.15 (s, 3H, CH_3), and 1.33 (s, 12H, $O_2C_2(CH_3)_4$). $^{11}B\{^1H\}$ δ: 31.2 (br). $^{13}C\{^1H\}$ δ: 169.4, 167.4, 157.6, 149.1, 138.9, 135.0, 131.7, 131 (br, *C*-B), 127.4, 123.3, 84.2, 28.0, and 25.0. IR (cm^{-1}) (Nujol): 2925, 2856, 1581 (C=N), 1463, 1377, 1358, 1336, 1270, 1173, 1134, 1092, 1016, 935, 845, 787, 729, and 656. Anal. calcd. (%) for $C_{19}H_{23}N_2BCl_2O_2Pt$, C 38.79, H 3.95, N 4.76; found: C 38.70, H 3.99, N 4.76.

X-ray crystallography

Crystals of **3b** and **4a** were grown from saturated CH_2Cl_2 solutions at 5 °C. Single crystals were coated with Paratone-N oil, mounted using a glass fibre, and frozen in the cold stream of the goniometer. A hemisphere of data was collected on a Bruker AXS P4/SMART 1000 diffractometer using ω and θ scans with a scan width of 0.3° and 30 s exposure times. The detector distances were 4 (**3b**) and 5 cm (**4a**). The data were reduced (33) and corrected for absorption (34). The structures were solved by direct methods and refined by full-matrix least squares on F^2 (35). All non-hydrogen atoms were refined anisotropically. Hydrogen atoms were located in Fourier difference maps and refined isotropically (**3b**) or included in calculated positions and refined using a riding model (**4a**).

Cell culture

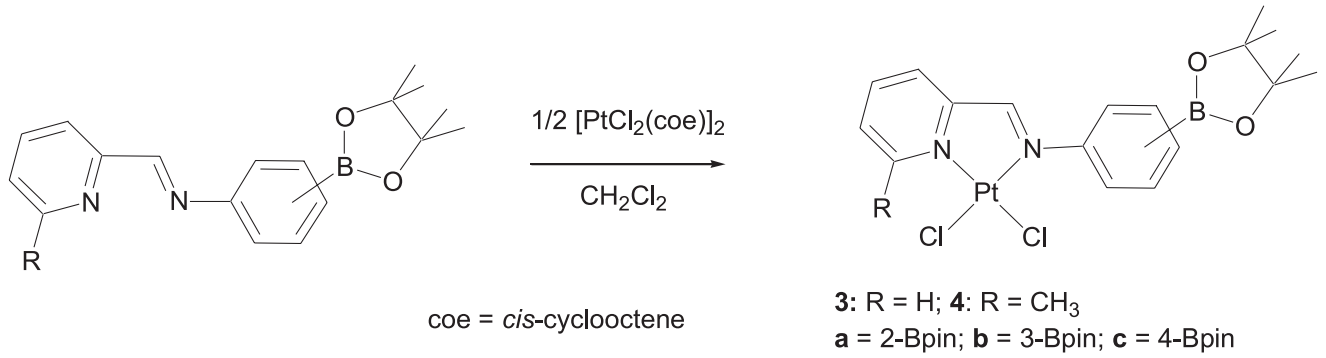
OV2008 (human ovarian carcinoma) and the analogous cisplatin-resistant cell line C13 were a generous gift from Dr. Barbara C. Vanderhyden of the Centre for Cancer Therapeutics, Ottawa Regional Cancer Centre, Ont. Both cell lines were cultured in complete RPMI-1640 medium with L-glutamine, supplemented with 5% fetal bovine serum, penicillin (50 units/mL), and streptomycin (50 mg/mL). Cells were incubated in a humidified atmosphere of 5% CO_2 at 37 °C and were subcultured twice weekly using trypsin-EDTA.

Cell growth inhibition assay

Cells were seeded in 96-well plates at a concentration of 0.1–1.0 × 10^4 cells/well in 200 µL of complete media and incubated for 24 h at 37 °C in a 5% CO_2 atmosphere to allow for cell adhesion. Stock solutions (15 mmol/L) of the compounds made in DMSO were filter sterilized, then diluted to 10 mmol/L in phosphate buffered saline (PBS, 0.02 mol/L phosphate, 0.11 mol/L NaCl, pH 7.0, sterile). The 10 mmol/L solutions were diluted to 50 µmol/L and 1.4 mmol/L in complete media for treatment against OV2008 and C13 cell lines, respectively, where 20 µL of compound solutions were added to 180 µL of fresh medium in wells to give final concentrations of 5 µmol/L against

© 2004 NRC Canada

Fig. 2. Synthesis of platinum complexes **3–4**.



OV2008 and 140 μmol/L for C13. All assays were performed in two independent sets of quadruplicate tests. Control groups containing no drug were run in each assay, along with standards of cisplatin and a previously studied *cis*-dichloro(pyridin-2-ylcarboxaldimine)platinum(II) complex (**2**).

Following 48 h of exposure, each well was carefully rinsed with 200 μL of PBS solution. 3-(4,5-dimethylthiazol-2-yl)-2,5-diphenyltetrazolium bromide (MTT) solution (50 μL, 1 mg/mL doubly distilled (dd)H_2O) along with 200 μL of fresh, complete media were added to each well, and plates were incubated for 45 min. Following incubation, the media was removed and the purple formazan precipitate in each well was solubilized in 200 μL of DMSO. Absorbances were measured using a VersaMax tunable microplate reader (Molecular Devices, Sunnyvale, Calif.) at 570 nm. Reduction of cell proliferation was determined as a fraction of the absorbance values for each drug treatment (T) by the mean absorbance of the no-drug control (C), and calculated using the expression 1 – T/C × 100%. Data from the separate trials were combined using a *t*-test ($P < 0.05$).

Results and discussion

Ligands

Aniline derivatives containing boronate ester groups were used, in place of the related boronic acids, in an attempt to increase the solubility of the ligands and the subsequent platinum complexes in organic solvents, and to prevent unwanted formation of anhydrides often seen in reactions with the acids (36, 37). Addition of these primary amines to 2-pyridinecarboxaldehydes gave the corresponding pyridinecarboxaldimine ligands (N–N_{Bpin}) in high yield (38–41). All new ligands were characterized by multinuclear NMR spectroscopy. For example, a singlet at ca. δ 8.4 ppm is observed in the ^{1}H NMR spectra for the imine methine peak and a broad peak at ca. δ 30 ppm in the ^{11}B NMR spectra for these ligands is indicative of a three coordinate boron atom. This latter result suggests that no appreciable inter- or intramolecular interaction between the Lewis-acidic boron and the basic imine or pyridine functionality is occurring in solution (42).

Platinum complexes

We have found that platinum complexes containing boronate ester appendages ($PtCl_2$(N–N_{Bpin}), Fig. 2) could be readily prepared by addition of pyridin-2-ylcarboxaldimine ligands to CH_2Cl_2 solutions of $[PtCl_2(coe)]_2$ (43).

All new platinum complexes have been characterized by a number of physical methods, including multinuclear NMR spectroscopy. A significant downfield shift in the ^{1}H NMR is observed for the imine proton upon coordination of the ligand to the metal center. For instance, the singlet at δ 8.36 ppm for the free 2-C_5H_4NCH=N[2-$C_6H_4BO_2C_2Me_4$] ligand shifts to 9.35 ppm in complex **3a**. Platinum satellites are also observed for this resonance ($J_{H\text{-}Pt}$ = 92 Hz) upon complexation of the ligand to the metal. Similar trends are observed for the pyridine hydrogen alpha to the nitrogen atom as the chemical shift changes from δ 8.50 to 9.50 ppm ($J_{H\text{-}Pt}$ = 62 Hz). Two distinct Bpin resonances are observed in both the ^{1}H (δ: 1.21 and 1.15 ppm) and ^{13}C{^{1}H} (δ: 25.4 and 25.1 ppm) NMR spectra for complex **3a**, arising from inequivalent methyl groups (Fig. 3). It is therefore possible that two of the Bpin methyl groups are lying over the plane of the platinum atom in a manner similar to that observed for AMD473.

Although we were unable to obtain single crystals of **3a** to verify if an appropriate conformational prerequisite for the shielding effect was occurring, complex **3b** has been characterized by an X-ray diffraction study (Fig. 4). Crystallographic data are given in Table 1.[3] The nitrogen–platinum bonds of 2.023(2) Å (pyridine) and 2.023(3) Å (imine) are similar to those reported in other platinum systems (37–39). Slightly longer Pt—N bond distances are observed in related five coordinate Pt(II) (37, 38) and Pt(IV) complexes (42). The imine C(7)—N(8) distance of 1.298(3) Å is in the range of accepted carbon–nitrogen double bonds (43). Interestingly, the angle between the aromatic ring on the imine nitrogen and the N(1)-Pt-N(8) plane is 108.1°, a trend that is observed in related diimine systems (44). Indeed, this structural feature has been used to create active and selective catalyst precursors for the polymerization of alpha olefins, where ortho substitution of the aniline group with bulky groups is believed to shield and stabilize the metal center.

[3] Supplementary material may be purchased from the Depository of Unpublished Data, Document Delivery, CISTI, National Research Council Canada, Ottawa, ON K1A 0S2, Canada. The material can also be obtained electronically at http://www.nrc.ca/cisti/irm/unpub_e.shtml. Crystallographic information has also been deposited with the Cambridge Crystallographic Data Centre (CCDC 239618 and 239619). Copies of the data can be obtained free of charge via www.ccdc.cam.ac.uk/conts/retrieving.html (or from the Cambridge Crystallographic Data Centre, 12 Union Road, Cambridge CB2 1EZ, UK; fax: +44 1223 336033; or deposit@ccdc.cam.ac.uk).

© 2004 NRC Canada

Fig. 3. Representative ^{1}H NMR spectrum of compound **3a** in DMSO-d_6, showing an expansion of the aromatic (Ar) region.

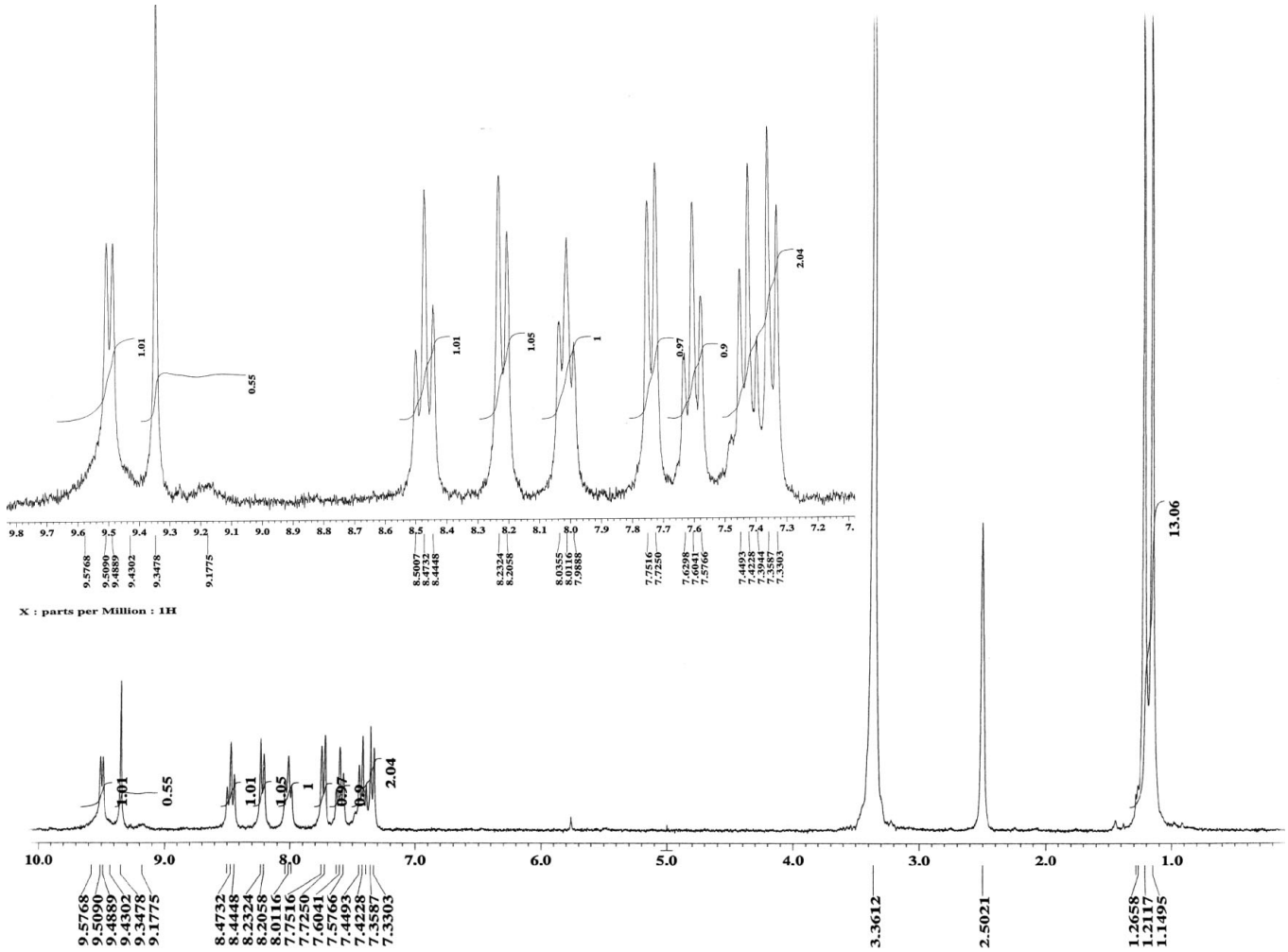
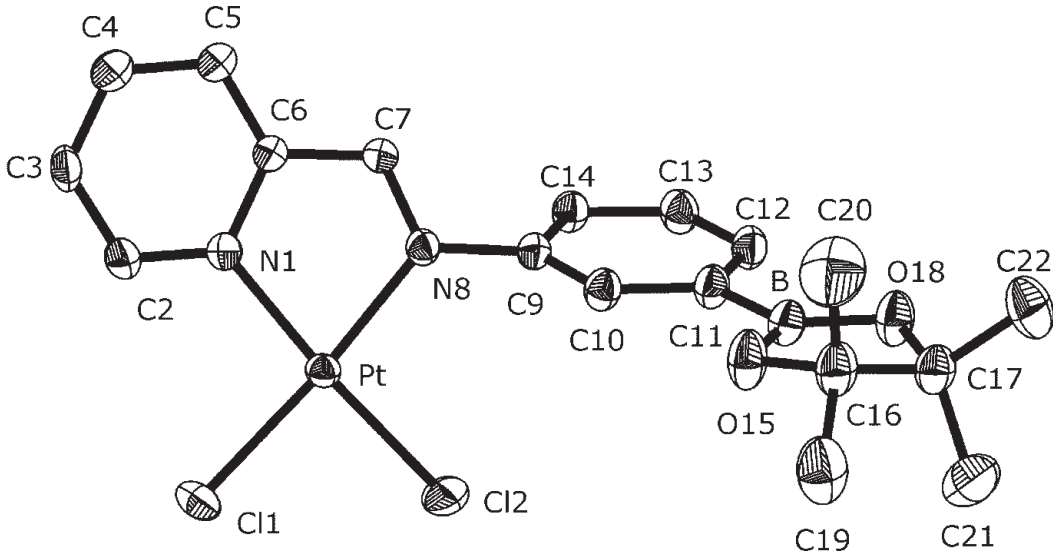


Fig. 4. A view of complex **3b**, with displacement ellipsoids drawn at the 30% probability level. H atoms have been omitted. Selected bond distances and angles; Pt—N(8) 2.023(3), Pt—N(1) 2.023(2), Pt—Cl(2) 2.2844(8), Pt—Cl(1) 2.3011(7), C(7)—N(8) 1.298(3), B—O(15) 1.374(4), B—O(18) 1.376(4), and C(11)—B 1.564(4) Å; N(8)-Pt-N(1) 80.17(9), N(8)-Pt-Cl(2) 95.36(7), N(1)-Pt-Cl(2) 175.43(7), N(8)-Pt-Cl(1) 175.04(6), N(1)-Pt-Cl(1) 94.88(7), Cl(2)-Pt-Cl(1) 89.59(3), O(15)-B-O(18) 113.7(3), O(15)-B-C(11) 121.7(3), and O(18)-B-C(11) 124.5(3)°.



© 2004 NRC Canada

Table 1. Crystallographic data collection parameters for **3b** and **4a**.

Complex	**3b**	**4a**
Chemical formula	$C_{18}H_{21}BCl_2N_2O_2Pt$	$C_{19}H_{23}BCl_2N_2O_2Pt$
Formula weight	574.17	588.19
Crystal system	Monoclinic	Orthorhombic
Space group	P2(1)/c	P2(1)2(1)2(1)
a (Å)	14.8642(8)	10.8778(5)
b (Å)	9.8220(5)	13.3995(7)
c (Å)	15.5384(9)	15.0437(8)
β (°)	109.936(1)	90
V (Å^3)	2132.6(2)	2192.73(19)
Z	4	4
$\rho_{calcd.}$ (mg m^{-3})	1.788	1.782
Crystal dimensions (mm)	0.075 × 0.3 × 0.375	0.05 × 0.1 × 0.45
Temperature (K)	173(1)	198(1)
Radiation	Mo Kα (λ = 0.71073 Å)	Mo Kα (λ = 0.71073 Å)
μ (mm^{-1})	6.844	6.658
Total reflections	22 717	14 427
Total unique reflections	7634	4878
Observed reflections ($F_o > 4\sigma(F_o)$)	6653	4772
No. of variables	249	244
R_{int}	0.0368	0.0179
Theta range (°)	2.50 to 32.50	2.04 to 27.50
Largest difference peak/hole, e (Å^{-3})	4.777/–3.473	0.769/–0.462
S (Goodness-of-fit) on F^2	1.048	0.869
R_1[a] ($l > 2\sigma(l)$)	0.0330	0.0132
wR_2[b] (all data)	0.0903	0.0317

[a] $R_1 = \Sigma(|F_o| - |F_c|) / \Sigma|F_o|$.

[b] $wR_2 = (\Sigma[w(F_o^2 - F_c^2)^2] / \Sigma[F_o^4])^{1/2}$, where $w = 1/[\sigma^2(F_o^2) + (0.0637 \cdot P)^2]$ (**3b**) and $w = 1/[\sigma^2(F_o^2)]$ (**4a**), where $P = (\max(F_o^2, 0) + 2 \cdot F_c^2)/3$.

The boronate ester group in **3b** is roughly coplanar with the aromatic group in order to maximize the donation from the ring *p*π electrons to the empty *p* orbital on boron. No significant interaction of the bulky pinacol group is observed, however, with the metal center.

We carried out an X-ray diffraction study on **4a** to see if the boronate ester group in the ortho position could effectively crowd the platinum atom in a fashion similar to the methyl group of AMD473. The molecular structure of **4a** is shown in Fig. 5 and its crystallographic data is summarized in Table 1. While similar trends observed for **3b** are found in **4a**, inequivalent platinum nitrogen distances are observed, Pt—N(9) 1.9936(19) Å (imine) and Pt—N(1) 2.057(2) Å (pyridine). The longer Pt—N(1) bond reflects the large strain due to the presence of the methyl group in the ortho position to the binding atom in the pyridine ring. Bond angles in **4a** are also similar to those found in **3b** and the twist angle to the phenyl ring in **4a** is 64.7°. Unfortunately, however, there appears to be no significant interaction of the Bpin group with the platinum center. For instance, two of the methyl groups of the Bpin moiety lie over the Pt with long Pt—C(20) and Pt—C(21) distances of 5.133 and 6.023 Å, and the Pt—O and Pt—B distances are 4.158 and 4.483 Å, respectively, and are too far away for any significant interaction. These results suggest that the ortho Bpin groups in these complexes may not shield the platinum atom as effectively as the methyl group in AMD473.

Cytotoxic activity

We have tested the cytotoxic activity of all new platinum complexes against both cisplatin-sensitive and cisplatin-resistant human ovarian cells (Table 2), OV2008 and C13, respectively, at concentrations corresponding to cisplatin's IC_{50} value against either cell line (45–49). While no activity was observed against cisplatin-sensitive cells OV2008, compounds **3a** (with the Bpin group in the ortho position, Entry 3), **3b** and **4b** (with the Bpin group in the meta position, Entries 4 and 7, respectively) showed only minimal activity against cisplatin-resistant cell line C13. Interestingly, the analogous picoline complex **4a** showed diminished activity as compared with **3a**. In general, the presence of the Bpin groups in these complexes seems to greatly reduce their activity, compared to the non-borylated analogue **2**. It is possible that the Lewis-acidic boron atom in these complexes is competing with, and concomitantly deactivating the platinum centre, by coordinating to the nitrogen donors in biomolecules. Further in vitro studies are therefore needed to address the structure activity relationships in these complexes in order to design a potent drug candidate.

Conclusion

Pyridinecarboxaldimines derived from the condensation of 2-pyridinecaboxaldehydes and aminoboronate esters $H_2NC_6H_4Bpin$ have been prepared in high yields and used as

© 2004 NRC Canada

Fig. 5. A view of complex **4a**, with displacement ellipsoids drawn at the 30% probability level. H atoms have been omitted. Selected bond distances and angles; Pt—N(9) 1.9936(19), Pt—N(1) 2.057(2), Pt—Cl(2) 2.2830(7), Pt—Cl(1) 2.2981(6), C(8)—N(9) 1.291(3), B—O(16) 1.3704, B—O(19) 1.366(4), and C(11)—B 1.555(4) Å; N(9)-Pt-N(1) 80.10(8), N(9)-Pt-Cl(2) 92.51(6), N(1)-Pt-Cl(2) 172.45(6), N(9)-Pt-Cl(1) 174.05(6), N(1)-Pt-Cl(1) 100.01(6), Cl(2)-Pt-Cl(1) 87.18(2), O(19)-B-O(16) 113.0(3), O(19)-B-C(11) 121.4(3), and O(16)-B-C(11) 125.6(2)°.

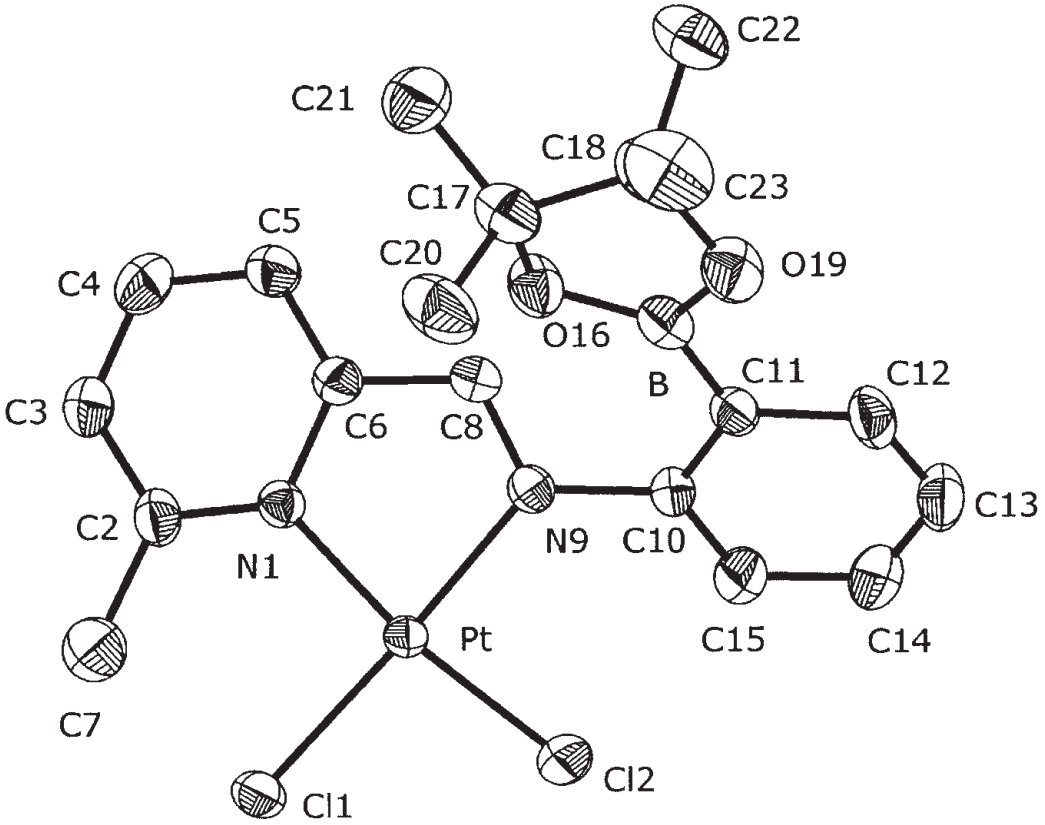


Table 2. Percent reduction of cell proliferation of cisplatin-sensitive (OV2008) and cisplatin-resistant (C13) cancer cells to compounds at 5 and 140 μmol/L, respectively (n = 8; ± SD).

Entry	Compound	OV2008	C13
1	Cisplatin	44±11	41±8
2	**2**	21±3	37±8
3	**3a**	0	56±10
4	**3b**	0	39±10
5	**3c**	0	0
6	**4a**	0	12±8
7	**4b**	0	35±9
8	**4c**	0	0

ligands for platinum. The resulting metal complexes have shown negligible cytotoxicity against both cisplatin-sensitive and cisplatin-resistant human ovarian cells, OV2008 and C13, respectively, where the addition of a Lewis-acidic boron moiety appears to deactivate the metal complexes ability to coordinate to DNA.

Acknowledgements

We thank Pfizer, Inc. for a Summer Undergraduate Research Fellowship (HAD), the Research Corporation (Cottrell College Science Award), the Natural Sciences and Engineering Research Council (NSERC), Canada Research Chair/Canadian Foundation for Innovation/Atlantic Innovation Fund programs, and Mount Allison University (MAU) for financial support. We also thank Roger Smith and Dan Durant (MAU) for expert technical assistance, Dr. Barbara C. Vanderhyden of the Centre for Cancer Therapeutics (Ottawa Regional Cancer Centre, Ont.) for providing us with the OV2008 and C13 cell lines, Steve Geier for his help with the manuscript, and anonymous reviewers for their helpful comments.

References

1. N. Miyaura and A. Suzuki. Chem. Rev. **95**, 2457 (1995).
2. C. Morin. Tetrahedron, **50**, 12521 (1994).
3. G.S. Weston, J. Blázquez, F. Baquero, and B.K. Shoichet. J. Med. Chem. **41**, 4577 (1998).
4. V.S. Stoll, B.T. Eger, R.C. Hynes, V. Martichonok, J.B. Jones, and E.F. Pai. Biochemistry, **37**, 451 (1998).
5. J. Adams, M. Behnke, S. Chen, A.A. Cruickshank, L.R. Dick, L. Grenier, J.M. Klunder, Y. Ma, L. Plamondon, and R.L. Stein. Bioorg. Med. Chem. Lett. **8**, 333 (1998).
6. C. Gao, B.J. Lavey, C.L. Lo, A. Datta, P. Wentworth, Jr., and K.D. Janda. J. Am. Chem. Soc. **120**, 2211 (1998).
7. W. Han, J.C. Pelletier, L.J. Mersinger, C.A. Kettner, and C.N. Hodge. Org. Lett. **1**, 1875 (1999).

© 2004 NRC Canada

8. J.D. Cox, N.N. Kim, A.M. Traish, and D.W. Christianson. Nat. Struct. Biol. **6**, 1043 (1999).
9. W. Yang, X. Gao, and B. Wang. Med. Res. Rev. **23**, 346 (2003).
10. T. Pandey and R.V. Singh. Synth. React. Inorg. Met.-Org. Chem. **30**, 855 (2000).
11. V.M. Dembitsky and M. Srebnik. Tetrahedron, **59**, 579 (2003), and refs. therein.
12. J.D. Dunitz, D.M. Hawley, D. Miklos, D.N.J. White, Y. Berlin, R. Marusic, and V. Prelog. Helv. Chim. Acta, **54**, 1709 (1971).
13. H. Nakamura, Y. Kitahara, T. Okasaki, and Y. Okami. J. Antibiot. **30**, 714 (1977).
14. G.W. Kabalka, B.C. Das, and S. Das. Tetrahedron Lett. **42**, 7145 (2001).
15. A.H. Soloway, W. Tjarks, B.A. Barnum, F.-G. Rong, R.F. Barth, I.M. Codogni, and J.G. Wilson. Chem. Rev. **98**, 1515 (1998).
16. J. Thomas and M.F.Hawthorne. Chem. Commun. 1884 (2001).
17. P.R. Westmark and B.D. Smith. J. Am. Chem. Soc. **116**, 9343 (1994).
18. G.T. Morin, M.-F. Paugam, M.P. Hughes, and B.D. Smith. J. Org. Chem. **59**, 2724 (1994).
19. E.R. Jamieson and S.J. Lippard. Chem. Rev. **99**, 2467 (1999).
20. J. Reedijk. Chem. Rev. **99**, 2499 (1999).
21. E. Wong and C.M. Giandomenico. Chem. Rev. **99**, 2451 (1999).
22. H. Rauter, R.D. Domencio, E. Menta, A. Oliva, Y. Qu, and N. Farrell. Inorg. Chem. **36**, 3919 (1997).
23. Y.-P. Ho, S.C.F. Au-Yeung, and K.K.W. To. Med. Res. Rev. **23**, 633 (2003).
24. N. Poklar, D.S. Pilch, S.J. Lippard, E.A. Redding, S.U. Dunham, and K.J. Breslauer. Proc. Natl. Acad. Sci. U.S.A. **93**, 7606 (1996).
25. E.T. Martins, H. Baruah, J. Kramarczyk, G. Saluta, C.S. Day, G.L. Kucera, and U. Bierbach. J. Med. Chem. **44**, 4492 (2001), and refs. therein.
26. J.L. Butour and J.-P. Macquet. Eur. J. Biochem**. 78**, 455 (1977).
27. K. Neplechová, J. Kašpárková, O. Vrána, O. Nováková, A. Habtemariam, B. Watchman, P.J. Sadler, and V. Brabec. Mol. Pharmacol. **56**, 20 (1999).
28. A.C.G. Hotze, Y. Chen, T.W. Hambley, S. Parsons, N.A. Kratochwil, J.A. Parkinson, V.P. Munk, and P.J. Sadler. Eur. J. Inorg. Chem. 1035 (2002).
29. H. Brunner, M. Schmidt, and H. Schönenberger. Inorg. Chim. Acta, **123**, 201 (1986).
30. S. Otto, A. Roodt, and L.I. Elding. J. Chem. Soc. Dalton Trans. 2519 (2003).
31. O. Baudoin, D. Guénard, and F. Guéritte. J. Org. Chem. **65**, 9268 (2000).
32. L.G. Nikolcheva, C.M. Vogels, R.A. Stefan, H.A. Darwish, S.J. Duffy, R.J. Ireland, A. Decken, R.H.E. Hudson, and S.A. Westcott. Can. J. Chem. **81**, 269 (2003).
33. SAINT 6.02, Bruker AXS, Inc., Madison, Wisc., USA. 1997–1999.
34. G.M. Sheldrick, SADABS, Bruker AXS, Inc., Madison, Wisc., USA. 1999.
35. G.M. Sheldrick, SHELXTL 5.1, Bruker AXS, Inc., Madison, Wisc., USA. 1997.
36. V. Martichonok and J.B. Jones. J. Am. Chem. Soc. **118**, 950 (1996).
37. C.M. Vogels, L.G. Nikolcheva, D.W. Norman, H.A. Spinney, A. Decken, M.O. Baerlocher, F.J. Baerlocher, and S.A. Westcott. Can. J. Chem. **79**, 1115 (2001).
38. C.R. Baar, L.P. Carbray, M.C. Jennings, and R.J. Puddephatt. J. Am. Chem. Soc. **122**, 176 (2000).
39. S.-J. Kim, N. Yang, D-H Kim, S.O. Kang, and J. Ko. Organometallics, **19**, 4036 (2000).
40. (*a*) A. Kundu and B.P. Buffin. Organometallics, **20**, 3635 (2001); (*b*) B. P. Buffin, E.B. Fonger, and A. Kundu. Inorg. Chim. Acta, **355**, 340 (2003).
41. M. Crespo, X. Solans, and M. Font-Bardía. Organometallics, **14**, 355 (1995).
42. H. Nöth and B. Wrackmeyer. *In* Nuclear magnetic resonance spectroscopy of boron compounds. Springer, Berlin. 1978.
43. M.P. Shaver, C.M. Vogels, A.I. Wallbank, T.L. Hennigar, K. Biradha, M.J. Zaworotko, and S.A. Westcott. Can. J. Chem. **78**, 568 (2000).
44. S.D. Ittel, L.K. Johnson, and M. Brookhart. Chem. Rev. **100**, 1169 (2000).
45. M.S. Robillard, M. Bacac, H. van den Elst, A. Flamigni, G.A. van der Marel, J.H. van Boom, and J. Reedijk. J. Comb. Chem. **5**, 821 (2003).
46. A. Trevisan, C. Marzano, P. Cristofori, M.B. Venturini, L. Giovagini, and D. Fregona. Arch. Toxicol. **76**, 262 (2002).
47. M.D. Todd, X. Lin, L.F. Stankowski, Jr., M. Desai, and G.H. Wolfgang. J. Biomol. Screening, **5**, 259 (1999).
48. S.M. Evans, A. Casartelli, E. Herreros, D.T. Minnick, C. Day, E. George, and C. Westmoreland. Toxicol. in Vitro, **15**, 579 (2001).
49. R.A. Houghten, C. Pinilla, J.R. Appel, S.E. Blondelle, C.T. Dooley, J. Eichler, A. Nefzi, and J.M. Ostresh. J. Med. Chem. **42**, 3743 (1999).

© 2004 NRC Canada

Crystal structure, spectroscopic studies, and nonlinear optical (NLO) properties of Schiff base metal complexes containing an N, S donor ligand

Zhao–Ming Xue, Ying-Wen Tang, Jie–Ying Wu, Yu–Peng Tian, Min–Hua Jiang, H.-K. Fun, and A. Usman

Abstract: A new ligand, 4-dipropylaminobenzaldehyde thiosemicarbazone (abbreviated as HL), and its complexes ML_2 (M = Ni, Pd, and Cu) have been synthesized and fully characterized by elemental analyses, EI-MS, IR and UV–vis spectroscopy, and photoluminescence measurements. All of the compounds exhibit a blue–green color with dual fluorescence in DMF solution. The quantum yield ratio ($\Phi'(CT)/\Phi(LE)$) decreases in the order $NiL_2 > HL > PdL_2 > CuL_2$. The ligand HL crystallizes in the monoclinic system, space group $P2_1/n$, with a = 15.1680, b = 8.5573, and c = 25.3920 Å, β = 100.3457°, and V = 3242.2 Å^3. The nickel complex (NiL_2) crystallizes in the triclinic system, space group $P\bar{1}$, with a = 8.3093, b = 9.7540, and c = 10.2802 Å, α = 101.383°, β = 107.693°, γ = 96.703°, and V = 764.12 Å^3. In these complexes, HL has lost a proton from its tautometric thiol form and acts as a single negatively charged bidentate ligand coordinating to the nickel ion via the mercapto sulfur and β-nitrogen atoms. The geometry around Ni(II) is almost square-planar with two equivalent Ni—N and two equivalent Ni—S bonds. The monomeric structure of HL or NiL_2 is extended into an infinite two-dimensional network via hydrogen bonds. The two-photon absorption of HL and ML_2 solutions (in DMF) was measured at 532 nm by the open-aperture Z-scan technique.

Key words: crystal structure, metal complex, dual fluorescence, NLO.

Résumé : On a réalisé la synthèse d'un nouveau ligand, la thiosemicarbazone du 4-dipropylaminobenzaldéhyde (abrév.: HL), et de ses complexes ML_2 (M = Ni, Pd et Cu) qu'on a caractérisés par analyse élémentaire, par spectroscopie « EI-MS », IR et UV–visible ainsi que par des mesures de photoluminescence. En solution dans le DMF, tous les composés présentent une couleur bleu-vert avec double fluorescence. L'ordre des rapports des rendements quantiques ($\Phi'(CT)/\Phi(LE)$) est $NiL_2 > HL > PdL_2 > CuL_2$. Le ligand HL cristallise dans le système monoclinique, groupe d'espace $P2_1/n$ avec a = 15,1680, b = 8,5573 et c = 25,3920 Å, β = 100,3457° et V = 3242,2 Å^3. Le complexe de nickel (NiL_2) cristallise dans le système triclinique, groupe d'espace $P\bar{1}$, avec a = 8,3093, b = 9,7540 et c = 10,2802 Å, α = 101,383°, β = 107,693° et γ = 96,703° et V = 764,12 Å^3. Le ligand HL a perdu un proton à partir de sa forme tautomère thiol et il agit vis-à-vis du nickel comme un ligand bidentate portant une seule charge négative qui conduit à une coordination avec l'ion nickel par le biais des atomes de soufre du mercapto et de l'azote en β. La géométrie autour du Ni(II) est pratiquement plan-carré avec deux liaisons Ni—N et Ni—S équivalentes, respectivement. La structure monomère de HL et de NiL_2 se répercute dans un réseau bidimensionnel infini par le biais de liaisons hydrogènes. L'absorption de deux photons à partir de solutions de HL et de NiL_2 (dans le DMF) a été mesurée à une longueur d'onde d'environ 532 nm par la technique du balayage Z à grande ouverture.

Mots clés : structure cristalline, complexe métallique, double fluorescence, NLO.

[Traduit par la Rédaction]

Received 5 January 2003. Published on the NRC Research Press Web site at http://canjchem.nrc.ca on 3 February 2005.

Z.-M. Xue,[1] Y.-W. Tang, J.-Y. Wu, and Y.-P. Tian.[2,3] Department of Chemistry, Anhui University, Hefei, 230039, China.
M.-H. Jiang. State Key Laboratory of Crystal Materials, Shandong University, Jinan, 250100, China.
H.-K. Fun and A. Usman. X-ray Crystallography Laboratory, School of Physics, Universiti Sains Malaysia, 11800, Penang, Malaysia.

[1]Corresponding author (e-mail: zmxue@ahu.edu.cn).
[2]Corresponding author (e-mail: yptian@ahu.edu.ca).
[3]Also at State Key Laboratory of Crystal Materials, Shandong University, Jinan, 250100, China, and State Key Laboratory of Coordination Chemistry, Nanjing University, Nanjing, 210093, China.

Introduction

There have been extensive studies of π-conjugated organic compounds concerning their large two-photon absorption (TPA) (1–4) and dual fluorescence phenomena (5–8). In contrast, TPA of transition metal complexes has received little attention (9, 10) and there has been virtually no report on dual fluorescence. In recent years, π-conjugated metal complexes have found applications in many areas of chemistry and materials science. For example, luminescent metal compounds can function as emitters in light-emitting devices (11). They are known to be very stable to intense irradiation in the near-infrared region and have been investigated as promising optical limiting materials (12, 13). To our knowledge, a metal complex with both efficient dual fluorescence and TPA has not been reported. The organic chromophore 4-

 doi: 10.1139/V04-142 © 2004 NRC Canada

dipropylaminobenzaldehyde thiosemicarbazone, which is a π-electron delocalized system containing mixed sulfur and nitrogen donors, was considered as a potential new efficient compound for obtaining one-photon- and two-photon-excited dual fluorescence (14) and prepared in our laboratory. Following the success of our initial work (15–18), we are particularly interested in further using it as a ligand to coordinate to transition metal ions to form metal complexes that show efficient dual fluorescence and TPA. We have selected Ni^{2+}, Pd^{2+}, and Cu^{2+} as the central metal ions to form metal complexes with it. In this paper, we present the dual fluorescence and two-photon absorption properties of the complexes.

Theory

Dual fluorescence

4-(*N*,*N*-Dimethylamino)benzonitrile (DMABN) is the prototype of a group of organic donor–acceptor compounds that can undergo intramolecular charge transfer (ICT) in the excited singlet state. In polar solvents, it exhibits dual fluorescence. Apart from normal emission from the locally excited (LE) state, which is also present in the gas phase and in nonpolar solvents, the spectrum observed in polar solvents exhibits a second, anomalous strongly red-shifted band, which is attributed to a charge-transfer (CT) state (19). This phenomenon has been mostly explained by the twisted intramolecular charge transfer (TICT) mechanism (20). In the TICT model, a 90° twist of the dimethylamino group with respect to the phenyl ring was considered to have occurred in the CT state of DMABN. The dimethylamino group was thereby assumed to be electronically decoupled from the rest of the molecule — the principle of minimum overlap. The CT/LE fluorescence quantum yield ratio $\Phi(CT)/\Phi(LE)$ increases with the efficiency of the ICT reaction.

Experimental

General procedures

All chemicals and solvents were dried and purified by usual methods. Elemental analyses were performed with a Perkin-Elmer 240 instrument. IR spectra were recorded with a Nicolet FT-IR 170SX instrument (KBr discs) in the 4000–400 cm^{-1} region. UV–vis spectra were recorded with a Shimadzu UV-265 spectrophotometer. The photoluminescence measurements were carried out in DMF solutions, and the spectra were collected with a Perkin-Elmer LS55 spectrofluorimeter. Mass spectra were obtained with a ZAB-HS mass spectrometer (FAB source).

Strategy of syntheses of HL and ML_2

4-Dipropylaminobenzaldehyde and 4-dipropylaminobenzaldehyde thiosemicarbazone (HL) were synthesized as described previously (14).

Syntheses of ML_2

$M(OAc)_2{\cdot}nH_2O$ (M = Ni(II), Cu(II)) or $PdCl_2(CH_3CN)_2$ (1 mmol) and HL (2 mmol) were disso1ved in ethanol (50 mL). After refluxing for 4 h, the mixture was cooled to room temperature. The precipitate was thoroughly washed with ethanol three times and dried in vacuo over P_2O_5. Yield 90%. Anal. calcd. for $C_{28}H_{42}N_8S_2Ni$ (%): C 54.63, H 6.83, N 18.21; found: C 54.64, H 6.82, N 18.24. mp 249~250 °C. Black crystals of NiL_2 were isolated by slow evaporation of a CH_2Cl_2 solution covered with ethanol. Anal. calcd. for $C_{28}H_{42}N_8S_2Pd$ (%): C 50.11, H 6.23, N 17.31; found: C 50.23, H 6.34, N 17.41. Anal. calcd. for $C_{28}H_{42}N_8S_2Cu$ (%): C 53.66, H 6.67, N 18.54; found: C 53.82, H 6.74, N 18.32.

X-ray crystal structure determinations

A crystal of HL with approximate dimensions 0.50 × 0.28 × 0.20 mm^3 and a crystal of complex NiL_2 with approximate dimensions 0.44 × 0.38 × 0.22 mm^3 were used for the X-ray structure determinations. Data were collected on a Siemens SMART-CCD area detector diffractometer using Mo Kα radiation in ω-scan mode at 293 K. The data collection covered a hemisphere of reciprocal space by a combination of three sets of exposures; each set had a different φ angle (0.88° and 180°) for the crystal and each exposure of 10 s. The crystal-to-detector distance was 4 cm, and the detector swing angle was –35°. Coverage of the unique set is over 99% complete. Crystal decay was monitored by repeating 30 initial frames at the end of data collection and analyzing the duplicate reflections and was found to be negligible.

The unit cell parameters were determined using SMART (21). The three sets of data collected were reduced using the program SAINT (22). The structure was solved with direct methods using the program SHELXTL (23). All the non-hydrogen atoms were located from the trial structure and then refined anisotropically with SHELXTL using a full-matrix least-squares procedure. Weighting schemes of $w = 1/[\sigma^2(F_o^2) + (0.0777P)^2]$, with $P = [(F_o)^2 + 2(F_c)^2]/3$, and $w = 1/[\sigma^2(F_o^2) + (0.1207P)^2]$, with $P = [(F_o)^2 + 2(F_c)^2]/3$, were applied for HL and NiL_2, respectively. The hydrogen atoms were geometrically fixed at calculated positions attached to their parent atoms and were treated as riding on them.

Results and discussion

Description of the structures of HL and NiL_2

Selected crystallographic experimental data for HL and NiL_2 are given in Table 1. The ORTEP diagrams of HL and NiL_2 with the atom numbering schemes are shown in Fig.1. Selected bond lengths and angles are listed in Tables 2 and 3. A view of the molecular packing of HL in the crystal is given in Fig. 2. Additional crystallographic data are available as Supplementary material.[4]

The ORTEP drawing of HL shows that there are two different structures of HL, cis and trans (refer to the structures of dipropyl). The corresponding bond lengths and angles of

[4] Supplementary data may be purchased from the Directory of Unpublished Data, Document Delivery, CISTI, National Research Council Canada, Ottawa, ON K1A 0S2, Canada (http://www.nrc.ca/cisti/irm/unpub_e.shtml for information on ordering electronically). CCDC 200310 and 200311 contain the crystallographic data for this manuscript. These data can be obtained, free of charge, via www.ccdc.cam.ac.uk/conts/retrieving.html (or from the Cambridge Crystallographic Data Centre, 12 Union Road, Cambridge CB2 1EZ, U.K.; fax +44 1223 336033; or deposit@ccdc.cam.ac.uk).

© 2004 NRC Canada

Table 1. Selected crystallographic experimental data for HL and NiL_2.

	HL	NiL_2
Formula	$C_{28}H_{44}N_8S_2$	$C_{28}H_{44}N_8S_2Ni$
Formula weight	556.85	615.54
Crystal system	Monoclinic	Triclinic
Space group	$P2_1/n$	$P\bar{1}$
Crystal dimensions (mm)	0.50 × 0.28 × 0.20	0.44 × 0.38 × 0.22
a (Å)	15.1680(8)	8.3093(1)
b (Å)	8.5573(5)	9.7540(3)
c (Å)	25.3920(10)	10.2802(2)
α (°)	—	101.383(1)
β (°)	100.3457(5)	107.693(1)
γ (°)	—	96.703(1)
V (Å^3)	3242.2(3)	764.12(3)
Z	4	1
μ (mm^{-1})	0.194	0.804
d (calcd.) (g cm^{-3})	1.145	1.338
F(000)	1208	328
Unique reflections	8221	3565
Reflections observed	22 330	5423
R	0.0769	0.0927
R_w	0.1598	0.2282
$\Delta(\rho)_{max,min}$ (e Å^{-3})	0.331, –0.337	0.929, –1.179

Table 2. Selected bond lengths (Å) for HL and NiL_2.

	HL	NiL_2
Ni(1)—N(2)		1.937(3)
Ni(1)—N(2A)		1.937(3)
Ni(1)—S(1)		2.1629(14)
Ni(1)—S(1A)		2.1629(14)
S(1)—C(8)	1.683(4)	1.722(4)
N(1)—C(3)	1.369(4)	1.358(6)
N(1)—C(12)	1.457(5)	1.448(8)
N(1)—C(9)	1.480(5)	1.628(10)
N(2)—C(7)	1.255(4)	1.299(5)
N(2)—N(3)	1.372(4)	1.401(5)
N(3)—C(8)	1.334(4)	1.279(6)
N(4)—C(8)	1.327(4)	1.356(6)
C(1)—C(2)	1.371(4)	1.383(6)
C(6)—C(7)	1.452(5)	1.450(6)

Table 3. Selected bond angles (°) for HL and NiL_2.

	HL	NiL_2
N(2)-Ni(1)-N(2A)		180.00(2)
N(2)-Ni(1)-S(1)		85.09(10)
N(2A)-Ni(1)-S(1)		94.91(10)
N(2)-Ni(1)-S(1A)		94.91(10)
N(2A)-Ni(1)-S(1A)		85.09(10)
S(1)-Ni(1)-S(1A)		180.00(6)
C(8)-S(1)-Ni(1)		97.50(15)
C(7)-N(2)-Ni(1)		124.60(3)
N(3)-N(2)-Ni(1)		120.3(3)
C(3)-N(1)-C(12)	122.5(3)	123.0(5)
C(3)-N(1)-C(9)	120.0(3)	121.1(5)
C(12)-N(1)-C(9)	117.5(3)	115.4(5)
C(7)-N(2)-N(3)	115.1(3)	115.1(3)
C(8)-N(3)-N(2)	122.5(3)	113.5(3)

the two structures are not distinctly different. The bond lengths of N(2)—N(3) (1.372 Å) and C(8)—N(3) (1.334 Å) suggest that these bonds have some double bond character but are nearly single bonds. The lengths of S(1)—C(8) (1.683 Å) and C(7)—N(2) (1.255 Å) suggest that these bonds have some double bond character. All the carbon atoms in the benzene ring are almost coplanar (mean deviation form the plane 0.0071 Å), and C(7), N(2), N(3), C(8), N(4), and S(1) are also nearly coplanar (mean deviation from the plane 0.0091 Å). The dihedral angle of the two planes is 3.31° and shows that they are nearly coplanar. All these crystallographic data suggest that there is a highly π-conjugated and electron-delocalized system in the molecule.

The nickel atom is coordinated in a square-planar configuration with two equivalent Ni—N bonds (l.937 Å) and two equivalent Ni—S bonds (2.l63 Å). The HL has lost a proton from its tautomeric thiol form and acts as a single negatively charged bidentate ligand coordinating to the nickel ion via the mercapto sulfur and β-nitrogen atoms. S(1), N(2), S(1a), N(2a), and Ni(II) are almost coplanar, as are S(1), C(8), N(3), N(2), and Ni(II) (mean deviation from the plane 0.0048 Å), and these two planes form a dihedral angle of 9.6°. The very small dihedral angle indicates the high extent of delocalization of electrons in the π-conjugated system of the two Schiff base ligands and the coordination system.

The monomeric structure of HL is extended into an infinite two-dimensional network via hydrogen-bond contacts between two neighboring molecules (Fig. 3). There are no intramolecular donor hydrogen bonds. A similar case exists for NiL_2. For HL, four hydrogen atoms attached to amino nitrogen atoms N(3A), N(3B), N(4A), and N(4B) have the potential to form donor hydrogen bonds (Fig. 3). Two hydrogen atoms attached to N(4A) and N(3B) formed intermolecular donor hydrogen bonds of the types 4AB (N(4A)-H···S(1B) (1 – x, 1 – y, 1 – z)) and 3BA (N(3B)-H···S(1A) (1 – x, 1 – y, 1 – z)). The N···S separations are 3.478(3) Å for N(4A)···S(1B) and 3.472(6) Å for N(3B)···S(1A). The N-H···S angles are 161.7(4)° for N(4A)-H···S(1B) and 157.6(6)° for N(3B)-H···S(1A). Two hydrogen atoms attached to N(3A) and N(4B) also formed intermolecular donor hydrogen bonds of the types 3AB (N(3A)-H···S(1B) (1 – x, –y, 1 – z)) and 4BA (N(4B)-H···S(1A) (1 – x, –y, 1 – z)). The N···S separations are 3.430(4) Å for N(3A)···S(1B) and 3.614(0) Å for N(4B)···S(1A). The N···S angles are 156.1(0)° for N(3A)-H···S(1B) and 163.6(2)° for N(4B)-H···S(1A).

For NiL_2, one hydrogen atom attached to amino nitrogen atom N(4) has the potential to form a donor hydrogen bond. The hydrogen atom attached to N(4) formed an intermolecular donor hydrogen bond of the type N(4)-H···N(3) (–x, –1 – y, –z). The N(4)···N(3) separation is 3.307(4) Å, and the N(4)-H···N(3) angle is 149.8(1)°.

It is interesting to compare the structure of HL in the free state with that in the nickel complex. The largest difference is found in the bond lengths around C(8). In the free ligand, the bond distances of C(8)—N(3) (1.334 Å) and C(8)—S(1) (1.683 Å) suggest that C(8)—N(3) has nearly single bond character and C(8)—S(1) has nearly double bond character,

© 2004 NRC Canada

Fig. 1. ORTEP drawings of HL and NiL_2 with the atom numbering schemes.

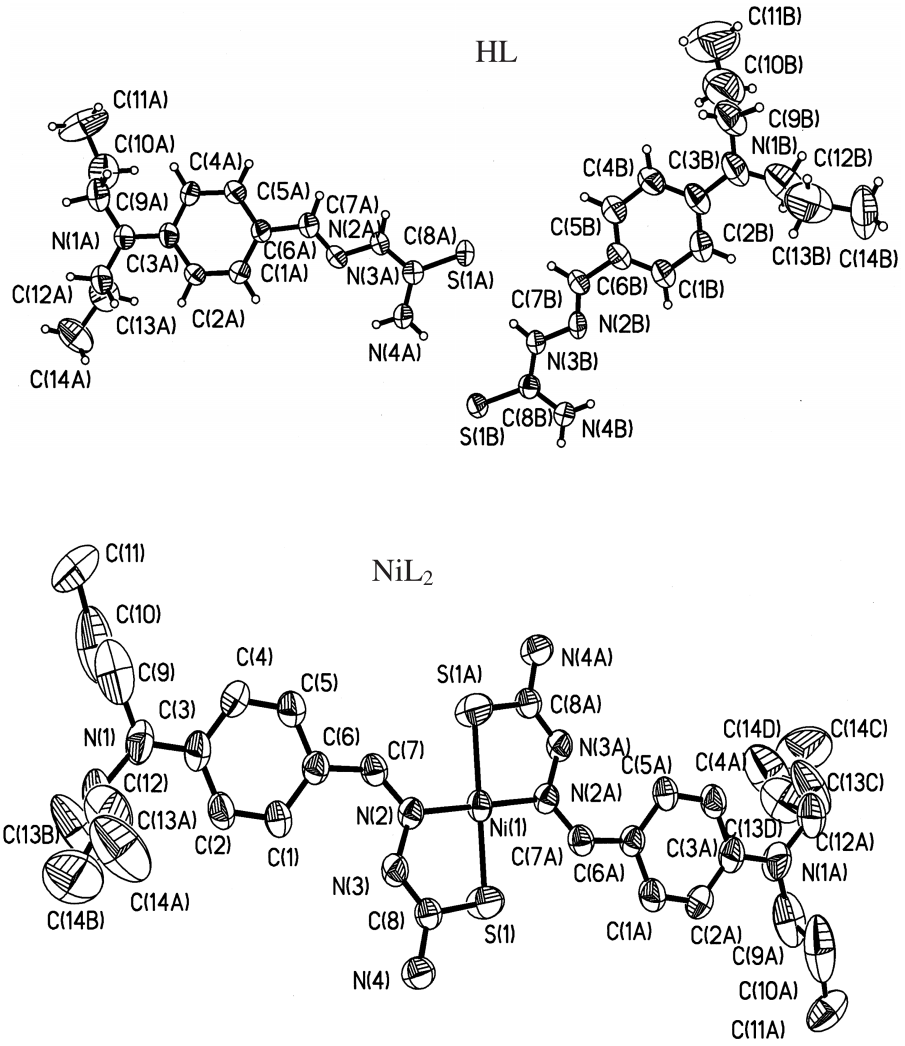
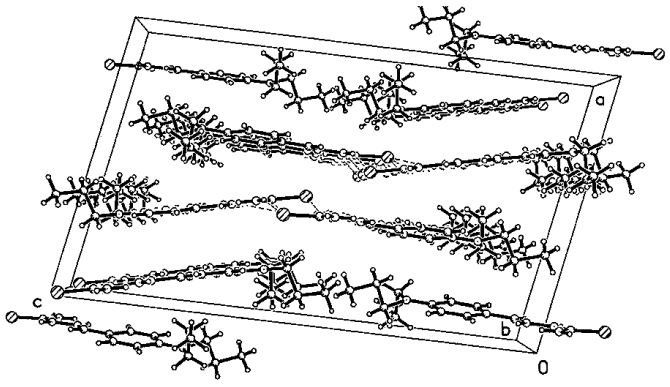


Fig. 2. A view of the molecular packing of HL in the crystal.



while in the complex the bond distances of C(8)—N(3) (1.279 Å) and C(8))—S(1) (1.722 Å) show that C(8)—N(3) is a double bond and C(8)—S(1) is a single bond. Comparing the bond lengths for C(7)—N(2) and C(6)—C(7) in HL with those in NiL_2, C(7)—N(2) is a shorter bond in HL (1.225 Å) than in NiL_2 (1.299 Å) and the C(6)—C(7) bonds are almost the same length (1.452(5) and 1.450(6) Å, respectively). These results, together with the spectral characterization of the nickel complex, indicated the presence of the C–S–M group formed by enolization of the -NH-C=S group in the free ligand to -N=C-SH and coordination to the metal ion through the sulfur after deprotonation (24, 25).

The deprotonation and formation of the metal complexes made the configuration of the ligand quite different. The ligand undergoes some conformational changes during the complex formation. Figure 4 shows the superposition of the ligand in the complex and in the free state. The major conformational changes are in the $NH_2NHC(S)NH_2$ moiety. The trans → cis and cis → trans (referring to the structure of NC(S)N) transitions around certain bonds facilitate the coordination of HL to the metal ion as a bidentate ligand via the β-nitrogen atom and the thio S atom.

FT-IR spectroscopy of HL and ML_2

FT-IR data for HL and ML_2 (M = Ni, Pd, Cu) are listed in Table 4. The spectrum of HL exhibits a strong band at 3152 cm^{-1}, which can be assigned to $\nu_{N\text{-}H}$ of the free ligand. The peak disappears in the IR spectra of the metal complexes, which suggests that the proton on the α-nitrogen

© 2004 NRC Canada

Fig. 3. H-bonds between two neighboring HL molecules.

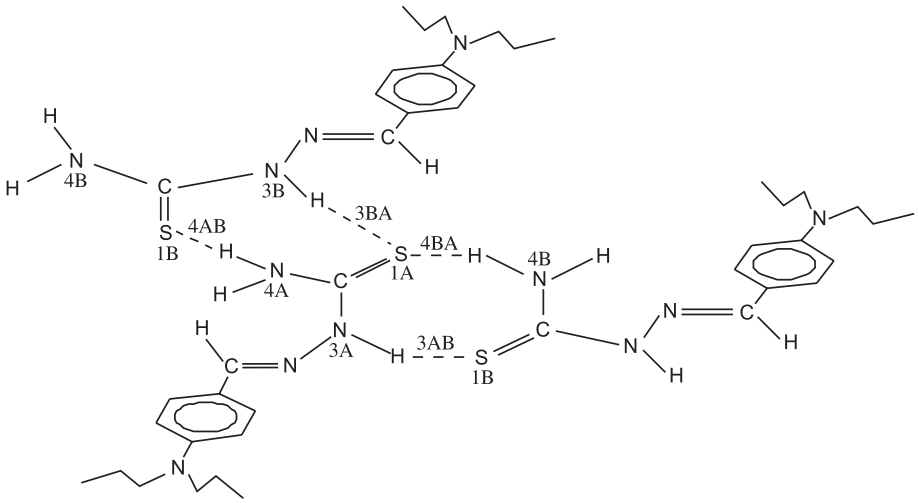
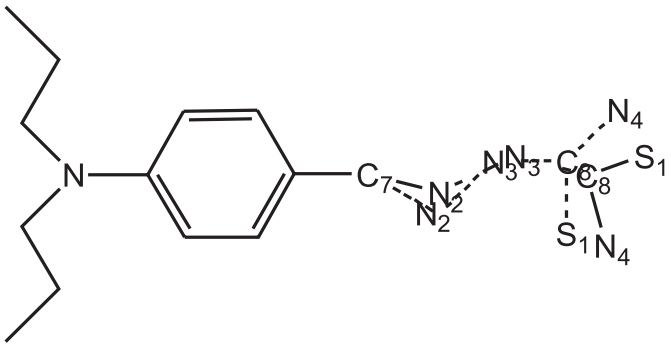


Fig. 4. Superposition of the ligand molecule in the complex (solid lines) and the free state (dashed lines).



atom is lost upon complex formation with the metal ion. A strong band at 1291 cm^{-1} in the IR spectrum of HL is assigned to $\nu_{C\text{-}N}$. This band is shifted to higher frequencies by ca. 11–19 cm^{-1} in the IR spectra of the metal complexes. This increase of $\nu_{C\text{-}N}$ on complexation is attributed to an increase of the C(8)—N(3) bond order as a result of deprotonation of the α-nitrogen atom. This tendency of HL to deprotonate may be attributed to the stabilization of the deprotonated form by conjugation of the -C=N-N=C– group. A strong band at 1046 cm^{-1} in the IR spectrum of HL is tentatively assigned to $\nu_{C=S}$. This band is absent in the spectra of the metal complexes. This observation can be explained by the change in the nature of the C(8)—S(3) bond on coordination of the ligand through the sulfur atom. This is proven by the crystal structure determinations for HL and NiL_2, which yielded C(8)—S(3) bond lengths of 1.683(4) and 1.722(4) Å, respectively. The peak at ca. 1589 cm^{-1} may be safely assigned to the C(7)=N(2) stretching vibration of the azonal group, since the frequency of this band is lowered by ca. 14–18 cm^{-1} in the spectra of the metal complexes. This decrease in $\nu_{C=N}$ on complexation is attributed to a decrease in the C=N bond order as a result of M–N bond formation. The very strong peak at ca. 1518 cm^{-1} in the IR spectra of HL is attributed to the aromatic C=C vibration. The band is very little affected upon complex formation.

Table 4. FT-IR data of HL and ML_2.

	$\nu_{N\text{-}H}$	$\nu_{C=S}$	$\nu_{C=N}$	$\nu_{C\text{-}N}$	$\nu_{N\text{-}N}$	ν_{Ph}
HL	3152	1046	1589	1291	955	1518
NiL_2	—	—	1571	1312	965	1516
PdL_2	—	—	1578	1299	964	1514
CuL_2	—	—	1576	1298	965	1516

These FT-IR data for HL and ML_2 (M = Ni, Pd, Cu) as well as the results of elemental analyses and MS, together with the crystal structures of HL and NiL_2, show that the Schiff base ligand formed stable metal complexes with the three metal ions. The ligand HL was deprotonated on complexation to the divalent M(II), forming the stable neutral complex ML_2 (as shown in Scheme 1).

Absorption spectra

The electronic absorption spectra of HL, NiL_2, PdL_2, and CuL_2, measured in DMF solution (d_0 = 1.0 × 10^{-5} mol/L), are shown in Fig. 5. HL, NiL_2, PdL_2, and CuL_2 all exhibit an intense and low-lying (near-UV region) absorption band and at least two peaks between 250 and 380 nm, with tailing at long wavelengths. The large molar absorption coefficients (log ε = 3.8–4.8) of the near-UV band are indicative of highly π-onjugated systems. The two peaks at shorter wavelengths are at 264 and 366 nm for HL, 267 and 377 nm for NiL_2, 266 and 374 nm for PdL_2, and 266 and 376 nm for CuL_2. The shorter-wavelength peak in each couple is the $\pi \rightarrow \pi^*$ absorption of larger π-conjugated systems, and the second peak is the $n \rightarrow \pi^*$ absorption associated with *p*–π conjugation of nitrogen lone-pair electrons with benzene. An additional peak due to a metal-to-ligand charge transfer (MLCT) absorption is observed at 425, 393, and 394 nm in the spectra of NiL_2, PdL_2, and CuL_2, respectively. There is no linear absorption in the wavelength range from ~500 to 800 nm.

Comparing the two peaks between 250 and 380 nm in the spectra of HL with those in the spectra of ML_2, the shorter-wavelength peak for ML_2 is red-shifted by about 2–3 nm compared to that of HL, and the longer-wavelength peak is red-shifted by about 8~11 nm. Such red shifts are consistent

© 2004 NRC Canada

Scheme 1. Strategy of syntheses of HL and ML_2.

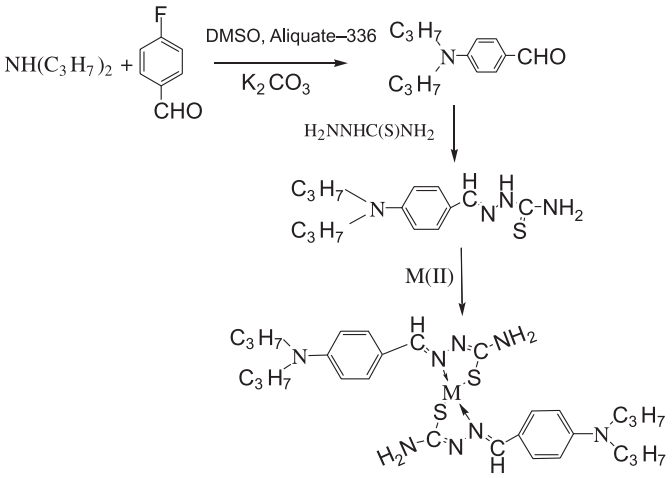
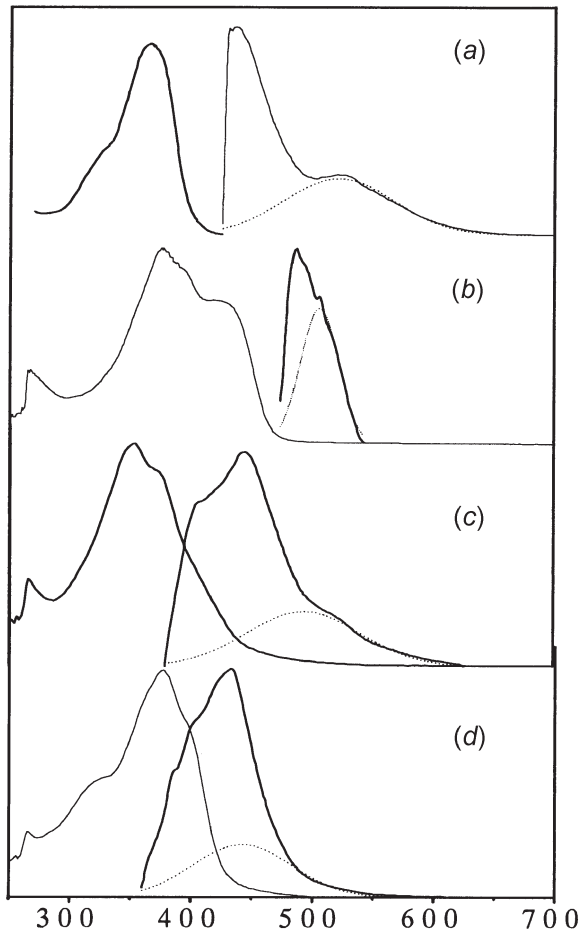


Fig. 5. Room-temperature UV–vis absorption and emission spectra of HL and ML_2 in DMF solution: (*a*) HL, one-photon excitation (OPE) at 400 nm; (*b*) NiL_2, OPE at 400 nm; (*c*) PdL_2, OPE at 434 nm; (*d*) CuL_2, OPE at 337 nm. Dotted curves represent "anomalous" emission from the CT state.



with the fact that when the N and S atoms of HL are coordinated to M(II), the new rings enhance the π-electron delocalization along the unsaturated system and reinforce the electronic density on the larger π-conjugated system and the *p*–π conjugation.

Fig. 6. Open-aperture Z-scan data. Normalized transmittance of ML_2.

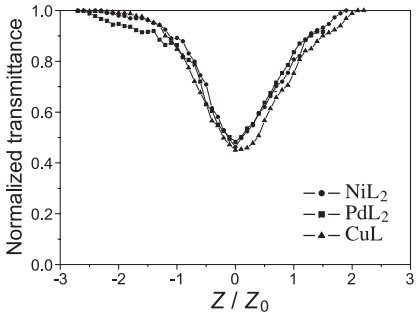


Table 5. TPA coefficients β and cross sections σ (in DMF solution).

	β (cm/GW)	$\sigma \times 10^{46}$ (cm^4 s/photon)
HL	—	—
NiL_2	0.47	0.84
PdL_2	0.48	0.98
CuL_2	0.51	0.99

One-photon-excited dual fluorescence

The one-photon steady-state emission spectra of HL, NiL_2, PdL_2, and CuL_2, measured in DMF solutions (d_0 = 1.0×10^{-7} mol/L), are shown in Fig. 5. HL, NiL_2, PdL_2, and CuL_2 emit a blue–green color with dual peaks and a large Stokes shift (LE peak, ~30–180 nm) when irradiated (one-photon processes) by UV at 400, 320, 320, and 337 nm, respectively. The characteristic benzaldehyde moiety bands had peaks at 523 and 430 nm for HL, 507 and 488 nm for NiL_2, 493 and 444 nm for PdL_2, and 444 and 434 nm for CuL_2. The quantum yield ratio $\Phi'(CT)/\Phi(LE)$ ($d_0 = 1.0 \times 10^{-7}$ mol/L) decreased in the order NiL_2 (2.12) > HL (0.79) > PdL_2 (0.45) > CuL_2 (0.43).

Two-photon absorption

The two-photon absorptions of HL and ML_2 solutions (in DMF) were measured by use of the open-aperture Z-scan technique (26) at a wavelength of 532 nm and are shown in Fig. 6. The normalized transmittance $T(z)$ in Fig. 6 was analyzed theoretically with the following equation:

$$T(z, s = 1) = \sum_{m=0}^{\infty} \frac{[1 - q_0(z)]^m}{(m+1)^{3/2}} \qquad \text{for } |q_0| < 1$$

where $s = 1$ indicates an open aperture, and $q_0(z) = \beta I_0(t) L_{\text{eff}}/(1 + z^2/z_0^2)$,where β is the TPA coefficient, $I_0(t)$ is the intensity of the laser beam at the focus ($z = 0$), $L_{\text{eff}} = [1 - \exp(-\alpha_0 L)]/\alpha_0$ is the effective thickness with α_0 the linear absorption coefficient and L the sample thickness, z_0 is the diffraction length of the beam, and z is the sample position. Nonlinear absorption of ML_2 in an open-aperture Z-scan, which is used to observe third-order phenomena that all molecules exhibit, can be explained mainly by the TPA mecha-

© 2004 NRC Canada

nism. Numerical calculations were performed using the optimal value for the parameter β. The best-fit values for the TPA cross section $\sigma = h\nu\beta/(N_A d_0 10^{-3})$ for HL and ML_2 are listed in Table 5. From the results above, it can be seen that the complexes have obvious two-photon absorption. However, the ligand has no two-photon absorption.

Conclusions

We have synthesized a new class of novel blue luminescent complexes based on a Schiff base. All compounds emit a blue-green color with dual fluorescence in DMF solution and show a large Stokes shift (LE peak, ~30–180 nm). The quantum yield ratio Φ′(CT)/Φ(LE) ($d_0 = 1.0 \times 10^{-7}$mol/L) decreases in the order NiL_2 (2.12) > HL (0.79) > PdL_2 (0.45) > CuL_2 (0.43). All of the compounds exhibit good one-photon fluorescent properties. The complexes have more highly π-conjugated and electron-delocalized systems than the free ligand and also have strong third-order nonlinear optical properties.

Acknowledgements

This work was supported by the National Natural Science Foundation of China (50272001, 50335050, 50325311) and the Natural Science and Person with Ability Foundation of Anhui Province (03044701, 2002Z021). H.K.F. thanks the Malaysian Government and Universiti Sains Malaysia for the research grant R&D No. 305/PFIZIK/610961.

References

1. Y. Ren, Q. Fang, W.T. Yu, H. Lei, Y.P. Tian, M.H. Jiang, Q.C. Yang, and T.C.W. Mak. J. Mater. Chem. **10**, 2025 (2000).
2. G.Y. Zhuo, X.M. Wang, D. Wang, C. Wang, X. Zhao, Z.S. Shao, and M.H. Jiang. Opt. Laser Technol. **33**, 209 (2001).
3. S.J. Chung, T.C. Lin, K.S. Kim, G.S. He, J. Swiatkiewice, P.N. Prasad, G.A. Baker, and F.V. Bright. Chem. Mater. **13**, 4071 (2001).
4. J.W. Baur, M.D. Alexander, Jr., M. Banach, L.R. Denny, B.A. Reinhardt, and A. Vaia. Chem. Mater. **11**, 2899 (1999).
5. L.R. Ling and Y.B. Jiang. Sci. China, Ser. B, **2**, 110 (2000).
6. F.D. Lewis and T.M. Long. J. Phys. Chem. A, **102**, 5327 (1998).
7. Y.V. Il'ichev, W. Kühnle, and K.A. Zachariasse. J. Phys. Chem. A, **102**, 5670 (1998).
8. Z.R. Grabowski, K. Rotkiewicz, W. Rubaszewska, and E. Kirkor-Kaminska. Acta Phys. Pol. A, **54**, 767 (1978).
9. J. Dai, G.Q. Bian, X. Wang, Q.F. Xu, M.Y. Zhou, M. Munakata, M. Maekawa, M.H. Tong, Z.R. Sun, and H.P. Zeng. J. Am. Chem. Soc. **122**, 11 007 (2000).
10. N. Lemaitre, A.D. Attias, I. Ledoux, and J. Zyss. Chem. Mater. **13**, 1420 (2001).
11. R.C. Kwong, S. Laman, and M.E. Thompson. Adv. Mater. **12**, 1134 (2000).
12. M.K.M. Low, H.W. Hou, H.G. Zheng, W. Wong, G.X. Jin, X.Q. Xin, and W. Ji. Chem. Commun. 505 (1998).
13. S. Shi, W. Ji, S.H. Tang, J.P. Lang, and X.Q. Xin. J. Am. Chem. Soc. **116**, 3615 (1994).
14. Z.M. Xue, Y.P. Tian, D. Wang, and M.H. Jiang. Dalton Trans. 1373 (2003).
15. Z.M. Xue, Y.P. Tian, D. Wang, Y.M. Yi, and M.H. Jiang. Sci. China, Ser. B, **5**, 505 (2003).
16. Z.M. Xue, X.J. Zhang, Y.P. Tian, Z.Q. Liu, and M.H. Jiang. Chin. J. Inorg. Chem. **10**, 1009 (2002).
17. Z.M. Xue, X.J. Zhang, Y.P. Tian, J.Y. Wu, M.H. Jiang, and H.K. Fun. Chin. J. Struct. Chem. **3**, 265 (2003).
18. Z.M. Xue, Y.P. Tian, D. Wang, and M.H. Jiang. Chin. Chem. Lett. **5**, 525 (2003).
19. E. Lippert, W. Lüder, F. Moll, W. Nägele, H. Boos, H. Prigge, and I. Seibold-Blankenstein. Angew. Chem. **73**, 695 (1961).
20. K. Rotkiewicz, K.H. Grellmann, and Z.R. Grabowski. Chem. Phys. Lett. **19**, 315 (1973).
21. Siemens. SMART [computer program]. 1996.
22. Siemens. SAINT [computer program]. 1996.
23. G.M. Sheldrick. SHELXTL [computer program]. 1997.
24. Y.P. Tian, C.Y. Duan, Z.L. Lu, and X.Z. You. Polyhedron, **13**, 2263 (1996).
25. Y.P. Tian, C.Y. Duan, and X.Z. You. Transition Met. Chem. **23**, 17 (1998).
26. J. Zhou, E.Y.B. Pun, and X.H. Zhang. J. Opt. Soc. Am., Sect. B, **18**, 1456 (2001).

© 2004 NRC Canada

Chemical-shift link to the Kamlet–Taft β parameter

Keith C. Brown, Muhsin El-Bermani, and John A. Weil

Abstract: In investigating liquid-phase proton NMR spectra of 2,2-dimethyl-1-(2,4,6-trinitrophenyl)hydrazine in various solvents, we have found an interesting correlation, at sufficiently low temperatures *T*, between the chemical-shift difference (splitting) of the picryl proton peaks, measured as *f*(*T*), and the Kamlet–Taft hydrogen-bonding basicity parameter β. The observed solvolytic effect offers a convenient way of determining and checking the value of the empirical parameter β. The phenomenon discloses that the molecular geometric configuration is affected vividly by hydrogen bonding with the surrounding solvent molecules. It follows that the internal conformation interchange taking place (in a higher *T* range) is not in fact solely a unimolecular property.

Key words: picryl proton NMR, chemical shift, solvent effects, hydrogen bonding, Kamlet–Taft β.

Résumé : Lors d'une étude en phase liquide des spectres RMN du proton de la 2,2-diméthyl-1-(2,4,6-trinitrophényl)hydrazine dans divers solvants, on a observé une corrélation intéressante, à des températures *T* suffisamment basses, entre la différence de déplacement chimique (dédoublement) des pics des protons picryles, mesurée sous la forme de *f*(*T*), et le paramètre β de basicité par formation de liaison hydrogène de Kamlet–Taft. L'effet solvolytique observé offre une méthode de déterminer et de vérifier la valeur du paramètre empirique β. Le phénomène montre que la configuration géométrique moléculaire est grandement affectée par les liaisons hydrogènes avec les molécules de solvant avoisinantes. Il s'en suit que l'échange de conformation interne que se produit à des températures plus élevées n'est pas uniquement une propriété unimoléculaire.

Mots clés : RMN du proton du picryle, déplacement chimique, effets de solvant, liaison hydrogène, paramètre β Kamlet–Taft.

[Traduit par la Rédaction]

Introduction

The 2,2-dialkyl- and 2,2-diaryl-1-(2,4,6-trinitrophenyl)hydrazines have been the subject of various liquid-phase nuclear magnetic resonance (NMR) studies (1–3), especially because their internal "hindered rotations" are clearly evident from such spectroscopy. Furthermore, some of these species are important because they form stable free radicals (hydrazyls) via oxidation, i.e., by loss of a hydrogen atom from the hydrazinic nitrogen attached to the picryl group, as studied by electron paramagnetic resonance (EPR) spectroscopy.

For decades now, both ^{1}H and ^{13}C NMR spectroscopy at various frequencies and temperatures have been utilized to investigate the internal conformation switching within various picrylamines and also within the above-cited picrylhydrazine molecules (1), with special emphasis on 2,2-diphenyl-1-picrylhydrazine. In particular, study of the collapse of the AB quartet observed at low sample temperature *T* to a broad single peak (coalescence) and eventual sharpening of this peak with increasing *T* has been very fruitful (3). A study (2) of the effect of the solvent on the activation parameters revealed correlation of these with the solvent's hydrogen-bonding basicity, as measured by the Kamlet–Taft β parameter (see refs. 4 and 5; see ref. 6 for a recent review of solvent polarity scales).

The solvent parameter β has been proven by many research groups to be meaningful and useful, in that many solute physical properties (namely, infrared line positions, electronic transition frequencies, and ^{19}F NMR chemical shifts) have shown very good linear relationships with β (5, 7, 8). In the present paper, we present recent data obtained with 2,2-dimethyl-1-(2,4,6-trinitrophenyl)hydrazine (DMPH), which reveal that the chemical-shift difference δ for the two picryl-proton peaks, measured in deuterated solvents at temperatures below the onset of the intramolecular reorientation effects, correlates nicely with β. In principle, any picrylamine RNH(Picr) (Picr = 2,4,6-trinitrophenyl) with a sufficiently bulky group R could serve as a suitable solute for the type of NMR work described herein (including replacement of the 4-substituent in Picr).

We do not have knowledge of how deuteration affects the β values of the solvents and trust that this fine point can be addressed in future research. For that matter, we do not know of any review adequately discussing the general accuracy of parameter β as listed multiply in the literature.

As part of the overall project, an X-ray-diffraction structural study of DMPH has recently been published by us (9).

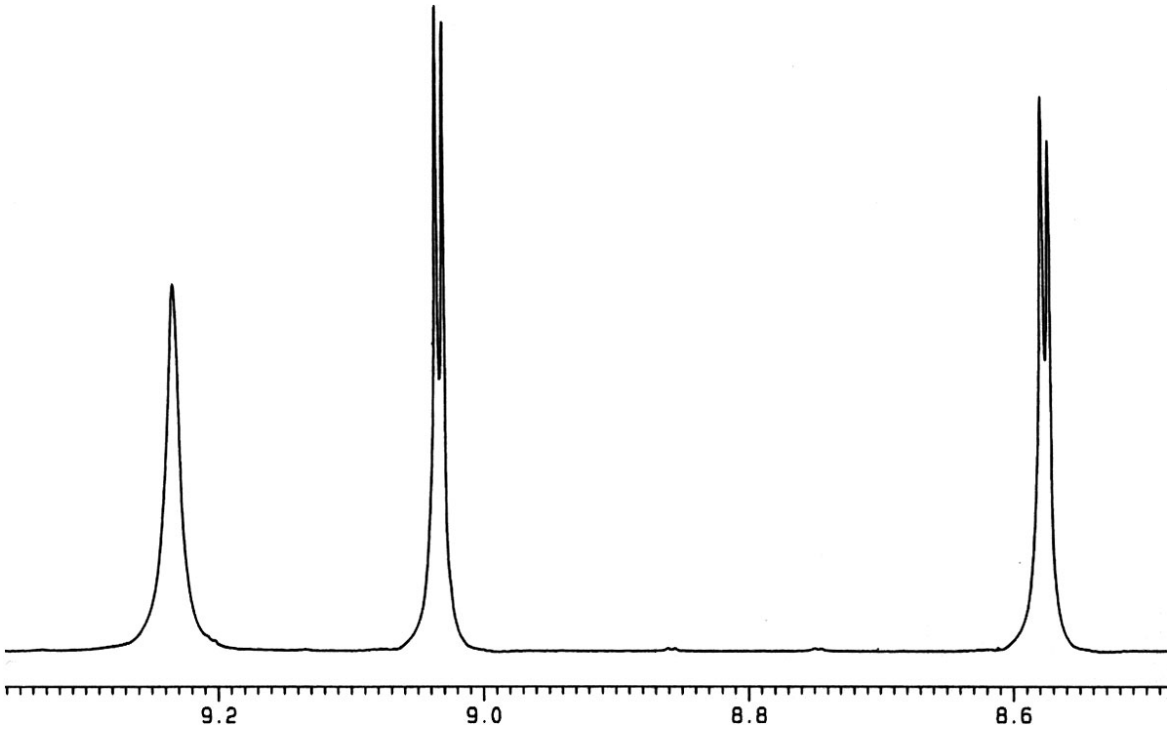
Received 19 May 2004. Published on the NRC Research Press Web site at http://canjchem.nrc.ca on 18 January 2005.

K.C. Brown, M. El-Bermani, and J.A. Weil.[1] Department of Chemistry, University of Saskatchewan, 110 Science Place, Saskatoon, SK S7N 5C9, Canada.

[1]Corresponding author (e-mail: john.weil@usask.ca).

 doi: 10.1139/V04-149 © 2004 NRC Canada

Fig. 1. The N–H and picryl (AB quartet) region of the ^{1}H NMR spectrum of DMPH in acetonitrile-d_3 at 240 K, taken at ν_0 = 500.13 MHz. The N–H peak occurs at 9.2338 ppm, center of doublet A at 9.0390 ppm, and center of doublet B at 8.576 ppm; all chemical shifts from TMS. The ^{13}C satellites (singlets and doublets, respectively) are barely visible, at 50.0 Hz from the N–H peak and at ca. 86 Hz from each picryl doublet.



Thus, appreciable information about its likely conformation(s) in liquid solution is available. One aspect of our interest is that DMPH, unlike its analogues, does not readily oxidize to form a hydrazyl free radical.

Experimental

The NMR spectra were taken on a Bruker DRX spectrometer operating at ν_0 = 500.13 MHz, without sample spinning, using either probe TXI or BBI. The variable-temperature unit on it is a BVT-3000.

The solvents used were commercially available deuterated materials, These perdeutero solvents, obtained from Sigma-Aldrich, were used as received. All the DMPH solutions were yellow–orange in color.

The temperatures used were below those temperatures at which DMPH "conformerization" began to be evident in the NMR spectra but of course were all above the solvent's melting point. The temperatures measured were judged to be accurate to better than ±1 K.

While investigating the conformerization kinetics, we noted the striking temperature dependences of $\nu_0\delta$ in some of the solvents used and deemed this latter effect worthy of separate study, as presented herein. Thus, we focus attention herein onto the chemical-shift difference δ between the proton NMR peaks arising from the two picryl protons of DMPH. Whenever spin–spin splitting into doublets was evident, the average position of these was taken. A typical spectrum is shown in Fig. 1.

We observed, in a series of samples of DMPH, prepared with various concentrations (10^{-3}–10^{-1} mol/L) both in acetone and in toluene-d_8, that δ did not vary appreciably within this range.

Results

The centers of the multiplet peaks A and B were measured, ignoring any ^{1}H–^{1}H spin–spin splittings present (resolved or not). The peak spacings between A and B equal the shift difference $\nu_0\delta$ to good approximation, since spin–spin coupling parameter J_{AB} is relatively small (ca. 2.6 Hz) compared to $\nu_0\delta$ (e.g., see ref. 10, p. 69). The spacings $\nu_0\delta$ were plotted (Fig. 2) against the sample temperature T, excluding the higher-temperature data where the points curve downward dramatically as a result of the onset of doublet collapse caused by the conformation-transfer phenomenon. Such plots were produced for the 8 solvents investigated (Table 1). Since the plots proved to deviate appreciably from being linear, two types of best-fit parameters were obtained, using both a linear and a quadratic polynomial. Thus, δ was fitted to the relations (*i*) $\delta_0 + \sigma T$ as well as (*ii*) $q_0 + q_1 T + q_2 T^2$, with T expressed in kelvins. Both functions gave quite satisfactory fits.

The values of the intercept and of the slope parameters obtained in this way were plotted against β. All these coefficients showed similar and gratifying correlations with β. A convenient way to present the results is to evaluate the fitted shift at T = 300 K (see Table 1) from the above relations. These data are given in Table 1, for relation (*i*), and are depicted in Fig. 3. We note the excellent correlation. The same is true for relation (*ii*).

© 2004 NRC Canada

Table 1. Certain properties of the picryl-proton chemical-shift difference behavior (at ν_0 = 500.13 MHz) of DMPH solutions and of the solvents, arranged in order of increasing β.

Solvent	mp[a] (K)	β	Temp. range (K)	Number of data points	Chemical-shift difference $\nu_0\delta$ at 300 K[b] (Hz)	Slope $\nu_0\sigma$ (Hz/K)	Intercept $\nu_0\delta_{\beta=0}$[c] (Hz)	RMS error in $\nu_0\delta$ (Hz)
Tetrachloromethane	250.4	0.00	264–280	9	374.0	–0.411±0.022	497.3±6.0	0.296
Trichloromethane-d_1	209.0	0.00	230–275	10	376.5	–0.297±0.006	465.6±1.5	0.204
Dichloromethane-d_2	178.1	0.00	220–280	27	363.0	–0.095±0.002	391.5±0.4	0.132
Toluene-d_8	178.0	0.11	200–270	15	345.0	0.507±0.025	192.9±5.9	1.941
Ethanenitrile-d_3	228.0	0.31	240–278	16	260.8	0.526±0.006	103.0±1.6	0.282
2-Propanone-d_6	179.0	0.48	244–274	16	225.6	1.253±0.011	–150.3±3.0	0.396
Tetrahydrofuran-d_8	172.0	0.55	242–274	17	215.6	1.289±0.037	–171.1±9.1	3.040
Dimethylformamide-d_7	212.0	0.69	230–266	19	127.1	1.77±0.02	–404.0±5	0.960

[a]The melting point temperatures (mp) are for the deuterated solvents.
[b]This temperature was chosen as being a convenient standard reference point. Closely analogous results were obtained at other choices, at lower temperatures, within the thermal region actually measured. Thus at 270 K, for example, $\nu_0\delta$ = 329.8 Hz for toluene-d_8.
[c]We note that intercept parameter $\nu_0\delta_\beta$ = 0 represents an extrapolation over a very large thermal range and thus may have limited physical meaning.

Fig. 2. Typical plot of the chemical-shift difference $\nu_0\delta$ of the picryl protons 3 and 5, as a function of sample temperature, for DMPH in acetone-d_6. Curve best-fit via Program "Origin 7".

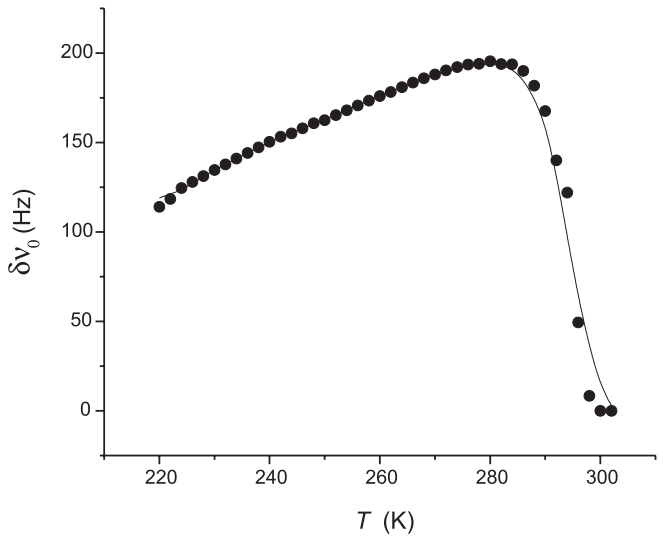
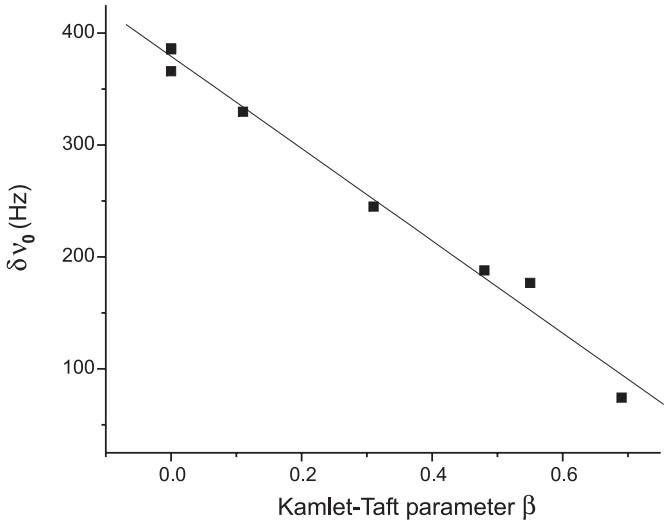


Fig. 3. The chemical-shift differences $\nu_0\delta$, calculated for 300.0 K using the best-fit data in Table 1, plotted against the Kamlet–Taft β values of the solvents used and listed therein. The best-fit straight line yielded slope –328 ± 20 Hz/β and intercept $\nu_0\delta_{\beta=0}$ = 374 ± 7 Hz, with an rms error of 12.74 Hz. For comparison, we cite that at 270.0 K, slope –412 ± 21 Hz/β and intercept $\nu_0\delta_{\beta=0}$ = 379 ± 8 Hz were found, with an rms error of 13.2 Hz.



With dimethylformamide-d_7, the highest-β solvent investigated, the slope of δ plotted against T is sufficiently large (Table 1) and the liquid-phase range available was sufficient that δ was found to cross through 0, at T = ca. 236 K. Ball-and-stick molecular models of DMPH and DMF indicate that there may be a close-fit dimer of these two, featuring two standard O···H hydrogen bonds between them.

Incidentally, we note that the chemical shifts between the methyl peaks and the picryl peaks A and B of DMPH, when plotted against T, show that both the latter peaks vary thermally in a parallel manner (as ascertained in chloroform-d and toluene-d_8).

We also have observed, somewhat to our surprise, that the two methyl groups in DMPH act as completely equivalent at even the lowest temperatures investigated, in the various solvents utilized, as investigated by us via ^{1}H NMR as well as ^{13}C NMR spectroscopy.

Discussion

It is thought that the inequivalence of the "meta" protons (3 and 5) in the picryl ring arises primarily from differences in the orientations of the "ortho" nitro groups (at carbons 2 and 6) (1, 11). This then gives rise to nonzero values of δ. In turn, the two nitro groups differ in orientation because one of these (either one) is H-bonded to the N–H proton (9). We have published some detailed quantum-mechanical modeling of the internal hindered reorientation for the closely related molecule 2-propanone-(2,4,6-trinitrophenyl)hydrazone (11). We also believe that there is competition for the hydrazinic H-bond between the adjacent nitro group and whatever solvent molecule is nearby.

© 2004 NRC Canada

Table 2. Solvent-dependent chemical shifts (ppm, relative to TMS) of the ^{1}H NMR lines of picryl A and B, N–H, and $N(CH_3)_2$ protons (at 500.13 MHz), all measured at 270 K for DMPH in various solvents.

Solvent	Picryl line A	Picryl line B	N–H	$N(CH_3)_2$
Tetrachloromethane	9.196	8.423	9.022	2.667
Trichloromethane-d_1	9.247	8.465	9.065	2.617
Dichloromethane-d_2	9.222	8.487	9.044	2.605
Toluene-d_8[a]	8.285	7.645	8.474	1.933
Ethanenitrile-d_3	9.037	8.568	9.147	2.111
2-Propanone-d_6	9.074	8.749	9.583	2.642
Tetrahydrofuran-d_8	9.076	8.776	9.406	2.567
Dimethylformamide-d_7	9.026	8.883	10.030	2.646

[a]The toluene-d^8 ^{1}H peaks for DMPH (checked at several concentrations) are all shifted upfield (smaller chemical shifts relative to TMS) by ca. 0.8 ppm from those predicted from the above table, likely due to the aromatic ring-current effect. Happily, this phenomenon does not affect the chemical-shift difference δ. We note that the toluene-d_8 peaks do occur as listed in the literature.

The two picryl-proton multiplets shift observably with β (Table 2) relative to the null of chemical shift (TMS), with the higher-field peak (B) moving more dramatically. It has been suggested (2) that peak A arises from the proton next to the nitro group H-bonded to the N–H group, but further study is called for. As β increases, the shift difference δ moves toward zero; i.e., the two nitro groups 2 and 6 act more alike, presumably because the N–H proton has been captured by the solvent molecule.

The methyl-peak positions (relative to null) for the various solvents, at say 300 K, show little correlation with β (Table 2). However, the N–H proton peak does show a steady shift to lower magnetic fields as β is increased, suggesting increased hydrogen bonding to the solvent molecules (see ref. 12, p. 407).

DMPH in the solid state contains no solvent molecules when crystallized out of absolute ethanol (9). However, other picrylhydrazines such as 2,2-diphenyl-1-picrylhydrazines readily incorporate solvent molecules upon crystallization (13). With DMPH, there is crystallographic evidence that considerable nonclassical hydrogen bonding between molecules occurs, and this may well be the cause of much of its crystal stability. Thus, there are no fewer than nine distances of < 2.9 Å between nitro-group oxygens and methyl protons on adjacent molecules, and the N–H proton, besides forming its major H-bond to its nearest nitro-group oxygen (on the same molecule), also is at 2.6 Å from a nitro-group oxygen of a neighbor molecule.

It is interesting to note (Table 1) that the three halogenic solvents exhibit the largest shift differences δ among the set investigated. They have the smallest β values and thus compete least with the nitro group for hydrogen bonding to the N–H protons of DMPH. They alone yield slopes of δ vs. T that are negative, presumably due to a thermal decrease in the difference in the environments at the picryl protons.

Obviously, both the parameter δ as measured herein and the parameter β as tabulated in the literature are subject to uncertainties. We have listed in Appendix A some of the factors coming to mind that are relevant to this topic.

The thermal behavior of δ in various solvents as presented herein will allow us to carry out a more accurate analysis of the conformerization kinetics, planned for the future. Thus, we are now in a better position to derive and present quantitative results describing DMPH's internal conformerization and plan to make these available in a subsequent publication.

Conclusions

The present measurements demonstrate that certain convenient NMR chemical-shift measurements correlate very well with the Kamlet–Taft solvolytic β, allowing checks and new evaluations of this parameter. They strengthen the belief that β is a meaningful empirical descriptor of solvent properties. They reveal, clearly, that the hindered rotations in DMPH and related hydrazines are affected by hydrogen bonding to the solvent. This realization, with use of the temperature dependences found, will make evaluation of the conformerization kinetics more accurate.

Acknowledgements

We are grateful to the Natural Sciences and Engineering Research Council (NSERC) of Canada for some support. We also thank Ms. Y. Upadrashta for her assistance with this project. The expertise provided by Professor J.W. Quail on certain crystallographic matters also proved to be most valuable.

References

1. J. Heidberg, J.A. Weil, G.A. Janusonis, and J.K. Anderson. J. Chem. Phys. **41**, 1033 (1964).
2. R.L. Tyson and J.A. Weil. J. Phys. Chem. **94**, 3951 (1990). Note that in Table IX, the second $\Delta H^{\ddagger}$ should read $\Delta G^{\ddagger}$.
3. K.C. Brown, R.L. Tyson, and J.A. Weil. J. Chem. Ed. **75**, 1632 (1998). Please note an unfortunate flaw therein: in eq. 2b, the second ± should be ∓.
4. M.J. Kamlet and R.W. Taft. J. Am. Chem. Soc. **98**, 377 (1976).
5. M.J. Kamlet, J-L.M. Abboud, M.H. Abraham, and R.W. Taft. J. Org. Chem. **48**, 2877 (1983).
6. A.R. Katritzky, D.C. Fara, H. Yang, K. Tämm, T. Tamm, and M. Karelson. Chem. Rev. **104**, 175 (2004).
7. T. Yokohama, R.W. Taft, and M.J. Kamlet. J. Am. Chem. Soc. **98**, 3233 (1976).
8. M.J. Kamlet, J.-F. Gal, and P.-C. Maria. J. Chem. Soc., Perkin Trans. 2, 1583 (1985).

© 2004 NRC Canada

9. J.W. Quail, J.A. Weil, and M.P. Singh. Acta Crystallogr., Sect. C, **C56**, 235 (2000).
10. R. Chang. Basic principles of spectroscopy. Robert E. Krieger, Huntington, N.Y. 1978.
11. K.C. Brown, B.R. Nelson, J.W. Quail, B.E. Robertson, J.A. Weil, and Z. Zimpel. Can. J. Chem. **77**, 1295 (1999).
12. J.A. Pople, W.G. Schneider, and H.J. Bernstein. High-resolution nuclear magnetic resonance. McGraw-Hill, New York. 1959.
13. H. Wang, B.E. Robertson, and J.A. Weil. J. Inclusion Phenom. Mol. Recognit. Chem. **10**, 203 (1991).

Appendix A. Some possible sources of uncertainty and error in the NMR analysis presented herein

1. NMR spectroscopy:
   (*a*) Choice of spectrometer frequency ν_0.
   (*b*) Machine stability of ν_0.
   (*c*) Temperature stability; uncertainty in actual value at sample.
   (*d*) Effect of choice of probe (Bruker TXI or BBI, both 5 mm).
   (*e*) Effect of shimming and stability thereof on peak-position data.
   (*f*) Measurement uncertainty of AB peak positions.
   (*g*) Effect of glass NMR tube on β, on solvent viscosity, and on δ.
2. Dependence of δ on solute concentration not included.
3. Effect on δ of other solvent (non-H-bonding) properties.
4. Temperature dependence of J_{AB} not included.
5. Existence of J_{ABC} not included (see ref. 2).
6. Solvent purity, including effect of air and traces of water.
7. Solute purity.
8. Effect of the choice of group R in the solute RNH(Picr), including the effect of multiple H-bonding sites in each solute molecule.
9. Literature data of β, including $\beta(T)$ and $\beta(^2H)$.

© 2004 NRC Canada

Chemical oxidation of fluoroanilines to fluoroazobenzenes and fluorophenazines with potassium ferricyanide and potassium hydroxide

Elisa Leyva, Concepción Medina, Edgar Moctezuma, and Socorro Leyva

Abstract: The oxidation of several fluoroanilines with potassium ferricyanide and potassium hydroxide is described. In this oxidation, the major products are fluoroazobenzenes. In the case of 2-fluoro-substituted anilines, heterocyclic fluorophenazines were obtained in low to moderate yields. The optimal conditions for the reaction and the mechanism are presented.

Key words: oxidation, fluoroanilines, fluoroazobenzenes, fluorophenazines.

Résumé : On décrit l'oxydation de plusieurs fluoroanilines avec du ferricyanure de potassium et de l'hydroxyde de potassium. Dans cette oxydation, les produits principaux sont des fluoroazobenzènes. Dans le cas des 2-fluoroanilines, des fluorophénazines hétérocycliques ont été obtenues avec des rendements allant de faibles à moyens. On présente les conditions optimales et le mécanisme de cette réaction.

Mots clés : oxydation, fluoroanilines, fluoroazobenzènes, fluorophénazines.

[Traduit par la Rédaction]

Introduction

Fluoroazobenzenes are extensively used as dyes and analytical reagents (1). They are also useful as materials with nonlinear optical properties (2–5). These fluorocarbon compounds exhibit the properties of water and oil repellency, high lubricity, and thermal and chemical stability (6). They are useful synthetic intermediates. Decafluoroazobenzene has been used as a precursor of several hydroxyfluoroazobenzenes that have been evaluated as inhibitors of steroid biosynthesis (7).

The oxidation of substituted anilines to azobenzenes with a variety of oxidizing agents, such as barium manganate (8), lead tetraacetate (9), sodium hypochlorite (10) and manganese dioxide (11), has been reported. However, the oxidation of fluoroanilines with inorganic oxidants in aqueous solution is complicated by the poor solubility of anilines under these conditions. The addition of an organic solvent inmiscible with the aqueous phase slows the reaction further, since the solubility of the fluoroanilines is inhibited. The oxidation of pentafluoroaniline under phase-transfer conditions (12) gave decafluoroazobenzene in only 28% yield. Tatlow and coworkers (13) reported the formation of decafluoroazobenzene (18%) and octafluorophenazine (6%) during the electrochemical oxidation of pentafluoroaniline.

Received 29 June 2004. Published on the NRC Research Press Web site at http://canjchem.nrc.ca on 18 January 2005.

E. Leyva,[1] C. Medina, E. Moctezuma, and S. Leyva. Facultad de Ciencias Químicas, Universidad Autónoma de San Luis Potosí, Av. Dr. Manuel Nava 6, Zona Universitaria, San Luis Potosí, S.L.P, 78210, Mexico.

[1]Corresponding author (e-mail: elisa@uaslp.mx).

The oxidation of aromatic anilines with potassium ferricyanide and KOH was first reported by Goldstein and McNelis (14). Mesidine was oxidized by this reagent in a methanol–water mixture at 45 °C for 10 days to give the corresponding azobenzene. In a short communication, we reported the oxidation of fluoroanilines with this oxidant (15). In the present paper, we report the oxidation of several fluoroanilines **1** to azobenzenes **2** and phenazines **3** by means of potassium ferricyanide and KOH. The optimal conditions for this reaction and the mechanism are presented.

Results and discussion

In general, the oxidation of fluoroanilines with inorganic oxidants in aqueous media gives very low yields due to the poor solubility of anilines under these conditions. The addition of an inmiscible organic solvent does not improve the yields. In our hands, several fluoroanilines **1a**–**1h** (Scheme 1) reacted with potassium ferricyanide to give the corresponding fluoroazobenzenes **2a**–**2h** in good to moderate yields when a mixture of ethanol and water was used as the solvent. All the fluoroanilines had good solubility in the solvent mixture used, although some are not very soluble in other solvents such as dichloromethane.

For each aniline **1a**–**1h**, the main product was the corresponding fluoroazobenzene **2a**–**2h** (Table 1). A particularly high yield (94%) was obtained with 4-fluoroaniline **(1c)**. Even the oxidation of pentafluoroaniline **(1h)** gave decafluoroazobenzene **(2h)** in higher yield than that previously reported (12). With 2-fluoro-substituted anilines **1a**, **1d**, **1e**, **1f**, and **1h**, in addition to the fluoroazobenzenes **2**, the corresponding phenazines **3** were also obtained in variable amounts as yellow crystalline compounds. With 2,4-

 doi: 10.1139/V04-150 © 2004 NRC Canada

Scheme 1.

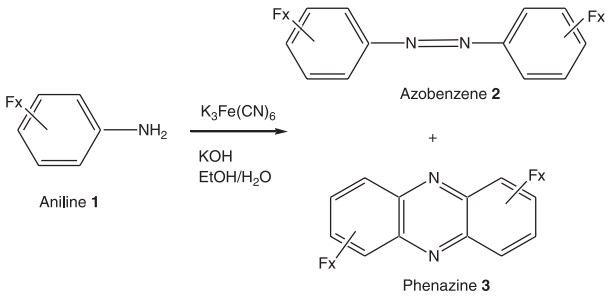


Table 1. Products formed in the oxidation of fluoroanilines**.**

	Yield (%)	
Aniline **1**	Azobenzene **2**	Phenazine **3**
1a: 2-Fluoroaniline	52	Trace
1b: 3-Fluoroaniline	50	None
1c: 4-Fluoroaniline	94	None
1d: 2,4-Difluoroaniline	52	20
1e: 2,5-Difluoroaniline	62	Trace
1f: 2,6-Difluoroaniline	65	25
1g: 3,4-Difluoroaniline	60	None
1h: Pentafluoroaniline	60	25

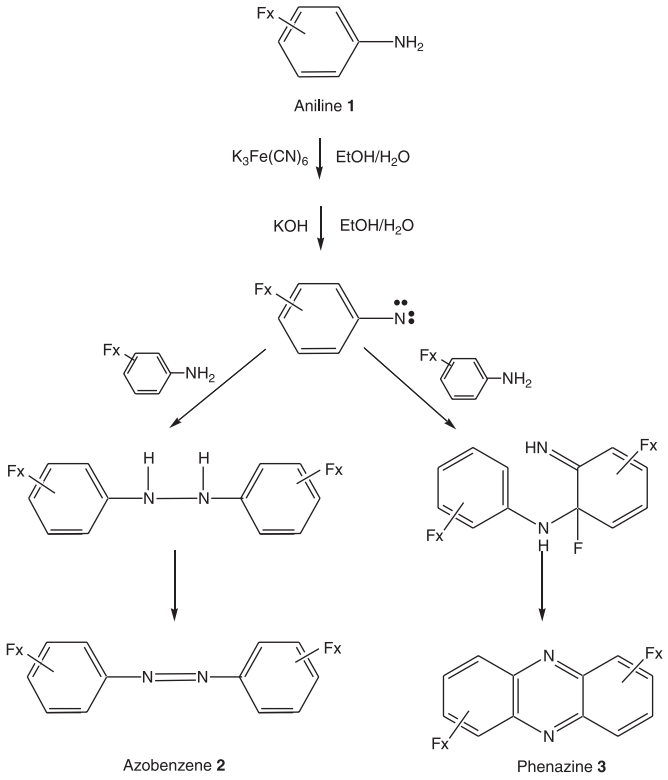
difluoroaniline (**1d**), phenazine **3d** was obtained in moderate yield. In the case of anilines with two *o*-fluoro substituents, the yields of phenazines were slightly higher.

The formation of the products observed in the oxidation of fluoroanilines can be explained by a mechanism involving a singlet fluorophenylnitrene as an intermediate (Scheme 2). Under these conditions, the fluorophenylnitrene would form from the fluoroaniline by reaction with potassium ferricyanide and KOH. Singlet fluorophenylnitrene is anticipated to be an ambident electrophile because the electron deficiency of the nitrogen could be neutralized by attack of a nucleophile not only on nitrogen but also on the ortho position of the aromatic ring. Nucleophilic attack by remaining fluoroaniline on nitrogen would give the fluorohydrazobenzene, which would oxidize to form the fluoroazobenzene. On the other hand, the electron-deficient singlet fluorophenylnitrene could be attacked at the ortho position of the aromatic ring by the nucleophilic aniline. Elimination of HF, heterocyclic ring closure, and further elimination of HF would give the phenazine **3**. In agreement with this mechanism is the observation that several equivalents of oxidant are required for the reaction to occur. A similar mechanism has been proposed for the oxidation of pentafluoroaniline to decafluoroazobenzene with sodium hypochlorite (12). Consistent with the proposed intermediacy of fluorophenylnitrene in this oxidation is the reported formation of both decafluoroazobenzene and octafluorophenazine in the thermal decomposition of azidopentafluorobenzene in the presence of pentafluoroaniline, where singlet nitrene is considered to be an intermediate (16).

Conclusions

The oxidation of fluoroanilines with potassium ferricyanide and KOH in an ethanol–water mixture gives the corresponding fluoroazobenzene in good to moderate yields. With 2-fluoro-substituted anilines, the corresponding fluorophenazines are also obtained in variable amounts. With 2,4-difluoroaniline, the phenazine is obtained in moderate yield. In the case of anilines with two *o*-fluoro substituents, the yields of phenazines are slightly higher.

Scheme 2.



Experimental section

General methods

All melting points were measured with a Fisher-Johns apparatus. IR spectra were recorded on a Nicolet 205 FT-IR spectrometer. UV–vis spectra were determined on a Shimadzu UV-2401PC spectrophotometer. ^{1}H NMR spectra were obtained on a Varian EM-200 using deuterated chloroform as solvent and were recorded in ppm from tetramethylsilane. ^{19}F NMR spectra were obtained on a Bruker AC 250 with a QNP probe and were recorded in ppm from trifluoroacetic acid or hexafluorobenzene. Mass spectra were obtained with a Hewlett Packard Model 5971 gas chromatograph equipped with a Hewlett Packard 5972 quadrupole mass detector. The chromatographic separation was performed on a capillary column (crosslinked 5% phenyl methyl silicone, 0.2 mm i.d. 0.33 μm × 25 m) using helium as carrier gas.

General procedure for oxidation

A given fluoroaniline (0.01 mol) was dissolved in an ethanol–water (1:1) mixture. Then, potassium hydroxide (0.018 mol) in a 1:1 ethanol–water mixture was added. Finally, potassium ferricyanide (0.04 mol) was added slowly. The resulting mixture was kept under reflux for 6 h. After this time, the mixture was filtered to remove the remaining

© 2004 NRC Canada

oxidant and extracted with dichloromethane. The organic phase was washed several times with water and dried with anhydrous sodium sulfate. The solvent was removed in a rotary evaporator, and the resulting mixture was passed through a silica gel column using hexane as the solvent to obtain the corresponding fluoroazobenzene as a crystalline orange solid. In the case of 2-fluoro-substituted anilines, fluorophenazines were obtained in low to moderate yields as yellow crystalline solids.

2,2′-Difluoroazobenzene (2a)

Orange crystals; yield 52%; mp 94–96 °C. IR (neat, cm^{-1}) 1219 (C–F). ^1H NMR ($CDCl_3$) δ (ppm): 7.5 (m, 4H, aromatic CH), 7.73 (m, 2H, aromatic), 8.05 (td, 2H, aromatic). ^{19}F NMR ($CDCl_3$), δ (ppm): –121.3 (s, 2F). EI-MS (70 eV) *m/z*: 218 (45%) [M^+], 123 (48%) [$M^+ - C_6H_4F$], 95 (100%) [$M^+ - C_6H_4FN_2$], 75 (25%) [$M^+ - C_6H_5F_2N_2$]; exact mass for $C_{12}H_8F_2N_2$: 218.0653; observed: 218.0663.

3,3′-Difluoroazobenzene (2b)

Orange crystals; yield 50%; mp 70–72 °C. IR (neat, cm^{-1}) 1247 (C–F). ^1H NMR ($CDCl_3$) δ (ppm): 7.24 (m, 2H, aromatic), 7.52 (q, 2H, aromatic), 7.62 (dd, 2H, aromatic), 7.78 (d, 2H, aromatic). ^{19}F NMR ($CDCl_3$) δ (ppm): –108 (s, 2F). EI-MS (70 eV) *m/z*: 218 (32%) [M^+], 123 (22%) [$M^+ - C_6H_4F$], 95 (100%) [$M^+ - C_6H_4FN_2$], 75 (24%) [$M^+ - C_6H_5F_2N_2$]; exact mass for $C_{12}H_8F_2N_2$: 218.0653; observed: 218.0655.

4,4′-Difluoroazobenzene (2c)

Orange crystals; yield 94%; mp 99–100 °C. IR (neat, cm^{-1}) 1231 (C–F). ^1H NMR ($CDCl_3$) δ (ppm): 7.3 (dd, 4H, aromatic), 8.04 (dd, 4H, aromatic). ^{19}F NMR ($CDCl_3$) δ (ppm): –106 (s, 2F). EI-MS (70 eV) *m/z*: 218 (29%) [M^+], 123 (20%) [$M^+ - C_6H_4F$], 95 (100%) [$M^+ - C_6H_4FN_2$], 75 (18%) [$M^+ - C_6H_5F_2N_2$]; exact mass for $C_{12}H_8F_2N_2$: 218.0653; observed: 218.0650.

2,2′,4,4′-Tetrafluoroazobenzene (2d)

Orange crystals; yield 52%; mp 150–152 °C. IR (neat, cm^{-1}) 1270 (C–F). ^1H NMR ($CDCl_3$) δ (ppm): 7.01 (m, 4H, aromatic), 7.85 (m, 2H, aromatic). ^{19}F NMR ($CDCl_3$) δ (ppm): –101.2 (s, 2F) –116.3 (s, 2F). EI-MS (70 eV) *m/z*: 254 (40%) [M^+], 141 (45%) [$M^+ - C_6H_3F_2$], 113 (100%) [$M^+ - C_6H_3F_2N_2$]; exact mass for $C_{12}H_6F_4N_2$: 254.0466; observed: 254.0407.

2,2′,5,5′-Tetrafluoroazobenzene (2e)

Orange crystals; yield 62%; mp 128–130 °C. IR (neat, cm^{-1}) 1253 (C–F). ^1H NMR ($CDCl_3$) δ (ppm): 7.25 (m, 4H, aromatic), 7.54 (m, 2H, aromatic). ^{19}F NMR ($CDCl_3$) δ (ppm): –116.3 (s, 2F), –127.8 (s, 2F). EI-MS (70 eV) *m/z*:254 (45%) [M^+], 141 (50%) [$M^+ - C_6H_3F_2$], 113 (100%) [$M^+ - C_6H_4FN_2$]; exact mass for $C_{12}H_6F_4N_2$: 254.0466; observed: 254.0477.

2,2′,6,6′-Tetrafluoroazobenzene (2f)

Orange crystals; yield 65%; mp 121–123 °C. IR (neat, cm^{-1}) 1017 (C–F). ^1H NMR ($CDCl_3$) δ (ppm): 6.85 (m, 4H, aromatic), 7.20 (m, 2H, aromatic). ^{19}F NMR ($CDCl_3$) δ (ppm): –125.3 (s, 4F). EI-MS (70 eV) *m/z*: 254 (47%) [M^+], 141 (72%) [$M^+ - C_6H_3F_2$], 113 (100%) [$M^+ - C_6H_3F_2N_2$]; exact mass for $C_{12}H_6F_4N_2$: 254.0466; observed: 254.0476.

3,3′,4,4′-Tetrafluoroazobenzene (2g)

Orange crystals; yield 60%; mp 70–72 °C. IR (neat, cm^{-1}) 1275 (C–F). ^1H NMR ($CDCl_3$) δ (ppm): 7.36 (m, 2H, aromatic), 7.78 (m, 4H, aromatic). ^{19}F NMR ($CDCl_3$) δ (ppm): –129.3 (s, 2F), –132.4 (s, 2F). EI-MS (70 eV) *m/z*: 254 (41%) [M^+], 141 (45%) [$M^+ - C_6H_3F_2$], 113 (100%) [$M^+ - C_6H_3F_2N_2$]; exact mass for $C_{12}H_6F_4N_2$: 254.0466; observed: 254.0471.

2,2′,3,3′,4,4′,5,5′,6,6′-Decafluoroazobenzene (2h)

Red–orange crystals; yield 60%; mp 142–143 °C. IR (neat, cm^{-1}) 1258 (C–F). ^1H NMR ($CDCl_3$) δ (ppm): 7.36 (m, 2H, aromatic), 7.78 (m, 4H, aromatic). ^{19}F NMR ($CDCl_3$) δ (ppm): –151.9 (m, 6F), –164.7 (m, 4F). EI-MS (70 eV) exact mass for $C_{12}F_{10}N_2$: 361.9901; observed 361.9890.

3,8-Difluorophenazine (3d)

Yellow crystals; yield 20%; mp 169–171 °C. IR (neat, cm^{-1}) 1535 (C=C), 1478 (C=C), 1638 (C=N), 1201 (C–F). ^1H NMR ($CDCl_3$) δ (ppm): 8.35 (m, 1H, aromatic), 8.42 (m, 1H, aromatic), 8.54 (m, 1H, aromatic), ^{19}F NMR ($CDCl_3$) δ (ppm): –125 (s, 2F). EI-MS (70 eV) exact mass for $C_{12}H_6F_2N_2$: 216.0499; observed 216.0480.

2,7-Difluorophenazine (3e)

Yellow crystals; yield 25%; mp 205–206 °C. IR (neat, cm^{-1}) 1533 (C=C), 1487 (C=C), 1639 (C=N), 1104 (C–F). ^1H NMR ($CDCl_3$) δ (ppm): 8.25 (m, 1H, aromatic), 8. 55 (m, 1H, aromatic), 8.65 (m, H, aromatic). ^{19}F NMR ($CDCl_3$) δ (ppm): –123.5 (s, 2F). EI-MS (70 eV) exact mass for $C_{12}H_6F_2N_2$: 216.0499; observed 216.0489.

2,3,4,5,7,8,9,10-Octafluorophenazine (3h)

Yellow crystals; yield 25%; mp 233–234 °C. IR (neat, cm^{-1}) 1638 (C=C), 1478 (C=C), 1201 (C–F). ^{19}F NMR ($CDCl_3$) δ (ppm): –155.5 (s, 2F), –157 (s, 2F), –162.4 (s, 2F), 166 (s, 2F). EI-MS (70 eV) exact mass for $C_{12}F_8N_2$: 323.9934; observed 323.9920.

Acknowledgements

Financial support by the National Council for Science and Technology (CONACyT) of Mexico (Grant 0762-M9109) is gratefully acknowledged. We thank Professor Miguel A. García-Garibay from the University of California at Los Angeles for help with MS measurements.

References

1. H.W. Russ and H. Tappe. Eur. Pat. Appl. EP 629, 667 (1994).
2. Y. Onogi, T. Hayashi, Y. Mizushima, and M. Yamamoto. Nippon Kagaku Kaishi, 815 (1990).
3. H. Yamamoto and A. Nishida. Nippon Kagaku Kaishi, 2338 (1985).
4. H. Sakai, J. Anzai, A. Ueno, and T. Osa. Nippon Kagaku Kaishi, 1194 (1985).
5. K. Kimura, T. Suzuki, and M. Yokoyama. Solid State Ionics, **40,** 666 (1990).

© 2004 NRC Canada

6. N. Yoshino, M. Kitamura, T. Seto, Y. Shibata, M. Abe, and K. Ogino. Bull. Chem. Soc. Jpn. **65,** 2141 (1995).
7. M. Jarman, S.E. Barrie, J.J. Deadman, J. Houghton, R. McCague, and M.G. Rowlands. J. Med. Chem. **33,** 2452 (1990).
8. H. Firouzabadi and Z. Mostafavipoor. Bull. Chem. Soc. Jpn. **56,** 914 (1983).
9. J.M. Birchall, R.N. Haszeldine, and J.E.G. Kemp. J. Chem. Soc. C, 449 (1970).
10. J. Burdon, C.J. Morton, and D.F. Thomas. J. Chem. Soc. 2621 (1965).
11. O.H. Wheeler and D. Gonzalez. Tetrahedron, **20,** 189 (1964).
12. J.J. Deadman, M. Jarman, R. McCague, R. McKenna, and S. Neidle. J. Chem. Soc. Perkin Trans. 2, 971 (1989).
13. A.G. Hudson, A.E. Pedler, and J.C. Tatlow. Tetrahedron Lett. **17,** 2143 (1968).
14. S.L. Goldstein and E.J. McNelis. J. Org. Chem. **38,** 183 (1973).
15. E. Leyva, E. Monreal, C. Medina, and S. Leyva. Tetrahedron Lett. **38,** 7847 (1997).
16. R.E. Banks and A. Prakash. J. Chem. Soc. Perkin Trans. 1, 1365 (1974).

© 2004 NRC Canada

A novel crown ether generation containing the pyrilium heteroaromatic cation — Synthesis, characterization, and solid-phase ^{13}C NMR[1]

Abolghasem Moghimi, Majid Faal Rastegar, and Mehdi Ghandi

Abstract: The synthesis and structural characterization of two members, **5** and **6**, of a novel generation of crown ethers containing the pyrilium cation are reported. These two compounds contain two and three benzo-9-crown-3 (B9C3) units, respectively, connected to the 2 and 6 or 2, 4, and 6 positions of a central pyrilium cation. The crown ethers **5** and **6** were obtained from the condensation reaction of appropriate aldehydes and methyl ketones in the presence of $POCl_3$. A variety of physicochemical methods including electrospray mass spectroscopy, solution ^1H and ^{13}C NMR, and solid-phase ^{13}C NMR were applied for structural characterization. The ^1H and ^{13}C NMR studies indicate rapid rotation of the B9C3 unit about the C–C bond that connects the two units to each other. The solid-phase ^{13}C NMR spectra of these two crown ethers reveal that there are deviations from planarity for the two phenyl rings attached at the 2 and 6 positions of the central pyrilium cation.

Key words: crown ether, pyrilium, solid-phase NMR, crownpyrilium, heteroaromatic.

Résumé : On a réalisé la synthèse et la caractérisation de deux nouveaux termes, **5** et **6**, d'une nouvelle génération d'éthers couronnes contenant le cation pyrillium. Ces deux composés contiennent deux et trois unités de benzo-9-couronne-3, B9C3, reliées aux positions 2 et 6 ou 2, 4 et 6 d'un cation pyrillium central. Les éthers couronnes **5** et **6** ont été obtenues par une réaction de condensation des aldéhydes ou des méthylcétones appropriés en présence de $POCl_3$. La caractérisation de la structure a été réalisée à l'aide de diverses méthodes physicochimiques, dont la spectroscopie de masse avec ionisation par électronébulisation, la résonance magnétique nucléaire du ^1H et du ^{13}C en solution et la RMN du ^{13}C en phase solide. Les études de RMN du ^1H et du ^{13}C indiquent que l'unité B9C3 donne lieu à une rotation rapide autour de la liaison C–C qui réunit les deux unités l'une à l'autre. La RMN du ^{13}C en phase solide de ces deux éthers couronnes révèle que les deux noyaux phényles attachés aux positions 2 et 6 du cation pyrillium central ne sont pas planaires.

Mots clés : éther couronne, pyrillium, RMN en phase solide, couronnepyrillium, hétéroaromatique.

[Traduit par la Rédaction]

Introduction

The synthesis and X-ray crystal structures of a novel crown ether generation containing different heteroaromatic cations such as pyrilium, thiopyrilium, and pyridinium was recently reported by our research group (1). We call these new crown ethers *crownpyrilium*, *crownthiopyrilium*, and *crownpyridinium dyes*. Crown ethers (2) and heteroaromatic cations (3) are two important classes of organic compounds and, as such, their synthesis and structural properties have been extensively investigated. Owing to their specific metal ion complexing ability and high extraction efficiency, crown ethers have been widely used as suitable neutral carriers in such important applications as selective metal transport through liquid membranes (4), preparation of ion-selective membrane sensors, (5), and phase transfer catalysis (6). Heteroaromatic cations have been applied as active materials in laser dyes, photosensitizers, and organic conductors (7). In a recent article, a class of pyrilium dyes with high efficiency in lasing and two-photon absorption fluorescence has been reported (7*a*). A search of the literature indicates that there are limited reports on the synthesis of pyrilium, thiopyrilium, and pyridine corands (8*a*, 8*b*) as well as hemispherand-like macrocycles containing the pyrilium subunit (8*c*, 8*d*).

The crown ether unit in the crownpyrilium compounds is expected to have the potential to form a host–guest complex with inorganic and organic cations, while the heteroaromatic cationic unit can behave as an anion receptor or interact with those functional groups that have the capability to form hydrogen bonds. Thus, these compounds are prominent in the design of ditopic artificial receptors for amino acid recognition, which is currently an area of great interest (9). In our

Received 22 March 2004. Published on the NRC Research Press Web site at http://canjchem.nrc.ca on 18 January 2005.

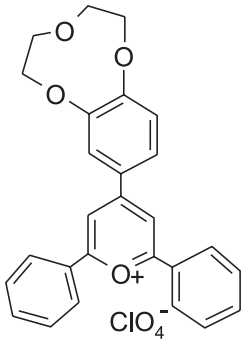
A. Moghimi.[2] Department of Chemistry, University of Imam Hossein, P.O. Box 16575–347, Tehran, Iran.
M.F. Rastegar. Department of Chemistry, Carleton University, Ottawa, ON K1S 5B6, Canada.
M. Ghandi. Department of Chemistry, University of Tehran, Tehran, Iran.

[1]Part II in a series on "A novel crown ether generation containing heteroaromatic cations." For the previous paper in this series, see ref. 1.

[2]Corresponding author (e-mail: samoghimi@yahoo.com).

 doi: 10.1139/V04-144 © 2004 NRC Canada

Fig. 1. Chemical structure of 2,6-diphenyl-4-B9C3-pyrilium perchlorate **1**.



1

previous paper (1), three new crown ethers, in which a benzo-9-crown-3 (B9C3) unit was attached to the 2,6-diphenyl heteroaromatic cation units at the 4-position, were investigated. Compound **1** (Fig. 1) is an example of these compounds. Spectrophotometric studies in methanol solution revealed that this class of crownpyrilium dyes can be successfully applied to selective amino acid recognition. Thus, the crown cavity in the corresponding laser dye systems is expected to play a unique role in both the fine adjustment of the absorption and emission spectra as well as the fluorescence enhancement, as was observed in the case of crownpyrilium dye **1**. The excitation and emission spectra of **1** revealed that this crown ether has an absorbance at about λ_{max} = 450 nm and a fluorescence at about λ_{max} = 580 nm, and the fluorescence intensity is sensitive to the concentration of an appropriate amino acid. This rather interesting behaviour attracted our attention, and we became more interested in extending this field of research by preparing and characterizing other similar compounds. Therefore, in this paper, we wish to report the synthesis of crownpyriliums **5** and **6** (Scheme 1), using the same synthesis methodology as applied previously in the preparation of **1**, and to discuss their solid-phase NMR spectra. The excitation properties will also be discussed and compared with those of **1**.

Experimental

Instrumentation

Solution NMR spectra were recorded on a 400-MHz Bruker AMX-400 spectrometer. Samples for both ^{1}H and ^{13}C NMR were prepared in $CDCl_3$ or DMSO-d_6 solution at a concentration of 0.1 mol/L, and their spectra were obtained in 5-mm tubes. All chemical shifts are reported in ppm downfield from Me_4Si (TMS). The mass spectra were recorded on a MS80RFA mass spectrometer by electron ionization (EI) at 70 eV and positive ion electrospray (ES). The IR spectra were obtained with a Shimadzu FTIR spectrometer using KBr discs. The melting points were measured on a digital Electrothermal 9000 apparatus and are uncorrected. Elemental analyses were performed at Ottawa University. The solid-phase ^{13}C NMR spectra were obtained at 50.3 MHz using a Bruker ASX-200 spectrometer under the same conditions as described previously (1). The spinning rate was 5 kHz. Chemical shifts were measured relative to external hexamethylbenzene (HMB) (methyl resonance at 16.9 ppm) and then converted to the TMS scale. The dipolar dephasing experiment was carried out by interruption of the ^{1}H decoupling for 40 μs immediately following the cross-polarization sequence.

Materials

B9C3 crown ether **2** (10), HCO-B9C3 crown ether **3** (11), and pyrilium crown ether **1** (1) were synthesized following the procedures described previously. Other reagents were purchased from Merck.

Synthesis of 4′-acetyl-B9C3 (4)

A 500-mL flask was charged with B9C3 (9 g, 0.05 mol), 150 mL of nitrobenzene, and 13.4 g (0.1 mol) of $AlCl_3$ under nitrogen. Acetyl chloride (4.2 g, 0.05 mol) was then added dropwise to the mixture, in an ice bath, over 30 min while stirring. The reaction was allowed to proceed at 0 °C for 3 h and subsequently at room temperature overnight. Then 150 mL of water was added to the mixture to quench the reaction followed by steam distillation. The aqueous solution thus obtained was extracted with CH_2Cl_2 (3 × 150 mL), and the combined organic extracts were dried over anhydrous sodium sulphate. After filtration and solvent removal, 10.1 g of light-brown oil was obtained. The oil was extracted with boiling hexane (3 × 150 mL). Upon cooling the hexane solution, 8.4 g (75.7%) of 4′-acetyl-B9C3 was obtained as light-yellow cubic crystals.

^{1}H NMR ($CDCl_3$) (ppm) δ_H: 7.64, 7.60, 7.58, 6.99, 4.59, 4.28, 3.93, and 3.90. ^{13}C NMR ($CDCl_3$) (ppm) δ_C: 196.5, 155.7, 150.6, 132.6, 125.1, 124.1, 121.9, 75.1, 72.7, 72.2, and 71.8. EI-MS *m/z* (%): 224 (M + 2, 0.5), 223 (M + 1, 3.7), 222 (M, 27.9), 207, 193, 178, 163, 149, 135, 107, 94, 79, 69, 63, 51, and 44. Anal. calcd. (%) for $C_{12}H_{14}O_4$: 222.10876; found: 222.08792.

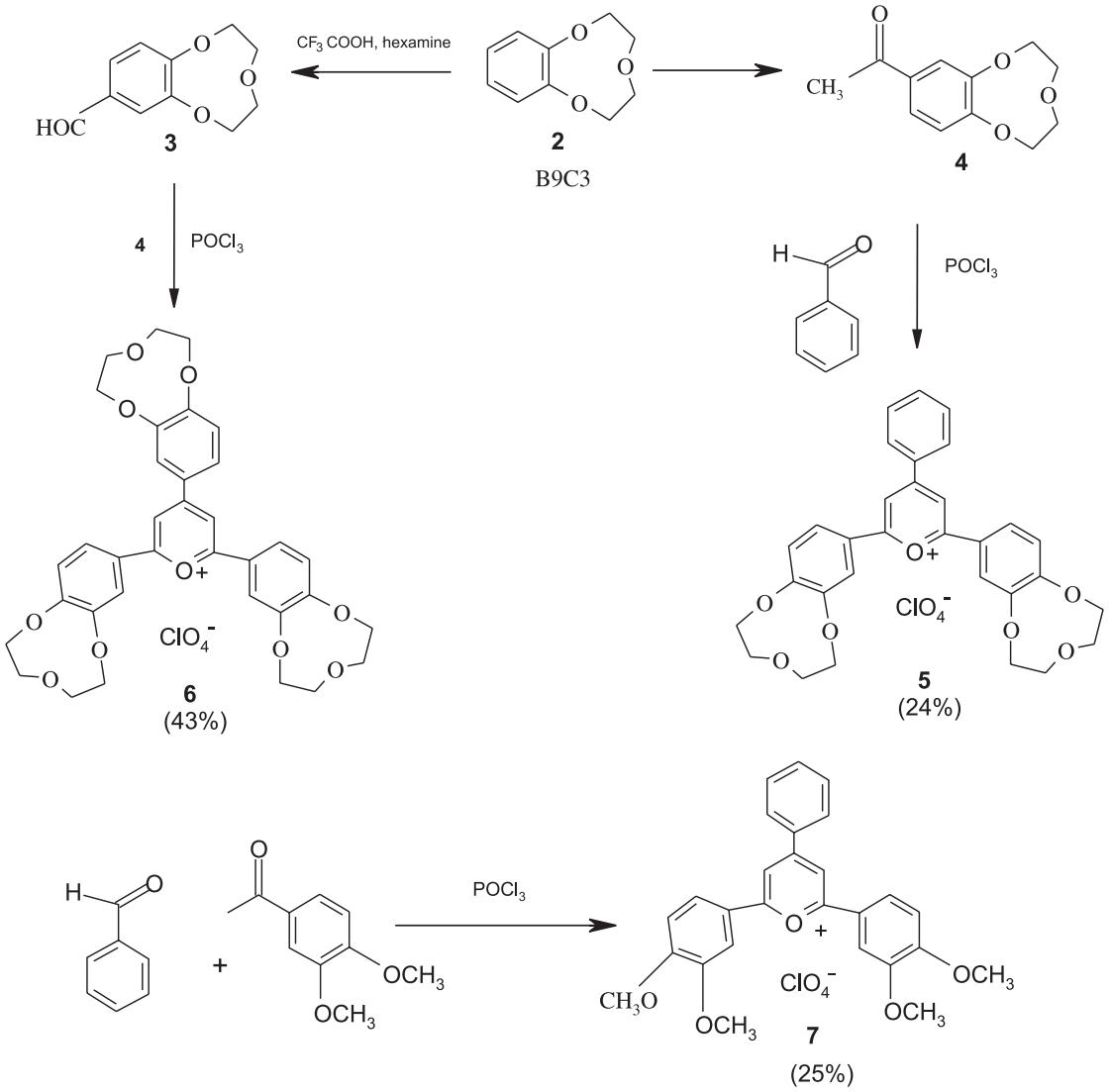
Synthesis of 2,6-bis(B9C3)-4-phenylpyrilium perchlorate (5)

Crown ether **4** (6.66 g, 30 mmol) was added to benzaldehyde (1.8 g, 15 mmol) in a 50-mL flask. The reaction mixture was cooled in an ice/water bath, and 5.37 g (35 mmol) of $POCl_3$ was added dropwise to the mixture. The reaction mixture, while stirring, was then warmed in a water bath (50–60 °C). The stirring was continued for 3 h followed by evaporation of excess $POCl_3$ on a rotary evaporator. The residue was dissolved in 200 mL of hot absolute ethanol and was heated to boiling. Next, 3 mL of 60% perchloric acid was added to the hot ethanol solution, and the solution was then allowed to cool to room temperature. The crystalline product was filtered, washed with diethyl ether, and finally vacuum dried. The orange crystalline product was recrystallized from acetic acid. After suction filtration and washing the orange needle crystals with diethyl ether, 2.2 g (24%) of **5** were obtained (mp 158–159 °C).

^{1}H NMR (DMSO-d_6) (ppm) δ_H: 8.9 (s, 2H, CH pyrilium), 8.5 (d, 2H, $^3J_{HH}$ 7.6 Hz), 8.2 (d, 2H, $^4J_{HH}$ 2.2 Hz), 8.1 (dd, 2H, $^3J_{HH}$, 8.4 Hz, $^4J_{HH}$ 2.2), 7.8 (t, 1H, $^3J_{HH}$ 7.3 Hz), 7.7 (dd, $^3J_{HH}$ 7.6 Hz, $^3J_{HH}$ 7.3 Hz), 7.2 (d, 2H, $^3J_{HH}$ 8.4 Hz), 4.7 (m, 4H), 4.4 (m, 4H), and 3.9 (m, 8H). ^{13}C NMR (DMSO-d_6) (ppm) δ_C: 168.5, 163.4, 156.9, 151.3, 134.7, 132.7, 129.7, 129.6, 125.0, 124.7, 123.2, 122.8, 113.5, 74.9, 72.0, 71.1,

© 2004 NRC Canada

Scheme 1. Synthesis route for **5**–**7**.



and 70.8. EI-MS *m*/*z* (%): 410 (1.5), 252 (80), 167 (53), 152 (12), 109 (100), 91 (27), and 45 (26). ES-MS *m*/*z* (%): 515.0 (M + 2, 7.1%), 514.0 (M + 1, 33.4%), 513.0 (2,6-di(B9C3)-4-phenylpyrilium cation, 100%), 329.9, and 304.1. FAB-MS *m*/*z* (%): 513.2 (2,6-di(B9C3)-4-phenylpyrilium cation, 25%), 462.2 (2%), 370.2 (4%), 278.1 (7%), 186.1 (25%), 149.1 (10%), and 75.0 (100). Anal. calcd. (%) for $C_{31}H_{29}O_{11}Cl$: C 60.73, H 4.73; found: C 59.50, H 4.67.

Synthesis of 2,4,6-tri(B9C3)-pyrilium perchlorate (6)

Crown ethers **4** (8.88 g, 40 mmol) and **3** (4.16 g, 20 mmol) in a mole ratio of 2:1 were mixed and well ground and were then placed in a 50-mL flask. Then 6.9 g (45 mmol) of $POCl_3$ was added dropwise to the reaction mixture. The mixture, while stirring, was warmed in a water bath (50–60 °C). The stirring was continued for 2 h followed by evaporation of excess $POCl_3$ on a rotary evaporator. The residue was dissolved in 250 mL of hot absolute ethanol and was heated to boiling. Then 5 mL of 60% perchloric acid was added to the hot ethanol solution, which was then allowed to cool to room temperature. The red crystalline product was filtered, washed with diethyl ether, and finally vacuum dried to obtain 6.2 g (43%) of **6** (mp 149–150 °C).

^{1}H NMR (DMSO-d_6) (ppm) δ_H: 8.74 (s, 2H, CH pyrilium), 8.34 (d, 1H, $^4J_{HH}$ = 2.2 Hz), 8.25 (dd, 1H, $^3J_{HH}$ = 8.7 Hz, $^4J_{HH}$ = 2.2 Hz), 8.20 (d, 2H, $^4J_{HH}$ = 2.2 Hz), 8.06 (dd, 2H, $^3J_{HH}$ = 8.7 Hz, ^4J = 2.2 Hz), 7.25 (d, 2H, $^3J_{HH}$ = 8.7 Hz), 7.22 (d, 1H, $^3J_{HH}$ = 8.7 Hz), 4.73 (m, 2H), 4.69 (m, 4H), 4.36 (m, 6H), and 3.87 (m, 12H). ^{13}C NMR (DMSO-d_6) (ppm) δ_C: 167.6, 161.7, 157.2, 156.6, 151.4, 151.3, 126.8, 126.4, 126.0, 124.7, 124.3, 123.4, 122.8, 122.4, 112.0, 75.0, 74.7, 72.0, 71.9, 71.3, 71.0, 70.9, and 70.8. ES-MS *m*/*z* (%): 615.0 (2,4,6-tri(B9C3)-pyrilium, 100), 517.0 (1), 369.0 (13), and 151.8 (2).

Synthesis of 2,6-bis(dimethoxyphenyl)-4-phenylpyrilium perchlorate (7)

This compound was prepared following a similar procedure to that used in preparing compound **5**. Yield 25%, mp 227–228 °C.

^{1}H NMR (DMSO-d_6) (ppm) δ_H: 8.82 (s, 2H, CH pyrilium), 8.43 (d, 2H, $^3J_{HH}$ = 7.5 Hz, ph), 8.15 (dd, 2H, $^3J_{HH}$ = 8.8 Hz,

© 2004 NRC Canada

$^4J_{HH}$ = 2.0 Hz,), 7.85 (d, 1H, $^3J_{HH}$ = 2.0 Hz), 7.72–8.84 (m, 3H, ph), 7.30 (d, 1H, $^3J_{HH}$ = 8.7 Hz), 3.97 (s, OCH_3), and 3.95 (s, OCH_3). ^{13}C NMR (DMSO-d_6) (ppm) δ_C: 168.6, 163.0, 154.8, 149.4, 134.3, 132.7, 129.5, 129.4, 123.7, 121.1, 112.8, 112.3, 110.2, 56.1, and 55.9.

Results and discussion

Synthesis and MS analysis

The synthetic pathway is shown in Scheme 1. The cyclization reaction of catechol and bis(dichloroethyl ether) under high dilution conditions in water as solvent (2*m*) followed by formylation of the resulting B9C3 with hexamine in the presence of CF_3COOH afforded compound **3** (4′-HCO-B9C3) in an overall 22.5% yield (1). Compound **4** was obtained in 75.7% yield from the acylation of B9C3 using acetyl chloride and $AlCl_3$ in nitrobenzene solvent. Among a number of procedures used in the literature for the synthesis of pyrilium cations (8), the condensation of appropriate aldehydes and ketones in the presence of $POCl_3$ was chosen to prepare the perchlorate salts of 2,6-diphenyl-4-B9C3-pyrilium (**1**), 2,6-di-B9C3-4-phenylpyrilium (**5**), 2,4,6-tri-B9C3-pyrilium (**6**), and 2,6-bis(dimethoxyphenyl)-4-phenyl-pyrilium perchlorate (**7**), which were obtained in yields of 29, 24, 43, and 25%, respectively. The melting points of the resulting pyrilium cations **1**, **5**, and **6**, (i.e., 248–250, 158–159, and 149–150 °C, respectively) decrease with increasing number of B9C3 units connected to the central pyrilium cation.

For the structural characterization of the resulting crown-pyrilium cations, MS and NMR spectroscopy were applied. Since it has been noted that EI-MS is not a suitable technique for structural characterization of organic salts such as heteroaromatic cations (1, 12), and considering that fast atom bombardment mass spectrometry (FAB-MS) and ES-MS have been successfully applied for some heteroaromatic cations (13, 14), the latter two methods were applied to both **5** and **6**. The appropriate base peaks at *m/z* = 513 and 615.0 in the ES-MS spectra that correspond to the naked 2,6-di-B9C3-4-phenylpyrilium and 2,4,6-tri-B9C3 pyrilium cations, respectively, were then detected. The elemental analysis data for **5**, $C_{31}H_{29}O_{11}Cl$, was found to be reasonably in agreement with the expected formula.

UV–vis spectroscopy

The UV–vis spectra of crownpyriliums **1**, **5**, and **6** and pyrilium **7** were recorded in MeOH to compare the absorption data and investigate the influence of the B9C3 substitution at the 2, 4, and 6 positions of pyrilium. The absorption data are collected in Table 1. The λ_{max} values are in the order of **5** > **6** > **1**. The influence of the crown cavity on the UV absorption characteristics of the pyrilium moiety is of particular interest. Comparison of the absorption data for each crownpyrilium (**5** and **6**) and their closely related methyl ether pyrilium derivative (**7**) indicates that there are noticeable differences between these compounds. As is clear from Table 1, pyrilium **7** shows a red shift in comparison with crownpyriliums **5** and **6**. This implies that the oxygen atoms directly attached to the phenyl rings in **7** behave as a better electron-donating group than the crownpyriliums **1**, **5**, and **6**. This might be due to the orientation of oxygen lone pairs imposed by the nine-membered ring crown ether in these compounds.

Table 1. UV-vis data for crownpyriliums **1**, **5**, and **6** and pyrilium **7**.

Compound	Solvent	Absorptions (nm)
1	CH_3OH	208, 274, 418
	C_2H_5OH	206, 277, 422
5	CH_3OH	208, 325, 388, 484
6	CH_3OH	208, 307, 440
7	CH_3OH	334, 409, 502

Table 2. Selected ^1H and ^{13}C NMR data of aromatic regions of compounds **5** and **7** to highlight the role of the two nine-membered B9C3 rings in **5** and the tetramethoxy groups in **7** on the chemical shifts (ppm).

	^{13}C (ppm)			^1H (ppm)		
H_i or C_i[a]	**5**	**7**	$\Delta\delta C$[b]	**5**	**7**	$\Delta\delta H$[b]
6, 24	122.8	112.8	–10.0	7.25	7.30	+0.05
26	123.2	112.8	–10.4	—	—	—
8, 16	124.7	121.1	–3.6	—	—	—
12, 14	113.5	110.2	–3.3	8.90	8.82	–0.08
5, 23	156.9	154.8	–2.1	—	—	—
9, 17	125.0	123.7	–1.3	8.25	7.85	–0.40
10, 18	151.3	149.4	–1.9	—	—	—

[a]The atom numbering for the pyrilium ring and phenyl groups in compound **7** is considered to be similar to that of compound **5**.
[b]Chemical shift differences (in ppm) between resonances of **7** and those of **5**.

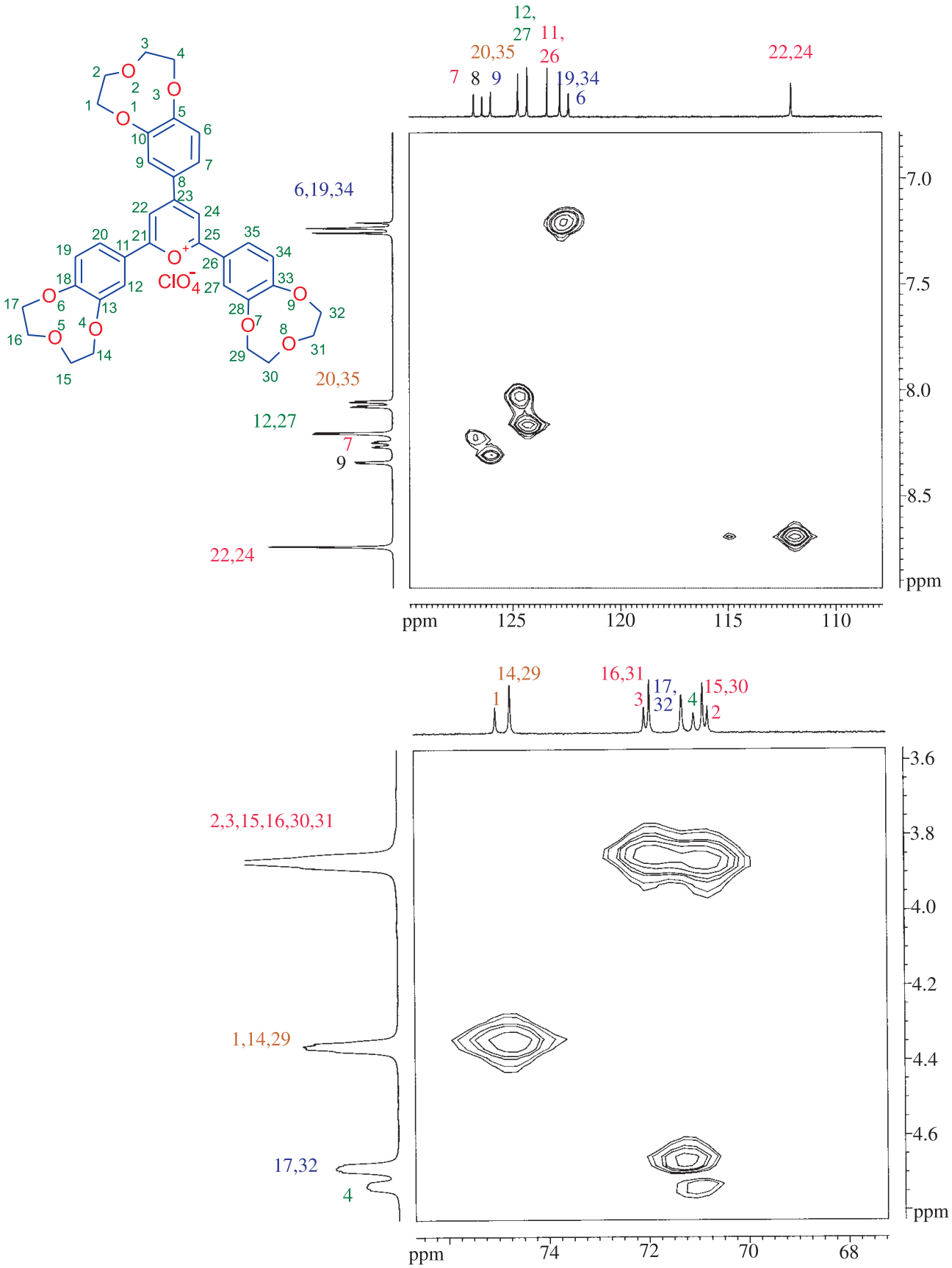
Solution ^1H and ^{13}C NMR

Proton and ^{13}C NMR spectra of **5** and **6** were recorded in DMSO-d_6. The analysis of the resulting data was performed using the known characteristic resonances of compound **1** (1) as well as the NMR data obtained for compound **7** and the two-dimensional NMR spectra. A typical two-dimensional ^1H-^{13}C HETCOR is given in Fig. 2 for compound **6**. Both **5** and **6** show a distinct singlet signal at about 9 ppm in their ^1H NMR spectra for the two pyrilium ring protons, which are equivalent as a result of fast B9C3 rotation on the NMR time scale. Other easily distinguishable ^1H resonances are the three and four multiplets in the 3.6–4.8 ppm region corresponding to the crown ether methylene protons of **5** and **6**, respectively. The more deshielded methylene resonances are due to the directly attached CH_2O groups on the phenyl rings. These well-separated peaks characterize the remote electronic effect of the pyrilium unit as an efficient electron-withdrawing group. The 8 and 12 CH_2O carbons in **5** and **6** clearly show 4 and 8 resolved ^{13}C resonances, respectively. The AMX spin system pattern for the three protons of the 4′-substituted- B9C3 benzene rings can be easily identified in the aromatic region. Based on known ^1H and ^{13}C NMR resonances, the other resonances were assigned using two-dimensional spectra. As shown in Fig. 2, for instance, the ^{13}C methylene and aromatic resonances can be identified from the ^1H-^{13}C HETCOR.

An interesting fact to be noted is that the chemical shifts for pyrilium and the three phenyl rings at the 2, 4, and 6 positions are influenced quite differently from those of the two

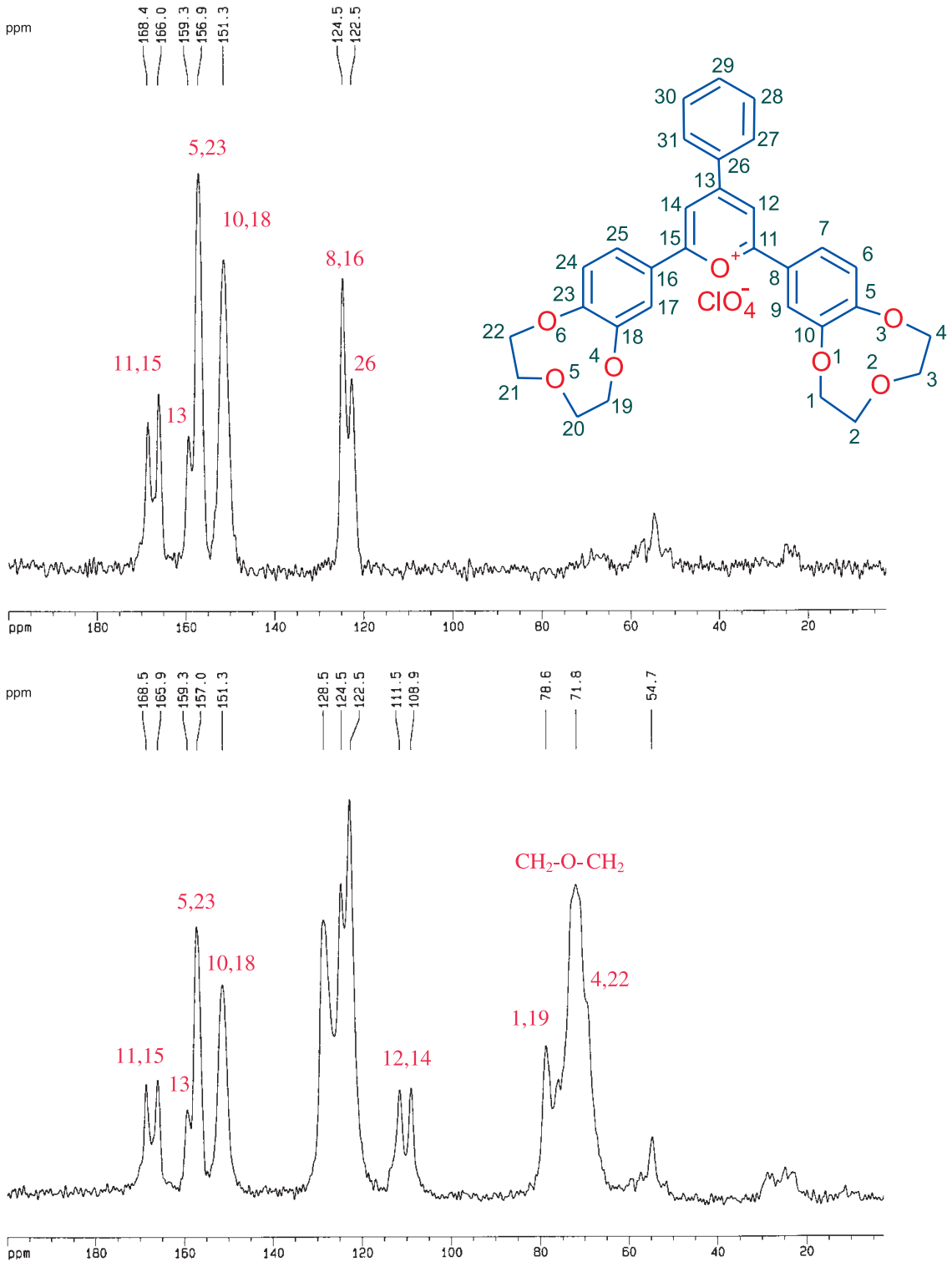
© 2004 NRC Canada

Fig. 2. The two-dimensional ^{1}H-^{13}C HETCOR for **6**.



© 2004 NRC Canada

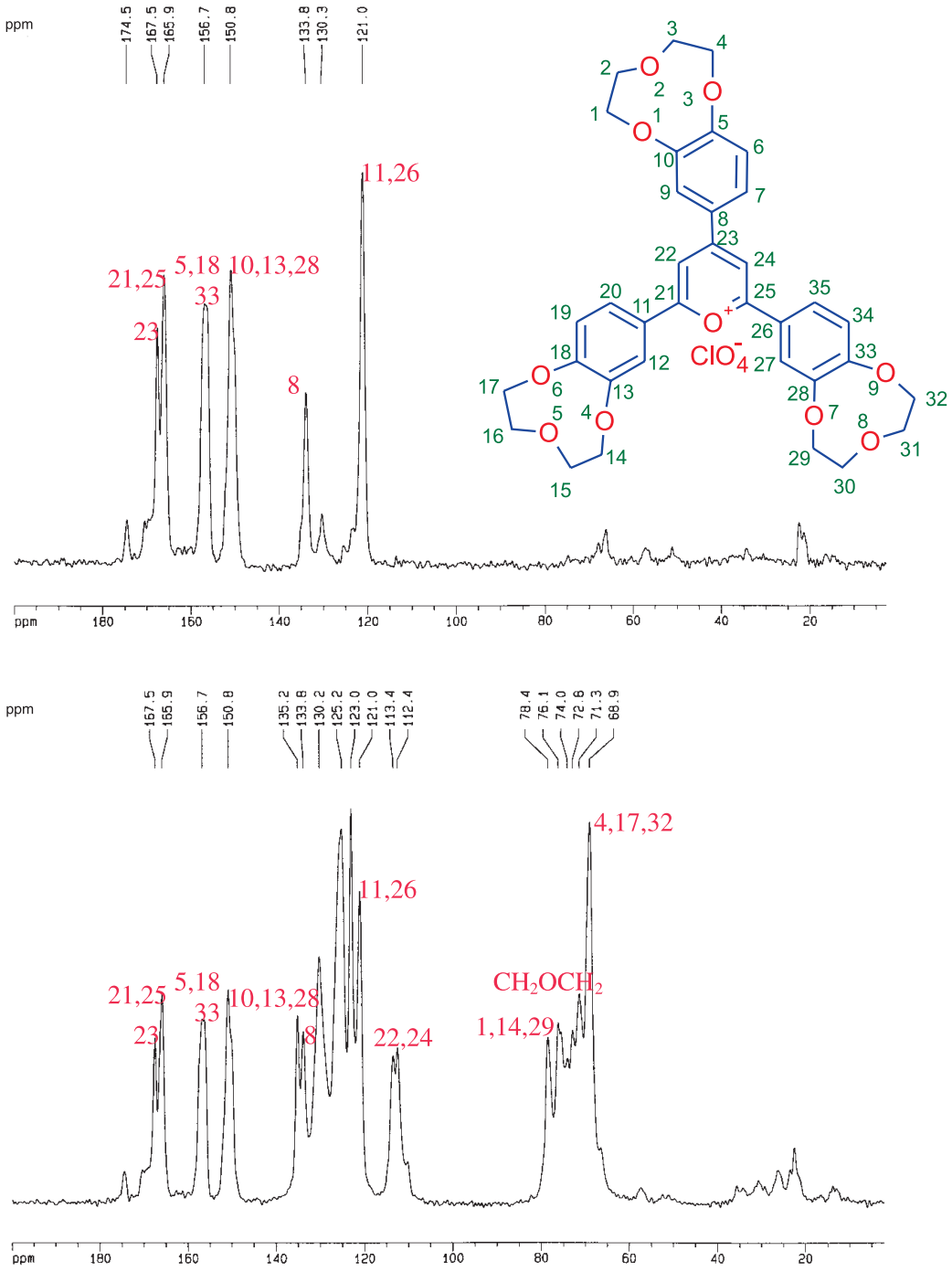
Fig. 3. Normal (*bottom*) and dipolar dephased (*top*) solid-phase ^{13}C NMR spectra of **5**.



nine-membered rings of B9C3 in **5** and **6** and the four methoxy groups in **7**. To obtain an estimate for the contribution of the B9C3 crown ring on the NMR resonances of compound **5**, NMR data for compound **7** were obtained under the same conditions as used for compound **5**, and some of these NMR data are listed in Table 2. As seen, large chemical shift differences ($\Delta\delta C$) are observed for the carbon atoms at the 6 and 26 positions, while there are moderate differences for those at positions 8 and 12. The downfield shifts indicated in Table 2 reveal the lesser electron-donating ability of the nine-membered crown ring as compared to the methoxy groups. This could be the result of the restricted orientation of attached oxygen atoms to the phenyl rings in **5** and **6** that results from the rigid nine-membered ring crown

© 2004 NRC Canada

Fig. 4. Normal (*bottom*) and dipolar dephased (*top*) solid-phase ^{13}C NMR spectra of **6**.



cavity. This supports our explanation for the UV–vis absorption. Considering the fact that particular guests, such as Be^{2+} (5*c*), can strongly interact with the crown cavity, one would expect that fine adjustment of both absorption and emission bands could be achieved by choosing an appropriate combination of guest and concentration.

Solid-phase ^{13}C NMR

Since our efforts to obtain single crystals of **5** and **6** for X-ray analysis failed, solid-phase ^{13}C NMR was chosen to obtain some insight into the solid-state structures of **5** and **6**. The normal and dipolar dephased solid-phase ^{13}C NMR spectra of **5** and **6** are presented in Figs. 3 and 4, respectively. To analyze the solid-phase NMR spectra, the previously reported solid-phase ^{13}C NMR data for B9C3, B9C3-d_4 (10), 4′-HCO-B9C3, and 4′-HCO-B9C3-d_4 (11), as well as the solution ^{13}C NMR data and dipolar dephased ^{13}C CPMAS spectra obtained in the present study, were all considered.

It was noticed that the overall spectral patterns are more or less similar to the one previously reported for crownpyrilium **1** (1). The nonprotonated carbons are readily

© 2004 NRC Canada

distinguishable in the dipolar dephased spectra. Examination of the ^{13}C CPMAS spectra reveals three distinct regions: a 67–79 ppm region for crown cavity CH_2O carbons, a 150–169 ppm region for nonhydrogenated phenyl carbons attached to oxygen atoms and the carbons α and γ to the pyrilium O^+ as a result of the inductive and resonance effects of pyrilium, and finally a 110–137 ppm region for the remaining, mostly CH, carbons.

As expected, the number of CH_2O resonances in **6** is greater than in **5**. The corresponding carbons in **1** have shown only one broadened singlet signal at 76.7 ppm (1). The deshielded resonances in the aliphatic CH_2O region correspond to the CH_2O carbons para to the pyrilium rings.

The multiplicity in the solid-state spectra of crown-pyrilium **5** and the chemical shift difference for the two C11 and C15 pyrilium carbons, i.e., 2.4 ppm, might be due to the lack of symmetry in its solid-phase structure. It is noted that the $\Delta\delta C$ values for the two C5 and C10 methylene carbons in **5** and the two corresponding C13 and C18 carbons in **6** are 5.6 and 5.9 ppm, respectively. Interestingly, these solid-phase $\Delta\delta C$ values are very close to the corresponding values in solution ^{13}C NMR spectra, indicating the similarities between the factors influencing the chemical shifts of these carbon atoms.

Conclusion

Two members, **5** and **6**, of a novel generation of crown ethers containing the pyrilium cation can be synthesized by the same strategy, and different crownpyrilium compounds containing two and three B9C3 units connected at the 2 and 6 or 2, 4, and 6 positions of a central pyrilium cation can be successfully synthesized. These novel crown ethers are obtained from the condensation reaction of appropriate aldehydes and methyl ketones in the presence of $POCl_3$. Other members of this crown ether generation with larger size crown cavity are expected to be synthesized by following the same synthetic method. The crown ether units in these compounds are potentially capable of forming host–guest complexes with inorganic and organic cations while the heteroaromatic cationic unit is suitable for binding with anions. Both ES-MS and FAB-MS methods are suitable for the characterization of this class of crown ethers. The ^1H and ^{13}C NMR studies indicate rapid rotation of the B9C3 unit about the C—C bond that connects the B9C3 units to the central pyrilium ring. The solid-phase ^{13}C NMR spectra of these compounds, as well as the X-ray crystal structure of **1**, reveal that there are deviations from planarity for the two phenyl rings attached at the 2 and 6 positions of the central pyrilium cation. The fluorimetric titration of **5** and **6** with some amino acids has indicated that these molecules can indeed function as host molecules. Further details will be published elsewhere.

Acknowledgements

The authors wish to gratefully acknowledge support for this work by the Research Council of the University of Tehran and to thank Prof. G. W. Buchanan of Carleton University, Ottawa, Canada, for the NMR and MS spectra and elemental analysis.

References

1. A. Moghimi, M.F. Rastegar, M. Taghizadeh, A. Yari, M. Shamsipur, G.P.A. Yap, and H. Rahbarnoohi. J. Org. Chem. **67**, 2065 (2002).
2. (*a*) C.J. Pedersen. J. Am. Chem. Soc. **89**, 2495 (1967); (*b*) C.J. Pedersen. J. Am. Chem. Soc. **89**, 7017 (1967); (*c*) C.J. Pedersen. J. Org. Chem. **36**, 1690 (1971); (*d*) G. Dotsevi, D.J. Cram, and Y. Sogah. J. Am. Chem. Soc. **97**, 1259 (1975); (*e*) F. Vogtle, M.W. Muller, and W.H. Watson. Top. Curr. Chem. **125**, 131 (1984); (*f*) J.S. Bradshaw, K.E. Krakowiak, R.M. Izatt, R.L. Bruening, and B.J. Tarbet. J. Heterocycl. Chem. **27**, 347 (1990); (*g*) G. Gokel. *In* Crown ethers and cryptands. Royal Society of Chemistry, Cambridge. 1991. pp. 22–36; (*h*) C.I. Ratcliffe, J.A. Ripmeester, G.W. Buchanan, and J.K. Denik. J. Am. Chem. Soc. **114**, 3294 (1992); (*I*) G.W. Buchanan, A.B. Driega, A. Moghimi, C. Bensimon, and K. Bourque. Can. J. Chem. **71**, 951 (1993); (*j*) R.M. Izatt, K. Pawlak, J.S. Bradshow, and R.L. Bruening. Chem. Rev. **95**, 2529 (1995); (*k*) G.W. Buchanan, M.F. Rastegar, and G.P.A. Yap. J. Mol. Struct. **605**, 1 (2002); (*l*) C.I. Ratcliffe, G.W. Buchanan, and J.K. Denik. J. Am. Chem. Soc. **117**, 2900 (1995); (*m*) G.W. Buchanan, M. Lefort, A. Moghimi, and C. Bensimon. J. Mol. Struct. **415**, 267 (1997); (*n*) G.W. Buchanan. Prog. Nucl. Magn. Reson. Spectrosc. **34**, 327 (1999); (*o*) G.W. Buchanan, M.F. Rastegar, and G.P.A. Yap. Can. J. Chem. **79**, 195 (2001); (*p*) A. Moghimi, M.F. Rastegar, M. Ghandi, G.W. Buchanan, and H. Rahbarnoohi. J. Mol. Struct. **526**, 185 (2000).
3. (*a*) M. Weissenfels, M. Pulst, and D. Greif. Sulfur Reports, **15**, 161 (1993); (*b*) J. Kuthan. Adv. Heterocycl. Chem. **34**, 145 (1983); (*c*) J. Kuthan, P. Sebek, and S. Bohm. Adv. Heterocycl. Chem. **59**, 179 (1994); (*d*) G. Doddi and G. Ekcolani. Adv. Heterocycl. Chem. **60**, 65 (1994); (*e*) S.V. Krivun, S.N. Baranov, and A.I. Buryak. Khim. Geterotsikl. Soedim. **7**, 132 (1971); (*f*) Chem. Abstr. **57**, 026 678, 1962; Jpn. Kokai Tokkyo Koho, Japanese Patent 26 678, 1982; Chem. Abstr. **114**, 143 078q, 1991; Chem. Abstr. **115**, 183 033y, 1991; Chem. Abstr. **119**, 282 020f, 1993; Chem. Abstr. **78**, 29 545c, 1973.
4. (*a*) R.M. Izatt, G.A. Clark, J.S. Bradshaw, J.D. Lamb, and J.J. Christensen. Sep. Purif. Methods **15**, 21 (1986); (*b*) K. Kimura and T. Shano. *In* Cation binding by macrocycles. *Edited by* Y. Inoue and G.W. Gokel. Marcel Dekker, New York. 1990; (*c*) M. Dozol. *In* New separation chemistry techniques for radioactive waste and other specific applications. *Edited by* L. Cecille, M. Casaraci, and L. Pietrelli. Elsevier, Amsterdam. 1991; (*d*) H.C. Visser, D.N. Reinhoudt, and F. de Jong. Chem. Soc. Rev. **23**, 75 (1994).
5. (*a*) P. Bulhmann, E. Pretsch, and E. Bakker. Chem. Rev. **98**, 1593 (1998); (*b*) M.R. Gangali, A. Rouhollahi, A.R. Mardan, M. Hamzeloo, A. Moghimi, and M. Shamsipur. Microchem. J. **60**, 122 (1998); (*c*) M.R. Gangali, A. Moghimi, and M. Shamsipour. Anal. Chem. **70**, 5259 (1998); (*d*) A. Rouhollahi, M.R. Gangali, A. Moghimi, G.W. Buchanan, and M. Shamsipur. J. Inclusion Phenom. Mol. Recognit. Chem. **70**, 5259 (1998); (*e*) M.A. Arnold and M.E. Meyerhoff. Crit. Rev. Anal. Chem. **20**, 149 (1988).
6. J.A. Moore and E.M. Partain. *In* Crown ether and phase transfer catalysis in polymer science. *Edited by* L.G. Mathias and C.E. Carraher, Jr. Plenum Press, New York. 1984. p. 291.
7. (*a*) M. Fakis, J. Polyzos, G. Tsigardias, J. Parthenios, A. Fragos, V. Giannetas, P. Persephonis, and J. Microyannidis. Chem. Phys. Lett. **323**, 111 (2000); (*b*) H.Z. Wang, F.I. Zao,

© 2004 NRC Canada

Y.J. He, X.G. Zheng, X.G. Huang, and M.M. Wu. Opt. Lett. **23**, 777 (1998); (*c*) F.J. Duarte. Laser Focus World, **31**, 187 (1995); (*d*) D.M. Teegarden, W.G. Herkstoreter, and W.C. McColgin. J. Imaging Sci. Technol. **37**, 149 (1993); (*e*) F.P. Schafer. *In* Springer series on topics in applied physics. 3rd ed. Vol. 1. Springer, Berlin. 1990; (*f*) M.R. Detty and S.L. Gibson. Organometallics, **11**, 2147 (1992); (*g*) M.R. Detty and P.B. Merkel. J. Am. Chem. Soc. **112**, 3845 (1990); (*h*) K. Iwata, T. Hagiwara, and H. Matsuzawa. J. Polym. Sci. Polym. Chem. Ed. **24**, 1043 (1986); (*I*) P.M. Borsenberger and D.C. Hoesterey. J. Appl. Phys. **51**, 4248 (1980); (*j*) Japanese Patent 8 226 678, 1996; Japanese Patent 126 655, 2001; German Patent 3 832 940, 1989; Japanese Patent 303 362, 1963; German Patent 3 832 903, 1989; German Patent 3 630 389, 1987; Japanese Patent 146 061, 1959; U.S. Patent 4 384 034, 1983; U.S. Patent 4 368 329, 1983; Japanese Patent 126 655, 2001; Japanese Patent 13 792, 1963; Eur. Patent 319 296, 1989; U.S. Patent 5 019 549, 1991; U.S. Patent 4 125 414, 1978.

8. (*a*) G. Doddi, G. Ercolani, and P. Mencarelli. Tetrahedron, **47**, 1977 (1991); (*b*) U. Eisner and T. Krishnamurthy. J. Org. Chem. **37**, 150 (1972); (*c*) P.J. Dijkstra, Jr., H.J. Den Hertog, J. Van Eerden, S. Harkema, and D.N. Reinhoudt. J. Org. Chem. **53**, 374 (1988); (*d*) P.J. Dijkstra, B.J. van Steen, B.H.M. Hams, H.J. den Hertog, Jr., and D.N. Reinhoudt. Tetrahedron Lett. **27**, 3183 (1986); (*e*) G. Doddi, G. Ercolani, and P. Nunziante. J. Chem. Soc. Perkin Trans. 2, 1427 (1987); (*f*) R. Wizinger and P. Ulrich. Helv. Chim. Acta, **39**, 207 (1956); (*g*) B.E. Maryanoff, J. Stackhouse, G.H. Senkler, and K. Mislow. J. Am. Chem. Soc. **97**, 2718 (1975); (*h*) R. Wizinger, S. Losinger, and P. Ulrich. Helv. Chim. Acta, **39**, 5 (1956); (*i*) Japanese Patent 26 678, 1982.
9. (*a*) H. Chen, S. Ogo, and H. Fish. J. Am. Chem. Soc. **118**, 4993 (1996); (*b*) T.N. Reetz, J. Huff, and R. Goddart. J. Am. Chem. Soc. **116**, 11 588 (1994). (*c*) F.P. Schmidtchen. Tetrahedron Lett. **25**, 4361 (1984); (*d*) E. Kimura, H. Fujioka, and M. Kodoma. J. Chem. Soc. Chem. Commun. 1158 (1986). (*e*) M.A. Hossain, and H.-J. Schneider. J. Am. Chem. Soc. **120**, 11 208 (1998).
10. G.W. Buchanan, A.B. Driega, A. Moghimi, C. Bensimon, R.A. Kirby, and T.D. Bouman. Can. J. Chem. **71**, 1983 (1993).
11. G.W. Buchanan, M. Rastegar, and G.P.A. Yap. J. Mol. Struct. **561**, 43 (2001).
12. V.C. Cordischi, G. Doddi, and F. Stegel. J. Org. Chem. **47**, 3496 (1982).
13. F. De Angelis, G. Doddi, and G. Ercolani. J. Chem. Soc. Perkin Trans. 1, 633 (1987).
14. R. Cotton, A. D'Agostino, and J.C. Traeger. Mass Spectrom. Rev. **14**, 79 (1995).

© 2004 NRC Canada

Synthesis and characterization of a series of 4-methyl-1-[2-aryl-1-diazenyl]-1,4-diazepanes and 1,4-di-[2-aryl-1-diazenyl]-1,4-diazepanes[1]

Shasta Lee Moser and Keith Vaughan

Abstract: 1-Methylhomopiperazine was coupled with a series of diazonium salts to afford the 4-methyl-1-[2-aryl-1-diazenyl]-1,4-diazepanes (**6**), a new series of triazenes. These compounds are, in the main, stable crystalline solids (some of the series are stable oils), and they have been characterized by ^{1}H and ^{13}C NMR spectroscopy, IR spectroscopy, and mass spectrometry. NMR assignments were determined by 2D NMR and variable-temperature NMR experiments and by comparison with model compounds. A second series of new compounds, namely, 1,4-di-[2-aryl-1-diazenyl]-1,4-diazepanes (**5**), were prepared by coupling unsubstituted homopiperazine (1,4-diazepane) with 2 molar equivalents of the diazonium salt and were similarly characterized. The crystal and molecular structure of the parent member of this bis-triazene series (**5**, X = H) has been determined by single-crystal X-ray diffraction analysis.

Key words: triazene, bis-triazene, diazenyl, bis-diazenyl, diazonium salt, NMR, diazepane.

Résumé : On a couplé la 1-méthylhomopipérazine avec une série de sels de diazonium pour obtenir des 4-méthyl-1-[2-aryldiazén-1-yl]-1,4-diazépanes (**6**), une nouvelle série de triazènes. Ces composés sont généralement des solides cristallins stables (quelques-uns sont des huiles stables) et on les a caractérisés par spectroscopie RMN du proton et du carbone-13, spectroscopie IR et spectrométrie de masse. Les attributions des bandes de RMN ont été assistées par des expériences de RMN 2D et de RMN à températures variables ainsi que par comparaison avec des composés modèles. On a préparé et caractérisé de la même manière une seconde série de nouveaux composés, des 1,4-di-[2-aryldiazén-1-yl]-1,4-diazépanes (**5**), par couplage de l'homopipérazine non substituée (« 1,4-diazépane ») avec deux équivalents molaires du sel de diazonium. Faisant appel à la diffraction des rayons X sur des cristaux uniques, on a déterminé la structure cristalline et moléculaire du composé fondamental de la série des bis-triazènes (**5**, X = H).

Mots clés : triazène, bis-triazène, diazényle, bis-diazényle, sel de diazonium, RMN, diazépane.

[Traduit par la Rédaction]

Introduction

The term *bis-triazene* has been coined to describe any molecule that contains two triazene units in the same molecule, with a link or spacer between the triazene moieties. Recent progress in the synthesis of bis-triazenes has been reviewed (1), and the variety of known bis-triazenes can be described by the general structures **1** and **2**. In bis-triazenes of type **1,** the triazenes are linked at the N3 of each triazene unit through the spacer (2, 3) whereas in bis-triazenes of type **2** the spacer is attached at the N1 of each triazene unit (4). Mixed bis-triazenes of type **3**, where the triazene is linked at N1 via a spacer to the N3 of the second triazene, are at present unknown.

Previously (2), we reported on the synthesis and characterization of the series *N*,*N*′-bis(aryldiazenyl)-*N*,*N*′-(dimethyl)ethan-1,2-diamines (**4**), which are bis-triazenes of type **1**. These bis-*N*-aryldiazenyl compounds showed some novel features in the NMR spectra, which were interpreted as arising from the rotational equilibrium in the triazene moiety. A natural extension of this previous work presented itself to us in the form of *N*,*N*′-bis(aryldiazenyl)homopiperazines (**5**), systematically known as the 1,4-di-[2-aryl-1-diazenyl]-1,4-diazepanes. There is one previous report of the synthesis of a bis-triazene of type **5**, namely, the unsubstituted parent compound **5k** (5). In the course of this undertaking, it seemed appropriate to synthesize the simpler mono-triazenes, the 4-methyl-1-[2-aryl-1-diazenyl]-1,4-diazepanes (**6**), which might serve as model compounds for the bis-triazenes (**5**). Another model system for comparison would be the *N*,*N*′-bis(aryldiazenyl)piperazines (**7**).

Furthermore, the triazenes of types **5** and **6** are members of a larger class of 1-aryldiazenyl-(1,*x*)-diazacycloalkanes that we are studying in a comprehensive manner. Very recently (6), we reported on the synthesis and characterization of a series of 1-methyl-4-[2-aryl-1-diazenyl]piperazines (**8**),

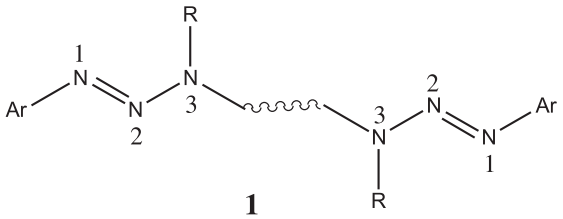
Received 3 June 2004. Published on the NRC Research Press Web site at http://canjchem.nrc.ca on 18 January 2005.

S.L. Moser and K. Vaughan.[2] Department of Chemistry, Saint Mary's University, Halifax, NS B3M 3X6, Canada.

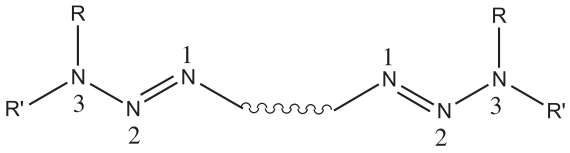
[1]Part II in a series of studies on triazene derivatives of (1,*x*)-diazacycloalkanes.

[2]Corresponding author (e-mail: keith.vaughan@smu.ca).

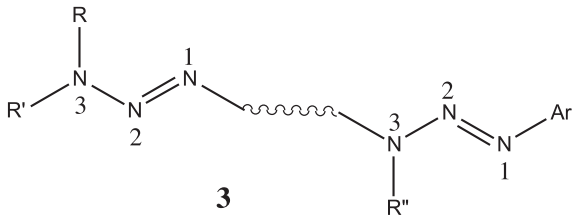
 doi: 10.1139/V04-153 © 2004 NRC Canada



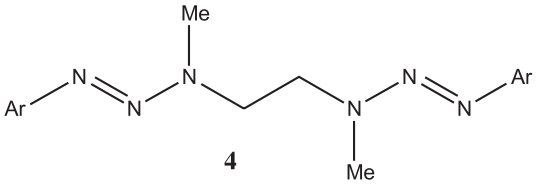
1



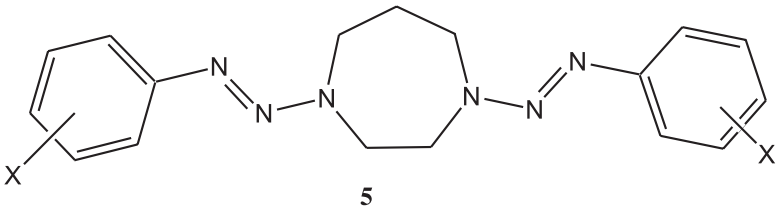
2



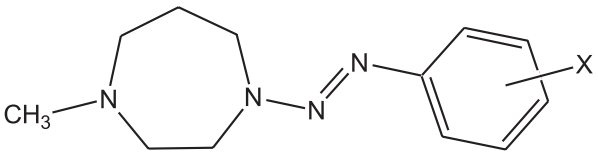
3



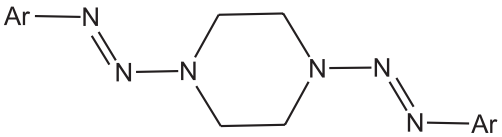
4



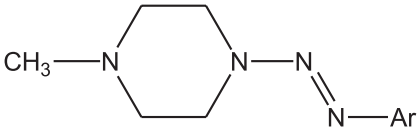
5



6



7



8

which exhibit important spectroscopic features in relation to the characterization of the triazenes **5** and **6**. Moreover, these new triazenes of types **5** and **6** are derivatives of the perhydro-1,4-diazepine (diazepane), a heterocyclic ring system with significant medicinal importance. Many well-known clinical tranquilizers, e.g., librium and valium, are 1,4-diazepine derivatives (7), and some benzodiazepines have been shown to be antitumour antibiotics (8). Thus, it is just conceivable that the new triazenes **5** and **6** may have useful biological activity.

Experimental

All reagents were reagent-grade materials purchased from Sigma-Aldrich Canada and were used without further purifi-

© 2004 NRC Canada

Table 1. Physical data of the 1,4-di-[2-aryl-1-diazenyl]-1,4-diazepanes (**5**).

Compound	Substituent X	Yield (%)	mp (°C)	Recrystallization solvent	IR bands (cm^{-1})[a]
5a	*p*-CN	70	213–215	EtOH/EtOAc	2221 (CN) 839 (OOP)
5b	*p*-NO_2	89	251–253	EtOAc	1326/1509 (NO_2) 851 (OOP)
5c	*p*-CO_2Me	82–94	162–164	EtOH/EtOAc	1715 (C=O) 820 (OOP)
5d	*p*-CO_2Et	78–87	103–105	EtOH	1710 (C=O) 857 (OOP)
5e	*p*-$COCH_3$	58–85	156–158	EtOH	1670 (C=O) 850 (OOP)
5f	*p*-$CONH_2$	11[b]	265–267	EtOAc	3364/3221 (NH) 1661 (C=O) 856 (OOP)
5g	*p*-SO_2NH_2	59	162–169	EtOH	3250/3350 (NH) 845 (OOP)
5h	*p*-Br	58–86	109–110	EtOH	826 (OOP)
5i	*p*-CH_3	75	104–106	EtOH	825 (OOP)
5j	*p*-OCH_3	56–93	123–124	EtOH	1151/1121 (CO) 835 (OOP)
5k	H	30	113–115[c]	EtOH	696, 768 (OOP)
5l	*o*-CN	53–62	129–131	EtOH	2219 (CN) 758 (OOP)
5m	*o*-NO_2	69–93	113–115	EtOH	1323/1528 (NO_2) 743 (OOP)
5n	*o*-Br	75–81	102–104	EtOH	760 (OOP)
5o	*o*-CO_2Me	16	71–76	—	1719 (C=O) 774 (OOP)

[a] OOP, out-of-plane bending vibration.
[b] Low yield due to low recovery during recrystallization.
[c] Lit. mp 118 °C (from ref. 5).

cation. Melting points were determined on a Fisher–Johns melting point apparatus and are uncorrected. Infrared spectra were obtained using Nujol mulls or KBr discs on a Bruker Vector 22 spectrometer. Proton and ^{13}C NMR spectra were obtained with either (*i*) Bruker AC 250- and 500-MHz spectrometers at the Atlantic Regional Magnetic Resonance Center at Dalhousie University or (*ii*) the Anasazi 60-MHz EFT spectrometer at Saint Mary's University (SMU). Chemical shifts were recorded in $CDCl_3$ solutions at 20 °C (unless specified otherwise) and are relative to Me_4Si as internal standard. Elemental analyses were performed by the Canadian Microanalytical Service Ltd. (Delta, B.C.). Accurate mass measurements were made on a CEC 21–110B mass spectrometer operated at a mass resolution of 8000 (10% valley) by computer-controlled peak matching to appropriate PFK reference ions. Spectra were obtained using electron ionization (EI) at 70 V and a source temperature of 175 °C, with samples being introduced by means of a heatable quartz probe. The standard deviation of mass measurement is ±0.0008 amu, which is an average of 3.6 ppm over the mass range of 100–300 amu.

General procedure

1,4-Di-[2-aryl-1-diazenyl]-1,4-diazepanes (5a–5o)

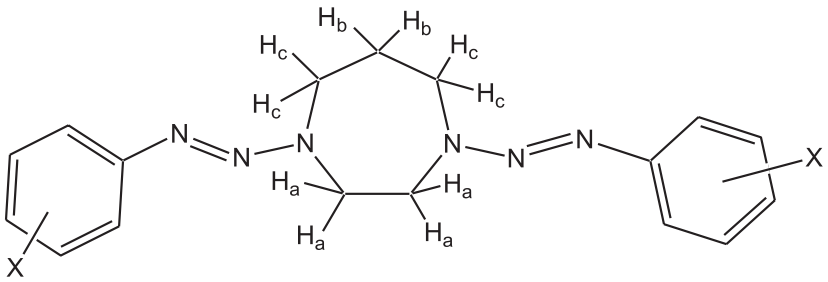
The aromatic primary amine (0.02 mol) was dissolved in 20 mL of 3 mol/L hydrochloric acid, with the aid of heat if necessary, and the resulting solution was cooled in an ice/salt bath to 0 °C. The solution was diazotized with a solution of sodium nitrite (1.52 g) in water (10 mL) while maintaining the temperature below 5 °C, and then stirred for a further 30 min in the cold. The solution was then neutralized with saturated sodium bicarbonate solution, after which the neat homopiperazine (1.1 g, 0.011 mol) was slowly added to the mixture. After stirring for a further 30 min, the mixture was further neutralized with saturated sodium bicarbonate solution and then left to stir until precipitation was deemed to be complete (1–3 h). The solid product was filtered under suction, dried, and recrystallized from an appropriate solvent. Physical data of the products, i.e., yield, mp, recrystallization solvent, and IR data, are listed in Table 1. Table 2 is a list of ^1H NMR chemical shift data, with appropriate assignments, and ^{13}C NMR data are listed in Table 3. The elemental analysis of selected compounds in this series are reported in Table 4. High-resolution EI mass spectral data of selected compounds of type **5** are given in Table 5.

4-Methyl-1-[2-aryl-1-diazenyl]-1,4-diazepanes (6a–6n)

The aromatic primary amine (0.01 mol) was dissolved in 10 mL of 3 mol/L hydrochloric acid, with the aid of heat if necessary, and the resulting solution was cooled in an ice/salt bath to 0 °C. The solution was diazotized with sodium nitrite (0.76 g) in water (10 mL) while maintaining the temperature below 5 °C, and then stirred for a further 30 min in the cold. The mixture was then neutralized with saturated aqueous sodium bicarbonate, after which the neat

© 2004 NRC Canada

Table 2. ^{1}H NMR chemical shift data (ppm) in $CDCl_3$ of the 1,4-di-[2-aryl-1-diazenyl]-1,4-diazepanes (**5**).



Compound	Substituent X	Aromatic[a]	H_a 4H	H_b 2H	H_c 4H	X
5a	*p*-CN	7.60 (d, *J* = 8.2) 7.46 (d, *J* = 8.2)	4.20 (s)	2.13 (br)	4.03 (br t)	—
5b	*p*-NO_2	8.21 (d, *J* = 7.5) 7.51 (d, *J* = 7.5)	4.25 (s)	2.16 (br)	4.08 (br) 3.95 (br)	—
5c	*p*-CO_2Me	8.00 (d, *J* = 8.55) 7.44 (d, *J* = 8.55)	4.18 (s)	2.16 (br)	4.01 (br)	3.91 (s, 6H) (OMe)
5d	*p*-CO_2Et	8.01 (d, *J* = 8.5) 7.44 (d, *J* = 8.2)	4.18 (s)	2.14 (br)	3.98 (br)	1.39 (t, 6H) 4.36 (q, 4H)
5e	*p*-$COCH_3$	7.93 (d, *J* = 8.5) 7.46 (d, *J* = 8.5)	4.19 (s)	2.14 (br)	4.04 (br t)	2.59 (s, 6H)
5f	*p*-$CONH_2$	7.35 (d, *J*= 8) 7.86 (d, *J* = 8)	4.19 (s)	2.0 (v br)	4.0 (v br)	8.28 (br)
5g	*p*-SO_2NH_2	7.78 (d, *J* = 8.6) 7.46 (d, *J* = 8.6)	4.04 (s)	1.75 (br)	3.76 (br)	5.2 (br, NH_2)
5h	*p*-Br	7.46 (d, *J* = 8.1) 7.31 (d, *J* = 8.1)	4.19 (s)	2.10 (br)	4.05 (br t)	—
5i	*p*-CH_3	7.31 (d, *J* = 8.2) 7.13 (d, *J* = 8.2)	4.09 (s)	2.11 (quin)	3.93 (t)	2.34 (s, 6H) (tolyl CH_3)
5j	*p*-OCH_3	7.37 (d, *J* = 9.1) 7.08 (d, *J* = 9.2)	4.08 (s)	2.11 (quin)	3.92 (t)	3.81 (s, 6H) (OCH_3)
5k	H	7.11 (t, *J* = 7.0), 7.29 (t, *J* = 8) 7.35 (t, *J* = 8)	4.08 (s)	2.06 (quin)	3.93 (t)	—
5l	*o*-CN	7.61 (br t, *J* = 7.2) 7.50 (br t, *J* = 7) 7.49 (br t, *J* = 7.3), 7.19 (m)	4.17 (br) 4.27 (br)	2.20 (quin) 2.41 (quin)	3.93 (t) 4.03 (t) 4.06 (t)	—
5m	*o*-NO_2	7.23 (br t, *J* = 7.5) 7.45 (m), 7.47 (m) 7.70 (t, *J* = 7.9)	4.11 (s) 4.13 (s)	2.12 (quin) 2.25 (quin)	3.81 (t) 3.92 (t) 3.98 (t)	—
5n	*o*-Br	7.03 (br t, *J* = 7) 7.22 (br t, *J* = 7) 7.35 (d, *J* = 7.9) 7.59 (d, *J* = 7.6)	4.12 (br s) 4.25 (br s)	2.20 (br) 2.0 (br)	3.96 (br)	—
5o	*o*-CO_2Me	7.26–7.75 (m)	4.12 (s)	2.2 (br)	3.95 (br t)	3.90 (s)

[a]Coupling constants (*J*) in Hz.

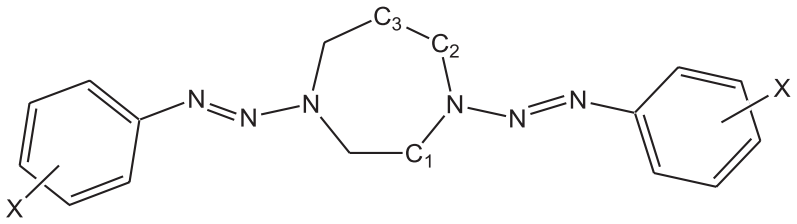
1-methylhomopiperazine (1.4 mL, 0.011 mol) was slowly added to the mixture. After stirring for a further 30 min, the mixture was further neutralized with saturated sodium bicarbonate solution and then left to stir until precipitation was deemed to be complete (1–3 h). The solid product was filtered under suction, dried, and recrystallized from an appropriate solvent. In some cases, notably the ones with an ortho substituent in the aryl group, the product was an oil in which case separation was achieved by extraction into dichloromethane. Physical data of the products, i.e., yield, mp recrystallization solvent, and IR data, are listed in Table 6. Tables 7 and 8 contain lists of the ^{1}H and the ^{13}C NMR chemical shift data, respectively, with appropriate assignments, for the triazenes of series **6**. High-resolution EI mass spectral data of selected compounds of type **6** are given in Table 5.

Discussion

Bis-diazonium coupling of an arenediazonium salt with homopiperazine (1,4-diazepane) (**9**) proceeded smoothly in aqueous solution to afford good yields of the 1,4-di-[2-aryl-1-diazenyl]-1,4-diazepanes (**5**). These bis-triazenes are stable, crystalline solids (Table 1) that recrystallize readily

© 2004 NRC Canada

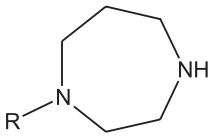
Table 3. ^{13}C NMR chemical shift data (ppm) in $CDCl_3$ of the 1,4-di-[2-aryl-1-diazenyl]-1,4-diazepanes (**5**).



Compound	Substituent X	C_1[a]	C_2[a]	C_3	Aromatic	X
5a	*p*-CN	54.2 (51.7)	44.1 (46.2)	26.1	119.6, 121.4 133.3, 153.8	108.7 (CN)
5d	*p*-CO_2Et	53.5 (br)	46.0 (br)	25 (w, br)	120.4, 127.3 130.5, 153.9	166.3 (C=O) 14.3 (CH_3) 60.6 (OCH_2)
5e	*p*-$COCH_3$	54.0 (56.8)	46.3 (44.0)	30.8	120.8, 129.8 134.6, 154.3	197.6 (C=O) 26.2 (CH_3)
5f	*p*-$CONH_2$	53.7 (w)	47.8 (w)	30.8	120.2, 129.0 131.0, 153.0	168.8 (C=O)
5h	*p*-Br	53.8 (br)	46.6 (br)	25.5 (br)	119.2, 122.5 132.1, 149.7	—
5i	*p*-CH_3	—[b]	49.0 (br)	25.8 (br)	120.3, 129.2 135.1, 148.2	20.7 (CH_3)
5j	*p*-OCH_3	—[b]	49.4 (br)	25.9 (w)	114.3, 121.8 144.7, 158.1	55.7 (OCH_3)
5k	H[c]	53.8 (56.8)	43.5 (46.3/54)	—[d]	120.7, 126.6 129.5, 150.8	—
5l	*o*-CN	54.3	—[b]	26 (br)	117.6, 125.6 133.3	—[b]
5m	*o*-NO_2	53.4 (51.3/56.8)	46.5 (45.4/47.5)	25.2	119.8, 123.6 125.2, 132.3 143.4, 144.8	—
5n	*o*-Br	53.1 (w)	45.9 (w)	24.3 (w)	118.6, 120.0 126.7, 127.7 132.9, 147.8	

[a]Numbers in parentheses are for the minor rotamer.
[b]Signal not observed.
[c]Spectrum recorded in acetone-d_6 at 213 K.
[d]Under acetone peak.

from ethanol or ethyl acetate or a mixture of the two, with the exception of the anthranilate derivative **5o**, which would not recrystallize. (Characterization of **5o** is based on NMR and mass spectral data of the crude compound.) Infrared spectra of the bis-triazenes confirmed the presence of the functional group X in the aryl moiety and also exhibited the appropriate out-of-plane (OOP) bending vibration band.



9 R = H

10 R = Me

Proton NMR spectra of the bis-triazenes (**5**) (Table 2) provide evidence for the characterization of these new compounds. The chemical shift of the four equivalent protons in the two-carbon spacer between nitrogens (H_a) occurs in the range 4.08–4.25 ppm. This observation correlates favourably with the chemical shift reported (2) for the methylene protons in bis-triazenes of type **4** and with the observed chemical shift (ca. 4.0 ppm) of the piperazine ring protons of the bis-triazene of type **7**.[3] The protons in the three-carbon spacer of the homopiperazine ring predictably give two signals at ca. 2.1 (H_b) and 4.0 (H_c), with a 1:2 integral ratio. However, the multiplicity of these signals is not evident in most spectra owing to line broadening; when the multiplicity is evident, e.g., in the spectra of **5j**, **5k**, and **5l**, the expected triplet–quintuplet pattern is evident. In several of these spectra, some chemical shifts are doubled, which suggests the existence of a mixture of conformational isomers.

[3] V.R. Little, R. Tingley, and K. Vaughan, unpublished results, and ref. 9.

© 2004 NRC Canada

Table 4. Elemental analysis of selected examples of the triazene series **5**.

		Calcd. (%)			Found (%)		
Compound	Formula	C	H	N	C	H	N
5c	$C_{21}H_{24}N_6O_4$	59.4	5.7	19.8	59.0	5.7	20.1
5d	$C_{23}H_{28}N_6O_4$	61.05	6.2	18.6	60.9	6.2	18.6
5l	$C_{19}H_{18}N_8$	63.7	5.06	31.3	63.3	5.05	31.2

Table 5. High-resolution electron-ionization (EI) mass spectral data for selected compounds of series **5** and **6**.

Compound	Formula	Calcd. mass (amu)	Found mass (amu)
5a	$C_{19}H_{18}N_8$	358.1654	358.1636
5e	$C_{21}H_{24}N_6O_2$	392.1960	392.1949
5h	$C_{17}H_{18}N_6Br_2$	463.9959	463.9929
5i	$C_{19}H_{24}N_6$	336.2062	336.2045
5j	$C_{19}H_{24}N_6O_2$	368.1960	368.1960
5k	$C_{17}H_{20}N_6$	308.1749	308.1743
5m	$C_{17}H_{18}N_8O_4$	398.1451	398.1447
5n	$C_{17}H_{18}N_6Br_2$	463.9959	463.9950
5o	$C_{21}H_{24}N_6O_4$	424.1859	424.1875
6a	$C_{13}H_{17}N_5$	243.1484	243.1476
6b	$C_{12}H_{17}N_5O_2$	263.1382	263.1392
6c	$C_{14}H_{20}N_4O_2$	276.1586	276.1587
6f	$C_{13}H_{19}N_5O$	261.1589	261.1595
6h	$C_{12}H_{17}N_4Br$	296.0636	296.0618
6j	$C_{12}H_{17}N_4Cl$	252.1142	252.1138

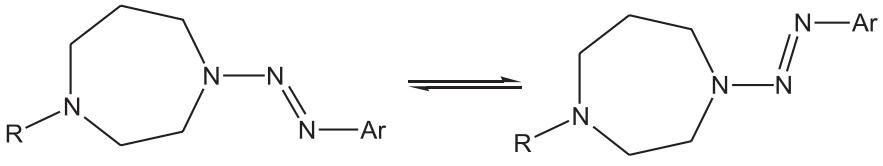
The origin of the line broadening and frequency doubling in these proton spectra is probably a combination of conformational and rotational phenomena. The seven-membered homopiperazine ring could have numerous conformations, and it seems likely that the universal line broadening in the ^{1}H NMR spectra of series **5** is caused by the dynamic equilibrium between these conformations. However, the doubling of the NMR frequencies is most likely attributable to the restricted rotation around the N(2)–N(3) bond of the triazene moiety (10), resulting in the equilibrium shown in eq. [1]. This equilibrium is affected strongly by the nature and location of the substituent X in the aromatic ring, which would explain why the doubling of signals is more evident in the bis-triazenes with ortho substituents.

Table 3 shows the ^{13}C NMR data obtained for a number of the bis-triazenes of series **5**. Acquisition of the ^{13}C NMR data was severely limited by the low solubility of the bis-triazenes and by extreme broadening of the signals, presumably due to the combination of conformational and rotational phenomena referred to earlier. However, the chemical shift data are consistent within the series and in comparison with other triazenes. The observed chemical shift range of the ring carbon atoms (C1 and C2) adjacent to the triazene moiety is ca. 47 and 54 ppm. In the triazene of type **8**, the piperazine ring carbons adjacent to the triazene resonate at ca. 47 ppm (6), and in the bis(aryldiazenyl)piperazines (**7**), the piperazine ring carbons give a signal in the range 46–48 ppm.[4] The central carbon (C3) of the propane bridge in the ring of **5** resonates in the range 25–30 ppm, which seems appropriate for this chemical environment and is similar to the chemical shift (25 ppm) of the analogous carbon (C5) in the model triazene (**6**) (see Table 8). The ^{13}C NMR spectra of the bis-triazene of series **5** do show doubling of some signals, presumably due to the rotational equilibrium shown in eq. [1].

The speculation that two forms of the bis-triazene exist was confirmed by a variable-temperature NMR study with the *p*-cyano derivative **5a**. At 303 K, the ^{1}H spectrum of **5a** has broad signals at 2.13 (H_b) and 4.02 (H_c) ppm. As the temperature is lowered, these signals resolve at 283 K into two broad signals each; at this temperature the sharp signal at 4.18 ppm, assigned to the H_a protons, also resolves into two signals. At 263 K, the fine structure of the signals is evident; further lowering of the temperature to 243 K does not change the spectrum significantly. At 236 K, the 2.13 ppm signal of H_b resolves into a broad signal at 2.14 ppm and an apparent quintuplet at 2.29 ppm. The 4.02 ppm signal of H_c resolves into a triplet at 3.87 ppm (J = 6.0 Hz) and a quintuplet at 4.08 ppm (J = 5.7 Hz). The signal of the H_a protons resolves into two singlets of unequal intensity at 4.20 and 4.23 ppm. The aromatic signals resolve into a system with eight lines.

As part of the study of the characterization of the bis-triazene series **5**, it seemed appropriate to synthesize and characterize the simple triazene series **6**, to be used as model compounds. 1-Methylhomopiperazine (**10**) was coupled in a 1:1 molar ratio with a series of diazonium salts. The physical properties of the 4-methyl-1-(2-aryldiazenyl)-1,4-

[1]



11a **11b**

[4] V.R. Little, R. Tingley, and K. Vaughan, unpublished results.

© 2004 NRC Canada

Table 6. Physical data of the 4-methyl-1-[2-aryl-1-diazenyl]-1,4-diazepanes (**6**).

Compound	Aryl substituent X	Yield (%)	mp (°C)	Recrystallization solvent	IR (cm^{-1})
6a	*p*-CN	77–91	68–70	Hexanes	2218
					838
6b	*p*-NO_2	58–82	89–91	Hexanes	1514
					1392
					855
6c	*p*-CO_2Me	78–85	75–77	Hexanes and petroleum ether	1709
					856
6d	*p*-CO_2Et	81	Oil		1712
					860
6e	*p*-$COCH_3$	75	Oil		1673
					845
6f	*p*-$CONH_2$	92	144–146	Ethanol	1677
					866
6g	*p*-SO_2NH_2	36	107–110		833
6h	*p*-Br	83	45–48	Petroleum ether	834
6i	*p*-CH_3	67	Oil		823
6j	*p*-Cl	60	37–39	Crystals grew from crude oil	833
6k	H	62	Oil		763
6l	*o*-CN	66	60–65	Crystals grew from crude oil	2224
					762
6m	*o*-NO_2	81	Oil		1526
					1351
					751
6n	*o*-Br	79	Oil		755

diazepanes (**6**) are listed in Table 6. Many of these products are oils, and the solid compounds are relatively low-melting materials, which recrystallize with difficulty from nonpolar solvents. On the other hand, the high level of solubility of these compounds made it possible to obtain good ^{13}C NMR spectra in concentrated solution in $CDCl_3$ using the SMU in-house low-frequency Anasazi EFT spectrometer.

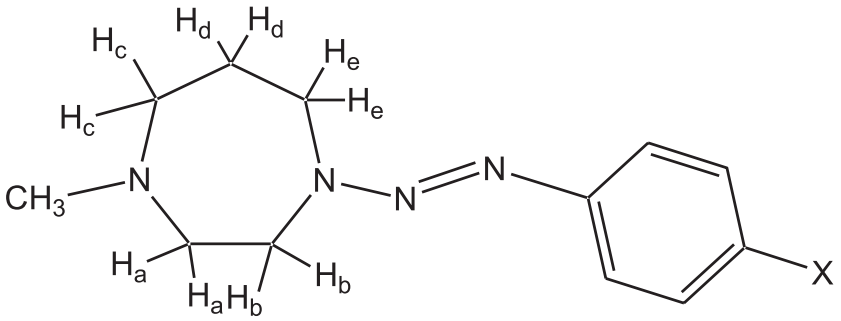
The assignment of chemical shifts in the ^1H and ^{13}C NMR spectra of the triazene series **6** was made possible by analysis of several 2D NMR spectra of the *p*-cyano derivative (**6a**). Significantly, the signals at 2.72 and 4.17 ppm correlate with each other but not with any other signals. These signals can be assigned to the H_a and H_b protons, respectively, in the major rotamer of the mixture; the assignment of the lower-field 4.17 ppm signal to H_b instead of H_a is based on an intuitive consideration of its proximity to the triazene moiety. Also, the smaller signals at 2.81 and 3.93 ppm correlate only with each other, so these signals can be assigned to H_a and H_b, respectively, in the minor rotamer. It can also be seen that the signals at 2.09, 2.64, and 3.85 ppm correlate with each other and can be assigned to H_d, H_e, and H_c, respectively, in the major rotamer, again based intuitively on the proximity of the protons to the triazene moiety and the N1 nitrogen of the homopiperazine ring. That leaves the signals at 1.96, 2.63, and 4.09 ppm to be assigned to H_d, H_e, and H_c, respectively, in the minor rotamer. It should be noted that the contour plots for the 2.63 and 2.64 ppm signals are barely separated in the 2D spectrum.

The heteronuclear single quantum coherence (HSQC) spectrum of **6a** provides information about proton–carbon linkages and thereby provides a means of assigning the ^{13}C signals to respective carbons as shown in Table 8. In the major rotamer, the 2.09 ppm ^1H signal correlates with the carbon signal at 25.3 ppm, which thus can be assigned to C5. The 2.64 and 2.63 ppm signals of H_e correlate with both the 58.86 and 58.37 ppm carbon signals, so these carbon signals can be assigned to C4 in the major and minor rotamers, respectively. The signal of H_a at 2.72 ppm correlates with the 59.08 ppm carbon signal, which must be assigned to C2. Similar analysis assigns the signal at 54.8 ppm to C3 and at 49.0 to C6 in the major rotamer; the assignment of the ^{13}C signals of the minor rotamer follows a similar pattern. These results are surprising in that the low-field signals, 58.86 and 59.08 ppm, are assigned to the carbons *furthest away* from the triazene moiety. Intuitively, these signals would be assigned to the carbon adjacent to the electron-withdrawing triazene moiety, but these results and conclusions are consistent with a similar analysis of the piperazine series **8** (6), in which the higher-field carbon signal was assigned to the carbon atom adjacent to the triazene moiety.

Table 7 shows the complete chemical shift data from the ^1H NMR spectra of the triazene series **6**. The NMR spectra suggest very clearly that there are two different forms of these molecules, and, surprisingly, a complete set of signals is seen clearly for each form in the ambient temperature spectra. The two forms are present in unequal amounts; the ratio of the major to the minor form was estimated, by measurement of the relative heights of the peaks, to be about 2:1. In Table 7, the chemical shifts of the major form are presented in the top line of the entry for each compound, followed by those of the minor form in parentheses. The multiplicity of the signal is shown in the lower line of each

© 2004 NRC Canada

Table 7. ^{1}H NMR chemical shift data (ppm) in $CDCl_3$ of the 4-methyl-1-[2-aryl-1-diazenyl]-1,4-diazepanes (**6**).

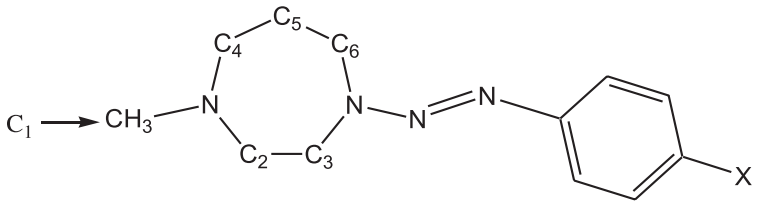


Comp.	Substituent X	Aromatic[a]	H_a[b]	H_b[b]	H_c[b]	H_d[b]	H_e[b]	N–CH_3	X
6a	*p*-CN	7.58 (d, *J* = 8)	2.72 (2.81)	4.17 (3.93)	3.85 (4.09)	2.09 (1.96)	2.64 (2.63)	2.40 (2.43)	—
		7.46 (d, *J* = 8)	5 lines	5 lines	5 lines	10 lines	5 lines	(s)	
6b	*p*-NO_2	8.19 (d, *J* = 9)	2.79 (2.87)	4.24 (3.99)	3.88 (4.13)	2.15 (2.03)	2.70	2.44 (2.47)	—
		7.49 (d, *J* = 9)	(br t)	5 lines	(br t)	9 lines	(br t)	(s)	
6c	*p*-CO_2Me	8.00 (d, *J* = 8.6)	2.72 (2.81)	4.18 (3.93)	3.84 (4.09)	2.09 (2.00)	2.64	2.39 (2.42)	3.90 (s)
		7.44 (d, *J* = 8.6)	(br t)	(br t)	(br t)	(m)	(br t)	(s)	
6d	*p*-CO_2Et	8.01 (d, *J* = 8.55)	2.70 (2.79)	4.16 (3.91)	3.83 (4.07)	2.06 (1.93)	2.61	2.37 (2.41)	1.38 (t)
		7.44 (d, *J* = 8.55)	(br t)	(br t)	(br t)	(br m)	(br t)	(s)	4.35 (t)
6e	*p*-$COCH_3$	7.93 (d, *J* = 8.4)	2.70 (2.79)	4.16 (3.92)	3.83 (4.07)	2.07 (1.93)	2.61	2.37 (2.41)	2.56 (s)
		7.46 (d, *J* = 8.3)	(br t)	(br t)	(br t)	(br m)	(br t)	(s)	
6f	*p*-$CONH_2$	7.79 (d, *J* = 8.5)	2.72 (2.82)	4.18 (3.93)	3.84 (4.09)	2.09 (1.96)	2.64	2.40 (2.43)	1.76 (s)
		7.46 (d, *J* = 8.5)	(br t)	(t)	(t)	(br m)	(br t)	(s)	
6g	*p*-SO_2NH_2	7.88 (d, *J* = 8.5)	2.79 (br)	4.37 (br t)	3.13 (br)	2.2 (br)	—[c]	—[d]	—
	(in DMSO-d_6)	7.30 (d, *J* = 8.5)							
6h	*p*-Br	7.42 (d, *J* = 8.8)	2.69 (2.77)	4.13 (3.88)	3.79 (4.04)	2.06 (1.94)	2.62 (t)	2.39 (br s)	—
		7.28 (d, *J* = 8.4)	(br t)	(br t)	(br t)	(br)			
6i	*p*-CH_3	7.31 (d, *J* = 8.2)	2.66 (br)	4.07 (br)	3.79 (4.03)	1.99 (br)	2.56 (br t)	2.34 (s)	2.30 (s)
		7.10 (d, *J* = 8.2)			(br)				
6j	*p*-Cl	7.34 (d, *J* = 8.8)	2.65 (2.72)	4.09 (3.84)	3.76 (3.99)	2.01 (1.88)	2.57 (br t)	2.34 (s)	—
		7.25 (d, *J* = 8.8)	(br t)	(br t)	(br t)	(br)			
6k	H	7.42 (br t)	2.69 (br)	4.11 (br)	3.81 (br)	2.03 (br)	2.59 (br t)	2.37 (s)	—
		7.39 (br d)							
		7.31 (t, *J* = 7.7)							
		7.11 (tt, *J* = 6.6)							
6l	o-CN	8.49 (dd, *J* = 2.0 and 6.6)	2.73 (2.84)	4.19 (4.01)	3.91 (4.10)	2.11 (1.98)	2.64 (t)	2.40 (2.43)	—
			(t)	(t)	(t)	(br m)		(s)	
		8.28 (d, *J* = 8.1)							
		7.49–7.86 (m)							
		7.25 (t, *J* = 7.4)							
6m	o-NO_2	7.64 (dd, *J* = 1.1, 8.0)	2.69 (2.76)	4.14 (3.87)	3.80 (4.05)	2.03 (2.61)	2.60 (2.61)	2.37 (2.39)	—
			(t)	(t)	(t)	(br m)	(br t)	(s)	
		7.51 (dt,*J* = 1.3, 6.9)							
		7.44 (dt, *J* = 1.3, 8.2)							
		7.15 (dt, *J* = 1.6, 8.0)							
6n	o-Br	7.56 (br d, *J* = 7.9)	2.67 (2.79)	4.13 (3.94)	3.86 (4.04)	2.06 (1.91)	2.59 (t)	2.36 (2.39)	—
		7.39 (dt, *J* = 1.5, 6.8)	(t)	(t)	(t)	(br m)		(s)	
		7.22 (dt, *J* = 1.1, 8.0)							
		6.95 (dt, *J* = 1.4, 8.0)							

[a]Coupling constants (*J*) in Hz.
[b]Numbers in parentheses are for the minor rotamer.
[c]Signal not resolved; may be under the shoulder of the DMSO peak.
[d]Under DMSO peak.

© 2004 NRC Canada

Table 8. ^{13}C NMR chemical shift data (ppm) in $CDCl_3$ of the 4-methyl-1-[2-aryl-1-diazenyl]-1,4-diazepanes (**6**).



Compound	Substituent X	C_1	C_2[a]	C_3	C_4[a]	C_5[a]	C_6[a]	Aromatic	X
6a	*p*-CN	46.7	59.1	54.8	58.9	25.3	49.1	119.6, 121.0	107.7 (CN)
			(53.8)		(58.4)	(29.0)	(48.4)	133.0, 154.4	
6b	*p*-NO_2	46.5	53.6	54.9	58.6	25.3	49.1	120.7, 124.8	—
						(28.7)		144.4, 156.4	
6c	*p*-CO_2Me	46.7	59.3	54.5	58.9	25.3	48.9	120.2, 126.4	51.9 (OMe)
			(53.8)			(29.0)	(48.0)	130.6, 154.8	167.1 (C=O)
6f	*p*-$CONH_2$	46.3	58.1	54.2	58.7	24.5	49.0	120.2, 129.1	168.8 (C=O)
			(53.4)			(28.7)	(48.2)	130.6, 153.6	
6h	*p*-Br	46.6	58.1	54.2	58.7	25.4	48.0	117.9, 122.0	—
								131.6, 150.0	
6i	*p*-CH_3	46.4	53.6 (br)	56 (br)	58.6	26.0 (br)	49.1 (br)	120.3, 129.3	20.9 (CH_3)
								134.4, 148.8	
6k	H	46.5	59.3	54.0	58.8	25.3	48.4	120.3, 125.1	—
			(52.8)			(28.8)		128.7, 151.0	

[a] Upper numbers belong to the major rotamer while lower numbers in parentheses are for the minor rotamer.

entry. In most of the compounds in the series, the methylene protons, H_a and H_b, appear as triplets with some line broadening and an unusual feature — the triplets are inside out; the inner peak is smaller than the outer peaks! This phenomenon is seen throughout the series from **6a** to **6o**; many of the triplets (multiplets) are inside out. An example of a spectrum of one of these triazenes (**6n**) is shown in Fig. 1.

The coupling constants of the homopiperazine ring protons in the triazenes (**6**) are in the range 3.8–4.6 Hz for J_{ab}, 4.9–5.2 Hz for J_{de}, and 5.8–6.2 Hz for J_{cd}. Analysis of these coupling constants confirmed the chemical shift assignments that were based on the 2D NMR spectrum and listed in Table 7. For example. in the spectrum of **6b** the 2.79 and 4.24 ppm signals have the same *J* value, i.e., 4.6 Hz; the minor peaks associated with these signals, 2.87 and 3.99 ppm, also have the same *J* value, 5.2 Hz. Careful measurement of these coupling constants corroborates the pairing of the signals from the major and the minor forms. For example, in the spectrum of **6b**, the 4.24 ppm major signal is paired with the 3.99 ppm minor signal, and not with the 4.13 ppm minor signal; the latter is correctly paired with the 3.88 ppm major signal.

The structures of several of the bis-triazene series **5** have been corroborated by elemental analysis (Table 4) and by high-resolution EI mass spectrometry (Table 5). Principal fragments in the mass spectra of **5** arise from cleavage of one of the *N*-aryldiazenyl bonds to give two fragments. All compounds showed molecular-ion peaks except **5b**, **5f,** and **5g**, but the observed fragments in the low-resolution spectra of **5b**, **5f,** and **5g** confirmed the structures. In the spectrum of **5b**, the base peak at *m/e* 150 is assigned to the fragment $O_2NC_6H_4N_2^+$, and the peak at *m/e* 247 is the mass of the *N*-(aryldiazenyl)homopiperazine fragment (less one H atom). Compound **5f** fragments in the same way to give fragments at *m/e* 148 and 245, and the sulfonamide **5g** gives fragments at *m/e* 184 and 283.

The X-ray crystal structure of the unsubstituted bis-triazene (**5k**) has been determined (11). The ORTEP diagram of this molecule is shown in Fig. 2. Full details of this structure will be published elsewhere.

Conclusion

The results reported in this paper, which is Part II of a new series (6), describe a new series of novel bis-triazenes (series **5**) and a new series of novel heterocyclic triazenes (series **6**). In the course of characterizing these two families of compounds, much has been learned about the spectroscopic correlation of the ring carbon atoms of the homopiperazine rings and of the protons attached to them. Together with the results reported in Part I, in which two series of *N*-aryldiazenylpiperazines were described (6), a significant body of knowledge is being established. The synthetic methodology is being laid as a foundation for future work, and a useful correlation of NMR spectroscopic chemical shifts (both ^1H and ^{13}C) is being established. This will provide a basis for future projects involving the synthesis of new analogues of these triazenes and bis-triazenes.

Acknowledgements

The authors are grateful to the Natural Sciences and Engineering Research Council of Canada (NSERC) for a Discovery Grant to the principal author (K.V.) and to the Faculty of

© 2004 NRC Canada

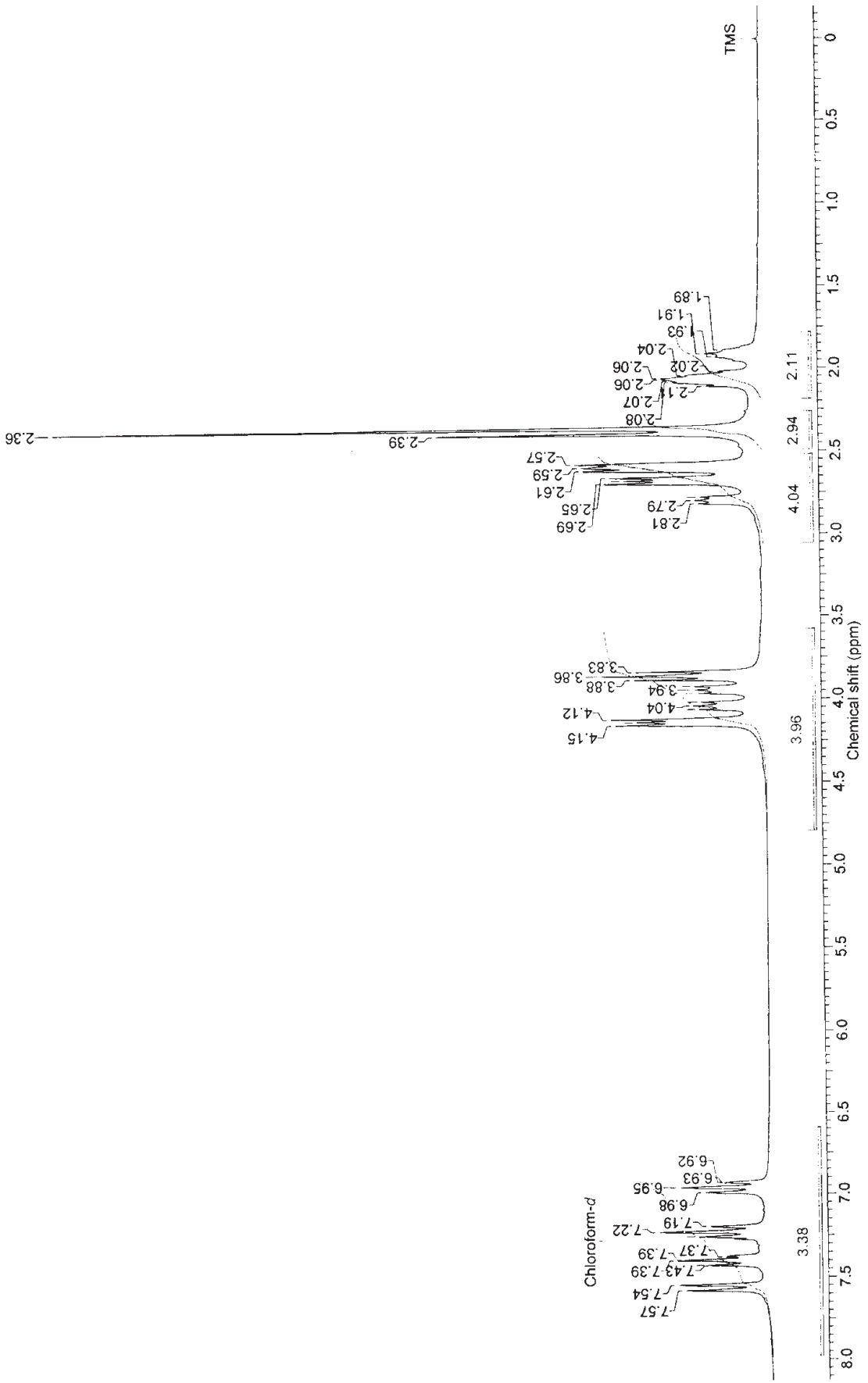
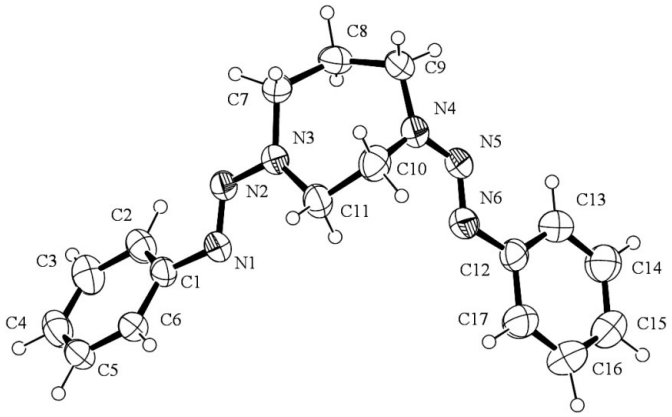


Fig. 1. Full ^{1}H NMR spectrum of 4-methyl-1-[2-(*o*-bromophenyl)-1-diazenyl]-1,4-diazepane (**6n**) in $CDCl_3$.

© 2004 NRC Canada

Fig. 2. ORTEP diagram of 1,4-di-(2-phenyl-1-diazenyl)-1,4-diazepane (**5k**).



Graduate Studies and Research at SMU for a Summer Research Award (2003) to S.L.M. We are also grateful to the Atlantic Region Magnetic Resonance Centre at Dalhousie University for providing NMR spectra and to Dalhousie University for providing mass spectral data. In particular, we would like to thank Dr. Bob Berno for assistance with interpretation of the NMR spectral data and Mr. Xiao Feng for assistance with the mass spectra.

References

1. K. Vaughan. Org. Prep. Proced. Int. **33**, 59 (2001).
2. D.L. Hooper, I.R. Pottie, M. Vacheresse, and K. Vaughan. Can. J. Chem. **76**, 125 (1998).
3. M.B. Peori, K. Vaughan, and D.L. Hooper. J. Org. Chem. **63**, 7437 (1998).
4. D.S. Brown, M.P. Merrin, and K. Vaughan. Proc. N.S. Inst. Sci. **40**, 67 (1995).
5. W. Esch and W. Marckwald. Chem. Ber. **33**, 761 (1900).
6. V.R. Little and K. Vaughan. Can. J. Chem. **82**, 1294 (2004).
7. M.J. Williams. J. Med. Chem. **26**, 619 (1983).
8. D.E. Thurston and D.S. Bose. Chem. Rev. **94**, 433 (1994).
9. E. Yanarate, A. Disli, and Y. Yildirir. Org. Prep. Proced. Int. **31**, 429 (1999).
10. T. Axenrod, P. Mangiaracina, and P.S. Progosin. Helv. Chim. Acta, **59**, 1655 (1976); M. Barra, S. Srivastava, and E. Brockman. J. Phys. Org. Chem. In press.
11. V. Bertolasi, S.L. Moser, and K. Vaughan. J. Chem. Crystallogr. In press.

© 2004 NRC Canada

Using ellipsoids to model charge distributions in gas phase protein complex ion dissociation

Susan Csiszar and Mark Thachuk

Abstract: Gas phase protein complex dissociation was modelled using ellipsoids on which discrete charges were placed in randomly chosen charge sites. A number of sizes, shapes, orientations, and types of ellipsoids were considered. For each case, charge transfer parameters and electrostatic energies were calculated as a function of the fractional surface area. It was found that to within 10–15%, the charge on product ions after dissociation is distributed according to their fractional surface area. This can imply, for example, that in experiments measuring the dissociation of homodimers, charge asymmetries of greater than 10–15% in the product ions signal that one of the ions has greatly increased its surface area, such as would occur with unfolding. This assumes that proton transfer occurs on a timescale fast enough that the dissociation products adopt the minimum electrostatic energy configuration. Calculation of this energy shows that it is minimized when one or more of the monomers is in an extended conformation.

Key words: protein complex dissociation, ellipsoid charge model, charge asymmetry.

Résumé : On a développé un modèle de la dissociation d'un complexe de protéine, en phase gazeuse, en faisant appel à des ellipsoïdes sur lesquelles on a placé des charges ponctuelles sur des sites chargés choisis au hasard. On a considéré un certain nombre de tailles, formes, orientations et types d'ellipsoïdes. Dans chaque cas, on a calculé les paramètres de transfert de charge et d'énergies électrostatiques en fonction de la superficie de la surface fractionnaire. On a trouvé que, dans des limites allant de 10 à 15 %, la charge sur les ions produits après dissociation est distribuée suivant la superficie de leur surface fractionnaire. Par exemple, ceci pourrait impliquer que, dans des expériences de mesures de dissociation d'homodimères, la présence d'asymétries de charge supérieures à 10 à 15 % pourrait indiquer que la superficie de la surface d'un des ions a connu une forte augmentation, tel que cela se produit lorsqu'une protéine se déplie. Cette conclusion implique que le transfert de proton se produit à une échelle de temps qui est suffisamment rapide pour que les produits de dissociation adoptent une configuration d'énergie électrostatique minimale. Le calcul de cette énergie montre qu'elle est minimale lorsqu'un ou deux des monomères existe dans une conformation étendue.

Mots clés : dissociation d'un complexe de protéine, modèle avec charge éllipsoïdale, asymétrie de charge.

[Traduit par la Rédaction]

Introduction

The advent of electrospray ionization (1) has led to the development of numerous advances in mass spectrometry, and has allowed for the study of non-covalent complexes, especially those with biological significance (2–12). Recently, a series of experiments (13–21) have examined the dissociation of charged protein complexes in the gas phase, including the charge and mass distributions of the product ions. In several systems, it has been observed that charge distributions can be quite asymmetric. For example, Schwartz et al. (17) studied the streptavidin tetramer and found that the tetramer dissociation into monomer and trimer ions was favoured over the dissociation into two dimer ions, that is,

[1] $$[4M + 14H]^{14+} \rightarrow [M + 7H]^{7+} + [3M + 7H]^{7+}$$

Received 21 June 2004. Published on the NRC Research Press Web site at http://canjchem.nrc.ca on 25 January 2005.

S. Csiszar and M. Thachuk.[1] Department of Chemistry, University of British Columbia, Vancouver, BC V6T 1Z1, Canada.

[1]Corresponding author (e-mail: thachuk@chem.ubc.ca).

in which 4M, 3M, and M represent the tetramer, trimer, and monomer, respectively, and *n*H represents the number, *n*, of protons bound to each species. This dissociation path is asymmetric in two ways; the masses of the two fragments are unequal and the charge distribution is also asymmetric in the sense that the monomer has a greater charge per mass than the trimer. Heck and co-workers (19) performed similar experiments on dimers and hence ensured the protein complex would dissociate into equal monomer fragments. Four different dimers were studied. They found that dissociation products of dimers of either *E. coli* Glyoxalase I or horse heart cytochrome *c* had quite asymmetric charges, while those of dimers of either human Galectin I or hen egg lysozyme were distributed symmetrically. Similar asymmetries have been observed with tetrameric avidin (16), tetramers of a variety of hemoglobins (16, 18), and pentamers of Shiga-like toxin I (20). Recently, Jurchen and Williams (21) have performed a series of sustained off-resonance irradiation collision activated dissociation (SORI-CAD) experiments in which several variables were systematically investigated. It was found for the dissociation of dimers of cytochrome *c* that the charge asymmetry in the products depends upon the initial charge state of the ion complex, with lower charges giving more asymmetry. As well, it was shown that dissocia-

 doi: 10.1139/V04-154 © 2004 NRC Canada

tions that occurred with higher internal energy (due to greater collision-induced heating) tended to give more symmetric dissociation products. The supposition from these experiments was that the dissociation occurs via a transition state that includes the unfolding of one of the monomers in the dimer. This was tested by examining complexes with varying degrees of conformational rigidity.

While the dissociation of these complexes involves many different time scales, and many types of interactions, one significant influence must be due to the Coulombic interactions of the charges present, since there is no surrounding medium to ameliorate them (as there would be in solution). The goal of the present work is to model these electrostatic interactions using discretely charged ellipsoids of varying shapes, sizes, and orientations.

This analysis was conducted for spheres with the charged droplet model (CDM) of Ryce and Wyman (22). The CDM models the fission of a spherical liquid drop into two droplets by considering the charge distribution among the two droplets. The CDM uses continuous charge distributions and assumes that charge transfer between the droplets can occur at any distance. Since the model considers the drop undergoing fission into two droplets connected by a thin bridge, charge can flow through this bridge between the droplets. The bridge is not explicitly modelled. A CDM has been formulated both with and without the explicit treatment of charge polarization. Essentially, for each droplet size and separation, the total energy, which is considered as the sum of the electrostatic energy and that due to surface tension, is minimized as a function of charge per droplet. The analysis produces analytic expressions for the fraction of charge associated with each child droplet.

When the CDM is applied to proteins, it fails to predict the observed results. Schwartz et al. (17) showed that the model agrees qualitatively with their results but not quantitatively, and Heck and co-workers (19) showed that the CDM does not agree at all with their results if one assumes that the dissociation produces equal mass fragments, for which case the charge distribution is predicted to be symmetric.

To refine somewhat the CDM, a new model is proposed here which approximates the nature of proteins more accurately, by using discrete charges and ellipsoidal shapes. Details of this model, and results of its predictions, are discussed in the following sections.

Results and discussion

Discretely charged ellipsoid model

In the discretely charged ellipsoid model (DCEM), the shapes of protein monomers are approximated as ellipsoids, both of the prolate and oblate varieties. Prolate or oblate ellipsoids are generated by rotating an ellipse about its major or minor axis, respectively. By varying the lengths of the major and minor axes, ellipsoids with many different sizes and shapes can be generated.

On each ellipsoid are placed a particular number of charge sites. These are randomly placed by choosing from a random number generator the spheroidal coordinates of each site. Two ellipsoids are placed in contact with a fixed relative orientation and size. Charges are then placed among the charge sites. Typically there are many more charge sites than charges. A computer program was written that recursively considers every possible charge arrangement and then finds the one with the lowest energy. This brute force approach guarantees that the absolute minimum energy configuration is always found. Unfortunately, no simple analytic expressions exist for charge distributions between ellipsoids. Even for ellipsoids with continuous charge distributions and restricted orientations, analytic expressions lead to complex formulae involving a series of elliptic integrals (23). For discrete charges, no simple expressions exist for the minimum charge distribution, not even for spherical systems. Thus, one is forced to adopt a completely numerical approach.

Note that only one charge is allowed per charge site, and that in the calculation of the electrostatic energy, a dielectric constant of unity is used, and thus the effect of differing dielectric constants within the body of the ellipsoid (protein) is not explicitly treated. This is not to imply that the protein would not affect the electrostatic energy calculation. A uniform dielectric constant would simply lead to an overall scaling of the energies, changing their absolute values but leaving their relative values the same. The difficulty is that the line of separation of some charges lies solely within one ellipsoid or another but there are others that lie between two different ellipsoids. These latter charges really do interact through free space. There should be, in principle, differing electrostatic energy factors depending upon the specific locations of the charges. This is a very complex calculation and it was not performed in the present case. For this reason, the calculated electrostatic energies should be used in a qualitative fashion with their absolute magnitudes being treated as upper limits to the true energies. However, their relative values should be more quantitative.

All charge sites are placed on the surface of the ellipsoid. While it is certainly the case in proteins that all protonation sites do not lie on the surface, the mechanism of the electrospray process tends to produce charges located there. As such, protonation sites that lie on the surface will tend to be protonated in preference to those buried within the core. However, even if a charge did become localized away from the surface, its effect could still be felt at the surface itself. Thus, in the DCEM, the surface charge sites could represent actual protonation sites, or may represent sites on the surface at which the effect of buried charges is most pronounced. For each fixed ellipsoid orientation and size, many instances of the energy minimization are performed each with differing randomly selected charge sites, and the resulting energies and charge distributions are averaged. By averaging over many different random configurations of charge sites, the dependence on this random choice should be minimized in the results. In most cases, 50 such initial configurations are used in the averaging process and, in most cases, the distributions are found to be quite narrow. In other words, the division of charge among the product ions depends only weakly on the particular location of the random charge sites, although the energy associated with this division can vary somewhat, depending upon the particular random distribution of charge sites.

In this particular study, the dissociation of two identical monomers is considered. So, the volume of each monomer is fixed to the same value, as is the number of charge sites on each. This again is a simplification of a true protein system

© 2004 NRC Canada

in which the volume and number of charge sites can vary with conformation. However, the charge asymmetries of the product ions in the DCEM were found to be only weakly dependent upon the volume and number of charge sites of the monomers.

In order to quantify the charge asymmetry, two parameters (charge transfer parameters) will be defined. The first is identical to that used by Ryce and Wyman (22), namely

$$[2] \qquad \varepsilon_V = g - f_V$$

in which the fractional charge g is defined as

$$[3] \qquad g = \frac{q_1}{q_1 + q_2}$$

with q_1 and q_2 being the charges on the product ions. The fractional volume f_V is defined as

$$[4] \qquad f_V = \frac{r_1^3}{r_1^3 + r_2^3}$$

in which r_1 and r_2 are the radii of the product ions. The charge transfer parameter, ε_V, as defined above, is only valid for spheres since the expression for f_V is only valid in this case. For other shapes, one would have to properly determine the fractional volume of each product ion. The value of the ε_V gives a measure of the deviation of charge symmetry as compared with the fractional volume of the product ions. In other words, if the charges on the product ions are distributed in the same way as their volumes then the $\varepsilon_V = 0$. A non-zero value of the ε_V implies that one product has received more charge than would be expected from its fractional volume. If a uniform density is assumed between the precursor and product ions, then the fractional volume is synonymous with the fractional mass of each product ion.

In the DCEM, as in the CDM, all charges are located on the surface, so it is more relevant from a physical point of view to use surface charge densities when comparing different systems. In fact, for all the ellipsoids used in the present work, the volumes of each product ion are held fixed. All scenarios would then give $f_V = 0.5$ regardless of the shape or orientation of the ellipsoid. Clearly, in this case, the ε_V is not going to be a sensitive enough probe of charge asymmetry. Rather, an analogous parameter using surface area ratios is defined instead, that is

$$[5] \qquad \varepsilon_S = g - f_S$$

in which the fractional surface area f_S is defined as

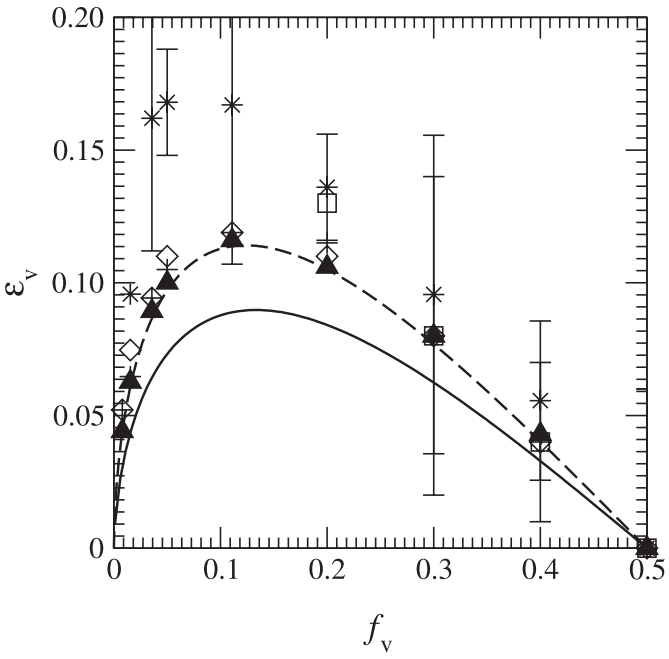
$$[6] \qquad f_S = \frac{S_1}{S_1 + S_2}$$

with S_1 and S_2 being the surface areas of the product ions. Unless otherwise stated, quantities with the subscript 1 will be associated with the product ion having the smallest volume and (or) surface area.

Spheres

Before considering the results for ellipsoidal systems, data was obtained for two spherical systems so that the DCEM and CDM results could be compared. The results of the comparison can be found in Figs. 1 and 2. A plot of the ε_V as a function of the fractional volume between two spheres that are touching is illustrated in Fig. 1, while in Fig. 2 the same results are expressed in terms of the surface area quantities, ε_S and f_S. All results are for touching spheres ($\alpha = 1$ in the notation of ref. 22).

Fig. 1. Plots of the charge transfer parameter, ε_V, as a function of the fractional volume, f_V, for two touching spheres. The solid line shows the prediction of the charged droplet model (CDM) with an approximation of uniform charge density. The dashed line gives the exact CDM prediction, including the effects of charge polarization. The results of the discretely charged ellipsoid model (DCEM) have 9 charges distributed among the two spheres. These DCEM results were determined in two ways; keeping the charge site density constant (stars) and varying the charge site density (open squares). The error bars represent the range of values possible as the location of the charge sites vary. The results of a dynamic model, which allows charge to move continuously on the surface of the sphere, are shown for 100, 200, and 1000 charges by open diamonds, pluses, and filled triangles, respectively.

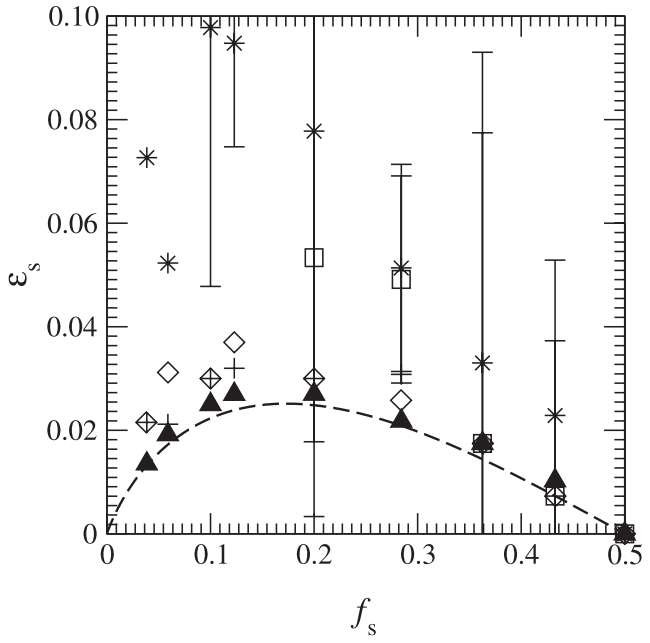


The DCEM values were calculated with 9 charges distributed among the two spheres with 10 charge sites per sphere for the $f_V = f_S = 0.5$ data points. For the other points, two different sets of data were taken; one with a constant and one with a varying charge site density. In the former case, the number of charge sites per surface area was kept constant as the sizes of the spheres changed. In the latter case, the number of charge sites was increased linearly with the radius of the sphere.

Two curves representing the CDM results are also given. The solid line plots the prediction using the approximation that the surface charge density on each sphere is uniform. The dashed line plots the results for the exact electrostatic solution, thereby allowing for charge polarization effects. The difference between the solid and dashed lines then represents the change in charge transfer after the charges on

© 2004 NRC Canada

Fig. 2. Plots of the charge transfer parameter, ε_S, as a function of the fractional surface area, f_S, for two touching spheres. The symbols and error bars are defined as in Fig. 1.



each sphere are allowed to interact with each other and distort each other's charge distribution.

It is straightforward to show that the CDM with the approximation of uniform charge densities predicts that $\varepsilon_S = 0$ for all f_S in Fig. 2. The predictions for the exact solutions of the CDM are more subtle to obtain, especially in the case of two touching spheres, so this procedure will be briefly outlined below.

Following the notation of ref. 22, given a value of f_V or f_S, one can determine the value of λ which equals r_1/r_2. The value of g can be determined from eq. [20] of ref. 22, and is given by

$$[7] \qquad g = \frac{1}{1 + \left(\frac{SU - T}{S - T}\right)}$$

We wish to determine the value of the right-hand side of eq. [7] in the limit of two touching spheres, namely $\alpha = 1$. In this limit, the values of β, μ, and μ' in ref. 22 all tend towards zero, and the expressions for S, U, and T that depend upon these parameters develop a singularity that must be removed by a proper limiting procedure. This is accomplished by expanding trigonometric hyperbolic functions in a Taylor series and retaining those terms involved with the singularity. When this is done consistently, the following results are obtained, namely

$$[8] \qquad \lim_{\beta \to 0} = \frac{1}{1+\lambda} \qquad \lim_{\beta \to 0} \frac{\mu'}{\beta} = \frac{\lambda}{1+\lambda}$$

$$[9] \qquad \lim_{\beta \to 0} (SU - T) = \frac{1}{\lambda} - \frac{\lambda}{(1+\lambda)^2} \quad \sum_{n=1}^{\infty} \frac{1}{n\left(n + \frac{\lambda}{1+\lambda}\right)}$$

$$[10] \qquad \lim_{\beta \to 0} (S - T) = 1 - \frac{1}{(1+\lambda)^2} \quad \sum_{n=1}^{\infty} \frac{1}{n\left(n + \frac{1}{1+\lambda}\right)}$$

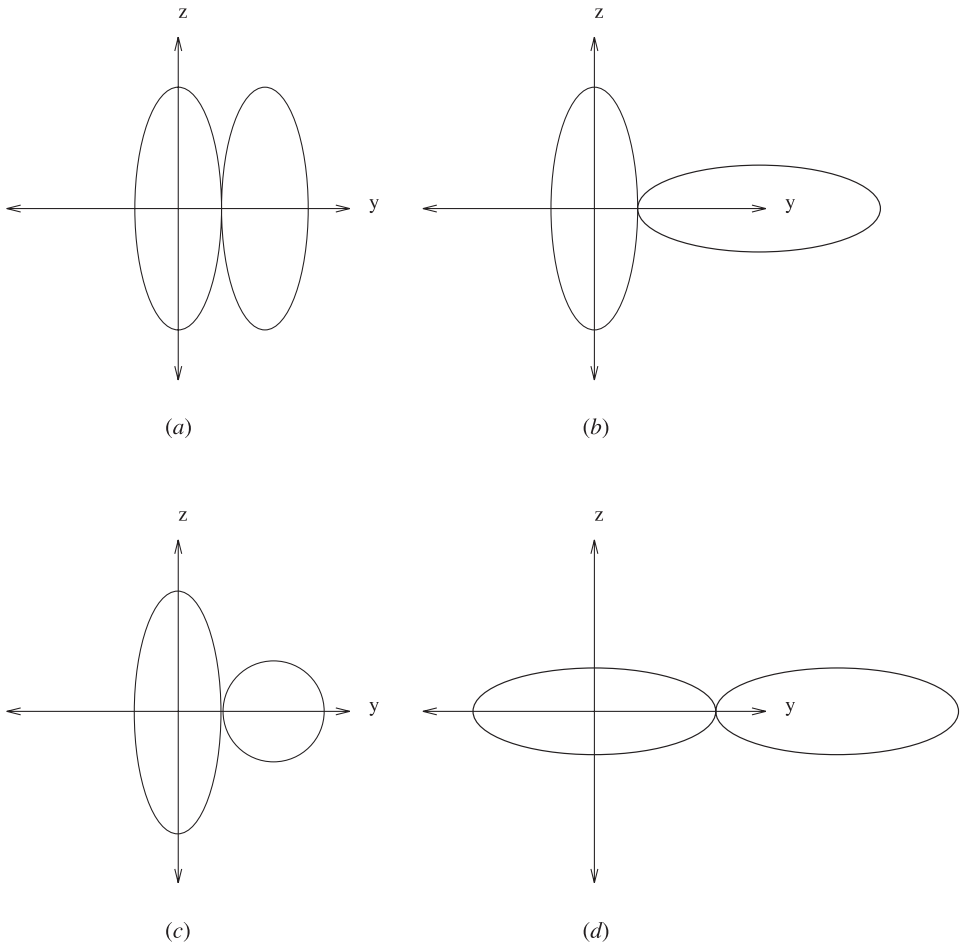
The right-hand sides of eqs. [9] and [10] are well-behaved functions of λ that can be evaluated with known numerical routines. Substituting the results from eqs. [9] and [10] (which are only valid in the limit of two touching spheres) into eq. [7], and then employing eqs. [2] and [5] allows one to calculate the values for the dashed curves in Figs. 1 and 2.

The other three curves in Figs. 1 and 2 arise from a dynamic model. In order to investigate the effects of charge discreteness, many more charges were added to the system. Rather than use a brute force minimization method, for which the calculation time grows considerably with the number of charges considered, a new model was devised to determine the minimum energy charge configuration. This model works by restricting charges to the surface of the spheres and giving the charges an initial velocity and a drag force. The charges eventually come to rest when the drag force and electrostatic force balance each other. This gives the configuration with the minimum electrostatic energy. Studies were done with 100, 200, and 1000 charges distributed among the two spheres. With this dynamic model, the charges are allowed to move to any position on the surface of the sphere, so that explicit charge sites are not used. In principle, these results should then approach the exact CDM ones once the number of charges becomes sufficiently large to adequately approximate a continuous distribution. Examination of the results in Figs. 1 and 2 shows that indeed this is the case when 1000 charges are used.

A number of conclusions can be drawn from Figs. 1 and 2. First, in all cases, there is a positive charge transfer towards the smaller sphere, that is this smaller sphere should carry more charge than predicted simply by its fractional volume or surface area. Second, it is important to consider polarization effects when determining minimum charge configurations. These effects account in total for the non-zero values of the ε_S and about 20% or so of the value of the ε_V. Third, the values of the ε_S are uniformly smaller than the ε_V. This implies that generally speaking, the charges distribute themselves more according to the fractional surface area of the spheres rather than their fractional volume. This is to be expected since the charges in all cases are located on the surface. Thus, the ε_S is the preferred charge transfer parameter to use when examining charge configurations. Fourth, while the results for several hundreds of charges are essentially identical to the results for continuous charge distributions, this is not the case when only a few charges are present. Both figures show large fluctuations in the ε_V and ε_S for the DCEM results which use only 9 charges. These fluctuations arise simply from the discreteness of the charge and the configurational restrictions imposed by the location of charge sites. Great care should be taken when using models based on continuous charge distributions for predicting results when a small finite number of charges are involved. In other words, charge asymmetry can arise simply because a system has a small number of discrete charges restricted to a small number of charge sites.

© 2004 NRC Canada

Fig. 3. The four orientations studied for the ellipsoid geometries. Note: In orientation (*c*) the major axis of the ellipsoid to the right is perpendicular to the plane of the page.



Ellipsoids

Different types of systems can be studied by varying the shapes and the relative orientations of ellipsoids. The shapes of the ellipsoids can be varied in two ways. The relative lengths of the major and minor axes can be varied, or the ellipsoid can be changed from one type to another, that is from prolate to oblate or vice versa. All these variations were examined.

Figure 3 shows the four different relative orientations of each ellipsoidal system studied. This figure shows prolate ellipsoids explicitly. The orientations for oblate ellipsoids are analogous, except with the roles of the major and minor axes interchanged. Data was calculated for systems consisting of two prolate ellipsoids, two oblate ellipsoids, and two ellipsoids one of each type. For each of the systems consisting of two of the same ellipsoid type, data was calculated for the four orientations shown in Fig. 3. For the mixed systems, one of the types was never rotated while the other ellipsoid was rotated according to orientations (*a*) through (c). In all calculations, the ellipsoid on the left was always held fixed while the size of the ellipsoid on the right was varied to give differing f_S values. For all cases, the ellipsoids are positioned so that they touch at the points shown in Fig. 3.

The volumes of the ellipsoids were held fixed at 19 720.17 $Å^3$, even when their sizes were changed. This value was chosen to mimic horse heart cytochrome *c*. In general, ellipsoids have three axes. In the present work, the two smaller axes (the minor axes) were set to the same length. To obtain ellipsoids with the same volume but different surface areas, the ratio of the major to minor axis was first increased, and then their absolute values were adjusted to keep the ellipsoid volume constant. In other words, the relative shapes of the ellipsoids change in this process. All the ellipsoids have 15 charge sites and 11 charges are distributed among both of them. These numbers are of the same order of magnitude as those found for protein systems and, at the same time, are computationally viable. In the lower panels of Figs. 4–7 charge transfer parameters, ε_S, are plotted as a function of f_S for the orientations shown in Fig. 3 for four different ellipsoidal systems, corresponding to two prolate ellipsoids, two oblate ellipsoids, a constant oblate – varying prolate ellipsoid pair, and a constant prolate – varying oblate ellipsoid pair, respectively.

The values of the ε_S are negative in Figs. 4 and 6, indicating charge transfer to the ellipsoid whose surface area is increasing. In both these cases, this ellipsoid is of the prolate type. On the other hand, when an oblate ellipsoid is increasing in surface area, as in Figs. 5 and 7, the ε_S is positive, indicating charge transfer to the fixed ellipsoid (which is of the oblate type in one case, and prolate in the other). Thus,

© 2004 NRC Canada

Fig. 4. Plots of electrostatic energy and ε_S as a function of the f_S for two prolate ellipsoids in contact, as predicted by the DCEM configured with 15 charge sites per ellipsoid and 11 charges in total distributed among the two ellipsoids. In the top panel, the upper points give the total electrostatic energy of the minimum energy configuration, while the lower points give the total interaction energy (that is the electrostatic energy due to charge pairs between ellipsoids). Results for orientations (*a*), (*b*), (*c*), and (*d*) (defined in Fig. 3) are given by open circles, pluses, stars, and open squares, respectively.

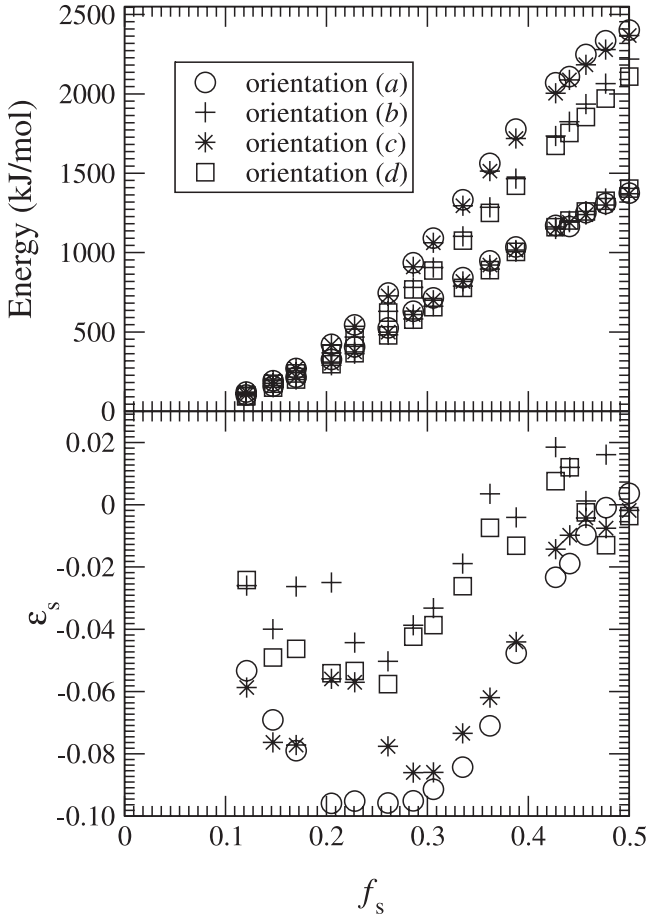
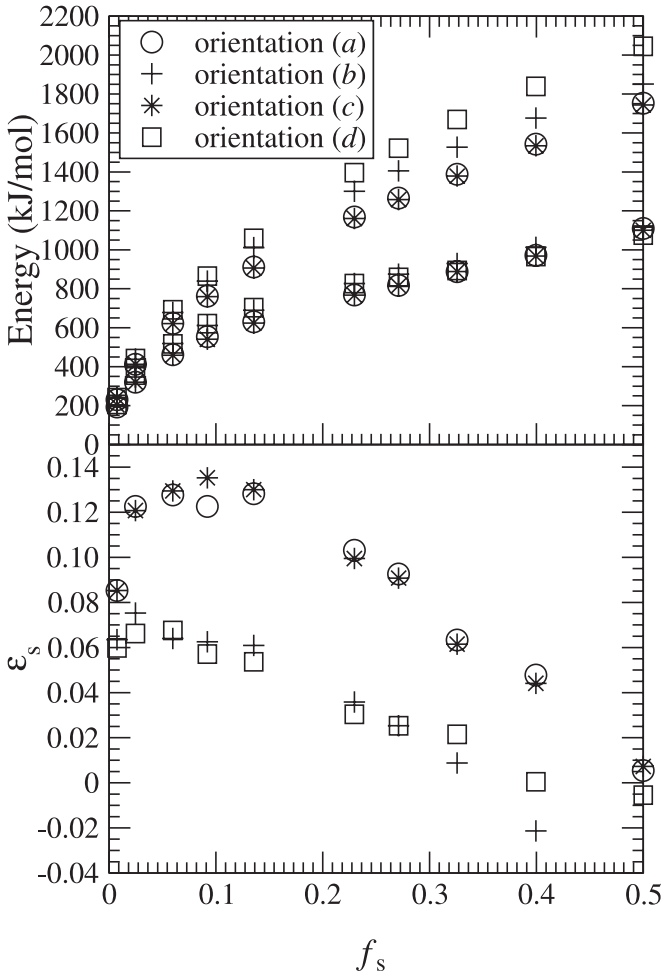


Fig. 5. The symbols are as defined in Fig. 4, except that these values correspond with two touching oblate ellipsoids.



the direction of the charge transfer depends upon the type of the ellipsoid with the larger surface area, not on the one with the smaller surface area. A larger prolate ellipsoid gains charge while an oblate ellipsoid loses charge, relative to its fractional surface area. For a fixed volume, in the way that the shapes of the ellipsoids were changed here, the larger prolate ellipsoids tend to be longer and pencil-like while the larger oblate ellipsoids tend to be flatter and disk-like. The longer shape of the prolate ellipsoid allows for greater separation of charges and hence charge transfer is favoured, as compared with the oblate ellipsoids.

Generally speaking, orientations (*a*) and (*c*) each produce about the same charge transfer and this is larger than orientations (*b*) and (*d*). This is expected because in orientations (*a*) and (*c*), the two ellipsoids are on average closer to each other than in orientations (*b*) and (*d*). This should lead to greater charge polarization in the former case, which as already seen in Figs. 1 and 2, leads to greater charge transfer. When the ε_S is negative, the maximum in charge transfer occurs when $f_S \approx 0.3$, while when the ε_S is positive, the maximum occurs when $f_S \approx 0.1$.

Two energies are plotted in the upper panels of Figs. 4–7. The uppermost points show the total electrostatic energy of the average minimum charge configuration. This energy was calculated by summing all the Coulombic pair interactions using a dielectric constant of unity. The lowermost points show the interaction energy between the ellipsoids, in other words, the sum of the pair interactions between charges on different ellipsoids. This interaction energy is the potential energy that would be available if the ellipsoids were separated to an infinite distance. The difference between these two sets of points is the self-energy of the ellipsoids, that is the Coulombic repulsive potential among the charges in each ellipsoid. This self-energy cannot be changed unless the shape of the ellipsoid changes, or charge transfer occurs.

Examining the upper panels in Figs. 4–7 shows a number of trends. First, although there is some variation in the total energy, there is essentially no variation in interaction energy with respect to the orientation of the ellipsoids. The differences in total energy arise solely from differences in the self-energies of each ellipsoid. However, there is substantial variation in interaction energy depending upon the type of

© 2004 NRC Canada

Fig. 6. The symbols are as defined in Fig. 4, except that these values correspond with two touching ellipsoids — the one on the left being oblate (with fixed dimensions) and the one on the right being prolate (with changing dimensions as reflected by the f_S).

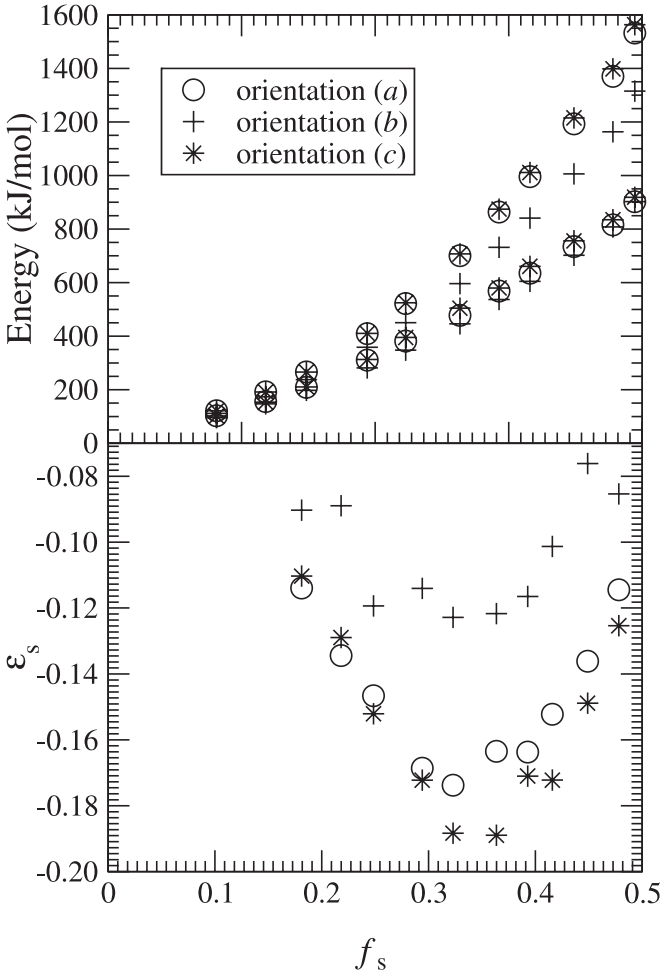
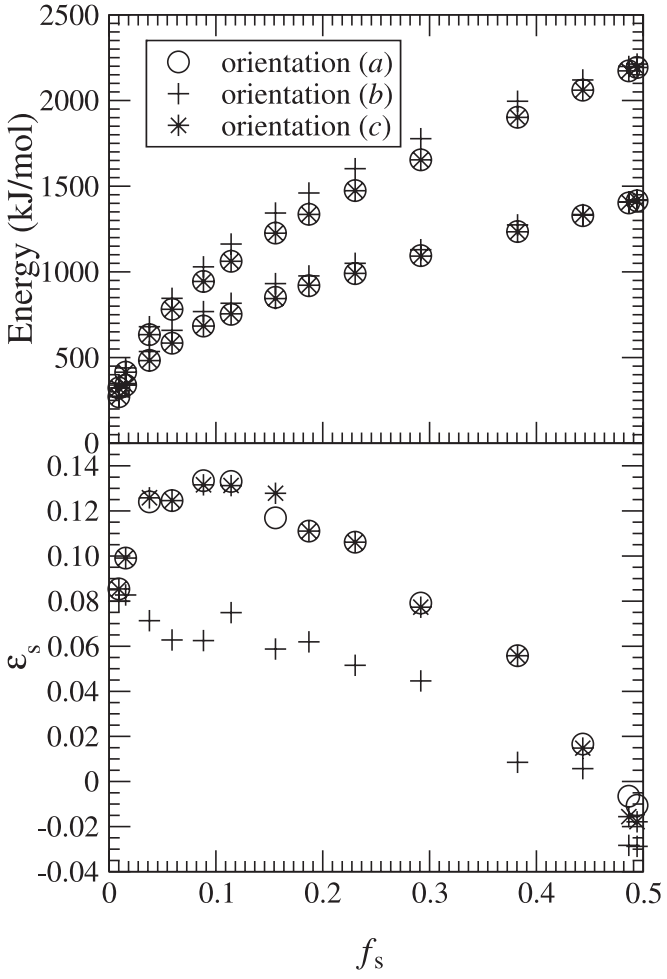


Fig. 7. The symbols are as defined in Fig. 4, except that these values correspond with two touching ellipsoids — the one on the left being prolate (with fixed dimensions) and the one on the right being oblate (with changing dimensions as reflected by the f_S).



ellipsoidal system. The highest interaction energies occur when the ellipsoid with the smaller surface area is prolate (Figs. 4 and 7). Interaction energies about 30% smaller occur when the ellipsoid with the smaller surface area is oblate (Figs. 5 and 6).

In all cases, the highest energies occur with $f_S = 0.5$, that is when both ellipsoids are the same. It is always energetically favourable for one ellipsoid to increase its surface area, thereby allowing lower energy charge configurations to become accessible. In principle, the energy would also be lower if both ellipsoids increased their surface areas, although this particular case was not calculated.

Application of the DCEM to protein complex dissociation

The DCEM describes the behaviour of discrete charges distributed among charge sites residing on the surface of ellipsoids of varying sizes and shapes. This is relevant to the dissociation of gas-phase protein complexes provided several assumptions are made.

The first assumption is that the mechanism for protonation of the complex always results in the lowest electrostatic energy configuration. This assumption is necessary because all the results presented here are for minimum energy charge configurations, that is charges that have been allowed to adopt the lowest energy configuration for a given set of charge sites. If intramolecular proton transfer occurs in the gas phase, and changes in a monomer occur during the dissociation process, then this assumption implies that the charges move to adopt the lowest energy configuration, even when conformation changes occur. On the other hand, if charges remain fixed on charge sites, then this assumption implies that the positions of these charges, (for example, determined during the electrospray process) are in the minimum energy configuration. A variety of intermolecular proton exchange mechanisms have been proposed in the gas phase (24). Some of these may be relevant for intramolecular proton exchange if appropriate conformational changes occur in a monomer or between monomers in a complex. Gas phase hydrogen/deuterium exchange experiments on cytochrome *c* have indicated that protons are mobile on the protein (25–27). Other experiments have shown that proton transfer can depend and be sensitive to experimental conditions (14, 28).

© 2004 NRC Canada

The second assumption is that the Coulomb interactions dominate the energetics in the dissociation process. Clearly, many types of interactions are present in protein complexes, and the electrostatic contributions considered here form one part of these. Some calculations (29, 30) have indicated that this assumption becomes more valid the larger the charge on the complex. However, it is also known that the dissociation process must overcome an activation barrier. Arrhenius parameters have been determined experimentally for several systems (20, 31) and indicate that dissociation is accompanied by large entropy changes, as would be present if part of the complex moved to a more extended configuration.

To the extent that these two assumptions are valid, several conclusions can be drawn. First, because the values of the ε_S were always less than about 0.1–0.15, it follows that to within about 10–15%, regardless of the particular shape or orientation of monomers in a protein complex, the fractional charge of a product ion is the same as its fractional surface area. Recall that the charge transfer parameters measure the deviation from this balance. In other words, if the dissociation of a homodimeric complex occurs with charges on the product ions that differ from each other by more than 15%, then one of the product ions increased its surface area. The greater the charge difference between the products, the greater the change in surface area that must have resulted.

This is consistent with the supposition of Jurchen and Williams (21) who propose that protein unfolding must accompany complex dissociation when the charges produced are asymmetric. Such unfolding greatly increases the surface area of one of the product ions. Note that this charge asymmetry can occur only if one, not both, of the monomers unfolds.

Similarly, if a multimeric complex dissociates into a monomer and a remaining complex, each carrying away equal charges, then the current results imply that the surface area of the monomer and remaining complex must be approximately equal, that is the monomer must undergo conformational changes that greatly increase its surface area. In all these cases, the product with the greater surface area carries the larger charge. In this context, surface area refers to the area of a convex surface that would encase a protein complex or monomer. This conclusion is consistent with the electrostatic Coulombic repulsion energy calculations of Klassen and co-workers (20) for B_5^{n+} ions of Shiga-like toxin I. They showed that while it is energetically unfavourable to charge enrich one monomer in the complex, such an enrichment could be driven by entropy resulting from conformational changes in the monomer, such as unfolding. This enrichment essentially transfers a significant amount of the Coulombic repulsion into intermolecular repulsion between the monomer and remaining complex, thereby favouring loss of the monomer and leaving the remaining complex with a greatly reduced intramolecular electrostatic repulsion.

At a finer level, conclusions are more speculative. Generally speaking, a value of the ε_S determined from experimental measurements would probably have errors comparable to the values seen in Figs. 4–7, so that in practice it will be difficult to extract any information about the relative orientations of the units in the complex. The sign of the ϵ_S appears to be more robust, indicating that greater charge asymmetries are possible if the larger ion is prolate shaped, as opposed to oblate shaped. However, the energetics of a particular scenario may not necessarily favour this degree of charge asymmetry. These results then imply that the energetics and charge asymmetry in complex ion dissociation depend only weakly on the relative orientations or shapes of the component monomers.

These results also indicate that fractional surface areas should be the preferred physical parameter to use when evaluating charge asymmetries, rather than fractional volumes. This follows mainly from the observation that at close distances, charges tend to distribute themselves more according to surface area than volume.

Second, the unfolding of a monomer and the resulting charge redistribution is greatly favoured energetically. Even considering the rather crude energy calculations presented in Figs. 4–7, many hundreds of kJ/mol of potential energy are available to help the system move towards the state where at least one of the products is unfolded to give a greater surface area. For the dissociation of a homodimer, the unfolding of both monomer units would in turn produce an even lower electrostatic energy, although the DCEM would predict a symmetric charge distribution in this case. Thus, if asymmetric charge distributions are observed, the DCEM would predict the unfolding of only one of the monomer units in this case.

While the DCEM can be used to explain some aspects of the dissociation of gas phase protein complexes, it provides only static information. In particular, it contains no dynamic information and is not able to address any questions concerning the manner in which the complex moves from one configuration to another, or how the unfolding of one monomer unit might be coupled with the dissociation of the complex. For example, whether monomer unfolding occurs prior to charge transfer, or concomitant with charge transfer cannot be distinguished. It also does not address any kinetic barriers that might exist between different states.

However, the goal of the DCEM is not to fully explain protein dissociation events but rather to provide a model for understanding the electrostatic interactions in such events at a level of description that is closer to reality than spherical models, such as the CDM. While the DCEM can provide some insight into the dissociation mechanism of protein complexes in the gas phase, more refined protein models are needed. Such models are currently being developed in our group to address dynamic issues.

Acknowledgements

This work was supported by a grant from the Natural Sciences and Engineering Research Council of Canada (NSERC) and the Canada Foundation for Innovation.

References

1. J.B. Fenn, M. Mann, C.K. Wong, and C.M. Whitehouse. Science (Washington, D.C.), **246**, 46 (1989).
2. M.C. Fitzgerald, I. Chernushevich, K.G. Standing, C.P. Whitman, and S.B.H. Kent. Proc. Natl. Acad. Sci. U.S.A. **93**, 6851 (1996).
3. J.A. Loo. Mass Spectrom. Rev. **16**, 1 (1997).
4. J.E. Bruce, V.F. Smith, C. Liu, L.L. Randall, and R.D. Smith. Protein Sci. **7**, 1180 (1998).

© 2004 NRC Canada

5. A.A. Rostom, M. Sunde, S.J. Richardson, G. Schreiber, S. Jarvis, R. Bateman, C.M. Dobson, and C.V. Robinson. Proteins: Structure, Function, and Genetics Suppl. **2**, 3 (1998).
6. T.D. Veenstra. Biophys. Chem. **79**, 63 (1999).
7. J.A. Loo. Int. J. Mass Spectrom. **200**, 175 (2000).
8. A. Dobo and I.A. Kaltahov. Anal. Chem. **73**, 4763 (2001).
9. V. Gabelica, C. Vreuls, P. Filée, V. Duval, B. Joris, and E. De Pauw. Rapid Commun. Mass Spectrom. **16**, 1723 (2002).
10. A. Mohimen, A. Dobo, J.K. Hoerner, and I.A. Kaltashov. Anal. Chem. **75**, 4139 (2003).
11. W.P. Griffith and I.A. Kaltashov. Biochemistry, **42**, 10024 (2003).
12. H. Xiao, I.A. Kaltashov, and S.J. Eyles. J. Am. Soc. Mass Spectrom. **14**, 506 (2003).
13. Y. Deng, H. Pan, and D.L. Smith. J. Am. Chem. Soc. **121**, 1966 (1999).
14. S.J. Eyles, J.P. Speir, G.H. Kruppa, L.M. Gierasch, and I.A. Kaltashov. J. Am. Chem. Soc. **122**, 495 (2000).
15. M.R. Mauk, A.G. Mauk, Y.-L. Chen, and D.J. Douglas. J. Am. Soc. Mass Spectrom. **13**, 59 (2002).
16. K.J. Light-Wahl, B.L. Schwartz, and R.D. Smith. J. Am. Chem. Soc. **116**, 5271 (1994).
17. B.L. Schwartz, J.E. Bruce, G.A. Anderson, S.A. Hofstadler, A.L. Rockwood, R.D. Smith, A. Chilkoti, and P.S. Stayton. J. Am. Soc. Mass Spectrom. **6**, 459 (1995).
18. C. Versluis and A.J.R. Heck. Int. J. Mass Spectrom. **210/211**, 637 (2001).
19. C. Versluis, A. van der Staaij, E. Stokvis, A.J.R. Heck, and B. de Craene. J. Am. Soc. Mass Spectrom. **12**, 329 (2001).
20. N. Felitsyn, E.N. Kitova, and J.S. Klassen. Anal. Chem. **73**, 4647 (2001).
21. J.C. Jurchen and E.R. Williams. J. Am. Chem. Soc. **125**, 2817 (2003).
22. S.A. Ryce and R.R. Wyman. Can. J. Phys. **48**, 2571 (1970).
23. H. Schultheis and R. Schultheis. J. Math. Phys. **16**, 905 (1975).
24. S. Campbell, M.T. Rodgers, E.M. Marzluff, and J.L. Beauchamp. J. Am. Chem. Soc. **117**, 12840 (1995).
25. D. Suckau, Y. Shi, S.C. Beu, M.W. Senko, J.P. Quinn, F.M. Wampler, and F.W. McLafferty. Proc. Natl. Acad. Sci. U.S.A. **90**, 790 (1993).
26. T.D. Wood, R.A. Chorush, F.M. Wampler, D.P. Little, P.B. O'Connor, and F.W. McLafferty. Proc. Natl. Acad. Sci. U.S.A. **92**, 2451 (1995).
27. F.W. McLafferty, Z. Guan, U. Haupts, T.D. Wood, and N.L. Kelleher. J. Am. Chem. Soc. **120**, 4732 (1998).
28. R.J. Anderegg, D.S. Wagner, C.L. Stevenson, and R.T. Borchardt. J. Am. Soc. Mass Spectrom. **5**, 425 (1994).
29. K.B. Shelimov, D.E. Clemmer, R.R. Hudgins, and M.F. Jarrold. J. Am. Chem. Soc. **119**, 2240 (1997).
30. Y. Mao, M.A. Ratner, and M.F. Jarrold. J. Phys. Chem. B, **103**, 10017 (1999).
31. N. Felitsyn, E.N. Kitova, and J.S. Klassen. J. Am. Soc. Mass Spectrom. **13**, 1432 (2002).

© 2004 NRC Canada

A novel unexpected two-dimensional layer-like luminescent dysprosium coordination polymer $[Dy_2(phth)_3H_2O]_n$ by hydrothermal synthesis

Yi-Shan Song, Bing Yan, and Zhen-Xia Chen

Abstract: Assembling potassium acid phthalate (KHphth) and dysprosium nitrate, a novel luminescent two-dimensional layer-like dysprosium coordination polymer with the formula $[Dy_2(phth)_3H_2O]_n$ has been synthesized by a hydrothermal process. It is unexpected that the complex exhibits a new coordination mode with phthalate and an asymmetrical structure for the two dysprosium fragments in the molecular unit. The title coordination polymer crystallizes in the monoclinic system, space group $P2_1/c$, with lattice parameters a = 7.913(2) Å, b = 26.360(7) Å, c = 11.563(3) Å, β = 106.864(3)°, V = 2308.3(11) Å^3, D_c = 2.404 Mg/m^3, Z = 4, $F(000)$ = 1576, GOF = 1.079, R_1 = 0.0282. The luminescence spectrum shows that the blue emission intensity of the $^4F_{9/2} \rightarrow {}^6H_{15/2}$ transition is stronger than the yellow emission intensity of the $^4F_{9/2} \rightarrow {}^6H_{13/2}$ transition.

Key words: dysprosium (III), two-dimensional layer-like coordination polymer, molecular structure, luminescence, hydrothermal synthesis.

Résumé : L'assemblage du phtalate acide de potassium (KHphth) et du nitrate de dysprosium par un procédé hydrothermique conduit à la synthèse d'un nouveau polymère luminescent de coordination du dysprosium, à couche bidimensionnelle, de formule $[Dy_2(phth)_3H_2O]_n$. Il n'était pas prévu que ce complexe présenterait un nouveau mode de coordination avec le phtalate et une structure asymétrique comportant deux fragments de dysprosium par unité moléculaire. Le polymère de coordination mentionné dans le titre cristallise dans le système monoclinique, groupe d'espace $P2_1/c$, avec a = 7,913(2) Å, b = 26,360(7) Å et c = 11,563(3) Å, β = 106,864(3)°, V = 2308,3(11) Å^3, D_c = 2,404 Mg/m^3, Z = 4, $F(000)$ = 1576, GOF = 1,079 et R_1 = 0,0282. Le spectre de luminescence montre que l'intensité de l'émission dans le bleu de la transition $^4F_{9/2} \rightarrow {}^6H_{15/2}$ est plus grande que celle de l'émission dans le jaune de la transition $^4F_{9/2} \rightarrow {}^6H_{13/2}$.

Mots clés : dysprosium(III), polymère de coordination à couche bidimensionnelle, structure moléculaire, luminescence, synthèse hydrothermique.

[Traduit par la Rédaction]

Introduction

In the past few decades, lanthanide complexes have received much attention because of their interesting photophysical properties, which have potential application in the active centers for luminescent materials or in luminescent probes for chemical or biological macromolecules (1–6). Consequently, considerable studies have been focused on the design and assembly of lanthanide complexes with organic ligands such as aromatic carboxylic acids, β-diketones, cryptands, calixarenes, and heterocyclic ligands. Especially the lanthanide complexes with aromatic carboxylic acids readily form dimeric or infinite-chain polymeric structures, which show higher thermal or luminescent stabilities for practical application than other lanthanide-complex systems (7–10). Among the various types of carboxylic acids, benzenedicarboxylate dianions are widely used in the construction of coordination polymers owing to their capability of acting as bridging ligands in various coordination modes (11).

Many coordination polymers of lanthanides with benzenedicarboxylate ligands such as phthalates as bridging groups between metal centers have been reported, and there has been much interest in the preparation of lanthanide aromatic carboxylates under hydrothermal conditions (12–22). In the work reported in this paper, we synthesized a novel dysprosium coordination polymer, $[Dy_2(phth)_3H_2O]_n$ (phth = phthalate), by a hydrothermal process and studied its photophysical properties. Unexpectedly, we found a new coordination mode of phth anions in the structure, which leads the title complex to form a novel two-dimensional layer-like structure. In addition, the dysprosium coordination polymer exhibits strong luminescence of Dy^{3+}.

Received 21 April 2004. Published on the NRC Research Press Web site at http://canjchem.nrc.ca on 29 January 2005.

Y.-S. Song and B. Yan.[1] Department of Chemistry, Tongji University, Shanghai, P.R. China.
Z.-X. Chen. Department of Chemistry, Fudan University, Shanghai, P.R. China.

[1]Corresponding author (e-mail: byan@tongji.edu.cn).

 doi: 10.1139/V04-148 © 2004 NRC Canada

Table 1. Crystal data and structure refinement for the title complex.

Complex	$[Dy_2(phth)_3(H_2O)]_n$
Formula	$C_{24}H_{14}Dy_2O_{13}$
Relative molecular weight *M*	835.35
Colour	Colorless
Temperature (K)	293(2)
Radiation	MoKα (λ = 0.71073 Å)
Crystal system	$P2_1/c$
Space group	Monoclinic
a (Å)	7.913(2)
b (Å)	26.360(7)
c (Å)	11.563(3)
β (°)	106.864(3)
Volume (Å^3)	2308.3(11)
Z	4
Calculated density (Mg/m^3)	2.404
Absorption coefficient (mm^{-1})	6.500
F(000)	1576
Crystal dimensions (mm)	0.15 × 0.05 × 0.03
θ range for data collection (°)	1.55–26.01
Reflections collected/unique	10446/4514 (*R*(int) = 0.0251)
Completeness to 2θ = 26.00	99.2%
Absorption correction	None
Max. and min. transmission	0.8289 and 0.4423
Refinement method	Full-matrix least-squares on F^2
Data/restraints/parameters	4514/2/360
Goodness-of-fit on F^2	1.079
Final *R* indices ($I > 2\sigma(I)$)	R_1 = 0.0282, wR_2 = 0.0652
Largest diff. peak and hole (e. Å^{-3})	0.981 and –1.332

Table 2. Atomic coordinates (10^4) of equivalent isotropic displacement parameters (10^3 Å^2) for the title complex.

Atom	*x*	*y*	*z*	*U*(eq)[a]
Dy(1)	850(1)	7261(1)	6583(1)	15(1)
Dy(2)	4019(1)	6951(1)	4856(1)	17(1)
C(1)	3396(6)	8311(2)	7428(4)	21(1)
C(2)	2693(6)	8674(2)	6404(4)	22(1)
C(3)	2732(8)	9173(2)	6757(5)	35(1)
C(4)	2008(9)	9547(2)	5947(6)	43(2)
C(5)	1273(9)	9435(2)	4743(6)	45(2)
C(6)	1290(8)	8941(2)	4355(5)	33(1)
C(7)	2005(6)	8552(2)	5179(4)	21(1)
C(8)	2138(6)	8044(2)	4677(4)	19(1)
C(9)	–2736(6)	7830(2)	4862(4)	18(1)
C(10)	–3275(6)	8369(2)	4604(4)	20(1)
C(11)	–2678(7)	8729(2)	5502(5)	35(1)
C(12)	–3290(9)	9219(2)	5329(6)	48(2)
C(13)	–4475(8)	9358(2)	4247(6)	42(2)
C(14)	–5063(7)	9006(2)	3346(5)	31(1)
C(15)	–4483(6)	8513(2)	3510(4)	20(1)
C(16)	–5095(6)	8141(2)	2506(4)	18(1)
C(17)	7843(6)	6344(2)	5746(4)	20(1)
C(18)	8136(6)	5934(2)	4923(4)	21(1)
C(19)	6909(7)	5545(2)	4680(5)	33(1)
C(20)	7070(8)	5128(2)	3972(6)	42(2)
C(21)	8467(8)	5114(2)	3490(6)	38(1)
C(22)	9669(7)	5504(2)	3711(5)	31(1)
C(23)	9555(6)	5912(2)	4423(4)	20(1)
C(24)	10957(6)	6310(2)	4554(4)	20(1)
O(1)	4861(5)	8397(2)	8164(3)	28(1)
O(2)	2398(4)	7964(1)	7658(3)	22(1)
O(3)	2579(4)	7666(1)	5399(3)	19(1)
O(4)	1909(5)	8000(1)	3575(3)	27(1)
O(5)	–1108(4)	7726(1)	5150(3)	25(1)
O(6)	–3901(5)	7513(1)	4834(3)	29(1)
O(7)	–4200(5)	7786(1)	2356(3)	28(1)
O(8)	–6611(4)	8234(1)	1709(3)	20(1)
O(9)	6283(4)	6425(1)	5721(3)	25(1)
O(10)	9151(4)	6564(1)	6455(3)	23(1)
O(11)	10653(4)	6779(1)	4685(3)	21(1)
O(12)	12436(4)	6170(1)	4490(3)	27(1)
O(13)	–1063(5)	7645(2)	7564(3)	28(1)

[a] *U*(eq) is defined as one-third of the trace of the orthogonalized *Uij* tensor.

Experimental

Synthesis of $[Dy_2(phth)_3H_2O]_n$

Aqueous solutions of $Dy(NO_3)_3{\cdot}6H_2O$ (139 mg, 0.3 mmol) and KHphth (61 mg, 0.3 mmol) were mixed in 10 mL of deionized water. After stirring for 30 min, the mixture was placed in a 25-mL Teflon-lined reactor and heated at 160 °C in an oven for 3 days. Upon slow cooling to room temperature, pillar-like crystals of the title complex suitable for X-ray diffraction analysis were obtained. Anal calcd. (%) for $C_{24}H_{14}Dy_2O_{13}$: C 34.48, H 1.68; found: C 35.69, H 1.52. IR data: 1414.9 cm^{-1} ($\nu_s COO^-$), 1541.5 cm^{-1} ($\nu_{as} COO^-$).

X-ray crystallography

X-ray diffraction data were obtained for a crystal with dimensions 0.15 mm × 0.05 mm × 0.03 mm on a CCD area detector four-circle diffractometer with graphite-monochromated MoKα radiation. The data were collected by the ω–2θ scan technique. The structure was solved by direct methods. All non-hydrogen atoms were refined anisotropically by full-matrix least-squares methods. The hydrogen atoms were added geometrically and not refined. The final *R* and R_w were 0.0404 and 0.1016, respectively. All calculations were performed using SHELXS-97 and SHELXL-97 (23, 24). Details of data collection and refinement are given in Table 1. Atomic coordinates and selected interatomic distances and angles are presented in Tables 2 and 3, respectively. Full crystallographic data (excluding structure factors) for the structure reported in this paper have been deposited as Supplementary material.[2]

[2] Supplementary data may be purchased from the Directory of Unpublished Data, Document Delivery, CISTI, National Research Council Canada, Ottawa, ON K1A 0S2, Canada (http://www.nrc.ca/cisti/irm/unpub_e.shtml for information on ordering electronically). CCDC 225117 contains the crystallographic data for this manuscript. These data can be obtained, free of charge, via www.ccdc.cam.ac.uk/conts/retrieving.html (or from the Cambridge Crystallographic Data Centre, 12 Union Road, Cambridge CB2 1EZ, U.K.; fax +44 1223 336033; or deposit@ccdc.cam.ac.uk).

© 2004 NRC Canada

Table 3. Selected bond distances (Å) and bond angles (°) for the title complex.

Bond lengths (Å)			
Dy(1)—O(10)#1	2.256(3)	Dy(2)—O(6)#4	2.218(4)
Dy(1)—O(5)	2.271(3)	Dy(2)—O(9)	2.257(3)
Dy(1)—O(4)#2	2.315(3)	Dy(2)—O(3)	2.377(3)
Dy(1)—O(8)#3	2.365(3)	Dy(2)—O(12)#1	2.384(4)
Dy(1)—O(13)	2.366(4)	Dy(2)—O(8)#3	2.388(3)
Dy(1)—O(2)	2.366(3)	Dy(2)—O(1)#5	2.423(4)
Dy(1)—O(3)	2.443(3)	Dy(2)—O(2)#5	2.503(3)
Dy(1)—O(11)#1	2.502(3)	Dy(2)—O(11)#1	2.652(3)
		Dy(2)—O(7)#3	2.909(4)
Bond angles (°)			
O(10)#1-Dy(1)-O(5)	97.14(12)	O(8)#3-Dy(2)-O(2)#5	138.64(11)
O(5)-Dy(1)-O(4)#2	149.23(13)	O(1)#5-Dy(2)-O(2)#5	52.68(11)
O(10)#1-Dy(1)-O(8)#3	91.92(12)	O(6)#4-Dy(2)-O(11)#1	147.76(12)
O(5)-Dy(1)-O(8)#3	136.97(12)	O(9)-Dy(2)-O(11)#1	125.35(12)
O(4)#2-Dy(1)-O(8)#3	73.66(12)	O(3)-Dy(2)-O(11)#1	66.88(11)
O(10)#1-Dy(1)-O(13)	85.81(13)	O(12)#1-Dy(2)-O(11)#1	51.24(11)
O(5)-Dy(1)-O(13)	73.92(13)	O(8)#3-Dy(2)-O(11)#1	64.22(10)
O(4)#2-Dy(1)-O(13)	75.34(13)	O(1)#5-Dy(2)-O(11)#1	112.34(11)
O(8)#3-Dy(1)-O(13)	148.93(12)	O(2)#5-Dy(2)-O(11)#1	74.42(10)
O(10)#1-Dy(1)-O(2)	151.65(12)	O(6)#4-Dy(2)-O(7)#3	72.86(12)
O(5)-Dy(1)-O(2)	95.75(12)	O(9)-Dy(2)-O(7)#3	67.22(12)
O(4)#2-Dy(1)-O(2)	74.15(12)	O(3)-Dy(2)-O(7)#3	71.35(11)
O(8)#3-Dy(1)-O(2)	95.70(12)	O(12)#1-Dy(2)-O(7)#3	117.44(11)
O(13)-Dy(1)-O(2)	73.68(13)	O(8)#3-Dy(2)-O(7)#3	47.47(11)
O(10)#1-Dy(1)-O(3)	137.61(12)	O(1)#5-Dy(2)-O(7)#3	136.50(11)
O(5)-Dy(1)-O(3)	74.35(12)	O(2)#5-Dy(2)-O(7)#3	161.10(11)
O(4)#2-Dy(1)-O(3)	125.97(12)	O(11)#1-Dy(2)-O(7)#3	107.56(10)
O(8)#3-Dy(1)-O(3)	70.86(11)	C(1)-O(1)-Dy(2)#2	93.6(3)
O(2)-Dy(1)-O(3)	70.38(11)	C(1)-O(2)-Dy(1)	134.7(3)
O(10)#1-Dy(1)-O(11)#1	69.17(11)	C(8)-O(3)-Dy(2)	120.3(3)
O(8)#3-Dy(1)-O(11)#1	67.00(11)	C(8)-O(3)-Dy(1)	127.8(3)
O(13)-Dy(1)-O(11)#1	138.76(12)	C(9)-O(5)-Dy(1)	137.5(3)
O(3)-Dy(1)-O(11)#1	68.45(11)	C(9)-O(6)-Dy(2)#1	177.8(3)
O(6)#4-Dy(2)-O(9)	85.34(13)	C(16)-O(8)-Dy(1)#6	122.0(3)
O(6)#4-Dy(2)-O(3)	83.65(13)	C(16)-O(8)-Dy(2)#6	101.9(3)
O(9)-Dy(2)-O(3)	138.55(12)	C(17)-O(10)-Dy(1)#4	141.1(3)
O(3)-Dy(2)-O(12)#1	117.60(12)	C(24)-O(12)-Dy(2)#4	100.9(3)
O(6)#4-Dy(2)-O(8)#3	119.73(13)	Dy(1)-O(13)-H(13A)	115(5)
O(3)-Dy(2)-O(8)#3	71.61(12)	Dy(1)-O(2)-Dy(2)#2	129.64(15)
O(6)#4-Dy(2)-O(1)#5	82.23(14)	Dy(2)-O(3)-Dy(1)	101.06(12)
O(3)-Dy(2)-O(1)#5	141.13(12)	Dy(1)#6-O(8)-Dy(2)#6	103.05(12)
O(9)-Dy(2)-O(2)#5	127.70(12)	Dy(1)#4-O(11)-Dy(2)#4	92.38(10)

Note: Symmetry transformations used to generate equivalent atoms: for #1, $-x + 2$, y, $-z + 3/2$; for #2, $-x + 2$, $-y$, $-z + 2$; for #3, x, $-y$, $z - 1/2$; for #4, $x + 1$, y, z; for #5, x, $-y + 3/2$, $z - 1/2$; for #6, $x - 1$, $-y + 3/2$, $z - 1/2$.

Physical measurements

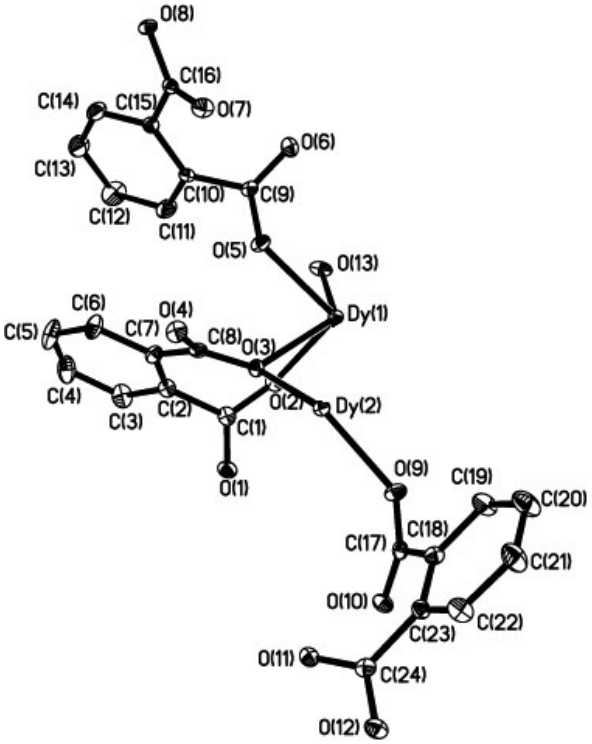
Elemental analyses (C, H, N) were determined on an Elementar Cario EL elemental analyzer. Infrared spectroscopy on KBr pellets was performed on a Nexus 912 AO446 FT-IR spectrophotometer in the range of 4000–400 cm^{-1}. Low-temperature luminescence (excitation and emission) spectra (77 K) for a solid sample of the title complex were measured with a Perkin-Elmer model LS-55 spectrophotometer.

Results and discussion

The asymmetric unit of the title complex, shown in Fig. 1, contains two dysprosium ions. X-ray diffraction crystal structure analysis reveals that it leads to a two-dimensional layer-like structure with the formula $[Dy_2(phth)_3H_2O]_n$. There are two types of metal environment in the structure of the title complex. The Dy(1) ion is eight-coordinated by eight oxygen atoms from five phth anions and has one coordinated water molecule, and the coordination geometry can be described as a distorted square monoantiprism geometry (Fig. 2*a*). The Dy(2) ion is nine-coordinated by nine oxygen atoms from six phth anions, and the coordination geometry can be described as a tricap-trigonal prism geometry (Fig. 2*b*). The distance between the Dy(1) ion and the Dy(2) ion is 3.7208(7) Å. It is interesting that a water molecule is coordinated only to the Dy(1) ion. In the coordination envi-

© 2004 NRC Canada

Fig. 1. The asymmetric unit of $[Dy_2(phth)_3H_2O]_n$ coordination polymer.



ronment of Dy(1), four oxygen atoms (O2, O3, O10, O11) from two phth anions are bound to the Dy(1) ion, among which the two pairs of chelating oxygen atoms (O2 and O3, O10 and O11) each come from different carboxylate groups of one phth anion. The distance between the Dy(1) ion and these oxygen atoms ranges from 2.256(3) to 2.502(3) Å, and the bond angle consisting of Dy(1) and the oxygen atoms from one phth anion are 70.38(11)° and 69.17(11)°, respectively. In addition,, three oxygen atoms (O4, O5, O8) from three chelating phth anions are bound to the Dy(1) ion, with the distance between Dy(1) and these oxygen atoms ranging from 2.271(3) to 2.365(3) Å, and there is one coordinated oxygen atom from the water molecule (O13), with the Dy(1)—O(13) distance being 2.366(4) Å. The average Dy(1)—O distance bond is 2.360 Å. In the coordination environment of Dy(2), six oxygen atoms (O1, O2, O7, O8, O11, O12) from three phth anions are bound to Dy(2), among which each pair of chelating oxygen atoms (O1 and O2, O7 and O8, O11 and O12) comes from the same carboxylate group. The distance between Dy(2) and these oxygen atoms ranges from 2.388(3) to 2.909(4) Å, and the bond angle consisting of Dy and the oxygen atoms from one phth anion ranges from 47.47(11) to 52.68(11)°. In addition, three oxygen atoms (O3, O6, O9) from three chelating phth anions are bound to the Dy(2) ion, with the bond distance ranging from 2.218(4) to 2.377(3) Å. The average Dy(2)—O bond distance is 2.456 Å, which is longer than the average Dy(1)—O bond distance. The reason is essentially that the chelating oxygen atoms belong to one carboxylate group, which prolongs the distances of the coordination bond.

All phth anions are completely deprotonated, and all the oxygen atoms take part in the coordination to the central metal. It can be considered that three phth anions are present in one unit of $[Dy_2(phth)_3H_2O]_n$, and it is noteworthy that they coordinate to the Dy ions in three different modes (Scheme 1):

(*a*) Bridging/chelating pentadentate and chelating monodentate (Scheme 1*a*): Oxygen atom 2 and oxygen atom 3 bridge three central metals (Dy1, Dy2, Dy2#). Dy1 and Dy2 are in one asymmetric unit, and Dy2# is in another unit, which has the same coordination environment as Dy2. In addition, oxygen atom 1 and oxygen atom 2 chelate Dy2#, while oxygen atom 4 is coordinated to Dy1#.

(*b*) Bridging/chelating tridentate and chelating bidentate (Scheme 1*b*): Oxygen atom 7 and oxygen atom 8 chelate/bridge Dy1 and Dy2, while oxygen atom 5 and oxygen atom 6 are connected to Dy1# and Dy2#, respectively.

(*c*) Bridging/chelating tetradentate and chelating monodentate (Scheme 1*c*): Oxygen atom 10, oxygen atom 11, and oxygen atom 12 chelate/bridge Dy1 and Dy2, while oxygen atom 9 is coordinated to Dy2#.

From Scheme 1, we can see that three units are bridged in coordination modes (*a*) and (*b*), while two are bridged in mode (*c*). To our knowledge, coordination modes (*b*) and (*c*) have been seldom reported, and coordination mode (*a*) has never been observed in ref. 9. All coordination modes of phth anions result in a two-dimensional layer structure (Fig. 3). Consequently, the three oxygen atoms O3, O8, and O11 actually link two dysprosium ions of one unit, and only O(2) bridges dysprosium ions of adjacent units; the other oxygen atoms use the chelating monodentate mode.

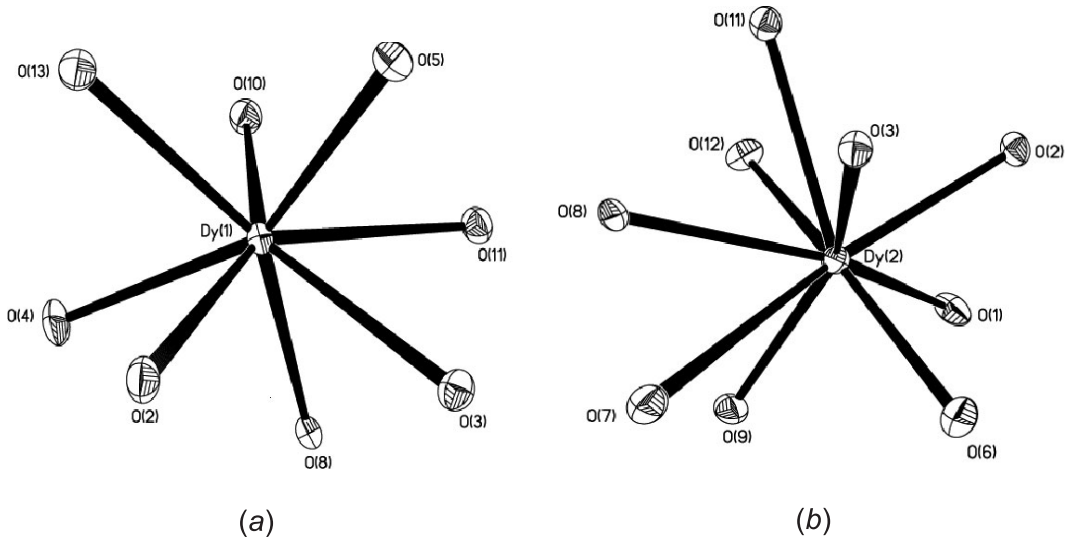
The carboxylic group forms one type of intermolecular hydrogen bond, which is the O(13)—H(13A)···O(7)#2 or O(13)—H(13B)···O(11)#7 intermolecular hydrogen bonding between the oxygen atoms of the bridged phth ligands and the oxygen atoms of the coordinated water molecules in the adjacent layers. Distances and angles of these hydrogen bond interactions are presented in Table 4. Such intermolecular hydrogen bonding links the adjacent layers, and, accordingly, a three-dimensional network (Fig. 4) is established and stabilizes the whole structure.

The UV–vis absorption spectrum for the title complex in water (10^{-4} mol L^{-1}) exhibits dominant absorption peaks in the narrow UV region between 200 and 330 nm, and the maximum absorption peaks are located at around 297 nm, which can be attributed to the characteristic absorption of the H_2phth ligand. The results indicate that H_2phth is the energy donor and luminescence sensitizer of the Dy^{3+} ion.

The phosphorescence spectrum of the title complex was measured (Fig. 5). From the phosphorescence emission, it is indicated that three apparent phosphorescence bands appear and the maximum phosphorescence wavelengths are at 402 and 415 nm, which correspond to the characteristic 0–0 and 0–1 transitions of the H_2phth ligand. The shortest wavelength of the phosphorescence emission band is assumed to be the 0–0 transition, so the energy of the lowest triplet state of H_2phth can be determined to be 24 875 cm^{-1}. The energy difference between this triplet state and the emitting levels of Dy^{3+} (20 875 cm^{-1}) was calculated to be 4000 cm^{-1}. According to the energy transfer and intramolecular energy mechanism (25–27), it can be predicted that the triplet-state energy of H_2phth is more suitable for the luminescence of the dysprosium ion.

© 2004 NRC Canada

Fig. 2. The two types of coordination polyhedra of the dysprosium ions in $[Dy_2(phth)_3(H_2O)]_n$.



Scheme 1. Coordination modes of phthalate groups in the title complex.

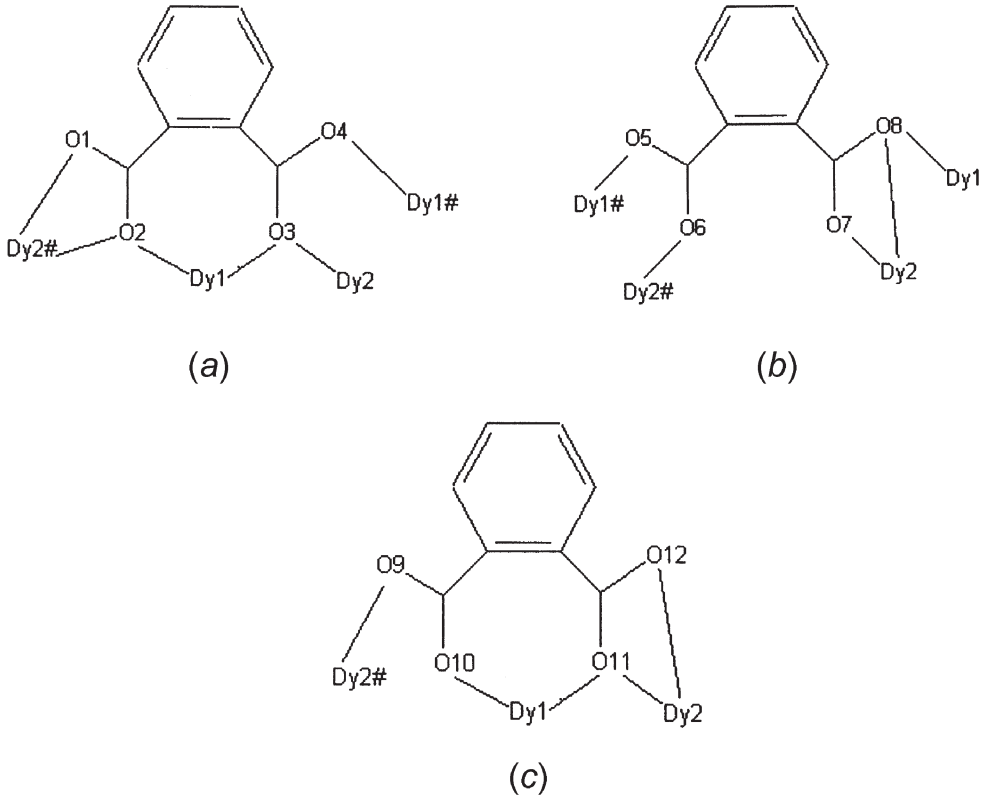


Table 4. Distances (Å) and angles (°) of hydrogen bond interactions for the title complex.

D—H···A	*d*(D—H) (Å)	*d*(H···A) (Å)	*d*(D···A) (Å)	∠(DHA) (°)
O(13)—H(13A)···O(7)#2	0.79(2)	1.89(2)	2.676(5)	170(7)
O(13)—H(13B)···O(11)#7	0.80(2)	2.09(2)	2.870(5)	167(6)

Note: Symmetry transformations used to generate equivalent atoms: for #2, $-x + 2$, $-y$, $-z + 2$; for #7, $x - 1$, $-y + 3/2$, $z + 1/2$.

The excitation spectrum of $[Dy_2(phth)_3H_2O]_n$ (Fig. 6, inset) shows that the title complex has effective energy absorption mainly in the UV region of 230–350 nm, and the excitation bands consist of five main peaks, at 241, 256, 260, 305, and 330 nm, respectively. We further measured the corresponding emission spectra by selective excitation at

© 2004 NRC Canada

Fig. 3. Two-dimensional layer structure of $[Dy_2(phth)_3H_2O]_n$ coordination polymer.

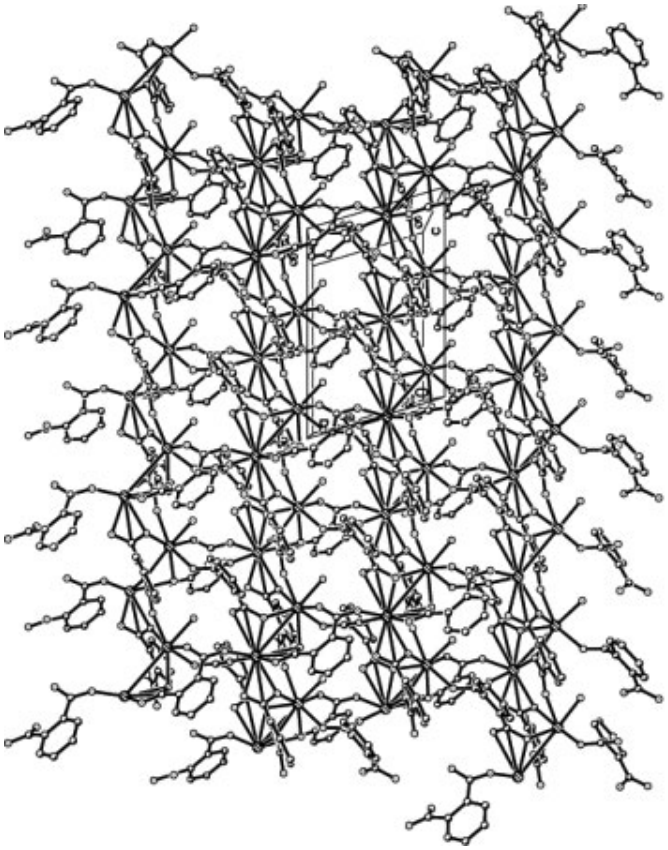


Fig. 4. The packing view of the unit cell for $[Dy_2(phth)_3H_2O]_n$ coordination polymer.

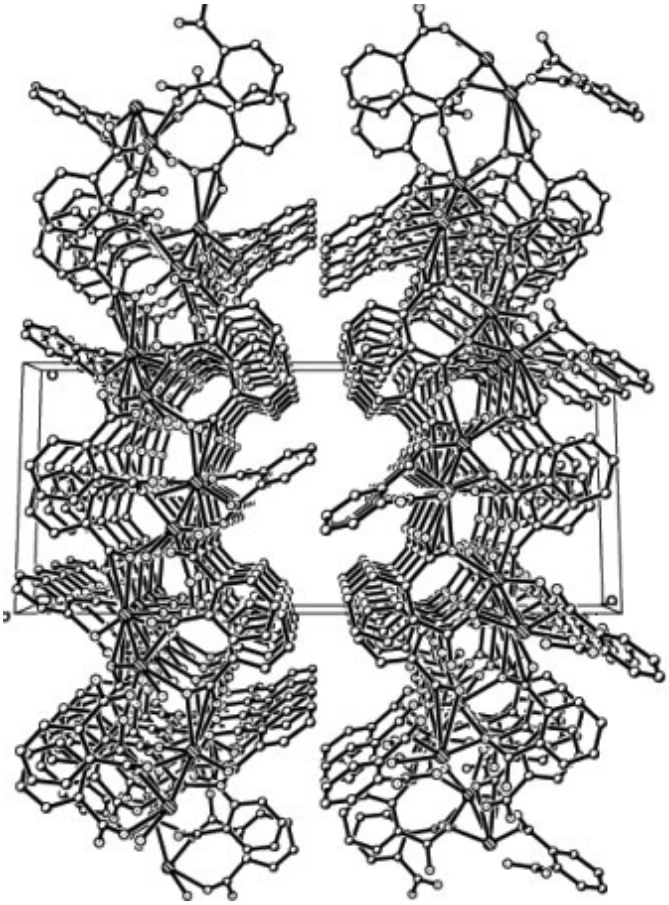
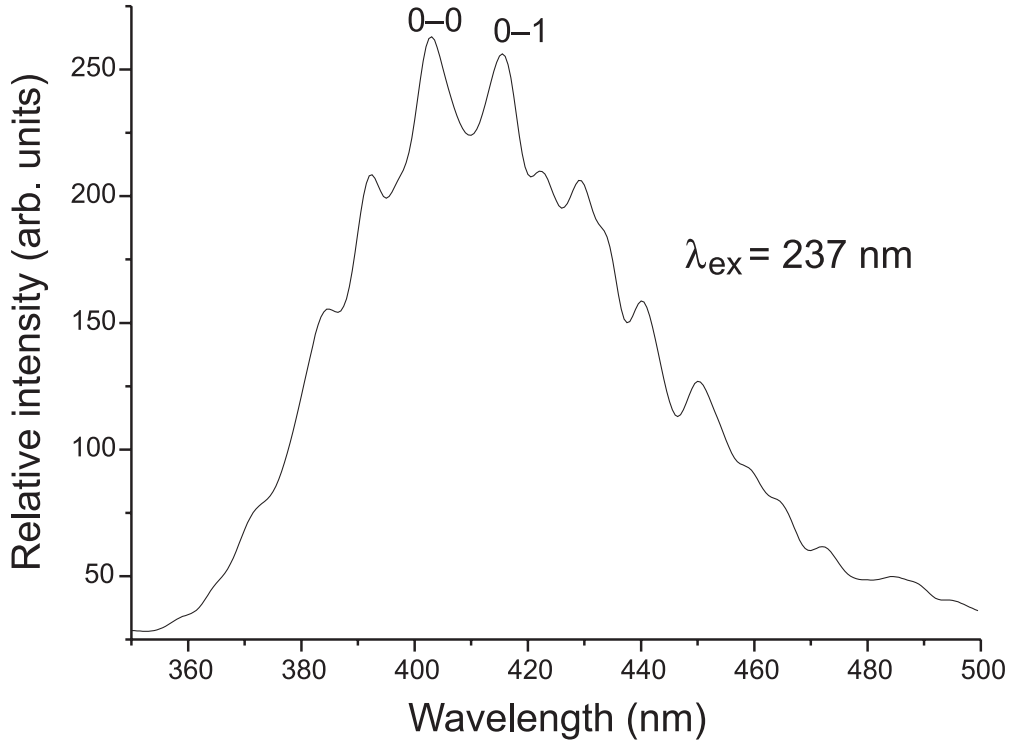
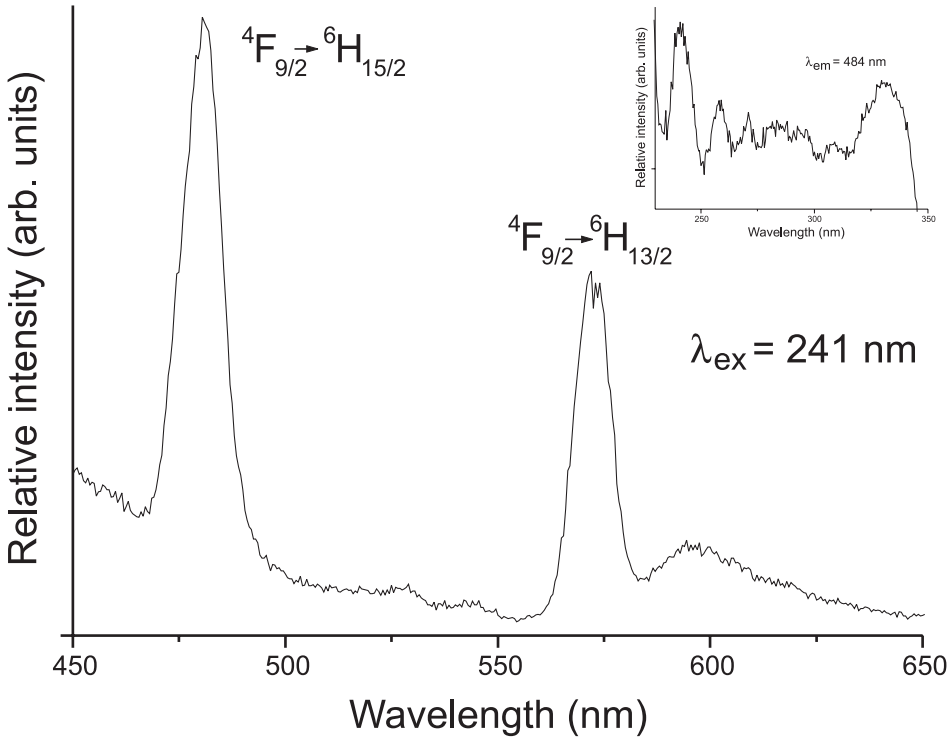


Fig. 5. Phosphorescence spectra of $[Dy_2(phth)_3H_2O]_n$ coordination polymer.



© 2004 NRC Canada

Fig. 6. Luminescence spectrum of $[Dy_2(phth)_3H_2O]_n$ coordination polymer. Inset: excitation spectrum.



the five different excitation wavelengths, and they showed similar emission position, except for some slight differences in luminescent intensities. This indicates that the five excitation bands are all the effective energy excitation for the luminescence of Dy^{3+} ions. The emission spectrum of the title complex exhibits two apparent emission bands under 241-nm excitation (Fig. 6), and the maximum emission wavelengths are at around 480 and 572 nm, respectively, which are attributed to the characteristic emission for $^4F_{9/2} \rightarrow {}^6H_J$ (J = 15/2, 13/2) transitions of the Dy^{3+} ion. The luminescence spectrum shows that the blue emission intensity of the $^4F_{9/2} \rightarrow {}^6H_{15/2}$ transition is stronger than the yellow emission intensity of the $^4F_{9/2} \rightarrow {}^6H_{13/2}$ transition.

Acknowledgement

The authors gratefully acknowledge the financial support from the National Natural Science Foundation of China (20301013).

References

1. T.A. Peter, B. Yan, and H.J. Zhang. J. Mater. Sci. **35**, 4325 (2000).
2. B. Yan. Mater. Lett. **57**, 2535 (1998).
3. T. Jin, S. Tsutsumi, Y. Deguchi, K.I. Machida, and G.Y. Adachi. J. Alloys Compd. **252**, 59 (1997).
4. C.F. Meares and T.G. Wensel. Acc. Chem. Res. **17**, 202 (1984).
5. Y.X. Ci, Y.Z. Li, and W.B. Chang. Anal. Chim. Acta, **248**, 589 (1991).
6. L.K. Scott and W D. Horrocks. J. Inorg. Biochem. **46**, 193 (1992).
7. L.P. Jin, S.X. Lu, and S.Z. Lu. Polyhedron, **15**, 4069 (1996).
8. E.P. Marinho, D.M. Araujo Melo, L.B. Zinner, K. Zinner, E.E. Castellano, J. Zukerman-Schpector, P.C. Isolani, and G. Vicentini. Polyhedron, **16**, 3519 (1997).
9. A. Fernandes, J. Jaud, G.J. Dexpert, and C.C. Brouca. Polyhedron, **20**, 2385 (2001).
10. B. Yan and Q.Y. Xie. J. Mol. Struct. **688**, 73 (2004).
11. Y.H. Wan, L.P. Zhang, and L.P. Jin. J. Mol. Struct. **658**, 253 (2003).
12. L.P. Zhang, Y.H. Wan, and L.P. Jin. J. Mol. Struct. **646**, 169 (2003).
13. E.R. Birnbaum and D.W. Darnall. Bioinorg. Chem. **3**, 15 (1973).
14. V.K. Chitale and K.S. Pitre. J. Inst. Chem. (India), **53**, 263 (1981).
15. R.A. Torres and G.R. Choppin. Radiochim. Acta, **35**, 143 (1984).
16. G.R. Choppin, E.N. Rizkalla, T.A. Al-Ansi, and A. Dadgar. J. Coord. Chem. **3**, 297 (1994).
17. Y.H. Wan, L.P. Jin, and K.Z. Wang. J. Mol. Struct. **649**, 85 (2003).
18. E. Suresh, K. Boopalan, R.V. Jasra, and M.M. Bhadbhade. Inorg. Chem. **40**, 4078 (2001).
19. J. Tao, M.L. Tong, and X.M. Chen. J. Chem. Soc., Dalton Trans. 3669 (2000).
20. D.F. Sun, R. Cao, Y.C. Liang, Q. Shi, W.P. Su, and M.C. Hong. J. Chem. Soc., Dalton Trans. 2335 (2001).
21. T.M. Reineke, M. Eddaoudi, M. Fehr, D. Kelley, and O.M. Yaghi. J. Am. Chem. Soc. **121**, 1651 (1999).
22. D.T. Vodak, M.E. Braun, J. Kim, M. Eddaoudi, and O.M. Yaghi. Chem. Commun. 2534 (2001).
23. G.M. Sheldrick. Acta Crystallogr., Sect. A, **A46**, 467 (1990).
24. G.M. Sheldrick. SHELXS-97 [computer program]. Gottingen University, Gottingen, Germany (1997).
25. S. Sato and M. Wada. Bull. Chem. Soc. Jpn. **43**, 2403 (1970).
26. B. Yan, H. Shao, H.J. Zhang, S.B. Wang, and J.Z. Ni. Chin. J. Inorg. Chem. **14**, 407 (1998).
27. B. Yan, H.J. Zhang, and J.Z. Ni. Chem. Res. Chin. Univ. **14**, 245 (1998).

© 2004 NRC Canada

Scavenging of photogenerated singlet molecular oxygen and superoxide radical anion by sulpha drugs — Kinetics and mechanism

Marta Díaz, Marta Luiz, Sonia Bertolotti, Sandra Miskoski, and Norman A. García

Abstract: The ability of the sulfanilic antibiotics (SDs), dapsone (DAP), sulfisoxazole (SFX), sulfadiazine (SFD), and sulfanilic acid (SFNA) to act as scavengers of the visible-light-photogenerated species superoxide radical anion ($O_2^{\bullet-}$) and singlet molecular oxygen ($O_2(^1\Delta_g)$) was studied employing the natural pigment riboflavin (Rf) and the artificial dye Rose Bengal as photosensitisers. A complex mechanism, common to all the SDs studied, was elucidated through stationary photolysis, polarographic detection of oxygen uptake, fluorescence spectroscopy, time-resolved phosphorescence detection of $O_2(^1\Delta_g)$, and laser flash photolysis. Visible-light irradiation of aqueous and aqueous methanolic solutions of Rf (ca. 0.02 mmol/L) plus SD (ca. 0.5 mmol/L) photogenerated excited singlet and triplet Rf (^{1}Rf* and ^{3}Rf*). Under these experimental conditions, only ^{3}Rf* is quenched either by oxygen, giving rise to $O_2(^1\Delta_g)$ by electronic energy transfer to dissolved ground-state oxygen, or by SD, yielding semireduced Rf through an electron-transfer process. Complementary experiments performed in pure water employing superoxide dismutase and sodium azide inhibition of oxygen uptake, in parallel with laser flash photolysis data, showed that $O_2^{\bullet-}$ is also formed, probably due to the reaction of the anion radical from Rf with dissolved oxygen, yielding also neutral, ground-state Rf. Both active oxygen species, namely, $O_2^{\bullet-}$ and $O_2(^1\Delta_g)$, are quenched by the SDs and, as a result, photodegradation of the SDs — each to a different extent — and photodegradation of the sensitiser itself were observed. The SDs that kinetically behave as the better physical quenchers of $O_2(^1\Delta_g)$, which are in principle good candidates as photoprotectors, namely, DAP and SFD, suffer photooxidation, exhibiting high to moderate oxygen consumption rates due to the $O_2^{\bullet-}$ oxidative pathway, whereas for SFNA and SFX, oxidation predominantly occurs through an $O_2(^1\Delta_g)$-mediated mechanism. Microbiological results for SFX, taken as a representative SD, indicate that the photodegradation of the drug, upon visible-light Rf-sensitised irradiation, is accompanied by a net loss in bacteriostatic activity.

Key words: photooxidation, singlet oxygen, superoxide radical anion, sulpha drugs.

Résumé : Utilisant comme sensibilisateur la riboflavine (Rf), un pigment naturel, et le Rose du Bengale, un colorant artificiel, on a étudié les possibilités des antibiotiques sulfaniliques (« SD »), soit dapsone (DAP), sulfisoxazole (SFX), sulfadiazine (SFD) et l'acide sulfanilique (SFNA), à agir comme pièges pour l'anion radical du superoxyde ($O_2^{\bullet-}$) et l'oxygène moléculaire ($O_2(^1\Delta_g)$), des espèces photogénérées par la lumière visible. On a élucidé le mécanisme complexe, commun pour toutes les espèces « SD » étudiées, par le biais de la photolyse stationnaire, de la détection polarographique de l'absorption d'oxygène, de la spectroscopie de fluorescence, de la détection de la phosphorescence résolue en fonction du temps du $O_2(^1\Delta_g)$ et de la photolyse éclair au laser. L'irradiation, à l'aide de lumière visible, de solutions aqueuses et méthanoliques aqueuses contenant environ 0,02 mmol/L de riboflavine et environ 0,5 mmol/L de « SD » conduit à la photogénération des états singulet et triplet excités de la riboflavine (^{1}Rf* et ^{3}Rf*). En travaillant dans ces conditions expérimentales, seul l'état triplet ^{3}Rf* est désactivé soit par l'oxygène, conduisant à $O_2(^1\Delta_g)$ par un transfert d'énergie électronique vers l'oxygène à l'état fondamental dissous, ou par les « SD », conduisant à une riboflavine partiellement réduite par le biais d'un processus de transfert d'électron. Des expériences complémentaires, effectuées dans de l'eau pure en utilisant de la dismutase de superoxyde et de l'azoture de sodium pour inhiber l'absorption de l'oxygène et en parallèle avec des données de photolyse éclair au laser, ont permis de montrer qu'il se forme aussi du $O_2^{\bullet-}$, probablement par la réaction de l'anion radical de la riboflavine avec de l'oxygène dissous, qui conduit aussi à la formation de riboflavine neutre, dans son état fondamental. Les deux espèces actives, soit le $O_2^{\bullet-}$ et le $O_2(^1\Delta_g)$, sont désactivées par les « SD » et il en résulte une photodégradation des « SD », chacun à un degré différent, ainsi qu'une photodégradation du sensibilisateur. En raison de la voie oxydante du $O_2^{\bullet-}$, les dérivés qui d'un point de vue cinétique sont les meilleurs désactivateurs physiques du $O_2(^1\Delta_g)$, soit DAP et SFD, et qui pourraient éventuellement être les meilleurs photoprotecteurs subissent des photooxydations accompagnées de vitesses de consommation de l'oxygène

Received 12 May 2004. Published on the NRC Research Press Web site at http://canjchem.nrc.ca on 29 January 2005.

M. Díaz and M. Luiz. Departamento de Química, Facultad de Ciencias Naturales, Universidad Nacional de la Patagonia San Juan Bosco, 9000 Comodoro Rivadavia, Argentina.
S. Bertolotti, S. Miskoski, and N.A. García.[1] Departamento de Química, Universidad Nacional de Río Cuarto, 5800 Río Cuarto, Argentina.

[1]Corresponding author (e-mail: ngarcia@exa.unrc.edu.ar).

 doi: 10.1139/V04-146 © 2004 NRC Canada

qui vont d'élevées à modérées; par ailleurs, avec le SFNA et le SFX, l'oxydation prévalente se produit par un mécanisme impliquant le $O_2(^1\Delta_g)$. Les résultats microbiologiques obtenus avec le SFX, utilisé comme modèle représentatif des antibiotiques sulfaniliques, indiquent que la photodégradation du médicament sous l'influence d'une irradiation avec de la lumière visible et sensibilisée par de la riboflavine s'accompagne d'une perte nette de son activité bactériostatique.

Mots clés : photooxydation, oxygène singulet, anion radical superoxyde, antibiotiques sulfaniliques.

[Traduit par la Rédaction]

Introduction

The scavenging action of daylight-photogenerated oxygen active species by pharmacological agents is increasingly being investigated (1). The main motivation for these studies is the evaluation of the potential antioxidative activity of the substrates and the extent and nature of possible photodamage as a result of their interactions with the oxidative species. The substrates can physically quench photogenerated oxidants and (or) simply undergo oxidation, lowering their specific therapeutic effects. In this context, the prevalence of physical quenching is an interesting possibility, since in this way the oxidative species are eliminated without any chemical transformation of the drugs.

The most frequent mechanism of daylight-promoted production of oxidative agents is represented by the photosensitised process by which absorption of daylight by a coloured species generates its electronic excited states and, under aerobic conditions, may initiate a cascade of photoprocesses, some of which frequently involve the production of transient oxidative species. A natural visible-light-absorbing pigment of particular interest is vitamin B_2, or riboflavin (Rf), which generates the oxidative species singlet molecular oxygen ($O_2(^1\Delta_g)$) and superoxide radical anion ($O_2^{\bullet-}$) with quantum yields of 0.48 and 0.009, respectively (2). Rf has been postulated as a possible sensitiser for the photooxidative degradation of numerous biologically relevant natural substrates and drugs (3, 4).

An important family of compounds, transparent to daylight, is made up of the antibiotics and bacteriostatics derived from sulfanilic acid, termed sulpha drugs (SDs), which belong to a known class of biologically active and commercially valuable substrates (5). The understanding of their behaviour in the presence of photogenerated oxidative species, and particularly kinetic and mechanistic information on possible oxidative processes, may be of great interest in pharmaceutical and medical fields, in relation to the potential occurrence of photoreactions in the presence of photosensitisers able to absorb daylight. The aim of the present study was to analyse the behaviour of the SD derivatives sulfanilic acid (SFNA), dapsone (DAP), sulfadiazine (SFD), and sulfisoxazole (SFX) (Scheme 1) under visible-light photoirradiation and in the presence of two different types of photosensitisers: the natural pigment Rf and, for comparative purposes, the synthetic dye Rose Bengal.

Materials and methods

Chemicals

Dapsone, sulfadiazine, sulfisoxazole, sulfanilic acid, riboflavin, D_2O (99.9%D), superoxide dismutase (SOD), and sodium azide (NaN_3) were purchased from Sigma. Rose Bengal was from Aldrich, and furfuryl alcohol (FFA) was from Riedel deHaën. Water was triply distilled, and MeOH (HPLC quality) was from Sintorgan (Buenos Aires, Argentina). In some experiments, water was replaced as a solvent by 1:1 (*v*/*v*) MeOH–water to increase the solubility of the SD. D_2O was employed instead of H_2O in the time-resolved phosphorescence detection (TRPD) experiments to lengthen the $O_2(^1\Delta_g)$ lifetime (6). The pH 7 and pD 7 buffered solutions were prepared according to a literature procedure (7).

Instrumentation and methods

Absorption and fluorescence measurements

Ground-state absorption measurements were carried out with a Hewlett Packard 8452A diode array spectrophotometer. For the static Rf fluorescence experiments, a Shimadzu RF5301-PC spectrofluorimeter was used; measurements were performed at 25 ± 1 °C on air-equilibrated solutions. Excitation and emission wavelengths were 445 and 515 nm, respectively. The Stern–Volmer constants (K_{SV}) for the interaction of the SD with the singlet excited state of Rf (^{1}Rf*) were determined by evaluation of the static fluorescence intensity of Rf in the presence (I) and in the absence (I_0) of SD, through a Stern–Volmer treatment (eq. [1]).

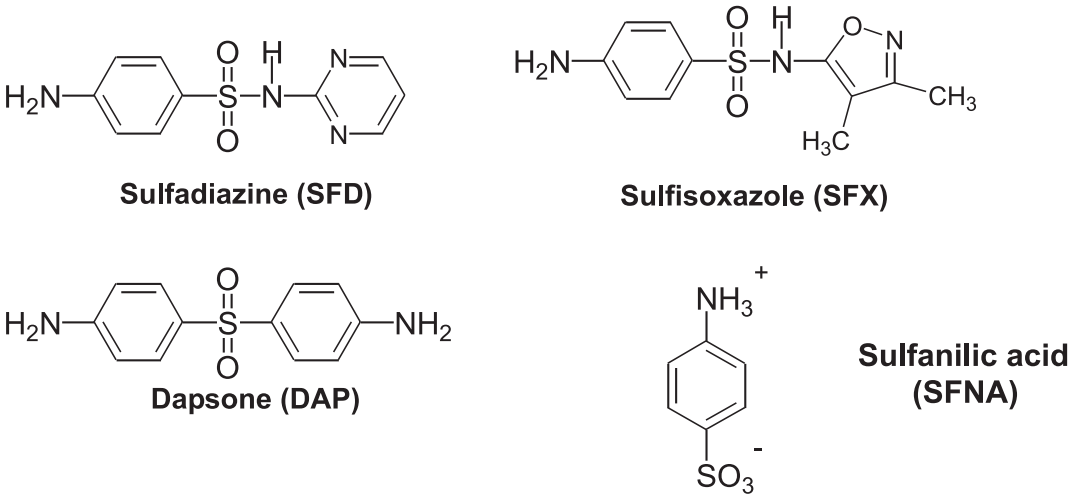
$$[1] \qquad I_0/I = 1 + K_{SV}[SD]$$

Static photolysis and determination of k_r

Static aerobic and anaerobic photolysis of aqueous and methanolic solutions containing SD and the sensitisers Rf and Rose Bengal was carried out in a home-made photolysis unit, previously described (8). Cut-off filters (420 nm) ensured that the light was absorbed only by the sensitiser. Anaerobic and aerobic photodecomposition rates of Rf were determined by evaluation of the initial slopes of Rf consumption (decrease of absorbance at 446 nm) vs. irradiation time. The rate constants of the chemical reaction of SD with $O_2(^1\Delta_g)$, k_r, were determined using Rose Bengal as a sensitiser and actinometric methods (9), which are based on the comparison of the slopes of the time course (first-order plots) of oxygen uptake by the substrate and by a reference compound with a known k_r value (k_{rR}). The ratio of the first-order slopes of oxygen uptake by SD and the reference, both determined at identical substrate concentration (5×10^{-4} mol/L), is equal to k_r/k_{rR}, assuming that the SD:O_2 stoichiometry is 1:1 and that the reaction of $O_2(^1\Delta_g)$ with the quencher is the only pathway for oxygen consumption. FFA, a pH-independent photooxidizable compound (10), was used as a reference with $k_{rR} = 1.2 \times 10^8$ L mol^{-1} s^{-1}. The oxygen

© 2004 NRC Canada

Scheme 1. Structures of the sulpha drugs employed.



consumption was monitored with a specific electrode (Orion 97–08).

Time-resolved phosphorescence detection of $O_2(^1\Delta_g)$ and determination of k_t

The laser-kinetic spectrophotometer for TRPD has been previously described (11). Briefly, it consisted of a Nd:YAG laser (Spectron) as the excitation source. The output at 532 nm was employed to excite Rose Bengal. The emitted radiation (mainly 1270 nm) was detected, after passing through appropriate filters, at right angles using an amplified Judson J16/8Sp germanium detector. The output of the detector was coupled to a digital oscilloscope and to a personal computer for processing the signal. To get a good signal-to-noise ratio, 16 shots were usually averaged, from which the decay times were calculated. The sensitiser, Rose Bengal, had an $A_{532} \cong 0.4$.

The $O_2(^1\Delta_g)$ lifetimes were evaluated in in the presence (τ) and in the absence (τ^0) of the quencher, SD. The data were plotted according to a simple Stern–Volmer treatment (eq. [2]):

$$[2] \qquad 1/\tau = 1/\tau^0 + k_t[SD]$$

where k_t is the overall rate constant for $O_2(^1\Delta_g)$ quenching (processes (8), (9), and (10) in Scheme 2, discussed in the Results section) and is given by $k_t = k_r + k_q$. The rate constants k_r and k_q refer to the chemical (reactive) and physical quenching, respectively, of $O_2(^1\Delta_g)$.

Laser flash photolysis experiments and determination of k_{q3}

N_2-saturated aqueous solutions of Rf (0.01 mmol/L) were photolysed using a flash photolysis apparatus. A nanosecond Nd:YAG laser system (Spectron) at 355 nm was the excitation source, employing a 150-W xenon lamp as analysing light. The detection system comprised a PTI monochromator and a red-extended photomultiplier (Hamamatsu R666). The signal, acquired and averaged by a digital oscilloscope (Hewlett-Packard 54504A), was transferred to a PC via a HPIB parallel interface, where it was analysed and stored. The disappearance of the Rf excited triplet state (^{3}Rf*), generated by the 355-nm laser pulse, was monitored from the first-order decay of the absorbance at 670 nm, a wavelength at which interference from other possible species is negligible. The decay of ^{3}Rf* was measured at low Rf concentration (typically 0.02 mmol/L) and at low enough laser energy to avoid undesirable effects such as self-quenching and triplet–triplet annihilation. The lifetime of ^{3}Rf* was evaluated in the presence (τ_3) and in the absence (τ_3^0) of the quencher, SD. The data were plotted according to a Stern–Volmer treatment (eq. [3]):

$$[3] \qquad 1/\tau_3 = 1/\tau_3^0 + k_{q3}[SD]$$

To obtain SD concentrations higher than those allowed by the solubility of SD in water, the solvent mixture MeOH–H_2O (1:1, *v*/*v*) was employed in the determinations of the interactions of the antibiotics with singlet and triplet excited states of Rf.

Microbiological determinations

The antibacterial activity of SFX was evaluated at different irradiation times, employing the agar-well diffusion method (12) and using the standard strain *Pseudomonas aeruginosa* (ATCC 27853). The nutritive agar was inoculated with a water suspension of the microorganism from irradiated and nonirradiated pH 7 aqueous solutions, in the presence of Rf ($Abs_{445\ nm} = 0.5$) and SFX 0.5 mmol/L), and incubated at 37 °C for 48 h, after which the diameter of the inhibitory *halo* was measured.

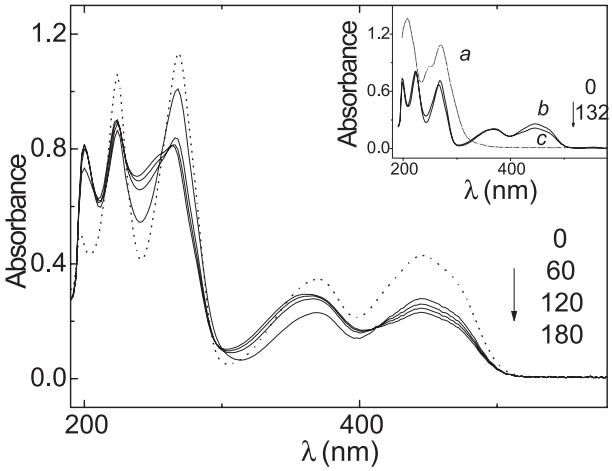
Results

No perturbations indicative of any kind of ground-state association between SDs and Rf within the concentration range used for the photochemical experiments employing either pH 7 H_2O or 1:1 (*v*/*v*) MeOH–H_2O as solvent were observed in difference spectra (SD (0.4–1 mmol/L) + Rf (0.01–0.04 mmol/L) vs. Rf).

Figure 1 shows the time evolution of the spectral changes produced in the Rf-sensitised aerobic irradiation of a MeOH–water solution of SFD (0.3 mmol/L) containing Rf at a concentration of ca. 0.02 mmol/L. It is evident that both the sensitiser and the substrate were transformed as a result of

© 2004 NRC Canada

Fig. 1. Time evolution of the absorption spectrum of SFD (0.3 mmol/L) + Rf (0.02 mmol/L) upon Rf-sensitised photoirradiaton in MeOH–H_2O. The dotted spectrum is that of Rf (ca. 0.03 mmol/L) in 1:1 (*v*/*v*) MeOH–H_2O. Inset: Time evolution of the absorption spectrum of SFD + Rf upon Rf-sensitised photoirradiation in H_2O (*b*, *c*). The upper trace (*a*) in the inset is a spectrum of SFD vs. H_2O (molarity not determined), included for comparative purposes. Numbers on the spectra represent irradiation time in seconds.



the photoirradiation. The same was true when SFD was replaced by SFX, DAP, or SFNA.

When aerated individual solutions of any of the three SD derivatives (0.4 mmol/L) and Rf (0.02 mmol/L) in pH 7 water were irradiated with visible light, oxygen consumption was observed (see Fig. 2*c* for a typical case). The relative rates of oxygen uptake are shown in Table 1. In the presence of NaN_3 (1 mmol/L), the rate of oxygen uptake was decreased but not suppressed (Fig. 2*b*). The salt NaN_3 is a selective quencher of the species $O_2(^1\Delta_g)$, with reported k_t values of $5 \times 10^8 - 15 \times 10^8$ L mol^{-1} s^{-1} in water (6). Concentrations of NaN_3 of the order of 1 mmol/L have been used previosuly to ascertain whether $O_2(^1\Delta_g)$ participates in a given reaction mechanism (6, 13, 14). A relatively low rate of oxygen uptake was observed in an aqueous solution containing Rf alone (0.02 mmol/L) (Fig. 2*a*).

In the presence of SOD (14 μg/mL), the rate of oxygen consumption in photoirradiated solutions of SFD (0.5 mmol/L) plus Rf (0.02 mmol/L) clearly decreased as compared to that in similar runs in the absence of the enzyme. This effect was practically absent in the corresponding runs with SFNA and SFX, and an intermediate situation (small decrease in the oxygen consumption rate) was observed for DAP (see data in Table 1). SOD, which catalyses the dismutation of $O_2^{\bullet-}$, has been utilised (15–18) as a quencher of $O_2^{\bullet-}$-mediated photooxidations, in similar concentrations to those employed in this work.

It is known that in the absence of oxygen, Rf photodegrades from its excited triplet state (^{3}Rf*), and the rate of this process can be determined from the initial evolution of the visible-absorption bands as a function of irradiation time (19). Figure 3 shows these spectral changes in 1:1 (*v*/*v*) methanol–water solutions through which N_2 was bubbled. In the presence of low concentrations of any SD (in the

Fig. 2. Oxygen consumption vs. irradiation time for (*a*) Rf (0.02 mmol/L), (*b*) SFX (0.4 mmol/L) + Rf (0.02 mmol/L) + NaN_3 (1 mmol/L), and (*c*) SFX (0.4 mmol/L) + Rf (0.02 mmol/L); solvent: H_2O.

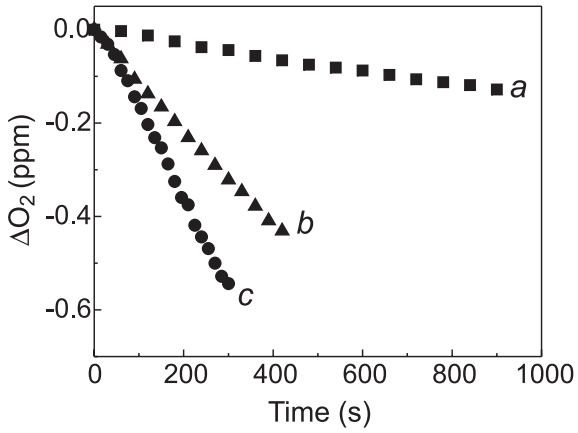
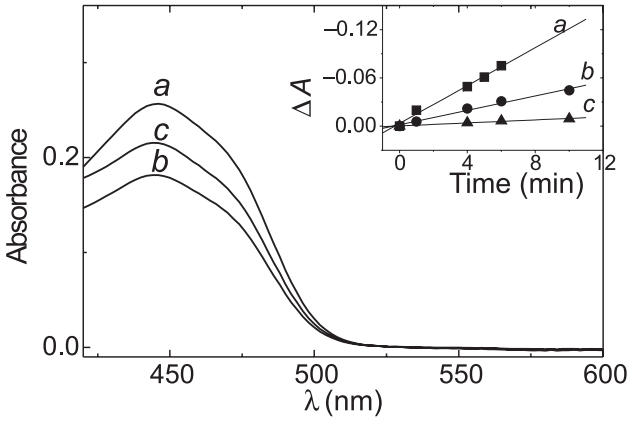


Fig. 3. Evolution of the 445-nm band of Rf in 1:1 (*v*/*v*) MeOH–H_2O upon irradiation with visible light (cutoff 400 nm). (*a*) Rf (0.015 mmol/L) not irradiated; (*b*) Rf (0.015 mmol/L) irradiated for 6 min; (*c*) Rf (0.015 mmol/L) + SFD (0.05 mmol/L), irradiated for 6 min. Inset: Rate of decrease of the 445-nm absorption band of Rf (0.015 mmol/L) upon irradiation with visible light in 1:1 (*v*/*v*) MeOH-H_2O. (*a*) Rf (0.015 mmol/L) alone; (*c*) Rf (0.015 mmol/L) + SFD (0.05 mmol/L); (*b*) Rf (0.015 mmol/L) + SFNA (0.05 mmol/L).



mmol/L range), the photodegradation rate of Rf was clearly decreased, suggesting a probable quenching of ^{3}Rf* by the SD. A typical illustration of this behaviour for SFD and SFNA is shown in the inset of Fig. 3.

Three experimental facts can be established through the combined analysis of the above results: (*a*) SD and Rf photodegrade upon visible-light irradiation in the presence of oxygen; (*b*) oxygenated species participate in the processes; and (*c*) electronically excited states of Rf participate in the generation of oxidative species and (or) in the photodegradation of the SD.

Results were interpreted and discussed on the basis of the kinetic scheme presented as Scheme 2. It shows the possible set of photoprocesses that could take place when a solution containing Rf and SD is irradiated with visible light in the

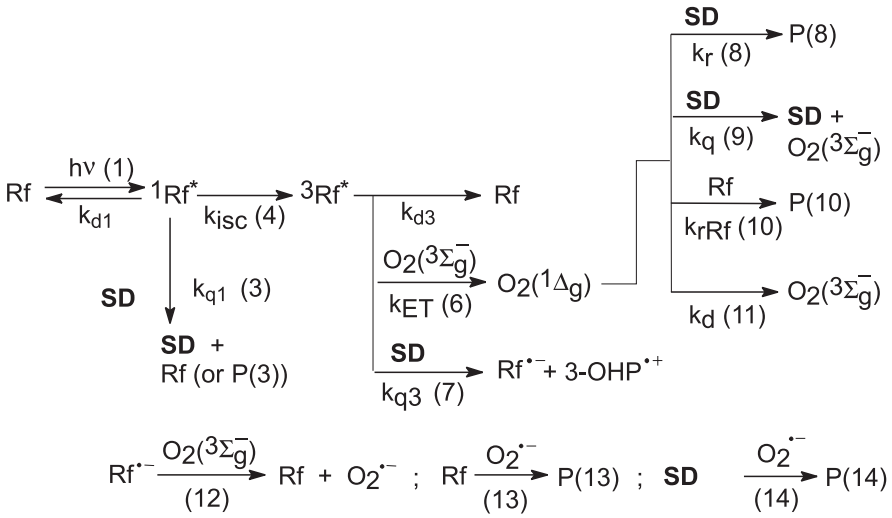
© 2004 NRC Canada

Table 1. Rate constants for the reactive (k_r) and overall (k_t) interaction of sulfanilic acid derivatives (SDs) with $O_2(^1\Delta_g)$ in H_2O and D_2O, respectively, ratio k_r/k_t, relative rates of oxygen uptake by the SD upon Rose Bengal (RB) and Rf sensitisation, and rate constants for the quenching of the singlet excited state (k_{q1}) and the triplet excited state (k_{q3}) of Rf by SD in 1:1 (*v*/*v*) MeOH–H_2O.

					Relative rate of oxygen consumption			
SD	Solvent	$k_r \times 10^7$ (L mol^{-1} s^{-1})	$k_t \times 10^7$ (L mol^{-1} s^{-1})	k_r/k_t	RB	Rf	$k_{q1} \times 10^9$ (L mol^{-1} s^{-1})	$k_{q3} \times 10^9$ (L mol^{-1} s^{-1})
SFNA	Water, pH/pD 7	0.33	0.70	0.47	0.12	0.035		
	Water, pH/pD 7 + SOD[a]					0.035		
	MeOH–water, 1:1						4.17	2.13
DAP	Water, pH/pD 7	0.20	1.21	0.16	0.074	0.29		
	Water, pH/pD 7 + SOD[a]					0.24		
	MeOH–water, 1:1						6.52	1.40
SFD	Water, pH/pD 7	0.23	1.17	0.19	0.083	1		
	Water, pH/pD 7 + SOD[a]					0.67		
	MeOH–H_2O, 1:1						5.57	1.17
SFX	Water, pH/pD 7	2.7	11.3	0.24	1	0.29		
	Water, pH/pD 7 + SOD[a]					0.29		
	MeOH–water, 1:1						4.76	1.27

[a]SOD 14 μg/mL.

Scheme 2. Possible reaction pathways for the Rose Bengal- and riboflavin-sensitised photooxidation of sulpha drugs.

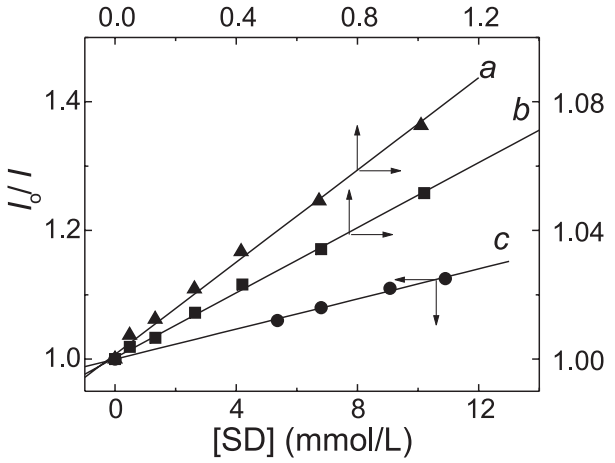


presence of oxygen. The initially generated excited singlet state ^{1}Rf* (process 1) can decay to the ground state (process 2), can be quenched by SD (process 3), or can undergo intersystem crossing to the excited triplet state ^{3}Rf* (process 4). The latter decays to the ground state or yields products (process 5), can be quenched by ground-state oxygen ($O_2(^3\Sigma_g^-)$) (process 6) dissolved in the medium, generating $O_2(^1\Delta_g)$ by energy transfer, or can be quenched by SD, yielding semireduced Rf ($Rf^{\bullet-}$) (process 7). $Rf^{\bullet-}$ can generate $O_2^{\bullet-}$ by reaction with molecular oxygen (process 12). The species $O_2(^1\Delta_g)$ can react with either SD (process 8) or Rf (process 10) or can be physically quenched by either SD (process 9) or the medium (process 11). In parallel, the generated species $O_2^{\bullet-}$ can react with Rf (process 13) or with SD (process 14).

To elucidate the reaction mechanism involving SD and Rf, under visible-light irradiation, we investigated the behaviour of electronically excited states of Rf and their potential interactions with ground-state SD in the absence and in the presence of dissolved molecular oxygen. Rf has a fluorescence emission band centered at 515 nm, with a fluorescence quantum yield of 0.25 (20, 21). In the presence of SD in concentrations much higher than 1 mmol/L, the stationary Rf-fluorescence emission intensity decreased, but the shape of the emission spectrum did not change. The Stern–Volmer constants for this interaction, K_{SV}, were determined (Fig. 4). Assuming that the fluorescence inhibition is a consequence of the quenching of ^{1}Rf* by SD, the K_{SV} values obtained will be equal to the ratio k_{q1}/k_{d1}, where k_{q1} and k_{d1} are the respective rate constants for the quenching of ^{1}Rf* by SD and for the deactivation of ^{1}Rf* (processes 3 and process 2, respectively, in Scheme 2). The respective k_{q1} values were obtained employing the literature value of 5.75 ns for $1/k_{d1}$ (22) and are shown in Table 1. These results indicate that ^{1}Rf* is practically unaffected by the presence of SD under the experimental conditions employed in static photolysis

© 2004 NRC Canada

Fig. 4. Stern–Volmer plots for the static fluorescence quenching of Rf (0.01 mmol/L) in 1:1 (*v*/*v*) MeOH–H_2O. (*a*) DAP; (*b*) SFD; (*c*) SFX.



(observation of the spectral changes and oxygen uptake experiments). As an example, less than 2% ^{1}Rf* is quenched in the presence of DAP (the most efficient quencher of ^{1}Rf*) at a concentration of 0.5 mmol/L, whereas for the quenching of 50% ^{1}Rf*, a DAP concentration of 30 mmol/L is necessary.

The interaction between ^{3}Rf* and SD (process 7) was studied through laser flash photolysis experiments in the absence of oxygen. The monoexponential decay curves indicated that the ^{3}Rf* lifetime appreciably decreased in the presence of any SD in the submillimolar concentration range. As before, a Stern–Volmer treatment (Fig. 5, inset) yielded the corresponding values of the bimolecular rate constant k_{q3} for the interaction (Table 1).

The transient absorption spectrum of the Rf solution 5 μs after the laser pulse (Fig. 5, trace *a*) is similar to that reported for ^{3}Rf* (22–24). A different spectrum was observed in the presence of 0.5 mmol/L of either of the two SDs studied (as illustrated in Fig. 5 (trace *b*) for the case of SFX), with a shape similar to that described (25) to account for electron-transfer processes to ^{3}Rf* from electron-donor substrates such as 2,6-dimethylphenol (26) and nucleotides (24), with the simultaneous generation of the well-known radical anion $Rf^{\bullet -}$ (24, 27, 28). The transient spectrum reported for $Rf^{\bullet -}$ (25), which possesses a non-pronounced maximum in the range of 530 nm, a region where the absorption of triplet Rf is comparatively low, and a smooth decrease up to ca. 700 nm, is closely coincident with trace *b* of Fig. 5.

As mentioned in the Introduction, the species $O_2^{\bullet -}$ and $O_2(^1\Delta_g)$ are usually present in aerobic Rf-phosensitised processes (27). Rf itself is also a moderate quencher of $O_2(^1\Delta_g)$ (Scheme 2, process 10), with a k_{rRf} value of 6×10^7 L mol^{-1} s^{-1}. To selectively study the potential contribution of the $O_2(^1\Delta_g)$-mediated process to the overall phototransformation of SD, TRPD and oxygen uptake experiments employing the sensitiser Rose Bengal were performed. This dye is possibly the most widely employed photosensitiser in $O_2(^1\Delta_g)$-mediated reactions, with a quantum yield of 0.76 for the generation of the oxygenated species (29). All SDs quenched the phosphorescence emission of $O_2(^1\Delta_g)$ to various extents (Fig. 6, inset). Table 1 shows the respective k_t values for the four SDs.

Fig. 5. Transient absorption spectra of Rf (0.02 mmol/L) in argon-saturated aqueous solution, in 1:1 (*v*/*v*) MeOH–H_2O: (*a*) 5 μs after the laser pulse, in the absence of SFX; (*b*) 30 μs after the laser pulse, in the presence of SFX (0.1 mmol/L). Inset: Stern–Volmer plot for the quenching of Rf excited triplet state by SFNA (*a*) and SFX (*b*).

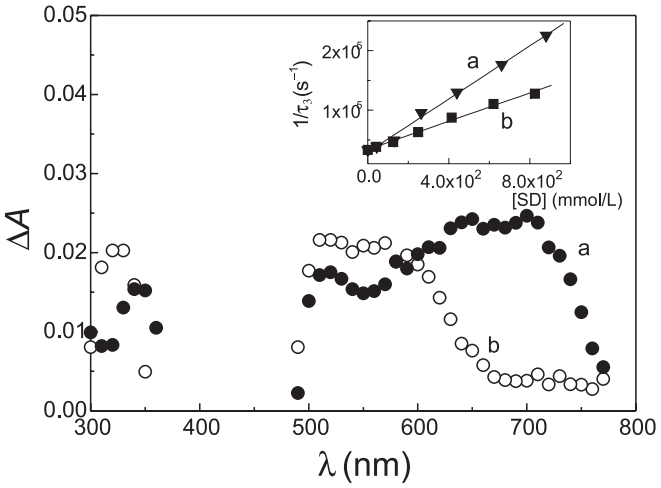
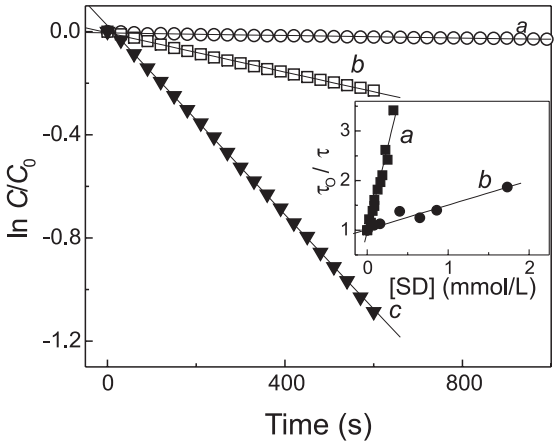


Fig. 6. First-order plots for oxygen uptake by SDs and the reference compound FFA (C_0 and C are the respective dissolved oxygen concentrations before photolysis and after photolysis) upon photoirradiation in 0.4 mmol/L aqueous solution in the presence of Rose Bengal ($Abs_{530\ nm}$ = 0.5) as a sensitiser: (*a*) DAP, (*b*) SFX; (*c*) FFA. Inset: Stern–Volmer plots for the phosphorescence quenching of $O_2(^1\Delta_g)$ in D_2O: (*a*) SFX; (*b*) SFNA.

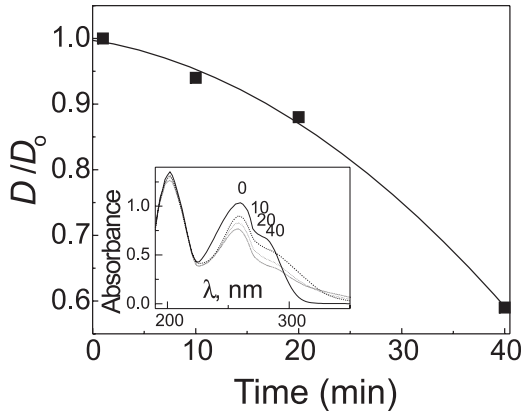


From oxygen uptake experiments (Fig. 6), kinetic data on the reactivity of SD towards $O_2(^1\Delta_g)$ were evaluated. The resulting k_r values are also shown in Table 1. In ancillary experiments performed in the presence of 1 mmol/L NaN_3, oxygen uptake by SD upon Rose Bengal sensitisation was practically eliminated, demonstrating the exclusive occurrence of the $O_2(^1\Delta_g)$-mediated mechanism, as unambiguously confirmed by the TRPD experiments.

Finally, the impact of the Rf-sensitised irradiation of SDs on their bacteriostatic power was tested. Figure 7 shows a plot of the ratio of the normalised diameter of the bacterista-

© 2004 NRC Canada

Fig. 7. Plot of the ratio of the normalised diameter of the bacteristatic inhibitory *halo* before photolysis (D_0) to that after photolysis (D) of a pH 7 aqueous solution of Rf ($Abs_{445\ nm}$ = 0.5) and SFX (0.5 mmol/L), as a function of photoirradiation time. Inset: Evolution of the absorption spectrum of the pH 7 aqueous solution of Rf ($Abs_{445\ nm}$ = 0.5) and SFX 0.5 mmol/L. Numbers on the spectra represent irradiation times in minutes.



tic inhibitory *halo* before photolysis to that after photolysis of a solution of SFX and Rf as a function of photoirradiation time. The results clearly show a decrease of the bacteriostatic activity of SFX due to the phototransformation, which was monitored through the respective absorption spectra of the nonirradiated and irradiated solutions.

Discussion

The data in Table 1 demonstrate that the relative rates of oxygen consumption in experiments employing Rose Bengal as a sensitiser do not parallel the respective data employing Rf sensitisation. One possible explanation for this discrepancy could be the operation of different mechanisms of oxygen uptake in the oxidation of SDs. When Rose Bengal is employed as a sensitiser, the relative reactivity via the $O_2(^1\Delta_g)$-mediated mechanism is important. In the case of Rf sensitisation, the experiments involving inhibition of oxygen uptake by NaN_3 and SOD demonstrate that a second mechanism, besides the $O_2(^1\Delta_g)$-mediated mechanism, could be operating. Although Rf is a fairly good generator of $O_2(^1\Delta_g)$ (2), it has been reported that several substrates are also oxidized by an Rf-sensitised process involving $O_2^{\bullet-}$ (30–32). Nevertheless, the direct generation of $O_2^{\bullet-}$ by Rf (step not included in Scheme 2) can be practically disregarded owing to the low quantum yield reported for such a process (2). Even so, its generation is possible through process 7, followed by process 12. The spectral evidence shown in Fig. 5 demonstrates the presence of the intermediate $Rf^{\bullet-}$. As indicated in Scheme 2, $^3Rf^*$ can be quenched by $O_2(^3\Sigma_g^-)$, producing $O_2(^1\Delta_g)$ (process 6), or by SD (process 7). It is currently accepted that the rate constant k_{ET} of process 6 is ca. 1/9 that of the diffusional value in the solvent used (33). Assuming a value for k_{ET} of 8×10^8 L mol^{-1} s^{-1}, i.e., 1/9 of the average diffusional rate constants in H_2O and MeOH (34), as well as an oxygen concentration in air-saturated MeOH–H_2O solutions of 1.2 mmol/L (35), it can be inferred that at an SD concentration of 0.4 mmol/L — similar to the concentration employed in the oxygen uptake experiments — the rate of process 7 ($k_{q3} \times$ [SD]), with a mean value of 1.5×10^9 L mol^{-1} s^{-1} for k_{q3} (Table 1), is only 20% lower than the rate of generation of $O_2(^1\Delta_g)$ (process 6) ($k_{ET} \times [O_2(^3\Sigma_g^-)]$). In other words, the species $Rf^{\bullet-}$ and $O_2(^1\Delta_g)$ seem to be generated to a similar degree, through process 6 and process 7, respectively.

In previous work (30, 36), we demonstrated the photochemical production of the species $Rf^{\bullet-}$ in several systems. It is known that under aerobic conditions $Rf^{\bullet-}$, in a subsequent step, produces the radical anion $O_2^{\bullet-}$, with a reported rate constant value of 1.4×10^8 L mol^{-1} s^{-1} for process 12. This reaction at the same time regenerates ground-state Rf, a crucial step in living organisms for which $O_2^{\bullet-}$ is a key intermediate in the oxygen redox chemistry (37). Hence, the oxygen consumption upon Rf-sensitised irradiation of SD could be due to two different mechanisms, and the prevalence of a given mechanism could depend on the reactivity of the oxygenated species towards the different substrates. Regarding the structure–reactivity analysis for the $O_2(^1\Delta_g)$ mechanism in the Rose Bengal-sensitised photoirradiation, it can be observed that SFNA, which contains the molecular moiety common to all SDs, interacts with $O_2(^1\Delta_g)$, and no substantial differences in k_t are observed to result from substitution by the groups aniline (DAP) or aminopyrimidine (SFD). On the other hand, both the overall and reactive interaction with $O_2(^1\Delta_g)$ dramatically increased upon incorporation of the isoxazole moiety as a substituent, as in the case of SFX. Nevertheless, according to the k_r/k_t ratio, higher photooxidation efficiency was exhibited by SFNA, whereas relatively low values of this ratio, and close to each other, were obtained for DAP and SFD. This means that DAP and SFD are fairly good photoprotectors against $O_2(^1\Delta_g)$, provided that they scavenge the oxidative species with a minimum of effective photodegradation. From a combined analysis of these results, and taking into account the inhibitory effect of SOD in the oxygen uptake experiments, it arises that only SFD and DAP are good reactants towards $O_2^{\bullet-}$, whereas the main source of oxygen uptake for SFX and SFNA is represented by the reaction with $O_2(^1\Delta_g)$.

Nevertheless, and regarding the potential activity of SDs as antioxidants, it is difficult to select the best photoprotector, simultaneously active against the oxygenated species $O_2(^1\Delta_g)$ and $O_2^{\bullet-}$. Those SDs that behave as the better $O_2(^1\Delta_g)$ physical quenchers concurrently exhibit high oxygen consumption rates due to the $O_2^{\bullet-}$ oxidative pathway.

Finally, the microbiological results for SFX, taken as a representative model for SDs, are self-explanatory: the photodegradation, upon Rf-sensitised visible-light irradiation of the drug is accompanied by a net loss of bacteriostatic activity.

Acknowledgements

Thanks are given to Consejo Nacional de Investigaciones Científicas y Técnicas (CONICET), Agencia Nacional de Promoción Científica y Tecnológica (ANPCyT), Secretarías de Ciencia y Técnica of the Universidad Nacional de Río Cuarto (SECyT UNRC), and Universidad Nacional de La Patagonia, SJB (SECyT UNP), all from Argentina, for financial support. The helpful assistance of Dr. Osvlado Córdoba, in the microbiological determinations, is acknowledged.

© 2004 NRC Canada

References

1. A. Albini and E. Fasani (*Editors*). Drugs: photochemistry and photostability. The Royal Society of Chemistry, Cambridge. 1998. Chap. 2. p. 51.
2. C.M. Krishna, S. Uppuluri, P. Riesz, J.S. Zigler, and D. Balasubramanian. Photochem. Photobiol. **54**, 51 (1991).
3. R.C. Straight and J.D. Spikes. *In* Singlet oxygen. Vol IV. *Edited by* A.A. Frimer. CRC Press, Boca Raton, Fla. 1985. Chap. 2
4. A.M. Edwards and E. Silva. J. Photochem. Photobiol. B, **63**, 126 (2001).
5. W.K. Joklik, H.L. Willett, and D.B. Amos (*Editors*). Zinsser' s microbiology. 20th ed. Appleton & Lange, Norwalk, Conn. 1992. p. 191.
6. F. Wilkinson, W.P. Helman, and A. Ross. J. Phys. Chem. Ref. Data, **24**, 663 (1995).
7. R.C. Weast and H.J. Astle (*Editors*). Handbook of chemistry and physics. 62nd ed. CRC Press, Boca Raton, Fla. 1981.
8. S. Miskoski and N.A. García. Collect. Czech. Chem. Commun. **56**, 1838 (1991).
9. C.S. Foote and T.Y. Ching. J. Am. Chem. Soc. **97**, 6209 (1975).
10. W.R. Hagg and J. Hoigné. Environ. Sci. Technol. **20**, 341 (1986).
11. S. Criado, S.G. Bertolotti, and N.A. García. J. Photochem. Photobiol. B, **34**, 79 (1996).
12. C. Pérez, M. Pauli, and P. Bazerque. Acta Biol. Med. Exp. **15**, 113 (1990).
13. R.M. Baxter and J.H. Carey. Nature (London), **306**, 575 (1983).
14. L. Zang and H.P. Misra. J. Biol. Chem. **267**, 17 547 (1992).
15. R.M. Baxter and J.H. Carey. Nature (London), **306**, 575 (1983).
16. L.-Y. Zang and H.P. Misra. J. Biol. Chem. **267**, 17 547 (1992).
17. P.G. Tratniek and J. Hoignè. Environ. Sci. Technol. **25**, 1596 (1991).
18. S. Criado, S. Bertolotti, and N.A. García. J. Photochem. Photobiol. B, **34**, 79 (1996).
19. B.J. Fritz, K. Matsui, S. Kasai, and A. Yoshimura. Photochem. Photobiol. **45**, 539 (1987).
20. P.F. Heelis. *In* Chemistry and biochemistry of flavoenzymes. Vol. 1. *Edited by* F. Muller. CRC Press, Boca Raton, Fla. 1991. pp. 171–193.
21. P.F. Heelis. Chem. Soc. Rev. **11**, 15 (1982).
22. S.G. Bertolotti, C.M. Previtali, A.M. Rufs, and M.V. Encinas. Macromolecules, **32**, 2920 (1999).
23. W.M. Moore and R.C. Ireton. Photochem. Photobiol. **25**, 347 (1977).
24. C. Lu, W. Lin, W. Wang, Z Han, S. Yao, and N. Lin. Phys. Chem. Chem. Phys. **2**, 329 (2000).
25. B. Orellana, A.M. Rufs, M.V. Encinas, C.M. Previtali, and S. Bertolotti. Macromolecules, **32**, 6570 (1999).
26. P.F. Heelis. Chem. Soc. Rev. **11**,15 (1982).
27. J.N. Chacon, J. McLearie, and R.S. Sinclair. Photochem. Photobiol. **47**, 647 (1988).
28. C. El Hanine-Lmoumene and L. Lindqvist. Photochem. Photobiol. **66**, 591 (1997).
29. F. Amat-Guerri, M.C. López-González, R. Martínez-Utrilla, and R. Sastre. J. Photochem. Photobiol. A, **53**, 199 (1990).
30. S.G. Bertolotti, C.M. Previtalli, A.M. Rufs, and M.V. Encinas. Macromolecules, **32**, 2920 (1999).
31. S. Criado, A. Pajares, J. Gianotti, G. Stettler, J.P. Escalada, S. Bertolotti, F. Amat-Guerri, and N.A. García. J. Photochem. Photobiol. B, **71**, 19 (2003).
32. I. Gutiérrez, S. Criado, S. Bertolotti, and N.A. García. J. Photochem. Photobiol. B, **62**, 133 (2001).
33. M. Koizumi, S. Kato, N. Mataga, T. Matsuura, and I. Isui. Photosensitised reactions. Kagakudogin, Kyoto, Japan. 1978.
34. J.G. Calvert and J.N. Pitts. Photochemistry. Wiley, New York. 1966.
35. S.L. Murov. Handbook of photochemistry. Marcek Dekker, New York. 1973.
36. E. Haggi, S. Bertolotti, S. Miskoski, F. Amat-Guerri, and N.A. García. Can. J. Chem. **80**, 62 (2002).
37. J.R. Kanofsky. Free Radical Res. Commun. **12–13** (Pt 1), 87 (1991).

© 2004 NRC Canada

Efficient photodecarboxylation of 3- and 4-acetylphenylacetic acids in aqueous solution

Lawrence A. Huck, Musheng Xu, Kaya Forest, and Peter Wan

Abstract: The photochemistry of 3- and 4-acetylphenylacetic acids (**6** and **7**) has been studied in aqueous solution. This work is a continuation of research efforts aimed at understanding the structural effects on the efficacy for benzyl carbanion photogeneration via photodecarboxylation. The nitro group (at the 3- and 4-positions) is known to be an exceptionally good activating group on the benzene ring — because of its enhanced electron-withdrawing effect in the excited triplet state — for photodecarboxylation and the related photo-retro-aldol type process. It is shown in this work that the acetyl group is an equally good activating group for the photodecarboxylation. Thus, the photochemistry of **6** and **7** parallels much of what was observed for the corresponding nitrophenylacetic acids **1** and **2**. Both **6** and **7** photodecarboxylate efficiently (Φ_d = 0.60 and 0.22, respectively, at pH 7) via the carboxylate form, to give observable (by laser flash photolysis) benzyl carbanion or related intermediates. The meta isomer **6** displays an acid-catalyzed pathway for photodecarboxylation at pH < 3 and along with its enhanced overall reactivity, is consistent with a meta effect of the acetyl group. Triplet state reactivity is inferred from sensitization and laser flash photolysis experiments. Based on the results of this work, the acetyl group may now be viewed as an "enhanced" electron-withdrawing group (in the excited state) when attached to a benzene ring (i.e., in acetophenone derivatives) that is capable of inducing ionic reactions, which is not the traditional photochemistry that is expected from such compounds.

Key words: photodecarboxylation, acid catalysis, acetophenone, photogenerated carbanion, enol, enolate.

Résumé : On a étudié la photochimie des acides 3- et 4-acétylphénylacétiques (**6** et **7**) en solution aqueuse. Ce travail est une continuation des efforts de recherche déployés pour comprendre les effets structuraux sur l'efficacité de la photogénération du carbanion benzyle par le biais d'une photodécarboxylation. Il est connu que, en raison de l'augmentation de leur effet électroaffinitaire dans l'état triplet excité, les groupes nitro (en positions 3 et 4) activent le noyau benzénique d'une façon exceptionnelle lors de réactions de photodécarboxylation et autres processus apparentés du type photo-rétro-aldolique. Dans ce travail, on a démontré que le groupe acétyle est aussi un bon groupe activant pour la réaction de photodécarboxylation. La photochimie des composés **6** et **7** est donc parallèle à ce qui a été observé avec les acides nitrophénylacétiques correspondants, **1** et **2**. Les composés **6** et **7** se décarboxylent d'une façon efficace (Φ_d = 0,60 et 0,22 respectivement, à un pH de 7), par le biais de la forme carboxylate, pour conduire à la formation du carbanion benzyle et d'autres intermédiaires apparentés qui peuvent être observés par photolyse éclair au laser. À des pH < 3, l'isomère méta, **6**, donne lieu à une photodécarboxylation impliquant une catalyse acide et, combiné avec sa plus grande réactivité globale, cette observation est en accord avec un effet méta du groupe acétyle. On déduit la réactivité de l'état triplet d'expériences de sensibilisation et de photolyse éclair au laser. Sur la base des résultats de ce travail, on peut considérer que, dans l'état excité, l'effet électroaffinitaire d'un groupe acétyle attaché à un noyau benzénique (comme dans les dérivés de l'acétophénone) est rehaussé, qu'il est capable d'induire des réactions ioniques ce qui ne correspond pas à la photochimie traditionnelle à laquelle on peut s'attendre avec de tels composés.

Mots clés : photodécarboxylation, catalyse acide, acétophénone, carbanion photogénéré, énol, énolate.

[Traduit par la Rédaction]

Introduction

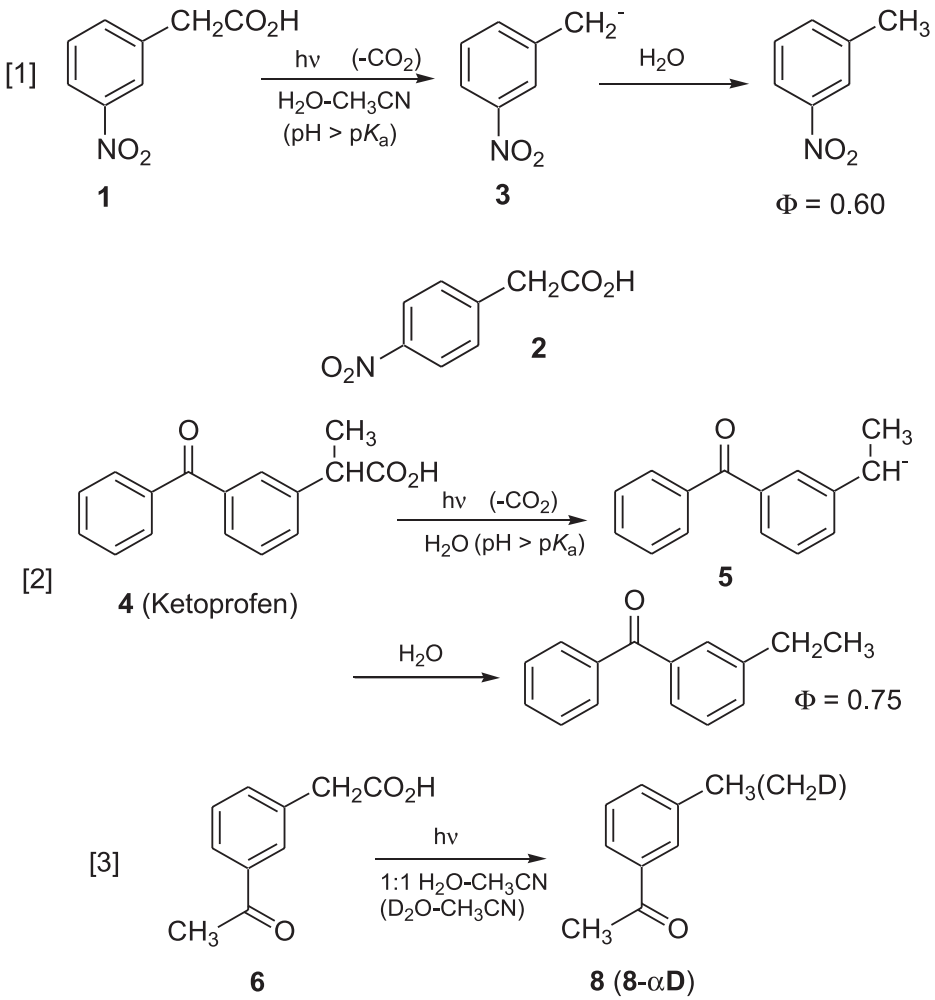
Decarboxylation is one of the simplest extrusion reactions in organic chemistry with wide-relevance in both organic synthesis (1) and in biological chemistry (1, 2). Photodecarboxylation is also well-known and has been studied extensively for a variety of organic substrates, where a number of mechanistic pathways are known to operate for the loss of CO_2 initiated by light (3). With respect to the photodecarboxylation of aromatic compounds, phenylacetic acids have been the most studied as they provide the obvious basis for Hammett-type studies, by varying substituents on the phenyl ring (3). Although we are not aware of any extended systematic studies in this approach — perhaps thwarted by the fact that the parent and many simple alkyl-substituted phenylacetic acids react with only low quantum efficiency (Φ < 0.02) (3) — it is known that 3- and 4-nitrophenylacetic acids (**1** and **2**, respectively, and related compounds) both react with very high quantum efficiency in the carboxylate form (Φ = 0.6) (4) via nitrobenzyl carbanion intermediates (e.g.,

Received 19 April 2004. Published on the NRC Research Press Web site at http://canjchem.nrc.ca on 3 February 2005.

L.A. Huck, M. Xu, K. Forest, and P. Wan.[1] Department of Chemistry, Box 3065, University of Victoria, Victoria, BC V8W 3V6, Canada.

[1]Corresponding author (e-mail: pwan@uvic.ca).

 doi: 10.1139/V04-122 © 2004 NRC Canada



3-nitrobenzyl carbanion (**3**) in eq. [1]). More recently, we have shown (5) that both the benzoyl (PhCO) and acetyl (CH_3CO) moieties also act as "enhanced" electron-withdrawing groups (when attached to a benzene ring) in the excited state, capable of mediating highly efficient photodecarboxylations of the corresponding substituted phenylacetic acid, providing a rational explanation for the previously reported efficient photodecarboxylation of ketoprofen (**4**) (via benzyl carbanion **5**, eq. [2]), a nonsteroidal anti-inflammatory drug that is known to be phototoxic (6). In this work, we detail our complete results on a study of the photodecarboxylation of 3- and 4-acetylphenylacetic acids (**6** and **7**, respectively) and show that their photochemical behaviour essentially *parallels* that observed for the corresponding nitro-substituted compounds **1** and **2**. Moreover, the results show that the acetyl group may be thought of as an enhanced "electron-withdrawing" group in the excited state, capable of inducing photochemistry that would not have been normally be anticipated when these compounds are viewed as substituted acetophenones.

Results and discussion

Product studies

The substrates for study (**6** and **7**) were readily prepared from the corresponding methylacetophenones (**8** and **9**) by initial NBS bromination of the methyl group, followed by substitution of the bromine by cyanide ion, and subsequent acid hydrolysis. Photolysis of **6** in H_2O–CH_3CN (1:1, pH 7, water portion, 10^{-3} mol L^{-1}, 254 or 300 nm, Rayonet RPR 100 photochemical reactor, 1–10 min, deoxygenated by argon purge) gave exclusively the corresponding photodecarboxylation product **8** in high yield (>80%, eq. [3]). Quantitative conversion was observed at sufficiently long photolysis times. No reaction was observed in the absence of light or when photolyzed in neat CH_3CN, the latter consistent with photoreactivity via the carboxylate ion (vide infra). Photolysis in D_2O–CH_3CN (1:1, pD 1 and 7) gave exclusively the corresponding α-deuterated product **8-αD**, consistent with the formation of a benzyl-carbanion-type intermediate in the photodecarboxylation. The overall reaction yield was only about 10%–20% lower in D_2O, indicative of a secondary solvent isotope effect for reaction, although the exact source of this effect is not known.

Similar photolysis of the para-isomer **7** gave two products at all conversions, the expected photodecarboxylation product **9** and a "dimer" **10** (formally derived from the coupling of two 4-acetylphenylmethyl radicals) (eq. [4]). Independent photolysis of **9** did not produce **10**. Photolysis in D_2O–CH_3CN gave the α-deuterated product **9-αD**, consistent with the formation of a benzyl-carbanion-type intermediate; no deuterium was incorporated into dimer **10**. The ratio of

© 2004 NRC Canada

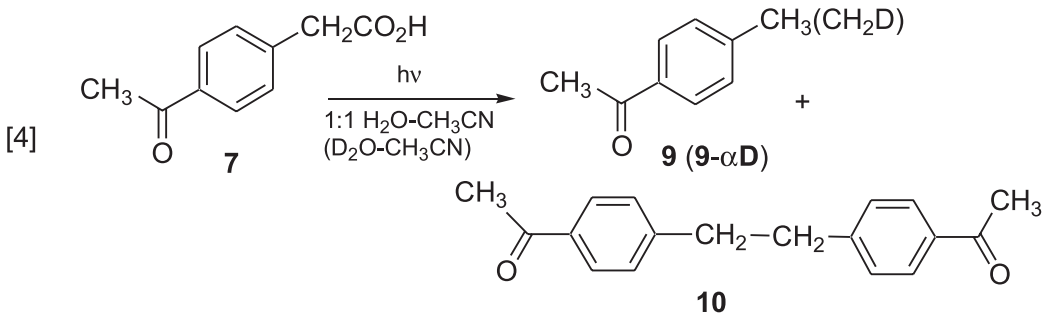
[4] 

Table 1. Ratio of products **9** vs. **10** observed in the photodecarboxylation of **7**.[a]

pH[b]	**9** (%)	**10** (%)
2.5	90	10
3.2	83	17
5.2	80	20
7.0	78	22
8.0	79	21
10.2	77	23
12.0	72	28

[a]Relative yields were calculated by ^{1}H NMR. Estimated errors: ±10% of quoted value. Conversions were 30%–70%. The relative yields were independent of conversion.
[b]pH of the aqueous portion (H_2O–CH_3CN, 1:1).

products **9** vs. **10** was found to be pH dependent (Table 1), with increasing yield of the dimer **10** (maximum relative yield ≈ 30%) with increasing pH. This trend is consistent with a mechanism in which the initially formed benzyl carbanion intermediate (**19a**) can react via two pathways, simple protonation to give **9** and a more complex "bimolecular" pathway (disproportionation-type route, vide infra) to give **10**. The protonation pathway would be favoured at lower pH, and this was indeed observed. Since the dimer **10** was observed as a photoproduct under relatively low lamp intensities (Rayonet photochemical reactor), it is unlikely that it arises via secondary photolysis of the anticipated intermediate carbanion (**19a**) of the photodecarboxylation (vide infra).

The above results observed for 4-acetylphenylacetic acid (**7**) is very similar to what is known in the photodecarboxylation of 4-nitrophenylacetic acid (**2**) (4) (Scheme 1). Photodecarboxylation of **2** gave a mixture of the expected 4-nitrotoluene (**11**) via simple protonation of the initially formed 4-nitrobenzyl carbanion (**12**) and a "dimeric" product (4,4′-dinitrobibenzyl, **13**). The relative yield of dimer **13** is enhanced at higher pH, becoming the major (>80%) product at pH > 10. Thermally generated **12** (via the deprotonation of **11** using strong bases and where there is no possibility of photoexcitation of the carbanion **12**) also gave **13** (7). The mechanism for the formation of **13** from **12** appears to be complex. Radical ions are believed to be involved (7) as strong EPR signals are observed. For the photodecarboxylation pathway, Craig and Pace (8) suggested the possibility of dimerization of the initially formed **12** based on kinetic studies for its decay, to give the radical dianion **14** (expected to be EPR active and consistent with the EPR signals observed) (8), which on work-up, is oxidized to give **13**. The very long lifetime of photogenerated **12** ($\tau \approx 60$ s, aqueous solution, pH 7) (7) would indicate slow reaction via simple protonation of the anion (carbon protonation is generally "slow" even in thermodynamically favourable cases), and hence, the possibility of dimerization to give radical dianion **14**. Such a mechanism does not operate for the 3-isomer **1** since the corresponding benzyl carbanion intermediate **3** is expected to be shorter lived. Indeed, the 3-nitrobenzyl carbanion (**3**) has never been detected as a transient, although the reason for this is still not clear.

The high yields and clean photochemistry observed for both **6** and **7** is further evidence for the enhanced activating effect of the acetyl group for photodecarboxylation. Moreover, no products were observed that are derived from the photochemistry of the carbonyl end of the molecule (e.g., via photoreduction or hydrogen abstraction), which is consistent with the notion that this group participates only as an enhanced electron-withdrawing group. Without the acetyl group, phenylacetic acid itself photodecarboxylates with only marginal quantum yields (<0.02) (3). That there is substantial charge transfer character (with negative charge polarized towards the carbonyl oxygen) in the reactive excited state of these compounds is further evidenced by observation of acid catalysis for the photodecarboxylation of **6** (vide infra).

Quantum yields

Quantum yields for photodecarboxylation were measured as a function of pH, using the photodecarboxylation of ketoprofen (**4**, $\Phi_d = 0.75$ (*6a*)) as a secondary standard (Fig. 1). H_2O–CH_3CN (1:1, v/v) was employed as the solvent in these studies because of experimental difficulties in performing semipreparative photolysis in 100% water. All the quoted pH are of the aqueous portion prior to mixing except for pH 4–8, where the pH was measured in the mixed solvent as adjustment to the pH had to be made with NaOH upon dissolution of the substrate. Since the quantum yield plot is for qualitative purposes only, the exact pH values are of less consequence. The quantum yields for photodecarboxylation (Φ_d) for both **6** and **7** are substantial at pH 7 (0.60 and 0.22, respectively), indicative of the highly activating nature of the acetyl group. For both compounds, the highest quantum yields were observed for the carboxylate form of the molecule (in the region where pH > pK_a; estimated pK_a for these compounds ≈ 3 to 4). Indeed, this is suggestive that only the carboxylate form is reactive in photodecarboxylation, as is the case for most arylacetic acids reported to date (3, 4). This is indeed the case for the para isomer **7** since the quantum yield vs. pH plot for this compound approaches zero at

© 2004 NRC Canada

Scheme 1.

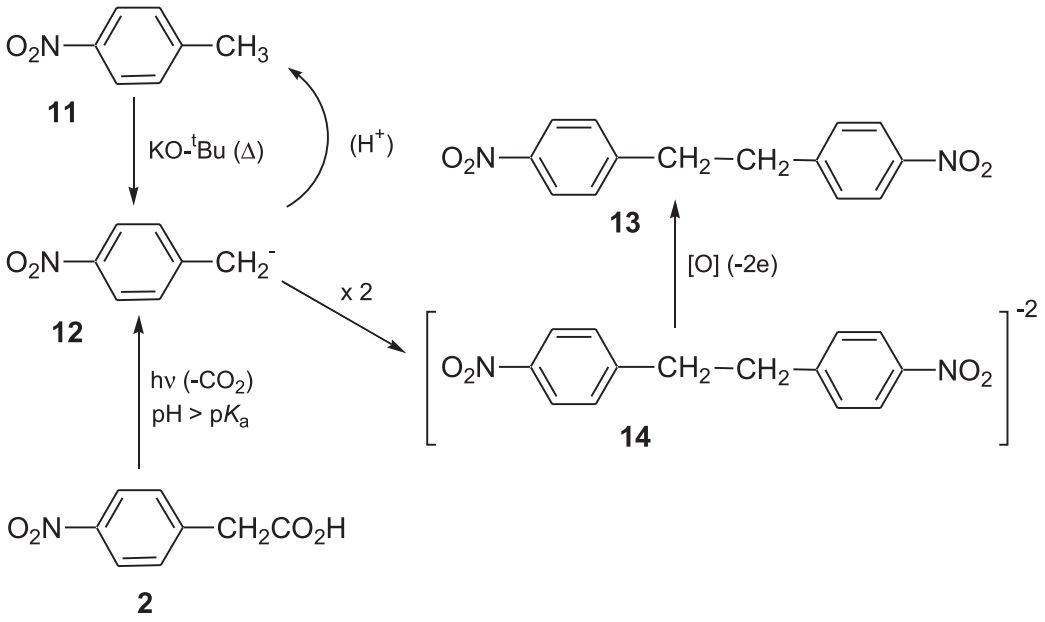
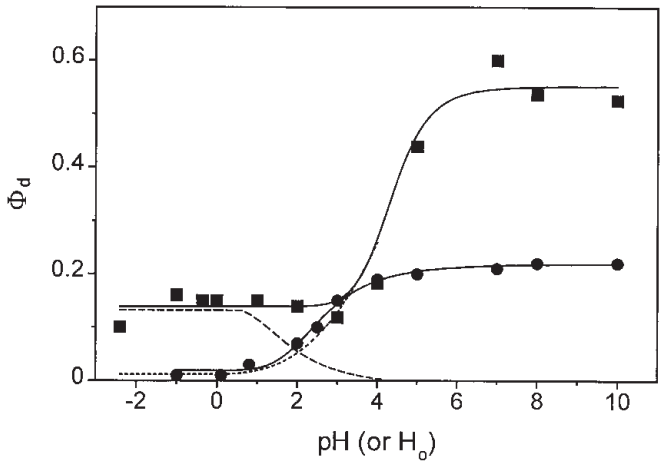


Fig. 1. Plots of quantum yields for photodecarboxylation (Φ_d) vs. pH for acetylphenylacetic acids **6** (squares) and **7** (circles) in H_2O–CH_3CN (1:1). The short-dashed line shows the expected trend for **6** if acid catalysis does not operate; the long-dashed line shows the resolved acid-catalyzed photodecarboxylation pathway.



pH < 1. For 3-acetylphenylacetic acid (**6**), the quantum yield is substantial (≈0.13) in acidic solution, which is indicative of an acid-catalyzed mechanism that operates only for the meta isomer. As shown in Fig. 1, the short-dashed line represents the expected trend in the absence of an acid-catalyzed pathway. The long-dashed line is the "resolved" contributing acid-catalyzed pathway. The "plateau" region observed in the pH 2 to H_o –2 region is therefore the sum of the acid- and "base"-catalyzed mechanisms. It should be emphasized at this point that product studies of **6** in the acid region discussed here also gave only one photoproduct (viz., **8**). Additionally, photolysis of **6** at pD 1 (where the mechanism is believed to be almost exclusively in the acid-catalyzed regime) gave **8**-α**D** exclusively. That is, the quantum yield vs. pH plot observed for **6** in Fig. 1 over the entire pH region is due to photodecarboxylation and not some other contributing photochemical reaction that may have been overlooked in the product studies.

The above "unusual" photoreactivity displayed by the meta acid **6** may be interpreted as another example of the well-known "meta effect" for the photochemistry of substituted benzenes that has been well-documented and studied by Zimmerman (9). That is, the meta-acetyl group in **6** can activate (in the excited state, by electron withdrawal) the corresponding attached acetic acid moiety more than a corresponding para-acetyl group. This results in a more reactive compound (as manifested in the higher quantum yields observed for **6** at all pH) as well as the operation of an observable acid-catalyzed pathway (vide infra).

Nanosecond laser flash photolysis (LFP) and reaction mechanisms

Although the results presented so far, based on product studies and quantum yield measurements vs. pH, show a close analogy in photochemical behaviour between the nitrophenylacetic acids (**1** and **2**) and the acetylphenylacetic acids (**6** and **7**), LFP results show mechanistic details for **6** and **7** that appear to be more complex than those reported for **1** and **2**. LFP studies of **6** and **7** were first performed in dry CH_3CN, where there is no photoreaction. Only one strong and broad ($\Delta OD \approx 0.12$) transient formed immediately after the laser pulse was observed for both compounds, with λ_{max} 330 nm (Fig. 2, shown for **7**), which was efficiently quenched by oxygen. This transient exhibited the same decay kinetics over the 330–430 nm region of the spectrum and hence assignable to one transient. For **6**, the lifetime (all single exponential fits) was 800 ns under N_2 and 50 ns under O_2; for **7**, 1200 ns under N_2 and 170 ns under O_2. This transient is assigned to the triplet state, in agreement with the known triplet state absorption for acetophenone itself (λ_{max} 330 nm (10)), although there is a

© 2004 NRC Canada

Fig. 2. Transient observed on LFP of **7** in 100% CH_3CN (266 nm excitation, N_2 purged). The signal at 340 nm is assigned to the triplet state. (130 ns (◆), 220 ns (□), 410 ns (●), 3000 ns after the laser pulse (×)). Inset: first-order decay at 340 nm; $\tau \approx 1000$ ns.

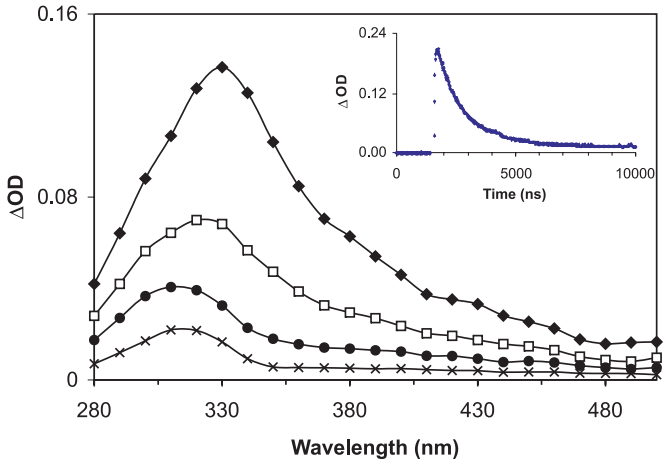
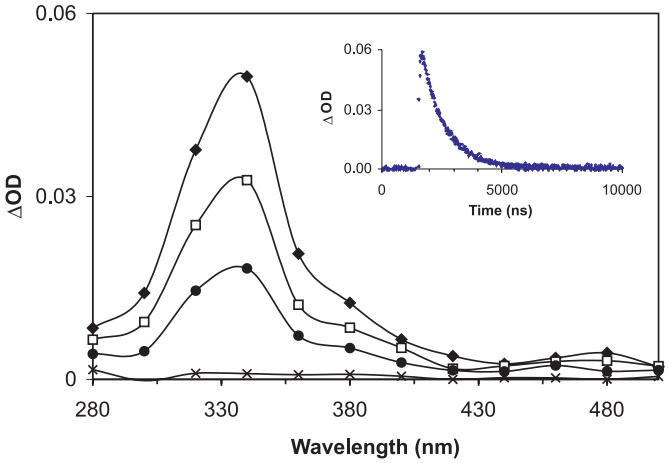


Fig. 3. Transient observed on LFP of **6** in H_2O–CH_3CN (1:1, pH 7) (266 nm excitation, N_2 purged). The transient is assigned to carbanion **15** or **16**. The decay is first order (130 ns (◆), 280 ns (□), 480 ns (●), 3000 ns after the laser pulse (×)). Inset: first-order decay at 340 nm; $\tau \approx 400$ ns.



weak residual longer lived signal at ca. 310 that was not assigned.

LFP studies of **6** and **7** were then carried out in H_2O–CH_3CN (1:1, at several different pH), a solvent where these compounds photodecarboxylate efficiently (except for **7** at pH < 2). The transient observed immediately upon the laser pulse for **6** in pH 7 is shown in Fig. 3. The spectral band is narrower and weaker than that observed in 100% CH_3CN, with λ_{max} at 340 nm. The same decay kinetics (single exponential decay) was observed across the whole spectral range with no significant residual signals. In addition, the transient is significantly longer lived in D_2O (about twofold) and is somewhat sensitive to oxygen but not to the same extent as the transient observed in 100% CH_3CN (Table 2). Therefore, although this transient has absorption in about the same spectral region as the triplet state assigned above, it *cannot* be the triplet state. Indeed, the absence of the triplet state in aq. CH_3CN would suggest that it may be the reactive state in the photodecarboxylation, given that aromatic ketones are known to intersystem cross very efficiently. Triplet sensitization experiments were carried out in which D_2O–CD_3CN (1:1) was replaced with D_2O–acetone-d_6 (1:1, with λ_{ex} = 300 nm), which resulted in 30% higher yield (when acetone-d_6 was used). Since most of the exciting light is absorbed by acetone in these experiments, the inference is that the triplet state of **6** is reactive towards photodecarboxylation, consistent with the LFP data. However, we cannot rule out reaction from the singlet state, although such a pathway is probably insignificant.

Table 2. Lifetimes of observed transients for **6** and **7** by LFP.

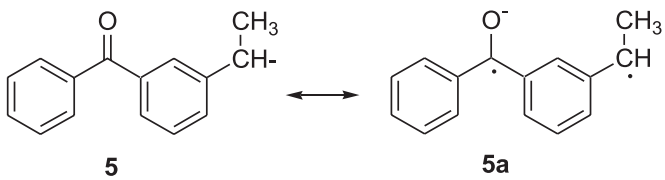
	Observed lifetimes (ns)[a]			
λ[b]	**6** (In H_2O)[c]	**6** (In D_2O)[c]	**7** (In H_2O)[c]	**7** (In D_2O)[c]
310			4600 (600)	4400 (630)
320			3400 (400)	3200 (460)
340	390 (220)	910 (190)	1800 (260)	1700 (300)
400	460 (140)	920 (190)	1700 (420)	3900 (710)

[a]Lifetimes obtained from first-order decays at the respective wavelength under N_2, except for 310, 320, and 340 nm of **7**, which did not obey first-order kinetics and the lifetimes are estimated based on force fitting to a single exponential decay. Values in brackets obtained under O_2. Estimated error: ±10% of quoted value. All transients were observed immediately after the laser pulse.

[b]Wavelength at which decay was monitored. Corresponds to λ_{max} for **6** at 340 nm and for **7** at 310 and 400 nm (shoulder).

[c]At pH(D) = 7. Cosolvent is 50% CH_3CN.

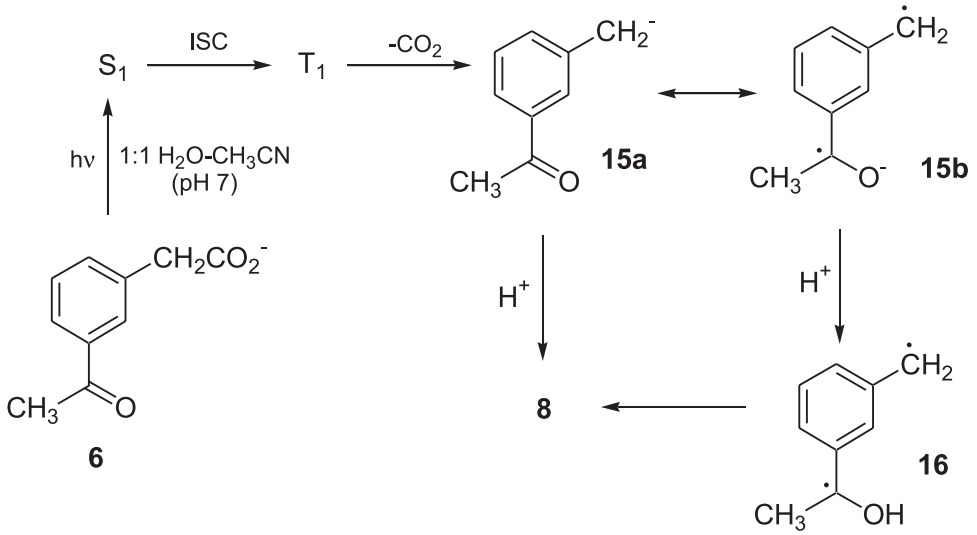
Scaiano and Monti and their respective co-workers (6*b*–6*d*) have carried out extensive LFP studies of the photodecarboxylation of ketoprofen (**4**), a reaction that is closely related to the ones being studied in the present work. They assigned a transient with λ_{max} at 330 and 580 nm as owing to carbanion **5**, although its spectral characteristics suggested that this anion might have substantial contribution from the radical anion (non-Kekulé) resonance form **5a**.



Lifetimes of this species has been reported to be about 200 ns in aqueous solution with much longer lifetimes when photogenerated in some organic solvents (6*b*–6*d*). In addition, a simple benzyl anion is known to absorb at ca. 350 nm (11). In view of these literature precedents and the observed primary solvent isotope effect on decay of the observed 340 nm LFP transient for **6**, it seems reasonable that it be assigned to (singlet ground state) benzyl carbanion **15a/15b** (Scheme 2). It is assumed that if the benzyl carbanion was initially photogenerated in its triplet state that intersystem crossing has occurred during the laser pulse. We cannot rule out formation of the corresponding (ground state) non-Kekulé enol **16** at this pH since the pK_a of some aromatic ketyls are known to be in the 7 to 8 range (6*c*). Indeed,

© 2004 NRC Canada

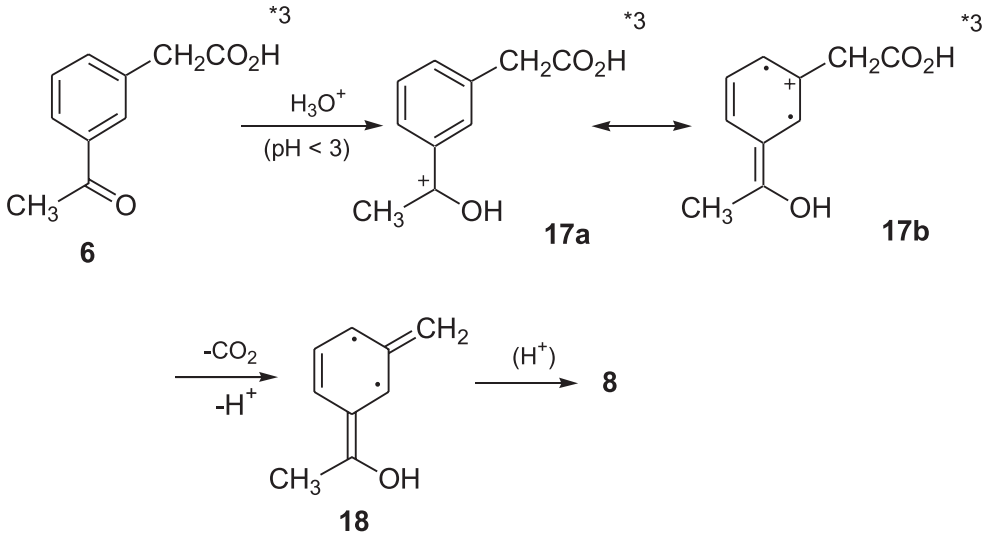
Scheme 2.



protonation at oxygen would be diffusion controlled in this case (at pH 7 or lower), further arguing that the transient may actually be the non-Kekulé biradical **16**. This species would still be quenchable by oxygen and sensitive to D_2O. LFP studies at pH 3 gave essentially the same transient but at pH 0, only very weak signals were observed, consistent with a change in reaction mechanism as required from data presented in Fig. 1. The acid-catalyzed photodecarboxylation pathway is given in eq. [5]. Support for this mechanism comes from the recent work of Wirz and co-workers (12) who showed that aromatic ketones such as benzophenone and acetophenone are readily photoprotonated via the triplet excited state, giving rise to reactive electronically excited carbocations that can undergo overall hydration (which for the parent systems studied are entirely reversible). In the case of acetophenone – phenylacetic acid **6**, such a photoprotonation would give rise to **17a/17b**, since Wirz and co-workers (12) have also shown that most of the positive charge of such cations reside at the meta positions (a form of meta activation (9)). An activated species such as **17b** would be expected to decarboxylate (with concerted loss of the carboxylic acid proton to water), to generate a species such as **18** (which may or may not be identical to **16**). In any event, in an acid medium, we anticipate that **18** will quickly form **8**. This mechanistic scheme also gives an explanation as to why acid catalysis for photodecarboxylation was not observed for the para-acid **7** since the positive charge of the protonated species would not be expected to be localized significantly at the para position. The question of why the quantum yields measured in acid reach a plateau below pH 1 (Fig. 2) can be explained simply by noting that **17a/17b** can deactivate back to ground state **6** without continuing on to **18**. In addition, triplet excited state **6** could also suffer simple nonproductive quenching by protons, which would compete with the acid-catalyzed photodecarboxylation process itself. Thus, one would not expect the quantum yields to continue to rise until quantum yield of unity is reached.

LFP results for the para-isomer **7** are more complex. Although strong signals (ΔOD up to 0.1, Fig. 4) were observed immediately upon the laser pulse, three major transients could be discerned at 310, 355, and 400 nm (Table 2). At least two transients are contained within the broad absorp-

[5]



© 2004 NRC Canada

Scheme 3.

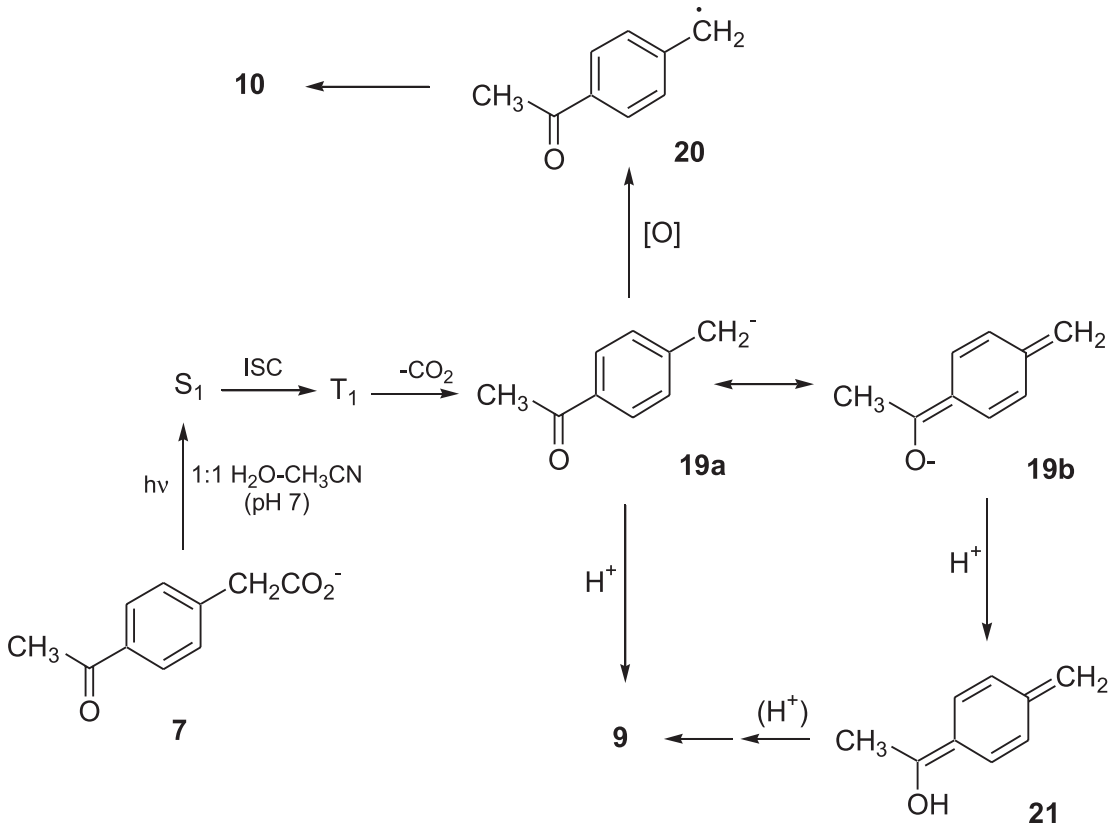
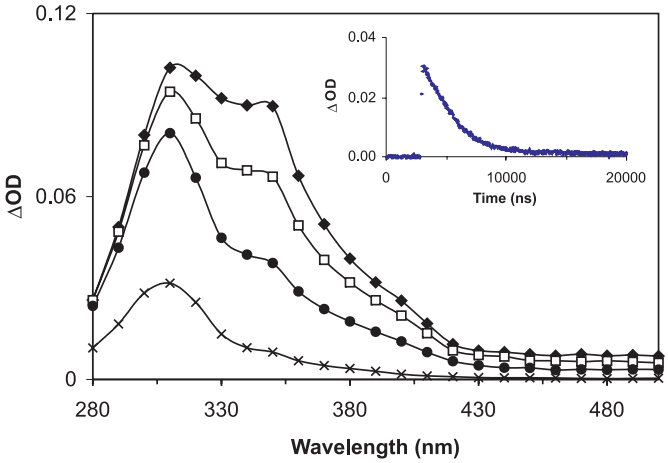


Fig. 4. Transients observed on LFP of **7** in H_2O–CH_3CN (1:1, pH 7, 266 nm excitation, N_2 purged); 500 ns (◆), 800 ns (□), 1600 ns (●), 13 000 ns after the laser pulse (×)). The transient at 400 nm (shoulder) is assigned to **19** or **21** and decays with first-order kinetics (inset) with $\tau \approx 1700$ ns.



tion in the 300–380 nm region, where the decays do not obey simple first-order kinetics, likely caused by the overlapping absorptions; only the 400 nm transient exhibited first-order decay. This increased complexity is not surprising since this compound gave two photoproducts (**9** and **10**) at all pH. Analogous experiments to **6** (vide supra) were performed to identify as many of the observed transients as possible, within the scope of the time resolution of the laser equipment. When H_2O was replaced with D_2O, an increase in lifetime (by about twofold) of the 400 nm transient was observed, while the lifetimes of the other transients were essentially unaffected. The products of the photodecarboxylation of **7** are formally derived from a benzyl carbanion **19** (to give **9**) and a benzyl radical **20** (to give **10**). Therefore, we assign the 400 nm transient to (ground state) carbanion **19a/19b** (Scheme 3), although we cannot rule out that it is in fact the corresponding enol **21**. The mechanism of photodecarboxylation of **7** (Scheme 3) proceeds in a similar fashion as proposed for **6**. After extrusion of CO_2 (via the carboxylate form), a benzyl carbanion (**19**) is generated, which can follow two possible routes to the product. It is either carbon protonated immediately to give **9** or is protonated at the oxygen to give enol **21**. Either pathway eventually leads to product **9**. The LFP transient at 400 nm could be reasonably assigned to either **19** or **21**. Compared to the analogous transient **15/16** for the meta acid **6**, the present transient is longer lived since the structure would have better resonance stablization. Improved resonance stabilization also explains the observed red shift (≈60 nm) of this transient.

The benzyl radical **20** is likely contained within the broad strong 300–380 nm absorption. These transients are all sensitive to oxygen, as would be required for such a radical. The parent benzyl radical itself is known to absorb at ≈315 nm (11). Although our results cannot discern among the various mechanisms possible for formation of **10,** we propose that one possible pathway is formation of **20** via oxidation of **19** (either by residual oxygen or by absorption of a photon). Another possibility is the coupling of two mole-

© 2004 NRC Canada

cules of **19**, giving a diradical dianion, which is then oxidized, similar to that proposed for **2** (Scheme 1). However, the much shorter lived **19** (1700 ns) compared to the para nitro analogue **12** (60 s) makes this less likely. However, it would appear that the longer lifetime of **19** compared to the corresponding meta carbanion **15** does allows for the minor "radical" pathway giving rise to the corresponding dimer **10**.

Summary

We have shown that acetophenone derivatives **6** and **7** undergo efficient photochemistry that is best rationalized as being due to the enhanced electron-withdrawing character of the acetyl group in the triplet excited state. The photochemistry mirrors some of the observed behaviour for the much-studied nitrophenylacetic acids **1** and **2**. The triplet state is reactive, although we cannot rule out residual singlet state reaction. Our results suggest that new types of photochemistry via ionic intermediates may be available for aromatic ketones, which will require a reevaluation of the present theoretical understanding of ketone photochemistry, at least in polar solvents such as water.

Experimental

General

^{1}H NMR spectra were recorderd on a Bruker AC300 (300 MHz) instrument in $CDCl_3$ unless otherwise specified. MS and HR-MS were obtained on a Kratos Concept H (EI) instrument. UV–vis spectra were recorded on a Varian Cary 5 instrument. Acetonitrile (HPLC or spectral grade) used for LFP experiments was dried by distillation from calcium hydride. Organic extracts were dried over anhydrous magnesium sulfate and filtered. pH(D) values were measured using a Fisher Accumet 915 pH meter.

Materials

3-Acetylphenylacetic acid (6)

3-Methylacetophenone (Aldrich, 5.17 g, 38 mmol) was added to a solution consisting of 100 mL CCl_4, 1.2 equiv. *N*-bromosuccinimide (8.23 g, 46 mmol), and a catalytic amount of benzoyl peroxide, and refluxed for 20 h under N_2. The bromination product was isolated by first evaporation of the solvent and subsequent dissolution in CH_2Cl_2 (with back-wash with water). This crude material was then dissolved in 10% H_2O–CH_3CN and refluxed for 4 h with 1.1 equimolar of NaCN. The resulting crude cyano derivative was hydrolyzed directly with concd. HCl (refluxed in 50 mL for 5 h). The crude acid product was isolated by evaporation of the solvent to give a brown solid, which was then dissolved in a minimum of hot water, filtered, and cooled. The crude product was recrystallized again in water to yield a white powder (0.38 g, 12% overall yield); mp (uncorrected) 96–99 °C (lit. value (13) 106 °C). ^{1}H NMR (300 MHz) δ: 2.59 (s, 3H, CH_3), 3.71 (s, 2H, $ArCH_2$), 7.43 (m, 2H, ArH), 7.86 (m, 2H, ArH), 10.8 (in acetone-d_6, br, COOH). ^{13}C NMR (250 MHz) δ: 26.6 (CH_3), 40.7 (CH_2), 127.5 (ArCH), 128.9(ArCH), 129.3 (ArCH), 133.8 (*ipso*), 134.1(ArCH), 137.5 (*ipso*), 176.6 (CO_2H), 197.9 (R_2CO). HR-MS calcd. for $C_{10}H_{10}O_3$: 178.0630; found: 178.0631.

4-Acetylphenylacetic acid (7)

The desired product was synthesized in a similar procedure and with comparable yield to **6** previously. The compound is a white powder, mp (uncorrected) 106–108 °C (lit. value (13) 119 °C). ^{1}H NMR (300 MHz, $CDCl_3$) δ: 2.58 (s, 3H, CH_3), 3.70 (s, 2H, $ArCH_2$), 7.36 (d, J = 8 Hz, 2H, ArH), 7.92 (d, J = 8 Hz, 2H, ArH), 12.4 (in acetone-d_6, br, COOH). ^{13}C NMR (250 MHz) δ: 26.6 (CH_3), 40.8 (CH_2), 128.7 (CH), 129.7 (CH), 136.2 (*ipso*), 138.6 (*ipso*), 176.1 (CO_2H), 197.8 (R_2CO). HR-MS calcd. for $C_{10}H_{10}O_3$: 178.0630; found: 178.0629.

Product studies

Preparative photolyses for **6** and **7** were carried out with samples (10–100 mg) dissolved in the appropriate solvent (40–100 mL) and transferred to a 100 mL quartz tube. The solution was irradiated in a RPR-100 photochemical reactor fitted with 254 nm or 300 nm lamps with continuous cooling (by a cold finger) and purging by a stream of argon for approximately 10 min before and continuously during irradiation (via a long stainless steel needle). Photolysis times ranged from 1 to 30 min, depending on the conversion desired, the efficiency of the reaction, and the size of the sample. After photolysis, aqueous samples were acidified (if necessary) and extracted with CH_2Cl_2. Direct evaporation of the organic solvent was used when samples were irradiated in wholly organic solvents. As the photoproducts are somewhat volatile, the temperature was kept under 30 °C during evaporation and the flask was returned to atmospheric pressure as soon as the solvent was removed. Typical experiments are described in the following.

Photolysis of 6 (pH 7)

Compound **6** (50 mg) was dissolved in 100 mL of H_2O–CH_3CN (1:1) and the pH was adjusted to 7 using aq. NaOH. The solution was irradiated using 4 × 254 nm lamps for 15 min. After photolysis, the solution was made acidic with concd. HCl (to pH < 2) and extracted with CH_2Cl_2 (3 × 40 mL). The solvent was dried over $MgSO_4$ and concentrated on a rotary evaporator. The ^{1}H NMR (300 MHz) was obtained in $CDCl_3$ and gave a spectrum identical to that of the commercial 3-methylacetophenone δ: 2.40 (s, 3H, $ArCH_3$), 2.58 (s, 3H, $COCH_3$), 7.37 (m, 2H, ArH), 7.74 (m, 2H, ArH). Conversion to **8** was 100%. MS (*m*/*z*): 134 (M^+).

Photolysis of 6 (pH ≈ 0)

Compound **6** (50 mg) was dissolved in 10% H_2SO_4–CH_3CN (1:1). Procedure as for pH 7 previously. The NMR spectrum of the product was the same as pH 7, with unreacted **6**. Conversion to **8** was 15% by ^{1}H NMR.

Photolysis of 6 (pD 7)

Compound **6** (100 mg) was dissolved in 100 mL of D_2O–CH_3CN (1:1) and the pD was adjusted to 7 with a solution of NaOD–D_2O. The ^{1}H NMR (300 MHz) spectrum of the photoproduct (76% yield) was identical to that of commercial 3-methylacetophenone except that the aromatic methyl group was monodeuterated (product **8**-α**D**). It was separated from the product mixture using column chromatography (CH_2Cl_2, R_f = 0.73): δ: 2.38 ("t", 2H, J = 2 Hz, $ArCH_2D$), 2.58 (s, 3H, $COCH_3$), 7.34 (m, 2H, ArH), 7.74 (m, 2H, ArH).

© 2004 NRC Canada

Photolysis of 7

Compound **7** (100 mg) was dissolved in 80 mL of H_2O–CH_3CN (1:1) and the pH was adjusted to 7.5 using aq. NaOH. The solution was irradiated using 254 nm lamps for 30 min. After photolysis, the solution was made acidic with concd. HCl (so the pH < 2) and extracted with CH_2Cl_2 (3 × 40 mL). The solvent was dried with $MgSO_4$ and concentrated. The products were separated by preparative TLC (5% EtOAc–CH_2Cl_2) to give two photoproducts, 4-methylacetophenone (**9**, 78%) and a dimer **10** (22%). The ^{1}H NMR (300 MHz) spectrum of **9** was identical to that of the commercial 4-methylacetophenone δ: 2.25 (s, 3H, $ArCH_3$), 2.42 (s, 3H, $COCH_3$), 7.20 (d, J = 8 Hz, 2H, ArH), 7.80 (d, J = 8 Hz, 2H, ArH). MS (EI, m/z): 134 (M^+). Dimer **10**: ^{1}H NMR (300 MHz) δ: 2.58 (s, 6H, CH_3CO), 3.00 (s, 4H, $ArCH_2$-), 7.20 (d, 4H, J = 8 Hz, ArH), 7.85 (d, 4H, J = 8 Hz, ArH). MS (EI, m/z): 266 (M^+).

Triplet sensitization of 6

Compound **6** (9.1 mg) was dissolved in 3.0 mL of D_2O–CD_3CN (2:1). Two aliquots (0.5 mL) were removed and diluted, one was with 0.5 mL CD_3CN and the other with 0.5 mL acetone-d_6. The solutions (8×10^{-3} mol L^{-1}) were placed into NMR tubes and purged with argon. The solutions were photolyzed for 90 s (8 × 300 nm lamps). Photodecarboxylation yields (by ^{1}H NMR) were 33% and 43% for D_2O–CD_3CN vs. D_2O–acetone-d_6 solutions, respectively.

Quantum yields

Photodecarboxylation quantum yields for **6** and **7** were determined using relative methods that involved comparison of the yields of decarboxylated product between ketoprofen (**4**) with a known quantum yield (secondary actinometric standard) of 0.75 (6) and those of the compounds in question, as determined by ^{1}H NMR integration. A known amount of standard was dissolved in CH_3CN–H_2O (1:1, 2×10^{-3} mol L^{-1} adjusted to pH 7) and photolyzed as above for 1 min (4 lamps, 254 nm). An equimolar amount of the compound of unknown quantum yield was irradiated under the same conditions and decarboxylation determined by ^{1}H NMR integration of the benzyl methyl protons.

Nanosecond laser flash photolysis (LFP)

LFP studies were carried out at the University of Victoria laser flash photolysis facility. A Spectra-Physics Nd:YAG laser (266 nm, ~10 ns, <30 mJ/pulse) was used for excitation and signals were digitized with a Tektronix TDS 520 recorder. Samples of OD ~ 0.4 at 266 nm were prepared and irradiated in 7 mm quartz cells. Flow cells were used to obtain spectra and kinetic data. Runs using static cells in aqueous solution gave irreproducible results because of efficient depletion of substrate because of efficient photochemical decarboxylation. Solutions were purged (with N_2 or O_2) prior to and continuously during LFP studies.

Acknowledgments

The Natural Sciences and Engineering Research Council of Canada (NSERC) and the University of Victoria are acknowledged for continued support of this research. We thank Matt Lukeman for help with some initial LFP experiments.

References

1. M.B. Smith and J. March. Advanced organic chemistry. 5th ed. Wiley-Interscience, New York. 2001.
2. A. Williams. Concerted organic and bio-organic mechanisms. CRC Press, Boca Raton, Florida. 2000.
3. D. Budac and P. Wan. J. Photochem. Photobiol. A, **67**, 135 (1992).
4. (*a*) J.D. Margerum and C.T. Petrusis. J. Am. Chem. Soc. **91**, 2467 (1969); (*b*) P. Wan and S. Muralidharan. J. Am. Chem. Soc. **110**, 4336 (1988); (*c*) J. Morrison, H. Osthoff, and P. Wan. Photochem. Photobiol. Sci. **1**, 384 (2002).
5. M. Xu and P. Wan. J. Chem. Soc. Chem. Commun. 2147 (2000).
6. (*a*) L.L. Costanzo, D. DeGuidi, G. Conderelli, A. Cambria, and M. Fama. Photochem. Photobiol. **50**, 359 (1989); (*b*) G. Cosa, L.J. Martinez, and J.C. Scaiano. Phys. Chem. Chem. Phys. **1**, 3533 (1999); (*c*) S. Monti, S. Sortino, G. DeGuidi, and G. Marconi. J. Chem. Soc. Faraday Trans. **93**, 2269 (1997); (*d*) M. Laferrière, C.N. Sanramé, and J.C. Scaiano. Org. Lett. **6**, 873 (2004).
7. (*a*) G.A. Russell and E.G. Janzen. J. Am. Chem. Soc. **89**, 300 (1967); (*b*) E. Buncel and B.C. Menon. J. Am. Chem. Soc. **102**, 3499 (1980).
8. B.B. Craig and M.D. Pace. J. Chem. Soc. Chem. Commun. 1144 (1987).
9. (*a*) H.E. Zimmerman. J. Phys. Chem. A, **102**, 5616 (1998); (*b*) H.E. Zimmerman. J. Am. Chem. Soc. **117**, 8988 (1995).
10. S.L. Murov, I. Carmichael, and G.L. Hug. Handbook of photochemistry. 2nd ed. M. Dekker, New York. 1993. p. 101.
11. F.L. Cozens, W. Ortiz, and N.P. Schepp. J. Am. Chem. Soc. **120**, 13 543 (1998).
12. M. Ramseier, P. Senn, and J. Wirz. J. Phys. Chem. A, **107**, 3305 (2003).
13. D. Papa, E. Schwenk, and A. Klingsberg. J. Am. Chem. Soc. **68**, 2133 (1946).

© 2004 NRC Canada

Synthesis and thermolysis of a spiro-fused oxadiazoline — Evidence for sequential formation of carbene and oxirane intermediates, and for oxirane dimerization

Arkadiusz Klys, Wojciech Czardybon, John Warkentin, and Nick Henry Werstiuk

Abstract: The spiro-fused oxadiazoline, 3,4-diaza-2,2-dimethyl-1,6,10-trioxaspiro[4.5]dec-3-ene, when thermolysed in a sealed tube in benzene-d_6 at 110 °C, afforded acetone and an apparent oxirane intermediate (2,2-dimethyl-1,4,8-trioxaspiro[2.5]octane) that could not be isolated. Attempts to isolate the oxirane gave a dimer (8,8,11,11-tetramethyl-1,5,7,10,12,16-hexaoxadispiro[5.2.5.2]hexadecane) as the major product. The oxirane is thermally stable at 110 °C but it is very sensitive to water, as indicated by its gradual disappearance after the tube was opened. The dimer of the oxirane is believed to form from a cation arising from the ring-opening of the oxirane when it reacts with moisture. This cation then reacts with the oxirane itself to regenerate water, which is effectively a catalyst for conversion of the oxirane to the dimer.

Key words: carbene, dioxacarbene, dialkoxyoxirane, oxadiazoline, 2,5-dihydrooxadiazole.

Résumé : Opérant dans un tube scellé, en solution dans du benzène-d_6 et à une température de 110 °C, on a réalisé la thermolyse de l'oxadiazoline à fusion spiro, 3,4-diaza-2,2-diméthyl-1,6,10-trioxaspiro[4.5]déc-3-ène, qui conduit à la formation d'acétone et d'un intermédiaire qui n'a pas été isolé et qui serait le 2,2-diméthyl-1,4,8-trioxaspiro[2.5]octane. Des essais en vue d'isoler l'oxirane ont conduit à la formation, comme produit majeur, du dimère 8,8,11,11-tétraméthyl-1,5,7,10,12,16-hexaoxadispiro[5.2.5.2]hexadécane. L'oxirane est thermiquement stable à 110 °C, mais il est très sensible à l'eau, comme on peut en déduire de sa disparition graduelle une fois que le tube est ouvert. On croit que le dimère de l'oxirane se forme à partir d'un cation qui se formerait à partir d'une ouverture de cycle de l'oxirane par réaction avec de l'eau. Ce cation pourrait alors réagir avec l'oxirane lui-même pour régénérer l'eau qui ne serait de fait qu'un catalyseur dans la conversion de l'oxirane en dimère.

Mots clés : carbène, dioxacarbène, dialkoxyoxirane, oxadiazoline, 2,5-dihydrooxadiazole.

[Traduit par la Rédaction]

Introduction

Many 2,2-dialkoxy-5,5-dialkyl-Δ^3-1,3,4-oxadiazolines (**1**), also known as 2,5-dihydro-2,2-dialkoxy-5,5-dialkyl-1,3,4-oxadiazoles, have been prepared and thermolyzed in benzene solution at temperatures near 110 °C (1). Their thermolysis is generally formulated as involving a 1,3-dipolar cycloreversion, by loss of N_2, to form a carbonyl ylide intermediate (**2**). Experimental evidence for a possible carbonyl ylide intermediate has been presented in only a few instances (2), suggesting that they are short-lived, if they bear two alkoxy groups, or that they are not real. Recent computational results[2] suggest that whether or not an ylide is a real intermediate in thermolysis of some oxadiazolines depends on the level of theory employed. In any case the ultimate products of oxadiazoline fragmentation are N_2, a ketone, and a dialkoxycarbene (**3**). An ylide intermediate, if real, fragments rapidly to the latter two products, Scheme 1. The carbene, a nucleophile, could then add to the ketone carbonyl group, either in a stepwise process via intermediate **4** or in a concerted reaction leading directly to oxirane **5**.

The existence of a ylide intermediate in oxadiazoline thermolysis has been questioned, on the basis of results of computation at a low level of theory. Smith (3) proposed a concerted reaction to afford a dialkoxycarbene without the intermediacy of a carbonyl ylide. If that were the case, products from apparent ylide intermediates could still arise via **4** or **5**, from attack of the carbene on the ketone, if **5** were to open to **2**.

We now present evidence for the formation of carbene **8** and oxirane **9** intermediates in the thermolysis of the spiro-fused oxadiazoline **6**, Scheme 2. Although a carbonyl ylide

Received 7 May 2004. Published on the NRC Research Press Web site at http://canjchem.nrc.ca on 3 February 2005.

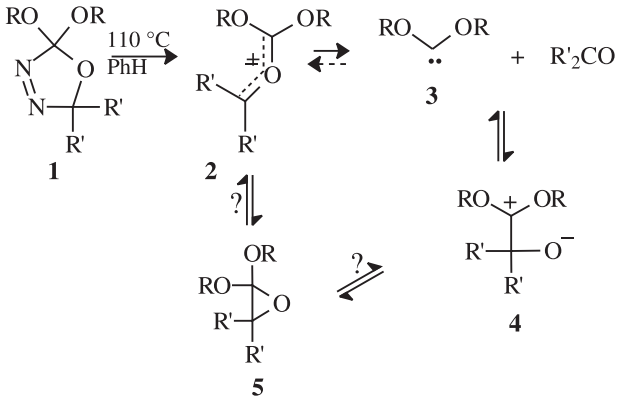
A. Klys, W. Czardybon, J. Warkentin,[1] and N.H. Werstiuk. Department of Chemistry, McMaster University, Hamilton, ON L8S 4M1, Canada.

[1]Corresponding author (e-mail: warkent@mcmaster.ca).

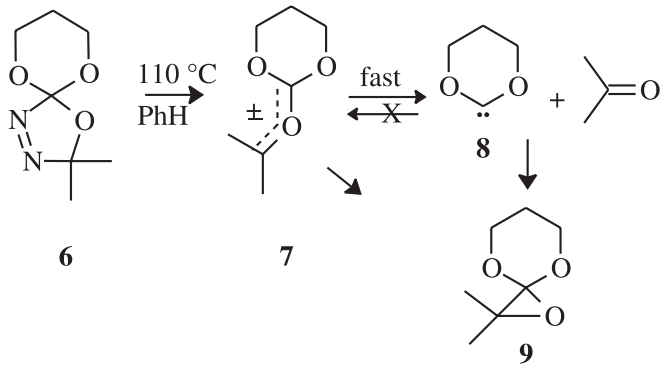
[2]W. Czardybon, J. Warkentin, and N.H. Werstiuk. Unpublished computations.

 doi: 10.1139/V04-158 © 2004 NRC Canada

Scheme 1.



Scheme 2.



intermediate **7** is possible from a mechanistic point of view, there is not any experimental evidence for it in this case.

Results and discussion

Oxadiazoline **6** was prepared by hydrazinolysis of carbonate **10**, conversion of the product (**11**) to the isopropylidene hydrazone **12**, oxidative cyclization of **12** to **13** with $Pb(OAc)_4$ in dichloromethane (2*b*), and acid catalysed cyclization of **13** to **6**, Scheme 3. Heating of a benzene solution of **6** (72 h) at 110 °C in a sealed tube gave a major product (ca. 60% by GC) and several minor products, one of which had a longer GC retention time. The initial major product was transformed, at room temperature, into the latter minor product after the tube was opened. Sometimes this process took a few hours and sometimes about one day. It is probably related to the rate at which the solution absorbed water from the atmosphere after the reaction tube was opened. Chromatography of the initial reaction mixture caused the same transformation.

We suggest the following interpretation of these results, Scheme 4. Thermolysis of **6** leads to loss of N_2 to form carbonyl ylide **7**. Fragmentation of **7** to **8** is probably slowed, relative to the rate of fragmentation of analogous ylides that lead to an acyclic dialkoxycarbene, because carbene **8** is U-shaped. The U-conformation of allyloxymethoxycarbene lies about 11 kcal mol^{-1} higher in energy than the W-conformation (4). That energy difference could mean that the transition state for formation of a U-shaped dialkoxycarbene from a carbonyl ylide is higher in energy than an analogous transition state for fragmentation to a W-shaped dialkoxycarbene. Nevertheless, a large fraction of the ylide fragments to the carbene (**8**) and acetone, as discussed below.

The longer lifetime of **7** could lead to some closure to oxirane **9**, which was a major initial product, but **9** must also come from attack of the carbene on acetone, as indicated by the results of inclusion of 1,1,1-trifluoroacetone, at two different concentrations, during the thermolysis. With a 5-fold excess of trifluoroacetone (0.5 mol/L), oxiranes **9** (3 parts) and **14** (7 parts) as well as diol **18** (4 parts) were the major products obtained before workup. With a 10-fold excess of trifluoroacetone (1.0 mol/L), oxirane **9** was not detected but **14** and **18** were observed in approximately a 4:3 ratio. Workup led to the conversion of **14** to a single diastereomer of **15** and to the loss of **18**. Products from **18** were not identified. The fact that formation of **9** was suppressed at the higher concentration of trifluoroacetone must mean that most of the **9** observed when trifluoroacetone was absent, or present at a low concentration, arose from addition of the free carbene (**8**) to acetone. Thus, fragmentation of presumed ylide **7**, although slowed because of the conformation imposed on carbene **8**, must still be fast relative to electrocyclic ring closure of **7** to **9**. Oxirane **9** must be formed primarily by reaction of carbene **8** with acetone. Trifluoroacetone, when present at a relatively high concentration, is expected to trap essentially all of the free carbene to form **14**. How **14** reacts to afford **15** is not known.

We did not find any **17**, which should have been present if **9** were in equilibrium with **16**, nor was any **20** detected. Compound **20** would be an expected product from the alternative ring opening of **9** to ylide **7**.

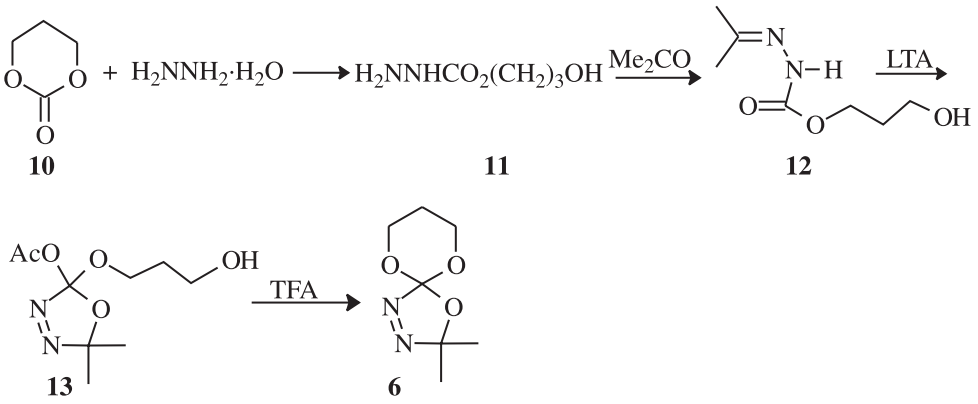
The finding of **9** and **14** is supported by precedent. One cyclic dialkoxyoxirane model (**24**) for **9** is known (5), and one 2,2-dimethoxyoxirane **25** has been reported (1*g*). In the absence of water, **9** must be relatively stable, since it can survive heating of **6** at 110 °C in benzene for 72 h. Oxirane **9** cannot undergo reversible ring opening rapidly, either to the carbonyl ylide **7** or to the isomeric zwitterion **16**, because those intermediates would react with trifluoroacetone.

In the presence of moisture, which enters slowly from the atmosphere once the sealed tube has been opened, oxirane **9** undergoes ring opening to the dihydroxy compound **18**, which must itself be in equilibrium with oxirane **9**, via cationic intermediate **19**, Scheme 4. Cation **19** reacts with oxirane **9** to afford 8,8,11,11-tetramethyl-1,5,7,10,12,16-hexaoxadispiro[5.2.5.2]hexadecane (**22**) the structure of which was secured by means of single crystal X-ray diffraction. Presumably the mechanism of formation of **22** involves intermediate **21**. Such a reaction would be unlikely in the presence of excess water, because there would not be any oxirane available, but it is likely when the available water is that absorbed from the atmosphere. Water is probably catalytic at very low concentrations, promoting the conversion of **9** to **22** without being consumed significantly. Lactone **23** is presumably the result of partial hydrolysis of **22** during the workup.

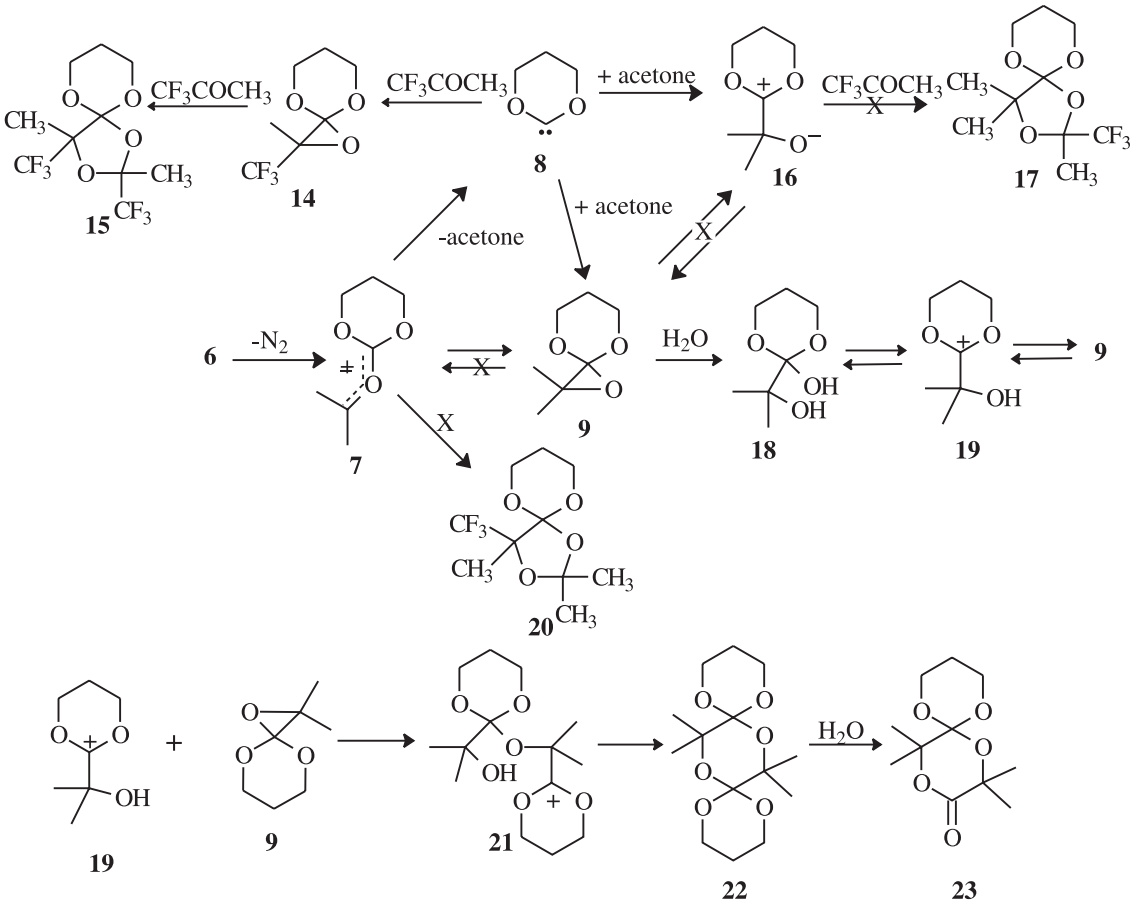
The present results may be surprising in view of the fact that oxadiazoline **26**, upon thermolysis in benzene, was reported (2*b*) to afford the carbene dimer **27** (ca. 20%), Scheme 5. An oxirane dimer, analogous to **22**, was not re-

© 2004 NRC Canada

Scheme 3.



Scheme 4.



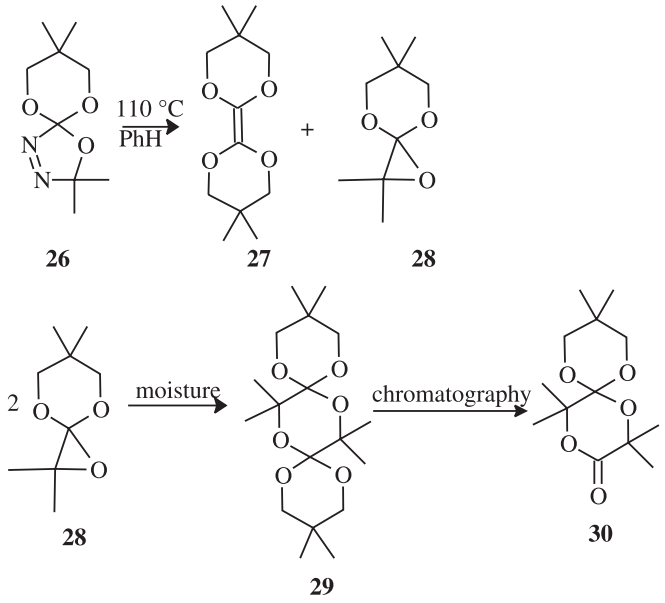
ported and in the present case, a carbene dimer was not isolated from thermolysis of **6**. Checking the NMR spectra and mass spectra again confirmed that the compound isolated from **26** was indeed **27**. However, **27** was obtained in only about 20% yield and only one additional, minor product (**30**) was identified. Compound **30**, analogous to **23**, is presumably derived from dimerization of oxirane **28** to **29** and partial hydrolysis of the latter, Scheme 6 (2*b*). The presumed intermediates, **28 and 29**, were not seen. Similarly, the thermolysis of **6** in the absence of trifluoroacetone gave many products that could have included the dimer of **8**.

In conclusion, it is likely that **6** and **26** undergo thermolysis by analogous mechanisms, affording products from the appropriate carbenes and from reaction of those carbenes with acetone. Although not all of the products were isolated and identified by different workers, there is no conflict between the results from thermolysis of **6** and **26**, which are expected to be qualitatively the same. However, it appears that the products are very sensitive to the humidity and to the adsorbent used in chromatographic separations.

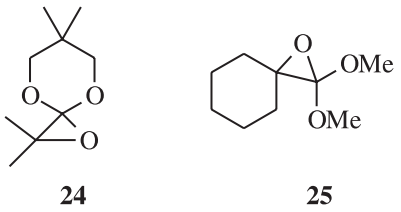
Catalysis of organic reactions by water is rare but not new. It is believed to occur, for example, during chlorination of olefins (6) and in the ketonization of enols (7). In the present case, water protonates and opens a highly reactive dialk-

© 2004 NRC Canada

Scheme 5.



Scheme 6.



oxyoxirane and the cationic intermediate attacks an oxirane molecule to afford an oxirane dimer.

Experimental

^{1}H NMR spectra run in benzene-d_6 are referenced to the signal for residual H in the solvent, set at 7.15 δ for benzene. ^{13}C NMR spectra were run in $CDCl_3$ and are referenced to the solvent signal at 77.16 δ for the center line.

1,3-Dioxan-2-one

1,3-Propanediol (15.6 g, 0.20 mol) and diethyl carbonate (30 g, 0.25 mol) in a 100 mL round-bottom flask fitted with a distillation column, were treated with freshly prepared NaOMe made from Na (0.18 g) and MeOH (3 mL). The solution was slowly heated to 100 °C and alcohols (methanol and ethanol, 70–85 °C at the top of the column) were collected. The temperature in the flask was slowly increased to 170 °C over a 5 h period. During this time about 80% of the product distilled at 130–150 °C. After cooling, the column was removed, excess diethyl carbonate and a trace amount of ethanol were distilled out (oil pump) and the product was distilled at 130–160 °C. Some fractions crystallized spontaneously; those that did not were dissolved in ether and the solutions were cooled to –55 °C to cause crystallization. The total yield of white crystalline product (8) was 7.65 g (30%), mp 45–46 °C. ^{1}H NMR (200 MHz, $CDCl_3$) δ: 2.13 (quint, ^3J = 5.6 Hz, 2H) and 4.44 (t, ^3J = 5.6 Hz, 4H).

Synthesis of hydrazinecarboxylic acid, 3-hydroxypropyl ester (11)

To compound **10** (2.0 g, 20 mmol) in 10 mL of ethanol, in a round-bottom flask with an efficient condenser, was added hydrazine hydrate (98%, 20 mmol) during 20 min. After refluxing for 18 h the volatiles were evaporated leaving a colourless oil (2.7 g, 99%) that solidified in the freezer (9). ^{1}H NMR (200 MHz, $CDCl_3$) δ: 1.75 (quint, ^3J = 6.3 Hz, 2H), 3.57 (t, ^3J = 6.3 Hz, 2H), and 4.08 (t, ^3J = 6.3 Hz, 2H).

Synthesis of 12

After acetone (15 mL) and **11** (1.0 g, 7.5 mmol) had formed a homogeneous solution (30–45 min), it was treated overnight with anhydrous Na_2SO_4. Decanting and evaporation of the acetone left **12** as a colourless oil (1.29 g, 99%). ^{1}H NMR (200 MHz, $CDCl_3$) δ: 1.83 and 1.91 (s and m, 5H), 2.05 (s, 3H), 3.72 (t, ^3J = 5.8 Hz, 2H), and 4.40 (t, ^3J = 5.8 Hz, 2H).

Synthesis of 6

To an ice-cooled heterogeneous mixture of $Pb(OAc)_4$ (LTA) (7.4 g, 16.5 mmol) in dry CH_2Cl_2 (15 mL) was added slowly, during 1h, a solution of **12** (2.5 g, 14.4 mmol) in 10 mL of CH_2Cl_2. Glacial acetic acid (two drops) was added and the yellow mixture was stirred for 4 h at 0 °C and for 16 h at room temperature. Filtration through Celite, washing with a $NaHCO_3$ solution (5%, 2 × 50 mL), drying over Na_2SO_4, and concentration gave a crude material **13** that was dissolved in CH_2Cl_2 (20 mL). Trifluoroacetic acid (3 drops) was added and, after stirring for 90 min, thin layer chromatography (TLC) analyses showed that conversion of **13** to **6** was complete. Concentration and column chromatography on silica gel (hexane/EtOAc = 4:1) gave **6** that could be crystallized from pentane at –55 °C to give 0.55 g (22%) of pure **6,** mp 63–64 °C. ^{1}H NMR (200 MHz, $CDCl_3$) δ: 1.53 (s, 6H), 1.88 (m, 1H), 2.17 (m, 1H), 4.20 (m, 2H), and 4.60 (m, 2H). The methyl groups of the oxadiazoline ring of a close analog of **6** absorb at δ = 1.52 (1*b*).

Thermolysis of 6 in benzene

A solution of **6** (344 mg, 2.0 mmol) in dry benzene was sealed into a glass tube and the tube was immersed in an oil bath at 110 °C for 72 h. One major product was detected by GC along with two minor products having longer retention times. A GC-MS gave a mass of 144 for the major product, which is consistent with oxirane **9**. The major product was transformed into one of the minor products as the feedstock aged. Isolation of the growing minor product and single crystal X-ray diffraction showed it to be **22**. The other material with a long retention time was identified as **23** on the basis of spectroscopy and analogy. A compound similar to **23**, except for a phenyl substituent, has been reported (2*b*). Chromatography (Chromatotron, SiO_2) afforded primarily the material with the longer GC retention time.

Compound 9

Compound **9** could not be isolated. In the ^{1}H NMR spectrum of the crude (200 MHz, C_6D_6) there was a strong singlet signal at 0.42 δ that disappeared slowly when the tube was opened. GC-MS *m/z*: 144 (M^+), 143 $(M-1)^+$,129 $(M-Me)^+$, 114 $(M-CH_2O)^+$, and 87 ($C_4H_7O_2^+$, 100%).

© 2004 NRC Canada

Compound 22

^{1}H NMR (500 MHz, C_6D_6) δ: 0.72 (d, J = 12 Hz, 2H), 1.68 (s, 12H), 1.73 (m, 2H), 3.44 (m, 4H), and 4.10 (t, J = 12 Hz, 4H). ^{13}C NMR (75 MHz, $CDCl_3$) δ: 24.76, 24.86, 30.21, 59.47, 79.13, and 108.43. MS (CI, NH_3) m/z: 289 $(M + H)^+$ (100), 288 (M^+, 14), 145 $(M/2 + H)^+$ (37), and 128 (33). The molecular structure of **22** was secured by means of single crystal X-ray diffraction.

Compound 23

^{1}H NMR (200 MHz, C_6D_6) δ: 1.35 (m (br), 2H), 1.44 (s, 6H), 1.51 (s, 6H), 3.28 (m, 2H), and 3.78 (m, 2H). ^{13}C NMR (50.3 MHz, $CDCl_3$) δ: 23.8, 24.3, 28.6, 29.8, 60.3, 84.9, 108.0, and 172.5. MS (EI) m/z: 231 (M + 1), 215, 200, 172, 164, 129, 103, and 70 (100%); MS (CI, NH_3) m/z: 231 $(M + H)^+$ (100), 173 (3), 145 (13), and 128 (34).

Thermolysis of 6 in benzene containing 1,1,1-trifluoroacetone in 5-fold excess

A solution of **6** (172 mg, 1.0 mmol) in benzene (10 mL) containing 1,1,1-trifluoroacetone (560 mg, 5.0 mmol) was heated as described above. Three products, with GC retention times (rt) of 5.2, 6.1, and 6.9 min were obtained. The fraction with rt = 6.9 min was collected and shown to be **15** (one diastereomer) by means of NMR spectroscopy (^{1}H, ^{19}F) and mass spectrometry. The mass spectra of the other fractions did not match the expectation for **17** which, like **15**, should have provided $(M + H)^+$ and $(M + NH_4)^+$ signals in the CI, NH_3 spectra.

Compound 15

^{1}H NMR (200 MHz, C_6D_6) δ: 1.38 (s, 3H), 1.43 (s, 3H), 1.52 (m, 2H), 3.34 (m, 2H), 3.74 (m, 2H). ^{19}F NMR (188.3 MHz, $CDCl_3$, ref. external $CFCl_3$ at –71.3 δ) δ: –78.82 (s), and –78.84 (s). MS (CI, NH_3) m/z: 328 $(M + NH_4)^+$ (12), 311 $(M + H)^+$ (100), 241(37), and 199 (15).

Compound 18

This material was not isolated in pure form. Structure **18** was assigned tentatively on the basis of its GC retention time, its mass spectrum (GC-MS) in which $(M\text{-}H_2O)^+$ was prominent at m/z = 144, and the ^{1}H NMR spectrum (200 MHz, C_6D_6) of a crude sample, that showed absorption at δ = 0.72, 1.74 (s, 5H), 3.41(m, 4H), 4.33 (s, 1H), and 5.95 (s, 1H). As expected for structure **18**, the compound was very unstable.

Thermolysis of 6 in benzene containing 1,1,1-trifluoroacetone in 10-fold excess

A solution of **6** (172 mg, 1.0 mmol) in benzene (10 mL) containing 1,1,1-trifluoroacetone (1.12 g, 10 mmol) was heated as described above. Two products were identified by GC as **15** and, tentatively, as the trifluoromethyl analogue of **18**.

Acknowledgements

The authors are grateful for continued financial support from the Natural Sciences and Engineering Research Council of Canada (NSERC). We thank Dr. Jim Britten for the X-ray structure of **22**.

References

1. See, for example: (*a*) N. Merkley, D.L. Reid, and J. Warkentin. Tetrahedron Lett. **43**, 1927 (2002); (*b*) N. Merkley and J. Warkentin. http://www.Arkat-usa.org/ark/journal/Volume2/Part3/Tee/001/001_index.htm ARKIVOC [online], **2**, 12 (2001); (*c*) N. Merkley, P.C. Venneri, and J. Warkentin. Can. J. Chem. **79**, 312 (2001); (*d*) N. Merkley and J. Warkentin. Can. J. Chem. **78**, 942 (2000); (*e*) N. Merkley, M. El-Saidi, and J. Warkentin. Can. J. Chem. **78**, 356 (2000); (*f*) M. Dawid, G. Mloston, and J. Warkentin. J. Org. Lett. **3**, 2455 (2001); (*g*) M. Dawid, P.C. Venneri, and J. Warkentin. Can. J. Chem. **79**, 110 (2001); Addendum, **79**, 1294 (2001); (*h*) V. Nair, S. Bindu, and L. Balagopal. Tetrahedron Lett. **42**, 2043 (2001); (*i*) P.C. Venneri and J. Warkentin. Can. J. Chem. **78**, 1194 (2000); (*j*) J.A. Dunn, J.P. Pezacki, M.J. McGlinchey, and J. Warkentin. J. Org. Chem. **64**, 434 (1999); (*k*) J.H. Rigby, S. Laurent, A. Cavezza, and M.J. Heeg. J. Org. Chem. **63**, 5587 (1998); (*l*) H.M. Muchall, N.H. Werstiuk, B. Choudhury, J. Ma, J. Warkentin, and J.P. Pezacki. Can. J. Chem. **76**, 238 (1998); (*m*) J.H. Rigby, A. Cavezza, and M.J. Heeg. J. Am. Chem. Soc. **120**, 3664 (1998); (*n*) J.P. Ross, P. Couture, and J. Warkentin. Can. J. Chem. **75**, 1331 (1997); (*o*) P. Couture, D.L. Pole, and J. Warkentin. J. Chem. Soc., Perkin Trans. 2, 1565 (1997); (*p*) D.L. Pole and J. Warkentin. J. Org. Chem. **62**, 4065 (1997); (*q*) J.H. Rigby, A. Cavezza, and G. Ahmed. J. Am. Chem. Soc. **118**, 12848 (1996); (*r*) K. Kassam, D.L. Pole, M. El-Saidi, and J. Warkentin. J. Am. Chem. Soc. **116**, 1161 (1994); (*s*) M. El-Saidi, K. Kassam, D.L. Pole, T. Tadey, and J. Warkentin. J. Am. Chem. Soc. **14**, 8751 (1992).
2. (*a*) P. Couture, M. El-Saidi, and J. Warkentin. Can. J. Chem. **75**, 326 (1997); (*b*) N. Merkley and J. Warkentin. Can. J. Chem. **80**, 1187 (2002).
3. W.B. Smith. J. Org. Chem. **60**, 7456 (1995).
4. D.L. Reid and J. Warkentin. J. Chem. Soc., Perkin Trans. 2, 1980 (2000).
5. M.S. Newman and E. Kilbourn. J. Org. Chem. **35**, 3186 (1970).
6. V.A. Tikhomirov, V.V. Smirnov, and I.V. Rostov. Zh. Fiz. Khim. **70**, 183 (1996); Chem. Abstr. 124, 288 514 (1996).
7. O.N. Ventura, A. Lledos, R. Bonaccorsi, J. Bertran, and J. Tomasi. Theor. Chim. Acta, **72**, 175 (1987).
8. S. Sarel, J. Katzhendler, and L.A. Poles. J. Chem. Soc. B, 1847 (1971); S. Li and P. Deslongchamps. Tetrahedron Lett. **35**, 5641 (1994).
9. M. Yan, Z. Zhang, X. Lei, Y. Xi, and Y. Xu. Yaoxue Xuebao, **20**, 219 (1985); Chem. Abstr. 104, 109 566 (1986).

© 2004 NRC Canada

Effects of di-, tri-, and tetraethylene glycols on the thermodynamic and micellar properties of Triton X-100 in water

Gwen MacIsaac, Aiysha Al-Wardian, Karen Glenn, and Rama M. Palepu

Abstract: Micellar and surface thermodynamic properties of aggregation of Triton X-100 (TX-100) in mixed solvent systems containing di-, tri-, and tetraethylene glycol with water have been investigated by employing surface tension, density, and fluorescence methods. The differences in Gibbs energies of micellization between water and binary solvent mixtures were determined to evaluate the influence of the co-solvent on the micellization process. From the surface tension measurements, the effects of the co-solvent on parameters such as surface excess, minimum area per molecule, and surface pressure indicate that the surface activity of the surfactant decreases with increasing concentration of the glycol co-solvent. Partial specific volumes, obtained from density measurements, indicate that the fraction of solvent molecules interacting with the micelles by hydrogen bonding vary with the type of additive. Fluorescence studies reveal that quenching of the pyrene probe by cetyl pyridinum chloride in TX-100 micelles is accompanied by simultaneous static and dynamic processes.

Key words: Triton X-100, glycols, thermodynamics, micelles, fluorescence quenching.

Résumé : Faisant appel à des méthodes de tension superficielle, de densité et de fluorescence, on a étudié les propriétés thermodynamiques micellaires et de surface d'un agrégat de Triton X-100 dans des solvants mixtes contenant des di-, tri- et tétraéthylèneglycols et de l'eau. Afin de pouvoir évaluer l'influence du cosolvant sur le processus de micellisation, on a déterminé les différences dans les énergies de Gibbs de micellisation entre l'eau et des mélanges de solvants binaires. Sur la base de mesures de tension superficielle, les effets du cosolvant sur de paramètres tels que l'excès de surface, la superficie minimale par molécule et la pression de surface semblent indiquer que l'activité de surface de l'agent de surface diminue avec une augmentation de la concentration du glycol agissant comme cosolvant. Les volumes spécifiques partiels, obtenus à partir de mesures de densité, indiquent que la fraction de molécules de solvant interagissant avec les micelles par liaison hydrogène varie avec le type d'additif. Les études de fluorescence révèlent que le piégeage de la sonde pyrène par le chlorure de pyridinium de cétyle des micelles de Triton X-100 s'accompagne de processus simultanés statiques et dynamiques.

Mots clés : Triton X-100, glycols, thermodynamique, micelles, piégeage de fluorescence.

[Traduit par la Rédaction]

Introduction

The self-aggregation of surfactant molecules is known to be highly dependent on the nature of the dispersion medium (1–3). Considerable research has been conducted on the effects of polar organic solvents, such as glycerol, formamide, and ethylene glycol, on the micellization process (4, 5). Studies of the micellar aggregation of surfactants in polar solvents mainly employ ionic surfactants (6–19). However, the effects of polar solvents on the micellar properties of non-ionic surfactants have been less extensively investigated and some of the results are contradictory (20–25). Penfold et al. (24) reported an increase in the micellar size on the addition of ethylene glycol, sorbitol, or glycerol, while Cantú et al. (22) observed that the micellar size of octaoxyethylene *n*-dodecyl ether ($C_{12}E_8$) decreased with the addition of glycerol. Similar decreases in micellar sizes for Pluronic P105 were also observed by Alexandridis and Yang (25). As part of a program dealing with the effects of glycols on the micellar and thermodynamic properties of poly-oxyethylene sorbitan-fatty acid esters (Tweens) and *p-tert*-octylphenoxy polyethylene ether (TX-100) in aqueous media (26–28), we present in this paper a study of the effects of diethylene glycol (DEG), triethylene glycol (TEG) and tetraethylene glycol (TTEG) co-solvents on the micellar properties of TX-100 in water. The non-ionic surfactant TX-100 is widely used to separate proteins from cell membranes (29, 30), extract DNA (31), etc. Mixed micelles of TX-100 with various lipid-like substances are extensively employed in many chemical and industrial applications (32–34). The effective-

Received 28 June 2004. Published on the NRC Research Press Web site at http://canjchem.nrc.ca on 8 February 2005.

G. MacIsaac, A. Al-Wardian, K. Glenn, and R.M. Palepu.[1] Department of Chemistry, St. Francis Xavier University, Antigonish, NS B2G 2W5, Canada.

[1]Corresponding author (e-mail: rpalepu@stfx.ca).

 doi: 10.1139/V04-157 © 2004 NRC Canada

ness of mixed micelle systems for these applications depends on the micelle size, shape. and other solution properties. In this study we report on both bulk and surface thermodynamic properties of TX-100 in the presence of glycol oligomer co-solvents employing surface tension, density, and fluorescence methods.

Experimental

Materials

All chemicals employed were of analytical grade quality. The surfactant TX-100 (Sigma) and the glycols (Aldrich) were used as supplied. Pyrene (Sigma) was purified by sublimation and recrystallized from ethanol. Cetyl pyridinum chloride (CPC) from Sigma was recrystallized from acetone.

Methods

Surface tension measurements were carried out on a Fisher 21 Tensiomat (model 21) equipped with a 13-mm diameter Pt-Ir ring. Details of the experimental procedure for the surface tension measurements are given in our earlier study (27).

Density measurements were carried out with an Anton-Paar DMA 5000 densimeter. The instrument was calibrated with air and water at 298.15 K. The temperature was controlled within ±0.001 °C.

Fluorescence measurements were carried out employing a Spex Fluoro Max-3 Spectrofluorometer. The emission spectrum of pyrene was measured in the 360 to 400 nm range by exciting pyrene probe molecules at 340 nm. The concentration of pyrene in the micellar solutions was of the order of 10^{-3} mmol/L. Surfactant concentrations for the determination of micro-polarity were of the order of 25 mmol/L. The quencher CPC concentration was varied in the range 0.1 to 0.9 mmol/L for the quenching studies and for aggregation number determination.

Results

Critical micelle concentration

A representative plot of surface tension (γ) for solutions of TX-100 in mixtures of water and glycols as a function of the surfactant concentration is presented in Fig. 1. The intersection point is taken as the critical micelle concentration (cmc) of TX-100. The small dip in the surface tension plots near the intersection point is attributed either to a trace of surface active impurity or because of the composition distribution arising from varying degrees of ethoxylation in TX-100 (35). The cmc values obtained from the surface tension measurements are presented in Table 1.

The cmc values in the presence of additives at 298 K were also determined by the variation in I_1/I_3 ratio (intensity ratio I_1 at 372 nm and I_3 at 304 nm) of pyrene with the concentration of surfactant. This method is based on the dependence of the I_1/I_3 ratio on the vibrational structure of the microenvironment of the probe. In the absence of micelles, the probe senses a polar environment, leading to higher values of the I_1/I_3 ratio. In the presence of micelles, the probe may reside in the palisade region of the micelles where the polarity is decreased, resulting in a lower I_1/I_3 ratio. The I_1/I_3 ratio as a function of surfactant concentration in various

Fig. 1. Representative surface tension plot of TX-100 in 10% DEG (□), TEG (●) and TTEG (Δ) at 303 K.

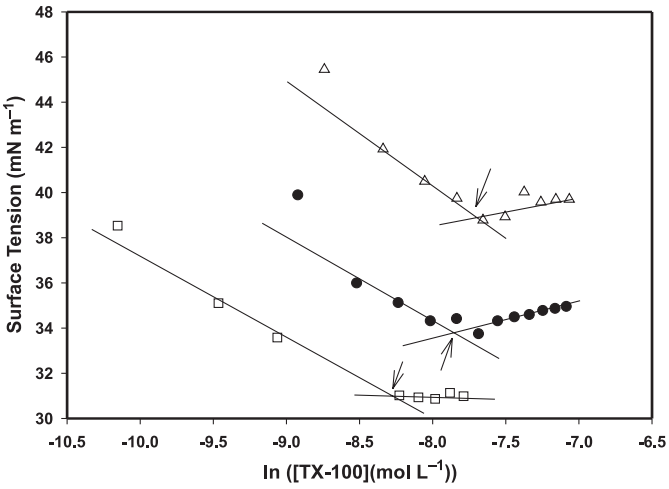


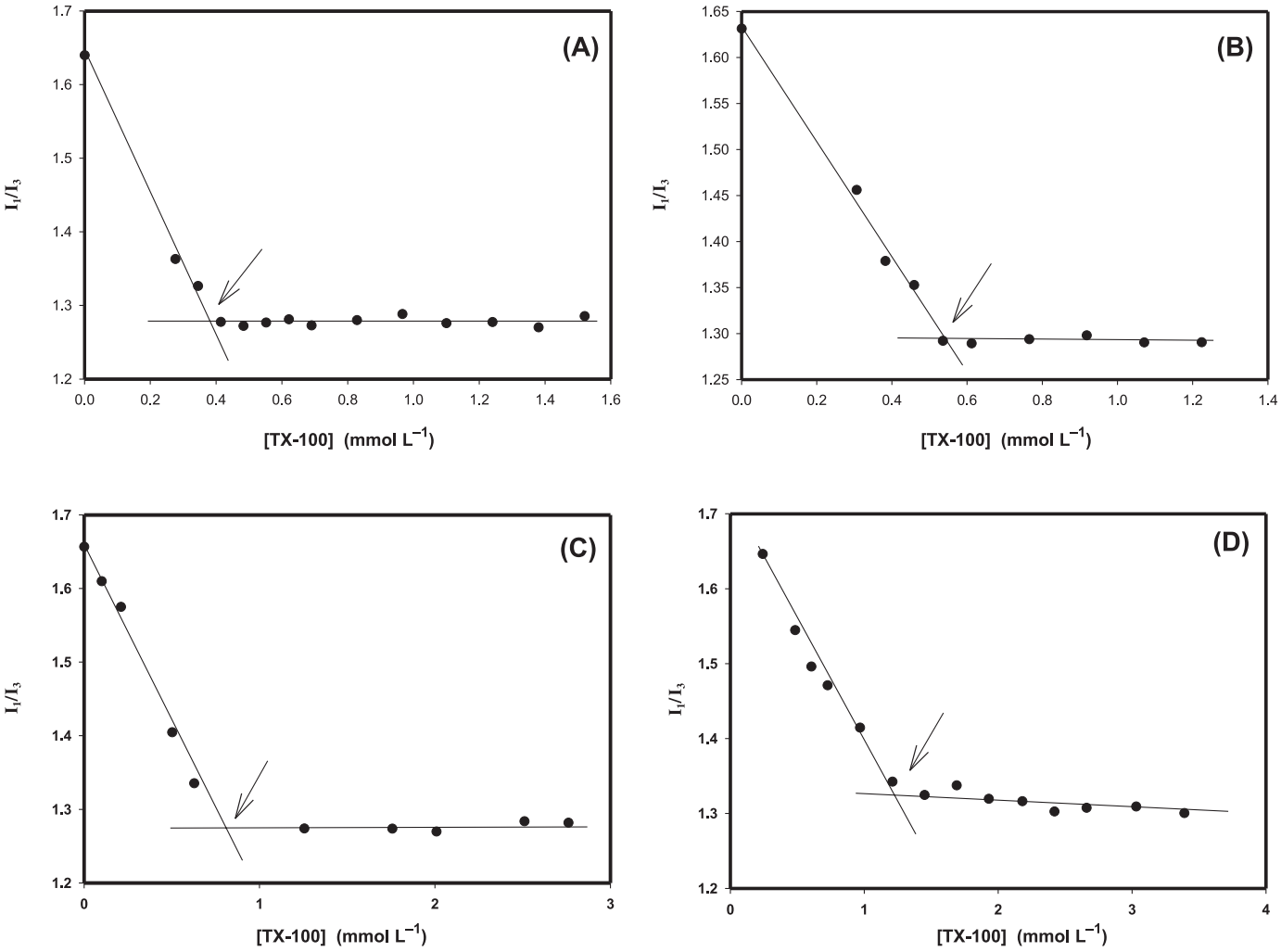
Table 1. Critical micelle concentration (cmc) of TX-100 in diethylene (DEG), triethylene (TEG), and tetraethylene glycol (TTEG) and water mixtures.

System	Glycol (wt%)	T (K)	cmc[a] (mmol/L)	cmc[b] (mmol/L)
DEG	0	298	0.24	0.3
		303	0.23	
		308	0.2	
	5	298	0.21	0.27
		303	0.23	
		308	0.29	
	10	298	0.36	0.43
		303	0.37	
		308	0.38	
	15	298	0.4	0.46
		303	0.42	
		308	0.45	
	20	298	0.57	0.62
		303	0.68	
		308	0.79	
TEG	5	298		0.45
	10	298	0.41	0.52
		303	0.44	
		308	0.47	
	15			0.77
	20			1.18
TTEG	5	298		0.4
	10	298	0.42	0.49
		303	0.47	
		308	0.53	
	15	298		0.93
	20	298		1.25

[a]Surface tension.
[b]Pyrene probe.

© 2004 NRC Canada

Fig. 2. Critical micelle concentration (cmc) determination of TX-100 in TEG and water mixtures: 5% (A), 10% (B), 15% (C), and 20% (D) at 298 K employing the I_1/I_3 ratio method.



glycol and water mixtures is presented in Fig. 2. The surfactant concentrations at the break point, as indicated in the plots, were taken as the cmc values. The characteristic vibrational structure of pyrene was not modified by the added glycol, except for a very small change in the I_1/I_3 ratio.

Surface properties

The surface excess concentration Γ_{max} and minimum area per molecule A_{min} at the air/solvent interface were obtained (36) by solving the following the equations

$$[1] \qquad \Gamma_{max} = -\frac{1}{RT}\left[\frac{\partial\gamma}{\partial \ell nc}\right]_{P.T.}$$

$$[2] \qquad A_{min} = \frac{1}{N_A\Gamma_{max}}$$

and the results are presented in Table 2. The symbols in eqs. [1] and [2] have the usual meanings. The values of surface pressure at the cmc (π_{cmc}) were obtained by employing eq. [3]

$$[3] \qquad \pi_{cmc} = \gamma_0 - \gamma_{cmc}$$

where γ_0 and γ_{cmc} are the surface tension of the pure solvent and the value at the cmc, respectively.

Thermodynamics of micellization

The Gibbs free energy of micellization (ΔG°_{mic}) was calculated using an equation based on the phase separation model (36)

$$[4] \qquad \Delta G^\circ_{mic} = RT \ln X_{cmc}$$

where X_{cmc} is the cmc value on the mol fraction scale.

The enthalpy (ΔH°_{mic}) and entropy (ΔS°_{mic}) of micellization were calculated using the following equations.

$$[5] \qquad \Delta H^\circ_{mic} = -RT^2\left(\frac{\partial \ell n X_{cmc}}{\partial T}\right)_P$$

$$[6] \qquad \Delta S^\circ_{mic} = (\Delta H^\circ_{mic} - \Delta G^\circ_{mic})/T$$

Finally, the effect of the co-solvent on the free energy of transfer ($\Delta\Delta G^\circ_{mic}$) process was obtained from the following equation.

© 2004 NRC Canada

Table 2. Thermodynamic parameters of micellization of TX-100 in diethylene (DEG), triethylene (TEG), and tetraethylene glycol (TTEG) and water mixtures.

System	Glycol (wt%)	T (K)	$-\Delta G^{\circ}_{mic}$ (kJ mol^{-1})	$-\Delta H^{\circ}_{mic}$ (kJ mol^{-1})	ΔS°_{mic} (J K^{-1} mol^{-1})	$\Delta\Delta G^{\circ}_{mic}$ (kJ mol^{-1})
DEG	5	298	30.9	2.5	95.3	–0.3
		303	31.1			0.1
		308	31.2			1
	10	298	29.4	4.3	84.2	1.2
		303	29.9			1.3
		308	30.3			1.8
	15	298	29.1	9	67.4	1.5
		303	29.4			1.8
		308	29.7			2.4
TEG	10	298	29.1	10.4	62.8	1.5
		303	29.4			1.8
		308	29.7			2.4
TTEG	10	298	29	19	34	1.6
		303	29.2			2
		308	29.4			2.7

Note: Uncertainties: ±0.5 kJ mol^{-1} for ΔG°_{mic} and ΔH°_{mic}; 5 JK^{-1} mol^{-1} for ΔS°_{mic}.

Table 3. Surface properties of TX-100 in diethylene (DEG), triethylene (TEG), and tetraethylene glycol (TTEG) and water mixtures.

System	Glycol (wt%)	T (K)	$\Gamma_{max} \times 10^6$ (mol m^{-2})	$A_{min} \times 10^{20}$ (m^2)	π_{CMC} (mN m^{-1})	ΔG°_{ad} (kJ mol^{-1})
DEG	0	298	1.82	91	40.1	–52.6
		303	1.9	87	42.6	–53.6
		308	2	83	42.3	–53.3
	5	298	1.37	121	27.2	–50.7
		303	1.32	126	23.5	–48.9
		308	1.2	138	12.5	–46.7
	10	298	1.36	123	22.4	–45.8
		303	1.06	157	16.9	–45.8
		308	1.04	159	11.3	–41.2
	15	298	0.85	195	20.4	–53.1
		303	0.82	204	14	–46.4
		308	0.72	230	12.7	–47.4
	20	298	0.8	207	16.6	–45.4
		303	0.71	233	12	–45.0
		308	0.65	256	11.4	–45.7
TEG	10	298	1.33	125	27.7	–42.5
		303	1.03	161	25.7	–43.4
		308	0.95	175	22.8	–47.8
TTEG	10	298	1.27	130	28.1	–42.5
		303	1.16	143	25.4	–43.4
		308	0.77	217	23	–47.8

$$[7] \qquad \Delta\Delta G^{\circ}_{mic} = \Delta G^{\circ}_{mic}(\text{glycol} + H_2O) - \Delta G^{\circ}_{mic}(H_2O)$$

The Gibbs energy of adsorption (ΔG°_{ad}) was obtained from

$$[8] \qquad \Delta G^{\circ}_{ad} = \Delta G^{\circ}_{mic} - \frac{\pi_{cmc}}{\Gamma_{max}}$$

and the results are listed in Table 3 along with other thermodynamic properties.

In the calculation of the ΔG°_{ad}, the standard state is defined as having the surface covered with a monolayer of amphiphile at a surface pressure equal to zero (37).

Discussion

In the presence of glycol additives, the cmc values increase considerably. The increase is attributed to the structure-breaking ability of the glycol additives (26). The increase in the cmc is larger than for ionic surfactants (17). Glycols may be considered as co-solvents in the present

© 2004 NRC Canada

study as well as structure-breaking solutes, thereby decreasing the hydrophobic effect. The cmc values obtained by the fluorescence method are slightly higher than those obtained by the surface tension method. The differences in the cmc values determined by the different techniques are attributed to the response of each technique to the individual property (36).

The increase in cmc values with temperature at a given concentration of glycol is due to the disruption of the solvent structure with temperature. It is therefore expected that the ΔG°_{mic} values would become less negative at higher temperature in the presence of the additive. However, the slightly more negative values of the ΔG°_{mic} at higher temperature in the presence of additive indicate that the change in the ln X_{cmc} term is more than compensated for by the change in the RT term, thereby resulting in a more negative value of ΔG°_{mic} (38). Also, at a given concentration of glycol additive, the ΔG°_{mic} values become less negative with increasing number of ethylene member groups in the glycol oligomers.

The ΔH°_{mic} is negative and follows the order TTEG > TEG > DEG. The ΔS°_{mic} values are positive and follow the order DEG > TEG > TTEG, indicating a decrease in hydrophobic interactions on the addition of glycol. The considerably lower values of the ΔS°_{mic} for the TTEG additive indicate that the TTEG is more effective in decreasing the hydrophobic effect compared to the other two additives. The values of the $\Delta\Delta G^{\circ}_{mic}$ are positive in all cases, further substantiating the hypothesis that the addition of glycol decreases the hydrophobic interactions due to improved solvation (39).

The values of Γ_{max} and π_{cmc} decrease with increasing diethylene glycol content and are lower for 10% TEG and TTEG aqueous mixtures when compared to the values for TX-100 in water. One can infer the hydrocarbon moiety of the glycols interacts with the backbone of the glycols, thereby shifting surfactant molecules from the interface to the bulk solution. This results in an increase in the minimum area per surfactant molecule and a decrease in the Γ_{max} with the addition of glycol oligomers. The effect of temperature (Table 3) indicates poor packing at the liquid/air interface. The more negative values of ΔG°_{ad} (Table 3) compared to ΔG°_{mic} (Table 2) indicate that more work has to be performed when micelles are formed from the monomeric surfactant molecules at the interface to the micellar state in the mixed solvent system.

The partial specific volume (v) of the micelle may be considered as the volume occupied per gram of dry micelle. The values of v for TX-100 in 10% DEG, TEG, and TTEG aqueous mixtures were calculated by employing the equation

$$[9] \qquad v = \frac{1}{\rho_0}\left(1 - \frac{\partial \rho}{\partial c}\right)$$

where ρ_o and ρ are the densities of solvent and micellar solution, respectively and c is the concentration of TX-100 solution in g/mL. The plot of density as a function of surfactant concentration in different glycol and water mixtures is presented in Fig. 3. The values of the partial specific volumes calculated from the slopes of the plots are presented in Table 4. The partial specific volumes of TX-100 changed slightly on addition of DEG, TEG, and TTEG. The values

Fig. 3. Density plots for determination of the partial specific volume (v).

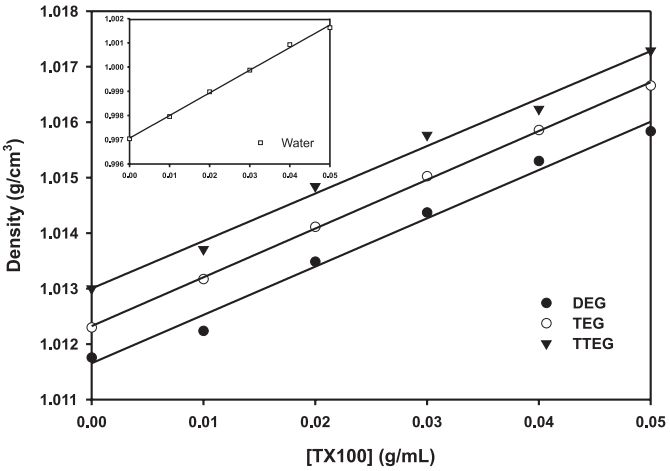


Table 4. Partial specific volume (v), I_1/I_3 ratio, and modified quenching SV constants (dynamic - K_{SV} and static - K_S) for pyrene probe by cetyl pyridinum chloride (CPC) in TX-100 micellar media.[a]

System	Glycol (wt%)	v (mL g^{-1})	I_1/I_3	K_{SV} (L mol^{-1})	K_S (L mol^{-1})
DEG	5		1.26		
	10	0.989	1.35	890	889
	15		1.41		
	20		1.46		
TEG	5		1.28		
	10	0.9877	1.38	665	826
	15		1.45		
	20		1.49		
TTEG	5		1.3		
	10	0.9871	1.41	1120	1131
	15		1.47		
	20		1.51		

Note: diethylene (DEG), triethylene (TEG), and tetraethylene glycol (TTEG) and water mixtures.

[a]TX-100 micelles in water: PSV = 0.9135 mL g^{-1}, I_1/I_3 = 1.20, K_{SV} = 827 L mol^{-1}, K_S = 815 L mol^{-1}.

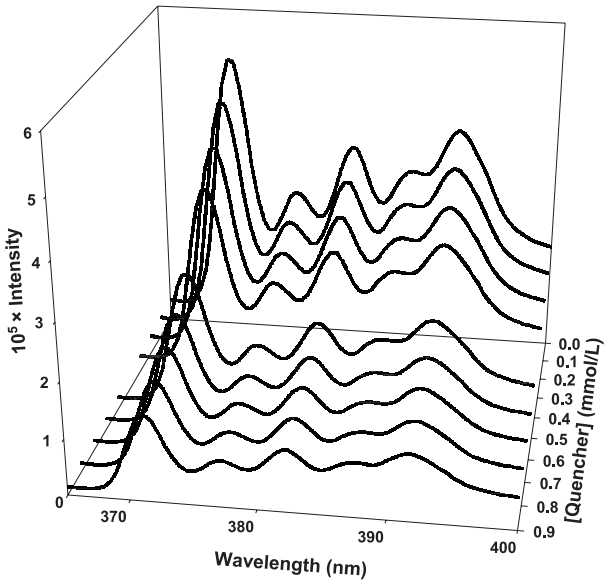
follow the order DEG > TEG > TTEG > H_2O. This indicates that part of the micellar solvation of TX-100 micelles (via hydrogen bonding) is mildly affected by the addition of DEG, TEG, and TTEG (40).

Fluorescence measurements were undertaken to determine the micropolarity of the pyrene resident in the palisade layer and to determine the aggregation numbers of the micelles in the mixed solvent system. The I_1/I_3 values of the probe in 25 mmol/L TX-100 in various glycol and water mixtures are presented in Table 4. The I_1/I_3 ratio indicates that the probe is sensing a more polar environment with increasing glycol content. This may be attributed to the decrease in the aggregation number and the steric hindrance associated with the quenching process (17).

Attempts to determine the aggregation numbers for the TX-100 micelles in the presence of glycols employing the static quenching method (41) were unsuccessful. Pyrene and

© 2004 NRC Canada

Fig. 4. 3D plot of fluorescence quenching of pyrene probe as a function of cetyl pyridinum chloride (CPC) concentration in 10% aqueous DEG solution.



CPC were used as probe and quencher, respectively. Fluorescence quenching of the pyrene probe as a function of CPC concentration in the TX-100 micellar medium is presented in Fig. 4. The aggregation numbers obtained by this method were considerably low for the TX-100 micelles and there is no definite dependence of aggregation numbers on the concentration of the glycol additives. To rationalize the situation, the quenching data were analysed in terms of the Stern–Volmer (SV) equation. The analysis indicates that the quenching in our system was accompanied by simultaneous dynamic and static processes. Taking both processes (42) into account, the modified SV equation

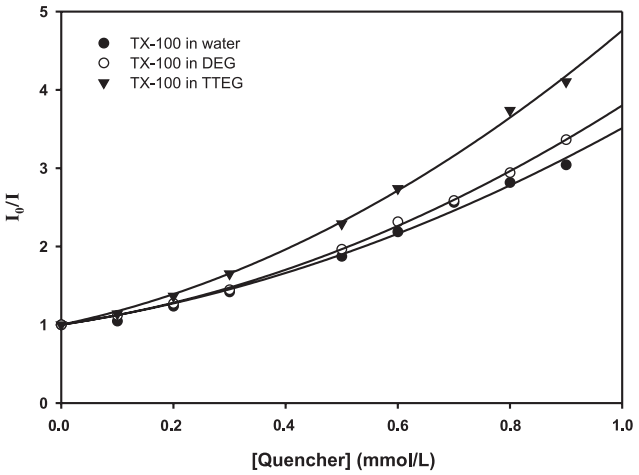
$$[10] \quad I_0/I = (1 + K_{SV}[Q])(1 + K_S[Q])$$

was fitted to the experimental data, where [Q] is the quencher concentration and the K_{SV} and K_S values represent the dynamic and static quenching constants, respectively. The modified SV equation is second order with respect to [Q], which accounts for its upward curvature (Fig. 5). The values of K_{SV} and K_S were determined by employing a nonlinear least squares method and are presented in Table 4. For all of our systems, the K_{SV} and K_S are similar in magnitude, so dynamic and static quenching processes both play important roles.

Conclusions

From the study of the effect of glycols on the micellization of TX-100, we have observed that the micellization process is less favourable in the presence of glycols. This is attributed to the structure-breaking abilities of glycols. In the presence of these additives the surface activity of TX-100 is also reduced. The minimum surface area increases with the glycol content in the mixture. Fluorescence studies indicate that the change in micropolarity sensed by the pyrene probe is due to improved solvation of the micelles. The quenching process of the pyrene probe by

Fig. 5. Stern–Volmer (SV) plot (modified) for the quenching of TX-100 by CPC.



CPC is accompanied by simultaneous dynamic and static processes.

Acknowledgements

RMP acknowledges an operating grant from the Natural Sciences and Engineering Research Council of Canada (NSERC) and A.A.W and K.G. are grateful for the Undergraduate Student Research Award (USRA) from NSERC for the years 2003 and 2004, respectively.

References

1. C. Tanford. *In* The hydrophobic effect: formation of micelles and biological membranes. 2nd ed. Wiley, New York. 1980.
2. J.N. Israela Chevili. Intermolecular and surface forces. Academic Press, New York. 1985.
3. D. Myers. Surfactants science and technology. 2nd ed. VCH, New York. 1992.
4. T. Wärnheim. Curr. Opin. Colloid Interface Sci. **2**, 473 (1997).
5. R. Zana. Colloids Surf. A, **27**, 123 (1997).
6. R. Nagarajan and C.C. Wang. Langmuir, **16**, 5242, (2000).
7. L.G. Ionescu and D.S. Fung. J. Chem. Soc., Faraday Trans. 1, **77**, 2907 (1981).
8. S. Backlund, B. Bergenställ, O. Molander, and T. Wärnheim. J. Colloid Interface Sci. **131**, 393 (1989).
9. W. Binana-Limbele and R. Zana. Colloid Polym. Sci. **267**, 440 (1989).
10. M. Sjöberg, V. Henriksson, and T. Wärnheim. Langmuir, **6**, 1205 (1990).
11. H. Gharibi, R. Palepu, D.M. Bloor, D.G. Hall, and E. Wyn-Jones. Langmuir, **8**, 782 (1992).
12. M.S. Bakshi. J. Chem. Soc., Faraday Trans. **89**, 4323 (1993).
13. A. Callaghan, R. Doyle, E. Alexander, and R. Palepu. Langmuir, **9**, 3422 (1993).
14. R. Palepu, H. Gharibi, D.M. Bloor, and E. Wyn-Jones. Langmuir, **9**, 110 (1993).
15. R. Nagarajan and C.C. Wang. J. Colloid Interface Sci. **178**, 471 (1996).
16. D.J. Lee and W.H. Huang. Colloid Polym. Sci. **274**, 160 (1996).
17. K. Gracie, D. Turner, and R. Palepu. Can. J. Chem. **74**, 1616 (1996).
18. C.C. Ruiz. J. Colloid Interface Sci. **221**, 262 (2000).

© 2004 NRC Canada

19. M.S. Akhter and S.M. Alawi. Colloids Surf. A, **173**, 95 (2000).
20. A. Ray. Nature (London), **231**, 313 (1971).
21. A. Ray and G. Némethy. J. Phys. Chem. **75**, 809 (1971).
22. L. Cantú, M. Corti, V. Degiorgio, H. Hoffman, and W.J. Ulibricht. J. Colloid Interface Sci. **116**, 384 (1987).
23. M. Jonströmer, M. Sjöberg, and T. Wärnheim. J. Phys. Chem. **94**, 7459 (1990).
24. J. Penfold, E. Staples, I. Tucker, and P. Cummins. J. Colloid Interface Sci. **185**, 424 (1997).
25. P. Alexandridis and L. Yang. Macromolecules, **33**, 5574 (2000).
26. C.C. Ruiz, J.A. Molina-Bolivar, J. Aguiar, G. MacIsaac, S. Moroze, and R. Palepu. Langmuir, **17**, 6831 (2001).
27. C.C. Ruiz, J.A. Molina-Bolivar, J. Aguiar, G. MacIsaac, S. Moroze, and R. Palepu. Colloid Polym. Sci. **281**, 531 (2003).
28. K.M. Glenn, S. Moroze, S.C. Bhattacharya, and R. Palepu. J. Dispersion Sci. Technol. **26**, 79 (2005).
29. G.C. Krescheck and J. Hwang. Chem. Phys. Lipids, **76**, 193 (1995).
30. K.S. Patra, A. Alonso, and F.M. Goñi. Biochim. Biophys. Acta, **112**, 1373 (1998).
31. M. Altschuler, D.K. Heddens, R.R. Diveley, and G.C. Krescheck. Biotechniques, **17**, 434 (1994).
32. E.H. Crook, D.B. Fordyce, and G.F. Trebbi. J. Phys. Chem. **67**, 1987 (1963).
33. A. Ray and G. Némethy. J. Am. Chem. Soc. **93**, 6787 (1971).
34. R.J. Robson and E.A. Dennis. J. Phys. Chem. **81**, 1075 (1977).
35. L. Mei, R. Yahya, H. Xiaoyu, and M.A. Winnik. J. Colloid Interface Sci. **230**, 135 (2000).
36. M.J. Rosen. Surfactants and interfacial phenomena. Wiley, New York. 1978.
37. M.J. Rosen, M. Duhamayake, and A.W. Cohen. Colloids Surf. A, **5**, 159 (1982).
38. S.B. Sulthana, S.G.T. Bhat, and A.K. Rakshit. Langmuir, **13**, 4562 (1997).
39. S.B. Sulthana, S.G.T. Bhat, and A.K. Rakshit. Colloids Surf. A, **111**, 57 (1996).
40. H. Schott. J. Colloid Interface Sci. **173**, 265 (1995).
41. N.J. Turro and A.J. Yekta. J. Am. Chem. Soc. **100**, 5951 (1978).
42. G.B. Behera, B.K. Mishra, P.K. Behera, and M. Panda. Adv. Colloid Interface Sci. **82**, 1 (1999).

© 2004 NRC Canada

Chiral bidentate *N*-heterocyclic carbene complexes of Rh and Pd

Li Ren, Austin C. Chen, Andreas Decken, and Cathleen M. Crudden

Abstract: The synthesis of a new chiral, bidentate oxazoline/imidazolidene carbene precursor is described. This species is reacted with various metal salts in the presence of a base to generate rhodium and palladium complexes, which are characterized spectroscopically and crystallographically.

Key words: chiral *N*-heterocyclic carbene, rhodium, palladium, oxazolidine, asymmetric catalysis.

Résumé : On décrit la synthèse d'un nouveau précurseur chiral et bidentate du carbène oxazoline/imidazolidène. On a fait réagir cette espèce avec divers sels métalliques, en présence de base, pour générer des complexes du rhodium et du palladium qu'on a caractérisés par des méthodes spectroscopiques et cristallographiques.

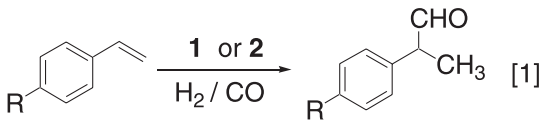
Mots clés : carbène chiral *N*-hétérocyclique, rhodium, palladium, oxazolidine, catalyse.

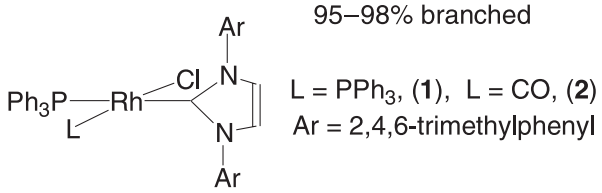
[Traduit par la Rédaction]

Introduction

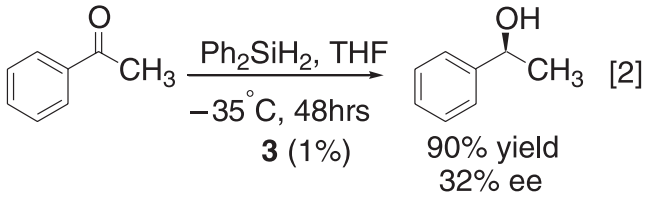
The use of *N*-heterocyclic carbenes as ligands for transition metals has experienced a renaissance of late (1). These ligands display intriguing properties relative to the more commonly employed phosphine ligands. Most importantly, the binding constants of carbene ligands with catalytically active transition metals such as Ru are approximately double that of the related phosphine ligands (2, 3). Carbene ligands have proven to be extremely useful in important reactions such as Ru–catalyzed metathesis reactions (4) and Pd–catalyzed coupling reactions (5).

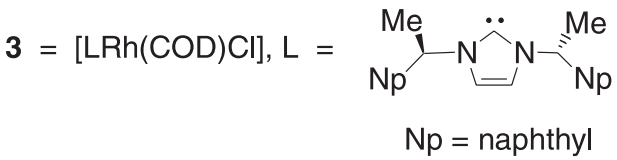
We have reported that mixed rhodium complexes **1** and **2**, which contain both phosphine and *N*-heterocyclic carbene ligands, are effective catalysts for the hydroformylation of vinyl arenes, giving the branched isomer with up to 98:2 selectivity (eq. [1]) (6). The activity of the carbene/phosphine complex (**2**) was twice that of the related bis-phosphine ([$RhCl(CO)(PPh_3)_2$]) under identical conditions. Furthermore, the carbene complex was more selective for the branched isomer than the bis-phosphine complex (96:4 vs. 88:12). With the regioselectivity and reactivity of these complexes established for the important hydroformylation reaction, we began the more challenging task of preparing chiral versions of these carbene complexes.





Several examples of chiral *N*-heterocyclic carbenes and their corresponding metal complexes have been reported in the literature (7–13) and an increasing number are being tested in catalytic reactions (14–20). In 1997, Herrmann reported the hydrosilylation of acetophenone with chiral monodentate carbene complex **3**, which proceeded in 32% enantiomeric excess (ee) (eq. [2]) (14*b*). The hydrosilylation of cyclohexylmethyl ketone was also examined with chiral





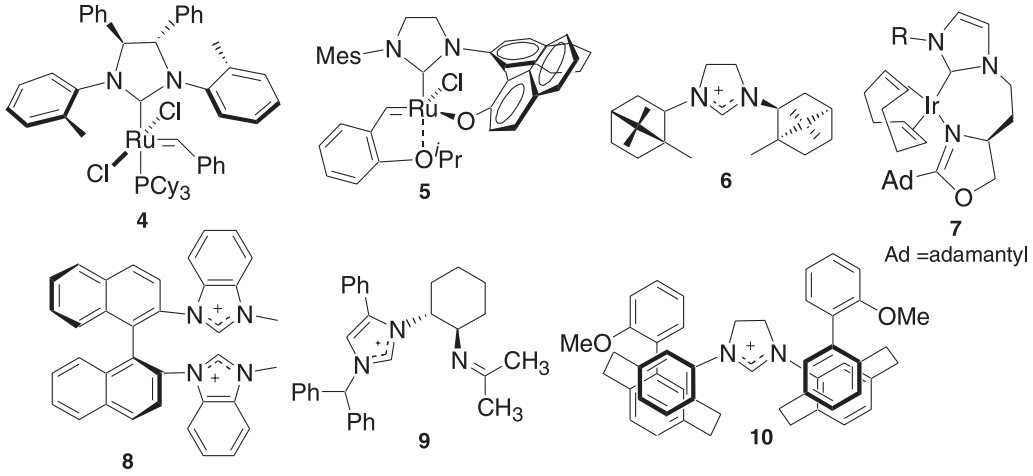
Received 4 February 2004. Published on the NRC Research Press Web site at http://canjchem.nrc.ca on 9 February 2005.

L. Ren, A.C. Chen, A. Decken,[1] and C.M. Crudden.[2,3] Department of Chemistry, University of New Brunswick, P.O. Box 45222, Fredericton, NB E3B 6E2, Canada.

[1]Author to whom questions concerning crystallography should be addressed.
[2]Current address: Department of Chemistry, Queen's University, Kingston ON K7L 3N6, Canada.
[3]Corresponding author (e-mail: Cruddenc@chem.queensu.ca).

 doi: 10.1139/V04-165 © 2004 NRC Canada

Chart 1. Successful chiral *N*-heterocyclic carbene complexes and carbene precursors.

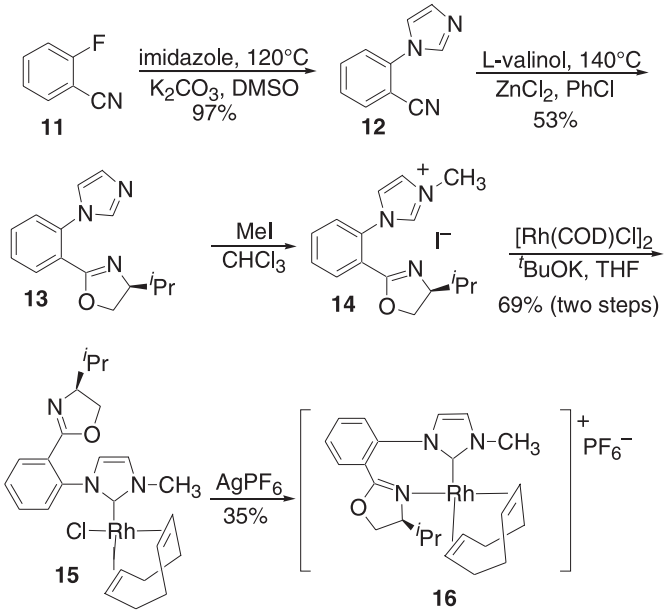


triazolium complexes and proceeded with up to 44% ee (14*c*, *d*).

Grubbs (15), Hoveyda (16), Hartwig (17), and Burgess (18) have reported carbene ligands that give high enantioselectivity for metathesis, arylation of ketones, and hydrogenation reactions, respectively (Chart 1). Recent reports from the groups of Shi (19), Douthwaite (14*h*), and Andrus (20) have described more complex carbenes that provide >90% ee in hydrosilylation, allylic alkylation, and enone arylation, respectively. Although high selectivities have been obtained using these catalysts for specific reactions, substrate generality still needs improvement.

Inspired by the successes of Pfaltz (21) and Brunner (22) with chiral phosphine/oxazoline ligands, we have prepared carbene ligands that have a chiral oxazoline as the second point of ligation. Related oxazoline/carbene complexes have been prepared by Herrmann (14), and complex **7** was introduced by Burgess during this study (18). With the aim of increasing the transfer of chiral information by increasing the rigidity between the carbene and the oxazoline, we embarked on the synthesis of carbene precursor, **14**.

Scheme 1. Synthesis of Rh complex **16**.



Results and Discussion

Beginning with commercially available 2-fluorobenzonitrile (**11**), nucleophilic aromatic displacement of the fluoride with imidazole proceeded quantitatively yielding **12** (Scheme 1). Subsequent condensation with optically pure valinol (23) followed by methylation with methyl iodide furnished carbene precursor **14**.

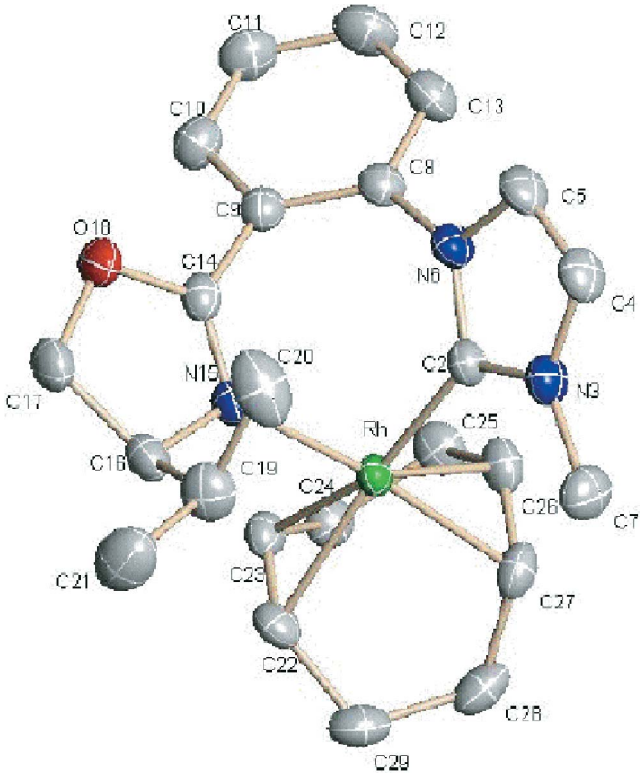
Although attempts to prepare and isolate the free carbene were unsuccessful, rhodium carbene complex **16** could be obtained in two steps from $[Rh(\eta^4\text{-}1,5\text{-}COD)(\mu\text{-}Cl)]_2$ and **14**. Thus, reaction of crude **14** and the rhodium complex in the presence of potassium *t*-butoxide followed by chlorine abstraction with silver hexafluorophosphate generated **16**. The ^{13}C NMR spectrum of this material contained a signal at 181 ppm, corresponding to the ligated carbene carbon, with a distinctive rhodium-carbon coupling constant of 50 Hz.

X-ray quality crystals[4] of **16** were obtained by recrystallizing the air-stable, yellow rhodium complex from dichloromethane/hexane. The crystal structure (see Fig. 1) revealed that the rhodium adopts a distorted square planar geometry with combined angles of 359.2°. The bite angle of the carbene-imidazoline ligand in complex **16** is 84.2°. As expected, the carbene–rhodium bond ((Rh—C(2) = 2.0150(16) Å) is much shorter than the oxazoline nitrogen–rhodium bond ((Rh—N(15) = 2.0954(14) Å). A stronger trans influence of the carbene ligand could be inferred from the longer distances separating the rhodium and the olefinic carbons trans to the carbene ((Rh—C(22) = 2.2085(16) Å, Rh—C(23) = 2.2097(17) Å) relative to those trans to the

[4] Crystal data for **16**: $C_{24}H_{31}F_6N_3OPRh$, crystal size 0.125 mm^3 × 0.150 mm^3 × 0.275 mm^3, orthorhombic, $P2_12_12_1$, a = 11.6588(4) Å, b = 13.3143(5) Å, c = 16.6038(6) Å, $\alpha = \beta = \gamma = 90°$, V = 2577.39(16) Å^3, Z = 4, 2θ (max) = 32.50°, ω and φ scans, 28 697 reflections scanned, 8910 unique reflections (R_{int} = 0.0179), T = 173(2) K, full-matrix least-squares on F^2, wR_2 = 0.0547, R_1 = 0.0231. Full details of the crystallographic analysis of **13** are described in the Supporting information.[6]

© 2004 NRC Canada

Fig. 1. View of the cation of **16**. Thermal ellipsoids are at the 30% probability level and hydrogen atoms have been removed for clarity.



oxazoline nitrogen ((Rh—C(26) = 2.1206(17) Å, Rh—C(27) = 2.1509(18) Å). However, the carbon–carbon double bond trans to the oxazoline ((C(26)—C(27) = 1.390(3) Å) is slightly longer than the C=C bond trans to the carbene ((C(22)—C(23) = 1.374(3)Å).

The corresponding palladium complex **17** could be prepared from either palladium acetate or [Pd(η^4-1,5-COD)Cl_2] (Scheme 2). Specifically, treatment of imidazolium salt **14** with [Pd(η^4–1,5–COD)Cl_2] in the presence of potassium *tert*-butoxide at room temperature, or simply heating **14** in DMSO with palladium acetate gave the same palladium-carbene iodide complex **17** (24). This structure was unambiguously demonstrated by X-ray crystallography[5] (see Fig. 2). The palladium, with the sum of the angles equal to 359.98°, is in a nearly perfect square-planar environment. Like its rhodium analogue, the palladium–iodide bond trans to the carbene (Pd—I(2) = 2.6571(3) Å) is longer than that trans to the oxazoline nitrogen (Pd—I(1) = 2.5657(3) Å). It is also noteworthy that within each asymmetric unit are two independent molecules with almost identical metric parameters. The main difference between them lies in the disposition of the two methyl residues of the isopropyl group (θ (C(21)—C(19)—C(20) = 112.0(4)° and C(41)—C(39)—C(40) = 115.3(4)°).

The catalytic activity of the new chiral rhodium-carbene

Scheme 2. Synthesis of Pd complex **17**.

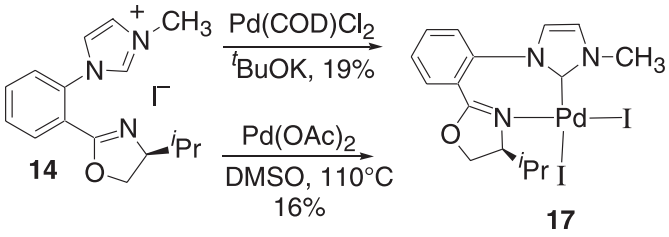
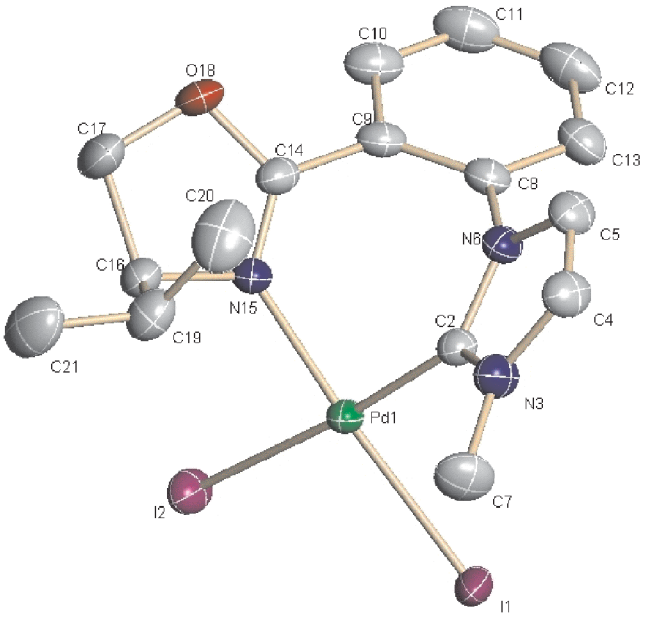


Fig. 2. View of the cation of **17**. Thermal ellipsoids are at the 30% probability level and hydrogen atoms have been removed for clarity.



complex **16** was evaluated in hydroboration and hydrosilylation reactions. Despite the chelating, monomeric form of the catalysts, the enantioselectivity of the described reactions never exceeded 10% ee. It is especially noteworthy that the bidentate ligand proved to be inferior to the monodentate ligand **3** in the hydrosilylation reaction under very similar conditions. One key difference between complex **16** and Herrmann's catalyst **3** is the C_2-symmetry of the latter species. This cannot be the sole reason for the poor performance of this species, as Pfaltz and co-workers (21) and Brunner (22) have shown that C_2-symmetry is not a necessary parameter for asymmetric induction. Regardless, it is clear that Herrmann's catalyst creates a chiral environment more effectively than the carbene derived from **14**.

Our synthetic method requires that the second group introduced onto the imidazole ring be a reactive electrophile. In this case methyl iodide was employed, with the consequence that the coordination site cis to the carbene is relatively unhindered. This may be the reason for the poor asymmetric induction observed in the reactions of complex **16**.

[5] Crystal data for **17**: $C_{32}H_{38}I_4N_3OPd$, crystal size 0.175 mm^3 × 0.250 mm^3 × 0.325 mm^3, monoclinic, *P*2(1), *a* = 8.8335(4) Å, *b* = 14.3771(7) Å, *c* = 15.7653(7) Å, α = γ = 90°, β = 99.630(1)°, *V* = 1973.98(16) Å^3, *Z* = 2, 2θ (max) = 30.00°, ω and φ scans, 19 249 reflections scanned, 10 005 unique reflections (R_{int} = 0.0168), *T* = 296(1) K, full-matrix least-squares on F^2, wR_2 = 0.0450, R_1 = 0.0206. Full details of the crystallographic analysis of **14** are described in the Supporting information.[6]

© 2004 NRC Canada

Conclusions

In conclusion, a chiral, bidentate oxazoline/carbene precursor can be prepared in three simple steps from commercially available starting materials. Herrmann's in situ deprotonation method obviates the need for the synthesis of the free carbene. The Rh catalyst **16** was examined in the hydrosilylation of acetophenone and the hydroboration of styrene. Although the catalyst was active, it gave less than 10% ee under all experimental conditions examined.

Experimental Section

General methods and materials

All solvents were dried according to standard procedures immediately prior to use and, where necessary, were purged using repeated freeze–pump–thaw cycles. Acetophenone was distilled under argon from phosphorous pentoxide. Styrene was fractionally distilled under a partial vacuum and percolated through a column of dry, neutral alumina immediately prior to use. Catecholborane was distilled from a partial pressure of argon to remove $B_2(catechol)_3$ and stored under argon in a Schlenk flask at –25 °C. All other reagents were used as received.

Instrumentation

Proton and ^{13}C NMR spectra were recorded on a Varian 400 MHz instrument using the solvent resonance as the internal standard. Gas chromatography (He carrier, 12.5 psi of head pressure (1 psi = 6.894 757 kPa), 1.14 mL/min flow) was performed with flame ionization (FI) detection using a split/splitless injector (split ratio 50) and hexane solutions. Retention times are given in min. All analyses were carried out using a 2,3-di-*O*-acetyl-6-*O*-*tert*-butyldimethylsilyl-β-cyclodextrin column (30 m, 0.25 mm diameter, 0.25 μm thickness).

Crystallography

Single crystals of **16** were coated with Paratone-N oil, mounted using a glass fibre and frozen in the cold nitrogen stream of the goniometer. Single crystals of **17** were coated with Paratone-N oil and mounted on a glass fibre with epoxy glue. A hemisphere of data was collected on a Bruker AXS P4/SMART 1000 diffractometer using ω and θ scans with a scan width of 0.3° and 30 s (for **16**) or 10 s (for **17**) exposure times. The detector distance was 4 cm. The data were reduced (SAINT) (25) and corrected for absorption (SADABS) (26). The structure was solved by direct methods and refined by full-matrix least squares on F^2(SHELXTL) (27). All non-hydrogen atoms were refined anisotropically. Hydrogen atoms were included in calculated positions and refined using a riding model for **17**. For **16**, hydrogen atoms were found in Fourier difference maps and refined isotropically. Thermal ellipsoid plots are at the 30% probability level. In some plots, hydrogen atoms have been omitted for clarity.

(2-Cyanophenyl)imidazole (12)

A 100 mL flame-dried, round-bottomed flask was charged with 3.634 g of 2-fluorobenzonitrile (**11**, 30 mmol), 3.064 g of imidazole (45 mmol), and 8.293 g of potassium carbonate (60 mmol) in 30 mL of DMSO. The reaction mixture was stirred at 120 °C under argon for 36 h. The reaction mixture, after cooling to room temperature, was poured into 50 mL of water to precipitate **12** as a white powder. The resulting suspension was filtered, washed, and dried in vacuo to give 4.894 g (97% yield) of the desired product. ^1H NMR (400 MHz, $CDCl_3$) δ: 7.88 (s, 1H), 7.85 (dd, 1H, J = 1.6, 7.6 Hz), 7.77 (dt, 1H, J = 1.6, 7.6 Hz), 7.56 (dt, 1H, J = 1.2, 7.6 Hz), 7.49 (dd, 1H, J = 1.2, 8.4 Hz), 7.38 (t, 1H, J = 1.2 Hz), and 7.30 (t, 1H, J = 1.2 Hz). ^{13}C NMR (100 MHz, $CDCl_3$) δ: 139.4, 136.7, 134.5, 134.3, 130.8, 128.4, 125.6, 119.6, 115.8, and 108.1

2-[(4S)-4-Isopropyloxazolyl]phenyl imidazole (13)

Zinc chloride (0.331 g, 2.43 mmol) was fused in a 250 mL flame-dried, round-bottomed flask. Then 4.083 g of (2-cyano-phenyl)imidazole (**12**, 24.3 mmol), 3.756 g of L-valinol (36.4 mmol), and 80 mL of chlorobenzene were added sequentially. The reaction mixture was left stirring at 140 °C under argon for 60 h. Following removal of the volatiles in vacuo, the pinkish residue was taken up in 100 mL of dichloromethane and washed with water (30 mL × 3). The aqueous wash was back-extracted with another 100 mL of dichloromethane. The organic layers were combined and dried over magnesium sulfate. Filtration and concentration in vacuo afforded a viscous oil that was identified as a mixture of unreacted starting material and desired product. Due to its very low solubility in ether, the starting material was removed by trituration with diethyl ether. Filtration, followed by concentration of the filtrate in vacuo afforded 3.276 g of the desired product (53% yield). ^1H NMR (400 MHz, $CDCl_3$) δ: 7.87 (dd, 1H, J = 1.2, 7.6 Hz), 7.62 (d, 1H, J = 0.8 Hz), 7.56 (dt, 1H, J = 2.0, 7.6 Hz), 7.48 (dt, 1H, J = 1.2, 7.6 Hz), 7.34 (dd, 1H, J = 1.2, 8.0 Hz), 7.14 (d, 1H, J = 1.2 Hz), 7.10 (t, 1H, J = 1.2 Hz), 4.22 (dd, 1H, J = 7.6, 8.8 Hz), 4.01–3.89 (m, 2H), 1.80–1.70 (m, 1H), 0.94 (d, 3H, J = 6.8 Hz), and 0.88 (d, 3H, J = 6.8 Hz). ^{13}C NMR (100 MHz, $CDCl_3$) δ: 161.8, 137.6, 131.5, 131.1, 129.2, 129.1, 128.5, 126.8, 120.6, 120.5, 72.7, 70.7, 32.7, 18.7, and 18.3.

1-(2-[(4S)-4-Isopropyloxazolyl]phenyl)-3-methyl imidazolium iodide (14)

255 mg of 2-[(4*S*)-4-isopropyloxazolyl]phenyl imidazole (**13**, 1.0 mmol) was dissolved in 20 mL of chloroform in a 50 mL round-bottomed flask. Excess methyl iodide (852 mg, 6.0 mmol) was then added dropwise to this mixture. After stirring for 16 h in the dark at room temperature, the volatiles were removed in vacuo to afford 395 mg of the desired product, which could not be purified by column chromatography or recrystallization. The crude material thus obtained was spectroscopically pure and was used in the next step without further purification. ^1H NMR (400 MHz, $CDCl_3$) δ: 9.69 (s, 1H), 8.09–8.06 (m, 1H), 7.86–7.83 (m, 1H), 7.73–7.66 (m, 2H), 7.52–7.48 (brs, 1H), 7.25 (s, 1H), 4.37 (dd, 1H, J = 8.0, 9.2 Hz), 4.27 (s, 3H), 4.02–3.89 (m, 2H), 1.68–1.60 (m, 1H), 0.86 (d, 3H, J = 2.8 Hz), and 0.84 (d, 3H, J = 2.8 Hz). ^{13}C NMR (100 MHz, $CDCl_3$) δ: 158.9, 138.3, 133.0, 132.5, 131.4, 131.1, 128.3, 124.2, 123.6, 123.0, 73.4, 70.3, 37.6, 32.9, and 18.7 (2).

© 2004 NRC Canada

(η^4-1,5-Cyclooctadiene)(1-(2-[(4S)-4-isopropyloxazolyl]phenyl)-3-methylimidaz-olin-2-ylidene)rhodium-(I)-hexafluorophosphate (16)

In a 100 mL flame-dried, round-bottomed flask, 0.572 g of $[Rh(COD)Cl]_2$ (1.16 mmol) was dissolved in 15 mL of THF. Under vigorous stirring and an argon purge, 325 mg of potassium *tert*-butoxide (2.90 mmol, 1.25 equiv.) was then added. The resulting suspension was stirred at room temperature for 10 min and then transferred via cannula into another 100 mL flame-dried, round-bottomed flask containing 920 mg of 1-(2-[(4*S*)-4-isopropyloxazolyl]phenyl)-3-methyl imidazolium iodide (**14**, 2.32 mmol) dissolved in 5.0 mL of THF. After stirring under argon at room temperature for 40 h, the solvent was removed and the product was purified by column chromatography, eluting with solvent systems of increasing polarity (pure dichloromethane to 10% methanol in dichloromethane). The neutral rhodium(I) complex **12** was isolated as an orange foam in 69% yield (821.2 mg). This was then redissolved in 20 mL of THF and 402.7 mg of silver hexafluorophosphate (1.59 mmol) was added. A white precipitate formed immediately. After stirring for 1 h, the suspension was filtered through a sintered glass funnel and the filtrate concentrated in vacuo. The resulting residue was then purified by column chromatography, eluting with solvent systems of increasing polarity (pure dichloromethane to 2% methanol in dichloromethane). Crystallization from dichloromethane/hexane furnished the desired product as yellow crystals (500 mg, 35% yield). ^{1}H NMR (400 MHz, $CDCl_3$) δ: 7.89 (dd, 1H, J = 1.6, 8.0 Hz), 7.79 (dt, 1H, J = 1.6, 7.6 Hz), 7.65 (dt, 1H, J = 1.2, 8.0 Hz), 7.48 (dd, 1H, J = 1.2, 8.0 Hz), 7.28–7.24 (m, 2H), 4.88–4.80 (m, 1H), 4.73 (dd, 1H J = 9.2, 10.4 Hz), 4.49–4.41 (m, 1H), 4.27 (dd, 1H, J = 7.2, 9.2Hz), 4.10–4.03 (m, 4H), 3.84–3.77 (m, 1H), 3.71–3.64 (m, 1H), 2.52–2.34 (m, 2H), 2.13–1.63 (m, 6H), 0.88 (d, 3H, J = 6.8 Hz), and 0.79 (d, 3H, J = 6.8 Hz). ^{13}C NMR (100 MHz, $CDCl_3$) δ: 181.1 (d, $J_{Rh\text{-}C}$ = 50.2 Hz), 162.9, 137.7, 133.6, 130.6, 129.1, 126.3, 124.6, 123.73, 123.69, 98.8 (d, $J_{Rh\text{-}C}$ = 7.2 Hz), 95.7 (d, $J_{Rh\text{-}C}$ = 7.2 Hz), 79.3 (d, $J_{Rh\text{-}C}$ = 13.6 Hz), 72.1, 71.4, 71.2 (d, $J_{Rh–C}$ = 5.6 Hz), 37.7, 32.6, 31.9, 30.8, 29.6, 27.9, 17.2, and 17.1.

(1-(2-[(4S)-4-Isopropyloxazolyl]phenyl)-3-methylimidazolin-2-ylidene) palladium-(II)-diiodide (17)

In a 100 mL round-bottomed flask, 348.3 mg of $Pd(COD)Cl_2$ (1.22 mmol) was dissolved in 15 mL of THF. To this was added 161.6 mg of potassium *tert*-butoxide (1.44 mmol). An immediate colour change from yellow to black was observed. After stirring at room temperature for 10 min, the reaction mixture was transferred via cannula into another 100 mL flame-dried, round-bottomed flask containing 474 mg of 1-(2-[(4*S*)-4-isopropyloxazolyl]-phenyl)-3-methyl imidazolium iodide (**14**, 1.2 mmol) in 5.0 mL of THF. The resulting mixture was then stirred for another 24 h. The solvent was then removed and the residue purified by column chromatography, eluting with solvent systems of increasing polarity (6:1 hexane/dichlormethane to pure dichloromethane). The desired product was then crystallized from dichloromethane/hexane yielding dark orange crystals (100 mg, 19% yield).

Alternatively, the same complex can be prepared as follows: In a 100 mL flame-dried, round-bottomed flask, 0.444 g of 1-(2-[(4*S*)-4-isopropyloxazolyl]phenyl)-3-methyl imidazolium iodide (**11**, 1.12 mmol) and 0.251 g of palladium acetate (1.12 mmol) was dissolved in 10 mL of DMSO. The reaction mixture was stirred under argon at 50 °C for 2 h and then at 110 °C for another 48 h. The solvent was then removed and the residue purified by column chromatography, eluting with pure dichloromethane. The desired product was then crystallized from dichloromethane/hexane yielding dark orange crystals (102 mg, 16%). ^{1}H NMR (400 MHz, $CDCl_3$) δ: 7.88 (dd, 1H, J = 1.6, 7.6 Hz), 7.80 (dt, 1H, J = 1.6, 8.0 Hz), 7.66 (dt, 1H, J = 1.2, 8.0 Hz), 7.55 (dd, 1H, J = 1.2, 8.0 Hz), 7.23 (d, 1H, J = 2.0 Hz), 7.19 (d, 1H, J = 2.0 Hz), 5.24 (ddd, 1H, J = 3.2, 3.6, 3.6 Hz, 1H), 4.64 (dd, 1H, J = 9.2, 10.4 Hz), 4.34 (dd, 1H, J = 6.8, 9.2 Hz), 4.16 (s, 3H), 2.40 (m, 1H), 0.88 (d, 3H, J = 6.8 Hz), and 0.60 (d, 3H, J = 6.8 Hz). ^{13}C NMR (100 MHz, $CDCl_3$) δ: 162.4, 136.9, 134.1, 131.0, 129.5, 126.7, 124.3, 123.8, 122.2, 72.6, 70.4, 40.7, 30.4, 17.9, and 14.8.

Hydroboration of styrene

In a 10 mL flame-dried, round-bottomed flask, 12.5 mg of rhodium complex **9** (0.01 mmol) was suspended in 2 mL of dried, deoxygenated THF. Freshly purified styrene (0.11 mL, 0.96 mmol) was then added to the reaction vessel and the mixture was stirred at room temperature for 10 min. Upon cooling to the desired temperature (0 °C or –30 °C) catecholborane (0.16 mL, 1.5 mmol) was added dropwise as a solution in 1 mL of THF over 20 min. Care was taken to minimize the variation in internal reaction temperature during this addition. After 16 h, 2 mL of methanol was added. The temperature was brought to 0 °C and the boronate ester was treated, under an atmosphere of nitrogen, with 1 mL of a 2 mol/L aqueous sodium hydroxide solution and 0.2 mL of hydrogen peroxide (30% (*w*/*v*)). The resulting black reaction mixture was then diluted with ether and the organic layer was separated. The aqueous layer was extracted further with ether (5 mL × 3). The organic extracts were combined, washed with brine (5 mL), and dried over magnesium sulfate. Filtration through a sintered glass funnel, followed by concentration of the resulting mixture in vacuo yielded the crude alcohols. The linear-to-branched ratio was elucidated from ^{1}H NMR of the crude product mixture with a 30 s delay inserted between each acquisition. Spectroscopically pure 1-phenylethanol was obtained by flash chromatography with 4:1 hexane/ether as eluent and its enantiomeric purity was determined by chiral GC (temperature protocol, 80 °C, 3 min, then increase 1 °C per min to 130 °C; retention times (*R*) = 33.5 min, (*S*) = 35.4 min). The following results were obtained at 0 °C: 58% combined yield, branched:linear = 55:45, ee = 7%.

Hydrosilylation of acetophenone

In a 25 mL flame-dried, round-bottomed flask was dissolved 27 mg of rhodium complex **9** (0.04 mmol) in 2 mL of deoxygenated, dried THF. Then 0.5 mL of freshly purified acetophenone (4.3 mmol) was added to the reaction mixture and the resulting pale yellow solution was cooled to –25 °C. Next 0.8 mL of diphenylsilane (4.3 mmol) was added neat, dropwise, over a period of 15 min and the reaction mixture was stirred under argon at –25 °C for 41 h. Hydrolysis of the silyl ether was accomplished through the addition of 1 mL

© 2004 NRC Canada

of methanol and a few crystals of *p*-toluenesulfonic acid. Complete hydrolysis was achieved after 10 h at room temperature. Spectroscopically pure 1-phenylethanol was obtained by flash chromatography with 4:1 hexane/ether as eluent (141 mg, 27% yield, 34% conversion by NMR). Enantiomeric excess (2%) was determined by chiral GC (temperature protocol, 80 °C, 3 min, then increase 1 °C per min to 130 °C; R = 33.5 min, S = 35.4 min).

Supplementary material

Supporting information available lists details of the crystal structure determination for compounds **13** and **14**.[6]

Acknowledgements

The Natural Sciences and Engineering Research Council of Canada (NSERC) is gratefully acknowledged for support of this research in terms of equipment and operating grants to CMC, and a postgraduate scholarship to ACC. The Canada Foundation for Innovation is also thanked for funding this research. The University of New Brunswick and BioChem Pharma are thanked for scholarships to LR and ACC.

References

1. For reviews see: (*a*) W.A. Herrmann, K. Öfele, D.v. Preysing, and S.K. Schneider. J. Organomet. Chem. **687**, 229 (2003); (*b*) W.A. Herrmann. Angew. Chem. Int. Ed. **41**, 1290 (2002); (*c*) T. Weskamp, V.P.W. Bohm, and W.A. Herrmann. J. Organomet. Chem. **600**, 12 (2000); (*d*) M. Regitz. Angew. Chem. Int. Ed. **35**, 725 (1996).
2. Binding constants of *N*-heterocyclic carbenes and phosphines with transition metals have been determined using calorimetry. ΔH of stabilization (kcal/mol) of IMes = 15.6, other heterocyclic carbenes = 18.6~21.2, PCy_3 = 9.4. (*a*) J. Huang, H.-J. Schanz, E.D. Stevens, and S.P. Nolan. Organometallics, **18**, 2370 (1999); (*b*) J. Huang, E.D. Stevens, S.P. Nolan, and J.L. Petersen. J. Am. Chem. Soc. **121**, 2674 (1999); (*c*) A.C. Hillier, W.J. Sommer, B.S. Yong, J.L. Petersen, L. Cavallo, and S.P. Nolan. Organometallics, **19**, 4327 (2003).
3. For binding constants determined by density functional theory (DFT) calculations, see T. Weskamp, F.J. Kohl, W. Hieringer, D. Gleich, and W.A. Herrmann. Angew. Chem. Int. Ed. **38**, 2416 (1999).
4. (*a*) M. Scholl, T.M. Trnka, J.P. Morgan, and R.H. Grubbs. Tetrahedron Lett. **40**, 2247 (1999); (*b*) M. Scholl, S. Ding, C.W. Lee, and R.H. Grubbs. Org. Lett. **1**, 953 (1999); (*c*) M.S. Sanford, J.A. Love, and R.H. Grubbs. J. Am. Chem. Soc. **123**, 6543 (2001); (*d*) J.A. Love, M.S. Sanford, M.W. Day, and R.H. Grubbs. J. Am. Chem. Soc. **125**, 10103 (2003); (*e*) L. Ackermann, A. Furstner, T. Weskamp, F.J. Kohl, and W.A. Herrmann. Tetrahedron Lett. **40**, 4787 (1999); (*f*) T. Weskamp, W.C. Schattenmann, M. Spiegler, and W.A. Herrmann. Angew. Chem. Int. Ed. **37**, 2490 (1998); (*g*) J. Huang, E.D. Stevens, S.P. Nolan, and J.L. Petersen. J. Am. Chem. Soc. **121**, 2674 (1999); (*h*) A. Fürstner, L. Ackermann, B. Gabor, R. Goddard, C.W. Lehmann, R. Mynott, F. Stelzer, and O.R. Thiel. Chem. Eur. J. **7**, 3236 (2001).
5. For applications of the Suzuki–Miyaura reaction see: (*a*) G. Altenhoff, R. Goddard, C.W. Lehmann, and F. Glorius. Angew. Chem. Int. Ed. **42**, 3690 (2003); (*b*) C. Zhang, J. Huang, M.L. Trudell, and S.P. Nolan. J. Org. Chem. **64**, 3804 (1999); (*c*) C.W.K. Gstöttmayr, V.P.W. Böhm, E. Herdtweck, M. Grosche, and W.A. Herrmann. Angew. Chem. Int. Ed. **41**, 1363 (2002); (*d*) For the Sonogashira coupling see: M. Eckhardt and G.C. Fu. J. Am. Chem. Soc. **125**, 13642 (2003); (*e*) For the Kumada coupling see A.C. Frisch, F. Rataboul, A. Zapf, and M. Beller. J. Organomet. Chem. **687**, 403 (2003); (*f*) For aminations of aromatic halides see S.R. Stauffer, S. Lee, J.P. Stambuli, S.I. Hauck, and J.F. Hartwig. Org. Lett. **2**, 1423 (2000); (g) M.S. Viciu, R.A. Kelly III, E.D. Stevens, F. Naud, M. Studer, and S.P. Nolan. Org. Lett. **5**, 1479 (2003); (*h*) M.S. Viciu, R.F. Germaneau, O. Navarro-Fernandez, E.D. Stevens, and S.P. Nolan. Organometallics, **21**, 5470 (2002).
6. A.C. Chen, L. Ren, A. Decken, and C.M. Crudden. Organometallics, **19**, 3459 (2000).
7. (*a*) A.W. Coleman, P.B. Hitchcock, M.F. Lappert, R.K. Maskell, and J.H. Müller. J. Organomet. Chem. **250**, C9 (1983); (*b*) M.F. Lappert. *In* Transition metal chemistry. *Edited by* A. Muller and E. Diemann. Verlag Chemie, Weiheim, Germany. 1981.
8. For a review of chiral carbene complexes see: M.C. Perry and K. Burgess. Tetrahedron: Asymmetry, **14**, 951 (2003).
9. W.A. Herrmann, L.J. Goossen, and M. Spiegler. Organometallics, **17**, 2162 (1998).
10. D.S. Clyne, J. Jin, E. Genest, J.C. Gallucci, and T.V. RajanBabu. Org. Lett. **8**, 1125 (2000).
11. C. Bolm, M. Kesselgruber, and G. Raabe. Organometallics, **21**, 707 (2002).
12. J. Huang, L. Jafarpour, A.C. Hillier, E.D. Stevens, and S.P. Nolan. Organometallics, **20**, 2878 (2001).
13. *(a)* M.C. Perry, X. Cui, and K. Burgess. Tetrahedron: Asymmetry, **13**, 1969 (2002); (*b*) F.M. Rivas, A. Giessert, and S.T. Diver. J. Org. Chem. **67**, 1708 (2002); (*c*) F.M. Rivas, U. Riaz, A. Giessert, J.A. Smulik, and A.T. Diver. Org. Lett. **3**, 2673 (2001); (*d*) L.G. Bonnet, R.E. Douthwaite, and R. Hodgson. Organometallics, **22**, 4384 (2003).
14. (*a*) W.A. Herrmann, L.J. Goossen, C. Kocher, and G.R. Artus. Organometallics, **16**, 2472 (1997); (*b*) W.A. Herrmann, L.J. Goossen, C. Kocher, and G.R. Artus. Angew. Chem. Int. Ed. **35**, 2805 (1996); (*c*) D. Enders and H. Gielen. J. Organomet. Chem. **617**, 70 (2001); (*d*) D. Enders, H. Gielen, J. Runsink, K. Breuer, S. Brode, and K. Boehn. Eur. J. Inorg. Chem. 913 (1998); (*e*) H. Seo, H.-J. Park, B.Y. Kim, J.H. Lee, S.U. Son, and Y.K. Chung. Organometallics, **22**, 618 (2003); (*f*) F. Guillen, C.L. Winn, and A. Alexakis. Tetrahedron: Asymmetry, **12**, 2083 (2001); (*g*) J. Pytkowicz, S. Roland, and P. Mangeney. Tetrahedron: Asymmetry, **12**, 2087 (2001); (*h*) L.G. Bonnet, R.E. Douthwaite, and B.M. Kariuki. Organometallics, **22**, 4187 (2003); (*i*) A.A.D. Tulloch, A.A. Danopoulos, G.J. Tizzard, S.J. Coles, M.B. Hursthouse, S. Hay-Motherwell, and W.B. Motherwell. Chem. Commun. 1270 (2001); (*j*) F. Glorius, G. Altenhoff, R. Goddard, and C. Lehmann. Chem. Commun. 2704 (2002); (*k*) S. Gischig and A. Togni. Organometallics,

[6] Supplementary data may be purchased from the Directory of Unpublished Data, Document Delivery, CISTI, National Research Council Canada, Ottawa, ON K1A OS2, Canada (http://www/nrc.ca/cisti/irm/unpub_e.shtml for information on ordering electronically). CCDC 253890 and 253891 contain the crystallographic data for this manuscript. These data can be obtained, free of charge, via www.ccdc.cam.ac.uk/conts/retrieving.html (or from the Cambridge Crystallographic Data Centre, 12 Union Road, Cambridge CB2 lEZ, U.K.; fax +44 1223 336033; or deposit@ccdc.cam.ac.uk).

© 2004 NRC Canada

23, 2479 (2004); (*l*) W.A. Herrmann and C. Kocher. Angew. Chem. Int. Ed. **36**, 2162 (1997).
15. (*a*) T.J. Seiders, D.W. Ward, and R.H. Grubbs. Org. Lett. **3**, 3225 (2001); (*b*) M. Scholl, S. Ding, C.W. Lee, and R.H. Grubbs. Org. Lett. **1**, 953 (1999).
16. J.J. Van Veldhuizen, S.B. Garber, J.S. Kingsbury, and A.H. Hoveyda. J. Am. Chem. Soc. **124**, 4954 (2002).
17. S. Lee and J.F. Hartwig. J. Org. Chem. **66**, 3402 (2001).
18. (*a*) X. Cui and K. Burgess. J. Am. Chem. Soc. **125**, 14212 (2003); (*b*) M.T. Powell, D.-R. Hou, M.C. Perry, X. Cui, and K. Burgess. J. Am. Chem. Soc. **123**, 8878 (2001); (*c*) M.C. Perry, X. Cui, M.T. Powell, D.-R. Hou, J.H. Reibenspies, and K. Burgess. J. Am. Chem. Soc. **125**, 113 (2003).
19. W.-L. Duan, M. Shi, and G.-B. Rong. Chem. Commun. 2916 (2003).
20. Q. Chai and M.B. Andrus. Angew. Chem. Int. Ed. **42**, 5871 (2003).
21 O. Loiseleur, M. Hayashi, N. Schmees, and A. Pfaltz. Synthesis, 1338 (1997).
22. H. Brunner. *In* Methoden der Organischen Chemie (Houben-Weyl). 4th ed. Vols. B and E 21. Thieme-Verlag, Stuttgart. 1995. pp. 4074–4081, and refs. cited therein.
23. (*a*) J.V. Allen, S.J. Coote, G.J. Dawson, C.G. Frost, C.J. Martin, and M.J. Williams. J. Chem. Soc., Perkin Trans. 1, 2065 (1994); (*b*) C. Bolm, K. Weickhard, M. Zehnder, and T. Ranff. Chem. Ber. **124**, 1173 (1991).
24. The coordination properties of the anion X^- determine whether it enters the inner coordination sphere of the resulting carbene complex; the most commonly used azolium iodides normally yield iodo complexes in which the iodide has replaced other ligands (e.g., chloride), see ref. 9. For an example of a $Pd(carbene)_2I_2$ complex and its application in the Heck reaction see: W.A. Herrmann, M. Elison, J. Fischer, C. Kocher, and G.R.J. Artus. Angew. Chem. Int. Ed. **34**, 2371 (1995).
25. SAINT 6.02 [computer program]. Bruker AXS, Inc., Madison, Wisconsin, USA. 1997-1999.
26. G. Sheldrick. SADABS [computer program]. Bruker AXS, Inc., Madison, Wisconsin, USA. 1999.
27. G. Sheldrick. SHELXTL 5.1 [computer program]. Bruker AXS, Inc., Madison, Wisconsin, USA. 1997.

© 2004 NRC Canada

RAPID COMMUNICATION / COMMUNICATION RAPIDE

Synthesis and X-ray crystal structure of $Cr(NR_2)_3$ (R = CH(Me)Ph)

Ryan S. Samuel, Brian O. Patrick, and Kevin M. Smith

Abstract: The reaction of $CrCl_3$ with three equivalents of the lithium salt of [*R*-(*R**,*R**)]-(+)-bis(α-methylbenzyl)amine produces the trigonal planar Cr(III) tris(amido) complex. The X-ray structure of $Cr[N\{CH(Me)Ph\}_2]_3$ is reported.

Key words: chromium, X-ray crystal structure, amido ligands, chiral ligands.

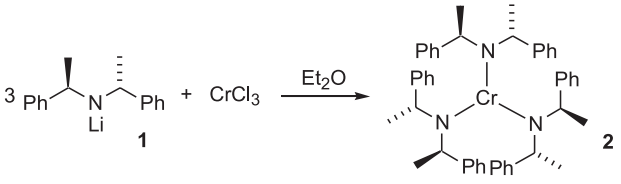
Résumé : La réaction du $CrCl_3$ avec trois équivalents du sel de lithium de la [*R*-(*R**,*R**)]-(+)-bis(α-méthylbenzyl)amine conduit à la formation du complexe tris(amido) Cr(III) à plan trigonal. On a déterminé la structure du $Cr[N\{CH(Me)Ph\}_2]_3$ par diffraction des rayons X.

Mots clés : chrome, structure cristalline, diffraction des rayons X, ligands amido, ligands chiraux.

[Traduit par la Rédaction]

Chiral lithium amide bases have been widely employed by organic chemists in asymmetric synthesis (1). For example, the lithium salt of [*R*-(*R**,*R**)]-(+)-bis(α-methylbenzyl)-amine (**1**) has been used in the synthesis of planar chiral complexes by the enantioselective directed ortho-metallation of prochiral (arene)$Cr(CO)_3$ compounds (2). Although transition metal amido complexes are widely recognized for their exceptional stoichiometric (3, 4) and catalytic (5–7) reactivity, to the best of our knowledge chiral amide **1** has not been used as a ligand for a transition metal. In this report we describe the preparation and X-ray crystal structure of a chiral Cr(III) tris(amido) complex.

The achiral $Cr[N(CHMe_2)_2]_3$ complex was first reported over 35 years ago (8), one of the first three-coordinate complexes stabilized by bulky monodentate anionic ligands (9, 10). The relative stability of this trigonal planar Cr(III) complex with respect to β-H elimination (11) and its utility as a precursor to a range of Cr(VI) (12) and Cr(II) (13) amido complexes prompted us to prepare the corresponding chiral $Cr[N\{CH(Me)Ph\}_2]_3$ complex **2** as shown in eq. [1].

[1] 

In an inert atmosphere glovebox, 10.88 mmol (2.518 g) of solid lithium amide **1**, obtained by deprotonation of commercially available [*R*-(*R**,*R**)]-(+)-bis(α-methylbenzyl)amine with *n*-BuLi, was added portionwise to a suspension of 3.26 mmol (0.516 g) of anhydrous $CrCl_3$ in 30 mL of Et_2O. After stirring for 5 days, the solvent was removed in vacuo, and the residue was extracted with pentane and filtered through Celite supported on a sintered glass frit. The very dark-red–brown filtrate was concentrated under reduced pressure until a precipitate began to form. After addition of 5 mL of toluene, the solution was cooled to –32 °C for 2 days to provide 0.117 g (0.161 mmol, 5% yield based on $CrCl_3$) of dark-brown crystals of $Cr[N\{CH(Me)Ph\}_2]_3$ suitable for single-crystal X-ray diffraction. Anal. calcd (%) for $C_{48}H_{54}CrN_3$: C 79.52, H 7.57, N 5.80; found: C 79.71, H 7.86, N 5.93. IR (KBr) (cm^{-1}): 3056 (m), 3026 (m), 2973 (s), 2837 (m), 2360 (m), 1600 (w), 1492 (m), 1452 (m), 1370 (m), 1315 (m), 1269 (m), 1269 (m), 1205 (w), 1096 (s), 1064 (s), 1040 (m), 1028 (m), 993 (m), 892 (s), 757 (s), 697 (s). UV–vis (pentane): λ_{max} (ε) 345 nm (6126 L mol^{-1} cm^{-1}), 467 nm (5884 L mol^{-1} cm^{-1}). Mp: 187–193 °C.

Compound **2** is highly air- and water-sensitive and is very lipophilic: attempts to recrystallize pentane solutions of **2** at –30 °C led to the deposition of amorphous, semisolid material. However, the addition of toluene to saturated room-temperature pentane solutions of **2** followed by cooling did lead to the isolation in low yield of crystals suitable for X-ray analysis. A similar strategy has previously been reported

Received 5 October 2004. Published on the NRC Research Press Web site at http://canjchem.nrc.ca on 24 December 2004.

R.S. Samuel and K.M. Smith.[1] Department of Chemistry, University of Prince Edward Island, 550 University Avenue, Charlottetown, PE C1A 4P3, Canada.
B.O. Patrick. Department of Chemistry, University of British Columbia, Vancouver, BC V6T 1Z1, Canada.

[1]Corresponding author (e-mail: kmsmith@upei.ca).

 doi: 10.1139/V04-166 © 2004 NRC Canada

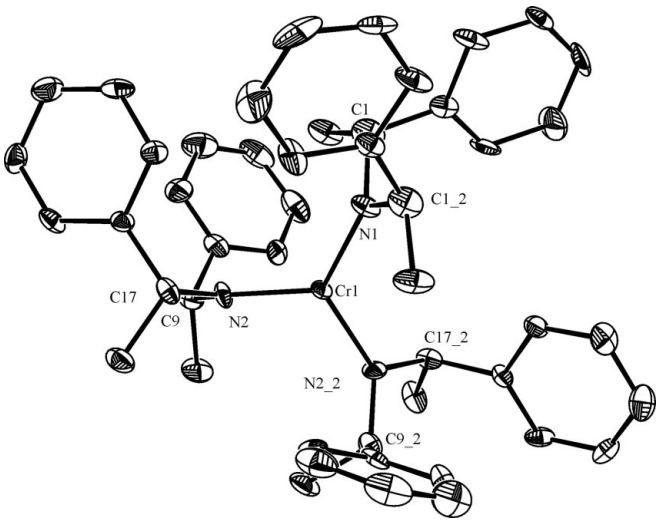
Table 1. Crystallographic data for $Cr[N\{CH(Me)Ph\}_2]_3$.

Crystal	**2**
Empirical formula	$C_{48}H_{54}CrN_3$
Formula mass	724.94
Colour, habit	Black, block
Crystal dimensions (mm)	0.50 × 0.40 × 0.20
Crystal system	Monoclinic
Space group	*C*2 (no. 5)
Z	4
a (Å)	17.671(2)
b (Å)	11.806(2)
c (Å)	19.740(2)
α (°)	90
β (°)	105.60(1)
γ (°)	90
Temperature (K)	173(2)
Volume (Å^3)	3966.5(9)
D_{calcd} (Mg m^{-3})	1.214
Radiation	Mo Kα (λ = 0.71069 Å)
Absorption coeff. (μ) (mm^{-1})	0.325
F(000)	1548.00
θ range for data collection (°)	2.0–27.7
Observed reflections	14 944
Independent reflections	4780 (R_{int} = 0.066)
Data/restraints/parameters	4780/0/479
Maximum shift/error	0.00
Goodness-of-fit on F^2	1.19
Final *R* indices [$I > 2\sigma(I)$]	R_1 = 0.066, wR_2 = 0.182
R indices (all data)	R_1 = 0.068, wR_2 = 0.183
Largest diff. peak and hole (e Å^{-3})	0.52 and –0.43

by Köhn et al. (14), who used Me_6Si_2 to aid in the crystallization of $Cr[N(SiMe_3)_2]_3$. Owing to the paramagnetic nature of the system, we are unable to confirm that the low isolated yield of crystals of **2** is due entirely to its evident lipophilicity, or if decomposition processes such as an H-atom abstraction from an amido ligand (11, 15) or oxidation of Cr (16) are occurring during or after the synthesis of **2**.

The X-ray diffraction measurements of **2** were made on a Rigaku/ADSC CCD area detector. The material crystallizes as a two-component twin, related by a 180° rotation about an axis perpendicular to the (0,0,–1) plane. The twin law was determined by and the integration carried out using the Twinsolve function of CrystalClear (17). The structure was solved by direct methods (18) using non-overlapped data from component 1, while a full-matrix least-squares refinement was carried out using all data, both overlapped and non-overlapped, from both components (19). The material crystallizes with two half-molecules in the asymmetric unit, each residing on a twofold rotation axis. Non-hydrogen atoms were refined anisotropically, while hydrogen atoms were added in calculated positions. The crystallographic data for **2** are shown in Table 1, and the ORTEP diagram of **2** with significant bond lengths and angles is shown in Fig. 1.

Fig. 1. ORTEP diagram of **2** (50% ellipsoids). Selected bond lengths (Å) and angles (°): Cr(1)—N(1) 1.91(1), Cr(1)—N(2) 1.858(6), N(1)—C(1) 1.451(9), N(2)—C(9) 1.486(10), N(2)—C(17) 1.48(1), N(1)–Cr(1)–N(2) 122.6(2), N(2)–Cr(1)–N(2_2) 114.8(4), Cr(1)–N(1)–C(1) 125.1(4), C(1)–N(1)–C(1_2) 109.7(8), Cr(1)–N(2)–C(9) 129.5(5), Cr(1)–N(2)–C(17) 118.2(5), C(9)–N(2)–C(17) 112.2(6).



The CIF tables of the crystal structure determination have been deposited as Supplementary material.[2]

Owing to the presence of the chiral amido ligands, complex **2** crystallizes in the chiral space group *C*2. While the trigonal arrangement of three C_2 symmetrical ligands about the Cr center could potentially result in a molecule with D_3 symmetry, complex **2** displays only a single crystallographic C_2 axis, lying along the Cr(1)–N(1) bond. Both the Cr center and the N atoms display trigonal planar geometries, with the sum of the bond angles around these atoms being very close to 360°.

The molecular structure of **2** is similar to that of achiral $Cr(NR_2)_3$ complexes, where NR_2 are the amido ligands derived from deprotonation of bis(trimethylsilyl)amine (14), diisopropylamine (20), *N*-*tert*-butyl-3,5-dimethylaniline (9), *N*-adamantyl-3,5-dimethylaniline (16), 2,2,6,6-tetramethylpiperidine (16), or dicyclohexylamine (21). The relatively short Cr—N bond lengths in **2** are very similar to those found for other $Cr(NR_2)_3$ complexes and are indicative of chromium–amido π-bonding interactions. The dihedral angles between the planes containing the N and Cr atoms fall in the range of 61.0°–64.2°, very close to the optimum angle of 62° calculated by Alvarez and co-workers using density functional theory on the sterically unhindered model compound $Cr(NH_2)_3$ (22).

In the past five years, chromium complexes with chiral ligands have been employed in a wide range of catalytic applications. In particular, chiral Cr(salen) complexes have been characterized as belonging to the class of "privileged

[2] Supplementary data may be purchased from the Directory of Unpublished Data, Document Delivery, CISTI, National Research Council Canada, Ottawa, ON K1A 0S2, Canada (http://www.nrc.ca/cisti/irm/unpub_e.shtml for information on ordering electronically). CCDC 255457 contains the crystallographic data for this manuscript. These data can be obtained, free of charge, via www.ccdc.cam.ac.uk/conts/retrieving.html (or from the Cambridge Crystallographic Data Centre, 12 Union Road, Cambridge CB2 1EZ, U.K.; fax +44 1223 336033; or deposit@ccdc.cam.ac.uk).

© 2004 NRC Canada

chiral catalysts" (23), owing to their utility in such mechanistically unrelated processes as asymmetric epoxide ring opening with Me_3SiN_3 (24), copolymerization of epoxides and CO_2 (25), and reductive coupling of organic halides and aldehydes (26, 27). While new chiral chromium complexes continue to be developed (28), to the best of our knowledge, **2** is the first chromium complex with a chiral amido (NR_2^-) ligand (29).

Given the single electron transfer reactivity exhibited by $Ti[N(R)Ar]_3$ complexes with organic substrates (30), $Cr(NR_2)_3$ complexes such as **2** may potentially serve as catalysts for pinacol coupling reactions. The first enantioselective Cr catalyst for this process was very recently reported (31). While the Cr(II) disilylamido complex $Cr[N(SiMe_3)_2]_2(THF)_2$ reacts readily with alcohols (32, 33), including salicylaldimines,[3] the corresponding Cr(III) complex $Cr[N(SiMe_3)_2]_3$ does not react under similar conditions. Preliminary results suggest that both $Cr(N^iPr_2)_3$ and **2** react with salicylaldimines, although unlike $HN(SiMe_3)_2$, the $HN[CH(Me)R]_2$ by-products of the amine elimination reactions are sufficiently strong Brønsted bases to deprotonate acidic salicylaldimines.[3] LoCoco and Jordan have recently demonstrated how chiral amido ligands can be used as directing groups for the enantioselective synthesis of chiral organometallic complexes of zirconium (34). Complex **2** is also of interest in the context of chromium amido complexes as pre-catalysts for ethylene polymerization (35, 36).

Although asymmetric processes mediated by chiral transition-metal complexes are of considerable academic and industrial interest, inorganic chemists have yet to explore the coordination chemistry of chiral amido ligands (29, 34) despite the widespread use of chiral lithium amide bases in organic chemistry. Recently, another reagent used in conjunction with BuLi in enantioselective ortho-metallation reactions, (–)-sparteine, has found use in the preparation of well-defined transition-metal compounds (37, 38). Perhaps amido ligands such as **1** may yet find applications as chiral ancillary ligands in C–C bond forming reactions mediated by chromium (26) or other early transition metal complexes.

Acknowledgements

This work was supported by the University of Prince Edward Island and the Natural Sciences and Engineering Research Council of Canada (NSERC).

References

1. P. O'Brien. J. Chem. Soc., Perkin Trans. 1, 1439 (1998).
2. S.E. Gibson and H. Ibrahim. Chem. Commun. 2465 (2002).
3. C.C. Cummins. Chem. Commun. 1777 (1998).
4. C.R. Clough, J.B. Greco, J.S. Figueroa, P.L. Diaconescu, W.M. Davis, and C.C. Cummins. J. Am. Chem. Soc. **126**, 7742 (2004).
5. L.H. Gade. Chem. Commun. 173 (2000).
6. A. Fürstner, C. Mathes, and C.W. Lehmann. Chem. Eur. J. **7**, 5299 (2001).
7. V. Ritleng, D.V. Yandulov, W.W. Weare, R.R. Schrock, A.S. Hock, and W.M. Davis. J. Am. Chem. Soc. **126**, 6150 (2004).
8. E.C. Alyea, J.S. Basi, D.C. Bradley, and M.H. Chisholm. J. Chem. Soc., Chem. Commun. 495 (1968).
9. C.C. Cummins. Prog. Inorg. Chem. **47**, 685 (1998).
10. P.P. Power. J. Organomet. Chem. **689**, 3904 (2004).
11. Y.-C. Tsai, M.J.A. Johnson, D.J. Mindiola, and C.C. Cummins. J. Am. Chem. Soc. **121**, 10 426 (1999).
12. A.L. Odom and C.C. Cummins. Polyhedron, **17**, 675 (1998).
13. E.W. Jandciu, J. Kuzelka, P. Legzdins, S.J. Rettig, and K.M. Smith. Organometallics, **18**, 1994 (1999).
14. R.D. Köhn, G. Kociok-Köhn, and M. Haufe. Chem. Ber. **129**, 25 (1996).
15. H. Cai, X. Yu, T. Chen, X.-T. Chen, X.-Z. You, and Z. Xue. Can. J. Chem. **81**, 1398 (2003).
16. K.B.P. Ruppa, K. Feghali, I. Kovacs, K. Aparna, S. Gambarotta, G.P.A. Yap, and C. Bensimon. J. Chem. Soc., Dalton Trans. 1595 (1998).
17. CrystalClear 1.3.6 [computer program]. Molecular Structure Corporation, The Woodlands, Tex. 1998–2004.
18. A. Altomare, M. Cascarano, C. Giacovazzo, and A. Guagliardi. J. Appl. Crystallogr. **26**, 343 (1994).
19. G.M. Sheldrick. SHELXL-97 (Release 97–2) [computer program]. University of Göttingen, Germany. 1997.
20. D.C. Bradley, M.B. Hursthouse, and C.W. Newing. J. Chem. Soc., Chem. Commun. 411 (1971).
21. D. Reardon, I. Kovacs, K.B.P. Ruppa, K. Feghali, S. Gambarotta, and J. Petersen. Chem. Eur. J. **3**, 1482 (1997).
22. A.A. Palacios, P. Alemany, and S. Alvarez. Inorg. Chem. **38**, 707 (1999).
23. T.P. Yoon and E.N. Jacobsen. Science (Washington, D.C.), **299**, 1691 (2003).
24. E.N. Jacobsen. Acc. Chem. Res. **33**, 421 (2000).
25. D.J. Darensbourg, R.M. Mackiewicz, A.L. Phelps, and D.R. Billodeaux. Acc. Chem. Res. **37**, 836 (2004).
26. A. Fürstner. Chem. Rev. **99**, 991 (1999).
27. M. Bandini, P.G. Cozzi, and A. Umani-Ronchi. Chem. Commun. 919 (2002).
28. (*a*) Z.-K. Wan, H. Choi, F.-A. Kang, K. Nakajima, D. Demeke, and Y. Kishi. Org. Lett. **4**, 4431 (2002); (*b*) H. Choi, K. Nakajima, D. Demeke, F.-A. Kang, H.-S. Jun, Z.-K. Wan, and Y. Kishi. Org. Lett. **4**, 4435 (2002); (*c*) A. Berkessel, D. Menche. C.A. Sklorz, M. Schröder, and I. Paterson. Angew. Chem. Int. Ed. **42**, 1032 (2003); (*d*) M. Inoue, T. Suzuki, and M. Nakada. J. Am. Chem. Soc. **125**, 1140 (2003); (*e*) M. Kurosu, M.-H. Lin, and Y. Kishi. J. Am. Chem. Soc. **126**, 12 248 (2004).
29. A. Shafir, D. Fiedler, and J. Arnold. Chem. Commun. 2598 (2003).
30. T. Agapie, P.L. Diaconescu, D.J. Mindiola, and C.C. Cummins. Organometallics, **21**, 1329 (2002).
31. N. Takenaka, G. Xia, and H. Yamamoto. J. Am. Chem. Soc. **126**, 13 198 (2004).
32. B. Horvath and E.G. Horvath. Z. Anorg. Allg. Chem. **457**, 51 (1979).
33. A. Kayal and S.C. Lee. Inorg. Chem. **41**, 321 (2002).
34. M.D. LoCoco and R.F. Jordan. J. Am. Chem. Soc. **126**, 13 918 (2004).
35. H. Ikeda, T. Monoi, K. Ogata, and H. Yasuda. Macromol. Chem. Phys. **202**, 1806 (2001).
36. K.H.D. Ballem, V. Shetty, N. Etkin, B.O. Patrick, and K.M. Smith. Dalton Trans. 3431 (2004).
37. S.C. Bart, E.J. Hawrelak, A.K. Schmisseur, E. Lobkovsky, and P.J. Chirik. Organometallics, **23**, 237 (2004).
38. R.M. Trend and B.M. Stoltz. J. Am. Chem. Soc. **126**, 4482 (2004).

[3] R.S. Samuel, M.C. McInnis, L.S. Dickieson, B.A. Dykerman, B.O. Patrick, and K.M. Smith. Manuscript in preparation.

© 2004 NRC Canada

AWARD LECTURE / CONFÉRENCE D'HONNEUR

2004 Bader Award Lecture
Metal-ion-catalyzed acyl and phosphoryl transfer reactions to alcohols: La^{3+}-promoted alcoholysis of activated amides, carboxylate esters, and neutral organophosphorus esters[1]

R. Stan Brown, Alexei A. Neverov, Josephine S.W. Tsang, Graham T.T. Gibson, and Pedro J. Montoya-Pelaez

Abstract: Unlike metal-ion-catalyzed hydrolysis processes, metal-ion-catalyzed methanolysis processes have received scant attention in the literature particularly from the standpoint of mechanistic studies. La^{3+}, introduced into methanol solution as its triflate or perchlorate salt, is particularly effective in promoting methanolysis reactions of unactivated and activated esters, phosphate triesters, and activated amides such as acetyl imidazoles and lactams. Studies of the kinetics of methanolysis of these substrates as a function of solution pH and $[La^{3+}]$ indicate that the solution comprises lanthanum dimers with one to five associated methoxides ($La_2^{3+}(^{-}OCH_3)_{1-5}$), the most catalytically active form being $La_2^{3+}(^{-}OCH_3)_2$, which is produced at near neutral pH in methanol (8.4). Mechanisms for all the acyl and phosphoryl transfer reactions are proposed where the metal ion serves a dual role of acting as a Lewis acid to activate the C=O or P=O system to nucleophilic attack by a metal-coordinated methoxide nucleophile. In cases where direct comparisons can be made, the La_2^{3+} catalyst system is more active for the methanolysis of nonactivated substrates than for activated substrates. Another general characteristic of this system is that the catalytic rate constant for the metal complex exceeds the second-order rate constant for free methoxide, in some cases by as much as 4600-fold. Overall the catalytic effects exhibited by the La_2^{3+} system is spectacular for such substrates as paraoxon, where as little as 2 mmol L^{-1} $La(OTf)_3$ in the presence of equimolar $NaOCH_3$ accelerates the methanolysis by 10^9-fold relative to the background reaction at neutral pH and ambient temperature.

Key words: kinetics of methanolysis, metal ion catalysis, lanthanides, methanolysis of carboxylate esters and phosphate esters.

Résumé : Contrairement aux processus d'hydrolyse catalysés par des ions métalliques, les processus de méthanolyse catalysés par les ions métalliques n'ont pratiquement pas été étudiés, en particulier, d'un point de vue mécanistique. Les ions La^{3+}, introduits dans des solutions méthanoliques sous la forme de triflate ou de perchlorate, sont particulièrement efficaces pour promouvoir les réactions de méthanolyses d'esters, activés ou non, de triesters de l'acide phosphorique et d'amides activés, tels les acétyl imidazoles et les lactames. Des études cinétiques des méthanolyses de ces substrats en fonction du pH de la solution et de la concentration en ions La^{3+} indiquent que la solution comprend des dimères du lanthane associés à un à cinq ions méthylates ($La_2^{3+}(^{-}OCH_3)_{1-5}$), la forme catalytiquement la plus active étant $La_2^{3+}(^{-}OCH_3)_2$ qui se forme à un pH pratiquement neutre, qui dans le méthanol est 8,4. Pour toutes les réactions de transfert d'acyle ou de phosphoryle, on propose des mécanismes dans lesquels l'ion métallique joue un double rôle comme acide de Lewis pour activer le système C=O ou P=O à l'attaque nucléophile par un méthanolate nucléophile coordiné à un métal. Dans les cas où on peut faire des comparaisons directes, le système de catalyseur à base de La_2^{3+} est plus actif pour la méthanolyse de substrats non activés par rapport aux substrats activés. Une autre caractéristique générale de ce système est que la constate de vitesse catalytique pour le complexe métallique est supérieure à la

Received 9 August 2004. Published on the NRC Research Press Web site at http://canjchem.nrc.ca on 26 January 2005.

R.S. Brown,[2] A.A. Neverov, J.S.W. Tsang, G.T.T. Gibson, and P.J. Montoya-Pelaez. Department of Chemistry, Queen's University, Kingston, ON K7L 3N6, Canada.

[1]Bader Award presentation at the 87th Canadian Chemistry Conference and Exhibition, London, Ontario, Canada, 1 June 2004.
[2]Corresponding author (e-mail: rsbrown@chem.queensu.ca).

 doi: 10.1139/V04-167 © 2004 NRC Canada

constante de vitesse du deuxième ordre de l'ion méthanolate libre et que dans certains cas, le rapport entre ces deux constante est de 4600. Dans l'ensemble, les effets catalytiques présentés par le système La_2^{3+} est spectaculaire pour des substrats tel le paroxon avec lequel une quantité aussi faible que 2 mmol L^{-1} de $La(OTf)_3$, en présence d'une quantité équimolaire de $NaOCH_3$, accélère la méthanolyse par un facteur de 10^9 par rapport à la réaction de référence, à un pH neutre et à la température ambiante.

Mots clés : cinétique de la méthanolyse, catalyse par des ions métalliques, lanthanides, méthanolyse d'esters d'acides carboxyliques et phosphoriques.

[Traduit par la Rédaction]

Introduction

Metal-catalyzed hydrolytic reactions of esters, amides (1), and phosphorus esters (2) have been studied for many years and, in general, these are relatively well-understood processes. These reactions involve catalytically active M^{x+}-($^-$OH) species where the metal ion serves several purposes such as: (*i*) decreasing the pK_a of the metal-associated HOH so that a M^{x+}-coordinated hydroxide can be formed at reduced pH; (*ii*) a bifunctional role for $M^{x+}(^-OH)$ acting as a Lewis acid and provider of the coordinated hydroxide to attack the C=O or P=O group; (*iii*) a possible additional role for the metal ion of promoting accelerated breakdown of any intermediates through coordination of the leaving group to the metal ion. By contrast, transition or lanthanide metal-catalyzed alcoholysis reactions, while being important industrial processes for carboxylate esterification or transesterification (3) are less understood with respect to mechanistic aspects and, as far as we are aware, have not been applied to phosphoryl transfer processes except in our labs. Buncel and co-workers (4) have extensively investigated the ethanolysis of phosphinate and phosphate esters promoted by alkali metal ethoxides, but these reactions occur under highly basic conditions through the intermediacy of $M_n^+(^-OEt)_m$ clusters, whereas the M^{2+}- and M^{3+}-catalyzed methanolysis reactions we discuss below occur under essentially neutral pH conditions.

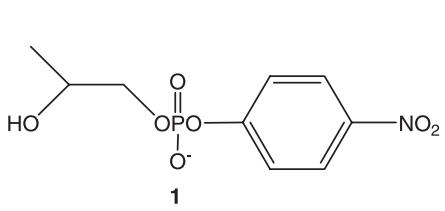
One might expect that M^{x+}-promoted alcoholysis reactions will be subject to the same mechanistic generalities as M^{x+}-promoted hydrolysis reactions. The bulk of our studies show that this is the case although, as will be shown below, there are important mechanistic and practical differences, which in certain ways simplify mechanistic study of the alcoholysis processes and circumvent at least two of the problems associated with metal hydroxides. First, in water at pH values above the pK_a of the M^{x+}(HOH), the active metal hydroxides form oligomeric–polymeric gels or precipitates that complicate the mechanistic analyses. In some cases this can be overcome by complexing the metal ion to ligands that block the oligomerization and prevent the precipitation of the metal hydroxides. However, this approach introduces other problems: for the most part the ligands employed are those that are readily available or easily synthesized and not necessarily the ideal ones for controlling geometry and reactivity of the complexes. Second, metal hydroxides in water are not particularly effective intermolecular catalysts and so the most effective catalytic systems are ones where the metal ion is held, through transient or fixed association with some proximal binding group, close to the scissile C=O or P=O linkage.

Moving to alcohol solvents ameliorates the above problems but requires due consideration of other factors, namely control and measurement of pH in alcohol solutions (5). Bosch and co-workers (6) have recently described simplified methods for determining the ^s_spH [3] in methanol solution, which have greatly enabled our work by allowing control of the $[CH_3OH_2^+]$ through the use of buffers in methanol, and now one can perform detailed mechanistic studies in methanol under buffered conditions as simply as one can in water. There is an additional consideration stemming from the fact that the autoprotolysis constant for methanol is $10^{-16.77}$, which means that neutral ^s_spH in methanol is ~8.4 (6). Using potentiometric titration in methanol we have determined the ^s_spK_a values for formation of the metal bound alkoxides of several transition and lanthanide metal ions (7). Interestingly, in the case of La^{3+}, catalytically active dimers such as $La_2^{3+}(^-OCH_3)_{1,2,3\ldots}$ are formed spontaneously in solution without the need for any binding ligands. Methanol, as a solvent, has additional benefits related to its low dielectric constant relative to that of water (31.5 vs. 78 (8)), which favours enhanced substrate solubility, greater ion-pairing between the catalytic metal ion and any anionic substrates, and greater Lewis acid interaction between neutral substrates and metal ions. Thus, as will be shown later, many acyl and phosphoryl transfer reactions to methanol can be greatly accelerated by $M^{x+}(^-OCH_3)$ species in contrast to the hydrolytic reactions in water where the $M^{x+}(^-OH)$ species have little or no activity.

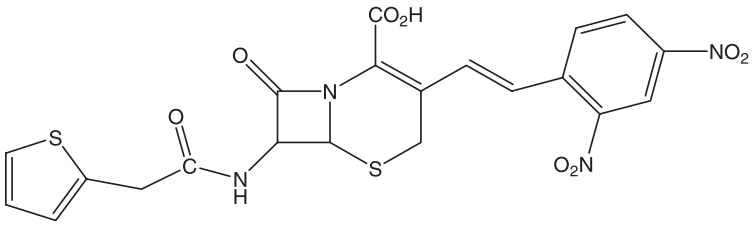
La^{3+} catalysis of acyl or phosphoryl transfer falls into two general classes. In the first category are substrates that ionize to give carboxylate or phosphate anions that bind very tightly to the metal ion and then are subject to rapid metal-catalyzed methanolysis. For example, La^{3+} can provide up to 10^{10}-fold acceleration of the methanolysis of diphenyl phosphate, di-*p*-nitrophenyl phosphate, and methyl *p*-nitrophenyl phosphate (9), and an impressive 4.6×10^{10}-fold acceleration of the methanolysis of RNA analogue β-hydroxypropyl-*p*-nitrophenyl phosphate (**1**) relative to the methoxide reac-

[3] For the designation of pH in nonaqueous solvents we use the forms described by Bosch and co-workers (6) based on the recommendations of the IUPAC (*In* Compendium of Analytical Nomenclature. Definitive Rules 1997. 3rd ed. Blackwell, Oxford, UK. 1998). If one calibrates the measuring electrode with aqueous buffers and then measures the pH of an aqueous buffer solution, the term ^w_wpH is used; if the electrode is calibrated in water and the "pH" of the neat buffered methanol solution then measured, the term ^s_wpH is used; and if the electrode is calibrated in the same solvent and the pH reading is made, then the term ^s_spH is used.

© 2004 NRC Canada



1



2

tion (10). More recently, we found that La^{3+} promotes the methanolysis of nitrocefin (**2**) by 10^5-fold relative to the methoxide reaction at a near neutral $^{s}_{s}$pH of 8 (11). Much of this work was reviewed recently (12) and thus will not be repeated here.

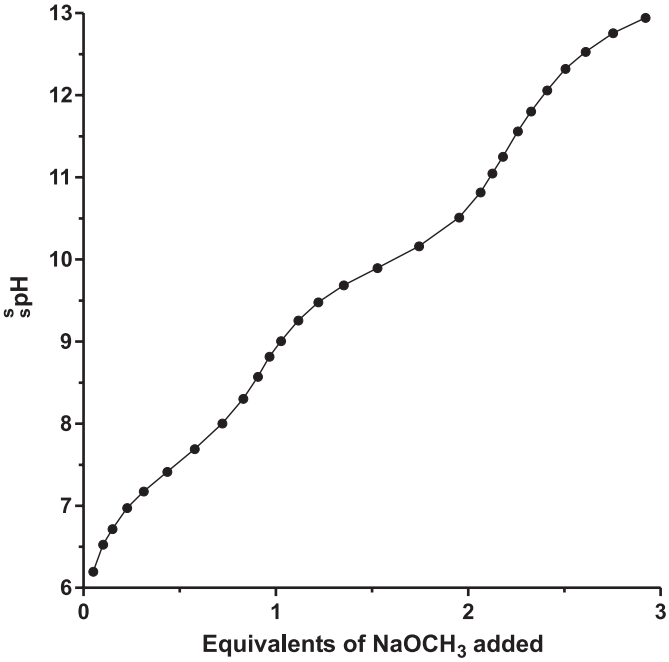
In the second category are neutral substrates such as carboxylate esters (13), phosphate triesters (14), activated amides such as acetyl imidazole and its pentamino Co^{III} derivative (15), and neutral β-lactams (11). These substrates have no strong binding with the metal ion and, after acyl or phosphoryl transfer to methanol, form products that are still neutral and thus will not be inhibitory as they bind to the metal ions with affinities similar to the original starting materials. It is these reactions that interest us here and in what follows we will give a chronological account of the major discoveries stemming from our studies of the La^{3+} catalysis of acyl and phosphoryl transfer from neutral substrates.

Results and discussion

Potentiometric titration of La^{3+} in methanol

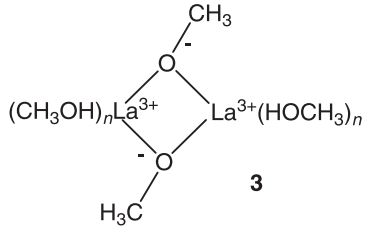
We have applied the methods described by Bosch and coworkers (6) to the potentiometric titration of several transition and lanthanide metal ions in methanol (7) and presented in Fig. 1 is a typical titration curve for La^{3+} introduced as its triflate salt. A cursory visual inspection of the profile indicates that there is an event consuming 1 equiv. of methoxide–La^{3+} with an apparent $^{s}_{s}pK_a$ ~ 7.5 and a second consuming 1.5 equiv. of methoxide–La^{3+} with an apparent $^{s}_{s}pK_a$ of ~10.4. Notable is the rather steep appearance of the titration curve, which suggests that dimeric or oligomeric species are formed. In the simplest analysis we proposed (13, 15) that in the neutral $^{s}_{s}$pH region the species formed is a bis-methoxy bridged La^{3+} dimer (**3**, $(La^{3+})_2(^{-}OCH_3)_2$) while in the high $^{s}_{s}$pH domain the species is $(La^{3+})_2(^{-}OCH_3)_5$. While not specified in those early studies, in the intermediate $^{s}_{s}$pH domain there must be La^{3+} complexes with intermediate numbers of methoxides and later we present a more sophisticated analysis that indicates that dimers containing one to five methoxides are present, the relative amounts of which are $^{s}_{s}$pH dependent.

Fig. 1. Potentiometric titration curve ($^{s}_{s}$pH vs. equiv. of added methoxide) of 1.33×10^{-3} mol L^{-1} $La(OTf)_3$ in methanol.

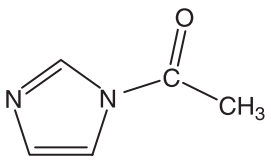


Acetyl imidazole

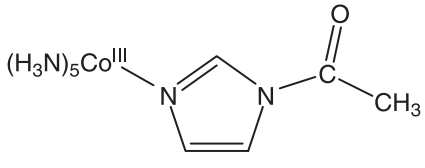
While it is an atypical amide, acetyl imidazole (**4a**) serves as a useful starting point for investigating the generalities of La^{3+}-catalyzed methanolysis since it is: (*i*) highly activated toward nucleophilic attack on the C=O and toward departure of the leaving imidazole; (*ii*) its hydrolytic mechanisms are well-studied and thus readily compared with the methanolysis processes; and (*iii*) its hydrolysis is *not* catalyzed by metal ions in water unless there is a proximal binding site, which places the bound metal ion in proximity to the C=O linkage (15). Shown in Fig. 2 is a typical set of plots of the k_{obs} for methanolysis of **4a** and **4b** vs. $[La^{3+}]$ at two $^{s}_{s}$pH values. Similar graphs are seen at different $^{s}_{s}$pH values and all have the common features of upward curvatures at low $[La^{3+}]$, followed by a linear plot at higher $[La^{3+}]$ (shown in Fig. 4 of ref. 15). The upward curvature suggests the involvement of a process that is higher than first order in



3



4a



4b

© 2004 NRC Canada

Scheme 1.

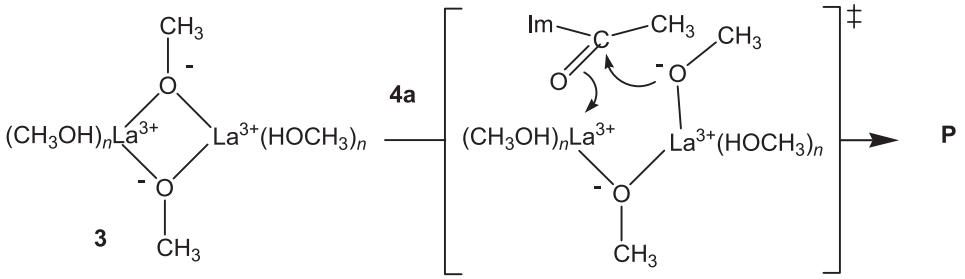


Fig. 2. Plots of pseudo-first-order rate constants vs. $[La^{3+}]$ for the methanolysis of AcIm (**4a**, ■, right axis, ${}^{s}_{s}pH = 6.7$) and $AcImCo(NH_3)_5^{3+}$ (**4b**, ●, left axis, ${}^{s}_{s}pH = 7.6$, I = 0.2 ($NaClO_4$)) at 25 °C (from ref. 15).

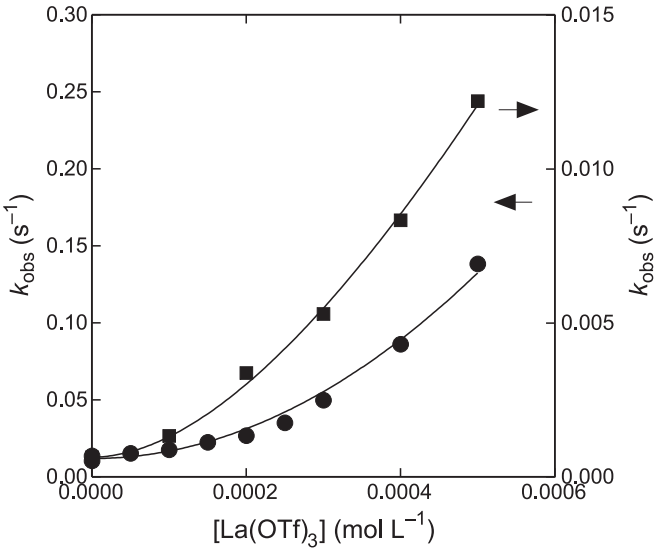
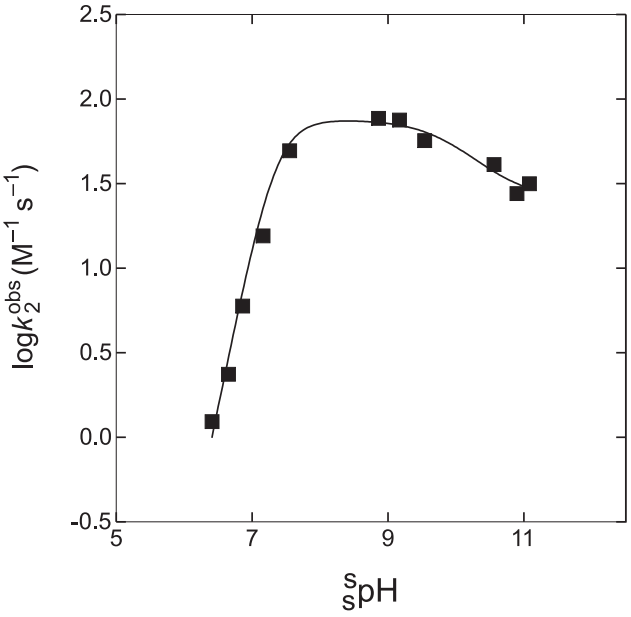


Fig. 3. Plots of the log of the second-order rate constant (k_2^{obs}) vs. ${}^{s}_{s}pH$ for $La(OTf)_3$-catalyzed methanolysis of AcIm (■) and $AcImCo(NH_3)_5^{3+}$ (●). Curves are the result of NLLSQ fitting of the experimental data to eq. [7] in ref. 15.



$[La^{3+}]$, possibly one involving a dimer of La^{3+}, and if its formation constant is large, e.g., $\geq 10^5$ M^{-1}, then above ~1 to 2×10^{-4} mol L^{-1} $[La^{3+}]$, the dimer is fully formed and the plot becomes linear. The slopes of the linear parts of the graphs at each ${}^{s}_{s}pH$ we define as k_2^{obs}, the observed second-order rate constant for $La_2{}^{3+}$-catalyzed methanolysis of **4a** and **4b**, and when $\log k_2$ is plotted as a function of ${}^{s}_{s}pH$ as in Fig. 3, it immediately becomes clear that there is an ascending wing of slope 2, followed by a plateau above ${}^{s}_{s}pH$ of ~7.5–7.8. There are two important points to be made concerning this plot. First, both **4a** and **4b** adhere to the same general plots with a kinetic ${}^{s}_{s}pK_a$ similar to the ${}^{s}_{s}pK_a$ determined via titration, and second, the ascending slope of 2 in each case indicates that the catalytically competent form acting on both substrates must have two methoxides. This also rules out any type of catalysis where the distal imidazole N is involved with La^{3+} as the pentamino Co^{III} blocks access to that site but the catalytic curve for **4b** has the same general ${}^{s}_{s}pH$ dependence as does **4a**. Fits of the kinetic data to equations developed in ref. 15 provide the lines through the data in Fig. 2 with the best-fit ${}^{s}_{s}pK_a$ value of 7.27 ± 0.15 and respective maximum second-order rate constants of 1.5×10^3 and 1.42×10^2 M^{-1} s^{-1} for methanolysis of **4a** and **4b** catalyzed by the $(La^{3+})_2(^{-}OCH_3)_2$ dimer. Based on the above experimental results, we propose that the catalytic mechanism proceeds as in Scheme 1 where the dimer **3** opens one of the methoxy–La^{3+} bridges to reveal a species capable of both Lewis acid activation of the C=O, and delivery of a La^{3+}-coordinated methoxide to the carbon. Notable is the fact that while the unaided $^{-}OCH_3$ nucleophile is 5900-fold more reactive with **4b** than with **4a** (k_{OCH_3} = 4.69×10^7 vs. 7.9×10^3 M^{-1} s^{-1} (15)) the catalysis afforded by **3** is 10-fold more effective for the neutral substrate **4a** than for the positively charged substrate **4b**, in line with the mechanism suggested in Scheme 1 since the Lewis acid interaction with the C=O of **4b** is expected to be poorer than with **4a**.

Methanolysis of carboxylate esters and β-lactams

The suggestion that the mechanism for La^{3+}-catalyzed methanolysis of acetyl imidazole proceeded through a transition state where the catalyst exercises a dual role of Lewis acid and delivery of nucleophile suggested that the same catalyst should be capable of promoting the methanolysis of other neutral C=O containing entities such as carboxylate esters and β-lactams. Our initial investigation probed the ability of the La^{3+} system to promote the methanolysis of various esters such as **5**–**11** to investigate the electronic and structural effects on catalysis (13). The kinetics of

© 2004 NRC Canada

Scheme 2.

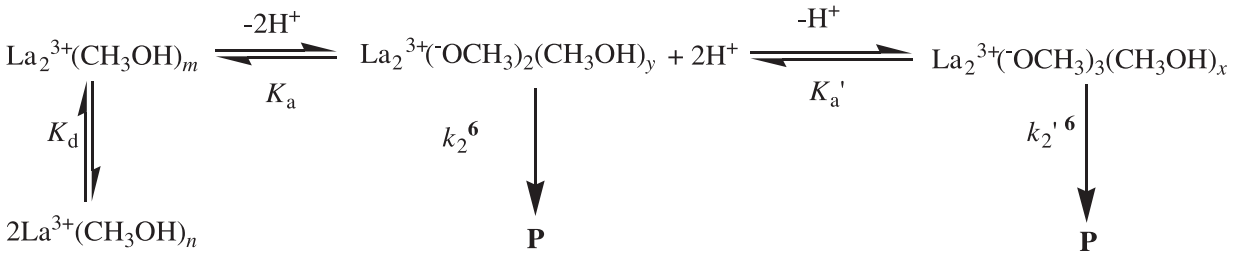
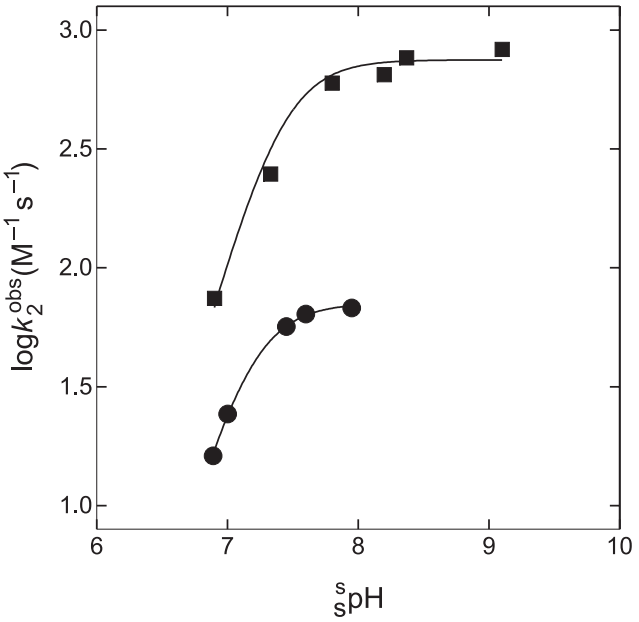
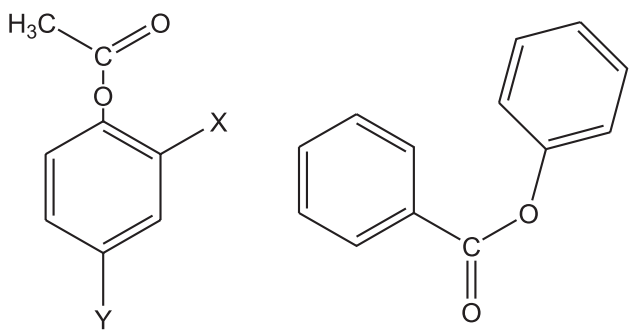


Fig. 4. A plot of the $\log k_2^{obs}$ (referring to the rate constant attributable to La^{3+} dimer) vs. $^{s}_{s}$pH for the La^{3+}-catalyzed methanolysis of *p*-nitrophenyl acetate (**6**); T = 25 °C (from ref. 13). Line through the data computed on the basis of fit to the kinetic equation derived for the process in Scheme 2.



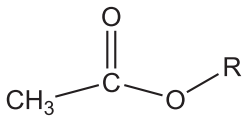
methanolysis of *p*-nitrophenyl acetate (**6**) were investigated for the $^{s}_{s}$pH and [La^{3+}] dependence under buffered conditions. These studies showed that the active catalyst was in general accord with that active for the acetyl imidazole series since in both cases there was an upward curvature in the plots of k_{obs} vs. [La^{3+}] eventually leading to linear dependencies at all $^{s}_{s}$pH values, the gradient of which is taken to be the k_2 value for La_2^{3+} catalysis. Shown in Fig. 4 is a logk_2 vs. $^{s}_{s}$pH plot for the catalyzed methanolysis of **6**, which shows an initial slope of 2, followed by a plateau and then a drop suggestive of a decreased catalytic ability of whatever La^{3+} species is formed at higher $^{s}_{s}$pH. Overall the process is modeled according to the simplified process given in Scheme 2 where the dominant catalytic species is $(La^{3+})_2(^{-}OCH_3)_2$ and the reduced activity form is exclusively $(La^{3+})_2(^{-}OCH_3)_3$. Fitting the data to the appropriate expression derived for the process in Scheme 2 (13) yields the line through the data in Fig. 4 and the computed $^{s}_{s}pK_a$ ($^{s}_{s}pK_a'$) and $k_2^{\mathbf{6}}$ ($k_2'^{\mathbf{6}}$) values of 7.35 ± 0.1 (10.2 ± 0.4) and 72 ± 1 M^{-1} s^{-1} (11.9 ± 4.5 M^{-1} s^{-1}).

Since the maximal kinetic activity appears to be in the plateau region of $^{s}_{s}$pH 8–10 (neutrality is $^{s}_{s}$pH = 8.4), the kinetics for the other esters were investigated in that region with the various rate constants being given in Table 1. Comparing the rate constants for La^{3+}-catalyzed methanolysis with the rate constant for methoxide attack on a given ester ($k_2^{ester}/k_{OMe^-}^{ester}$) makes it apparent that the less-activated aryl esters are more susceptible to catalyzed alcoholysis than the activated esters, a fact first noted in this study (13) and a following one investigating Eu^{3+}-catalyzed methanolysis of **6** and **7** (16) and subsequently described for an example of Cu^{2+}-catalyzed methanolysis of methyl acetate vs. *p*-nitrophenyl acetate (17). In fact, for esters **7**–**10**, the $k_2^{ester}/k_{OMe^-}^{ester}$ values are >1 if La^{3+} is used, as is the case for Eu^{3+}-catalyzed methanolysis of phenyl acetate. At first this seems peculiar since a normal Brønsted relationship would suggest that the methoxide bound to a metal ion would be a worse nucleophile than free methoxide. However, this can be taken as good evidence for the dual role for the catalyst in providing Lewis acid activation of the C=O unit and intramolecularly supplying the nucleophile (18). For the nonactivated esters



5 X=Y=NO_2
6 X=H, Y=NO_2
7 X=Y=H

8



9 R= Et
10 R= *i*Pr
11 R= *t*Bu

© 2004 NRC Canada

Table 1. Maximal second-order rate constants for $(La^{3+})_2(CH_3O^-)_2$-catalyzed methanolysis, and second-order rate constants for methoxide attack on esters **5**–**11**; T = 25 °C (from ref. 13).

Substrate	${}^{s}_{s}pH_{max}$	k_2^{ester} (M^{-1} s^{-1})[a]	$k^{ester}_{OCH_3}$ (M^{-1} s^{-1})	$k_2^{ester}/k^{ester}_{OCH_3}$	Acceleration[b]
5	9.8	29±2	410[c]	0.07	42 000
6	8 to 9	72	220±100[d]	0.6–0.225	243 000
7	8.8	58±3	2.66[e]	21	18 750 000
8	8.7	3.0±0.06	0.338±0.006[f]	8.9	5 300 000[g]
9	8.5[h]	0.143	$(5.7\pm0.2)\times10^{-2}$[f]	2.5	2 300 000
10	8.5[h]	0.0083	$(7.0\pm0.1)\times10^{-3}$[f]	1.2	1 120 000
11	8.5[h]	$<<5.7\times10^{-6}$	$(2.0\pm0.1)\times10^{-4}$[f]	<<0.03	

[a]Esters **5**–**8** were determined by UV kinetics in CH_3OH; **9**–**11** were determined from ^1H NMR in d_4-methanol as described in the text.

[b]Catalytic value at ${}^{s}_{s}pH$ 8.5, in the presence of 5×10^{-3} mol L^{-1} $(La^{3+})_2(CH_3O^-)_2$. Background rate computed from $k^{ester}_{OCH_3}$ assuming the value for solvent reaction at ${}^{s}_{s}pH$ 8.5 is entirely attributed to CH_3O^- + ester; the autoprotolysis constant of methanol is $10^{-16.77}$ (6).

[c]V. Machacek, S. Mareckova, and S. Vojeslav. Collect. Czech. Chem. Commun. **44**, 1779 (1979).

[d]27.4 °C. R.L. Schowen and C.G. Behn. J. Am. Chem. Soc. **90**, 5839 (1968).

[e]C.G. Milto, M. Gresser, and R.L. Schowen. J. Am. Chem. Soc. **91**, 2047 (1969).

[f]Reference 13.

[g]Acceleration computed at ${}^{s}_{s}pH$ 8.7.

[h]${}^{s}_{s}pH$ estimated from the titration curve of La^{3+} and set by 1:1 $La^{3+}/^-OCH_3$ stoichiometry.

the catalysis afforded in the neutral ${}^{s}_{s}pH$ region relative to the background reaction is quite spectacular, varying from (1–20) × 10^6-fold at room temperature, which, as far as we are aware, represents the greatest acceleration reported for any intermolecular metal-catalyzed acyl transfer reaction.

The likely mechanism for the transesterification involves a preequilibrium binding of the ester to one of the metal ions in the La^{3+} dimer followed by breaking of one of the methoxy–La^{3+} bonds on the way to a transition structure analogous to what we proposed in Scheme 1 for the methanolysis of acetyl imidazole. The reason why the catalysis is so large in methanol and so poor in water likely stems from a composite of effects such as increased preequilibrium association of the La^{3+} complex with the ester C=O and a less well solvated $(La^{3+})_2(^-OCH_3)_2$ in the reduced dielectric medium leading to enhanced electrophilic–nucleophilic properties. Indeed, such an ensemble coordinatively stabilizes both the tetrahedral intermediate and the transition state leading to it. For esters having good leaving groups such as *p*-nitrophenyl acetate, once the tetrahedral intermediate is reached its subsequent breakdown to expel the *p*-nitrophenoxy group probably does not require assistance by the metal ion. However, in the case of nonactivated esters such as ethyl acetate, microscopic reversibility arguments require that if the La^{3+} mediates the delivery of methoxide to form the tetrahedral intermediate (T_o^-), then its decomposition via expulsion of ethoxide must also be La^{3+}-mediated, which requires a translocation of the metal ion between the labile alkoxy groups. Interestingly, we have been unable to observe any reaction with tertiary esters such as *tert*-butyl acetate, probably because of a combination of rate-retarding electronic and steric effects where the translocation of the metal ion to the *tert*-butoxy group in the tetrahedral intermediate is precluded.

The study of the La^{3+}-catalyzed methanolysis of β-lactams **12** and **13** proved very interesting from kinetic and analytical standpoints (11) because it pointed out for the first time that the La^{3+} catalyst may comprise dimeric forms in addition to the originally assumed $La_2{}^{3+}(^-OCH_3)_2$. Although the general traits of curvature in the plots of k_{obs} vs. low $[La^{3+}]$ followed by a linear dependence at high $[La^{3+}]$ were evident, the plots of $\log k_2$ vs. ${}^{s}_{s}pH$ (see Fig. 5) did not show the initial slope of 2 as was so evident in the acetyl imidazole and ester cases. This suggested that the species responsible for the catalysis were somewhat different from that initially assumed in the case of esters and acetyl imidazole.

The answer to this dilemma required a more extensive analysis of the titration curves for La^{3+} in methanol, in particular determining the formation constants for the various $La_2{}^{3+}(^-OCH_3)_{1,2,3...}$ forms and their concentrations as a function of ${}^{s}_{s}pH$ under conditions

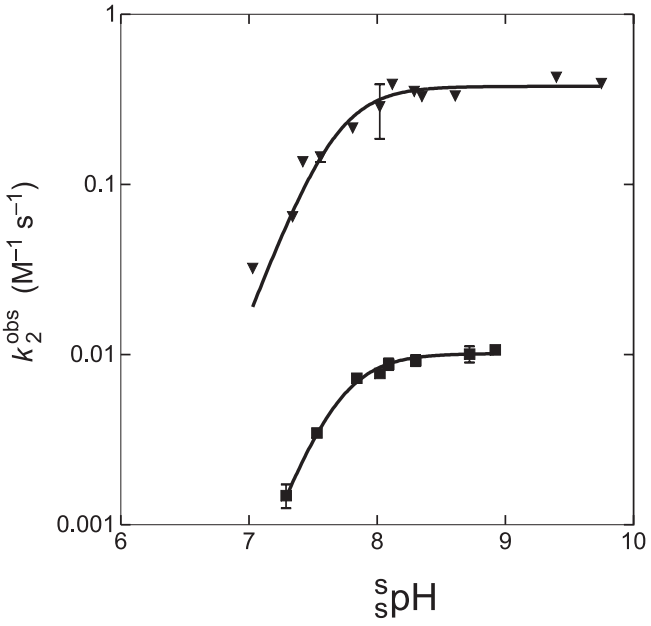
$$[1]\qquad La_2{}^{3+}(^-OCH_3)_n \rightleftharpoons 2La^{3+} + nOCH_3{}^-$$

$$[2]\qquad {}^{s}_{s}K_n = [La^{3+}{}_2(^-OCH_3)_n]/[La^{3+}]^2[OCH_3{}^-]^n$$

that mirror those present in the kinetic studies. In a detailed study of the titration of various transition and lanthanide metal ions in methanol (7) we used the computer program Hyperquad (19) to analyze the La^{3+} potentiometric titration data by fitting these to the dimer model presented in eq. [1], where n assumes values of 1–5, to give the stability constants (${}^{s}_{s}K_n$) that are defined in eq. [2]. From the five computed stability constants, $\log {}^{s}_{s}K_{1-5}$ = 11.66 ± 0.04, 20.86 ± 0.07, 27.52 ± 0.09, 34.56 ± 0.20, and 39.32 ± 0. 26, respectively, one can compute the concentrations of the various $La_2{}^{3+}(^-OCH_3)_n$ forms as a function of ${}^{s}_{s}pH$ at $[La(OTf)_3]_{total}$ = 2×10^{-3} mol L^{-1} using HySS, a component of the Hyperquad suite of programs (19). For ease of visualization, the species distribution diagram is shown in Fig. 6 where it is evident that dimeric forms containing one to five methoxides are successively formed at increasing ${}^{s}_{s}pH$. It is possible to analyze the kinetic data as a linear combination of the contributions of the various dimeric forms determined by their individual rate constants and concentrations at a given ${}^{s}_{s}pH$ according to eq. [3] where $k_2{}^{2:1}$, $k_2{}^{2:2}$, and $k_2{}^{2:n}$ are the second-order rate constants for the dimer containing one, two, and n (up to five) methoxides and $[La(OTf)_3]_t$ is the

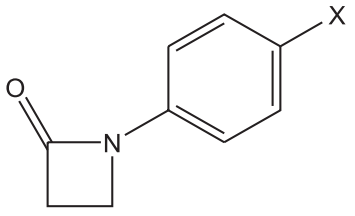
© 2004 NRC Canada

Fig. 5. Plots of the k_2^{obs} vs. $^{s}_{s}$pH for the La^{3+}-catalyzed methanolysis of β-lactams **12** (■) and **13** (▼) at 25 °C under buffered conditions. Lines through the data are computed on the basis of fits to eq. [5] containing up to three $La_2^{3+}(^{-}OCH_3)_n$ species (vide infra).



$$[3] \qquad k_2^{obs} = (k_2^{2:1}[La_2^{3+}(^{-}OCH_3)_1] + k_2^{2:2}[La^{3+}{}_2(^{-}OCH_3)_2]... \; k_2^{2:n}[La_2^{3+}(^{-}OCH_3)_n])/[La(OTf)_3]_t$$

total amount of La^{3+} in solution. It should be recognized that each $La_2^{3+}(^{-}OCH_3)$ species is operative in a different $^{s}_{s}$pH range, and so one can only perform satisfactory fits to a given species when the kinetic data are acquired in the appropriate $^{s}_{s}$pH domain. In the case of **12**, for which limited kinetic data are available, a satisfactory plot (not shown) is obtained using only $La_2^{3+}(^{-}OCH_3)_2$, but for lactam **13**, where there is a slightly more extended $^{s}_{s}$pH range for the kinetic points, the plot shown in Fig. 7 is nicely analyzed as originating from the collective contributions from the three dimeric forms $La_2^{3+}(^{-}OCH_3)_{1,2,3}$. The computed rate constants for these forms reacting with **13** are given in Table 2.



12 X = H
13 X = NO_2

There are additional points of note stemming from what we observe for the lactams. First, as part of this study we attempted to catalyze the methanolysis of **12** and **13** using Zn^{2+} in methanol solvent containing 0 to 1 equiv. of methoxide, but no catalysis was observed. However, in the presence of La^{3+} strong catalysis was observed, a phenomenon probably associated with the dual catalytic nature of the active dimeric forms that act both as Lewis acids and deliverers of the methoxide nucleophile. For the two lactams, $La_2^{3+}(^{-}OCH_3)_2$ is the dominantly active species with computed second-order rate constants of 0.026 and 0.98 M^{-1} s^{-1} for the methanolysis of **12** and **13**, respectively. For **13** there

Fig. 6. A species distribution diagram for various $La_2^{3+}(^{-}OCH_3)_{1,2,3...}$ forms as a function of $^{s}_{s}$pH, computed from the formation constants defined in eqs. [1] and [2], $[La(OTf)_3] = 2 \times 10^{-3}$ mol L^{-1}.

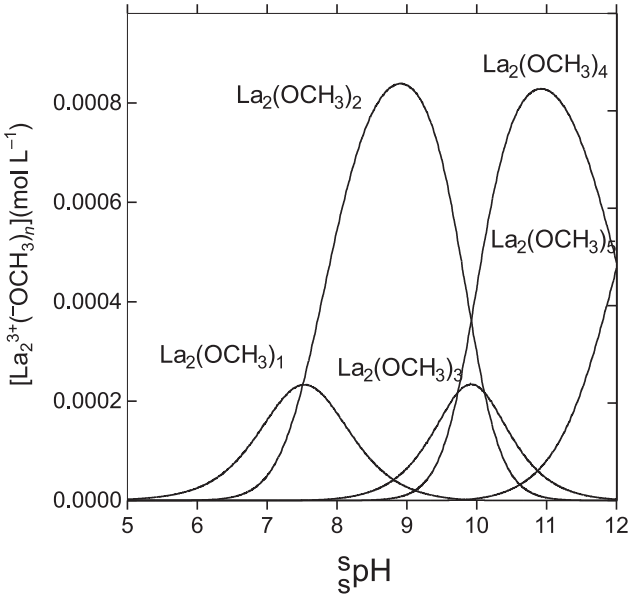
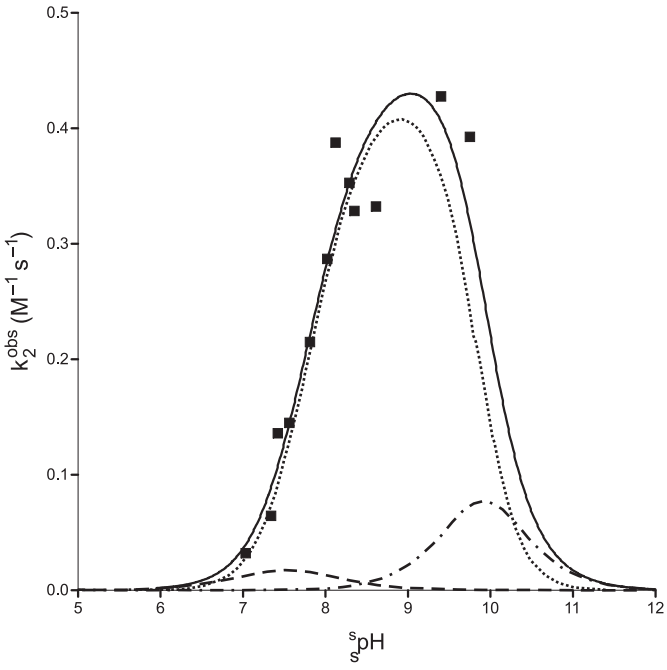


Fig. 7. Plot of the contributions of various $La_2^{3+}(^{-}OCH_3)_n$ forms to the k_2^{obs} for La^{3+}-catalyzed methanolysis of **13** as a function of $^{s}_{s}$pH. Solid line gives the combined effects of various species computed according to the fits to eq. [3]; contribution of $La_2^{3+}(^{-}OCH_3)_1$ (— — —); contribution of $La_2^{3+}(^{-}OCH_3)_2$ (···); contribution of $La_2^{3+}(^{-}OCH_3)_3$ (·—·—·); included as (■) are the actual k_2^{obs} kinetic data.



© 2004 NRC Canada

Table 2. Computed rate constants for $La_2^{3+}(^-OCH_3)_n$ species to the methanolysis of **12** and **13** determined through fits of k_2^{obs} at each ^s_spH to eq. [3].[a]

$La_2^{3+}(^-OCH_3)_n$ species		$k_2^{2:n}$ (M^{-1} s^{-1})
12	$^-OCH_3$	$k^{\mathbf{12}}_{OCH_3} = 0.0026$
	$La_2^{3+}(^-OCH_3)_2$	$k_2^{2:2} = 0.026\pm0.003$
13	$^-OCH_3$	$k^{\mathbf{13}}_{OCH_3} = 0.43$
	$La_2^{3+}(^-OCH_3)_1$	$k_2^{2:1} = 0.06\pm0.01$
	$La_2^{3+}(^-OCH_3)_2$	$k_2^{2:2} = 0.98\pm0.11$
	$La_2^{3+}(^-OCH_3)_3$	$k_2^{2:3} = 1.23\pm0.13$

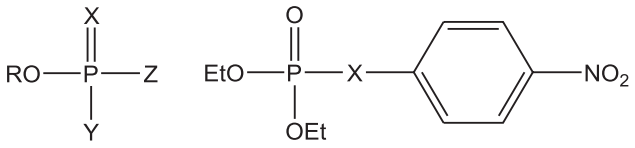
[a]Errors computed from the average % deviation in the fitted numbers calculated by eq. [3] from the actual kinetic data reported in ref. 11.

are some uncertainties in the $k_2^{2:2}$ and $k_2^{2:3}$ terms, which could have been reduced by obtaining the kinetic data over a wider ^s_spH range, but inclusion of the $k_2^{2:3}$ term is justified since its omission leads to a poorer overall fit. Also for **13**, the rate constant for $La_2^{3+}(^-OCH_3)_3$ is larger at 1.23 M^{-1} s^{-1} than the term for $La_2^{3+}(^-OCH_3)_2$, but overall the trimethoxy form does not contribute so much to the kinetics because its concentration is lower than that of $La_2^{3+}(^-OCH_3)_2$. These constants can be compared with the second-order rate constants for the methoxide reactions, 0.0026 and 0.43 M^{-1} s^{-1}, respectively, for **12** and **13** (20)[4] once again showing that the dimeric catalysts with metal-bound methoxides are actually more reactive than free methoxide. The overall catalytic effect of the composite reactions catalyzed by all the species can be judged in comparison to the base-catalyzed reaction at a neutral ^s_spH of 8.4, where the [$^-OCH_3$] is 4.27 × 10^{-9} mol L^{-1} and a 1 mmol L^{-1} solution of catalyst (generated from 2 mmol L^{-1} of La(OTf)$_3$) accelerates the methanolysis of **12** by ~2 × 10^7-fold and **13** by ~5 × 10^5-fold. Interestingly, there is a 40-fold larger catalytic effect for the less reactive lactam, which probably results from a fine balance of electronic effects on the preequilibrium binding of the lactam to metal ion (expected to be less favourable for the nitro derivative) followed by a rate-limiting attack on the coordinated C=O (expected to be faster for the nitro derivative).

It now becomes apparent that for La^{3+}-catalyzed methanolysis of acyl transfer the $(La^{3+})_2(^-OCH_3)_n$ speciation changes as a function of ^s_spH and the possibility exists that each of these can be catalytically active. In a given case, the observed ^s_spH/rate constant profile must be viewed as a sum of contributions determined by the individual rate constants and the concentration of each of the active species. Since La^{3+} dimers with one to three associated methoxides have activity with lactam **13** there is no reason to suspect that the La^{3+}-catalyzed methanolysis of esters such as *p*-nitrophenyl acetate **6** should not be mediated by other dimers such as $(La_2^{3+})(^-OCH_3)_{1,3,4,5}$. Accordingly, we reanalyzed the kinetic data for methanolysis of **6** shown in Fig. 4 by fitting of the k_2 values as a linear combination of rate constants for the various $La_2^{3+}(^-OCH_3)_n$ species as shown in eq. [3] to provide rate constants of (91.8 ± 8.8) M^{-1} s^{-1} for $La_2^{3+}(^-OCH_3)_2$ and (38.0 ± 5.6) M^{-1} s^{-1} for $La_2^{3+}(^-OCH_3)_4$ with no apparent involvement of $La_2^{3+}(^-OCH_3)_3$. Subsequently, we will see that catalysis by several dimers is a prevalent phenomenon for phosphoryl transfer from neutral phosphate triesters, and in fact that at high ^s_spH the situation becomes complicated by the deleterious formation of oligomers of reduced catalytic activity.

Paraoxon (15) and its thiol derivative, *O*,*O*-diethyl *S*-*p*-nitrophenyl phosphorothioate (16)

Activated neutral organophosphate, phosphinate, and phosphonate esters (OP esters) of the general form **14** are potent acetylcholinesterase inhibitors if they contain at least one leaving group whose conjugate acid has a pK_a of 8 or less (21). These have important uses as animal and crop protectants (22) and as chemical warfare (CW) agents (23). The OP family includes the insecticides parathion (RO=Z=OEt; X=S; Y=$OC_6H_4NO_2$) and paraoxon (**15**), as well as the alkylphosphonofluoridate nerve G-agents, for example Soman (RO=$(CH_3)_3CCH(CH_3)O$; Z=CH_3; X=O; Y=F) and Sarin (RO=$(CH_3)_2CHO$; Z=CH_3; X=O; Y=F), and finally the V-agents such as VX (Z=Et; X=O; Y=$SCH_2CH_2N(CH(CH_3)_2)_2$). OP compounds of these types are among the most deadly of man-made materials since all are designed to effect a single biological outcome, namely death of the target organism because of acute respiratory failure after exposure.



14 **15** X = O **16** X = S

In many cases, the toxic uses as pesticides are considered beneficial, at least to man, as they assure larger crop yields, generally healthier animals, and reduce the incidence of insect infestation and insect-borne diseases. Despite these seemingly beneficial properties, world usage of organophosphate pesticides is declining due to their persistence in foodstuffs and the environment and also because of unselective negative effects on non-target species. Nevertheless, the most recent statistics available indicate that in 1999 some 9 000 000 pounds (1 pound = 0.45 kg) of these were used in the US, comprising 72% of all insecticides used commercially, in home and garden, and the government sector (24). By some estimates world use is roughly 10 times this amount, or 90 000 000 pounds per year (1 pound = 0.45 kg), and there is increasing concern over soil and water contamination that arises from spills and improper use.

Because of their toxicity and the attention drawn to them by the 1992 Chemical Weapons Convention Treaty (25) that requires total destruction of chemical weapons stockpiles by the signatories by 2007, considerable effort has been directed toward methods of facilitating the controlled decomposition of the OP CW materials particularly through hydrolysis and oxidation (23, 26). Although some very effective methods for destruction of organophosphorus materi-

[4]By way of comparison, the HO^- reaction in water on **12** and **13** has reported second-order rate constants of 1.3 × 10^{-3} and 50 × 10^{-3} M^{-1} s^{-1}, respectively (A.P. Laws and M.I. Page. J. Chem. Soc. Perkin Trans. 2, 1577 (1989)).

© 2004 NRC Canada

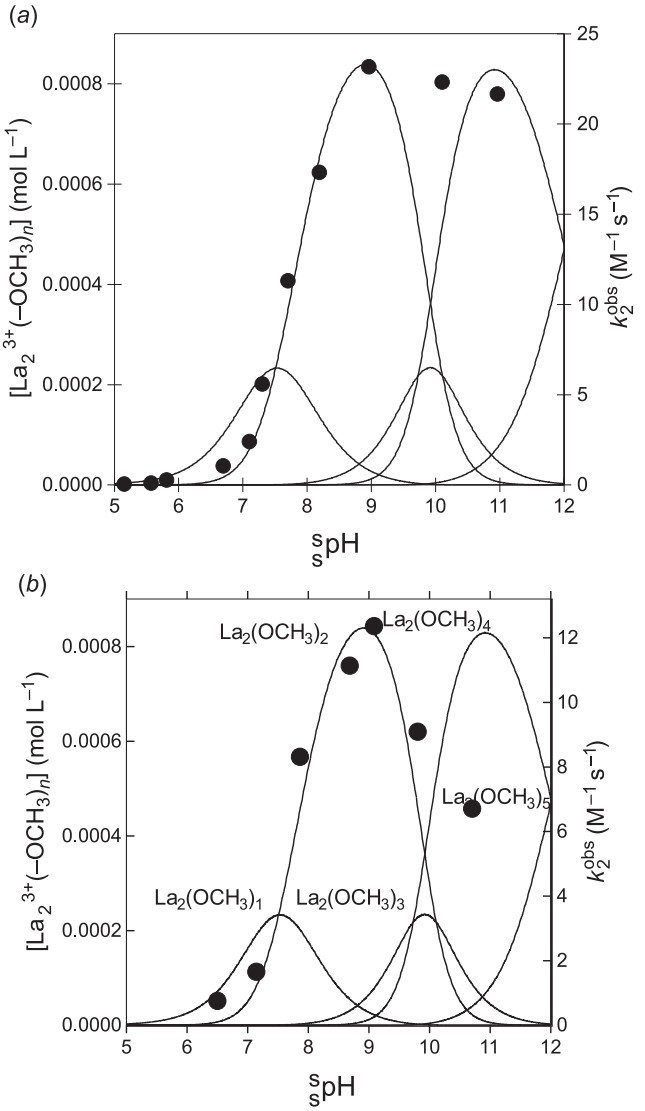
als are available, none is applicable to all situations or classes of compounds. At the present time the task of destruction of these materials is a problem of gigantic proportions given looming deadlines, the amounts of materials to be handled, and the fact that no ideal methodology exists when one considers all factors including the disposal of the end products of reaction. For example, the US and Russia have declared that their respective stockpiles of OP CW material comprise some 25 000 tons (27) and 32 000 tons (28), and destruction using conventional means of burning and (or) hydrolysis is projected to cost some $24 billion US and $20 billion US, respectively, probably requiring at least to 2012 to complete. Even so, the existing methodologies are not without problems given the technical difficulties of purification of waste stream from hydrolysis, or public outcry from burning.

It appeared to us that La^{3+}-catalyzed alcoholysis reactions might offer an attractive alternative to the present hydrolysis and burning strategies. The ideal benefits would be rapid conversion of the starting materials to nontoxic neutral phosphate or phosphonate alkoxy esters, which can be disposed of using conventional burning, a reaction medium that solvates the starting materials efficiently, and the ability to provide an effective process for the decomposition of V-agents (29).[5] As simulants for the methanolysis of the G-agents and V-agents, respectively, we studied the La^{3+}-catalyzed methanolysis of the insecticide paraoxon **15** (14) and its phosphorothioate derivative **16** (30) as a function of ${}^{s}_{s}$pH and $[La^{3+}]$.

As is the case for the La^{3+}-catalyzed methanolysis of esters and activated amides, plots of k_{obs} vs. $[La^{3+}]$ for methanolysis of both **15** and **16** showed upward curvature at low $[La^{3+}]$ followed by linear domains at higher concentrations. The gradients of the linear portions at each ${}^{s}_{s}$pH were taken as the second-order rate constants (k_2^{obs}) for La^{3+}-dimer catalyzed methanolysis of each species and when these are overlaid on the La^{3+}-speciation diagram as illustrated in Figs. 8*a* and 8*b*, it can be seen that the maximum activity stems from the $(La^{3+})_2(^{-}OCH_3)_2$ and $(La^{3+})_2(^{-}OCH_3)_4$ forms. As is shown in Fig. 9 for **16**, the k_{obs} vs. $[La^{3+}]$ plots at the highest ${}^{s}_{s}$pH values (~11) exhibit an apparent saturation behaviour consistent with the formation of oligomeric forms of $La_x^{3+}(^{-}OCH_3)_n$ similar to what we have seen previously for Eu^{3+}-catalyzed methanolysis of esters (16). To obtain the k_2^{obs} values at high ${}^{s}_{s}$pH for inclusion in Figs. 8*a* and 8*b* one needs either to determine the slope of the k_{obs} vs. $[La^{3+}]$ plots at $[La^{3+}] < 2 \times 10^{-4}$ mol L^{-1}, or perform the kinetic experiments in the presence of a ligand, such as 18-crown-6, which will break up the oligomers, thus minimizing the oligomer formation. An approach similar to this was used by Gómez-Tagle and Yatsimirsky (31) to stabilize a bis-hydroxy-bridged La^{3+} dimer by coordinating each of the metal ions to bis-tris propane as in **17,** which stabilized the dimeric form and made it soluble in the buffered aqueous solution. The Fig. 9 data indicate that the k_{obs} values obtained in the presence of 18-crown-6 lie on the same straight line obtained at low k_{obs} vs. free $[La^{3+}]$ suggesting that its presence does not affect the catalytic viability of the La^{3+} species to any great extent. The slope of this line is taken as the k_2^{obs} for $(La^{3+})_2(^{-}OCH_3)_n$ catalysis of the methanolysis of **16**.

The k_2^{obs} kinetic data in Figs. 8*a* and 8*b* can be fit to the linear combination of La_2^{3+} species given in eq. [3] to provide the rate constants for each of the reactive forms $(La_2^{3+}(^{-}OCH_3)_n)$ responsible for the catalyzed methanolysis

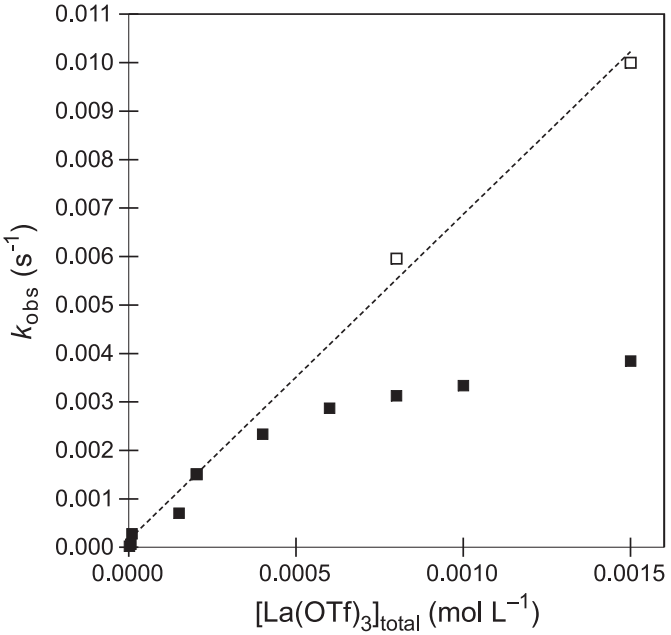
Fig. 8. Speciation diagram for the distribution of $La_2^{3+}(^{-}OCH_3)_n$ forms (n = 1–5) as a function of ${}^{s}_{s}$pH. Speciation calculated (7) for $[La(OTf)_3] = 2 \times 10^{-3}$ mol L^{-1}. Data represented as (●) correspond to second-order rate constants (k_2^{obs}) for La^{3+}-catalyzed methanolysis of (*a*) **15** (data from ref. 14, right vertical axis) and (*b*) **16** (data from ref. 30).

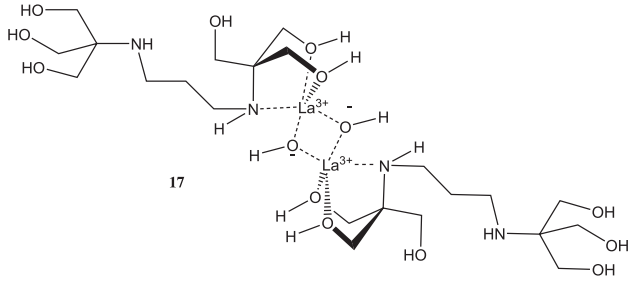


[5] In certain cases, alcoholysis may proceed with different selectivity than hydrolysis as is known to be the case for the uncatalyzed methanolysis of the V-agents where the reaction with alkoxide proceeds largely to displace the SR^{-} group leading to phosphonate oxyesters. For example, when V-agents are hydrolyzed with hydroxide in water about 90% of the product arises from P–SR cleavage, and 10% from P–OR cleavage, but the latter product is toxic and unreactive to further hydrolysis as it is a phosphonic acid derivative. Methanolysis reactions, even if they lead to some P–OR cleavage, cannot produce nonreactive phosphonic acid intermediates and thus should lead to complete destruction of the starting material.

© 2004 NRC Canada

Fig. 9. Plot of k_{obs} vs. [La(OTf)$_3$] for the methanolysis of *O*,*O*-diethyl *S*-(*p*-nitrophenyl phosphorothioate (**16**, 8.1 × 10^{-5} mol L^{-1}) in 1:1 Et_3N–$HClO_4$ buffer $^{s}_{s}$pH 10.7, *T* = 25 °C, data obtained without 18-crown-6 (■); data obtained with added 18-crown-6, 1:1 with added [La^{3+}] (□).





17

of **15** and **16**, the various values being given in Table 3. From these computed rate constants and the speciation as a function of $^{s}_{s}$pH are constructed the plots showing the individual kinetic compositions comprising the overall k_2^{obs} vs. $^{s}_{s}$pH profile, which are shown in Figs. 10*a* and 10*b*.

The appearance of the plots indicates there is a rather large plateau region for each ester between $^{s}_{s}$pH 8 and 11. In the case of paraoxon, a 2 mmol L^{-1} solution of La^{3+} (corresponding to 1 mmol L^{-1} dimer) gives a $t_{1/2}$ of ~20 s at $^{s}_{s}$pH 8.3, which amounts to an acceleration of 10^9-fold relative to the background methoxide reaction ($k^{\mathbf{15}}_{OCH_3}$ = 0.011 M^{-1} s^{-1}), which is computed to have a $t_{1/2}$ of ~600 years at that same $^{s}_{s}$pH. The catalysis for the thioate derivative **16** is also impressive: a 2 mmol L^{-1} solution of La^{3+} at $^{s}_{s}$pH 8.3 gives a $t_{1/2}$ of ~31 s, which amounts to an acceleration of 5.4 × 10^7-fold relative to the background reaction ($k^{\mathbf{16}}_{OCH_3}$ = 0.12 M^{-1} s^{-1}), which is computed to have a $t_{1/2}$ of ~54 years at that $^{s}_{s}$pH.

Table 3. Computed second-order rate constants ($k_2^{2:n}$) for the $La_2^{3+}(^{-}OCH_3)_n$-catalyzed methanolysis of paraoxon **15** and its thiolate derivative **16** obtained through fits of k_2^{obs} at each $^{s}_{s}$pH to eq. [3].[a]

$La_2^{3+}(^{-}OCH_3)_n$ species		$k_2^{2:n}$ (M^{-1} s^{-1})
Paraoxon[b] (**15**)	$^{-}OCH_3$	$k^{\mathbf{15}}_{OCH_3}$ = 0.011
	$La_2^{3+}(^{-}OCH_3)_1$	$k_2^{2:1}$ = 15.8±2.9
	$La_2^{3+}(^{-}OCH_3)_2$	$k_2^{2:2}$ = 51.1±1.1
	$La_2^{3+}(^{-}OCH_3)_3$	$k_2^{2:3}$ = 35.6±6.5
	$La_2^{3+}(^{-}OCH_3)_4$	$k_2^{2:4}$ = 49.7±1.4
O,*O*-Diethyl *S*-*p*-nitrophenyl phosphorothioate[c] (**16**)	$^{-}OCH_3$	$k^{\mathbf{16}}_{OCH_3}$ = 0.12
	$La_2^{3+}(^{-}OCH_3)_1$	$k_2^{2:1}$ = 11.6±5.3
	$La_2^{3+}(^{-}OCH_3)_2$	$k_2^{2:2}$ = 28.4±1.2
	$La^{3+}{}_2(^{-}OCH_3)_4$	$k_2^{2:4}$ = 16.1±1.6

[a]Errors computed from the average % deviation in the fitted numbers calculated by eq. [3] from the actual kinetic data.
[b]Paraoxon data in part from ref. 14 and in part (high pH) from this work.
[c]From ref. 30.

To check for catalytic turnover, we investigated by ^{31}P NMR the methanolysis of a 10-fold excess of **15** or **16** buffered at $^{s}_{s}$pH ~8.8 in the presence of La(OTf)$_3$. In the two cases, the starting materials were gone in less than 10 min and 103 s, respectively (14, 30). In a third experiment with the far less reactive *O*,*O*-diethyl *S*-phenyl phosphorothioate in 100-fold excess over the La^{3+}, we observed that the reaction was essentially complete within 70 min indicating that 100 turnovers had occurred within that time, and importantly that the products do not inhibit the reaction (30).

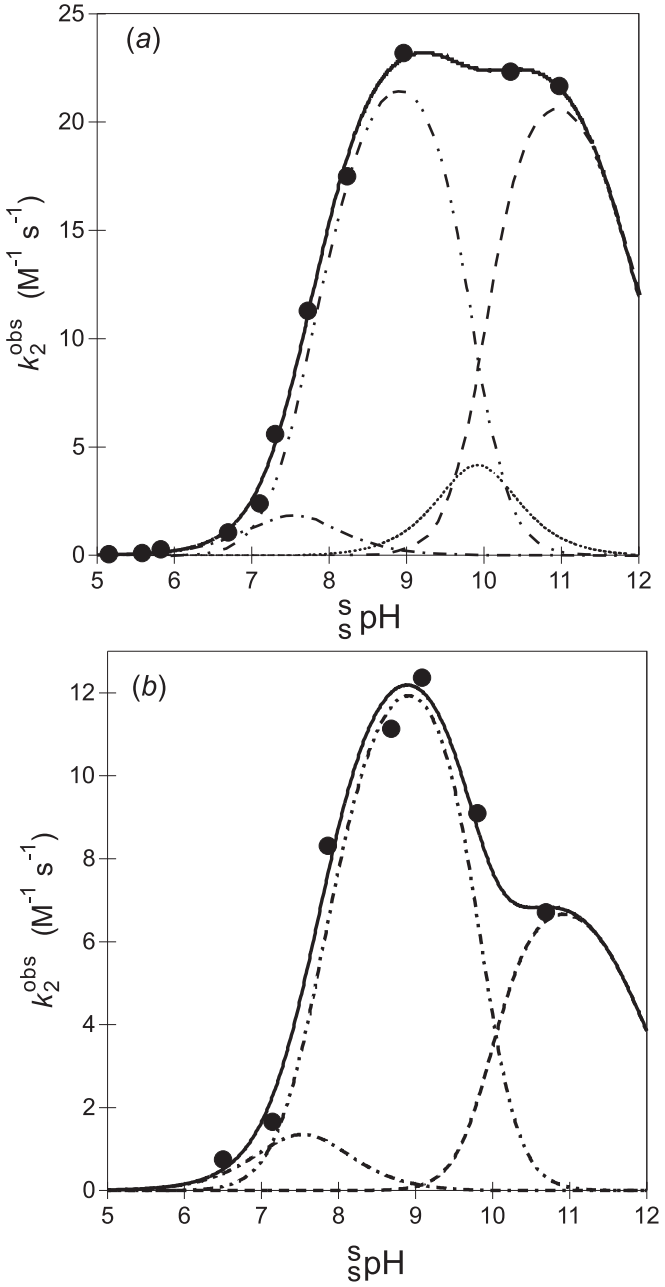
Do other metal ions exhibit exalted catalysis of alcoholysis of carboxylate and phosphate esters?

As indicated above, we have studied the methanolysis of certain esters (most extensively *p*-nitrophenyl acetate) promoted by Eu(OTf)$_3$ (16). Detailed kinetic studies conducted as a function of [Eu^{3+}] and $^{s}_{s}$pH revealed that the active form of the catalyst is the monomeric form $Eu^{3+}(^{-}OCH_3)$ that, at higher $^{s}_{s}$pH, gives way to an inactive form of stoichiometry $Eu^{3+}(^{-}OCH_3)_2$, which seems to exist in solution as an oligomer ($(Eu^{3+}(^{-}OCH_3)_2)_n$). Highest activity for the Eu^{3+} system is obtained in a $^{s}_{s}$pH 7.1–7.2 solution, midway between the two macroscopic kinetic $^{s}_{s}pK_a$ values of $^{s}_{s}pK_a^{\mathbf{1}}$ = 6.33 ± 0.06 and $^{s}_{s}pK_a^{\mathbf{2}}$ = 8.02 ± 0.10 for formation of the mono and dimethoxy forms. The catalysis of the methanolysis of esters such as *p*-nitrophenyl acetate (**6**), phenyl acetate (**7**), and ethyl acetate (**9**) at the $^{s}_{s}$pH maximum of 7.12 is substantial, being 8 530 000-fold, 95 000 000-fold, and 7 813 000-fold, respectively.[6] The efficiency of this catalyst and the fact that it operates as a monomer suggest that it

[6]The acceleration is computed relative to the reaction of methoxide at $^{s}_{s}$pH 7.12, where the [CH_3O^-] = 2.24 × 10^{-10} mol L^{-1}, using the second-order rate constants for methoxide attack on **6**, **7**, and **9** of 220, 2.66, and 5.7 × 10^{-2} M^{-1} s^{-1}, respectively (see Table 1) and the second-order rate constants (k_2^{max}) determined in the Eu work of 42, 11.7, and 1 × 10^{-2} M^{-1} s^{-1}, respectively.

© 2004 NRC Canada

Fig. 10. Kinetic plot of the overall second-order rate constant for $La_2^{3+}(^{-}OCH_3)_n$-catalyzed methanolysis of: (*a*) **15** (k_2^{obs}) as a function of $^{s}_{s}$pH showing the best-fit kinetic contributions of each dimer bearing one to four methoxides and (*b*) **16** (k_2^{obs}) as a function of $^{s}_{s}$pH showing the best-fit kinetic contributions of dimers bearing one, two, and four methoxides.



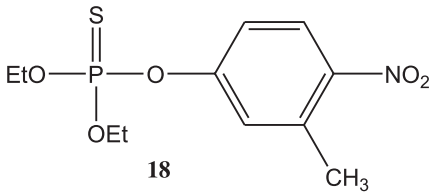
might have quite different selectivities than does the La^{3+} dimer catalyst.

In a preliminary screening we have looked at the ability of a series of lanthanide and transition metal ions, introduced as their triflate salts, to catalyze the ethanolysis of paraoxon (**15**). Since all the La^{3+}-catalyzed methanolysis reactions discussed above showed maximal catalytic activity at a $[La^{3+}]/[^{-}OCH_3]$ of 1.0, we studied the ethanolysis reactions under three conditions where the $[M^{x+}]/[NaOEt]$ ratio varied from 0.5 to 1.0 to 1.5.[7] For all the lanthanides, the maximum constants were obtained when the ratio was 1.0. Shown in Table 4 are the pseudo-first-order rate constants from which it can be determined that all the lanthanides have some activity, the best being La^{3+}, while some of the transition metal ions catalyze the reaction as well. Interestingly, when we investigated the ethanolysis of the P=S derivative fenitrothion (**18**), none of the lanthanides promoted the reaction, presumably because of the fact these are considered "hard" in the Pearson "hard soft" sense (32), although two of the softer transition metal ions (Zn^{3+} and Cu^{2+}) did, which prompted us to study the alcoholysis reactions promoted by transition metal ions in more detail.

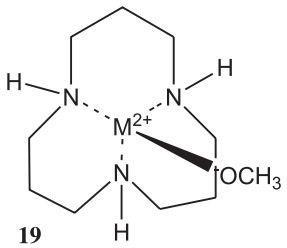
Table 4. Summary of observed rate constants for Ln^{3+}- and M^{2+}-catalyzed ethanolysis of paraoxon (**15**); T = 25 °C, determined at $[M^{x+}]$ = [NaOEt] = 10^{-3} mol L^{-1}.

Metal ion	$10^4 k_{obs}$ (s^{-1})
La^{3+}	9.1
Pr^{3+}	4.2
Nd^{3+}	4.1
Gd^{3+}	3.7
Sm^{3+}	3.1
Eu^{3+}	1.5
Tb^{3+}	2.4
Ho^{3+}	1.7
Dy^{3+}	1.1
Er^{3+}	1.0
Tm^{3+}	0.82
Zn^{2+}	0.62
Y^{3+}	0.54
Yb^{3+}	0.43
Ni^{2+}	0.20
Cu^{2+}	NA

Note: NA = not available.



18



19

[7] W. Desloges, A.A. Neverov, and R.S. Brown. Unpublished results.

© 2004 NRC Canada

Table 5. Second-order catalytic rate constants for **19**:$Cu^{2+}(^{-}OCH_3)$ and **19**:$Zn^{2+}(^{-}OCH_3)$ reacting with paraoxon (**15**) and fenitrothion (**18**); T = 25 °C.

Catalyst	$^{s}_{s}$pH at 0.5 equiv. of base	K_{dis} $(M^{-1})^a$	k_m(**15**) $(M^{-1}\ s^{-1})^a$	k_m (**18**) $(M^{-1}\ s^{-1})^a$	Relative selectivity^b
$^{-}OCH_3$		NA	1.1×10^{-2}	$(7.2\pm0.2)\times10^{-4}$	1
$Cu^{2+}(^{-}OCH_3)^c$	6.86 ± 0.2	<0.005	0.22±0.02	0.79±0.03	55
$Zn^{2+}(^{-}OCH_3)^d$	~8	<0.005	2.0±0.04	0.19±0.01	1.5
19:Cu^{2+}:$(^{-}OCH_3)^e$	8.75 ± 0.1	NA	2.76±0.17	12.2±0.4	67
19:Zn^{2+}:$(^{-}OCH_3)^f$	9.3	NA	0.85±0.01	$(4.8\pm0.2)\times10^{-2}$	0.86
$La_2^{3+}(^{-}OCH_3)_2$		NA	47.2±2.3	—	~0

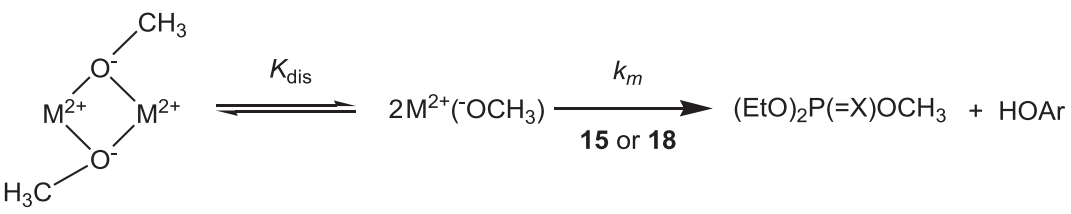
[a]Dimer dissociation constant (K_{dis}) and conditional second-order rate constant (k_m) for reaction with monomer defined as in eq. [4]. NA means nonapplicable since there is no observable dimerization under the specific conditions. The K_{dis} of <0.005 indicates very strong dimerization and is quoted as an upper limit based on an iterative fitting procedure that provided the lowest standard deviations.
[b]Defined as $(k_m(\mathbf{18})/k_{OCH_3}(\mathbf{18}))/(k_m(\mathbf{15})/k_{OCH_3}(\mathbf{15}))$.
[c]Based on NLLSQ fits of k_{obs} vs. $[Cu^{2+}]_t$ data at a [methoxide]/$[Cu^{2+}]_t$ ratio of 0.5 (see ref. 33*a*).
[d]Based on NLLSQ fits of k_{obs} vs. $[Zn^{2+}]_t$ data at a [methoxide]/$[Zn^{2+}]_t$ ratio of 0.3 (see ref. 33b).
[e]Based on linear fits of k_{obs} vs. [**19**:Cu^{2+}:$(^{-}OCH_3)]_t$ data at a methoxide]/$[Cu^{2+}]_t$ ratio of 0.5.
[f]Based on linear fits of k_{obs} vs. [**19**:Zn^{2+}:$(^{-}OCH_3)]_t$ data at a methoxide]/$[Zn^{2+}]_t$ ratio of 1.0.

More recent studies have concentrated on the effect of Zn^{2+} and Cu^{2+} and some of their complexes with phenanthroline, 2,9-dimethylphenanthroline, 2,2′-bipyridyl and 1,5,9-triazacyclododecane, each as their mono-methoxy forms ($L:M^{2+}(^{-}OCH_3)$), to promote the methanolysis of **15** and **18** (33), a variety of carboxylate esters (34), and phosphate triesters[8] where the leaving group is varied. The above Zn^{2+} and Cu^{2+} complexes are reactive as monomers, but in the case of the phenanthroline and bipyridyl complexes, form unreactive dimers as in eq. [4], which limits the catalytic efficiency. However, when bound by the tridentate ligands such as dipicolylamine or triazacyclododecane (eg. **19**) the complexes are monomeric and prove to be efficient catalysts for both phosphate esters. Given in Table 5 are the second-order catalytic rate constants (k_m) for complex **19** along with those for the copper and zinc methoxides, and the rate constants for methoxide attack on the two phosphates (33). Uncatalyzed attack of CH_3O^- on paraoxon (**15**) is faster by roughly 15-fold than on **18**. The $Cu^{2+}(^{-}OCH_3)$ system alone or bound in the form of **19** is more effective for **18** than **15**, while the $Zn^{2+}(^{-}OCH_3)$ systems have similar selectivity for the P=O and P=S esters. This is quantified by the relative selectivity (RS) parameter given in Table 5, which compares the relative reactivity of the $M^{2+}(^{-}OCH_3)$ reactions and free methoxide attack on the P=S and P=O substrates $((k_m(\mathbf{18})/k_{OCH3}(\mathbf{18}))/(k_m(\mathbf{15})/k_{OCH_3}(\mathbf{15})))$. The RS parameters clearly correlate with the hard/soft properties (32) of the metal ion. The hard ion La^{3+} exhibits exclusive selectivity for the P=O substrate (RS ~ 0), while the softer Zn^{2+} ion shows almost equal affinity for P=O and P=S substrates (RS ~ 1). Of the three ions, Cu^{2+} appears to be the softest and exhibits high selectivity for the P=S substrate with RS values from ~55–70. It is also of note that all the metal-catalyzed rate constants listed in Table 5 exceed those for the free methoxide, indicating that the metal ions, even in the case of the monomeric forms, must be involved in a dual role of Lewis acid and delivery of the methoxide nucleophile.

Conclusions

Our recent work on the La^{3+}-catalyzed methanolysis of neutral esters, lactams, activated amides, and phosphate triesters has revealed cases where the activities of the metal ion are much more prominent than in aqueous solution. Indeed in aqueous solution, metal ion catalysis of acyl or phosphoryl transfer is poor or nonexistent unless there is some proximal binding group that positions the metal ion close to the scissile bond. Metal ions in water are also well-known to have limited or little solubility at high pH because of formation of the metal-hydroxo forms, but in our experience metal alkoxides are soluble throughout the $^{s}_{s}$pH region where the important catalysis is observed. Our original kinetic work with acetyl imidazole and esters indicated that the active form was a La^{3+} dimer having two associated methoxides. Subsequently, a more detailed speciation analysis revealed that in the concentration range where the kinetic studies were performed, there were five $^{s}_{s}$pH dependent dimeric forms of general structure $La_2^{3+}(^{-}OCH_3)_n$, n = 1–5. Maximum catalysis is observed in the neutral $^{s}_{s}$pH region of 8–10, with the dominant active form being $La_2^{3+}(^{-}OCH_3)_2$. Depending upon what substrate is being investigated, the

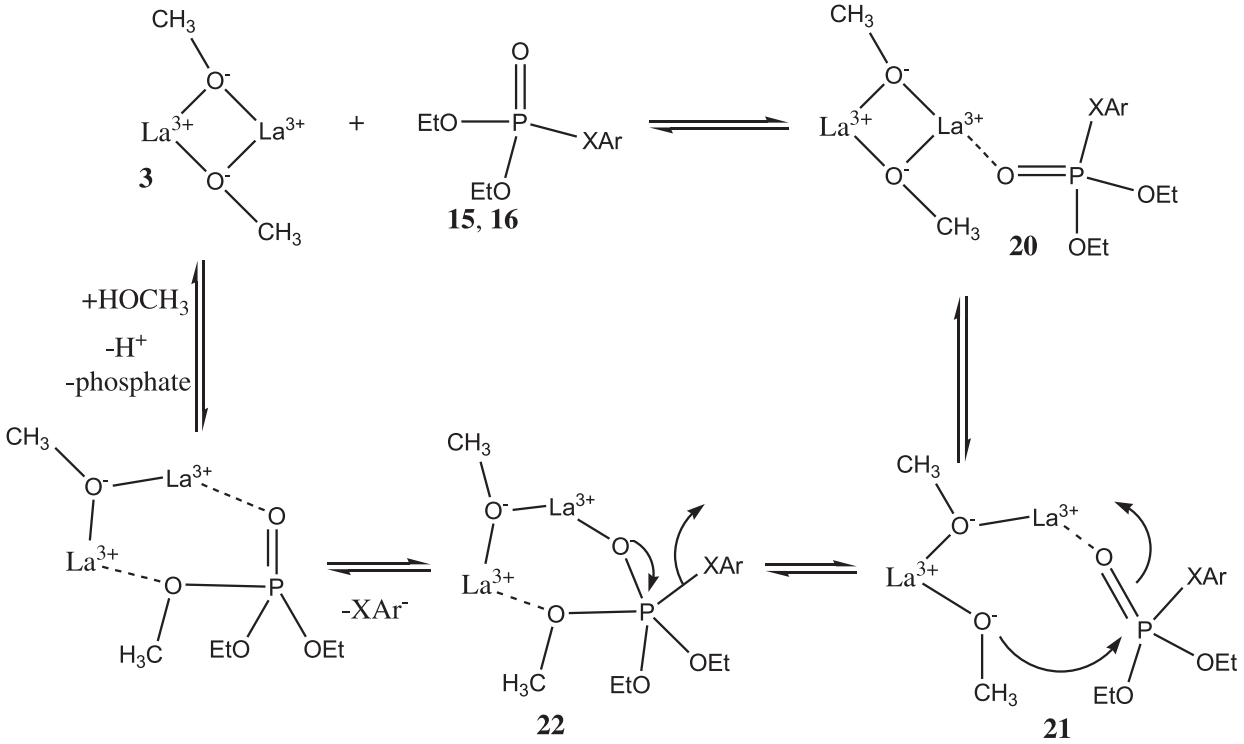
[4]



[8]J.S.W. Tsang, A.A. Neverov, T. Liu, and R.S. Brown. Submitted.

© 2004 NRC Canada

Scheme 3. Methanols of solvation omitted for clarity.



ssspH/rate profiles vary in shape in a nonobvious, but easily analyzed way, which attributes the overall curve to the sum of the contributions of each dimeric form.

1. All evidence points to a common mechanism for the catalysis exhibited by the $La_2^{3+}(^{-}OCH_3)_n$ system acting on all the neutral C=O and P=O substrates we have investigated, which is best illustrated for the phosphorus esters in Scheme 3 using the La^{3+} dimer with two methoxides (**3**). It is difficult to envision any mechanism that does not involve a preequilibrium binding of the substrate to **3** to form the transient complex **20**. While we have never observed saturation kinetics we assume that switching the medium from water to the less polar alcohol increases the equilibrium binding constant thus providing one method of increasing the reaction rate. Because the methoxide in **20** is bound between two electropositive La^{3+} ions, it is unlikely that it is sufficiently nucleophilic to attack an unactivated ester or phosphate (35), so we propose that one of the methoxide–La^{3+} bonds is transiently cleaved as in **21** to reveal a Lewis acid activated P=O adjacent to a metal-bound methoxide nucleophile. Nucleophilic attack creates the five-coordinate intermediate **22**, which in the case of good aryloxy or thioaryloxy leaving groups, probably decomposes without the requirement for La^{3+} assistance. Turnover to reform **3** is accomplished by methanol addition, deprotonation, and release of the transiently bound trialkoxy phosphate ester product.
   In the case of unactivated carboxylic acid esters such as ethyl acetate, the La^{3+}-catalyzed transesterification is very effective and probably proceeds in much the same way involving a tetrahedral intermediate bound to one of the La^{3+} ions in the complex. Any proposed mechanism involving formation of an intermediate that requires delivery of a La^{3+}-bound methoxide must, by microscopic reversibility, require the departure of a La^{3+}-bound ethoxide, but for better leaving groups such as aryloxy, assistance of departure might not be required. Current work in our laboratories is aimed at determining the effects of changing the leaving groups in carboxylic and phosphorus esters in the hopes of shedding light on the mechanistic differences between the two classes of compounds (34).[8]
2. Another feature of the dimeric La^{3+} system is the fact that the k_2/k_{OCH_3} or $k_2^{2:n}/k_{OCH_3}$ ratios for many of the nonactivated esters, the lactams, and the phosphates are greater than unity. In fact, where direct comparison can be made, the k_2/k_{OCH_3} ratio is greater when the substrate is less activated. For example, the k_2/k_{OCH_3} ratios are 21 and 0.07 for phenyl acetate and dinitrophenyl acetate, respectively, and ~10 and 2 for the $k_2^{2:2}/k_{OCH_3}$ ratio with lactams **12** and **13**. Since normal Brønsted considerations suggest that a methoxide bound to an electropositive metal ion is less nucleophilic than free methoxide, a dual role for the catalyst is implied where Lewis acid activation is concurrent with nucleophilic delivery of methoxide. That the catalysis is actually more effective for the less-activated substrates suggests that there is a counterbalance of electronic effects on the binding (activation) step and nucleophilic delivery step.
3. La^{3+} catalysis of the methanolysis of the phosphate triesters is quite spectacular in terms of the rate enhancements relative to the background reactions. In addition, the $k_2^{2:n}/k_{OCH_3}$ values (n = 2–4) are very large, ranging from ~3200–4600 for paraoxon to 135–230 for the phosphorothioate derivative **16**. As far as we know,

© 2004 NRC Canada

these are among the largest ratios reported for any metal-ion-catalyzed phosphoryl transfer,[9] which points to the fact that metal-ion-catalyzed alcoholysis processes are possessed of special catalytic benefits for such systems.

4. As a final point of note, the catalytic system described herein can be made simply in situ for preparative work by formulating a 2–20 mmol L^{-1} solution of $La(OTf)_3$ in methanol and treating with 1 equiv. of $NaOCH_3$. The $^{s}_{s}$pH of this solution is close to neutrality (8.4).

Acknowledgements

The authors gratefully acknowledge the continuing financial support of the Natural Sciences and Engineering Research Council of Canada (NSERC) and Queen's University. In addition, GTTG acknowledges the financial support of NSERC through the Canada Graduate Scholarships Program. RSB acknowledges the excellent collaborations with numerous undergraduate, graduate, post-doctoral researchers and research associates whose names appear on the publications from this group. For the more recent work concerning the methanolysis of phosphate triesters, the authors acknowledge the financial support of the United States Department of the Army, Army Research Office, Grant No. W911NF-04-1-0057.[10]

References

1. (*a*) T.J. Przystas and T.H. Fife. J. Chem. Soc. Perkin Trans. 2, 393 (1990), and refs. cited therein; (*b*) J. Suh. Acc. Chem. Res. **25**, 273 (1992), and refs. cited therein; (*c*) P. Tecilla, U. Tonellato, F. Veronese, F. Fellugg, and P. Scrimin. J. Org. Chem. **62**, 7621 (1997); (*d*) J. Chin, V. Jubian, and K. Mrejen. J. Chem. Soc. Chem. Commun. 1326 (1990); (*e*) L. Meriwether and F. Westheimer. J. Am. Chem. Soc. **78**, 5119 (1956); (*f*) T.J. Grant and R.W. Hay. Aust. J. Chem. **18**, 1189 (1965); (*g*) J.T. Groves and R.M. Dias. J. Am. Chem. Soc. **101**, 1033 (1979); (*h*) J.T. Groves and R.R. Chambers. J. Am. Chem. Soc. **106**, 630 (1984); (*i*) J.T. Groves and J.R. Olson. Inorg. Chem. **24**, 2715 (1985); (*j*) L. Sayre, K.V. Reddy, A.R. Jacobson, and W. Tang. Inorg. Chem. **31**, 935 (1992); (*k*) T.H. Fife. Acc. Chem. Res. **26**, 325 (1993); (*l*) T.H. Fife and R. Bembi. J. Am. Chem. Soc. **115**, 11 358 (1993); (*m*) T.N. Parac and N.M. Kostić. J. Am. Chem. Soc. **118**, 51 (1996); (*n*) L. Singh and R.N. Ram. J. Org. Chem. **59**, 710 (1994); (*o*) P.A. Sutton and D.A. Buckingham. Acc. Chem. Res. **20**, 357 (1987); (*p*) E. Kimura, I. Nakamura, T. Koike, M. Shionoya, Y. Kodama, T. Ikeda, and M. Shiro. J. Am. Chem. Soc. **116**, 4764 (1994); (*q*) T. N. Parac, G.M. Ullman, and N.M. Kostić. J. Am. Chem. Soc. **121**, 3127 (1999), and refs. cited therein; (*r*) A.M. Ridder and R.M. Kellogg. *In* Comprehensive supramolecular chemistry. Vol. 4. Supramolecular reactivity and transport: Bioorganic systems. *Edited by* Y. Murakami. Elsevier Science Ltd., Oxford. 1996. Chap. 11; (*s*) J. Chin. Acc. Chem. Res. **24**, 145 (1991), and refs. cited therein.

2. (*a*) A. Blasko and T.C. Bruice. Acc. Chem. Res. **32**, 475 (1999), and refs. cited therein; (*b*) N.H. Williams, B. Takasaki, M. Wall, and J. Chin. Acc. Chem. Res. **32**, 485 (1999), and refs. cited therein; (*c*) R.A. Moss, B.D. Park, P. Scrimin, and G. Ghirlanda. J. Chem. Soc. Chem. Commun. 1627 (1995); (*d*) R.A. Moss, J. Zhang, and K. Bracken. J. Chem. Soc. Chem. Commun. 1639 (1997); (*e*) J. Sumaoka, S. Miyama, and M. Komiyama. J. Chem. Soc. Chem. Commun. 1755 (1994); (*f*) J.R. Morrow, J.A. Buttrey, and K. Berback. Inorg. Chem. **31**, 16 (1992); (*g*) J.R. Morrow, L.A. Buttrey, V.M. Shelton, and K.A. Berback. J. Am. Chem. Soc. **114**, 1903 (1992); (*h*) K.P. McCue and J.R. Morrow. Inorg Chem. **38**, 6136 (1999); (*i*) L.L. Chappell, D.A. Voss, Jr., W.DeW. Horrocks, Jr., and J.R. Morrow. Inorg. Chem. **37**, 3989 (1998); (*h*) R. Breslow and B. Zhang. J. Am. Chem. Soc. **116**, 7893 (1994); (*i*) N. Takeda, M. Irisawa, and M. Komiyama. J. Chem. Soc. Chem. Commun. 2773 (1994); (*j*) R.W. Hay and N. Govan. J. Chem. Soc. Chem. Commun. 714 (1990); (*k*) H.-J. Schneider, J. Rammo, and R. Hettich. Angew. Chem. Int. Ed. Engl. **32**, 1716 (1993); (*l*) K.G. Ragunathan and H.-J. Schneider. Angew. Chem. Int. Ed. Engl. **35**, 1219 (1996); (*m*) P. Gómez-Tagle and A.K. Yatsimirsky. J. Chem. Soc. Dalton Trans. 2957 (1998); (*n*) P. Molenveld, J.F.J. Engberson, and D.N. Reinhoudt. J. Org. Chem. **64**, 6337 (1999), and refs. cited therein; (*o*) S.-I. Kondo, K. Shinbo, T. Yamaguchi, K. Yoshida, and Y. Yano. J. Chem. Soc. Perkin Trans. 2, 128 (2001); (*p*) K.P. McCue and J.R. Morrow. Inorg. Chem. **38**, 6136 (1999).

3. (*a*) G.W. Parshall and S.D. Ittel. Homogeneous catalysis: The applications and chemistry of catalysis by soluble transition metal complexes. 2nd ed. Wiley Interscience, New York. 1992. pp. 269–296; (*b*) M.G. Stanton, C.B. Allen, R.M. Kissling, A.L. Lincoln, and M.R. Gagné. J. Am. Chem. Soc. **120**, 5981 (1998), and refs. cited therein; (*c*) J. Otera. Chem. Rev. **93**, 1449 (1993); (*d*) T. Okano, K. Miyamoto, and J. Kiji. Chem. Lett. 246 (1995); (*e*) B.C. Ranu, P. Dutta, and A. Sarkar. J. Org. Chem. **63**, 6027 (1998); (*f*) L. Baldini, C. Bracchini, R. Cacciapaglia, A. Casnati, L. Mandolini, and R. Ungaro. Chem. Eur. J. **6**, 1322 (2000); (*g*) R. Cacciapaglia, S. Di Stephano, E. Kelderman, and L. Mandolini. Angew. Chem. Int. Ed. **38**, 349 (1999); (*h*) R. Cacciapaglia, L. Mandolini, R. Arnecke, V. Böhmer, and W. Vogt. J. Chem. Soc. Perkin Trans. 2, 419 (1998); (*i*) P. Breccia, R. Cacciapaglia, L. Mandolini, and C. Scorsini. J. Chem. Soc. Perkin Trans. 2, 1257 (1998); (*j*) W.M. Stevels, M.J.K. Ankoné, P.J. Dijkstra, and J. Feijen. Macromolecules, **29**, 8296 (1996); (*k*) N.J. Hinde and C.D. Hall. J. Chem. Soc. Perkin Trans. 2, 1249 (1998), and refs. cited therein; (*l*) J. Otton, S. Ratton, V.A. Vasnev, G.D. Markova, K.M. Nametov, V.I. Bakhmutov, L.I. Komarova, S.V. Vinogradova, and V.V. Korshak. J. Polym. Sci. Part A: Polymer Chem. **26**, 2199 (1988).

4. (*a*) V.K. Balakrishnan, J.M. Dust, G.W. vanLoon, and E. Buncel. Can. J. Chem. **79**, 157 (2001); (*b*) R. Nagelkerke, M.J. Pregel, E.J. Dunn, G.R.J. Thatcher, and E. Buncel. Org. React. (N.Y.), **29**, 11 (1995); (*c*) E.J. Dunn and E. Buncel. Can. J. Chem. **67**, 1440 (1989); (*d*) E.J. Dunn, R.Y. Moir, E. Buncel, J.G. Purdon, and R.A.B. Bannard. Can. J. Chem. **68**, 1837 (1990); (*e*) M.J. Pregel and E. Buncel. J. Chem. Soc. Perkin

[9] Recent work from our laboratories has shown that transition metal ion complexes, for example the 1,5,9-triazacyclododecane complexes of Cu^{2+}:$^{-}OCH_3$ or Zn^{2+}:$^{-}OCH_3$, provide very efficient catalysis of the methanolysis of paraoxon and fenitrothion (34*a*, 34*b*), with k_2/k_{OCH_3}-ratios as high as 17 000-fold for reaction with fenitrothion (**18**).

[10] The content of the information does not necessarily reflect the position or the policy of the federal government, and no official endorsement should be inferred.

© 2004 NRC Canada

Trans. 2, 307 (1991); (*f*) M.J. Pregel, E.J. Dunn, and E. Buncel. J. Am. Chem. Soc. **113**, 3545 (1991); (*g*) M.J. Pregel, E.J. Dunn, R. Nagelkerke, G.R.J. Thatcher, and E. Buncel. Chem. Soc. Rev. 449 (1995).
5. R.G. Bates. Medium effects and pH in non-aqueous solvents. *In* Solute-solvent interactions. *Edited by* J.F. Coetzee and C.D. Ritchie. Marcel Dekker, New York. 1969. p. 45.
6. (*a*) E. Bosch, F. Rived, M. Roses, and J. Sales. J. Chem. Soc. Perkin Trans. 2, 1953 (1999); (*b*) F. Rived, M. Rosés, and E. Bosch. Anal. Chim. Acta, **374**, 309 (1998); (*c*) E. Bosch, P. Bou, H. Allemann, and M. Rosés. Anal. Chem. **68**, 3651 (1996); (*d*) I. Canals, J.A. Portal, E. Bosch, and M. Rosés. Anal. Chem. **72**, 1802 (2000).
7. G.T.T. Gibson, A.A Neverov, and R.S. Brown. Can. J. Chem. **81**, 495 (2003).
8. H.S. Harned and B.B. Owen. *In* The physical chemistry of electrolytic solutions. ACS Monograph Series 137. 3rd ed. Reinhold Publishing, New York. 1957. p. 161.
9. A.A. Neverov and R.S. Brown. Inorg. Chem. **40**, 3588 (2001).
10. J.S.W. Tsang, A.A. Neverov, and R.S. Brown. J. Am. Chem. Soc. **125**, 1559 (2003).
11. P. Montoya-Pelaez, G.T.T. Gibson, A.A. Neverov, and R.S. Brown. Inorg. Chem. **42**, 8624 (2003).
12. R.S. Brown and A.A. Neverov. J. Chem. Soc. Perkin Trans. 2, 1039 (2002).
13. A.A. Neverov, T. McDonald, G. Gibson, and R.S. Brown. Can. J. Chem. **79**, 1704 (2001).
14. J.S. Tsang, A.A. Neverov, and R.S. Brown. J. Am. Chem. Soc. **125**, 7602 (2003).
15. A.A. Neverov and R.S. Brown. Can. J. Chem. **78**, 1247 (2000).
16. A.A. Neverov, G. Gibson, and R.S. Brown. Inorg. Chem. **42**, 228 (2003).
17. R. Cacciapaglia, S. Di Stephano, F. Fahrenkrug, U. Lüning, and L. Mandolini. J. Phys. Org. Chem. **17**, 350 (2004).
18. (*a*) J. Chin. Acc. Chem. Res. **24**, 145 (1991); (*b*) S.H. Gellman, R. Petter, and R. Breslow. J. Am. Chem. Soc. **108**, 2388 (1986); (*c*) P. Scrimmin, G. Ghinlanda, P. Tecilla, and R.A. Moss. Langmuir, **12**, 6235 (1996); (*d*) J.R. Morrow and W.C. Trogler. Inorg. Chem. **28**, 2330 (1989); (*e*) R.W. Hay and N. Govan. Polyhedron, **17**, 463, 2079 (1998).
19. P. Gans, A. Sabatini, and A. Vacca. Talanta, **43**, 1739 (1996).
20. T.J. Broxton and L.W. Deady. J. Org. Chem. **39**, 2767 (1974).
21. (*a*) R.A. Main and F. Iverson. Biochem. J. **100**, 525 (1966); (*b*) J. Emsley and D. Hall. *In* The chemistry of phosphorus. Wiley, New York. 1976. p. 494.
22. (*a*) A. Toy and E.N. Walsh. *In* Phosphorus chemistry in everyday living. 2nd ed. American Chemical Society, Washington, D.C. 1987. Chaps. 18–20; (*b*) L.D. Quin. *In* A guide to organophosphorus chemistry. Wiley, New York. 2000; (*c*) M.A. Gallo and N.J. Lawryk. *In* Organic phosphorus pesticides. The handbook of pesticide toxicology. Academic Press, San Diego, Calif. 1991.
23. (*a*) Y.-C. Yang, J.A. Baker, and J.R. Ward. Chem. Rev. **92**, 1729 (1992); (*b*) Y.-C. Yang. Acc. Chem. Res. **32**, 109 (1999); (*c*) Y.-C. Yang. Chem. Ind. (London), 334 (1995).
24. US Environmental Protection Agency. About Pesticides, Industry Sales and Uses. Available from http://www.epa.gov/oppbead1/pestsales/99pestsales/usage1999_3.html [accessed August 2004].
25. Conference on Disarmament. The Convention of the Development, Production, Stockpiling and Use of Chemical Weapons and on Their Destruction. CD/1170. Geneva, August 1992. Available from http://www.dfait-maeci.gc.ca/nndi-agency/cwc_1-en.asp.
26. H. Morales-Rojas and R.A. Moss. Chem. Rev. **102**, 2497 (2002), and refs. cited therein.
27. G.S. Pearson and R.S. Magee. Pure Appl. Chem. **74**, 187 (2002).
28. Russian Munitions Agency. Chemical Disarmament. Available from http://www.munition.gov.ru/eng/zapasho.html [accessed August 2004].
29. Y.-C. Yang, F.J. Berg, L.L. Szafraniec, W.T. Beaudry, C.A. Bunton, and A. Kumar. J. Chem. Soc. Perkin Trans. 2, 607 (1997), and refs. cited therein.
30. J.S.W. Tsang, A.A. Neverov, and R.S. Brown. Org. Biomol. Chem. **2**, 3457 (2004).
31. P. Gómez-Tagle and A.K. Yatsimirsky. Inorg. Chem. **40**, 3786 (2001).
32. M.B. Smith and J. March. Advanced organic chemistry. 5th ed. Wiley Interscience, New York. 2001. pp. 338–342, and refs. cited therein.
33. (*a*) A.A. Neverov and R.S. Brown. Org. Biomol. Chem. **2**, 2245 (2004); W. Desloges, A.A. Neverov, and R.S. Brown. Inorg. Chem. **43**, 6752 (2004).
34. A.A. Neverov, N. Sunderland, and R.S. Brown. Org. Biomol. Chem. **3**, 65 (2005).
35. (*a*) N.H. Williams, W. Cheung, and J. Chin. J. Am. Chem. Soc. **120**, 8079 (1998); (*b*) D. Wahnon, A.-M. Lebuis, and J. Chin. Angew. Chem. Int. Ed. Engl. **34**, 2412 (1995).

© 2004 NRC Canada

NOTE OF APPRECIATION / NOTE DE RECONNAISSANCE

The quality of the papers in this journal depends a great deal on the efforts of those who agree to act as critical readers of manuscripts. The editors gratefully acknowledge the following who helped us between 1 November 2003 and 31 October 2004:

La qualité des articles publiés dans notre revue dépend beaucoup de ceux qui acceptent de faire une lecture critique des manuscrits. Les directeurs scientifiques expriment leur reconnaissance aux personnes suivantes qui nous ont aidés, du 1er novembre 2003 au 31 octobre 2004 :

Abraham, M.H.
Abrams, M.
Abrams, S.R.
Acree, W.E.
Adam, A.
Adams, R.D.
Akrivos, P.D.
Alberto, R.
Alloin, F.
Andersen, R.J.
Anderson, S.L.
Andrushchenko, V.
Apblett, A.
Appleton, T.
Arnold, W.
Aroca, R.F.
Arteca, G.A.
Atwood, J.
Auclair, K.
Back, T.G.
Bain, A.D.
Baker, J.
Balfour, W.J.
Ballini, R.
Banfi, L.
Banks, J.
Barclay, L.R.C.
Barra, M.
Barrett, C.J.
Barthel, J.
Batteas, J.
Becker, U.
Begovic, N.
Bellissent-Funel, M.
Bennet, A.J.
Benson, G.C.
Berg, D.J.
Bergens, S.H.
Bernard, G.
Bernard, G.M.
Bernath, P.F.
Bhattacharyya, D.
Birss, V.L.
Bitterwolf, T.
Bixon, M.
Bizzotto, D.
Blair, S.L.
Blandamer, M.J.
Bobbo, S.
Bodwell, G.J.
Boeré, R.T.
Bolm, C.
Boncella, J.M.
Bond, A.M.
Boutalib, A.
Brennan, J.D.
Briganti, G.
Brolo, A.G.
Brooks, R.L.
Brosa, C.
Brossard, L.
Brown, R.S.
Buncel, E.
Burford, N.
Burns, C.
Butler, I.S.
Cai, X.
Canty, A.
Carreno, C.
Castellucci, E.M.
Caulton, K.G.
Cha, J.K.
Chalikian, T.V.
Chan, T.H.
Chandrasekhar, S.
Charette, A.B.
Charlton, J.L.
Chauder, B.
Cheetham, A.K.
Chen, A.
Chen, D.D.Y.
Chen, L.-C.
Chen, P.
Chenevert, R.
Chin, J.
Chirik, P.
Chisholm, M.
Chivers, T.
Clark, J.
Clearfield, A.
Clyburne, J.
Constas, S.
Conway, B.E.
Cook, G.
Cormier, J.F.
Corriu, R.J.P.
Cowie, M.
Cox, R.A.
Cramb, D.T.
Creager, S.E.
Crich, D.
Crudden, C.M.
Crutchley, R.J.
Cullen, J.M.
Cummins, C.C.
Curan, D.P.
Cvetovich, R.
da Silva Pereira, M.I.
Dagdigian, P.J.
Dalgarno, A.
Damha, M.J.
Danhardt, G.
Daoust, B.
Das, B.
Dash, U.N.
Dauban, P.
Davidson, E.R.
de la Hoz, A.
de Lijser, P.
de Mattos, M.C.S.
de Vicente, M.E.S.
Dean, P.A.W.
Dembinski, R.
Demoustier-Champagne, S.
Deslongchamps, G.
Devlin, J.
Diaz, L.
Dibble, P.
Dibble, T.S.
Dilworth, J.R.
Dimmock, J.R.
Ding, K.
Domanska, U.
Dougherty, R.C.
Douglas, D.
Douheret, G.
Doye, S.
Drake, J.E.
Dubois, M.
Dupont, J.
Dust, J.M.
Eagan, T.
Eisenberg, R.
Eland, J.H.D.
Ellis, B.
Ellis, T.H.
Elsevier, C.J.
Englezos, P.
Eschenmoser, A.
Esko, J.D.
Espenson, J.
Evans, W.J.
Fagnou, K.R.
Fahrni, C.J.
Fairbanks, A.J.
Faller, J.
Fallis, A.G.
Farrell, J.
Fedorak, P.
Fekner, T.
Fenniri, H.
Field, R.W.

© 2004 NRC Canada

Findlay, J.A.
Firouzabadi, H.
Foght, J.M.
Fotakis, C.
Fournier, R.
Francisco, J.S.
Franck, R.W.
Fraser-Reid, B.
Fray, D.J.
Friedrich, B.
Fryzuk, M.D.
Fujita, K.
Furst, W.
Gambarotta, S.
Gao, J.
Garrett, T.
Gassa, L.M.
Gates, B.
Gates, D.
Gauld, J.
Gedye, R.N.
Georg, G.
Ghali, E.
Giannis, A.
Gibson, V.
Gielen, M.
Gigandet, M.P.
Glinski, J.
Goddard, J.D.
Goldberg, K.
Gough, K.
Gould, E.S.
Graham, D.J.
Granger, P.
Grant, A.
Grant, E.R.
Green, J.
Green, J.R.
Grevels, F.-W.
Gribble, G.
Griffiths, K.
Grindley, T.B.
Grossert, J.S.
Gudmundsdóttir, A.
Gudmundsson, J.S.
Guedel, H.U.
Guthrie, J.P.
Gutowski, M.
Haddleton, D.M.
Haley, M.M.
Hambley, T.
Hanan, G.S.
Hanson, J.
Hara, S.
Harrington, D.A.
Harrison, P.H.M.
Hart, J.P.
Harvey, P.D.
Harvey, R.
Hasegawa, T.I.
Heck, A.
Hefter, G.
Heintz, A.
Helquist, P.
Henry, B.R.
Herring, R.
Hicks, R.G.
Hidai, M.
Hillhouse, G.
Hofman, T.
Holdcroft, S.
Holland, P.
Horton, D.
Horváth-Szabó, G.
Houk, K.N.
Hu, X.K.
Huang, Y.
Hudson, R.H.E.
Hughes, R.P.
Huisgen, R.
Hussey, C.L.
Hutchings, G.J.
Imae, T.
Imamoto, T.
Iwanek, W.
Iwao, M.
Jablonski, C.
Jaenicke, S.
James, B.R.
Jasra, R.V.
Jenkins, P.
Jessop, P.
Jetter, R.
Jiménez, E.
Johnson, K.E.
Johnson, S.
Jones, M.
Jones, R.H.
Jones, W.
Jordan, R.
Jordan, R.B.
Jorgenson, K.
Joule, J.
Juaristi, E.
Julien, C.
Jung, M.E.
Jura, M.
Kakefuda, A.
Kang, Y.K.
Kappe, C.O.
Karlsson, L.
Katsuki, T.
Kawaguchi, K.
Kazlauskas, R.
Kazmaier, U.
Keay, B.A.
Keillor, J.
Kelly, L.A.
Kende, A.
Kennedy, D.
Kennepohl, P.
Kerns, R.J.
Kertesz, M.
Khlebnikov, A.
King, J.
King, J.F.
Kirby, A.J.
Kitsopoulos, T.
Klassen, J.
Klobukowski, M.
Koch, S.A.
Kolandaivel, P.
Komadel, P.
Korolev, V.P.
Koser, G.
Kotovych, G.
Kozak, C.
Kraatz, H.-B.
Kresge, A.J.
Krishna, P.
Krull, U.J.
Kubiak, C.P.
Lai, Y.-H.
Langler, R.F.
Laschat, S.
Lautens, M.
Lay, P.A.
Leaist, D.
Leclerc, M.
Lee, D.G.
Lee, J.
Lennox, B.
Leone, S.R.
Lessard, J.
Leung, T.K.
Lever, A.B.P.
Levy, D.H.
Lewars, E.
Lewis, F.D.
Leznoff, C.
Leznoff, D.B.
Li, J.Y.
Li, Y.
Lipson, R.
Lipson, S.J.
Loeb, S.J.
Loock, H.P.
Lopes, A.
Lopez, S.
Loppnow, G.R.
Lou, B.
Loupy, A.
Lu, J.
Lu, Z.
Lucy, C.
Macartney, D.H.
MacFarland, D.
MacLachlan, M.J.
MacMillan, A.
Madou, M.
Maier, M.
Makosza, M.
Malatesta, F.
Manners, I.
Marcaccini, S.
Marder, S.R.
Marshall, P.
Martinez-Palou, R.
Masakatsu, S.
Matt, D.
Mattos, O.R.
McAuley, A.
McClelland, R.A.
McConville, D.
McDonald, R.

© 2004 NRC Canada

McGarvey, D.J.
McIndoe, J.S.
McIndoe, S.
McKellar, A.R.W.
Meier, K.
Mellet, C.O.
Ménard, H.
Merkt, F.
Merrill, R.
Meyers Kelley, A.
Mezey, P.G.
Mihichuk, L.M.
Miller, J.D.
Miller, M.J.
Miller, T.
Mindiola, D.
Mitchell, R.H.
Mizobe, Y.
Mo, O.
Moazzen-Ahmadi, N.
Monteiro, M.
Moore, J.S.
Morill, J.S.
Morris, R.H.
Morrow, J.R.
Moss, R.A.
Muchall, H.M.
Muniz-Miranda, M.
Murphy, C.
Nelson, T.D.
Nesper, R.
Neusser, H.J.
Ng, C.Y.
Ni, Y.
Nichols, R.J.
O'Connel, J.P.
Ojima, I.
Okimoto, M.
Olah, G.
Oleschuk, R.D.
Osman, R.
Oswal, S.L.
Otter, A.
Ozerov, O.
Padwa, A.
Pagni, R.
Paizs, B.
Palaniappan, S.
Palepu, R.
Paleta, O.
Palmer, D.
Palmer, D.A.
Palmieri, G.
Pannell, K.H.
Papoian, G.A.
Parusel, A.B.J.
Parvez, M.
Patey, G.
Penner, G.H.
Perrin, C.L.
Peters, D.G.
Peters, J.C.
Pettit, G.R.
Peyerimhoff, S.D.
Piers, W.E.
Pincock, J.
Pinnavaia, T.
Pinto, B.M.
Pizzo, F.
Placido, J.
Poe, A.J.
Poirier, M.D.
Poirier, R.A.
Pomeroy, R.K.
Pottie, I.
Pottie, I.D.
Power, W.P.
Pratt, S.T.
Pritchard, H.O.
Pulay, P.
Quadrelli, E.A.
Quail, J.W.
Queguiner, G.
Rainwater, J.C.
Ranu, B.
Rard, J.A.
Räsänen, M.
Ratcliffe, C.I.
Ratner, M.A.
Rauzy, E.
Rayner, C.M.
Reber, C.
Redington, R.L.
Regen, S.L.
Reid, P.
Reynolds, W.F.
Rice, J.
Richard, J.P.
Rigby, J.H.
Riguera, R.
Riordan, C.G.
Ripmeester, J.A.
Roberts, S.M.
Robinson, W.
Rochon, F.D.
Rogers, R.D.
Roscoe, S.G.
Rossi, R.A.
Roy, R.
Rutherford, M.
Saliner, A.G.
Salvadori, P.
Sandler, S.I.
Sankar, M.
Saracco, G.
Sastry, N.V.
Satsuma, A.
Saunders, J.
Sayari, A.
Schaefer, H.F.
Schafer, L.
Schepp, N.P.
Scherson, D.A.
Schmalz, H.-G.
Schmieder, P.K.
Schneider, S.
Schott, H.
Schreimer, D.
Schrock, R.R.
Schurko, R.
Scott, L.
Scott, P.
Scott, S.
Sears, D.
Sears, T.
Selassie, C.
Selinsky, B.S.
Sen, D.
Serrano Granados, D.
Setser, D.W.
Sharma, V.K.
Shelef, M.
Sherman, J.C.
Shi, Y.J.
Shibasaki, M.
Shibaski, M.
Shimizu, G.H.K.
Shimizu, M.
Simard, S.
Singh, V.K.
Skelton, B.W.
Snider, B.
Softley, T.P.
Solladie, G.
Soloshonok, V.A.
Sorensen, T.S.
Soutar, I.
Spenser, I.D.
Spino, C.
Spivey, A.V.
Srinivasan, K.V.
Steer, R.P.
Stephan, D.W.
Stephanidou-Stephanatou, J.
Stephens, C.
Stork, G.
Stryjek, R.
Stynes, D.V.
Sukenik, C.N.
Sun, C.-M.
Sundberg, R.J.
Swaddle, T.W.
Switzer, J.
Szarek, W.A.
Tabrizian, M.
Tahmassebi, D.
Takats, J.
Tamura, K.
Taniguchi, Y.
Tanner, M.E.
Tao, F.-M.
Tatsumi, K.
Tavares do Amaral, A.
Taylor, R.
Tee, O.S.
Templeton, J.L.
Thompson, A.
Thompson, K.
Thompson, R.
Thompson, R.C.
Threadgill, M.D.
Tian, Z.-Q.
Tidwell, T.T.
Tilset, M.
Torres, T.

© 2004 NRC Canada

Trabanco, A.A.
Tretiak, S.
Trindle, C.
Trost, B.
Trszczanowicz, A.J.
Trudeau, M.
Truhlar, D.G.
Tuczek, F.
Tunon, I.
Tykwinski, R.
Uedaira, H.
Uneyama, K.
Vaidyanathan, R.
van Eldik, R.
van Hieningen, A.
vanLoon, G.W.
Vaughan, K.
Vedejs, E.
Veinot, J.G.C.
Velasco, I.
Verrall, R.E.
Viskolcz, B.
Volpe, P.L.O.
Voyer, N.
Vrabec, J.
Wagner, B.D.
Waldron, K.C.
Walrafen, G.E.
Wan, P.
Wang, Z.Y.
Ward, D.E.
Wardlaw, D.M.
Warkentin, J.
Warren, T.H.
Wasylishen, R.E.
Watson, J.K.G.
Weaver, D.F.
Weinberg, N.
Westaway, K.C.
Westcott, S.A.
Wetmore, S.D.
White, M.G.
White, R.L.
Wiberg, K.B.
Williams, C.
Williams, R.V.
Williams, V.
Wilson, P.D.
Winkelman, J.
Winnewisser, M.
Winnik, M.A.
Winter, C.H.
Wiseman, P.W.
Wisner, J.
Wolf, M.
Wolkenberg, S.
Wolzcanski, P.
Woo, H.G.
Wood, P.
Woolley, E.M.
Workentin, M.
Wormald, C.J.
Wuest, J.D.
Yamane, T.
Yang, D.S.
Ye, Z.-G.
Yost, R.A.
Yu, H.-Z.
Yurkinskii, V.P.
Zard, S.
Zaworotko, M.
Zehnacker, A.
Zgierski, M.
Zhao, Z.
Ziegler, T.
Zielkiewicz, J.
Ziurys, L.M.

© 2004 NRC Canada